ExHFT-7

7th World Conference on Experimental Heat Transfer, Fluid Mechanics and Thermodynamics

28 June - 03 July 2009, Krakow, Poland

Proceedings

Editors:
J.S. Szmyd, J. Spałek, T.A. Kowalewski

ExHFT-7

7th World Conference on Experimental Heat Transfer, Fluid Mechanics and Thermodynamics

28 June - 03 July 2009, Krakow, Poland

ExHFT-1 Dubrovnik (1988)
ExHFT-2 Dubrovnik (1991)
ExHFT-3 Honolulu (1993)
ExHFT-4 Brussels (1997)
ExHFT-5 Thessaloniki (2001)
ExHFT-6 Matsushima (2005)

ExHFT-7

7th World Conference on Experimental Heat Transfer, Fluid Mechanics and Thermodynamics

28 June - 03 July 2009, Krakow, Poland

Proceedings

Editors:
J.S. Szmyd, J. Spałek, T.A. Kowalewski

ISBN 978-83-7464-235-4

AGH University of Science and Technology Press
al. Mickiewicza 30, 30-059 Krakow
tel. 012 617 32 28, tel./fax 012 638 40 38
e-mail: redakcja@wydawnictwoagh.pl
http://www.WydawnictwoAGH.pl

Preface

This Conference CD-ROM Proceedings contains the papers presented at the seventh World Conference on Experimental Heat Transfer, Fluid Mechanics and Thermodynamics (ExHFT-7) held in Krakow, Poland from 28 June – 03 July 2009.

The World Conferences on Experimental Heat Transfer, Fluid Mechanics and Thermodynamics have been taking place since 1988, a full twenty years. This year's Follows successful conferences in Dubrovnik (1988, 1991), Honolulu (1993), Brussels (1997), Thessaloniki (2001), and Matsushima (2005).

ExHFT-7 is being organized under the auspices of the Assembly of World Conferences on Experimental Heat Transfer, Fluid Mechanics and Thermodynamics. The goal of this conference is to provide a forum for the exposure and exchange of ideas, methods and results in heat transfer, fluid mechanics and thermodynamics.

Conference topics include, but are not limited to: Fundamentals: Heat and Mass Transfer, Fluid Mechanics, Thermodynamics, Measurement Techniques, Interdisciplinary Areas in Heat and Fluid Flow, Reaction and Combustion, and Turbulence, Applications: Aerospace Technology, Advanced Energy Systems, Advanced Environmental Systems, Biotechnology and Medical Systems, Cryogenics, Education, Fuel Cell Systems, Interactive Computational and Experimental Methodologies, Manufacturing Processes, Material Processing, Micro Electronic Equipment, Micro-Electro-Mechanical Systems, Miniaturized Systems for Chemistry and Life Sciences, Nanotechnology.

Within the general subjects of this conference three mini-symposia are organized. The topics include: Biological Systems, Fuel Cell Systems, and Micro- and Nano-scale Systems.

Twelve state-of-the-art keynote papers are delivered by world leading experts and two lectures by Nusselt-Reynolds Prize winners.

All contributed papers were peer reviewed. Recommendations were received from Lead Scientists and the Advisory Board. Accordingly, of the 398 eligible extended abstracts submitted 350 contributions were invited to prepare full papers. Through a review process by International Scientific Committee, 270 papers were selected for presentation at ExHFT-7. All contributions were prepared by the authors in a camera ready form. The total number of submitted and accepted papers for this year's conference represents a significant increase over previous ExHFT conferences, which speaks to the great vitality of experimental heat transfer, fluid mechanics and thermodynamics.

We hope that this proceedings will be used not only as a document of the event but also to assess achievements and new paths to be taken in heat transfer, fluid mechanics and thermodynamics research.

Finally, we would like to congratulate the winners of the 2009 Nusselt-Reynolds Prize, Professors Dimos Poulikakos and Katepalli R. Sreenivasan.

Janusz S. Szmyd
Józef Spałek
Tomasz A. Kowalewski

Acknowledgments

We would like to express our thanks to our colleagues from the Assembly of World Conferences on Experimental Heat Transfer, Fluid Mechanics and Thermodynamics, as well as from International Scientific Committee i.e. Lead Scientists and the Advisory Board.
Their advice and efforts have helped us to overcome the problems normally associated with organising international meetings.

Special thanks goes to Lead Scientists for their work in encouraging the submission of papers and the subsequent review of all papers. Their contribution cannot be overestimated.

The ExHFT-7 Conference was organised by the AGH University of Science and Technology and Jagiellonian University. The demanding work involved could not have been done without the contribution of so many individuals from both institutions as well as numerous external co-workers. Without their extremely valuable help such a meeting would be impossible. Thank you all so much!

Janusz S. Szmyd
Józef Spałek
Tomasz A. Kowalewski

Honorary Committee

Rector
Professor Antoni Tajduś
AGH - University of Science and Technology

Rector
Professor Karol Musioł
Jagiellonian University

Organizing Committee

Prof. Janusz S. Szmyd - Conference Chairman
(AGH - University of Science and Technology)
This e-mail address is being protected from spam bots, you need JavaScript enabled to view it
Prof. Jozef Spalek - Conference Co-Chairman
(Jagiellonian University)
This e-mail address is being protected from spam bots, you need JavaScript enabled to view it
Prof. Tomasz A. Kowalewski - Conference Co-Chairman
(IPPT PAN, Polish Academy of Sciences)
This e-mail address is being protected from spam bots, you need JavaScript enabled to view it
Maciej Pilch - Conference Manager
(Jagiellonian University Events Office)

Members

Dr. Marek Jaszczur (AGH - University of Science and Technology)
Dr. Elzbieta Fornalik (AGH - University of Science and Technology)
Dr. Robert Podsiadly (Jagiellonian University)
Dr. Janusz Donizak (AGH - University of Science and Technology)
Dr. Adam Holda (AGH - University of Science and Technology)
Dr. Andrzej Ziemba (AGH - University of Science and Technology)
Joanna Hoszko (Jagiellonian University)
Anna Tylek (Jagiellonian University)
Elzbieta Koszalka (AGH - University of Science and Technology)
Anna Urbanik (AGH - University of Science and Technology)
Grzegorz Brus (AGH - University of Science and Technology)
Lukasz Pyrda (AGH - University of Science and Technology)
Remigiusz Nowak (AGH - University of Science and Technology)
Witold Wrobel (AGH - University of Science and Technology)

Scientific Committee

J. S. Szmyd Conference (Chairman),
T.A. Kowalewski (Conference Co-Chairman)

Lead Scientists

G. Amberg (Sweden)
F. Arinc (Turkey)
H. Auracher (Germany)
B. Azzopardi (UK)
J. Banaszek (Poland)
A. Bar-Cohen (USA)
M. Behnia (Australia)
V. Bontozoglou (Greece)
A. H. Castillejos (Mexico)
G.P. Celata (Italy)
T. Chmielniak (Poland)
A. Clausse (Argentina)
P. Coelho (Portugal)
A. Coronas (Spain)
W.J.A. Dahm (USA)
P. Di Marco (Italy)
N. Djilali (Canada)
S. Drobniak (Poland)
M.S. El-Genk (USA)
F.A. Franca (Brazil)
S. Fujikawa (Japan)
C.W.M van der Geld (The Netherlands)
A. Gelfgat (Israel)
L. Guo (China)
M. Hajj (USA)
G. Hetsroni (Israel)
K. Hishida (Japan)
Y. Hwang (USA)
J.M. Hyun (South Korea)
T. Inoue (Japan)
A. M. Jacobi (USA)
L. Jacquin (France)
S.G. Kandlikar (USA)
C. Kapusta (Poland)
C.J. Kim (USA)
H. Kobayashi (Japan)
A.K. Kolar (India)
J. S Lee (South Korea)
S.J. Lee (South Korea)
P. Le Quéré (France)
E. Leonardi (Australia)
A.I. Leontiev (Russia)
X.G. Liang (China)
A. Majumdar (USA)
S. Maruyama (Japan)
A.F. Massardo (Italy)
T.H.van der Meer (The Netherlands)
D. Mewes (Germany)
J.P. Meyer (South Africa)
J. Mikielewicz (Poland)
G.L. Morini (Italy)
H. Müller-Steinhagen (Germany)
D.B. Murray (Ireland)
V.E. Nakoryakov (Russia)
T. Niimi (Japan)
A.J. Nowak (Poland)
B. Palm (Sweden)
J. Patterson (Australia)
A. Pollard (Canada)
A.T. Prata (Brazil)
J. Rose (UK)
S.K. Saha (India)
Y. Sakai (Japan)
W. Schneider (Austria)
T.W. Simon (USA)
A. Solan (Israel)
T-H. Song (South Korea)
A.C.M. Sousa (Canada)
A. van Steenhoven (The Netherlands)
P. Stephan (Germany)
B. Sundén (Sweden)
K. Takeishi (Japan)
W.Q. Tao (China)
Y. Utaka (Japan)
L. Vasiliev (Belarus)
V.V. Wadekar (UK)
C.C. Wang (Taiwan)
J.I. Yanagihara (Brazil)
H. Yoshida (Japan)
X. Zhang (China)
S.M. Zubair (Saudi Arabia)
I. Zun (Slovenia)

Advisory Board

Assembly of World Conferences on Experimental Heat Transfer, Fluid Mechanics and Thermodynamics

Session Topics

Nusselt Reynolds Prize Winners

NRL	Nusselt Reynolds Prize Lectures

Invited Speakers

KL	Keynote lectures

Mini Symposia

BS	Biological Systems
FCS	Fuel Cell Systems
MNS	Micro- and Nano- scale Systems

Technical Sessions

AEES	Advanced Energy and Environmental Systems
AT	Aerospace Technology
CM	Computational Methodology
EXM	Experimental Methodology
FM	Fluid Mechanics
HMT	Heat and Mass Transfer
HT	Heat Transfer
LES	Large Eddy Simulation in heat transfer and fluid mechanics
MA	Miscellaneous Applications
MEMS	Micro- Electro- Mechanical Systems
MP	Material Processing
MT	Measurement Techniques
THE	Thermodynamics
TUR	Turbulence

Contents

Nusselt- Reynolds Prize Lectures

ON EMERGING MICRO- AND NANOSCALE TECHNOLOGIES FOR ENERGY APPLICATIONS

Dimos Poulikakos
Laboratory of Thermodynamics in Emerging Technologies
Mechanical and Process Engineering Department
ETH Zurich

ABSTRACT. This paper highlights the main points of my keynote lecture for the 2009 Nusselt-Reynolds Prize and contains examples of experimental aspects of my current research in heat transfer and transport phenomena at the interface of energy applications and micro- and nanoscale technologies. It is not the scope of this paper to present an exhaustive account of all current and past activities related to its title. It is rather an account of current research in my laboratory in this area, containing both the underlying scientific challenges as well as the hoped final outcome in terms of applications. To this end, examples from the areas of energy conversion, as well as energy transport will be discussed. In the area of energy conversion an original, deformable, direct methanol micro-fuel cell will be presented made of lightweight, flexible, polymer-based materials. A basic understanding and control of two-phase flows (in this case methanol and carbon dioxide) in microchannels as well as novel materials processing and microfabrication methods are directly related to the performance of such energy conversion devices. In the area of energy conservation and reuse, examples from the information technology will be employed. Specifically, new concepts of liquid (water) cooling of chips reaching heat removal rates in excess of 700 W/cm^2 in domains with restricted heights of the order of one mm will be presented. These concepts include optimized, nature-inspired microchannel designs for liquid transport, combined with ultra-high heat flux impinging micro-jet cooling. One additional advantage of using water to cool high density electronics is energy reuse, due to the potentially much higher exergy content of the coolant compared to toady's air cooled technologies. The last part of the paper focuses on the employment of functional nanostructures such as carbon nanotubes and nanowires of conductive and semi-conductive materials for the efficient transport of electricity and heat and the need for the development of novel technologies for the manufacturing, characterisation as well as handling of such nanostructures.

Keywords: *energy, micro-fuel cells, electronics cooling, nanotechnology, carbon nanotubes*

INTRODUCTION

Energy has emerged as arguably the most important challenge facing humanity in the 21st century (see for example the list in Fig. 1). This fact has reinvigorated the energy debate and research worldwide, bringing to the forefront the multifaceted nature of the scientific and social problems involved, resulting from a rapidly growing, energy hungry world population. At the outset of the scientific debate and depending on its context, a number of basic facts have to be understood. For the energy-engineering scientist, the following are of paramount importance:

* Corresponding author: Prof. Dimos Poulikakos
Phone: + (41)-44-3914641, Fax: + (41)-44-6322738
E-mail address: dimos.poulikakos@ethz.ch
www.ltnl.ethz.ch

-The issue of *quality* is essential in understanding e-The continuous scientific challenge is the *conversion* of various forms of "lower" quality energy (thermal, chemical, nuclear, solar, etc.), to the "highest" quality mechanical or electrical energy.

-Every time we convert we lose in overall quality (2nd Law of Thermodynamics). Hence, we must convert as efficiently and as little as possible (conservation) with due respect to the environment.

Thermal engineering is at the center of just about every energy activity, because thermal energy, its production, transfer, harvesting, control, and storage are necessary steps on the way to conversion to electrical or mechanical energy. In addition, thermal energy is often used directly in a large variety of heating and cooling applications, related or not related to conversion or utilization of other forms of energy.

1.ENERGY
2.WATER (More than 1B people lack access to safe water)
3.FOOD
4.ENVIRONMENT
5.POVERTY (3B people living on less than $2/day)
6.TERRORISM & WAR
7.DISEASE
8.EDUCATION
9.DEMOCRACY
10. POPULATION (Could go to 10 Billion in the 21st Century ~ 6.4B people in 2004)

Figure 1. Humanity's Top Ten Grand Challenges in the 21st Century (List by R. E Smalley).

It is therefore a natural consequence that the areas of thermodynamics, heat transfer and related fluid dynamics have been at the center of intellectual activity in engineering sciences and have produced a plethora of advances that have served humanity for many years, including those of pioneers in the field such as Wilhelm Nusselt and Osborn Reynolds in the past century.

In this lecture I will attempt to give some examples of current heat transfer research as we enter the 21st century that are directly related to the issue of energy as I described it above. These examples stem from my own activities as well as those of my scientific collaborators. At the beginning of the 21st century we are fortunate to have at our disposal tools and technologies, which the pioneers in the field of heat transfer could not even dream about. To this end, the issue of enabling micro- and nanotechnology for energy applications is central to all the topics I will cover in this lecture. Today, we are able, for example, to analyse and control transport of fluids and heat in channels that are not only smaller than the human hair, but they are beyond the realm of continuity, going down to diameters of molecular dimensions. We can investigate and quantify the transport of heat through the interface between two materials from the atomic viewpoint. Such developments create a new perspective and can give birth to new ideas to confront the energy challenge.

The paper and the lecture are structured as follows: Starting with the area of microscale energy conversion, a deformable, direct methanol micro-fuel cell will be presented, made of lightweight, flexible, polymer-based materials. The importance and control of two-phase flows (methanol and carbon dioxide) in the microchannels of the anode of the fuel cell is directly related to the performance of such energy conversion devices. Next, the area of ultra high heat flux cooling in small spaces will be discussed as well as its implications in energy conservation, in particular as it relates to information technology. Specific concepts include optimized, nature-inspired microchannel designs for liquid transport, combined with ultra-high heat flux impinging micro-jet cooling. One additional advantage of

using water to cool high density electronics is energy reuse, due to the potentially much higher exergy content of the coolant compared to toady's air cooled technologies. The last part of the paper focuses on the employment of nanostructures for novel energy applications, such as, carbon nanotubes and nanowires of conductive and semi-conductive materials for the efficient transport of electricity and heat and the need for the development of novel technologies for the characterisation as well as handling of such nanostructures.

ENERGY CONVERSION: A DEFORMABLE, DIRECT METHANOL MICRO- FUEL CELL

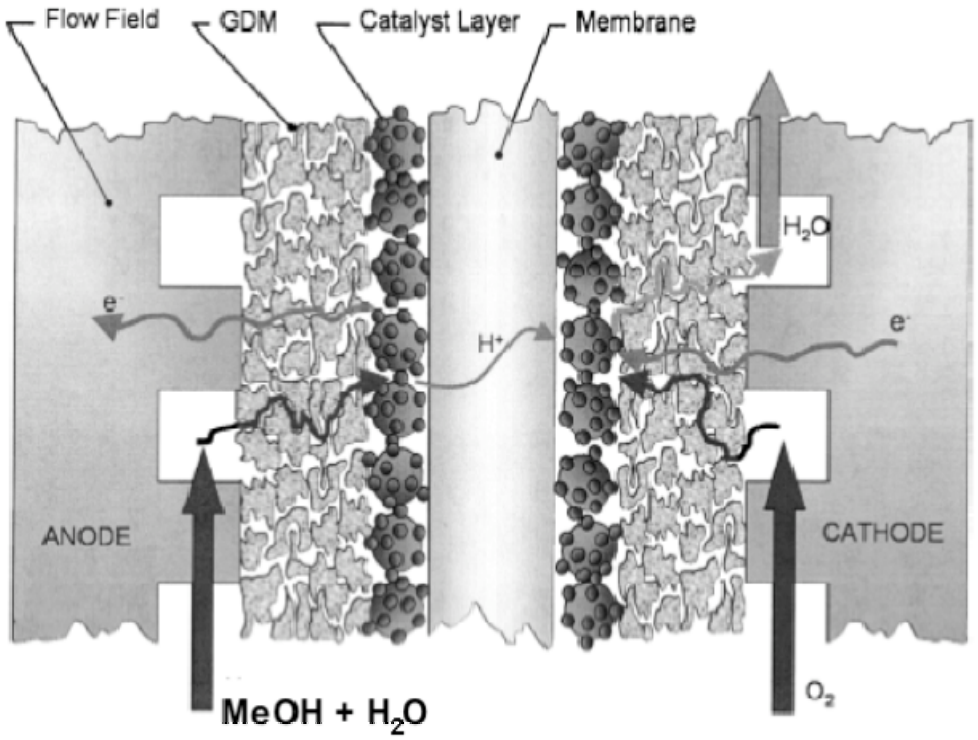

Figure 2. Operating Principle of a direct Methanol Fuel Cell

The schematic in Fig. 2 above shows the operating principle of a direct methanol fuel cell (DMFC). While progress has been made toward the realization of such transportable devices with traditional materials, there is a need for the integration of devices in personal, also wearable environments that are non-flat, undergo deformations and prefer to carry only a limited weight. This gave impetus for the creation of the flexible direct methanol fuel cell shown in Figure 3.

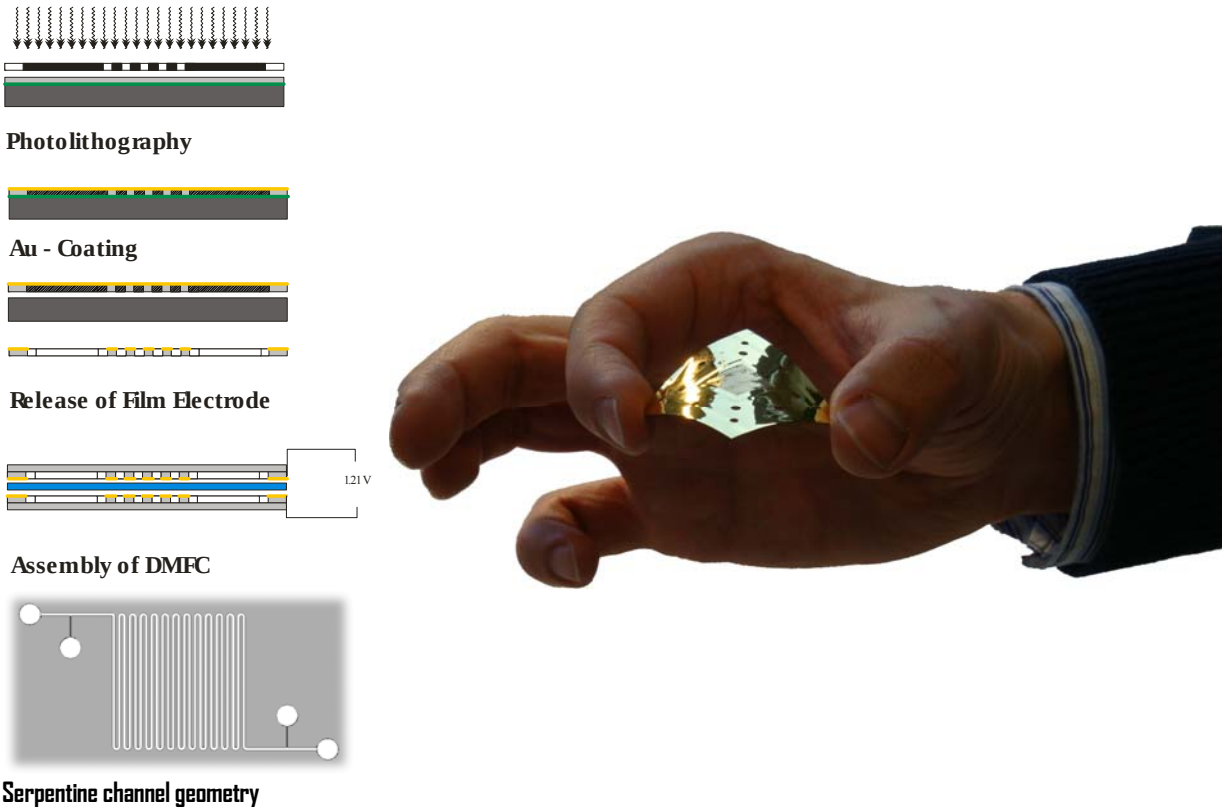

Figure 3. Assembly and photograph of a flexible, small-scale fuel cell on polymer based materials, showing also the serpentine channel geometry for the anode and cathode.

The critical point in the manufacturing of such a device is the combination of metals (gold) and polymers required for the cell anode and cathode see Ref. [1]. A standard microfabrication/MEMS technique [2], based on photolithography was applied to manufacture micro-sized channel networks, see the fabrication steps in Figure 3. In a first step, a 500 ± 25 µm thick, p-doped, double side polished, 4" silicon wafer with a resistivity of up to 30 ohm · cm was coated with at 10 µm thick layer of a negative photoresist (AZ® 4562, MicroChem). In the subsequent photolithographic procesS step (MA6, Süss Micro Tec), the mask polarity of the deployed high resolution quartz mask (ML&C) patterns the photoresist during the UV exposure. A dry etching procedure was performed using an inductive coupled plasma system (ICP, Surface Technology Systems) resulting in a rectangular shaped channel cross-section with a depth and width of 200 µm.

The surface roughness of the channel walls is defined by the cycle length of the involved "Bosch process" and the mask resolution, and does not exceed 1 µm. By the iteration of the abovementioned steps at the backside of the silicon wafer, fluid inlets, outlets and pressure ports are incorporated. After dicing the wafer into predefined microchannel chips, PEEK (Upchurch Scientific®) fluid connectors were sealed to the inlet, outlet and pressure tubes by epoxy. After the anode and cathode of the fuel cell were manufactured in the abovementioned manner, they were processed together sandwiching in between a standard polymer electrolyte membrane, on one side of which an appropriate catalyst was layered. An example of the performance of the resulting fuel cell is shown in Fig. 4. The corresponding flow fields in the fuel cell anode microchannels are shown in Fig. 5, Refs. [1,3]. The darker areas denote gas regions (carbon dioxide). It is clear that the presence of gas disrupts the electrical performance of the fuel cell and may strongly reduce the produced power [1,3] (compare Figs. 4 and 5).

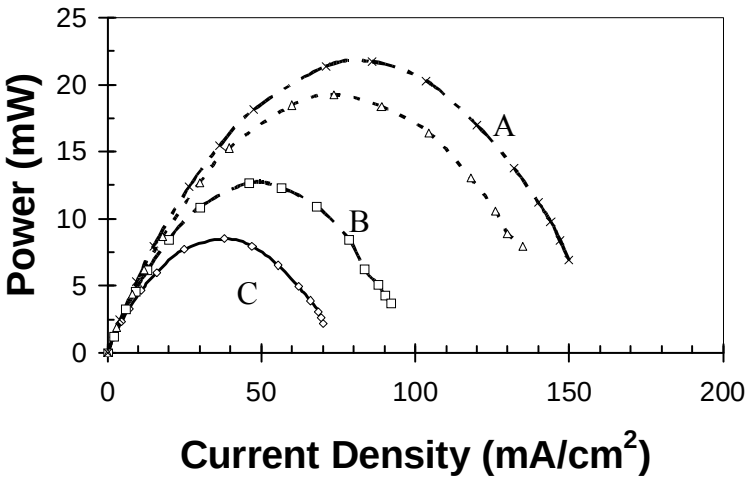

Figure 4. Performance curves of a flexible micro-DMFC from [3].

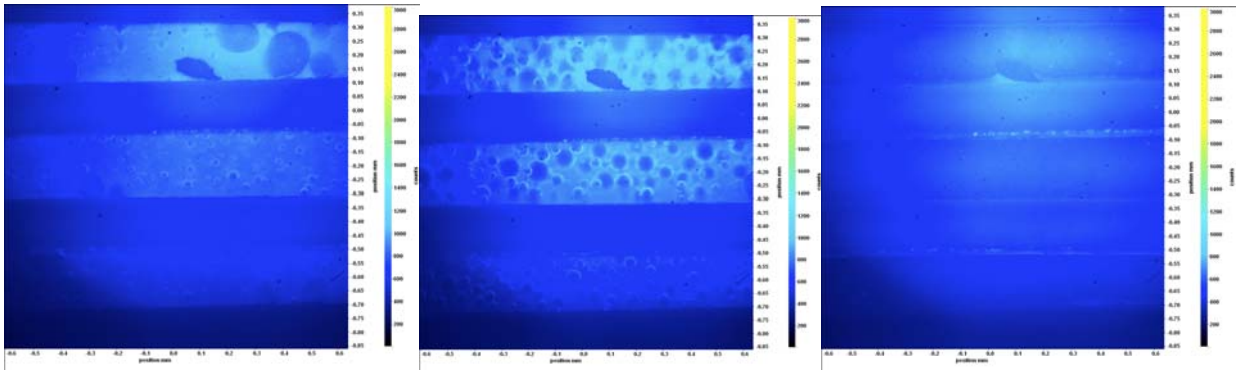

(a) (b) (c)

Figure 5. Flow configurations in the fuel cell microchannels corresponding to the designated curves, (a) A, (b) B, (c) C, in Figure 4, from [1,3].

THERMAL ENERGY TRANSFER: MICROCHANNEL ULTRA HIGH HEAT FLUX COOLING DEVICES FOR ELECTRONICS

The past few decades have seen a rapid growth in the computational power of processor chips, which may continue as predicted by Moore's law. The exponential increase in transistor density and storage density as well as the faster clock speed, however, cause serious problems in the thermal management of microelectronic devices. The miniaturization trend renders the thermal management challenging, especially when strict limitation of space and operating costs are applied. Until now the CPUs are cooled using large air heat sinks, but this will not be sufficient for cooling the next generation of microchips [4,5], particularly in compact multichip modules and 3-D microelectronic packages. Hence, novel cooling methods with thin form factors and high cooling performance are needed urgently.

We demonstrated an ultra thin heat sink for electronics, combining optimized impinging slot-jets, micro-channels and manifolds for efficient cooling. The design is optimized for a 2 x 2 cm^2 chip and provides a total thermal resistance of 0.087 cm^2K/W for flow rates < 1 l/min and an overall

pressure drop < 0.1 bar**.** This results in a maximum cooling capacity of 750 W/cm^2 for a temperature difference between fluid inlet and chip of 65K.

No previous studies in the literature considered the influence of the manifold on the hydrodynamic and thermal performance of the heat sink. This simplification is appropriate if there are no size restrictions in the third dimension. With denser packages, there is a demand for thin and efficient heat sinks with only lateral access for fluid supply and return. For these systems the optimum choice of design parameters can only be determined by combined analysis of the performance of a unit cell of the heat transfer structure and the design of the manifold.

We have demonstrated through modelling and experiments, [6,7], that combining heat transfer micro-channels containing slot-jets structures bringing coolant to the hot surface with manifold channels for the coolant transport, allows the optimization of an overall heat sink performance (Figure 6). First, we introduced a three-dimensional model of a unit cell of the heat transfer structure to solve the conjugate heat transfer problem for the micro-channel/jet flow. We then studied the basic physical phenomena of a unit cell and its dependency on the volumetric flow rate. We varied the length, channel width, fin thickness to channel width ratio and inlet/outlet width for a constant volumetric flow rate to determine the sensitivity of the heat sink to the individual design variables. In a second step we constructed a three-dimensional model considering the flow in the manifold channels and the heat transfer structure [6]. This model is applied to study the capability of the manifold to uniformly distribute the liquid coolant and to demonstrate that a design with tapered inlet and expanding outlet manifold channels provides uniform fluid distribution. The model results were confirmed by experiments [7].

The design consists of a manifold system with lateral fluid supply-and-return, which feeds an array of parallel micro-channels where the heat transfer is performed (Figure 6). Fluid enters the inlet manifold channels from the side. Along the inlet manifold channels the flow uniformly branches into the subsequent heat transfer structures through slit nozzles at the bottom wall of the manifold channels. The parallel micro-channels are orthogonal to the manifold channels. Hence, the flow direction after impingement on the hot surface at the bottom of the heat transfer channels is perpendicular to the one of the manifold system. While travelling along the heat transfer micro-channels, the fluid removes the heat, leaves the heat transfer micro-channel structure upwards through slit nozzles and merges into the outlet manifold channels, which guide the fluid to a lateral return (see Figure 6). The entire chip area can be cooled by just one of these systems, comparable from a manufacturing standpoint to a parallel channel network with a lateral manifold system as it was studied in one of our earlier papers [5]. It is possible that many of these systems are arranged in parallel to reduce the overall pressure drop and bulk thermal resistance of the heat sink.

Figure 7a shows streamlines starting from points equally spaced over the inlet surface. The flow enters the heat transfer structure through the inlet nozzle and impinges on the channel bottom wall where it undergoes a 90 deg. change of momentum. The vorticity with its axis transverse to the flow in the streamwise direction generates recirculation near the inner corner at the channel entrance, where the fluid velocity is much slower (Figure 7b). As the fluid flows along the channel, a hydrodynamic boundary layer develops. Towards the end of the channel the fluid is drained to the outlet nozzle with a stagnation zone formed in the channel region opposite to the outlet nozzle.

Figure 7c shows the static pressure contours at the center-plane of the heat transfer unit cell. From this Figure it becomes obvious that the hydrodynamic performance of the unit cell is dominated by the pressure drop across the inlet and outlet nozzles and not by the pressure drop along the channel.

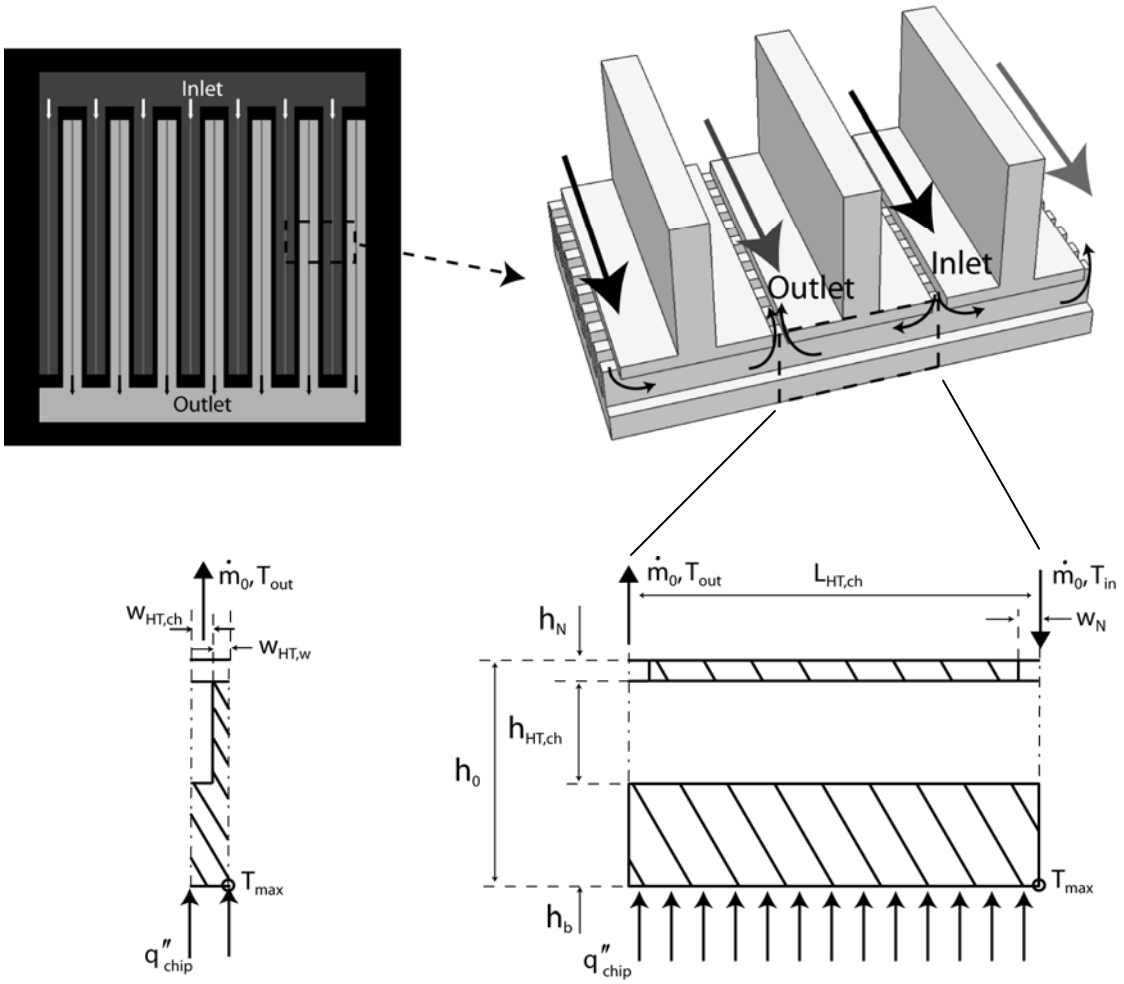

Figure 6. Schematic of a manifold micro-channel heat sink a) top view on manifold, b) isometric section view c) unit cell of the heat transfer structure side view d) unit cell of the heat transfer structure front view. From Ref. [6].

In order to analyze the thermal performance further, we present temperature contours in the solid and the fluid domains at the center-plane of the heat transfer unit cell in Figure 7d. Cold fluid enters the heat transfer structure through the inlet nozzle and impinges on the bottom channel face opposite to the inlet nozzle. The impinging jet inhibits the growth of hydrodynamic and thermal boundary layers, resulting in a small diffusion length from the solid wall to the convective flow and thus in an enhanced heat transfer rate.

Many more details on the performance of this ultra-high heat flux heat sink can be found in [6, 7]. In the following, we compare the efficiency of the different heat sink designs. The efficiency of a heat sink is defined by the ratio of the removed heat flux for a certain invested pumping power. The ability to remove a certain heat flux scales directly with the total thermal resistance of the system. For this reason we compare in Fig. 8 the total thermal resistance of the different designs as a function of idealized pumping power, *P*, which is defined as

$$P = \Delta p \dot{V}_{tot} . \qquad (1)$$

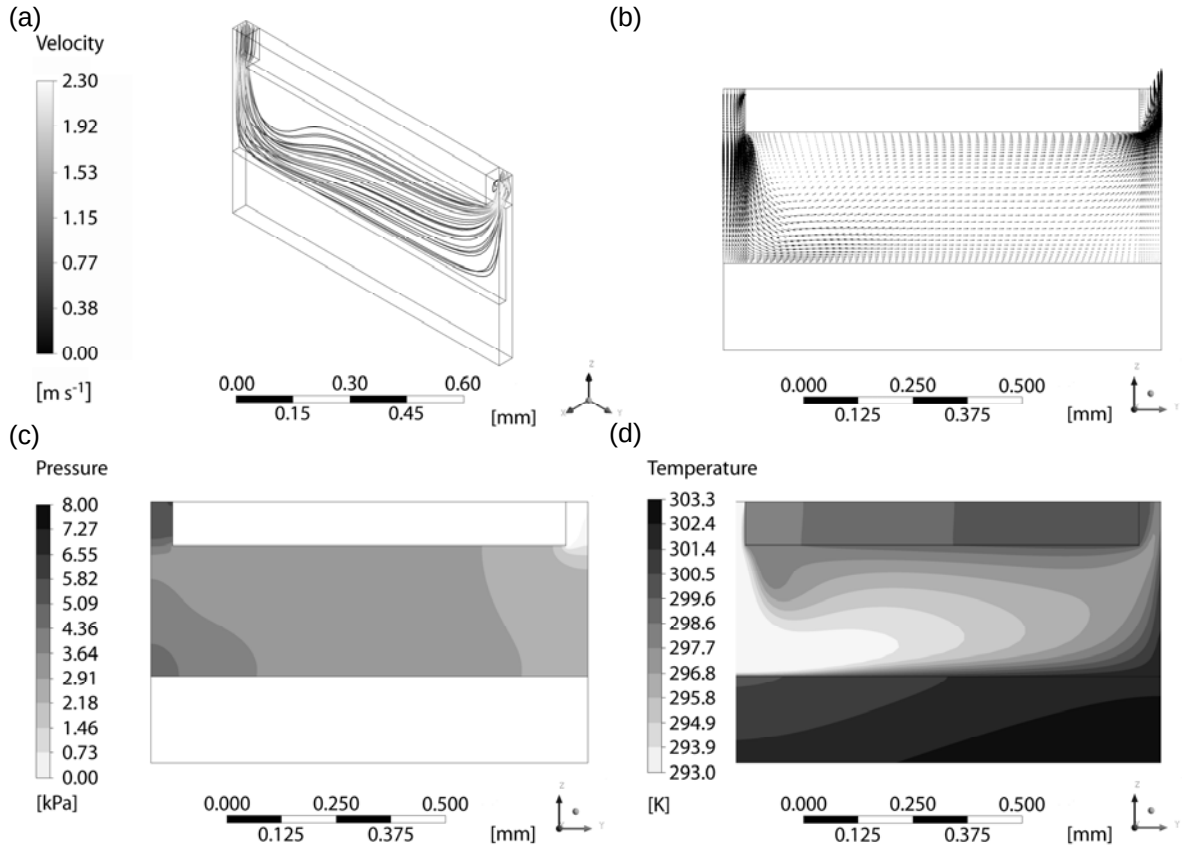

Figure 7: Spatial visualization of basic physical phenomena for a representative case at the center XZ-plane – a) streamlines starting from points being equally distributed over the inlet surface, b) velocity vectors, c) pressure contours and d) temperature contours – computed by means of three-dimensional model of the unit cell of the heat transfer structure. From Ref. [6].

In the case of high pumping powers and correspondingly high volumetric flow rates, the design with the smallest channel width of the heat transfer structure namely $w_{HT,ch}$ = 25 μm performed most efficient, although it had the highest hydrodynamic resistance (Fig. 8). At a constant pumping power, the volumetric flow rate was lower for the test-vehicle with $w_{HT,ch}$ = 25 μm than for the other two with larger channels and consequently it provided a higher bulk thermal resistance. However, due to the lower convective thermal resistance of this test-vehicle, the available thermal mass flux was used more efficiently resulting in higher outlet temperatures for a constant heat flux. When the pumping power was reduced, the increase of total thermal resistance of the test-vehicle with $w_{HT,ch}$ = 25 μm was more pronounced compared to the other two devices. Since its convective thermal resistance was lower than that of the other devices, the transition at which the bulk thermal resistance became the dominant part in the resistance chain occurred at higher volumetric flow rates and, consequently, at higher pumping powers.

In all, the total thermal resistance of the test-vehicle with $w_{HT,ch}$ = 25 μm showed a stronger dependence on the pumping power. For pumping powers below 0.06 W it would be beneficial to increase the channel width of the heat transfer structure from $w_{HT,ch}$ = 25 μm to $w_{HT,ch}$ = 50 μm in order to reduce the hydrodynamic resistance and at the same time the bulk thermal resistance. At this point the increase of the convective thermal resistance due to an enlargement of the channel width would be compensated by the reduction of the bulk thermal resistance [7].

Further, we demonstrate the potential of the heat sink design to be used in combination with elevated inlet temperatures to reduce the datacenter energy costs and to allow energy reuse. We studied the influence of increased fluid inlet temperatures on the performance of the best performing test-vehicle with a channel width of $w_{HT,ch}$ = 25 µm. Figure 9a depicts the pressure drop and the total thermal resistance of this device as a function of fluid inlet temperature at a constant volumetric flow rate of 1 l/min and a constant heat flux density of 100W/cm^2. An increase of fluid inlet temperature from 20°C to 70°C lowered the pressure drop across the heat sink about 40% due to a 60% reduction of the dynamic viscosity of water.

The pressure drop reduction was not linear as the dynamic viscosity of water decays exponentially with temperature. On the other hand, the total thermal resistance of the heat sink was increased by about 12%, being mainly attributed to a 20% reduction of the silicon's thermal conductivity. A reduction of the thermal conductivity of silicon contributed to an increase of the conduction thermal resistance of the silicon base causing a 6% increase of total thermal resistance [7]. In addition, the fin efficiency was decreased causing a reduction of the convective thermal resistance. On the other hand, the fluid thermal conductivity was increased by about 10% resulting in an increased convective heat transfer. However, the total thermal resistance of the heat sink was only slightly affected by the convective thermal resistance as the latter has only a share of 20% in the chain of thermal resistances. The volumetric heat capacity of the fluid decreased by about 2%, which directly affected the bulk thermal resistance of the system.

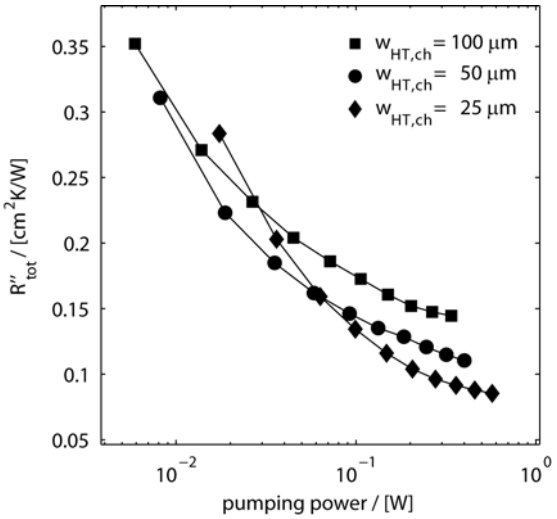

Figure 8. Maximum total thermal resistance as a function of pumping power for varying channel width $w_{HT,ch}$. From Ref. [7].

To evaluate the enhancement in efficiency of the heat sink due to elevated inlet temperatures we determined the relative coefficient of performance, COP, being normalized to the COP at 20°C [7]. The coefficient of performance is defined by the ratio of the removed heat for an invested pumping power. Hence, we write the relative coefficient of performance for a constant maximum temperature difference between heater and fluid inlet as (the symbols are self explanatory, P stands for power and R for thermal resistance)

$$\frac{COP}{COP_{20}} = \frac{\dot{q}_{heater}}{P}\frac{P_{20}}{\dot{q}_{heater,20}} = \frac{P_{20}}{P}\frac{R''_{tot,20}\Delta T_{\max}}{R''_{tot}\Delta T_{\max,20}} = \frac{P_{20}}{P}\frac{R''_{tot,20}}{R''_{tot}} \qquad (1)$$

Figure 9b depicts the relative enhancement in COP as a function of fluid inlet temperature. Due to the nonlinear behaviour of the pressure drop as a function of inlet temperature (Fig. 9a) we

observed a saturation behaviour for the COP. At inlet temperatures above 60°C, the pumping power reduction and the increase of total thermal resistance were balanced. Hence, a further rise of the inlet temperature did not influence the efficiency of the heat sink. Concluding, the performance of the heat sink could be enhanced by more than 40% for a 50°C rise of the fluid inlet temperature (compared to an inlet temperature of 20°C), resulting in a maximum heater temperature of 81°C for a fluid inlet temperature of 70°C.

NANOTECHNOLOGY FOR THE EFFICIENT TRANSPORT OF ENERGY: NANOENGINEERING WITH CARBON BASED ELECTRONICS

A very important part of the energy challenge in the 21st century is energy transport in the form of electricity including the related heat transfer issues. Nanotechnology has a lot to offer here, in particular in terms of nanoengineered materials and interfaces between different materials featuring desired properties, far superior to those of bulk materials. To this end, novel characterization methods need to be developed in parallel, for the accurate determination of the properties of such nanomaterials. In this lecture, I will focus on the topic of determination of the thermal conductivity of a very promising multifunctional kind of nanomaterial, namely, the carbon nanotube [8,9].

Theories and experiments showed that carbon nanotubes have remarkable thermal properties. However, both the experimental data and the theoretical predictions are scattered over 1 order of magnitude. In recent experiments, the reported thermal conductivities for multiwall carbon nanotubes at room temperature are in the range 400- 3000 W/mK, likely depending on the type and size of carbon nanotubes (CNTs) utilized, which give rise to different mean free paths of the energy carriers.

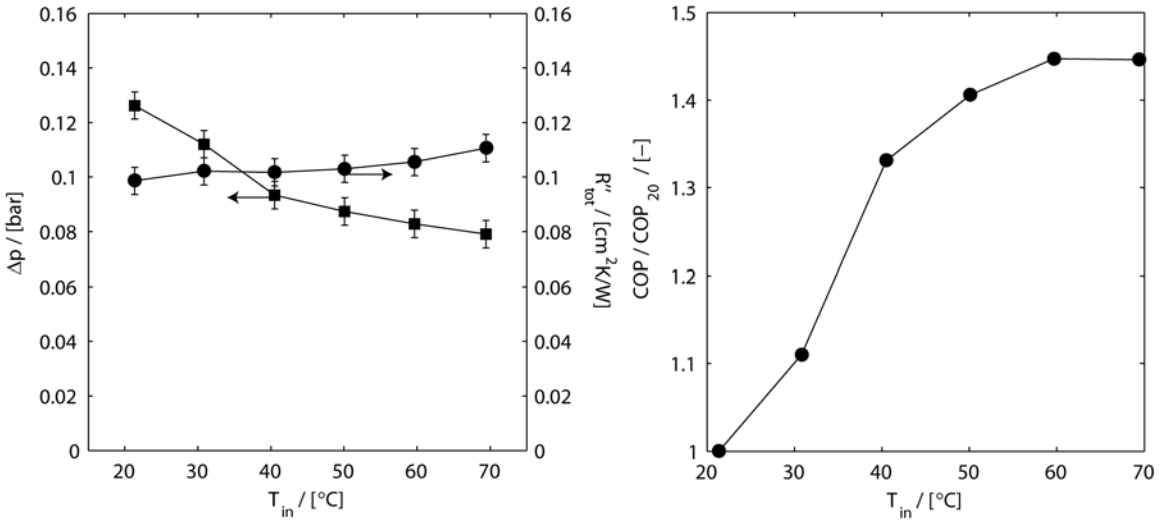

Figure 9: (a) total pressure drop and maximum total thermal resistance and (b) relative COP as a function of fluid inlet temperature for $w_{\mathrm{HT,ch}} = 25\mu m$, $\dot{q}''_{\mathrm{heater}} = 100 W/cm^2$ and $\dot{V} = 1 l/\mathrm{min}$. From Ref. [7].

There is still a need for a reliable and reproducible measurement technique to test the theoretical predictions and to provide fundamental thermophysical data for an efficient design of carbon nanotube based nanoelectronics. To fully understand the fundamental heat transport characteristics in the mesoscopic scale, reliable data of thermal conductivity for various sizes of nanotubes should

be collected in a reasonably precise manner. To this end, we developed a novel measurement technique based on the four-point-probe third-harmonic (3-ω) method with assistance of a focused ion beam (FIB) source for the fabrication of the needed experimental device [8,9].

We have employed the four-point 3-ω method for a carbon nanotube. However, the proposed method can be easily implemented to other nanosystems. With this method, the contact resistance was eliminated and spurious signals caused by it could be avoided. Hence, the contact contribution can be neglected in both the electrical and the thermal network. To construct a four-wire connection, a simple nanofabrication process was developed in which FIB milling was performed on a prefabricated microdevice (Fig. 10). The control of individual carbon nanotubes was realized by dielectrophoresis (Fig. 10). By applying a constant amplitude ac current through the carbon nanotube, we could generate a temperature rise fluctuating at the second harmonic and measure the 3-ω signal, which is used to compute the thermal conductivity. The multiwalled carbon nanotube used in this study shows a dissipative nature. MWCNTs are diffusive conductors. As a consequence, the one-dimensional heat diffusive equation along the nanotube suspended between two metal electrodes can be utilized to obtain a closed form solution of the third harmonic response [8,9].

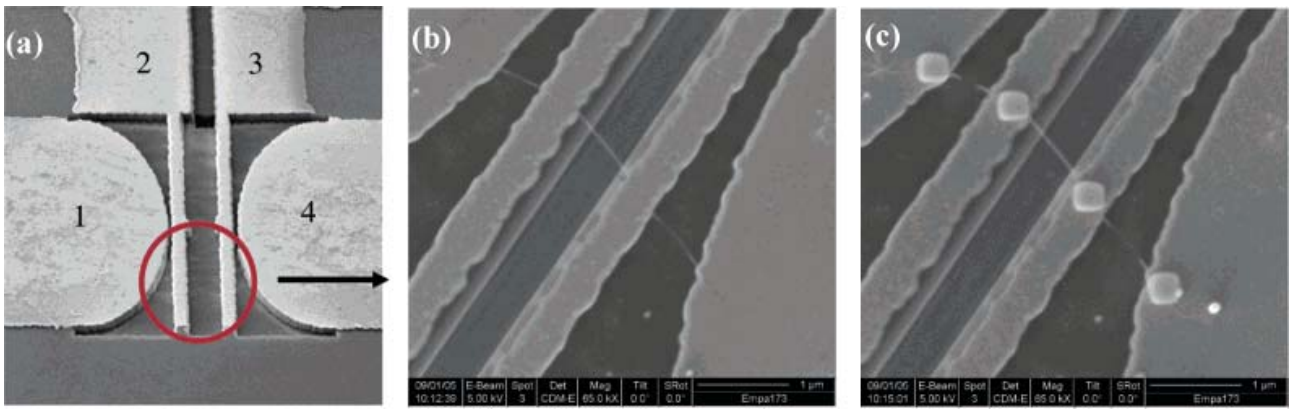

Figure 10. A series of pictures of a four-point-probe 3-ö experiment: (a) four-wire construction by focused ion beam milling; (b) selective deposition of single CNT by dielectrophoresis; (c) electron beam soldering at four contacts. From Ref. [8].

The measured value for the CNTs investigated in [8] is 300 W/mK. The dissipative nature of phonon transport has been verified with the measurement of 3-ω signal, which follows the third power law [8,9].

CLOSING REMARKS

Energy is arguably the most important technical and scientific challenge facing humanity as we enter the 21st century. Significant progress is required in all areas of energy conversion, energy transport and energy storage and conservation. Due to our increasingly mobile society, the capability of decentralized, transportable and personal power generation is becoming a major driver for emerging energy technologies. All the above must be achieved with a great sensitivity to the environmental impact of energy technologies, as the warning signals of the harmful impact of human activities on the environment have reached the danger level. Micro- and Nanotechnologies can significantly contribute to the emergence of the next generation of energy devices in particular

through the enabling of manufacturing of devices and materials with superior performance. Examples of such devices and materials were shown in the course of the lecture. Significant advances in experimental heat transfer and the related thermodynamics are central issues in many novel energy applications and in combination with the great potential of nanotechnology, they can surely be a major contributor to overcoming the energy challenge in years to come.

REFERENCES

1. C. Weinmueller, N. Hotz, A. Mueller and D. Poulikakos, "On two-phase flow patterns and transition criteria in aqueous methanol and CO2 mixtures in adiabatic, rectangular microchannels", International Journal of Multiphase Flow (2009), doi: 10.1016/j.ijmultiphaseflow.2009.03.010.

2. Madou, M. J., "Fundamentals of microfabrication: the science of miniaturization", CRC Press, Boca Raton, London, New York, Washington D.C., 2002.

3. C. Weinmueller, 2009, "Deformable, Direct Methanol Micro- Fuel Cells", PhD Thesis, Mechanical and Process Engineering Department, ETH Zurich.

4. Sauciuc et al., "Air-cooling extension – performance limits for processor cooling applications", in: 19th IEEE SEMI-THERM Symposium, 2003.

5. W. Escher , B. Michel and D. Poulikakos "Efficiency of optimized bifurcating tree-like and parallel microchannel networks in the cooling of electronics", Int. Journal of Heat and Mass Transfer 52 (2009) 1421–1430.

6. W. Escher, B. Michel1 and D. Poulikakos, "A novel high performance, ultra thin heat sink for electronics" International Journal of Heat and Mass Transfer, in press.

7. W. Escher, T. Brunschwiler, B. Michel and D. Poulikakos, "Experimental Characterization of An Ultra Thin Manifold Micro-channel Heat Sink", Journal of Heat Transfer, in review, (2009).

8. T. Y. Choi, D. Poulikakos, J. Tharian and U. Sennhauser, "Measurement of Thermal Conductivity of Indivisual Carbon Nanotubes by the 4-point 3-omega Method," Nanoletters, Vol. 6, No. 8, 1589-1593, 2006.

9. Choi Tae-Youl, D. Poulikakos, J. Tharian and U. Sennhauser, "Measurement of thermal conductivity of individual multi-walled carbon nanotubes by the 3-ω Method" Applied Physics Letters, 87, 013108, 2005.

NUSSELT AND REYNOLDS NUMBERS IN THERMAL CONVECTION AT VERY HIGH RAYLEIGH NUMBERS

K.R. Sreenivasan
International Centre for Theoretical Physics
Trieste, Italy

ABSTRACT. By taking advantage of the unique properties of cryogenic helium gas, a concerted experimental effort has been made to study thermal convection over eleven decades of the Rayleigh numbers upwards of a million. The Nusselt and Reynolds numbers have been measured. The measurements are compared with theoretical results wherever possible. The results of these investigations will be discussed. Some aspects of quantized vorticity below the lambda point in liquid helium will also be presented. The talk will not assume any special knowledge of cryogenic helium.

Keywords: *Thermal convection, vorticit,*

* Corresponding author: Prof. K.R. Sreenivasan
Phone: +(39)-040-2240-251
E-mail address: krs@ictp.it
http://www.ictp.it/~krs

Keynote Lectures

REALIZATION OF FUSION AS THE ULTIMATE ENGERGY SOURCE FOR HUMANITY

M. A. Abdou
Center for Energy Science and Technology Advanced Research (CESTAR), Los Angeles, USA
University of California-Los Angeles, Los Angeles, California, U.S.A.

ABSTRACT. Fusion promises to be the ultimate energy source for mankind, but the scientific and technological challenges are enormous. ITER, now being constructed in France is a major step in fusion research. But the most challenging stage of fusion development still lies ahead: the development of Fusion Nuclear Science and Technology (FNST). This stage will aim at developing the nuclear components surrounding the plasma, which are exposed to an extreme environment of high surface and volumetric heating, intense radiation fluxes, strong 3-component magnetic field, and many thermal/chemical/mechanical/electromagnetic interactions. The presence of these multi-function components in the unique and complex fusion environment leads to many new multi-physics, multi-scale phenomena and synergistic effects that require extensive worldwide R&D programs to understand and predict. A facility for development of FNST is required in addition to ITER.

Keywords: *Fusion, FNST, ITER, CTF, DEMO*

INTRODUCTION

Fusion has great potential to be a sustainable energy source with no emission of greenhouse or other polluting gases. However, fusion development has taken a relatively long time. When the viability, practicality, and economic competitiveness of fusion will be demonstrated is an open question. Our success in realizing practical fusion in the 21st century will depend in large measure on our understanding of the enormous engineering challenges that a fusion energy system involves and addressing them in an extensive R&D program, including the construction and operation of the appropriate facilities in a timely manner.

Fusion development from 1950 until today can be characterized as “exploring the physics of plasmas.” Fusion is now entering a new phase that can be generally called “exploring the physics of fusion.” This phase may take about 20 years with the primary research activities focused on the construction and operation of ITER, under construction by an international consortium in Cadarache, France, and the

*Corresponding Author : Prof. M.A. Abdou
Phone: (310) 206-0501, Fax: (301) 825-2599
Email : abdou@fusion.ucla.edu

National Ignition Facility (NIF) being constructed by the US in Livermore, California. ITER and NIF will investigate the physics of burning fusion plasmas in magnetic and inertial fusion, respectively.

The most challenging phase of fusion development will most likely be the R&D on Fusion Nuclear Science and Technology (FNST). This phase will aim at developing the nuclear components surrounding the plasma, which are exposed to an extreme environment of high surface and volumetric heating, intense radiation fluxes, strong 3-component magnetic field, and many thermal/chemical/mechanical/electromagnetic interactions. Nuclear components are located inside the vacuum vessel where tolerance for failure is low.

There are five pillars of a fusion energy system: *1-Confined and Controlled Burning Plasma, 2-Tritium Fuel Self-Sufficiency, 3-Efficient Heat Extraction and Conversion, 4-Safe and Environmentally Advantageous, 5-Reliable System Operation.* FNST plays the key role in all the last four pillars, i.e. 2-5. Yet, FNST has not yet received the priority and the resources needed in the world fusion program. The blanket is a central component of FNST. Yet, no fusion blanket has ever been built or tested. There exist no facilities that provide the necessary environment for meaningful testing of the fusion nuclear components.

ITER will provide the first fusion nuclear environment in which blankets can be tested and data relevant to FNST obtained. While testing in ITER provides very important information on FNST, it is severely limited. Development of FNST will require a new facility designed specifically to test and develop fusion nuclear components. This type of facility for fusion nuclear science and technology is often called CTF (Component Testing Facility) or VNS (Volumetric Nuclear Source).

WHAT IS FUSION NUCLEAR TECHNOLOGY?

Fusion Nuclear Technology (FNT) includes all components from the edge of the plasma to the toroidal field coils, i.e. First Wall/Blanket, vacuum vessel and shield components, and other plasma interactive/high heat flux components (divertor, r.f. antennas/launchers/waveguides, diagnostics). These components are illustrated in a vertical cross section of a tokamak reactor in Fig.1. Other components coupled to and affected by the nuclear environment include Tritium Processing Systems, Instrumentation and Control Systems, Remote Maintenance Components, and Heat Transport and Power Conversion Systems. Many technical areas are essential to FNT; for example, neutronics, materials, thermomechanics, thermofluids, magnetohydrodynamics, safety, solid mechanics, radiation effects and chemistry.

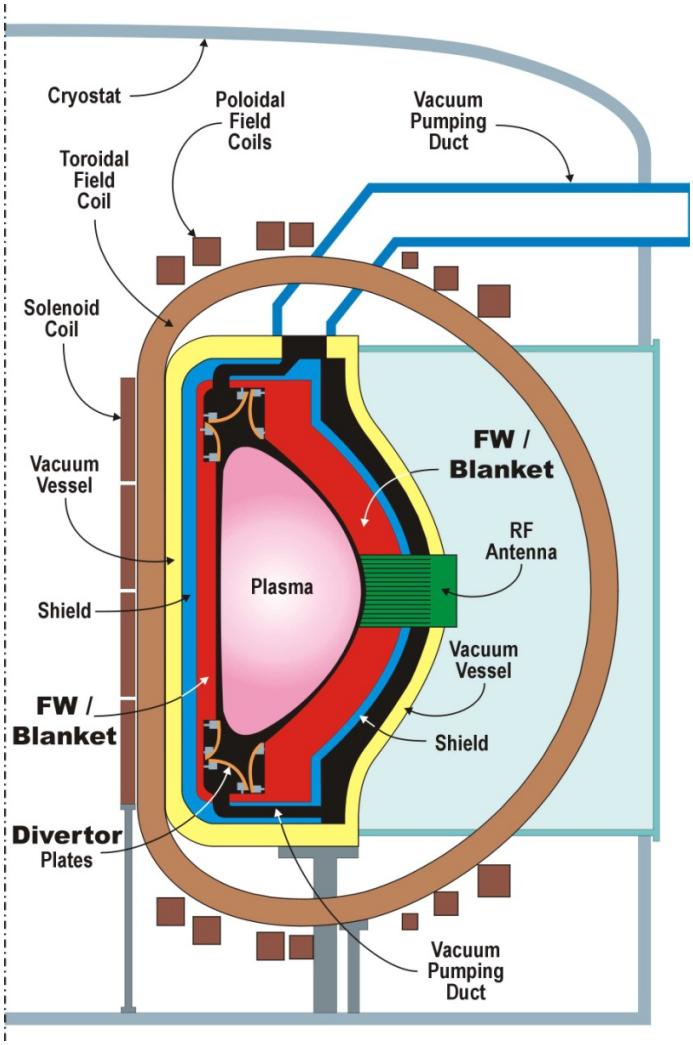

Figure 1**.** Vertical Section of a Tokamak Reactor that shows the fusion nuclear components

FNT components, particularly the blanket/first wall/divertor must operate safely and reliably in a harsh environment. Yet, no fusion blanket has ever been built or tested. Blanket systems have many possible designs, materials, and configurations. Many blanket concepts have been proposed worldwide, see Table 1, each having its own balance of feasibility and attractiveness issues. Only after stages of fusion environment testing can an informed down-selection be made. The large number of concepts and wide range of issues are best screened by utilizing the resources and the ingenuity of the world's FNT programs.

Table 1
Blanket concepts proposed by ITER Parties for ITER testing [5]

Concept	**Acronym**	**Materials**	**Proposing Party**
Helium-Cooled Ceramic Breeder	HCCB	RAFS Structure Be multiplier, Ceramic breeder (Li_2TiO_3, Li_4SiO_4, Li_2O) Helium coolant and purge	EU, KO, CN, (JA,US, RF, IN)* *Supporting Role
Water-Cooled Ceramic Breeder	WCCB	RAFS structure Be multiplier, Ceramic breeder (Li_2O) Water coolant, He purge	JA
Helium-Cooled Lead-Lithium	HCLL	RAFS structure Molten Pb-17Li breeder/multiplier Helium coolant	EU, CN
Dual-Coolant Lead-Lithium	DCLL	RAFS structure SiC flow channel inserts Molten Pb-17Li breeder/coolant Helium coolant	US, CN (EU, JA, IN)* *Supporting Role
Helium-Cooled Molten Lithium	HCML	RAFS structure Lithium breeder Helium coolant	KO
Self-Cooled Lithium	Li/V	Vanadium alloy structure Insulator barrier (*e.g.*, AlN) Lithium breeder/coolant	RF
Lead-Lithium Ceramic Breeder	LLCB	RAFS structure Dual coolant Lead Lithium and Helium Dual breeder Lead Lithium and Ceramic	IN

ITER AND TEST BLANKET MODULE (TBM)

ITER is a tokamak, in which strong magnetic fields confine a torus-shaped fusion plasma. It will be the first fusion reactor to create more energy than it uses. The objectives set out for ITER are basically two: 1) programmatically, to demonstrate the scientific and technological feasibility of fusion energy for peaceful purposes; and 2) technically, to demonstrate extended burn of DT plasmas, with steady state as the ultimate goal; to Integrate and test all essential fusion power reactor technologies and components, and to demonstrate safety and environmental acceptability of fusion. Breeding blankets represent one of the major technological breakthroughs required from passing from ITER to the next step, usually called DEMO, a demonstration reactor able to furnish electric power to the grid. For this reason, among the technical objectives of ITER it is specifically stated that "*ITER should test tritium breeding module concepts that would lead in a future reactor to tritium self-sufficiency and to the extraction of high-grade heat and electricity production.*"

Test Blanket Modules (TBMs) inserted in ITER represent a principal strategy by which ITER will provide the first experimental data on the potential of fusion as an energy source. TBMs are essential to answering two critical questions about fusion as an energy source: "*Can tritium be produced in the blanket at a rate sufficient to supply tritium to fuel the plasma?"* and *"Can heat be extracted from the blanket, simultaneously with tritium breeding, at temperatures high enough for efficient electricity generation?"* This is why successful TBM experiments in ITER represent an essential step on the path to DEMO in all the ITER Parties' fusion development plans. A *principal mission* of the ITER Test Blanket Module (TBM) Program is to develop, deploy, and operate ITER TBM experiments that provide unique experimental data on, and operational experience with, the integrated function of blanket and first wall (FW) components and materials in a true fusion environment. This data is essential for validation of the scientific understanding and predictive capabilities; demonstration of the principles of tritium self-sufficiency in *practical* systems; development of the technology necessary to install breeding capabilities in next-step machines; and providing the first integrated experimental results on reliability, safety, environmental impact, and efficiency of fusion energy extraction systems.

The overall ITER operational plan through the first ~10 years is preceded by one year of integrated commissioning of in-vessel components. The 10-year plan includes 2.5 years of initial H-H operation; a brief D-D phase; and an approximately six-year-long D-T phase. During the D-T phase, typical operating conditions for the TBMs include an average FW surface heat flux of 0.27 MW/m^2 (during a plasma pulse), a neutron wall load of 0.78 MW/m^2 (during a plasma pulse), and a pulse length of 400 s (or longer) with a duty cycle of 22% (or higher). These parameters are used in the conceptual designs of Parties' TBMs. Other important conditions of ITER that allow for meaningful integrated testing of blanket components and material systems include a strong magnetic field (~ 5 T) of the same order as in power plants, and off-normal plasma events such as disruptions, ELMs, VDEs, *etc*.

Three 1.75 m wide × 2.2 m high equatorial ports have been allocated by ITER for TBM testing. Test modules must be recessed 50 mm from the nominal surface of the first wall of the ITER shielding blanket in order to reduce plasma-wall interaction effects, including the maximum disruption energy load (0.55 MJ/m^2 over 1-10 ms). Correspondingly, a 2 mm beryllium protection layer on the FW is requested.

Each TBM is supported by a water-cooled steel frame that has a thickness of 200 mm on each side of the TBM and a backside shield behind each TBM. The TBM is inserted from the plasma side into the frame and supported from behind by attachment to the backside shield block with flexible supports. Each frame can hold two vertically or horizontally oriented TBM backside shield pairs. This combined unit is known as the TBM port plug, and provides a standardized interface with the ITER basic

structure, including thermal insulation of the basic machine from the TBM. The port plug is inserted though the bioshield and into the port as a single unit.

Each TBM system includes several associated sub-systems, such as coolant loops, tritium management equipment, a liquid breeder loop (in liquid breeder TBMs), instrumentation packages and control systems, and safety systems. These sub-systems will need to interface with the ITER facility and services, including remote handling equipment, the hot cell facility, the ITER standard cooling system, the HVAC, diagnostic, and control and safety systems, each with its corresponding operational procedures and limitations. Any equipment and interfaces necessary for a particular TBM will have to match the space and services available at each test port. Three blanket options, in which liquid metal MHD plays an important role in determining blanket performance, have been proposed for testing in ITER. They are a helium-cooled PbLi (HCLL), a dual-cooled PbLi (DCLL), and a dual-function PbLi (DFLL) blanket concept. The common MHD problems among the three concepts relate to the MHD flow distribution for complex flow elements including toroidal manifold flow distribution, contractions/expansions in poloidal plane, and MHD velocity profile in electrically-coupled multiple ducts. In the HCLL blanket, liquid metal circulation is primarily required for tritium removal. Larger flow rates are desirable in order to keep the tritium permeation losses low. A specific MHD question on the HCLL concept addresses the coupled effect of the MHD velocity magnitude and profile on alleviating the tritium permeation problem. The basic idea of the DCLL blanket is to use helium to remove all heat deposited in the blanket structure (including the surface heat flux on the first wall), and a flowing, self-cooled, PbLi alloy breeder to remove nuclear heat generated in the breeding zone – at a high temperature for efficient power conversion. The DCLL concept consists of PbLi channels contained within a helium-cooled structure made of reduced activation ferritic steel (RAFS). A unique MHD problem for this particular concept relates to the effect of natural convection on the MHD flow and temperature distributions. Both DCLL and DFLL concepts require the use of an insulator such as SiC/SiC flow channel insert (FCI) for pressure drop and thermal loss control. Such a FCI performs two important functions: (a) the FCI thermally insulates the PbLi so that its temperature can be considerably higher than the surrounding structure, and (b) the FCI also provides electrical insulation between the PbLi flow and the thick, load-bearing RAFS walls to reduce the MHD pressure drop to a manageable level, even in high magnetic field regions. MHD related R&Ds have been identified under the IEA collaborative efforts, including toroidal expansion and toroidal manifold MHD experiments.

In addition, it is necessary to ensure that the TBMs are compatible with the tokamak operation. Several issues driven by the interaction of the test blanket module and the magnetic field that must be characterized and investigated during the hydrogen plasma operation phase including:

- interference of the test modules with plasma confinement, including the effects of ferritic/martensitic steels on the ITER magnetic confinement fields;
- operation of the test modules, diagnostics, and supplementary equipment in a strong magnetic field;
- test module structural loads and corresponding responses owing to surface heat flux on the test module first wall during normal plasma discharges, and including spatially non-uniform heat fluxes, for instance, from plasma MARFEs;
- test module structural loads and corresponding responses during tokamak startup and shutdown, including transient events like plasma disruptions; and
- material erosion and transport from the test module first wall and the necessity of using a beryllium protective layer (current requirement is for a 2 mm Be layer).

These issues also present challenging opportunities for the PAMIR Community.

FRAMEWORK FOR FNT DEVELOPMENT

The technical foundations for the fusion nuclear technology development path to DEMO are based on many previous technical studies led by the US and other countries over three decades. Examples of references that provide the technical basis are References [1], [2], and [3]. These comprehensive studies concluded that blanket development is one of the key components on the critical path to DEMO. The major elements of the proposed blanket development path to DEMO are illustrated in Fig. 2. They are:

Base R&D activities with nuclear and non-nuclear experiments in *non-fusion* facilities; and modeling and computer simulations

Testing Blanket Modules (TBM) in ITER during Phase 1 of operation

Continuous transfer of information from ITER TBM and base R&D into the refinement of blanket designs and the construction of blanket test modules, and possibly breeding blankets, in CTF

Testing in CTF that addresses the engineering development and reliability growth of blankets to a level sufficient to design, construct and operate full breeding blankets in DEMO.

It is important to understand the relationship and incremental role of each of these elements. A detailed description is given in reference 6.

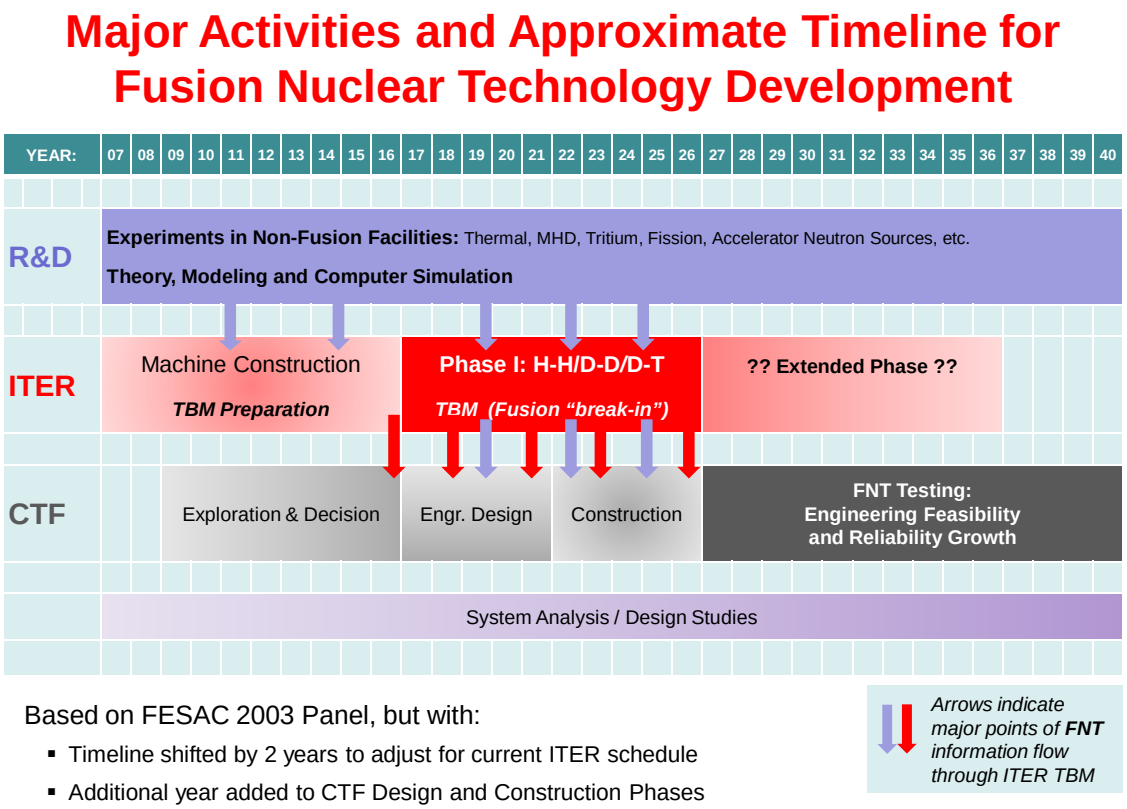

Figure 2. Major Activities and Approximate Timeline for FNT Development

These main FNT development path elements are made up of many progressive R&D activities, as illustrated in Fig. 3. Note that tests in non-fusion facilities are limited to single-effect and some multiple-interaction tests. Fusion tests are needed to cover several multiple-interaction tests, integrated tests, and component tests.

In partial analogy to experience from technology development in other fields, we propose that testing and development of FNT (primarily the blanket) in fusion facilities proceed in three stages: (I) initial fusion environment "break-in"; (II) engineering feasibility and performance verification; and (III) component engineering development and reliability growth, as illustrated in Fig.4.

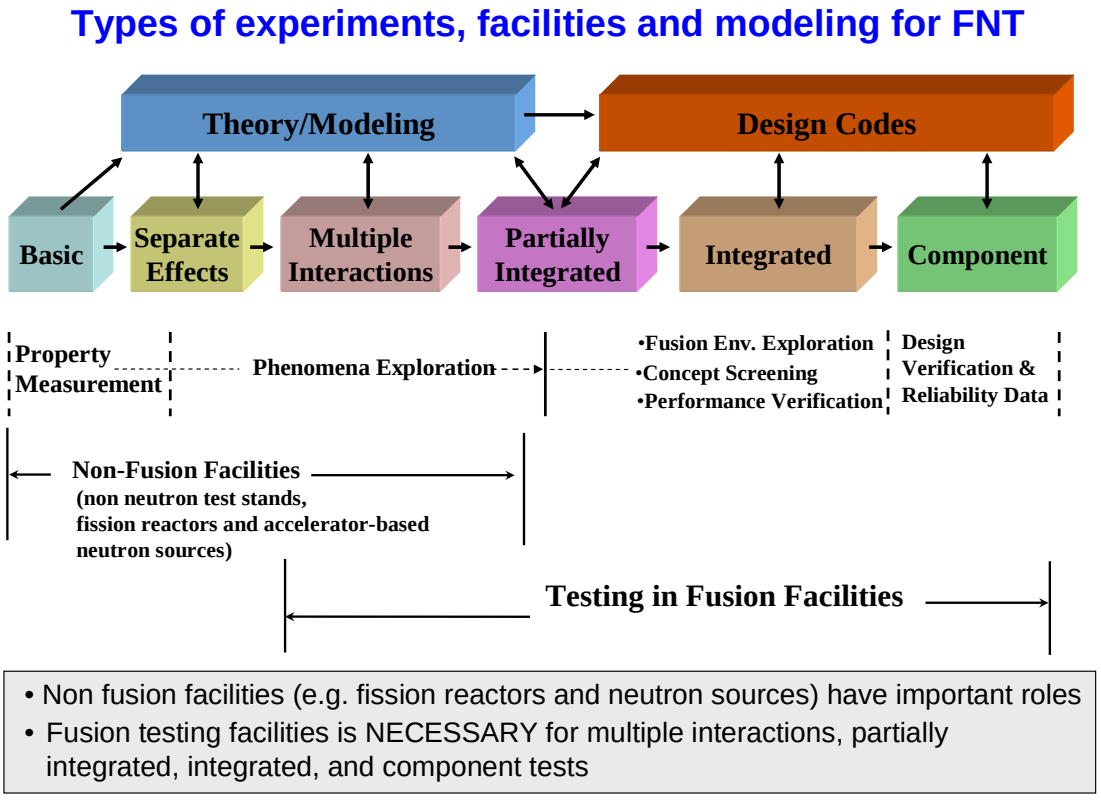

Figure 3. Types of Experiments, Facilities, and Modeling for FNT

We note again that FNT components such as the blanket have never been tested before in any fusion facility. Therefore, the Stage I testing should be focused on calibration and exploration of the fusion environment, including uncovering unexpected synergistic effects and testing experimental techniques and diagnostic tools (e.g. how to measure and collect data, interpret and extrapolate results, and include the effects of the fusion environment on instrumentation tools). Part of the Stage I fusion environment exploration is screening a number of candidate design concepts. Only a limited number of concepts are tested in Stage II, which aims at engineering feasibility and performance verification. Modules with a representative size should be used in this stage to ensure that all the key aspects of subsystem interactions are tested. Results of tests in Stage II should permit selection of a very small number of concepts, but selection of a single concept is too risky, prior to performing reliability growth tests in

Stage III. Stage III tests focus on true engineering development where actual prototypical components are tested and an aggressive design/test/fix iterative program is instituted. The extensive reliability testing required to achieve blanket availability goals is one of the primary reasons why blanket testing determines the critical path for FNT development.

The role of ITER TBM is to provide the Stage I testing needs, while the CTF mission is to perform the testing required in Stages II and III.

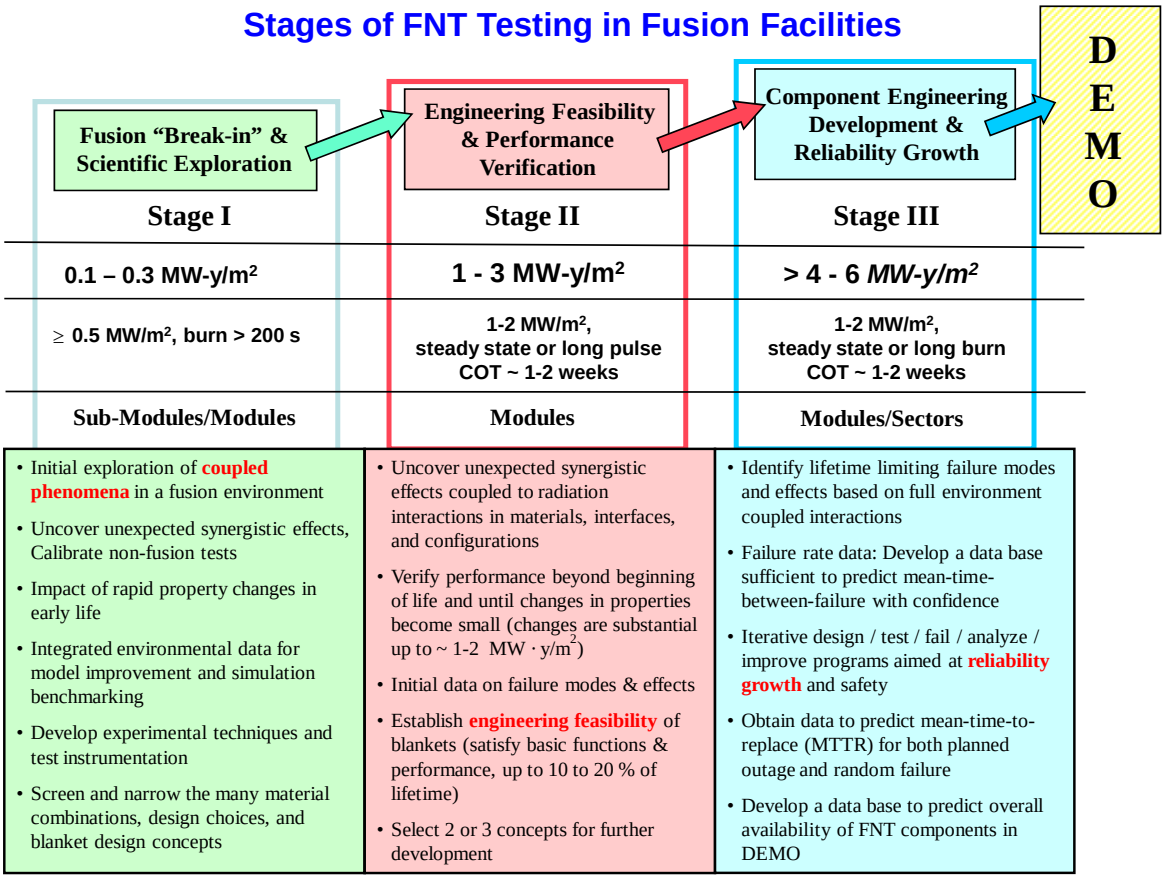

Figure 4. Stages of FNT Testing in Fusion Facilities

DEMO GOALS

DEMO requirements are a strong driver for the need for such an FNT development path, as described above. Previous system and planning studies provide general goals and features of DEMO. All studies and planning activities conclude that the DEMO must achieve tritium self-sufficiency. Another conclusion is that at least one option must be validated for each component prior to construction of DEMO. The goal of fusion R&D plans around the world is the operation of a demonstration power plant (Demo), which will enable the commercialization of fusion energy. The target date is typically 20-40 years from now. Early in its operation the Demo will show net electric power production, and ultimately it will demonstrate the commercial practicality of fusion power. It is anticipated that several such fusion demonstration devices will be built around the world. In order for a future fusion industry to be competitive, the Demo must:

a) achieve tritium self sufficiency; b) be safe and environmentally attractive;
c) extrapolate to competitive cost for electricity; d) use the same physics and technology as the first generation of competitive commercial power plants to follow; and
e) achieve availability of ~ 50%, and extrapolate to commercially practical levels.

The most difficult and time consuming stage in FNT development is expected to be the "reliability growth phase." Prior studies, *e.g.* Refs. [1] and [4], have shown that the availability of the blanket system must be higher than 88% to meet a Demo target availability goal of 50%. Since the time to replace blankets is long (weeks), the Mean-Time-Between Failures (MTBF) must be long to achieve such a high availability target goal. Current assessments, again see *e.g.* Ref. 1, show that (A) the MTBF for a single blanket module must be considerably longer than its fluence lifetime, and (B) the required blanket system MTBF is longer than what is achievable based on extrapolations from other technologies. Therefore, an aggressive reliability growth program needs to be pursued for the blanket, which will require a large testing area and long testing time to achieve a reasonable confidence level. This is one of the major objectives of CTF. Early data from R&D and ITER TBM should help screen blanket concepts in order to allow CTF to focus quickly on engineering development and reliability growth testing of a very small number of blanket concepts (preferably two).

CONCLUSIONS

Fusion nuclear components must operate safely and reliably in a harsh environment. No fusion blanket has ever been built or tested. Hence, their integrated function and reliability are by no means assured. ITER presents the first opportunity to test blanket materials and components in an actual fusion environment after many years of research, development and design in domestic programs. ITER test blanket module (TBM) testing represents a critical step toward establishing the principles of tritium self-sufficiency and energy extraction – on which the feasibility of deuterium-tritium fusion energy production relies. The role of ITER TBM is to provide the Stage I Fusion Break-in testing needs. The CTF mission is to perform the testing required in Stages II and III.

Fusion Nuclear Science and Technology (FNST) development is the most difficult challenge remaining in the practical realization of fusion as a practical energy system. The cost of R&D and the time to DEMO and commercialization of fusion energy will be determined largely by FNST.

REFERENCES

1. Abdou, M.A. et al., Results of an International Study on a High-Volume Plasma-Based Neutron Source for Fusion Blanket Development, *Fusion Technology*, 29, pp 1-57, 1996.

2. Abdou, M.A. et al., Technical Issues and Requirements of Experiments and Facilities for Fusion Nuclear Technology, *Nuclear Fusion*, 27, No. 4, pp 619-688, 1987.

3. A Study of the Issues and Experiments for Fusion Nuclear Technology, *Fusion Technology*, 8, pp 2595-2645, 1985.

4. A Plan for the Development of Fusion Energy: Final Report to FESAC, March 2003.

5. US ITER Test Blanket Module (TBM) Program, Volume I: Technical Plan and Cost Estimate Summary, *UCLA-FNT-216*, 2007.

6. Workshop on the Role of the ITER TBM in Fusion Nuclear Technology Development, May 30 – June 1, 2007, *UCLA-FNT-218*, 2007.

Solar Hydrogen Production

H. Müller-Steinhagen*, M. Neises, M. Roeb, C. Sattler
Deutsches Zentrum für Luft- und Raumfahrt e.V. (DLR)
Institute of Technical Thermodynamics, Germany

Abstract. The potential of hydrogen to become the energy carrier of the future is widely accepted. Today more than 90% of hydrogen is produced from fossil sources, mainly by steam reforming of natural gas and by coal gasification. To finally benefit from hydrogen as a fuel, it has to be produced in large quantities without emission of greenhouse gases. Solar thermal processes have the potential to be the most efficient technologies for large scale hydrogen production in the future. Therefore, high temperature solar technologies are under development for the different steps on the way to renewable hydrogen. This paper discusses the general research strategy for a spectrum of solar processes incorporating carbonaceous materials as well as splitting of pure water.

Keywords: *solar, hydrogen, thermochemical cycles, CSP, steam methane reforming*

INTRODUCTION

The potential of hydrogen to become the energy carrier of the future is widely accepted. At present, about 50 million tonnes of hydrogen are produced per year, with an annual increase of about 6 % [12]. More than 90% of this amount is produced from fossil sources, the other 10% mainly by electrolysis using power from the grid. 95 % of the hydrogen is directly used in chemical industry for the production of ammonia, methanol, and for refining.

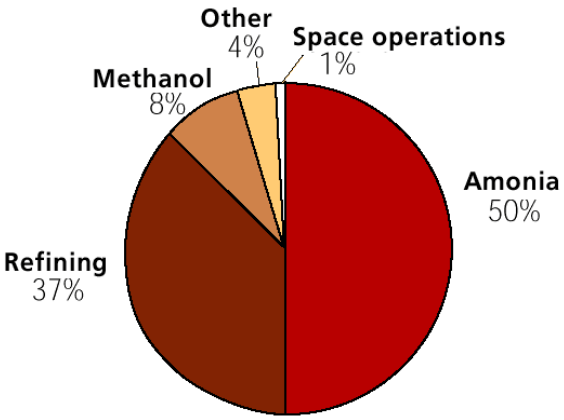

Figure 1: Use of hydrogen in 2002 [1].

Today the only energetic use of hydrogen worth mentioning is as a propellant in space operations for example in rocket engines like the Vulcain of the Ariane-5 [3,4].

* Corresponding author: Prof. Dr. Dr.-Ing. habil. H. Müller-Steinhagen
Phone: + (49)-711-6862-358, Fax: + (49) -711-6862-712
E-mail address: hans.mueller-steinhagen@dlr.de

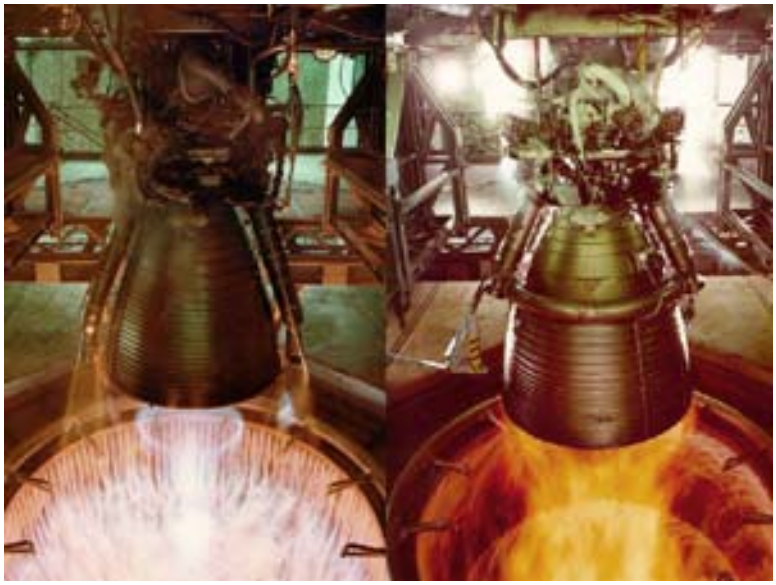

Figure 2: Vulcain-1 (left) and Vulcain-2 (right) rocket engines heat-up test at DLR Lampoldshausen, Germany.

Therefore, the change to a hydrogen based energy economy which is worldwide supported and already prepared by international initiatives such as the International Partnership for the Hydrogen Economy, IPHE [5,6], the International Energy Agency, IEA [7], or the European Hydrogen and Fuel Cell platform and the Joint Technology Initiative [8,9,10,11,12] will be very challenging. To finally benefit from hydrogen as an energy carrier, especially for transport sector, it has to be produced without greenhouse gas emission. To become accepted by users, it will initially have to become desirable and available for niche applications, and then affordable to reach the mass market. Also, the basic supply infrastructure will have to be established.

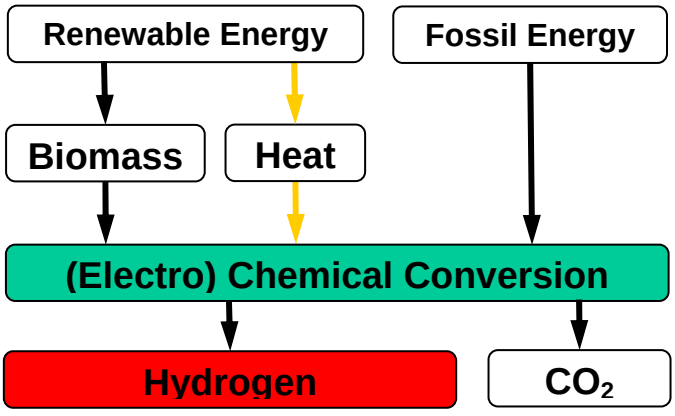

Figure 3: Hydrogen production routes.

These criteria have to be connected by a strategy incorporating transition steps. The efficiency and applicability of the chosen production processes as well as technologies for storage and conversion are the most important conditions for a successful implementation of a hydrogen economy. On this pathway, the focus will move from desirable, available and applicable to efficient, affordable, and sustainable.

In the present paper, cost estimates from many different sources for industrial scale production of hydrogen are provided. Most of the prices are based on models and theoretical studies. Therefore,

they are neither consistent nor real values. Nevertheless, they indicate that numerous authors care about market introduction of hydrogen as an energy carrier, and demonstrate the importance of the harmonization of the calculation procedures.

CURRENT INDUSTRIAL HYDROGEN PRODUCTION

Steam methane reforming (SMR)

SMR is currently the least expensive and most common method for hydrogen production. The feedstock is mainly natural gas (NG), which is primarily composed of methane mixed with some heavier hydrocarbons and CO_2 as well as some impurities which need to be removed [13].

Initially, NG is hydrogenated at 350-450 °C to convert sulphur impurities into H_2S which is removed over a ZnO bed forming ZnS and H_2O. Upon preheating at 450 to 650 °C NG is injected into the reforming reactor together steam in excess of stoichiometry. The reactor pressure varies from 2 to 3 MPa and its temperature from 850 to 950 °C. Most of the industrial SMR is done in externally heated tubular reactors using catalysts.

The reforming reaction never reaches completion. It yields a gas mixture of H_2, CO, H_2O, CH_4, and CO_2. This has to be processed over several steps to obtain sufficiently pure H_2. The first step is the water gas shift (WGS) reaction where CO is converted into CO_2 producing additional H_2, followed by the separation of H_2 and acid gases (CO_2 and remaining H_2S).

(1) $$CO + H_2O \rightarrow CO_2 + H_2$$

Classical regenerative chemical or physical absorption techniques are used for this purpose. The final step allows the separation of the remaining impurities from H_2 using a Pressure Swing Adsorption (PSA) unit. This PSA works at 2 to 2.5 MPa based on the selective adsorption on a molecular sieve. Three to four columns are used for continuous hydrogen production, working in alternative mode: while one is adsorbing and purifying the gas, the others are regenerated (depressurization, rinsing, pressurization). Standard PSA units achieve H_2 purities above 99.9 %.

Depending on the plants and their optimization levels (gases recirculation loop, heat exchangers), the thermal efficiency varies from 65 to 75 % [1]. The production of 1 kg H_2 by means of SMR yields 9.42 kg of CO_2 emissions [14]. The production cost of hydrogen is between 5.97 and 7.46 $/GJ (0.57 and 0.74 €/kg) [15].

Coal gasification

The oldest technology for hydrogen production is coal gasification. Here, coal is introduced into a gasifier at temperatures between 750 and 1500 °C, depending on reactor type, with air or oxygen as reactants and steam as temperature moderator. Three types of reactors are commonly used:

- fixed bed (Lurgi)
- fluidized bed (Winkler/Lurgi)
- entrained flow (Koppers-Totzek, Texaco)

These reactors work under different operating pressures:

- atmospheric (Koppers-Totzek – 1480 °C)
- up to 10 MPa (Texaco at 4.2 MPa – 1350/1450 °C)

[1] Thermal efficiencies for steam methane reforming and coal gasification have been calculated using data extracted from the *E3 Database* (software tool to create energy chains for individual processes, used in the project HYWAYS), which provides an assessment of consumables for a given plant, in particular natural gas consumption in kWh per kWh of produced hydrogen.

The produced syngas consists primarily of H_2, CO, CH_4 and CO_2. After several separation and purification steps, technically pure hydrogen is obtained. Industrial plants have thermal efficiencies ranging from 45 % to 60 % [1] depending on the requirement of coal crushing, O_2 supply and/or gas compression units. For Koppers-Totzek (58%) and Texaco (63%) more precise values are available [45]. Typical amounts of CO_2 emissions are about 23 kg CO_2 / kg H_2 [16]. Hydrogen cost for a coal gasification plant with a production of 2.8 million Nm³/day amounts to 11.57 $/GJ H_2 (1.15 €/kg), the underlying coal price in this case is unknown [15]. Today, there are large coal gasification plants in Europe, South Africa and the USA, and technologies for gasification of coal are the subject of significant R & D efforts by the coal industry.

The Lurgi Process (Fixed-Bed)

Different descriptions of the Lurgi Process are reported. For example, the reactor has been described as fixed-bed and as well as moving bed. The present authors decided to use the more plausible fixed bed option. The original Lurgi gasifier was developed in 1936. In a vertical water cooled pressure vessel coal is intermittently charged from above through a lock-hopper. The coal movement is controlled by a distributor. Steam and O_2 (or air) are injected through a rotary bottom grate, which is also used for the extraction of the residual dry-ash. The Lurgi gasifier requires large quantities of steam to reduce the combustion zone temperature below the ash fusion temperature. The temperature is about 1000 °C near the bottom and about 500 °C near the top. Because of the low temperature and the lack of O_2 in the devolatilization zone, the product gas contains a high content of hydrocarbon liquids which are separated by cooling. A standard Lurgi unit is 4 m in diameter and has a nominal dry gas capacity of 55,000 m³/h (= 600 t/d moisture ash free coal) [17].

The Winkler Process (Fluidized-Bed)

Fluidized bed systems are operated between 800 and 1100 °C, depending on the coal reactivity, to avoid ash fusion in the gasifier. At these temperatures, the coal is converted primarily into CO, H_2 and CO_2 and small amounts of CH_4. The coal is supplied as a powder and maintained in a suspended state of continuous random motion, by the gasified agent [17].

Due to the fact that gasifier exhaust temperatures match hot gas clean-up and purification temperatures, these systems have a better overall efficiency than entrained flow systems, which require cooling before clean-up. In comparison to moving bed reactors, fluidized bed units have higher coal mass flow rate, thus reducing the size and the cost of the unit. Low temperature and high pressure fluidized bed gasification processes produce more CH_4 and synthesis gas, thus requiring less O_2 and having an increased efficiency. However, there are also several disadvantages such as narrow particle size distribution, agglomeration of feed coal which lowers the gasification rate, and high dust content of the raw gas due to the grading effect of the gas stream [17].

A typical Winkler gasifier is 5.5 m in diameter and 23 m high. It can gasify approximately 1100 t/d of coal under atmospheric pressure [17].

The Koppers-Totzek Process (Entrained-Bed)

Coal is first pulverized then gasified in a mixture of steam and air (or O_2). The products must be cooled down before purification, which reduces the thermal efficiency. These entrained flow systems produce only little CH_4, are relatively compact, and have short reaction times because of their high operating temperatures (1040 – 1540 °C). The gasifiers are insensitive to almost all pulverized coal with a certain particle size. Due to the requirement of a high temperature and therefore a high O_2 consumption, the process has a lower thermal efficiency than fluidized and moving bed systems. The synthesis gas is relatively free of tars, hydrocarbons heavier than CH_4 and nitrogen compounds.

Most of the Koppers-Totzek gasifiers are using two burner heads. They have an internal diameter of up to 3.5 m, a height of about 7.5 m, and an internal volume of approximately 28 m³. Their nominal

dry gas capacity is 17000 m³/h (= 210 t/d of moisture-ash-free coal. Additionally, four-burner-head models with 56 m³ are in operation and a six–burner gasifier is being developed [17].

IMPLEMENTING CONCENTRATED SOLAR ENERGY

The success of a hydrogen economy is dependent on the availability of the energy carrier H_2. Since the present infrastructure is mainly based on (non-renewable) fossil resources, it may be logical to start from this point. Sequestration of CO_2 is a widely discussed opportunity to reduce greenhouse gas emissions (GHG) but research is at the very beginning. Concentrated solar technologies on the other hand are in operation and under further development for since several decades. Hence, it is advantageous to combine the established production processes with (renewable) solar energy to firstly reduce GHG emissions. This initial application of solar technology will foster the possibility to develop processes that ultimately are based on water splitting, only.

At present some fossil/solar hybrid processes are already under development.

Solar Tower Power Plants

The basis for using solar thermal technologies in bulk conversion technologies is their ability to provide heat at a temperature level of at least 900 °C in the multi MW range.

Figure 4: First commercial solar tower power plants PS-10 in operation and PS-20 under construction (Seville, Spain).

All solar technologies described in the following are based on technology derived from solar tower (or central receiver) power plants. The inauguration of the first commercial solar tower power plant PS-10 in June 2007 near Seville, Spain, demonstrated that this technology has the potential to generate electricity in large-scale facilities. It now has to show that it can also be integrated into more complex processes.

CARBON BASED TRANSITION PROCESSES

Since SMR is the most common process for hydrogen production it is obvious that the first intermediate technology to be worked on was the solar steam reforming of methane-rich gas. This technology is already on a several 100 kW scale. It combines the economical efficiency of SMR with solar thermal heat leading to partially renewable hydrogen production with reduced CO_2 emissions. Besides NG, other fossil resources like coal or petcoke are also under investigation for solar thermal conversion. A further step will be the decomposition of methane into hydrogen and carbon. With this, less resource intensive hydrogen is produced and the carbon remains as a solid which may either be used or stored. Solid storage is much easier than the sequestration of gaseous CO_2. The use of biomass as feedstock may enhance the sustainability of all hybrid processes.

Solar Reforming of Natural Gas

Using a solar thermal reactor, many of the required unit operations are similar to industrial SMR. Natural gas is converted using concentrated solar energy to generate a hydrogen rich gas. Afterwards, the WGS-reaction is applied. The reforming of natural gas using solar energy has been investigated since the 1980s. Reformer efficiencies from 85-90 % are reported. Basic solar plant costs have been estimated at 1322 €/kW_e for a 100 MW_e central receiver gas turbine plant. Solar heat is delivered at 0.0164 \$/kWh_{th} (0.0135 €/kWh_{th}) which finally results in H_2 production costs of 0.0264 \$/kWh_{th} (0.73 €/kg) [18]. These numbers are very optimistic compared to the industrial process, but show that the gap between fossil and fossil/solar hybrid is quite small.

The technical feasibility of solar reforming with LPG as feed stock and combustion of the product gases in a gas turbine to generate electricity was successfully demonstrated in the SOLASYS project. During the solar reforming test period, the solar reformer was operated in the power range 100-220 kW producing synthesis gas at 8.5 bar and 760 °C [19,20]. Currently, within the European project SOLREF, this process is further developed.

Recently, the 400 kW_{th} SOLREF reactor was installed on the solar tower of the Weizmann Institute of Science (WIS), Rehovot Israel. The plant is designed to be very close to an industrial installation. Forthcoming test campaigns will demonstrate how such installations can be operated under semi-industrial conditions.

Figure 5: The SOLREF reactor installed on the WIS solar tower.

Solar Gasification and Reforming of Petcoke

Solar reforming of petcoke uses fossil fuels that are not suitable for conventional refining. Upgrading with concentrated solar power as energy source may make large carbon resources accessible. The gasification process strongly depends on its temperature, pressure and C/O_2 ratio. The chemical product of the process is synthesis gas. Above 1000 °C, gasification yields a pure gas phase containing H_2 and CO. Solar energy acts as carbon saver since 50% of feedstock is substituted.

Solar and simulated solar heated gasification of petcoke samples from the Orinoco Basin was successfully performed at laboratory scale and at 5 kW solar furnace scale by ETH Zurich, CIEMAT, and PDVSA [21]. The hydrogen generation cost are estimated to about 2.1 €/kg H_2 [22].

Solar-assisted Coal Gasification

Solar-assisted coal gasification is closely related to the conventional process, but the use of solar energy results in a significant contribution of about 30 % renewable energy to the products. Unlike SMR, coal gasification involves solid materials, and thus the design of a solar-driven coal gasification reactor is much more technically challenging [23].

Some small-scale R&D work has been done by the Research Centre for Carbon Recycling and Utilization at the Tokyo Institute of Technology. In their experiments, molten salts provide a thermal storage system that allows the reaction to proceed in a stable manner under the conditions of intermittent solar energy supply. These conditions have been studied at laboratory scale. Due to the utilization of molten salt and the better contacting of CO_2 with the coal particles in the melt, higher reaction rates have been achieved [23].

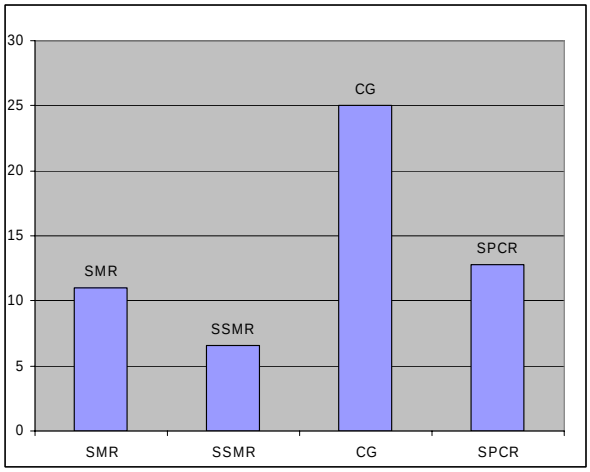

Figure 6: CO_2 production in carbon containing processes [kg CO_2 /kg H_2].

WATER BASED PROCESSES

Long term technologies should be solely based on the water splitting reaction.

(2) $$H_2O \rightarrow H_2 + 1/2\,O_2$$

Electrolysis powered by renewable (or nuclear) energy seems to be the way since it is an established technology. However, since the 1970s extensive work was done on thermal processes because they are predicted to have higher efficiencies and lower cost. The easiest reaction for the production of hydrogen is the thermal decomposition of water (eq. 2) which directly yields pure hydrogen [24]. However because of unfavourable thermodynamics, relevant yields can only be achieved at very high temperatures above 2500 °C, resulting in tremendous technological problems with materials selection and the attempt to incorporate solar energy as the driving energy for the reaction [25].

Especially in the 1970s to 1990s significant work was done on this problem [26, 27, 28, 29, 30, 31, 32, 33]. The feasibility of water-splitting was demonstrated experimentally at the Weizmann Institute of Science in Israel [33] and in France [34].

Current efforts on the solar chemistry for water splitting and hydrogen production are focused on processes for water splitting at lower temperatures [35].

Metal/Metal oxide Thermochemical Cycles

From all technological possibilities the most interesting is the thermochemical two-step water splitting process using redox systems. According to this idea, during the first step (water splitting)

the reduced and therefore activated material (usually a metal oxide) is oxidized by taking oxygen from water and producing hydrogen according to the reaction:

(3) $$MO_{reduced} + H_2O \rightarrow MO_{oxidized} + H_2$$

During the second step (re-generation) the material is reduced to be used again, delivering some of the oxygen of its lattice according to the reaction:

(4) $$MO_{oxidized} \rightarrow MO_{reduced} + O_2$$

The advantage of this process is the production of pure hydrogen without having to separate hydrogen and oxygen. The challenge is the realisation of a two-step process consisting of a splitting and a regeneration step. The redox materials that have been evaluated consist of oxide pairs of multivalent metals (Fe_3O_4/FeO [36], Mn_3O_4/MnO [37, 38]) or systems of metal oxide/metal (e.g. ZnO/Zn [39, 40]). Water splitting is taking place at temperatures below 900K while the reduction of the metal oxide, i.e. the regeneration, takes place at much higher temperatures. Using solar concentrated energy at temperatures above 1600 °C, Fe_3O_4 can be transformed into FeO. This is followed by the exothermic reaction of FeO and H_2O at much lower temperatures where H_2 and Fe_3O_4 are generated. The concept has been proven experimentally [41 , 42]; however the regeneration temperatures are still high, imposing a barrier to the integration of two-step water splitting processes a concentrating solar systems. Also, knowledge gaps in chemical thermodynamics and their impact on reactor design and process performance exist for these extreme conditions [36].

With an activated redox system, the reaction temperature for the two-step water-splitting process can be reduced. Within the scope of the EU-funded HYDROSOL project, the H_2 production was proven at experimental scale [43]. The reactor system works on a level of 15 kW_{th} in a quasi-continuous way. It consists of two reactors in which both reaction steps are carried out in parallel.

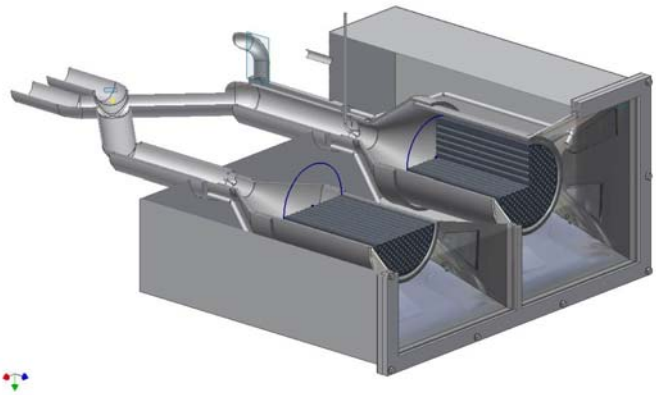

Figure 7: Reactor for quasi continuous H_2 production.

In a test campaign using the solar furnace at DLR Cologne (see Fig. 8), the reactor efficiency η_r of the research reactor and the efficiency related to the higher heating value of the produced hydrogen η_{HHV} were determined.

(5) $\eta_r = Q / P_s$

(6) $\eta_{HHV} = Q_H / P_s$

$Q = \Sigma H_{products,\ reactor\ exit} - \Sigma H_{educts,\ reactor\ entry}$
Q_H = higher heating value of H_2 produced
Ps = radiation power

For η_r for the whole process 24 % were achieved over one day. The efficiency of the production of hydrogen (related to the higher heating value) η_r was 4.4 %. This is a good starting point for the

improvement of this process, considering that the reactor is of very small scale and neither the reactor nor the redox system is optimized as yet. In addition, Kolb et al [44] predicted the potential of such technology when implemented in a multi-Megawatt solar tower system. According to their analysis annual solar-to-hydrogen efficiencies are 5-7 percentage-points higher than those of a comparable solar plant producing electricity and applying alkaline electrolysis for hydrogen production.

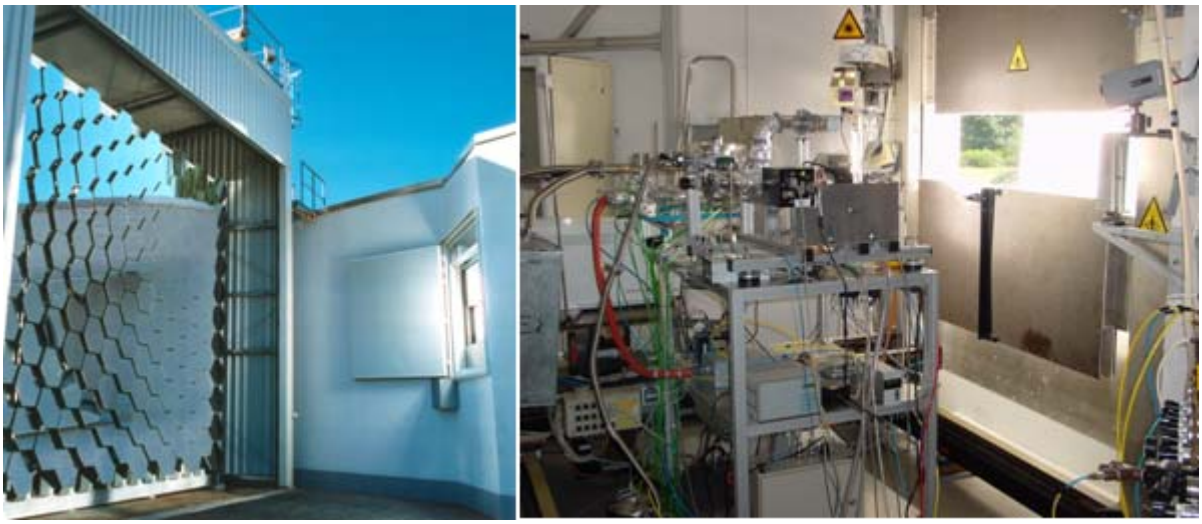

Figure 8: Hydrogen production in the DLR solar furnace, Cologne Germany.

Based on the prototype reactor tested in the solar furnace a scale-up step has been carried out. A 100 KW_{th} pilot plant has been developed and built. It was installed and inaugurated in March 2008 at the Small-Solar-Power-System (SSPS) on the Plataforma Solar de Almería (PSA), Spain (**Figure 9**).

Figure 9: Pilot plant for two-step water splitting during test operation.

In summer 2008 a detailed thermal qualification campaign of the pilot plant took place, using uncoated ceramic honeycombs as absorbers. Some main aspects of these tests were the development and validation of operational and measurement strategies, the gain of knowledge on the dynamics of the system, in particular during thermal cycling, the determination of the controllability of the whole system, and the validation of the control concept. The thermal tests allowed to improve, refine and finally demonstrate the process strategy and showed the feasibility of the implemented control concept. It could be shown that rapid change-over between the modules is a central benefit for the performance of the process. This reduces the time period with lower hydrogen production or ineffective regeneration of the modules. To achieve a faster switching of the temperature levels, the

number of heliostats changing in focus should be as high as possible until the target temperatures are reached. **Figure 10** shows the temperature progression over some cycles and the number of heliostats necessary to keep and adjust the two different temperature levels in both chambers of the reactor.

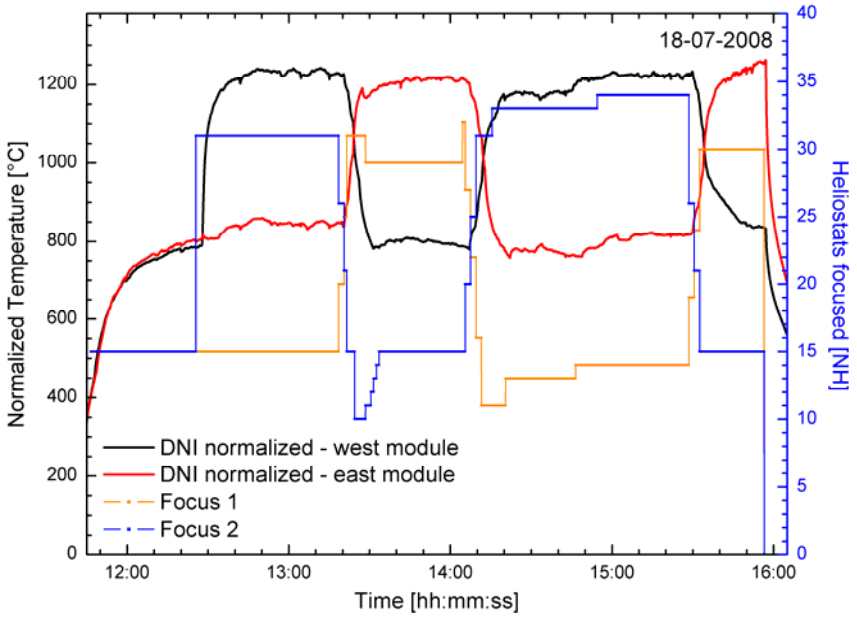

Figure 10: Thermal cycling of the reactor and number of heliostats needed to power and control the process.

In November 2008 the absorber was replaced and honeycombs coated with redox material were installed. This allowed carrying out first tests of hydrogen production by water splitting. The tests were successful – some first cycles could be run without problems. Significant amounts of hydrogen were produced with a conversion of steam of up to 30 %.

Extensive work has also been carried out on the Zn/ZnO cycle. Its first step is the thermal dissociation of ZnO into Zn and O_2 at about 2000 °C. In the second step Zn is hydrolysed at 450 °C generating H_2 and ZnO. The Zn/ZnO cycle can reach a maximum exergy conversion efficiency of 29% and a solar thermal efficiency of 40% [39]. A study for a 90 MW solar reactor operated at 2000 °C was reported by Fahrni [45]. Solar H_2 production costs for this large scale plant with an annual production rate of 61 million kWh_{th} were estimated between 0.13 and 0.15 $/$kWh_{th}$ (3.58-4.12 €/kg). If electric energy generated by fuel cells would be used the price would be 0.33 $/$kWh_{th}$ (9.08 €/kg).

Sulfur Cycle Family

Many of the promising thermochemical cycles for water splitting use sulphur based systems. Much of work was done in the European Joint Research Centre in Ispra, Italy, which focused on the use of nuclear heat [46]. Since the sulphuric acid decomposition process is carried out at the maximum temperature level of high temperature reactors and in a corrosive atmosphere, it constitutes the main problem in the coupling. Since nuclear heat is and will be limited to temperatures below 950°C which might be possible with a GEN IV reactor, concentrated solar energy is able to perform these processes much more efficiently. The reason for this is an exponential rise of the reaction rate with increasing temperature [47]. Industrially the process is carried out in several steps, between 300 and 1000 °C. One option to carry out this process by solar radiation is the Solar CRISTINA Process [48]. Basically, carbon steel and refractory bricks can be used for the equipment. Energy is transferred by direct contact between the hot air vector and the reactants; thus direct contact heat transfer equipment can conveniently be used. Since the solar heat source is intermittent and

thermochemical processes are conceived to operate continuously, it will be necessary to provide continuity by storing thermal energy, chemical energy, chemicals, etc.

Hybrid Sulfuric Acid Cycle (Westinghouse, ISPRA Mark 11)

The Westinghouse cycle is a hybrid electrochemical thermochemical cycle consisting of two steps [49]. Catalysts are available for accelerating the rate of SO_3 reduction coupled to a nuclear heat source at a temperature level of 850 °C. As described above, the use of catalysts may not be necessary if higher temperatures can be provided by concentrated solar radiation. Electrical power is required for the electrolysis. Nevertheless, the overall process is calculated to be more efficient than direct water electrolysis [50]. For SO_2 electrolysis, carbon-supported platinum catalysts were employed to prepare the electrodes [51]. Ceramics such as silicon carbide, silicon nitrite, and cermets possess excellent resistance to H_2SO_4 corrosion at ambient temperature and at low acid concentration [52].

(7) $2\ H_2O + SO_2 \rightarrow H_2SO_4 + H_2$ electrolysis, 80°C

(8a) $H_2SO_4 \rightarrow H_2O + SO_3$ > 450°C

(8b) $SO_3 \rightarrow SO_2 + ½\ O_2$ >800°C

The cycle has the potential for achieving high thermal efficiencies above 40 % while using common and inexpensive chemicals. The material selection for the decomposition of the H_2SO_4 is the main challenge of the process [49,50].

Conceptual designs and cost estimates indicate that the product gas separation can be done conventionally and economically [50]. The H_2 production costs were calculated alternatively at 0.0596 \$/Nm³ H_2 (0.55 €/kg) [52] or 8.4\$/GJ H_2 (0.83 €/kg) [53].

Sulfur-Iodine Cycle (General Atomics, ISPRA Mark 16)

The sulphur-iodine (IS) process also known as the ISPRA Mark 16 and General Atomics (GA) process is a “pure” thermochemical cycle [39,46,54]. Originally it was intended to couple the cycle to a nuclear heat source, but more recently the coupling to a solar thermal plant was designed because of higher efficiencies at temperatures above 1000 °C [49,55,56,57].

The three reactions are performed in separate sections of the apparatus, the Bunsen reaction and the sulphuric acid decomposition run in parallel to avoid SO_2 storage [58]. The IS feasibility was successfully demonstrated in a glass, quartz and Teflon laboratory-scale apparatus [49], on the solar power tower of the Georgia Institute of Technology [59], and within the European HYTHEC project in the solar furnace of DLR in Cologne, Germany [60,61].

For large scale application, heat generation by a 2400 MW_t modular helium reactor (H2-MHR) which should be able to provide temperatures up to 900 °C was proposed. The overall efficiency for this reactor was calculated to 42 % at 850 °C. It is assumed that efficiencies up to 52 % may be achievable with a reactor outlet temperature of 950 °C [59]. The decomposition of H_2SO_4 and HI was found to be a challenging procedure causing severe corrosion problems [49]. The experimental problems and the less promising results of the economic calculations led to abandoning the activities on the Mark 16 cycle by GA. Recently it is again in the focus of intensive research.

Within the EU funded project HYTHEC sulphuric acid splitting could be shown in a continuously working solar receiver reactor in the solar furnace of DLR over a time period of 75 hours. Complete vaporisation of concentrated sulphuric acid in and at a porous absorber made of SiSiC was achieved at temperatures between 1000 °C and 1250 °C. Sulphuric acid was homogeneously decomposed without the use of catalysts with conversions between 20 and 55 % at different operating points confirming the positive influence of increased temperatures. The throughput of the solar reactor was limited by the capacity of the vaporiser used. No visible corrosion occurred in the reaction zone of the reactor [61].

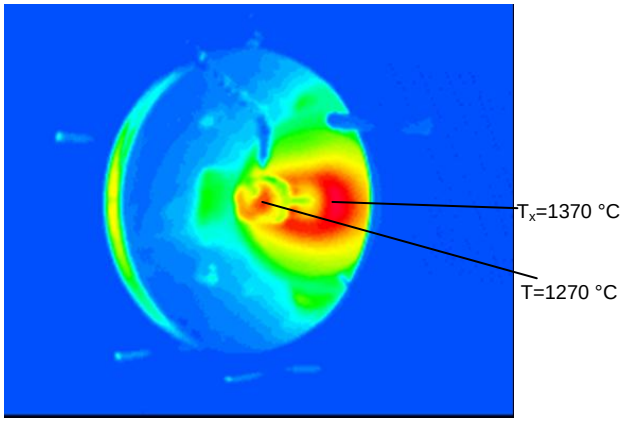

Figure 11: Solar H_2SO_4 splitting in a volumetric reactor in the DLR solar furnace, Cologne, Germany.

The hydrogen production costs by a solar driven IS process are calculated at 45.7 $/GJ (4.53 €/kg). The solar heat costs were estimated at 260 $/$MW_{th}$ (215 €/MW_{th}) [57]. The coupling to the H2-MHR would result in H_2 production cost between 11.84 and 16.75 $/GJ (1.17-1.66 €/kg) depending on the kind of installation [59].

CONCLUSIONS

The present paper summarizes and compares the available technologies for the production of hydrogen, as well as the related R&D efforts. To optimize and accelerate the availability of environmentally benign hydrogen, it will initially be necessary to combine established technologies like steam-methane reforming with solar energy. Subsequently, further development will proceed successively to renewable hydrogen production without CO_2 emissions. This pathway has to be adapted to comply with geographical, political and economical circumstances. All proposed solar technologies have to be implemented in the sunbelt of the earth. While there will occur regional differences, the technological challenges have to be solved in a joint effort. Considering the scope of the technological challenge and the associated costs, it will be important to pool the efforts presently undertaken all over the world, in order to improve the most promising processes and make them available for the market.

ACKNOWLEDGMENTS

The authors would like to thank the European Commission for funding the projects SOLASYS, SOLREF, SOLHYCARB, HYDROSOL, HYDROSOL 2, HYTHEC, HYCYCLES, and INNOHYP-CA.

REFERENCES

1 Heinloth, K., „Die Energiefrage: Bedarf und Potentiale, Nutzen, Risiken und Kosten“, 2. Edition, Vieweg+Teubner, 2003, ISBN 3528131063

2 B. Kruse, Grinna, S., Buch, C. Translated to English by Jenifer Høibråten and Diana Oeding., "Hydrogen," *The Bellona Foundation, Oslo, Report 6*: 2002, February 13, 2002.

3 C. Rothmund, "Forty years of French-German cooperation in space propulsion," Acta Astronautica, vol. 55, pp. 707-715, 2004.

4 C. Bonnal, Eymard, M., Soccodato, C., "Future launchers strategy : the Ariane 2010 initiative," *Acta Astronautica*, vol. 48, pp. 885-893, 2001.

5 "Summit establishes international hydrogen economy partnership," *Fuel Cell Bulletin*, vol. 2004, pp. 5-6, 2004.
6 International Partnership for the Hydrogen Economy URL: http://www.iphe.net
7 International Energy Agency URL: http://www.iea.org
8 S. Barrett, "The European hydrogen and fuel cell Strategic Research Agenda and Deployment Strategy," *Fuel Cell Bulletin*, 2005, 5, pp. 12-19, 2005.
9 S. Barrett, "Progress in the European Hydrogen & Fuel Cell Technology Platform," *Fuel Cell Bulletin*, vol. 2005, 4, pp. 12-17, 2005.
10 European Hydrogen and Fuel Cell Technology Platform URL: http://www.hfpeurope.org
11 European Hydrogen and Fuel Cell Technology Platform Key Documents https://www.hfpeurope.org/hfp/keydocs
12 European Industry Grouping for a Fuel Cell and Hydrogen Joint Technology Initiative http://www.fchindustry-jti.eu/.
13 B. C. Palm T., Sauar E., "Bellona Report 3:1999, "Green Heat and Power", Eco-effective Energy Solutions in the 21st Century," June 2000.
14 SLS Partners Inc.http://www.slspart.com/hydrogen_fm.html.
15 C.E.G. Padró and V. Putsche, "Survey of the Economics of Hydrogen Technologies", Technical Report, September 1999 NREL/TP-570-27079
16 B. Gaudernack, S. Lynum, Natural Gas utilization without CO2 Emissions, *Energy Conv. Management* 38, Suppl., S165-S172; 1997.
17 D. Vamvuka, Gasification of Coal, "Clean Use of Coals. Low-Rank Technologies", Multi Science Publishing Co. Ltd., 515-581, 2000.
18 J. H. Edwards, Do, K.T., Maitra, A.M., Schuck, S., Fok, W. , Stein, W., "The use of solar based CO2/CH4 reforming for reducing greenhouse gas emissions during the generation of electricity and process heat," *Energy Convers. Mgmt*, vol. 37, pp. 1339-1344, 1996.
19 S. Möller, D. Kaucic, C. Sattler, "Hydrogen Production by Solar Reforming of Natural Gas: A Comparison Study of Two Possible Process Configurations," *Journal of Solar Energy Engineering*, vol. 128, pp. 16-23, 2006.
20 SOLREF Homepage http://www.solref.dlr.de/solref/
21 D. Trommer, F. Noembrini, M. Fasciana, D. Rodriguez, A. Morales, M. Romero, A. Steinfeld, "Hydrogen production by steam-gasification of petroleum coke using concentrated solar power—I. Thermodynamic and kinetic analyses," *Int. J. Hydrogen Energy*, 30, 605-618, 2005.
22 CIEMAT, personal communication.
23 J.H. Edwards, W. Stein, A Review of Technologies for Using Solar Thermal Energy to produce Hydrogen, CSIRO Energy Technology, Newcastle, 2005.
24 E.A. Fletcher, R.L. Moen, "Hydrogen and Oxygen from water," *Science*, 197, 1050-1056, 1977.
25 J.E. Funk, M.G. Bowman, M.G., "Renewable hydrogen energy from solar thermal central receiver systems," Proc., 3rd International Symposium on Hydrogen from Renewable Energy, Honolulu, HI, 201-213, 1986.
26 E. Fletcher, "System for obtaining hydrogen and oxygen from water with the solar energy." U.S.: The regents of the University of Minnesota, 1977.
27 E. Bilgen, Ducarroir, M., Foex, M., Sibieude, F., "Use of solar energy for direct and two-step water decomposition cycles," *International Journal of Hydrogen Energy*, 2, 251-257, 1977.
28 R.B. Diver, S. Pederson, T. Kappauf, E.A. Fletcher, Hydrogen and oxygen from water–VI. Quenching theeffluent from a solar furnace. *Energy*, 12, 947–955, 1983.
29 S. Ihara, "On the study of hydrogen production from water using solar thermal energy," *Int. J. Hydrogen Energy*, 5, 527-534, 1980.
30 E. Bilgen, Solar hydrogen production by direct water decomposition process: a preliminary engineering assessment. *Int. J. Hydrogen Energy*, 9, 53–58, 1984.

31 J. Lédé, J. Villermaux, R. Ouzane, M.A. Hossain, R. Oahes, Production of hydrogen by simple impingement of a turbulent jet of steam upon a high temperature zirconia surface. *Int. J. Hydrogen Energy*, 12, 3–11, 1987.

32 G. Olalde, D. Gauthier, A. Vialaron, Film boiling around a zirconia target. Application to water thermolysis. *Adv. Ceramics*, 24, 879–883, 1988.

33 Kogan A., "Direct solar thermal splitting of water and on site separation of the products – II-experimental feasability study," *International Journal of Hydrogen Energy*, vol. 23, pp. 89-98, 1998.

34 C. Etiévant, Solar high-temperature direct water splitting — a review of experiments in France, *Solar Energy Materials*, 24, 1-4, 413-440, 1991.

35 B.M. Abraham, F. Schreiner, F., "General principles underlying chemical cycles which thermally decompose water into the elements," *Industrial and Engineering. Chemistry, Fundamentals*, 13, 4, 305-310, 1974.

36 A. Steinfeld, S. Sanders, R. Palumbo, "Design aspect of solar thermochemical engineering – A case study: Two-step water splitting cycle using the Fe_3O_4/FeO redox system", *Solar Energy*, 65, 1, 43-53, 1999.

37 M. Sturzenegger, P. Nüesch, "Efficiency analysis for a manganese-oxide-based thermochemical cycle," *Energy* 24, 959-970, 1999.

38 C. Perkins, A.W. Weimer, Likely near-term solar-thermal water splitting technologies, *International Journal of Hydrogen Energy*, 29, 1587-1599, 2004.

39 A. Steinfeld, "Solar hydrogen production via a two-step water splitting thermochemical cycle based on Zn/ZnO redox reactions," International Journal of Hydrogen Energy, 27, 611-619, 2002.

40 S. Möller, R. Palumbo, Solar thermal decomposition kinetics of ZnO in the temperature range 1950-2400 K. *Chemical Engineering Science*, 56, 4505-4515, 2001.

41 T. Kodama, High-temperature solar chemistry for converting solar heat to chemical fuels, *Progress in Energy and Combustion Science*, 29, 567-597, 2003.

42 H. Aoki, H. Kaneko, N. Hasegawa, H. Ishihara, A. Suzuki, Y. Tamaura, Y., The $ZnFe_2O4$/(ZnO+Fe_3O_4) system for H_2 production using concentrated solar energy, *Solid State Ionics*, 172, 113-116, 2004.

43 M. Roeb, C. Sattler, R. Klüser, N. Monnerie, L. de Oliveira, A.G. Konstandopoulos, C. Agrafiotis, V.T. Zaspalis, L. Nalbandian, A.M. Steele, P. Stobbe, P. "Solar Hydrogen Production by a Two-Step Cycle based on Mixed Iron Oxides" *Journal of Solar Energy Engineering*, 128, 2, 125-133, 2006.

44 G. Kolb, R. Diver, "Screening Analysis of Solar Thermochemical Hydrogen Concepts", *SANDIA REPORT SAND2008-1900*, March 2008.

45 R. Fahrni, Hydrogen Production-An overview of hydrogen production methods and costs today, ETH Zurich, 2002.

46 G. E. Beghi, "A decade of research on thermochemical hydrogen at the joint research centre, ISPRA," *International Journal of Hydrogen Energy*, 11, 761-771, 1986.

47 E. Lüpfert, K.-H. Funken, "The high temperature dissociation of waste sulphuric acid with concentrated solar radiation", Solar Thermal Concentrating Technologies: *Proceedings of the 8th International Symposium*, Köln, Germany, Oct. 6-11, M. Becker, M. Böhmer eds., C.F. Müller, Heidelberg, ISBN 3-7880-7616-X, 3, 1277-1291, 1996.

48 E. Bilgen, "A hybrid thermochemical hydrogen producing process based on the Cristina-Mark cycles," *Int. J. Hydrogen Energy*, 11, 241-256, 1986.

49 IAEA-TECDOC-1085, May 1999 – International Atomic Energy Agency, Hydrogen as an energy carrier and its production by nuclear power; International Atomic Energy Agency.

50 L.E. Brecher S. Spewock C.J. Warde C.J., The Westinghouse sulfur cycle for the thermochemical decomposition of water, *1st World Hydrogen Energy Conference, Conference Proceedings*, 1, 1976.

51 P.W.T Lu, Technological aspects of sulfur dioxide depolarized electrolysis for hydrogen production, Int. J. Hydrogen Energy, 8, 10, 773-781, 1983.

52 G.H. Farbman, The conceptual design of an integrated nuclear-hydrogen production plant using the sulfur cycle water decomposition system, *Report NASA-CR-134976*, 1976.
53 D. Van Velzen, “Cost comparison of different methods of producing hydrogen,“ Wasserstoff, Energieträger der Zukunft, Votragsveröff. T-1-309-101-1, 1981.
54 J.R. Schuster, Status of thermochemical water-splitting development at General Atomics, GA-A14666, General Atomics 1977.
55 General Atomics, "High-pressure catalytic metal reactor in a simulated solar central receiver (GA-A18285)," GA-A18285, 1986.
56 C. W. Pretzel, J.E. Funk, "The Development Status of Solar Thermochemical Hydrogen Production," Sandia National Laboratories, Albuquerque, NM and Livermore CA SAND86-856 UC-62c, 1987.
57 K.-F. Knoche, "Thermochemical H2 - Production with a solar driven Sulfur-iodine-process," *Solar thermal energy utilization, DLR*, vol. 4, pp. 441-498, 1988.
58 S. Kubo, H. Nakajima, S. Kasahara, S. Higashi, T. Masaki, H. Abe, K. Onuki, “A demonstration study on a closed-cycle hydrogen production by the thermochemical water-splitting iodine–sulfur process,” Nuclear Engineering and Design, 233, 347-354, 2004.
59 K. R. Schultz, "Use of the modular helium reactor," presented at World Nuclear Association Annual Symposium, London, 2003.
60 A. Le Duigou, J.M. Borgard, B., Larousse, D. Doizi, R. Allen, B.C. Ewan, G.H., Priestman, R. Elder, G. Cerri, C. Salvini, A. Giovannelli, G. De Maria, M. Roeb, A. Noglik, P.M. Rietbrock, S. Mohr, L. de Oliveira, N. Monnerie, M. Schmitz, C. Sattler, A. Orden, D. de Lorenzo, J. Cedillo, S. Dechelotte, O. Baudouin, “HYTHEC : An EC funded search for a long term massive hydrogen production route using solar and nuclear technologies”, *Int. J. Hydrogen Energy*, 32, 1516-1529, 2007.
61 M. Roeb, A. Noglik, P.M. Rietbrock, S. Mohr, L. de Oliveira, C. Sattler, G. Cerri, G., de Maria, A. Giovanelli, A. Buenaventura, D. de Lorenzo, “HYTHEC: Development of a dedicated solar receiver-reactor for the decomposition of sulphuric acid,” *Proceedings of EHEC conference*, Zaragossa, Spain, 22-25 November 2005.

BOILING IN MICRO-CHANNELS

G. Hetsroni*
Department of Mechanical Engineering, Technion - Israel Institute of Technology,
32000, Haifa, Israel

ABSTRACT. Boiling heat transfer in micro-channels is a subject of intense academic and practical interest. Though many heat transfer correlations have been proposed, most were empirically formulated from experimental data. However, hydrodynamic and thermal aspects of boiling in micro-channels are not well understood. Moreover, there are only a few theoretical models that link the heat transfer mechanism with flow regimes in micro-channels. Also, there are discrepancies between different sets of published results, and heat transfer coefficients have either well exceeded, or fallen far below, those predicted for conventional channels. Here we consider these problems with regard to micro-channels with hydraulic diameters ranging roughly from 5 μm to 500 μm, to gain a better understanding of the distinct properties of the measurement techniques and uncertainties, the conditions under which the experimental results should be compared to analytical or numerical predictions, boiling phenomenon, as well as different types of micro-channel heat sinks. Two-phase flow maps and heat transfer prediction methods for vaporization in macro-channels are not applicable in micro-channels, because surface tension dominates the phenomena, rather than gravity forces. The models of convection boiling should correlate the frequencies, sizes and velocities of the bubbles and the coalescence processes, which control the flow pattern transitions, together with the heat flux and the mass flux. Therefore, the vapour bubble size distribution must be taken into account. The flow pattern in parallel micro-channels is quite different from that in a single micro-channel. At same values of heat and mass flux, different, time dependent, flow regimes occur in a given micro-channel. At low vapour quality, heat flux causes a sudden release of energy into the vapour bubble, which grows rapidly and occupies the entire channel cross section. The rapid bubble growth pushes the liquid-vapour interface on both caps of the vapour bubble, at the upstream and the downstream ends, and leads to a reverse flow. We term this phenomenon as explosive boiling. One of the limiting operating conditions with flow boiling is the critical heat flux (CHF). The CHF phenomenon is different from that observed in conventional size channels.

Keywords: *micro-channel, boiling, pressure drop, heat transfer, fluctuation*

INTRODUCTION

To achieve higher heat dissipation rates for micro-electronic and optical technologies, the fundamentals of two-phase heat transfer in micro-channels are being studied ever more extensively. Micro-channel heat sinks are devices that provide liquid or two-phase flow through parallel channels of diameter less than, say, 1mm. These systems are ideally suited for devices where high heat flux is dissipated from small surface area of high performance supercomputers, optical devices,

* Corresponding author: Prof. G. Hetsroni
Phone: + (972)-4-8292058, Fax: + (972)-4-8238101
E-mail address: hetsroni@techunix.technion.ac.il

electric vehicles and advanced military avionics. The hydraulic diameter of micro- channels, d_h, is in the range 10- 500 μm, the length, L, is in the range 10-15 mm.

Qu and Mudawar [1] presented and discussed experimental results, which provide physical insight into the unique nature of saturated flow boiling heat transfer in a water-cooled micro- channel heat sink. Contrary to macro- channel the heat transfer coefficient was shown to decrease with increasing thermodynamic equilibrium quality. This unique trend was attributed to appreciable droplet entrainment and onset of annular flow regime. Such a trend was also reported by Hetsroni et al. [2]. On the other hand, Bertsch et al. [3] found that heat transfer coefficient first rises steeply as vapour quality increases from a subcooled value, and again drops sharply with further increases in vapour quality. Agostini et al. [4] presented experimental results on flow boiling of refrigerants R236fa and R245fa in silicon heat sinks. Three significant heat transfer trends were identified: the heat transfer coefficient was independent of the heat flux, increased or decreased with heat flux.

An annular flow model was developed by Qu and Mudawar [5] to predict the saturated flow boiling heat transfer coefficient. Laminar liquid and vapor flow, smooth interface, and strong droplet entrainment and deposition effects were incorporated into the model.

Kandlikar and Balasubramanian [6] presented the flow boiling correlations to transition, laminar and deep laminar flows in micro-channels. The flow boiling correlations for large diameter tubes were modified for flow boiling in micro- channels. It was concluded that boiling was more nucleate dominant for low Reynolds numbers (Re< 100) in micro- channels. Thome et al. [7] proposed a new heat transfer model for evaporation in the elongated- bubble regime in micro- channels. The model describes the transient variation in local heat transfer coefficient during the sequential and cyclic passage of a liquid slug, an evaporating elongated bubble and a vapour slug. The time averaged local heat transfer coefficient calculated using this model was compared by Dupont et al. [8] to 1591 experimental data which cover tube diameters from 0.77 to 3.1 mm. The data were obtained for the following seven fluids: R- 11, R- 12, R- 113, R- 123, R- 134a, R- 141b, and CO_2. The new model predicts 67% of the database to within +- 30%.

Zhang et al. [9] proposed a correlation for flow boiling heat transfer in mini-channels. However, the realistic prediction of flow boiling heat transfer coefficients is possible only for a set of experimental data selected by the authors of these models. For example, the mean relative error of prediction of recent experimental data presented by Agostini et al. [4] by different investigations is: Thome et al. [7] +4%, Kandlikar and Balasubramanian [6]-23%, Lee and Mudawar [10] -609%, Zhang et al. [9] +35%.

An important aspect of flow boiling in micro-channels is the pressure fluctuations, because these fluctuations can lead to instabilities in flow. Pressure fluctuations and corresponding temperature oscillations are associated with boiling in micro- channels to a greater extend than in conventional channels. This is because the flow velocities are very low, and bubble formation can cause a significant disruption of low-quality flow. The periodic wetting and rewetting phenomena were observed by Hetsroni et al. [2, 11, 12, 13], Zhang et al. [14], Steinke and Kandlikar [15]**.** The explosive vaporization and significant pressure drop fluctuations were observed by Hetsroni et al. [2, 12]. Flow pattern, observed in these studies and reported also by Kandlikar [16], revealed a flow reversal in some channels with expanding bubbles pushing the liquid- vapor interface in both upstream and downstream directions. Lee et al. [17, 18] studied experimentally bubble dynamics in a single trapezoid micro-channel and in two parallel micro-channels with a hydraulic diameter of 41.3 μm. Bubble nucleation and growth in parallel micro-channels were observed for some cases with the wall temperature lower than the saturation temperature corresponding to the system pressure. It was reported by Bergles and Kandlikar [19] that CHF in micro-channels under

conditions of low mass flux and low quality may be a result of instabilities rather than conventional dryout mechanism.

The main purpose of the present study is to highlight the dynamics of vapour bubble, and heat transfer coefficient under condition boiling regime in micro-channels.

DYNAMICS OF VAPOR BUBBLE

The bubble dynamics in a confined space, in particular in micro-channels, is quite different from that in unconfined still fluid. In micro-channels the bubble evolution depends on a number of different factors such as existence of solid walls restricting bubble expansion in the transversal direction, a large gradient of the velocity and temperature field, etc. Some of these problems were discussed by Kandlikar [16], and Dhir [20]**.** A detailed experimental study of bubble dynamics in a single and two parallel micro-channels was performed by Lee et al. [21] and Li et al. [22].

Dimensional Analysis. Yarin et al. [23] presented the functional equation for the rate of bubble growth as follows

$$\frac{dr}{dt} = f(q, h_{LG}, \rho_L, \rho_G, \mu_L, k_L, c_{pL}, d_0, d_*, \sigma, \Delta T_S, g, t, U) \tag{1}$$

where dr/dt is the rate of bubble growth, t is the time.

Among the dimensional variables of the problem, five parameters which have independent dimensions may be chosen, and then equation (1) may be written in dimensionless form. Choosing parameters p_L , c_{pL} , U, ΔT_S , d_* and taking into account the π-theorem, equation **(**1) can be represented as:

$$\Pi = \varphi(\Pi_1, \Pi_2, ...\Pi_9) \tag{2}$$

where $\Pi = \frac{\dot{r}}{U}$, $\Pi_1 = \frac{q}{\rho_L U c_{pL} \Delta T_S}$, $\Pi_2 = \frac{h_{LG}}{c_{pL} \Delta T_S}$, $\Pi_3 = \frac{\rho_G}{\rho_L}$, $\Pi_4 = \frac{\mu_L}{\rho U d_*}$, $\Pi_5 = \frac{k_L}{\rho_L c_{pL} U d_*}$, $\Pi_6 = \frac{d_0}{d_*}$,
$\Pi_7 = \frac{\sigma}{\rho U^2 d_*}$, $\Pi_8 = \frac{g d_*}{U^2}$, $\Pi_9 = \frac{\tau U}{d_*}$, $\dot{r} = \frac{dr}{dt}$

Analysis of experimental data presented by Lee et al. [21] revealed that the parameters $\Pi_3 - \Pi_9$ did not change significantly, and the parameter Π_2 depends mainly on the wall access temperature, $\Delta T_S = T_W - T_S$. We assumed that $\Pi_2 \approx$ const. Thus, one can consider Π_1 as the dimensionless parameter that determines the rate of bubble growth in the linear regime:

$$\frac{dr}{dt} = \varphi(\Pi_1) \tag{3}$$

Experimental Data. Single micro-channel. Data by Lee et al. [21] and Li et al. [22] contain the results related to bubble dynamics in a single micro-channel.

In the range of $\Pi_1 = 0.00791 - 0.0260$ linear behavior of the bubble radius was observed, when $\Pi_1 > 0.0260$ exponential bubble growth took place (Figure 1**).**

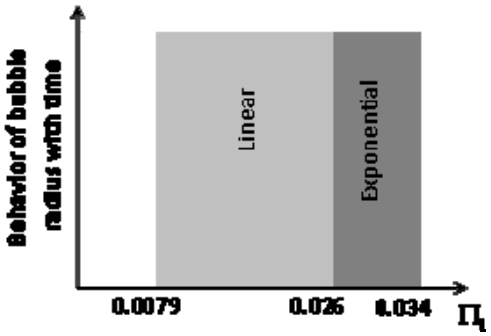

Figure 1. Behaviour of bubble change of radius vs. time. The values of $\prod_1$ were calculated from experimental data.

Parallel micro-channels. The bubble dynamics under conditions corresponding to flow in two parallel trapezoidal micro-channels with hydraulic diameter 47.7 μm was studied by Li et al. [22]. The bubbles in two parallel micro-channels generally grow in a similar way to that in a single micro-channel. The authors also reported the presence of two-phase flow instability.

Hetsroni et al. [11] studied bubble growth in 26 parallel horizontal triangular micro-channels of d_h = 103 μm and length of 10 mm. Temporal variation of bubble size is shown in Figure 2**.** Figures 2a, b show the variation of bubble size in the streamwise direction L_p, and in the spanwise direction L_n, respectively.

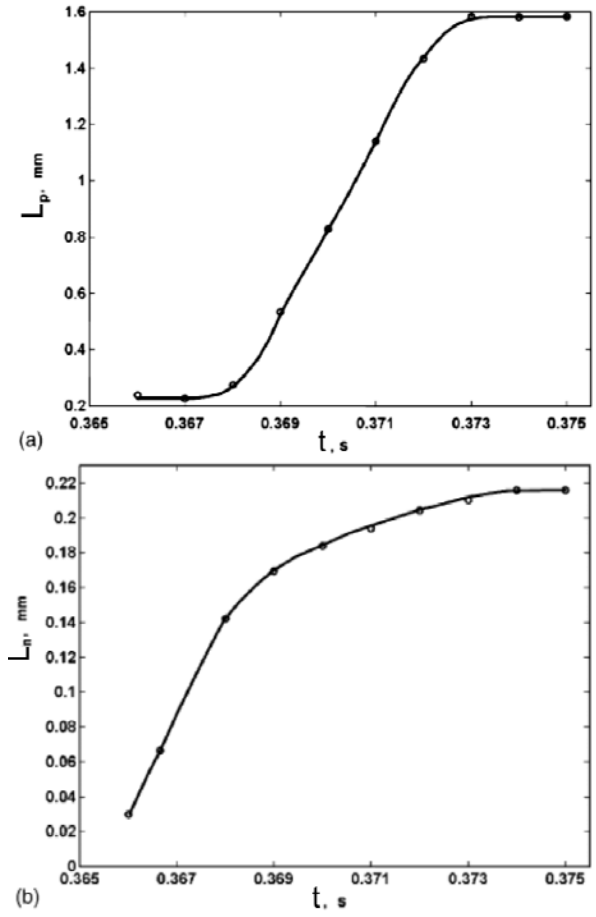

Figure 2. Temporal variation of vapour bubble size: (**a**) streamwise direction, L_p (**b**) spanwise direction, L_n. U_{LS} = 0.046 m/s, q = 8×10^4 w/m^2.

The observed ratio $f = L_p/L_n$, is quite different from that reported for subcooled flow boiling of water in tubes of 17–22 mm inner diameter. Prodanovic et al. [24] reported that this ratio was typically around 0.8 for experiments at 1.05–3 bar.

Bubble velocity. Figure 3 shows the velocity of the displacement of the bubble tail in the streamwise direction U_b (m/s) versus the bubble lifetime t, at fixed conditions as described above, i.e., $q = 8\times10^4$ W/m^2, $U_{LS} = 0.046$ m/s. One may conclude that the velocity of bubble displacement varies, depending on the range of lifetime. In region A of the boiling process, during the period of about 0.005 s from the appearance of the first bubble, ONB, the bubble velocity is equal to the superficial liquid velocity. It should be noted that the term ONB, known as the onset of nucleate boiling, was borrowed from the terminology of subcooled flow boiling in larger tubes. Region B is characterized by a sharp increase in the bubble velocity, namely the bubble is accelerated in the streamwise flow direction. Figure 3 shows that in this region the bubble velocity increases about threefold, during a time interval of about 0.003 s. After the time when U_b reaches maximum value it remains constant, as shown in Figure 3**,** region C.

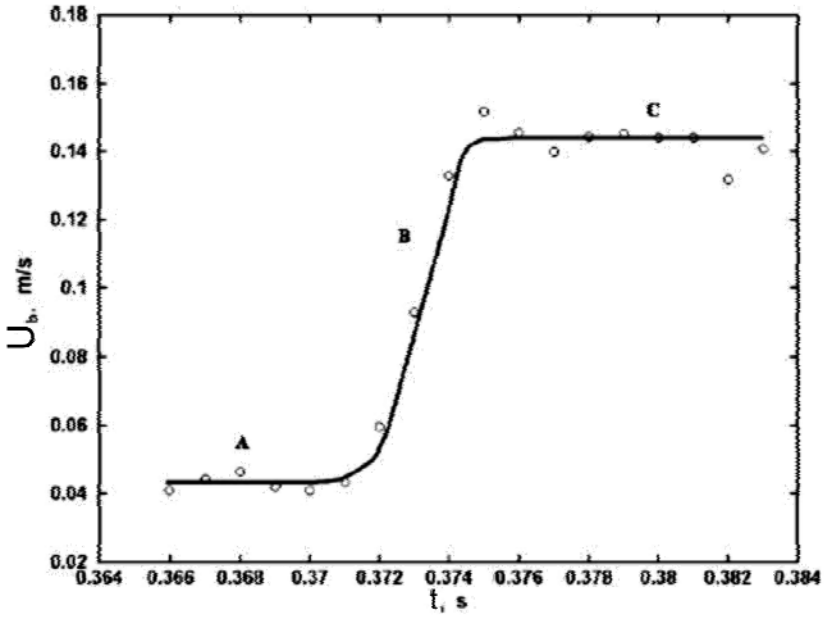

Figure 3. The velocity of bubble displacement. $U_{LS} = 0.046$ m/s, $q = 80$ kW/m^2.

Such a behaviour agrees with results reported by Agostini et al. [25]. The collision of elongated bubble has been studied by Revellin et al. [26] along adiabatic glass micro-channels of 509 and 709 μm internal diameters for refrigerant R-134 a. A model for the collision of elongated bubbles in micro-channels was proposed to predict the bubble length distribution at the exit of the micro-evaporator.

In micro-channels, bubbles cause a significant volume change (relative to the channel size). As a result, pressure fluctuations were observed. The temporal behaviour of the pressure drop is shown in Figure 4.

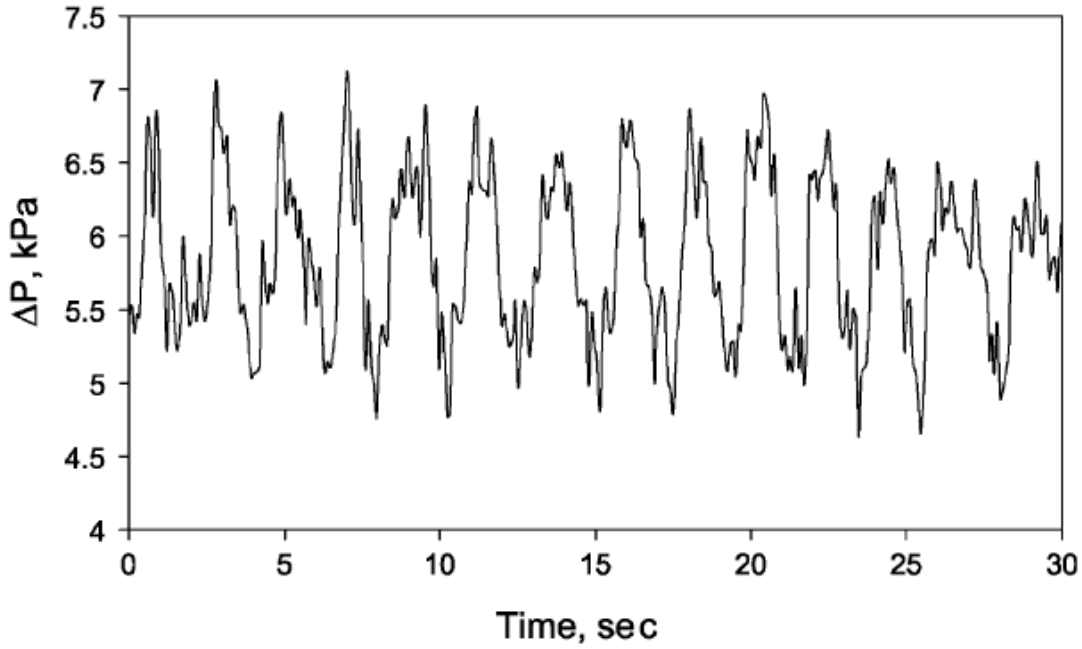

Figure 4. Pressure drop fluctuations. U_{LS} = 0.14 m/s, q = 220 kW/m^2.

The pressure spike introduces a disruption in the flow. Depending on the local conditions, the excess pressure inside the bubble may overcome the inertia of the incoming liquid and the pressure in the inlet manifold, and cause a reverse flow of varying intensity, depending on the local conditions. There are two ways to reduce the flow instabilities: reduce the local liquid superheat at the ONB and introduce a pressure drop element at the entrance of each channel, Kandlikar [27]. Kakac and Bon [28] reported that density-wave oscillations were observed also in conventional size channels. Introduction of additional pressure drop at the inlet (small diameter orifices were employed for this purpose) stabilized the system.

Simultaneous visualizations and measurements were done by Wang et al. [29] to investigate effects of inlet/outlet configurations on flow boiling instabilities in parallel micro-channels having a length of 30 mm and a hydraulic diameter of 186 μm. It was found that nearly steady flow boiling existed in the parallel micro-channels through an inlet restriction.

HEAT TRANSFER

The heat transfer coefficient of boiling flow through a horizontal rectangular channel with low aspect ratio (0.02–0.1) was studied by Lee and Lee [30]**.** The detail experimental study of flow boiling heat transfer in two-phase heat sinks was performed by Qu and Mudawar [5]. It was shown that the saturated flow boiling heat transfer coefficient in a micro-channel heat sink is a strong function of mass velocity and depends only weakly on the heat flux. This result, as well as the results by Lee and Lee [30]**,** indicates that the dominant mechanism for water micro-channel heat sinks is forced convective boiling but not nucleate boiling.

Heat transfer characteristics for saturated boiling were considered by Yen et al. [31]. From this study of convective boiling of HCFC123 and FC72 in micro-tubes with inner diameter 190, 300 and 510 μm one can see that in the saturated boiling regime, the heat transfer coefficient monotonically decreased with increasing vapour quality, but is independent of mass flux.

The convective and nucleate boiling heat transfer coefficient was the subject of experiments by Grohmann [32]. The measurements were performed in micro-tubes of 250 and 500 μm in diameter. Nucleate boiling metastable flow regimes were observed. Heat transfer characteristics at the nucleate and convective boiling in micro-channels with different cross-sections were studied by Yen et al. [33].

Several popular macro-channel correlations, and recently recommended small-channel correlations, were examined by Lee and Mudawar [34]. Predictions were adjusted for the three-sided wall heating and rectangular geometry.

Experiments by Lee and Mudawar [34] reveal the range of parameters at which heat transfer is controlled by nucleate boiling or annular film evaporation. The first of these processes occurs only at low qualities (x< 0.05) corresponding to very low heat fluxes; the second one at moderate (0.05<x<0.55) or high (x>0.55) qualities that correspond to higher heat fluxes. New correlations were suggested by Lee and Mudawar [34]. They are based on the Martinelli parameter X and account for micro-channel effects not represented in the prior correlations.

The work by Steinke and Kandlikar [15] focused on obtaining heat transfer data during flow boiling in micro-channels. An experimental investigation was performed for flow boiling using water in six parallel, horizontal micro-channels with a hydraulic diameter of 207 μm. The ranges of parameters are: mass flux from 157 to 1782 kg/m^{2}s, heat flux from 5 to 930 kW/m^2, inlet temperature of 22°C, quality from sub-cooled to 1.0, and atmospheric pressure at the exit.

$$h_{tp} = 0.6683\,Co^{-0.2}(1-x)^{0.8} f_2 h_L + 1058\,Bo^{0.7}(1-x)^{0.8} F \cdot h_L \tag{4}$$

$$Co = \left(\frac{\rho_G}{\rho_L}\right)^{0.5} \left(\frac{1-x}{x}\right)^{0.8} \tag{5}$$

$$Bo = \frac{q}{G h_{LG}} \tag{6}$$

where Co is the convection number given in equation (5), Bo is the boiling number given in equation (6), f_2 is the multiplier, h_L is the heat transfer coefficient with all liquid flow, and x is the quality. The F number for water is 1.0 and the f_2 is multiplier is 1.0 for micro-channel flow.

The empirical correlation obtained by Steinke and Kandlikar [15] predicts a heat transfer coefficient about twice higher than that measured by Qu and Mudawar [5] during flow boiling of water (x<0.15) and during flow boiling of R-134a (x = 0.4–0.8). This correlation also overpredicts the experimental data obtained by Yen et al. [31] during convective boiling of HCFC123 and FC72 in d=190 μm tubes in the range of x=0.4–0.9.

Critical Heat Flux of Flow Boiling. Zhang et al. [35] proposed a correlation for CHF under condition of saturated boiling:

$$Bo = 0.0352\left[We + 0.0119\left(\frac{L}{d_h}\right)^{2.31}\left(\frac{\rho_G}{\rho_L}\right)^{0.361}\right]^{-0.295} \times \left[\left(\frac{L}{d_h}\right)^{-0.311}\left(2.05\left(\frac{\rho_L}{\rho_L}\right)^{0.170} - x_{in}\right)\right] \tag{7}$$

where $Bo = q_{crit} / (h_{LG} G)$ is the boiling number, $We = (G^2 d_h) / (\sigma \rho_L)$ is the Weber number, q_{crit} is the critical heat flux, h_{LG} is the latent heat of vaporization, G is the mass flux, x_{in} is the thermodynamic equilibrium quality at the inlet, ρ_G and ρ_L are the densities of saturated vapor and liquid, respectively, d_h is the hydraulic diameter, L is the heated length, and σ is the surface tension.

Hall and Mudawar [36] provided a comprehensive review of the current state of knowledge of subcooled CHF for water flow boiling in channels, and proposed a statistical correlation with five parameters based on almost all available subcooled CHF databases in the literature:

$$Bo = \frac{C_1 We^{C_2} (\rho_L / \rho_G)^{C_3} [1 - C_4 (\rho_L / \rho_G)^{C_5} x_{in}]}{1 + 4 C_1 C_4 We^{C_2} (\rho_L / \rho_G)^{C_3 + C_5} (L / d_h)} \tag{8}$$

where the Weber number $We = G^2 d_h / (\rho_L \sigma)$, $C_1 = 0.0722$, $C_2 = -0.312$, $C_3 = -0.644$, $C_4 = 0.900$, and $C_5 = 0.724$. The correlation was developed using a total of 4860 data points and predicted CHF with a rms error of 14.3% in the following parametric ranges: $0.1 < P_0 < 20$ MPa, $0.25 < d_h < 15.0$ mm, $2 < L/d_h < 200$, $300 < G < 30000$ kg/m^2 s, $-2.00 < x_{in} < 0.00$, and $-1.00 < x_{out} < 1.00$.

A theoretical model for the prediction of the critical heat flux of refrigerants flowing in heated, round micro-channels has been developed by Revellin and Thome [26]. The model is based on the two-phase conservation equations and includes the effect of the height of the interfacial waves of the annular film. Validation has been performed by comparing the model with experimental results presented by Wojtan et al. [37], Qu and Mudawar [38], Bowers and Mudawar [39], Lazareck and Black [40]. More than 96% of the data for water and R-113, R-134a, R245fa were predicted within ±20%.

Explosive Boiling of Water in Parallel Micro-Channels. The thermo-hydrodynamic processes of boiling in a micro-channel heat sink were subject to a number of experimental investigations performed during the last decade. Periodic wetting and rewetting phenomena were observed by Hetsroni et al. [11, 12], Zhang et al. [14], Steinke and Kandlikar [15], and Kandlikar and Balasubramanian [6].

Quasi-Periodic Boiling in a Certain Single Micro-Channel of a Heat Sink. The main parameters that affect the explosive boiling oscillations (EBO) in an individual channel of a heat sink such as hydraulic diameter, mass flux, and heat flux were studied by Hetsroni et al. [11-13].

Period between successive events. Figure 5 shows the dependence of the dimensionless period of phase transformations (i.e., the time between bubble venting), t^*, on boiling number Bo ($t^* = t/Ud_h$, $Bo = q/Gh_{LG}$, where t is the period between successive events, U is the mean velocity of single-phase flow in the micro-channel, d_h is the hydraulic diameter of the channel, q is heat flux, m is mass flux, h_{LG} is the latent heat of vaporization). The dependence of t^* on Bo can be approximated, with a standard deviation of 16%, by

$$t^* = 0.000030 \, \mathrm{Bo}^{-2} \tag{9}$$

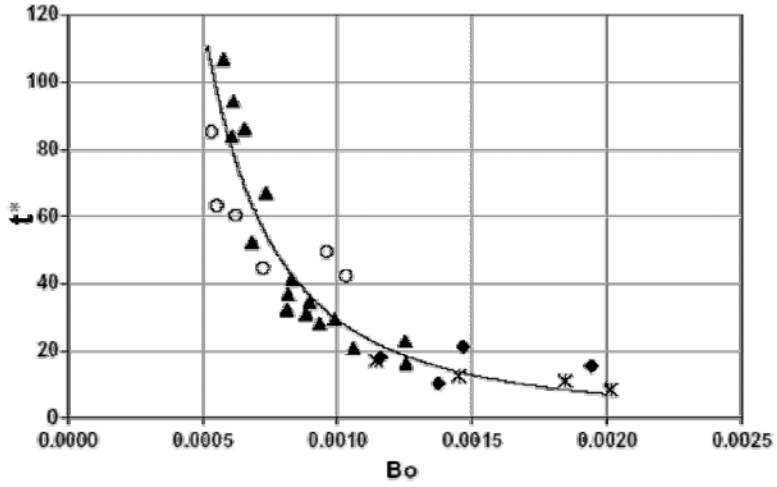

Figure 5. The dependence of the dimensionless time interval between cycles on the boiling number: circles (o) represent d_h=100 μm, water, triangles (▲) represent d_h=130 μm, water, diamonds (♦) represent d_h=220 μm, water, star (∗) represents d_h=220 μm, ethanol.

The Initial Thickness of the Liquid Film. The term initial liquid film thickness is defined as the average thickness of fluid, evenly distributed during the period t, over the surface of the circular micro-channel, after venting of the elongated bubble.

The average liquid thickness δ, can be calculated as:

$$\delta = qt / \rho_L h_{LG} \tag{10}$$

Figure 6 shows the dependence of the dimensionless initial liquid thickness of water and ethanol δ^*, on the boiling number Bo, where $\delta^* = \delta U / \nu$, U is the mean velocity of single-phase flow in the micro-channel, and ν is the kinematic viscosity of the liquid at saturation temperature. The dependence of δ^* on Bo can be approximated, with a standard deviation of 18%, by:

$$\delta^* = 0.00015\ \mathrm{Bo}^{-1.3} \tag{11}$$

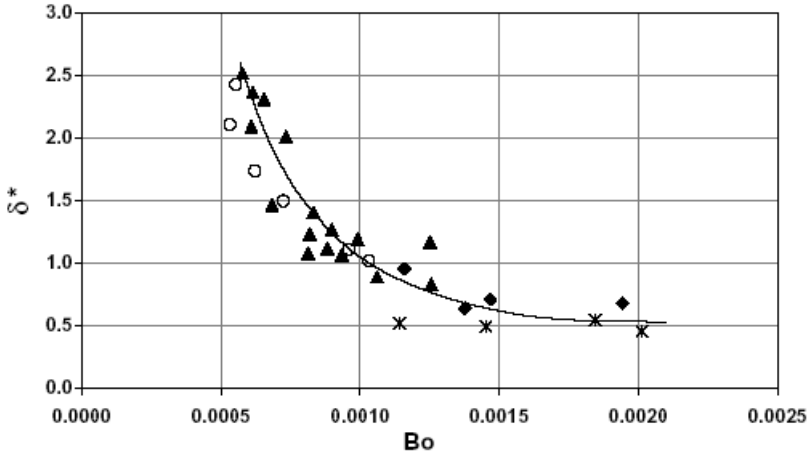

Figure 6 Dependence of the dimensionless initial film thickness on the boiling number: *circles* (o) represent d_h=100 μm, water, *triangles* (▲) represent d_h=130 μm, water, *diamonds* (♦) represent d_h=220 μm, water, *star* (∗) represents d_h=220 μm, ethanol.

The initial thickness of the liquid film is a key parameter of the explosive boiling. The term initial liquid film thickness is defined as the average thickness of fluid, evenly distributed during period *t*, over the surface of the circular micro-channel, after venting of the elongated bubble. This surface is located downstream of the ONB and may be characterized by the heated length and hydraulic diameter. This point may be discussed in some detail with regard to the beginning of the critical heat flux (CHF) regime. The variation of the initial thickness of the film of water versus the heat flux is depicted in Figure 7. For explosive boiling the film thickness decreases with increasing heat flux from 125 to 270 kW/ m^2 from about 8 to 3 μm. This range of values is on the same order of magnitude as those given by Moriyama and Inoue [41] and by Thome et al. [7] for R-113 in small spaces (100–400 μm). Decreasing liquid film thickness with increasing heat flux is a distinct feature of dryout during explosive boiling. Under the conditions at which the instantaneous temperature of the heater surface exceeds 125°C, the value of δ was in the range of 3±0.6 μm. This value may be considered as minimum initial film thickness. If the liquid film reached the minimum initial film thickness δ_{min}, CHF regime occurred. According to Thome et al. [7] δ_{min} is assumed to be on the same order of magnitude as the surface roughness. The values of the minimum initial film thickness calculated by Thome et al. [7] for R-113 at saturation temperature 47.2°C was in the range of 1.5–3.5 μm.

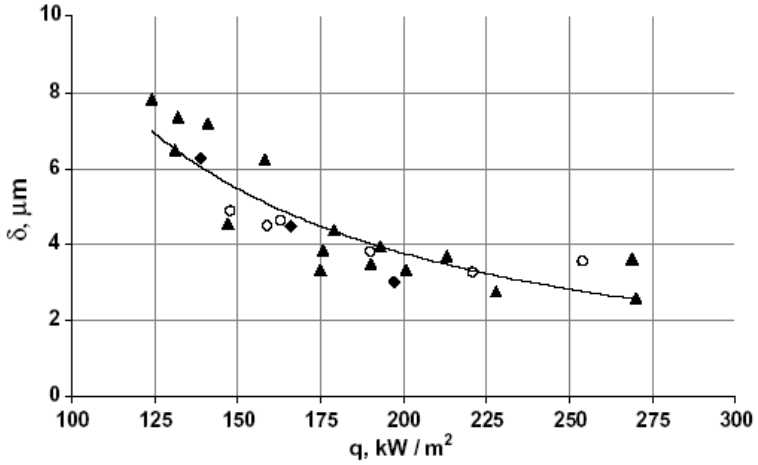

Figure 7 The variation of the initial film thickness for water versus heat flux: *circles* (o) represent d_h=100 μm, water, *triangles* (▲) represent d_h=130 μm, water, *diamonds* (♦) represent d_h=220 μm, water.

System that Contains a Number of Parallel Micro-Channels. Hetsroni et al. [11-13] also studied the effect of EBO in individual channels on the average characteristics of the whole heat sink: total pressure drop and temperature fluctuations on the heater, and the heat transfer coefficient. The high-frequency oscillations in individual micro-channels are superimposed and lead to total low-frequency pressure drop and temperature oscillations of the system.

Fluctuation of pressure drop, fluid and heated wall temperatures. The experimental investigations of boiling instability in parallel micro-channels were carried out by simultaneous measurements of temporal variations of pressure drop, fluid and heater temperatures. The channel-to-channel interactions may affect pressure drop between the inlet and the outlet manifold as well as associated temperature of the fluid in the outlet manifold and heater temperature. Figure 8 illustrates this phenomenon for pressure drop in the heat sink that contains 13 micro-channels of d_h = 220 μm at mass flux G = 93.3 kg/m^2 s and heat flux q = 200 kW/m^2. The temporal behaviour of the pressure drop in the whole boiling system is shown in Figure 8a**.** The considerable oscillations were caused by the flow pattern alternation, that is, by the liquid/two-phase alternating flow in the micro-

channels. The pressure drop FFT is presented in Figure 8b. Under condition of the given experiment, the period of pressure drop fluctuation is about t = 0.36 s.

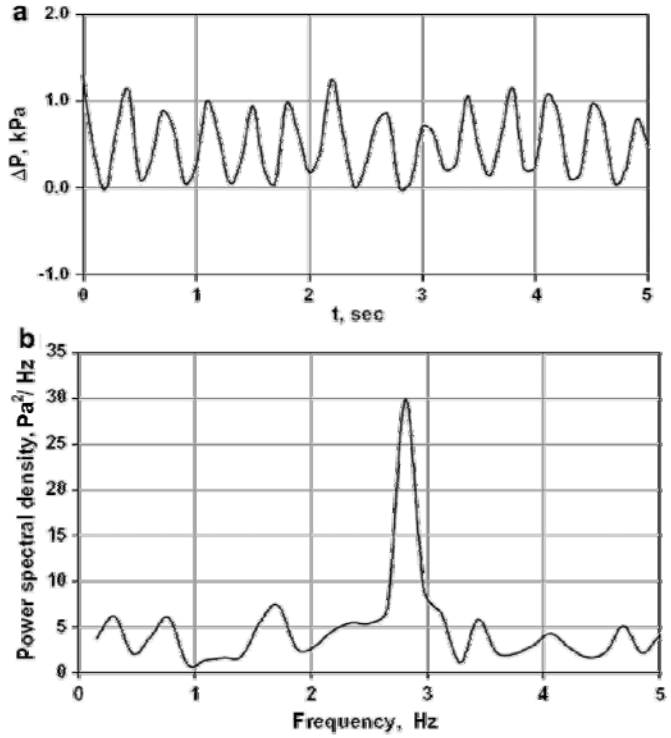

Fig8. Time variation of pressure drop at q = 200 kW/m^2: (**a**) pressure drop fluctuations, (**b**) pressure drop amplitude spectrum.

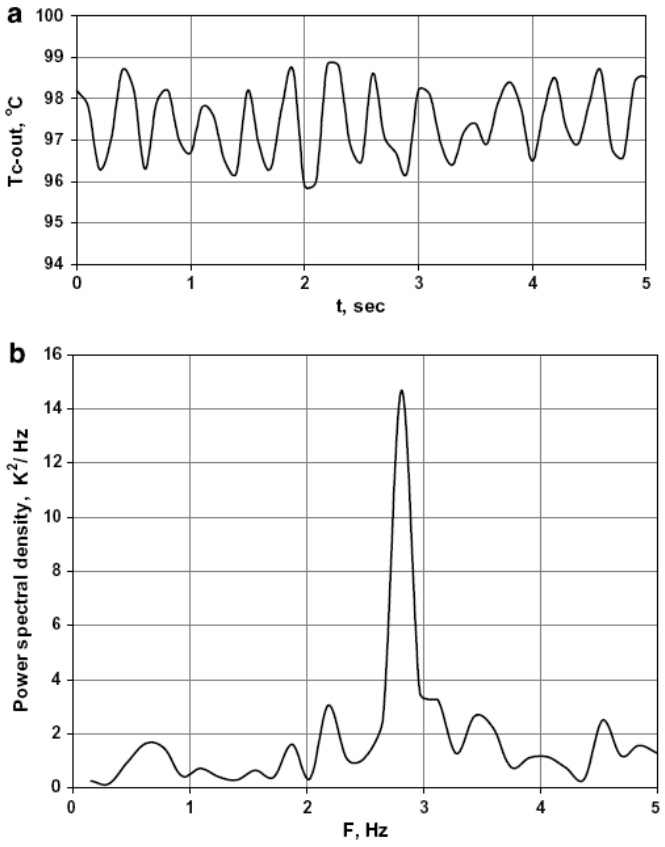

Fig 9. The Time variation of the fluid temperature at the outlet manifold q=200 kW/m^2: (**a**) temperature fluctuations, (**b**) temperature amplitude spectrum**.**

The pressure drop fluctuation provides an insight into the temperature behaviour of the fluid in the outlet manifold. The pressure drop fluctuation frequency represents the oscillations in the system. Figure 9a, b shows the time variation and FFT of the fluctuation component of the fluid temperature. In Figure 9a one can observe that the average fluid temperature at the outlet manifold is less than the saturation temperature. This results in the fact that only single liquid comes to the outlet manifold through some of the parallel micro-channels.

The time variation of the mean and maximum heater temperature is presented in Figure 10. The mean heater temperature (i.e., the average temperature of the whole heater) changed in the range of $\Delta T_{av} = 10$ K. The maximum heater temperature changed in the range of $\Delta T_{max} = 6$ K. Comparison between Figs. 8, and 9, shows that the time period (frequency) is the same for the pressure drop and the fluid temperature at the outlet manifold, and the mean and maximum heater temperature fluctuations. It also allows one to conclude that these fluctuations are in phase. When the heat flux is increased, at constant value of mass flux, the oscillation amplitudes of the pressure drop, the fluid and the heater temperatures also increase.

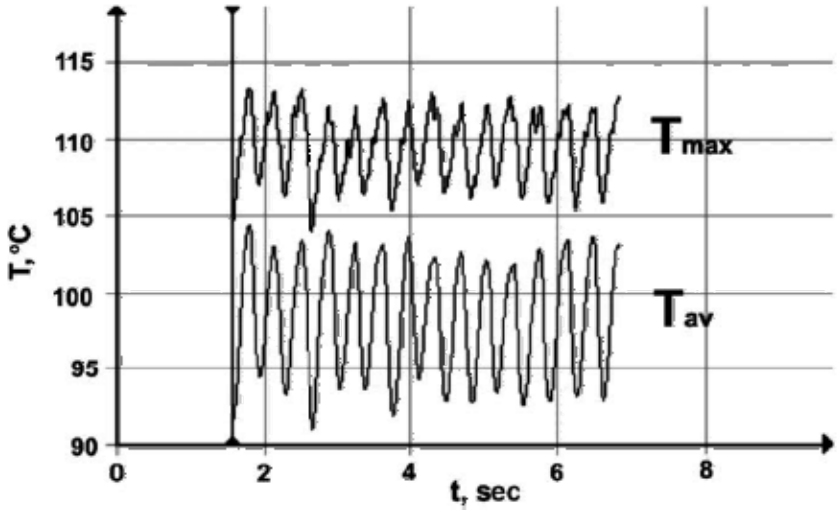

Figure 10. Time variation of average and maximum heater temperature at $q = 200$ kW/m^2.

Average Heat Transfer Coefficient. In the range of quality x=0.01-0.08 it was observed that at the same boiling number and inlet temperature, an increase in diameter shifts the ONB further from the inlet. The region of the local dryout decreases and the average heated surface temperature decreases as well. Under this condition the heat transfer coefficient increases with increased hydraulic diameter. In order to take into account the effect of surface tension and micro-channel hydraulic diameter, we have applied the Eotvos number $Eo = g(\rho_L - \rho_G)d_h^2/\sigma$. Figure 11 shows the dependence of the Nu/Eo on the boiling number Bo, where $Nu = hd_h/k_L$ is the Nusselt number, h is the heat transfer coefficient, and k_L is the thermal conductivity of fluid. All fluid properties are taken at the saturation temperature. This dependence can be approximated, with a standard deviation of 18%, by the relation:

$$Nu/Eo = 0.030\, Bo^{-1.5} \tag{10}$$

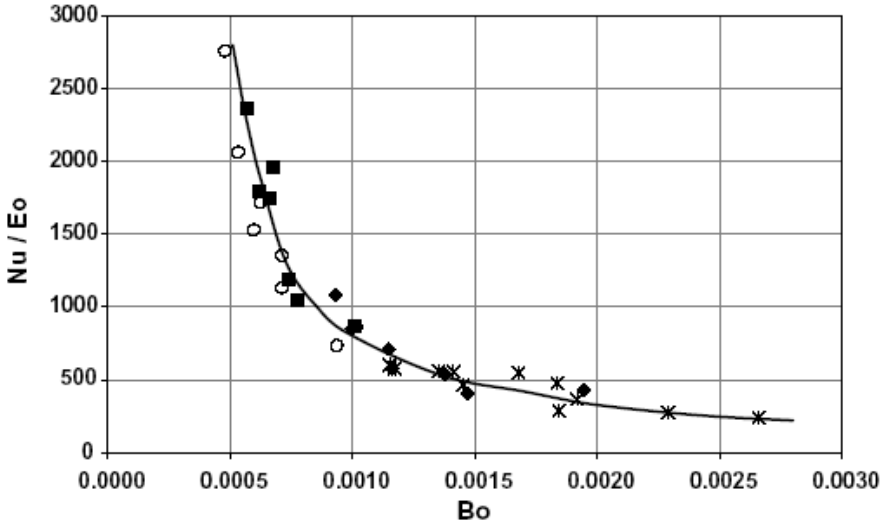

Fig 11. The dependence of *Nu / Eo* on the *Bo*: *circles* (o) represent d_h=100 μm, water, *triangles* (▲) represent d_h=130 μm, water, *diamonds* (♦) represent d_h=220 μm, water, *star* (∗) represents d_h=220 μm, ethanol.

CONCLUSIONS

Bubble dynamics in a confined space. Dimensional analysis shows that the variation of the bubble radius with time depends on the parameter $\Pi = q/(\rho_L U c_{pL} \Delta T_S)$. In the range of Π=0.0079–0.026, linear behaviour was observed, and when Π>0.026 exponential bubble growth took place.

Heat transfer in two-phase flow boiling. The extent to which an incoming liquid will be vaporized is a design variable that depends on the intended application. In micro-scale refrigeration systems, the change in vapour quality may be substantial, on the order of 0.8 for example. In electronics cooling applications, the equilibrium vapour quality may remain at 0, or be very small; in those designs, the aim is to capture the high-heat transfer coefficients of subcooled flow boiling, without the added complexities of net vapour generation (e.g., the need to incorporate a condenser). The distinction between low and high-quality outflow affects heat transfer coefficients. Experiments by Lee and Mudawar [34] revealed the range of parameters at which heat transfer was controlled by nucleate boiling or annular film evaporation. The first of these processes occurred only at low qualities ($x < 0.05$), the second one at moderate ($0.05 < x < 0.55$) or high ($x > 0.55$) qualities. New correlations were suggested by Lee and Mudawar [34]. They are based on the Martinelli parameter and may be used for two-phase flow boiling of water and refrigerant R-134a.
Critical Heat Flux

Several thousand CHF points have been reported in the boiling literature of the past 50 years. Most of these data were obtained with stable flow in single conventional size circular tubes and conventional size channels. The tubes were usually of uniform wall thickness, and direct electrical heating was utilized to simulate the constant heat flux. The correlation suggested by Zhang et al. [35], (equation (7)) gives the best agreement with experimental data on saturated CHF in channels of 0.33–6.22 mm. There is a significant difference between experimental results of CHF obtained in a single micro-channel of d_h = 0.5 mm and in the block that contained twenty-one 0.215 × 0.21 mm channels.

The study of CHF in micro-channels has not received much attention in the literature. Single-tube CHF data are not available for micro-channels with hydraulic diameters less than 0.3 mm. Under

conditions of explosive boiling, Hetsroni et al. [13] suggested that the initial thickness of the liquid film may by considered as a key parameter that affects CHF in the system containing a number of parallel micro-channels of $d_h = 0.1–0.22$ mm. New experiments should be performed to validate the dimensionless groups suggested for the evaporating interface near the heated wall and CHF for single micro-channels, as well as for blocks that contain parallel micro-channels.

Flow instability. The channel-to-channel interactions may affect pressure drop between the inlet and the outlet manifolds, as well as associated temperature of the fluid in the outlet manifold and the temperature of the heater. The frequency and the phase are the same for all these fluctuations. They increase at a constant value of mass flux with increasing heat flux. The large heated wall temperature fluctuations are associated with CHF. As the heat flux approached CHF, the parallel-channel instability, which was moderate over a wide range of heat fluxes, became quite intense and must be associated with maximum temperature fluctuation of the heated surface.

REFERENCES

1. Qu, W., Mudawar, I., Measurement and prediction of pressure drop in two-phase micro-channel heat sinks. *Int. J. Heat Mass Transfer* Vol. 46, pp. 2737–2753, 2003
2. Hetsroni, G., Mosyak, A., Segal, Z., Ziskind, G., A uniform temperature heat sink for cooling of electronic devices. *Int J Heat Mass Transfer* Vol. 45, pp. 3275–3286, 2002
3. Bertsch, S. S., Groll, E. A., Garimella, S. V., Refrigerant flow boiling heat transfer in parallel micro-channels as a function of local vapor quality. *Int. J. Heat Mass Transfer* Vol. 51, pp. 4775-4787, 2008.
4. Agostini B, Revellin R, Thome J., Elongated bubbles in micro-channels. Part I: Experimental study and modeling of elongated bubble velocity. *Int. J. Multiphase Flo*w Vol. 34, pp. 590-601, 2008
5. Qu, W., Mudawar, I., Flow boiling heat transfer in two-phase micro-channel heat sink. I: Experimental investigation and assessment of correlation methods. *Int. J. Heat Mass Transfer* Vol. 46, pp. 2755–2771, 2003
6. Kandlikar, S. G., Balasubramanian, P., An extension of the flow boiling correlation to transition, laminar and deep laminar flows in mini-channels and micro-channels. *Heat Transfer Eng* Vol. 25, pp. 86–93, 2004
7. Thome, J. R, Dupont, V., Jacobi, A. M., Heat transfer model for evaporation in micro-channels. Part I: Comparison with database. *Int. J. Heat Mass Transfer* Vol. 47, pp. 3375–3385, 2004
8. Dupont, V., Thome, J. R., Jacobi, A. M., Heat transfer model for evaporation in micro-channels. Part II Comparison with database. *Int. J. Heat Mass Transfer* Vol. 47, pp. 3387-3401, 2004
9. Zhang, W., Hibiki, T., Mishima, K., Correlation for flow boiling heat transfer in mini-channels. *Int. J. Heat Mass Transfer* Vol. 47, pp. 5749-5763, 2004
10. Lee, J, Mudawar, I., Two-phase flow in high-heat-flux micro-channel heat sink for refrigeration cooling applications. Part I: pressure drop characteristics. *Int. J. Heat Mass Transfer* Vol. 48, pp. 928–940, 2005
11. Hetsroni, G., Mosyak, A., Segal, Z., Pogrebnyak, E., Two-phase flow pattern in parallel micro-channels. *Int. J. Multiphase Flow* Vol. 29, pp. 344–360, 2003
12. Hetsroni, G., Mosyak, A., Pogrebnyak, E., Segal, Z., Explosive boiling of water in parallel micro-channels. *Int. J. Multiphase Flow* Vol. 31, pp. 371–392, 2005
13. Hetsroni, G., Mosyak, A., Pogrebnyak, E., Segal, S., Periodic boiling in parallel micro-channels at low vapor quality. *Int. J. Multiphase Flow* Vol. 32, pp. 1141–1159, 2006

14. Zhang, L., Koo, J-M., Jiang, L., Asheghi, M., Goodson, K. E., Santiago, J. K., Measurements and modeling of two-phase flow in micro-channels with nearly constant heat flux boundary conditions. *J. Microelectromech. Syst* Vol. 11, pp. 12–19, 2002
15. Steinke, M., Kandlikar, S. G., An experimental investigation of flow boiling characteristics of water in parallel micro-channels. *Trans ASME J Heat Transfer* 126:518–526, 2004
16. Kandlikar, S. G., Fundamental issues related to flow boiling in mini-channels and micro-channels. *Exp. Thermal Fluid Sci.* Vol. 26, pp. 389–407, 2002
17. Lee, H. J., Lee, S. Y., Pressure drop correlations for two-phase flow within horizontal rectangular channels with small heights. *Int. J. Multiphase Flow* Vol. 27, pp. 782–796, 2001
18. Lee, H. C., Oh, B. D., Bae, S. W., Kim, M. H., Single bubble growth in saturated pool boiling on a constant wall temperature surface. *Int. J. Multiphase Flow* Vol. 29, pp. 1857–1874, 2003
19. Bergles A. E., Kandlikar, G. G., On the nature of critical heat flux in micro-channels. *J. Heat Transfer* Vol. 127, pp. 101-107, 2005
20. Dhir, V. K., Boiling heat transfer. *Ann Rev Fluid Mech* Vol. 30, pp. 365–4011998
21. Lee, P. C., Tseng, F. C., Pan, C., Bubble dynamics in microchannels. Part 1: single microchannel. *Int. J. Heat Mass Transfer* Vol. 47, pp. 5575–5589, 2004
22. Li, H. Y., Tseng, F. C., Pan, C., Bubble dynamics in micro-channels. Part II: two parallel micro-channels. *Int. J. Heat Mass Transfer* Vol. 47, pp. 5591–5601, 2004
23. Yarin, L. P, Mosyak, A. Hetsroni, G., Fluid Flow, Heat Transfer and Boiling in Micro-channels, Springer Verlag, 2008
24. Prodanovic, V., Fraser, D., Salcudean, M., On transition from partial to fully developed subcooled flow boiling. *Int. J. Heat Mass Transfer* Vol. 45, pp. 4727–4738, 2002
25. Agostini, B., Thome, J. R., Fabbri, M., Michel, B., Calmi, D., Kloter, U., High heat flux flow boiling in silicon multi-micro-channels. Part I: Heat transfer characteristics of refrigerant R236fa. *Int. J. Heat Mass Transfer* Vol. 51, pp. 5400-5414, 2008
26. Revellin, R., Thome, J., A theoretical model for the prediction of the critical hat flux in heated micro-channel. *Int. J. Heat and Mass Transfer* Vol. 51, pp. 1216-1225, 2008
27. Kandlikar, S. G., Nucleation characteristics and stability considerations during flow boiling in micro-channels. *Exp. Thermal and Fluid Science* Vol. 30, pp. 441-447, 2006
28. Kakac, S., Bon, B., A review of two-phase flow dynamic instabilities in tube boiling systems. *Int. J. Heat Mass Transfer* Vol. 51, pp. 399-433, 2008
29. Wang, G., Cheng, P., Bergles, A. E., Effects of inlet outlet configurations on flow boiling instability in parallel micro-channels. *Int. J. Mass Transfer* Vol. 51, pp. 2267-2281, 2008
30. Lee, H. J., Lee, S. Y., Heat transfer correlation for boiling flows in small rectangular horizontal channels with low aspect ratios *Int. J. Multiphase Flow* Vol. 27, pp. 2043–2062, 2001
31. Yen, T-H., Kasagi, N., Suzuki, Y., Forced convective boiling heat transfer in micro-tubes at low mass and heat fluxes. *Int. J. Multiphase Flow* Vol. 29, pp. 1771–1792, 2003
32. Grohmann, S., Measurement and modeling of single-phase and flow-boiling heat transfer in micro-tubes. *Int. J Heat Mass Transfer* Vol. 48, pp. 4072–4089, 2005
33. Yen, T-H., Shji, M., Takemura, F., Suzuki, Y., Kasagi, N., Visualization of convective boiling heat transfer in single micro-channels with different shaped cross-sections. *Int. J. Heat Mass Transfer* Vol. 49, pp. 3884–3894, 2006
34. Lee, J, Mudawar, I., Two-phase flow in high-heat-flux micro-channel heat sink for refrigeration cooling applications. Part II: heat transfer characteristics. *Int. J. Heat Mass Transfer* Vol. 48, pp. 941–955, 2005
35. Zhang, W., Hibiki, T., Mishima, K., Mi, Y., Correlation of critical heat flux for flow boiling of water in mini-channels. *Int. J. Heat and Mass Transfer* Vol. 49, pp. 1058–1072, 2006
36. Hall, D. D, Mudawar, I., Critical heat flux (CHF) for water flow in tubes—II. Subcooled CHF correlations. *Int J Heat Mass Transfer* Vol. 43, pp. 2605–2640, 2000
37. Wojtan, L., Revellin, R., Thome, J., Investigation of critical heat flux in single uniformly heated micro-channels. Exp. Therm, *Fluid Sci.* Vol. 30, pp. 765-774, 2006

38. Qu, W., Mudawar, I., Measurement and correlation of critical heat flux in two-phase micro-channel heat sinks. *Int. J. Heat Mass Transfer* Vol. 47, pp. 2045-2059, 2004
39. Bowers, M. B., Mudawar, I., High flux boiling in low flow rate, low pressure drop mini-channel and micro-channel heat sinks. *Int. J. Heat Mass Transfer* Vol. 37, pp. 321-332, 1994
40. Lazarek, G. M., Black, S. H., Evaporative heat transfer, pressure drop and critical heat flux in a small vertical tube with R-113. *Int. J. Heat Mass Transfer* Vol. 25, pp. 945–959, 1982
41. Moriyama, K., Inoue, A., Thickness of the liquid film formed by growing bubble in a narrow gap between two horizontal plates. *J. Heat Transfer Trans* ASME Vol. 118, pp. 132–139, 1996

QUANTITATIVE TEMPERATURE AND THERMAL CONDUCTIVITY PROFILING WITH THERMOCOUPLE SCANNING THERMAL MICROSCOPE PROBE

O. M. Kwon[1], J. S. Lee[2*]
[1]Korea University, Seoul, Korea
[2]Seoul National University, Seoul, Korea

ABSTRACT. Quantitative temperature and thermal conductivity profiling technique is presented, which eliminates the influence of heat transfer through the air, and measures the temperature and thermal conductivity of a sample from a tip-sample heat transfer only, operating thermocouple scanning thermal microscope (SThM) probe in both passive and active modes. We describe the principle of the technique through a rigorous theoretical analysis of the heat transfer that occurs during measurement. The spatial resolution of this technique is demonstrated by obtaining the thermal conductivity profile of samples in which a thin silicon oxide layer is sandwiched between single crystal silicon layers. Thermal conductivity distributions are quantitatively profiled for samples with a 1.4 μm-thick silicon oxide layer and a 200 nm-thick oxide layer. For a sample with a 100 nm-thick silicon oxide layer, only the existence of a region with lower thermal conductivity could be identified. Based on our results, the spatial resolution of this technique is estimated to be around 150 nm.

Keywords: *Scanning thermal microscope, thermocouple probe, quantitative profiling, temperature, thermal conductivity*

INTRODUCTION

The scanning thermal microscope (SThM) is a type of scanning probe microscope (SPM) that maps out the temperature and/or the thermal property of a sample surface by scanning a sharp SThM probe with a temperature sensor at the tip. The tip-sample contact force is controlled by an atomic force microscope (AFM) [1, 2]. Since a SThM can measure temperature and thermal properties with the highest known spatial resolution, it has been used for such diverse applications as the detection of the failure of electronic devices [3], locating a hot spot in an operating metal-oxide semiconductor field effect transistor [4], imaging the phonon temperature distribution of electrically-heated carbon nanotube (CN) circuits [5], imaging the temperature distribution inside a vertical-cavity surface-emitting laser [6], polymer light-emitting diodes [7], thermal conductivity distribution of biological samples [8], and nondestructive evaluation of subsurface microelectronic structures [9].

Despite the high spatial resolution of SThM, its usefulness has been limited because of its lack of quantitative measurement. In an effort to improve quantitative temperature measurement, Luo *et al.* developed a resistance network model based on the assumption that when a probe makes contact with a sample surface, heat transfers from the sample to the base of the cantilever without any leakage to the surrounding air [10]. According to this model, if the thermal resistance of the SThM probe cantilever and tip-sample contact are measured correctly, a quantitative temperature

* Corresponding author: Prof. J. S. Lee
Phone: + (82)-2-880-7117, Fax: + (82)-2-883-0179
E-mail address: jslee123@snu.ac.kr

profile of the sample can be obtained from the temperature distribution measured by the thermocouple junction at the end of the SThM probe tip.

However, Shi *et al.* observed experimentally that the temperature measured by the thermocouple junction of a SThM probe depends on the size of the sample, even if the temperature of the sample is the same [11]. This is because most of the heat transfers not through the tip-sample contact, but through the air gap between the sample and the SThM probe. Hence, it became clear that merely by multiplying a certain proportionality constant by the temperature distribution measured by the thermocouple of the SThM probe, a correct quantitative temperature profile of the sample cannot be obtained.

Conventionally, thermocouple SThM probes have been used mostly for temperature imaging, whereas thermo-resistive SThM probes are used for thermal property imaging. However, both thermocouple and thermo-resistive probes can be operated in either a passive mode or an active mode. Hence, in principle, both probes can measure either temperature or thermal properties.

Recently, Roh *et al.* developed a technique, named the 2ω method [12, 13], that can image a local thermal property by taking advantage of a thermocouple SThM probe that had already shown a spatial resolution of around 100 nm in local temperature measurement [14]. The 2ω method can map out the local thermal property by monitoring the amplitude of the 2ω signal from the thermocouple junction of a probe heated by an alternating current (ac) with a frequency of 1ω. The spatial resolution of this technique is around 200 nm. However, the spatial resolution of the 2ω method is severely limited by heat transfer through the air gap between the probe and sample, which turned out to be much larger than the heat transfer through the contact between the probe tip and the sample. Moreover, heat transfer through the air prevents quantitative interpretation of the measured data.

Therefore, for the quantitative profiling of temperature or thermal properties, the influence of air should be carefully removed. A direct approach would be to carry out the measurement in a vacuum. However, measurement in vacuum can entail several problems. First, it might reduce measurement sensitivity since, in a vacuum, the water film that enhances the heat transfer through the tip-sample contact in an atmospheric environment disappears. Second, a new position control mechanism for the SThM probe should be employed, since the laser beam deflection technique widely used for SThM probe position control in an atmospheric environment would not be effective in a vacuum due to significant heating caused by the laser beam. Third, for measurement in a vacuum, the necessary equipment and the measurement process are more expensive.

However, if the sensitivity of the SThM probe is sufficiently improved to detect even the smallest signal generated by heat transfer through the tip-sample solid-solid contact, then measurement in a vacuum can have the following advantages: first, the spatial resolution might be improved further, since the diameter of the tip-sample contact would be significantly reduced without the water film; and second, measurement in a vacuum would allow differentiation of the energy transport through the solid-solid contact from energy transport through solid-liquid-solid contact. Therefore, a vacuum measurement using SThM can potentially be a scientifically useful tool.

For quantitative local thermal conductivity measurements, thermo-resistive probes have been used. The thermo-resistive probe can be operated in either ac or direct current (dc) mode. In dc mode, the thermal conductivity of the sample is obtained from the amount of the power estimated to be transferred to the sample, while the SThM probe is operated in constant temperature mode. Ruiz *et al.* argued the power transferred to the sample is the difference between the power required to maintain the temperature of the thermo-resistive element at a predetermined constant value in contact with the sample, and the power out of contact [15]. Introducing a generalized thermal conductivity approach, Tsukruk *et al.* refined the model suggested by Ruiz *et al.* [16]. Through analytical and numerical thermal modelling of the tip and sample, Lefevre *et al.* showed that a major portion of the power (~ 66 %) goes to the silver coating of the probe wire [17]. However, the method proposed by Ruiz *et al.* has been used without much modification.

For the ac mode of measurement, unlike the dc mode of measurement that requires calibration for the particular probe used, it is supposed to be an advantage that the thermal conductivity of a sample can be extracted from a certain functional relation existing between the heating frequency and the amplitude of temperature oscillation without any calibration of the probe being used. Fiege *et al.* reported that the 3ω method was applied in SThM with a resistive probe for quantitative measurement of the thermal conductivity of gold, silver, and a CVD diamond film with a spatial resolution of approximately 30 nm [18]. However, Lefevre *et al.* later argued with a thermal modelling of the SThM set up that the conventional 3ω method cannot be applied to the SThM setup [19]. Anyway, any other experimental results that can reverse this argument are hard to find ever since.

Since thermo-resistive SThM probes, especially the Wollaston wire probe, are very robust and can be operated in both passive and active modes, they have been used widely for the characterization of thermal properties. However, if the size of the thermo-resistive element of the probe were reduced to improve its spatial resolution, its sensitivity would decrease because a thermo-resistive SThM probe is a line sensor based on a line-heating and line-sensing scheme. In addition, in order to keep the electrical resistance of the lead line smaller than that of thermo-resistive element, the metal lead line should remain thick enough, but this prevents proper thermal insulation of the sensing thermo-resistive element. The thermal sensor should be thermally insulated to the greatest extent possible to enhance its sensitivity: without adequate sensitivity, spatial resolution cannot be improved.

Since the thermocouple SThM probe is, in principle, a point sensor, the size of its sensing part can be reduced without sacrificing sensitivity. The size of the sensing part of the current thermocouple SThM probe is already quite small, and the thermal insulation of the thermocouple junction is good--it is located at the end of the silicon oxide tip whose thermal conductivity is about 1.4 W/m-K. With the rapid evolution of nanofabrication techniques, the thermocouple junction at the end of the tip will become sharper and smaller, and this would enhance sensitivity and spatial resolution even further.

In this study, we suggest a quantitative temperature and thermal conductivity profiling technique with the thermocouple SThM probe, which has advantages in spatial resolution and sensitivity, by removing the influence of air in the environment while operating the probe in both passive and active modes.

PRINCIPLE OF QUANTITATIVE MEASUREMENT

Recently, Kim *et al.* demonstrated, both theoretically and experimentally, a double scan technique that can profile temperature only from the heat transfer through the tip-sample contact by the subtraction of the signal due to the heat transfer through the air [20]. In this study, we demonstrate theoretically and experimentally that this technique can be extended to quantitative thermal conductivity profiling. For a rigorous description of the measurement principle, the heat transfer between a thermocouple SThM probe and a sample is schematically shown in Figure 1. The principle of the technique is as follows.

First, the topography of the sample and the dc thermoelectric signal from the thermocouple junction are measured simultaneously by scanning the probe on the sample surface in controlled force-contact mode. The dc thermoelectric signal measured at this time, as shown schematically in Figure 1, is the signal due to both the heat transfer through the tip-sample contact and the heat transfer through the air. In contact mode, the governing equation for the temperature distribution in the probe is

$$\frac{d}{d\xi}\left[\sum A_i(\xi)k_i\frac{dT_c(\xi)}{d\xi}\right]-p(\xi)h_{eff}(\xi)[T_c(\xi)-T_{sub}(\xi)]+g\left(\xi\right)=0 \tag{1}$$

where ξ represents a position in the probe, T_c is the local temperature in the probe in contact mode, A_i is the cross section of each material in the probe, k_i is the thermal conductivity of each material, p

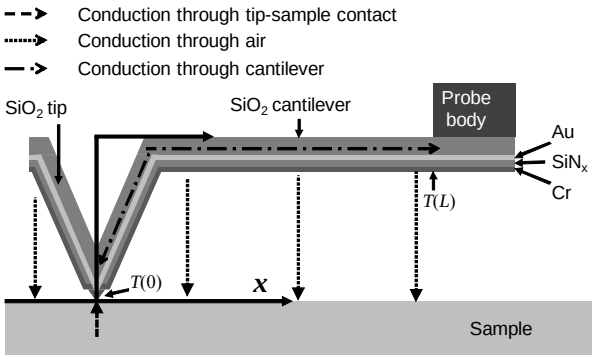

Figure 1. SThM probe in contact with sample and various heat transfer paths around the probe.

is the perimeter of the probe related to the surface exchanging heat flux with the sample, h_{eff} is the effective heat transfer coefficient between the probe and the sample, T_{sub} is the local temperature of the sample, and g is the heat generation per unit length of probe. During passive mode operation for temperature profiling, g=0, but during active mode operation for thermal conductivity, profiling g would be nonzero in the active mode. The boundary condition for equation (1) is

$$\sum A_i k_i \frac{dT_c(0)}{d\xi} = Q_{ts} = G_{ts}(T_c(0) - T_{sub}(0)),\ T_c(L) = T_b \tag{2}$$

where Q_{ts} is the heat flux through the tip-sample contact, G_{ts} is the tip-sample conductance, and T_b is the temperature at the cantilever base contacting the silicon body.

Second, the SThM probe is scanned along the same line as the first scan at a constant height above the sample surface using the topography data obtained from the first scan. The thermoelectric signal measured at this time is due to the heat transfer through the air only, because the tip is not in contact with the sample in the lift mode. In lift mode, the governing equation is

$$\frac{d}{d\xi}\left[\sum A_i(\xi) k_i \frac{dT_l(\xi)}{d\xi}\right] - p(\xi) h_{eff}(\xi)[T_l(\xi) - T_{sub}(\xi)] + g(\xi) = 0 \tag{3}$$

where T_l is the local temperature in the probe in lift mode. The value of h_{eff} in equation (3) is assumed to be the same as that in equation (1). Since the tip is not in contact with the sample, by definition there is no heat transfer through the tip-sample contact. Therefore, the boundary condition of equation (3) is

$$\sum A_i k_i \frac{dT_l(0)}{d\xi} = 0,\ T_l(L) = T_b \tag{4}$$

Then, the difference between the thermoelectric signal obtained in the first scan by contact mode and the signal in the second scan by lift mode is the signal due to the heat transfer through the tip-sample contact only. The equation governing the difference between the temperature in contact mode and the temperature in lift mode can be obtained by subtracting equation (3) from equation (1):

$$\frac{d}{d\xi}\left[\sum A_i(\xi) k_i \frac{dT_{cl}(\xi)}{d\xi}\right] - p(\xi) h_{eff}(\xi) T_{cl}(\xi) = 0 \tag{5}$$

where T_{cl} is T_c - T_l. The boundary condition of this equation is obtained by subtracting equation (4) from equation (2):

$$\sum A_i k_i \frac{dT_{cl}(0)}{d\xi} = Q_{ts} = G_{ts}(T_c(0) - T_{sub}(0)),\ T_{cl}(L) = 0 \tag{6}$$

Unlike equations (1) and (3), equation (5) is homogeneous. Therefore, its solution $T_{cl}(\xi)$ is linearly proportional to Q_{ts} in the whole domain. This linear relationship also holds at the end of the tip (ξ = 0), where the nano-thermocouple junction is located. Hence,

$$Q_{ts} = C\left(T_l(0) - T_c(0)\right) \tag{7}$$

where C is a proportionality constant whose dimension is [W/K]. From equations (2) and (7), the local temperature of the sample T_{sub} is

$$T_{sub}(0) = T_c(0) + \frac{C}{G_{ts}}\left(T_c(0) - T_l(0)\right) \tag{8}$$

Since equation (8) holds regardless of the location of the tip-sample contact x, the temperature profile of the sample is

$$T_{sub}(x) = T_c(x) + \varphi\left(T_c(x) - T_l(x)\right) \tag{9}$$

where φ is a dimensionless constant defined as C/G_{ts}, $T_{sub}(x)$ is the local temperature of the sample, and $T_{c,l}(x)$ is the temperature of the probe at the end of the tip ($\xi = 0$) in contact or lift mode when the tip-sample contact is made at x.

The derivation leading up to equation (9) is exact except for one assumption: that the value of h_{eff} in equation (3) is the same as that in equation (1). One possible approach to minimizing the error caused by this assumption is to keep the height for the lift mode scan as small as possible. However, this approach makes the measurement quite difficult, and cannot remove the error completely.

Another more effective approach can be explained using Figure 2. As a heater line used as a sample moves closer to the end of the SThM tip, the temperature measured by the thermocouple probe rises almost linearly until the sample makes contact with the end of the SThM tip. Therefore, the temperature that would be measured at the height of zero just before the tip-sample contact is made can be obtained from the simple extrapolation of the temperatures measured at two different heights. Thus, we have

$$T_l(x) = T_{l_1} + \frac{\left[T_{l_1}(x) - T_{l_2}(x)\right] l_1}{l_2 - l_1} \tag{10}$$

where T_l is the local temperature just before the tip-sample contact is made, and T_{l1} and T_{l2} are the temperatures measured at lift heights l_1 and l_2, respectively.

Next, the local thermal conductivity of the sample can be obtained as follows. According to the theory of scanning spreading resistance microscopy [21], which is commonly used to measure the local electrical conductivity of semiconductors, the following relation is satisfied:

$$I = \frac{1}{R_{elec}}(V_{sub} - V_{ground}), \quad R_{elec} = \frac{1}{4a\sigma} \tag{11}$$

where I represents the electrical current through the tip-sample contact, R_{elec} is the electrical spreading resistance, V_{sub} is the voltage of the sample at the contact, V_{ground} is the ground voltage, a is the radius of the contact, and σ is the local electrical conductivity of the sample. As the driving potential of electrical current is voltage, the driving potential of heat flux is temperature. From this analogy, we see that the following relation is also satisfied:

$$Q_{ts} = \frac{1}{R_{th}}(T_{sub} - T_\infty), \quad R_{th} = \frac{1}{4ak} \tag{12}$$

where Q_{ts} represents the heat flux through the tip-sample contact, R_{th} is the thermal spreading resistance, T_{sub} is the temperature of the sample at the contact, T_∞ is the temperature of the surroundings, a is the radius of the contact, and k is the local thermal conductivity of the sample.

Hence, from equations (7), (9), and (12), we obtain

$$\frac{1}{k} = \frac{4a}{C}\left[\frac{T_c - T_\infty}{T_l - T_c} - \frac{C}{G_{ts}}\right] \tag{13}$$

In terms of the thermoelectric voltage measured from the SThM probe, equation (13) can be rewritten as

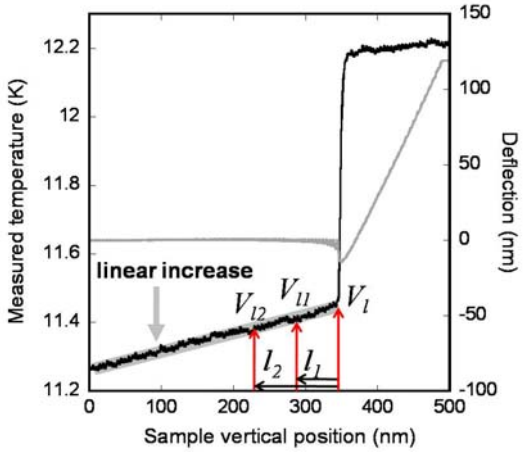

Figure 2. Cantilever deflection and temperature measured by SThM probe as a function of the vertical position of a heater line used as a sample.

$$\frac{1}{k} = \frac{4a}{C}\left[\frac{V_c + (T_b - T_\infty)S}{V_l - V_c} - \frac{C}{G_{ts}}\right] \tag{14}$$

where S is the thermopower of the thermocouple junction of the SThM probe. Hence, by measuring V_l and V_c, we can obtain the local thermal conductivity of the sample.

EXPERIMENTAL RESULTS

Quantitative temperature profiling

The experimental setup for quantitative temperature profiling is depicted in Figure 3 (a), and consists of a preamplifier, a signal access module (SAM), a SThM probe, and a scanning probe microscope (SPM). Scanning electron microscope (SEM) pictures of the SThM probe used in this experiment are shown in Figure 1 (b). To reduce the heat transfer through the air and the cantilever, the height of the probe tip was increased to 12 μm and the cantilever material was changed from silicon nitride to silicon oxide, whose thermal conductivity is much lower than that of silicon nitride. The design and fabrication of this probe is reported in [22]. Since the dimensionless constant φ defined as C/G_{ts} in equations (8) and (9) differs for each SThM probe, it should be measured for each probe [20]. The dimensionless constant φ for the probe used in this experiment is 10.9 K/K, as shown in Figure 3 (c).

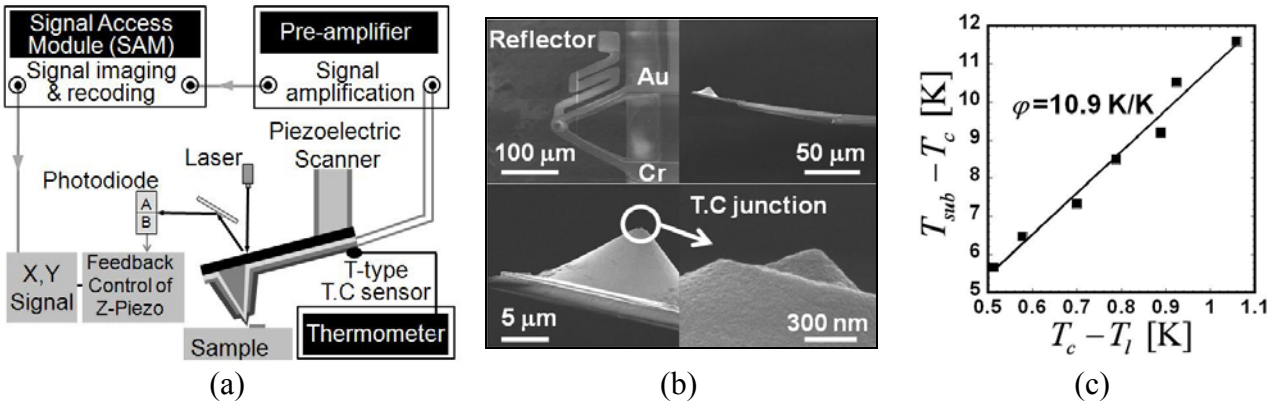

(a) (b) (c)

Figure 3. (a) Schematic diagram of experimental setup for temperature profiling. (b) SEM images of full SiO2 SThM probe: top view (upper left), side view (upper right), probe tip (lower left), thermocouple junction (lower right). (c) The difference between the temperature of the sample and that measured in contact mode as a function of temperature jump during tip-sample contact.

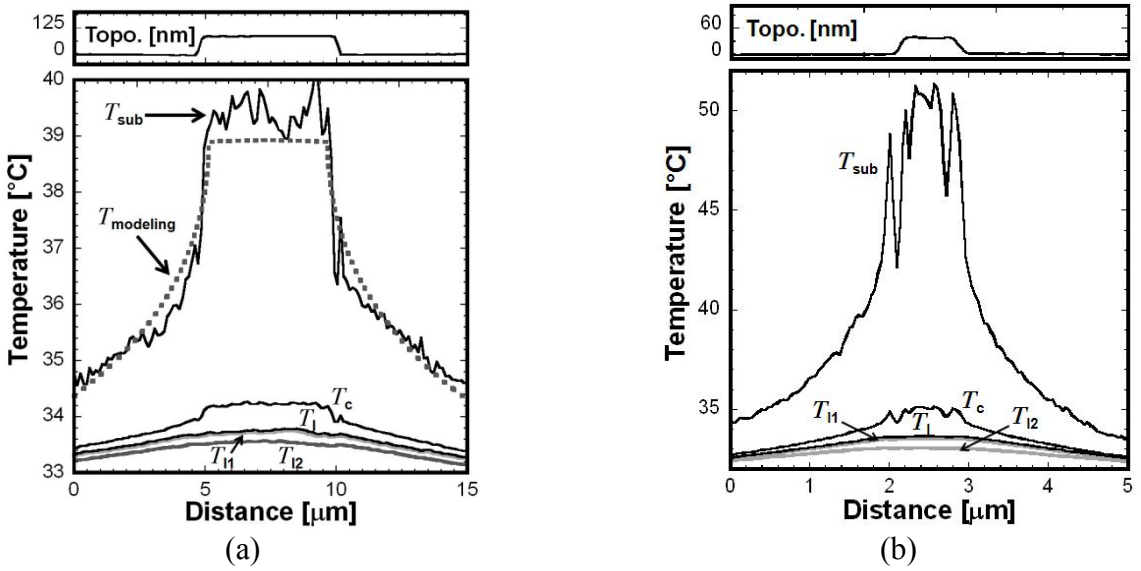

Figure 4. The temperature profile around an electrically heated aluminum line measured in contact mode T_c, the profiles obtained at lift heights of l_1 and l_2 T_{l1} and T_{l2}, the profile obtained by equation (10) T_l, and the temperature profile of the substrate obtained by equation (9) T_{sub} (a) for 5 μm wide line (b) for 500 nm wide line.

The temperature profile around an electrically heated aluminum line measured in contact mode T_c, the profiles obtained at lift heights of l_1 and l_2 T_{l1} and T_{l2}, the profile obtained by equation (10) T_l, and the temperature profile of the substrate obtained by equation (9) T_{sub} are compared in Figure 4. To confirm that the temperature profile is quantitatively correct, the temperature profile by modeling T_{model} was also compared for 5 μm wide aluminum line in Figure 4 (a). The amount of heat generation in the heater required in the modeling was obtained from the current and voltage applied to the aluminum line heater.

The temperature profile obtained using equation (9) is much closer to the modeling result than the profile obtained by direct contact mode measurement. Therefore, this technique has an advantage in quantitative temperature profiling using SThM by significantly reducing the influence of heat transfer through the air.

Quantitative thermal conductivity profiling

The experimental setup for quantitative thermal conductivity profiling is depicted in Figure 5 (a), which consists of a function generator, a preamplifier, a signal access module (SAM), a Wheatstone bridge circuit, a SThM probe, and a scanning probe microscope (SPM). The function generator was used to apply a high frequency ac bias to heat the thermocouple of the SThM probe. The Wheatstone bridge was used to remove the dominant ac voltage, and thereby improve the measurement sensitivity of the dc thermoelectric voltage generated from the thermocouple junction of the SThM probe. The dc thermoelectric voltage from the thermocouple junction was fed into the SAM and became simultaneously available with the topography signal of the SPM.

The heating of the thermocouple junction of the SThM probe is not exactly point-heating, because the junction of the probe is heated by the Joule effect. However, the current density increased approaching the junction and eventually maximized at the junction, whose diameter is about 350 nm for the particular probe used. Since the temperature peaked sharply at the junction (where the thermoelectric signal is measured), this technique is very close to a point-heating and point-sensing scheme.

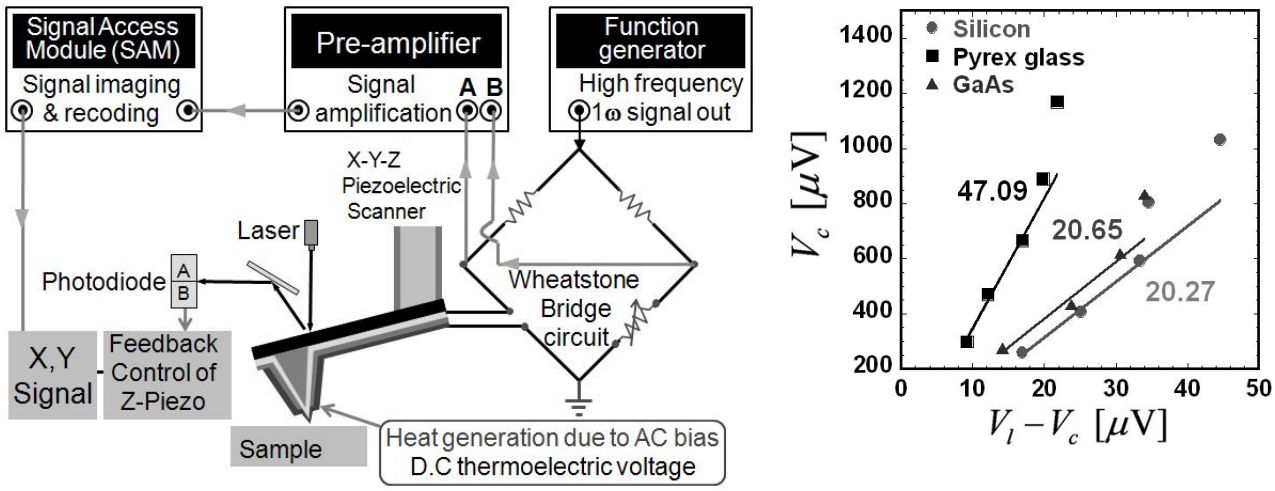

(a) (b)

Figure 5. (a) Schematic diagram of experimental setup for thermal conductivity profiling. (b) Thermoelectric voltage generated from the thermocouple junction of the probe in contact with sample V_c as a function of the difference between the one in lift mode and the one in contact V_l - V_c.

In order to obtain local thermal conductivity quantitatively from equation (14), we determined C/a and a dimensionless constant C/G_{ts}. To do so, we rewrote equation (14) as

$$V_c = \left(\frac{C}{4ak} + \frac{C}{G_{ts}} \right) (V_l - V_c) - (T_b - T_\infty) S \tag{15}$$

and determined these two constants experimentally from the proportionality of V_c with respect to V_l - V_c. Silicon and Pyrex glass were used as the samples because their thermal properties are well known. The experimentally-obtained relation between V_c and V_l - V_c is shown in Figure 5 (b). From Figure 5(b), C/a and C/G_{ts} were determined to be 151 W/m-K and 20.0 K/K, respectively, for this particular probe. To ensure that these constants are valid, the same experiments were carried out for a GaAs sample whose thermal properties are also well known. The experimentally-obtained slope and the slope obtained from equation (15) match quite closely.

To estimate the spatial resolution of our technique, the thermal conductivity distributions across the samples, within which a thin silicon oxide layer was sandwiched between single crystal silicon layers, are profiled as shown in Figure 6. From the C/a and C/G_{ts} values measured above for this particular probe, and V_l and V_c, the thermal conductivity profiles were obtained using equation (14).

For the sample of 1.4 μm silicon oxide layer with tip-sample contact made only on the silicon oxide layer, thermal conductivity was measured to be around 1.4 W/m-K, which is known to be that of silicon oxide, as shown in Figure 6 (a). Hence, we show that this technique is quantitative. However, we also note that near the interface of silicon and silicon oxide, the measured thermal conductivity changes rather smoothly. This appears to be because, while the tip is positioned near the interface, both the silicon and silicon oxide regions are within the tip-sample contact and influence the heat flux from the tip to sample, as shown in Figure 6.

To estimate the spatial resolution of this technique more accurately, the thermal conductivity distributions across the samples with 200 nm-thick and 100 nm-thick silicon oxide layers were also obtained, and are shown in Figure 6(b) and (c) respectively. For the 200 nm-thick sample, the thermal conductivity of silicon oxide could be measured quantitatively near the center of the silicon oxide layer. However, for the 100 nm-thick sample, the measured thermal conductivity was not quantitatively correct, although the SThM probe could detect a region of lower thermal conductivity. From these results, the spatial resolution of this particular probe for quantitative measurement seems to be about 150 nm.

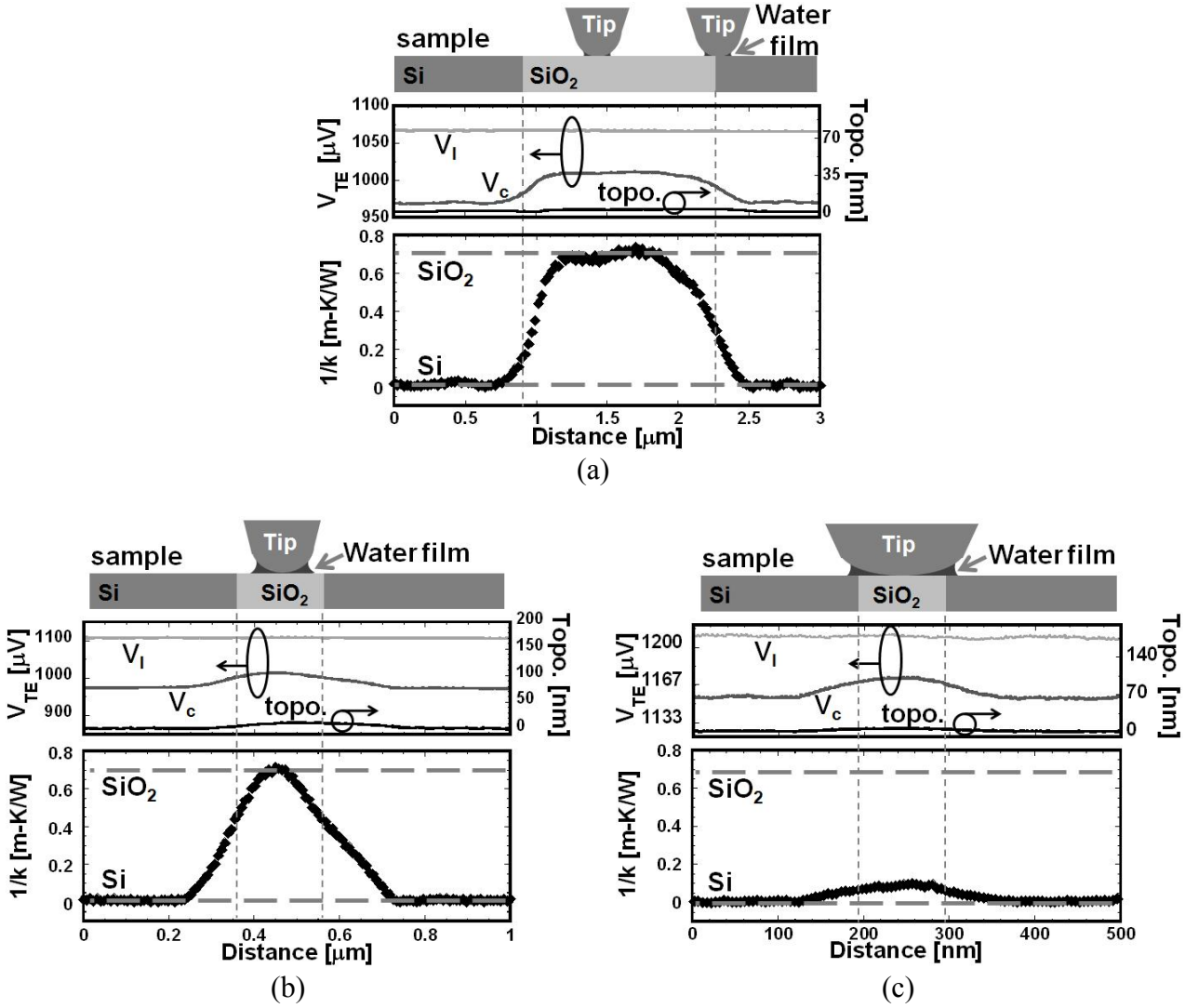

Figure 6. Thermoelectric voltage profile generated from the thermocouple junction of the SThM probe in lift mode V_l, the profile in contact mode V_c, the topography of the sample (upper), the thermal conductivity profile converted from V_c and V_l using equation (14) (lower) for (a) 1.4 μm-thick silicon oxide sample. (b) 200 nm-thick silicon oxide sample. (c) 100 nm-thick silicon oxide sample

CONCLUSIONS

In this study, we developed a quantitative temperature and thermal conductivity profiling technique which eliminates the influence of heat transfer through the air, and measures the temperature and thermal conductivity of a sample from the tip-sample heat transfer only, operating thermocouple SThM probe in both passive and active modes. The principle of our technique was explained through a rigorous analysis of the heat transfer phenomena occurring during measurement. We experimentally determined two characteristic constants of the particular SThM probe used. The spatial resolution of this technique was demonstrated by obtaining the thermal conductivity profiles of samples in which a thin silicon oxide layer was sandwiched between single crystal silicon layers. For samples with a 1.4 μm-thick silicon oxide layer and a 200 nm-thick oxide layer, the thermal conductivity distributions were quantitatively profiled. However, for a sample with a 100 nm-thick silicon oxide layer, the obtained profile was not quantitative. From the experimental results obtained thus far, the quantitative spatial resolution of this technique is estimated to be around 150 nm. In order to further improve spatial resolution, the tip radius of the completed thermocouple SThM probe should be decreased.

REFERENCES

1. Majumdar, A., Scanning Thermal Microscopy, *Annu. Rev. Mater. Sci.*, Vol. 29, pp 505-585, 1999.
2. Pollock, H. M. and Hammiche, A., Micro-Thermal Analysis: Techniques and Applications, *J. Phys. D*, Vol. 34, pp R23-R53, 2001.
3. Lai J. et al., Thermal Detection of Device Failure by Atomic Force Microscopy, *IEEE Electron Device Lett.*, Vol. 16, pp 312-314, 1995.
4. Kwon, O. and Majumdar A., Cross-sectional Thermal Imaging of a Metal-Oxide-Semiconductor Field-Effect Transistor, *Microscale Thermophys Eng.*, Vol. 7, pp 349-354, 2003.
5. Shi, L. et al., Scanning Thermal Microscopy of Carbon Nanotubes Using Batch-fabricated Probes, *Appl. Phys. Lett.*, Vol. 77, No. 26, pp 4295–4297, 2000.
6. Luo, K. et al., Scanning Thermal Microscopy of a Vertical-Cavity Surface-Emitting Laser, *Appl. Phys. Lett.*, Vol. 71, No. 12, pp 1604-1606, 1997.
7. Choi, S. H. et al., the Effect of Electrode Heat Sink in Organic-Electronic Devices, *Appl. Phys. Lett.*, Vol. 93, 183301, 2008.
8. Haeberle, W. et al., Nanometer-scale Heat-Conductivity Measurements on Biological Samples, *Ultramicroscopy*, Vol. 106, pp 678-686, 2006.
9. Kwon, O. et al., Scanning Thermal Wave Microscopy (STWM), *J. Heat Transf.*, Vol. 125, No. 1, 2003.
10. Luo, K. et al., Sensor Nanofabrication, Performance, and Conduction Mechanisms in Scanning Thermal Microscopy, *J. Vac. Sci. Technol. B* , Vol. 15, No. 2, pp 349–360, 1997.
11. Shi, L. et al., Thermal Transport Mechanisms at Nanoscale Point Contacts, *J. Heat Transf.*, Vol. 124, No. 2, pp 329-337, 2002.
12. Roh, H. H. et al., Novel Nanoscale Thermal Property Imaging Technique: The 2 omega Method. I. Principle and the 2 omega Signal Measurement, *J. Vac. Sci. Technol. B*, Vol. 24, pp 2398-2404, 2006.
13. Roh, H. H. et al., Novel Nanoscale Thermal Property Imaging Technique: The 2 omega Method. II. Demonstration and Comparison, *J. Vac. Sci. Technol. B*, Vol. 24, pp 2405-2411, 2006.
14. Shi, L. et al., Design and Batch Fabrication of Probes for Sub-100 nm Scanning Thermal Microscopy, *J. Microelectromech. S.*, Vol. 10, No. 3, pp 370-378, 2001.
15. Ruiz, F. et al., Determination of the Thermal Conductivity of Diamond-like Nanocomposite Films Using a Scanning Thermal Microscope, *Appl. Phys. Lett.*, Vol. 73, No. 13, pp 1802-1804, 1998.
16. Tsukruk, V. V. et al., Microthermal Analysis of Polymeric Materials, *Thermochim. Acta*, Vol. 395, pp 151-158, 2002.
17. Lefevre, S. et al., Thermal Conductivity Calibration for Hot Wire Based dc Scanning Thermal Microscopy, *Rev. Sci. Instrum.*,Vol. 74, No. 4, pp 2418-2423, 2003.
18. Fiege, G. B. M. et al., Quantitative Thermal Conductivity Measurements with Nanometre Resolution, *J. Phys. D: Appl. Phys.*, Vol. 32, No. 5, pp L13-L17, 1999.
19. Lefevre, S. et al., 3ω-scanning thermal microscope, *Rev. Sci. Instrum.*, Vol. 76, No. 3, 033701, 2005.
20. Kim, K. et al., Quantitative Scanning Thermal Microscopy Using Double Scan Technique, *Appl. Phys. Lett.*, Vol. 93, No. 20, 203115, 2008.
21. Mazur, R. G. and Dickey, D. H., A Spreading Resistance Technique for Resistivity Measurement on Silicon, *J. Electrochem. Soc.*, Vol. 113, pp 255-259, 1966.
22. Kim, K. et al., Thermal Design and Batch Fabrication of Full SiO_2 Probes for Sensitivity Improvement, *Proceedings of The Seventh JSME-KSME Thermal and Fluids Engineering Conference*, Sapporo, Japan, Oct. 13-16, 2008, H132.

HEAT TRANSFER IN PATIENTS UNDER HYPOTHERMIC CONDITIONS

F.E.M. Janssen, G.M.J. Van Leeuwen and A.A. van Steenhoven *
Department of Mechanical Engineering
Eindhoven University of Technology, the Netherlands

ABSTRACT. Most bio-heat transfer models for patients under hypothermic conditions contain three sub-models: a passive heat transfer model, an active coupling between local blood flow and temperature, and a pharmacological model to incorporate the effects of drugs. In this paper an illustrative example will be given focussed on scalp cooling to prevent chemotherapy induced hair loss. Scalp cooling can reduce hair loss. Unfortunately, the efficacy of scalp cooling varies strongly. A systematic evaluation of the current hypothesis for the hair preservative effect of scalp cooling is necessary for a better understanding of the various important parameters of scalp cooling. To quantify the contribution of the putative mechanisms of scalp cooling, a computational model was developed, partly based on experimental data. With the complete model, we evaluated the effect of several scalp cooling protocol parameters.

Keywords: *Bio-heat transfer, Scalp cooling, Pharmacokinetic model*

INTRODUCTION

Chemotherapy induced hair loss is a feared side effect of cancer treatment [1]. Scalp cooling during the administration of cytotoxic drugs can reduce this hair loss [2]. Cooling can be achieved by means of a cap, that is pre–cooled in a freezer or that exchanges coolant with a reservoir. The current hypothesis for the hair preservative effect of scalp cooling is that cooling of the scalp skin reduces blood flow (perfusion) and chemical reaction rates [3]. Reduced perfusion leads to less cytotoxic drugs available for uptake, while the reduced temperature decreases uptake of and damage by chemotherapy. Altogether, less damage is done to the hair cells, and the hair is preserved.

To support this hypothesis, we conducted a series of in vitro biological cell experiments in an earlier study [4], in which local tissue concentrations were related to cell damage at different temperatures. A typical result is given in figure 1. Cell survival significantly increased with decreasing doxorubicin concentrations. When compared to an exposure temperature of 37°C, a decrease in temperature also has a significant increasing effect on cell survival. No significant differences were found between exposure temperatures of 22°C and 10ºC. At a concentration of 0.5 µg ml^{-1}, cell survival increased from 41% (37°C) to 85% and 89% by reducing temperature to 22°C and 10°C, respectively.

However, the effect of scalp cooling in clinical practice varies strongly [5]. A systematic evaluation of the current hypothesis is necessary for a better understanding of the various important parameters of scalp cooling.

* Corresponding author: Prof. A.A. van Steenhoven
Phone: + (31)-40-2472132, Fax: + (31)-40-2475399
E-mail address: a.a.v.steenhoven@tue.nl

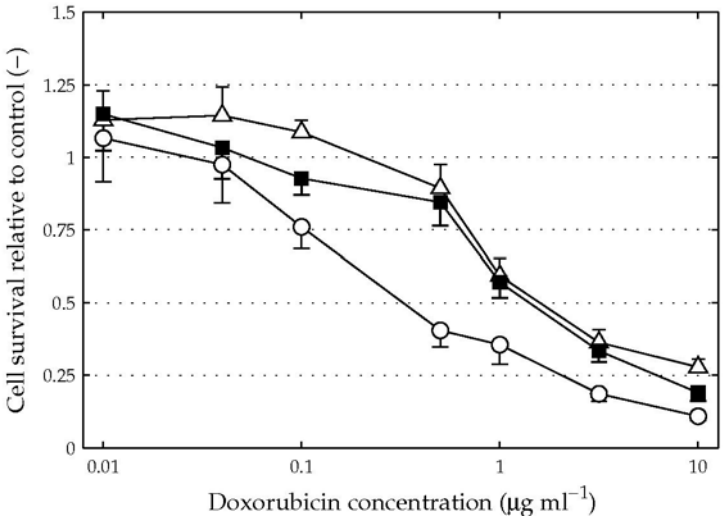

Figure 1. Cell viability as a function of doxorubicin concentration and exposure temperature Δ= T_L (10ºC), ■= T_M (22ºC) and ○ = T_H (37ºC). Data points show the mean and standard error of 8 replicates. The fits are shown for 37ºC (—), 22ºC (-·-) and 10ºC (--). Adapted from [4]

In the present study, we want to quantify the contribution of the putative mechanisms by which scalp cooling prevents hair loss. To that end, a computational model has been developed based on the current hypothesis of the mechanisms of scalp cooling. The full computational model consists of sub–models that describe heat transfer in the human head, perfusion through the scalp skin as function of temperature and transport of doxorubicin (a specific chemotherapy agent) in the human body. Experiments have validated and improved the different computational models. As the heat transfer model and the skin perfusion relation is already published elsewhere [6, 7], we will here mainly focus on the pharmacokinetic model.

METHODS

Heat transfer model

Although more complicated models can be used to analyze heat transfer in perfused tissues [8], in this study a one dimensional heat transfer model was used, that uses the Pennes' equation to describe heat transfer in the human head during scalp cooling. The model consists of several tissue layers, representing the brain, skull, fat, skin, hair and cold cap. Model properties are shown in table 1, in which q_m represents the metabolic heat production and w_b the perfusion. For a more detailed description of the heat transfer model of the head, the reader is referred to [6]. Parameter studies with the heat transfer model showed that key parameters that determine the actual skin temperature during scalp cooling are the size of both the sub–cutaneous fat–layer and the hair–layer.

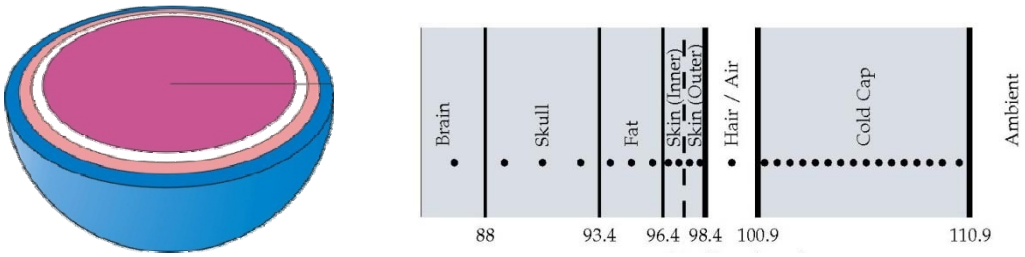

Figure 2. Schematic representation of the outer part of the heat transfer model

Table 1
Thermophysical Tissue Parameters used in the Heat Transfer Model (from [6])

	d (mm)	k (W/m·K)	c (J/ kg·K)	ρ (kg/m^3)	q_m (W/m^3)	w_b (kg/m^3·s)
Brain	88.0	0.5	3800	1000	8800	8.5
Skull	5.4	1.0	1700	1500	130	0.150
Fat	3.0	0.2	2390	1050	130	0.2
Inner skin	1.0	0.384	3570	1130	500	1.5
Outer skin	1.0	0.384	3570	1130	0	0.0
Hair	2.5	0.04	1000	1	0	0.0
Cold Cap	10.0	0.500	4300	1000	0	119.0

Relationship between temperature and blood flow

As an input in the heat transfer and pharmacokinetic models a relation is needed between local skin temperature and local skin perfusion. In an earlier study [7], we established such a relationship using laser Doppler flowmetry and thermocouple measurements and the result is given in figure 3.

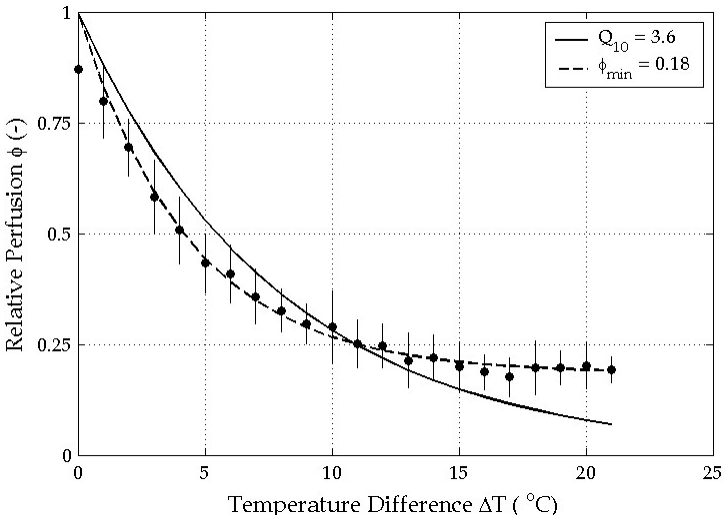

Figure 3. Average temperature difference and perfusion and best fits for minimum perfusion, Φ_{min}(—) and Q_{10} (--). Adapted from [8].

Relative perfusion as a function of the temperature difference appeared to be well described by:

$$\emptyset_w = \frac{w_b}{w_{b,0}} = \emptyset_{min} + (1 - \emptyset_{min}) e^{\left(-\frac{T_0 - T}{\Theta}\right)} \quad (1)$$

in which $w_{b,0}$ and T_0 are the perfusion and temperature in neutral state. The limit in perfusion, Φ_{min}, was found to be equal to 18%, and the rate of change, Θ, was found to be equal to 4.3ºC, indicating that 95% of the drop in perfusion is reached for a temperature difference of approximately 13ºC.

Pharmacokinetic model

An eight–compartment physiologically based pharmaco-kinetic (PBPK-) model for doxorubicin was developed. It is largely based on a previous model for doxorubicin [9], with some modifications. A schematic of this model is shown in figure 4.

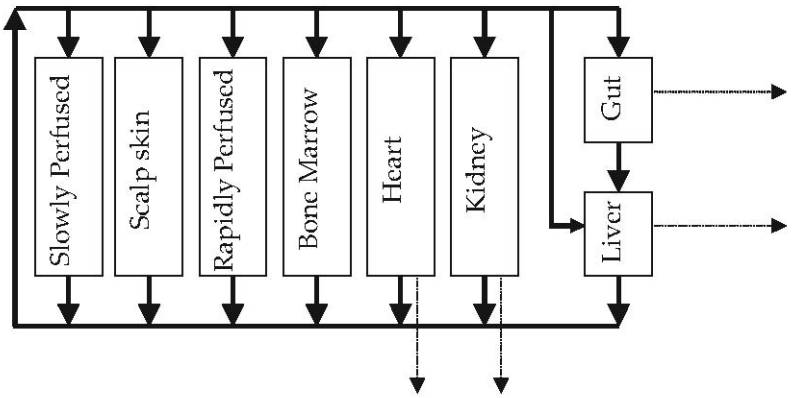

Figure 4. Schematic representation of the PBPK model for doxorubicin.
Solid lines represent the blood circulation, dashed lines represent the metabolic and excretory pathways that eliminate doxorubicin from the body. Adapted from [9].

The standard model represents a female with a body mass of 70 kg and a body height of 1.67 m, which is in agreement with the mean of the Dutch female population in 2002. For each compartment, a generic tissue mass balance for doxorubicin is formulated:

$$\frac{dA_T}{dt} = W_B (C_A - C_V) - M \tag{2}$$

in which A_T (mol) is the amount of doxorubicin in the tissue, W_B (m^3 s^{-1}) is the volumetric blood flow rate through the tissue, C_A and C_V (mol m^{-3}) are the arterial concentration entering the tissue and the venous concentration leaving the tissue, respectively, and M (mol s^{-1}) is the rate of metabolism and/or excretion of doxorubicin in the tissue. Values for blood flow and tissue volume used in the standard model are shown in table 2.

Table 2
Tissue Properties used in the Pharmacokinetic Model.

	W_B (1/min)	V_T (l)	T_{DNA} (μM)	T_{CAL} (μM)
Liver	0.35 ± 0.05	1.82 ± 0.28	23.7 ± 2.3	44.6
Heart	0.26 ± 0.04	0.35 ± 0.04	8.3 ± 4.0	43.8
Kidney	1.05 ± 0.08	0.28 ± 0.03	16.2 ± 2.2	52.3
Bone Marrow	0.29 ± 0.02	1.47 ± 0.14	19.1 ± 13.7	25
Gut	1.17 ± 0.11	1.19 ± 0.13	25.2 ± 2.3	25
Slowly Perfused	1.57 ± 0.15	51.2 ± 5	4.5	15
Scalp Skin	0.29 ± 0.03	2.89 ± 0.28	4.5 1	5
Blood	5.84	5.53	-	-

Values for perfusion and volume are obtained from [10], values for binding capacity are taken from [9]. Values are shown as mean ± standard deviation.

To account for saturable chemical-specific binding, a partitioning coefficient K_p was introduced [9], which relates the venous concentration to the tissue concentration:

$$C_V = \frac{1}{K_p} C_T \tag{3}$$

Here the partitioning coefficient is mathematically represented by [11]:

$$K_p = \left(1 + \frac{T_{DNA}}{K_{DNA} + C_T} + \frac{T_{CAL}}{K_{CAL} + C_T}\right) \tag{4}$$

with T_{DNA} and T_{CAL} the DNA and cardiolipin binding capacity available and K_{DNA} and K_{CAL} the binding affinities of doxorubicin to DNA and cardiolipin, respectively (see table 2), and C_T the doxorubicin tissue concentration $C_T = A_T/V_T$. The affinity constants for DNA and cardiolipin are set to K_{DNA} = 200 nM and K_{DNA} = 400 nM, respectively (see table 3).

Table 3
Body Properties used in the Pharmacokinetic Model.

Parameter	Symbol	Standard model
Body Mass [1]	m_b	70 kg
Height [1]	h_b	1.69 ± 0.2 m
BMI [1]	-	24.5 ± 1.7 kg m^{-2}
Surface Area	-	1.8 m2
Cardiac Output [2]	W_{CO}	5.8 l min^{-1}
Dox fraction bound to blood [3]	F_B	0.7
Affinity constant for DNA [3]	K_{DNA}	200 nM
Affinity constant for cardiolipin [3]	K_{CAL}	400 nM
Fraction renal blood flow cleared [3]	F_f	0.1

[1] Based on data obtained from Statistics Netherlands (CBS)
[2] Value obtained from [10] and [3] based on data from [9].

Binding to proteins in the blood is also accounted for. It is assumed that only unbound drug concentration in the blood C_A is available for uptake in the tissue – except for the liver, where total drugs C_{BL} is available for uptake. The fraction of doxorubicin that is bound to plasma proteins is equal to F_B =0.7 [9]. The blood compartment mass balance may now be specified as:

$$\frac{dA_B}{dt} = \sum_i W_{B,i} C_{V,i} - C_A W_{CO} - W_{B,L}(C_{BL} - C_A) \tag{5}$$

where $W_{CO} = \Sigma W_{B,i}$ is the total cardiac output. With A_B (mol) the amount of doxorubicin in the blood, the total arterial concentration C_{BL} and unbound arterial concentration C_A are defined as:

$$C_{BL} = \frac{A_B}{V_B}$$
$$C_A = C_{BL}(1 - F_B) \tag{6}$$

In some tissues doxorubicin is metabolized to non–harmful products. In the liver, kidney and the heart, doxorubicin is metabolized to doxorubicin aglycone (AG), which can be described by a linear process:

$$M_{AG} = K_{AG} C_T V_T \tag{7}$$

Other metabolic processes include the metabolism by aldo–keto reductase (AKR) to doxorubicinol in the liver and the kidney, and excretion in the faeces by P–glycoprotein (PGP) in the liver and the gut. Michaelis–Menten kinetics may be used to describe these processes:

$$M_{AKR,PGP} = \frac{V_{max-AKR,PGP} C_T}{K_{M-AKR,PGP} + C_T} \tag{8}$$

Finally, excretion of doxorubicin by filtration in the urine in the kidney compartment is modelled by:

$$M_f = P_f W_B C_A \tag{9}$$

Values for metabolic activity that are used in the pharmacokinetic model under standard conditions are shown in table 4. For each tissue compartment, see equations 2 and 5, a single ordinary differential equation (ODE) is obtained. The complete set of ODEs is solved using MATLAB.

Table 4
Doxorubicin Specific Metabolic and Excretory Parameters used in the pharmacokinetic model.

	AG[1]	AKR[2]		PGP[2]	
	K_m	K_m	V_m	K_m	V_m
Liver	12104	275	1804	10	300
Kidney	484	539	3161	10	100
Heart	760	-	-	-	-
Gut	-	-	-	0.2	80

[1] The first order rate constant K_m for metabolism to aglycone (AG) is expressed in (h^{-1} kg tissue^{-1}).
[2] The activities for aldo–keto reductase (AKR) and P–glycoprotein (PGP) are expressed as K_m (μM) and V_m (μmol h^{-1} kg tissue^{-1}).

RESULTS

Validation

Unfortunately, there is hardly any data available describing the doxorubicin concentration in time for individual organs in humans. Currently, only blood serum levels in time are available in literature. This means that the results of the model can only be compared to these blood serum levels, and that the model cannot be validated on the scale of individual organs. However, the concentration in the blood serum is a direct result of the distribution, metabolism and excretion of doxorubicin in individual organs. When the model accurately predicts blood serum levels, it is very likely that the concentration levels in each individual organ are of the correct order. Therefore, we compared blood serum levels from the study of Andersen [12] with results from our model. Figure 5 shows the blood plasma concentration (mean ± SD) of 24 patients receiving a dose of 50 mg m^{-2} as a 10 minute infusion. The results of our model describe the measured data well; peak concentration, first half–life time and final half–life time are predicted within the range of intra–individual variation.

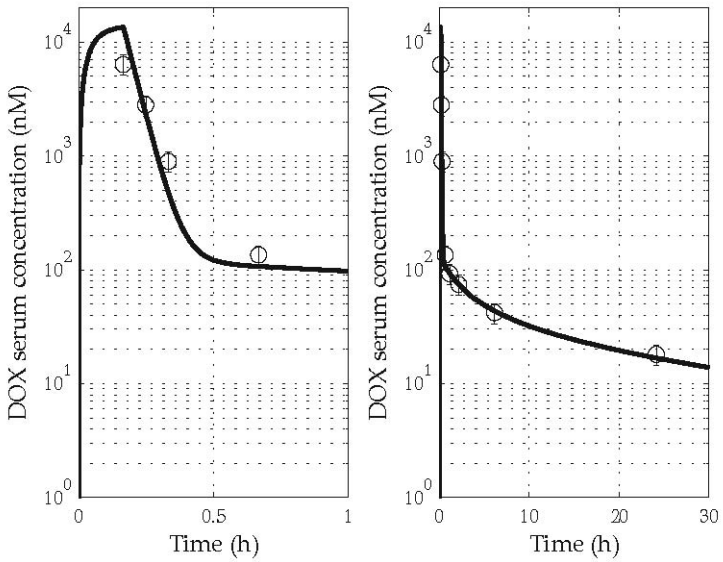

Figure 5: Blood plasma concentrations obtained by the pharmacokinetic model (–) compared to the average blood plasma concentration (○, mean ± SD) of 24 patients receiving a dose of 50 mg m^{-2} [12]. The left figure shows a time range of 30 hours, the right figure shows the first hour only.

Scalp cooling under standard conditions

The model was used for a first investigation of the effects of scalp cooling on local scalp skin concentrations. A standard chemotherapy procedure was modelled, in which the patient receives a total dose of 75 mg m^{-2} doxorubicin, intra–venously administered in a period of 2 hours. The effect of scalp cooling was compared to no cooling. In the scalp cooling case, perfusion to the scalp skin was reduced to 20% during administration of chemotherapy and the subsequent 2 hours, for a total period of 4 hours. The results of these simulations are shown in figure 6.

Blood serum levels are continuously high during the 2 hours of administration, after which they show a rapid fall. The concentration in the scalp skin is a little higher than the blood serum concentration and it stays relatively high for the complete simulation period. Doxorubicin concentration in the scalp is significantly lower when scalp cooling is applied, compared to no scalp cooling. After a certain period, no distinction in scalp skin concentration can be made between the two cases. When no cooling is applied, the maximum concentration in the scalp is equal to 1.66 μg ml^{-1} and the average concentration during the first 24 hours is 0.61 μg ml^{-1}. With scalp cooling, the maximum concentration is 0.48 μg ml^{-1} and the average concentration equals 0.38 μg ml^{-1} . Thus, reducing the perfusion by a factor of 5, see figure 3, reduces the maximum concentration by a factor of 3.5 and the average concentration by a factor of 1.6. As seen from figure 1, such a reduction can have a notable effect on cell survival.

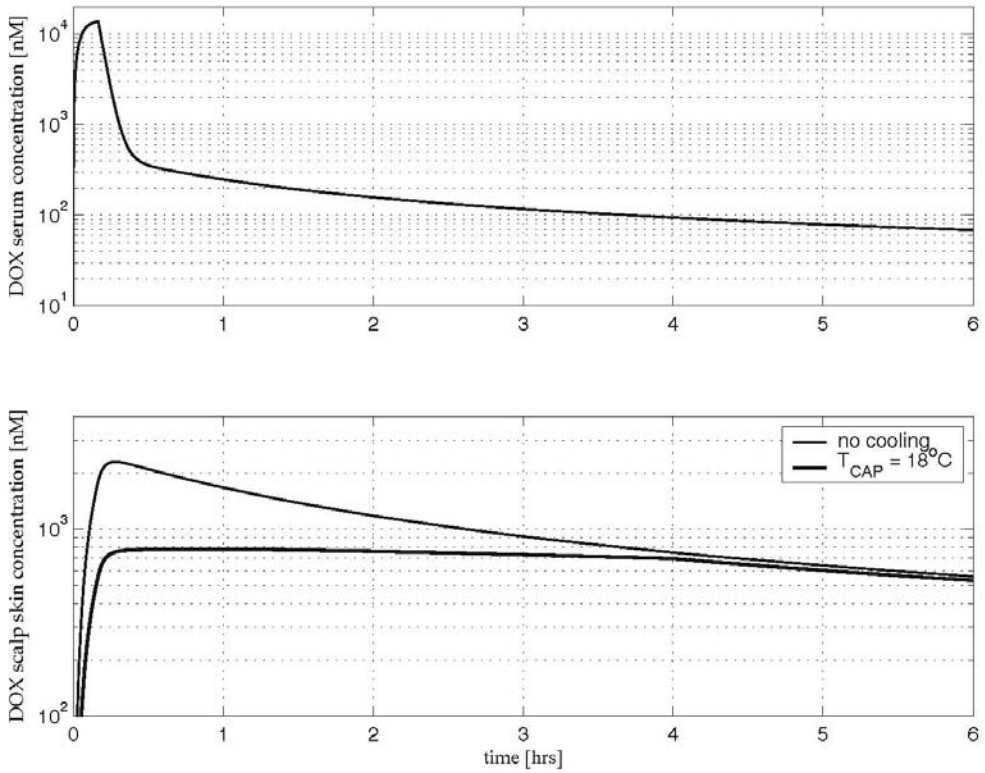

Figure 6: Model prediction of doxorubicin serum levels C_{serum} (top) and scalp skin concentration C_{scalp} (bottom) after a 2 hour intra– venous administration of a total dose of 75 mg m^{-2} doxorubicin. The bottom figure shows the effect of cooling the scalp to 19.2°C for 4 hours during administration on scalp skin concentration, compared to no cooling at all.

Parameter study

In a parameter study we investigated some important parameters in the physiologically based pharmacokinetic model for doxorubicin, see also [13]. The effect of these parameters on maximum and average scalp skin concentration during scalp cooling was evaluated. In the simulations, we used a skin temperature of T = 19.2ºC and a minimum perfusion value of Φ_{min} = 0.20. As an example, values used and results for tissue perfusion are shown in table 5. Changes in these perfusion rates are compensated by changing perfusion or volume of the rapidly perfused compartment, such that cardiac output and total body volume of the model remain the same. When the standard deviation was unknown, we used the mean value and a variation of 20% to define the lower and upper limit.

The parameter study [13] shows that the most important parameters influencing maximum doxorubicin concentration in the scalp skin during scalp cooling are the perfusion of both the scalp skin and the liver, the body mass, the body height and the fraction of doxorubicin bound to the blood. Maximum modelled doxorubicin concentration is 0.56 μg ml-1, for an increase in scalp skin perfusion from 0.23 to 0.35 l min^{-1}. A decrease in perfusion to 0.23 l min^{-1} results in a concentration of 0.42 g ml^{-1}, which is the lowest peak concentration in the parameter study. This influence of perfusion was as expected, since the concentration is flow limited. The influence on average doxorubicin concentration in the scalp skin is a bit lower, however, seeing that results range from 0.35 to 0.40 μg ml^{-1}.

Table 5
Effect of Changes in Tissue Perfusion (W_B) on Maximum Scalp Skin Concentration (C_{max}) and Average Scalp Skin Concentration C_{avg} during Cooling (T = 19.2°C, Φ_w =0.27).

	W_B (l min^{-1})		C_{max} (μg ml^{-1})		C_{avg} (μg ml^{-1})	
	down	up	down	up	down	up
Liver	0.25	0.45	0.52	0.45	0.40	0.35
Heart	0.18	0.34	0.49	0.47	0.38	0.37
Kidney	0.89	1.21	0.50	0.47	0.39	0.36
Bone marrow	0.25	0.33	0.48	0.48	0.38	0.38
Gut	0.95	1.37	0.51	0.46	0.39	0.36
Slowly perfused	1.27	1.87	0.50	0.47	0.37	0.38
Scalp skin	0.23	0.35	0.42	0.56	0.35	0.39

Up and down correspond to increasing or decreasing a parameter, respectively. Responses of the model under standard conditions are C_{max} = 0.48μg ml^{-1} and C_{avg} =0.38 μg ml^{-1}

CONCLUSION AND DISCUSSION

In this paper, we developed a computational model for mass transport of chemotherapy in the human body during scalp cooling. Doxorubicin is used as a chemotherapeutic agent. In the model, we used a lumped–parameter approach with the assumption that doxorubicin exhibits flow–limited characteristics. Comparisons of the pharmacological model of doxorubicin to plasma concentration data showed that the model was able to predict these concentrations well. Therefore, the model was used to investigate the effect of scalp cooling, especially the effect of reduced tissue perfusion, on local tissue concentrations.

The results of the model show that during scalp cooling, maximum tissue concentrations may be reduced by a factor of 3.5 when perfusion is reduced by a factor of 5. The average concentration was reduced by a factor of 1.6. As illustrated in figure 1, these reductions can have a dramatic influence on cell survival, especially when an additional effect of temperature on metabolism is present. The parameter study showed that important parameters in the model are the perfusion of both the scalp skin and the liver, the body mass and the body height. Other important parameters are the fraction of doxorubicin bound to the blood and the volume of the scalp skin.

One limitation of the pharmacological model used is that the only effect of scalp cooling that is modelled is reduced tissue perfusion. Due to cooling, mass transfer characteristics may change. In a study on the temperature dependent dermal absorption of chloroform, a large decrease in skin permeability with decreasing temperature was found [14]. In our model, the effect of reduced temperature might be modelled using a temperature dependent partition coefficient K_p (see equation 4). For this, however, knowledge of the temperature dependency of these coefficients for doxorubicin is needed. Currently, this data is unavailable. Therefore, any reduced uptake of doxorubicin due to reduced temperature is unaccounted for in the current model. This means that predicted tissue concentrations by the model might be higher than in reality.

In parallel studies, we are now extending the developed model to complete cooling of patients undergoing cardiac surgery with the emphasis on influence of anaesthesia [15,16] and individualised human thermoregulation [17].

REFERENCES

1. Katsimbri, P., Bamias, A. and Pavlidis, N., Prevention of chemotherapy-induced alopecia using an effective scalp cooling system, *Eur. J. Cancer,* 36, 766–771, 2000
2. Protiere, C., Evans, K., Camerlo, J., d'Ingrado, M.P., Macquart-Moulin, G., Viens, P., Maraninchi, D. and Genre, D., Efficacy and tolerance of a scalp-cooling system for prevention of hair loss and the experience of breast cancer patients treated by adjuvant chemotherapy, *Support Care Cancer,* 10, 529–537, 2002
3. Bulow, J., Friberg, L, Gaardsting, O. and Hansen, M., Frontal subcutaneous blood flow, and epi-and subcutaneous temperatures during scalp cooling in normal man Scand. *J. Clin. Lab. Invest.,* 45, 505–508, 1985
4. Janssen, F.E.M., Bouten, C.V.C., van Leeuwen, G.M.J. and van Steenhoven, A.A., Effects of temperature and doxorubicin exposure on keratinocyte damage in vitro*, In Vitro Cell Dev. Bio.l Anim.*, 44, 81-86, 2008
5. Grevelman, E.G. and Breed, W.P.M., Prevention of chemotherapy-induced hair loss by scalp cooling*, Ann. Oncol.,* 16, 352-358, 2005
6. Janssen, F.E.M. and Van Leeuwen, G.M.J. and van Steenhoven, A.A., Modelling of temperature and perfusion during scalp cooling, *Phys. Med. Biol.,* 50, 4065–4073, 2005
7. Janssen, F.E.M., Rajan, V., Steenbergen, W., van Leeuwen, G.M.J. and van Steenhoven, A.A., The relationship between local scalp skin temperature and cutaneous perfusion during scalp cooling, *Physiol. Meas*., 28, 829-839, 2007
8. Stanczyk, M., Van Leeuwen, G.M.J. and van Steenhoven, A.A., Discrete vessel heat transfer in perfused tissuemodel comparison, *Phys. Med. Biol.* 52 1–13, 2007
9. Gustafson, D., Rastatter, J., Colombo, T. and Long, M., Doxorubicin pharmacokinetics: Macromolecule binding, metabolism, and excretion in the context of a physiologic model, *J. Pharm. Sc.,* 91, 1488–1501, 2002
10. Brown, R., Delp, M., Lindstedt, S., Rhomberg, L. and Beliles, R., Physiological parameter values for physiologically based pharmacokinetic models, *Tox. Ind. Health,* 13, 407–484, 1997
11. Leung, H., Paustenbach, D., Murray, F., and Andersen, M., A physiological pharmacokinetic description of the tissue distribution and enzyme-inducing properties of 2,3,7,8-tetrachlorodibenzo-p-dioxin in the rat. *Toxicology and Applied Pharmacology*, 103, 399–410, 1990.
12. Andersen, A., Holte, H. and Slørdal, L., Pharmacokinetics and metabolism of doxorubicin after short–term infusions in lymphoma patients, *Cancer Chem. Pharm.* 44, 422–426, 1999
13. Janssen, F.E.M., Modelling physiological and biological aspects of scalp cooling, Eindhoven University of Technology, *PhD thesis*, 2007
14. Corley, R., Gordon, S., and Wallace, L., Physiologically based pharmacokinetic modelling of the temperature–dependent dermal absorption of chloroform by humans following bath water exposures. *Toxicological Sciences*, 13–23, 1953
15. N.M.W. Severens, W. van Marken Lichtenbelt, A.J.H. Frijns, A.A. van Steenhoven, B.A.J.M. de Mol, D.I. Sessler, A model to predict patient temperature during cardiac surgery, *Phys. Med. Biol.,* 52, 5131-5145, 2007
16. N.M.W. Severens, W. van Marken Lichtenbelt, G.M.J. van Leeuwen, A.J.H. Frijns, A.A. van Steenhoven, B.A.J.M. de Mol, H.B. van Wezel, D.J. Veldman, Effect of forced-air heaters on perfusion and temperature distribution during and after open heart surgery, *Eur J Cardiothorac Surg*, 32, 888-895, 2007
17. W. van Marken Lichtenbelt, A.J.H. Frijns, A.M.J. van Ooijen, D. Fiala, A.M. Kester , A.A. van Steenhoven, Validation of an individualized model of human thermoregulation for predicting responses to cold air, *Int. J. Biometeorology*, 51, 169-179, 2007

MOLECULAR TRANSPORT PHENOMENA AND THE KINETIC BOUNDARY CONDITION AT THE VAPOR-LIQUID INTERFACE

S. Fujikawa*
Division of Mechanical and Space Engineering, Hokkaido University, Sapporo, Japan

ABSTRACT. The kinetic boundary condition at the interface of a vapor and its condensed phase for the Boltzmann equation, and evaporation and condensation coefficient are discussed in detail on the basis of the author's recent studies. By molecular dynamics simulations, the kinetic boundary condition is found to be the product of three one-dimensional Maxwellian distributions for the three velocity components of vapor molecules and a factor including a well-defined condensation coefficient. The condensation coefficient of water is successfully determined by fusing experimental data acquired by the shock tube into numerical simulations of the Gaussian-BGK Boltzmann equation. It is found that, in conditions of weak condensation near the equilibrium state, the condensation coefficient of water is equal to the evaporation coefficient (=unity) evaluated by molecular dynamics simulations at the equilibrium state and it decreases as the vapour-liquid system deviates from the equilibrium state. The boundary conditions for the Navier-Stokes-type set of equations are also derived by the perturbation analysis.

Keywords: *evaporation, condensation, kinetic boundary condition, molecular dynamics, molecular gas dynamics*

INTRODUCTION

In fluid dynamics and molecular gas dynamics, boundary conditions are of paramount importance because they have relevance to the drag and lift exerted on bodies and heat and mass transfer across boundaries. Especially, in cases where the boundary condition is for the interface of a vapor and its liquid phase, it involves some difficult problems, which have been discussed for more than one century and are not yet made clear [1-3]. This is because the derivation of the boundary condition requires detailed information of molecular phenomena at the interface, whilst the governing equations (the Navier-Stokes equations in fluid dynamics and the Boltzmann equation in molecular gas dynamics) can be derived from macroscopic or microscopic conservation laws.

As shown in Fig. 1, the regions of both sides of the interface of a vapor and its liquid phase consist of three regions, i.e., (i) a transition region where the density varies continuously from the liquid phase to the vapor one, (ii) a nonequilibrium vapor region with a temporal scale of mean free time and a spatial one of mean free path, and (iii) a local equilibrium vapor region **(**continuum region**)**. The interface of the vapor and its liquid phase is defined as that between the transition region and the nonequilibrium region, and it is in a nonequilibrium state [4].

Physical phenomena in these regions obey different governing equations, e.g., molecular dynamics (MD) in the transition region, molecular gas dynamics in the nonequilibrium region, and fluid dynamics in

* Corresponding author: Prof. S. Fujikawa
Phone: + (81)-11-7066429, Fax: + (81)-11-7066429
E-mail address: fujikawa@eng.hokudai.ac.jp

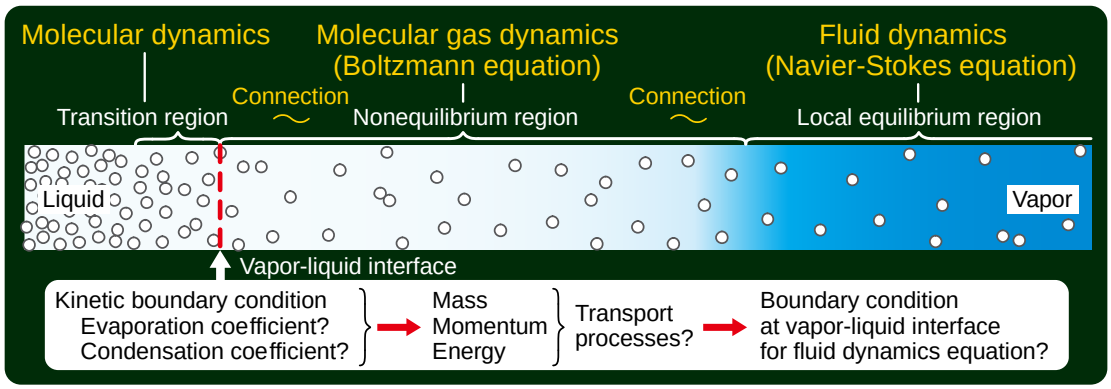

Figure 1. The interface of the vapor and its condensed phase, and the three regions of both sides of the interface. Physical phenomena in these regions obey different governing equations, molecular dynamics in the transition region, molecular gas dynamics in the nonequilibrium region, and fluid dynamics in the equilibrium region.

the equilibrium region. Gas flows accompanied with mass, momentum, and energy transport at the interface are accurately described by molecular gas dynamics based on the Boltzmann equation. Then, the Boltzmann equation requires the boundary condition called the kinetic boundary condition (KBC). The KBC has two problems unresolved [4]. One is whether or not the KBC available and believed reliable is physically correct. The other is that the KBC contains two unknown parameters called evaporation and condensation coefficient [3, 4]. These coefficients have been investigated for more than one century, and they have not been determined accurately [3,5,6].

Fujikawa and his group have long engaged in accurate determination of evaporation and condensation coefficient by their original method based on molecular dynamics and molecular gas dynamics where simulation data of the latter are fused with experimental ones acquired by a shock tube [7-11]. The present paper is concerned with the author's state-of-the-art studies of the boundary condition for the Boltzmann equation, the boundary condition for the Navier-Stokes-type set of equations, and the evaporation and condensation coefficient of water.

MOLECULAR DYNAMICS

Formulation of the kinetic boundary condition

In this section, using MD simulations, we present a new KBC for the Boltzmann equation at the stationary interface of argon vapor and its condensed phase. The conventional KBC available and believed reliable, an only model, is [3, 12]:

$$f^{\text{out}} = [\alpha\rho^* + (1-\alpha)\sigma]\hat{f}^*(T_\ell) \qquad (\xi_z > 0), \tag{1}$$

$$\sigma = -\sqrt{\frac{2\pi}{RT_\ell}}\int_{\xi_z<0}\xi_z f^{\text{coll}} d\xi, \tag{2}$$

where f^{out} is the velocity distribution function of molecules leaving the interface, $\rho^*\hat{f}^*(T_\ell) = \rho^*\exp[-(\xi_x^2+\xi_y^2+\xi_z^2)/(2RT_\ell)]/[(2\pi RT_\ell)^{3/2}]$ is the equilibrium distribution function with the saturated vapor density ρ^* at the temperature of the condensed phase T_ℓ, f^{coll} is the distribution function of molecules incident on the interface, ξ_x and ξ_y are the molecular velocity components tangential to the interface, ξ_z is the normal component, R is the gas constant per unit

mass, and α is a parameter between zero and unity. The simpleness of equation (1) with (2) is suitable for analytical studies and a number of problems have been solved with this KBC [3, 12, 13].

However, equation (1) assumes, without being verified, that f^{out} is in proportion to $\hat{f}^*(T_\ell)$. On this assumption, the lack of necessary information of phenomena at the interface is augmented by the introduction of a parameter α ; the mass flux across the interface is then given as $\alpha(\rho^* - \sigma)\sqrt{RT_\ell/(2\pi)}$. Historically, α has been called the condensation coefficient and its value, e.g., for water, has excited much controversy [6]. Unless the validity of equation (1) is proven, however, such controversy may be unfruitful. Although some authors recently addressed the KBC at the interface with MD methods [14, 15], they could not reach the physically correct KBC owing to their ambiguous definitions of the evaporation and reflection of molecules [16, 17].

In the kinetic theory, the velocity distribution function f^{out} should be a function of the temperature T_ℓ at the interface and the velocity distribution function f^{coll} of molecules incident on it, in addition to the molecular velocity $\boldsymbol{\xi}$, i.e., $f^{\text{out}} = f^{\text{out}}(\boldsymbol{\xi}, T_\ell, f^{\text{coll}})$. We therefore investigate $f^{\text{out}}(\boldsymbol{\xi}, T_\ell, f^{\text{coll}})$ for various f^{coll} and a specified $T_\ell = 85$ K (near the triplepoint of argon) in nonequilibrium steady MD simulations for the argon vapor-liquid two-phase system, thereby constructing the physically correct form of KBC at the interface for argon.

The distribution function f^{out} has turned out to be expressed by

$$f^{\text{out}} = \frac{\rho_{\text{out}}}{(2\pi \text{R})^{3/2} T_\ell \sqrt{T_\ell}} \exp\left(-\frac{\xi_x^2 + \xi_y^2}{2RT_t} - \frac{\xi_z^2}{2RT_\ell} \right), \tag{3}$$

for $\xi_z > 0$, where $\rho_{\text{out}} = 2\int_{\xi_z>0} f^{\text{out}} d\boldsymbol{\xi}$ and $T_t = (1/R)\int_{\xi_z>0} \xi_x^2 \hat{f}^{\text{out}} d\boldsymbol{\xi}$ is calculated in the MD simulation ($\hat{f}^{\text{out}} = f^{\text{out}} / (\int_{\xi_z>0} f^{\text{out}} d\boldsymbol{\xi})$) . The reduced temperature $\hat{T}_t = T_t / T_\ell$ as a function of the energy flux of incoming molecules across the interface is shown in Fig. 2. We split f^{out} into two parts, i.e., $f^{\text{out}}\left(T_\ell, f^{\text{coll}}\right) = f^{\text{out}}\left(T_\ell, 0\right) + \left[f^{\text{out}}\left(T_\ell, f^{\text{coll}}\right) - f^{\text{out}}\left(T_\ell, 0\right) \right]$. The first term is independent of f^{coll} and is called the spontaneous evaporation [16]. All the effects of f^{coll} are confined into the second term, and hence it may be called the reflection. This is the only splitting that distinguishes the evaporation from the reflection without ambiguity. According to this splitting, the outgoing mass flux $\langle J_{\text{out}} \rangle = \int_{\xi_z>0} \xi_z f^{\text{out}} d\boldsymbol{\xi}$ can also be split into $\langle J_{\text{out}} \rangle = \langle J_{\text{evap}} \rangle + \langle J_{\text{ref}} \rangle$, where $\langle J_{\text{evap}} \rangle = \int_{\xi_z>0} \xi_z f^{\text{out}}(T_\ell, 0) d\boldsymbol{\xi}$ and $\langle J_{\text{ref}} \rangle = \int_{\xi_z>0} \xi_z [f^{\text{out}}(T_\ell, f^{\text{coll}}) - f^{\text{out}}(T_\ell, 0)] d\boldsymbol{\xi}$. From the balance of the mass fluxes across the interface, the difference between the incoming mass flux $\langle J_{\text{coll}} \rangle$ and the reflection mass flux $\langle J_{\text{ref}} \rangle$ should condense onto the interface. We can therefore define the condensation mass flux as $\langle J_{\text{cnds}} \rangle = \langle J_{\text{coll}} \rangle - \langle J_{\text{ref}} \rangle$. These relations enable us to rewrite $\langle J_{\text{out}} \rangle$ into $\langle J_{\text{out}} \rangle = \langle J_{\text{evap}} \rangle + \langle J_{\text{coll}} \rangle \left(1 - \langle J_{\text{cnds}} \rangle / \langle J_{\text{coll}} \rangle\right)$. Furthermore, since equation (3) yields $\langle J_{\text{out}} \rangle = \rho_{\text{out}} \sqrt{RT_\ell/(2\pi)}$, we can eliminate $\langle J_{\text{out}} \rangle$ to give

$$\rho_{\text{out}} = \frac{\langle J_{\text{evap}} \rangle}{\sqrt{RT_\ell/(2\pi)}} + \left(1 - \frac{\langle J_{\text{cnds}} \rangle}{\langle J_{\text{coll}} \rangle}\right) \frac{\langle J_{\text{coll}} \rangle}{\sqrt{RT_\ell/(2\pi)}}. \tag{4}$$

This naturally leads to the introduction of the evaporation coefficient α_e and the condensation coefficient α_c defined as [16]

$$\alpha_e = \frac{\langle J_{\rm evap} \rangle}{\rho^* \sqrt{RT_\ell/(2\pi)}}, \qquad \alpha_c = \frac{\langle J_{\rm cnds} \rangle}{\langle J_{\rm coll} \rangle}, \tag{5}$$

and by using equation (2), we obtain $\rho_{\rm out} = \alpha_e \rho^* + (1-\alpha_c)\sigma$. In Ref. [16], we have studied $\langle J_{\rm evap} \rangle$ and α_e by the vacuum evaporation simulation for argon, and demonstrated that α_e is a function of the temperature in the condensed phase alone.

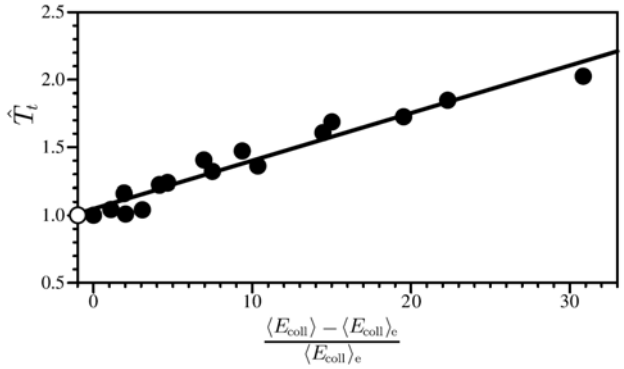

Figure 2. The reduced temperature $\hat{T}_t = T_t / T_\ell$ as a function of the energy flux of incoming molecules across the interface [4]. The open circle denotes the result of vacuum simulation [16].

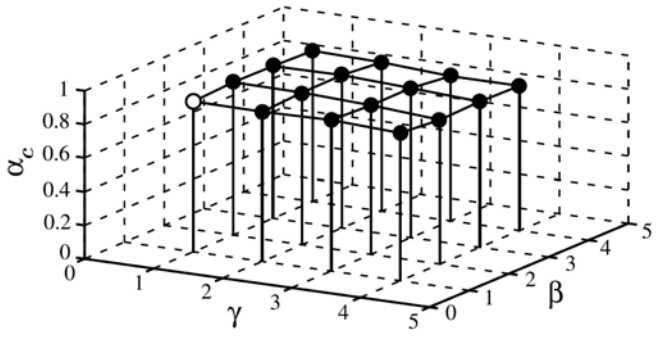

Figure 3. The condensation coefficient α_c versus β and σ which are parameters representing the deviation from the equilibrium state [4]. The open circle denotes the equilibrium state where α_c is equal to the evaporation coefficient α_e from their definitions.

The condensation coefficient α_c evaluated with the use of $\langle J_{\rm cnds} \rangle = \langle J_{\rm coll} \rangle - \left(\langle J_{\rm out} \rangle - \langle J_{\rm evap} \rangle \right)$ is plotted in Fig. 3, which clearly shows that α_c is almost equal to $\alpha_e = 0.868$ at $T_\ell = 85$K [16]. We emphasize that if α_c is a constant, it must be equal to α_e. Consequently, from equations (3)-(5), the physically correct KBC at the interface is determined as

$$f^{\text{out}} = \frac{[\alpha\rho^* + (1-\alpha)\sigma]}{(2\pi R)^{3/2} T_t \sqrt{T_\ell}} \exp\left(-\frac{\xi_x^2 + \xi_y^2}{2RT_t} - \frac{\xi_z^2}{2RT_\ell} \right), \tag{6}$$

for $\xi_z > 0$, where we have used the result in Fig. 3, i.e., $\alpha = \alpha_e = \alpha_c$. It is obvious that conventional model (1) with (2) is recovered in the limit of the equilibrium state, i.e., $T_t = T_\ell$.

In summary, using steady nonequilibrium MD simulations of the vapor-liquid two-phase system of argon, we construct the physically correct KBC at the interface in the form of equation (6). The new KBC is similar to the conventional one in the sense that f^{out} is the product of one-dimensional Maxwellian distributions. However, it does not contain any arbitrary parameters: α should be the evaporation coefficient defined in equation (5), and T_t is the linear function of $\langle E_{\text{coll}} \rangle$ as verified in Fig. 2. In particular, Fig. 3 brings the long lasting controversy over α to an end.

CONDENSATION IN SHOCK TUBE AND MOLECULAR GAS DYNAMICS

Condensation in shock tube

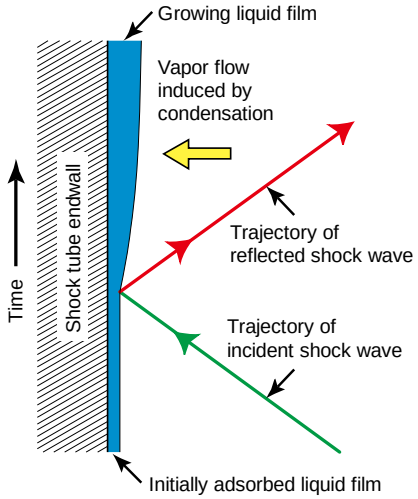

Figure 4. The growth of the liquid film on the shock tube end wall behind the reflected shock wave.

A shock tube is a suitable device to realize a nonequilibrium state at the interface between the vapor and its condensed phase [7-11]. Figure 4 shows the propagation process of shock waves in the vapor advancing toward and reflecting from the endwall of the shock tube. Just at the instant when the shock wave is reflected at the endwall on which an adsorbed liquid film with a thickness of a molecular scale exists initially, the pressure, temperature and density of the vapor far from the endwall increase rapidly and these are held at higher values compared with the initial ones. However, the vapor temperature adjacent to the endwall changes little because the endwall made of a thick glass has a large heat capacity compared with that of the vapor, whereas the vapor pressure increases almost to the pressure in the main stream. Thus, the vapor becomes supersaturated at the surface of the adsorbed liquid film, and it begins to condense in the form of a liquid film on the adsorbed film. The liquid film grows with the lapse of time to a macroscopic scale.

Shock tube

Figure 5 shows a horizontal type of shock tube used in the experiment, in which the optical interferometer is incorporated for the measurement of liquid film thickness [11]. The length of the low pressure section (test section, attained vacuum level =1.0×10^{-2} Pa) is 2830 mm, and the length of the high pressure section is 2600 mm. Two sections are connected coaxially, and a thin aluminum diaphragm is sandwiched between them. The cross section of the shock tube is the circle

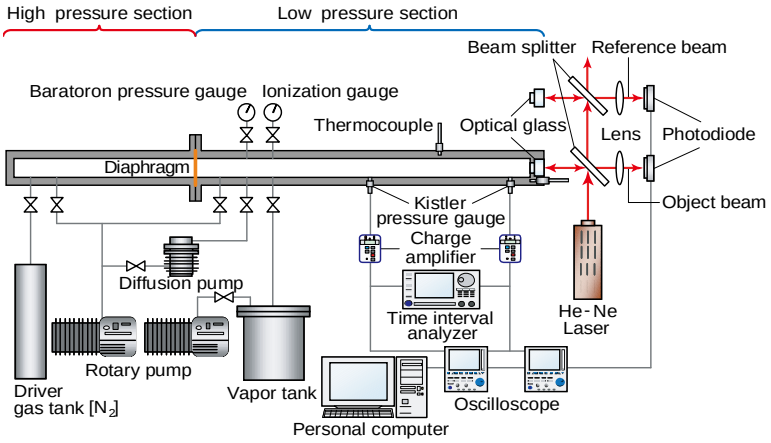

Figure 5. The shock tube and optical interferometer.

of 74.3 mm in diameter. The endwall of the test section consists of a quartz glass with the thickness of 15 mm, and its surface is polished at the flatness level of $\lambda/20$ (λ=632.8 nm) to prevent the diffused reflection of a laser beam for optical measurement and to make the laser-shed region of a liquid film on the surface as uniform as possible. The Mach number of the incident shock wave is estimated from the distance (=1000 mm) between two pressure gauges (type 701A Kistler Instrument AG, Winterthur, Switzerland) and the passage time of the shock wave between them.

The variation in time of a liquid film thickness is obtained by the measurement of light reflectance from the optically transparent film system, because the growing film, together with the glass endwall, forms a kind of interferometer. In the measurement of light reflectance, the following special device is made to eliminate systematic noises from the light reflectance. A light beam from the light source is divided into two beams; one is the physical beam containing information of the liquid film thickness and the other is the reference one which is subtracted from the light reflectance of the physical beam in order to eliminate the noises. The physical and reference beams are detected by two photodiodes, respectively.

Molecular gas dynamics analysis

As shown in Fig. 6, a steady shock wave with plane front in the vapor is formed far from the endwall and propagates toward it. In front of this incident shock wave with Mach number M, the molecular distribution function is a stationary Maxwellian with the temperature T_0 and the density ρ_0. Behind the shock wave, the distribution function is also Maxwellian with the temperature T_b, the density ρ_b and the velocity v_b. These quantities both in front of and behind the shock wave can

be connected by Rankine-Hugoniot relations. An adsorbed liquid film is supposed to exist initially on the endwall, as it does actually.

After the shock wave is reflected at the endwall, condensation takes place in the form of a liquid film on the surface of the initially adsorbed liquid film, and the liquid film grows with the lapse of time. The temperatures of the liquid film and endwall change due to the release of latent heat of condensation. Therefore, we need to solve the Boltzmann equation for the vapor together with the heat conduction equations for the liquid film and endwall. We assume that this phenomenon is a one-dimensional problem. The coordinate X stems from the interface moving due to condensation. The Gaussian BGK-Boltzmann equation is adopted as the governing equation for the water vapour

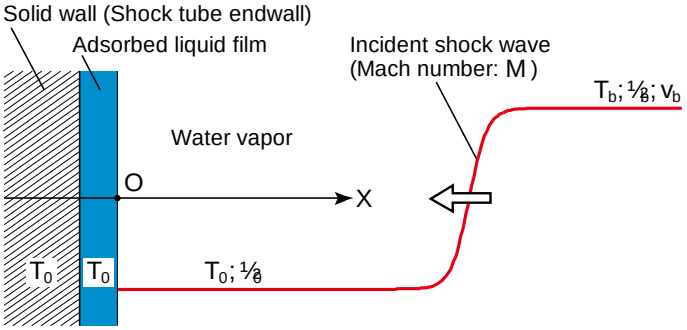

Figure 6. The schematic diagram of numerical model of film condensation on the shock tube endwall behind the reflected shock wave.

and given by [18]

$$\frac{\partial f}{\partial t}+(\xi_x-v_\ell)\frac{\partial f}{\partial X}=\frac{p}{\mu(1-v+\theta v)}(G(f)-f), \tag{7}$$

where $f(X,t,\boldsymbol{\xi},\eta)$ is the molecular distribution function, t is the time, $\boldsymbol{\xi}=(\xi_x,\xi_y,\xi_z)$ is the molecular velocity in which ξ_x,ξ_y,ξ_z are the x-, y-, z-components, η is the internal energy parameter, v_ℓ is the velocity of the moving interface, p is the pressure, $\mu(T)$ is the viscosity coefficient which is a function of the temperature T, and v and θ are constants. The function $G(f)$ in the right hand side of equation (7) is given by

$$G(f)=\rho f_{\mathrm{tr}}^{G} f_{\mathrm{int}}^{G}, \tag{8}$$

$$f_{\mathrm{tr}}^{G}=\frac{1}{\sqrt{\det(2\pi\tau_{ij})}}\exp\left(-\frac{1}{2}(\xi_i-v_i)\tau_{ij}^{-1}(\xi_j-v_j)\right), \tag{9}$$

$$f_{\mathrm{int}}^{G}=\frac{1}{\Gamma\left(\frac{n}{2}+1\right)(RT_{\mathrm{rel}})^{n/2}}\exp\left(-\frac{\eta^{2/n}}{RT_{\mathrm{rel}}}\right), \tag{10}$$

where ρ is the density, f_{tr}^{G} is the translational distribution function of polyatomic molecules, f_{int}^{G} is the distribution function of internal motions, det is the determinant, Γ is the gamma function, R is the gas constant per unit mass and n is the internal degrees of freedom of molecules which are taken to be 3 for water so that the theoretical specific heat ratio $(\gamma = 8/6)$ can coincide with the experimental one. The other quantities are defined by

$$\rho = \iint f \mathrm{d}\boldsymbol{\xi}\mathrm{d}\eta\,,\ \rho v_x = \iint \xi_x f \mathrm{d}\boldsymbol{\xi}\mathrm{d}\eta\,,\ \frac{3}{2}RT_{\mathrm{tr}} = \frac{1}{\rho}\iint \frac{1}{2}(\xi_i - v_i)^2 f \mathrm{d}\boldsymbol{\xi}\mathrm{d}\eta\,,$$

$$\frac{n}{2}RT_{\mathrm{int}} = \frac{1}{\rho}\iint \eta^{2/n} f \mathrm{d}\boldsymbol{\xi}\mathrm{d}\eta\,,\ T = \frac{3}{n+3}T_{\mathrm{tr}} + \frac{n}{n+3}T_{\mathrm{int}}\,,\ p = \rho RT\,,$$

$$T_{\mathrm{rel}} = \theta T + (1-\theta)T_{\mathrm{int}}\,,\ \rho\Theta_{ij} = \iint (\xi_i - v_i)(\xi_j - v_j) f \mathrm{d}\boldsymbol{\xi}\mathrm{d}\eta\,,$$

$$\tau_{ij} = (1-\theta)[(1-\nu)RT_{\mathrm{tr}}\delta_{ij} + \nu\Theta_{ij}] + \theta RT\delta_{ij}\,,$$

where v_x is the velocity component in the x direction, T_{tr} is the translational temperature, T_{int} is the internal temperature, T_{rel} is the relaxation temperature, $\rho\Theta_{ij}$ is the stress tensor, τ_{ij} is the corrected tensor and δ_{ij} is the Kronecker's delta. The integration with respect to $\boldsymbol{\xi}$ is carried out over the whole space of $\boldsymbol{\xi}$ unless otherwise stated, and the integration with respect to η is carried out in the domain of $[0,\infty)$.

The Gaussian-BGK Boltzmann equation is solved with the following kinetic boundary condition for molecules going out from the interface into the vapour phase [6]:

$$f^{\mathrm{out}} = [\alpha_{\mathrm{e}}\rho^{*} + (1-\alpha_{\mathrm{c}})\sigma] f_{\mathrm{tr}}^{\mathrm{eq}} f_{\mathrm{int}}^{\mathrm{eq}} \quad (\xi_x > v_\ell), \tag{11}$$

$$f_{\mathrm{tr}}^{G} = \frac{1}{(2\pi RT)^{3/2}} \exp\left(-\frac{(\xi_x - v_\ell)^2}{2RT_\ell} - \frac{\xi_y^{\,2} + \xi_z^{\,2}}{2RT_\ell} \right), \tag{12}$$

$$f_{\mathrm{int}}^{G} = \frac{1}{\Gamma\left(\frac{n}{2}+1\right)(RT_\ell)^{n/2}} \exp\left(-\frac{\eta^{2/n}}{RT_\ell} \right), \tag{13}$$

where α_{e} is the evaporation coefficient, α_{c} is the condensation coefficient, $\rho^{*} = p^{*}/RT_\ell$ is the saturated vapor density at the temperature T_ℓ of the liquid film surface, p^{*} is the saturated vapor pressure evaluated from Antoine's formula, and

$$\sigma = -\sqrt{\frac{2\pi}{RT_\ell}} \int_{\xi_x < v_\ell} (\xi_x - v_\ell) f^{\mathrm{coll}} \mathrm{d}\boldsymbol{\xi}\mathrm{d}\eta\,, \tag{14}$$

where f^{coll} is the molecular distribution function incident on the interface. The condensation coefficient is determined from the net condensation mass flux at the interface. The flux $\rho_\ell v_\ell$ can be given by the mass conservation equation at the interface:

$$\rho_\ell v_\ell = (\alpha_{\mathrm{c}}\sigma - \alpha_{\mathrm{e}}\rho^*)\sqrt{\frac{RT_\ell}{2\pi}}, \tag{15}$$

where ρ_ℓ is the density of the liquid film. When the vapor-liquid system is in the equilibrium state, $\rho^* = \sigma$ and $\rho_\ell v_\ell = 0$ and hence $\alpha_{\mathrm{e}} = \alpha_{\mathrm{c}}$. Making use of equation (15) allows us to eliminate the evaporation coefficient α_{e} and the condensation coefficient α_{c} from equation (11) and leads to

$$f^{\mathrm{out}} = \left(\sigma - \rho_\ell v_\ell \sqrt{\frac{2\pi}{RT_\ell}}\right) f_{\mathrm{tr}}^{\mathrm{eq}} f_{\mathrm{int}}^{\mathrm{eq}} \qquad (\xi_x > v_\ell). \tag{16}$$

Therefore, once v_ℓ is experimentally given as a function of time, the Boltzmann equation can be uniquely solved with the distribution function f^{out} given by equation (16). In consequence, $\rho_\ell v_\ell$, T_ℓ, ρ^* and σ in equation (15) become known, and the unknowns in equation (15) are only α_{e} and α_{c}. Note that α_{e} is a function of T_ℓ alone from its definition. Therefore α_{c} can be evaluated from equation (15) by using the value of α_{e} which has been estimated by the recent molecular dynamics simulations for water [17]. The use of this value of α_e will be justified by the experiment.

Results

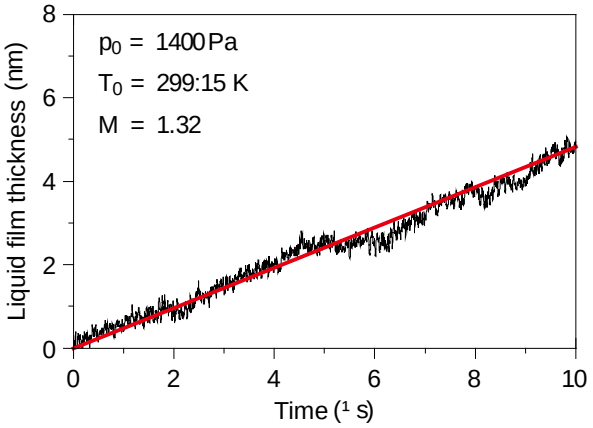

Figure 7. The time evolution of the liquid film thickness.

Figure 7 shows the variation in time of the liquid film thickness. Note that the origin of the time is reset at the condensation onset. The red solid line is an approximated curve for the converted experimental data. The slope of the curve means the moving velocity of the surface of liquid film v_ℓ. It is found that the curve can be approximated well by a straight line, i.e., v_ℓ is constant for a short time. By using the velocity v_ℓ for the boundary condition given by equation (16), the numerical simulation is conducted and the value of the condensation coefficient can be uniquely deduced.

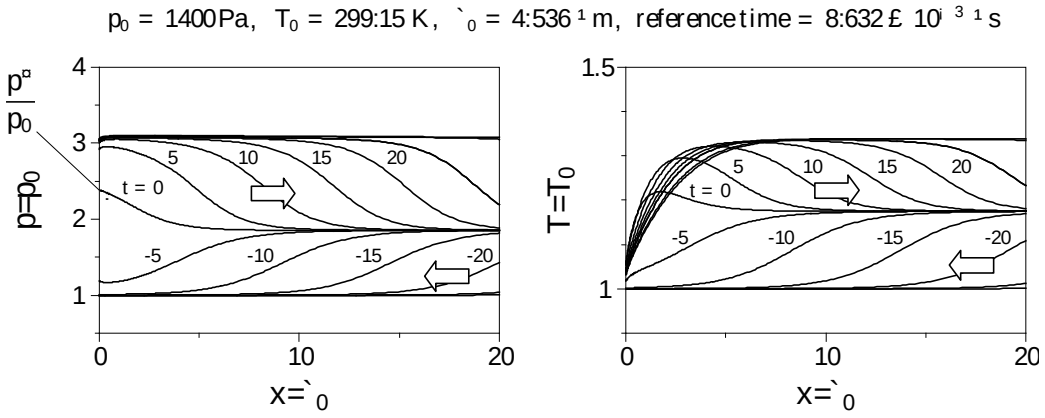

Figure 8. The propagation process of the shock waves advancing toward and reflecting from the shock tube endwall: (a) pressure profiles; (b) temperature profiles. The time is normalized by the reference time. The condition is the same as that in Fig. 7.

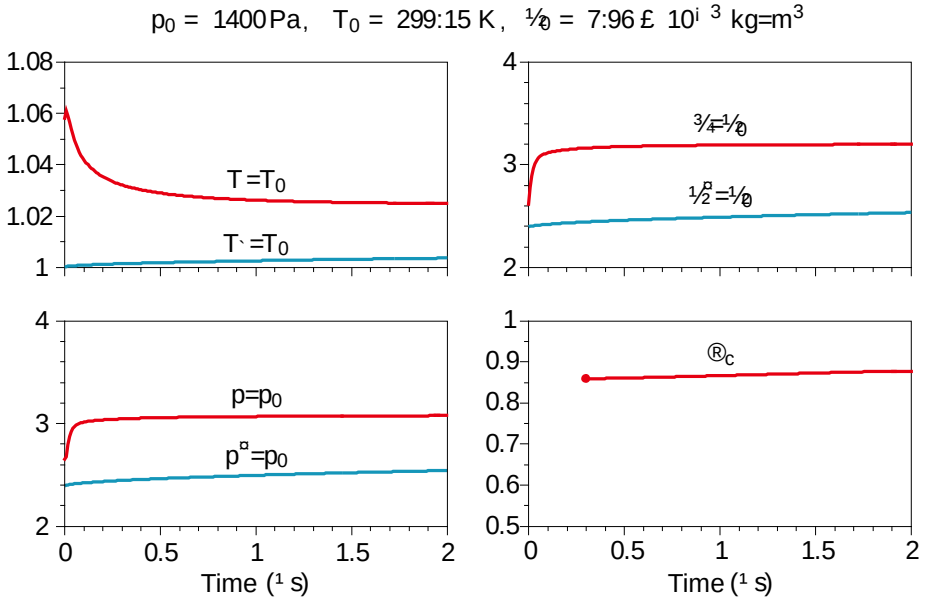

Figure 9. The variation in time of macroscopic quantities at the interface and the determined condensation coefficient α_c. The red circle at the left end on the α_c - line is the starting time of the acquisition of α_c. The condition is the same as that in Fig. 7.

Figure 8 shows the propagation process of the shock waves advancing toward and reflecting from the boundary: (a) pressure profiles, (b) temperature profiles. The abscissas of (a) and (b) are both the distance from the liquid film surface in the vapor. The time indicated for each profile in (a) and (b) is normalised by the reference time. The pressure at the interface rises gradually during the incidence and reflection process of the shock waves and it approaches a constant. On the other hand, the temperature profiles show that the thermal boundary layer including the Knudsen layer, which is the nonequilibrium region of vapor near the interface, is formed behind the reflected shock wave.

Figure 9 shows the variation in time of macroscopic quantities at the interface. After the onset time of condensation, the temperature T, the pressure p, and σ set in an almost steady state immediately.

Then, from Fig. 9(a), we can see that the variation in the liquid film temperature T_ℓ is about 0.5 % for 2 μs. Therefore, those of the saturated vapor pressure p^* and the saturated vapor density ρ^* are about 8 %. As a result, from equation (15), the condensation coefficient α_c may be regarded as a constant value for 2 μs after the condensation onset.

Figure 10 shows the relationship between the condensation coefficient and σ/ρ^*. The σ/ρ^* of the abscissa denotes the ratio of the collision mass flux $\sigma\sqrt{RT_\ell/(2\pi)}$ onto the interface to the mass flux $\rho^*\sqrt{RT_\ell/(2\pi)}$ at the equilibrium state. We can see that the condensation coefficient of water approaches unity as σ/ρ^* does unity, i.e., the equilibrium state. The red circle at $\sigma/\rho^*=1$ is the value (1.00 at 300K) of α_e, estimated by the MD simulation [17]. The red solid line is drawn by the method of least-squares so as that it coincides with the above value of α_e at the equilibrium state. This asymptotic behaviour of α_c approaching α_e, as σ/ρ^* does unity, may justify the use of α_e evaluated by the MD simulation. The condensation coefficient of water can be expressed by the following equation:

$$\alpha_c = \frac{\rho^*}{\sigma}(\alpha_e - A) + A, \tag{17}$$

where α_e=1.00 and A = 0.47. Consequently, we can estimate the condensation coefficient of water by using equation (17) in weak condensation states at the room temperature. For comparison, the condensation coefficient of methanol is shown by blue circles and the blue line ($\alpha_e = 0.86$ at $\rho^*/\sigma = 1.0$). We can notice that there is a significant difference between water and methanol.

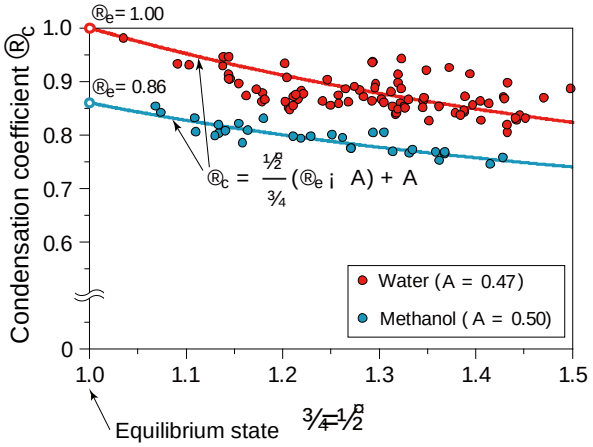

Figure 10. The condensation coefficient versus σ/ρ^* for water (red circles). For comparison, the condensation coefficient of methanol is shown (blue circles) [20]. The σ is calculated from equation (14).

MOLECULAR GAS DYNAMICS AND BOUNDARY CONDITION FOR FLUID-DYNAMICS-TYPE SET OF EQUATIONS

Asymptotic analysis

We will deal with a time-independent problem for weak evaporation or condensation where the half-infinite extent of a vapor with the pressure p_∞, the temperature T_∞ and the density ρ_∞ is in contact with its half-infinite liquid phase with the constant temperature T_ℓ [21]. Evaporation or condensation takes place at the interface between the vapor and the liquid, depending on whether or

not the pressure at the interface is lower than the saturated vapor pressure $\rho^*(T_\ell)$ at the temperature T_ℓ. We will adopt the Gaussian-BGK Boltzmann equation applicable to a polyatomic gas [18] and derive the boundary condition at the boundary for fluid-dynamic-type, i.e., Navier-Stokes-type, set of equations.

The following assumptions are made: (i) the interface is planar and at rest, and hence the phenomenon in question is spatially one-dimensional, dependent on the X axis normal to the interface. (ii)the vapor is the ideal gas. (iii) the boundary condition is Eq.(11) for the case of $\alpha_e = \alpha_c = \alpha$ and $v_\ell = 0$.

The Gaussian-BGK Boltzmann equation is equation (7). We will study the time-independent solution for weak evaporation or condensation on the basis of the asymptotic theory for small Knudsen numbers. According to Sone's book [12], we will seek a moderately varying solution of the Gaussian-BGK Boltzmann equation in a power series (S expansion) as

$$\phi = k\phi_{S1} + k^2\phi_{S2} + \cdots, \quad k = \frac{\sqrt{\pi}}{2}\frac{\lambda_0}{L} = 1, \tag{18}$$

where $\phi = (f - f_0)/f_0$ is the nondimensional distribution function$\left[\phi = O(k)\right]$, f_0 the equilibrium distribution function in the reference equilibrium state (the subscript 0 represents the reference equilibrium state), ℓ_0 the mean free path in the reference state, and L the characteristic length of the system. The mean free path is given by

$$\ell_0 = (1 - \nu + \theta\nu)\frac{\mu_0}{p_0}\frac{2}{\sqrt{\pi}}\sqrt{2RT_0}. \tag{19}$$

Corresponding to the expansion (18), the macroscopic variables are also expanded in k.

The resulting fluid-dynamic-type set of equations are

$$\frac{\partial P_{S1}}{\partial x_i} = 0, \tag{20}$$

$$\frac{\partial u_{iS1}}{\partial x_i} = 0, \tag{21}$$

$$u_{jS1}\frac{\partial u_{iS1}}{\partial x_j} = -\frac{1}{2}\frac{\partial P_{S2}}{\partial x_i} + \frac{\mathrm{Pr}}{2}\frac{\partial^2 u_{iS1}}{\partial x_j^2}, \tag{22}$$

$$u_{iS1}\frac{\partial \tau_{S1}}{\partial x_i} = \frac{1}{2}\frac{\partial^2 \tau_{S1}}{\partial x_i^2}, \tag{23}$$

$$\frac{\partial u_{iS2}}{\partial x_i} + u_{iS1}\frac{\partial \omega_{S1}}{\partial x_i} = 0, \tag{24}$$

$$u_{jS1}\frac{\partial u_{iS2}}{\partial x_j}+(u_{jS2}+\omega_{S1}u_{jS1})\frac{\partial u_{iS1}}{\partial x_j} = -\frac{1}{2}\frac{\partial}{\partial x_i}\left(P_{S3}\frac{\mathrm{Pr}}{2}\frac{\partial^2\tau_{S1}}{\partial x_j^2}\right)+\frac{\mathrm{Pr}}{2}\frac{\partial^2 u_{iS2}}{\partial x_j^2}+\frac{\mathrm{Pr}}{2}\frac{\partial}{\partial x_i}\left[\beta\tau_{S1}\left(\frac{\partial u_{iS1}}{\partial x_j}+\frac{\partial u_{jS1}}{\partial x_i}\right)\right], \tag{25}$$

$$u_{jS1}\frac{\partial \tau_{S2}}{\partial x_i}+(u_{jS2}+\omega_{S1}u_{jS1})\frac{\partial \tau_{S1}}{\partial x_j}-\frac{2}{5+n}u_{jS1}\frac{\partial P_{S2}}{\partial x_j} = \frac{\mathrm{Pr}}{5+n}\left(\frac{\partial u_{iS1}}{\partial x_j}+\frac{\partial u_{jS1}}{\partial x_i}\right)^2+\frac{1}{2}\frac{\partial^2}{\partial x_i^2}\left(\tau_{S2}+\frac{\beta}{2}\tau_{S1}^2\right), \tag{26}$$

where $x = X/L$ and $\omega_{Sm}, \tau_{Sm}, P_{Sm}$ and $u_{iSm}(m=1,2)$ are expansion coefficients of the nondimensional density $\omega=(\rho-\rho_0)/\rho_0$, the temperature $\tau=(T-T_0)/T_0$, the pressure $P=(1+\omega)(1+\tau)-1$, and the velocity $u_i = v_i/\sqrt{2RT_0}$, respectively. The viscosity is assumed as $\mu=\mu_0(1+\tau)^\beta$. We should remark that (i) equations (20)-(26) are the same as those for the BKW model [19], if we set $n=0$ (monatomic gas), $\mathrm{Pr}=1$ and $\beta=1$; (ii) the temperature associated with translational motion T_{tr} and that with internal motion T_{int} are equal to T up to the order shown above.

Knudsen layer

The Knudsen layer analysis can also be carried out in the same way as that given in Sone's book [12], and thereby the Knudsen layer corrections and the boundary condition for the fluid-dynamic-type equations can be obtained. The result in the leading order of approximation is

$$(u_{iS1}-u_{wi1})t_i = 0, \tag{27}$$

$$u_{iK1} = 0, \tag{28}$$

$$\begin{pmatrix} P_{S1}-P_{w1} \\ \tau_{S1}-\tau_{w1} \\ \omega_{K1} \\ \tau_{\mathrm{tr}K1} \\ \tau_{\mathrm{int}K1} \end{pmatrix} = u_{iS1}n_i \begin{pmatrix} C_4^*-2\sqrt{\pi}\dfrac{1-\alpha}{\alpha} \\ d_4^* \\ \Omega_4^* \\ \Theta_{4\mathrm{tr}}^*(y) \\ \Theta_{4\mathrm{int}}(y) \end{pmatrix}. \tag{29}$$

Here, (i) $u_{iS1,}$ T_{S1} and P_{S1} are evaluated at the interface; (ii) u_{wi1}, T_{w1} and P_{w1} are, respectively, the first expansion coefficients of the nondimensional velocity and temperature of interface, and the saturated vapor pressure at the temperature, e.g., $v_\ell/\sqrt{2RT_0} = ku_{wi1}+\cdots$ and so on; (iii) u_{iK1}, ω_{K1}, $\tau_{\mathrm{tr}K1}$ and $T_{\mathrm{int}K1}$ are, respectively, the Knudsen layer corrections for the velocity, density and temperature associated with translational and internal motions; (iv) n_i and t_i are unit vectors normal and tangential to the interface, respectively; (v) y is the coordinate stretched in the n_i

direction, $x_i n_i = ky$. The values of slip coefficients C_4^* and d_4^* and the functional forms of Knudsen layer functions $\Omega_4(y), \Theta_{4\mathrm{tr}}^*(y)$ and $\Theta_{4\mathrm{int}}^*(y)$ are dependent on the parameters θ and ν and the internal degrees of freedom n.

We set $\theta = 0.6471, \nu = -0.5$ and $n = 6$ corresponding to methanol vapor at room temperature, $\mathrm{Pr} = 0.86$ and the radio of specific heats 1.22. In that case, we obtain

$$C_4^* = -2.0723, \qquad d_4^* = -0.2185, \tag{30}$$

and

$$\Omega_4^*(0) = 0.475, \quad \Theta_{4\mathrm{tr}}^*(0) = -0.083, \quad \Theta_{4\mathrm{int}}^*(0) = 0.145. \tag{31}$$

The slip coefficients and the Knudsen layer functions for the BKW model and for the usual Boltzmann equation for hard-sphere gas are precisely determined and tabulated in Sone's book [12]:

$$\begin{aligned} &C_4^* = -2.1412, \quad d_4^* = -0.4557, \quad \Omega_4^*(0) = 0.37815, \quad \Theta_4^*(0) = 0.05206, \quad (\text{hard}-\text{sphere}), \\ &C_4^* = -2.13204, \quad d_4^* = -0.44675, \quad \Omega_4^*(0) = 0.36303, \quad \Theta_4^*(0) = 0.03717, \quad (\text{BKW}). \end{aligned} \tag{32}$$

As seen from equations (30)-(32), C_4^* for the Gaussian-BGK model for the polyatomic gas (methanal) is rather close to those for the monatomic gas. The coefficient d_4^* for the polyatomic gas is, however, about half of that for the monatomic gas. Derivation of the coefficients for water vapor is now under progress.

One-dimensional steady and weak evaporation or condensation

The one-dimensional steady solution for weak evaporation or condensation is clearly explained based on the S expansion, and the result is directly applied to the present case. For the given conditions at infinity, (p_∞, T_∞), and the liquid temperature at the interface T_ℓ, the solution in the vapor phase can be written as

$$\frac{p - p_\infty}{p^*} = \frac{p_\infty - p^*}{p^*} \left[\frac{\Omega_4^*(y) + \dfrac{3}{3+n}\Theta_{4\mathrm{tr}}^*(y) + \dfrac{3}{3+n}\Theta_{4\mathrm{int}}^*(y)}{C_4^* - 2\sqrt{\pi}\dfrac{1-\alpha}{\alpha}} \right], \tag{33}$$

$$\begin{aligned} \frac{T - T_\infty}{T_\ell} = &\left(\frac{p_\infty - p^*}{p^*} \frac{d_4^*}{C_4^* - 2\sqrt{\pi}\dfrac{1-\alpha}{\alpha}} - \frac{T_\infty - T_\ell}{T_\ell} \right) \exp\left(\frac{p_\infty - p^*}{p^*} \frac{1}{C_4^* - 2\sqrt{\pi}\dfrac{1-\alpha}{\alpha}} \frac{4X}{\sqrt{\pi}\ell_0} \right) \\ &+ \frac{p_\infty - p^*}{p^*} \frac{1}{C_4^* - 2\sqrt{\pi}\dfrac{1-\alpha}{\alpha}} \left[\frac{3}{3+n}\Theta_{4\mathrm{tr}}^*(y) + \frac{n}{3+n}\Theta_{4\mathrm{int}}^*(y) \right], \end{aligned} \tag{34}$$

$$\frac{v}{\sqrt{2RT_\ell}} = \frac{p_\infty - p^*}{p^*} \frac{1}{C_4^* - 2\sqrt{\pi}\dfrac{1-\alpha}{\alpha}}, \tag{35}$$

where $y = 2X/(\sqrt{\pi}\ell_0)$ is the mean free path of the saturated vapor at the temperature T_ℓ and, hereafter, v denotes the velocity component normal to the interface. Thus, p, T and v everywhere in the vapor phase are determined by p_∞, T_∞ and T_ℓ, the slip coefficients and C_4^* and d_4^*, the Knudsen layer functions, and the condensation coefficient (= the evaporation coefficient) α.

CONCLUSIONS

The state-of-the-art studies of evaporation and condensation based on molecular dynamics (MD), molecular gas dynamics and the shock-tube experiment have been presented by focusing on the kinetic boundary condition (KBC) at the interface of the vapor and its condensed phase, and the evaporation and condensation coefficient. The principal results can be summarized as follows.

(1) The physically correct kinetic boundary condition (KBC) is formulated by MD simulations. This KBC is similar to the conventional model, but not contain any arbitrary parameters.
(2) Molecular gas dynamics simulations and experiments by shock tube make it possible to obtain the correct values of evaporation and condensation coefficient of water; the evaporation coefficient is just unity, and the condensation coefficient is equal to the evaporation coefficient at the equilibrium state and it decreases with increasing in the nonequilibriun degree.
(3) One-dimensional steady and weak evaporation or condensation has been analyzed and the boundary condition for the Navier-Stokes-type set of equations has been obtained by the perturbation analysis.

Precise analysis of evaporation and condensation very near the equilibrium state is in progress based on molecular gas dynamics [22], and the corresponding experiment using sound resonance is also in progress. [23]. These studies are expected to clarify the more exact value of the evaporation coefficient very near the equilibrium state. The evaporation coefficient, surface tension coefficient and saturated vapour pressure of a nanodroplet are investigated in detail by molecular dynamics simulations [24].

ACKNOULEDGEMENTS

This work has been done with the author's former colleagues, Dr. Takeru Yano (Professor of Osaka University), Dr. Tatsuya Ishiyama (Assistant Professor of Tohoku University) and Dr. Kazumichi Kobayashi (Assistant Professor of Osaka Prefecture University). It is also indebted to Dr. Masao Watanabe (Associate Professor of Hokkaido University) and to the author's many graduate students, especially Messrs. Hisao Yaguchi, Shigeto Nakamura, Masashi Inaba and Daigo Yamano. It was financially supported by the Grant in Aid for Scientific Research of the Japan Society for the Promotion of Science (JSPS) from 2005 to 2008 (Grant No.17360074). The author would like to express his deepest gratitude to his former and present colleagues, graduate students and JSPS.

REFERENCES

1. Hertz, H., Über die Verdunstung der Flüssigkeiten, insbesondere des Quecksilbers, im luftleeren Raume, *Ann.Phys.und Chemie*, Vol.17, pp.177-200, 1882.
2. Knudsen, M., Die Maximale Verdampfunggeschwindigkeit des Quecksilbers, *Ann.Phys.und Chemie*, Vol.47, pp.697-708, 1915.
3. Cercignani, C. *Rarefied Gas Dynamics*: *From Basic Concepts to Actual Calculations*, Cambridge University Press, 2000.

4. Ishiyama, T., Yano, T. and Fujikawa, S., Kinetic Boundary Condition at a Vapour-liquid Interface, *Phys. Rev. Letts*, Vol.95, pp.084504-1-084504-4, 2005.
5. Cammenga, H. K., Evaporation Mechanism of Liquids, *Current Topics in Material Science*, Vol.5, pp.335-448, 1980.
6. Marek, R. and Straub, J., Analysis of the Evaporation Coefficient and the Ccondensation Coefficient of Water, *Int. J. Heat and Mass Transf*. Vol.44, pp.39-53, 2001.
7. Fujikawa, S., Okuda, M., Akamatsu, T. and Goto, T., Non-equilibrium Vapour Condensation on a Shock-tube Endwall behind a Reflected Shock Wave, *J. Fluid Mech.*, Vol.183, pp.293-324, 1987.
8. Maerefat, M., Fujikawa, S., Akamatsu, T., Goto, T. and Mizutani, T., An Experimental Study of Non-equilibrium Vapour Condensation in a Shock-tube, *Exp.in Fluids*, Vol.7, pp.513-520, 1989.
9. Maerefat, M., Fujikawa, S. and Akamatsu, T., Non-equilibrium Condensation of Water and Carbon Tetrachloride Vapour in a Shock-tube, *Exp.in Fluids*, Vol.9, pp.345-351, 1990.
10. Fujikawa, S., Yano, T., Kobayashi, K., Iwanami, K. and Ichijo, M., Molecular Gas Dynamics Applied to Phase Change Processes at a Vapor-liquid Interface: Shock-tube Experiment and MGD Computation for Methanol, *Exp.in Fluids*, Vol.37, pp.80-86, 2004.
11. Kobayashi, K., Watanabe, S., Yamano, D., Yano, T. and Fujikawa, S., Condensation Coefficient of Water in a Weak Condensation State, *Fluid Dyn.Res.*, Vol.40, pp.585-596, 2008.
12. Sone, Y., *Kinetic Theory and Fluid Dynamics*, Birkhauser, 2002.
13. Sone, Y., *Molecular Gas Dynamics*: *Theory*, *Techniques*, *and Applications*, Birkhauser, 2006.
14. Nagayama, G. and Tsuruta, T., A General Expression for the Condensation Coefficient Based on Transition State Theory and Molecular Dynamics Simulation, *J. Chem. Phys.*, Vol.118, pp.1392-1399, 2003.
15. Meland, R., Frezzotti, A., Ytrehus, T. and Hafskjold, B., Nonequilibrium Molecular-dynamics Simulation of Net Evaporation and Net Condensation, and Evaluation of the Gas-kinetic Boundary Condition at the Interphase, *Phys. Fluids*, Vol.16, pp.223-243, 2004.
16. Ishiyama, T., Yano, T. and Fujikawa, S., Molecular Dynamics Study of Kinetic Boundary Condition at an Interface between Argon Vapor and Its Ccondensed Phase. *Phys. Fluid*s, Vol.16, pp.2899- 2906, 2004.
17. Ishiyama, T., Yano, T. and Fujikawa, S. 2004. Molecular Dynamics Study of Kinetic Boundary Condition at an Interface between Polyatomic Vapor and Its Condensed Phase, *Phys. Fluids*, Vol.16, pp.4713-4726, 2004.
18. Andries, P., Le Tallec, P., Perlat, J. -P., Perthame, B., The Gaussian-BGK Model of Boltzmann Equation with Small Prandtl Number. *Eur. J. Mech. B Fluids*, Vol.19, pp.813-830, 2000.
19. Onishi, Y. and Sone, Y., Kinetic Theory of Slightly Strong Evaporation and Condensation－Hydrodynamic Equation and Slip Boundary Condition for Finite Reynolds Number－, *J. Phys. Soc. Jpn*. , Vol.47, pp.1676-1685, 1979.
20. Mikami, S., Kobayashi, K., Ota, T., Fujikawa, S., Yano, T. and Ichijo, M., Molecular Gas Dynamics Approaches to Interfacial Phenomena Accompanied with Condensation, *Exp.Therm. and Fluid Sci.* Vol.30, pp.795-800, 2006.
21. Yano, T., Kobayashi, K. and Fujikawa, S., Condensation of Methanol Vapor onto Its Liquid Film on a Solid Wall behind a Reflected Shock Wave, *Rarefied Gas Dynamics, AIP Conference Proceedings,* Vol.762, pp.208-213, 2005.

22. Inaba, M., Fujikawa, S. and Yano, T., Molecular Gas Dynamics on Condensation and Evaporation of Water Induced by Sound Waves, *Rarefied Gas Dynamics* (AIP), Vol.1084, pp.671-676, 2008.
23. Nakamura, S., Yano, T., Watanabe, M. and Fujikawa, S., A Novel Sound Resonance Method for Measurement of Evaporation Coefficient, *Proceedings of ExHFT-7*, Krakow, June 28-July 3, 2009, in this CD-ROM.
24. Yaguchi, H., Yano, T. and Fujikawa, S., Molecular Dynamics Study of Vapour-liquid Equilibrium State of an Argon Nanodroplet and Its vapor (in Japanese), *Trans. of JSME*, Ser.B, 2009, in press.

BOILING AND TWO-PHASE FLOW IN NARROW GAPS – WITH APPLICATION TO THERMAL PACKAGING OF CHIP STACKS

A. Bar-Cohen[1*], K.J.L. Geisler[2], E. Rahim[1]
[1]University of Maryland, College Park, MN, USA
[2]General Dynamics Advanced Information Systems, Bloomington, MN, USA

ABSTRACT. Application of the available theories, correlations, and experimental data for pool and flow boiling as well as convective transport in narrow gaps, to a notional 3D chip stack configuration, reveals that single phase natural convection cooled die stacks can be expected to dissipate in the range of 25 MW/m^3 when immersed in candidate Fluorinert™ electronics cooling liquids, while optimum pool boiling configurations are shown to dissipate 200 to 400 MW/m^3 over a wide range of system pressures. Alternatively, chip stacks optimized for single phase forced convection are predicted to yield volumetric heat transfer rates from 100 to 300 MW/m^3, and flow boiling configurations are demonstrated to exceed 1 GW/m^3. Optimum die spacings for both single and two phase cooling are found to be in the range of 0.2 mm to 0.6 mm for typical microelectronics geometries. Heat transfer performance maps summarizing the upper limits for each of these immersion cooling approaches are presented.

Keywords: *chip stack, liquid cooling, electronics, boiling, heat transfer*

INTRODUCTION

While homogeneous and heterogeneous chip stacks are a crucial building block in advanced microsystem architectures, effective thermal management of stacked chips remains a most difficult challenge. In addition to providing increased packaging density, 3D die stacking, as illustrated in Figure 1, accommodates shorter interconnect distances between devices, reduced power dissipation and improved electrical performance. A first-order approach for cooling these devices is to rely on conduction through the various layers up to the top of the package and/or down to the underlying PCB. More advanced thermal packaging approaches might include between-die solid conductors to improve lateral heat spreading to the package periphery [1], but the relatively low thermal conductivity of the electrical insulators typically considered for this role would be expected to yield large temperature gradients. On the other hand, immersion cooling techniques, which provide fluid flow in the narrow channels formed between stacked dies and high heat transfer coefficients directly on the die surfaces, could be very efficient in dissipating high volumetric heat generation rates, isothermalizing the silicon layers, and accommodating Joule heating in high current-density interconnects.

Single phase natural convection in dielectric liquids provides a quantitative baseline for direct liquid cooling of 3D chip stacks. Nucleate pool boiling also includes the advantages of passive, buoyancy-driven flow, but with significantly increased heat transfer rates above natural convection. Further enhancement in the dissipated heat flux and volumetric heat transfer rates can be achieved by the introduction of forced flow through the narrow channels in the chip stack, both single phase forced convection and, even more, flow boiling. Using available heat transfer coefficient correlations, the

* Corresponding author: Prof. Avram Bar-Cohen
Phone: + (1)-301-405-3173, Fax: + (1)-301-314-9477
E-mail address: abc@umd.edu

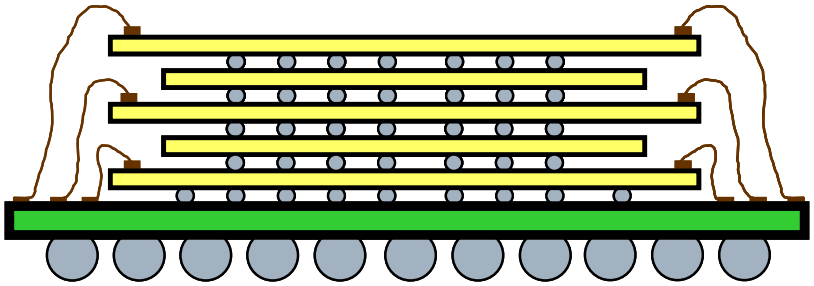

Figure 1. Illustrated 3D stacked die package

maximum achievable heat transfer rates from individual chips, optimal gap dimensions, and upper performance limits for immersion cooling of 3D chip stacks can be determined. Sample results for representative 3D chip stacks immersed in saturated FC-72 are generated, and performance maps summarizing the upper limits for each of these cooling approaches are presented and discussed.

Single phase natural convection in dielectric liquids provides a quantitative baseline for direct liquid cooling of 3D chip stacks. Nucleate pool boiling also includes the advantages of passive, buoyancy-driven flow, but with significantly increased heat transfer rates above natural convection. Further enhancement in the dissipated heat flux and volumetric heat transfer rates can be achieved by the introduction of forced flow through the narrow channels in the chip stack, both single phase forced convection and, even more, flow boiling. Using available heat transfer coefficient correlations, the maximum achievable heat transfer rates from individual chips, optimal gap dimensions, and upper performance limits for immersion cooling of 3D chip stacks can be determined. Sample results for representative 3D chip stacks immersed in saturated FC-72 are generated, and performance maps summarizing the upper limits for each of these cooling approaches are presented and discussed.

PASSIVE IMMERSION COOLING

Passive techniques, which require no input power, are often desired for improved reliability and ease of implementation when compared to active, forced flow approaches. While heat transfer performance may be relatively limited, capabilities may be sufficient for certain application classes, in particular portable and/or consumer electronic products.

Single phase natural convection

Single phase natural convection is the easiest form of direct liquid cooling to implement and provides a lower bound for pool boiling and a benchmark solution for other advanced cooling approaches. An illustration of the basic geometry of a vertically-oriented die stack appears in Figure 2. The gravity vector is taken to be parallel to the die length, L, and perpendicular to the stack height, H.

Following the composite Nusselt number correlation derivations of Bar-Cohen and Rohsenow [2] and including the Prandtl number correction of Bar-Cohen and Schweitzer [3], Geisler [4] derived and validated a composite Nusselt number correlation for symmetrically-heated, vertical microchannels immersed in saturated FC-72 at atmospheric pressure, based on the use of the fully-developed and isolated plate asymptotes, as

$$\mathrm{Nu}_\delta \equiv \frac{h\delta}{k} = \left[\left(\frac{24}{\mathrm{El}} \right)^2 + \frac{0.705^{-2}}{\sqrt{\mathrm{El}}} \right]^{-1/2} \tag{1}$$

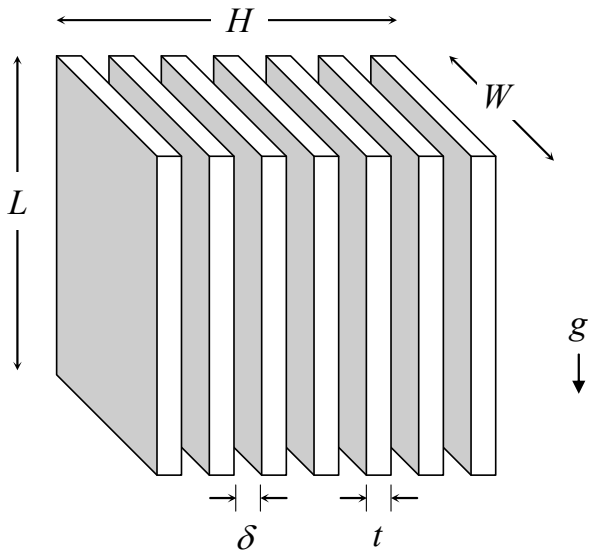

Figure 2. Die stack geometry and nomenclature

where the Elenbass number, El, is defined as,

$$\mathrm{El} \equiv \mathrm{Ra}_L \frac{\delta^4}{L^4} = \frac{c_p \rho^2 g \beta (T_{\mathrm{die}} - T_{\mathrm{amb}}) \delta^4}{\mu k L} \tag{2}$$

Following Elenbaas [5], the heat transfer coefficient defined by equation (1) includes the fluid temperature rise in the channel and is, therefore, based on the temperature difference between the channel wall and the fluid at the channel inlet. Figure 3 contains a graph of the composite Nusselt number relation, equation (1), along with the associated fully developed and isolated plate limits. The transition region from fully developed to isolated plate behavior is shown to occur in the range of Elenbaas numbers from 10 to 200.

Using the definitions of the Nusselt number and heat transfer coefficient, the total heat transfer rate from an array of vertical dies can be written as

$$q = 2LWHk\Delta T\left(\frac{\mathrm{Nu}_\delta}{\delta(\delta + t)}\right) \tag{3}$$

where the dies are $L \times W$ in size with thickness t, and H is the height of the entire stack—as illustrated in Figure 2. Optimum die spacings, which maximize the volumetric cooling rate from a chip stack may be found by substituting the channel Nusselt number expression, equation (1), into equation (3), taking the derivative of the resulting expression with respect to δ, and setting the result equal to zero. This process yields the following transcendental equation.

$$\left(2\delta + 3t - a^{-2}\mathrm{El}^{3/2}\delta\right)_{\mathrm{opt}} = 0 \tag{4}$$

where

$$a = 24 \cdot 0.705 = 16.92 \tag{5}$$

The optimum Elenbaas number in the thin die limit, equation (4) with $t = 0$, is marked in Figure 3. This optimum point (El = 69.0, Nu = 1.66) is clearly shown to occur in the transition region between the fully developed channel and isolated plate limits. The subtle effect of die thickness on optimum spacing is shown in Figure 4. As die thickness increases, fewer dies can be accommodated in a fixed stack height or volume, and larger gaps—with their associated higher heat transfer coefficients—are needed to maximize the stack volumetric heat transfer rate. It should be noted, however, that since both the die thickness and the larger gap lead to a smaller number of chips per unit volume, and since the heat transfer coefficient increase is modest, the total chip stack heat transfer rate—even at the optimum spacing—decreases as the die thickness increases.

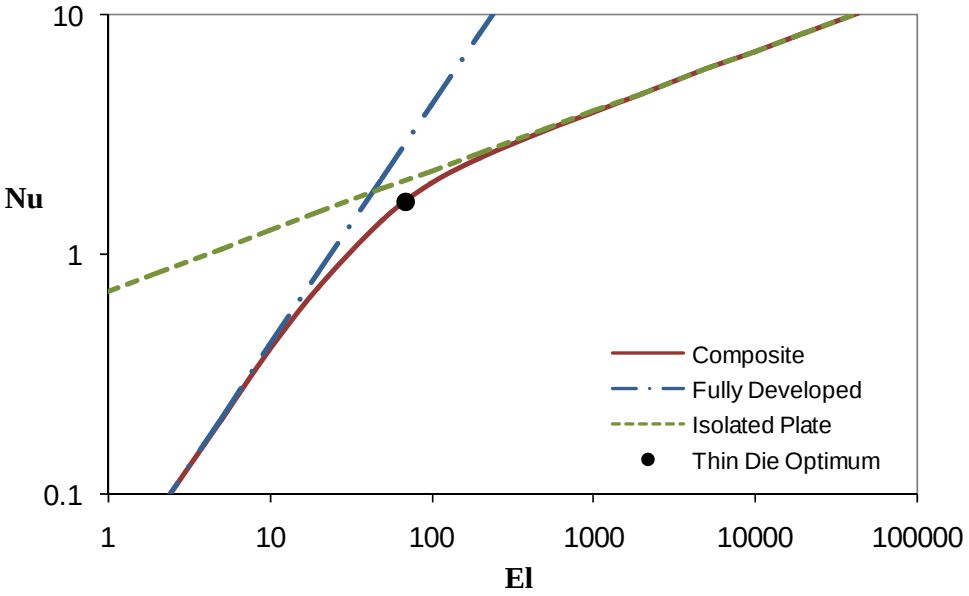

Figure 3. Isothermal Nusselt number correlations for symmetrically heated channels immersed in saturated FC-72 at atmospheric pressure

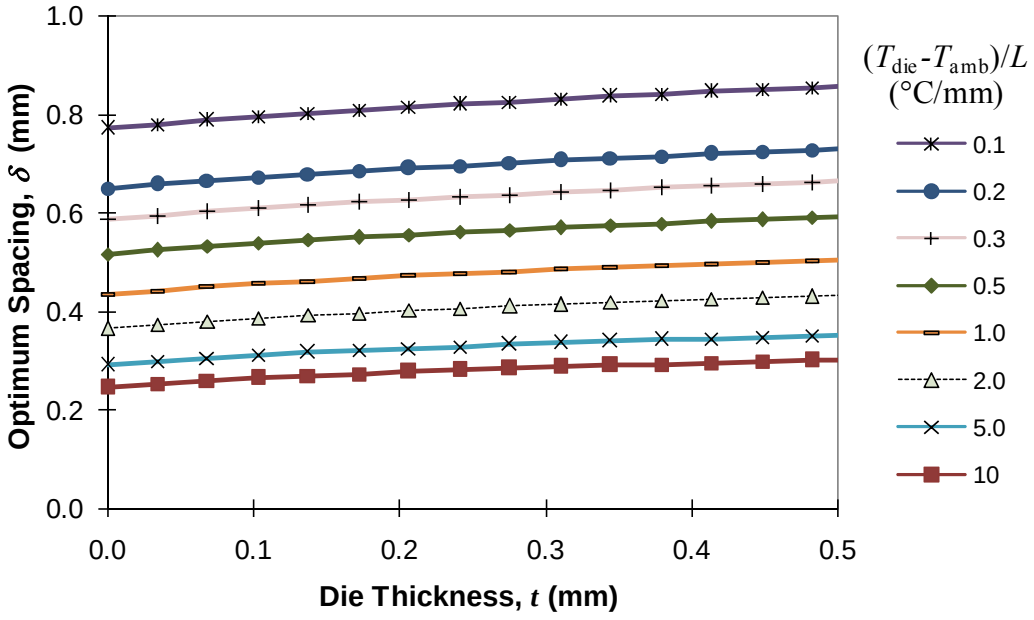

Figure 4. Optimum spacing as a function of die thickness for natural convection in saturated FC-72 at atmospheric pressure

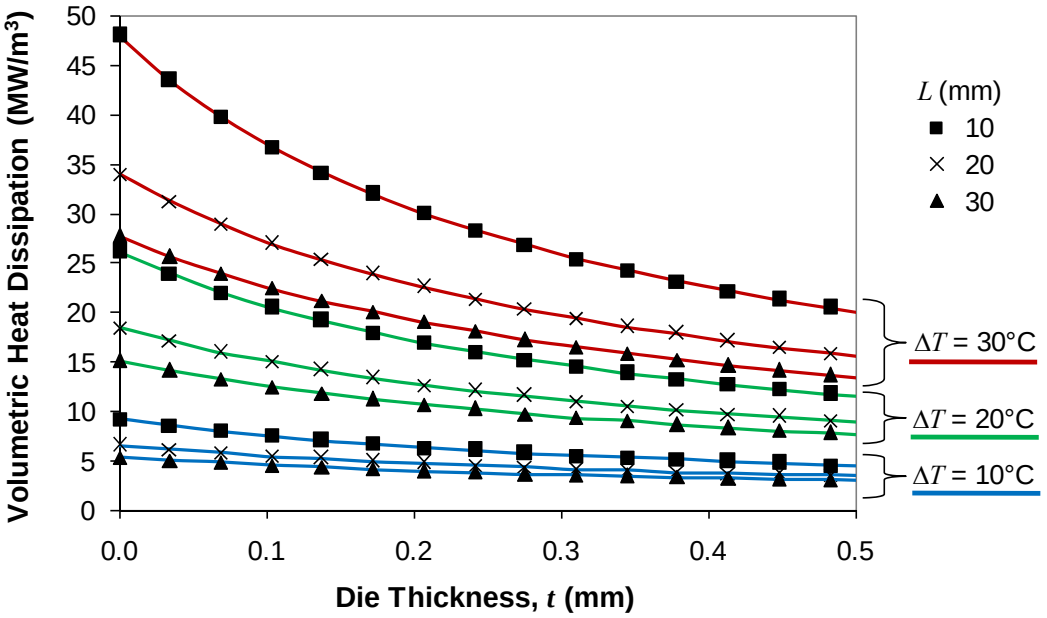

Figure 5. Natural convection volumetric heat dissipation rates for optimum die stacks in saturated FC-72 at atmospheric pressure

Figure 5 shows the volumetric heat dissipation rates, as a function of die thickness for optimally-spaced die stacks, obtained with equation (4). Over the geometric parameter ranges of interest ($t < 0.5$ mm, $L = 10$–30 mm, and $\Delta T = 10$–30°C), optimum die spacings are found to range from 0.25 mm to 0.85 mm, while volumetric heat dissipation rates reach several tens of MW/m^3. While volumetric heat transfer rates for vanishingly thin die immersed in FC-72 can be expected to reach as high as 50 MW/m^3, for more typical configurations where die thickness is approximately equal to these optimum spacings, volumetric dissipation rates are reduced to approximately half of the thin die values, *i.e.* falling in the vicinity of 25 MW/m^3.

Pool Boiling

Unfortunately, the desirable chemical inertness and electrically insulating characteristics of candidate immersion fluids also tend to be accompanied by relatively poor thermal properties. As a consequence, even the optimum natural convection heat transfer coefficients result in cooling rates that are insufficient to meet the demanding requirements of high performance microprocessors. Fortunately, nucleate boiling, which provides significant increases in heat flux with very modest increases in surface temperature, may be employed to significantly enhance heat transfer rates from microelectronics immersed in dielectric liquids.

The upper limit of nucleate boiling is the Critical Heat Flux (CHF), representing the point where the large volume of generated vapor prevents fresh liquid from replenishing the supply at the surface. As a result, the surface becomes blanketed by a thin layer of vapor and increases greatly in temperature. As this temperature excursion can be on the order of 100°C or more, electronics cooling applications are most often restricted to the single phase and nucleate boiling regimes, with CHF as an absolute upper limit. The well known Kutateladze-Zuber CHF relation [6] was developed for saturated pool boiling on large, thick, upward-facing horizontal plates.

$$q''_{\text{K-Z}} = \frac{\pi}{24} C_{\text{lg}} \sqrt{\rho_{\text{g}}} [\sigma_{\text{l}} g(\rho_{\text{l}} - \rho_{\text{g}})]^{1/4} \tag{6}$$

The Zuber analytical treatment considered the Taylor instability criterion for coalesced bubble vapor columns and defined CHF as occurring when the liquid-bubble interface becomes unstable. More recent research has suggested that, for horizontal heaters, lateral bubble coalescence creates dry patches on the surface that eventually reach the Leidenfrost temperature and cause CHF [7]. Mudawar *et al*. [8] derived an interfacial lift-off model for CHF on vertical surfaces based on an analysis of Kelvin-Helmholtz waves. Their resulting equation is identical in form to equation (6), despite being based on a different mechanism. Regardless of its derivation, equation (6) remains relatively accurate and, in particular, captures the effect of pressure on CHF.

In confined die stack geometries, boiling activity can be expected to produce axial quality and vapor fraction gradients, leading to distinct two phase flow regimes. The presence of this vapor will increase fluid buoyancy in the channel. But as boiling activity increases, the growing vapor fraction may eventually lead to dry out (premature CHF) at the heated surfaces, beginning at or near the channel exit, and causing severe heat transfer degradation. Based on earlier work by Monde *et al*. [9] and Bonjour and Lallemand [10], Geisler and Bar-Cohen [11] correlated CHF for symmetrically heated channels as

$$q''_{\text{chan}} = q''_{\text{K-Z}}\left[1+\gamma\left(\frac{L}{\delta}\right)^{1.517}\right]^{-1} \tag{7}$$

where

$$\gamma = 1.08\times10^{-4}\left(\rho_{\text{l}}/\rho_{\text{g}}\right)^{1.343(p/p_c)^{0.252}} \tag{8}$$

The volumetric cooling rate attained at critical heat flux (CHF) may be expressed as

$$\left(\frac{q}{V}\right)_{\text{CHF}} = \frac{Aq''_{\text{CHF}}}{V} = \frac{2nLWq''_{\text{CHF}}}{nLW(\delta+t)} = q''_{\text{CHF}}\frac{2}{(\delta+t)} \tag{9}$$

where n is the number of dies, $H/(\delta+t)$, and q"$_{\text{CHF}}$ is the pool boiling critical heat flux.

Geisler and Bar-Cohen [12] combined equations (6) and (7) with a factor from the literature based on heated surface properties that captures the reduction in CHF expected with decreasing die thickness [7], yielding

$$\left(\frac{q}{V}\right)_{\text{CHF}} = \frac{\pi}{24}\frac{C_{\text{lg}}\sqrt{\rho_{\text{g}}}[\sigma_{\text{l}}g(\rho_{\text{l}}-\rho_{\text{g}})]^{1/4}}{1+\gamma(L/\delta)^{1.517}}\left(\frac{t\sqrt{(\rho c_p k)_{\text{h}}}}{t\sqrt{(\rho c_{\text{p}}k)_{\text{s}}}+0.1}\right)\left(\frac{2}{\delta+t}\right) \tag{10}$$

Figure 6 shows volumetric heat dissipation results for 20 mm long dies immersed in saturated FC-72 at atmospheric pressure as predicted by equation (10). At vanishingly small channel spacings, CHF goes to zero, while the array volume asymptotes to a constant $V=nLWt$. At large spacings, corresponding to $L/\delta < 10$, boiling channels achieve their large spacing CHF limit, and additional spacing increases provide no improvement in overall heat transfer but continue to increase the array volume. Thus, an optimum channel spacing exists in the range $0 < \delta < L/10$ where volumetric heat dissipation is maximized. Peak heat dissipation rates range from 200 to 300 MW/m^3—an order of magnitude higher than can be achieved in single phase natural convection.

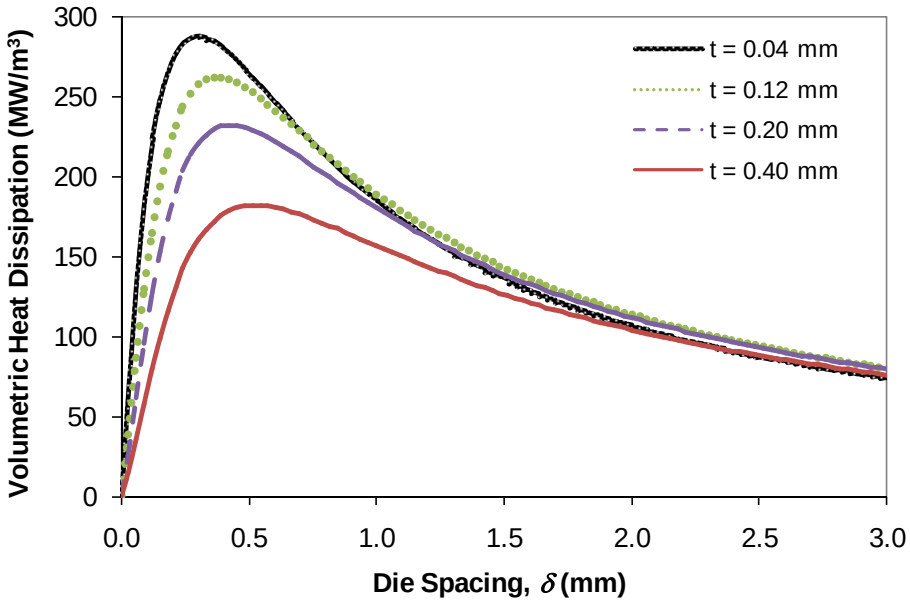

Figure 6. Volumetric heat dissipation at CHF for 20 mm long stacked silicon dies immersed in saturated FC-72 at atmospheric pressure

Optimum die spacings that maximize volumetric heat dissipation may be found by taking the derivative of equation (10) with respect to channel spacing and setting it equal to zero. Algebraic manipulation yields

$$\left(\frac{L}{\delta_{\text{opt}}}\right)=\left[1.517\gamma\left(1+\frac{t}{\delta_{\text{opt}}}\right)-\gamma\right]^{-1/1.517} \tag{11}$$

Figure 7 shows optimum spacing results, calculated using equation (11) over a range of die length and thickness for saturated FC-72 at atmospheric pressure ($\gamma = 0.002412$). As in the case of single phase optimization, as die thickness increases, the number of dies and, hence, gaps per unit volume decreases, thus decreasing the volumetric penalty of larger spacings, while providing modestly higher heat transfer coefficients. It is interesting to note that optimum die spacings are, thus, approximately half a millimeter for both single phase natural convection and pool boiling.

The optimum spacing found with equation (11) can then be used in equation (10) to find the maximum volumetric heat dissipation for a given die length and thickness. Figure 8 shows loci of maxima found in this manner for silicon dies immersed in saturated FC-72 at atmospheric pressure over an unrealistically wide die thickness range of 0.004–4 mm (for illustrative purposes). Optimum volumetric heat dissipation rates are clearly on the order of several hundred MW/m^3. The 280MW/m^3 peak in the $L = 20$ mm curve of Figure 8 occurs at approximately $\delta = 0.3$ mm and $t = 0.04$ mm. For die lengths of 10 and 30 mm, volumetric heat dissipation is a maximum for $t \approx 0.03$ and 0.05 mm, respectively. Fortunately, it can be shown that, in terms of die thickness, the peak volumetric cooling rates are relatively broad and that the effusivity effect on CHF does not significantly counteract the volumetric benefits of decreasing die thickness until $t < 10$ μm [4].

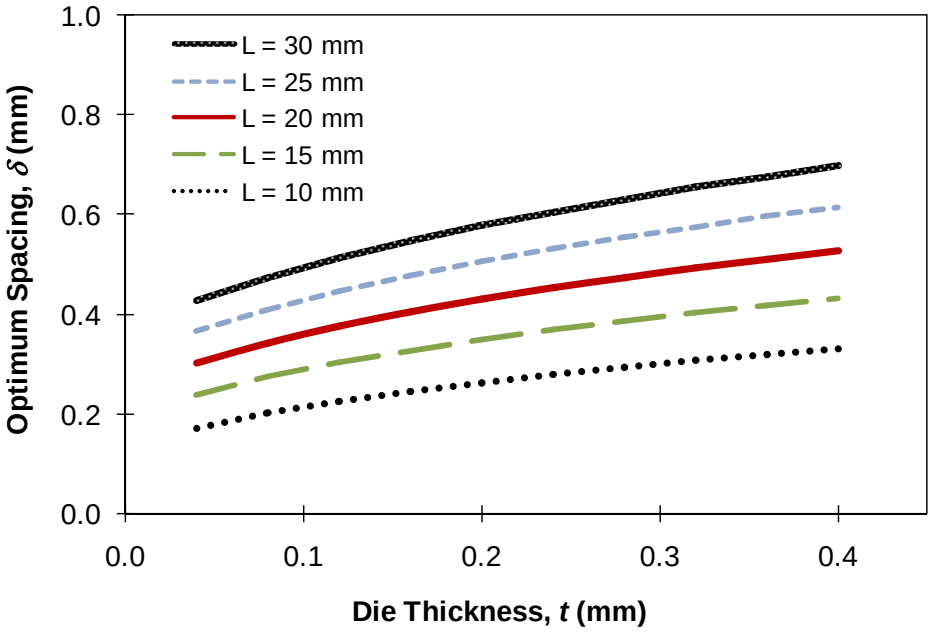

Figure 7. Optimum die spacing calculated using equation (11) for saturated FC-72 at atmospheric pressure

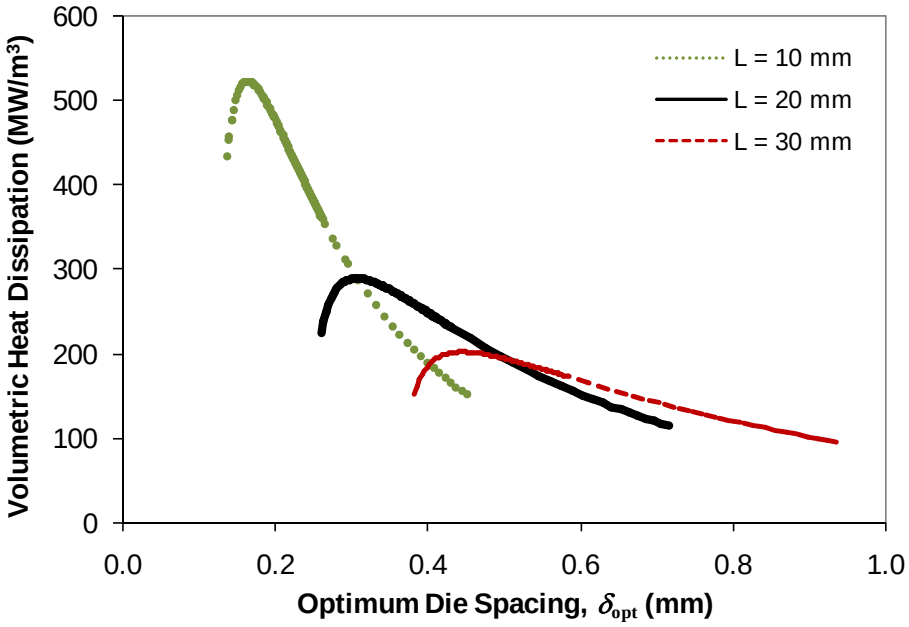

Figure 8. Optimum die spacing and maximum pool boiling volumetric heat dissipation for stacked dies of thickness ranging from 0.010 to 1 mm immersed in saturated FC-72 at atmospheric pressure

SINGLE PHASE MICROCHANNEL COOLERS

Introduction

Attention now shifts to direct liquid cooling approaches which require active pumping of the working fluid, starting with single phase forced convection. Microfabrication techniques have been used to create microchannel heat sinks and coldplates since the early 1980's [13]. Such liquid cooled microchannel coolers are characterized by sub-millimeter gaps and large channel aspect ratios. Flow in such channels results in very thin boundary layers and convective heat transfer coefficients that easily exceed the natural convection values cited above and may rival the highest heat transfer rates achievable in pool boiling. Applying this technique to 3D chip stacks, the entire stack may be seen to be analogous to a microchannel cooler, with dielectric liquid forced between the tightly-spaced chips.

Governing equations

The thermal behavior of single phase flow in high aspect ratio microchannels formed between parallel plates or within a chip stack may be predicted with the Kakac *et al*. [14] isoflux equations for the heat transfer coefficients attained in developing laminar flow. The average Nusselt number, based on the hydraulic diameter and divided into three flow length segments, is given by:

$$\mathrm{Nu}_{D_\mathrm{h}} = 2.236x^* - 0.333 \ \text{ for } \ x^* < 0.001 \tag{12}$$

$$\mathrm{Nu}_{D_\mathrm{h}} = 2.236x^* - 0.333 + 0.9 \ \text{ for } \ 0.001 < x^* < 0.01 \tag{13}$$

$$\mathrm{Nu}_{D_\mathrm{h}} = 8.235 + 0.0364/x^* \ \text{ for } \ x^* > 0.01 \tag{14}$$

where

$$\mathrm{Nu}_{D_\mathrm{h}} \equiv \frac{hD_\mathrm{h}}{k} \tag{15}$$

$$x^* = \frac{L/D_\mathrm{h}}{\mathrm{RePr}} \tag{16}$$

and

$$D_\mathrm{h} = 2\delta \ \text{ (for } \delta << W\text{)} \tag{17}$$

As the reader might anticipate from the analyses shown in the previous sections, to a good first approximation flow in volumetrically-optimized microgaps within a chip stack approach fully developed conditions at the channel exit. Consequently, in determining average heat transfer coefficients for optimized configurations, only the $x^* > 0.01$ segment, equation (14), is required.

The Reynolds number, which is based on hydraulic diameter, may be expressed in terms of mass flux, G (kg/m^{2}s), as

$$\mathrm{Re} = \frac{G2\delta}{\mu} \tag{18}$$

With the Nusselt number correlations provided above, the wall heat transfer coefficient is based on the average temperature of fluid in the channel, $(T_{out}+T_{in})/2$, where

$$\left(T_{\text{out}} - T_{\text{in}}\right) = \frac{q}{c_p G \delta W} \tag{19}$$

Combining this equation with the definition of the heat transfer coefficient yields:

$$q = \left(T_{\text{die}} - T_{\text{in}}\right) W \left(\frac{1}{2Lh} + \frac{1}{2c_p G \delta} \right)^{-1} \tag{20}$$

Considering that the volume of a single channel is $LW(\delta+t)$, volumetric heat dissipation may be expressed as

$$\frac{q}{V} = \frac{\left(T_{\text{die}} - T_{\text{in}}\right)}{L\left(\delta + t\right)} \left(\frac{1}{2Lh} + \frac{1}{2c_p G \delta} \right)^{-1} \tag{21}$$

where

$$h = \frac{\text{Nu}k}{D_{\text{h}}} = \frac{8.235k}{2\delta} + 0.0364 \frac{2G\delta c_p}{L} \tag{22}$$

Heat transfer rates

Sample results for the dependence of volumetric heat dissipation on die spacing are shown in Figure 9 for saturated FC-72 at atmospheric pressure, assuming a die length of 20 mm and thickness of 0.3 mm, with an average die temperature 30°C above the inlet, and for various channels mass fluxes. These data demonstrate than when mass flux, G, (and, therefore, average channel velocity) is fixed, there exists an optimum spacing which maximizes the volumetric heat transfer. For the examples shown in Figure 9, the optimum spacings are near 0.1 mm, and volumetric heat dissipation rates approach 250 MW/m^3.

In order to find these optima explicitly, one can take the derivative of equation (21) with respect to channel spacing and set it equal to zero. This process yields the following fourth order polynomial in δ.

$$\frac{8 \cdot 0.0364^2 + 4 \cdot 0.0364}{8.235} \Gamma \delta^4 - \frac{2}{t} \delta^3 + \left(4 \cdot 0.0364 - 1\right) \delta^2 + \frac{8.235}{2\Gamma} = 0 \tag{23}$$

where

$$\Gamma = \frac{G c_p}{kL} \tag{24}$$

Detailed expressions for the coefficients in equation (23) are shown to demonstrate their lineage back to the Nusselt number correlation, equation (14). Unfortunately, analytical solutions to the roots of equation (23) are prohibitively complex. Numerical solution of equation (23) must be pursued carefully, not only to select the proper root, but also to ensure convergence, as the values of

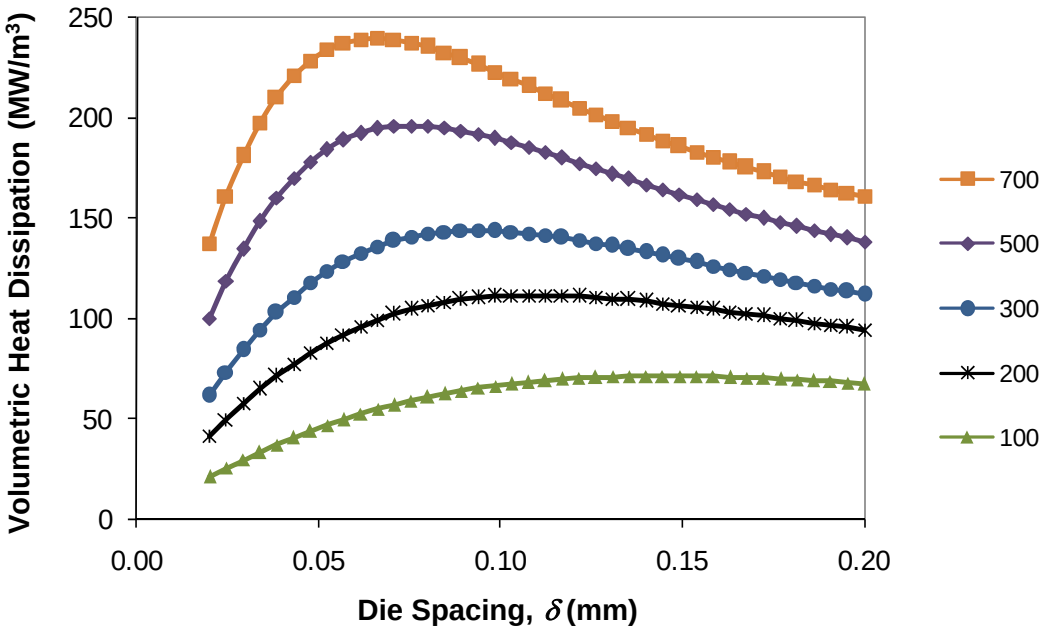

Figure 9. Volumetric heat dissipation results for single phase forced convection cooled die stacks with $L = 20$ mm, $t = 0.3$ mm, and $\Delta T = 30°C$

the polynomial coefficients may differ by fifteen to twenty orders of magnitude. It is interesting to note that the optimum spacing is only dependent on temperature through the temperature dependence of the fluid thermal conductivity and specific heat. Further, the relationship between die thickness and optimum spacing depends only on Γ. Figure 10 shows the results of numerical solution of equation (23) and demonstrates that over a wide parametric range, optimum spacings fall between 0.02 mm and 0.2 mm.

Figure 11 shows volumetric heat dissipation rates as a function of die thickness for optimally-spaced stacks of 20 mm long dies in saturated FC-72 at atmospheric pressure, with an average die to inlet temperature rise of 30°C. Over a range of mass flux from 100 to 700 kg/m^{2}s and die thicknesses between 0.1 and 0.5 mm, heat transfer rates are shown to range from 100 to 500 MW/m^3—comparable to the results shown in the previous section for die stacks optimized for pool boiling. For a given set of conditions, the single phase forced convection provides less heat transfer per die than pool boiling, but the optimum spacing is smaller so the net result is comparable volumetric heat transfer. Over a wider parametric range ($L = 10$–30 mm, and $\Delta T = 10$–$30°C$), optimum die spacings range from 40 to 190 μm, while volumetric heat dissipation rates span 13 to 850 MW/m^3. Corresponding Nusselt numbers are in a very narrow range, 8.6 ± 0.3, signifying near fully developed channel flow ($x^* = 0.06$–0.2). Reynolds numbers are deep into the laminar regime, less than 300, validating the appropriateness of the various correlations employed.

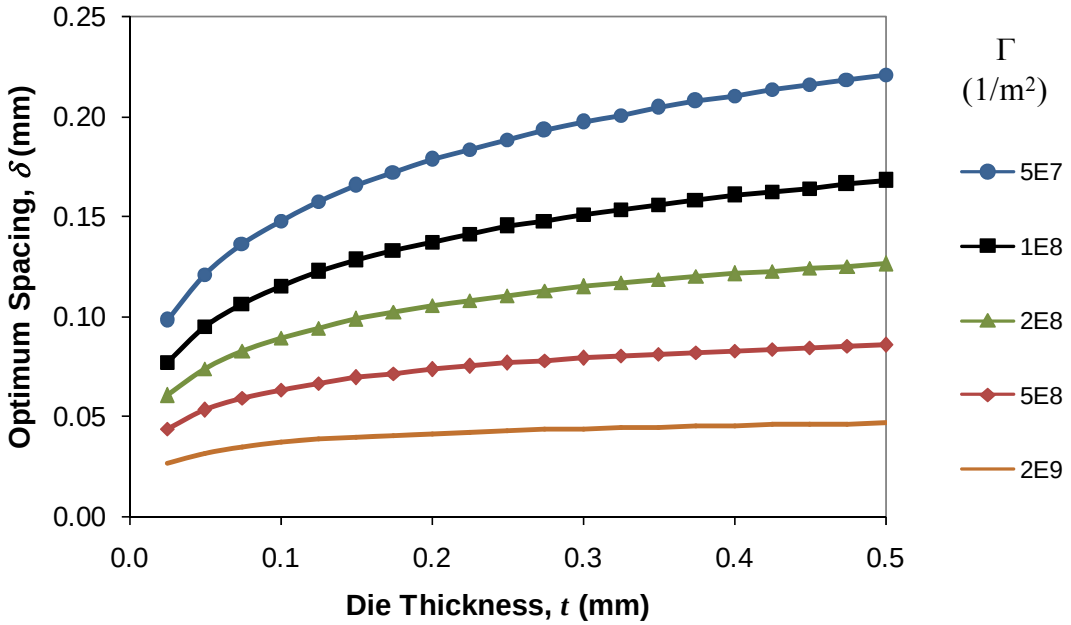

Figure 10. Optimum spacing as a function of die thickness for single phase forced convection in saturated FC-72 at atmospheric pressure

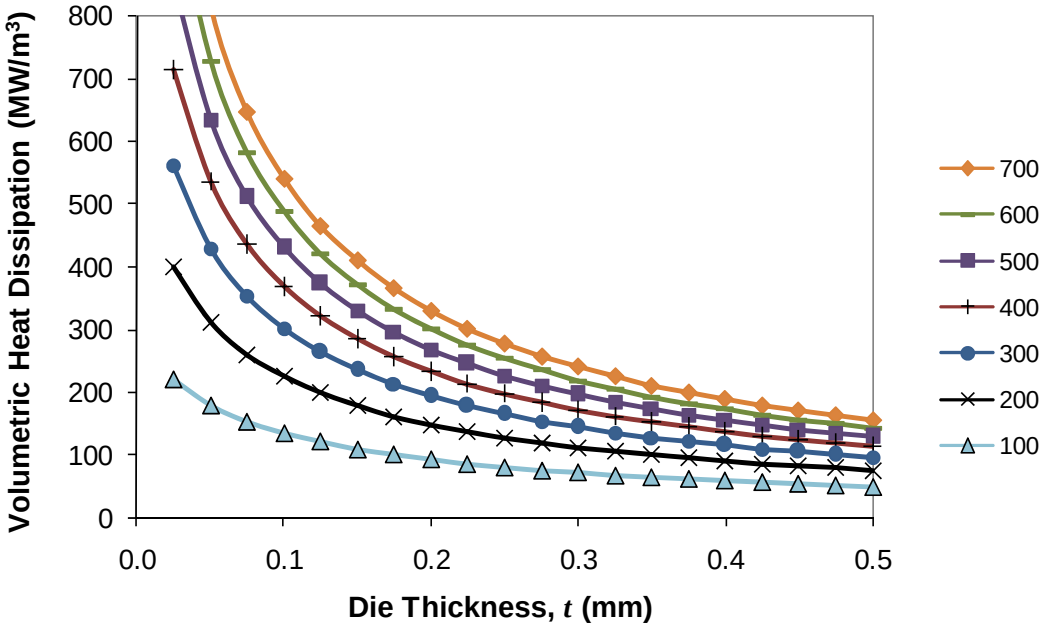

Figure 11. Single phase forced convection volumetric heat dissipation rates for optimum die stacks in saturated FC-72 at atmospheric pressure, $L = 20$ mm, $\Delta T = 30°C$.

FLOW BOILING

Introduction

The relatively high heat transfer rates attainable with nucleate pool boiling and forced convection of dielectric liquids flowing through miniature channels, respectively, makes the forced evaporative flow of such liquids in a heated microgap channel between chips a most promising candidate for the thermal management of advanced semiconductor devices. Interestingly, gas-driven flow of a dielectric liquid through miniaturized channels, formed by the microgaps between gallium arsenide chips and adjacent circuit boards, was used to provide thermal management for a compact, three-dimensional, high performance module in the Cray-3 computer developed in the 1990's [15]. Regrettably, few validated correlations exist for flow boiling in miniature channels, but understanding and identification of the prevailing flow regimes can facilitate a regime-informed extrapolation of available data and traditional flow boiling correlations to the prediction of heat transfer rates in the gaps formed between chips in a 3D stack.

Flow regimes

The inherent complexity of two-phase thermal transport and its parametric sensitivities in miniature channel flow can be expected to lead to substantial variations in the heat transfer coefficient as the vapor quality increases from near-zero (saturated liquid) to near-unity (saturated vapor) conditions. The physics-based models used in the Taitel and Dukler flow regime maps appear to offer the best basis for determining the prevailing flow regimes in evaporating refrigerant and dielectric liquid flow within miniaturized channels [16].

As an example, Kim *et al*. [17] performed an exploratory experimental study of the thermofluid characteristics of flow boiling in a 10 mm wide by 37 mm long (in the flow direction) microgap channel. The asymmetrically heated channel, formed between a heated copper surface and an acrylic visualization window, was tested in a horizontal orientation. Channel spacings of 110, 210, and 550 μm were investigated. The inlet temperature of the coolant was maintained at 25 ± 0.2°C, with mass flux varying from 56 kg/m^{2}s to 1270 kg/m^{2}s. Figure 12 provides a Taitel-Dukler flow regime map for FC-72 flowing at 133 kg/m2s through the 110 μm microgap channel studied by Kim *et al*. [17]. While the four primary flow regimes—*i.e*. Stratified, Intermittent, Bubble, Annular—are identified on the map, for the 210 and 500 μm channels and for liquid volumetric flow rates from 0.17 ml/s to 0.83 ml/s, the liquid and vapor superficial velocities lead to microchannel operation exclusively in the Intermittent and Annular flow regimes.

Heat transfer limits

Building on the foregoing success in validating a flow-regime-informed approach to the analysis and evaluation of the two-phase heat transfer coefficients in miniature channels, Bar-Cohen and Rahim [16], examined the predictive accuracy of five classical two-phase heat transfer correlations, namely those due to Chen [18], Kandlikar [19], Gungor-Winterton [20], Gungor-Winterton Revised [21], and Shah [22].

The comparison of the correlations to the available miniature channel data for refrigerants and dielectric liquids was conducted by dividing the available data into three categories: Intermittent Flow, Annular Flow-low quality, and Annular Flow–moderate quality. The peak heat transfer coefficient reported for each set of conditions was used as the criteria for separating the "low quality" and "moderate quality" sub-regimes of annular flow. When the data are aggregated in this "regime-sorted" manner, Bar-Cohen and Rahim [16] showed that selecting the best fitting of the classical correlations for each of the flow regime categories, yields predictive agreement with regime-sorted heat transfer coefficients that does not depart significantly from the agreement found in large pipes and channels. In particular, the dominant, low quality Annular data was found to be

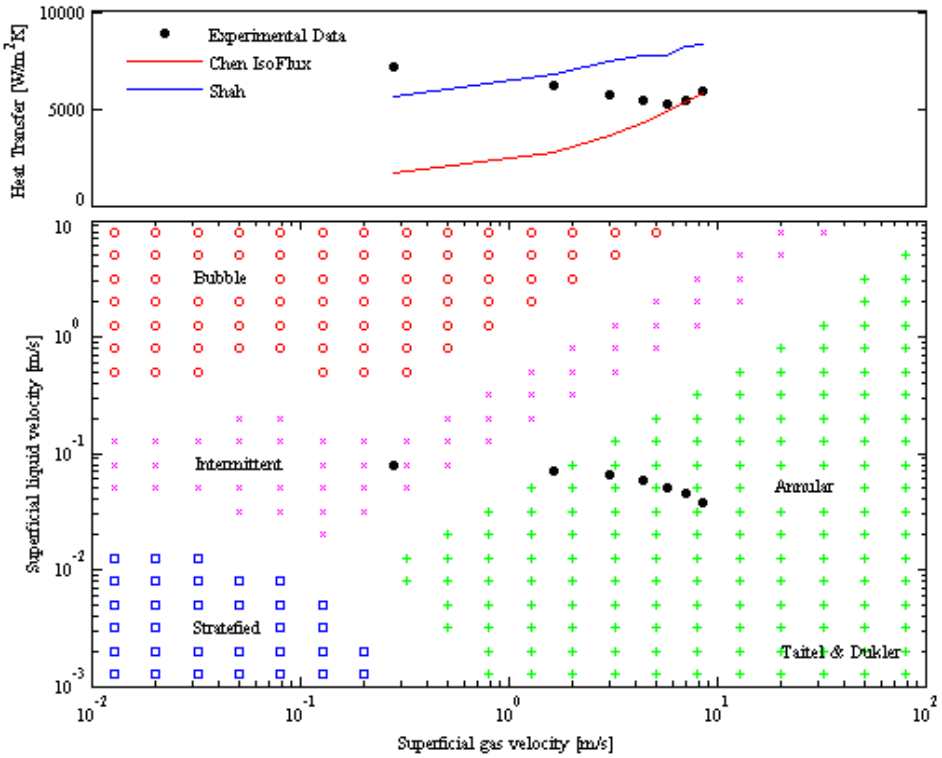

Figure 12. Heat transfer coefficient comparison and Taitel-Dukler flow regime map for 110 μm channel, with data representing a mass flux of 133.3 kg/m^{2}s and heat flux of 16.8 kW/m^2

correlated by the Chen correlation to within an average discrepancy of just 24% and standard deviation of 31%, while the Shah correlation provides agreement to within an average discrepancy of 32% and standard deviation of 40% for data in the Intermittent regime.

The measured values of the area-averaged experimental heat transfer coefficients from Kim *et al.* [17], spanning a range of 5 kW/m^{2}K to 7.5 kW/m^{2}K as a function of superficial vapor velocity (or quality), are shown in Figure 12 above the flow regime map, along with predictions based on the Shah [22] and Chen [18] correlations. In agreement with expectations, all but one of these heat transfer coefficient values are seen to be bounded by these two correlations.

Performance limits and optimum spacings

Based on the foregoing, it would appear that the highest heat transfer rates in two-phase flow through miniature channels will be attained in the annular regime, relying on the evaporation of vanishingly thin liquid films. Previous work has shown that the venerable Chen correlation can predict the heat transfer coefficients in this regime, prior to local dryout, with a standard deviation of 31%. The Chen correlation finds the two phase heat transfer coefficient as the sum of the nucleate boiling contribution (microscopic contribution, or h_{mic}) and the convective boiling contribution (macroscopic contribution, or h_{mac}).

$$h_{\mathrm{TP}} = h_{\mathrm{mic}} + h_{\mathrm{mac}} \tag{25}$$

The microscopic contribution was found as

$$h_{\mathrm{mic}} = 0.00122\left[\frac{k_{\mathrm{l}}^{0.79} c_{p,\mathrm{l}}^{0.45} \rho_{\mathrm{l}}^{0.49}}{\sigma^{0.5} \mu_{\mathrm{l}}^{0.29} h_{\mathrm{lg}}^{0.24} \rho_{\mathrm{g}}^{0.24}}\right]\left[T_{\mathrm{w}} - T_{\mathrm{sat}}(P_{\mathrm{l}})\right]^{0.24}\left[P_{\mathrm{sat}}(T_{\mathrm{w}}) - P_{\mathrm{l}}\right]^{0.75} S \tag{26}$$

where S is the suppression factor which was originally presented by Chen in a graphical format. The empirical fit of the suppression factor as introduced by Collier was used in this study as

$$S\left(\mathrm{Re}_{\mathrm{tp}}\right)=\left(1.25+2.56\times10^{-6}\,\mathrm{Re}_{\mathrm{tp}}^{1.17}\right)^{-1} \tag{27}$$

The macroscopic contribution was found using the Dengler-Addoms correlation with a Prandtl number correction factor to generalize the correlation beyond water as a working fluid.

$$h_{\mathrm{mac}}=h_{\mathrm{l}}F\left(X_{tt}\right)\mathrm{Pr}_{\mathrm{l}}^{0.296} \tag{28}$$

where the empirical fit of the enhancement factor, F, as a function of the Martinelli parameter, X_{tt}, provided by Collier was used in this study as

$$F\left(X_{tt}\right)=1 \text{ for } X_{tt}^{-1}\le 0.1 \tag{29}$$

$$F\left(X_{tt}\right)=2.35\left(0.213+\frac{1}{X_{tt}}\right)^{0.736} \text{ for } X_{tt}^{-1}>0.1 \tag{30}$$

The macroscopic contribution was found to be dominating in the micro channel flow boiling as the nucleate boiling is suppressed because of the very thin liquid film and the insufficient super heat at the channel (die) wall.

Volumetric heat transfer rates, obtained via the Chen correlation, for microgap channels of 50 μm to 1.3 mm, operating with mass fluxes of 100 to 1000 kg/m^{2}s are shown in Figure 13. These values are based on the maximum heat transfer coefficient for values of mass flux and channel gap in such a way not to exceed a wall temperature of 85$^{\mathrm{o}}$C, for a single channel between two dies of 20 mm by 20 mm each.

As can be seen in Figure 13, to the accuracy of the Chen correlation used, an optimum gap of approximately 0.150 to 0.200 mm appears to exist for the two-phase cooling of such a chip stack and to be nearly insensitive to mass flux. A maximum volumetric heat dissipation of 2.1 GW/m^3 is achievable with a mass flux of 1000 kg/m^{2}s of FC-72 in a 0.150 mm single gap channel. This volumetric cooling rates drops quickly as the mass flux decreases and the gap size increases. Thus, at a mass flux of 100 kg/m^{2}s the optimum gap yields a volumetric cooling rate of 200 MW/m^3 and for gaps of approximately 1 mm, even the highest mass flux of 1000 kg/m^{2}s yields cooling rates below 200 MW/m^3.

PERFORMANCE MAPPING

In addition to the range of possible volumetric cooling rates discussed in the individual sections above, it is instructive to make a direct comparison of the heat densities associated with the four considered heat transfer modes through the use of performance maps. Since it is often not possible to capture the full value or cost associated with a particular cooling technique with just one pair of metrics, several performance maps will be discussed. For purposes of this comparison, it will be assumed that saturated FC-72 at 1 atm is the working fluid and that the chips are 20 mm square and 0.3 mm thick with an allowed maximum chip surface temperature of 85°C. Fluid flow rates and velocities for natural convection and pool boiling are determined by the physics of these buoyancy-driven flows, while for the forced flow approaches, flow rate or inlet velocity must be specified.

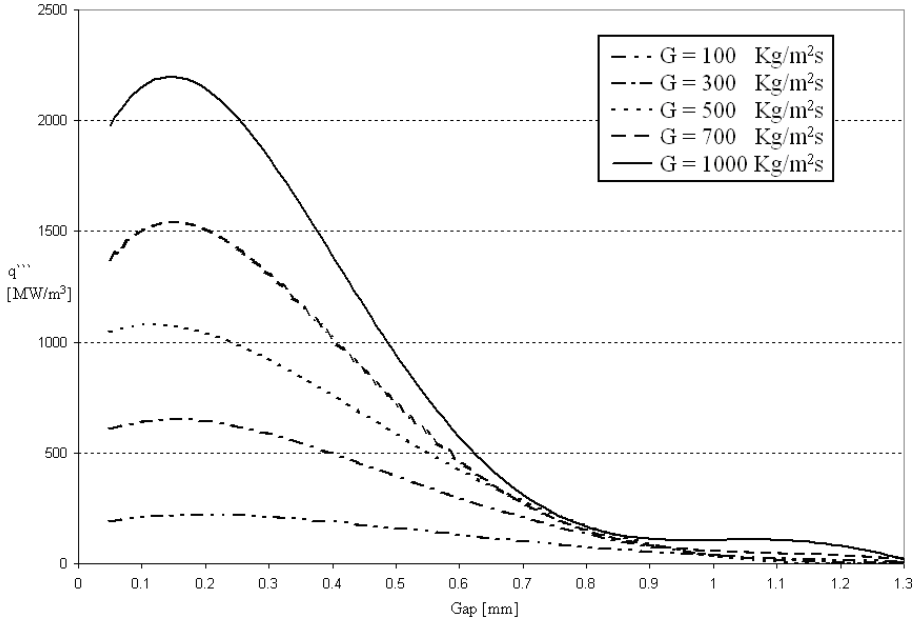

Figure 13. Volumetric heat dissipation in two-phase flow of FC-72 in a single channel mini gap

Figure 14 shows a 3D chip stack immersion cooling performance map, expressed in terms of volumetric heat dissipation versus gap dimension. In Figure 15, the data behind Figure 14 is displayed in terms of chip surface heat flux. Since in a given application the total (volumetric) flow rate available to a stack can be expected to be determined by system-level capabilities and considerations, the forced flow curves in Figure 14 are based on a condition of fixed volumetric flow rate per gap. For the case of fixed volumetric flow rate, V, the Reynolds number, equation (18), can be shown to be independent of chip spacing:

$$\mathrm{Re} = G\left(\frac{2\delta}{\mu}\right) = \left(\frac{\rho V}{\delta W}\right)\left(\frac{2\delta}{\mu}\right) = \frac{2\rho V}{\mu W} \tag{31}$$

For single phase forced convection, the transition to turbulence is expected to begin at a Reynolds number of 2300. Beyond this point, the McAdams equation for turbulent single phase forced convection is employed

$$\mathrm{Nu}_{D_h} = 0.023\,\mathrm{Re}_{D_h}^{0.8}\,\mathrm{Pr}^{0.333} \tag{32}$$

For the conditions and geometry on which the curves of Figure 14 are based, the transition to turbulence occurs between 6 and 7 mL/s.

Clearly, as expected, in Figures 14 and 15 the highest volumetric heat dissipations and highest chip surface heat fluxes are achieved with flow boiling. Likewise, single phase natural convection provides the lowest heat transfer capability of the four modes shown. For gap spacings in the 0.2 to 0.3 mm range, single phase forced convection and pool boiling provide roughly equivalent performance, with pool boiling improving at larger spacings and forced convection improving with reductions in gap size. As discussed in earlier sections, volumetric heat dissipation for the two passive cooling modes peaks at gap spacings near 0.5 mm, with sharply reduced performance below 0.2 mm for natural convection and 0.1 mm for pool boiling. On the other hand, for the active cooling modes (forced convection and flow boiling), both chip stack volumetric heat dissipation and chip surface heat flux are maximized at small gap spacings and decrease with increasing gap size.

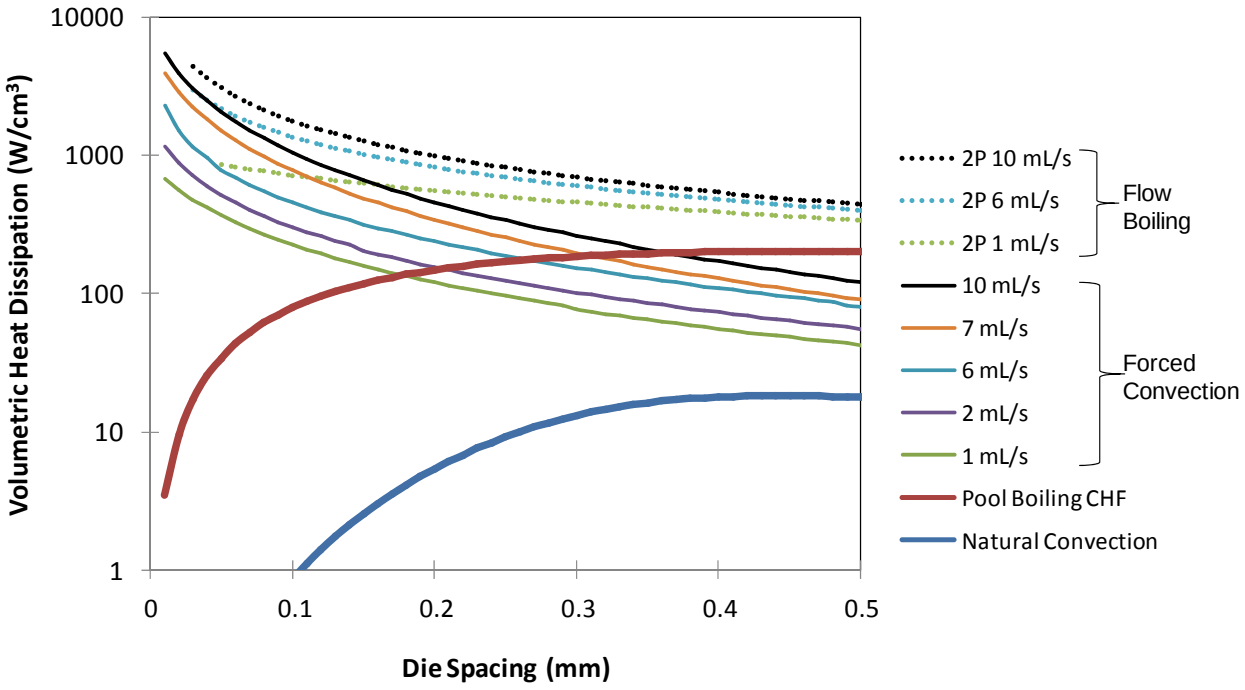

Figure 14. Volumetric heat dissipation performance map, fixed volumetric flow rate

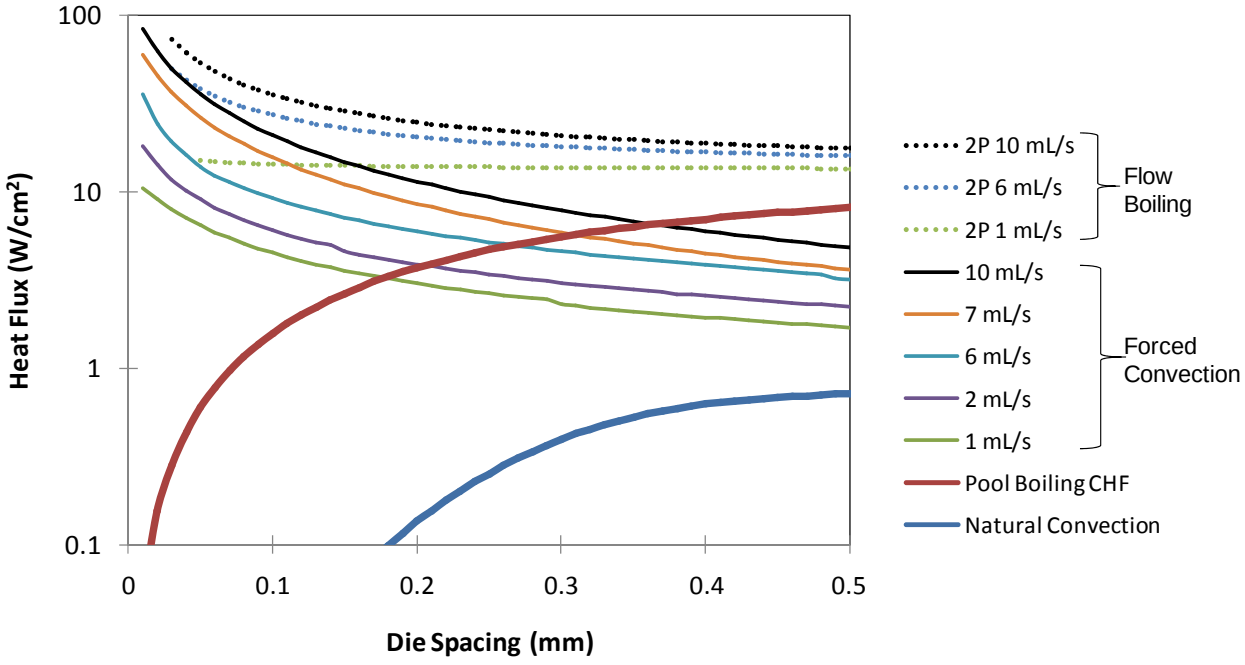

Figure 15. Heat flux performance map, fixed volumetric flow rate

Passive techniques (natural convection and pool boiling) require no input power and may be easier to implement but provide somewhat limited heat transfer capability. It should be noted that proven immersion cooling enhancement techniques (*e.g.* liquid subcooling, liquid mixtures, surface modifications, *etc.*) could be employed to push these limits significantly higher. While the greatest heat transfer performance is achieved with forced flow approaches with very small spacings, channel pressure drop and, therefore, pumping power requirements can be expected to increase drastically with increasing flow rates and decreasing gap sizes. As the curves of Figures 14 and 15 are based on a fixed volumetric flow rate condition, reducing the gap size by a given factor increases the liquid velocity at the channel inlet by that same factor.

Figure 16 shows a performance map for volumetric heat dissipation like Figure 14 but, in this case, based on a condition of fixed gap inlet velocity. The natural convection and pool boiling curves are unchanged, but the forced flow curves display different features. The single phase forced convection curves are the most changed. With inlet velocity fixed, heat transfer capability drops dramatically at the smallest die spacings as the sensible heat rise in the fluid limits performance. In terms of both volumetric heat dissipation and chip surface heat flux, local maxima are observed at die spacings ranging from 0.02 to 0.05 mm. A reduction and subsequent increase and second local maxima is later observed at higher die spacings. Since velocity is constant for these calculations, Reynolds number increases with increasing spacing, and this second peak represents the transition to turbulence. While turbulent flow provides greatly increased heat transfer performance, its associated increased pressure drop characteristics may render it impractical for some applications.

In all of the performance maps, Figures 14-16, and regardless of the flow condition imposed, flow boiling curves are terminated on the low end as flow exit quality is necessarily limited to values less than 1. The main result of holding inlet velocity constant in Figure 16 for flow boiling is that the curves are flatter and display a subtle maximum in the vicinity of this limit.

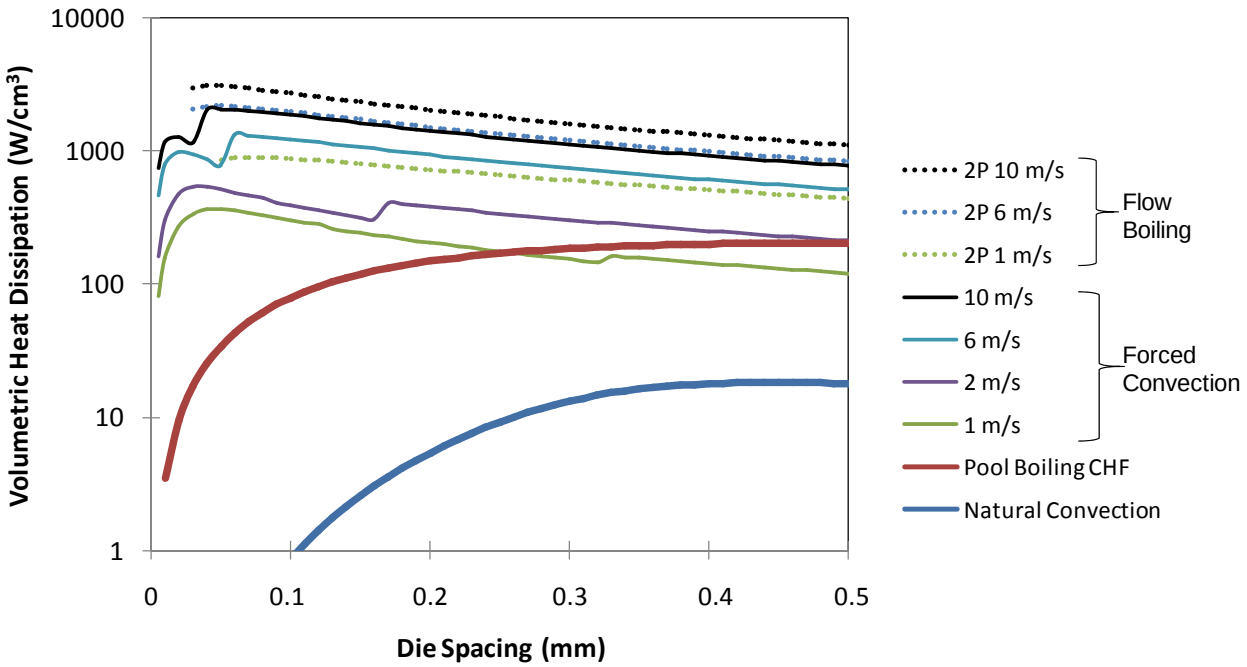

Figure 16. Volumetric heat dissipation performance map, fixed gap inlet velocity

CONCLUSIONS

The foregoing has explored the thermal management potential of direct liquid cooling of 3D chip stacks, a crucial building block in advanced microsystem architectures of the future. The introduction of miniature liquid passages between adjacent chips, providing convective and/or ebullient heat transfer, along with buoyant fluid flow in these narrow gaps, was shown to offer a most promising alternative to conduction cooling of three-dimensional chip stacks. It was shown that cooling densities ranging from 25 MW/m^3 (or $25W/cm^3$) for natural convection, to 200 to 400 MW/m^3 for pool boiling, to 100 to 300 MW/m^3; for forced convection, and in excess of 2 GW/m^3 for flow boiling could be achieved using FC72 as the dielectric coolant. Optimum die spacings for both single and two phase cooling were found to be in the range of 0.2 mm to 0.6 mm for typical microelectronics geometries.

It may, thus, be surmised that passive immersion cooling—relying on natural convection and/or pool boiling—could provide the requisite thermal management capability for 3D chip stacks anticipated for use in much of the portable equipment category. Alternatively, pumped flow of dielectric liquids through the microgaps in 3D stacks, providing single phase and/or flow boiling heat absorption, could meet many of the most extreme thermal management requirements for high-performance 3D microsystems.

However, due to the thermofluid complexity of ebullient phenomena and the paucity of data for pool and flow boiling of dielectric liquids in microgaps, much more fundamental research is needed to solidify the physical understanding of these phenomena and to underpin the basic relations needed for the design and optimization of 3D immersion cooled microsystems.

NOMENCLATURE

El	Elenbaas number
F	forced convection enhancement factor
G	mass flux, kg/m2s
n	number of dies
Nu	Nusselt number
Pr	Prandtl number
Ra	Rayleigh number
S	nucleate boiling supression factor
t	die thickness, m
X_{tt}	Martinelli parameter
x^*	dimensionless channel length

Greek

δ	die/channel spacing, m
Γ	single phase optimization parameter
γ	fluid density parameter
ψ	two phase enhancement ratio

Subscript

amb	ambient
CHF	critical heat flux
h	heater
mac	macroscopic
mic	microscopic
opt	optimum
sat	saturated
tp	two phase

REFERENCES

1. Gerlach, D. and Joshi, Y.K., 2006, Parametric thermal modeling of 3D stacked chip electronics with interleaved solid heat spreaders, Proceedings of the Tenth Intersociety Conference on Thermal and Thermomechanical Phenomena in Electronic Systems, 1208–1212.
2. Bar-Cohen, A. and Rohsenow, W.M., 1984, Thermal optimum spacing of vertical, natural convection cooled, vertical plates, Journal of Heat Transfer, 106, 116-122.
3. Bar-Cohen, A. and Schweitzer, H., 1985, Convective immersion cooling of parallel vertical plates, IEEE Transactions on Components, Hybrids, and Manufacturing Technology, CHMT-8(3), 343-351.
4. Geisler, K.J.L., 2007, Buoyancy-Driven Two Phase Flow and Boiling Heat Transfer in Narrow Vertical Channels, Ph.D. Thesis, Department of Mechanical Engineering, University of Minnesota. http://www.menet.umn.edu/~kgeisler
5. Elenbaas, W., 1942, Heat dissipation of parallel plates by free convection, Physica, 9(1), 665–671.
6. Zuber, N., 1958, On the Stability of Boiling Heat Transfer, Transactions of the ASME, 80(1), 711-720.
7. Arik, M., and Bar-Cohen, A., 2003, Effusivity-based correlation of surface property effects in pool boiling CHF of dielectric liquids, International Journal of Heat and Mass Transfer, 46, 3755–3764.
8. Mudawar, I, Howard, A.H., and Gersey, C.O., 1997. An analytical model for near-saturated pool boiling critical heat flux on vertical surfaces, International Journal of Heat and Mass Transfer, 40(10), 2327–2339.
9. Monde, M., Kusuda H., and Uehara, H., 1982. Critical heat flux during natural convective boiling in vertical rectangular channels submerged in saturated liquid, Journal of Heat Transfer, Vol. 104, no. 2, pp. 300–303.
10. Bonjour, J. and Lallemand, M., 1997. Effects of confinement and pressure on critical heat flux during natural convective boiling in vertical channels, International Communications in Heat and Mass Transfer, Vol. 24, no. 2, pp. 191–200.
11. Geisler, K.J.L., and Bar-Cohen, A., 2009. Confinement effects on nucleate boiling and critical heat flux in buoyancy-driven microchannels, International Journal of Heat and Mass Transfer, 52 (2009), 2427–2436, doi:10.1016/j.ijheatmasstransfer.2009.02.001.
12. Geisler, K.J.L., and Bar-Cohen, A., 2009. Passive immersion cooling of 3-D stacked dies, IEEE Transactions on Components and Packaging Technologies, article in press, 10.1109/TCAPT.2008.2006186.
13. Phillips, R.J., 1990, Microchannel Heat Sinks, Chapter 3 in Advances in Thermal Modeling of Electronic Components and Systems, Volume 2, A. Bar-Cohen and A.D. Kraus, eds., ASME Press, New York.
14. Kakac, S., Shah, R.K., and Aung, W., 1987, Handbook of Single-Phase Convective Heat Transfer, John Wiley & Sons, New York.
15. Bar-Cohen, A., Sherwood, G., Hodes, M., and Solbrekken, G., 1995, Gas-Assisted Evaporative Cooling of High Density Electronic Modules, IEEE Transactions on Components, Hybrids, and Manufacturing Technology, Vol. 18, no. 3, pp. 502-509.
16. Bar-Cohen, A., E. Rahim, 2009. Modeling and prediction of two-phase microgap channel heat transfer characteristics, Heat Transfer Engineering, Vol. 30, no. 8, pp. 601.
17. Kim, D.W., Rahim, E., and Bar-Cohen, A., 2007, Thermofluid Characteristics of Two-Phase Microgap Coolers, InterPACK 2007, Vancouver, BC, Canada.
18. Chen, J. C., 1966, Correlation for Boiling Heat Transfer to Saturated Fluids in Convective Flow, Industrial and Engineering Chemistry, Process Design and Development, (5)3, 322-329.

19. Kandlikar, S.G. and Balasubramanian, P., 2004, An extension of the flow boiling correlation to transition, laminar, and deep laminar flows in minichannels and microchannels, Heat Transfer Engineering, Vol. 25, no. 3, pp. 86-93.
20. Gungor, K.E., and Winterton, R.H.S., 1986, A General Correlation for Flow Boiling in Tubes and Annuli, International Journal of Heat and Mass Transfer, Vol. 29, no. 3, pp. 351-358.
21. Gungor, K.E., and Winterton, R.H.S., 1987, Simplified General Correlation for Saturated Flow Boiling and Comparisons of Correlations with Data, Chemical Engineering Research and Design, Vol. 65, no. 2, pp.148-156.
22. Shah, M. M., 1976, A New Correlation for Heat Transfer during Boiling Flow through Pipes, ASHRAE Transactions, (82)2, 66-86.

THE INFLUENCE OF BOUNDARY CONDITIONS ON TURBULENT JETS

Andrew Pollard[1]
Department of Mechanical and Materials Engineering
Queen's University at Kingston, ON, CANADA K7L-3N6

ABSTRACT In this paper free round turbulent jets and the influence of boundary conditions are considered. The boundary conditions include altering the exit conditions of the mean and turbulence quantities, altering the vorticity generation at the exit through the introduction of tabs and altering the entrainment by the introduction of walls. The notion of a mixing transition is reviewed using new experimental data obtained using a novel flying hot wire experiment. Various structure eduction schemes are applied to the near field of a jet to assist in the identification of important features in the flow.

Keywords *Round jets, boundary conditions, hot wire anemometry, wall jets, jets with tabs, structure eduction*

INTRODUCTION

The round turbulent jet is basic to our understanding of turbulence, and the addition of physico-chemical phenomena such as mixing and combustion greatly complicate this canonical flow, see Pollard and Candel [1]. A free jet can be created rather straightforwardly: blow a fluid through a "nozzle" and it happily reacts with its surroundings by entraining the ambient fluid. What this paper attempts to review are: what are the influences of the initial conditions of the jet itself (mean and turbulence velocity distributions across the jet at the exit of the nozzle); what are the influences brought to the jet by altering the external ambient fluid or boundary conditions; what structural changes occur to the turbulence in each of these cases and what are the effects of Reynolds number on the preceding as well as on turbulence length scales.

The self-similar far field and propagation of inlet effects

Traditional similarity solution for the far field of a round jet has been shown by George [2] to be flawed. He postulated another approach that may be taken to achieve a self-similar solution: the "traditional" approach, which assumes a point source of momentum that is independent of source conditions, does not account for the "considerable evidence that the growth rates in jets arising from different source conditions are (also) different". The inclusion of initial conditions and no *a-priori* assumptions about the functional dependence of U_S, R_S and δ is required. To achieve solutions that result in self-similarity the solution must account for a dynamic relative balance at any given axial and radial location and must include *source conditions*, George [2] derived the following:

[1]Corresponding author: Prof. Andrew Pollard
Phone: +(1) 613-533-2569, Fax: +(1) 613-533-6489
E-mail address: pollard@me.queensu.ca
Note that portions of this paper were presented at CHT'08, Marrakech, Morocco 2008.

$-f^2 + (f'/\eta)\int_0^\eta f\eta\, d\eta = \left\{R_S / (U_S^2 d\delta/dx)\right\}(\eta g_{12})'/\eta$ which all jets must obey if they are self-similar, with the differences being only an amplitude factor due to the {.} term. That is, all mean and Reynolds stress profiles arising from different experiments will be the same profile *shape* and the same Reynolds stress profile shape, but the amplitudes will vary due to the {.} factor. The overarching conclusion reached by George and his group was "the Reynolds stress which when plotted as $\overline{uv}/U_C^2$ will vary from experiment to experiment (*sic)* because its own scale represented in these variables is $U_S^2 \frac{d\delta}{dx}$".

Reynolds number effects

A jet becomes fully turbulent when the Reynolds number exceeds ~10^4, Ricou and Spalding [3]. It is approximately at and beyod this Re that the entrainment of ambient, quiescent fluid saturates so that the mass flow rate across any cross-section becomes constant. Below this Re, the mass flux increases with decreasing Re. What has not been addressed completely in the literature is why Re> ~10^4 is needed to achieve fully turbulent flow.

There is a large corpus of literature that explore experimentally the turbulent round jet over a variety of axial extents and Reynolds numbers, see Ball and Pollard [4]; however, most of these studies consider a variety of axial locations at which some basic quantities are assembled and presented, such as mean velocity decay rates, turbulence stress distributions etc and correlations. The invention of PIV and 3-D versions of it have provided increased opportunity to explore vorticity and other multi-dimensional features, see for example, Weisgraber and Liepmann [5] and most recently Ganapathisubramani *et al.* [6].

If inlet conditions are important, as argued by George [2], then the effects of Re can only be compared using data from experimental rigs that are either the same or enough details are known that all other effects may be eliminated. Panchapakesan and Lumley [7] and Hussein *et al.* [8] considered two different Reynolds numbers (1.1×10^4 and 9.55×10^4, respectively); Hussein *et al*. briefly discuss the effects of Reynolds number as the reason for the differences between their results and Panchapakesan and Lumley [7]. Dimotakis [9] has argued that most shear flows undergo a "mixing transition" to achieve a universal behaviour for the turbulence, and the Reynolds number ($U\delta/\nu$) for this to occur must be greater than $1\text{-}2\times10^4$, which is in accord with Ricou and Spalding [3].

A Brief History of the Near to Intermediate Field of a Turbulent Round Jet

The near to intermediate field of a round jet has been the subject of many investigations. It is convenient to classify these into three main categories (a) characterisation, (b) phase averaged properties and (c) coherent structure identification using minimal spatial and temporal averaging.

(a) Characterisation

Perhaps the most influential paper that characterised a round jet was that of Wygnanski and Fiedler [10]. This paper provided extensive time-averaged distributions of turbulent stresses, skewness and flatness factors, spatial- and auto-correlations, various spatial scale lengths, spectra and estimates of convection velocities. While those data obtained were carefully obtained, they were inconsistent when

subjected to closure of the mean momentum equation for a jet that issued into an infinite environment, George et al. [11] (see George [2]) and this is because the jet used by Wygnanski and Fiedler did not issue into an infinite environment. That is, the data reliably characterise the flow used, but not that of a "free" jet. The latest paper that attempts to examine Reynolds numbers effects on round jets is Malmstrom *et al.* [12]; however, they did not address the question "why Re~$2x10^4$?"

(b) Conditional sampling and phase-averaged properties

The recognition that turbulence contains "structure" was firmly established with the flow visualisation of a supersonic mixing layer, Brown and Roshko [13]. This discovery, and the advent of computer controlled data acquisition set the stage for a new era in turbulence research. Yule [14] investigated the near field of a round jet using conditional sampling hot wire methods. Phased-averaged details for a round jet emerged from Hussain's laboratory, see *e.g.* Hussain and Zaman [15,16]. Conditional averaging use ensemble averages based on the use of a trigger-event; and, as will be returned to later, this introduces some considerable subjectivity since to educe a structure the trigger-event should be associated with that structure. Or, in other words, the structure educed will depend on the scheme used. Phase-averaging decomposes the instantaneous velocity signal $\mathbf{u}(\mathbf{t})$=(U+u', V+v', W+w') into global time-mean, a periodic "coherent" or ensemble average part, and the background "random" part. Note that because of this procedure, only the total signal can close the Navier-Stokes equations.

Hussain and Zaman [15,16] considered jets with mean Re_D ~ 25,000 and a variety of exit boundary layer thicknesses at the nozzle exit (momentum thickness $0.0203 < \Theta < 0.0511$). The jet was "forced" at the preferred mode. The preferred mode refers to the Strouhal number $St_D=fD/U_O$, where f is the excitation (forcing) frequency; the preferred mode St_D~0.3. The mean flow profile instability leads to the formation of coherent structures, which are characteristically transient, and which metamorphose into other "structures" as they evolve with distance downstream. A good example is the work of Yule [14] wherein "cartoons" attempt to point out the basic vortex structures and their interaction in the near-field before the establishment of "full" turbulence beyond the potential core. These structures evolve from the basic instability within the shear layer of the jet. Jet instability can be either convective or absolute; that is, convective is rather more parabolic in nature while absolute is equivalent to elliptic where a perturbation can travel both up and down-stream. In the near field of a jet, >25% of the energy in the flow is contained in the coherent part of the flow, Fiedler [17]. Thus, turbulence energy is distributed through mean, coherent and incoherent components. For future reference, since coherent energy is prominent in the near field, this provides the opportunity for passive and active control. However, phase-averaged structures are educed from data that give no or very little insight into the time domain. A Large Eddy Simulation of a round jet provides opportunities to explore the rich landscape of features as illustrated in figure 1.

(c) Turbulence structure and structure eduction methods

Irrespective of the method used, whether it is theory, experiment or computation, the Navier-Stokes must be satisfied (*often a failure by experimentalists*). And, if the solutions to the Navier-Stokes equations are at hand, say from a direct numerical simulation, the energy contained in the variety of spatial and temporal scales are fully available for interrogation.

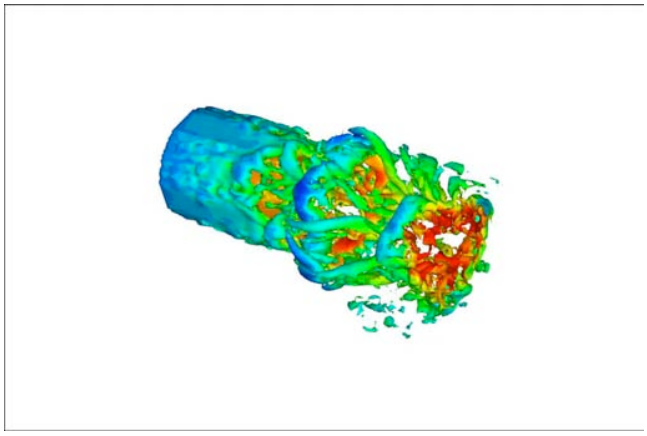

Figure 1: Instantaneous isosurfaces of vorticity magnitude, Large Eddy Simulation of round jet at Re_D = 68,000 using reprocessed data from McIlwain and Pollard [18].

The distribution of energy, however, is complexly intertwined throughout the terms and the spectrum of length scales in for example the transport equation for turbulence energy. Various methods have been used to identify these length scales and the energy budgets have been established for various points in a turbulent jet (but not for a wide range of Re). The most insight into the dynamics of a turbulent jet has been through the application of structure eduction methods using simulation data and the application of say, the proper orthogonal decomposition, to analyse time varying data obtained using rakes of 138 hot wires, Citriniti and George [19].

Coherent structures are related to the vorticity and strain in the flow field. The eigenvalue equation corresponding to the velocity gradient tensor $\nabla u_{ij} = \partial u_i / \partial x_j$ is $\lambda^3 - I_3\lambda^2 + I_2\lambda - I_1 = 0$ where the coefficients I_i represent the three invariants of the tensor. Specifically,

$$I_1 = R = \det(\partial u_i / \partial x) = (\lambda_1\lambda_2\lambda_3) = \frac{1}{3}(\lambda_1^3 + \lambda_2^3 + \lambda_3^3) \quad ,$$

$$I_2 = Q = \frac{1}{2}\left\{(\frac{\partial u_i}{\partial x_j})^2 - \frac{\partial u_i}{\partial x_j}\frac{\partial u_j}{\partial x_i}\right\} = \lambda_1\lambda_2 + \lambda_2\lambda_3 + \lambda_3\lambda_1 = -\frac{1}{2}(\lambda_1^2 + \lambda_2^2 + \lambda_3^2) = \frac{1}{2}P^2 - \frac{1}{2}\left\{\frac{\partial u_i}{\partial x_j}\frac{\partial u_j}{\partial x_i}\right\}$$

$$I_3 = P = \frac{\partial u_i}{\partial x_j} = \lambda_1 + \lambda_2 + \lambda_3 \,,$$

where R, Q and P are alternate symbols often used in the literature. Note that large positive values of Q (see for example Hunt *et al.* [20]) suggest significant enstrophy, see below, (Davidson [21]). Note that $\partial u_i / \partial x_j = S_{ij} + \Omega_{ij}$ represents the sum of the rate of strain and rotation tensors. The negative second eigen-value method $-\lambda_2$ of Jeong and Hussein [22] requires that the second eigenvalue of $S_{ij}^2 + \Omega_{ij}^2$ be negative.

There are other fields that can help to draw out some of the structural dynamics in turbulence. These include vorticity magnitude, helicity, palinstrophy, enstrophy, the Lamb vector, the dissipation of enstrophy all of which (including the eigenvalue-based methods mentioned earlier) require the specification of a threshold level for the eduction to be “useful”. These vorticity-based techniques are defined as:

Vorticity: $\vec{\omega} = \vec{\nabla} x \vec{v}$

Vorticity magnitude: $$\left|\vec{\omega}\right| = \left\{ (\frac{\partial w}{\partial y} - \frac{\partial v}{\partial z})^2 + (\frac{\partial u}{\partial z} - \frac{\partial w}{\partial x})^2 + (\frac{\partial v}{\partial x} - \frac{\partial u}{\partial y})^2 \right\}^{1/2}$$

Helicity: $$\xi = \vec{v} \bullet \vec{\omega} = u\omega_x + v\omega_y + w\omega_z$$

Palinstrophy: $$\Pi = \frac{1}{2}\left|\vec{\nabla} \times \vec{\omega}\right|^2$$

Enstrophy: $$E = \left\{ \frac{1}{4}(\omega_X^4 + \omega_Y^4 + \omega_Z^4) + \omega_X^2\omega_Y^2 + \omega_Y^2\omega_Z^2 + \omega_X^2\omega_Z^2 \right\}^{1/2}$$

Lamb vector: $$\vec{\Lambda} = \vec{v} \times \vec{\omega}$$

Dissipation of enstrophy: $$\Delta = \left\{ \frac{\partial \omega_Z}{\partial y} - \frac{\partial \omega_y}{\partial z} \right\}^2 + \left\{ \frac{\partial \omega_x}{\partial z} - \frac{\partial \omega_z}{\partial x} \right\}^2 + \left\{ \frac{\partial \omega_y}{\partial x} - \frac{\partial \omega_x}{\partial y} \right\}^2$$

A new method has been proposed by Larcheveque and Larcheveque [23] that purports to not require the setting of a threshold. The basis for the method involves expressing the surface of constant vorticity in the basis of eigenvectors of the Hessian matrix $H_{ij}(\omega) = \frac{\partial^2 \omega}{\partial x_i \partial x_j}$. An isosurface is where the difference between the vorticity magnitude at any two points, say M and M_O equals zero. This can be expanded in terms of a vector connecting any two points on the surface $\overrightarrow{MM_O}$ as follows: $\omega_M - \omega_{M_O} = \overrightarrow{MM_O} \bullet \vec{\nabla}(\omega_{M_O}) + \frac{1}{2}\overrightarrow{MM_O}^T H(\omega)_{M_O} \overrightarrow{MM_O}$. A useful property of this equation is that when it is written as the basis of eigenvalues of the Hessian the following quadratic is obtained: $\lambda_1(X + \frac{a}{\lambda_1})^2 + \lambda_2(Y + \frac{b}{\lambda_2})^2 + \lambda_3(X + \frac{c}{\lambda_3})^2 = \frac{a^2}{\lambda_1} + \frac{b^2}{\lambda_2} + \frac{c^2}{\lambda_3}$. The invariants determine the shape of the structures, which are highlighted in the following table.

	I_1	I_2	I_3
Pancake vortices	<0	>0	<0
Tubular vortices	<0	>0	≥0
Rotational sheets	<0	≤0	≥0
Planar sheets	<0	≤0	≥0

Table 1: Invariants for different vortex structures, after Larcheveque and Larcheveque (2007) [23].

The Navier-Stokes may be recast into $\frac{\partial \vec{u}}{\partial t} - \vec{\Lambda} = -\nabla h - \nu(\nabla \times \nabla \times \vec{u})$, Mallinson [24] and the viscous dissipation term is twice the square root of the palinstrophy, which itself appears in the transport equation for enstrophy, see Davidson [21].

NUMERICAL SIMULATIONS

There have been numerous investigations of round jets that rely on Reynolds averaged Navier-Stokes modelling of turbulence. I have chosen not to include them here.

Large eddy and direct numerical simulations (LES/DNS) of free jets continue to emerge in the literature. For LES, these include Olsson and Fuchs [25], McIlwain and Pollard [18], Bogey and Bailly [26], Uddin and Pollard [27-29] and Kim and Choi [30]. These simulations cover a wide range of initial conditions and Reynolds numbers, but save for Uddin and Pollard [27-29] all focus on the near field (typically x/D<15). For DNS, the Reynolds number and the integration domain are small, typically Re<2500 and x/D<40. The reason for the low Re, is due purely to spatial and temporal resolution requirements of DNS. That is, it can be demonstrated (see Reynolds [31]) that the number of CV's required scales with $L / \lambda_k \approx Re^{3/4}$, where L is the domain size length scale and λ_k is the Kolmogorov length scale, and the time step scales with $Re^{1/2}$, so that memory scales with $Re^{9/4}$ and CPU time scales with $Re^{11/4}$. To place this into perspective, to perform one DNS of the flow over a commercial airliner at cruise conditions would take about a 10^9 years using existing computer technology.

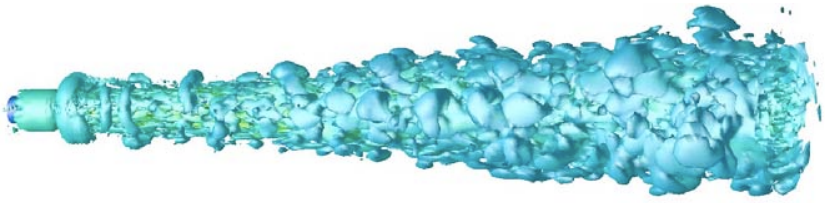

Figure 2: LES of a round jet, Re_D~7000, {unpublished work by Golanski and Pollard}.

A sample LES of a free round jet is illustrated in figure 2. This jet covered 0<x/D<35, using 256x120x64 control volumes in x-r-θ coordinate directions. The MPI parallel code uses second order differencing with a three-step fractional step method. Structure is educed using the Laplacian of the pressure (see Dubief and Delcayre [33]), normalized by the square of the mean exit velocity. The magnitude of the Laplacian (in this case 0.05) varies and is "coloured" by the magnitude of the streamwise velocity and this provides different levels of "colour" to the isosurfaces.

The data from McIlwain and Pollard [18] have been interrogated using the above noted schema; these are displayed in figure 3. Figure 3(a-h) use the same database to educe "structure". In Figure 3(a-e), the Q value, enstrophy, negative second eigenvalue, palinstrophy and helicity are displayed. These figures have employed different threshold magnitudes, while in figure 3(a) Q was coloured by the velocity magnitude. Clearly Q, $-\lambda_2$ and E all provide very similar "pictures" of the structure. The palinstrophy, which mimics the viscous dissipation of enstrophy (and similarly in the transformed Navier-Stokes equation that contains the Lamb vector) possess a finer scale; however, as this is LES, this is misleading as dissipation is not resolved. The complex vortex structure is evident, as well as the "flotsam" that indicates regions of fluid rotation vs. fluid stretching/compression. The Q-value reinforce the braid-like structures near x/D~4, which are opposite in sign to helicity. The palinstrophy

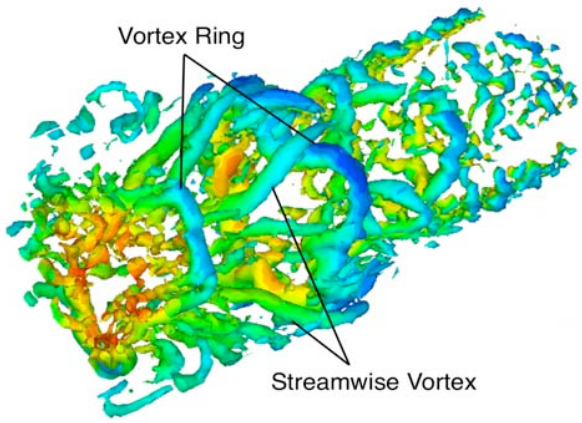

Figure 3a: Q-value

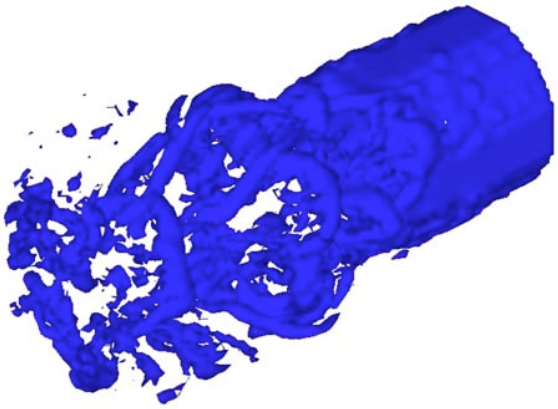

Figure 3b: Enstrophy

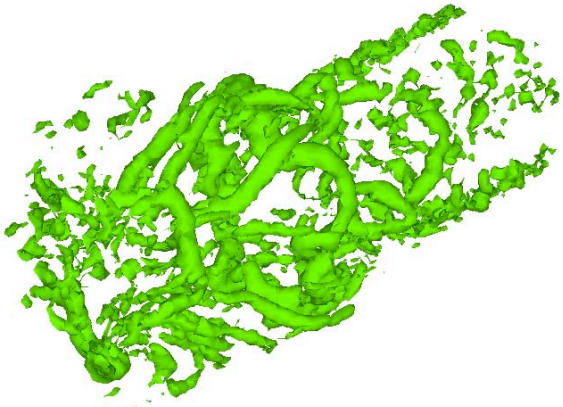

Figure 3c: Negative second eigenvalue

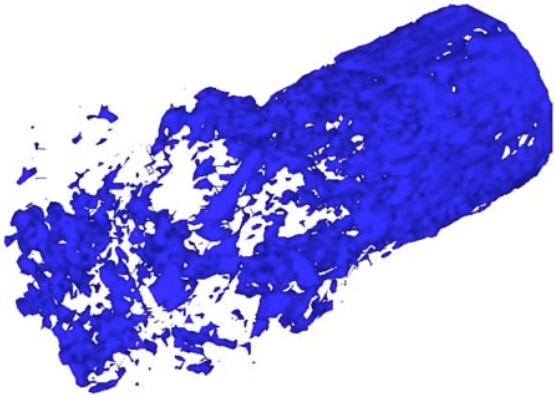

Figure 3d: Palinstrophy

Figure 3e: Helicity

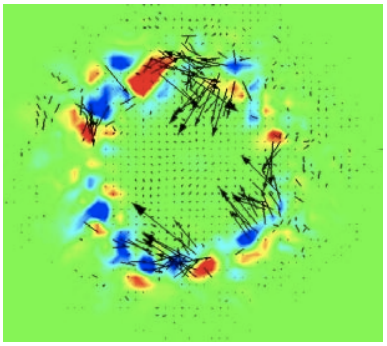

Figure 3f: Helicity and Lamb vector, x/D=1.6

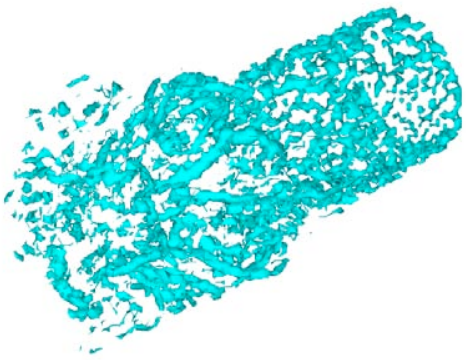

Figure 3g: Larcheveque and Larcheveque method, pancake vortices

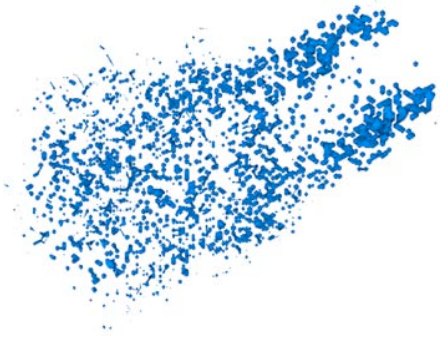

Figure 3h: Larcheveque and Larcheveque method, planar sheet vortices

field provides a richer background link to the Lamb vector. Interestingly, Davidson [21] states (pg 210) "(*sic*) regions of high helicity tend to correspond to regions of low (*sic)* Lamb vector (for a given energy and enstrophy). However, (*sic*) the Lamb vector corresponds to the non-linear term in the Navier-Stokes equations which, in turn, drives the energy cascade. So perhaps regions of high helicity tend to exhibit a somewhat depleted energy cascade, with a relatively low value of ε (dissipation)".

In figure 3(f), the jet cross-sectional plane at about x/D=3 is displayed using the helicity concomitantly with the Lamb vector. The helicity magnitude indicates the alignment between the velocity and vorticity vectors so the blue and the red colours indicate ±180 phase. The Lamb vector (arrows in fig. 3f) is the cross product of the velocity and vorticity vectors and thus the arrows indicate translation magnitude for a given vorticity; that is, the arrows suggest flow into the centre of the jet, which is clearly non-axisymmetric.

Figure 3(g, h) displays the application of the Larcheveque and Larcheveque method for the pancake and planar vortex sheet vortices. While the pancake vortices clearly indicate recognisable structure, the planar sheets do not.

Effects of mean and turbulence inlet distributions on free turbulent round jet.

Recently, Uddin and Pollard [27, 28, 29] performed LES of a round jet within a mild co-flow. The work considered the effects of initial conditions on the evolution of the mean and Reynolds shear stresses in the near to far field. The Reynolds number was ~7,200, and utilized 1024x144x72 CV's and over 125,000 CPU hours on 16 CPU HPC facility were required to run all four cases.

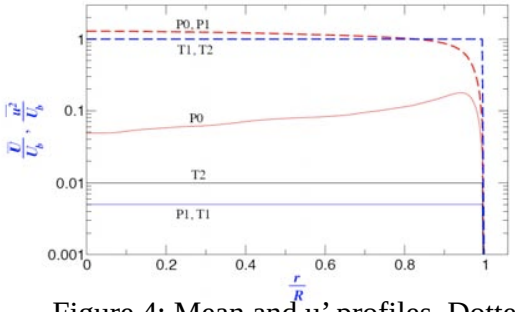

Figure 4: Mean and u' profiles. Dotted and solid lines represent mean and RMS quantities respectively.

The inlet conditions are provided in Figure 4. T1 represents a

synthesised top hat mean velocity with a time averaged streamwise intensity of 0.05%, which corresponds to the experimental conditions of Nickels and Perry [34]; T2 is T1, but with a turbulence intensity of 1%; P0 is fully developed pipe flow obtained from separate LES and P1 is same as P0 with an average streamwise turbulence intensity of 1%.

Data are scaled using Townsend's approach $\Delta^2 = \int_0^\infty \{U(r) - U_1\} r^2 \, dr \,/ \int_0^\infty \{U(r) - U_1\} \, dr$, where U, U_1 are the mean velocity of the jet and co-flow respectively (U/U_1=11). The mean axial velocity and the Reynolds shear stress distributions (f(r)) are not at all influenced by altering the inlet conditions; however, as can be observed in the plots of Reynolds normal stresses, there are significant effects, see figure 5. These are not just scaling issues, as noted by George [2]. It may be that the Reynolds number is too low (does not exceed the "mixing transition" $Re>10^4$), or that the simulations are influenced by the external co-flow, which will result in the far field "jet" to become a wake-like.

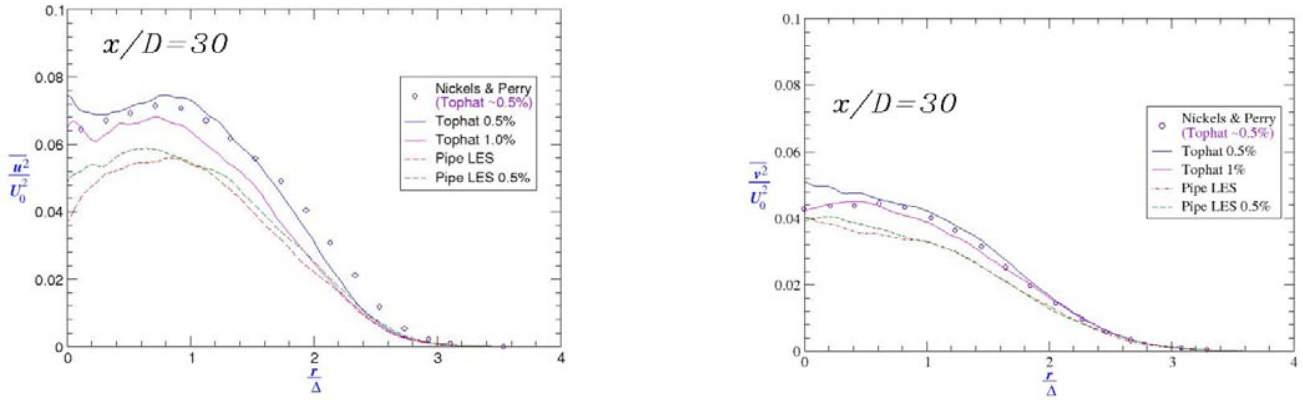

Figure 5: Axial (u') and transverse (v') turbulence intensities for LES of round jet, Uddin and Pollard [27]

Figure 6: LES of round jet; note the fading of structure as the jet fluid evolves downstream

Malmstrom *et al.* [12] concluded, without reference to George *et al.*, that "outlet turbulence could have such an influence (mean axial velocity decay rate coefficient decrease for Re<~20,000).

There remains some considerable opportunity to explore the intermediate field of a round jet (say at x/D<40) to determine how the various structures that have been identified in the simulations evolve and especially as a function of Reynolds number, Ball and Pollard [4]. Given that structures identified

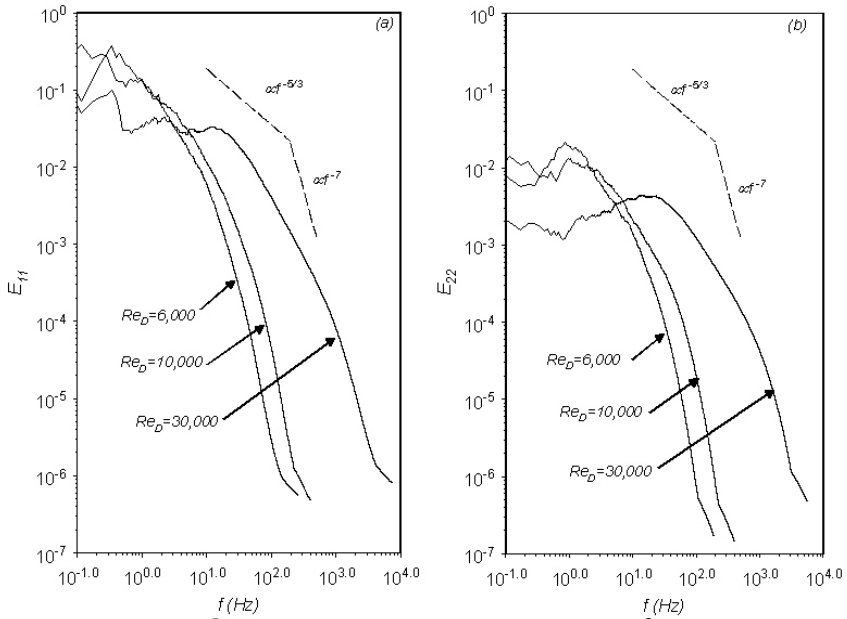

Figure 7: Velocity spectra at *r/D=0* at *x/D=10* for *Re*$_D$*=6,000, 10,000* and *30,000*. (a) *u*-spectra, (b) *v*-spectra.

alter their magnitudes as they are advected downstream, it is very difficult to "track" them, see figure 6.

Dimotakis [9] has proposed that the finding of Ricou and Spalding may be traced not to the large scale structure in the flow, which are peculiar to the geometry considered, rather to the physical significance of the various scales of the turbulence and their Reynolds number scaling. That is, there is a decoupling between the large scales and those free from the effects of viscosity. Starting with the theory presented in Kolmogorov [35], Dimotakis linked the outer scale, δ, to a variety of other length scales; *i.e.* , and using some additional scaling arguments, arrived at:

$$\mathrm{Re}^{-3/4} < \frac{\lambda_k}{\delta} \approx 50\,\mathrm{Re}^{-3/4} < \frac{\lambda}{\delta} < \frac{\lambda_L}{\delta} \approx 5.0\,\mathrm{Re}^{-1/2} < 1$$

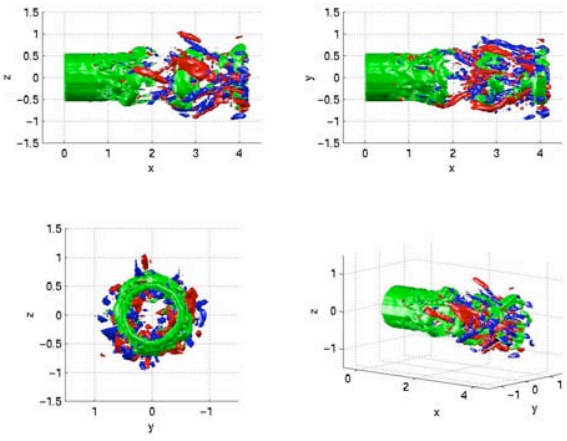

Figure 8: Round jet streamwise (Red{+}, blue{-}) and azimuthal (green) vorticity magnitude in LES of round jet 0<x/D<5. McIlwain *et al.* [38]

where $\mathrm{Re} = \frac{U\delta}{\nu}$, and λ_k, λ_V and λ_L are the Kolmogorov, viscous and the Leipmann-Taylor microscale and λ is a range of scales that are unaffected by the outer scale. Dimotakis suggests that $\lambda_L / \lambda_V > 0.1\mathrm{Re}^{1/4}$ or that $\mathrm{Re}>10^4$, or the number of viscous scales within a Taylor microscale and then argues that "viscous decoupling of the outer and inner scales of turbulence as responsible for the transition criterion" or mixing transition. To test Dimotakis' hypothesis, Fellouah and Pollard [36, 37] considered the round jet using a novel flying hot wire experimental facility. This work considered 6,000 < Re_D <100,000, using the same set-up, data acquisition systems etc. over 0.04 < x/D < 25. Data were obtained using single and cross hot wires. They have

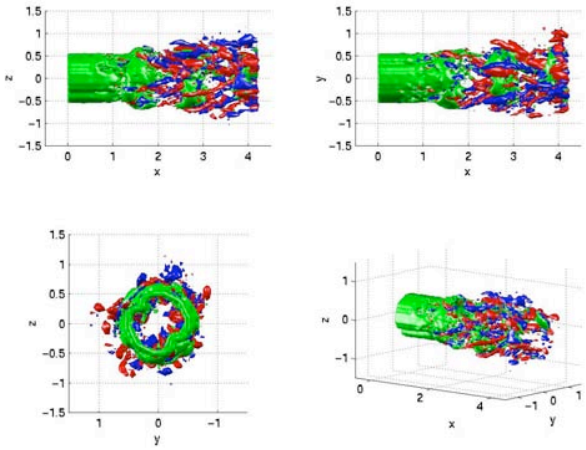

Figure 9: Round jet with two tabs. Streamwise (Red{+}, blue{-}) and azimuthal (green) vorticity magnitude in LES of round jet 0<x/D<5 with 2 tabs at 135^o and 315^o. Note increased appearance of streamwise vorticity (same contour levels) as compared to free round jet in Fig. 8.

demonstrated that the mixing transition is non-local and that it appears to occur at the appearance of the -5/3 inertial subrange rather than at the transition between the inertial and dissipation (k^{-7}) ranges. Figure 7 provides the velocity spectra on the jet centreline *x/D=10*, and for the three Reynolds numbers considered. It is clear the mixing transition, which demarcates *Re=10,000* and *Re=30,000*, display very different velocity spectral energy content, most noticeably at *x/D=10*. The inertial sub-range is certainly evident at *Re=30,000* than at the lower Reynolds numbers, while the dissipation range is in greater evidence for the lower, sub-mixing transition Reynolds numbers. Dimotakis argues that the mixing transition should occur when there is a separation between the large and viscous scales and free from viscous effects; that is between the inertial sub-range and the dissipation range. Based on those data presented here, it is the appearance on the inertial sub-range itself that may indicate the mixing transition, Fellouah and Pollard [36].

Effects of passive interaction with the exit flow of a round jet

McIlwain, Holme, Waterman and Pollard [38] introduced delta tabs to better understand the physics of inlet conditions on the formation and evolution of structure in a jet. The jet was forced at a Strouhal frequency of 0.35 and the jet was populated with either 1, 2, 3 or 4 tabs located at 45^o, 135^o 225^o and 315^o, respectively. Reynolds numbers for all jet simulations was kept at 68,000. Through direct comparison with simulation data, and using exactly the same structure eduction scheme and threshold levels, McIlwain *et al.* determined that when tabs are used the zeroth mode (the ring vortex) in the near field is significantly distorted in the azimuthal direction and this gives rise to increased appearance of streamwise "braids", see figures 8 and 9. McIlwain *et al.* calculated the entrainment for each case considered and determined that the rate of entrainment increased as the number of tabs was increased, relative to the free-jet, no-tab case. There is little difference in the rate of entrainment between the round jet without tabs and the round jet with one tab. However, the mass flow rate of the round jet with four tabs is 10% greater than either of the other two flows at *x/D* = 3.0 and 12% greater at *x/D* = 4.2. Between 0.0 < x/D < 2.5, the flow rate of all three jets is similar.

The round jet with four tabs entrains approximately 6% more fluid compared to the other two flows. All flows with tabs indicate an increase in the rate of entrainment as the rings are torn apart particularly at *x/D* = 2.5 for the jet with four tabs, and at *x/D* = 3.0 for the single and two-tab flows. This location also corresponds to the point where the braid-shaped structures begin to dominate the flow field. In the jet with four tabs, the braid-shaped structures that form at the bulges in the shear layer cause the rings to break apart faster, and appear to be responsible for the increased entrainment. This result supports

previous findings that the streamwise braid-shaped structures have greater effect on flow entrainment than the azimuthal ring-shaped structures.

Effects of walls on the evolution of a "free" jet

Ewing and Pollard [39] postulated a model for the anisotropic spread rate based on the structural features uncovered in some experiments. This hypothesis was based on the interaction of the zero'th mode vortex (Kelvin-Helmholtz) with the wall, see figure 10.

The anisotropic spread rate, which is a well known phenomenon in 3D wall jets, see Launder and Rodi [40]. However, Ewing and Pollard [39] captured the main reason for this.

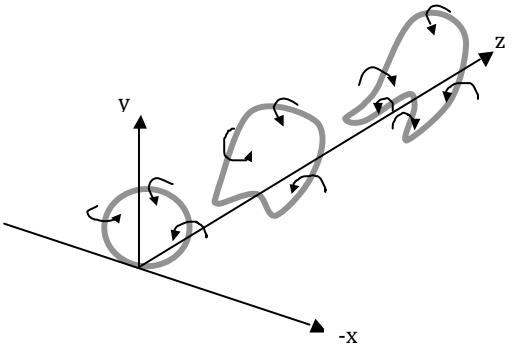

Figure 10: Breakdown of round jet in proximity to a wall, located at y=0, as hypothesised by Ewing and Pollard [39]

In my laboratory, investigations that used both experimental and computational approaches have been used to explore this feature of wall jets. In figure 11, the rather smeared views of a round wall jet (on the wall case) taken at different times on the same axial plane clearly demonstrate that the anisotropic picture suggested in earlier work is probably due to the integrated effects of measurements rather than the conditional "snap-shot" that reflects the periodic structure. Figure 11 (top) suggests anisotropy in the spreading while clearly its neighbour (bottom) doesn't. Further investigation and better time-resolved flow visualization, see figure 12, for the off-the-wall case, indicates vortex structure that reinforces the spatial and temporal anisotropic behaviour. To quantify some features of the vortex structure, Benaissa *et al.* 41] used rakes of hot wires and conditional averaging to deduce the angles and other features of the main structures in the wall jet. This time delay is associated with the angle α noted in the flow visualisation. An estimate of the angle based on this time delay of 2.4 ms is 45. This estimate is based on a convection velocity (Taylor's frozen turbulence hypothesis) of 10 m/s (velocity at $y_{1/2}$). For the spread in the span wise direction, conditional averages in the Z direction a suggest a shorter time delay in this direction estimated to be 1.4 ms., thus $\beta \sim 25^{o}$. The far-field anisotropic spread rate is, on average, $\frac{\partial y_{1/2}}{\partial x} = 0.048 \pm 0.003$ and $\frac{\partial z_{1/2}}{\partial x} = 0.26 \pm 0.02$. The experimental data suggest a complex vortex interaction

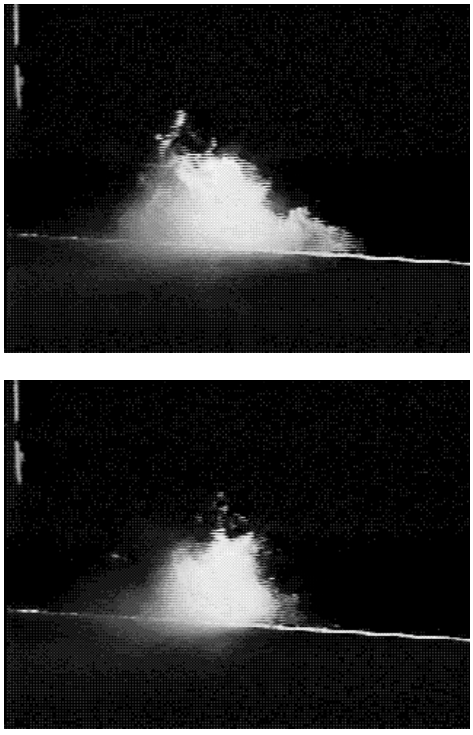

Figure 11: Smoke visualisation of round wall jet. The two images represent, at x/D=10, side lobe ejection (top) and no-side lobe ejection, (bottom).

mechanism, further details of which have explored using large eddy simulation in Pollard *et al.* [42].

Pollard *et al.* [42] considered a square wall jet, as a substitute for the round jet. Briefly, the ring vortices that emerge from the orifice begin to change into horseshoe vortices at a streamwise location of approximately z/D=7, for the "on-the-wall" case, which is the same location at which the streamwise braids begin to dominate the flow. It also appears that the vortex inclines towards the wall as it develops downstream. The top of the horseshoe vortex moves faster than the base, which is slowed down by the viscous effects near the wall. This causes the stretching of the legs of the structure and the formation of quasi-streamwise vortices.

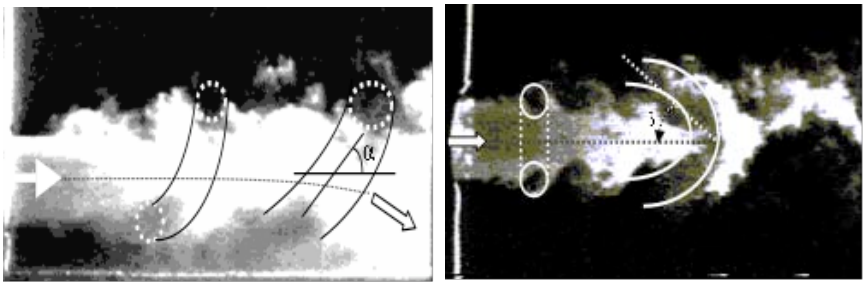

Figure 12: Elevated wall jet. Round jet located at h/D=1 (wall to jet centreline) above the wall. The cartoon superimposed on the visualisations indicate the supposed vortex structure. The angles were determined using conditional averaging of hot wire signals, see Benaissa *et al.* 2004.

The comparison between the plots of Q-value and streamwise vorticity, see figure 13, reveals that the largest lateral spread rate appears in the region where streamwise vortices are the most present in the coherent structures. Thus, the inclination of horseshoe structures and their alignment in the streamwise direction could explain the large lateral growth rate. The increase in the inclination of structures would enhance the size of lateral ejection explaining the significant increase in the lateral spread rate as the flow evolves downstream.

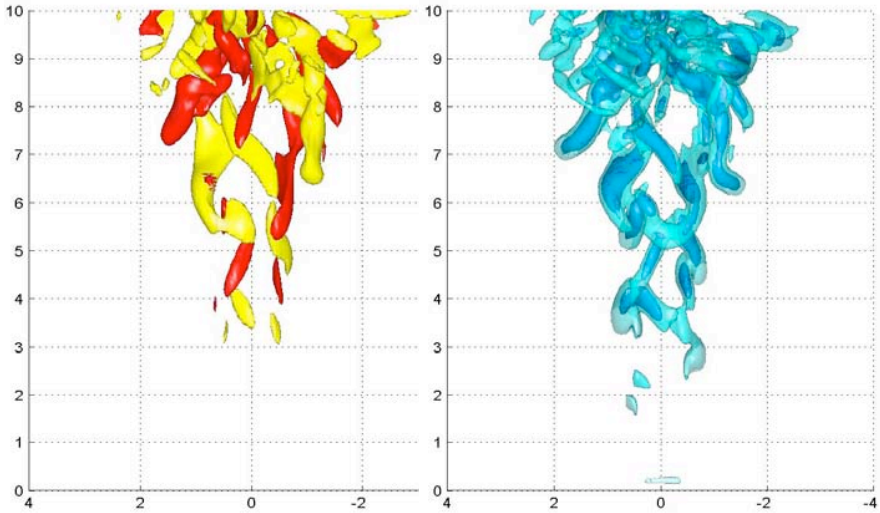

Figure 13: Plan view of streamwise vorticity (left) and Q (right) for on the wall square wall jet case. The streamwise vorticity colours indicate +/- sense of rotation.

The wall jet, when elevated from the wall more clearly demonstrates the complex vortical behaviour of the jet, and gives tantalising indications of the vortex structure found by Ewing and Pollard [39], see figure 14.

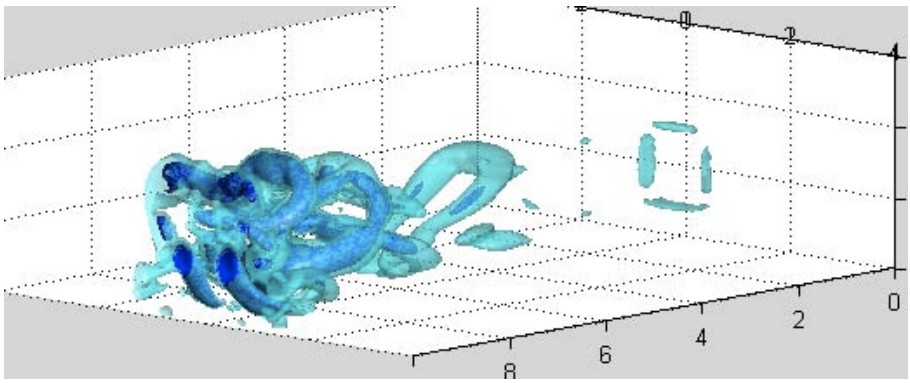

Figure 14: Off-the-wall h/D=1 case. Q-values. The two arrows indicate the tails of two legs of a horseshoe vortex, which spread laterally. This lateral spread enhances the anisotropic spread rate of the wall jet. There are hints of vortex structure suggested by Kasagi [43] for "alternate modes" in a bifurcating jet.

SUMMARY REMARKS

The round jet has been revisited. The hypothesis, which needs to be proved, is: turbulence "structure" dominates any high Re flow, and as exemplified by the influence of interference by tabs and walls, the initial structure evolves uniquely dependent upon the boundary conditions. More important, as Re increases, the turbulence structure evolves to a "state" that limits a particular flow-regime to super-saturate entrainment of irrotational fluid. This suggests that the entrainment, as governed by the circulation of individual structures evolves to a maximum and limiting entrainment-enabling state. The mixing transition ideas of Dimotakis have been further explored.

As with computers, experimental methods continue to increase in capacity. The recent paper by Ganapathisubramani *et al.* [6] considers three dimensional, **time-resolved** PIV. They considered a round jet at Re_D=5100 (Re_λ~150). They acquired all 9 components of the velocity gradient tensor at x/D~35. They educed structure using essentially the same method as McIlwain and Pollard [18] and inferred small scale vortex strength around vortex-tube-like structures or "worms" (after Jimenez *et al.* [44]). They additionally focused on the alignment (dot product) between the vorticity vector and the eigenvectors of the rate of strain tensor. The angle between the eigenvector and vorticity vector is φ they deduced that the vorticity vector aligns with strain (*i.e.* cos φ=1) and least likely (*i.e.* cos φ=0) with compressive strain and indeed the vorticity vector "is perpendicular to the principal compressive strain." They also had enough data to calculate the dissipation, which, from an experimental investigation, is a significant accomplishment. Unfortunately, the paper does not consider the role of these fine-scale structures on entrainment. However, the paper does suggest that the hypothesis put forward above has merit and indeed, my laboratory is pursuing this now.

This paper has considered a "simple" question, drawn from an observation by Ricou and Spalding. The paper has provided tantalizingly glimpses of what is posited as the rich structural landscape of this flow. Through theory, simulations and experiments we have learned that turbulence has a memory of its origins and that to alter the initial and boundary conditions the structure of the turbulence is altered.

ACKNOWLEDGEMENTS

It is with pleasure that I acknowledge the assistance of Ms. Emily Sheridan, Drs. H. Fellouah and F. Golanski and Mr. C.G. Ball who provided some of their unpublished research results. This paper was prepared while the author was on sabbatical at the University of Auckland, New Zealand, and ably hosted by Professor G.D. Mallinson. I have enjoyed continued funding from the Natural Science and Engineering Research Council of Canada. I also acknowledge the significant computational resources provided to my students and laboratory by the High Performance Computing Virtual Laboratory (www.hpcvl.org).

REFERENCES

1. A. Pollard and S. Candel (eds) (2002) Turbulent Mixing and Combustion, Proceedings of the IUTAM Symposium, Kingston, Ontario 3-6 June, 2001, Kluwer Academic Publishers. (ISBN 1-4020-0747-7).
2. W.K. George (1989) The self preservation of turbulent flows and its relation to initial conditions and coherent structures, in *Advances in Turbulence*, Hemisphere Publishing Corp., New York. W.K. George and R. Arndt (eds.) pp 39-73.
3. F. Ricou and D.B. Spalding (1961) Measurements of entrainment by axisymmetric turbulent jets, J. Fluid Mechanics, **11**:21-32.
4. C.G. Ball and A. Pollard (2009) A review of experimental and computational studies of turbulent round jets, Computational and Experimental Fluid Dynamics Laboratory Report, No. 01/09, Department of Mechanical and Materials Engineering, Queen's University at Kingston (see http://me.queensu.ca/people/pollard)
5. T. H. Weisgraber and D. Liepman (1998), Turbulent structure during transition to self-similarity in a round jet, Expt. Fluids, **24**:210-224
6. B. Ganapathisubramani, K. Lakshminarasimhan and N.T. Clemens (2008) Investigation of the three dimensional structure of fine-scales in a turbulent jet by using cinematographic stereoscopic PIV, J. Fluid Mech. **598**:141-175.
7. N.R. Panchapakesan and J.L. Lumley (1993) Turbulence measurements in axisymmetric jets of air and helium 1. Air-jet. J. Fluid Mechanics **246:**197–223.
8. H. J. Hussein, S.P. Capp and W.K. George (1994) Velocity measurements in a high Reynolds number, momentum-conserving, axisymmetric, turbulent jet, J. Fluid Mech. **258**:31-75.
9. P. Dimotakis (2000) The mixing transition in turbulent flows, J. Fluid Mechanics, **409**:69-98.
10. I. Wygnanski and H.E. Fiedler (1969) Some measurements in a self preserving jet, J. Fluid Mechanics, **38**:577-612.
11. W.K. George, S.P. Capp, A.A. Seif, C.B. Baker and D.B Taulbee (1988) A study of the turbulent axisymmetric jet J. Eng. Sci., King Saud Univ. **14**(1): 85-93.
12. T. G. Malmström, A. T. Kirkpatrick, B. Christensen, and K. D. Knappmiller (1997), Centreline velocity decay measurements in low-velocity axisymmetric jet, J. Fluid Mech. **346**: 363.
13. G. Brown and A. Roshko (1974) On density effects and large structure in turbulent mixing layers, J. Fluid Mechanics **64**:775-816.
14. A. Yule (1978) Large-scale structure in the mixing layer of a round jet. J. Fluid Mech*anics* **89**:413–432.
15. A.K.M.F. Hussain and K.B.M.Q. Zaman (1981) Vortex pairing in a circular jet under controlled excitation. Part 2. Coherent structure dynamics, J. Fluid Mech. **101**(3):493-644
16. A.K.M.F. Hussain and K.B.M.Q. Zaman (1981) The preferred mode of the axisymmetric jet, J. Fluid Mech. **110**:39-81.

17. H.H. Feidler (1998) Control of free turbulent shear flows, in: Flow Control: Fundamentals and Practices, Lecture Notes in Physics, Monograph, Berlin, M. Gad-el-Hak, A. Pollard and J-P. Bonnet (eds) pp335-430.
18. S. McIlwain and A. Pollard (2002) Large eddy simulation of the effects of mild swirl on the near field of a round free jet, Phys. Fluids **14**(2):653-661.
19. J. H. Citriniti and W.K. George (2000) Reconstruction of the global velocity field in the axisymmetric mixing layer utilising proper orthogonal decomposition, J. Fluid Mechanics, **418**:137-166.
20. J.C.R. Hunt, A.A. Wray and P. Moin (1998) Eddies, stream and convergence zones in turbulent flows, *Proceedings of the 1988 Summer Programme*, Centre for Turbulence Research, Stanford University, pp. 193-208.
21. P. A. Davidson (2004) *Turbulence-An introduction for scientists and engineers,* Oxford UP.
22. J. Jeong and A.K.M.F. Hussain (1995) On the identification of a vortex, J. Fluid Mechanics
3. **285**:69-94.
23. L. Larcheveque and M. Larcheveque (2007) New Criteria for the Eduction of Three Dimensional Turbulent Structures, *Proceedings, Turbulent Shear Flow Phenomena 5,* TU Munchen, Garching,
4. 27-29 August, Friedrich, Adams, Eaton, Humphrey, Kasagi and Leschziner (eds), Volume 2,
5. pp555-560.
24. G.D. Mallinson (2006) CFD visualisation: challenges of complex 3D and 4D data fields, Keynote lecture, CFD 2006, Kingston, Canada (to appear in Int'l J. CFD 2008).
25. M. Olsson and L. Fuchs (1996) Large eddy simulation of the proximal region of a spatially developing circular jet, Phys. Fluids, **8**(8):2125-2137.
26. C. Bogey and C. Bailly, Large eddy simulations of transitional round jets: influence of the Reynolds number on flow development and energy dissipation, Phys. Fluids, **18**:065101
27. M. Uddin and A. Pollard (2005) Effect of initial conditions in the near and far fields of a co-flowing jet, Proceedings, TSFP-4, Williamsburg, Virginia, Gatski *et al. (eds)*
28. M. Uddin and A. Pollard (2006) MPI scalability of a large memory LES code, Int'l. J. High Performance Computing and Networks, **4**(5/6):295-302.
29. M. Uddin and A. Pollard (2007) Self-similarity of coflowing jets: the virtual origin, Phys. Fluids, **19**(1):068103_1-068103_4.
30. J. Kim and H. Choi (2009) Large eddy simulation of a circular jet: effect of inflow conditions on the near field, J. Fluid Mechanics, **620**:383-411.
31. W.C. Reynolds (1990), "The potential and limitations of direct and large eddy simulations", *Whither Turbulence? Turbulence at the Crossroads*, Springer-Verlag, Berlin, pp.313-343.
32. F. Golanski and A. Pollard (2008) DNS and LES of a round free jet: the role of structure in its spatial evolution, in preparation.
33. Y. Dubief and F. Delcayre (2000) On coherent vortex identification in turbulence, J. Turbulence, DOI: 10.1088/1468-5248/1/1/011
34. T. Nickels and A. E. Perry (1996) An experimental and theoretical study of the turbulent co-flowing jet, J. Fluid Mechanics, **309**:157-182.
35. A.N. Kolmogorov (1941) Local structure of turbulence in an incompressible viscous fluid at very high Reynolds numbers, Dokl. Akad. Nauk. SSSR **30**, 299
36. H. Fellouah and A. Pollard (2009) Reynolds number effects within the development region of a turbulent round free jet, accepted for publication, Int'l. J. Heat and Mass Transfer.
37. H. Fellouah and A. Pollard (2009) Velocity spectra in the developing region of a round jet, in preparation for submission to Experiments in Fluids.

38. S. McIlwain, T. Holme, S. Waterman and A. Pollard (2002) Effects of one, two and quadruple tabs on the mixing and entrainment in the near field of a round jet, pp 377-386, in Pollard and Candel (eds) Turbulent Mixing and Combustion, Proceedings of the IUTAM Symposium, Kingston, Ontario 3-6 June, 2001, Kluwer Academic Publishers. (ISBN 1-4020-0747-7).
39. D. Ewing and A. Pollard (1997) Evolution of the large scale motions in a three dimensional wall jet, Paper AIAA-97-1964, 28th AIAA Fluid Dynamics Conference, Snomass, Colorado.
40. B.E. Launder and W. Rodi (1983) The Turbulent Wall Jet, Progress in Aerospace Sciences, **19**(2-4): 81-128
41. A. Benaissa, B. Fleck and A. Pollard (2004), Wall Effects on Axi-symmetric Jet Evolution, Intl. J. Transport Phenomena, **6**(4):323-331.
42. A. Pollard, M. Uddin and J. Braly (2004) Large eddy simulation of 3D square wall jets, Proceedings, CFD'04, the 12th Annual conference of the CFD Society of Canada, Ottawa. (see www.cfdsc.ca)
43. N. Kasagi (2005) Toward smart control of turbulent jet mixing and combustion, Intl. Conf. Jets, Wakes and Separated Flows, Oct. 2005, Toba-shi, Mie, Japan.
44. J. Jimenez, A.A. Wray, P.G. Saffman and R.S. Rogallo (1993) The structure of intense vorticity in isotropic turbulence, J. Fluid Mech. **255**:65-90.

ON HEAT TRANSFER AND FLUID FLOW IN RIBBED DUCTS USING LIQUID CRYSTAL THERMOGRAPHY AND PIV MEASUREMENTS

B. Sundén*
Lund University, Department of Energy Sciences, Division of Heat Transfer, P.O. Box 118, Lund, SE-22100 Sweden

ABSTRACT. Enhancement of forced convection is important in many engineering applications. Surface modifications like rib-roughening are commonly used in applications such as compact heat exchangers and gas-turbines. This paper gives a brief summary of heat transfer and fluid flow in ribbed ducts using liquid crystal thermography and PIV measurements. Details of the flow pattern and the influence of rib configuration and arrangement on heat transfer are discussed. Nevertheless, our understanding of the flow physics in ribbed channels is not yet complete and further studies are needed.

Keywords: *ribbed ducts, heat transfer, flow pattern, liquid crystal thermography, PIV measurements*

INTRODUCTION

Periodic ribs are often used in the design of heat exchanger channels in order to enhance the heat transfer rate and thus to improve the overall process efficiency. Historically ribs have been introduced in the cooling passages of gas turbine blades because of the extremely high thermal loads and reduced dimensions. It has been found that the main thermal resistance to the convective heat transfer is due to the presence of viscous sub-layer on the heat-transferring surfaces. The presence of ribs makes the viscous sub-layer break down by virtue of flow separation and reattachment, which reduces the thermal resistance and considerably enhances the heat transfer. However, the use of ribs gives rise to higher friction and hence higher pumping power. Thus, many experimental studies have been carried out to determine the rib configuration and arrangement that produce optimum effects. Among the parameters affecting the heat transfer characteristics, the ratio of the rib height to channel height (e/H) [1-5] and the rib pitch to height (P/e) [1-3, 6] are important ones. In general, an increase in the rib height increases the heat transfer. It is also found that if the core flow is strongly perturbed by the presence of high ribs there appears to be a more sharp increase of the flow resistance than the enhancement of heat transfer. The optimum e/H is known to be around 0.1 [1]. There also exists an optimum pitch, since the pitch should be longer than the reattachment length formed behind the rib. The ratio of the rib pitch to height recommended is about 10 for the Reynolds range of interest [1]. Since the optimum values of the aforementioned parameters are well established through extensive experimental data, we shall give more attention to other geometric parameters.

Heat transfer in a ribbed channel is locally deteriorated immediately behind the ribs (i.e. hot spots) due to the formation of a corner eddy. The heat transfer in this region is essentially dominated by conduction since the flow is nearly stagnant relative to the mainstream flow. Attempts have been made to overcome the adverse effect by changing the geometry of the rib cross section. Han et al. [7] applied

* Corresponding author: Prof. B. Sundén
Phone: + (46)-46-222 86 05, Fax: + (46)-46-222 47 17
E-mail address: bengt.sunden@energy.lth.se

modelling clay to fill the corners of the rectangular ribs to create two distinct geometries. It was found that the clay has a modest effect on the heat transfer coefficients, and the influence of the rib shape on the heat transfer coefficients disappears at higher Reynolds number where the flow is in the completely rough regime. Lockett and Collins [8] reported that the hot spots were alleviated when the more streamlined (or rounded) ribs were used. Moreover, they found that the heat transfer distribution depends on the Reynolds number for the rounded rib, but independent for square-rib geometry. Taslim and Korotky [9] pointed out that the rounded ribs deteriorate the heat transfer performance. Liou and Hwang [10] showed that semicircular ribs result in a lower heat transfer rate than the conventional square rib. Chandra et al. [11] studied the effect of rib profiles on the heat transfer rate. They found that square ribs produce higher heat transfer augmentation than any other rib profile. Therefore, they claimed that the greater number of sharp corners of a rib yield increasingly higher heat transfer coefficient and friction factor. Contrary to the conclusions of Chandra et al. [11], Ahn [12] argued that the triangle-ribbed shape has the highest heat transfer performance. More recently, Ahn et al. [13] performed large eddy simulation of flow and heat transfer in a channel roughened by square and semicircular ribs. They found that the two ribs produce nearly the same heat transfer, but the semicircular ones yield lower drag than the square one. As is clear from the above-mentioned results, the effects of rib cross-sectional shape on the heat transfer characteristics is still open to debate.

In addition to varying the rib cross section profile, another way to avoid hot spots is to replace the solid-type ribs by perforated ribs. Because part of the air flow passes through the perforated ribs and directly impinges on the recirculating region behind the rib, the hot spots may not arise. Hwang and Liou [14, 15], employed the holographic interferometry to measure the heat transfer characteristics in a channel with perforated ribs. The results indicated that the perforated ribs have the advantages of eliminating the hot spots and providing a superior heat transfer performance. Meanwhile, Liou and Wang [16] and Liou et al. [17] investigated the heat transfer and friction characteristics in a duct with detached ribs. It was found that the thermal performance was better for the detached-ribbed duct flows than in the attached-ribbed duct flows. Basically, the hot spots around the concave corners behind the attached ribs were absent for the detached-ribbed duct flows. Later on, Liou et al. [18] compared the thermal performance between the detached solid-rib array and the detached perforated-rib array. They concluded that the duct flow with solid-type ribs is superior compared to a duct with perforated ribs. However, Kukreja and Lau [19] pointed out in their experiments that the perforated ribs are not as good as solid ribs in enhancing heat transfer. Although perforated ribs caused lower pressure drop, they did not improve the thermal performance. Increasing the size of the holes, the number of the holes, or the total hole area did not increase the overall heat transfer. More recently, Moon and Lau [20] carried out experiments to determine the average and local heat transfer between two blockages with holes. They showed that the local heat transfer distribution is strongly dependent on the configuration of the hole array in the blockages. In general, the smaller holes cause higher heat transfer enhancement, but also significantly larger increase of pressure drop than larger holes. These seemingly controversial results call for further studies to investigate the detailed flow fields and heat transfer distribution in ducts roughened with perforated-type ribs.

Apart from the transverse pattern, ribs can also be arranged in inclined as well as V-shaped configurations. It is postulated that the secondary flow induced by the inclined and V-shaped ribs affects the heat transfer significantly. Han et al. [7] found that the highest heat transfer for a given friction power is achieved with ribs with 45° angle of attack. In a similar investigation Han et al. [21] studied the heat transfer characteristics in square channels with parallel, crossed and V-shaped angled ribs, respectively. They found that the V-shaped ribs directed opposite to the main flow provide the highest heat transfer enhancement while the V-shaped ribs pointing the flow direction generate the largest pressure drop penalty. It was conjectured that differences in the secondary flow are the explanation for the observed results. Lau et al. [22] came up with same conclusions as Han

et al. [21] in their experimental studies. They showed that the V-shaped ribs pointing upstream with 60° attack angle gave the highest heat transfer coefficients. Taslim et al. [3] performed an experimental investigation using liquid crystal thermography to determine the local heat transfer coefficients in a square duct with angled, V-shaped and discrete ribs on two opposite walls. They reported that the heat transfer is highest for V-shaped ribs pointing downstream, which is obviously contrary to the results of Han et al. [21]. Applying the same measurement technique as Taslim et al. [3], Gao and Sundén [23] found that V-shaped ribs pointing downstream are superior to the V-shaped ribs pointing upstream in enhancing the heat transfer. Recently, by performing numerical simulations, Jia et al. [24] supported the statement that the V-shaped ribs pointing downstream produce higher heat transfer coefficients. They supposed that the discrepancy is probably attributed to the insufficient number of sampling points in the Han et al. [21] measurements in which thermocouples were utilized.

With rapid development of measurement techniques, great opportunities are opened up to map the detailed temperature distribution on a surface and gain insight of the flow structures in complex flows. This will significantly enhance our understanding of the flow and heat transfer characteristics in ribbed ducts and shed light on the design optimization of the various cooling systems. In this paper, focus is on the applications of the liquid crystal thermography (LCT) and particle image velocimetry (PIV) in research concerning the heat transfer and fluid flow in ribbed ducts. Part 2 gives brief descriptions of LCT and PIV. In Part 3, recent developments are presented and discussed. The conclusions are placed in Part 4.

EXPERIMENTAL SETUP AND PROCEDURES

Liquid Crystal Thermography

Liquid crystal thermography is based on substances called thermochromic liquid crystals. Basically, liquid crystals are substances in an intermediate phase that is between the pure solid and pure liquid phases, thus sharing some of the properties of both liquids and crystals. Liquid crystals are conventionally divided into three classes, which are termed as smectic, nematic and cholesteric according to the molecular structures. The cholesteric liquid crystals are often used as temperature sensors because the molecules can selectively reflect visible light depending on the surrounding temperature. At temperatures below the critical value (event temperature), a liquid crystal is in the solid state and will appear transparent. Once the temperature is above the threshold, the liquid crystal material will reflect a unique wavelength of visible light when illuminated by white light and viewed under fixed optical conditions. As temperature rises, the reflected colour will change. Finally, when the temperature exceeds the clearing point, the material will enter the pure liquid state and will revert back to being transparent. Therefore, this character enables cholesteric liquid crystals to serve as an effective temperature-sensing medium.

LCT is an economical and affordable technique compared with the infrared thermal imaging method. A resolution of less than 0.1 ˚C is easily obtainable for narrow band liquid crystals. In addition, its short response time, in the order of 0.1 sec, means that it can respond to the temperature change very quickly. However, liquid crystals can only be used at relatively low temperatures. For example, the active bandwidths of most commercially available LCT products are limited to the temperature range from -30 ˚C to 120 ˚C. Over the development of LCT, several methods have been employed to interpret the colour of liquid crystals. Currently, the hue-temperature calibration method is most commonly used due to its high resolution in heat transfer research field. Figure 1 shows the profile of hue-temperature relation. It is found that the hue is fairly linear with temperature in the range of 30 to 130, which corresponds to the temperature range of 35 ˚C to 37 ˚C. Above 38 ˚C, the hue value is not quite sensitive to the variation of temperature.

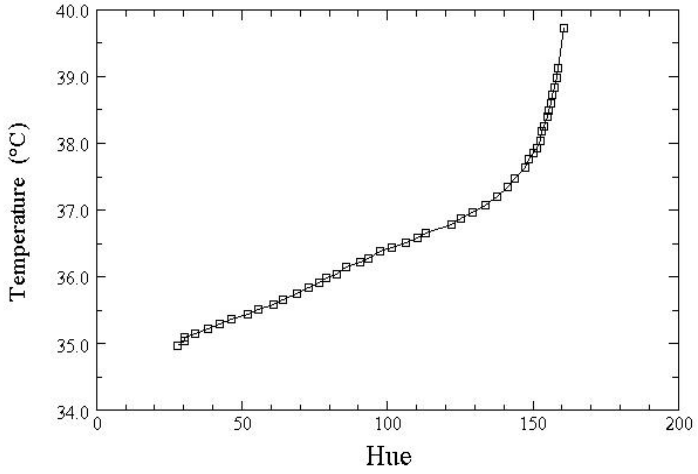

Figure 1 Hue-temperature calibration

Data Reduction

The heat transfer result is presented in terms of local Nusselt number, that is,

$$Nu = \frac{(Q_{el} - Q_{loss}) \cdot D_h}{(T_w - T_{bulk}) \cdot k_f \cdot A} \tag{1}$$

where Q_{el} is the measured input power to the heater, Q_{loss} is the dissipation rate in terms of radiative heat transfer to the surroundings and the conductive heat transfer through the back of the heated surface. In estimating the radiative heat loss, the surface and air bulk temperature are considered as constant when taking into account the fact that the air temperature rise from entrance to exit is less than 2 °C. For polished Inconel, the emissivity is approximately equal to 0.05. The conduction heat leakages are calculated from the temperature difference across the heated wall. Two thermocouples are installed at the back of the heated surface. The sum of the two terms is found to be less than 6% of Q_{el}. In Eq. (1), k_f is the air thermal conductivity and A is the area of the heating surface; T_w is the surface temperature indicated by the liquid crystal, and T_{bulk} is the local air bulk-mean temperature. All the thermal properties are evaluated at the air bulk-mean temperature. The experimental uncertainty is also analysed. Based on the normal distribution with 95% confidence, the uncertainty in local Nusselt number is estimated to be within ±6%. This value takes into account such independent variables as electric current, resistance of heater, liquid crystal thermographic reading, air bulk temperature, and dissipation rate.

Particle Image Velocimetry

PIV techniques have been developed in the last two decades and became widely used in the study of fluid mechanics. PIV is often used to measure the instantaneous velocity field in a 2D plane with relatively high spatial resolution. The velocity is computed by finding the displacement of tracer particles in a given time interval. The basic principle of PIV is presented in Figure 2. The measured flow is seeded with small tracer particles. These seeding particles are supposed to faithfully follow the motions of the fluid. A pulsed light sheet is used to illuminate the interesting area of the flow field twice to catch the flow movement. The light scattered by the tracer particles is recorded on a CCD sensor. The digital PIV recording is then divided into small interrogation windows. The calculation of the particle displacement is done by cross-correlating the two corresponding interrogation windows. Using the fast Fourier transformation (FFT), the position of the highest peak in the correlation domain indicates the mean displacement of the particles in a particular

interrogation window. Repeating the process, the displacement vectors of all interrogation windows are finally transformed into a complete instantaneous velocity map.

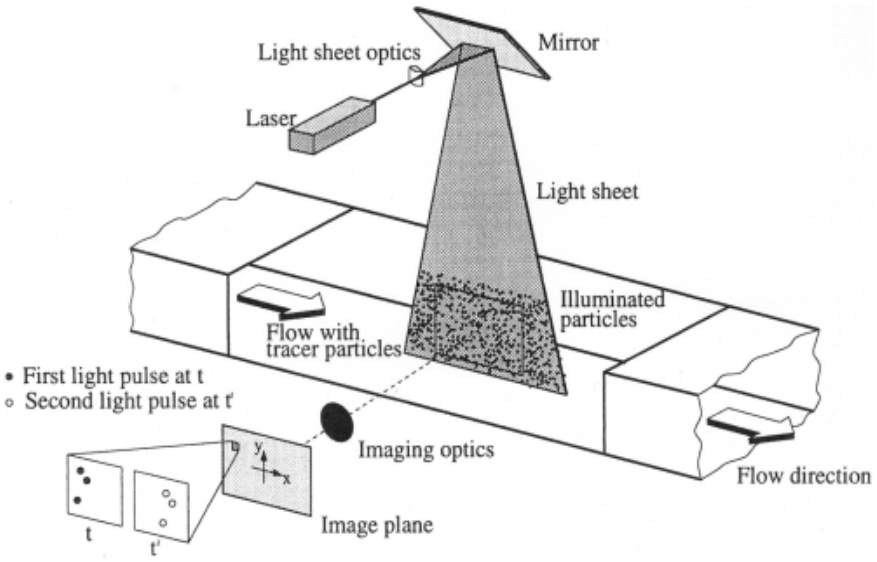

Figure 2 Basic principle of PIV

Measurement Procedure

A commercially available PIV system developed by Dantec Dynamics has been used in our recent present investigations. The system is arranged to measure the velocity fields in the vertical symmetry plane and the horizontal plane of the ribbed channel. Oil-based aerosol with mean particle diameter of 1μm is generated by a TSI 9306 six-jet atomizer. The concentration of the seeding particles is regulated by the compressed air pressure and the number of Laskin nozzles. In order to get homogeneous trace particles, the channel inlet is preceded by a plenum with two screens. A Quantel Q-switched Nd:YAG laser provides the pulsed illumination with a wavelength of 532 nm. The duration of each pulse is 10 ns and the maximum output energy is 120 mJ. The light-sheet thickness in the test section is kept at 0.8 mm. A digital camera containing a CCD chip with 1280 × 1024 pixels and a Nikon AF Micro 60f/2.8D lens with an optical filter are used to record the particle images. Typically, the magnification factors range from 50 μm/pixel to 70 μm/pixel.

The time interval between laser pulses is set such that the particles move at most 8 pixels between the pair of images. In our experiments, the time interval varies from 10 to 20 μs depending on the velocity magnitude and the desired resolution. Within each window, the number of seeding particles is greater than 5 and the particle image size projected onto the CCD sensor is approximately 3 pixels. FFT-based cross-correlation coupled with a two-dimensional Gaussian fit is applied to find the correlation peak position. Assuming that the measured particle displacement is accurate to the extent between 0.01 to 0.1 pixels, which is the commonly accepted range, the experimental uncertainty in the instantaneous velocity measurement is estimated to be less than 2%. The sample size is another error source for the mean and fluctuating velocity statistics. In the present study, 500 images are generated for each measurement plane. The uncertainties of the velocity gradient $\frac{d<u>}{dy}$ and shear stress $<-u'v'>$ are estimated to be within 5% and 10%, respectively.

RECENT WORKS

Separated Flow and Heat Transfer in a Ribbed Channel

Although the repeated ribs may be considered as a roughness elements, it may also be viewed as a problem in boundary layer separation and reattachment [25]. The heat transfer enhancement mechanism from separation and reattachment is not yet clear since the physics of the flow associated with separation is complex in nature. Usually, the flow in channels fitted with transverse periodic ribs is used as a simple model to study the effect of separation on the heat transfer. Unlike the flow over a backward-facing step, the flow over a rib is more complicated since it displays an additional separation bubble in the region upstream of the rib. According to Bradshaw and Wong [26], the flow over a rib (or fence) involves two 'strong perturbations' (two separation bubbles) and is an extremely difficult flow to understand. In general, the flow separates at the edge of the rib, forming a widening free shear layer which reattaches downstream on the floor. The separated shear layer splits into two parts at the reattachment point, where one part of the flow is deflected upstream into the recirculating region; the other part of the flow redevelops downstream to form a new boundary layer which grows in thickness. The wall shear stress is vanishing at the reattachment point. Further downstream, due to the adverse pressure gradient caused by the next rib, the flow separates once again and forms a secondary separation bubble. Figure 3 plots the overall streamlines between consecutive ribs in a ribbed channel. In this figure, the ribs obstruct the channel by 15% of its height and are arranged 12 rib heights apart. The Reynolds number, based on the bulk-mean velocity and the height of the channel, is 22,000. All the following results presented in this section are based on this rib arrangement and flow condition.

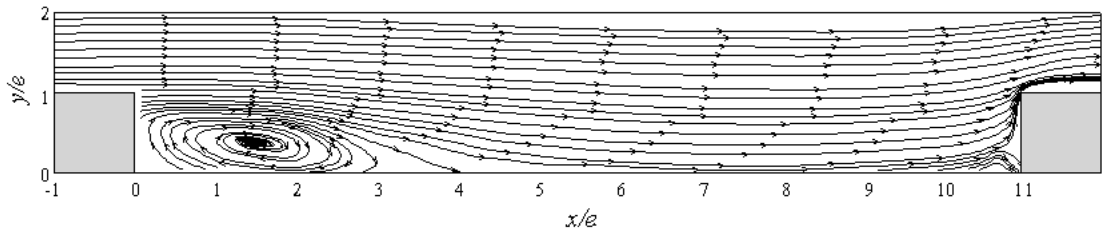

Figure 3 Global flow features between two consecutive ribs, Wang et al. [27]

Figure 4 shows the map of the heat transfer enhancement between two ribs. The spatial variations of local heat transfer clearly reveal the footprints of flow separation, reattachment and redevelopment. It clearly shows that the maximum heat transfer occurred at the reattachment region. Further downstream, the Nusselt number is decaying gradually because the new boundary layer grows in thickness. However, the Nusselt number is rising up in the vicinity of the downstream rib.

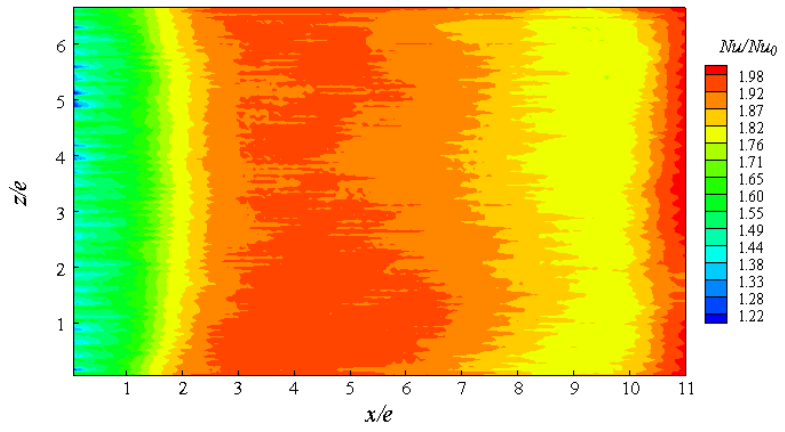

Figure 4 Nusselt number in the region between two consecutive ribs, Wang and Sundén [28]

Heat transfer is strongly dependent on the inner-wall flow features. In order to exhibit this relationship, Figure 5 displays the profiles of skin-friction coefficient and Nusselt number along the centerline between two consecutive ribs. This figure conveys the impression that the location of the maximum heat transfer coefficient is quite consistent with the reattachment point (x/e = 3.6) within the permissible measurement errors. At the reattachment point, the wall shear stress vanishes. In the post-reattachment region ($4 < x/e < 8$), the steep rise of the skin-friction factor is accompanied with the gradual decrease of heat transfer coefficient.

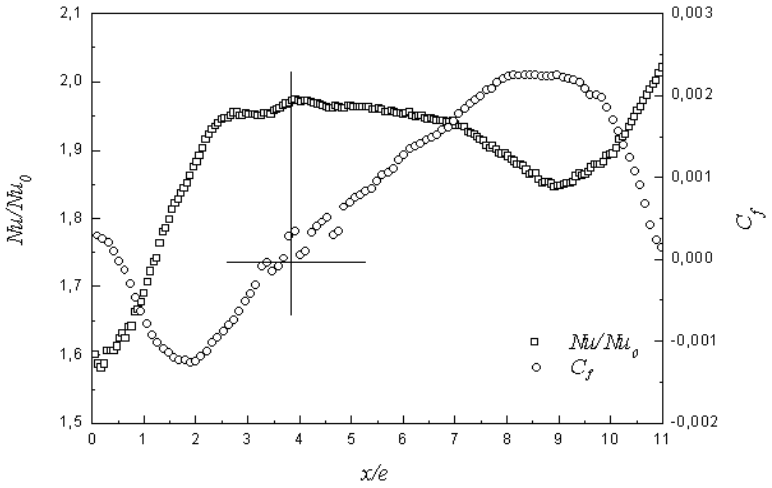

Figure 5 Comparison between the skin-friction factor and Nusselt number along the centreline, Wang [26]

Figure 6 shows the features of the maximum shear stress plotted against streamwise distance. The general level of the maximum shear stress rises gradually with increasing distance up to the reattachment point, and then decreases rapidly between x/e = 3.7 and 4.7. Following the rapid decay after reattachment, a short plateau is observed in the region $5 < x/e < 6.5$.

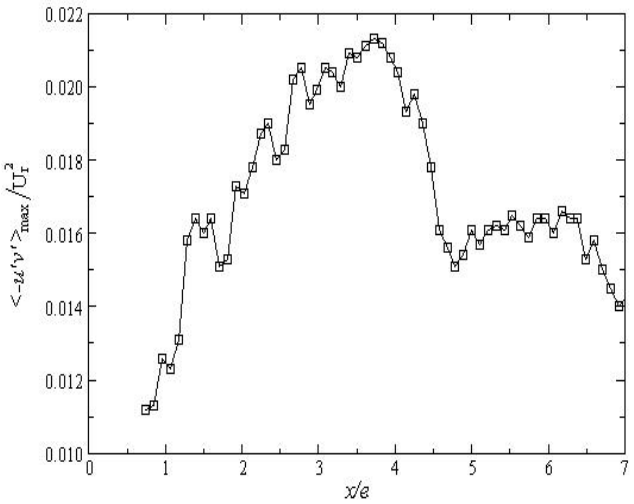

Figure 6 Maximum Reynolds shear stress distribution, Wang and Sundén [28]

For a two-dimensional flow, the turbulence kinetic energy production is approximated as

$$Q_{en} = < -u'v' > \frac{\partial U}{\partial y}$$

Figure 7 gives the turbulent kinetic energy production. It is evident that the quantities exhibit distinct peaks at *y/e* = 1 for the region upstream of the reattachment point (*x/e* = 2 and 3.6). Further inspection of the maximum turbulence production shows that the peak is approximately coincident with the inflexion point. This means that the velocity gradient $\frac{dU}{dy}$ at the inflexion point plays a dominant role in the production of turbulence as flow separation occurs.

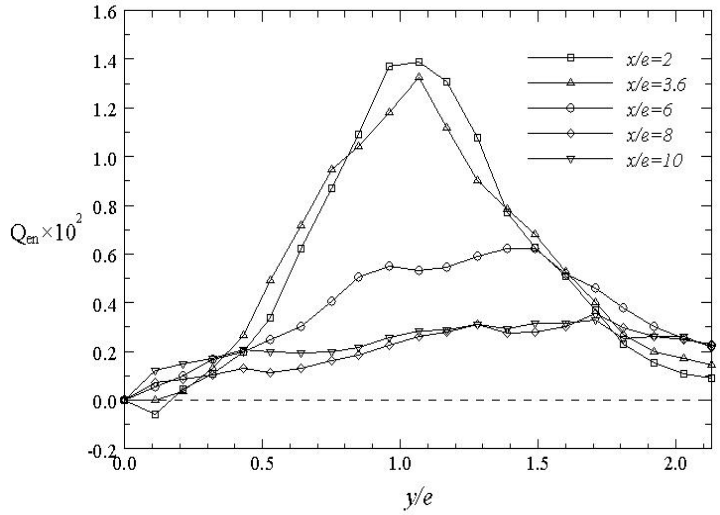

Figure 7 Turbulence kinetic energy production, Wang and Sundén [28]

Two-point correlations are instrumental in studying flow structures because they reveal how coherent the flow structure is over a certain distance. The size of the structures is roughly twice the distance between the origin and the point where the correlation coefficient levels off to zero. The two-point correlation coefficient is defined as

$$R_{u_i u_i, x_j} = \frac{< u'_i(x_{j0}) u'_i(x_j) >}{\sqrt{< u'^2_i(x_{j0}) >} \sqrt{< u'^2_i(x_j) >}}$$

where u_i' is an instantaneous velocity fluctuation, and x_{j0} is a fixed location. The distance between the two points is expressed by $r_{x_j} = x_j - x_{j0}$. Figure 8 shows the distribution of the streamwise velocity correlation $R_{uu,z}$ in the spanwise direction. Four points (*x/e*, *y/e*) in the symmetry plane are selected as origin, *i.e.*, A (0.5, 1), B (5.5, 2), C (5.5, 1) and D (8, 1), respectively. Apart from point A, which is immediately downstream separation, the other three are located in the post-reattachment zone. It is apparent that all the points at *y/e* = 1 show a similar size of the spanwise structures and the correlation virtually vanishes at 1.3*e*. For point B, however, the correlation length is approximately 1.7*e*. In addition, it is noticed that all the points demonstrate pronounced negative values down to −0.2 for large spanwise separation. This is likely caused by the streamwise eddies which are inclined in the vertical direction.

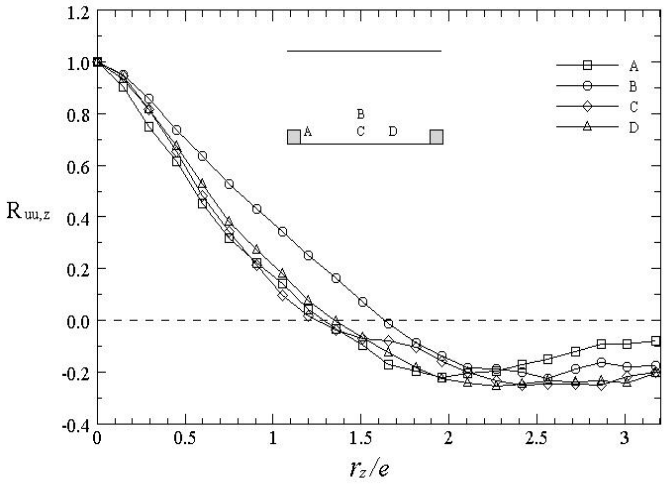

Figure 8 Spanwise *u'* correlation coefficient at different points (*x/e*, *y/e*) in the flow field, A (0.5, 1), B (5.5, 2), C (5.5, 1), D (8, 1), Wang and Sundén [28]

When the flow separates at the edge of a rib, spanwise vortices are generated in the shear layer due to the Kelvin-Helmholtz instability. To identify these vortical structures in an instantaneous velocity field, one should vary the reference frame velocity. When the reference frame velocity matches the convection velocity of an eddy, it becomes recognizable as a roughly circular pattern. This method of visualization is called Galilean decomposition. Figure 9 shows an instantaneous velocity vector field in which the reference frame moves at U_f = 5.0 m/s. The figure clearly displays two distinct vortices being shed downstream of the rib. The vortices have a size approximately one-half of a rib height and are inclined at approximately 20° with respect to the *x*-axis.

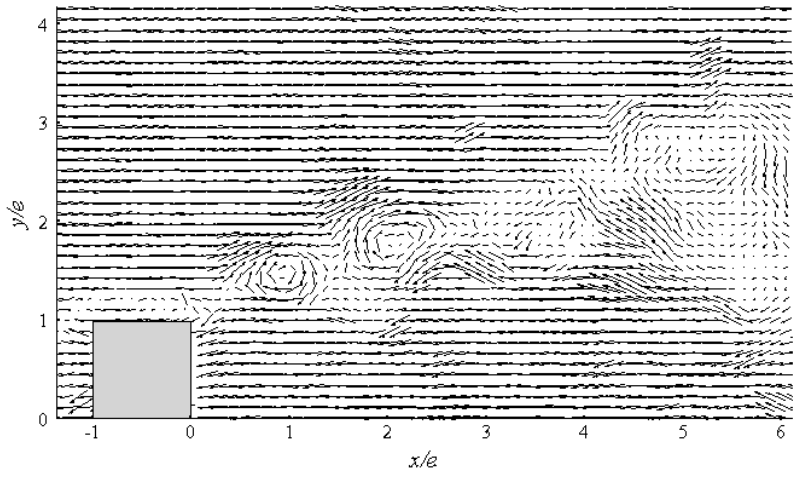

Figure 9 Galilean transformation for visualizing vortices, Wang and Sundén [28]

The Effect of Rib Cross Section Profile

Wang and Sundén [30] investigated the heat transfer characteristics in a square channel with various-shaped ribs. Four geometries were considered in their study, that is, square, triangular, trapezoidal with decreasing height in the flow direction, and the trapezoidal with increasing height in the flow direction. The results showed that the trapezoidal ribs with increasing height in the flow direction provide the highest heat transfer enhancement and are likely to be used to suppress the local hot spots occurring

immediately downstream the rib. Figure 10 shows the comparison of heat transfer among the various rib shapes.

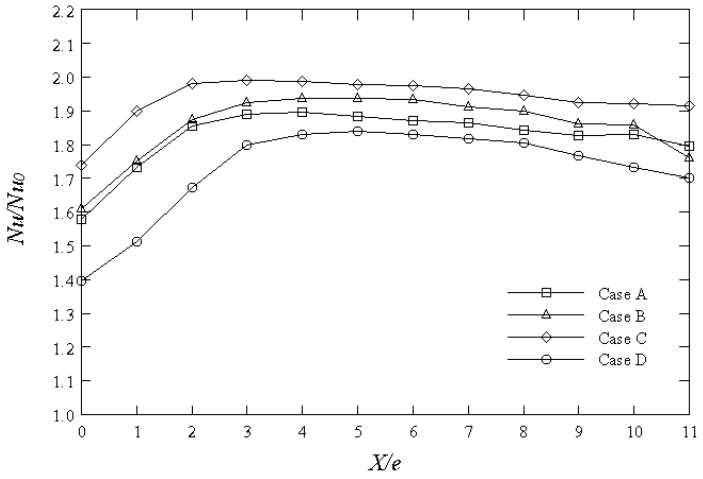

Figure 10 Local heat transfer along the centreline; Case A, square ribs; Case B, Triangular ribs; Case C, trapezoidal ribs with decreasing height in the flow direction; Case D, trapezoidal ribs with increasing height in the flow direction, Wang and Sundén [30]

Based on the experimental work of Wang and Sundén [30], Kamali and Binesh [31] performed numerical simulations to study the heat transfer and friction factor in a channel roughened with various-shaped ribs. They found good agreement between the predicted results and the measurements. Figure 11 shows the streamlines of the reprehensive cases for Re = 20000, e/H = 0.1 and P/e = 12 in their simulations. Of the four cases, the flow over the square rib appears to be the most complex; since the rib face is perpendicular to the flow direction, sizable primary and secondary recirculation regions form near the front and rear corners at the rib bottom are recognized. The size of the recirculation zone, however, is largest for the trapezoidal rib with increasing height in the flow direction and smallest for the square rib.

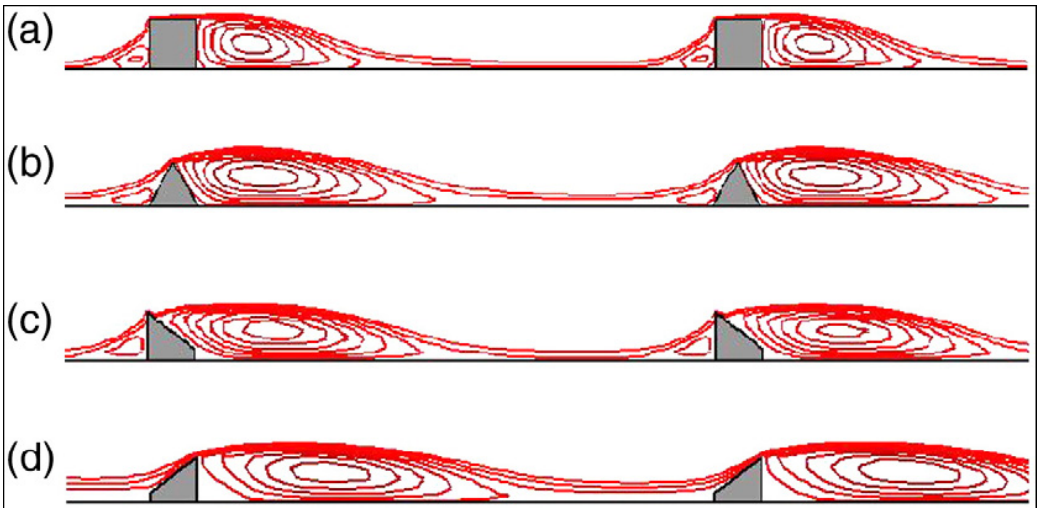

Figure 11 Streamlines for representative ribs, Kamali and Binesh [31]

Effect of Rib Arrangement

Gao and Sundén [32] carried out experiments to investigate the heat transfer in a rectangular duct roughened by V-shaped ribs. The aspect ratio of the duct is 1/8. The rib height-to-hydraulic diameter ratio is 0.06, with an attack angle of 60°. The pitch ratio is 10. Figure 12 shows the RGB images taken for the V-shaped ribs pointing upstream at *Re* = 6000. The significant spanwise variation of the heat transfer coefficients is noticeable. The V-ribs generate two double-cell counter-rotating vortices that extend over the whole cross section. Figure 4 shows the RGB images taken for the V-shaped ribs pointing downstream at *Re* = 6000. It is clear that the spanwise heat transfer coefficients are totally different from that of the V-ribs pointing upstream. For the central part where the V-ribs pointing upstream induced the highest heat transfer coefficients, the V-ribs pointing downstream produce the lowest heat transfer coefficients. For both the bottom and top side, where the V-ribs pointing upstream induced the lowest heat transfer coefficients, the V-ribs pointing downstream produce the highest heat transfer coefficients. For the V-ribs pointing downstream, two double-cell counter rotating vortices are generated but with opposite direction.

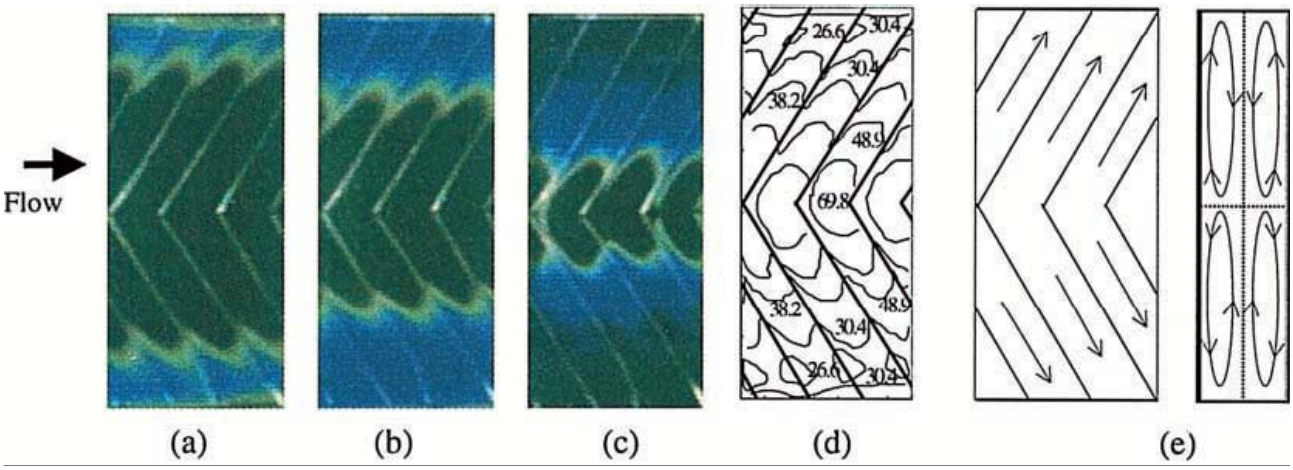

Figure 12 V-shaped ribs pointing upstream at *Re* = 6000. (a) q_w= 354 W/m^2, (b) q_w= 437 W/m^2, (a) q_w= 660 W/m^2, (d) Local Nusselt number contours, (e) Schematic pattern of secondary flow induced by V-ribs, Gao and Sundén [32]

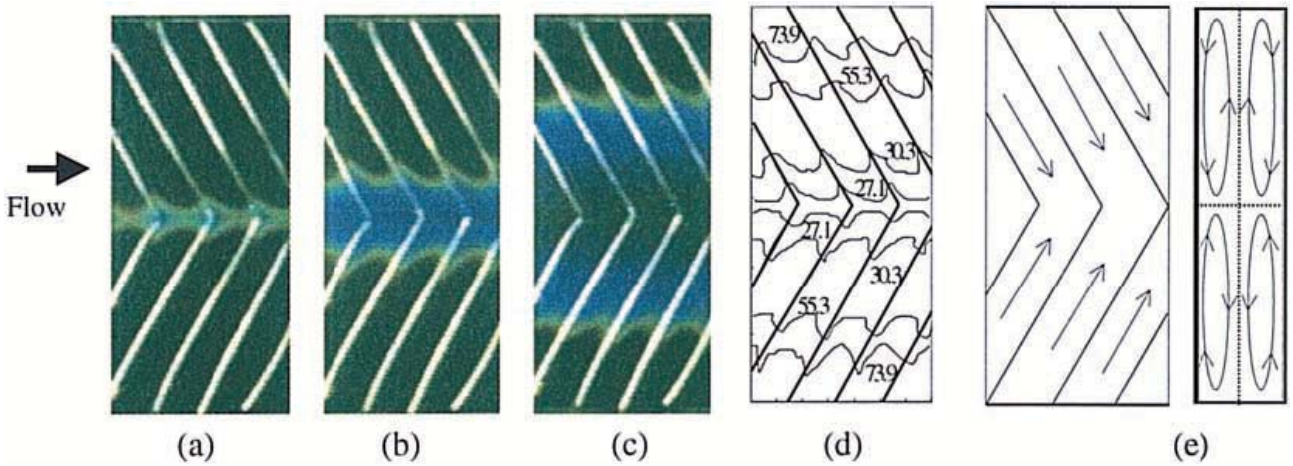

Figure 13 V-shaped ribs pointing downstream at *Re* = 6000. (a) q_w= 383 W/m^2, (b) q_w= 455 W/m^2, (a) q_w= 575 W/m^2, (d) Local Nusselt number contours, (e) Schematic pattern of secondary flow induced by V-ribs, Gao and Sundén [32]

The averaged Nusselt numbers plotted against Reynolds number are illustrated in Figure 14. Compared with the smooth channel, the heat transfer is appreciably enhanced in the channel roughened by V-shaped ribs. In the tested Reynolds number range, the enhanced heat transfer caused by the V-ribs pointing downstream is higher than those caused by the V-ribs pointing upstream.

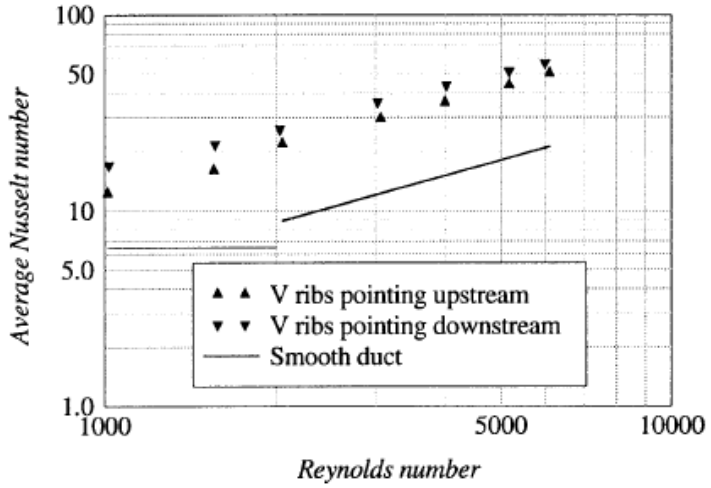

Figure 14 Average Nusselt number versus Reynolds number, Gao and Sundén [32]

CONCLUSIONS

Heat transfer and fluid flow in ribbed channels continue to be a topic of considerable practical and theoretical interest. The present paper has only briefly touched on a very few of the many areas involving the enhancement of heat transfer and separated flow in ribbed ducts. Further research and studies are needed to gain the sight into the physical process and shed light on the design optimization of the future cooling systems.

ACKNOWLEDGEMENTS

Financial support from Swedish Research Council (VR) and Swedish Energy Agency (STEM) is kindly acknowledged.

REFERENCES

1. Han, J. C., Heat Transfer and Friction in Channels with Two Opposite Rib-Roughened Walls, *Trans. ASME J. Heat Transfer*, Vol. 106, pp. 774-781, 1984.
2. Liou, T. M., and Hwang, H. H., Turbulent Heat Transfer Augmentation and Friction in Periodic Fully Developed Channel Flows, *Trans. ASME J. Heat Transfer,* Vol. 114, pp. 56-64, 1992.
3. Taslim, M. E., Li, T., and Kercher, D. M., Experimental Heat Transfer and Friction in Channels Roughened with Angled, V-Shaped, and Discrete Ribs on Two Opposite Walls, *Trans. ASME J. Turbomachinery*, Vol. 118, pp. 20-28, 1996.
4. Taslim, M.E., and Wadsworth, C. M., An Experimental Investigation of the Rib Surface-Averaged Heat Transfer Coefficient in a Rib–Roughened Square Passage, *Trans. ASME J. Turbomachinery*, Vol. 120, pp. 564-570, 1997.
5. Han, J. C., and Park, J. S., Developing Heat Transfer in Rectangular Channels with Rib Turbulators, *Int. J. Heat Mass Transfer*, Vol. **31**, pp.183-195, 1988.

6. Rau, J. G., Cakan, M., Moeller, D., and Arts, T., The Effect of Periodic Ribs on the Local Aerodynamic and Heat Transfer Performance of a Straight Cooling Channel, *Trans. ASME J. Turbomachinery*, Vol. 120, pp. 368-375, 1998.
7. Han J. C., Glicksman, L. R., and Rohsenow, W. M., An Investigation of Heat Transfer and Friction for Rib-Roughened Surfaces. *Int. J. Heat Mass Transfer*, Vol. 21, 1143-1156, 1978.
8. Lockett J. F, and Collinsm, M. W., Holographic Interferometry Applied to Rib-Roughness Heat Transfer in Turbulent Flow, *Int. J. Heat Mass Transfer*, Vol. 33, pp. 2439-2449, 1990.
9. Taslim, M. E., and Korotky, G. J., Low-Aspect-Ratio Rib Heat Transfer Coefficient Measurements in a Square Channel, *Tran. ASME J. Turbomach.*, Vol. 120, pp. 831-838, 1998.
10. Liou T. M., and Hwang J. J., Effect of Ridge Shapes on Turbulent Heat Transfer and Friction in Rectangular Channel, *Int. J. Heat Mass Transfer*, Vol. 36, pp. 931-940, 1993.
11. Chandra, P. R., Fontenot, M. L., and Han, J. C., Effect of Rib Profiles on Turbulent Channel Flow Heat Transfer, *AIAA J. Thermophysics and Heat Transfer*, Vol. 12, pp. 116-118, 1998.
12. Ahn S. W., The Effect of Roughness Type on Friction Factors and Heat Transfer in Roughened Rectangular Duct. *Int. Comm. Heat Mass Transfer*, Vol. 28, pp. 933-942, 2001.
13. Ahn, J., Choi, H., and Lee, J. S., Large Eddy Simulation of Flow and Heat Transfer in a Channel Roughened by Square or Semicircle Ribs, *Trans. ASME J. Turbomach.*, Vol. 127, pp. 263-269, 2005.
14. Hwang, J. J., and Liou, T. M., Heat Transfer in a Rectangular Channel with Perforated Turbulence Promoters Using Holographic Interferometry Measurement, *Int. J. Heat Mass Transfer*, Vol. 38, pp. 3197-3207, 1995.
15. Hwang, J. J., and Liou, T. M., Effect of Permeable Ribs on Heat Transfer and Friction in a Rectangular Channel, *Trans. ASME J. Turbomach.*, Vol. 117, pp. 265-271, 1995.
16. Liou, T. M., and Wang, W. B., Laser Holographic Interferometry Study of Developing Heat Transfer in a Duct with a Detached Rib Array, *Int. J. Heat Mass Transfer,* Vol. 38, pp. 91-100, 1995.
17. Liou, T. M., Wang, W. B., and Chang, Y. J., Holographic Interferometry Study of Spatially Periodic Heat Transfer in a Channel with Ribs Detached from one Wall, *Trans. ASME J. Heat Transfer*, Vol.117, pp.32-39, 1995.
18. Liou, T. M., Shuy, W. J., and Tsao, Y. H., Effect of Rib Height and Pitch on the Thermal Performance of a Passage Disturbed by Detached Solid Ribs, *Trans. ASME J. Turbomach.*, Vol. 120, pp. 581-588, 1998.
19. Kukreja, R. T., and Lau, S. C., Distribution of Local Heat Transfer Coefficient on Surface with Solid and Perforated Ribs, *J. Enhanced Heat Transfer*, Vol. 5, pp. 9-21, 1998.
20. Moon, S. W., and Lau, S. C., Heat Transfer Between Blockages with Holes in a Rectangular Channel, *Trans. ASME J. Heat Transfer*, Vol. 125, 587-594, 2003.
21. Han, J.C., and Zhang, Y. M., and Lee, C. P., Augmented Heat Transfer in Square Channels with Parallel, Crossed and V-shaped Angled Ribs, *Trans. ASME J. Heat Transfer*, Vol. 113, pp. 590-596, 1991.
22. Lau, S. C., Kukreja, R. T., and McMillan, R. D., Effects of V-Shaped Rib Arrays on Turbulent Heat Transfer and Friction of Fully Developed Flow in a Square Channel, *Int. J. Heat Mass Transfer*, Vol. 34, pp. 1605–1616, 1991.
23. Gao, X., and Sundén, B., Heat Transfer and Pressure Drop Measurement in Rib-Roughened Rectangular Ducts, *Exp. Therm. Fluid Sci.*, Vol. 24, pp. 25-34, 2001.
24. Jia, R., Sunden, B., and Faghri, M., Computational Analysis of Heat Transfer Enhancement in Square Ducts with V-shaped Ribs: Turbine Blade Cooling, *Trans. ASME J. Heat Transfer*, Vol. 127, 425-433, 2005.
25. Webb, R. L., Eckert E. R. G., and Goldstein, R. J., Heat Transfer and Friction in Tubes with Repeated-Rib Roughness, *Int. J. Heat Mass Transfer*, Vol. 14, pp. 601-617, 1971.
26. Bradshaw, P., and Wong, F. Y. F., The Reattachment and Relaxation of a Turbulent Shear Layer, *J. Fluid Mech.* Vol. 152, pp. 113-135, 1972.

27. Wang, L., Hejcik, J., and Sundén, B., PIV Measurement of Separated Flow in a Square Channel with Streamwise Periodic Ribs on One Wall, *Trans. ASME J. Fluids Engineering*, Vol. 129, pp. 834-841, 2007.
28. Wang, L., and Sundén, B., Experimental Investigation of Local Heat Transfer in a Square Duct with Continuous and Truncated Ribs, *Exp. Heat Transfer*, Vol. 18, pp 179-197, 2005.
29. Wang, L., Experimental Studies of Separated Flow and Heat Transfer in a Ribbed Channel, Doctoral thesis, Lund University, 2007.
30. Wang, L., and Sundén, B., Experimental Investigation of Local Heat Transfer in a Square Duct with Various-Shaped Ribs, *Heat Mass Transfer*, Vol. 43, pp. 759-766, 2007.
31. Kamali, R., and Binesh, A. R., The Importance of Rib Shapes on the Local Heat Transfer and Flow Friction Characteristics of Square Ducts with Ribbed Internal Surface, *Int. Comm. Heat Mass Transfer*, Vol. 35, pp. 1032-1040, 2008.
32. Gao, X., and Sundén, B., Heat Transfer Distribution in Rectangular Ducts with V-shaped Ribs, *Heat Mass Transfer*, Vol. 37, pp. 315-320, 2001.

MASS TRANSPORT PHENOMENON ON FUEL CELLS AND CO_2 UNDERGROUND SEQUESTRATION

S. Hirai[1] *, S. Tsushima[1]
[1]Tokyo Institute of Technology

ABSTRACT. The global warming caused by the production of carbon dioxide (CO2) from burning fossil fuels is getting widespread international attention. A significant reduction in the volume of CO2 emissions to the atmosphere is requiring urgent solution. There are number of ways by which CO2 emissions can be reduced, improvement of energy efficiency, use of renewable energy, and carbon sequestration. In this article, we describe two realistic countermeasures, CO2 capture and sequestration (CCS) and hydrogen fuel-cell energy system to mitigate global warming. In both fields, mass transport plays a key role for improvement and prediction of the systems. We present experimental and numerical investigations on mass transport process in both CCS and polymer electrolyte membrane fuel cells (PEMFCs).

Keywords: *mass transport, CO_2 capture and sequestration, fuel cell, polymer electrolyte membrane*

INTRODUCTION

Modern civilization is being maintained by a large consumption of the fossil fuel, and it is being predicted that CO_2 concentration, now at 370-380ppm, would become several times larger in future. Therefore, it is immediately required to take global warming measures. CO_2 capture and sequestration (CCS) and hydrogen fuel-cell energy system have been gathering much attention as realistic countermeasures to mitigate global warming.

CO_2 underground sequestration is CO_2 captured from large-scaled power plants injected into aquifers. Captured CO_2 can also be utilized for enhanced oil recovery (EOR). In the aquifers, CO_2 possibly rises upward due to buoyancy effect. Therefore, more recently, residual gas trapping mechanism at the aquifers is also investigated for secure geological storage of CO_2 in the underground [1]. For long-term sequestration of CO_2, fundamental understanding on CO_2-water two-phase flow behaviors in porous rock materials is inherently needed.

Hydrogen energy systems also have been gathering much attention in term of efficient utilization of fossil fuel and energy security. Polymer electrolyte membrane fuel cells (PEMFCs) are considered power sources for vehicle and on-site power generation in the future. For implementation of PEMFCs, further improvement on energy efficiency and power density as well as robustness and durability of the system are needed. Water inside the fuel cells plays a key role for both cell performance and durability, motivating experimental and numerical studies on water transport in PEMFCs.

* Corresponding author: Prof. S. Hirai
Phone: + (81)-3-5734-3336, Fax: + (81)-3-5734-3336
E-mail address: hirai@mes.titech.ac.jp

In the following sections, we describes our research activities in CCS and fuel cells, focusing on mass transport process with advanced in-situ diagnostics, which are applied to acquire fundamental understanding.

CO_2 UNDERGROUND SEQUESTRATION

MRI visualization of CO_2–water behaviors in a rock-core sample

We performed MRI visualization of a rock-core after CO_2 injection. Noninvasive measurement of a water distribution is one of the advantages of the MRI technique. Nuclei with non-zero spin angular momenta have an intrinsic magnetic dipole moment. In a static magnetic field, B_0, each nuclear spin precesses with frequency, $\omega_0=\gamma B_0$, where ω_0 is called the Larmor frequency and γ is the gyromagnetic ratio, characteristic of the nuclei being studied. The Larmor frequency for protons at 7.05 T, which is the strength of magnetic field used in our MRI system (Varian Unity Inova model 300/150 SWB), is about 300 MHz. By applying a radio frequency magnetic field at the Larmor frequency, the nuclear magnetic resonance signal due to precession is observed after the magnetization is rotated away from the static field. In MRI, spatial information is converted into the MR signals by applying a gradient magnetic field. Hence, the distribution of proton density can be imaged in any cross-section. In our experiments, the gradient coils provided a maximum gradient strength of 0.24 T/m.

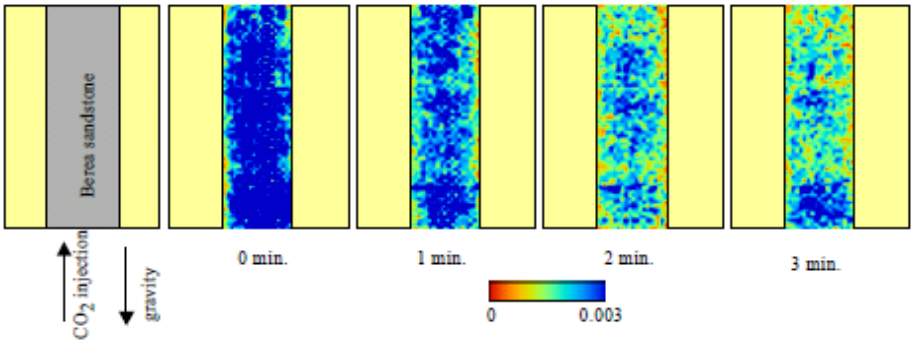

Figure.1 Distribution of water in Berea sandstone core at 9.0MPa, 42°C with CO_2 injection

In preliminary experiments, we confirmed that the MR signal intensity from any local position was proportional to the water content in the porous medium. This means that measured MR signal intensity reflects local water saturation, which is defined as the fraction of the void volume occupied by water [2], in the porous media. In the experiments with CO_2 injection, we measured the initial MR signal intensity distributions in the porous medium filled with water. Then, we started to supply CO_2 into the porous medium with time-series acquisition of MR images. As shown in Fig.1, the injected CO_2 would replace some water in the porous medium thus decreasing the MR signal intensity. The local water saturation in the porous medium can be defined as the ratio of MR signal intensity with the CO_2 gas to that without gas. MRI results were analyzed for the coreflood interpretation method to determine the local Darcy phase velocities and capillary dispersion rate for a range of water saturations. As shown in our previous study [1], we successfully estimated the properties of two-phase flow such as Darcy phase velocities and the capillary dispersion rate function on a basis of the *in-situ* saturation profiles obtained by MRI.

Super-atomization of liquid CO_2 for stable geological storage

As the caprock structures exists only few sites in areas surrounding Japan, it is necessary to develop a new geological storage technique. We proposed a technique of trapping super-atomized liquid

CO_2 in a porous structure to realize stable geological storage and boost the efficiency of storage. The atomized liquid CO_2, which is the same scale as the gap diameter in the aquifer might be trapped stably by the interface tension.

In our previous study [3], the super-atomization process and the emulsion stability have been examined experimentally. The liquid CO_2 was atomized by using a static mixer placed in a closed circulatory channel. In order to measure the size of the super-atomized liquid CO_2, dynamic light scattering was employed. Since water and liquid CO_2 are mutually immiscible, a surfactant (trisiloxane) was added to assist the atomization of liquid CO_2.

As the result, the liquid CO_2 could be atomized by getting through the static mixer, however its lifetime was about 20 seconds without surfactant. On the other hand, liquid CO_2 was super-atomized in the presence of the surfactant and long lifetime was achieved. In the presence of 2.0 mass% surfactant concentrations, the liquid CO_2 was super-atomized with an average diameter of 5 μm and lifetime of the atomized state was for 120 min. The diameter of the super-atomized liquid CO_2 was same scale as the gap diameter in the aquifer. Additionally, the lifetime is substantially long for CO_2 injection process. For these experimental results, a feasibility of stable CO_2 geological storage has been suggested.

WATER TRANSPORT AND DEGRADATION ANALYSIS IN PEMFC

MRI visualization of water content in a polymer electrolyte membrane in an operational fuel cell

In PEFCs, appropriate water management to maintain polymer electrolyte membrane (PEM) hydrated is of great importance, because the ion conductivity of membrane is lower at lower water content. Consequently, it is of great interest to water content and water transport process in PEMs during fuel cell operation. We thus have been developing an in-situ visualization technique using magnetic resonance imaging (MRI) for measurement of water content distribution in PEMs in through-plane and in-plane direction under fuel cell operation. We succeeded in visualization of transversal water content distributions in a membrane during fuel cell operation by designing a fuel cell that can operate in an MRI system [4]. It was shown that water concentration gradient established in the membrane with increase of cell current due to an electro-osmotic effect. This MRI observation was also compared with numerical simulation for validation [5]. We also examined lateral water content distributions with different flow pattern, *i.e.* a parallel flow and a serpentine flow by using three-dimensional (3D) MRI visualization. We confirmed that a parallel flow configuration shows different membrane hydration from a parallel flow [6].

<u>High-resolution MRI</u>

An especially challenging issue in MRI visualization for PEMFCs is achievement of higher spatial resolution, which is necessary to obtain fundamental insights into water transport processes in PEMs that are practically used for industrial applications. Figure 2 shows high-resolution MRI results of transversal water content distribution in a 117-μm-thick membrane. We achieved MRI visualization of 10-μm-boxel width along the through-plane direction in the membrane using a high-sensitivity radio frequency (RF) coil system and a specially designed PEMFC for MRI measurement.

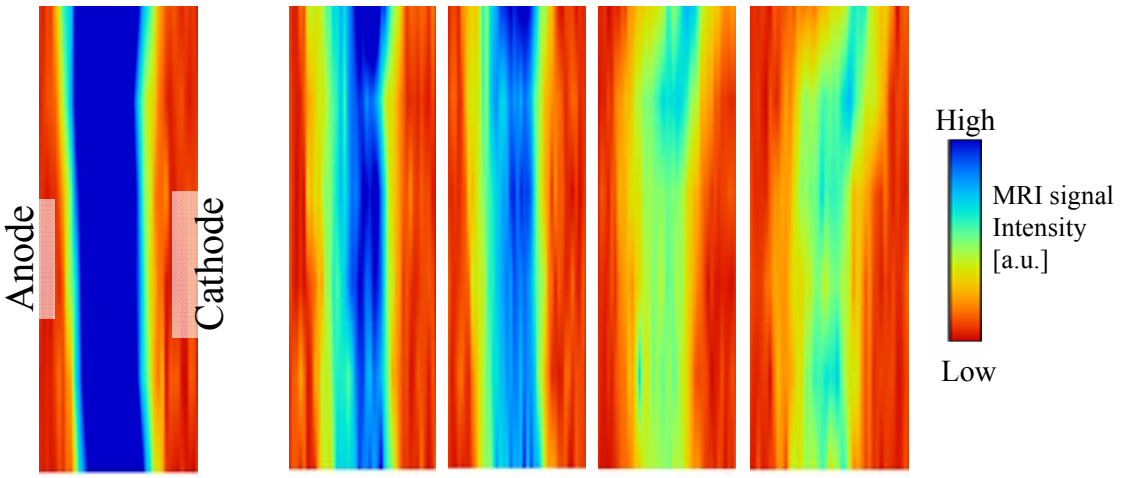

(a) 0 [A/cm^2] (b) 0.1 (c) 0.2 (d) 0.3 (e) 0.4

Figure 2. MRI visualization of transversal water content distribution in a polymer electrolyte membrane with 117 μm-thickness under fuel cell operation

Reduction of the membrane thickness might flatten the water content profile in the membrane because of enhancement of water back-diffusion from the cathode to the anode. However, MRI visualization shows partial dehydration at the membrane's anode side with increased cell current, as observed in the 340-μm-thick membrane, which reflects that electro-osmotic drag remains influential on water content profiles in the membrane during fuel cell operation. Our next target for development of MRI visualization techniques is 5-μm-boxel width in the 50-μm-thick membrane.

Nuclei-labeling MRI (NL-MRI)

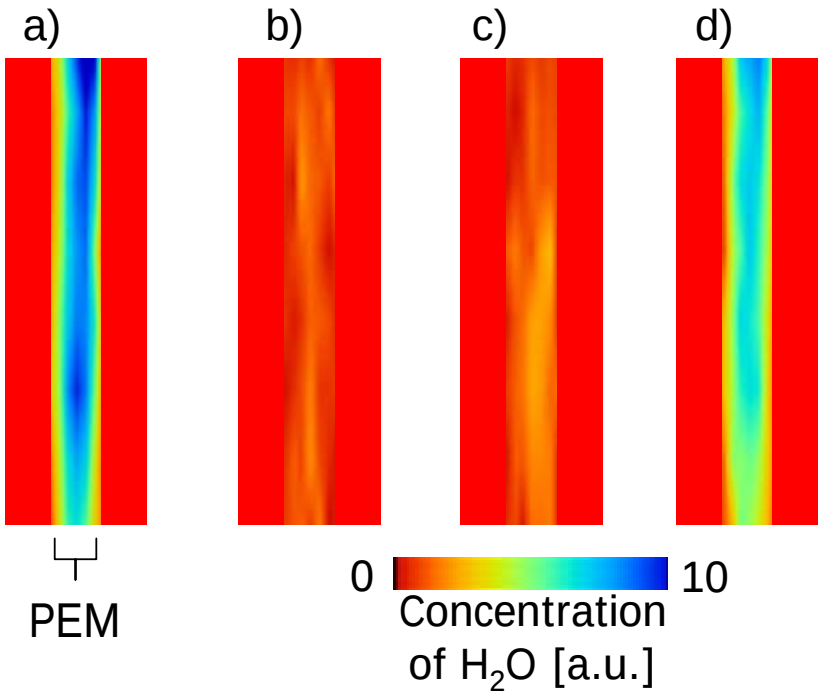

Figure 3. NL-MRI results in the membrane The anode is on the left side. (a) normal operation (b) effect of anode humidification (c) effect of cathode humidification (d) effect of supplied hydrogen.

Our recent MRI application with isotope-labeling techniques enabled us to examine water sources for membrane hydration [7]. Neither D_2 nor D_2O is visible using ^{1}H-MRI, but fuel cell operation is not affected by the isotope. Using various combinations of D_2 fuel and D_2O for inlet humidification, it is possible to isolate each water source and transport mechanism.

Without nuclei labeling, a conventional MRI technique can only obtain overall water content distributions resulting from all water sources and transport processes. However, the water vapor in the cathode and fuel to the anode can be labeled with deuterium. Because deuterium can not be visualized by ^{1}H-MRI as a result of the difference of the nuclear magnetic resonance frequency, what is obtained using this technique is the distribution of water (H_2O) that has been absorbed in the anode side. In other words, we can ascertain the effect of water vapor from the anode side on hydration of PEM without disturbing the membrane's natural hydration state. Using other combinations of isotope-labeled fuel and humidification water, it is possible to isolate and study each water source and transport effect during PEMFC operation.

Figure 3 shows cross-sectional MR images of a membrane operated with different nuclei-labeling experiments. The fuel cell was operated at 60°C with 84% relative humidity maintained at the anode and the cathode inlet. As presented in Figure 2(d), water observed inside the membrane apparently originates in the supplied hydrogen, which indicates that supplied water vapor was not absorbed directly into the membrane and thus played a role in suppressing water discharge as vapor from the membrane. In fact, NL-MRI yields direct insight that is valuable for discussion of the membrane hydration path in operational PEMFCs.

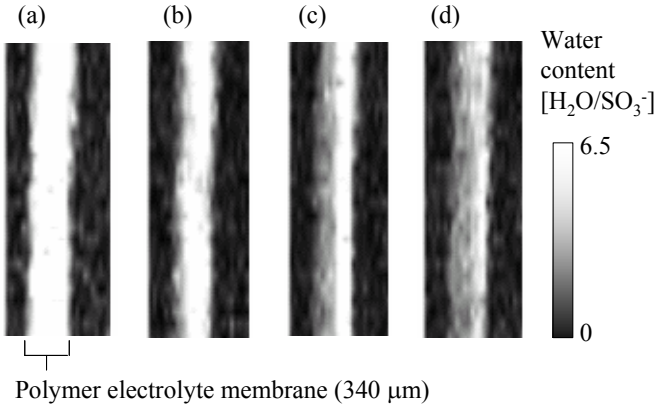

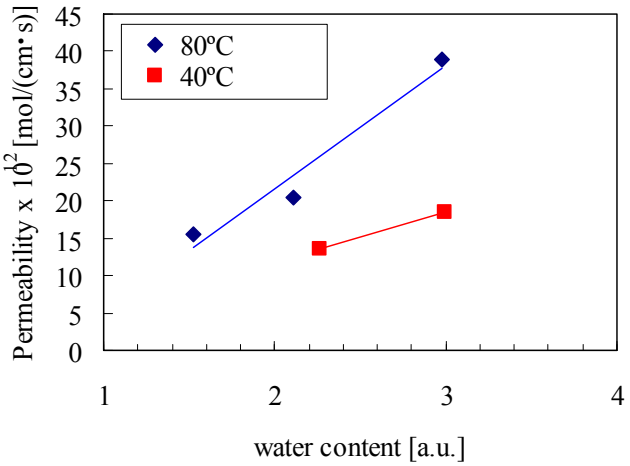

Figure 4. Hydrogen permeability under fuel cell operation at 0.1 A/cm^2 with water content measured by MRI.

Membrane degradation analysis using MRI

We also applied MRI for PEM degradation analyses. Actually, MRI was used to monitor water contents in the membrane during fuel-cell operation. We also used direct gas mass spectroscopy (DGMS) to investigate hydrogen crossover in the membrane. The averaged water content in the membrane was obtained from this MRI result. It is depicted along with hydrogen permeability through the MEA in Figure 4. Hydrogen permeability increases with water content in the membrane, suggesting that the hydrophilic domain of the membrane plays an important role for hydrogen permeation processes [8].

CONCLUSION

We described our research activities in CCS and fuel cells, focusing on mass transport process with advanced *in-situ* diagnostics, e.g. MRI, TDLAS and DGMS which are applied to acquire fundamental understanding on CO_2 and water transport.

ACKNOWLEDGEMENT

This work was partially supported by JSPS, NEDO and RITE. The author gratefully acknowledges all members sharing their time in RCCRE in Tokyo Tech.

REFERENCES

1. Suekane, T., Ishii, T., Tsushima, S., and Hirai, S., Migration of CO_2 in Porous Media Filled with water, *J. Thermal Sci. Tech.*, Vol. 1, pp 1-11, 2006.
2. Bear, J., Dynamics of Fluids in Porous Media, Dover, 441, 1972.
3. Uemura S., Suzuki, K., Tsushima, S., and Hirai, S., Study on the Ultramicronization of liquid CO2 for stable geological storage, Proc 45th National Heat Transfer Symp., Vol.1, pp 119-120, 2008.
4. Tsushima, S., Teranishi, K., and Hirai, S., Magnetic Resonance Imaging of the Water Distribution within a Polymer Electrolyte Membrane in Fuel Cells, *Electrochem. Solid-State Lett.*, Vol.7, No.9, A269-A272, 2004.
5. Teranishi, K., Tsushima, S., and Hirai, S., Analysis of Water Transport in PEFCs by Magnetic Resonance Imaging Measurement, *J. Electrochem. Soc.*, Vol.153, No.4, A664-668, 2006.
6. Tsushima, S., Nanjo, T., Nishida, K., and Hirai, S., Investigation of the Lateral Water Distribution in a Proton Exchange Membrane in Fuel Cell Operation by 3D-MRI, *ECS Trans.*, Vol.1, No.6, pp 199-205, 2005.
7. T. Kotaka, S. Tsushima, and S. Hirai, *ECS Trans.* **11**-1, 445 (2007).
8. S. Tsushima, T. Nanjo, and S. Hirai, *ECS Trans.*, **11**-1, 435 (2007).

RECENT ACHIEVEMENTS IN MULTI-SCALE MODELLING AND SIMULATIONS OF MAGNETOFLUIDDYNAMIC PHENOMENA:

FROM ORIGIN OF PLANETARY MAGNETIC FIELDS TO IMPROVED MAGNETIC DRUG TARGETING

S. Kenjeres[1, *]
[1]Department of Multi-Scale Physics, Faculty of Applied Sciences and J.M. Burgerscentre for Fluid Dynamics, Delft University of Technology, Delft, The Netherlands

ABSTRACT. The paper reviews some of the recent results in modelling and simulations of flow and heat transfer of the electrically conductive fluids interacting with electromagnetic fields. Despite the differences in flow geometries and huge disparity of the length- and time-scales, ranging from astrophysical to biomedical applications, it is demonstrated that magnetofluiddynamic (MFD) phenomena are characterised by two fundamental features – a time-dependent spiralling flow patterns and non-homogeneous distributions of the magnetic fields. Some representative examples of both one- and two-way coupled MFD phenomena are considered: electromagnetically driven vertical turbulent flows with and without heat transfer in a generic setup, turbulent magnetic dynamo under realistic experimental conditions (the Riga-dynamo experimental setup), and finally, simulations of the magnetic particle deposition in the realistic human blood vessels subjected to the locally imposed strong magnetic gradients (magnetic drug targeting). In all considered cases, a good agreement between available experimental results and numerical simulations is obtained, proving accuracy and potentials of the multi-scale modelling approach in simulating complex MFD phenomena.

Keywords: *fluid flow and turbulence, magnetic field, Lorentz force, magnetic dynamo, magnetic drug targeting;*

INTRODUCTION

In this paper, fundamental interactions between fluid flow, turbulence and electromagnetic fields are addressed. These interactions are essential for possible explanations of a fascinating number of phenomena in nature and technology, ranging from origin of magnetic fields in universe to the most recent advancements in medical applications through magnetic drug targeting techniques. Control of flow, turbulence and heat transfer of electrically conductive working fluids is a basic prerequisite for the design and optimization of many technological processes. Examples include electromagnetic braking of continuous steel casting, free-surface stabilization of the aluminum reduction cells, joining metals by arc welding, crystal growth, electromagnetic mixing and steering in metallurgy, and liquid metal blankets in new generation of fusion reactors, space craft-propulsion systems, satellite navigation, etc. The magnetofluiddynamics (MFD) (or traditionally called magnetohydrodynamics or MHD) is a typical example of the multi-physics phenomena – fluid flow, heat transfer and turbulent transport as a part of the fluid dynamics on one side, and on the other side, magnetic fields and electric currents as a part of the electromagnetism. We will demonstrate, that

* Corresponding author: Dr. Sasa Kenjeres
Phone: + (31)-15-2783649, Fax: + (31)-15-2782838
E-mail address: S.Kenjeres@tudelft.nl

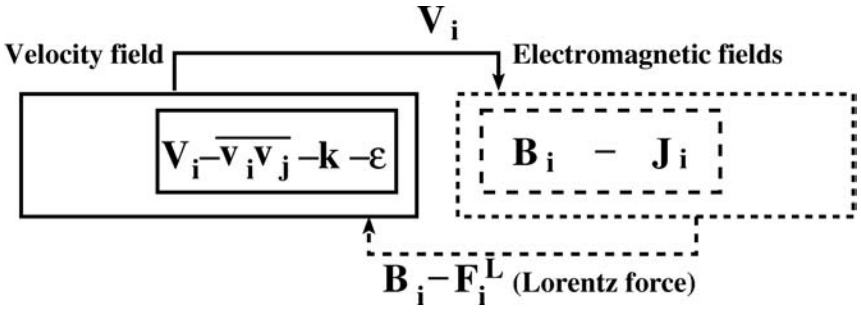

Figure 1. The general overview of the fluid flow, turbulence and electromagnetic fields interactions: the one-way interaction ($V_i \rightarrow B_i$) and the two-way interactions ($V_i \rightarrow B_i$, $B_i \rightarrow V_i$).

despite enormous disparity of characteristic length and time scales and intensity of interactions, all above mentioned phenomena are characterised by two essential features – time-dependent spiralling flow patterns and non-homogeneous distributions of electromagnetic fields.

General classification of electrically conducting fluid flows in the presence of electromagnetic fields can be based on the value of the Reynolds magnetic number $Re_m=V\,D/\lambda$, which represents the ratio between magnetic advection and diffusion, where $\lambda=1/(\mu_0\,\sigma)$ is magnetic diffusivity and μ_0 and σ are magnetic permeability and electric conductivity of the working fluid, respectively. The typical velocity and length scale (size of domain) are V and D, respectively. For $Re_m << 1$, the interactions between electromagnetic fields and fluid flow are one-way only, excluding the effects of the fluid velocity (V_i) onto the distributions of magnetic (B_i) and electric (J_i) fields. Under such conditions, the system of Maxwell's equations can be significantly simplified and only one additional equation for electric potential has to be introduced to fully close the system of equations. In contrast to that, two-way interactions occur for $Re_m > 1$, i.e. a fully coupled system of momentum and magnetic induction equations has to be solved. For both one- and two-way coupled systems, velocity and electromagnetic fields are interconnected through the Lorentz force ($F_L=J \times B$). In order to reach significantly large values of Re_m, the product V D has to be large, since the magnetic diffusivity is given as a property of fluid. By increasing a velocity and/or the dimension of the system, we are easily approaching a turbulent flow regime, characterized by a high hydrodynamic Reynolds number $Re = V\,D\,/\,\nu$ where ν is the fluid kinematic viscosity. The general overview of interactions between fluid flow, turbulence and electromagnetic field is shown in Fig.1.

Due to the fact that fluid flow will be primarily in the fully developed turbulent regime and because of our present inability to computationally resolve all characteristic flow and turbulence scales in time and space, the modelling of the unresolved scales remains one of the big challenges in the MFD phenomena. In this study we will adopt a multi-scale approach, i.e. the energetically most dominant flow and turbulence structure will be fully resolved by numerical mesh while the subscale structures will be represented by a turbulence model. The standard representation of the subscale turbulence structures primarily developed for the pressure driven flows is not suitable for the flows subjected to or driven by strong body forcing – as in case of the electromagnetic forcing. This required development of the novel electromagnetically extended subscale turbulence closures – and we will address some of our most recent achievement in this direction. In order to demonstrate recent achievements in mutually coupled magnetofluiddynamic phenomena of electrically conductive fluids, three examples are selected:

- Electromagnetically driven vortical turbulent flows with and without heat transfer,
- Turbulent Magnetic Dynamo,

- Magnetic Drug Targeting.

In the first example, a generic setup with imposed electromagnetic forcing is studied both experimentally and numerically. The electromagnetic forcing imposed by different combinations of permanent magnets and electrodes is constant in time, i.e. one-way interactions are considered. Flow and turbulence structure reorganization are analysed and their influence on the wall-heat transfer is studied. The second application addresses challenging magnetic dynamo phenomenon where by imposing mechanically driven turbulent spiralling flow of sodium, a self-generated and self-sustained magnetic field is created in laboratory conditions (the Riga-dynamo setup). Here, a fully coupled mechanism is considered, i.e. two-way interactions are simulated. The final example addresses application of a locally distributed magnetic field (originating from the permanent magnets or the state-of-art superconductive magnets) in capturing small (nano- or micro-scale diameter) magnetic particles released in a blood stream. Here, in addition to solving the fluid flow equations, equations describing the distributions of magnetic particles are introduced too. In this case we are dealing with one-way coupled phenomena. The major challenge (in addition to the complex geometry of typical blood vessels) lies in necessity to include combined effects of the magnetization and Lorentz force on blood flow because of the non-negligible electric conductivity of blood.

MATHEMATICAL EQUATIONS AND SUBSCALE/SUBGRID TURBULENCE CLOSURE

The governing fluid momentum, temperature and magnetic induction equations together with divergency-free conditions for velocity (**U**) , magnetic field (**B**) and total electric current (**J**) that describe the two-way coupled fluid flow/electromagnetic interactions can be written as:

$$\frac{\partial \widehat{U}_i}{\partial t} = \frac{\partial}{\partial x_j}\left[\nu\left(\frac{\partial \widehat{U}_i}{\partial x_j}+\frac{\partial \widehat{U}_j}{\partial x_i}\right)-\widehat{U}_i\widehat{U}_j\right]-\frac{1}{\rho}\frac{\partial \hat{P}}{\partial x_i}+\frac{1}{\rho}\varepsilon_{ijk}\widehat{J}_j\widehat{B}_k-\beta g_i\left(\hat{T}-T_{REF}\right) \quad (1)$$

$$\frac{\partial \hat{T}}{\partial t}=\frac{\partial}{\partial x_j}\left(\frac{\nu}{\mathrm{Pr}}\frac{\partial \hat{T}}{\partial x_j}-\hat{T}\widehat{U}_j\right),\quad \frac{\partial \widehat{B}_i}{\partial t}=\frac{\partial}{\partial x_j}\left(\frac{1}{\mu_0\sigma}\frac{\partial \widehat{B}_i}{\partial x_j}-\widehat{B}_i\widehat{U}_j+\widehat{U}_i\widehat{B}_j\right),\quad \frac{\partial \widehat{U}_i}{\partial x_i}=0,\quad \frac{\partial \widehat{B}_i}{\partial x_i}=0,\quad \frac{\partial \widehat{J}_i}{\partial x_i}=0 \quad (2)$$

Here "^" stands for the instantaneous variables. Any instantaneous variable can be expressed as a sum of an averaged (mean) and a fluctuating contribution (Reynolds decomposition). The last two terms in Eq.(1) represent the Lorentz (electromagnetic) and the thermal buoyancy (gravitational) force, respectively. By performing filtering of the equations above, i.e. by performing ensemble or time-averaging of equations in the case of Reynolds-Averaged Navier-Stokes (RANS) approach or by performing spatially averaging over a control volume in the case of Large-Eddy Simulations (LES), additional terms representing subscale (RANS) or subgrid (LES) contributions will appear. Since in the present study we will deal primarily with the turbulence associated with the velocity and turbulence fluctuations, the higher order moments associated with the velocity and temperature fields will be modelled, whereas the magnetic field fluctuations will be directly resolved. This approach is justifiable for the working regimes characterised by high Re and small or moderate values of $\mathrm{Re_m}$. For situations with high $\mathrm{Re_m}$ additional models dealing with magnetic stresses and cross-correlations between velocity and magnetic fields should be introduced.

Large-Eddy Simulation: Subgrid Turbulence Model

Expressions in the subgrid turbulence contributions in the momentum and temperature equations must be provided in order to have a fully closed system of equations. In the present investigations, the subgrid turbulent stress and subgrid turbulent heat flux are evaluated from the magnetically extended

Table 1
Specification of the T-RANS model coefficients

$C_{\varepsilon 1}$	$C_{\varepsilon 2}$	C_L	σ_k	σ_ε	C_μ
1.44	1.92	0.025	1.0	1.3	0.09

eddy-viscosity based Smagorinsky [1] model of Shimomura [2] and a simple gradient diffusion of temperature, Kenjeres [3], respectively:

$$\tau_{ij} = \frac{1}{3}\tau_{kk}\delta_{ij} - \nu_t S_{ij},\ S_{ij} = \frac{1}{2}\left(\frac{\partial U_i}{\partial x_j} + \frac{\partial U_j}{\partial x_i}\right),\ \nu_t = \nu_s \exp\left[\frac{-\frac{\sigma}{\rho}\left(C_m\Delta\right)^2 \mid B_0 \mid^2}{\nu_s}\right],\ \nu_s = \left(C_s\Delta\right)^2\left(S_{ij}S_{ij}\right)^{1/2} \quad (3)$$

$$C_s = C_{s0}\left[1 - \exp\left(\frac{-x_i^{N+}}{25}\right)\right]^2,\ \mid B_0 \mid = \sqrt{B_i^2},\ \tau_{\theta i} = -\frac{\nu_t}{\mathrm{Pr}_t}\frac{\partial T}{\partial x_i} \quad (4)$$

Here, U_i and T are resolved velocity and temperature fields, respectively. The van Driest [4] damping function based on the non-dimensional wall distance is introduced in order to provide a proper near-wall behaviour of the turbulent viscosity. The standard values of the SGS model coefficients are used, C_{s0}=0.1, C_m=1.4, Pr_t=0.86. The characteristic spatial filter Δ is calculated as $\Delta = \Delta V^{1/3}$ where ΔV is the control volume.

Transient Reynolds-Averaged Navier-Stokes: Subscale Turbulence Model

In cases where the application of LES is not possible, for example for flows characterised by high Re or where the accurate predictions of the wall-heat transfer will require full resolving of the near-wall regions, application of the transient Reynolds-Averaged Navier-Stokes (T-RANS) approach is only viable option, Kenjeres and Hanjalic [5], Hanjalic and Kenjeres [6]. Now, a subscale model of unresolved (subscale) flow and turbulence structures needs to be introduced. The eddy-viscosity based two-equations k-ε model is introduced with additional source/sink terms representing the electromagnetic contributions, Kenjeres and Hanjalic [7]. The equations of the T-RANS model with specification of model coefficients are given next:

$$\tau_{ij} = \frac{3}{3}k\delta_{ij} - \nu_t\left(\frac{\partial U_i}{\partial x_j} + \frac{\partial U_j}{\partial x_i}\right),\nu_t = C_\mu\frac{k^2}{\varepsilon} \quad (5)$$

$$\frac{\partial k}{\partial t} = \frac{\partial}{\partial x_j}\left(\nu\frac{\partial k}{\partial x_j} + D_k^t - U_j k\right) - \tau_{ij}\frac{\partial U_i}{\partial x_j} - \varepsilon - P_k^b \quad (6)$$

$$\frac{\partial \varepsilon}{\partial t} = \frac{\partial}{\partial x_j}\left(\nu\frac{\partial \varepsilon}{\partial x_j} + D_\varepsilon^t - U_j\varepsilon\right) - C_{\varepsilon 1}\tau_{ij}\frac{\partial U_i}{\partial x_j}\frac{\varepsilon}{k} - C_{\varepsilon 2}\frac{\varepsilon^2}{k} - P_\varepsilon^b \quad (7)$$

$$D_k^t = \frac{\nu_t}{\sigma_k}\frac{\partial k}{\partial x_j},\ D_\varepsilon^t = \frac{\nu_t}{\sigma_\varepsilon}\frac{\partial \varepsilon}{\partial x_j},\ P_k^b = \frac{\sigma}{\rho}B_0^2 k\exp\left(-C_L\frac{\sigma}{\rho}B_0^2\frac{k}{\varepsilon}\right),\ P_\varepsilon^b = P_k^b\frac{\varepsilon}{k} \quad (8)$$

Here, $(P_k - P_\varepsilon)^b$ are the electromagnetic source/sink terms and turbulent diffusion terms $(D_k - D_\varepsilon)^t$ are calculated by applying simple gradient hypothesis.

NUMERICAL METHOD

The above presented set of equation is discretized by applying a finite-volume approach. The recently developed finite-volume based Navier-Stokes/Maxwell's solver can be applied for any three-dimensional non-orthogonal geometry distributed over many multi-blocks (locally structured) or on a fully unstructured mesh. The local grid refinements can be activated in the pre-specified blocks. The solver can be executed in serial or parallel mode. The latter involves the domain decomposition based message passing interface (MPI) directives. All transport variables are located in the geometrical centre of such control volumes (collocated variable arrangement). In order to prevent a decoupling between the velocity and pressure fields (checkerboard pressure oscillations) the Rhie–Chow interpolation is used in the pressure-correction equation. The corrected velocity and pressure fields are iteratively calculated by the semi-implicit method for pressure-linked equations (SIMPLE) algorithm. The numerical accuracy of the entire discretized system is of the second-order. The time integration is performed by the fully implicit second order scheme based on three consecutive time steps. The diffusive terms are discretized by the second-order central differencing scheme. The remaining convective terms are calculated by the monotonicity preserving total variation diminishing (TVD) schemes. The linearized system of equations is then solved using Stone's strongly implicit procedure (SIP) based on an incomplete lower-upper (LU)-factorization. Additional numerical details are given in Kenjeres and Hanjalic [8], [9], [10].

ELECTROMAGNETICALLY DRIVEN VORTICAL FLOWS

One of the most beautiful examples of mutual interdependency between flow, turbulence and electromagnetic fields can be found inside of whirlpool galaxies, Soward *et al.* [11]. Based on astrophysical observations and satellite measurements a link between spiralling pattern of the dust clouds inside of galaxy and underlying magnetic field is confirmed. This fundamental paradigm connecting spiralling flows (in both laminar and turbulent flow regimes) with electromagnetic fields will be in focus of our investigations. As an example, the spiral arms and dust clouds inside of whirlpool galaxy M51 are shown in Fig.2a. Inspired by this beautiful example from nature, a similar attempt in generating swirling flows by imposed electromagnetic forcing is performed on a laboratory scale. By imposing different configuration of arrays of permanent magnets of opposite polarities and oppositely charged electrodes, different multi-vortex patterns of electrically conductive working fluid confined in a simple rectangular tank can be easily generated.

An example of such an electrically driven flow that closely resembles above mentioned whirlpool galaxy is shown in Fig.2b,c. Here, flow is visualised by a laser induced fluorescence (LIF) technique of a dye colour released in an electrically conductive fluid (water with electrolyte solution), Verdoold *et al.* [12]. The Lorentz force is generated by combining two permanent magnets with opposite polarities that are located below the lower wall of the rectangular tank and two oppositely charged (with DC current) electrodes that are located in the upper part of the side walls. The dimensions of the tank are 0.6x0.6x0.155 m^3.The permanent magnets have dimensions 0.084x0.040x0.040 m^3 and are arranged in arrays of alternating polarity. The distance between each magnet is 0.040 m, resulting in a maximum magnetic field strength of 1.0 T inside the tank. The controllable DC current could be varied between 0.5 and 10 A. Due to the relatively large electrical current, induction effects can be neglected and Ohm's law can be approximated by $J \sim \sigma E$. Then, the resulting Lorentz force for the present range of experiments can be expressed as $F^L = ExB$, which is constant in time. Water with 7% Na_2SO_4 electrolyte solution is used as a working fluid, with electric conductivity $\sigma = 5.5$ S/m.

The sketch of this combination with applied DC current of I=10 A is shown in Fig.3-above. The value of the Reynolds number based on the maximum velocity reaches value of Re=8000 indicating

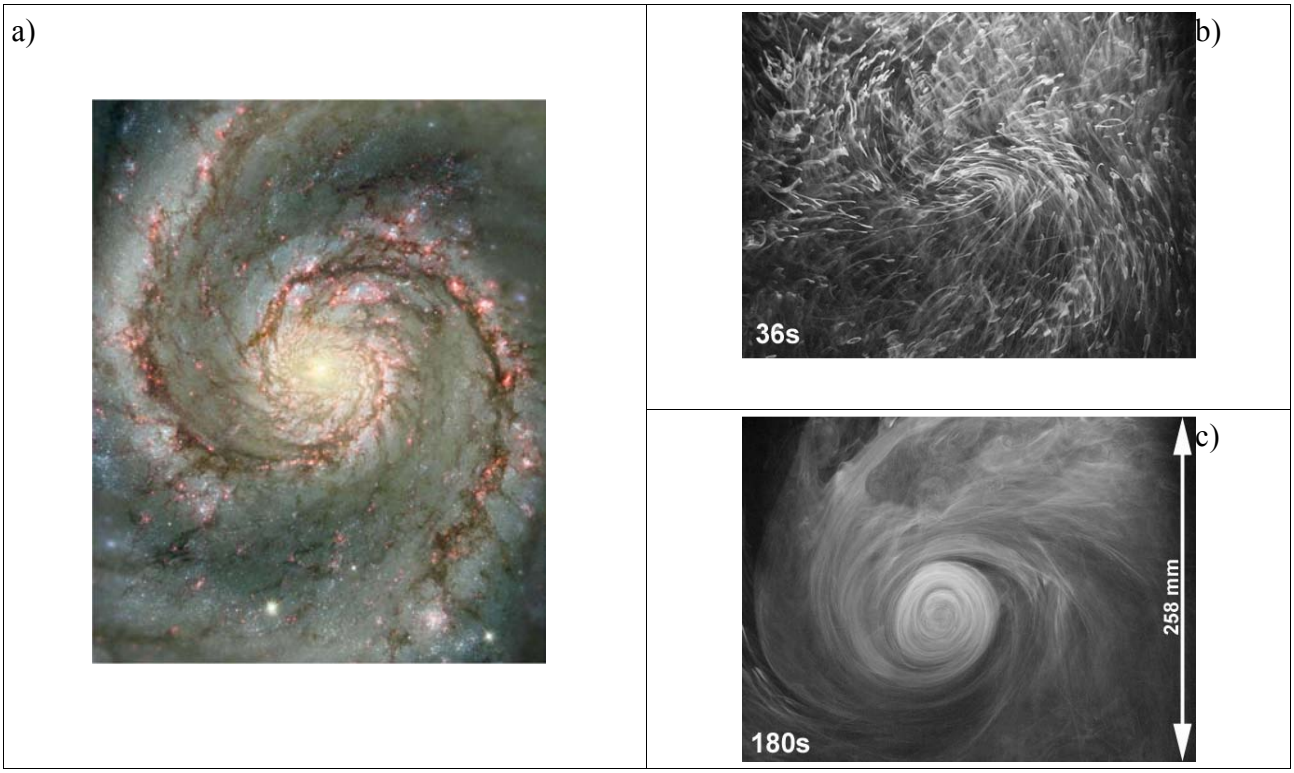

Figure 2. Left- The spiral arms and dust clouds inside of whirlpool galaxy M51 (radius ~38000 light years), image credit NASA and The Hubble Heritage Team (STScI/AURA); Right- a laser induced fluorescence visualisation of the electromagnetically driven draft-tornado (radius ~130 mm) in laboratory conditions (generated by a combination of 2-permanent magnets with |B|=1 T below lower wall and 2-electrodes with I=10 A along the side walls): initial (-b) and fully developed state (-c), Verdoold *et al.* [12].

turbulent flow regime (at least in regions with the intensive forcing). In the early stage of the forcing, some of the initially created spiralling arms of the centrally created vortex start to be visible, Fig.2b. In the fully developed state a very close resemblance with a whirlpool galaxy is obtained, Fig.2c. Note that these visualisations were performed in the top plane of the setup – providing just two-dimensional flow imprints (in the top plane). In order to be able to provide full three-dimensional time-dependent insights into flow and turbulence of such electromagnetically driven vortical flows under different forcing conditions, series of LES are performed, Kenjeres *et al.* [13]. Results of the above analysed configuration with 2-permanent magnets and 2-electrodes are shown in Fig. 3-below. The time-averaged resolved velocity and pressure fields are used for depicting three-dimensional flow structure. The velocity vectors in the central horizontal plane together with isosurfaces of pressure are shown in Fig.3a. The centrally located low-pressure regions indicate intensive swirling fluid motion. Similarly, a stream-traces coloured with velocity magnitude are shown in Fig.3b. A typical tornado-like structure is clearly visible. The high velocity in the proximity of the lower wall is simply result of the strong electromagnetic forcing that decays as the distance from the wall increases. Also the presence of the spiralling arms is nicely visible in the lower part of the centrally located vortex. In addition to the qualitative observations, numerical simulations are also validated against flow measurements obtained by particle imaging velocimetry (PIV) technique. The profiles of the circumferentially averaged magnitude of the horizontal velocity along the vortex diameter at two characteristic vertical locations (z=0.025 and 0.040 m) are shown in Fig.4-left. It can be seen that the peak value stays approximately constant with wall distance, whereas its location gradually moves towards the outer edge of the vortex. A good agreement between PIV and LES is obtained, especially with respect to the exact peak value, while some discrepancies are visible at locations towards the vortex edge. The time-averaged vertical profiles of the horizontal velocity at two different locations are shown in Fig.

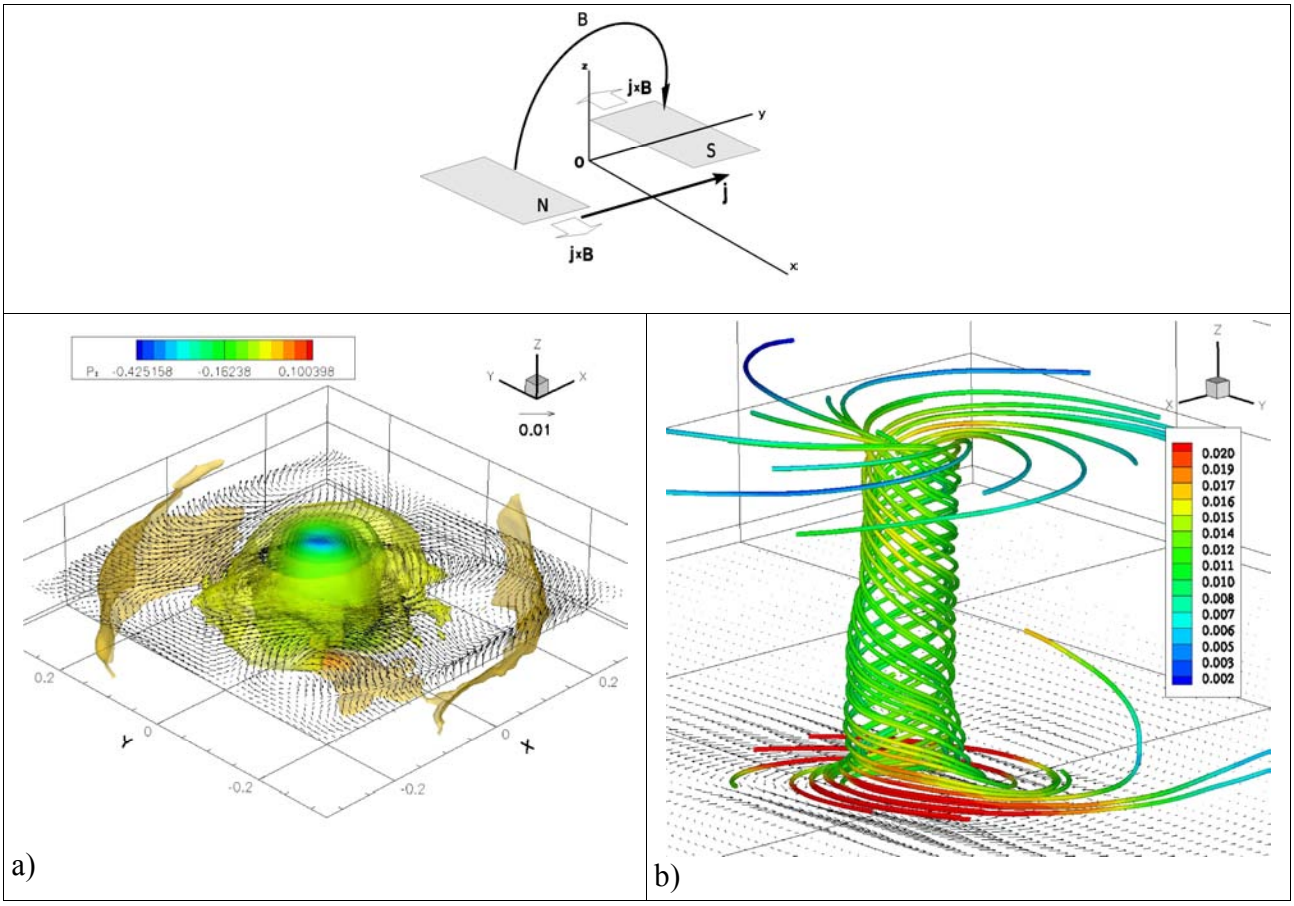

Figure 3. Sketch of distributions of magnetic and electric field lines as well as of resulting Lorentz force for configuration with 2-permenent magnets (B=1 T) and 2-electrodes (I=10 A) distributed along the side walls (x=-0.3 and 0.3 m) – above; Time-averaged LES results of the velocity vectors in the central horizontal plane and isosurfaces of low-pressure region (in Pa) (below-a) and zoom-in of the stream-traces coloured by the velocity magnitude (in m/s) (below-b), Kenjeres *et al.* [13].

4-right. Note that the measured vertical profiles do not span the entire height of the setup. The locations of the velocity peak values in the proximity of the lower wall are nicely captured at both locations. At x =-0.05 m some deviations between PIV and LES can be observed in the upper part for z > 0.075 m. The velocity peak value is slightly underestimated at x = 0.05 m, but the qualitative shape of the profile is well captured. It can be concluded that combined experimental and numerical studies of the electromagnetically driven flows in a generic setup proved that despite its geometrical simplicity, this setup can be used for fundamental studies of the interactions between flow, turbulence and electromagnetic fields. By changing the intensity of the applied DC electric current, different flow regimes (laminar, transitional or fully turbulent) can be achieved in different parts of the setup. Generally very good agreement between measurements and simulations is obtained for velocity field components at different locations proving validity of the preformed LES.

After this initial validation, the studies of the heat transfer are performed next, Kenjeres [3]. In addition to the supplying the heat flux through the lower hot wall and by cooling the upper wall, also a multi-array of the permanent magnets with opposite polarities is imposed. This is done in order to effectively control the wall-boundary layers along the lower horizontal thermally active wall. In total 35 magnets of opposite polarities (of identical specification as already mentioned for the isothermal studies) are used. The different intensities of supplied electric current through electrodes are applied, i.e. I=0, 1 and 10 A. The temperature difference between lower hot and top

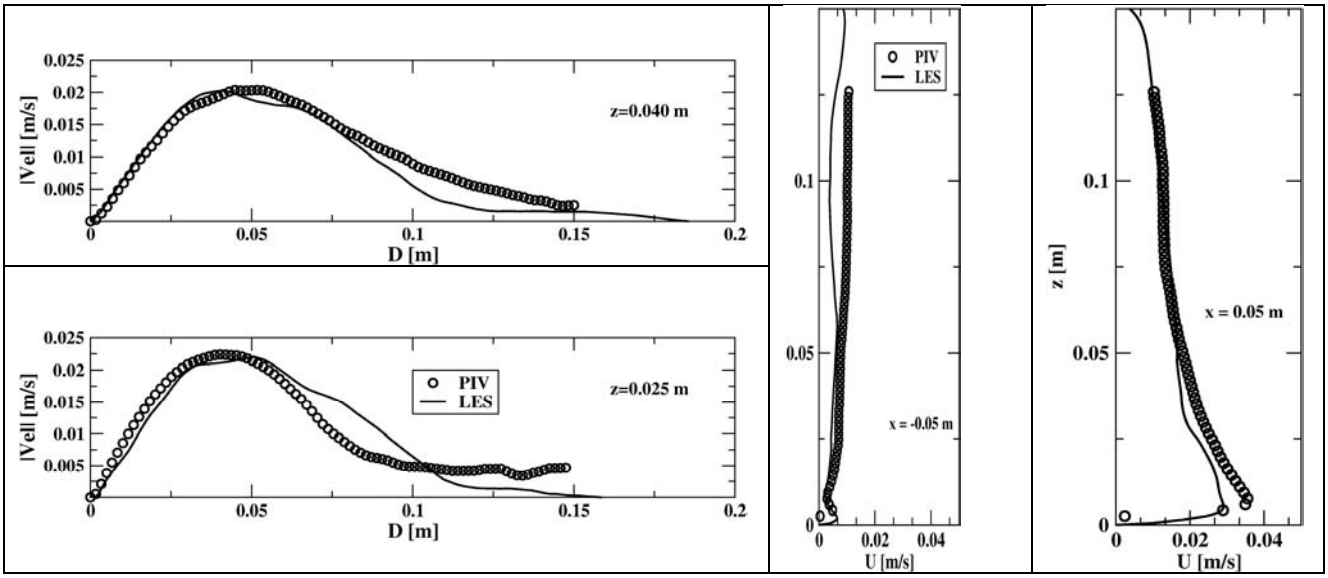

Figure 4. Comparison between PIV measurements and LES results for electromagnetically driven draft-tornado situation presented in previous figure; Left- circumferentially averaged modulus of velocity profiles at two characteristic vertical locations, z=0.025 and 0.040 m; Right- the vertical profiles of horizontal velocity component at two characteristic locations, x=-0.05 and 0.05 m, Kenjeres *et al*. [13].

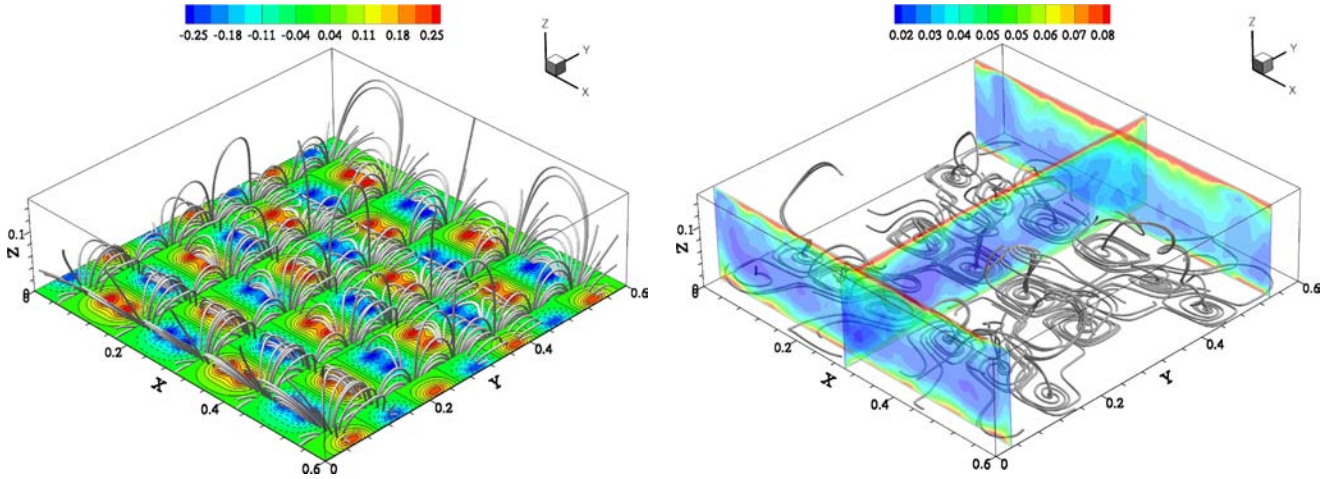

Figure 5. A wall-bounded [4:4:1] aspect ratio enclosure heated from below and cooled from top, filled with an electrically conductive locally fluid (electrolyte solution) subjected to locally generated Lorentz force originating from a multiple-array of the permanent magnets located below the lower wall and two electrodes along the side walls (x=0 and 0.6 m); Left- magnetic flux lines (gray lines) and the contours of the horizontal magnetic field at the lower wall (in T); Right- the stream-traces (gray lines) of the resolved velocity field and contours of the non-dimensional temperature variance in characteristic vertical planes, Kenjeres [3].

cold wall generates Ra=10^7 and Pr=7. An impression of the flow structures and imposed magnetic field is shown in Fig. 5. The magnetic field is visualized by plotting the spatial distributions of the magnetic flux lines, Fig.5-left. It can be seen that the strongest concentration of the flux lines is in the proximity of the lower horizontal wall and that gradually decays as the distance from wall increase. It indicates that the strongest forcing will occur in the regions close to the lower wall, i.e. the wall boundary layers will be mostly affected by imposed electromagnetic forcing. The generated flow structures are shown in Fig.5-right. The multiple spiraling vertical structures generated by strong shearing in horizontal planes are dominant flow structures. The strong temperature

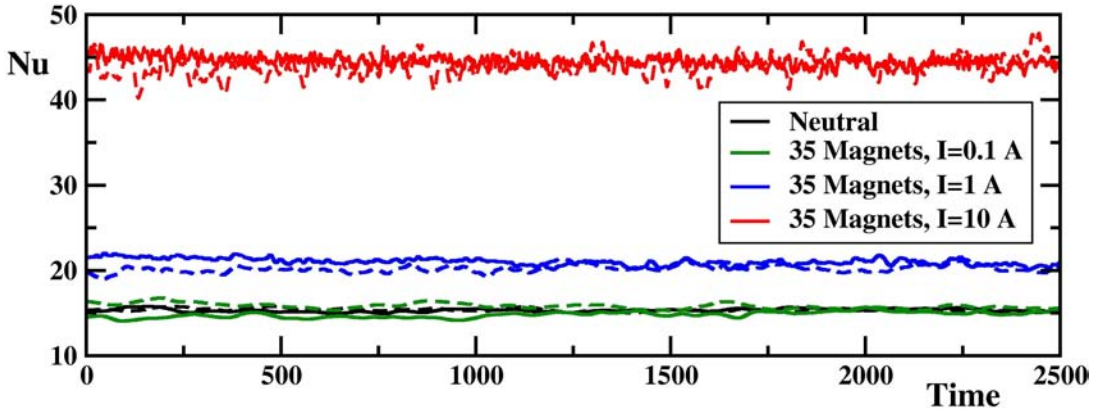

Figure 6. Time evolution of the Nusselt numbers along the top- (dashed lines) and bottom-wall (solid lines) for configuration shown in previous figure for different strengths of the imposed DC current, I= 0, 0.1, 1 and 10 A, Ra=10^7, Pr=7, Kenjeres [3].

fluctuations are located in the thin thermal boundary layers along the thermally active walls, as indicated by contours of the temperature variance in characteristic vertical planes, Fig.5 -right.

The time-evolutions of the Nusselt number along the top- and bottom-wall are shown in Fig. 6. The value of Nu=15.35 for the neutral situation agrees well with experimentally obtained correlations Nu =$0.145Ra^{0.29}$=15.54 (Tanaka and Miyata [14]) and Nu=$0.183Ra^{0.278}$=16.1 (Chu and Goldstein [15]). Also good agreement is obtained with DNS results of Nu =15.75 (Kerr and Herring [16]). It can be seen that flow and turbulence reorganization in the presence of external electromagnetic fields has a significant impact on the wall-heat transfer. The imposed current of I=1 A (that generates mean motion with Re=1300) gives 34% enhancement of the total heat transfer coefficient, while I=10 A (that generates mean motion with Re=4500) gives an impressive 188% increase. The significance of the obtained heat transfer enhancement can be compared with values obtained in Uda *et al.* [17] where an enhancement of 5–10% was experimentally obtained in annular turbulent flow $5x10^3<Re<10^5$ of lithium subjected to a magnetic field B_0=0.8 T.

MAGNETIC DYNAMO

The process of partial conversion of the mechanical energy of the moving electrically conductive fluid into magnetic energy is called magnetic dynamo. It is believed that ability of the turbulent motion of an electrically conductive fluid to generate and to maintain a magnetic field against its natural decay is the crucial mechanism responsible for generation and sustenance of magnetic fields in galaxies, stars and planets (including Earth's magnetic field creation), Soward *et al.* [11], Busse [18].

A validation of realistic simulations of the Earth's magnetic field generation can be only indirect, e.g. by comparing the recorded magnetic field distributions at the Earth surface. In order to provide direct and valid proofs of the magnetic dynamo mechanism, it is necessary to have well-defined and controlled working conditions, while retaining the basic physics of the dynamo phenomenon. A general concept of the magnetic dynamo inside of the simplified vertical column of an electrically conductive fluid (that is present in the liquid metallic outer core) driven by combined effects of thermal and concentration (composition) buoyancy, as well as subjected to the rotational effects due to the rotation of Earth, are shown in Fig. 7-left, Busse [18]. This simplified concept is mimicked by the Riga-dynamo setup shown in Fig.7-right, Gailitis *et al.* [19], [20]. Here, the mechanical forcing of working fluid by thermal and concentration (composition) buoyancy is simply replaced by strong

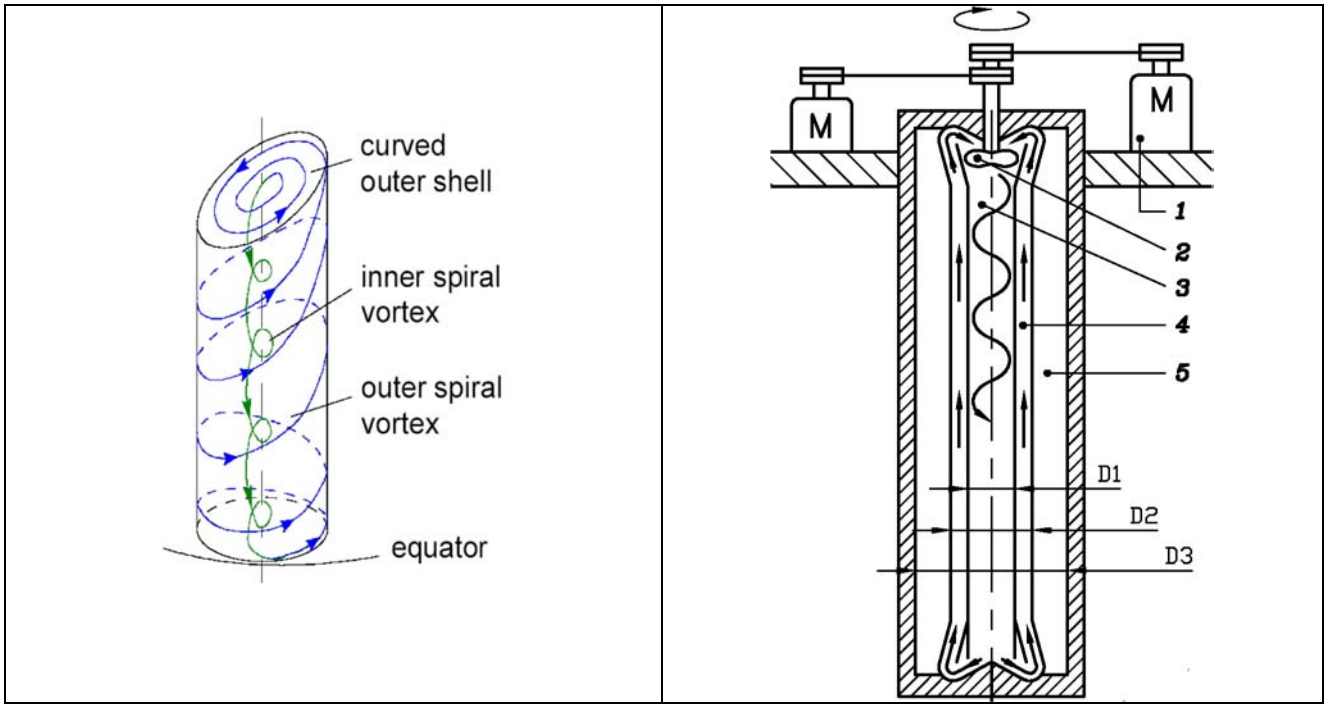

Figure 7. Left- a concept of the magnetic dynamo inside of the simplified vertical column of a conductive fluid driven by thermal and concentration buoyancy inside of Earth; Right- sketch of the Riga-dynamo experimental setup, Gailitis et al [19], [20]: 1- two engines (M) with 100 kW to drive propeller; 2- propeller; 3- inner cylinder with intensive swirling motion; 4- outer passage with back-flow; 5- surrounding ring of sodium at rest; D1=0.21 m, D2=0.4 m, D3=0.8 m are characteristic dimensions of the inner, outer and surrounding cylinder, respectively. The typical vertical length is L=3 m.

mechanical forcing by a centrally located propeller in the upper part of the inner cylinder. The propeller is driven by two electric motors with a power up to 100 kW each. The sodium is used as a working fluid because of its excellent electric conductivity properties, i.e. its use will provide the best probability to reach critical dynamo threshold under experimental conditions. After strongly swirling flow in the inner cylinder, fluid turns in a 180 degrees bend and reaches the outer cylinder and a closed loop of fluid motion is established. All around this central annular passage there is an additional ring of sodium at rest. Its role is to reduce possible escaping of the self-generated magnetic field in the surrounding environment.

It is recalled that the flow inside of the setup is in highly turbulent regime ($Re=3.5x10^6$) so it is necessary to simulate this flow with a turbulence model. Since the both direct numerical (DNS) and large-eddy simulation (LES) are out of reach for such high values of Re, we applied a novel electromagnetically extended subscale model in transient mode (T-RANS approach), Kenjeres and Hanjalic [7], [9], [10]. On other hand, the estimated range of $15<Re_m<20$ makes it possible to fully numerically resolve self-generated magnetic field in time and space – so no additional modelling of the magnetic turbulence is needed. This hybrid T-RANS/DNS approach for simultaneous solving of the two-way coupled fluid flow, turbulence and self-generated electromagnetic fields made it possible to simulate realistic experimental working conditions for the first time. Before performing the fully coupled two-way interactions, validity of the eddy viscosity based two equations k-e turbulence model (EVM) is tested by simulating a 1:2 scale-down experimental setup with water as working medium and results are compared with available experimental measurements and results obtained by more advanced full second moment closure (SMC) model. The axial and tangential velocity profiles at three characteristic vertical locations (y=+0.5, 0, -0.5 m) are shown in Fig.8. It

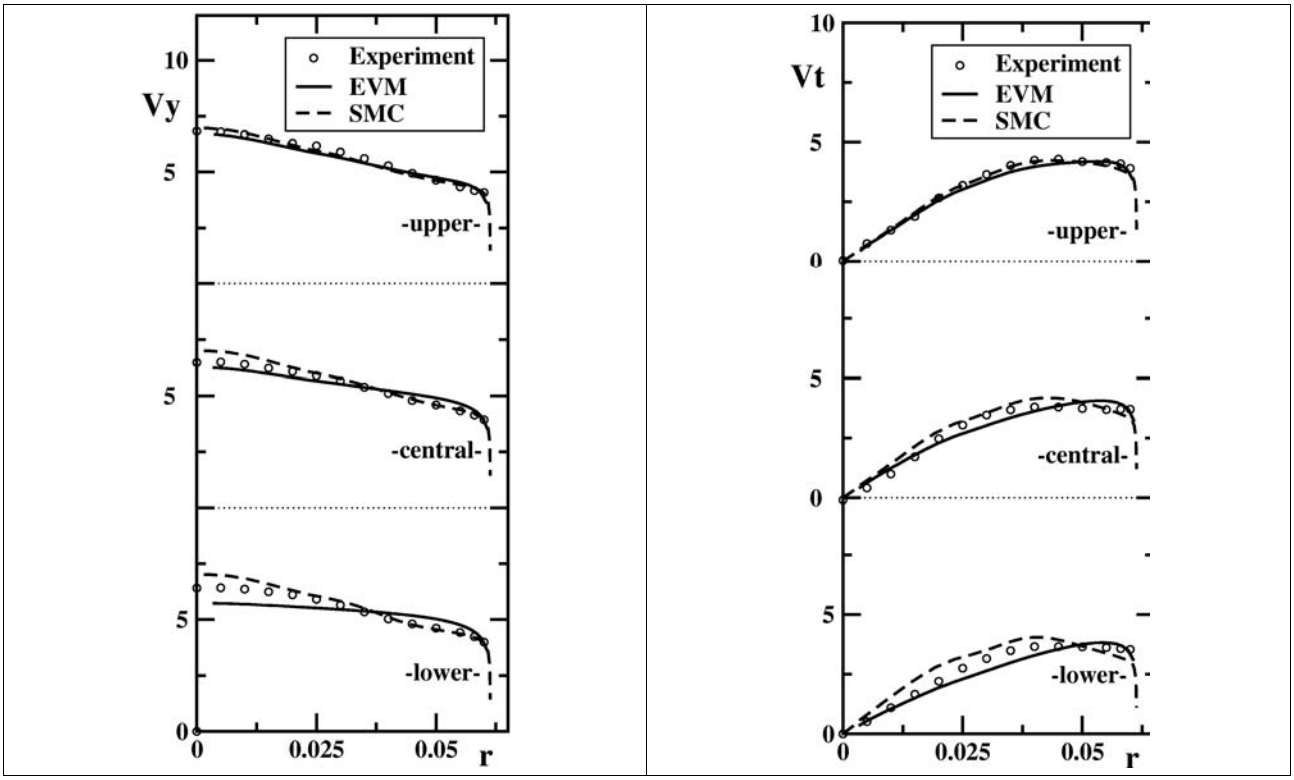

Figure 8. Comparison of experimental (LDA) and numerically obtained (with eddy-viscosity EVM and second-moment-closure SCM) velocity profiles in a 1:2 scaled-down Riga-dynamo setup with water as working medium; Left- axial velocity, Right- tangential velocity (both in m/s), Kenjeres and Hanjalic [10].

can be seen that the EVM performs quite well under defined working swirling conditions at all three locations giving good agreement with both experimental and SMC data. Since the more advanced SMC model requires solving 6 additional PDEs, the simpler EVM proved to be the best compromise between accuracy of the physical representation and numerical robustness and efficiency. Based on this performance, this model is used for the follow-up simulations. After this preliminary validation, a fully coupled solver is activated and results of simulations are shown in Fig.9. A snapshot of the intensive swirling flow pattern in the inner cylinder generated by propeller and visualised by stream-traces coloured by the axial velocity component is shown in Fig.9-left. The corresponding structure of the self-generated magnetic field (visualised by magnetic flux lines coloured by the axial magnetic field component) is shown in Fig.9-right. While the flow pattern is confined in the inner and outer cylinders, the self-generated magnetic field is allowed to leave the computational domain as indicated by the open magnetic flux lines. It is important to note differences in flow and magnetic field distributions – if magnetic filed will be simply driven by convective contribution of the velocity field, they will exhibit very similar spatial distributions. In contrast to that, very different structures are observed indicating importance of the magnetic flux stretching term as a primary mechanism behind the self-generation of magnetic field. Contours of the self-generated and self-sustained magnetic field components (tangential and radial) in the central horizontal (x-z) plane at the characteristic time instant during saturation regime are shown in Fig.10.

The resulting self-generated and self-sustained magnetic field profiles are shown in Fig.11. Here, the symbols represent the experimentally recorded maximum values at the particular radial locations for different propeller rotation rates - ranging from 1900 to 2500 rpm, Gailitis *et al* [19], [20]. All profiles are rescaled with the maximum value along the radial direction. It can be seen that

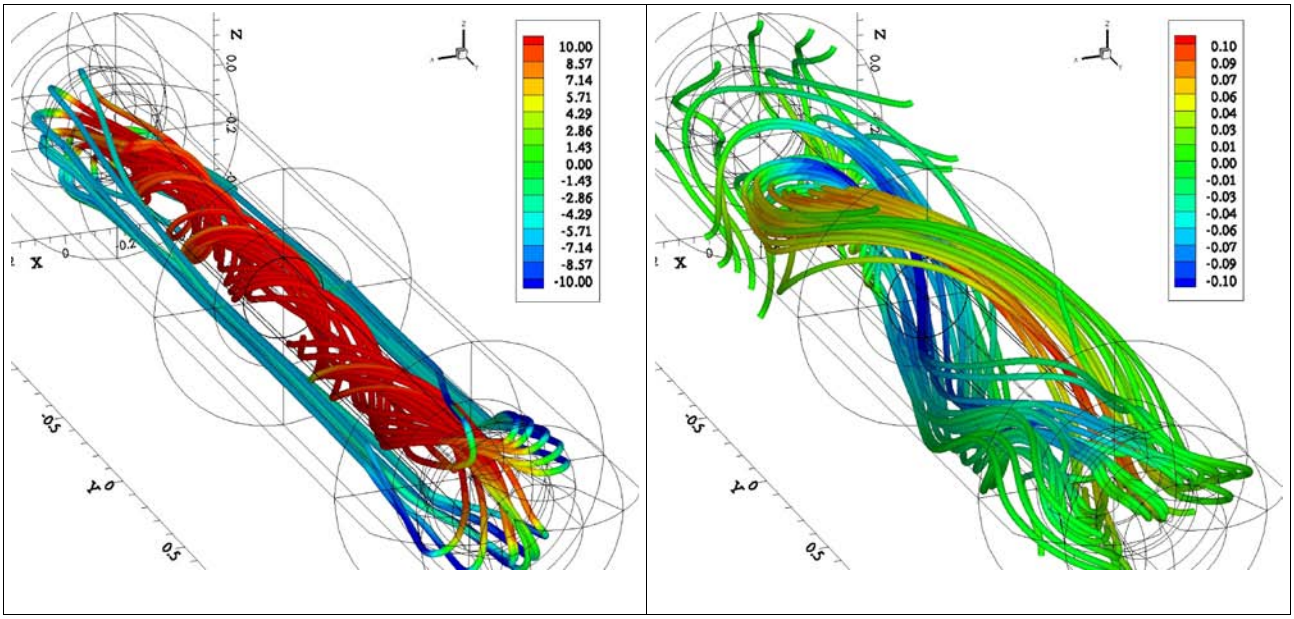

Figure 9. Left- Swirling flow pattern in the inner cylinder generated by propeller (stream-traces coloured by axial velocity, in m/s); Right- self-generated magnetic field magnetic (magnetic flux lines coloured by the axial magnetic filed, in T) – a snapshot of the simulated three-dimensional fields, $Re=3.5x10^6$, $Re_m=18$, Kenjeres and Hanjalic [10].

for both the axial and radial magnetic field component, the experiments show a slight deviation in the profile symmetry. In contrast to the experimental profiles, the numerical results show perfect symmetry indicating full convergence of the magnetic induction equation. The magnetic field profiles indicate that after t=5.5 sec, a fully saturated regime is achieved. A very good agreement between the experiments and simulations is observed for the axial magnetic filed component, Fig.11-left. The results for the radial magnetic field component show a larger scatter, but again, agreement can be considered as good, Fig.11-right. In contrast to the zero axial magnetic fields at the outer boundary of the surrounding sodium at rest, the radial component correctly shows a final value. This boundary value is slightly under-predicted as compared with measurements, but shows clearly that the boundary condition for the vertical magnetic field is properly imposed. In contrast to the monotonic time evolution of the axial magnetic field profiles, the radial profiles show an interesting variation in the radial location of the peak value. The peak value travels from the centre of the outer cylinder for earlier time instants (cycle 10–cycle 15) and finally settles at the middle radial distance in the inner cylinder, Fig.11-right.

In contrast to the measurements of magnetic field components that are restricted to one-dimensional recordings (time dependency), the numerical simulations can provide full three dimensional spatial distributions. Kenjeres and Hanjalic [9], [10]. In Fig.12-left, the isosurfaces of the radial magnetic field of opposite signs (red and blue) are shown together with stream-traces of the instantaneous velocity field (grey tubes) at different time instants, i.e. t= 2, 2.5 and 7.5 s, respectively. The strongest self-amplification takes place in the lower part of the set-up and then it moves upwards. In order to demonstrate effects of the generated Lorentz force on turbulent kinetic energy (TKE) of underlying velocity field, three dimensional distribution of TKE is shown in Fig.12-right. It can be clearly observed that a 'gap' is appearing in the lower part of the inner cylinder as time progress. This indicates that the levels of the turbulent kinetic energy are reduced in this region by an active action of the Lorentz force. In contrast to that, TKE levels in the outer cylinder show periods with suppression or enhancement – depending for which selected time instants these values are shown.

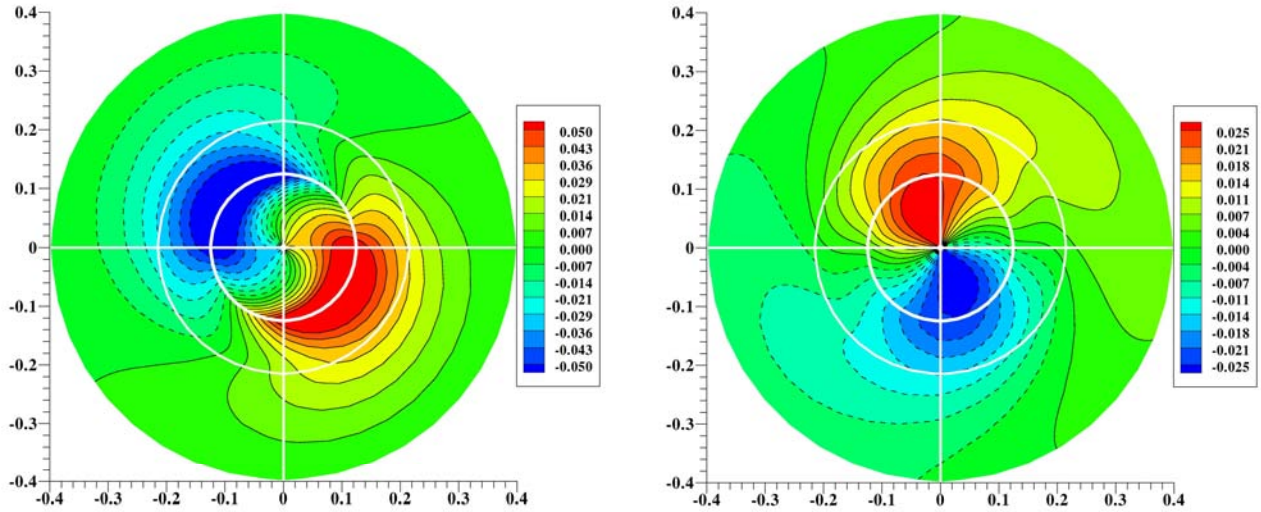

Figure 10. Contours of the self-generated and self-sustained magnetic field at particular time instant during saturation regime in the central horizontal (x-z) plane (y=-0.5 m): tangential (-left) and radial (-right) magnetic field component (in T), Kenjeres and Hanjalic [10].

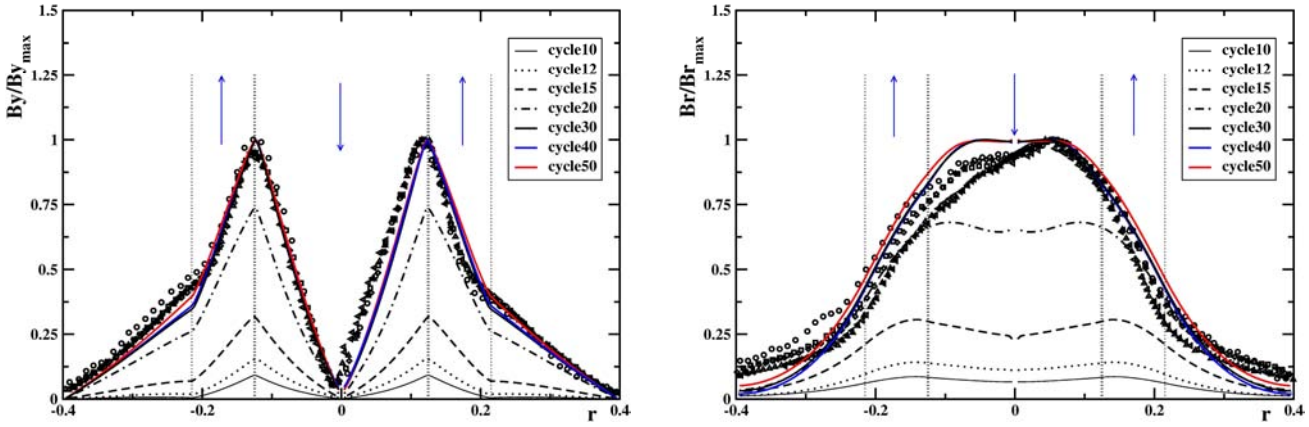

Figure 11. Time-evolution of the magnetic field component profiles in the central horizontal (x-z) plane (y=-0.5 m): axial (-left) and radial (-right) component (in T). Note that the cycle time instants actually correspond to the following time instants: cycle 5 = 1 s, cycle 10 = 2 s, cycle 15 = 2.85 s, cycle 20 = 3.5 s, cycle 30 = 5.5 s, cycle 40 = 7.5 s, cycle 50 = 9.5 s, respectively, Kenjeres and Hanjalic [10].

Finally, it can be concluded that presented numerical simulations based on a hybrid T-RANS/DNS approach for velocity (T-RANS) and magnetic field (DNS) succeeded in replicating numerically a magnetic-dynamo mechanism in a turbulent flow regime as observed in the Riga-dynamo experimental setup. This was achieved without imposing any external excitation or artificial inputs for electromagnetic fields. It is shown that such an approach clearly demonstrated not only its potentials to reproduce process of the self-generation and self-sustenance of a magnetic field, but also captured distributions and magnitude of the magnetic field components in close agreement with available experimental data.

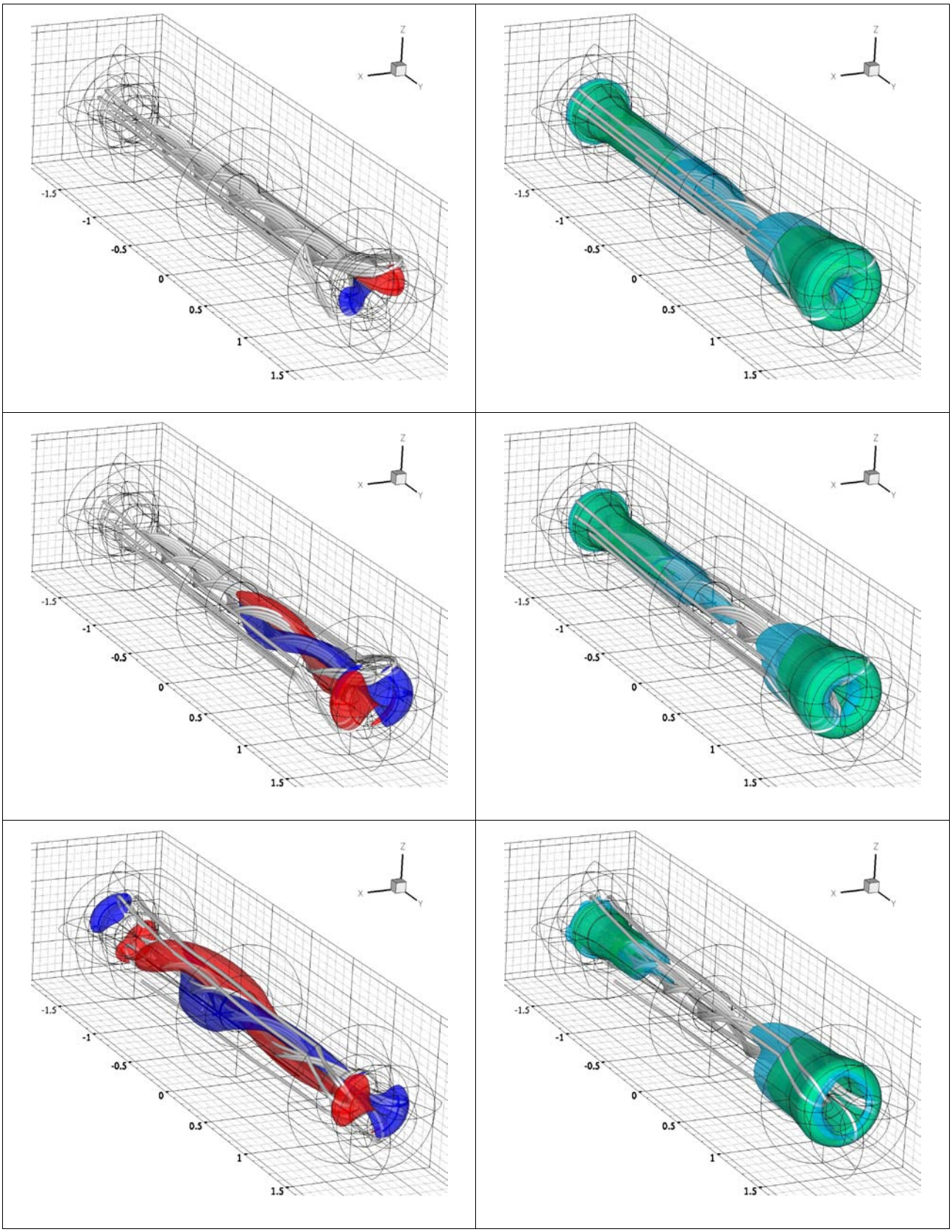

Figure 12. Time evolutions (from top to bottom, Time= 2, 2.5 and 7.5 sec, respectively) of the radial magnetic field component (B_r= + 0.05 T – red, -0.05 T – blue) (-left) and of the turbulent kinetic energy (iso-surface k= 2.5 m^2/s^2 is light blue and k= 1 m^2/s^2 is light green (-right).

MAGNETIC DRUG TARGETING

At present, one of the main problems of chemotherapy is often not the lack of efficient medical drugs, but our inability to precisely deliver these drugs in sufficiently high concentrations in areas affected by disease. The concept of the magnetic drug targeting (MDT) is to insert a small magnetic particles as carriers of medical drug into blood flow and to locally apply magnetic field gradients over an area of interest that these particle will be locally captured and accumulated in these regions, Alexiou [21], [22], [23], Torchilin [24]. Two major goals can be achieved: a huge (tenfold) increase in local concentrations of medical drugs and significant reduction of the freely circulating drugs. Due to latter, toxic effects of medical drugs on healthy organs will be drastically reduced. It is not difficult to imagine that blood flow in realistic blood vessels will exhibit complex three-dimensional patterns with characteristic imprints of spiralling motion, Kenjeres [25]. Distribution of magnetic particles released in blood flow will strongly depend from the underlying flow patterns. By imposing external magnetic field gradients, through generated magnetization force, distributions of the magnetic particles can be significantly affected. For sufficiently strong magnetization force, magnetic particles can be efficiently captured from the blood flow and deposited along the blood vessel walls at the pre-defined locations in desired regions. In contrast to the previously analysed cases where the underlying fluid flow was affected by magnetic fields, here we introduce additional equation for the magnetic particle trajectories in presence of magnetization force:

$$m\frac{d^2r}{dt^2} = F_D + F_M \tag{9}$$

where r(t) is the particle location and F_D and F_M are the drag and magnetization forces, respectively. The drag force is defined by Stokes expression (that is valid for $Re_p=\rho \mid u_p - u_f \mid D / \mu << 1$) as

$$F_D = 3\pi\mu D\left(u_p - u_f\right) \tag{10}$$

where u_p and u_f are velocity of the particle and fluid, respectively. The magnetization force acting on particles can be expressed as

$$F_M = \mu_0 M \cdot \nabla H \cdot V_P \tag{11}$$

where M is the magnetization, H is the auxiliary magnetic field, μ_o is the magnetic permeability of vacuum and V_p is the volume of the particle. The particle velocity (under assumption that the particle inertia can be neglected) can be estimated as a sum of the fluid velocity u_f and a 'magnetic velocity' u_m as

$$u_p = u_f + u_m = u_f + \frac{F_M}{3\pi\mu D} \tag{12}$$

The capture efficiency of magnetic particles by an imposed magnetic field is simply calculated as a ratio between number of particles deposited along the vessels walls and total number of the released particles

$$\eta = \frac{n_{dep}}{n_{in}} = \frac{n_{in} - n_{out}}{n_{in}} \tag{13}$$

In order to demonstrate basic concepts of the magnetic drug targeting technique, we simulated a realistic case of blood flow inside of human left coronary artery (LCA) where magnetic particles with different diameters were released, Haverkoort and Kenjeres [26]. A magnetic field distribution from a recently developed superconducting magnet that generates sufficiently strong gradients was imposed and capturing efficiency for different particle diameters is analyzed. Numerical mesh used for computations is shown in Fig.13-left. This geometry was created by averaging angiograms (medical imaging technique to obtain geometry of the blood vessels) of 83 healthy patients in order to get a single representative dataset, Giannoglou *et al.* [27].

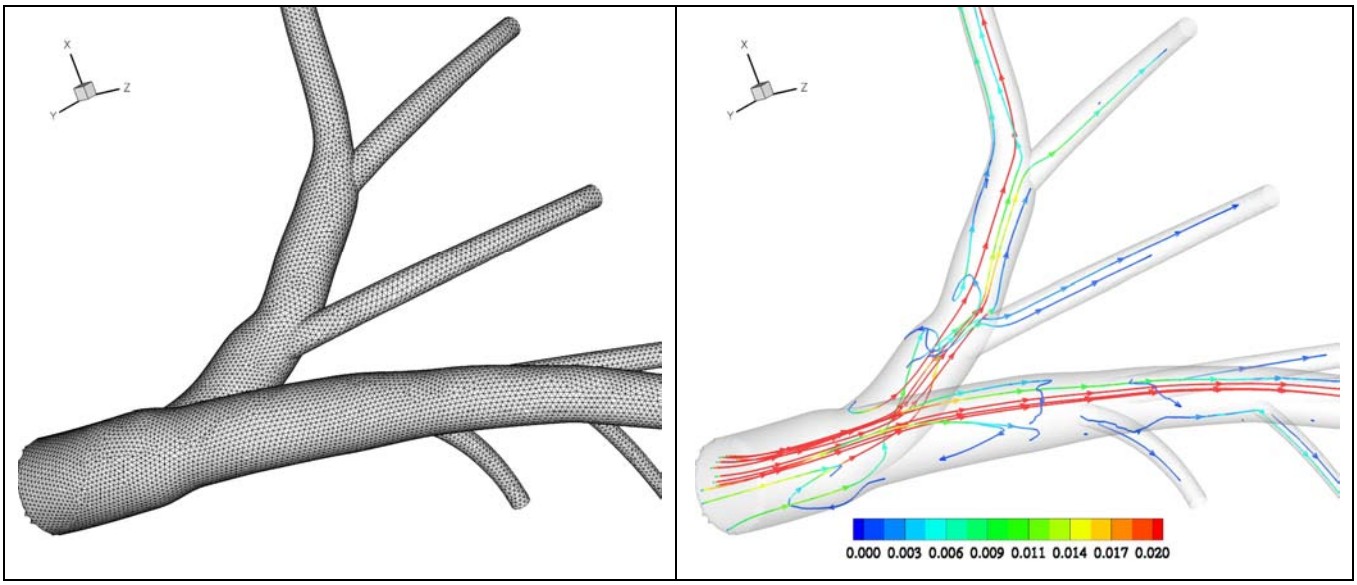

Figure 13. Numerical mesh used for computations of blood flow inside a simplified model of the multi-branching left-coronary artery (LCA) (generated as a typical configuration by averaging geometrical data of 83 healthy patients) (-left) and visualization of the flow pattern at particular time instant of the pulsating heartbeat cycle (stream-traces coloured by magnitude of the velocity), Haverkort and Kenjeres [26].

Characteristic heartbeat cycle was simulated by imposing a periodically changing (with a characteristic time period of t = 1s that corresponds to the real cardiac cycle) flattened inlet radial velocity profile at the inlet plane of the coronary artery:

$$u_f(r,t) = \frac{4}{3} u_{in}(t) \left[1 - \left(\frac{r}{R} \right)^6 \right] \tag{14}$$

The average Reynolds number based on inlet parameters is estimated to be in 100< Re<500 range. The flow rate was forced to distribute over the several outlets according to Murray's law (proportional to r^3 – where r is the outlet radius). The initial diameter of the left coronary artery is ~4.5 mm while the multiple outlets reduce their diameters up to 0.9 mm and total length of approximately 12 cm. Eqn.(9) is numerically integrated using the forth-order Runge-Kutta scheme. The momentum equation is integrated in time with a typical time step corresponding to $1/100^{th}$ of the characteristic period of the cardiac cycle (t=0.01 s). A snapshot of the characteristic flow pattern that corresponds to a period of deceleration of blood flow is shown in Fig.13-right. It can be seen that due to multi-branching geometry and adverse pressure gradients (during the period of deceleration in the cardiac cycle) flow reversals with already mentioned spiralling imprints are clearly visible. In parallel with solving the time-dependent velocity and pressure fields, distributions of the different classes of magnetic particles are also tracked and their deposition along the artery walls is analyzed. The imposed magnetic field originates from a state-of –the-art superconducting magnet that gives $|B|_{max}$~2.5 T at a distance of approximately 4.5 cm from the patient chest – mimicking a real application. In Fig.14-above, contours of the magnetisation force are shown. Fur such an imposed magnetic field, deposition efficiency is calculated and shown in Fig.14-below – for different time instants. It is immediately clear that the magnetic field significantly increases the deposition efficiency compared to the neutral situation (magnetic field off), Fig.14-left and Fig.14-right. The capturing efficiency for different particle diameters is shown in Fig.15. Different lines indicate different orientation of the superconducting magnet. Compared to the neutral case for which practically no significant levels of the deposition rates are observed, the case with active magnet reaches capturing efficiencies between 10 and 35 %- for the biggest particle diameters in 2 to 4 μm range. This result is very encouraging for possible future medical applications

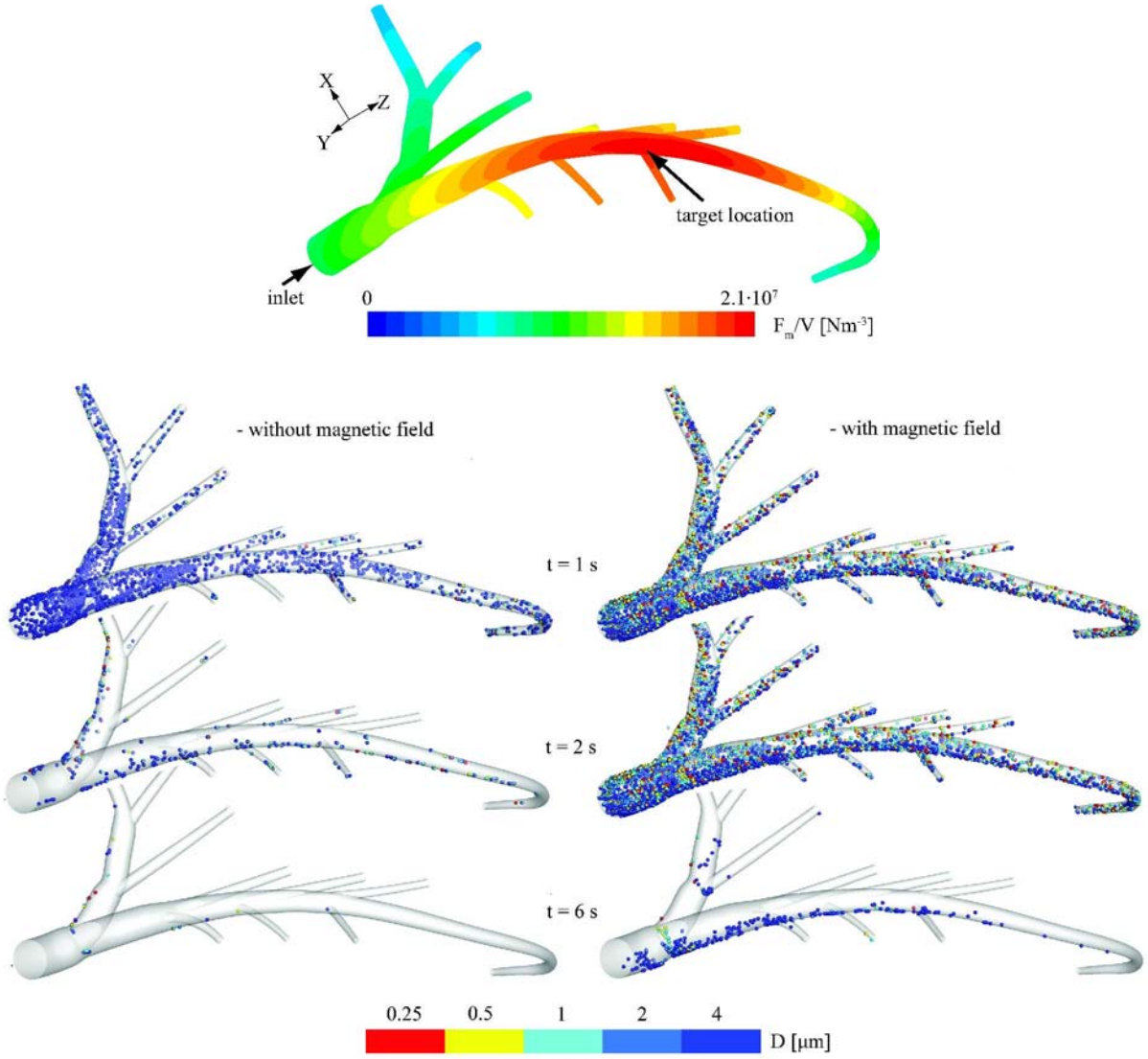

Figure 14. Simulations of the time dependency of magnetic particles depositions along the walls of the left coronary artery (LCA) subjected to an external magnetic field originating from a state-of-the-art superconducting magnet (with $|B|_{max}$~2.5 T) (different colours indicate different particle diameters – not to scale), Haverkoort and Kenjeres [26].

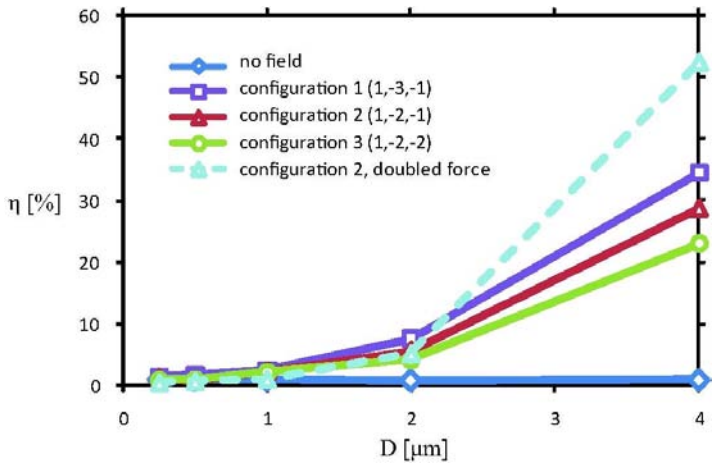

Figure 15. The capturing efficiency of magnetic particle carriers released in the left-coronary-artery (LCA) as a function of a particle diameter D for various superconducting magnet orientations, Haverkoort and Kenjeres [26]

of the magnetic drug targeting approach in fighting arteriosclerosis even for such challenging flow situations as occurring in the coronary arteries.

CONCLUSIONS

An overview of the recent achievements in the multi-scale modelling and simulations of complex interactions between fluid flow, heat transfer, turbulence and electromagnetic fields is presented. Three different classes of problems are considered including both the one- and two-way coupled interactions: 1- the single and multiple vortical flow patterns (draft tornados) generated by imposed electromagnetic field in a generic setup with and without heat transfer; 2- the mechanism of the self-generation of the magnetic field by turbulent swirling flow of liquid sodium in the Riga-dynamo experimental setup; 3- the magnetic capturing of nanoparticulates as a medical drug carriers released in a time-dependent pulsating blood flow inside of the left coronary artery. For first two applications, an extensive validation of the adopted multi-scale modelling approach is performed against available experimental results. A good agreement with available flow and magnetic field profiles are obtained for both configurations proving accuracy and potentials of the numerical simulations. The simulations also revealed some interesting phenomena for the very first time. A significant wall-heat transfer enhancement is obtained (up to 200%) in turbulent flow regime caused by targeted electromagnetic control of the wall-boundary layers. A fully integrated two-way coupled simulation of the experimental magnetic dynamo revealed process of the self-generation and self-sustenance of magnetic field under realistic working conditions. In contrast to the experimental data that are usually limited to the single point measurements in time, the numerical simulations provided a complete three-dimensional picture of flow and magnetic structures and their dynamical (time-dependent) evolutions. The last application demonstrated potentials of using numerical simulation in optimising the process of the local delivery of the medical drugs carried by magnetic nanoparticulates. The capturing efficiency is significantly increased when strong magnetic gradient are imposed even in such challenging case of the left coronary artery, demonstrating potentials of magnetic drug targeting technique in treating cardiovascular diseases.

REFERENCES

1. Smagorinsky, J., General circulation experiments with the primitive equations. I. The basic experiment, *Mon. Weather Rev.* 91, pp.99-164, 1963.
2. Shimomura, Y., Large eddy simulation of magnetohydrodynamic turbulent channel flow under a uniform magnetic field, *Physics of Fluids* 3 (12), pp. 3098–3106, 1991.
3. Kenjeres, S.,"Electromagnetic enhancement of turbulent heat transfer", Phys. Rev. E., Vol.78, Issue 6, Art. No.066309, pp.1-5, 2008.
4. van Driest, E. R., On turbulent flow near a wall, *J. Aero. Sci.* 23, pp.1007-1011, 1956.
5. Kenjeres, S. and Hanjalic, K., "Transient analysis of Rayleigh–Benard convection with a RANS model", *Int. J. Heat and Fluid Flow* 20, pp.329–40, 1999.
6. Hanjalic, K., and Kenjeres, S., "T-RANS simulation of deterministic eddy structure in flows driven by thermal buoyancy and Lorentz force", *Flow, Turbulence and Combustion* 66, pp. 427–51, 2001.
7. Kenjeres, S. and Hanjalic, K., "On the implementation of effects of Lorentz force in turbulence closure models", *Int. J. Heat Fluid Flow* 21, pp. 329–37, 2000.
8. Kenjeres, S. and Hanjalic, K., "LES, T-RANS and hybrid simulations of thermal convection at high *Ra* numbers", *Int. J. Heat Fluid Flow* 27, pp.800–10, 2006.
9. Kenjeres, S. and Hanjalic, K., "Numerical simulation of a turbulent magnetic dynamo", *Phys. Rev. Lett.* 98, pp.1–4, 2007.
10. Kenjeres, S. and Hanjalic, K.,"Numerical insights into magnetic dynamo action in turbulent regime", *New J. Phys.* 9, pp.306 1–29, 2007.

11. Soward A. M., Jones, C. A., Hughes, D. W. and Weiss, O., Editors, *Fluid dynamics and dynamos in astrophysics and geophysics*, CRC Press , 2005.
12. Vedoold, J., Rossi, L.R.C., Tummers, M.J., Hanjalic, K., "Towardselectromagnetic control of thermal convection", *Proceedings of the ISFCMV Conference*, Sorrento, Italy, 2003.
13. Kenjeres, S., Verdoold, J., Tummers, M. J., Hanjalic, K. and Kleijn, C. R. (2009), "Numerical and Experimental Study of Electromagnetically Driven Vortical Flows", *Int. J. of Heat and Fluid Flow, in press,* 2009.
14. Tanaka, H., and Miyata, H., "Turbulent natural-convection in a horizontal water layer heated from below", *Int. J. Heat and Mass Transfer*, Vol. 23 (9), pp.1273-1281, 1980.
15. Chu T. and Goldstein, R. J., J., "Turbulent convection in a horizontal layer of water", J. Fluid Mech. 60, pp.141-159, 1973.
16. Kerr, R. M. and Herring, J. R.,"Prandtl number dependence of Nusselt number in direct numerical simulations", *J. Fluid Mech.* 419, pp.325-344, 2000.
17. Uda, N., Yamaoka, N., Horiike, H. and Miyazaki, K.,"Heat transfer enhancement in lithium annular flow under transverse magnetic field", *Energy Convers. Manage*., Vol. 43, Issue 3, pp. 441-447, 2002.
18. Busse, F. H., "Homogeneous dynamos in planetary cores and in the laboratory", *Annu. Rev. Fluid Mech.* 32, pp.383-408, 2000.
19. Gailitis, A., et al., "Detection of a flow induced magnetic field eigenmode in the Riga dynamo facility", *Phys. Rev. Lett.* 84**,** pp.4365-4368, 2000.
20. Gailitis A., et al., "Magnetic field saturation in the Riga dynamo experiment", Phys. Rev. Lett. 86, pp. 3024-3027, 2001.
21. Alexiou, C., Arnold, W., Klein, R.J., Parak, F.G., Hulin, P., Bergemann, C., Erhardt, W., Wagenpfeil, S., Lubbe, A.S., "Loco-regional cancer treatment with magnetic drug targeting", Cancer Research 60 (23), pp.6641–6648, 2000.
22. Alexiou, C., Schmidt, A., Klein, R., Hulin, P., Bergemann, C., Arnold, W., "Magnetic drug targeting: biodistribution and dependency on magnetic field strength", Journal of Magnetism and Magnetic Materials 252 (1–3), pp.363-366, 2002.
23. Alexiou, C., Jurgons, R., Schmid, R.J., Bergemann, C., Henke, J., Erhardt, W., Huenges, E., Parak, F., "Magnetic drug targeting-biodistribution of the magnetic carrier and the chemotherapeutic agent mitoxantrone after locoregional cancer treatment", Journal of Drug Targeting 11 (3), pp.139–149, 2003.
24. Torchilin, V. P., Ed., "*Nanoparticulates as Drug Carriers*", Imperial College Press, 2006.
25. Kenjeres, S., "Numerical analysis of blood flow in realistic arteries subjected to strong non-uniform magnetic fields", *Int. J. Heat and Fluid Flow*, Vol. 29, Issue 3, pp.752-764., 2008.
26. Haverkort, J. W. and Kenjeres, S., "Optimizing drug delivery using non-uniform magnetic fields: a numerical study", *Proceedings of the 4th European Congress for Medical and Biomedical Engineering, Engineering for Health*, EMBC 2008, 23-27 November 2008, Antwerp, Belgium, pp.1-4, 2008.
27. Giannoglou, G. D., Soulis, J. V., Farmakis, T. M. and Louridas, G. E., "Molecular viscosity distribution in the left coronary artery tree", *Comp. in Caridiol*., Vol.30, pp.641-644, 2003.

DROPLET MICROFLUIDICS: FUNDAMENTALS AND APPLICATIONS

P. Garstecki, Krzysztof Churski
[1]Institute of Physical Chemistry, Polish Academy of Sciences,
Kasprzaka 44/52, 01-224 Warsaw, Poland

ABSTRACT. Microfluidic systems offer perfect control over formation of bubbles and droplets. In my lecture I will discuss the physical mechanisms underlying this control and the use of multiphase microfluidic systems for preparation of droplets, compound droplets, capsules and particles. Microfluidic systems allow also for a control of transport of droplets through topologically non-trivial microfluidic networks of channels. In such systems the droplets present in the network affect their trajectories via long-range interactions mediated through the pressure field in the channels. These interactions lead to fascinating dynamic behaviours. The recently developed techniques for computer controlled formation of droplets and guiding them through the channels open up completely new possibilities for constructing automated chips for analytical and synthetic chemistry.

Keywords: *microfluidics, droplets, automated systems, lab on chip*

Microfluidic systems offer perfect control over the processes of formation of droplets and bubbles. In the microfluidic devices it is possible to precisely tune all important characteristics of the emulsions: the volume, volume fraction and the frequency of formation [1-3] of droplets. It is also possible to form bimodal, multimodal and continuous distributions [4,5] of sizes, or to prepare emulsions comprised of distinct families of droplets of different sizes and chemical composition, and to tune their ratios of sizes and stoichiometry [6]. Also the architecture of individual droplets can be tuned: from multiple emulsions (i.e. drops-in-drops), with tuned hierarchy and stoichiometry [7,8], to preparation of capsules and solid particles [9,10].

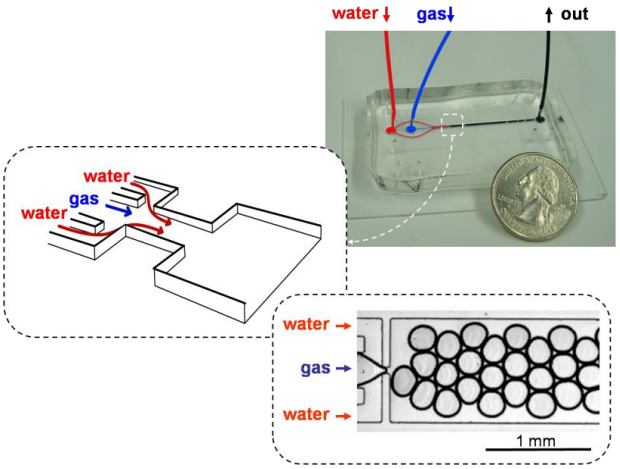

Figure 1. A planar microfluidic flow focusing system producing bubbles of Nitrogen in aqueous solutions of surfactant [1].

* Corresponding author: Prof. X . Yxy
Phone: + (11)-12-345678, Fax: + (11)-12-3456789
E-mail address: my-email@address.edu.pl

These characteristics, coupled with a detailed understanding of break-up in confined systems [11-14], prompt for applications in i) preparation of 'perfect' emulsions and their derivatives for use in pharmacology, cosmetics, and food industries, and ii) use of droplets as micro-reaction-beakers for automated, parallel chemical and biochemical analyzes and for chemical synthesis.

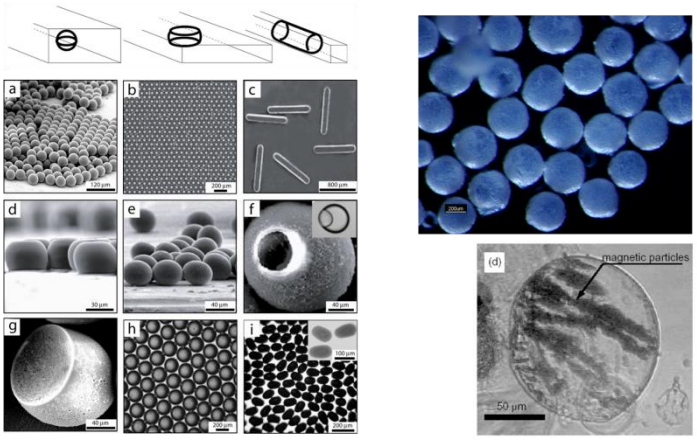

Figure 2. Examples of use of microfluidic methods of forming droplets for formulation of new materials: anisotropic particles [10] (left pane) and polymeric capsules [9] (right pane).

In the lecture I will discuss the mechanism behind the observed monodispersity of the droplets and bubbles formed in microfluidic systems. This mechanism rests on the stability of interfaces in confined geometries of microfluidic junctions [11, 12, 15] and on the separation of time-scales between fast equilibration of the interface and disturbances in the pressure field, and slow progression of the flow (as reflected by usually small values of the capillary number). The ability to form perfectly monodisperse foams and emulsions [11,12,15] and further particles [10], capsules [9] and compound droplets [16-18] may lead to applications in formulation of new materials for use in pharmacy, cosmetics and food industries.

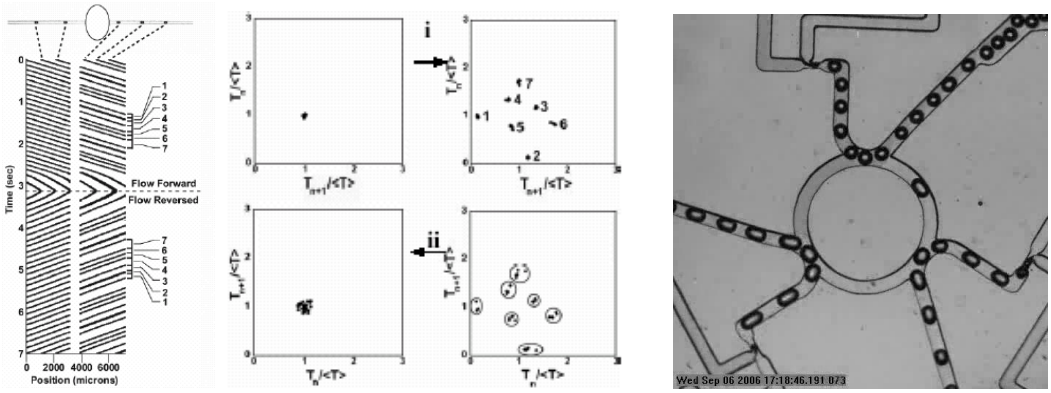

Figure 3. (left) demonstration of reversibility of the complex flows of droplets in microfluidic networks [21], (right) a microfluidic ring oscillator [22]

Another use of microfluidic droplet systems is to perform reactions within droplets [19]. Several simple demonstrations of analytical, and synthetic screens have been reported [19]. Extending the current capabilities of microfluidic droplet based systems for more advanced applications in chemistry requires i) understanding of the dynamics of transport of droplets through networks of microchannels [20-23]., and ii) construction of tools for computer controlled formation and guiding of droplets. Recent experiments [20] have demonstrated that the properties of flow of droplets in capillaries (e.g. the increased resistance to flow introduced by the droplets) can be used to perform elementary but non

trivial schemes of processing of sequences of droplets, as for example coding and decoding [21] or logic operations [22]. These demonstrations, together with the apparent robustness of such operations to experimental disturbances or noise [21] suggest that it should be possible to design and operate automated chips performing non trivial operations (e.g. merging, splitting, distributing in the network) on the micro reaction vessels (droplets). I will describe the current state of art in formation of droplets on demand in microfluidic systems and the prospects for designing fully automated combinatorial lab-on-chip systems.

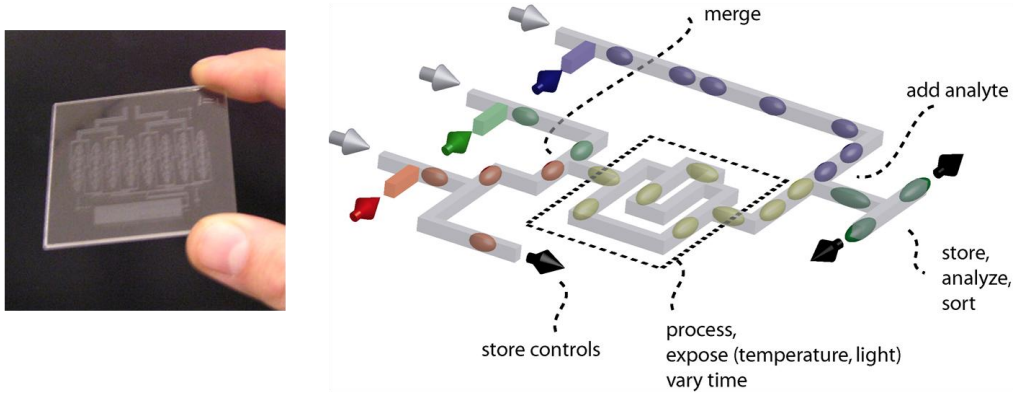

Figure 4. Vision of an automated chip to perform complicated chemical protocols on droplets.

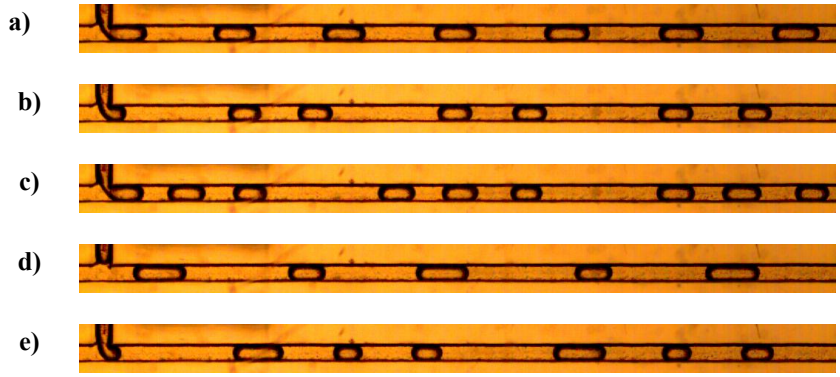

Figure 5.Examples of sequences of droplets formed with a droplet-on-demand system. a) monodisperse droplets produced at a constant interval, b) monodisperse droplets formed at two different intervals, c) packs of three monodisperse droplets separated by a longer interval, d) droplets of two different volumes produced all at the same intervals and e) packs of three droplets, with the first two droplets having one volume, and the third droplet having a larger volume.

REFERENCES

1. P. Garstecki, I. Gitlin, W. Diluzio, E. Kumacheva, H.A. Stone, G.M. Whitesides Appl. Phys. Lett. 85, 2649 (2004)
2. T. Thorsen, R. W. Roberts, F. H. Arnold, S. R. Quake, Phys. Rev. Lett. 86, 4163 (2001)
3. S. L. Anna, N. Bontoux, H. A. Stone, Appl. Phys. Lett. 82, 364 (2003)
4. P. Garstecki, M. Fuerstman, G.M. Whitesides, Nature Physics, 1, 168-171 (2005)
5. P. Garstecki, M. Fuerstman, G.M. Whitesides, Phys. Rev. Lett. 94, 234502 (2005)
6. M. Hashimoto, P. Garstecki, G.M. Whitesides Small, 3, 1792-1802 (2007)
7. Z. Nie, S.Q. Xu, M. Seo et al., JACS 127, 8058-8063 (2005)
8. A. Utada, E. Lorenceau, D.R. Link, P.D. Kaplan, H.A. Stone, D.A. Weitz, Science 308, 537-541 (2005)
9. S. Takeuchi, P. Garstecki, D.B. Weibel, G.M. Whitesides, Adv. Mater. 17, 1067 (2005)

10. S. Xu, Z. Nie, M. Seo, P.C. Lewis, E. Kumacheva, P. Garstecki, D.B. Weibel, I. Gitlin, G.M. Whitesides, H.A. Stone, Angew. Chem. Int. Ed. 44, 724 (2005)
11. P. Garstecki, H.A. Stone, G.M. Whitesides Phys. Rev. Lett. 94, 164501 (2005)
12. P. Garstecki, M. Fuerstman, H.A. Stone, G.M. Whitesides, Lab Chip 1, 437 (2006)
13. M. De Menech, P. Garstecki, F. Jousse, H.A. Stone, J. Fluid Mechanics, 595, 141-161, (2008)
14. Z. Nie, M. Seo, S. Xu, P. C. Lewis, M. Mok, E. Kumacheva, G. M. Whitesides, P. Garstecki, H. A. Stone, Microfluidics and Nanofluidics, 5, 585-594 (2008)
15. B. Dollet, W. Van Hoeve, J.P. Raven, P. Mrmottant, M. Versluis, Phys. Rev. Lett., 100, 034504 (2008)
16. A.S. Utada, E. Lorenceau, D.R. Link, P.D. Kaplan, H.A. Stone, D.A. Weitz, Science, 308, 537-541 (2005)
17. M. Seo, C. Paquet, Z.H. Nie, S.Q. Xu, E. Kumacheva, Soft Matter, 3, 986-992 (2007)
18. S. Okushima, T. Nisisako, T. Torii, T. Higuchi, Langmuir, 20, 9905-9908 (2004)
19. H. Song, D. L. Chen, R. F. Ismagilov, Angewandte Chemie International Edition, 2006, 45, 7336-7356
20. F. Jousse, R. Farr, D.R. Link, M.J. Fuerstman, P. Garstecki, Phys. Rev. E 74, 036311 (2006)
21. M. Fuerstman, P. Garstecki, G.M. Whitesides, Science, 315, 828-832 (2007)
22. M. Prakash, N. Gershenfeld, Science 315, 832-835 (2007)
23. M. Schindler, A. Ajdari, Phys. Rev. Lett. 100, 044501 (2008)

Biological Systems

EFFECT OF SKIN TEXTURE ON RADIATIVE CHARACTERISTICS OF HUMAN SKIN

J. Yamada[1], K. Nakamura [1], M. Kaizuka [1], K. Kikuchi [2], S. Takata [2, *]
[1] Shibaura Institute of Technology, Tokyo, Japan
[2] Shiseido, Co., Ltd., Tokyo, Japan

ABSTRACT. It is thought that the skin texture on human skin influences its appearance and a fine texture of skin makes the skin beautiful. However, it has not been clarified how the skin texture influences its appearance. In this study, to clarify the scattering characteristics at the skin surface, an experimental study using an optical prism with skin structure has been performed, and to understand the experimental results, three numerical models have been developed. A model takes into account comparatively large skin structure, which is called "skin texture," and another model considers the finer structure called "microstructure." The other is a combined model of the two models. The results predicted by the models that consider the microstructure are in good agreement with the experimental one. This reveals that the skin texture does not affect the light scattering by skin surface, but the microstructure finer than the skin texture.

Keywords: *Radiation, Radiative Properties, Human skin, Skin Texture, Appearance*

INTRODUCTION

A phrase "kime komayakana" is one of expressions to describe beautiful human skin in Japan. The word "kime" represents grooves on the skin surface, and the word "komayaka" means that the grooves or the structure confined by grooves are fine or small. Since a skin with the fine structure looks beautiful, the phrase "kime komayakana" may be used for representing beautiful skin. We are not sure of this, however, it is empirically thought the structure on skin surface affects appearance of human skin. Therefore, many studies have been carried out so far.

In those studies, researchers try to clarify the effect of the surface structure on appearance for human skin. However, since the reflection by human skin contains surface reflection at the skin surface and internal scattering inside the skin, the appearance does not depend on only the skin surface but also inside optical characteristics of human skin. This means that observation or experimental study using actual human skin cannot clarify the effect of the surface structure of the skin on its appearance.

The final goal of this study is to clarify what and what optical characteristics beautiful skin comes from, and to develop cosmetics that reproduce the optical characteristics of beautiful skin. To do this, it is necessary to individually evaluate how the surface reflection and the internal scattering influence the appearance of human skin. The purpose of this study is to experimentally investigate the optical characteristics of skin surface and to clarify the effect of the surface structure on the optical characteristics by using numerical models.

* Corresponding author: Prof. J. Yamada
Phone: + (81)-3-5859-8011, Fax: + (81)-3-5859-8001
E-mail address: jyamada@sic.shibaura-it.ac.jp

In this study, to set the surface reflection by the skin structure apart from the internal scattering inside the skin, an optical prism having a surface structure of skin is prepared and a scattering characteristic is measured. In order to understand what the measured scattering characteristic comes from, three models are proposed and compared with the measured results. A model taking into account microstructure much smaller than the skin grooves is in good agreement with the measured results.

SCATTERING CHARACTERISTICS OF SKIN SURFACE

To avoid the effect of the internal scattering inside the skin and to evaluate the effect of the surface reflection at the skin surface, an optical prism on which a surface structure of skin was printed was fabricated (Fig. 1). When the skin surface on the prism is irradiated by incident light, a part of the light penetrates into the prism. However, the light is not scattered in the prism because the prism is transparent. Using this prism, the scattering characteristics of the skin surface can be evaluated.

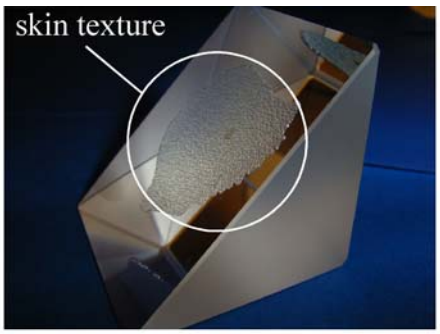

Fig. 1 Surface Structure of Skin Printed on an Optical Prism

The prism is made of BK7, and its reflective index is close to the refractive index of human skin, which depends on the water content and is around 1.5. The surface structure of skin is fabricated by UV light curable resin AT3925M (NTT Advanced Technology, Co., LTD.) on the prism surface. The refractive index of this resin can be controlled. In this study, the refractive index of the resin is adjusted to that of prism so that difference in refractive index between the resin and the prism is not given rise to. The skin structure printed on the prism is taken from an inner arm of man aged 22 years.

In the experiment, the skin surface on the prism is irradiated by parallel beam having a diameter of 5 mm and the light reflected by the surface structure is measured. A He - Ne Laser (632.8 nm) is used as the incident beam, and an optical fiber with a receiving lens having narrow view angle (0.6×10^{-3} sr) is used to detect the reflected light. The measurements are performed 6 times at different positions.

To evaluate the appearance of skin, the bi-directional reflectance is adopted. The definition of the bi-directional reflectance, ρ'', is [1]

$$\rho''(\theta_{in},\theta_r,\phi_r) = \pi I(\theta_r,\phi_r)/q_{in}(\theta_{in}) \tag{1}$$

where q_{in} is the radiative flux of the incident light, and I is the intensity of reflected light. θ_{in}, θ_r, ϕ_r are the polar angles of incident light and reflected light, and the azimuthal angle measured from the direction of the incidence, respectively. The measured results are converted to the bi-directional reflectance. The profiles of the bi-directional reflectance on the incident plane, which contains both the axis of the incident beam and the axis normal to the surface, are shown in Fig. 2.

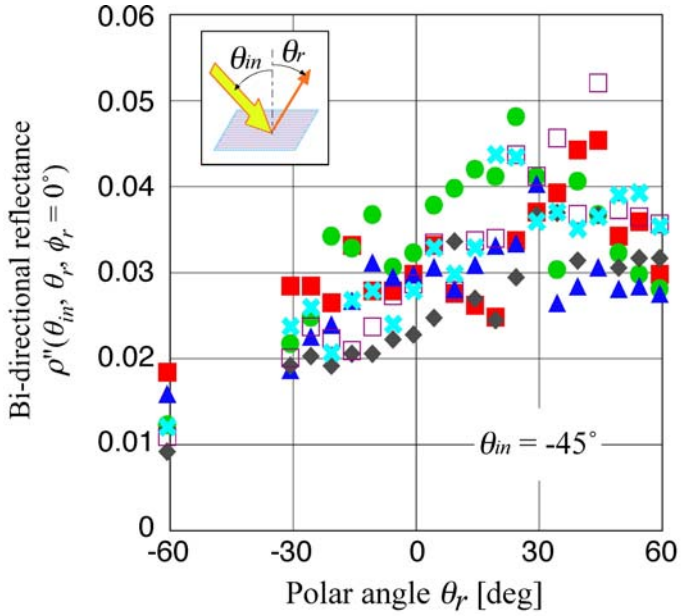

Fig. 2 Experimental results for Reflection by Surface Structure of Skin

The results of θ_{in}, = -45˚, which is the incident angle of light, are shown in this figure. Any peak cannot be seen around 45˚ in θ_r, which is the specular direction corresponding to the incident direction. This means the skin surface diffusely reflects the incident light, and it is found that the skin surface has an optical characteristic that the strongly reflection occurs in the direction along the surface (large θ_r).

In this study, to understand what these scattering (reflection) characteristics come from, three models are proposed and compared with the measured results. The numerical models will be described in the following.

NUMERICAL MODELS FOR SKIN STRUCTURE

Geometric configuration for the surface structure is measured using a confocal laser-scanning microscope (CLSM) to construct the numerical models. The result is shown in Fig. 3. The imaged area of skin is about 2.5 x 2.5 mm^2. Brightness in this figure represents depth of structure. Deep grooves are brightly shown. It can be seen that there are comparatively larger grooves configuring

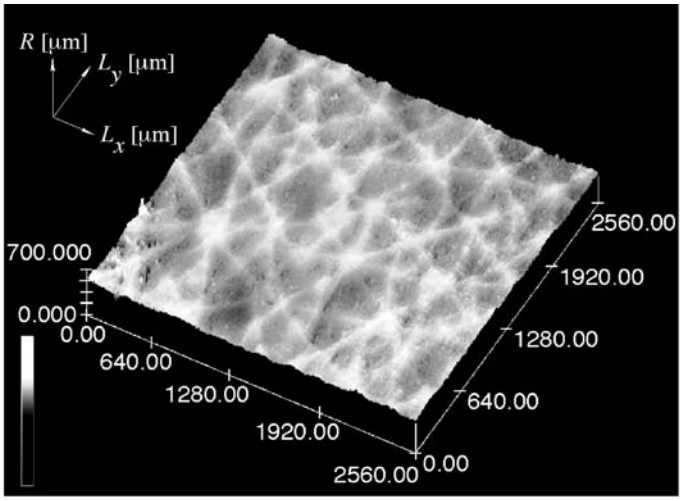

Fig. 3 Surface Structure of Skin Imaged by a Confocal Laser-scanning Microscope

triangle networks and smaller structures over the surface. In this study, larger groove structure is called "skin texture" and smaller structure is called "microstructure."

Numerical models have been constructed based on the CLSM image. Figure 4 shows a model (Model A) that takes into account only the "skin texture." The "microstructure" is not considered in this model. The depth of grooves and the size of the triangle network have determined from the CLSM image. It is assumed that the scattering at the surface is induced by the reflection and the refraction at the interface between the two media that have different refractive indexes. The reflection and the refraction are assumed to follow the geometric optics governed by Fresnel's relations.

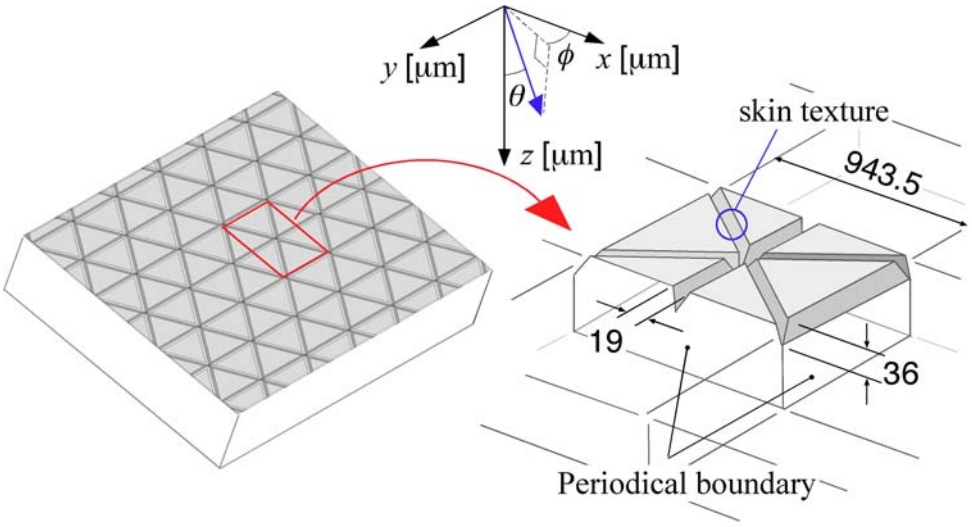

Fig. 4 Model A: Numerical Model Taking into Account "Skin Texture"

Another model (Model B) does not take into account the " skin texture" but the "microstructure." In this model, it is assumed that the scattering at the surface with the "microstructure" is induced by the reflection and the refraction at the interface. This is the same as Model A. However, the actual microstructure is not placed on the surface. The microstructure is treated statistically. The concept and the feature of this model are as follows.

When an ideally fine beam of light hitting on the skin surface meets a small element of surface on microstructure, the light is reflected by or transmitted through the small surface element. If it is assumed that the reflection and/or the transmission follow geometric optics, as mentioned before, only the direction of the small surface element is necessary to determine the reflected or transmitted direction. Generally, since the skin surface is widely irradiated, the incident radiation hits many small surface elements on microstructure that are oriented at varied directions, if we know the directions of the small surface elements, we can evaluate the radiation scattering. Therefore, we propose a method for statistically determining the directions of small surface elements on microstructure. In this study, we give the probability for the direction of the small surface element that the incident light hits.

To give the probability for the direction of the small surface elements, we utilize the geometric configuration of the microstructure measured by the CLSM. The CLSM image stores digital data for height of the surface structure every 2.5 μm. When a surface element is taken by neighboring three data points, as shown in Fig. 5, the direction, the polar and the azimuthal angles, θ_e and ϕ_e of the surface element can be determined. We checked up on the directions of the whole surface elements imaged by the CLSM and derived the probability density function for the direction of the surface elements, $p(\theta_e, \phi_e)$. When $\Delta M(\theta_e, \phi_e)$ is the number of surface elements that face to a

small solid angle, $\Delta\Omega_e$ around θ_e and ϕ_e, and the total number of the surface elements is M_{tot}, the probability density function, $p(\theta_e, \phi_e)$ is determined by

$$p(\theta_e, \phi_e) = \lim_{\Delta\Omega_e \to 0} \frac{\Delta M(\theta_e, \phi_e)}{M_{tot}\Delta\Omega_e} \tag{2}$$

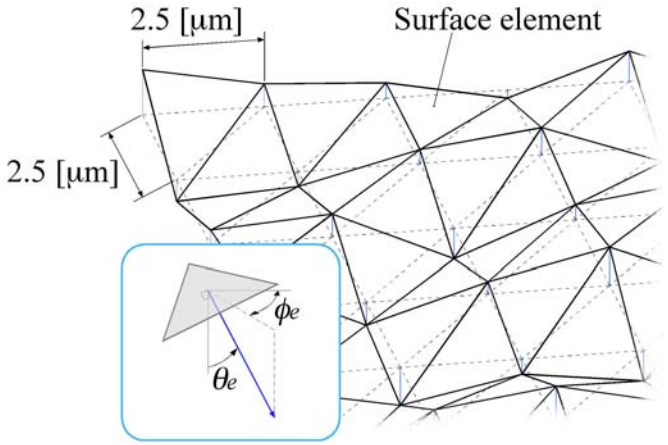

Fig. 5 Model B: Numerical Model Taking into Account "Microstructure"

When the incident light hits a surface element, the direction of the surface element is not determined by the above probability density function, because it also depends on the projected area to the incident direction of the surface element. Therefore, by taking into account the projected surface area, the probability density function for the incident light with the incident angle of θ_{in} is given by,

$$f(\theta_e, \phi_e, \theta_{in}) = \lim_{\Delta\theta_e \to 0, \Delta\phi_e \to 0} \frac{\int_{\Delta\Omega_e} p(\theta,\phi)\, A(\theta,\phi,\theta_{in})\, d\Omega}{\sin\theta_e \Delta\theta_e \Delta\phi_e} \cdot \frac{1}{\oint_{\Omega=2\pi} p(\theta,\phi) A(\theta,\phi,\theta_{in}) d\Omega} \tag{3}$$

where $\Delta\theta_e$ and $\Delta\phi_e$ are the small increments of angle around θ_e and ϕ_e, respectively, and $\Delta\Omega_e = \sin\theta_e \Delta\theta_e \Delta\phi_e$.

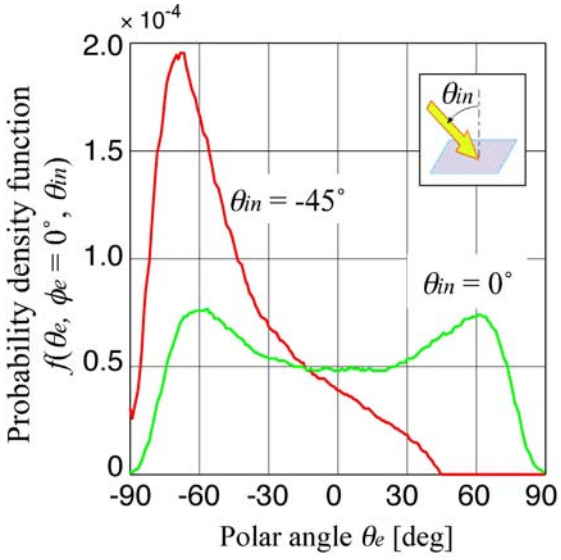

Fig. 6 Probability Density Function for Orientation Angle of Surface Elements on Microstructure

The probability density functions for θ_{in} = 0˚ and -45˚are shown in Fig. 6. It is found that the function is symmetric for the normal incidence of light (θ_{in} = 0˚) because the surface elements are randomly oriented in the azimuthal direction and is azimuthal symmetric. It is also found that the function is zero for 45˚ < θ_e when θ_{in} = -45˚. The reason for this is the incident light does not hit surface elements oriented to a polar angle larger than 45˚.

The third model (Model C) is a combined model of Model A and Model B. This model takes into account both the "skin texture" and the "microstructure."

RESULTS AND DISCUSSION

The bi-directional reflectances of the three models are numerically evaluated using a Monte Carlo method. The results are shown in Fig. 7. In this calculation, it is assumed that the incident light is parallel and uniform and has an incident angle of 45˚ so that the results can be compared with the experimental results.

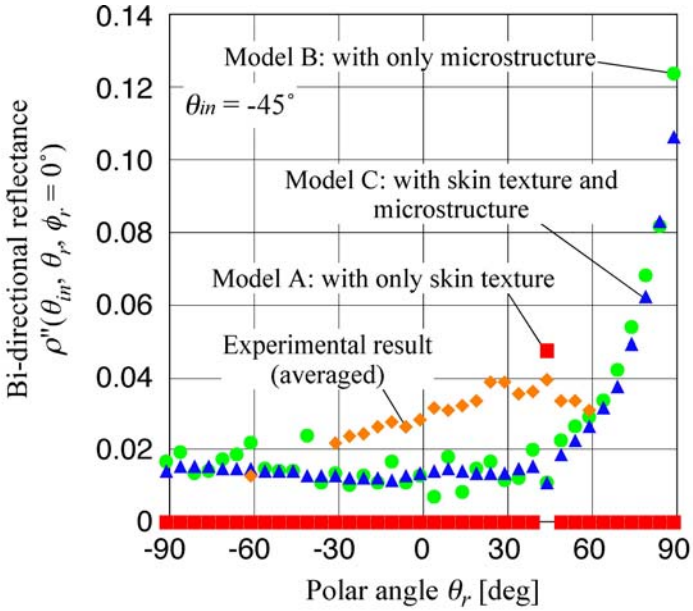

Fig. 7 Comparison between Numerical Results and Experimental Results

For Model A, the profile of reflected light depends on the incident axis of light and the orientation of the skin texture. Although the skin texture on an actual skin is randomly oriented, the skin texture in the model is not. Therefore, in the calculation, we calculate the profiles of reflected light varying orientation of the skin texture all over the azimuthal directions and average the calculated profiles. The resultant profile is shown in Fig. 7 with red square symbols.

Figure 7 reveals that the numerical results using Model A does not agree with the experimental result at all. Since we do not consider the "microstructure" in this model, only the strong specular reflection occurs. A peak in the numerical results represents the strong specular reflection. On the other hand, it is found that the numerical results for Model B and C, shown with green circle and blue triangle, respectively, are in good agreement with the experimental results in magnitude, although the profiles are not. Furthermore, it is found that the numerical results of Model B and C are almost the same. This means the scattering by the skin surface does not depend on the "skin texture" but the "microstructure."

There are discrepancies between the numerical results and experimental ones in profile of the bi-directional reflectance. Especially, the increase at large polar angles in the numerical results cannot

be seen in the experimental results. This can be due to diffraction effects that are not considered in the numerical models.

CONCLUSIONS

To clarify the scattering characteristics at the skin surface, an experimental study using an optical prism with skin texture has been performed, and to understand the experimental results, three numerical models have been developed in this study. A model takes into account comparatively large skin structure, which is called "skin texture," and another model considers the finer structure called "microstructure." The other is a combined model of the two models. The results predicted by the models that consider the microstructure are in good agreement with the experimental one. This reveals that the skin texture does not affect the light scattering by skin surface but the microstructure finer than the skin texture.

ACKNOLEDGEMENT

This study is supported by the Ministry of Education, Science and Culture of Japan under Grant. No. 17206019 and No. 19360103.

REFERENCES

1. Brewster, M. Q., Thermal Radiative Transfer & Properties, John Wily § Sons, Inc., New York, 1992

EXPERIMENTAL SIMULATION OF A THERMALLY SIGNIFICANT BLOOD VESSEL IN A TISSUE SUBJECTED TO CRYO-SURGERY

N. Rybko, A. Shitzer*, D. Degani
Department of Mechanical Engineering
Technion, Israel Institute of Technology, Haifa, Israel 32000

ABSTRACT. The influence of a thermally significant blood vessel on a tissue phantom, during freezing by a liquid Nitrogen operated, circular, surface cryo-probe was investigated. The medium used in the experiments was a 0.2% mass concentration Bacto Agar/distilled water solution. The blood vessel was simulated by a 5.4/6 mm ID/OD brass-alloy tube. The experiments were conducted under several flow rates of constant temperature water in the embedded tube: no flow, 30, 100 and 200 ml/min. Cryo-probe cooling rates applied on the surface of the medium varied from -4.4°C/min to -9.2°C/min. The advancement of the frozen front was tracked by thermocouples placed in the medium. Results indicate reductions in the extents of the total frozen areas under the cryo-probe of about 42% due to the highest flow rate vs. no-flow in the tube, and 53% by applying the highest vs. the lowest cryo-probe cooling rate.

Keywords: *phase change; cryo-surgery; liquid Nitrogen; thermal perturbation; embedded tube.*

INTRODUCTION

Cryo-surgery is a medical technique used for destroying undesired tissues by the application of controlled localized freezing. The treatment is performed by a cryo-probe, which may be placed either in contact with the tissue surface, or inserted into the targeted tissue. The treatment can be applied as a stand-alone or in conjunction with other conventional surgical techniques. Current applications of cryo-surgery include the treatment of a variety of malignancies in the liver, prostate, skeleton bones, womb, skin and benign hemorrhoids. Although this technique has many advantages, it still falls short of being the treatment of choice, especially because of the uncertainty regarding its long term effects and success rate.

Investigators suggest several criteria for the success of the treatment. Apparently, the most important of these is the cooling rate maintained at the tissue freezing front [1]. Experimental evidence obtained from tissue cultures, suggests that at both very high cooling rates, of hundreds of degrees Celsius per minute, and at very low cooling rates, of up to several degrees Celsius per minute, the tissue may be lethally damaged as a result of two different mechanisms. Another important criterion for the success of the cryo-surgical procedure is the minimal temperature reached in the tissue during the treatment. Current practices assume maximal tissue-specific "lethal" temperatures of -5°C to -50°C [2].

Thermal perturbations which are present in the treated region, e.g., large blood vessels (artery or vein) that traverse the targeted area, may distort the temperature field and modify the rate and extent of freezing. This thermal perturbation could affect the achievement of the desirable end result, or it could prevent parts, or even the whole volume of the malignant tissue from being frozen. Thus,

* Corresponding author: Prof. A. Shitzer
Phone: + (972)-4-8292841, Fax: + 972-(4)-8295711
E-mail address: mersasa@tx.technion.ac.il

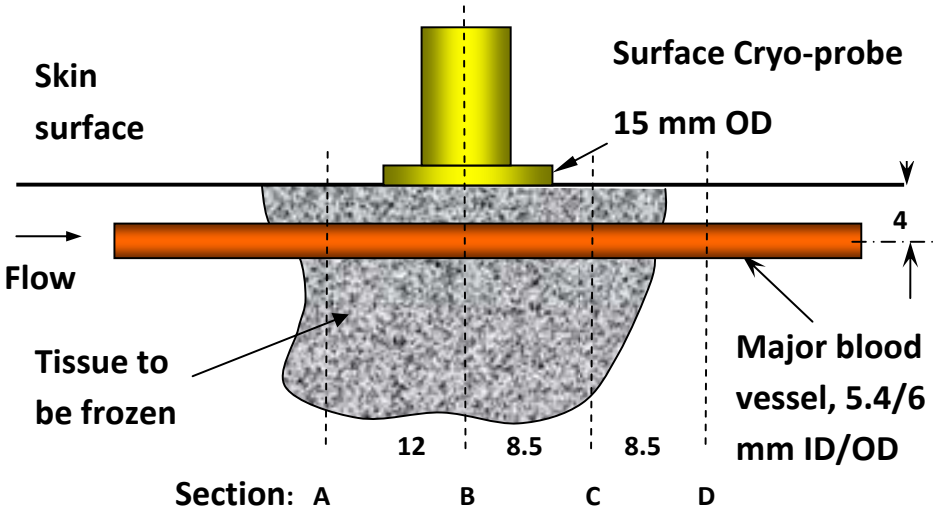

Figure 1. Schematic view of the tumor, blood vessel and surface cryo-probe

understanding the evolution of the temperature field that develops in the vicinity of a cryo-probe in the presence of such a thermal perturbation could be useful in the design and application of a cryo-surgical procedure and increase its probability for greater success.

The purpose of this study is to investigate experimentally the influence of a simulated thermally significant blood vessel on a tissue phantom, while it is being frozen by a circular, liquid Nitrogen operated, surface cryo-probe (Figure 1). The medium used in the freezing experiments was a 0.2% mass concentration Bacto Agar/distilled water solution. The thermo-physical properties of this solution closely approximate those of a biological tissue. The blood vessel is simulated by a 5.4/6 mm ID/OD brass-alloy tube.

EXPERIMENTS

Experimental setup

Detailed description of the experimental setup is given by Rybko [3] and by Massalha and Shitzer [4]. Only essential details are repeated here. The setup consisted of the following four subsystems (see Figure 2):

Liquid nitrogen (LN_2) freezing system. The cryo-surgical system (Model CS-13-A, RICOR, Israel) consisted of an LN_2 storage Dewar, a flat, circular, surface cryo-probe (brass, 15 mm OD) connected to an insulated, flexible delivery tube and a PC-based control system.

Test section. A rectangular support frame, made of two plexiglass plates, held both the embedded tube (the "heat source") and the thermocouple wires. The embedded tube, simulating large blood vessels in the human body, was made of a thin wall circular brass-alloy tube 5.4/6 mm in diameters. The tube was placed at a centerline depth of 4 mm parallel to the surface of the PCM on a plane coinciding with the centerline of the cryo-probe. The tube was perfused by 26ºC constant temperature water. The test section was filled with the phase-changing medium (PCM, 0.2% mass concentration Bacto Agar/distilled water solution) and was placed in an inner cylindrical container which was fitted, flush at the top, inside an insulated, outer cylindrical container. The free volume between the bottoms and sides of the two metal containers was used for circulating temperature-controlled water to maintain a constant temperature at the outer surfaces of the PCM contained

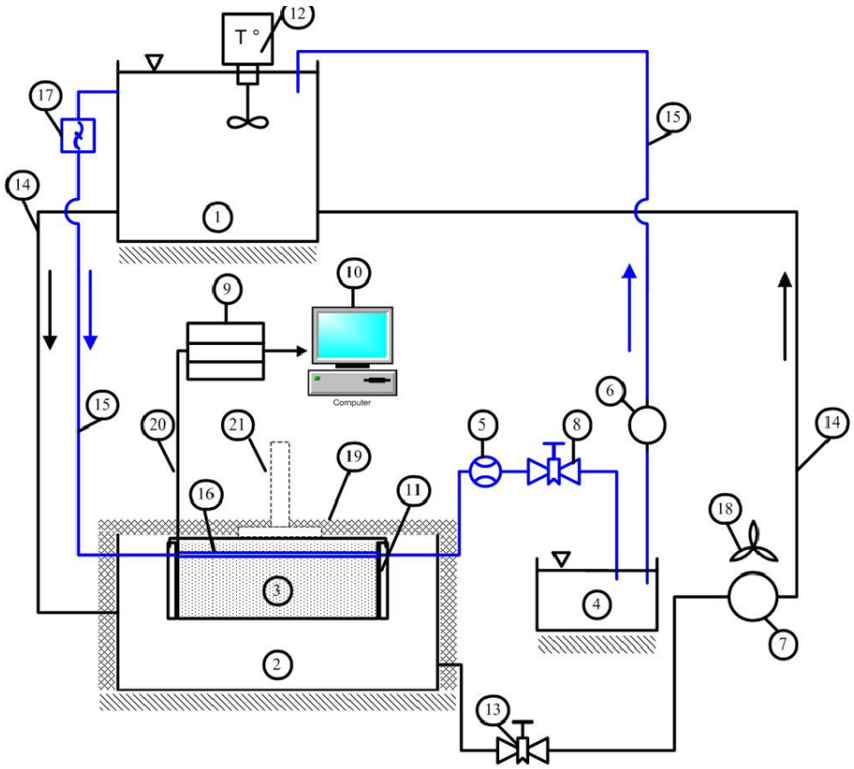

1 Constant temperature water container, **2** Water circulating container, **3** PCM and embedded tube container, **4** Water collecting container, **5** Turbine flow meter, **6** Return pump, **7** Circulation pump, **8** Flow regulating valve, **9** Thermocouple sampling multiplexer **10** PC, **11** Plexiglass frame, **12** Controlled electrical heater and water stirrer, **13** Regulating valve, **14** 25 mm ID tygon tube, **15** 6 mm ID tygon tube, **16** Brass alloy tube simulating a blood vessel, **17** Water filter, **18** Fan, **19** Polyurethane insulation, **20** Thermocouple wires, **21** Surface cryo-probe

Figure 2. Schematic layout of the experimental setup.

inside the inner container. A schematic layout of the test section is shown in Figure 2.

The water circulating system. Constant temperature water was supplied to the embedded tube and into the volume between the outer and inner containers. Water flow rate in the embedded tube was continuously monitored by a turbine flow meter.

Temperature measuring system. A total of 40 Teflon-coated, Type K (chromel-alumel) thermocouples (TCs), made of 0.25 mm wires with 0.076 mm coating (OMEGA Engineering), were used: 7 to measure the temperatures of the water flowing through the embedded tube (Figure 3) and the remaining 33 to monitor the temperatures of the PCM (Figure 4). The thermocouple junctions were welded by an electrical arc and were placed in the PCM on four separate planes perpendicular to the
embedded tube (Sections A to D in Figure 1). Placement was done at alternate lateral locations on a 5x5 mm grid to minimize thermal perturbations, as shown in Figure 4. Two additional Type T (copper- constantan) TCs were inserted into the bottom part of the cryo-probe. The thermocouple wires were

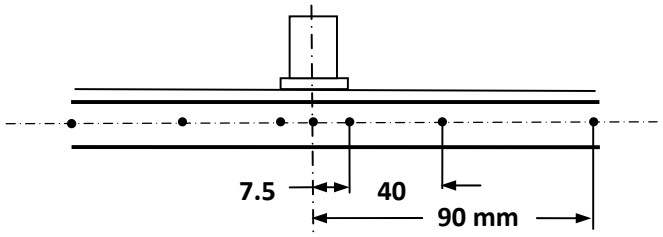

Figure 3: Thermocouple placements in the embedded tube

connected to a PC through a multiplexer and were scanned every 1 sec with a sampling rate of 25 samples/sec.

Experimental procedure

The experiments were conducted under several flow rates of constant temperature water in the embedded tube: without flow, 30, 100 and 200 ml/min. Cooling rates applied on the surface of the PCM by the cryo-probe varied from -4.4°C/min to -9.2°C/min. Tracking the advancement of the frozen front was done by the aforementioned TCs. Each experiment was performed with the same initial and boundary conditions, which were achieved by circulating water at a uniform temperature of 26°C through the system for several hours prior to the initiation of the freezing process.

RESULTS

Figure 5 shows the effects of the highest flow rate used in the embedded tube, 200 ml/min, on the propagating temperature fronts at the various measuring sections in the PCM. These fronts were drawn by interpolating the readings of the various TCs. Results are shown at 1055 seconds after the initiation of the cooling process when the cryo-probe temperature reached -95ºC. Section B, which coincides with the cryo-probe centerline, and which was instrumented with the most thermocouple junctions, exhibits temperature regions from 20ºC to -60ºC. A symmetrical pattern is established in

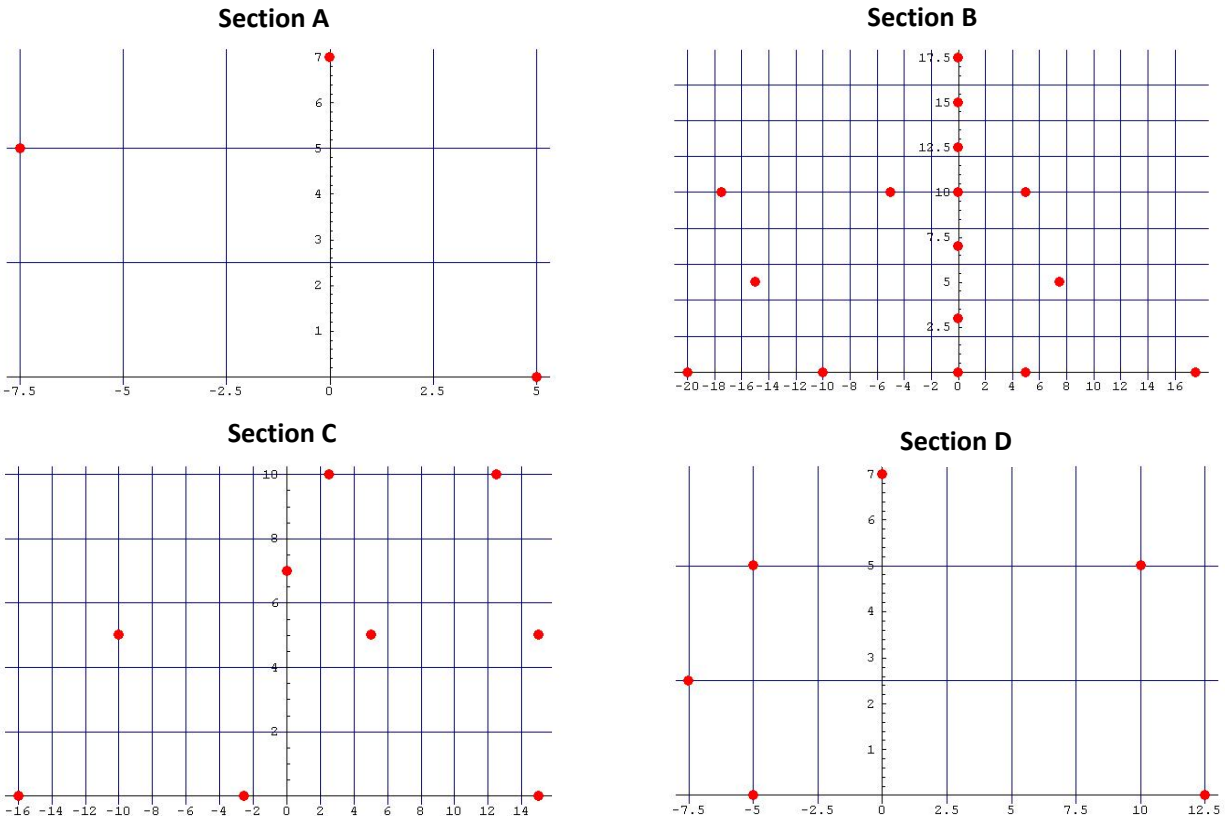

Figure 4. Thermocouple placement in the PCM (hereinafter cryo-probe placed at (0,0))

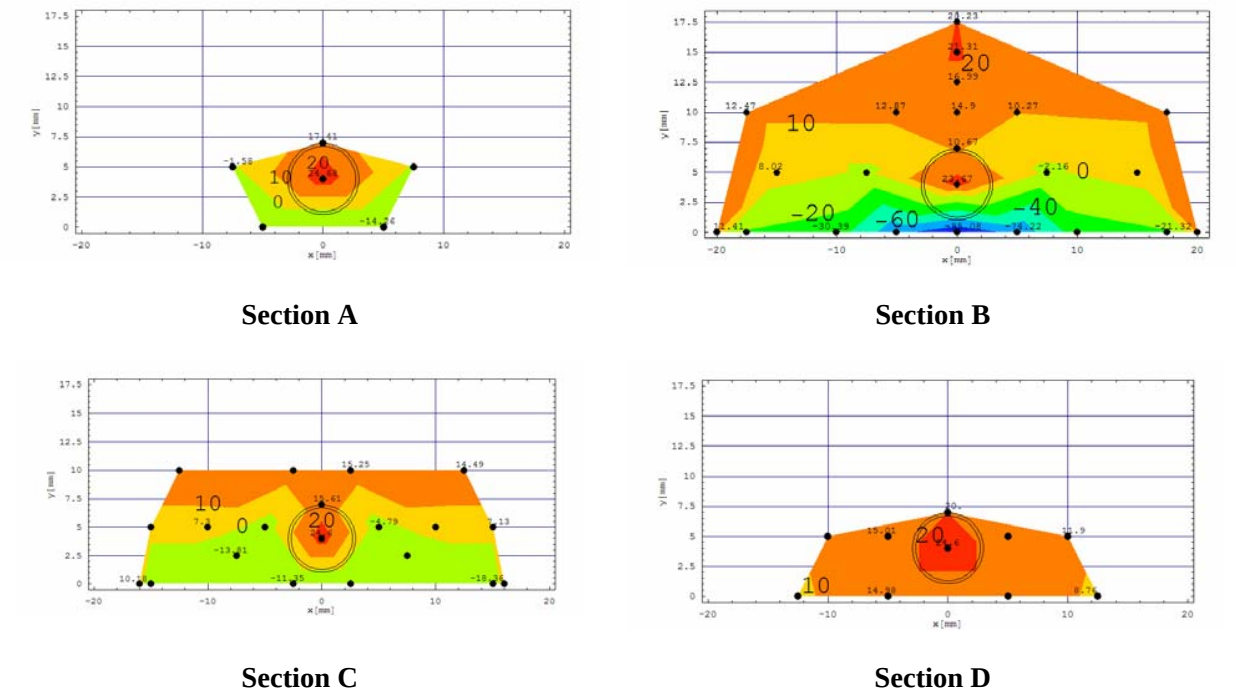

Figure 5. Effect of 200 ml/min flow rate in the tube on temperature distributions in the PCM at the various measuring sections. Cryo-probe temperature -95ºC after 1055 seconds

the PCM with the isothermal boundaries spreading sideways due to the heating effect of the embedded tube. No temperatures below freezing are observed above the tube (figures 4 to 7 are inverted with the cryo-probe assumed to be placed at (0,0), as per Figure 4). Temperature variations in the other sections are less pronounced with temperatures staying above -20ºC in Sections A and C. Temperatures below 0ºC were not detected in Section D located 17 mm from the cryo-probe centerline.

The effects of the various flow rates in the tube on temperature distributions in Section B of the PCM are shown in Figure 6. In the experiment without flow in the tube, the area that reached temperatures lower than -40°C (considered as “lethal” temperature in certain applications) was about 30% of the total frozen area at that Section. This area was smaller, at about 16 to 20% of the total frozen area, in the experiments with the various flow rates in the tube. At the lowest flow rate used, 30 ml/min, partial freezing was observed to occur inside the tube. As was to be expected, the experiment without flow in the tube differed significantly from the other experiments. In this experiment, the tendency of the frozen region to form a spherical-like ice ball was clearly seen (top left, Figure 6) and the stagnant water in the tube froze completely. Seen clearly in this figure are also the "suppression" and sideways spreading effects of the increased flow rates on the advancement of the freezing front into the PCM.

The effects of cryo-probe cooling rates on the temperature distributions in Section B in the PCM are shown in Figure 7. Three cooling rates were employed: -9.2, -6.6 and -4.4°C/min. In all cases the final cryo-probe temperature was -95ºC and the flow rate in the tube was 200 ml/min. This condition dictated different experimental times for the various cooling rates; the lower the rate the longer the application time. Due to this operational strategy, the largest frozen area was obtained

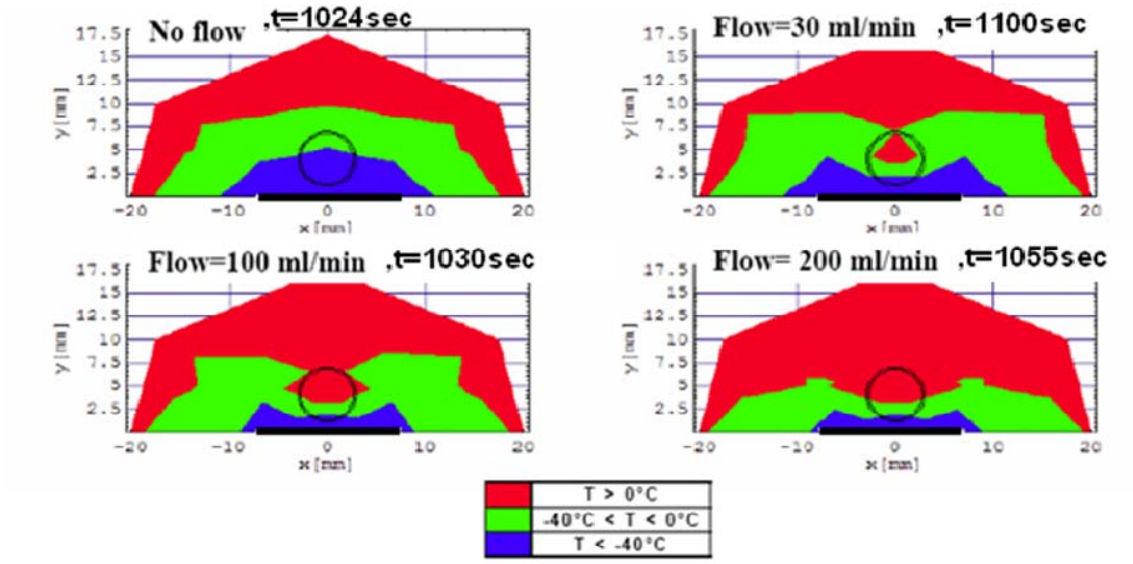

Figure 6. Effects of flow rates in the tube on temperature distributions in the PCM. Section B.

for the lowest cooling rate used which was operated for the longest time. Table 1 summarizes the total frozen areas, and the relative areas that reached the "lethal" -40ºC observed in Section B for all flow and cooling rates employed.

Finally, Figure 8 shows temperatures measured along the centerline of the embedded tube for the various flow rates. Connecting lines are drawn for illustration purposes and do not reflect actual variations. Data are shown after about 1000 seconds of operation when the temperature of the cryo-probe had reached -100ºC. It is seen that for both the case without flow in the tube, and the lowest flow rate used (30 ml/min), water temperatures fell below freezing in the tube. The higher flow rates used prevented this from occurring and, furthermore, resulted in essentially constant water temperatures in the tube.

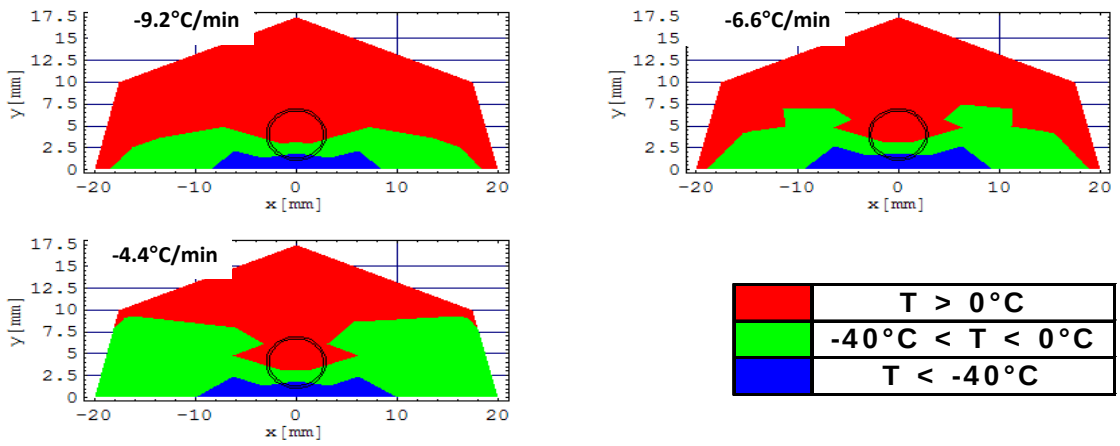

Figure 7. Effects of cryo-probe cooling rates on temperature distributions in the PCM. Section B.

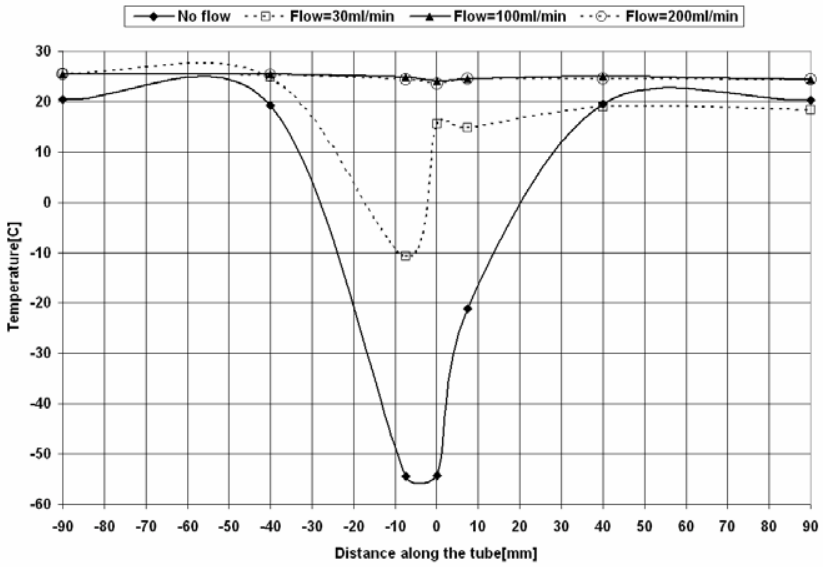

Figure 8. Temperature distributions along the centerline of the embedded tube for the various flow rates when the cryo-probe temperature reached -100ºC (after about 1000 seconds).

TABLE 1
Total frozen areas and areas below -40ºC in Section B for different flow and cooling rates.

	Total frozen area (mm^2)	*Frozen area below -40ºC (mm^2)*	*Percentage frozen area below -40ºC (%)*
Flow rate (ml/min)		Cooling rate = - 9ºC/min	
0	257	76	30
30	270	54	20
100	216	35	16
200	148	28	19
Cooling rate (ºC/min)		Flow rate = 200 ml/min	
-9.2	131	26	20
-6.6	175	33	19
-4.4	281	30	17

CONCLUSIONS

The effects of an embedded, warm-fluid carrying tube during freezing of a phase-changing medium (PCM) were studied experimentally. Freezing was performed by a surface cryo-probe operated by liquid Nitrogen. Two parameters were varied: (a) flow rate in the embedded tube, and, (b) cooling rate of the cryo-probe surface. In the first series of experiments cryo-probe cooling rate was maintained at -9ºC/min. As was to be expected, increasing the flow rate of the warm fluid in the tube, diminished the extent of the total frozen volume in the PCM. In the plane coinciding with the tube centerline, total frozen area decreased from about 257 mm^2 for no flow in the tube, to 148 mm^2 for

200 ml/min flowing in the tube, a 42% area reduction. Similar frozen area reduction proportions were obtained for the areas bounded by -40ºC which is considered to be the "lethal" temperature for cell destruction in certain cryo-surgical applications. The second series of experiments consisted of a constant flow rate of 200 ml/min in the tube. Cooling rates applied by the cryo-probe until the final cryo-probe temperature reached -95ºC, ranged from -4.4ºC/min to -9.2ºC/min. Under these conditions the largest frozen area in the above plane was obtained for the lowest cooling rate, which was operated for the longest time, at some 281 mm^2. The highest cooling rate produced only 131 mm^2 of frozen area, a 53% area reduction. Results for the areas bounded by the "lethal" temperature were significantly different with only a 13% area reduction for these two cooling rates. Results of this study quantify the effects of both these parameters which should be considered during the planning and application of cryo-surgical procedures.

ACKNOWLEDGEMENT

This study was supported in part by the James H. Belfer Chair in Mechanical Engineering, Technion, Israel Institute of Technology.

REFERENCES

1. Critser, J. K. and Mobraaten, L.E., Cryopreservation of Murine Spermatozoa. *ILAR J. Cryobiology of Embryos, Germ Cells, and Ovaries***,** Vol. 41, No. 4, pp. 197-206, 2000.

2. Gage, A., A. and Baust, J., Review: Mechanisms of Tissue Injury in Cryosurgery. *Cryobiology***,** Vol. 37, pp. 171-186, 1998.

3. Rybko, N., Experimental Simulation of a Thermally Significant Blood Vessel in a Tissue Undergoing Freezing, *M.Sc Thesis*, Technion, Israel Institute of Technology, Mech. Eng. Dept., Haifa, 2007.

4. Masslha, L. and Shitzer, A., Freezing by a Flat, Circular Surface Cryoprobe of a Tissue Phantom with an Embedded Cylindrical Heat Source Simulating a Blood Vessel. *ASME J. Biomech. Eng.*, Vol. 126, No. 6, pp. 736-744, 2004.

ELECTRICAL CLASSIFICATION OF SINGLE RED BLOOD CELL DEFORMABILITY IN HIGH SHEAR MICRO-CHANNEL FLOWS

Y. Katsumoto, K. Tatsumi*, T. Doi, K. Nakabe
Kyoto University, Kyoto, Japan

ABSTRACT. Measurement of human red blood cell (RBC) deformability in a micro-channel using electric micro-sensors is proposed and carried out in this study. The time series of the electric resistance is measured using an alternative current vs. voltage (I-V) method as the RBCs deformed by high shear flows individually pass between the electrodes. The resistance distributions vary in relation with the RBC shape, which depends on the cell deformability under the condition of a constant shear stress produced by the flow. Experiment is carried out with the samples of normal and glutaraldehyde treated (rigidized) RBC to evaluate the feasibility of the present method.

Keywords: *Micro-channel, Red blood cell, Deformability, Micro electric resistance sensor*

INTRODUCTION

Measurement of the deformability of a red blood cell (RBC) is an important issue in terms of not only investigating the hydrodynamic characteristics of the blood such as fluid viscosity and electric permeability[1], but also diagnosing initial symptoms of diseases in clinical investigation. For example, in *Plasmodium falciparum*, which is one of the most virulent diseases causing severe anaemia in number of tissues and organs[2], the deformability of the RBC is significantly reduced due to the increase of the internal viscosity and rigidization of the cytomembrane caused by having the plasmcytoskeleton of the RBC bounded with the neoantigens during the parasite, even in the early 'ring' stage[3]. Therefore, developing a technique which can evaluate the deformability of the RBC with low cost, short time and simplified procedure would provide a large contribution in the medical fields particularly in clinical testing[3,4].

There are several typical measuring schemes to evaluate the RBC deformability. The one using viscometer[5] evaluates the deformability of the bulk RBC solutions from the fluid viscosity. The one using a rheometer with coaxial rotating cylinder applies shear stress on the RBC and measures the deformability visually[6]. Measurement using optical tweezers[7] or micro-glass pipettes[8] stretches single RBC and evaluates the extension rate. However, the accuracy of the former two measuring schemes is low especially when the number density of infected RBC is small. This is not preferable for clinical test of diseases in the early stages. On the other hand, the latter two can evaluate the deformability of each single RBC whereas the available sampling number of RBC is limited.

The motivation of the present study is to develop a micro sensor which can measure the deformability of a single RBC using hydrodynamic stresses and electrical sensors applied in a micro-channel. Recently, Korin et al.[9] visualized the behaviour of RBCs in a micro-channel and measured the cell deformation by analysing the images of the cells stretched by the high shear flow. The usage of the micro-channel has the advantage in reducing the cost, measuring time, and sample volumes. Their method, however, requires high spatial resolution image recording equipment, which may increase the cost and impair the compactness of the application. In contrast, the sensor proposed in the present study is based on an electrical measurement to evaluate the RBC deformation. Namely, micro platinum membrane electrodes are attached to the channel bottom wall

* Corresponding author: Dr. K. Tatsumi
Phone: + (81)-75-7535209, Fax: + (81)-75-7535209
E-mail address: tatsumi@mbox.kudpc.kyoto-u.ac.jp

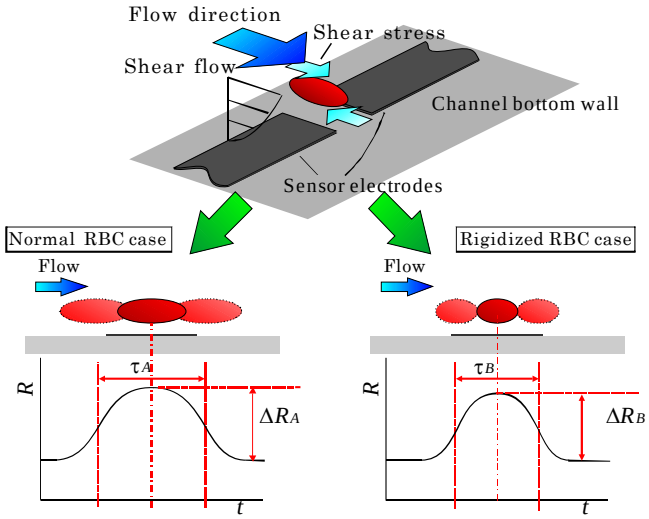

Figure 1. Concept of the measuring method of RBC deformability.

of the sensor, and the time-sequential signals of electric resistance are measured as the RBC crosses the electrodes. Compared with the aforementioned optical measurements, the present method can decrease the size and cost of the device markedly. A higher affinity to the existing RBC counting equipments is also another advantage. In this paper, experiment is carried out to evaluate the feasibility of the sensor proposed in this study. Micro-channel with the micro membrane electrodes is fabricated, and the electric resistances of the RBC crossing the electrodes are measured and analysed using the samples of normal human RBC and glutaraldehyde-treated rigidized RBC.

MEASUREMENT PHYSICS

The electric conductivity of the RBC cytomembrane is approximately 1×10^{-6}S/m, which is small enough to be considered as an insulating material compared with the cytoplasm and normal saline solution. When a low frequency AC electric field is applied around the RBC suspended in a solution, the current is interfered mainly by the cytomembrane. In this case, the cell shape also affects the distribution of the current density, in other words, the electric resistance monitored between the electrodes changes depending on the cell shape.

Figure 1 shows the schematic of the measuring method proposed in this study. A pair of platinum membrane electrodes is attached to the bottom wall of a micro-channel, and the time-sequential signals of the electric resistance between the electrodes are measured. When RBCs are suspended in the micro-channel flow, the resistance between the electrodes increases significantly as the RBC passes between them due to its high electric insulating property. While the RBCs flow in the channel, they are stretched and deformed attributed to the high shear stress provided by the steep velocity gradient of the flow. The profile of the measured resistance is affected not only by the fluid properties but also by the size, position and shape of the RBC. If the position of the RBC passing between the electrodes can be precisely controlled, then the shape of the RBC, which also represents the deformability of the RBC, can be evaluated by analysing the resistance signals.

When an electric field is, thus, applied to the RBC by using the sensor shown in Fig. 1, the parallel circuit between the electrodes consists of cytoplasm, cytomembrane, solvent, and the electric double layer formed at the electrode surface as shown in Fig. 2(a). This circuit can also be simplified as parallel components of variable resistance and capacitance connected in series with the component of the electric double layer, presenting the change in the electric characteristics as the RBC passes between the electrodes.

As one can see, the accuracy of the measurement largely relies on how large the difference between the resistances of the buffer solution and the RBC membrane is. If a solution of high ionic concentration, such as isotonic sodium chloride solution, is used, however, the effect of the electric double layer cannot be neglected. This problem can be solved by applying a high frequency AC electric field to the electrodes and reducing the capacitance of the electric double layer. In contrast,

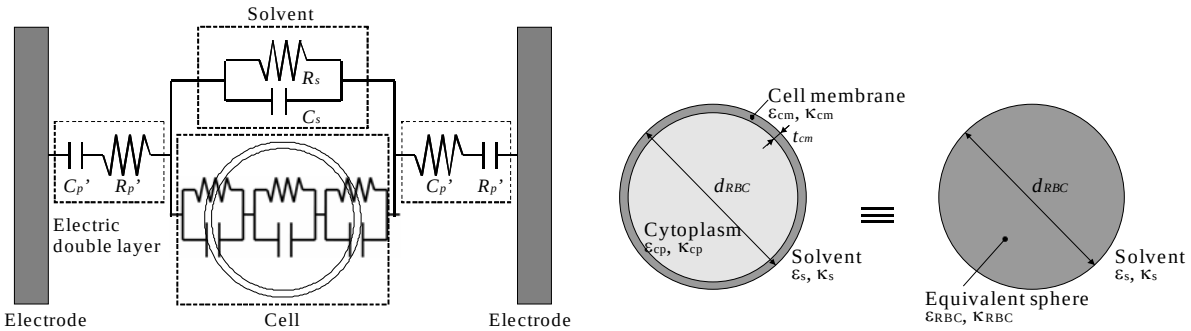

(a) Equivalent circuit (b) Cell model

Figure 2. (a) Equivalent circuit model of the sensor with an RBC suspended in a solvent, (b) Cell model simplified as a sphere in the numerical simulation.

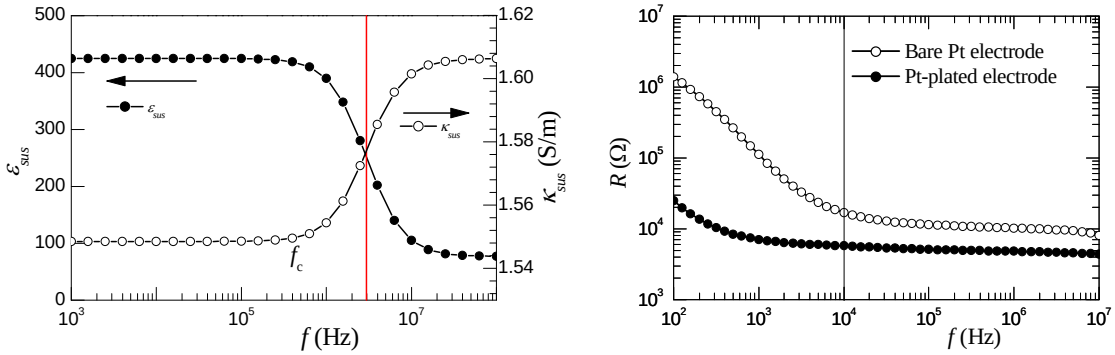

(a) Effects of f on ε and κ (sim.) (b) Effects of f on R (exp.)

Figure 3. AC frequency effects on (a) permittivity ε and conductivity κ of RBCs suspended in PBS (simulation), and (b) the resistance of the PBS without RBC (experiment).

since the cell membrane has electrically insulation properties, an increase in the frequency of the electric field can incur a decrease of the cell resistance. Therefore, there is a trade-off problem in determining the frequency range to be applied on the electrodes.

The maximum limit of the frequency is obtained from the numerical simulation calculating the impedance characteristic of RBCs suspended in the solution using the model proposed by Katsumoto et al.[10]. This model treats the RBC as a 6μm diameter sphere shown in Fig. 2(b) having the frequency-dependent complex permittivity derived form from the Maxwell-Wagner equation.

Figure 3(a) depicts the results of the computation showing the effects of the frequency, f, on ε and κ, respectively. κ increases with f in the area above several MHz in the figure showing the relaxation behaviour of the solution. This indicates that the cytomembrane acts as an insulator when the frequency is low, while the cytoplasm is directly measured when the frequency is high. As mentioned above, the present sensor shows a higher performance with larger difference in the solution and RBC. Therefore frequency of several tens of kHz is suitable for the sensors. The lower limit of the frequency to be applied will be discussed shortly.

EXPERIMENTAL SETUP

Figure 4 and Table 1 show the schematic and dimensions of the channel and sensor electrodes used in this study, respectively. The channel width is 1mm and is much larger than the channel heights H_1 and H_2. Therefore, the channel flow can be considered as two-dimensional flow, and the RBC is deformed receiving the shear stress in the streamwise direction.

The channel has three inlets, and RBCs suspended in phosphate buffer saline (PBS: Amresco) solution are supplied from the center inlet while PBS solution only is supplied from the side ones. Due to the low Reynolds number of the flow in the micro-channel, the flow is in laminar regime and the molecular diffusion of the flow supplied from the center inlet becomes small. Therefore, by

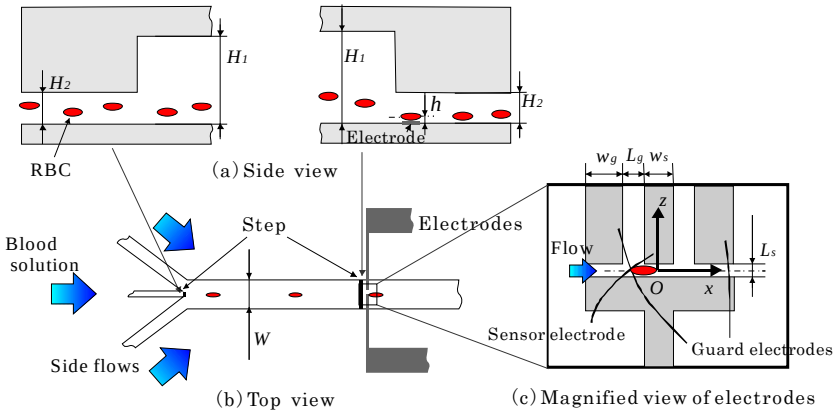

Figure 4. Schematic of the micro-channel and sensor electrodes.

Table 1. Parameters of the micro-channel and electrodes (μm).

W	H_1	H_2	L_s	L_g	w_s	w_g
1000	52	10	5.2	2.3	14.8	14.6

changing the flow rate of each side flow, the spanwise position of the RBC passage can be controlled to pass the center of the electrodes. These fluids are supplied by syringe pumps (Nihon Kohden: CFV-3200, Harvard Apparatus: econoflo) with flow rates of 0.01 and 1.0μl/min.

When the RBC is placed in the channel shear flow, the RBC receives a lift force attributed to the so-called Fåhraeus effect[11]. This lift force moves the RBC away from the channel wall on which the sensor electrodes are embedded. Apparently, this leads to a decrease of the measuring resistance and the sensor S/N ratio. To tackle this problem, the channel heights at the center inlet and at the electrodes are smaller than the other parts of the channel, i.e. backward-facing and forward-facing steps are installed in the downstream of the center inlet and immediately upstream of the electrodes, respectively. The RBC is, thus, supplied from the inlet in a lower position, and the downwash flow at the forward-facing step carries the RBC toward the bottom wall. This spanwise and downward positioning of the RBC passage can control the relative distance between the RBC and electrodes.

The micro-channel illustrated in Fig. 4 is made of poly-dimethylsiloxane (PDMS) and is fabricated by using SU-8 (MicroChem) as a casting mold. To fabricate the SU-8 mold, an optical mask, on which the channel pattern is printed, is prepared first. Then, SU-8 layer spincoated on a slide glass is exposed to the UV light through the mask. After the post baking and etching processes, an SU-8 mold is obtained. PDMS in liquid phase is then poured over the SU-8 mold, and is rigidized and ripped off. The PDMS channel is then attached to a slide glass, on which the platinum membrane patterns of electrodes are formed. These electrodes are fabricated through a sputtering and lift-off processes using a sputtering equipment (ULVAC KIKO: SCOTT-C3) and ZPN (ZEON) resist.

The electrodes are serially connected to the shunt resistance for detection. Sinusoidal wave of AC voltage is applied to these resistances under the condition of 10kHz using a function generator (NF: WF-1973). By measuring the phases of the shunt resistance and applied voltages, the resistance measurement accuracy is enhanced.

As shown in Fig. 4, guard electrodes are placed on both sides of the sensor electrode (the one used for detection). Voltage is charged to these guard electrodes through an FET input Op-amp possessing the same electric potential with the sensor electrode. The electric fluxes from the guard electrodes will suppress the fringe effect of the fluxes from the sensor electrode. This leads to a narrow distribution of the current density in the streamwise direction and enhances the sensitivity.

To evaluate the impedance characteristic of the electrodes, the electric resistance between the electrodes embedded in the channel filled with PBS solution is first measured by using an impedance analyser (Agilent: 4294A). Figure 3(b) shows how the frequency of the applied AC voltage, f , affects the resistance, R. The open and solid circles in the figure present the results using platinum bare electrodes and platinum black plated ones, respectively. The Pt-plated electrodes represent those with Pt nano particles attached on the surface using the following plating process.

Namely, first filling the channel with a solution of hexachloroplatinic (H_2PtCl_6) 30mg/mL and lead acetate $(CH_3COO)_2Pb$ 0.3mg/mL, and then applying 2V DC voltage between the electrodes.

As shown in Fig. 2(a), when f is not sufficiently high, an electrical double layer is formed at the electrode surfaces, which leads to a reduction in the resistance measurement performance. This can be observed in Fig. 3(b), where the resistance R plotted with the open circles decreases as f increases and then becomes constant. As mentioned above, 10kHz AC electric field is applied in this study. This is, however, not large enough to suppress the appearance of the electric double layer as can be found in Fig. 3(b), i.e. R measured under the condition of f = 10kHz is larger than the values in higher frequency region. To tackle this problem, the aforementioned Pt-black plating is conducted on the electrode surface in this study. A layer of Pt nano-particles will be formed on the surface as a porous media, and the surface area is increased by this structure resulting in the reduction of the electric double layer effect. In this case, the frequency range from which R begins to increase is shifted toward the lower f side and R is small and uniform under the condition of f = 10kHz compared with the case of bared electrodes. It should be noted that the reason why the resistance in the plated case are lower than those of the bare electrodes is attributed to the fact that the plate is formed uniformly on the surface and the distance between the electrodes is decreased.

Along with the above electric measurements, optical measurement is carried out using a microscope (Olympus: IX-71) and halogen lamp as the light source for the purpose of verifying the position and shape of the RBC when passing between the electrodes. An objective lens (Olympus: LMPLFLN100X, ×100 magnification and NA = 0.8) and a high speed camera (Vision Research: Phantom V7.3) are used to record the images. The frame rate of the camera is 1000 frames/s and the CCD resolution is 800×650 pixels. The optical resolution of the image is 0.21μm/pixel. The focusing depth of the image Δz is 1.669μm calculated from the following equation:

$$\Delta z = \frac{\lambda_0 n}{NA^2} + \frac{n}{MNA} e \tag{1}$$

e and M are the smallest distance that can be resolved by the detector, and lateral magnification, respectively. λ_0 and n are the wave length of light in air and refraction index.

Korin et al. [13] reported that shear stress required to deform an RBC with a deformation index DI=0.5 in a micro-channel is approximately 15Pa. Here, DI is defined as $DI = (a-b)/(a+b)$, where a and b are the long and short axes of the RBC, respectively. When water is used as the working fluid, it is not suitable to obtain this value of shear stress by increasing the flow rate because of the time resolution of the measurement using the high-speed camera and electric sensors. Polyvinylpyrrolidone (PVP: MW 3.6×10^5, Nacalai tesque) is, therefore, mixed with the working fluid to increase the viscosity, by which sufficient shear stress is achieved to deform the RBC.

RBC treatment is carried out by the following procedure. 10μl sample blood is collected from a healthy human volunteer. The blood is first suspended in 1ml PBS, and then centrifuged during 10min with 1000G to separate the RBC from other substances, i.e. plasma, plaque and leucocytes. Supernatant solution is removed, and 0.1ml PBS is added to the collected RBC. 0.4ml PBS with 10wt% PVP is added to the solution, and RBC suspended solution of PBS with 8wt% PVP is prepared and used as the normal RBC suspended working fluid.

Rigidized RBCs are prepared by treating the cells with glutaraldehyde. Glutaraldehyde (Nakalai tesque: 25% solution) is first diluted with PBS by 0.025wt%. The RBC separated from other substances in the same way shown above is then added to this solution and settled for 30min under room temperature. The solution is, then, centrifuged during 10min with 1000G. After removing the supernatant solution, 1ml PBS is added. Once again the solution is centrifuged and the supernatant solution is removed. Finally, 0.1ml PBS and 0.4ml PBS with 10wt% PVP are respectively added to the solution, and, thus, PBS solution of 8wt% PVP with rigidized RBC is prepared.

EXPERIMENTAL RESULTS

Figures 5(a) and (b) show the snapshots presenting the behaviour of the normal and rigidized RBCs passing between the electrodes, respectively. The flow direction is from the left to the right, and the

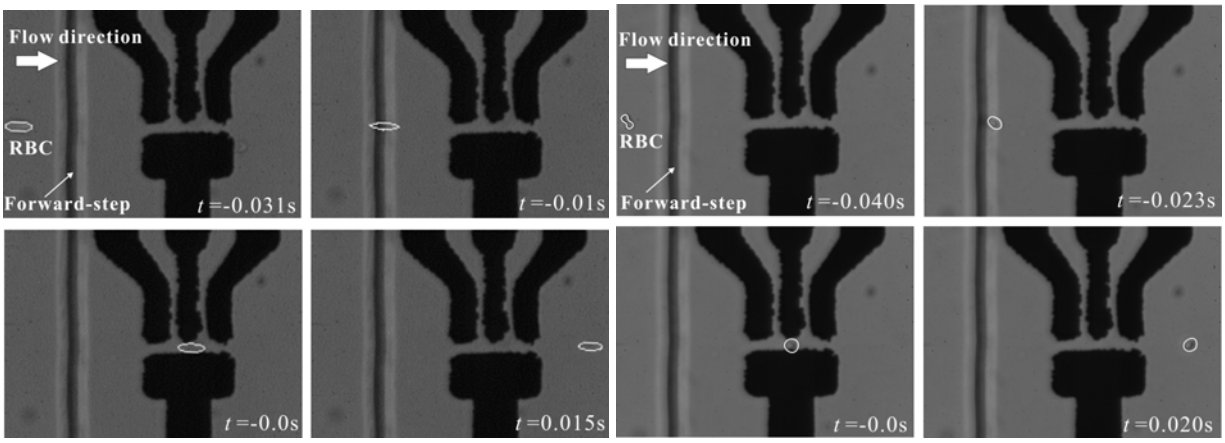

(a) Normal RBC case (b) Rigidized RBC case

Figure 5. Snapshots of RBCs passing between the electrodes.

Table 2. Averaged value of the major and minor axes of the RBC and deformation index, *DI*.

	Normal RBC	Rigidized RBC
a [μm]	14.54	7.37
b [μm]	4.65	7.35
DI	0.52	0.00

arrow indicates the location of the forward-facing step. Although not shown here, the height of the RBC passage, *h*, was obtained visually by measuring the distance between the points focused on the RBC and bottom wall. *h* was nearly constant for all RBC measured as h=5μm. It should be noted that the degree of the error in *h* is approximately equal to the aforementioned focusing depth Δz.

In the figure, the RBC is deformed and stretched in the streamwise direction owing to the two-dimensional shear flow in the channel. In Fig. 5(a), the RBC deforms most when passing the forward-step. This is due to downward flow generated at the step by which not only the shear stress is increased, but also the RBC is carried to the area of larger shear stress located close to the bottom wall. The deformation rate gradually decreases as the RBC flows to the downstream. This can be attributed to the Fåhraeus effect[11], namely, a lift force works on the RBC and the RBC moves toward the channel center resulting in a reduction of the shear stress.

In contrast with the normal RBC case, the rigidized RBC shown in Fig. 5(b) maintains a biconcave surface and no deformation of the cell is observed. The RBC rotates as it flows, which is a motion so called 'flipping'. When a normal RBC is suspended in a shear flow, the cytomembrane not only deforms but also rotates together with the cytoplasm. This is called 'tank treading motion' of the cell, which prevents the cell to flip[12]. Since the shape of the cytomembrane in the rigidized RBC case is fixed, the tank treading motion cannot be generated and the flipping motion takes place.

Table 2 shows the averaged value of the long and short axes of the RBC, *a* and *b*, and the deformation index, *DI* , obtained from the visualization results. As mentioned above, rigidized RBCs show no deformation and have a circle projection shape. Therefore *a* and *b* are identical in this case. On the other hand, since the normal RBC is deformed, *a* is almost three times larger than *b*. *DI* is approximately 0.5 in the normal RBC case.

Figure 6 shows the distributions of ΔR_{max} and δ of the normal and rigidized RBCs. ΔR_{max} and δ are the maximum value and half bandwidth of the resistance peak distributions obtained when each RBC passes the electrodes, respectively. During the experiment, variation in the RBC spanwise position when passing the electrodes is observed. This is attributed to the width of the center inlet of the channel, which is 50μm and is much larger than the gap between the electrodes, L_g =5μm . To discuss this effect, the spanwise position of the cell, y_{RBC}, is taken as the abscissa in the figure. The lines in the figure present the results obtained by using the least-square method (L.S.M.) in each RBC case.

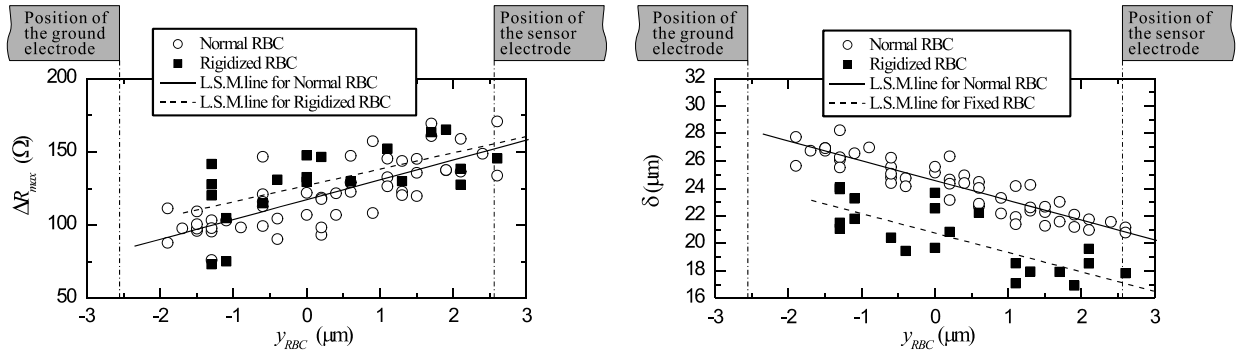

(a) Relation between ΔR_{max} and y_{RBC} (b) Relation between δ and y_{RBC}

Figure 6. Distributions of peak resistance ΔR_{max} and half bandwidth δ against spanwise location of RBC, y_{RBC}.

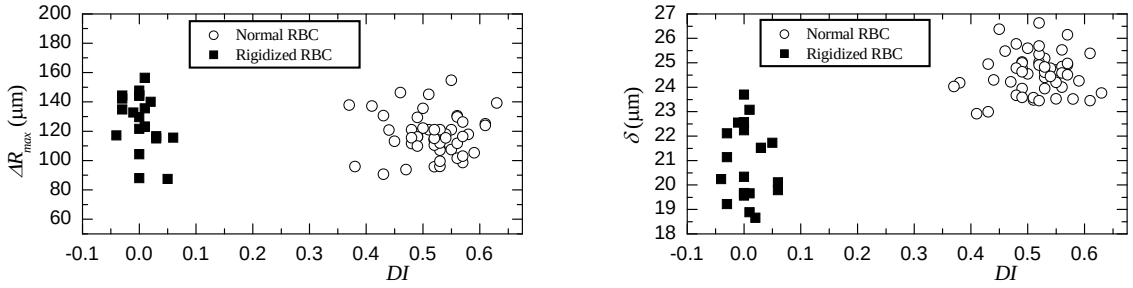

(a) Relation between ΔR_{max} and *DI* (b) Relation between δ and *DI*

Figure 7. Distributions of modified ΔR_{max} and δ against deformation index *DI*.

In Fig. 6 (a), ΔR_{max} decreases as the RBC position y_{RBC} is closer to the ground electrode. On the other hand, δ increases as y_{RBC} decreases as shown in Fig. 6(b). This can be attributed to the following reason: As seen in Figs. 4 and 5, the sensor side consists of three electrodes, the sensor and guard electrodes, while the ground side has a single electrode. The effect of the guard electrodes reducing the fringe components of the electric flux deteriorates in the ground side. Namely, the current density distribution becomes wide and the value decreases in the position close to the ground electrode. The amount of electric flux blocked by the RBC, therefore, decreases, which leads to a decrease in the resistance particularly the maximum value, ΔR_{max}. On the other hand, since the current density distribution is wider at the location close to the ground electrode, δ increases.

As shown in Fig. 6, y_{RBC} appears to affect ΔR_{max} and δ linearly. Therefore, the linear component using the L.S.M. line in the figure is subtracted from each value, and is shown in Fig. 7 in relation with *DI*. Since only two kinds of RBCs, normal and glutaraldehyde-treated ones, are measured in the experiment, two large groups are found in the area close to *DI* = 0.0 and 0.5.

To evaluate the variation of the samples in each RBC case, coefficient of variance, $Cv=\sigma/m\times100$, is shown in Table 3. σ and m are the standard deviation and arithmetic average of the distributions, respectively.

In Fig. 7(a), ΔR_{max} of both RBCs show similar values and overlap with each other. Furthermore, *Cv* of ΔR_{max} shown in Table 3 is relatively large in both RBC cases, indicating that the variation of the samples is large.

On the other hand, a difference in the groups of δ for the normal and rigidized RBCs is recognizable in Fig. 7(b) indicating the fact that there is a correlation between δ and *DI*. Furthermore, *Cv* shown in Table 3 is small compared with those of ΔR_{max} . These results point out that the half bandwidth δ is more reasonable as an index to evaluate the shape, i.e. deformability of the RBC, than ΔR_{max}.

The reason why δ shows a better characteristic than ΔR_{max} is due to current density distribution between the electrodes. ΔR can be more sensitive with the RBC height position *h*. Therefore, even when the RBC height position is controlled by the step flow, small variation in *h* can vary ΔR_{max}

Table 3. Coefficient of variance for ΔR_{max} and δ

	ΔR_{max}		δ	
	Normal RBC	Rigidized RBC	Normal RBC	Rigidized RBC
Cv (%)	12.1	15.4	3.42	7.39

largely enough to make the difference of the RBC shape ambiguous. δ, however, depends more on the current density distribution in the streamwise direction, which is less affected by other parameters.

CONCLUSIONS

A micro sensor consisted of micro-channel and electric sensors, which can measure the deformability of a single RBC was proposed and evaluated in this study. The sensor was fabricated and its feasibility was examined using normal and rigidized human red blood cells. The major results are stated as follows:

1. The frequency of the sensor AC voltage was determined numerically and experimentally. Together with the Pt-black plated on the electrodes, frequency specification of 10kHz reduced the influences of the electric double layer formed on the electrodes and dielectric relaxation appearing around the cell membrane, which led to the increase of the sensor sensitivity.
2. The backward- and forward facing steps, and the side flows applied in the micro-channel were effective to control the height and spanwise positions of the RBC in order to closely pass the area between the sensor electrodes.
3. A good correlation was observed between the half bandwidth of the time-sequential signals of the resistance and the deformation index. In contrast, the correlation between the peak value of the resistance and deformation index was considerably small. This characteristic was strongly attributed to the current density distribution formed between the electrodes. Consequently, the feasibility of the present sensor was verified from the results.

ACKNOWLEDGEMENT

This study was financially supported by The Japanese Ministry of Education, Culture, Sports, Science.

REFERENCES

1. Sugihara-Seki, M. and Fu, B. M., Blood Flow and Permeability in Microvessels, *Fluid Dynamics Research*, Vol. 37, pp. 82-132, 2005.
2. Miller, L. H., Baruch, D. I., Marsh, K. and Doumbo, O. K., The Pathogenic Basis of Malaria, *Nature*, Vol. 415, pp. 673-679, 2002.
3. Dondorp, A. M., Kager, P. A., Vreeken, J. and White, N. J., Abnormal Blood Flow and Red Blood Cell Deformability in Severe Malaria, Parasitology Today, Vol. 16, pp. 228-232, 2000.
4. Lim, C. T., Zhou, E. H. and Quek, S. T., Mechanical Models for Living Cells – a Review, *J. Biomechanics*, Vol. 39, pp. 195-216, 2006.
5. Chien, S., Biophysical behavior of Red Cells in Suspension, *In the Red Blood Cell* (*Ed. Surgenor, D. M.*), Vol. 2 (1975), Academic Press, New York, pp. 1031-1133, 1975.
6. Dobbe, J. G. G., Streekstra, G. J., Hardeman, M. R., Ince, C. and Grimbergen, C. A., Measurement of the Distribution of Red Blood Cell Deformability Using an Automated Rheoscope, *Cytometry*, Vol. 50, pp. 313-325, 2002.
7. Hénon, S., Lenormand, G., Richert, A. and Gallet, F., A New Determination of the Shear Modulus of the Human Erythrocyte Membrane Using Optical Tweezers, *Biophysical J.*, Vol. 76, pp. 1145-1151, 1999.
8. Mohandas, N. and Evans, E., Mechanical Properties of the Red Blood Cell Membrane in Relation to Molecular Structure and Genetic Defects, *Annual Reviews*, Vol. 23, pp. 787-818, 1994.
9. Korin, N., Bransky, A. and Dinnar, U., Theoretical Model and Experimental Study of Red Blood Cell (RBC) Deformation in Microchannels, *J. Biomechanics*, Vol. 40, pp. 2088-2095, 2007.
10. Katsumoto, Y., Hayashi, Y., Oshige, I., Omori, S., Kishii, N., Yasuda, A. and Asami, K., Dielectric sytometry with THree-dimensional Cellular Modelling, *Biophysical J.*, Vol. 95, pp. 3043-3047, 2008.
11. Goldsmith, H. L., Cokelet, G. R. and Gaehtgens, P., Robin Fåhraeus: Evolution of His Concepts in Cardiovascular Physiology, *American J. Physiological Society*, Vol. 257, pp. 1005-1015, 1989.
12. Olla, P., The Lift on a Tank-Treading Ellipsoidal Cell in a Shear Flow, *J. Physics 2 France*, Vol. 7, pp. 1533-1540, 1997.

IN VIVO MEASUREMENT OF BLOOD FLOW IN MICRO-CIRCULATION SYSTEMS OF A CHICKEN EMBRYO

S. J. Lee[1, *], J. Y. Lee[1]
[1]Center for Biofluid and Biomimic Research, Dept. of Mechanical Eng., Pohang, Republic of Korea.

ABSTRACT. The micro-circulation system of a living biological creature plays an important role in maintaining the metabolism and transport nutrients and wastes. In addition, the hemodynamic characteristics of blood flow such as wall shear stress and flow rate are important factors that affect angiogenetic process and control the vasomotion and dilatation of the vessel adaptively. These governing factors of blood flows in the micro-circulation system are crucial in the development of the cardiovascular system as well as for the proper functioning of an organism, especially when the blood flow is related to circulatory vascular diseases. Moreover, the structural characteristics of blood vessels (Murray's law and bifurcation pattern) are significantly influenced by the hemodynamic characteristics. Therefore, it is important to measure the blood flow *in vivo* and determine its relation to the structural rules of the vessel. In this study, we measured the blood flow in the extraembryonic arterial blood vessels of chicken embryos and investigated the hemodynamic characteristics and the structural rules of the vessels along the bifurcation cascade. Velocity field information of the blood flow was measured using a micro-PIV technique and the temporal characteristics were obtained using a high-speed CMOS camera. The mean velocity in the arterial blood vessels decreased and Womersley number (α) calculated based on the pulsating frequency and diameter of the vessel also decreased, as the bifurcation cascaded. The ratio of Murray's law was very close to the theoretical value of 1 when the vessel diameter was small (50 μm ≤ D_0 ≤ 100 μm). However, the value deviates from 1 as D_0 increases. The bifurcation angles are wider when the D_0 is smaller and becomes narrower as D_0 increased.

Keywords: *In vivo measurement, Blood flow, Arterial bifurcation, Micro-circulation, Constructal Rule*

INTRODUCTION

Arteries are important in the cardiovascular system and easily adapt to varying flow and pressure conditions by enlarging or shrinking to meet hemodynamic demands. Blood flow in arterial blood vessels is basically an unsteady pulsatile flow, with flow characteristics becoming more complicated due to the non-Newtonian properties of blood [1-3]. In addition, the hemodynamic characteristics of blood flow change significantly in the arterial bifurcation cascade, and these changes play a major role in the pathology of atherosclerosis [4].

Over the past 80 years, several studies have been conducted to test Murray's law [5,6] as well as different minimum principles. Nonetheless, only a few have focused on the bifurcation angle as a geometrical governing factor. The bifurcation angle of the vascular system is an important geometric factor that affects hemodynamic properties, flow conditions and other transport

* Corresponding author: Prof. S. J. Lee
Phone: + (82)-54-2792169, Fax: + (82)-54-2793199
E-mail address: sjlee@postech.ac.kr

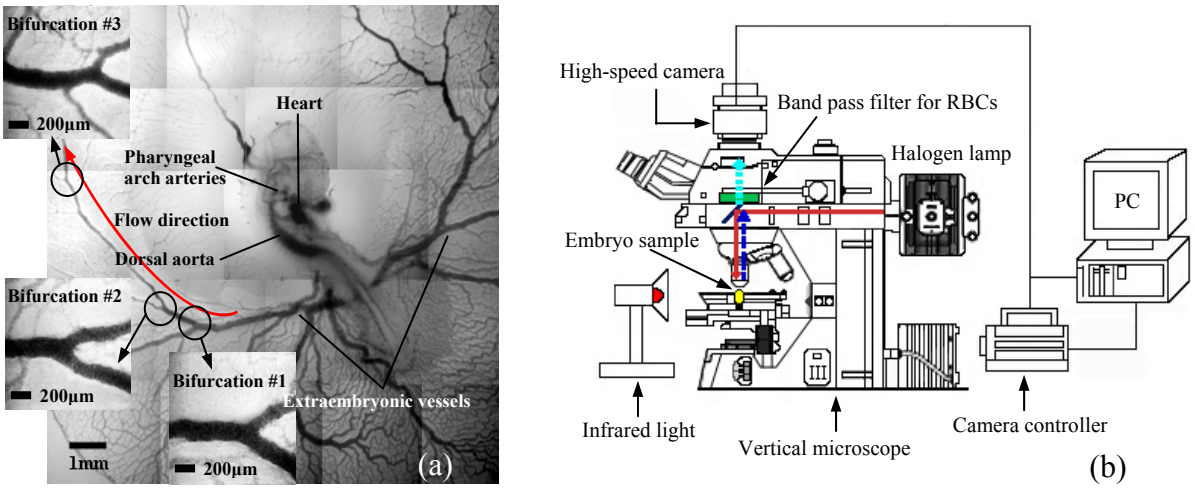

Figure 1. (a) Chicken embryo after approximately 72 hours of incubation, (b) schematic diagram of a micro-PIV system used for *in vivo* measurement of arterial pulsatile blood flow

phenomena in blood flows [7]. In addition, their effects on blood flow are believed to play a major role on developmental growth, angiogenesis, and vascular networking.

We therefore have used the micro-PIV technique to measure quantitative velocity fields of pulsatile blood flow in the extraembryonic arterial blood vessels of Hamburger and Hamilton [8] (HH)-stage 18 chicken embryos with high spatial and temporal resolutions, especially in the arterial bifurcation cascade. We have analyzed the complex pulsatile flow phenomena in the arterial bifurcation cascade. In order to understand the cardiovascular circulation system in detail, it is necessary to investigate the design rules related to the bifurcation angle and its relationship to the diameter of blood vessels. For this reason, we measured not only the diameters of blood vessels to test Murray's law, but also the angles of the arterial bifurcations. The bifurcation angle (θ) was analyzed according to the diameter of the parent vessel (D_0) and the diameter ratio of the daughter branches (D_2/D_1). The bifurcation angle was used to compare the measured diameter of the vessel with the theoretically optimal diameter estimated from the principle of minimum work.

METHODS AND MATERIALS

Chicken Embryos

Chicken embryos were obtained at early stages of development, within the first 3 days of incubation. Since these embryos are very sensitive to variations in temperature, humidity and environmental conditions, all experiments were performed in a room maintained at constant temperature and humidity, and infrared light was applied to maintain each embryo at a constant temperature of 37ºC. To prevent desiccation of the embryos, the vitelline surface region of each, containing the extraembryonic blood vessels, was covered with a thin film of sterile-filtered mineral oil [9]. Fig. 1(a) shows a typical chicken embryo after 72 hours of incubation; each sectional image was taken with a 4× objective lens. Although the embryo and the extraembryonic blood vessels were small, the components of the circulatory system, including the chambered heart, arterial vessels and venous vessels, could be visualized clearly on the vitelline surface. Blood flow inside the extraembryonic blood vessels of a chicken embryo at an early developing stage can be visualized clearly by optical methods *in vivo* and the whole velocity fields of the unsteady pulsatile blood flow in extraembryonic arteries can be measured non-invasively using the temporally-

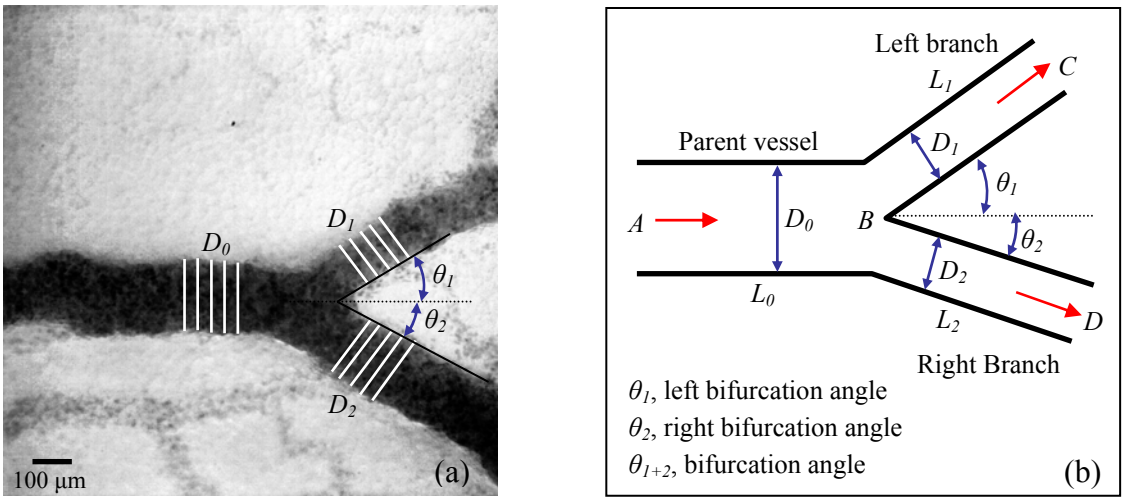

Figure 2. A typical microscopic image of extraembryonic arterial bifurcation (a) and geometric parameters of the branching pattern of vessel (b)

resolved *in vivo* micro-PIV system (Fig. 1(b)). The main target of this study, the arterial bifurcation cascade, is also shown in Fig. 1(a) along the main lumen.

Measurement Technique and Experimental Set-up

Fig. 1(b) shows a schematic diagram of the micro-PIV system used in this study. The *in vivo* micro-PIV system used in this study consists of a vertical microscope (*Nikon Eclipse 80i*), a high-speed CMOS camera (*PCO 1200hs*), a halogen lamp and a PC for data processing and control. RBCs inside blood vessels were used directly as tracer particles, making the injection of chemical tracers unnecessary.

To analyze the unsteady pulsatile flow, blood flow images of red blood cells (RBCs) were captured using a high-speed CMOS camera at 250 fps (frames per second) to achieve sufficiently high temporal resolution with a spatial resolution of 14.6 μm × 14.6 μm. To obtain an instantaneous velocity field from two consecutive flow images, the fast Fourier transform (FFT) based cross-correlation PIV algorithm was applied. The size of the interrogation window was 24 × 24 pixels, with a 50% overlap. The spacing between two adjacent vectors was 12 pixels, corresponding to about 14.6 μm. In this experimental condition, we were able to measure the dimensions very precisely because 1 image pixel captured by the CMOS camera corresponded to 1.219 μm. Figs. 2(a) and (b) show a typical microscopic image of the arterial bifurcation and the schematic diagram for geometric parameters of the branching pattern, respectively. The dimensions were measured at five different locations near the bifurcation in each blood vessel to smooth out the nonuniformities as did by Taber et al. [10]. In order to avoid undesirable effects such as shrinkage and deformation of blood vessels accompanied by desiccation, the vitelline surface was covered with a thin film of sterile-filtered mineral oil because the configuration and dimension of the blood vessels are the most important factors in this experiment. In addition, the lower part of the egg was submerged in a constant-temperature bath to maintain the temperature within the range of 37-38ºC, the same temperature range as in the egg incubator.

RESULTS AND DISCUSSION

Fig. 3 shows the time-averaged mean velocity vector fields and vorticity contours at each bifurcation. The vorticity (ω_z) was calculated from velocity field data using the secondary data

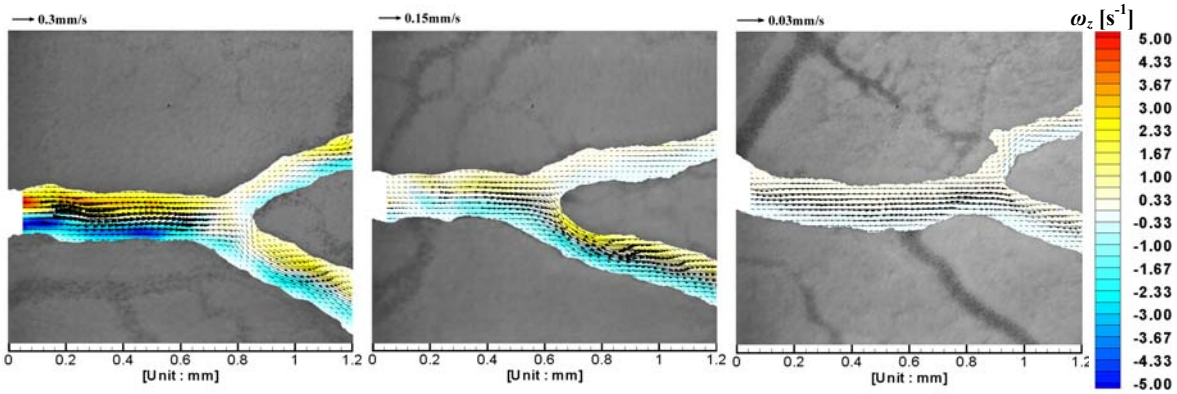

(a) Bifurcation #1 (b) Bifurcation #2 (c) Bifurcation #3

Figure 3. Mean velocity fields and vorticity contours at arterial bifurcations

Table 1
Global average of bifurcation parameters

Bifurcation parameter	Global dimension
Ratio of Murray's law α (= $D_0^3/(D_1^3+D_2^3)$)	1.053 ± 0.188
D_2/D_1	1.001 ± 0.349
Left bifurcation angle θ_1 (degree)	37.434 ± 23.689
Right bifurcation angle θ_2 (degree)	39.726 ± 22.506
Bifurcation angle θ_{1+2} (degree)	77.161 ± 26.171

reduction procedure. Although the blood vessels were bifurcated and the instantaneous flow showed noticeable pulsatility, the time-averaged velocity vectors were distributed smoothly in the mean velocity field without any noticeable flow separation or secondary flow, even in the regions of bifurcation. These hemodynamic characteristics can be mainly attributed to the basic properties of low-Reynolds number flow (Re « 1).

As the bifurcation cascaded, the magnitudes of the local mean velocity ($U_{L,mean}$, in mm/s) rapidly decreased from 0.475 ± 0.538 mm/s to 0.020 ± 0.230 mm/s. This was due to the increase in total cross-sectional area of the vessels and the accumulation of pressure loss due to flow resistance along the blood vessels. Vorticity (ω_z, in s^{-1}) was higher in regions near the vessel wall due to large velocity gradients (Fig. 3), but relatively low at the central regions of the blood vessels. In the human blood circulation system, the total cross-sectional area of capillaries is about ten times larger than that of arterial blood vessels. The mean velocity and pulsatility must therefore be reduced significantly to satisfy the continuity of the blood flow through bifurcations. This causes unsteady pulsatile flow in arterial blood vessels to be altered gradually to a slow steady flow, as blood flow approaches the capillary blood vessels. This may be a type of natural physiological regulation, because gases, nutrients and waste materials can be exchanged efficiently through the thin permeable walls of the capillaries under these flow conditions.

The global average of the geometric parameters of the arterial bifurcations is listed in Table 1. For the HH-stage 18 chicken embryos tested in this study, the mean value of the ratio of Murray's law ($\alpha = D_0^3/(D_1^3 + D_2^3)$) was 1.053 ± 0.188. This value is very close to the theoretical value of unity given by Murray's law. In addition, the branch diameter ratio $D_2/D_1 = 1$, indicating that the global bifurcation system is symmetric ($D_2 = D_1$). Therefore, the bifurcation angle θ_{1+2} (≈ 77º, also see Fig. 4(c)) is also close to the theoretical value of the symmetric bifurcation (≈ 75º; Murray

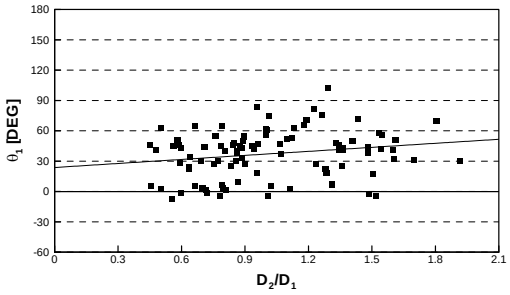

(a) Bifurcation angle of the left branch

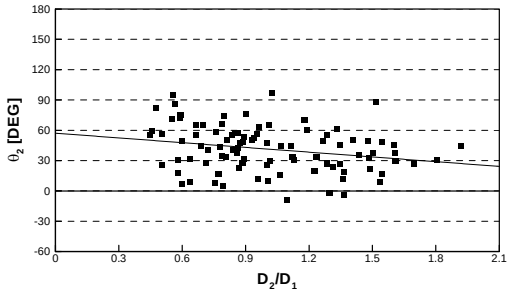

(b) Bifurcation angle of the right branch

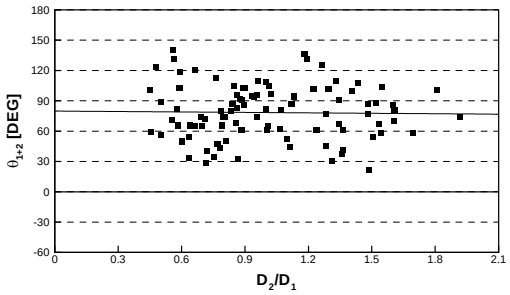

(c) Combined bifurcation angle

Figure 4. (a)~(c) Bifurcation angle of the left branch (θ_1), the right branch (θ_2) and the combined bifurcation angle (θ_{1+2}), respectively

[5,6]). However, the right bifurcation angle θ_2 is slightly larger than the left bifurcation angle θ_1. Other geometrical parameters such as D_1/D_0, D_2/D_0 and γ (cross-sectional area ratio) also have similar values of symmetrical bifurcation ($D_1/D_0 = D_2/D_0 = 2^{-1/3} \approx 0.794$ and $\gamma = 2^{1/3} \approx 1.260$).

Fig. 4 shows the variations of measured bifurcation angles (θ_1, θ_2 and θ_{1+2}) according to the diameter ratio (D_2/D_1). As the diameter ratio D_2/D_1 increased, the left bifurcation angle θ_1 slightly increased, while the right bifurcation angle θ_2 slightly decreased. Therefore, due to mutual compensation, the combined bifurcation angle θ_{1+2} is maintained at a nearly constant value of 77º, close to the theoretical bifurcation angle of 75º for a symmetric bifurcation, as shown in Table 1. From Figs. 4(a) and 4(b), we can see that the bifurcation angle (θ_1 or θ_2) of a branch vessel is larger when the diameter of the corresponding branch (D_1 or D_2) is small. The most common approach to testing the validity of Murray's law is to utilize the dependence of branching angle at a branch point on the relative size of the daughter vessels. A number of alternative formulations of the relation are possible; all predict that daughter vessels with smaller radii should make steeper angles to the parent vessels. The results shown in Figs. 4(a) and 4(b) support well the predictions on the bifurcation angle relation of daughter vessels. In addition, the combined bifurcation angle (θ_{1+2}) is nearly constant, regardless of the ratio of the branch's diameter (Fig. 4(c)). These results indicate that the geometric parameters of the vascular system are strictly regulated by the constructal rules of morphogenesis.

CONCLUSION

In this study, we obtained the velocity field information in the extraembryonic blood vessels of chicken embryos under *in vivo* condition. As bifurcation cascades, the mean velocity and pulsatility in the arterial vessel decrease, indicating flow becomes steady state apparently as the vessel diameter decreases. This flow phenomenon satisfies the Murray's law because it is based on the Hagen-Poiseuille's law. This is attributed to the fact that Poiseuille's formula postulated in the derivation of Murray's law is best approximated for vessels of smaller diameter. The unsteady pulsatile flow in arterial blood vessels becomes a slow steady flow or suppressed to a laminar flow, as the blood flow approaches capillary blood vessels.

The structural characteristics follow well the constructal rule (Murray's law), especially when D_0 is small. The bifurcation angle increased as D_0 decreases. It seems reasonable to utilize geometric information of the vascular system and its rules for the design of fluid transport systems, especially for micro-scale fluidic devices. The structural design of microchannels with bifurcation or confluence and complicatedly-connected microchannel networks in Lab-on-a-chip and μ-TAS (total analysis system) would be potential applications.

ACKNOWLEDGEMENTS

This work was supported by Creative Research Initiatives (Diagnosis of Biofluid Flow Phenomena and Biomimic Research) of MEST/KOSEF.

REFERENCES

1. Ku, D. N., Blood flow in arteries, *Annu. Rev. Fluid Mech.*, Vol. 29, pp. 399-434, 1997.
2. Zamir, M., The physics of coronary blood flow. New York: Springer, 2005.
3. Zamir, M. and Ritman, E. L., The physics of pulsatile flow. American Institute of Physics, 2000.
4. Malek, A. M., Alper, S. L. and Izumo, S., Hemodynamic shear stress and its role in atherosclerosis, *JAMA*, Vol. 282, pp. 2035-2042, 1999.
5. Murray, C. D., The physiological principle of minimum work applied to the angle of branching of arteries, *J. Gen. Physiol.*, Vol. 9, pp. 835-841, 1926.
6. Murray, C. D., A relationship between circumference and weight in trees and its bearing on branching angles, *J. Gen. Physiol.*, Vol. 10, pp. 725-729, 1927.
7. Cho, Y. I., Back, L. H. and Crawford, D. W., Experimental investigation of branch flow ratio, angle, and Reynolds number on the pressure and flow fields in arterial branch model, *Trans. ASME, J. Biomech. Eng.*, Vol. 107, pp. 257-267, 1985.
8. Hamburger, V. and Hamilton, H., A series of normal stages in the development of the chick embryo, *J. Morphol.*, Vol. 88, pp.49-92, 1951.
9. Vennemann, P., Kiger, K. T., Lindken, R., Groenendijk, B. W., Stekelenburg-de Vos S., ten Hagen, T. M., Ursem, N. C., Poelmann, R. E., Westerweel, J. and Hierck, B. P., In vivo micro particle image velocimetry measurements of blood-plasma in the embryonic avian heart, *J. Biomech.*, Vol. 39, pp. 1191-1200, 2006.
10. Taber, L. A., Ng, S., Quesnel, A. M., Whatman, J. and Carmen, C. J., Investigating Murray's law in the chick embryo, *J. Biomech.*, Vol. 34, pp. 121-124, 2001.

PRECISE AND RAPID COOLING OF SKIN TISSUE FOR CRYOSURGERY UTILIZING PELTIER EFFECT IN EXTREMELY LOW TEMPERTURE

H. Takeda[1, *], J. Okajima[1], S. Aiba[2], A. Komiya[3], S.C. Mishra[4], S. Maruyama[3]
[1]Development of Mechanical Systems and Design, Tohoku University, Sendai, Japan
[2]Department of Dermatology, Tohoku University, Sendai, Japan
[3]Institute of Fluid Science, Tohoku University, Sendai, Japan
[4]Department of Mechanical Engineering, Indian Institute of Technology Guwahati, India

ABSTRACT. This paper reports an experimental study of skin cooling for precise cryosurgery. The Peltier cryoprobe developed in the previous study has facilitated accurate control of heat transfer for precise cryosurgery. Cooling performance of the cryoprobe was estimated through the experiment utilizing pig skin. The maximum cooling rate (255°C/min) was found at −40 °C, and this value was found adequate for the skin cryosurgery. Thermophysical characteristics of different parts of the skin were found to be different. Thermophysical characteristics between after and before the freezing/thawing cycle were also observed to be different. However, these differences were not significant. Experimental results were found to be in a good agreement with the numerical results.

Keywords: *Precise Control, Rapid Cooling, PID Controller, Skin Cryosurgery, Peltier Effect*

INTRODUCTION

Cryosurgery is one of the treatment methods in which undesired tissue such as a cancerous tissue is frozen and destroyed. The advantages of the cryosurgery are: (i) focal and central application causes less damage to the normal tissue than resection, (ii) operation time is short, (iii) tissue recovery time is relatively short (iv) retreatment is highly feasible and (v) tumors near large blood vessels can be treated [1]. Despite these advantages, owing to the uncertainty and less repeatability, applications of the cryosurgery have been limited. In the skin surgery, cryosurgery is applied only to an early stage cancer or verruca. The main problem in the existing cryosurgery cooling methods is associated with an inadequate control of the cooling sequence. Therefore, development of a cryoprobe with precise control of heat transfer would allow precise treatment and, thereby, widen the application of the cryosurgery.

For precise control of heat transfer as well as rapid cooling, Maruyama et al. [2, 3] used the Peltier element, which is normally used as a device for actively controlling heat transfer in the steady-state. They found that both precise control of heat transfer and rapid cooling could be realized by utilizing the Peltier effect and by maintaining the heat sink at the cryogenic temperature. They developed a cryoprobe using Peltier elements and dry ice (solid carbon dioxide) as the low temperature heat sink [4]. Takeda et al. [5] developed the model of the cryoprobe in which cooling performance was improved utilizing Peltier module and liquid nitrogen as a cryogen. To control surface temperature precisely, they also developed a control system [5]. Through the experiment utilizing an agar, it was shown in the previous study [4, 5] that the cryoprobe can control imperceptible frozen region even thinner than 300μm and it can prevent freezing of the peripheral region of the affected tissue.

* Corresponding author: H. Takeda
Phone: + (81)-22-217-5244, Fax: + (81)-22-217-5244
E-mail address: heroki@pixy.ifs.tohoku.ac.jp

Because of its porous structure and water transportation, as far as thermal response is concerned, the skin tissue is different from an agar. Therefore, the estimation of the Peltier cryoprobe has to be conducted utilizing skin tissue for the application to an actual operation.

The first objective of this study is to estimate the cooling performance and controllability of the cryoprobe by utilizing a piece of pig skin. The suitability of the cryoprobe for actual cryosurgery is then discussed in accordance with the experimental results. Since effective thermophysical properties may change with repeated freezing/thawing and they may be different for different position in the skin, the second objective is, therefore, to evaluate the effect of the locations in the biological tissue.

EXPERIMENTAL METHOD

The cooling experiment was conducted utilizing the Peltier cryoprobe and the jig for injection of thermocouples. Principal concepts of the Peltier cryoprobe and the jig are explained in the following sections.

Peltier Cryoprobe

The schematic diagram and photograph of the cryoprobe are shown in Figs. 1(a) and 1(b), respectively [10]. Utilizing the Peltier effect and cryogenic heat sink, the cryoprobe can control heat transfer precisely and achieve rapid cooling. The Peltier module (KSMH01031F-ABE, KELK Ltd.) of 8 mm long × 8 mm wide and 1.65 mm high is attached between the heat sink and the cooling section. The diameter of the cooling section is 5 mm and the T-type thermocouple is attached to monitor the surface temperature for feedback control. To maintain a constant low temperature, the volume of the heat sink is a comparatively large. Liquid nitrogen is employed as a refrigerant in the cryoprobe and it cools the heat sink by pool boiling. The vessel is insulated by vacuumed co-axial pipes. Therefore, the side wall of the vessel is thermally insulated. The surface of the handle was found so warm that the operator could grab it with his hand. The vessel, in which liquid nitrogen can be maintained for about 30 minutes during the operation, has a volume of about 250 ml.

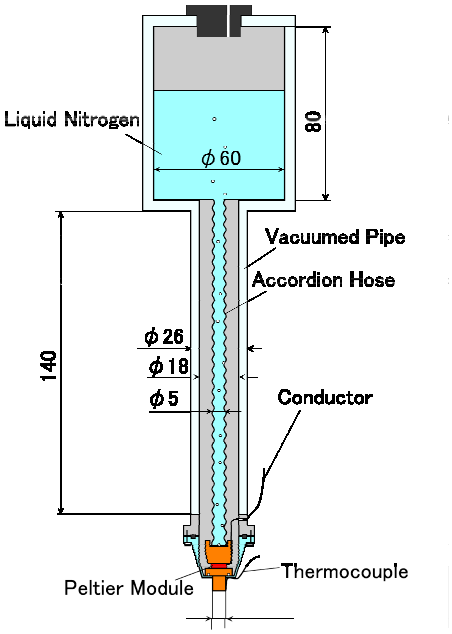

(a) Schematic diagram of the Peltier cryoprobe

(b) Photograph of the Peltier cryoprobe

Figure 1. Peltier cryoprobe

Experimental Procedure

In order to measure the temperature variations in the skin block, thermocouples were installed to the points beneath cooling point utilizing the jig developed in this study. Figure 2(a) shows schematic diagram of the jig. The L-shaped jig has 5 guide holes of diameter $\phi = 0.5$ mm at 1 mm, 3 mm, 5 mm, 7 mm and 10 mm depths, respectively. Injection needles were installed into the specimen until the tops of the needle reached beneath the cooling point. After that, T-type thermocouples ($\phi = 0.050$ mm) covered with $\phi = 0.28$ mm × $\phi = 0.20$ mm of polyimide tubes were installed through the injection needle. After that, as shown in Fig. 2(a), injection needles were pulled backward to keep the thermocouples embedded in the meat. By utilizing the jig, thermocouples were installed parallel precisely beneath the cooling points. Schematic diagram of the cross section around the periphery of the cooling section of the cooling experiment is shown in Fig. 2(b). Although thermocouples were installed through the guide hole, the depths of the thermocouples were not exactly the same as the depths of the guide hole because the skin surface was distorted by the pressure of the injection needles. Therefore, after the cooling experiment, the skin was cut and depths of the thermocouples were measured.

In order to estimate the cooling performance of the Peltier cryoprobe and evaluate thermophysical characteristics of the human skin, we utilized the pig skin. This was done for the reason that many characteristics such as structure, mechanical properties and thermophysical properties of the pig skin are similar to those of the human skin. Several blocks of the pig skin were picked up from buttocks and shoulders of the pig. Cross sectional of each block of the pig skin was 50 mm ×50 mm square and its thickness was 10 mm. The skin blocks were shaved and according to the procedure explained above, thermocouples were installed. Next, the cooling section was attached and cooling sequence was applied to the skin surface. The sequence of the experiment was controlled by the PID controller. In the initially, heat flux from the cooling section into the heatsink was cut off by setting the temperature of the cooling section equal to the surface temperature of the specimen. After the cooling started, temperature of the cooling section was controlled so as to maintain it at a set value. The cooling rate, end temperature (lowest temperature during the operation), hold time (time period for which the surface temperature was maintained at the end temperature) and heating rate could be set during the operation. Cooling was obtained by applying constant electric current on the Peltier module or by the PID controller. In order to estimate the cooling performance, the cooling experiment by applying constant electric current was also conducted. After the experiment, the blocks were cut and the depths of the thermocouples were measured.

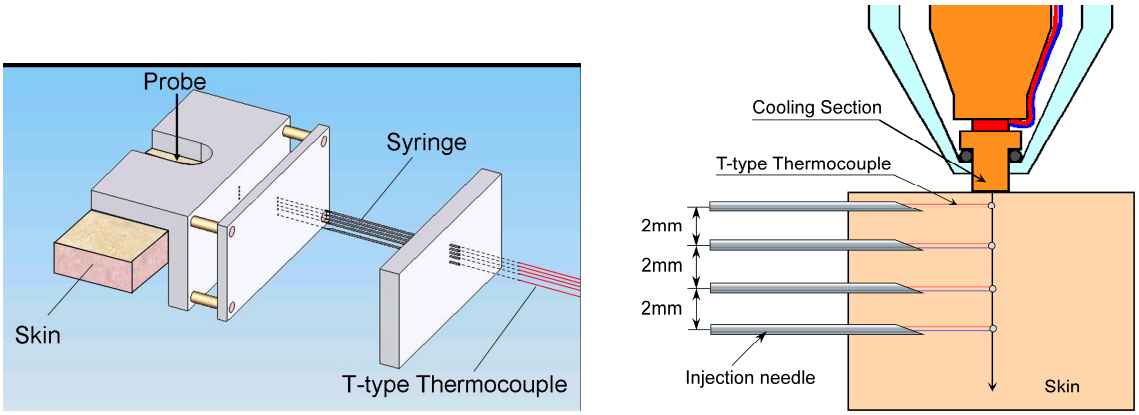

(a) Schematic diagram of the jig for the thermocouple injection

(b) Schematic diagram of the cross section in the periphery of the cooling section

Figure 2. Schematic diagram of the experimental set up

RESULTS AND DISCUSSIONS

In the cooling experiment utilizing PID controller or constant electric current, cooling performance of the Peltier cryoprobe and the characteristics of the pig skin were estimated. To assure reliability, experimental results were compared with those of the numerical simulation.

Estimation of Cooling Performance

Our previous results [5] utilizing an agar indicated that the cooling rate and the lowest temperature were maximized when an electric current of 1.0 A was applied to the Peltier module. In the present work, therefore, in order to estimate maximum cooling performance for the skin tissue and to measure the variation of the surface temperature with time, measurements were made by applying 1.0 A electric current. Variation of temperature with time is shown in Fig. 3. Solid line shows average temperature over 4 experiments and broken lines show the maximum and the minimum errors assuming that all data distributes as t-distribution. It is observed from the figure that the dispersion of temperature variation increased gradually after the freezing. Such a dispersion was not observed in the experiment of the cooling of an agar. This difference is because water component of the skin tissue is different at different positions, and after the freezing, latent heat of water strongly affects temporal variation of temperature of the cooling section. Therefore, it is impossible for the feed forward cooling system such as the conventional cooling method utilizing cotton or cooling probe with liquid nitrogen to conduct repeatable cooling sequence. It indicates that the Peltier cryoprobe with a PID controller has advantages for precise operation.

Figure 4 shows the relationship between the surface temperature and the cooling rate applying constant 1.0 A current that provides the maximum cooling rate of the Peltier cryoprobe. It is seen from the figure that the cooling performance decreases with decrease in temperature of the cooling section. This is for the reason that the temperature gradient in the Peltier elements becomes small as the surface temperature decreases. The cooling rate reaches 0 °C/min at –120 °C, so the cryoprobe cannot cool the skin tissue lower than –120 °C. Around –10 °C, there is a discontinuity of the cooling rate because there was immediate temperature increase due to ice nucleation in the skin. The graph also shows that the cooling rate lower than the maximum cooling rate (colored region in Fig. 4) can be controlled freely by applying appropriate electric current higher than 1.0 A. In cryosurgery, lethal temperature is in the range from -20 °C to -40 °C [6] and the cooling rate in this temperature range is very important. In this temperature range, our cryoprobe the cooling rate ranges from 360 °C/min to 255 °C/min. This cooling rate is sufficient for the cryosurgery [6, 7].

Figure 5 shows one of the results of the controlled cooling sequence (180 °C/min cooling to –30 °C, holding 120 s, and heating by 300 °C/min, in this case). It is seen from the results that a precise control of the cooling sequence can be achieved when the overshoot at the cooling is lower than 2 °C. Except the data logger's inherent error, the error at the steady-state was found to be less than ±0.1 °C. The same experiments were repeated and the difference of surface temperature of each experiment was found to be lower than 0.2 °C in the steady-state as well as in the transient state. Therefore, unlike a feed-forward cooling systems, with the present cryoprobe, the cooling sequence is repeatable. The figure also shows temperature variation with time of every location including the surface. During 100 s of the cooling time, the temperature difference between any two depths is found to be very high, even higher than 10 °C. This situation is advantageous for controlling the imperceptible necrotized area because it means that a high temperature difference can be achieved in a thin region. For example, assuming the lethal temperature is –20 °C, necrotized area is around 1.0 mm in this experiment. There is a little possibility for temperature of 2.0 mm depth to decrease lower than –20 °C even in the case having the maximum error. Therefore, we consider that the necrotized area can be controlled precisely less than mm order.

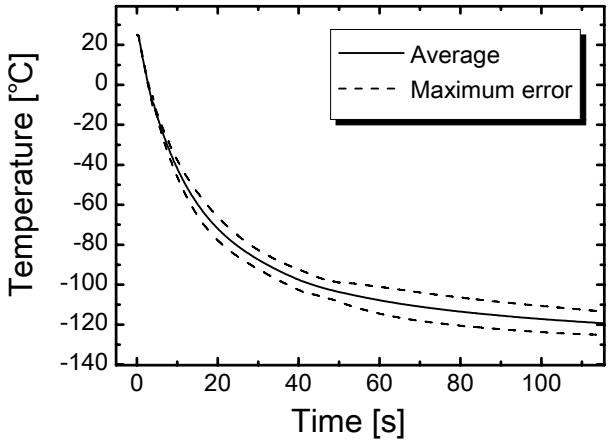

Figure 3. Surface temperature variation of pig skin with time of the cooling section at -1.0A

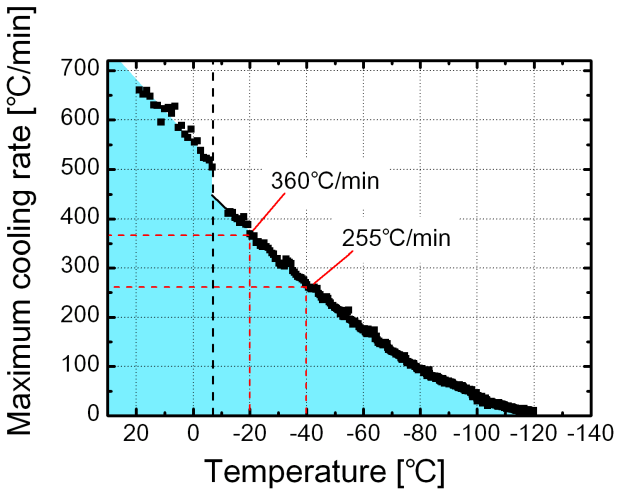

Figure 4. Relationship between temperature and maximum cooling rate

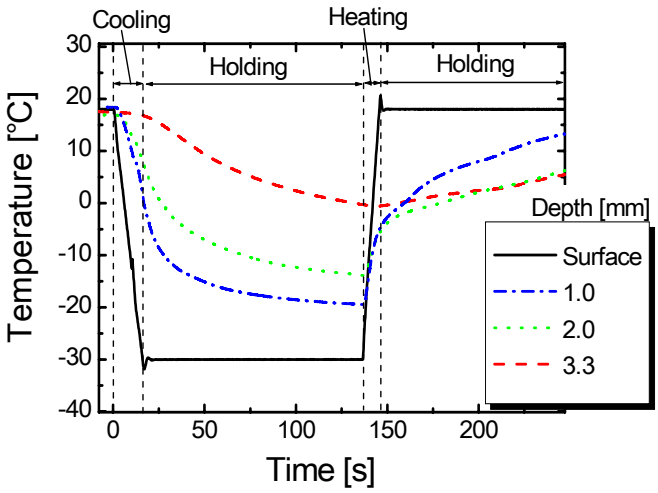

Figure 5. Temperature variation of pig skin at a several depths with time of cooling sequence

Estimation of the characteristics of the skin tissue

Second objective of the experiment of the skin cooling is to estimate the characteristics of the skin tissue. For the precise and repeatable cryosurgery, it is important to know the repeatability of the cooling sequence and the difference between skins of different parts. An agreement of the numerical simulation with the experimental results means that the frozen depth and inner temperature can be predicted before the operation and an appropriate cooling sequence can be decided before the actual operation.

In order to evaluate the difference of the thermophysical properties between skins of different parts, during the cooling, by applying constant 1.0 A current, surface temperature variation with time was compared. Results are shown in Fig. 6. As observed and explained in Fig. 3, temperatures at different locations are different. However, comparing the temperature profiles between different parts, e.g. shoulder and buttock in this case, we could not find significant difference. From the results, we can expect that thermophysical properties of different parts of the skin are similar and we can measure thermophysical properties of the skin from different parts. To confirm this assumption, evaluations of more samples of different parts are needed, but at least in the case of shoulder and buttock, the difference between local positions was more dominant than the difference between other parts.

In the research by Bischof et al. [8], the latent heat of tissue was observed to become higher once the tissue underwent freezing/thawing cycle because of the destruction of the cell membrane. In order to destroy undesired tissue, certainly it is necessary to repeat freezing/thawing cycle in cryosurgery. Therefore, it is important to investigate how large the change of latent heat affects temperature variation of the inner part of the skin. In the present experiment, controlled cooling and heating sequence was repeated several times and results are presented in Fig. 7. In the graph, the solid lines show temperature variation at 1 mm depth and the dashed lines show the same at 3 mm depth. From the figure, it is observed that temperature during the 3rd cooling is slightly higher than during the 1st cooling. However, the difference was less than 2°C at 1 mm depth. This difference can be neglected in the actual cryosurgery because there are many other factors such as anisotropy and random structure of the skin which make it difficult to predict frozen region or inner temperature.

Finally, temperature distributions of each cooling time were compared with numerical results. For the comparison, experimental results are from the controlled cooling and heating experiment for which the results are shown in Fig. 5. The computational results are based on the enthalpy method for the frozen region [9], and relationship between temperature and enthalpy in the mushy region was reconstructed from the experimental results through tissue cooling [5]. Thermophysical properties utilized in the calculation were that of a general tissue. The calculation did not consider matter diffusion or nano-scale structure but utilized effective thermophysical properties. Surface temperature measured in the experiment was utilized as boundary conditions. Axisymmetric numerical calculation was applied in this study. The results are shown if Fig. 8. Calculation results and experimental results are found to reasonably agree quantitatively. However, to see qualitatively, some results had difference more than 5 °C. Considerable reasons of the difference are, (1) the depths of the thermocouples were not accurate because of deformation of the skin and (2) thermophysical properties utilized in the calculation was not accurate. We could not clarify which result (experiment or calculation), or neither of them, is reliable. In order to realize more precise operation, we need further research such as measurement of thermophysical properties of the skin or more accurate temperature measurement. If we can predict temperature profile precisely, the precise control of freezing region or necrotized region will be predicted in actual cryosurgery by combining heat transfer control by the Peltier cryoprobe and the numerical calculation.

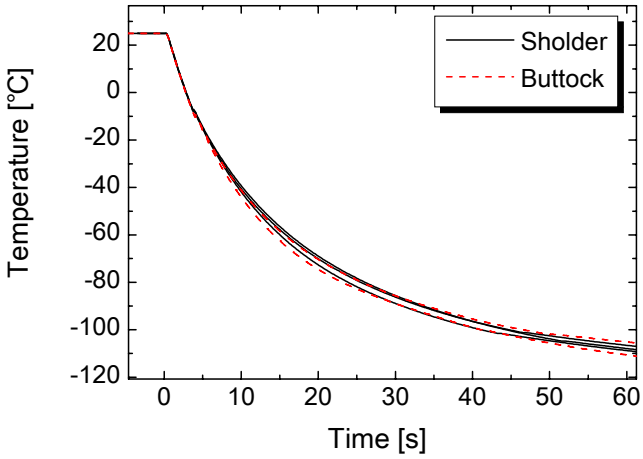

Figure 6. Variation with time of surface temperature of different skin parts during cooling by constant electric current

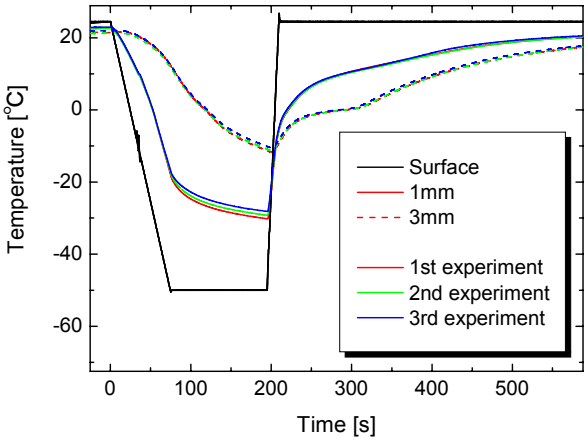

Figure 7. Variation with time of surface and inner temperature in the experiment of repeat freezing/thawing

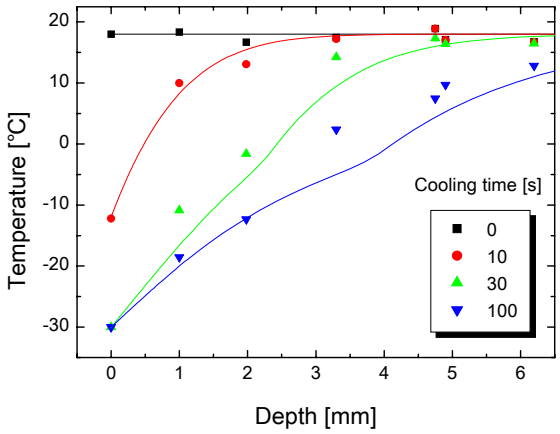

Figure 8. Comparison of numerical simulation and experimental results in temperature distribution of the skin for each cooling time (plots are experimental results and lines are numerical result)

CONCLUSIONS

The cooling performances of the Peltier cryoprobe were estimated utilizing pig skin blocks. The experiment utilizing constant electric current showed sufficient cooling rate and the lowest temperature for the cryosurgery. The cooling rate was up to 255 °C/min at -40 °C and the lowest temperature was -120 °C. The controllability of the cooling sequence was also confirmed and the temperature variation of the points beneath the cooling surface indicated the possibility to control imperceptible necrotizing thickness. Thermophysical characteristics were also evaluated and the results showed that thermophysical properties were not significantly different between the parts (shoulder and buttock) and between freezing times. Experimental result agreed well with numerical simulation developed in the previous study. It indicates that the freezing region or necrotized region can be predicted and controlled precisely by combining heat transfer control with the Peltier cryoprobe and numerical simulation.

REFERENCES

1. Rubinsky, D. and Onik, G., Cryosurgery: Advances in the Application of Low Temperature to Medicine, *Int. J. Refrig.*, Vol. 14, pp 190-199, 1991.
2. Maruyama, S., Active Heat Transfer Control by Non-Equilibrium Thermoelectric Device, *Proceedings of 33rd National Heat Transfer Symposium on Japan*, pp 127-128, 1996, in Japanese.
3. Maruyama, S., Nino, E. and Ruocco, G., Analysis of a Thermoelectrical Device for Active Heat Transfer Control, *Int. J. Therm. Sci.*, Vol. 40, pp 911-016, 2001.
4. Maruyama, S., Makoto, T., Sakai, S. and Fujima, K., Development and Heat Transfer Control of Cauter Using Non-Equilibrium Peltier Element, Proceedings of 40th National Heat Transfer Symposium on Japan, pp 555-556, 2002, in Japanese.
5 Takeda, H., Maruyama, S., Aiba, S. and Komiya, A., Precise Control of Frozen Region During Cryosurgery Utilizing Peltier Effect, *Proceedings of The ASME-JSME 2007 Thermal Engineering and Summer Heat Transfer Conference*, HT2007-32651, CD-ROM, 2007.
6 Rubinsky, B., Cryosurgery, *Annu. Rev. Biomed. Eng.*, Vol. 2, pp 157-187, 2000.
7 Gage, A.A. and Baust, J., Mechanisms of Tissue Injury in Cryosurgery, Cryobiology, Vol. 37, pp 171-186, 1998.
8 Bischof, J.C., Micro and Nanoscale Phenomena in Bioheat Transfer, *Heat Mass Transfer*, Vol. 42, pp 955-966, 2006.
9 Voller, V.R. and Swaminathan, C.R., Treatment of Discontinuous Thermal Conductivity in Control-Volume Solutins of Phase-Change Problems, *Num. Heat Transfer*, Part B, Vol. 24, pp 161-183, 1993.

ACOUSTIC CHARACTERISTICS OF ULTRASOUND IN WATER CONTAINING LIPID MICROBUBBLES

R. Imai, H. Nakagawa, T. Kanagawa, M. Watanabe and S. Fujikawa*
Division of Mechanical and Space Engineering,
Graduate School of Engineering, Hokkaido University, Sapporo, 060-8628, Japan

ABSTRACT. The resonant frequencies of lipid bubbles are measured from attenuation of ultrasound pulse propagating through the test cell filled with normal saline or lipid bubble solution. The attenuation spectrum has two dominant peaks in the frequency range of 0 through 15 MHz due to the energy absorption by lipid bubble resonant oscillations. The two peaks of attenuation spectrum are observed near the bands of 1.4 MHz and 11.5 MHz, respectively. The peaks of attenuation spectrum decrease with the decrease in the concentration of the lipid bubble solution. Furthermore, the strong attenuation is confirmed to be hardly affected by the length through the lipid bubbles. We conclude that the two peaks in the attenuation spectrum obtained are related to the effect of the existence of lipid bubbles.

Keywords: *Ultrasound, Lipid microbubble, Drug delivery system*

INTRODUCTION

Bubbles have been widely used in various fields, for instance, from marine engineering to medical engineering. One of the most characteristic features observed in the practical bubble application is a wide range of bubble diameter. Diameters of bubbles are of the order of millimeters when bubbles are used for the drag reduction of large vessel. On the other hand, they are of the order of nanometers when bubbles are used for clinical applications such as the contrast agents.

In the field of medical engineering, the application of bubbles to Drug Delivery System (DDS) has attracted great attention as the administration of next generation. DDS with bubbles of nanometer size is expected to be a noninvasive clinical treatment. Capsules of nanometer size, which contain exogenous gene such as anticancer drug, are administered in blood. These capsules are transported to target sites and impregnate in the disorder cells efficiently.

There exist bubbles wrapped in biomedical materials, i.e., lipid. The lipid bubbles are used as the transport carrier of DDS. However, dynamic properties of these lipid bubbles are not yet made clear. DDS with lipid bubbles uses actively the resonance of bubbles in order to increase the efficiency of gene injection in the disordered cell, because oscillations of lipid bubbles are easily excited with sufficiently small driving forces at resonant conditions.

In this study, acoustic characteristics of lipid bubbles are experimentally investigated in the vicinity of the resonance. The resonant frequencies of lipid bubbles are evaluated by measuring the attenuation of the propagating broadband ultrasound waves through the water containing lipid bubbles.

* Corresponding author: Prof. S. Fujikawa
Phone: + (81)-11-706-6429, Fax: + (81)-11-706-6429
E-mail address: fujikawa@eng.hokudai.ac.jp

EXPERIMENTAL METHOD

Lipid bubble

We use lipid bubbles in a liquid. A lipid bubble is composed of a kind of shell made of lipid layer, in which both gas and liquid are contained. The lipid bubble is made from a liposome. Figure 1 shows schematic diagrams of a lipid bubble. The liposome used in the present experiment is first made of lipid with DSPC (DiStearoyl Phosphatidyl Choline) and then modified by PEG (PolyEthlen Glycol Distearate). With the treatment, the liposome can exist stably in blood. The liposome becomes easily incorporated with ligand that is able to bind disease-related markers on bubble surfaces.

The liposome is produced by the reverse phase evaporation method. The inside of liposome produced by this method is liquid phase (Figure 1 (a)); hence liquid should be replaced by C_3F_8 (Perfluorocarbon) gas (Figure 1 (b)). The C_3F_8 gas is first injected into a glass receptacle containing a liposome solution, and then the receptacle is wobbled using an ultrasonic cleaner (Ultrasound cleaner 2510-J-DTH, Bransonic Co., Ltd.) until the solution in the receptacle becomes opaque. As shown in Figure 1 (b), it is supposed that replacement from the contained liquid to the gas within the liposome is attained by micelle formation inside the liposome [1]. The C_3F_8 gas enables lipid bubbles containing this gas to be used as an ultrasound contrast agent [2]. It is also necessary to equalize the size distribution of lipid bubbles by using the 20 kHz ultrasound probe. The lipid bubbles with larger diameters are assumed to be destroyed by this procedure. Figure 2 shows the distribution of lipid bubble diameter.

The solution containing lipid bubbles is diluted with the PBS (Phosphate Buffered Saline), and thus, solutions of different concentrations are obtained. The stock solution of lipid bubbles before diluted contains DSPC of 1 mg in its 1 ml. In this study, lipid bubble solutions with the concentration of 1000 ppm, 1333 ppm, 2000 ppm, and 4000 ppm are used. The experimental test cell which is the container made of the Polyvinylidene Chloride film (Saran Wrap, Asahi Kasei Co., Ltd.) is filled with lipid bubble solution. Ultrasound passes through this film.

Figure 3 shows the scanning electron micrograph of the liposome.

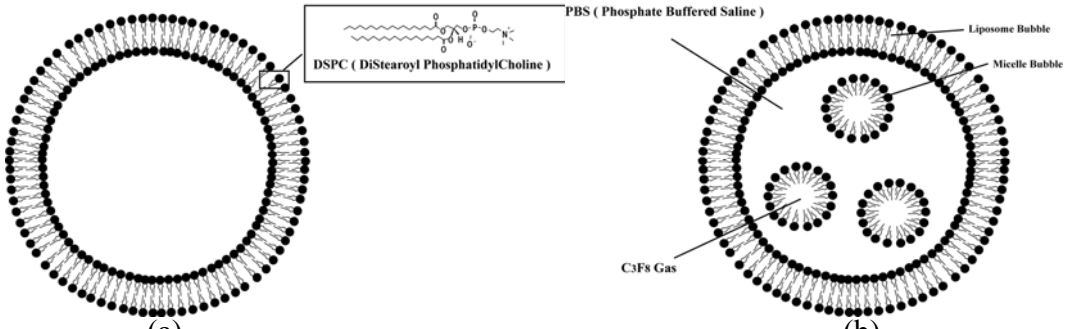

Figure 1. Schematic diagrams of a lipid bubble: (a) before gas replacement, (b) after gas replacement of liquid phase inside a liposome.

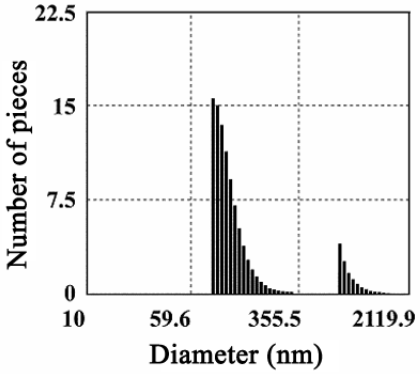

Figure 2. Distribution of lipid bubble diameter.

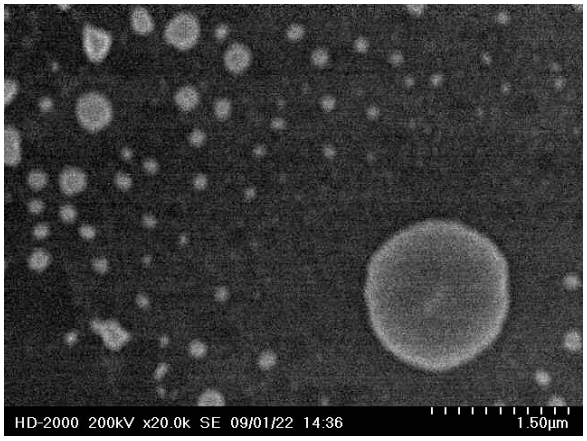

Figure 3. The scanning electron micrograph of the liposome.

Experimental apparatus and method

Experimental apparatus

Figure 4 shows the experimental apparatus, which is similar to that used by Hoff et al. [3]. This apparatus consists of a pulser/receiver, a coaxial cable relay for selecting transducers, four transducers (Panametrics Videoscan V306-SU, V382-SU, V326-SU and V312-SU), and a digital oscilloscope (LeCroy9410, LeCroy Co., Ltd.). The pulser/receiver and oscilloscope were connected to a PC.

Central frequencies of four types of broadband ultrasound transducers are 2.25MHz, 3.5MHz, 5.0MHz, and 10.0MHz, respectively. The four transducers are unfocused, 2.25 MHz with 13 mm aperture diameter, 3.5 MHz with 13 mm aperture, 5.0 MHz with 10 mm aperture, and 10.0 MHz with 6 mm aperture diameter. They are mounted in parallel in a water tank made of acrylic.

The test cell is filled with normal saline or the diluted lipid bubble solution. The lengths of the cell are 31.5 mm or 15.0 mm, and the distances from transducers to the experimental cell are 100 mm. The back wall of the water tank acts as an acoustic reflector, and is placed 150 mm from the transducer faces as shown in Figure 4. This acoustic reflector is made of steel.

Experimental method

The transducers are excited by the pulser which sends broadband ultrasound short pulses at 50 pulses per second. These pulses propagate through the experimental cell containing a lipid bubble solution separated from the ambient water by a very thin plastic film. These pulses are reflected at the back wall of the water tank, and then received by the transducer again. That is, the pulses pass through the cell twice; hence the total sound path lengths through the cells of 31.5 mm and 15.0 mm become 63.0 mm and 30.0 mm, respectively. The received pulses are amplified by the receiver and transferred to the oscilloscope. The oscilloscope is set to display only the reflection off the back wall of the chamber. The pulses are digitized in the oscilloscope at a sampling rate of 20 GS/s, and transferred to PC.

Signal processing of the received pulses is carried out using MATLAB software (The Math Works, Inc., Natick, MA). The power spectra are calculated by the Fast Fourier Transformation of received pulses in the cases of with and without lipid bubbles in the cell, respectively. Figure 5 shows an example of received pulses and their power spectra, without and with lipid bubbles in the cell with 31.5 mm in length. The attenuation spectra are calculated by the normalization, i.e., dividing the difference of power spectra both with and without lipid bubbles by the total sound path length through the cell, which is either 63.0 mm or 30.0 mm.

The evaluation ranges of broadband ultrasound transducers are from 1.4 to 3.0MHz, from 2.0 to 5.0MHz, from 3.0 to 8.0MHz, and from 6.0 to 14.0MHz, respectively, which correspond to their central frequencies 2.25MHz, 3.5MHz, 5.0MHz, and 10MHz. The overlaps of the curves obtained by different transducers assure the consistency of the experiment.

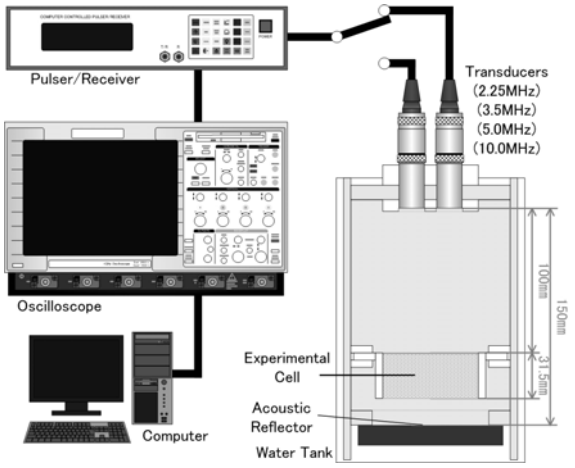

Figure 4. Schematic of the experimental apparatus.

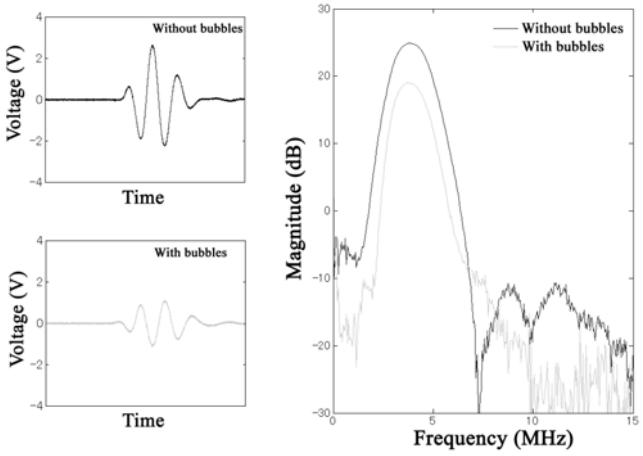

Figure 5. An example of received pulses and their power spectra measured with 3.5 MHz transducer. The left diagrams show received pulses passed through the cell twice: The upper and lower figures shows received pulses without and with lipid bubbles, respectively. The right diagram shows their power spectra, without and with lipid bubbles in the experimental cell.

RESULTS

First, we measured power spectra both with and without lipid bubbles, and calculated the attenuation spectrum, which is defined as the division of the difference between them by the total sound path length through the experimental cell, with both acoustic energy and the path length of the experimental call fixed as 100 μJ and 31.5 mm, respectively. The attenuation spectrum, which is used as the index of the difference of the acoustic characteristics between with and without lipid bubbles, is shown in Figure 6 in the case of the lipid bubble solution concentration of 1333 ppm.

Figure 6 is a typical example of the attenuation spectrum. It should be emphasized that, in this frequency range (0-15 MHz), this attenuation spectrum has two peaks. The larger attenuation is observed around the frequency of 1.4 MHz, the other is observed around the frequency of 11.5 MHz. It is understood that the existence of these peaks in the attenuation spectrum is due to the acoustic energy absorption by the lipid bubbles with resonant oscillations; hence the resonant frequencies of the solution of lipid bubbles are evaluated as approximately around the frequencies of 1.4 MHz and 11.5 MHz. These two peaks should be closely related with the distribution characteristics of the lipid bubble diameter, as already shown in Figure 2. Thereafter, these two peaks of the attenuation spectrum are discussed in the context of the acoustic characteristics of the lipid bubbles.

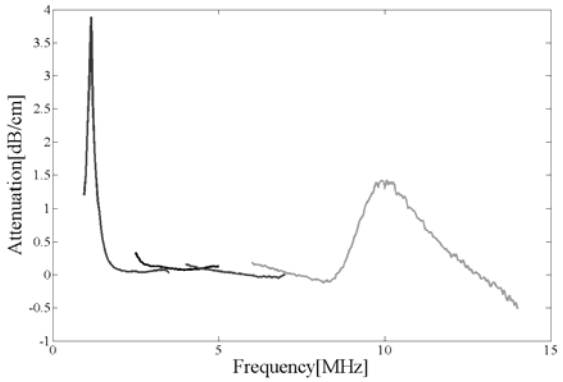

Figure 6. Acoustic attenuation spectra: with acoustic energy of 100 μJ, cell thickness of 31.5 mm, concentration of 1333 ppm.

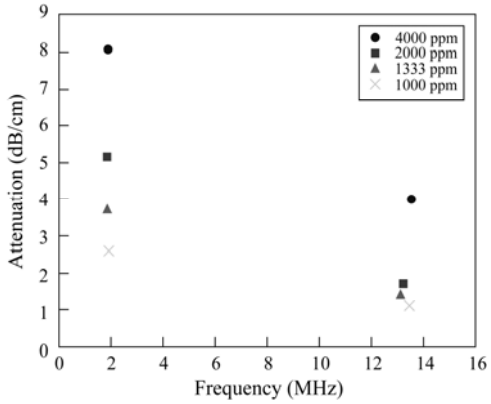

Figure 7. Peak attenuation with acoustic energy of 100 μJ, cell thickness is 31.5 mm, concentrations of 1000 ppm, 1333 ppm, 2000 ppm, and 4000 ppm.

Figure 7 shows the effects of concentration of the lipid bubble solution on the magnitudes of the attenuation at the two peaks of the attenuation spectrum. Here, the acoustic energy and the length of the experimental cell are fixed as 100 μJ and 31.5 mm, as before. Four types of lipid bubble solutions with the concentration of 1000 ppm, 1333 ppm, 2000 ppm, and 4000 ppm are used. It should be noted that the magnitudes of the attenuation at both of the two peaks decrease with the decrease in the concentration of the lipid bubble solution. The concentration of the solution is proportional to number of lipid bubbles per unit volume, and consequently to the amount of energy absorbed by the resonant frequencies of the lipid bubbles.

In order to discuss the effects of the total sound path length, we compare the attenuation spectra obtained by using two cells with different lengths of 31.5 mm and 15.0 mm, respectively. Figure 8 shows the effects of cell length on the magnitude of the attenuation at the two peaks of the attenuation spectrum, in the case that the acoustic energy is 100 μJ and the concentration of the lipid bubble solution is 2000 ppm. There exist little influences of the difference in the cell length; hence the magnitude of the attenuation peak is independent of the total path length through the lipid bubble solution.

As has been already discussed, the two dominant peaks in the attenuation spectrum obtained by this experiment are related to the resonance of the lipid bubbles. A resonant frequency increases with the decrease in the diameter of bubbles. Therefore, the resonant frequency observed in the vicinity of 1.4 MHz and 11.5 MHz may be contributed by lipid bubbles with diameter of 1.5 μm of 200 nm, respectively. It should be noted that this discussion should be improved by incorporating the multiple bubble effects.

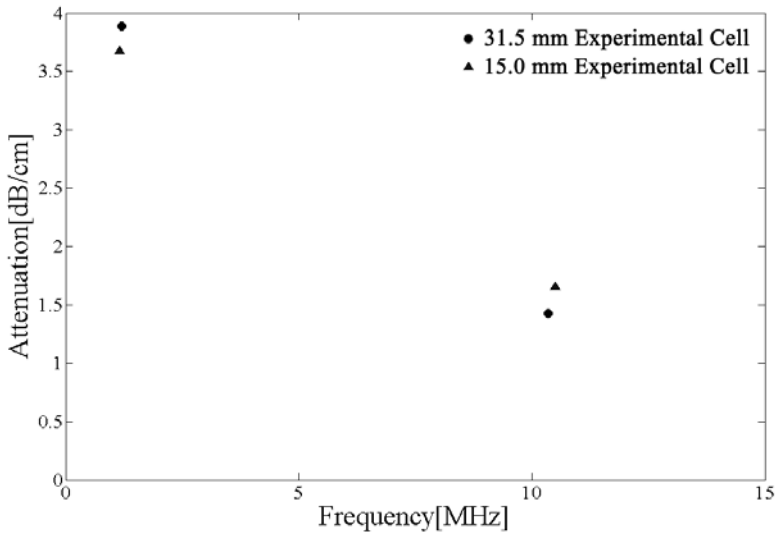

Figure 8. Acoustic attenuation spectra with acoustic energy of 100 μJ concentration of 1333 ppm, cell thickness of 31.5 mm and 15.0 mm.

CONCLUSIONS

We have experimentally studied the resonant frequencies of the lipid bubbles and obtained the following results:

(1) The attenuation spectrum, which is defined as the division of the difference of power spectra between with and without lipid bubbles by the total sound path length through the experimental cell, has two dominant peaks.

(2) The strong attenuations are observed at two different frequencies, around 1.4 MHz and 11.5 MHz, respectively.

(3) The strong attenuation decreases with the decrease in the concentration of the lipid bubble solution.

(4) The strong attenuation is independent of the path length through the lipid bubbles.

ACKNOWLEDGEMENTS

This work was carried out by the aid of Research on Advanced Medical Technology, Ministry of Health, Labor and Welfare (H19-nano-010). The authors would like to express their deepest gratitude towards this grant. Authors would also like to express their gratitude for the help of Hokkaido Innovation through NanoTechnology Support (HINTS, Nanotechnology Network Project Supported by the Ministry of Education, Culture, Sports, Science and Technology).

REFERENCES

1. Suzuki, R., Oda, Y., Namai, E., Takizawa, T., Negishi, Y., Utoguchi, N., Tachibana, K., and Maruyama. K., Development of Site Specific Gene Delivery System with Sonoporation, *J. Pharm. Soc. Jpn*., Vol. 128, No. 2, pp 187-192, 2008.
2. Maruyama, K., Suzuki, R., Takizawa, T., Utoguchi, N., and Negishi, Y., Drug and Gene Delivery by "Bubble Liposomes" and Ultrasound, *J. Pharm. Soc. Jpn.*, Vol. 127, No. 5, pp 781-787, 2007.
3. Hoff, L, Sontum, P. C., and Hovem, J. M., Oscillations of Polymeric Microbubbles: Effect of the Encapsulating Shell, *J. Acoust. Soc. Am.*, Vol. 107, No. 4, pp 2272-2280, 2000.

BOILING HEAT TRANSFER IN SMALL CHANNEL FOR DEVELOPMENT OF ULTRAFINE CRYOPROBE

J. Okajima[1]*, S. Maruyama[2] and A. Komiya[2]
[1]School of Engineering, Tohoku University, Miyagi, Japan
[2] Institute of Fluid Science, Tohoku University, Miyagi, Japan

ABSTRACT. Boiling heat transfer experiment for the development of ultrafine cryoprobe was conducted. The structure of ultrafine cryoprobe which is the co-axial double tube was simulated. To visualize the phenomena, water under the low pressure condition was used as working fluid. The inner diameter of needle section is 1.2mm. Two types inner tube were made and it was evaluated the effect obtained by the difference of inner tube diameter. The emission of small bubbles from inner tube to glass tube was observed by visualization experiment. Furthermore temperature measurement with heat flux obtained on the needle surface was conducted. The relationship between needle surface temperature and heat flux elucidates that needle surface temperature of thinner inner tube is lower despite lower flow rate. This fact indicates that pressure drop of inner tube or the state of water at the exit of inner tube is important for cooling needle.

Keywords: *Boiling heat transfer, Rapid cooling, Small channel, Cryosurgery*

INTRODUCTION

Cryosurgery is one of the surgical treatments, which utilize frozen phenomena of the tissue for removing lesions. The advantages of cryosurgery are minimal invasiveness, low bleeding, and short period for recovery[1]. Cryoprobe that is the cooling equipment for cryosurgery is usually cooled by Joule-Thomson effect of the high pressure refrigerant and its outer diameter is 3-8mm. Conventional cryoprobe has enough cooling power but poor heat transfer controllability. To overcome this problem, our group has developed novel type cryoprobe which can control heat transfer precisely by utilizing Peltier module[2]. The treatment effect of this cryoprobe was confirmed by animal experiment[3]. Furthermore less invasiveness and application to small lesion which can not be treated by conventional method are required for the development of cryosurgery. To satisfy these requirements, downsizing of cryoprobe is focused as one of the solution. On the other hand, cooling power of cryoprobe decreases as downsizing. Because surface area of cryoprobe and flow rate of refrigerant decreases. Therefore downsized cryoprobe using Joule-Thomson effect might generate insufficient cooling power for cryosurgery[4]. Therefore large heat transfer coefficient is required to downsizing cryoprobe to obtain sufficient cooling power.

To overcome these problems, we consider the concept of novel type cryoprobe “cooling needle” which has less than 1mm diameter and uses boiling heat transfer. We investigated the relationship between heat transfer coefficient of cooling needle and frozen region in biological tissue when the diameter of cooling needle is 0.5mm. As a result, large heat transfer coefficient which is equivalent to outer boiling heat transfer coefficient is required to generate the sufficient frozen region[5].

The knowledge of boiling heat transfer in microchannel is important for the development of cooling needle because the size of fluid channel inside cooling needle is small. Many investigations

* Corresponding author: Mr. J. Okajima
Phone: + (81)-22-514-5244, Fax: + (81)-22-514-5244
E-mail address: okajima@pixy.ifs.tohoku.ac.jp

about boiling heat transfer in microchannel have been conducted. A criterion to differentiate between macroscale and microscale of two-phase flow and heat transfer was discussed by Kew et al[6]. and Kandlikar et al[7]. Kew et al. defined threshold diameter by using confinement number *Co* When confinement number becomes less than 0.5, the two-phase flow and heat transfer is classified into microscale phenomena. Confinement number is expressed as;

$$Co = \sqrt{\frac{\sigma}{g\left(\rho_L - \rho_V\right) D_h^{\,2}}}\,, \tag{1}$$

where σ [N/m], g [m/s^2], ρ [kg/m^3] and D_h [m] are surface tension, gravitational acceleration, density and hydraulic diameter, respectively. Subscript L and V are liquid and vapor, respectively. On the other hand Kandlikar et al. classified scale effect by hydraulic diameter of channel: conventional channel (> 3mm), minichannel (200μm-3mm), microchannel (10μm-200μm), transitional channel (0.1μm-1μm) and molecular nanochannel (< 0.1μm). Many experiments of boiling heat transfer in microchannel was conducted[8][9] and various correlations were proposed by using these experimental data. Chen proposed a correlation[10] which uses Lockhart and Martinelli parameter[11] to judge the laminar or turbulent flow in the both of liquid and gas phase. This correlation was improved by Zhang et al[12]. On the other hand Kandliker et al. also proposed a correlation[13] which used liquid phase Raynolds number to judge the flow condition. The both correlations define that two-phase flow heat transfer coefficient consists of nucleate boiling and single phase forced convective heat transfer coefficient. Furthermore Thome et al. analysed theoretically heat transfer phenomena of two-phase slug flow in microchannel[14]. However the boiling heat transfer mechanism in microchannel has not been fully understood. Additionally the correlations of boiling heat transfer which are given so far might not apply to cooling needle because experimental conditions of these studies are different from cooling needle. Therefore boiling phenomena in cooling needle should be clarified experimentally.

The final goal of our study is to conduct the cryosurgery by using cooling needle which has sufficient cooling power and to achieve the heat transfer control of cooling needle by controlling boiling phenomena in cooling needle. For that purpose, the behaviour of boiling flow and its heat transfer in cooling needle has to be clarified at first. The objective of this study is to evaluate the transient temperature response and transient boiling characteristics of cooling needle. As a first step, water with low pressure is used for refrigerant of cooling needle. The effects obtained by the difference of inner tube diameter are evaluated by visualization of boiling flow and measurement of temperature of cooling needle.

PRINCIPLE OF HEAT TRANSFER IN COOLING NEEDLE

Cooling needle has the co-axial double tube structure as shown in Fig.1. When refrigerant which is high pressure, high temperature and liquid state comes into inner tube, large pressure drop occurs. Furthermore the refrigerant expands on the exit of inner tube. This process is isenthalpic expansion therefore temperature and pressure decreases. The refrigerant becomes two-phase flow in the outer tube. This boiling phenomenon forcibly occurs due to the pressure difference between inlet and outlet tube. Therefore refrigerant absorbs the heat equivalent to evaporative latent heat which is required for phase change of refrigerant. As a result, surrounding of cooling needle is cooled. Its cooling power depends on the state of refrigerant (subcooled or saturated) or the flow state (single or two phase). The boiling phenomenon in cooling needle is different from boiling phenomena in conventional boiling experiment in microchannel in several points as follows;

1. Condition to reach saturation state in outer tube is not increment of quality by input heat flux but pressure drop by thin inner tube.
2. The enthalpy of refrigerant on the exit of inner tube is not corresponding of enthalpy on the inlet due to heat exchange to fluid flow in outer tube and frictional pressure drop in inner tube.
3. Boiling phenomena around tip of needle is the most important to use in cryosurgery.

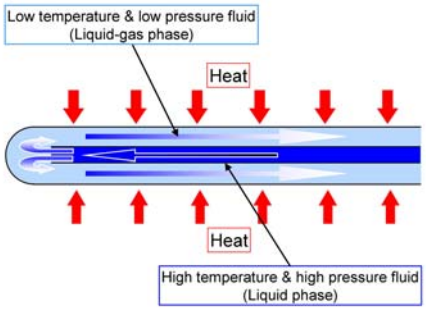

Figure 1. The cooling mechanism in cooling needle

EXPERIMENTAL APPARATUS

Figure 2 shows the schematic of the experimental apparatus. Working fluid is water. The apparatus consists of temperature-controlled reservoir, electromagnetic valves, needle section, liquid nitrogen (LN2) trap and oil-sealed rotary vacuum pump. Temperature-controlled reservoir is heated by the electrical heater to keep the temperature at 100°C. Therefore the pressure in the reservoir is kept at 0.1 MPa which is saturation pressure of water at 100°C. The oil-sealed rotary vacuum pump is used for keeping low pressure at nearly 0 Pa in outlet and LN2 trap avoids of indraft of water to vacuum pump. The electromagnetic valves can open the both of upstream and downstream flow pathes at a time. Temperature, pressure and flow rate were measured by thermocouple, bourdon tube pressure gauge and rotameter, respectively.

The needle section consists of glass pipe (1.2mm inner diameter, 2mm outer diameter) and nylon inner tube as shown in Fig. 3. Figure 4 shows the threshold diameter between microscale and macroscale two-phase calculated by Eq. (1). PROPATH[15] was used for the thermophysical properties of water. According to classification proposed by Kew et al., two-phase flow in glass pipe which is used in this experiment is classified into microscale phenomena. In addition, according to classification proposed by Kandlikar[7], this glass pipe is classified into minichannel. By using glass pipe, the flow pattern of boiling flow can be observed by digital high-speed microscope (KEYENCE Co., Ltd. VW-6000). Two types nylon inner tube were made by extending with heating. The dimensions of inner tubes are listed in Table 1. The values of the dimension of inner tube were determined by digital high-speed microscope. The needle section is partially heated as constant heat flux condition by nichrome wire supplied DC current as shown in Fig. 3. The length of heated area is 5mm. Thermocouple for measurement of needle surface temperature was set between glass pipe surface and nichrome wire. When temperature of the needle surface was measured, glass pipe was insulated thermally.

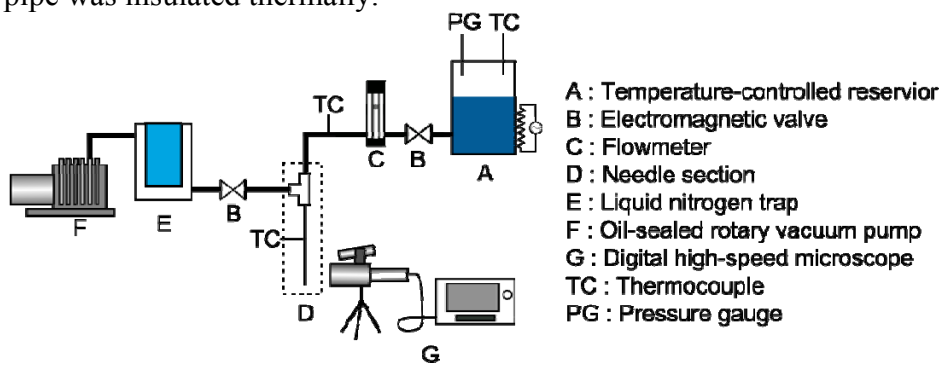

Figure 2. Schematic diagram of experimental apparatus

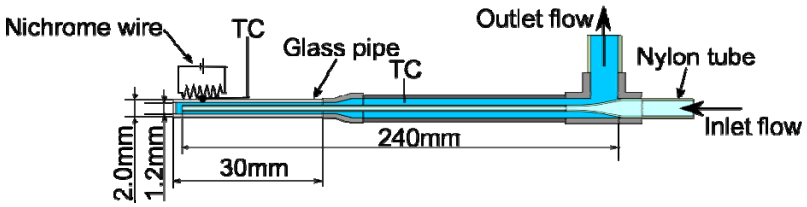

Figure 3. The details of needle section

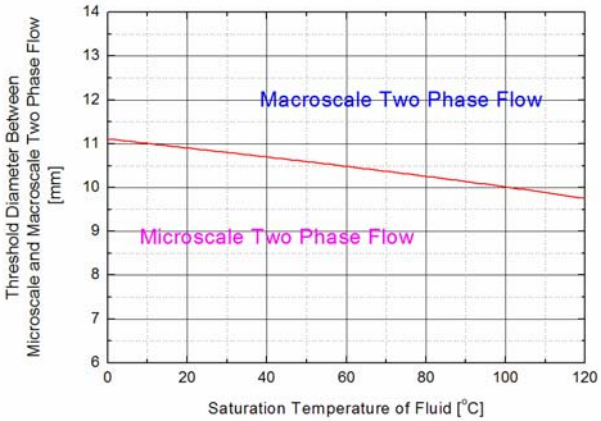

Figure 4. Threshold diameter between microscale and macroscale two-phase flow calculated from confinement number

Table 1. The dimensions of inner tube

	Outer diameter [μm]	Inner diameter [μm]	Thickness [μm]
Inner tube A	410	340	70
Inner tube B	190	145	45

RESULT AND DISCUSION

Visualization result -bubble generation process

Figures 5 and 6 show the visualization results of boiling flow pattern. These snapshots were taken by digital high-speed microscope. The frame rate and shutter speed were set 1000 fps and 1/4000 s, respectively. The differences of inner tube influence on boiling flow pattern as shown in Figs. 4 and 5. The flow rates of inner tube A and B are 5.0 ml/min and less than 0.5 ml/min, respectively. The flow rate in the case of inner tube A was much larger than inner tube B because of the difference of inner diameter. The value of flow rate in the case of inner tube B was not determined because the minimum range of flowmeter is 0.5 ml/min. In the both cases, the emission of small bubbles from inner tube was observed. This phenomenon indicates that water became the saturation state on the exit of inner tube. In the case of inner tube A, the bubble was released from the tip of needle in 40ms. However, in the case of inner tube B, the bubble expanded on the tip of needle. Furthermore the quantity of liquid in glass pipe in the case of inner tube B was less than the case of inner tube A because of the difference of flow rate as shown in Figs. 5 and 6. In addition, small bubbles were observed in the liquid slug in the both cases. This phenomenon also indicates that water in glass pipe became saturation condition.

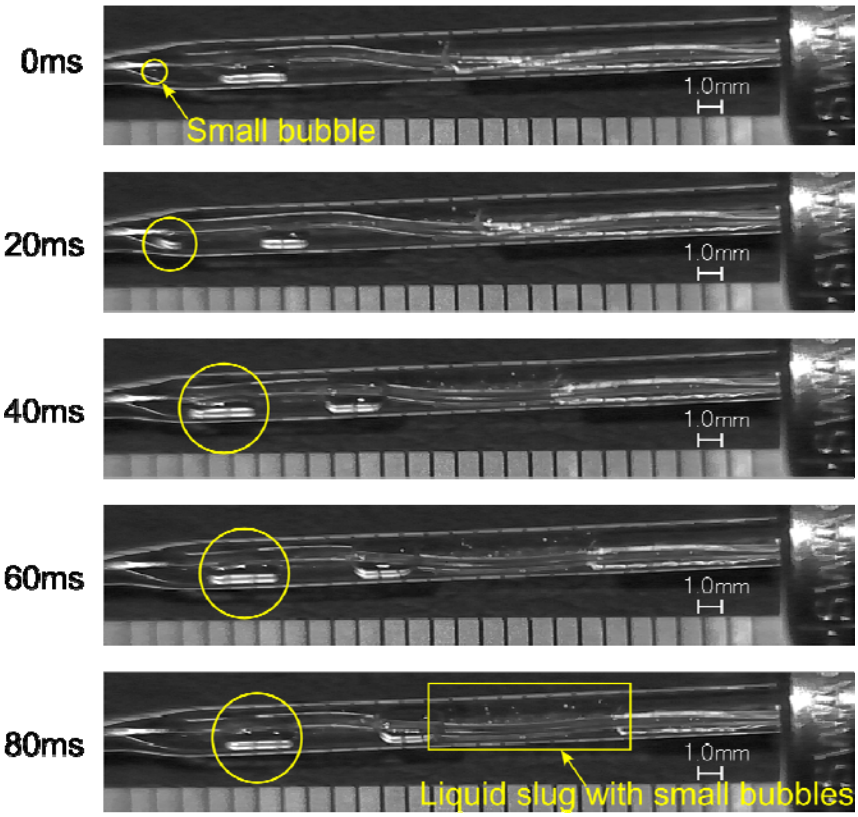

Figure 5. Visualization of bubble generation process in the case of inner tube A

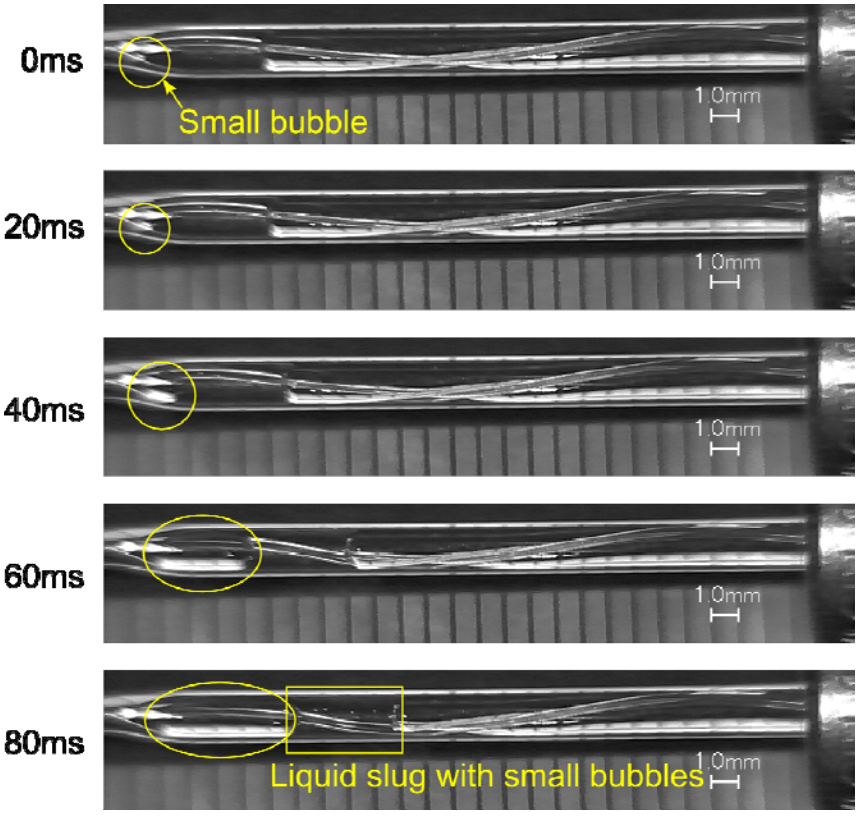

Figure 6. Visualization of bubble generation process in the case of inner tube B

Temperature measurement without heating

Figure 7 shows the time variation of temperature of inlet, outlet and needle surface in the case of inner tube A and B, respectively. Needle surface temperature was measured with insulating around the needle. The time 0 s was defined as the moment when valve was opened. In spite of higher inlet temperature in the case of inner tube B than inner tube A, needle surface and outlet temperature of inner tube B was lower than inner tube A. Here it is assumed that convergence temperature of needle surface in Fig. 7 is the saturation temperature of the water in the tip of needle. By this assumption, the properties of saturated water on the exit of inner tube can be calculated.

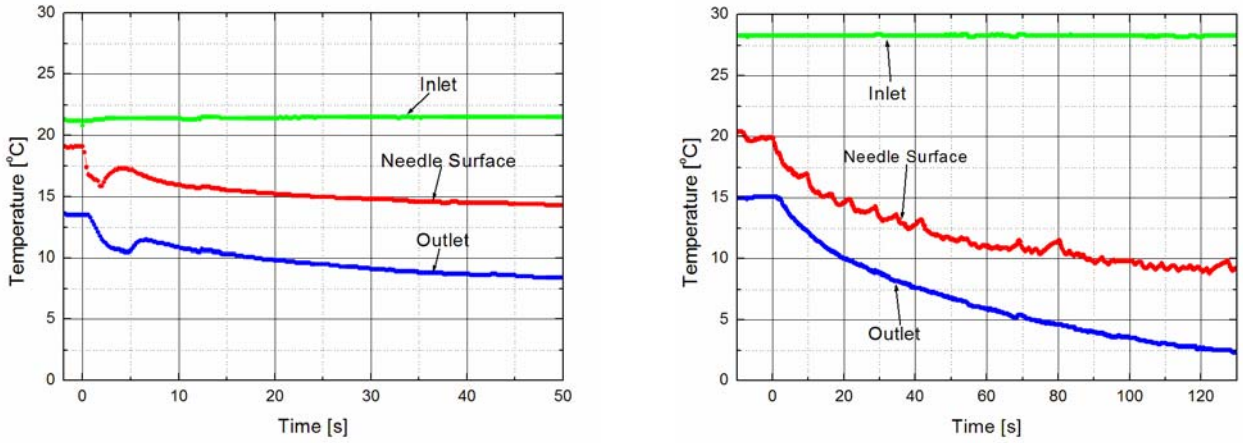

(a) inner tube A (b) inner tube B

Figure 7. Time variation of temperature without heating on the needle surface

Temperature measurement with heating

Figure 8(a) shows transient temperature response of needle surface under various heat fluxes in the case of inner tube A. In this experiment, needle surface was heated before opening the electromagnetic valves. Afterward both of electromagnetic valves were opened. Figure 8 shows cooling process by boiling heat transfer. Furthermore needle surface temperature converges at constant value. This steady state temperature depends on the heat flux. During experiment needle surface temperature was controlled without exceeding 100°C because heat-resisting temperature of nylon tube is around 100°C. In addition, Fig. 8(b) shows transient temperature response under the various heat fluxes in the case of inner tube B. In the case of inner tube B, needle surface temperature did not increase by heat flux like the case of inner tube A because boiling phenomena even continued after valve close. Therefore transient process could not be observed. As a consequence, only steady state temperature of needle surface was measured under various heat fluxes as shown in Fig. 8(b). The needle with inner tube B could absorb larger heat flux than inner tube A.

Figure 9 shows the relationship between needle surface temperature, heat flux and vapor quality at the tip of needle. Thermodynamic equilibrium vapor quality x is defined as follows,

$$x = \frac{h - h_L}{h_{LV}}, \tag{2}$$

$$h = h_{in} + \frac{1}{\dot{M}} \int_S q dS , \tag{3}$$

where h [J/kg], $\dot{M}$ [kg/s], q [W/m^2] and S[m^2] are enthalpy, mass flow rate, heat flux and heat transfer area, respectively. In addition, h_L, h_{LV} and h_{in} are the enthalpy of saturated liquid, the latent heat of vaporization and the enthalpy of the fluid at inlet condition. In this study, h_{in} means the enthalpy of water on the exit of inner tube, therefore it corresponds to h_L. Heat transfer area S denotes the heating

area as shown in Fig. 3. It is assumed that flow rate of inner tube B is 0.5ml/min and saturation temperature of water in outer tube is equivalent to measured temperature in Fig. 7. It is obvious that needle surface temperature of inner tube B is lower than inner tube A. Flow rate of inner tube B is much smaller than inner tube A. However cooling power of inner tube B is larger than inner tube A. Futhermore vapor quality at the tip of needle in the case of inner tube B is much larger than inner tube A. The differences of needle surface temperature and vapor quality between inner tube A and B is caused by the difference of flow rate. This fact indicates that pressure drop of inner tube or the state of refrigerant at the exit of inner tube is important for cooling needle. Therefore the design of inner tube is one of significant factors to realize cooling needle for cryosurgery.

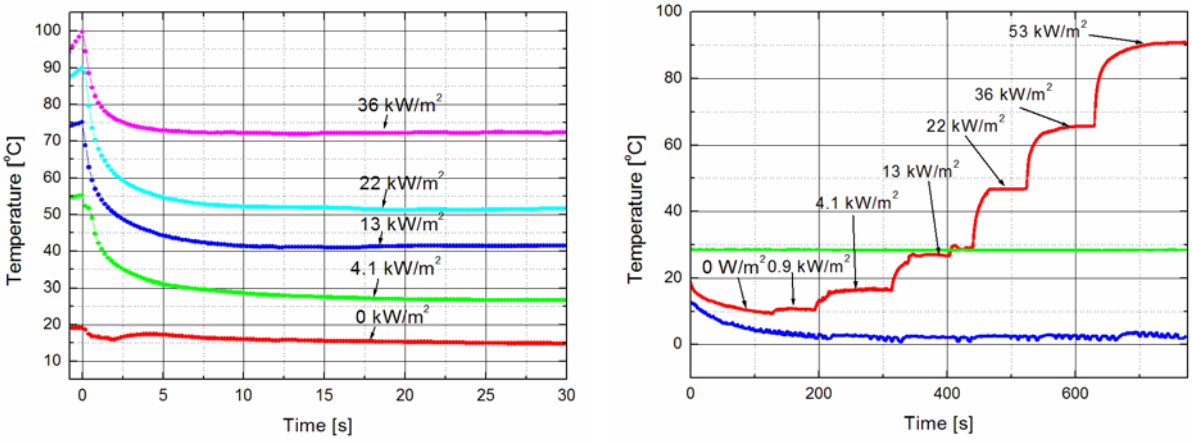

(a) inner tube A (b) inner tube B

Figure 8. Transient temperature response of needle surface under the various heat fluxes

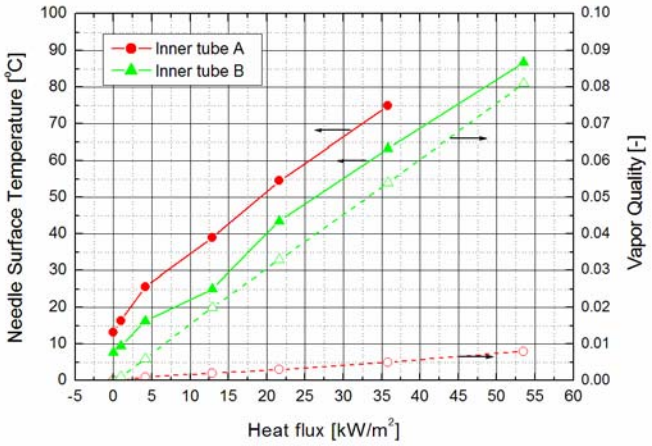

Figure 9. The relationship between needle surface temperature and heat flux

CONCLUSION

Boiling heat transfer experiment for developing cooling needle was conducted. The effect that the difference of inner tube diameter obtains was considered. Several results as follows are obtained.

- The emission of small bubbles from inner tube to glass tube was observed by visualization experiment. This phenomenon indicates that water became the saturation state on the exit of inner tube.
- Time variation of temperature of inlet, outlet and needle surface was measured. The needle surface and outlet temperature of thinner inner tube was lower.

- Temperature measurement with heat flux obtained on the needle surface was conducted and vapor quality was calculated. The relationship between needle surface temperature and heat flux elucidates that needle surface temperature of thinner inner tube is lower despite lower flow rate. This fact indicates that the pressure drop of inner tube or the state of refrigerant at the exit of inner tube is important for cooling needle.

ACKNOWLEDGEMENT

This work was supported by a Grant-in-Aid for JSPS Fellows [20·7374] from the Japan Society for the Promotion of Science.

REFERENCE

[1] J. Bishof et al., "A Morphological Study of Cooling Rate Response in Normal and Neoplastic Human Liver Tissue: Cryosurgical Implications", *Cryobiology* (1993), Vol. 30, pp. 482-492.

[2] H. Takeda et al., "Precise Control of Cooling and Heating Rate Utilizing Peltier Cryoprobe for cryosurgery", Proceedings of the 19th International Symposium on Transport Phenomena (2008), pp. 141.

[3] H. Takeda et al., "Evaluation of the Peltier Cryoprobe Availability through Animal Experiments", *Proceedings of Fifth International Conference on Flow Dynamics* (2008), OS8-14.

[4] J. Okajima et al., "Evaluation of the Relation between Frozen Regions and Heat Transfer Coefficient of Cooling Needle", *Proceedings of Fourth International Conference on Flow Dynamics* (2007), OS7-3.

[5] J. Okajima et al., "Possibility of Micro-Cryosurgery Utilizing Cooling Needle", *Proceedings of 16th International Conference on Mechanics in Medicine and Biology* (2008), pp. 6B-2.

[6] P. A. Kew et al., "Correlations for the prediction of boiling heat transfer in small-diameter channels", *Applied Thermal Engineering* (1997), Vol. 17, pp. 705-715.

[7] S. G. Kandlikar et al., "Evolution of Microchannel Flow Passages -Thermohydraulic Performance and Fabrication Technology", *Heat Transfer Engineering* (2003), Vol. 24, No. 1, pp. 3-17.

[8] J. R. Thome, "Boiling in microchannels: a review of experiment and theory", *International Journal of Heat and Fluid Flow* (2004), Vol. 25, pp. 128–139.

[9] G. Ribatski et al., "An analysis of experimental data and prediction method for two-phase frictional pressure drop and flow boiling heat transfer in micro-scale channels", *Experimental Thermal and Fluid Science* (2006), Vol. 21, pp. 1-19.

[10] J. C. Chen, "Correlation for boiling heat transfer to saturated fluids in convective flow", *Industrial & Engineering Chemistry Process Design and Development* (1966), Vol. 5, No. 3, pp. 322-329.

[11] R. W. Lockhart et al., "Proposed correlation of data for isothermal two-phase, two-component flow in pipes", *Chemical Engineering Progress* (1949), Vol. 45, No. 1, pp. 39-48.

[12] W. Zhang et al., "Correlation for flow boiling heat transfer in mini-channels", *International Journal of Heat and Mass Transfer* (2004), Vol. 47, No. 26, pp. 5749-5763.

[13] S. G. Kandlikar et al., "An extension of the flow boiling correlation to transition, laminar, and deep laminar flows in minichannels and microchannels", *Heat Transfer Engineering* (2004), Vol. 25, No. 3, pp. 86-93.

[14] J. R. Thome et al., "Heat transfer model for evaporation in microchannels. Part I: presentation of the model", *International Journal of Heat and Mass Transfer* (2004), Vol. 47, pp. 3375-3385.

[15] PROPATH Group, "PROPATH: A Program Package for Thermophysical Properties", version 13.1, July, 2008.

DYNAMICS OF NANOFIBERS CONVEYED BY LOW REYNOLDS NUMBER FLOW IN A MICRO-CHANNEL

K. Sadlej*, E. Wajnryb, M.L. Ekiel-Jezewska, T. A. Kowalewski
IPPT PAN, Polish Academy of Sciences, Warsaw, Poland

ABSTRACT. In this paper we aim on creating an experimental and numerical model of nano and microfilaments suspended in a confined Poiseuille flow. The experimental data obtained for short nanofibres will help elucidate fundamental questions concerning mobility and deformation of biological macromolecules due to hydrodynamic stresses from the surrounding fluid motion. Nanofibres suspended in the microchannel flow are obtained by electrospinning polymer solutions. Their typical dimensions are 100-1000μm (length) and 0.1-1μm (diameter). Typical for macromolecules, folding and unfolding sequences are observed and correlated with local flow gradients. This behaviour is compared with predictions of the Stokesian bead-spring model modelling dynamic behaviour of the fibre suspended in a Poiseuille flow between two infinite parallel walls.

Keywords: nanofibres suspension, microchannels, filaments dynamics, Stokesian dynamics

INTRODUCTION

Microfluidics is a rapidly growing field of basic and applied research, predominantly driven by the tight demands of biotechnology [1]. The well-known "lab-on-a-chip" (LOC) concept embraces the goal of integrating a bio-laboratory on a single microfluidic chip. Recent developments of the LOC technology provide possibility for handling not only single cells but to use the microfluidic systems for manipulating, sorting and analysing individual biomolecules. Devices consisting of nanoscale pores are being pursued as probes of molecular structure [1,2]. Single, double or triple DNA strands passing nanopores are observed to extract the identity of DNA bases [3,4]. Rapid measurements of DNA fragment size, of their folding and unfolding sequences represent challenging target for present single molecule studies. Development and availability of highly sensitive experimental tools permits to follow transient behaviour of single macromolecules in nearly native environment. However, such studies are still very tedious and expensive, and available experimental data are mostly quantitative, not accurate enough to be used for validating numerical models. In addition modelling of microbiological processes involve complex molecular interactions difficult for direct modelling due to prohibitive number of molecules involved and time scales far beyond those available for simulation methods at molecular level [5,6]. On other hand coarse, long time scale behaviour of macromolecules can be usually relatively well described using simple Stokesian fluid dynamics. Understanding slender filament dynamics in Stokesian flow may elucidate fundamental questions about mobility and deformation of biological macromolecules due to hydrodynamic stresses from the surrounding fluid motion. Moreover, by combining hydrodynamic interactions with molecular models one may aim to achieve a multiscale description of biologically driven process.

* Corresponding author: dr. K. Sadlej
Phone: + (48)-22-8269803, Fax: + (48)-22-8269815
E-mail address: ksadlej@ippt.gov.pl

Having all above arguments in mind the present paper aims on creating an experimental and numerical model allowing to obtain quantitative data on hydrodynamics of nano and microfilaments suspended in a confined Poiseuille flow. Microscopic data are obtained for the fluid - filament interactions, including their lateral migration, wall effects, and folding-unfolding sequences. To evaluate the importance of hydrodynamic interactions a macroscopic model is developed for modelling dynamic behaviour of a single fibre in a Poiseuille flow.

EXPERIMENTAL

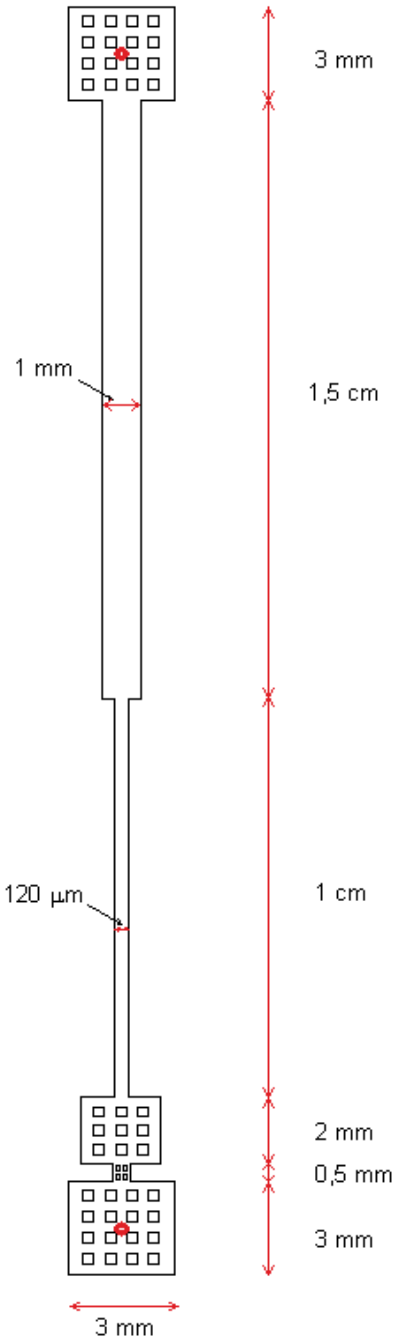

The main part of the experimental set-up consists of a microscope, a laser light source and a high speed digital camera. The flow is observed using a 10x (NA 0.3 / WD 17.30 mm) microscope lens covering an area of *854 µm x 683 µm.* Short illumination time is achieved by using a single pulsed Nd:YAG laser, delivering 1 mJ energy at 532 nm wavelength and 1kHz repetition rate (Ekspla Ltd). The flow is illuminated and observed through the upper wall of the channel. By traversing the field of observation in the horizontal and vertical direction, the position of the interrogated flow plane is selected. For the recording of images a high-speed 10bit *PCO 1200HS* camera with 1280 x 1024 pixels resolution is used. In most cases the flow was driven by syringe micro-pump permitting flow rate variation from 1 $\mu m^3/s$ to 1 mm^3/s.

The micro and nano filaments used in the experiment are produced by electrospinning polymer solutions [7]. Two types of polymers, polycaprolactone (PCL) and poly-L-lactide (PLLA), are used to form short, insoluble in water filaments. Small amount of rhodamine is added to the polymer solution to make produced filaments visible under a fluorescence microscope. By modifying electrospinning parameters, it is possible to produce filaments of diameters varying from 100 nm to 5 µm. The aspect ratio of filaments is then in the range from 50 to several thousands. In fact it is difficult to obtain short pieces of filaments and several scenarios of microfluidic separators are applied to preselect randomly chopped continuous nanofibres before they are used for the experimentation. The flow is studied in different channels created in a PDMS mould. The typical channel dimension is 100µm. Fluorescence of filaments suspended in the flow is excited by Nd:Yag laser and emitted red light (610nm) is collected by the camera using appropriate filters. Translocation of filaments within the channel and their shape evolution are evaluated using image processing software.

Fig. 1 Schematic of the microchannel used for studying nanofibre translocation in the flow.

Figure 1 shows typical shape of microchannel used for investigating single fibre dynamics. The straight parts of the microchannel allow for studying fibre interaction with a Poiseuille flow, structured obstacles in form of pillars are used to analyse possibility of fibre sorting.

NUMERICAL

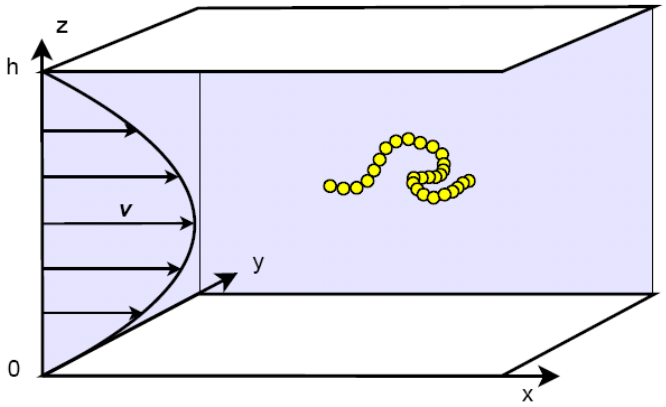

Fig. 2. Coordinate system of the numerical model

The bead-spring model is used for modelling the dynamic behaviour of fibres in a Poiseuille flow inside a microchannel modelled by two infinite parallel walls (Fig. 2). The regime of low Reynolds number of a particle is considered and the Brownian motion of particles is neglected resulting in a description based on the stationary Stokes equations

$$\begin{aligned} \eta\nabla^2\mathbf{v} - \nabla p &= \mathbf{0}, \\ \nabla\cdot\mathbf{v} &= 0, \end{aligned}$$

where η is the fluid viscosity, p is the pressure and **v** is the fluid velocity field. These equations must be supplemented by stick boundary conditions for the fluid velocity field on fibre and wall surfaces, as well as the condition of vanishing fluid flow disturbance far away from the fibre. In the model adopted, each fibre strand is constructed out of N solid non-deformable spherical particles which can move with respect to each other [8]. The spheres are lined up and connected by fictitious springs with equilibrium length l_0, a parameter of the model. Although external, non-hydrodynamic forces or torques applied to the fibre are absent, each segment of it feels elastic and bending forces defined for each fibre conformation and forces resulting from hydrodynamic interactions between segments of the fibre and with the flow itself. The derivation of the dynamical behaviour of the fibre realizes the following procedure. For each fixed configuration the instantaneous hydrodynamic forces exerted by the fluid on the particles are calculated. Then the velocity of each bead is linearly proportional, through the mobility matrix dependent on the exact position of all fibre segments, to the sum of these forces and the elastic and bending forces exerted on each fibre segment. Both the hydrodynamic forces and the mobility matrix are determined numerically by the HYDROMULTIPOLE algorithm [9], which implements the theoretical multipole method [10] of calculating hydrodynamic interactions between bodies within Stokesian dynamics. In this particular case, the wall effects where evaluated by the single-wall superposition. The evolution of the fibre is then determined by time stepping the set of coupled differential equations for each fibre-segment position. The calculations have been performed for several initial configurations, different fibre aspect ratios (number of beads) and different flexibilities.

RESULTS

Preliminary experiments with single nanofibres are performed to collect knowledge about different flow scenarios. Steady and pulsating flow is generated to analyze behaviour of suspended

nanofibres. In most cases after single nanofibre is localized in viewing area of the camera, the flow is stopped and reversed. Such push-pull motion permitted to observe selected object without changing position of the channel. Figures 3 and 4 show examples of collected images of nanofibres acquired under fluorescent microscope. The motion of short (0.1 mm) fragments through the multi pillar structure (Fig. 3a) exhibits characteristic fibre bending.
For longer fragments (above 0.5 mm) looping of the fibre tails is observed. Long fragments are often trapped or their relative motion is slowed down. This effect can be used to sort out selected fibre fragments before they enter the straight part of the microchannel (comp. Fig. 1). Fibres conveyed through the straight channel are usually deformed by flow shear stress (comp. Fig. 3b, Fig. 4). This behaviour shows several similarities to confinement-induced coiling-recoiling of DNA molecules.

The sequence of images shown in Fig. 4 is extracted from the longer movie illustrating complex dynamics of nanofibre fragment located about 40μm from the channel wall. It is interesting to note that average velocity of the fibre is similar to that of tracer particle located close to the flow axis (Fig. 4). By tracing displacement of both tails of the tangled fibre it is found that its part being closer to the wall is apparently nearly 20% faster than the other one. This striking behaviour seems to be confirmed by our numerical model (comp. Fig. 5).

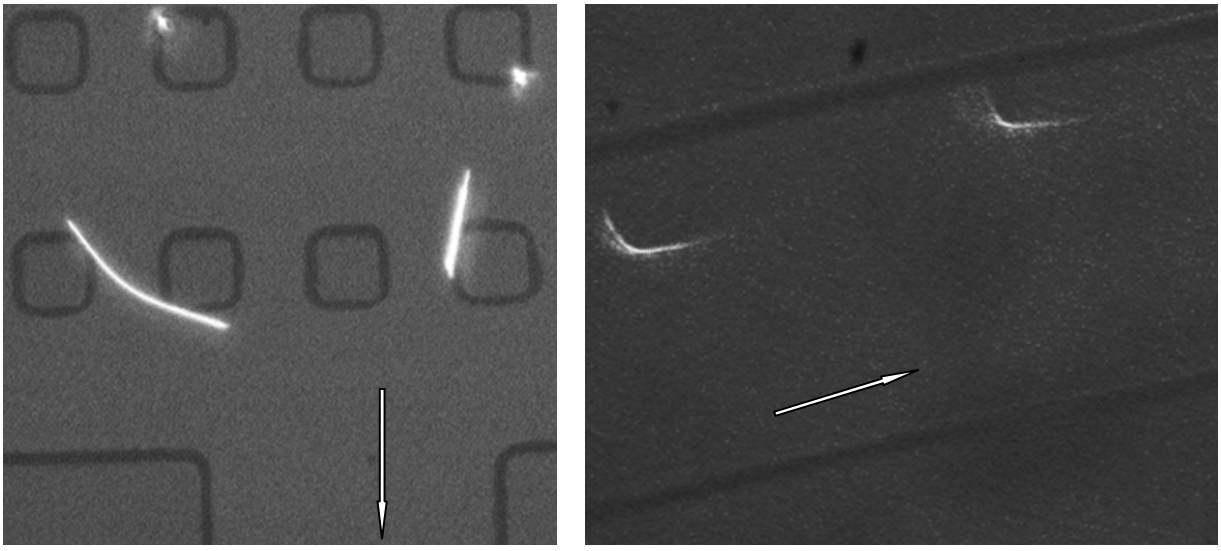

a b

Fig. 3. Fluorescent filaments passing multi-pillar separator (a), and conveyed close to the channel wall (b). Image width corresponds to 0.3mm.

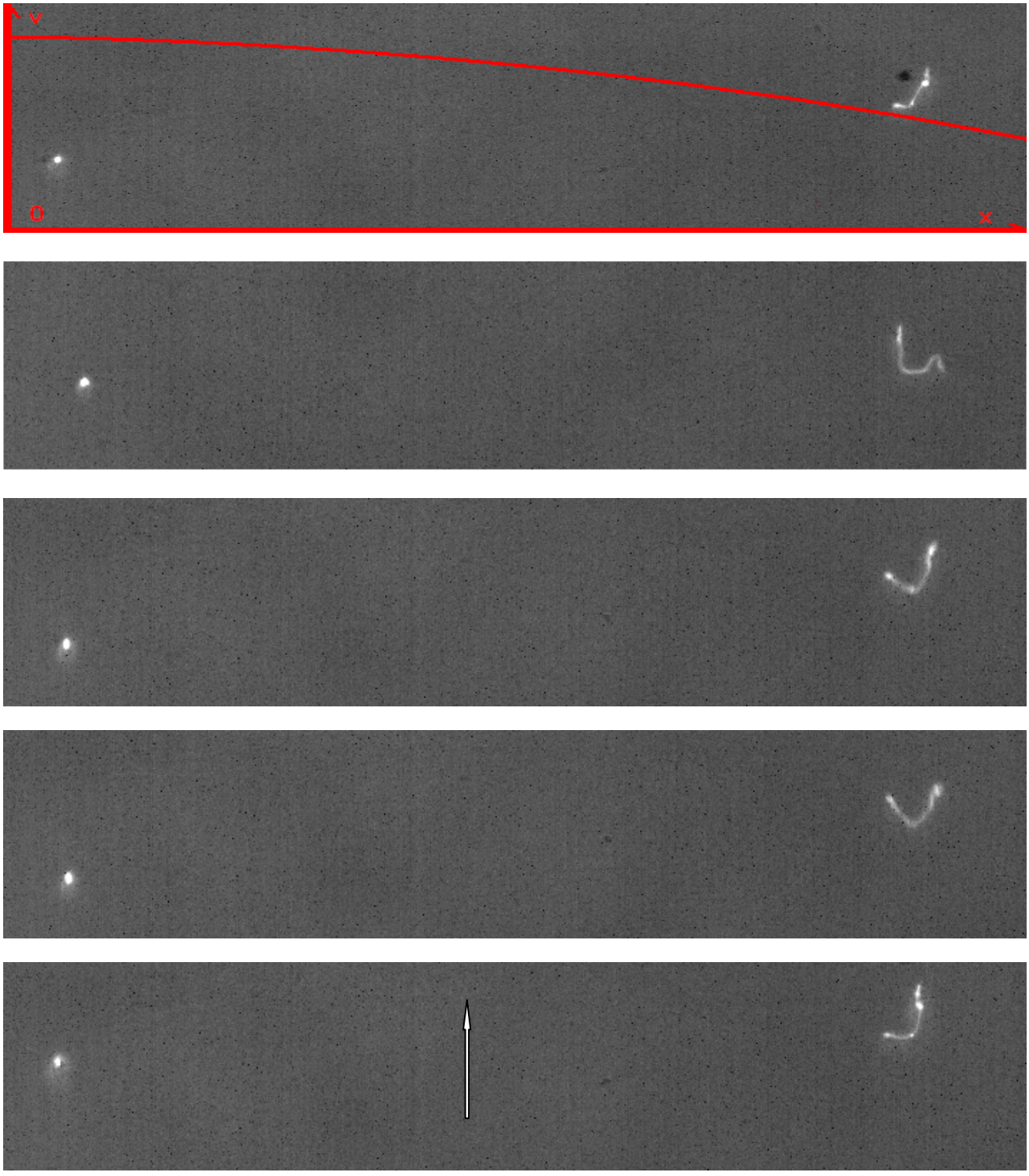

Fig. 4. A sequence of images of a nanofibre conveyed by a pulsating Poiseuille flow. The microchannel width is 2mm and the mean flow velocity is 40μm/s. Channel axis is on the left side, less than one half of the channel is visible. Poiseuille velocity profile is indicated by the red line. The bright spot on the left is a fluorescent particle used to measure local flow velocity.

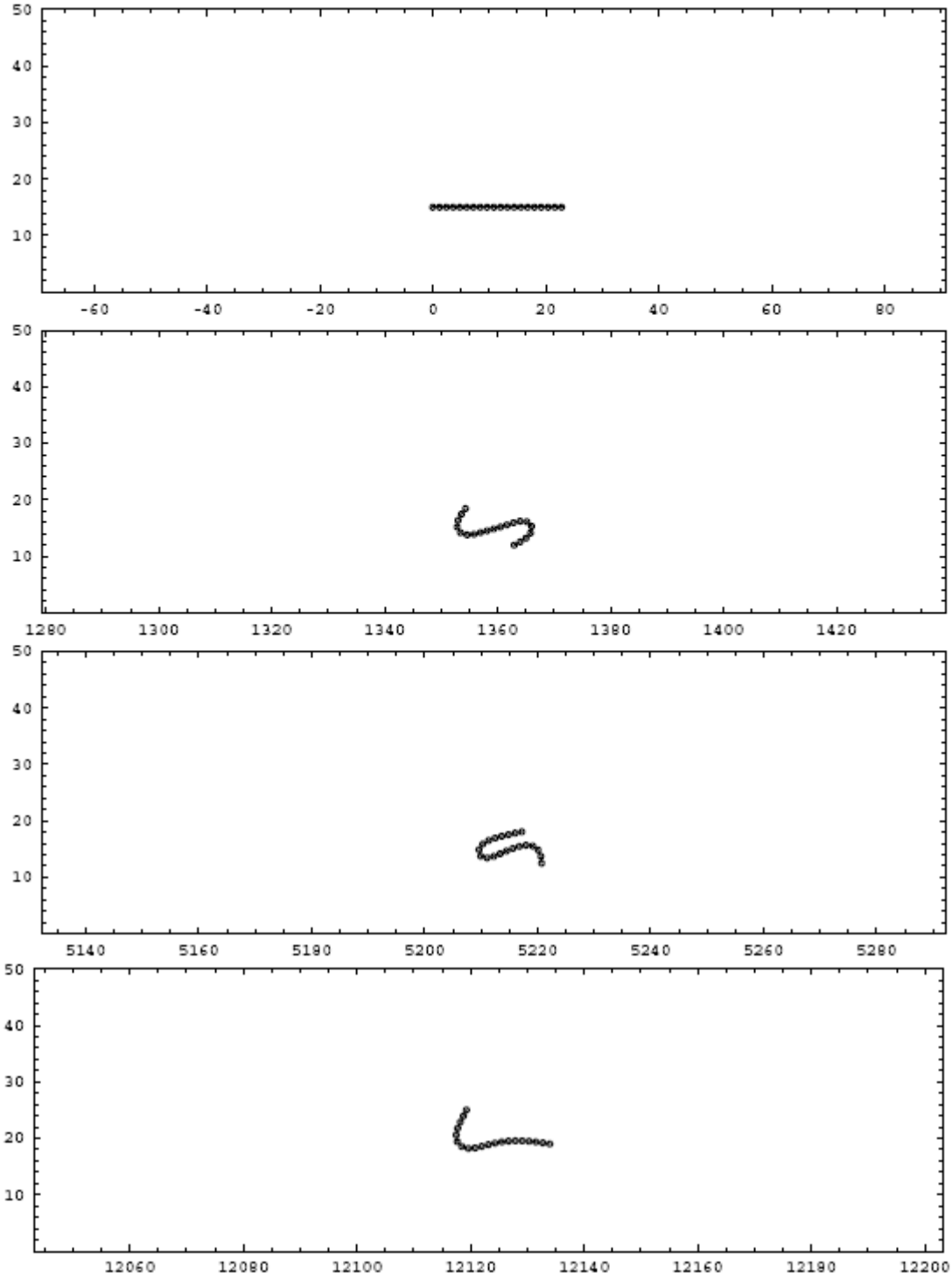

Fig. 5. Numerical modelling: flipping/tumbling motion of a fibre conveyed along the channel wall. Travelled distance given in fibre diameter units; initial fibre position $z = 15$. Number of beads $N = 20$, distance between walls $h = 50$ (fibre diameter units).

Several simulation runs performed for short "strings of beads" conveyed by Poiseuille flow gave us very promising results, reproducing the typical evolution of a fibre shape observed in the experiment. However, at the moment quantitative comparison with the experiment is limited by lack of elastic data for the available filaments. Hence, the present aim is to estimate unknown elastic properties of the physical filament by try-and-error simulation of observed filament. We have therefore preformed simulations for fibres of different length and flexibility. These have provided some interesting conclusions summarized below:

1. The motion of a single fibre strand in Poiseuille flow shows a generic behaviour. Independently of the initial configuration, it fairly rapidly (depending on its length and degree of entanglement), straightens out along the streamlines. It then begins a flipping or tumbling motion, which is almost periodic. Almost, not exactly, because the fibre has a tendency to migrate toward or away from the wall, moving through areas of different flow velocities.
2. Migration of fibres towards the centre of the channel is present only when the initial distance from the wall is large enough (typically larger then approximately 5 fibre diameters). The migration speed then decreases with distance from the wall.
3. Greater stiffness of the fibre hinders flipping on small distances from the wall and increases the flipping period elsewhere.
4. Longer fibres migrate faster towards the middle of the channel and take much longer time to flip while bending. This is shown in Fig. 6, where the distance between the first and last segment of the fibre is plotted for the whole flipping period. The short fibre (5 beads) behaves as a solid rod rotating in the flow, whereas for the long fibre (40 beads) nearly periodic stretching and winding is visible.

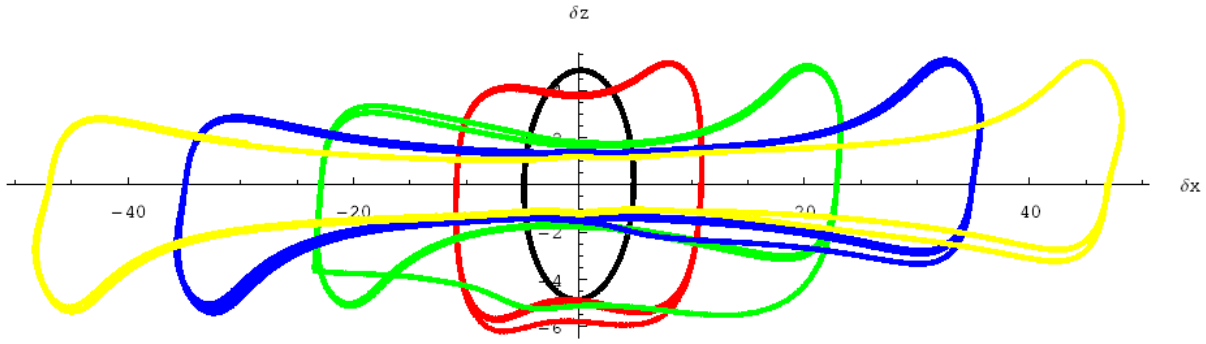

Fig. 6. Numerical modelling: evolution of the distance (δx , δz) between both ends of the fibre conveyed by the flow in x direction. Initially fibre is aligned with the flow (δz =0). The equilibrium distance between fibre segments is $l_0 = 1.2$. Five different fibre lengths marked by colours: black: N = 5, red: N = 10, green: N = 20, blue: N = 30, yellow: N = 40. Shorter fibres tend to stay straighter during flipping. In particular, for N = 5 the fibre virtually does not fold at all. The plotted evolution curve (black) is then almost a perfect circle.

CONCLUSIONS

Our preliminary experimental and numerical studies demonstrate the possibility of evaluating the dynamics of long filaments conveyed in the Poiseuille flow. Several observed features show convincing similarities to confinement induced deformations of biopolymers or DNA strands. Further study is planned to elucidate details necessary for quantitative analysis of this phenomena.

NOMENCLATURE

h	distance between walls, fibre diameter units
N	number of beads, relative length of the fibre.
x, z	coordinates along the channel and across the channel, distance in fibre diameter units.
δx , δz	distance between both ends of the fibre, fibre diameter units

ACKNOWLEDGMENTS

This investigation was supported by the Polish Ministry of Science and Education program *Biowizja.* The authors thank Diana Lamparska and Krzysztof Zembrzycki for their invaluable help in the experimental work.

REFERENCES

1. Mijatovic D., Eijkel J. C. T., van den Berg A., Technologies for nanofluidic systems: top-down vs. bottom-up—a review, *Lab Chip* 5, pp.492–500, 2005.
2. Maleki-Jirsaraei N. Sarbolouki M,-N., Rouhani S., Simulation of DNA electrophoresis through Microstructures, *Electrophoresis* 28, pp. 301–308, 2007
3. Joo Ch., Balci H., Ishitsuka Y., Buranachai Ch.,Ha, Advances in Single-Molecule Fluorescence Methods for Molecular Biology, *Annu. Rev. Biochem.* 77 pp. 51–76, 2008.
4. Craighead H., Future lab-on-a-chip technologies for interrogating individual molecules, *Nature* 442, 387-393, 2006
5. Kreuzer H.J. M. Grunze M., Stretching of single polymer strands:A first-principles theory Europhys. Lett. 55, pp. 640–646, 2001
6. Dai L., Mu Y., Nordenskio L. van der Maarel J.R.C., Molecular Dynamics Simulation of Multivalent-Ion Mediated Attraction between DNA Molecules, *Phys Rev. Let.* 100, 118301, 2008.
7. Kowalewski T.A., Błoński S., Barral S., Experiments and modelling of electrospinning process, *Bull. Pol. Acad. Scs.* 53, pp.385-394, 2005
8. Dhont J. K.G., Briels W.J.. Rod-like Brownian Particles in Shear Flow. WILEY-VCH Verlag Berlin GmbH, 1988.
9. Ekiel-Jeżewska M.L., Wajnryb E., Q. *J. Mech. Appl. Math.*, 59:563–585, 2006.
10. Cichocki B., Jones R. B., Kutteh R., Wajnryb E., *J. Chem. Phys.*, 112:2548, 2000.

EXPERIMENTAL MEASUREMENTS OF SHEAR STRESS IN A TUBULAR AIR LIFT MEMBRANE SYSTEM

N. Rios[1,*], C.C.V. Chan[2], P. R. Berube[2], I. Nopens[1]
[1]Department of Applied Mathematics, Biometrics and Process Control (BIOMATH). Coupure Links 653, B-9000, Ghent, Belgium
[2]University Department of Civil Engineering, The University of British Columbia, 6250 Applied Science Lane, Vancouver, BC, V6T 1Z4, Canada.

ABSTRACT. Application of a two-phase slug flow in side-stream membrane bioreactors (MBRs) has proven to increase the permeate flux and decrease fouling through a better control of the cake layer. Literature has shown that the hydrodynamics near the membrane surface have an impact on the degree of fouling by imposing high shear stress near the surface of the membrane. An experimental program was developed to investigate the shear stress imposed on the surface of a membrane under different two-phase flow conditions (gas an liquid), by varying the flow of each phase. Due to the random behaviour of the shear stress values, caused by the continuous passing of bubbles and difference in size (coalescence), the results were analysed using histograms of shear stress distributions (SSD). A bi-modal SSD was observed, with one peak corresponding to the shear induced by liquid flow, and the other induced by gas flow. This distribution could be modelled using two Gaussian relationships. Literature suggests that fouling control is expected to be optimal when the shear induced by liquid flow is approximately equal to that induced by gas flow. Therefore, the Gaussian relationships could be used to identify the two-phase flow conditions that optimize fouling control.

Keywords: *Side-stream membrane bioreactor, gas-liquid slug flow, wall shear stress, bi-modal distribution*

INTRODUCTION

Bearing in mind the more stringent effluent quality standards imposed by the EU Water Framework Directive (EU-WFD), treatment efficiencies need to be improved. These improvements can be achieved both in terms of biological removal efficiency as well as in the sludge-water separation step. For the last step two types of technologies exist, the Conventional Activated Sludge (CAS) systems where the separation is brought about by gravity (Figure 1, a) and the Membrane Bioreactors (MBR) where the separation is achieved by filtration (Figure 1, b and c). The latter has proven to be a good alternative to achieve high effluent quality compared to the CAS. However, a common problem encountered with MBR systems is fouling of the membrane resulting in a frequent need for membrane cleaning to remove the accumulate foulants [1], making it a less appealing alternative in terms of cost-effectiveness. This has been the limiting factor in the full-scale application of these systems. There are two types of MBR, one has the membrane inside the bioreactor, commonly called immersed membrane bioreactor (iMBR) (Figure 1, b); and the other has the membrane outside the bioreactor, named side-stream membrane bioreactor (sMBR) (Figure 1, c). This work focuses on the latter type.

* Corresponding author: Nicolas Rios
Phone: +32 9 264 59 35, Fax: +32 9 264 62 20
E-mail address: nriosrat@biomath.ugent.be

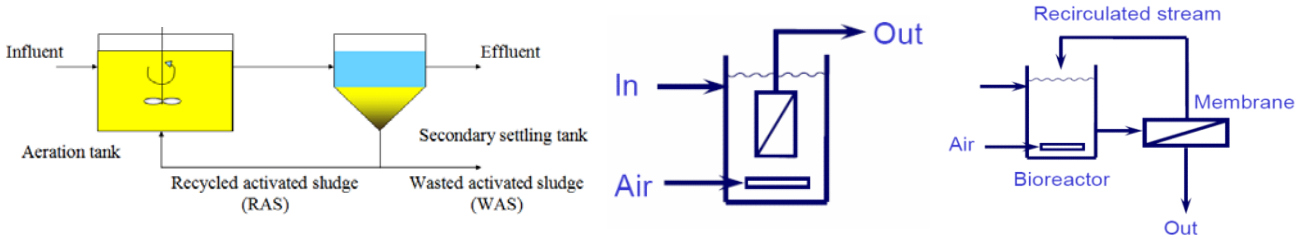

Figure 1. (a) Conventional Activated Sludge (CAS), (b) Immersed and (c) side-stream MBR [1]

The hydrodynamics near the membrane surface play an important role in fouling control. To reduce the fouling near the membrane surface, air is often introduced in the sludge flow to create a gas-liquid two-phase slug flow [2], which increases the surface shear stress. These shear stresses increase the mass transfer of foulants away from the membrane surface. However, the mechanism governing the mass transfer of foulants under two-phase flow conditions are poorly understood, and therefore, a trial-and-error approach is used to optimize the hydrodynamics of two-phase flow near a membrane surface.

In the slug flow that typically builds up, three different zones can be distinguished (Figure 2): 1) the falling film zone, i.e. the zone where the bubble is passing, 2) the wake zone, i.e. the zone just behind the bubble where mixing of liquid and gas takes place and 3) the liquid slug zone.

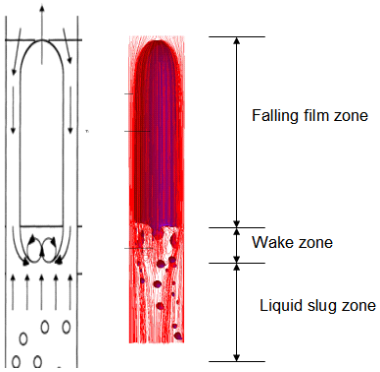

Figure 2. Zones in the slug flow [3] (left) and numerical simulation of a Taylor bubble rising through stagnant glycerine in a vertical tube [4] (right)

Experimental studies on hydrodynamics of two-phase flow have been reported in literature using shear probes [5, 6]. The method uses an electrolyte solution with a well known stoichiometry reaction which allows to correlate the diffusion (mass transfer) with a difference in electrical potential [7]. However, a more comprehensive hydraulic model of two-phase flow along a membrane is needed to better understand the mechanisms and allowing for better control of the fouling phenomenon.

MATERIALS AND METHODS

Description of the Setup

A description of the setup is given in Figure 3. For the present study, a Plexiglas tube, similar in geometry to the airlift tubular membranes of interest, was used. The tube has a length of 2 m with an inner diameter of 9.9 mm. In the middle of the tube (1 m) a flow cell is present which contains 2 electrochemical shear probes (cathode). A stainless steel pipe fitting is located downstream of the pipe

(at top of the pipe apparatus, anode). A temperature controlled water bath (20°C) is used to keep the temperature of the electrolyte solution flowing through the system constant. A MasterFlex pump is used to recirculate liquid in the system and a rotameter (range 0 to 1 L min^{-1}) is used to measure the liquid flow rate, whereas a gas flow meter (range 0 to 0.33 L min^{-1}) is used to measure the flow rate of the nitrogen gas. Nitrogen gas was used instead or air to avoid the oxidation of the electrolyte solution. A gas-liquid separator tank, which is used to store the electrolyte solution, feeds the tube with liquid and closes the loop.

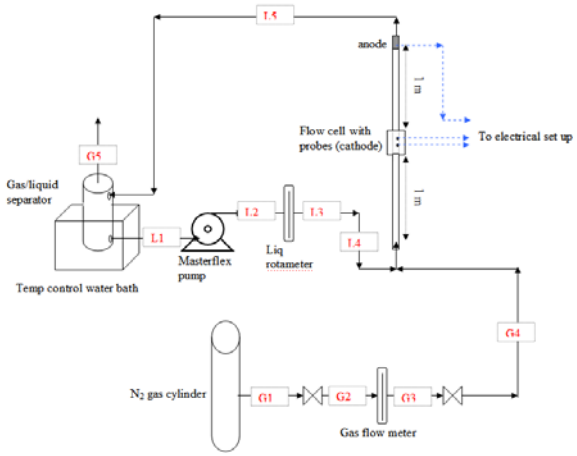

Figure 3. Description of the electrochemical shear measurement.

The electrolyte solution is pumped to the tube with specific flow rates (0.1, 0.2, 0.3, 0.4 and 0.5 L min^{-1} or 0.022, 0.043, 0.065, 0.087 and 0.108 m s^{-1}), which are monitored with the liquid rotameter. The nitrogen gas is pumped to the tube directly from a gas cylinder at different flow rates (0.1, 0.2 and 0.3 L min^{-1} or 0.022, 0.043 and 0.065 m s^{-1}), monitored by the gas flow meter. Water with the electrolyte solution and nitrogen are pumped inside of the tube at the bottom. This leads to a total of 15 possible gas-liquid flow rates, corresponding to the expected operating range in full-scale airlift tubular membrane systems, that were investigated. For each combination, surface shear stresses were measured for a period of 10 seconds, and recorded at a frequency of 1000 Hz [8]. For each combination six repetitions were performed. The flow cell has two shear probes to allow determination of the direction of the flow. When both probes in the flow cell are connected to the circuit simultaneously, the probe that is upstream (relative to the direction of flow) measures a higher magnitude of shear signal compared to the probe that is downstream of the flow. This occurs because the downstream probe is in the diffusional wake of the upstream probe [9].

Shear probes and shear stress

The shear signals recorded in Labview are in units of Voltage. This voltage can be transformed into shear stress (τ) using the following relation [7]:

$$\tau = \mu_L \left[\frac{4.64\,V}{\nu_e F \pi d_e^{\frac{5}{3}} C_o D^{\frac{2}{3}} R G} \right]^3 \qquad (1)$$

where V is the voltage signal (V), R is the resistance (Ω), G is the amplifier gain (=1000), ν_e is the number of electrons involved in the reaction (=1), F is the Faraday constant (=96 500 C mol^{-1}), d_e is the diameter of the probe (m), C_o is the bulk concentration of ferricyanide (=3 mol m^{-3}), D is the diffusion coefficient of ferricyanide ($7.14 \cdot 10^{-10}$ m^2 s^{-1}) and μ_L is the dynamic viscosity of the solution (= 0.001 Pa s).

RESULTS AND DISCUSSION

Shear profiles in two-phase vertical pipe flow

Typical results obtained using the electrochemical shear probes, and the corresponding shear stresses, are presented in Figure 4 a and b, respectively.

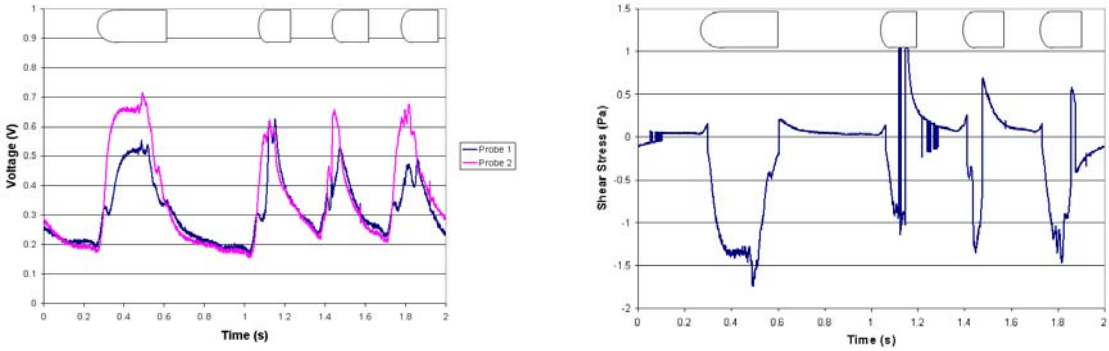

(a) (b)

Figure 4. a) Raw voltage signal for the two probes and b) conversion to shear stress for a water-N_2 combination of 0.1-0.1 L min^{-1} during a period of 2 s. (Note that the figure contains schematics of the slugs and their impact on the shear stress)

In Figure 4, the valleys in the shear stress are the bubbles and the plateaus are the liquid slug. Gas slugs rising in the vertical tubes were observed to periodically coalesce when downstream slugs 'catch-up' with upstream slugs. The coalescence occurs because two bubbles join together when the space between them gets shorter and the trailing bubble reaches the wake of the leading bubble, which makes the trailing bubble accelerate and finally coalesce with the leading bubble. This is the reason why the shear stress patterns induced by successive slugs are not similar. As a result, the pattern of shear forces in successive shear events, induced by rising gas slugs by the electrochemical shear probe, varied considerably over time. In addition to being used to validate the CFD model, shear stress distributions (SSD) were used to explore the effect of the different experimental conditions investigated on the resulting shear stresses. The SSDs with bins of 0.5 Pa were derived in the range -3 and 3 Pa (Figure 5). The histograms summarise two things: 1) the range of SSD that the membrane surface experiences and 2) the frequency or the duration of this exposure. SSD for the different gas-liquid flows are shown in Figure 5.

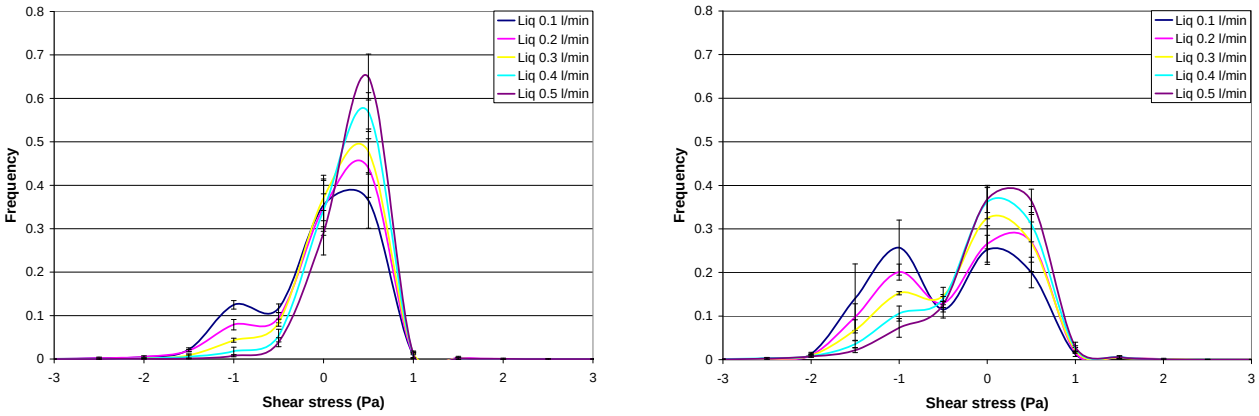

(a) (b)

Figure 5. SSD for two different gas flow rates (a) 0.1 and (b) 0.3 l min^{-1} with five liquid flow rate combinations.

For all cases, it is possible to distinguish clearly two peaks in the distributions (bi-modal distribution): a first peak occurs at a marginally positive shear value and is caused by the liquid slug; whereas a second peak occurs at a negative shear value and is caused by the gas slugs. The magnitude of the frequency for both peaks is, however, different for the different gas-liquid flow rate combinations. At low gas flow rates, the liquid slug peak is more pronounced (Figure 5a) and the magnitude of the frequency of the liquid peaks increase with the liquid flow rates. Similar findings can be observed in Figure 5b. However, at higher gas flow rates, the peaks become more balanced.

A number of studies have suggested that fouling control can be correlated to the variability in the magnitude of surface shear stresses [10]. Therefore, conditions that maximize the occurrence of both positive (liquid flow) and negative (bubble flow) shear conditions are likely to promote better fouling control. For all experimental conditions investigated, a bi-modal SSD was observed (Figure 5). An empirical relationship was developed to model the bi-modal SSD based on the Gauss distribution for the different experimental conditions investigated using the following equation:

$$f(\tau) = \underbrace{\frac{A_1}{w_1\sqrt{0.5\pi}}\exp\left[-\frac{(\tau-\tau_1)^2}{w_1^2}\right]}_{Gas\ slug} + \underbrace{\frac{A_2}{w_2\sqrt{0.5\pi}}\exp\left[-\frac{(\tau-\tau_2)^2}{w_2^2}\right]}_{Liquid\ slug} \quad (2)$$

The parameter $A_i / w_i\sqrt{0.5\pi}$ is the height of the curve's peak, τ_i is the position of the centre of the peak, and w_i controls the width of the curve. From the previous equation, there are six parameters that need to be defined (A_1, A_2, w_1, w_2, τ_1 and τ_2). The 15 SSD that were obtained from the different combinations investigated were fitted by equation (2) using Sigmaplot v10 obtaining an R-squared of 0.999 for all the combinations. Linear correlations for the different parameters were tested based on the liquid (u_{SL}) or gas (u_{SG}) superficial velocity as follows:

$$A_1 = m_1 u_{SG} + b_1 \quad (3) \qquad w_1 = m_3 u_{SL} + b_3 \quad (5) \qquad \tau_1 = m_5 u_{SL} + b_5 \quad (7)$$

$$A_2 = m_2 u_{SG} + b_2 \quad (4) \qquad w_2 = m_4 u_{SG} + b_4 \quad (6) \qquad \tau_2 = m_6 u_{SL} + b_6 \quad (8)$$

The coefficients of the slope (m_i) and intercept (b_i) are presented in Table 1.

Table 1.
Slope and intercept coefficients for equations (3) to (8)

	m_i	b_i	r^2
A_1	2.4122 ± 0.4593	0.0606 ± 0.0215	0.6797
A_2	-4.1921 ± 1.1033	0.5387 ± 0.0516	0.6104
w_1	5.3298 ± 0.8327	0.6167 ± 0.0598	0.7591
w_2	3.9621 ± 1.3383	0.3413 ± 0.0626	0.7103
τ_1	9.8327 ± 1.6658	-1.2210 ± 0.1196	0.7283
τ_2	0.5881 ± 0.2629	0.2135 ± 0.0189	0.2965

The correlations obtained are shown in Table 1, and present low R-squared values. This was due to the fact that the six parameters in equation (2) were modelled with a linear relationship, and each parameter was defined in terms of the superficial liquid or gas velocities (no combinations). This was done on purpose to keep the model structure simple.

The SSD obtained using equations 2 to 8 were compared to those obtained experimentally (Figure 6). At relatively high gas flow rates, the frequencies obtained using equations (2) to (8) and experimentally were relatively similar, deviating by less than approximately 5 %. However, at relatively low gas flow rates, the differences were slightly higher, exceeding 10 %.

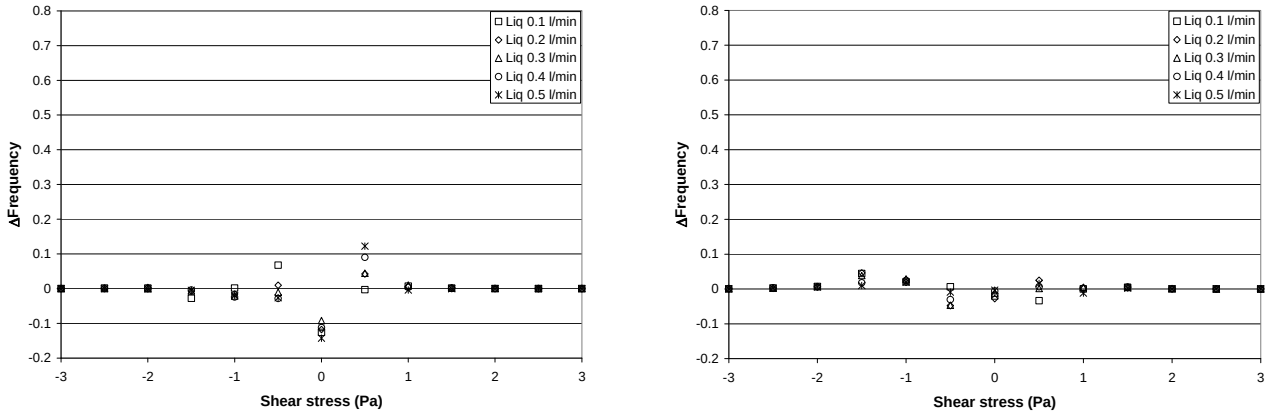

(a) (b)

Figure 6. Difference in frequency from SSD between experimental and correlations for two different gas flow rates (a) 0.1 and (b) 0.3 L min^{-1} with five liquid flow rate combinations.

The results suggest that equations (2) to (8) were able to predict the experimental data accurately. Therefore, these equations can be used to identify one exact set of operating conditions that make the gas and liquid flow rates generate similar peaks in the bi-modal SSD. The balance of the liquid and gas peaks are in terms of the curve height ($A_i / w_i \sqrt{0.5\pi}$), the width (w_i) and the centre of the peak (τ_i). However, the last term (τ_i) cannot be fixed in the equation due that the centre of the positive and negative peaks occurs in different places (positive and negative shear stress). Therefore, two velocities combinations were identified within the range of the operational conditions investigated and used to reproduce the SSD. They are presented in Figure 7.

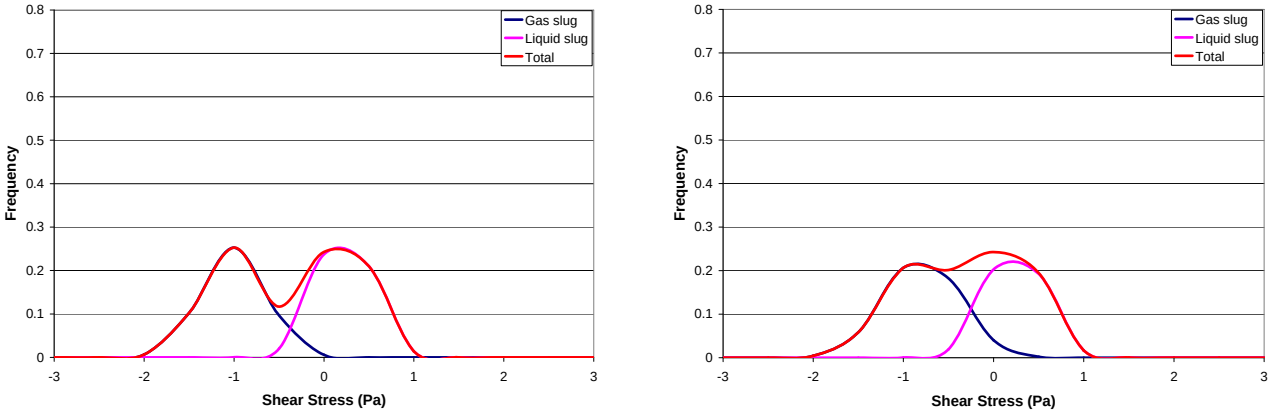

(a) (b)

Figure 7. SSD for different liquid-gas flow rates: (a) 0.10-0.32 and (b) 0.20-0.36 L min^{-1}

From Figure 7, it is possible to observe three curves, derived from equation (2). Where the first peak is the gas slug, the second is the liquid slug and the third line is the sum of both. Similar values were found between the height and the width of these curves to have a balance liquid and gas slug

peaks in terms of frequency. Nevertheless, a perfect match was not possible within the experimental range and a slightly extrapolation for the gas flow rate was made. From Figure 7a, the ratio between the liquid and the gas flow rate is 3.2 times, which means that to equilibrate the peaks at this specific liquid flow rate it is necessary to have 3.2 times more flow rate of the gas compared to the liquid. For Figure 7b, a ratio of 1.3 was found, where the flow rate of the liquid was double but the gas flow rate kept almost similar as for the case of Figure 7a. From these results, it is possible to observe that the liquid flow rate doubled but that the gas flow rate increased only 10 % to balance the two peaks.

Another factor to consider in optimising fouling control is the energy consumption, which can be expressed in terms of pressure drop using the correlation developed by [11] for two-phase flow. These equations will not be discussed further in the paper. A sum up of the pressure drop in function of the gas-liquid flow rates is presented in Table 2.

Table 2.
Two-phase pressure drop

Liquid flow rate L min^{-1}	Gas flow rate L min^{-1}	Pressure drop kPa	Liquid flow rate L min^{-1}	Gas flow rate L min^{-1}	Pressure drop kPa	Liquid flow rate L min^{-1}	Gas flow rate L min^{-1}	Pressure drop kPa
0.1	**0.32**	**4.89**	0.2	0.2	10.12	0.4	0.2	13.48
0.1	0.3	5.16	0.3	0.3	10.19	0.5	0.2	14.45
0.1	0.2	6.78	0.4	0.3	11.63	0.3	0.1	15.07
0.2	0.3	8.17	0.3	0.2	12.13	0.4	0.1	16.08
0.2	**0.36**	**9.36**	0.5	0.3	12.71	0.5	0.1	16.76
0.1	0.1	10.06	0.2	0.1	13.40			

When the pressure drop is low the energy requirements to pump the liquid and gas through the tube are lower. From Table 2, the highlighted values correspond to the liquid-gas combinations that were found as optimal combinations. From this analysis the optimal combinations result in lower pressure drop in the tube. For instance, comparing the use of liquid-gas 0.1-0.32 l min^{-1} requires 5 % less energy than 0.1-0.3 l min^{-1} and has a better remove of particles due to the balance of shear stress in the membrane surface. Finally, this correlation can be used to determine the more efficient liquid-gas ratio to increase the removal of particles at the membrane surface and to optimize the energy consumption in terms of pressure drop.

CONCLUSIONS

Due to the coalescence of bubbles, the shear stress is excessively random; therefore, SSDs are used to quantify the shear stress the tube surface is exposed to. Two peaks were found, one due to the liquid and a second due to the gas slugs. At different gas-liquid flow rates combinations, these peaks change in terms of frequency. At high liquid flow rates the liquid peak increases and the gas peak decreases. At high gas flow rates, the gas peak increases, however the liquid pick does not disappear. The bi-modal behaviour was correlated with two Gauss distributions, one for each peak. A total of six parameters were needed to describe the two Gauss distributions, each of these parameters were correlated with a linear regression function of the superficial liquid or gas velocity. A comparison between the numerical correlation and the experimental data was made and presented an error less than 15 %. The numerical correlation was used to find balanced peaks in the Gauss distribution in terms of

height and width. It was found that this new correlation can help to identify the optimal gas and liquid flow rates that minimize fouling and decrease energy requirements in terms of pressure drop.

NOMENCLATURE

A_i	height of the peak in the Gauss curve
C_o	bulk concentration of ferricyanide ions (mol m^{-3})
d_e	diameter of the probe (m)
D	diffusion coefficient of ferricyanide (= $7.14 \cdot 10^{-10}$ m^2 s^{-1})
F	Faraday constant (= 96 500 C mol^{-1})
G	amplifier gain (= 1000)
R	resistor in the circuit (Ω)
$u_{SL,G}$	superficial velocity of liquid or gas (m s^{-1})
v_e	number of electrons involved in the reaction (= 1)
V	measured shear signal (V)
w_i	width of the Gauss curve.
τ	wall shear stress (Pa)
τ_i	position of the centre of the peak in the Gauss curve

REFERENCES

1. S. Judd, The MBR Book: Principles and Applications of Membrane Bioreactors for Water and Wastewater Treatment. Elsevier, Amsterdam, 2006.
2. Z.F. Cui, S. Chang, and A.G. Fane, The use of gas bubbling to enhance membrane processes, J. Membr. Sci., 221 (2003) 1-35.
3. R. Ghosh, Z.F. Cui, Mass transfer in gas-sparged ultrafiltration: Upward slug flow in tubular membranes, J. Membr. Sci., 162 (1999) 91.
4. T, Taha, Z.F. Cui, CFD modelling of slug flow in vertical tubes, Chem. Eng. Sci., 61 (2006) 676-687.
5. V.E. Nakoryakov, O.N. Kashinsky, A.V. Petukhov and R.S. Gorelik, Study of local hydrodynamic characteristics of upward slug flow, Exp. Fluids, 7 (1989) 560-566.
6. D. Zheng, D. Che, Experimental study on hydrodynamic characteristics of upward gas-liquid slug flow, Int. J. Multiphase Flow, 32 (2006) 1191-1218.
7. C. Gaucher, P. Legentilhomme, P. Jaouen, J. Comiti, J. Pruvost, Hydrodynamics study in a plane ultrafiltration module using an electrochemical method and particle image velocimetry visualization. Experiments in Fluids 32 (2002), 283-293.
8. C.C.V. Chan, P.R. Berube, E.R. Hall, Shear profiles inside gas sparged submerged hollow fiber membrane modules. J. Membr. Sci., 297 (2007) 104-120.
9. P.R. Berube, G. Afonso, F. Taghipour, C.C.V. Chan, Quantifying the shear at the surface of submerged hollow fiber membranes. J. Membr. Sci., 279 (2006) 495-505.
10. G. Ducom, F.P. Puech, C. Cabassud. Gas/liquid two-phase flow in a flat sheet filtration module: Measurement of local wall shear stresses. Can. J. Chem. Eng., 81 (2003) 771-775
11. J.R. Thome, Engineering Data Book III. Wolverine Tube Inc. 2008.

SCREENING DIAGNOSTICS OF ERYTHROCYTIC SOLUTIONS BASED ON DISSIPATIVE PATTERNS BEHAVIOUR IN THE PRESENCE OF A MAGNETIC FIELD

A.A. Bozhko[1, *], G. Kirko[2]

[1] Perm State University, Perm, Russia
[2] Perm State Academy Medical, Perm, Russia

ABSTRACT. The influence of a uniform magnetic field on the behaviour of erythrocyte solutions made of fresh blood samples is investigated. It is found that the dissipative structures in these solutions taken from different donors differ from each other. Subsequently, it is shown that the application of a magnetic field parallel to the surface of a solution can be successfully used for express screening diagnostics of samples.
Keywords: *erythrocyte solution, dissipative patterns, magnetic field, express diagnostics*

EXPERIMENTAL APPARATUS

Observations of the qualitative state of erythrocytes can be used to conduct a rapid analysis of blood samples including different kinds of anaemia whose presence may change the size and shape of erythrocytes. The erythrocytes typically have the shape of a disk with the diameter of 7.2-7.9 μm and the mean thickness of 2 μm. Erythrocytes consist mainly of hemoglobin. It is composed of one albumen molecule of globulin and four molecules of iron-bearing compound of hem. That is why the solution of erythrocytes is very sensitive to an imposed magnetic field. It is known that the increase in erythrocyte size is indicative of the deficiency of vitamin B_{12}, while the prevalence of small size erythrocytes may be a symptom of iron-deficiency anaemia and inborn microspherocytosis. The current paper reports an experimental study of the response of dissipative patterns in thin layers of erythrocyte solution to the applied magnetic field.

Experiments were performed in a layer of erythrocytes suspended in 0.9% solution of *NaCl*. Fresh blood samples were used. In order to obtain stable solutions blood was centrifuged at 3000 rpm in a salt solution. Subsequently, a few heparin crystals were added to prevent fibrin formation. Such erythrocyte solutions remain stable for up to an hour i.e. much longer than the duration of the conducted experiments typically running for about three minutes.

Small volume of erythrocyte solution (0.2-0.4 ml) was poured in a Petri dish (with the diameter of 9.5 cm and the height of 1.5 cm) filled with *NaCl* solution so that the thickness of a resulting mixture did not exceed 3.5 mm. The vessel was fixed in the center of two Helmholtz pairs of coils that were oriented orthogonally to each other. Helmholtz coils were able to create magnetic field of up to 10 mT perpendicular or parallel to the open surface of a Petri dish. The arising flow structures were filmed using a video camera, which was placed 1 meter away from the surface of a Petri dish so that it occupied the complete video image. A lighting unit was placed under the dish.

* Corresponding author: Dr A.A. Bozhko
Phone: + (7)-342-2396836, Fax: + (7)-342-2371611
E-mail address: bozhko@psu.ru

EXPERIMENTAL RESULTS

Dissipative structures in erythrocite solution were first experimentally observed in absence of a magnetic field [1]. A close-up of such structures is shown in Figure 1. The light regions in the photograph correspond to high density of erythrocytes. Erythrocytes are virtually absent along the dark lines and their intersections (symbol EL). The observed structures were similar to Benard convection cells [2] with a characteristic size of the order of the layer thickness.

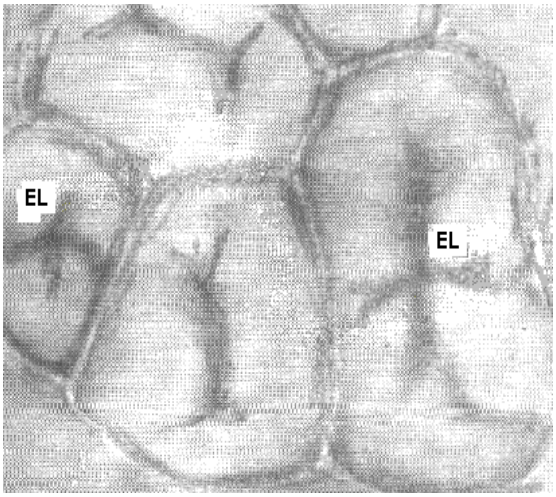

Figure 1. Dissipative patterns in an erythrocyte layer observed in absence of magnetic field. View from above. The characteristic cell diameter is about 7 mm.

Further experiments showed that convection patterns in erythrocyte solution are influenced strongly by a magnetic field which is parallel to the free surface. Typical non-stationary dissipative patterns observed in this case are shown in Figure 2. When magnetic field is just switched on small cells and narrow winding rolls with the width of about 2 mm are observed. As time progresses cells merge into rolls which align with the applied magnetic field. The transverse size of rolls increases more than four times during the exposure to magnetic field. The optimal alignment of initially disordered patterns with the direction of magnetic field is achieved at magnetic field strength of 10 mT. Similar patterns arising when the horizontal component of magnetic field is increased were reported in [3] for a free-surface layer of a colloidal dispersion of magnetic nanoparticles (also referred to as magnetic fluid [4]) placed in a magnetic field of nearly the same strength (7.7 mT): once the magnetic field is applied the hexagonal convection patterns stretch and finally form ridges aligned with magnetic field. The observed spatio-temporal patterns were correlated with the erythrocyte sizes found in blood samples received from different donors.

The same experimental set up was used to study flow patterns in magnetic fluids. In this case salt solution was replaced with kerosene. A Petri dish then was placed in the center of Helmholtz coils and a few droplets (0.2-0.4 ml) of a ferrofluid were added to kerosene. Over the time of about 5 minutes ferrofluid formed a layer of uniform thickness. Subsequently, a magnetic field of a similar strength to that used in the erythrocytic solution experiments was applied. The structures observed in a magneto-colloid mixture were found to be very similar to those seen in Figure 2.

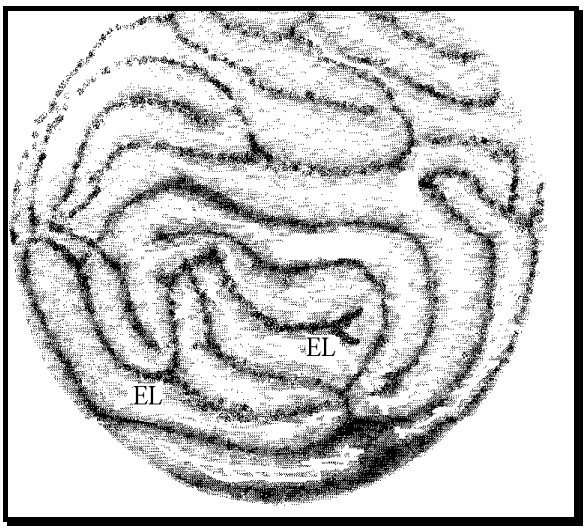

Figure 2. Dissipative structures observed in an erythrocyte layer 70 seconds after the magnetic field of 6.4 mT was applied in the plane of the photograph. View from above. The diameter of the observed area is 9.5 cm.

CONCLUSIONS

At present we are conducting systematic experiments aiming at compiling a comprehensive catalogue of patterns which would enable preliminary diagnostics of a human condition. Similarities between the patterns arising in erythrocytic and ferromagnetic mixtures indicate that the previously accumulated knowledge in the area of ferrohydrodynamics [4] can provide valuable guideance for accomplishing this task.

ACKNOWLEDGEMENTS

The authors would like to express their sincere appreciation to Dr G.I. Malkova, A.B. Lomov and E.N. Laptev of the Blood Research Laboratory at Perm State Medical Academy for their assistance with experiments. The work was supported by the Russian Foundation for Basic Research and Government of Perm Region, Russia, under grant № 07-08-96039.

REFERENCES

1. Laizan, L.K., Menshikov, I.V. Dissipative patterns in erythrocytic dredges, *Bulletin of Udmurt University*, Vol. 5, Issue 2, pp. 117-126, 1993.
2. Benard, H. Les tourbillons cellulaires dans une nappe liquide, *Revue general des Sciences, pures et appliquees*, Vol. 11, pp. 1261-1271, 1900.
3. Groh, C., Richter, R., Rehberg, I., Busse, F.H. Reorientation of a hexagonal pattern under broken symmetry: the hexagon flip, *Phys. Rev. E,* Vol. 76, pp. 055301-(1-4), 2007.
4. Rosensweig, R. E. *Ferrohydrodynamics,* Cambridge University Press, Cambridge, England, 1985.

ANALYSIS OF THERMAL EFFECTS IN HUMAN BODY EXPOSED TO EM RADIATION

E. Kurgan, P. Gas *
AGH University of Science and Technology
Deptartment of Electrical and Power Control Engineering
al. Mickiewicza 30, 30-059 Kraków, Poland

ABSTRACT. In this article distribution of the electromagnetic field components and temperature are calculated. Knowledge of temperature distribution in human body is of great importance in hyperthermial treatment of tumors. First distribution of induced current density in tissues is calculated and next bioheat equation is solved. Computed temperature distribution allow as optimal determination of electric parameters exciting coil in such a way that temperature attain its maximum value in the tumor and surrounding tissues. At the end sensitivities of the maximum temperature distribution in the body from different model parameters are calculated.

Keywords: *hyperthermia, Specific Absorption Rate, finite element method.*

INTRODUCTION

Hyperthermia is a medical therapy of tumor treatment through increasing the tissue temperature in specific part of the human body, which can have fewer side effects than other traditional methods as chemotherapy or radiotherapy. It is well known that continuous temperature in range 42–46 C will cause necrosis of living cells, resulting in a permanent damage cell functions, or at least increasing heat-induced sensitization of tumor cells to ionizing radiation and to certain chemical drugs. Up to now, many different methods have been devised to raise temperature either locally in selected parts of particular organs or over the whole body. A main advantage of electromagnetic (EM) hyperthermia is its ability to control the destruction process by a single electromagnetic applicator. In ideal case, concentrating power on a tumor selectively heats it to temperatures high enough to destroy cancerous cells without overheating and damaging the surrounding healthy tissues. Different heating methods are used to heat the superficial and deep placed tumors. Resistive heating with external electrodes, microwaves or ultrasound are usually used. Such techniques, however, may cause problems in heating deeply situated tumors, due to unavoidable overheating adjacent healthy tissues. In recent years interest in improving hyperthermia techniques has gained substantial attention in searching for new methods that can result in depth and uniform tissue heating. Invasive methods include heating with deep implanted electrodes, invasive microwave antennas, thermal seed heating, etc. To avoid pain caused by such methods, great efforts have recently been made to use radio frequency (RF) tissue heating.

Electromagnetically induced current in radiofrequency range has recently become the preferred mode of energy delivery for the tumor destruction or sensitization. The high current density near the tumor generates heat which rapidly increases the tissue temperature, causing desiccation and protein structural change in macromolecules. In comparison with other methods as, for example, high-

* Corresponding authors: Eugeniusz Kurgan, Piotr Gas
Phone: (+48 12) 6173857
E-mail address: kurgan@agh.edu.pl, piotr.gas@agh.edu.pl

energy direct-current, the advantages of radiofrequency radiation therapy are that energy can be delivered in a graded manner by changing exciting current density, it does not require general anesthesia, it can produce a homogeneous region of necrosis. The synergistic behavior between hyperthermia and chemo- and radiotherapy is a well-known phenomenon and in the last time hyperthermia experiences increasing attention of medical world.

This paper describes, through numerical finite element modeling and computer simulation, distribution of electromagnetic variables such as magnetic vector potential, electric field strength, induced current density, which are used next as starting point in calculation of heat sources in human body. In order to calculate a full investigation of the temperature variation in human tissues, one needs to take into account tissue composition, blood perfusion rate, heat conduction effects of various tissues, and heat generation due to metabolic processes. All these factors are covered in bioheat equation.

In regional hyperthermia systems, low frequency radio waves are employed to obtain significant penetration depths to heat deep-seated tumors. In this publication, inductive noninvasive applicators are employed what is highly desirable in clinical applications. The current applicators using in this study have circular shape and are placed around a patient. However, it is extremely difficult to design general-purpose antenna which can heat a tumor located anywhere within the body. The heat generation can one control with adequately placed thermometer. On the other hand, the temperature measurements also have severe problems. From one side only invasive methods are available today to measure the temperature distributions inside tissues and from the other side thermometers themselves can significantly change heat generation.

In this article distribution of the electromagnetic field components and temperature are calculated. Knowledge of temperature distribution in human body is of great importance in hyperthermial treatment of tumors. First distribution of induced current density in tissues is calculated and next bioheat equation is solved. Computed temperature distribution allow as optimal determination of electric parameters exciting coil in such a way that temperature attain its maximum value in the tumor and surrounding tissues.

MAIN EQUATIONS

Around the human body a cylindrical coil with excitation current is placed as in Figure 1.

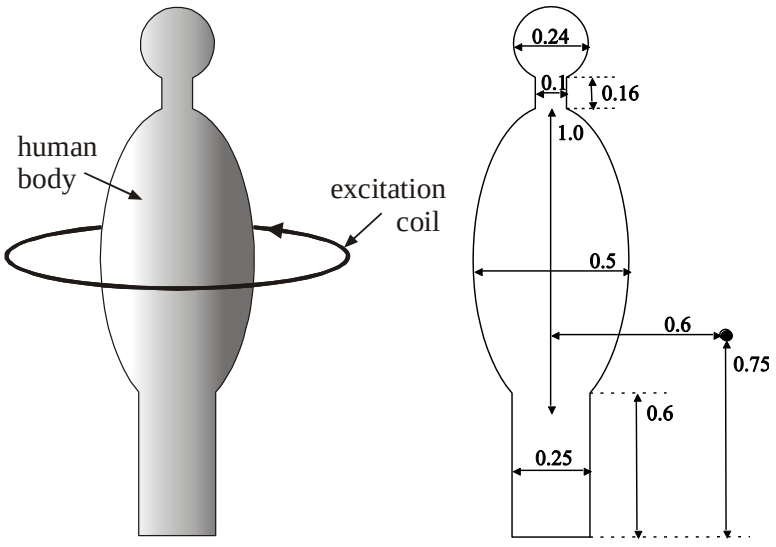

Figure 1. Schematic view of human body surrounded by wire with excitation current. Dimensions are given in meters.

The human body is considered as homogeneous medium with averaging material parameters. The current is flowing in clock-wise direction. The radius of this coil has value r_1. The exciting current in the coil generates sinusoidal electromagnetic field, which next induces eddy currents in human body. These currents are sources of heat and after some transient time, a temperature distribution in body is established. In order to calculate temperature, first distribution of electromagnetic field generated by circular coil with exciting current has to be calculated. Let us start with Maxwell's equations in time domain:

$$\nabla \times \mathbf{H} = \mathbf{J}_\mathrm{i} + \mathbf{J}_\mathrm{c} + \frac{\partial \mathbf{D}}{\partial t} \tag{1}$$

$$\nabla \times \mathbf{E} = -\frac{\partial \mathbf{B}}{\partial t} \tag{2}$$

where $\mathbf{J}_\mathrm{i}$ is an impressed current, which can be treated as a source of the electromagnetic field, and which results from charges placed outside computational domain, $\mathbf{J}_\mathrm{c}$ is a conduction current caused by electric field strength accordingly with differential Ohm's law, and other vectors have their usual meaning. Magnetic vector potential is defined as

$$\mathbf{B} = \nabla \times \mathbf{A} \tag{3}$$

Introducing (3) into (2) (3)we get

$$\nabla \times \mathbf{E} = -\frac{\partial}{\partial t}\left(\nabla \times \mathbf{A}\right) = -\nabla \times \frac{\partial \mathbf{A}}{\partial t} \tag{4}$$

and finally

$$\nabla \times \left(\mathbf{E} + \frac{\partial \mathbf{A}}{\partial t} \right) = 0 \tag{5}$$

We can introduce potential V as

$$-\nabla V = \mathbf{E} + \frac{\partial \mathbf{A}}{\partial t} \tag{6}$$

Field intensity can be express now as

$$\mathbf{E} = -\nabla V - \frac{\partial \mathbf{A}}{\partial t} \tag{7}$$

In two dimensional problems we can assume that $\nabla V = 0$, so in this case

$$\mathbf{E} = -\frac{\partial \mathbf{A}}{\partial t} \tag{8}$$

Taking into account, that $\mathbf{J}_\mathrm{c} = \sigma\,\mathbf{E}$, and $\mathbf{D} = \varepsilon\mathbf{D}$ and introducing (8) into (1) yields

$$\nabla \times \mathbf{H} = \mathbf{J}_\mathrm{i} + \sigma\mathbf{E} + \varepsilon \frac{\partial \mathbf{E}}{\partial t} \tag{9}$$

and

$$\nabla\times\left(\frac{1}{\mu}\nabla\times\mathbf{A}\right)=\mathbf{J}_{\mathrm{i}}-\sigma\frac{\partial\mathbf{A}}{\partial t}-\varepsilon\frac{\partial^2\mathbf{A}}{\partial t^2} \tag{10}$$

If in time domain in sinusoidal steady state magnetic vector potential is given by function

$$\mathbf{A}(\mathbf{r},t)=A_m(\mathbf{r})\cos[\omega t+\varphi(\mathbf{r})] \tag{11}$$

then we can introduce complex amplitude

$$\tilde{\mathbf{A}}(\mathbf{r},t)=\hat{\mathbf{A}}(\mathbf{r})e^{j\omega t} \tag{12}$$

where phasor $\hat{\mathbf{A}}(\mathbf{r})$ is a complex number dependent from spatial coordinates $\mathbf{r} = (x, y, z)$. Magnetic vector potential in time domain $\mathbf{A}(\mathbf{r}, t)$ is related with complex amplitude $\tilde{\mathbf{A}}(\mathbf{r},t)$ by

$$\mathbf{A}(\mathbf{r},t)=\mathrm{Re}\left[\hat{\mathbf{A}}(\mathbf{r})e^{j\omega t}\right] \tag{13}$$

Introduction (13) into (10) gives

$$\nabla\times\left(\frac{1}{\mu}\nabla\times\hat{\mathbf{A}}\right)-\left(\omega^2\varepsilon+j\omega\sigma\right)\hat{\mathbf{A}}=\hat{\mathbf{J}}_{\mathrm{i}} \tag{14}$$

In two dimensions we assume symmetry with respect to coordinate φ, so magnetic vector potential can be written as

$$\hat{\mathbf{A}}=A_\varphi(r,z)\mathbf{e}_\varphi \tag{15}$$

Because also

$$\hat{\mathbf{J}}_{\mathrm{i}}=J_{\mathrm{i}}\mathbf{e}_\phi \tag{16}$$

thus equation (14) can be written in simpler form

$$-\left[\frac{\partial}{\partial r}\left(\frac{1}{\mu r}\frac{\partial\left(rA_\phi\right)}{\partial r}\right)+\frac{\partial}{\partial z}\left(\frac{1}{\mu r}\frac{\partial\left(rA_\phi\right)}{\partial z}\right)\right]-\left(\omega^2\varepsilon+j\omega\sigma\right)A_\phi=J_{\mathrm{i}} \tag{17}$$

As boundary condition we assume zero potential no symmetry axis z. The above equation is solved by finite element method over given computational domain. If $\sigma >> \omega\varepsilon$ then displacement current can be neglected.

Unlike the computation of the electric currents in body, for which agreement exists accordingly a derived physical model, no clear consensus exists for an appropriate mathematical model for the evaluation of temperature field distribution in biological tissues. An extremely important work in the modeling of heat transfer in biological tissues was done over half a century ago by Pennes. The equation, which he derived, is named bioheat equation, and it can be derived from the classical Fourier law of heat conduction. This model is based on the simple assumption of the energy exchange between the blood flowing in vessels and the surrounding the tumour tissues. Pennes model may provide suitable information on temperature distributions in whole body, organ under consideration, and tumour analysis under study.

Pennes model states, that the total heat exchange between tissue surrounding a vessel and blood flowing in it, is proportional to the volumetric heat flow and the temperature difference between the blood and the tissue. The expression of Pennes bioheat equation in a body with uniform material properties in steady state is given by

$$\nabla\left(-k\nabla T\right)=\rho_b C_b \omega_b (T_b - T) + Q_{ext} + Q_{met} \tag{18}$$

where T is temperature [K], k − the tissue thermal conductivity [W/(m·K)], ω_b − the blood perfusion rate [1/s], C_b − the blood specific heat, T_b − the blood vessel temperature, Q_{met} − the metabolic heat generation rate [W/m^3], and Q_{ext} − the external heat sources [W/m^3].
The usual boundary condition associated with the heat transfer process in the context of hyperthermia can be given by

$$\mathbf{n}\cdot\left(-k\nabla T\right)=h(T_{air} - T) \tag{19}$$

on boundary Γ, where h is the heat transfer coefficient [W/(m^2·K)], T_{air} is the temperature of the surrounding air [K].

The limitations associated with bioheat equation were pointed out in [17]. One of the most serious limitations results from the fact that the perfusion rate is not generally independent from temperature. Instead, the human thermoregulatory system generally responds to increased heat generation in an tissue by attempting to increase blood flow to that part of body. In regional hyperthermia, the most common modelling choice is to assume that the blood perfusion rate in the Pennes model is constant. Several experiments, however, have shown that the response of organ to heat generation is dependent, even at moderate temperatures in the range 41–43°C. Nevertheless, we further assume constant value of blood perfusion rate. Both equations (17) and (18) are simultaneously solved by finite element method.

COMPUTATIONAL RESULTS

The hyperthermia arrangement in two dimensions as given in fig.1 is considered. The dimensions and physical parameters of the model are given in following tables (Tables 1 – 2):

Table 1
PHYSICAL PARAMETERS OF TISSUES
TAKEN INTO NUMERICAL MODEL

Tissue	ε_r	σ [S/m]	k [W/(m·K)]	Q_{met} [W/m^3]
Human body	29.6	0.053	0.22	300

Table 2
PHYSICAL PARAMETERS OF BLOOD
TAKEN INTO BIOHEAT EQUATION

Tissue	ρ_b [kg/m^3]	C_b [J/(kg·K)]	T_b [K]	ω_b [1/s]
Blood	1060	3639	310.15	in body 0.005

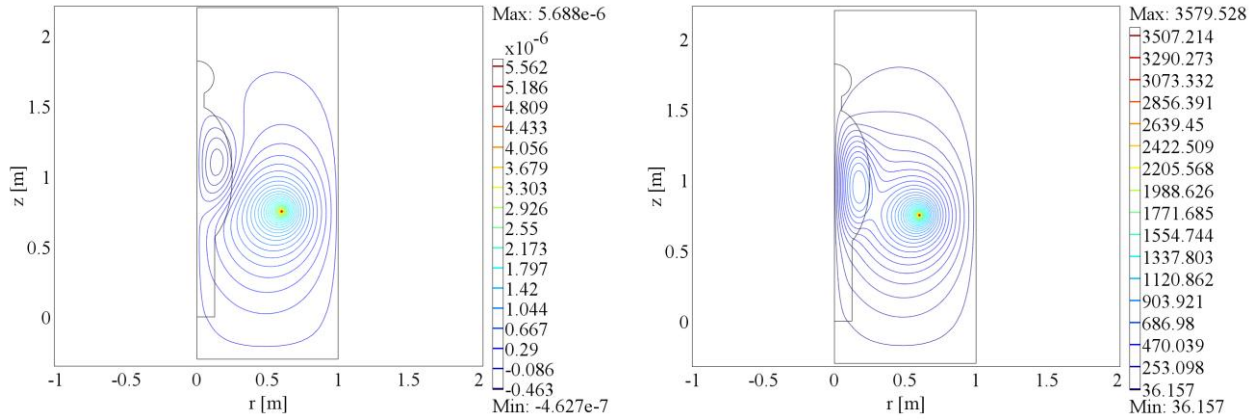

Figure 2. Equipotential lines of magnetic vector potential A_ϕ (left)
and equipotential lines of modulus of the electric field strength E_ϕ (right).

The whole computational domain was divided into triangular finite elements and appropriate boundary conditions were introduced. The exciting current in the coil is I_{max} = 4.5 [A], and frequency is f = 100 [MHz]. Moreover, the heat transfer coefficient is h = 10 [W/(m^2·K)] [25], and the air temperature surrounding the body is T_{air} = 293.15 [K]. Radius of the exciting coil with current I_{max} has value r = 0.6 [m].

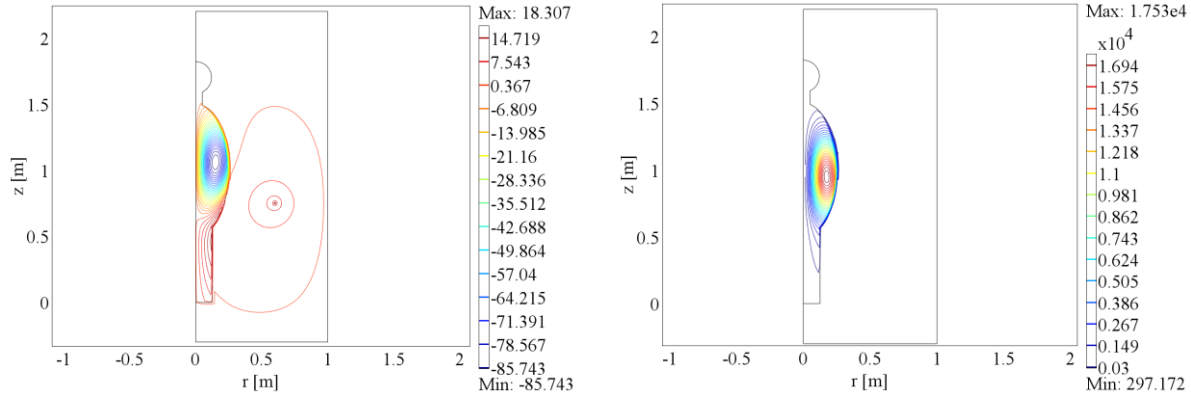

Figure 3. Equipotential lines of total current density (left)
and equipotential lines of resistive heating (right).

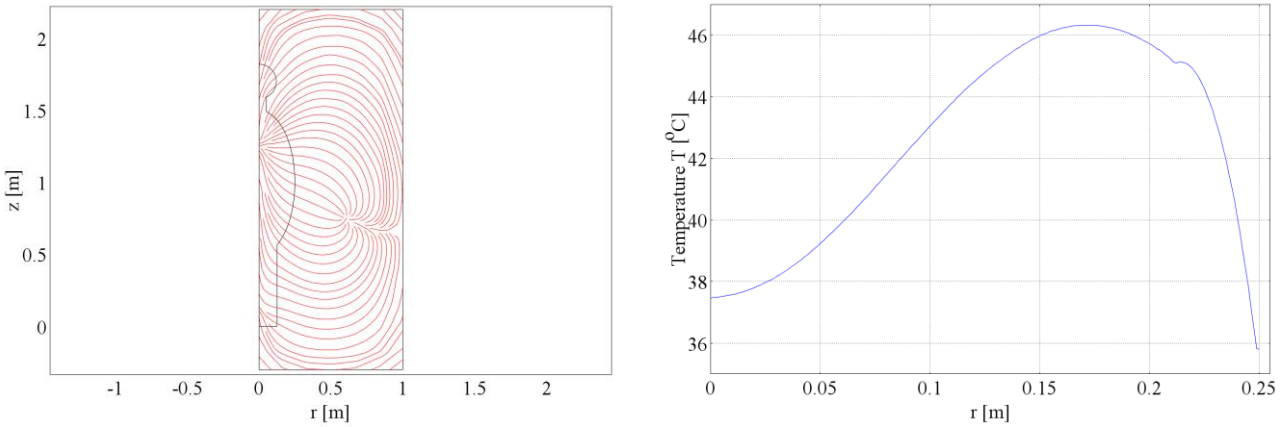

Figure 4. Streemlines of the total energy flow (left) and temperature distribution
along line from point (0,0.95) to point (0.25, 0.95) (right).

First magnetic vector potential A_ϕ is calculated from the equation (17), and next modulus of the electric field strength E_ϕ, computed with formula $E_\phi = j\omega \cdot A_\phi$ (Figure 2). Total induced current density in human body is calculated from the equation $J_z = (\omega^2\varepsilon + j\omega)\cdot A_\phi$ and then resistive heat source $Q_{ext} = 0.5\ \mathrm{Re}[J_\phi (E_\phi^* + \sigma^{-1} J_{i\phi}^*)]$ (Figure 3). At the end bioheat equation was solved. Figure 4 shows power density streamlines from field source to human body. One can see that energy really flows from energy source, in this case exciting coil, to human body.

At Figure 5 six temperature distributions for different blood perfusion rates ω_b and exciting current I_{max} are shown. Calculations were made for frequency f = 500 [kHz] with condition that in every case maximal temperature has the value T_{max} = 46°C. When blood perfusion rate is increased exciting current should be also adequately corrected as it is shown in Figure 5.

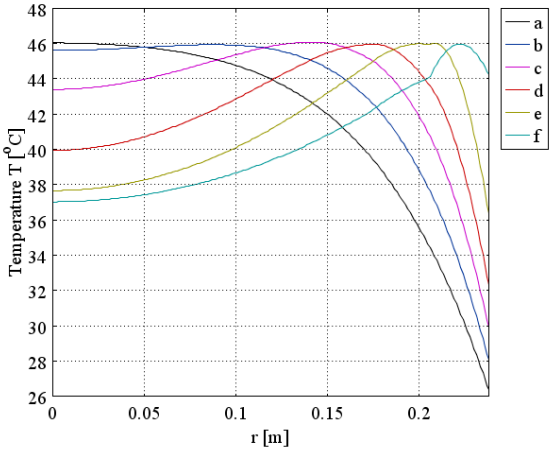

Lines	ω_b [1/s]	I_{max} [A]
a	0.000005	545
b	0.00001	720
c	0.00002	925
d	0.00005	1240
e	0.0002	2060
f	0.005	8450

Figure 5.Temperature distribution along path from (0, 0.85) to (0.2386, 0.85).

In Fig. 6 and 7 sensitivities of the maximum temperature T_{max} along path from (0, 0.85) to (0.2386, 0.85) from exciting frequency f, exciting current in the coil I_{max}, perfusion rate ω_b and surface heat transfer coefficient h are shown.

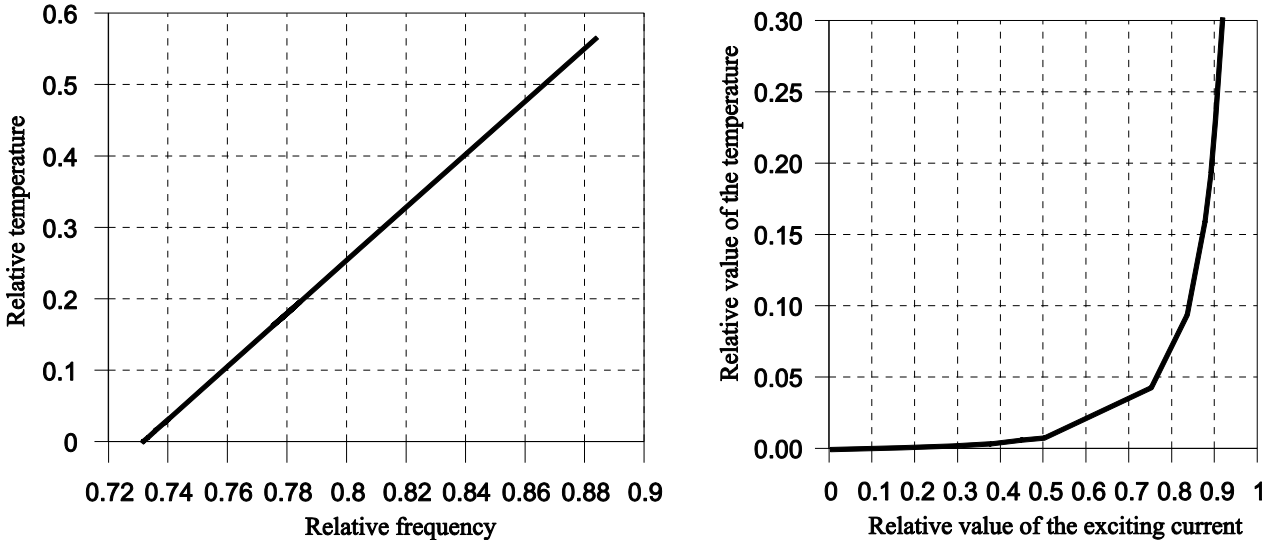

Figure 6. Relative maximum temperature distribution along path from (0, 0.85) to (0.2386, 0.85) from relative frequency (left) and relative value of exciting current I_{max} (right).

All four figures present dependence between relative maximum temperature in human body in relation to relative values of model parameters:

$$\frac{\Delta T_{\max}}{T_{\max}} = f\left(\frac{\Delta\omega}{\omega}\right) \tag{20}$$

where ω is here any model parameter.

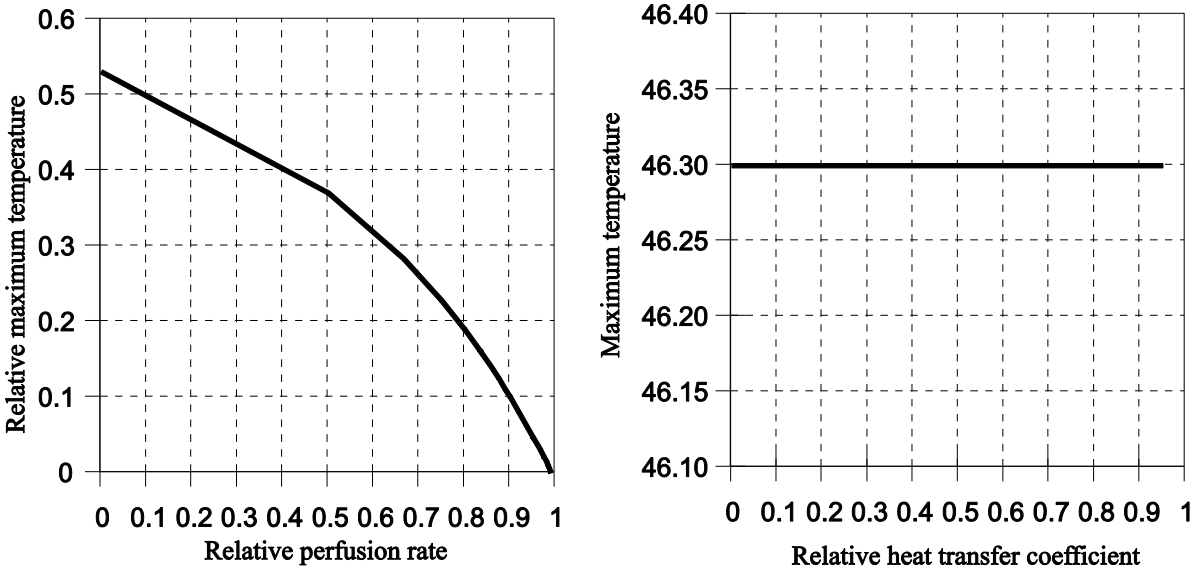

Figure 7. Relative maximum temperature distribution along path from (0, 0.85) to (0.2386, 0.85) from relative perfusion rate (left) and maximum temperature from relative heat transfer coefficient (right).

CONCLUSIONS

In this study, numerical simulations electromagnetic field and temperature distribution in human tissues was performed. A two-dimensional analysis has been applied to compute the electric current fields and the temperature distributions inside tissues. The developed procedure is general and could be used to evaluate temperature distributions for arbitrary coils configurations, also in the case when coils are placed at different angels compared with human body, have different radius and different conducting currents. The described method could be used to optimize the position, exciting current amplitude and phases of coils, and to give better control to the temperature distributions throughout the tumor volume. Numerical results show that there is a considerable variation of the temperature parallel to the coil plane, which signifies the importance of the two-dimensional model employed in this paper. This approach is expected to be valuable in improving optimal distribution of the temperature in tumor and surrounding tissues when tumor is placed deep in body. There is direct proportionality between relative temperature and exciting frequency ω. Thus through frequency change one can adjust temperature in the body (Fig.6). Exciting current $I_{\max}$ has influence on body temperature, when it is greater than 0.3. Blood perfusion rate generally diminishes body temperature (Fig 7) and heat transfer coefficient h has not visible influence on temperature distribution.

REFERENCES

1. Jackman, W. M., Wang, X., Friay, K. J., Roman, C. A., Moulton, K. P., Beckman, K. J., McClelland, J. H., Twidale, N., Hazlitt, H. A., Prior, M. I., Margolis, P. D. , Calame, J. D., Overholt, E. D. and Lazzara R., Catheter ablation of accessory atrioventricular pathways (Wolff-Parkinson-White syndrome) by radiofrequency current,' *New Engl. J. Med.*, Vol. 324, pp 1605-1611, 1991.
2. Calkins, H., Sousa, J., El-Atassi, R., Rosenheck, S., de Buitleir, M., Kou, W. H., Kadish, A. H. , Langberg, J. J. and Morady, F., Diagnosis and cure of the Wolff-Parkinson-White syndrome or paroxysmal supraventricular tachycardias during a single electrophysiologic test, *New Engl. J. Med.*, Vol. 324, pp 1612-1618, 1991.
3. Jazayeri, M. R. , Hempe, S. L., Sra, J. S., Dhala, A. A., Blanck, Z., Deshpande, S. S., Avitall, B., Krum, D. P., Gilbert, C. J. and Akhtar, M., Selective transcatheter ablation of the fast and slow pathways using radiofrequency energy in patients with atrioventricular nodal reentrant tachycardia, *Circ.*, Vol. 85, pp 1318-1328, 1992.
4. Klein, L. S., Shih, H. T., Hackett, F. K., Zipes, D. P. and Miles, W. M., Radiofrequency catheter ablation of ventricular tachycardia in patients without structural heart disease, *Circ.*, Vol. 85, pp 1666-1674, 1992.
5. Huang, S. K., Graham, A. R., Lee, M. A., Ring, M. E., Gorman, G. D. and Schiffman, R., Comparison of catheter ablation using radiofrequency versus direct current energy: Biophysical, electrophysiologic and pathologic observations, *J. Am. Coll. Cardiol.*, Vol. 18, pp 1091-1097, 1991.
6. Haines, D. E. and Watson, D. D., Tissue heating during radiofrequency catheter ablation: A thermodynamic model and observations in isolated perfused and superfused canine right ventricular free wall, *Pace*, Vol. 12, pp 962-976, 1989.
7. Hindricks, G., Haverkamp, W., Glker, H., Rissel, U., Budde, T., Ritcher, K. D., Borggrefe, M. and Breithardt, G., Radiofrequency coagulation of ventricular myocardium: Improved prediction of lesion size by monitoring catheter tip temperature," *Eur. Heart J.*, Vol. IO, pp 972-984, 1989.
8. Wittkampf, F. H. M., Hauer, R. N. W. and Robles de Medina, E. O., Control of radiofrequency lesion size by power regulation, *Circ.*, Vol. 80, pp. 962-968, 1989.
9. Bardy, G. H., Sawyer, P. L., Johnson, G. W. and Reichenbach, D. D., Radiofrequency ablation: Effect of voltage and pulse duration on canine myocardium, *Am. J. PhysioL*, Vol. 258, pp HI899-HI905, 1990.
10. Haines, D. E. and Verrow, A. F., Observations on electrode-tissue interface temperature and effect on electrical impedance during radiofrequency ablation of ventricular myocardium, *Circ*., Vol. 82, pp 1034-1038, 1990.
11. Strohbehn, J. W. and Roemer, R. B., A survey of computer simulations of hyperthermia treatments," *IEEE Trans. Biomed. Eng.*, Vol. BME-31 , pp 136-149, 1984.
12. Erez, A. and Smitzer, A., Controlled destruction and temperature distributions in biological tissues subjected to monoactive electrocoagulation, *J. Biomechan. Eng.*, Vol. 102, pp 42-49, 1980.
13. Hayes, L. J., Diller, K. R., Pearce, J. A., Schick, M. R. and Colvin, D. P., Prediction of transient temperature fields and cumulative tissue destruction for radiofrequency heating of a tumor, *Med. Physics*, Vol. 12, pp 684-692, 1985.
14. Strohbehn, J. W. and Douple, E. B., Hyperthermia and cancer therapy: A review of biomedical engineering contributions and challenges, *IEEE Trans. Biomed. Eng.*, Vol. BME-31, pp 779-782, 1984.
15. Hahn, G. M., *Hyperthermia and Cancer*, Plenum, New York, 1982.
16. Storm, F. K., Elliot, R. S., Harrison, W. H. and Morton, D. L., Clinical RF hyperthermia by magnetic-loop induction: A new approach to human cancer therapy, *IEEE Trans. Microwave Theory Tech.*, Vol. 82, pp 1149-1158, 1982.

17. Guy, A. W., Lehmann, J. F. and Stonebridge, J. B., Therapeutic applications of electromagnetic power, *Proc. IEEE*, Vol. 62, pp 55-75, 1974.
18. Christensen, D. A. and Dumey, C. H., Hyperthermia production for cancer therapy: A review of fundamentals and methods, *J. Microwave Power*, vol. 16, pp 89-105, 1981.
19. Astrahan, M. A., A localized current field hyperthermia system for use with 192-iridium interstitial implants, *Med. Phys.*, Vol. 9, pp 419-424, 1982.
20. Gerner, E. W., Connor, W. G., Boone, L. M., Doss, J. D., Mayer, E. G. and Miller, R. C., The potential of localized heating as an adjunct to radiation therapy, *Radiology*, Vol. 116, pp 433-439, 1975.
21. Strohbehn, J. W., Temperature distributions from interstitial RF electrode hyperthermia systems: Theoretical predictions, *Int. J. Radiut. Oncol. Biol. Phys.*, Vol. 9, pp 1655-1667, 1983.
22. Doss, J. D., Calculation of electric fields in conductive media, *Med. Phys.*, Vol 9, pp 566-73, 1982.
23. Spiegel, R. J., A review of numerical models for predicting the energy deposition and resultant thermal response of humans exposed to electromagnetic fields, *IEEE Trans. Microwave Theory Tech.*, Vol. 32, No. 8, pp 730-746, 1984.
24. Caorsi, S., Electromagnetic heating of layered biological systems with nonlinear thermoregulatory properties, *Radio Sci.*, Vol. 19, pp 1199-1204, 1984.
25. Foster, K. R., Ayyaswamy, P. S., Sundararajan, T. and Ramakrishna, K., Heat transfer in surface-cooled objects subject to microwave heating, *IEEE Trans. Microwave Theory Tech.*, Vol. MTTMTT-30, pp 1158-1 166, 1982.
25. Zhong-Shan Deng, Jing Liu, Mathematical modeling of temperature mapping over skin surface and its implementation in thermal disease diagnostics, *Computers in Biology and Medicine*, vol. 34, pp. 495–521, 2004

Fuel Cell Systems

HYDROGEN STORAGE PROPERTIES OF GRAPHITE INTERCALATED WITH LITHIUM BY MECHANICAL ALLOYING

A. Takasaki* and, R. Era
Shibaura Institute of Technology, Tokyo, Japan

Abstract. We attempted to intercalate lithium, which has a strong chemical affinity with hydrogen, in graphite structure by mechanical alloying (MA). The graphite powders were firstly mechanical alloyed with lithium hydride (LiH) powders, and then were dehydrogenated in a vacuum. The amount of lithium was varied from $C_{92}Li_8$ to $C_{88}Li_{12}$ by changing the amount of LiH. Although the graphite structure turned into a turbostratic one after earlier MA, the aromatic carbon layers still remained even after longer MA. The graphite interlayer spacing increased with increasing MA time. The interlayer spacing for the $C_{92}Li_8$ powders varied largely, that were about 0.665 nm before MA and about 0.725 nm after MA for 40 h, showing the intercalation of lithium between the graphite interlayers after dehydrogenation. After rehydrogenation at a temperature of 303 K and an initial hydrogen pressure of 4 MPa, the $C_{92}Li_8$ powders absorbed about 1.6 wt.% hydrogen, while the pure graphite, the $C_{90}Li_{10}$ and the $C_{88}Li_{12}$ powders absorbed only about 0.6 wt% hydrogen. No formation of LiH was observed after rehydrogenation. Hydrogen desorption for the $C_{92}Li_8$ powders occurred at 469 K, while those for the $C_{90}Li_{10}$ and the $C_{88}Li_{12}$ powders occurred at more than 473 K. The $C_{92}Li_8$ powders exhibited the best hydrogen storage properties among the powder mixtures.

Keywords: *hydrogen storage, graphite, lithium hydride, mechanical alloying*

INTRODUCTION

Hydrogen storage is one of important technological issues for the application of the fuel cell. Several kinds of hydrogen storage methods are now being proposed, in which the storage in a high-pressure tank seems to be most simple and convenient, but there are potential problems, i.e. very low volumetric density for hydrogen storage and dangerousness. The hydrogen storage in solid materials such as metal hydrides, which has been studied actively by materials scientists and engineers, is very safe and normally shows high volumetric density, but suffer from lower gravimetric density.

Hydrogen storage in carbonaceous materials has firstly been reported by Dillon et. al.[1] for single walled nanotubes. Since then study for hydrogen storage in carbonaceous materials, like carbon nanofibers [2] and nanostructured graphite produced by mechanical milling in hydrogen atmosphere [3], etc., has been widely performed. However, there is still controversy about the hydrogen capacities. Because carbon is one of light elements, higher hydrogen capacities that are the amount of hydrogen stored per unit weight is expected, even if it takes some hydrogen atoms.

Mechanical alloying (MA) of Mg with graphite (approximately $C_{47}Mg_{53}$) in nitrogen atmosphere was reported to result in the generation of large amounts of dangling carbon bonds in the graphite, providing suitable sites for hydrogen atoms, in which at least two hydrogen states have been

* Corresponding author: Prof. A. Takasaki
Phone: + (81)-3-5859-8059, Fax: + (3)-3-5859-8001
E-mail address: takasakil@shibaura-it.ac.jp

reported to exist; one in the form of C-H bonding in the nanostructured graphite and the other as a hydride in Mg [4]. We have previously reported that the graphite interlayer (graphene) spacing in the graphite structure was expanded by a combination of addition of small amount of Mg and MA, leading the hydrogen capacity about 1 wt.% at 308 K [5]. This suggests that Mg atoms were intercalated between the graphite interlayer in the graphite structure and attracted hydrogen into the interlayer. In this study, we attempted to substitute Li for Mg, and mechanically alloy and hydrogenate the graphite/Li powder mixtures after MA because the Li is a lighter element than Mg so that higher hydrogen capacity in weight percent would be anticipated.

EXPERIMENTAL PROCEDURES

Commercially pure graphite and LiH powders were used as starting materials in this study (Li powders were not used because they are very active in an atmospheric condition). The purities of graphite and LiH powders were 99.9 % and 95 % respectively, and the mean grain diameters were 20 μm and 30 μm respectively.

By adjusting the powder mixtures with a final chemical composition of $C_{100-x}Li_x$ ($0 \leq x \leq 12$) after dehydrogenation of LiH, the powder mixtures were poured into stainless-steel vials ($45cm^3$) with some stainless-steel balls. The ball-to-mixture weight ratio was approximately 20:1. The vials containing the powder mixtures and the balls were evacuated by a rotary-pump and then back-filled with an argon gas (99.99999 %) several times in a glove box, and the final argon gas pressure was kept to be 0.1 MPa. MA was carried out by a Fritsch Pulverisette 7 planetary ball mill. The maximum ball acceleration was 15g. To avoid any temperature increases during MA, the alloying period of 0.5 h was alternated with an equal rest time.

After MA the powder mixtures were dehydrogenated in a vacuum at an elevated temperature, and then rehydrogenated at 308 K at an initial hydrogen pressure of 4 MPa in a pressure-composition-isotherm (PCT) equipment (Sieverts type apparatus). The hydrogen capacities of the powder mixtures after dehydrogenation were calculated from the pressure change in the PCT measurement. Thermal analyses such as thermogravimetry/differential thermal analysis (TG/DTA) and differential scanning calorimetry (DSC) were also performed for the powder mixtures after rehydrogenation to investigate the hydrogen desorption properties. X-ray diffraction measurements were made with Cu-Kα radiation to identify the phases before and after MA for several times, and before and after rehydrogenation.

RESULTS AND DISCUSSION

Figure 1 shows X-ray diffraction patterns for $C_{88}Li_{12}$ powder mixtures before and after MA for several MA times. The X-ray intensity of the prominent peak for the graphite, (002), decreases with increasing MA time up to 40 h, although other peaks for the graphite and LiH almost disappear after earlier MA (about 8 h). The graphite structure seems to be decomposed and turned into a turbostratic structure (i.e. structure whose chemical bonding between the graphite interlayer are broken because of a weak van der Waals' secondary bonding but the bonding in the aromatic carbon layers (graphene) still exits because of a strong covalent bonding) by MA process. The (002) peak for the graphite also shifts to lower angles with increasing MA times, indicating an expansion of the graphite interlayer spacing. The graphite interlayer spacing as a function of MA time for all powder mixtures are shown in Figure 2. The interlayer spacing seems to increase with increasing MA time up to 40 h. The spacing for the $C_{92}Li_8$ powders, particularly, varied largely between before and after MA, which was about 0.665 nm before MA and about 0.725 nm after MA for 40 h (about a 9 % increase). The spacing for $C_{92}Li_8$ after MA for 40 h is the highest among the powder mixtures. An expansion of

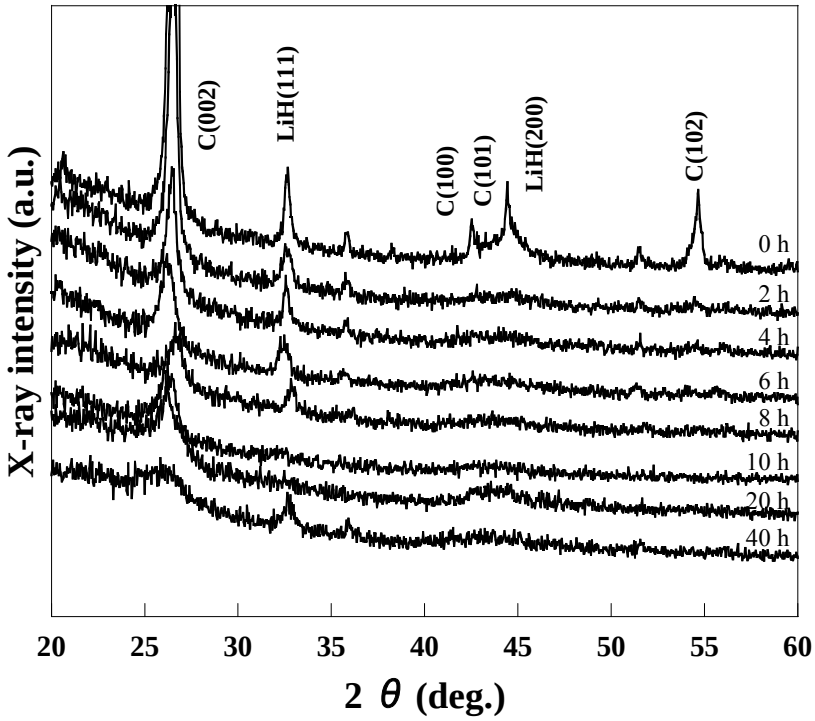

Figure 1. X-ray diffraction patterns for for $C_{88}Li_{12}$ powder mixtures before and after MA for several MA times.

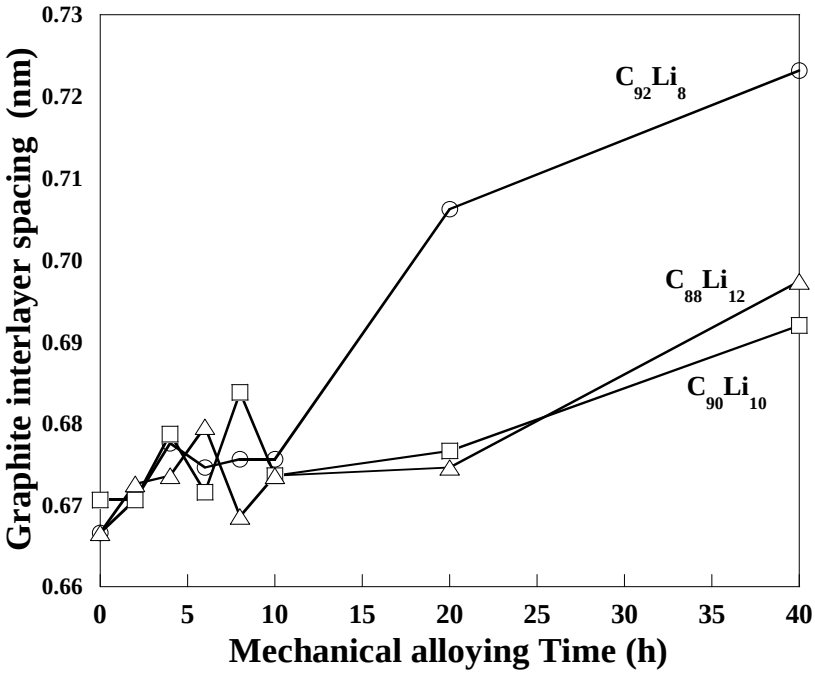

Figure 2. The graphite interlayer spacing as a function of MA time for all powder mixtures.

graphite interlayer was reported for graphite without any additives after MA under hydrogen atmosphere for earlier milling time [3]. However, it is suggested that the Li must be intercalated

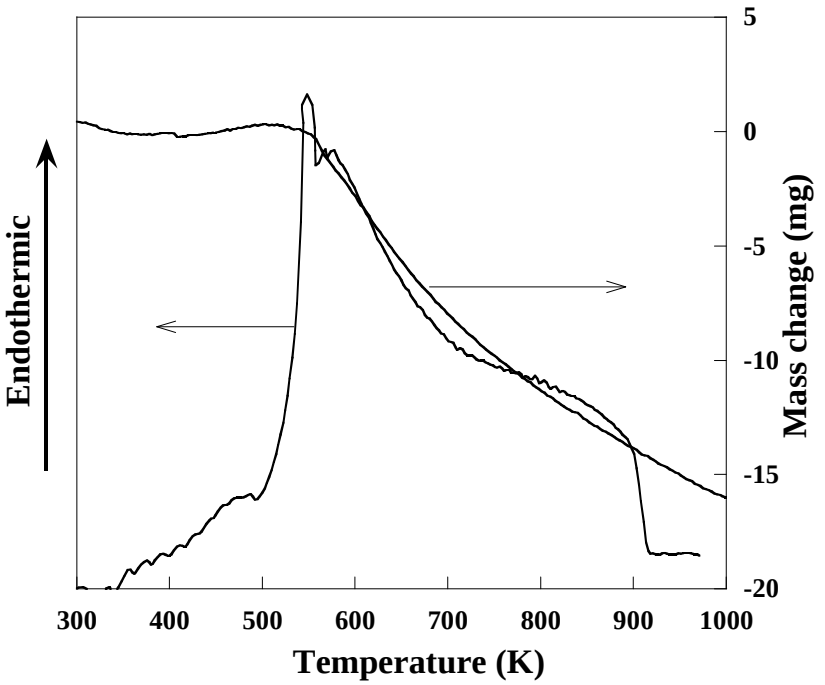

Figure 3. Thermogravimetry/ differential thermal analyses curves for $C_{92}Li_8$ powder mixture after MA for 40 h.

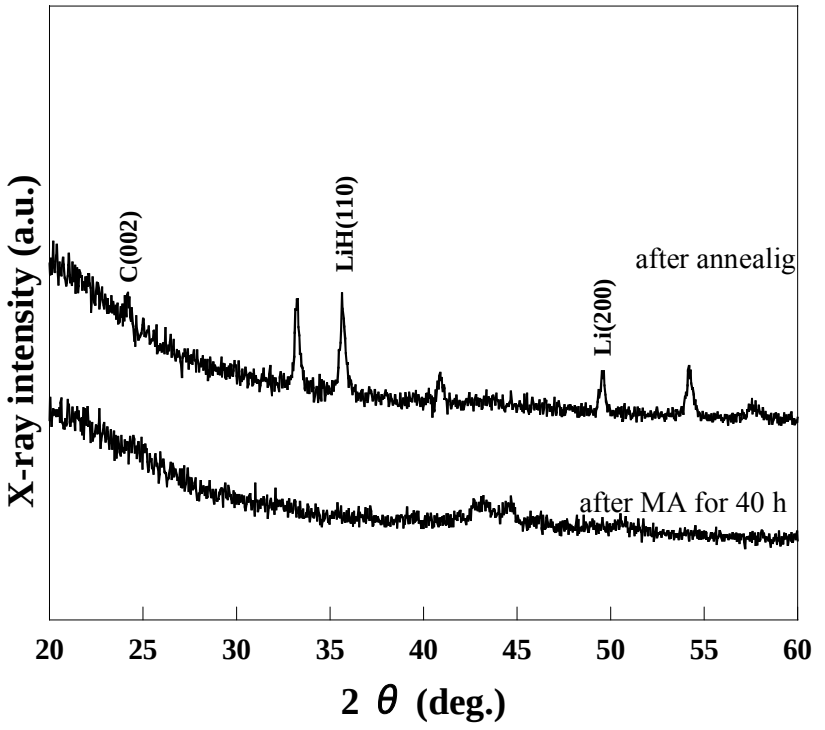

Figure 4. X-ray diffraction patterns for $C_{92}Li_8$ powder mixture before and after the first dehydrogenation after MA.

between the graphite interlayers after dehydrogenation process of the powder mixtures, because the interlayer spacings are dependent on both the chemical composition and MA time in this study.

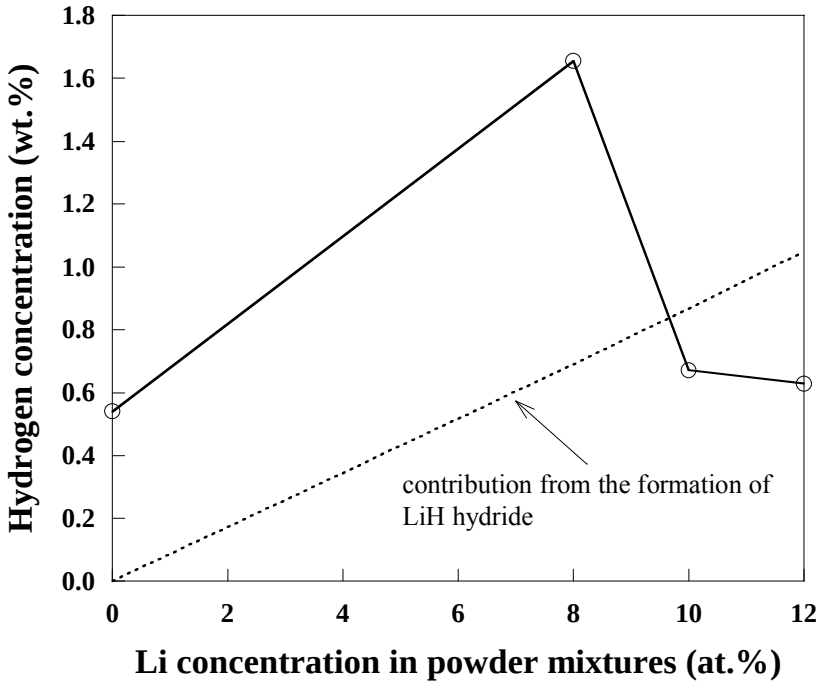

Figure 5. Hydrogen concentration (open circles) in the powder mixtures as a function of Li concentration in the powder mixtures after MA for 40 h. The data shown with dashed line indicate the hydrogen concentration in the powder mixtures if Li existed in the powders is assumed to turn back into LiH hydride.

Figure 3 shows TG/DTA curves for $C_{92}Li_8$ powder mixture after MA for 40 h. The mass of the powder mixture initiates to decrease at a temperature of about 573 K with an endothermic reaction, indicating the decomposition of LiH in the powder mixtures. From these results, all the powder mixtures after MA were dehydrogenated at a temperature of 773 K for 5 h in a vacuum. Figure 4 shows X-ray diffraction patterns for $C_{92}Li_8$ powder mixture before and after the first dehydrogenation after MA. No X-ray diffraction peaks for LiH were observed even before hydrogenation, and several peaks for Li were observed after dehydrohenation, indicating that the dehydrogenation was performed sufficiently at 773 K for 5 h in a vacuum. Some peaks which are not indexed seem to be due to an oxide formation during heating.

After dehydrogenation of the powder mixture, all powders were rehydrogenated in a PCT apparatus to investigate their hydrogenation properties at a temperature of 308 K and an initial hydrogen pressure of 4 MPa. Figure 5 shows hydrogen concentration (open circles), measured from pressure change, in the powder mixtures as a function of Li concentration in the mixtures after MA for 40 h. The $C_{92}Li_8$ powder absorbed about 1.6 wt.% hydrogen whereas the pure graphite, $C_{90}Li_{10}$, $C_{88}Li_{12}$ powders absorbed about 0.6 wt% hydrogen. The data shown with dashed line in Figure 5 indicate the hydrogen concentration in the powder mixtures if one assumes that the Li existed in the powders turned back into LiH hydride during rehydrogenation (although we did not observe a LiH formation (see Figure 6)). Even if we assume the formation of LiH, $C_{92}Li_8$ mixture absorbed more than the level of hydrogen capacity due to the LiH formation, suggesting that hydrogen absorption occurred in the graphite structure. Fig. 6 shows X-ray diffraction patterns for $C_{90}Li_{10}$ powder mixtures before and after hydrogenation in PCT apparatus. Even after rehydrohenation, no X-ray diffraction peaks corresponding to the LiH hydride are observed for all the powder mixtures. Thus it is implied that hydrogen absorption was occurred in the graphite structure by extending the graphite interlayer spacing.

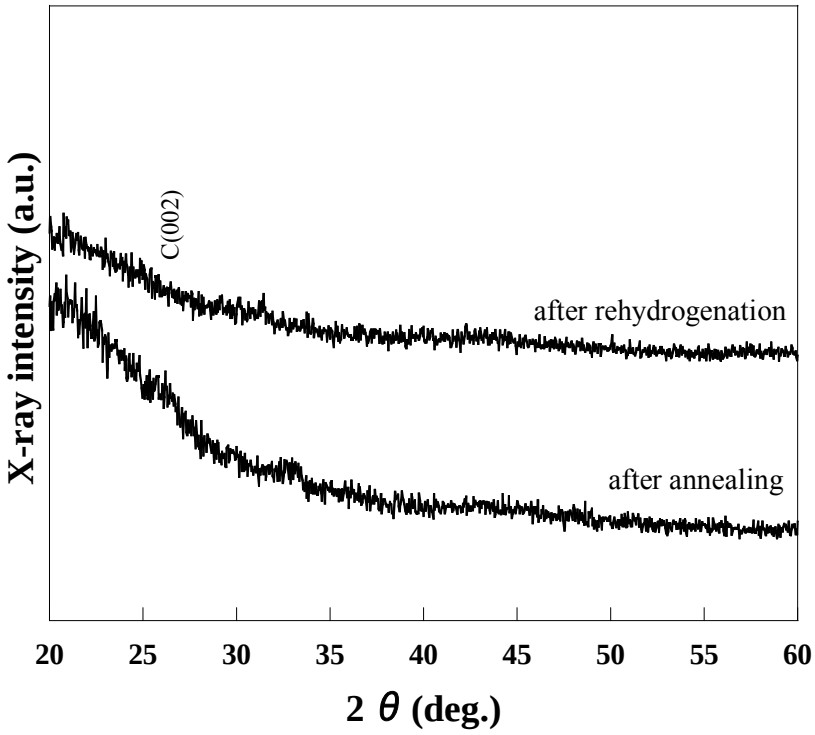

Figure 6. X-ray diffraction patterns for $C_{90}Li_{10}$ powder mixtures before and after hydrogenation.

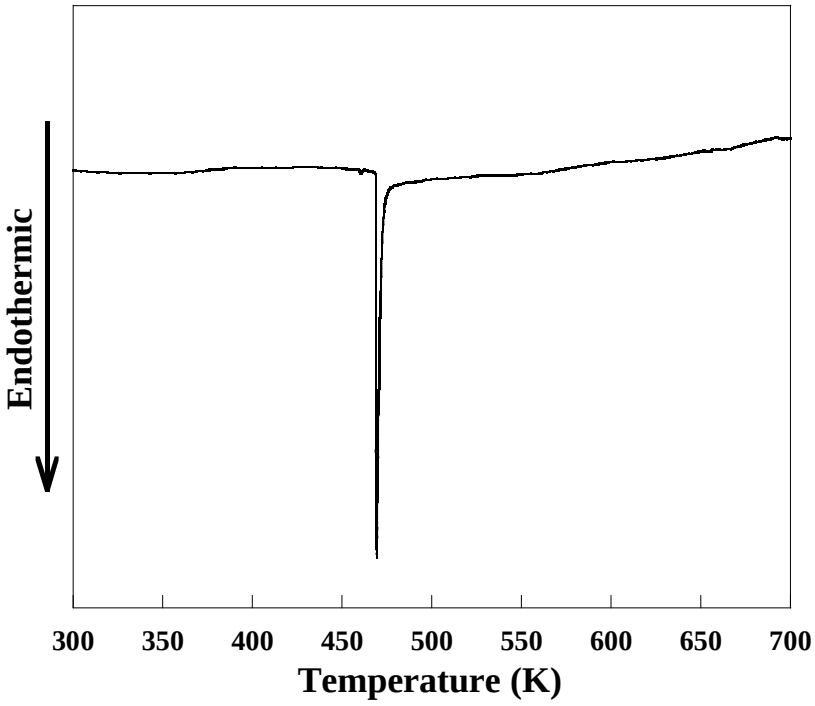

Figure 7. Differential scanning calorimetry curve for $C_{92}Li_8$ powder mixtures mechanically alloyed for 40 h after rehydrogenation.

Figure 7 shows DSC curve for $C_{92}Li_8$ powder mixtures, which were mechanically alloyed for 40 h, after rehydrogenation. The $C_{92}Li_8$ powder seems to desorb hydrogen at temperatures lower than 473 K. However, the $C_{90}Li_{10}$ and the $C_{88}Li_{12}$ powder mixtures desorbed hydrogen much higher

than that for $C_{92}Li_8$ mixtures, which were about 530 K and 490 K respectively, indicating that the $C_{92}Li_8$ powders exhibit the best hydrogen storage properties among the powder mixtures in this study. Two types of hydrogen coordinations, hydrogen in the graphite layers and that with the C-H covalent bonding, were reported for graphite after MA under hydrogen atmosphere [3]. At least two types, C-H bonding and hydriding of Mg, were also reported for nanocomposites obtained by MA of graphite and Mg [4]. Because the C-H bonding and Mg-H hydriding are due to strong chemical bonding, their hydrogen desorption normally occurred at higher temperatures. The hydrogen deosprtion temperature for the present powder mixtures, particularly for $C_{98}Li_8$, is lower than those, suggesting strongly that hydrogen absorption occurred in the graphite interlayers.

CONCLUSIONS

Mechanical alloying (MA) for the powder mixtures consisted of graphite and lithium hydride (LiH) powders ($C_{100-x}Li_x$ ($0 \leq x \leq 12$)) was attempted to intercalate lithium in graphite structure after dehydrogenation. The results obtained are summarized as follows;

1. Although the graphite structure turned into a turbostratic structure after earlier MA, aromatic carbon layers still remained even after MA for 40 h because of the strong covalent bonding. The graphite interlayer (graphene) spacing increased with increasing MA time. The interlayer spacing for the $C_{92}Li_8$ powders after MA for 40 h, which was the highest among the powder mixtures, increased about 9 % from that before MA, indicating the intercalation of lithium between the graphite interlayer after dehydrogenation.
2. After rehydrogenation at a temperature of 308 K and an initial hydrogen pressure of 4 MPa, the $C_{92}Li_8$ powders absorbed about 1.6 wt.% hydrogen, but the pure graphite, the $C_{90}Li_{10}$ and the $C_{88}Li_{12}$ powders absorbed only about 0.6 wt% hydrogen. No formation of LiH was observed after rehydrogenation.
3. An accelerated hydrogen desorption occurred endothermically at 469 K for the $C_{92}Li_8$ powders, while those for the $C_{90}Li_{10}$ and the $C_{88}Li_{12}$ powders occurred at 530 K and 490 K respectively.

ACKNOWLEDGEMENTS

This work was partially supported by the European Commission (project *Dev-BIOSOFC*, FP6-042436, MTKD-CT-2006-042436).

REFERENCES

1. A.C. Dillon, K.M. Jones, T.A. Bekkedahl, C.H. Kiang, D.S. Bethune, M.J. Heben, *Nature*, vol. 386, pp. 377, 1997.
2. A. Chambers, C. Park, R. Terry, K. Baker, N.M. Rodriguez, *J. Phys. Chem. B*, vol. 102, pp. 4253, 1998.
3. S. Orimo, G. Majer, T. Fukunaga, A. Züttel, L. Schlapbach, H. Fujii, *Appl. Phys. Let.*, vol. 75, pp. 3093, 1999.
4. H. Imamura, M. Kusuhara, S. Minami, M. Matsumoto, K. Masanari, Y. Sakata, K. Itoh, T. Fukunaga, *Acta Mater.*, vol. 51, pp.6407-6414
5. A. Takasaki, Y. Furuya, M. Katayama, *J. Alloys Comps.*, vol.446-447, pp.110-113, 2007

TRANSIENT THERMAL EFFECTS IN A FUEL PROCESSOR FOR HIGH TEMPERATURE SOFC STACKS

A. Ferretti[1], A. Traverso[1,*], G.J.Saunders[2]
[1]University of Genoa, Thermochemical Power Group (TPG), Genoa, Italy
[2]Rolls-Royce Fuel Cell Systems Limited, Loughborough, United Kingdom

ABSTRACT. Fuel processing is a fundamental step in any fuel cell system fuelled with hydrocarbons. This work focuses on the development of the model of one reactor of the Fuel Processor unit being developed by Rolls-Royce Fuel Cell Systems Limited: the SCSO (Selective Catalytic Sulphur Oxidation). The transient model has been validated against experimental data: attained results are shown to demonstrate both the accuracy of results and the validity of modelling approach.

Keywords: heat transfer modelling, transient, fuel processor, solid oxide fuel cells

INTRODUCTION

The Fuel Processor unit is complementary to the high temperature Fuel Cell system and its relevance should not be underestimated. The modelling activity, in which this work is placed, helps along the development of such system. The final purpose of this work was to build a transient model of the desulphuriser, suitable for the development of the control system of the actual Fuel Processor. More precisely it was thought as a predicting tool for tuning control parameters and strategies.
The model has been developed as a new component of Matlab-Simulink external library named TRANSEO, which is a comprehensive tool, built in the last ten years at TPG, and still growing. It is based on the C language and it has been used for previous works on microturbine-based energy cycles: accuracy of existing components has already been proved, hence the choice to continue developing it throughout this work.

SCSO SUB-SYSTEM MODELLING AND VALIDATION

System overview

The SCSO is one of the Fuel Processor subsystems and its task is to make the raw natural gas from the network consistent with the high temperature solid oxide fuel cell requirements in terms of composition, pressure and temperature. Two main requirements are pursued: reduction of sulphur and higher hydrocarbon contents in the pipeline natural gas. Sulphur is usually present as odorants, organic sulphur compounds like THT (tetrahydrotiophene) commonly used in most European countries, OBE (dimethyl and diethyl sulphide) used in UK and mercaptans used together with THT in the US. The level of sulphur varies from country to country and it is neither constant within the same country, ranging between 2 ppm and 16 ppm. From studies on the actual Fuel Cell system, it

* Corresponding author: Prof. A . Traverso
Phone: + (39)-010-3532455, Fax: + (39)-010-3532566
E-mail address: alberto.traverso@unige.it

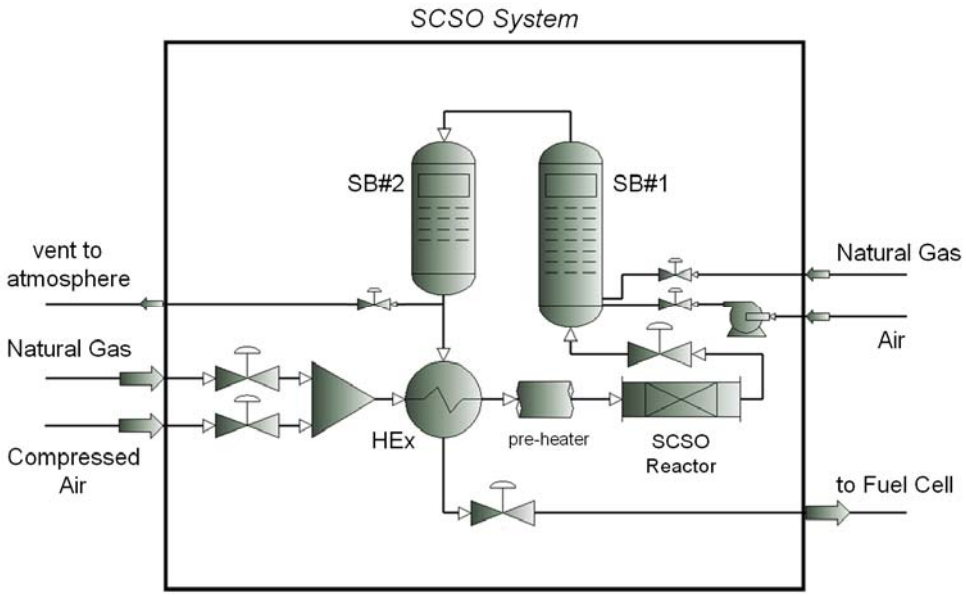

Figure 1. Simplified layout of the desulphurisation subsystem

resulted that a sulphur concentration of approximately 100 ppb has to be assumed as the target concentration in the fuel stream that must be achieved after the desulphurization process. Higher hydrocarbons (C_2-C_6) in the natural gas have a decomposition temperature much lower than methane: feeding a higher-hydrocarbons-rich natural gas to a high temperature SOFC system may result in carbon deposition in any point where thermal cracking temperature is exceeded. Therefore, for commercial systems, very low sulphur and higher hydrocarbons concentration in methane has to be obtained and natural gas has to be maintained below critical temperature before any mixing with a steam- or oxygen-rich stream. To overcome such problems, the SCSO technology combines the fuel with a sub-stoichiometric amount of oxygen and uses a sulphur tolerant monolith catalyst to oxidize selectively the sulphur compounds to sulphur oxides (SO_2 and SO_3 referred to collectively as SO_x). The SO_x species are then absorbed (chemical adsorption) downstream by two different inexpensive low capacity (6.5 gS/100g adsorbent) particulate adsorbents (SO_3 can displace SO_2 and therefore it has to be removed upstream on a different bed).
Sorbent beds are required to be warmed up with hot air during the start-up phase: two burners are placed inside the sorbent bed vessels to operate until the designed temperature is achieved. During such a warm-up the two vessels are being isolated from the rest of the system since burners are designed to operate at atmospheric pressure to reduce both costs and control issues.
The model refers to the actual layout of the SCSO subsystem from the 250kWe Fuel Processor. Most of control or safety components such as vents or check valves have been neglected, as the main goal was the validation against experimental data during normal operation.

STANDARD REACTING PIPE MODEL

The “Standard Reacting Pipe” TRANSEO component is a multipurpose time-dependent model, representing most of the actual parts of the system: empty pipes, electrical heaters and reactor itself. By now, only the selective catalytic sulphur oxidation and the catalytic partial oxidation are implemented but other reactions/reactors will be added soon. The “Standard Reacting Pipe” model can be used to predict the transient behaviour of an empty pipe, in its simplest form, as well as a chemical reactor implementing user-defined reactions. The aim, in fact, was to create the transient model of a pipe with also the capability of calculating temperature and composition changes due to various reaction sets. Since the reduction of the calculation time was a necessary requirement, a “lumped-volume” model has been adopted [6]: it is a simplified scheme, based on

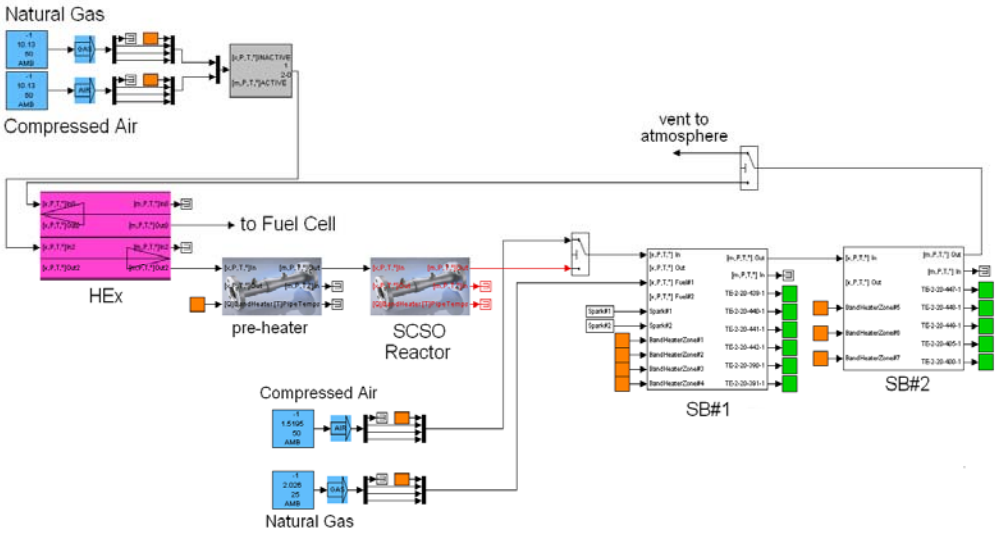

Figure 2. Matlab/Simulink model of the complete subsystem

the hypothesis of semi-ideal gas, that allows the use of large time steps. The lumped-volume model (Figure 3) is formed by an off-design model that behaves as an actuator disk, followed by a duct, with constant equivalent cross-sectional area and length, for the fluid dynamic delay. In this way, a sort of superposition of the effects is carried out: the actuator disk responds rigidly to the inlet and lumped-volume conditions (these represented its boundary conditions), while its effect is delayed by the equivalent duct that follows. The actuator disk is actually the place where the involved reactions happen. On the other hand, heat transfer is modelled with a more detailed approach in this work, since the heat transfer/storage/loss are the main phenomena to be captured by the model.

Heat Transfer Model

The heat transfer model adopted in the "Standard Reacting Pipe" was based on the one from the original pipe component of the TRANSEO library, which implemented a basic heat transfer: heat exchange between gas stream and wall, and heat losses towards the environment. In the "Standard Reacting Pipe" such model has been upgraded. As the real system involved not negligible catalyst and insulation masses, to best represent its behaviour, the transient effect due to the thermal capacitance of multiple layers of different materials has been implemented. While the real geometry for both the metal and insulation layers have been taken into account, for the catalyst the complex geometry of the real system had to be simplified. The SCSO reactor catalyst, in fact, implemented a micro channel geometry while the sorbent beds contained packed spheres. These two complex configurations have been simplified through the use of an additional concentric circular layer between the pipe and the gas stream. The thickness of such layer was determined spreading the calculated (from data) volume of catalyst onto the inner surface of the pipe (it acts as fixed external radius for the inner layer). The catalyst-fluid surface of heat exchange was not bound to this simplified geometry but it was left to be defined by the user as a parameter from the Simulink component mask. The heat transfer was modelled also considering the effect of the electrical band heaters: they are used to heat the gas stream and to keep the different components (i.e. reactor and sorbent beds) at operating temperature also in no flow conditions (zero space velocity).

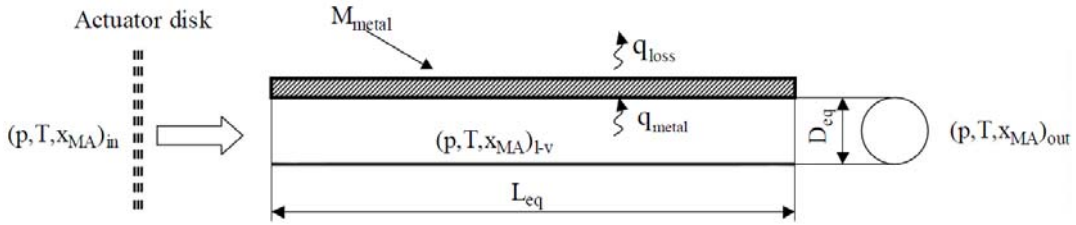

Figure 3. Lumped-volume model [6]

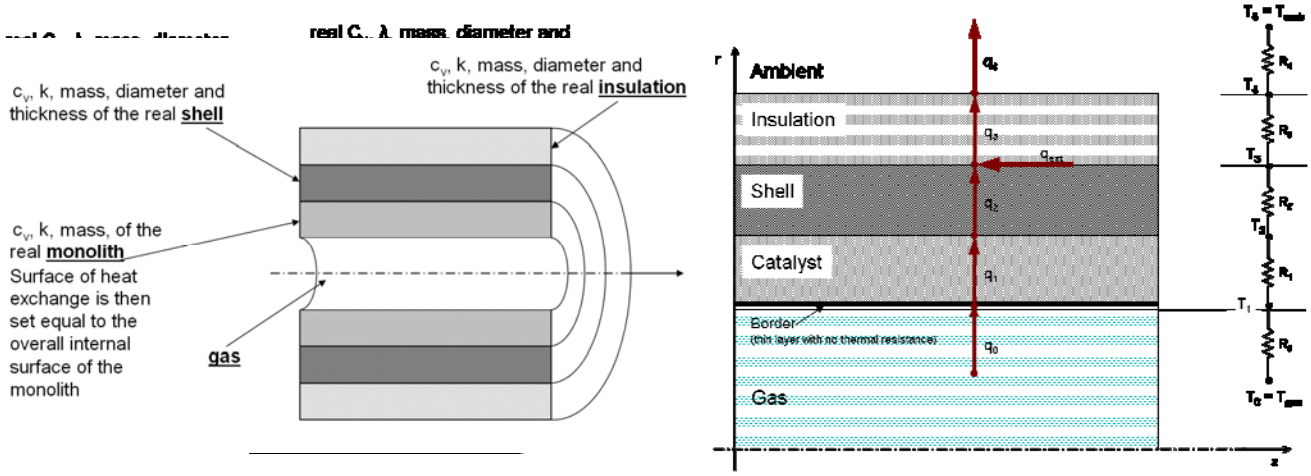

Figure 4. Simplified geometry adopted (left) and heat transfer model (right)

To simulate this effect an external heat rate in the heat transfer scheme has been added between the metal and insulation layers, where the heaters are actually placed.
A general relationship between Nu, Re and Pr numbers is adopted. Dividing the general relationship by the on-design values of Nu, Re and Pr numbers (i.e. the Nu, Re and Pr numbers calculated at on-design conditions), it is possible to derive (1). Such an equation expresses the relationship of the convective heat transfer coefficient h with the current and on-design values Re', Pr' and k'. The user only needs to introduce the reference value for the convective coefficient, that is h', and the exponents "a" and "b", together with the on-design operating parameters (mass flow or velocity, pressure, temperature). By assuming standard composition for the flow (air at ISO conditions), the tool is automatically capable of calculating the remaining on-design numbers to be employed in (1). Such an approach is employed here because the aim is to simulate the transient and off-design behaviour of the system, rather than designing it: thus, geometry and design operating conditions can be considered known.

$$h = h' \cdot \frac{k}{k'} \cdot \left(\frac{\mathrm{Re}}{\mathrm{Re}'}\right)^a \left(\frac{\mathrm{Pr}}{\mathrm{Pr}'}\right)^b \tag{1}$$

Energy equations for the gas stream and for the solid layers, considering the assumptions of the model and its geometry, reduce respectively to (2) and (3).

$$\frac{\partial\left(\rho c_v T A_c\right)}{\partial t} = -\frac{\partial\left(\dot{M} c_p T\right)}{\partial z} + q \tag{2}$$

$$\frac{\partial\left(M c_v T\right)}{\partial t} = q \tag{3}$$

In the following equations the calculation nodes (Figure 4) are referred to with the use of the subscript i. The heat exchange rates q_i must be explicitly indicated, as reported in (4).

$$q_i = \frac{1}{R_i}\left(T_i^{\,n+1} - T_{i+1}^{\,n+1}\right) \qquad \text{for } 0 \le i \le 4 \tag{4}$$

Thermal resistances R_i (5) for the solid layers are calculated consistently with the actual cylindrical geometry.

The inner resistance is calculated starting from the convective coefficient and area of heat exchange; the external resistance is derived from the thermal conductance parameter which is to be provided by the user from the component mask in Simulink.

$$\begin{cases} R_0 = \dfrac{1}{h \cdot A} \\ R_i = \dfrac{1}{2\pi\lambda_i L} \cdot \ln \dfrac{r_{i+1}}{r_i} \qquad \text{for } 1 \le i \le 3 \\ R_4 = \dfrac{1}{U_4} \end{cases} \tag{5}$$

Since the reduction of the calculation time is a necessary requirement when plant simulations are carried out, it was decided to adopt an implicit scheme for calculating the temperatures at the *n+1* (i.e. current, unknown) time, as it allows the use of greater time steps of integration without compromising the stability of the results. All the previous sets of equations are then being used in the system (6).

$$\begin{cases} \left[1 + \dfrac{m_{out} c_p dt}{c_{v0} M_0} + \dfrac{dt}{c_{v0} M_0 R_0}\right] \cdot T_0^{n+1} + \left[-\dfrac{dt}{c_{v0} M_0 R_0}\right] \cdot T_1^{n+1} = T_0^n + \left[\dfrac{m_{in} c_{pin} dt}{c_{v0} M_0}\right] T_{totin} \\ \left[-\dfrac{dt}{c_{vx} M_x R_0}\right] \cdot T_0^{n+1} + \left[1 + \dfrac{dt}{c_{vx} M_x R_0} + \dfrac{dt}{c_{vx} M_x R_1}\right] \cdot T_1^{n+1} + \left[-\dfrac{dt}{c_{vx} M_x R_1}\right] \cdot T_2^{n+1} = T_1^n \\ \left[-\dfrac{dt}{c_{v1} M_1 R_1}\right] \cdot T_1^{n+1} + \left[1 + \dfrac{dt}{c_{v1} M_1 R_1} + \dfrac{dt}{c_{v1} M_1 R_2}\right] \cdot T_2^{n+1} + \left[-\dfrac{dt}{c_{v1} M_1 R_2}\right] \cdot T_3^{n+1} = T_2^n \\ \left[-\dfrac{dt}{c_{v2} M_2 R_2}\right] \cdot T_2^{n+1} + \left[1 + \dfrac{dt}{c_{v2} M_2 R_2} + \dfrac{dt}{c_{v2} M_2 R_3}\right] \cdot T_3^{n+1} + \left[-\dfrac{dt}{c_{v2} M_2 R_3}\right] \cdot T_4^{n+1} = T_3^n + \left[\dfrac{dt \cdot q_{ext}}{c_{v2} M_2}\right] \\ \left[-\dfrac{dt}{c_{v3} M_3 R_3}\right] \cdot T_3^{n+1} + \left[1 + \dfrac{dt}{c_{v3} M_3 R_3} + \dfrac{dt}{c_{v3} M_3 R_4}\right] \cdot T_4^{n+1} = T_4^n + \left[-\dfrac{dt}{c_{v3} M_3 R_4}\right] \cdot T_5 \end{cases} \tag{6}$$

It is possible to write (6) as the product of a matrix representing the constant coefficients and the unknown term vector: the result is the vector of the known (i.e. at the previous time step) terms. The matrix turns out to be tri-diagonal and so it is possible to find the value of the T_i^{n+1} elements of the unknown vector using the Gauss method. The boundary conditions and the additional q_{ext} in (7) are being considered in the vector of the known terms.

$$\begin{bmatrix} [...] & [...] & 0 & 0 & 0 \\ [...] & [...] & [...] & 0 & 0 \\ 0 & [...] & [...] & [...] & 0 \\ 0 & 0 & [...] & [...] & [...] \\ 0 & 0 & 0 & [...] & [...] \end{bmatrix} \cdot \begin{bmatrix} T_0^{n+1} \\ T_1^{n+1} \\ T_2^{n+1} \\ T_3^{n+1} \\ T_4^{n+1} \end{bmatrix} = \begin{bmatrix} T_0^n + [...] \cdot T_{totin} \\ T_1^n \\ T_2^n \\ T_3^n + [...] \cdot q_{ext} \\ T_4^n + [...] \cdot T_5 \end{bmatrix} \tag{7}$$

VALIDATION

Approach

The model has been validated against experimental data retrieved from a representative test that took place in late 2007 in Canton, Ohio, at Rolls-Royce Fuel Cell Systems US laboratories. It was a 120h test on the 250kWe Fuel Processor and it included a complete test on the SCSO subsystem. Warm-up, part and full load operation and cool-down phases were tested and recorded with 2s sample time. During the first 27 hours of the test, the system was operating the warm-up cycle. Pressure was atmospheric and the two sorbent beds were isolated from the rest of the system (Figure 1). Two different ignitions of the burner (only one of the two burners was used) are visible at hour 2nd and 16th (Figure 6). At the hour 27th the burner was turned off and the band heaters temperature control loop started. It maintained the set-point temperature and at the hour 42nd the system pressurised: it was ready for the reactor light-off that took place in 90 minutes time. The system operated until the hour 82nd at various loads and then it was cooled down.
Validation has been performed in two steps: firstly, single blocks of the system layout have been verified, secondly the complete system layout has been tested. In such a way, in the first part of validation a number of unknown parameters could be assumed, while in the second part prediction of system behaviour could be verified. For brevity, since this paper mainly focuses on the heat transfer model, the results will be explained but the validating process will not be described. More details on the validating process and additional results will be included in [1].

Final Results

Once the validation of single components was carried out, the model of the entire subsystem layout was built (Figure 2). The inputs from experimental data (orange blocks in Figure 2) were the methane and main air streams, the methane and air streams to the burners and the output signal of the controllers to the electrical heaters (i.e. reactor pre-heater, sorbent bed #1 zones 1-4 and sorbent bed #2 zones 1-3). Results on the temperatures of the reactor are shown in Figure 5. The graph on top refers to the temperatures of the gas streams, except one (dotted line) that represents the measurement of the thermocouple placed on the outer shell: the matching with experimental can be

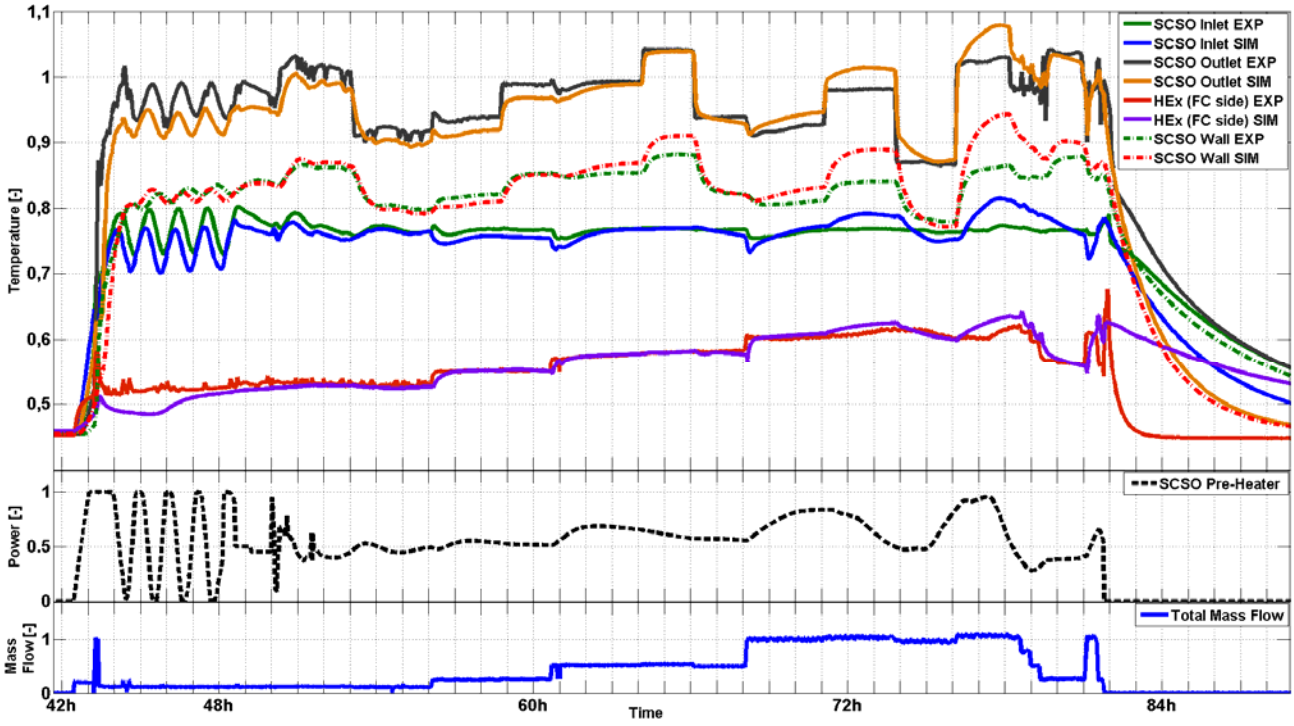

Figure 5. SCSO reactor gas and wall temperature validation

considered acceptable. It is worth saying that during the analysis of the reactor on its own, the model results were much closer to the experimental data: it is in fact easily noticeable that the calculated SCSO outlet temperature (orange) is largely affected by the upstream error from the recuperator and pre-heater components. The control signal of the SCSO pre-heater from the test is plotted below in Figure 5 and it explains the behaviour of the reactor inlet temperature in the last part of the chart: the value measured during the test (green) is almost constant while the model (blue) is prone to the heater effect. At the bottom the total flow rate during this part of the test (i.e. operation phase) is plotted. The validation of the SCSO wall temperature required an analysis on the flow regime (i.e. Reynolds number) as at first there was a significant mismatch between the model and experimental data. Such investigation revealed a laminar flow in every condition of the test. The Dittus-Boelter equation used for calculating the off-design convective coefficient was not valid anymore and Nu was instead considered constant [5]. The model with the new settings confirmed the analysis results and its wall temperature got closer to the experimental data.
Figure 6 shows the sorbent beds gas measurement points considered during the validation: the first just after the first burner, the second at the outlet of the first vessel and the third at the end of the second vessel. Results achieved show an acceptable overall behaviour of the model during the whole test length. Nonetheless a delay effect on the gas temperatures is visible in the second and third plot of Figure 6. The model yields a larger error when space velocity is negligible. This is reasonable as in such condition the influence of the free convection mechanism (not considered in the developed heat transfer model) become relevant. Also wall temperatures for all the sorbent beds heating zones have been validated, showing results consistent with those presented in this paper. They are plotted and discussed further in [1].

CONCLUSIONS

The validation of the model helped in better understanding and quantifying the phenomena undergoing in the different components of the rig: considering the test duration (120hours) and the variety of operating conditions (warm-up, hot stand-by, part and full load operation) the model prediction can be considered acceptable. Such validation confirms the validity of the heat transfer model adopted and also the effectiveness of the TRANSEO code as base for future developments.

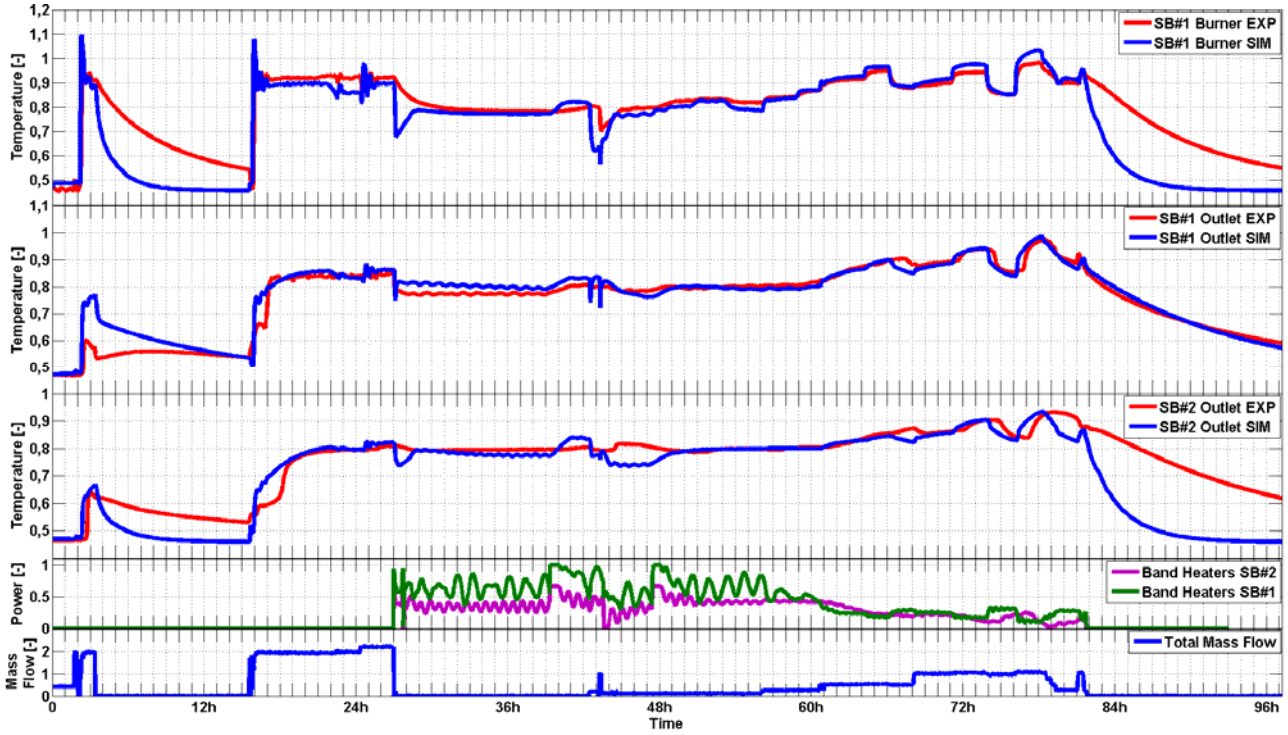

Figure 6. Sorbent beds #1 & #2 gas temperature validation

Nomenclature:

	Description		Description
SOFC	Solid oxide fuel cell	HEx	Heat exchanger (gas-gas counter-flow)
SCSO	Selective catalytic sulphur oxidation	X_{MA}	Mass fraction (composition)
SB#1	Sorbent Bed 1	ppm	Parts per million (concentration)
SB#2	Sorbent Bed 2	ppb	Parts per billion (concentration)

ACKNOWLEDGMENTS

The technical and financial support of Rolls-Royce Fuel Cell Systems Limited is greatly acknowledged. This work has been partially funded by European Community's Sixth Framework Programme through the European Marie-Curie Action ToK-IAP "EnSOFC", contract no. MTKI-CT-2006-042298. The content of this work reflects exclusively the authors' view. The European Community is not liable for any use of the information contained here.

REFERENCES

1. A. Ferretti, A. Traverso, G. J. Saunders, Transient model validation of a desulphuriser system, *European Fuel Cell Forum Paper*,2009.

2. F. Ghigliazza, A. Traverso, M. Pascenti, A. F. Massardo, Micro Gas Turbine Real-Time Modeling: Test Rig Verification, *ASME Paper GT2009-59124*, 2009.

3. F. Cerutti, An External Fuel Processor for a SOFC hybrid system, *PhD Thesis*, 2007.

4. L. Magistri, M. Bozzolo, O. Tarnowsky, G. Agnew, A.F. Massardo, Design and Off-Design Analysis of a MW Hybrid System Based on Rolls-Royce Integrated Planar Solid Oxide Fuel Cells, *Journal of Gas Turbines and Power,* Vol. 129, pp. 792-797, 2007.

5. F. P. Incropera, D. P. DeWitt, T. L. Bergman, A. S. Lavine, *Introduction to Heat Transfer*, Fifth Edition, J. Wiley & Sons Inc., pp 475-477, 2007.

6. A. Traverso, A. F. Massardo, R. Scarpellini, Externally Fired micro-Gas Turbine: Modelling and experimental performance*, Applied Thermal Engineering, Elsevier Science*, 26, 1935–1941, 2006.

7. A. Traverso, TRANSEO code for the dynamic performance simulation of micro gas turbine cycles", *ASME Paper GT2005-68101*, 2005.

8. A. Kidnay, W. Parrish, *Fundamentals of Natural Gas Processing*, Taylor & Francis Group , 2005.

9. A. F. Massardo, Integrated Planar Solid Oxide Fuel Cell (IP-SOFC) Hybrid Systems: Design, Off-Design, Transient Modelling and Validation, invited lecture, The 21st Century COE Program Mechanical Systems Innovation, *Energy Innovation Projects*, University of Tokyo, Japan, 2005.

10. A. F. Massardo, High Temperature Fuel Cell Pressurised Hybrid Systems: Modelling, Testing and Future Developments, invited lecture, *3rd CO2 Conference*, Trondheim, Norway, 2005.

11. F. Marsano, L. Magistri, M. Bozzolo, O. Tarnowski, Influence of Fuel Composition on Solid Oxide Fuel Cell Hybrid System Layout and Performance, *ASME Paper GT2004-53853*, 2004.

12. J. Lampert, Selective catalytic oxidation: a new catalytic approach to the desulfurization of natural gas and liquid petroleum gas for fuel cell reformer applications, *Journal of Power Sources*, Volume 131, Issues 1-2, 2004.

13. R. H. Perry, D. W. Green, *Perry's Chemical Engineers' Handbook*, Seventh Edition, McGraw Hill, 1998.

EVALUATION OF CATHODE MESOSCALE STRUCTURE CONTROL OF SOFC

A. Konno[1,*], A. Kuroyanagi[1], H. Iwai[1], M. Saito[1], H. Yoshida[1]
K. Kodani[2], K. Yoshikata[2]
[1]Kyoto University, Kyoto, Japan
[2]Dai Nippon Printing Co., Ltd., Kyoto, Japan

ABSTRACT. The effects of cathode mesoscale structures on the SOFC performance are experimentally investigated. Preliminary scale analysis using the characteristic lengths based on the conservation equations for electron, ion and gas phases shows that the ionic transport is the rate-limiting process of the transport phenomena in electrode under a standard SOFC condition and thus the active reaction area exists in the vicinity of the electrode-electrolyte interface. The electrode-electrolyte interface is modified by introducing mesoscale structures to the electrode and its effects on the cell performance are examined by conducting power generation tests for the cells with two types of mesoscale grooves. Enhancement of the power generation performance was observed for the grooved cells.

Keywords: *SOFC, Power generation performance, Cathode mesoscale structure, Scale analysis*

INTRODUCTION

Enhancement of the power generation density is important for the development of solid oxide fuel cells (SOFCs). To increase the power generation density, there have been many investigations from various angles including thin-film electrolyte, development of high conductivity electrolyte materials [1], improvement of electrode [2] and multi-layer electrode for electrochemical reaction and gas diffusion [3, 4]. The key step in the electrochemical power generation of SOFCs is the electrochemical reaction at electrodes. It proceeds at three-phase boundary (TPB) where the oxygen ion, the electron and the reaction gas meet. TPB near the electrode-electrolyte interface is believed to be active and such region in the electrode is sometimes called as active reaction area. It is expected that such active reaction area could be expanded by modifying the electrode-electrolyte interface shape.

We have previously investigated the effects of anode mesoscale structures on power generation density of SOFC [5, 6]. The characteristic length of mesoscale structure is smaller than the macroscopic shape of a cell (~1mm) and larger than the microstructure of electrodes such as the grain size of the electrodes (~1μm). As one of the simplest mesoscale geometries we introduced small grooves machined on the electrolyte to enlarge the anode-electrolyte interface area and found that the anode with such mesoscale structure achieved larger power density compared with a standard flat anode. However it should be kept in mind that the enlargement of electrode-electrolyte interface by introducing mesoscale structures does not always give a positive result. The mesoscale structure causes the change of electrode and electrolyte thickness as well as the electrode-electrolyte interface area. The ohmic loss and concentration overpotential in the electrode increase with the increase of the electrode thickness. The ohmic loss for ionic conduction in the electrolyte is also increased with electrolyte thickness. The active reaction area is strongly affected by these changes of overpotentials, because it is

* Corresponding author: Mr. A. Konno
Phone/FAX: + (81)-75-7535203
E-mail address: konno@t06.mbox.media.kyoto-u.ac.jp

directly related the ohmic loss of electrode and electrolyte, activation overpotentials and concentration overpotentials. From the previous numerical simulations [6, 7], it is found that the active reaction area distributes non-uniformly when the cell has mesoscale grooves and it expands into the groove bottom. Groove shape and depth are found to be very important parameters for discussions on the effective grooves to enlarge the active reaction area.

In this study, we firstly make a scale analysis using the characteristic lengths based on the conservation equations of electron, oxide ion and gas phase to estimate a suitable length scale of mesoscale structure. On that basis, we evaluate the cathode mesoscale structure by conducting power generation experiments of electrolyte supported button cells. Two types of the cathode mesoscale structures are realized by adopting different groove shapes on electrolyte surface. The power generation tests using each cell are conducted and the effects of the grooves on the power generation performance are discussed.

SCALE ANALYSIS

In this section we try to estimate the active reaction area in a simple analysis assuming an electrode consisting of three phases that are the electronic conducting phase, the ionic conducting phase and gas phase. The electrode reaction depends on the transport phenomena in three phases and the electrochemical reactions occur at three-phase boundary. It is believed that the electrochemical reaction is particularly prominent near the electrode-electrolyte interface. Costamagna el al. [8] and Chan and Xia [9] predicted the active reaction area and the electrode performance by the numerical analysis considering transport phenomena of two electrical potential phases or three phases. We try to estimate the active reaction area using the characteristic lengths from the conservation equation of these three phases. From each conservation equation (equation (1)), the orders of electronic, ionic and gas phase characteristic length can be expressed as equation (2).

$$\sigma_{el}\frac{\partial^2\phi_{el}}{\partial x^2}=i_{tpb},\quad \sigma_{io}\frac{\partial^2\phi_{io}}{\partial x^2}=i_{tpb},\quad D_{eff}\frac{\partial^2 C_j}{\partial x^2}=\frac{i_{tpb}}{nF} \tag{1}$$

$$l_{el}\sim\sqrt{\frac{\sigma_{el}\phi_{el}}{i_{tpb}}},\quad l_{io}\sim\sqrt{\frac{\sigma_{io}\phi_{io}}{i_{tpb}}},\quad l_{gas}\sim\sqrt{\frac{nFD_{eff}C_j}{i_{tpb}}} \tag{2}$$

where σ_i is effective conductivity at phase i, ϕ_i is electric potential at phase i, i_{tpb} is electrochemical reaction rate per unit volume, n is number of electron carried by chemical species, F is Faraday constant, D_{eff} is effective diffusivity of porous electrode, C_j is molar concentration of chemical species j at gas phase. Relative comparison among three characteristic lengths shows that oxide ion transport is the rate-limiting step in the electrodes. As the electrochemical reaction rate per unit volume is same in the formulas of the characteristic lengths (equation (2)), ratios of the characteristic lengths can be written as effective conductivities and diffusivity as follows.

$$\frac{l_{el}}{l_{io}}=\sqrt{\frac{\sigma_{el}\phi_{el}}{\sigma_{io}\phi_{io}}}\approx\sqrt{\frac{\sigma_{el}}{\sigma_{io}}},\quad \frac{l_{gas}}{l_{io}}\sim\sqrt{\frac{nFD_{eff}C_j}{\sigma_{io}\phi_{io}}}=\sqrt{\frac{nFD_{eff}P_j}{R_0T\sigma_{io}\phi_{io}}} \tag{3}$$

The values of these two ratios are estimated using electrical and thermo-physical properties of standard electrode materials [10-12]. Assumed electrode materials are Ni-YSZ cermets and LSM-YSZ composite as anode and cathode material, respectively. As the electrode is porous, the value of effective ionic conductivity is assumed to be one-tenth of ionic conductivity of a dense electrolyte. Effective diffusivity is calculated as $D_{eff}=\varepsilon/\tau\, D_{ij}$, where ε is porosity, τ is tortuosity factor and D_{ij} is the binary diffusivity between chemical species i and j ($\varepsilon = 0.3$, $\tau = 3$). ϕ_{io} uses 1V for the reference voltage. From the estimation of the ratios at general operating conditions of SOFC, the order of ratio l_{el}/l_{io} is 10^3 for anode and 10^2 for cathode, respectively. It shows that electron transport in the

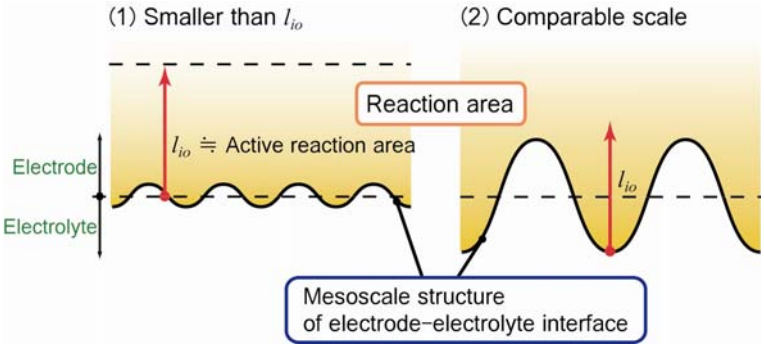

Figure 1. Active reaction area of the cells applied (1) mesoscale structure smaller than ionic characteristic length and (2) the structure comparable to ionic characteristic length

electrode is sufficiently fast and therefore it is not the rate-limiting process. On the other hand, the orders of l_{gas}/l_{io} is 10 for anode and 1~10 for cathode, respectively. It shows that the oxide ion transport is of the primary importance and probably the rate-limiting process yet the gas phase transport may affect the reaction area and the electrode performance depending on the operating conditions. The gas phase transport becomes important when the gas concentration is low and/or the gas diffusivity is low due to inefficient microstructure of electrode (equation (2)). When the oxide ion transport is the rate-limiting process, the active reaction area is limited to the neighboring area of the electrode-electrolyte interface. It is expected that the thickness of the reaction area is close to the ionic characteristic length.

In this study we apply mesoscale structure to enhance cell performance by increasing the electrolyte-electrode interface area. To improve cell performance, the scale of the electrode mesoscale structure should be larger than the ionic characteristic length. The mesoscale structure that is smaller than the ionic characteristic length will be buried in the active reaction area and therefore enlargement of electrolyte-electrode interface has little effect on the power generation performance as shown in Figure 1. Mesoscale structures larger than the characteristic length of ion transport are effective and suitable for the electrode performance enhancement.

In the following experiments, LSM cathode is used for electrode material. It is known that LSM is a mixed ionic and electronic conducting material but the ionic conductivity is negligibly small under a standard operating condition of SOFC [13]. Ionic characteristic length of LSM cathode is quite short and therefore it is expected that the cathode electrochemical reactions occur only in the vicinity of the electrode-electrolyte interface. Cathode mesoscale structures of tens of micron scale are employed in the experiment expecting structures of this size can improve the power generation performance by the electrode-electrolyte interface enlargement.

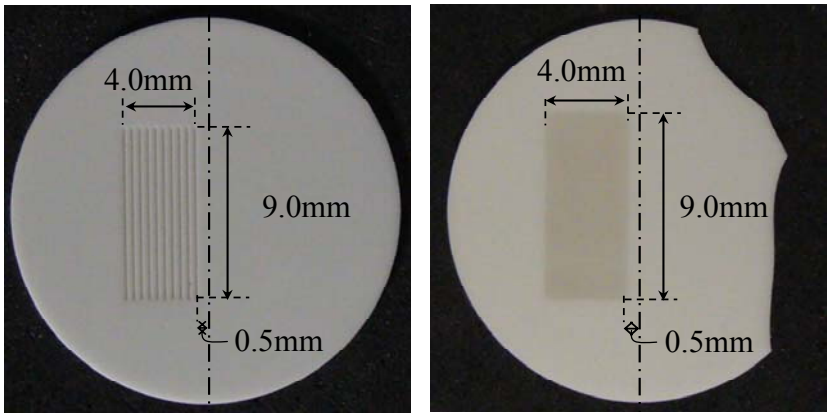

(a) Large grooves (b) Small grooves

Figure 2. Top view of electrolyte with grooves

EXPERIMENTAL SETUP

Cell fabrication

Electrolyte-support button cells are used as test cells. Figure 2 shows the button type electrolyte made of Yttria stabilized Zirconia (YSZ, Tosoh, Japan). Its thickness is 0.5mm. The grooves are machined on one side of the electrolyte to realize the mesoscale structure. Two types of grooves are tested in this study, namely, large groove and small groove. The groove shape parameters are listed in Table 1. The area enlargement factor in the table is defined as a ratio of electrode-electrolyte interface area of grooved part to that of the flat part. Figure 3 shows cross sectional views of large and small grooves.

NiO-YSZ is used for the anode material. It is prepared from NiO powder (Wako Pure Chemical Industries, Japan) and 8mol% YSZ powder (Tosoh, Japan) by ball milling (Ni:YSZ=1:1, volume ratio) and pre-sintered at 1500°C for 5 hours. NiO-YSZ powder is mixed with poly-ethylene glycol, screen printed on the electrolyte surface and sintered at 1400°C for 5 hours. The cathode material is prepared using $La_{0.7}Sr_{0.3}MnO_x$ powder (AGC Seimi Chemical Co., Japan). It is mixed with

Table 1 Shape parameters of grooves

	Depth (μm)	Width (μm)	Interval (μm)	Area enlargement factor
Large grooves	210	210	220	1.58
Small grooves	60	60	50	1.72

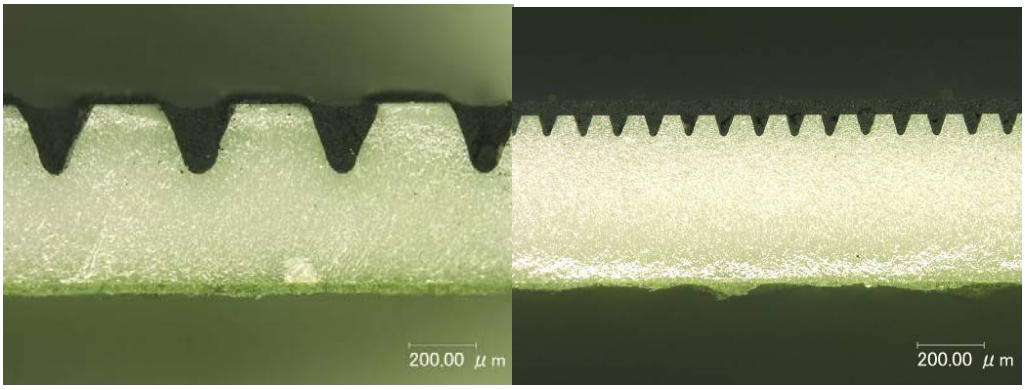

(a) Large grooves (b) Small grooves

Figure 3. Cross sectional view of the cell with grooves on cathode side.

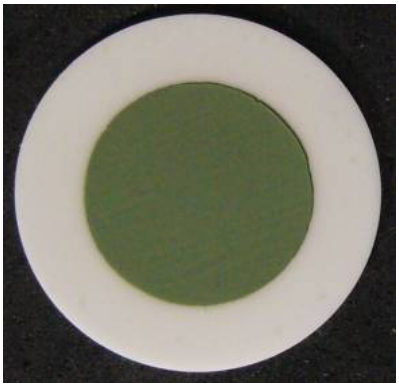

Figure 4. Anode side of test cell

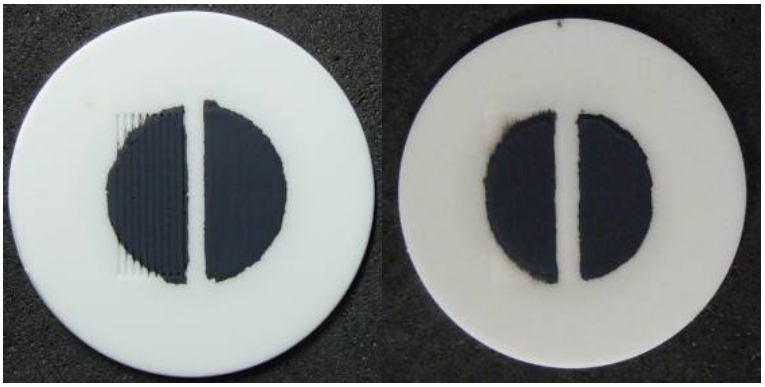

Figure 5. Cathode side of test cell

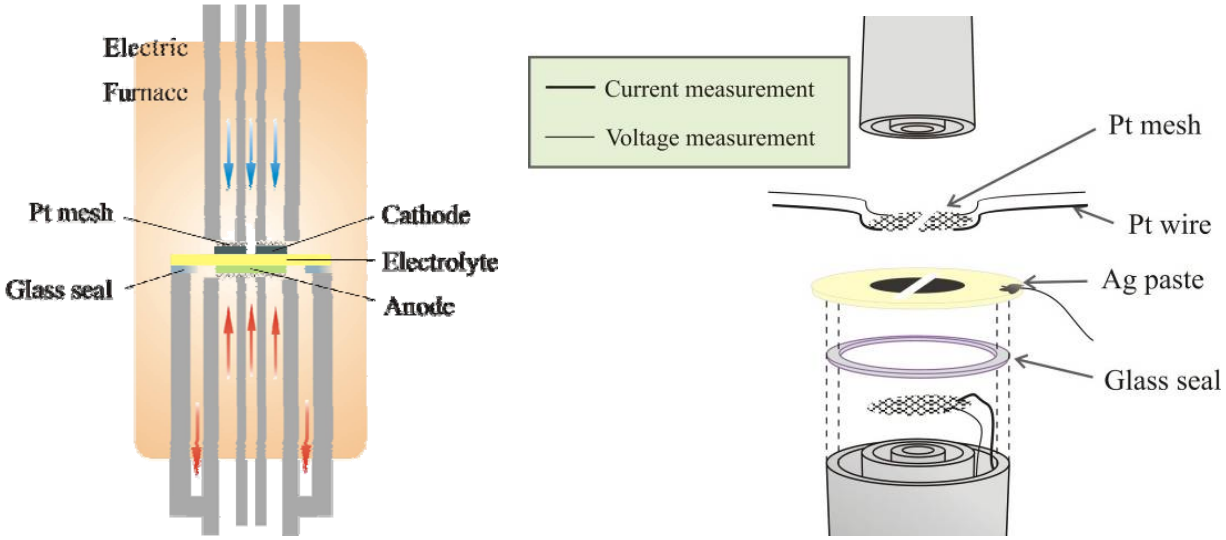

Figure 6. Test section of power generation setup

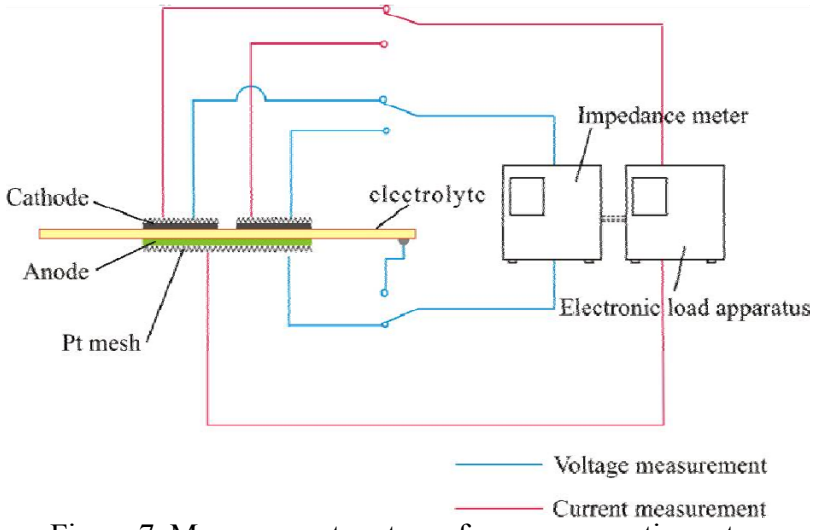

Figure 7. Measurement system of power generation setup

poly-ethylene glycol, screen printed on cathode side of electrolyte and sintered at 1150^{o}C for 5 hours. Figure 4 and 5 shows anode and cathode electrodes fabricated on each side of the test cells. As shown in Figure 5, cathode electrode is segmented into two parts. One side covers the flat surface and the other covers the grooved surface.

Power generation testing

Figure 6 shows the test section of the experimental button cell setup in this study. A button cell is sandwiched by co-axial ceramic tubes. On the anode side, the fuel is supplied through the inner tube. It turns and flow through the outer tube to be exhausted. On the cathode side, air as oxidant is supplied through the double tube and is directly exhausted in the furnace. The air flow rate is controlled by mass flow controller. The fuel is a mixture of hydrogen and nitrogen. Its concentration is controlled by mass flow controllers. Anode side outer tube is tightly connected to the cell by glass sealing to prevent gas leakage. The test section is placed in an electric furnace to maintain the operating temperature. It is confirmed prior to the experiments that the both fuel and air feeding tubes have enough length for preheating the flows.

To collect the current from the electrodes, thin platinum mesh is physically contacted to the electrode surfaces as shown in Figure 6. As the cathode is divided into two parts in this study, two sets

of current collectors are carefully placed on each cathode so that there is no electrical contact between two electrodes. The segmented cathode electrodes are evaluated one by one to find if there is any difference between them. Platinum wire of 0.5mm in diameter is connected to each platinum mesh. For voltage measurement, thinner platinum wire of 0.2mm in diameter is also connected to each platinum mesh. An impedance meter (KIKUSUI KFM2150) and an electronic load (KIKUSUI PLZ164WA) is used for the power generation testing as shown in Figure 7 to obtain *i-V* characteristics. Current density is defined as a measured current divided by a projected electrode area. The projected area is measured by means of image processing. The experiments were conducted varying the operating temperature (800, 850 and 900°C). Three individual cells are tested for large (GL1, GL2 and GL3) and small grooves (GS1, GS2 and GS3), respectively.

RESULTS AND DISCUSSION

Fundamental characteristics

Fundamental power generation characteristics are examined for both large and small grooved cells. Figure 8 shows *i-V* characteristics of large grooves (a) and small grooves (b) at operating temperature of 800°C. Terminal voltage decreases as the current density increases. The current density of grooved side is always larger than that of the flat side at any terminal voltage. This is a common

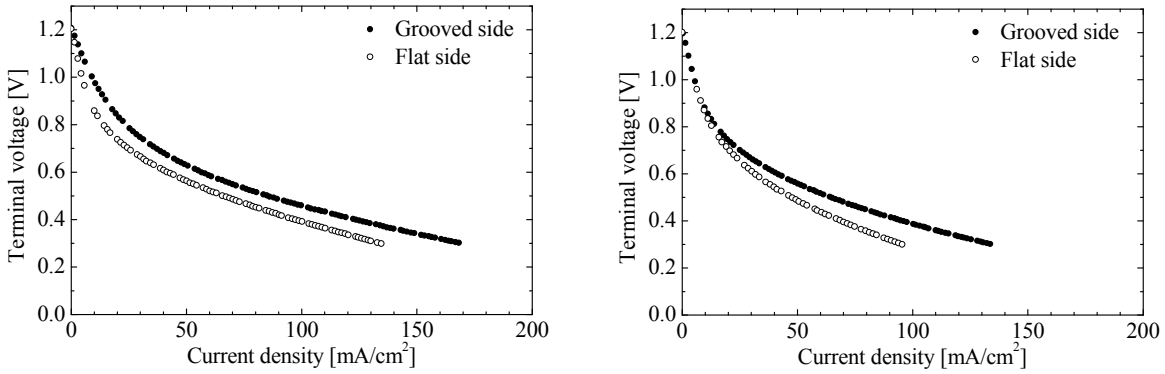

(a) Large grooves (GL1) (b) Small grooves (GS1)

Figure 8. *i-V* characteristics at operating temperature 800°C and hydrogen concentration 100%

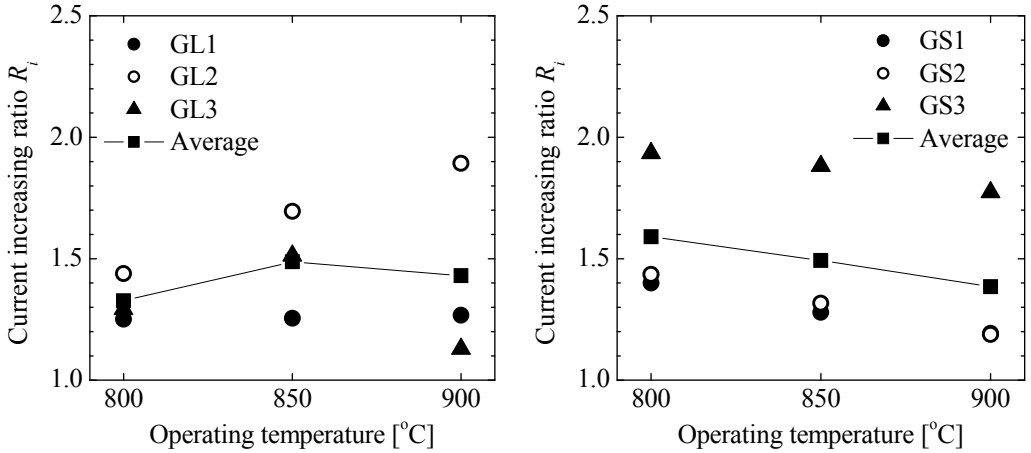

(a) Large grooves (b) Small grooves

Figure 9. Effect of operating temperature on current increasing ratio at hydrogen concentration 100%

tendency for all cells tested in this study. It shows that the cathode grooves improve the power generation performance of the cell.

Current density increasing ratio

To evaluate the effect of mesoscale grooves at different operating temperature, the current density increasing ratio R_i is defined as equation (4).

$$R_i = \frac{\text{Current density of grooved side}}{\text{Current density of flat side}} \tag{4}$$

The current density increasing ratio denotes enhancement of current density from a flat electrode to a grooved electrode at same terminal voltage. In the following discussion, the terminal voltage is fixed at 0.3V. Figure 9 shows the current density increasing ratio for both large grooves (a) and small grooves (b) at different operating temperature. In all cells, the current density increasing ratio is larger than unity. It shows that the mesoscale groove yields an enhancement of the power generation performance. In the case of the large grooves shown in Figure 9 (a), there seems no clear trend induced by the operating temperature. The average values of the current increasing ratio are 1.33, 1.49 and 1.43 at 800, 850 and 900^{o}C, respectively. In the case of the small grooves, the current density increasing ratio tends to decrease as the operating temperature is increased as seen in Figure 9 (b). The average values of the ratio are 1.59, 1.49 and 1.38 at 800, 850 and 900^{o}C, respectively. It is observed, however, that there are clear differences among the cells implying needs for more testing. The averaged current density increasing ratios take lower values than the averaged enlargement factors in both large and small groove cases. This is not surprising because the current density increasing ratio is affected by not only the enlargement of electrode-electrolyte interface area but also by the mean electrolyte thickness and the mean electrode thickness. Electrochemical reaction is enhanced near the groove bottom where the electrolyte is locally thin, while gas diffusion resistance is increased due to thicker electrode.

CONCLUSIONS

The effects of cathode mesoscale structure control on power generation performance are experimentally investigated. Scale analysis by characteristic lengths of the transport phenomena in the electrode was conducted to discuss the suitable size of mesoscale structure. The power generation experiments using cells with two different cathode grooves were conducted to evaluate the effect of cathode mesoscale grooves on the power generation performance.

(1) Preliminary scale analysis revealed that the ionic transport is the rate-limiting process among electron, oxide ion and gas phase transport in the electrodes under a standard cell condition.
(2) The power generation experiments showed that the cathode mesoscale grooves affect the cell performance. The current density is enhanced more than 30% compared with a standard flat electrode at terminal voltage of 0.3V.

ACKNOWLEDGEMENT

This research was partially supported by the European Commission (project Dev-BIOSOFC, FP6-042436, MTKD-CT-2006-042436), the NEDO project “Development of SOFC System Technology” and the Kansai Research Foundation for technology promotion (KRF).

REFERENCES

1. Ishihara, T., Matsuda, H. and Takita, Y., Doped $LaGaO_3$ perovskite type oxide new oxide ionic conductor, *Journal of the American chemical society*, Vol. 116, pp 3801-3803, 1994.
2. Kenjo, T. and Nishiya, M., $LaMnO_3$ air cathodes containing ZrO_2 electrolyte for high temperature solid oxide fuel cells, *Solid State Ionics*, Vol. 57, pp 295-302, 1992.
3. Murray, E. P., Tsai, T. and Barnett, S. A., Oxygen transfer processes in $(La,Sr)MnO_3/Y_2O_3$-stabilized ZrO_2 cathodes: an impedance spectroscopy study, *Solid State Ionics*, Vol. 110, pp 235-243, 1998.
4. Haanappel, V. A. C., Mertens, J., Rutenbeck, D., Tropartz, C., Herzhof, W., Sebold, D. and Tietz, F., Optimization of processing and microstructural parameters of LSM cathodes to improve the electrochemical performance of anode-supported SOFCs, *Journal of Power Sources*, Vol. 141, pp 216-226, 2005.
5. Iwai, H., Inuyama, K., Kuroyanagi, A, Yoshida, H., Kodani, K. and Yoshikata, K., Effects of mesoscale structure of anode electrode on SOFC performance, *Proc. of 18th International Symposium on Transport Phenomena*, pp 1647-1653, 2007.
6. Iwai, H., Inuyama, K., Kuroyanagi, A., Saito, M., Yoshida, H., Performance prediction of SOFC with anode mesoscale structure control, *Proc. of 5th European Thermal-Sciences Conference*, 2008.
7. Konno, A., Iwai, H., A., Saito, M., Yoshida, Numerical simulation of SOFC performance Affected by cathode mesoscale-structure control, *Proc. of 6th International Fuel Cell Science, Engineering and Technology Conference*, FuelCell2008-65246, 2008.
8. Costamagna, P., Costa, P. and Antonucci, V., Micro-modelling of solid oxide fuel cell electrodes, *Electrochimica Acta*, Vol. 43, No. 3-4, pp 375-394, 1998.
9. Chan, S.H., and Xia, Z.T., Anode micro model of solid oxide fuel cell, *Journal of the Electrochemical Society*, Vol. 148, No. 4, pp 388-394, 2001.
10. Perry, R.H., Perry's chemical Engineers' Handbook 7th edition, McGraw-Hill, New York, 1997.
11. Costamagna, P. and Honegger, K., Modeling of solid oxide heat exchanger integrated stacks and simulation at high fuel utilization, *Journal of the Electrochemical Society*, Vol. 145, No. 11, pp 3995-4007, 1998.
12. Minh, N.Q. and Takahashi, T., Science and technology of ceramic fuel cells, Elsevier, 1995.
13. Østergård, M.J.L. and Mogensen, M., ac impedance study of the oxygen reduction mechanism on $La_{1-x}SrMnO_3$ in solid oxide fuel cells, *Electrochimica Acta*, Vol. 38, No.14, pp 2015-2020, 1993.

STUDIES ON FLOW STRUCTURES IN MODEL CHANNELS OF A DISK SHAPE PLANAR SOFC

K. Tsunoda[1 *], Y. Mukai[2], K. Kinomura[3]
[1] Shibaura Institute of Technology, Tokyo, Japan
[2] Mitsubishi Heavy Industries, LTD., Kobe, Japan
[3] Tokyo Institute of Technology, Yokohama, Japan

ABSTRACT. A flow between two parallel disk shape plates at low Reynolds numbers (*Re*<100), which simulates a flow in the disk shape planar-type solid oxide fuel cell (SOFC), was experimentally investigated. Flow patterns at various flow rates were measured by using particle image velocimetry (PIV). In the channel installed flat plate current collectors, a velocity field indicated a stable radial flow pattern for a moderate Reynolds number, however, velocity gradient occurred along the radial direction. Since this result suggested the necessity of improvement of the channel shape, we designed a new channel with circle involute shape current collectors. In the new channel, a swirl flow occurred and maintained constant speed toward the channel exit. Furthermore, we confirmed that the velocity fields were remarkably improved and flow uniformity was achieved over the wide range of Reynolds numbers. This is because a flow passage consisting of two adjacent involute curves is equivalent to a constat-area channel due to the geometrical property of the involute curve.

Keywords: *Particle Image Velocimetry, Radial Flow, Swirl Flow, Solid Oxide Fuel Cell, Disk Shape Channel*

INTRODUCTION

Since solid oxide fuel cell (SOFC) using an oxygen-ion conducting electrolyte is operated at a high temperature, thermal management of the cell becomes an important issue. For instance, thermal stresses due to the temperature non-uniformity are unfavorable phenomena to cell's reliability. To solve this kind of problem, detailed information about the fluid dynamic phenomena occurring in the cell is required, because temperature distribution is strongly related to the velocity field. Furthermore, in order to achieve a homogeneous fuel supply to the electrode and to remove the heat generated in the cell, the uniformity of flow distribution is highly desirable.

Among several types of cell geometries, disk shape planar SOFC is prospective in a point that it can produce high electric power density [1]. Another advantage of disk shape SOFC is geometrical flexibility on flow passage. Therefore, it is expected to realize uniform fuel and air flows by optimizing a flow passage in the case of disk shape SOFC. However, it is difficult to confirm flow uniformity in practical operation.

In the present study, we investigated detailed flow structures between two parallel disk shape plates at low Reynolds numbers (*Re*<100) to simulate the practical operation in case of SOFC. The Reynolds number based on the fuel or air flow velocities was determined from electric current density, fuel utilization factor, and air utilization factor. In the experiment, airflow at room temperature was supplied to the model channel and flow patterns in the channel were measured by using particle image velocimetry (PIV) at various flow rates. In practical SOFC unit, a current

* Corresponding author: Prof. K. Tsunoda
Phone: + (81)-3-5859-8015, Fax: + (81)-3-5859-8001
E-mail address: ktsunoda@sic.shibaura-it.ac.jp

collector is an important component, because it can be used not only for conducting the electric current but also for determining the flow uniformity. Therefore, we installed current collectors with circle involute shape in the model channel, and tried to improve the flow uniformity by the optimization of flow passage.

EXPERIMENTAL SETUP

Figure 1(a) shows an experimental model of the disk shape SOFC channel employed in the present study. It has almost the same size as typical disk shape SOFC unit (outer diameter: D_O = 90 mm) and consists of a fuel channel and an air channel [2, 3, 4]. In the fuel channel, a working gas enters from the center hole (inner diameter: D_f = 24 mm) of the bottom disk, and then flows outward. Twelve air injection holes with a width of 4mm are drilled into the outer rim surface of the air channel at a regular interval. A working gas fed into the upper section of the air channel flows inward, changes its direction at the inner rim of a separation disk (inner rim diameter: D_i = 30 mm), and flows back through the lower section of the air channel. The fuel channel has a height of H_f = 5 mm or 2 mm, and both of the upper and lower air channels have heights of H_a = 2 mm, respectively. As shown in Fig. 1(a), the origin of coordinate system was chosen at the center of the bottom disk, and r and θ denote the radial and circumference directions, respectively.

Current collectors installed in the fuel channel and in the lower section of the air channel have a function of collecting the electric current. Furthermore, current collector acts as a guide for gas flow and determines the flow uniformity. Figure 2 shows two types of current collector examined in the present experiment. For one case, four flat plates are placed along the radial direction (hereafter referred to as "radial-type"). For the other case, eight curve plates having a circle involute surface geometry are regularly arranged (hereafter referred to as "involute-type"). The width of current collector is 2 mm for both cases. The height of the fuel channel is 2 mm when involute-type current collectors are installed. We adopt the curvilinear coordinate system (ξ,η) illustrated in Fig. 1(b), where ξ is measured along a circle involute and η is measured at right angles to it, respectively. The origin of ξ-axis is set on the circumference of the base circle, and ξ_0 is arc length between point O' and point P. A width between adjacent involute curve η_0 is given by $\eta_0 = r_i\alpha$.

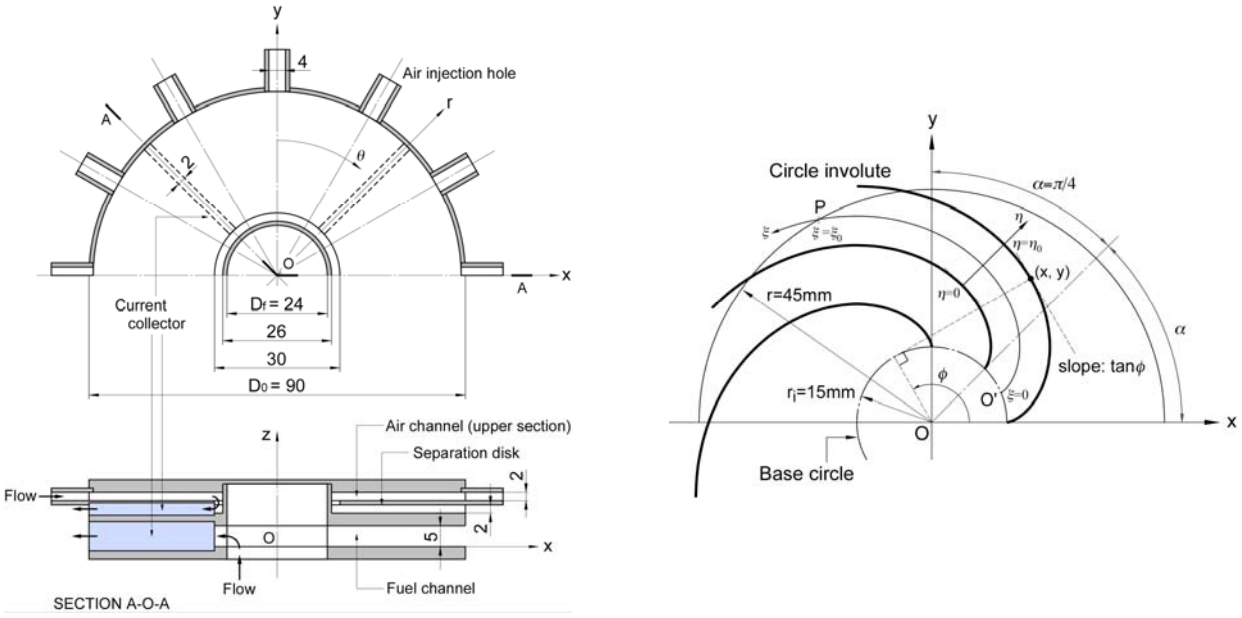

(a) Plane and cross-sectional views of the channel (b) Illustration of the circle involute

Figure 1. Experimental model of the disk shape channel

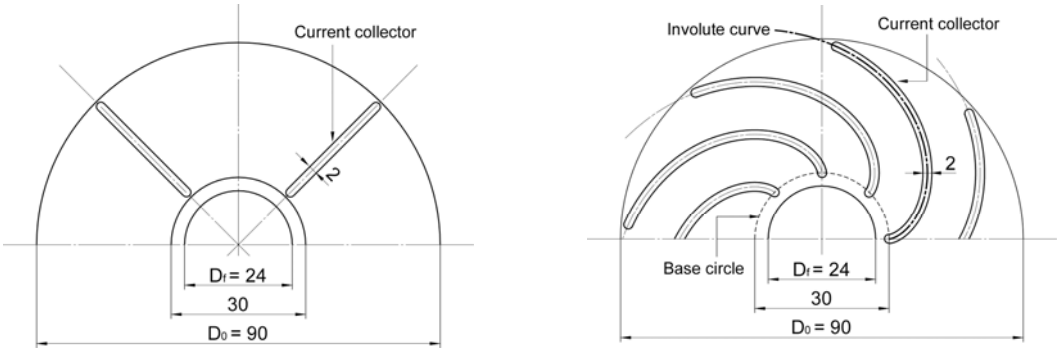

Figure 2. Arrangement of current collectors (Left: radial-type, Right: involute-type)

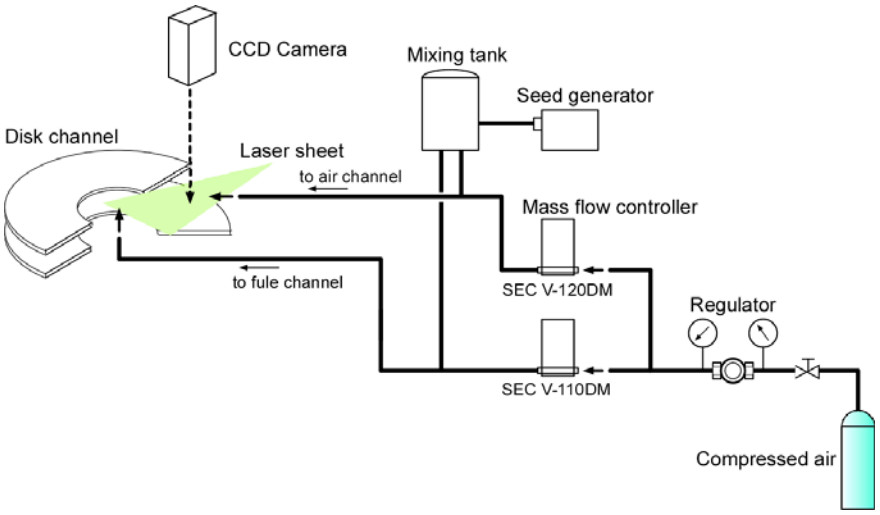

Figure 3. Schematic of the experimental setup

Figure 3 shows a schematic of the experimental setup. In order to give a detailed description of a flow field, instantaneous velocity vectors were measured by using PIV. The working gas is supplied from a compressed air cylinder at room temperature and seeded with tracer particles having about 10μm in diameter. Flow rates of the working gas in the fuel channel and in the air channel are controlled by mass flow controllers (HORIBA STEC, SEC-V110DM, SEC-V120DM). A light source of the PIV system is a double-pulsed Nd:YAG laser with an energy of 400 mJ per pulse (Spectra-Physics, PIV400). The pulsed laser beam is formed into light sheet having about 0.75 mm in thickness. This light sheet enters channel and illuminates the horizontal plane parallel to the disk plate. Light scattered from the particles in the field of view (60mm × 60mm) is captured by CCD camera (TSI, Model630046) settled above the channel and a series of particle images are recorded on PC. Instantaneous velocity vectors are deduced from successive particle images by using statistical correlation techniques with the aid of commercial software (Lavision, DaVis FlowMaster 7.1).

In order to simulate the practical operation in case of SOFC, experiments were performed at low Reynolds numbers of $1 \leq Re \leq 43$ in the fuel channel and $12 \leq Re \leq 92$ in the air channel, respectively. The Reynolds number is defined by $Re=U_f H_f / \nu$ or $Re=U_a H_a / \nu$. Here U_f and U_a denote respectively the velocities at the fuel channel inlet and air channel inlet, and are calculated from the operating condition of electric current density of 5000 A/m^2, fuel utilization factor of 0.5-0.8 and air utilization factor of 0.2-0.3. The above mentioned Reynolds numbers correspond to flow rates of 0.1 l/min $\leq Q_f \leq$ 3.0 l/min in the fuel channel and 1.0 l/min $\leq Q_a \leq$ 8.0 l/min in the air

channel. According to the method of ANSI/ASME PTC 19.1-1985 [5], uncertainty interval associated with the instantaneous velocity estimated at 95% coverage is evaluated as $0.04U_f$.

RESULTS AND DISCUSSION

Flow patterns in the disk channel with radial-type current collector

Fuel channel Figure 4 shows time-mean velocity vectors and contours in the horizontal plane at Q_f = 0.5 *l*/min. This flow rate corresponds to Reynolds number of 7. Time-mean values are calculated by ensemble averaging 50 instantaneous velocity fields. Although it is not shown here, the instantaneous velocity fields are almost identical to the time-mean flow representations. Therefore, we discuss overview of flow patterns on the basis of time-mean flow fields in the present paper. As seen in Fig. 4(a), in the middle horizontal plane (z=2.5 mm), the working gas flows radially and decelerates gradually toward the channel exit. However, a little higher velocities appear along the radial directions of θ = –26° and 28°. We can also see that low velocity regions are present near the current collectors owing to boundary layers developed on the current collector surfaces. Fig. 4(b) shows velocity field in the horizontal plane at z=4.5 mm which corresponds to the position of 0.5 mm apart from anode surface of the practical SOFC. Flow velocity decreases over the whole region of the channel by the effect of boundary layer on the disk plate. We found from a series of experiments that a relatively uniform radial flow was attained at Reynolds number of about 7 but occurrence of velocity gradient along the radial direction can not be avoided in the fuel channel.

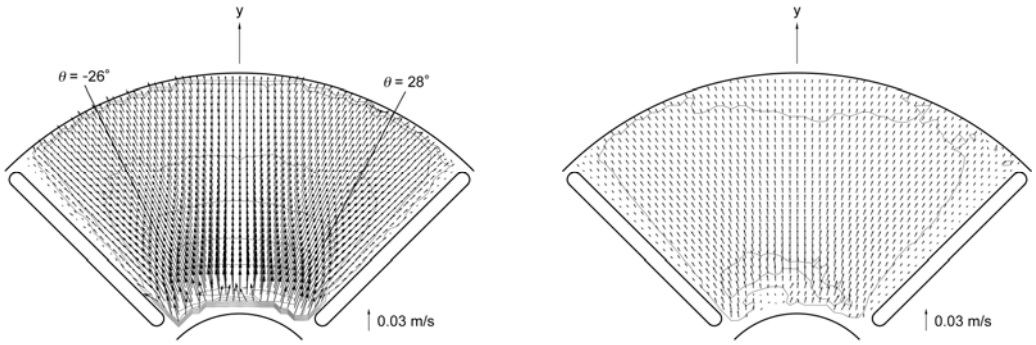

(a) z=2.5 mm (b) z=4.5 mm

Figure 4. Velocity fields in the horizontal plane of the fuel channel at Q_f = 0.5 *l*/min

.

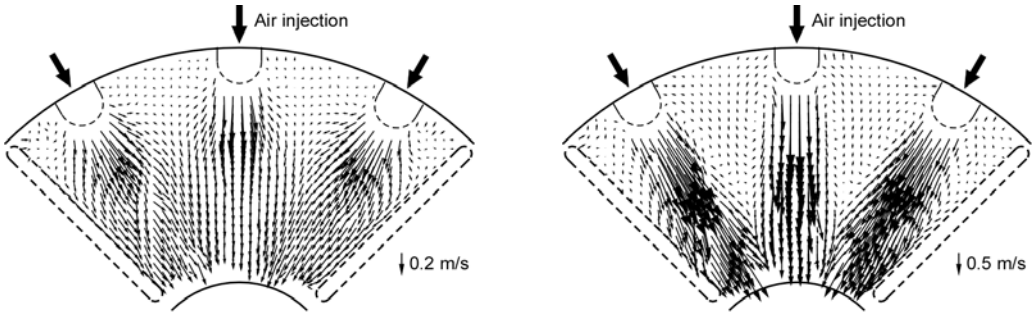

(a) Q_a = 2.0 *l*/min (b) Q_a = 8.0 *l*/min

Figure 5. Velocity fields in the middle horizontal plane of the upper section of the air channel

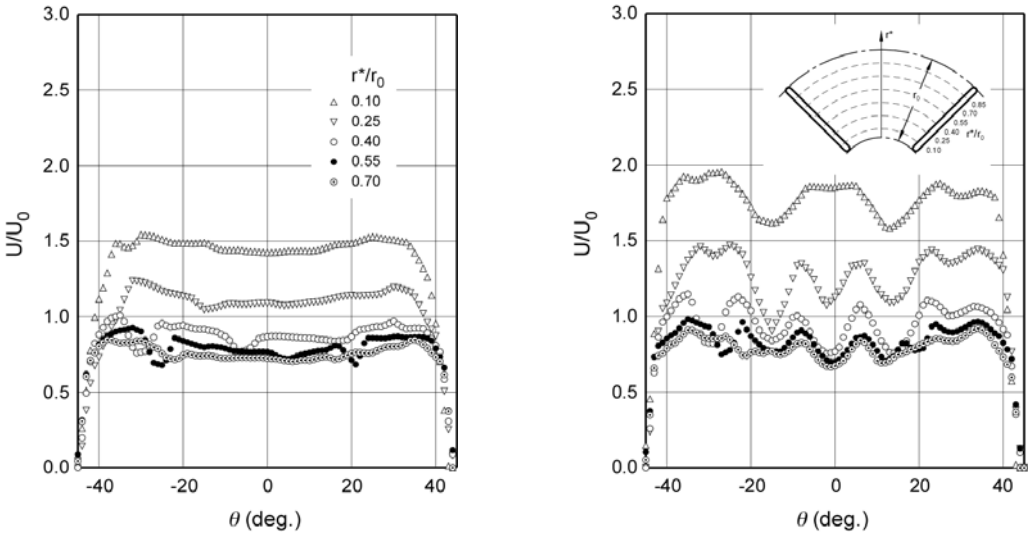

(a) Q_a =2.0 *l*/min (b) Q_a =8.0 *l*/min

Figure 6. Velocity profiles along the circumference direction in the lower section of the air channel

<u>*Upper section of the air channel*</u> Figure 5 shows velocity vectors in the middle horizontal plane of the upper section of the air channel at Q_a=2.0 and 8.0 *l*/min. These flow rates correspond to *Re*=23 and 92, respectively. The air supplied from injection hole, which shows jet-like behavior, flows to inner rim of the separation disk and strikes inner cylindrical surface. After that, jet-like flow spreads over the inner cylindrical surface and strikes it uniformly for the case of Q_a=2.0 *l*/min. On the other hand, at Q_a=8.0*l*/min, jet-like flow strikes on narrow area of the inner cylindrical surface and returned flow gives rise to a large-scale vortex between adjacent jet-like flows. This flow pattern is similar to multiple impingement jet, and is induced by the interaction between jet-like flows from adjoining air injection holes.

<u>*Lower section of the air channel*</u> Figure 6 shows velocity profiles in the middle horizontal plane of the lower section of the air channel at Q_a=2.0 and 8.0 *l*/min. Here, *U* is calculated by $U = (u_x^2 + u_y^2)^{1/2}$ from PIV data, and U_0 is estimated by flow rates and channel cross-sectional area at *r* =15 mm. At Q_a=2.0 *l*/min, uniform radial flow is realized in the lower section of the air channel. However, at Q_a=8.0 *l*/min, it is found that high-speed regions exist along the radial directions of $\theta \approx 0°$ and ±27°. This is because a high-momentum fluid produced by the fluid impingement onto the inner cylindrical surface enters lower section of the air channel. Therefore, the optimum flow field in the air channel is obtained at lower flow rates that correspond to a range of *Re* of 12-46. These results suggest the necessity of improvement of the channel shape and injection method of air.

Flow patterns in the disk channel with involute-type current collector

As mentioned above, in the case of radial-type channel, velocity gradient occurs along the downstream direction. This is because a cross-sectional area of the disk channel increases along the radial direction. Accordingly, in order to improve flow uniformity in a disk channel, we designed a flow passage with circle involute shape current collectors (Fig. 2).

<u>*Fuel channel*</u> Figure 7 shows velocity vectors in the middle horizontal plane of the fuel channel at Q_f = 0.3 and 3.0 *l*/min. These flow rates correspond to *Re* = 4 and 43, respectively. We can see from Fig. 7(a) that a swirl flow occurs between adjacent current collectors and maintains nearly constant speed toward the channel exit. In addition, the flow pattern seen in Fig. 7(a) is still present at higher flow rate (higher Reynolds number) as seen in Fig. 7(b). It is clearly shown from these features that the velocity field is significantly improved and flow uniformity can be achieved over the wide range of Reynolds numbers by introducing the circle involute shape current collectors. This is because a

flow passage consisting of two adjacent circle involutes is equivalent to constat-area channel due to the geometrical property of circle involute.

In order to clarify flow uniformity, velocity profiles along the direction perpendicular to the current collector surface (i.e. η-direction) are shown in Fig. 8. Here, velocity profiles are plotted at dimensionless streamwise locations of ξ/ξ_0=0.1, 0.25, 0.4, 0.55, 0.7 and 0.85. As shown in Fig. 8(a), in the case of Q_f = 0.3 *l*/min, a maximum of U/U_0 =1.9 is reached near η/η_0=0.3 at ξ/ξ_0=0.1. In the region of 0.25 ≤ ξ/ξ_0≤ 0.55, U/U_0 is about 1.5 except near the current collectors where it falls rapidly to zero. However, in the downstream from a trailing edge of current collector (ξ/ξ_0> 0.7), the working gas is decelerated owing to the increase in channel cross-sectional area. From these characteristics, we can find that deceleration of the working gas is suppressed over a large part of the channel and the area of uniform velocity field in the involute-type channel extends wider than that in the radial-type channel. A peak of the velocity profile is observed close to η/η_0=0.3 at ξ/ξ_0=0.1 and close to η/η_0=0.5 at ξ/ξ_0=0.55, respectively. This flow feature indicates that the path of a working gas does not precisely follow the circle involute. As shown in Fig. 8(b), in the case of Q_f =3.0 *l*/min, velocity profiles show good similarity at ξ/ξ_0≤ 0.55, and the velocity at ξ/ξ_0=0.7 is higher than that for the case of Q_f =0.3 *l*/min. Comparing Fig. 8(b) with Fig. 8(a), the velocity field at higher flow rate of Q_f =3.0 *l*/min still exhibits the global features occurring at lower flow rate of Q_f =0.3 *l*/min, but flow uniformity is slightly enhanced with increase in flow rate.

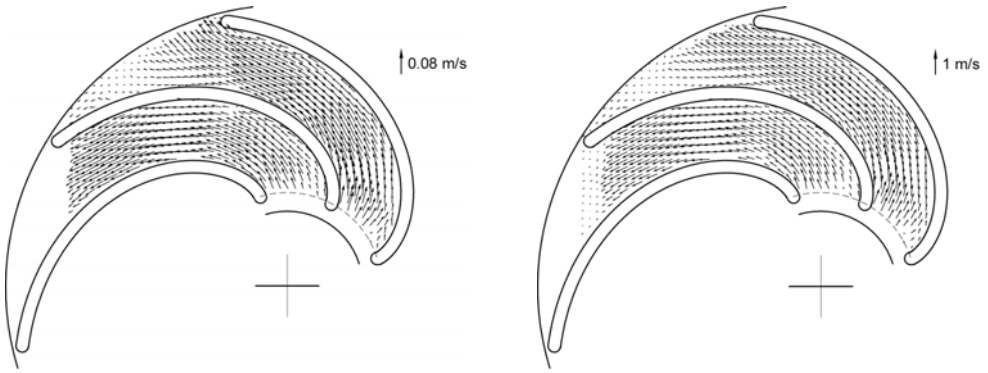

(a) Q_f =0.3 *l*/min (b) Q_f =3.0 *l*/min

Figure 7. Velocity fields in the middle horizontal plane of the fuel channel

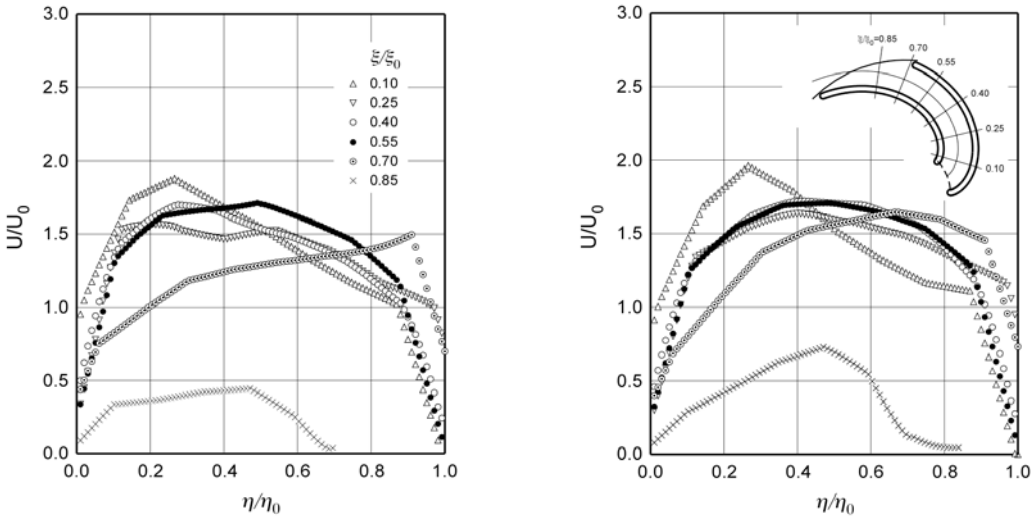

(a) Q_f =0.3 *l*/min (b) Q_f =3.0 *l*/min

Figure 8. Velocity profiles along the η-direction at several locations of ξ/ξ_0 in the fuel channel

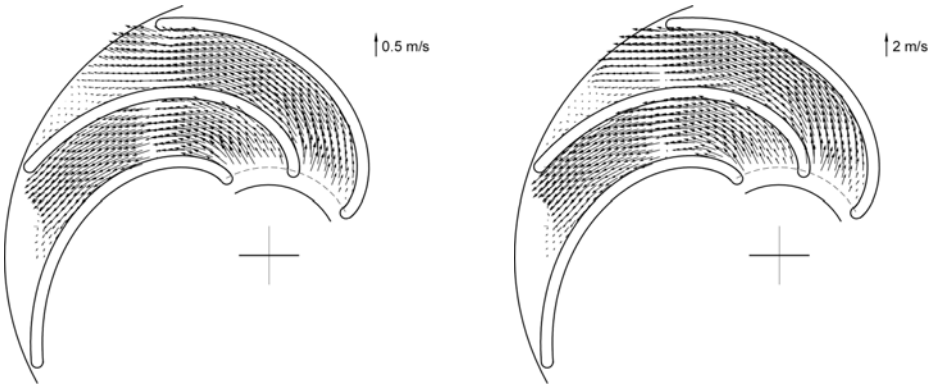

(a) Q_a =2.0 *l*/min (b) Q_a =8.0 *l*/min

Figure 9. Velocity fields in the middle horizontal plane of the lower section of the air channel

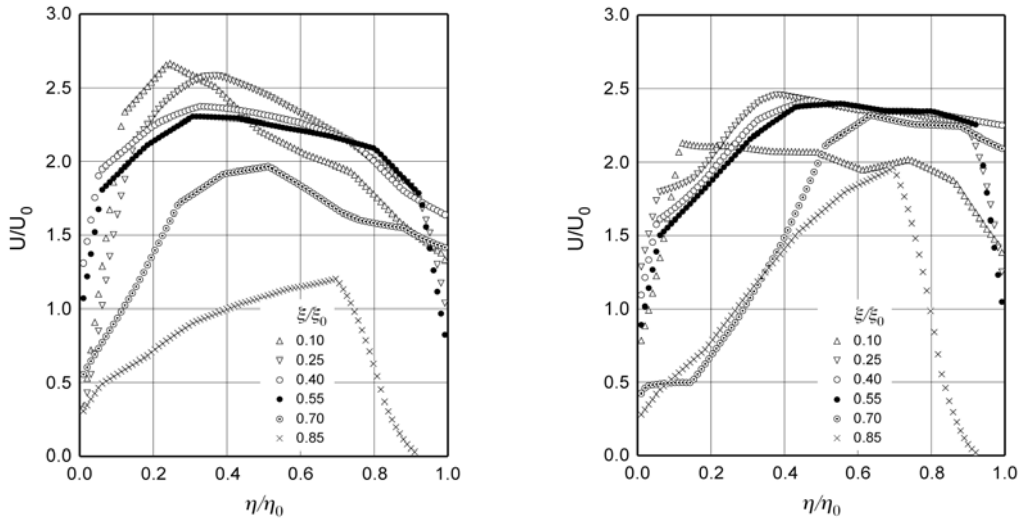

(a) Q_a =2.0 *l*/min (b) Q_a =8.0 *l*/min

Figure 10. Velocity profiles along the η-direction at several locations of ξ/ξ_0 in the lower section of the air channel

Lower section of the air channel In the present experiment, velocity fields in the horizontal plane of the upper section of the air channel are not effectively affected by introducing the involute-type current collectors, and have similarity to velocity fields shown in Fig. 5. Hence, we focus on the velocity fields in the lower section of the air channel.

Velocity vectors in the middle horizontal plane of the lower section of the air channel at Q_a =2.0 and 8.0 *l*/min are compared in Fig. 9. These flow rates correspond to *Re*=23 and 92, respectively. Measured velocity fields are nearly identical regardless of flow rates and a strong resemblance can be observed between the velocity fields in Fig. 7 and those in Fig. 9.

Figure 10 shows velocity profiles along the η-direction at several dimensionless streamwise locations to investigate flow uniformity in more detail. In the case of Q_a =2.0 *l*/min, a maximum of U/U_0 exceeds 2.5 at ξ/ξ_0=0.1 and 0.25, and reaches about 2.3 at ξ/ξ_0=0.4 and 0.55. The position to achieve maximum velocity is around η/η_0=0.3 at $0.1 \leq \xi/\xi_0 \leq 0.55$. In the case of Q_a =8.0 *l*/min, U/U_0 is about 2.1 over the wide range of η/η_0 at ξ/ξ_0=0.1, whereas U/U_0 reaches up to 2.4 for $0.5 < \eta/\eta_0 < 0.9$ at $0.25 \leq \xi/\xi_0 \leq 0.55$. In addition, no apparent streamwise variation of U/U_0-profile is found in the region of $0.25 \leq \xi/\xi_0 \leq 0.55$. Comparing Fig. 10(a) and Fig. 10(b), flow uniformity is

enhanced at $0.25 \leq \xi/\xi_0 \leq 0.55$ and velocity increases at downstream part of the channel ($\xi/\xi_0 \geq 0.7$) with increase in flow rate. In addition, we can find that, in the case of higher flow rate, the η/η_0 location to achieve maximum velocity shifts toward positive η-direction and a gas flow deflects away from the involute curve. A fluid motion toward the η-direction is estimated by the η-component of the momentum equation. For simplicity, we consider the η-component of Euler's equation of motion [6]:

$$\frac{\partial U_\eta}{\partial t} + \frac{R}{R+\eta} U_\xi \frac{\partial U_\eta}{\partial \xi} + U_\eta \frac{\partial U_\eta}{\partial \eta} - \frac{U_\xi^{\,2}}{R+\eta} = -\frac{1}{\rho}\frac{\partial P}{\partial \eta} \tag{1}$$

where U_ξ and U_η are the velocity components in the ξ- and η-directions, P is the pressure, ρ is the density, and R is the curvature of circle involute at (ξ, 0), respectively. From equation (1) we see that, in the flow field where U_ξ is dominant compared with U_η, the pressure gradient along the negative η-direction plays primary role in a centripetal force to maintain a swirl motion. In case of higher flow rate, a momentum of fluid increases and the influence of pressure gradient on the fluid motion relatively weaken accordingly. Consequently, the gas flow strays from the involute curve.

CONCLUSIONS

A detailed flow structure between two parallel disk shape plates was investigated by using the particle image velocimetry. The experiment was performed at low Reynolds numbers (Re<100) to simulate the practical operation in SOFC. When we installed radial-type current collector in the disk channel, unfavorable flow deceleration occurred toward downstream direction. However, in the case of applying an involute-type current collector, a flow velocity was kept at nearly constant value toward the channel exit. This trend was observed regardless of flow rates, and hence flow uniformity was achieved over the wide range of Reynolds numbers by introducing the circle involute shape current collector. This is because a flow passage consisting of two adjacent involute curves functions as a constat-area channel due to the geometrical property of the involute curve.

REFERENCES

1. Dang, Z., Iwai, H. and Suzuki, K., Numerical Modeling of a Disk Shape Planar SOFC, Second International Conference on Fuel Cell Science, Engineering and Technology, pp 361-368, 2004.
2. Mizutani, Y., Hisada, K., Ukai, K., Yokoyama.M. and Sumi, H., Experiences With the First Japanese-Made Solid-Oxide Fuel-Cell System, *Trans. ASME, J. Fuel Cell Science and Technology*, Vol. 2, No. 3, pp 179-185, 2005.
3. Costamagna, P. and Honegger, K., Modeling of Solid Oxide Heat Exchanger Integrated Stacks and Simulation at High Fuel Utilization, Journal of Electrochemical Society, Vol.145, No.11, pp 3995-4007, 1998.
4. Bossel, U., Portable 1 kW SOFC Generator Operated on Methanol, Proceedings of the Fuel Cell World, pp 206-213, 2003.
5. ANSI/ASME PTC 19.1-1985, Measurement Uncertainty, Supplement on Instruments and Apparatus, Part 1, 1986.
6. Schlichting, H., *Boundary-Layer Theory*, McGraw-Hill, pp 67-68, New York, 1979.

MEASUREMENT AND MODELLING OF HEAT AND MASS TRANSPORT CHARACTERISTICS INSIDE PEMFC SYSTEMS

T. Araki*, So Manabe, Yuki Uemura, Kenji Ohora
Yokohama National University, Yokohama, Japan

ABSTRACT. To grasp and generalize effects of the local mass and energy transport on transient performance of PEMFC, we have measured voltage and membrane resistivity responses. Also, unsteady numerical model, which solved mass, electrical charge, and energy conservation equations had been developed. As necessary parameters for developing them, we measured properties of water content of MEA, MEA resistivity, the activation over-voltage, and mass transfer coefficients at boundaries etc. The measured and calculated transient responses were agreed well in many operating conditions. Especially complicated voltage responses with liquid water droplet evaporation could be numerically estimated.

Keywords: *PEMFC, Heat and mass transfer, unsteady power generating characteristics, water evaporation*

INTRODUCTION

Applications of PEMFC as good alternatives to conventional power generators are promising especially for vehicles and distributed stationary power generators. In PEMFCs, the water plays a significant role in proton conductivity of polymer electrolyte membrane (PEM) and reactant gas transport in channel and gas diffusion layers (GDL). However, mass, especially water, transport phenomena in each layers of PEMFC are so complicated as shown in Fig.1. For instance, the water is transported from the anode to cathode by electro-osmotic drag, and generated water at the cathode is diffused back toward the anode, and there are transport resistances at any boundaries between layers. Due to the importance of water transport factors, such as diffusion coefficient and electro-osmotic coefficient of water vapor through a membrane, have important effects on the performance of PEMFC, these factors have been measured in our previous reports.

Water transport phenomena in steady states have been cleared so far on some level, however, the water transport characteristic in transient state is still unclear, even transient state observed frequently during PEMFC operation such as start up and load change. The voltage, membrane resistivity and outlet gas humidity responses after supplying gas humidity stepwise change were measured. It is true that the supplying humidity change is not frequently occurred in actual PEMFC operation, however, the effect of water transport can be easily inspected by under these conditions.

To discuss more detail of effects of the local water transport on performance of PEMFC, we have developed unsteady numerical model, which solved mass conservation equations and

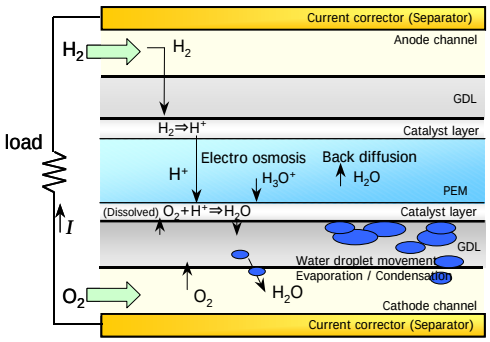

Fig.1 General factors of water transport inside PEMFC

* Corresponding author: Prof. T. Araki
Phone: + (81)-45-339-3920, Fax: + (81)-45-339-3920
E-mail address: taraki@ynu.ac.jp

charge conservation equations in gas channel, GDL and MEA. As necessary parameters for developing them, we measured properties of Water content of MEA, MEA resistivity, the activation over-voltage, and overall mass transfer coefficient etc..

EXPERIMENTAL SETUP AND NUMERICAL MODEL

Experimental apparatus

Overview of experimental apparatus is shown in Fig. 2. Two sets of gas supplying systems (gas cylinders, mass flow controllers, humidifiers etc.) are placed on anode and cathode respectively, and supplied gaseous conditions could be changed quickly by use of four-way selector valves. The humidity change was mainly applied in present study for discussing water transport inside cell. Single cell was tested and it included membrane electrode assembly (MEA), gas diffusion layer (GDL), gas distributors (current collector), and end plates. The active area of MEA was 10cm^2, and its thickness was about 50μm. Carbon papers of 200μm thickness were used as GDL. The gas distributors were designed as single serpentine groove which length is 25cm with square cross section (1.0mm ×1.0mm). Supplied gaseous species are hydrogen and oxygen for decreasing effect of diffusion overpotential. Cell temperature was maintained at 70^{o}C by a constant temperature device. Dew point meters were used to measure relative humilities at inlet and outlet of anode and cathode. To control and measure accurate current/voltage polarization curves, the fuel cell was connected to a bipolar power supply. Membrane resistance were recorded by LCR meter connected with PC.

Numerical model

Investigating detailed transient of overvoltage distribution, it is needed to study not only experimentally but also numerically. Then, we have developed a transient two and three dimensional numerical model in PEMFC which includes equivalent circuit, conservation of mass and charge. Most of equations and algorithm of this model are as reported previously[1].

Electrical characteristics. As electrical parameters, activation overpotential, resistivities of membrane and GDL, and capacitance of electrical double layers have v\been measured. For example, measuring methods of activation overpotential are explained. Activation overpotential was measured with various supplied gaseous relative humidity (RH). Pure hydrogen and oxygen were used to eradicate the influence of concentration overvoltage, and relatively high flow rates of 1000 cc/min were supplied to even water content at MEA as far as possible. Current density was controlled at 0.1 A/cm^2. Fig.3 shows activation overpotential as a function of current density with

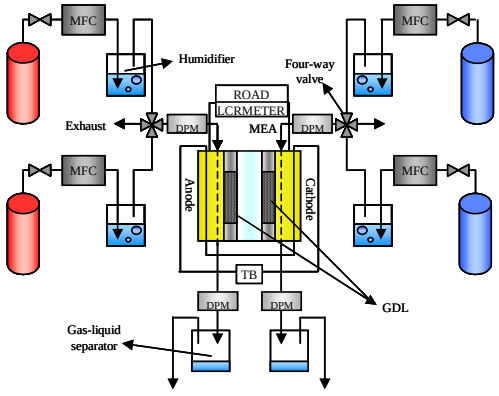

Fig. 1 Experimental apparatus

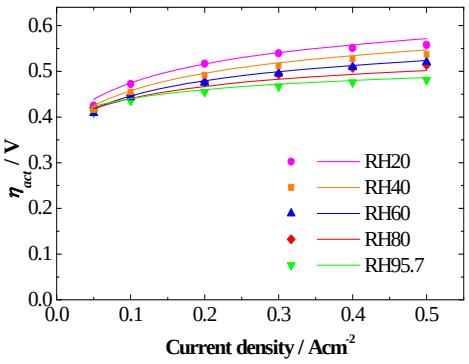

Fig.2 Effects of relative humidity on Activation overpotential

various supplied gaseous humidity. The activation overpotential increases as the supplied gaseous relative humidity decrease. The approximation, equation 1, was obtained by fitting results.

$$\eta_{act} = A + B \ln i \quad (1)$$

$$A = -1.4\times10^{-3}\,\mathrm{RH} + 0.6392\,,\ B = -3\times10^{-6}\mathrm{RH}^2 - 5\times10^{-5}\mathrm{RH}$$

Water transport characteristics. Overall mass transfer coefficient at the MEA/GDL interface, equation 2, was calculated from results of transient response MEA water content or resistivity after sudden supplied gas humidity change.

$$K_g = 1.0\times10^{-3}\ \mathrm{m/s},\ K_m = 1.19\times10^{-6}\ \mathrm{m/s} \quad (2)$$

Values of other properties such as the diffusion coefficients, electro osmotic drag coefficient, are used same as reported [2].

RESULTS AND DISCUSSIONS

Voltage responses after humidity change in dry condition

Transient cell voltage responses after sudden supplied gaseous humidity changes were measured Relatively low fuel and oxidant utilization ratio, in other words, high flow rates of supplied gases 100 cc/min, and low current density of 0.1 A/cm^2 were applied to keep test cell dry. Circle dots in Fig. 3 shows measured voltage response after supplied gaseous relative humidity (RH) change from 20% to 60% in (a) and from RH60% to RH20% in (b), respectively. Voltage increased after upward humidity change (a) due to decrease of resistivity and resistive overpotential. In figure (b) voltage decreased adversely. Downward change showed little bit slower response, however difference of time constants were not so big in these lower humidified conditions; no liquid water inside GDL.

Numerical voltage responses in same conditions were also plotted in Fig. 3 with lines. Cell voltages at steady state and time constants agreed well. Differences of the amount of 10 mV is enough small compared with experimental errors and repeatability.

For investigating mass transport in detail, the water concentration contours at t=0.0s, 1.0s, 5.0s, and 30s after humidity change from RH60 to RH60 are shown in Fig.4. Because water concentration in MEA was much higher than that of vapor, they were converted to gaseous equilibrium value at cell temperature (70^{o}C). At t=1.0s, the concentration of water vapor in GDL and channel changed significantly, but the concentration in MEA hardly changes. This means large part of mass transport resistance exists at MEA/GDL interface consists of CL and MPL.

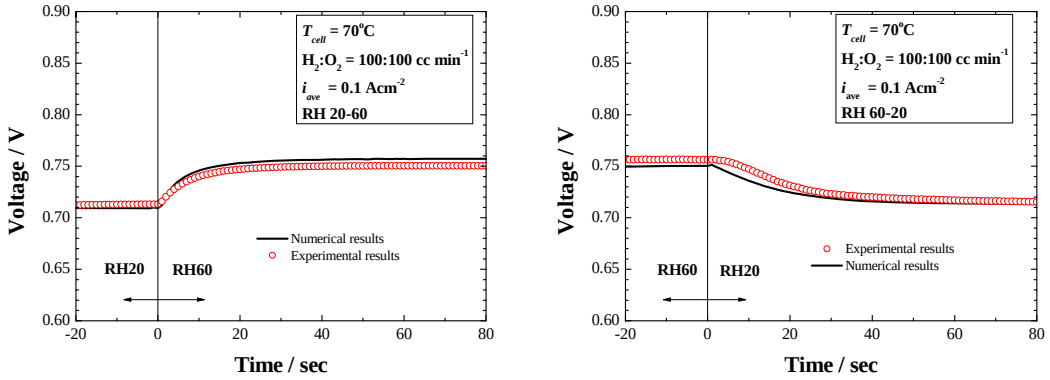

(a) upward change (RH20 to RH60) (b) downward change (RH60 to RH20)

Fig. 3 Voltage response after sudden supplied gas humidity change

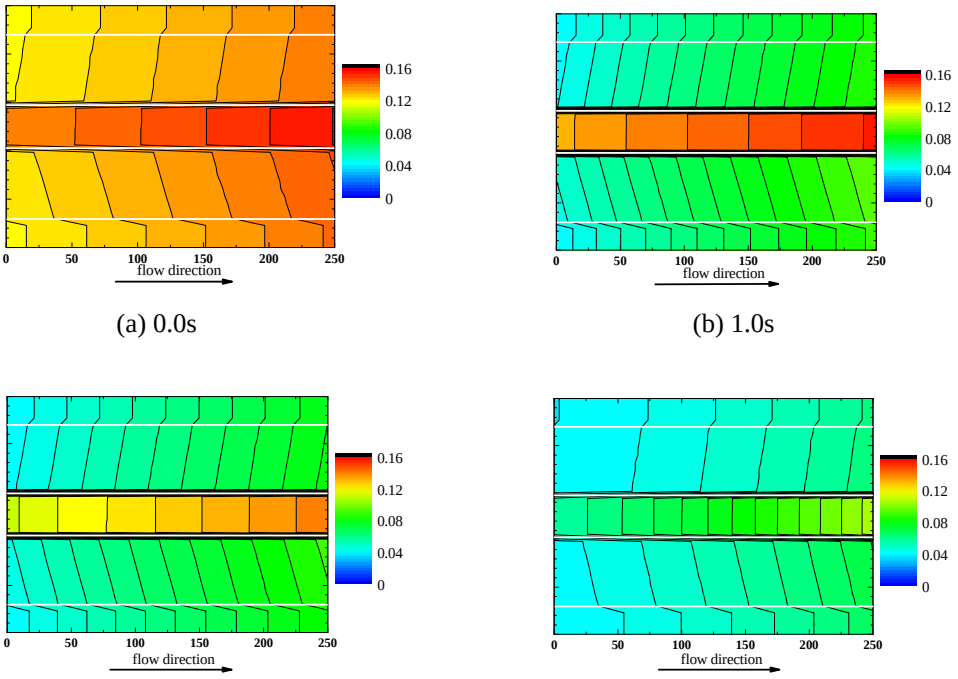

(a) 0.0s (b) 1.0s

(c) 5.0s (d) 30s

Fig. 4 Water concentration contours after sudden supplied gas humidity change from RH60 to RH20

Consequently, time constants of cell voltage was mainly influenced by mass transport resistance at MEA/GDL under these conditions. This illation can be understood more easily from Fig. 5, which shows water concentration profiles in normal to PEM direction at 200mm from inlet.

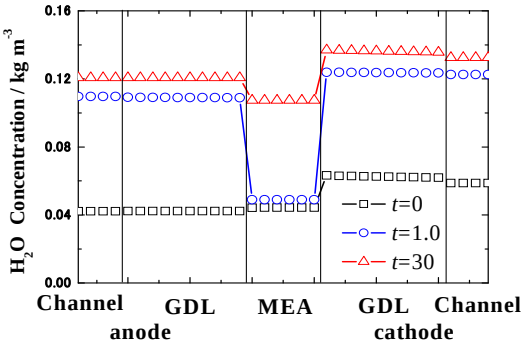

Fig.5 H_2O concentration profiles from anode to cathode at 200mm of the channel length

Voltage responses after humidity change with liquid water

The voltage responses in previous section were fast, because of a little amount of water in a cell. The responses could be extremely slowed if water droplets located in GDL or channel. Thus, experiments had been conducted in higher humidified conditions (or more current density, which means greater amount of generated water), to confirm and discuss effects of accumulated water. Fig. 6 shows voltage responses in various current densities ranging from 0.1 to 0.5A/cm^2. Responses after moisturize change and dryer change with low current density (0.1 A/cm^2) were fast and comparable with the dry conditions in previous section. On the contrary, it is clearly seen that the responses after desiccate change with higher current densities were very slow and completely unlike previous conditions. Please note that, the time axis is ten times extended compared with Fig. 3. These delays were subject to the accumulated water and its slow evaporation. Moreover, complicated voltage responses with inflexion points were observed. The inflection points could be accounted from the difference of evaporating speed at each layer or location. During water droplets exist in a cell, the membrane did not dried up and membrane resistivity did not change rapidly, however, after the instant of liquid water disappear from GDL or channel, the PEM dried up faster due to a thinness of PEM and low amount of water content.

We have also conducted numerical analysis considering amount of accumulated water in GDLs. The numerical responses are plotted in Fig. 7 with experimental responses. The numerical voltage response also showed some inflections and basically agreed with experiment. Thus, adequacy of our model was confirmed in those experimental conditions. Examining the results more minutely, experimental voltage drew away from numerical after 100s and reached steady state much slower than numerical voltage. These differences are probably owing to 3 dimensional effects. As shown blue arrow in Fig. 8, liquid water accumulated under rib is needed to transported long way to transport to channels and takes long time to completely evaporated. Then, the experimental responses need more time to reach steady state. Meanwhile, we constructed a 2 dimensional model in this study and did not considered such effects, then, .numerical response was estimated a little bit

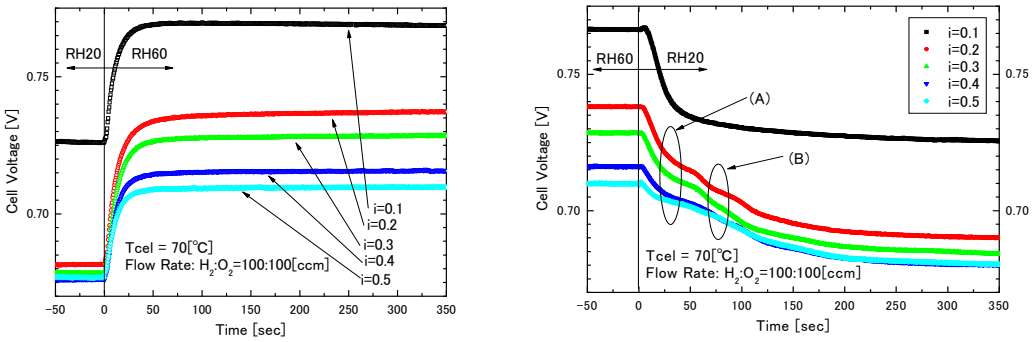

(a) upward change (RH20% to 60%) (b) downward change (RH60% to 20%)

Figure 6 Voltage responses in various current densities ranging from 0.1 to 0.5A/cm^2

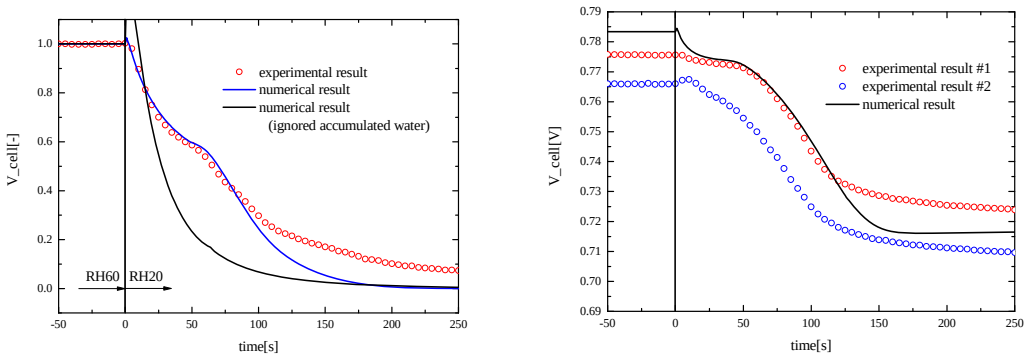

(a) RH60% to 20% with 0.3A/cm^2 (b) RH95.8% to 20% with 0.1A/cm^2

Figure 7 Comparison of numerical and experimental voltage responses

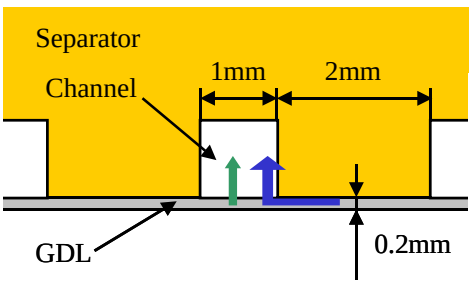

Figure 8 Effect of rib on water evaporation

quicker.

Energy transport

The temperature distributions in actual working cell have been also calculated and measured. The examples of calculated temperature distributions are shown in Fig. 9. The temperature at cathode catalyst layer seems to be highest in these results.

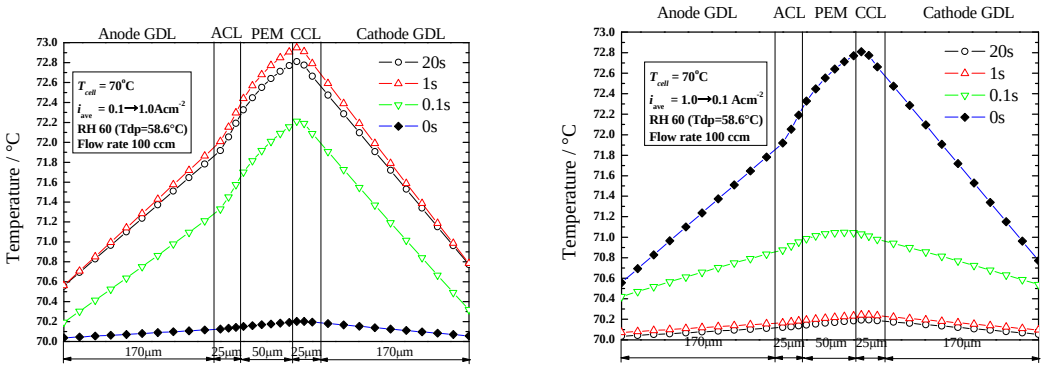

Figure 9 Temperature profile after load current density change
from 0.1 [A/cm^2] to 1.0 [A/cm^2](left side) and from 1.0 [A/cm^2] to 0.1 [A/cm^2](right side)

CONCLUSIONS

Voltage transient responses of PEMFC were investigated experimentally and numerically. In dry condition, the voltage responses were affected strongly by transport resistances at OEM-GDL, and they mainly dominate reaction time. The voltage responses with accumulated water droplets were extremely delayed and complicated. Some inflection points were observed, and they depend on locations of water accumulated position and its length of diffusion path.

ACKNOWLEDGMENT

This research is partly supported by The New Energy and Industrial Technology Development Organization (NEDO) and JSPS (KAKENHI).

REFERENCES

1. Araki, T., *et al.*, Mass transfer characteristics inside PEMFC and its unsteady power generation analysis, *Trans. IEEJ*, 128, pp. 571-578, 2008. *in Japanese*.
2. Onda, K. *et al.*, , Analysis of Current Distribution at Polymer Electrolyte Fuel Cell in Use of Measured Membrane Properties and Comparison with Measured Current Density, *J. Electrochem. Soc.*, Vol. 154, No. 2, pp.B247-B257, 2007.

STEAM REFORMING OF DIMETHYL ETHER WITH CATALYTIC COMBUSTION IN A SMALL ANNULAR TUBE

M. Saito[1, *], N. Kubo[1], Y. Kataoka[1], Y. Lee[1], K. Teramoto[1], H. Iwai[1], H. Yoshida[1]
[1]Kyoto University, Kyoto, Japan

ABSTRACT. Recently, hydrogen has attracted much attention as a fuel, particularly for fuel cells. If small equipment that can supply hydrogen is realized, its applications can be greatly extended. The steam reforming of dimethyl ether (DME) is expected to be used for the production of hydrogen. In this study, we fabricated a small DME reformer. Catalytic combustion is used as a heat source because the steam reforming of DME is an endothermic reaction. The reformer has the structure of a double tube, in which steam reforming of DME occurs in the outer channel, and the catalytic combustion occurs in the inner channel. At a sufficiently high temperature, DME was almost completely reformed. However, it is necessary to avoid an excessively high temperature because the formation of CO and CH_4 increases. Thus, temperature control is important for the steam reforming of DME.

Keywords: *fuel reforming, catalytic combustion, dimethyl ether*

INTRODUCTION

Hydrogen utilization is now recognized as a key technology for efficient energy conversion. The steam reforming of dimethyl ether (DME) is expected to be used for the production of hydrogen [1]. DME can be reformed at lower temperatures than hydrocarbons. Moreover, its portability is good because it is a liquid fuel and its toxicity and corrosivity are far less than those of methanol.

We designed a small DME reformer based on a self-sustaining reaction. The steam reforming of DME is an endothermic reaction. Therefore, catalytic combustion is used as a heat source. We fabricated a small reformer with an annular tube structure, and examined the conversion of DME for varying temperature profiles.

CONCEPT AND DESIGN

Steam reforming of DME

The overall reaction of DME steam reforming is expressed as follows:

$$CH_3OCH_3 + 3H_2O = 6H_2 + 2CO_2 - 123.84\ [\text{kJ/mol}] \quad (1)$$

In general, the steam reforming of DME progresses with in consecutive steps.

$$CH_3OCH_3 + H_2O = 2CH_3OH - 24.68\ [\text{kJ/mol}] \quad (2)$$

$$CH_3OH + H_2O = 3H_2 + CO_2 - 49.58\ [\text{kJ/mol}] \quad (3)$$

* Corresponding author: Mr. M. Saito
Phone: + (81)-75-7535203, Fax: + (81)-75-7535203
E-mail address: msaito@mech.kyoto-u.ac.jp

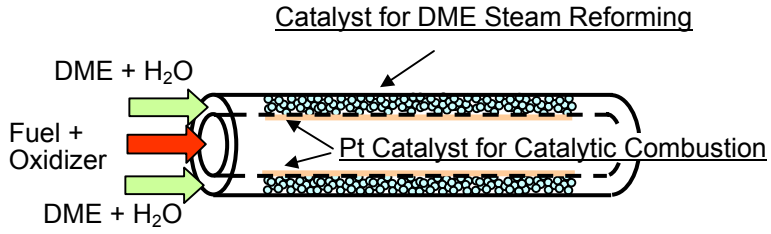

Figure 1. Conceptual figure of DME steam reformer

The first step is the hydrolysis of DME, which is well known to be enhanced by solid-acid catalysts [2]. The second step is the steam reforming of methanol, which proceeds in the presence of metal catalysts [3, 4], particularly Cu catalysts [2, 5]. As indicated in reactions (2) and (3), both reactions are endothermic.

When the temperature is high, a reverse water-gas shift reaction takes place.

$$H_2 + CO_2 = CO + H_2O - 41.17\ [\text{kJ/mol}] \tag{4}$$

This reaction is undesirable, because H_2 is consumed and CO is produced. Furthermore, the decomposition of DME is also expected to occur at higher temperatures.

$$CH_3OCH_3 = CH_4 + CO + H_2 \tag{5}$$

Thus, for the collection of H_2, temperature control is important to avoid excessive temperature rises.

Catalytic combustion

As described in the previous section, thermal energy must be added to enable the steam reforming of DME. We considered that catalytic combustion is a suitable heat source in a small reformer. In a small volume, it is difficult to sustain gas-phase combustion, because the heat loss is relatively large owing to the high specific surface area. On the other hand, the large specific surface area is an advantage for catalytic combustion [6]. Moreover, catalytic combustion can be maintained under a lean fuel condition and at a low temperature [7], so that it is possible to generate the heat to achieve the moderate temperature required for reforming DME.

Annular tube reformer

For our small DME reformer based catalytic combustion, we adopted the annular structure shown in Fig. 1. To reduce the heat loss, the channel used for catalytic combustion is installed on the inside of the reformer, and the released heat is recovered for the steam reforming of DME in the outer channel.

There are various choices for the fuel used in the catalytic combustion, for example, part of the unreformed DME, part of the reformed hydrogen or residual hydrogen from a fuel cell system. In the present experiment, we introduce hydrogen into the channel used for catalytic combustion independently of the reformed gas obtained by DME steam reforming.

EXPERIMENTS ON ANNULAR TUBE REFORMER

Apparatus

Figures 2 and 3 show schematic diagrams of the experimental apparatus. It has the structure of a double tube, in which the steam reforming of DME occurs in the outer channel, and the catalytic combustion occurs in the inner channel. The outer quartz tube has an inner diameter of 6.0 [mm] and an outer diameter of 8.0 [mm]. The inner stainless-steel tube, whose inner surface is coated with a Pt catalyst for catalytic combustion, has an inner diameter of 2.0 [mm] and an outer diameter of 4.0 [mm].

A mixture of DME, H_2O and balance N_2 is introduced into the outer channel, in which the reforming catalyst is packed. We fabricated the Cu-Fe spinel-type oxide catalyst referred to in the paper by Tanaka et al. [2]. The flow rate of H_2O in the liquid phase is controlled by a syringe pump, and the water vapor after heating is mixed with DME and N_2. To enable catalytic combustion, a mixture of H_2 and air flows into the inner channel and reacts on the inside surface coated with the Pt catalyst.

The gases for reforming and catalytic combustion are independently fed into each channel. The length of the Pt catalyst on the inner tube for catalytic combustion is 100 [mm]. To determine the amount of catalyst suitable for reforming DME, the length of catalyst packed in the outer channel was varied. We set it to 30, 50 and 100 [mm] in this experiment.

We set eight thermocouples at intervals of 10 [mm] in the catalyst for reforming DME. The thermocouple used to measure the temperature of catalytic combustion in the inside channel has a transverse mechanism that enable it to be moved to an arbitrary position.

The composition of reformed gas was analyzed by gas chromatography (Shimadzu, GC-8APT) with a thermal conductivity detector after the water trap. A Molecular Sieve 5A column was used to separate H_2, O_2, N_2, CH_4 and CO, and a Porapak Q column was used to separate CO_2 and DME. The exhaust gas after catalytic combustion was also analyzed by gas chromatography to confirm the completeness of the reaction.

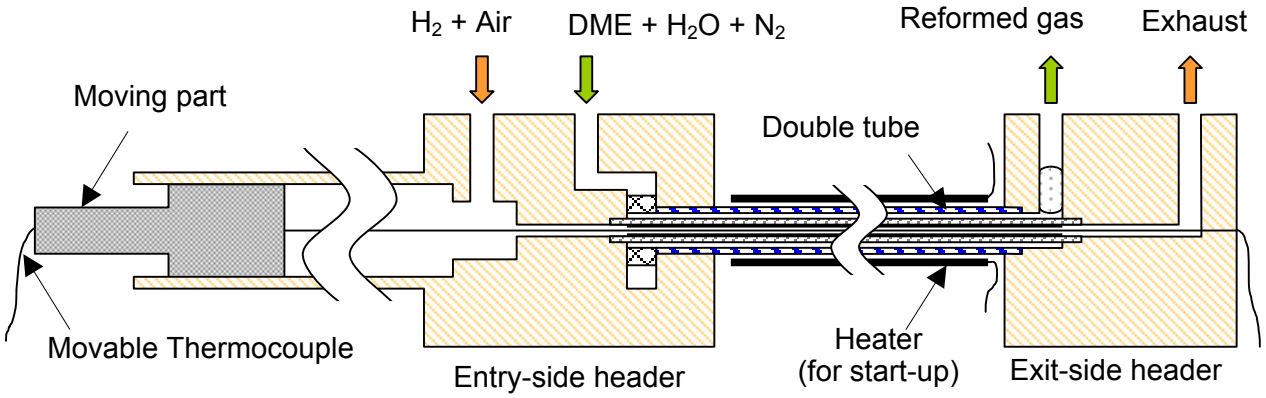

Figure 2. Schematic diagram of experimental apparatus

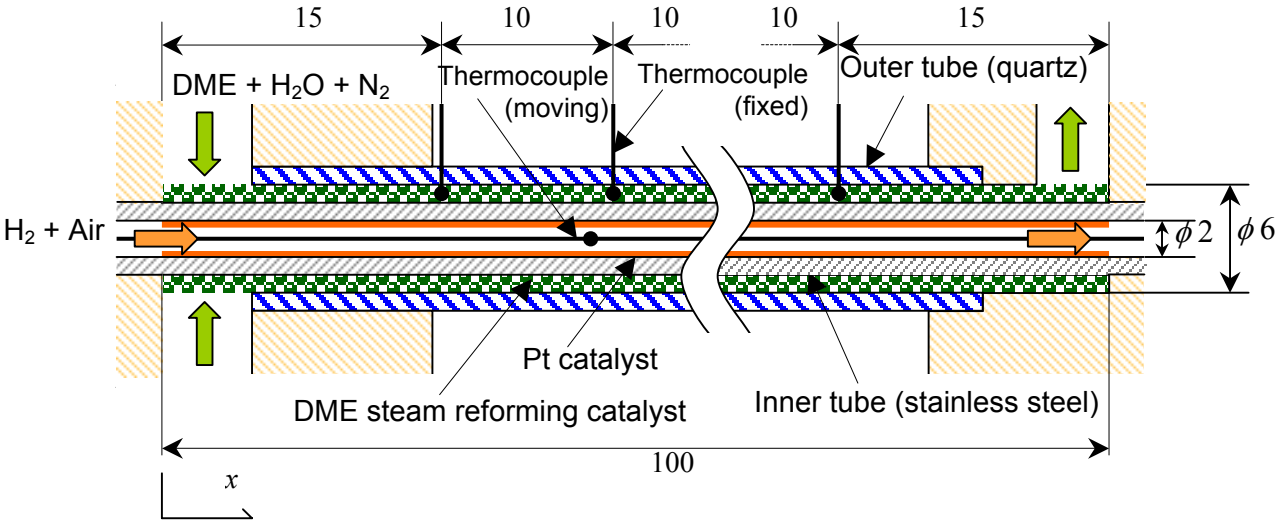

Figure 3. Test section

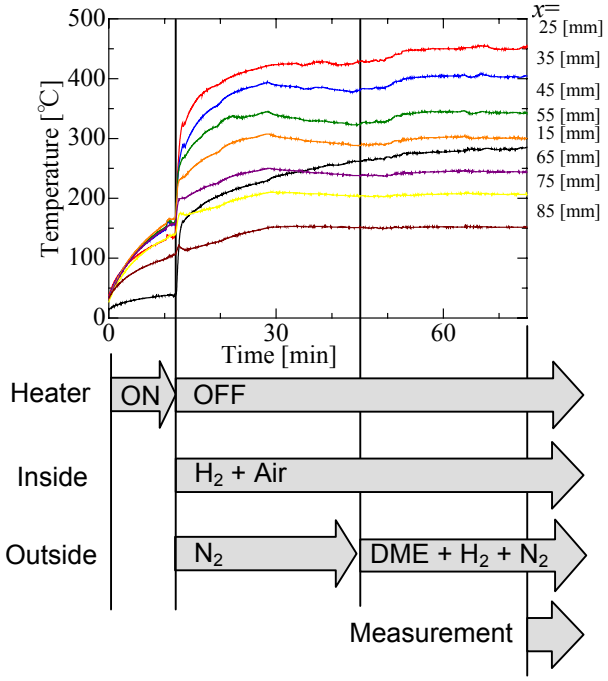

Figure 4. Experimental procedure

Procedure

Figure 4 shows the experimental procedure and the corresponding changes in temperature. The position of x is defined as the distance from the inlet as shown in Fig. 3.

This apparatus should be thermally self-sustaining during reforming. However, for start-up, the test section must be heated by using nichrome wire heater. When the heater was turned off, we introduced the mixture used for catalytic combustion into the inner channel. After the catalyst reached a sufficient temperature, the reformed gas was introduced. We measured the temperature and the concentration of the gases in the steady state, in which the amplitude of temperature variation had settled to within 0.5 [°C].

Results and discussion

Prior to discussing the experimental results, "space velocity", which is often used for the evaluation of catalysts, is defined as follows:

$$\text{Space velocity } [\text{h}^{-1}] = \frac{\text{Flow rate of reformed gas } [\text{m}^3/\text{h}]}{\text{Volume of catalyst } [\text{m}^3]} \quad . \tag{6}$$

Space velocity denotes the amount of reactants that can be treated per unit volume of catalyst. The larger this value, the better the performance of the catalyst.

Figure 5 shows an example of temperature profiles of the inner channel for catalytic combustion. The temperature was measured by moving the thermocouple in 5 [mm] steps. The temperature during reforming was lower than those before and after reforming. This temperature difference indicates that the heat released from catalytic combustion was used for the endothermic reaction of steam reforming of DME. We found that there is a region where the reaction does not take place. Because no residual hydrogen was detected by analysis with gas chromatography, it can be deduced that the catalytic combustion had been completed within the first 30 [mm], and the decline in temperature was caused by heat loss.

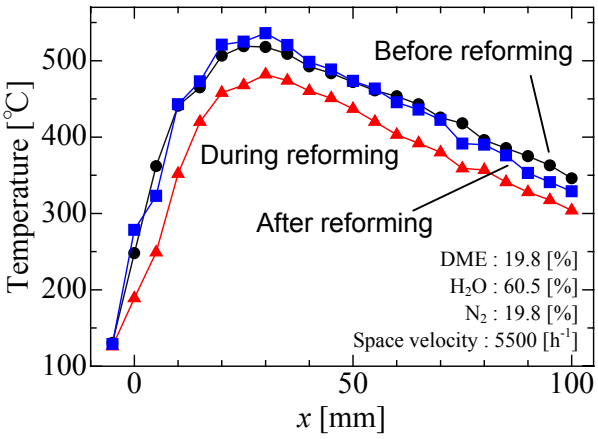

Figure 5. Temperatures of the inner channel

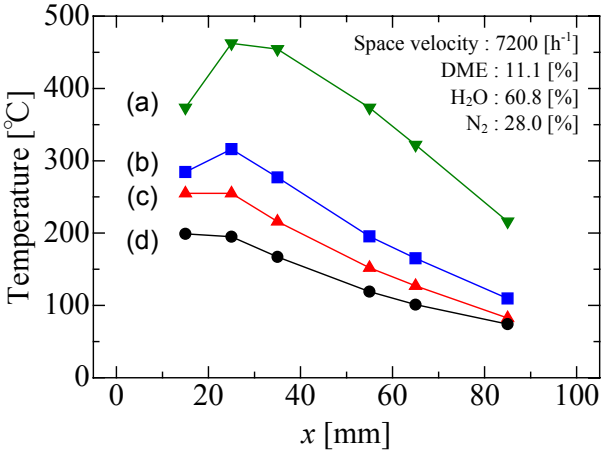

		Catalytic combustion		Steam reforming
		Equivalence ratio	Flow rate [l/min]	DME conversion [%]
(a)	▼	0.72	2.58	98.1
(b)	■	0.65	1.27	75.3
(c)	▲	0.56	1.22	65.0
(d)	●	0.46	1.17	0.0

Figure 6. Temperature profiles of the reforming catalyst and DME conversion for each temperature profile

The temperature profiles of the reforming catalyst are shown in Fig. 6, along with a table of the conditions of catalytic combustion and DME conversion. DME conversion is defined as follows:

$$\text{DME conversion}\,[\%] = 100 \cdot \frac{F_{\text{DME},\,in} - F_{\text{DME},\,out}}{F_{\text{DME},\,in}}\ , \tag{7}$$

where $F_{\text{DME},\,in}$ and $F_{\text{DME},\,out}$ are the volumetric flow rates of DME at the inlet and outlet of the reformer, respectively, which were calculated using the data obtained from gas chromatography.

The equivalence ratio and flow rate of the gas used for catalytic combustion in the inner channel had a strong effect on the temperature of the catalyst used for reforming DME in the outer channel.

Under condition (d), DME was not reformed, because the temperature was low throughout the channel. With increasing temperature, DME conversion increased, until it was almost completely reformed under condition (a) with a sufficiently high temperature. It was found that, for DME reforming, the temperature of the catalyst should be at least 250 [°C].

We changed the length of the DME catalyst to estimate a suitable amount of DME catalyst and size of the reformer. Figure 7 shows DME conversion and the concentrations of H_2, CO, CO_2 and CH_4 for DME catalyst of 30, 50 and 100 [mm] length. Only CO, CO_2 and CH_4 were detected by gas chromatography as single-carbon species.

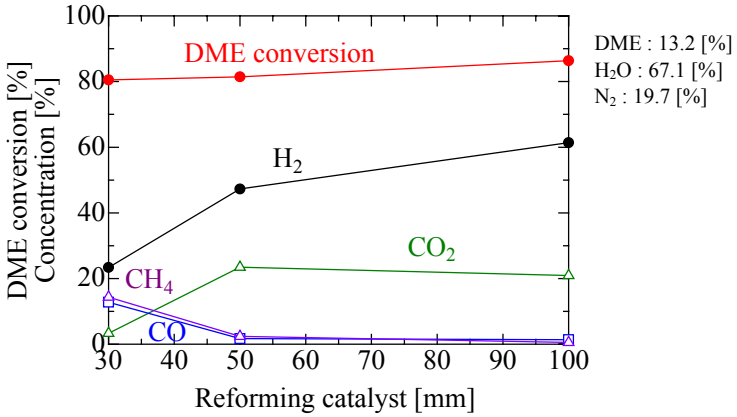

Figure 7. DME conversion and concentration of each species with varying catalyst length

There is little difference in DME conversion for different lengths of catalyst. However, when the catalyst length is 30 [mm], the concentrations of H_2 and CO_2 decreased markedly and those of CO and CH_4 increased. This indicates that 30 [mm] of catalyst is insufficient to complete the reaction of steam reforming and that the residual DME was decomposed into CO and CH_4 by reactions (4) and (5). As a result, we found that 50 [mm] is a suitable length of DME catalyst.

EXPERIMENTS ON A REFORMER INVOLVING TEMPERATURE CONTROL

Apparatus

In accordance with the results in the previous section, we designed and fabricated a new reformer with 50 [mm] length, as shown in Fig. 8. It has a pseudo-triple tube structure, which consists of an outer channel, an inner channel and an inner rod coated with the Pt catalyst for catalytic combustion.

To produce various temperature profiles, we can easily exchange the inner rod to one with a different coating distribution. We prepared four types of rods as also shown in Fig. 8. Although a heterogeneous reaction on a surface is generally a disadvantage in catalytic combustion, it is used as an advantage in this research to easily select the heat generation area.

Results and discussion

Figure 9(a) shows temperature profiles of the DME catalyst for each inner rod. The conditions except for the type of inner rods are fixed. It was found that a high temperature could be realized around the coated Pt catalyst and that Type B had a flatter temperature profile.

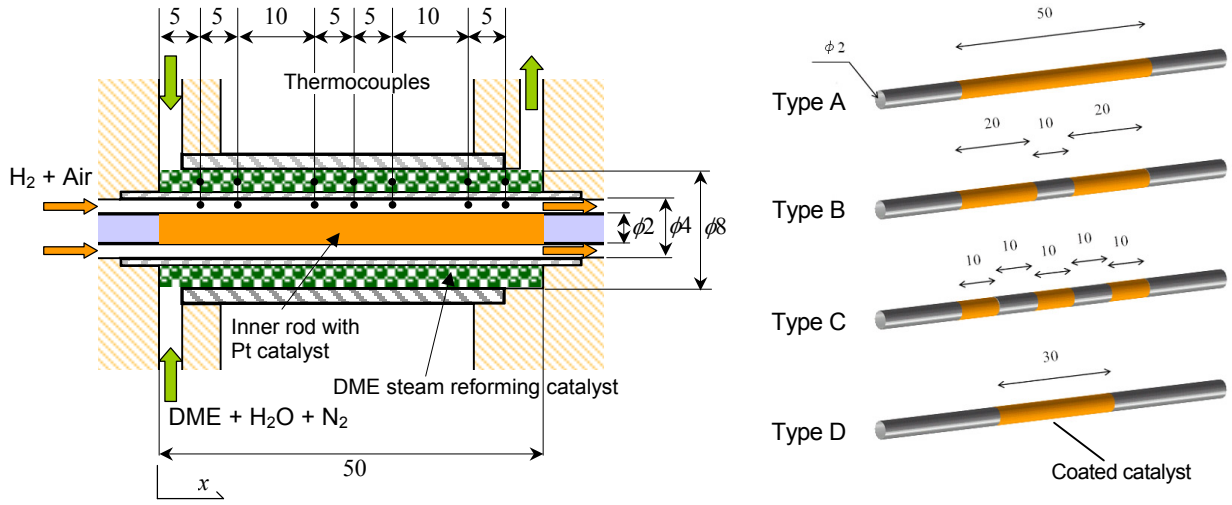

Figure 8. Schematic diagram of improved experimental apparatus

Figure 9(b) shows DME conversion for the four types of rods with varying temperature. While the temperature profile is different for each rod as shown in Fig. 9(a), the maximum temperature throughout the channel is adapted as a temperature in Fig. 9(b). DME conversion increases with the temperature. Note that Type B achieves the highest DME conversion in spite of the lowest temperature. This result agrees with the finding in Fig. 9(a) that Type B had the flattest temperature profile and maintained the largest region for effective reforming.

Figure 10 shows DME conversion and the concentration of each species for Type B. As expected, DME conversion and H_2 concentration increased with temperature because the reforming reaction was activated. Although CO and CH_4 concentrations also increased, it can be considered that their production is sufficiently small regardless of complete DME conversion. Thus, temperature control to achieve a flat profile is an effective method for ensuring the high production of H_2 and the suppression of undesirable species such as CO and CH_4.

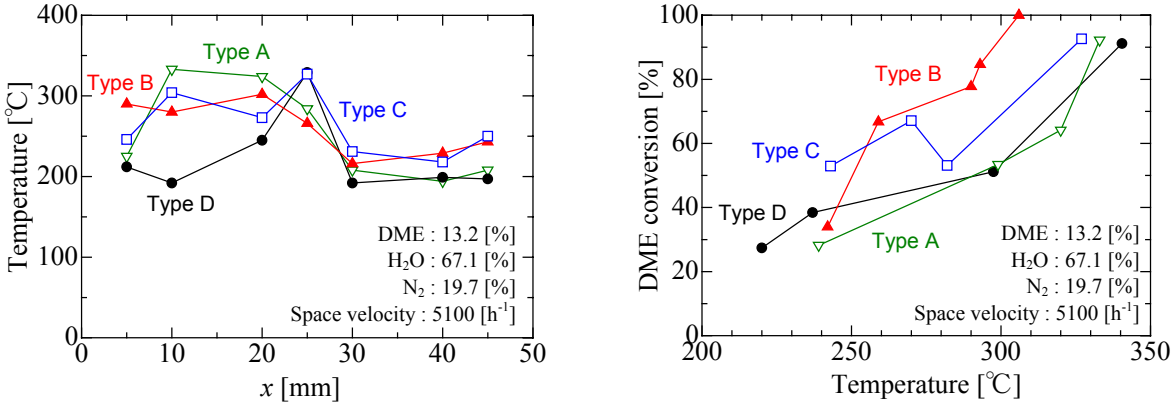

Figure 9. Temperature profiles and DME conversion for the four types of rods

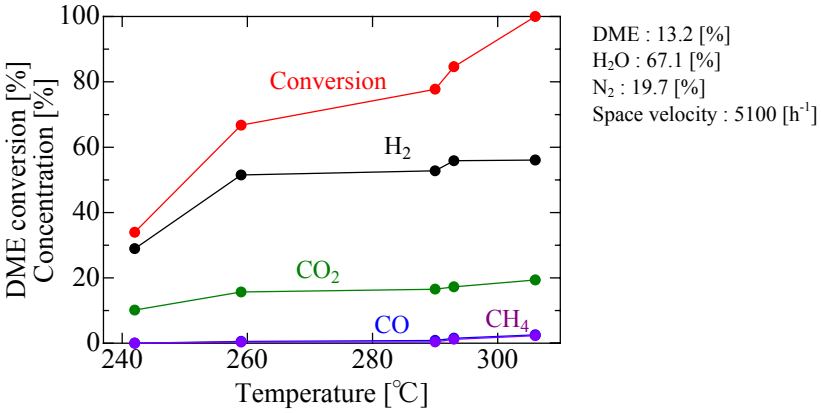

Figure 10. DME conversion and concentration of each species for Type B

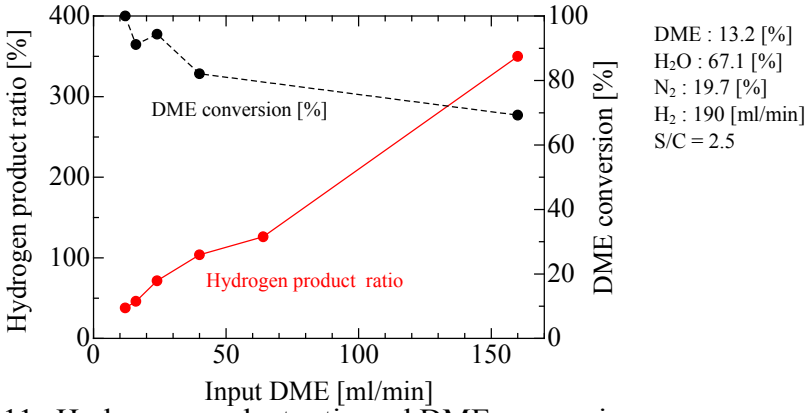

Figure 11. Hydrogen product ratio and DME conversion

Figure 11 shows the hydrogen product ratio and DME conversion for Type B. The hydrogen product ratio is defined as follows:

$$\text{Hydrogen product ratio}\,[\%] = 100 \cdot \frac{\text{Hydrogen produced from DME reforming}\,[\text{ml/min}]}{\text{Hydrogen used for catalytic combustion}\,[\text{ml/min}]} \quad (8)$$

This ratio indicates that how much hydrogen is produced from DME reforming in comparison with hydrogen used for catalytic combustion. If the hydrogen product ratio is smaller than 100 %, which occurs for a low flow rate of DME, this reforming system cannot be established because the hydrogen consumed in the catalytic combustion cannot be compensated by that produced during reforming. With increasing DME input, although DME conversion decreases owing to the short residence time, the hydrogen input ratio is improved. In the case of a DME input of 160 [ml/min], even if only 28.4 % of the hydrogen produced is used in the catalytic combustion, this reformer can maintain a self-sustaining reaction.

CONCLUSION

To produce hydrogen in a small device, we designed and fabricated a DME reformer, in which catalytic combustion is used as a heat source. The reformer has a structure of double tube, in which the steam reforming of DME occurs in the outer channel, and the catalytic combustion occurs in the inner channel. From experiments on the proposed reformer, the following findings were obtained: (1) The temperature of the reforming catalyst was controlled by the catalytic combustion in the inner channel. (2) At a sufficiently high temperature, DME was almost completely reformed. (3) To suppress the formation of CO and CH_4 while achieving high DME conversion, a flat temperature profile is desirable because the effective reforming region is large. (4) Under suitable conditions, the operation of the reformer is self-sustaining

ACKNOWLEDGEMENT

This work was supported by Grant-in-Aid for Young Scientists (B) (No.20760132) from the Japanese Ministry of Education, Culture, Sports, Science and Technology.

REFERENCES

1. P. K. Cheekatamarla and C.M. Finnerty, Reforming catalysts for hydrogen generation in fuel cell applications, Journal of Power Sources, vol. 160, pp. 490-499, 2006.
2. Y. Tanaka, R. Kikuchi, T. Takeguchi1 and K. Eguchi, Steam reforming of dimethyl ether over composite catalysts of γ-Al_2O_3 and Cu-based spinel, Applied Catalysis B: Environmental, vol. 57, pp. 211–222, 2005.
3. T. Mathew, Y. Yamada, A. Ueda, H. Shioyama, T. Kobayashi and C. S. Gopinath, Effect of support on the activity of Ga_2O_3 species for steam reforming of dimethyl ether, Applied Catalysis B: Environmental, vol. 300, pp. 58-66, 2006.
4. N. Laosiripojana and S. Assabumrungrat, Catalytic steam reforming of dimethyl ether (DME) over high surface area Ce–ZrO_2 at SOFC temperature: The possible use of DME in indirect internal reforming operation (IIR-SOFC), Applied Catalysis A: General, vol. 320, pp. 105–113, 2007.
5. K. Faungnawakij, N. Shimoda, T. Fukunaga, R. Kikuchi and K. Eguchi, Cu-based spinel catalysts CuB_2O_4 (B = Fe, Mn, Cr, Ga, Al, $Fe_{0.75}Mn_{0.25}$) for steam reforming of dimethyl ether, Applied Catalysis A: General, vol. 341, pp. 139–145, 2008.
6. M. Saito, T. Genko, S. Tomita, H. Iwai, H. Yoshida, Experimental and numerical study of catalytic combustion using heat recirculation in a double tube, Proceedings of the 2nd International Forum on Heat Transfer, 2008.
7. L. D. Pfefferle and W. C. Pfefferle, Catalysis in Combustion, Catalyst Review - Science and Engineering, vol. 29, pp. 219-267, 1987.

SYNTHESES OF NANO CATALYSTS AT MULTI-BUBBLE SONOLUMINESCING CONDITION

Hyo Won Kim[1], Ki Moon Kang[1] and Ho-Young Kwak[1],*
[1]Mechanical Engineering Department, Chung-Ang University
Seoul 156-756, Korea

ABSTRACT. Synthesis of supported Ni catalysts with a core/shell structure at the multibubble sonoluminescence (MBSL) condition and their catalytic tests for methane decomposition by partial oxidation were performed in this study. The catalysts prepared were analyzed by XRD, TEM and XPS. Without doping the third components, the supported catalyst of core/shell structure made with 10% Ni loading on Al_2O_3 yields 96% conversion efficiency of methane at reaction temperature of 800ºC and shows excellent thermal stability for the first 40 h. In addition, the uniform layer of Ni particles on the surface of support material hindered coke formation and sintering process, which enhances thermal stability for the catalysts.

Keywords: *Core/shell structure, Multibubble sonoluminescence, Partial oxidation of methane, Supported Ni catalysts*

INTRODUCTION

Methane is known to be an ideal source for hydrogen production due to its enormous reserves. Furthermore, it has the highest H/C ratio so that it reduces air pollutants while produces more hydrogen. Steam methane reforming (SMR) which produces 50% pure hydrogen consumption over the world is a conventional process for converting hydrocarbons into synthetic gas [1]. However this process is highly endothermic so that water must be heated to the reaction temperature of 1073K [2]. An alternative to SMR is the catalysts partial oxidation (CPO) of methane. This reaction shows mild exothermicity, high conversion and selectivity of hydrogen and H_2/CO ratio of 2.0, which is proper value for Fischer-Tropsch reaction. Furthermore, CPO process does not produce CO_2 emission. Detailed reaction involved in the process given was discussed by Otsuka et al. [3].
It is well known that supported Ni catalysts are effective for CPO except the noble metal-based catalysts whose high cost prevent from widespread industrial applications. However deactivation of the supported Ni catalysts occurs due to coke formation on Ni surface and sintering so that various

* Corresponding author: Prof. H. Y. Kwak
Phone: +82-2-820-5278, Fax: +82-2-826-7464
E-mail address: kwakhy@cau.ac.kr,

additives have been used to improve metal dispersion and minimize coke formation [4,5,6]. Usually the supported nickel catalysts were prepared by impregnation of supports with an aqueous solution or $Ni(NO_3)_2 \cdot 6H_2O$ followed by calcination of the impregnated materials at high temperature. A uniform dispersion of Ni particles on the surface of the supported materials is required for better performance for the catalysts.

Sonoluminescence (SL) is a light emission phenomenon associated with the catastrophic collapse of micro bubble oscillating under an ultrasonic field. The intense local heating and high pressure inside the bubble and liquid adjacent to the bubble wall from such collapse can give rise to unusual effects in chemical reactions and such sonochemical process has been proven to be a useful technique to create novel materials with unusual properties.

Sonochemistry is an application of sonoluminescence (SL), a light emission phenomenon associated with catastrophic collapse of a gas bubble oscillating under an ultrasonic field. The intense local heating and high pressure inside the bubbles and liquid adjacent the bubble wall form such a collapse that it can give rise to unusual effects in chemical reactions [7], and the sonochemical process has been proven to be a useful technique in making specialty nanomaterials. Recently observed results [8] of the peak temperature and pressure from the sonoluminescing gas bubble in sulfuric acid solutions were predicted [9] accurately by the hydrodynamic theory for sonoluminescence phenomena [10,11,12]. The estimated temperature and pressure in the liquid zone around the collapsing bubble with equilibrium radius 5 ㎛ (an average radius of bubbles generated in a sonochemical reactor at a driving frequency of 20 kHz and an input power of 179 W [13]) is about 1000º C and 500 atm, respectively[10]. A lot of transient bubbles which are generated and collapsed and synchronized with the applied ultrasound facilitate the transient supercritical state [14] in the liquid layer where rapid chemical reactions can take place. In fact, various core-shell structures of nanoparticles were prepared at the MBSL condition [15].

In this paper, we present a study on efficient synthesis of new nano materials of various kinds in MBSL conditions. In particular, the results of Ni-based nano catalysts for hydrogen production will be presented, as these catalysts have the potential to mass produce hydrogen which is touted as the driver of the future energy industry. The sonochemical method at MBSL condition can produce nanolayers of Ni particles that are uniformly formed on the supported material. Such nanolayers and structure of Ni particles on the supported particle may help enhance the activity and stability of the catalysts.

EXPERIMENTAL

Catalysts preparation

Figure 1 shows an experimental apparatus for an MBSL system consisting of a cylindrical quartz cell into which a 5 mm diameter titanium horn (Misonix XL2020, USA) is inserted. This system was operated at 20 kHz and 220 W. The solution in the test cell was kept at 1.4 atm with argon gas and the temperature of the solution inside the cell was kept to around 50º C by a circulating water bath, which is the optimal condition for the coating process [16].

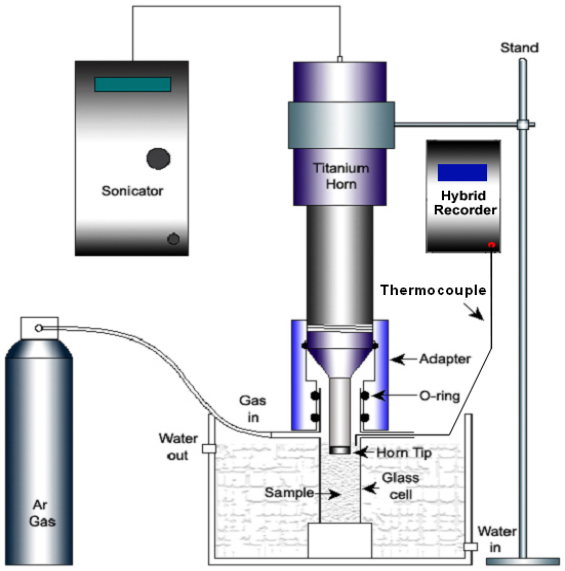

Figure 1. Experimental set up for multibubble sonoluminescence (MBSL)

For preparation of supported Ni catalysts, the supported material used is γ-Al_2O_3 (Aldrich) which has a large active surface area and thermal stability at high temperature [4]. Ni $(NO_3)_2 \cdot 6H_2O$ (Junsei, 0.7 mmol), NaOH (Aldrich,1.4 mmol) and γ-Al_2O_3 (2 mmol) in distilled water were sonicated for 20 minutes at the aforementioned MBSL condition to synthesize Ni/Al_2O_3, a catalyst with core/shell structure. The powders were separated by centrifuge and dried in an oven at 105ºC for 12 hr, subsequently calcined at 700~900ºC for 4h.

Characterization of catalysts

The supported Ni catalysts were characterized by various instruments, such as X-ray diffraction (Rigaku 12KW, Japan), high resolution transmission electron microscope (JEOL, TEM-3010, 300kV) and XPS(ESCA 2000).

Catalytic reaction

Partial oxidation of methane with air was performed in a fixed bed quartz reactor (8 mm ID, 500 mm height) at a reaction temperature of 700º C or 800ºC and atmospheric pressure and flow rate of 30 ml/min (GHSV= 17900/h). The weight of the catalyst employed is about 100 mg. Quartz wool was used as a distributor in the fixed bed reactor. The outlet gas products were analyzed on-line by a GC equipped with a thermal conductive detector (TCD). The conversion efficiency of methane is defined as

CH_4 conversion: $(F_{in,CH_4} - F_{out,CH_4}) / F_{in,CH_4}$ (1)

where F_i is the molar flow rate of i-species.

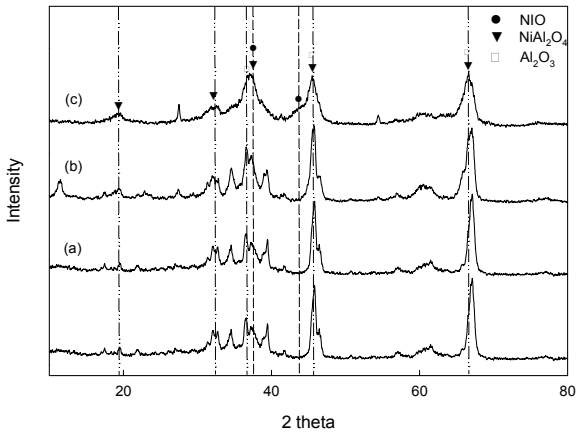

Figure 2. XRD patterns for Ni/Al_2O_3 nanopowder calcined at 700□ which depend on Ni-loading: 5 wt%, (b) 10 wt% and(c) 20 wt%. The XRD pattern at bottom is shown for Al_2O_3.

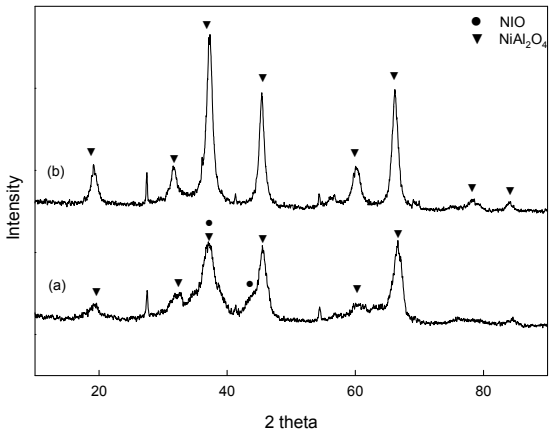

Fig.3. XRD patterns for 20 wt% Ni/Al_2O_3 nanopowder depending on calcination temperature: (a) 700□, (b) 900□.

Figure 2 shows the XRD pattern for Ni/Al_2O_3 nanoparticles calcined at 700º C depending on their Ni loadings. For the supported Ni catalysts with Ni loading of 5% and 10%, the characteristic peak indentified as NiO at $2\theta = 37.04^o$ appears slightly and the Al_2O_3 peaks at $2\theta = 37.04^o$, and 67.37^o can be seen clearly. With 20% of Ni loading, the catalyst displays NiO characteristic peaks at $2\theta = 37.04^o$ and, 43.30^o corresponding to the (111) and (200) planes. Also the catalysts with 20% Ni loading show some peaks representing the spinel structure of $NiAl_2O_4$. With an increase of Ni loading, the characteristic peaks representing NiO and $NiAl_2O_4$ appear more clearly. As shown in Fig. 3, the catalysts with 20% Ni loading calcined at 900□ have characteristic peaks for the spinel structure of $NiAl_2O_4$ corresponding to the (111), (220), (311), (400), (511), (440), (553) and (444) planes.

Figure 4 shows high resolution TEM images of Ni-based catalysts prepared by the sonochemical method at the MBSL condition, followed by calcination at 700□. With increase in Ni loading, the thickness of the Ni layer on Al_2O_3 also increases. The thickness of the Ni layer is about 1.4 nm for 5%, 2.6 nm for 10% and 3.6 nm for 20% Ni loadings. As shown in Fig. 4(d), the supported catalyst shows that Ni/Al_2O_3 transformed to the spinel structure, $NiAl_2O_4$, when it calcined at 900□. The conversion efficiency of methane increased at higher Ni loading. The CH_4 conversion efficiency of the catalyst with 20% Ni-loading, a spinel structure $NiAl_2O_4$ oxide at reaction temperature, 700□ is about 86 %, which is higher efficiency compare to the results obtained in previous works [17]. However, the catalysts show complete deactivation after 13 hours methane reforming, which is due to carbon nano-fiber formation on the surface of the supported material as shown in Fig. 5(a). A Ni particle is present at the tip of the carbon namo-fiber , which was observed

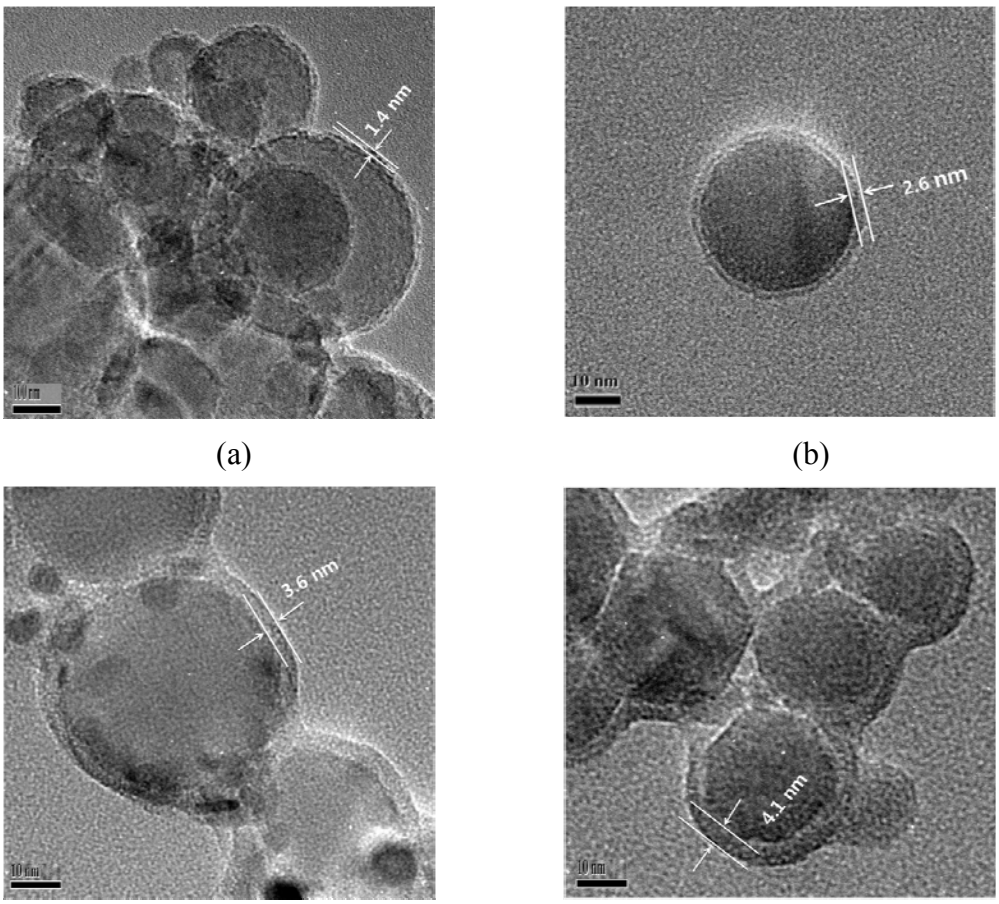

(a) (b)

(c) (d)

Figure 4. TEM image of Ni/Al_2O_3 nanopowder calcined at 700□ depending on Ni loading: (a) 5 wt% Ni/Al_2O_3, (b) 10 wt% Ni/Al_2O_3 and (c) 20 wt% Ni/Al_2O_3 and (d) $NiAl_2O_4$ spinel structure calcined at 900□.

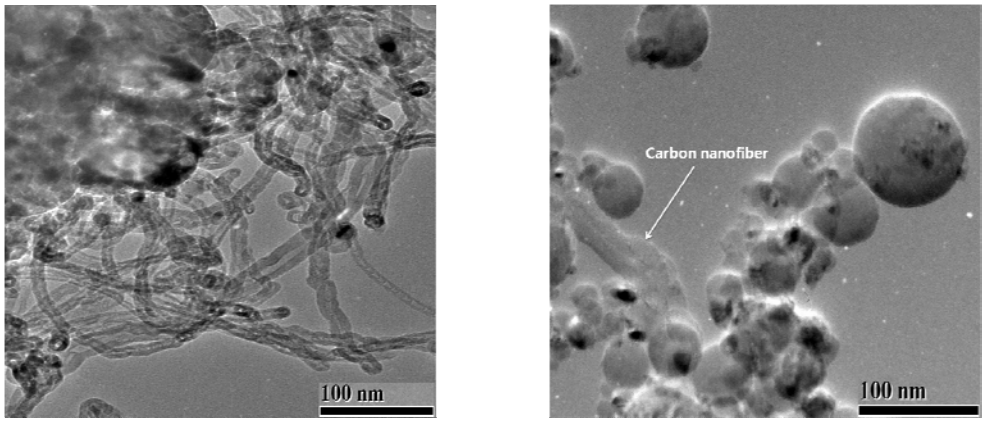

(a) (b)

Figure 5. TEM image (a) of carbon nano-fiber formation on the surface of the catalyst $NiAl_2O_4$ with 20% Ni loading after 13 h run at reaction temperature of 700□ and TEM images of the supported Ni catalysts after 40 h run for (b) 10 wt%

in the previous works [18,19].

The conversion efficiency for the catalyst with 10% Ni loading at reaction temperature 800□ is about 96% as can be seen in Fig. 6. Furthermore, the supported Ni-based catalyst with core/shell structure shows good thermal stability in the first 40 h. This is because carbon nano-fiber did not form on the surface of the coated Ni-layer of the catalyst with 10% Ni content after 40 h run as can be seen in Fig. 5(b). Quite different pattern of carbon nano-fiber formed and grew at the site where NiO particles were present in the catalyst [17]. These are quite remarkable results among the results for the supported Ni-based catalysts prepared by other researchers [2,5]. For the magnesia supported nickel catalysts, the maximum methane conversion reached was about 94% [2]. Even for the Ni-based catalyst with doping of molybdenum (to prevent coke formation) the efficiency of methane conversion shows a maximum of 92% at the start, decreasing to 83% after 60 hours run [7]. From analyses by XRD, TEM and XPS, observed TPR pattern for the supported Ni catalyst with 5 and 10% Ni loadings we found that coexistence of NiO and NiOx species and the NiOx species which interact strongly with the supporting material play a very effective role in the partial oxidation of methane and they contribute to the thermal stability of the catalyst [17]. In fact, a similar TPR pattern was obtained for Ni/θ-Al_2O_3 catalyst by Roh et al. [20]. The maximum CH_4 conversion obtained in their study is 88% with a 12% Ni/θ-Al_2O_3 catalyst.

It is known that the sintering process occurs due to the microcrystalline nickel oxide particles which lead to aggregation of Ni particle at high temperature [4]. However, the drop in Ni/Al ratio due to the sintering process of Ni particles was not occurred for the supported Ni catalysts with the core/shell structure prepared in this study. The uniform coating layer of Ni particle on the catalysts with the core/shell structure prevents from the aggregation of Ni particles. Also it is noted that carbon deposition easily takes place on the surface of the supported Ni catalyst, Ni/ γ-Al2O3. The uniform dispersion of the Ni particles on the supported Ni catalyst with the core/shell structure prohibits the coke formation on the surface of the catalyst.

CONCLUSIONS

Supported Ni-based catalysts with a core/shell structure were prepared using a sonochemical method at the MBSL condition. Supported Ni-based catalyst of core/shell structure produced good conversion efficiency of CH4, at about 80% at reaction temperature of 700º C and 96% at reaction temperature of 800º C. The existence of NiO and NiOx on the surface of Ni/Al_2O_3 catalyts and the uniform layer of Ni particles on the Al_2O_3 support contribute to better conversion efficiency of methane and thermal stability of catalysts.

ACKNOWLEDGEMENTS

This work has been supported by Seoul R&D program (2006) and by a grant from the Electric

Power Research Institute (EPRI) in the USA, under contract EP-P19394/C9578.

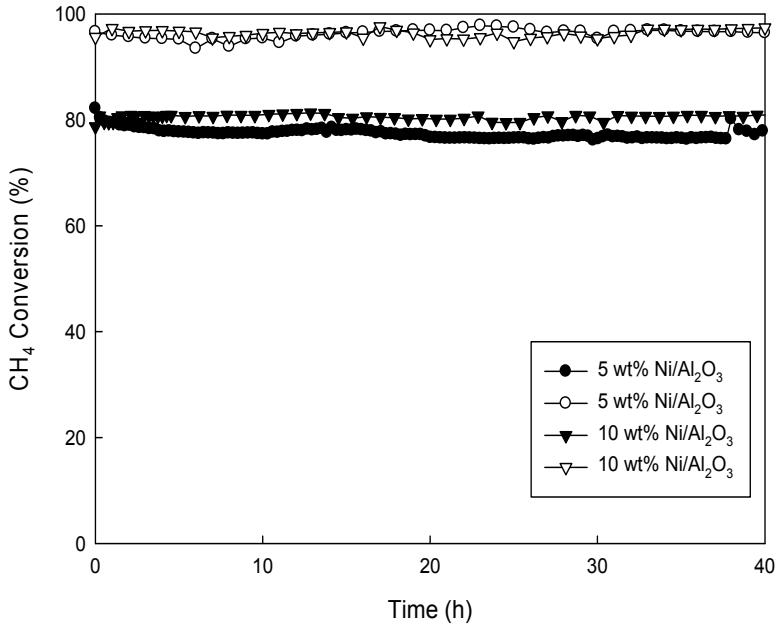

Figure 6. CH_4 conversion with time for a stream over supported Ni-based catalysts with 5% and 10% Ni loadings depending on reaction temperature: (a) 700□(solid symbols) and (b) 800□(empty symbols).

REFERENCES

1. Xu, J.C., Yeung, M.Y., Ni, J., Meunier, F., Acerbi, N., Fowles, M., and Tsang, S.C., Methane steam reforming for Hydrogen Production using low Water-ratios without Carbon Formation over Ceria Coated Ni Catalysts, *Appl. Catal. A*, Vol. 345, pp 119-127, 2008.
2. Requies, J.M., Cabrero, A., Barrio, V.L., Guemez, M.B., Cambra, J.F., Arias, P.L., Perez-Alonso, F.J., Ojeda, M., Pena, M.A., and Fierro, J.L.G., Partial Oxidation of Methane to Syngas over Ni/MgO and Ni/La_2O_3 Catalysts, *Appl Catal A*, Vol. 289, pp 214-223, 2005.
3. Otsuka, K., Takenaka, S., and Ohtsuki, H., Production of pure hydrogen by cyclic decomposition of methane and oxidative elimination of carbon nanofibers on supported-Ni-based catalysts, *Appl Catal A*, Vol. 273, pp 113-124, 2004.
4. Xu, Z., Li, Y., Zhang, J., Chang, L., Zhou, R., and Duan, Z., Bound-state Ni species- a superior form in Ni-based catalyst for CH_4/CO_2 reforming, *Appl Caltal A*, Vol. 210, pp 45-53, 2001.
5. Cai, X., Dong, X., and Lin, W., Effect of CeO_2 on the catalytic performance of Ni/Al_2O_3 for

autothermal reforming of methane, *J. Natural Gas Chem.*, Vol. 17, pp 98-102, 2008.

6. Koo, K.Y., Roh, H.S., Seo, Y.T., Seo, D.J., Yoon, W.L., and Park, S.B., A highly effective and Stable Nano-sized Ni/MgO-Al_2O_3 Catalyst for Gas to Liquids (GTL) Process, *Int. J. Hydrogen Energy*, Vol. 33, pp 2036-2043, 2008.
7. Suslick, K.S., Sonochemistry, *Science*, Vol. 247, pp 1439-1445, 1990.
8. Flannigan, D.J., Hopkins, S.D., Camara, C.G., Putterman, S.J., and Suslick, K.S., Measurement of pressure and density inside a single sonoluminescing bubble, *Phys. Rev. Lett*., Vol. 96, pp 204301-204304, 2006.
9. Kim, K.Y., Byun, K.T., and Kwak, H., Characteristics of sonoluminescing bubbles in aqueous solutions of sulfuric acid, *J. Phys. Soc. Jpn*. Vol. 75, pp 114705-114711, 2006.
10. Kwak, H., and Yang, H., An aspect of sonoluminescence from hydrodynamic theory, *J. Phys. Soc. Jpn.* Vol. 64, pp 1980-1992, 1995.
11. Kwak, H., and Na, J.H., Hydrodynamic solutions for a sonoluminescing gas bubble, *Phys. Rev. Lett*., Vol. 77, pp 4454-4457, 1996.
12. Kwak, H., and Na, J., Physical processes for single bubble sonoluminescence, *J. Phys. Soc. Jpn*. Vol. 66, pp 3074-3083, 1997.
13. Tsochatzidis, N.A., Guirad, P., Wihelm, A.M., and Delmas, H., Determination of velocity, size and concentration of ultrasonic cavitation bubbles by the phase-Doppler technique, *Chem. Eng. Sci.*, Vol. 56, pp 1831-1840, 2001.
14. Hua, I., Hochemer, R.H., and Hoffmann, M.R., Sonolytic hydrolysis of pnitrophenyl acetate—the role of supercritical water, *J. Phys. Chem.,* Vol. 99, pp 2335-2342, 1995.
15. Kwak, H., Shim, I.W., Byun, K.T., and Lee, S.S., Method of manufacturing layered nano structures and layered nano structures prepared thereby. Pending in USA papent,
16. Lee, S.S., Seo, K.W., Yoon, S.H., Shim, I.W., Byun, K.T., and Kwak, H., CdS Coating on TiO_2 nanoparticles under multibubble sonoluminescence condition, *Bull. Korean Chem. Soc.* Vol. 26, pp 1579-1581, 2005.
17. Kim, H.W., Kang, K.M., and Kwak, H., Preparation of supported Ni catalysts with a core/shell structure and their catalytic tests of partial oxidation of methane, accepted for *Int. J. Hydrogen Eng.,* 2009.
18. Takenaka, S., Tomikubo, Y., Kato, E., and Otsuka, K., Sequential production of H_2 and CO over supported Ni catalysts, *Fuel*, Vol. 83, pp 47-57, 2004.
19. Chen, J., Quao, Y., and Li, Y., Promoting effects of doping ZnO into coprecipitated Ni-Al_2O_3 catalyst on methane decomposition to hydrogen and carbon nanofibers, *Appl. Catal, A* , Vol. 337, pp 148-154, 2008.
20. Roh, H.S., Jun, K.W., Dong, W.S., Baek, S.C., and Park, S.E., Methane reforming reactions over stable Ni/θ-Al_2O_3 catalysts, *J. Ind. Eng. Chem*. Vol. 8, pp 464-471, 2008.

EXPERIMENTAL AND NUMERICAL STUDIES ON REACTION KINETICS OF METHANE/STEAM REFORMING ON Ru/Al_2O_3 CATALYST

G. Brus[1,*], T. Ichikawa[2], Y. Noro[2], S. Kimijima[2], J.S. Szmyd[1]
[1]AGH - University of Science and Technology, Krakow, Poland
[2]Shibaura Institute of Technology, Tokyo, Japan

ABSTRACT. In the present paper, experimental and numerical studies on a methane/steam reforming process on Ru/Al_2O_3 catalyst have been conducted. The gas mixture composition and flow rate were measured at the outlet of the reformer to establish the methane/steam reforming rate and kinetics of the reforming reaction. Determining the reaction kinetics is of great significance in the design process of industrial reactors. To optimize reactor parameters such as diameters, catalyst density, catalyst distribution, steam/carbon ratio and intensity of fuel flow, detailed data about reaction kinetics is required. In the present paper, kinetics of methane/steam reforming on the Ru/Al_2O_3 catalyst was experimentally investigated. Measurements including different thermal boundary conditions, fuel flow rate and steam-to-methane ratios were performed. The reforming rate equation derived from experimental data was used in the numerical model to predict synthetic gas composition at the outlet of the reformer.

Keywords: *SOFC, Fuel Cells, methane/steam reforming, Ru/Al_2O_3 catalyst, reforming system*

INTRODUCTION

Industrial methane/steam reforming using Ni as the catalyst is preformed around 850 ^oC with a steam-to-carbon ratio of between 2 and 5 to prevent carbon deposition. Carbon formation is a major problem during methane/steam reforming reaction based on Ni catalysis. Carbon formation occurs between nickel and metal-support and creates fibers which damage the catalytic property of the reactor. It was found that by replacing Ni with a noble metal such as Rh, Ru, Pd, Ir and Pt, coke formation could be minimised [1]. From all noble metals suggested for the methane reformer, Ru seems to be the cheapest [1]. The price of catalyst material is an important consideration in industrial processes, where some materials can be rejected because of their relatively high cost. At the same time, Ru exhibits better catalytic properties for reforming reaction than do Pt, Pd, Ir, and it exhibits similar properties to Rh. The Ru/Al_2O_3 catalyst is also more durable than Ni when it comes to thermal shock and temperature fluctuations [1]. To this point, most publications on the topic have primarily investigated the kinetic properties of methane-steam reforming on Ni catalyst [1-5], which is the catalyst most often used for commercial reactors in hydrogen production. Different kinetics have been reported by the various research groups working on methane/steam reforming based on nickel catalyst [2-5]. The reaction order and kinetic parameters may be significantly different from one catalyst to another [1]. Experiments on Ni catalyst have been carried out by Achenbach and Riensche [2] to determine the kinetics of the methane/steam reforming process at anode materials of a solid oxide fuel cell. Their tests [2] showed that the partial pressure of H_2O has no catalytic effect on the reaction. Achenbach and Riensche [2] have proposed an equation for reforming kinetics in the form of the Arrhenius-type

* Corresponding author: MSc Grzegorz Brus
Phone: + (48)-12-6173279, Fax: + (48)-12-6172685
E-mail address: brus@agh.edu.pl

independence of the partial pressure of H_2O, which is proportional to methane (CH_4) partial pressure. An alternative model of methane reforming reaction rate on a nickel-based catalyst was proposed by Odegard *et al*. [3]. Both of the proposed models assume reforming kinetic in Arrhenius type form and independence of the steam's partial pressure. An increasing number of papers have been devoted to methane/steam reforming on ruthenium catalyst. Kinetic analysis on low-temperature methane/steam reforming using a ruthenium-supported catalyst has been studied by Itoh *et al*. [6]. The reaction rate of methane/steam reforming at low temperature was measured to establish the rate of expression. A few models have also been proposed based on the Langmuir-Hinshelwood mechanism [6]. An equilibrium case of methane/steam reforming reaction based on Ru/Al_2O_3 catalyst has been studied by the Kimijima Group [7] and an equilibrium numerical model of the reforming reaction was developed. The numerical results have been compared with experimental data and good agreement found.
Determination of the reaction kinetics is significant in the design of industrial reactors. To optimize reactor parameters such as diameters, catalyst density, steam-to-carbon ratio and intensity of fuel flow, detailed data about reaction kinetics is required. In the present paper, experimental study on methane/steam reforming on Ru/Al_2O_3 catalysts was experimentally investigated. The gas mixture composition and flow rate were measured at the outlet of the reformer to establish the rate at which methane reforms and the kinetics of the reforming reaction.

EXPERIMANTAL INVESTIGATION

Experimental procedure

A schematic view of the experimental setup is shown in figure 1. A stainless steel reformer was located in an electrical furnace, which can be heated up to 1000^{o}C. The maximum working temperature of pre-heater and after-heater is 400^{o}C; however, for all experimental investigations presented in this paper, the temperature of pre- and post-heater was maintained at 200^{o}C. High purity methane was the fuel used in the experiment. It was supplied to the reformer via flow controller and an evaporator, which was also used as a pre-heater. Water was fed to the system with a pump. The gas composition after the reforming process was analysed by gas chromatography prior to which the steam had been separated by cooling down the gas mixture to 2 ^{o}C. The reforming reaction tube was partially filled with Ru/Al_2O_3 and partially with Al_2O_3 as will be precisely described in subsequent sections of this paper.
Ruthenium-supported alumina is a new type of catalyst material used for the methane/steam reforming reaction. Figure 2A shows a typical reaction tube, where a catalyst supported on metallic particles is located inside the reaction tube. The catalyst is spherical in shape and has a 3-mm diameter, and the Ru-Al density is 0,0025 g mm^{-3}. In the presented investigation the original spherically shaped particles were crushed into micro-particles roughly 300 μm in size and were located in the reaction tube as shown in figure 2B. To prevent large temperature gradients in the reformer, modifications of the reaction tube were applied. To avoid a cooling effect of the entering fluid, the reformer was partially filled with Al_2O_3, as shown in figure 2B. In this solution, a mixture of gases before getting to the reaction zone was pre-heated by electric furnace to the reaction temperature. To control thermal conditions of the experiment, four thermocouples were located in the experimental set-up, as shown in figure 1 (marked as "T"). To derive correct kinetics data, the reaction has to occur in a whole volume of catalyst. This can be accomplished by maintaining the reforming conversion rate at a low level. To achieve a low level of methane conversion, the fuel was additionally mixed with nitrogen (see figure 2B). Nitrogen does not have a direct influence on the reforming reaction but the partial pressure of the components changed, which results in a decrease in both the reaction and methane conversion rates.

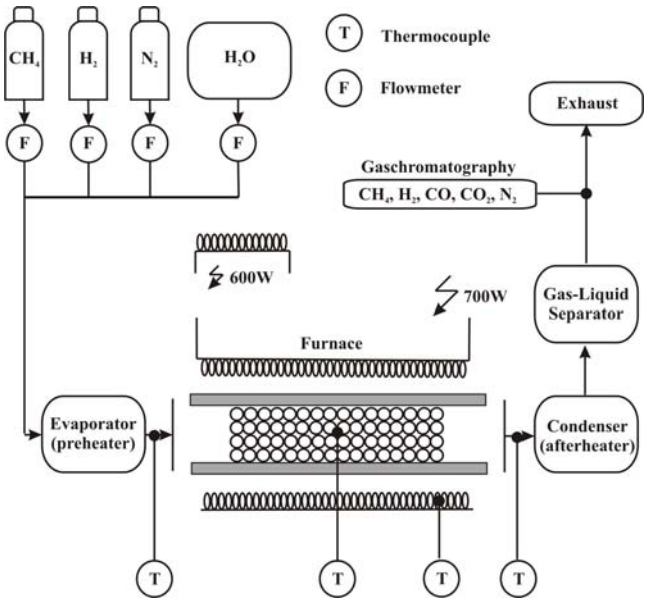

Figure 1. Schematic view of the experimental set-up

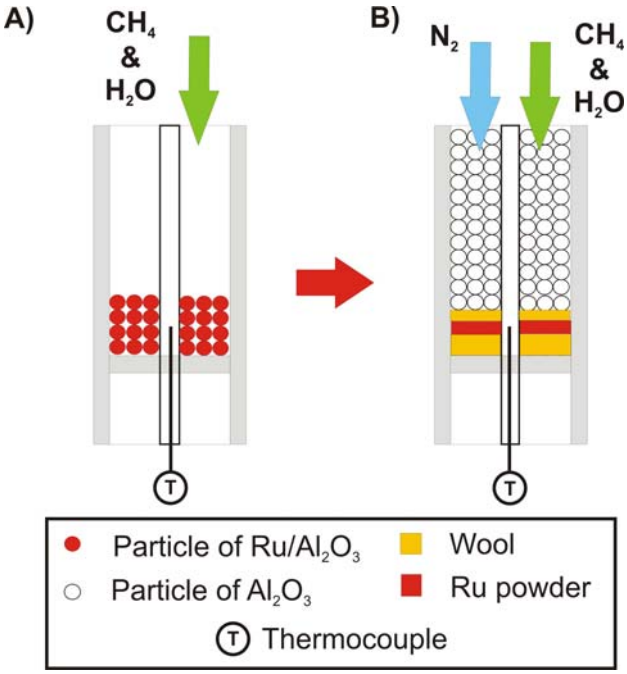

Figure 2. Schematic view of the reaction tube. A) Typical reaction tube. B) Modified reaction tube.

Methodology

The methane/steam reforming process is widely considered the conventional process for producing hydrogen [4], [5]. In the reforming process of methane with steam, the dominant reactions are the following two [8]:

fuel reforming reaction

$$CH_4 + H_2O \rightarrow 3H_2 + CO \tag{1}$$

shift reaction

$$CO + H_2O \leftrightarrow H_2 + CO_2 \tag{2}$$

It follows from the stoichiometry of the steam/methane reforming reaction that the reaction rate expression can be approximated using the equation

$$r_{CH_4} = k\left(p_{CH_4}\right)^a \left(p_{H_2O}\right)^b, \tag{3}$$

where; $k = A \cdot \exp\left(-E / RT\right)$

where k is the reforming reaction constant, p_{CH4} and p_{H2O} are partial pressures [Pa] of methane and water, respectively, a and b are dimensionless coefficients responding to the reaction order, A is the pre-exponential factor, E the activation energy [J mol^{-1}], R the universal gas constant [J mol^{-1} K^{-1}] and T the reaction temperature [K].

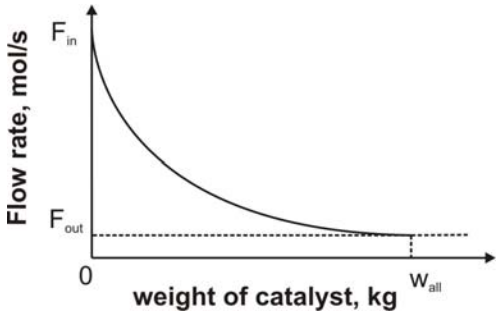

Figure 3. Methane flow rate as a function of catalyst weight

Equation (3) can be rewritten as the relationship between the molar flow rate of methane and the weight of the used catalyst. Figure 3 presents the relationship between the molar flow rate of methane and the weight of the catalyst used. As can be seen from figure 3, for given inlet flow rate of methane, increasing the amount of catalyst results in a decrease in the methane outlet flow rate as an effect of methane's higher conversion rate. However, for some amount of catalyst, marked on figure 3 as w_{all}, there is no more change in the conversion rate. The equilibrium occurs and outlet flow rate remains constant. Therefore, the non-equilibrium reaction rate can be described as a ratio between the change in the flow rate of methane and the change in the amount of catalyst. The mathematical form of this relation can be expressed as

$$r_{\text{CH}_4} = -dF_{\text{CH}_4} / dw_{cat}\,, \tag{4}$$

where $F_{\text{CH}_4} = F^{\text{in}}_{\text{CH}_4} \cdot (1-x)$,

where F_{CH_4} is the methane flow rate, [mol/s] x is a dimensionless amount of reacted methane in the reforming reaction, and w_{cat} is the weight of catalyst used, [kg].

By combining equations (3) and (4), the following equation was formulated:

$$k = \left(F^{\text{in}}_{\text{CH}_4} / w_{cat}\right) \cdot \int_0^{x_{out}} \left(1 / k\left(p_{\text{CH}_4}\right)^a \left(p_{\text{H}_2\text{O}}\right)^b\right) \cdot dx \tag{5}$$

From the stoichiometry of reaction (1) and (2) the partial pressures can be defined as

$$p_{\text{CH}_4} = \left(n_{\text{CH}_4} / n_{\text{all}}\right) \cdot P = \left[(1-x)/(1+SC+NC+2x)\right] \cdot P\,, \tag{6}$$

$$p_{\text{H}_2\text{O}} = \left(n_{\text{H}_2\text{O}} / n_{\text{all}}\right) \cdot P = \left[(SC-x-y)/(1+SC+NC+2x)\right] \cdot P\,, \tag{7}$$

where n_{all} is the total amount of product at the outlet of the reaction tube, P is total pressure [Pa], n_{CH4}, n_{H2O} are, respectively, the methane and water fractions at reformer output, x is a fraction of reacted methane, y is a fraction of reacted carbon monoxide, SC is the steam-to-carbon ratio and NC is the nitrogen-to-carbon ratio. n_{all} was derived from stoichiometry of reactions (1) and (2).

Introducing equations (6) and (7) into equation (5) yields the final form of the equation for the reaction constant:

$$k = \left(F^{\text{in}}_{\text{CH}_4} / w_{cat}\right) \cdot \int_0^{x_{out}} \left((1+SC+NC+2x)^{a+b} / P^{a+b} (1-x)^a (SC-x-y)^b\right) \cdot dx \tag{8}$$

where, a and b are coefficients related to the reaction order.

By following Itoh *et al*. [6] the methane conversion rate x is determined by the outlet quantity and can be calculated

$$x = \left(x_{CO} + x_{CO_2}\right) / \left(x_{CH_4} + x_{CO} + x_{CO_2}\right) \tag{9}$$

The shift reaction occurs very quickly, so the conversion rate can be estimated from the equilibrium equation

$$K_{shift}\left(x - y\right)\left(SC - x - y\right) = y \cdot \left(3x + y\right) \tag{10}$$

where: $K_{shift}=\exp[-\Delta G/(RT)]$
where ΔG is the change of standard Gibbs free energy of shift reaction, R is the universal gas constant [J mol^{-1} K^{-1}] and T is the reaction temperature [K].
Because the reaction constant does not depend on the *SC* and *NC* ratios, *a* and *b* can be found [9]. *K* is constant if *a* and *b* are set correctly. The real values of *a* and *b* are the ones which result in the smallest *k* derivation for different *SC* and *NC* ratios. Equation (8) was solved numerically for various values of *a* and *b* and for the different *SC* and *NC* ratios. The range from -1.0 to 2.0 has been chosen as a common range for reaction order according to already published data; figure 4 shows the results of computation. The smallest reaction constant deviation was found to be 0.3 and 0.1 for *a* and *b*, respectively.
To develop a fully kinetic model of the reforming reaction on the Ru catalyst, the relationship between the reaction temperature and reaction constant has been investigated. The effect of the temperature on the reaction was studied by increasing the temperature from 550°C to 725°C. Results of the experiment are presented in the form of Arrhenius plot, as shown in figure 5.

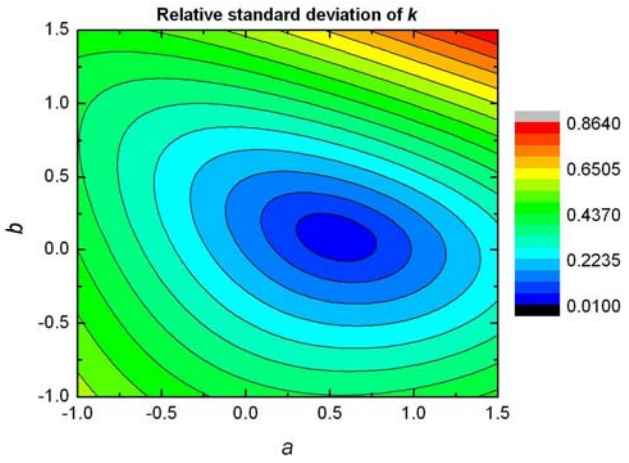

Figure 4. Relative standard deviation of *k*

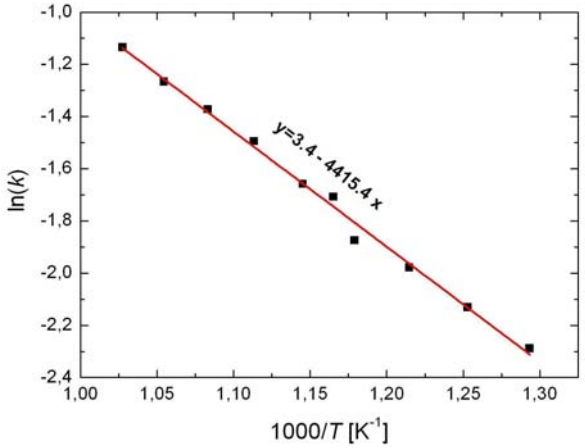

Figure 5. Arrhenius plot for Ru/Al_2O_3

To the experimental data a straight line was fitted as a result of approximation. The equation for the straight line for the experiment takes the form of Arrhenius equation and can be expressed

$$\ln k = \ln A - \left(E / R\right) \cdot \left(1 / T\right) \tag{11}$$

Where T [K] is the temperature of fuel conversion, R = 8.314472 [J mol^{-1} K^{-1}] is the universal gas constant, A is called the pre-exponential factor and corresponds to the intercept of line at 1/T=0 and E [J mol^{-1}] which is obtained from the slope of the line in the activation energy of the steam reforming reaction. Thus the kinetic of the methane/steam reforming reaction can be described by reforming rate [mol s^{-1} g^{-1}] based on the experimentally obtained data by following equation:

$$R_{st} = 29.96 \cdot \exp\left(-36711.89 / RT\right) \cdot p_{CH_4}^{0.3} \cdot p_{H_2O}^{0.1} \tag{12}$$

MATHEMATICAL MODEL FOR THE FUEL REFORMING PROCESS

The steam reforming reaction described by equation (1) is a slow and highly endothermic reaction; therefore a kinetic expression is required to calculate the reaction rate. Also, how methane is reformed inside the reformer is dependent on the local conditions including not only temperature but also the partial pressure of each chemical species and the density of the catalysis [10]. The water-gas shift reaction described by equation (2) is a fast and weak exothermic reaction and can be assumed to be in equilibrium at the reforming temperature [8].

In this paper, the reaction rates of the two main reactions (equations (1) and (2)) R_{st} and R_{sh} are calculated

$$R_{st} = w_{cat} \cdot 29.96 \cdot \exp\left(-36711.89 / RT\right) \cdot p_{CH_4}^{0.3} \cdot p_{H_2O}^{0.1} \tag{13}$$

$$R_{sh} = K_{sh}^{+} p_{CO} p_{H_2O} - K_{sh}^{-} p_{H_2} p_{CO_2} \tag{14}$$

Equation (13) is based on the experimentally obtained data and was described in the previous paragraph, where, w_{cat}, is catalyst weight [g], T [K] is temperature of fuel conversion, R = 8.314472 [J mol^{-1} K^{-1}] is the universal gas constant, p_{CH4} the partial pressure of methane [Pa] and p_{H2O} the partial pressure of steam [Pa]. The catalyst weight w_{cat} is an important parameter because control of its distribution can be used as a means to changing the distribution pattern of the reformer temperature.

K_{sh}^{+} and K_{sh}^{-} denote the rate constants of forward and backward water-gas shift reactions. The water shift reaction given by equation (2) reaches equilibrium rapidly; therefore CO_2, H_2, CO and H_2O must satisfy the equilibrium equation. Chemical equilibrium is represented by the equilibrium constant, which is a function of temperature and is equal to the ratio between the reactants' partial pressures and the products' partial pressures.

$$K_{sh} = K_{sh}^{+} / K_{sh}^{-} = (p_{CO_2} p_{H_2}) / (p_{CO} p_{H_2O}) = \exp(-\Delta G_{sh}^{0} / RT) \tag{15}$$

where ΔG_{sh}^{0} is the change of standard Gibbs free energy in the shift reaction.

This equilibrium constant given by equation (15) is introduced into equation (14) to calculate the rate of the shift reaction.

The change of each chemical species caused by the fuel reforming reaction (equation (11)) and shift reaction (equation (12)) are derived from the reactions' stoichiometry and are calculated as follows:

$$\Delta \dot{n}_{H_2} = 3x + y \tag{16}$$

$$\Delta \dot{n}_{CO} = x - y \tag{17}$$

$$\Delta \dot{n}_{CO_2} = y \tag{18}$$

$$\Delta \dot{n}_{CH_4} = -x \tag{19}$$

$$\Delta \dot{n}_{H_2O} = -x - y \tag{20}$$

RESULTS

Numerical simulation is a useful tool for designing SOFC reformer processes. In the numerical model presented in this paper, gas composition at the outlet of the reformer can be predicted based on the inlet conditions. Examples of numerical results and their comparison with the experimental data are shown in figures 7 and 8. In the present paper, the effect of the temperature on the steam reforming reaction was studied by increasing reaction temperature from 500 ^{o}C to 700 C. The data shows the outlet dry gas composition to be a function of reaction temperature. Predictably, the outlet molar fraction of

methane decreases with increasing reaction temperature and the opposite behavior can be observed for the molar fraction of hydrogen. As observed in figures 6 and 7, the amount of carbon monoxide increases as the reaction temperature increases. This observation is significant because in contrast to the low-temperature fuel cell, the carbon monoxide does no poison the high temperature solid oxide fuel cell anode but can be electrochemically converted as a fuel [2].

An important requirement for kinetic experiments is catalytic stability. In the presented investigation the condition of catalyst was periodically checked and no degradation was observed.

The quality of numerical computations can be presented by a correlation plot of the measurements against the numerical model. An example of such a comparison can be seen in figure 8 where the experimental results were set against calculated reforming conversion rates. The points situated on the line present a perfect fit between the experimental and numerical results. Most of the points are located on the line or in its vicinity. The presented correlation plot indicated that the quality of the numerical model is satisfactory and can be used to predict the outlet gas composition for the methane/steam reforming process.

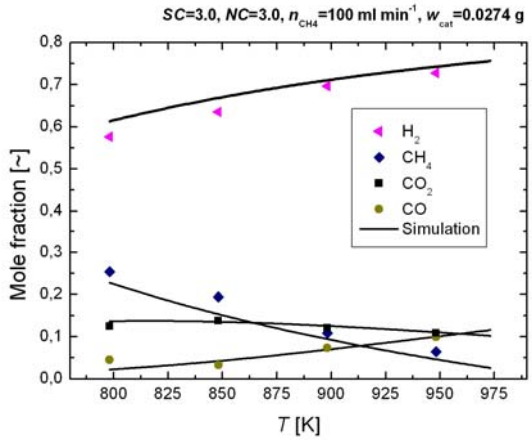

Figure 6. Experimental results compared to numerical simulation for methane inlet flow rate 100 ml min^{-1}

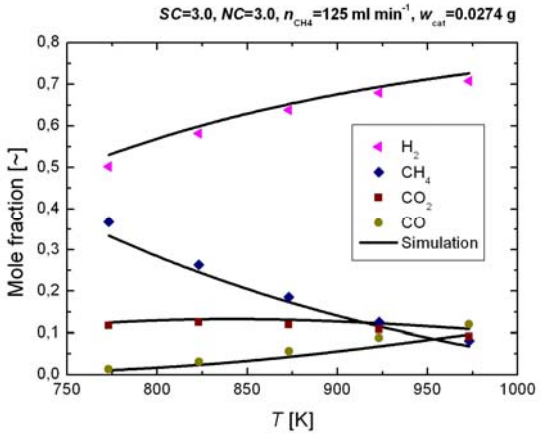

Figure 7. Experimental results compared to numerical simulation for methane inlet flow rate 125 ml min^{-1}

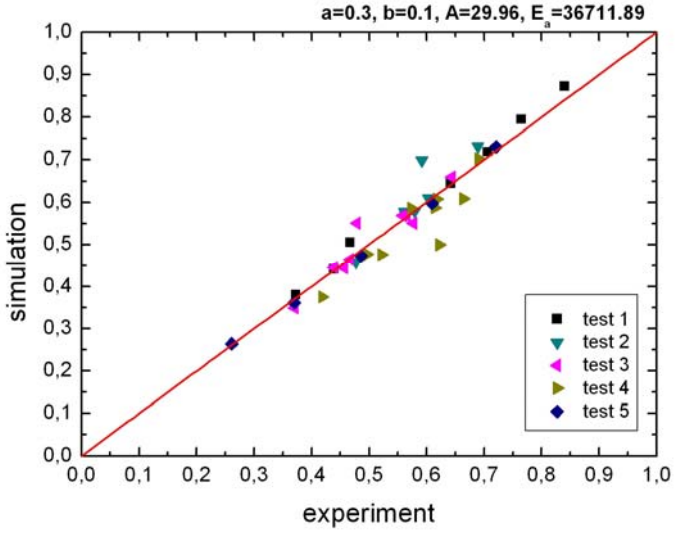

Figure 8. Correlation plots of the measured conversion rate against the model's

CONCLUSIONS

In the presented paper experimental and numerical studies on the fuel reforming process on an Ru/Al_2O_3 catalyst have been investigated. The gas mixture composition and flow rate were measured at the outlet of the reformer to establish the methane reforming rate and kinetics of the reforming reaction. The experimental set-up was built to investigate results for different thermal boundary conditions, the fuel flow rate and the steam-to-methane ratios. The reforming rate equation derived from experimental data was used in the mathematical model to predict syngas composition at the outlet of the reformer for the isothermal fuel reforming process. It was shown that the results of numerical computations are a good fit to the experimental data. Obtained results indicate how important parallel, numerical and experimental studies are in designing SOFC reformers. It was also shown that successful predictions of the outlet gas composition for different modelling conditions can be made.

ACKNOWLEDGMENTS

This research was partially supported by the European Commission (project *Dev-BIOSOFC*, FP6-042436, MTKD-CT-2006-042436).

REFERENCES

1. Berman A., Karn R.K., Epstein M., Kinetics of steam reforming of methane on Ru/Al_2O_3 catalyst promoted with Mn oxides, J. Applied Catalysis, Vol. 285, pp 73-83, 2005
2. Achenbach E., Methane/steam reforming kinetics for solid oxide fuel cells, J. Power Sources, vol. 49, pp 333-348, 1994
3. Odegard R., Jornsen E., Karoliussen H., Methane reforming on Ni/zirconia SOFC anodes, in M. Dokiya, O Yamoto, H. Tagawa, S.C. Singhal Eds., *Proceedings of 4th International Symposium on Solid Oxide Fuel Cells*, Penninyton, NJ, pp 810-819, 1995
4. Xu J., Froment G.F., Methane steam reforming; methanation and water-gas shift: I intrinsic kinetics, AIChE Journal, vol. 35, pp 88-96, 1989
5. Xu J., Froment G.F., Methane steam reforming; II Difusional limitations and reactor simulation, AIChE Journal, Vol 35, pp 97-103, 1989
6. Itoh N., Yamamoto T., Sato T, Yu W., Ohmori T., Kinetic Analysis on Low-Temperature Steam Reforming of Methane Using a Ruthenium Supported Catalyst, J. Japan Institute of Energy, vol. 85, pp 307-313, 2006 (in Japanese).
7. K. Ichikawa, S. Kimijima, Experimental Study on Methane Reforming for indirect Internal Reforming SOFC, *Proceedings of National Congress of Japan Society of Mechanical Engineering*, August 3-7, 2008 (in Japanese).
8. S. Nagata, A. Momma, T. Kato, Y. Kasuga, J. Power Sources, 101 (2001) 60-71.
9. D. Sekine, Experimental study on the steam reforming for small-scale SOFC, *Bachelor Thesis*, Tokyo University, 2005 (in Japanese)
10. Suzuki K., Iwai H., Nishino T., in: Suden B., Faghir M. (Eds.), Transport Phenomena in Fuel Cells, WIT Press, Lund, p. 95, 2005

EFFECT OF SEPARATOR RIB ON WATER FORMATION IN POLYMER ELECTROLYTE FUEL CELL

H. Tanigawa[1,*], Y. Miyazaki[1], T. Tsuruta [1]
[1] Department of Mechanical and Control Engineering, Kyushu Institute of Technology, Kitakyushu, Japan

ABSTRACT. Water management is very important in the development of the Polymer Electrolyte Fuel Cells (PEFC) with high performance and high reliability. Three-dimensional numerical and experimental study has been done for the different type of flow passages. Two kinds of flow passages, that is, serpentine-type and straight type were selected. It is found that the separator rib plays as the covering to reduce water escaping from the GDL to the channel. The moisturizing effect in the straight-type channel is higher than that in the serpentine-type channels, but the draining effect in the serpentine-type channel is better than that in the straight-type channel.

Keywords: *Polymer Electrolyte Fuel Cell, Lattice Gas Automaton, Condensation*

INTRODUCTION

Polymer Electrolyte Fuel Cells (PEFCs) have attractive interest for portable, automotive and residential applications. Water management is important in the Polymer Electrolyte Fuel Cell (PEFC) operating at room temperature. The reaction between proton and oxygen produces water and condensation occurs in the cathode side of the PEFC. If the water droplets cover the gas diffusion layer (GDL) the supply of oxygen to the membrane would be limited, then the power generation rate of the PEFC decreases. On the other hand, in a dryout condition, the polymer electrolyte membrane (PEM) shows lower electrolytic conductivity. Many researches on the water management for the PEFCs have been conducted experimentally, theoretically and numerically. For example, in the experimental studies, the water distribution was measured by MRI imaging [1, 2], optical visualization [3~5] and neutron imaging [6~9]. The numerical works have been carried out on the transport characteristics in the cell and the effects of water distribution were discussed by using the finite element method [10], the control volume method [11,12] and the lattice boltzmann method [13]. The purpose of the present paper is to make clear these problems by using the Lattice Gas Automaton (LGA) method. First, we have developed a three-dimensional LGA simulation method for the analysis of the transport phenomena inside the cells. The flooding and the plugging phenomena are studied focusing on the effect of separator ribs. Secondly, the visualization experiments have been conducted to verify the simulation results. We use two kinds of flow passage, that is, the serpentine-type and the straight-type are selected and the performances are compared.

NUMERICAL METHOD

Figure 1 shows the numerical simulation system. Three-dimensional simulations are carried out by using the Lattice Gas Automaton (LGA) method. Simple and local rules are applied for

* Corresponding author: Dr. H. Tanigawa
Phone: + (81)-93-884-3136, Fax: + (81)-93-884-3136
E-mail address: tanigawa@mech.kyutech.ac.jp

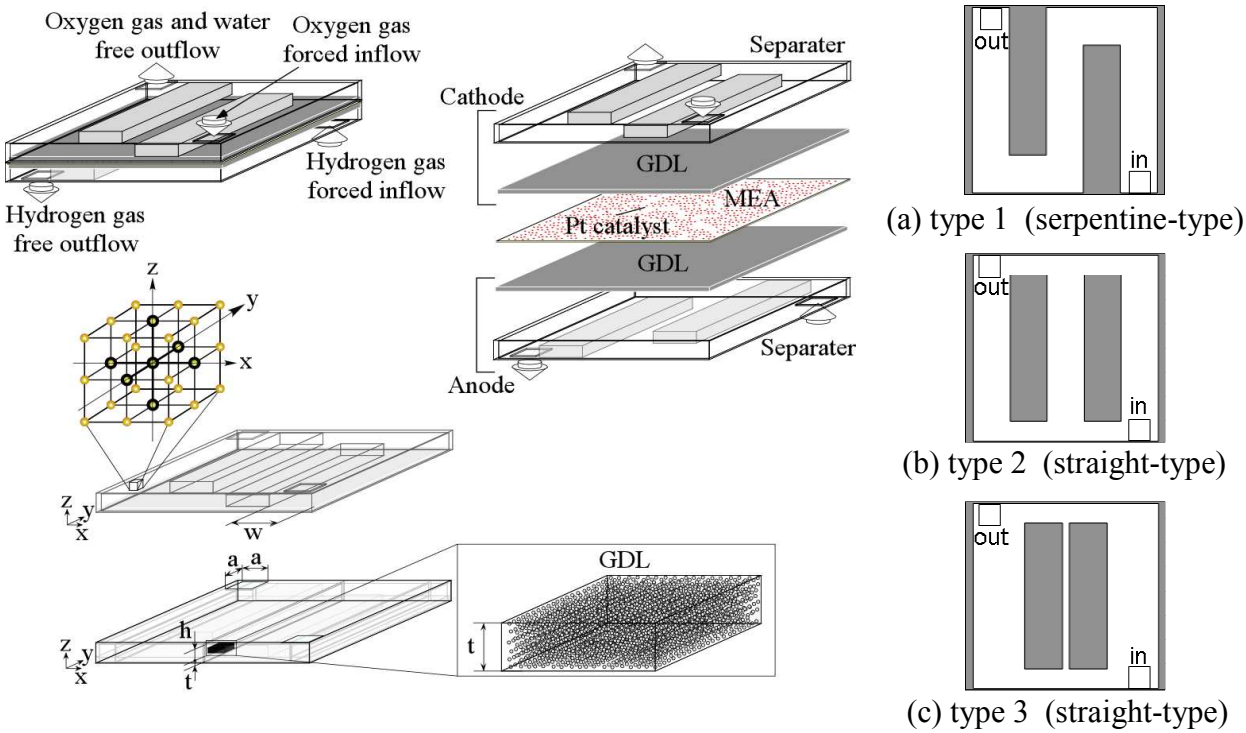

Figure 1. Analytical model

fluid particles and dominant flow pattern is calculated as self-organized macroscopic phenomenon. In this study, we use the HPP model [14] for the collision rule between particles. Also, the LG model [15] is used for the phase change by introducing an interaction length to consider the attractive force between the particles.

In the simulation on the cathode and anode side transport phenomena, we use four kinds of particles, i.e. oxygen, hydrogen, hot water and cold water for the serpentine-type and the straight-type flow passages. The oxygen and hydrogen particles are supplied to the entrance at each time-step. The GDL is modelled by porous layer made of solid particles arranged at random (porosity ε=0.8). The thickness of the MEA is assumed to be zero. In order to simulate the cell reaction at the MEA the catalyst particles are supplied randomly on the MEA surface. The number density of catalyst node to the total node number is set at α=0.2% in this study. The reaction occurs when the oxygen gas and the hydrogen gas encounter to the catalyst and they change to a hot water particle. In the LGA method, 6 particles can exist at one lattice point. We consider the effect of water vapor saturation by setting a saturation particle number Nsat at the lattice point. That is, if the number of the hot water particles exceeds Nsat, then excess particles change to the cold water particles. This scheme corresponds to the condensation. For a boundary condition at the electrode surface, an interaction length between the cold water particle and the solid surface is used in the similar way to the interaction length between the water particles [16]. The electrode surfaces are considered as hydrophilic and GDL is hydrophobic. The reaction rate is defined as a ratio of the number of reaction node to the catalyst node.

EXPERIMENTAL METHOD

Figure 2 shows the structure of the PEFC in this experiment. MEA is sandwiched between two carbon GDLs and two current collectors. The current collector has ϕ2.3 mm holes in an alternate arrangement. The active area of the cell is 16[cm^2]. As shown in Fig.2, we use two kinds of flow passage, that is, the serpentine-type and the straight-type are selected. The serpentine-type has an 8[mm] width channel and rib. In the straight-type, the width of the channel and rib are change to 12[mm], 4[mm] and 16[mm], respectively. The channel heights of both type are as same as 1[mm]. The both separators are made of polycarbonate for image measurements.

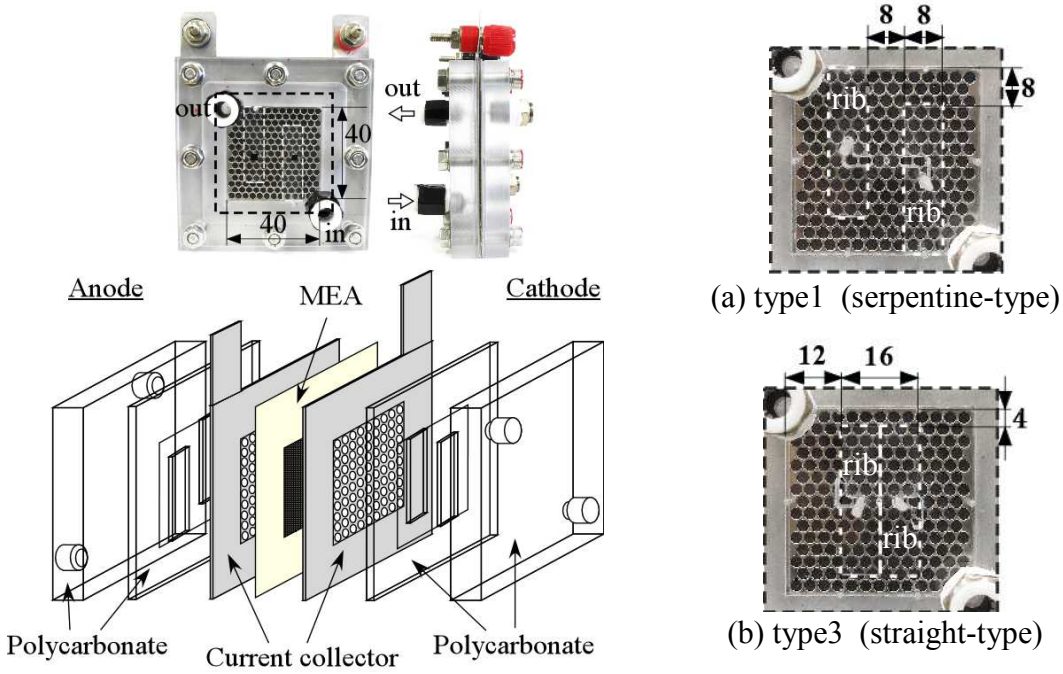

Figure 2. Polymer electrolyte Fuel cell

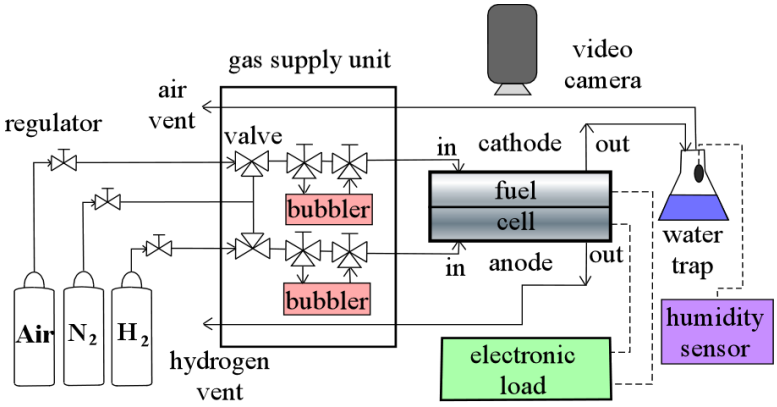

Figure 3. Experimental apparatus

Figure 3 shows the experimental apparatus. The PEFC is horizontally installed so that the cathode side might turn to a top. The experimental conditions are as follows; the current density 200 [mA/cm^2], the hydrogen gas flow rate 0.1 [l/min], the air flow rate 0.2 [l/min], and the room temperature 21 [^{o}C]. The outputs are measured with the fuel cell evaluation system. In the observation tests, distributions of the water at the cathode side are recorded with the digital video camera.

RESULT AND DISCUSSION

In Fig. 4, the numerical flow patterns are visualized. In the straight-type channel the gas selects a shortcut to the exit and flows into one side. The flow in the serpentine type channel the gas can not select the path and U-shape turning raises the flow resistance.

Figure 5 shows the time transients of the reaction rate. In the steady state condition, the reaction rate for the straight-type channel is lower than that for the serpentine-type. In the straight-type channel, the stagnation area is formed in the cell area as shown in Fig.4(b). These areas are not effective for the cell reaction. This is the reason why the straight-type channel shows the lower reaction rate.

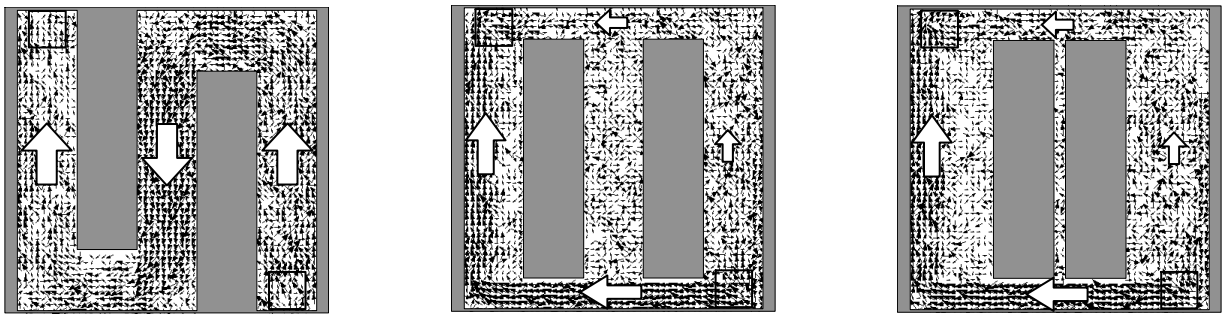

(a) type 1 (b) type 2 (c) type 3

Figure 4. Flow patterns (cathode, numerical, t=156,000[cycle])

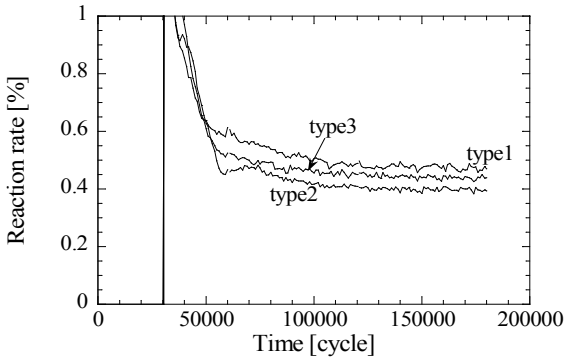

Figure 5. Time transients of the reaction rate [%] (numerical)

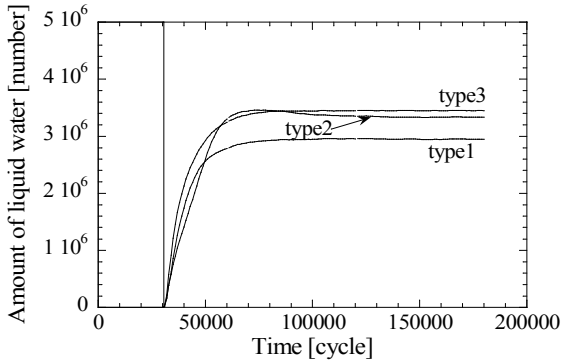

Figure 6. Time transients of the amount of liquid water in GDL (numerical)

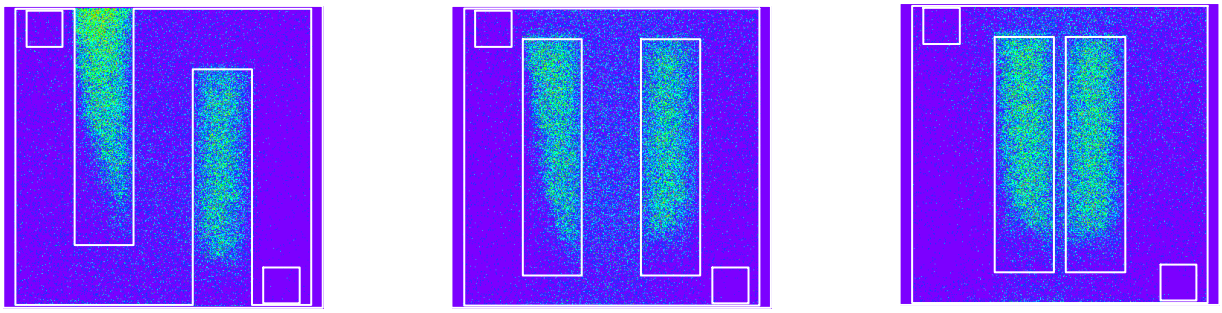

(a) type 1 (b) type 2 (c) type 3

Figure 7. Water distributions (cathode, numerical)

Figure 6 shows the time transients of the amount of liquid water in GDL. The both straight-type channels show larger water content than the serpentine-type channel. We can understand the reason from Fig. 7 which visualizes the water distributions for each channel type at the time t=180,000 cycle. The cold water is observed at the separator rib for each channel. We can see that the separator rib plays as the covering to reduce the escape of water from the GDL to the channel. Then, in the straight-type channel, the stagnation area is not effective for the drainage of the water droplets. On the other hand, in the serpentine flow channel, the gas-flow blows up the water droplets and the reaction area is kept uncovered. This is the reason why the straight-type channel shows larger water content than the serpentine-type.

Experimental images of the cathode side are presented in Fig.8. The condensed water is observed underneath the separator rib at the steady-state. We are sure that the separator rib plays as the covering shown by the numerical results.

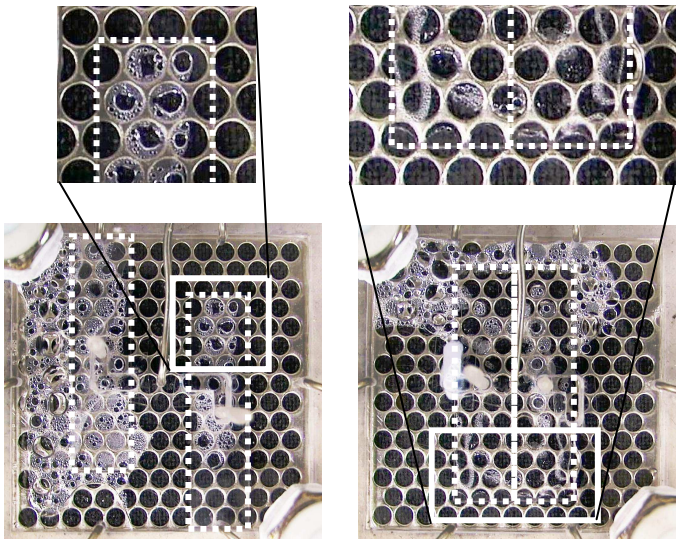

(a) type 1 (b) type 3

Figure 8. Water distributions (experimental, 992[min])

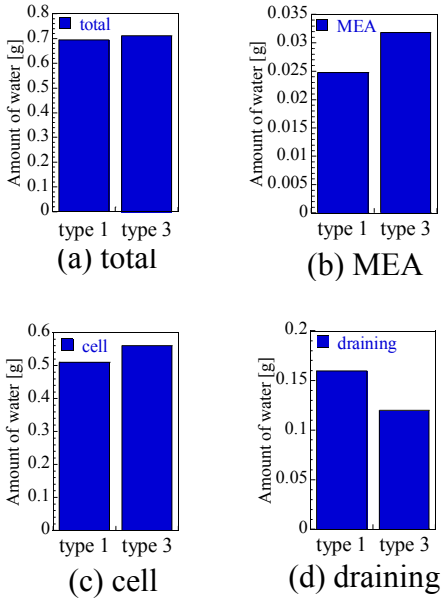

(a) total (b) MEA (c) cell (d) draining

Figure 9. The amount of produced water (experimental, 992[min])

Figure 9 shows the amount of produced water for each channel type at the time after 16 hour. The straight-type channel shows larger water content inside the cell than the serpentine-type channel, but the serpentine-type channel shows larger draining than the straight-type channel. The results show that the moisturizing effect in the straight-type channel is higher than that in the serpentine-type channels, but the draining effect in the serpentine-type channel is higher than that in the straight-type channel.

CONCLUSIONS

Experimental and three-dimensional numerical studies have been done for the different type of flow passages of the PEFC. It is found that the separator rib plays as the covering to reduce the escape of water from the GDL to the channel. The moisturizing effect in the straight-type channel is marked as compared with the serpentine-type channels, but the draining effect in the serpentine-type channel is better than that in the straight-type channel.

NOMENCLATURE

Nsat : saturation particle number
t : non-dimensional time (cycle)
α : number density of catalyst node (%)

ACKNOWLEDGMENTS

This work was financially supported by the research and development of polymer electrolyte fuel cell from the New Energy and Industrial Technology Development Organization (NEDO), Japan.

REFERENCES

1. Bedet, J., Maranzana, G., Leclerc, S., Lottin, O., Moyne, C., Stemmelen, D., Mutzenhardt, P. and Canet, D., Magnetic resonance imaging of water distribution and production in a 6cm^2 PEMFC under operation, *International Journal of Hydrogen Energy*,33, pp 3146-3149, 2008.
2. Hirai, S. and Tsushima, S., Laser Measurement Techniques and MRI visualization for Fuel Cell and CO_2 sequestration R&D, *Proceedings of Thermal Engineering Conference '07*, No.07-5, pp 39-42, 2007.
3. Ous, T. and Arcoumanis, C., Visualisation of water droplets during the operation of PEM fuel cells, *Journal of Power Sources*,173, pp 137-148, 2007.
4. Liu, X., Guo, H., Ye, F. and Ma, C.F., Water flooding and pressure drop characteristics in flow channels of proton exchange membrane fuel cells, *Electrochimica Acta*,52, pp 3607–3614, 2007.
5. Bazylak, A., Sinton, D. and Djilali, N., Dynamic water transport and droplet emergence in PEMFC gas diffusion layers, *Journal of Power Sources,* 176, pp 240-246, 2008.
6. Owejan, J.P. , Trabold, T.A. , Jacobson, D.L. , Arif, M. and Kandlikar, S.G., Effects of flow field and diffusion layer properties on water accumulation in a PEM fuel cell, *International Journal of Hydrogen Energy*,32, pp 4489-4502, 2007.
7. Turhan, A., Heller, K., Brenizer, J.S. and Mench, M.M., Passive control of liquid water storage and distributionin a PEFC through flow-field design, *Journal of Power Sources*,180, pp 773–783, 2008.
8. Chen, Y.-S., Peng, H., Hussey, D.S., Jacobson, D.L., Tran, D.T., Abdel-Baset, T. and Biernacki, M., Water distribution measurement for a PEMFC through neutron radiography, *Journal of Power Sources*,170, pp 376–386, 2007.
9. Hartnig, Ch., Manke, I., Kardjilov, N., Hilger, A., Grünerbel, M., Kaczerowski, J., Banhart, J. and Lehnert, W., Combined neutron radiography and locally resolved current density measurements of operating PEM fuel cells, *Journal of Power Sources*,176, pp 452–459, 2008.
10. Hwang, J.J., Chao, C.H., Chang, C.L., Ho, W.Y. and Wang, D.Y., Modeling of two-phase temperatures in a two-layer porous cathode of polymer electrolyte fuel cells, *International Journal of Hydrogen Energy*,32, pp 405 – 414, 2007.
11. Jung, H.-M., Lee, K.-S. and Um, S., Macroscopic analysis of characteristic water transport phenomena in polymer electrolyte fuel cells, *International Journal of Hydrogen Energy*,33, pp 2073 – 2086, 2008.
12. Jung, C.-Y., Lee, C.-S. and Yi, S.-C., Computational analysis of transport phenomena in proton exchange membrane for polymer electrolyte fuel cells, *Journal of Membrane Science*,309, pp 1–6, 2008.
13. Inoue, G., Yoshimoto, T., Matsukuma, Y. and Minemoto, M., Development of simulated gas diffusion layer of polymer electrolyte fuel cells and evaluation of its structure, *Journal of Power Sources* ,175, pp 145–158, 2008.
14. Hardy, J., de Pazzis, O. and Pomeau, Y., Molecular dynamics of a classical lattice gas: Transport properties and time correlation functions, *Phys. Rev. A*, 13, pp 1949-1961, 1976.
15. Appert, C. and Zaleski, S., Lattice gas with a liquid-gas transition, *Physical Review Letters*, Vol.64, No.1, pp 1-4, 1990.
16. Tanigawa, H. and Tsuruta, T., Lattice gas analysis on two-phase flow in cathode of polymer electrolyte fuel cells, *Proceedings of the 7th ASME-JSME Thermal Engineering Conference*, HT2007-32759(CD-ROM), pp 1-7, 2007.

ELECTROLYTE-SUPPORTED SOLID OXIDE FUEL CELL WITH COMPOSITE CATHODE

K. Świerczek[1], W. Zając[1], J. Durnaś[1], J. Kołacz[1], J. Molenda[2,*]
[1]AGH University of Science and Technology, Faculty of Material Science and Ceramics, al. Mickiewicza 30, 30-059 Krakow, Poland
[2]AGH University of Science and Technology, Faculty of Energetics and Fuels, al. Mickiewicza 30, 30-059 Krakow, Poland

ABSTRACT. In this work we present an evaluation of ceria-based electrolyte-supported Intermediate Temperature Solid Oxide Fuel Cell (IT-SOFC) with composite, perovskite cathode possessing mixed ionic-electronic conductivity. A custom-made, testing unit is described and the operational parameters (OCV, current – voltage characteristics, cell power) measured in 600 – 675°C range are presented. Additionally, the measured impedance spectra of the cell allowed to determine the temperature dependence of the ohmic resistance, the charge transfer resistance and the diffusion resistance of the cell.

Keywords: *IT-SOFC, cell construction, ceria-based electrolyte, mixed ionic-electronic conductivity perovskite*

INTRODUCTION

One of a crucial issues of SOFC technology is to lower an operational temperature of the working cell. For a conventional cell, built using zirconia-based electrolyte, lanthanum strontium manganite cathode and nickel-zirconia cermet anode, the working temperature is around 900 – 1000°C. New materials, which are being developed nowadays, should allow to decrease the operational range down to 600 – 800°C. Among many gains arising from such a lowering, one should point out a slower chemical and thermal degradation of the cell components, a possibility of utilization of a cheaper and more environmentally friendly materials, especially for interconnectors, a shorter warm-up time, compatibility with internal fuel reforming and reduced problems with cell stack sealing and gas system [1, 2]. However, several important problems must be overcome, which are connected mainly to a lower catalytic activity of the electrode materials and a lower electrical conductivity of the solid electrolyte. This creates an urgent necessity of developing new materials with sufficient catalytic and transport properties in the lower temperature range.
In this work we show results of testing of a home-made, single cell, SOFC unit based on new, promising cathode and electrolyte materials. The influence of main operational parameters i.e. temperature and fuel flow on the performance of the cell are presented.

EXPERIMENTAL

Cathode and electrolyte materials were obtained using sol-gel and coprecipitation methods, details can be found elsewhere [3, 4]. In this work we focused on new and promising perovskite materials with $La_{0.4}Sr_{0.6}Co_{0.2}Fe_{0.8}O_3$ and $Sm_{0.6}Sr_{0.4}Co_{0.2}Fe_{0.8}O_3$ chemical composition and the electrolyte

* Corresponding author: Prof. J. Molenda
Phone: + (48)-12-6172026, Fax: + (48)-12-6172522
E-mail address: molenda@agh.edu.pl

material with $Ce_{0.85}Gd_{0.15}O_{1.925}$ composition [4-6]. These materials were found to be chemically inert to each other at high temperatures and seem to be promising in terms of a long-term stability of the cell [7]. The cell performance was studied using custom-made SOFC testing unit shown in Figure 1. The anode was fuelled with dry hydrogen, with flow changing in the range of 10 – 100 cm^3min^{-1}, whereas air was provided at the cathode side, with flow rate about 500 cm^3min^{-1}. The measurements of the electrochemical properties of the cell were carried out using Solartron SI 1287 electrochemical interface and Solartron 1252A frequency response analyzer. In order to evaluate the operational parameters of the cell, current – voltage and power density characteristics as well as impedance spectra were recorded.
The cell was constructed as:

- composite: 85wt.% $La_{0.4}Sr_{0.6}Co_{0.2}Fe_{0.8}O_3$, 15wt.% $Sm_{0.6}Sr_{0.4}Co_{0.2}Fe_{0.8}O_3$ as the cathode,
- $Ce_{0.85}Gd_{0.15}O_{1.925}$ gas-tight sinter as the electrolyte (about 0.8mm thick),
- 40:60 8YSZ-NiO reduced to 8YSZ-Ni cermet as the anode.

The sintering process of the cell was conducted with separate firings of the anode (1200°C) and the cathode (1100°C).

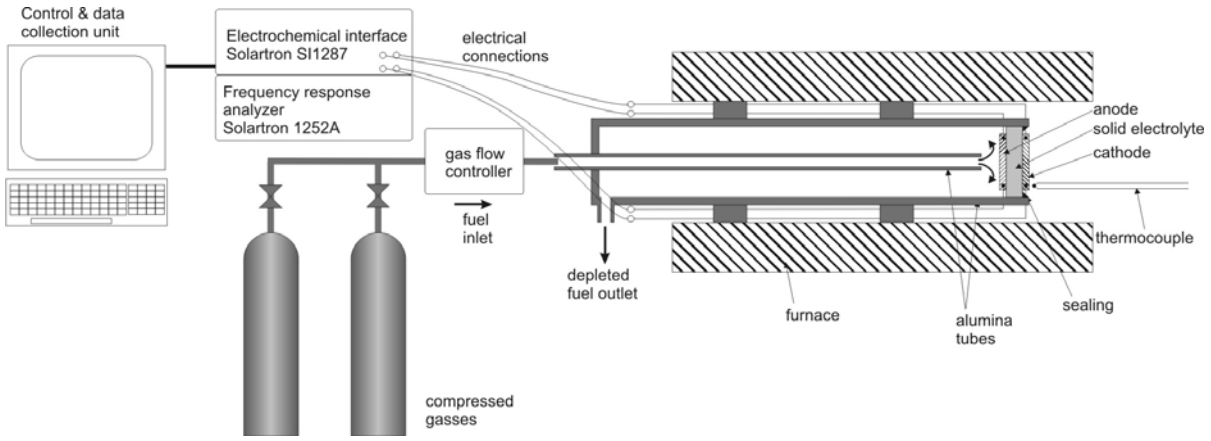

Figure 1. Schematics of the custom-made SOFC testing unit.

RESULTS AND DISCISSION

One of the most important features concerning materials used for SOFC technology is their electrical conductivity. In the case of the electrolyte it has to be purely ionic and should be as high as possible. In the case of the cathode material an utilization of mixed ionic-electronic conductivity was found to be beneficial, as it allows for the oxygen reduction reaction to take place all over the surface of the cathode, and therefore may allow for a better efficiency of the working cell [2]. The temperature dependence of the electrical conductivity of the cathode and electrolyte materials used for the cell construction are shown in Figure 2. Analyzing the data, two important issues may be noticed. Due to a relatively high activation energy of the ionic conductivity of the electrolyte material, its resistance increases rapidly with a decreasing temperature and therefore, the ohmic losses of the cell may become considerable. In the case of the cathode materials, the existence of a rather slightly pronounced maximum (or inflection) on the electrical conductivity dependence indicate an appearance of the oxygen vacancies at this temperature [2, 5]. The deviation from the oxygen stoichiometry increases with the increasing temperature, but the total conductivity decreases, due to the trapping of the created electrons on a high valence 3*d* metals [2]. The appearance of the oxygen vacancies indicate the existence of the mixed ionic-electronic conductivity in the perovskite material.

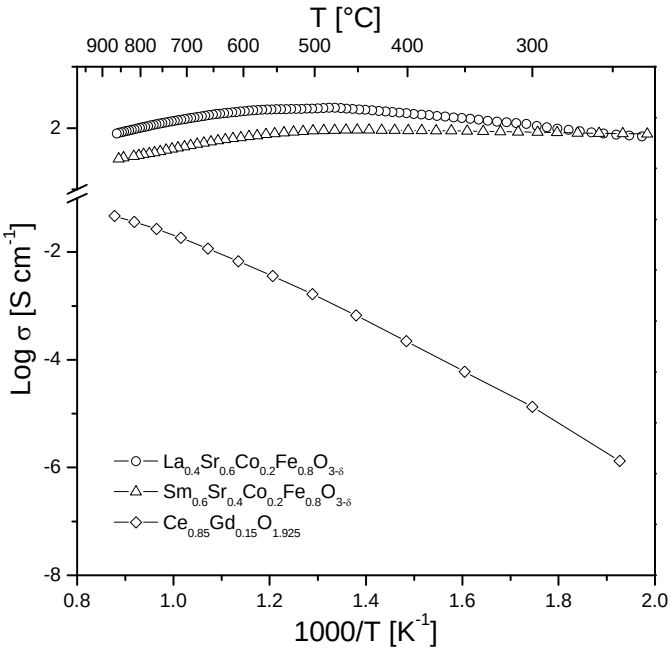

Figure 2. Electrical conductivity as a function of temperature for $La_{0.4}Sr_{0.6}Co_{0.2}Fe_{0.8}O_{3-\delta}$, $Sm_{0.6}Sr_{0.4}Co_{0.2}Fe_{0.8}O_{3-\delta}$ and $Ce_{0.85}Gd_{0.15}O_{1.925}$.

The impedance spectra recorded for the cell in 600 – 675°C temperature range are depicted in Figure 3. The obtained data were fitted using a typical equivalent circuit used for SOFC (Figure 4) [8]. The spectra consist of two depressed semi-circles shifted to the right from the origin. A clearly visible coil element is also present. R_{ohm} represents all of the ohmic resistances present in the cell, it can be however ascribed to the electrolyte resistance mainly. R_{ct} is related to the charge transfer resistance and R_d represents diffusion resistance [9]. Figure 5. presents the temperature dependence of the obtained R_{ohm}, R_{ct} and R_d values. The obtained results suggest that the cell performance is R_{ohm} limited in the whole temperature range. This in turn imply that the decrease of the electrolyte thickness should lead to a higher effectiveness of the working cell.

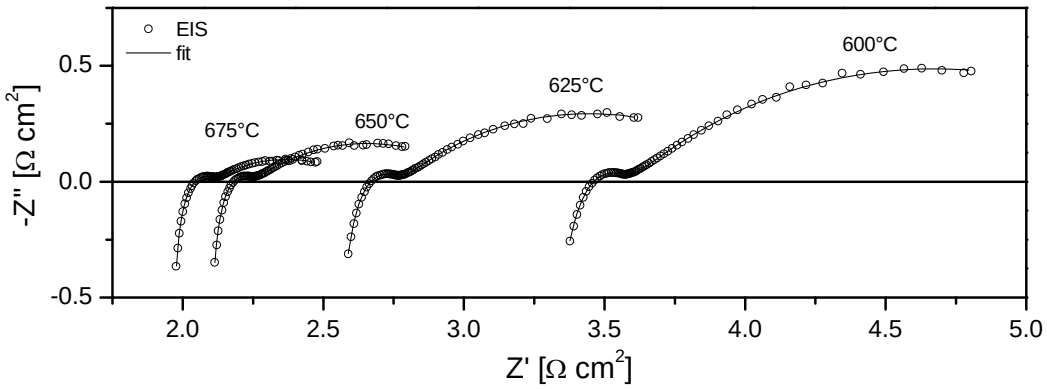

Figure 3. Impedance spectra of the measured cell.

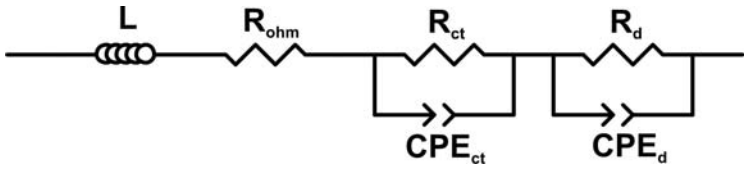

Figure 4. Equivalent circuit used for data analysis.

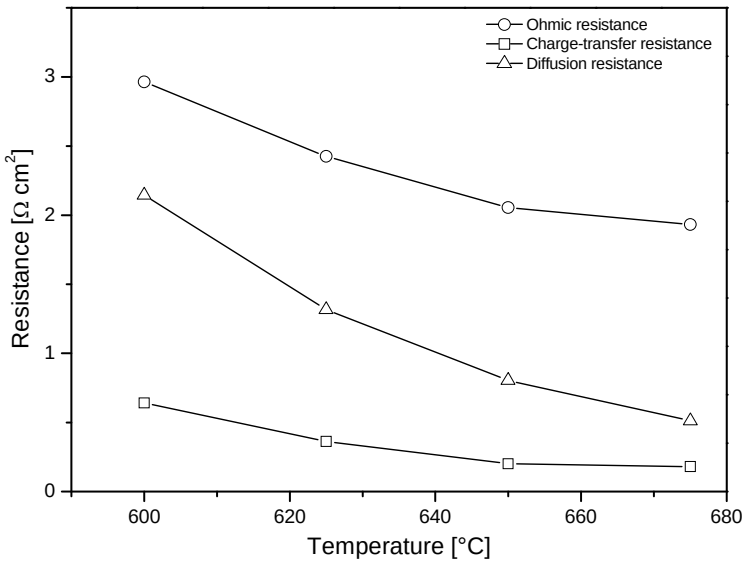

Figure 5. R_{ohm}, R_{ct} and R_d dependence on temperature.

The recorded OCV values (Figure 6) were relatively close to the theoretical ones, proving that the electrolyte layer was gas-tight and that the electronic component of the electrical conductivity of the electrolyte is rather marginal. A fairly weak dependence of OCV versus H_2 flow, for flow rates over 40 cm^3min^{-1}, was measured. However, low flow rates (especially 10 cm^3min^{-1}) seem to be not sufficient for our cell construction. The flow rate of 40 cm^3min^{-1} appears to be a good compromise between the cell voltage and the fuel utilization.

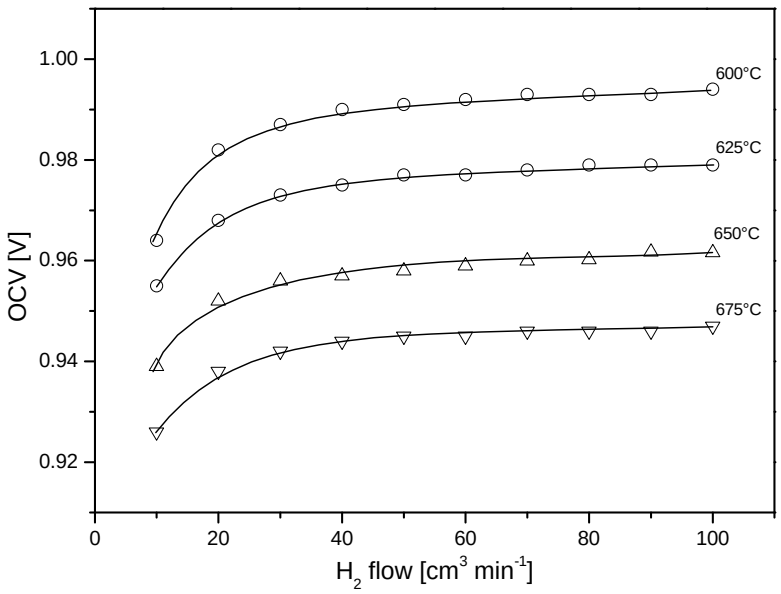

Figure 6. OCV values as a function of the H_2 flow recorded in 600 – 675°C temperature range.

The measured in 600 – 675°C temperature range and for 40 cm^3min^{-1} fuel flow rate values of voltage and power density vs. current density are presented in Figure 7a. A typical increase of the maximum power of the cell with the increasing temperature was obtained. Figure 7b shows the evolution of voltage and power characteristics as a function of H_2 flow. The results additionally confirm that 40 cm^3min^{-1} fuel flow is optimal for the cell construction. The maximum values dependence vs. flow are shown in Figure 7c.

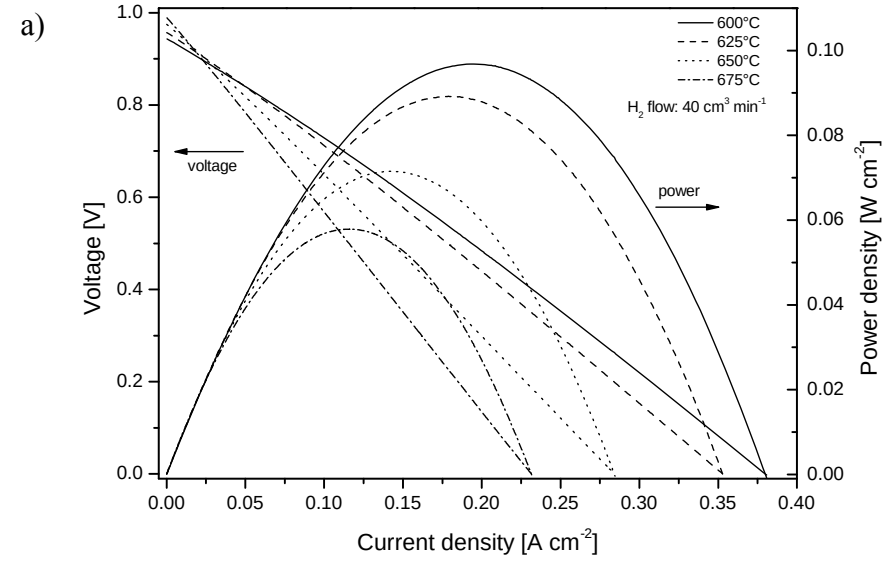

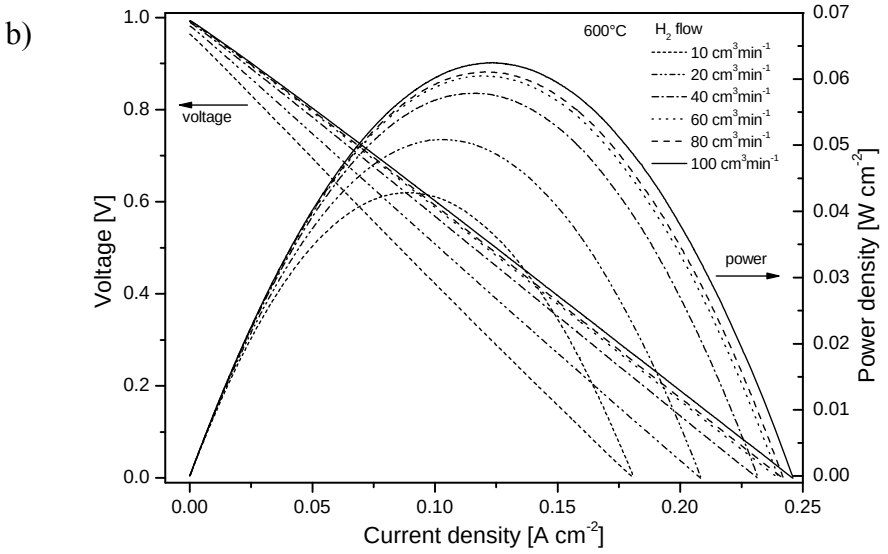

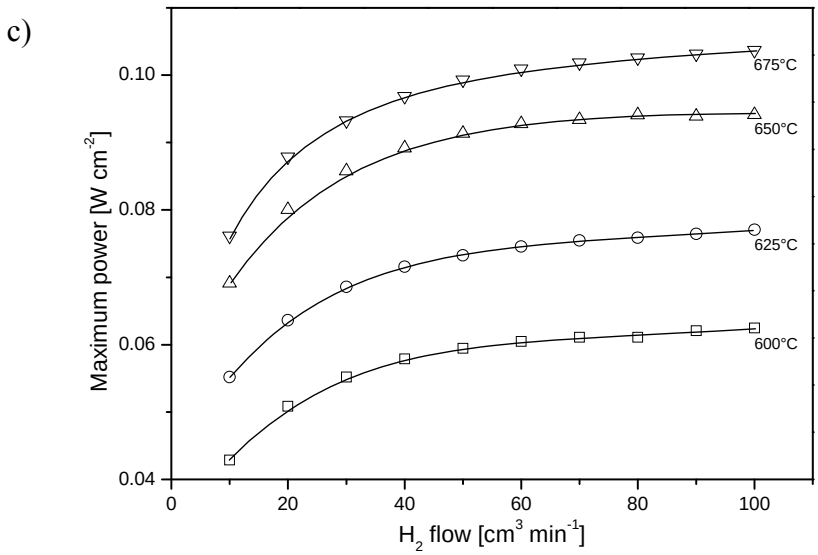

Figure 7. (a) Voltage and power density vs. current density recorded in 600 – 675°C temperature range for fuel flow rate of 40 cm^3min^{-1} and (b) at 600°C for fuel flow rate in the range 10 – 100 cm^3min^{-1}. (c) Maximum power as a function of H_2 flow for 600 – 675°C temperature range.

CONCLUSIONS

The presented results of the electrochemical characterization of the working, composite cathode 85wt.% $La_{0.4}Sr_{0.6}Co_{0.2}Fe_{0.8}O_3$, 15wt.% $Sm_{0.6}Sr_{0.4}Co_{0.2}Fe_{0.8}O_3$, CGO15 electrolyte and 8YSZ-Ni anode, SOFC cell are encouraging and suggest that further improvements can be achieved. The used materials seem to be attractive in terms of their performance in the cell, especially, their electrical conductivity seems to be sufficient. The impedance spectra analysis indicate that the performance of the cell is limited by its ohmic resistance, which can be associated with the thickness of the electrolyte. A significant improvement of the working cell parameters, especially power density, may be expected when thinner electrolyte would be used. For our custom-made SOFC testing unit hydrogen fuel flow equal 40 cm^3min^{-1} seem to be the optimal one.

ACKNOWLEDGEMENT

This work was supported by Polish Ministry of Science and Higher Education under grants N N507 4441 33 and N N507 1573 33.

REFERENCES

1. Ivers-Tiffée, E., Weber, A., Herbstritt, D., Materials and technologies for SOFC-components, *J. of the Europ. Ceramic Soc.* Vol. 21, pp 1805-1811, 2001.
2. Molenda, J., Świerczek, K., Zając, W., Functional materials for the IT-SOFC, *J. Power Sources*, Vol.173, pp 657-670, 2007.
3. Świerczek, K., Marzec, J., Pałubiak, D., Zając, W., Molenda, J., LFN and LSCFN perovskites — structure and transport properties, *Solid State Ionics*, Vol. 177, pp 1811-1817, 2006.
4. Zając, W., Molenda, J., Electrical conductivity of doubly doped ceria, *Solid State Ionics*, Vol. 179 pp 154-158, 2008.
5. Świerczek, K., Gozu, M., Structural and electrical properties of selected $La_{1-x}Sr_xCo_{0.2}Fe_{0.8}O_3$ and $La_{0.6}Sr_{0.4}Co_{0.2}Fe_{0.6}Ni_{0.2}O_3$ perovskite type oxides, *J. Power Sources*, Vol. 173, pp 695-699, (2007).
6. Świerczek, K., Pelic, B., Molenda, J., Wybrane właściwości fizykochemiczne perowskitów serii $Sm_{1-x}Sr_xCo_{0.2}Fe_{0.8}O_{3-\delta}$, *Materiały Ceramiczne* (2009) - accepted for publication
7. Zając, W., Świerczek, K., Molenda, J., Thermochemical compatibility between selected $(La,Sr)(Co,Fe,Ni)O_3$ cathodes and rare earth doped ceria electrolytes, *J. Power Sources* Vol. 173, pp. 675-680, 2007.
8. Perry Murray, E., Barnett, S.A., $(La,Sr)MnO_3$-$(Ce,Gd)O_{2-x}$ composite cathodes for solid oxide fuel cells, *Solid State Ionics*, Vol. 143, pp. 265-273, 2001.
9. Piao, J., Sun, K., Zhang, N., Xu, S., A study of process parameters of LSM and LSM-YSZ composite cathode films prepared by screen-printing, *J. Power Sources*, Vol. 175, pp. 288-295, 2008.

METHANE/STEAM REFORMING KINETICS FOR SOLID OXIDE FUEL CELLS ON Ni/YSZ CATALYST

T. Ichikawa[1], G. Brus[2,*], Y. Noro[1], S. Kimijima[1], J.S. Szmyd[2]
[1] Shibaura Institute of Technology, Tokyo, Japan
[2] AGH - University of Science and Technology, Krakow, Poland

ABSTRACT. This paper presents experimental and numerical studies on the fuel reforming process on an Ni/YSZ catalyst. Nickel is widely known as a catalyst material for Solid Oxide Fuel Cells. Because of its prices and catalytic properties, Ni is used in both electrodes and internal reforming reactors. However, using Ni as a catalyst carries some disadvantages. Carbon formation is a major problem during a methane/steam reforming reaction based on Ni catalysis. Carbon formation occurs between nickel and metal-support, creating fibers which damage the catalytic property of the reactor. To prevent carbon deposition, the steam-to-carbon ratio is kept between 3 and 5 throughout the entire process. To optimize the reforming reactors, detailed data about the entire reforming process is required. In the present paper kinetics of methane/steam reforming on the Ni/YSZ catalyst was experimentally investigated. Measurements including different thermal boundary conditions, the fuel flow rate and the steam-to-methane ratios were performed. The reforming rate equation derived from experimental data was used in the numerical model to predict synthetic gas composition at the outlet of the reformer.

Keywords: *SOFC, fuel cells, methane/steam reforming, Ni/YSZ catalyst, reforming*

INTRODUCTION

The majority of commercial reactors in hydrogen production use methane/steam reforming on nickel catalyst. To design reforming reactors properly, detailed data about reaction kinetics are required. The kinetics of methane/steam reforming on Ni catalyst have been studied by many groups of researchers [1-6]. However, there is some disagreement as to the reported reaction order and activation energy of methane/steam reforming. Various researchers working on methane/steam reforming based on nickel catalyst [1-6] have reported different kinetics. The methane/steam reforming is an important part of the fuel conversion process for high temperature fuel cells such as Solid Oxide Fuel Cell. The high working temperature of an SOFC makes hydrocarbons the most suitable fuel in achieving high efficiency from natural resources [7]. For hydrocarbon-based fuel, three types of fuel conversion can be considered in reforming reactions: external, indirect internal and direct internal reforming systems. High-temperature SOFC eliminates the need for an expensive external reforming system. The possibility of using internal reforming is one of the advantages of high temperature fuel cells. Strong endothermic fuel reforming reactions can be thermally supported by the heat generated due to the sluggishness of electrochemical reactions, diffusion of participating chemical species and ionic and electric resistance. However, when operating at high temperatures, thermal management becomes an important issue. To carry out thermal management properly, detailed modelling and numerical analyses of the phenomena occurring inside the reformer are required. In the present paper, kinetics of methane/steam reforming on Ni/YSZ catalysts was

* Corresponding author: MSc Grzegorz Brus
Phone: + (48)-12-6173279, Fax: + (48)-12-6172685
E-mail address: brus@agh.edu.pl

experimentally investigated. The gas mixture composition and flow rate were measured at the outlet of the reformer to establish the methane reforming rate and kinetics of the reforming reaction. Based on experimental data, a mathematical and numerical model of the reforming reaction has been developed. The numerical model was compared to the experimental results and good agreement was found.

EXPERIMENTAL INVESTIGATION

Experimental procedure and facility

A schematic view of the experimental setup is shown in figure 1. A stainless steel reformer was located in an electrical furnace, which can be heated up to 1000°C. The maximum working temperature of pre-heater and after-heater is 400°C; however, for all experimental investigations presented in this paper, the temperature of pre- and post-heater was maintained at 200°C. High purity methane was the fuel used in the experiment. It was supplied to the reformer via a flow controller and evaporator, which was also used as a pre-heater. Water was fed to the system with a pump. The gas composition after the reforming process was analysed by gas chromatography prior to which the steam had been separated by cooling down the gas mixture to 2 °C. The reforming reaction tube was filled by nickel supported on yttria-stabilized zirconia. Figure 2A shows a typical reaction tube, where a catalyst supported on metallic particles is located in a reaction tube. For the presented investigation, a catalyst material was taken from an unused SOFC unit. The catalyst was a tubular-shape anode and consisted of 40% Ni and 60% YSZ. In the presented investigation the original tubular shape anodes were crushed into micro-particles roughly 300 μm in size and were located in the reaction tube as shown in figure 2B. To prevent large temperature gradients in the reformer, modifications of the reaction tube have been applied. To avoid a cooling effect of entering fluid, the reformer was partially filled with Al_2O_3 as shown in figure 2B. In this solution a mixture of gases before getting to the reaction zone was pre-heated by electric furnace to the reaction temperature. To control the thermal condition of the experiment, four thermocouples were placed in the experimental set-up as shown in figure 1 (marked as "T").

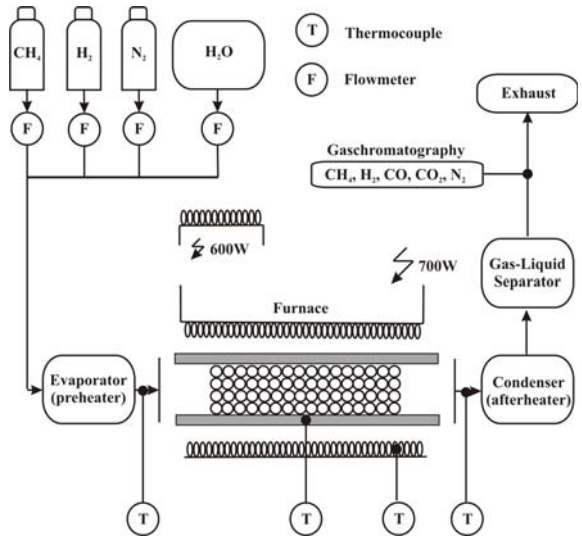

Figure 1. Schematic view of the experimental setup

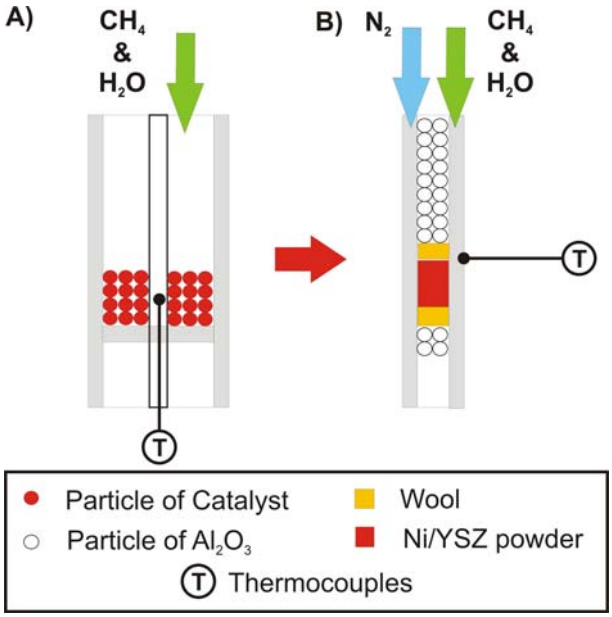

Figure 2. Schematic view of reaction tube. A) Typical reaction tube. B) Modified reaction tube.

To derive correct kinetics data, the reaction has to occur in a whole volume of catalyst. This can be accomplished by keeping the reforming conversion rate low. To achieve a low level of methane conversion, the fuel was additionally mixed with nitrogen (see figure 2B). Nitrogen does not directly influence the reforming reaction but the partial pressure of the components changed, which decreases both the reaction rate and methane conversion rate.

Methodology

The methane/steam reforming process is widely known as a conventional process for producing hydrogen [4], [5]. In the reforming process of methane with steam, the dominant reactions are the following two [8]
fuel reforming reaction

$$\mathrm{CH_4 + H_2O \rightarrow 3H_2 + CO}, \tag{1}$$

shift reaction

$$\mathrm{CO + H_2O \leftrightarrow H_2 + CO_2} \tag{2}$$

It follows from the stoichiometry of the steam/methane reforming reaction that the reaction rate expression can be approximated with this equation:

$$r_{\mathrm{CH_4}} = k\left(p_{\mathrm{CH_4}}\right)^a \left(p_{\mathrm{H_2O}}\right)^b, \tag{3}$$

where $k = A \cdot \exp\left(-E / RT\right)$

Where k is the reforming reaction constant, p_{CH4} and p_{H2O} are partial pressures of methane and water, respectively, [Pa], a and b are dimensionless coefficients responding to the reaction order, A is a pre-exponential factor, E is the activation energy, [J mol^{-1}], R the universal gas constant, [J mol^{-1} K^{-1}] and T the reaction temperature, [K]

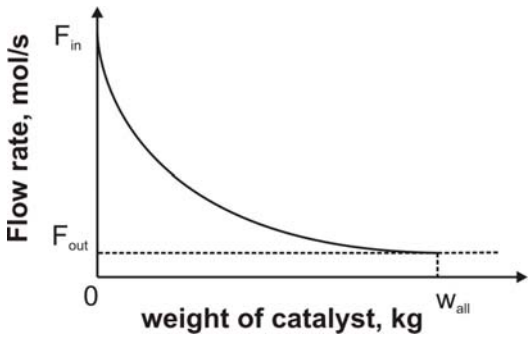

Figure 3. Methane flow rate as a function of catalyst weight

Figure 3 presents the relationship between the molar flow rate of methane and the weight of catalyst used. As can be seen for the given inlet flow rate of methane, increasing the amount of catalyst results in a decrease in the methane outlet flow rate as an effect of the higher conversion rate of methane. However, for some amount of catalyst, marked on figure 3 as w_{all}, there is no more change in the conversion rate. The equilibrium occurs while the outlet flow rate stays constant. Therefore the non-equilibrium reaction rate can be described as a ratio between the change in the flow rate of methane and the change in the amount of catalyst. Mathematically, this is written

$$r_{\mathrm{CH_4}} = -dF_{\mathrm{CH_4}} / dw_{cat}, \tag{4}$$

where

$F_{CH_4} = F^{in}_{CH_4} \cdot (1-x)$, where F_{CH_4} is the methane flow rate, [mol/s] and x is a dimensionless amount of reacted methane in the reforming reaction, w_{cat} is the weight of catalyst used, [kg].
By combining equations (3) and (4), the following equation was formulated:

$$k = \left(F^{in}_{CH_4} / w_{cat}\right) \cdot \int_0^{x_{out}} \left(1/k\left(p_{CH_4}\right)^a \left(p_{H_2O}\right)^b\right) \cdot dx \tag{5}$$

From the stoichiometry of reactions (1) and (2), the partial pressures can be defined as

$$p_{CH_4} = \left(n_{CH_4} / n_{all}\right) \cdot P = \left[(1-x)/(1+SC+NC+2x)\right] \cdot P\,, \tag{6}$$

$$p_{H_2O} = \left(n_{H_2O} / n_{all}\right) \cdot P = \left[(SC-x-y)/(1+SC+NC+2x)\right] \cdot P\,, \tag{7}$$

where n_{all} is the total amount of product at the outlet of the reaction tube, P is total pressure [Pa], n_{CH4}, n_{H2O} are, respectively, the methane and water fractions at the reformer output, x is a fraction of reacted methane, y is a fraction of reacted carbon monoxide, SC is the steam-to-carbon ratio and NC is the nitrogen-to-carbon ratio. n_{all} was derived from stoichiometry of reactions (1) and (2).
Introducing equations (6) and (7) into equation (5) yields the final form of the equation for the reaction constant:

$$k = \left(F^{in}_{CH_4} / w_{cat}\right) \cdot \int_0^{x_{out}} \left((1+SC+NC+2x)^{a+b} / P^{a+b} (1-x)^a (SC-x-y)^b\right) \cdot dx \tag{8}$$

where, a and b are coefficients related to the reaction order.
By following Itoh et al. [6] the methane conversion rate x is determined by the outlet quantity and can be calculated as

$$x = \left(x_{CO} + x_{CO_2}\right) / \left(x_{CH_4} + x_{CO} + x_{CO_2}\right) \tag{9}$$

The shift reaction occurs very fast and therefore the conversion rate can be estimated from the equilibrium equation

$$K_{shift}(x-y)(SC-x-y) = y \cdot (3x+y) \tag{10}$$

where:

$$K_{shift} = \exp\left[-\Delta G / (R \cdot T)\right], \tag{11}$$

where ΔG is the change of the standard Gibbs free energy of the shift reaction, R is the universal gas constant, [J mol^{-1} K^{-1}] and T is the reaction temperature, [K].
Because the reaction constant does not depend on the SC and NC ratios, a and b can be found [9]. K will be constant if a and b are set correctly. The real values of a and b are those that result in the smallest k derivation for different SC and NC ratios. Equation (8) was solved numerically for various values of a and b and for the different SC and NC ratios. The range from -1.0 to 2.0 has been chosen as a common range for reaction order according to already published data; figure 4 shows the results of computation. The smallest reaction constant deviation was found to be 0.3 and 0.1 for a and b, respectively.

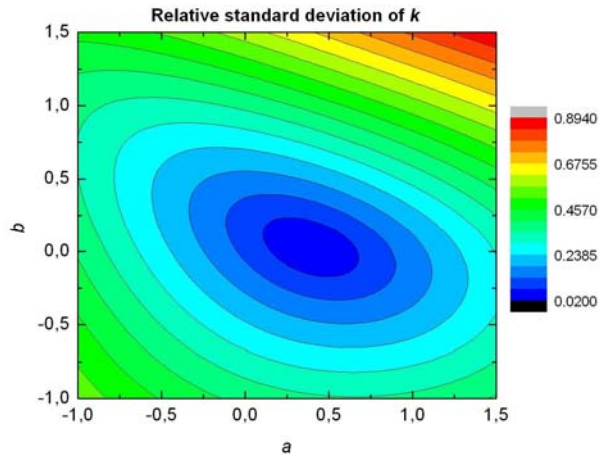

Figure 4. Relative standard deviation of *k*

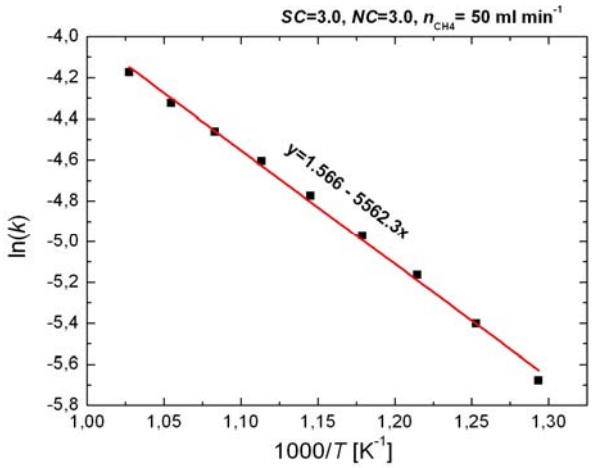

Figure 5. Arrhenius plot for Ni/YSZ

To develop a full kinetic model of the reforming reaction on the Ni/YSZ catalyst, the relationship between the reaction temperature and reaction constant has been investigated. The effect of the temperature on the reaction was studied by increasing the temperature from 500°C to 700°C. The results of the experiment are presented as an Arrhenius plot, as shown in figure 5.
A straight line was fitted to the experimental data as a result of approximation. The equation for the straight line for this experiment takes a form of Arrhenius equation and can be described

$$\ln k = \ln A - \frac{E}{R} \cdot \frac{1}{T} \tag{12}$$

Where T [K] is the temperature of fuel conversion, R = 8.314472 [J mol^{-1} K^{-1}] the universal gas constant, A is called the pre-exponential factor and corresponds to the intercept of line at 1/T=0 and E [J mol^{-1}], which is obtained from the slope of the line, is the activation energy of the steam reforming reaction.

Thus the kinetic of the methane/steam reforming reaction can be described by a reforming rate [mol s^{-1} g^{-1}] based on the experimentally obtained data by following this equation:

$$R_{st} = 4.79 \cdot \exp\left(-46223.11 / RT\right) \cdot p_{\mathrm{CH_4}}^{0.37} \cdot p_{\mathrm{H_2O}}^{0.05} \tag{13}$$

MATHEMATICAL MODEL FOR THE FUEL REFORMING PROCESS

The steam reforming reaction described by equation (1) is a slow and highly endothermic reaction; therefore a kinetic expression is required to calculate the reaction rate. How methane is reformed inside the reformer is dependent on the local conditions, including not only temperature but also the partial pressure of each chemical species and density of the catalysis [10]. The water-gas shift reaction described by equation (2) is a fast and weak exothermic reaction and can be assumed to be in equilibrium at the reforming temperature [8].
In the presented paper the reaction rates of the two main reactions (equations (1) and (2)) R_{st} and R_{sh} are calculated

$$R_{st} = 4.79 \cdot \exp\left(-46223.11 / RT\right) \cdot p_{\mathrm{CH_4}}^{0.37} \cdot p_{\mathrm{H_2O}}^{0.05} \tag{14}$$

$$R_{\mathrm{sh}} = K_{\mathrm{sh}}^{+} p_{\mathrm{CO}} p_{\mathrm{H_2O}} - K_{\mathrm{sh}}^{-} p_{\mathrm{H_2}} p_{\mathrm{CO_2}} \tag{15}$$

Equation (14) is based on the experimentally obtained data and was described in the previous paragraph, where, w_{cat}, is catalyst weight [g], T [K] the temperature of fuel conversion, R = 8.314472 [J mol^{-1} K^{-1}] the universal gas constant, p_{CH4} the partial pressure of methane [Pa] and p_{H2O} the partial

pressure of steam [Pa]. The catalyst weight w_{cat} is an important parameter because control of its distribution can be used as a means of changing the distribution pattern of the reformer temperature.

K_{sh}^{+} and K_{sh}^{-} denote the rate constants of forward and backward water-gas shift reactions. The water shift reaction given by equation (2) reaches equilibrium rapidly; therefore CO_2, H_2, CO and H_2O have to satisfy the equilibrium equation. Chemical equilibrium is represented by the equilibrium constant which is a function of temperature and is equal to the ratio of the reactants' to the products' partial pressures.

$$K_{sh} = K_{sh}^{+} / K_{sh}^{-} = (p_{CO_2} p_{H_2}) / (p_{CO} p_{H_2O}) = \exp(-\Delta G_{sh}^{0} / RT) \tag{16}$$

where ΔG_{sh}^{0} is the change of standard Gibbs free energy of shift reaction.

This equilibrium constant, given by equation (16), is introduced into equation (15) to calculate the rate of the shift reaction.

The change of each chemical species caused by the fuel reforming reaction (equation (11)) and shift reaction (equation (12)) are derived from the reactions' stoichiometry and are calculated as follows:

$$\Delta \dot{n}_{H_2} = 3x + y \tag{17}$$

$$\Delta \dot{n}_{CO} = x - y \tag{18}$$

$$\Delta \dot{n}_{CO_2} = y \tag{19}$$

$$\Delta \dot{n}_{CH_4} = -x \tag{20}$$

$$\Delta \dot{n}_{H_2O} = -x - y \tag{21}$$

RESULTS

This paper has presented experimental and numerical studies on the fuel reforming process on an Ni/YSZ catalyst. The gas mixture composition and the flow rate were measured at the outlet of the reformer to establish the methane-steam reforming rate and kinetics of the reforming reaction. Measurements including different thermal boundary conditions, the fuel flow rate and the steam-to-methane ratios were performed. The reforming rate equation derived from experimental data was used in the numerical model to predict synthetic gas composition at the outlet of the reformer. Figure 6 presents a mole fraction of fuel in the outlet of the reformer as a function of reaction temperature. As can be seen in the figure 6, numerical results, presented as a constant line, fit the experimental data well. Figure 6 indicates that the amount of carbon monoxide increases with the reaction temperature. This is significant because in contrast to the low temperature fuel cell, the carbon monoxide does not poison the high temperature solid oxide fuel cell anode but can be electrochemically converted as a fuel [2]. In figure 7 an effect of the methane flow rate on the steam reforming reaction was studied by increasing the inlet methane flow rate from 50 ml min^{-1} to 150 ml min^{-1}. As can be seen in figure 7, the inlet flow rate of methane has a small influence on the outlet mole fraction of CO and CO_2. The existing disagreement between the experimental and numerical data is a result of a high conversion rate. The relatively large amount of catalyst and low flow rate of methane results in a shift reaction (1) to the left side and cannot be precisely described by the numerical model used. The quality of the numerical computations can be presented by a correlation plot of the measurements against the numerical model. The example of numerical results and their comparisons with the experimental data are shown in figures 8, where the experimental results were set against the calculated reforming conversion rates. The points situated on the line present a perfect fit between

the experimental and numerical results. Most of the points are located on the line or in its vicinity. Good agreement between the experimental and numerical results was obtained.

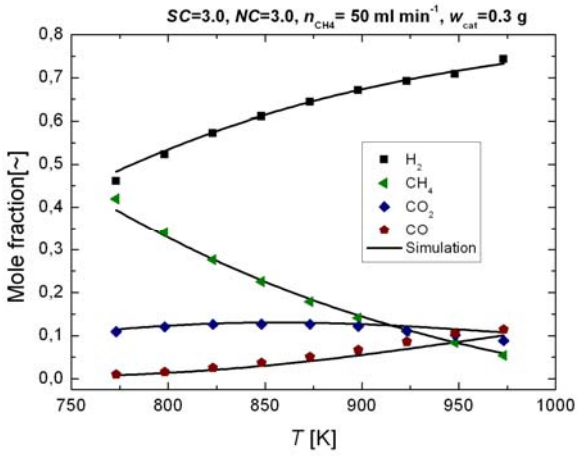

Figure 6. Experimental results in comparison with numerical simulation. Mole fraction of fuel in the outlet of the reformer as a function of reaction temperature.

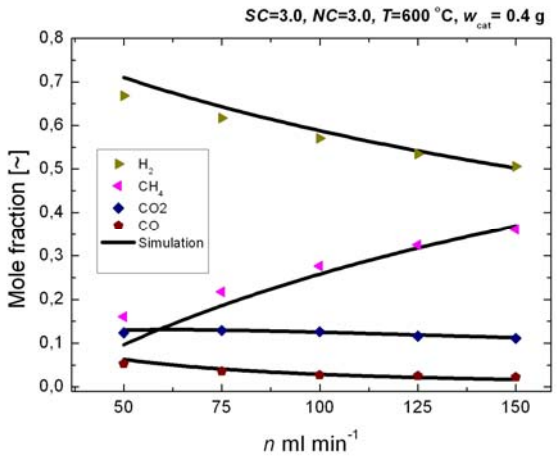

Figure 7. Experimental results in comparison with numerical simulation. Mole fraction of fuel in the outlet of the reformer as a function of inlet methane flow rate.

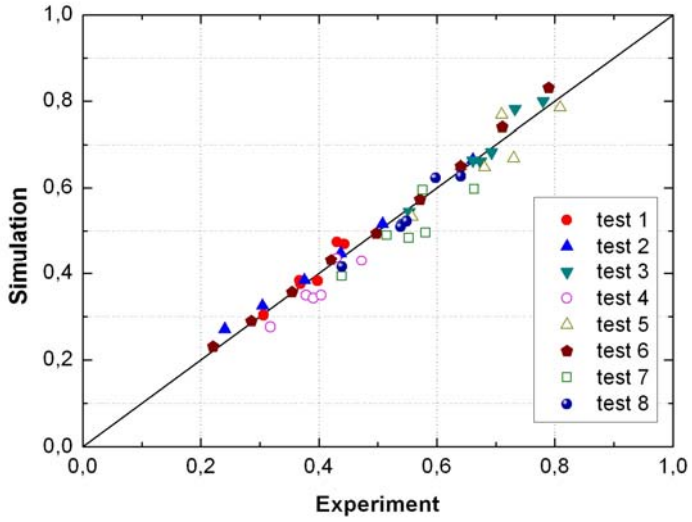

Figure 8. Experimental results in comparison to calculated reforming conversion rates.

CONCLUSIONS

This paper has presented experimental and numerical studies on the fuel reforming process on an Ni/YSZ catalyst. The gas mixture composition and the flow rate were measured at the outlet of the reformer to establish the methane reforming rate and kinetics of the reforming reaction. The experimental setup was built to investigate results for different thermal boundary conditions, the fuel flow rate and the steam-to-methane ratios. The reforming rate equation derived from experimental data was used in the mathematical model to predict the synthetic gas composition at the outlet of the reformer for the isothermal fuel reforming process. It was shown that the results of numerical computations fit the experimental data well. The obtained results show how important parallel, numerical and experimental studies are in the process design of SOFC reformers. It was also shown that applying a combined approach leads to the successful prediction of the outlet gas composition for different modelling conditions.

ACKNOWLEDGMENTS

This research was partially supported by the European Commission (project Dev-BIOSOFC, FP6-042436, MTKD-CT-2006-042436).

REFERENCES

1. Xu J., Froment G.F., Methane steam reforming; methanation and water-gas shift: I intrinsic kinetics, AIChE Journal, vol. 35, pp 88-96, 1989
2. Xu J., Froment G.F., Methane steam reforming; II Difusional limitations and reactor simulation, AIChE Journal, Vol 35, pp 97-103, 1989
3. Lee A.L, Zabransky R.F., Huber W.J., Internal Reforming Development for Solid Oxide Fuel Cells, Ind. Eng. Chem. Res., Vol. 29, pp 766-773, 1990
4. Achenbach E., Methane/steam reforming kinetics for solid oxide fuel cells, J. Power Sources, vol. 49, pp 333-348, 1994
5. Odegard R., Jornsen E., Karoliussen H., Methane reforming on Ni/zirconia SOFC anodes, M. Dokiya, O Yamoto, H. Tagawa, S.C. Singhal Eds., Proc. 4th International Symposium on Solid Oxide Fuel Cells, Penninyton, NJ, pp 810-819, 1995
6. K. Ahmed, K. Foger, Kinetics of internal steam reforming of methane on Ni/YSZ-based anodes for solid oxide fuel cells, Catalysis Today, 63 (2000) 479-487
7. K. Eguchi, in: K. Suzuki (Eds.) International Workshop on Fuel Cell and Fuel Cell Hybrid Systems, Energy Flow Research Center, Research Organization for Advanced Engineering, Tokyo, (2004) 13.
8. S. Nagata, A. Momma, T. Kato, Y. Kasuga, Numerical Analysis of output characteristic of tubular SOFC with internal reformer, J. Power Sources, 101 (2001) 60-71.
9. D. Sekine, Experimental study on the steam reforming for small-scale SOFC, *Bachelor Thesis*, Tokyo University, 2005 (in Japanese)
10. Suzuki K., Iwai H., Nishino T., in: Suden B., Faghir M. (Eds.), Transport Phenomena in Fuel Cells, WIT Press, Lund, p. 95, 2005

Micro- and Nano- scale Systems

SURFACE TENSION DOMINATED CONDENSATION IN MICROCHANNELS

H. S. Wang, J. W. Rose *
Queen Mary, University of London, Mile End Road, London E1 4NS, UK

ABSTRACT. A wholly theoretical model for condensation in rectangular and triangular cross section microchannels has been developed by the authors (Wang and Rose [5]). This takes account of the effects of gravity, streamwise shear stress on the condensate surface and, most importantly, the transverse pressure gradient due to surface tension in the presence of change in condensate surface curvature. Numerical results have been generated for various channel shapes, sizes, fluids, vapour-to-surface temperature differences and vapour mass fluxes. It is found that, over a certain length of channel, the local mean (around the channel perimeter) heat-transfer coefficient is essentially independent of gravity (including inclination of the channel) and surface shear stress and depends only on surface tension. Dimensional analysis for the surface tension dominated region leads a relation between the Nusselt number and a single dimensionless group analogous to that occurring in the simple Nusselt theory except that the gravity is replaced by surface tension. Data for 7 fluids, 5 temperature differences, 7 channel geometries and 5 channel inclinations are well correlated by a Nusselt-like equation with Nusselt number dependant on one dimensionless group involving surface tension and vapour-to-surface temperature difference. This is a step towards the objective of summarising the results of numerical solutions for the whole channel, including those positions along the channel where gravity and shear stress also play important roles, by algebraic equations.

Keywords: *Condensation*, *Microchannel*, *Surface tension*, *Theory*, *Correlation*

INTRODUCTION

Refrigeration and air conditioning, account for a significant proportion of electricity usage, and consequently for fuel consumption and associated CO_2 emissions. Improvement in design and performance of refrigeration plant can make a significant contribution to mitigation of these problems. Condensers employing microchannel tubes such as those shown in Fig. 1 have been used successfully in automotive air conditioners for around 20 years and have proved both compact and effective.

Fig. 1 Multi-port extruded tube, Koyama et al. [1]. Typical channel dimension around 1 mm.

Available experimental heat-transfer data for condensation in microchannels are relatively few and widely scattered. Vapour-side, heat-transfer coefficients have, with a few exceptions (Koyama et al. [1], Cavallini et al. [2] generally been inferred from overall measurements by subtraction of thermal resistances and/or using "Wilson plot" techniques; such data have high uncertainty.

* Corresponding author: Prof. John W Rose
Phone: + (44)-20-78825275, Fax: + (44)-20-89831007
E-mail address: j.w.rose@qmul.ac.uk

Four correlations based on data for R134a (Wang et al. [3], Koyama et al. [1], Cavallini et al. [2], Bandhauer et al. [4] and one theoretical solution (Wang and Rose [5]) have been proposed. For R134a the correlations have been shown (Su [6], Su et al. [7-8]) to be broadly in agreement with each other and with the theoretical solution (see Fig. 2). Wide differences are seen when the correlations and theory are used for other fluids as (see Fig. 3).

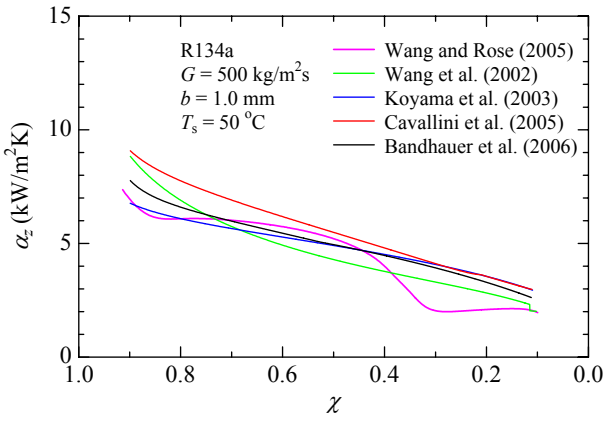

Fig. 2 Comparison of correlations and theory for R134a

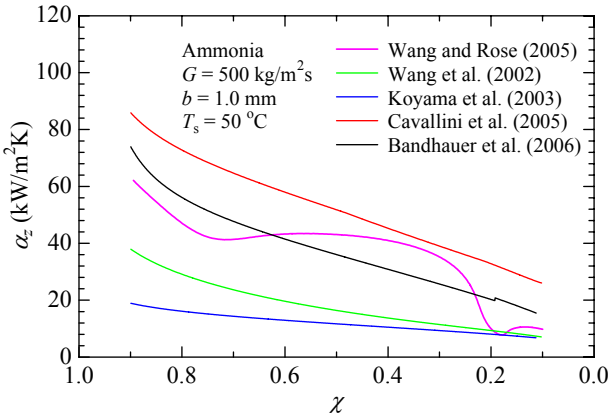

Fig. 3 Comparison of theory and correlations for ammonia

The theory has no empirical input and numerical solutions can readily be obtained for any fluid and any channel cross section with a vertical axis of symmetry. Solutions have been obtained for a range of channel geometries, fluids, mass fluxes, vapour-to-surface temperature differences and channel inclinations (Wang and Rose ([5, 9-11], Wang et al. [12], Su et al. [7-8]). The theory requires numerical solution of the differential equation for the condensate film thickness and consequently is not so convenient for use in design and optimisation as algebraic equations. The present paper describes an approach towards summarising theoretical results by approximate algebraic equations.

THEORY

The co-ordinate scheme for rectangular and triangular channels are shown in Fig. 4.

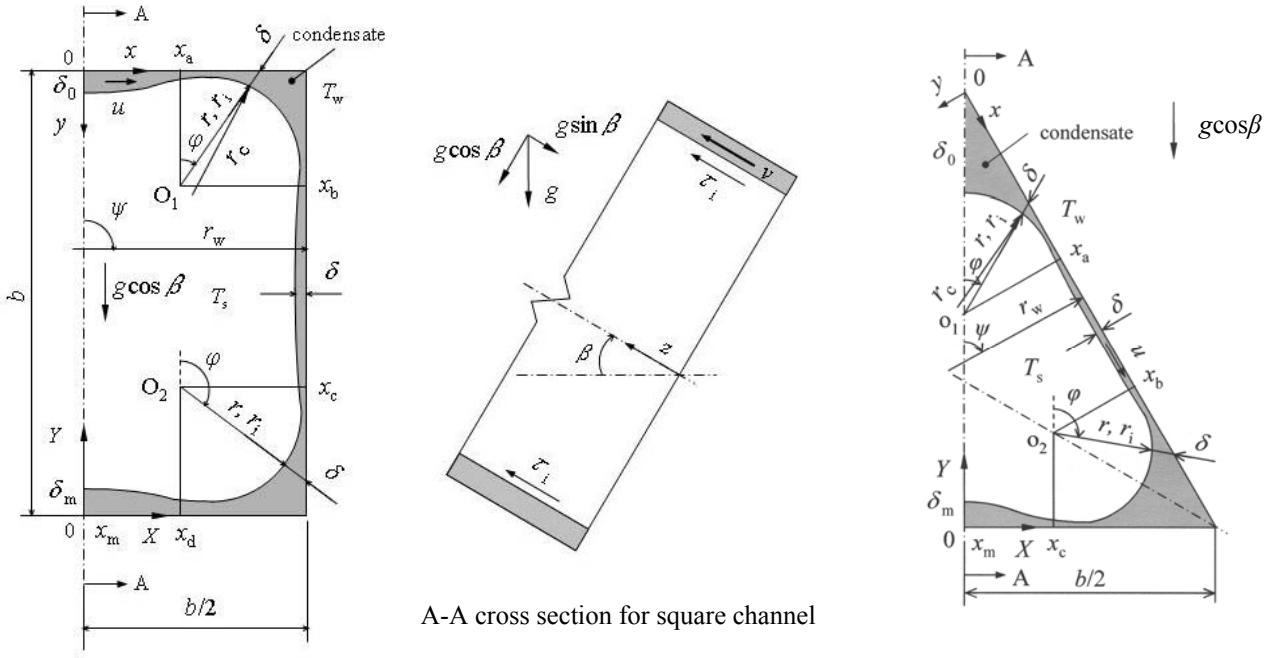

Fig. 4 Co-ordinate scam in the theory of Wang and Rose [5, 9]

When the transverse pressure gradient due to surface tension, and the streamwise shear stress on the condensate surface are included in an otherwise Nusselt treatment of the condensate film on the channel surface (see Wang and Rose [5, 9]) the differential equation for the condensate film thickness, δ, on the channel wall is found to be:

$$\frac{(\rho_l - \rho_v)g\cos\beta}{3\nu_l}\frac{\partial}{\partial x}(\delta^3\sin\psi) + \frac{\sigma}{3\nu_l}\frac{\partial}{\partial x}\left\{\delta^3\frac{\partial}{\partial x}\left(\frac{1}{r_c}\right)\right\} + \frac{1}{2\nu_l}\frac{\partial\left(\tau_i\delta^2\right)}{\partial z} - \frac{(\rho_l - \rho_v)g\sin\beta}{3\nu_l}\frac{\partial}{\partial z}\left(\delta^3\right)$$

$$-\frac{1}{3\nu_l}\frac{\partial}{\partial z}(\delta^3\frac{\mathrm{d}P_v}{\mathrm{d}z}) = \frac{1}{(1+\zeta\lambda_l/\delta)}\frac{\lambda_l(T_s - T_w)}{h_{fg}\delta} \qquad (1)$$

where

$$\frac{1}{r_c} = \frac{\partial^2\delta/\partial x^2}{\left\{1+\left(\partial\delta/\partial x\right)^2\right\}^{3/2}} \qquad (2)$$

z and x are the streamwise and transverse co-ordinates, T_s and T_w are the vapour and wall temperatures, τ_i is the streamwise surface shear stress on the condensate surface, P_v is the vapour pressure, ν_l and λ_l are the condensate kinematic viscosity and thermal conductivity, h_{fg} is the specific latent heat of evaporation, ζ is a minor correction term for the interface temperature discontinuity (see Wang and Rose [5]) and r_c is the radius of curvature of the condensate surface in the transverse plane.

Equation (1) is valid (to the same degree as the classical Nusselt theory) for the annular or annular/stratified flow regime. An equivalent equation in polar co-ordinates, used to treat corners and for a circular channel, is given by Wang and Rose [5]. Modified polar coordinate equations to include channel inclination are given by Wang and Rose [9]. Solution of Eq. (1) requires an estimate of the streamwise surface shear stress distribution on the condensate surface. In the solutions obtained to date this has been obtained using standard approximate methods (see Cavallini et al. [13]) which take account surface transpiration (condensation). The model has been used to predict a wide range of results for typical conditions. Results are found to be only marginally affected by moderate arbitrary changes in the streamwise shear stress so that the accuracy of the streamwise shear stress estimate is of secondary importance.

SURFACE TENSION DOMINATED REGIME

A particularly important finding is the fact that the solutions show the transverse (to the flow direction) pressure gradient due to surface tension dominates over both gravity and streamwise shear stress in certain circumstances. In this regime the mean (around the channel perimeter) heat-transfer coefficient remains virtually constant for some distance along the channel. When gravity is set to zero the heat-transfer coefficient in this regime is essentially unaffected. When the vapour flow rate is increased so as to increase the streamwise shear stress on the condensate surface, the heat-transfer coefficient is not increased, rather the length of channel over which the coefficient remains high is increased.

Figure 5 shows, for a triangular channel and for the conditions indicated, that the heat-transfer coefficient is essentially independent of gravity for distances from the channel inlet between about 80 mm and 210 mm. Figures 6a and 6b give solutions for different vapour mass fluxes for triangular and square channels. These indicate that, while the heat-transfer coefficient near the

channel inlet is affected by vapour mass flux (surface shear stress), there exist ranges of mass flux where the heat-transfer coefficient is essentially constant (independent of both vapour shear stress and gravity); the distances along the channel where this is so increases with increasing vapour mass flux. Fig. 7 demonstrates, for the case of the square channel, that the condensate film profiles are closely similar at z = 95 mm when G =300 kg/m^2 s and at z = 489 mm when G = 1000 kg/m^2 s. This is due to the fact that the vapour shear stress has appreciable effect on the liquid film near the corners while having little effect along the channel walls where the film flow is dominated by transverse surface tension generated pressure gradient.

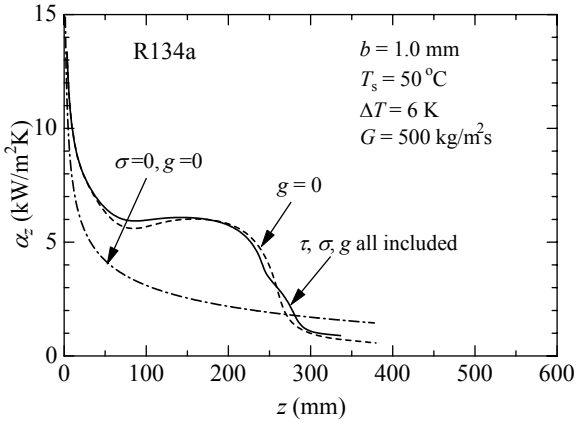

Fig. 5 Mean heat-transfer coefficient along upright triangular channel (Wang and Rose [5])

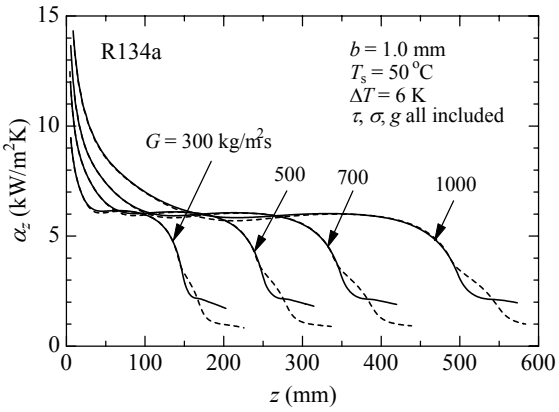

Fig. 6a Mean heat-transfer coefficient along triangular channel for different vapour mass fluxes (dashed line vertex up, solid line vertex down; Wang and Rose [5])

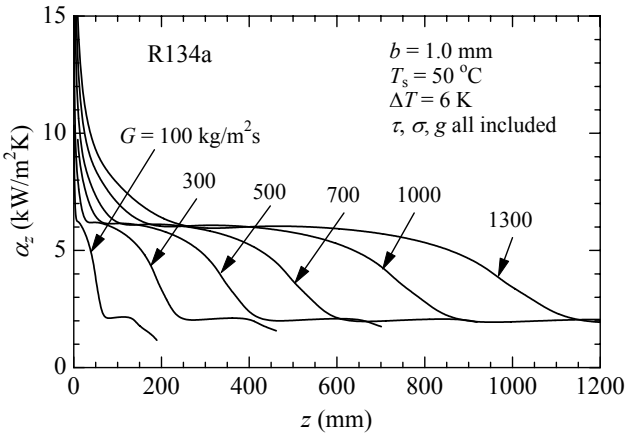

Fig. 6b Mean heat-transfer coefficient along square channel for different vapour mass fluxes (Wang and Rose [5])

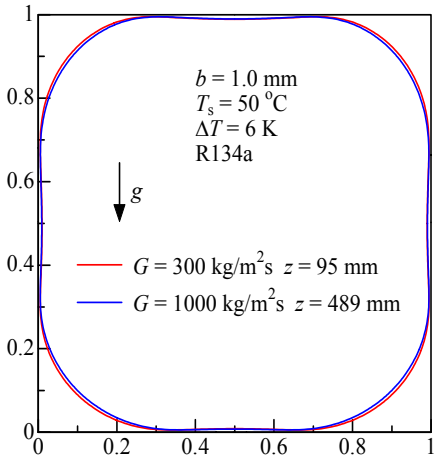

Fig. 7 Condensate film profiles at two vapour flow rates and two distances along thew channel

Figure 8 shows results for different vapour-to-surface temperature differences for a square channel. It is seen, that the heat-transfer coefficient is higher at low ΔT as expected owing to lower condensation rates and consequently thinner condensate films. It is also seen that the range of distance from the channel inlet over which the heat-transfer coefficient is essentially independent of z is larger at lower ΔT. Figure 9 gives results for square channels of different dimensions. Regions where the heat-transfer coefficient is essentially independent of gravity are identifiable for channels with side 2 mm or smaller. For larger channels it appears that the transverse surface tension effect is small. The heat-transfer coefficient where surface tension dominates increases strongly with decrease in channel dimension while the distance over which the coefficient remains high decreases with decreasing size due to flooding of the channel.

Figure 10 shows results for different channel inclinations. Again, a range of inclinations can be seen where the heat-transfer coefficient is independent of inclination for some distance along the channel. Figure 11 gives results for various fluids showing in all cases a range of distance where the heat-transfer coefficient is almost constant. This is least evident for the case of carbon dioxide.

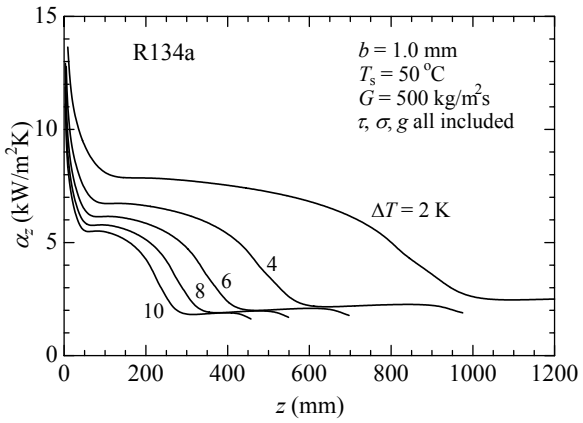

Fig. 8 Mean heat-transfer coefficients for square channel at different vapour-to-surface temperature differences (Wang and Rose [5])

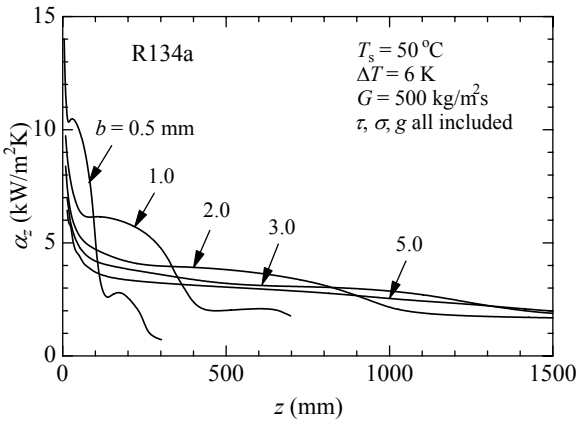

Fig. 9 Mean heat-transfer coefficients for square channels of different size (Wang and Rose [5])

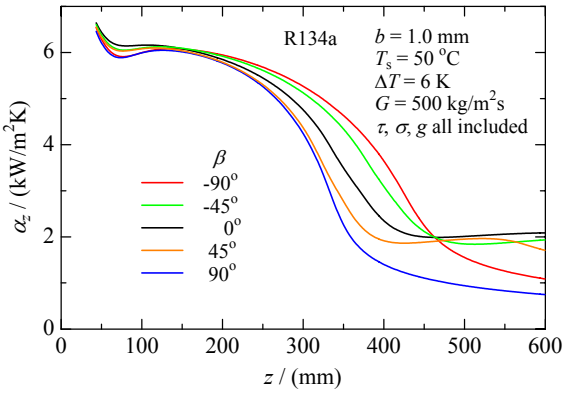

Fig. 10 Mean heat transfer coefficient for different channel inclinations (negative angles β indicate downflow) (Wang and Rose [9])

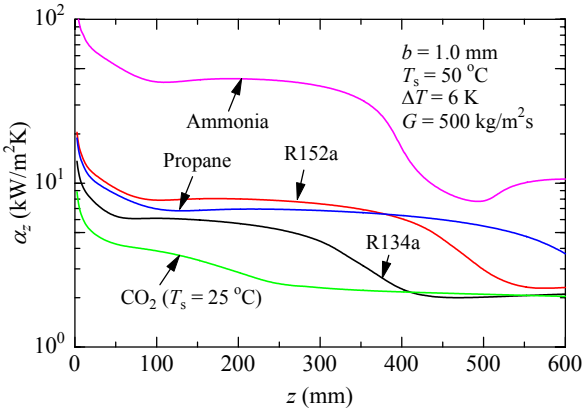

Fig. 11 Mean heat transfer coefficient for different fluids (Wang et al. [12])

DIMENSIONAL ANALYSIS FOR THE SURFACE TENSION DOMINATED PART OF THE CHANNEL

Here, as in the Nusselt problem, inertia and convective effects in the film are neglected together with gravity so that the mean condensate film thickness is governed by surface tension, viscosity and the rate at which liquid condenses on unit area of the surface V. Thus the effective mean thickness of the condensate may be written

$$\delta = \xi(\sigma, \mu, x, V) \tag{3}$$

where x is the relevant linear dimension.

Dimensional analysis then gives

$$\frac{\delta}{x} = f\left(\frac{\sigma}{\mu V}\right) \tag{4}$$

We now suppose, as is often done when correlating heat-transfer data, that this function takes the form

$$\frac{\delta}{x} = A\left(\frac{\sigma}{\mu V}\right)^{p} \tag{5}$$

where A and p are constants.

Then, as in Nusselt, we neglect convection in the condensate film and write

$$V = \frac{m}{\rho} = \frac{q}{\rho h_{fg}} = \frac{\lambda \Delta T}{\delta \rho h_{fg}} \tag{6}$$

Substituting volume condensation rate per area V in Eq. (5) and rearranging gives

$$Nu = C\left(\frac{\rho\, h_{fg} \sigma\, x}{\mu\, \lambda\, \Delta T}\right)^{n} \tag{7}$$

where $C = A^{1/(p-1)}$ (8)

and $n = p/(p-1)$ (9)

For the case of the triangular and square channel the relevant linear dimension is the side of the channel b so we have

$$Nu = C\left(\frac{\rho\, h_{fg} \sigma\, b}{\mu\, \lambda\, \Delta T}\right)^{n} \tag{10}$$

Values of the heat-transfer for the surface tension controlled region have been identified as closely as possible from all of the results obtained to date and plotted as shown in Fig. 12. (For rectangular channels the geometric mean of the lengths of the two sides has been used for b). It may be seen that the data for all cases (7 fluids, 7 channel geometries, 5 values of ΔT in the range 2-10 K) are satisfactorily fitted by

$$Nu = 1.43\left(\frac{\rho\, h_{fg} \sigma\, b}{\mu\, \lambda\, \Delta T}\right)^{1/4} \tag{11}$$

which may be compared with the Nusselt equation for gravity controlled condensation on a vertical flat plate

$$Nu = 0.943\left(\frac{g \Delta \rho\, h_{fg} L^{3}}{\mu\, \lambda\, \Delta T}\right)^{1/4} \tag{12}$$

where L is the height of a vertical condensing surface.

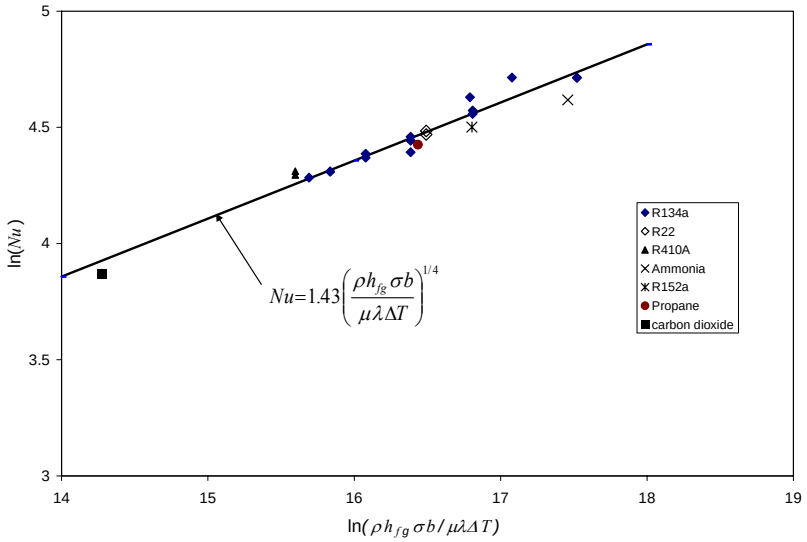

Fig. 12 Correlation of results for surface tension dominated region

CONCLUSION

For condensation in sufficiently small channels, solutions of the differential equation for the annular flow regime indicate ranges of the relevant variables where the transverse flow, due to the pressure gradient resulting for surface tension in the presence of surface curvature, dominates. For these circumstances, where gravity and streamwise shear stress on the condensate film due to vapour flow have negligible effect on the heat-transfer coefficient, a simple Nusselt-like correlation has been obtained. The same result has been found in an approximate analysis which does not invoke dimensional analysis (Wang and Rose [11]). This is a first step towards the objective of summarizing the theoretical results in the form of simple equations for ready use in design and optimization.

NOMENCLATURE

A	constant, see Eq. (5)
b	side length of channel
C	constant, see Eq. (7)
G	mass flux of vapour
g	specific force of gravity
h_{fg}	specific enthalpy of evaporation
m	condensation mass flux
n	constant, see Eq. (7)
p	constant, see Eq. (5)
P_v	vapour pressure
P_s	saturation pressure
q	heat flux
r_c	radius of curvature of the condensate surface in the channel cross-section, see Fig.4
r	radial polar co-ordinate, see Fig.4
r_i	distance from origins O_1 , O_2 to vapour-liquid interface, see Fig.4
r_w	radius of curvature of channel surface in the channel cross-section, see Fig.4
T_s	saturation temperature
T_w	tube wall temperature
u	condensate velocity along channel surface in x-direction or φ direction, see Fig.4
U_v	local bulk vapor velocity
V	volume condensation flux on condensate surface

v	condensate velocity along channel surface in z-direction, see Fig.4
x	linear dimension, see Eq. (4)
x, y	coordinates along and normal to channel surface, see Fig.4
x_a, x_b, x_c, x_d	x coordinates at the foot of the perpendicular from origins O_1 and O_2, see Fig.4
x_m	x coordinate at centre of bottom surface, see Fig.4
X, Y	fixed coordinates, see Fig.4
z	streamwise coordinate, see Fig.4

Greek symbols

α_z	average heat-transfer coefficient over perimeter of channel at location z
δ	condensate film thickness
ΔT	vapour-surface temperature difference
λ	condensate thermal conductivity
μ	condensate viscosity
ν	condensate kinematic viscosity
β	inclination of channel to horizontal
ρ	condensate density
σ	surface tension
τ	vapour shear stress at vapour-liquid interface
φ	angle, polar co-ordinate, see Fig.4
φ_a, φ_b, φ_c, φ_d	angles corresponding to x_a, x_b, x_c, x_d, see Fig.4
ψ	angle between the normal of channel surface and Y coordinate, see Fig. 4

REFERENCES

[1] Koyama, S., Kuwahara, K., Nakashita, K. and Yamamoto, K., (2003b), An experimental study on condensation of refrigerant R134a in a multi-port extruded tube, *Int. J. Refrig.*, **24**, 425-432.

[2] Cavallini, A., Del Col, D., Doretti, L., Matkovic, M., Rossetto, L. and Zilio, C., (2005), A model for condensation inside minichannels, Proc. of HT05 National Heat Transfer Conf., ASME, San Francisco, paper HT2005-72528.

[3] Wang Wei-Wen, W., Radcliff, T. D. and Christensen, R. N., (2002), A condensation heat transfer correlation for millimetre-scale tubing with flow regime transition, *Experimental Thermal and Fluid Science*, **26**, 473-485.

[4] Bandhauer, T. M., Agarwal, A. and Garimella, S., (2006), Measurement and modelling of condensation heat transfer coefficients in circular microchannels, ASME J. Heat Transfer, 128(10), 1050-1059.

[5] Wang, H. S. and Rose, J. W. (2005). Film condensation in microchannels – a theoretical model for rectangular section. *Trans. ASME J. Heat Transfer*, **127**, 1096-1105.

[6] Su, Q., 2007, Experimental investigation of condensation in microchannels. PhD Thesis, Univ. London.

[7] Su, Q., Yu, G. X., Wang, H. S. and Rose, J. W., 2008, Correlations and Theory for Microchannel Condensation, 6th Int. Conf. on Nanochannels, Microchannels and Mini-channels, 19-21 June, Germany.

[8] Su, Q., Yu, G. X., Wang, H. S. and Rose, J. W., (2009), Microchannel Condensation: Correlations and Theory, Int. J. Refrig., under review.

[9] Wang, H. S. and Rose, J. W. (2006a), Film condensation in microchannels: effect of tube inclination. Proc. Fourth ASME International Conference on Nanochannels, Microchannels and Minichannels. June 19-21, 2006 Limerick, Ireland. Paper ICNMM2006-96049.

[10] Wang, H. S. and Rose, J. W. (2006b). Film condensation in horizontal microchannels. Int. J. Thermal Sciences, **45**, 1205-1212.

[11] Wang, H. S. and Rose, J. W. (2009), Correlation of theoretical results for condensation in microchannels, in preparation.

[12] Wang, H. S., Ding, J and Rose, J. W. (2007). Heat transfer during annular film condensation in microchannels: calculations for R152a, R134a, R22, R410, propane, ammonia and carbon dioxide. Proc. 6th Int. Conf. on enhanced, compact and ultra compact heat exchanger: ECI. Potsdam, 12-16 Sept.

[13] Cavallini, A., Del Col, D., Doretti, D., Longo, G. A. and Rossetto, L. (1999), A new computational procedure for heat transfer and pressure drop during refrigerant condensation inside enhanced tubes, J. Enhanced Heat Transfer, **6**. 441-446.

TURBULENCE IN MICRO-CHANNELS

T. A. Kowalewski*, S. Blonski
IPPT PAN, Polish Academy of Sciences, Warsaw, Poland

ABSTRACT. Fluid mechanics in small channels, i.e. channels of micrometer size, is dominated by surface effects and often exhibits striking differences of flow characteristics when compared with macro scale. One of important microfluidic problems is flow destabilization and occurrence laminar-turbulent transition. In this paper we describe our experimental and numerical attempts to understand growth of flow instabilities and development of turbulent structures in small channels. In the first configuration flow of water through 1mm long and 0.4mm high microchannel formed between two planes is investigated varying Reynolds number from 1000 to 6770. Fluorescent traces are used for flow visualization and microPIV acquisition of temporary velocity fields. The microPIV data are used to evaluate turbulent flow characteristics. Our experimental study shows that destabilization of flow in such a micro-channel does not necessarily occurs when it is usually expected. Nearly laminar flow structure is present within the channel even for the highest investigated flow Reynolds number. These findings are confirmed by numerical simulation performed using finite volume code.
On the other hand it appears possible to achieve unstable flow pattern even for quite low Reynolds number flow regime by proper modification of the channel walls. In the second experimental and numerical study we demonstrate that appropriately chosen wall waviness of the micro-channel may lead to flow destabilization already at quite low flow Reynolds number (~100).

Keywords: *microchannels, microPIV, turbulence, flow instability*

INTRODUCTION

The advances of microfluidics allow for the manufacturing micro-reactors, micro-scaled cooling devices or small liquid atomisers. These devices are characterised by a large surface-to-volume ratio, hence provide possibility for larger heat fluxes or offer large catalytic surface for reactions. In most of these applications flow unsteadiness or turbulence is desirable, however not easy to achieve in small scales. The design and optimisation of microfluidic devices is usually based on our knowledge gained for macro scale hydrodynamics. However, it can be expected that small channel hydrodynamics has to be reconsidered in different contexts: relative large surface area can be responsible for delayed (or accelerated) laminar-turbulent transition [1-8]; wall roughness becomes elevated relative to small channel size and may influence laminar-turbulent transition [9]; appropriate wall corrugation can be used to activate flow instability and effectively diminish critical Reynolds number [10].
In spite of the existence of numerous experimental and theoretical investigations, a number of principal problems related to laminar-turbulent transition in micro scales are not fully resolved. There are contradictory data on transition from laminar to turbulent flow. Some studies indicate that the transition from the laminar to the turbulent flow in micro-scale passages takes place at critical Reynolds numbers, ranging from 300 to 2000. The reported values are lower than those known from the conventional theory for large-size tubes. In particular, Wu and Little [1,2] experimentally observed that in glass and silicon microchannels having hydraulic diameters between 45.5 μm and

* Corresponding author: Prof. T.A. Kowalewski
Phone: + (48)-22-8269803, Fax: + (48)-22-8269815
E-mail address: tkowale@ippt.gov.pl

83.1 μm, the flow was laminar for Re < 1000 and became fully turbulent for Re > 3000. Choi et al. [3], analysing microtubes with a hydraulic diameter of 53 μm and 81.2 μm, indicated that the transition to turbulent flow occurs at Re = 2000. However, they found that this value decreases for smaller microchannels (Re = 500 for D_h = 9.7 μm and 6.9 μm). These and following measurements were performed by employing "classical" experimental methodology, i.e. detecting global effects like pressure drop, heat fluxes or mixing effectiveness. In small channels entrance effects and probe size may largely modify measurements, as indicated by Celata et al. [4]. Only quite recently it appeared possible to acquire detailed information on the temporary velocity flow fields within micro channel. Time-dependent measurements of the velocity field within microchannels by means of the microPIV technique have been performed to access the laminar/turbulent transition range [5-8]. These measurements, in principle, are able to resolve not only the integral information on the laminar/turbulent transition, they can, moreover, provide local information on both mean and fluctuating velocity contributions. Hence, information on the developing flow, on the spatial distribution of the mean flow, on the spatial distribution of turbulent fluctuations and stresses, and on the intermittent flow is accessible. Li et al. [5] measured time-dependent velocity fields in a rectangular microchannel of 320 x 330 μm^2 cross section. They discuss profiles of the mean axial velocity, of the axial and transversal velocity fluctuations, and reported good agreement with findings known for macroscopic channels. Quite recently Wibel and Ehrhard [6] in their very careful microPIV study of velocity fluctuations confirmed that the laminar/turbulent transition in 133μm channels occurs in the range $1900 \leq Re \leq 2220$, in reasonable agreement with macroscopic findings. Moreover, the profiles of the turbulent quantities are reported in good agreement with findings within macroscopic channels. All reported investigations deal with well developed flow in a long channel. However, due to high pressure drop only very short micro channels can be used in practical realization. In our micro-PIV study of high Reynolds number flow in very short micro channel [7,8] delayed occurrence of turbulence was reported. This finding is subject of the present paper as well.

The occurrence of laminar/turbulent transition can be strongly modified by wall roughness, which becomes an issue for small channels [9]. On the other hand it was predicted by Szumbarski [10,11] that controlled wall waviness may lead to flow destabilization already at Reynolds number close to 100. The outcome of our numerical and experimental study of this remarkable feature is reported in the second part of the present paper.

EXPERIMENTAL

Apparatus

The main part of the experimental set-up consists of a microscope, a laser light source and a digital camera. The flow is observed using 10x (NA 0.3 / WD 17.30 mm) microscope lens and area covered by the camera is *854 μm x 683 μm.* Short illumination time is achieved by using a pulsed light of Nd:YAG laser, delivering 30 mJ energy at 532 nm wavelength (New Wave Research, Inc.). The flow is illuminated and observed through the upper window of the channel. By traversing the field of observation in the horizontal and vertical direction, the position of the interrogated flow plane was selected. For the recording of images a high-resolution (1280 x 1024 pixels) 12bit *PCO SensiCam* camera was used. When coupled with the double pulse laser the system permits acquisition of two images at the minimum time interval of 200 ns, exposition time of 5 ns, and about 3.75 Hz repetition rate. The micro-PIV measurements were performed for pure water seeded with fluorescent tracers, polystyrene spheres of 2 μm in diameter (Duke Scientific Inc.). The particle volumetric concentration was very low (<0.0001%wt), hence they did not affect the flow structure. Unlike typical PIV methods, microPIV does not utilize a thin laser sheet to illuminate the seeding particles [12]. The whole investigated volume is flooded with the laser light using beam expander and the microscope objective. Two low pass filters, mounted between the objective and the camera, permit only the fluorescent red light to pass, while preventing the green laser light to be detected by the camera. The micro-PIV images present well detectable bright spots of the seeding

particles. The accuracy of the velocity measurement depends on several experimental factors (quality of the images, seeding concentration, particle displacement), as well as on the vector evaluation procedure. Using in house developed software and by evaluating uniform, predefined flow of water through the micro-channel, the error of velocity measurement was estimated to be below 5%.
In most cases the flow was driven by the micro pump (Cole-Palmer Inst.) permitting flow rate variation from $Q_V = 0.02$ cm^3/s to 70 cm^3/s. For the highest measured flow rates (200 cm^3/s) pressurized supplying system was used [7].

Short channel turbulence
The flow of pure water was studied using in a flat model of an emulsifier, described already in details [7,8]. It consists of a small channel formed between two glass plates and a triangular processing element creating the rapid flow contractions (Fig. 1). Dimension of the two gaps created between glass plates and processing element (triangular obstacle) are 0.4mm in height, 1mm in length and 15mm in width. The flat geometry and two glass windows permit application of optical methods for measuring flow velocity fields (microPIV method) within the gap (P_1,$P_{1\text{-}2}$,P_2) as well as nearly 4 mm upstream (P_0) and 3mm, 5mm, and 8mm downstream (P_3,P_4,P_5). The flow rate used varied from *16 to 204 cm^3/s*, and the corresponding Reynolds number based on the microchannel height varied from *1000 - 6770*. For the highest flow rate the both symmetrical microchannels (upper and lower gap) were supplied, whereas in other cases only interrogated upper gap was open for the flow.

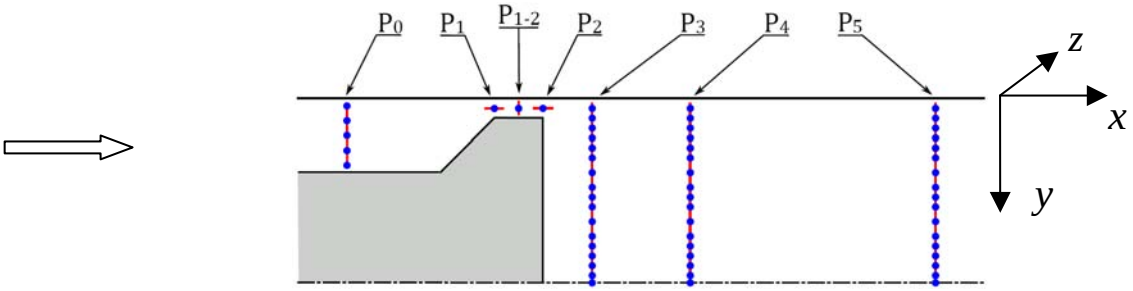

Figure 1. Schematic drawing of the channel and locations P_0 - P_5 interrogated by the PIV method. The flow is driven from left to right. Distances are measured from the gap exit (*x = 0*) and the top wall (*y=0*). At location P_0 (*x = -4 mm*) PIV covers 5 planes between top and bottom wall; at P_1 and P_2 PIV interrogation planes are in the mid-height of the gap (*y = -0.2 mm*), covering partly gap inlet and outlet, respectively; at $P_{1\text{-}2}$ measurements are located in the middle of the length of the microchannel (*x = -0.5 mm*) and cover three vertical positions *y = -0.1 mm*, *y = -0.2 mm* and *y = -0.3mm*. P_3 - P_5 indicate location of PIV interrogation planes used to measure velocity distribution from the top wall to the flow axis (*y = 0 : -3.75 mm*). They are located at distances *x = 1 mm* (P_3), *x = 3 mm* (P_4), and *x = 8 mm* (P_5) from the gap exit.

Corrugated wall
A simple model of the wavy channel formed between two plates has been machined in polycarbonate using micro-machining technique. The average channel height is *793 µm*, its width is *33.6 mm*, and the length *75 mm*. Surface of the bottom wall is modulated by 20 rows (comp. Fig. 2). They create spanwise periodic structure with channel depth varying from *0.4mm* to *1mm*. The upper wall of the channel is flat to permit optical measurements. An average flow velocity in the corrugated channel varied from about *0.76 mm/s* to *2.6 m/s*, which corresponds to Reynolds number based on the average channel height *Re=0.6* and *Re=2100*, respectively. The channel length is probably too short to allow for fully developed flow instabilities to occur spontaneously. However, it is assumed that initial spanwise flow disturbances generated by the strongly divergent flow inlet may become amplified by the wall waviness, if the theoretical prediction [10,11] is correct. The

microPIV velocity measurements and the flow visualisation of single florescent traces are done. These experiments aim identification of the critical Reynolds number. The microPIV measurements provide quantitative data about development of flow field disturbances. Long time exposure of single florescent traces are used to indicate possible spatial fluctuations of observed streaklines.

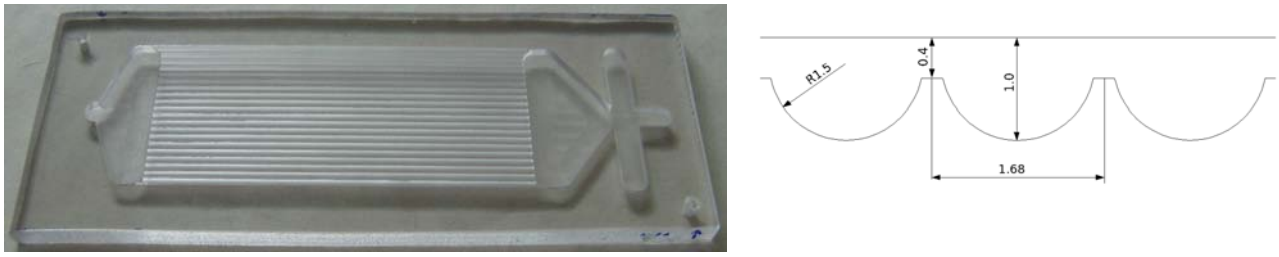

Figure 2. Left: experimental channel with 20 spanwise wall corrugations. The top wall is flat for better optical access; right: cross section of the channel with dimensions of the corrugations (in mm).

NUMERICAL

Finite–volume package Fluent 6.3 (Ansys Inc.) is used to generate the computational grid and to perform stability analysis using unmodified three-dimensional set of Navier-Stokes equations (DNS). The DNS model allows obtaining accurate, unsteady solution of unmodified Navier-Stokes equations by resolving the whole range of spatial and temporal scales of the turbulence. In our case the main aim of the simulation is to identify presence of instability modes and the critical Reynolds number for their amplification. All the spatial scales of the turbulence must be resolved in the computational mesh. Hence, very fine mesh and small time steps are used (typical 10^{-7}s). The direct numerical simulation (DNS) performed with the classical finite volume code implemented in *Fluent* is time consuming and vulnerable. Nevertheless, it appeared that for both investigated geometries it was possible to obtain reasonable solutions reproducing typical for the turbulence flow characteristics.

Short microchannel. The numerical domain used in the simulations of flow in the short microchannel describes full 3D geometry of the whole device, including 97.5 mm long inlet and 78.5 mm long outlet. Preliminary estimation of the Kolmogorov scales shows that smallest flow structures should be about 1μm in size with time scale below 1μs. According to this estimation structural hexahedron mesh with boundary layer was generated in the gap and in the vicinity of the processing element. The tetrahedron mesh was used in the remaining parts of the computational domain. It was found that sufficient accuracy of the numerical model was obtained for the gap mesh of 50x60x50 nodes (smallest distance between gap mesh nodes was about 3μm), fine enough to resolve expected Kolmogorov microscale. The total number of computational cells for the whole domain was over 1.7 mln. Detailed parameters used for modeling flow in the short microchannel are those collected in [8]. Simulations performed covered four flow rates, corresponding to the microchannel Reynolds number 1000, 1800, 3300 and 6770.

Corrugated wall. Numerical simulation of instabilities growth in the channel must assume long enough (theoretically infinite) channel length. Hence, computational domain used for simulating flow in the corrugated channel assumed periodic boundary conditions for the inlet and outlet. For the spanwise direction two sets of performed computations included either periodic boundary conditions or two side walls limiting computational domain [11]. For the first case (fully periodic boundary conditions) total number of elements was about 0.4mln. Inclusion of side walls increased this number from 0.7mln for five corrugation periods to 23.4mln elements for full 20 periods of wall corrugation. The last configuration reproduces the experimental geometry. However, due to

prohibitive computational time most of the numerical solutions are obtained for fully periodic computational domain or domain with five periods of corrugation limited by two side walls.

RESULTS

Short microchannel

In order to quantify the turbulence in the channel, the ensemble-averaged velocity fields are calculated at each of seven selected location before, within, and behind the microchannel (Fig. 1). Measurements were repeated up to hundred times at the same position to obtain sufficient statistics [8]. With 5 flow rates, 70 areas interrogated by microPIV measurements, and in average 50-100 measurements taken for each position, the total number of evaluated flow fields exceeds 50,000.

Velocity measurements performed at two positions P_1 and P_2 within the gap indicate that the flow through the gap is practically laminar, even for the highest applied flow rate no large temporal flow field fluctuations could be found. The streamwise velocity of the flow rapidly increases in the vicinity of the entrance to the gap, but turbulent fluctuations remain low despite high flow Reynolds number (6770). Velocity measurements at the gap exit (P_2) show development of the first instabilities (Fig. 3a). Behind the gap streamwise flow velocity decreases and strong recirculation zone with the reversal of flow can be found in the region behind the processing element [7,8]. The turbulent fluctuations of the velocity field and break-up of the flow symmetry, observed in this region, indicate that probably transition from laminar to turbulent flow regime occurs there.

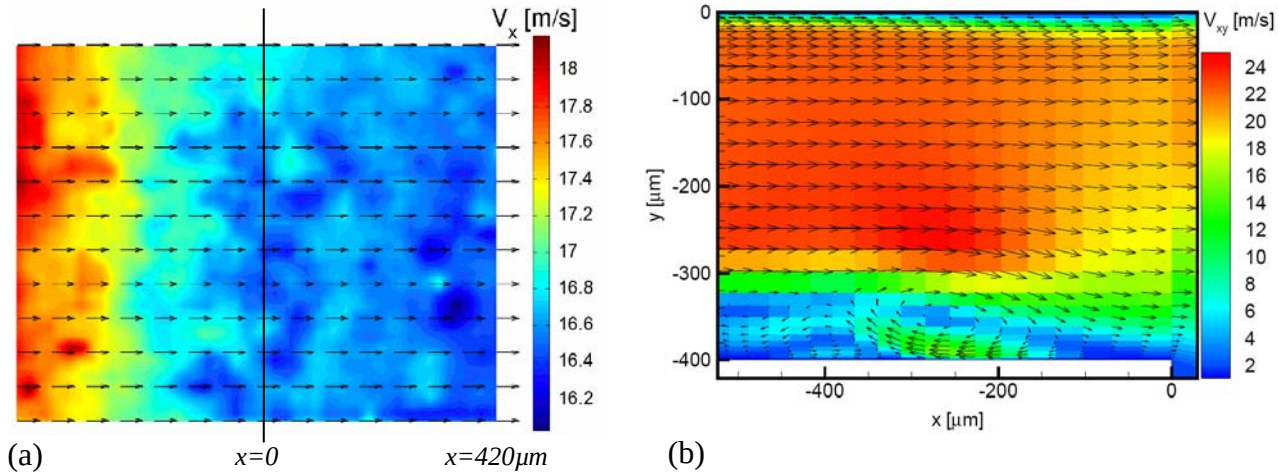

Figure 3. (a) - flow structure measured by micro-PIV at the *x-z* horizontal plane located in the mid-height (*y=-0.2 mm*) of the outlet region of microchannel (half of the field covers region in the microchannel and half behind it). (b) - temporary flow structure at the vertical symmetry plane of outlet region of the microchannel obtained form DNS simulation. Contours colored by the velocity magnitude.

Numerical modeling confirms main details of the velocity flow field measured by the micro-PIV method. For the highest flow rate a small vortex in the bottom part of microchannel outlet region (Fig. 3b) could be found. It indicates place where flow destabilization is initiated, propagating downstream to the outer region. Both experimental data (Fig. 4a) and DNS simulations (Fig. 4b) indicate that intensity of turbulence (turbulence energy tke_{xz}) remains relatively low before and in the microchannel, rapidly increasing downstream from the gap. However, the turbulent kinetic energy values estimated form the numerical model and from the PIV measurement are only in a qualitative agreement (Fig.4b). Visible quantitative differences are believed to be mainly due to limited accuracy of the micro-PIV measurements and missing data for the third velocity component (comp. [7,8]).

The numerical data are used to reevaluate Kolmogorov microscales within the microchannel. It appears that even for the highest Reynolds number Kolmogorov length and time scales amount within the gap about 1mm and 1s, respectively. It confirms experimental findings that in spite of relatively high Reynolds number the velocity fluctuations are very small and flow within the microchannel seems to be laminar.

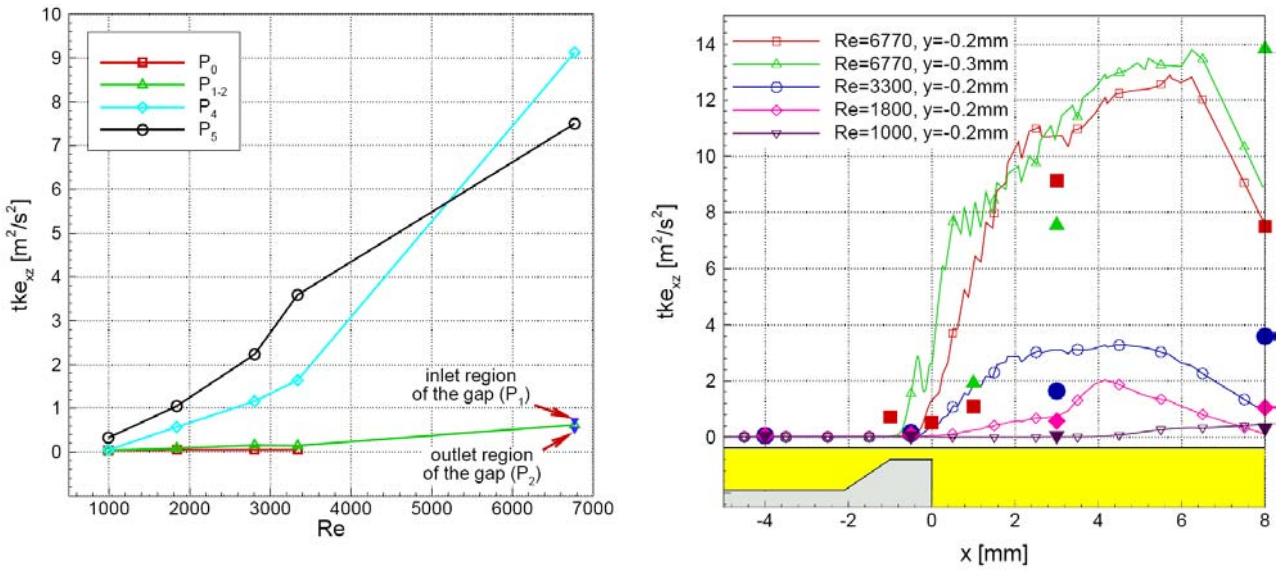

(a) (b)

Figure 4. (a) - turbulent kinetic energy tke_{xz} as a function of Reynolds number evaluated from the PIV data *0.2 mm* below the top wall (*y = -0.2 mm*) at 4 different locations along the experimental model ($P_0 – P_5$); (b) – variation of turbulent kinetic energy tke_{xz} evaluated from DNS results along the computational domain, given for two vertical positions: *y=-0.2 mm* (red line) and *y=-0.3 mm* (green line) below the top wall. Filled symbols indicate corresponding experimental data.

Corrugated wall

The transversal flow disturbances are generated across the whole channel width, interacting in a complex way with all 20 corrugations (Fig. 2). Flow pattern in the corrugated channel was visualized using long time exposure (120 ms) of single florescent traces. These experiments allow for fast identification of the critical Reynolds number. At low flow rates the particle tracks exhibit straight lines. Increasing flow rate the wavy character of particle tracks reveals emerging transversal flow disturbances. Our preliminary experimental study [11] shows that transversal velocity fluctuations can be visualized by particle tracking at least for the flow Reynolds number *Re = 120* (Fig. 5). The wavy motion of the tracer implies presence of the transversal velocity component.

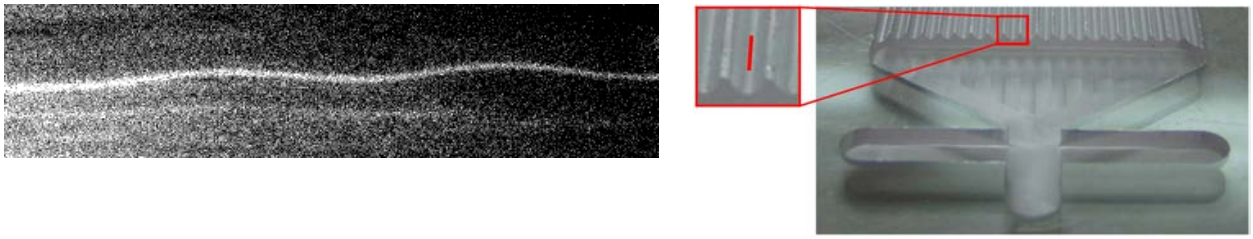

Figure 5: Left: trace of the fluorescent particle recorded in the corrugated channel (Fig. 2). The image width corresponds to 0.3mm, illumination time is *0.12s*, flow Reynolds number *Re = 120*. Right: position in the channel, where particle trace was recorded.

Micro-PIV measurements performed within the channel were used to obtain the flow disturbances. Proper understanding of the full structure of the analysed flow needs recombination of several sets of single flow fields obtained at different locations across the channel, and at its different depths. The typical disturbed velocity field structure obtained by means of micro-PIV is given in Fig. 6a. The mean flow is subtracted to reveal transversal velocity components. Due to the small interrogated flow area (0.85 mm x 0.68 mm) only flow in the vicinity of a single corrugation can be shown. Nevertheless, one may find that local spanwise flow disturbances are present, indicating emerging flow instabilities.

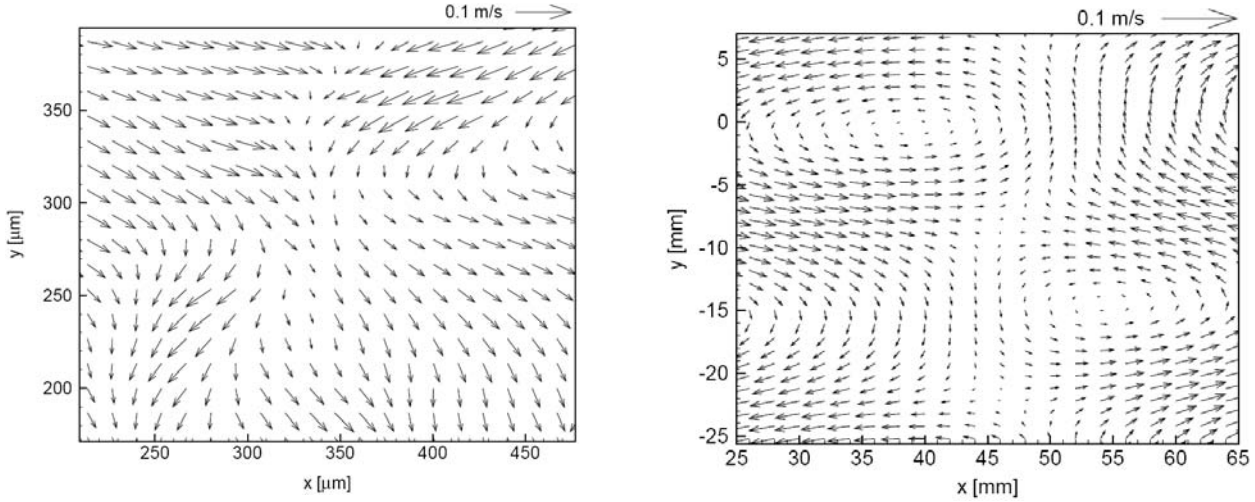

Figure 6. (a) Velocity field fluctuations measured in the corrugated channel *0.2 mm* below the upper wall, Reynolds number *Re = 200*; (b) - flow fluctuation predicted by the numerical simulations for the symmetry plane, flow Reynolds number *Re = 100*.

Numerical simulations performed for the corrugated channel confirmed generation of transversal instability modes for flow Reynolds number as low as *100*. It was found that for the flow with Reynolds number *Re = 100* small initial flow disturbances are quickly amplified and after about 200 s fully developed unsteady flow is observed [11]. The flow velocity field extracted from the numerical solution for the channel central cross-section (Fig. 6b) well reproduces predicted by the linear stability analysis space periodic counter-rotating vortices [10] travelling in the streamwise direction. It seems evident that the introduced wall waviness generates spanwise instabilities propagating along the channel and disturbing the flow structure. The new unstable flow pattern, which emerges form the unstable mode have complex three-dimensional structure promoting mixing properties of the channel flow. It is interesting to note that numerical model indicates that presence of the side walls (confined channel) does not significantly change this picture.

CONCLUSIONS

Experimental and numerical investigations demonstrated that flow pattern within the short, nearly two-dimensional microchannel remains laminar even for Reynolds number well above 6000. Obviously small channel dimensions are responsible for damping the development of classical cascade of turbulent vortices. This fact may have an important impact on design of emulsifiers [8], or microchannel heat exchangers. On the other hand it is shown that proper modification of the micro-channel walls may lead to flow destabilization already at Reynolds numbers about 100. This effect predicted by the theoretical study [10] is confirmed both numerically and experimentally.

NOMENCLATURE

tke_{xz}	$= \left\langle V_x'^2 \right\rangle + \left\langle V_z'^2 \right\rangle$, Turbulent Kinetic Energy for x - z horizontal plane [m^2 s^{-2}].
Re	Reynolds number based on the channel height.
Q_V	volumetric flow rate [m^3 s^{-1}].
$V_{x,y,z}$, $V'_{x,y,z}$	components of the velocity and of the fluctuating part of the velocity, respectively.
x, y, z	coordinates along the channel, across the channel, and perpendicular to channel cross-section in Fig. 1; x - z PIV interrogated planes.

ACKNOWLEDGMENTS

This investigation was supported by the Polish Ministry of Science and Education under project *Enhancement of the mixing process in micro-flows,* grant No.: N501008733.

REFERENCES

1. Wu P., Little W. A., Measurement of Friction Factors for the Flow of Gases in Very Fine Channels used for Microminiature Joule-Thompson Refrigerators, *Cryogenics*, vol. 23, pp. 273–277, 1983.
2. Wu P., Little W.A., Measurement of Heat Transfer Characteristics of Gas Flow in Fine Channel Heat Exchangers Used for Microminiature Refrigerators, *Cryogenics*, vol. 24, pp. 415–420, 1984.
3. Choi S.B., Barron R. F., Warrington R. O., Liquid Flow and Heat Transfer in Microtubes, Micromechanical Sensors, Actuators and Systems, *ASME DSC*, vol. 32, pp. 123–128, 1991.
4. Celata G.P., Cumo M., McPhail S., Zummo G., Characterization of Fluid Dynamic Behavior And Channel Wall Effects in Microtubes, *Int. J. Heat Fluid Flow*, vol. 27, pp. 135-143, 2006.
5. Li H., Ewoldt R., Olsen M.G, Turbulent and Transitional Velocity Measurements in a Rectangular Microchannel Using Microscopic Particle Image Velocimetry, *Exp. Therm. Fluid Scie.*, vol. 29, pp.435-446, 2005.
6. Wibel W., Ehrhard P., Experiments on the Laminar/turbulent Transition of Liquid Flows in Rectangular Microchannels. *Heat Transfer Eng.*, vol. 30 pp. 70-77, 2009.
7. Kowalewski T.A., Błoński S., Korczyk P., Turbulent Flow in a Microchannel, *Proc. of ASME ICNMM2006,* CD-ROM paper 96090, pp. 1-10, University of Limerick, Ireland, 2006.
8. Blonski S., Korczyk, P.M., Kowalewski T.A., Analysis of Turbulence in a Micro-channel Emulsifier, *Int. J. Therm. Scie.*, 46, pp. 1126-1141, 2007.
9. Kandlikar S.G., Roughness Effects at Microscale – Reassessing Nikuradse's Experiments on Liquid Flow in Rough Tubes. *Bull. Pol. Ac.: Tech.*, vol. *53*, pp. 343-349, 2005.
10. Szumbarski J., Instability of Viscous Incompressible Flow in a Channel with Transversely Corrugated Walls, *Journal of Theoretical and Applied Mechanics* 45(3), pp. 659-683, 2007
11. Kowalewski T.A, Szumbarski J., Blonski S., Low-Reynolds-Number Instability of the Laminar Flow between Wavy Walls, *Proc. of ASME ICNMM2008*, CD-ROM proceedings ISBN 0-7918-3826-9, paper 62070, pp.1-8, TU Darmstadt, Germany, 2008.
12. Santiago J.G., Wereley S.T., Meinhart C.D., Beebe D.J., Adrian R.J., A Micro Particle Image Velocimetry System, *Exp. Fluids*, vol. 25, pp. 316-319, 1998.

PRESSUE SENSITIVE MOLECULAR FILM FOR MEASUREMENT IN MICRO-FLOWS

Y. Matsuda[1*], T. Uchida[1], S. Suzuki[1], H. Yamaguchi[1], H. Mori[2], T. Niimi[1]
[1] Department of Micro-Nano Systems Engineering, Nagoya University, Japan
[2]Fluid Engineering Lab, Department of Mechanical Engineering, Kyushu University, Japan

ABSTRACT. The pressure-sensitive paint (PSP) has potential as a diagnostic tool for pressure measurement in the high Knudsen number regime, because it works as a so-called "molecular sensor". However, there are few reports concerning application of the PSP to micro-flows, because the conventional PSP is too thick owing to polymer binder. In our previous work, we have adopted Langmuir-Blodgett (LB) technique to fabricate a pressure sensitive molecular film (PSMF). In this study, we constructed four samples of PSMFs whose luminophore was Pt(II) Mesoporphyrin IX (PtMP), Pt(II) Mesoporphyrin IX dimethylester (PtMPDME), Pt(II) Protoporphyrin IX (PtPP) and Cu(II) Mesoporphyrin IX dimethylester (CuMPDME), respectively. The pressure sensitivity of those PSMFs were tested, and it is clarified that the PSMF composed of PtMP has the highest pressure sensitivity among the four and has equivalent pressure sensitivity of conventional polymer PSPs (e.g. PtOEP/GP-197). Moreover, we have applied PSMF to pressure measurement of a gas flow through the 170μm width micro-channel, and the pressure distribution on the surface along the channel was successfully obtained.

Keywords: Pressure-Sensitive Paint, High Knudsen Number Flow, Micro Flow, LB Film

INTRODUCTION

For the development of micro- and nano-technology with small characteristic length and semiconductor process technology under high vacuum environments, it has been strongly desired to understand thermo-fluid phenomena around a device such as magnetic head slider of hard disk drive, micro thruster for micro satellite, and semiconductor thin film fabrication system and so on. Optical measurement techniques based on emission and absorption of photons by molecules are useful tools for the experimental analyses of high Knudsen number flows. However, the experimental techniques are behind in development compared with numerical simulation techniques. In particular, there are no appropriate techniques for measurement of gas pressure on a solid surface inside micro-systems. To measure pressure distribution in high Knudsen number regimes, we have adopted a pressure sensitive paint (PSP) technique [1]-[2]. Because the PSP works as a so-called "molecular sensor", it seems suitable for analyses of high Knudsen number flows, which require diagnostic tools in the molecular level. However, application of the PSP to micro-devices is very difficult, because the conventional PSPs are very thick compared to the dimension of micro-devices owing to the use of polymer binders. Moreover, they do not have sufficient spatial resolution for pressure measurement of micro-flows because of the aggregation of luminescent molecules in polymer binders [3].

In the previous study, we have developed pressure sensitive molecular films (PSMFs) by using Langmuir-Blodgett (LB) technique [4] to construct ordered molecular assemblies, and have tested

* Corresponding author: Dr. Y. Matsuda
Phone: + (81)-52-789-2701, Fax: + (81)-52-789−3124
E-mail address: y.matsuda@nagoya-u.jp

the PSMF to clarify the feasibility of the pressure measurement around micro-devices [5]. PSMF with nanometer order thickness and high spatial resolution is suitable for analyses of micro-flows. The PSMF based on Pd(II) Mesoporphyrin IX (PdMP), which is used as luminescent molecules, has been fabricated and it is clarified that the pressure sensitivity of PSMF of PdMP is sufficiently high [5]. However, the PSMF composed of PdMP cannot be applicable to the pressure range higher than 130 Pa due to saturation of oxygen quenching of PdMP; this is caused by the long life time of PdMP, which is so long (1.0msec [6]) that most of luminescent molecules are quenched. It is desired for PSMF to work around the atmospheric pressure, because the most micro-devices are used in the atmospheric pressure. In order to fabricate a useful PSMF for atmospheric pressure range, we constructed four samples of PSMFs composed of Pt(II) Mesoporphyrin IX (PtMP), Pt(II) Mesoporphyrin IX dimethylester (PtMPDME), Pt(II) Protoporphyrin IX (PtPP) and Cu(II) Mesoporphyrin IX dimethylester (CuMPDME), respectively. Those luminescent molecules have shorter life time compared with PdMP (e.g. the life time of PtMPDME and CuMPDME are 0.14msec and 0.1msec, respectively [6]).

RELATION BETWEEN PRESSURE AND LUMINESCENT INTENSITY

The pressure measurement technique using PSP is based on oxygen quenching of luminescent molecules. PSP is composed of luminescent molecules and a binder material to fix the luminescent molecules to a solid surface. When the PSP layer applied to the surface is illuminated by UV light, the luminescent molecules are excited by absorption of photon energy, and then the molecules emit phosphorescence. On the other hand, oxygen molecule with triplet ground state acts as a quencher of the luminescence. As a result, the phosphorescence intensity decreases as an increase in partial pressure of oxygen. Pressure on the solid surface can be deduced from the relationship between pressure and the luminescence intensity (Stern-Volmer plot [1]).

$$\frac{I_{ref}}{I} = \sum_{n=0}^{N} A_n \left(\frac{P}{P_{ref}} \right)^n , \tag{1}$$

where I is the luminescence intensity and P is the oxygen pressure. I_{ref} is the luminescence intensity at the known reference pressure P_{ref}. The coefficients A_n are the constants called as Stern-Volmer coefficients determined by calibration tests. The luminescence intensity I of the ideal PSP (N = 1) depends inversely on P following to Eq. (1), but the actual PSPs have nonlinear dependence of I^{-1} on P. In practice, a second-order polynomial (N = 2) is commonly used. In the PSMF, however, the relation of the luminescence intensity I and P is different from that of PSP, because the quenching rate of PSMF is dominated by adsorbed oxygen molecules on the surface of PSMF. The adsorption quantity is determined by Langmuir adsorption isotherm. Then, the relationship between pressure P and the luminescence intensity I can be written as following equation.

$$\frac{I_{ref}}{I} = B_0 + B_1 \frac{P / P_{ref}}{P / P_{ref} + \alpha} , \tag{2}$$

where B_n are the Stern-Volmer coefficients.

EXPERIMENTAL METHODS

Fabrication of pressure sensitive molecular film

In this study, we have adopted Langmuir-Blodgett (LB) method to fabricate a pressure sensitive molecular film (PSMF) with ordered molecular structure applicable to pressure measurement around micro-devices. The LB method provides us with capability to construct ordered molecular assemblies. LB films are fabricated according to the following procedure. At first, a drop of a dilute solution of amphiphilic molecules in a volatile solvent is spread on the interface between air and subphase. After the solvent is evaporated, a monolayer of the molecules remains on the interface. The monolayer is transferred to a substrate with compressing the monolayer so as to control the order of the molecules (see Fig. 1).

Experimental apparatus

Figure 2 shows the experimental apparatus composed for this study. The PSMF samples were applied to glass plates, and the specimens were set inside a vacuum chamber evacuated by a scroll pump (ULVAC DVS-631) and a turbo molecular pump (ULVAC UTM-1500). Pure oxygen gas was supplied into the chamber, and the pressure in the chamber is monitored by a capacitance manometer and an ionization vacuum gauge. A xenon-arc lamp (USHIO UXL-500SX) with a band-pass filter (400±20 nm) was used as an excitation light source illuminating the specimen via an optical fiber. The luminescence was filtered by a long-pass filter (600 nm) to eliminate the light from the xenon-arc lamp, and was detected by an EM-CCD camera (Andor Technology DV887AC-UV, 512×512 pixels, 14 bit). The image of the luminescence was processed by a personal computer.

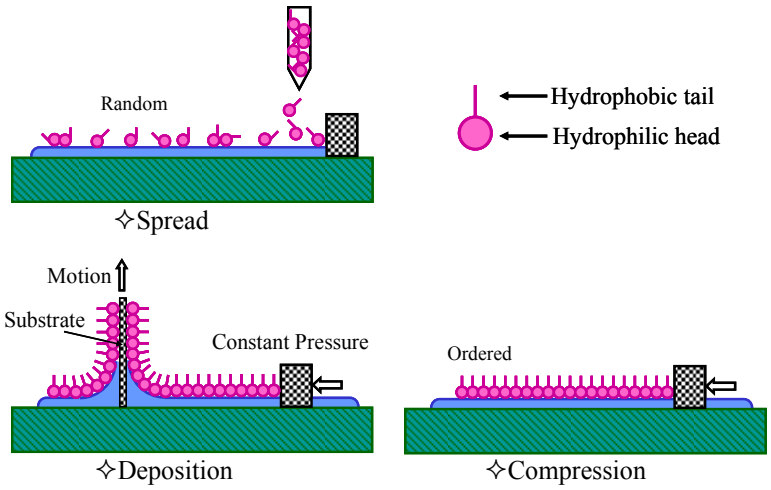

Figure 1. A schematic process of LB method.

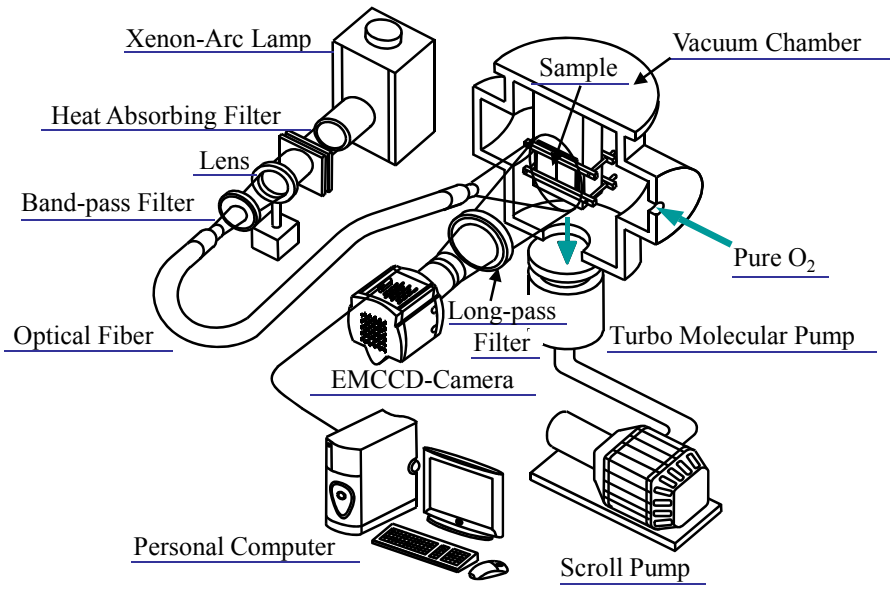

Figure 2. Experimental apparatus.

RESULTS AND DICUSSIONS

Pressure sensitivity of pressure sensitive molecular film

Figure 3 shows the pressure sensitivities of the PSMFs composed of PtMP, PtMPDME, PtPP and CuMPDME below 21kPa (equal to the partial pressure of oxygen in atmospheric pressure). The horizontal axis of the Stern-Volmer plot is the normalized pressure p/p_{ref} and the vertical axis is the inverse luminescent intensity ratio I_{ref}/I, where I_{ref} is the reference luminescent intensity at the reference pressure p_{ref}=1.0x10^{-2} Pa. It is clarified that the pressure sensitivity of PSMF-PtMP is highest among the four tested PSMFs and is comparable to that of conventional PSPs (e.g. PtOEP/GP-197[1]). In contrast, PSMF-PtPP and PSMF-CuMPDME have little pressure sensitivity. These results indicate that both PtPP and CuMPDME are nearly insensitive to oxygen molecule.

Pressure measurement in micro-channel gas flow

As an application of our PSMF to pressure measurement of micro-scale gas flows, we measured the pressure distribution of the micro-channel. The high pressure camber of the micro-channel is connected to the supply port of mixed gas (N_2: 79%, O_2: 21%) and the low pressure camber is connected to the outer port evacuated by vacuum pump. The channel width is 170μm and the length is 270μm. The stagnation and the downstream pressure were set at 11.5kPa and 1.4kPa, respectively. Since both the inlet port and outlet port are attached far from the micro-channel, the effect of inlet and outlet condition can be negligible. The luminescent of PSMF is detected by a fluorescence microscope.
Figure 4(b) shows the pressure fields of micro-channel obtained by the measurement using the PSMF-PtMP and by Direct Simulation Monte Carlo (DSMC) method [7]. Both results obtained by PSMF and DSMC are in agreement with each other. These results show the usefulness of our PSMF for measurement of micro-scale gas flows, although PSMF result contains noticeable noise, because the amount of luminescent molecules of PSMF is smaller than that of conventional PSP.

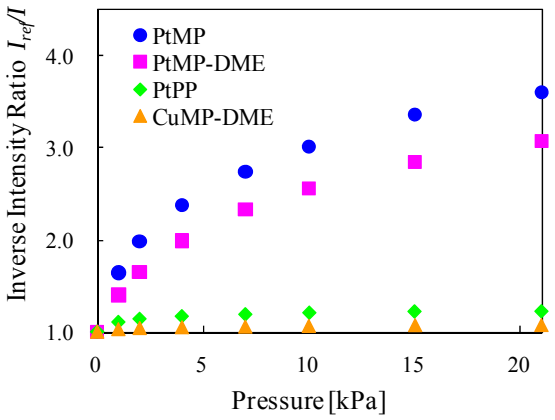

Figure 3. Stern-Volmer plots of PSMFs.

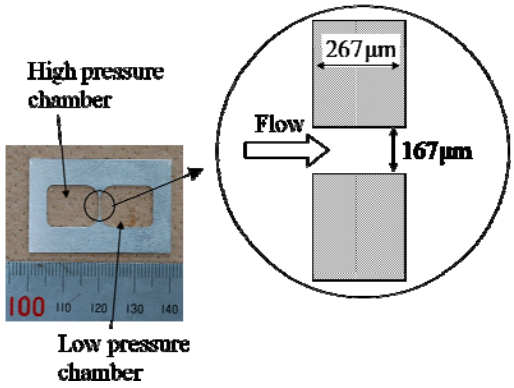

(a) Geometric configuration of micro-channel.

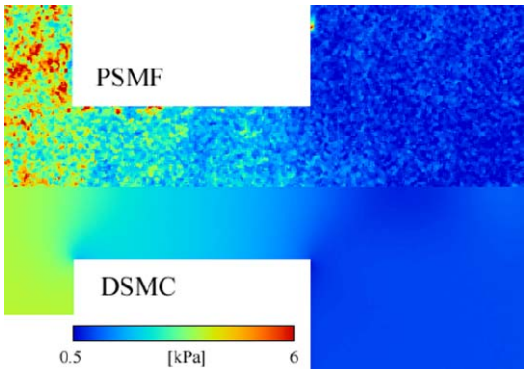

(b) Pressure field of micro-channel.

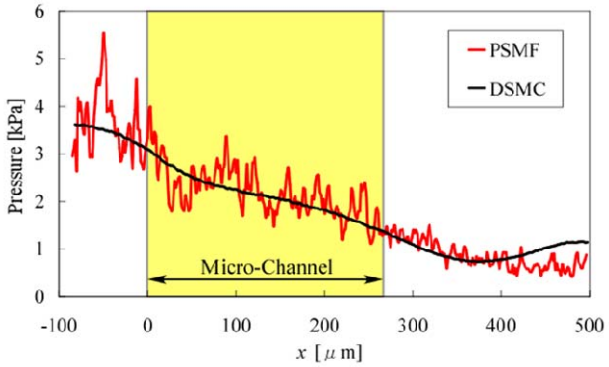

(c) Pressure distribution along the canter line of the channel.

Figure 4. Pressure fields of micro-channel obtained by PSMF-PtMP.

CONCLUSIONS

In this study, the following results are obtained:

1. We fabricated PSMF composed of Pt(II) Mesoporphyrin IX (PtMP). It is shown that PSMF of PtMP has higher pressure sensitivity compared with PSMF of Pd(II) Mesoporphyrin IX (PdMP) below 11kPa, and PSMF of PtMP has enough pressure sensitivity in the range from 0kPa to 21kPa of oxygen pressure.
2. The pressure distribution of micro-scale gas flow was measured using PSMF, showing the usefulness of our PSMF for measurement of micro-scale gas flow.

REFERENCE

1. T. Liu, T. Champbell, S. P. Burns and J. P. Sullivan., Temperature- and pressure-sensitive paints in aerodynamics, *Applied Mechanics Reviews*, Vol. 50, pp 227-246, 1997.
2. J. H. Bell, E. T. Schairer, L. A. Hand and R. D. Mahta., Surface pressure measurements using luminescent coatings, *Annual Review of Fluid Mechanics*, Vol. 33, pp 155-206, 2001.
3. H. Mori, T. Niimi, M. Hirako and H. Uenishi., Molecular number flux detection using oxygen sensitive luminophore, *Physics of Fluids*, Vol. 17, 100610, 2005.
4. A. Ulman, *An Introduction to Ultrathin Organic Films From Langmuir-Blodgett to Self-Assembly*, Academic Press, San Diego, 1991.
5. Y. Matsuda, H. Mori, T. Niimi, H. Uenishi and M. Hirako., Development of pressure sensitive molecular film applicable to pressure measurement for high Knudsen number flows, *Experiments in Fluids*, Vol. 42, pp 543-550, 2007.
6. R.S. Becker, Metalloporphyrins. Electronic spectra and nature of perturbations. I. Transition metal ion derivatives, *The Journal of Physical Chemistry*, Vol. 67, No. 12, pp2662-2669, 1963.
7. G.A. Bird, *Molecular Gas Dynamics and the Direct Simulation of Gas Flows*, Oxford University Press, New York, 1994.

MICROLAYER CONFIGURATION IN NUCLEATE POOL BOILING FOR WATER

Y.Utaka[1,*], K.Nakamura[2], Y.Kashiwabara[1]
[1]Yokohama National University, Yokohama, Japan
[2]Hitachi Appliances, Hitachi, Japan

ABSTRACT**.** The objective of the study is to clarify the configuration of a microlayer formed between the vapor bubble and the heat transfer surface in nucleate pool boiling of an isolated bubble region. The microlayer thickness was measured using specially devised measurement system by applying the laser extinction method. A thin optic fiber in a thin stainless tube was inserted into the liquid pool with the gas blowing both for preventing the getting wet of fiber made of fluorinated glass and removing the liquid in the path of laser light. The process of bubble growth was recorded with the two high speed cameras. It was elucidated that the thickness of the initially formed microlayer was decided uniquely. The thickness was between 1 μm and 8 μm and was increased with the increase of distance between incipient bubble site and measuring position regardless of heat flux in this experiment.
Keywords: *pool boiling, phase change, microlayer, isolated bubble region, laser extinction method*

INTRODUCTION

Nucleate boiling is a widely used in industry due to its good heat transfer characteristics. However, there are unknown factors about the heat transfer mechanisms of nucleate boiling due to the physicochemical factors, such as in the process of the bubble nucleation, bubble growth, bubble behavior, phase changes at the liquid-vapor interface.

As the mechanisms of heat transfer in nucleate boiling, the convective heat transfer and the latent heat transfer have been proposed. The mechanism of the convective heat transfer is based on the diffusion of thermal boundary layer by bubble behavior and sensible heat transport. The mechanism of the latent heat transfer is based on the conversion of sensible heat stored in superheated liquid layer to bubble growth and vaporization of the microlayer formed between the growing bubble and heat transfer surface. Although the mechanisms of heat transfer in nucleate boiling were examined from viewpoint of the above, the quantitative discussions were insufficient. Especially, the heat transfer characteristics of microlayer evaporation, in which a large amount of heat transport occurs by latent heat of evaporation, are thought to be important. Therefore, clarification of the configuration of the microlayer is of fundamental importance.

Concerning the thickness of the microlayer in nucleate boiling, the presence of the microlayer was clarified, and its thickness of 4.2 μm for water in the gap between the heat transfer surface and the window parallel to the surface by the interferometric method was measured by Sharp [1]. Jawurek [2] measured the microlayer thickness of 0.5 μm for ethanol on a glass surface. Furthermore, Voutsinos and Judd [3] measured the thickness of dichloromethane to be 1 μm to 6 μm, and the thickness increased with the increase of distance from the bubble incipient site. Also, the theoretical

* Corresponding author: Prof. Yoshio. Utaka
Tel/Fax: + (81)-45-339-3909
E-mail: utaka@ynu.ac.jp

model was proposed by Cooper and Lloyd [4] for the prediction of microlayer thickness, experimental validation of the prediction does not show sufficient correspondence.

In this study, the laser extinction method was used with a specially device to make non-contact measurements using a thin optic fiber in a thin stainless tube with a gas blowing. By applying this method, the objective of this study is to clarify the characteristics of the microlayer configuration by direct measurement of the thickness of the microlayer formed underneath the vapor bubble and by observation and measurement of vapor bubble behaviors using two high-speed cameras.

NOMENCLATURE

A : extinction coefficient [m^{-1}]

h : height from the heat transfer surface to the optic fiber front edge [m]

I : laser intensity through microlayer [-]

I_0 : reference laser intensity [-]

q : heat flux [W/m^2]

r_L : distance between bubble site and measurement position [m]

R_M : radius of microlayer on heat transfer surface [m]

R_{Mmax} : maximum radius of microlayer [m]

t : elapsed time from generation of bubble [s]

t_g : elapsed time before formation of initial microlayer [s]

δ : microlayer thickness [m]

δ_0 : initial microlayer thickness [m]

EXPERIMENTAL APPARATUS AND METHOD

Figure 1 shows the experimental apparatus used in the present study. The apparatus is composed of a boiling system for water at atmospheric pressure and a measurement system for the transmission ratio of laser light. As the heat transfer plate, a 2-mm-thick quartz glass plate with high transparency for laser light was attached to the bottom of the boiling chamber. The test water in the boiling chamber was maintained at the saturation temperature by heating with surrounding electric heater. The rear side of the cavity on the heat transfer surface was heated by impinging a jet of hot nitrogen gas from a nozzle having an inner diameter of 2 mm at an angle of 60° for bubble generation from the fixed point. The mechanism for the adjustment of the position of fiber optic equipment was placed on top of boiling container. The velocity of the nitrogen jet was approximately 180 m/s, and the temperature of the jet was changed from 513 to 673 K for adjustment of the heat flux. Heat flux was determined by iteration for the overall heat transfer system using the heating-side heat transfer coefficient obtained from the flow rate and the temperature of the nitrogen jet, and the boiling heat transfer coefficient from the boiling characteristic curve [5].

A helium-neon laser light with a wavelength of 3.39 μm and a detector made of Pb-Se were used in the laser light transmission ratio measurement system. Fig.2 shows the principle of the laser extinction method used to measure the thickness of the microlayer. The intensity of the laser light is

reduced by scattering and adsorption in the microlayer formed under the bubble on the heat transfer surface, and the intensity ratio of transmitted light to incident light can be determined. Laser light from an oscillator was concentrated and directed through a 94 μm diameter optical fiber with high transmission for infrared light. The intensity of transmitted light, I_0, was determined by detecting the intensity through the air and a dry heat transfer plate. The thickness of the microlayer could then be determined by application of Lambert's law, as shown in equation (1):

$$e^{-A\delta} = \frac{I}{I_0} \tag{1}$$

where A is the extinction coefficient of water, which is 5.42×10^4, as measured by Utaka-Nishikawa [6].

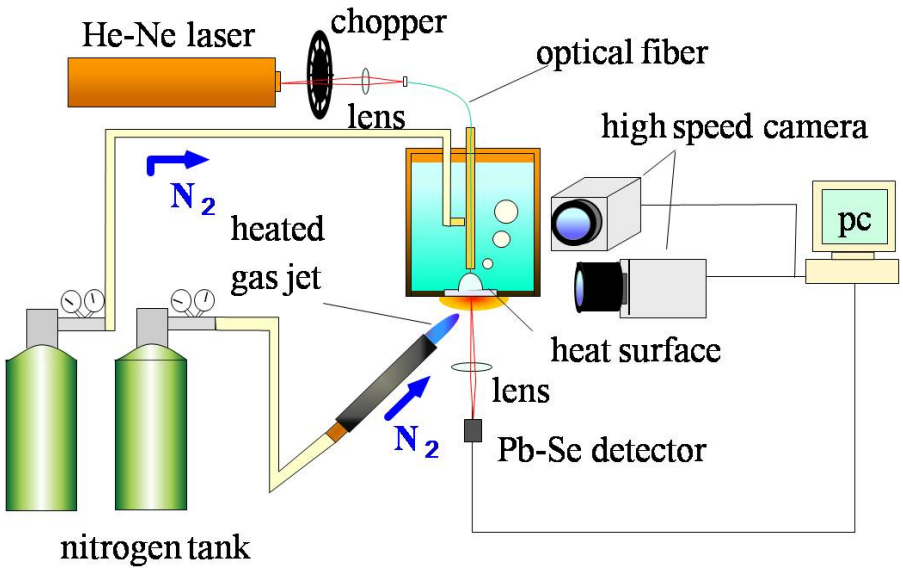

Figure 1. Schematic diagram of experimental apparatus

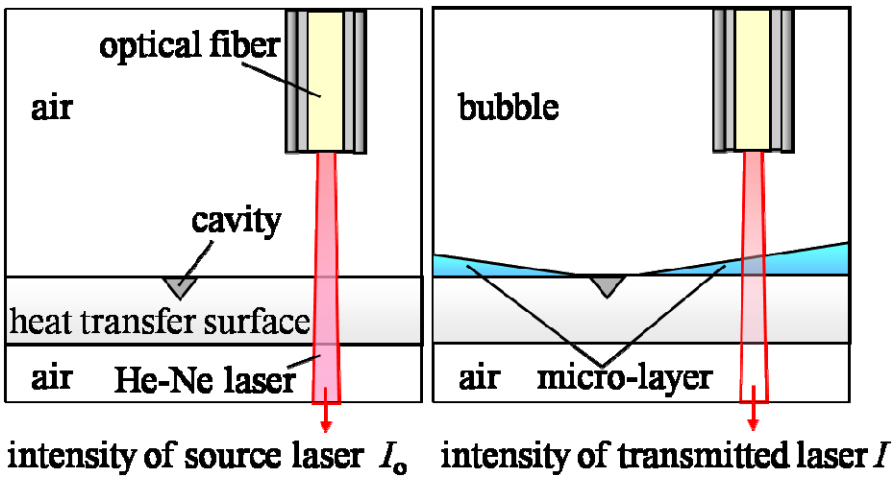

Figure 2. Principle of the laser extinction method

The laser extinction method used in the present study is based on the nature of extinction of infrared light in the test liquid, so that the bulk liquid must be removed from the pathway of the laser in the pool and optical fiber made of fluorinated glass must be prevented the getting wet. Therefore, a thin stainless steel tube having a diameter of 0.4 mm was used to cover the optical fiber and confine the nitrogen gas blowing in the apparatus, as shown in Figure 3. The detailed structure of the laser light emitting apparatus is shown in Figure 4, in which the optical fiber is installed inside the thin stainless steel tube and located at the position of bubble generation. The gas blown through this tube coalesced with the vapor bubble, so that the effect of the bulk liquid could be removed. Furthermore, there was a possibility that a thin liquid film could form between the nitrogen gas bubble and the vapor bubble. Therefore, fine wires having diameters of 70 μm were attached to the tip of the stainless steel tube in order to break the film.

The aspect of boiling was simultaneously recorded with laser signal by using two high-speed digital cameras with a maximum frame rate of 5,000 fps at two orthogonally oriented directions from the plane of the heat transfer surface, and this data was used to develop the distance measurement from the incipient bubble point.

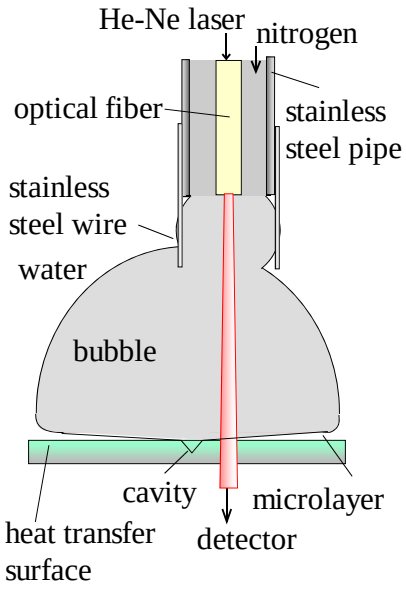

Figure 3. Method for measurement of the microlayer thickness

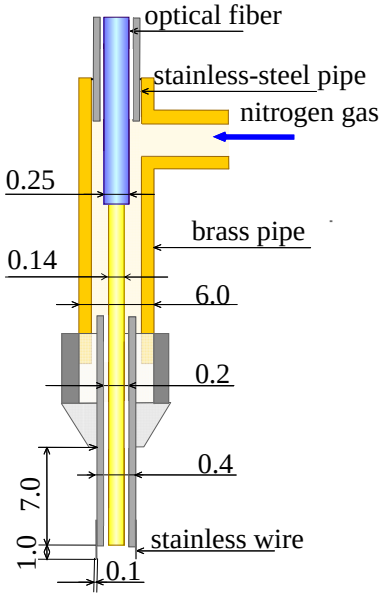

Figure 4. Details of the fiber equipment (dimensions are in mm)

EXPERIMENTAL RESULT AND DISUCUSSION

Effect of the height from the heat transfer surface to the optical fiber front edge

Measurements were performed for three heat flux conditions by varying the distance from the incipient bubble site to the light axis on the surface r_L , and the distance between the tip of the optical fiber and the heat transfer surface *h*, as shown in Figure 5. In general, since there is a spread angle from the fiber exit, it is possible to minimize the irradiation area by shortening the distance from the heat transfer surface. However, in the range of smaller *h*, that is, when the tip of the fiber is near the heat transfer surface, the fiber apparatus prevents nucleation of the bubble due to the disturbance of the superheated layer near the surface. Therefore, the experiment was carried out with a distance *h* of greater than 2.3 mm. Next, measurement of the laser irradiation area and intensity distribution on the surface was performed in order to determine the measurement area for the microlayer thickness. Figure 6 shows the intensity distribution on the surface, which confirms the straight nature of the laser light in this system. This indicates that the effect of changing *h* is not significant in the range *h* > 2.3 mm. The irradiation area was 0.3 mm in diameter for the case of *h* = 3.3 mm, which was a typical distance used in the present study.

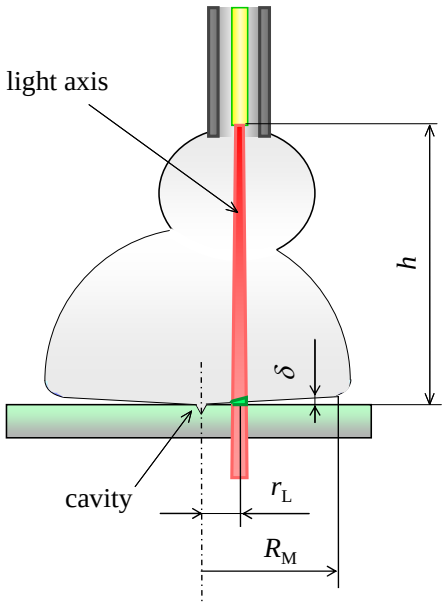

Figure 5. Parameter notation

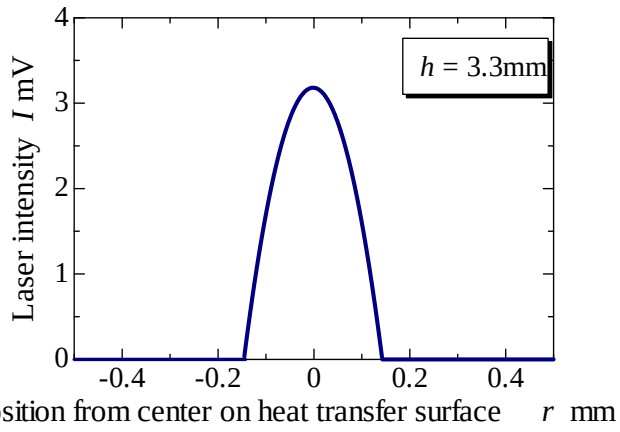

Figure 6. Distribution of laser intensity

Variation of microlayer thickness

Figure 7 shows a typical example of variation in microlayer thickness when the height of the fiber h = 3.3 mm the distance from the incipient site r_L = 0.39 mm and the heat flux q = 50 kW/m^2. It is impossible to measure the thickness of the microlayer, because there is bulk liquid present between the bubbles of gas and vapor, and most of the laser light fraction is absorbed and scattered by the bulk liquid immediately after bubble generation. After just a few moments, the effect of the bulk liquid disappears, with partial extinction of the laser light by the microlayer, so that measurement of the microlayer thickness becomes possible when the vapor bubble reaches the thin stainless steel tube in which the optical fiber is installed. The initial microlayer thickness was approximately 1.5 μm, and the thickness was reduced by the effect of evaporation over time. Since the film thickness was zero at approximately t = 20 ms, a dryout area appeared.

As shown in Figure 8, the initial microlayer thickness δ_0 can be defined as the thickness appearing at the time just after the microlayer forefront moves past the measurement point and the microlayer is formed. In most cases, it is not possible to measure the thickness of the initial microlayer. Therefore, the initial microlayer thickness is determined by extrapolation of the linear line fitted using the least squares method to the domain of the straight change. The average value of correction used for the microlayer thickness was approximately 0.5 μm.

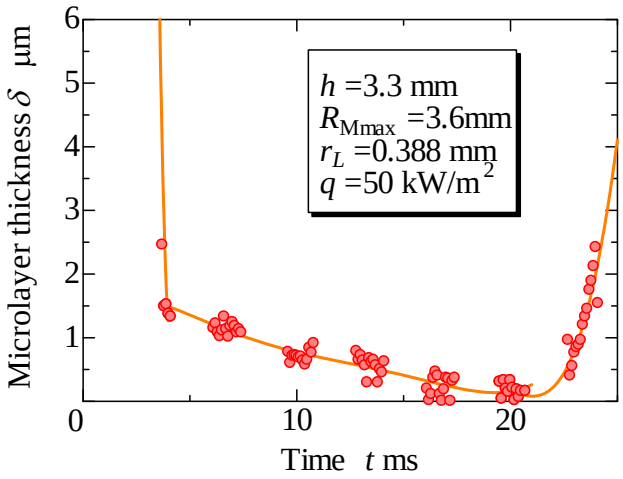

Figure 7. Variation of microlayer thickness

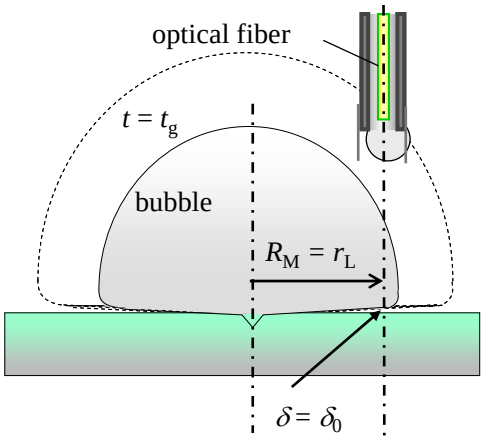

Figure 8. Definition of the initial microlayer thickness measurement

Distribution of microlayer thickness

Figure 9 shows the variation of initial microlayer thickness δ_0 as a function of the measurement position r_L. The microlayer grew to a radius of around 2-4 mm on the heat transfer surface. The radius of microlayer was approximately 80% of the vapor bubble radius in the horizontal direction. The initial microlayer thickness δ_0 was increased with the increase of the distance from the bubble initiation site, and its thickness was approximately 1-8 μm. Furthermore, since the effect of heat flux on the microlayer thickness was slight, the linear curve shown in Figure 9 was fitted to all data by the least squares method under the assumption of zero film thickness $\delta_0 = 0$ at the incipient bubble site $r_L = 0$. The relationship between the distance from the incipient bubble site and the microlayer thickness is expressed by equation (2):

$$\delta_0 = 3.14 \times 10^{-3} \times r_L \tag{2}$$

Investigation of the precision of measurement

The variation of the extinction rate of the laser due to the change in microlayer thickness was determined in this measurement. The small irradiation area of the heat transfer surface was achieved by investigation of the relationship between the height of the laser exit from the optical fiber and the area of irradiation of the laser. Therefore, the dominant factor concerning the measurement accuracy was the fluctuation of the laser intensity and the characteristics of the detector. The variation of the detected laser intensity was measured by irradiating the laser to the detector under conditions to similar the experimental conditions. As a result, the maximum fluctuation of the detected intensity was 8.6%, as shown in Figure 10. This fluctuation value converted to a microlayer thickness of ±1.7 μm calculated from equation (1), as shown by the broken line in Figure 9. The microlayer thickness distribution expressed by equation (2) is thought to be reliable, because the error investigated above was relatively large compared to other error factors, and more than 90% of measured data were in the area between the two broken lines in Figure 9.

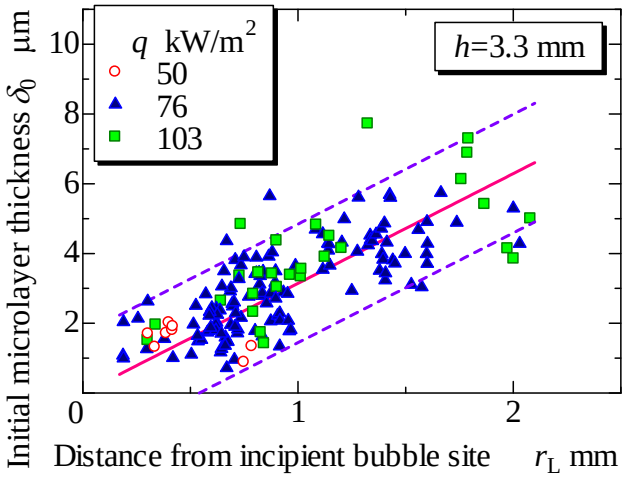

Figure 9. Variation of initial microlayer thickness with respect to the distance from the incipient bubble site

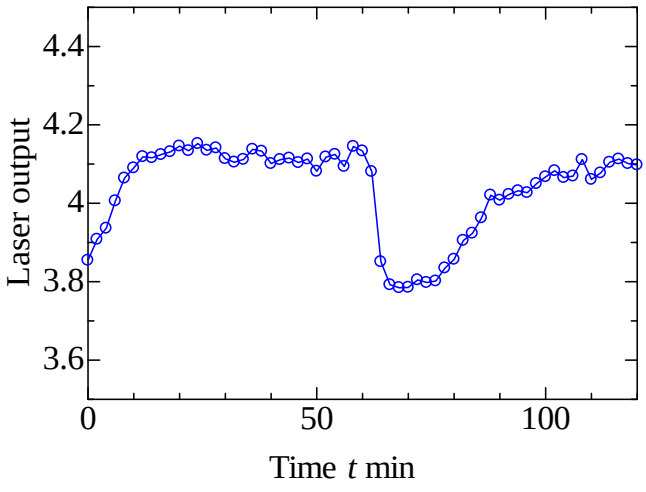

Figure 10. Variation of laser output with respect to time

CONCLUSIONS

The laser extinction method was used to elucidate the characteristics of the microlayer configuration in nucleate pool boiling by direct measurement of the microlayer thickness formed underneath the vapor bubble. The special device used both a thin optic fiber and a gas blowing system. The results are summarized as follows:

(1) The initial microlayer thickness was approximately 1-8 μm.
(2) The heat flux appeared to have little effect on the initial microlayer thickness.
(3) The initial microlayer thickness was increased with the increase of the distance from bubble initiation site. The relationship between the distance from the incipient bubble site and the microlayer thickness was expressed by the following equation:

$$\delta_0 = 3.14 \times 10^{-3} \times r_L .$$

(4) The microlayer thickness was reduced by the effect of evaporation.

ACKNOWLEDGMENTS

The authors would like to thank Mr.Akinori.Sakurai, Mr.Kunitoshi Itagaki and Mr.Hideyuki Sonoda, who were graduate students of Yokohama National University, for helping the experiment. The present study was supported in part by a Grant-in-Aid for Scientific Research from the Ministry of Education, Culture, Sports, Science and Technology, Japan [(B)17360096].

REFERENCES

1. Sharp, R.R., The nature of Liquid Film Evaporation During Nucleate Boiling, NASA TN D-1997, Lewis Research Center, Cleveland, Ohio, 1964.
2. Jawurek, H.H., Simultaneous Determination of Microlayer Geometry and Bubble Growth in Nucleate Boiling, Int. J. Heat Mass Transfer, Vol.12, pp.843-848, 1969.
3. Voutsinos, C.M. and Judd, R.L., Laser Interferometric Investigation of the Microlayer Evaporation Phenomenon, J. Heat Transfer, Vol.97, No.1, pp.88-92, 1975.
4. Cooper, M.G., Lloyd, A.J.P., The Microlayer in Nucleate Pool Boiling, Int. J. Heat and Mass Transfer, Vol.12, pp.895-913, 1969.
5. Kutateladze, S.S., Heat Transfer in Condensation and Boiling, Translation Series, AEC-tr-3770, pp.129, 1959.
6. Utaka, Y. and Nishikawa, T., Unsteady Measurement of Condensate Film Thickness for Marangoni Condensation by Using Laser Absorption Method, Transactions of the Japan Society of Mechanical Engineers (Series B), Vol. 68, No. 672, pp.2292-2299, 2003.

A NOVEL PARTICLE MIXING METHOD WITH FREQUENCY SELECTION BASED ON AC ELECTROKINETICS

D. Akutsu*, M. Motosuke and S. Honami
Tokyo University of Science, Tokyo, Japan

ABSTRACT. In a microfluidic device, the utilization of electrokinetics is effective for fluid or particle control. Under high frequency alternating-current (AC) electric field over kilohertz, the effect of polarization emerges and the electric charge of particle can be neglected. The control of particles can be achieved in the condition with low voltage. In this frequency range, two kinds of phenomena involving dielectrophoresis and electrothermal effect exist. The purpose of this study is to investigate the potential of particle mixing technique based on the frequency-dependent AC electrokinetics. The behavior of polystyrene submicron particles suspended in water under the AC electric field with high frequency (1 ~ 300 kHz) was evaluated by means of micron-resolution particle image velocimetry. As a result, particle movement indicates drastic change with applied frequency. In addition, the quantitative assessment of mixing effect was conducted.

Keywords: *Microfluidics, AC electrokinetics, Particle mixing, Joule heating*

INTRODUCTION

The microfluidic devices have attracted considerable attention and have broadened their application fields in biology, chemistry, medical and mechanical engineering. However, there is a problem that a stable laminar flow in the channel inhibits the sorting and mixing of suspended particles. Therefore, efficient and versatile technique for microparticle control is strongly required. Many studies on particle control in the microfluidic device have been suggested and researched. For instance, a mixing promotion using the microchannel with a certain three-dimensional shape fabricated by MEMS (Micro Elecro-Mechanical Systems) technology has been studied [1]; however, the mixing method with complicated structure is lack of durability and tends to generate undesired pressure loss in the area for mixing. Also, there are other particle manipulation techniques with direct-current (DC) electrokinetics which include electrophoresis and electroosmosis [2]. In these methods, the influence of temperature rise in solution cannot be negligible because high voltage applied is needed in a minute area [3]. In the present study, we have focused on the high-frequency alternating-current (AC) electrokinetics. In the operation method using the AC electric field over kilohertz, charge of particle is cancelled and the effect of polarization becomes dominant. So, electrically neutral particle can be used in this frequency range. Phenomena under the AC electric field for particle manipulation focused in this study are dielectrophoresis (DEP) and electrothermal effect (ET). These phenomena are induced by low voltage with a simple electrode pattern. These phenomena occur simultaneously when an appropriate frequency is selected. The intensity and direction of these effects are determined by applied frequency and electrical properties of fluid and particle. Therefore, an appropriate selection of the frequency at each solution is essential for the particle mixing in the microfluidic device. In order to establish a novel mixing technique based on AC electrokinetics, it is necessary to understand the behavior of particles both under DEP and ET force. The evaluation of the mixing

* Corresponding author: D. Akutsu
Phone: + (81)-3-32604272, Fax: + (81)-3-52130977
E-mail address: mot@rs.kagu.tus.ac.jp

effect including the frequency dependence is also needed. The objective of this study is the investigation of particle movement in detail and the evaluation of the mixing effect under the frequency dependent AC electrokinetics.

AC ELECTROKINETICS

Dielectrophoresis (DEP)

Dielectrophoresis is a phenomenon in which a force is exerted on a dielectric particle under nonuniform electric field. Since the polarization of the particle generates DEP force [4], the particle does not have to be charged. DEP force acting on a sphere particle suspended in a medium is given as follows.

$$\mathbf{F}_{\mathrm{DEP}} = \frac{1}{4}\pi\varepsilon_m d^3 \,\mathrm{Re}\left[\frac{\varepsilon_p^* - \varepsilon_m^*}{\varepsilon_p^* + 2\varepsilon_m^*}\right]\nabla|\mathbf{E}|^2 \tag{1}$$

$$\varepsilon^* = \varepsilon - \frac{\sigma}{\omega} j \tag{2}$$

Subscript *m* and *p* means medium and particle, respectively. The fractional factor in brackets is known as Clausius-Mossotti factor $K(\omega)$. Positive DEP occurs when $\mathrm{Re}[K(\omega)] > 0$, the particle is attracted to the area of high electric field. The converse of this is negative DEP which occurs when $\mathrm{Re}[K(\omega)] < 0$, the particle is toward the area of low electric field. The polarity of electric field does not have an effect on DEP force. The intensity and direction of the force strongly depend on the applied frequency and the electrical properties of fluid and particle.

Electrothermal effect (ET)

Electrothermal effect is a convection flow driven by electric field. This phenomenon is caused by gradient in electrical properties due to a nonuniform temperature field by the Joule heating [5]. The ET force acting on fluid becomes,

$$\mathbf{F}_{\mathrm{ET}} = -\frac{1}{2}\left\{\left(\frac{\nabla\sigma_m}{\sigma_m} - \frac{\nabla\varepsilon_m}{\varepsilon_m}\right)\cdot\mathbf{E}\frac{\varepsilon_m\mathbf{E}}{1+(\omega\tau)^2} + \frac{1}{2}|\mathbf{E}|^2\nabla\varepsilon_m\right\} \tag{3}$$

The first and second term in equation (3) represents the Coulomb force and the dielectric force, respectively. The intensity and direction of ET flow are also controlled by the frequency; positive- and negative- ET can be generated. In the positive ET, a body force exerts the fluid to flow from higher temperature area to lower one along the applied electric field gradient, and negative ET induces reversely-directed flow with positive ET.

Combination of DEP and ET

The two phenomena of DEP and ET occur simultaneously in a practical microfluidic device under AC electric field with nonuniformity. Four pattern of combination can be considered; p-/n- DEP and p-/n- ET. The contribution of each effect can be determined by the balance of electrical properties in particle and fluid associated with a frequency selection.

EXPERIMENTAL SETUP

Microfluidic device

A microfluidic device used in this study is fabricated with photo- and soft-lithography (see Figure 1). The microchannel structure made of PDMS (polydimethylsiloxane) is placed on a flat glass substrate with electrodes. The scale of the microchannel is 200 μm in width, 40 or 50 μm in height and 40 mm in length. The PDMS channel has a thin wall in one side. The substrate has an electrode pattern made of ITO (indium tin oxide). The electrode pattern is comb-shaped with the space of 25 μm. Two kinds of electrode patterns are fabricated, and the line of electrodes is 25 μm (narrow type) and 2 mm (wide type). PMMA (polymethylmethacrylate) reservoirs with inner diameter of 8 mm are served as the inlet and outlet. A difference in the liquid surface level at each reservoir causes stable pressure-driven flow in the microchannel. A fully developed laminar channel flow can be obtained in a measurement section because Reynolds number is 3×10^{-3}. The applied voltage and frequency were controlled by a function generator (FG) with the voltage of 1 ~ 3 $V_{p\text{-}p}$ at the frequency of 1 ~ 300 kHz.

Working fluid

Distilled water is used as the working fluid. Fluorescent polystyrene particles (PS) with the diameter of 720 nm are seeded to observe the particle behavior. Volume fraction of particles in the working fluid was approximately 0.048 %. Table 1 indicates the electrical properties of the working fluid and particle. Electrical conductivity of the fluid is measured and other properties are reference values [6].

Table 1
Electrical properties of working fluid

Conductivity (mS/m)		Relative permittivity	
Fluid	Particle	Fluid	Particle
1.4	10	67	2.25

Micro-PIV setup

As the measurement method, micro-PIV (particle image velocimetry) technique was employed in this study. This technique is based on the volume illumination and the detection of the movement of fluorescent particles in the focal plane of an objective lens. Figure 2 shows a schematic of the experimental system. This system has been developed around an inverted microscope. A continuous mercury lamp is used as an illumination source. The microscope consists of an objective lens (Obj; 20×, *NA* 0.4), a filter cube, and a zoom lens (ZL; 2.5×). The filter cube has an exciter filter (ExF), an emitter filter (EmF) and a dichroic mirror. We have developed a lateral observation arrangement by

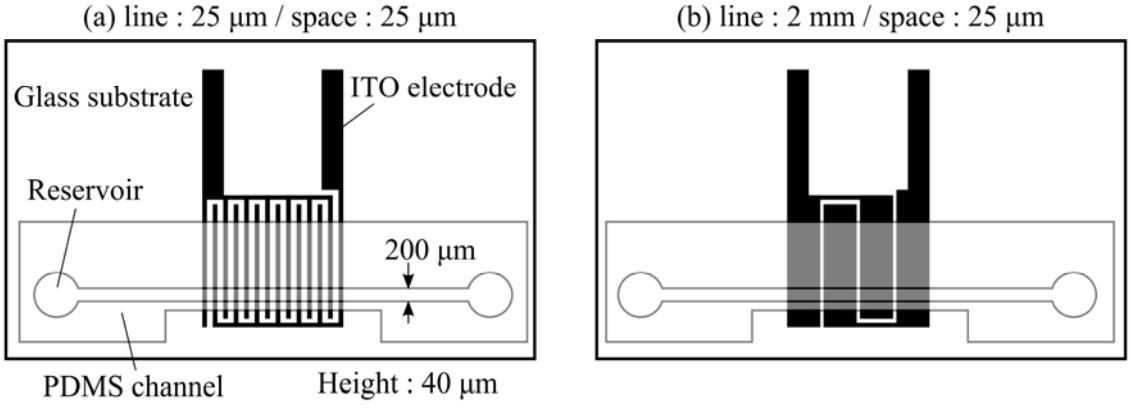

Figure 1. Microfluidic device (a) Narrow type (b) Wide type

using a minute reflection prism to obtain the particles movement in the cross-section normal to the electrode substrate. In this setup, the particle behavior is observed through the side PDMS wall (See Figure 3). The fluorescent image of PS is collected by Obj via the prism, and then coupled to a CCD camera (640×480 pixels, 12 bit). The excitation and emission wavelength of the fluorescent particles is 468 and 508 nm, respectively. Time interval between two images in a pair was 35 ms. In order to reduce the effect of diffusion due to the Brownian motion of the particles, time-average processing between 200 image pair is performed.

RESULTS AND DISCUSSIONS

Observation of frequency-dependent particle position

In order to observe the frequency-dependent AC electrokinetics in the fabricated microfluidic device, distributions of the particles were observed from the lower side of the microchannel. Each particle image was acquired immediately above 30 second after the voltage application. Figure 4 shows the distributions of fluorescent intensity in streamwise direction of the channel and the CCD images with the voltage of 1 $V_{p\text{-}p}$. The flow velocity at the center of the channel was about 50 μm/s. Here, the narrow electrode pattern with line of 25 μm is used. From Figure 4, it is obvious that the particle position is strongly influenced by the frequency. At 1 kHz, the peak fluorescent intensity

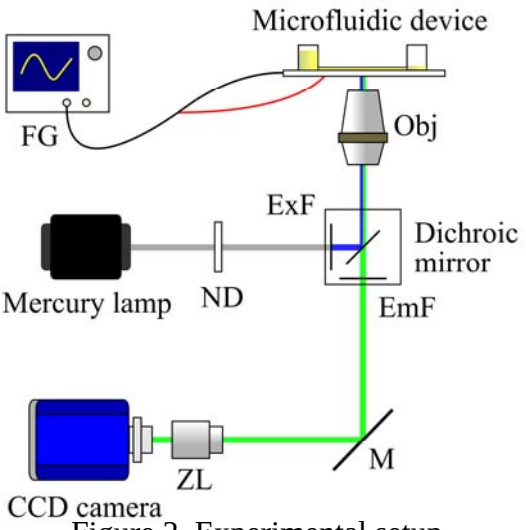

Figure 2. Experimental setup

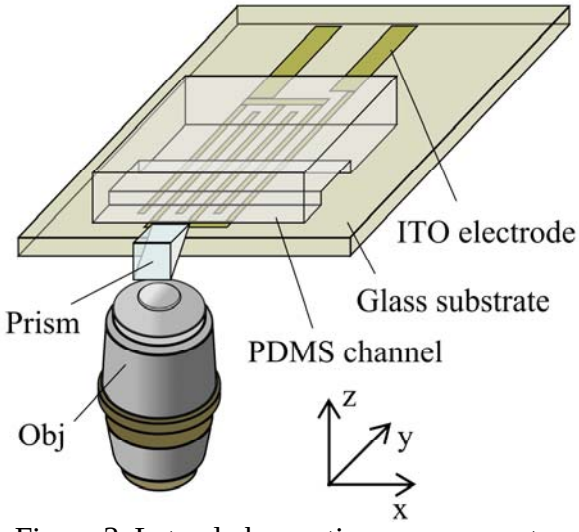

Figure 3. Lateral observation arrangement

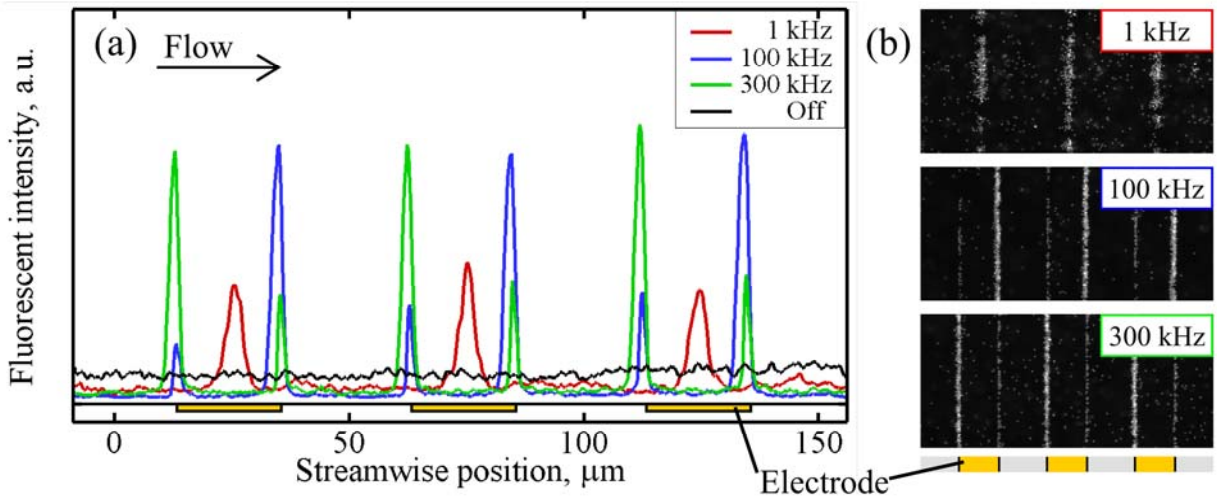

Figure 4. Particle distribution with different applied frequency
(a) Fluorescent intensity distribution (b) CCD image

was located on the center of each electrode. On the other hand, at 100 and 300 kHz, the peak was at the electrode edge. This frequency-dependence is due to the difference in the contribution of DEP and ET on the particle behavior. At 1 kHz, the particle motion along the electrode surface is recognized before the collection on the center of electrode; this is considered as the positive ET convection. At 100 and 300 kHz, particles gather around the electrode edge as if they experience the attraction force toward the edges. The origin of the attraction force and counterflow is DEP and ET, respectively. At 100 kHz, the particles move to the electrode gap due to the positive ET convection as well as the positive DEP. Therefore, the fluorescent intensity is higher at the upstream edge of the electrode gap because the relative velocity of particle becomes lower around the upstream edge. At 300 kHz, since the negative ET convection force acts on the particle, the fluorescent intensity is higher at the downstream edge of the electrode gap. These results indicate the two phenomena of DEP and ET have different features.

Validity of lateral observation arrangement

The microfluidic device used in this study consists of the different materials PDMS and glass. Therefore, in the case of using the lateral observation arrangement, it can be considered that difference of the refraction indices might distort the image in heightwise direction. As a preliminary step for the measurement of particle velocity from the side wall of the channel, the validity of measurement with the lateral observation setup was investigated. The thickness of the side PDMS wall around center of the microchannel was made to 125 μm. Figure 5 shows a velocity profile in the microchannel measured from the side wall. The measured velocity distribution indicates a good agreement with Poiseuille flow without distortion in heightwise direction.

Behavior of particle subjected to AC electric field

ET convection. The micro-PIV measurement with the lateral observation was carried out to confirm the detail of the particle behavior. In this experiment, the particle images without the flow were acquired. Figure 6 indicates the velocity field of the particles with 1 $V_{p\text{-}p}$ at 1 kHz. The counter-rotating behavior with strong tangential flow on the electrode surface is observed. This flow pattern agrees with the characteristics of the flow induced by ET effect. X-component velocity distributions in heightwise cross-section at the center of the rotation (x = ± 19 μm) are shown in Figure 7. Figure 8 depicts the z-component velocity distribution in the cross-section passing the rotational center (z = 7.3 μm). The particle velocity in x-component around the electrode plane is about 60 μm/s, and this is higher than the z-component one. In the vicinity of the edge, it is confirmed that the particles approach the electrode edges as shown in two valleys of the heightwise velocity in Figure 8. Therefore, these results indicate that the particle is subjected to the resultant force of the body force

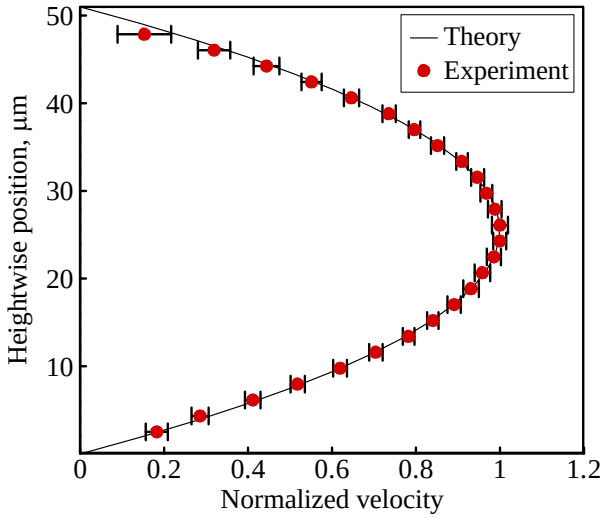

Figure 5 Channel flow measured from side wall

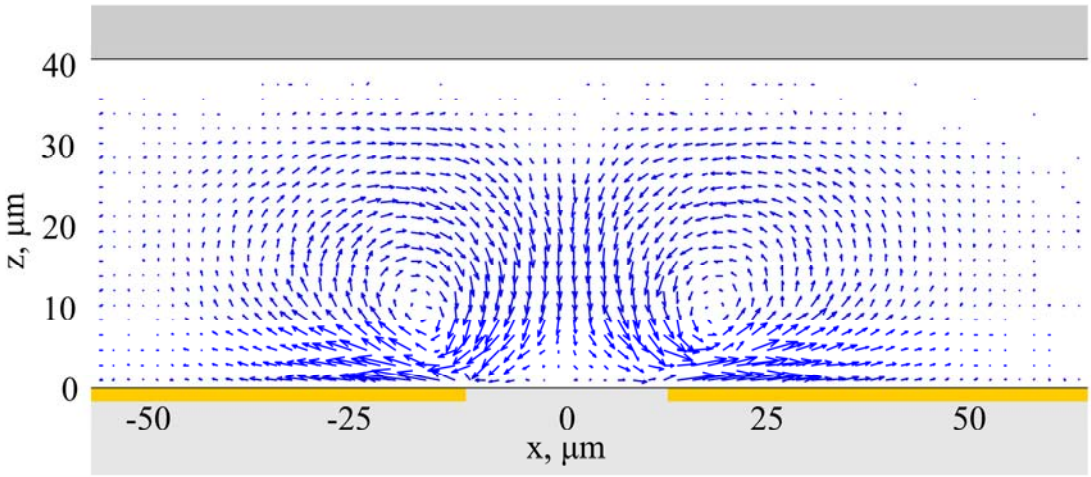

Figure 6. Particle velocity field at 1 kHz with 1 V_{p-p}

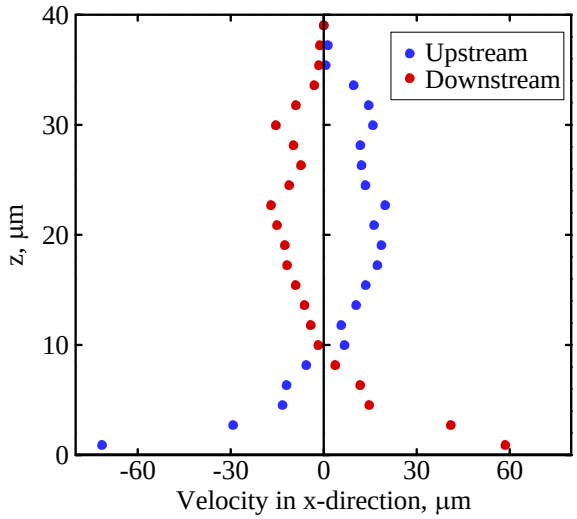

Figure 7. Heightwise distributions of particle velocity at the rotational center

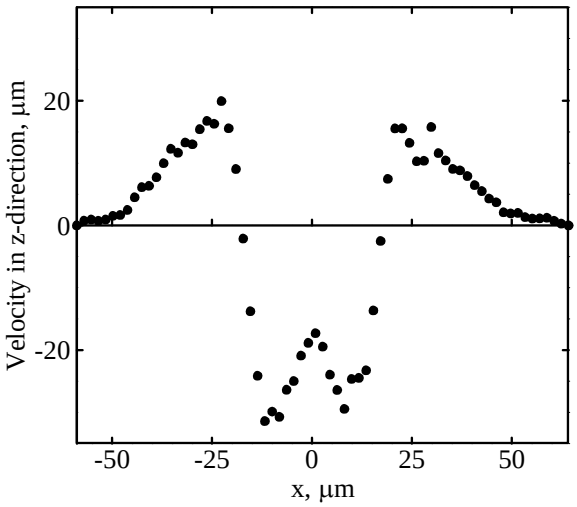

Figure 8. Streamwise distribution of particle velocity at the rotational center

by ET convection and the dielectrophoretic force by DEP attraction. It can be said that the measurement field is dominated by positive ET under the applied frequency of 1 kHz.

Evaluation of particle mixing. In order to evaluate the effect of the particle mixing, comparison with the spontaneous diffusion by Brownian motion was performed. The root mean square displacement of the particle due to Brownian motion is given by,

$$\Delta l = \sqrt{\frac{2k_B T}{3\pi d\eta}\Delta t} \tag{4}$$

In this study, for the quantitative assessment of the particle mixing, we define the mixing coefficient as a ratio of the particle migration distance under electric field to the Brownian displacement,

$$\phi = \frac{v\Delta t}{\Delta l} \tag{5}$$

Here, the mixing coefficient per unit time was evaluated. Figure 9 shows the contour of streamwise- and heightwise- component of mixing coefficient at 1 kHz. In x-component, there are two local peaks with high mixing coefficient around the electrode surface. The similar experiments in the frequency range of 1 ~ 100 kHz are carried out. The spatial-averaged mixing coefficient in all the measurement area and the electrode gap region was calculated. The relation between the averaged mixing coefficient and the applied frequency is shown in Figure 10. In this range, the mixing coefficient is increased as the frequency is decreased. The high heightwise mixing effect can be obtained at the gap area under 30 kHz. It is confirmed that the mixing with the low voltage of 1 V_{p-p} is possible.

DEP attraction. Next, the applied frequency was switched to 300 kHz. Since the significant behavior of the particles was not confirmed, the applied voltage was elevated to 3 V_{p-p}. In this condition, the particle behavior differs much from the that at 1 kHz. Figure 11 shows the particle velocity field with 3 V_{p-p} at 300 kHz. The particles migrate toward the electrode edges, and weak upward flow at the center of the electrode gap is recognized. The nearer the electrode edge, the stronger the DEP force acting on the particle is. The particle velocity around the electrode edges is about 9 μm/s. It is considered that the particle is exerted by the negative ET and the positive DEP.

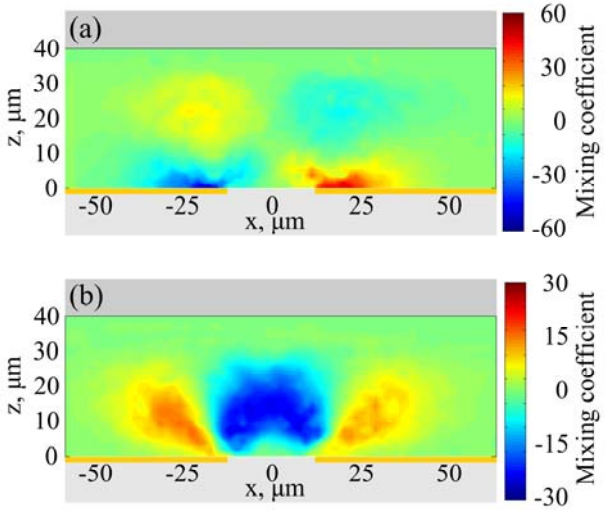

Figure 9. Spatial distribution of mixing coefficient
(a) Streamwise component
(b) Heightwise component

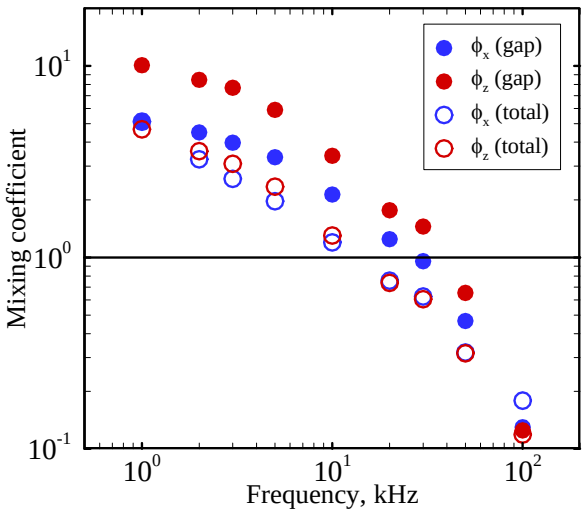

Figure 10. Frequency dependence of average mixing coefficient at 1 ~ 100 kHz with 1 V_{p-p}

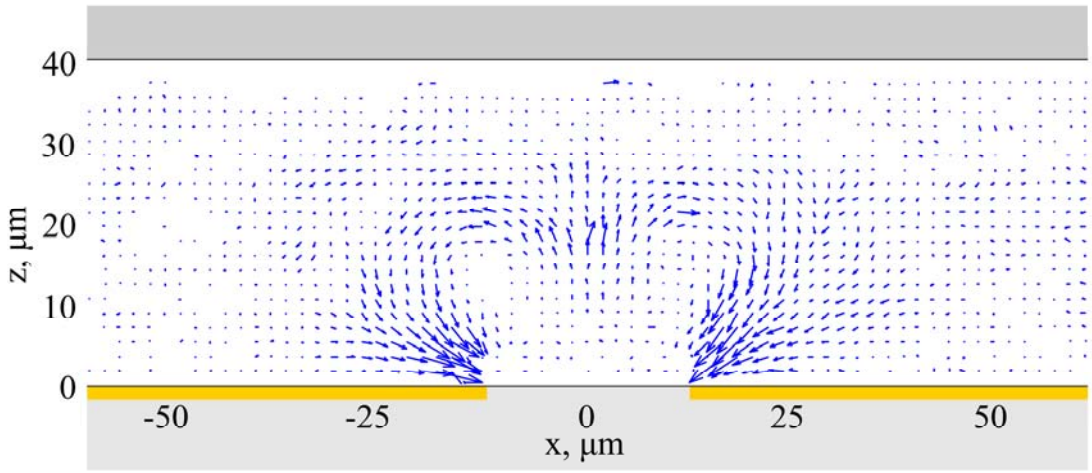

Figure 11. Particle velocity field at 300 kHz with 3 V_{p-p}

The particles are convected by the negative ET and finally attracted to the electrode edges. Therefore, it can be said that this behavior is efficient movement as mixing rather than collection.

CONCLUSIONS

In this study, the particle mixing based on AC electrokinetics is investigated. It is confirmed that the difference of the particle behavior depending on the applied frequency is caused by the frequency-dependent contribution of dielectrophoresis and electrothermal effect. The distributions of the fluorescent intensity indicate that the positive DEP is dominant in the range of 100 ~ 300 kHz and the cross frequency which changes the ET direction exists between 100 and 300 kHz. The measurement result of the particle velocity field indicates that these two forces act on the particle simultaneously. The efficient particle operation for mixing is evaluated by the mixing coefficient, and it is confirmed that the coefficient increases as the frequency decreases. Finally, our results imply the validity of the innovative mixing control with frequency selection.

NOMENCLATURE

d	particle diameter	m
E	electric field	V/m
j	imaginary number	-
k_B	Boltzmann's constant	-
Δt	observation period	s
T	absolute temperature	K
v	particle velocity	m/s
Δl	displacement associated with Brownian motion	m
x	streamwise coordinate	m
y	spanwise coordinate	m
z	heightwise coordinate	m
ε	relative permittivity	-
η	viscosity of fluid	Pa·s
σ	electric conductivity	S/m
τ	charge relaxation time of fluid	s
ϕ	mixing coefficient	-
ω	angular frequency	1/s

REFERENCES

1. R. H. Liu, Passive Mixing in a Three-dimensional serpentine microchannel, *Journal of Microelectromechanical Systems*, Vol. 9, No. 2, pp. 190-197, 2000.
2. I. Glasgow, Electroosmotic mixing in microchannels, *The Royal Society of Chemistry 2004*, Vol. 4, pp. 558-562, 2004
3. X. Xuan, Electroosmotic flow with Joule heating effects, *The Royal Society of Chemistry 2004*, Vol. 4, pp. 230-236, 2004
4. T. B. Jones, Electromechanics of particles, pp. 34-48, 2005
5. A. Ramos, Ac electrokinetics: a review of forces in microelectrode structures, *Journal of Physics D: Applied Physics*, Vol. 31, pp. 2338-2353, 1998
6. J. Y. Jung, Separation of microparticles and biological cells inside an evaporating droplet using dielectrophoresis, *Analytical Chemistry*, Vol. 79, No. 13, pp. 5087-5092, 2007

EXPERIMENTAL MEASUREMENT OF ENERGY ACCOMMODATION COEFFICENT FOR METAL SURFACE BY LOW-PRESSURE METHOD

H. Yamaguchi[1, *], Y. Aoki[1], Y. Matsuda[1], T. Niimi[1]
[1]Nagoya University, Nagoya, Japan

ABSTRACT. The energy accommodation coefficients for metal surface have been measured by the Low-Pressure method. The energy accommodation coefficient was deduced from the pressure dependence of the heat flux between concentric cylinders. Experimental results are reported for argon and oxygen in contact with a platinum surface. The surface temperature dependence of the energy accommodation coefficients is also studied, and discussed in comparison with previous results.

Keywords: *Energy accommodation coefficient, Low-Pressure method, Gas-surface interaction, Heat flux, High Knudsen number flow*

INTRODUCTION

Heat transfer to and from surfaces in micro flow fields has been an important research field because of problems in removal of heat generated in micro-devices along with the progress in micro- and nano-technology. In micro gas flows, the molecular mean free path, λ, becomes comparable to the characteristic length of the system, L. Knudsen number, Kn, which is defined as a ratio of the molecular mean free path to the characteristic length of the system, is large in these so-called "high Knudsen number flows". Noncontiuum effects appear in high Knudsen number flows, and gas-surface interaction becomes dominant over the flow field compared to interactions between gas molecules.

Gas-surface interaction phenomena have been investigated for a long time. Detailed information about the interaction has been investigated using molecular beam scattering experiments and molecular dynamics simulations. However, for a simple thermal design of a system, the accommodation coefficient, which illustrates overall gas-surface interaction without any detailed processes, is the most widely used empirical parameter. The energy accommodation coefficient, α, is defined as

$$\alpha = \frac{E_i - E_r}{E_i - E_s}, \tag{1}$$

where E_i is the averaged incident energy, E_r is the averaged reflected energy, and E_s is the averaged energy when the reflected molecules are in equilibrium at the surface temperature.

The energy accommodation coefficient has been experimentally measured with several methods in a variety of gas-surface combinations. However, there are few reports on the energy accommodation coefficient of non-metallic surfaces, which are important materials for micro- and nano-technology. Therefore, we set our final goal as the measurement of the energy accommodation

* Corresponding author: Dr. H. Yamaguchi
Phone: + (81)-52-789-2701, Fax: + (81)-52-789-3124
E-mail address: hiroki@nagoya-u.jp

coefficients on non-metallic surfaces. To establish a measurement scheme, the energy accommodation coefficient was measured experimentally for a metal surface in this research.

LOW PRESSURE METHOD

The energy accommodation coefficient was measured following the Low-Pressure method [1]. In this method, the energy accommodation coefficient is obtained from the temperature dependence of the heat flux between two surfaces with a certain temperature difference in the free-molecular flow regime. Experimental setup was designed as the geometry of two concentric cylinders with a gas filled gap. In the free-molecular flow regime, theoretical heat flux between two cylinders, q, as in Figure 1 depends on gas-surface interaction, i.e. the energy accommodation coefficient.

The radii of the inner cylinder and the outer cylinder are defined as r and R, respectively. The temperature of the inner cylinder, T_H, is higher than that of the outer cylinder, T_C. The gas between the cylinders is quiescent, thus conduction is dominant in the heat transfer between the cylinders: convection is negligible.

The heat flux between concentric cylinders is described depending on the gas phase flow regime. In the free-molecular limit, q_{FM}, where $Kn \gg 1$ and in the continuum limit, q_C, $Kn \ll 1$, the description is exactly shown [1,2]:

$$q_{FM} = \frac{1}{2}\alpha\left(1+\frac{\zeta}{4}\right)\frac{\bar{c}}{T}p\left(T_H - T_C\right), \tag{2}$$

$$q_C = \frac{k}{r\ln\left(R/r\right)}\left(T_H - T_C\right), \tag{3}$$

where ζ is the number of internal degrees of freedom of gas molecules, $\bar{c}$ is the mean speed of the gas molecules, T is the average temperature of the gas, and k is the gas thermal conductivity. q_{FM} is proportional to the pressure, p, whereas q_C is independent of p.

In the transitional regime between the two limits, the heat flux, q, is often approximated as [2],

$$\frac{1}{q} = \frac{1}{q_{FM}} + \frac{1}{q_C}. \tag{4}$$

Since the condition for a free-molecular flow is quite severe in our experimental measurements, the analytical form extended to the transitional regime, eq. (4), was employed to derive the energy accommodation coefficient in this research.

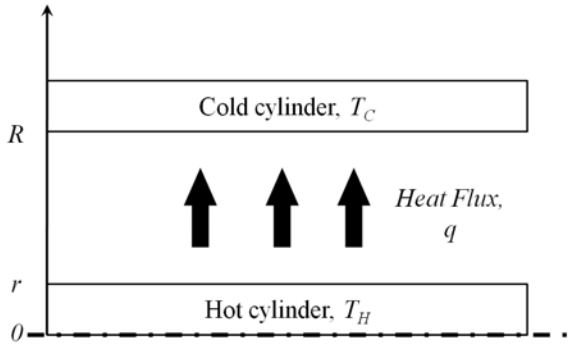

Figure 1. Schematic image of the geometry of concentric cylinders.

EXPERIMENTAL SETUP

The concentric cylinders were realized with a non-treated thin platinum wire and a Pyrex cylinder in this research. The radii of the wire and the cylinder were 25 μm and 6 mm, respectively. Argon and oxygen were chosen as a test gas. The pressure was ranged from the free-molecular to the transitional regime, and was measured with MKS 627B Baratron pressure transducer. The temperature of the Pyrex cylinder was uncontrolled and was measured by K-type thermocouple. The temperature of the thin platinum wire was controlled by an analog bridge circuit, which was similar to that used in the hot-wire airflow meter or the Pirani gauge, and the heat transfer was calculated from the electrical power consumption of the wire. The temperature was deduced theoretically from the resistance of the wire using the temperature dependence of the specific electric resistance of platinum.

RESULTS AND DISCUSSIONS

Heat Flux between Cylinders

The heat flux between the thin platinum wire and the Pyrex cylinder is proportional to the pressure in the low pressure range, and asymptotically increase to a constant value. The measured heat flux and the fitted analytical curve by eq. (4) to determine the energy accommodation coefficient for argon at the surface temperature of about 450 K are plotted in Figure 2 with red circles and blue solid line, respectively. From these results, the energy accommodation coefficient was obtained to be 0.822 in this case, which is smaller than unity.

Temperature Dependence of Energy Accommodation Coefficient

The energy accommodation coefficient is known to be affected by surface conditions, such as temperature, roughness, and so on. To investigate the temperature dependence, the temperature of the thin platinum wire was changed from about 300K up to about 600K. The obtained energy accommodation coefficients are plotted in Figure 3 with the results given in the previous report [3]. They show quite similar with previous reported results, and the energy accommodation coefficients decrease as the surface temperature increases. The results for oxygen shows smaller value compared with that for argon.

Energy Accommodation Coefficient of Platinum Surface

For metal engineering surfaces, the energy accommodation coefficient is often assumed to be unity, i.e. the scattering process is modeled by the diffuse reflection. However, it must be inappropriate from these results. The energy accommodation coefficient varies according to the gas species and the surface temperature, and the temperature dependence is also different from one to one.

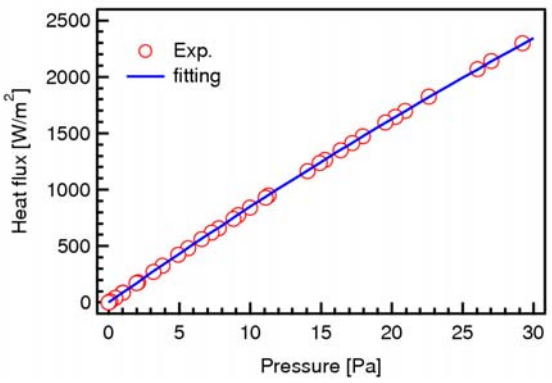

Figure 2. Pressure dependence of heat flux between cylinders for argon at the surface temperature of about 450 K.

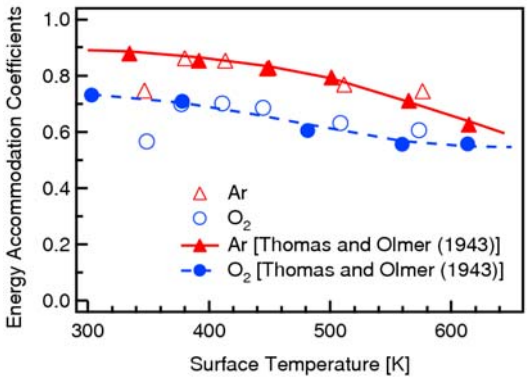

Figure 3. Temperature dependence of energy accommodation coefficients.

Since the gas-surface interaction significantly influences the micro-flow field, the energy accommodation coefficient for various pairs of gas and surface should be experimentally investigated in detail further.

CONCLUSIONS

The energy accommodation coefficients for non-treated platinum surface have been measured by the Low-Pressure method with the simple concentric cylinder geometry. The energy accommodation coefficient was obtained from the pressure dependence of the heat flux between the cylinders. The energy accommodation coefficients are reported for argon and oxygen for wide range of surface temperature, which show good agreement with previously reported results. The energy accommodation coefficients show decreasing against the surface temperature increase, and the tendency is deferent for argon and oxygen.

ACKNOWLEDGEMENT

This research was supported by a Grant-in-Aid for Scientific Research from the MEXT and JSPS, Japan.

REFERENCES

1. Goodman, F.O. and Wachman, H.Y., *Dynamics of Gas-Surface Scattering*, Academic Press (1976).
2. Trott, W.M., Rader, D.J., Castañeda, J.N., Torczynski, J.R. and Gallis, M.A., AIAA2007-4039 (2007).
3. Thomas, L.B. and Olmer, F., *Journal of American Chemical Society*, **65**, pp.1036-1043 (1943).

NONCONTAT MANIPULATION OF MICROFLOW BY PHOTOTHERMAL CONTROL OF VISCOUS FORCE

M. Motosuke[1, *], J. Shimakawa[1], D. Akutsu[1], S. Honami[1]
[1]Tokyo University of Science, Tokyo, Japan

ABSTRACT. This paper describes the experimental validation of a novel noncontact microflow manipulation by the local control of the viscous force. This technique relies on the photothermal technique to induce a local viscosity distribution in microflow. The absorption of focused laser beam generates the change in the viscosity of the fluid corresponding to the temperature rise. The temperature and velocity was measured by the micron-resolution particle image velocimetry and laser-induced fluorescence, respectively. Measurement results indicate that the local variation of the viscosity due to the temperature rise can cause the change in flow structure. At the high temperature area, the streamwise velocity was increased. In addition, the agreement between the experimental results and numerical simulation clarifies that the primary factor for the change of the microflow structure is the locally controlled viscous force.

Keywords: *microfluidics, viscosity, photothermal effect, local property control*

INTRODUCTION

Microfluidic system has recently emerged owing to the development of micro- / nano- fabrication technology, and attracted considerable attention from biological, medical, chemical and engineering fields [1]. The miniaturized system offers several advantages over conventionally sized one, including small sample volume, short reaction time, portability and potential for parallel operation. In microscale, the effect of properties on transport phenomena becomes dominant; heat conduction, mass diffusion, interfacial tension and viscous force often dominate the system [2]. An appropriate control on the property can be an effective thermal and fluid handling method especially for the microfluidic device. In this study, we have focused on the local control of the viscosity, because the viscous force is dominant in low Reynolds number flow in the microdevice. A local spot with different viscosity can yield a spontaneous shear force, and then it may cause the change in flow structure. In order to induce the local viscosity distribution in a liquid flow, the photothermal effect which is a property variation due to the light-induced temperature change [3], is utilized. The viscosity of liquid is known as the temperature-sensitive property, and the method using the viscosity change by the temperature variation can be applied in various liquids. In addition, an optical based technique has attractive features such as non-intrusive and high temporal- / spatial-resolution, and also has a possibility for a flexible flow control. In the present paper, we discuss a potential of the noncontact control of the flow behavior in a microfluidic device by changing the viscosity in the liquid by means of photothermal effect. The temperature field of a liquid flow in a microfluidic device was measured, and the corresponding velocity measurement in the field with the local viscosity change was performed. Furthermore, the temperature and velocity profiles were compared with those from the numerical simulation.

* Corresponding author: Dr. M. Motosuke
Phone: + (81)-3-32604272, Fax: + (81)-3-52130977
E-mail address: mot@rs.kagu.tus.ac.jp

EXPERIMENTAL SYSTEM

Microfluidic device

In this study, a microchannel structure made of PDMS (polydimethylsiloxane) elastomer was fabricated by soft lithography [4]. PDMS has highly transparent in visible wavelength [5] so that an optical access for heating or measurement is possible. Figures 1 and 2 show the fabrication process and a schematic of the microchannel. A master mold is fabricated by the standard photolithography process with SU-8 photoresist on a silicon wafer. Then the PDMS mold with the negative relief structure is prepared by casting over the master mold. The PDMS mold is placed on the glass substrate and sealed. The difference in liquid surface levels between inlet and outlet reservoirs causes the stable pressure-driven flow in the microchannel. The microchannel has rectangular cross section with 50 μm in height, 200 or 500 μm in width, and the length is 40 mm. The Reynolds number in the present experimental condition was less than 0.1.

Heating optical setup

Figure 3 (a) indicates the overview of heating optical system. In the experimental system, a compact diode laser (LD) with the wavelength of 635 nm is used as the heating source. The LD beam is focused by an objective lens (Obj 1) and irradiated into the microchannel. The irradiation timing and power of LD beam can be controlled by a function generator (FG). The use of low magnification lens with long focal length enables the suitably constant beam waist within the microchannel. Therefore, the temperature rise of the fluid around the center in heightwise direction is assumed to be uniform.

Temperature and velocity measurement system

A schematic of the measurement system for temperature and velocity is shown in Figure 3 (b); measurement is conducted from the lower part of the microchannel. The temperature measurement is performed by micro-LIF (laser-induced fluorescence), which uses a temperature-sensitive fluorophore dissolved in the liquid [6]. The temperature of fluid can be determined by utilizing the inverse function of the calibration function f_c which relates the fluorescent intensity to the temperature of the solution, as presented in equation (1).

$$T = f_c^{-1}\left\{\frac{I(T) - I_d}{I_{ref} - I_d}\right\} \tag{1}$$

Here, the fluorescent intensity for the calibration was normalized by that at a reference temperature after subtracting the background intensity. Although rhodamine B is a popular fluorescent dye with strong temperature dependence in the fluorescent intensity [7], slight absorption in the wavelength of the heating laser in this study (635 nm) might affect the emission intensity distribution. Thus, fluorescein (FL) which does not absorb the LD wavelength was used as the temperature sensitive

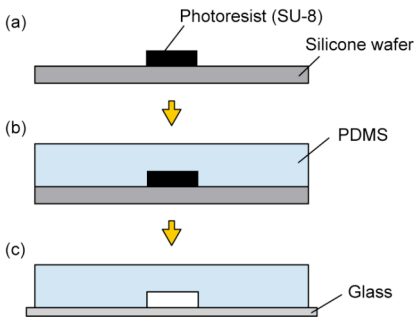

Figure 1. Fabrication process of soft lithography (a) Relief structure (b) Casting (c) Sealing

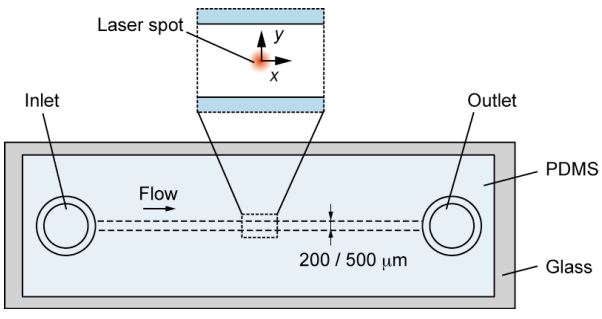

Figure 2. Schematic of PDMS microchannel

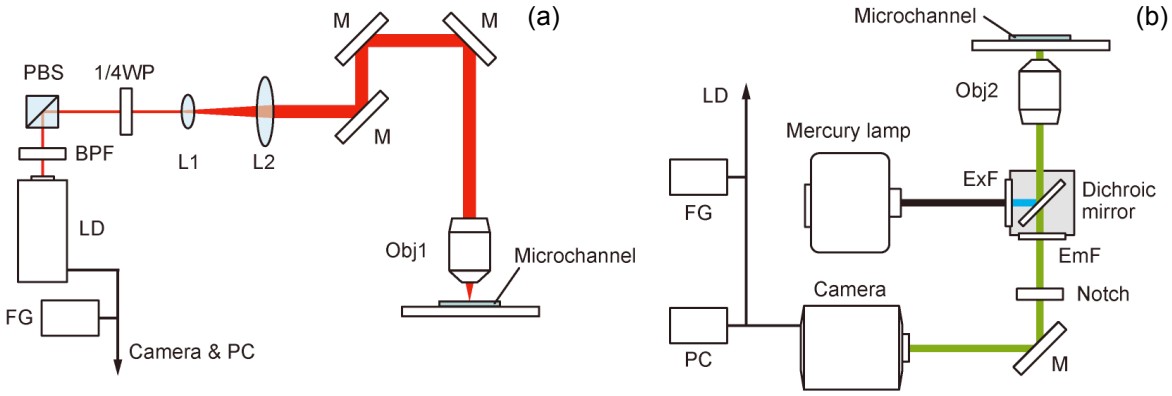

Figure 3. Schematic of experimental setup (a) Heating system (b) Measurement system

fluorescent dye. In addition, fast lifetime of fluorescence in FL of 3-4 ns is suitable to apply the dynamic flow field. The velocity field is measured by micro-PIV (particle image velocimetry), in which the velocity can be obtained by the image processing for the motion of fluorescent tracer particles in the focal plane of an objective lens [8]. Fluorescent polystyrene particles with the nominal diameter of 700 nm are used as tracer. Considering the specification of the objective lens for velocity measurement having a magnification of 40 and NA of 0.95 (air immersion), the measurement depth defined by following equation (2) [9] results in 3.0 μm.

$$\Delta z = \frac{3n\lambda}{\mathrm{NA}^2} + \frac{2.16 d_p}{tan\theta} + d_p \qquad (2)$$

Time-averaging procedure is used in the image processing to reduce the random Brownian motion of tracer particles. By adopting this, RMS value in a measured velocity field can be reduced from 5.5 (instantaneous) to 0.4 % (100 pairs averaged). Both in micro- PIV/LIF system, a mercury lamp is used as the illumination source, and an excitation filter extracts the wavelength for the excitation of fluorescent dye or particle. Fluorescent image is obtained by a Peltier-cooled CCD camera or a CMOS camera with an image intensifier. A notch filter inserted in front of the camera is designed to eliminate only the LD wavelength. The excitation and emission peak wavelengths of the fluorescent dye for temperature measurement and the particle for velocity measurement are indicated in Table 1. Because of the similar bands for the temperature and velocity measurement, the same optical system including filters can be used in this study. The measurement section in heightwise direction was set at the center of the microchannel, $z = 25$ μm.

Table 1
Properties of fluorescent dye and particle

	Temperature	Velocity
Material	Fluorescein	Polystyrene
Size (nm)	0.14 (soluble)	700
Excitation wavelength (nm)	494	468
Emission wavelength (nm)	521	508

Working fluid

The working fluid is buffer solution, hydrodynamically regarded as water. In order to absorb the wavelength of the heating beam, non-fluorescent absorption dye of Brilliant Blue FCF (BB) is added. BB has strong absorption band in the wavelength range over 600 nm. Thus, BB aqueous solution can be heated by the irradiation of LD in the present setup without an interference with the wavelength for excitation and emission to measure the temperature or velocity. Since fluorescein

has strong pH dependence on the fluorescent intensity, it is necessary to prevent pH variation according to the temperature change. In this study, tetra-borate buffer solution (pH 9.18) was employed; the effect of the variation in the fluorescent intensity due to pH variation corresponding to the temperature change on the measurement value of the fluid temperature was estimated to be less than 1 K.

RESULTS AND DISCUSSION

Temperature calibration experiment

As a preliminary step to measure the temperature of the working fluid from the fluorescent intensity, the calibration experiment was conducted with a constant temperature plate connected to the circular water bath. The temperature range for the calibration was 283 to 343 K. Figure 4 presents the temperature dependence of fluorescent intensity in several concentration of absorption dye, BB. The concentration of FL is fixed to 0.1 mM. The higher temperature dependence in higher BB concentration implies a little overlap in the distributions between the absorption of BB and the emission of FL. This is recognized as a slight decay at high wavelength in the fluorescent spectrum obtained by a spectroscope. There is no shift around the peak wavelength of FL emission in the present temperature range. There are two ways to deal with this issue; one is to use another emission filter (EmF) transmitting narrowly around the peak emission wavelength, and the other is to obtain the calibration function at each BB concentration. In this study, the calibration curve for each BB concentration is approximated by the third-order polynomial fit to determine the relationship between temperature and the fluorescent intensity normalized by the value at 298 K.

Change in microflow structure with local temperature distribution

Figure 5 shows the temperature field measured by micro-LIF and the relative velocity field where the relative velocity between the velocity with and without the laser heating is indicated. The reference velocity at the center span, u_{ref}, was approximately 1800 μm/s and the concentration of BB was 0.5 mM. The focused beam diameter was 7 μm, and the laser power at immediately above the microchannel was 4 mW. It is clear that the flow velocity is increased at around the high temperature area. In this result, the increment in the streamwise velocity was about 7 % of u_{ref}, and the temperature rise at the position was around 30 K. This change in the flow behavior is induced by adding the local temperature rise in microflow. Figure 6 depicts the laser-induced velocity variation in streamwise and spanwise velocities at x = 0 and ± 40 μm. The streamwise velocity variation upstream of the heated area was higher than the downstream one, as shown in Figure 6 (a). This is attributed to the difference of the temperature rise in the streamwise direction due to the convection toward downstream. Moreover, there was the decrease in the velocity away from the heating spot in spanwise direction. The spanwise velocity profiles in Figure 6 (b) means a

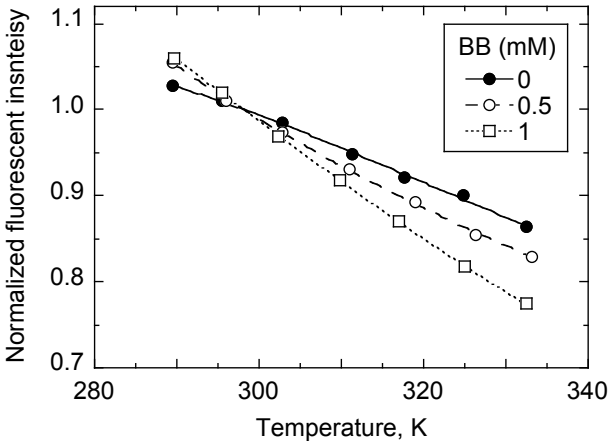

Figure 4. Calibration curves with FL concentration of 0.1 mM

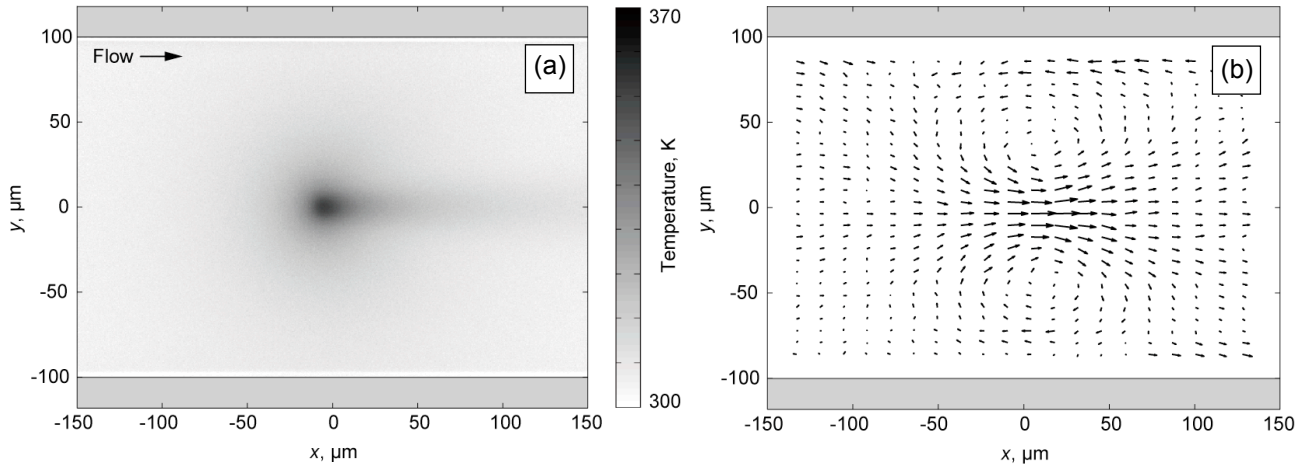

Figure 5. Temperature and velocity field with laser irradiation
(a) Temperature (b) Relative velocity

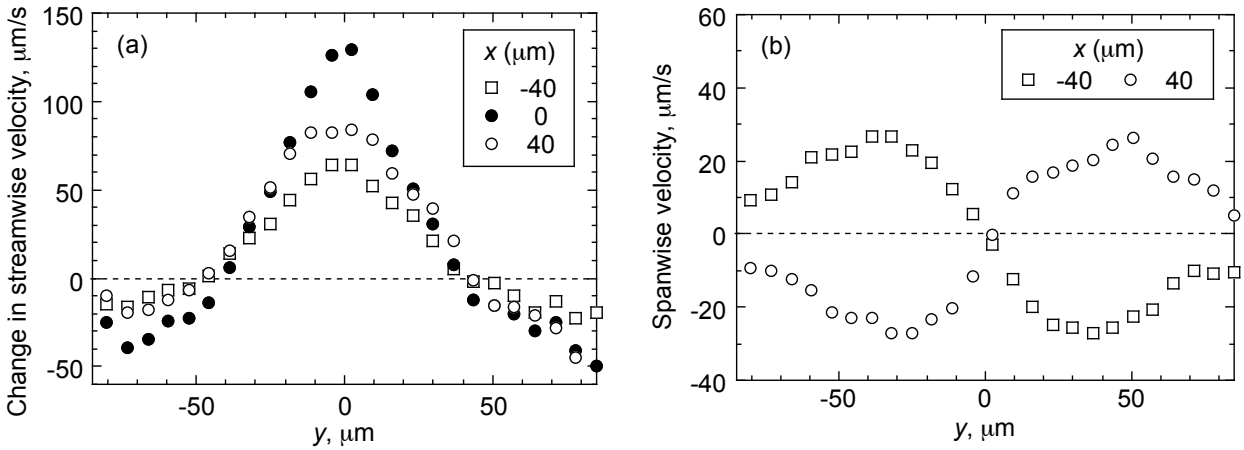

Figure 6.Profiles of velocity change with laser heating at $x = 0$ and ± 40 μm
(a) Streamwise component (b) Spanwise component

convergence flow into the center span at upstream region and an outflow at downstream area. In addition, it is found that the flow field in spanwise direction has a symmetric structure. This behavior can be explained as the nature of continuum. Since the area with high temperature has low viscosity, fluid tends to flow into the region with a low flow resistance. After passing the low viscous area, then, the spreading flow occurs. For further investigation, the effect of the focused laser irradiation near the sidewall of the cannel was investigated. Figure 7 depicts the velocity field including the dependence of the laser power. Here, PDMS microchannel with 500 μm in width was used. For the measurement without change in the measurement depth, Δz, a relay lens with magnification of 0.7 was set in light path between the objective lens and the camera. The heating beam diameter and u_{ref} was 50 μm and 1300 μm/s, respectively. The velocity variation similar to that shown in Figure 4 (b) can be observed, and the maximum velocity at the region of the laser heating is increased with the increase of the irradiating laser power. Accordingly, the reduction of the velocity is increased. Furthermore, the position where the streamwise velocity does not change is independent of the laser power. In order to examine the influence of u_{ref} on the change in flow structure, the velocity measurements with different u_{ref} was performed. For an appropriate evaluation, the same microchannel was used under the same heating condition, and u_{ref} set here was 1420 and 3200 μm/s. As a result, there is no variation in the induced velocity profile by the laser heating against u_{ref}. In a preliminary experiment, the similar changes of the velocity profiles were observed with u_{ref} of 10, 50 or 100 μm/s. Given the same viscosity distribution in the fluid, this u_{ref}

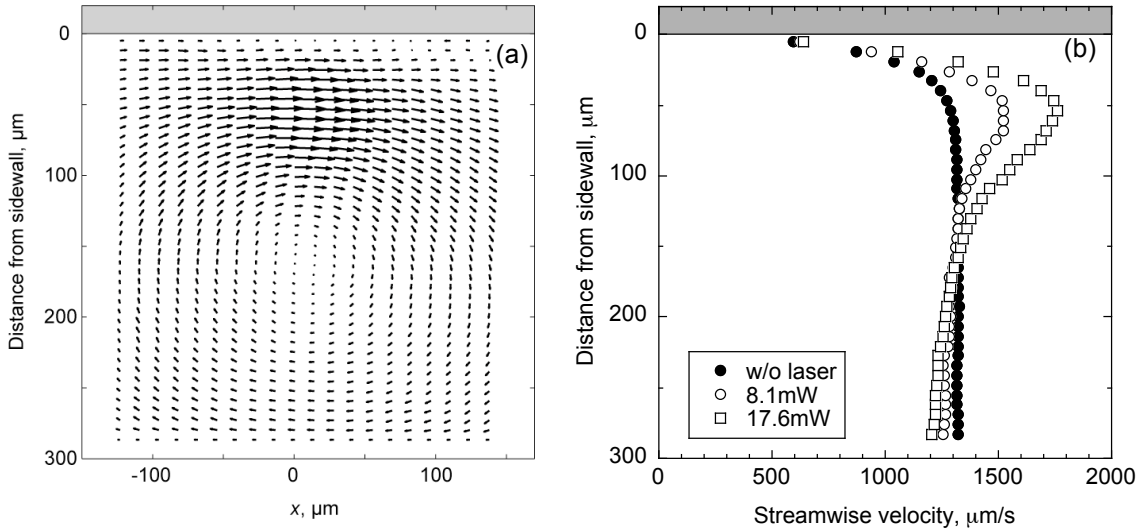

Figure 7. Microflow behavior with local temperature distribution near sidewall (a) Relative velocity field (b) Comparison of streamwise velocity at $y = 0$ without laser and with different irradiation power

independence is reasonable under the literalized Stokes equation which is valid in low Reynolds number flow [10]. From these experimental results, it is confirmed that the generation of local temperature distribution causes the change in microflow structure.

Comparison between experimental and numerical results

The main factor which causes the velocity variation under the local temperature rise is assumed to be the distribution of the viscous force. However, above-mentioned results are not sufficient to uniquely characterize the origin of the change in microflow structure, because the temperature change can provoke the variation in other properties. In this study, a comparison with the numerical simulation was performed. The geometry of the microchannel model was a three-dimensional straight channel with the same cross-sectional area as the PDMS channel of 200 μm in width and 50 μm in height. The Navier-Stokes, continuity and energy conservation equations were coupled. The heat source considered here has the Gaussian intensity distribution as in the TEM_{00} mode of the laser beam. The beam diameter was set at 7 μm, which was the same as the experimental condition. In this calculation, the heat generation density was adjusted to fit the temperature data measured by

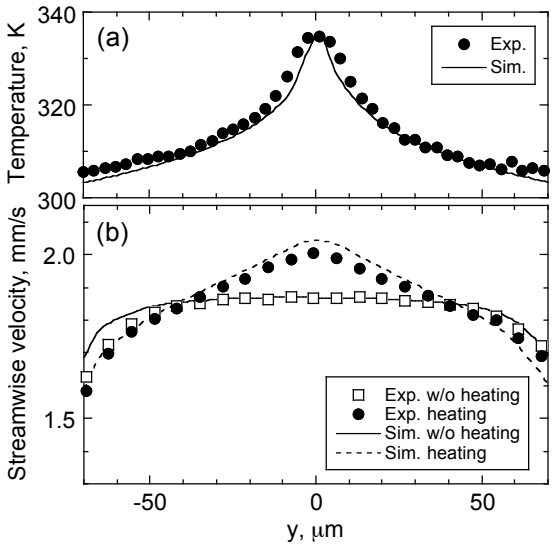

Figure 8. Comparison of temperature and velocity profiles between experiment and simulation (a) Temperature (b) Streamwise velocity

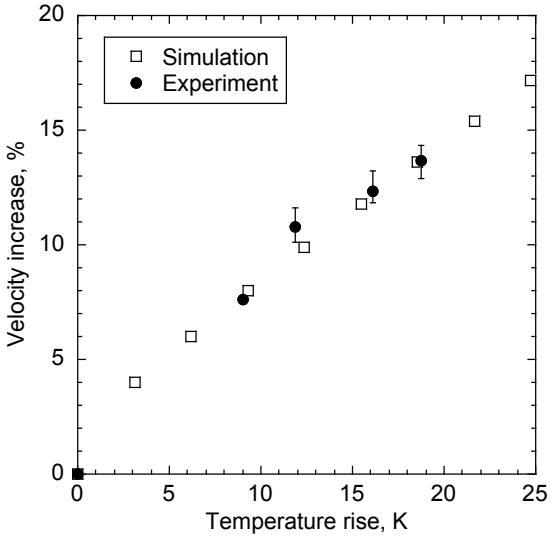

Figure 9. Dependence of temperature rise by laser heating and the induced velocity increase at beam spot

micro-LIF, because this parameter strongly depended on the optical transmitting or scattering characteristics of PDMS microchannel. Working fluid was water, and only the temperature dependence of the viscosity was considered. Numerical analysis was conducted with the finite element simulation software *COMSOL Multiphysics*. Figure 8 shows experimental and simulated results of the temperature and streamwise velocity profiles at $x = 0$ (beam spot position). Both simulated velocity profiles with and without heating indicate good agreement with those in the experimental results. This agreement means that the primary factor to induce the velocity change is the local variation of the liquid viscosity. The relationship between the maximum temperature rise at the beam spot and the corresponding velocity increase is depicted in Figure 9. The tendency of the positive dependence of the temperature rise which is controlled by the beam intensity on the velocity increment can be obtained in both results. A slight departure from the linear relationship is attributed to the nonlinearity in the temperature dependence of the viscosity. These numerical investigations elucidate the role of the local change in viscosity on the flow structure in the microfluidic device.

CONCLUSIONS

An investigation of a potential of the photothermally-induced distribution of the viscosity for the manipulation of the liquid flow in a microfluidic device was conducted. Micro- PIV and LIF was utilized for the velocity and temperature measurement of the microflow undergoing the local heating. At the heated area where the working fluid has low viscosity, the velocity was increased due to the local reduction of the flow resistance. The distribution of the viscosity also yields an accompanying flow both upstream and downstream of the high temperature region. It was found that the primary factor causing the change in flow structure was the distribution of temperature-dependent viscosity. The velocity fields obtained by the present experiment agree well with those from the numerical simulation considering the temperature dependence of the viscosity. This flow behavior owing to the local temperature change can be controlled by the irradiation condition including the beam parameter or the impinging location.

NOMENCLATURE

d_p	particle diameter	m
I	light intensity	-
I_d	background light intensity	-
I_{ref}	light intensity at reference temperature	-
n	refractive index	-
NA	numerical aperture	-
T	temperature	K
u	streamwise velocity	m/s
u_{ref}	streamwise velocity at channel center	m/s
x	streamwise direction	m
y	spanwise direction	m
z	heightwise direction	m
Δz	measurement depth	m
λ	wavelength	m
θ	collection angle	rad

REFERENCES

1. P. Tabeling, *Introduction to Microfluidics*, Oxford University Press, 2005.
2. P. B. Bird, W. E. Stewart, E. N. Lightfoot, *Transport Phenomena 2nd ed.*, John Wiley & Sons, Inc., 2002.

3. D. P. Almond, P. M. Pater, *Photothermal Science and Technology*, Chapman & Hall, 1996.
4. Y. Xia, G. M. Whitesides, Soft Lithography, Annual Review of Material Science, Vol. 28, pp. 153-184, 1998.
5. J. C. McDonald, G. M. Whitesides, Poly(dimethylsiloxane) as a Material for Fabricating Microfluidic Devices, *Accounts of Chemical Research*, Vol. 35, No. 7, pp. 491-499, 2002.
6. D. Ross, M. Gaitan, L. Locascio, Temperature Measurement in Microfluidic Systems Using a Temperature-Dependent Fluorescent Dye, *Analytical Chemistry*, Vol. 73, No. 17, pp. 4117-4123, 2001.
7. K. Karstens, K. Kobs, Rhodamine B and Rhodamine 101 as Reference Substances for Fluorescence Quantum Yield Measurements, *Journal of Physical Chemistry*, Vol. 84, No. 14, pp. 1871-1872, 1980.
8. J. G. Santiago, S. T. Wereley, C. D. Beebe, R. J. Adrian, A Particle Image Velocimetry System for Microfluidics, *Experiments in Fluids*, Vol. 25, No. 4, pp. 316-319, 1998.
9. C. D. Meinhart, S. T. Wereley, M. H. B. Gray, Volume Illumination for Two-dimensional Particle Image Velocimetry, *Measurement Science and Technology*, Vol. 11, No. 6, pp. 809-814, 2000.
10. L. D. Landau, E. M. Lifshitz, *Fluid Mechanics*, Pergamon Press, 1959.

MODELLING PRESSURE FLUCTUATIONS DURING FLOW BOILING IN MICROCHANNELS WITH INLET COMPRESSIBILITY AND RESISTANCE

S. Gedupudi, T. G. Karayiannis, D. B. R. Kenning*
School of Engineering and Design, Brunel University, Uxbridge, Middlesex, UB8 3PH, U.K.

ABSTRACT. Confined bubble growth during flow boiling at low pressures in microchannels generates pressure fluctuations that may cause transient flow reversals that disturb the flow distribution in heat sinks formed of parallel channels joined by plena. A simple model is developed for the effects of upstream compressibility and flow resistance at the channel inlet on the magnitude of the pressure transient during the growth of one bubble in a single channel. Preliminary results are presented.

Keywords: *flow boiling, microchannel, heat sink, pressure fluctuations*

INTRODUCTION

Flow boiling at near atmospheric pressure in assemblies of closely-spaced, parallel micro-channels connected by inlet and outlet plena is a promising method of cooling micro-electronic devices at high heat fluxes. The growth of long confined bubbles causes local fluctuations in pressure that may cause temporary reversals of the inlet flow, triggering transient dryout and driving liquid and/or vapour through the plenum towards other channels. The flow reversals may be suppressed by a large frictional resistance at the entry to each channel, e.g. [1-4]. The design guidance is that the time-averaged pressure drop across this resistance should be similar to the pressure drop along the channels. Elimination of flow reversal does not eliminate the pressure fluctuations within channels, which may still influence heat transfer and in extreme cases cause structural damage. Pressure fluctuations have been measured at different axial locations in studies of single channels [5-10] dependent on the compressibility in the upstream boundary conditions, which may result from the pump characteristics or trapped bubbles of vapour or gas. The pressure variations were also measured and simulated by a 1-D model for the special case of bubble growth in an initially uniformly superheated channel with one sealed end (no inlet compressibility, no inlet flow) [11]. 1-D models with different approximations have been developed for oscillatory heat pipes [12].

It is of practical importance to improve the understanding of the effects of bubble-driven pressure fluctuations in assemblies of parallel channels. Parametric studies with 1-D models with simplified physics are less demanding computationally than fully 3-D simulations. A 1-D model for the pressure variations during the growth of a single vapour bubble in a single channel for the special conditions of constant inlet flow (i.e. no inlet compressibility) and constant exit pressure, with features suggested by experimental observations of bubble growth and supported by some 3-D numerical simulations, was presented in [13,14]. The new features of the model, specific to channels of rectangular cross-section of high aspect ratio, are: (i) confinement in two stages, first "partial confinement" by the minor dimension, then "full confinement" by the major dimension of the cross-section, (ii) growth driven by a constant heat flux only to the area of the bubble surface pressed against the heated wall of the channel. Viscous forces are assumed negligible compared to

* Corresponding author: Prof. D.B.R. Kenning.
Phone: + (44)-1895267120 Fax: + (44)-1895256392
E-mail address: david.kenning@brunel.ac.uk

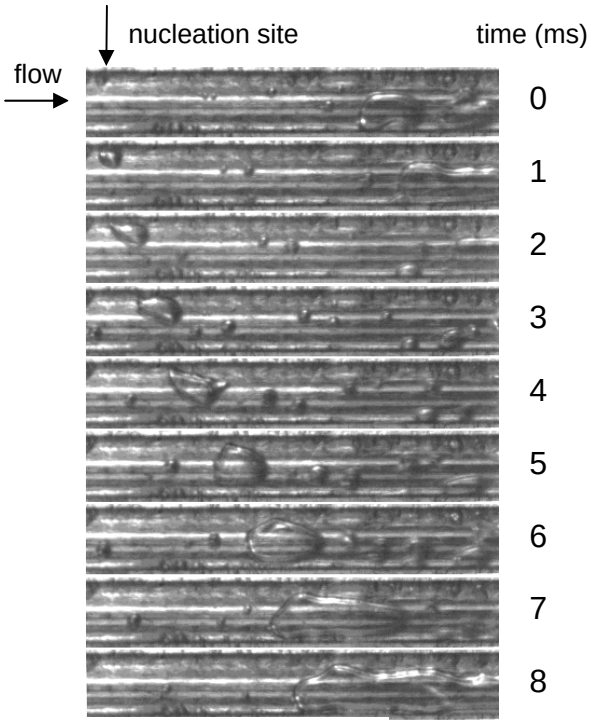

(a) q 219 kW/m^2
U_l 0.7 m/s, ΔT_{sub} 7K

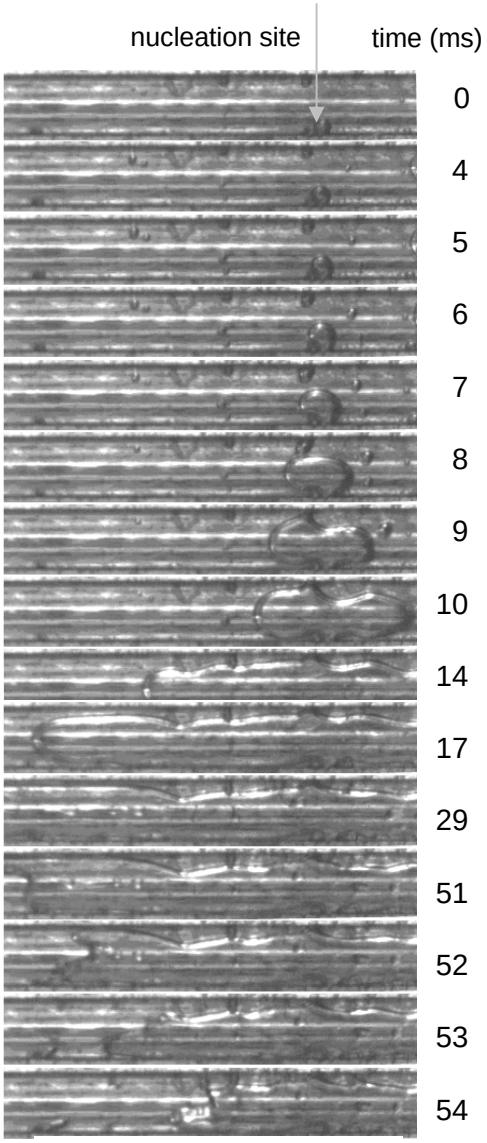

(b) q 173 kW/m^2
U_l 0.7 m/s, ΔT_{sub} 7K

Figure 1. Experimental bubble growth.
(a) No upstream compressibility
(b) With subcooled boiling in preheater

inertial forces. The vapour density is assumed (a) constant, or (b) equal to the saturated vapour density for the instantaneous pressure in the bubble. Variable vapour density is more realistic for the large pressure changes at high heat fluxes and reduces the predicted amplitude of the pressure variations. However, it introduces some modelling problems for a smooth transition to full confinement, discussed in [11] and not yet fully resolved. Using the model with constant vapour density, it was shown that the amplitude of the pressure variation increased with the length of the liquid slug downstream of the bubble nucleation site and with the wall heat flux driving exponential bubble growth.

In this paper, the model for constant density is extended by the addition of sub-models for upstream compressibility in the plenum and a flow resistance at the inlet to the channel. Figure 1 illustrates the sensitivity of bubble motion to apparently minor changes in the rig design that introduced upstream compressibility during experiments on rigorously degassed water boiling at 1.1 bar pressure in a test channel of rectangular section 1.6 mm wide, 0.38 mm deep and 40 mm long, machined in an electrically heated copper block, with a glass window on one side. Reduction in the heat transfer area of the preheater in the external circuit some distance before the test section created compressible vapour due to local subcooled boiling. Further particulars are given in [13].

Examples of bubble growth are shown in Figure 1, (a) with the larger preheater, no upstream compressibility and (b) with subcooled boiling in the smaller preheater creating upstream compressibility despite the same rigorous degassing procedure. In both cases, partial confinement occurred within 2 ms of detectable nucleation but growth to full confinement took 7 - 9 ms. In (a), the growing bubble was pushed downstream by the incoming liquid immediately. Rapid axial

growth only in the downstream direction occurred after full confinement. Nucleation of succeeding bubbles occurred at intervals of about 13 ms, corresponding approximately with the estimated time for the bubble to reach the channel exit. In (b), growth of the partially confined bubble occurred nearly symmetrically in the upstream and downstream directions. Rapid upstream growth occurred after full confinement. The upstream end of the bubble moved out of view at 19 ms and did not return for a further 30 ms. The downstream end of the bubble rapidly moved out of view. The period between nucleation events at the same site was not regular. Recordings at lower magnification showed that more than one nucleation site was active in the channel for both conditions (a) and (b). For the images shown in cases (a) and (b), nucleation sites were located at about 17 mm and 20 mm from the inlet respectively.

1-D MODEL FOR CONFINED GROWTH, WITH UPSTREAM COMPRESSIBILITY

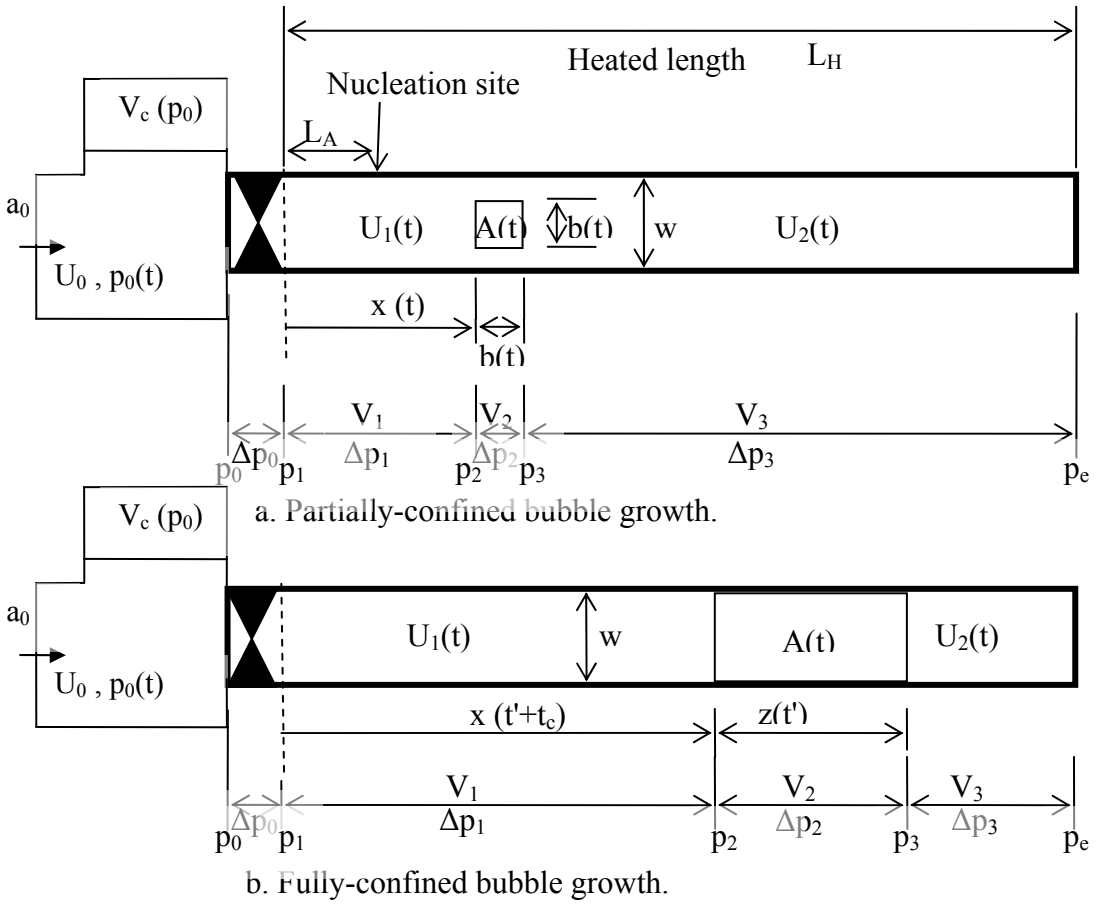

Figure 2. Bubble growth models.

The two-stage model for partially and fully confined growth is summarised in Figure 2. The channel is of rectangular section, width w, depth h << w and heated length L_H. Heat input is on one of the sides w, with an adiabatic window on the opposite side and negligible heat input on sides h. A single nucleation site is located at L_A from the inlet. A constant volumetric flow rate U_0 a_0 is delivered by the pump to the upstream plenum of cross-sectional area a_0 >> wh so that $p_0(t)$ is the stagnation pressure. A restriction at the channel inlet imposes a frictional resistance with constant loss coefficient F based on the velocity U_1 in the channel so that, depending on the direction of U_1,

$$p_0 - p_1 = [1 + FS(\rho_f/\rho_l)]\, \rho_l\, U_1^2\, /2, \quad \text{where } S = |U_1| / U_1 \qquad (1)$$

ρ_f depends on whether liquid or vapour phase is passing through the constriction. In the present model, it is assumed that only liquid enters or leaves the upstream end of the channel. Models for flow reversal with vapour passing through the inlet will be developed later.
The plenum is connected to a compressible volume $V_C(t)$ defined by a sub-model, so that

$$(U_0 a_0) + dV_C/dt = whU_1 \quad (2)$$

Sources of compressibility include presence of vapour or noncondensable gas, connections to parallel channels, pump characteristics, and sub-cooled boiling in the preheater upstream of the channel. In the present model, the only source is assumed to be due to non-condensable gas with initial volume V_{Ci} , as in the Brutin et al. experiments [8]. Assuming an isothermal process,

$$p_0 V_C = p_{0i} V_{Ci}, \; dV_C/dt = -C\, dp_0/dt, \quad C = p_{0i} V_{Ci}/p_0^2 \approx V_{Ci}/p_e \text{ for small changes} \quad (3)$$

$$\text{From (1) – (3),} \quad \frac{dp_1}{dt} = \left(\frac{U_0 a_0 - whU_1}{C} \right) - (1+FS)\rho_l U_1 \frac{dU_1}{dt} \quad (4)$$

Partially-confined growth (PC)

The earliest stage of unconfined growth from a nucleus with dimensions << h is neglected. When the bubble is confined fully along the depth h, except for very thin liquid films between the bubble and the surfaces w, it is assumed that the bubble length and width b(t) are equal. Neglecting the volume of the thin liquid films on sides w, the volume of the bubble V(t) is hb^2. Assuming constant heat flux q through the single contact area b^2 and neglecting the change of ρ_v and h_{lv} with pressure,

$$b = he^{t/(2\tau)}, \quad \tau = \rho_v h_{lv} h/q \quad (5)$$

$$\text{From continuity,} \quad U_2 = U_1 + \left(h^2/w\tau\right)e^{t/\tau} \quad (6)$$

From conservation of momentum, neglecting friction and assuming that the upstream end of the bubble moves at U_1 and the average velocities of the bubble and the liquid alongside are $(U_1+U_2)/2$, the pressure differences over the control volumes V_1, V_2 and V_3, are given by

$$\Delta p_1 = \rho_l \left(U_1 \frac{dx}{dt} + x \frac{dU_1}{dt} \right) + \left(0 - \rho_l U_1^2\right) = \rho_l \left(x \frac{dU_1}{dt} \right) \quad (7)$$

$$\Delta p_2 = \left\{ \left[\left(\rho_l \frac{db}{dt} \right) - (\rho_l - \rho_v) \frac{2b}{w} \frac{db}{dt} \right] \frac{(U_1 + U_2)}{2} + \left[(\rho_l b) - (\rho_l - \rho_v) \frac{b^2}{w} \right] \frac{1}{2} \left(\frac{dU_1}{dt} + \frac{dU_2}{dt} \right) \right\} \quad (8)$$

$$\Delta p_3 = \rho_l \left[U_2 \left(-U_1 - \frac{db}{dt} \right) + (L_H - x - b) \frac{dU_2}{dt} \right] + \left[\rho_l U_2^2 - 0 \right] \quad (9)$$

From the above equations, with r as the ratio of vapour density to liquid density, ρ_v / ρ_l ,

$$\frac{dU_1}{dt} = \frac{\left(\frac{p_1(t) - p_e}{\rho_l} - U_1 \left[r \frac{h^2}{w\tau} e^{t/\tau} \right] - e^{t/\tau} \frac{h^2}{w\tau^2} (L_H - x) + e^{3t/2\tau} \frac{3h^3}{4w\tau^2} - e^{2t/\tau} \frac{h^4}{w^2\tau^2} r \right)}{\left[L_H - (1-r) \frac{h^2}{w} e^{t/\tau} \right]} \quad (10)$$

Fully-confined growth (FC)

Fully-confined bubble growth commences from the time t_c at which b = w. Let $t' = t - t_c$. The contact area A = w z (t'), where z is the length of the bubble, and from the bubble growth equation

$$z = we^{t'/\tau} \quad (11)$$

$$\text{From continuity,} \quad U_2 = U_1 + \frac{dz}{dt'} = U_1 + \left(\frac{w}{\tau} \right) e^{t'/\tau} \quad (12)$$

From the momentum equation, assuming that the ends of the bubble move at U_1 and U_2 and its average velocity is $(U_1+U_2)/2$, the pressure differences over the control volumes V_1, V_2 and V_3 are

$$\Delta p_1 = \rho_l\left(U_1\frac{dx}{dt} + x\frac{dU_1}{dt}\right) + \left(0 - \rho_l U_1^2\right) = \rho_l\left(x\frac{dU_1}{dt}\right) \quad (13)$$

$$\Delta p_2 = \left\{\left[\left(\rho_v\frac{dz}{dt}\right)\frac{(U_1+U_2)}{2}\right] + \left[(\rho_v z)\frac{1}{2}\left(\frac{dU_1}{dt}+\frac{dU_2}{dt}\right)\right]\right\} + \{0-0\} \quad (14)$$

$$\Delta p_3 = \rho_l\left[U_2\left(-\frac{dx}{dt}-\frac{dz}{dt}\right) + (L_H - x - z)\frac{dU_2}{dt}\right] + \left[\rho_l U_2^2 - 0\right] = \rho_l\left[(L_H - x - z)\frac{dU_2}{dt}\right] \quad (15)$$

$$\frac{dU_1}{dt'} = \frac{\left(\frac{p_1(t)-p_e}{\rho_l} - U_1\frac{rw}{\tau}e^{t'/\tau} - (L_H - x)\frac{w}{\tau^2}e^{t'/\tau} + (1-r)\frac{w^2}{\tau^2}e^{2t'/\tau}\right)}{\left[L_H - (1-r)we^{t'/\tau}\right]} \quad (16)$$

The equations are solved by a finite difference method. The incoming flow a_0U_0 and the exit pressure p_e are assumed to be constant. The initial conditions are assumed to be $p_1 = p_e$, $U_1 = a_0U_0 / wh$, neglecting any impulsive changes associated with the initial unconfined growth of the bubble.

SIMULATIONS FOR WATER AT 1 BAR

Conditions

The simulations in this paper correspond to the flow conditions of the visualizations in Figure 1 : water in a channel 0.38 x 1.5 x 40 mm, constant exit pressure of 1 bar, constant inlet flow to the plenum equivalent to a liquid velocity U_1 = 0.7 m/s in the channel. The vapour density is assumed constant and viscous forces are neglected. The nucleation site is placed at the mid-point of the channel, unless otherwise mentioned. At present, the simulation is terminated when either end of a bubble reaches the end of the channel. Simulations for multiple bubbles are under development.

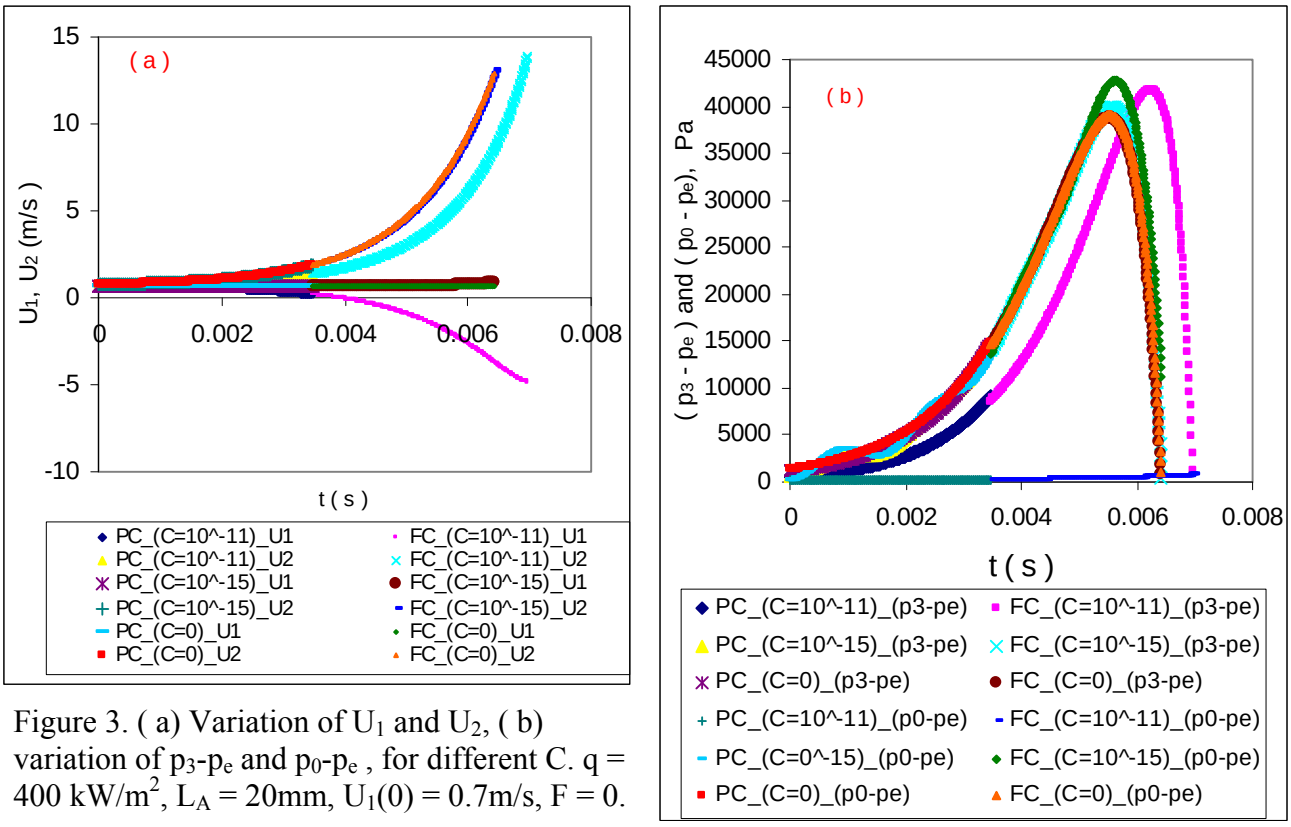

Figure 3. (a) Variation of U_1 and U_2, (b) variation of p_3-p_e and p_0-p_e , for different C. q = 400 kW/m^2, L_A = 20mm, $U_1(0)$ = 0.7m/s, F = 0.

Simulations of the liquid velocities U_1, U_2 on each side of the bubble, the bubble pressure p_3 and the pressure in the inlet plenum p_0 at a heat flux of 400 kW/m^2 are shown in Figure 3 for C = 0, 10^{-11} and 10^{-15}, corresponding respectively to trapped gas volumes in the inlet plenum of 0 (original model in [14]), 1000 mm^3 and 0.1 mm^3 (from Eq.(3)). For comparison, the volume of liquid displaced from the channel to the plenum by movement of one end of the bubble through 20 mm is 11.4 mm^3.

The simulations for C = 10^{-15} are very similar to those for C = 0, except for a small oscillatory component at a frequency of approximately 660 Hz, of the same order as the estimate of 850 Hz for the natural frequency of a spring – mass system using the mass of the upstream liquid column in the channel. The plenum pressure (p_0) is nearly equal to the bubble pressure (p_3). For relatively large upstream compressibility, C = 10^{-11}, the upstream velocity U_1 reverses after about 4 ms , after which growth is nearly symmetrical in the upstream and downstream directions. The bubble pressure rise is reduced and the plenum pressure remains nearly constant. In all the figures, only the total pressure drop ($p_0 - p_e$) and pressure drop at the downstream end of the bubble ($p_3 - p_e$) are shown, and the pressure drop at the upstream end of the bubble ($p_0 - p_3$) can be obtained from it. The pressure drop across the bubble ($p_2 - p_3$) is negligible, at least for the constant vapour property considered in the present model. The simulations show that in the presence of upstream (or inlet) compressibility, the pressure drop at the upstream end will be of the same order of magnitude as that at the downstream end, though they may differ in signs, which makes the total pressure drop between the inlet and outlet much smaller than that for without inlet compressibility. This also shows that for upstream (or inlet) compressibility, the local pressure fluctuations within the channel will be much higher than that between the two channel ends. The amplitude of these pressure fluctuations may be grossly underestimated by experimental measurements of the pressure difference between the inlet and outlet plena.

Additional simulations (not shown here) confirm that the initial asymmetry in growth and the associated delay in flow reversal are modified by changes in the initial incoming flow rate. The amplitude of the bubble pressure within the channel depends strongly on the heat flux, being much smaller at 100 kW/m^2, Figure 4. Also there is no flow reversal for 100 kW/m^2. The simulations performed so far do not exhibit the eventual return of liquid observed in Figure 1(b). Further investigation is required over a wider range of parameters. It may be necessary to use the non-linear version of the compressibility model in Eq.(3), so that the compressibility decreases as reverse flow proceeds, or a different sub-model that is more representative of the subcooled boiling that is the source of compressibility in these particular experiments.

For relatively large compressibility C = 10^{-11}, which maintains the pressure in the inlet plenum nearly constant, a large inlet resistance factor F = 40 reduces the reverse flow into the inlet

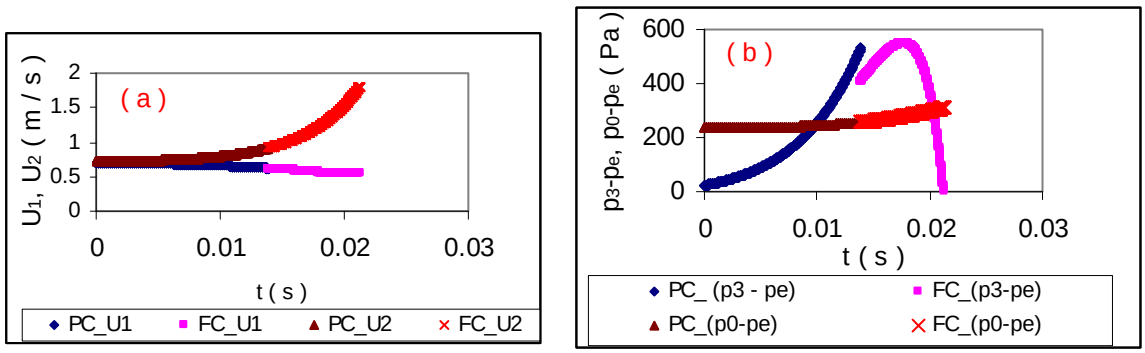

Figure 4. (a) Variation of U_1 and U_2, (b) variation of p_3-p_e and p_0-p_e , for q = 100 kW/m^2, L_A = 20mm, $U_1(0)$ = 0.7m/s and C=10^{-11}, F = 0. Compare with q = 400 kW/m^2 and C=10^{-11} in Figure 3.

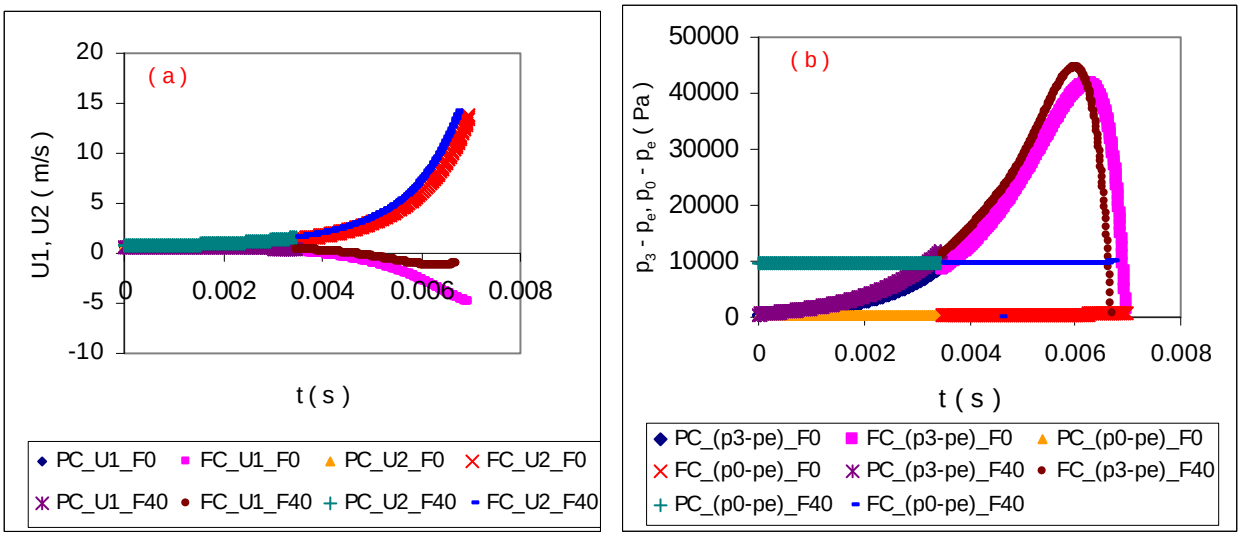

Figure 5. (a) Variation of U_1 and U_2, (b) variation of p_3-p_e and p_0-p_e , for F = 0, 40. q = 400 kW/m^2, L_A = 20mm, $U_1(0)$ = 0.7m/s and C = 10^{-11}.

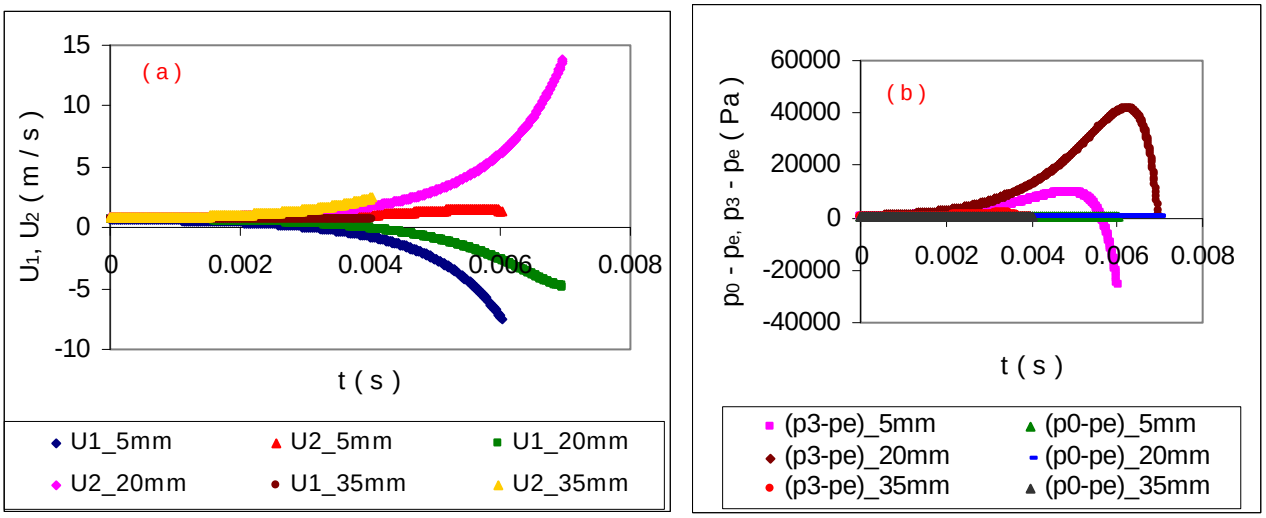

Figure 6. (a)Variation of U_1 and U_2, (b) variation of p_3-p_e and p_0-p_e, for different L_A (5, 20, 35 mm) . q = 400 kW/m^2, U_1 (0) = 0.7 m/s, C = 10^{-11}, F = 0.

plenum but increases slightly the maximum pressure within the channel, Figure 5. Figure 6 shows that the position of the nucleation site influences the reverse flow, with the nucleation site close to inlet showing more flow reversal (negative U_1) than the one at the middle, while the one close to the outlet hardly shows any flow reversal. In the experiments with inlet compressibility, it was observed that the bubbles near the channel inlet and middle grew in both upstream and downstream directions, with irregular periods between nucleation events, whereas those near the outlet only grew in downstream direction with more regular nucleation. The pressure fluctuation ($p_3 - p_e$) caused by the bubble near the outlet is very small compared to that caused by the bubbles near the inlet and middle. However, ($p_0 - p_e$) is very small and similar for all three cases, Figure 6b. The present model considers only single bubble. But in reality, there will be multiple bubbles and their interactions can also influence flow reversal. As the amplitude of pressure fluctuations and their frequencies increase with the heat flux, it will becomes necessary to consider the variation of vapour density and saturation temperature with pressure, not considered in the present bubble growth model.

CONCLUSIONS

A simple model has been developed for the pressure fluctuations and flow reversal caused by the growth of a single vapour bubble in a single micro-channel of rectangular cross-section with upstream compressibility and inlet flow resistance. Preliminary simulations have revealed the interactions between these external influences and conditions within the channel such as the heat flux and the position of the nucleation site. Further development of the model is required to include viscous forces, pressure-dependent vapour properties, different models for compressibility and multiple bubbles that may eventually guide the design of the plena for multichannel heat sinks.

REFERENCES

1. Koşar, A., Kuo, C. J. and Peles, Y., Suppression of boiling flow oscillations in parallel micro-channels by inlet restrictions, *Trans. ASME, J. Heat Transfer*, Vol. 128, pp. 251-260, 2006.
2. Mukherjee, A. and Kandlikar, S.G., Numerical study of the effect of inlet constriction on bubble growth during flow boiling in microchannels, *3rd International Conference on Microchannels and Minichannels*, ICMM2005-75143, Toronto, Ontario, Canada, 2005.
3. Kandlikar, S.G., Kuan, W.K., Willistein, D.A. and Borrelli, J., Stabilization of flow boiling in microchannels using pressure drop elements and fabricated nucleation sites, *Trans. ASME, J. Heat Transfer*, Vol. 128, pp. 389-396, 2006.
4. Lee, P.C. and Pan, C., Boiling heat transfer and two-phase flow of water in a single shallow microchannel with a uniform or diverging cross-section, *J. Micromech. Microengineering*, Vol. 18, 025005, 2008.
5. Kenning, D.B.R. and Yan, Y., Saturated flow boiling of water in a narrow channel: experimental investigation of local phenomena, *IChemE Trans. A, Chem. Eng. Research and Design*, Vol. 79, pp. 425-436, 2001.
6. Wen, D.S., Kenning, D.B.R. and Yan, Y., Flow boiling of water in a narrow vertical channel at low mass flux: observations of local phenomena, *Proc.12th Int. Heat Transfer Conf.* Grenoble, Vol. 3, pp. 773-778, 2002.
7. D. Brutin, Topin, F. and Tadrist, L., Experimental study of the unsteady convective boiling in heated minichannels, *Int. J. Heat Mass Transfer*, Vol.46, pp. 2957-2965, 2003.
8. Brutin, D. and Tadrist, L., Pressure drop and heat transfer analysis of flow boiling in a minichannel; influence of the inlet condition on two-phase flow stability, *Int. J. Heat Mass Transfer*, Vol. 47, pp. 2365-2377, 2004.
9. Zhang, L., Goodson, K.E.,and Kenny, T.W., *Silicon Microchannel Heat Sinks, Theories and Phenomena,* Springer Verlag, Berlin, Heidelberg, New York, 2003.
10. Zhang, L., Wang, E.N., Goodson, K.E.,and Kenny, T.W., Phase change phenomena in silicon microchannels, *Int. J. Heat Mass Transfer*, Vol. 48, pp.1572–1582, 2005.
11. Kenning, D.B.R., Wen, D.S., Das, K.S. and Wilson, S.K. Confined growth of a vapour bubble in a capillary tube at initially uniform superheat: experiments and modelling, *Int. J. Heat Mass Transfer*, Vol. 49, pp. 4653-4671, 2006.
12. Shafii, M.B., Faghri, A. and Zhang, Y., Thermal modeling of unlooped and looped pulsating heat pipes, *Trans. ASME, J. Heat Transfer*, Vol. 123, pp. 1159-1172, 2001.
13. Zu, Y.Q., Gedupudi, S., Yan, Y.Y., Karayiannis, T.G. and. Kenning, D.B.R., Numerical simulation and experimental observations of confined bubble growth during flow boiling in a mini-micro channel with a rectangular cross-section of high aspect ratio, *Proc. 7th Int. ASME Conf. on Nanochannels, Microchannels and Minichannels,* paper no. ICNMM2009-82118, Pohang, June 22-24, 2009.
14. Gedupudi, S., Zu, Y.Q., Karayiannis, T.G., Kenning, D.B.R. and Yan, Y.Y., 1-D modelling and 3-D simulation of confined bubble formation and pressure fluctuations during flow boiling in a mini-micro channel with a rectangular cross-section of high aspect ratio, *Proc. 7th Int. ASME Conf. on Nanochannels, Microchannels and Minichannels,* paper no. ICNMM2009-82119, Pohang, June 22-24, 2009.

μ– SCALE LIF AND PIV INVESTIGATION OF MIXING IN A RIBBED MICROMIXER

Mohammed Asfer, P. K. Panigrahi *
Mechanical Engineering Dept,
IIT Kanpur, U.P. 208016 (INDIA)

ABSTRACT. Mixing of binary or multi component fluid streams is an essential feature of many microfluidic systems i.e. DNA purifications, polymerase chain reaction (PCR), protein folding etc. However, mixing rates are governed by molecular diffusion for low Reynolds number micro flows and in the absence of enhanced mixing techniques, mixing lengths and residence times can be much longer than the requirement of most applications. The present study presents a passive mixing strategy for mixing between acetone-water and glycerol-water injected into the Y-shaped inlet of the micromixer. The mixing-channel of the micromixer is a PDMS microchannel of 30μm (depth) × 220μm (width) cross section with micro-ribs located on both the sidewalls of the mixing-channel. The width and height of ribs on the mixing-channel walls are equal to 30μm and 20μm respectively. The mixing performance between two fluid streams has been visualized and quantified by the μ-LIF (Laser Induced Fluorescence) technique. It has been observed that mixing index increases due to the presence of micro ribs and the mixing index at the outlet of the micromixer is 17.36% and 33.98% more than that without ribs (smooth micromixer) for acetone-water and glycerol-water respectively. The mixing index for glycerol-water flow is lower than that of the acetone-water solution. The μ-PIV (particle image velocimetry) results provide detailed flow field near the micro-ribs responsible for the mixing enhancement between the fluid streams. Overall, the present study demonstrates the influence of micro-ribs, fluid properties (viscosity ratio) and flow condition i.e. velocity ratio on mixing performance between two fluid streams.

Keywords: *μ-LIF, μ-PIV, micromixer, micro ribs, two-fluid mixing*

INTRODUCTION

Mixing in microscale is primarily driven by diffusion and therefore is slower compared to that in the macroscopic length scales. Therefore, many high performance passive and active mixing schemes have been investigated in literature to overcome the limitations imposed by the laminarity of micro flows. It is not always feasible to use mechanical agitation at the microscopic scale. The fabrication of passive structures through micro fabrication techniques has its own limitations. Two common arrangements for introducing the two fluid streams are T-shaped and L-shaped micromixer. The mixing is not so significant except at higher Reynolds numbers in T-shaped mixer. In L-shaped conduits, the bend induced vortices at low values of Reynolds number decay before they have an opportunity to significantly stir the fluid. In the experiments of Johnson *et al*. (2002) and Stroock *et al*. (2002), a series of micro ridges were fabricated on the bottom of a polydimethylsiloxane (PDMS) channel at an oblique angle to the flow direction. The mixing enhancement between two-fluids was attributed to the helical secondary flow generated along the ridges on the surface of the channel. The increase in the depth or frequency of micro ridges

* Corresponding author: Prof. P. K. Panigrahi
Phone: + (91)-512-2597686, Fax: + (91)-512-2597408
E-mail address: panig@iitk.ac.in

increases the strength of the helical flow and the rate of mixing in the mixing channel**.** Ou *et al*. (2007) experimentally studied a series of ultra hydrophobic surfaces with diagonal microridges fabricated on the bottom wall of a Y-shaped channel and observed a reduction in the mixing length as much as ten times compared to a smooth hydrophobic surface. They demonstrated maximization in mixing by changing the geometry of the surface structure due to the generation of most favorable slip velocity along the shear-free air-water interface aligned obliquely to the flow direction. They observed the mixing to be less sensitive to the area ratio of the shear-free air-water interface compared to the angle of the microridges. Also the mixing mechanism suggests that fluorescent tagged and untagged fluids stacked vertically leads to enhanced mixing even for micro ridges aligned at 90^o to the flow direction compared to the horizontal stacking. Hu *et al*. (2006) investigated the mixing of pure water and acetone solution under different Reynolds numbers and acetone solution concentration. The mixing efficiency decreases with increase of acetone solution concentration and mixing efficiency equal to 98% was observed for the proposed micro mixer. Liu *et al*. (2004) carried out numerical study of mixing between pure water and a solution of glycerol in different micromixers. They observed that at Re=1, the mixing performance for both herringbone and serpentine mixer varies inversely with mass fraction of glycerol due to the dominance of molecular diffusion. However, at Re=10, opposite trend was observed for serpentine mixer which was attributed to the enhancement of flow advection at large mass fraction. Hoffmann *et al*. (2006) used both μ-LIF and μ-PIV techniques for investigating liquid-liquid mixing in T-shaped micromixers. Lindken *et al*. (2005) used a stereoscopic μ-PIV technique to investigate the three dimensional nature of flow in a T-shaped micromixer. Asfer *et al*. (2008) used μ-PIV technique for investigating the effect of repeated transverse micro-ribs on laminar flows in PDMS microchannel. The above literature survey demonstrates the role played by concentration field (two dimensional or three dimensional), the velocity field (two dimensional or three dimensional) and the surface geometry modification as the source for enhanced mixing between the fluid streams. However, no systematic study is available on the influence of relative physical property of the two fluid streams i.e. viscosity ratio and the flow properties i.e. velocity ratio on mixing enhancement between two fluid streams.

The preset study investigates the influence of fluid properties of the two mixing streams on the mixing behavior in a passive ribbed micro mixer with Y-type inlet. A series of micro ribs are oriented at an angle of 90^o to the flow direction on both sidewalls of the mixing-channel. The mixing of two miscible fluids (1) DI water and a solution of acetone in water, and (2) DI water and a solution of glycerol in water has been studied experimentally. The mass fraction (φ) of acetone and glycerol in water has been set equal to 0.2. The mixing performance of the micromixer has been visualized and quantified using the Laser induced Fluorescence (μ-LIF) technique. The Particle Image Velocimetry (μ-PIV) has been used to study the role played by the flow field on mixing of the micromixer.

EXPERIMENTS

Fabrication of micromixer

Micromixers used in the present experiments were fabricated by using PDMS replica moulding technique at Stanford Microfluidics Foundry (Dept. of Bio-engineering, Stanford University). Two types of micromixers were used: (1) smooth micromixer and (2) micromixer with rectangular ribs on the sidewalls of the mixing-channel. Both the ribbed and smooth micromixer has Y-type inlet and mixing-channel cross-section is equal to 220 μm (width) ×30 μm (depth). Ribs are 20 microns in height and 30 microns in width with a spacing of 70 microns between each rib. The schematic drawing of the micro channel and the microscope image of the ribbed section of the micromixers used in the present study are shown in figure 1 (a) and (b) respectively.

Experimental set up and conditions

The experimental apparatus shown in figure 2 consists of two parts: (a) the flow delivery system and (b) the micro-LIF/PIV system. A double-syringe pump (Injectomate 216, Vital Bio-systems

co.) was used to supply the fluids to the two inlets of the micromixer. The range of flow rates that can be obtained from this pump is 0.1-99 ml/hr with an accuracy of ≤ 2 %. The micromixer was

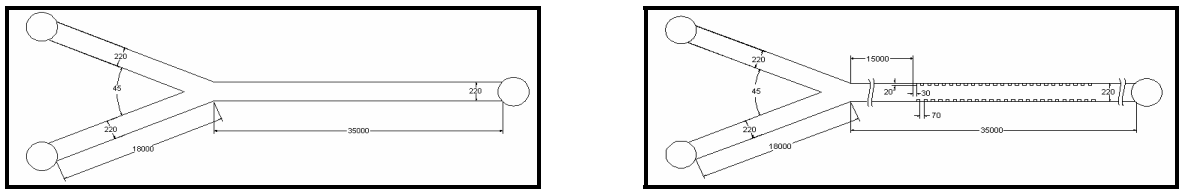

(a)

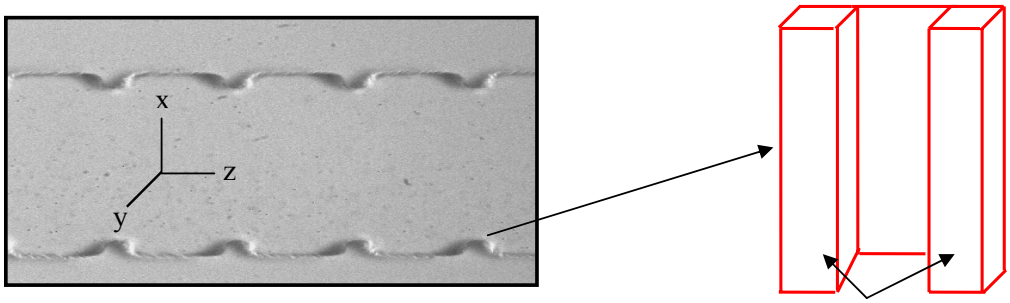

(b)

Figure 1. Micromixer geometry (a) smooth and ribbed micromixer (b) Microscope image of the ribbed section of the mixing-channel

kept over the stage of the inverted microscope (Leica Microsystems; DMI 5000M) and connected to the flow delivery system with flexible tubing. In order to prevent building up of any contaminants in the system, pure water was first pumped through the micromixer to expel stagnant contaminants. For μ-LIF measurements, one inlet stream was marked with the fluorescent dye (Rhodamine 6G). The excitation and emission wavelengths of the fluorescent dye are between 460-560 nm and 540-640 nm respectively. Illumination of the flow is achieved by using the light source (halogen lamp 12 V, 100W) with the epifluorescent filters and microscope objective. The concentration images of flow are recorded using a 12-bit 1344×1024 pixels digital CCD camera (HiSense Mk II) and then acquired in the PC for subsequent mixing analysis. For quantitative estimation of mixing, the grey values of the recorded concentration images at different positions (in relation to length of the mixing channel) are investigated by using the DynamicStudio analysis software (Dantec dynamics Inc.). For μ-PIV study, deionized water is used as the working fluid, seeded with a dilution of 1:20 fluorescent carboxylate-modified microspheres (diameter ≈ 1μm, Molecular probes, Inc). This particle concentration is selected as it is the maximum seeding load for acceptably low noise levels under the current illumination conditions. Tracer particles are visualized under bright field illumination mode with a high-power LED serving as light source. The light source and camera are synchronized by a timer box (Dantec dynamics Inc.) The timing between two consecutive LED pulses is set such that the tracer particles moved approximately 1/4th of an interrogation window between the pulses. A standard adaptive cross correlation technique is used to obtain the instantaneous flow field in the mixing channel. The Reynolds number in the respective leg of the Y-inlet is calculated using $\mathrm{Re} = \frac{u_{avg} D_H}{\nu}$ where u_{avg} is the average fluid velocity in the channel, D_H hydraulic diameter and ν kinematic viscosity of fluid. For the solutions of Acetone and Glycerol with a mass fraction φ=0.2 the kinematic viscosity ν is calculated as 0.7962×10^{-6} and 1.8296×10^{-6} m^2/s respectively.

Mixing performance evaluation

Evaluation criterion for the performance of two-fluid mixing inside micromixer has been based on the uniformity of the concentration inside the micro channel. Liu *et al*. (2004) assessed two-fluid mixing in micromixers through measurements of the deviation of the pixel intensity I_i values in a given image from average intensity value I_{mean}, i.e.

$$C_{dev} = \frac{\sqrt{\frac{1}{N}\sum_{i=1}^{N}(I_i - I_{mean})^2}}{2^n - 1} \quad (1)$$

where N is the total number of pixels and n' the grey bit number of the image under analysis. To compare the mixing performance of the mixers under a range of conditions C_{dev} is further normalized as follows to give the mixing index,

$$C_{mix} = \frac{(C_{dev\_inlet} - C_{dev})}{C_{dev\_inlet}} \quad (2)$$

Where C_{dev_inlet} and C_{dev} are the values at the inlet and at the position of interest (in relation to mixing-channel length) respectively. If two fluids are fully mixed in the mixing-channel, the intensity I_i in equation (1) is the same for every pixel, and consequently C_{mix} is equal to 1 and for no mixing it is zero. The concentration field is calculated based on the calibration between dye concentration and intensity values (grey values) of pixels. Figure 3 shows a linear relationship between the intensity of the fluorescent image and the dye concentration for both acetone and glycerol solution in the concentration range of 0-29.2 μmol/lit.

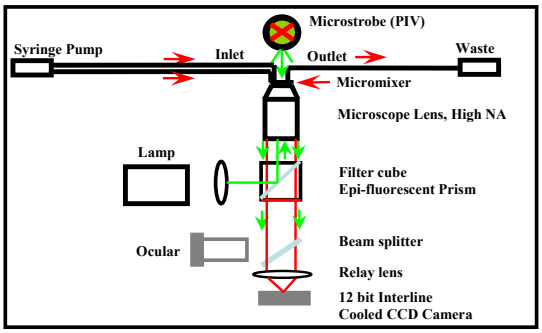

Figure 2. Schematic of the experimental setup used for μ-LIF/PIV

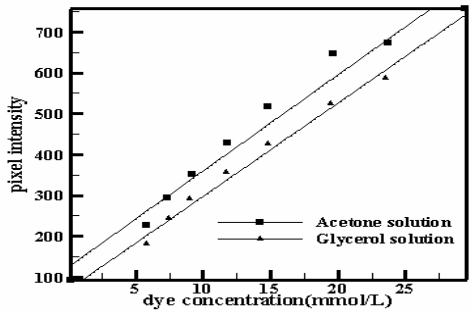

Figure 3. Calibration curve between pixels intensity and dye concentration

RESULTS AND DISCUSSION

LIF Results

The mixing performance of ribbed micromixer for acetone-water and glycerol-water solution under different flow conditions has been investigated using LIF technique. The positions of interface between the two fluid streams with respect to one of the sidewalls for different flow conditions are presented in Table 1. The Reynolds number is calculated based on the flow rate in respective leg of the Y-channel. The position of the interface with respect to the ribbed surface is expected to play an important role as there is a possibility of cross flow generation near the interface. Table 1 shows the interface to be located at about 24.36 and 26.66 μm for the acetone-water flow at $Re_{acetone}$ = 2.8 and 4.0, and Re_{water} = 20.8 and 29.5 respectively. For the glycerol-water flow, the interface is located at about 31.4 and 34.96 μm at $Re_{glycerol}$ = 1.2 and 1.7, and Re_{water} = 20.8 and 29.5 respectively. For the same velocity ratio (VR = 9.17), the interface of glycerol-water is located farther (31.4 μm) from the side wall compared to that of acetone-water (24. 36 μm). It should be remembered that the rib

height is equal to 20 μm and therefore the acetone-water interface is located closer to the rib compared to that of glycerol-water.

For the velocity ratio, VR=9.17, the mixing index results have been reported in Figure 4 (a) and (b) for acetone-water and glycerol-water respectively. The mixing index variation along the mixing-channel of a smooth micromixer under the same experimental conditions is also shown for comparison with that of ribbed micromixer. The mixing index at the end of the mixing-channel increases in streamwise direction for both acetone-water and glycerol–water flow. The mixing index in the ribbed section is higher than that of the smooth channel for acetone-water flow. The mixing index at the exit of the channel is also largest for the higher Reynolds number case. The corresponding fluorescence images of concentration field at different streamwise locations of the mixing-channel are shown in figure 5**.** The interface between the two fluids is sharper in the entrance region of the Y-channel clearly showing the two-fluid region. In the ribbed and post-rib region, the interface region is comparatively blurred due the mixing between the two-fluids. The water flow side in the ribbed region of acetone-water flow shows higher light intensity compared to that in the pre-rib region and also the ribbed-region of glycerol-water flow due to superior mixing. Overall observation from the visualization images of figure 5 corresponds well to that of mixing index in Figure 4.

The PIV measurements show parabolic velocity profile indicating higher mean fluid velocity at the center of the channel compared to that in the near the wall region. The interface in the present flow is located closer to the wall resulting in lower velocity at the interface. Hence, the mixing is expected to be influenced by both convection and diffusion. The residence time for diffusion near the wall is high because of low velocity as compared to the center region of the mixing channel. The numerical predictions for smooth T-mixer shows increase in the mixing length requirement for complete mixing between two fluid streams with increase in Re. The present study shows more mixing for the same mixing-channel length with increase in Re due to the presence of ribs. This can be attributed to larger effect of ribbed structures on the interface of the two fluid streams at higher Re compared to the lower Re case due to more stretching and thinning of fluids occurring in the near ribbed wall region. The stretching and thinning of fluids near the ribbed wall produces stronger transverse velocity component as compared to the smooth micromixer contributing to higher mixing between the two fluid streams. The mixing index at the outlet of the mixing-channel is about 17.36% and 33.98% more compared to the smooth micromixer for acetone- water and glycerol- water flow respectively. Thus, the influence of ribbed region is also a function of the nature of the fluid.

Table 1 Interface locations (δ) between the two fluid streams (acetone- water and glycerol- water) as a function of Reynolds number.

Velocity ratio (VR)	Reynolds no. (Acetone- water)	Interface location (μm)	Reynolds no. (Glycerol- water)	Interface location (μm)
9.17	$Re_{acetone}$ =2.8 Re_{water} =20.8	26.66	$Re_{glycerol}$ =1.2 Re_{water} =20.8	34.96
9.17	$Re_{acetone}$ = 4.0 Re_{water} =29.5	24.36	$Re_{glycerol}$ =1.7 Re_{water} =29.5	31.40

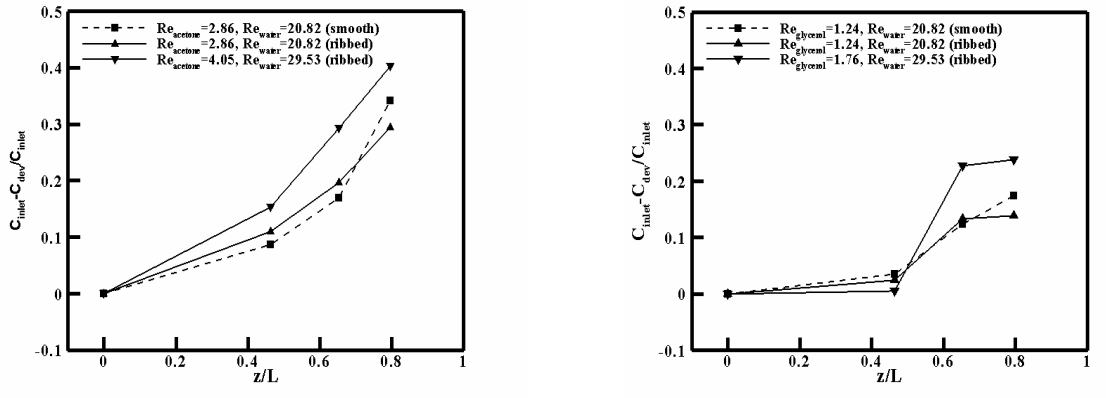

(a) (b)

Figure 4. Variation of mixing index along the mixing channel length for ribbed micromixer for VR=9.17 (a) acetone- water (b) glycerol- water

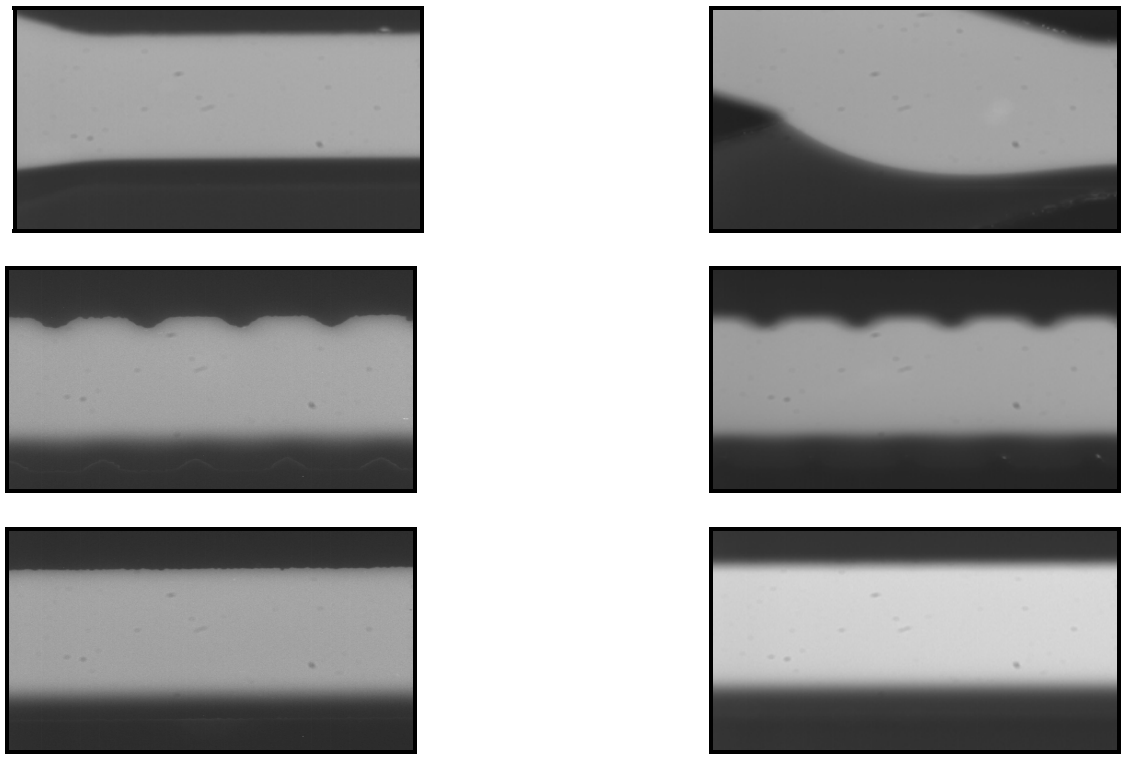

(a) (b)

Figure 5. Fluorescence images of (a) acetone- water and (b) glycerol- water at Y-inlet (Top), ribbed (middle) and post-rib locations (bottom) of the micromixer.

PIV Results

The velocity field from PIV measurements is useful for understanding the role played by convection on mixing between the two streams. The flow in the smooth region of the mixing-channel is fully developed due to long length of the channel prior to the ribbed region. Figure 6 shows the normalized u and v velocity field in the inter-rib region between 3rd and 4th ribs for both acetone-water and glycerol-water flow. The normalization has been carried out using the maximum u-velocity. The centerline velocity (u_{max}) is equal to 0.0223 ms^{-1} and 0.019 ms^{-1} for acetone-water

and glycerol-water flow respectively. The measurements are reported in the half-width region of the channel i.e. from mixing-channel centerline to the lower ribbed wall at different streamwise locations (z/h) in the inter-rib regions. The streamwise velocity profile shows a gradual decrease in magnitude from the channel centerline towards the lower ribbed wall, however there is no significant variation along the streamwise directions. The nature of the u-velocity profile is not exactly parabolic as in the smooth region of the mixing-channel, which can be attributed to the presence of micro ribs on the sidewalls of the mixing-channel. The transverse v-velocity changes its sign from negative to positive along the streamwise directions in the inter-rib region. The v-velocity magnitude is stronger between z/h= 0.6 to 1.2 compared to that between z/h=0 to 0.3 in the inter-rib region which can attributed to the different flow behavior in the upstream and downstream portion of the inter-rib region. The average v-velocity magnitude for the acetone-water flow is more than that of glycerol-water flow. There is also a general increase in the v-velocity magnitude in ribbed micromixer compared to that of the smooth micromixer. The higher v-velocity is attributed towards better mixing enhancement between the two fluid streams. This observation from velocity field correlates well with the observation from LIF measurements. The u-velocity vector field and v-velocity magnitude contours in the inter-rib region for acetone-water and glycerol-water flow are shown in figure 7. There is in general higher magnitude of both u and v-velocity for the acetone-water flow case compared to that of the glycerol-water. There is no significant difference in u-velocity between the acetone-water and glycerol-water flow case. The gradient in u-velocity is observed for both the flow. However, the overall v-velocity magnitude is higher for the former case compared to the later. Therefore, the higher v-velocity fields due to the rib near the interface between two-fluid is attributed to higher mixing.

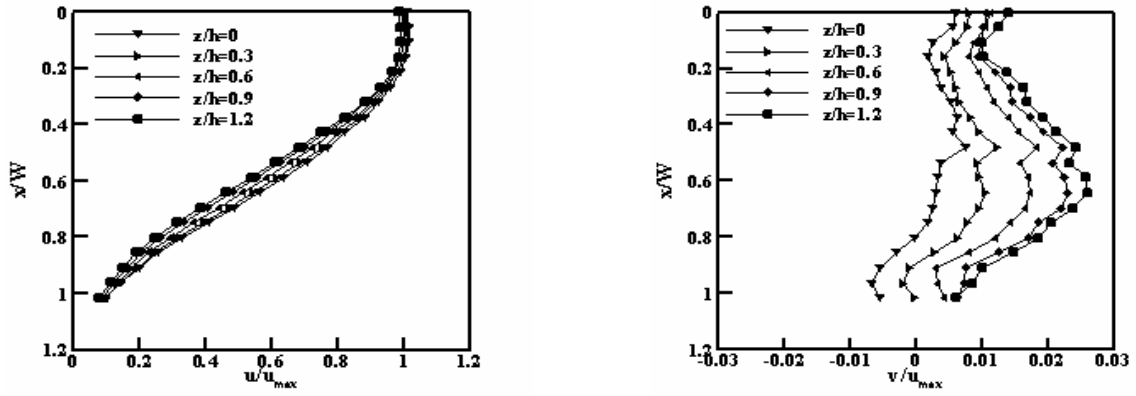

(a)

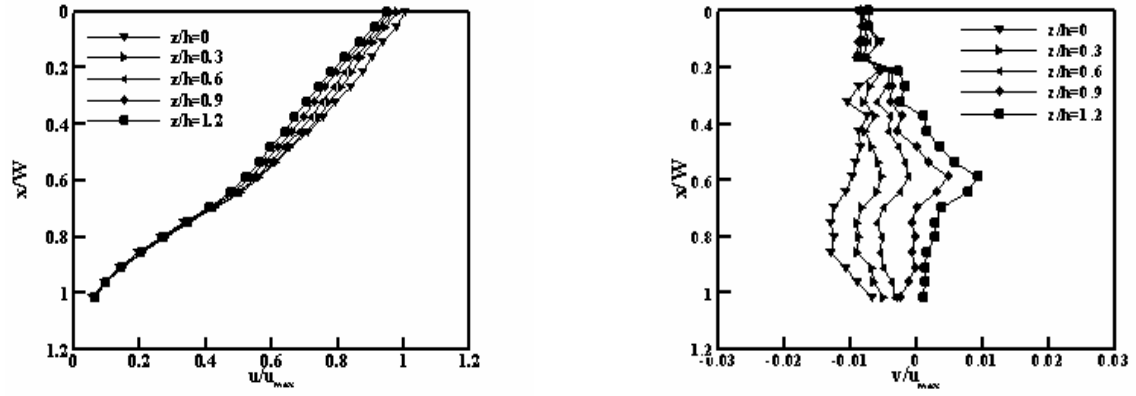

(b)

Figure 6. The normalized u- and v- velocity profile in the inter-rib region between 3rd-4th ribs for (a) acetone-water and (b) glycerol-water

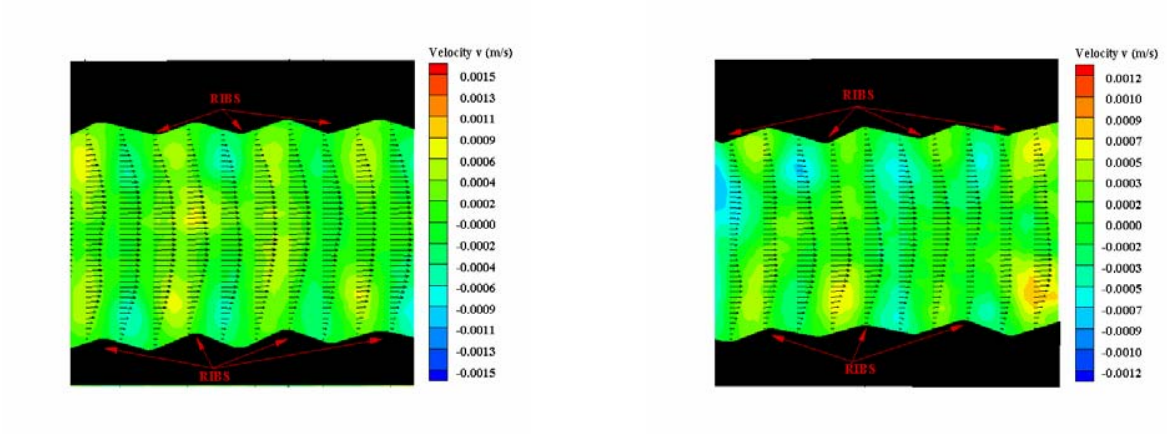

(a) (b)

Figure 7 The u-velocity vectors and v-velocity magnitude contours in the inter-rib region between for (a) acetone- water and (b) glycerol-water flow.

SUMMARY

The present study reports the effect of surface modification, i.e. micro ribs on mixing between two different fluids (acetone-water and glycerol-water solution) by using the "micro-laser induced fluorescence'' (μ-LIF) and "micro particle image velocimetry'' (μ-PIV) techniques. The ribs on the side walls of the microchannel aligned at an angle of 90^o to the flow direction lead to stretching and thinning of fluid elements, which efficiently reduces the mixing length requirement for complete mixing compared to that of smooth micromixer. The mixing between the two streams is higher at higher Reynolds number for both acetone-water and glycerol-water flow case. The mixing is lower for glycerol-water case compared to that of the acetone-water at same velocity ratio between the two streams. The μ-PIV results demonstrates a strong transverse velocity component as compared to smooth micromixer leading to higher stretching and thinning of liquid elements near the interface and hence mixing enhancement between the two fluid streams.

REFERENCES

1. Johnson, T. J, Ross, D. and Locascio, L. E., Rapid microfluidic mixing, *Anal Chem*., 74(1), pp 45- 51, 2002.
2. Stroock, A. D, Dertinger, S. K, Whitesides, G. M. and Ajdari, A., Patterning Flows Using Grooved Surfaces, *Anal Chem.*, 74(20), pp 5306-5312, 2002.
3. Jia, Ou. Geoffrey, R. Moss. and Jonathan, P. Rothstein., Enhanced mixing in laminar flows using ultrahydrophobic surfaces, *Physical Review*, E 76, 016304, 2007.
4. Hu, Y. H, Chang, M. and Lin, K. H., A study of two fluids mixing in a helical- type micromixer, J. of Physics: Conference series, 48, pp 531-536, 2006.
5. Liu, Y. Z, Kim, B. J. and Sung, H. J., Two-fluid mixing in a microchannel, Int. J. of Heat and Fluid Flow, 25, pp 986-995,2004
6. Hoffmann, M, Schluter, M. and Rabiger, N., Experimental investigation of liquid-liquid mixing in T-shaped micro-mixers using μ-LIF and μ-PIV, Chem. Engineering Science, pp 2968-2976, 2006.
7. Lindken, R, Westerweel, J. and Wieneke B., Stereoscopic micro particle image velocimetry, Experiments in Fluids, 41, pp 161-171, 2006.
8. Asfer, M., Panigrahi, P. K."Micro-PIV study of flow inside micro channel with surface mounted repeated transverse ribs", ASME Micro/Nano Scale Heat Transfer Conference, Tainan, Taiwan, January 6-9 (2008).

HEAT TRANSFER PROPERTIES OF NANODIAMOND-ENGINE OIL NANOFLUID FLOWING IN A MICROFIN TUBE

M.Ghazvini*, M.A.Akhavan-Behabadi, M.Raisee, E.Rasouli
Faculty of Mechanical Engineering, University College of Engineering, University of Tehran, Iran

ABSTRACT. Heat transfer enhancement of engine oil-nanodiamond nanofluid with different particle concentration under constant heat flux is investigated, experimentally. The test section is a horizontal microfin tube of 8.92 mm I.D., 9.52 mm O.D. and 1025 mm length. The nanofluid flowing inside the tube is heated by an electrical coil heater wrapped around it. Experiments are carried out under three different constant heat fluxes of 3, 8 and 13.5 kW/m^2 and Reynolds numbers up to 100. Experimental results clearly indicate a heat transfer enhancement of up to 55% due to the presence of nanoparticles in the base fluid. This heat transfer augmentation increases with an increase in Reynolds number and heat flux. The performance analysis of adding nanodiamond to engine oil flowing inside a microfin tube shows that, by increasing the Reynolds number, the performance index is increased; it means that the use of nanoparticles as additives to enhance heat transfer coefficients, is recommended specially at high Reynolds numbers.

Keywords: *Nanofluid, Microfin tube, Enhancement, Convective heat transfer, Laminar flow*

INTRODUCTION

Ultrahigh-performance cooling is one of the most vital needs of many industrial technologies. However, to develop an energy-efficient heat transfer fluid that is required for ultrahigh-performance cooling, the low thermal conductivity is a primary limitation. The produce of metallic or nonmetallic particles of nanometer dimensions can be achieved by modern nanotechnology. Nanomaterials have unique mechanical, optical, electrical, magnetic, and thermal properties. Nanofluids are made by suspending nanoparticles with average sizes below 100 nm in traditional heat transfer fluids such as water, oil, and ethylene glycol. Fluids with suspended solid particles are expected to have better heat transfer properties compared to conventional heat transfer fluids. These special properties make nanofluid a revolutionary coolant for future devices.

In addition, another way of enhancing heat transfer is extending the heat transfer surfaces; it provides a better contact between the fluid and the carrier. The microfin tubes are widely used in different heat exchangers because of their good enhancement capability and relatively low pressure drop in comparison with the other conventional extended surfaces.

Nanofluids found to possess long time stability and large efficient thermal conductivity [1]. Lee [2] reported that suspension of 4% volume fraction of CuO 35 nm particles in ethylene glycol shows 20% increase in thermal conductivity. Since the theoretical models such as Maxwell correlation [3] cannot determine exactly the thermal conductivity of nanofluids, therefore it is necessary to study about thermal conductivity enhancement mechanisms of this kind of fluids. Chopkar et al [4] prepared nanofluids by dispersing about 0.2–1.5% volume fraction of Al_2Cu and Ag_2Al nanoparticles in water

* Corresponding author: M. Ghazvini
Phone: + (98)-911-3933391
E-mail address: mghazvini@ut.ac.ir

and ethylene glycol. They characterized the size/microstructure of nanoparticles by X-ray diffraction and transmission electron microscopy, and measured the thermal conductivity of nanofluid using a modified thermal comparator. Moreover, Nie et al. [5] in a paper discussed several proposed mechanisms of thermal conductivity enhancement in nanofluids using a mathematical and analytical approach.

There are relatively few studies involved in describing fluid flow and convective heat transfer performance of the nanofluids. Li and Xuan [6] studied convective heat transfer of 35 nm Cu/ water nanofluid and showed that the suspended nanoparticles remarkably enhance heat transfer process with smaller volume fraction of Cu nanoparticles.

Some other experimental or theoretical investigations indicated that the Nusselt number of the nanofluids increases with increasing volume fraction of the nanoparticles [7, 8]. However Pak and Cho [9] expressed that the convective heat transfer coefficient of Al_2O_3 /water and TiO_2 / water nanofluids with concentration of 3.0% volume was 12.0% smaller than that of pure water. Putra [10] reported suppression of natural convection heat transfer by nanofluid of Al_2O_3 / water and CuO/ water and concluded that this could be due to nanoparticles settling and velocity difference between nanoparticles and main fluid. Nanofluid boiling process was investigated experimentally by several researchers. Das et al. [11] observed nanofluids boiling performance deterioration.

As far as the numerical predictions for forced convection of nanofluids is concerned, only recently a few papers have been published. Maiga et al. [12] presented numerical results for laminar and turbulent nanofluid flow through a uniformly heated tube using the Fluent code; however, no comparison between their numerical and experimental data was reported. Akbarinia and Behzadmehr [13] have numerically studied laminar mixed convection of a nanofluid consisting of water and Al_2O_3 in a curved tube. No comparison with experimental data was reported in their work. Recently, Raisee and Moghaddami [14] numerically studied laminar forced convection of nanofluids through circular pipes using two different models. Comparisons of numerical results with experimental data showed that it is necessary to include the effects of Brownian motion in modeling of viscosity and thermal conductivity to achieve reliable predictions.

Al-Fahed and Chamra [15] experimentally investigated the heat transfer and pressure drop of oil flow in plain tubes, microfin tubes and in tubes with twisted tape inserts. They reported that heat transfer enhancement and pressure drop of microfin tube flow were more than those of plain tube. Also, Afroz and Miyara [16] tested water flow in microfin tubes and found similar results.

The objective of the present work is to study the convective heat transfer characteristics of nanodiamond / engine oil nanofluid flowing inside a microfin tube.

EXPERIMENTAL FACILITY AND PROCEDURE

Figure 1 shows the schematic diagram of experimental set-up. The flow loop is consists of test section, cooler, receiver, gear pump, flow measuring apparatus, various thermocouples and flow controlling system. In order to control the fluid flow rate a reflux line with a valve is used. The test section is a horizontal microfin tube of 8.92 mm I.D., 9.52 mm O.D. and 1025 mm length. The microfin tube is a copper tube having internal microfins with triangular fin cross-sections. The geometrical parameters of microfin tube are shown in Figure 2.

The nanofluid flowing inside the tube is heated by an electrical heating coil wrapped around it. The test section (tube and heater) is completely insulated with glass wool pads. Two K-type thermocouples are used to measure the bulk temperatures of nanofluid flow at inlet and outlet of test section. Also, six

pairs of K-type thermocouples are mounted with uniform distances of 125 mm on the external surface of the test tube to measure the wall temperatures.

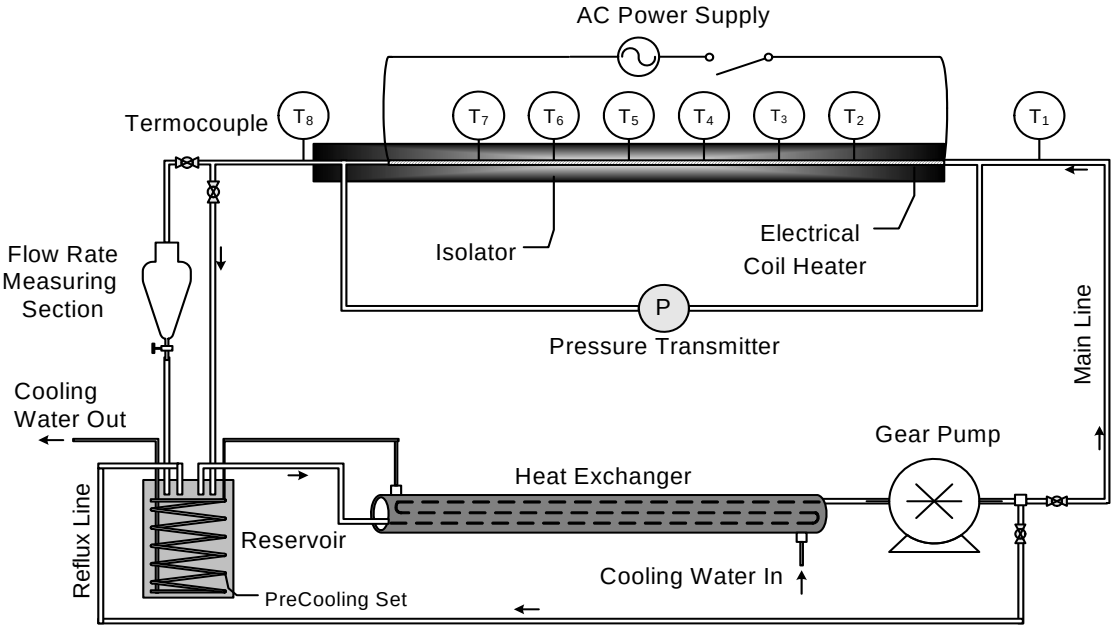

Figure 1. Schematic diagram of experimental set-up.

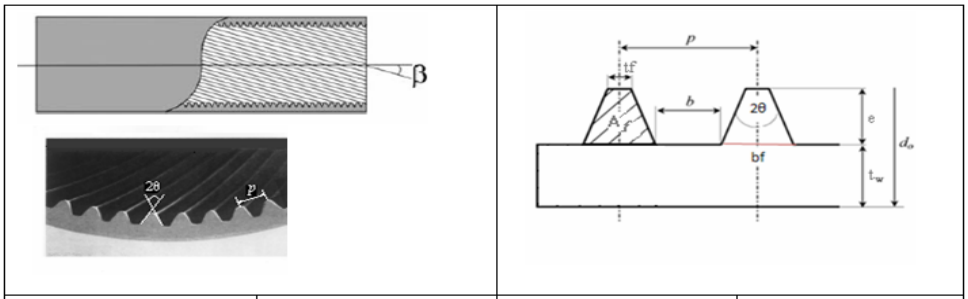

Outside diameter	$d_o = 9.52mm$	Fin tip	$tf = 0.096mm$
Wall thickness	$t_w = 0.3mm$	Fin pitch	$p = 0.48mm$
Fin height	$e = 0.25mm$	Helix angle	$\beta = 15^\circ$
Number of fin	$n = 55$	Fin tip angle	$2\theta = 15^\circ$
Fin base	$bf = 0.207mm$	Fin area	$A_f = 0.379$
Pipe length	L= 1200 mm	Area enhancement	$\varepsilon_a = 1.63$

Figure 2. Geometrical parameters of microfin tube.

In the present work, nanodiamond-engine oil nanofluid is used as the working fluid. Nanofluids with different diamond nanoparticles concentrations of 0.2%, 0.5%, 1.0%, and 2.0% weight fractions in 20W50 engine oil are used. The nanofluid is prepared and dispersed using mechanical (ultrasonic vibrator) and chemical (adding dispersant) treatments. Flow measuring section is consisted of a 500 cm^3 glass vessel with a valve at its bottom. The flow rate is directly computed by measuring the time required to fill the glass vessel. The constant exerted heat fluxes are 3, 8 and 13.5 kW/m^2 with

Reynolds numbers varying from 2 to 100. Furthermore, the thermal conductivity and specific heat of nanofluids are measured using KD2 and DSC F3 Maia apparatuses, respectively.

RESULTS AND DISCUSSION

Specific heat

A differential scanning calorimeter was used to measure the heat capacity of different nanofluids and the pure engine oil. Based on the collected data, different correlations were developed to predict the specific heat of pure engine oil and nanofluids. Table 1 demonstrates the correlations for pure engine oil and 1% weight fraction nanofluid.

Table 1
Specific heat as a function of Temperature

Fluid	Correlation
Pure Engine Oil	$Cp = 1.77 + 1.18\times10^{-2}T - 2.02\times10^{-4}T^2$
1% Nanofluid	$Cp = 2.07 - 2.30\times10^{-3}T + 1.19\times10^{-4}T^2$

Thermal conductivity

The thermal conductivity of nanofluids were measured at several temperatures. Using the present data, the following correlation was developed to estimate the thermal conductivity of nanofluids:

$$k_{nf} = 0.126 + 0.074\varphi - 0.056\varphi^2 + 0.015\varphi^3 \quad (1)$$

where φ is the weight fraction of nanoparticles.

Convection heat transfer

During all the test runs, the Reynolds number is small enough so that the flow can be considered as fully-developed; however, the Prandtl number of engine oil is about 1500 and the temperature field is in thermally developing condition.

Equation (2) is used to calculate the local convection heat transfer coefficient.

$$h(x) = \frac{\dot{m}c_p}{\dot{m}c_p (T_s - T_i)/q'' - Px} \quad (2)$$

Where, T_s and q" are taken from experimental data.

To calculate the mean heat transfer coefficient, the following expression is used.

$$\bar{h} = \frac{1}{L}\int_0^L h(x)\,dx \quad (3)$$

The variation of local convection heat transfer coefficient along the tube for pure engine oil and different nanofluids is presented in Figure 3. The results are for Peclet number of 10000 and heat flux of 8 kW/m^2. A significant enhancement is seen as a result of utilizing nanofluid instead of pure

engine oil. This enhancement is about 41% for the nanofluid with 2% weight fraction in comparison with pure engine oil at x=0.2 m.

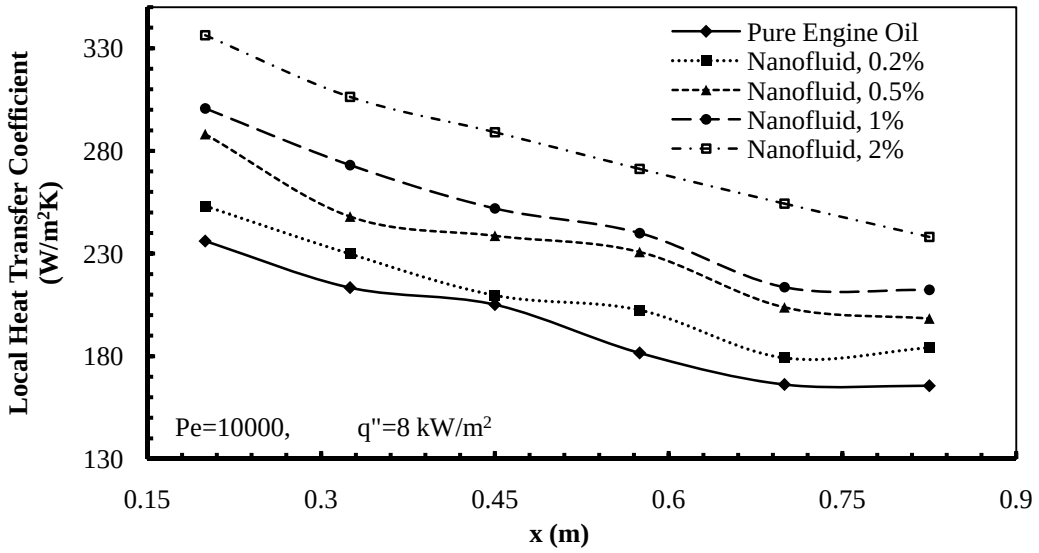

Figure 3. Local heat transfer coefficient as a function of *x* for different nanofluids

Figure 4 shows the variation of mean heat transfer coefficient as a function of weight fraction in two Peclet numbers of *Pe*=10000 and *Pe*=15000, and two heat fluxes of 3 and 13.5 kW/m^2. The effect of nanoparticles in enhancing heat transfer can be easily seen in this figure. In addition, one can note the effect of heat flux changes on the heat transfer coefficient. For microfin tube, the highest heat transfer enhancement is about 55% which is belonged to 2% nanofluid at heat flux of 3 kW/m^2. Moreover, higher Peclet number leads to a higher heat transfer coefficient.

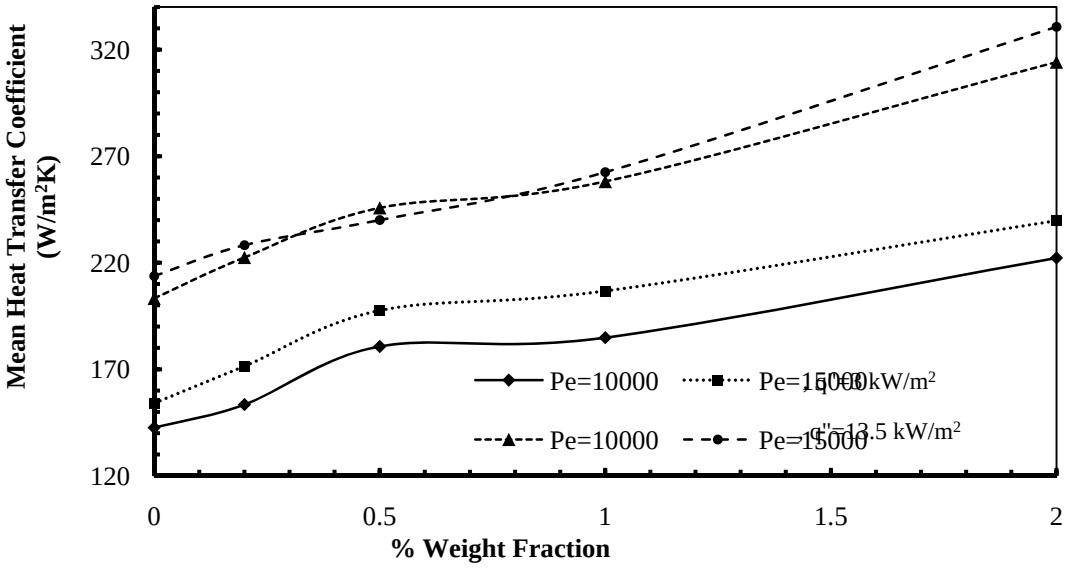

Figure 4. Variation of mean heat transfer coefficient with weight fraction

Performance analysis

In order to analyse the performance of a system using microfin tube and nanofluid together, the increase of pressure drop as a result of adding nanoparticle should also be considered. Utilizing the experimental data of pressure drop exists for the same set-up and flow conditions, the performance index (η) is calculated using Equation (4).

$$\eta = \frac{\left(\frac{h_{nf}}{h_f}\right)}{\left(\frac{\Delta P_{nf}}{\Delta P_f}\right)} = \frac{R_h}{R_{\Delta P}} \tag{4}$$

According to the above correlation, if the index is more than one, using nanofluid is efficient. Figure 5 shows the performance index for different working conditions. As it is seen, by increasing the Reynolds number, the performance index increases. Therefore, using both of nanofluid and microfin tube to enhance heat transfer coefficient is recommended specially at Reynolds Numbers more than 10.

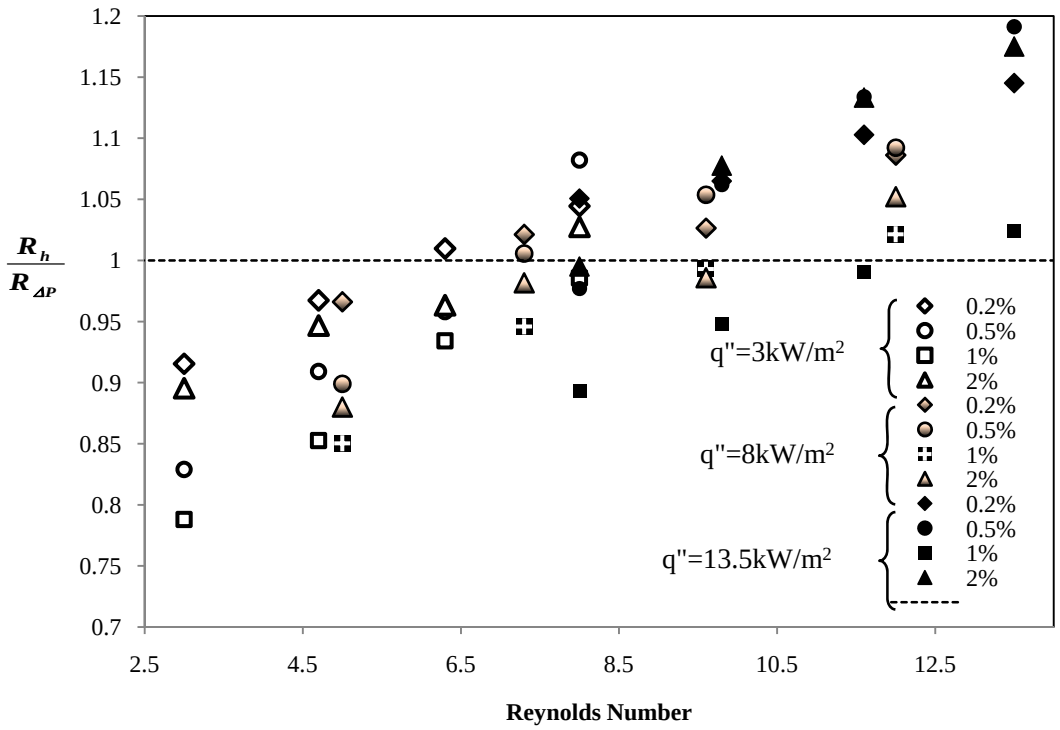

Figure 5. Performance index as a function of Reynolds number

CONCLUSION

The following conclusions are achieved from the present experimental work:

1) The use of nanofluid instead of pure fluid and microfin tube instead of smooth tube, enhances the heat transfer coefficients significantly. The rate of enhancement is more in lower heat fluxes.
2) Higher Reynolds (Peclet) numbers and higher heat fluxes lead to higher heat transfer coefficients.

3) The maximum heat transfer enhancement is about 55% which is belonged to nanofluid of 2% weight fraction at heat flux of 3 kW/m^2.
4) The performance analysis of adding nanodiamond to engine oil flowing inside a microfin tube shows that, by increasing the Reynolds number, the performance index is increased; it means that the use of nanoparticles as additives to enhance heat transfer coefficients, is recommended specially at high Reynolds numbers.

REFERENCES

1. Khanafer, K., Vafai, K., and Lightstone, M., Buoyancy-driven heat transfer enhancement in a two-Dimensional enclosure utilizing nanofluids, *Int. J. Heat Mass Trans.* Vol. 46 (19), pp. 3639–3653, 2003.
2. Lee, S., Choi, S.U.S., Li, S., and Eastman, J.A., Measuring thermal conductivity of fluids containing oxide nanoparticles, *J. Heat Trans.*, Vol. 121, pp. 280–289, 1999.
3. Maxwell, J., *A Treatise on Electricity and Magnetism*, 2nd ed., Oxford University Press, Cambridge,UK, 1904.
4. Chopkar, M., Kumar, S., Bhandari, D.R., Dasd, P.K., and Manna I., Development and characterization of Al_2Cu and Ag_2Al nanoparticle dispersed water and ethylene glycol based nanofluid, *J. Materials Sci. Eng. B*, Vol. 139, pp. 141–148, 2007.
5. Nie, C., Marlow, W.H., and Hassan, Y.A., Discussion of proposed mechanisms of thermal conductivity enhancement in nanofluids, *Int J. Heat Mass Trans*., Vol. 51, pp. 1342–1348, 2008.
6. Xuan, Y., and Li, Q., Investigation on convective heat transfer and flow features of nanofluids, *J. Heat Trans*., Vol. 125, pp. 151–155, 2003.
7. Koo, J., and Kleinstreuer, C., Laminar nanofluid flow in micro heat sinks, *Int. J. Heat Mass Trans.*, Vol. 48, pp. 2652–2661, 2005.
8. Yang, Y., Zhang, Z.G., Grulke, E.A., Andersen, W.B., and Wu, G., Heat transfer properties of nanoparticle-in-fluid dispersions (nanofluids) in laminar flow, *Int. J. Heat Mass Trans.*, Vol. 48 (6), pp. 1107–1116, 2005.
9. Pak, B.C., and Cho, Y., Hydrodynamic and heat transfer study of dispersed fluid with submicron metallic oxide particles, *Exp. Heat Trans*., Vol. 11 (2), pp. 151–170, 1998.
10. Putra, N., Roetzel, W., and Das, S.K., Natural convection of nanofluids, *Heat Mass Trans*., Vol. 39 (8), pp. 775–784, 2003.
11. Das, S.K., Putra, N., and Roetzel, W., Pool boiling characteristics of nano-fluids, International *J. Heat Mass Trans*., Vol. 46 (5), pp. 851–862, 2003.
12. Maiga, S. E. B., Nguyen, C. T., Galanis, N., and Roy, G., Heat transfer behavours of nanofluids in a uniformly heated tube, *J. Superlatice Microstructures*, Vol. 35, pp. 543-557, 2004.
13. Akbarinia, A., and Behzadmehr, A., Numerical study of laminar mixed convection of a nanofluid in horizontal curved tubes, *App. Thermal Eng*., Vol. 27, pp. 1327-1337, 2007.
14. Raisee, M., and Moghaddami, M., Numerical Investigation of Laminar Forced Convection of Nanofluids through Circular Pipes, *J. Enhanced Heat Trans*., Vol. 15(4), pp. 335-350, 2008.
15. Al-Fahed, S., Chamra, L.M. and Chakroun, W., Pressure drop and heat transfer comparison for both microfin tube and twisted-tape inserts in laminar flow, *Exp. Thermal and Fluid Sci.* Vol. 18, 323-333, 1999.
16. Afroz, M.M. Hasan, and Miyara, A., Friction factor correlation and pressure loss of single-phase flow inside herringbone microfin tubes, *Int. J. Refrigeration* Vol. 30, No. 7, pp.1187-1194, 2007.

Advanced Energy and Environmental Systems

INVESTIGATIONS ON THE DELIVERING BEHAVIOUR OF MULTIPHASE SCREW PUMPS

A. Scharf[1], G. Aleksieva[1], J. Lewerenz[2], D. Mewes[1]*
[1]Institute of Multiphase Processes, Leibniz University Hannover, Germany
[2]Bornemann Pumps, Obernkirchen, Germany

ABSTRACT. Multiphase screw pumps are used for the delivery of gas-liquid-flows even at high gas rates. In order to estimate their delivering behaviour a model is derived, which is based on mass and energy balances for single closed chambers formed by the intermeshing and counter-rotating screws. Thereby the pressure profiles inside the pumps are predicted, which determine the mechanical loads to the rotating and static components as well as the delivered volume flows. In order to verify the calculated results, the pressure profiles are measured along the inside of the cylindrical casing in dependence of several characteristic operating modes of multiphase screw pumps.

Keywords: *multiphase pump, screw pump, multiphase flow*

INTRODUCTION

Multiphase pumping is applied in the oil and natural gas exploring and conveying industry especially in offshore applications. By means of multiphase transport cost-intensive separation units on offshore platforms can be avoided, because the gas-liquid-mixtures can be conveyed directly to central separation units located onshore. As a consequence the number of platforms is reduced, which leads to a saver and more efficient offshore oil production.

Multiphase screw pumps can handle gas-liquid-flows with gas volume fractions up to 0.95 and withstand even temporary dry runs. Furthermore, screw pumps are suitable for the delivery of high-viscous fluids since they operate without valves.

In Figure 1 the design of a screw pump is presented.

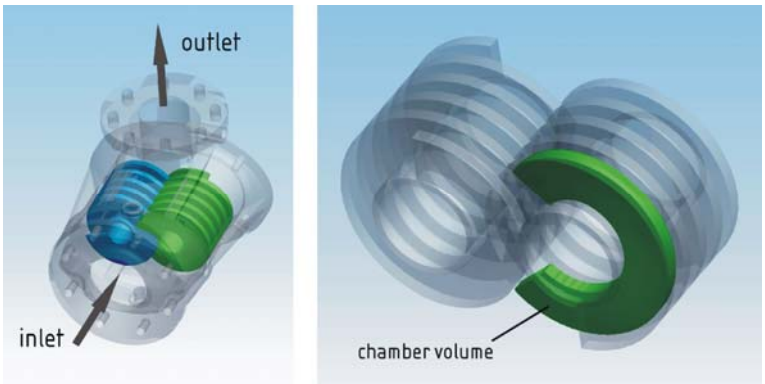

Figure 1. Twin screw pump and position and shape of a chamber

* Corresponding author: Prof. Dr.-Ing. Dr. h.c. Dieter Mewes
Phone: + (49)-511-762-3638, Fax: + (49)-511-762-3031
E-mail address: mewes@ifv.uni-hannover.de

The multiphase mixture entering the pump gets into the chambers formed by the intermeshing screws and the enclosing housing (cp. Figure 1). Due to the rotation of the screws, the chambers are closed at the suction side of the pump and move along the screw axis towards the outlet. At the discharge side, the chambers open and the gas-liquid-mixtures are released through the outlet.

Since the rotation of the screws is contactless, several gaps are located between the intermeshing screws and between the screws and the housing. Three different types of gaps occur and are shown schematically in Figure 2.

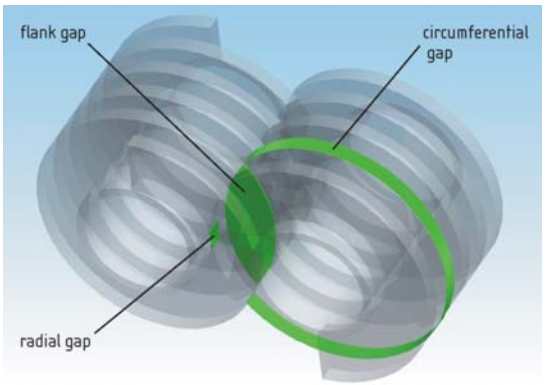

Figure 2. Gap types in a screw pump

The circumferential gap is an annular gap between the tip circle of a screw and the inner wall of the housing. The radial gap is placed between the tip circle of one screw and the root circle of the opposed screw. The flank gap is a lenticular gap, which is placed between the flanks of adjacent intermeshing screws.

During the movement of a chamber along the axis of the intermeshing screws, the chamber pressure increases. This leads to pressure differences between adjacent chambers and thus to internal backflows of the gas-liquid-mixture through the different types of gaps. The gap flows determine the shape of the resulting pressure profiles along the screw axis.

The pressure profiles are highly affecting the delivery flows as well as the mechanical loads to the pump's components. In order to estimate the delivering behaviour of screw pumps the calculation of the pressure profiles are done by mass and energy balances for closed chambers. In order to verify the calculated pressure profiles the pressure build-up is measured in a multiphase screw pump for different operational conditions and compared to the calculated results.

There are several attempts to describe the delivering behaviour of multiphase screw pumps by the transport equations for momentum, mass and energy. Etzold [1] calculates the change of pressure in closed chambers inside the pump and the loss flows by setting up boundary conditions for continuous pressure raise in the closed chambers while moving from the inlet to the outlet. Furthermore, Etzold [1] reduces the boundary value problem to an initial value problem, which he solves iteratively. Körner [2] and Wincek [3] use similar approaches but calculate two separate cases with an integer number of stages, which are below and above the real number of stages. Weighting these two cases according to the real number of stages leads to an approximate solution. Feng, Yueyuan, Ziwen and Pengcheng [4] present a model, by which the backflow within the screw pump depending on the rotational angle is determined. There is two-phase flow in the radial and flank gaps and pure liquid flow in the circumferential gaps. The effect of acceleration pressure drop on the gap flows is neglected. Nakashima [5] chooses a different approach by deviding the multiphase pumping operation into an arrangement of fundamental processes like separation, pumping, compression and mixing. Nakashima applies the process simulator HYSYS for solution.

Naujoks [6] applies a chamber model to calculate the delivering behaviour of screw compressors, which considers the reduction of the chamber volume. Neumann [7] calculates the delivering behaviour of screw compressors by means of mass and energy balances, including heat transfer across the chamber boundaries.

MATHEMATICAL FORMULATION

The volume flow of the multiphase mixture at inlet conditions

$$\dot{V} = \dot{V}_{theo} - \dot{V}_{loss} - \dot{V}_{rec} \tag{1}$$

is determined by the difference between the theoretical displacement volume flow $\dot{V}_{theo}$ and the loss flow

$$\dot{V}_{loss} = \dot{V}_{l,loss} + \dot{V}_{g,loss} \tag{2}$$

and the recirculation flow $\dot{V}_{rec}$. The theoretical displacement volume flow is a function of the shape and the rotational frequency of a twin screw pump. In order to estimate the performance of a pump the volumetric efficiency

$$\eta_{vol} = \frac{\dot{V}_{theo}}{\dot{V}} \tag{3}$$

is defined as the ratio of the theoretical displacement volume flow $\dot{V}_{theo}$ and the actual displacement volume flow of the pump $\dot{V}$. Within some special designed pumps, separated liquid is recirculated from the outlet to the inlet. This flow is defined as recirculation flow. This design helps to enhance the sealing of the gaps inside the pump for high gas volume fractions. The loss flow is directed across the closed chambers inside the pump via different gaps back to the inlet of the pump. It can be of multiphase type and caused by two components. One is pressure driven and the other component is due to the rotation of the screws a shear flow induced one [8].

Time intervalls model the movement of the chambers along the rotating screws. For each time intervall mass and energy balances are set up for each closed chamber. Those are considered as open systems (Figure 3). The differential equation for the change of liquid mass inside a closed chamber gives

$$\frac{dM_{l_i}}{dt} = \sum_{in} \dot{M}_{l_i} - \sum_{out} \dot{M}_{l_i} \tag{4}$$

and for the mass change of gas

$$\frac{dM_{g_i}}{dt} = \sum_{in} \dot{M}_{g_i} - \sum_{out} \dot{M}_{g_i} \tag{5}$$

i has the meaning of the chamber index. Eq. 4 and Eq. 5 mean that the amount of each phase in a closed chamber is only changed by the incoming and the outgoing mass flows crossing the gaps.

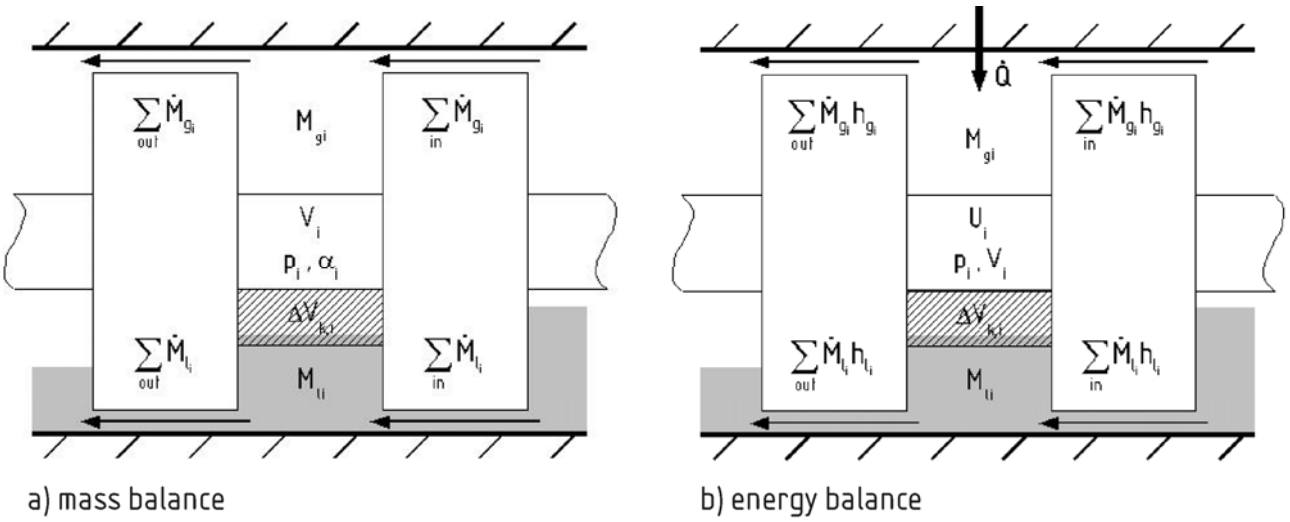

Figure 3. Closed chamber as an open mass system (a) and a transient thermodynamic system (b)

Since enthalpy is transferred between adjacent chambers via the gap streams, a closed chamber is considered as a transient open thermodynamic system (Figure 3 (b)).

The energy blance for a closed chamber is

$$\frac{dU_i}{dt} = \sum_{in}\left(\dot{M}_{l_i} h_{l_i} + \dot{M}_{g_i} h_{g_i}\right) - \sum_{out}\left(\dot{M}_{l_i} h_{l_i} + \dot{M}_{g_i} h_{g_i}\right) + \dot{Q} + \dot{W}_v \qquad (6)$$

the change of the internal energy U_i by time is determined by the sum of incoming and outgoing enthalphy flows. The heat flow $\dot{Q}$ is crossing the chamber boundary and W_v is the requested power for compressing the gas phase. The heat flow $\dot{Q}$ is caused by the friction in bearings and sealings. It is measured in dependence on the rotational frequency. The additional power of compression is caused by the reduction of the chamber volume while moving along a screw with declining pitch.

The algorithms for calculating the delivering behaviour are taken from an existing numerical program called SiMuS (simulation of multiphase screw pumps) and published in [9]. As input data geometrical and operational parameters have to be provided. Output values are for example volume flow, volumetric as well as thermodynamic efficiency and pressure distribution within the pump.

The internal backflows between adjacent chambers through the different gaps affect the shape of the resulting pressure profile along the screw axis. Thus it is important to calculate the different gap flows precisely [10]. In the current applied equations all gap flows are assumed to be pure liquid according to a hypothesis mentioned by many authors [1], [2], [3]. A gap flow consists of two components. One is pressure driven and the other component is due to the rotation of the screws a shear flow induced one.

EXPERIMENTAL SETUP

In order to verify the calculated pressure profiles the pressure build-up along the screw axis is measured by means of a test rig. The corresponding flow chart is shown in Figure 4.

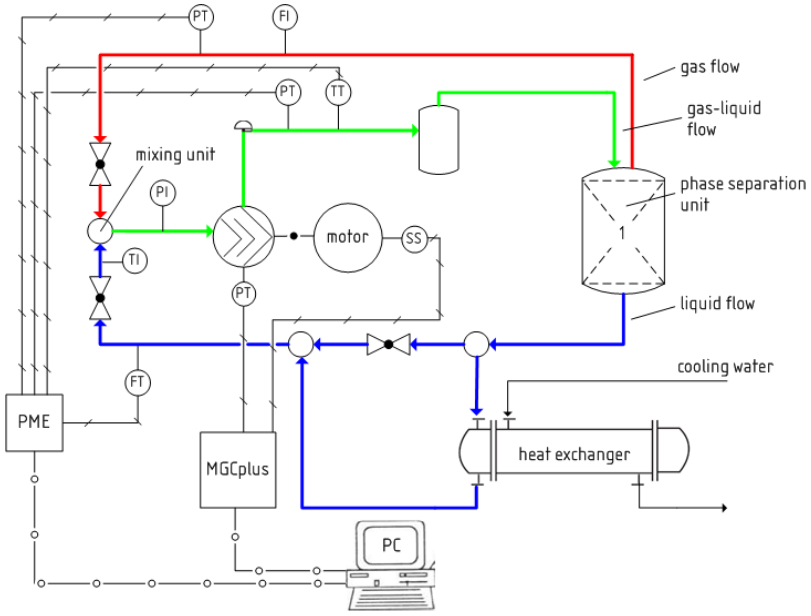

Figure 4. Flow chart of the test facility

The gas and liquid flows are mixed in a Y-mixing unit, downstream of which the gas-liquid-mixture enters the pump. After leaving the pump, the pressurised fluid flows into a small vessel, in which liquid accumulates at the bottom for external recirculation. Downstream the phases are separated in a separation unit by means of a structured packing and further internals, which extend the hold-up time of the liquid phase in the vessel. The temperature of the liquid phase is determined by a tube heat exchanger. Valves in the gas and liquid stream determine the pressure build-up in the pump. The rotational frequency of the motor and thus of the screws is determined by a frequency converter.

The signals of temperature, flow rate and pressure metering points are processed by means of the software Catman Professional 5.0.

The used pump is a SL 125 Twin Screw Pump, produced by Bornemann Pumps GmbH (Figure 5).

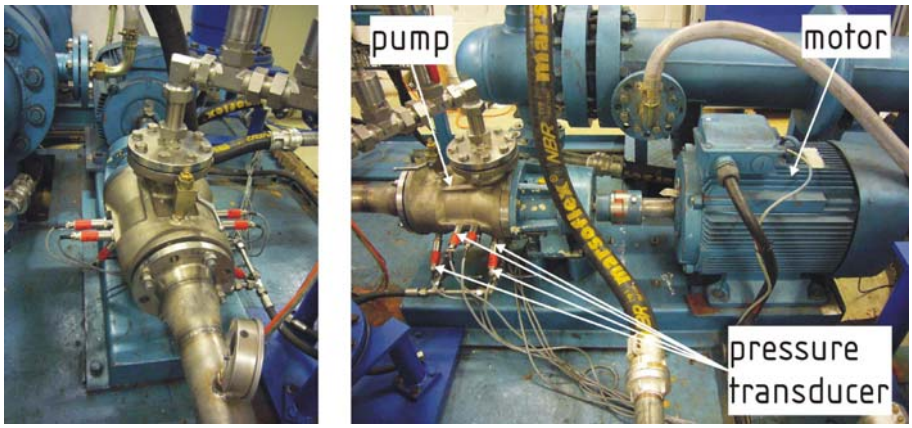

Figure 5: Used screw pump with installed pressure transmitters

The red labelled instruments are seven pressure transducers. In dependence on the rotation angle of the screws a pressure profile is obtained by combining and synchronising the time-dependent signals of all seven pressure transducers.

RESULTS

In context of the experimental investigation the influence of the

- rotational frequency of the screws
- pressure difference over the pump
- gas volume fraction of the mixture
- the design of the screws (degressive/constant pitch)

on the pressure profile along the screw axis are observed. Thereby the gas volume fraction turns out to influence on the pressure profile. In Figure 6 measured pressure profiles along the screw axis are presented as a function of the gas volume fraction. The measured pressure profiles are not measured over the whole length of the screw. For increasing gas volume fractions the pressure profile becomes more progressive ($0.00 \leq \alpha \leq 0.74$), which leads to less loss flow due to the lower pressure build-up close to the suction side ($0 \text{ mm} \leq z \leq 23 \text{ mm}$). Over a certain gas volume fraction of the mixture ($\alpha > 0.74$) the pressure profile becomes linear again.

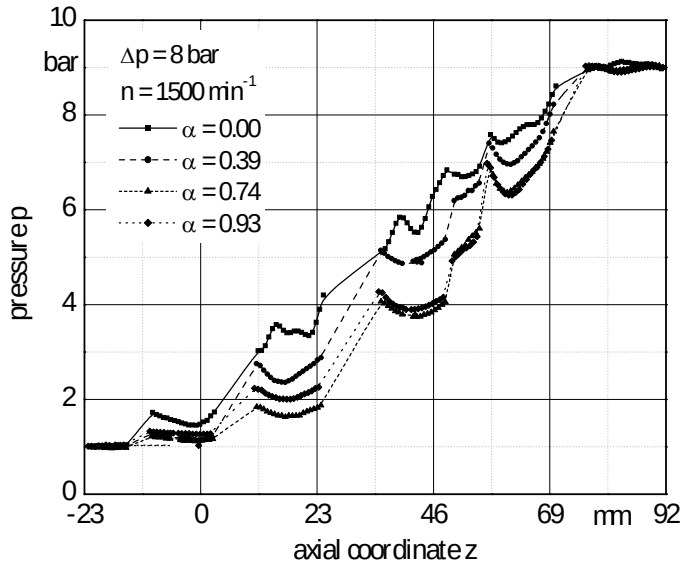

Figure 6. Measured pressure profiles as a function of the gas volume fraction

The corresponding volumetric efficiencies are presented in Figure 7 as functions of the gas volume fractions and the rotational frequencies of the screws. Since the screw pump does operate without recirculation the amount of liquid conveyed in the chambers does not seal the gaps properly with liquid. This leads to higher gaseous gap flows and thus to a higher loss flow for very high gas volume fractions.

In Figure 8 measured and calculated pressure profiles are shown for a medium gas volume fraction ($\alpha = 0.39$) and for a high gas volume fraction ($\alpha = 0.93$). Since the calculations are conducted for screws with the constant pitch of 23 mm the vertical lines are separating the adjacent chambers from each other. After 3.28 rotations (3.28 chambers) a chamber is opened to the discharge side and the pressure increases rapidly to the discharge pressure. The calculations are conducted with and without considering the flow through the flank gaps.

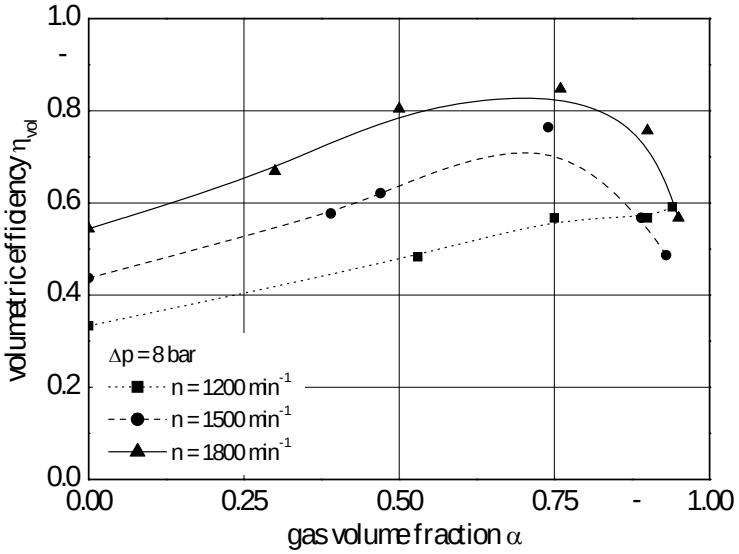

Figure 7. Measured volumetric efficiency as a function of the gas volume fraction

The differences between measured and calculated pressure profiles are smaller, if the flow through the flank gaps is taken into account. The consideration of the flank gaps leads to an interaction between the pressure profiles of both screws. This is why besides the opening of the last chamber the opening of the opposed screw's last chamber also leads to pressure increases in all chambers at a certain rotation angle. Without considering the flank gaps the received pressure profiles are too progressive, which leads to an underestimation of the pump's loss flow and thus to an overestimation of the pump performance. Since the pressure profiles become more linear by considering the flank gaps the difference of the calculated results with and without the flank gaps becomes bigger for increasing gas volume fractions (cp. $\alpha = 0.93$).

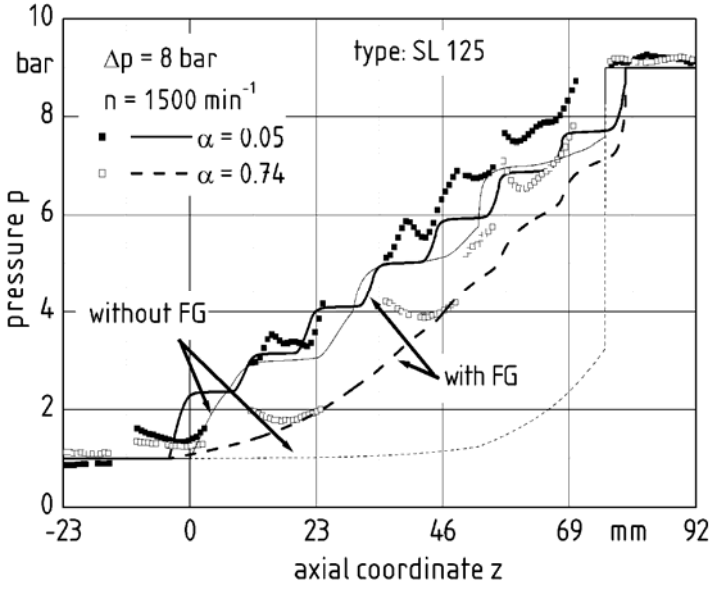

Figure 8. Measured and calculated pressure profiles

CONCLUSIONS

The calculation model allows to obtain the pressure build-up and the delivery flow of a multiphase screw pump in dependence on the screw design and the operating conditions. By means a new

designed experimental setup the pressure build-up and the delivery flow are measured and compared to the calculated results. The comparison is done with and without considering the flow through the flank gaps in the calculation model. The measured pressure profiles indicate that the flow through the flank gaps affects the delivering behaviour of a screw pump significantly. By considering the flow through flank gaps, the obtained pressure profiles match the experimental data. Furthermore the experimental investigation shows the necessity for a recirculation system. Without any recirculation flow, the different gaps are not sufficiently sealed with liquid over a certain gas volume fraction. This leads to an increasing loss flow. Consequently the volumetric efficiency of a screw pump without a recirculation system decreases for very high gas volume fractions.

ACKNOWLEDGEMENTS

The authors would like to thank the Bornemann Pumps GmbH for the close cooperation and technical support for the experimental investigations and the German Federal Ministry of Economics and Technology for the financial support of this project.

REFERENCES

1. Etzold, S.: Verlustanalyse von Schraubenspindelpumpen bei Mehrphasenförderung; PhD Thesis, VDI Verlag Reihe1 Nr. 221, Düsseldorf 1993

2. Körner, H.: Zum Förderverhalten von Schraubenspindelpumpen für Zweiphasengemische hohen Gasgehalts; PhD Thesis, University of Erlangen, Erlangen 1998

3. Wincek, M.: Zur Berechnung des Förderverhaltens von Schraubenspindelpumpen bei der Förderung von Flüssigkeits/Gas-Gemischen; PhD Thesis, University of Erlangen, Erlangen 1992

4. Feng, C., Yueyuan, P., Ziwen, X., Pengcheng, S.: Thermodynamic performance simulation of a twin-screw multiphase pump; Proc. Instn. Mech. Engrs. 215 (2001) E, 157-163

5. Nakashima, C. Y., Junior S. d. O., Caetano E. F.: Thermodynamic model of a twin-screw multiphase pump; ASME ETCE, Houston 2002

6. Naujoks, R.: Zustandsänderungen in trockenlaufenden Schraubenmaschinen – ein Vergleich von Rechnung und Experiment; PhD Thesis, University of Dortmund, VDI Verlag Reihe 7 Nr. 69, Dortmund 1982

7. Neumann, G.: Berechnete, prozessbeeinflussende Strömungsvorgänge in Schraubenmaschinen; PhD Thesis, University of Bochum, Bochum 1986

8. Tiedt, W.: Berechnung des laminaren und turbulenten Reibungswiderstandes konzentrischer und exzentrischer Ringspalte; Technischer Bericht Nr. 4, Institut für Hydraulik und Hydrologie, Darmstadt 1968

9. Rausch, T.: Thermofluiddynamik zweiphasiger Strömungen in Schraubenspindelpumpen; PhD Thesis, University of Hannover, Hannover 2006

10. Scharf, A., Rausch, T., Aleksieva, G., Reichwage, M., Mewes, D.: Effect of gap flows inside a multiphase screw pump on the conveying characteristic; ICMF, Leipzig 2007

HEAT RECOVERY FROM A 1 MW CLASS GAS ENGINE CHP SYSTEM: 1/5 SCALE MODEL TEST

J. Ahn[1,*], H. J. Kim[1], K. S. Choi[1], D. S. Song[1]
[1]Korea Institute of Energy Research, Daejeon, Korea

ABSTRACT. The present study has been conducted to develop a heat recovery system for a 1 MW class gas engine based cogeneration system. In the cogeneration system, heat is recovered from two parts of the engine, which are jacket water and exhaust gas. The heat from the jacket water is recovered by a plate type heat exchanger and used for the room heating and/or hot water supply. The heat from the exhaust gas is used to generate steam. For both of the heat recovery devices, 1/5 scaled experiments are performed and the results are compared to the conventional correlations for the design.

Keywords: *Combined Heat and Power (CHP), Heat Recovery Steam Generator (HRSG), Heat Transfer*

INTRODUCTION

With the pursuit of high quality and reliability of electricity, the distributed energy system is proposed to be constructed in place of the conventional centralized system. Many kinds of energy sources including renewable ones have been considered for the distributed system and the combined heat and power (CHP) system based on the reciprocating engine has appeared to be one of the most feasible solutions within the current state of the art. Among the fuels for the engines for power generation, LNG has big merits not only for its economic feasibility but also for the environmental issues, since the exhaust gas contains less pollutants and carbon dioxide (CO_2).

In the CHP system, the heat is obtained by recovering the thermal energy from the cooling water and the exhaust gas of the engine, while it generates the electricity. The engine is rather fixed for its capacity and maker. The heat recovery system, however, has some room for engineering to be adjusted to the characteristics of the site such as its seasonal variation of energy demand. The energy demand of the site should be well analysed to decide a proper core engine and system configuration. After the decision, the heat recovery system is supposed to be engineered to maximize the economic feasibility.

The gas engine is mostly used for the site, whose electricity demand is less than 5 MW. A relatively small system of several hundreds kW class is mostly installed at a site with the thermal energy demand as a form of hot water. However, sites for MW class system, which is the scope of the present study, often have some demand for steam, e.g. a hospital with steam based sterilizers. Since the temperature from the cooling water of the engine is not high enough to boil the water, the steam is generated by recovering the thermal energy from the exhaust gas as illustrated in Fig. 1.

The core engine of the present CHP system has been chosen as 1 MW class Waukesha 15V150LTD [1]. Based on its engineering data, the energy balance has been analysed and depicted in Fig. 1(b). The heat recovered from the cooling water and the exhaust gas of the engine is 487 and 621 kW, respectively. Prior to the design of the full scale system, 1/5 scaled model experiments have been conducted for each heat exchanger in the present study. The design and off-design performance for

* Corresponding author: Dr. J. Ahn
Phone: + (82)-42-8603328, Fax: + (82)-42-8603098
E-mail address: jahn@kier.re.kr

each heat exchanger have been obtained and compared with the conventional correlations, which have been used for the thermal design of the system.

EXPERIMENTAL SETUP

Heat Recovery from Engine Jacket Coolant

Since water is used as coolant for the engine jacket for the present study, its thermal energy is recovered as a form of hot water through a heat exchanger. The working fluid at both sides of the heat exchanger is water, so that a plate type heat exchanger (Figure 2(b)) is mostly adopted. The heated water from the recovery system is supplied directly to the household demand or used for the room heating as shown in Figure 2(a). For both of the cases, the low temperature part is supposed to have more flow rate and less temperature difference between inlet and outlet compared to the high temperature part, i.e. the engine coolant side. The difference should affect the heat transfer characteristics and they need to be considered in designing the heat recovery system.

To study the performance of a plate type heat exchanger at an operating condition similar to a CHP system, the test rig is devised to form closed circuits for hot and cold side as depicted in Figure 3(a). The coolant from the gas engine is supplied at the flow rate of 10 t/h and temperature of 98^{o}C. The flow rate at the hot side is 2 t/h in the present experiment, which corresponds 1/5 scale of the real application. The water from the hot side is supplied from a boiler, whose control system has been modified to achieve the temperature over 90^{o}C. The cold side, which corresponds to the energy demand site in the CHP system, has temperature controlled drains to investigate the effects of energy demand of the site. An extra valve has been installed at the inlet of the burner of the boiler to simulate the partial load condition of the engine.

The temperature at the exit and inlet of the heat exchanger has been measured by RTD (Resistance Temperature Detect) to evaluate its design and off-design performance. The flow rate at each side has been measured by an electro magnetic flow sensor. A gas analyser has been installed at the exhaust gas exit of the boiler to check its combustion characteristics (Figure 3(a)).

Model Heat Recovery Boiler

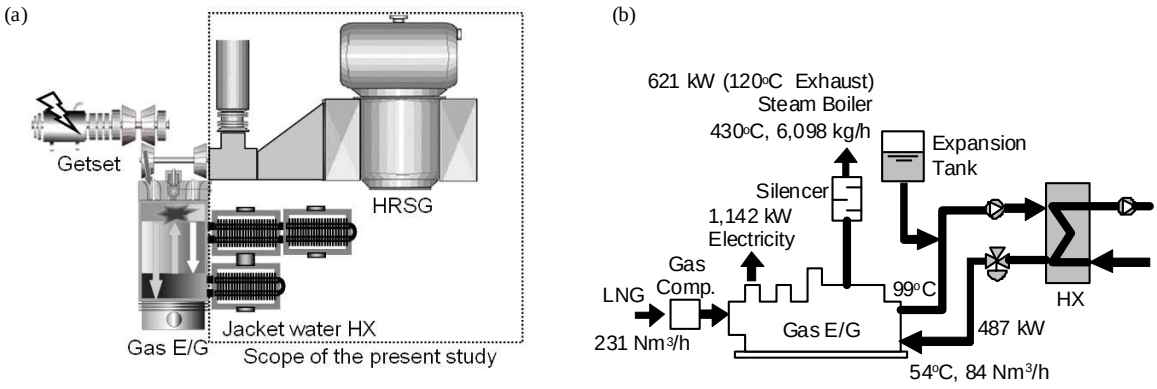

Figure 1 Gas engine CHP system; (a) system composition; (b) energy balance

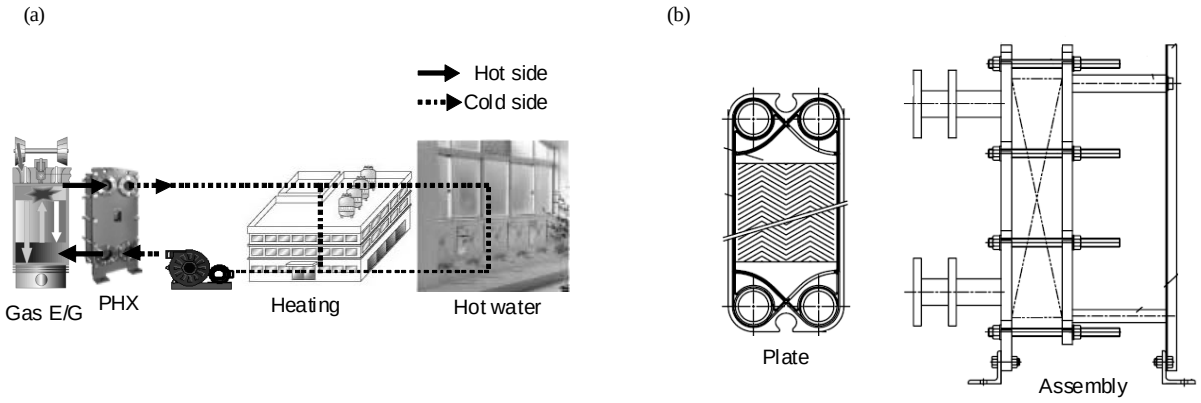

Figure 2 Heat recovery from the jacket water; (a) system configuration; (b) heat exchanger

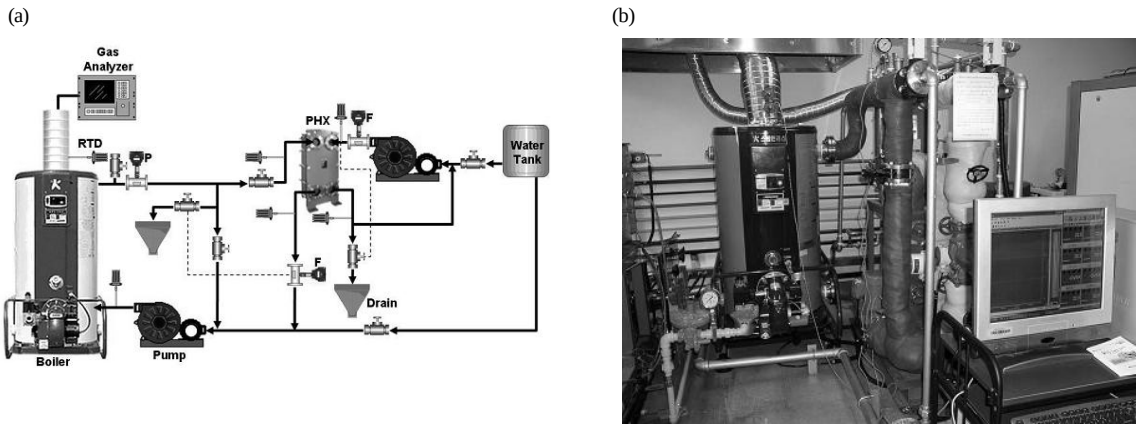

Figure 3 Test rig for the jacket water heat recovery; (a) schematics; (b) photograph

In the present CHP system, the thermal energy from the exhaust gas of the engine is recovered in the form of steam by a water tube type boiler, where fins can be installed at the evaporator section to efficiently recover heat from the exhaust gas with low temperature compared to the combustion gas directly from a burner for a conventional boiler. The evaporator section is a bundle of finned tube as shown in Figure 4(a). The bulk temperature of exhaust gas should decrease as it flows downstream. By considering the temperature change, finned tubes in the downstream have two times larger fin density as shown in Figure 4(b). The bundles with two types of finned tubes are composed into two separate modules as shown in Figure 4(a) to achieve more sophisticated design data from each module.

The exhaust gas to supply the model waste heat boiler is obtained from combustion gas of LNG, which is the fuel for the present gas engine. The burner is placed in a combustion chamber, surrounded by a furnace type boiler (Figure 5). The combustion gas is firstly cooled by the water outside and then diluted by additional air with the flow rate of 330 kg/h, which is supplied by a blower at the exit of the combustion chamber. Finally, the combustion gas is cooled through a heat exchanger until 430^{o}C, which is prescribed as the temperature of exhaust gas of the engine.

The water is supplied to each module separately to keep the water level at the steam separator, so that its flow rate indicates the amount of evaporation. The evaporation is also calculated from the change of enthalpy of the exhaust gas, which is measured by the thermocouples installed among the riser tubes.

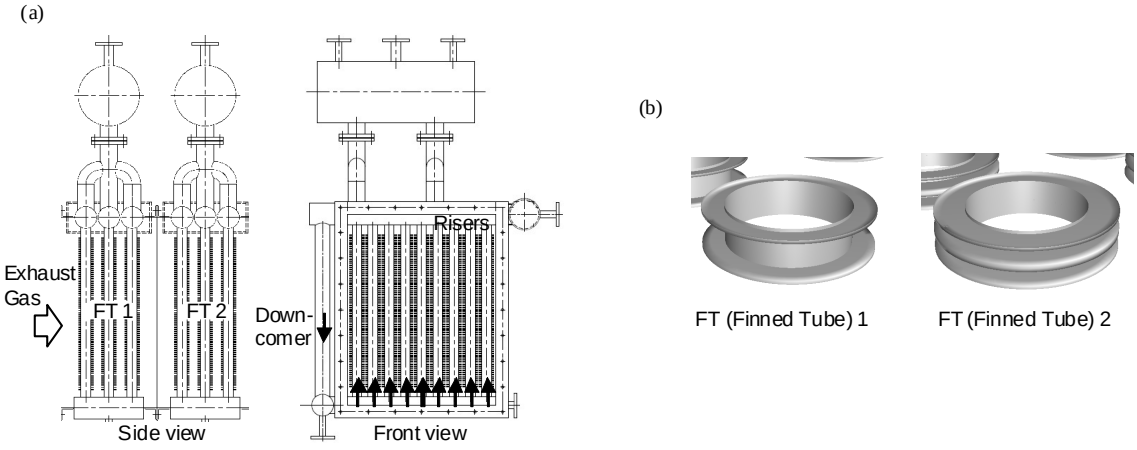

Figure 4 Heat exchange module for waste heat boiler; (a) schematics; (b) finned tube details

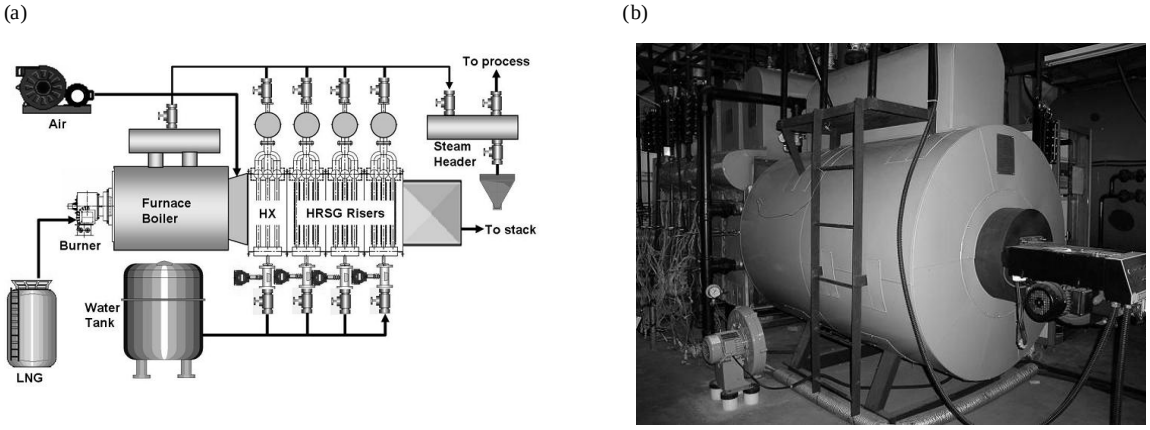

Figure 5 Experimental setup for the waste heat boiler; (a) schematics; (b) photograph

The heat transfer coefficient is as well evaluated from the gas temperature to be compared with the conventional correlation to predict it around the tube banks.

RESULTS AND DISCUSSION

Performance of Plate Type Heat Exchanger for the Heat Recovery from the Engine Coolant

The engine in the present study controls its coolant by adjusting its flow rate according to its operation load [1]. In the experiment, 2 m^3/h of water is supplied at the full load, while the flow rate is reduced 1 m3/h at the load of 50%. When the flow at the cold side is supplied at the room temperature, the heat exchanger shows high efficiency near unity for the low flow rate at the cold side of 2 m^3/h. The efficiency is deteriorated with the increase of the flow rate at the cold side. It decreases to 0.8 at the operation load of 50% when the cold side flow rate is 4 m^3/h.

The efficiency of heat exchanger is deteriorated when the water at the cold side is supplied at the higher temperature of 40 ^oC as shown in Figure 6 (a). With the higher inlet temperature at the cold side, the efficiency becomes more sensitive to the operation load of the engine. At the load of 50%, the heat exchanger efficiency is observed to decrease below 70%.

Figure 6(b) shows the surface margin from the experiment comparing with the prediction based on the correlation [3]. The experimental data deviate from the prediction as the flow rate at the cold

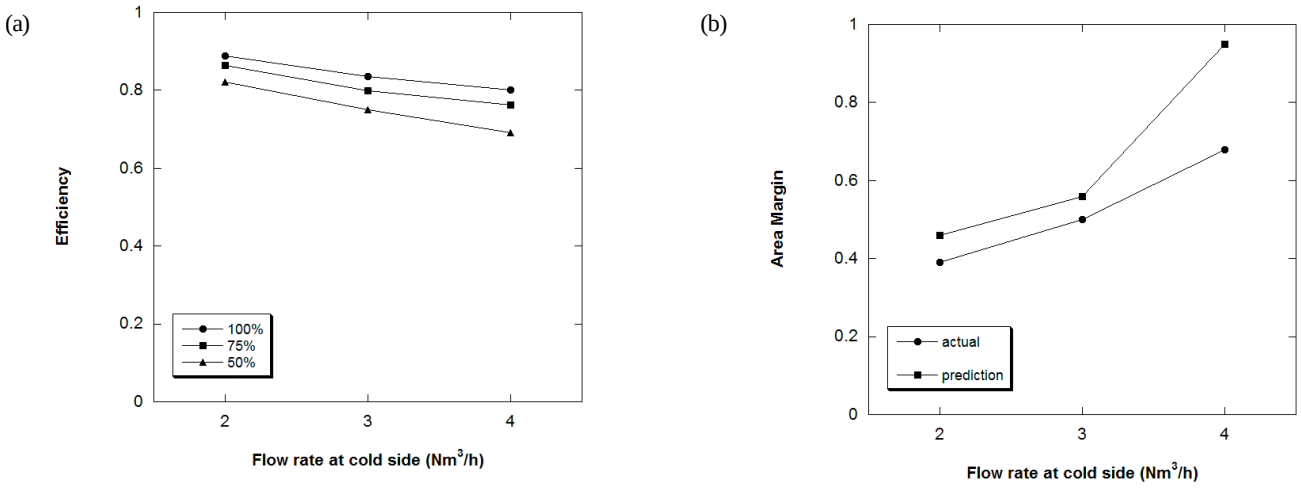

Figure 6 Jacket water heat recovery performance; (a) efficiency; (b) area margin

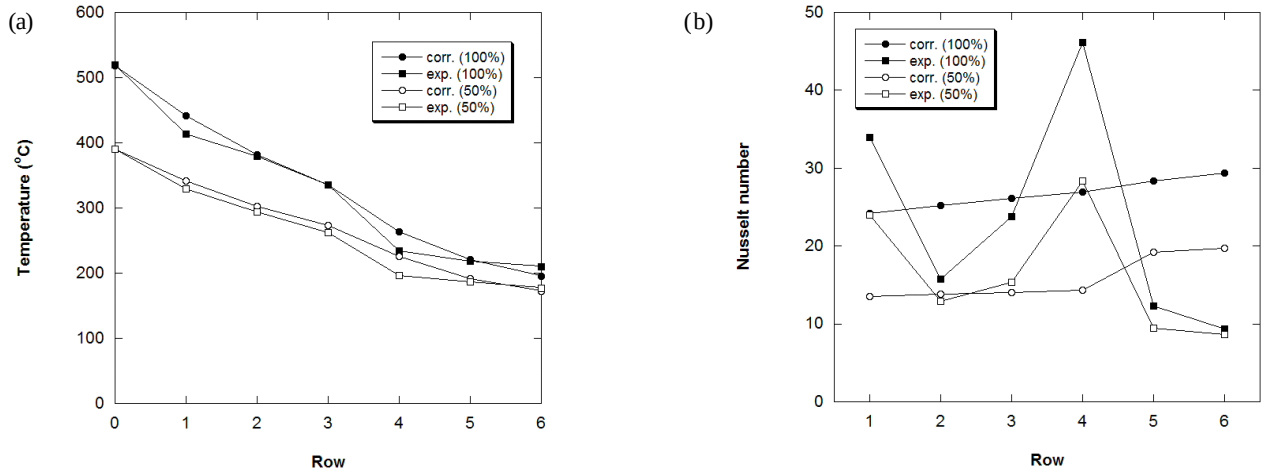

Figure 7 Jacket water heat recovery performance; (a) efficiency; (b) area margin

side increases from 2 m^3/h to 4 m^3/h. The surface margin, however, tends to increase as the flow rate at the cold side increase so that the heat exchanger will not be insufficient even at the off-design operation. Kumar's correlation [3] over-predicts the surface margin by 15% at the design point.

Performance of the Model Heat Recovery Boiler

The riser tubes of the model heat recovery boiler in the present study are designed to have different fin density along the streamwise direction as shown in Figure 4. The fin density is decided to yield uniform evaporation rate at each module based on Zhukauskas' correlation [4, 5]. The exhaust gas temperature variation along the streamwise direction agrees well with the prediction from the correlation as shown in Figure 7(a). However, the temperature from the experiment is lower than the prediction at the 1st and 4th row, where the fin density changes.

The Nusselt number evaluated from the enthalpy change of the exhaust gas shows much higher values than the Zhukauskas' correlation at the 1st and 4th row (Figure 7(b)). This trend is considered

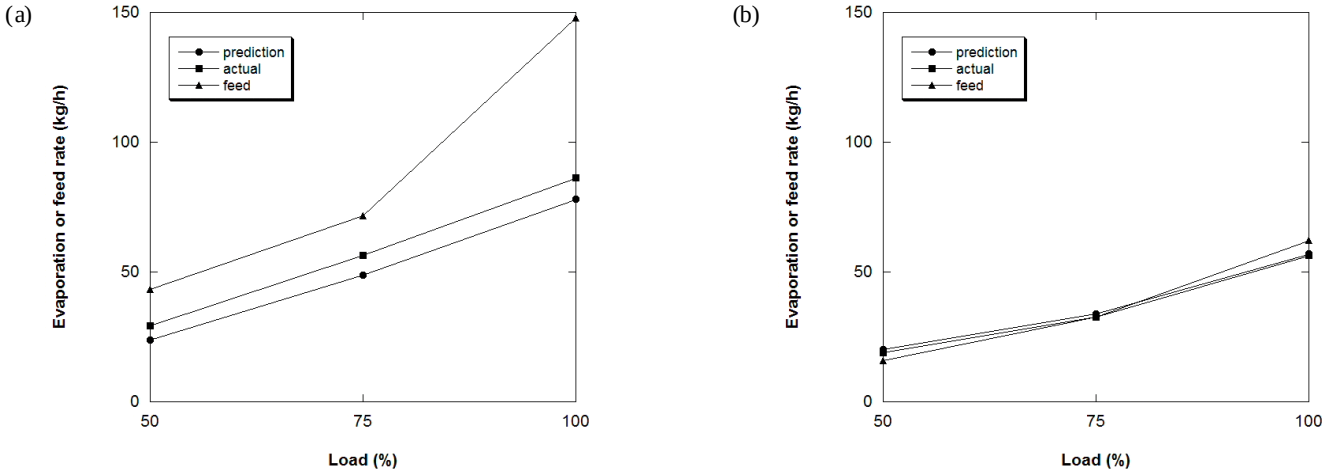

Figure 8 Evaporation rate; (a) at finned tube 1; (b) at finned tube 2

to be caused by the increase of the fin density at the location, which should accelerate the flow. Numerical simulation about the flow and heat transfer around this geometry is going to be conducted to clarify the mechanism.

The amount of evaporation is evaluated from the change in the enthalpy of the exhaust gas and compared to the flow rate of the feed water in Figure 8. They agree well and accurately predicted by the correlation for the module at the downstream (Figure 8(b)). However, the feed water supply is more than evaporation at the upstream module (Figure 8(a)). The droplet may not be completely separated at the drum so that the water feed may not be exactly balanced with the evaporation. This problem will be further explored by measuring the steam quality at the exit of the drum.

CONCLUSIONS

1. The heat exchanger efficiency of the engine coolant heat recovery system can decrease by 30%, in case the cold side water is supplied with the elevated temperature of 40^{o}C with the engine operation load of 50%.
2. Since the surface margin increases for the off-design operation, the heat recovery from the jacket water with plate type heat exchanger can be designed based on the Kumar's correlation.
3. For the finned-tube type heat exchanger, Nusselt number is under-predicted by conventional Zhukauskas' correlation where fins are newly installed.
4. Steam separation has been deteriorated at the upstream evaporators because of non-uniform heating.

REFERENCES

1. Dresser Inc., *Waukesha APG Series Gas Engine Catalogue 1390-1530 BHP*, 2006.
2. Taibong Industry Inc., *Plate Heat Exchanger Catalogue*
3. Kumar, H., The Plate Heat Exchanger: Construction and Design, *Proceedings of 1st U.K. National Conference on Heat Transfer*, Paper No. 86, 1984.
4. Ahn, J., Kim, J. J. and Kang, S. B., Heat Transfer Module for Multi-Burner Water Tube Boiler: 0.5 t/h Class Model Simulation, *Proceedings of SAREK 2007 Winter Annual Meeting*, 2007.
5. Incropera, F. P. and De Witt, D. P., *Fundamentals of Heat and Mass Transfer 3rd Ed.*, John Wiley & Sons, 1990.

INFLUENCE OF THE FLUID PROPERTIES ON CO-CURRENT TWO-PHASE FLOWS IN A HORIZONTAL CHANNEL CONNECTED TO A RISER

C. Vallée[1,*], T. Seidel[1], D. Lucas[1], M. Beyer[1], H.-M. Prasser[2], H. Pietruske[1], P. Schütz[1], H. Carl[1]

[1]Forschungszentrum Dresden-Rossendorf, Institute of Safety Research, Dresden, Germany
[2]ETH Zürich, Dept. of Mechanical and Process Engineering, Institute of Energy Technology, Zürich, Switzerland

ABSTRACT. In order to investigate the two-phase flow behaviour in a complex reactor-typical geometry and to supply suitable data for CFD code validation, a model of the hot leg of a pressurised water reactor was built at Forschungszentrum Dresden-Rossendorf (FZD). The hot leg is composed of a horizontal pipe, a 50° upward bend and an inclined riser. The hot leg model is operated in the pressure chamber of the TOPFLOW facility of FZD, which is used to perform high-pressure experiments under pressure equilibrium with the inside atmosphere of the chamber. Consequently, parts of the flat test section could be equipped with large windows for the application of optical observation techniques, also at reactor typical boundary conditions.

Co-current flow experiments were performed in the hot leg model, simulating a two-phase natural circulation in the primary circuit of a PWR. The experiments were done with air and water at 3.0 bar and room temperature as well as with steam and water at pressures up to 50 bar and the corresponding saturation temperature (i.e. up to 264°C). The probability distribution of the water level measured in the RPV simulator was used to characterise the flow in the hot leg. It was found that the form of the distribution informs about the stationarity of the water flow to the steam generator: the broader the distribution, the more discontinuous the transport of water over time. This tendency was confirmed by the high-speed video observations, which were also used to identify the flow regime. Furthermore, generally the distributions are flatter for the cold experiments than for the hot ones. This shows that, due to the lower surface tension and viscosity, the transport of water induced by the gas is more constant in time for the steam/water flow.

Keywords: *two-phase flow, co-current flow, fluid properties, hot leg, pressurised water reactor*

INTRODUCTION AND MOTIVATION

In the event of a loss-of-coolant-accident (LOCA) in a pressurised water reactor (PWR), emergency strategies have to be mapped out in order to guarantee the reliable removal of the decay heat from the reactor core. During a hypothetical small break LOCA with failure of the high pressure emergency core cooling system, the decay heat has to be released to the secondary circuit over the steam generators (SG). Therefore, the primary circuit is designed to favour a natural circulation if the main coolant pumps are not available. Furthermore, if steam is generated in the primary circuit due to its depressurisation, stratified two-phase flow regimes can occur in the main cooling lines. The intermittent flow regimes especially could affect the core cooling and are consequently relevant for the

* Corresponding author: C. Vallée
Phone: + (49) 351-260-3227, Fax: + (49) 351-260-2818
E-mail address: c.vallee@fzd.de

reactor safety. Therefore, the flow in hot leg geometries were investigated over the last decades in dedicated test facilities. Gardner (1989) and Petritsch & Mewes (1999) for example performed experiments with air and water in test sections with reduced scales. Extensive investigations were also conducted at original power plant scale in the Upper Plenum Test Facility (UPTF) with steam and water at pressures up to 15 bars (Weiss, 1992).

The objectives of the previous experiments were the validation and optimisation of accident management strategies as well as the development of models for the numerical simulation of LOCA scenarios. Currently, the state of the art calculation programs are so-called one-dimensional system codes, like *ATHLET* or *RELAP5*, which are principally based on empirical correlations and not on physical models. Consequently, the system codes are not able to simulate the flow phenomena, which limits their output possibilities to macroscopic effects. These limitations are particularly pronounced for the flows dominated by 3D effects, which require the use of a computational fluid dynamics (CFD) approach. However, the actual CFD codes applied to two-phase flows do not meet the high level of confidence needed in the field of nuclear reactor safety. Especially the closure models for interfacial transfer and turbulence field coupling embedded in CFD must be validated to allow reliable simulations. Therefore, high-resolution experimental data is needed for comparison with CFD calculations.

For the investigation of two-phase flows, the thermal fluid dynamics test facility TOPFLOW (Transient twO Phase FLOW) was built at Forschungszentrum Dresden-Rossendorf (FZD). This allows generic and applied experiments at boundary conditions typical for the power and process industries. The facility is equipped with a 4 MW electrical heater, which allows to produce steam flow rates up to 1.5 kg/s at the maximum operating pressure of 70 bar and the corresponding saturation temperature of 286°C (Prasser et al., 2006). TOPFLOW has become the major experimental facility of the *German CFD-network* initiated by the GRS (Gesellschaft für Anlagen und Reaktorsicherheit mbH).

In recent years, the TOPFLOW facility was extended with a pressure chamber which is used to perform high-pressure experiments under pressure equilibrium with the inside atmosphere of the chamber. For the first experiments, a model of the hot leg of a pressurised water reactor equipped with large windows was mounted in the chamber. The interfacial structure was visualised with a high-speed camera during co-current flow experiments under reactor typical boundary conditions (steam/water at pressures up to 50 bar and saturation temperature). First, the particularities of the new operation technique developed at FZD will be presented in details. As an example, one co-current flow experiment will be shown. From the water level measured in the reactor pressure vessel simulator, probability distributions were calculated and analysed. Furthermore, the characteristics of the distributions will be interpreted with the help of the high-speed camera images.

EXPERIMENTAL SETUP AND OPERATION PARTICULARITIES

High pressure experiments under pressure equilibrium

Usually, experiments with steam and water at power plant typical boundary conditions implicate to deal with two main constraints: the high pressure and the high temperature. These harsh boundary conditions limit strongly the measuring techniques to be considered and consequently the experimental investigation possibilities. In order to reduce somewhat these requirements, a new operation technique was developed at FZD which makes it possible to perform high-pressure steam/water experiments under pressure equilibrium.

Therefore, the test section is installed in the pressure chamber of the TOPFLOW test facility of FZD (Fig. 1). For steam/water experiments, a special heat exchanger condenses the exhaust steam from the

test section directly in the pressure chamber. This heat exchanger is designed with two openings and connects the test section to the pressure chamber. As a consequence, the condenser unit is operated with two gases: the steam to condense and a non condensable gas (air or nitrogen) which fills the pressure chamber. Both gases stratify because of the density difference: the lighter steam is injected from the top and the heavier non condensable gas stays at the bottom. The stratification layer in the condenser unit allows a self-regulation of the cooling power of the heat exchanger according to the arriving steam flow rate. In fact, by displacing the stratification layer up and down, the steam uncovers exactly the heat exchanger surface needed for its full condensation. In order to allow the free movement of the stratification layer inside the condenser unit while changing the steam flow rate, the cold end of the heat exchanger is permanently connected to the inner atmosphere of the chamber over large pipes (see Fig. 1), which guarantees the full pressure equilibrium at all times. The chamber can be pressurised with compressors up to 50 bar either with air for cold experiments or with nitrogen for steam experiments. Thanks to this experimental method, the test section does not have to support overpressures and can be designed with thin materials. Furthermore, this allows for example to equip the test section with large windows for optical observations of the flow.

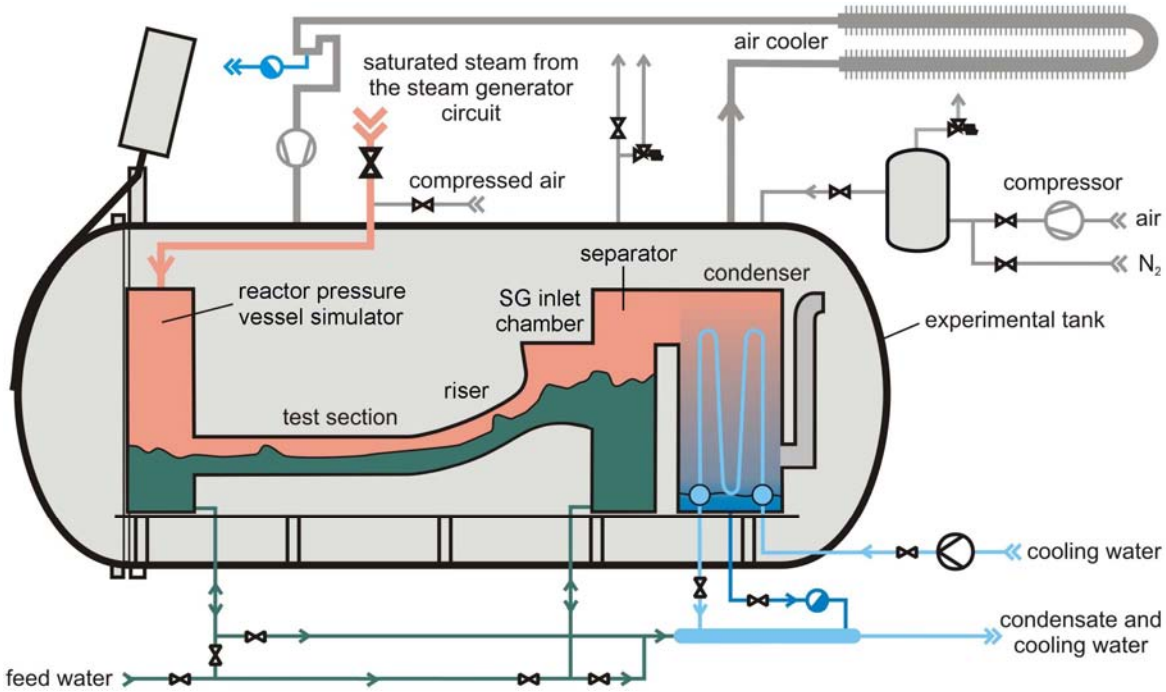

Figure 1. Schematic view of the experimental apparatus in the pressure chamber

Insulation of the test-section at high pressure levels

During steam/water experiments, all the components of the test section are heated up to the saturation temperature of water, i.e. to a maximum of 264°C at 50 bar. Because it is intended to put standard electronic measuring devices (e.g. high-speed video camera) inside the pressure chamber, the temperature of the atmosphere should be kept below their common maximum operation temperature of 50°C. Therefore, the warm components must be insulated and the inevitable heat losses removed to the outside.

First of all, conventional insulation materials like glass wool and mineral wool were used. During commissioning tests, these materials were found to present worse insulation properties with increasing pressure conditions and became insufficient at higher pressure levels. Due to the increasing gas density as well as to the increasing temperature of the components, the density difference between the cold and warm gas increases rapidly with the pressure. As a result, natural convection starts within the fibre packages of the material and reduces strongly its insulation properties. Many different commercial

materials were tested under high pressure conditions in house because of the lack of technical information delivered for our application by the manufacturers. Finally, compact micro glass-fibre materials were found to be suitable and were applied very carefully to the hot components. These materials were successfully tested in the pressure chamber up to the nominal pressure of 50 bar and showed good insulation properties.

Furthermore, the heat inevitably loosed through the insulation material is removed by an air/air heat exchanger installed on the roof of an auxiliary wing of the building. A forced convection of the gas inside the chamber is established by a pressure-proof electrical fan mounted in the circulation pipe (see Fig. 1).

One additional issue was to enable the observation of the hot steam/water flow without inducing substantial heat losses. For this, the high density difference between the hot and cold gas observed at high pressures was used as an advantage. In fact, the transparent part of the test section was surrounded with an insulation cap where the hot gas forms a stable stratification and stays like in a hot-air balloon. The insulation cap is only open to the bottom, which implies to place the camera vertically. Therefore, a 45° inclined mirror was placed under the insulation cap in order to deflect the light from the test section to the camera.

The hot leg model: test section and instrumentation

The test section of the hot leg model is schematically shown in Figure 2. The main components consist of the test section itself, the reactor pressure vessel simulator located at the lower end of the horizontal channel and the steam generator (SG) separator connected to the SG inlet chamber. The test section reproduces the hot leg of a PWR from the German *Konvoi* type at a scale of 1:3. In order to provide optimal observation possibilities, the test section is not composed of pipes like in the original power plant, it is a 50 mm thick channel representing a cut through the vertical mid-plane of the hot leg and of the steam generator inlet chamber. Consequently, the test section is composed of a horizontal rectangular channel, a bend that connects it to an upward inclined and expended channel, and a quarter of a circle representing the steam generator inlet chamber. The horizontal part of test section is 2.12 m long and has a rectangular cross section of 0.05 x 0.25 m². The riser is 0.23 m long, has an inclination of 50° to the horizontal plane and an expansion angle of 7.5°. Moreover, the SG and RPV simulators are identical vessels with 0.8 x 0.5 x 1.55 m³ (D x W x H) cubic shape. As shown in Figure 2, the test section is equipped with glass side walls in the bended region of the hot leg and of the steam generator inlet chamber in order to allow visual observation.

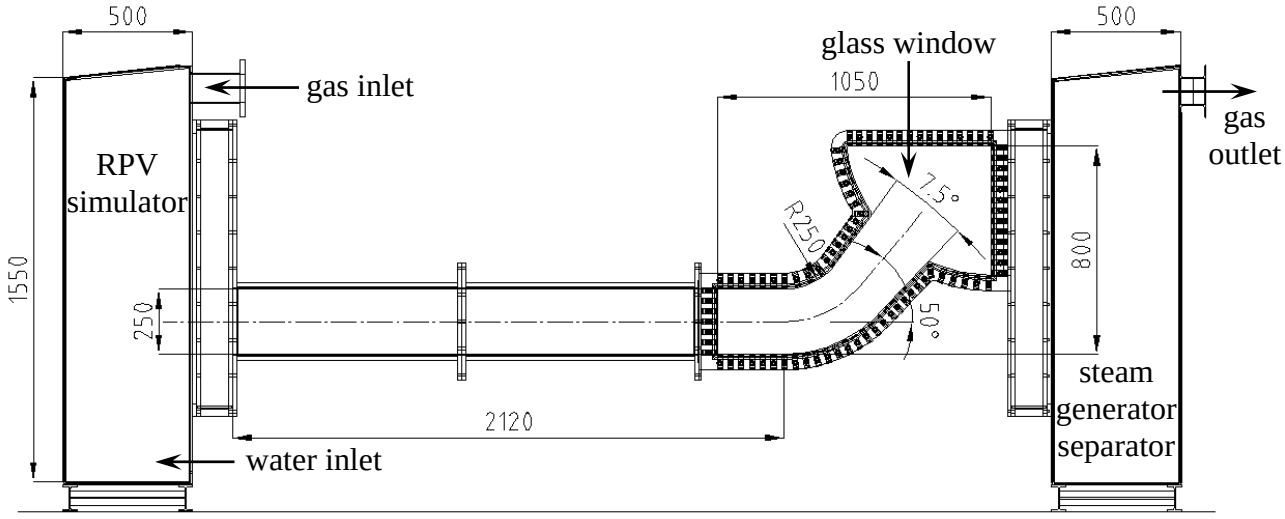

Figure 2. Schematic view of the hot leg model test section (dimension in mm)

The boundary conditions and global flow parameters were measured: a vortex meter was used to measure the injected water mass flow rate. The injected air mass flow rate was measured and controlled using thermal mass flow meters and the steam flow rate was measured with ISA-nozzles. The temperatures of the gas as well as of the water were measured at different positions by thermocouples. The water levels in both separators were determined by the measurement of the differential pressure between the top and the bottom of the vessels with differential pressure transducers. The differential pressure between the SG and RPV separators was measured by a differential pressure transducer. The signals of these global parameters were transmitted to a personal computer via a data acquisition system running at 1 Hz. Additionally to these measurands, a high-speed video camera was used to record the flow behaviour. The camera was put into a small pressure vessel equipped with a sight glass and was operated at frequencies of 100 Hz and a shutter speed of 1/500 to 1/1000 s.

CO-CURRENT FLOW EXPERIMENTS

Experimental procedure and test matrix

During the experiments, a constant flow rate of each fluid was injected in the RPV simulator (see Fig. 2) and flowed through the test section to the SG separator. In this tank, the liquid phase is separated from the gas, which flows to the condenser unit. The water is stored in the SG separator so that the water level increase can be used to check the mass balance. Because an accumulation of water in the SG separator could influence the two-phase flow in the test section, special attention was paid to the water level in this tank. The experiments were completed as soon as the water in the SG separator reached the level of the steam generator inlet chamber. Table 1 shows an overview of the varied boundary conditions. The co-current flow experiments were performed with air and water at 3.0 bar and room temperature as well as with steam and water at pressures up to 50.0 bar and the corresponding saturation temperature. In the experimental series, the water mass flow rate was varied between 0.3 and 0.9 kg/s and the gas mass flow rate between 0.01 and 0.84 kg/s.

Table 1
Co-current flow experiments in the hot leg model: overview of the test matrix

Gas [-]	Pressure level [bar]	Temperature [°C]	Water flow rate [kg/s]	Gas flow rate [g/s]	Number of runs [-]
air	3.0	19 – 25	0.32 – 0.91	11 – 144	12
steam	15.0	198	0.30 – 0.92	35 – 400	18
steam	30.0	233	0.28 – 0.91	75 – 500	15
steam	50.0	263	0.27 – 0.91	76 – 840	16

Example of co-current flow experiment

As an example, one co-current flow experiment was chosen to illustrate the observed phenomena. This run was performed at a system pressure of 30.0 bar and a temperature of about 230°C, which is close to the saturation conditions. The mass flow rates were 0.30 kg/s for the water and 0.15 kg/s for the steam. Figure 3 shows the evolution in time of the water level in the separators and of the pressure drop over the test section. It is remarkable that the water level in the SG separator increases stepwise. This indicates that despite of the constant inlet flow rates, the water transport to the SG separator is discontinuous. This behaviour explains the periodic variation of the water level in the RPV simulator between 640 and 660 mm as well as the regular increase of the pressure drop over the test section.

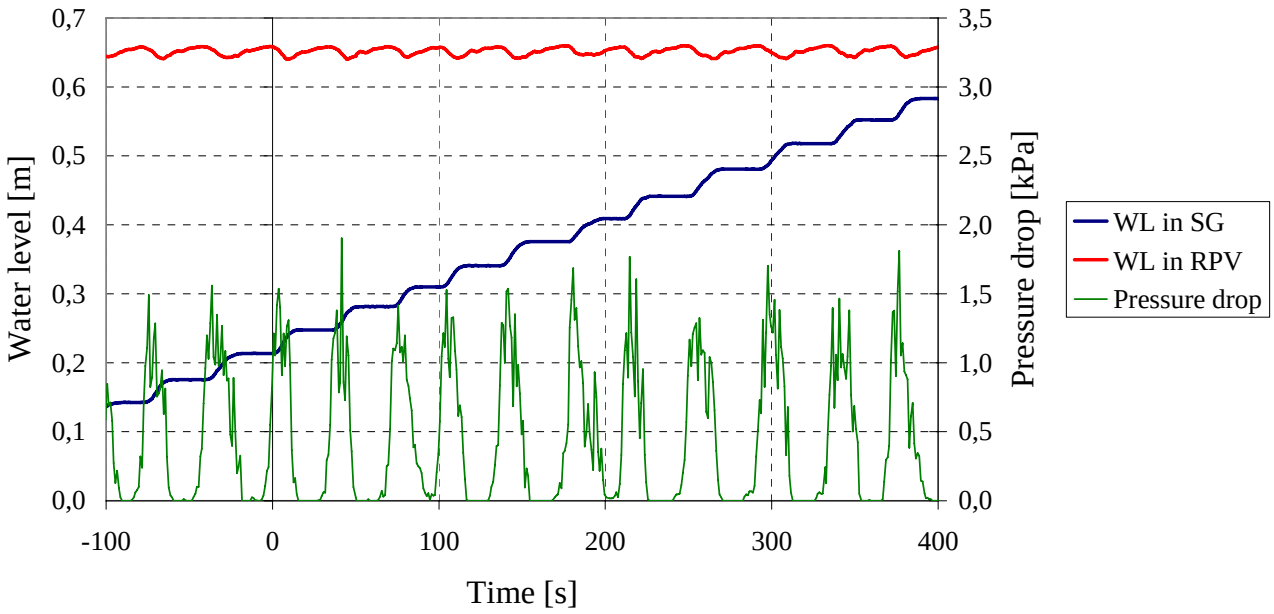

Figure 3. Evolution of the water levels and pressure drop in time during a co-current flow experiment at 30.0 bar and 230°C, with $\dot{m}_L = 0.30$ kg/s and $\dot{m}_G = 0.15$ kg/s

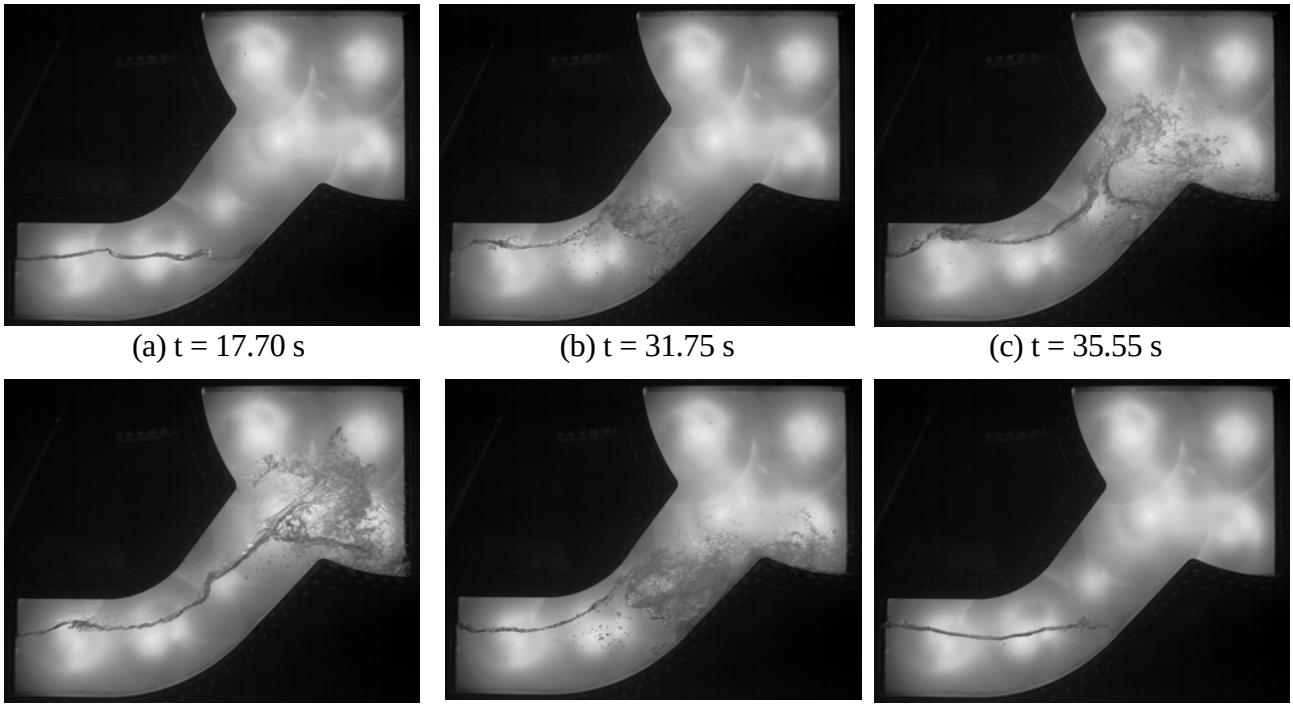

(a) t = 17.70 s (b) t = 31.75 s (c) t = 35.55 s

(d) t = 41.60 s (e) t = 46.80 s (f) t = 50.00 s

Figure 4. Evolution of the interphase structure during a co-current flow experiment at 30.0 bar and 230°C, with $\dot{m}_L = 0.30$ kg/s and $\dot{m}_G = 0.15$ kg/s

According to the flow structures observed with the high-speed camera over one period (c.f. Fig. 4), the following two flow regimes were observed:

1. First, for t < 31.6 s, the flow in the horizontal part of the channel is stratified wavy (Fig. 4-a) and no water is transported to the SG separator. This flow regime is characterised by a negligible pressure drop over the test section.
2. Afterwards, the water level reached in the horizontal part of the hot leg obstructs the steam flow enough to generate instable wave growth to plugs (Fig. 4-b and 4-c). Consequently, water is transported to the SG separator and the pressure difference between the separators increases

and becomes unstable. For 40 < t < 45 s, the plugs become bigger (Fig. 4-d) and the amount of water transported is higher than the injected flow rate. Therefore, the water level in the RPV simulator decreases, affecting the plug flow regime which can not be sustained after about 48 s (Fig. 4-e).

Subsequently, the flow in the horizontal part of the hot leg quiets and comes back to a wavy flow (Fig. 4-f), before the sequence starts over.

Evolution of the probability distribution of the water level measured in the RPV simulator

In order to reflect the variation over the time of the water level measured in the RPV simulator as shown in section 3.2., a statistical approach is proposed. The probability density distribution of the water level was calculated over the available measuring time (about 250 to 800 s, depending mainly on the water flow rate). The water level in the RPV simulator *l* was scaled relatively to the height *H* of the horizontal part of the hot leg model as follows:

$$L = \frac{l - L_H}{H - L_H} \tag{1}$$

with L_H the level of the lower edge of the horizontal channel.

The evolution of the probability distribution with the varied boundary conditions (shown in Table 1) is presented in Figure 5: the row defines the gas and pressure/temperature conditions, the column the water mass flow rate. The exact flow rates measured during each experiment are listed in Table 2, where the runs are numbered according to the diagram letter followed by the number of the curve. Figure 5 shows that the water level in the RPV simulator, and consequently in the test section, decreases with an increase of the gas flow rate. Furthermore, the form of the distribution varies with the boundary conditions: the air/water experiments at 3.0 bar with $\dot{m}_L \approx 0.3$ kg/s (Fig. 5-a) present very large and flat distributions whereas peaked curves were obtained with steam and water at 50.0 bar and $\dot{m}_L \approx 0.9$ kg/s (Fig. 5-f). The form of the distribution informs about the stationarity of the water flow to the steam generator: the broader the distribution, the more discontinuous the transport of water over time (see distribution 3 in Fig. 5-c, which corresponds to the example shown in section 3.2.). In this case, the broad distribution indicates that plug flow transports spontaneously more water to the SG separator than the water flow rate injected in the RPV simulator. This behaviour could mean that the water flow rate naturally entrained by the gas flow can not be reduced below a minimum value. In fact, when the injected water flow rate is lower than this value, the inequality in the input and output mass flow rates leads to an intermittent discharge of the water in the horizontal channel and consequently to a broad probability distribution.

A comparison between the columns of Figure 5 shows that at the same pressure and temperature boundary conditions, an increase of the water flow rate tends to sharpen the probability distributions of the water level. According to the theory developed in the previous paragraph, an increase of the water flow rate above the minimum possible discharge water flow rate leads to a continuous water transport and consequently to a peaked distribution. This could be the case between the experiments a-1 and b-1. However, some broad distributions become only slightly sharper with the increase of the water flow rate (e.g. experiments c-3 and d-3). This behaviour could be explained by the resulting reduction of the duration while no water is transported, which corresponds to the time during that waves at the water surface can quiet. Therefore, a higher water flow rate increases the probability for sustaining instabilities at the free surface to lead to an earlier begin of the next plug flow period.

The left column in Figure 5 shows the variation of the distributions with the pressure at a constant water mass flow rate of about 0.3 kg/s. It was observed that the distributions become more peaked and narrow with increasing pressure. However, the temperature was varied with the pressure and therefore

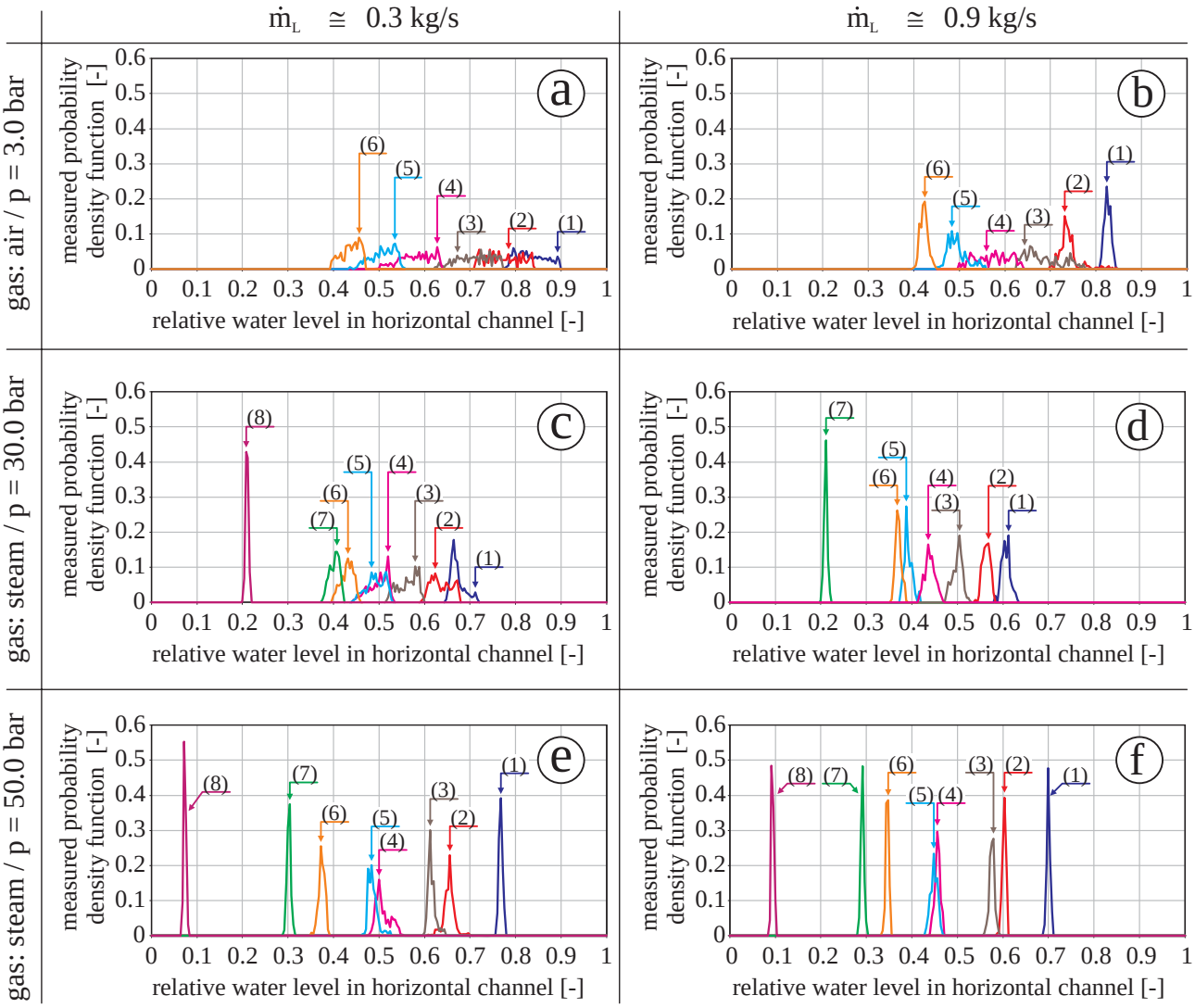

Figure 5. Evolution of the frequency distribution of the water level in the RPV simulator during co-current flow experiments under variation of the gas flow rate, for different water flow rates as well as pressure and temperature levels

Table 2
Boundary conditions of the experiments presented in Figure 5

Exp. number	Mass flow rate [kg/s]		Exp. number	Mass flow rate [kg/s]		Exp. number	Mass flow rate [kg/s]		Exp. number	Mass flow rate [kg/s]	
[-]	Gas	Water	[-]	Gas	Water	[-]	Gas	Water	[-]	Gas	Water
a-1	0.011	0.32	b-6	0.144	0.89	d-3	0.15	0.88	e-7	0.51	0.28
a-2	0.022	0.33	c-1	0.075	0.31	d-4	0.20	0.85	e-8	0.84	0.27
a-3	0.036	0.33	c-2	0.10	0.28	d-5	0.25	0.91	f-1	0.076	0.90
a-4	0.072	0.33	c-3	0.15	0.30	d-6	0.31	0.85	f-2	0.13	0.81
a-5	0.108	0.33	c-4	0.20	0.29	d-7	0.50	0.84	f-3	0.15	0.91
a-6	0.144	0.32	c-5	0.20	0.28	e-1	0.076	0.30	f-4	0.25	0.79
b-1	0.011	0.91	c-6	0.25	0.30	e-2	0.13	0.28	f-5	0.25	0.90
b-2	0.022	0.90	c-7	0.32	0.28	e-3	0.15	0.29	f-6	0.43	0.79
b-3	0.036	0.90	c-8	0.50	0.29	e-4	0.25	0.27	f-7	0.50	0.80
b-4	0.072	0.89	d-1	0.075	0.90	e-5	0.25	0.30	f-8	0.84	0.81
b-5	0.108	0.88	d-2	0.10	0.86	e-6	0.43	0.27			

the viscosity and the surface tension. Table 3 shows that especially the liquid viscosity as well as the surface tension decrease substantially between 20 and 264°C. This can explain the more continuous transport of the water to the SG separator by the gas flow at higher pressure and temperature levels. Moreover, this trend is not influenced by an increase of the water flow rate to about 0.9 kg/s (see right column of Fig. 5).

Table3
Variation of the fluid properties according to IAPWS-IF97

Gas [-]	Pressure level [bar]	Temperature [°C]	Density (L / G) [kg/m³]	Dynamic viscosity (L / G) [Pa.s]	Surface tension [N/m]
air	3.0	20.0	999.4 / 3.568	$1.20\cdot10^{-3}$ / $1.79\cdot10^{-5}$	0.073
steam	15.0	198.3	866.6 / 7.593	$1.36\cdot10^{-4}$ / $1.57\cdot10^{-5}$	0.038
steam	30.0	233.9	821.9 / 15.00	$1.14\cdot10^{-4}$ / $1.69\cdot10^{-5}$	0.030
steam	50.0	263.9	777.4 / 25.35	$1.00\cdot10^{-4}$ / $1.80\cdot10^{-5}$	0.023

Comparison with high-speed video observations

In order to interpret the evolution of the form of the distributions shown in Figure 5 with the gas flow rate, typical flow pictures taken during different co-current flow experiments are presented in Figure 6. As an example, the experiments were chosen at the extrema of the available boundary conditions.

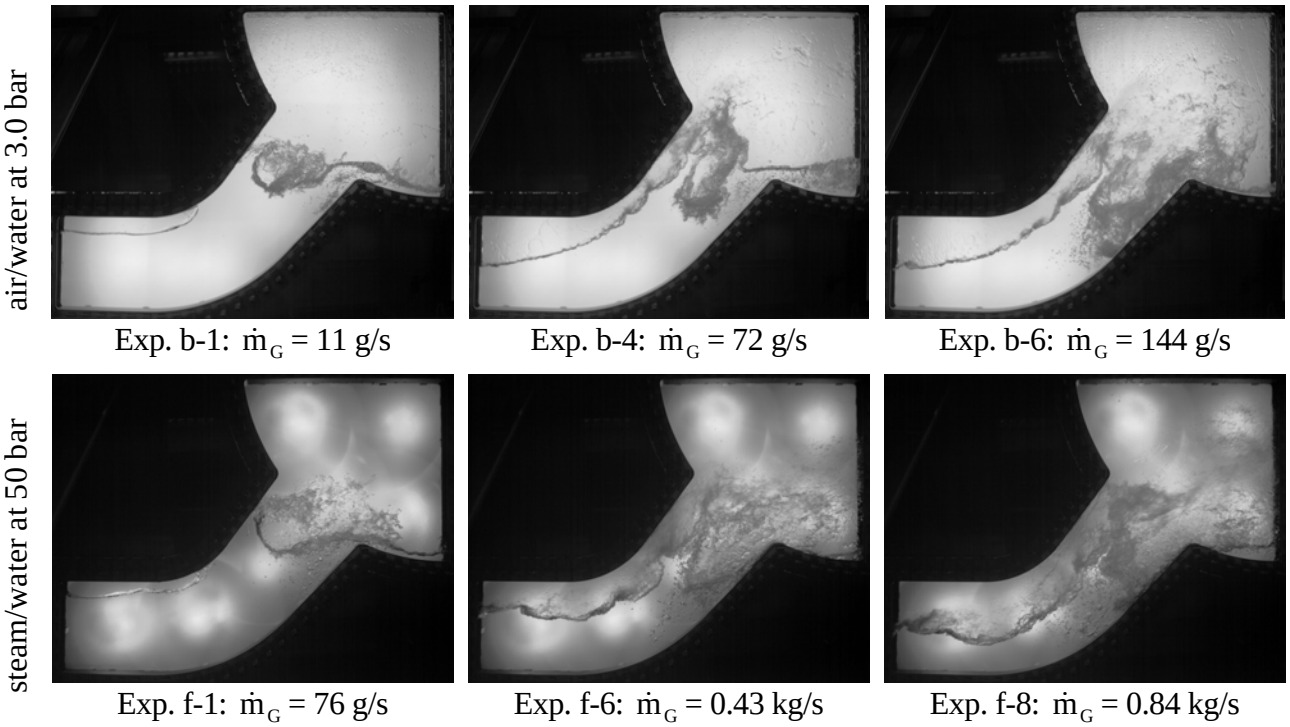

Figure 6. Typical flow pictures taken during different co-current flow experiments with $\dot{m}_L \approx 0.90$ kg/s

At low gas flow rates, the flow regime was identified as elongated bubble flow (Fig. 6, left column) and as slug flow at high gas flow rates (Fig. 6, right column). The probability distributions corresponding to these experiments are peaked. In the case of elongated bubble flow, the transport of water is continuous due to overflow as can be seen in the images. During slug flow, the transport of water occurs with droplets that detach from the wave front, which is also a continuous mechanism. At

intermediate gas flow rates (Fig. 6, middle column), the water transport is periodic and the probability distribution of the water level is flat, like in the experiment presented in section 3.2. These observations allow to conclude that a change in the form of the probability distribution from peaked over flat to peaked indicates a flow regime transition.

SUMMARY AND CONCLUSIONS

Co-current flow experiments were performed in a model of the hot leg of a pressurised water reactor, simulating a two-phase natural circulation in the primary circuit. The experiments were done with air and water at 3.0 bar and room temperature as well as with steam and water at pressures up to 50 bar and the corresponding saturation temperature (i.e. up to 264°C). Over this range of boundary conditions, the main fluid properties vary significantly. The frequency distribution of the water level measured in the RPV simulator was used to characterise the flow in the hot leg. It was found that the form of the distribution informs about the stationarity of the water flow to the steam generator: the broader the distribution, the more discontinuous the transport of water over time. Generally, the distributions are broader for the cold experiments than for the hot ones. This shows that, due to the lower surface tension and viscosity, the transport of water induced by the gas is more constant in time for the steam/water flows. Furthermore, the high-speed video observations were used to identify the flow regime. This shows that a change in the form of the probability distribution coincides with a flow regime transition: from elongated bubble flow at low gas flow rates to slug flow at high gas flow rates.

ACKNOWLEDGMENTS

This work is carried out in the frame of a current research project funded by the German Federal Ministry of Economics and Labour, project number 150 1329.

The authors would like to thank the TOPFLOW team for their work on the test facility and the preparation of the experiments, by name Klaus Lindner, Heiko Rußig, Marko Tamme and Steffen Weichelt.

REFERENCES

1. Gardner, G. C., Air-water model studies of cocurrent flow into and along a PWR hot leg to the steam generator, Nuclear Engineering and Design, Vol. 117/3, pp 251-261, 1989.
2. Petritsch, G. and Mewes, D., Experimental investigations of the flow patterns in the hot leg of a pressurized water reactor, *Nuclear Engineering and Design*, Vol. 188/1, pp 75-84, 1999.
3. Prasser, H.-M., Beyer, M., Carl, H., Manera, A., Pietruske, H., Schütz, H., Weiß, F.-P., The multipurpose thermalhydraulic test facility TOPFLOW: an overview on experimental capabilities, instrumentation and results. *Kerntechnik*, Vol. 71/4, pp 163-173, 2006.
4. Weiss, P., UPTF-TRAM Versuch A2. Ausbildung der Schichtenströmung in der heißseitigen Leitung, SIEMENS/KWU Quick Look Report S554/92/012, Erlangen, Germany, 1992.

FAST PYROLISYS CHARACTERISTICS OF BIOMASS IN A BUBBLING FLUIDISED BED REACTOR

Hang Seok Choi[1,*], Yeon Seok Choi[1], Seock Joon Kim[1], Hoon Che Park[2], So Young Han[1]
[1]Environmentla Systems Research Division, Korea Institute of Machinery and Materials, Daejeon, South Korea
[2]Graduate School of Mechanical Engineering, Chungnam National University, Daejeon, South Korea

ABSTRACT. Thermal conversion of woody biomass into liquid oil has been fulfilled to investigate the effects of pyrolysis and condensing conditions. A bubbling fluidised bed reactor having cylindrical shape was used to give fast pyrolysis condition to sample biomass maintaining reaction temperature around 500°C and commonly used spiral quenching system was applied to condensing volatile gases issuing from the reactor. In the present study, flow and physical parameters such as wood and nitrogen supply rates, biomass supply rate, pyrolysis temperature and condensing temperature, etc. were considered to elucidate the thermal characteristics of volatile generation and its condensation. Especially, the focus was given to the condensing of volatile which was mixed with various gases having different molecular weights, which means different boiling point. From the results, the effects of heating and condensing heat transfer on the thermal conversion of biomass are fully investigated in the bubbling fluidised bed reactor. Also, the physical and chemical properties of the collected biocrude oil were figured out through various analysis techniques.

Keywords: *biocrude oil, biomass, fast pyrolysis, fluidised bed, heat transfer*

INTRODUCTION

Recently, the price of fossil fuels is rapidly increased and furthermore the conventions on climate change become more and more severe, especially for greenhouse gases which are mainly produced by using fossil fuels. Hence, to overcome this environmental problem caused by fossil fuels, biomass is one of the promising renewable energy sources and in particular, thermal conversion of biomass has been investigated in many countries [1-4]. Among the thermal conversion methods, in the present study, fast pyrolysis method is adopted for thermal conversion of biomass into biocrude oil and this biocrude oil can be directly used for heat and power generation and furthermore applied to bio-refinery [2]. The fast pyrolysis method is the rapid heating of biomass without oxygen resulting in conversion of biomass into volatile gases, non-condensable gases and char. In the method, higher heating rate to biomass and short vapour residence time are the main issues for increasing oil yield and its quality. In the present study, to fundamentally scrutinize the pyrolysis characteristics of biomass, a cylindrical bubbling fluidised bed reactor is devised and used for fast pyrolysis experiment. The effects of flow and physical parameters for production of biocrude oil are investigated and the chemical compound and physical characteristics of the collected biocrude oil are scrutinized. In the results, the flow characteristics of fluidised bed, vapour residence time, reaction temperature and condensing temperature are the major factors for controlling the yield of biocrude oil and furthermore condensing heat transfer plays an important role for elevating the quality of biocrude oil.

* Corresponding author: Dr. Hang Seok Choi
Phone: + (82)-42-868-7398, Fax: + (82)-42-868-7284
E-mail address: hschoi@kimm.re.kr

Table 1
Physical characteristics of woody biomass (saw dust of bald cypress)

Moisture (wt. %)		20.9
Ash (wt. %)		0.12
Heating Value (kcal/kg)		4,187
Element (wt. %)	C	47.12
	H	6.00
	N	0.11
	O	46.77

EXPERIMANTAL METHOD

The fast pyrolysis system is mainly composed of working fluid (nitrogen) injection device, biomass supply device, bubbling fluidised bed, condenser and measuring sensors for flow and temperature, etc. as depicted in Figure 1. To maintain constant pyrolysis temperature inside the bubbling bed, electrical heating furnace is used and the thermocouple is inserted into the center of the bubbling bed and the temperature control unit of the system adjusts the target pyrolysis temperature using the thermocouple signal. At the bottom of the bubbling fluidised bed reactor, a plenum chamber is made for pre-heating of nitrogen. The heated nitrogen is delivered to the bed for fluidisation and N_2 is adopted for maintaining pyrolysis condition without O_2. For the sample material of the present pyrolysis experiment, well-dried sawdust is used and the physical characteristics of the saw dust are illustrated in Table 1. For each experiment, totally 100g saw dust is consumed, respectively. In the fast pyrolysis experiment, major physical parameters that may affect heating rate of biomass and consequent thermal conversion of it are chosen such as pyrolysis temperature and condensing temperature. Also, the flow parameters associated with vapour residence time are nitrogen volume flow rate and biomass feeding rate. These physical and flow parameters are considered in the present experimental study to investigate the pyrolysis characteristics associated with the flow and heat transfer features of the bubbling fluidised bed reactor.
Also, the analysis of physical characteristics and chemical compounds of the collected biocrude oil is performed.

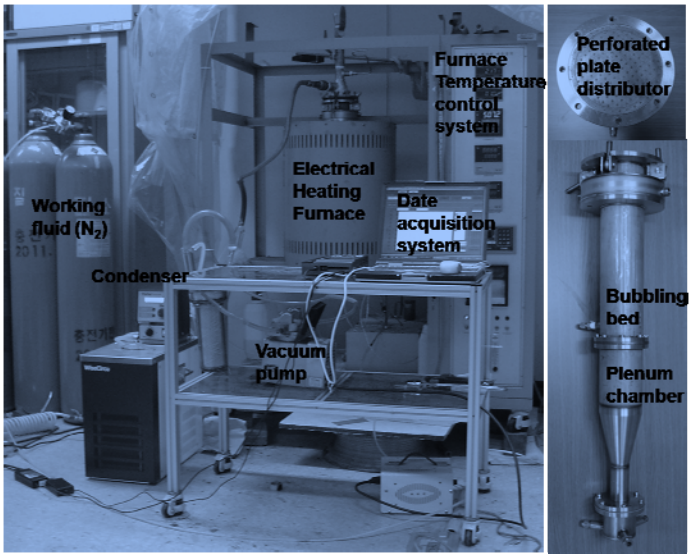

Figure 1. Experimental apparatus and bubbling fluidised bed reactor

To measure the moisture content, Karl Fisher Titration method is used and for heating value, low heating value is measured by LECO AC-350 instrument. To find out the weight of solid contained in the collected biocrude oil, the filter of pore size 0.1 μm is adopted and for ash, to prevent the splashing of the sample, moisture and the volatile gases having low boiling point are evaporated then after combustion at 770 □, the weight of remnant is evaluated. The chemical elements for C, H, O, N and S are measured by thermo elementary analyser, FLASH EA1112 and the chemical compounds of biocrude oil are gauged by gas chromatography with mass selective detector.

RESULTS AND DISCUSSIONS

Figure 2 shows the effect of flow parameters i.e., inert gas (N_2) and biomass supply rates for biocrude oil yield, which is measured as Yield (wt. %) = the weight of collected biocrude oil / supplied biomass weight ×100 and "wt." means weight. As increasing N_2 supply rate from 10 to 15 *lpm*, the yield of biocrude oil is increased and then from 15 to 25 *lpm* it is decreased. Hereinafter, "*lpm"* indicates liter per minute. This can be explained that with increasing flow rate over 10 *lpm*, fluidization of sand is started and steady bubbling fluidisation is made around 15 *lpm*. Here, steady bubbling fluidisation means the flow motion representing spatially and temporally random distribution of bubbles in the bed and this is confirmed by cold flow test considering gas volume expansion at hot gas condition. In this case, sand and biomass may be well mixed by steady bubbling fluidisation and the heat transfer from sand to biomass is expected to be distributed uniformly over whole biomass surface. After 15 *lpm*, the flow transition from bubbling to slugging and finally turbulent motion occurs and then the efficient mixing between sand and biomass and consequent heat transfer are expected to be lowered compared with those of random bubbling fluidisation [5, 6]. Hence, for all the experimental tests appeared here, the N_2 supply rate is fixed as 15 *lpm*, the pyrolysis temperature is also kept constant as 480 □ and biomass supply rate is 3.33 *g/min* except for their tests. For biomass supply rate, biocrude oil production is increased with increasing the supply rate. This may be connected with vapour residence time in the reactor because long residence time may induce the secondary vapour cracking reaction [7, 8].

Figure 3 shows the effects of physical parameters such as pyrolysis temperature and condensing temperature. For pyrolysis temperature which is measured in the center of the bed, the production of biocrude oil is increased with increasing pyrolysis temperature until 500 □ and then decreased.

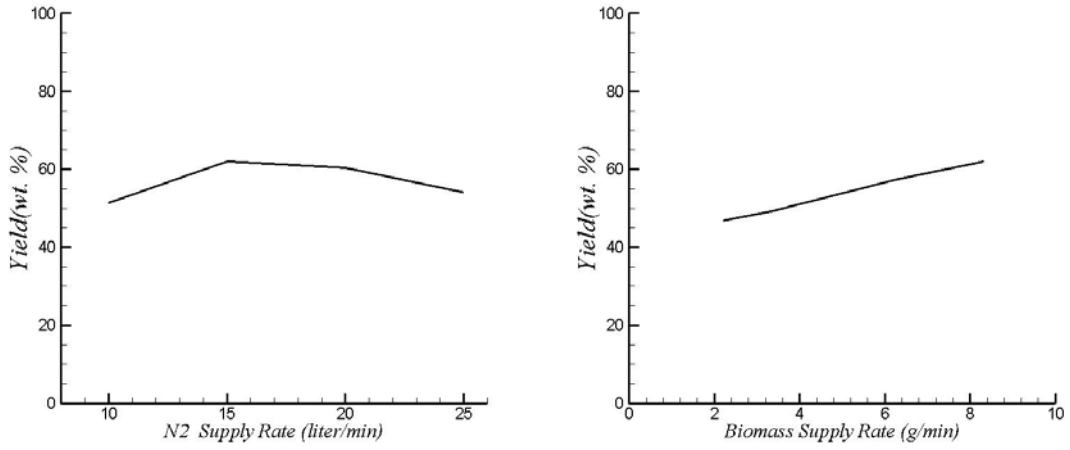

(a) (b)

Figure 2. The effect of flow parameters; (a) for N_2 supply rate, (b) for biomass supply rate

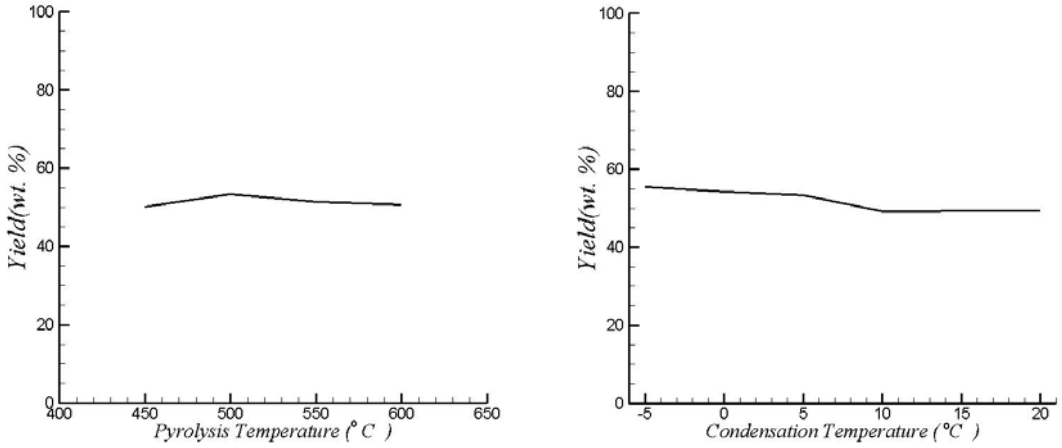

(a) (b)

Figure 3. The effect of physical parameter; (a) for pyrolysis temperature, (b) for condensation temperature

From the pyrolysis kinetics of wood, it can be explained that as increasing reaction temperature above 500 □, the secondary reaction of primary tar becomes active and according to reaction kinetics, tar is cracked into non-condensable gas and char, etc. [7, 8]. Then the yield of biocrude oil is decreased. For the condensing temperature of produced condensable gases, it is decreased gradually from 20 □ to -5□ to investigate the effect of condensing temperature for the condensable gases having different boiling points. With increasing condensing temperature, the yield of biocrude oil becomes larger because the condensation heat transfer between hot gases and cold water is more and more activated in the heat exchanger and at the lower temperature case the vapour gases having light molecules can be condensed. It is noted that for the same flow rate of cold water, the decrease of cold water temperature leads to increase of heat flux from hot gas to cold water because of higher temperature difference.

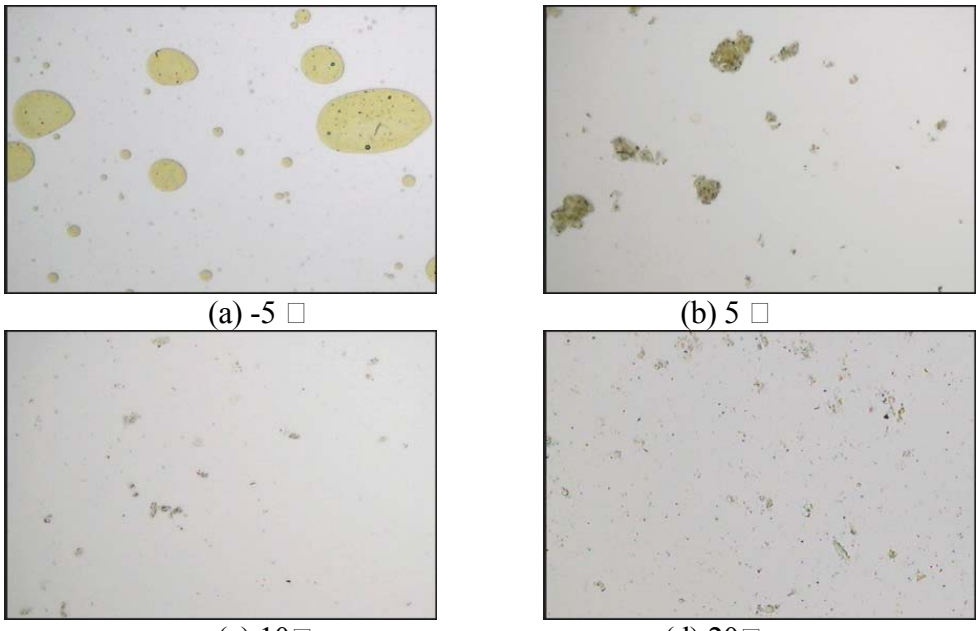

(a) -5 □ (b) 5 □

(c) 10□ (d) 20□

Figure 4. The microscopic features of the produced biocrude oils for different condensing temperature

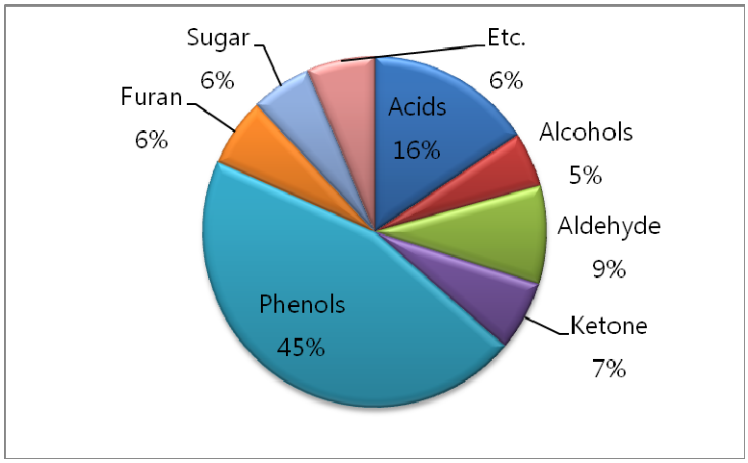

Figure 5. Chemical compounds of collected biocrude oil

However, it should be noted that the rapid quenching of hot vapours consisting of many different chemical species may result in a drop of biocrude oil quality. It will be discussed in the following. Figure 4 represents the microscopic pictures of the collected biocrude oil for different condensing temperature cases, which are enlarged 100 times. As can be seen in the figure, the solid particles such as char or a conglomerated lump appears remarkably below 5 □ and the size and population become larger and more frequent, respectively.

Table 2 shows the physical properties of collected biocrude oil at 3.33g/min for biomass supply rate, 15 *lpm* for N_2 supply rate, 480□ for pyrolysis temperature and 10□ for condensing temperature. This oil is brown liquid with pungent odour and compared with heavy oil for reference. Especially, the collected biocrude oil shows the lower PH and lower heating value compared with heavy oil but it contains no N and S, which are the source of NOx and SOx. In Table 2, it also has oxygen and this can explain the low heating value of biocrude oil. In Figure 5, the chemical compounds of biocrude oil are illustrated and organic compounds more than 100 ones are detected from the collected biocrude oil and it is mainly composed of organic acid, alcohols, sugar, aldehyde, ketone, phenols and furan, etc.

Table 2
Physical characteristics of biocrude oil

Contents		Biocrude Oil	Heavy Oil
Moisture (wt. %)		26.96	0.01
Density (kg/m^3)		1.22	0.9
Viscosity(cp)		-	180(50℃)
PH(20□)		2.40	-
LHV(kcal/kg)		3625	9700
Solids (wt. %) -0.1μm		0.068	-
Ash(wt. %)-770□		0.015	-
Element (wt. %)	C	43.30	85.2
	H	7.56	11.2
	O	49.14	1.0
	N	-	0.3
	S	-	2.3

Phenols have the largest portion of total chemical compounds however these portions become different case by case according to sample biomass material.

CONCLUSIONS

In the present study, the effects of flow and physical parameters for production of biocrude oil from biomass are scrutinized by fast pyrolysis experiment. For flow parameters, the optimum value of N_2 flow rate for the highest yield of biocrude oil is around 15 *lpm* corresponding to steady bubbling fluidization condition of the reactor. The increase of biomass feeding rate into pyrolysis reactor elevates the production rate of biocrude oil. Maximum pyrolysis temperature for its peak production is located just below at 500 □ and it is closely related to the secondary cracking mechanism of tar. For the effect of condensing temperature, the yield of biocrude oil is increased with decreasing the temperature but it is noted that below 0 □, a conglomerated lump appears remarkably, which is composed of solids as char. From the chemical and physical analysis of the collected biocrude oil, the biocrude oil shows a lower heating value compared with heavy oil but it has been reported by many researchers that there is high possibility of the oil for the application to heat and power and furthermore bio-refinery [1,2].

REFERENCES

1. Yaman, S., Pyrolysis of Biomass to Produce Fuels and Chemical Feed stocks, *Journal of Energy Conversion and Management*, Vol. 45, pp 651-671, 2004.
2. Brammer, J. G., Lauer, M. and Bridgwater, A. V., Opportunities for Biomass-derived "Bio-oil" in European Heat and Power Markets, *Energy Policy*, Vol 34, pp 2871-2880, 2006.
3. Zhang, H., Xiao, R., Huang, H. and Xiao, G., Comparison of Non-catalytic and Catalytic Fast Pyrolysis of Corncob in a Fluidised Bed Reactor, *Bioresource Technology*, Vol. 100, pp. 1428-1434, 2009.
4. Asadullah, M., Rahman, M. A., Ali, M. M., Rahman, M. S., Motin, M.A., Sultan, M. B. and Alam, M. R., Production of Bio-oil from Fixed Bed Pyrolysis of Bagasse, *Fuel*, Vol. 86, pp. 2514-2520, 2007.
5. Yates, J.G., Effects of Temperature and Pressure on Gas-Solid Fluidization, *Chemical Engineering Science*, Vol. 51, pp. 167-205, 1996.
6. Kurosaki, Y., Ishiguro, H. and Takahashi, K., Fluidization and Heat Transfer Characteristics around a Horizontal Heated Circular Cylinder Immersed in a Gas Fluidized Bed, *Int. J. Hat Mass Transfer*, Vol. 31, pp. 349-358, 1988.
7. Blasi, C.D., Analysis of Convection and Secondary Reaction Effects within Porous Solid Fuels Undergoing Pyrolysis, *Combustion Science and Technology*, Vol. 90, pp. 315-340, 1993.
8. Liden, A. G., Berruti, F. and Scott, D. S., A Kinetic Model for the Production of Liquids from the Flash Pyrolysis of Biomass, *Chem. Eng. Comm.*, Vol. 65, pp. 207-221, 1988.

EXCHANGE FLOW IN A RESERVOIR MODEL EXPERIENCING DIURNAL TEMPERATURE CHANGES AT THE WATER SURFACE

Tomasz P Bednarz*, John C Patterson, Chengwang Lei, Feng Xu
School of Engineering & Physical Sciences, JCU, Townsville QLD 4811, Australia

ABSTRACT. In the present experiment, a reservoir model is subjected to diurnal temperature changes at the water surface. The transient thermal forcing acting on the system results in an unsteady quasi-periodic flow response. During the heating phase, a stable stratification of the water body is develops and during the cooling phase a very unstable rapid flow mixing over local water depth can be clearly observed. The thermal instabilities that occur after the thermal forcing switches from heating to cooling play an important role in breaking up a residual circulation and initiating a reverse flow. Inversely, when the system is in the heating phase, a stable large-scale convective roll is clearly observed. Understanding of the flow mechanisms pertinent to this problem is important for predicting the transport of nutrients and/or pollutants across reservoirs. Accordingly, the transient flow characteristics are analysed based on the temperature and velocity fields extracted non-invasively from experimental photographs of thermo-chromic liquid crystal patterns using concurrent Particle Image Thermometry and Particle Image Velocimetry techniques. The present work extends our previous experimental and numerical investigations of the exchange flows in reservoirs.

Keywords: e*xchange flows*, *unsteady natural convection*, *PIT*, *PIV*, *image processing*

INTRODUCTION

The mechanisms that govern the transport of heat and mass in the near shore regions of lakes and reservoirs are of great significance for proper understanding and management of these resources. In a typical diurnal cycle, the ambient temperature changes periodically, resulting in varying thermal forcing acting on the water body. This has a direct impact on the convective circulation in the water, and can cause transport of small suspended pollutant or biological particles or dissolved constituents into or from deep water regions. Therefore an understanding of transport phenomena driven by the external thermal forcing is essential for understanding particle transport.

During a typical fine day, absorption of solar radiation entering through the water surface results in relatively warm shallow regions and a stable stratification in deep regions [1, 2]. In shallow waters, the water depth is less than the penetration depth of solar radiation, and thus a fraction of the radiation reaches the bottom where it is absorbed and re-emitted into the water layer above the bottom. This bottom heating is a destabilizing mechanism, which competes with the stable stratification. The bottom heating however, will not occur during cloudy weather and in this caseonly a vertical stable stratification will occur as the result of the ambient temperature increasing. This case is the focus of the present experimental results. Conversely, during the night, near-shore horizontal temperature gradients are developed from unequal cooling rates since the shallow region cools relatively faster than the deeper region. The result is a cold water undercurrent proceeding toward the deeper regions. At the same time, cooling at the water surface may generate plunging plumes from the surface. The cooling configuration is potentially unstable in a Rayleigh-Benard sense, depending on the cooling rate [3, 4]. Typical flow characteristics observed during the cooling phase is depicted in Figure 1.

* Corresponding author: Dr Tomasz P Bednarz
Phone: + (61)-7-47815218, Fax: + (61)-7-47816788
E-mail address: tomasz.bednarz@jcu.edu.au

In natural water bodies, all the above-mentioned mechanisms work together in a complex way over diurnal cycles. This problem has attracted significant research attention over the last two decades. Lei & Patterson investigated by numerical simulations the flow response to periodic heating and cooling by means of a varying surface heat flux, including depth-dependent absorption during the heating phase [5]. The results showed a time lag in the overall flow response when thermal forcing is switched between heating and cooling. This outcome is consistent with the field observations of Adams & Wells [6] and Monismith et al. [7], and the analysis of Farrow & Patterson [8] and Farrow [9]. They also concluded that, during both the cooling and heating phases, thermal instabilities break the residual circulation and reverse the flow in deep waters.

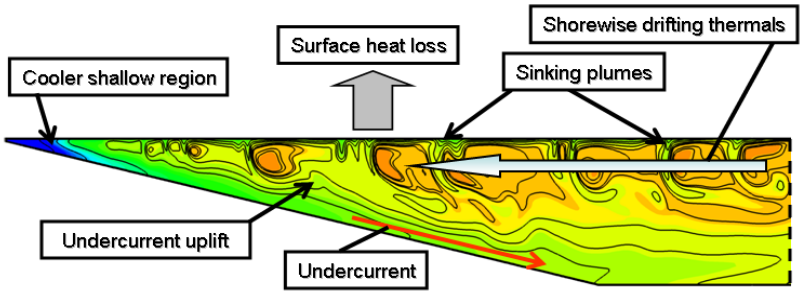

Figure 1. Flow characteristics observed during cooling experiments [3].

The present work extends, through physical experiments, the previous numerical investigations in a reservoir model with a periodic forcing applied at the water surface. In this case, the periodic forcing is by means of a varying surface temperature, corresponding to the effects of a varying ambient temperature but with no radiation input, as might be experienced during cloudy atmospheric conditions.

EXPERIMENTAL APPARATUS AND PROCEDURES

Experimental setup

The experimental apparatus used in the present study is shown in Figure 2(a). An enclosure, a chamber which provides alternate heating and cooling to the water surface and a wedge are all made of transparent Perspex except the lower surface of the chamber. The cavity is 30 cm long, 6 cm wide and 1.5 cm high. A wedge of an inclination 0.1 is placed inside the enclosure and fixed to the bottom and sidewalls. The heating and cooling chamber has two inlets and two outlets, respectively, each located at the centres of the vertical walls. The lower surface of the chamber is a copper plate painted black, through which the water in the experimental cavity is heated or cooled by water of a varying temperature passing through the chamber. All those parts are then joined together with eight screws.

Figure 2(b) shows the experimental setup of which the main part is the model described above. For visualization purpose the enclosure is filled with distilled water premixed with thermo-chromic liquid crystal slurry KXN-20/30 with a concentration approximately 0.1 ml per litre of water. The heating and cooling chamber is connected through hoses to a thermo-stating water bath (Julabo HE of 2000-W heating capacity) controlled by a personal computer. The central vertical cross-section of the enclosure is illuminated by a white light sheet generated by a halogen lamp of a 150-W Liesegang 3000AF projector, located about 2 m from the mirror, which is placed underneath the enclosure. A thin slit film is placed at the film location of the projector so that a thin light sheet is obtained over a long distance. The horizontal light sheet is reflected by the mirror and then redirected vertically to illuminate the entire middle section of the enclosure. The thickness of the light sheet is about 4 mm. All experimental photographs are taken by a high-resolution 12.8 Mega-Pixel of 4368×2912 pixels, SLR digital camera Canon EOS 5D with Canon EF 70-200 f/2.8L lens. The time interval between consecutive experimental shots is controlled using Canon TC-80N3 timer remote controller. The shutter speed of the camera is set to 1/4 s, the focal length to 200 mm, ISO speed to 800 and the lens aperture to f/4.0.

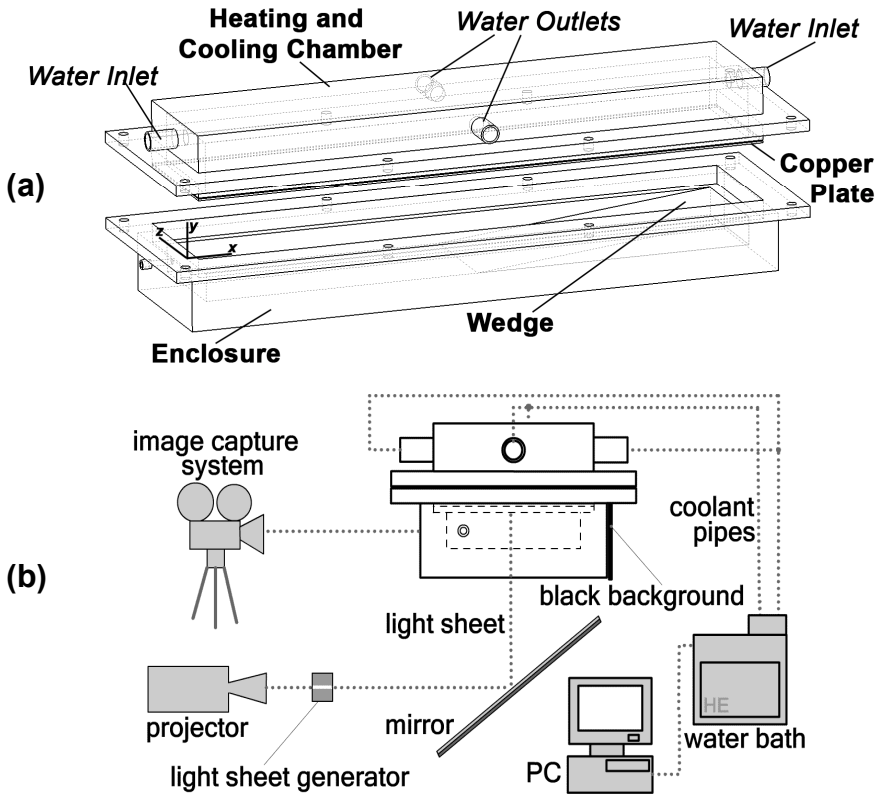

Figure 2. (a) Experimental model, (b) Setup for flow visualisation and temperature control.

Concurrent PIV / PIT measurements and flow visualization

The present experiment includes flow visualization and simultaneous temperature and velocity measurements with the application of thermo-chromic liquid crystals (TLCs). This approach uses two main features of the TLCs, that is, their colour response to local temperature changes and their seeding particle appearance. The first feature can be used to directly convert colour information captured by a digital camera into temperature values, the so-called Particle Image Thermometry (PIT), using hue-temperature calibration curve as described in [10-13]. If the TLC particles are sufficiently large (50-100 μm), they can also be successfully used as tracers of the flow field. The motion of scattering particles in an illuminated plane can be successfully analysed to provide instantaneous velocity vector maps in a cross-section of the flow field. The Particle Image Velocimetry (PIV) technique is based on image processing and pattern recognition algorithms and is described in [13-15]. Therefore, the general procedures for the concurrent PIV/PIT measurements include seeding the flow field with the TLC particles, illuminating a desired cross-sectional plane, and acquiring well focused photographs with sharp colours and clear patterns of the seeding particles. Then proper image processing techniques are applied to the experimental photographs (due to limitation of this paper, the visualisation procedures are not described here). The benefit of the concurrent PIV/PIT measurements is obvious: the temperature and velocity fields can be measured simultaneously, and the measurements are totally non-invasive.

Experimental conditions

For characterization of the natural convection flow in such a reservoir model, four non-dimensional parameters are defined. These quantify the important fluid, flow and geometrical properties of the system. These are: the Prandtl number (*Pr*) which characterizes the ratio of momentum diffusion to thermal diffusion, the Grashof number (*Gr*) which characterizes the ratio of buoyancy to viscous forces and therefore the relative strength of the thermal forcing, the aspect ratio

(A) which defines the geometry of the cavity, and the bottom slope (A_s) which characterizes the inclination of the slope:

$$Pr = \frac{\nu}{k}; \quad Gr = \frac{g\beta \Delta T H^3}{\nu^2}; \quad A = \frac{H}{L} = 0.05; \quad A_s = \frac{H}{L_s} = 0.1 \tag{1}$$

where ν is the kinematic viscosity, k is the thermal diffusivity, g is the gravity acceleration, β is the thermal expansion coefficient, ΔT is the maximum temperature difference ($\Delta T = T_{max} - T_{min}$), where T_{max} and T_{min} are respectively the maximum and minimum temperatures in the whole thermal cycle.

The present experiments were carried out in the reservoir model subject to periodic heating and cooling at the water surface as seen in Figure 3 for $Pr = 6.82$ and $Gr = 3.52 \times 10^4$. This can be related to a real situation with a very small temperature change over the diurnal cycles. The achieved period P of the thermal forcing in the laboratory environment was 14 minutes. Initially, the fluid in the enclosure was kept isothermal at 20.9 ºC for about 20 minutes ($t < 0$) before the periodic change of the water bath temperature was applied to the system ($t \geq 0$). The image capture started after ~34 minutes seen as $t/P = 0$ in Figure 3, i.e., after the start-up effect was minimized and the system response had become quasi steady. The points {a}–{e} marked on the imposed surface temperature curve in Figure 3 denote the times described below to quantify the flow development in a thermal forcing cycle with one additional time {f} for checking repeatability of the flow response.

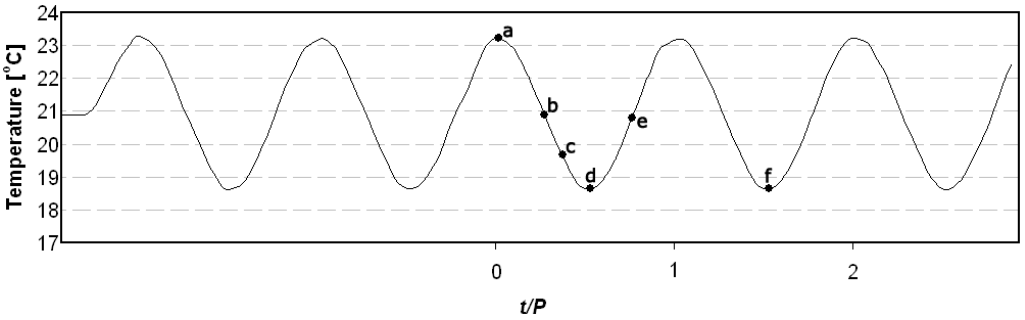

Figure 3. Time history of the temperature at the water surface.

EXPERIMENTAL RESULTS

In this section, the results of simultaneous flow and temperature measurements using TLCs are presented. Figure 4 shows six experimental unprocessed photographs corresponding to the times (a) to (f); Figure 5 presents corresponding isotherms extracted using the PIT technique; Figure 6 shows the results of PIV measurements with contours of the horizontal velocity component (left column) and the streamlines (right column).

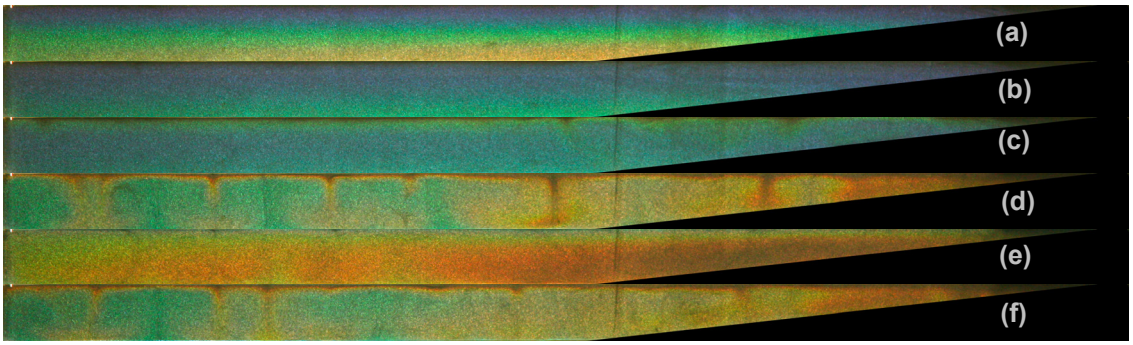

Figure 4. Raw photographs of the observed flow at $Pr = 6.82$ and $Gr = 3.52 \times 10^4$.

At the time instant {a}, the water surface temperature reaches a value of 23.3°C. The heating rate reaches its maximum value and the upper layer is clearly warmed, leaving the relatively colder fluid formed at the previous cooling stage below it (those affected layers will be described later for {e}). A

stable stratification of the temperature is established over almost the entire water body except a small region affected by cooling in the preceding cycle, as seen in Figures 4(a) and 5(a). Figure 6(a) show that a large counter-clockwise convective roll is created in the enclosure. The streamlines confirm that relatively warmer fluid is moving up along the bottom slope and moving out toward the deep-end under the water surface. The strongest flow is observed below the water surface (Figure 6a). However, the overall flow strength is very weak at this stage.

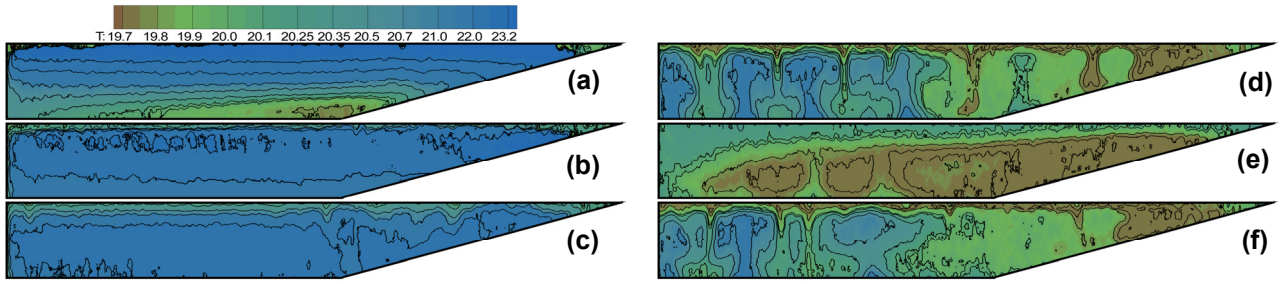

Figure 5. Temperature contours.

At the time instant {b}, the cooling effect at the water surface is distinct, but the majority of the water body is still vertically stratified, as seen in Figures 4(b) and 5(b). A clockwise convective roll has been created and occupies the half of the enclosure (deep water region) as seen in Figure 6(b). The strongest flow takes place beneath the surface above the slope (Figure 6b). In the rest of the enclosure (the deeper region), the flow becomes very weak as cooling proceeds as seen from the streamline contours.

At the time instant {c} convective instability below the water surface can be clearly observed (Figures 4c and 5c). Since the cooling is from the top, the fluid immediately below the surface becomes denser and heavier relative to the interior region. Thermal instabilities occur, in the form of Rayleigh-Bernard plumes when the local Rayleigh number in the surface layer exceeds a critical value, as determined in [3, 4]. At this stage, the plumes are relatively weak and are just starting to penetrate the local water depth. They will intensify as the cooling at the water surface continues. In the region above the slope, where the instabilities at this time are the strongest, intensive mixing is observed from the streamlines in Figure 6(c). In the deep water region, the clockwise convective roll developed earlier still dominates the flow.

At the time instant {d}, the surface temperature reaches its minimum of 18.6^{o}C. Distinct plunging thermals can be observed at this time (Figures 4d and 5d). These thermals penetrate the local water depth in the form of Rayleigh-Benard convection, carrying colder surface water to the bottom, where they are prone to overturning and mixing with the ambient fluid. The cooling of the water body occurs at a faster rate in the shallow region, as the thermals have less distance to travel through, and thus a horizontal temperature gradient is established in that region. Figures 6d suggest that the Rayleigh-Benard convective circulations occur in the whole fluid body, enhancing the local mixing. This is also confirmed by the streamline contours.

At the time instant {e}, the temperature at the water surface is increasing, and a layer of relatively warmer fluid is forming just beneath the water surface. There are no distinct plunging thermals present in the enclosure at this stage, and the convective motion is much weaker compared with that at time instant {c}, as seen in Figure 5. A cold undercurrent proceeding down the bottom slope can be seen in Figure 6e and is evolved into a clockwise convective circulation taking place on the right-hand side region of the reservoir model. The heating from the water surface slowly stabilises the convective motion.

For comparison purposes, the temperature and flow structures at time instant {f}, corresponding to {d}, is presented. As seen in Figures 4-6f the general characteristics of the temperature and flow fields at time instant {f} is very similar to that described for time instant {d}. However, at time instant {f}, the plunging thermals appear in slightly different locations from those appearing at time instant {d}.

This is due to the randomness of the Rayleigh-Benard instabilities and the three-dimensionality of the flow.

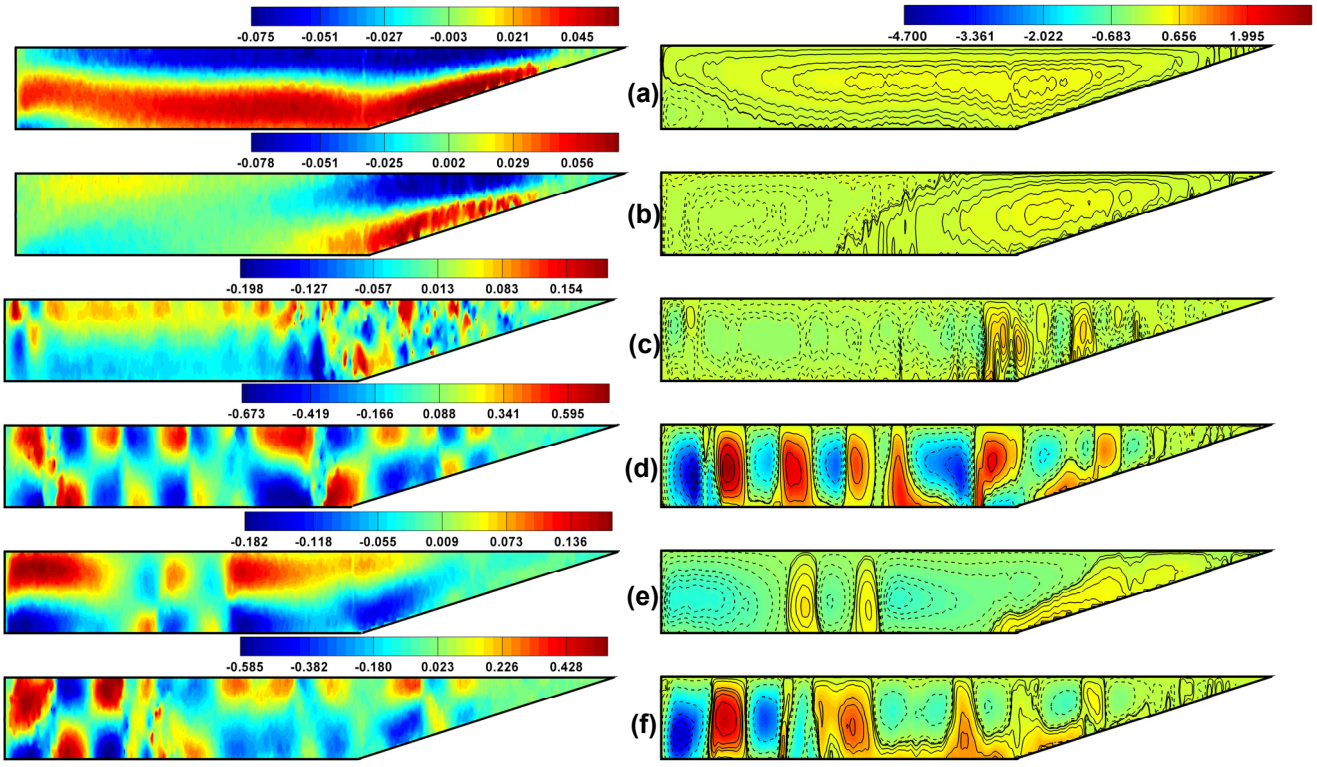

Figure 6. Horizontal velocity component contours (left column) and streamlines (right column).

Horizontal exchange flow rate

The horizontal volumetric flow rate per unit width across a vertical sectional plane at a given x location is defined as [1-3]:

$$Q(x) = \frac{1}{2}\int_{-h_x}^{0} |u|\, dy \tag{2}$$

where h_x is the local water depth at a given x location, and $Q(x)$ quantifies the horizontal exchange flow at that location. An averaged volumetric flow rate Q_m is obtained by integrating these quantities along the horizontal direction.

$$Q_m = \frac{1}{L}\int_{0_x}^{L} Q(x)\, dx \tag{3}$$

Figure 7 plots the time history of the horizontal exchange flow rate calculated for the Grashof number $Gr = 3.52\times10^4$ along with the time history of the water surface temperature measured during the experiments. In this plot, the exchange flow rate Q_m is normalized using the scale ~k, and the time is normalized by the period P of the thermal forcing cycles. The horizontal solid line in Figure 7(a) represents the mean temperature in the reservoir model. Accordingly, a temperature value above the horizontal line represents day-time heating, and a temperature value below the horizontal line represents night-time cooling. The cycles in both figures start when the temperature at the water surface is at the maximum value. At $t/P = 0.25$, the thermal forcing is switching from the day-time heating to the night-time cooling, whereas at $t/P = 0.75$ the switching is from night-time cooling to daytime heating. The horizontal flow rate Q_m is calculated from the PIV data after the fluid flow is assumed to be in a quasi steady state. The point $t/P = 0$ in Figure 7 corresponds to time instant {a} marked in Figure 3.

It is seen in Figure 7(b) that two minima and two maxima of Q_m appear over one thermal forcing cycle from $t/P = 0$ to 1.0. At $t/P = 0$ a small maximum of Q_m is observed. This time instant

corresponds to the heating up stage and the maximum is in phase with the thermal forcing. At this time, a weak anti-clockwise convective circulation is present. When the surface temperature starts to decrease, the warm upper layer of the water body continues to grow downwards and a convective circulation is still present as described above. The exchange flow rate Q_m remains at approximately the same level for some time until at around $t/P = 0.16$ when it starts to decrease. Slightly after $t/P = 0.26$ the averaged horizontal flow rate reaches a minimum, and this moment approximately corresponds to the switch from day-time heating to the night-time cooling. Also at this time, plunging thermals are observed in the system. Further cooling at the water surface results in enhanced local mixing in the enclosure. As a consequence, the calculated exchange flow rate increases abruptly and reaches a maximum at around $t/P = 0.5$, when the surface cooling peaks. Subsequently, the cooling from the top surface remains in place for some time although the water surface temperature is actually increasing. Another minimum of Q_m is observed at $t/P = 0.86$, indicating that there is a time lag of the flow response to the switch of the thermal forcing from cooling to heating, which corresponds approximately to 11% of the forcing period. After $t/P = 0.86$, Q_m increases to reach another maximum at $t/P = 1.0$ that corresponds to the maximum heating rate.

It is also noticeable in Figure 7 that the overall strength of the circulation in the heating phase is significantly weaker than that in the cooling phase. This indicates that during cloudy whether conditions, i.e., when solar radiation is not present, the cooling effect dominates the convective motion in reservoirs.

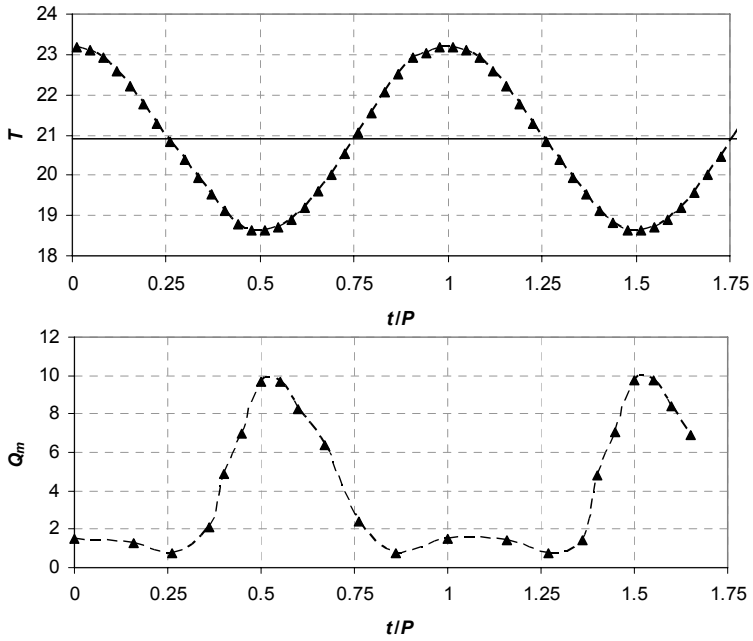

Figure 7. Time histories of (a) temperature at the water surface; (b) horizontal exchange flow rate.

CONCLUSIONS

In this study, the quasi-steady natural convection flow in a reservoir model subject to periodic thermal forcing at the water surface is described based on experimental flow visualisation and quantitative temperature and velocity measurements by means of concurrent Particle Image Thermometry and Particle Image Velocimetry. The present experiment has revealed the general characteristics of the flow development relevant to cloudy atmospheric conditions when solar radiation is not present in the system and the flow is driven solely by the ambient temperature changes. It is observed that the primary convective circulation in the reservoir changes its direction when the thermal forcing switches from cooling to heating and vice versa. It is also revealed that there is a time lag of the flow response to the switch of the thermal forcing from cooling to heating which is approximately

11% of the forcing period in the present case. The calculated horizontal exchange flow rate based on the measured velocity field showed that the overall strength of the circulation in the heating phase is significantly weaker than that in the cooling phase, suggesting that during cloudy conditions, the cooling effect dominates the convective motion in reservoirs

REFERENCES

1. Lei, C. and Patterson, J. C., Natural convection in a reservoir sidearm subject to solar radiation: experimental observations, *Experiments in Fluids*, Vol. 32, pp 590-599, 2002.
2. Lei, C. and Patterson, J. C., Natural convection in a reservoir sidearm subject to solar radiation: a two-dimensional simulation, *Numerical Heat Transfer Part A*, Vol. 42, pp 13-32, 2002.
3. Bednarz, T. P., Lei, C. and Patterson, J. C., A numerical study of unsteady natural convection induced by iso-flux surface cooling in a reservoir model, *International Journal of Heat and Mass Transfer*, Vol. 52, pp 56-66, 2009.
4. Bednarz, T. P., Lei, C. and Patterson, J. C., An experimental study of unsteady natural convection in a reservoir model cooled from the water surface, *Experimental Thermal and Fluid Science*, Vol. 32, pp 844-856, 2008.
5. Lei, C. and Patterson, J. C., Natural convection induced by diurnal heating and cooling in a reservoir with slowly varying topography, *JSME International Journal Series B – Fluids and Thermal Engineering*, Vol. 49, pp 605-615, 2006.
6. Adams, E. E. and Wells, S. A., Field measurements on side arms of Lake Anna Va, *Journal of Hydraulic Engineering*, Vol. 110, pp 773-793, 1984.
7. Monismith, S. G., Imberger, J. and Morrison, M. L., Convective motions in the sidearm of a small reservoir, *Limnology and Oceanography*, Vol. 35, pp 1676-1702, 1990.
8. Farrow, D. E., Periodically forced natural convection over slowly varying topography, *Journal of Fluid Mechanics*, Vol. 508, pp 1-21, 2004.
9. Farrow, D. E. and Patterson, J. C., On the response of a reservoir sidearm to diurnal heating and cooling, *Journal of Fluid Mechanics*, Vol. 246, pp 143-161, 1993.
10. Bednarz, T. P., Lei, C. and Patterson, J. C., Particle image thermometry for natural convection flows, *16th Australasian Fluid Mechanics Conference*, Gold Coast, December 2-7.
11. Stasiek, J. A., Thermochromic liquid crystals and true colour image processing in heat transfer and fluid-flow research, *Heat and Mass Transfer*, Vol. 33, pp 27-39, 1997.
12. Stasiek, J. A., Thermochromic liquid crystals applied for heat transfer research, *Opto-Electronics Review*, Vol. 10, pp 1-10, 2002.
13. Park, H.G, Dabiri, D. and Gharib, M., Digital particle image velocimetry / thermometry and application to the wake of a heated circular cylinder, *Experiments in Fluids*, Vol. 30, pp 327-338, 2001.
14. Bednarz, T. P., Lei, C. and Patterson, J. C., An experimental study of unsteady natural convection in a reservoir model subject to periodic thermal forcing using combined PIV and PIT techniques, *Experiments in Fluids*, 2009, in press.
15. Raffel, M., Willert, C. and Kompenhans, J., Particle image velocimetry, Springer-Velag, 1998.

EVALUATION OF METHODS OF THE IN-CONTAINMENT HEAT TRANSFER COEFFICIENT DETERMINATION FOR LOSS-OF-COOLANT ACCIDENTS SIMULATION PURPOSES

T. Bury*
Silesian University of Technology, Gliwice, Poland

ABSTRACT. This work deals with thermal-hydraulic analyses of loss-of-coolant accidents within containments of pressurized water reactors. Such accidents are initiated by a rupture of the primary cooling circuit. For obvious reasons courses of these accidents can not be analysed by means of a full scale physical experiments. The mathematical modelling and numerical simulations are widely used for these purposes. It was found that the very difficult problem is to properly determine the heat transfer coefficient from in-containment gaseous atmosphere to walls and structures. This issue has been thoroughly investigated on a special test station at the Lucas Height Research Centre in Sydney, and results of the experiment have became a basis for numerical codes validation and development within the framework of the CASP-3 project. The main aim of this work is to validate a domestic computer code called HEPCAL and also to evaluate different methods for the heat transfer coefficient calculation. The results obtained shown that the use of standard correlations for Nusselt number gave effects the most comparable to the experimental ones.

Keywords: *pressurized water reactor, LOCA, heat transfer coefficient, CASP-3, numerical simulations*

INTRODUCTION

A rupture of the primary cooling circuit initiates one of the most dangerous accident which may happen in a pressurized water nuclear reactor unit. The worst scenario assumes the double ended break of the main coolant pipeline. It causes the loss of nearly whole coolant inventory in a few to a few dozen seconds. Some radioactive products of the coolant activation and fission products may be released from the primary circuit along with the coolant. To prevent release of these products and dangerous progress of the accident the reactors are fitted with the containment systems - hermetic buildings which enclose the primary circuit and all the safety and auxiliary systems. The whole is often called as the accident localization system. The coolant flowing out of the primary circuit evaporates immediately due to pressure difference and a mixture of air, steam and hydrogen fills up the containment building causing a rapid growth of the internal pressure and temperature. This is so-called loss-of-coolant accident (LOCA).

It is obvious that thermal-hydraulic analyses of such accidents can not be performed by means of a full scale physical experiments. Thus, the mathematical modelling and numerical simulations are widely used for these purposes. The nuclear industry developed two groups of the computer codes for thermal-hydraulic analyses of LOCA: one-dimensional system codes (also referred as lumped parameter codes) and three-dimensional field codes (mostly based on CFD). The lumped parameter codes reached high degree of maturity up to now and these codes are in common use and are also accepted by many nuclear authority bodies as proper tools for safety evaluation purposes.

* Corresponding author: Dr T. Bury
Phone: + (48)-32-2372051, Fax: + (48)-32-2372872
E-mail address: Tomasz.Bury@polsl.pl

Determination of a heat transfer coefficient from internal atmosphere to walls and structures is one of the most significant problems in thermal-hydraulic analyses of LOCA. This problem was investigated in detail on the special test station in Lucas Heights Science and Technology Center in Sydney (Australia) in the frameworks of the CASP-3 project (Containment Analysis Standard Problem).

The aim of this work was to simulate the CASP-3 experiment using the lumped parameter code HEPCAL as a part of the code validation process. Three versions of code have been used for simulations. Three different ways of the heat transfer coefficient determination from the gaseous atmosphere to walls and structures have been applied to these code versions.

THE CASP-3 PROJECT

The experiment performed by the Australian Atomic Energy Commission has been used by the OECD/CSNI Working Group on Water Reactor Containment Safety as Containment Analysis Standard Problem No. 3 [2]. The experiment was performed in October 1981 on the Lucas Heights blowdown/containment rig.

Test rig description

The general arrangement of the test rig with localizations of the measuring points is shown in Figure 1. The pressure vessel is insulated and contains an electric heater to boil water and raise pressure. The outlet pipe is heated by an electric heater tape wound around the pipe and is thermally insulated. The pipe is blocked by a cooper disc which is ruptured to start the blowdown [3]. The main element of the test rig is the containment model: steel vessel divided onto two compartments connected through the orifice plate and the pipe. The vessel is not insulated, it is freestanding within a large building. A circular deflector disperses the incoming blowdown flow around the chamber and prevents large crossflows at the intercompartment orifice.

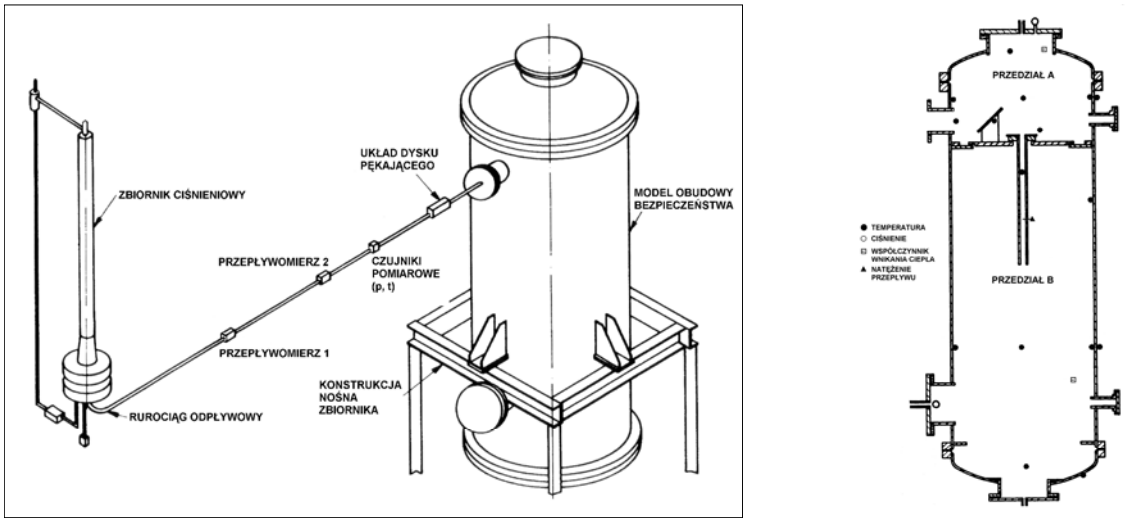

Figure 1. Test station – general view (left) and the containment vessel cross section with localization of measuring points (right)

The measurement instrumentation allow to record pressure, temperature, flow and heat transfer coefficient data.

Analyzed experiment scenario

The initial conditions are gathered in Table 1. Data related to the blowdown flow are presented in Figures 2 and 3.

Table 1
Initial conditions for the CASP-3 experiment [2,3]

Item		Value
Pressure vessel		
	Pressure, kPa	10 400
	Temperature, ºC	314
	Water mass, kg	8.5
Containment (both compartments)		
	Pressure, kPa	100.0
	Temperature, ºC	16.3
	Humidity, %	100
Ambient conditions		
	Pressure, kPa	99.3
	Temperature, ºC	16.5

The experiment was initiated by the rupture of the cooper disk (see Figure 1). The water from the pressure vessel started to evaporate immediately due to the pressure difference. The steam release into the compartment A lasted for 43 s. The recording period was 48 s – it started 5 s before the rupture. The coolant mass flow rate and its specific enthalpy is shown in Figures 2 and 3.

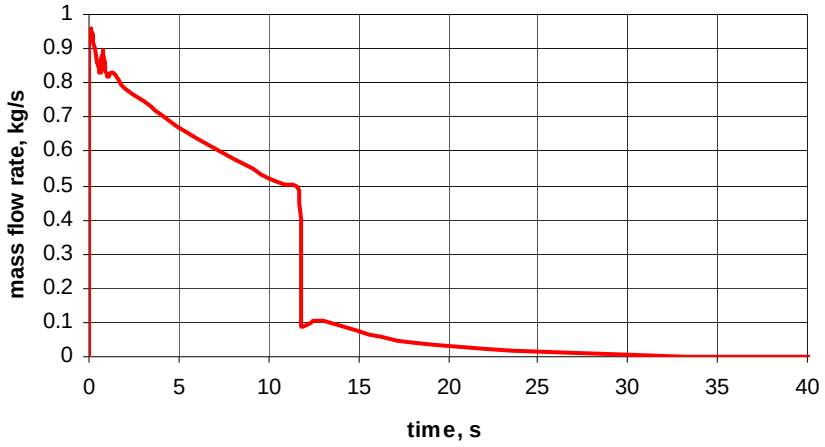

Figure 2. The steam mass flow rate during experiment [2]

The parameters shown in Figures 2 and 3 are very important for numerical simulations - the stand as the boundary conditions.

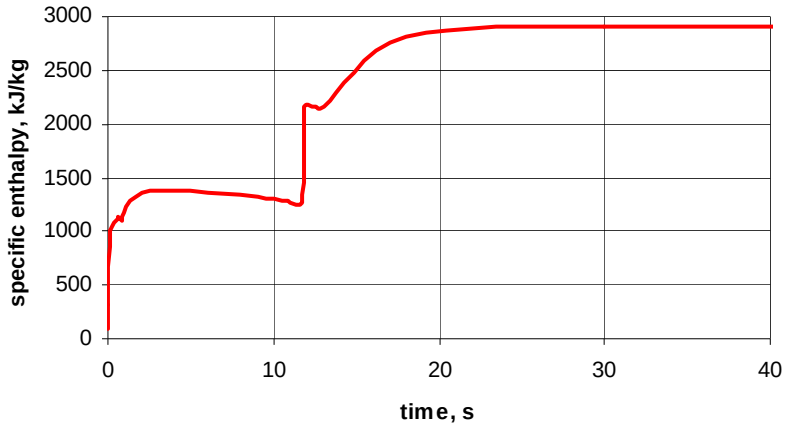

Figure 3. The steam specific enthalpy [2]

NUMERICAL MODEL

HEPCAL computer code

The results received here are an effect of simulations performed using the code HEPCAL, worked out at the Institute of Thermal Technology of the Silesian University of Technology [4,5]. Three versions of the code have been used which differ of the heat transfer coefficient determination methods (details given in the next subsection) [6]. This is a lumped parameter system code using so-called control volume method to reproduce physical phenomena.

The whole containment is simulated by a couple of zones (volumes), connected to each other in the given way. Usually the geometry and dimensions of a control volume correspond to the real dimensions of the specified compartment of the accident localization system. The control volumes are connected through opened channels, orifices, valves, membranes or siphon closures. For each zone homogeneous conditions (perfect mixing) are assumed. The mathematical basics of the model describing changes of thermodynamic parameters present equations of mass and energy balance for specified phases and equations of state [4-6]. The equations of mass and energy balance apply to the time step $\Delta\tau$, however the equations of state concern to the end of each time step. All the equations are nonlinear and their form depend on the state of the specified agents in the control volume. The basic set of equations constituting the mathematical model consists of:

- equations of the energy and mass balance for each control volume,
- equations describing intercompartment flows,
- equations of state for the specified gaseous agents (air, steam, hydrogen),
- equations describing additional phenomena, e.g. heat transfer to walls and structures.

The model applied in the HEPCAL code allows to determine the thermal parameters (temperature, pressure, density) in the specified volumes and the mass and energy flow rates between the control zones. The spraying system work is taken into account, and also heat transfer between phases and heat accumulation in the structures of the containment.

The calculations of the unknown quantities are realized in several steps. First, all the mass and energy fluxes are calculated (the leakage of coolant from the primary circuit, the flow rates of agents through the valves, orifices, water flow rate in the spraying system, heat accumulation in walls and structures). Heat transfer between gaseous and liquid phase is also determined. All these calculations refer to the thermal parameters at the beginning of time step and allow to determine the

internal energy of gas and liquid at the end of time step. Eventually, one obtains a set of *n* nonlinear equations which is being solved using the Newton-Rapshon method. At the last step of calculations all the remaining quantities (partial pressures, total volumes of gas and water etc.) are calculated. The computational procedure is repeated in the each time step for each control volume.

According to the code requirements the considered model of the containment has been subdivided onto two compartments, which correspond to the real partitions of the model.

Determination of the heat transfer coefficient

The heat transfer coefficient from internal atmosphere to containment walls and structures was calculated using three methods:

- Marshall-Holland's formula,
- Tagami's relationships,
- standard correlations for Nusselt number considering the mass and energy transport related to steam condensation or evaporation.

The first two method have been implemented into the HEPCAL-AU version of the code, and the last one in the HEPCAL-AD version [6].

The Marshall-Holland's correlation relies on experimental results [2] and it depends the heat transfer coefficient value HTC of the current mass of the air m_a and steam m_s into the considered control volume:

$$HTC = C \cdot \left(\frac{m_s}{m_a} \right)^{0,8} \tag{1}$$

The constant C in equation (1) is equal to 320 for concrete walls and 450 for steel walls. It is however not explicitly indicated either the phase change is considered or not. Moreover, the heat transfer coefficient value computed by this formula is limited to 1580 W/(m^2·K) in the HEPCAL code.

The maximum value of the heat transfer coefficient determined by Tagami's relationships is a function of the energy release rate from the primary circuit to the control volume [7]:

$$HTC_{\max} = f\left(\frac{energy\ released\ to\ the\ containment}{containment\ volume \cdot time\ of\ \ peak\ \ pressure\ appearance} \right) \tag{2}$$

Experiments have shown that the maximum pressure value is reached at the end of the blowdown phase of the accident usually. The maximum value of the heat transfer coefficient is given by the following formula:

$$HTC_{\max} = 425 \cdot \left(\frac{E_{coolant}}{V \cdot \tau_{blowdown}} \right)^{0,6} \tag{3}$$

where $E_{coolant}$ stands for the energy released along with the coolant from the primary circuit, V is the volume of the control zone where the break takes place and $\tau_{blowdown}$ is the blowdown phase time (it amounts to about 20 s for a large break LOCA and rises while the break became smaller).

The researches realized by Tagami [7] have proved that the growth of the heat transfer coefficient during the blowdown phase has a parabolic trend and it can be written by the equation:

$$HTC = HTC_{max}\sqrt{\frac{\tau}{\tau_{blowdown}}} \tag{4}$$

The heat transfer coefficient value falls down after the blowdown phase till the stagnation phase is achieved. This decrease is described by the following relationship:

$$HTC = HTC_{stag} + \left(HTC_{max} - HTC_{stag}\right)\cdot e^{-0,05\cdot\left(\tau-\tau_{blowdown}\right)} \tag{5}$$

The value of the heat transfer coefficient stabilizes in the stagnation phase and it is calculated as:

$$HTC_{stag} = 11,3 + 283,4\frac{m_s}{m_a} \tag{6}$$

The heat transfer coefficient values computed according to equations (3) - (6) are right for the steel walls. The values equal to 40% of them are assumed for the concrete walls.

The standard correlations for Nusselt number have been implemented into the HEPCAL-AD code. These relationships are well known (for example from [8]) and are not repeated in this paper. An important feature of this code version is taking into account the mass transfer during a change of phase. The attempt assumed in the numerical model differs slightly from a full mass and heat transfer analogy. The details may be found in [6].

RESULTS OF SIMULATIONS

The most important results obtained from numerical simulations are the heat transfer coefficient trends during the analysed experiment scenario. These trends are shown in Figure 4 - computational outcomes are compared with the experimental ones.

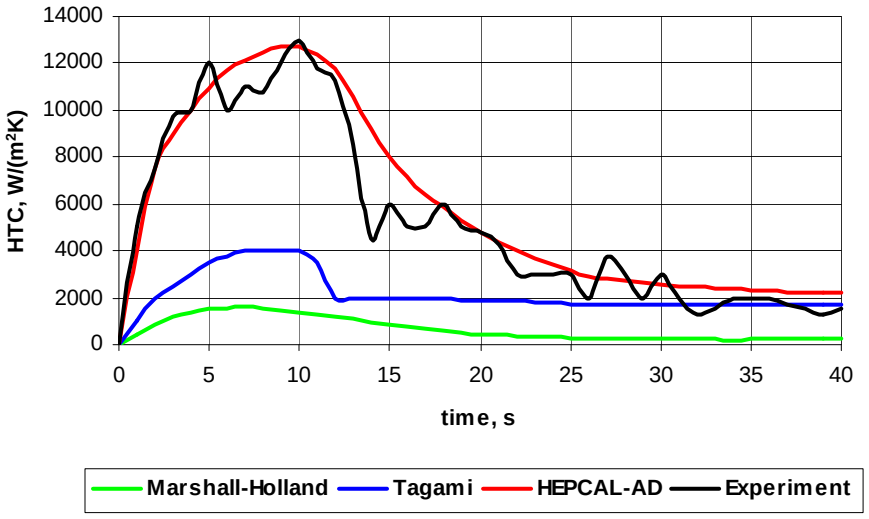

Figure 4. Heat transfer coefficient trend in compartment A

The worst results have been obtained using the Marshall-Holland formula. Tagami's relationships also give values of the heat transfer coefficient far below the measured data, but the trend is more similar to

the experiment. The best results have been achieved by applying standard equations for Nusselt numbers and considering the steam condensation on the containment model walls. Seems that the empirical correlations do not properly consider the phase change - this process significantly increases the heat transfer intensity.

The internal pressure is one of the most interesting parameters regarding thermal-hydraulic analyses of loss-of-coolant accidents within containments of nuclear reactors. The pressure trends in both compartments obtained by applying the HEPCAL-AD code are presented in Figures 5 and 6. One may note that the HEPCAL code results are in quite good conformity with the experiment.

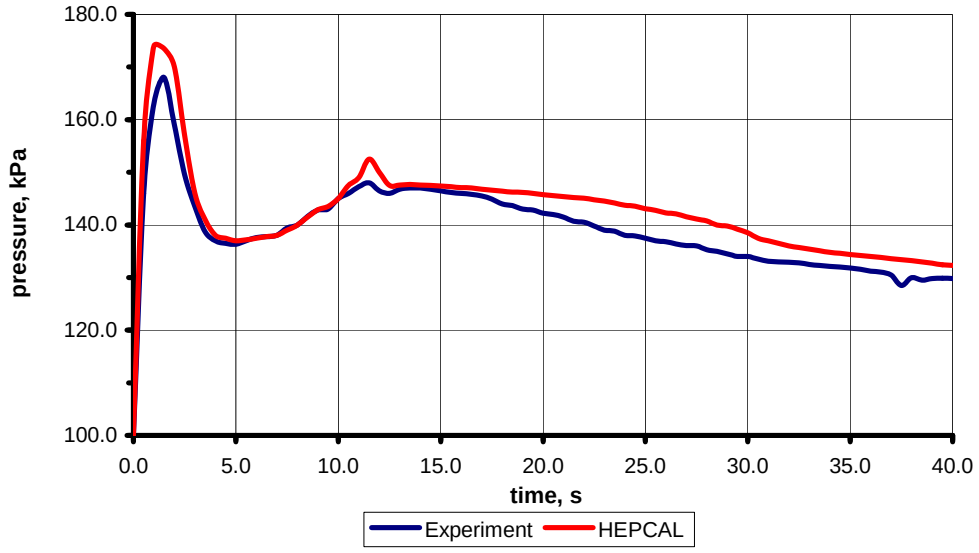

Figure 5. Pressure in compartment A

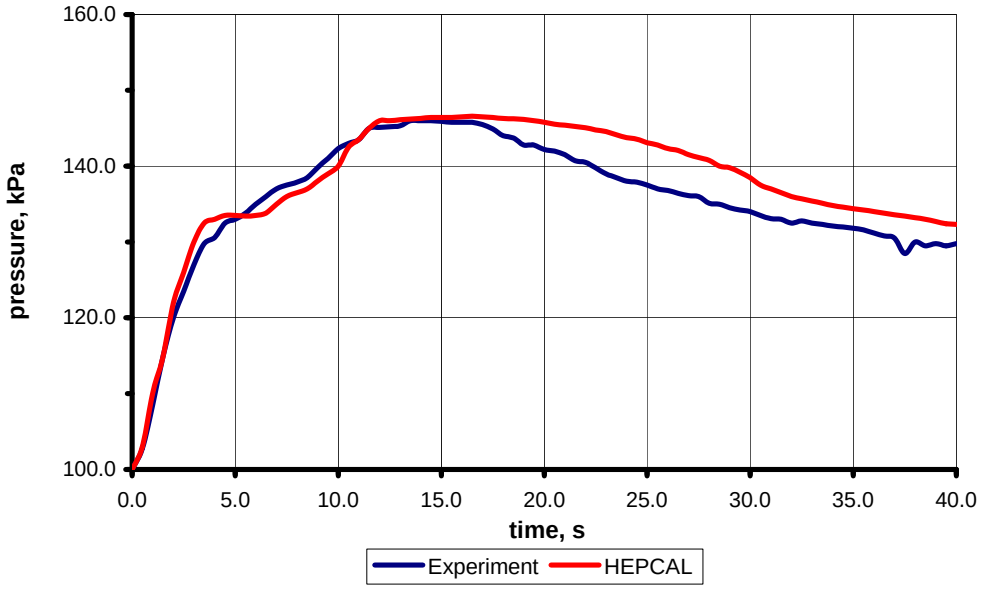

Figure 6. Pressure in compartment B

CONCLUSIONS

The main aim of this work has been to evaluate different methods for determination of the heat transfer coefficient from internal atmosphere to containment walls and structures. The analysis has been performed based on experimental results taken from the CASP-3 project. This experiment has been simulated using the domestic code HEPCAL. The heat transfer coefficient was calculated using three methods. Results of simulations were then compared with experimental data.

The usage of the standard correlations for Nusselt number and considering the mass transfer related to the steam condensation gave a comparable results only. Application of the methods based on empirical correlations for the heat transfer coefficient calculation resulted in its values much smaller than experimental. A probable reason for such situation is neglected or not fully implemented phase change phenomena. Although the empirical equations are very convenient to implement into the code and their application makes the simulation shorter, they may lead to wrong results. The third applied method for the heat transfer coefficient determination has given best results in the analysed case, but usage of this method requires a lot of data which may be not always available for a real plant simulation.

ACKNOWLEDGEMENTS

This work has been realized under the contract No. N N512 374535 financed by the Ministry of Science and Higher Education.

REFERENCES

1. OECD, International Standard Problems: brief descriptions (1975-1997), OECD - CSNI Report NEA/CSNI/R(1997)3, Paris, 1997.
2. Marshall J., Holland P.G., Woodman W., OECD/CSNI Containment Analysis Standard Problem No. 3. Experimental Results, CASP3-1. OECD, Paris, 1981.
3. Marshall J., Woodman W., Comparison report on Containment Analysis Standard Problem No. 3, OECD, Paris, 1983.
4. Fic A., Skorek J., Mathematical model of transient thermal and flow processes in containment of a PWR nuclear reactor, *Archiwum Energetyki*, vol. 1-2, 1993.
5. Skorek J., Składzien J., Thermal Analysis of the Loss-of-Coolant accident within the containment of the WWER-440 and WWER-1000 nuclear reactors, *Computer Assisted Mechanics and Engineering Sciences* vol.1 No. 3/4, 1994.
6. Bury T., Analysis of thermal and flow processes within containments of water nuclear reactors during loss-of-coolant accidents. *PhD thesis*, Institute of Thermal Technology, Silesian University of Technology, Gliwice 2005.
7. Tagami T., Interim Report on Safety Assessment and Facilities. Establishment Project in Japan for Period Ending June 1965 (No. 1), Japanese Atomic Energy Research Institute, Tokio, 1965.
8. Welty J.R., Wicks C.E., Wilson R.E., Rorrer G., *Fundamentals of momentum, heat and mass transfer*, Jonh Wiley and Sons, Inc., 2001.

ENERGETIC AND ECONOMIC ANALYSIS OF A SMALL-SCALE TRIGENERATION PLANT WITH A LIQUID DESICCANT COOLING SYSTEM

M. Badami*, A. Portoraro[1]
[1] Dipartimento di Energetica, Politecnico di Torino, Torino, Italy

ABSTRACT. A small-scale trigeneration plant with 126/220/210 kW of electrical, heating and cooling capacities respectively is presented in the paper. The plant is going to be installed in the Politecnico di Torino (Turin, Italy) premises. The plant is characterized by an innovative natural gas fired internal combustion engine, that has been coupled to a liquid LiCl-water desiccant cooling system. The system is able to provide 20.000 m^3/h of cooled air to a building where there are several teaching classrooms. In this work, the main characteristics of the plant and the energetic performance are described. A detailed economic study, which has the aim of evaluating the financial profitability of the installation, is also presented.

Keywords: *Trigeneration, Combined Heat Cooling and Power (CHCP), Desiccant Cooling, Economic assessment, Energy Market*

PLANT DESCRIPTION

A small-scale trigeneration plant has been set up and installed at the Politecnico di Torino, Turin, Italy. The study, the design and the development of this installation is part of the HEGEL Project (High Efficiency polyGEneration Applications), that is a project co-financed by the European Commission within the 6th Framework Programme, under priority 6.1. The plant has been conceived to provide an air – conditioning service to a small building (about 2.105 m^2, see Figure 1), where several teaching classrooms are located.

Figure 1. The building

* Corresponding author: Prof. M . Badami
Phone: + (39)-011-0904516, Fax: + (39)-011-0904599
E-mail address: marco.badami@polito.it

The main components of the plant are the cogenerator, which was developed and setup by the FIAT Research Centre (Turin, Italy), and the desiccant cooling system. Several humidifiers and exchangers are also needed to refine the temperature and humidity of the air supplied to the building. A schematic diagram of the installation is provided in Figure 2.

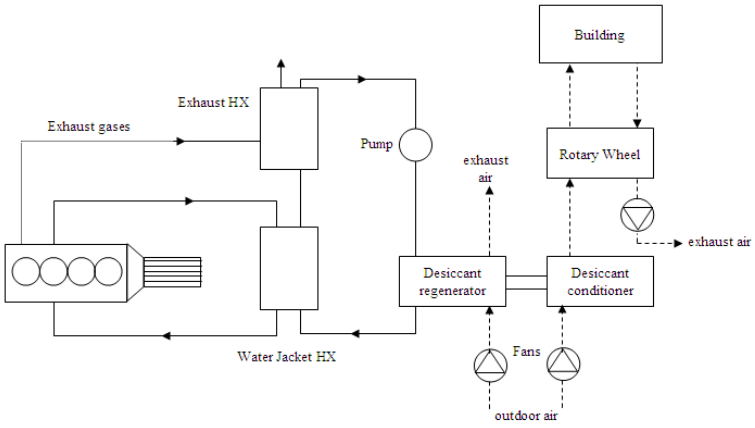

Figure 2. Schematic diagram of the trigeneration plant

The innovative natural gas combined heat, cooling and power (CHCP) system has electrical, heating and cooling capacities of 126/220/210 kW, respectively (see Figure 3). The heat is recovered from the engine through a water/water exchanger and a gas/water heat exchanger. The first one recovers heat from the engine cooling water, the second from the flue gases. The cogenerator has an electronic power unit, made up of an AC/DC-DC/AC converter, which allows the engine to operate at variable speed, while delivering 50 Hz AC to the grid. Due to the power electronics, the engine can operate at part load conditions by varying the rotating speed. This strategy allows the engine to achieve higher part load efficiency than conventional cogenerators [1] (see Figure 4).

Figure 3. The cogenerator

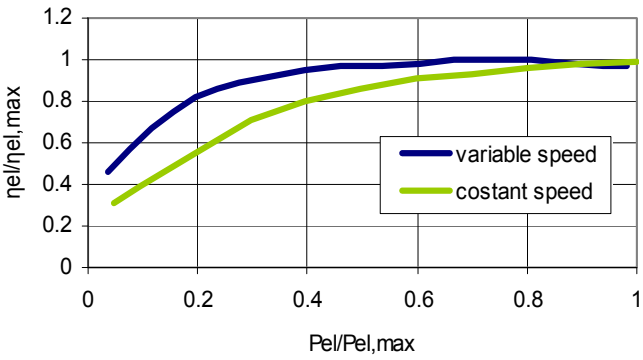

Figure 4. Part load efficiency of the CHP

The heat recovered from the engine is exploited in a Thermally Activated Technology (TAC) device, that is, the desiccant cooling unit. This unit is composed of two sections: a conditioner and a regenerator. The conditioner is able to produce a cooling effect from the dehumidification obtained through the sorption of the humidity in an external airflow of 20.000 m^3/h, by a LiCl-water solution. Then, the moisture is desorbed from the solution in the regenerator, by means of a second external 20.000 m^3/h air flow (see Figures 5 and 6). A rotary heat exchanger has been placed between the supply airstream, which is already treated inside the conditioner, and the return air flow. The heat is

transferred from the supply to the return stream. Moreover, a humidifier, placed after the rotary wheel, further decreases the supply air temperature (evaporative cooling).

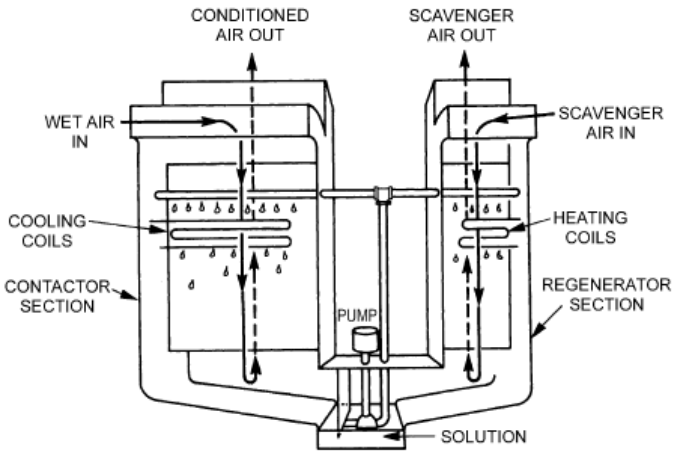

Figure 5. Flow Diagram of the Liquid-Absorbent Dehumidifier [2000 ASHRAE Systems and Equipment Handbook, 22.2]

Figure 6. A liquid desiccant unit

ENERGETIC ANALYSIS

The energetic analysis of the plant has been performed on nominal data provided by the cogenerator (see Table 1) and the desiccant unit (see Table 2) manufacturers.

Table 1
Main cogenerator data

Engine type	Otto 4T
Displacement	5883 cm^3
Fuel	Natural Gas
Generator	Asynchronous water-cooled
Power electronics	AC/DC - DC/AC converter
Electric power	126 kW
Thermal power	220 kW
Fuel input power	427 kW
Electrical efficiency	0.295
Thermal efficiency	0.515
Energy Utilization Factor	0.810

Table 2
Main Desiccant unit data (single unit)

Number of units employed	4
Desiccant solution type	LiCl-water
Nominal air capacity (conditioner)	5000 m3/h
Nominal air capacity (regenerator)	5000 m3/h
Net weight	540 kg
Operating weight (including LiCl)	690 kg
Dimensions (L/W/H)	2240/1420/1575 mm
Nominal latent cooling capacity	~ 42 kW

The electrical, thermal and cooling power characteristics of the trigeneration plant are reported in Table 3.

Table 3
Electrical and thermal balance of the trigeneration plant

Cogenerator rated power	126 kW_{el}
Desiccant unit requirements	15.8 kW_{el}
Other plant component requirements	19.4 kW_{el}
CHCP net electrical rated power	90.8 kW_{el}
CHP recovered thermal power	220 kW_{th}
Cooling power supplied by the desiccant system	168 kW_{el}
Cooling power supplied by the rotary heat exchanger	42 kW_c
CHCP total cooling power	210 kW_c

The main hypotheses considered in this study are:

- as the plant capacities are much lower than the electrical, thermal and cooling load of the Politecnico di Torino user's, the whole energy production is considered to be self consumed inside the internal electric and thermal grids of the Politecnico;
- during the summer season, the plant is only turned on to guarantee the base load (about 600 hours). During these hours, the rated cooling power (210 kW) is entirely exploited. When only part of the maximum cooling power is needed, the plant is turned off, and the partial load is satisfied by a traditional vapour compression refrigeration group;
- the heat recovered from the engine during the summer season is all sent to the desiccant system to produce the cooling effect;
- during the entire considered period, the plant always works at rated power.

On the basis of the above presented hypotheses, the following yearly working hours can be assumed:

- Winter: about 1.900 h (13 hours/day for 6 days/week, for 6 months);
- Summer: about 600 h (10 hours/day for 5 days/week, for about 3 months)

Considering the aforementioned operating hours, and the nominal power reported in Table 3, the plant energy production can be calculated. The results are summarized in Table 4:

Table 4
CHCP plant energy production during the year

	Operating hours	Electrical production	Thermal production	Cooling production
	h	MWh_{el}	MWh_{th}	MWh_c
Winter	1900	236	412	-
Summer	600	55	133	127
Total	2500	E_{el} = 236+55	E_{th} = 412+133 E^*_{th} = 412	E_c = 127

A recognized way of assessing the energetic performance of a cogeneration / trigeneration plant, proposed by the European Union (EU), is through the calculation of the Primary Energy Savings (PES). The amount of PES provided by a CHP plant can be calculated on the basis of equation (1) [2]. A traditional boiler $\eta_{th,s}$ = 0.9 and an electrical efficiency value $\eta_{el,s}$ = 0.525 of the separate production

plant have been considered For the calculations, as indicated in [3]. Moreover, the Decision of the EU introduces two correction factors on the $\eta_{el,s}$ value:

- One factor is related to the average yearly temperature (12.5 °C registered in Turin in the year 2008);
- The other factor is related to the tension at which the electrical power is produced by the plant (380 V);

The electrical efficiency value for the separate production becomes [3]:

$$\eta_{el,s} = \{52.5 + [(15 - 12.5) \cdot 0.1]\} \cdot 0.860 = 45.4\% \quad (1)$$

Therefore:

$$PES = 1 - \frac{E_{fuel}}{\frac{E_{el}}{\eta_{el,s}} + \frac{E_{th}}{\eta_{th,s}}} = 15.2\% \quad (2)$$

where E_{fuel} is the total fuel energy input in the specified reference period (1 year); E_{el} is the total net electricity production and E_{th} is the total thermal energy recovered from the engine, in the reference year.
The regulations provided in European Union Directive 2004/08/CE, have set two different primary energy savings thresholds, which will be valid from the 1st January 2011; when the PES index is greater that the threshold, the plant is recognised as a "high efficiency cogeneration" plant. The two thresholds values are:

- PES > 0, when the rated electrical power of the cogenerator is less than 1 MW_{el};
- PES > 10% in the other cases.

In the present application, where the electrical rated power is 126 kW, there should be a PES > 0.
The calculation of the energy terms in equation (2) should be performed by considering a specified reference period (for instance, 1 year). Moreover, in this formulation, according to the Decision of the European Commission 2008/952/CE of 19th November 2008, the heat employed to produce a cooling effect can be considered as useful thermal energy. No cooling efficiencies of reference are indicated, and only the total amount of heat exploited is considered.
Some Authors [3] have suggested alternative methodologies to calculate the savings offered by a CHCP plant, and in particular they highlighted the cooling production efficiency. A Trigeneration Primary Energy Savings index (TPES) is introduced, which is defined as follows:

$$TPES = 1 - \frac{E_{fuel}}{\frac{E_{el}}{\eta_{el,s}} + \frac{E^*_{th}}{\eta_{th,s}} + \frac{E_c}{\eta_{c,s}}} \quad (3)$$

In this formulation, E_{el} is again the net electrical power produced by the CHCP during the considered period (one year); E^*_{th} is the useful thermal energy output produced by the cogenerator, excluding the part exploited in the desiccant unit during the summer season (with reference to Table 4, E^*_{th} = 412 MWh); E_c is the cooling energy produced by the plant over the year.
$\eta_{th,s}$ and $\eta_{el,s}$ are the separate thermal and electrical production efficiencies, while $\eta_{c,s}$ is the traditional reference efficiency for cooling power generation [2], which can be expressed as:

$$\eta_{c,s} = \eta_{el,s} * COP_s \quad (4)$$

where COP_s is the coefficient of performance of one equivalent compression electric refrigerator group. In the calculation, COP_s is assumed equal to 2.7.
From equations (3), (4), it results that:

$$TPES = 1 - \frac{E_{fuel}}{\frac{E_{el}}{\eta_{el,s}} + \frac{E^*_{th}}{\eta_{th,s}} + \frac{E_c}{\eta_{el,s} * COP_s}} = 12.1\% \quad (5)$$

It should be pointed out that the primary energy savings not only depend on the performance of the plant, but also on the efficiencies of the reference situation with separate production of heat and power. Figure 7 shows the PES = 0, PES = 10% and PES = 20% curves in a plan where X and Y axes are η_{el} and η_{th} respectively. The PES point is represented for the selected separated efficiencies. The position of the TPES point over the map has been determined by means of the two electrical and thermal equivalent production efficiencies, defined by equations (6).

$$\eta^{eq}_{el} = \frac{E_{el} + E_c / COP_s}{E_{fuel}}; \qquad \eta^{eq}_{th} = \frac{E^*_{th}}{E_{fuel}} \quad (6)$$

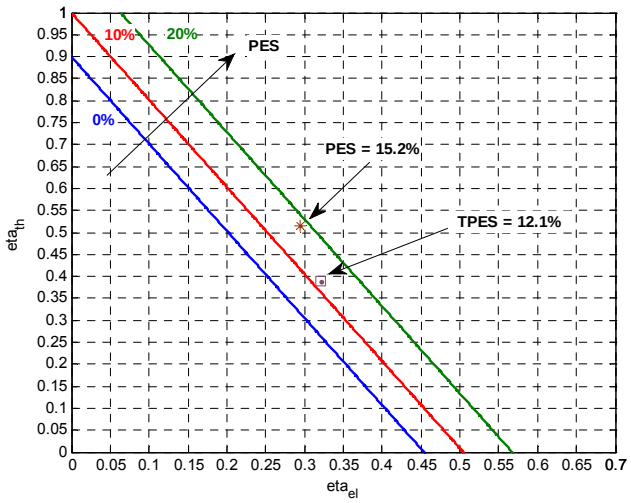

Figure 7. Primary Energy Savings curves in function of the electrical and thermal efficiency of the cogenerator, for $\eta_{el,s} = 0.454$ and $\eta_{th} = 0.9$

ECONOMIC ANALYSIS

An economic profitability analysis of the installation was carried out. The prices of buying/selling electricity, the personnel and maintenance costs and the fuel costs were considered, while the purchase and self-production of electrical, thermal and cooling energy were contextualized in the energy market of reference. Moreover, national subsides from Italian Legislation were taken into account in the calculations (the Government provides some money benefits for each toe of primary energy saved [5]). Some insurance and general costs were considered, and these were both assumed equal to 5% of the total costs. All the profit and cost unit prices are reported in Table 5.
The unit prices of the electrical and thermal energy represent the cost of the actual supply. Different costs were considered for the electricity supply, as the Italian National Electric System is organized in time bands. Furthermore, the actual Italian legislation foresees the detaxation of the natural gas

employed for cogeneration purposes (0.25 Sm^3 for each produced kWh_{el} should be paid without inland duties). Therefore, two different natural gas costs are presented.

Table 5
Profit and cost unit prices

Revenues	
Electrical energy price (self-consumption) [8.00 – 19.00]	166.3 €/MWh_{el}
Electrical energy price (avoided purchase) [8.00 – 19.00]	141.3 €/MWh_{el}
Electrical energy price (self-consumption) [other hours]	166.3 €/MWh_{el}
Electrical energy price (avoided purchase) [other hours]	158.9 €/MWh_{el}
Thermal energy price (from district heating service)	65 €/MWh_{th}
Subsidies	
Italian Legislation Subsidies (referred to February '09)	~ 80 €/toe
Costs	
Natural gas (with detaxation)	0.360 €/Sm^3
Natural gas (with detaxation)	0.569 €/Sm^3
Personnel	4 h/week, with a full cost of 40.000 €/year
CHP maintenance cost	16.0 €/MWh_{el}
Desiccant unit maintenance cost	8.0 €/MWh_c
National duty on electricity consumption	3.10 €/MWh_{el}
Regional tax on electricity consumption	11.36 €/MWh_{el}
General cost	5% of total costs

The avoided costs were calculated from these unit prices, and considering the energetic production of the plant reported in Table 4. The economic profitability was assessed, by means of two indices that are usually employed to evaluate the convenience of investment with high initial capital costs [6]: the Simple Payback period (SPB) and the Internal Rate of Return. The simple payback is the amount of time it will take to recover installation costs, based on annual energy cost savings. The SPB is calculated as the ratio of the annual energy cost savings, over the initial installation cost.

$$SPB = I / (R_i + S_i - C_i) \quad (5)$$

Where I is the total initial investment, R_i is the total revenue, S_i is the total subsidy and C_i is the total plant costs in the year i.

The IRR instead is the average annual return earned through the life of an investment. The IRR is the value of the discount rate s that satisfies equation (6) for a given N, where N is the total plant life, in years. For the calculations, N = 15 years is assumed.

$$\sum_{i=1}^{N} \frac{Ri + Si - Ci}{(1+s)^i} = 0 \quad (6)$$

Due to the high volatility of the fuel cost over the last few years, the profitability analysis of the investment has been related to several natural gas cost values. The estimation of the plant investment cost is marked by a vertical dotted band [6], and the results of the economic simulation are reported in Figures 9 and 10.

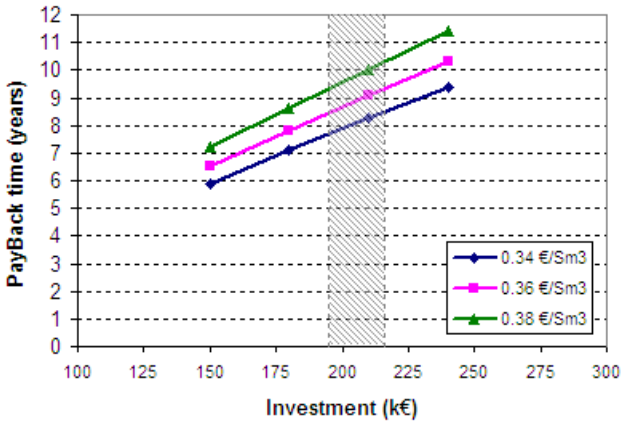

Figure 9. Payback time of the investment for different natural gas cost

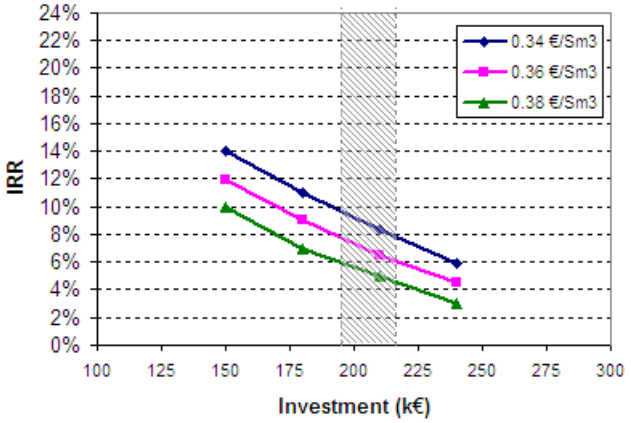

Figure 10. IRR at 15 years of the investment for different natural gas costs

CONCLUSIONS

A small-scale trigeneration plant, with a natural gas ICE and a liquid desiccant cooling system, is presented in the paper. An energetic analysis, based on the nominal data of the cogenerator and of the desiccant unit, has been performed. The Primary Energy Savings achievable from the plant operation have been calculated, referring both to EU Directive 2004/8/CE and to another methodology proposed in literature. The results of the comparison are described and discussed in detail. An economic analysis has also been carried out; the paper describes the main hypotheses, and illustrate the methodology adopted to assess the profitability of the investment. Two commonly used indices have been calculated, the Simple Payback Period and the Internal Rate of Return. As the fuel cost has had a high volatility in recent months due to the international market situation, the paper has the aim of illustrating the relationship between such indicators and the fuel cost. National Subsidies have also been considered in the study.

ACKNOWLEDGMENTS

The support provided for this work under EU Sixth Framework Programme Priority 6.1 (contract TREN/05/FP6EN/S07.56687/020153, HEGEL Project, “High Efficiency polygeneration appLications) is gratefully acknowledged. The Authors also wish to express their thanks also to Dr. Pasquale Campanile, Dr Franco. Anzioso and Dr. Paolo Chiantore from FIAT Research Centre, Turin (Italy) for their support and collaboration.

REFERENCES

1. Badami, M., Casetti, A., Campanile, P., Anzioso, F., Performance of an innovative 120 kWe natural gas cogeneration system, Energy 32 (2007) 823-833.
2. Directive 2004/8/EC. On the promotion of cogeneration based on a useful heat demand in the internal energy market. European Parliament and Council; 11 February 2004.
3. Decision of the European Commission 2007/74/CE of 21st December 2006
4. Chicco, G. and Mancarella, P., *Trigeneration primary energy saving evaluation for energy planning and policy development*, Energy Policy 35 (2007) 6132–6144.
5. See also http://www.mercatoelettrico.org/En/Default.aspx
6. Irving, G., *Modern cost-bene6t methods: an introduction to financial, economic and social appraisal of development projects*, in: The MacMillan Press, Ltd., London/UK, 1978.

METAL FOAM CONDENSERS FOR MINIATURE-SCALE REFRIGERATION SYSTEMS

G. B. Ribeiro, J. R. Barbosa Jr.*, A. T. Prata
Federal University of Santa Catarina, Florianópolis, Brazil

ABSTRACT. This study consists of an experimental analysis of the thermal-hydraulic performance of microchannel condensers with open-cell metal foams to enhance the air side heat transfer. The condensers were designed to be part of a miniature-scale refrigeration system. Three different metal foam samples were tested with distinct numbers of pores per inch (10 and 20) and porosity (89.30 and 94.70%). A conventional condenser with plain fins was also tested for a performance comparison. On the refrigerant side, seventeen micro-channels with diameter of 1.5 mm were used in all condensers. The experimental apparatus is composed of an air loop (a closed-loop wind tunnel calorimeter) and a refrigerant loop which allows the specification of the mass flow rate and the thermodynamic state of the refrigerant at the condenser inlet. Iso-butane (R-600a) was used as the working fluid. The experiments were performed at the condensing temperature of 90°C, with coolant inlet temperature of 50°C. Air side flow rates ranged from 1.4×10^{-3} m^3/s to 3.3×10^{-3} m^3/s. The refrigerant mass flow rate was maintained at 2.9×10^{-4} kg/s. The heat transfer rate, the overall thermal conductance *UA*, the Colburn factor *j*, the friction factor *f* and the pumping power were calculated as part of the analysis of the prototypes.

Keywords: *condenser, metal foam, porous media, miniature refrigeration system*

INTRODUCTION

The current generation of transistors used in computer processors are responsible for severe rates of heat dissipation per unit area which, if not appropriately controlled, can reduce the performance and compromise the reliability of electronic devices. Thus, the heat management of processors has become a cornerstone of computer technology. A large number of studies have been devoted to engineering the removal of heat from these devices. According to Ortega and Birle [1], natural and forced convection of air are no longer capable of maintaining the processor temperature below acceptable values.

Cooling technologies as diverse as liquid jet and spray impingement, liquid loops and heat pipes have been considered for high heat flux applications. According to Trutassanawin and Groll [2], the vapor compression refrigeration cycle is the only technology capable of removing high heat fluxes in a high-temperature environment. However, space restrictions (which impose a limit on the size of the refrigeration system) are among the most challenging aspects on this thermal solution. Therefore, the design of compact components of the cycle, such as compressors and heat exchangers, is essential for advancing the technology.

This paper presents an experimental analysis of compact microchannel condensers for a miniature-scale refrigeration system. Copper metal foams were used as extended surfaces for enhancing the air side heat transfer. Metal foams have several attributes often pursued in high performance heat

* Corresponding author: J. R. Barbosa Jr.
Phone: + 55 48 3721 9397, Fax: + 55 48 3234 5166
E-mail address: jrb@polo.ufsc.br

exchangers, such as a large surface area per unit volume, a high thermal conductivity of the solid matrix and large heat transfer coefficients.

Floyd et al. [3] investigated analytically and experimentally the behaviour of copper metal foam heat exchangers in an impinging water flow arrangement, for which a performance similar to that of a microchannel heat exchanger has been observed. They also showed that the foam porosity has a high influence on the surface temperature and on the water flow rate. Haack et al. [4] presented an overview of metal foam materials for high performance heat exchangers. They showed that, for a fixed coolant flow rate, both the heat exchanger effectiveness and the pressure drop increase with decreasing pore size. Boomsma et al. [5] presented an experimental apparatus for evaluating metal foam heat exchangers. In their tests, the performance of aluminium metal foam exchangers under forced convection was compared with that of commercial heat exchangers, using water as coolant. The thermal resistance of the metal foam heat exchangers was 2 to 3 times lower than that of the commercial heat exchanger for a fixed pumping power.

In the present paper, the influence of the number of pores per inch (PPI) and of the porosity on the performance of metal foam condensers is investigated experimentally for conditions typical of small scale refrigeration systems for electronic cooling applications. The heat transfer and the air side pressure drop were observed to increase with the number of PPI and decrease with increasing porosity.

EXPERIMENTAL APPARATUS

Air loop

The air loop is presented schematically in Figure 1. It consists of a thermally insulated, fully instrumented, closed loop wind tunnel calorimeter. Two direct current (DC) blowers with a variable power input control were used to supply air through the test section. In order to measure the air flow rate, four calibrated nozzles with different diameters were installed together with two differential pressure transducers; one of them measures the pressure difference between the inlet of the nozzles and the atmospheric pressure, and the other measures the pressure drop across the nozzles. A humidity transducer was also placed upstream of the nozzles.

A two-transducer arrangement identical to the one described above was used in the test section to measure the condenser pressure drop. On the whole, fifteen T-type thermocouples were installed in the air loop. Five of them were installed upstream of the condenser test section and another five were positioned downstream of the condenser. Three thermocouples were placed outside the air loop for room temperature control. The two remaining thermocouples were used to measure the air temperature upstream of the nozzles. To control the inlet temperature, a set of electric heaters and a cooling coil connected to a thermostatic bath were used. The use of diffusion baffles, porous media and a fan ensures the uniformity of air temperature and velocity at the tunnel cross section.

Refrigerant loop

The refrigerant loop is shown schematically in Figure 2. A variable-speed compressor was used to pump iso-butane (R-600a) through the loop and an oil filter was used to separate residual oil from the discharged refrigerant. An accumulator was placed downstream of the condenser. The expansion device is a hand-operated needle valve. The refrigerant mass flow rate was measured with a Coriolis-type mass flow meter placed between the accumulator and the needle valve.

Resistance temperature detectors (RTDs) were placed upstream of the compressor and mass flow meter. At the condenser inlet, the pressure was measured by means of an absolute pressure transducer. Two immersion-type thermocouples were installed upstream and downstream of the condenser. The tests conditions are controlled through proportional-integral-derivative (PID)

microcontrollers. The compressor inlet temperature, the mass flow meter inlet temperature and the condenser inlet temperature were controlled by electric heaters positioned around the connection tubing. The condenser inlet pressure was controlled by an electric heater wrapped around the accumulator. The specification of the test conditions is such that the refrigerant is in the superheated vapour state at the inlet of the mass flow meter and of the compressor.

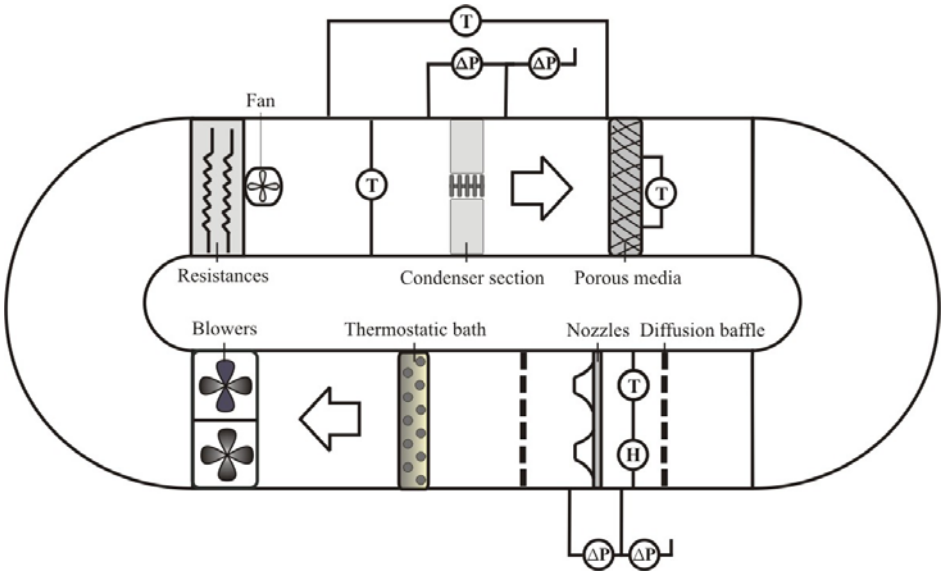

Figure 1. Schematic representation of the air loop

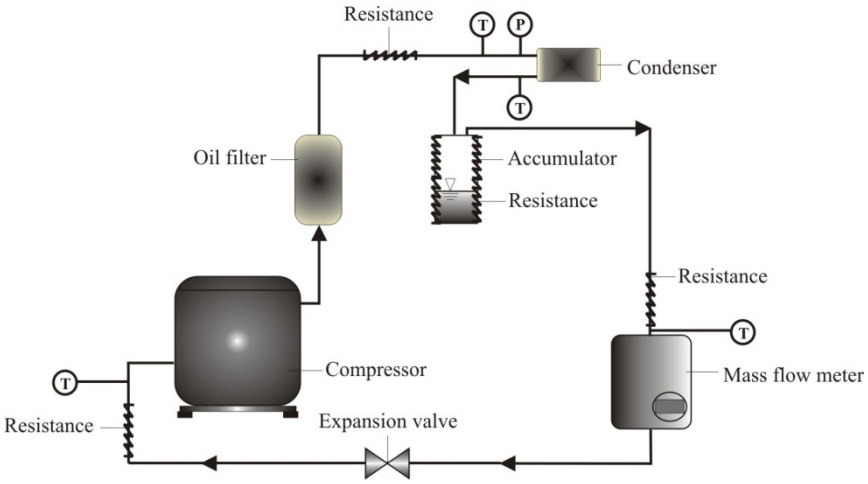

Figure 2. Schematic representation of the refrigerant loop

METAL FOAM CONDENSERS

All condensers were manufactured from copper, and three metal foam samples were used with different number of pores and porosity. The number of pores is defined as the quantity of pores encountered in an inch of structure, whereas the porosity can be defined as the volume fraction occupied by the fluid. Here, numbers of pores per inch (PPI) equal to 10 and 20, and porosities of 89.30 and 94.70% were used. The metal foams were brazed at the top and bottom of a 3 mm thick copper plate with seventeen circular parallel microchannels with a diameter of 1.5 mm.

As illustrated in Figure 3, air flows through the porous media, extracting heat from the refrigerant fluid that flows (in a cross-flow arrangement) inside the microchannels. The length (in the direction of the air flow), height and width of the metal foam samples brazed on the plate were 35, 7 and 48 mm, respectively. A condenser with sixty 0.5 mm thick, brazed plain fins was tested for performance comparison purposes. All prototypes had the same frontal area.

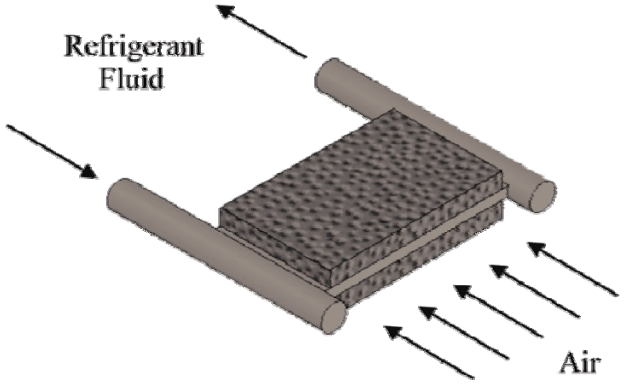

Figure 3. Illustration of a metal foam condenser

EXPERIMENTAL PROCEDURE

To evaluate the performance of the miniature-scale condensers, a condensing temperature of 90°C was used for all experimental runs. A 2°C inlet superheat was maintained during all tests. The air inlet temperature was kept at 50°C, whereas the air flow rate was set at three different values: 1.4×10^{-3} m^3/s, 2.3×10^{-3} m^3/s and 3.3×10^{-3} m^3/s. The refrigerant mass flow rate was kept at 2.9×10^{-4} kg/s. Overall, three different conditions were evaluated for each condenser. Each test was performed twice, which resulted in six tests for each heat exchanger.

DATA REDUCTION

The heat transfer rate measured on the air side $\dot{Q}_{air}$ is calculated through equation (1), where $\dot{M}_{air}$ is the air mass flow rate, $c_{p,air}$ is the specific heat, and $T_{in,air}$ and $T_{out,air}$ are the air inlet and outlet temperatures respectively.

$$\dot{Q}_{air} = \dot{M}_{air} c_{p,air} (T_{out,air} - T_{in,air}) \tag{1}$$

Similarly, the heat rejection from the refrigerant side $\dot{Q}_{ref}$ can be evaluated from

$$\dot{Q}_{ref} = \dot{M}_{ref} (h_{in,ref} - h_{out,ref}) \tag{2}$$

where $\dot{M}_{ref}$ is the refrigerant mass flow rate, and $h_{in,ref}$ and $h_{out,ref}$ are the enthalpies at inlet and outlet of the condenser. The overall heat conductance UA can be obtained from the ratio of the heat transfer rate $\dot{Q}_{air}$ and the logarithmic mean temperature difference, ΔT_{lm}.

$$UA = \dot{Q}_{air} / \Delta T_{lm} \tag{3}$$

As proposed by Boomsma et al. [5], the following dimensionless quantities can be used to correlate the air-side heat transfer and pressure drop

$$f = \frac{\Delta p_{cond}}{\left(L_{cond} / D_h\right)\left(\rho_m u_{air}^2 / 2\right)} \tag{4}$$

$$\rho_m = (\rho_{in,air} + \rho_{out,air}) / 2 \tag{5}$$

$$D_h = 4A_{pm} / L_{cond} \tag{6}$$

$$u_{air} = \dot{V}_{air} / A_{pm} \tag{7}$$

where f is the friction factor, $\dot{V}_{air}$ is the air flow rate and A_{pm} is the frontal area of the porous media. In the equations above, $\rho_{in,air}$ and $\rho_{out,air}$ are the inlet and outlet air densities, respectively, L_{cond} is the heat exchanger length along the air flow, and Δp_{cond} is the measured pressure drop.

The Colburn *j*-factor was calculated as follows

$$j = \frac{h_{air} A_{pm} \,\mathrm{Pr}_{air}^{\,2/3}}{\dot{M}_{air} c_{p,air}} \tag{8}$$

where h_{air} is the heat transfer coefficient from the air side calculated in the form [5]

$$h_{air} = \frac{\dot{M}_{air} c_{p,air} (T_{out,air} - T_{in,air})}{A_{con}\left(T_{cond} - T_{air,in}\right)} \tag{9}$$

A_{con} is the interface area between the porous media and condenser plate, and T_{cond} is the condensing temperature. The Reynolds number, as suggested by Kaviany [6], can be obtained from

$$\mathrm{Re} = \frac{\rho_m u_{air} \sqrt{K}}{\mu_m} \tag{10}$$

$$\mu_m = (\mu_{in,air} + \mu_{out,air}) / 2 \tag{11}$$

where $\mu_{in,air}$ and $\mu_{out,air}$ are viscosity of the air at the inlet and outlet, respectively, and K is the permeability of the metal foams. The permeability can be calculated from a linear regression of Darcy's law as follows

$$\dot{V}_{air} = -\frac{KA_{pm}}{\mu_m L_{cond}} \Delta p_{cond} \tag{12}$$

The air side pumping power $\dot{W}$ is calculated from

$$\dot{W} = \Delta p_{cond} \dot{V}_{air} \tag{13}$$

RESULTS

As part of the validation procedure of the experimental setup, the energy balance on both sides of the condenser, i.e., the air side and the refrigerant side, were compared yielding a deviation of ±10%. The main source of uncertainty was the heat loss from the air loop to the environment through the duct walls. It should be noted that the refrigerant side heat transfer rate was measured only at conditions where the refrigerant was a subcooled liquid at the condenser outlet. An uncertainty propagation analysis was performed based on the data reduction equations. The estimated measurement uncertainties of the pressure drop, friction factor, heat transfer, *UA* and Colburn factor were ±1.2%, ±2.1%, ±5.0%, ±5.7% and ±5.7%, respectively.

The effect of the number of pores can be analysed by a direct comparison between condensers A and B. Similarly, the influence of the porosity can be evaluated by comparing condensers B and C. Figure 4 shows the pressure drop as a function of the air volumetric flow rate for the three metal foam condensers. As expected, the pressure drop increases with the increasing air flow rate. By comparing condenser A and B, it can be seen that increasing the number of pores increases the pressure drop. Furthermore, decreasing the porosity increases the pressure drop, as seen in Figure 4.

Results for the friction factor are shown in Figure 5. The friction factor decreases with increasing Reynolds number. Like the pressure drop, the condenser with the higher number of pores and the lower porosity presents the highest friction factor. The metal foam condenser with lower porosity and higher number of pores presented a more compact solid matrix and more tortuous air flow passages, making the fluid flow more difficult.

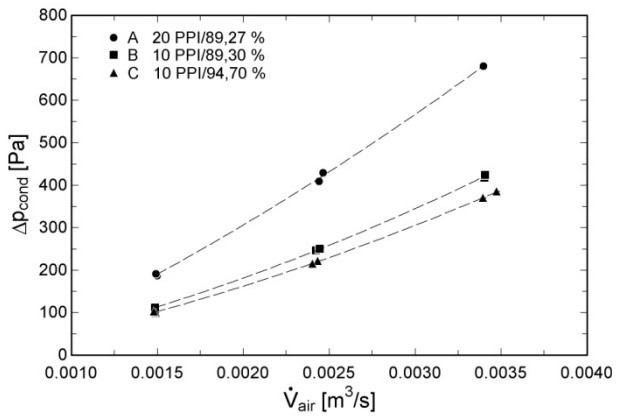

Figure 4. Pressure drop versus air flow rate

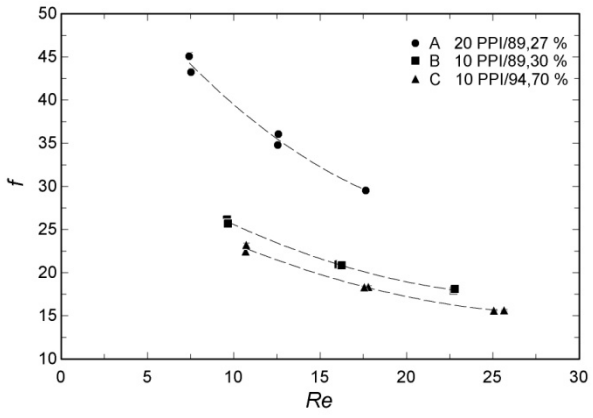

Figure 5. Friction factor versus Reynolds number

Figures 6 and 7 show the heat transfer rate and the overall thermal conductance *UA* as a function of the air flow rate. As expected, the heat transfer rate increases with increasing air flow rate. In Figure 6, condenser A presented higher heat transfer rates than condenser B. Thus, a higher number of pores resulted in higher heat transfer rates. Similarly, lower porosity also resulted in higher heat transfer rates.

It can be seen in Figure 7 that, as expected, *UA* increases with increasing air flow rate. Like the heat transfer rate, the metal foam condensers with a higher number of pores and a lower porosity presented higher heat transfer coefficients. The increase in the number of pores for a fixed porosity

results in a higher interface area between the solid matrix and the air. The decrease in porosity for a fixed number of pores results in a smaller area available for heat transfer. However, it also results in a larger volume of the solid matrix. This larger volume has become more significant for the heat transfer due to a low thermal resistance between the refrigerant fluid and the coolant.

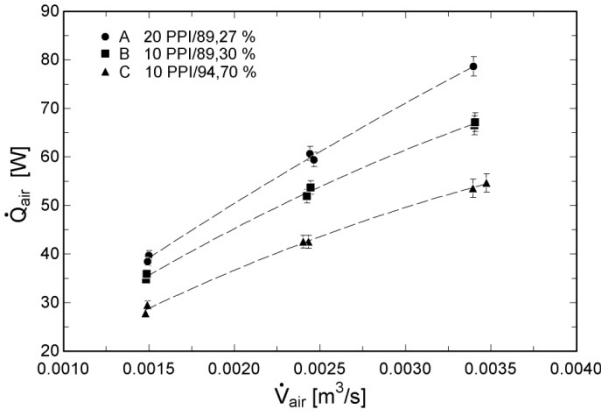

Figure 6. Heat transfer versus air flow rate

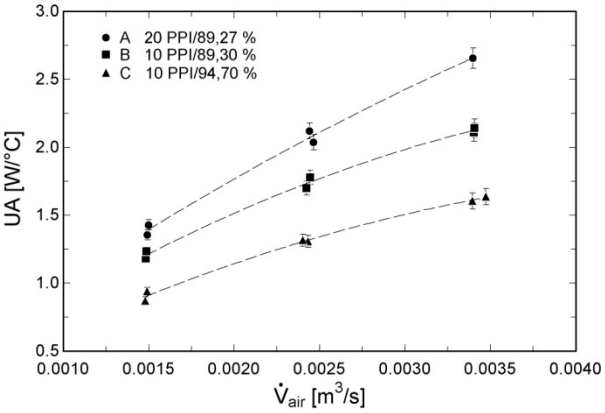

Figure 7. *UA* versus flow rate

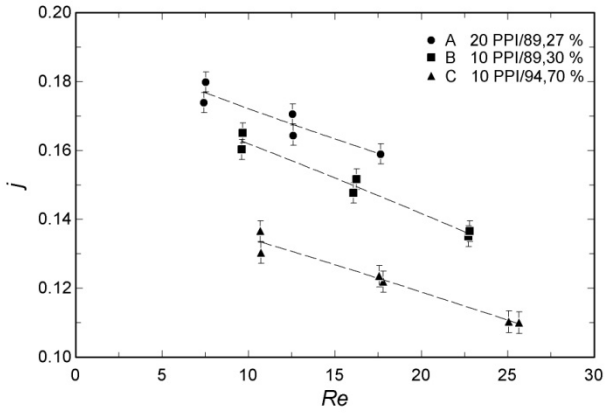

Figure 8. Colburn factor versus Re

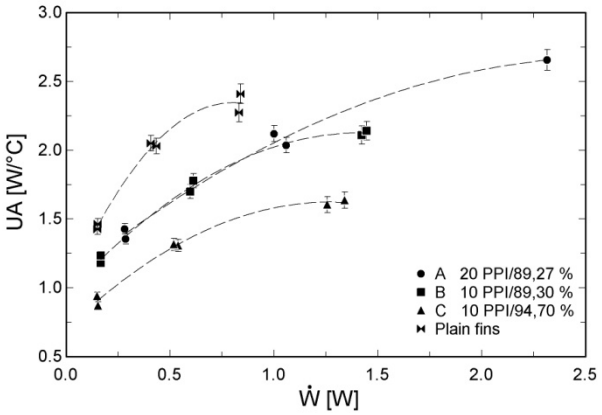

Figure 9. *UA* versus pumping power

The results of the Colburn *j*-factor as function of the Reynolds number are shown in Figure 8. Like the friction factor, the *j*-factor decreases with increasing Reynolds number. It can be concluded that the increase in the number of pores and the decrease in porosity results in higher Colburn factors. Hence, a higher number of pores and a lower porosity improved the thermal performance of the metal foam condensers investigated here.

Figure 9 presents *UA* as a function of the required pumping power. For the lower values of pumping power, condensers A and B presented a similar behaviour. Higher values of thermal conductance could be obtained with condenser A, but at the expense of a more elevated pumping power. By comparing condensers B and C, it can be seen that a lower porosity resulted in a higher thermal conductance, for approximately the same pumping power. In addition, Figure 9 also shows that the required pumping was lower in the conventional (plain fin) condenser than in the metal foam condensers. So, at least for the conditions investigated, the use of a metal foam condenser in a miniature-scale refrigeration system may not be advantageous.

CONCLUSIONS

In order to consider the feasibility of their application as part of a small scale refrigeration system, a series of tests was performed to assess the thermal-hydraulic performance of three metal foam condensers using air as coolant. The number of pores per inch (PPI) and the porosity were varied and their influence on the condensers' performance was analysed.

A refrigerant loop facility that uses iso-butane as refrigerant and a wind tunnel calorimeter to control the air flow conditions were utilized for the miniature-scale heat exchangers performance evaluation. The condensing temperature used in the experiments was 90°C and the air inlet temperature was set at 50°C. Three different air flow rates and one refrigerant mass flow rate were tested.

It was observed that the increasing the number of PPI and decreasing the porosity resulted in a higher air-side pressure drop and in a higher overall thermal conductance. For a fixed pumping power, the overall thermal conductance of the metal foam condensers was lower than that of a plain fin condenser with similar characteristics.

ACKNOWLEDGEMENTS

This study was performed under a joint research programme between the Federal University of Santa Catarina and EMBRACO. The support from Eng. Augusto P. Zimmermann (EMBRACO) is greatly appreciated. Financial support from CNPq and FINEP is also acknowledged.

REFERENCES

1. Ortega, A., and Birle, J. R., The evolution of Air Cooling in Electronic Systems and Observations about its Limits, *Proc. 18th National & 7th ISHMT-ASME*, Guwahati, pp K114-K126, 2006.
2. Trutassanawin, S. and Groll, E., Numerical analysis of a miniature-scale refrigeration system (msrs) for electronic cooling, *International Refrigeration and Air Conditioning Conference*, Purdue, R173, pp 1-10, 2004.
3. Floyd, D. E., Topolski, M. J and Darabi, J., Design and evaluation of copper metal foams in cold plates, *ASME International mechanical engineering congress and exposition*, Chicago, 2006.
4. Haack, D. P., Butcher, K. R., Kim, T., Lu, T. J., Novel lightweight metal foam heat exchangers, *ASME International mechanical engineering congress and exposition*, Orlando, 2000.
5. Boomsma, S. S., Poulikakos, D., Zwick, F., Metal foam as compact high performance heat exchangers, *Mechanics of materials*, Vol. 35, pp 1161-1176, 2003
6. Kaviany, M. *Principles of Heat Transfer in Porous Media*, 2nd Edition, Springer, 1995.

MODEL OF SUPERCRITICAL TWO-PHASE STEAM-WATER INJECTOR

R. Matysko[1], D. Butrymowicz[*1], W. Angielczyk[2], M. Trela[1], M. Bergander[3]

[1]Institute of Fluid-Flow Machinery of Polish Academy of Sciences, Gdansk, Poland,
[2]Université catholique de Louvain, TERM Division, Louvain-la-Neuve, Belgium
3University of Hartford, 200 Bloomfield Avenue, West Hartford, CT 06117, USA

ABSTRACT. Two-phase steam-water injectors may be applied as a feeding pump device or as a condensing device in many applications. In such injectors steam is a motive fluid while cold water is a secondary fluid. One-dimensional model of two-phase injector has been proposed in the paper. Model is based on two-fluid model of two-phase flow along with a set of closure equations. The results of calculations have been compared with experimental results showing reasonably good agreement.

Keywords: *two-phase flow, injector, two-fluid model, condensation*

INTRODUCTION

Steam –water two-phase injector investigated in the present paper consists of motive steam nozzle, water nozzle, mixing chamber and diffuser. Two different kinds of such injector may be distinguished with respect to the arrangement of the steam nozzle: with a central or outer (annular) nozzle. Figure 1 shows a schematic sketch of the injector with the central arrangement of the steam nozzle which is investigated in the paper. In this case steam is a motive fluid while water is a secondary fluid.

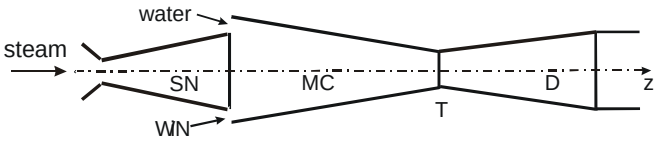

Figure 1. Schematic sketch of steam-water injector:
SN – steam nozzle, MC – mixing chamber, D - diffuser, T- throat, WN – water nozzle.

Having a converging-diverging nozzle shape, the steam is accelerated to the supersonic velocity at the inlet to the mixing chamber. Transfer of heat, momentum (due to the temperature and velocity differences) and mass (due to condensation of steam on water) occur in the mixing chamber. Usually the condensation process is terminated at the throat, followed by a rapid increase of pressure in this region called the shock wave. Then, water is decelerated in the diffuser, which causes a further increase of pressure.

It is seen that the steam injector can be simultaneously used as a water pump and/or a heat exchanger. The exemplary applications of such injector are presented in Fig. 2. The injector can be used as a pumping device in safety passive systems in nuclear power stations (Fig. 2a) in order to

* Corresponding author: D. Butrymowicz
Phone: + (48)-58-6995299, Fax: + (48)-58-3416144
E-mail address: butrym@imp.gda.pl

deliver cooling water to the reactor under breakdown conditions. The other possible application is shown in Fig. 2b where the injectors are used as a feedwater heaters, i.e. as a condensing devices (mixing condensers). Details concerning such applications can be found in papers by Cattadori [5] and Narabayasi [7].

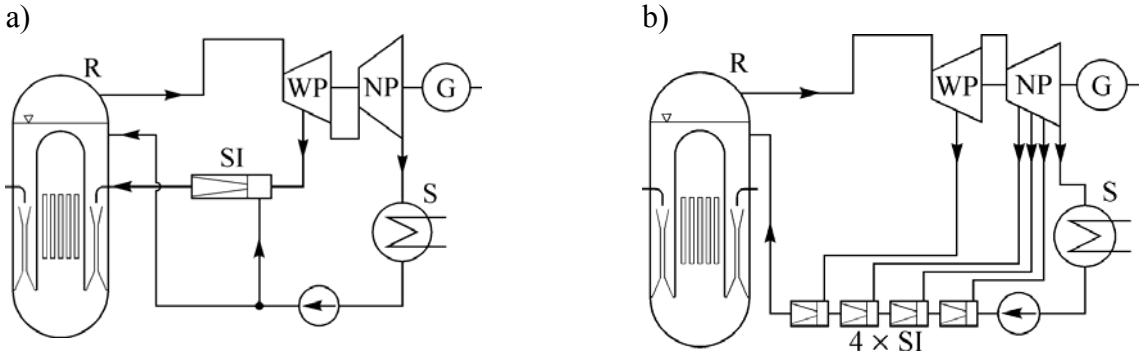

Fig. 2. Exemplary applications of two-phase injectors in nuclear power systems: a) as a cooling water feeding device; b) as a feedwater heating device; R – nuclear reactor; WP – high pressure turbine; NP – low-pressure turbine; S – condenser; G – electric generator.

In many applications of two-phase injector in power generation systems dedicated codes are used to calculate the injector, e.g. RELAP, TRAC, CATHARE – see papers by Pokharna [8]; Carlson [4], Bestion [1]. Various models of two-phase flow are used in order to describe operation of component of power generation systems, mainly: homogenous based on three equations of conservation of mass, energy, and momentum, and two-fluid models based on six equations of conservation for both phases with interphase transport equation, see Ishii [8].

MODEL ASSUMPTIONS

The present paper deals with modelling of two-phase supercritical injector. Two-fluid steady-state model of two-phase flow has been applied for the injector along with closure equations based on the so-called WAHA-3 code equations [11].

The following general assumption has been applied:

- model is steady state;
- all parameters may be averaged through the cross-section area of low, i.e. one dimensional model is applied;
- vapour phase is saturated;
- liquid phase is subcooled.

Moreover, separated flow model have been applied for the closure equations describing the following model quantities: CVM – virtual mass, S – stratification parameter, C_i – interphase shear stress, F_{wall} – flow resistance at the wall. The closure equations of the WAHA-3 code have been used in our calculations [11].

FORMULATION OF THE MODEL

The model of the two-phase stream-water supercritical injector is formulated below. This model consists of the following conservation equations:

a) mass conservation for gas phase:

$$\frac{d}{dz}\left(A\rho_g v_g \alpha\right) = A\Gamma \tag{1}$$

b) mass conservation for liquid phase:

$$\frac{d}{dz}\left(A\rho_l v_l(1-\alpha)\right) = -A\Gamma \tag{2}$$

c) momentum conservation for gas phase:

$$\frac{d\left(A\alpha\rho_g {v_g}^2\right)}{dz} + A\alpha\frac{dp}{dz} + A\cdot C_{VM}\left(v_l\frac{dv_g}{dz} - v_g\frac{dv_l}{dz}\right) + Ap_i\frac{d\alpha}{dz} = \\ = A\alpha\rho_g g\cos\theta - AC_i|v_r|v_r + A\Gamma v_i - AF_{g,wall} \tag{3}$$

d) momentum conservation for liquid phase:

$$\frac{d\left(A(1-\alpha)\rho_l {v_l}^2\right)}{dz} + A(1-\alpha)\frac{dp}{dz} - A\,C_{VM}\left(v_l\frac{dv_g}{dz} - v_g\frac{dv_l}{dz}\right) - Ap_i\frac{d\alpha}{dz} = \\ = A(1-\alpha)\rho_l g\cos\theta + AC_i|v_r|v_r - A\Gamma v_i - AF_{l,wall} \tag{4}$$

e) energy conservation for liquid phase:

$$\frac{d\left(A(1-\alpha)\rho_l e_l v_l\right)}{dz} + \frac{d\left(A(1-\alpha)pv_l\right)}{dz} = AQ_{il} - A\Gamma\left(h_l + \frac{v_l^2}{2}\right) + A(1-\alpha)\rho_l g v_l\cos\theta \tag{5}$$

In conservation equation for liquid phase e_l is the sum of specific internal energy and kinetic energy:

$$e_l = h_l - \frac{p}{\rho_l} + \frac{{v_l}^2}{2} \tag{6}$$

It is import ant to note, that vapour is saturated. Because of relation between temperature and pressure under saturated state: $T_s = f(p); T_g = T_s$, there is one independent variable less. Therefore, in this case five conservation equations have been used. The following vector of the state variables is proposed for considered case of the ejector:

$$\varepsilon = \left(\alpha, p, v_g, v_l, h_l\right)^T \tag{7}$$

The further simplifications are possible in the particular case of the ejector. We have assumed that vapour phase is always saturated, therefore:

$$\rho_g = \rho_g(p, x=0)\,. \tag{8}$$

Liquid chase may be treated as incompressible. Taking into consideration above additional assumption the following set of conservations equations have been developed:

a) mass conservation for gas phase:

$$A\rho_g v_g\frac{d\alpha}{dz} + Av_g\alpha\frac{d\rho_g}{dp}\frac{dp}{dz} + A\rho_g\alpha\frac{dv_g}{dz} = A\Gamma - v_g\alpha\rho_g\frac{dA}{dz} \tag{9}$$

b) mass conservation for liquid phase:

$$A\rho_l(1-\alpha)\frac{dv_l}{dz} - Av_l\rho_l\frac{d\alpha}{dz} = -A\Gamma - v_l\rho_l(1-\alpha)\frac{dA}{dz} \tag{10}$$

c) momentum conservation for gas phase:

$$A\alpha\left(v_g^2\frac{d\rho_g}{dp} + 1\right)\frac{dp}{dz} + \left(Av_g^2\rho_g + Ap_i\right)\frac{d\alpha}{dz} + \left(2Av_g\alpha\rho_g + AC_{vm}v_l\right)\frac{dv_g}{dz} - AC_{vm}v_g\frac{dv_l}{dz} = \\ Ag\alpha\rho_g\cos\theta - v_g^2\rho_g\alpha\frac{dA}{dz} - AF_{g,wall} - AC_i|v_r|v_r + Av_i\Gamma \tag{11}$$

d) momentum conservation for liquid phase:

$$A(1-\alpha)\frac{dp}{dz} - \left(Av_l^2\rho_l + Ap_i\right)\frac{d\alpha}{dz} - AC_{vm}v_l\frac{dv_g}{dz} + \left(2Av_l\rho_l(1-\alpha) + AC_{vm}v_g\right)\frac{dv_l}{dz} = \\ Ag(1-\alpha)\rho_l\cos\theta - v_l^2\rho_l(1-\alpha)\frac{dA}{dz} - AF_{l,wall} + AC_i|v_r|v_r - Av_i\Gamma \tag{12}$$

e) energy conservation for liquid phase:

$$A\rho_l(1-\alpha)\left(h_l+\frac{3v_l^2}{2}\right)\frac{dv_l}{dz}-Av_l\rho_l\left(h_l+\frac{v_l^2}{2}\right)\frac{d\alpha}{dz}+Av_l\rho_l(1-\alpha)\frac{dh_l}{dz}=$$
$$Agv_l(1-\alpha)\rho_l\cos\theta-v_l\rho_l(1-\alpha)\left(h_l+\frac{v_l^2}{2}\right)\frac{dA}{dz}+AQ_{il}-A\Gamma\left(h_l+\frac{v_l^2}{2}\right) \quad (13)$$

The above set of equations can be transform into the matrix form:

$$B\frac{d\varepsilon}{dz}=C\,, \quad (14)$$

and it further can be transformer to the following relation:

$$B^{-1}B\frac{\partial\varepsilon}{\partial z}=B^{-1}C\,. \quad (15)$$

The injector may be treated as the momentum exchanger, therefore a key role in the model play the closure equations, especially for variable in momentum conservation equations. The following terms influence on momentum transfer between two phases in the model:

- $\Gamma(v_i-v_k)$ is the momentum transfer between phases at the interface; here Γ is vapour mass condensed. In our case we assume that: $v_i=v_l$ and v_k is the velocity of phase (liquid or vapour).
- $AC_i|v_r|v_r$ describe the frictional stress at the interface. Here: $v_r=v_g-v_l$.
- $A(1-S)C_{VM}\left(v_l\frac{\partial v_g}{\partial z}-v_g\frac{\partial v_l}{\partial z}\right)$ describes momentum transported with virtual mass due to movement of vapour bubbles. Term $(1-S)$ describes influence of flow structure on momentum transfer. The stratification parameter S enables the discussed set of equations is hyperbolic, Drew in [6].
- $Ap_i\frac{\partial\alpha}{\partial z}$ is the term where the so-called interphase pressure is used. In our case the interphase pressure has not a strict physical interpretation and is used in order to ensure the hyperbolic character of the discussed set of equations. For the separated two-phase flows the following relation is proposed by Tiselj in [11]

$$p_i=\alpha(1-\alpha)\Delta\rho g D_h \quad (16)$$

- The stratification parameter S defined by Carlson in [4] and Tiselj in [11] is used in the paper. The parameters C_{VM} and p_i depends on the stratification parameter. For separated flow $S=1$. The consequence of separated flow is diminishing of influence of C_{VM} on momentum transfer as well as increasing of the role of p_i. The following relation is proposed by Tiselj in [11]:

$$S=S_nX_iX_{\rho v}X_\alpha X_{1-\alpha} \quad (17)$$

where the factors describe influence of various effects on the flow structure:
S_n - factor of Kelvin-Helmholtz instability;
X_i - factor of channel inclination;
$X_{\rho v}$ - factor of very high mass fluxes;
X_α - factor of very high or very small void fraction;

Condensation heat transfer plays a key role for the operation of the discussed injector. Based on the systematic experimental investigations Trela and Butrymowicz [12] proposed the following correlation describing condensation heat transfer in the injector:

$$Nu = 210.8943 \cdot 10^{-6}\ \mathrm{Re}_v^{0.8-3.09561\Delta-0.134536X} \\ Ja^{-1.86626+8.948750\Delta-0.067246X}\, Oh^{-0.362097-8.86765\Delta-0.211543X}. \tag{18}$$

in the above equation is used dimensionless water feeding gap thickness:

$$\Delta = \frac{\delta}{D_{th}}. \tag{19}$$

The further details of the model are presented in the report of Butrymowicz et al. [3].

RESULTS OF NUMERICAL CALCULATIONS

Two geometry configurations of the injector are presented in Fig. 3. There is a cylindrical throat of the mixing chamber in the case 'B' while in the case 'A' there is a sharp-edge throat. The case 'A' was investigated previously by the authors in paper [13]. The numerical calculations have been carried out for the geometry of the injector investigated in [2]. The calculations of the operation of steam-water injector have been carried out for the operating parameters used in the experiments [2]. The operating parameters for various geometries are given in Table 1.

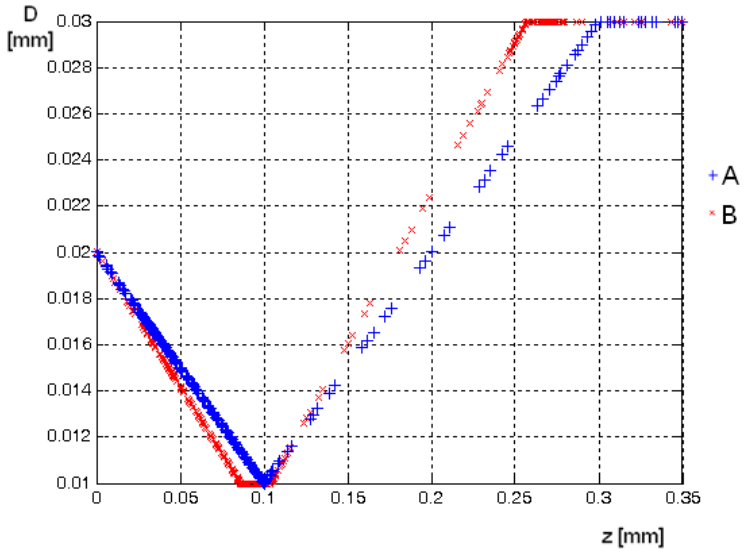

Fig. 3. Geometry of mixing chamber and diffuser with mesh grid of investigated injector. A - injector with sharp-edge throat; B - injector with cylindrical throat

Table 1. Operating parameters for the injector calculations

ejector with sharp-edge throat			ejector with cylindrical throat		
run No.	discharge pressure $[Pa]$	volume rate of liquid $[dm^3/h]$	run No.	discharge pressure $[Pa]$	volume rate of liquid $[dm^3/h]$
A	$p_{out} = 448500$	$\dot{Q}_l = 4895.8$	A	$p_{out} = 492925$	$\dot{Q}_l = 4692$
B	$p_{out} = 349000$	$\dot{Q}_l = 4876.2$	B	$p_{out} = 454552$	$\dot{Q}_l = 4769.6$
C	$p_{out} = 199100$	$\dot{Q}_l = 4000.7$	C	$p_{out} = 388463$	$\dot{Q}_l = 4710.0$
D	$p_{out} = 191700$	$\dot{Q}_l = 3005.8$	D	$p_{out} = 279994$	$\dot{Q}_l = 4777.8$

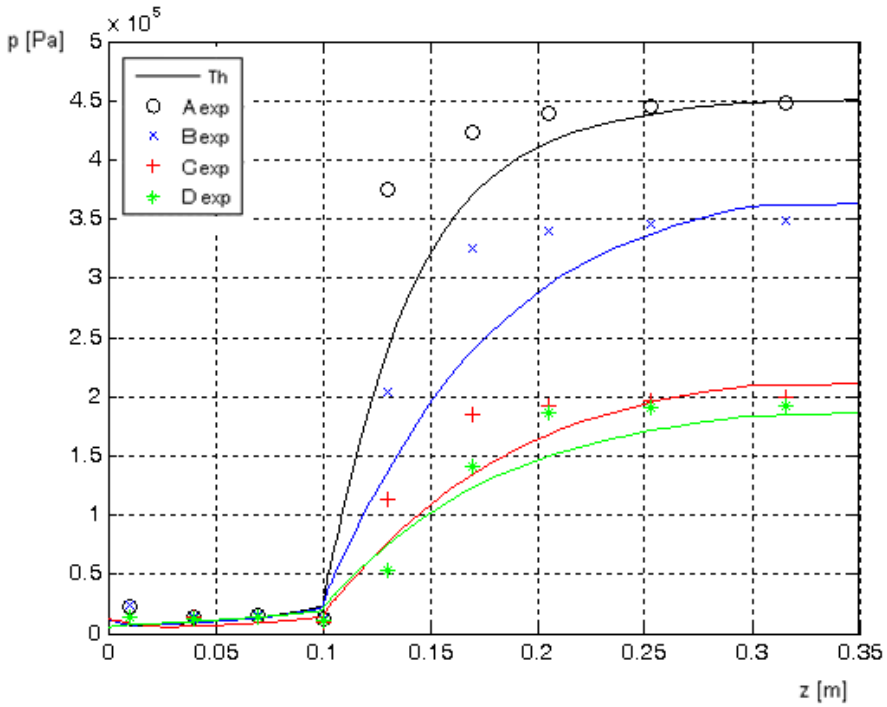

Fig. 4. Comparison of pressure profile calculated (lines) with experimental data for ejector with sharp-edge mixing chamber throat.

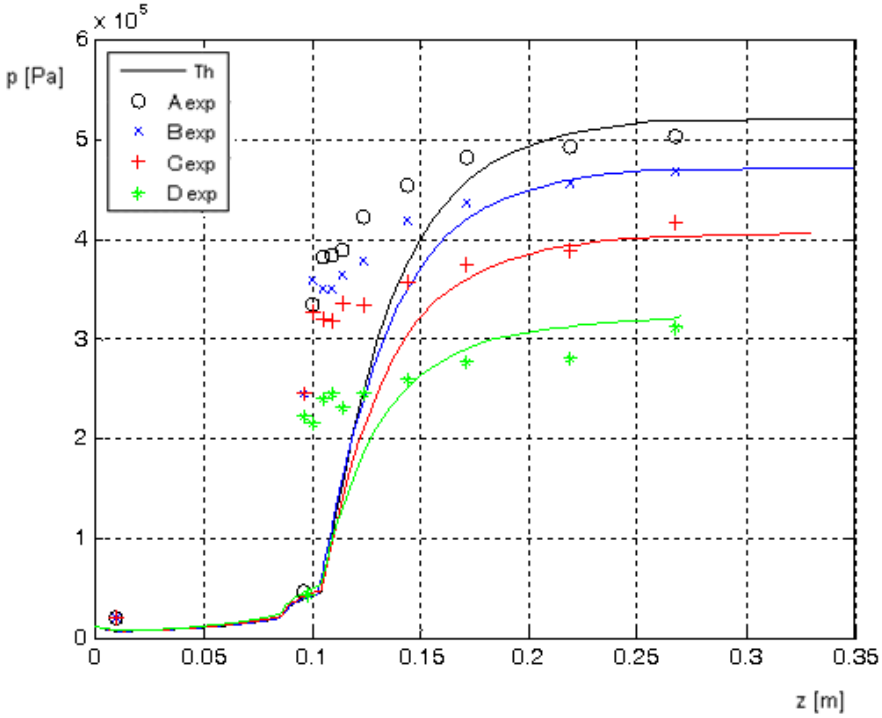

Fig. 5. Comparison of pressure profile calculated (lines) with experimental data for ejector with cylindrical throat of mixing chamber

The calculation results are compared with experimental data in Fig. 4 and 5 for the case of sharp-edge throat and cylindrical throat of mixing chamber, respectively. A reasonably good agreement between calculation results and experiments was shown for the case 'A'. In the case 'B' however, the calculated discharge pressure agrees very well with experiments, there is not very good prediction of the position of condensation shock wave (see Fig. 5). In the case 'B' experiments proved that shock-wave produce relatively higher pressure gradient in comparison with case 'A' which has been also obtained in presented calculations.

CONCLUSIONS

Two-fluid model have been applied to calculate pressure distribution in two-phase injector along with a set of closure equations used in the WAHA-3 code [11]. There is reasonably good agreement between experimental data and calculation results. However, there is a clear need to improve stratification model in order to better describe pressure rise within condensation shock wave, especially in the case of the injector with cylindrical throat of the mixing chamber.

NOMENCLATURE

A	-	surface area cross-section, m^2
B	-	Matrix, see Eq. (14)
c	-	specific heat, J/(kg·K)
C	-	source-terms vector
C_i	-	interfacial friction coefficient
C_{VM}	-	virtual mass coefficient, kg/m^3
D	-	diameter, m
e	-	specific total energy, J/kg
F	-	volume specific wall friction force, N/m^3
g	-	gravity acceleration, kg/s^2
h	-	specific enthalpy, J/kg
h_{fg}	-	specific latent heat of vaporisation, J/kg
Ja	-	Jacob number, $c_{p,l}\left(T_g - T_l\right)/h_{fg}$
Nu	-	Nusselt number $\beta D/\lambda_l$
Oh	-	Ohnesorge number $\mu_l/\sqrt{\sigma D\rho_l}$
p	-	pressure, Pa
Re	-	Reynolds number $\rho v D/\mu$
S	-	stratification factor
v	-	velocity, m/s
Q	-	heat transfer rate per unit of volume [W/m^3]
X	-	Martinelli parameter;
x	-	quality
z	-	spatial coordinate, m

Greek symbols

α	-	void fraction;
β		heat transfer coefficient, $W/(m^2\cdot K)$
δ	-	liquid gap thickness, m
ε	-	vector of state variables
λ	-	thermal conductivity, W/(m·K)
Γ	-	vapor generation rate, $kg/(m^3\cdot s)$
θ	-	asimuth angle
μ	-	dynamic viscosity, kg/(m· s)
ρ	-	density, kg/m^3
σ	-	surface tension, N/m

Subsripts

g	-	gas
i	-	interface
l	-	liquid
r	-	relative quantity

s - saturation
th - throat.

REFERENCES

1. Bestion D. (2000) The phase appearance and disappearance in the CATHARE code, *Trends in Numerical and Physical Modeling for Industrial Multiphase Flows*, Cargase, France, pp. 1-10.
2. Buła M., Kwidziński R., Karwacki J., Trela M. (2003) Experimental investigations of distributions of temperature and pressure in stem injector (in Polish), *Technical Report of the Institute of Fluid-Flow Machinery,* No. 3448/2003, Gdansk, Poland.
3. Butrymowicz D., Matysko R., Angielczyk W. (2008) Application of two-fluid model for modelling of supercritital two-phase injector (in Polish), *Technical Report of the Institute of Fluid-Flow Machinery,* Gdansk, Poland.
4. Carlson K. E. et al. (1990) Relap5/Mod3 Code Manual, Vol. 1-7, *Nureg/CR-5535*, EG&G Idaho, Idaho Falls.
5. Cattadori G., Galbiati L., Mazzocchi L., Vanini P. (1995) A single-stage high pressure steam injector for next generation reactors: test results and analysis, *Int. Journal of Multiphase Flow*, Vol. 21, No 4, pp 591-606.
6. Drew D., Cheng L., Lahey R.T. (1979) The analysis of virtual mass effects in two-phase flow *Int J. Multiphase Flows*, Vol. 5, pp. 233-242.
7. Narabayashi T., Ohmori S., Mori M., Asanuma Y., Iwaki C. (2006) Development of multi-stage steam injector for feedwater heaters in simplified nuclear power plant, *JSME Journal*, pp. 368-376.
8. Ishii M., Hibiki T.: Thermo-Fluid dynamics of two-phase flow. *Springer* 2006
9. Pokharna H., Mori M., Ransom V.H. (1997) Regularization of Two-Phase Models: A comparison of Numerical and Differential Approaches. *Journal of Computational Physics* 134, pp. 282-295.
10. Prosperetti A., Satrape J.V.(1990) Stability of two-phase flow models. The IMA volumes in mathematics and its applications, Vol. 26, *Springer-Verlag*, New York.
11. Tiselj I. et al. (2004) WAHA3 Code manual. JSI Report, Ljubljana.
12. Trela M., Butrymowicz D. (2004), Investigations of heat transfer in supersonic steam-water injector, *Proceeding of the Int. Conference on Heat Transfer and Renewable Sources of Energy*, Międzyzdroje, Poland.
13. Butrymowicz D., Matysko R., Angielczyk W., Trela M. (2008) Model of Supercritical Two-phase Steam-water Injector, *5th International Conference on Transport Phenomena in Multiphase Systems*, Białystok, Poland, Vol. 2, pp. 411-415.

VAPORISATION OF HFC REFRIGERANTS AT HIGH TEMPERATURE

D. Del Col*, E. Lunardi, A. Padovan
Dipartimento di Fisica Tecnica
University of Padova, Padova, Italy

ABSTRACT. Several correlations are available in the open literature for computing the heat transfer coefficient during vaporisation inside plain channels. With respect to halogenated refrigerants, these correlations are usually compared to data taken in a limited range of saturation temperature and reduced pressure. More recently, the adoption of new refrigerants, such as high pressure HFCs and carbon dioxide, requires to largely extend the pressure range of application of such correlations. Besides, the design of evaporators for some heat pumping applications, where evaporation temperatures are set at higher values as compared to usual evaporating temperatures in air-conditioning, requires proper validation of the computing methods.
The present paper presents two sets of heat transfer coefficients measured at high saturation temperature in a 8 mm internal diameter tube with R134a and R410A. This database is characterized by reduced pressure spanning between 0.19 and 0.53. Mass velocity ranges between 200 and 600 kg $m^{-2}s^{-1}$ and heat flux between 14 and 31 kW m^{-2}. Present data are compared against four predicting models.

Keywords: *vaporisation, refrigerants, high pressure*

INTRODUCTION

Much research has been done in the field of in-tube flow boiling in the last decades and much experimental data regarding flow boiling in plain channels is now available, covering a large number of fluids. Nevertheless, with regard to halogenated refrigerants, most flow boiling data sets refer to a narrow range of saturation temperatures, which is typical of common refrigeration and air-conditioning applications. This also leads to a limited range of reduced pressure in the refrigerant vaporisation data sets.
Nowadays, the adoption of new refrigerants, such as carbon dioxide, with different thermodynamic and thermophysical properties, represents a challenge to the capability and accuracy of previous established correlations. In the case of carbon dioxide, for instance, 2°C saturation temperature corresponds to 3670 kPa saturation pressure and 0.5 reduced pressure, which is far higher as compared to common halogenated refrigerants.
An example of high evaporating temperature application of HFC refrigerants is represented by the heat pump clothes dryers, where the evaporating refrigerant subtracts heat from the hot air stream and thus the evaporating temperature can reach higher values as compared to conventional air-conditioning applications. In the recent years, there is an increasing interest on heat pump dryers due to the significant energy savings compared to standard electric resistance dryers.
A higher operating saturation pressure results in high vapour density, low surface tension, high vapour viscosity and low liquid viscosity, and thus yields flow boiling heat transfer and two-phase

* Corresponding author: Dr. D. Del Col
Phone: + (39)-049-8276891, Fax: + (39)-049-8276896
E-mail address: davide.delcol@unipd.it

flow characteristics quite different from those of conventional data. High pressure and low surface tension have major effects on nucleate boiling heat transfer characteristics.
The present paper reports new data, measured during flow boiling of R134a and R410A at high saturation temperature, which is interesting both for practical applications and for models assessment.
The heat transfer coefficients were measured during flow boiling of halogenated refrigerants inside a 8 mm plain copper tube. The test section is a counter flow tube-in-tube evaporator, where the refrigerant flows in the inner tube while the cooling water flows in the annulus.
This new data is compared against some models available in the literature with the aim of discussing the capability and the accuracy of those models in the prediction of the heat transfer coefficient for a wide range of reduced pressure. They are the correlations by Gungor and Winterton [1], Liu and Winterton [2], Kandlikar [3] and Wojtan et al. [4, 5].

EXPERIMENTAL APPARATUS

A schematic of the apparatus is provided in Figure 1. The experimental facility consists of two loops: the refrigerant loop and the water loop. In the first loop the refrigerant is pumped as subcooled liquid and then it is heated, and in some cases partially evaporated, in the preheater to achieve the desired quality at the inlet of the test section. The refrigerant enters the tube side of the test section at a known mass velocity and vapor quality and then it is vaporised against the cold water flowing in the annulus. After the two-phase mixture leaves the test section and goes to a braised plate type condenser, where it is fully condensed and subcooled. A bladder accumulator connected to a nytrogen bottle and a pressure regulator are installed in the refrigerant loop. The refrigerant flow can be independently controlled by a magnetic coupled gear pump.
The inlet vapor quality to the test section is determined by the heat extracted in the preheater, which can be controlled varying water temperature and flow rate. In the same way, the heat transfer rate in the test section can be varied by adjusting water temperature and flow rate. Thus vapor quality, mass velocity, and heat flux can be independently controlled.
The preheater and the test section are coaxial tube-in-tube heat exchangers, in which the refrigerant flowing inside the tube is heated and vaporised by hot water flowing in the annulus side. In the hot water circuit, an electrical heater supplies the water with the power transferred to the refrigerant. A by-pass system is used to vary the water flow rate. Water flow rates are measured by magnetic type flow meters.
The temperature of the hot water entering the preheater and the test section is controlled by a secondary water circuit. The water from the test section and from the electric boiler are mixed together in a storage tank, where the water temperature is maintained constant. Thermostatic control of the water is accomplished by adjusting the electrical power supplied to the heater.
The test section is divided into two different parts: a pre-conditioning section around 300 mm long, where the refrigerant flow, under vaporisation, achieves a fully developed flow regime, and the measuring section, around 1.0 m long, in which the heat transfer coefficient is measured. This structure is obtained using a single 1.6 m long inner tube and two separate heating water jackets, connected in series on the water side.
The inner tube, which is the test tube, is instrumented with eight copper-constantan (type T) thermocouples embedded in its wall to measure surface temperature. The thermocouples are inserted and soldered into four equidistant axial groves. Four thermocouples are located 100 mm past the inlet of the measuring section. The other four thermocouples are located 100 mm before the outlet.
The water temperature change in the test tube is measured by a four junction copper-constantan thermopile inserted into appropriate mixing chambers. A metal helix is wound around the test tube inside the annulus, in order to avoid stratification in the water flow and to get high heat transfer coefficient on the water side together with appropriate values for the water temperature decrease.

Two digital strain gauge pressure transducers (absolute and differential transducers) are connected to manometric taps to measure the vapour pressure upstream and downstream of the test tube. Refrigerant temperatures at inlet and outlet of the test section are measured by means of adiabatic sections, with thermocouples inserted into both the refrigerant flow and the tube wall.
The heat flow rate trasnferred in the test tube is derived from an enthalpy balance on the heating water side. The average heat transfer coefficient α is obtained from the equation:

$$\frac{q}{A} = \alpha \frac{(T_{w1} - T_{w2})}{ln \frac{T_{w1} - T_s}{T_{w2} - T_s}}$$

where q is the heat flow rate exchanged in the tube, A is the heat transfer surface area, T_s is the mean saturation temperature, T_{w1} and T_{w2} are the wall temperatures at inlet and outlet.
Enthalpy change and vapour quality change in the test section are obtained from the heat flow rate and the refrigerant mass flow rate, which is measured by a Coriolis effect mass flow meter having an accuracy of 0.4% of the measured value and inserted downstream of the pump.
All the thermocouples were calibrated using a bath with a Kaye reference thermometer (accuracy 0.02°C). The average accuracy for the thermocouples is estimated to be equal to 0.05°C. For the thermopiles, the average accuracy is around 0.03°C. Comparison between flow temperature and wall temperature inside the adiabatic sections gives a maximum deviation of 0.04 K.
The refrigerant pressure is measured at the inlet of the test section by a digital strain gauge transducer with an accuracy of ±2 kPa for low pressure fluids and ±7 kPa for high pressure fluids.
Experimental heat transfer coefficients are reduced from the measured values of saturation temperature and wall temperature. The saturation temperature is obtained from the pressure and is compared to the refrigerant temperature directly measured in the adiabatic sections before and after the test section. When saturated refrigerant flows in the tube, the difference between saturation temperature determined from pressure and directly measured refrigerant temperature was within the experimental uncertainty of the two sensors. For pure fluids, the two values differ by less than 0.1°C at high mass velocity. Higher deviations are found at low vapour quality, and are probably due to non-equilibrium in the flow and to local sub-cooling at the inlet of the test section. Since an important contribution to the experimental uncertainty is associated to the determination of the saturation temperature, the saturation to refrigerant temperature difference has been compared to the wall superheat for each test run: the data points characterized by ratios of temperature difference (saturation minus refrigerant) to wall superheat higher than 5% have not been considered in the present work.

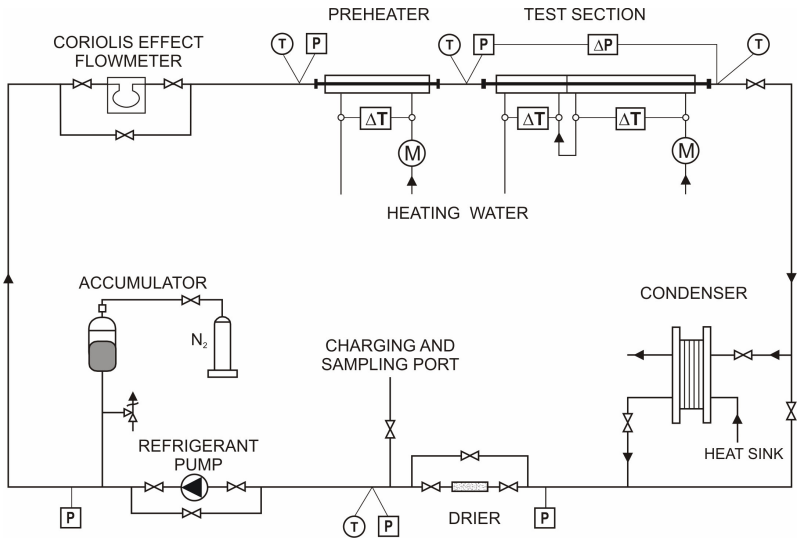

Figure 1. Sketch of the test rig

Table 1
Accuracy for sensors and parameters

Temperature	± 0.05°C	Temperature difference	± 0.03°C
Refrigerant flow rate	± 0.4%	Heat flow rate	± 4.6%
Vapour quality	± 0.05	Heat transfer coefficient	± 7.6%

The heat flux transferred to the refrigerant is derived from an enthalpy balance on the water side. Water flow rates in the test section and the preheater are measured by magnetic-type flow meters with an accuracy around ± 0.5% of the measured value. A Keithley data acquisition system is used to acquire the data.
The average uncertainty for the heat flow rate is around 4% while the average uncertainty for the heat transfer coefficient is around 6%. It was estimated from a propagation of error analysis that the heat transfer coefficients were measured to an accuracy ranging between 4.7 and 7.6 %. A list of accuracies for sensors and parameters is reported in Table 1.

Table 2
Experimental conditions of the present database

	G [kg m^{-2} s^{-1}]	q [kW m^{-2}]	x [/]	p_{RED} [/]
R134a	200-600	13.4-31.2	0.08-0.85	0.19-0.29
R410A	200-400	15.2-25.9	0.12-0.83	0.49-0.53

TEST RESULTS

The experimental data used in the present paper was taken during flow boiling of R134a and R410A inside a 8 mm plain commercial copper tube. The experimental heat transfer coefficients are quasi-local values, obtained during saturated flow boiling from the direct measurement of the wall temperature.
The experimental operating conditions in the present database is reported in Table 2. Mass velocity ranges from 200 up to 600 kg m^{-2}s^{-1}, the heat flux goes from 14 to 31 kW m^{-2} while the reduced pressure spans between 0.19 and 0.53. Data points cover the entire range of vapour quality. The wall superheat goes from 2.5 to 8 K.
R134a and R410A present different thermophysical properties: in fact at 40°C saturation temperature the reduced pressure is considerably higher for R410A, leading to a much higher vapor density (103 kg m^{-3} for R410A vs. 50 kg m^{-3} for R134a) and much lower vapour velocity in the tube, at same mass velocity.
Figure 2 reports the heat transfer coefficients measured during flow boiling of R134a at around 43°C saturation temperature, corresponding to 0.29 reduced pressure. Mass velocity G spans between 200 and 600 kg m^{-2}s^{-1}, while heat flux q goes from 14 to 30 kW m^{-2} . As one can see, the heat transfer coefficient is approximately constant up to 0.6 vapour quality, no matter what the mass velocity and heat flux conditions are. Recently, R134a data have been reported by Silva Lima et al. [6], showing the dependence of the heat transfer coefficients on saturation temperature (ranging between 5 and 20°C in their data). In their work it can be seen that the experimental *HTC* trend vs. vapour quality becomes more flat when increasing saturation temperature.
For the test runs performed at 400 kg m^{-2}s^{-1} and 26.5 kW m^{-2} average heat flux, the heat transfer coefficient shows an abrupt decrease at 0.85 vapor quality, due to the dryout of the liquid film at the wall. The strong effect of the heat flux on the heat transfer coefficient was evidenced by comparing data sets at same mass velocity but different heat flux.
In the test runs at G200-q14 and G400-q26.5 there is a local minimum, since the heat transfer coefficient decreases at low values of vapour quality and then increases with vapour quality. The

presence of this minimum is the result of the competition between nucleate and convective boiling mechanisms and was noted by other studies in the literature [6]. As the vapour quality increases, the flow pattern is expected to be annular type, the liquid film thickness decreases and the vapour velocity increases. Both phenomena promote heat transfer increase. By comparing the R134a test runs at *G*400 and *G*600, which have been performed at similar values of heat flux, one can see that heat transfer coefficients increase with mass velocity and the heat transfer increase due to mass flux increase depends on the vapour quality, showing a stronger effect of the convective mechanism at higher *G*.

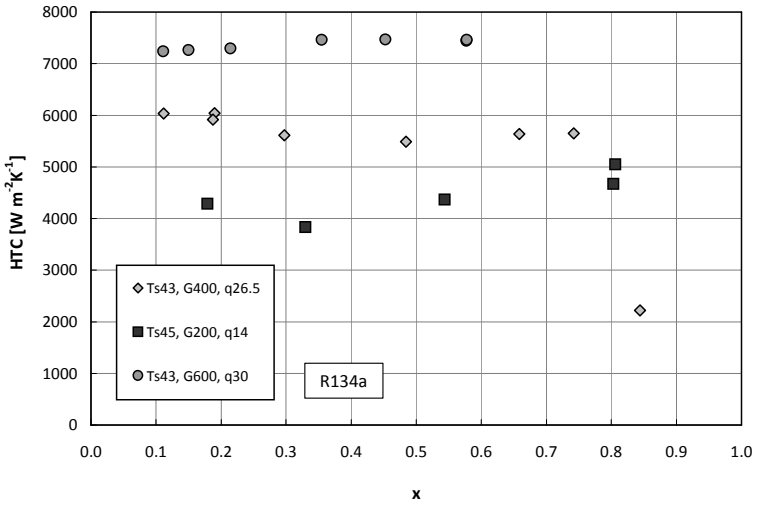

Figure 2. R134a heat transfer coefficients vs. vapour quality. Average values of saturation temperature *Ts*, mass velocity *G* and heat flux *q* are reported for each set.

Some values of heat transfer coefficient measured with R410A at around 40°C saturation temperature are plotted in Figure 3. Test results are reported for two values of mass velocity and heat flux. As compared to Figure 2, the experimental heat transfer coefficient diminishes when increasing vapour quality, for the entire range. This trend is not usual for halogenated refrigerants, whereas an increase of the heat transfer coefficient with vapour quality is usually expected. Nevertheless, this trend is similar to what one measured for the high pressure fluid carbon dioxide [7, 8]. Both papers [7, 8] have shown that the effect of mass velocity on the heat transfer coefficient of CO_2 is negligible at low vapour quality (up to 0.4), while the heat transfer is heat flux dependent, suggesting that the nucleate boiling mechanism is dominant in this region. For carbon dioxide, the drop in heat transfer coefficient is due to the large dominance of nucleate boiling at low vapour qualities and to partial dryout of the liquid film. The dominance of nucleate boiling at low qualities is caused by the thermophysical properties of the fluid, such as a low surface tension and a low liquid to vapour density ratio. These parameters are compared for R134a, R410A and CO_2 in Table 3, providing this way an explanation for the unusual behaviour of R410A and its similarity to CO_2 heat transfer experiments.
The *HTC* difference between the two test runs reported in Figure 3 is mainly due to the different heat fluxes, at low vapour quality, while at higher vapour quality both heat flux and mass flux may play a role since the rise of mass flux provides an enhancement of convective evaporation.

Table 3
Properties of saturated vapour

	R134a @ 40°C	R410A @ 40°C	CO_2 @ 0°C
Liquid to vapor density	22.9	9.4	6.4
Surface tension (N $m^{-3} \cdot 10^3$)	6.1	3.2	4.5

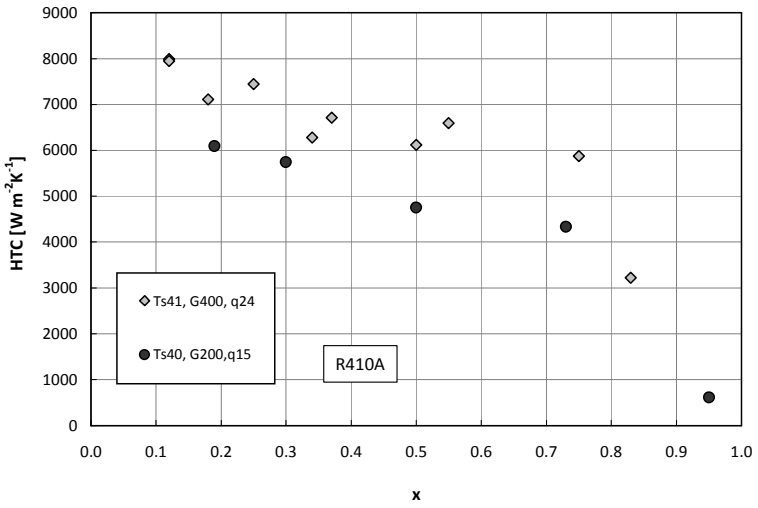

Figure 3. R410A heat transfer coefficients vs. vapour quality. Average values of saturation temperature *Ts*, mass velocity *G* and heat flux *q* are reported for each set.

ASSESSMENT OF CORRELATIONS

Four well-known models have been chosen for comparison with the present database. They are the correlations by Gungor and Winterton [1], Liu and Winterton [2], Kandlikar [3] and Wojtan et al. [4, 5]. All these models consider the Chen's basic postulate, which associates convective and nucleate boiling heat transfer mechanisms in the flow boiling heat transfer coefficient prediction.
The comparison was made for all the data points, excluding the tests with dryout and mist flow regimes for which those methods, except the one by Wojtan et al. [5] is not applicable. In total, 34 runs with R134a and 16 runs with R410A are compared against the models.
Table 4 reports average, mean absolute and standard deviations obtained from the comparison between experimental and calculated heat transfer coefficients for the two data sets.
Both the correlations by Gungor and Winterton [1] and by Liu and Winterton [2] are based on the superposition of the convective and the nucleate contribution. On average, the correlation by Gungor and Winterton underpredicts the experimental data by 20 % (Figure 4). The prediction capability is not significantly affected by any parameter (vapour quality, mass velocity, heat flux, reduced pressure), as suggested by the low value of standard deviation for both data sets. The correlation by Liu and Winterton provides a better agreement in the case of R134a data, but overpredicts most R410A experimental heat transfer coefficients (Figure 5).
When using the model by Wojtan et al. [4, 5], the prediction of the heat transfer coefficient is based on a diabatic two-phase flow pattern map. This map was significantly updated from previous work by Kattan et al. [9]. The stratified-wavy region has been subdivided into three sub-zones and the annular-to-dryout and dryout-to-mist transition curves have been added. The heat transfer coefficients are calculated from attribution of appropriate wet and dryout perimeters, obtained from the relative flow pattern. The authors have proposed an asymptotic model with exponent n = 3 for convective and nucleate boiling term of the heat transfer coefficient for the wet perimeter. The model by Wojtan et al. (Fig. 6) shows a similar behaviour as the Liu and Winterton correlation, providing a fair agreement with R134a data, but overestimating R410A by more than 20%.
Kandlikar [3] proposed a correlation for saturated two-phase flow boiling heat transfer inside horizontal and vertical tubes, which includes a fluid dependent parameter in the nucleate boiling term. Kandlikar [3] provided the fluid parameter for R134a which is equal to 1.63. The value for the azeotropic mixture R410A is taken from Wattelet et a. [10]: they determined a value of 3.3 using their data set. Although the average deviation between experiments and calculated values is low for both fluids, the Kandlikar correlation is not able to catch the experimental trend and the values of standard deviation are the highest among those models.

Table 4
Comparison between experiments and models

	R134a			R410A		
	e_R [%]	e_{AB} [%]	σ_N [%]	e_R [%]	e_{AB} [%]	σ_N [%]
Gungor and Winterton	-21,2	21,2	10,5	-18,7	18,7	8,9
Liu and Winterton	-14,0	14,2	9,0	22,4	24,3	20,7
Wojtan et al.	-12,3	16,4	14,0	27,3	28,0	22,1
Kandlikar *(*)*	-4,4	14,7	18,7	7,7	25,4	31,1

(*) The fluid dependent parameter for R410A in the Kandlikar correlation is taken from Wattelet et al. [10].
(**) $e_R = (1 / Np) \Sigma [(Nu_{CALC} - Nu_{EXP}) / Nu_{EXP}] \cdot 100$ (av. deviation); $e_{AB} = (1 / Np) \Sigma [| Nu_{CALC} - Nu_{EXP} | / Nu_{EXP}] \cdot 100$ (mean abs. deviation); $\sigma_N = \{ [\Sigma (e - e_R)^2] / (Np - 1) \}^{1/2}$ (standard deviation); $e = [(Nu_{CALC} - Nu_{EXP}) / Nu_{EXP}] 100$

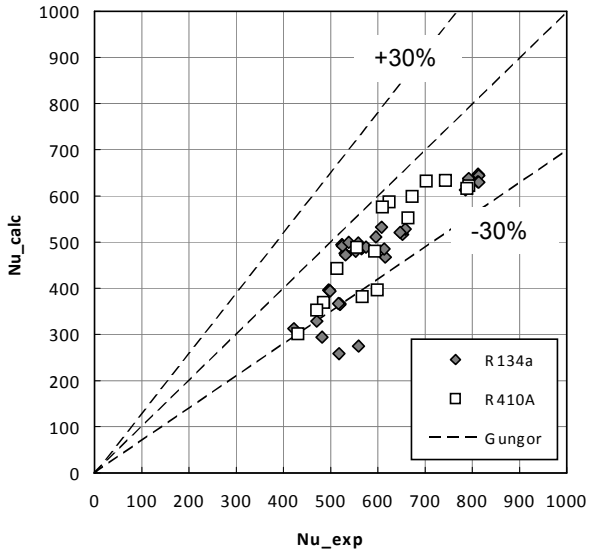

Figure 4. Comparison of experiments with model by Gungor and Winterton [1].

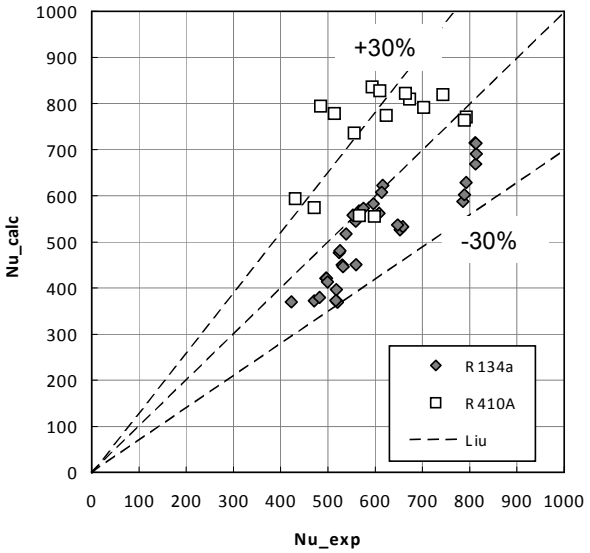

Figure 5. Comparison of experiments with model by Liu and Winterton [2].

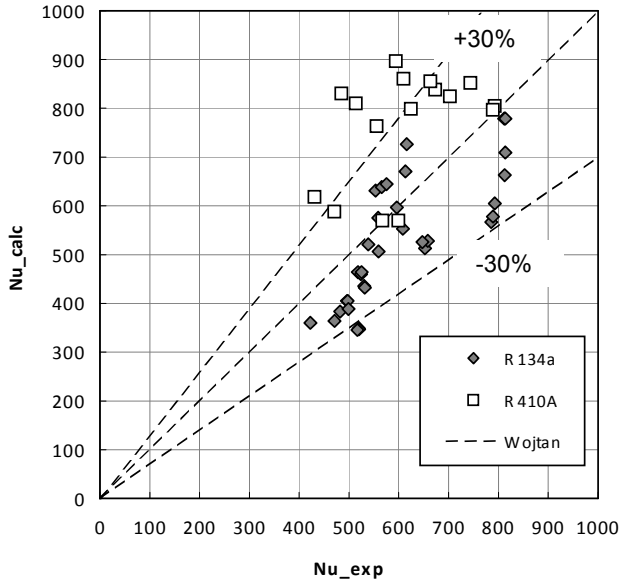

Figure 6. Comparison of experiments with model by Wojtan et al. [4, 5]

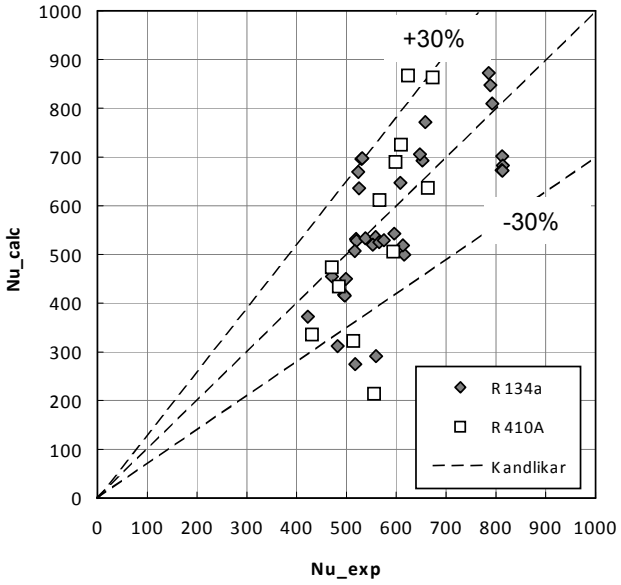

Figure 7. Comparison of experiments with model by Kandlikar [3].

CONCLUSIONS

New heat transfer data measured during flow boiling of R134a and R410A at high saturation temperature, and thus high reduced pressure, are presented in this paper. Experimental trends of heat transfer coefficient are roughly constant (R134a) or decrease (R410A) with vapor quality, showing that nucleate boiling must play a key role at these conditions. Experiments are compared against four correlations available in the open literature. Gungor and Winterton correlation shows little scattering but a general underprediction of experimental data. Both the models by Liu and Winterton and Wojtan et al. overpredict R410A heat transfer coefficients.

NOMENCLATURE

G	mass velocity [kg m^{-2} s^{-1}]
HTC	heat transfer coefficient [W m^{-2} K^{-1}]
Nu	Nusselt number
p_{RED}	reduced pressure
q	heat flux [kW m^{-2}]
T_s	saturation temperature [°C]
x	vapour quality

REFERENCES

1. Gungor K. E., R. H. S. Winterton, 1987, Simplified general correlation for saturated flow boiling and comparisons of correlations with data, Chemical Engineering Research & Design, v 65, n 2, p 148-156
2. Liu Z., R. H. S. Winterton, 1991, General correlation for saturated and subcooled flow boiling in tubes and annuli, based on a nucleate pool boiling equation, International Journal of Heat and Mass Transfer, v 34, n 11, p 2759-2766
3. Kandlikar S.G., 1990, A General Correlation for Saturated Two-Phase Flow Boiling Heat Transfer Inside Horizontal and Vertical Tubes, J. Heat Transfer, 112, pp. 219-228.
4. Wojtan L., Ursenbacher T., Thome J.R., 2005, Investigation of flow boiling in horizontal tubes: PartI – A new diabatic two-phase flow pattern map, Int. J. Heat Mass Transfer, 48, p 2955-2969.
5. Wojtan L., Ursenbacher T., Thome J.R, 2005, Investigation of flow boiling in horizontal tubes: PartII – Development of a new heat transfer model for stratified-wavy, dryout and mist flow regimes, Int. J. Heat Mass Transfer, 48, p 2970-2985.
6. Silva Lima R. J., Quibén J. M., Thome J. R., 2009, Flow boiling in horizontal smooth tubes: New heat transfer results for R-134a at three saturation temperatures, Applied Thermal Engineering 29 1289–1298.
7. Oh H.-K., Hak-Geun Ku, Geon-Sang Roh, Chang-Hyo Son, Seung-Jun Park, 2008, Flow boiling heat transfer characteristics of carbon dioxide in a horizontal tube, Applied Thermal Engineering 28, 1022–1030.
8. Yun R., Yongchan Kim, Min Soo Kim, Youngdon Choi, Boiling heat transfer and dryout phenomenon of CO_2 in a horizontal smooth tube, 2003, International Journal of Heat and Mass Transfer 46, 2353–2361.
9. Kattan N., Thome J.R., Favrat D., 1998, Flow boiling in horizontal tubes: Part 3 – Development of a new heat transfer model based on flow pattern, Journal of Heat Transfer, Vol. 120, 156-165.
10. Wattelet J.P., J.C. Chato, B.R. Christoffersen, J.A. Gaibel, M. Ponchner, P.J. Kenny, R.L. Shimon, T.C. Villaneuva, N.L. Rhines, K.A. Sweeney, D.G. Allen, T.T. Heshberger, Heat Transfer Flow Regimes of Refrigerants in a Horizontal tube Evaporator, ACRC TR-55, University of Illinois at Urbana-Champaign, 1994.

EXPERIMENTAL EVALUATION OF A DIRECT EXPANSION EVAPORATOR USING MULTIPLE U-TUBE HEAT EXCHANGERS IN PARALLEL

B. Beauchamp[1], L. Lamarche[1,*], S. Kajl[1]
[1]Ecole de technologie supérieure, Montreal, Canada

ABSTRACT. This paper presents the experimental evaluation of a thermostatic expansion valve (TXV) - dry evaporator system using multiple U-tube heat exchangers in parallel. The system studied is part of a commercially available direct expansion ground source heat pump system. When operated in heating mode, this heat pump uses multiple U-tube heat exchangers in parallel and each U-tube is controlled by an independent TXV. Experimental measurement showed that the actual TXV-evaporator system presents TXV hunting and refrigerant flow mal-distribution behaviour. Those phenomena are both known to impact the operating stability and cooling capacity of a heat pump and should not be accepted as normal operating characteristic of a system. Several experimental tests were made to obtain stable operating conditions of the system by adjusting the TXV's static superheat spring of the parallel U-tubes. Despites the attempts made, the system never reached at stable operating behaviour. This undesirable operating behaviour can lead liquid refrigerant entering the compressor and cause damage. Furthermore, cooling capacity and system performance can be severely penalized.

Keywords: *Direct Expansion, Evaporator, Thermostatic expansion valve, Ground heat pump, Ground heat exchanger*

INTRODUCTION

Ground-coupled heat pumps are attractive, efficient systems for residential and commercial air conditioning applications. Vertical direct-expansion ground heat pumps (DX-GCHP) are recently receiving a particular attention since they are considered to have a lower installation cost and similar performance compared to conventional secondary ground loop heat pumps. A DX-GCHP has its evaporator/condenser directly inserted into the boreholes and being an integral part of the refrigeration cycle therefore eliminating the secondary loops components. Furthermore, the drilling cost of a DX-GCHP should be lower than that of a conventional heat pump since the DX ground exchanger is usually smaller as a result of the copper tube used and the phase change flowing fluid [1]. The long remote buried evaporator/condenser needs particular attention to ensure proper system performance as opposed to conventional ground heat pump with a secondary ground loop [2, 3].

* Corresponding author: M. L. Lamarche
Phone: + (1)-514-396-8858, Fax: + (11)-514-396-8530
E-mail address: louis.lamarche@etsmtl.ca

Because of the increasing interest for DX-GCHP and the lack of documentation found in the literature for those systems, it is relevant to conduct detailed experimental studies describing their performance and thermal behavior.

TXV - evaporator system stability was investigated by a number of researchers [4,5,6]. These studies clearly show that it is the combination of the TXV and evaporator characteristics that influences the stability of the control loop system. As noted above, the vertical buried heat exchanger of the type of heat pump studied in the present paper can be constituted of long copper tubing (in the range of 65 to over 110 meters long). Furthermore, each vertical U-tube constituting the evaporator has its independent operating TXV. Several researches have been conducted on refrigerant flow mal-distribution but concerned parallel paths from a manifold after a unique and single TXV [7,8,9]. Therefore, the particular TXV - evaporator configuration experimented in this paper followed with the slow transient heat transfer from the boreholes to the ground was not found to be investigated.

This paper first presents the particular evaporator constituted of multiple parallel U-tubes each controlled by an independent TXV. Followed is an experimental evaluation of the hunting behavior of the TXV - evaporator system for a unique U-tube. Finally, hunting behavior and refrigerant flow mal-distribution of multiple parallel U-tubes are presented.

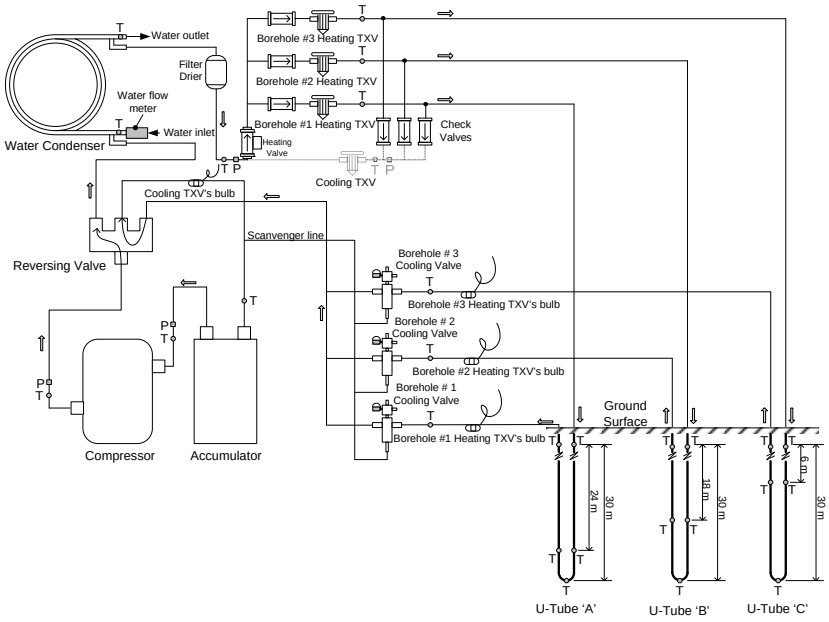

Figure 1. Schematic of the heat pump operated in heating mode

OPERATION OF THE HEAT PUMP IN HEATING MODE

To realize experimental measurements, a commercially available heat pump was instrumented and installed in the laboratories of the university. The system is a direct expansion ground source heat pump with a 10 kW nominal heating capacity using refrigerant R22 as the working fluid. It is a *ground direct expansion-to-water* system. The heat pump is instrumented with 4 refrigerant pressure transducers and 15 refrigerant temperature transducers of type 'K'. Water flow rate is acquired using a turbine type flow meter. The compressor power is acquired using an ammeter probe and a voltmeter. The heat pump is connected to three copper U-tubes of 30 m length each inserted in a different borehole drilled at a 30 degree angle from vertical. Each U-tube includes one

12.7 mm (referred as vapor line) and one 9.5 mm (referred as liquid line) outside diameter tube. Five thermocouples of type 'T' are installed on each U-tube and are located at the inlet, the bottom and the exit of each U-tube and at depths (both pipes) of 24, 18 and 6 meters respectively for U-tube 'A', 'B' and 'C'.

When the heat pump is used in heating mode (figure 1), all the ground loops (so-called evaporator) are activated. The check valves, downstream of the cooling TXV, restrict the refrigerant from flowing through this TXV. Liquid refrigerant passes through the opened heating valve, is throttled through 3 heating TXVs and flows toward the ground loops via the liquid lines. Low pressure refrigerant then vaporizes in the ground loops and flows toward the vapor line header.

As depicted in figure 1, the evaporator is configured with 3 U-tubes connected in parallel and each controlled by an independent TXV. As per manufacturer's instruction, this particular configuration was realized to 'independently' control the refrigerant flow in each U-Tube. However, as it will be presented later, the dynamics behavior of each U-tube is influenced by the operating characteristic of the other U-tubes.

The *Danfoss* thermostatic expansion valves are externally equalized, unbalanced port, ballast charge and are rated at 2.5 kW each. This kind of TXV responds to three forces (figure 2). The spring force (F_s) results from the superheat spring adjustment and tends to close the valve. The superheat pressure force (F_b) results from the remote bulb pressure applied on the effective diaphragm area. This force is applied on the top of the diaphragm and tends to open the valve. The evaporator exit pressure force (F_e) results from the outlet evaporator pressure applied on the effective diaphragm area. This force is applied on the bottom of the diaphragm and tends to close the valve. Furthermore, in an unbalanced port TXV fluctuations in the condenser pressure can influence the power balance and cause instability. In fact, the differential pressure force (F_{dp}) resulting from the high and low side differential pressure force applied on the effective port area tends to open the valve and affects the valve superheat settings.

EXPERIMENTAL CONDITIONS

Based on experimental results previously obtained by the authors, the system operating condition in heating mode presented instabilities. Investigation was therefore necessary to analyse the possible causes of the instabilities. At first instance, experimental tests were conducted for an evaporator configured using only one U-tube. The remaining U-Tubes were kept closed. This configuration is appropriate for analysing the hunting behaviour of a TXV - evaporator system. Finally, experimental tests were conducted for an evaporator configured using 3 U-tubes in parallel to analyse the dynamic control loop nature of such a TXV - evaporator system and possible refrigerant flow mal-distribution.

When conducting the tests, the only parameter that could be externally adjusted is the spring force of the TXVs. When the spring adjustment screw is completely turned counter clockwise, the static superheat spring force is at its minimum setting. Static superheat can be increased but turning the adjustment screw clockwise. As per TXV's manufacturer, one clockwise turn adjustment should result in approximately 2.5 °C increase in operating superheat. The initial TXV spring setting is factory set at 4 turns from the completely turned counter clockwise position.

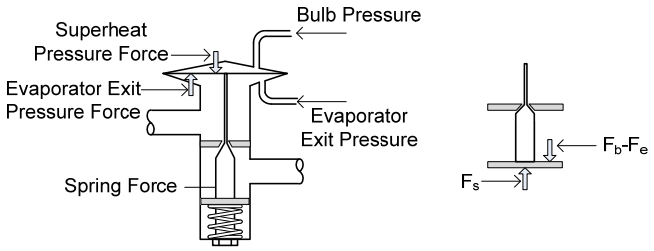

Figure 2. Schematic diagram of the thermostatic expansion valve (TXV)

Evaporator configured using one (1) U-Tube

Experimental tests have been conducted using only one (1) U-tube as depicted in figure (3). Under this configuration, the evaporator is not constituted of parallel branches. The tests have been conducted from an initial spring adjustment screw completely turned counter clockwise. The system was operated continuously and the spring screw was adjusted between 1/2 and 1 turn clockwise after 3 operating oscillations of the TXV were observed or after approximately 10 minutes if not oscillations occurred. Table 1 shows the tests spring screw adjusting parameters. For a spring screw setting varying between 0 and 2 turns, the evaporator outlet superheat is zero degree. A superheat of zero degree is not an appropriate operating condition for the heat pump as this could lead to compressor failure by liquid flooding this component. Furthermore, for the tests realized, the maximum number of turns that could be realized within the operating limits of the system was 8 turns. Over 8 turns, the system reached the maximum allowable high operating pressure (2150 kPa).

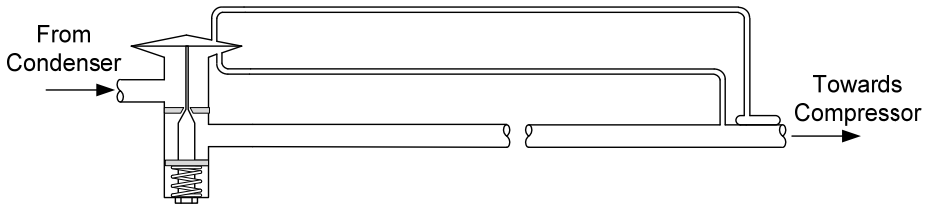

Figure 3. Schematic TXV - evaporator system configured using one U-tube

Table 1
Tests with evaporator configured using (1) one U-Tube: spring screw adjusting parameters

Adjustement No.	Time (minutes)	Number of turn from the completely counter clockwise position
1	0	0
2	33	1
3	43.3	2
4	54.2	3
5	76.7	4
6	98.9	5
7	124.6	6
8	161.6	7
9	195.7	8

The experimental data resulting from the operation of the system (with spring screw setting between 3 and 8 turns) with only one U-tube used in the evaporator are presented in figure 4. When the spring setting varies between 3 to 8 turns, the evaporator outlet superheat modulates severely. The cyclic behaviour of the measured evaporator outlet superheat is known as expansion valve hunting. Hunting is characterized by a cyclic action of the expansion valve resulting in the cyclic overfeeding and

underfeeding of the evaporator with liquid refrigerant. Hunting is known to considerably degrade the refrigerating capacity of the evaporator and to potentially lead to compressor failure by liquid flooding this component. Several possibilities are known to cause expansion valve hunting:

i. Incorrect sensor bulb location.
ii. Over-sized expansion valve
iii. Undersized evaporator tubing
iv. Thermostatic expansion valve adjustment
v. Time lag and transportation lag
vi. Flow mal-distribution in multi-circuit evaporator

For the experimental tests conducted using only one (1) U-tube in the TXV - evaporator system the following causes are not investigated: (i) incorrect sensor bulb location, (ii) over-sized expansion valve and (iii) undersized evaporator tubing. Furthermore, flow mal-distribution in multi-circuit evaporator is not applicable when only one (1) U-tube is used. Therefore, were investigated only: (iv) thermostatic valve adjustment and (v) time lag and transportation lag.

For the test presented, the static superheat spring was adjusted between 0 to 9 turns. It is a common troubleshooting procedure to adjust the static superheat spring when the TXV - evaporator system does not presents normal operating conditions. As depicted in figure 4, stable operating conditions with a minimum (non-zero) superheat value was not achieve. The system operated with either zero degree of superheat or under hunting conditions. Furthermore, high oscillations in the difference between high and low pressure are observed and could have lead to instabilities since the TXV in not a balanced port valve.

Under certain assumptions [5], the dynamic of a TXV - evaporator system can be represented using three different time constants and a transportation lag. The time constants represent the motion of the transition point, the thermal capacity of the tube wall and the TXV itself. It has been noted that it is the combination of all the time constants that can lead to system instabilities. Those time constants delay the time between a change in the TXV mass flow rate and its influence on the evaporator outlet superheat. The transportation lag in the TXV - evaporator system is caused by the time required by the change in refrigerant flow to travel the length of evaporator. It is mainly the evaporator length divided by the velocity of the refrigerant flow. This lag is quite complex to evaluate because of the two-phase flow characteristic. Important transportation lag is nevertheless known to be a cause of instability [4,5].

Based on the experimental results, the combined effects of the time constants and the transportation lag is estimated in the range of 6 to 12 minutes depending of the operating characteristics. Reported time constant [4,5,6], are usually in the order of 5 to 120 seconds. Transportation lag is usually considered to be around 5 seconds.

The experimental results demonstrate that the actual TXV- evaporator system exhibits unusual long time and transportation lag. It is not the scope of this paper to investigate the detailed cause of these particular phenomena. Nevertheless, long evaporator piping and slow transient ground heat transfer are believed to contribute significantly to the important lag observed.

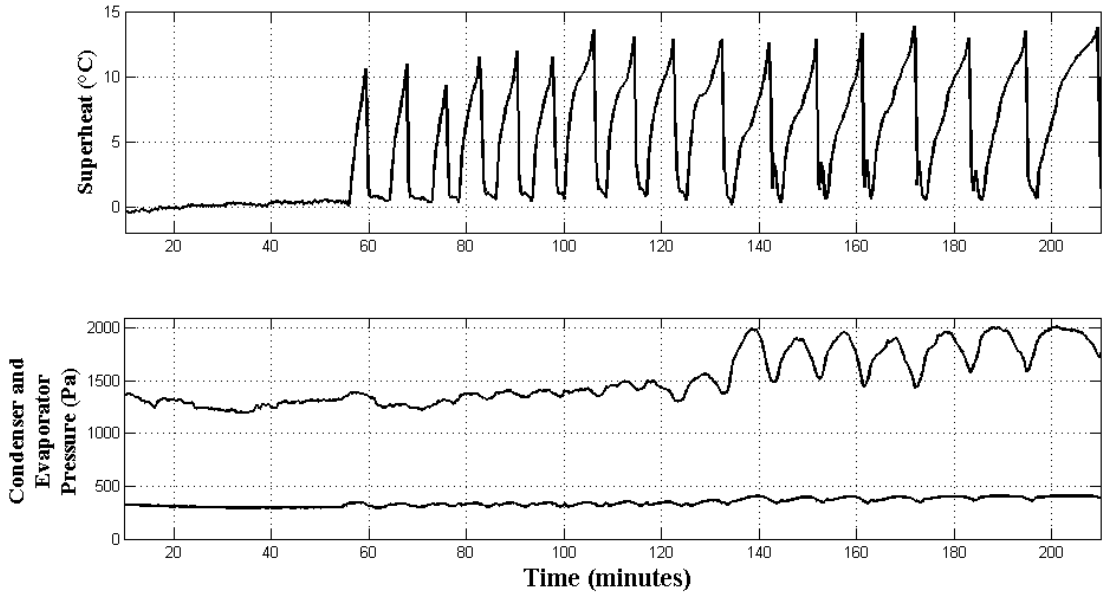

Figure 4. Superheat, Condenser and Evaporator pressures for evaporator tested with one U-tube

Evaporator configured using three (3) U-Tubes

Experimental tests have been conducted using three (3) U-tubes as depicted in figure (5). The tests have been conducted from TXV's initial spring adjustment screw turned 4 turns from the completely counter clockwise position. Under this configuration, the evaporator is constituted of parallel branches and is as per manufacturer's setting. The system was operated continuously and the different TXV spring screws were slowly adjusted in order to reach a global stable operation of the system and the three (3) U-tubes.

The U-tubes outlet superheats are evaluated with the measured outlet temperature (T_A, T_B and T_C) and the evaluated saturation temperature at the corresponding suction line pressure (P_{suc}). The suction line superheat is evaluated with the measured suction line temperature (T_{suc}) and the evaluated saturation temperature at the corresponding suction line pressure (P_{suc}). The suction line superheat is the resulting superheat from the operation of the three U-tubes and is of importance to insure no liquid refrigerant is directed towards the compressor.

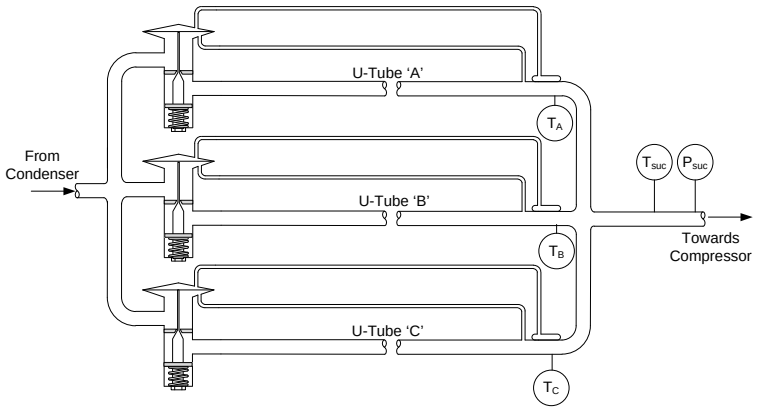

Figure 5. Schematic of the heat pump operated in heating mode

The first test series was conducted during 60 minutes. The system was operated continuously and was set as per manufacturer's instructions. No adjustment of the static superheat was realized.

Figure 6 shows the operating superheat of each U-tube and the common suction line. U-Tube 'A' and 'B' exhibit a thermostatic valve hunting behaviour as depicted in their excessively modulating outlet superheat. The quasi constant evaluated operating superheat of U-Tube 'C' indicates that the refrigerant flow in this U-Tube is low or non-existent. The common suction line superheat is observed to be a function of the operating characteristic of U-Tube 'A' and U-Tube 'B' only. This flow mal-distribution behaviour in the parallel paths was observed on several experimental tests realized by the authors.

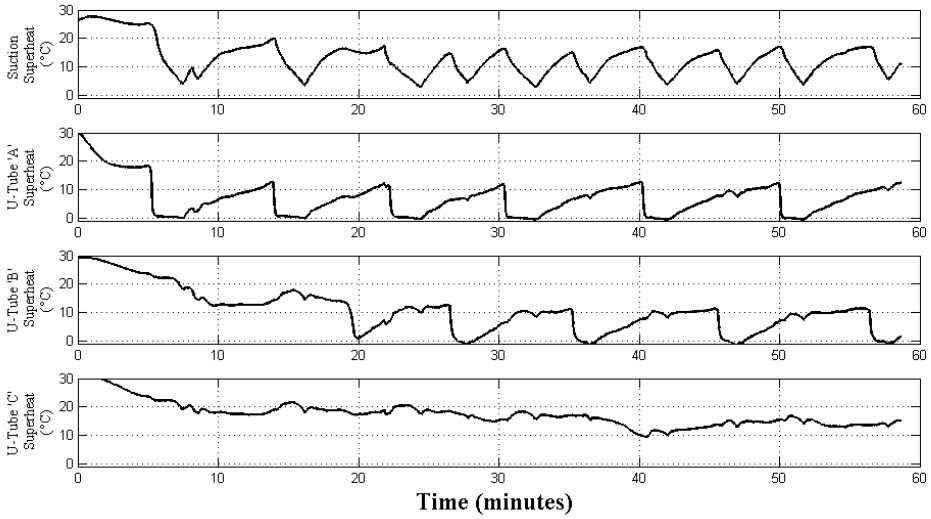

Figure 6. Operating superheat of first test series using multiple U-Tube

The second test series was conducted during about 720 minutes (12 hours). The system was operated continuously and the TXVs static superheats were manually adjusted with the purpose of obtaining a stable operating superheat for each U-tube and the common suction line. The results in figure 7 indicate that a stable operating condition was never reached. The three TXV presents an undesirable hunting characteristic with superheat oscillating between zero to about 18 °C. The common suction line superheat was also oscillating but the minimum observed value was about 5 °C therefore indicating that compressor was not fed with liquid refrigerant. The operational superheats measured again suggest that refrigerant flow mal-distribution is present in the evaporator parallel paths.

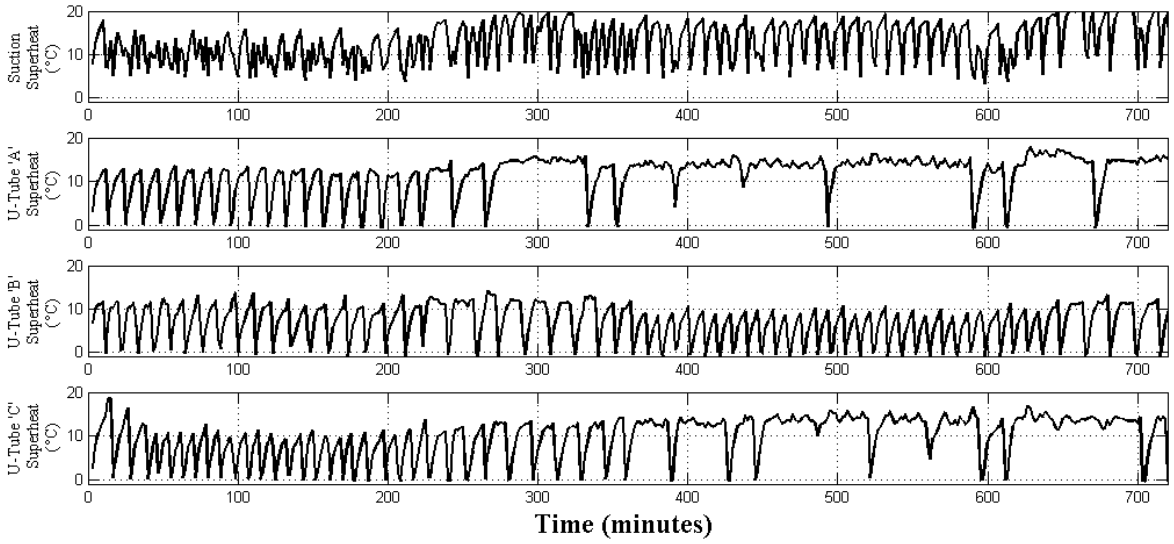

Figure 7. Operating superheat of second test series using multiple U-Tube

CONCLUSIONS

The experimental evaluation of a thermostatic expansion valve (TXV) - dry evaporator system using multiple U-tube heat exchangers in parallel was presented. The observed operating characteristic clearly indicate that this system present severe TXV hunting and refrigerant flow mal-distribution in the evaporator parallel paths. These two undesirable operational conditions are known to penalize and degrade the thermal performance of an evaporator and the whole refrigeration system. Further experimental and theoretical researches are now undertaken to investigate the detailed causes of these particular phenomena.

REFERENCES

1. Mei V.C. and Baxter V.D., *Experimental study of direct-expansion ground coil heat exchangers*. ASHRAE Trans. 96, 1990, 821–828.
2. HALOZAN H. and RIEBERER R., *Direct-expansion ground-coupled heat pumps*. IEA Heat Pump Centre Newsletter, Vol. 23, No. 4. 2005, 30-32.3.
3. HALOZAN H. and Svec O., *Heat pump systems with direct expansion ground coils.* Final Report of Annex 15, IEA, Paris.
4. Ghaled A.I. *Effect of sudden changes in evaporator external parameters on a refrigeration system with an evaporator controlled by a thermostatic expansion valve,* International Journal of Refrigeration, Volume 24, Issue 6, September 2001, Pages 566-576
5. Stoecker W.F. *Stability of an evaporator - expansion valve control loop*. Fourth techinical session of tha ASHRAE 73d Annual meeting in Toront, On. Canada, no. 2007, June 1966.
6. Broersen P.M.T. *Hunting of evaporators controlled by a thermostatic expansion valve*. Transactions of the ASME, Journal of dynamic system measurement and control 1980, Vol. 102, 130-135.
7. Kim, J.-H. et al., *A hybrid method for refrigerant flow balancing in multi-circuit evaporators: Upstream versus downstream flow control,* International Journal of Refrigeration (2009), doi:10.1016/j.ijrefrig.2009.01.013
8. Kim J.H. *Evaluation of a hybrid method for refrigerant flow balancing in multi-circuit evaporators*, International Journal of Refrigeration (2009), doi:10.1016/j.ijrefrig.2009.01.016
9. Jianying G. *Effects of air flow maldistribution on refrigeration system dynamics of an air source heat pump chiller under frosting conditions.* Energy Conversion and Management, Volume 49, Issue 6, June 2008, Pages 1645-1651

AEES-12

ExHFT-7
28 June – 03 July 2009, Krakow, Poland

NUMERICAL MODELING OF MULTI-MATERIAL ACTIVE MAGNETIC REGENERATION

K.K. Nielsen[1,2,*], K. Engelbrecht[2], C.R.H Bahl[2], A. Smith[2], N. Pryds[2], J. Hattel[1]

[1]Department of Mechanical Engineering, Technical University of Denmark
Building 425, Niels Koppels Allé, DK-2800 Kgs. Lyngby, Denmark
[2]Fuel Cells and Solid State Chemistry Division
Risø National Laboratory for Sustainable Energy
Technical University of Denmark - DTU, Frederiksborgvej 399, DK-4000, Denmark

ABSTRACT. Magnetic refrigeration is a potentially environmentally-friendly alternative to vapour compression technology that is presented in this paper. The magnetocaloric effect in two magnetocaloric compounds in the $La(Fe,Co,Si)_{13}$ series is presented in terms of their adiabatic temperature change and the specific heat as a function of temperature at constant magnetic field. A 2.5-dimensional numerical model of an active magnetic regenerative (AMR) refrigerator device is presented. The experimental AMR located at Risø DTU has been equipped with a parallel-plate based regenerator made of the two materials. Experimental zero heat-load temperature spans are presented for different operating conditions and the results are compared to predictions of the numerical model. It is concluded that the model reproduces the experimental tendencies and when including thermal parasitic losses to ambient and the predictions from the model are within 1.5 K of the experimental results.

Keywords: *active magnetic regeneration, numerical modeling, magnetocaloric effect*

INTRODUCTION

Magnetic refrigeration and some of the challenges

Magnetic refrigeration is a research field covering a wide range of different physical disciplines. The basic physical property on which magnetic refrigeration is based is the magnetocaloric effect (MCE). This effect is exhibited by magnetic materials where increased ordering may be introduced by applying a magnetic field, thus lowering the magnetic entropy. This makes the MCE an inherently fundamental quantum mechanical effect. If the field is applied under adiabatic conditions the temperature of the material will rise. In order to maintain constant total entropy the decrease of the magnetic entropy must be compensated by an increase of the lattice and electron entropies thus increasing the temperature. This makes the MCE observable on the macroscopic level. The MCE is reversible for many magnetocaloric materials of interest but some materials exhibit some magnetic hysteresis [1].

For refrigeration applications the MCE can be used with the magnetocaloric material (MCM) as a refrigerant to accept a cooling load over a temperature span. However, the magnitude of the MCE is rather small – with an adiabatic temperature change with magnetization on the order a few K per tesla of magnetic flux density. This obviously limits the applicability of the MCE as a potential refrigerant. However, by implementing a regenerative, or active magnetic regeneration (AMR), cycle the

* Corresponding author: K.K. Nielsen
Phone: + 45 4677 4758
E-mail address: kaki@risoe.dtu.dk

technology can be used to absorb a cooling load at a temperature span that is higher than the adiabatic temperature change of the MCM. This process exploits the MCM in two ways; by using the MCE as work input to generate cooling and as a regenerator to store heat temporarily and build up a temperature gradient. This makes temperature spans larger than the adiabatic temperature change possible. The AMR process is composed of four sub processes. First the material is magnetized and thus the temperature in the solid regenerator rises. Second, a heat transfer fluid – typically water-based – is pushed through the material (which is designed in some porous configuration) from the cold to the hot end thus lowering the temperature of the material by rejecting heat to the ambient while still magnetized. The third step is demagnetization. This ensures the material to cool below the initial temperature. The fourth and final step is moving fluid towards the cold end, thus absorbing a heat load from the cooled space. Thus, magnetic refrigeration includes the fundamental MCE as well as macroscopic heat transfer and fluid dynamics.

The challenges are many within this area of research; issues like regenerator geometry (particle bed, parallel plates etc.), operating conditions (cycle frequency, fluid movement etc.) and the magnetocaloric properties of the MCM just to mention a few. The MCE is most pronounced over a relatively small temperature span around the Curie temperature (T_C) of the material (where a ferromagnetic material changes to its paramagnetic state). This limits the optimal operating temperature for any given MCM and thus constructing a regenerator of a series of materials each with its own working temperature range tuned to the local regenerator temperature experienced by each material can greatly increase the total MCE in the regenerator. This work is concerned with a first attempt to model an experimental setup with two materials configured in a parallel-plate stack of magnetocaloric plates of sintered La(Fe,Co,Si)13 made by Vacuumschmelze, Germany [2,3]. Using this material, experiments have been performed using the experimental AMR device located at Risø DTU, Technical University of Denmark. The device is a single regenerator reciprocating AMR that is discussed in more detail in [4] and [5]. Results of this and corresponding modeling results are the scope of this paper. Previous AMR modeling including comparisons with experimental results can be found in e.g. [6,7].

The magnetocaloric effect

The MCE is typically discussed in three different forms: The isothermal magnetic entropy change (ΔS_{mag}) when magnetizing a sample of a MCM, the adiabatic temperature change (ΔT_{ad}), i.e. the temperature change of a MCM when magnetized adiabatically and finally the specific heat capacity, c_H, as function of temperature, T, at constant magnetic field, H. The adiabatic temperature changes of two magnetocaloric materials are given in Figure 1. The materials are two different $La(Fe,Co,Si)_{13}$ compounds. The Fe/Co ratio has been varied in order to change the Curie temperature [2]. The figure shows the adiabatic temperature change when magnetizing from 0 T to 1.1 T. Some important details should be observed in the figure. Firstly, the clearly visible position of either material's transition temperature (in this case defined as the peak of the (ΔT_{ad}), curves). Secondly, the temperature ranges where each material exhibits a significant MCE overlap somewhat. Whether this overlap is sufficient for utilizing both materials in an effective refrigeration process is to be decided from modeling and experimental studies. In this paper we address some of these issues. It should be noted that the MCE for these materials is reversible. This is important since irreversibility associated with magnetization and demagnetization, known as magnetic hysteresis, is a serious degrading factor when considering the material's application as a refrigerant.

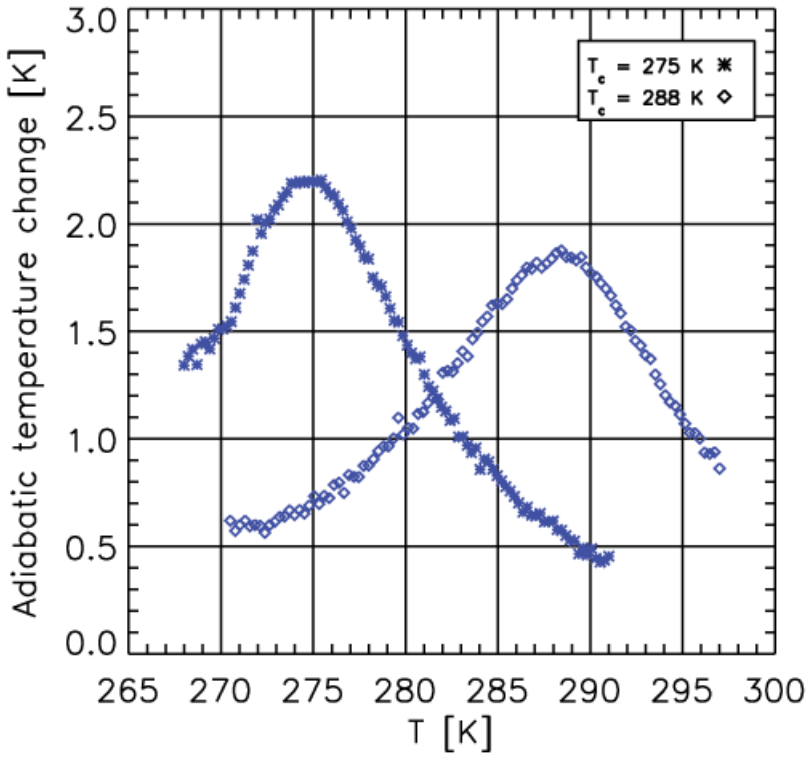

Figure 1: The adiabatic temperature change of two different compositions of $La(Fe,Co,Si)_{13}$ when magnetized from 0 to 1.1 Tesla. The indicated T_c in the figure legend is the Curie temperature of the materials.

The specific heat in an applied magnetic field has so far only been measured in detail on the compound with the low transition temperature and is given by [3]. Figure 2 shows the temperature dependence of the zero-field and the 1.0 T specific heat. Notice two important factors: First the peak value shifts significantly (3.5 K) between the two applied magnetic fields. Second, the zero-field specific heat has a higher and narrower peak than the 1.0 T specific heat curve has.

NUMERICAL AMR MODEL

The experimental device mentioned previously is modeled through a versatile 2.5-dimensional numerical model of a parallel plate AMR. The solution domains consist of a fluid domain and three solid domains; the MCM plate and a hot and cold heat exchanger (HEX). The governing equations are

$$\frac{\partial T_f}{\partial t} = \frac{k_f}{\rho_f c_{p,f}} \nabla^2 T_f + q_{bd,fc} + q_{bd,fh} + q_{bd,fMCM} + q_{loss,f} - u \frac{\partial T_f}{\partial x} \tag{1}$$

$$\frac{\partial T_{MCM}}{\partial t} = \frac{k_{MCM}}{\rho_{MCM} c_{H,MCM}} \nabla^2 T_{MCM} - q_{bd,fMCM} + q_{loss,MCM} \tag{2}$$

$$\frac{\partial T_c}{\partial t} = \frac{k_c}{\rho_c c_{p,c}} \nabla^2 T_c - q_{bd,fc} + q_{loss,c} \tag{3}$$

$$\frac{\partial T_h}{\partial t} = \frac{k_h}{\rho_h c_{p,h}} \nabla^2 T_h - q_{bd,fh} + q_{loss,h} \tag{4}$$

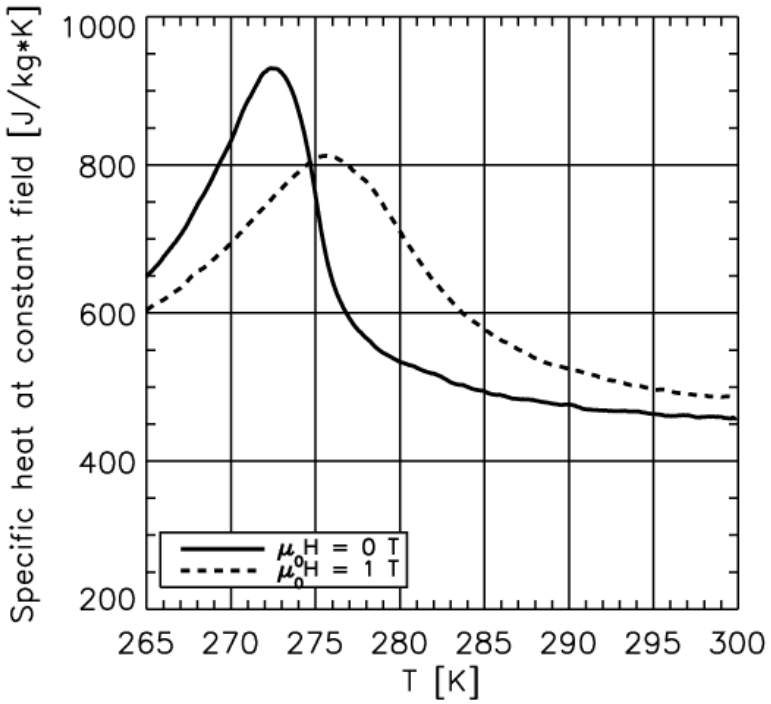

Figure 2: The specific heat capacity at constant magnetic field of the $La(Fe,Co,Si)_{13}$ sample with T_C = 275 K. Notice both the lower peak value as well as the lowering and broadening of the in-field specific heat.

The subscripts *f, MCM, c* and *h* indicate fluid, MCM, cold and hot HEX respectively. The thermal properties ρ and *k* denoting the mass density and the thermal conductivity have been introduced. The domains, as illustrated in Figure 3, are coupled via the boundary heat fluxes with subscripts *bd*.

The solution to Equations. (1)-(4) is determined for a number of cycles each divided in four sub processes further divided in time steps until cyclic steady-state is reached. The four sub-processes are: Magnetization (duration: τ_1 seconds), fluid flow from cold to hot end (hot blow, duration: τ_2 seconds), demagnetization (duration: τ_3 seconds) and finally flow from hot to cold end (cold blow, duration: τ_4 seconds). The cycle is assumed symmetric and thus $\tau_1 = \tau_3$ and $\tau_2 = \tau_4$. The numerical details can be found in [8]. The thermal properties used in the model are given in Table 1.

Thermal parasitic losses to the ambient are enabled through the q_{loss} terms in Equations. (1)-(4). These are formulated on the form

$$q_{loss} = \frac{T - T_\infty}{\sum_i R_i}. \tag{5}$$

The ambient temperature is denoted by T_∞ and the thermal resistances R_i are to be summed over for each numerical grid cell. An example of such a summation is

$$R_{fl,total} = \frac{1/2\Delta z_f}{k_f \Delta x \Delta y} + \frac{\Delta z_{pl}}{k_{pl} \Delta x \Delta y} + \frac{1}{h_{conv} \Delta x \Delta y}, \tag{6}$$

which is representative for the fluid channel. Here $\Delta x, \Delta y$ and Δz denote the dimensions of the grid cell and h_{conv} the passive convective heat transfer coefficient modeling the heat loss on the outside of the regenerator to the ambient.

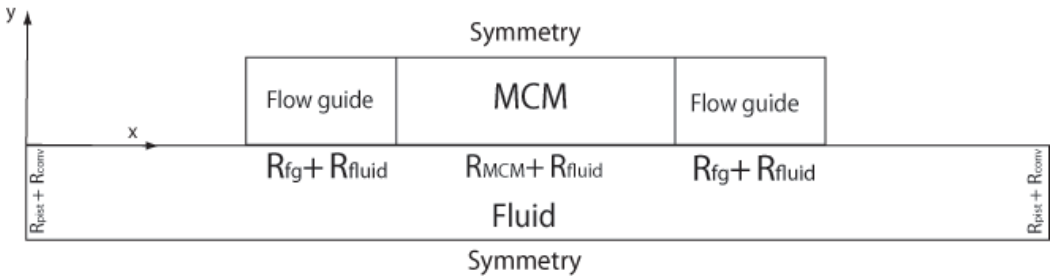

Figure 3: The four solution domains of the numerical AMR model. The domains denoted flow guide, are able to act as either passive plastic flow guides or as HEXs with perfect contact to the ambient (the hot HEX) or to a heat load (cold HEX). The symmetry lines indicate that only half a flow channel and half a solid domain are solved for. The indication of thermal resistances shows the internal thermal boundaries between the domains.

RESULTS

In the following results from both modeling and the experimental AMR device located at Risø DTU, are presented. The MCE was modeled discretely in the sense that at the first timestep of the AMR cycle the adiabatic temperature change from magnetizing was applied. Similarly, halfway through the modeled cycle (at the end of the hot blow) the adiabatic temperature change from demagnetizing was applied in one timestep. The specific heat was applied similarly. Here the data set from the 1.0 T measurements was used to temperature-interpolate the specific heat in the first half of the AMR cycle. In the last half of the cycle the zero-field specific-heat table was used. The adiabatic temperature change data is as previously shown in Figure 1. The specific heat is shown in Figure 2. However, since the specific heat of the high transition temperature material is not yet available, the specific heat data of the low-transition temperature material was used but shifted 13 K higher on the temperature scale (matching the difference between the peak values in the adiabatic temperature change values, see Figure 1).

The experimental approach is described thoroughly in both [4,5]. The range of the operating parameters are given in Table 2. Both experiments were performed with a regenerator using the two materials (each 20 mm long yielding in total a 40 mm long regenerator). The flow channel height was 0.5 mm and the thickness of the plates 0.9 mm. All experiments were performed at an ambient temperature, T_∞, approximately equal to 287 K, which was also used as the input ambient temperature to the model. A total of 11 plates were used.

The model is able to simulate thermal parasitic losses to the ambient modeled via thermal resistances as described in Equations. (5)-(6). Modeling both with and without this loss has been performed. The results from the two experimental situations are given in Figure 4 and Figure 5. Here it is clearly seen that including the thermal parasitic losses improves the model's ability to reproduce the experimental results.

Table 1
Thermal properties of the computational domains. Data for copper is used for the HEXs. The thermal conductivity of the MCM was estimated from the results of [9,10].

	ρ [kg/m^3]	c [J/kg·K]	k [W/m·K]
Fluid	1000	4200	0.6
MCM	7100	500-950	9
HEXs	8933	385	401
Housing	N/A	N/A	0.2

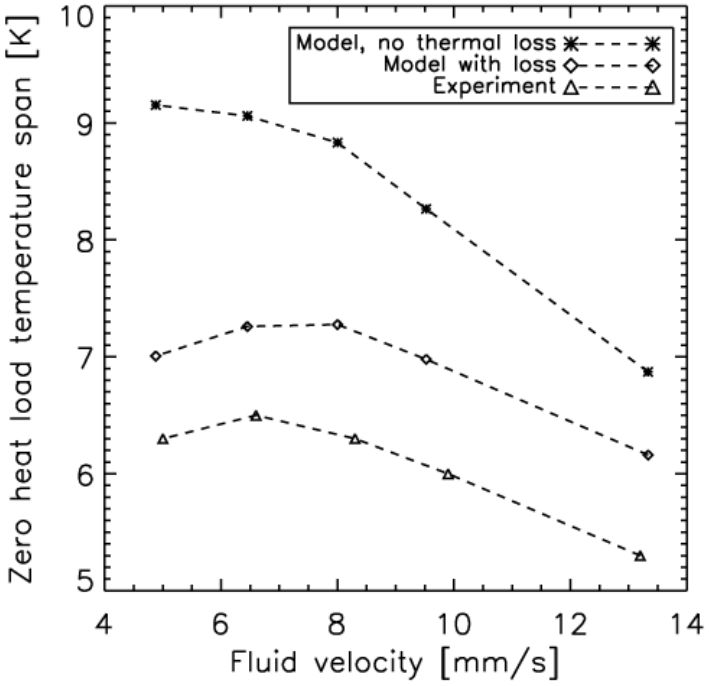

Figure 4: The no heat-load temperature span of experiment #1 (see Table 2 for details).

Overall, the predictions of the thermal loss model overestimate no more than 1.5 K in the worst case and in general about only 1 K, compared to the experimental results. The motivation for performing the two sets of experiments was to change the utilization defined as:

$$U = \frac{\rho_{fl} c_{p,fl} H_{fl} \Delta x}{\rho_{MCM} c_{H,MCM} H_{MCM} L_{MCM}}. \quad (7)$$

Where ρ_{fl} is the mass density of the heat transfer fluid, $c_{H,fl}$ is the specific heat of the fluid, H_{fl} is the thickness of the fluid channel, Δx is the stroke length, ρ_{MCM} is the mass density of the MCM, H_{MCM} is the thickness of the MCM plate, $c_{H,MCM}$ is the mean specific heat of the MCM, and L_{MCM} is the length of the MCM plate. Thus, the utilization expresses the fraction of thermal mass of fluid moved compared to the thermal mass of the MCM. The mean specific heat of the MCM was set to 550 J/kgK. Now, the two values of the utilization (which characterize the two experiments respectively) are kept constant by varying the fluid velocity and the timing of the AMR cycle. Thus, a low fluid velocity means a higher cycle time. Therefore, the fact that the model reproduces the experiment at low fluid velocities closer than at high is explained by the fact that thermal losses affect performance more in a slow cycle than a faster cycle. Also, the largest temperature span, and thus the highest conduction loss to the surroundings, is achieved with a relatively slow fluid velocity (not the slowest – the temperature span curves clearly have a peak fluid velocity).

Table 2
The operating parameters of the two experiments.

Experiment	Utilization [-]	Timing range [s]	Fluid velocity range [mm/s]
#1	0.51	5 s – 10.2 s	5.0 – 13.3
#2	0.81	7 s – 15.4 s	5.0 – 13.3

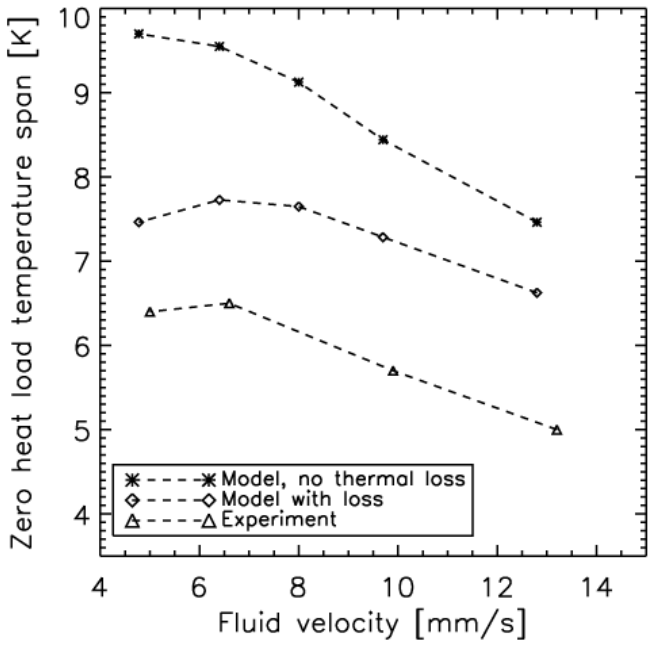

Figure 5: no heat-load temperature span of experiment #2 (see Table 2 for details).

DISCUSSION AND CONCLUSION

The comparison between experimental results and modeling of the experiment shows that the numerical AMR model presented here is able to reproduce the tendencies of the experiment. When including thermal losses to the ambient it is furthermore seen that the model results improve significantly in reproducing the experimental values. However, a discrepancy still exists. This may partially be explained by the use of the specific heat of the low-transition temperature material as the specific heat of the high-transition temperature material. Also the internal magnetic field in the MCM is somewhat reduced compared to the external field due to demagnetization [11]. Furthermore, the regenerator is comprised of 11 plates of MCM and will be subject to variation in thermal losses and spatially varying magnetic flux densities, which is not included by the model since the modelled geometry consists only of half a fluid channel and half a solid domain. Future work will include further modeling of the two-material regenerator in order to optimize for future choices of the transition temperatures of each individual material. As the maximum experimentally reached temperature span was about 6.5 K and the ambient was at 287 K the low-transition temperature material was clearly not as active as it could be and was thus not utilized fully.

ACKNOWLEGEMENT

We thank Mr. Jørgen Geyti for his technical help. Also, we thank Vacuumschmelze GmbH & Co. KG, 63450 Hanau, Germany for supplying the plates of $La(Fe,Co,Si)_{13}$. The authors further acknowledge the support of the Programme Commission on Energy and Environment (EnMi) (Contract No. 2104-06-0032), which is part of the Danish Council for Strategic Research.

REFERENCES

1. Gschneidner, K. A., V. K. Pecharsky, and A. O. Tsokol. "Recent Developments in Magnetocaloric Materials." *Rep. Prog. Phys.* 68 (2005):1479-1539.
2. Katter M., V. Zellmann, G.W. Reppel, and K. Uestuener. "Magnetocaloric properties of $La(Fe,Co,Si)_{13}$ bulk material prepared by Powder Metallurgy", *IEEE Trans. Magn.* 44 (2008) 3044.
3. Hansen, B. R., M. Katter, L. Theil Kuhn, C. R. H., A. Smith, and C. Ancona-Torres. "Characterization study of a plate of the magnetocaloric material La(Fe,Co,Si)13." 2009. *Proc. 3rd International Conference on Magnetic Refrigeration at Room Temperature, IIF/IIR.*
4. Bahl, C.R.H., T.F. Petersen, N. Pryds, and A. Smith. "A versatile magnetic refrigeration test device." *Review of Scientific Instruments* 79 (2008): 093906.
5. Engelbrecht, K., J. B. Jensen, C. R. H., and N. Pryds. "Experiments on a modular magnetic Refrigeration Device." 2009. *Proc. 3rd International Conference on Magnetic Refrigeration at Room Temperature, IIF/IIR.*
6. Dikeos, J., A. Rowe, and A. Tura. "Numerical Analysis of an Active Magnetic Regenerator (AMR) Refrigeration Cycle." *AIP Conference Proceedings* 823 (2006): 993-1000.
7. Engelbrecht, K.L., G.F. Nellis, S.A. Klein, and A.M. Boeder. "Modeling active magnetic regenerative refrigeration systems." Refrigeration Science and Technology Proceedings, 2005. 265-274.
8. Nielsen, K.K., R. Bjørk, C.R.H. Bahl, N. Pryds, A. Smith, and J. Hattel. "Detailed numerical modeling of a linear parallel-plate Active Magnetic Regenerator." *Accepted for publication in the International Journal of Refrigeration*, 2009.
9. Fujieda, S., Y. Hasegawa, A. Fujita, and K. Fukamichi. "Thermal transport properties of magnetic refrigerants La(Fex Si1-x)13 and their hydrides, and Gd5 Si2Ge2 and MnAs." *Journal of Applied Physics* (AIP, USA) 95 (2004): 2429-2431.
10. Fukamichi, K., A. Fujita, and S. Fujieda. "Large magnetocaloric effects and thermal transport properties of La(FeSi)13 and their hydrides." *Journal of Alloys and Compounds* (Elsevier, Switzerland) 408-412 (2006): 307-12.
11. Bahl, C.R.H., and K.K. Nielsen. "The effect of demagnetization on the magnetocaloric properties of gadolinium." *Journal of Applied Physics* 105 (2009): 13916.

PERFORMANCE OF DI COMPRESSION IGNITION ENGINE FUELLED WITH VEGETABLE OIL AND ITS ETHYL ESTER

L. Tarabet[1,*], S. Hanchi[1], M. Tazerout[2]
[1]Ecole Militaire Polytechnique, Bordj El Bahri, Algérie
[2]Ecole des Mines de Nantes, Nantes, France

ABSTRACT. Nowadays investigation about alternative sources of energy from species adapted in arid lands became a very important task for researches due to gradual depletion of world petroleum and the impact of environmental degradation. The aim of this study is to evaluate the effect of using the eucalyptus oil or its biodiesel on the DI compression ignition engine performances. Hence, a theoretical model, based on thermodynamic single zone model, is developed to simulate the engine cycle and to analyze the performance characteristics of the Diesel engine. The crude oil used in this work is extracted from sheets of eucalyptus trees. The biodiesel is obtained by transesterification of the oil with ethanol and catalyst (NAOH). In comparison with diesel fuel performances, the theoretical results showed that the biodiesel provides better performances than those of the eucalyptus crude oil.

Keywords: *biodiesel, combustion, thermodynamic model*

INTRODUCTION

We assist during these last years, to a climatic change due to a strong aggravation of the greenhouse effect caused mainly by the CO_2 emissions, which result from fossil hydrocarbon combustion. As result, intensive research is carried out to find appropriate substitution fuel to the fossil fuels. The use of the biofuels like ethanol, biogas, hydrogen, vegetable oil and the biodiesel in internal combustion engines is significant in this context [1-2].
The use of vegetable oil, biodiesel and animal fats for diesel engines applications is studied by various researchers. Some of the recent studies which dealt with transesterification, performance study and emission analysis are reported.
Dos Sontos [3] prepared biodiesel from the oil contained in the kernels of Terminalia Catappa fruits by transesterification with methanol and catalyst. It is reported that the oil extraction yield around 49% allow the possibility of economical exploitation, and its biodiesel physicochemical properties are close to the properties of Diesel fuel.
Pramanic [4] investigated the use of Jatropha curcas oil in diesel engine. It is found that the oil physicochemical properties are close to the properties of diesel fuel except for the viscosity which is much higher. The problem of high viscosity of this vegetable oil is resolved by blending the oil with diesel fuel in varying proportions. From the performance evaluation it is established that blends containing 40-50% of Jatropha oil can be substituted for diesel without any engine modification. In other previous works, the problem of vegetable oil high viscosity has been overcome by several techniques, such as preheating the oil, microemulsification with ethanol, transesterification or thermal cracking/pyrolysis [5-6].
Rakopoulos [7] developed a computational code based on thermodynamic multi-zone model for simulating the combustion process in the diesel engine fuelled with cottonseed oil or its methyl ester

* Corresponding author: PhD. L . Tarabet
Phone: + (213)-21-863469, Fax: + (213)-21-863404
E-mail address: ltarabet@Gmail.com

(biodiesel). It is found that the results from the relevant computer program for the in cylinder pressure, exhaust nitric oxide concentration (NO) and soot density are compared favorably with the corresponding measurements from an experimental investigation.
Considering the great number of eucalyptus trees available in the arid regions, we decide to study the possibility to use the oil contained in its leaves as an alternative solution to the diesel fuels. This vegetable oil is extracted by steam training. The Eucalyptus oil properties allowed us to envisage using it as fuel oil. But the greatest difference between Eucalyptus oil and diesel fuel is the viscosity. To overcome this problem, this oil is esterified with ethanol. In order to show the advantages of using this biodiesel in diesel engine, a thermodynamic single zone model was developed to simulate the engine cycle and to analyse the performances. We used an explicit solution method in solving the system of ordinary differential equations that obtained from the first law of thermodynamics. The reliability level of the mathematical model is verified by comparing the predicted parameters with the measured ones when the engine is fuelled with diesel fuel. After the confirmation that the predicted values of pressure are in good agreement with those obtained experimentally in different loads, we introduced the crude oil and biodiesel thermo-physical properties into the theoretical model, and then the performances are calculated for the different fuels (eucalyptus oil, biodiesel and Diesel).

MATHEMATICAL MODELING

Single zone thermodynamic model is used for analysing the performance characteristics of four strokes DI compression ignition engine. The model governing equations are derived by applying the thermodynamic First Law to the cylinder charge. The cylinder charge is supposed as a homogeneous gas mixture of fuel vapour and air. Pressure and temperature inside the cylinder are uniform and vary with crank angle. Specific heats of the gaseous mixture are temperature dependant.

Cylinder geometry

Using engine kinematics the cylinder volume at any crank angle can be computed using the following equation

$$V(\theta) = V_{clear} + \frac{\pi D^2}{4} L \left(1 + R\left(1 - \cos(\theta)\right) - \sqrt{1 - R^2 (\sin(\theta))^2}\right) \quad (1)$$

where V_{clear} is the clearance volume, and D, L, R are respectively the cylinder bore, the rod length and the ratio of connected rod length to crank radius.

Energy equation

The model is valid only for the period of the compression and expansion cycles. For the closed system, the Thermodynamic 1st Law gives

$$\delta Q - \delta W = dU \quad (2)$$

$$\left(\delta Q_{in} - \delta Q_{loss}\right) - p\,dV = m\,c_v\,dT \quad (3)$$

Table 1
Specification of the engine used

Make	LISTER-PETTER
Type	Naturally aspirated four stroke single cylinder compression ignition
Bore and stroke	95.3 mm × 88.9 mm
Compression ratio	18:1
Displacement volume	630 cc
Connecting rod length	165.3
Fuel injection timing	20° before TDC
Rated power output	2.8kW at 1500 rev/mn

From the ideal gas equation, $pV = m\,R\,T$, we can write

$$m\,dT = \frac{1}{R}\left(p\,dV + V\,dp\right) \tag{4}$$

and

$$dU = \frac{c_v}{R}\left(p\,dV + V\,dp\right) \tag{5}$$

Rearranging equation (2) provides

$$\left(\delta Q_{in} - \delta Q_{loss}\right) - p\,dV = \frac{c_v}{R}\left(p\,dV + V\,dp\right) \tag{6}$$

$$\left(1+\frac{c_v}{R}\right)p\,\frac{dV}{d\theta} = \left(\frac{\delta Q_{in}}{d\theta} - \frac{\delta Q_{loss}}{d\theta}\right) - \frac{c_v}{R}V\,\frac{dp}{d\theta} \tag{7}$$

Introducing $R = c_p - c_v$ and $\gamma = c_p / c_v$, we obtain

$$\frac{dp}{d\theta} = \frac{\gamma - 1}{V}\left(\frac{\delta Q_{in}}{d\theta} - \frac{\delta Q_{loss}}{d\theta}\right) - \gamma\frac{p}{V}\frac{dV}{d\theta} \tag{8}$$

Heat transfer

Cylinder wall heats transfers are represented using the heat transfer coefficient Woschni correlation [8].

$$\frac{dQ_{in}(\theta)}{d\theta} = \frac{h_g(\theta)S(\theta)\left(T_w - T(\theta)\right)}{\omega} \tag{9}$$

where S is the surface area in contact with the gases, T_w, the wall temperature and h_g is the heat transfer coefficient which is given as

$$h_g(\theta) = 3.26\times10^{-3}D^{-0.2}p(\theta)^{0.8}w(\theta)^{0.8}T(\theta)^{-0.55} \tag{10}$$

with the cylinder bore D taken as the characteristic length, w as a local average gas velocity in the cylinder which is expressed as

$$w = \left[c_1\overline{S}_p + c_2\frac{V_d T_r}{p_r V_r}\left(p - p_m\right)\right] \tag{11}$$

here V_d is the displaced volume, p the instantaneous cylinder pressure, p_r, V_r, T_r the pressure, the volume and temperature at reference state (inlet valve closing), and p_m is the atmospheric pressure.

For the compression period: $c_1 = 2.28$, $c_2 = 0$

For the combustion and expansion period: $c_1 = 2.28$ $c_2 = 3.24\times10^{-3}$

Heat release analysis

Heat release due to combustion is calculated using single Wiebe's heat release correlation [9]

$$\frac{dQ_{loss}}{d\theta} = m_f\,LHV\,\frac{dx(\theta)}{d\theta} \tag{12}$$

Table 2
Properties of Diesel fuel, eucalyptus oil and its biodiesel

Properties	Diesel	Eucalyptus oil	Biodiesel
Specific gravity	0.830	0.950	0.826
Viscosity (mm^2/s) at 40°C	3	30	4.78
Lower heating value (kJ/kg)	42500	37195	39760
Carbon content (wt. %)	86	77.1	77.0
Hydrogen content (wt. %)	14	11.5	12.18
Oxygen content (wt. %)	00	11.4	10.32
Sulphur content (wt. %)	0.29	00	00
Stoichiometric air-fuel ratio	15	12.57	12.48

where *LHV* denotes lower heating value, m_f the fuel mass, $\left[dx(\theta)/d\theta\right]$ the combustion rate obtained from the Wiebe function

$$\frac{dx(\theta)}{d\theta} = 6.908\frac{b+1}{\Delta\theta_d}\left(\frac{\theta-\theta_0}{\Delta\theta_d}\right)^m \exp\left[-6.908\left(\frac{\theta-\theta_0}{\Delta\theta_d}\right)^{m+1}\right] \tag{13}$$

In this relation θ_0 is the start of combustion, $\Delta\theta_d$ is the total combustion duration, while *a* and *m* are adjustable parameters. The fuel injected inside the cylinder is directly connected to the fuel/air equivalence ratio

$$\phi^{-1} = \frac{(A/F)_{actual}}{(A/F)_{stoich}}$$

Then:
$$m_f = \frac{\phi m_g}{(A/F)_{stoich}} \tag{14}$$

where m_g is the mass of air, which entering the cylinder.

Ignition delay
To determine the ignition delay, the Wolfer's empirical relation is used and expressed as [9]

$$\int_{t_{inj}}^{t_{ig}} \frac{dt}{t(p,T)} = \frac{1}{K_{t_{inj}}}\int_{t_{inj}}^{t_{ig}} \frac{dt}{(p(t))^{-q}\exp(E/RT(t))} = 1 \tag{15}$$

where t_{inj} is the time at witch injection starts, t_{ign} is the time at witch the ignition starts. The values of various constants appearing in the above equation are

K = 2272, q = -1.19, E/R = 4650.

SOLUTION PROCEDURE AND APPLICATIONS

The mathematical model results in set of ordinary differential equations. These equations must be integrated simultaneously by Runge Kutta method. Two types of applications were performed. The first has been conducted to verify the applicability and the reliability of the presented mathematical model by comparing the predicted parameters with the measured ones in the Diesel fuelling case. The specifications of the engine used for comparisons are given in Table1. The second is performed to examine the effects of fuelling the engine with the eucalyptus oil and its ethylic ester on its performances such as the specific fuel consumption and the efficiency.

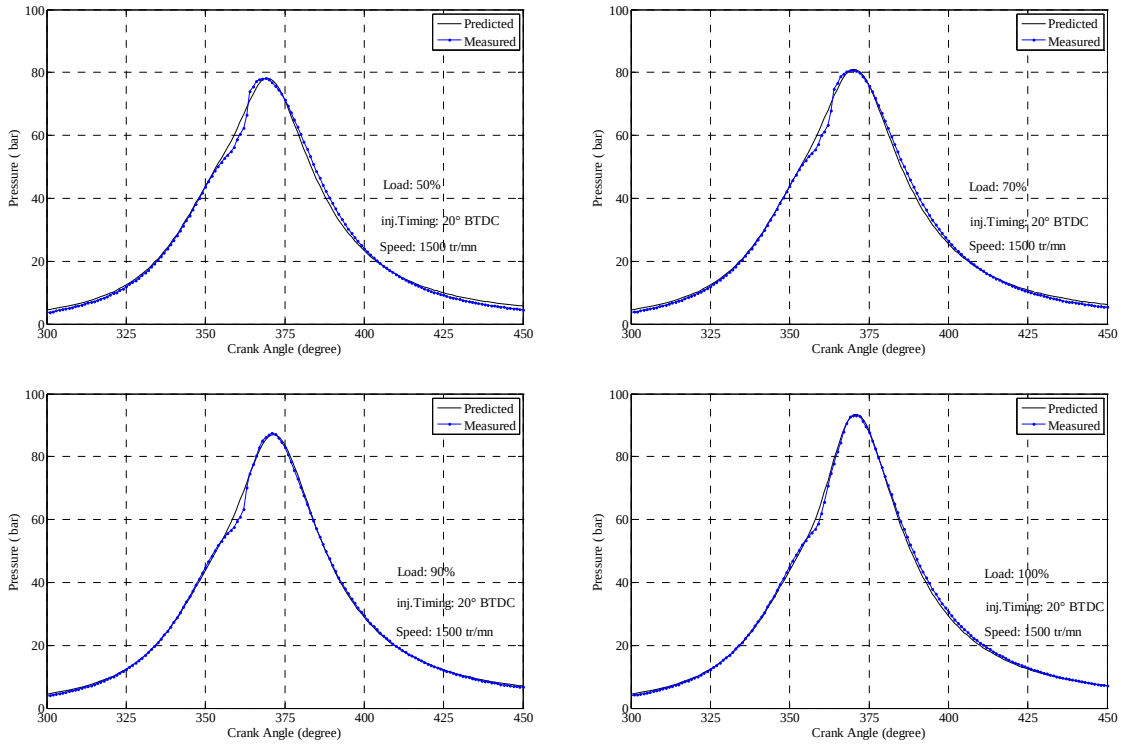

Figure 1: comparison of the predicted in cylinder pressure with the measured

The properties of the various fuels used in this study are measured at the Ecole des Mines of Nantes and are reported in the Table2. It is noticed, expect for the eucalyptus oil viscosity, that the other physicochemical properties of the crude oil and of its biodiesel are close with those of the Diesel fuel.

RESULTS AND DISCUSSIONS

Comparison with experimental data

To demonstrate the reliability of the mathematical model, predicted values of "in cylinder" pressure of the DI compression ignition fuelled with Diesel fuel are compared with measured ones in various engine loads. As seen from the Figure 1, the predicted "in cylinder" pressure are in good agreement with those experimentally obtained for all engine load. Thus, the simulation model can be applied for the different biofuels.

Parametric study

Compression ratio effect: The simulation model is run with compression ratio from 14:1 to 20:1 for the 3 different fuels. Figure 2 shows that for the compression ratio *CR=18*, the maximum "in cylinder pressure" is greatest in diesel fuel case due to their low volatility in comparison with eucalyptus crude oil and its biodiesel.

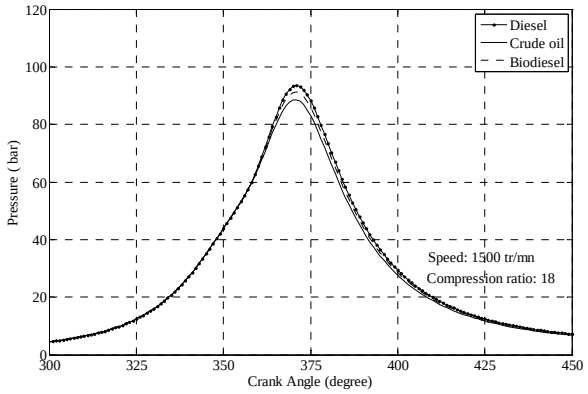

Figure 2: Variation of in cylinder pressure

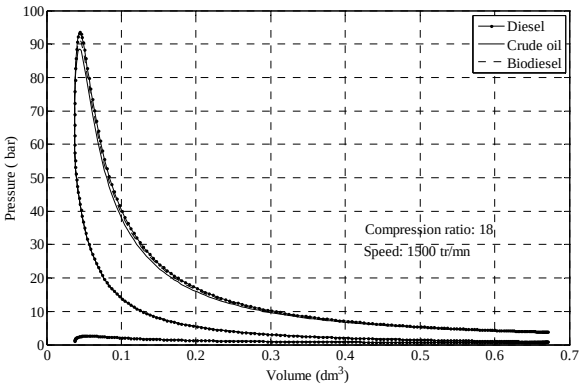

Figure 3: P-V diagram

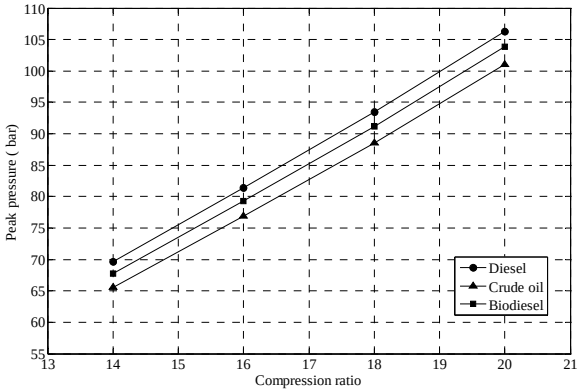

Figure 4: Effect of compression ratio on peak pressure at 1500rpm

The biodiesel peak pressure case is closer to the diesel fuel case one than to the eucalyptus crud oil. It can be seen also from the P-V diagram (Figure 3), that the enclosed area of the biodiesel fuel case is greater than the eucalyptus crude oil one.
In the Figure 4, the peak pressure inside the cylinder with various compression ratios is compared for the three fuels used. For all the fuels, the high pressure of compressed mixture is growth by 35% due to the compression ratio increasing.
Figure 5 shows that the indicated specific fuel consumption of the eucalyptus crude oil case is the highest in comparisons with the biodiesel and the diesel fuels cases. The indicated specific fuel consumption decreased on average by 16%, when the compression ratio is increased from 14 to 20 for all the fuels.
Figure 6 shows that the engine increasing compression ratio is expressed by an increasing in the indicated thermal efficiency for all the fuels. It can be seen also that the indicated thermal efficiency of biodiesel case is lower than that of diesel case, and higher than that of the crude oil. This is due to that the indicated thermal efficiency is directly dependant to the lower calorific value which is lowered by the presence of the higher percentage of oxygen molecule in the crude oil case and slightly lowered in the biodiesel case.

Engine speed effect: The performance evolution of DI compression ignition engine with respect to the engine speed is studied for the conventional diesel fuel, the eucalyptus crude oil and its ethylic ester (biodiesel).
From the Figure 7, the peak pressure of the mixture increased by 22% when the engine speed is 4000rpm. It can be seen also, that the biodiesel peak pressure is greater than that of the eucalyptus oil due to its higher calorific heating value which increase the heat release.
Figure 8 shows the engine power values for diesel fuel, eucalyptus crude oil and its biodiesel at different engine speeds. The maximum power values for the 3 fuels are obtained at 4000 rpm.

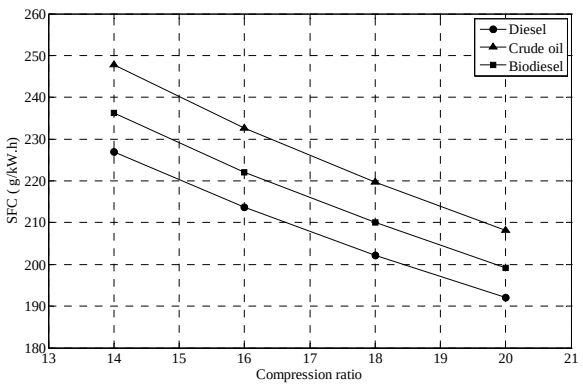

Figure 5: Variation of SFC with CR

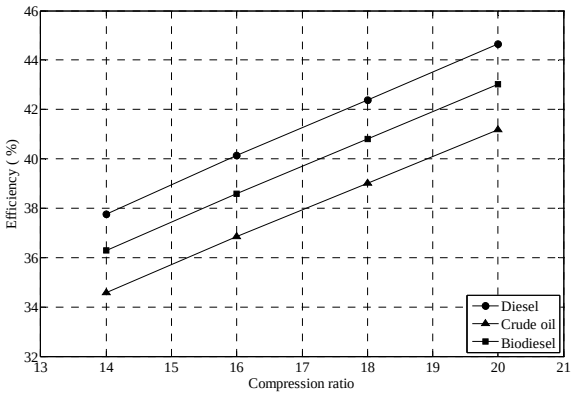

Figure 6: Variation of efficiency with CR

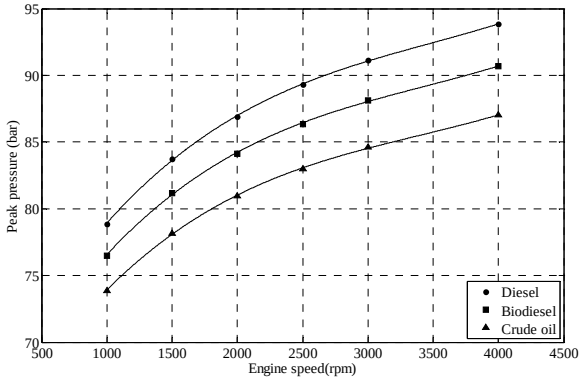

Figure 7: Effect of engine speed on peak pressure

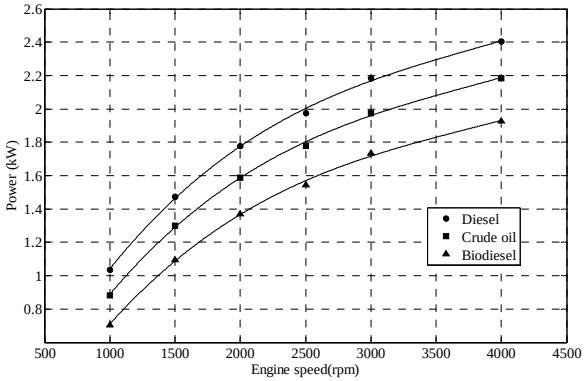

Figure 8: Variation of power values

According to these values, the traditional diesel fuel has the greatest power. It can be seen also that for all engine speed, that the power is decreased by 25% when the engine is fuelled by the crude oil and by 10% when it is fuelled by the biodiesel.

Figure 9 shows the specific fuel consumption (SFC) evolution with respect to the engine speed for these fuels. It can be seen that the SFC value is important at the lower engine speed, and decreased with engine speed increasing. At 4000 rpm, the minimum SFC value with conventional diesel fuel is 202.04 g/kW.h and with biodiesel and crude oil it is 222.41 g/kW.h and 251.99 g/kW.h, respectively.

Figure 10 shows the Efficiency evolution with respect to the engine speed for the 3 fuels. The power reduction due to the use of alternative fuel (eucalyptus or its biodiesel) is expressed by the efficiency decreasing. At 1000 rpm, the efficiency is decreased by 24 % and 10 % for the crude oil and its biodiesel respectively. But at higher engine speed (4000 rpm), the efficiency is slightly decreased by 10% and 5% for the crude oil and its biodiesel respectively.

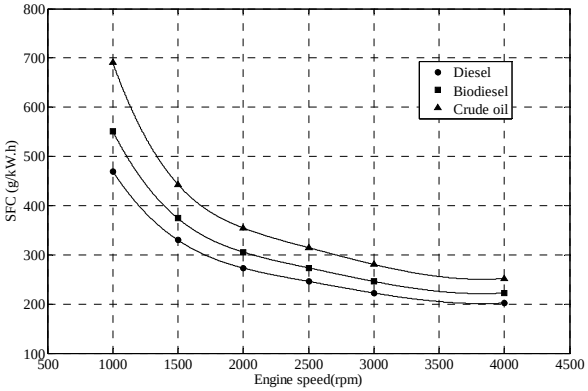

Figure 9: Variation of specific fuel consumption

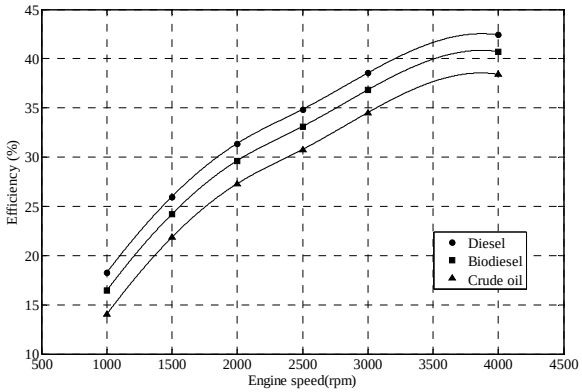

Figure 10: Variation of efficiency

CONCLUSION

The aim of the present investigation is to analyse numerically the usability of eucalyptus oil or its biodiesel as a substitute to diesel fuel in CI engine. A single zone thermodynamic model has been developed for theoretical determination of DI diesel engine cycles and engine performance parameters fuelled with various fuels. The numerical results obtained showed for the all treated cases that the engine performance characteristics follow the same trend. When the engine is fuelled with biodiesel, the performances are comparable to those of the diesel fuelling case. For the crude oil fuelling case, not only the performances are the lowest, but also its usability requires an implementation of an oil preheating system to reduce its high viscosity.
Finally, the reliability of the model is proven, and the biodiesel is an appropriate substitute to the diesel fuel.

REFERENCES

1. Humke, A.L., Barsic, N. J., Performance and emission characteristics of a naturally aspirated diesel engine with vegetable oils. *Transactions of Society of Automotive Engineers,* 1981; 810955.
2. Czerwinski, J., Performance of HD-DI diesel engine with addition of ethanol and rapeseed oil. *Trans. Soc. Automot. Eng,*. 1994; 940545.
3. Dos Sontos, I. C. F. Studies of Terminalia catappa L. oil: Characterization and biodiesel production, *Bioresource Technology*, No. 99, pp 6545-6549, 2008.
4. Pramanik, K., Properties and use of Jatropha curcas oil and diesel fuel blends in compression ignition engine, *Renewable energy*, No. 28, pp 239-248, 2003.
5. Senthil Kumar, M., Kerihuel, et al., Experimental investigations on the use of preheated animal fat as fuel in a compression ignition engine, *Renewable energy*, No. 30, pp 1443-1456, 2005.
6. Ramadhas, A.S., et al. Characterization and effect of using rubber seed oil as fuel in the compression ignition engines, *Renewable energy*, No. 30, pp 795-803, 2005.
7. Rakopoulos, C.D., et al., Development and application of multi-zone model for combustion and pollutants formation in direct injection diesel engine running with vegetable oil or its bio-diesel, *Energy Conversion & Management*, No. 48, pp 1881-1901, 2007.
8. Annand, W. J. D., Heat transfer in the cylinders of reciprocating internal combustion engines, *Proc. I. Mech. E*., Vo. 17, No. 36, pp 973-990, 1963.
9. Heywood, J. B., *Internal combustion engines fundamentals*, Mc-Graw Hill, 1988.
10. Descieux, D., One zone thermodynamic model simulation of an ignition compression engine, *App. Ther. Eng*. No .27, pp 1457–1466, 2007.

AN EXPERIMENTAL STUDY ON A SOLAR COLLECTOR AND BURNER COMBINED HEATING SYSTEM

H. S. Kim[1], N. Ryu[2] and Y. C. Park[3,*]
[1]Department of Applied Energy System, Graduate School, Jeju National University, Jeju, Korea
[2]R&D Division, Kangnam Co. Ltd., Changwon, Korea
[3]Department of Mechanical Engineering, Jeju National University, Jeju, Korea

ABSTRACT. The solar energy is limitless and pollution-free natural energy; however, the solar energy has not been utilized extensively due to its low density and restriction of availability.
The performance of the heating system with a burner and solar collectors is influenced by the efficiency. The solar collector and the thermal storage tank are controlled by different temperature controller. The controller has a temperature sensor which is being affected by the location of the sensor and also this location leads to make the properties of the controller.
This study was conducted to analyze operating characteristic of a solar assisted heating system for hot water supply and panel heating of a house. The main part of the system is a thermal storage tank which was designed to store energy that obtained from solar collectors and a burner. The heat exchanger is located on bottom of the storage tank which supplies solar energy to the water in the storage tank and is connected directly to the solar collectors. As an additional heat source, a burner was inserted to the top of the storage tank and supplies energy to water in the storage tank through indirect contact of the fire frame and stack flue. And also a small tank for hot water heating was attached at inside of the thermal storage tank. The water in the tank is heated by the water in the thermal storage tank.
In this study, the compact system with various heat sources and various function, performance test was conducted. As results, if design temperature of the boiler is increased, the efficiency of system is decreased. When the system uses hot water, system performance is decreased as increasing of the warm water usage. The developed system can be used as main heating equipment to the residential with the panel heating.

Keywords: *solar collector, burner, heating, experiment*

INTORDUCTION

Importation rate of fossil fuel or crude oil in Korea has been reduced a little due to development of gas field in outside country and participation in joint research petroleum business. However, 93-95% of consuming energy is relying on importation of the energy from other countries. The development of new and renewable energy are important issues in Korea not only necessity of the energy but also energy security of the country.
Research on fundamental technologies is not common due to demands for the predominant output or propagation of facility in the new and renewable energy industries. However, government will supply lots of fund to the renewable facility and R&D area to increase distribution rate of the new and renewable energy technology.

* Corresponding author: Prof. Y. C. Park
Phone: + (82)-64-7543626, Fax: + (82)-64-7563886
E-mail address: ycpark@jejunu.ac.kr

The solar is most applicable and accessible energy in renewable energy area by abundant solar distribution throughout the country. The rate of solar energy utilization is lower than the other renewable energy even though there is a lot of technology development for the solar energy area. The solar is limitless and pollution-free energy in the natural; however, the solar energy has not been utilized extensively due to its low density and restriction of availability.

Among the solar energy technology, water heating system is most popular device. It should be more useful if we extend the utilization of the solar energy from water heating application to panel heating for the residential house.

Ryu et. al. [1], Kim et. al. [2] and Paek et. al. [3] had studied a solar heating system to get optimum heat charge conditions for the thermal storage tank. They considered heat exchangers performance and design of return pipes that is a distributor of return water from residence panel. They delivered a more efficient thermal storage tank with changing the location of the return pipe at inside of the storage tank and system performance test was conducted with developed thermal storage tank.

Kim et. al.[4, 5] had constructed a heat pump system with solar collectors and a thermal storage tank as additional devices for a residential heating equipment. They alternated operating sequences from direct heat supply mode to heat pump operating mode for heat supply to the residence house from the thermal storage tank. The system controlled with well designed a differential temperature controller. As results, they show that it is possible to get more efficient thermal storage process with the developed differential temperature controller. And, there is more heat losses in the top side of thermal storage tank than bottom. It was founded that the energy bill can be saved about 30% with the solar collectors in the heat pump system compared with an electric heater and 90% of energy bill could be saved compared with an oil fired boiler.

As following researches, Park et. al.[6,7] had studied the same system with Kim's [4,5] to know optimum control temperature of the circulating pump in the solar collector. Han [8] had published a numerical calculation about effect of the water heating device on the system performance. Han [8] suggested that the water heating load is small enough to neglect compared with the heating load for the heating of the residential house.

This study was conducted to analyze operating characteristics of a solar assisted heating system for water heating and panel heating of a house. The main part of the system is a thermal storage tank which was designed to store energy that obtained from solar collectors and a burner. A heat exchanger located in bottom of the storage tank which supplies solar energy to the water in the storage tank and is connected directly with the solar collectors. As an additional heat source, a burner was inserted to the top of the storage tank and supplies energy to water in the storage tank through indirect contact of the fire frame and stack flue. And also a small tank for water heating was attached at inside of the thermal storage tank. The water in the water heating tank is heated by the water in the thermal storage tank itself.

In this study, an experimental study was conducted to improve efficiency of a heat storage tank with solar collector. Most of solar energy systems are used for water heating application with simple heat storage structures. However, by the solar energy application is extended to panel heating purposes, there is limitation in efficiency of the conventional heat storage tank. When the conventional heat storage tank used in solar assisted heating system, the water in the storage tank was heated in advance of heating operation by the solar heat, it makes reduction of utilization efficiency in the solar energy. Through analyzing flow characteristics and figuring problems out of a conventional heat storage tank, it is found that the system performance could be improved by optimization of the structure of the storage tank [9]. The experiments are conducted with real scale bases with designed thermal storage tank that has a distributor for return water from panel.

EXPERIMENTS

System configuration

The experimental apparatus is consisted with a 1.0 m^3 capacity thermal storage tank, solar collectors with 20 m^2 of surface area, a 5 RT capacity chiller to supply heat load to the system as work as thermal load at a residential house. The test rig is shown in Figure 1.

Solar heat of the solar collect is supplied to the thermal storage tank with control signal from a differential temperature controller. The controller checked a temperature difference between the solar collector fluid and water in the thermal storage tank. If the temperature difference between them reached at a specified temperate, the circulation pump started and supply the heat to the thermal storage tank through a heat exchanger which is inserted in the thermal storage tank.

On the other hand, room temperature controller controls another circulating pump for heat load. If the room temperature less than a specified setting temperature, the circulating pump starts and supplies the heat in the thermal storage tank to the heating load side. The heat load in this study is simulated by the chiller.

When the fluid temperature in the thermal storage tank has decreased to a specified degree, the burner started to increase the supply temperature of the thermal storage tank.

Hot water for shower and dish-washing can be supplied by a signal from the demand side opening of the valve. The heat of the hot water tank, which inserted in the thermal storage tank as shown in Figure 2, is indirectly supplied by the heat of the fluid in the thermal storage tank.

Experimental equipment

Solar collector. The solar collector which is used in this study is plate type solar collector with 20m^2 surface area. If we assume that a family with four persons are live in 90m^2, the house should be equipped about 6 to 10 pieces of solar collector to cover the heating load in the winter. Ten pieces of collectors are parallel aligned and inclined from the surface with 40^o.

Thermal storage tank. A tank in tank type thermal storage tank with a tank in coil type heat exchanger inserted was designed. The storage tank is consisted with a supply nozzle and a distributor type return

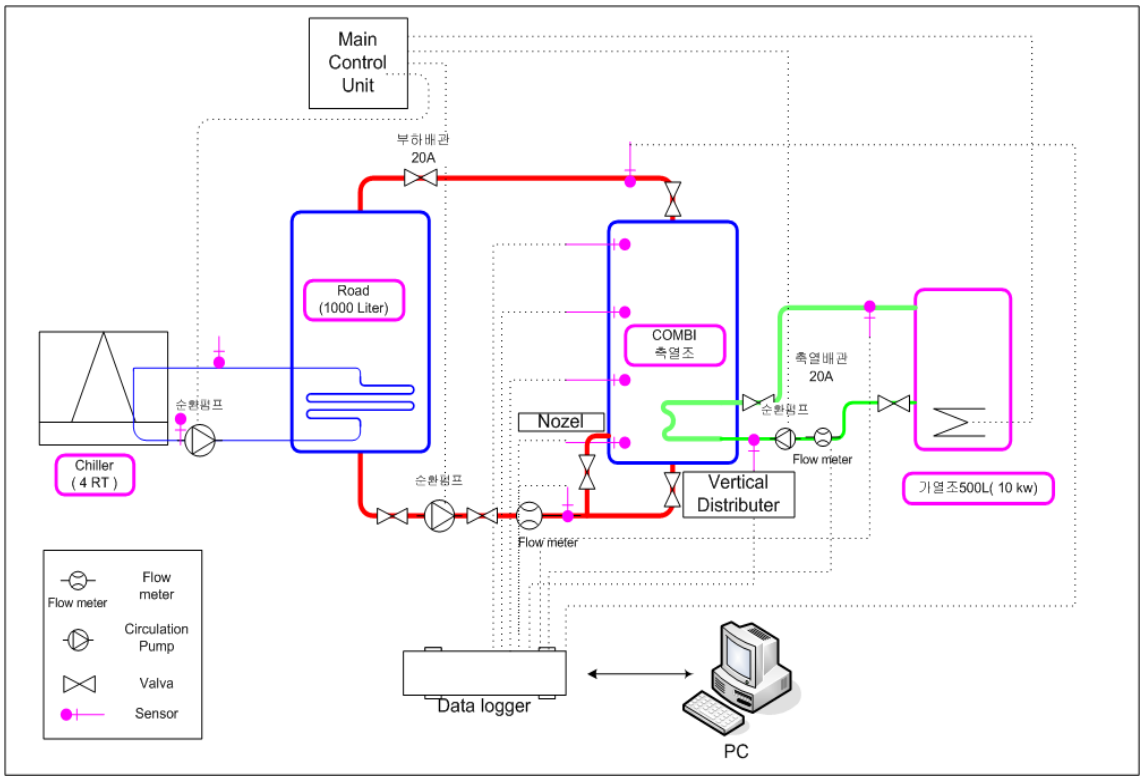

Figure 1. Schematic diagram of the experimental setup

nozzle for heating the panel of the residential house and couple of nozzles for hot water supply. Figure 2 shows the designed storage tank. The capacity of the storage tank is 1.0 m^3 and insulated with 50 mm thickness urethane foam.

Burner. The solar energy will be main heat source of the house. However, if the weather is not easy to get the heat from the sun in cloudy or rainy days, a burner is installed in the system to assist the deficient heat. To reduce the size of the system, the burner is inserted to the thermal storage tank as shown in Figure 2. The burner uses oil as fuel and a 17 W injector for the oil supply to the combustion chamber. The heat exchanger of the burner is modified to contact the flame with the fluid in the thermal storage tank and the stack of the flue gas bended 180^o from the flame direction.

Measurement devices

Temperature is measured with T-type thermocouple. The sheathed thermocouple is 200mm length and 1.6 phi diameter and inserted at all inlet and outlet of the component.

Electrical volume flow meters are installed at the solar collector outlet and return pipe to thermal storage tank from the heat load with 0-120 lpm flow range.

Solar radiation is measured with an Albedometer which is installed at the solar collector with 45^o inclination.

All measured data are achieved by a data logger (DR-230, Yokogawa) with 60 second time interval and stored at a personal computer simultaneously.

Experiment procedure

In this study, the setting temperature of the boiler is varied from 40 ^{o}C to 60 ^{o}C with 5 ^{o}C difference. The temperature difference setting between the solar collector and the thermal storage tank is fixed to 5 ^{o}C. And cut-off temperature values are 2^{o}C to avoid rapid hysteresis of the pump operation. The setting temperature of the main controller is varied with experiment.

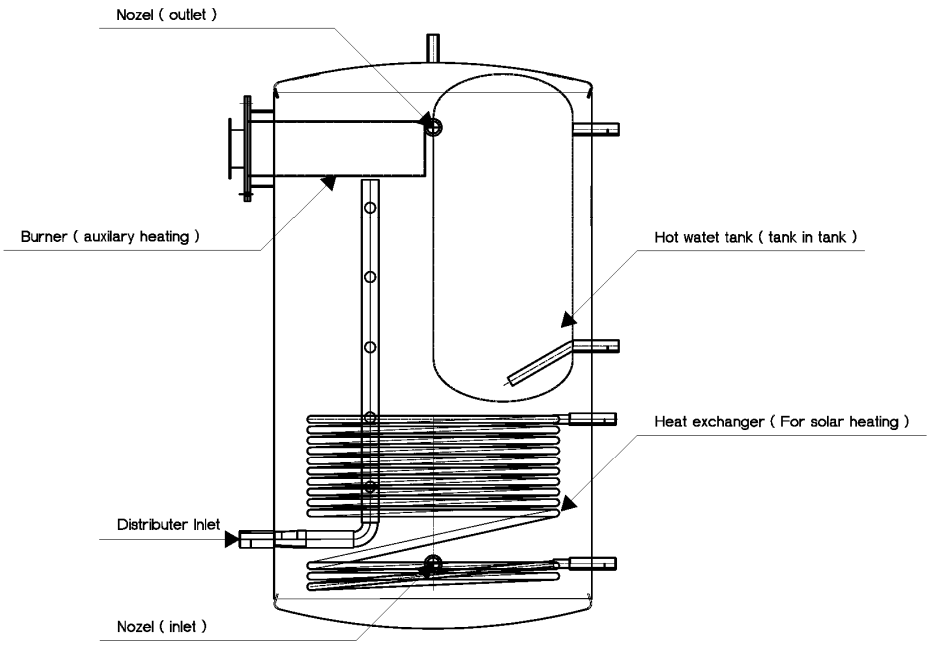

Figure 2. Schematics of the thermal storage tank

RESULTS AND DISCUSSION

Thermal storage tank performance

Solar energy utilization performance of the heat storage tank is improved with vertically installed distributor for return water compare to conventional horizontal type distributor's performance. It is found that the conventional heat storage tank is not suitable for heat storage tank for panel heating equipment and it is possible more improvement by modification of the heat storage tank.

The test conducted with variation of the volume flow rate of the supply heating water to the panel with changing of the return pipe installation method. When the thermal storage tank uses a nozzle type return pipe, the temperature of the fluid at 3/4 height of the tank (denoted to Tm_top in the Figure 2) decreases early stage of the operation and the fluid temperature at 2/4 and 1/4 height of the tank (denoted to Tm_bot and T bot in the Figure 2) increases by heat transfer from fluid at the 3/4 location. It is easy to understand the trend of temperature variation from right side graph in the Figure 3.

If the nozzle has replaced with the developed vertical type distributor, the heat transfer mechanism changes as shown in Figure 4. It shows that the temperature stratification with the height of the location is maintained for long time. Therefore, it is possible to supply a higher temperature fluid to the desired heat load rapidly without increasing all fluid temperature to the desired temperature.

Solar collector efficiency is calculated with equation (1). If the weather condition of Busan City in Korea is adapted to the equation (1), the efficiency of the solar collector with a developed vertical

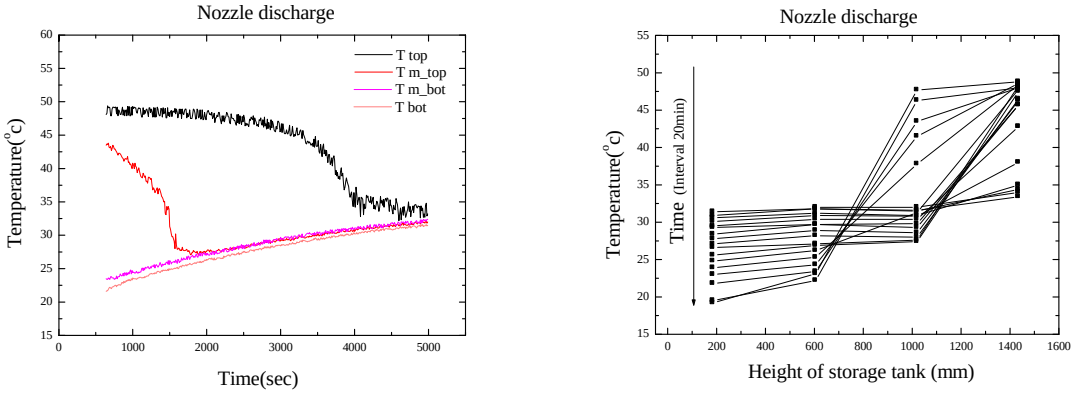

Figure 3. Temperature variation in the thermal storage tank with time in case of using a nozzle type return pipe

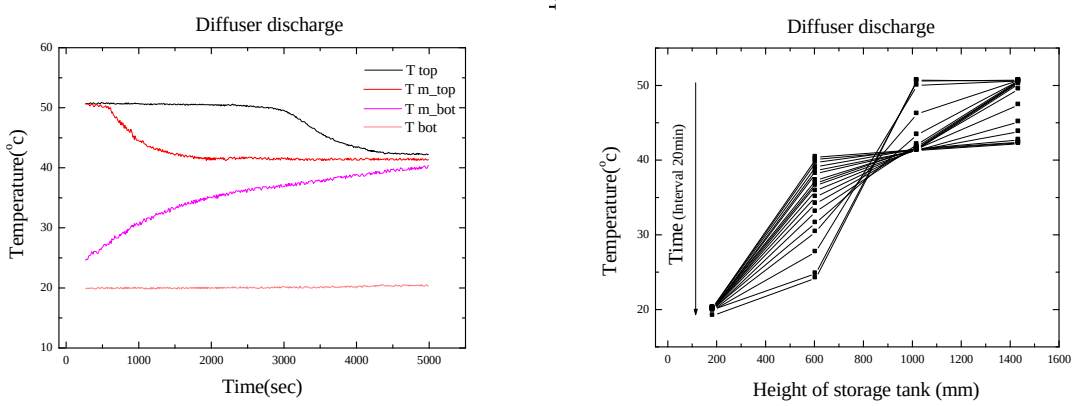

Figure 4. Temperature variation in the thermal storage tank with time in case of using a diffuser type return pipe

type distributor is increased about 7.25% than that of the nozzle type return pipe as shown in Table 1. The efficiency variation with temperature difference is shown in the Figure 5.

$$\eta = F_R(\tau\alpha) - F_R U_L\left(\frac{t_i - t_a}{It}\right) \tag{1}$$

Component performance

To know the performance of the thermal storage tank, heat loss through the wall of the thermal storage tank is needed. The storage tank was heated with auxiliary heating device up to 55°C and leaves the storage tank in the ambient temperature 26°C. It takes about 5 hours to release all energy in the storage tank as shown in Figure 6. The most of heat losses are occurs at the attaché part of the boiler in the storage tank due to that high temperature environment of that place makes difficulties for insulation. When the sun set downs at 6 o'clock, the temperature of the storage tank decrease about 18% from 55°C to 45°C during 1 hour until heating operation begins at 7 o'clock

Boiler performance is varied with maximum limit temperature settings. In this study, the control temperature set at 40 °C, 50 °C and 60 °C. When the boiler outlet water temperature reached at the specified temperature, the boiler stops and operating will began when the outlet temperature drops about 4 °C from the specified temperature. Fuel consumption is increased about 77% if the setting temperature increased from 40 °C to 50 °C and 81% of fuel consumption is increased when the setting temperature increased from 50 °C to 60 °C. The energy used to run the boiler with limit temperature 40

Table 1
Comparison between Theory and Experiment

Items		Value
$F_R(\tau\alpha)$		0.71
$F_R U_L$		-4.3
t_a		13°C
It		600[W/m^2]
t_i	Nozzle	37.6(Δt =7.6°C)
	Distributor	32.2 (Δt =2.2°C)
η	Nozzle	53.37%
	Distributor	57.24%

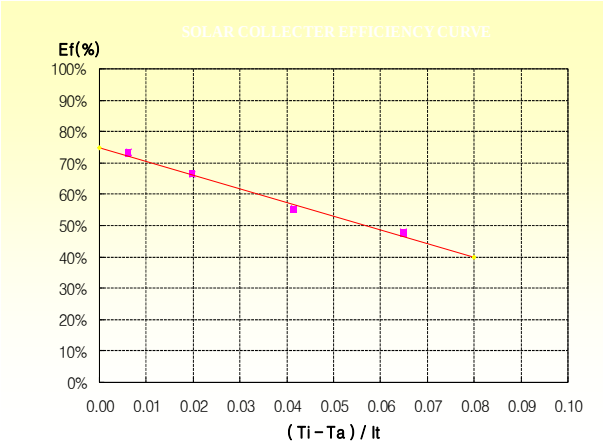

Figure 5. Efficiency variation with temperature difference between inlet of the collector and ambient temperature

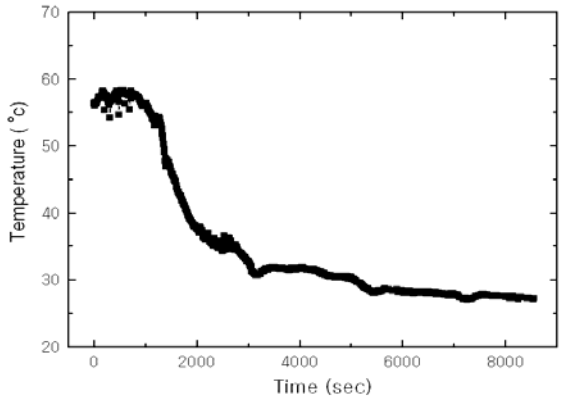

Figure 6. Heat loss variation of the thermal storage tank with time when the tank is exposed to the environment temperature

^{o}C , 50 ^{o}C and 60 ^{o}C is 6,427 kcal/day, 11,506 kcal/day and 20,855kcal/day, respectively. Figure 7 shows the temperature variation during the boiler performance test with time.

System performance

In this study, the system performance is tested with interval heat load to the system. Heat load is imposed 2 hours interval during daytime and 1 hour interval in the night. Figure 8 shows load, energy absorption from the sun and burner operation signals at 60^{o}C setting temperature of the boiler. The burner does not work during day time. However, in the night, the boiler runs accompany with the heating load. If the setting temperature varies from 40^{o}C, 50^{o}C and 60^{o}C, the solar fraction of the heating load is 97.9%, 84.5% and 59.5%, respectively.

When the system supplies hot water for shower and dish-washing, the energy consumption is measured with variation of flow rate of the hot water at 3 lpm, 5 lpm and 7 lpm. Figure 9 shows thermal storage fluid temperature variation with 7 lpm of supply water flow rate. The oil consumption increased with respect to the supply water flow rate. When the flow rate is set to 3 lpm, 5 lpm and 7 lpm, the oil consumption is 0.12 litter, 0.16 little and 0.22 litter during 20 minutes operation.

The total fraction of the solar energy in the system is shown in Figure 10. It shows that most of the month during a year could cover the heating load of the residential house by the energy from the sun except 5 months from October to March. However, during the winter season, the solar energy fraction to the heating load is about 47% approximately.

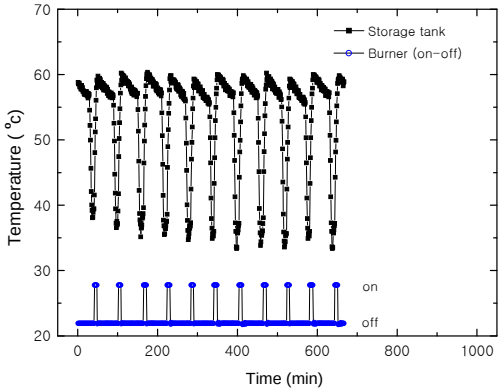

Figure 7. Temperature variation of the fluid in the thermal storage tank and signal of burner operation with time

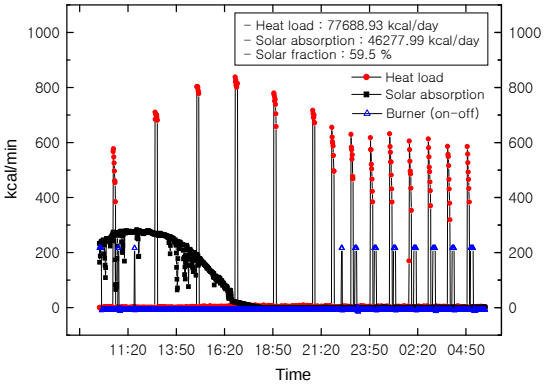

Figure 8. Heat load and solar absorption rate variation of the system during a day

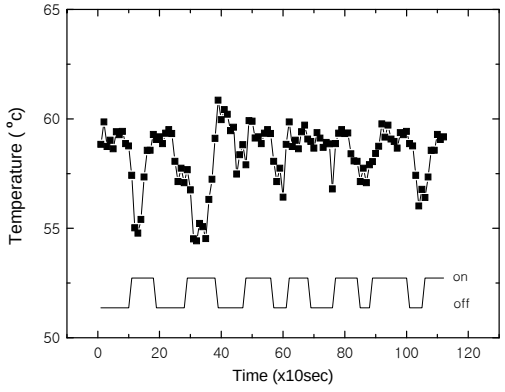

Figure 9. Efficiency variation with temperature difference between inlet of the collector and ambient temperature

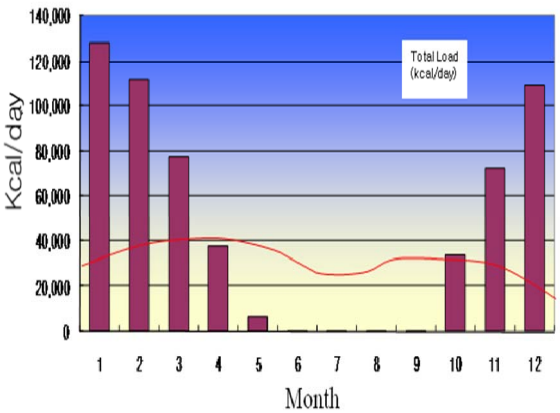

Figure 10. Efficiency variation with temperature difference between inlet of the collector and ambient temperature

CONCLUSIONS

The developed compact system with various heat source such as solar and burner and various function such as water heating and panel heating, performance test was conducted. The performance of the heating system with a burner and solar collectors is influenced by its efficiency. The solar collector and the thermal storage tank are controlled by different temperature controller. As results, if design temperature of the boiler is increased, the efficiency of system is decreased. When the system works as water heater, system performance is decreased as increasing of the water usage. The developed system can be used as main heating equipment to the residential house.
The results in this study could be used in development of solar assisted heating system for the residential house and will be basic technology in home appliance industries with solar energy. The information which arouse during the development will be reference in regulation rule making process. This study also will contribute to distribution of the new and renewable energy in the country.
It is found that the system developed in this study will be commercialized by the developing company with obtained know-how during the developing process if the market of the water and panel heating solar system have a good circumstance in the future.

ACKNOWLEDGEMENTS

Financial support of this research was provided by Energy Resources Technology Development Project (2005-02-0280-3-010) from Korea Energy Management Corporation.

REFERENCES

1. Ryu, N. J, Han, Y. and Park, Y. C., The Study on Efficiency Improvement of a Thermal Storage Tank for Solar Combined Heating System, Journal of the Korean Solar Energy Society, Vol. 25, No. 4, 2007 pp.43-49, 2007.
2. Kim, D. E., Peak G. D., Choi K. H. and Ryu N. J., Comparison of performance of heating systems with a solar collector, Korea Solar Energy Society, 2005 Autumn conference, pp.31-36, 2005.
3. Peak, G. D., Kim J. W., Eflita Yohana, N. J Ryu and K. H. Choi, Research on heating of all-terrain system with solar collector and liquid desiccant, 2005 spring conference, Korea Solar Energy Society, pp.176-181, 2005.
4. Kim J., Ko, G. S. and Park, Y. C., A study on the solar assisted heating system with refrigerant as working fluid, Journal of the Korean Solar Energy Society, Vol. 25, No. 4, pp.37-44, 2005.
5. Kim J., Ko, G. S. and Park, Y. C., A study on the operating strategic for solar assisted heating system, Korea Solar Energy Society, 2006 Autumn conference, pp.25-30, 2006.
6. Park, Y. C., Ko, G. S. and Han, Y., A Study on Hybrid Heating System with Anti-Superheating Devices, Journal of the Korean Solar Energy Society, Vol. 27, No. 2, pp.19-27, 2007.
7. Park, Y. C., Kim J. and Ko, G. S., A Study of Performance Characteristics on Hybrid Heat Pump System with Solar Energy as Heat Source, Journal of the Korean Solar Energy Society, Vol. 27, No. 1, pp.47-54, 2007.
8. Yuri H., A study on a hot water supply and panel heating system with a solar collector and burner combined thermal storage tank, master thesis, Cheju National University, 2008.
9. Ryu, N. J., A study on efficiency improvement of the heat storage tank for solar assisted heating equipment, master thesis, Pukyong University, 2006.

A STUDY ON RADIATIVE TRANSFER IN A TiO_2 PHOTOELECTRODE FOR THE DYE SENSITIZED SOLAR CELL PERFORMANCE ENHANCEMENT

M. Sangklinhom*, J. Yamada
Shibaura Institute of Technology, Tokyo, Japan

ABSTRACT. Nanoporous TiO_2 photoelectrodes of dye-sensitized solar cells (DSSC) fabricated from various sized TiO_2 particles were investigated to examine the effect of controlling radiative transfer on cell performance. The electrical performance of various cell types was measured. To clarify the effects of controlling radiative transfer on cell performance by using different TiO_2 particle sizes in multi-layered photoelectrodes, numerical simulation of the radiative transfer through TiO_2 photoelectrodes was developed. The results revealed that not only the total amount of light absorbed within the photoelectrode is important for improvement of the cell performance, but also that improved light absorption distribution within the photoelectrode is essential.

Keywords: *Dye sensitized solar cell, Radiative transfer, TiO_2 photoelectrode, numerical simulation*

INTRODUCTION

Dye-sensitized solar cells (DSSC) were first introduced in 1991 by O'Regan and Grätzel [1]. At that time, an energy conversion efficiency of 7.1% was reported, while nowadays the record efficiency has reached 11% [2], and the theoretical efficiency limit is above 30% for a single band gap junction [3], indicating that DSSCs are potential candidates for future solar energy conversion devices. However, significant improvement of the DSSC system is required for practical application.

The dye-sensitized TiO_2 photoelectrode, which is used to absorb incident light, is one of the main factors that plays an important role in efficiency improvement. The photoelectrode requires a large internal surface area to attach a large amount of dye molecules for electron generation, which can be achieved by using small TiO_2 particles (3-5 nm) [4]. The result is that a transparent photoelectrode can be obtained, but with poor light scattering characteristics. Simulations of light scattering in a TiO_2 photoelectrode of the DSSC has been reported for suitable mixtures of small (e.g., 20 nm in diameter) and larger TiO_2 particles (e.g., 250-300 nm in diameter) as effective light scattering particles that indicated significant enhancement of solar light absorption [5,6,7]. In addition, improvement of the TiO_2 photoelectrode has been reported using a double layer system [8], where the photoelectrode is separated into two layers; the first layer is a transparent layer composed of small TiO_2 particles (20 nm) and the second layer is a light-scattering layer composed of larger TiO_2 particles (400 nm). Other developing technologies, such as the multi-layer technique, where the structure of the TiO_2 photoelectrode consists of layers of different radius TiO_2 nanoparticles with a particular size [9], and the mixing of other metal oxides into the scattering

* Corresponding author: M. Sangklinhom
Tel: + (81)-3-5859-8023, Fax: + (81)-3-5859-8001
Email address: m606503@shibaura-it.ac.jp

layer have been reported [10]. These techniques have potential for the improvement of dye-sensitized TiO_2 photoelectrodes. However, in order to sustain efficient electron injection at the photoelectrode and electron re-generation from the counter electrode, the sufficient iodide and triiodide level should be maintained. But, the iodide concentration varies along the thickness of the photoelectrode [11]. The highest iodide concentration is at the photoelectrode side that closes to the counter electrode, and it is the shortest pathway for redox species between the two electrodes, electrons can quickly transfer from counter electrode to the photoelectrode. Therefore, the photoelectrode side that closes to the counter electrode would be the effective area for the electrons generation, the radiative transfer should be controlled to efficient the electron generation in this photoelectrode area.

In this study, an attempt was made to control the radiative transfer in a nanoporous photoelectrode prepared with TiO_2 particles of different sizes, since the scattering characteristic of the particles depend on size and shape. TiO_2 photoelectrodes composed of single, double, and triple layers were fabricated, where each layer has different sized TiO_2 particles. The electrical characteristics of a solar cell with the fabricated photoelectrodes were measured to evaluate the performance. A numerical code based on the Monte Carlo method was used to clarify the radiative transfer within the TiO_2 photoelectrodes. The results indicate that the solar cell performance is significantly affected by the photon absorption distribution within the TiO_2 photoelectrodes. The DSSC performance can be enhanced by using different particle sizes for each layer, in order to control the photon absorption distribution within the photoelectrode.

EXPERIMENTAL AND NUMERICAL SIMULATION

Fabrication of TiO_2 photoelectrodes

A conventional doctor blade technique was employed to fabricate single, double, and triple layer system nanoporous TiO_2 photoelectrode films. Commercially available TiO_2 powders (P-25, Nippon Aerosil) with an average particle diameter of 21 nm were used, which is a widely used particle size for transparent photoelectrode films of DSSCs. Other TiO_2 powders, ST-01, and CR-EL, with average diameter sizes of 7, and 250 nm, respectively, were obtained from Ishihara Sangyo Kaisha, Ltd., Japan. To prepare the TiO_2 paste, 1.0 g of powder was ground in a mortar with the addition of a drop of an acetic acid solution in purified water, 1.0 g of polyethylene glycol (PEG), and then 0.5 mL of Triton-X 100. The TiO_2 paste was spread on a transparent conductive oxide (TCO) coated glass substrate, and the film thickness controlled by the doctor blade. The TiO_2 film was dried at room temperature for several minutes and then heated at 450 °C for 1 h to form a nanoporous TiO_2 film. Covering the TiO_2 surface with dye was performed by soaking the film for more than 24 h in a solution of ruthenium N3 dye (Peccell Technologies, Japan). The dye was adsorbed on the TiO_2 nanostructure surface. A counter electrode was prepared by coating a 20 nm thick Pt catalyst layer by the sputtering technique. The dyed-TiO_2 photoelectrode was assembled with the counter electrode as a sandwich-type cell. The electrolyte (0.05 M of I_2 and 0.1 M of LiI dissolved in acetonitrile) was introduced into the cell as a redox mediator.

Measurement

The electrical characteristics of the fabricated DSSC solar cells were measured using a potentiostat (Hokuto Denko HAL3001) with irradiation using a 150 W Xenon lamp.

Numerical simulation

A numerical code for radiative transfer by the Monte Carlo method was developed to clarify the effect of radiation transfer in the photelectrodes. The radiative properties of a photoelectrode are required as input parameters; Mie theory is used to calculate the scattering and extinction efficiency of a single uncoated particle. And the TiO_2 particles covered by dye, the scattering and extinction efficiency were calculated using the "coated sphere" code [12]. The general principal of radiative transfer problem solving by the Monte Carlo method is already well known, and has been developed by many researchers in field, and this numerical code has developed related to the light transport in multi-layered media [13]. The following is a brief description for scoring the absorption quantity in the medium of the present radiation transfer simulation based on Monte Carlo method.

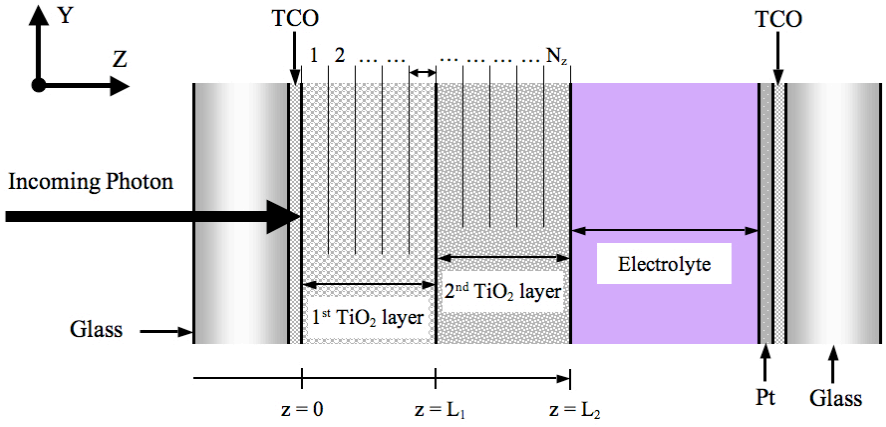

Figure 1. Schematic illustration of the TiO_2 photoelectrode (double-layered case) for the numerical simulation of radiative transfer based on the Monte Carlo method.

Launching a photon packet Each photon packet is initially assigned a weight W, which is equal to unity. The photon is injected orthogonally into the medium from the origin. The step size of the photon packet s, is calculated based on a uniformly distributed random number ξ, and a total interaction coefficient μ_t:

$$s = \frac{-\ln(\xi)}{\mu_t} \tag{1}$$

Photon absorption After the photon has taken a step, the photon weight will be reduced, due to absorption by the interaction site. A fraction of the photon present weight W, will be deposited in the local grid element. The amount of deposited photon weight ΔW, is calculated using

$$\Delta W = (\mu_a / \mu_t) W \tag{2}$$

where μ_a is an absorption coefficient, and μ_t is a total interaction coefficient or an extinction coefficient. This fraction of photon weight is scored as absorbance if the photon packet interaction site is in the medium:

$$A(z) = A(z) + \Delta W \tag{3}$$

Otherwise, if the photon packet exits the medium, the fraction of photon weight will be scored as reflectance or transmittance array, depending on where the photon packet exits.

The photon weight is then updated using

$$W = W - \Delta W \tag{4}$$

The photon packet with the new weight W, will undergo scattering at the interaction site and survive until the weight is too small or the photon packet has escaped the medium.

Internal photon distribution During the simulation, the absorbed photon weight is scored into the absorption array A(z), and is internally represented by $A[i_z]$, where i_z is the index for grid elements in the z direction and is computed from

$$i_z = \text{int}(z/L \times N_z) \tag{5}$$

where z is the distance from the origin to the photon packet interaction site, every photon that has taken a step, z will be re-evaluated. L is the thickness of the medium, and N_z is the total number of grid elements (sub-layers). The photon weight will be scored into the grid element absorption array as

$$A[i_z] = A[i_z] + \Delta W \tag{6}$$

The total photon weight absorbed in the medium A, is the summation of the total photon weight absorbed in each grid element $A[i_z]$, which is computed from

$$A = \sum_{i_z=1}^{N_z} A[i_z] \tag{7}$$

The absorption A, and $A[i_z]$, can be represented as the photon absorption probability in the medium and in each grid element (each sub-layer in Fig. 1.), respectively, by dividing by N (total photon weight).

$$A = A/N \text{ [-]} \tag{8}$$
$$A[i_z] = A[i_z]/N \text{ [-]} \tag{9}$$

where [-] represents dimensionless units.

Table 1.
Details of the photoelectrode types. The first number represents the first layer close to the glass substrate, as shown in Figure 1.

Photoelectrode type	Particle size in 1st layer (nm) / Thickness (μm)	Particle size in 2nd layer (nm) / Thickness (μm)	Particle size in 3rd layer (nm) / Thickness (μm)	Total thickness (μm)
7	7 / 15	-	-	15
21	21 / 15	-	-	15
7+21	7 / 5	21 / 10	-	15
21+7	21 / 5	7 / 10	-	15
7+250	7 / 15	250 / 3	-	18
21+250	21 / 15	250 / 3	-	18
21+7+250	21 / 5	7 / 10	250 / 3	18

RESULTS AND DISCUSSION

The measured electrical characteristics of the DSSCs are presented as current-voltage (*I-V*) curves in Fig. 2. The numerical simulation results of radiative transfer in the TiO_2 photoelectrodes are also shown here.

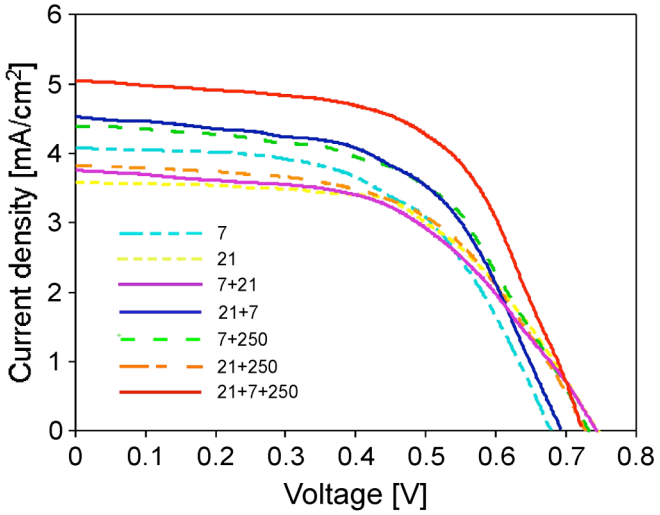

Figure 2. Measured *I-V* characteristics of DSSCs fabricated using different TiO_2 particle sizes for each photoelectrode layer. The numbers indicate the photoelectrode types given in Table 1.

Table 2.
Maximum electric power produced by the cells and the total photon absorption within the photoelectrode of the cells. Each group is ordered from high to low electric power.

Cell group	Photoelectrode type	Power, mW	Total absorption, %
A	21+7	1.759	15.95
	7	1.584	15.97
	21	1.505	15.39
	7+21	1.475	15.72
B	21+7+250	2.096	18.50
	7+250	1.765	18.26
	21+250	1.545	17.43

The cells were classified into two groups, *A* and *B*, as shown in Table 2. The cells in group *A* consist of single- and double-layered photoelectrodes without a scattering layer. The cells in group *B* consist of double and triple layered photoelectrodes with a scattering layer, that is, the layer composed of 250 nm TiO_2 particles.

The maximum electric power of each cell was calculated according to the measured *I-V* characteristics given in Figure 2. Figure 3 shows the spectral absorbance and internal photon absorption distribution within the photoelectrodes calculated using a numerical simulation code.

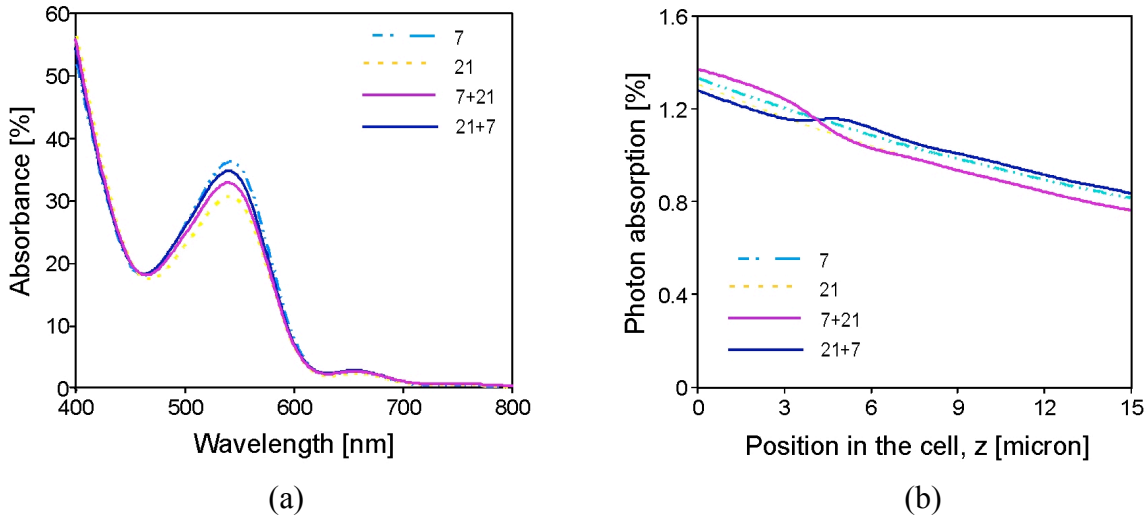

Figure 3. (a) Simulated spectral absorbance of single and double-layered photoelectrodes of group *A*, (b) photon absorption distribution profiles.

Considering the *I-V* characteristics in Fig. 2 and the total photon absorption in Table 2, the cell performance is dependent on the amount of photon or light absorbed within the photoelectrode of the cell. However, this is not the case for all cells examined. For example, considering the cells in group *A* of Table 2, the cell that has the highest efficiency (21+7-cell) does not have the highest photon absorption. In addition, the cell that has the lowest efficiency (7+21-cell) does not have the lowest photon absorption. To clarify this, the internal photon absorption within the photoelectrode was simulated, as shown in Figure 3(b).

Figure 3(b) shows the difference in absorptivity of each photoelectrode in each position of the cells in group *A*. Higher absorption in the deep region ($z > 5$ μm) significantly improves the cell performance more than high absorption in the shallow region ($z < 5$ μm). Considering the 21+7-cell, the cell has the highest photon absorption in the deep photoelectrode side ($z > 5$ μm) close to the electrolyte layer; therefore, it has the highest efficiency in group *A*, even though it has the lowest photon absorption in the shallow region ($z < 5$ μm). On the other hand, the 7+21-cell has the opposite absorptivity to that of the 21+7-cell; it is the least efficient cell in group *A*. This may also be due to the electron transfer mechanism; the shortest pathway for redox species between the photoelectrode and the counter electrode is the end of the photoelectrode close to the electrolyte layer side, and the longest pathway is the end of photoelectrode close to the TCO glass side (see Fig. 1). Therefore, if the radiative transfer to the deep photoelectrode region close to the electrolyte layer can be controlled, it might be effective to improve the cell efficiency, because electrons can be quickly transferred from the counter electrode to this photoelectrode area. As a result, we have shown that the highest efficiency solar cell is that which has the highest photon absorption in the deep region (Table 2, Fig. 3).

To support this reasoning of the light absorption effect, the effect on the illumination side to the photoelectrode has been proposed and discussed [11]. It is preferable to illuminate the cell from the counter electrode side (in this case, the photon absorption slope in Fig. 3(b) is the opposite side) for effective improvement of the cell efficiency. However, practically, illumination from the counter electrode side is not favorable, because it has higher incident light loss from passage through the counter electrode and bulk electrolyte layer. Therefore, illumination from the photoelectrode side is still preferable.

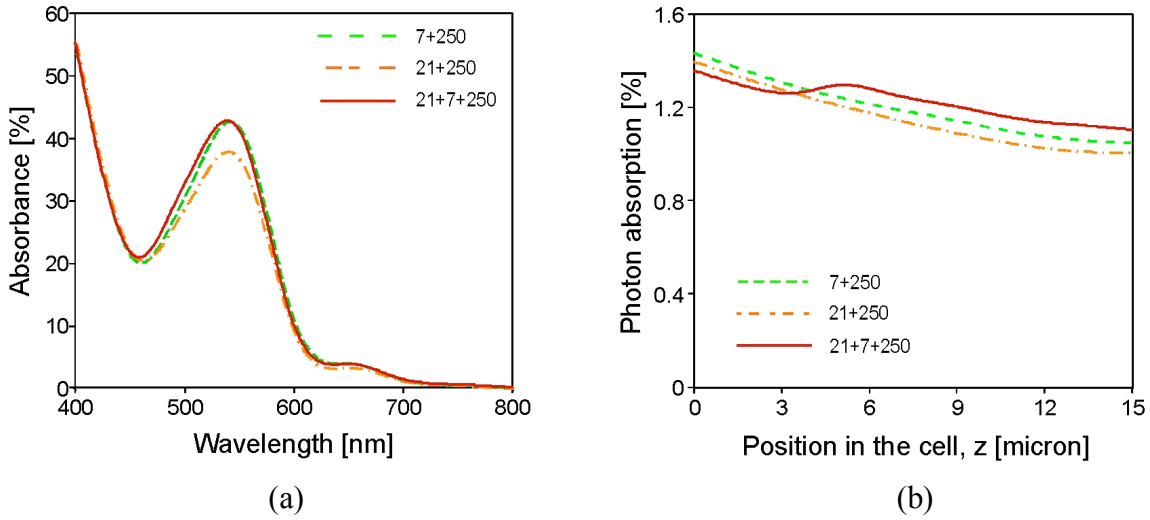

(a) (b)

Figure 4 (a) Simulated spectral absorbance of double and triple layered photoelectrode of group *B*, (b) photon absorption distribution profiles, the photon absorbed in the scattering layer is not included.

From the results, it is possible to control the radiative transfer by using different particle sizes for photoelectrode fabrication. Cells of double and triple layered photoelectrodes were fabricated (group *B*), and their performance was evaluated. The triple layered 21+7+250-cell has the highest efficiency of the cells examined in this study. This triple layered cell is a combination of the 21+7-cell in group *A* and a scattering layer. The numerical simulation results are shown in Fig. 4. It was revealed that the radiative transfer within the TiO_2 photoelectrode can be controlled, and the effect of the internal photon absorption distribution of the photoelectrode on the cell performance is supported. Therefore, the deep region close to the electrolyte layer should have high absorptivity in order to improve the cell performance.

CONCLUSION

The effect of radiative transfer in dye-sensitized solar cells was investigated. The amount of radiation absorbed in the deep region of the photoelectrode has an affect on cell performance. Therefore, control of the radiative transfer within the photoelectrode is essential for improved performance. We have proposed a method to control the radiative transfer for improvement of the cell performance using different TiO_2 particle sizes and a layered photoelectrode. However, to confirm these results, the influence of electrolyte-mass transport is currently under investigation.

REFERENCES

1. B. O'Regan, M. Gratzel, A low-cost, hight efficiency solar cell based on dye-sensitized colloidal TiO_2 films, *Nature* **353,** 737-740, 1991.
2. Y. Chiba, A. Islam, Y. Watanabe, R. Komiya, N. Koide, L. Han, Dye-sensitized solar cells with conversion efficiency of 11.1%, *JJAP*. Vol. 45, No. **25**, L638-L640, 2006.
3. W. Shockley, H. Queisser, Detailed Balance Limit of Efficiency of *p-n* Junction Solar Cells, *J. Appl. Phys*. **32**, 510-519, 1961.
4. J. Jiu, S. Isoda, M. Adachi, F. Wang, Preparation of TiO2 nanocrystalline with 3-5 nm and application for dye-sensitized slar cell, *J. Photochemistry. Photobiology A: Chemictry* **189**, 314-321, 2007.

5. J. Ferber, J. Luther, Computer simulations of light scattering and absorption in dye-sensitized solar cells, *Sol. Energy Mater. Sol. Cells.* **54**, 265-275, 1998.
6. W.E. Vargas, G.A. Niklasson, Optical properties of nano-structured dye-sensitized solar cells, *Sol. Energy. Mater. Sol. Cells*. **69**, 147-163, 2001.
7. Y. Tachibana, H. Y. Akiyama, S. Kuwabata, Optical simulation of transmittance into a nanocrystalline anatase TiO_2 film for solar cell applications, *Sol. Energy. Mater. Sol. Cells*. **91**, 201-206, 2007.
8. S. Ito, T. N. Murakami, P. Comte, P. Liska, C. Grätzel, M. K. Nazeeruddin, M. Grätzel, Fabrication of thin film dye sensitised solar cells with solar to electric power conversion efficiency over 10%, *Thin Solid Films*, **516**, 4613-4619, 2008.
9. Z. S. Wang, H. Kawauchi, T. Kashima, H. Arakawa, Significant influence of TiO_2 photoelectrode morphology on the energy conversion efficiency of N719 dye-sensitized solar cell, *Coordinat. Chem. Rev*. **248**, 1381-1389, 2004.
10. S. Hore, C. Vetter, R. Kern, H. Smit, A. Hinsch, Influence of scattering layers on efficiency of dye-sensitized solar cells, *Sol. Energy Mater. Sol. Cells.* **90**, 1176-1188, 2006.
11. N. Papageorgiou, M. Grätzel, P.P. Infelta, On the relevance of mass transport in thin layer nanocrystalline photoelectrochemical solar cells, *Sol. Energy Mater. Sol. Cells* **44** (1996) 405-438.
12. C.F. Bohren, D.R. Huffman, *Absorption and scattering of light by small particles.* John Wiley & Sons, Inc., 1998.
13. L. Wang, S.L. Jacques, L. Zheng, MCML-Monte Carlo modelling of light transport in multi-layered rissues, *Computer Methods and Programs in Biomedicine*. **47**, 131-146, 1995.

EVOLUTION OF VORTICITY CHARACTERISTICS IN THE WAKE OF WIND TURBINES

C. Masson*, S.-P. Breton, C. Sibuet Watters
École de technologie supérieure, Montréal, Canada

ABSTRACT. The two-bladed wind turbine tested in the wind tunnel of the Technical University of Delft (TUDelft), the NREL phase III three-bladed rotor, and the theoretical case of a finite wing in translation are studied using the actuator surface (AS) method, which represents blades by using singular surfaces of velocity and pressure discontinuities. A 3D in-house Control-Volume Finite-element method is used to solve the Navier-Stokes equations in RANS form with appropriate adaptations to accomplish the AS action on the flow. Circulation is calculated in the wake of the wing and turbine rotors by performing contour line integrals of the tangential velocities along circles in the wake, allowing to track vorticity evolution, and to verify if the AS method correctly predicts vorticity conservation in the wake. The simulated vorticity is found to be conserved in a satisfactory way in the wake in the case of the finite wing in translation and the NREL rotor. However, this is not the case concerning the TUDelft WT, where problems were also found when calculating the circulation from experimental velocities.

Keywords: *Wind Energy, Wake, Vorticity, Actuator Surface, CFD*

INTRODUCTION

Vortex Modeling of wind turbine (WT) wake aerodynamics poses interesting challenges, especially in the region of the near wake where the blades' trailing vorticity is concentrated in tip and root vortices, subject to important deformation and turbulent diffusion. Study of the near wake is important both for rotor and far wake aerodynamic analysis and is therefore of concern to both WT and wind farm design. While full RANS-CFD models are more and more used to study WT aerodynamics, their use is still computationally prohibitive, especially when simulating configurations of several WTs. The actuator surface (AS) method, which represents WT blades using singular surfaces of velocity and pressure discontinuities, is a promising method for the study of WT wake interactions within a wind farm. This model is directly inspired by vortex and actuator disk approaches towards the determination of the blade aerodynamics. The actuator surface represents a potentially interesting concept to add to CFD toolkits with comparative advantages over existing volume forces approaches. Indeed, the action of the modeled device is spread over a surface rather than a volume, preventing arbitrary choices of volume thickness and forces distributions with subsequent dependency in the flow solution or computational instabilities. Furthermore, the actuator surface is perfectly compatible with the vorticity principles of creation and evolution of vortices, and by Kutta-Jukowski law to lift production, whereas volume force approaches fail to always complain with such principles and as a consequence, may not reproduce the genuine characteristics of the flow.

Validations of the AS concept have been realized for simple analytical cases and for the case of the finite wing in translation [1, 2] as well as the experimental rotors of NREL and Delft Technical

* Corresponding author: Prof. C. Masson
Phone: + 1-514-396-8504, Fax: + 1-514-396-8530
E-mail address: christian.masson@etsmtl.ca

University [3], and have shown that the concept is useful to predict the flowfield and the values of induced drag or angles of attack. However, this method has not been validated yet for vorticity conservation, which could consist in a weakness. In this method, the presence of the blades is directly represented as vortices, making it similar to vortex wake methods, but contrarily to the latter, vortices are not directly represented in the wake, but are rather intrinsically handled by the CFD calculations. In this article, we will therefore focus on the capacity of the model to model vorticity in the wake, and correctly handle vorticity conservation throughout the wake. A method to calculate vorticity in the wake will be presented, after which the mathematical basis of the AS will be reviewed. Results will then be presented looking at vorticity evolution and conservation for three different cases, i.e. the finite wing in translation, the two-bladed TUDelft and three-bladed NREL phase III experimental rotors.

DESCRIPTION OF THE ACTUATOR SURFACE MODEL

Essential features of the actuator surface model

The actuator surface (AS) concept exposed here addresses the modeling of lifting devices aerodynamics, where strong viscous separation does not occur so that lift is linked to the circulation as in inviscid flow theory. In practice, for a wind turbine, using the AS to model the rotor aerodynamics consists in using an infinitely thin surface whose shape corresponds to the blade planform area, as shown in Figure 1. The AS is a vortex sheet that can be described by a vorticity vector $\vec{\gamma}$ which measures the integral sum of vorticity over the thickness of the sheet, if vorticity were spread over a finite thickness. Since here the sheet is infinitely thin, $\vec{\gamma}(x,y,z)$ is a Dirac-type function and has units of vorticity $\times$ distance.

Let (u,v,w) be the components of the Eulerian velocity field $\vec{V}$ in the (X,Y,Z) Cartesian system of coordinates (see Figure 1). It can be proven [4] that a particle of fluid that crosses the AS from $x < x_{AS}$ to $x > x_{AS}$ undergoes a sudden increase in velocity given by $\Delta\vec{V} = \vec{\gamma} \times \vec{n}_{AS}$, where $\vec{n}_{AS}$ is a unit vector normal to the AS (in the specific example of Figure 1, $\vec{n}_{AS}$ points in the X direction). When applying the principles of vorticity flux conservation to the vortex sheet, it is found that the divergence of the $\vec{\gamma}$ field must be null, hence:

$$\nabla \cdot \vec{\gamma} = 0 \tag{1}$$

This first equation implies that the distribution of discontinuities across the AS is constrained and not completely free; in practice, this equation serves to derive the lateral component of the velocity discontinuities while the component of the velocity jump along the aerodynamic lifting section is prescribed via knowledge of circulation from blade-element analysis (see section below).

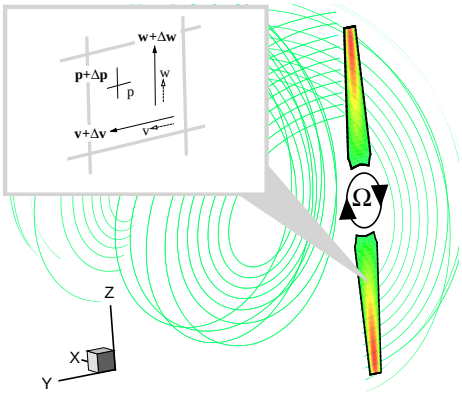

Figure 1. The actuator surface used to model wind turbine blade aerodynamics

A second consequence of the AS is to be analyzed dynamically. Indeed, a particle that crosses the AS undergoes step changes in velocities which must be related to an attached system of forces responsible for changing the particle's momentum. If the (*X*,*Y*,*Z*) system of Figure 1 is set to rotate at the same velocity as the AS modeling the wind turbine blades, it can be shown [3] that the force $\vec{f}_{AS}$ per unit area of the AS surface is given by:

$$\vec{f}_{AS} = -\rho \vec{V}_{rel,avg} \times \vec{\gamma} \tag{2}$$

where $\vec{V}_{rel,avg} = \left(\vec{V} + \Delta\vec{V}/2\right) - \vec{V}_{AS}$ is the average flow velocity relative to the AS and $\vec{V}_{AS}$ is the velocity of the AS at the point where $\vec{f}_{AS}$ is evaluated.

Velocity and pressure discontinuities, together with the associated system of forces (which is the force exerted by the AS on the flow per unit area of the AS), fully represent the action of the AS on the flow governed by the Navier-Stokes equations in the general form, or the Euler equations in this particular case. The determination of the AS loading starts with local blade-element analysis and calculation of the circulation around sections of the AS. In the next section, these steps are presented.

Determination of the AS loading

In this work, blade element analysis is used to determine the values of circulation along the airfoil sections of a wind turbine blade or a wing. The relative velocity seen by the blade, $\vec{V}_{rel}$, is evaluated from the flow solution calculated by the proposed numerical method, which solves the problem raised by the actuator surface whose loading depends on $\vec{V}_{rel}$ as well. This interdependence between actuator surface loading and flow velocities at the actuator surface results in an iterative process that takes place during the solution process.

In the case of the finite wing and the two-bladed turbine, relative velocities, as well as the angles of attack along the blade, are evaluated at the AS surface. In the case of the three-bladed turbine, where grid lines are not aligned with the blades (see below), flowfield characteristics are first determined on control points located 0.8 times the blade chord upstream of each blade. A correspondence between a point on an upstream line and a point on the blade is made through the distance from the root of the blade, measured in both cases on a line going perpendicularly towards the root. The relative velocity on a point *P* of an upstream line, $\vec{V}_{rel,\mathrm{P}}$, is found by an interpolation using the velocities calculated at the four closest grid points. This relative velocity, together with the pitch angle of the blade, and the local twist angle at a given distance from the root of the blade, is used to calculate an inflow angle at the position *P*, which is defined as the angle between the orientation of the local chordline of the blade and the relative velocity $\vec{V}_{rel,\mathrm{P}}$. The transition from an inflow angle at an upstream location to the angle of attack on a blade is made using the following transfer function, developed by NREL [5]:

$$\alpha = -5.427 \times 10^{-5} \alpha_m^3 + 6.713 \times 10^{-3} \alpha_m^2 + 0.617\ \alpha_m - 0.8293$$

With α the angle of attack, and α_m the inflow angle.

Using the definition of the lift coefficient and the Kutta-Joukowsky law, the circulation Γ can be written as [3]:

$$\Gamma = \frac{1}{2} c \left\| \vec{V}_{rel} \right\| C_l \tag{3}$$

Special care is needed in assuring a reasonable circulation distribution using blade elements as mentioned above in terms of numerical stability and physical accuracy. The simple use of blade elements as described above will not always guarantee a zero circulation at the blades tip and root, as expected in reality. Therefore, a zero circulation is imposed at the tip and root of the blades. Moreover, a radial distribution leading to too steep gradients might lead to too important velocity jumps that might prevent the calculation from converging. For example, the use of an elliptical distribution which leads to infinite circulation gradients at the tip and root of a blad or wing cannot be modelled in our method. For this reason, following the idea of Sant [6], an option is included that allows the circulation values at a chosen number of radial positions to be linked by cubic splines, leading to smoother variations of circulation along the blade. These two features were not implemented for the finite wing, where a smooth circulation distribution naturally fell to zero at the root and tip of the wing.

Distribution of discontinuities on planar actuator surface

Once the circulation Γ around a section of a planar AS is known, the task consists in distributing this circulation along the section in the most appropriate way, provided that $\int_0^c \Delta v dy = \Gamma$. In this work, a simple parabolic distribution is assumed to specify the Δv distribution along the chord. For the finite wing and the two-bladed rotor that are aligned with the grid lines (see below), the distribution of the lateral velocity discontinuity Δw can be deduced analytically from equation (1) and the boundary condition $\Delta w=0$ at $y=0$ [3]. For the three-bladed rotor, where the blades are not aligned with grid lines, the distribution of Δw is to be found from solving equation (1) numerically. This is done by integrating equation (1) on the surface S of each quadrilateral cell forming the rotor plane, which contains the actuator surfaces. Here, Green's theorem is used to transform this surface integral into a line integral along the cell contour C:

$$\iint_S \left(\frac{\partial \Delta w}{\partial y} - \frac{\partial \Delta v}{\partial z} \right) dydz = \oint \left(\Delta v dy + \Delta w dz \right) = 0 \tag{4}$$

Performing this line integral around each quadrilateral cell in the rotor plane will lead to a system of linear equations that is to be solved for Δw using the known Δv distribution, and imposing $\Delta w=0$ everywhere outside a given blade as a boundary condition. An explicit scheme is used in space to determine which values of Δv and Δw are to be used in calculating the integrals at the frontiers of each quadrangle, where upstream values at a given grid point are to act on the frontier downstream from this point.

The picture of the AS as a model for wind turbine aerodynamics is now complete. The reader is referred to [2, 3] for information about how to embed the AS model into a CFD method to solve for the flow around the AS, specifically the 3D Control-Volume Finite-Element Method (CVFEM) of Saabas & Baliga [7]. It is to be noted that in the following applications of the AS method, the system of reference is chosen fixed relative to the AS, hence the CVFEMs are used to solve for a steady flow.

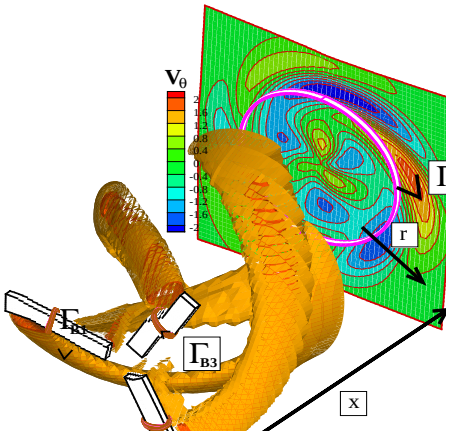

Figure 2. Illustration of the method used to calculate the vorticity in the wake of the turbine Γ_W

VORTICITY CONSERVATION ISSUES

The vortex system associated with a wind turbine rotor consists in bound vorticity that is attached to the blades, as well as trailing vortices forming the wake behind the rotor. This vorticity system originates at the blade from viscous forces affecting the flow close to its surface, in the boundary layer. The bound vorticity is modelled by the actuator surface itself in the AS method, which makes it in this sense similar to a vortex wake method. However, the trailing vortices are not represented as such in the wake of the turbine by this method as they are in a vortex wake method, but are rather intrinsically modelled by the CFD method. Helmholtz's third law for inviscid flows states that vortex filaments cannot end inside a fluid and must have the same strength throughout their lengths, imposing therefore vorticity conservation. This law applies to the studied case of blades or wings where viscous effects are approximated to be confined to the boundary layer and viscous forces are negligible elsewhere. In order for the AS method to be consistent, it must obey this law and predict vorticity conservation from its formation at the blade throughout its evolution in the wake of the blade. A method illustrated in Figure 2 was developed to verify if it is the case or not. It makes use of Green's theorem stating that the flux of vorticity through a circular surface as the one shown in the plane at the right of the figure is equal to the line integral of the tangential velocity around the perimeter of this surface. This line integral can therefore be used to find the circulation in the wake Γ_w at the axial position x of the circular plane relative to the plane of the rotor. If vorticity is conserved, and no wake expansion is present, the vorticity entering a circular plane of radius r should consist in three root vortices (for a three-bladed wind turbine), plus any change in the bound vorticity on the blades as one moves along the blades up to the position r, that would result in trailing vorticity leaving the blades into the wake. This is specifically equal to the addition of the bound vortices on the three blades Γ_{B1}, Γ_{B2} and Γ_{B3}, that can be calculated by performing contour line integrals around the blades as indicated in the figure. This method then makes it possible to track down vorticity evolution and verify if it fulfills Helmholtz's third law, keeping however in mind that wake expansion does occur, so that in reality one can only write $\Gamma_w \approx \Gamma_{B1} + \Gamma_{B2} + \Gamma_{B3}$.

RESULTS

Finite wing in translation

As a first verification, we study the distribution of vorticity in the wake of a finite wing. The actuator surface used to model the finite wing is a flat tapered plate parallel to the incoming flow. Four wing geometries are studied, all having identical span b of 10m and aspect ratio of 10, but different tip to root ratio (1.0; 0.8; 0.6; 0.4). The reader is referred to [2] for information and calculation parameters regarding the grid used to solve this problem. Let us only mention here that

grid lines follow the sides of the wing, and nodes are placed on the mid-chord of the wing to compute the induced angle α_i. The lift coefficient is then calculated using the thin airfoil relation $C_L = 2\pi(\beta - \alpha_i)$ where β is the wing pitch angle (here fixed to 5 degrees). Figure 3 shows the wake circulation Γ_W calculated at three downstream axial positions in the wake (2m, 10m and 100m) using the following equation :

$$\Gamma_W(x,y) = -\int_{-\infty}^{+\infty} w(x,y,z)dz \tag{5}$$

Where w is the component of the velocity measured along the z axis that is perpendicular to the AS (x is streamwise and y is spanwise, y=0 delimiting the middle of the wing). The results shown were obtained using the second order convection scheme available in the present numerical model [3]. Using the same reasoning than the one presented in the section above, we expect more or less that Γ_W be equal to the bound vorticity at the same spanwise location. This is indeed verified in Figure 3 where it is visible that in the near wake, distribution of wake closely matches the bound vorticity distribution, whereas further downstream the distributions are smeared out, due to numerical and viscous diffusion. However, the circulation is not found to reach zero for spanwise positions $y>b/2$, as it should. We believe that this undesired behavior is due to the choice of boundary conditions on the side of the calculation domain where velocities are imposed to be equal to the incoming velocity U_∞, which prevent the perturbations induced by the wing vortices system to be represented on the domain sides.

Wind turbines

The reader is referred to [3] for information regarding the discretization and grid parameters used to model the two-bladed TUDelft experimentatal rotor. Figure 4 shows the calculated Γ_W compared with the blade bound vorticity for this 0.6m-radius rotor at a tip-speed ratio of 8. The first order convection scheme available in the present numerical model [3] was used here. Results are also

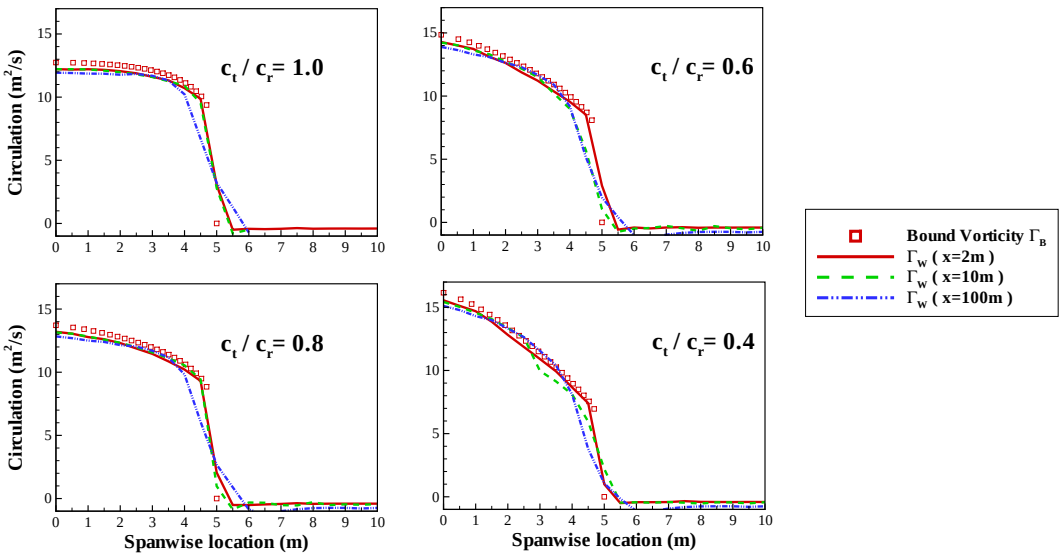

Figure 3. Results for the finite wing in translation

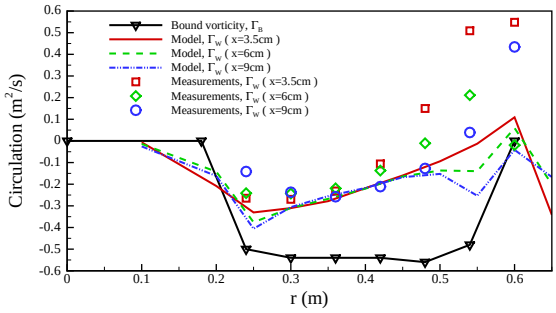

Figure 4. Results for the TUDelft experimental rotor

compared with experimental wake circulation values. The latter are obtained at three different downstream locations in the wake (d=3.5cm, 6cm and 9cm) by integrating around circular contours (as discussed in the section concerning vorticity conservation above) the tangential velocities measured using hot-wire anemometry, as described in [6]. It is observed that neither the simulation results nor the experimental results show satisfactory agreement between the circulations calculated in the wake and around the blades. It is however remarkable that numerical and experimental wake circulations agree well except at the wake outer boundary ($0.5 < r < 0.6$). Although we have not investigated this case in more details, we believe that this is essentially due to turbulent and viscous diffusion occurring in the wake of this rapidly rotating wind turbine (700rpm).

101x101x101 points are used to discretize the 3D grid around the three-bladed 10-m diameter (D) NREL rotor, with local refinement in the rotor plane. The rotor is represented by three rectangular ASs, each containing 110 nodes, and located in a 2D plane of dimension 4D x 4D oriented normally to the incoming flow. The 3D grid is obtained by extending this 2D plane 20D upwind and 1D downwind from the rotor plane. Figure 5 shows the circulation in the wake Γ_W compared with the blade bound vorticity for a tip speed ratio of 6. Results are shown for both the first and second order convection schemes available in the present numerical model [3]. The use of the second order convection scheme is seen to result in an improvement of the agreement between the bound circulation and the circulation in the wake. In previous studies, the second order convection scheme was also found to lead to more accurate results [3]. The shapes of the curves agree quite well, although a small difference in circulation amplitude is observed. The circulation at a radial position larger than the blade radius tends towards zero, which is expected. One has to note however that it should not reach 0 at a distance exactly equal to the radius of the blade due to wake expansion. The first order curves show that little dissipation is seen to occur as one moves further into the wake, but it is not possible at this moment to affirm if it consists in numerical or physical diffusion.

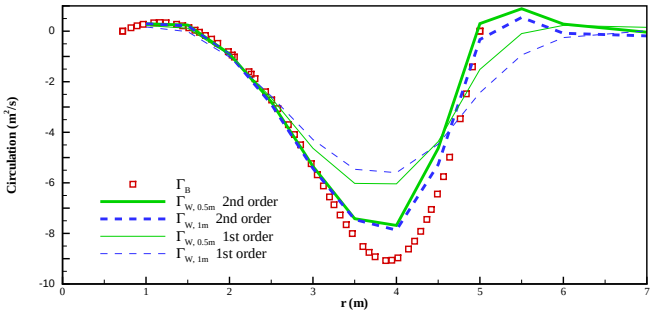

Figure 5. Results for the NREL experimental rotor Γ_W

CONCLUSION

The results obtained for the three-bladed rotating turbine and the finite wing in translation suggest that the AS method is able to correctly model and preserve vorticity in the wake, despite the fact that is does not explicitely model vortices in the wake, but leaves it in the hands of the CFD model. However, problems were obtained for the rapidly rotating TUDelft rotor concerning both the simulations and experimental results, and were expected to possibly be due to turbulent and viscous diffusion. Work will soon be performed to model the Mexico 4.5m diameter wind turbine recently tested in Europe's largest wind turbine, where velocities in the wake are measured using PIV, and should help in clearing that out. The nature of the diffusion that was observed in the wake still remains to be studied further in detail, as it was not possible at this time to determine it if consisted in numerical or physical diffusion. This is an important point that needs to be investigated to guarantee that the model is pertinent to study wind turbine wake aerodynamics.

ACKNOWLEGMENTS

We would like to thank TUDelft for providing access to their experimental data. This study received support from the Canada Research Chairs Program. S.-P. Breton would like to thank the Fonds Québécois de la recherche sur la nature et les technologies for financial assistance in the form of a post-doctoral scholarship.

REFERENCES

[1] Masson C. and Leclerc C., Toward blade-tip vortex simulation with an actuator-lifting surface model. *ASME Wind Energy Symposium,* American Institute of Aeronautics and Astronautics: Reno, Nevada, 2004, pp 300–308.

[2] Sibuet Watters C. and Masson C., Recent advances in modeling of wind turbine wake vertical structure using a differential actuator disk theory. *2nd conference: The Science of making Torque from Wind*, J. Phys.: Conf. Ser.: Danish Technical University, DK, 2007.

[3] Sibuet Watters C. and Masson C., Modelling of lifting devices aerodynamics using the actuator surface concept. *Submitted to the Int. J. Num. Methods in fluids*, 2008.

[4] Wu J.Z., Ma H.Y., Zhou M.D., *Vorticity and Vortex Dynamics*, Springer, 2006.

[5] Schepers J., Brand A., Bruining A., Graham J., Hand M., Infield D., Madsen H., Paynter R., Simms D., Final report of IEA annex XIV: Field rotor aerodynamics, *Technical Report ECN-C–97-027*, ECN 1997.

[6] Sant T., Improving BEM-based aerodynamic models in wind turbine design codes, *PhD Thesis*, Technical University of Delft, 2007.

[7] Saabas H., Control volume finite element method for three-dimensional, incompressible, viscous fluid flow, *PhD Thesis*, Mc Gill University, 1991.

STUDY ON THE HEAT TRANSFER CHARACTERISTICS IN THE LOWER SPLASH REGION OF CIRCULATING FLUIDIZED BED RISER

R.S. Patil[1], M. Pandey[1], P. Mahanta[1,*]
[1]Indian Institute of Technology, Guwahati, India

ABSTRACT. This paper presents the results of experimental studies on the wall to bed heat transfer behaviour in the lower splash region of a Cold Circulating Fluidized Bed (CCFB) riser of uniform cross sectional area (0.15 m × 0.15 m). Experiments were carried out with different superficial velocities of air (4.8 – 6.4 m/s) with a constant heat flux of 1600 W/m^2. Further, experiments were repeated with two different sand inventories of 10 kg and 16 kg with mean particle size of 271 μm. Heat transfer coefficient was evaluated along the riser height. Temperature distributions across the riser bed were also estimated at two locations along the riser height, i.e., 0.8 m and 1 m respectively. Trends obtained have been compared for different superficial velocities of air and sand inventories.

Keywords: *Circulating fluidized bed, heat transfer coefficient, bed temperature, riser*

INTRODUCTION

Use of circulating fluidized bed (CFB) boilers in power generation is gaining popularity because of its environmental compatibility and high efficiency. To increase the capacity of boiler, it is essential to increase the cross section of CFB boiler along with its height. However it is desirable to restrict the height of the furnace to about forty meters due to commercial constraints [1]. In such a case, additional heat transfer surface area is to be provided to complement the furnace wall area in order to accomplish the required heat absorption for the production of superheated steam. This is sought to be accomplished in practice by providing: (i) an External Heat Exchanger (EHE) at the bottom of the cyclone dipleg before recirculation of solids and/or (ii) in-furnace heat exchangers suspended in the core space of upper dilute zone of the riser in the form of wing walls, omega panels, and a division or a curtain wall. Knowledge of the heat transfer behaviour in different extraction methods is essential for a proper design and operation of a CFB boiler. Heat transfer characteristics at an axial tube located along the axis of the CFB riser were reported by Kolar and Sundaresan [1]. They have reported that heat transfer coefficient decreases with increase in superficial velocity and increases with increase in solid circulation rate.

Axial distributions of local heat transfer coefficient along the riser height in the upper dilute region of the riser were reported by Kolar [2], Basu [3], Zeng et al. [4], Bi et al. [5] and Ahn and Han [6].

Large-scale fluidized beds for commercial processes commonly require lager heat transfer surfaces. Design then demands that proper heat transfer coefficients be specified. Empirical correlations are unable to cover the wide range of variables and conditions encountered. Therefore, the mechanistic

* Corresponding author: Prof. P.Mahanta
Phone: + (91)-361-2583126, Fax: + (91)-361-2690762
E-mail address: pinak@iitg.ernet.in

model that incorporates the key factors influencing heat transfer to predict the heat transfer coefficient has been reported by Chen et al. [7].

From the literature review it is found that most of the heat transfer works on CFB were reported for the upper splash region of the riser. There will be erosion of the lower splash region during operation of CFB boiler, as lower splash region is having dense hot stream of coal, limestone and sand etc. For designing the entire CFB, the study on lower splash region is equally important and emphasis has been given in the present paper to find variation of heat transfer coefficient along the height of the heater and bed (air + solid mixture flow) temperature distribution across the heater. This will help in designing more efficient CFB boiler.

EXPERIMENTAL SETUP

The setup of CFB, designed and developed at IIT Guwahati, is shown in Figure 1. It consists of uniform cross sectional area (0.15 m × 0.15 m) made of plexiglass (to facilitate flow visualization). A positive displacement type blower powered by a 20 HP motor supplies air. Figure 1 indicates: 1.Motor, 2.Blower, 3.Bypass valve, 4.Main control valve, 5.Water manometer, 6.Orifice plate, 7.Riser column, 8.Cyclone separator, 9.Downcomer, 10.Sand measuring section, 11.Butterfly valve, 12.Distributor plate, 13.Aeration valve, 14.Insulated heater, and 15.Pressure tapings. Heater (shown in Figure 2) has 1.Nichrome wire, 2.Mica, 3.Mica, 4.Wall temperature thermocouple, 5.Asbestos sheet, 6.Ceramics wool, 7.MS wall, 8.Bed temperature thermocouples to measure the temperature at the along the height of the heater, and 9. Thermocouples used to measure the bed temperature across the heater at the sections taken 0.8 m and 1 m above the distributor plate perpendicular to the height of the heater.

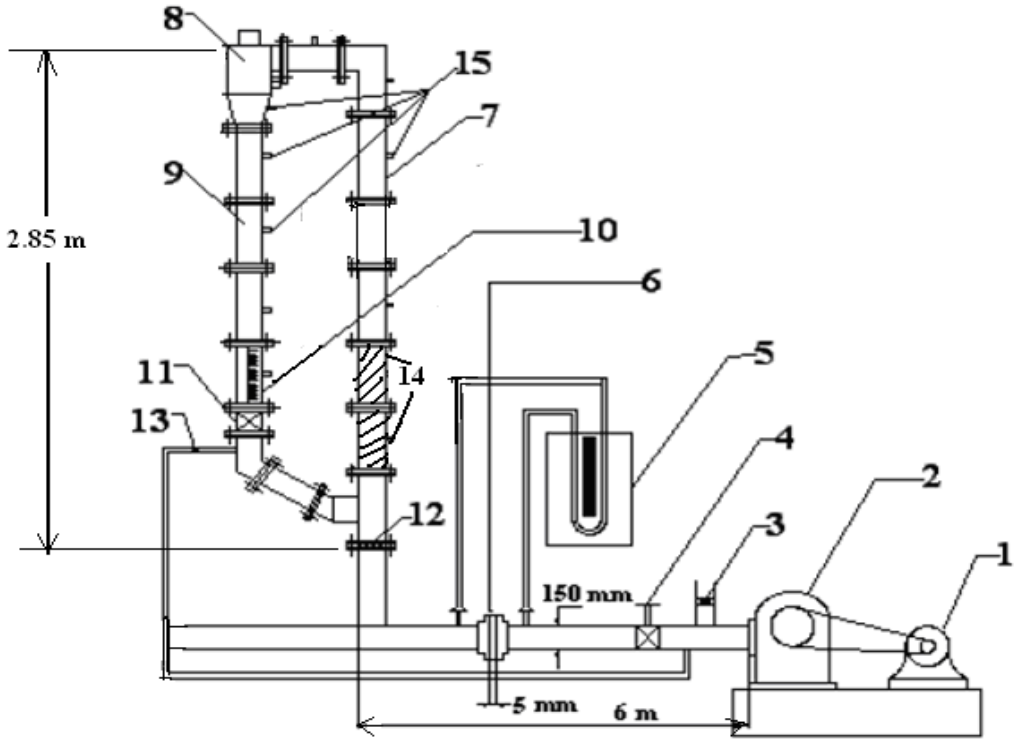

Figure 1. Experimental setup of Cold Circulating Fluidized Bed

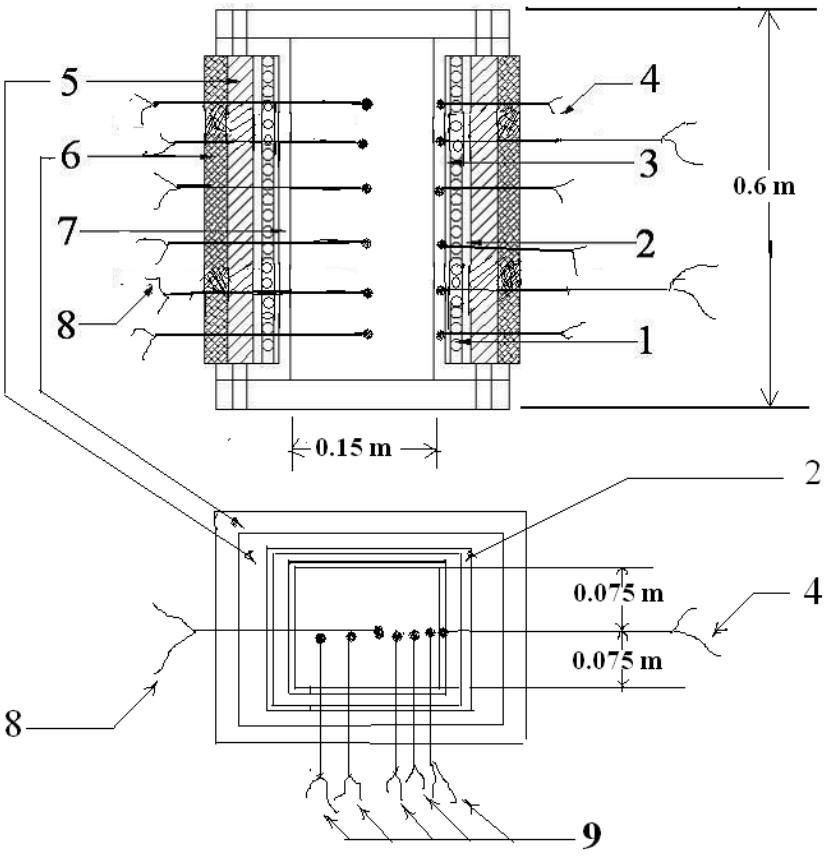

Figure 2. Heater

The main function of the heater (Figure 2) is to supply the heat flux externally for carrying out heat transfer studies. The heater has been fabricated from MS sheet of 2 mm thickness. Height of the heater was of 0.6 m and has been located 0.6 m above the distributor plate. Electric supply has been provided to the Nichrome wire of 2000 W capacity, wound on the mica sheet of 1.5 mm thickness which covers the MS wall of the heater. Another mica sheet, which acts as electric insulator, has been provided on the Nichrome wire. To avoid the heat losses by radiation, ceramic wool and 6 mm thick asbestos sheet has been provided on the mica sheet. Heat has been supplied to the wall of MS heater therefore wall to bed (solid + air mixture) heat transfer would occur at the heater. To measure the temperature of the surface of the heater and the bed temperature, calibrated T type thermocouples have been installed on the wall and inside the heater. The heat flux input to the heater wall has been controlled with the help of a variac.

Six thermocouples each have been used to measure the axial bed temperature and surface temperature of the riser column. These thermocouples have been placed at an equal distance of 0.85 m. Two cross sections have been taken in the heater at 0.8 m and 1 m above the distributor. Six thermocouples have been placed in each cross section to measure the non axial bed temperatures at non-dimensional distance of 0.3, 0.43, 0.5, 0.73, 0.83 and 0.9. Here the non-dimensional distance is the distance X (in m) measured from the left hand side wall of the heater to the thermocouple end, normalized with respect to the width B (0.15 m) of the heater.

HEAT TRANSFER STUDY

The heat transfer coefficient (h) [8] is calculated by

$$h = Q / A_S . (T_S - T_B) \quad W.m^{-2}.K^{-1} \qquad (1)$$

where T_B and T_S represent the bed and wall temperature, respectively, A_S is the surface area of the heater and Q is the heat supplied (in W) at heater, measured using a Wattmeter. T type calibrated thermocouples and data acquisition system with Dasy Lab software version 8.0 has been used to measure the T_S and T_B.

Experiments have been carried out at different superficial air velocities of 4.8 m/s, 5.4 m/s and 6.4 m/s, at the constant heat flux of 1600 W/m^2, for two different sand inventories of 10 kg and 16 kg having average particle size of 271 μm.

Following sections represent the results and discussions on bed temperature distribution and variation of heat transfer coefficient along the axis (height) of the heater.

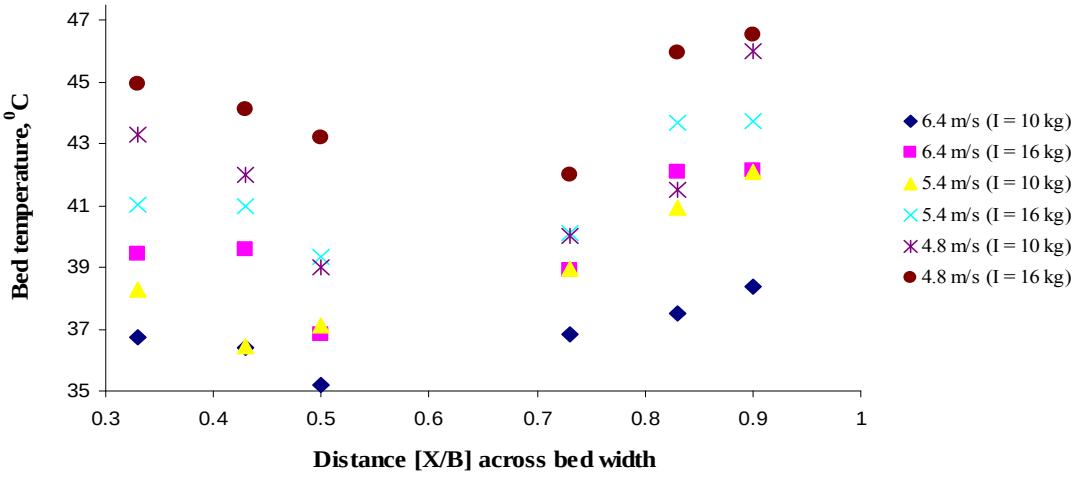

Figure 3. Bed temperature distribution at 0.8 m above the distributor plate

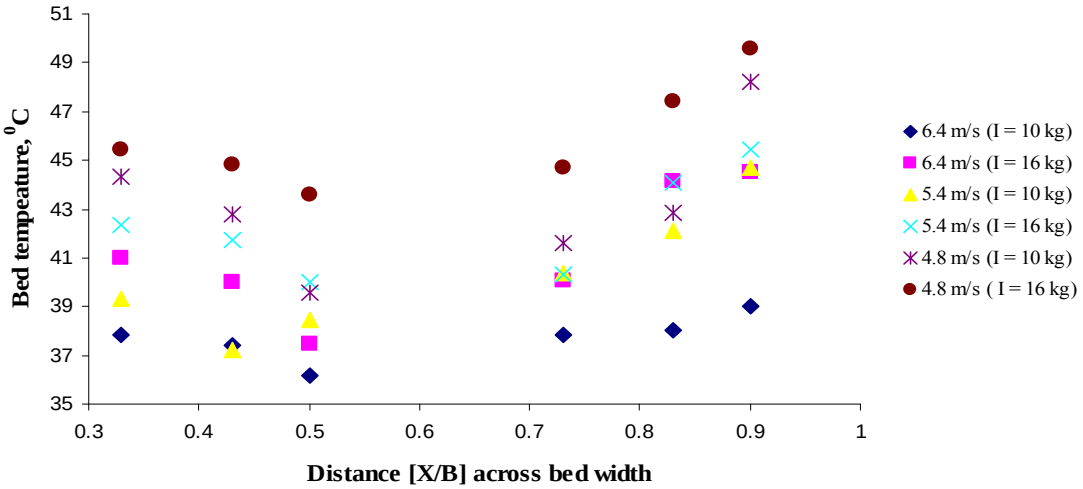

Figure 4. Bed temperature distribution at 1 m above the distributor plate

BED TEMPERATURE DISTRIBUTION ACROSS THE HEATER

Figure 3 and 4 indicates the bed temperature distribution for two cross sections taken at 0.8 m and 1 m above the distributor plate respectively. Bed temperature distribution have been compared for different fluidizing air velocities at two different sand inventories, I = 10 kg and I = 16 kg.

When superficial air velocity increases, bed temperature decreases and it was maximum near the both the heated walls of heater while less at the centre of heater. It has been observed that, for the same fluidizing velocity bed temperature increases with increase in inventory of sand.

It has been observed that corresponding bed temperatures were more at bed cross section taken at 1 m height above the distributor plate than respective bed temperatures measured at cross section taken at 0.8 m height above the distributor plate.

Bed temperature at right hand side wall was more than bed temperature at left hand side wall because of more particle concentration at right hand side wall due to incoming particles from dipleg, which were forced upward towards the right hand side wall in the riser by central high speed air flow coming from distributor plate. Thus particle concentration is important phenomena in bed temperature distribution.

HEAT TRANSFER COEFFICIENT DISTRIBUTION

Figure 5 indicates the axial distribution of heat transfer coefficient along the height of the heater. Heat transfer coefficient have been compared for different superficial air velocities at different sand inventories such as I = 10 kg and I = 16 kg.

It has been observed that, heat transfer coefficient increases with decrease in superficial velocity of air measured at the same sand inventory. It was observed that heat transfer coefficient measured at same superficial velocity of air but at different sand inventories decreases with decrease in sand inventory

At constant heat flux, the value of heat transfer coefficient decreases along the height of heater in the upward direction because of increase in temperature difference of wall and bed (T_S - T_B).

It has been observed that the heat transfer coefficient decreases rapidly in bottom dense zone as shown in Figure 5. It can be concluded that heat transfer coefficient decreases rapidly when the amount of sand particles in the mixture flow of air + sand decreases considerably. It means that sand particles had major role in carrying heat from wall of the heater.

CONCLUSIONS

Experiments based on the wall to bed heat transfer have been completed along the heater placed in the riser of the CFB. Bed temperature distributions across the heater have been obtained at two different sections, 0.8 m and 1 m above the distributor plate. Bed temperature decreases with increase in the superficial velocity of air and decrease in the sand inventory. Bed temperature at right hand side wall was more than bed temperature at left hand side wall because of more particle concentration at right hand side wall. Therefore particle concentration is important phenomena in bed temperature distribution.

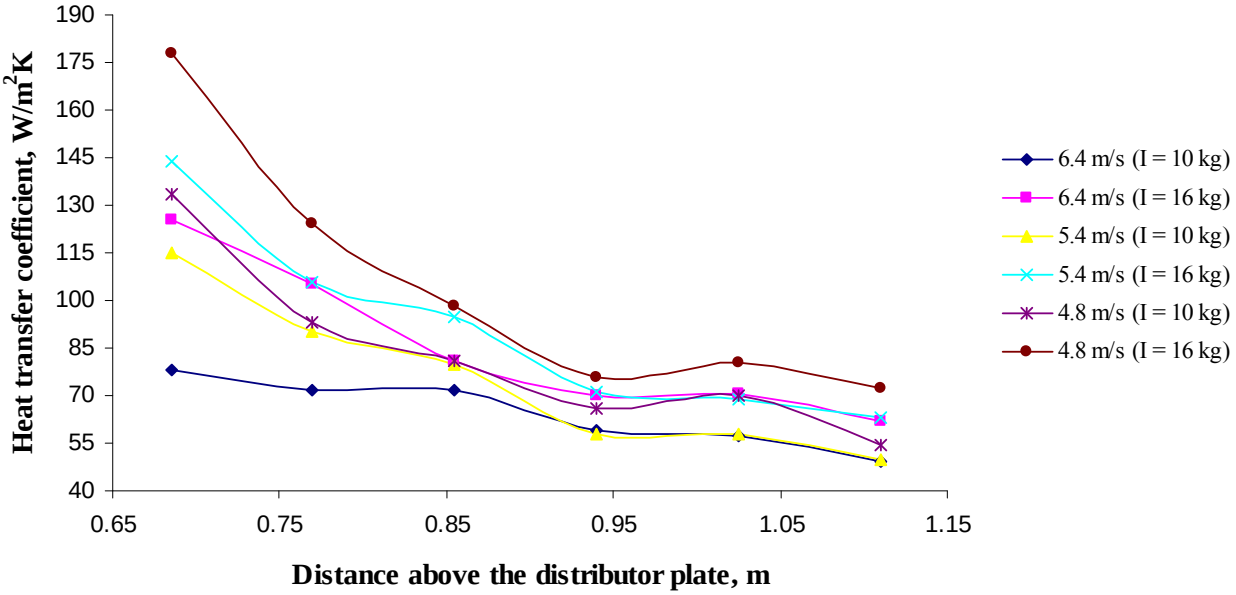

Figure 5. Axial distribution of the heat transfer coefficient along the height of the heater

Heat transfer coefficient has been estimated along the height of the heater. Heat transfer coefficient increases with decrease in the superficial velocity of air and increase in the sand inventory. It has been observed that the heat transfer coefficient decreases rapidly in the bottom dense portion of the riser. It can be concluded that heat transfer coefficient decreases rapidly when the amount of sand particles in the mixture (air + sand) flow decreases considerably. It means that sand particles had major role in carrying heat from wall of the heater. Thus study on estimation of the bed temperature and heat transfer coefficient in the lower portion of riser, which is comparatively hotter and denser region of solid particles, will be useful in designing more efficient CFB boiler.

ACKNOWLEDGEMENT

The experimental facility used in the present work was setup with financial support from the Ministry of HRD, Govt. of India.

REFERENCES

1. Kolar, A. K. and Sundaresan, R., Heat Transfer Characteristics at an Axial Tube in a Circulating Fluidized Bed Riser, *International Journal of Thermal Sciences*, Vol. 41, pp 673-681, 2002.
2. Kolar, A.K., Heat Transfer in Circulating Fluidized Bed Boilers: Perspective and Issues, *Proceedings of Fourth ISHMT-ASME Heat and Mass Transfer Conference,* Tata McGraw-Hill, India, 2000, pp 105-116.
3. Basu, P., Heat Transfer in High Temperature Fast Fluidized Beds, *Chemical Engrg. Sci.*, pp 3123–3136, 1990.
4. Zheng, Q.Y., Wang, X. and Li, X., Heat Transfer in Circulating Fluidized Bed, P. Basu, M. Horio, M. Hasatani (Eds.), *Circulating Fluidized Bed Technology III*, Pergamon Press, Canada, 1991, pp 263–268.

5. Bi, H., Jin Y., Yu, Z. and Bai, D., An Investigation of Heat Transfer in CFB, P. Basu, M. Horio, M. Hasatani (Eds.), *Circulating Fluidized Bed Technology III*, Pergamon Press, Canada, 1991, pp 233–238.
6. Ahn, G.R. and Han, G.Y., Bed-To-Immersed Tube Heat Transfer in a Circulating Fluidized Bed, *J. Chem. Engrg.,* Japan, Vol. 30, pp 421–426, 1997.
7. Chen, J.C., Grace, J.R. and Golriz, M.R., Heat Transfer in Fluidized Beds: Design Methods, *Powder Technology*, Vol. 150, pp 123-132, 2005.
8. Kunii, D., and Levenspiel, O., *Fluidization Engineering*, Butterworth-Heinemann, USA, 1991.

PERFORMANCE EVALUATION OF DIRECT STEAM GENERATION TROUGH SOLAR ENERGY GENERATION SYSTEM IN 30 CITIES OF CHINA

D.H. Mei, Y.L.He*, Y.B. Tao, W.Q. Tao
School of Energy and Power Engineering, Xi'an Jiaotong University, Xi'an, China

ABSTRACT. In this paper, the integrative theory-model-simulation (TMS) study is performed to investigate the performance of the saturated steam turbine cycle direct steam generation (DSG) trough solar energy generation system (SEGS). Based on the solar radiation data in 30 provincial capital cities in China, the running of the whole system is simulated and the yearly performance is calculated, and the effects of day-and-night, seasons, years and latitude on the performances are analyzed. At last, the SEGS is combined with the conventional energy system, and the influence of different conventional energy on the SEGS cost is discussed. All the results obtained by the evaluation carried out in this paper may be useful in the initial stage when an SEGS is being constructed in China.

Keywords: *solar energy generation system, system simulation, direct steam generation, direct solar radiation*

INTRODUCTION

Nowadays too high construction cost is one of the main factors that restrict the commercialization of solar thermal to electric energy conversion system(STEECS), or simply, solar energy generation system (SEGS). It is a promising method to reduce the construction cost by utilizing the technology of direct steam generation (DSG) in SEGS. In 2003, DSG was proven feasible in the horizontal trough collector in the Direct Solar Stem (DISS) of Spain[1]. Many researchers have conducted various studies on SEGS to improve its efficiency. Eck , Schmidt and Eickhoff, et al [2] studied the performance of compact gas-liquid separator on steady-state cases, and the result showed that the suitable value of steam quality in the inlet of the compact gas-liquid separator is 0.7-0.8. To the flow conditions inside the absorber tube, Eck and Steinmann [3] simulated and designed the DSG collector field based on the flow stratification of hot fluid and stability of absorber tube. Natan, Barnea and Taitel [4] investigated the variation of working fluid flow conditions inside the tube with that of direct solar radiation on different working fluid mass flow. Their results indicated that water tends to flow in the tube which gains less solar radiation. Eck, Steinmann and Rheinlander [5] also researched the difference between the performances of tilted and horizontal absorber tubes. It is found that horizontal absorber tube has better performance because of its smaller temperature gradient when the steam quality is not so small. And to the flow conditions of the working fluid in the collector field, Eck, Zarza and Eickhoff et al [1] concluded that recirculation method is the best one among the once-through, injection and recirculation methods. On the other hand, automatic-control mode is one of the key technologies in the DSG trough SEGS. Valenzuela, Zarza and Berenguel et al [6] analyzed the controlling mode when different flow method was used. All such research results are benefit to the improvement the efficiency of SEGS in some extent. Obviously

* Corresponding author: Prof. Y.L. He
Phone: + (86)-29-82663851 Fax:+ (86)-29-82669106
E-mail address: yalinghe@mail.xjtu.edu.cn

when a new SFGS is to be constructed, the site selection is an important factor to be taken into account. In the existing solar energy references very few systematically discussed this factor. In this paper, the 30 provincial capital cities in China are taken into account, a model of saturated steam turbine cycle DSG trough SEGS is built, the variation trend of the total efficiency of the system with the change of day, night, seasons, years and latitude is analysed by using the meteorological data from different places during different times. In order to overcome the drawback of instability and discontinuity of solar radiation, different conventional fuel systems are combined into the SEGS. And the influences of them on the economy of the system are also investigated.

TREATMENT OF METEOROLOGICAL DATA PROVIDED BY WEATHER STATION

In order to provide fundamental data for the simulation of the whole system performance, we collected the meteorological data from the weather station of 30 provincial capital cities in China. Self-compiling programs were established to treat the global and diffuse solar radiation for the hourly, daily, monthly and yearly solar radiation. From the treated meteorological data, it can be seen:

1. Solar radiation is zero in almost half of the year in these regions because of the influence of day and night. The ratio of effective direct solar radiation time T_u to the global solar radiation time T_t, which is expressed as ξ, is more than 50% in only a few regions (Table 1). These regions are Lhasa, Hohhot, Kunming, Lanzhou, Taiyuan, Shenyang, Shijiazhuang, Beijing and Changsha. According to Eck and Steinmann research results [3], there is no usage value when the direct solar radiation is less than 250 $\mathrm{W\cdot m^{-2}}$. This limitation is called as Two-hundred and Fifty Principle in this paper. The symbol T_u shown above is the time when the direct solar radiation is large than 250 $\mathrm{W\cdot m^{-2}}$, while T_t is the time when the direct solar radiation is not zero.

Table 1
The effective direct solar radiation time to the global solar radiation ratios in each region

City	Hongkong	Guangzhou	Kunming	Guilin	Fuzhou	Guiyang	Changsha	Nanchang
T_t/h	3282	3353	3717	3088	3264	3216	3357	3298
T_u/h	1638	1628	2389	1197	1512	1421	1819	1536
ξ	0.499	0.486	0.643	0.388	0.463	0.442	0.542	0.466
City	Chongqing	Lhasa	Hangzhou	Wuhan	Chengdu	Shanghai	Hefei	Nanjing
T_t/h	3272	3846	3219	3249	3226	3159	3271	3121
T_u/h	1465	2609	1619	1499	1388	1464	1648	1177
ξ	0.448	0.678	0.503	0.451	0.430	0.463	0.504	0.377
City	Xi'an	Zhengzhou	Lanzhou	Jinan	Xining	Taiyuan	Shijiazhuang	Tianjin
T_t/h	3335	3378	3682	3335	3412	3619	3531	3157
T_u/h	1438	1689	2176	1497	1759	2058	1882	1484
ξ	0.431	0.500	0.678	0.449	0.516	0.569	0.533	0.470
City	Beijing	Hohhot	Shenyang	Urumchi	Changchun	Harbin		
T_t/h	3535	3931	3477	3553	1830	3516		
T_u/h	1837	2570	1920	1740	1634	1695		
ξ	0.520	0.654	0.552	0.490	0.472	0.482		

2. The yearly direct solar radiation of these 30 regions is shown in Figure 1. The digits of 1~30 on the abscissa represent these 30 regions respectively with the latitude ordered from small to large. It can be seen that there is no direct relationship between the yearly direct solar radiation and the latitude. If the yearly direct solar radiation is regarded as the basis on which to choose the place for construction of a the SEGS, Lhasa, Hohhot, Kunming, Lanzhou, Taiyuan, Changsha, Shenyang, Shijiazhuang, Urumchi,

Beijing and Hefei can be considered, as the yearly direct solar radiation in these places is larger than $1.0\times10^{6}\ \mathrm{W\cdot m^{-2}}$.

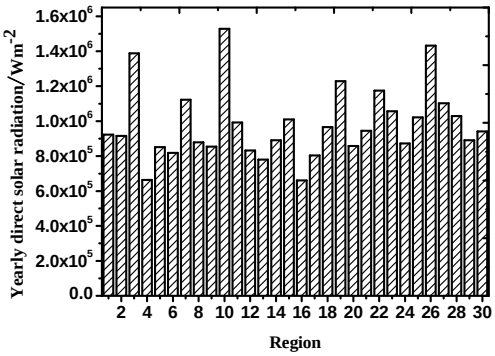

Figure. 1 Yearly direct solar radiation of the 30 regions

CONCEPTUAL COMPONENTS DESIGNOF THE SATURATED STEAM TURBINE CYCLE DSG TROUGH SEGS

In general, SEGS contains 6 parts: solar thermal collect subsystem, energy absorb and delivery subsystem, energy storage subsystem, steam generation subsystem, motive subsystem and power generation subsystem, and solar thermal collect subsystem and motive subsystem are the most important components. In this paper, these two components are designed to form the saturated steam turbine cycle DSG trough SEGS with other components.

Design of the DSG collector field

As mentioned above the feasibility of DSG has been proven in DISS project. In this paper, the collectors in the DISS project are used, and the parameters of these collectors [7] are shown in Table 2. Each collector was made up of eight thermal-absorbing units, and eight collectors were in series connection in the south-north direction. In order to make full use of the solar radiation, double-axis tracking system was selected to make sure that solar radiation beam is on the opening plane of the collector. According to Eck and Zarza's paper [8], there were nine collector-rows in the saturated steam turbine cycle, and the last collector in each row was connected to a header pipe; then the header pipes were connected to a vapor liquid separator, and the steam quality in whose inlet was 0.85. The saturated water from the vapor liquid separator was fed into the inlet of the collector field via pump and the saturated steam went to saturated steam turbine directly to work by expansion. Considering both the construction cost and steam quality, this paper takes the steam quality in the inlet of the vapor liquid separator being close to 0.85.

Table 2
Specification and performance parameter of the collector in DISS project

Item	Parameter
Total length of a collector: L /m	98.5
Opening width of a collector: W /m	5.76
Opening area of a collector: A_t /m^2	548.35
No. of thermal absorbing unit in a collector: N	8
Outer diameter of the absorber tube: D_o /m	0.07
Inner diameter of the absorber tube: D_i /m	0.055
Length of thermal absorbing unit: l /m	12.27
Optical efficiency of the collector: POE	0.765

The assumptions in the simplified model of the absorb tube are:

1. The glass casing is not considered, and the ceramal selective absorbing film is sticked to the outer surface of the absorber tube. The emissivity ε_{ab} of the film is given by equation (1) [9],

$$\varepsilon_{ab} = 0.00042 \times T_w - 0.0995 \tag{1}$$

In equation (1), T_w is the temperature on the outer surface of the tube, K.

2. The pipe wall thickness is neglected, and the mean value of inner and outer diameter is treated as the mean diameter of the tube.
3. Temperature in the cross section of the tube is invariable, and it only changes along the axial direction.
4. Temperature in the inlet of each calculation unit is regarded as the temperature on the surface of the unit.
5. Pressure drop along the whole tube and the thermal loss at the junction between every two tubes are not considered.

Usually in the DSG trough collector field, there are three sections: super-cooled water section, vapor-liquid mixture section and superheated steam section. In the super-cooled water and superheated steam sections, the absorber tube is divided into several calculation units, shown in Figure 2, where L and D are the total length and the diameter of the tube, and q is the density of direct solar radiation on the opening face of the collector. In each unit, T_{in}, T_{out} and Δl are the inlet and outlet temperature, axial length of the unit, respectively.

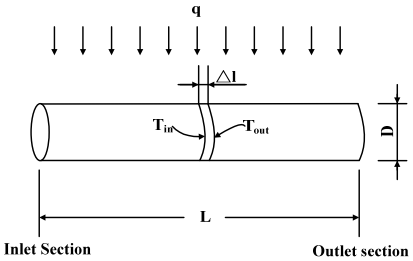

Figure. 2 Calculation diagram of the absorber tube

In these two sections, the temperature in the outlet of each calculation unit and the length of each section are calculated by

$$\Delta l \cdot W \cdot I_{dir} \cdot POE = q_m \left(h_o - h_i\right) + \sigma \varepsilon_{ab} A (T_w^{\,4} - T_e^{\,4}) + hA\left(T_w - T_e\right), \tag{2}$$

where q_m is the mass flow rate of the working fluid(water or steam) in this paper, W and A are the width of the opening face of the collector and the radiating area of each calculation unit respectively, h is the convection heat transfer coefficient between the tube and environment, σ is Stepan- Boltzmann constant, 5.67×10^{-8}. h_o and h_i are respectively the enthalpy of the working fluid in the outlet and inlet of each calculation unit. The water enthalpy can be determined by

$$h = 4348.52053T - 1.19399\times10^6,\ 283\text{K} < T < 553\text{K}, \tag{3}$$

and

$$h = 2482.16519T + 1.47293\times10^6,\ 563\text{K} < T < 1273\text{K}. \tag{4}$$

Equations (3) and (4) are valid only when p is 7 MPa, and they are both obtained by fitting according to the corresponding data between temperature and enthalpy on the water and steam thermodynamic property chart.

In vapor-liquid mixture region, the pressure and temperature of working fluid are invariable when all loss is not considered. So the temperature on the outer surface of the tube in this section is invariable based on the above-mentioned assumption. And the length of this section can be evaluated by

$$l_T \cdot I_{dir} \cdot POE = q_m (h^* - h') + \sigma \varepsilon_{ab} \pi D l_T (T_w^{\,4} - T_e^{\,4}) + h\pi D l_T (T_w - T_e), \tag{5}$$

where l_T is the length of this section, h^* and h' are the enthalpy of saturated steam and water respectively at the calculation point, and other parameters are the same with those in equation (2).

The program flow chart of designing the DSG collector field is shown in Figure 3.

Design of the saturated steam turbine cycle

In this paper, parameters of the SEGS in the design condition are as follows: I_{dir} is 850 $W \cdot m^{-2}$, T_e is 293K, the temperature of the given water T_{in} is 448K, and the efficiency of the generator is 0.96. The performance of the collector field and saturated steam turbine cycle at the design condition is indicated in Table 3.

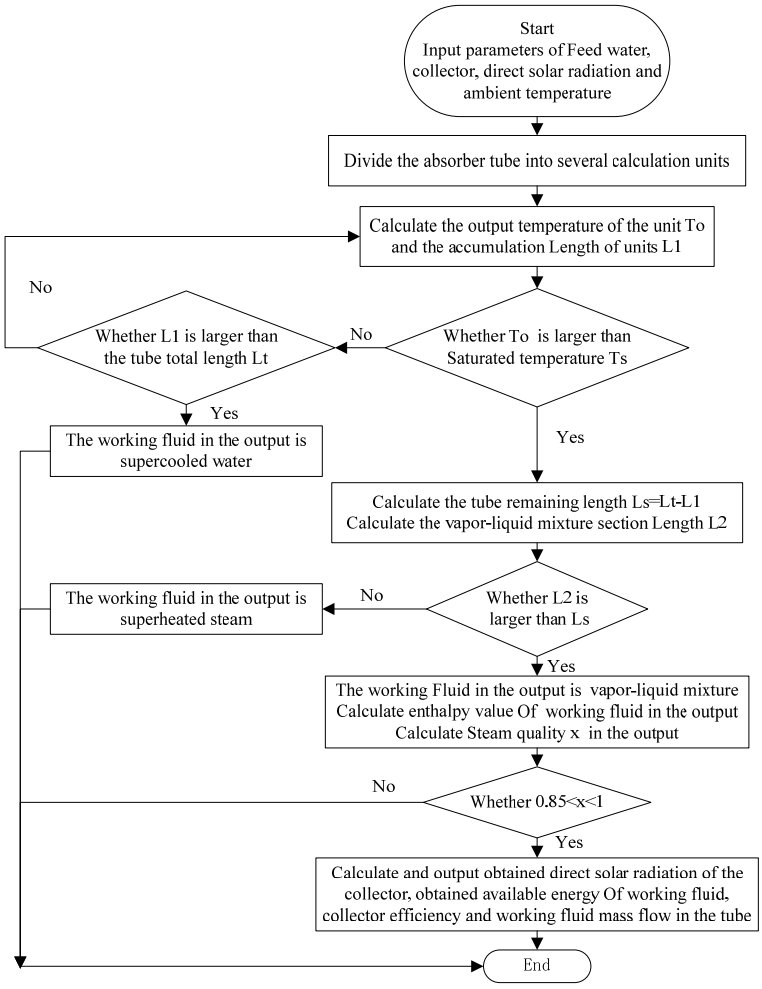

Figure. 3 Program flow chart of designing the DSG collector field

Table 3
Performance of DSG trough SEGS at design condition

Solar thermal collect subsystem	
Direct solar radiation gained in collector field I_t /MWh	124569
Thermal output in collector field Q /MWh	81927
Subsystem efficiency η_c	0.658
Saturated steam output in the field q_{mg} / $kg \cdot s^{-1}$	10.89
Power generation subsystem	
Power output P /MWh	19360
Subsystem efficiency η_{gs}	0.236
DSG trough SEGS	
Total system efficiency η_t	0.155

PERFORMANCE EVALUATION OF THE WHOLE SYSTEM

Performance evaluation of the system without conventional energy system

The motive subsystem designed preliminarily is connected with the DSG collector field and other components, and the performance of the saturated steam turbine cycle DSG trough SEGS, in different time and different regions, is evaluated based on the direct solar radiation in different time and different regions. From the simulation results, the major points are as follows.

1. The system efficiency reaches its peak value at noon, then decreases on both sides, and turn to zero at night as the density of the direct solar radiation is zero. Figure 4 and Figure 5 show the system efficiency of the SEGS and the direct solar radiation in Xi'an in June 22nd, 2002. The shape of these two curves are generally similar except that the efficiency is zero at 6:00 and 18:00 while the direct solar radiation is not zero at that time, just because of the Two-hundred and Fifty Principle.

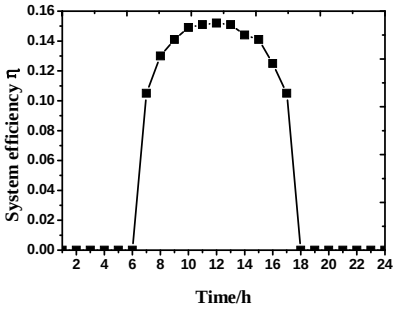

Figure.4 System efficiency of the SEGS in Xi'an in June 22nd, 2002

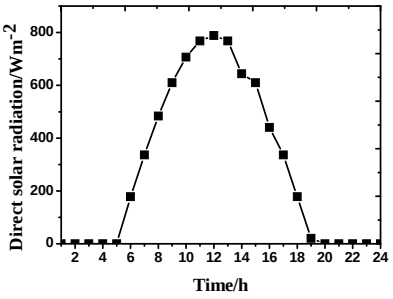

Figure.5 Direct solar radiation in Xi'an in June 22nd, 2002.

2. In accordance with the latitude from low to high in the order, Guangzhou (N23° 00'), Nanchang (N28° 40′), Xi'an (N34° 15'), Beijing (N39° 57') and Harbin(N45° 45') are selected as the places to build the SEGS and the evaluation of the performance is conducted. Figures 6, 7 and 8 indicate the variation of monthly effective working time, net generating capacity and system efficiency of the above five regions.

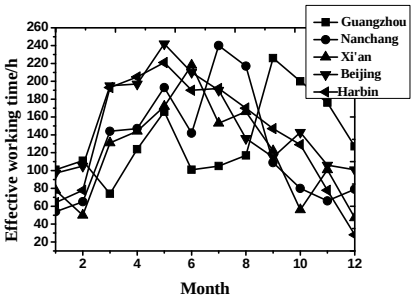

Figure. 6 Effective working time in different latitudes in 2002

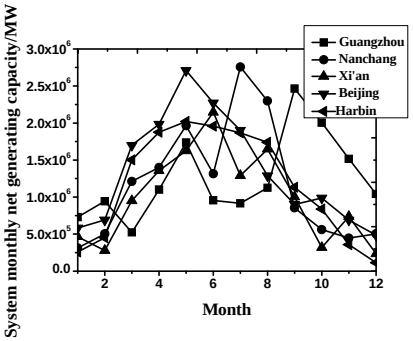

Figure. 7 Monthly net generating capacity in different latitudes in 2002

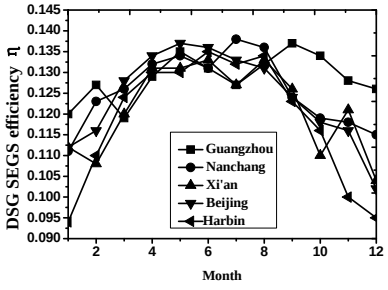

Figure. 8 System efficiency in different latitudes in 2002

It can be seen in Figure 6 that that the effective working time in low latitude regions is shorter than that in high latitude in summer, while opposite in winter. This may be related to the climate characteristics in China. China is in the East Asia monsoon climate zones. Annual rainfall reduces from the southeast coast to the northwest inland. The South not only takes a long rainy season, but also has a rainfall in summer and autumn in some places, while the north and northwest China has less rainfall. On the other hand, there is more snow weather in northern in winter.

From Figure 7 and Figure 8, some similarities between the variations of the monthly net generating capacity and system efficiency with that of latitude are shown. The monthly net generating capacity and system efficiency reduce with the rise of latitude. It can also be concluded that from summer and winter there is no appreciable change in system efficiency among low latitude regions, while there is an obvious change among high latitude regions.

3. The average efficiency of the system in different regions changes little in the year. As seen in Figure 9, average efficiency of the whole system in the 30 regions all keeps between 12.5% and 13.5%, the maximum of which is 13.5% in Lhasa and Changsha and the minimum is 12.5% in Guilin and Changchun. From this it can be seen that the average efficiency of the system can not be the main factor while the building address of the SEGS is being selected.

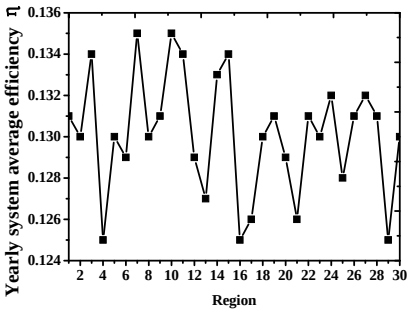

Figure. 9 Yearly system average efficiency of the 30 regions in 2002

Performance evaluation of the system with conventional energy system

It is well-known that the pure SEGS can not operate safely because of instability and discontinuity of solar radiation, leading the operating life of the system to reduce and the maintain cost to increase. In this paper, a conventional energy system is connected with the DSG trough SEGS. When the day and night, seasons and weather conditions change, automatic control device will drive the conventional energy system to work, such that the given water can reach the state requirements of main steam on the inlet of the saturated steam turbine on the designing condition. Hence the system can work steadily.

Diesel, natural gas and coal are selected as the optional conventional energy. The unit price and the combustion value of the three energies are shown in Table 4.

Table 4
Unit price and the combustion value of conventional energy

Conventional energy		Combustion value / $J \cdot kg^{-1}$	Unit price / $Yuan \cdot kg^{-1}$ 、 $Yuan \cdot m^{-3}$	Discount factor of standard coal
Coal	Bituminous coal	2.9×10^7	0.3	0.9285
	Anthracite	3.0×10^7	0.3	0.9855
	Coke	3.4×10^7	0.3	0.9285
Diesel		3.3×10^7	3.4	1.571
Natural gas		7.1×10^7	1.98	1.236

Lhasa is taken as the example, and the amount of the needed conventional energy and the economic cost are calculated. Table 5 indicates the calculation result. From this, it can be seen that when energy amount and economic cost are both considered, coke is a suitable choice when there are abundant coal resources, while natural gas can be selected when coal resources is going to be deficient. On the other hand, diesel is inadvisable as the conventional energy from these two factors. Generally speaking, what conventional energy will be selected depends on the realistic condition of the region where the SEGS is to be built, such as the types of mineral resources in and around the region, transport mode, etc.

Table 5
Amount and economic cost of needed conventional energy in Lhasa 2002

Conventional energy	Bituminous coal	Anthracite	Coke	Diesel	Natural gas
Amount	20033834kg	19366038kg	17087682kg	17605490kg	8182834m^3
Discounted standard coal amount/kg	18601414	19085230	15865913	27658224	10113982
Cost/Yuan	6010151	5809812	5126305	59858668	16202010

CONCLUSIONS

In this paper, the DSG trough SEGS is investigated, and the TMS analysis is conducted to investigate the performance of the saturated steam turbine cycle DSG trough SEGS. The hourly meteorological data of 30 cities in China provided by the weather station are adopted and treated with the self developed program, and the curves of solar radiation value with time and address are obtained. The whole DSG system model is built by the design of the collector field of SEGS and the saturated steam turbine system. Then, the running of the whole system is simulated, the yearly performance is calculated, and the effects of day-and-night, seasons, years and latitude on the performances analyzed according to the solar radiation data. At last, the SEGS is combined with the conventional energy system to discuss the influence of different conventional energy on the SEGS cost.

ACKNOWLEDGEMENTS

The present work is supported by the Key Project of National Natural Science Foundation of China (No.50736005),and National Basic Research Program of China (973 Program)(2007CB206902)

REFERENCES

1. Eck, M., Zarza, E., Eickhoff, M., Rheinlander, J., Valenzuela, L.. Applied research concerning the direct steam generation in the parabolic troughs. Solar Energy. 2003, 74 (4): 341-351.
2. Eck, M., Schmidt, H., Eickhoff, M., Hirsch, T.. Field test of water-steam separators for direct steam generation in parabolic troughs. Journal of Solar Energy Engineering. 2008, 130: 011002-1-011002-6.
3. Eck, M., Steinmann, W.-D.. Modelling and design of direct solar steam generating collector fields. Journal of Solar Energy Engineering. 2005, 127:371-380.
4. Natan, S., Barnea, D., Taitel, Y.. Direct steam generation in parallel pipes. International Journal of Multiphase Flow. 2003,(29): 1669-1683.
5. Eck, M., Steinmann, W-D., Rheinlander,J.. Maximum temperature difference in horizontal and tilted absorber pipes with direct steam generation. Energy. 2004,(29): 665-676.
6. Valenzuela, L., Zarza, E., Berenguel, M., Camacho, E.F.. Control concepts for direct steam generation in parabolic troughs. Solar Energy. 2005,(78): 301-311.
7. Zarza, E., Rojas, M.E., Gonzalez, L., Caballero, J.M., Rueda, F.. INDITEP: The first pre-commercial DSG solar power plant. Solar Energy, 2006, 80: 1270-1276.
8. Eck M., Zarza, E.. Saturated steam process with direct steam generating parabolic troughs. Solar Energy. 2006, (80):1424-1433.
9. Dudley, V., Kolb, G.., Sloan, M., Kearney, D.. (1994) SEGS LS2 solar collector – test results. Report of Sandia National Laboratories, SANDIA94-1884, U.S.A.

Aerospace Technology

CHARACTERISTICS OF FLOW FIELD AROUND WALL INJECTION INTERACTING WITH INCIDENT SOCK WAVE IN SUPERSONIC AIRSTREAM

S. Ishida, Y. Sakimitsu, H. Nakamura, Y. Ogami, T. Kudo, H. Kobayashi *
Institute of Fluid Science, Tohoku University, Sendai, Japan

ABSTRACT. Experimental and numerical studies were performed to explore flow interactions between an incident shock wave and the transverse fuel injection from a slot in supersonic airstream, which is expected to occur in a scramjet combustor. Results showed that the characteristic length of the recirculation zone which plays a significant role in flame holding in a scramjet combustor increased as the incident shock wave was introduced downstream of the injection slot, whereas these values approached to a constant value as the incident shockwave was introduced upstream of the injection slot. The variations of the characteristic length with the location of incident shock wave measured based on wall static pressures were in good agreement with the PTV measurement preformed previously. The differences in wall static pressures in combustion and non-combustion cases clearly indicated that the flame was held in the recirculation zone downstream of the injection slot.

Keywords: *supersonic combustion, wall injection, shock wave, reattachment point*

INTRODUCTION

Scramjet is one of the key technologies to develop a hypersonic air-breathing propulsion system. In a scramjet combustor, it is expected that many shock waves are generated and they affect the flow field, especially fuel-air mixing region dramatically. It is, therefore, of importance to investigate the interaction between an incident shock wave and fuel injected flows to develop a controllable supersonic combustor. In our previous studies on supersonic combustion for a wall injection [1], it was found that flame is not held when an incident shock wave was introduced upstream of the fuel injection slot. It was also found that, on the other hand, when the incident shock wave was introduced downstream of the injection slot, flame holding was possible even at low total temperature of the supersonic airstream [1]. Particle Tracking Velocimetry (PTV) was also performed to measure the scale of the recirculation zone downstream of the injection slot to investigate the flame holding mechanism [2].
In the present study, wall static pressures were measured to evaluate the characteristic length of the recirculation zone and compared to the characteristics of the wall-static-pressure profiles obtained by an unsteady numerical simulation. The characteristic length was also compared to that obtained by PTV experiments and the effect of the incident shock wave on the flame holding was discussed.

EXPERIMENTAL SETUP

Experiments were conducted using the supersonic combustion wind tunnel at the Institute of Fluid Science, Tohoku University. This wind tunnel is a blow-down type which releases exhaust gases to atmosphere. A storage heater is equipped to increase total temperature of the airstream. Outlet diameter

* Corresponding author: Prof. H. Kobayashi
Phone: + (81)-22-217-5272, Fax: + (81)-22-217-3523
E-mail address: kobayashi@ifs.tohoku.ac.jp

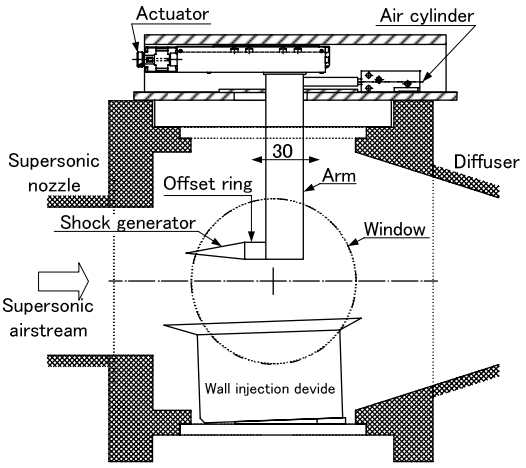

Figure 1. Schematic of the test section.

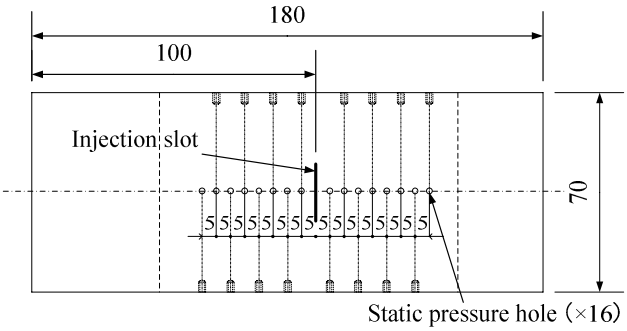

Figure 2. Drawing of the wall injection device.

of a supersonic nozzle exit is 135 mm and the test section is a semi-free-jet type. The Mach number was fixed at 2.5 in the present experiments.

A schematic of the test section is shown in Fig. 1. A wall injection device has a two-dimensional injection slot with a size of 0.5 mm × 20 mm and in total 16 holes to measure the wall static pressure as shown in Fig.2. Eight holes are lined up with 5 mm intervals both upstream and downstream of the injection slot. The diameters of the holes are 1 mm and the each hole is connected to a pressure sensor outside of the test section. A pre-burning chamber is located upstream of the fuel injection slot in the wall injection device for combustion experiments because the static temperature of the supersonic air-stream in this facility is lower than the auto-ignition temperature of hydrogen [1]. The injected gases for combustion experiment contain a large amount of unburned hydrogen at high temperature because the equivalence ratio of the gases supplied to the pre-burning chamber, ϕ, was sufficiently high ($\phi > 4$). In the case of non-combustion experiments, air was injected instead of the pre-burned hydrogen. Gas supplying tubes, pressure port, thermocouple, and electronic spark igniter were connected to the bottom of the pre-burning chamber. The wall injection device was installed into the test section with angle of +2 degrees in the direction of the supersonic airstream to prevent from boundary layer separation at the leading edge of the wall injection devise.

NUMERICAL METHOD

Two-dimensional compressive Reynolds Averaged Navier-Stokes (RANS) equations were used in the present study. These equations were solved using a finite volume method. The AUSM-DV method [3] for the convection terms and the MFGS method [4] for the time integral were used. For a turbulence model, the Wilcox's *k*-ω two-equation model [5] was employed.

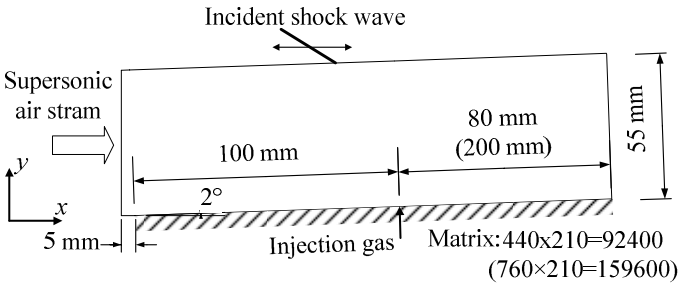

Figure 3. Schematic of the computational domain.

Figure 3 shows a schematic of the computational domain. Total width of wall is 180 mm and height of domain is 55 mm. It has 92,400 grid points in total and minimum grid interval near the wall is 10 μm. The Mach number, the total pressure, and the total temperature of the supersonic airstream were set to 2.5, 0.5 MPa and 673 K, respectively. The Mach number, the total pressure, and the total temperature of injected air conditions for non-combustion simulation were set to 1.0, 1.2 MPa and 300 K, respectively.

RESULTS AND DISCUSSION

Profiles of wall static pressures

Profiles of the wall static pressures with the distance from injection slot and the Schlieren images are shown in Fig. 4. Wall static pressures presented in the figure are time averaged values. Figure 4 (a), (b) and (c) are in the cases without an incident shock wave, with an incident shock wave introduced 9.2 mm upstream of the injection slot, with an incident shock wave introduced 20.5 mm downstream from the injection slot, respectively. The location of the incident shock wave, x_i, is defined as distance between the injection slot and the reaching point of the extrapolated line of the incident shock wave on the wall.

In the case of Fig. 4 (a), i.e., without incident shock wave, wall static pressures downstream of the injection slot are lower than 20 kPa and keep almost constant value (i.e., 35 kPa) after reattachment of the injected gas flow. This low pressure and low density condition might cause flameholding difficult. Upstream of the injection slot, meanwhile, the wall static pressures increases due to boundary layer separation and, from the point, an oblique shock wave is generated. The boundary layer separation of the airstream generates a recirculation zone between the separation point and the injection slot. The flow velocity inside the recirculation zone is lower than that of airstream.

In the case of Fig. 4 (b), i.e., x_i=-9.2 mm, wall static pressures behind the incident shock wave increases rapidly. Wall static pressures downstream of the shock wave are also higher than the case without incident shock wave (Fig.4 (a)). In this case, the separation point is located upstream of the measurement region, so that the pressure increase near the separation point could not be measured. The wall static pressures upstream of the injection slot are totally higher than those in other cases, and this conditions are advantageous for flameholding in terms of chemical reaction. In our previous study, however, flame-holding could not be attained in this condition [1]. The possible reason is that the injected hydrogen gas was not supplied enough for flameholding upstream as well as the static temperature of the supersonic airstream in the present test facility is not high.

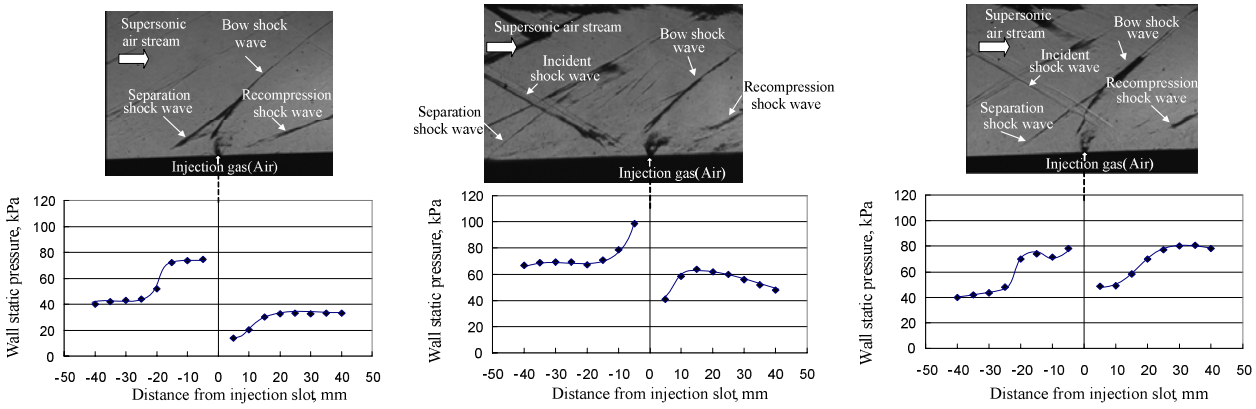

(a) without incident shock wave (b) x_i = - 9.2 mm (c) x_i = 20.5 mm

Figure 4. Wall static pressure profiles and corresponding schlieren images depending on the location of incident shock waves, x_i. The injected gas is air and the total pressure of the injected air is 1.2 MPa.

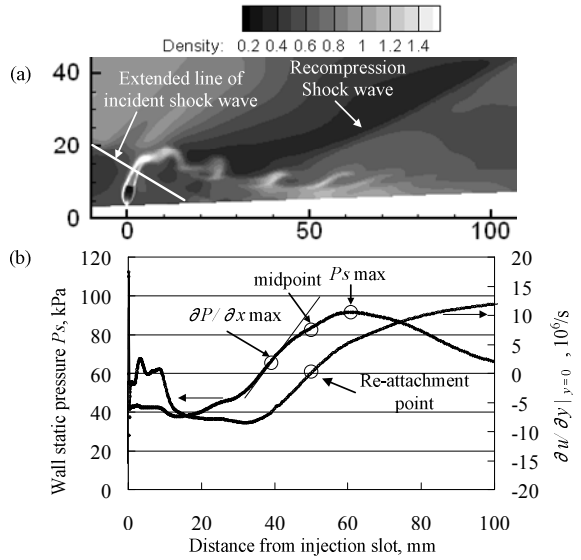

Figure 5. The method to define the characteristic length between the injection slot and the reattachment point using wall static pressure based on the unsteady numerical simulation: (a) contour of air density (x_i=15 mm); (b) relationship between time-averaged wall static pressures and $\partial u/\partial y$ at y=0.

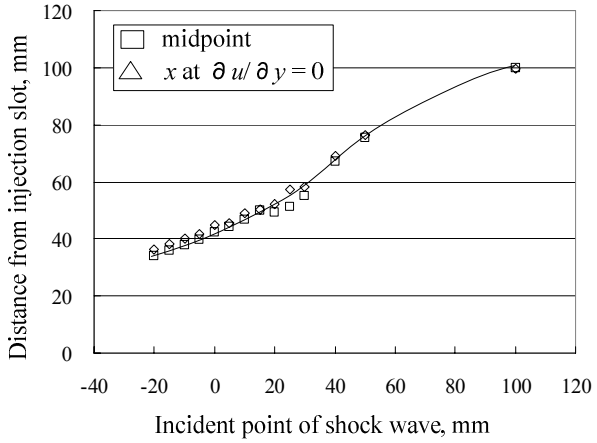

Figure 6. Relationship between the midpoint defined in Fig.5 and the point of ∂u/∂y=0 considered as reattachment point with the location of incident shock wave, x_i.

In the case of Fig. 4 (c), i.e., x_i=20.5 mm, when a shock wave was introduced downstream of the injection slot, wall static pressures downstream of the injection slot reached up to 80 kPa, which is the highest value in the present experiments. This is presumed to be one of the reasons why the flameholding was achieved in this condition [1]. Moreover, compared to the case of Fig. 4 (a), i.e., without incident shockwave, the separation point moved upstream. This result implies that the increase in the static pressure downstream of the injection slot also affects the static pressure upstream of the injection slot.

Figure 5(a) and (b) show instantaneous density profiles for x_i=15 mm and comparisons between the profiles of time averaged wall static pressure, P_s, and velocity gradient, ∂u/∂y at y=0, respectively, where u is the velocity component in the direction of airstream. Generally speaking, the reattachment point can be defined as the point where ∂u/∂y=0 at the wall, i.e., y=0. It is interesting to see that the midpoint between the maximum $\partial P_s/\partial x$ and the maximum P_s is well correspond to the reattachment

point, i.e., $\partial u/\partial y=0$. The increase in P_s downstream of the point is due to the recompression of the airstream where the recompression shock wave is formed and then P_s decreases again where the injected gas is accelerated near the wall. Therefore, it is reasonable to consider the reattachment point is located between $\partial P_s/\partial x$ point, i.e., the inflection point in P_s profile and the maximum P_s point.
To confirm how the midpoint corresponds to the reattachment point in other cases, variations of the midpoint and the reattachment point with locations of incident shock wave were plotted in Fig. 6. It is interesting to see that, regardless of the location of incident shock wave, the midpoint is in good agreement with the reattachment point. From these findings in the numerical simulations, in the present study, we have decided to determine the reattachment point from measured profiles of wall static pressures, that is, the midpoint is the reattachment point.
Measured discrete wall-static-pressure profiles were interpolated using a spline function, and then the midpoint was determined. In the case of the incident shock wave was introduced upstream of the injection slot, however, the profile of the wall static pressure does not have the inflection point of wall static pressure. Therefore, in those cases, the point of 5 mm downstream of the injection slot was assumed to be the inflection point of wall static pressure .

Comparison with the previous PTV measurements

Variations of the characteristic length with the location of incident shock wave measured using the above mentioned method are shown in Fig. 7. The results of PTV measurements reported previously [2] are also shown in the figure. Two cases of the injection pressure, 1.2 MPa and 1.6 MPa, are also compared there. When the incident shock wave was introduced to more than 10 mm downstream of the injection slot (x_i>10 mm), the characteristic length increased significantly. This means that the characteristic residence time becomes longer, thus the favourable condition for flameholding is realized. When the incident shock wave was introduced upstream of the injection slot, characteristic length does not change keeping a constant value of about 10 mm. These tendencies are in good agreement with the results of PTV measurements [2]. The difference between the characteristic length measured using wall static pressures and PTV measurements in the cases that the shock wave was introduced upstream of the injection slot seems to be due to the definition of the reattachment point because the inflection point in P_s profile could not be detected from measured wall static pressures and so it was assumed to be 5 mm downstream of the injection slot. These differences indicate that the point of maximum $\partial P_s/\partial x$ exists much closer to the injection slot. Figure 7 also shows interesting feature that the effect of the difference in total pressure of injection air is small in determination of the characteristic length.

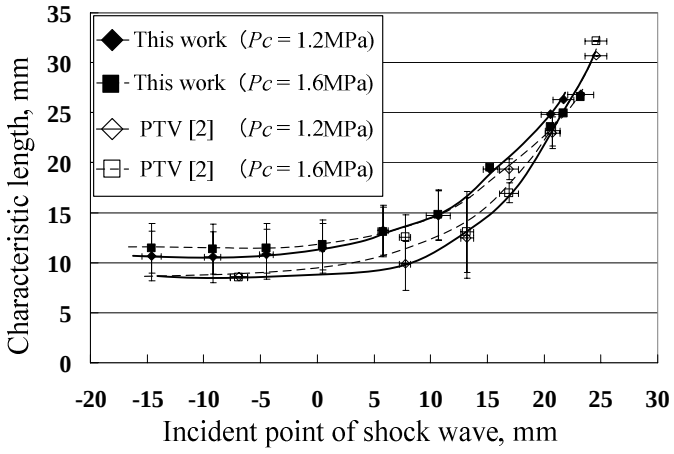

Figure 7. Variations of characteristic length with the location of incident shock wave.

Wall static pressure during combustion

Profiles of the wall static pressure were also measured during combustion. The experiments were conducted using the same procedure by Nakamura et al. [1], that is, the combustion experiments were performed moving the shock generator from downstream to upstream, thus the incident point of shock wave, x_i, moves after the supersonic wind tunnel started.

Figure 8 shows instantaneous profiles of wall static pressures during combustion. The initial location of incident shock wave is x_i=19.4 mm. The point of the maximum wall static pressure moves upstream as the location of incident shock wave, x_i, moves upstream. From comparison between the Schlieren images and wall static pressures, it was seen that the point of the maximum wall static pressure exists behind the recompression shock wave, being the same as the non-combustion cases. Just after flame extinction occurred, the wall static pressure downstream of the injection slot dropped rapidly. This transition of the wall static pressure indicates well that the flame is held in the recirculation zone downstream of the injection slot in the present experiment. The decrease in the wall static pressure after extinction moves the upstream separation point close to the injection slot, making the separation volume upstream of the injection slot smaller.

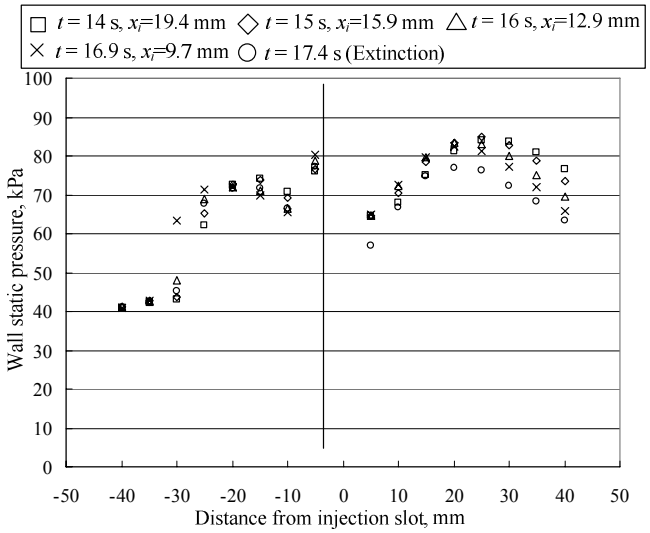

Figure 8. Variations of wall static pressures after the wind tunnel started in the case of combustion, where t is elapsed time. Flame was extinguished at t=17.4 s.

CONCLUSIONS

Experimental and numerical studies were performed to explore flow interactions between an incident shock wave and the transverse fuel injection from a slot in supersonic airstream in the cases of non-combustion and combustion. Based on the unsteady numerical simulations on the velocity profiles and wall static pressures, a method to determine the reattachment point of injected gas was proposed. The method could be applied to the experiments and a good agreement on the variations of the reattachment point between measured by wall static pressures and PTV measurements was obtained.

It was also confirmed that the characteristic length of the recirculation zone which plays a significant role in flame holding in supersonic airstream significantly increases as the incident shock wave was introduced downstream of the injection slot, whereas the length approaches to a constant value as the incident shockwave was introduced upstream of the injection slot. The change in the wall static pressures in combustion and non-combustion cases clearly indicated that the flame was held in the recirculation zone downstream of the injection slot.

REFERENCES

1. Nakamura, H., Sato, N., Kobayashi, H. and Masuya, G., Effect of the Location of an Incident Shock Wave on Combustion and Flow Field of Wall Fuel-Injection, *Transactions of the Japan Society for Aeronautical and Space Science*, Vol. 51, No. 173, pp.170-175, 2008.
2. Nakamura, H., Sato, H., Ishida, S., Ogami, Y. and Kobayashi, H., A Study of Interaction between Shock Wave and Cross-flow Jet Using Particle Tracking Velocimetry, *Transactions of The Japan Society for Aeronautical and Space Sciences*, 2009, (in press)
3. Wada, Y. and M. S. Liou, M. S., A Flux Splitting Scheme with High-Resolution and Robustness for Discontinuities, *AIAA Paper* 94-0083, 1994.
4. Shima, E, A simple Implicit Scheme for Struc-tured/Unstructured CFD, *Proceedings of 29th Fluid Dynamics Conference*, pp.325-328, 1997, (in Japanese).
5. Wilcox, D. C., *Turbulence Modeling for CFD*, 2nd ed., DCW Industries, La Canada, California, USA, 1998.

THE EXPERIMENTAL STUDY OF THE TRANSIENT AEROTHERMAL BEHAVIOR IN A TURBOFAN

D. Donjat[1*], P. Reulet[1], E. Divouron[2], E. Radenac[3], P. Millan[1]
[1]ONERA, DMAE, Toulouse, France
[2]SNECMA, Moissy-Cramayel, France
[3]ONERA, DEFA, Palaiseau, France

ABSTRACT. A synthesis of a complete experimental campaign on transient aerothermal behaviour in a complex cavity is presented. Due to the high complexity of the configuration, a set of validation experiments are defined following a unitary models block approach. Measurements are adapted to quantify the transient heat transfer until the thermal equilibrium in each selected case by using a phase-average approach. Transient cycles are defined according to the thermal response of the systems. An accurate evaluation of the systematical experimental errors is also conducted.

Keywords: *validation experiments, transient heat transfer, engine core compartment, phase-average measurements*

INTRODUCTION

For aircraft engine manufacturers, the improvement of turbofan efficiency imposes constant technological innovations which imply important and complex aero-thermal and thermo-mechanical modifications. Thus the reliability of engine is directly linked with the optimisation of the thermal environment during all flight phases. However, a lack of knowledge on the heat evolution during high transient flight phases as take-off often leads to unnecessarily large design margins that increase cost, weight and inefficiency. In this context, they are widely involved in research for transient conjugate heat transfer problem and are especially interested in both the characterisation of heat exchange during the engine speed changes in several critical areas and the development of methods to simulate such coupled phenomena.
We propose here to describe the methodology developed during a complete experimental campaign defined by ONERA, in association with major French aeronautical industries. The goal of this important work is to characterize accurately the transient aero-thermal evolution in a turbofan engine core compartment configuration for a full engine cycle. This campaign will also allow constituting an accurate database useful to validate the numerical models developed jointly.
The by-pass engine core compartment configuration was selected due to its criticality (see figure 1). Localized between the IFS and the primary flow casing, this system is in the vicinity of the combustion chamber and high pressure turbine. The high heat transfer induces complex aero-thermal behaviour. Despite global air cooling coupled with dedicated ventilations which are taken directly from the cold fan flow, the thermal conditions could be severe in transient engine phases for the different critical items installed in this part of the nacelle as valves, ECS pipes, bleed ducts, electronic control systems or turbine casing.

* Corresponding author: Dr. David Donjat
Phone: + (33)-562252808, Fax: + (33)-562252583
E-mail address: david.donjat@onera.fr

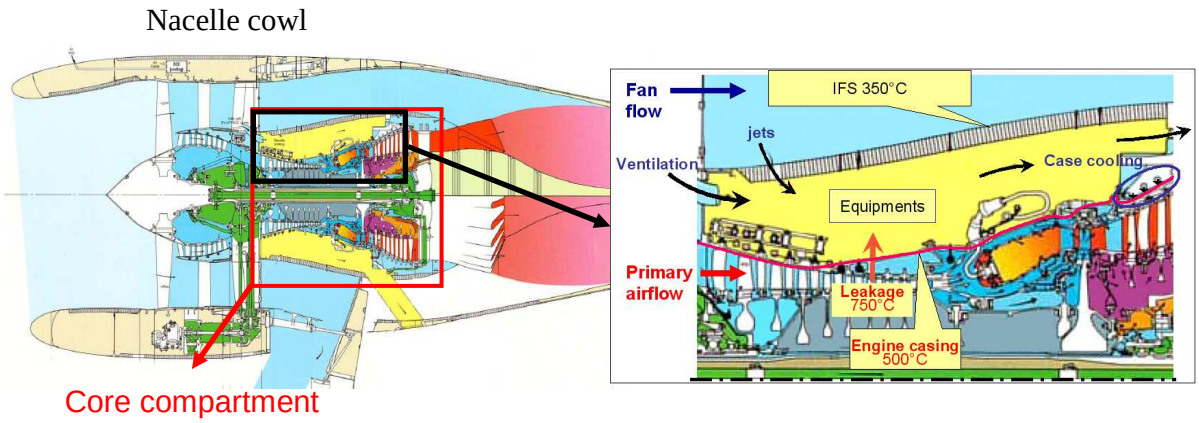

Figure 1. Nacelle core compartment – Aero-thermal behaviours

The definition of an experiment which models such complex and global aero-thermal problem, characterized by multi-physics phenomena with a high level of coupling, should follow the methodology defined by Oberkampf and Trucano [1]. They proposed to divide the system into several unitary models with simple geometries in order to separate each phenomenon following reference cases. At that point, correctly instrumented experiments are defined as accurate validation models. The figure 2 gives the decomposition of the nacelle core compartment aero-thermal configuration and the definition of an experimental campaign based on five different mock-ups to describe it particular aero-thermal behaviour.
In the following parts, we present two of them and discussed on the experimental methodology applied to study transient heat transfer.

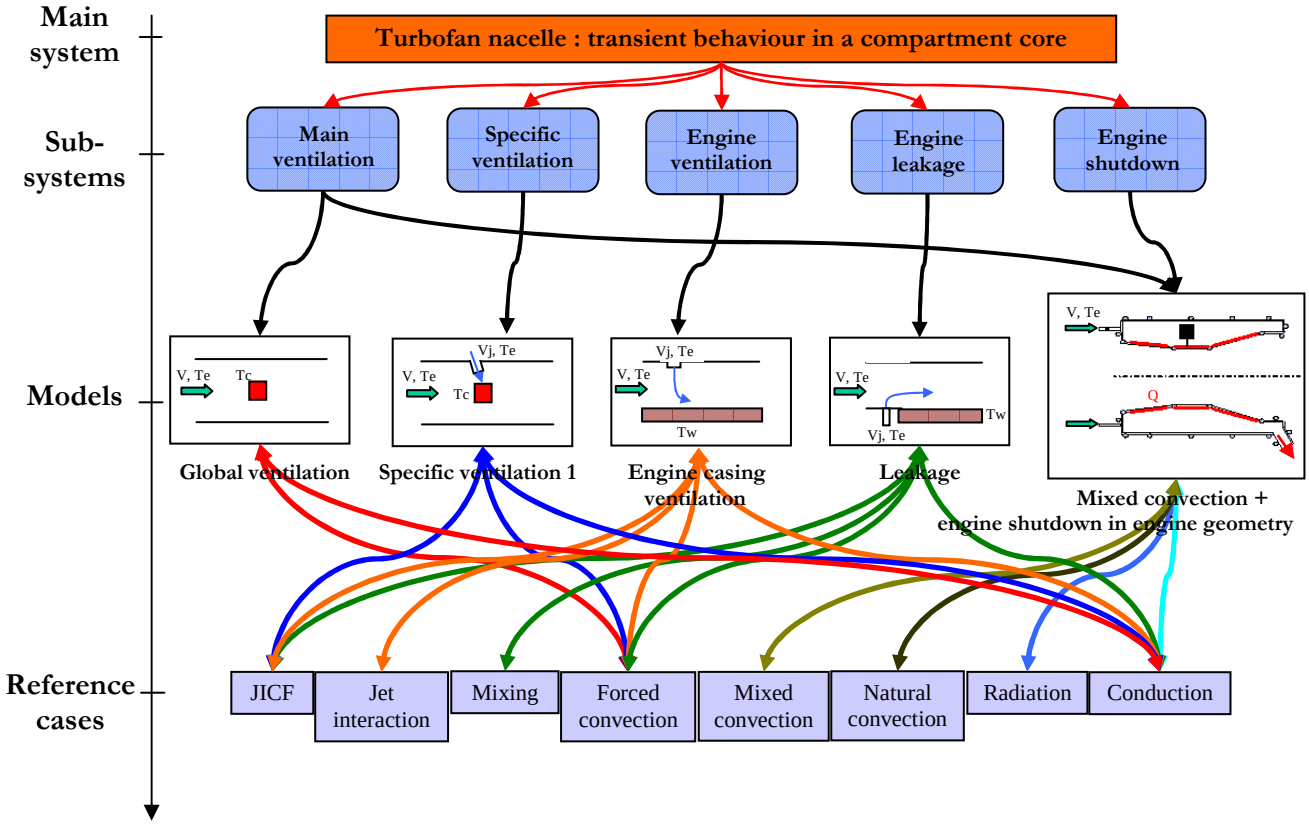

Figure 2. Decomposition of nacelle core compartment aero-thermal configuration in simplest models according to Oberkampf's block approach

DEFINITIONS OF EXPERIMENTS

Definition and experimental set-ups

"Engine casing ventilation" case. The case involves one or several vertical and cold jets discharging in a narrow channel cross flow at ambient temperature. They are in strong thermal interaction with a thick, opaque and homogenous flat plate heated on its back face at a constant temperature of 325 K as shown on figure 3(a). The target plate is made of a glass-ceramic Macor. This material is homogeneous, isotropic, and opaque for infrared radiation. But above all it allows the highest wall temperature evolution for our experimental conditions. The dimensions of jets and their positions above the target plate are defined to be representative of the engine real conditions. The mock-ups are integrated in an Eiffel wind tunnel with a test section 0.3 m high and 0.4 m wide. This kind of wind tunnel is well adapted for these experiments since there is no progressive heating of the flow. It produces a cross flow with a constant velocity. Moreover the temperature in the wind-tunnel room is controlled.

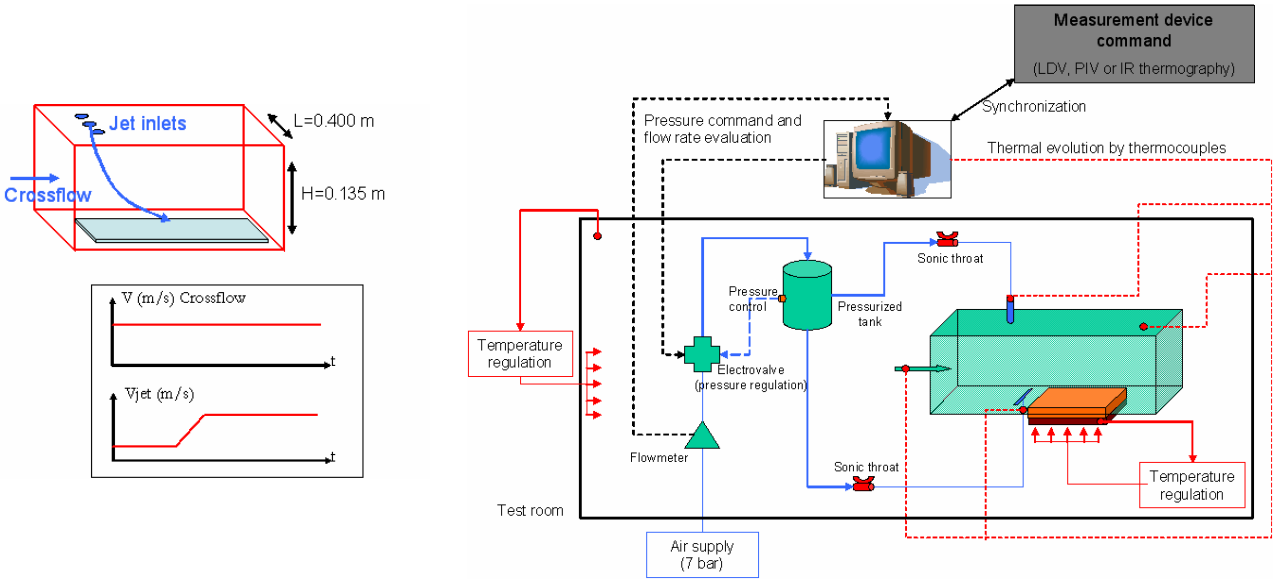

Figure 3. (a) Scheme of unsteady aerothermal validation experiment. (b) Experimental set-up and wind tunnel. Controls and regulations in the test cell

The geometric parameters as jet diameter d, relative position of jet and jet to impact side wall distance H are defined in order to respect similitude criteria. In particular, the ratio H/d is about 10 for an effective velocity ratio in the range from 6 to 7.5 with a main cross flow velocity of 4.2 m/s. The jet and cross flow temperatures are the same in order to avoid the phenomena of mixing and also simplify the validation. The thick flat plate (thickness e) is heated on its back side at constant uniform temperature T_e (with heating resistors controlled in temperature). The relative position of the jet always ensures an impact on the heated plate in the selected range of flow rates. The transient phase is based on the linear rising of jet velocity between two extreme values as shown on figure 3. Flow rate changes in 10s and each step is long enough to reach the thermal equilibrium for the heated plate. This flow rate evolution is well controlled and can be repeated a large number of times. An experimental set-up is developed to be compatible with phase-average measurements which need a complete synchronization between the test-section control computer and each acquisition device (see figure 3(b)). Moreover, for thermal measurements, this technique induces necessarily long time acquisitions. Besides all parameters have to be controlled and if necessary regulated, a complete characterization of the test-room is essential in particular in order to quantify experimental uncertainties. In this set-up, air which feed each jet comes from a controlled pressure

tank via a sonic throat. This solution allows the accurate control of jet velocity evolution with a fast proportional electro-valve. Moreover, jet nozzles are designed to ensure a rather uniform velocity on the whole jet exit surface. As both jet and main flow velocities are particularly critical variables, a flowmeter and a Pitot probe allow a permanent measure of them. In the same way, all temperatures (jet outlet, main flow, wind tunnel walls, glass-ceramic backside and test room) are acquired continuously.

"Convection in engine geometry" case. A simplified and modular half scale mock-up based on the CFM56-5C core compartment configuration is defined. It respects the form, the convective and turbulent flow specifications of the real configuration, but with temperature levels, heating power, mass flow rates, dimensions and cycle duration compatible with laboratory capacities. An illustration of the design is shown on figure 4.

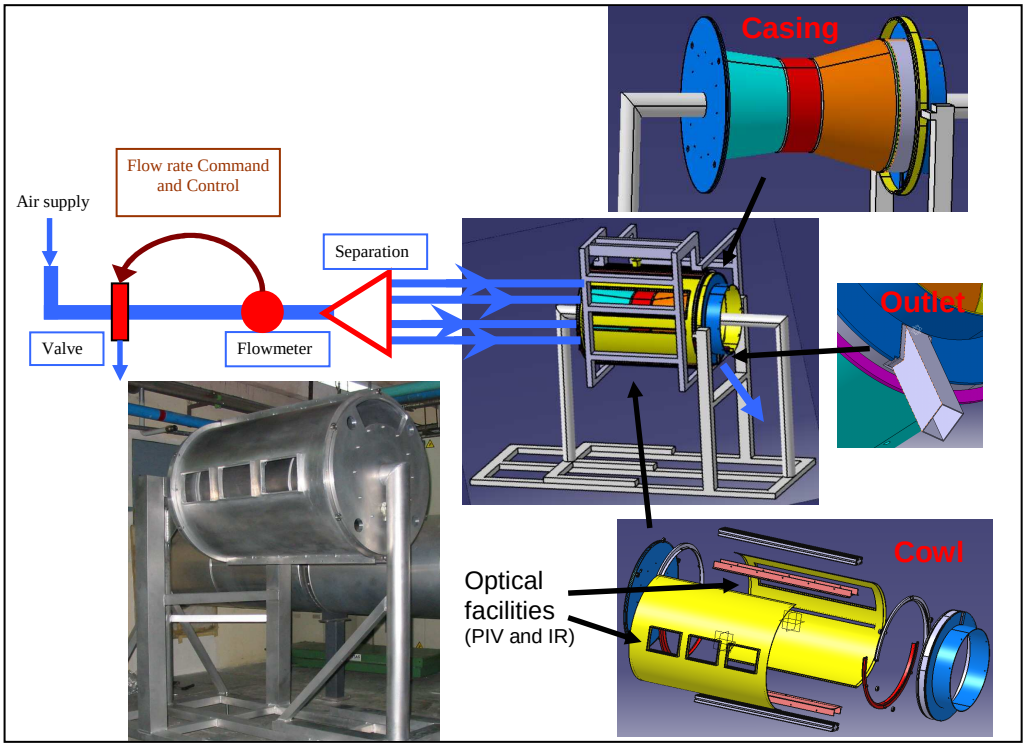

Figure 4. Nacelle core cavity set-up

It is made up with a cylindrical cowl with optical facilities built around a heated internal casing which model high pressure compressor, combustion chamber and high pressure turbine casings. By making a rotating cowl, the entire cavity is accessible by non intrusive optical measurement tools. Measurement localizations are referred with the angle of rotation (see figure 5). The entire cavity is either ventilated with four air inlets at ambient temperature (configuration C0) or not (natural convection configuration). For main ventilation studies, several items can be installed to generate realistic aero-thermal behaviour (configuration C1) as shown on figure 5(b).

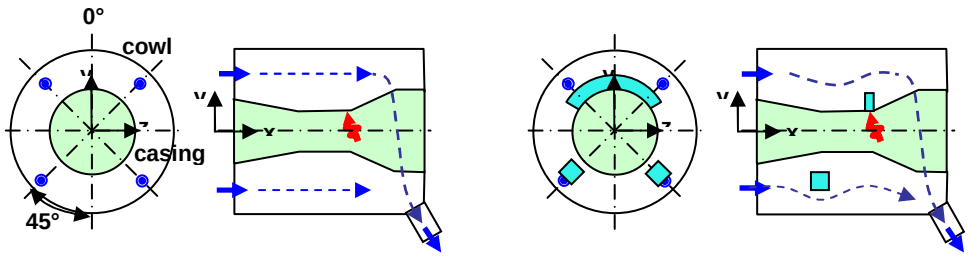

Figure 5. Configurations C0 (a) and C1 (b)

A dimensional analysis is made to select representative parameters as the ratio between internal casing radius and external IFS radius and either the Reynolds number (in the case of a forced convection configuration) or the Grashof number (in the case of natural convection configuration). Preliminary aerothermal calculations of the air flow and solid temperatures are done with stable mass flow rates and stable heating conductor surface flux on the inner wall of the casing. They allow imposing the more adequate powers in order to have the good wall temperatures, and the best materials to maximize thermal circumferential gradient (see table 1). The transient phase is based on the linear rising of inlet flow rate between GI and TO values in 8s (see figure 6).

Table 1
Typical temperatures for steady conditions

GROUND IDLE (GI)				TAKE OFF (TO)			
Mass Flow [g/s]	T1 [K]	T2 [K]	T3 [K]	Mass Flow [g/s]	T1 [K]	T2 [K]	T3 [K]
60	310	355	340	240	340	400	340

Phase-average measurements

In order to characterize dynamics and heat transfer during transient evolution, efficient techniques as PIV, LDV and infrared thermography are used. The measurements concern the flow velocity and turbulence, the heated plate wall temperature, and all the boundary conditions. For each configuration, steady dynamic and thermal conditions for both extreme flow rates are first quantified and the influence of operational conditions is estimated. In a second time, unsteady flow is measured with a phase-average approach to quantify the transient effects of either the test plate or the engine cavity casing.

PIV measurements. In each case, PIV measurements are performed with a 10 Hz double impulse YAG laser and a X-StreamVISION XS-5 camera coordinated by an IDT synchronizer. The post-processing software is IDT ProVision. Measurements are made in several axial and transverse planes through optical facilities and allow an accurate description of the flow topology. Mean fields are the result of an average based on several hundreds of image pairs validated by convergence study. The unsteady flow is measured with a phase-average approach on a number of cycles (as described on figure 2) consistent with steady measurements in order to quantify correctly the aero-thermal behavior. Length definition of cycles depends on both the configuration and the complexity of measurement process (see example on figure 6).

Infrared thermography measurements. Each test section is equipped with a ZnSe window which improves IR transmission. Infrared thermography measurements are realized with a Cedip Jade III LW camera with a 320*240 resolution. In parallel, several thermocouples follow the air temperature in jet and main flow and also on the test section wall temperature. They are used to quantify the wall temperature of all test section sides in order to check the adiabatic assumption and evaluate the radiative exchange error induced by using the Gebhart coefficient method. All these additional measurements are expected to quantify the systematic experimental errors.
In each case, the phase-average measurement is done with several cycles whose length is defined according to the evaluation of conduction characteristic time. For simple configurations, as jet impingement case, phase-average post-treatment is based on 350 acquired cycles with an acquisition frequency equal to 1 Hz. All the sequences are checked and validated in order to take into account the evolution of test-room conditions during the measurement. In this way, a criterion on the flow temperature is imposed and finally the phase-averaged post-treatment is done with less than 100 cycles of 660 s. However for the engine geometry mock-up, where transition conditions will be longer than in the simple cases (see figure 6), an other strategy is defined by using frame averaging in order to decrease the number of cycles. In our case, as the infrared camera is able to work at a frequency of 50 Hz, a 1Hz measurement is obtained by averaging 50 frames each second

in only one cycle. The accuracy of this approach is evaluated compared to the first method in the "engine casing ventilation" experiment and we obtain results quite consistent with an error lower than 0.3K.

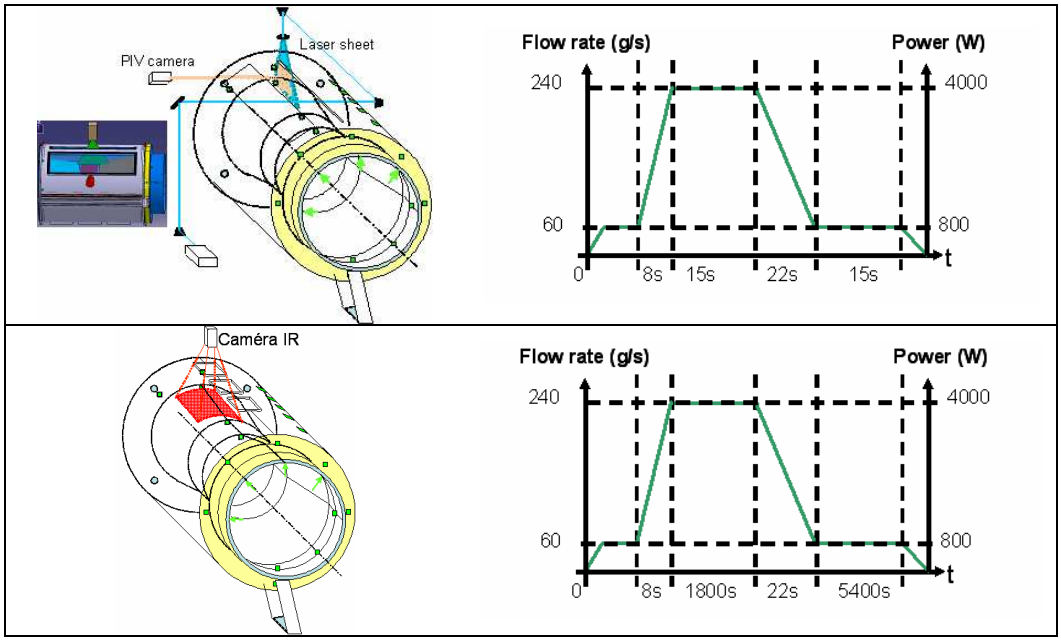

Figure 6. “Global ventilation” case – Adaptation of cycles for transient aerothermal measurements

RESULTS

“Engine casing ventilation” case – One jet in operation

The analyze of the main velocity field measured in the symmetrical plane for the both extreme flow shows the path and the impact of the jet on the heated plane with naturally an upstream position in the case of the higher flow rate. In both flow fields, the temperature profile looks quite symmetrical despite an accuracy of 0.8K for backside temperature condition. The impact of jet on the heated plate is detected and the impinging point on the material moves backward to the beginning of the material (from x=0.060 m to x=0.0 m), as confirmed by the study of the flow dynamics. In particular, for the higher flow rate condition, the decrease of the temperature is the result of the additional influence of the development of the boundary layer upstream and the jet impingement.

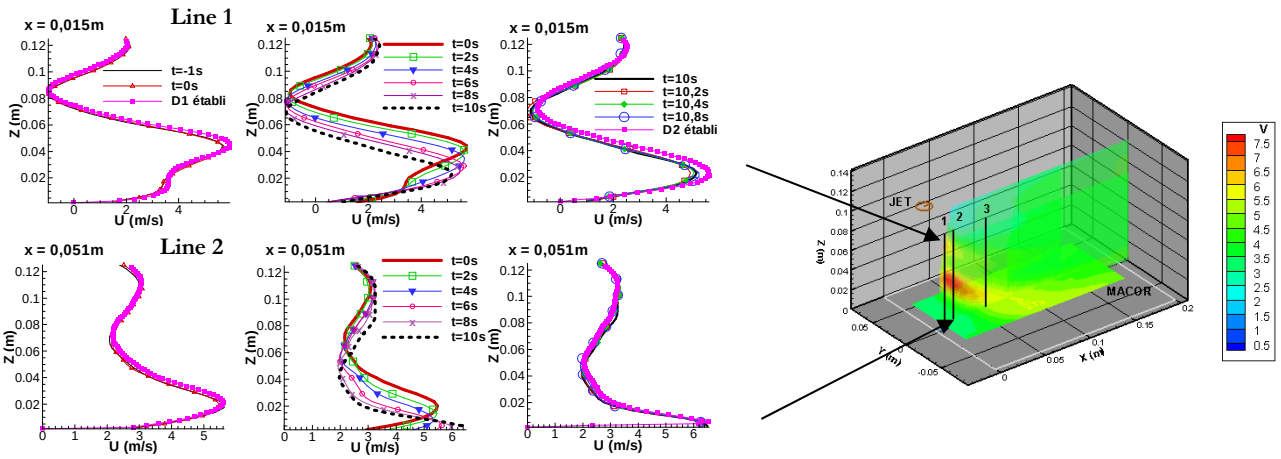

Figure 7. Main velocity field during transient evolution of jet flow rate

The maximum temperature difference between both extreme flow rates is about 8.8 K at x=0.014 m. The measurement statistic uncertainty is evaluated to be equal to 0.07 K. In the same way, the repeatability uncertainty due to the variation of measurement is less than 0.4 K. The velocity profile evolution during the unsteady period between -1s and 12s is shown on figure 7 according to two vertical lines localized in the symmetrical plane. First, axial velocity component profiles at the beginning (t=-1 to 0s) and at the end of the linear flow rate rising (t=10 to 10.8s) are compared to the steady case ones and show a good agreement (the maximal relative error is inferior to 8%).The velocity values at t=11.9s and t=9s are very similar, showing a fast transient evolution of velocities: we can consider that the dynamic equilibrium is reached instantaneously. During the flow rate linear evolution (t=0 to 10s), velocity profiles are given each 2s. The maximum of velocity induced by the jet is well detected and we can easily follow its vertical evolution during flow rate rising. As the jet speed increases, the impingement moves backward and strongly interacts with the boundary layer. Moreover the other influence of the jet is the deceleration of the higher part of the main flow due to an obstructing effect of the cross flow (velocity is from 2.6 to 4m/s, compared to the 4.2 m/s cross flow inlet).

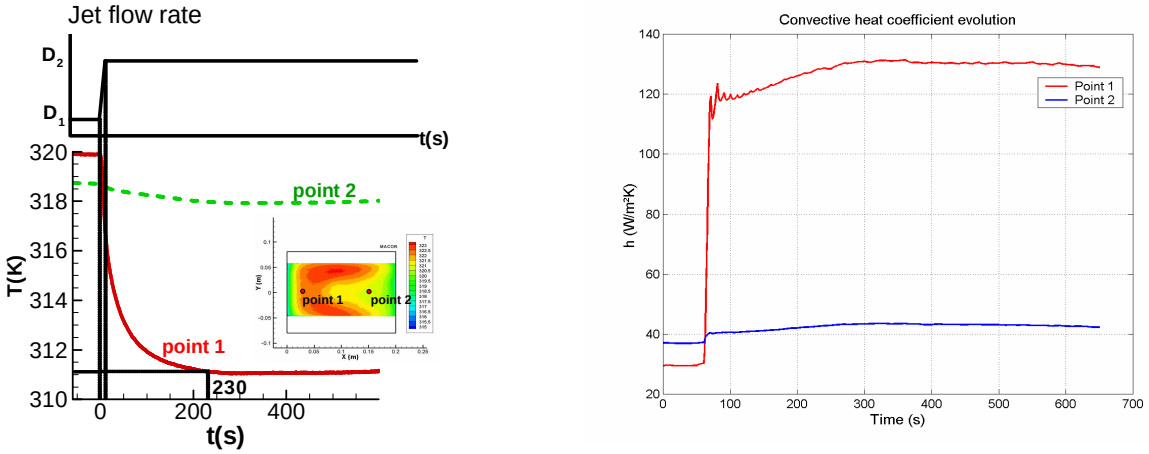

Figure 8. (a) Wall temperature evolution during transient experiment. (b) Convective heat coefficient evolution during transient experiment

The figure 8(a) shows the wall temperature at two distinct points during the transient phase. As the evolution of the flow field follows the jet flow rate increase, the convective conditions are quickly modified. Following the temperature evolution on point 1, which marks the impinging zone for the higher flow rate condition, the return to thermal equilibrium is reached in about 230 s. It is consistent with the theoretical estimation based on the conduction characteristic time (τ_c = 274 s). Moreover, the temperature fields obtained are used to evaluate the convective transfer coefficient during the transient phase (see figure 8(b)). This estimation is based on an inverse method developed in ONERA which resolve the heat conduction equation in the material with constant uniform temperature on rear face. It determines the heat flux evolution on front face (fluid – solid interface) to obtain the measured temperature evolution on this face.

“Convection in engine geometry” case

The figure 9 shows the main velocity field measured in axial planes for the both extreme flow and both configurations. The inlet jets in 45° and 135° are well detected. Between them, a large reverse flow appears in the entire cavity. The items involved in configuration C1 induce local modification of flow patterns. Based on thermal measurements, the resolution of an energetic balance in the cavity wall leads to convective heat coefficient evaluation (figure 10(a)). By following the evolution of the adimensional axial velocity defined with inlet value, the evolution of flow during transient phase is consistent and only items generate local dynamics evolution (see figure 10(b)).

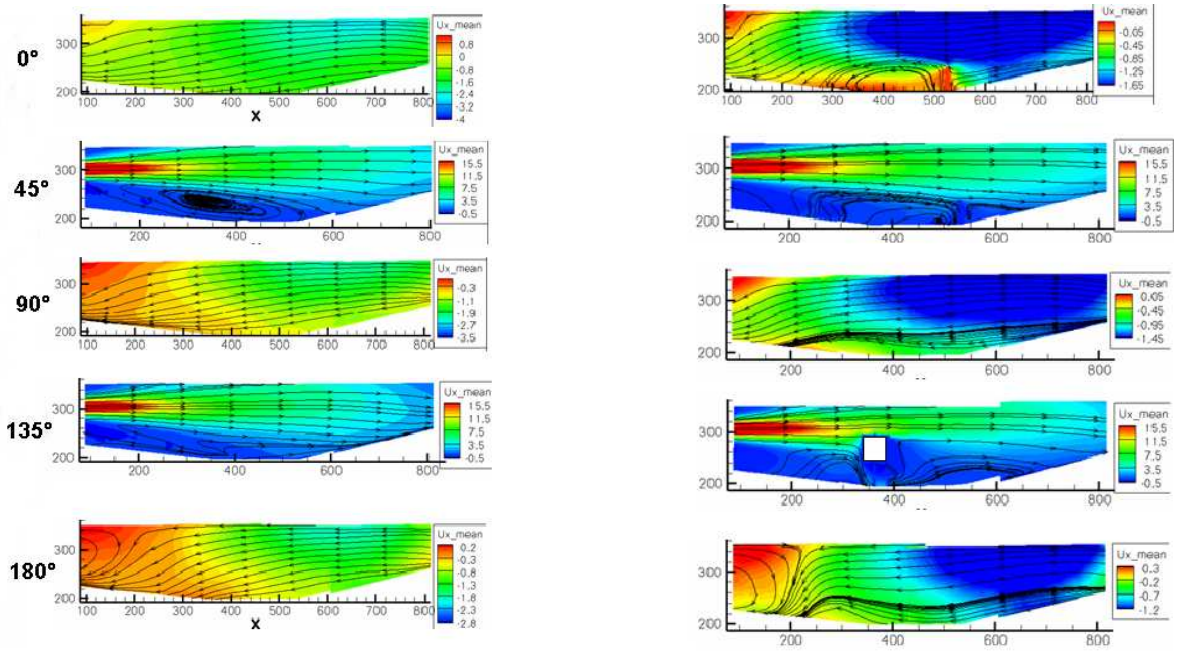

Figure 9. Axial velocity flow field for the both cases (left: case C0, right: case C1)

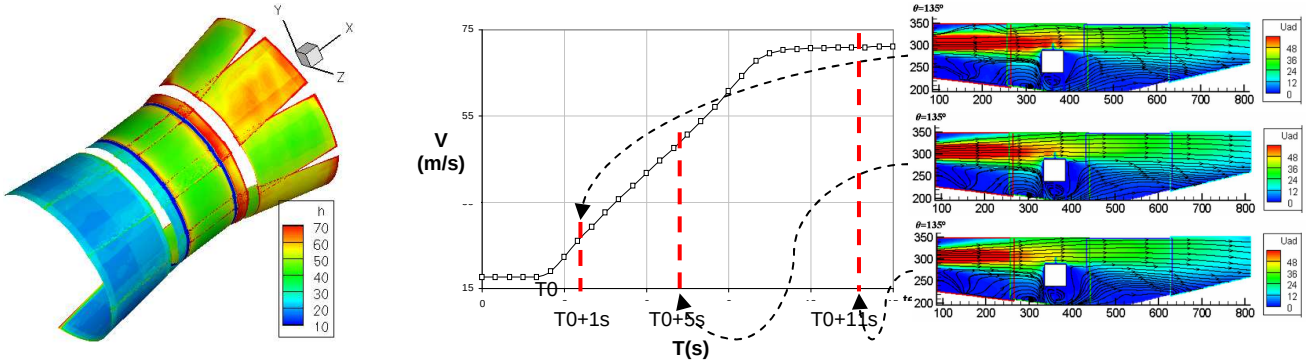

Figure 10. (a) C0 : Convective heat coefficient for stabilized TO (W/m²K).
(b) C1 : Evolution of axial velocity flow field during transient phase

CONCLUSIONS

In this paper, we present a methodology to experimentally describe the complex aerothermal behaviour of the nacelle core compartment during transient phases. Several simplified set-ups are defined to study each specific phenomenon (as cooling by air jet impact or global ventilation) which occurs in such complex system. The study of transient behaviours needs the adaptation of phase-average strategy. In each case, dynamics and wall temperature field characterizations are performed in order to highlight the strong link between the air flow and the wall temperature. These data are then used to evaluate the evolution of the heat coefficient during a transient phase. Specific post-processing is used in order to quantify measurements uncertainties and to evaluate corrections (as the closed cavity multi-reflection radiative heat transfer and its influence on the infrared measurement).

REFERENCES

1. Oberkampf W.L. and Trucano T.G., Verification and validation in computational fluid dynamics, Progress in Aerospace Sciences, 38, pp 209-272, 2002

EXPERIMENTAL AND NUMERICAL INVESTIGATION OF A NOVEL COMPRESSOR ENDWALL DESIGN

A. Hergt[1,*], W. Steinert[1], C. Dorfner[1], E. Nicke[1], M. Beversdorff[1]
[1] German Aerospace Center (DLR),
Institute of Propulsion Technology
Linder Hoehe, 51147 Cologne, Germany

ABSTRACT. The flow in an axial compressor row is characterized by the presence of several secondary flow effects. When it occurs, the corner separation between the endwall and the blade in a compressor row dominates and is responsible for a large part of total pressure losses. It is well known that this separation is driven by the interaction between the cross flow on the endwall and the blade boundary layer. Hence, a promising way to improve axial compressors is to shape not only the blade but also the endwall in a three dimensional way in order to influence the cross flow. This paper presents a recently developed novel endwall design and its detailed experimental and numerical investigation of the resulting flow effects.
A non-axisymmetric endwall groove, which generates an aerodynamic separator, was designed by means of the 3D-RANS flow solver TRACE linked with an automated multiobjective optimizer. This aerodynamic separator interacts with the cross flow on the endwall, which leads to a significant loss reduction, load redistribution and reduction of recirculation.
Object of the investigation is a highly loaded compressor cascade which is described in detail with respect to its flow phenomena and physics. The measurements by means of 3-hole and 5-hole-probes as well as Laser-Two-Focus technique is carried out at the transonic cascade wind tunnel of the DLR in Cologne in order to detect the flow structure of the blocked endwall cross flow as well as the redistribution of the corner separation. Comparing the experimental and numerical data shows good agreement and allows a comprehensive view on the flow.
The endwall cross flow, caused by the pressure compensation between two adjacent blades is blocked and deflected by a vortex (aerodynamic separator), which is generated at the separation edge of the newly designed endwall contour. These results are obtained by oil-flow patterns as well as pressure distribution measurements on the endwall.
Concerning the cascade performance a considerable influence of the novel endwall design was observed. A significant loss reduction was achieved as well as an increase of the pressure ratio and the flow turning was detected. In summary, it can be stated that non-axisymmetric contoured endwalls have shown their potential for compressor improvement, thus they offer an additional design space for modern turbomachinery.

Keywords: *non-axisymmetric, endwall, separator, axial-compressor, cross-flow*

INTRODUCTION

Nowadays, turbomachines play an important role in transportation and power generation in form of airplane propulsion and heavy-duty gas turbines. Against the background of fast-paced worldwide increase in demand for mobility and power, a further efficiency improvement of axial compressors

* Corresponding author: A. Hergt
Phone: + (49)-2203-601-2217, Fax: + (49)-2203-64395
E-mail address: alexander.hergt@dlr.de

is essential in order to reduce CO_2 and NOX emissions. An improvement of compressor efficiency is directly linked with the possibility of influencing secondary flow effects in blade cascades. This correlation was already identified in the early 1950´s. Since that time and still ongoing systematic studies [1], [2], [3] have been performed in order to understand these flow phenomena.
A significant secondary flow effect in the vane row of an axial compressor is the corner separation, which is defined as the separation between the endwall and the vane, because this separation is responsible for a large part of the aerodynamic losses. The corner separation is caused by the interaction of the endwall cross flow and vane boundary layer during the concurrent presence of a pressure gradient in flow direction. Hence the research in the recent past has focused on influencing cross flow by endwall modifications. It has been shown by Corral and Gisbert [4] and Duden et.al [5] that the application of these modifications in form of non-axisymmetric contoured endwalls can be very successful in turbine stages. Concerning axial compressors Dorfner et.al. [6], Harvey and Offord [7], [8], as well as Iliopoulou et al. [9] have recently shown that it is possible to achieve such good results also for compressors. In order to continue the efforts in improving compressor performance, the DLR 3D-RANS flow solver TRACE [10] was used and linked with an in-house automated multiobjective optimization tool by Voss et al. [11] and extended by Dorfner [12] to design a numerically optimized endwall contour. The development of this novel non-axisymmetric endwall groove generating an aerodynamic separator and its influence on compressor cascade performance was first-time presented by Dorfner and Hergt et.al. [13], [14].
The objective of the present work was to measure the resulting flow structure in the highly loaded compressor cascade with contoured endwall in order to describe and analyse the flow phenomena in detail. Therefore, measurements in the transonic cascade wind tunnel of the DLR in Cologne [15] were carried out. In this process the investigation was focused on detailed measurements by means of 3-hole and 5-hole-probes as well as Laser-Two-Focus method within the cascade passage close to the endwall. Furthermore, experimental flow visualisation by means of oil streak pattern allows the detailed interpretation and description of the resulting flow phenomena. The experiments were carried out at the aerodynamic design point (ADP) of the cascade at $M_1 = 0.69$.

BASELINE CASCADE AND NOVEL ENDWALL DESIGN

The baseline configuration is a high-speed compressor cascade with CDA airfoils. Its consists of 6 blades with 70 mm chord and 186 mm blade span and has flat endwalls. This cascade enables tests at realistic flow conditions, e.g. Mach number, thus transferability to real turbomachines is possible to a certain extent. The aerodynamic design point of the datum cascade with inlet Mach number $M_1 = 0.7$ and inlet flow angle $\beta_1 = 134.8°$ was chosen for the tests. At these flow conditions the measured Mach number distribution at midspan as well as the blade profile is shown in Fig 1. Further cascade design parameters are the stagger angle $\beta_{st} = 109.9°$, the pitch to chord ratio $t/c = 0.75$ and the blade aspect ratio $h/c = 2.4$. The incoming endwall boundary layer thickness amounts to 18 mm on each wall which is equivalent to 22% of the blade span.
As described in the introduction, the interaction of the endwall cross flow and vane boundary layer during the concurrent presence of a pressure gradient in flow direction is responsible for the existence of corner separation. In order to prevent this separation a novel endwall design in form of a non-axisymmetric endwall groove has been developed in a previous study [12], [13]. This groove creates a vortex with its separation edge, which acts as an aerodynamic separator and prevents the endwall cross flow from interacting with the blade suction side boundary layer. Goal of the present investigation was to measure and visualize the resulting flow phenomena in order to improve the understanding of the aerodynamic separator and validate the numerical results. For the investigation a contoured endwall (CEW) cascade including the baseline blade profiles was constructed. A symmetrical, identical grooved endwall is attached to both sides of the blades in the cascade wind tunnel. Figure 2 shows the cascade blades with one attached contoured endwall (CEW).

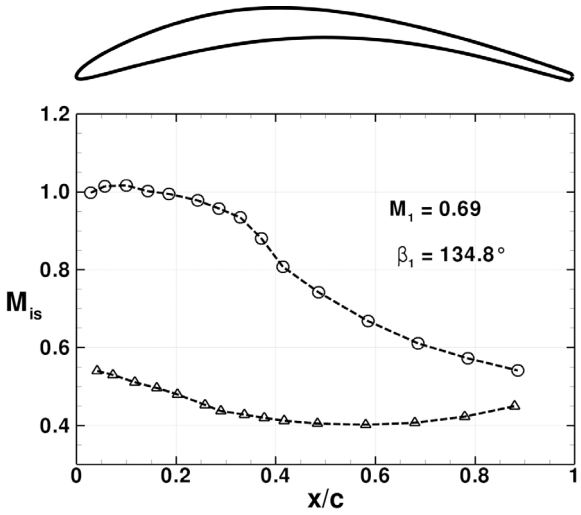

Figure 1: Profile (top) and measured Mach number distribution at midspan of the datum cascade

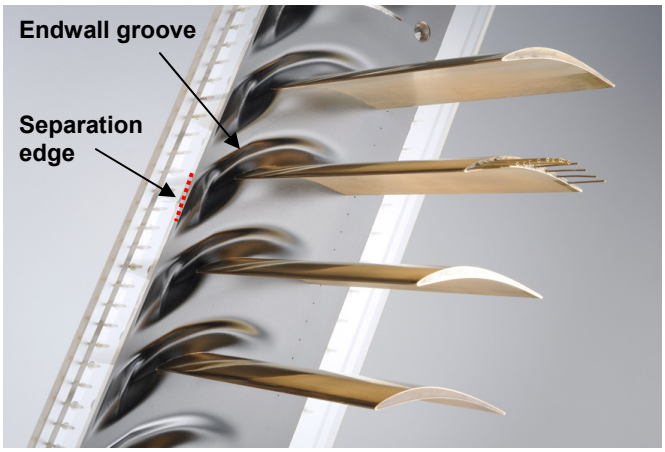

Figure 2: Cascade with non-axisymmetric endwall contouring

TEST FACILITY AND EXPERIMENTAL SETUP

The experiments were performed in the transonic cascade wind tunnel at the DLR in Cologne [15]. This tunnel is a closed loop, continuously running facility with a variable nozzle, an upper transonic wall, and a variable test section height. The air supply system enables an inlet Mach number range from 0.2 to 1.4 and a Mach number independent variation of the Reynolds number from 1×10^5 to 3×10^6. Figure 3 shows a cross section of the transonic cascade wind tunnel with the main inlet and outlet flow parameters.

For the present tests the blade chord Reynolds number was around 1×10^6. The inlet total temperature was about 300 K and the free stream turbulence level was around 0.6 percent. Two blades, in the center of the cascades, were instrumented at midspan on the pressure and suction side respectively.

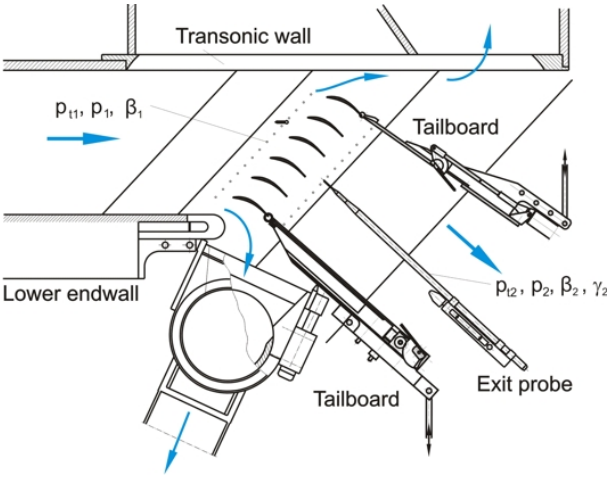

Figure 3: Cross section of the DLR transonic cascade wind tunnel

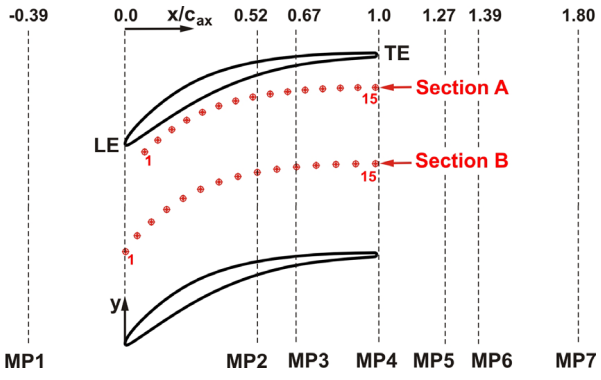

Figure 4: Location of pressure taps on the endwall (section A and B) and axial measurement planes (MP)

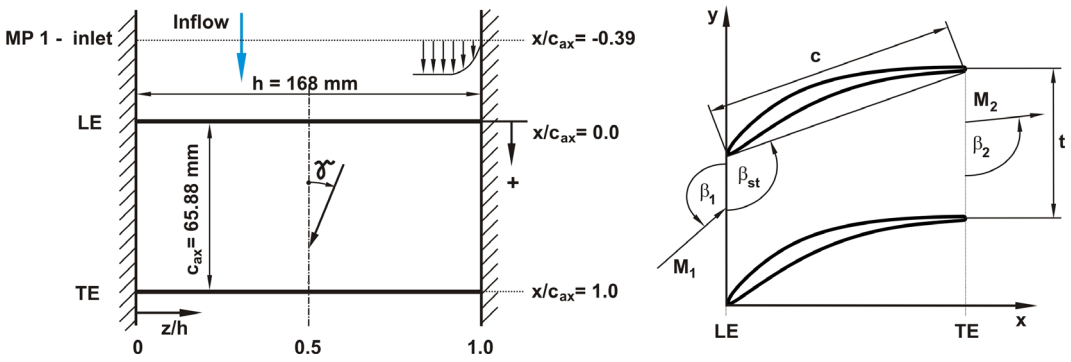

Figure 5: Cascade definition and parameter

Additionally, the spanwise flow symmetry in the datum cascade is verified by static taps on both endwalls near pressure and suction side. In order to verify spanwise flow symmetry in the CEW cascade, one blade in the center was instrumented at 10 percent and 90 percent span, since endwall instrumentation near suction side was impossible due to the contoured endwall. During the measurements of the datum and the CEW cascades, passage-to-passage flow periodicity was checked by traversing the wakes at midspan over the three middle passages as well as by measurement of the static pressure distribution across the inlet measurement plane (Fig. 5). Additionally, in the CEW cascade one blade passage was instrumented with 2 ×15 pressure taps, located as shown in Fig. 4 and denoted by section A and B. In this figure and in Fig. 5 also the measurement planes (MP1 to MP7) and cascade parameters and are given.
The test procedure is defined as follows: Generally, measurements were carried out at the ADP of the cascades with an inlet Mach number of 0.69 and included wake measurements with a combination of 3-hole and 5-hole probes at MP4, MP5, MP6 and MP7 in order to resolve the development of the wake against the axial distance and to indentify the losses. Additionally, 3-hole and 5-hole probe measurements were performed at MP2 and MP3 in order to resolve the development and effect of the aerodynamic separator on the endwall cross flow. These measurements are problematic due to the blockage of the pressure probes within the cascade. Hence, additional Laser Two Focus (L2F) [16] measurements were carried out at selective points in order to validate the pressure measurement. The one cascade endwall was flat and consists of acryl glass which allowed the optical accessibility for the tests. This means that the cascade endwall setup was asymmetric in this case, thus the cascade flow close to the endwalls was additionally checked. Thereby the flow close to the CEW endwall shows a good agreement with the results of the symmetric CEW cascade setup. The cascade loss measurements as well as the oil flow pattern were carried out with a symmetric cascade endwall setup.
Furthermore, the endwall pressure was measured at 2×15 pressure taps (Fig. 4) in order to validate the numerical results and to detect changes in the endwall pressure distribution due to the endwall groove. The estimated uncertainties of the test data at midspan are ± 0.2 deg for the inlet ant outlet flow angle as well as ± 0.002 for the midspan total pressure loss coefficient.

Numerical Setup

For comparison with the experimental results and in order to analyse the endwall flow in detail, steady numerical simulations with DLR's 3D-RANS flow solver TRACE, including k-*w* turbulence model, were carried out for both operating points at the measured inflow conditions. Concerning the convergence massflow as well as the global mean residual, which had to be less than $1x10^{-6}$, were checked. A fine multi-block grid of nearly 2 million nodes with an OCH topology was used in order to sufficiently resolve the blade and endwall boundary layer. Calculations with the fine grid as well as a coarse grid, in each case with and without wall functions, were carried out in order to check the grid independence. In the process the global values displayed very good agreement.

RESULTS AND DISCUSSION

The optimization and numerical results given by Dorfner et al. [12], [13] show that the novel endwall contour in form of a groove with a separation edge generates a vortex. This vortex acts as an aerodynamic separator and leads to a separation of the endwall cross flow above the endwall groove. Figure 6 shows the results of the 3-hole and 5-hole probe measurements in different axial cross sections (MP2 to MP7). These measured loss distributions illustrate the interaction of the aerodynamic separator with the endwall cross flow and the development of the loss wake behind the cascade. The measurement planes 2 and 3 range from y/t = 0.1 to 0.9 in which 0 and 1 represent the position of the trailing edges. In these planes a region with very high losses is visible close to the endwall (marked with I). Additionally, the rotational sense of the aerodynamic separator is marked on the planes for a better illustration. It shows that the endwall cross flow is prevented from interacting with the blade suction side boundary layer. The high loss region is detached from the blade suction side and results from the separation of the endwall cross flow above the groove. This is also illustrated in the measurement plane 4 directly behind the trailing edge. There, the high loss region caused by the corner separation is marked with III and the gap to the detached loss region is marked with II.

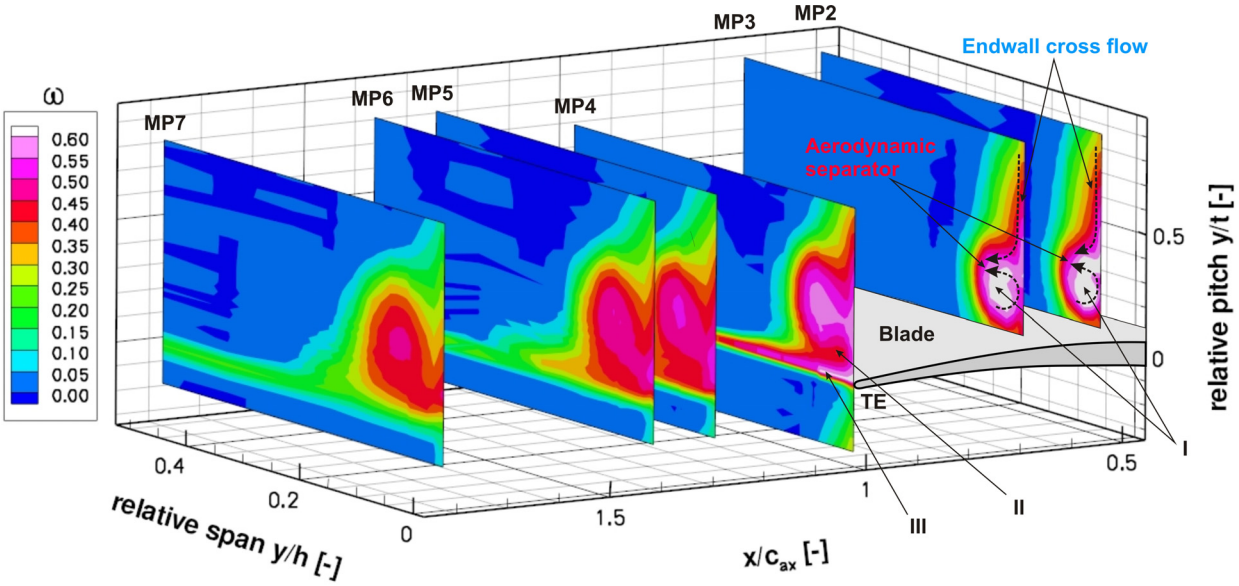

Figure 6: Measured total pressure loss distribution in different axial measurement planes.

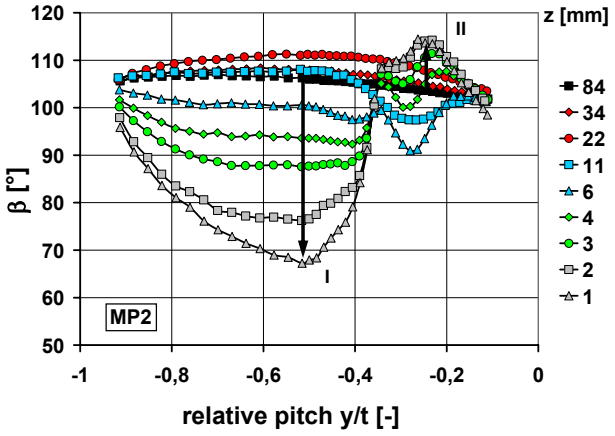

Figure 7: Measured pitchwise flow angle β distribution in MP2 at different spanwise positions

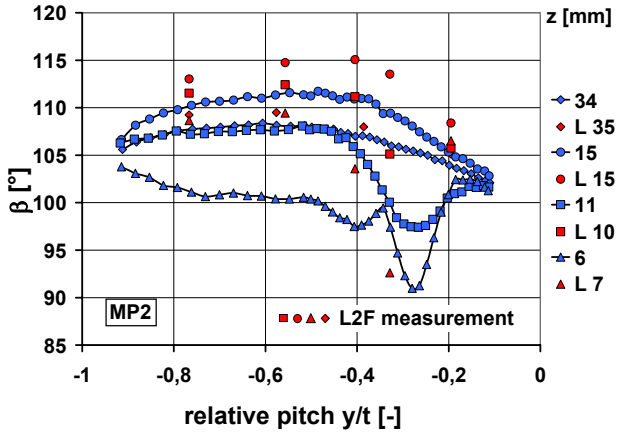

Figure 8: Comparison of measured pressure probe and L2F results for the flow angle β in MP2

Considering the wake behind the cascade it becomes apparent that the losses are not dominated by the corner separation. Close to the endwall the losses result from the kinetic losses induced by the aerodynamic separator. The pitchwise flow angle distributions which were measured in plane 2 and shown in Fig. 7 lead to the previous interpretations. Comparing the pitchwise flow angle distribution at midspan (z = 84 mm) and close to the endwall (z = 1 mm) the increase of overturning of the flow is observable. This overturning, marked I, represents the cross flow on the endwall above the groove. In the range of y/t = -0.1 to -0.4 an underturning is shown in Figure 7. The stepwise change of the flow angle close to the endwall at y/t = -0.4 compared to midspan can be explained by the interaction of the aerodynamic separator and the endwall cross flow. This interaction leads to the separation of the endwall boundary layer above the endwall groove at approximately y/t = -0.4.

In order to validate the pressure probe measurements within the cascade passage L2F measurements were carried out. Figure 8 shows a comparison of the results of the measurements. In this figure considerable differences are observable. At z = 34 mm the results show a good agreement, but towards the endwall the discrepancy increase. This results from uncertainty of the pressure measurement due to the blockage of the probes in the cascade passage as well as from the uncertainty of the L2F measurements caused by the light dispersion and high turbulence level close to the endwall, but the general tendency is comprehensible. Additionally, it has to be mentioned that the L2F measurements was not carried out at the same series of measurements. The oil flow pattern of Fig. 9 and Fig. 10 give an illustration of the flow path on the endwall of the datum and the CEW cascade.

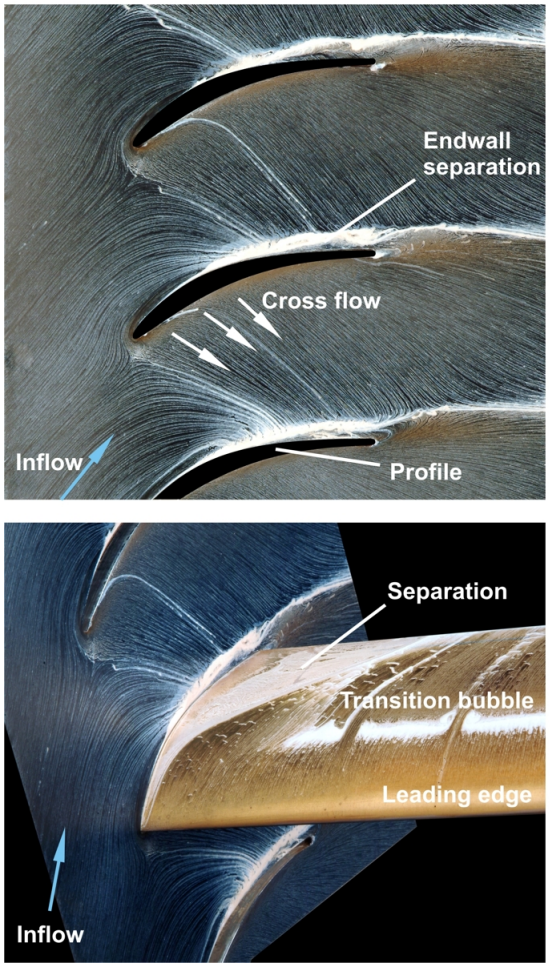

Figure 9: Oil-flow visualization on endwall (top) and blade suction side (bottom) datum cascade

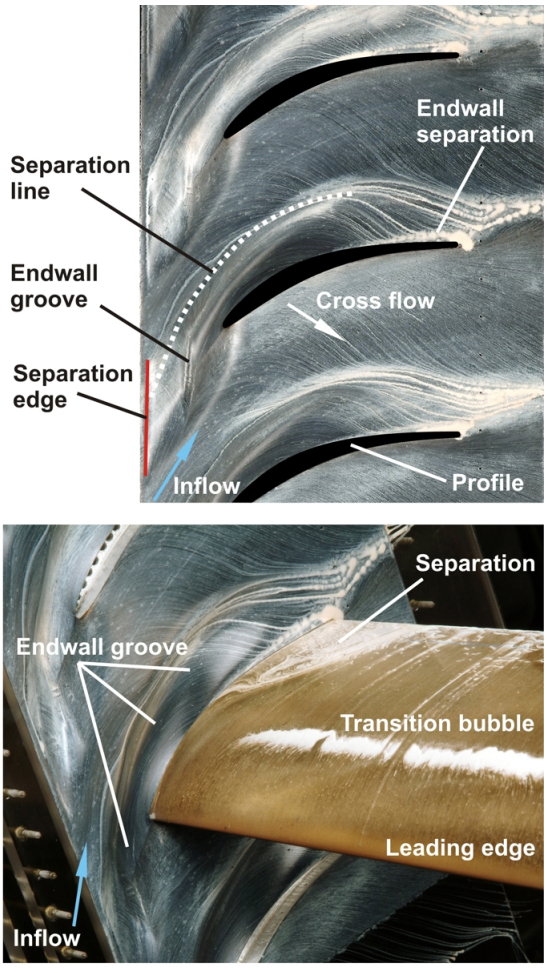

Figure 10: Oil-flow visualization on endwall (top) and blade suction side (bottom) CEW - cascade

In the case of the datum cascade low momentum fluid is forced towards the suction side corner, where this flow separates due to the high pressure gradient in flow direction. The typical flow pattern for these separations is visible in Fig. 9. The oil flow pattern of the CEW cascade with the endwall groove is shown in Fig. 10. In this figure the separation edge, where the vortex (aerodynamic separator) originates is visible. Furthermore the separation line above the Endwall is observable and it becomes apparent that the cross flow is blocked there. In addition the extension of the corner separation is significantly reduced for the CEW cascade in comparison with the datum cascade.

The changed flow patterns are also reflected in the static pressure distribution on the endwall as shown in Fig. 11, where the measurement plane 2 is marked by the dashed line at $x/c_{ax} = 0.52$. In this figure it is observable that the pressure distribution has generally changed. The pressure gradient between zone II and III is decreased as well as the curvature of the pressure profile in zone IV is smoothed, which leads to a pitchwise unloading of the endwall. The deflection of the flow within the endwall boundary layer is decreased in the case of contoured endwall. The change in pitchwise pressure gradient is also reflected in Fig. 12. It shows the comparison of the static pressure at endwall section A and B for the datum and the CEW cascade. The pressure difference or rather the driving force caused by the pressure gradient is decreased in zone II and III for the contoured endwall. It seems that the slight pressure change in zone I (Fig. 11 and Fig. 12) has no observable effect.

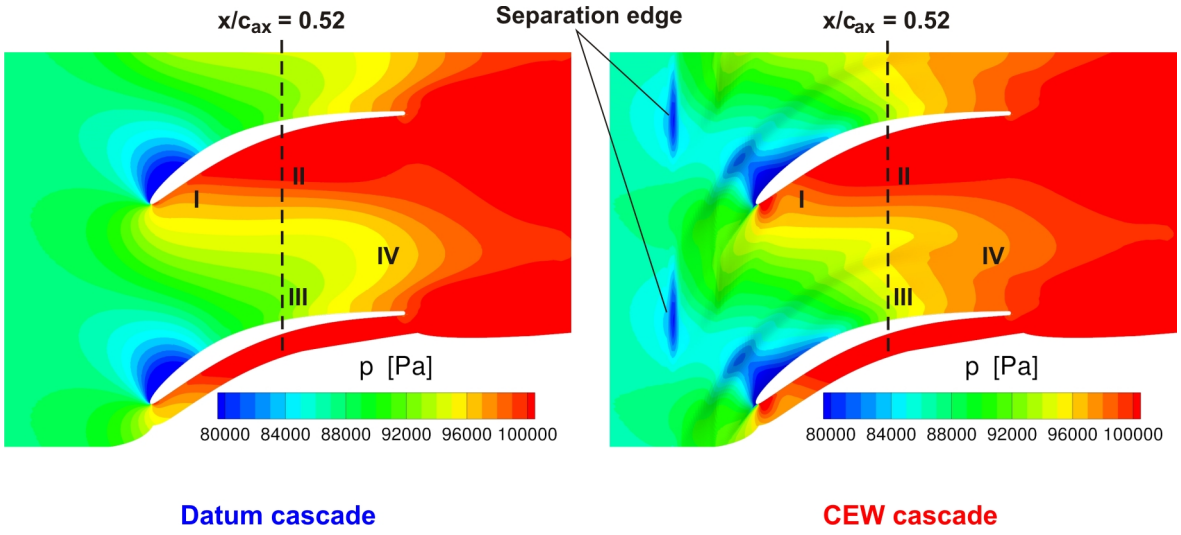

Figure 11: Numerical results of the static pressure distribution on the endwall of the datum and CEW cascade.

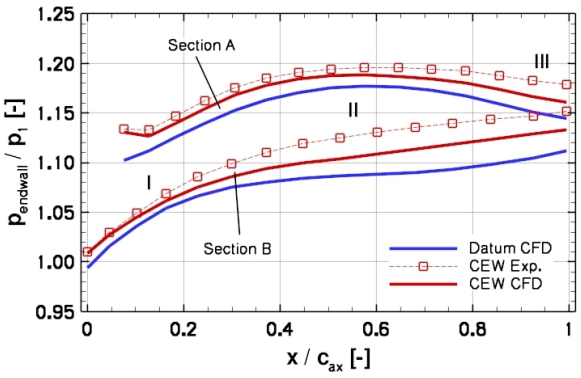

Figure 12: Measured and numerical results of the static pressure on endwall section A and B

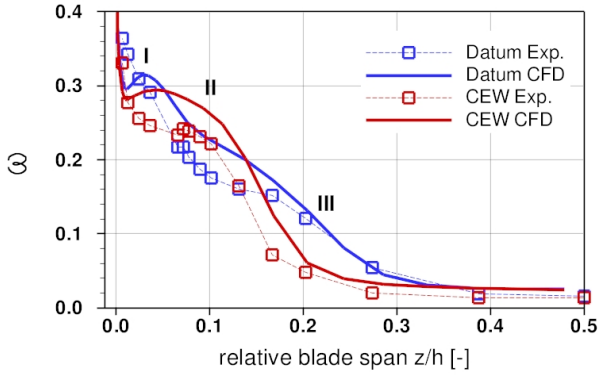

Figure 13: Measured and calculated spanwise loss distribution in MP6

Figure 13 shows the experimental and numerical results for the spanwise loss distribution (pitchwise averaged). This figure illustrates that the contoured endwall creates a redistribution and reduction of the losses near the endwall, whereas the losses at midspan (z/h = 0.5) remain unchanged. Between z/h = 0.15 and 0.3 (zone III in Fig. 12) as well as between the sidewall and 0.05 (zone I) the losses are decreased by a reduction of the corner separation. Due to the kinetic losses induced by the aerodynamic separator, a local slight loss increase is however observed in zone II of the Fig. 13. In summary a significant decrease of the total passage loss (mass averaged) is achieved in the range of 17 (Exp.) to 21 percent (CFD).

CONCLUSIONS

The flow phenomena of a novel numerically-optimized endwall contour have been investigated in detail in the presented paper. The experimental and numerical study deals with the influence of the developed aerodynamic separator on the endwall cross flow and the cascade loss behaviour.
Concerning the cross flow behaviour on the endwall it has been shown that the usual flow structure is significantly influenced by the aerodynamic separator, thus the strong interaction of low momentum endwall fluid with the suction side boundary layer and the resulting corner separation is considerably decreased.
Due to the decrease of the separation the losses are also significantly decreased. The separation is not completely suppressed by the aerodynamic separator, but the total passage loss is decreased around 20 percent at the aerodynamic design point of the cascade. In future, a detailed PIV study is going to be performed in order to resolve the vortex structure and the endwall separation of the cross flow.
In summary, non-axisymmetric contoured endwalls have shown their potential for compressor improvement and thus they offer an additional design space for modern turbomachinery and gas turbines.

NOMENCLATURE

Latin

c	profile chord length
h	blade span
M	Mach number
p	pressure
Re	Reynolds number based on chord length
t	pitch
x, y, z	cartesian coordinates

Greek

β	flow angle with respect to cascade front
γ	spanwise deflection angle
ω	total pressure loss coefficient

Abbreviations

ADP	aerodynamic design point
CDA	controlled diffusion airfoil
CEW	contoured endwall
MP	measurement plane
RANS	Reynolds-averaged Navier-Stokes

Subscrips

1	inlet plane
2	exit plane
ax	axial
is	isentropic
t	total, stagnation value

REFERENCES

1. Herzig, H., Hansen, A. and Costello, G., 1953. “Visualization of Secondary Flow in Compressor Cascades”. *Technical Report 1163, NACA.*
2. Schlichting, H. and Das, A., 1966. “Recent Research on Cascade-Flow Problems”. *Journal of Basic Engineering, ASME*, March, pp. 221-228.

3. Gbadebo, S., Cumpsty, N. and Hynes, T., 2005. "Three-Dimensional Separation in Axial Compressors". *Journal of Turbomachinery, ASME*, 127(2), April, pp. 331-339.
4. Corral, R. and Gisbert, F., 2008. "Profiled End Wall Design Using an Adjoint Navier-Stokes Solver". *Journal of Turbomachinery, ASME*, 130(2), April, pp. 021011-1 – 021011-8.
5. Duden, A., Raab, I. and Fottner, L., 1998. "Controlling the Secondary Flow in a Turbine Cascade by 3D Airfoil Design and Endwall Contouring". International Gas Turbine and Aeroengine Congress and Exposition, Stockholm, Sweden, June 2-5, ASME Paper 98-GT-72.
6. Dorfner, C., Nicke, E. and Voss, C., 2007. "Axis-Asymmetric Profiled Endwall Design by using Multi-Objective Optimisation Linked with 3D RANS-Flow-Simulation". ASME Turbo Expo, Montreal, Canada, May 14-17, ASME Paper GT2007-27268
7. Harvey, N., 2008. "Some Effects of Non-Axisymmetric End Wall Profiling on Axial Flow Compressor Aerodynamics Part I: Linear Cascade Investigation". ASME Turbo Expo, Berlin, Germany, June 9-13, ASME Paper GT2008-50990.
8. Harvey, N. and Offord, T., 2008. "Some Effects of Non-Axisymmetric End Wall Profiling on Axial Flow Compressor Aerodynamics Part II: Multi-Stage HPC CFD Study". ASME Turbo Expo, Berlin, Germany, June 9-13, ASME Paper GT2008-50991.
9. Iliopoulou, V., Lepot, I. and Geuzaine, P., 2008. "Design Optimisation of a HP Compressor Blade and its Hub Endwall". ASME Turbo Expo, Berlin, Germany, June 9-13, ASME Paper GT2008-50293.
10. Yang, H., Nürnberger, D. and Kersken, H.-P., 2006. "Towards Excellence in Turbomachinery Computational Fluid Dynamics: A Hybrid Structured-Unstructured Reynolds-Averaged Navier-Stokes Solver". *Journal of Turbomachinery, ASME*, 128(2), April, pp. 390-402.
11. Voss, C., Aulich, M., Kaplan, B. and Nicke, E., 2006. "Automated Multiobjective Optimisation in Axial Compressor Blade Design", ASME Turbo Expo, Barcelona, Spain, May 8-11, ASME Paper GT2006-90420.
12. Dorfner, C., 2009. "Entwicklung eines Verfahrens zur Konstruktion nicht-rotationssymmetrischer Seitenwandkonturen in axialen Verdichtern". PhD thesis, Ruhr-Universität Bochum.
13. Dorfner, C., Hergt, A., Nicke, E. and Mönig, R., 2009. "Advanced Non- Axisymmetric Endwall Contouring for Axial Compressors by Generating an Aerodynamic Separator Part I: Principal Cascade Design and Compressor Application". ASME Turbo Expo, Orlando, Fl, USA, June 8-12, ASME Paper GT2009-59383.
14. Hergt, A., Dorfner, C., Steinert, W., Nicke, E. and Schreiber, H.-A., 2009. "Advanced Non-Axisymmetric Endwall Contouring for Axial Compressors by Generating an Aerodynamic Separator Part II: Experimental and Numerical Cascade Investigation". ASME Turbo Expo, Orlando, Fl, USA, June 8-12, ASME Paper GT2009-59384.
15. Steinert, W., Fuchs, R. and Starken, H., 1992. "Inlet Flow Angle Determination of Transonic Compressor Cascade". *Journal of Turbomachinery, ASME*, 114(3), July, pp. 487-493.
16. Beversdorff, M., Maziol, L., Blaha, C., 1998. "Application of 3D-Laser Two Focus Velocimetry in Turbomachine Investigation", AGARD PEP Symposium, Brussels, Belgium, October 20-24, AGARD-CP-598

THE EFFECT OF LEADING EDGE TUBERCLE GEOMETRY ON THE PERFORMANCE OF DIFFERENT AIRFOILS

K. L. Hansen, R. M. Kelso and B. B. Dally
School of Mechanical Engineering
University of Adelaide, Adelaide, Australia

ABSTRACT. Results are presented of an experimental investigation on the effects of modification to the leading edge geometry of two NACA airfoils with different aerodynamic characteristics. The modification was inspired by the humpback whale flipper, which has rounded tubercles on its leading edge resembling the shape of a sine curve. Force measurements on both modified and unmodified 2-D airfoils show that tubercles are more beneficial for the NACA 65-021 airfoil than the NACA 0021 airfoil. Also, for smaller amplitude tubercles, the modified NACA 65-021 airfoil outperforms its unmodified equivalent for most angles of attack. Hydrogen-bubble visualisation was used to identify characteristic features of the flow for airfoils with tubercles. It appears that the velocity behind the troughs is greater than behind the tubercles themselves at the leading edge. Downstream from the leading edge, the flow from behind the peaks seems to be entrained into this region, giving rise to the formation of stream-wise vortices.

Keywords: tubercles, passive flow control, airfoil performance, delayed stall, enhanced lift

INTRODUCTION

Tubercles are leading-edge, rounded protuberances that alter the flow-field around an airfoil. The presence of tubercles on the humpback whale flipper, for example, has been associated with the tight turning manoeuvres that it is required to make as part of its feeding ecology [1]. It has been postulated that tubercles give rise to the formation of stream-wise vortices, which enhance momentum exchange within the boundary layer [1]. This can lead to improvements in foil performance, such as delayed stall and higher maximum lift coefficient, allowing a smaller foil surface to be utilised [2]. Hence, drag at the cruise condition and weight of the wing can be reduced.

A numerical study by Watts & Fish [3], which compared a NACA 63_4-021 airfoil with sinusoidally-shaped tubercles to an unmodified airfoil, reported a 4.8% increase in lift, 10.9% reduction in induced drag, and 17.6% increase in lift-to-drag ratio (L/D) at a 10-degree angle of attack. It was concluded that tubercles have a negligible effect on drag at zero angle of attack but may incur an 11% increase in form drag at a 10-degree angle of attack.

An experimental investigation undertaken by Miklosovic *et al.* [4] compared the lift and drag of idealised scale models (NACA 0020) of the humpback whale flipper with and without tubercles. Their results showed 40% increase in the stall angle, 6% increase in the total maximum lift coefficient and a decrease in drag in the post-stall regime. The lift-to-drag ratio was larger for the airfoil with tubercles for all angles except $10° \leq \alpha \leq 12°$. Stein and Murray [5] conducted experiments

Corresponding author: Kristy Hansen
Phone: + (618) 8303-3847, Fax: + (618) 8303-4367
E-mail address: khansen@mecheng.adelaide.edu.au

for $0° \leq \alpha \leq 12°$, using a two-dimensional airfoil with sinusoidal tubercles having amplitude and spacing equal to the average values for the humpback whale. Their results revealed that the modified airfoil experiences reduced lift and increased drag compared to the unmodified airfoil. Another study by Murray *et al.* [6], found that aerodynamic performance of a 3D foil with tubercles could be improved by increasing the sweep angle.

An investigation by Johari *et al.* [7] compared the effect of changing the spacing and amplitude of sinusoidal tubercles on a nominally two-dimensional NACA 63_4-021 airfoil without sweep or taper. They concluded that airfoils with tubercles achieve a lower stall angle and lower maximum lift coefficient, $C_{L_{max}}$, than their unmodified equivalent, which is consistent with the findings in [5]. However, improvements were noted in the post-stall regime in which the airfoils with tubercles had lift coefficients as much as 50% greater than the unmodified airfoil [7]. They also found that the smallest amplitude and shortest wavelength tubercles performed best in terms of stall angle and $C_{L_{max}}$. It was also concluded that varying the amplitude has more effect on airfoil performance than changing the wavelength of the tubercles. Tuft experiments [7] showed that separation originates in the troughs between the tubercles and that the flow remains attached at the tubercle peaks. Despite indications of an earlier separation at lower angles of attack for airfoils with tubercles, at post-stall angles, the flow over the tubercle peaks was still attached when the flow over the unmodified airfoil had completely separated.

A dye visualisation study [8] of the same airfoils found that separation regions behind the troughs appear to be bi-periodic, in that adjacent troughs have the same pattern as their second neighbour. This behaviour was attributed to the fluctuating flow field at the trailing edge of the airfoil. The presence of tubercles creates span-wise flow as a result of the varying leading-edge sweep and this was reported to give rise to the formation of counter-rotating stream-wise vortices. Custodio [8] postulates that these counter-rotating vortices generate vortex lift similar to that observed on a delta wing. However, Nierop *et al.* [9] claim that it is not possible for the tubercles to act as vortex generators since the wavelength and amplitude are much larger that the boundary layer thickness. They propose the explanation that the greater downwash behind the tubercles compared to the troughs leads to a reduction in the effective angle of attack and thus delayed stall in this region.

The purpose of the experimental investigation reported here is to quantify the aerodynamic benefits of sinusoidal tubercles for two different airfoils at low Reynolds numbers. The airfoils investigated here have different chord-wise positions of maximum thickness and are designed for different flow regimes. The study also aims to examine the effect of the tubercle's amplitude and wavelength on the performance of the airfoil and to identify characteristic flow patterns for airfoils with tubercles.

EXPERIMENTAL PROCEDURE

Tubercle configurations were modelled for two types of airfoil: NACA 0021 and NACA 65-021. The airfoils were machined from aluminium and anodised in matte black to ensure optimum visualisation of hydrogen bubbles. All airfoils have a mean chord of $\bar{c}$ = 70mm and span of s = 495mm, giving a plan-form area of $S = 0.035\text{m}^2$. Sinusoidal tubercle configurations are illustrated in Figure 1 and the dimensions are summarised in Table 1. The values used here for amplitude and wavelength are close to estimates taken from data of an actual whale flipper [1]. Drag and lift forces for eight different airfoils were measured in a wind tunnel. Flow visualisation using the hydrogen-bubble technique was also performed to observe the flow field around the airfoil and to highlight flow separation regions and vortex formation.

Table 1
Tubercle configurations and adopted terminology

0021 airfoils		**65-021 airfoils**	
Configuration	**Label**	**Configuration**	**Label**
0021 unmodified airfoil	0021 unmod	65-021 unmodified airfoil	65021 unmod
Amplitude 4mm (0.06c) Wavelength 15mm (0.21c)	A4W15	-	-
Amplitude 4mm (0.06c) Wavelength 30mm (0.43c)	A4W30	Amplitude 4mm (0.06c) Wavelength 30mm (0.43c)	6 A4W30
Amplitude 4mm (0.06c) Wavelength 60mm (0.86c)	A4W60	-	-
Amplitude 8mm (0.11c) Wavelength 30mm (0.43c)	A8W30	Amplitude 8mm (0.11c) Wavelength 30mm (0.43c)	6 A8W30

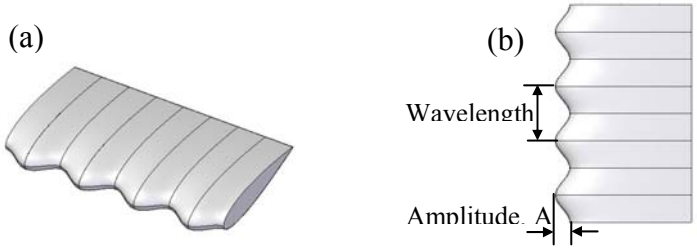

Figure 1. Section view of airfoil with tubercles (a) 3D view, (b) Plan view with characteristic dimensions

Force measurements

Force experiments were undertaken in the open section of the wind tunnel at the University of Adelaide, which has a 0.5m square cross-section and a turbulence intensity of ~0.8%. Maximum blockage occurs at α = 30º and is calculated to be 7% and thus small enough to be ignored in this investigation. The free-stream velocity was measured using a Pitot tube and the sampling rate was 1000 Hz. The data were averaged over one minute and collected via a National Instruments USB-6008/6009 data acquisition device. The Reynolds number based on the free-stream velocity of U_∞ = 25m/s and mean chord length was 120,000. The working section was bolted to the exit of the wind tunnel (Figure 2) and the top of the airfoil was located very close (5mm) to the ceiling of the duct to minimise three-dimensional effects. The foundation of the load cell consisted of a heavy steel base-plate to inhibit the effects of floor vibration and a stiff frame to minimise vibrational disturbances generated by the airflow (Figure 3). These vibrations could potentially cause inaccuracies in the measurements. The angle of attack for the airfoil was set using a Vertex rotary table with an estimated uncertainty of ±0.2 degrees. Lift, drag and moment measurements were conducted using a 6-component load cell from JR3 with external digital electronics. This was fixed to a rotary table and rotated together with the airfoil. Care was taken to ensure the airfoil was mounted as accurately as possible with regard to the free-stream flow. System calibrations showed that the load cell accuracy is within ± 1%.

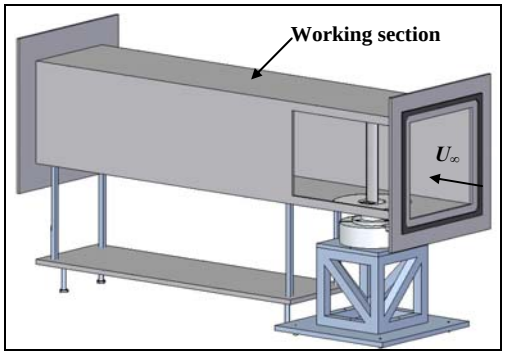

Figure 2. Sketch of experimental

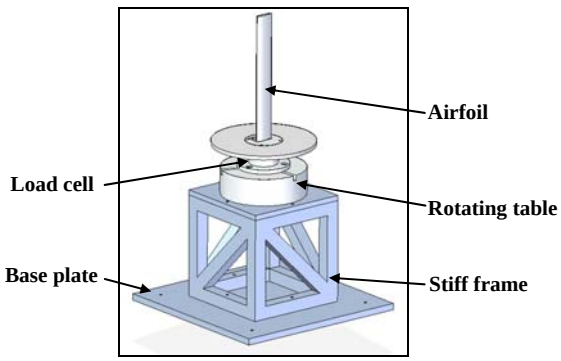

Figure 3. Load cell arrangement

The sampling period of the analogue-to-digital converter was 16ms, which ensured that at least 1000 samples were collected for each angle of attack. Due to the unsteady nature of the flow at post-stall angles, the number of collected samples was increased to 3000 for these cases.

Three sets of measurements were taken for each airfoil for the range of angles $-4° \leq \alpha \leq 30°$. The average results for the lift, drag and moment coefficients for the tested airfoils were then plotted and compared. The NACA 0021 and NACA 65-021 airfoils were analysed separately due to their different characteristics but the relative influence of the tubercles for the two airfoils was compared.

Hydrogen bubble visualisation

Hydrogen bubble visualisation was carried out in a 0.5m-square working section of a closed-return water channel of the University of Adelaide. The water tunnel velocity was selected to give optimum flow conditions for visualisation with the hydrogen bubble method. Thus velocities of U_∞= 70mm/s and 84mm/s were utilised, corresponding to Re = 4370 and 5250 respectively. A low current was passed through a sinusoidally-kinked platinum wire with diameter of 40μm, used to generate streak-lines. The flow was illuminated using a thin light sheet and digitally recorded via a SONY Mini-DV video camera, which was connected to a laptop computer. Footage was recorded from different orientations to highlight specific features. The side view shows the separation point; the top view shows variations in streak-line spacing alluding to local pressure and velocity variations and the angled top view enables identification of vortex structures. In all cases, the flow was visualised as close as possible to the mid-span location to minimise 3-D effects.

DATA ANALYSIS

For each airfoil, at each angle of attack (α), the chord-wise (F_C) and normal (F_N) forces were measured along with the moment about the span-wise axis, M_Z and converted to lift, drag and pitching moment. These were non-dimensionalised, giving the coefficients of lift and drag based on the dynamic pressure and plan-form area and pitching moment, based on the dynamic pressure, plan-form area and chord. Values of C_L, C_D and C_M for NACA 0021 are compared to published data [10]. Unfortunately, no data at the Re number of interest was found for the NACA 65-021 airfoil to compare with the results.

RESULTS

Force measurements

Lift coefficient (C_L). The lift coefficients are plotted against the angle of attack for the NACA 0021 airfoils in Figure 4. From the figure it is clear the airfoils with tubercles have lower C_{Lmax} values than the unmodified airfoil. However, the stall characteristics are much less abrupt. In comparison with

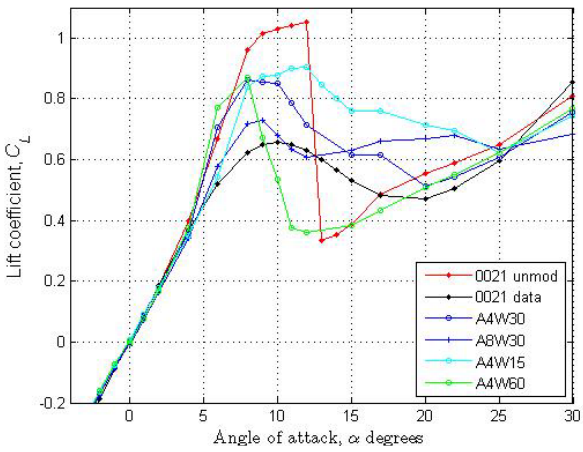

Figure 4. Lift Coefficient vs. Angle of Attack for NACA 0021

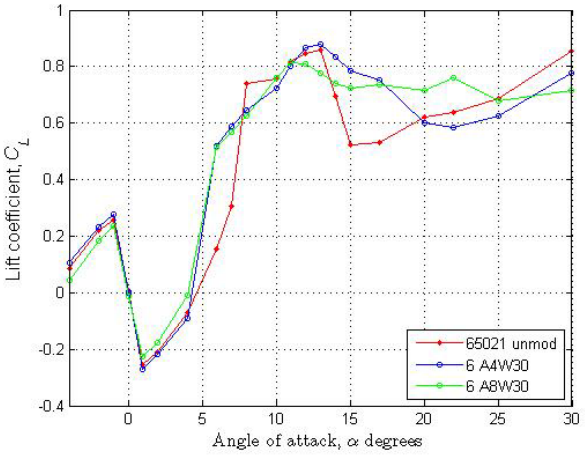

Figure 5. Lift Coefficient vs. Angle of Attack for NACA 65-021

the unmodified airfoil, the drop in C_L after stall (ΔC_L) is considerably less for the A8W30 airfoil with ΔC_L = 17% as opposed to ΔC_L = 68% for the unmodified airfoil. An interesting point is that there is a slight increase in the slope, $\partial C_L / \partial \alpha$ at around α = 4°, which is also evident in Miklosovic & Murray [11] and is perhaps a blockage effect.

Figure 5 indicates that the NACA 65-021 airfoils with tubercles achieve higher relative values of C_L for the majority of attack angles investigated in this study. Also, the lift characteristics are generally smoother for the modified airfoils. It can also be observed that for small angles of attack the NACA 65-021 airfoil generates a negative lift (for $0 < \alpha < 4$), which is attributed to an unexpected early separation of the laminar boundary layer on one side of the airfoil. This phenomenon is not observed, however, at larger angles of attack. This behaviour will be the subject of further investigation.

By increasing the amplitude of the tubercles, a smoother stall characteristic can be achieved but there is an associated penalty of a drop in $C_{L\,max}$ and a decrease in maximum stall angle. This can be seen in both Figure 4 and 5, where the post-stall C_L is higher for the A8W30 and 6 A8W30 airfoils in comparison to the A4W30 and 6 A4W30 airfoils. For both airfoils, the smaller amplitude tubercles achieve a larger C_{Lmax} and a higher maximum stall angle than the larger amplitude tubercles. It can be observed that the NACA 65-021 airfoil with smaller amplitude tubercles surpasses the unmodified airfoil in terms of performance, with its C_L value 3% and 17% higher for α = 13° and 14°, respectively. This indicates that there may be an optimum tubercle configuration for a particular airfoil and/or tubercles are more beneficial for certain airfoils.

It can be seen in Figure 4 that the wavelength of the tubercles noticeably influences the performance of the airfoil. As the wavelength is reduced, the stall angle increases and for the A4W15 airfoil, this angle is equal to that of the unmodified airfoil (i.e. α_{stall} = 12°). This result is in contradiction with other studies [7,9], which found that the varying the wavelength has negligible effects. In addition, the post-stall C_L is greater for the A4W15 airfoil compared to the other tubercle configurations, which illustrates that reducing the wavelength is beneficial for both the pre-stall and post-stall regimes. The effect of reducing the wavelength appears to be more advantageous than varying the amplitude, in terms of achieving both a higher $C_{L\,max}$ and favourable post-stall characteristics.

Drag coefficient (C_D). The results in Figures 6 and 7 indicate that at low angles of attack (i.e. $\alpha < 8°$), tubercles have a minimal effect on C_D for both airfoils. As the stall angle is approached, the tubercles act to increase the drag and thus reduce the extent of the drag bucket. At post-stall angles, tubercles achieve a favourable effect for all airfoils in terms of drag.

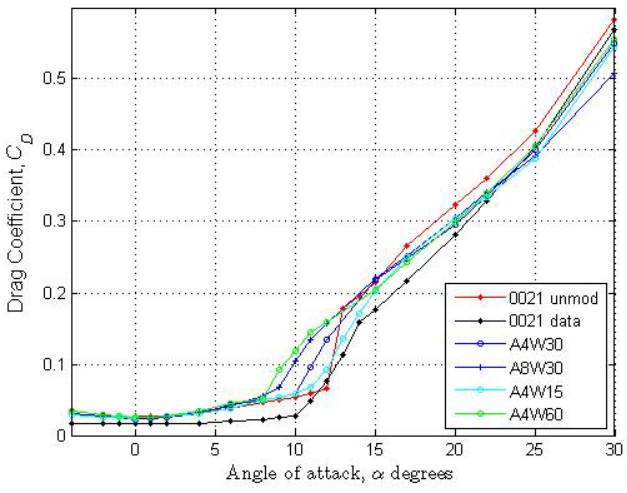

Figure 6. Drag Coefficient vs. Angle of Attack for NACA 0021

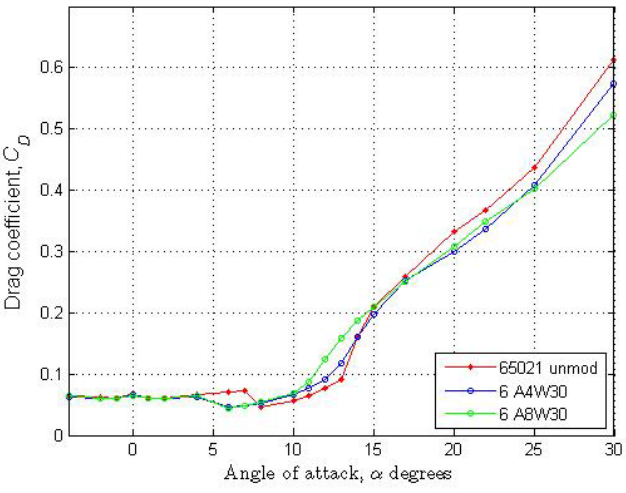

Figure 7. Drag Coefficient vs. Angle of Attack for NACA 65-021

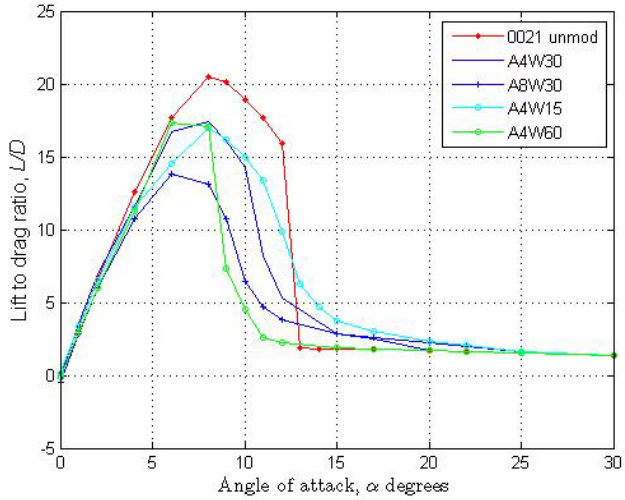

Figure 8. Lift-to-Drag Ratio vs. Angle of Attack for NACA 0021

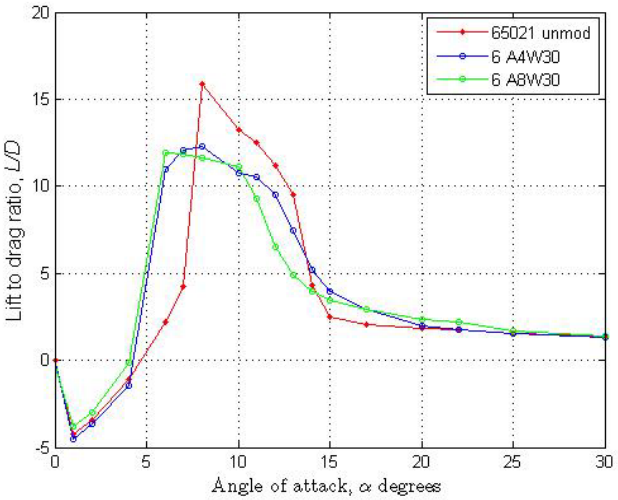

Figure 9. Lift-to-Drag Ratio vs. Angle of Attack for NACA 65-021

A lower drag is observed in the range 8º ≤ α ≤15º for the NACA 0021 airfoil having tubercles with smaller amplitude. For α < 8º, there is small difference in the drag characteristics and for α > 15º, the airfoil with larger tubercles exhibits a lower C_D. The NACA 65-021 airfoil shows a similar trend, although the range of lower C_D occurs at 8º≤ α ≤17º. Outside this range there is little difference in tubercle performance.

A comparison between tubercle wavelength configurations reveals that a smaller wavelength produces a significantly lower drag in the range 8º ≤ α ≤15º. In fact, for the angles excluding α = 10-12º, the A4W15 airfoil displays enhanced C_D performance when compared to the unmodified airfoil. At α > 15º, the larger wavelength configuration yields a slightly lower C_D.

Lift-to-drag *(L/D) ratio.* Figures 8 and 9 highlight the drag costs in producing lift, providing a measure of aerodynamic efficiency. It is observed that for both airfoils, incorporating tubercles gives a higher *L/D* ratio after stall. However, at lower angles of attack the unmodified airfoil is generally more efficient. The peak *L/D* ratio of 20.5 occurs at α = 8º for the unmodified NACA 0021 airfoil and it is 17% higher than the peak value for the A4W15, which represents the best tubercle configuration. After stall, the A4W15 airfoil demonstrates *L/D* ratios up to 70% higher than the unmodified airfoil.

For the NACA 65-021 airfoils, better *L/D* performance is noted in the range α < 8º and α > 14º for both airfoils with tubercles, compared to the unmodified airfoil. In general, smaller amplitude tubercles achieve a higher *L/D* than larger amplitude tubercles, especially in the range of 10º≤ α ≤15º. The peak *L/D* ratio for the unmodified airfoil of 15.9 also occurs at α = 8º, and is 23% higher than that for the 6 A4W30 airfoil. In the post-stall regime, the 6 A4W30 airfoil has *L/D* ratios up to 37% higher.

Pitching moment coefficient (C_M). The pitching moment coefficient, C_M relative to the quarter-chord position is plotted in Figures 10 and 11. The measured C_M displays more fluctuations than the data curve, however the overall trend is consistent. For small angles of attack (α < 4º), there is little difference in C_M between the unmodified airfoil and models with tubercles for the NACA 0021. At these angles, all airfoils experience a nose-up pitching moment.

Where as the unmodified airfoil drops to a negative C_M at α = 6º, the models with small wavelength or large amplitude tubercles remain positive. At stall, the unmodified airfoil rises to its maximum positive value but this rise is less pronounced for all airfoils with tubercles. In the post-stall region,

the majority of airfoils with tubercles have a less-negative C_M, which is an advantageous characteristic. Overall, changes in C_M are less abrupt for airfoils with tubercles.

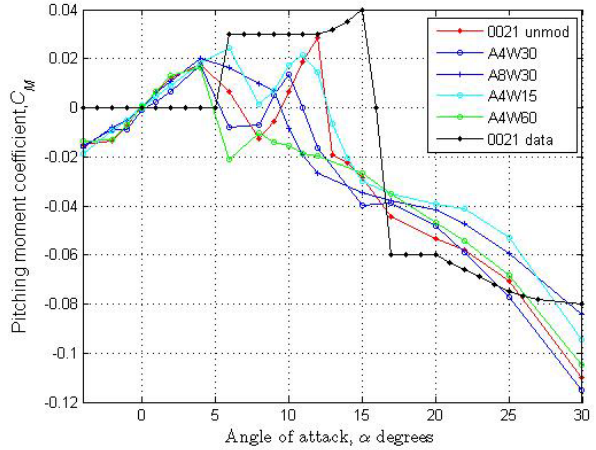

Figure 10. Pitching Moment Coefficient vs. Angle of Attack for NACA 0021

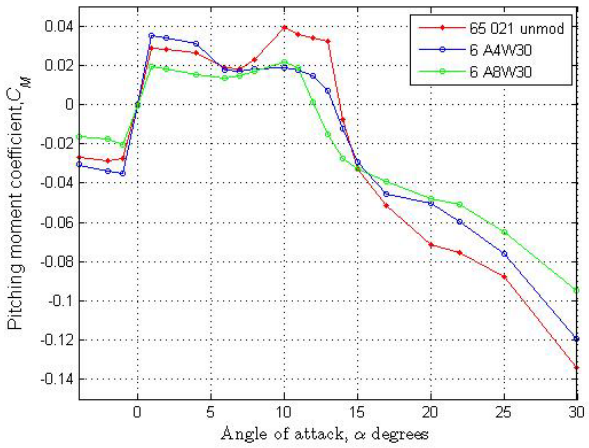

Figure 11. Pitching Moment Coefficient vs. Angle of Attack for NACA 0021

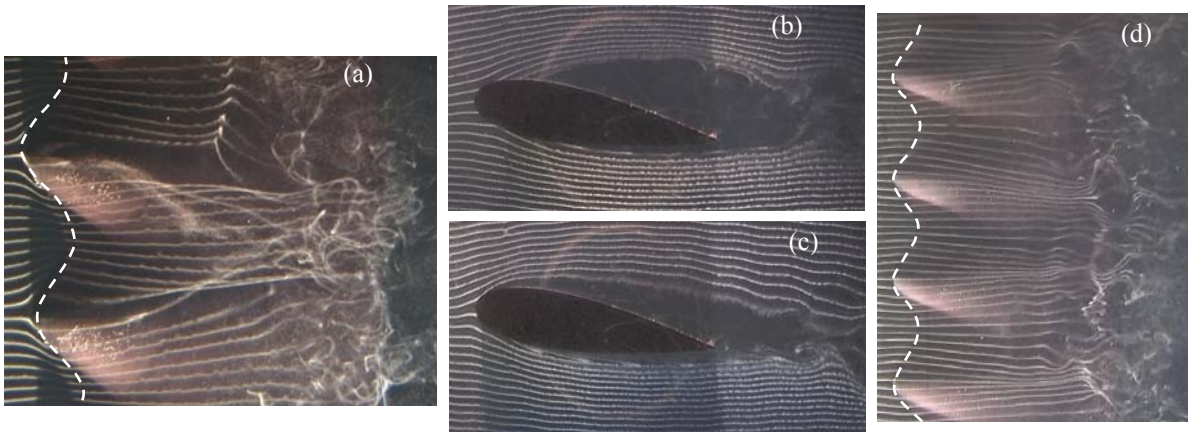

Figure 12. Hydrogen bubble visualisation (a) angled top view showing stream-wise vortices, (b) side view in plane of trough (c) side view in plane of peak and (d) top view depicting regions of acceleration. Dashed lines show the outline of the leading edge

Hydrogen bubble visualisation

Flow visualisation shows that stream-wise vortices form on either side of the troughs between tubercles, downstream of the leading edge (Figure 12(a)). It is also evident that the flow separates behind the tubercle troughs earlier than it separates behind the peaks. This can be seen in Figures 12(b) and 12(c), which show that the wake is wider behind the trough. Figures 12(a) and 12(d) suggests that the flow is accelerated in the troughs at the leading edge. This is indicated by the convergence of streak-lines in these regions. The influence of the stream-wise vortices can be seen in the convergence of streak-lines towards the tubercles. At the surface, the flow is expected to diverge away from the tubercles.

DISCUSSION

The mechanism by which tubercles alter the flow characteristics over airfoils is still not well understood. From the results presented here and also in [8] it is clear that tubercles give rise to the formation of stream-wise vortices. The acceleration of the flow in the troughs between tubercles is likely to lead to a region of low pressure in the troughs at the leading edge, which is consistent with [3]. The flow from behind the peaks seems to be entrained towards this apparent low-pressure region, giving rise to a pair of counter-rotating vortices behind each trough. It is unclear as to

whether these vortices induce a type of vortex lift as suggested in the literature [7,8,11] or if they increase the extent of flow attachment, thus delaying stall, through an augmented rate of momentum exchange within the boundary layer. According to Miklosovic *et al.* [11], the unsteadiness observed close to stall and in post-stall conditions showed signs of vortex-dominated flow. However, this was contradicted by the fact that the characteristic simultaneous increase of $C_{L\ max}$ and $C_{D\ min}$ did not occur [11]. It has been argued by van Nierop *et al.* [9] that it is implausible for tubercles to behave as vortex generators since their wavelength and amplitude are much larger than the boundary layer thickness and that instead, they alter the pressure distribution on the wing, increasing the extent of flow attachment. Despite this viewpoint, there seems to be a strong analogy between tubercles and counter-rotating vortex generators as described in [12].

In this study, it was observed that when the position of maximum thickness is further aft, increasing the extent of laminar flow, tubercles can be more beneficial. Since there is a more efficient exchange of momentum in a turbulent boundary layer [13], it is inferred that tubercles are more effective for a laminar boundary layer for which momentum exchange is poor. In regards to the smallest wavelength and amplitude being the most beneficial tubercle configuration, it is expected that associated stream-wise vortices are smaller, leading to a relatively lower form drag component. Additionally, since more vortices are generated per unit length of span for the smaller wavelength tubercles, this may result in greater momentum exchange.

CONCLUSIONS

The results for the NACA 0021 airfoil indicate that in the pre-stall regime there is marginal advantage in employing tubercles. At post-stall conditions, however, a large improvement in lift-to-drag ratio can be achieved and much smoother stall characteristics are observed. These results are consistent with results from [7]. The most beneficial configuration of the tubercles proves to be those with the smallest amplitude and narrowest wavelength. Results for the NACA 65-021 show that the position of maximum thickness has a noticeable effect on the performance of the tubercles. For this airfoil, tubercles maintain a higher lift-to-drag ratio for the majority of angles of attack, except near stall. For both airfoils, tubercles act to smooth out the pitching moment characteristics of the airfoil.

REFERENCES

1. Fish, F.E. and Battle, J.M., Hydrodynamic design of the humpback whale flipper, *J. Morp.*, 225:51-60, 1995.
2. Katz, J., Plotkin, A., Low Speed Aerodynamics, *Cambridge University Press*, 2001.
3. Watts, P. and Fish, F.E., The Influence of Passive, Leading Edge Tubercles on Wing Performance, *Proc. of Unmanned Untethered Submersible Technology (UUST)*, Durham, NH, August, 2001.
4. Miklosovic, D. S., Murray, M. M., Howle, L. E., and Fish, F. E., Leading Edge Tubercles Delay Stall on Humpback Whale Flippers, *Phys. Fluids* 16(5): L39-L42, 2004.
5. Stein, B. & Murray, M.M., Stall mechanism analysis of humpback whale flipper models, *Proc. of Unmanned Untethered Submersible Technology (UUST)*, Durham, NH, August 2005.
6. Murray, M.M., Miklosovic D.S., Fish, F.E., Howle, L.E., Effects of leading edge tubercles on a representative whale flipper model at various sweep angles, *Proc.of Unmanned Untethered Submersible Technology (UUST)*, Durham, NH, August 2005.
7. Johari, H., Henoch, C., Custodia, D. & Levshin, A., Effects of leading edge protuberances on airfoil performance, *AIAA Journal*, 45:11, November 2007.
8. Custodio, D., The effect of humpback whale-like leading edge protuberances on hydrofoil performance, *Thesis submitted to Worcester Polytechnic Institute*, December 2007.
9. van Niorop, E., Alben, S & Brenner, M.P., How bumps on whale flippers delay stall: an aerodynamic model, *Physical review letters*, PRL 100, 054502, February 2008.
10. Sheldahl, R. E. & Klimas, P. C., Aerodynamic Characteristics of Seven Airfoil Sections Through 180 Degrees Angle of Attack for Use in Aerodynamic Analysis of Vertical Axis Wind Turbines, *SAND80-2114*, Sandia National Laboratories, Albuquerque, New Mexico, March 1981.
11. Miklosovic, D.S. & Murray, M.M., Experimental evaluation of sinusoidal leading edges, *J. Aircraft*, 44:1404–1407, 2007.

12. Kermode, A.C., Mechanics of Flight, *Pitman Publishing Ltd*., London, 1972, pp. 350-352.
13. Marchaj, C.A., Aero-Hydrodynamics of Sailing, *Granada Publishing Ltd.*, Great Britain, 1979.

EXPERIMENTAL INVESTIGATION OF THE EFFECT OF HEAT TRANSFER ON PRESSURE DROP FOR A HEAT EXCHANGER FOR AERO ENGINE APPLICATIONS

C. Albanakis[1], D. Missirlis[1*], P. Storm[2], K. Yakinthos[1], A. Goulas[1]
[1]Laboratory of Fluid Mechanics & Turbomachinery, Department of Mechanical Engineering, Aristotle University of Thessaloniki, Egnatia street, 54124 Thessaloniki, Greece
[2]MTU Aero Engines GmbH, Dachauerstrasse 665, 80995 Munich, Germany

ABSTRACT. The present work is investigating the effect of heat transfer on the pressure drop for a heat exchanger designed to be used in an aero engine installation. The main idea of this technology is based on the use of an alternative thermodynamic cycle. The heat exchanger consists of elliptic tubes placed in a 4-3-4 staggered arrangement and is operating as a heat recuperator aiming at the exploitation of the thermal energy of the turbine exhaust gas to pre-heat the compressor outlet air before combustion and thus, to decrease fuel consumption and pollutant emissions. The operation of the heat exchanger is characterized by two basic parameters, the pressure loss and the heat transfer taking place. The presence of the heat exchanger introduces a pressure drop in the flow field, which can significantly affect the downstream flow development and the effectiveness of the thermodynamic cycle of the installation. The pressure drop induced by the heat exchanger depends on geometry-related parameters, such as the geometry and the arrangement of the tubes, and to operation-related parameters, such as the flow inlet conditions and the heat transfer taking place. For the proper evaluation of the performance of the heat exchanger both of these parameters should be considered. For this reason a wide range of experimental measurements was carried out in a wind tunnel where a test section of the heat exchanger was installed. The presence of the hot gas was modelled with preheated air while for the heat transfer cold water was circulated inside the elliptic tubes. The experimental measurements were performed with the use of a 3-hole pressure probe and a Pitot-static tube, while for the air temperature measurements, a K-type thermocouple was used. For the water temperature measurements, a Platinum Resistance Thermometers PT100 thermocouple was used. Various sets of detailed experimental measurements were performed including also isothermal measurements in order to have a reference point for the pressure drop of the flow through the heat exchanger when no heat transfer was taking place. The experimental measurements showed that the pressure drop was directly affected by the mean temperature of the air flow through the heat exchanger.

Keywords: *heat transfer, pressure drop, heat exchanger, aero engine*

INTRODUCTION

Despite the fact that modern civil aero engines are of a high technological level, there are still demands of lower fuel consumption and reduced pollutant emissions. Consequently, it is necessary for engineers to investigate new concepts which can contribute to the optimization of the overall

* Corresponding author: Dr. D . Missirlis
Phone: + (30)-2310-996033, Fax: + (30)-2310-996002
E-mail address: misirlis@eng.auth.gr

operation of an aero engine. Towards this direction, MTU Aero Engines have developed the concept of the intercooled recuperative aero engine (IRA), as shown in Figure 1.

A detailed description of this technology can be found in the works of Broichhausen et al. [1], Wilfert and Masse [2] and in the MTU Aero Engine internet site [3]. The main idea in such a concept is the use of an alternative, but more efficient, thermodynamic cycle for aircraft engines, which is based on recuperation. For this reason a system of heat exchangers, operating as heat recuperators, is mounted at the exhaust nozzle of the aircraft engine so as to exploit part of the thermal energy of the exhaust gas of the aero engine and obtain a better combustion with less pollutant emissions.

Each one of the heat exchangers is constructed by special profiled tubes of elliptic geometry placed in a 4-3-4 staggered arrangement, in order to minimize the pressure drop, and consist of two manifold collector tubes, Figure 2. During engine operation, the flow from the high-pressure compressor (HPC) enters the upper tube from both sides and is distributed into the U-shaped profiled tubes, which are brazed into the manifold tubes and form the core of the heat exchanger. The preheated air is collected in the lower manifold tube and it is guided back to the combustion chamber. At the same time, the hot exhaust gas from the low-pressure turbine flows upwards through the heat exchanger elliptic tubes and its temperature is decreased while heating-up the air inside the elliptic tubes. Additional details of the heat exchanger geometry and of this technology can be found in the works of Missirlis et al. [4], Yakinthos et al. [5] and Albanakis et al. [6].

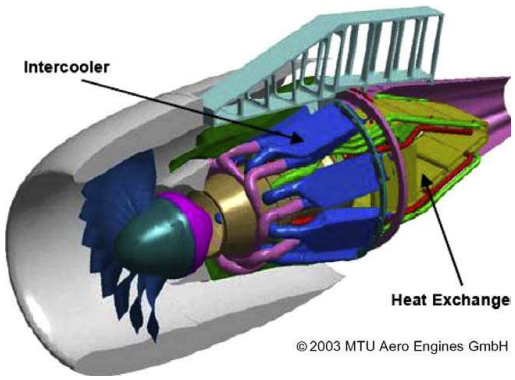

Figure 1. The intercooled recuperative aero engine

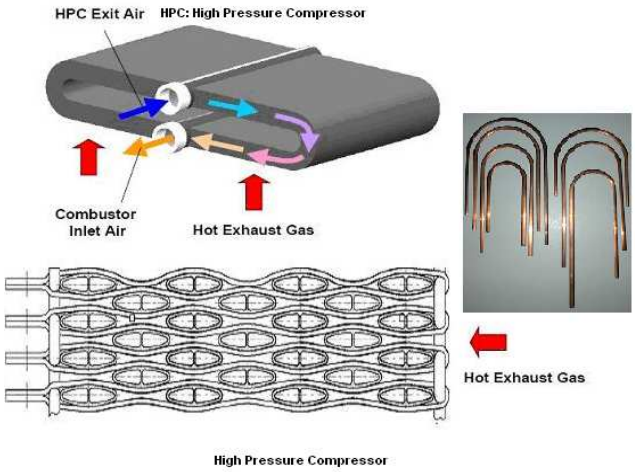

Figure 2. The heat exchanger and the U-shaped elliptic profiled tubes

EXPERIMENTAL SET-UP

To maximize the benefit of this technology it is necessary to investigate the hydraulic and thermal performance of these heat exchangers. For this reason, it was obligatory to carry out a wide range of experimental measurements sufficient enough to describe the operation of the heat exchanger. For the experimental measurements, a part of the heat exchanger corresponding to the straight part of the device was used as shown in Figure 3. The heat exchanger model was placed in a wind-tunnel with a rectangular cross-sectional area. Figures 3 and 4 show the test-rig with the heat-exchanger placed in the wind-tunnel. During the experimental measurements the hot gas has been generated with preheated air while, for the heat transfer, cold water was circulated inside the heat exchanger tubes. Additional details about the experimental setup can be found in the work of Albanakis et al. [6].

The measurement positions have been chosen to be 40mm upstream the model and 40mm downstream the model. The two positions were the same for both the velocity, pressure and temperature measurements. Additionally, in order to correlate the pressure drop between cases with and without heat transfer, two sets of pressure drop measurements have been carried-out, the first with no heat transfer (isothermal) and the second one with heat transfer (anisothermal).

The pressure drop measurements were performed with the use of a Pitot-static tube and a 3-hole pressure probe. The latter is capable of measuring total and static pressure, velocity and flow angle after a proper calibration. The probe consists of three small tubes, one central and two others which are placed in a symmetrical arrangement, as presented in Figure 5. Each of these tubes is capable of providing pressure values to a digital manometer attached to the probe. The final signal is transferred to a computer for further processing. The calibration procedure of the 3-hole probe is based on the suggestions of Gundogdu and Carpinlioglu [7], Morrison et al. [8] and it is similar to the one used in Missirlis et al. [4].

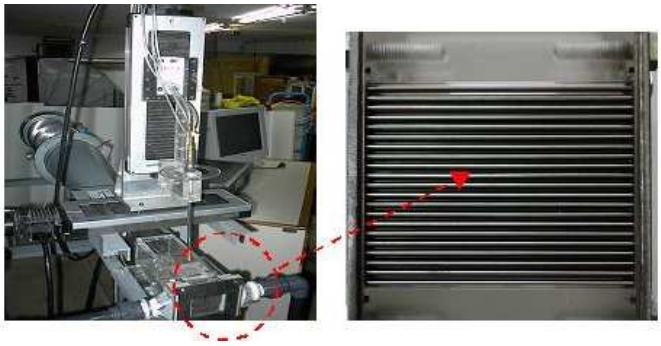

Figure 3. The test-rig with the heat exchanger

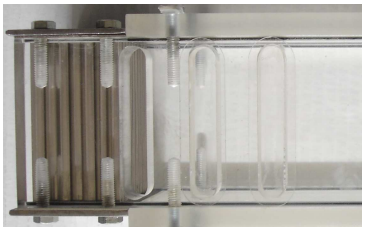

Figure 4. The test-rig with the heat exchanger

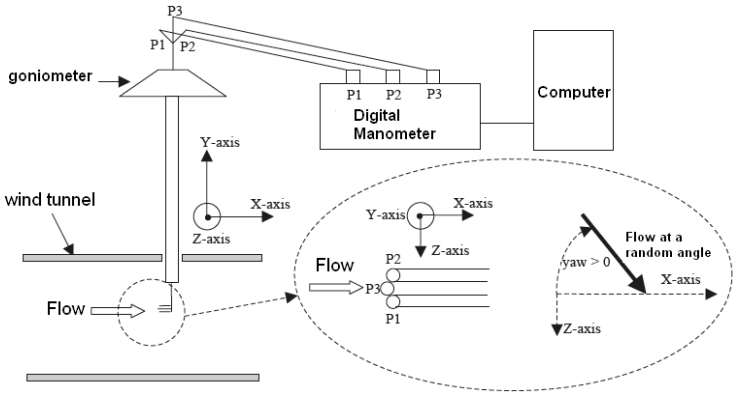

Figure 5. Diagram of the pressure probe operation

Regarding the calibration procedure, the side tubes P_1 and P_2 of the 3-hole pressure probe values will have equal values only when the tip of the probe is placed parallel to the local airflow direction. At this position, the pressure value of the center tube P_3 will be equal to the total pressure of the flow. This position is corresponding to the zero-degree position of the calibration. Thus, at the first step the probe is placed at airflow inside an empty wind tunnel and by changing the angle with the goniometer the zero-degree position is found and the P_1, P_2 and P_3 pressure values are recorded. From this position, the orientation of the probe is changed from +30 to -30 degrees (relatively to the zero-degree position) with a step of 5 degrees and each time the corresponding P_1, P_2 and P_3 values are recorded. Then, the following non-dimensional coefficients, as shown in equations (1), (2) and (3), are calculated for each angle.

$$Cp_{yaw} = (P_1 - P_2)/(P_3 - P_{ave}) \ , \quad P_{ave} = 0.5(P_1 + P_2) \tag{1}$$

$$Q_p = (P_3 - P_{ave})/(0.5\rho V^2) = (P_3 - P_{ave})/(P_{total} - P_{static}) \tag{2}$$

$$S_p = (P_{total} - P_3)/(P_3 - P_{ave}) \tag{3}$$

With the use of the measured values and polynomial curve fitting the functions of the coefficients towards the yaw angle are calculated as presented in Figure 6.

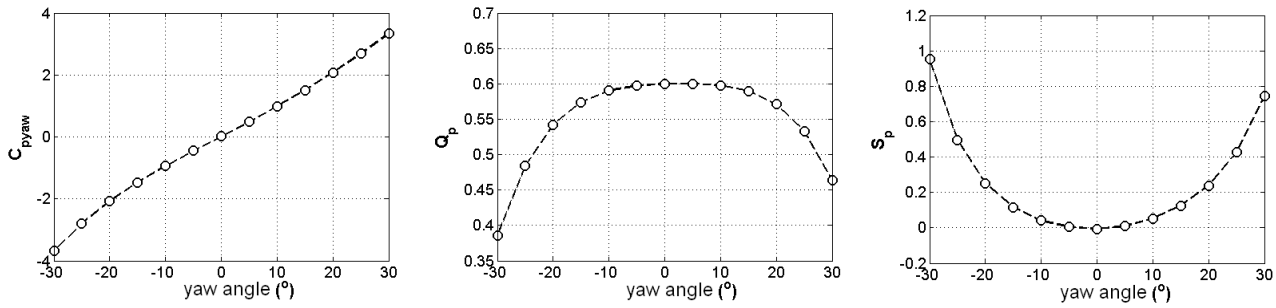

Figure 6. Plots Plots of the non-dimensionalized coefficients towards the flow angle

Hence, when the probe is placed in a random position inside a flow field in order to derive the total and static pressure, the yaw angle and the velocity components, the reverse procedure is followed. More specifically, since from a specific measurement the P_1, P_2 and P_3 pressure values are known, the C_{pyaw} can be easily calculated. In addition, from the curve fitting of the C_{pyaw} plot the yaw angle can be derived as a function of the C_{pyaw} and thus, the flow angle is also known. Furthermore, since the yaw angle is known, the Q_p and S_p coefficient can be calculated. At the final step, the values of the velocity, total and static pressure are calculated as presented in equations (4), (5) and (6) respectively:

$$V = \sqrt{\frac{P_3 - P_{ave}}{0.5\rho Q_p}} \tag{4}$$

$$P_{total} = S_p(P_3 - P_{ave}) + P_3 \tag{5}$$

$$P_{static} = P_{total} - \frac{1}{2}\rho V^2 \tag{6}$$

Regarding the air temperature measurements, a K-type thermocouple was used while for the water temperature measurements, a Platinum Resistance Thermometers PT100 thermocouple was used.

In order to ensure that the experimental measurements reflect the true average behavior of the heat exchanger it was necessary to proceed to a measurement step dependency study to determine the most appropriate measurement step size. After some preliminary measurements with different steps sizes at both measurement planes, it was decided to use a measurement step equal to 5 mm for the inlet and 2 mm for the outlet position since the use of these step values provided an accuracy corresponding to less than 1 Pa for the total and static pressure values and to approximately 0.01 m/s for the velocity magnitude.

MEASUREMENTS SET-UP AND RESULTS

The experimental measurements correspond to the following measurement sets:

- Isothermal measurements with T_{inlet}=T_{outlet}=20°C (293K)
- Isothermal measurements with T_{inlet}=T_{outlet}=40°C (313K)
- Isothermal measurements with T_{inlet}=T_{outlet}=60°C (333K)
- Isothermal measurements with T_{inlet}=T_{outlet}=80°C (353K)
- Anisothermal measurements with T_{inlet}=60°C and T_{outlet}=31°C (333K-304K), taking into account the heat transfer effect
- Anisothermal measurements with T_{inlet}=80°C and T_{outlet}=33°C (353K-306K), taking into account the heat transfer effect

The Reynolds number of the flow was defined by equation (7). For the experimental measurements of the present work, the corresponding Reynolds numbers were in the range of 3100 to 5500 which, based on suggestions of Umeda and Yang [9], are within the transitional regime.

$$\mathrm{Re} = \frac{u_{\max} D}{\nu} \tag{7}$$

where,

$u_{\max}$: is the maximum velocity which is based on the minimum free area available for fluid flow $A_{\min}$

D : is the diameter of the equivalent circular tube with the same perimeter as the one of the elliptic tubes

ν : is the fluid kinematic viscosity

Typical plots of the static pressure measurements are presented in Figure 7. Figure 8 shows the static pressure drop per unit length for the isothermal cases, when the inlet air temperature takes values of 20°C, 40°C, 60°C and 80°C, together with the static pressure drop for the two anisothermal cases of T_{inlet}=60°C and T_{outlet}=31°C and of T_{inlet}=80°C and T_{outlet}=33°C. In the same figure the polynomial fitting curves are plotted which in all cases are best described by a second order polynomial curve. As it can be seen, the effect of the air temperature is clearly shown and a larger value of temperature leads to a larger pressure drop. This conclusion is valid also for the anisothermal measurements when an effective weighted temperature (e.g. average temperature) between the inlet and outlet is taken into consideration. Thus, the anisothermal case of T_{inlet}=80°C and T_{outlet}=33°C, which corresponds to average air flow temperature of 56.5°C, is placed in the static pressure drop plot of Figure 8 lower than the one of 60°C.

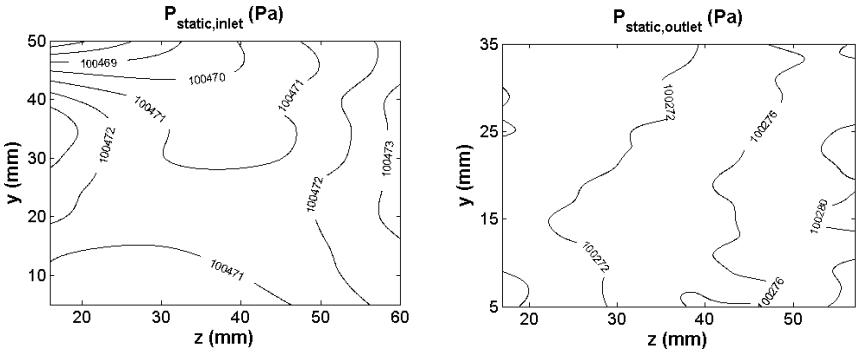

a) mass flow of $0.029\ kg/s$

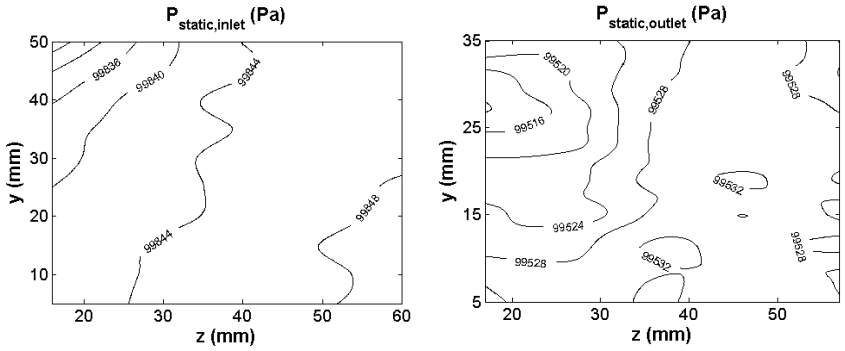

b) mass flow of $0.037\ kg/s$

Figure 7. Inlet and outlet static pressure isolines for the isothermal measurements of 20°C

A very small deviation from this trend is met only for the anisothermal case of T_{inlet}=60°C and T_{outlet}=31°C, which corresponds to average air flow temperature of 45.5°C and which is placed almost exactly on the static pressure drop curve of the 40°C, even though under the same approach a higher pressure drop should be expected. Additionally, in order to correlate the pressure losses with the average air flow velocity inside the heat exchanger, which is related to the average temperature and density of the flow inside the heat exchanger, the results of the experimental measurements were reprocessed and are presented in Figure 9. As it can be seen, all experimental measurements follow the same second order polynomial curve. This indicates that the static pressure drop is strongly affected by the average velocity of the air flow inside the heat exchanger regardless of whether heat transfer takes place or not.

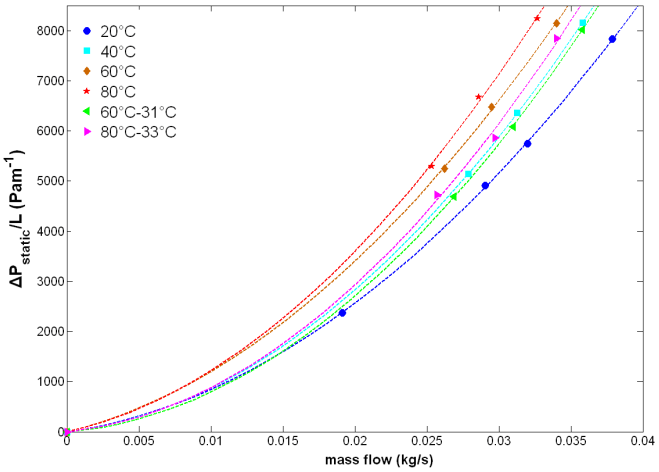

Figure 8. Comparison of the static pressure drop per unit length over mass flow for the isothermal and anisothermal cases

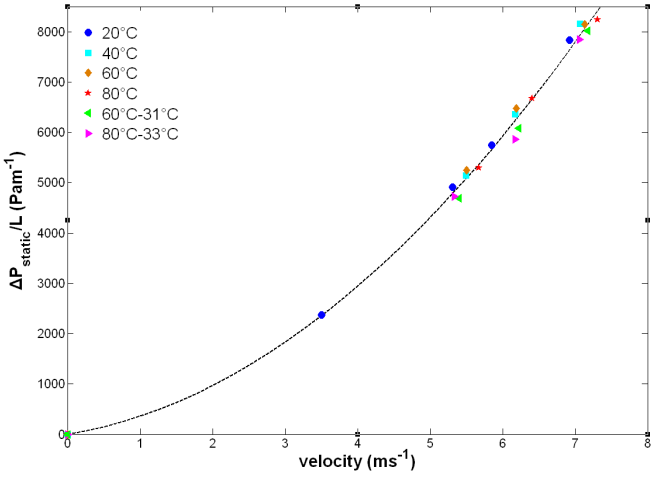

Figure 9. Static pressure drop over effective velocity

Consequently, since the correlation of the effective velocity with repect to pressure loss is known, it is relatively easy for the engineer to calculate the pressure losses due to the presence of the heat exchanger in the overall aero engine installation as long as the average air flow temperature can be estimated. The latter can be deduced from either the derivation of a Nusselt correlation from the

experimental anisothermal measurements or from a literature survey for similar setups (Kays and London [10], Zukauskas [11]).

CONCLUSIONS

In the present work, the performance of a heat exchanger designed for aero engines was investigated experimentally. The measurements show that the pressure drop is directly affected by the mean temperature of the air flowing through the heat exchanger. The static pressure drop could be described by a second order polynomial fitting curve and could be regarded as nearly independent of the inlet air temperature and heat transfer but strongly dependent on the average 'effective' velocity of the air flow inside the heat exchanger which is related to the average temperature and density of the flow inside the heat exchanger for the same mass flow at the inlet. Thus the measurements corresponding to the higher mean air flow temperature yield the higher pressure drop while the ones corresponding to the lower mean air flow temperature produce the lower pressure drop. Based on these conclusions a general pressure drop law can be derived which can sufficiently describe the pressure drop behaviour of the heat exchanger inside the aero engine installation.

ACKNOWLEDGMENTS

This paper is part of the 03ED research project implemented within the framework of the "Reinforcement Programme of Human Research Manpower" (PENED) and co-financed by National and Community Funds 25% from the Greek Ministry of Development-General Secretatiat of Research and Technology and 75% from E.U.-European Social Fund. MTU Aero Engines GmbH has also funded a part of this project.

REFERENCES

1. Broichhausen, K., Scheugenpflug, H., Ch. Mari, Barbot, A., Clean The European Initiative Towards Ultra Low Emission Engines, ICAS 2000, Harrogate, UK, 2000.
2. Wilfert, G., Masse, B., Technology integration in a low emission heat exchanger engine, in: Proceedings of the 8th CEAS European Propulsion Forum, Nottingham, UK, 2001.
3. http://www.mtu.de
4. Missirlis, D., Yakinthos, K., Palikaras, A., Katheder, K., Goulas, A., Experimental and numerical investigation of the flow field through a heat exchanger for aero-engine applications, Int. J. of Heat and Fluid Flow 26 (2005) 440–458.
5. Yakinthos, K., Missirlis, D., Palikaras, A., Storm, P., Simon, B., Goulas, A., Optimization of the design of recuperative heat exchangers in the exhaust nozzle of an aero engine, Applied Mathematical Modelling 31 (2007) 2524-2541.
6. Albanakis, C., Yakinthos, K., Kritikos, K., Missirlis, D., Goulas, A., Storm, P., The effect of heat transfer on the pressure drop through a heat exchanger for aero engine applications, Applied Thermal Engineering 29 (2009) 634-644.
7. Gundogdu, M.Y. and Carpinlioglu, M.O., A multi-tube pressure probe calibration method for measurements of mean flow parameters in swirling flows, Flow Measurements and Instrumentation 9 (1998) 243-248.
8. Morrison, G.L., Schobeiri, M.T., and Pappu, K.R., Five-hole pressure probe analysis technique, Flow Measurements and Instrumentation 9 (1998) 153-158.
9. Umeda, S., Yang, S.W., 1999. Interaction of von Karman vortices and intersecting main streams in staggered tubes bundles. Experiments in Fluids 26, 389–396.
10. Kays, W., London, A., 1984. Compact Heat Exchangers, third ed. McGraw Hill, New York.
11. A.A. Zukauskas, Convective heat transfer in cross-flow, in: S. Kakac, R.K. Shah,W. Aung (Eds.), Handbook of Single-Phase Convective Heat Transfer, Wiley, New York, 1987

AN INVESTIGATION INTO THE EFFECT OF THERMAL BOUNDARY CONDITIONS ON TRANSIENT NATURAL CONVECTION

T. Confrey[1,*], D. Newport[1], V. Egan[1], V. Lacarac[2]
[1]Stokes Institute, Dept. of Mechanical and Aeronautical Engineering,
University of Limerick, Limerick, Ireland
[2]Airbus UK, Filton, Bristol BS99 7AR, United Kingdom

ABSTRACT. The current paper presents a study on the effect of thermal boundary conditions on transient natural convection in an air filled rectangular enclosure. Experiments are carried out over a Grashof number range of 10^5-10^7 for an enclosure of aspect ratio of A = 0.25. The cavity is representative of an aircraft wing box resting on the apron where the top surface of the enclosure is exposed to solar loads. Experiments were carried out for the following three cases. In case one the top surface is heated to 100°C by means of a PID controlled heater mat, with conduction permitted through the side and bottom walls. For case two the top wall is again PID controlled, but an isothermal and constant temperature boundary condition was imposed on the bottom wall. Lastly for case three an isoflux boundary condition was imposed on the top wall, and again the bottom wall was isothermal and at constant temperature. Experimental methods employed included flow visualisation, particle image velocimetry and thermocouple measurements. Principal results indicate the existence of two counter acting flow circulations driven by the side wall, the flows were found to detach an adiabatic point adjacent to the side wall. The introduction of an isothermal bottom surface had the most effect on the flow structures, owing to elevated side wall temperatures. The interior air temperature distributions remained similar for each case.

Keywords: *natural convection, transient experiments, aircraft wing box compartment*

INTRODUCTION

Natural convection studies have received considerable attention over recent decades due to the broad range of engineering applications such as electronics cooling, solar collectors, nuclear reactors, fire research, pollution in lakes, chemical vapor deposition and ventilation in buildings. However, the application of aircraft compartment cooling has received little attention. This paper focuses on an aircraft wing box compartment subjected to solar loads directly on the upper wing surface. The aircraft is stationary on the apron for a time period relative to commercial aircraft turnaround time, and it is during this time that the aircraft experiences its most elevated temperatures. The wing box compartments are the location for many of the aircraft fuel tanks where heat generated is cooled by natural convection. With the replacement of traditional aircraft materials by advanced modern composite materials, a new thermal environment is introduced, where knowledge of such effects are desired. A transient experimental analysis of the natural convection behavior in a replica aluminum wing box heated only from above was carried out to deliver an in depth understanding of this phenomenon.

* Corresponding author: Thomas Confrey
Phone: + (353)-61-202471, Fax: + (353)-61-202393
E-mail address: Thomas.confrey@ul.ie

Review papers from Ostrach [1] and Catton [2] summarize the early enclosure natural convection investigations which proved to be the foundation of many of the studies to follow. Some of the most familiar and established studies on natural convection include those of Cormack *et al* [3, 4, 5], which also served as the basis for many of the early natural convection studies, particularly low aspect ratio studies. An abundance of studies on differentially heated cavities for various applications followed which included Ostrach [6] and Kimura and Bejan [7]. The first transient natural convection investigations include Patterson and Imberger's [8] scale analysis predictions of a low aspect ratio differentially heated cavity, and the closely related transient experimental analysis carried out by Yewell *et al* [9]. Ostrach [10] summarizes as extensively as possible the most relevant and significant studies of the early enclosure natural convection investigations era. The pertinent more recent studies on enclosure natural convection include investigations on the effect of varied boundary conditions on the fundamental natural convection fluid flow and heat transfer behavior. Das *et al* [11] studied a symmetrically side heated enclosure, Manca and Nardini [12] experimentally investigated an open ended cavity with a heated top wall and an unheated lower wall, where Anderozzi *et al* [13] carried out a similar numerical study. Other studies have focused on the effects wall boundary conditions such as conduction in the vertical walls [14] and the presence of non isothermal surfaces [15]. More relevant to the current study, Sadowski *et al* [16] experimentally investigated natural convection flow in an enclosure driven by a vertical wall with two separate uniform temperature sections of a vertical configuration, similarly Tscherry *et al* [17] investigated flow generated by colliding boundary layers along a vertical wall with two uniform temperature horizontal sections. Newport *et al* [18, 19] and Egan *et al* [20, 21] have carried out several in depth experimental and numerical studies relative to enclosure natural convection in aircraft compartments. Most relevant to the current study are the investigations carried out by Wu and Ching [22-24], where the effects of top wall temperatures on laminar natural convection in air filled cavities for varied aspect ratios was investigated.

The objectives of the current paper were to investigate the effects of varied thermal boundary conditions on the transient flow structures and temperature distributions in an air filled rectangular enclosure heated on the upper surface only. Experiments were carried out for the following three cases. For case one the top surface of the enclosure was heated to 100°C by means of a PID controlled heater mat, conduction through the side and bottom walls was permitted. For case two, wall conduction between the side and bottom walls was prohibited by placement of a rubber insulation material; forced convection cooling was also applied to the bottom surface resulting in an isothermal and constant temperature bottom surface at an average of 25°C. An isoflux boundary condition of 700 W/m^2 on the upper surface was then introduced for case three, the bottom surface is again isothermal and at constant temperature as per case two.

The paper is structured as follows. Details of the experimental set up and methods employed are described. The results from the analysis are presented on a case by case basis, and discussed comparatively. Flow visualization was employed to qualitatively investigate the transient evolution of the thermally induced flow structures. Particle image velocimetry was utilized to quantitatively measure the velocity fields to gain an understanding of the driving force behind the natural convection flow and thermocouple measurements delivered an insight into the transient wall and interior air temperature distributions. The conclusions are then offered upon closure.

EXPERIMENTATION

Thermocouple Measurements

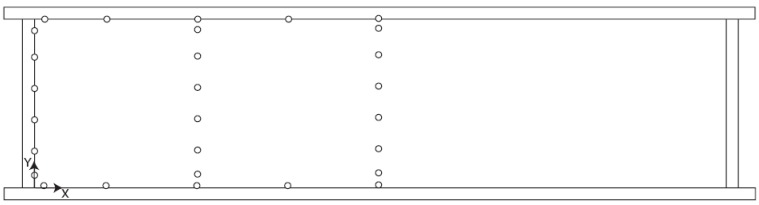

Figure 1. Test facility with thermocouple positions outlined

Experiments were conducted on an aluminium test facility as shown in Figure 1; the walls of the apparatus were made from 10 mm thick aluminium plates. The size of the apparatus was 620 mm (H) × 170 mm (L) × 620 mm (D). The interior enclosure size is 150 mm (H) × 600 mm (L) × 600 mm (D) yielding an aspect ratio of H/L = 0.25. The left and right side walls were made from 10 mm thick glass, thus allowing for optical access to view the flow structures within the enclosure. A 500W rubber heater mat was placed over the entire top surface area to achieve a boundary condition of 100°C. The test facility was insulated using 50mm fibre glass thermal insulation and the apparatus was placed on wooden slats to permit insulation of the bottom surface in case one, and the placement of a forced convection cooling mechanism for cases two and three. Dow Corning 340 Heat Sink Compound was applied at the end sections of each aluminium plate to minimize the thermal contact resistance and assist in conduction between each plate for case one, and only on the top end section for cases two and three. Thermocouples were used to record transient temperatures throughout the interior of the enclosure and on the inside wall surfaces. The thermocouples were mounted on a polycarbonate cross which was placed into the enclosure at a position of D=300mm. Surface measurements were recorded by fixing the thermocouples to the face of the respective surfaces using high temperature adhesive tape. K-type thermocouples were used for the measurements which were connected to an AGILENT data acquisition system. The thermocouples were calibrated using a LAUDA E100 thermocouple bath to an accuracy of ±0.5°C. The positions of the thermocouples are illustrated in Figure 1.

Particle Image velocimetry and Flow Visualisation

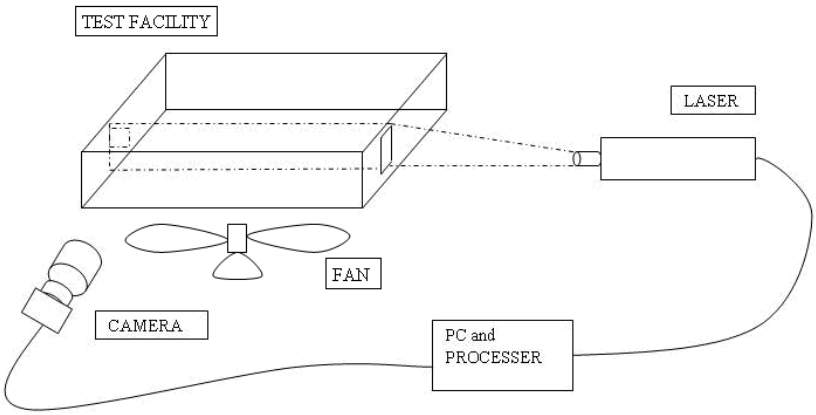

Figure 2. Experimental set up

Flow visualisation was employed to observe the flow structures from time zero to steady state temperature conditions. In the current experiments smoke was employed as a tracer fluid and entered the enclosure through a small opening in the left side glass panel. The illumination source used was a Nd:YAG laser of 532 nm wavelength. This produced a beam 2mm thick which entered the enclosure through a window in the rear aluminium panel as shown in Figure 2. The laser sheet illuminates the smoke particles revealing the natural convection flow structures. Flow visualisation images of size 115mm x 150mm (x × y) along the front wall were recorded using a 2 MP Power View CCD camera. Particle image velocimetry (PIV) was then employed to measure the instantaneous velocities of the particles. Images were processed using the TSI Insight 3G software. To ensure accurate measurements the resolution of the images was increased where the field of view was reduced to 58mm x 50mm. This was found to be sufficient to resolve the near wall velocity boundary layers which were recorded along the front vertical wall at heights of y = 130 mm, 85 mm and 30 mm.

RESULTS

This section is structured as follows. First the initial observations based on the measured transient Grashof numbers, boundary conditions and interior temperature distributions are discussed and defined. The results are then presented in order of case where the observed transient flow structures, measured velocity profiles and wall and interior air temperature distributions are discussed comparatively.

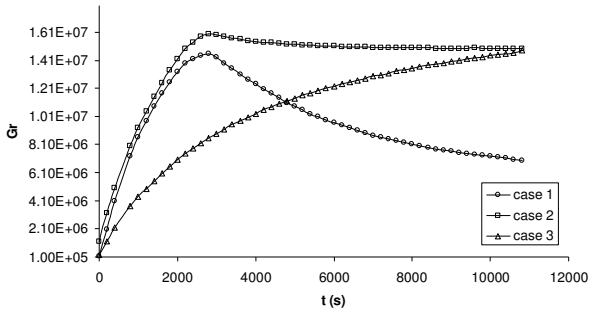

Figure 3. Transient Grashof number for cases 1-3

Experiments were carried out over the laminar Grashof range of 10^5-10^7 as shown in Figure 3. For case one the top surface was heated by means of a PID controlled heater mat, the time taken to reach the desired boundary condition of 100°C was 45 minutes (2700 seconds), conduction was permitted through the bottom surface hence reducing the temperature gradient relative to the height of the enclosure, where a gradual reduction in Grashof number was observed. For case two an isothermal and constant bottom surface temperature was introduced allowing the Grashof number to remain constant from 45 minutes onward. In case three a constant heat flux boundary condition was imposed on the top wall giving a Grashof number equal to that in case two at a steady state time of 180 minutes (10800 seconds).

The fluid flow and heat transfer was observed to be symmetrical about the vertical centreline of the enclosure where the vertical walls were found to be the main driving force behind the natural convection flow. The flow visualisation images presented in Figure 4 are representative of the flow structures adjacent to the front vertical wall. A degree of non isothermality was present on both the top and bottom surfaces. For the purpose of data analysis an averaged temperature surface boundary condition was calculated. The dimensionless local temperature is denoted by $T^* = (T_L-T_B)/(T_T-T_B)$ and is calculated based on the top and bottom surface temperatures at each transient instant, the dimensionless vertical height is denoted by $y^* = y/H$ and the corresponding horizontal position by $x^* = x/L$.

Case One

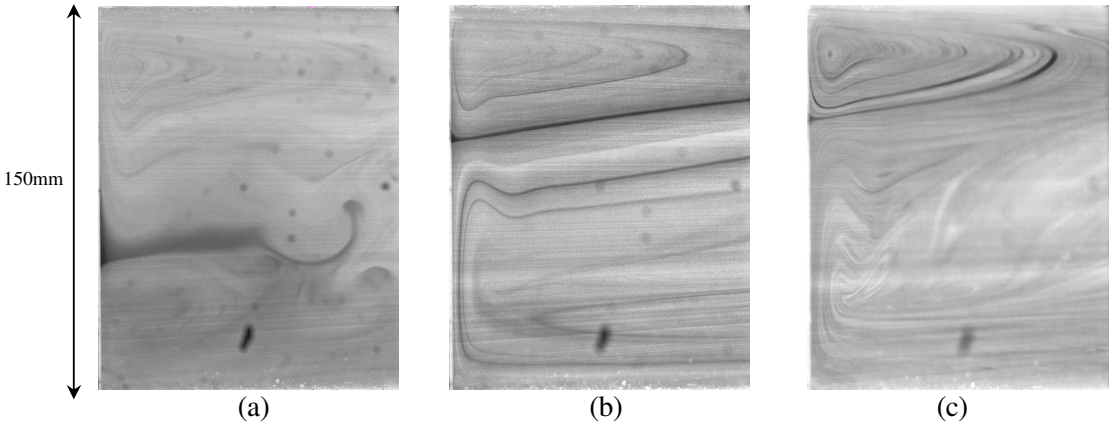

(a) (b) (c)

Figure 4. Flow Visualisation Images at (a) 5 (b) 45 and (c) 180 minutes

The transient flow structures for case one are shown in Figure 4. At 5 minutes the flow was observed to initiate from the centre of the heated top surface and act towards the cooler vertical side wall, the flow then proceeds to descend along the vertical wall where a definite detachment of the flow was observed. The fluid then becomes entrained in the natural convective circulation current completing the counter clockwise circulation evident in the upper left hand side of the enclosure. Below the point of detachment the air was observed to be almost stationary at this early transient stage as the fluid in this region of the enclosure is not exposed to any significant temperature gradient. At 45 minutes as shown in Figure 4 (b), the top surface is at 100°C, the flow structures are developed and the presence of two counter acting circulations along the vertical wall is clearly evident. In the upper region of the cavity the flow structures are the same as those observed at 5 minutes, however in the lower region of the cavity an upward flow has now developed opposing the downward fluid motion yielding a clockwise circulation in the lower region of the cavity. The detachment point of the flow has also increased in height compared to Figure 4 (a). The point of detachment is the exact location where the surface and fluid temperature in the immediate vicinity adjacent to the vertical wall are equal. Conduction through the vertical wall therefore becomes significantly influential in determining the exact location of the detachment point. At 180 minutes, on arrival of steady state, the only notable difference between the flow structures at 45 minutes is a further increase in the detachment point height suggesting that the transient conduction through the side wall has a significant effect on the adjacent natural convection circulations.

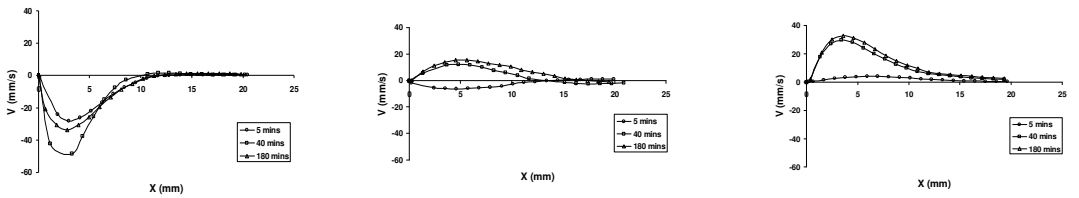

(a) (b) (c)

Figure 5. Velocity Profiles at (a) y=130mm (y*=0.86) (b) 85mm (y*=0.56) (c) 20mm (y*=0.13)

A quantitative insight into the fluid velocity and direction along the vertical wall was gained by particle image velocimetry measurements as shown in Figure 5. At a position of y = 130mm the fluid, at all times, is at a higher temperature than the vertical wall and hence is subjected to a negative buoyancy force as it is cooled and flows down towards the base of the compartment. The fluid velocity was

observed to increase from a minimum of -28 mm/s at 5 minutes to a maximum of -48 mm/s at 45 minutes which coincided with the top wall reaching 100°C. The velocity at 180 minutes then reduces to -33 mm/s due to the now constant top wall boundary condition and also the increased side wall temperature owing to the prolonged period of heating time from 45 minutes to steady state. The interaction between the wall and adjacent fluid temperature is further highlighted as influential in determining the fluid flow direction at this point. At a position of y = 85 mm a reversal of flow direction was observed, at 5 minutes a weak downward acting flow of -6 mm/s was overturned to an upward flow of 12 mm/s at 45 minutes which gradually increased marginally to 15 mm/s at 180 minutes. It is noted that at y = 20 mm the fluid flow is consistently acting upward where the velocity magnitudes are larger than at y = 85 mm. In the lower region of the cavity the side wall acts as a heating mechanism to the adjacent cooler fluid yielding the upward fluid motion, a decrease in velocity magnitude was observed at y = 85 mm due to the opposing force of the downward acting fluid in the upper region of the cavity where the side wall acts as a cooling mechanism to the adjacent warmer fluid in the vicinity of the heated top wall. The opposing flows meet at the adiabatic detachment point of zero velocity where they then act towards the core region of the enclosure and complete their respective circulations as observed previously.

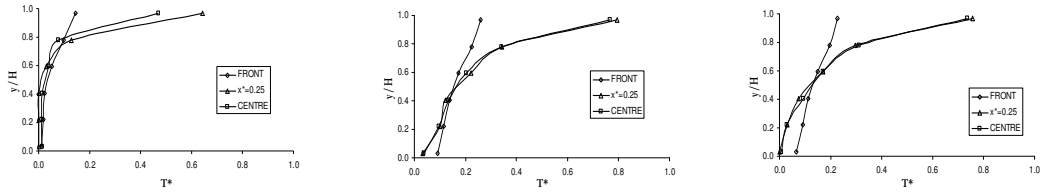

(a) (b) (c)

Figure 6. Temperature Distributions at (a) 5 (b) 45 and (c) 180 minutes

From analysis of Figure 5 an understanding of the transient flow structures has been gained. Shown in Figure 6 are measurements of the front vertical wall and the interior air temperature distributions at the vertical centreline and at x* = 0.25. At a time of 5 minutes and at y* > 0.75, the initial flow direction within the enclosure, is determined at an early stage as shown in Figure 6 (a). At just 5 minutes the interior air temperatures were found to be larger than that of the side wall indicating that the upper section of the wall acts as a cooling mechanism to the adjacent fluid yielding the downward acting flow. A small temperature gradient in the enclosure at y* < 0.45 was observed agreeing with previous flow visualisation images indicating only minor activity in the lower region of the enclosure at this time. At 45 minutes the presence of the two opposing heat transfer mechanisms is evident. The front wall temperature is lower than the fluid temperature at y* > 0.45 where the downward motion was previously observed and at y* < 0.45 the wall temperature is higher than the adjacent fluid where the previous upward motion was observed. The point at y* = 0.45 is deemed to be the location of the adiabatic detachment point. At 180 minutes similar behaviour was observed, however the detachment point has increased in height to y* = 0.55 again agreeing with the previously observed flow structures where the flow physics remained similar with only a small increase in detachment height being the notable difference. The detachment point was observed to be higher than y* = 0.45-0.55 in the flow visualisation images. Higher resolution temperature measurements in the immediate vicinity of the vertical front wall may permit a more accurate representation of the exact transient detachment locations; however the correct fundamental fluid flow and heat transfer behaviour concerning the enclosure as an entirety is sufficiently achieved.

Case Two

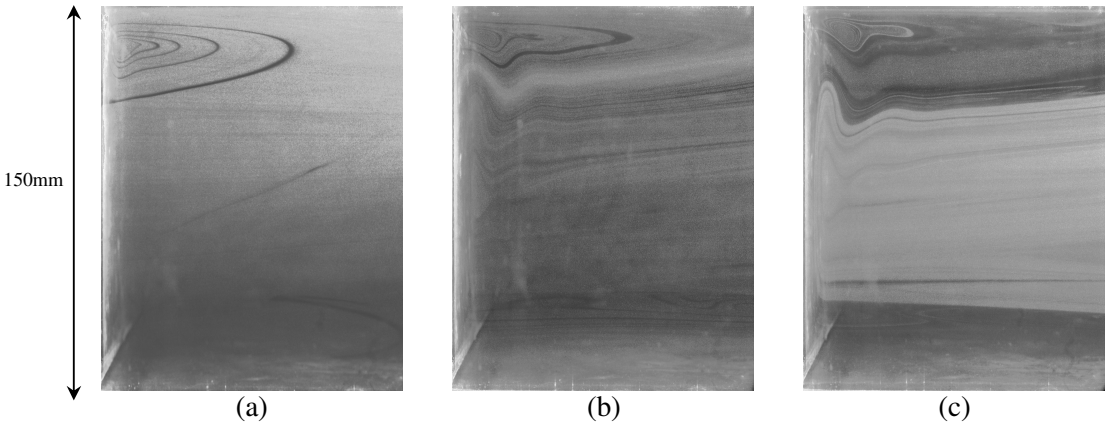

Figure 7. Flow Visualisation Images at (a) 5 (b) 45 and (c) 180 minutes

For case two the top surface remains heated to 100°C by means of PID control; however an isothermal and constant temperature bottom surface is introduced inhibiting conduction from the side walls to the bottom wall and the addition of forced convection cooling on the exterior of the bottom surface. The effect of such alteration of the boundary conditions on the evolved flow structures is illustrated in Figure 7. At 5 minutes the fundamental flow physics remains similar as in case one, with the notable difference being significant increase in the detachment point height along the vertical wall. As seen previously the front wall temperature is highly influential on the developed flow structures, therefore a higher detachment point indicates a higher wall temperature where the effect of a cooling mechanism on the warm fluid in the upper region of the cavity is reduced. Based on the flow visualisation observations it is suggested that reducing conduction from the side wall to the bottom wall induces elevated local side wall temperatures which effectively increase the adiabatic detachment point between the solid wall and the adjacent fluid. At 45 minutes the flow structures reveal a dominant clockwise acting circulation adjacent to the side wall where the detachment point is in close proximity to the heated top wall. The downward motion and counter clockwise circulation is still present but less prominent and less effective as acting as a cooling mechanism on the warm fluid in this region. Upon arrival of steady state at 180 minutes the downward fluid motion has been lessened to a zone of recirculation in the most upper part of the enclosure adjacent to the side wall, where the upward fluid motion dominates the flow adjacent to the vertical side wall.

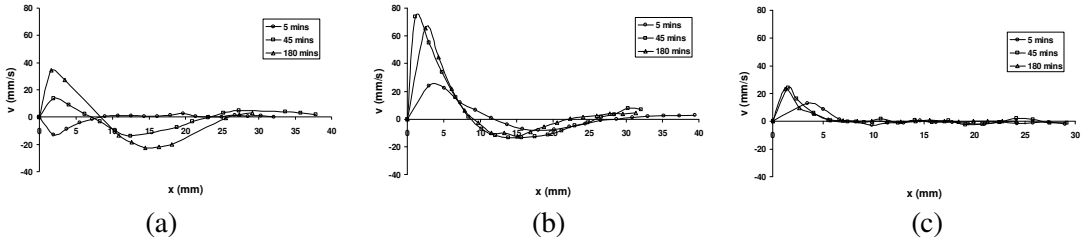

Figure 8. Velocity Profiles at (a) y=130mm (y*=0.86) (b) 85mm (y*=0.56) (c) 20mm (y*=0.13)

The experimentally measured velocity profiles at the side wall for case two are shown in Figure 8. At 5 minutes and at a location of y = 130 mm, the fluid is cooled by the vertical wall and has a velocity of -14 mm/s compared to -28 mm/s at the same position for case one. The reduction in velocity suggests a reduction in temperature gradient between the vertical sidewall and the adjacent fluid where the effect of the wall as a cooling mechanism has been reduced at this early transient stage. At 45 minutes and

180 minutes the fluid flow direction has been reversed with velocities of 13 mm/s and 34 mm/s recorded. At y = 85 mm the flow direction is again acting upward at all times, the minimum velocity of 26 mm/s occurring at 5 minutes and the maximum of 75 mm/s at 45 minutes. The fluid velocity then reduces to 65 mm/s at this location once reaching 180 minutes. The reduction in velocity is proportional to the imposed top wall boundary condition where the PID output is at 100% until the top surface reaches 100°C at 45 minutes, the output then reduces maintaining the desired constant temperature boundary condition until the arrival of steady state at 180 minutes. At the same position in case one, the velocity magnitudes were observed to be lower at all times, the elevated side wall temperatures observed in case two induce a higher temperature gradient between the side wall and the adjacent fluid which leads to higher velocity magnitudes in case two. At y = 20mm the flow was again found to be acting upward at each transient stage from a minimum of 13 mm/s at 5 minutes to 24 mm/s and 23 mm/s at 45 and 180 minutes.

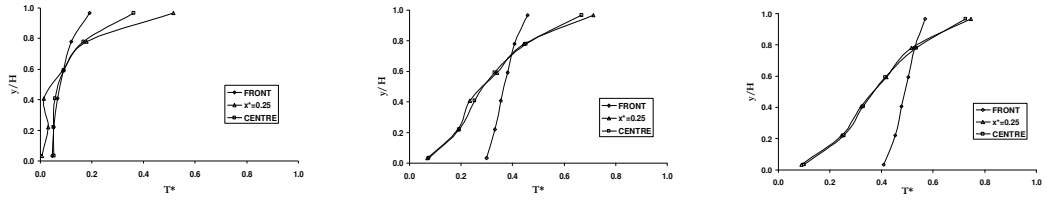

(a) (b) (c)

Figure 9. Temperature Distributions at (a) 5 (b) 45 and (c) 180 minutes

Shown in Figure 9, at 5 minutes the front surface temperature was observed to be at a maximum of T*=0.2, higher than in case one at a maximum of T*=0.15 at the same time. The previous fluid flow observations and velocity measurements are supported where an increase in detachment height from y* = 0.45 in case one at 5 minutes to y* = 0.6 in case two at 5 minutes was observed, owing to the increased front wall temperature. For case two, at 45 minutes the detachment height has increased to y* = 0.7 and again increases to y* = 0.8 at 180 minutes. The similarity in the trends between the interior temperature distributions at 45 minutes and 180 minutes for cases one and two also agrees with the previously observed similar flow structures. The only notable difference in each case is the small increase in the detachment height from 45 minutes to 180 minutes.

Case Three

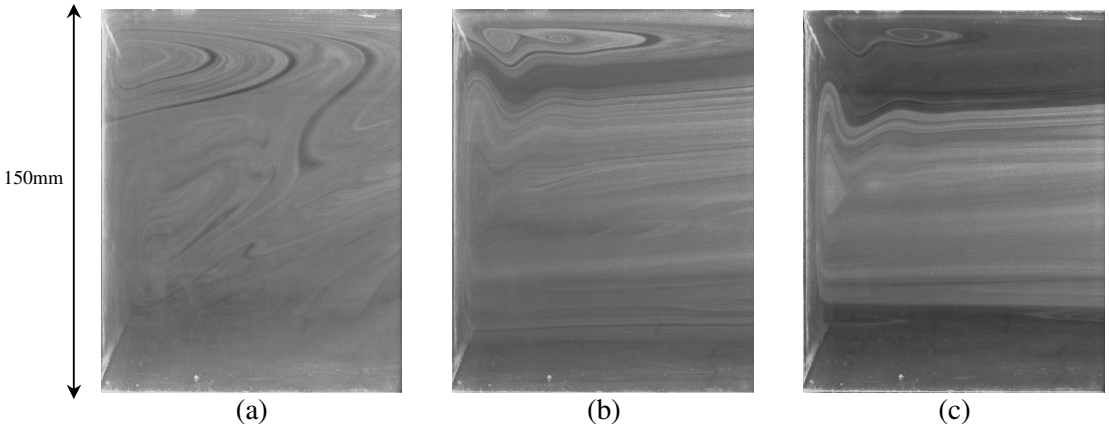

(a) (b) (c)

Figure 10. Flow Visualisation Images at (a) 5 (b) 45 and (c) 180 minutes

For case three a constant heat flux boundary condition of 700 W/m2 was imposed on the top wall, where the bottom surface is identical to that of case two, remaining isothermal and at constant temperature. It was observed that the flow physics between the three cases remains very similar, where the detachment point varies, dependant on the adjacent side wall temperature. For cases two and three the transient flow structures revealed a distinct similarity as shown in Figure 10. At five minutes the downward acting flow is present where the detachment points occur at approximately the same location, the flow then acts towards the core region where it becomes entrained and completes the counter clockwise circulation in the upper region of the enclosure. In the lower region of the enclosure the initial development of the upward acting flow occurs. At 45 and 180 minutes the flow structures for case three are fully developed and exhibit the same flow behaviour as that of case two where the increase of the detachment point is the only difference. This indicates that for different top surface boundary conditions, the temperature gradients in the enclosure are proportional inducing the same transient flow structures.

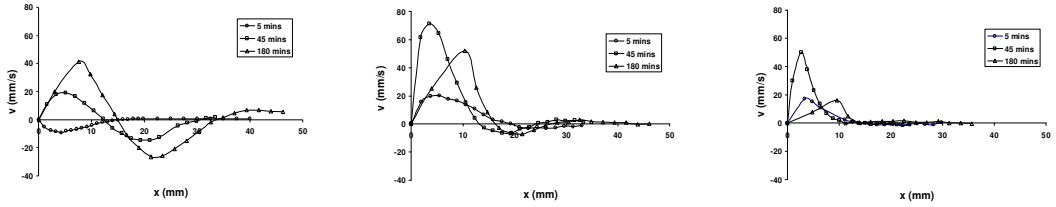

(a) (b) (c)

Figure 11. Velocity Profiles at (a) y=130mm (y*=0.86) (b) 85mm (y*=0.56) (c) 20mm (y*=0.13)

The transient velocity profiles measured for case three exhibit similar behaviour to that of case two as shown in Figure 11. At y = 130 mm the flow was observed to initially act downward at 5 minutes, where at 45 and 180 minutes the flow direction is then reversed as the side wall temperature and detachment height increase. The velocity was seen to gradually increase from a velocity of 18 mm/s at 45 minutes and 41 mm/s at 180 minutes. The transition was observed to be gradual for case three. For the PID controlled top surfaces of case one and case two a fluctuation was observed where the maximum velocity occurred at 45 minutes when the 100°C boundary condition was achieved. The velocity magnitudes indicate that the temperature gradient between the top surface and the adjacent side walls for case one and two were found to be at a maximum at 45 minutes, whereas for the isoflux case three the evolution was observed to gradual. At the positions of y = 85 mm and y = 20 mm the fluid adjacent to the side wall was observed to flow towards the top surface at all times recorded. The maximum velocity magnitudes at these locations occurred at 45 minutes and were observed to decrease on approach to steady state; a possible reason for this is that the side wall heats faster resulting in arrival at the thermal capacitance limit of the solid wall before the interior air. Therefore after 45 minutes the air continues heating at a faster rate than that of the adjacent solid wall which resulted in a decrease in the velocity magnitudes.

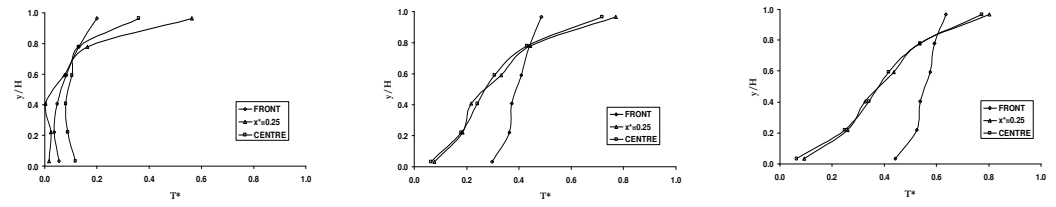

(a) (b) (c)

Figure 12. Temperature Distributions at (a) 5 (b) 45 and (c) 180 minutes

Figure 12 depicts the temperature distribution for case three; again the only notable difference is the increase in detachment height, again supporting the previously observed transient flow structures. The temperature distributions for case three exhibit the same heat transfer and flow physics as cases one and two.

For cases one to three, it was observed that the transient interior air temperatures trends are similar for each case. The front surface temperatures for cases two and three were observed to be higher than case one, resulting in the change in flow structures and the higher detachment point.

CONCLUSIONS

- An understanding of the fundamental heat transfer process and flow physics for an air filled enclosure heated from above only has been gained. The flow is fundamentally vertical about the vertical centreline where the side walls were observed to be the main driving force behind the flow. Two counter acting circulations existed adjacent to the side wall where the opposing flows detach at an adiabatic point along the side wall once the solid and fluid temperatures are equal.
- The effect of thermal boundary conditions on the flow structures and temperature distributions have been investigated. The flow physics and temperature distributions were shown to obey the same fundamental physics for each of the cases analysed.
- The introduction of an isothermal bottom surface was deemed to have the most significant effect on the induced flow structures, the local side wall temperatures were observed to increase effectively increasing the detachment point along the vertical wall.
- The elevated side wall temperatures reduced the cooling effect on the warm fluid in upper region of the enclosure. The counter clockwise acting circulation was reduced, where the dominant flow was the clockwise acting circulation acting from the lower region of the enclosure.

ACKNOWLEDGEMENTS

The author gratefully acknowledges the support of the Irish Research Council for Science, Engineering and Technology (IRCSET) and Airbus UK.

REFERENCES

1. Ostrach, S., 1972, “Natural Convection in Enclosures,” Advances in Heat Transfer, 8, pp. 209-229.
2. Catton, I., 1978, “Natural Convection in Enclosures,” *Proceedings of the 6th International Heat Transfer Conference*, Vol. 6, Hemisphere Publishing Corp., Washington, DC, pp. 13–30.
3. Cormack, D.E., and Leal, L.G., 1974, “Natural Convection in a Shallow Cavity with Differentially Heated End Walls. Part 1.
   Asymptotic Theory,” Journal of Fluid Mechanics, 65(2), pp. 209-229.
4. Cormack, D.E., Leal, L.G., and Seinfeld, J.H., 1974, “Natural Convection in a Shallow Cavity with Differentially Heated End Walls. Part 2. Numerical Solutions,” Journal of Fluid Mechanics, 65(2), pp. 231-246.
5. Imberger, J., 1974, “Natural Convection in a Shallow Cavity with Differentially Heated End Walls. Part 3. Experimental Results,” Journal of Fluid Mechanics, 65(2), pp. 247-260.
6. Ostrach, S., Loka, R.R., and Kumar, A., 1980, “Natural Convection in Low Aspect Ratio Rectangular Enclosures,” Heat Transfer Division of ASME, 8, pp. 1-10.

7. Kimura, S., and Bejan, A., 1980, "Experimental Study of Natural Convection in a Horizontal Cylinder with Different End Temperatures," Int. J. Heat and Mass Transfer, 23, pp. 1117-1126.
8. Patterson, J., and Imberger, J., 1980, "Unsteady Natural Convection in a Rectangular Cavity," J. Fluid Mechanics, 100(1), pp. 65-86.
9. Yewell, R., Poulikakos, D., and Bejan, A., 1982, "Transient Natural Convection Experiments in Shallow Enclosures," J. Heat Transfer, 104, pp. 533-538.
10. Ostrach, S., 1988, "Natural Convection in Enclosures," J. Heat Transfer, 110, pp. 1175-1988.
11. Das, S.P., Chakraborty, S., Dutta, P., 2002, "Natural Convection in a Two-Dimensional Enclosure Heated Symmetrically from Both Sides," *Int.Comm. Heat Transfer*, Elsevier Science Ltd, Vol. 29, pp. 345-354.
12. Manca, O., and Nardini, 2007, "Experimental Investigation on Natural Convection in Horizontal Channels with the Upper Wall at Uniform Heat Flux," Int. J. Heat and Mass Transfer, 50, pp. 1075-1086.
13. Anderozzi, A., Jaluria, Y., Manca, O., 2007, "Numerical Investigation of Transient Natural Convection in a Horizontal Channel Heated from the Upper Wall," J. Numerical Heat Transfer, 51, pp. 815-842.
14. Saeid, N.H., 2007, "Conjugate Natural Convection in a Porous Enclosure: Effect of Conduction in One of the Vertical Walls," Int. J. Thermal Sciences, 46, pp. 531-539.
15. Alawadhi, E.M, 2008, "Natural Convection Flow in a Cubical Enclosure with a Heated Strip," J. Thermophysics and Heat Transfer, 22(3), pp. 515-521.
16. Sadowski, D., Poulikakos, D., Kazmierczak, M., 1987 "Three Dimensional Natural Convection Experiments in an Enclosure," J. Thermophysics, 2(3), pp. 242-249.
17. Tscherry, J., Cooper, P., Soh, W.K, 2002, "Flow Generated by Colliding Laminar Natural Convection Boundary Layers," *Int. Comm. Heat Mass Transfer*, Elsevier Science Ltd, Vol. 29, pp. 67-76.
18. Newport, D., Confrey, T.W., Egan, V., Lacarac, V., 2008, "Measurement of Transient Natural Convection in Non-Ventilated Aircraft Compartments," *ASME-JSME Summer Heat Transfer Conference*, ASME, Jacksonville, Florida, USA.
19. Newport, D., Egan, V., Aguanno, M., Lacarac, V., Estebe, B., Murer, Y., 2008, "Thermally Induced Flow Structures in Aircraft Wing Compartments," *ASME-JSME Summer Heat Transfer Conference*, ASME, Jacksonville, Florida, USA.
20. Egan, V., Moore, D., Newport, D., Lacarac, V., Estebe, B., 2008, "An Analysis of Natural Convection in Leading Edge Wing Compartments," *ASME-JSME Summer Heat Transfer Conference*, ASME, Jacksonville, Florida, USA.
21. Egan, V., Newport, D., Lacarac, V., Estebe, B., 2008, "Velocity Field Measurements in Leading Edge Wing Compartments," *ASME-JSME Summer Heat Transfer Conference*, ASME, Jacksonville, Florida, USA.
22. Wu, W., Ewing, D., Ching, C.Y., 2006, "The Effect of the Top and Bottom Wall Temperatures on the laminar Natural Convection in an Air-Filled Square Cavity," Int. J. Heat and Mass Transfer, 49, 1999-2008.
23. Wu, W., and Ching, C.Y., 2007, "The Effect of the Top Wall Temperature on the Laminar Natural Convection in Rectangular Cavities with Different Aspect Ratios," *ASME-JSME Summer Heat Transfer Conference*, ASME, Vancouver, British Columbia, Canada.
24. Wu, W., Ewing, D., Ching, C.Y., 2008, "Investigation of a Large Top Wall Temperature on the Natural Convection Plume along a Heated Vertical Wall in a Square Cavity," Int. J. Heat and Mass Transfer, 51, 1551-1561.

INVESTIGATION OF FLOW FIELD BEHIND AN OSCILLATING AIRFOIL BELOW AND BEYOND STATIC STALL

H. Sadeghi[1*], M. Mani[2,]
[1] M.Sc Student, University of Amirkabir, Tehran, Iran
[2] Professor, Board member, Center of excellence in computational aerospace engineering, University of Amirkabir, Tehran, Iran

ABSTRACT. The unsteady flow field behind an oscillating airfoil, below and beyond static stall condition, has been investigated in a low speed wind tunnel by means of hot-wire anemometer. The airfoil was an EPPLER 361 oscillating in a pitching motion about the half chord axis at reduced frequency of 0.182. The amplitude of oscillation was 8 deg. To assess effect of mean incidence angle, the mean incidence of oscillation was varied 0-10 deg. Streamwise mean velocity profiles and turbulence intensity profiles at 0.25 chord distance behind trailing edge of airfoil were investigated. When the maximum dynamic angle of attack was below the static stall angle of attack, weak effects on the wake were found by increasing mean angle of attack. Instead, for higher angles of attack strong unsteady effects were appeared on the wake. Furthermore, variations of momentum deficit coefficients were discussed.

Keywords: *Oscillating Airfoil, Mean Incidence Angle, Static Stall, Unsteady Wake*

INTRODUCTION

In recent years considerable research has been conducted into the problem of unsteady aerodynamic of an oscillating airfoil, especially problem of airfoil stall. Most of the previous investigations were directed to unsteady wing loading and dynamic stall process, as reviewed by McCroskey [1]. Dynamic stall phenomenon appears on helicopters rotor blades, rapidly maneuvering aircraft, wind turbine and even insect wings. In many cases dynamic stall becomes the primary limiting factor in the performance of the associated vehicle or structure [2]. The mechanism of dynamic stall was first identified on helicopters. The importance of unsteady aerodynamics was considered by Harris and Pruyen [3] when helicopter designs were unable to predict the performance of high speed helicopters using conventional aerodynamics. Tolouei et al [4] investigated experimentally the unsteady pressure distribution over an EPPLER 361 airfoil. They found that pressure coefficients in the low angle of attack range showed little overshoot when compared with the static values, while for the large angle of attack cases the differences were significant. They considered that the large overshoot in the dynamic pressure coefficient for the high angle of attack case is probably due to the existence of the stable dynamic vortex, which is created near the leading edge and moves downstream. Mani et al [5] measured Surface static pressure distribution on the upper and lower sides of the model, during the oscillating motion. It was found that reduced frequency had strong effects on the pressure distribution, near the leading edge of the airfoil.

There are many practical situations where unsteady wakes are involved. The wake-blade interaction in turbo machinery flows is one example. Relatively scant attention has been given to the study of

* Corresponding author: Hamed Sadeghi
Phone: + (98)-911-1522207, Fax: + (98)-151-3212031
E-mail address: hamsadeghi@yahoo.com

oscillating wakes. Satyanarayana [6] measured unsteady wakes of airfoils and cascades under a sinusoidally varying gust flow. Time-mean and time-dependent wake profiles at low frequency behind the airfoil were reported in his work, and the distinctions between these were discussed. Panda and Zaman [7] studied the wake of a similar airfoil at mean angles of attack above the static stall angle by use of hot wire anemometry and flow visualization. They saw that in addition to the familiar dynamic stall vortex (DSV), an intense vortex of opposite sign originates from the trailing edge just when the DSV is shed. These two vortices take the shape of the cross section of a large mushroom. They also measure the vorticity flux shed into the wake and compute the circulatory part of the lift coefficient by means of Kutta-Joukowski theorem. Koochesfahani [8] studied experimentally the vortical flow patterns in the wake of a NACA0012 airfoil pitching at small amplitudes and showed that the oscillation wave form has an important effect in the vortical pattern shapes and mean velocity profiles in the wake. He found that there is a critical value for the oscillation frequency that the usual velocity defect profiles in the wake changes to excessive momentum similar to a jet flow and the airfoil produces trust force. Also, he showed that in special cases mean velocity profiles have two peak of velocity defect, that this is symptom of a double-wake structure. Recently, an experimental measurement of unsteady wake behind a sinusoidally unsteady airfoil was performed by Mani et al [9]. They were shown that the angle of attack and reduced frequency are the most important parameters which influence on the velocity profiles. Also, they found that the influence of angle of attack on the velocity profiles is to increase the momentum deficit and wake thickness.

The primary purpose of the present study is to investigate the characteristics of unsteady wake of an airfoil oscillating sinusoidally in pitch, below, near and beyond static stall condition. The airfoil was an EPPLER 361. The velocity in the wake was measured by means of hot-wire anemometer. The airfoil was given at different mean incidence angles, and the resulting wakes were investigated to understand the effects of them.

EXPERIMENTAL SETUP

The experiments were conducted in a TE-44/C PLINT low speed wind tunnel of Amirkabir University of Technology (AUT) having a rectangular test section of 0.45m×0.45m×1.2m. An airfoil of Eppler-361 profile was mounted horizontally in test section. The chord of the airfoil was 0.145 m, and the aspect ratio was 3.0. The gap between the airfoil and the side wall was 1 mm. The ratio of the chord length to the height of the test section was 1:3. Figure 1 shows a view of the airfoil in test section.

Figure 1. A view of airfoil in test section

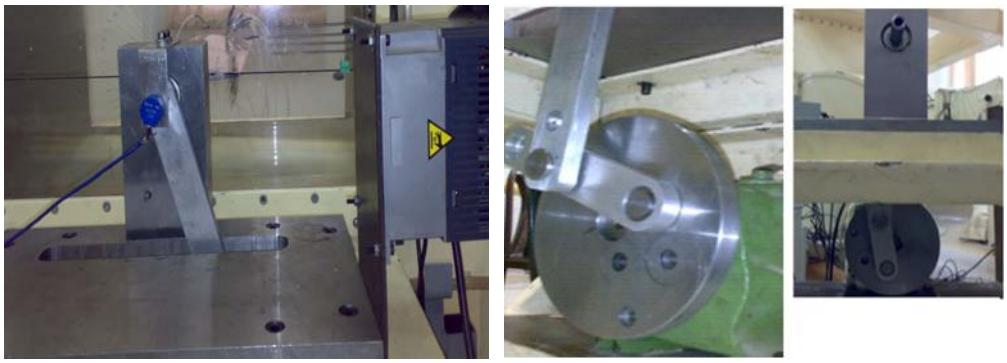

Figure 2. Views of oscillation system

Pitching oscillation about the half-chord axis was provided by a crank-connecting rod mechanism, driven by a variable-speed ac motor. Figure 2 shows the pictures of oscillation mechanism. The instantaneous angle of attack (dynamic angle), α , can be expressed as:

$$\alpha = \alpha_0 + A\sin 2\pi ft \tag{1}$$

Throughout the test, the oscillation amplitude was 8 deg. The mean incidence angles of attack were given four values of 0, 2.5, 5 and 10 deg. Therefore, during the test, instantaneous angle of attack of airfoil was varied from -8 to 18 degrees. It should be note that the static stall angle of this airfoil was about 12.5 °. The value of reduced frequency *k*, define as $k = 2\pi fC / 2U_\infty$, was considered about k =0.182. The tunnel speed and the frequency of oscillation were set at U_∞ =5 m/s and f =2 Hz, respectively. The corresponding Reynolds number, based on the chord length, was 50000.

A constant temperature hot-wire anemometer (CTAs) was employed for the velocity measurements. The hot-wire probes were mounted on a support in the center plane of the test section behind the airfoil as shown in Fig. 3. Each sensor of probe was made of tungsten and the diameter of sensor was about 5μm.The overheat ratio and DC offset voltage for each hot-wire sensor carefully adjusted such that each sensor nearly the same operating conditions. Data were acquired and processed by a 12 bit 16 channel A/D converter board capable of sample rates up to 200 kHz.

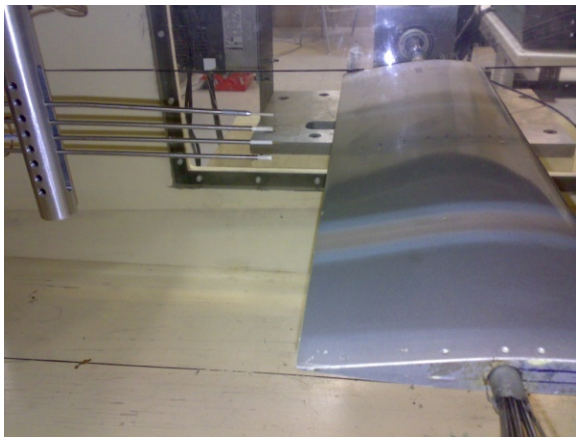

Figure 3. Model and hot-wire sensors

DATA ACQUISITION AND REDUCTION

A potentiometer model LT-M-0200-S was used to initiate data sampling. It was connected to the oscillation mechanism and its output voltage was synchronized with the CTA outputs. A personal computer (P4) with a 16 channel A/D converter board also processed the data. Data was taken, at a given probes location. Measurements were carried out for one downstream station. The vertical traverse was restricted from *Y/C*= -0.63 to +0.63 moved by every 50 mm for the measurements. The ensemble averaging procedure that has been adopted in the present experiment, where the samples in each bin are statistically independent because they were collected during different cycles, avoids statistical bios, as observed by lyn et al [10]. Statistical uncertainty in mean and r.m.s velocities depends on the number of sampled data, turbulence intensity and confidence level. For the present experiment, considering a typical value of 2000 sampled data, a confidence level of 95% and a local turbulence intensity of 30%, uncertainties of ±4% and ±5% are expected for the mean and r.m.s velocities, respectively.

EXPERIMENAL RESULTS AND DISCUSSION

The results of the investigation will be described in three main subsections. First, the effect of mean incidence angle on the wake will be studied while airfoil oscillates quite below static angle of attack ($\alpha < 12.5^{\circ}$). Then, the results will be investigated while maximum angle of attack is near static angle of attack. Finally, the wake will be studied when maximum angle of attack is quite beyond static angle of attack.

Maximum angle of attack below static stall

In this subsection, the results are obtained at two mean angles of 0° and 2.5° for oscillation amplitude of A=8°. The amplitude and mean angles of attack are selected such that during one oscillation cycle, the model would oscillate quite below static angle of attack.

Mean velocity profile. Figure 4 illustrates the mean velocity profiles at aforementioned mean angles. This figure shows very low increasing of velocity defect when mean incidence angle becomes larger.

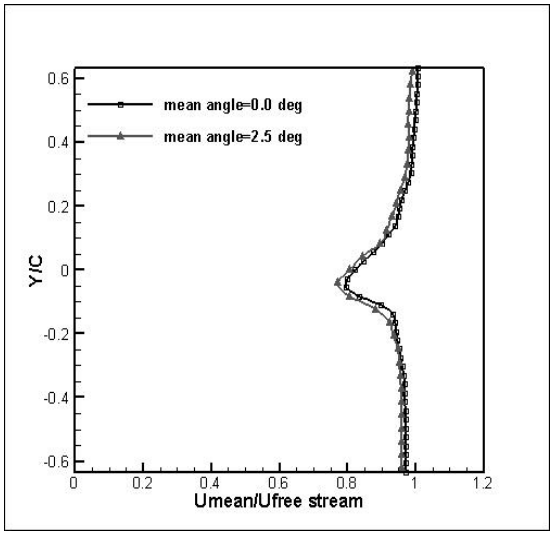

Figure 4. Mean velocity profiles at α_0=0° and 2.5°

Momentum deficit coefficient. The momentum deficit coefficients at aforementioned mean angles are obtained. It should be mention that the mean velocity profiles are used to estimate the momentum deficit on the airfoil [8]. The values of C_f for two mean angles of 0° and 2.5° are estimated about 0.13550 and 0.14235, respectively. It is found that momentum deficit coefficient increases only about 4.81 percent with increasing mean incidence angle.

R.M.S. velocity profile. Figures 5 shows the r.m.s. streamwise velocity profiles at two mean incidence angles at phase angle of 180°. Small differences are found in two profiles. Both profiles have well defined double peak structure at the same phase angle, and the position of each peak is very close for both mean angles.

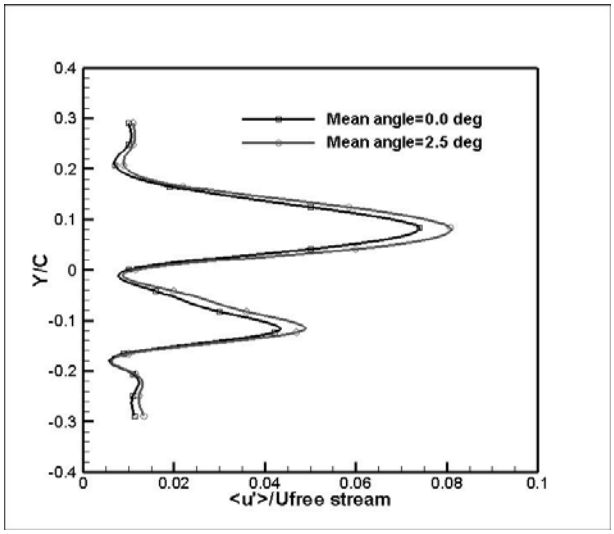

Figure 5. R.M.S. velocity profiles at α_0=0° and 2.5°, Phase ($2\pi ft$) =180°

The all above results totally confirm no particular effects on the wake profiles with increasing mean angle of attack. When airfoil oscillates below static stall angle of attack, flow remains attached throughout the oscillation cycle on the airfoil surface and vortices form the wake with arranged mutation. Therefore, the wake keeps almost the same structure in all angles below static stall.

Maximum angle of attack near static stall

In order to compare profiles, when maximum angle of attack exceeds static angle of attack slightly, mean angles of attack are set at 2.5° and 5° at oscillation amplitude A=8° , Fig. 5. In this case, airfoil could oscillate below static angle of attack at α_0 =2.5° and nearly beyond static angle of attack at α_0 =5°, respectively.

Mean velocity profile. The mean velocity profiles at two mean angles of 2.5° and 5° are plotted in Fig. 6. It is seen that the profiles are considerably different from each other. As seen in Fig. 6, the velocity defect and wake thickness increase with mean angle.

Momentum deficit coefficient. The momentum deficit coefficient for mean angle of 5° is obtained and is compared with the mean angle of attack of 2.5°. The value of C_f at α_0 =5° is estimated about 0.17372. The momentum deficit coefficient at the case of 5° increases about 18 percent against case of 2.5°. This increasing of momentum deficit coefficient is more considerable than previous case.

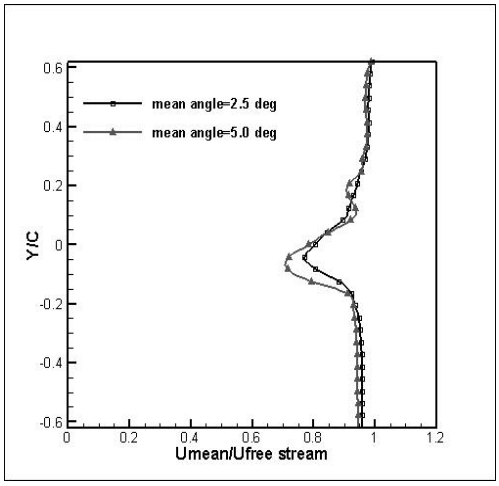

Figure 6. Mean velocity profiles at α_0=2.5° and 5°

R.M.S. velocity profile. Figures 7 shows the r.m.s. streamwise velocity profiles at two aforementioned mean incidence angles at phase angle of 180°. The manifest variations in turbulence intensities, especially in peaks of profiles and positions of them are observed as mean angle becomes larger.

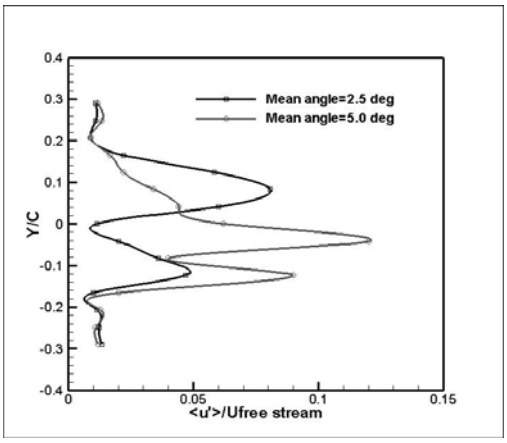

Figure 7. R.M.S. velocity profiles at α_0=2.5° and 5°, Phase ($2\pi ft$) =180°

All results in above subsection show the considerable variation in the wake as maximum angle of attack passes static angle of attack slightly. When airfoil exceeds static stall angle, flow reversal occurs in boundary layer. This eventuates that formed vortices in the wake become larger with irregular mutation.

Maximum angle of attack beyond static stall

Finally, mean angles of attack are selected such that the maximum angle of attack is quite beyond static angle of attack.

Mean velocity profile. Figure 8 shows a great increasing of the wake thickness and velocity defect with mean incidence angle. when the mean angle of attack is 10 °, a very broad region of large velocity defect and wake thickness is noted, which is absent for the cases of 0°, 2.5 °or 5 °.

Momentum deficit coefficient. The momentum deficit coefficient for the mean angle of 10° is estimated about 0.23469. It is found that momentum deficit coefficient increases surprisingly about 26 percent in comparison with the mean angle of 5°. This increasing of momentum deficit coefficient is very considerable than last cases. In fact, this shows the more decreasing of momentum around airfoil when maximum angle of attack is quite beyond static angle of attack.

R.M.S. velocity profile. Figure 9 illustrates the r.m.s. streamwise velocity profiles at two mean angles of 5 ° and 10°. It is seen that turbulence intensities in all positions for mean angle of 10 º in the wake increase excessively. Also, the double peaks structure of turbulence profiles disappears at mean angle of 10 º. This huge variation in turbulence structure in the wake indicates occurrence of a recent phenomenon.

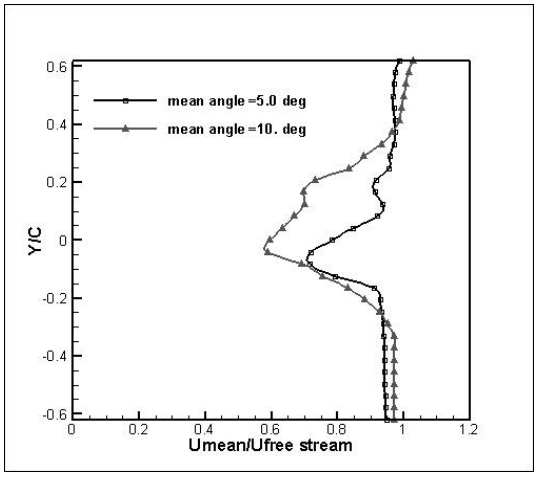

Figure 8. Mean velocity profiles at α_0=5° and 10°

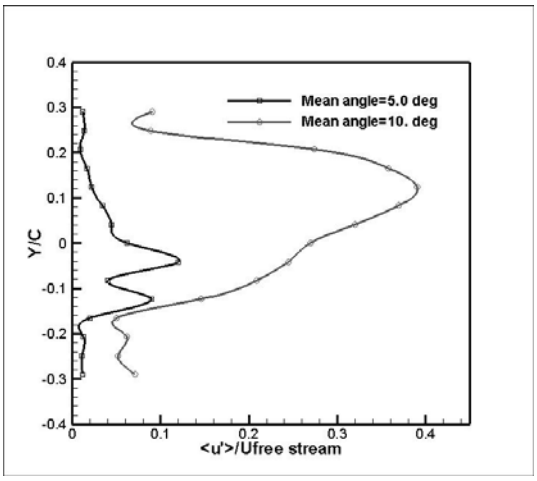

Figure 9. R.M.S. velocity profiles at α_0=5° and 10° Phase ($2\pi ft$) =180°

Above observations are evidences of a large region of separated flow on the airfoil surface or dynamic stall during the motion at α_0=10°. This huge separation causes that airfoil surface vortex goes into the wake and a sudden growth on vortices size, wake thickness and turbulence intensity appears.

CONCLUSIONS

The unsteady wakes developed behind an EPPLER 361 oscillating airfoil were characterized by using hot-wire anemometer. The results of the present investigation have revealed the different effects of changing mean angle on the wake profiles and momentum deficit coefficients. When maximum angle of attack was below the static angle, weak effects of mean angle increasing were observed. This is due to attached flow on the airfoil surface. The considerable effects were appeared after static angle whereas larger vortices formed the wake. A huge growth of wake thickness, turbulence intensity and momentum deficit were considered after special mean angle of attack to be result of large separation on the airfoil surface.

NOMENCLATURE

A	Oscillation Amplitude (degree)
C	Airfoil Chord (m)
C_f	Momentum deficit coefficient (non-dimension)
f	Frequency of oscillation (Hz)
k	Reduced frequency (non-dimension)
t	Time (s)
Y	Vertical distance from chord line (m)
U_{mean}	Streamwise mean velocity (m/s)
U_∞	Free stream velocity (m/s)
α	Instantaneous angle of attack or dynamic angle of attack (degree)
α_0	Mean incidence angle (degree)

REFERENCES

1. McCroskey, W. J., “Some Current Research in Unsteady Fluid Dynamics —The 1976 Free man Scholar Lecture,” ASME Transactions, Journal of Fluid Engineering, Vol. 99, March 1977, pp. 8-39.
2. Carr, L. W., “Progress in Analysis and Prediction of Dynamic Stall,” Journal of Aircraft, Vol. 25, Jan 1988, pp.6-17.
3. Harris, F. D. and Pruyn, R. R., Blade Stall-Half Fact, Half Fiction, Journal of American Helicopter Society, Vol. 13, No. 2, April 1968, pp. 27-48.
4. E. Tolouei, M. Mani, M. R. Soltani, M. Broomand, "Flow Analysis around a Pitching Airfoil" Paper# AIAA-2004-5200 23rd AIAA Applied Aerodynamics conference 16-19 August 2004 Rhode Island, U.S.A.
5. M. Mani, F. Ajalli, M.R. Soltani," An experimental investigation of the reduced frequency effects into pressure coefficients of a plunging airfoil "Seventh International Conference on Advances in Fluid Mechanics, 21, 23 May, 2008.
6. Satyanarayana, B., “Unsteady Wake Measurements of Airfoil and Cascades,” AIAA Journal, Vol. 15, May 1977, pp. 613-618
7. Panda, J., and Zaman, K.B.M.Q “Experimental Investigation of the Flow Field of an Oscillating Airfoil and Estimation of Lift from Wake Survays,” Journal of Fluid Mechanics, Vol. 265, 1994, pp. 65-95.
8. Koochesfahani, M. M, “Vortical Patterns in the Wake of an Oscillating Airfoil,” AIAA Journal, Vol. 27, No. 9, Sep. 1989, pp. 1200-1205.
9. M. Mani, F. Gudarzi, S.M.H.Karimian," Wake Analysis of a Plunging Airfoil" The 6th International Conference on heat Transfer, Fluid Mechanic and Thermodynamics, 30 June to 2 July 2008, South Africa.
10. D.A. Lyn, S. Einav, W. Rodi, J. Park, "A Laser Doppler Velocimetry study of ensemble-averaged characteristics of the turbulent near wake of square cylinder", J. Fluid mech. 304 (1995) 285-319

AN EXPERIMENTAL WAKE ANALYSIS OF A PITCHING AIRFOIL

H. Sadeghi[1*], M. Mani[2,]
[1] M.Sc Student, University of Amirkabir, Tehran, Iran
[2] Professor, Board member, Center of excellence in computational aerospace engineering, University of Amirkabir, Tehran, Iran

ABSTRACT. An experimental investigation was carried out to study the behaviour of the flow field in the wake of an oscillating airfoil in a subsonic wind tunnel. The airfoil was given the harmonic pitching motion about the half chord axis at various oscillation frequencies. The oscillation amplitudes were 8 and 10 deg, and the mean angle of attack was set at 2.5 deg. To assess the effect of Reynolds number, the measurements were performed at 3 different Reynolds numbers of 50000,100000 and 200000. Streamwise mean velocity profiles and turbulence intensity profiles were investigated at several vertically aligned points behind the airfoil at one-quarter chord downstream distance from trailing edge. The results revealed that with increasing oscillation frequency, the wake thickness and turbulence intensity decreased. Besides, it was found that increasing oscillation amplitude caused more increasing of the wake thickness, velocity defect and turbulence intensity in the wake. Furthermore, as an extension of the studying, an estimation of the momentum deficit coefficient was obtained.

Keywords: *Unsteady Wake, Frequency, Reynolds Number, Amplitude, EPPLER-361 Airfoil*

INTRODUCTION

The unsteady aerodynamic theory of oscillating airfoils has received considerable attention in past years. The classical unsteady aerodynamic theory of oscillating airfoils was developed as a result of interest in aircraft flutter problems by Theodorsen [1]. Later, Lighthill [2] extended this theory using propulsion modeling of certain spaces of aquatic animal, birds and insects. In comparison with the many theoretical and numerical studies that have been devoted to the subject of oscillating airfoil, quite a few experimental results appear to be available. Experimental unsteady aerodynamic researches have very important role in both understanding the essential physics of the problem and validating the results from the computational studies. Most of the previous investigations were directed to unsteady wing loading and dynamic stall process, as reviewed by McCroskey [3]. Recently, Tolouei et al [4] investigated experimentally the unsteady pressure distribution over an EPPLER 361 airfoil. They found that pressure coefficients in the low angle of attack range showed little overshoot when compared with the static values, while for the large angle of attack cases the differences were significant. They considered that the large overshoot in the dynamic pressure coefficient for the high angle of attack case is probably due to the existence of the stable dynamic vortex, which is created near the leading edge and moves downstream. Soltani et al [5] showed that by increasing the oscillation frequency, the motion of the airfoil could not adjusted the free-stream flow, and the hysteresis loop of pressure coefficient will change into straight line. In addition in high angles of attack the hysteresis loop grows, so that preventing wing stall and increasing the lift. But this is just applied to smaller speeds. Ajalli et al [6] showed that at different amplitudes for

* Corresponding author: Hamed Sadeghi
Phone: + (98)-911-1522207, Fax: + (98)-151-3212031
E-mail address: hamsadeghi@yahoo.com

unsteady airfoil, the hysteresis loops in the pressure data were both clockwise and counter clockwise when plotted against the equivalent angle of attack. It was found that heaving amplitudes had strong effects in pressure distribution, near the leading edge of the airfoil. Mani et al [7] measured Surface static pressure distribution on the upper and lower sides of the model, during the oscillating motion. It was found that reduced frequency had strong effects on the pressure distribution, near the leading edge of the airfoil.
In spite of less attention about studying the characteristic of the wake in comparison with the measuring the force on oscillating airfoils, several important researches have been conducted into the problem of downstream wake. Satyanarayana [8] measured unsteady wakes of airfoils and cascades under a sinusoidally varying gust flow. Time-mean and time-dependent wake profiles at low frequency behind the airfoil were reported in his work, and the distinctions between these were discussed. Koochesfahani [9] studied experimentally the vortical flow patterns in the wake of a NACA0012 airfoil pitching at small amplitudes and showed that the oscillation wave form has an important effect in the vortical pattern shapes and mean velocity profiles in the wake. He found that there is a critical value for the oscillation frequency that the usual velocity defect profiles in the wake changes to excessive momentum similar to a jet flow and the airfoil produces trust force. Also, he showed that in special cases mean velocity profiles have two peak of velocity defect, that this is symptom of a double-wake structure. Recently, an experimental measurement of unsteady wake behind a sinusoidally unsteady airfoil was performed by Mani et al [10]. They were shown that the angle of attack and reduced frequency are the most important parameters which influence on the velocity profiles. Also, they found that the influence of angle of attack on the velocity profiles is to increase the momentum deficit and wake thickness.

The objectives of the present study are to examine the unsteady wake of an airfoil oscillating sinusoidally in pitch at various conditions. The airfoil was EPPLER-361. The velocity in the wake was measured using the hot-wire anemometer. The airfoil was given at different oscillation frequencies, Reynolds numbers and oscillation amplitudes, and the resulting wakes (mean velocity profiles) were measured to understand the effects of them.

EXPERIMENTAL FACILITY

The experiments were conducted in the subsonic wind tunnel. The tunnel was of closed return type and had a test section of 0.457 m × 0.457 m × 1.2 m. The nozzle contraction of the tunnel was about 7.31, and the turbulence intensity was less than 0.1% in the test section. Figure 1 shows a view of the wind tunnel.

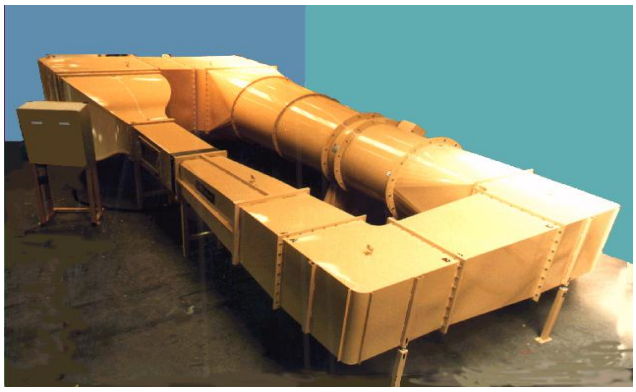

Figure 1. A schematic of wind tunnel

Figure 2. Views of oscillation system

An EPPLER 361 airfoil, with Chord of 0.145 m and a span of 0.45 m was used in the investigations. An especially oscillation mechanism capable of pitching the model at various amplitudes, mean angles of attack and oscillation frequencies was used in the present experiment. The pitch rotation axis was fixed at the wing half chord. Figure 2 shows the picture of oscillation mechanism. A constant temperature hot-wire anemometer (CTAs) was employed for the velocity measurements. The hot-wire probes were mounted on a support in the center plane of the test section behind the airfoil as shown in Fig 3. The traverse mechanism was used to shift sensors. The vertical traverse was restricted from *Y/C*= -0.63 to +0.63 moved by every 50 mm for the measurements.

EXPERIMENTAL PROCEDURE

The motion of the airfoil was sinusoidally pitching oscillation. The dynamic angle of attack, α, can be expressed as:

$$\alpha = \alpha_0 + A\sin 2\pi ft$$

During the test, the oscillation amplitudes were 8 deg and 10 deg, and the mean angle of attack was set at 2.5 deg. The values of oscillation frequency, *f*, were considered about f =1, 2 and 3 Hz. The free stream velocities were set at U_∞=5, 10 and 20 m/s and the corresponding Reynolds numbers were 50000, 100000 and 200000.

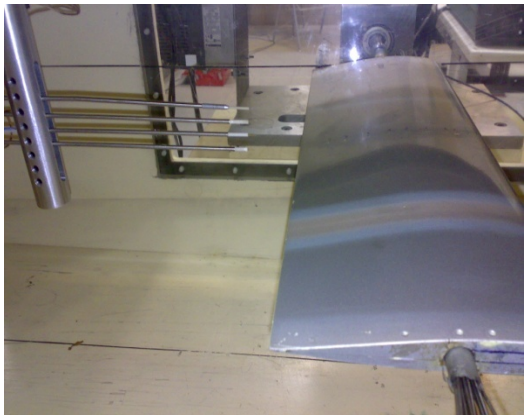

Figure 3. Model and hot-wire sensors

MEASURMENT ACCURACY

Comprehensive reviews of errors in hot-wire measurements and guidelines to evaluate them were given by Bruun [11]. For the present experiment, several works have been done to decrease errors. Hot-wire's sensors have been calibrated by wind tunnel before and after each experiment in order to minimize errors of variation of sensor's temperature. The ensemble averaging procedure that has been adopted in the present experiment, where the samples in each bin are statistically independent because they were collected during different cycles, avoids statistical bios, as observed by lyn et al [12]. Statistical uncertainty in mean and r.m.s velocities depends on the number of sampled data, turbulence intensity and confidence level. For the present experiment, considering a typical value of 2000 sampled data, a confidence level of 95% and a local turbulence intensity of 30%, uncertainties of ±4% and ±5% are expected for the mean and r.m.s velocities, respectively.

EXPERIMENTAL RESULTS AND DISCUSSION

Mean velocity profile

In this subsection, the results are described by streamwise mean velocity profiles in the wake. It is necessary to mention that streamwise mean velocity and vertical distance are non-dimensioned by free stream velocity and airfoil chord, respectively.

Effect of oscillation frequency. The mean velocity profiles at frequencies of f =1, f =2 and f =3 Hz for oscillation amplitude of A=8° and Reynolds of Re =50000 are plotted in Fig. 4. This Figure illustrates that the broadness of profiles or wake thickness becomes smaller slightly, when the oscillation frequency increases.

Effect of oscillation amplitude. Figure 5 illustrates the profiles at two oscillation amplitudes of 8° and 10° for frequency of f =2 Hz and Reynolds of Re =50000. It is seen that at case of 10 degree, the velocity defect and broadness of profile increases.

Effect of Reynolds number. To reveal the effect of Reynolds number on the wake of an oscillating airfoil, mean velocity profiles are plotted at 3 Reynolds numbers of Re =50000, Re =100000 and Re=200000 in Fig. 6. In this case, the oscillation amplitude and oscillation frequency are A=8° and f =2 Hz, respectively. This Figure shows that with increasing Reynolds number, velocity defect and wake thickness decrease.

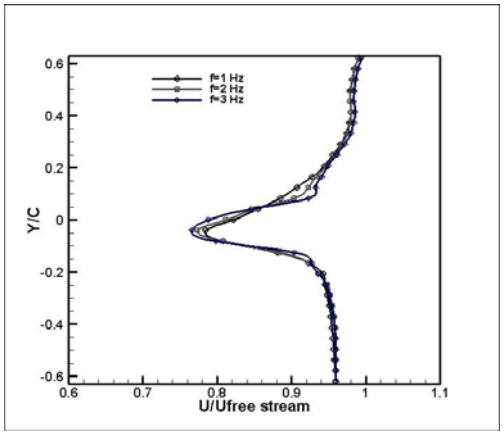

Figure 4. Mean velocity profiles at different frequencies

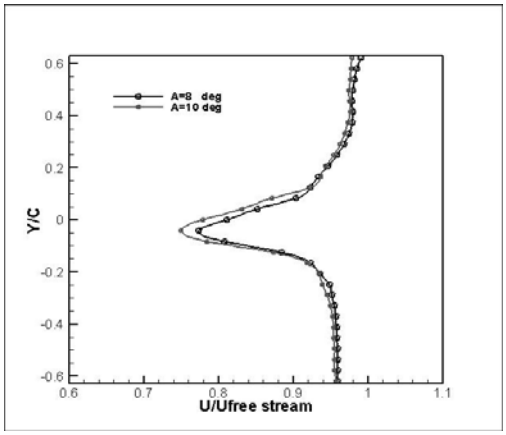

Figure 5. Mean velocity profiles at different amplitudes

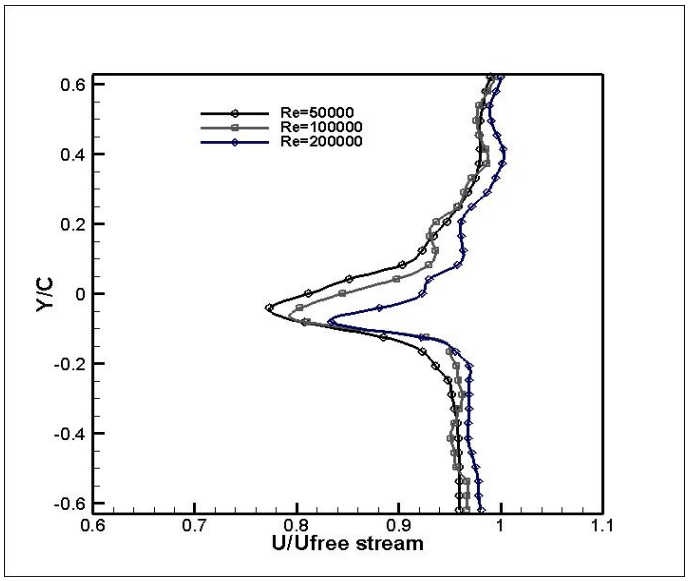

Figure 6. Mean velocity profiles at different Reynolds numbers

Momentum deficit coefficient

The mean velocity profile can be used to estimate the momentum deficit on the airfoil [9]. With usual normalization of the force with freestream dynamic head and the airfoil chord, the momentum deficit is given by

$$C_f = 2/C\int_{-\infty}^{\infty} U/U_\infty(1-U/U_\infty) \tag{2}$$

where the contribution due to the fluctuating quantities and the pressure term have been neglected.

Effect of oscillation frequency. Variation of momentum deficit coefficient with reduced frequency is depicted in Fig. 7. In this case, A =8° and Re =50000. This figure shows the considerable decreasing in momentum deficit coefficient with frequency. This demonstrates very important role of oscillation frequency that increasing frequency is the one of the most important factors to reduce momentum deficit and achieving thrust.

Effect of oscillation amplitude. Momentum deficit coefficients are compared for two different amplitudes in Fig. 8. In this case, f =2 Hz and Re =50000. It is found that, for the case of 10 degree, the momentum deficit coefficient increases about 10 percent against case of 8 degree. This demonstrates the considerable increasing of momentum deficit around airfoil with increasing oscillation amplitude.

Effect of Reynolds number. To assess the effect of Reynolds number on the Momentum deficit for the present oscillating airfoil, momentum deficit coefficients are compared at 3 Reynolds numbers, Fig. 9. In this case, the oscillation amplitude and oscillation frequency are A=8° and f =2 Hz, respectively. Figure 9 shows that with increasing Reynolds number, momentum deficit coefficient decreases.

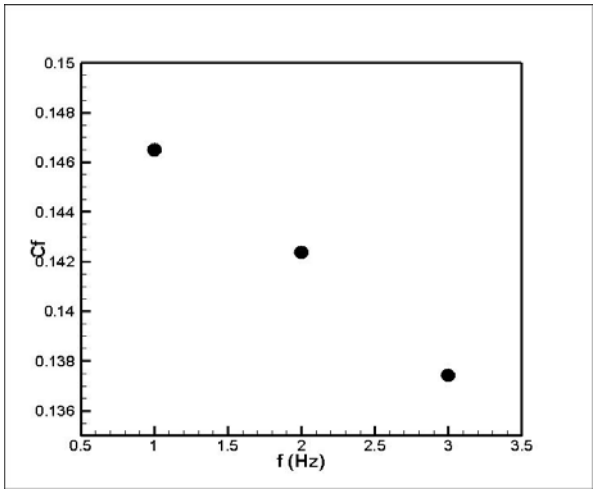

Figure 7. Variations of momentum deficit coefficients with frequencies

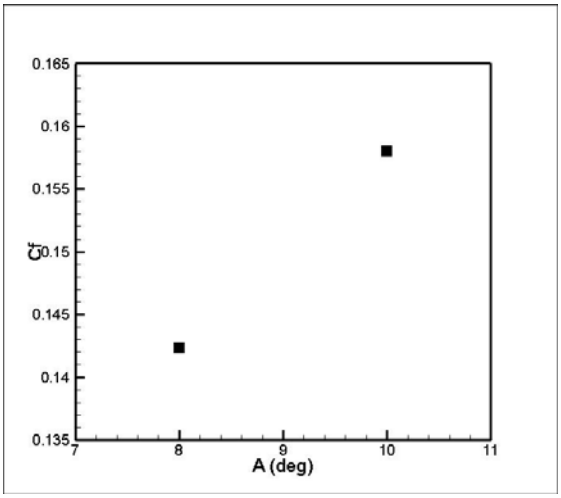

Figure 8. Variations of momentum deficit coefficients with amplitudes

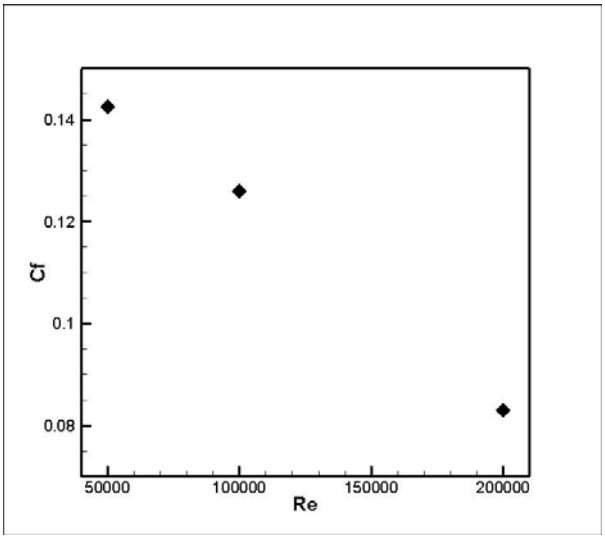

Figure 9. Variations of momentum velocity deficit coefficients with Reynolds numbers

R.M.S. velocity profile

In order to better identification and discussion of flow field in the wake, r.m.s. streamwise velocity profiles are obtained. It should be mention that r.m.s. streamwise velocity is $\sqrt{u'^2}/U_\infty$.

Effect of oscillation frequency. Figures 10 and 11 show r.m.s. streamwise velocity profiles at two different frequencies at two phase angles of 0° and 180°, respectively. In these cases, A=8° and Re =50000. The considerable differences in the pick of profiles and positions of them at f =1 Hz indicate the importance of history and state of fluid motion. It is clear from figures that with increasing frequency, profiles tend to have same behaviour. In fact, increasing frequency reduces history of fluid motion. These figures illustrate that the wake becomes less turbulent as the frequency increases. Increasing the rate of oscillating causes more stability in boundary layer and the rate of vortex formation is reduced around airfoil. This is due to delay in vortex initiation with increasing pitch rate. Therefore, vortices in the wake become smaller and wake thickness decreases.

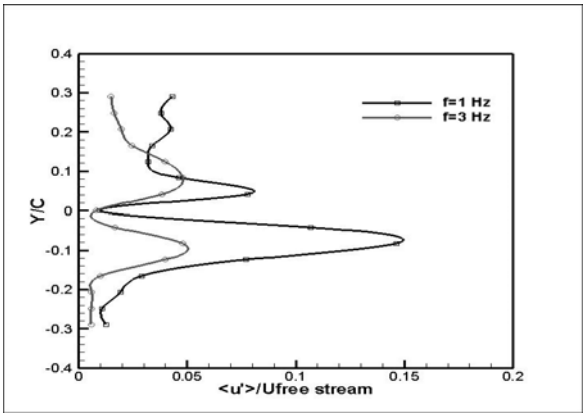

Figure 10. Streamwise r.m.s. velocity profiles Phase ($2\pi ft$) =0°

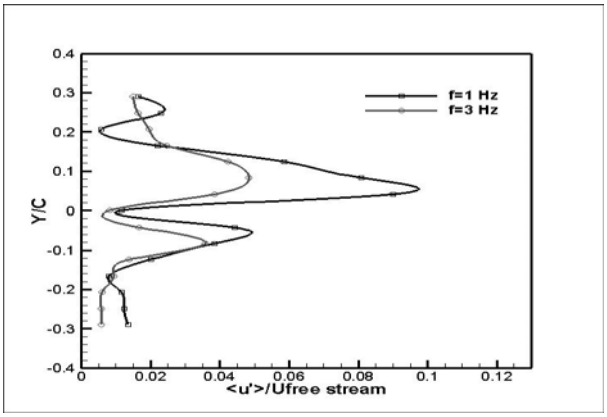

Figure 11. Streamwise r.m.s. velocity profiles Phase ($2\pi ft$) =180°

Effect of oscillation amplitude Figures 12 and 13 illustrate r.m.s. streamwise velocity profiles at two different amplitudes at two phase angles of 0° and 180°, respectively. In these cases, f =1 Hz and Re =50000. It is seen that in both figures with increasing oscillation amplitude, turbulence intensities in the wake increase. Increasing oscillation amplitude initiates vortex development earlier in the oscillating cycle and formed vortices in the wake become larger. So, it causes wake thickness and turbulence intensity increase.

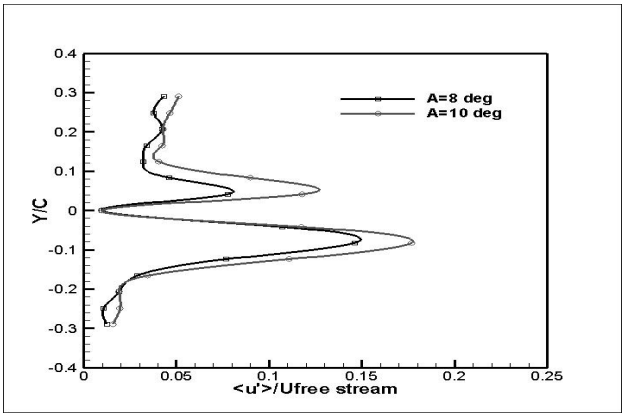

Figure 12. Streamwise r.m.s. velocity profiles Phase ($2\pi ft$) =0°

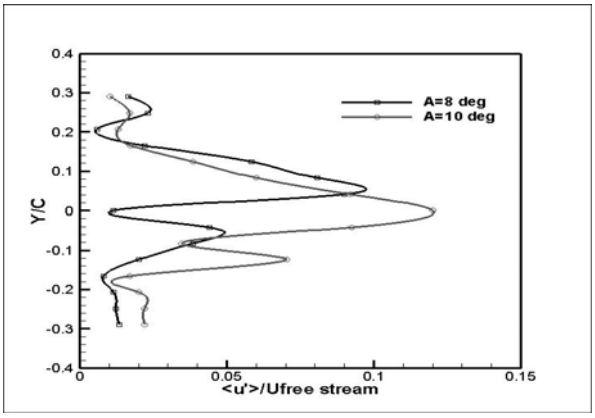

Figure 13. Streamwise r.m.s. velocity profiles Phase ($2\pi ft$) =180°

CONCLUSIONS

The mean velocity profiles, momentum deficit coefficients and r.m.s velocity profiles in the wake of an oscillating airfoil have been experimentally investigated, and the results have been revealed several interesting features. Increasing oscillation amplitude increased momentum deficit, wake thickness and turbulence intensity because of earlier vortex development in the oscillating cycle and formation of larger vortices in the wake. It was found that oscillation frequency has important role to reduce momentum velocity deficit and wake thickness due to delay in vortex initiation. Also, the results showed that with increasing Reynolds number, velocity defect and momentum deficit decreased.

NOMENCLATURE

A	Oscillation Amplitude (degree)
C	Airfoil Chord (m)
C_f	Momentum deficit coefficient (non-dimension)
f	Frequency of oscillation (Hz)
Re	Reynolds number (non-dimension)
U	Streamwise mean velocity (m/s)
U_∞	Free stream velocity (m/s)
u'	Turbulence intensity (m/s)
Y	Vertical distance from airfoil chord (m)
α_0	Mean incidence angle (degree)

REFERENCES

1. Theodorsen, T., "General Theory of Aerodynamic Instability and the mechanism of Flutter/NACA TR 496, 1935.
2. Lighthill, J., Mathematical Bio-fluid dynamics, SIAM, Philadelphia, 1975.
3. McCroskey, W. J., "Some Current Research in Unsteady Fluid Dynamics —The 1976 Free man Scholar Lecture," ASME Transactions, Journal of Fluid Engineering, Vol. 99, March 1977, pp. 8-39.
4. E. Tolouei, M. Mani, M. R. Soltani, M. Broomand, "Flow Analysis around a Pitching Airfoil" Paper# AIAA-2004-5200 23rd AIAA Applied Aerodynamics conference 16-19 August 2004 Rhode Island, U.S.A.
5. M. R .Soltani, M. Mani, E. Tolouei, "An Experimental Investigation of Surface Pressure Variation over an Oscillating Airfoil", The 11th Australian International Aerospace Congress, March 2005, Melbourne Australia.
6. F. Ajalli, M. Mani, M. Soltani "An Experimental Investigation of Pressure Distribution around a Heaving Airfoil" The 5th International Conference on heat Transfer, Fluid Mechanic and Thermodynamics, 1-4 July 2007, South Africa.
7. M. Mani, F. Ajalli, M.R. Soltani," An experimental investigation of the reduced frequency effects into pressure coefficients of a plunging airfoil "Seventh International Conference on Advances in Fluid Mechanics, 21, 23 May, 2008.
8. Satyanarayana, B., "Unsteady Wake Measurements of Airfoil and Cascades," AIAA Journal, Vol. 15, May 1977, pp. 613-618
9. Koochesfahani, M. M, "Vortical Patterns in the Wake of an Oscillating Airfoil," AIAA Journal, Vol. 27, No. 9, Sep. 1989, pp. 1200-1205.
10. M. Mani, F. Gudarzi, S.M.H.Karimian," Wake Analysis of a Plunging Airfoil" The 6th International Conference on heat Transfer, Fluid Mechanic and Thermodynamics, 30 June to 2 July 2008, South Africa.
11. H. H. Bruun, Hot-Wire Anemometry : Principles and Signal Analysis, OXFORD UNIVERSITY PRESS
12. D.A. Lyn, S. Einav, W. Rodi, J. Park, "A Laser Doppler Velocimetry study of ensemble-averaged characteristics of the turbulent near wake of square cylinder", J. Fluid mech. 304 (1995) 285-319

FEEDBACK CONTROL OF VORTEX SHEDDING BEHIND A SQUARE CYLINDER WITH INLINE OSCILLATIONS

Sushanta Dutta[1],* Krishnamurthy Muralidhar[2], Pradipta K. Panigrahi[3]
[1]Department of Mechanical & Industrial Engineering, IIT Roorkee, Roorkee, India
[2]Department of Mechanical Engineering, IIT Kanpur, Kanpur, India
[3]Department of Mechanical Engineering, IIT Kanpur, Kanpur, India

ABSTRACT. A feedback control experiment is conducted for flow past an oscillating square cylinder using PIV and HWA. The interest here is towards active control of the flow field that is likely to result in drag reduction at intermediate Reynolds numbers. Additionally, the dynamics of the flow phenomena for a square cylinder with oscillations in the direction of the incoming flow is also of interest. Experiments have been conducted at a Reynolds number of 175. The feedback loop consists of the hotwire probe, phase shifter available in labVIEW, a power amplifier and electromagnetic actuators. The detailed flow field has been investigated using PIV. Flow visualization images are also captured using laser light sheet and a CCD camera. The flow field has been investigated in terms of instantaneous as well as time-averaged velocity fields. The instantaneous flow field shows suppression of vortex shedding and reduction in velocity fluctuations in the presence of feedback. The periodic structure is disrupted in the presence of the feedback signal. The time averaged flow field shows the reduction in the size of the recirculation region with both open loop and feedback when compared to flow past a stationary cylinder.

Keywords: *Square cylinder, Inline oscillations, Feedback control, PIV, Hotwire anemometer.*

INTRODUCTION

Control of bluff body wakes is of fundamental interest as well as practical significance. Flow control can be employed to reduce the intensity of the wake in order to eliminate flow induced oscillation and reduce drag experienced by the object. A variety of control techniques have been proposed. These are classified as active and passive control strategies. In passive control, the flow geometry is altered and there is no external addition of energy. In active control, momentum is transferred over a portion of the boundary and net energy is transferred to the fluid. Active control can be classified as open and closed loop. A closed loop active control system uses actuators driven by external energy sources through a feedback signal collected from the flow field.

The choice of the transfer function connecting the velocity/pressure signal and the one driving the actuator is crucial for the effectiveness of a feedback signal (Zhang et al. 2005). For objects that are set in motion by the unsteady forces, literature shows that a control system will best perform when a combination of flow field information and body motion is used for control (Ikemoto et al. 2001). Tao et al. (1996) reported a feedback experiment with a hotwire probe wherein flow visualization was conducted using a dye injection technique for flow past a circular cylinder. The flow visualization images clearly showed complete suppression and enhancement for various feedback conditions. Roussopoulos (1993) studied feedback control of vortex shedding for flow past a circular cylinder at an intermediate Reynolds number using flow visualization and hotwire technique and was able to increase the critical Reynolds number of the onset of vortex shedding. A loudspeaker was used as an actuator and the hotwire sensor as control. The wake

* Corresponding author: Dr. Sushanta Dutta
Phone: + (91)-1332-285410, Fax: + (91)-1332-285665
E-mail address: duttafme.iitr@yahoo.com

unsteadiness could be controlled for up to 10 times the critical Reynolds number. Zhang et al. (2003, 2004) studied the control mechanism of vortex shedding for a spring loaded square cylinder whose top surface was perturbed using a piezo actuator. Both closed loop and open loop studies showed a reduction in the time-averaged drag coefficient. The open loop system can suppress vortex shedding only if it is outside the synchronization range. Within the synchronization range the open loop control enhances vortex shedding and hence, the structural vibration. On the other hand, the feedback signal from the flow suppresses vortex shedding by adjusting the phase of the forcing signal. Thus, the study revealed that closed loop control was more advantageous when compared to the open loop system. Wolfe and Ziada (2003) studied the effect of feedback control on vortex shedding from two tandem cylinders in cross-flow. Feedback control was applied for resonant and non resonant cases downstream of the cylinder. A synthetic jet was induced upstream through a narrow slit using a loudspeaker. The response of the downstream cylinder could be reduced up to 70% in the resonant and 75% for non-resonant experiments. Zhang et al. (2005) studied flow past a stationary cylinder with a perturbation of its top surface at a Reynolds number of 7400. The authors used closed loop control with PID controller to perturb the surface using piezo-ceramic actuators. The study showed that when the surface perturbation and the force due to vortex shedding are in opposed phase, there is a weakening of vortex shedding and a reduction in the fluctuating forces.

CONTROL SCHEME AND EXPERIMENTAL DETAILS

The present investigation is an experimental study wherein wake characteristics of an oscillating prismatic cylinder are obtained using particle image velocimetry (PIV). A low speed vertical test cell has been used for generating the base flow. The cylinder is square in cross-section and is mounted horizontally with its axis perpendicular to the flow direction. The cylinder is driven in a direction parallel to the incoming flow by electromagnetic actuators. The frequency of oscillation is determined by using a single wire hot-wire anemometer that detects wake unsteadiness. The details of the experimental setup are described in Dutta et al. (2007). The flow field is characterized in terms of time averaged as well as instantaneous quantities such as velocity vectors, rms velocity, vorticity contours center-line recovery of velocity. The time-averaged velocity vectors are used to determine the drag coefficient acting on the cylinder. The goal of the study is to explore conditions under which the cylinder experiences lower drag and its correlation to the vorticity field. The data analysis procedures are identical to those reported in Dutta et al.(2007).

The PIV system (*Oxford Lasers*, UK) used in the study consists of a double pulsed Nd :YAG laser (λ= 532 nm) of 15 mJ/pulse power, a Peltier-cooled 12 bit CDD camera with a frame speed of 8 Hz, a synchronizer, frame grabber and a dual processor PC. The CCD consists of an array of 1280×1024 pixels. The field of view for PIV measurements is 40×35 mm. In experiments the oil particle size was around 2-3 μm while the pixel size was 6.7 μm. The size of the particle image on the pixel array was estimated as 14-15 μm from a histogram distribution of light intensity over an interrogation spot. The velocity vectors are calculated from particle traces by the cross-correlation method. The interrogation size is 16×16 pixels and 5561 velocity vectors are obtained with a spatial resolution of 0.5 mm for velocity. The cylinder motion is generated by mounting the prism over two electromagnetic shakers (*Spanktronics*, India). The shaker frequency and amplitude are adjustable through a control unit that is interfaced to a PC. The PC also receives signals from a hot-wire probe and the control strategy is implemented in a *Labview* environment. Flow visualization is carried out using light sheet of the laser and the CCD camera that accompanies PIV measurements, but with a reduced particle number density. Time averages are calculated by working with an image sequence comprising 200 frames.

Experiments were conducted in the following manner. A hotwire probe was placed at $\boldsymbol{x/d}$ =5 downstream and $\boldsymbol{y/d}$=1.2 from the cylinder centre. A long hotwire signal (60000 points) sampled at 1000 values per second was collected in the near wake of a stationary cylinder. This data was subsequently used for generating the feedback signal for the oscillating of the cylinder. The signal was low-passed filtered at a cut off frequency of 100 Hz to remove the high frequency components.

The signal was amplified to the level acceptable to the actuator. A phase shift was given to the filtered signal before sending it to the actuator. By placing the time series of the filtered and amplified signal in a loop, it was possible to run the experiment for a long period of time. The schematic layout of the feedback circuit is shown in Figure 1(b). Results discussed below are for a phase shift of 180^o. The amplitude of oscillation is practically constant in the oscillation experiments with and without feedback.

UNCERTAINTY AND VALIDATION

The seeding of flow with oil particles, calibration, light sheet reflection, and image digitization affect PIV measurement. Room temperature and calibration affect the hotwire measurement. For the particle size utilized and the range of frequency in the wake, a slip velocity error of 0.3-0.5 % relative to the instantaneous local velocity is expected. In the present experiments, the effect of introducing particles is examined by conducting experiments at a fixed Reynolds number by varying the size of the cylinder and air speed. The streamline plot and the dimensionless size of the recirculation region were found to be identical. The *x* and *y* velocity profiles from the PIV measurements matched hotwire measurement very well in the far wake. From repeated measurements the uncertainty in drag coefficient measurement was estimated to be within 3-4 %.

Figure 1(a). Photograph of the setup

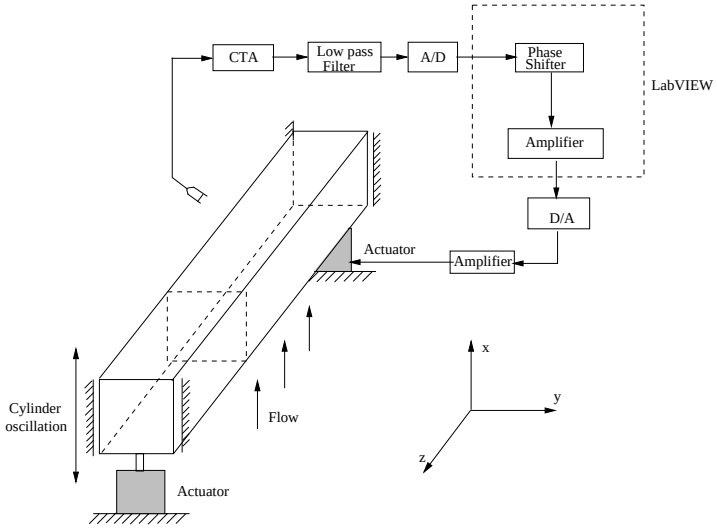

Figure 1(b). Schematic diagram of the feedback circuit

RESULTS AND DISCUSSIONS

Flow patterns are presented in terms of the time-averaged and instantaneous quantities recorded from experiments. Figure 2 shows the streamwise velocity signal as a function of time for stationary and oscillating cylinders, the latter with feedback. With feedback, the magnitude of velocity fluctuation is seen to be substantially reduced. Further, the spectral characteristics of the signal are also seen to be affected.

Table 1 presents the drag coefficient value for stationary and oscillating cylinders with and without feedback. Drag coefficient reported here arises from the combined effect of momentum deficit and time-averaged turbulent stresses at the outflow plane of the wake. It has been determined as a time-averaged quantity from a PIV data set of 200 images. The drag coefficient has been determined from the profiles of velocity and velocity fluctuations across the entire test cell at a streamwise location of $\boldsymbol{x}$=10.

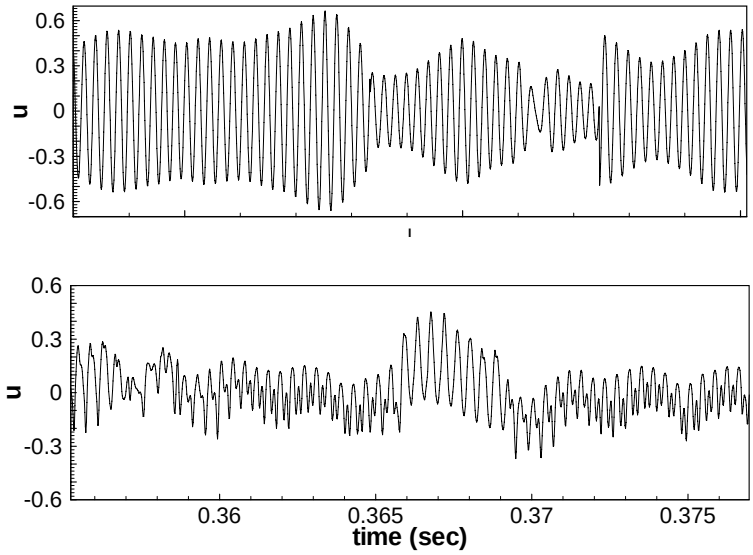

Figure 2. Typical time histories of the streamwise velocity component with (lower trace) and without (upper trace) perturbation. Time scales for the two traces are identical. Re=175.

The drag coefficient has been calculated from the extended formula

$$C_D = 2\int_{-\infty}^{\infty} \tfrac{u}{U}(1-\tfrac{u}{U})dy + 2\int_{-\infty}^{\infty} (\frac{\overline{v'^2} - \overline{u'^2}}{U^2})dy$$

The first term is the momentum deficit of the time-averaged flow field and the second term is the contribution of the turbulent fluctuations. In all experiments, the second term was found to be 10-15 % of the total drag.

TABLE 1

Drag coefficient (C_D) value for Stationary and Oscillating Cylinder (open loop and closed loop) at Re=175.

Cylinder motion	Stationary	Forced oscillations	With feedback
Drag coefficient (C_D)	1.42 ±3%	1.31±4%	1.35±4%

Figure **3** shows the time-averaged velocity vectors for stationary and oscillating cylinders, with and without feedback. From the figure it is seen that the near wake velocity is strongly affected by cylinder motion. The size of the velocity deficit zone (in blue) reduces in the presence of cylinder oscillation. The recirculation zone is quite small for the open loop system. With feedback, the size of the recirculation zone increases when compared to open loop oscillation. The size of the recirculation zone is related to base pressure and hence related to drag coefficient. Thus, for the choice of parameters, feedback does not appear to have a beneficial effect in diminishing the time-averaged drag coefficient beyond the value for forced oscillations. A similar conclusion was arrived at by Zhang et al. (2004). The proper choice of the feedback parameters is thus, crucial.

Figure 4 shows the time-averaged and fluctuating velocity components in the wake for three cases: when the cylinder is stationary, oscillatory and oscillations are with feedback. Measurements at the location x=**4** are reported.

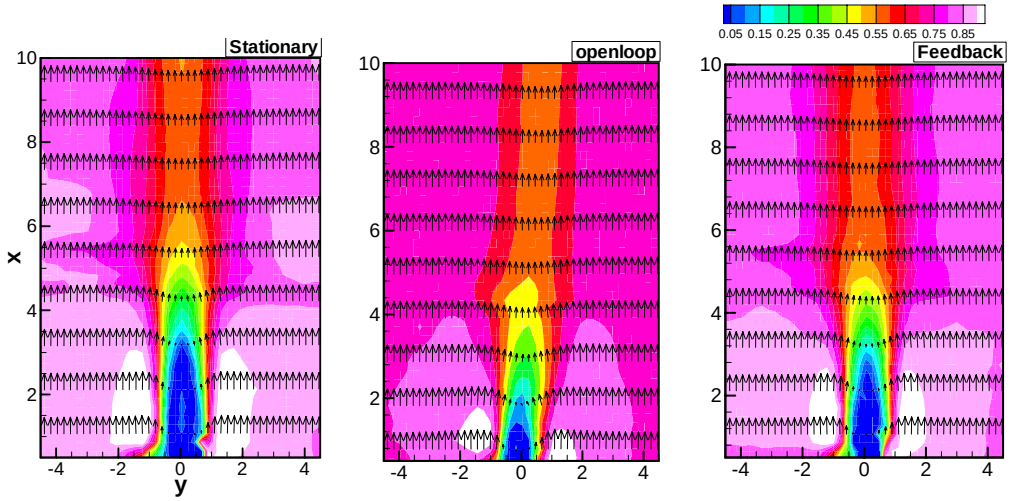

Figure 3. Time-averaged velocity vectors for stationary and oscillating cylinder (with and without feedback) at Re=175. The flooded contours represent the absolute velocity magnitude.

The mean velocity deficit is higher for the stationary cylinder when compared to the perturbed. The velocity deficit for the closed loop experiment is higher when compared to forced oscillations. The velocity deficit is a second measure of the time-averaged drag coefficient along with the wake size of the base region.

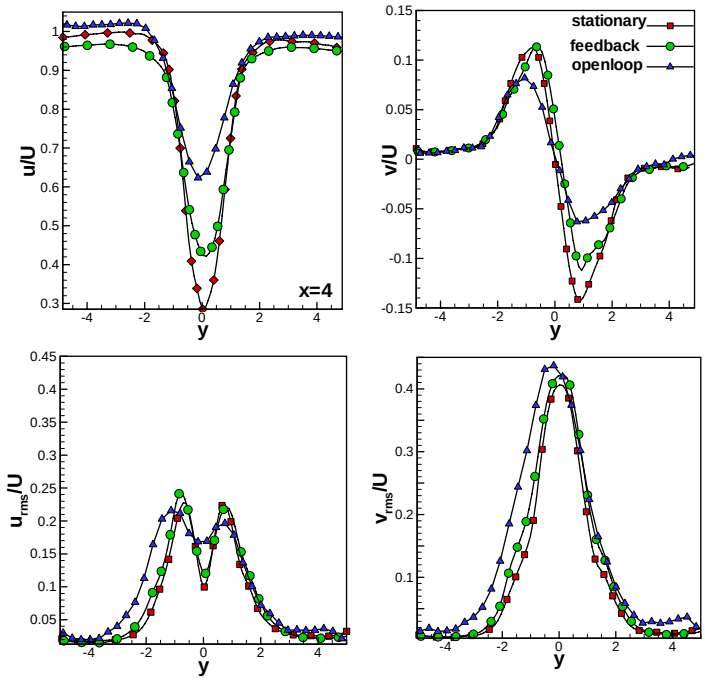

Figure 4. Comparison of time-averaged velocities $\boldsymbol{u}$ and $\boldsymbol{v}$, velocity fluctuations $\boldsymbol{u}_{\text{rms}}$ and $\boldsymbol{v}_{\text{rms}}$ for stationary and oscillating cylinders (with and without feedback) at a downstream location of $\boldsymbol{x}$ =4, Re=175.

Thus, for the present set of parameters, the control function (namely a phase shift of 180^{o}) is seen to be ineffective in reducing the time-averaged drag coefficient beyond what is seen for forced oscillations. In contrast, it is shown later from instantaneous flow visualization images (Figure 8) that vortex shedding is weakened with feedback.

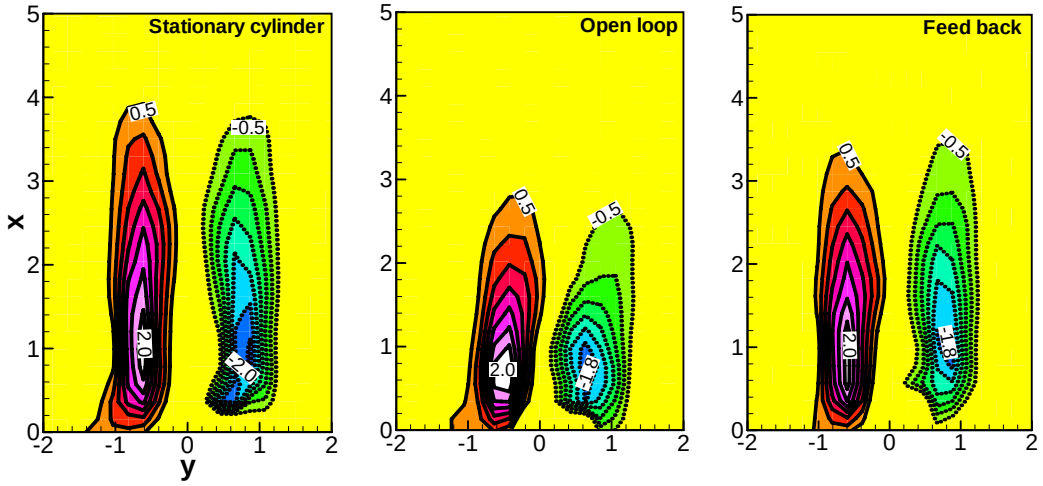

Figure 5. Time-averaged vorticity contours for stationary and oscillating cylinder (with and without feedback) at Re=175.

The strength of the velocity fluctuations diminish, as seen from the time traces of the velocity signal (Figure 2). The magnitudes of u_{rms} and v_{rms} were measured to be nearly equal for experiments with and without feedback, but smaller than for a wake of a stationary cylinder.

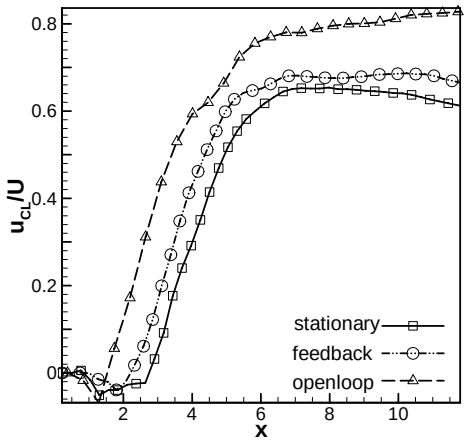

Figure 6. Centerline recovery of streamwise velocity for stationary and oscillating cylinder (with and without feedback at Re=175.

Figure 5 compares the dimensionless time-averaged spanwise (ω_z) vorticity contours for a stationary cylinder against open loop and feedback controlled oscillations. For the open loop, the vortices move close to the cylinder and the concentration of vortices near the cylinder increases. The concentration of the maximum vorticity zone in the near field region confirms the reduction in the size of the recirculation zone, Figure 3**.** With feedback control, the concentration near the cylinder marginally decreases, indicating that feedback negates some of the beneficial aspects of forced oscillations.

Figure 6 shows the centerline recovery of streamwise velocity for stationary and oscillating cylinders, with and without feedback. The centerline velocity dips to a minimum and then increases as fluid is entrained from the region outside the wake. The average centreline velocity is lower inside the recirculation zone, where the transverse velocity is high. The recovery is faster in the near field region and reaches an asymptotic value at around x =7. The rate of velocity recovery is seen to be high for the open loop system when compared to the stationary and feedback control experiments.

Figure 7 shows the instantaneous contours of spanwise vorticity for stationary and oscillating cylinders (with and without feed back) at selected instants of time. Positive vorticity corresponds to clockwise rotation and is indicated by solid lines whereas the negative spanwise vorticity corresponds to counter clockwise rotation and is indicated by dashed lines. When there is no perturbation, the vortices display the pattern of a Karman vortex street. With forced perturbation, the vortices get distorted. The vortices are shed much closer to the cylinder and the longitudinal spacing of the vortices decreases. With feedback controlled oscillations, the periodic structure is disrupted. Experiments showed that the structure thus generated is not continuous and has intermittency.

Figure 8 shows particle traces for stationary and the oscillation experiments for flow past a square cylinder. The top row shows a sequence of three instantaneous images for a stationary cylinder. Pure Karman vortex shedding flow pattern is seen from the images. The shedding mechanism is different for an oscillating cylinder when compared to the stationary. With oscillation at the vortex shedding frequency, vortex shedding is governed by the amplitude of oscillation of the cylinder. Vortices are shed from very near the cylinder. With the application of feedback to the actuator, vortex shedding is fully distorted and the wake size significantly reduces. This pattern was not continuously seen with feedback. Intermittently the vortex shedding such as that for a stationary cylinder was also seen.

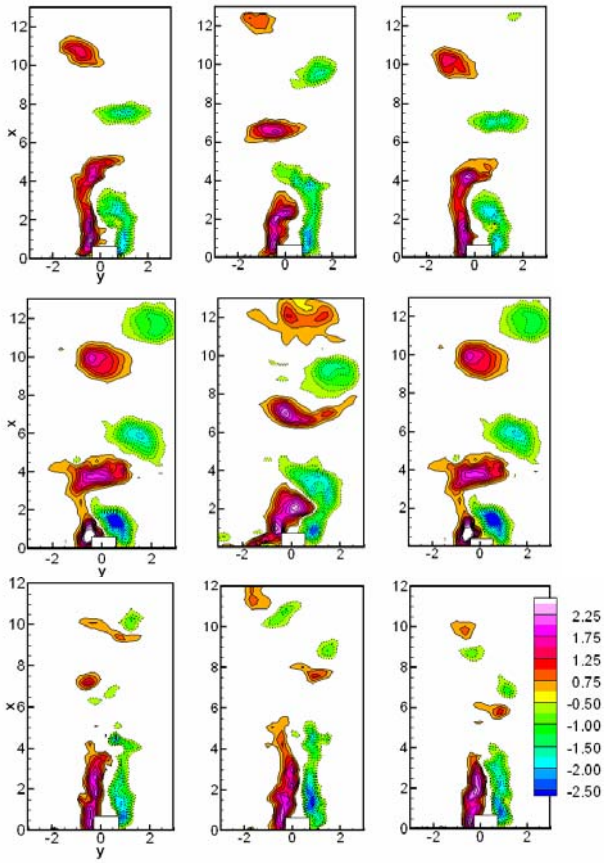

Figure7. Instantaneous spanwise vorticity contours for a stationary cylinder (top), oscillating cylinder without feedback (middle) and cylinder with feedback (bottom) cylinder at Re=175.

CONCLUSIONS

The flow field in the wake of a cylinder oscillated using feedback control was investigated in terms of instantaneous as well as time-averaged data. In the feedback mode, the cylinder was fed an 180^{o} phase shifted signal with respect to the velocity signal in the near wake. The instantaneous flow field showed suppression of vortex shedding and reduction in velocity fluctuations with feedback. The time averaged flow field showed a smaller recirculation region both with open loop and feedback when compared to a stationary cylinder. Keeping amplitude and frequency fixed, the time-

averaged wake size was seen to increase with feedback. However, the instantaneous velocity fluctuations were seen to be damped.

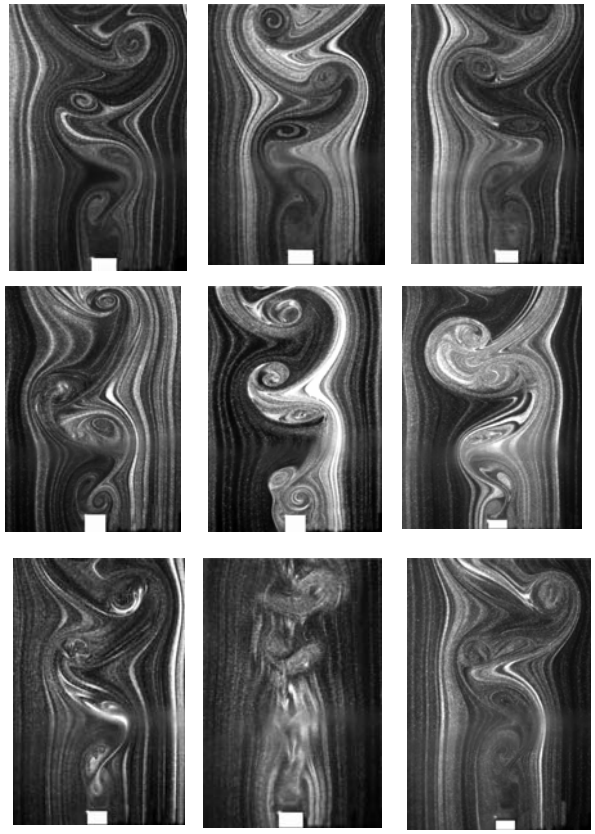

Figure 8. Flow visualization images for stationary (top row), open loop (middle row) and closed loop oscillation (bottom row). Images are phase matched.

REFERENCE

1. Adrian, R. J., Particle imaging techniques for experimental fluid mechanics, Ann. Review of Fluid Mechanics. Vol. 23, pp. 261-304, 1991
2. Dutta, S. Panigrahi, P. K., and Muralidhar, K., Sensitivity of a square cylinder wake to forced oscillations, ASME, J. Fluids Engg, Vol. 29, pp. 852-870, 2007.
3. Fujisawa, N., Kawaji, Y. and Ikemoto, K., Feedback control of vortex shedding from a cylinder by rotational oscillations, J. Fluids and Structures, Vol. 15, pp. 23-37, 2001.
4. Griffin O.M., Hall M.S., Review-vortex shedding lock-on and flow control in bluff body wakes. J. Fluid Engg., Transaction ASME, Vol. 113, pp. 526-537, 1991.
5. Roussopoulos, K., Feedback Control of Vortex Shedding at Low Reynolds Numbers, J. Fluid Mech., Vol. 248, pp. 267-296, 1993.
6. Tao, J. S., Huang X. Y. and Chan, W. K., A flow visualization study on feedback control of vortex shedding from a circular cylinder, J. Fluids and Structures, Vol. 10, pp. 965-970, 1996.
7. Wolfe, D., Ziada, S., Feedback control of vortex shedding from two tandem cylinders, J. Fluids and Structures, Vol. 78, pp. 579-592, 2003.
8. Zhang, M. M., Zhou, Y. and Cheng L., Closed-loop-controlled vortex shedding and vibration of a flexibly supported square cylinder under different schemes, Phys. Fluids, Vol.16, No. 5, pp 1439-1448, 2004.
9. Zhang, M. M., Zhou, Y. and Cheng, L., Spring Supported Cylinder Wake Control, AIAA Journal, Vol 41, pp. 1500-1506, 2003.
10. Zhang, M. M., Zhou, Y. and Cheng L., Closed-Loop-Manipulated Wake of a Stationary Square Cylinder, Expt. Fluids, Vol. 39, pp. 75-85, 2005.

Computational Methodology

DEVELOPMENT OF A SCALABLE 3-D GEOMETRIC MODEL FOR CFD FLOW SIMULATION OF SHAFT KILNS

Z. Xu*, H. Woche, and E. Specht
Institute of Fluid Dynamics and Thermodynamics, Otto von Guericke University Magdeburg, Magdeburg, Germany

ABSTRACT. The knowledge of temperature distribution and radial gas mixing plays a very important role in design of shaft kilns, yet is poorly understood. This is due to the geometric complexity and the movement of the lumpy processed material, which make it impossible to measure the main parameters, such as temperature, gas components, and velocity etc. The purpose of this study is to develop a three-dimensional geometric model that can be applied by computational fluid dynamics (CFD) to visualize the full flow structure in the important zone of the kilns. It is shown that tetra-based packed arrangement is suitable for model with spheres. The jet behaviour is independent of the loading height after expanding into a packed tube, so that 4 layers of particles up the burner system are assumed to be enough for modelling. A 9-layer wall segment model is developed finally and used for CFD simulation successfully. This geometric model has proved to be scalable and computationally less expensive.
Keywords: *Shaft kilns, CFD, packed bed, geometric model, flow simulation*

INTRODUCTION

Shaft kilns have wide use in industry, from the calcination of limestone, refractory material (magnesite, dolomite, corundum) to mineral wool manufacturing etc. The normal shaft kiln, basically a packed bed reactor, works on a very simple principle. The raw material is fed in at the top of the kiln and the product is withdrawn from the bottom. Heat to calcine the material is introduced roughly in the middle of the kiln through gas heating systems. The design of these systems, however, may fail to provide optimum combustion of gas in the calcining zone (injection zone) due to the significant influences of the processed material on the gas permeability. This results in decreased quality of products, reduced productivity, and low thermal efficiency [1]. The optimization is usually very empirical and costly because the industrial shaft kilns are large and complicated systems. Comparing with investigation in experimental manner, mathematical modelling is much more efficient. In fact, modelling has aided the design and operation of shaft kilns over the years. Many works have appeared in the literature [1-5]. But most of these studies are based on thermal balance and material balance of the kilns, whereas the knowledge on the in-kiln phenomena especially on the radial gas distribution and mixing is not sufficient. As demands on system performance increase, model needs to be able to give the radial distribution of the fluid in detail in order to acquire thorough knowledge of the problems, for instance, to localize regions of deficient heating or overheating. Computational fluid dynamics (CFD) is one of the critical "enabling technologies" for achieving this. It allows engineers to predict and design the desired fluid dynamics in geometrically complicated equipment [6-8].
Nowadays, none of the researchers attempted the CFD simulation of shaft kilns due to complex geometry definition, extremely computational cost, and limitations in computational power as well. The related studies are flow simulation in packed bed reactors using CFD approach. These works

* Corresponding author: Z. Xu
Phone: + (49)-391-6712421, Fax: + (49)-391-6712762
E-mail address: eric.zhiguoxu@gmail.com

reviewed by Dixon et al. [9-10], however, mainly focus on studying gas flowing through packed tubes which have a very low tube-to-particle diameter ratio (N), e. g. N=4.
The first step, also the most critical, in CFD simulation is geometric modelling. Correct definition of the geometry provides a more realistic scenario for simulation, and the technique used for constructing the geometry will ensure the feasibility of generating a mesh good enough to capture the full phenomena involved in the problem. Therefore, this work aims to develop a less expensive geometric model which can be used for simulating the flow structures in the industrial-scale shaft kilns by using CFD. With this intention, a geometry having a tube-to-particle diameter ratio of 20 was developed step by step in this paper. Simulations were carried out based on the geometry to demonstrate the viability of using CFD as a design tool for shaft kilns. Geometry and grid generation were executed by using Gambit 2.3.16, and all numerical simulations were performed with the commercial CFD code FLUENT6.2.16 on HP-Proliant-DL585 server (4×DualOperon885-2600MHz 32GB Memory).

DEVELOPMENT OF THE GEOMETRIC MODEL

Simplifications

For the first stage, the process and the characteristics of the kilns and processed materials were simplified, as clarified by the following:

(1) Fixed bed. In practice, the solid phase is moving downwards the kiln. But considering that the velocity is extremely slow, e.g. about 10 m/day in lime production, the bed is defined to be fixed.
(2) Regular packed Spheres. Due to the complicated packing structure in the shaft kilns, processed material granules are assumed to have uniform spherical geometry.
(3) No heat transfer between gas and solid. Heat transfer between two phases is complicated to simulate. To solve this process, the resolution near the wall should be fine enough, which will result in a prohibitively high computation cost. Therefore, no solid computation domain exists in the model.

Packed arrangement

To create the geometry, the first step is to select a proper packed arrangement. For regular packing, the packed arrangements are determined by three basic types of sphere cluster. According to the spatial structure of each sphere cluster, they are named tetra-based arrangement, hexa-based arrangement, and octo-based arrangement respectively.

Hexa-based arrangement. A hexa-based sphere cluster is formed by eight spheres with centres at the apexes of a cube, shown in Figure 1. Arrangement, constructed by this element structure, has a very simple structure and can be easily created. As can be seen in Figure 1, particles are piled up linearly. But it's also obvious that, channelling problem tends to occur with this geometry, which can lead to a non-representative flow pattern. The void fraction of this arrangement is about 0.48.

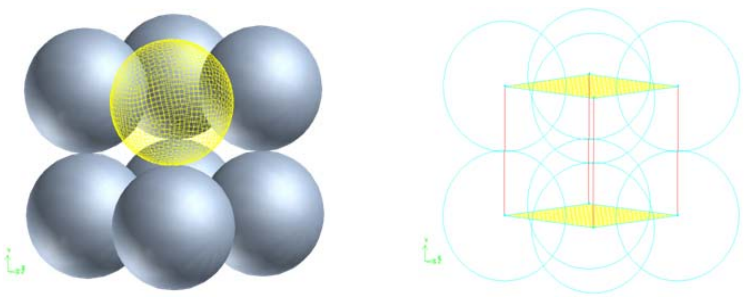

Figure 1. A single hexa-based sphere cluster

Octa-based arrangement. Figure 2 depicts an octa-based sphere cluster, which is constituted by six spheres with centres at the apexes of an octahedron. This arrangement has the same void fraction as the hexa-based structure, about 0.48. Comparing with the octa-space configuration, this structure is relatively complicated and more sensible for modelling. But channelling problem cannot be avoided taking place completely if gas flows in certain directions, indicated by the arrows in Figure 2. For normal shaft kilns, as being known, there is cooling air flowing axially from the bottom to the top and concurrently radial fuel injections from circumference. Therefore, this packed arrangement is not practicle as well.

Tetra-based arrangement. Apparently, a tetra-based structure consists of four particles with centres at the apexes of a tetrahedron. Figure 3 shows a single tetra-based sphere cluster. Comparing with the other arrangements, this configuration is more spatially stable and compact. Besides, channelling problem can be prevented by properly stacking the clusters, which gives this arrangement a big advantage. However, the densely structure also leads to a low void fraction, say, about 0.26 [11]. Given that that the normal porosity of the packed material in shaft kilns is around 0.4, the particle is shrunk to a certain extent to get a bigger void fraction. Consequently, there are no real "contacts" between particles in the model, and of course this will influence the flow pattern somewhat especially on the heat transfer mechanism. When heat transfer is considered in modelling, the geometrical arrangement should be carefully designed.

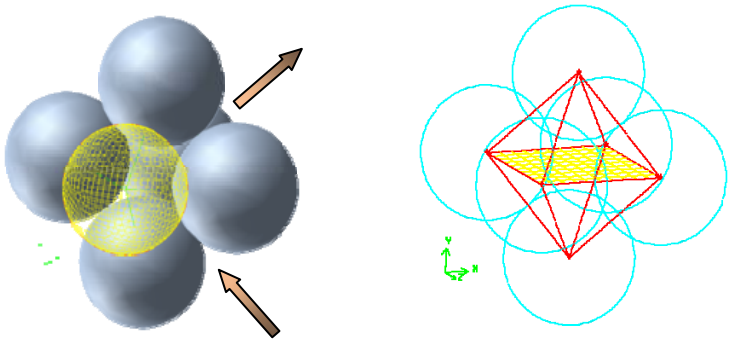

Figure 2. A single hexa-spaced sphere cluster

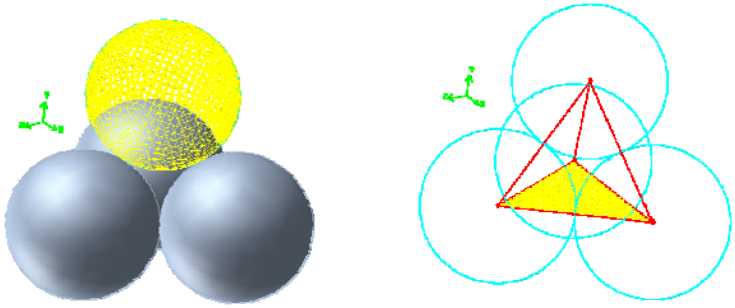

Figure 3. A single tetra-based sphere cluster

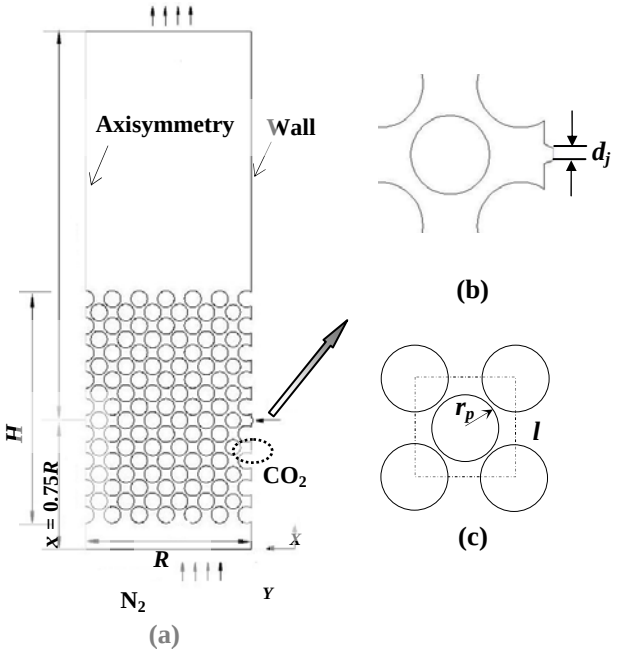

Figure 4. 2-D simulation geometry: (a) schematic of the geometry, (b) close view of the slot injector, (c) packed arrangement

Particle loading height

As mentioned in the introduction, the calcining zone is where engineers are interested in. To visualize the flow fields in this region is therefore the primary aim of CFD simulation. But one very important question in modelling is what the loading height (*H*) is needed to obtain results that are representative. In the industry, the shaft kiln can be up to 30 meters high. The tremendous number of particles will definitely make the computation prohibitive. In order to gain the effect of loading height on the behaviour of the fuel injector, simulations based on 2-D models were performed. Figure 4 shows the geometry, which consists of a half perpendicular plane of a packed tube (R=1.0 *m*), subtracted by circles corresponding to packed particles (d_p=100 *mm*), and inlets of N_2 and CO_2 corresponding to the cooling flow and fuel jet flow respectively. The particle loading height was created to 1.5 *m* and 4 *m* for study.

Figure 5 and Figure 6 show the temperature contours and mass fraction of CO_2 along the cross-section at x=0.75 *m* within the two packed tube. As can be noted, there is no obvious difference between the two cases, which indicates that the behaviour of the jet flow is independent of the loading height. Chukin et al. [12] once experimentally studied the effect of bed height on the gas distribution in a packed bed with jet flow from the bottom. After fifty experiments being performed, a conclusion was drawn that, after the gas jet finished expanding into the bed, increases or decreases of bed would not affect the gas-flow distribution within it.

The experimental data also showed that stabilization in the gas-flow distribution over the bed cross section began even at a height of ~15 *mm*. In other words, the height for jet expanding is about three to four layers in terms of the particle size (d_p=4.6-6.0 *mm*). As can be seen in Figure 5, the expansion of the CO_2 jet is diminishing after through 4 layers, which is in well agreement with the experiment. In contrast with jet from bottom, however, for the cases with circumferential jets the stabilization height depends on the injector-to-particle diameter ratio as well. Apparently, if the ratio is much great than 1, the results will be definitely not validate. Therefore, 4 layers up the burner system are assumed to be enough for modelling when the main focus is on the fuel injection zone and the burner-to-particle diameter ratio is around or less than 1.

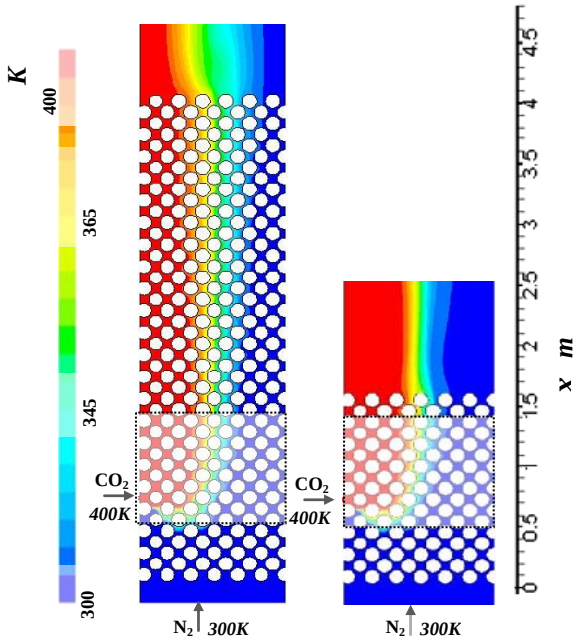

Figure 5. Temperature contours comparison V_{CO_2}/V_{N_2}= 4, v_{N_2}=0.5 *m/s*

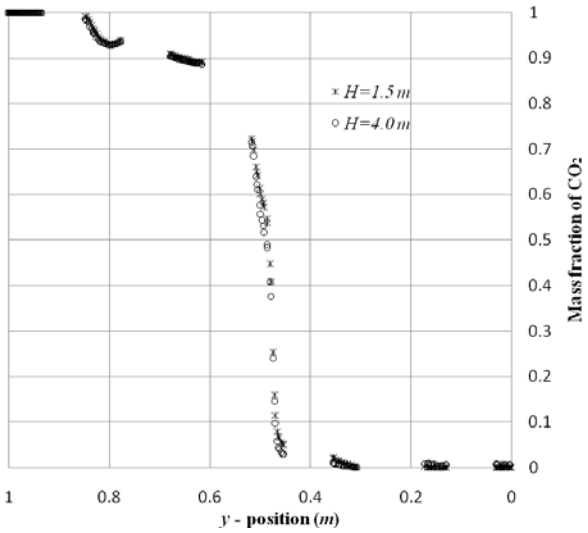

Figure 6. Mass fraction of CO_2 along the cross-section at *x*=0.75 *m*

Wall segment strategy

According to the study presented above, the height of the model can be reduced dramatically. Even with a low height, however, the particle number is still huge if the full cross-section of a kiln is to be modelled. Fortunately, shaft kilns usually have many burners which divided it into several periodic sections. Therefore the geometric model can be further reduced to a small wall segment by taking advantage of the flow symmetry. This strategy (WS model) has been widely used for CFD flow simulation of packed bed [13-15].

A shaft kiln with 12 circumferential burners is depicted in Figure 7, in which planes 1 through 4 indicate two sorts of symmetric or periodic faces. Figure 8 shows one of the 30° WS model for CFD simulation. The wall is subtracted by particles to avoid near-wall effect in this stage.

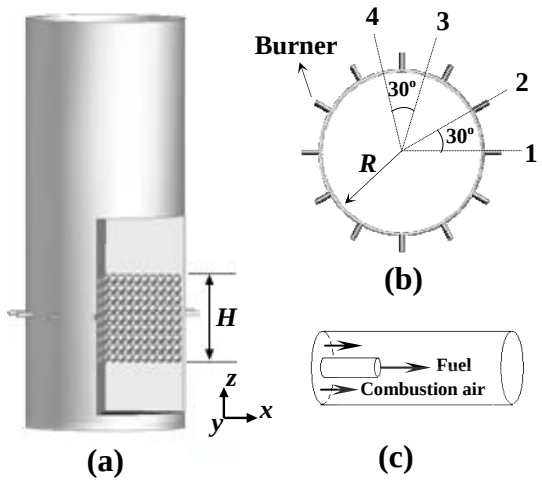

Figure 7. A scheme of shaft kiln (calcining zone): (a) front view, (b) top view, (c) close-up of burner

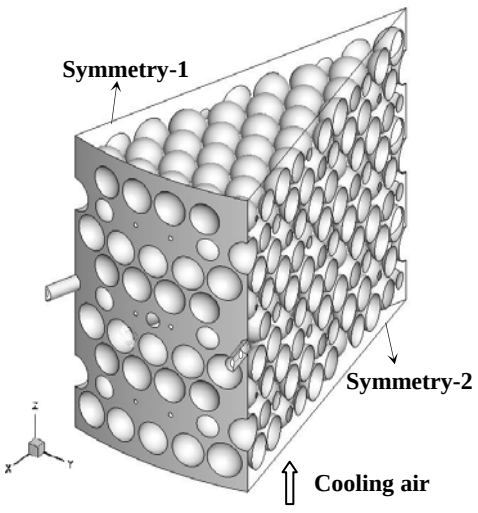

Figure 8. A WS model for simulation

Mesh design

Mesh is another essential parameter in CFD modelling. Theoretically, finer the mesh size, more accurate the solution is. However, it can lead to extremely high computational requirements as well. Therefore, a compromise has to be with respect to accuracy and computation cost. A graded mesh was created after the grid independence study. The mesh was designed with special attention paid on the small gaps between particles. Figure 9 shows the non-uniform surface mesh on the spheres. As can be noted, grid is finer in the small gaps and becomes coarser in the larger void area. The resulting mesh contains totally about 3,104,000 cells.

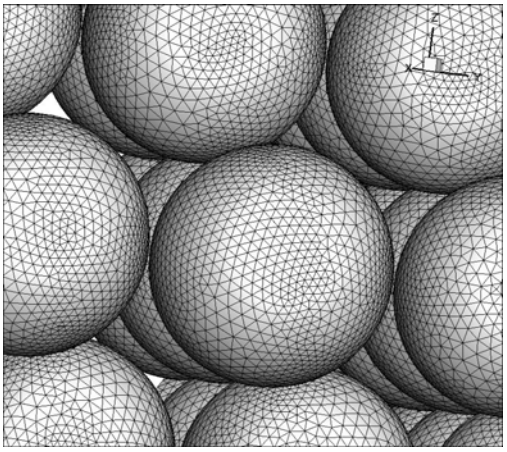

Figure 9. Graded mesh design on the surface of particles

CFD SIMULATION

In this section, some simulations and results based on the developed geometric model will be presented. So far, however, the simulations were carried out just to test the application of CFD approach on flow modelling of shaft kilns while with no intention to compute a real case. Thus the operating parameters defined in the simulation did not follow the industry production conditions.

Models and boundary conditions

The fluid was taken to be incompressible flow. The standard k-ε turbulence model and species transport model were employed to calculate combustion with methane and air as the fuel and oxidant. First-order upwind schemes were selected to compute the field variables. The pressure-velocity coupling algorithm was the SIMPLE scheme. Some geometric details and boundary conditions are listed in Table 1.

Table 1
Geometry dimension and boundary conditions

Inlet	D_h (m)	Velocity (m/s)	Temperature (K)
Fuel	0.02	60	315
Combustion air	0.04	40	315
Cooling air	2.0	0.34	600

In the table, D_h is hydraulic diameter and velocity is superficial velocity.

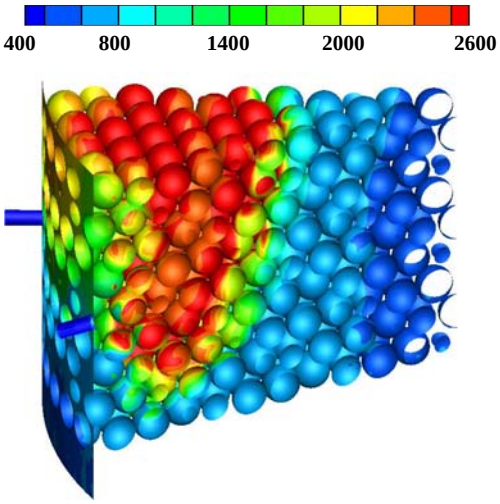

Figure 10. Temperature contours on the particles surface with combustion

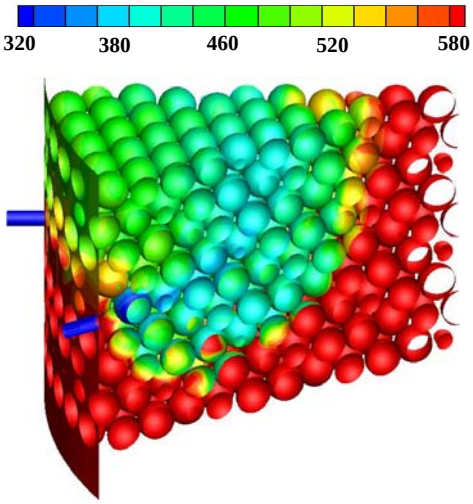

Figure 11. Temperature contours on the particles surface without combustion

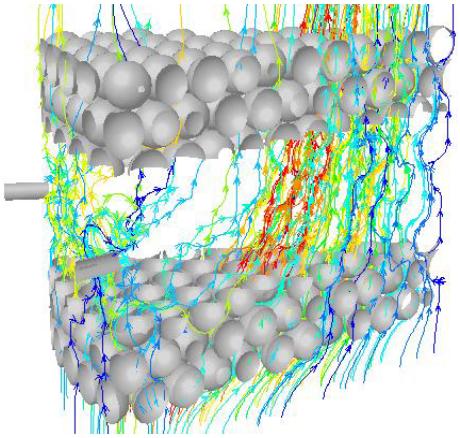

Figure 12. Path lines from the cooling-air inlet with combustion

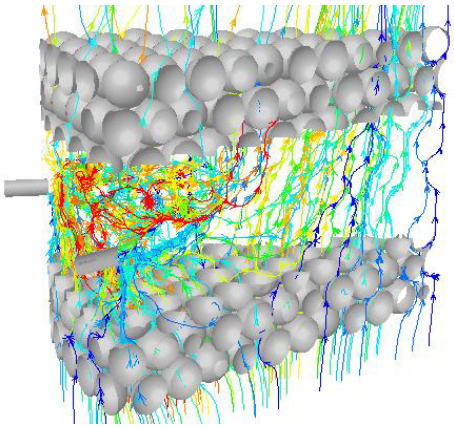

Figure 13. Path lines from the cooling-air inlet without combustion

Simulation results and postprocessing

Simulations were carried out initially to check the effect of combustion modelling on the computational time demand and the radial gas distribution. In one case, the gaseous fuel was ignited successfully by patching a high temperature, whereas in the other, simulation was performed with "cold-flow" (without reactions).

The results are presented in the form of temperature contour and path line plots to illustrate the qualitative features of temperature distribution and insight of the flow pattern, shown in Figure 10 to Figure 13. As expected, combustion modelling takes more iteration to obtain a converged solution due to the strong impact of the reaction on the flow pattern. Surprisingly, however, combustion does not improve the radial mixing. On the contrary, the mixing is worse in the combustion case. The explanation is beyond the present work. However, all the observations discussed above demonstrate that CFD modelling can provide highly detailed information on the in-kiln phenomena. The challenge for the future is to improve the model, including the shape of particles, the structure of packing and correspondingly the mesh design etc., to gain the knowledge that is accurate enough for design purposes.

SUMMARY

A scalable 3-D geometric model for simulating the flow in a shaft kiln has been developed in this paper. The model is reduced by taking advantage of the flow symmetry and the independence of jet behaviour on the loading height. This makes a great contribution to decrease the computational cost, and thereby the model can be scaled up for larger shaft kilns. To develop other packed arrangement, even a random structure, is the logically expansion of the present work. With verification and model improvement, computational fluid dynamics is expected to be a useful design tool for industrial shaft kilns.

REFERENCES

1. Unaspekov, B. A., and Strekalova, L. V., A Model Study of the Performance of a Kazogneupor Shaft Kiln, Refractories and Industrial Ceramics, Vol. 43, No. 7-8, pp 275-276, 2002.
2. Bes, A. , PhD Thesis, Univeristy of Magdeburg, Germany, 2006.
3. Yi, Z., Zhou, J., and Chen, H., Numerical Simulation of Thermal Process and Energy Saving of Lime Furnace, Journal of Central South University of Technology, Vol. 12, No. 3, pp 295-299, 2005.
4. Verma, C.L., Simulation of Lime Shaft Kilns Using Mathematical Modelling, Zement-Kalk-Gips 12, pp 576-582, 1990.
5. Yuan, A., The Optimization Research of Thermal Process in Lime Kiln, Metallurgical Energy, Vol. 18, No. 2, pp 34–38, 1999.
6. Salari, D., Niaei, A., and Nabavi, S. R., CFD Flow and Heat Transfer Simulation for Empty and Packed Fixed Bed Reactor in Catalytic Cracking of Naphtha, Proceedings of World Academy of Science, Engineering and Technology, Vol. 23, pp 67-70, 2007.
7. Smith, B., and Ranade, J., Computational Fluid Dynamics for Designing Process Equipment: Expectations, Current Status, and Path Forward. Ind. Eng. Chem. Res., Vol. 42, pp 1115-1128, 2003.
8. Dixon, A. G., and Nijemeisland, M., CFD As a Design Tool for Fixed-bed Reactors. Ind. Eng. Chem. Res., Vol. 40, pp 5246-5254, 2001.
9. Nijemeisland, M., Dixon, A.G., Comparison of CFD Simulations to Experiment for Convective Heat Transfer in a Gas-solid Fixed Bed, Chemical Engineering Journal, Vol. 82, pp. 231-246, 2001.
10. Nijemeisland, M., and Dixon, A.G., CFD Study of Fluid Flow and Wall Heat Transfer in a Fixed Bed of Sphperes, AIChE Journal, Vol. 50, No. 5, pp. 906-920, 2004.
11. Hendricks, R. C., Athavale, M. M., Lattime, S. B., and Braun, M. J., Virtual and Experimental Visualization of Flows in Packed Beds of Spheres Simulating Porous Media Flows, NASA/TM-207926, 1998.
12. Chukin V. V., and Kuznetsov R. F., Gas Distribution in a Packed Bed, Journal of Engineering Physics, Vol. 13, No. 1, pp 74-78, 1967.
13. Suekane, T., Yokouchi, Y., and Hirai, S., Inertial Flow Structures in a Simple-packed Bed of Spheres", Fluid Mechanics and Transport Phenomena, Vol. 49, No. 1, pp 10-17, 2003.
14. Kloeker, M., Kenig, E. Y., and Egorov, Y., CFD-based Study on Hydrodynamics and Mass Transfer in Fixed Catalyst Beds, Chem. Eng. Technol. Vol. 28, No. 1, pp. 31-36, 2005.
15. Taskin, M. E., Dixon, A. G., Stitt, E.H., and Nijemeisland, M., Approximation of Reaction Heat Effects in Cylindrical Catalyst Particles with Internal Voids Using CFD, International Journal of Chemical Reactor Engineering, Vol. 5, pp 1-15, 2007.

COMBINED EXPERIMENTAL AND NUMERICAL CHARACTERIZATION OF HEAT TRANSFER IN HERMETIC RECIPROCATING COMPRESSORS

T. Dutra, C. J. Deschamps*
Federal University of Santa Catarina, Florianopolis, Brazil

ABSTRACT. A combined experimental and numerical study is developed to characterize heat transfer in the shell of a hermetic reciprocating compressor adopted for household refrigeration, under actual operating conditions. For the first time, measurements of heat flux are carried out in several regions of the shell surface and validated through energy balances and numerical simulation. The results indicate the effect of lubricating oil as an agent in the heat transfer process. Additionally, local heat transfer coefficients inside the compressor are seen to be virtually not affected by the condensing and evaporating temperatures, which is a convenient aspect for numerical modelling.

Keywords: *heat flux measurement, hermetic compressor, heat transfer modelling.*

INTRODUCTION

In reciprocating compressors adopted for household refrigeration, great part of the energy used to compress the gas is converted into heat. If such an amount of heat is not sufficiently removed from the compressor internal ambient, its thermodynamic efficiency is greatly affected by gas superheating associated with heat transfer in the suction system. Heat transfer that takes place throughout the suction system walls is a function of gas temperature inside the compressor shell, which is a result of heat dissipated by heat sources, such as the compression chamber.

According to [1], gas superheating corresponds to 49% of the overall thermodynamic loss in small reciprocating compressors. Several attempts have been directed to provide a better understanding of heat transfer inside the compressor and, as a consequence, alternatives to reduce superheating. However, thermal analysis of compressors is a difficult task due to its geometric complexity, which does not allow simple modeling approaches. Moreover, the oil inside the compressor acts as a lubricating agent for bearings and also as a mean to directly transfer heat from the compressor kit to the shell. In order to find alternatives to reduce superheating losses, it is of fundamental importance the understanding of all relevant heat transfer phenomena acting on the gas during its path from the suction line up to the compression chamber.

A number of numerical models have been proposed in the literature to predict heat transfer in reciprocating compressors. Some of these models [2-3] are based on integral formulations, in which mass and energy balances are applied to a number control volumes specified in the compressor domain. The output data is the temperature level in each control volume. Other studies are based on differential formulations for the whole domain, including heat transfer in the compressor components and in the gas, but with a great computational cost [4]. Finally, a third group of methodologies [5, 6] combine integral and differential formulations in the form of a hybrid model.

* Corresponding author: Prof. C. J. Deschamps
Phone: + (55)-48-32345166, Fax: + (55)-48-32345691
E-mail address: deschamps@polo.ufsc.br

Heat transfer in reciprocating compressors has also been experimentally investigated [7, 8]. In such works, thermocouples are usually employed to measure the gas temperature in positions strategically chosen so as to evaluate heat transfer in different components through energy balances. However, thermocouples are not suitable when a more detailed analysis is required, such as the local characterization of heat exchange between the gas and surfaces.

This paper is concerned with an experimental investigation aimed at characterizing heat transfer in a small reciprocating compressor under actual operating conditions. Measurements are carried out in several regions of the compressor shell and validated by means of results from energy balances and numerical simulations. Additionally, data for heat flux and temperature are combined to obtain local heat transfer coefficients in some positions of the shell.

EXPERIMENTAL PROCEDURE

The internal and external surfaces of a hermetic reciprocating compressor shell were instrumented with heat flux sensors (HFS) and thermocouples. The internal surface was divided into eleven regions, whereas ten regions were used for the external surface, as can be seen on Figure 1. Each region was characterized by one HFS, with the exception of regions *i2* and *i3*, where two sensors were adopted instead. On the other hand, heat flux at the external regions *e6* and *e7* were evaluated from an analytical solution available for fins [9]. Most HFS's employed in the present work are provided with a thermocouple to measure also its surface temperature, with the exception of a different type of HFS needed at region *i11*.

A HFS is built from thermocouples in a serial association. The voltage output of a thermopile, E, is a function of the thermoelectric sensitivity of the materials, S_T, the number of thermocouple junctions, N, and the temperature difference between the HFS surfaces, ΔT, i.e. $E = N S_T \Delta T$. On the other hand, the one-dimensional steady-state heat flux perpendicular to the HFS surfaces, q'', depends on the HFS thermal conductivity, k, the HFS thickness, t, and the temperature difference between its surfaces ($q'' = k \Delta T / t$). Thus, by combining the aforementioned equations, one obtains a linear relation between heat flux and the voltage output ($q'' = E / S$), where S ($= N S_T t / k$) is the sensitivity of the HFS. The value of S is usually provided by the sensor manufacturer, but can also be obtained from a calibration procedure. In this study, some HFS's were calibrated and no difference higher than 10% was observed in relation to the values of S specified by the manufacturer. For this reason, the latter were considered in the measurements.

The instrumentation of HFS's on the internal surface of a compressor shell is not a simple task, due to the high temperature levels inside the compressor and the presence of lubricating oil. To circumvent such difficulties, an epoxy-adhesive was adopted to attach the HFS to the surfaces. Moreover, their wires were carefully positioned inside the compressor, as illustrated in Figure 2(a), so as to minimize changes in the lubricating oil flow path. This is a very important aspect, because the lubricating oil affects the heat transfer process inside the compressor. Figure 2(b) presents a three-dimensional schematic view of the compressor, with the identification of some of its main components, including an oil pump. As can be seen, the oil is stored at the carter in the lower region of the compressor shell and taken to the upper parts by centrifugal action of an oil pump.

Several thermocouples were also instrumented in the compressor internal ambient, in order to establish a suitable reference temperature, T_∞, to estimates the local heat transfer coefficient, h, in each region, i.e.:

$$h = \frac{q''}{T_S - T_\infty} \tag{1}$$

where T_S is the sensor surface temperature. It should be mentioned that in most regions inside the compressor there is a thin film of oil covering the surface, as illustrated in Figure 3. Therefore, since the reference temperature, T_∞, is measured in the gas, the heat transfer coefficient h should be in fact regarded as a global heat transfer coefficient. For the shell external surface there is no such an issue and the usual interpretation for the heat transfer coefficient holds.

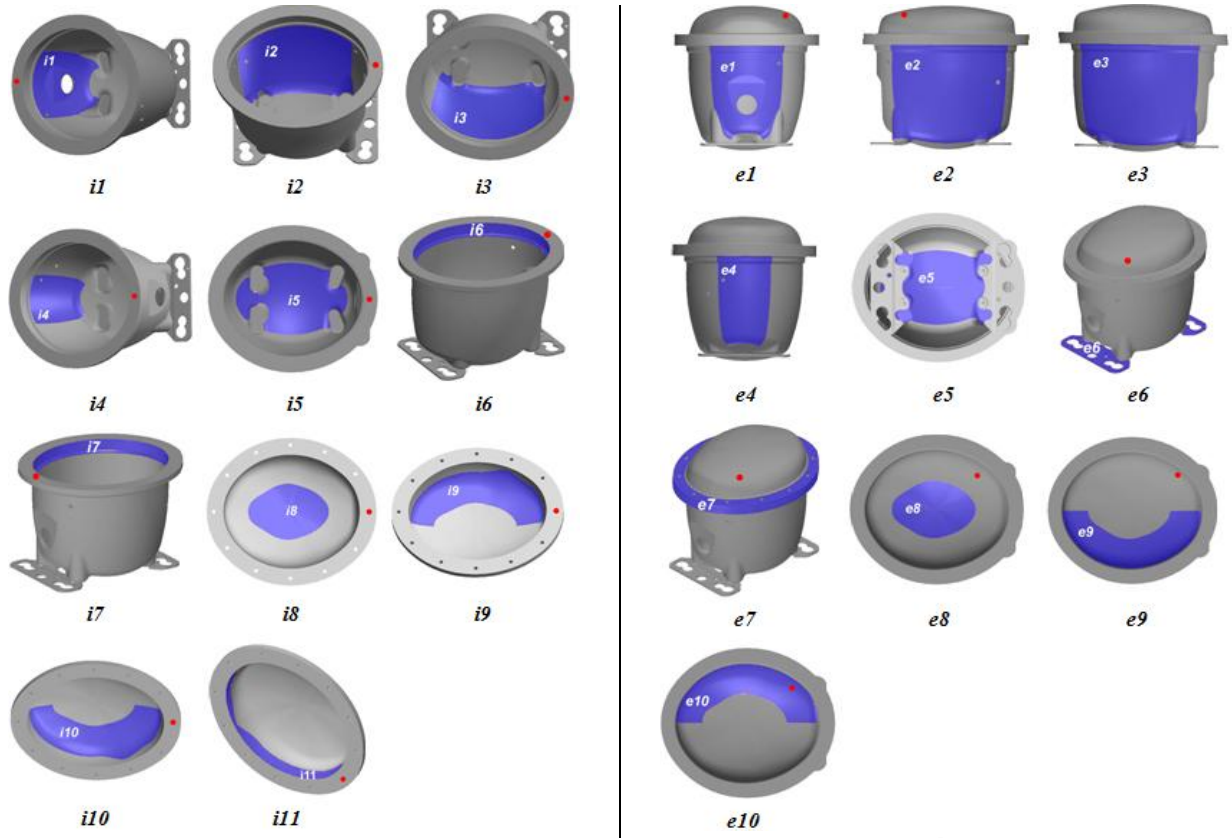

(a) (b)

Figure 1. Regions for measurements in the compressor shell: (a) internal surface; (b) external surface.

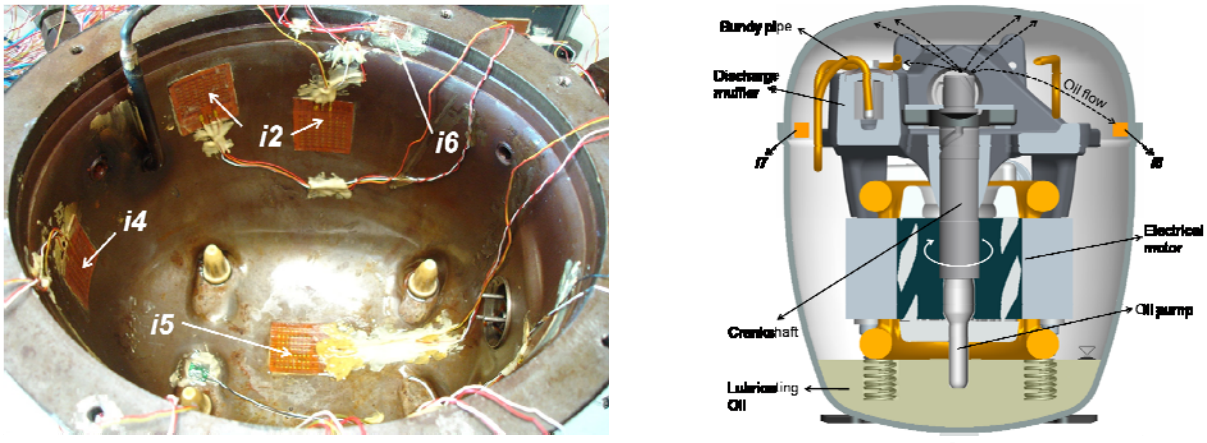

(a) (b)

Figure 2. (a) HFS's installed on the shell internal surface; (b) Compressor schematic view.

RESULTS AND DISCUSSIONS

A reciprocating compressor operating with R134a was selected for the analysis, being submitted to two operating conditions, represented by two pairs of evaporation and condensation temperatures: (-23.3ºC/40.5ºC) and (-10.0ºC/90.0ºC). All tests were conducted in a calorimeter facility following refrigerating conditions established by standards. The uncertainties associated with measurements taken with the calorimeter are $\pm$ 2% for mass flow rate and power consumption. Further details of the experimental facility can be found in [9]. The compressor was tested five times for each operating condition. Results for heat flux, temperature and heat transfer coefficient are presented with an uncertainty bar corresponding to a 95% confidence limit.

Validation of experimental results

The heat transfer rate rejected through the compressor shell, $\dot{Q}_C$, can be evaluated by summing up the contributions of local heat flux measured in each of the regions depicted in Figure 1. Hence,

$$\dot{Q}_C = \sum_{i=1}^{n} q''_i \, A_i \tag{2}$$

where q''_i is the local heat flux on the *i*-nth region of the shell surface with an area equal to A_i. Values of A_i needed in equation (2) are obtained from a CAD model.

The heat rejected through the compressor shell, $\dot{Q}_C$, can also be obtained from an energy balance applied to the compressor itself:

$$\dot{W}_C = \dot{m}\left(h_{DIS} - h_{SUC}\right) + \dot{Q}_C \tag{3}$$

where $\dot{W}_C$ is the compressor power consumption, $\dot{m}$ is the refrigerant mass flow rate and h_{SUC} and h_{DIS} are the refrigerant specific enthalpies at suction and discharge lines, respectively. The power consumption is measured with a power meter and the specific enthalpies are determined from measurements of temperature and pressure at suction and discharge lines. As Figure 4 shows, there is a satisfactory agreement between results for $\dot{Q}_C$ obtained from measurements, equation (2), and from the energy balance, equation (3). The larger deviation occurs for the value measured at external surface, which is approximately 15% higher than that returned from the energy balance.

It should be mentioned a number of uncertainty sources in the measurements, associated with the following aspects: i) accuracy of the heat flux sensor; ii) compressor instrumentation process; iii) contribution of thermal radiation; iv) selection of representative regions to quantify the total heat transfer rate through equation (2). As far as the heat flux sensor is concerned, the manufacturer specifies an accuracy of 5%. On the other hand, random errors associated with instrumentation were treated by repeating five times each test condition and then applying a 95% confidence limit to the average value. Thermal radiation is also an issue since there is a difficulty to characterize the emissivity of surfaces, especially inside the compressor where oil is present on almost all surfaces. Yet, for the external surface, infrared thermography was combined with thermocouples to quantify the emissivity. Finally, the number of regions in which HFS are assembled must enough to properly discretize the heat transfer that takes place on both surfaces of the compressor shell, as given by equation (2). Therefore, for the purpose of energy balance, measurement of heat transfer is not a trivial task since one should have information about the thermal field before installing the heat flux sensors. Naturally, if the aim is to obtain only local values for heat transfer, then this issue is not relevant. Considering all the aforementioned difficulties, the level of agreement between estimates for $\dot{Q}_C$ obtained from equations (2) and (3) are considered acceptable.

Local heat transfer analysis

Figures 5 and 6 show experimental results prepared to analyse the heat transfer process at the internal surface of the compressor shell. From Figure 5, one can clearly notice the presence of high flux rates at the border of the shell cover (*i9*, *i10*, *i11*) and region *i6*. This is so for regions *i9*, *i10* and *i11* because, after leaving the pump, the oil hits against the cover surface, forming an impinging jet in the form of volute that enhances heat transfer there. Moreover, heat transfer is increased in region *i6* by oil spatter, which is much more intense than in the opposite side *i7*. Figure 2(b) provides a schematic view of the oil spatter that takes place in the upper region of the compressor. As can be seen, some components inside the compressor, such as the discharge muffler and the bundy pipe, act as baffles, avoiding oil spatters on region *i7* with the same intensity as it occurs on *i6*.

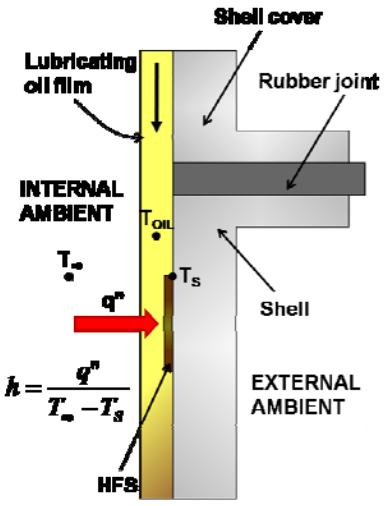

Figure 3. Lubricating oil film on the shell internal surface.

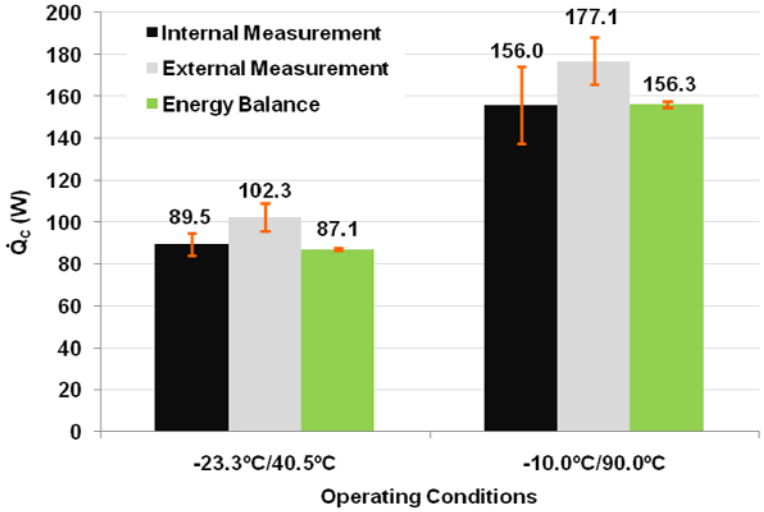

Figure 4. Compressor heat transfer rate at different operating conditions.

Figure 5(b) shows high values of heat transfer coefficients on surfaces *i9*, *i10* and *i6*, confirming the previously explained effect of the oil. For region *i11*, the heat transfer coefficient was not evaluated because, as already mentioned, the HFS installed there had no capability for temperature measurement. The results show that when the compressor operating condition is changed from -23.3ºC/40.5ºC to -10.0ºC/90.0ºC, there is an increase in the levels of heat transfer and temperature, although heat transfer coefficients remain almost constant. Therefore, such an increase in heat transfer can be attributed mainly to a shift in the compressor thermal profile, as one can verify by comparing Figures 6(a) and 6(b).

Turning the attention to the external surface, Figure 7 indicates a high intensity heat flux at regions *e2*, *e4*, *e5* and *e9*, mainly associated with higher heat transfer coefficients, as shown in Figure 8. Such regions belong to the compressor side that was exposed to the air flow stream from a fan installed inside the compartment in which the compressor is tested. The adoption of such a fan is a requirement of standards for compressor testing, which specifies that levels of temperature and air velocity inside the compartment must be controlled.

Although it is observed significant differences between local heat fluxes on the external and internal surfaces, heat flux levels on external surface are also increased when condition -23.3ºC/40.5ºC is changed to -10.0ºC/90.0ºC. This increase in the heat flux level is related to a temperature profile shift

on the external surface, as also verified for the internal surface, and for this reason the heat transfer coefficient virtually does not change.

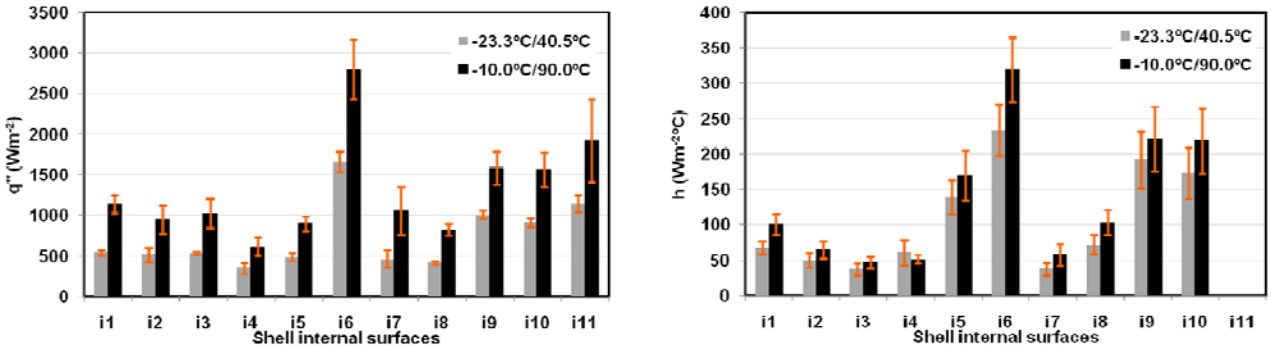

(a) (b)

Figure 5. Measurements at the shell internal surface: (a) heat flux; (b) heat transfer coefficients.

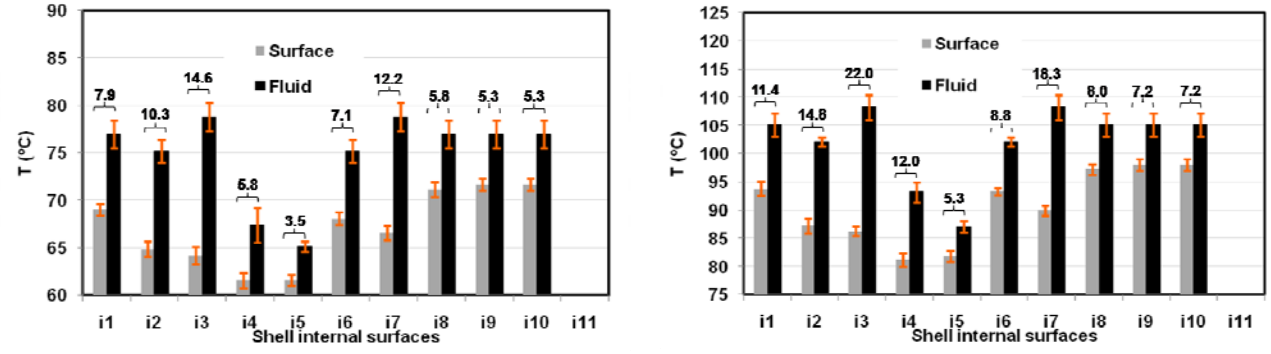

(a) (b)

Figure 6. Difference between the temperatures in the fluid and on shell internal surfaces: (a) -23.3ºC/40.5ºC; (b) -10.0ºC/90.0ºC.

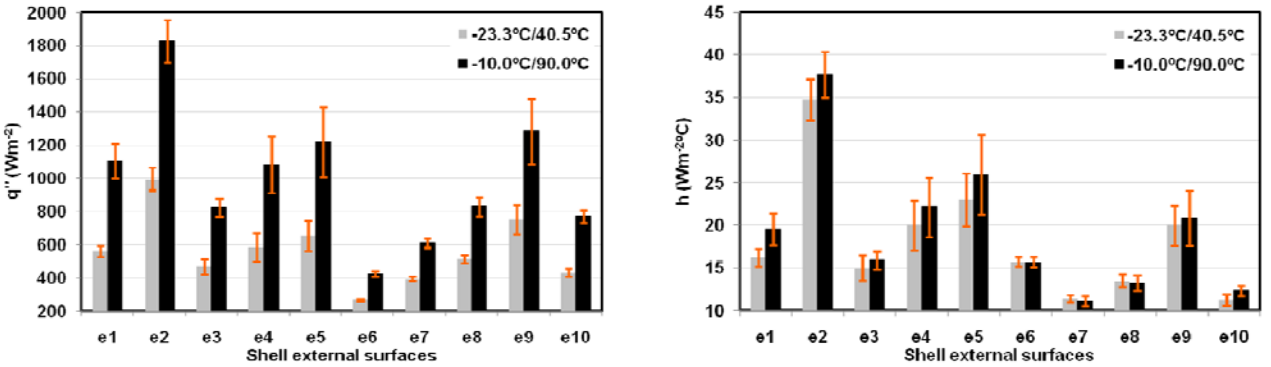

(a) (b)

Figure 7. Measurements at the shell external surface: (a) heat flux; (b) heat transfer coefficients.

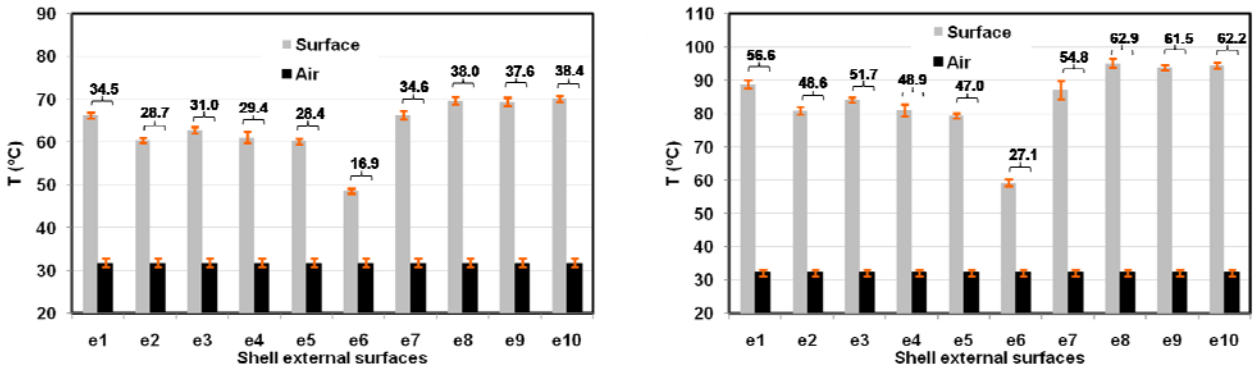

(a) (b)

Figure 8. Difference between the temperatures in the air and on shell external surfaces: (a) -23.3ºC/40.5ºC; (b) -10.0ºC/90.0ºC.

Numerical simulation

Heat conduction in the compressor shell was simulated with the commercial code FLUENT 6.3 [10], which adopts a finite volume methodology to discretize the governing equations. Boundary conditions of local convective heat transfer coefficient and ambient temperature were prescribed for both the internal and external surfaces, with reference to the experimental data. The three-dimensional geometry of the compressor shell was prepared and made available from CAD software. Two computational grids were tested for assessment of truncation errors, one with 1.3 x 10^6 and other with 2.7 x 10^6 volumes. Results for temperature [ºC] obtained with each grid were in an agreement within 1% in the whole domain and, therefore, the numerical solution was considered to be representative of the heat conduction equation.

Figure 9 shows a comparison between results for temperature field on the external surface of the compressor shell provided by the numerical prediction and measured with infrared thermography combined with thermocouples. Good agreement is seen between the experimental and numerical results, with a typical deviation of 2%. The greatest difference was found at the base plate, corresponding to approximately 5%. The level of agreement seen in Figure 9 provides further evidence about the measurement accuracy.

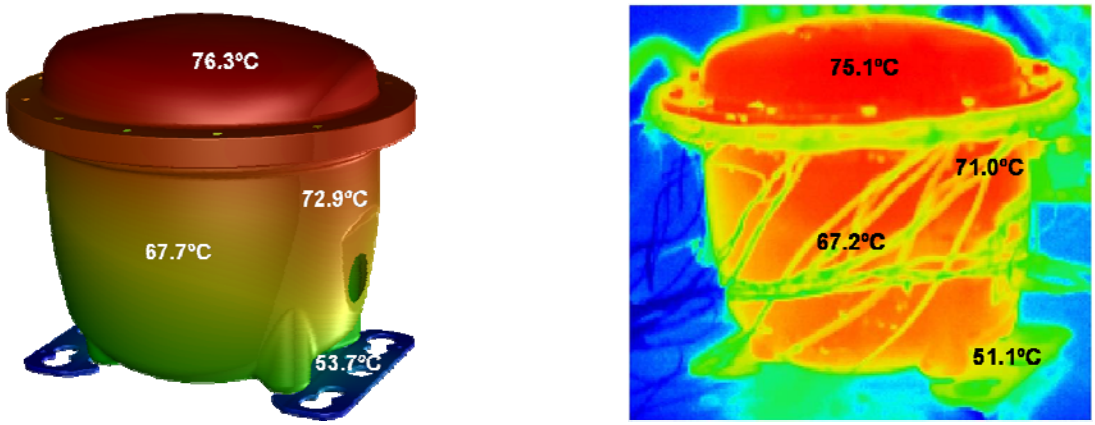

(a) (b)

Figure 9. Temperature field on the compressor shell (a) numerical prediction; (b) measurements.

CONCLUSIONS

An experimental investigation of heat transfer in the shell of a small reciprocating compressor has been reported. It was identified a number of factors that can negatively affect the measurements. The experimental data were validated with reference to results obtained from energy balances and numerical simulations. Heat flux sensors and thermocouples allowed the characterization of local heat transfer in several regions of the external and internal surfaces. The results showed a great effect of the lubricating oil in the heat transfer process. On the other hand, it was observed that local heat transfer coefficients are insensitive to the compressor operating conditions. This is an interesting aspect that makes it easy to characterize boundary conditions for numerical modelling of heat transfer in compressors. The experimental procedure presented in this paper was not available in the literature and, therefore, represents a valuable contribution for the analysis of superheating in compressors. The work will be extended to include measurements for other components of the compressor, such as suction and discharge mufflers, electrical motor and cylinder.

ACKNOWLEDGEMENTS

This study forms part of a joint technical-scientific program of the Federal University of Santa Catarina and EMBRACO. Support from FINEP (Federal Agency of Research and Projects Financing) and CAPES (Coordination for the Improvement of High Level Personnel) is also acknowledged.

REFERENCES

1. Ribas Jr., F. A., Deschamps, C. J., Fagotti, F., Morriesen, A., Dutra, T., Thermal Analysis of Reciprocating Compressors - A Critical Review. *Proc. Int. Compressor Engineering Conf. Purdue*, paper 1306, 2008.
2. Todescat, M. L., Fagotti, F., Prata, A. T., Ferreira, R. T. S., Thermal Energy Analysis in Reciprocating Hermetic Compressors. *Proc. Int. Compressor Engineering Conf. Purdue*, pp. 1419-1428, 1992.
3. Ooi, K. T., Heat Transfer Study of a Hermetic Refrigeration Compressor. *Applied Thermal Engineering*, 23, pp. 1931-1945, 2003.
4. Raja, B., Sekhar, S. J., Lal D. M., Kalanidhi, A. A., Numerical Model for Thermal Mapping in a Hermetically Sealed Reciprocating Refrigerant Compressor. *Int. J. Refrigeration* 26 (6), pp. 229-236, 2003.
5. Almbauer, R. A., Burgstaller, A., Abidin, Z., Nagy, D., 3-Dimensional Simulation for Obtaining the Heat Transfer Correlations of a Thermal Network Calculation for a Hermetic Reciprocating Compressor. *Proc. Int. Compressor Engineering Conf. at Purdue*, paper C079, 2006.
6. Ribas Jr, F. A., Thermal Analysis of Reciprocating Compressors. *Int. Conf. on Compressors and Their Systems*, London, pp. 277-287, 2007.
7. Meyer, W. A., Thompson, H. D., An Experimental Investigation into Heat Transfer to the Suction Gas in a Low-Side Hermetic Refrigeration Compressor. *Proc. Int. Compressor Engineering Conf. Purdue*, pp. 908-916, 1990.
8. Kim, S. H., Sim, Y. H., Youn, Y., Min, M. K., An Experimental Study on Internal Temperature Distribution and Performance Characteristics in a Reciprocating Compressor for a Domestic Refrigerator. *Proc. Int. Compressor Engineering Conf. Purdue* (1), pp. 245-252, 2000.
9. Dutra, T., Experimental Investigation of the Heat Transfer in Reciprocating Compressors Adopted for Household Refrigeration. *M.Sc. Thesis,* PPGEM, Federal University of Santa Catarina, 2008.
10. ANSYS, Inc. *FLUENT user's guide*, v. 6.2.16, Lebanon/NH, USA, 2006.

A MULTISCALE APPROACH FOR THIN-FILM SLUG FLOW

A. Carlson[*1], D. Lakehal[2] AND P. Kudinov[3]
[1] Linnè flow center, Department of Mechanics,
The Royal Institute of Technology, Stockholm, Sweeden
[2] ASCOMP GmbH, Zürich, Switzerland
[3] Division of Nuclear Power Safety,
The Royal Institute of Technology, Stockholm, Sweeden

ABSTRACT. A multiscale modeling approach is presented for multiphase flow phenomena featuring a thin-film bounding two phases. A Micro Scale Solver predicts the thin film dynamics, influenced by an antagonistic Van der Waals force and a stabilizing repulsive force, which is mapped onto a Macro Scale Solver through a multiscale coupling. Numerical experiments of thin-film slug flow in a micro-pipe demonstrate that the key to capture multiscale phenomena lies in the accurate modelling of the microscale parameters. Faitful results are obtained with the multiscale treatment for the modelling of slug flow with a 10.4 nm thin-film, where pure computational multi-fluid dynamics is deficient.
Keywords: *Multiscale coupling, two-phase flow, numerical simulations, Level Set method.*

INTRODUCTION

Typical microfluidics examples involving multiscale phenomena are flows with moving contact lines, boiling, droplet/bubble coalescence and break-up, ect. To accurately capture their physical behaviour it is crucial to describe the interaction between the different, macroscopic and microscopic length scales of these flows. This poses challenges on theoreticians as well as modellers since these phenomena are not often based on one theoretical framework. Molecular dynamics (MD) theory could capture effects on both the macro- and micro-scale, but large-scale molecular dynamics simulations are today not accessible due to excessive computational time. Macroscopic continuum theory does permit large-scale computations, but lack in capturing intermolecular effects at microscale. We propose in the present paper a multiscale modelling approach for multiphase flow phenomena featuring a microscopic thin-film that separates two phases. A multiscale coupling is introduced, linking a microscopic thin-film model including intermolecular forces and a continuum model describing the large-scale multiphase flow motions. The developed multiscale simulation platform is based on two solvers: a Sub-Grid-Scale (SGS) Mirco Scale Solver (MiSS) for the thin-film dynamics, and a Macro Scale Solver (MaSS) for the modelling of the macroscopic multiphase flow characteristics. The models are based on two different theoretical frameworks and are well documented in the literature; namely the Long Wave Theory and the Navier Stokes equations with a Level Set interface tracking formulation. Numerical experiments of thin-film slug flow are presented with the modelling of a 10.4 nm film.

Two-phase slug flow have features that makes it suitable to optimize heat and mass transport in channels and capillaries, and are for these purposes studied here. This flow regime is indeed attractive for numerous applications in biomedical engineering and micro-system technology. Between the interface of the elongated drops or bubbles and the channel surface a thin bounding liquid film is formed, and its existence is the determining factor for controlling the heat and mass transfer in the flow. In cases of high heat flux, of gas-liquid slug flow, a rupture of the thin-film could generate a rapid temperature increase in the solid, referred to as a *dry-out* phenomenon.

* Corresponding author: A. Carlson
E-mail address: andreaca@mech.kth.se

Slug flow in small channels has been subject of investigations since the pioneering work of Bretherton [4] and Taylor [1]. Based on hydrodynamic theory Bretherton related the liquid film thickness (h_b), between the channel surface and the bubble interface, to the Capillary (Ca) number, using $h_b = 0.83 * Ca^{2/3}$. $Ca = (\mu_l U_B)/\sigma$, where μ_l is the film viscosity, U_B is the bubble speed and σ is the surface tension coefficient. The capillary number expresses the relative importance of the surface tension force to the viscous force in the flow. Bretherton's correlation has recently been modified [1], based on the experimental results of Taylor [1], in order to account for a larger range of Ca-number flows. These continuum models seemingly only holds as long as Ca is greater than $\sim 10^{-3}$. For lower Ca numbers, these models fail to correctly estimate the film height. Bretherton pointed out that a disjoining pressure (from non-hydrodynamic forces) could be the cause of deviation from physical observations and the proposed correlation. This is an early evidence of the influence of intermolecular forces on the film in slug flow. The availability of various experimental [4, 15, 17] and numerical investigations [6, 10] on slug flow in small channels, does not give any qualitative information concerning the film height for low Ca-number slug flows. For this flow regime the length scale of the film (h) is well separated from the characteristic length scale (L) of the phenomena, where $h \ll L$. As the film height becomes close to 100nm, the validity of the continuum theory starts to lack a theoretical justification and a molecular dynamics description is needed to adequately describe the physical phenomena.

MODELING FRAMEWORK OF THE MACRO SCALE SOLVER (MaSS)

The interface tracking method

The theoretical framework of the MaSS is based on a single fluid formalism of the Navier Stokes equations for an incompressible interfacial two-phase flow,

$$\nabla \cdot \mathbf{u} = 0, \tag{1}$$

$$\rho(\phi)(\partial_t \mathbf{u} + \mathbf{u} \cdot \nabla \mathbf{u}) = -\nabla p + \nabla \cdot (\mu(\phi)(\nabla \mathbf{u} + (\nabla \mathbf{u})^T) + \delta \mathbf{F}_s, \tag{2}$$

$\delta \mathbf{F}_s = \sigma \mathrm{K} \cdot \mathbf{n} = \sigma \mathrm{K} \cdot \nabla \phi / |\nabla \phi|$ is the surface tension force acting on the interface δ_s with a curvature K and a normal **n**, here using the continuum surface force model by Brackbill et al. [3]. The Level Set method [16] is applied to track the evolution of the interface in time by solving an additional scalar advection equation, defined by

$$\partial_t \phi + \mathbf{u} \cdot \nabla \phi = 0, \tag{3}$$

where ϕ stands for the signed distance function to the interface, where $\phi=0$. The ϕ-function separates the two different phases with $\phi>0$ indicating the liquid phase and $\phi<0$ indicating the gas phase. To avoid distortion of the Level Set function as it is advected in time, a re-initialization procedure is solved in accordance with the method proposed by Sussman et al. [16].

The method as implemented in the CMFD solver TransAT (developed at ASCOMP Gmbh), which is based on the finite volume method and applied as the MaSS, has proven to be successful for many multiphase flow phenomena [6, 10]. Nevertheless, the method can be deficient for other flows, producing unphysical results without a sub-grid-scale multi-physics treatment of thin-films. This alleviate the DNS dilemma, since resolving all relevant length scales would generate a prohibitive computational costs due to the spatial and temporal resolution requirements (Δt, $\Delta x \sim 10^{-9}$).

MODELING FRAMEWORK OF THE MICRO SCALE SOLVER (MiSS)

A mechanistic thin-film model

The mathematical formulation of the MiSS is based on the Long Wave Theory (LWT), which is deduced by an asymptotical reduction of the Navier Stokes equations [14]. The LWT, with the modelling of molecular long- and short-range forces, has shown to correctly describe the microscopic thin-film morphology on a flat plate dominated by intermolecular forces [2]. This recent validation of the theory, through matching experimental results, makes it suitable as a theoretical framework for the Sub-Grid-Scale (SGS) modelling of thin films, influenced by intermolecular forces. In the present

work we confine ourselves to the treatment of relatively "thick" films (>10 nm), where also the LWT is valid. The Knudsen (Kn) number is often applied as measure to distinguish the continuum from the molecular flow field representation, Kn=λ/L. It is defined as the ratio of the molecular length scale (λ) (the mean free path) to the characteristic macroscopic length scale (L). For films larger than 10nm the Kn number regime between continuum mechanics and slip-flow applies, alleviating the need of a no-slip condition at the wall.

The long wave evolution equation describes the spatio-temporal evolution of a thin liquid film on a solid surface under the influence of intermolecular interactions [18]:

$$\mu\partial_t h(z,t) - \frac{1}{3}\partial_x\left[h(z,t)^3\partial_x(\Phi - \sigma\partial_x^2 h(z,t))\right] = 0, \tag{4}$$

representing three different phenomena in play; a pseudo-viscous force μh(z,t), the excess intermolecular force $\partial_x(h(z,t)^3\partial_x(\Phi))$ and the surface tension force $\partial_x(h(z,t)^3\sigma\partial^2{}_x h(z,t))$. The relative magnitude of the different terms controls the dynamics of the film. In Eq. 4 h is the film height, Φ represents the intermolecular interaction, μ and σ are the dynamic viscosity and the surface tension coefficient. The surface tension force acts as a stabilizing force of the film. The influence of the excess intermolecular forces have two contributions the antagonistic attractive Van der Waals force, and a stabilizing repulsive force. A Mie potential [8] is typically introduced in the thin-film equation for the modelling of the intermolecular interaction. The long range attractive Van der Waals potential $A/(12\pi h(z,t)^3)$ is modelled in concordance with Jain and Ruckstein [9]. The short range stabilizing repulsive potential $-B/h(z,t)^4$ is based on the analysis of Oron [13]. This results in a 3-4 intermolecular potential rather than the more frequently used 3-9 potential:

$$V'(h) = \Phi = \frac{A}{12\pi\cdot h(z,t)^3} - \frac{B}{h(z,t)^4}, \tag{5}$$

where A is the Hamaker constant and B is the repulsive forces coefficient. The Hamaker constant is a material property that controls the interaction force acting between two interfaces or an interface and a solid surface. Its sign determines if the Van der Waals interaction acting on the film is either attractive (positive A) or repulsive (negative A). A rigor modelling of the Hamaker constant is still an open question to be solved and beyond the scope of the present work. The application of the 3-4 potential circumvents the need for a transition region between the films large ridges and its stable minimum height in the pseudo-wetting scenario [13]. To ensure a correct order of magnitude of the retarding coefficient B, we use the measured value from Becker et al. [2] in the 4-potential: $B_B=6.3*10^{-76}Jm^6$. Although the materials here differ form the ones in the experiments of Becker et al. [2], the same coefficient in the 4-potential gives $B=nB_B^{3/8}= 8B_B^{3/8}$. n is a numerical parameter introduced in order to obtain a larger transition region for the pseudo wetting between stable flat films and the rupture regime.

The Sub-Grid-Scale (SGS) MiSS is based on the thin-film Eq. 4. Due to the stiff nature of the time dependent partial differential equation with higher order derivatives (4^{th} order), special care needs to be taken in the numerical solution method. The thin-film equation has been solved in MatLab by a finite difference method with a 4^{th} order stencil for the spatial derivatives. A Gear method was applied for the time marching [12], which is known to be optimal for the treatment of stiff problems. The code was validated against previously published results for the thin-film equation with the inclusion of the intermolecular Van der Waals potential (Burelbach et al. [5]).

MULTISCALE COUPLING METHODOLOGY

The application of the multiscale coupling between the MaSS and MiSS is motivated by two factors. First, such a coupling enables us to numerically investigate multi-physics phenomena taking place on different length and time scales, which does not lie in one theoretical framework. The virtue behind the multiscale methodology is the ability to model the microscale tendencies, which are captured, and then mapped onto the macroscale solution. As we will show below, this is the key to correctly capture the

flow of certain multi-physics phenomena. Secondly, the multiscale coupling seeks to obtain a high computational efficiency with the strict requirement that is [7]; *computational cost with a multiscale method << computational cost with pure micro solver*. This is obtained here by decoupling the two solvers in the multiscale coupling approach by exploiting the separation of both temporal and spatial length scales; the MiSS converges toward a steady-state solution, within one MaSS time step. As a result the MaSS is not restricted by the time step applied in the MiSS, $\Delta t_{MiSS} << \Delta t_{MaSS}$. A scheme of the multiscale coupling methodology is shown in Fig. 1. First, we check if the macroscale formulation would fail in the present model for physical phenomena with characteristic length scales less than ~100nm. This is done by checking whether the near wall cell is <200nm. If a multiscale treatment is not needed, which means that Δx_{wall}>200nm and no dry-out, pure macro scale simulations would apply. Should this not be true, a multiscale treatment is needed and some macroscale parameters are transferred from the MaSS to the MiSS. The parameters are the near wall mesh resolution, the unstable wave number, the film viscosity and the surface tension coefficient.

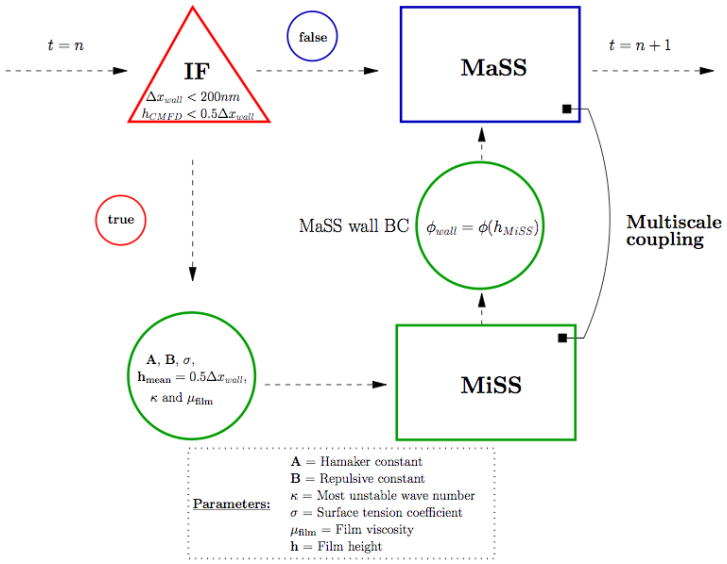

Figure. 1. Schematic description of the multiscale simulation platform.

The main feature with the multiscale coupling methodology is to substantially reduce computation time, without the sacrifice of key physics. For this purpose, MiSS computations are not performed at every time step. The minimum film height is extracted from a thin-film stability map pre-computed with the MiSS, based on variations in the Hamaker constant (all other parameters are kept constant), see Fig. 2. The microscale film height h, is mapped onto the macroscale flow field through a boundary condition applied in the MaSS, $\phi_{wall} = \phi(h_{MiSS})$. This is performed in the computations by the Level Set ϕ function, which locally represents the film height in the wall-normal direction of the near wall cell.

Thin-film stability map based in the Hamaker constant

Fig. 2 shows the thin-film stability map predicted by the MiSS, and is based on the Hamaker constant and the minimum film height. The film has a viscosity μ_s=0.002Pa*s and a surface tension coefficient σ=0.1Nm. Initially, the film has a long-wave disturbance

$$h(z,t) = h_{mean} \cdot (1 + \cos(\kappa^2 z / \pi)), \quad (6)$$

where κ is the most unstable wave number and the fastest growing linear mode [14], and h_{mean} is half of the near wall cell size, h_{mean} =83nm. The thin-film equation is solved in a spatial domain of z= h_{mean} [-π/κ, π/κ], with periodic boundary conditions at the edge of the domain. The thin-film equation is solved in Cartesian coordinates.

The MiSS, depending on the magnitude of the Hamaker constant, predicted three different film regimes. The typical thin-film morphology for these regimes is shown in Fig. 2. For A>9*10^{-19}J the

film is stable and flattens, meaning that the attractive intermolecular forces are not large enough compared with stabilizing (repulsive- and surface tension-) forces. In this case, the film will lubricate the pipe surface. The second pseudo-wetting regime was observed for $9*10^{-19}$J <A< $1.6*10^{-19}$J; see Fig. 2. In the pseudo-wetting scenario, the attractive forces accelerate the film towards the solid surface, and as it approaches its equilibrium minimum film height, the repulsive forces grow and decelerate the film motion. The film finally obtains its equilibrium configuration, with a flat region with the minimum film height that is bounded by large ridges; see centre of Fig. 2. In both the stable and pseudo-wetting regime, a stable minimum film height is obtained.

For the regime A>$1.6*10^{-19}$J, the minimum film height becomes less than 10nm, and the LWT starts to loose its validity. A transition region between thin films that can be described within the LWT and a molecular dynamics theory, is illustrated in Fig. 2 (right part). By further increasing the Hamaker constant, the unstable film rupture regime is reached, which would result in a *dry-out* condition. The right part in Fig. 2 describes the typical film shape as it ruptures. In this scenario, the film accelerates towards the surface due to the strong antagonistic attractive forces. The repulsive and surface tension forces do not manage to stabilize the film, which finally leads to a film rupture. At the point-of-rupture the thin-film equation diverges ($h \rightarrow 0$) and the LWT is no more justifiable, which implies that the exact time of rupture and film shape cannot be extracted with fidelity. Nonetheless, the important resulting micro scale information like: stable minimum film height or film rupture, are extracted from the thin-film stability map and coupled to the macro scale solver through a boundary condition on the pipe surface. For cases where the film ruptures, a contact line would be formed at the solid surface. The treatment and modelling of moving contact lines is assumed to be an important aspect in dry-out conditions; it is although not a subject in the present work.

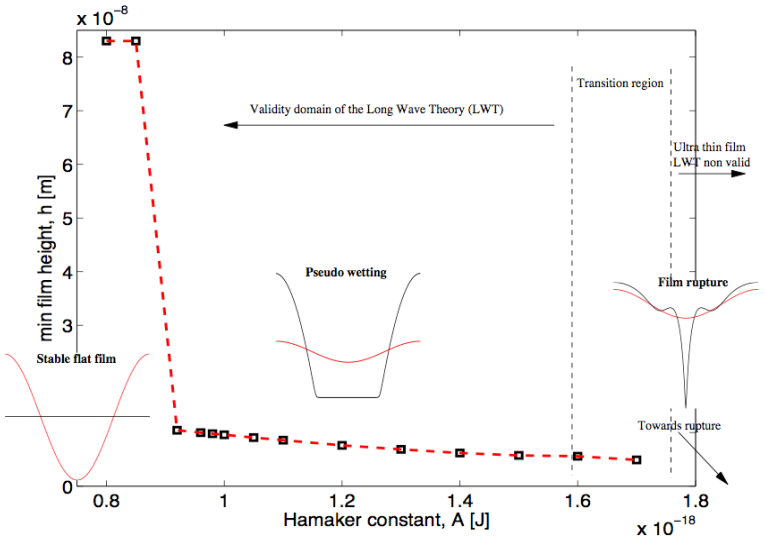

Figure. 2. Thin-film stability map based on Hamaker constant and min film height, $\Phi=A/(12\pi h^3) - B/h^4$.

MULTISCALE SIMULATION PLATFORM

Simulation setup and boundary conditions

Two-dimensional axis-symmetric simulations of a liquid-liquid slug flow in a pipe with D=10μm diameter have been performed. The simulation setup is shown in Fig. 3 with the boundary conditions. The outer annulus is feeding silicone oil with viscosity μ_s=0.002Pa*s and density ρ_s=950kg/m^3, and the small concentric pipe is feeding water with viscosity μ_w=0.001Pa*s and density ρ_w=998kg/m^3. The two phases have a surface tension coefficient of σ=0.1Nm, and with a Hamaker constant A=$9*10^{-19}$J, and a repulsive coefficient B=$8.3*10^{-23}$Jm. The simulations were performed on an equidistant mesh, with 60 cells over the pipe diameter, giving a mesh spacing $\Delta z=\Delta r$=168nm. These parameters give a prediction in the MiSS of a minimum film height of 10.4 nm, so that a thin oil film should sustain

between the pipe surface and the droplets. The inlet velocity for the silicone oil is set to U_s= 0.11m/s and for water U_w = 0.066m/s. We make the assumption that at t=0 the flow is not fully developed and that entrance edge effects can be ignored. Gravitational effects have been neglected in accordance with the limit derived by Bretherton [4]. The convergence criteria were set to 10^{-4}, and a dynamic time stepping scheme has been applied based on the Courant-Friedrich-Leavy (CFL) number with CFL_{max}=0.3 and CFL_{max}=0.1. A monotonic upwind scheme Hybrid Linear/Parabolic Approximation (HLPA) has been applied for the momentum equations with a Weighted Essential Non-Oscillatory (WENO) scheme for the Level Set function. A Strongly Implicit Procedure (SIP) solver [11] by Stone is used to solve the system of linear matrices. A first-order Euler scheme has been applied for the time integration and the pressure-velocity is decoupled with a Semi-Implicit Method for Pressure-Linked Equations (SIMPLE) [11].

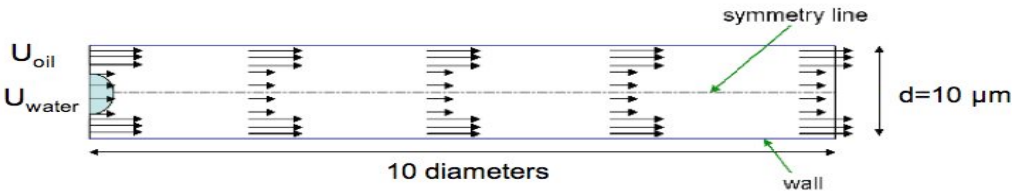

Figure. 3. Simulation setup and boundary conditions.

RESULTS

Comparison between CMFD and Multiscale simulation

The water and oil flow through the two inlets and new interfacial area is formed with the shape of a thumb (Fig. 4). At some point, there is an incipience of an interfacial disturbance that grows in time to finally result in the formation of a droplet. Droplets are in the present simulations generated with a nearly constant frequency. A more thorough description of the droplet formation and propagation can be found in the paper by Lakehal et al. [10].

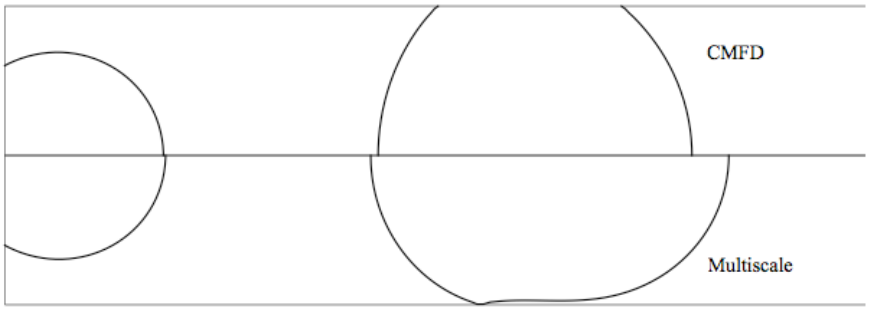

Fig. 4. Comparison of the two-phase flow predicted with pure CMFD (upper) and the multiscale simulation platform (lower), represented by the iso-contour of the zero level set function at t=398 µs.

Fig. 4 shows the multiphase flow characteristics in a section of the pipe that is corresponding to a length of three diameters. The upper subfigure is the prediction from the CMFD simulation and the lower subfigure is the prediction from the multiscale simulation platform. To the left of Fig. 4 one can observe the two inlets feeding water and oil, noticing that the interface has a nearly spherical shape due to the dominating capillary force. The upper subfigure shows the multiphase flow prediction with CMFD, a few instances after the first droplet has been formed. The droplet does not immediately wet the wall, but as it travels downstream it relaxes to its equilibrium shape, and the film between the surface and interface is thinned. This leads to a loss of the numerical accuracy of the thin-film. As it becomes less than half of the near wall cell size $h<0.5\Delta x_{wall}$, the droplet wets the pipe surface (see Fig. 4). As the interface comes in contact with the pipe surface, two contact lines are formed (see Fig. 4). In the present simulation an equilibrium contact angle formed between the tangent of the interface and the pipe surface of 140° has been introduced as a boundary condition. This event is characterized as a numerical dry-out since a wetting film should sustain. Further, as the film ruptures the droplet looses its

characteristic shape resulting in a change in the droplet curvature at its front and rear. By comparing the CMFD result with the multiscale simulation, we notice clearly that the film rupture process induces a mass loss in the droplet (Fig. 4). The lower subfigure in Fig. 4 shows a very different droplet shape, predicted with the multiscale simulation approach. As the droplets interface approaches the pipe surface, the film height is predicted by the MiSS and the imposed as a boundary condition for the MaSS simulation. The microscopic thin-film in the present case has a minimum film height of 10.4 nm. The re-initialization of the level-set function gives a smooth transition between the minimum film height and the outer macroscopic droplet shape. The multiscale simulation captures the wetting film and it conserves the droplet size. Comparing the droplet shape using CMFD and multiscale, with the experimental results of Sarrazin [15], reveals that the multiscale treatment provides a more faithful picture than pure CMFD, notice that these experiments were performed with slightly different non-dimensional numbers and channel size.

Although the multiscale coupling gives more physically realizable results, there are some weakness points that need to be emphasized. The coupling does in its present state generate spurious pressure and velocities in the narrow vicinity of the thin-film treatment zone. This directly affects the ability to meet a low convergence criterion ($<10^{-4}$), which is also difficult to control. The main reason for the production of spurious pressure and velocities is the way the film has been mapped onto the MaSS. In order to limit such numerical deficiencies, a mass and momentum balance needs to be introduced at the film through a rigorous coupling between the two solvers. The CMFD simulation produces also velocities that are not smooth at the contact lines.

Comparison of resolved MaSS thin-film and Multiscale simulation

Fig. 5 shows a comparison between a resolved CMFD simulation (upper subfigure) and a multiscale simulation on a coarse mesh (lower subfigure). The two simulations have strikingly similar predictions of the flow characteristics, with slight difference in the droplet size caused by a different pinch-off time and location. A higher mesh resolution subsequently reduces the numerical width of the interface, which is an important factor for coalescence predictions. Fig. 5 shows evidence of the different break-up scenarios, as the interface at the inlet in the multiscale simulation propagates further downstream than the resolved CMFD, at the same time. The CMFD result predict quite well the droplet shape on a fine mesh, although at the expense of an increased computational cost. The thin-film between the interface and the pipe surface is in the present simulation captured within one cell only. In order to fully resolve such a flow phenomenon the film should be resolved with approximately 10 cells, which is an absolute minimum in order to capture a laminar flow profile. This would increase the computational costs rather drastically. The key-point is although that pure CMFD lacks a theoretical sound thin-film prediction.

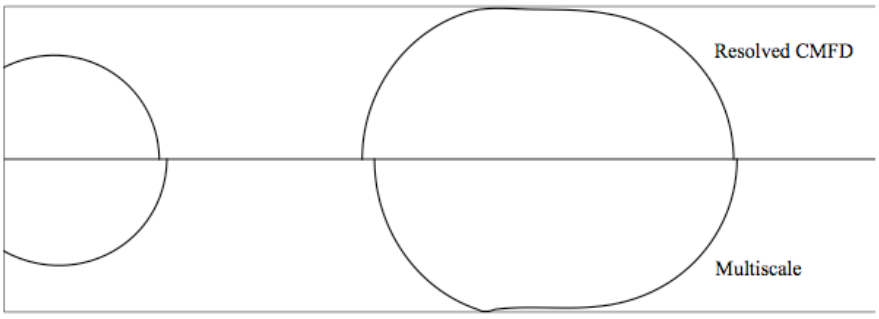

Figure. 5. Comparison of the flow characteristics predicted with CMFD on a fine mesh and the multiscale simulation on a coarser mesh, lines denote the iso-contour of the zero level set function at t=398μs.

CONCLUSION

In the present paper we have presented a multiscale modelling approach for interfacial flow phenomena endowed with a microscopic thin-film separating the two phases. A multiscale coupling is introduced between a Micro Scale Solver, which simulates the resulting thin-film dynamics, and a Macro Scale Solver for the macroscopic two-phase flow. The minimum thin-film height is seen as a sub-grid-scale variable that can evolve freely on the macro scale field through a wall boundary condition, without restricting the macroscopic time marching. This enables an efficient prediction of this class flow phenomena featuring complex physics without a unifying theoretical framework. A pure continuum model, in this case a CMFD method, will even in a direct numerical simulation lack a theoretical justification as intermolecular forces will be govern the phenomenon. A practical example of slug flow in a micro pipe has been presented, with the successful modelling of a 10.4 nm bounding thin-film formed between the slugs interface and the pipe surface. The numerical dry-out generated with CMFD on a coarse grid is an example of an unphysical solution. The multiscale simulation compares well with a resolved CMFD simulation. The multiscale simulation result also compare well with the droplet shape seen in the experiments by Sarrazin [15]. The presented computational capabilities are crucial in order to predict, inter-phase heat and mass transfer processes in micro channels that contains a two-phase flow.

REFERENCES

1. P. Aussillous and D. Quere. Quick deposition of a fluid on the wall of a tube. *PHYSICS OF FLUIDS*, 12(10):2367-2371, Oct 2000.
2. J. Becker, G. Grun, R. Seemann, H. Mantz, K. Jacobs, K. R. Mecke, and R. Blossey. Complex dewetting scenarios captured by thin-film models. *NATURE MATERIALS*, 2(1):59-63, Jan 2003.
3. J. U. Brackbill, D. B. Kothe, and C. Zemach. A continuum method for modeling surface-tension. *JOURNAL OF COMPUTATIONAL PHYSICS*, 100(2):335-354, Jun 1992.
4. F. P. Bretherton. The motion of long bubbles in tubes. *JOURNAL OF FLUID MECHANICS*, 10(02):166-188, 1961.
5. J. P. Burelbach, S. G. Bankoff, and S. H. Davis. Nonlinear stability of evaporating condensing liquid-films. *JOURNAL OF FLUID MECHANICS*, 195:463-494, Oct 1988.
6. A. Carlson, P. Kudinov, and C. Narayanan. Prediction of two-phase flow in small tubes: A systematic comparison of state-of-the-art CMFD codes. TP_F17, Proceedings 5th European Thermal-Sciences Conference, Stoffels, G-G.M., van der Meer, T.H. and van Steenhoven A.A, 2008.
7. W. E, B. Engquist, X. Li, W. Ren, and E. Vanden-Eijnden. Heterogeneous multiscale methods: A review. *COMMUNICATION IN COMPUTATIONAL PHYSICS*, 2(3):367-450, Jun 2007.
8. Jacob N. Israelachvili. *Intermolecular and surface forces*, volume 2. ed. Academic Press, 1992.
9. R. K. Jain and E. Ruckstein. Stability of stagnant viscous films on a solid-surface. *JOURNAL OF COLLOID AND INTERFACE SCIENCE*, 54(1):108-116, 1976.
10. D. Lakehal, G. Larrignon, and C. Narayanan. Computational heat transfer and two-phase flow topology in miniature tubes. *MICROFLUIDICS AND NANOFLUIDICS*, pages 261-271, 2008.
11. www.ascomp.ch/transat
12. The MathWorks. *MatLab 7.0.4*, 2005.
13. A. Oron. Three-dimensional nonlinear dynamics of thin liquid films. *PHYSICAL REVIEW LETTERS*, 85(10):2108-2111, Sep 2000.
14. A. Oron, S. H. Davis, and S. G. Bankoff. Long-scale evolution of thin liquid films. *REVIEWS OF MODERN PHYSICS*, 69(3):931-980, Jul 1997.
15. F. Sarrazin, K. Loubiere, L. Prat, C. Gourdon, T. Bonometti, and J. Magnaudet. Experimental and numerical study of droplets hydrodynamics in microchannels. *AICHE JOURNAL*, 52(12), 2006.
16. M. Sussmann, P. Smereka, and S. Osher. A level set approach for computing solutions to incompressible 2-phase flow. *JOURNAL OF COMPUTATIONAL PHYSICS*, 114(1):146-139, 1994.

17. G. I. Taylor. Deposition of a viscous fluid on the wall of a tube. *JOURNAL OF FLUID MECHANICS*, 10(02):161-165, 1960.
18. M. B. Williams and S. H. Davis. Non-linear theory of film rupture. *JOURNAL OF COLLOID AND INTERFACE SCIENCE*, 90(1):220-228, 1982.

RECONSTRUCTION OF THE HEAT TRANSFER COEFFICIENT FOR IMPINGEMENT HEAT EXCHANGE

A. Ryfa[1*], R. Bialecki[1,]
[1]Institute of Thermal Technology at Silesian University of Technology, Gliwice, Poland

ABSTRACT. The paper presents an application of the inverse technique for the heat transfer coefficient (HTC) retrieval for the single phase impingement heat exchange. Such heat transfer method involves a jet flow of fluid from nozzle to a target. A high velocity of the jet causes the destruction of the boundary layer at the targeted surface what leads to a very intensive heat transfer. The method presented here retrieves the HTC directly from the temperature measurements at the opposite side of the targeted object. In order to provide a sufficient amount of input data for the inverse procedure the thermal camera is involved in measurements. It allows distinguishing a large number of measurement points for every time instance. The superposition principle is used to decompose a searched boundary condition to a sum of known linear components multiplied by unknown coefficients. The difficulties that arise from non-linear dependency of the temperature on the HTC are bypassed by application of the definition of the convective boundary condition together with using the fact that the HTC is constant in time. The developed technique was used to retrieve the HTC for the air jet impingement heating on a flat surface.

Keywords: *heat transfer coefficient, inverse analysis, impingement, thermography*

INTRODUCTION

Jet impingement [1] technique consists in directing a jet flow from a nozzle to a target, typically a solid surface. The momentum of the jet destroys the boundary layer at the surface, leading to intensive heat exchange. The efficiency of this heat transfer arrangement makes jet impingement a popular method of intensive cooling and heating. Drying of textile or paper, cooling of electronic packages, cooling of slabs in steel industry, car or aircraft engines cooling are just few examples of applications of the jet impingement technique encountered in industry.
A straightforward technique of modelling jet impingement heat exchange is to apply the CFD analysis coupled with the heat conduction analysis in solid. However, especially for multiphase problems, this technique is both inaccurate and numerically very intensive. Thus, convective boundary condition, where heat transfer coefficient plays the central role, is frequently used in engineering practice. A convenient feature of the HTC is that while transient temperature and heat flux fields on the boundary may vary rapidly, HTC defined as their ratio remains often practically constant. Inverse analysis [2] applied to retrieving the convective heat condition is therefore an attractive alternative to coupled CFD simulations. The inconvenience of using inverse analysis is that it requires experiments in order to determine the value of HTC.
Standard inverse technique relies on separate evaluation of the temperature and heat flux distribution on the impinged surface [3]. The idea is to adjust the response of a heat conduction model in the solid to the measured temperatures. The free parameters in this optimization process are the coefficients describing the spatial and temporal distribution of boundary temperature and

* Corresponding author: mgr inż. Arkadiusz Ryfa
Phone: + (48)-32-2372316, Fax: + (48)-32-23728729
E-mail address: arkadiusz.ryfa@polsl.pl

heat flux on the surface impinged by the jet. Once the temperature and heat flux distributions are retrieved, the HTC distribution is evaluated from its definition, as a ratio of heat flux and temperature excess. The disadvantage of this approach is that the resulting distribution of the HTC is irregular, as both the temperature and heat flux may vary independently. The proposed method produces the spatial distribution of the HTC directly from transient temperature measurements. The paper is a follow up of our earlier work [3] where an implicit technique has been employed.

DEVELOPED METHOD

The HTC depends nonlinearly on the temperature and thus the inverse problem of retrieving HTC is nonlinear as well. Due to this fact the superposition principle cannot be applied directly. However, application of the definition of the convective boundary condition (1) allows overcoming this difficulty.

$$h = \frac{q}{T_f - T} \tag{1}$$

where T_f is bulk temperature of the fluid. The typical inverse procedures apply the Robin condition after the heat flux and boundary temperatures are retrieved. This method called indirect is explained in details in [3]. It requires solving of the optimization problem twice and allows on independent variation of the temperature and the heat flux. It leads, in the presence of the measurement errors, to solution that differs from the correct one. This paper concerns on the second possibility, which is the explicit method. The method allows obtaining spatial distribution of the HTC for impingement cooling solving the optimization problem only once. It uses a fact that the HTC for impingement cooling is constant in time and applies the convective boundary condition directly to the minimized objective function.

Lest take the boundary Γ of the domain Ω and divide it into two parts. On the first part Γ_R the heat flux is unknown. On the remaining portion of the boundary Γ_E, the BC's are known. The temperature at arbitrary point $\mathbf{r}_i$ is expressed as:

$$T(\mathbf{r}_i) = T_E(\mathbf{r}_i) + T_R(\mathbf{r}_i) \tag{2}$$

where the T_E is the temperature field corresponding to the zero flux prescribed at Γ_R and the BC on Γ_E and the internal heat generation unchanged. The second temperature field T_R corresponds to homogeneous BC's on Γ_E and real heat flux on Γ_R which is unknown. This flux is expressed as a linear combination of known trial functions N_j.

$$q_R(\mathbf{r}_i) = \sum_{j=1}^{J} q_j N_j \tag{3}$$

The trial functions are analog to shape functions arising in FEM and BEM techniques [3]. Each of them is associated with a certain spatial location that is decided by the user. It provides the necessary method flexibility and allows using any knowledge about the process for which the HTC is retrieved. From the linearity of the problem, it can be immediately seen that for a selected set of points $\mathbf{r}_{i:}$ $i=1,2,...N$

$$T(\mathbf{r}_i) = T_E(\mathbf{r}_i) + \sum_{j=1}^{J} q_j \Theta_j(\mathbf{r}_i),\ i = 1,2,...N \tag{4}$$

where Θ_j is a temperature field obtained assuming that the heat flux on Γ_R is just the trial function N_j. Equation (4) can be rewritten in a matrix form

$$\mathbf{T} = \mathbf{T}_E + \mathbf{J}\mathbf{q} \tag{5}$$

In the case under consideration, the sensitivity coefficient is the derivative of the temperature at a given point, with respect to the unknown parameter

$$j_{ki} = \frac{\partial T(\mathbf{r}_i)}{\partial q_k} \tag{6}$$

The sensitivity coefficients are just the entries of the matrix **J** being the auxiliary temperatures $\Theta_k(\mathbf{r}_i)$ entering equation (4). As the retrieved heat flux depends on the time, the temporal domain must also be discretized. Assume that the limits of the time steps used to approximate the temporal variation of the heat flux are denoted as $t_0, t_1,\ldots,t_k, t_{k+1}, t_U$ with u standing for the index of the time step while U the total number of thereof. The estimated heat flux distribution can then be expressed as a product of space and time dependent functions

$$q_R(\mathbf{r}_i,t) = \sum_{j=1}^{J}\sum_{u=1}^{U} q_j^u N_j(\mathbf{r}_i) M_u(t) \tag{7}$$

where M is a known trial function depending solely on time and q^u_j is unknown parameter describing the temporal and spatial distribution of the heat flux on Γ_R. Let the subscript p be associated with a pair of spatial trial function j and temporal trial function u as $p = u(U\text{-}1) + j$. Additionally, to simplify the notation let the $Q_p(\mathbf{r},t) = N_j(\mathbf{r})M_u(t)$. Using this notation, equation (7) can be rewritten in more compact form as:

$$q_P(\mathbf{r}_i,t) = \sum_{p=1}^{P} q_P Q_p(\mathbf{r}_i,t) \tag{8}$$

Analog to equation (4), the temperature at any point and time instant can be written as

$$T(\mathbf{r}_i,t) = T_E(\mathbf{r}_i,t) + \sum_{p=1}^{P} q_p \Theta_p(\mathbf{r}_i,t) \tag{9}$$

In the case under consideration, where the HTC is constant in time it is enough to employ only one time step. It causes that only two temporal values of heat flux and temperature are searched for each spatial location associated with trial functions. If the temperature at the boundary Γ_r has to be determined instead of the heat flux, the procedure is completely analogous. The problem remains linear and the only change is that in equations (3-9) the temperature T is used instead of the heat flux q.

The unknown coefficients are determined from least square fit of the model and the measurements

$$\min\phi = \sum_{i=1}^{I} [\hat{T} - T_{\mathrm{mod}}(T_{p1},\ldots T_{pJ}, T_{k1},\ldots T_{kJ})]^2 \tag{10}$$

To retrieve the HTC directly, the residuals for both heat flux and temperature parts have to be added (11). As the HTC is constant for a whole considered time the heat fluxes are then removed

$$\min\phi = \sum_{i=1}^{I} [\hat{T} - T_{\mathrm{mod}}(T_{p1},\ldots T_{pJ}, T_{k1},\ldots T_{kJ})]^2 + \sum_{i=1}^{I} [\hat{T} - T_{\mathrm{mod}}(q_{p1},\ldots q_{pJ}, q_{k1},\ldots q_{kJ})]^2 \tag{11}$$

from the optimization formula by applying the definition of the Robin (12) boundary condition what leads to its final form (13).

$$h_i = \frac{q_{ip}}{T_f - T_{ip}} = \frac{q_{ik}}{T_f - T_{ik}} \tag{12}$$

$$\min \phi = \sum_{i=1}^{I} [\hat{T} - T_{\mathrm{mod}}(T_{p1},...T_{pJ},T_{k1},...T_{kJ})]^2 + \sum_{i=1}^{I} [\hat{T} - T_{\mathrm{mod}}(h_1,...h_J T_{p1},...T_{pJ},T_{k1},...T_{kJ})]^2 \tag{13}$$

This optimization problem (13) can be solved by applying one of the available nonlinear programming procedures. In this case it was recast into a solution of a set of nonlinear equations by resorting to the necessary conditions for minimum. The result led to a set of *J* algebraic equations of *J* unknowns. Due to the aforementioned ill posedness of the problem, the solution of this set is very sensitive to input data errors. Here, the optimization was solved using modified Levenberg-Marquardt technique, which was originally developed for non linear systems and therefore it improves the stability of the solution in the presence of the measurement errors. The sensitivity coefficients i.e. the temperatures $\Theta_k(\mathbf{r}_i)$ entering equation (4) can be obtained using any available analytical or numerical methods. It is, however convenient to use numerical solution due to its universality with respect to domain shape and automation possibilities. Due to those advantages, in the case at hand the sensitivity matrix entries were calculated using a commercial FEM code MSC.Marc.

RECONSTRUCTION PROCEDURE

Experimental rig

The developed technique was used to retrieve the HTC for the air jet impingement heating on a flat surface. The test rig is presented in Figure 1. The compressed air is heated up by a heater to 50^{o}C.

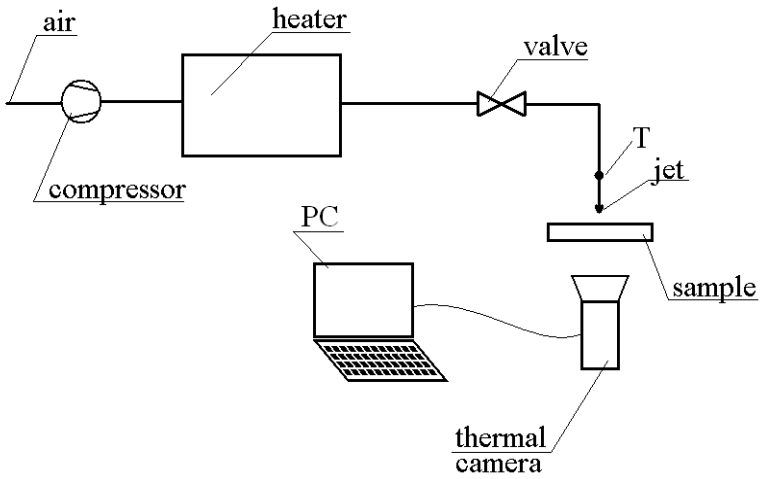

Figure 1. The test rig.

After constant air parameters are reached, the valve is opened and the air flows through nozzle towards the sample. The heated object is a steel cylinder of 60 mm diameter and 5 mm thickness. When the hot air impinges the front surface the sample starts heating up. The temperature measurements are taken with the SC-2000 thermal camera at the back surface of the sample. The images are picked up every 0.2 second. The influence of the nozzle diameter on the jet heating efficiency was tested by use of jets of diameters *d* equal respectively to 5, 6 and 7mm. For each nozzle the measurements lasts until the temperature field at the back of the sample does not change. However, for the inverse procedure only the initial part of the measurements, with the strongest temperature variation is taken. It improves stability and reduces the influence of the temperature errors on the solution. The thermography measurement technique offers a possibility of treating

each pixel of the registered thermal-image as a temperature sensor. For the applied grid resolution and measurement time it produced a set of nearly 2700 equations for determining the spatial distribution of the HTC.

Inverse procedure

The HTC is retrieved by two spatial trial functions of compact support (Figure 2). The description of such functions involves the definition of the sub domains where they do not vanish. In the problem at hand two domains have been defined. The central one is limited by a coaxial circle of a 25mm diameter with the centre at the impingement point, while second covers remaining portion of

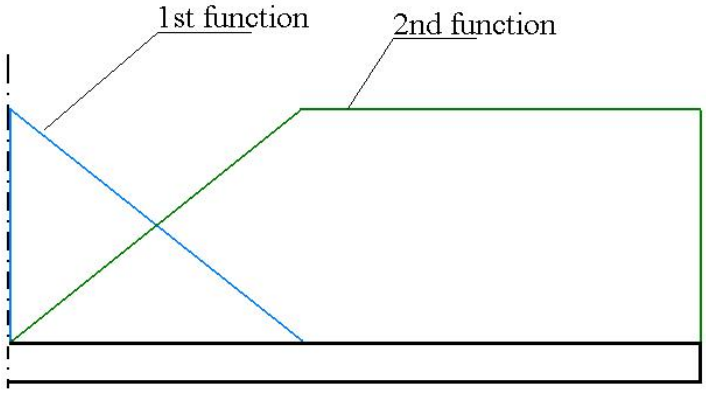

Figure 2. Functions used for HTC retrieval.

the object. The linear trial function is prescribed in the first zone, to retrieve the peak value of the HTC. In the second zone constant in space function is used, as the variation of the retrieved parameters is expected to be very low. It needs to be stressed, that the choice of the approximating functions is crucial for the results. On one hand a selected set of trial functions should produce a highly accuracy approximation of the retrieved function. The purpose is to obtain an accurate reproduction of searched film coefficient. On the other hand, reducing the number of unknowns generally improves the conditioning of the inverse problem. Thus, the number of trial functions used in the approximation of the reconstructed function should be low. Additionally, to reduce the ill posedness of the inverse problem, the trail functions should filter out the high frequency noise. Polynomial functions of low order, such as used in this case constant and linear functions are very suitable for this purpose.

RESULTS

The HTC was reconstructed for three different nozzle diameters between 5 and 7 mm and two nozzle-to-sample distances equal to 15mm and 18mm. The results are presented in Figures 3 and 4. The results show that the highest value of the HTC is at the impingement point. Then it gradually decreases when increasing radial distance. The minimal value is reached in the second zone of the impinged surface. The minimal HTC value is at the level of 10-15% of the peak one. Therefore the choice of constant trial function in that zone is justified because the possible spatial variation can be neglected. With the increase of the nozzle diameter the peak value of the HTC decreases. The radial decrease of the HTC is steeper while the minimal value increases significantly. It means that smaller nozzle can heat up more intensively the impingement region while surrounding area is less heated than for larger nozzle. Other factor with the significant impact on the heat exchange efficiency is the nozzle-to-sample distance (Figure 4). Increasing this distance decreases the peak HTC value of about 10-15%. It comes together with increase of the minimal HTC of value about 20-40%.

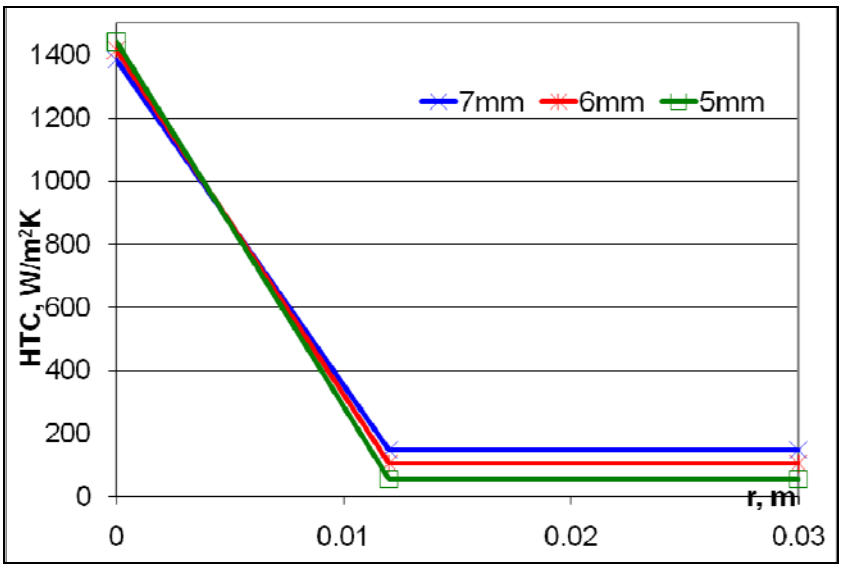

Figure 3. Retrieved HTC for different nozzle diameters.

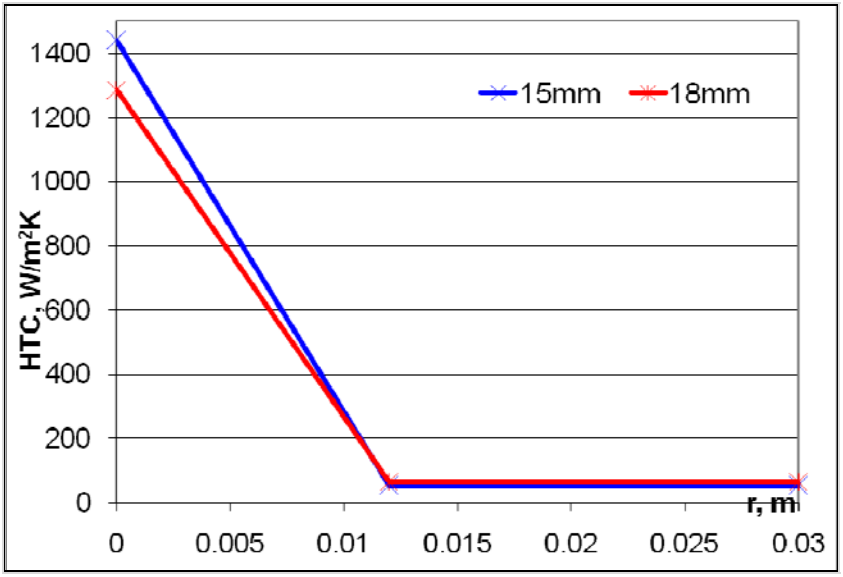

Figure 4. The influence of the nozzle-to-sample distance on the HTC for 5mm nozzle.

To verify the accuracy of the inverse procedure obtained values of the HTC were used as an input boundary condition in a direct heat conduction case called *check run*. The temperatures obtained from solution of this direct case were compared, with the measured temperatures $\hat{T}$. The quality of solution was then judged by mean temperature difference (14) calculated for all points at all time instances. The comparison is presented in Table 1.

$$\Delta = \frac{\sqrt{\sum_{i=1}^{I} (\hat{T} - T_{DIR})^2}}{I} \tag{14}$$

Additionally the measured temperatures at several locations, distributed at different distances from the impingement point were compared with those obtained from *check run* (Figure 5).

Table 1
Mean temperature difference between experiment and inverse analysis

nozzle (mm)	nozzle-to-surface distance (mm)	
	15	18
5	0.24	0.34
6	0.34	0.25
7	0.37	0.42

For all measurement series, the mean temperature difference is small. It means that the temperature field obtained from the *check run* is very similar to the one from measurement. It leads to conclusion that the retrieved convective boundary condition is also in good accordance with the actual one. The temperature time history for two points is presented in Figure 5. One of those points

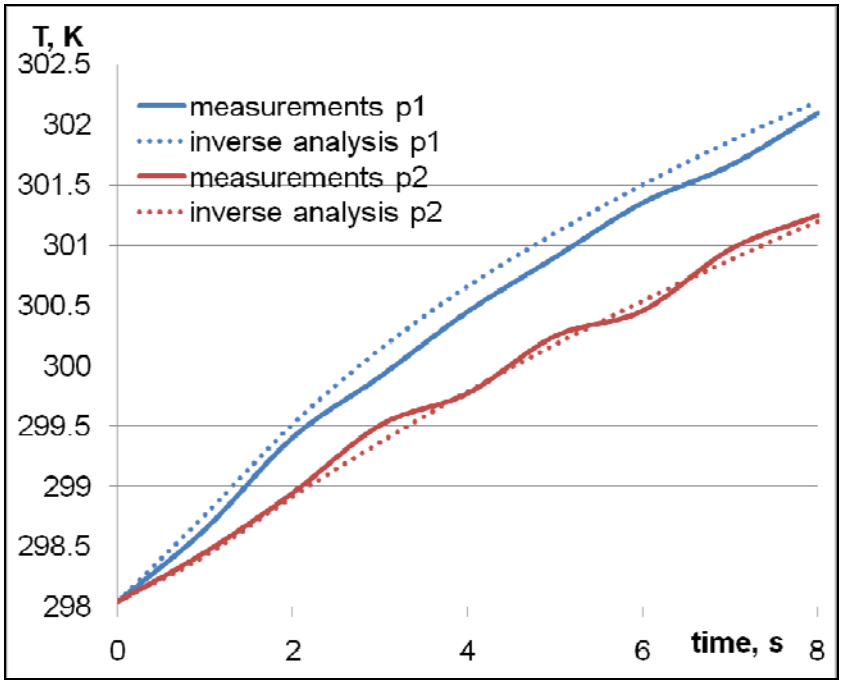

Figure 5. Comparison between measured and temperatures from model for 5mm jet.

lays in the impingement point, while second one 10mm from it. Both solid lines (measurements) show some minor oscillations that are most probably caused by radiation reflected from the measured surface. For both points there is a good agreement between measured and calculated temperature.

CONCLUSIONS

The results show that the proposed method is suitable for retrieving the spatial distribution of the HTC for the impingement phenomenon. The applied linear and constant trial functions are able to reproduce general shape and magnitude of HTC with good accuracy. Low temperature differences obtained from the comparison procedure proved correctness of main assumption of the method i.e. constancy of the HTC in time. The results proved that the inverse procedure is stable if only some precautions are taken. The main point here is to limit the number of the estimated degrees of

freedom to the necessary minimum. The by-products of the analysis are the smoothed sensitivity coefficients which are very helpful at the stage of planning the experiments. Values of those coefficients show the best places where the temperature sensors should be placed. The inverse problems are ill-posed what means the errors in input data are amplified during the solution procedure what often leads to instability of the solution. Simple trial functions used in the developed method filter out the high frequency errors and decrease influence of ill-conditioning on the solution.

NOMENCLATURE

N – spatial trial function,
M – temporal trial function,
$\mathbf{r}$ – vector coordinate, m
Δ – mean temperature difference, K
Γ – boundary,
Φ – minimized objective function, K^2
Θ – auxiliary temperature field, K
Ω – domain,
Superscripts:
m – mean,
mod – from model,

REFERENCES

1. N. Souris and H. Liakos and M. Founti. *Impinging Jet Cooling on Concave Surfaces*. Journal of American Institute of Chemical Engineers, 50(8): 1672-1683, 2004.
2. Ä Ozisik, N. M. and Orlande, R. B., *Inverse Heat Transfer Fundamentals and Applications*, Taylor and Francis, NY 2000.
3. A. Ryfa, R.A. Białecki, B. Facchini and L. Tarchi. *Application of the inverse analysis for the boundary condition retrieval*, IPDO Symposium Proceedings, Vol. 1, 114-121, 2007.

EXPERIMENTAL VALIDATION OF THE NUMERICAL MODEL OF THE HEAT TRANSFER COEFFICIENT CALCULATION FOR A CROSS FLOW HEAT EXCHANGERS

T. Bury*, J. Składzień, A. Sachajdak
Silesian University of Technology, Gliwice, Poland

ABSTRACT. The paper deals with the thermal analysis of a ribbed cross-flow heat exchanger of a gas-liquid type with non-uniform flow of the agents. The form and scope of the air inflow to the exchanger have been investigated on a special measuring rig. The results became the basis for elaboration of a computer code for thermal-hydraulic analyses of such type heat exchangers. The initial validation of this code has shown some differences between experimental and numerical results. The heat transfer coefficient at the gas side has been indicated as a possible reason of the recorded discrepancies. An enlarged model of the recurrent element of the heat exchanger under consideration has been built and mounted on an additional test station in order to check the numerical procedure responsible for determination of this parameter. A comparison of the experimental and numerical results shows satisfactory compliance. The numerical results are a little bit underestimated, but the relative differences of compared parameters are rather small. According to the results of analyses one may conclude that the CFD based numerical model accurately portrays the real phenomena.

Keywords: *cross-flow heat exchangers, heat transfer coefficient, numerical simulations, CFD, infra-red thermography*

INTRODUCTION

Among the currently applied heat exchangers with extended surface of the heat transfer the most important meaning have the plate exchangers (with the mixed current) and the ribbed cross-flow heat exchangers, which core has the form of a bunch of pipes with flat plate ribs. Small size, low weight and a high efficiency determine the strong position of such devices. A compact ribbed heat exchangers are commonly used in thermal technique, refrigeration, air-conditioning and automotive industry.

The paper presents a part of the research project related to thermal analysis of a ribbed cross-flow heat exchanger of a gas-liquid type with non-uniform flow of the agents. One of the most important parameters describing such heat exchangers is the heat transfer coefficient at the gas side. A variety of constructions being applied causes significant problems with determination of this coefficient. The problem is additionally complicated by a non-uniform flow of a gas. The last issue has been investigated in detail on a special test station in the Institute of Thermal Technology of the Silesian University of Technology [1]. The scope and form of this inequality have been measured on the test station shown in Fig. 1. The main element of the measuring system is a thermoanemometric sensor installed onto a measuring probe which shifting is controlled by a computer. It allows to determine velocity and temperature fields of the air at the exchanger inlet and outlet. The measurements

* Corresponding author: Dr T. Bury
Phone: + (48)-32-2372051, Fax: + (48)-32-2372872
E-mail address: Tomasz.Bury@polsl.pl

results have then became the basis for elaboration of the numerical model of the considered exchanger.

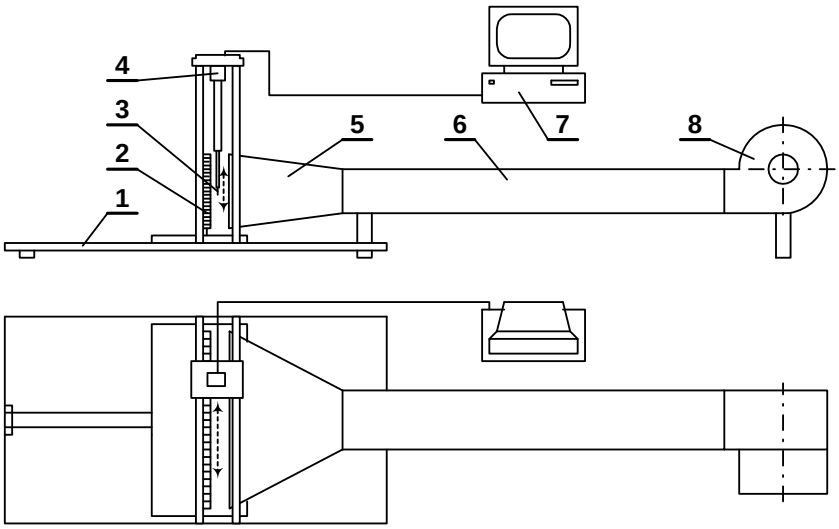

Figure 1. Test station - the air supply module (1 – support plate, 2 – heat exchanger, 3 – thermoanemometric sensor, 4 – measuring probe, 5 – diffuser, 6 – channel, 7 – control computer, 8 – fan)

The measurement within framework of [1] were performed without presence of a hot medium and the initial arrangement of the test station did not allow for validation of the computer code. It became possible after modernization of the experimental rig and installation of the hot water supply module – see Fig. 2. The validation procedure was performed by means of comparison of the experimental and numerical results. The total heat flux transported in the heat exchanger is the main compared parameter and it is the basis for evaluation of the code. A significant differences have been recorded between experimental and numerical data after the initial validation of the model [2]. A minor changes have been put into the code and the validation procedure was then repeated with usage of the infra-red thermography measurements results also [3]. The last stage of the research was the sensitivity analysis [4]. This analysis has shown that the heat transfer coefficient from ribbed surfaces to a gas may be a reason for recorded discrepancies between numerical and experimental results.

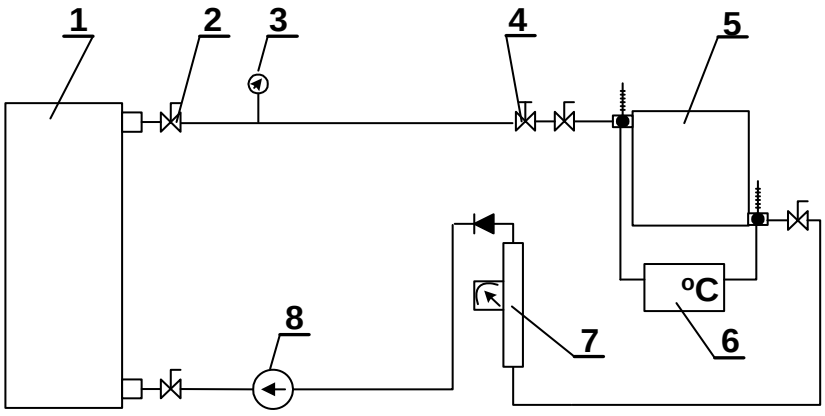

Figure 2. Test station – the water supply module (1 – electric heater, 2 – cut-out valve, 3 – manometer, 4 – control valve, 5 – heat exchanger, 6 – water temperature measuring system, 7 – flow meter, 8 – pump)

An enlarged special model of a fragment of the considered exchanger has been built in order to check the numerical procedure responsible for determination of the heat transfer coefficient from the ribs to the gas [5]. The verification of this procedure is the main aim of the investigations. The numerical model of the system under consideration is a part of the mentioned laboratory stand and contains the flow channel with the ribs. All the performed simulations have been realized using the measured air flux and the electric heaters surfaces temperature as the boundary conditions.

EXPERIMENTAL ANALYSIS

Test rig for investigations of the heat transfer conditions on a plate rib surface

The model consists of four plate ribs with respective pipe sections. Two electric heaters simulate the hot water flow inside the pipes. This model is placed in a flow channel with an observation window and it is cooled by the forced air flow (see Figure 2). The air flux and temperatures at the inlet and outlet are measured by thermocouples. The infra-red thermography technique is used for measurement of the temperature field on the surface of the first rib. Several thermocouples are also installed for measuring the temperature on the other ribs surfaces.
Two parameters have been set as independent during experiments: the temperature of the pipe internal wall and the air flow rate. Following parameters have been recorded during measurements:

- the air volumetric flow rate,
- the air temperature at the inlet and outlet of the ribs section,
- the electric heater surface temperature (assumed after as the pipe inner surface temperature)
- temperatures on the ribs surface in the measuring points,
- temperature distribution on the surface of the first rib.

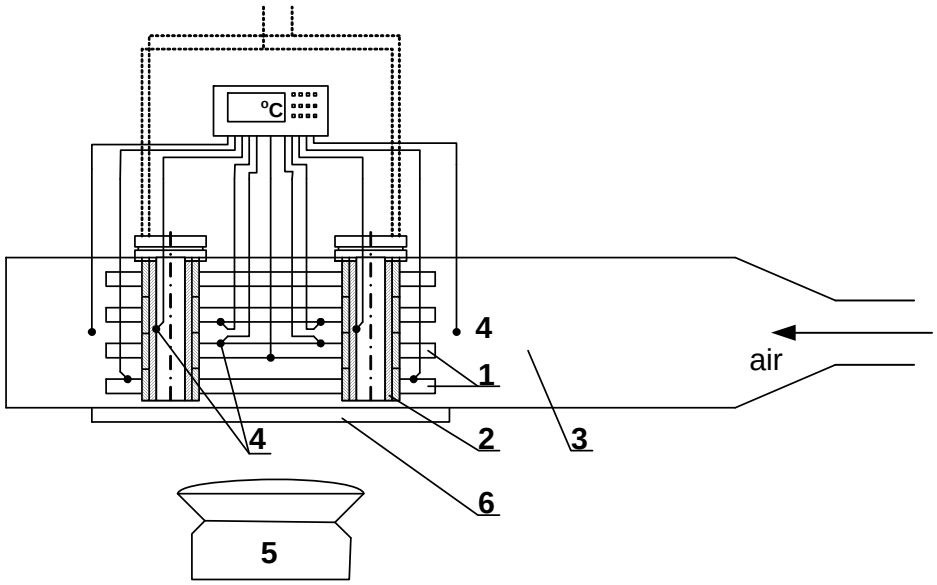

Figure 2. Simplified sketch of the test station (1 - ribs and pipe models, 2 - electric heaters, 3 - flow channel, 4 - thermocouples, 5 - infra-red camera, 6 - speculum)

Experimental results

Twenty five experiments have been realized in total (signed MS-1 to MS-25 respectively) during basic measurements. These experiment have been divided onto five measuring series differing with the set temperature of the electric heaters (from 50 to 90 degrees Celsius with ten degree step). Table 1 presents experimental results for two selected series. These results concerning two given

temperatures of the electric heaters surfaces (50ºC and 90ºC). This temperature are measured independently for each heat and is signed as t_{g1} and t_{g2} in Table 1. The air volumetric flow rate V_{air} has changed from 25m^3/h up to 45 m^3/h. The electric power N_g consumed by the heaters and the inlet and outlet air temperatures ($t_{air,in}$ and $t_{air,out}$ respectively) are also presented in Table 1.

Table 1
Selected experimental results

Experiment No.	V_{air} m^3/h	t_{g1} ^{o}C	t_{g2} ^{o}C	N_g W	$t_{air,in}$ ^{o}C	$t_{air,out}$ ^{o}C
MS-1	25.3	49.5	50.2	116.5	24.0	37.5
MS-2	30.1	49.2	50.6	122.6	24.0	35.9
MS-3	35.0	49.6	50.4	128.0	24.4	34.8
MS-4	40.3	49.1	50.5	132.4	24.5	33.4
MS-5	44.9	49.7	50.4	137.1	22.9	31.1
MS-21	25.3	93,7	90.4	192.0	23.9	44.8
MS-22	30.1	89.5	90.6	196.5	24.0	42.9
MS-23	34.9	90.8	90.5	200.5	24.0	40.7
MS-24	40.2	89.3	89.6	207.0	24.0	39.2
MS-25	45.1	89.7	90.6	215.8	24.5	38.3

The infra-red thermographic temperature distributions on the first rib surface are the main experimental results. Such a distribution for one of the measuring series is presented in Fig. 3.

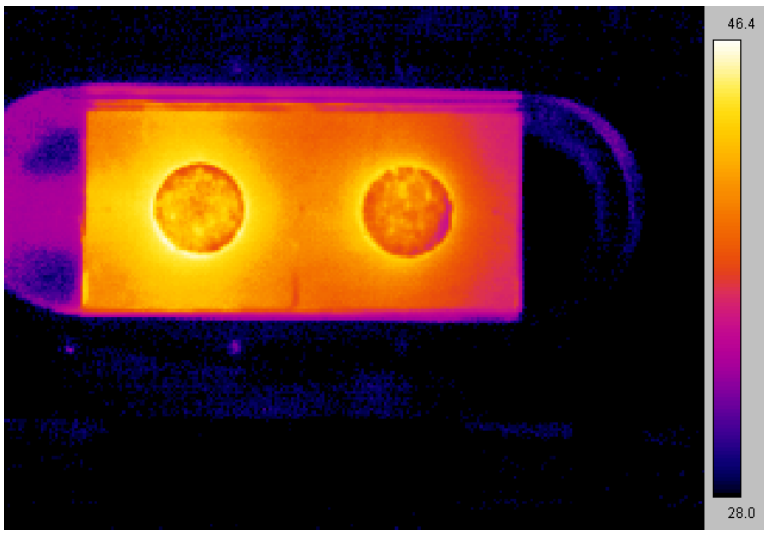

Figure 3. Sample infrared thermographic picture of the first rib surface – experiment MS-1

NUMERICAL SIMULATIONS

The geometry of the model has been created using Gambit preprocessor and it is shown in Figure 4 as well as the boundary conditions types. The numerical grid counts over 550 thousands of tetrahedral cells. Turbulence models tests have shown that the standard k-ε model gives the best results. All the performed simulations have been realized using the measured air flow rates and the

electric heaters surfaces temperature as the boundary conditions. A steady state conditions were assumed during computations.

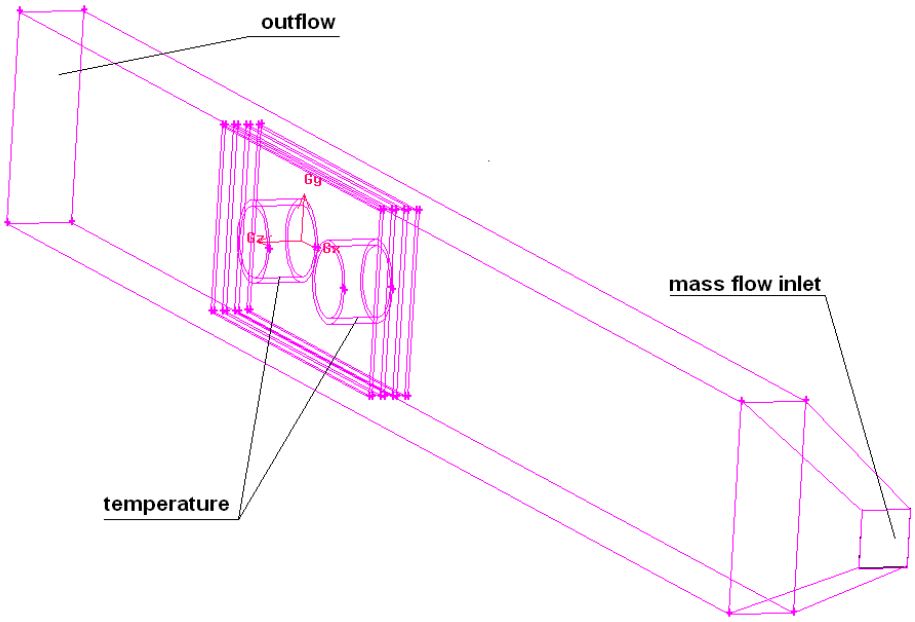

Figure 4. Geometry of the numerical model of the test rig and boundary conditions types

The CFD analysis gives the possibility to view fields of the most important parameters in different cross sections of the object under consideration. The air velocity distribution is shown in Fig. 5. The cross section plane is parallel to the flow direction and it crosses the second rib. One may note that the air inflow to the ribs section is quite well unified.

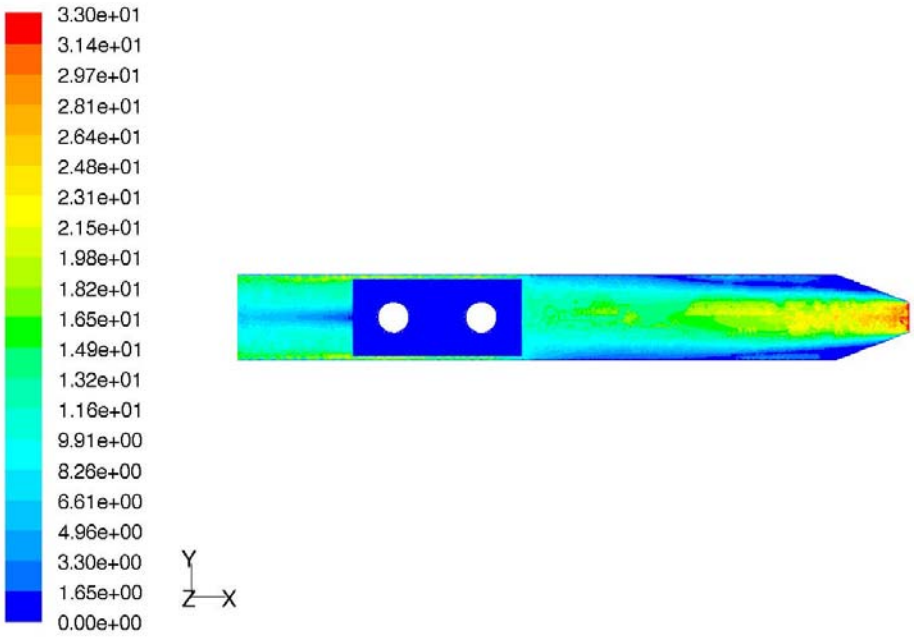

Figure 5. Distribution of the air velocity in the flow channel, m/s – calculations for experiment MS-1

The most interesting numerical results are the temperature distributions on the first rib surface, as well as the experimental results. These distributions may be next compared with the infra-red

thermography measurements. The sample first rib surface temperature field for experiment MS-1 is presented in Fig. 6.

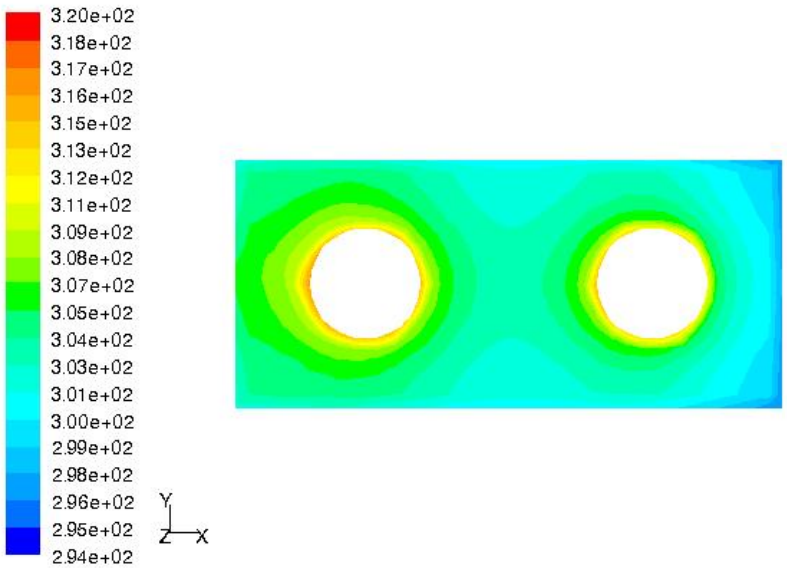

Figure 6. Temperature field on the first rib surface, K – calculations for experiment MS-1

COMPARATIVE ANALYSIS

The main goal of the analysis is to evaluate the numerical CFD model used for computations of the heat transfer coefficient at the gas side of the considered heat exchanger. A simple comparison of measured and computed temperatures for two analysed experiments is presented in Table 2. The subscripts at the temperature given in Table 2 mean the numbers of the thermocouples. The first three thermocouples are placed on the first rib visible surface and are also used for calibration of the infra-red camera. The calculated surface temperature values are a little bit underestimated, as well as the air outlet temperature. The last parameter is computed as the area weighted average value for the cross section placed 2 cm next to the ribs section.

Table 2
Sample comparison of experimental and numerical data for the rib temperature

		t_1, °C	t_2, °C	t_3, °C	t_4, °C	t_5, °C	t_6, °C	t_7, °C	$t_{air,out}$, °C
MS-4	Measurement	40,4	41,5	34,5	43,9	39,8	40,6	33,9	33,4
	Simulation	40,1	40,9	33,8	43,5	39,4	39,9	33,3	32,9
MS-22	Measurement	56,2	57,7	48,0	61,1	55,4	56,5	47,2	42,9
	Simulation	55,5	56,2	47,1	60,5	54,6	55,1	46,3	41,3

The most interesting is comparison of the temperature field for the first rib surface (see Figures 7 and 8). Due to a different colour scales a direct comparison is somewhat difficult.

The next step in the analysis was the computation and comparison of the total heat flow rate transported from the ribbed surface to the flowing air. The results for measuring series MS-1 to MS-5 are presented in Table 3. The total heat flux has been calculated twice based on the air enthalpy raise:

- considering the measured values of the volumetric air flow and its temperature measured at the inlet and outlet of the ribs section (Q_{air} in Table 3),
- taking into account the computed values of the mentioned parameters (Q_{Fluent} in Table 3).

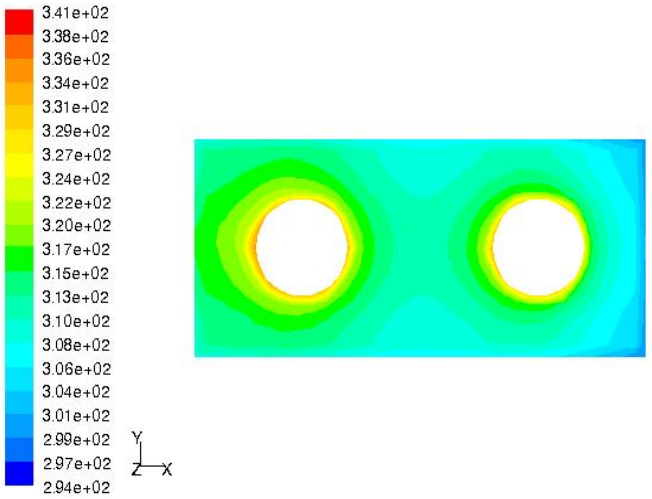

Figure 7. Calculated temperature field of the first rib surface for experiment MS-4

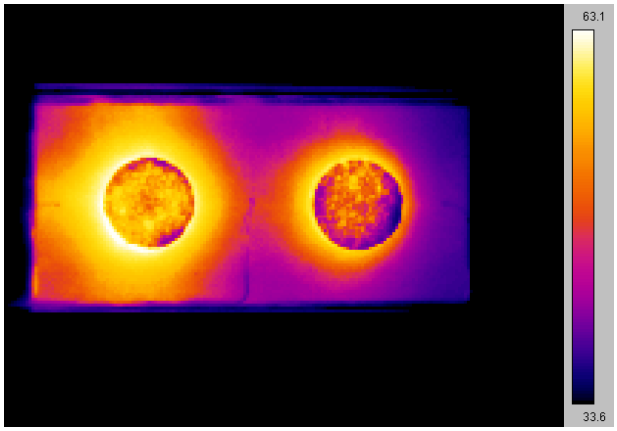

Figure 8. Measured temperature field of the first rib surface for experiment MS-4

Table 3
Comparison of experimental and computational data – heat flow rates

Measurement No.	**N_g W**	**Q_{air} W**	**Q_{Fluent} W**	**δ_{Qair} %**	**$\delta_{QFluent}$ %**
MS-1	116.5	111.8	104.5	4.03%	10.30%
MS-2	122.6	117.2	109.9	4.40%	10.36%
MS-3	128.0	119.0	111.7	7.03%	12.73%
MS-4	132.4	117.2	109.9	11.48%	16.99%
MS-5	137.1	120.9	113.6	11.82%	17.14%
MS-21	192.0	173.1	165.8	9.84%	13.65%
MS-22	196.5	186.2	178.9	5.24%	8.96%
MS-23	200.5	190.7	183.4	4.89%	8.53%
MS-24	207.0	200.0	192.7	3.38%	6.91%
MS-25	215.8	203.3	196.0	5.79%	9.18%

The relative differences (δ_Q) between experimental and numerical results have been calculated. The heat flow rates calculated based on the measured values, as it can be seen, is lower than the measured values of the electric power of the heaters. The obvious reason of this situation are the heat losses through the rear wall of the flow channel. The differences between experimental and computational heat flow rates calculated as the CFD results reach up to 18% for some cases, but the average difference is somewhat over 10%.

CONCLUSIONS

The main aim of the performed research has been to investigate if the numerical model of the recurrent fragment of the exchanger under consideration may be a useful and reliable tool for determination of the heat transfer coefficient at the gas side. The simple comparison of the experimental and numerical data shows satisfactory compliance of results. The numerical results are mostly a little bit underestimated, but the relative differences of compared parameters do not exceed 18%.

According to the results of analyses it may be noted that the CFD based numerical model portrays the physical phenomena with satisfying accuracy. A probable reason of the recorded discrepancies are some simplifications in the numerical model geometry and neglecting of the radiative heat transport.

ACKNOWLEDGEMENTS

This work has been realized under the contract No. 3T10B 062 29 financed by the Ministry of Science and Higher Education.

REFERENCES

1. Piątek R., Thermal analysis of plate fin and tube heat exchanger with unequal inlet of mediums, *PhD Thesis*, Institute of Thermal Technology, Silesian University of Technology, Gliwice, 2003.
2. Bury T., Piątek R., Składzień J., Experimental validation of the numerical thermal model of the cross-flow heat exchanger with unequal agent flow, *Proceedings of ECOS 2008 Conference*, Gliwice-Krakow, 2008, vol. 1, 329-336.
3. Bury T., Kruczek T., Application of infrared thermography for validation of numerical analyses results of a finned cross-flow heat exchanger with non uniform flow of the agents, *Proceedings of 9th International Conference on Quantitative InfraRed Thermography - QIRT 2008*, Krakow, 2008.
4. Bury T., Składzień J., Piątek R., Validation and sensitivity analysis of the mathematical model of a cross-flow heat exchanger with non-uniform flow of agents, *Proceedings of the Conference Energetyka 2008*, Wroclaw, 2008.
5. Bury T., Składzień J., The experimental and the numerical analysis of a ribbed heat exchanger with an unequal inlet of the air, *Heat Transfer and Renewable Sources of Energy 2006*, Międzyzdroje 2006, pp. 419-426.

MECHANISMS OF BUBBLE FRAGMENTATION IN FLASHING FLOWS

O. Ivashniov, M. Ivashneva*
MV Lomonosov State University, Moscow, Russia

ABSTRACT. The model of boiling flow considering bubbles break-up possibility was used to simulate the depressurization of a high-pressure vessel. The results of numerical experiment were in good agreement with that of a physical one and reveal the role of bubble fragmentation in the flow dynamics. The break-up induced by a centrifugal acceleration of the interfacial surface under a rapid bubble growth is the reason of the pressure rise and its maintenance at the level intermediate between the pressure of saturation and atmospheric one at the wave stage of efflux. The bubble fragmentation induced by the difference in phase velocities is 'responsible' for an explosive evaporation in moving front at the main stage of efflux.

Keywords: *flashing, fragmentation, bubble, boiling, intensification*

INTRODUCTION

In a normally working nuclear reactor the hot water is under high pressure. If there is damage water starts to flow out at a high speed. Owing to the drop of pressure this efflux is accompanied by boiling. To create a safety system a model for boiling liquid flow is necessary that comply with experimental data. The full-scale experiments are expensive and the models having a minimal number of non-physical coefficients are of special interest in the sight of physical experiments substitution by numerical ones. The opening of a high-pressure tube may considered to be a simplest model of reactor damage. This process simulation by the models of boiling flow based on the equations of conservation is given in [1]. The model considering the boiling to be equilibrium has no non-physical coefficients at all and the boiling centers number is chosen in the model permitting the liquid temperature to differ from that of vapor. According to the experiment (Figure 1), on the vessel opening, the pressure keeps a certain level which is lower than the pressure of saturation and falls down in the wave moving towards the closed tube side. The equilibrium model does not model the intermediate level keeping (it predicts the pressure fall up to the pressure of saturation) and the non-equilibrium model does not simulate boiling fronts predicting monotonous pressure diminution. The application of the last model for nozzle flows simulation [2] shows that the number of boiling centers must be chosen three orders of magnitude greater than that which gives the best correspondence for depressurization simulation. This difference and the fact that the numbers of centers are too great to be of physical reasoning: 10^6-10^9per liquid kilogram, gives the idea that the number is not a constant but a function determined by the bubble fragmentation. The results of the numerical modeling of high-pressure vessel depressurization using the boiling flow model which considers bubble fragmentation are presented in the paper.

BUBBLE FRAGMENTATION INDUCED BY THE DIFFERENCE IN PHASE VELOCITIES

For simulation there were used experimental results of Edwards & O'Brien [3]. A 4m-length tube with 7.5 cm internal diameter was initially occupied by hot water with temperature T_0=515 K. The pressure in the tube, P_0=7 MPa, was twice the pressure of saturation and water did not boil. The

* Corresponding author: Dr. M. Ivashneva
Phone: + 7(8332)-64-0149, Fax: + 7(8332)-64-4697
E-mail address: ivashneva-m@mail.ru

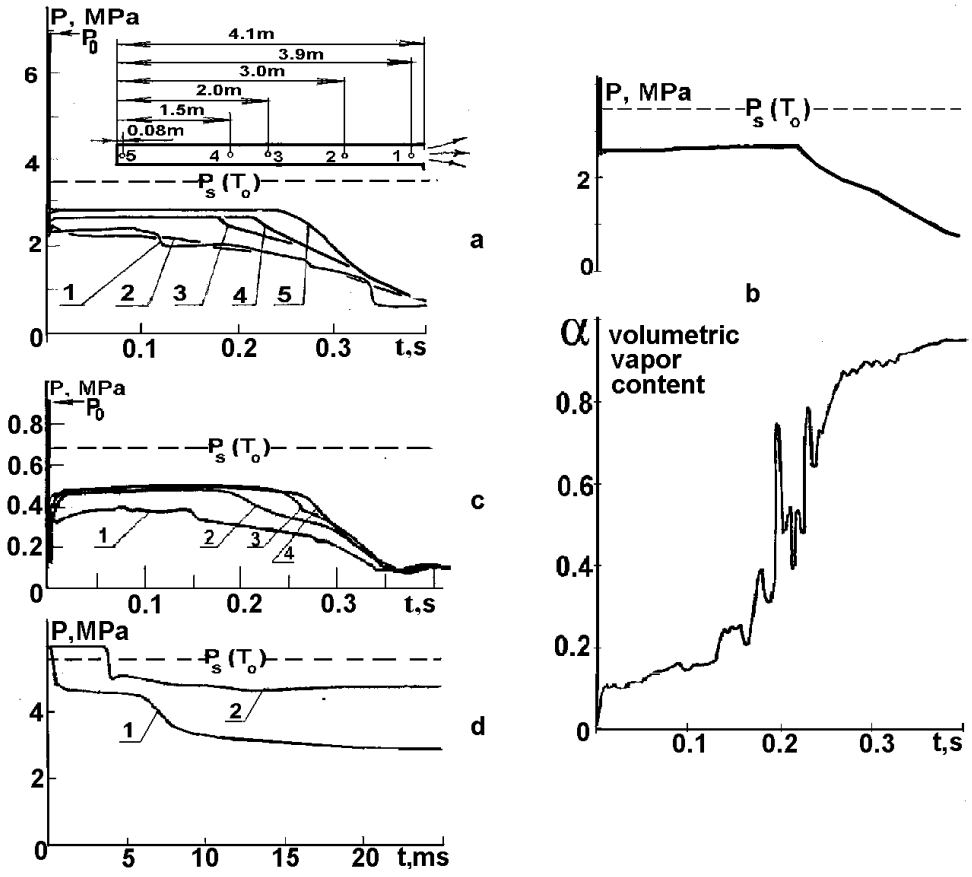

Figure 1. The experiments on high-pressure vessel depressurization. The experiment of Edwards & O'Brien (1970): (a) pressure oscillograms at five tube cross-section locations shown in the insert, (b) versus time curves for the pressure P and volumetric vapour content α in the 4th cross-section. The results of one from the experiments of Winters & Merte (1979) on the depressurization of the tube occupied with dichlorodifluoromethane (c). Pressure oscillograms at cross-sections located 6.3, 0.428, 0.792 and 1.156 m distant from the opened side (the curves 1-4). The experiments of Isaev (1980) on boiling CO_2 efflux (d). Pressure oscillograms at the tube cross-section 12 and 32 cm distant from an opened side (the curves 1 and 2).

right-hand end of the tube was closed with a glass disc. On destroying the disc the liquid efflux started. The pressure oscillograms measured at five tube cross-sections are shown by solid lines in the Figure 1(a). At the 4th point the volumetric vapour fraction was additionally measured (Figure 1(b)). It is seen than a uniform pressure 2.7 MPa which was less than the pressure of saturation was settled at points 3, 4, 5 practically at once after the vessel opening (i.e. in a short time of 3 ms necessary for the wave moving with a speed of sound in a pure liquid to travel the length of the channel). The pressure remained constant for a long time: only after 0.2 s did it start to decrease rapidly at the 3-rd point, and then at the 4-th and 5-th one. The front of pressure reduction was moving with the speed of only 12 m/s (Figure 1(a)). Decompression was accompanied by a large increase in the volumetric vapour content (Figure 1(b)).

We supposed that an explosive evaporation may be caused by the bubble fragmentation which being multiple resulted in a quick and effective increase in the interfacial surface. The model considering bubble fragmentation due to Kelvin-Helmholtz instability was constructed. It is the model of boiling flow of Nigmatulin and Soplenkovu [4] with the only exception that it 'allows' the change

in the bubble concentration. The model consists of the laws for conservation for the mixture mass, momentum and energy, vapor mass and the equation for the bubble number balance.

$$\frac{\partial \rho}{\partial t}+\frac{\partial(\rho u)}{\partial x}=0 \qquad \frac{\partial(\rho u)}{\partial t}+\frac{\partial\left(\rho u^2+P\right)}{\partial x}=-\xi\frac{\rho|u|u}{2D} \tag{1}$$

$$\frac{\partial}{\partial t}\left(\rho\left(i-\frac{P}{\rho}+\frac{u^2}{2}\right)\right)+\frac{\partial}{\partial x}\left(\rho u\left(i+\frac{u^2}{2}\right)\right)=0 \tag{2}$$

$$\frac{\partial\left(\rho_g\alpha\right)}{\partial t}+\frac{\partial\left(\rho_g\alpha u\right)}{\partial x}=jn \tag{3}$$

The intensity of the liquid evaporation into a bubble j is determined from the automodel solution of the problem about a heat growth of a vapor bubble in approximated form [7].

$$j=2\pi D_l a\rho_l \,\mathrm{Ja}\,\mathrm{Nu} \qquad \mathrm{Nu}=2+\left(\frac{6\,\mathrm{Ja}}{\pi}\right)^{2/3}+\frac{12\,\mathrm{Ja}}{\pi} \qquad \mathrm{Ja}=\frac{c_l\rho_l\left(T_l-T_s\right)}{\rho_g h} \tag{4}$$

where Ja is the Jakob number, $T_s(P)$ and T_l are the liquid temperatures on the bubble surface and in the distance from the bubble. Besides (4), the set of equations (1-3) is closed by the equations of state for liquid and vapor phases and by the caloric equation for the liquid.

There introduced the equation for bubble number balance. Phase by-passing is determined from the balance equation for the forces acting the bubble (the inertia of a bubble itself is neglected).

$$\frac{dc}{dt}=\psi \qquad f_A+f_m+f_\mu=0 \tag{5}$$

$$f_A=\rho_l\frac{4}{3}\pi a^3\frac{du}{dt} \qquad f_\mu=-\rho_l\frac{c_\mu}{2}\pi a^3\left|u_g-u\right|\left(u_g-u\right) \tag{6}$$

$$f_m=-\rho_l\frac{2}{3}\pi a^3\left(\frac{d_g u_g}{dt}-\frac{du}{dt}\right)-\frac{\rho_l}{2}\left(u_g-u\right)\frac{d_g}{dt}\left(\frac{4}{3}\pi a^3\right) \tag{7}$$

$$\mathrm{Re}\le 10.9: \quad c_\mu=\frac{16}{\mathrm{Re}}$$

$$10.9<\mathrm{Re}\le 1000: \quad c_\mu=\frac{48}{\mathrm{Re}}\left(1-\frac{2.2}{\sqrt{\mathrm{Re}}}\right) \quad \mathrm{Re}=2a\rho_l\frac{\left|u_g-u\right|}{\mu}$$

$$\mathrm{Re}>1000: \quad c_\mu=4.466\cdot 10^{-2}$$

The intensity of the bubble fragmentation is defined by a relax ratio.

$$\psi=\frac{c^*-c}{\tau^*} \tag{8}$$

c^* is the number of bubbles which would appear in the case of instantaneous break-up, τ^* is the character time of fragmentation. The parameters c^* and τ^* are determined from the solution of the problem about the growth of small indignations of a plane interfacial surface flowing round by the liquid. A dispersion analysis gives the law of the versus time dependence of the amplitude of a sine-shaped perturbation of the length λ:

$$\xi=K\exp\left[h\cdot t-\mathrm{i}\frac{2\pi}{\lambda}x\right] \qquad h(\lambda)=\pm\sqrt{\frac{4\pi^2}{\lambda^2}\frac{\rho_g\left(u_g-u_l\right)}{\rho_l}-\frac{8\pi^3}{\lambda^3}\frac{\sigma}{\rho_l}}$$

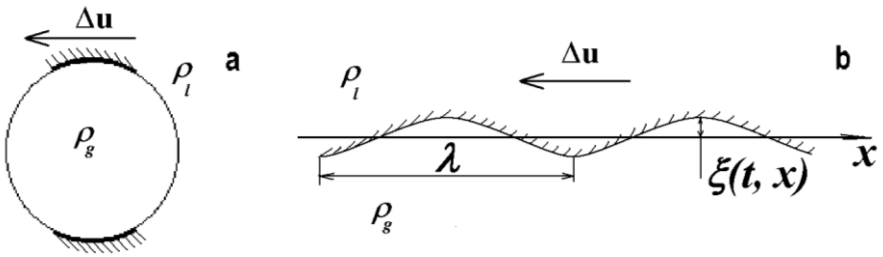

Figure 2. The schemes for the bubble break-up (a) and for the indignation development (b).

Considering a bubble to fragment by the wave with the fastest growing amplitude λ^* which cannot exceed the bubble diameter, $\lambda^* \le 2a$ [7], we obtain the criterion for the stability of the bubble overflowing by the liquid and the estimation for its critical value We^*.

$$\lambda^* = \frac{3\pi\sigma}{\rho_g\left(u_g - u_l\right)^2} \qquad We = \frac{2a\rho_g\left(u_g - u_l\right)^2}{\sigma} \qquad We^* = 3\pi$$

The number of bubble fragments, c^*/c, is estimated as the ratio of the bubble diameter to the length of the wave with the fastest growing amplitude The characteristic time of a bubble fragmentation is estimated as the time of e-fold growth of a harmonic perturbation of the length λ^*.

$$\frac{c^*}{c} = \frac{2a}{\lambda^*} = \frac{We}{We^*} \qquad \tau^* \approx \frac{1}{h\left(\lambda^*\right)} = \sqrt{\frac{\rho_l a^3}{\sigma}\left(\frac{We}{We^*}\right)^3}$$

The model has two free parameters: the initial number of boiling centers and the critical meaning of Weber number. The best correspondence to the experiment is achieved with their meanings: c_0=0.4 10^6kg^{-1}and We^*=1. The calculative parameters distribution within 0.1, 0.2 and 0.3 seconds since the vessel opening are shown in the Figure 3. The explosive evaporation in boiling fronts is repeated in a numerical experiment on high- pressure vessel depressurization.

The flow consists of three zones. The first one is between a closed tube side and the wave front. The concentration of bubbles and the liquid overheats are homogeneous over this zone (Figure 3, c,d) and the intensity of the mixture expansion due to boiling is homogeneous as well. Along the zone, the velocity is increasing according to a linear low from 0 to 10 m/s (Figure 3,f). The acceleration is about 100 m/s^2. The pressure gradient corresponding to such acceleration is approximately 0.1 MPa and is not noticeable versus the pressure level, 3 MPa. In the second zone, the parameters changes sharply. The number of bubbles is increasing by 6 orders of magnitude (Figure 3,c). A sharp increase in the interfacial surface due to multiple bubble fragmentation intensifies the boiling and the vapor content is increasing from 0.2 up to 0.8 (Figure 3,b). The temperatures of liquid and vapor equalize (Figure 3,d). The third zone is a zone of an equilibrium boiling, a centered wave of rarefaction.

Boiling fronts were observed in the experiments under the other initial water parameters [3] and with the other fluids [6, 7] as well (Figure 1,c,d). An explosive boiling in moving fronts is, thus, a specific feature of high-pressure vessel depressurization that is in agreement with its explanation from dynamic flow characteristics seen from the numerical experiment. The difference in phase velocities which is maximal at the channel exit causes a multiple bubble fragmentation following by a sudden increase in the interfacial area and a quick lost of liquid heat energy due to evaporation.

The evaporation results in the increase in the pressure, flow velocity and the conditions for the bubble fragmentation are created upstream. The wave travels transforming the potential energy of overheated liquid into the kinetic energy of flow.

The possibility of bubble fragmentation in speed flows agree with the data of Yamamoto et al., 2007.

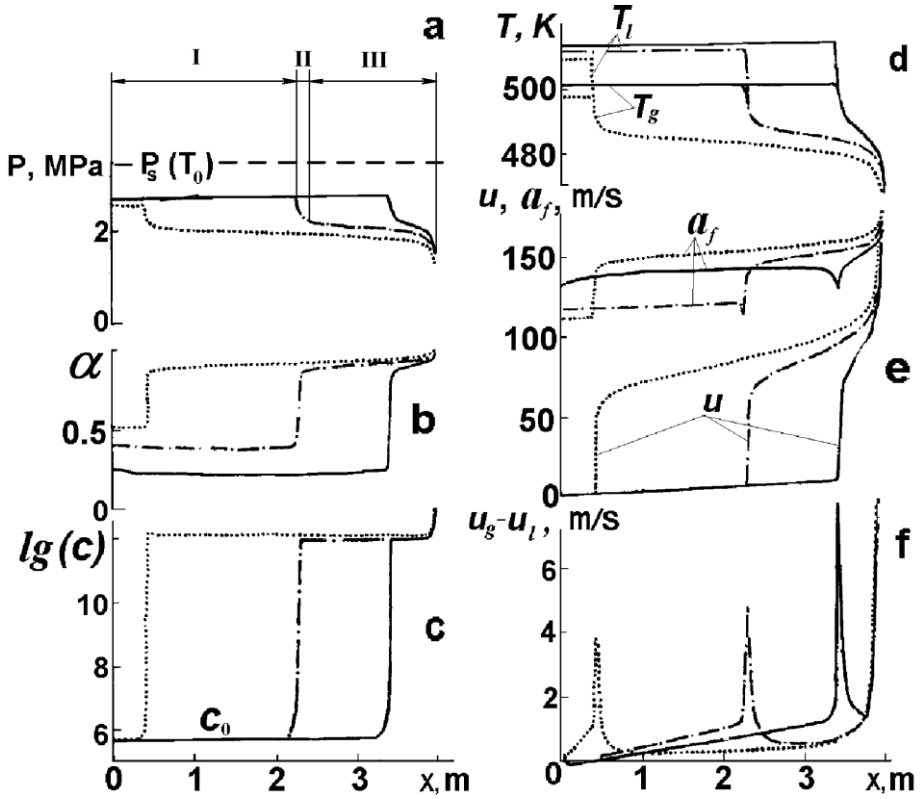

Figure 3. The boiling fronts under high-pressure vessel opening. Versus channel length distributions of the pressure (a), volumetric vapor content (b), the bubble number per mixture unit (c), liquid and vapor temperatures (d), the flow velocity and the frozen speed of sound (e), the difference in phase velocities (f) within 0.1, 0,2 and 0.3 ms since the depressurization (solid, dash and dotted lines, respectively).

Investigating the boiling flow structure at slow and pre-flashing regimes under the same volumetric vapor content [8] he found out that the vapor phase was significantly more dispersed under high-speed flow regimes.

FRAGMENTATION INDUCED BY RADIAL ACCELERATIONS OF BUBBLE SURFACE

In the Figure 1(a,c) the pressure behavior at the wave stage of depressurization looks like an instantaneous drop up to 2.7 MPa. Micro-scale pressure oscillogram fixed in the same experiment of Edvards & O'Brien (Figure 4,left, solid line) shows that it drops lower with a subsequent rising to this level. The bubble number chosen to simulate the pressure level is about a million per liquid kilogram. The liquid with such concentration of centers must not be clear that is not the case and we may suppose that this number is not 'initial'. The bubble number has time to increase within the wave stage of efflux. The reason of the increase is supposed to be the same as the increase in the number of boiling centers at the main stage of efflux, the bubble fragmentation. Within the time interval the pressure rise occurs the bubbles of a zero radius can only grow up to the dimensions of 0.1 mm in diameter. Neither of known schemes for bubble fragmentation (due to Kelvin-Helmholtz instability on the lateral surfaces of the bubble, the destabilization of head and tail surfaces induced by the flow acceleration) 'permits' the fragmentation of such small bubbles.

We have proposed that the development of the instability of the bubble surface may be caused by radial accelerations in the liquid surrounding the bubble (Figure 4,a).When the bubble acceleration is positive, $a > 0$, there is a negative pressure gradient in the surrounding liquid: the pressure decreases with a distance from the bubble center. The situation is qualitatively similar to that when a heavier liquid above a lighter one. They only differ in the forces that induce the pressure gradient.

It is reasonable to characterize the proposed type of instability by the Bond number as well, substituting the gravity for the inertia.

$$Bo = \frac{4a^2 \rho_l \dot{\omega}_a}{\sigma}, \qquad \dot{\omega}_a = \frac{d\omega_a}{dt}, \tag{9}$$

Constructing the fragmentation scheme we will use (as we do for the fragmentation scheme due to Kelvin-Hemholtz instability) the results of the solution of the problem about the growth of small perturbations of a flat interfacial surface under the action of the body force of $\dot{\omega}_a$ density (Birkhoff, 1960). A dispersion analysis gives the law of the versus time dependence of the amplitude of a sine-shaped perturbation of the length λ:

$$\delta = \delta_0 \exp\left[I\, t - \mathrm{i} \frac{2\pi}{\lambda} x \right] \qquad I(\lambda) = \sqrt{\frac{2\pi}{\lambda}\dot{\omega}_a - \frac{8\pi^3}{\lambda^3}\frac{\sigma}{\rho_l}}, \qquad \mathrm{i}^2 = -1$$

From the conditions $dI/d\lambda = 0$ and $d^2 I/d\lambda^2 < 0$, we find the length of the wave with the fastest growing amplitude:

$$\lambda^* = \sqrt{\frac{12\pi^2\sigma}{\rho_l}}$$

Supposing a bubble to break-up by the waves with the length λ^* which cannot exceed the bubble diameter, $\lambda \le 2a$ (Nigmatulin, 1989), we obtain the expression for the Bond number (9), the estimation for its critical value, $Bo^* = 4\pi^2$, the characteristic time of a bubble fragmentation and

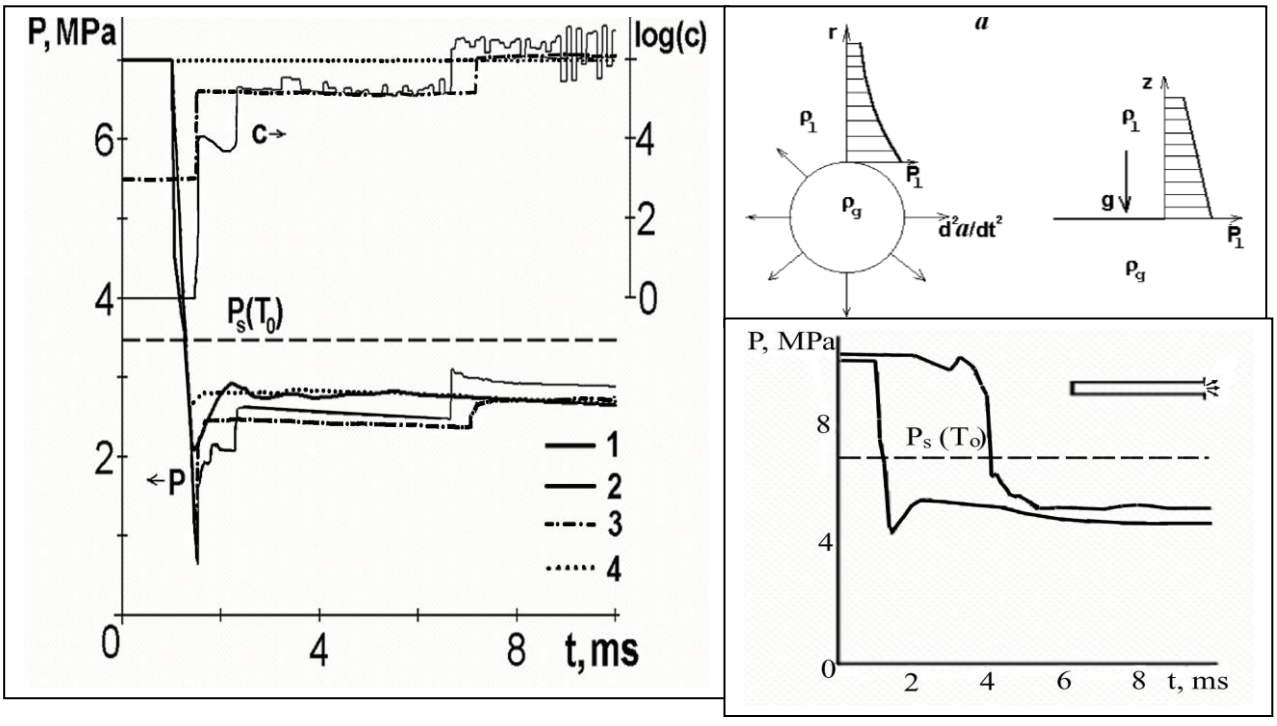

Figure 4 The scheme of the development of the bubble surface instability (a). Left-hand, small-scale pressure and bubble number oscillograms in cross-section 1.1 m from the open vessel end: 1, experiment; 2-4, calculations with the advanced model for different c_0 values: 1, 10^3, 10^6/kg. Right-hand bottom, versus time experimental pressure dependences: the tube of 7.5 cm diameter (left), 10.3 MPa, 559 K (Edwards and O'Brien, 1970); the tube diameter is 1.27 cm (right), 10.3 MPa, 563 K (Lienhard et al, 1978).

the number of bubble fragments.

$$\tau^* = \sqrt{\frac{\rho_l a^3}{\sigma}}\left(\frac{\mathrm{Bo}^*}{\mathrm{Bo}}\right)^{3/4} \qquad \frac{c^*}{c} = \frac{2a}{\lambda^*} \approx \sqrt{\frac{\mathrm{Bo}}{\mathrm{Bo}^*}}. \tag{10}$$

Within the framework of the homobaric model, we will calculate the radial acceleration of the phase interface from the equation for a bubble mass balance $dm_g/dt=j$, rewritten it in the form:

$$a\omega_a + \frac{1}{3}a^2\frac{\dot{P}}{P} = \frac{D_l}{2}\mathrm{Ja}\,\mathrm{Nu} \tag{11}$$

Differentiating (11) with respect to time gives:

$$a\dot{\omega}_a = \frac{D_l}{2}\left[\left(\mathrm{Nu}+\mathrm{Ja}\frac{d\,\mathrm{Nu}}{d\,\mathrm{Ja}}\right)\frac{d\,\mathrm{Ja}}{dt} - \frac{2}{3}\mathrm{Ja}\,\mathrm{Nu}\frac{\dot{P}}{P}\right] - \omega_a^2 - \frac{a^2\ddot{P}}{3P} + \frac{5a^2\dot{P}^2}{9P^2} \tag{12}$$

$$\frac{d\,\mathrm{Ja}}{dt} = -\frac{jn(i_g - i_l)}{\rho_g h(1-\alpha)} - \frac{c_l\rho_l}{\rho_g h}\left(\frac{T_l - T_s}{P} + \frac{dT_s}{dP}\right)\dot{P} \qquad \dot{P} = \frac{dP}{dt}, \quad \ddot{P} = \frac{d^2P}{dt^2}$$

$\dot{P}$, $\ddot{P}$ are substantial time derivatives of the pressure. These derivatives are expressed via time derivatives of specific volume with the equation of the mixture state. The equation below (where a_f is a 'frozen' speed of sound in the mixture) is derived from the equations of mass balance for mixture and vapor and state equations for liquid and vapor.

$$\frac{dP}{dt} = \rho^2 a_f^2\left(-\frac{dV}{dt} + 2\pi D_l a\,\mathrm{Ja}\,\mathrm{Nu}\,c\right) \qquad a_f = \left(\frac{\rho\rho_l(1-\alpha)}{\beta^2} + \frac{\rho\alpha}{P}\right)^{-1/2} \tag{13}$$

After differentiating (13) with respect to time, we obtain

$$\frac{d^2P}{dt^2} = \rho^2 a_f^2\left\{-\frac{d^2V}{dt^2} - \left(jc - \frac{2\chi}{P}\dot{P}\right)\frac{\dot{P}}{\rho_g P} + 2\pi D_l c\left[\omega_a\,\mathrm{Ja}\,\mathrm{Nu} + a\left(\mathrm{Nu}+\mathrm{Ja}\frac{d\,\mathrm{Nu}}{d\,\mathrm{Ja}}\right)\dot{\mathrm{Ja}}\right]\right\} \tag{14}$$

Using balance equations for the mixture mass and momentum (1) we may express the first and second substantial time derivatives of the specific mixture volume, $V = 1/\rho$, in term of the derivatives with respect to coordinate. For the parameter distribution known, time derivatives may, thus, be calculated for each time instant/step.

$$\frac{dV}{dt} = V\frac{\partial u}{\partial x}, \qquad \frac{d^2V}{dt^2} = V\left[\left(\frac{\partial u}{\partial x}\right)^2 - \frac{\partial}{\partial x}\left(V\frac{\partial P}{\partial x}\right)\right]$$

Thus all the parameters for Bond number estimation may be obtained with the equations (11)-(14).

Using the model version considering the possibility of bubble fragmentation caused by radial accelerations the wave stage of depressurization has been studied numerically. The vessel dimensions and the water parameters are taken from the same experiment of Edvards & O'Brien (1970): P_0=7 MPa, T_0=515 K. The no-flow condition is specified at the left-hand end of the channel. At the right-hand side, the pressure attains the atmospheric value within τ =0.256ms, and remains constant afterwards.

Calculated oscillograms for the pressure and bubble number in the cross-sections 3 m spaced from the closed vessel end for different initial concentrations of boiling centers and Bo^*=300 are plotted on the same graph in the Figure 4,left. It is seen that the pressure curves obtained for the meanings of initial centers concentration 1, $10^3$and 10^6 kg^{-1} approaches the same level (corresponding to that obtained in the experiment shown by a thick solid curve) in a few milliseconds. The 'behavior' of the bubble concentration is similar: with no dependence on the initial bubble number tasked the bubble concentration approaches the level 10^6 kg^{-1}.

This numerical experiment explains the contradiction in the mode of boiling centers induction revealed from the analysis of the experimental data. The pressure curves measured for the depressurization of a thin and thick tube (Figure 4,right) coincide in the 'steady' level installed at the wave stage. That means that the intensity of boiling does not depend on the area of the wall surface per liquid volume and may be a ground of the opinion that the bubbled appear in all the volume. However the experiments on the boiling in low-gravity [10] and in the drop isolated from the walls [11] do not show volume-induced bubbles. We may adopt the bubble concentrations tasked in numerical experiment to be the concentration of wall-induced bubbles. We see that the bubbles fragment until their concentration reaches the same level. The reason is that that the waves induced by fragmentation and caused the further fragmentation 'require' certain energy to spread [12]. Liquid energy 'wasted' on evaporation is proportional to the bubble concentration through the interfacial area. Since the limit concentration when the fragmentation is ceases does not depend on the initial one the system 'does not remember' the number of wall-induced bubbles that gives the impression that the bubbles are induced in the volume. The break-up of bubbles explains the boiling-up in the nozzles with a sharp entrance edge [4]. The coefficient of the stream narrowing shows the liquid to be pure and that permits to conclude that the liquid boils up in the absence of walls. A few bubbles appear on the walls does not influence on the liquid pureness and due to break-up their number increase in orders resulting in intensive boiling.

CONCLUSIONS

The model of boiling flow based on the equations of conservation which considers bubbles break-up possibility was used to study the depressurization of a high-pressure vessel. In numerical experiment we obtained the boiling non-equilibriumity with the pressure keeping a certain level at the wave stage and its sudden diminution in a moving front at the main stage of efflux that was in good agreement with the physical experiment. The numerical simulation of the high-pressure vessel depressurization has shown bubbles fragmentation to be an important mechanism of interfacial surface formation specific for flashing flows. A multiple bubble fragmentation induced by the accelerated movement of the surface of rapidly expanded bubble is a reason of the volume-type boiling up after the pressure drop.The bubble break-up induces by the difference in phase velocities is 'responsible' for an explosive evaporation in boiling fronts.

NOMENCLATURE

QUANTITY	SYMBOL	COHERENT SI UNIT
Bubble concentration per unit mass per unit volume ($n = c\,\rho$)	 c n	 1/kg $1/m^3$
Drug Coefficient $\begin{pmatrix} = 64/\mathrm{Re}_D \;\; for\; \mathrm{Re}_D \le 2300 \\ = 0.0278 \quad for\; \mathrm{Re}_D > 2300 \end{pmatrix}$	ξ	dimensionless
Dynamic liquid viscosity coefficient	μ	kg/(м s)
Force buoyancy virtual mass Stokes force	f_A f_m f_μ	$kg\ m/s^2$
Vapour content mass volumetric	 χ α	dimensionless
Intensity of bubble break-up	ψ	$kg^{-1}\ s^{-1}$
Length Bubble radius Channel diameter	 a D	 m m

Mixture density ($\rho = (1-\alpha)\rho_l + \alpha\rho_g$)	ρ	kg/m^3
Pressure	P	H/m^2
Rate of liquid evaporation into a bubble	j	kg/s
Reynolds Number for a channel $\left(= \frac{\rho_l D u}{\mu_l} \right)$	Re_D	dimensionless
Specific enthalpy liquid, vapour mixture ($i = (1-\chi) i_l + \chi i_g$)	i i_l and i_g i	m^2/c^2 m^2/c^2 m^2/c^2
Temperature liquid saturation	T T_l $T_s(P)$	K K K
Velocity flow velocity velocity of liquid, of bubbles velocity of bubble surface	 u u_l, u_g ω_a	 m/s m/s m/s
Viscous resistance Coefficient	c_μ	dimensionless

ACKNOWLEDJEMENTS

The work was supported by the Russian Foundation for Basic Research (grant No.08-08-00222).

REFERENCES

1. Ivashnyov, O.E., Ivashneva, M.N. and Smirnov, N.N. Slow waves of boiling under hot water depressurization, *J. Fluid Mechanics*, Vol. 413, pp 148-180, 2000.
2. Ivashnev, O.E. Specific features of the modelling of boiling-fluid flows, *Fluid Dynamics*, Vol. 43, No. 3, pp 390-401, 2008.
3. Edvards, A.R. and O'Brien, T.P. Studies on phenomena connected with the depressurization of water reactors, *J. Br.Nucl. Engng. Soc.*, Vol. 9, pp 125-135, 1970.
4. Nigmatulin, B.I. and Soplenkov, K.I. The study of an unsteady efflux of boiling liquid from channels in a thermodynamic non-equilibrium approximation, *Teplofizika Vysokikh Temperatur*, Vol. 18, pp 118-131, 1980.
5. Nigmatulin, R.I. *Dynamics of multiphase media*, Hemisphere, Washington, 1987.
6. Winters, W.S. and Merte, H. Experimental and nonequilibrium analysis of pipe blowdown. *Nucl. Sci. Engng.*, Vol. 69, pp 411-429, 1979.
7 Isaev, O.A. Liquid boiling under a fast pressure falls in an adiabatic unsteady stream. *PhD Thesis*, Sverdlovsk, 1980.
8. Yamamoto, T., Yeda, U., Ishihara I., Ozawa, M, Umekawa, H. and Matsumoto R. Flow boiling heat transfer of carbon dioxide at high pressure in horizontal mini-channels, *Proc. 6th Int. Conf. on multiphase flow*, Leipzig, Germany, July 9-13, 2007, pp 476-584.
9. Lienhard D., Alangir M. T., An initial stage of hot water depressurization under a sudden pressure drop, *Teploperedacha*, Vol. 100, N 3, pp 98-106, 1978.
10. Hanaoka, Y., Tokura, I. and Tonino, H. On incipience of bubble formation in depressurization Process under micro-gravity environment, *Proc. Workshop on Short-Term Experiments under Strongly Reduced Gravity Drop Tower Days* 1998 in Hakkaido, pp 98-101.
11. Shepherd, J.E. and Sturtevant, B, Rapid evaporation at a superheated limit, *J. Fluid Mech.*, Vol 121, pp 379-402, 1982.
12. Ivashnev, O.E. and Smirnov N.N., Appearance of nucleation shocks in a boiling liquid, *Fluid Dynamics*, Vol. 40, No. 3, pp 426-438, 2005.

NUMERICAL FLOW ANALYSIS FOR SETTLING POND DESIGN

D.K. Lee[1,*], Y.J. Kim[1,] and Y.D. Jo[1]
[1]Korea Institute of Geoscience & Mineral Resources (KIGAM), Daejeon, Korea Republic

ABSTRACT. Numerical flow analysis for settling pond design has been conducted to investigate the optimal flow characteristics, including the inflow rate and the shape and depth of a settling pond. Total area and maximum depth of the pond is 500 m^2 and 3 m respectively. We define retention time, retention time ratio, homogeneity index and inflow exchange efficiency for choosing the optimal conditions. As a result of this study, the optimum flow rate and width:length of the pond were found to be under 15 ℓ/sec and 1:5, respectively.

Keywords: *settling pond, inflow age, retention time*

INTRODCUTION

Iron exists in the ferrous form within the country's mine workings. Upon exposure to the surface the ferrous iron oxidizes to become ferric iron, a hydrolysis reaction which causes the precipitation of ferric hydroxide, these particles fall from the solution and join together to form a thick substance that coats the pond. A settling pond stores mine drainage within a given period for leading the precipitation of ferric hydroxide in mine drainage, so that remediation of contaminated effluents can be accomplished. The key to design of a settling pond is to ensure that the retention time of mine drainage in a pond is sufficiently long that iron precipitates will settle out effectively. In past retention time recommendations for such purposes have ranged from as little as 8 hours to more than 72 hours. It has revealed the existence of a relatively robust linear relationship between the percentage reduction in the influent iron concentration and nominal hydraulic retention time (Parker, 2003). In the UK Coal industry, basic water treatment design guidance for engineers was provided by NCB (1982). Total pond volume and flow rate are often designed on the basis of 48 hours retention time (Laine and Jarvis, 2003) and 100 m^2 of pond surface area for every liter/sec of drainage. The length to width ratio should be within the range 2:1 to 5:1 (NCB, 1982). The depth of the pond is usually set at around 3 m to to prevent re-suspension of settled particles due to wind (PIRAMID Consortium, 2003). The theoretical maximum concentration of ferrous iron that can be oxidized in a single aeration cascade is 50 mg/l. But practical experience suggests that 30 mg/l ferrous iron is a more realistic figure (NCB, 1982). For discharges with in excess of 30 mg/l it will be necessary to have a series of aeration cascades, with settling ponds in between. Until now, the nominal hydraulic retention time calculated simply as the ratio of the volume of mine drainage stored in a pond to the flow rate is used for design of a settling pond. The flow distribution characteristics in a pond varies as shape and depth of a pond and flow rate of mine drainage so that more sophisticated techniques such as application of the physics represented by Navier-Stokes equation are needed.

* Corresponding author: PhD. D.K. Lee
Phone: + (82)-42-868-3228, Fax: + (82)-42-868-3418
E-mail address: ldk@kigam.re.kr

MUMERICAL METHODS

Concept of inflow age

The concept 'air age' in the field of air conditioning was introduced to estimate the retention time of the inflow mine drainage. The air age means the time that the inflow air as shown in Figure 1 moves down to the point P and the retention time means the time that air flows down to the outlet. Fluid of this study is not air but mine drainage, thus the air age was renamed as 'inflow age' and used.

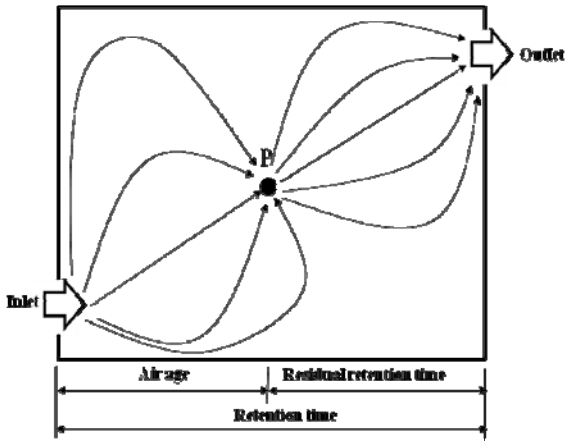

Figure 1. The concept of air age.

Suggestions of the estimating indices for settling pond design

Retention time

Retention time means the time needs that the inflow mine drainage from the entrance reaches to exit and is defined in this study as the areal average inflow age using the result of computational analysis.

Retention time ratio

Retention time ratio is a guideline showing how long does the inflow mine drainage stay in the pond and is defined as the ratio of nominal retention time to the retention time.

Homogeneity Index

Homogeneity index is defined as the value of the average retention time of the route with the minimum staying time from the entrance to the exit divided by the volume average retention time. The homogeneity index closer to 1 indicates that the distribution of the retention time has better homogeneous.

Inflow Exchange Efficiency

Inflow exchange efficiency is defined as the ratio of mean retention time and inflow exchange. Inflow exchange efficiency means the shortest time to take for the pond to be exchanged with the fresh inflow mine drainage and is defined as the ratio of the average retention time to the inflow exchange time.

Cases setting of a settling pond

A schematic of a settling pond is shown in Figure 2. Dimensions of inlet and outlet of the pond are the same as 0.3 m × 0.3 m. Area of the pond is 500 m^2 in all cases. Flow rate at inlet is determined on the basis of 100 m^2 of pond surface area for every liter/sec of mine drainage by NCB(1982). Table 1 gives all cases on flow rate and shape and depth of a settling pond.

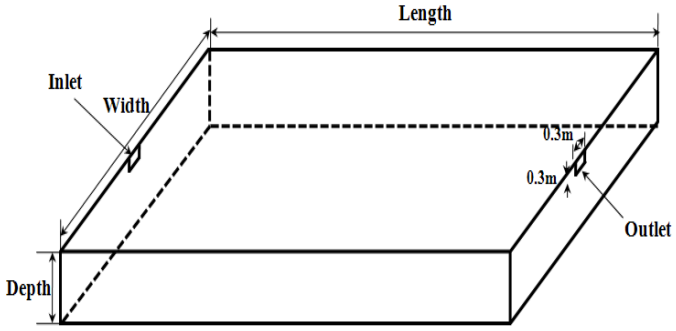

Figure 2. Schematic of a settling pond

Table 1. Cases of settling pond.

Case	Width:length	Flow rate(ℓ/sec)	Length(m)	Width(m)	Depth(m)
1	1:3	1	12.90	38.73	3
2	1:3	5	12.90	38.73	3
3	1:3	10	12.90	38.73	3
4	1:3	15	12.90	38.73	3
5	1:3	20	12.90	38.73	3
6	1:2	5	15.81	31.62	3
7	1:4	5	11.18	44.72	3
8	1:5	5	10.00	50.00	3
9	circle	5	25.23	-	3
10	1:2	5	15.81	31.62	2
11	1:3	5	12.90	38.73	2
12	1:4	5	11.18	44.72	2
13	1:5	5	10.00	50.00	2
14	circle	5	25.23	-	2
15	1:2	5	15.81	31.62	1
16	1:3	5	12.90	38.73	1
17	1:4	5	11.18	44.72	1
18	1:5	5	10.00	50.00	1
19	circle	5	25.23	-	1

Mesh construction

In the case that if both sides on the basis of the symmetric plane have the same shape and flow conditions, the analysis has been made only for half. The meshes were more denser at near inlet and outlet and the grid sizes were increased gradually as closer to the middle of the pond.

Numerical analysis method

Computational analyses were performed for the three governing equations as continuity equation, momentum equation and turbulent dissipation equation to predict the flow distribution, retention time and estimating indices in 3-dimensional settling pond. In this study, the flow rate in the settling pond was very low but the k-ε turbulent model was used in consideration of the sudden change in the velocity at the inflow part.

RESULTS AND DISCUSSION

Flow characteristics by the flow rate at inlet

Figure 3 shows the distributions of the velocity and the inflow age of the mine drainage in the pond according to the inflow rate. As shown in the figure, the velocity in the pond was generally increased by increase in the inflow rate and the distributions of the velocity at the mine drainage

inlet and outlet were symmetry with same trends. On the other hand, stagnant areas with relatively low velocity were formed at the corners of rectangular ponds. In most cases, the smallest inflow age could be seen along the straight line from the inlet to the outlet, while the farther from the straight line the higher age of inflow to be achieved. Especially because the corners of the rectangular ponds are the stagnant areas, the ages of inflow in this area are relatively quite high.

Figure 3. Distributions of velocity and inflow age according to inflow rate in settling ponds.

Case	inflow rate (ℓ/sec)	Velocity distribution	velocity (m/sec)	inflow age distribution	inflow age (hr)
1	1		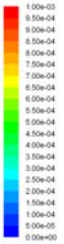	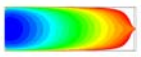	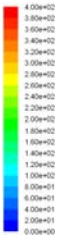
2	5				
3	10				
4	15				
5	20				

Figure 4(a) represents the relationship between the flow rate and the volumetric average velocity in the pond. The figure indicates that the volumetric average velocity and the flow rate are in proportional. Figure 4(b) shows the retention time verse the different flow rates for cases 1 to 5 with the depth of 3 m. It was found that the flow rate is in inversely proportional to the retention time in the figure. Figure 4(c) shows that the ratio of the retention time at the outlet to the nominal retention time. It was confirmed that the retention time increased as the flow rate increased.

The homogeneity index and the exchange efficiency versus the flow rate are presented in Figure 4(d) and Figure 4(e), respectively. It can be seen in the figure that the homogeneity index and the exchange efficiency nearly kept constant up to the flow rate of 15 ℓ/sec and was decreased from the flow rate of 20 ℓ/sec. It could be considered that the homogeneous index and the inflow exchange efficiency decreases as flow rate increase more than 15 ℓ/sec in the settling pond.

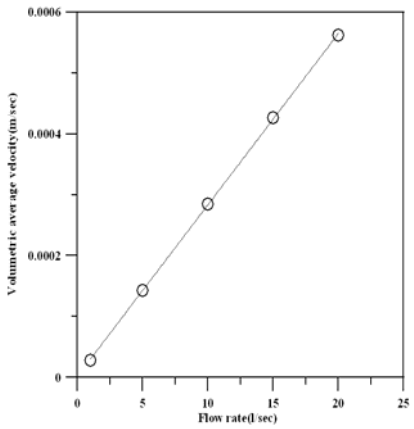

(a) Volumetric average velocity

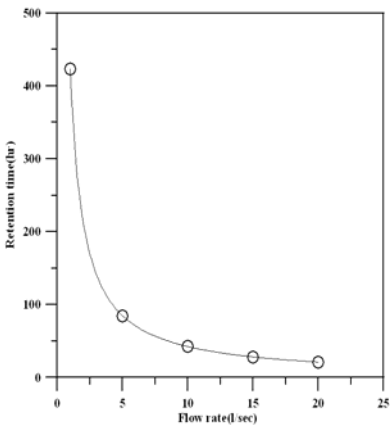

(b) Retention time

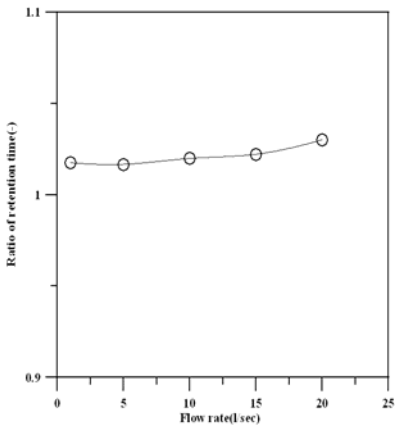

(c) Retention time ration

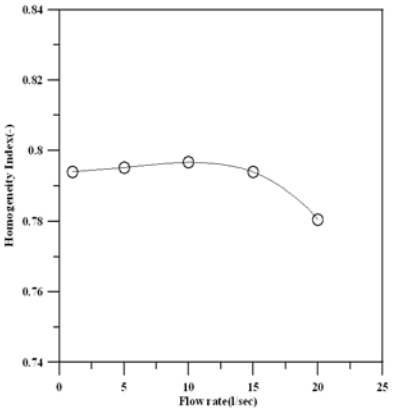

(d) Homogeneity index

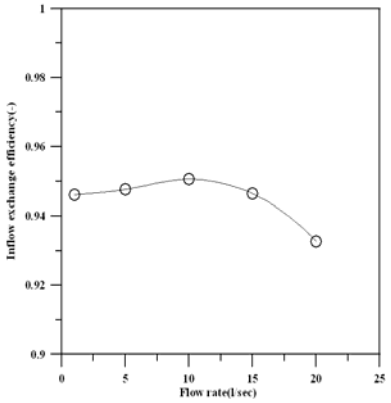

(e) Inflow exchange efficiency

Figure 4. Flow characteristics by inflow rate in a settling pond.

Flow characteristics by the shape of settling ponds

Figure 5 demonstrates the distributions of the velocity and the inflow age in the settling ponds with different shapes when the mine drainage inflows under the same condition with 5 ℓ/sec of flow rate in a settling pond with 500 m^2 of surface area. As the ratio of the length to the width is increased, the area of the stagnant region around the corners decreases and the velocity near the central region increases gradually. In the case that the settling pond has round-shape, the velocity is relatively lower than in the rectangular pond. For the distribution of the inflow age, as the ratio of the length to the width increases, a homogeneous distribution along the direction to outlet was found. However, if the settling pond is round shape, the inflow age is high along the both sides and it was found that the stagnant area is increased.

Figure 5. Distributions of velocity and inflow age according to shape and depth of settling ponds.

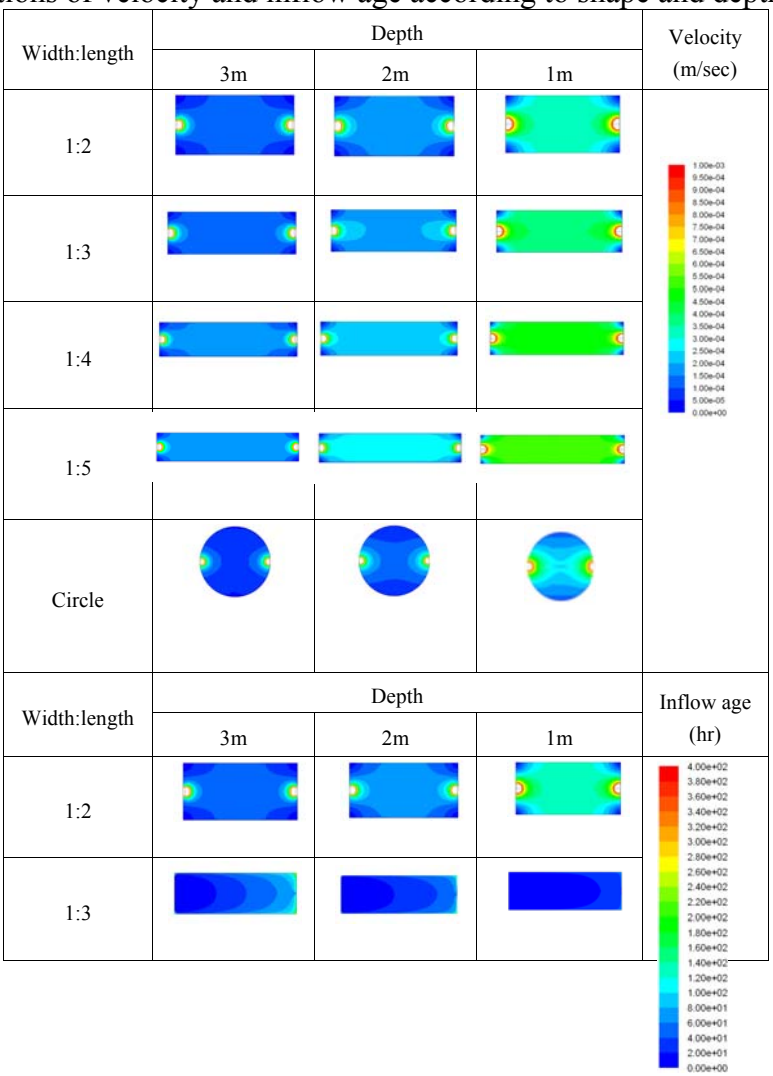

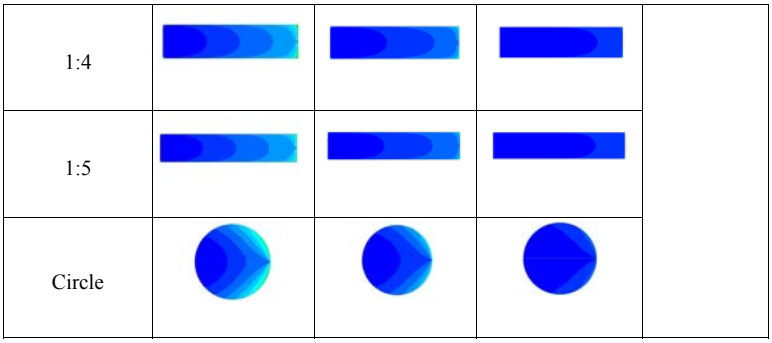

Figure 6(a) shows the relationship between shape of the pond and the volumetric average velocity. By increasing the ratio of length/width and also decreasing the depth as shown in the figure, the volumetric average velocity increased. It should be noted that the depth of the pond gave bigger effect than the ratio of length and width of the pond. However, the volumetric average velocity in the round pond was smaller than in the rectangular pond. Figure 6(b) represents the change of the retention time for the shape of the pond. As shown in the figure 6(b), if the depth of the pond in rectangular shape was constant, the retention time was not changed regardless the length/width ratio of the pond, while the retention time in the round pond was little higher than in the rectangular one. Therefore it was found out that there is no effect of the length/width ratio in the retention time in the rectangular pond. The retention time ratio for the different pond shapes were demonstrated in Figure 6(c). From the figure, it was found that the retention time ratio, except with 1 m of depth, decreased with the following sequence; the round-shaped pond, the rectangular ponds with the width:length of 1:2, 1:3, 1:4 and 1:5. The homogeneity index for the different pond shapes were shown in Figure 6(d). The smallest homogeneity index at the round pond and the increase in the homogeneity index by increase in the length/width ratio of the rectangular pond were found out from the figure. In Figure 6(e), the relationship between the shape of the pond and the inflow exchange efficiency was presented. As seen in the figure, the inflow exchange efficiency was increased as the length/ width ratio of the rectangular pond was increased. For the rectangular pond, the efficiency became to be lowest at the pond with the length/width ratio of 1:2 and became to be highest at the pond with the ratio of 1:5. On the other hand, for round pond the inflow exchange efficiency was lowest at the pond with 1 m of depth.

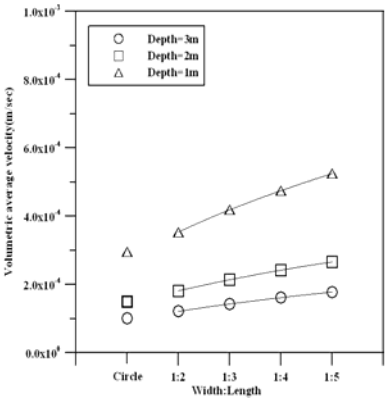

(a) Volumetric average velocity

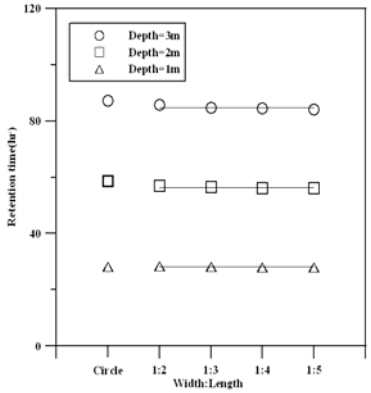

(b) Retention time

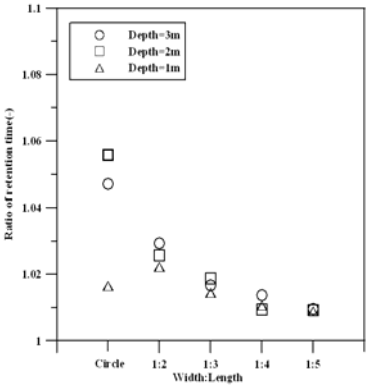

(c) Retention time ratio

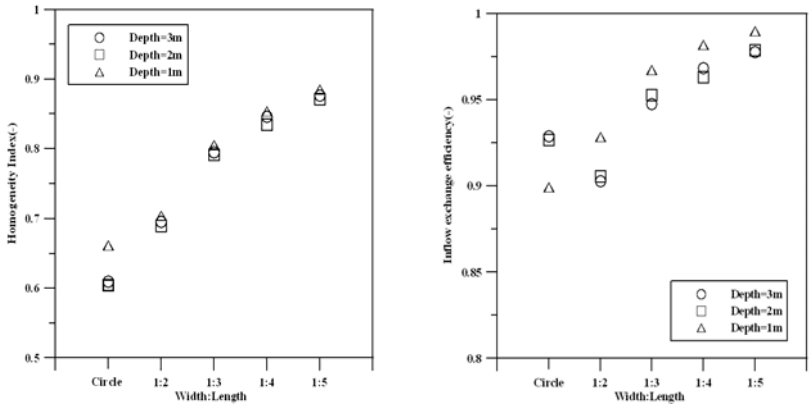

(d) Homogeneity index (e) Inflow exchange efficiency

Figure 6. Flow characteristics by shapes of settling ponds.

Flow characteristics by the depth of a settling pond

Figure 5 shows the distributions of the velocity and the age of inflow for the different depths when the mine drainage inflows under the same condition with the flow rate of 5 ℓ/sec in 500 m^2 of the pond area. As shown in the figure, for all of the pond shapes as the depth of the pond increased, the average velocity in the pond was rapidly decreased in the same inflow rate. Especially, when the depth of the pond increased in the rectangular pond, it was found that the range of stagnant region was expanded around the corner parts. The inflow age increased by increasing the depth of the pond as well, and the inflow age gave a high value at the stagnant region. Figure 7(a) represents the relationship of the volumetric average velocity and the depth for the different pond shapes. For the all cases in the figure, the volumetric average velocity decreased as the depth increased. In Figure 7(b), the relationship of the retention time to the depth for different pond shapes was demonstrated. The retention time was linearly proportional to the depth of the settling pond. For the rectangular ponds, similar linear relationships to the retention time regardless the shape of the pond was presented while for the round pond, the retention time was little higher than in the rectangular pond. Figure 7(c) gives the retention time ratio for the depth of different ponds. In the rectangular ponds with the width:length of 1:5, 1:4 and 1:3, the retention time ratio did not changed by the depth, but in the pond with the width:length of 1:2, the retention time ratio was slightly increased by the increase of the depth. However, in the round pond the retention time ratio showed a parabolic trend for the retention time ratio as the depth increased. The homogeneity index for the depth of different shaped ponds was illustrated in Figure 7(d). The homogeneity index has almost same values for all cases in the rectangular ponds, but in the round pond it gives the biggest value when the depth is 1 m and the homogeneity index tends to decrease as the depth increases. Figure 7(e) shows that the relationship of the inflow exchange efficiency to the depth for different pond shapes. The inflow exchange efficiency was decreased by increasing the depth of the rectangular settling pond. It was interesting to have an almost same efficiency value for the ponds with 2 m and 3 m of depths while the inflow exchange efficiency increment was higher for the pond with smaller length/width ratio of the rectangular pond. For the round pond, there was a trend that the inflow exchange efficiency increased as the depth increased.

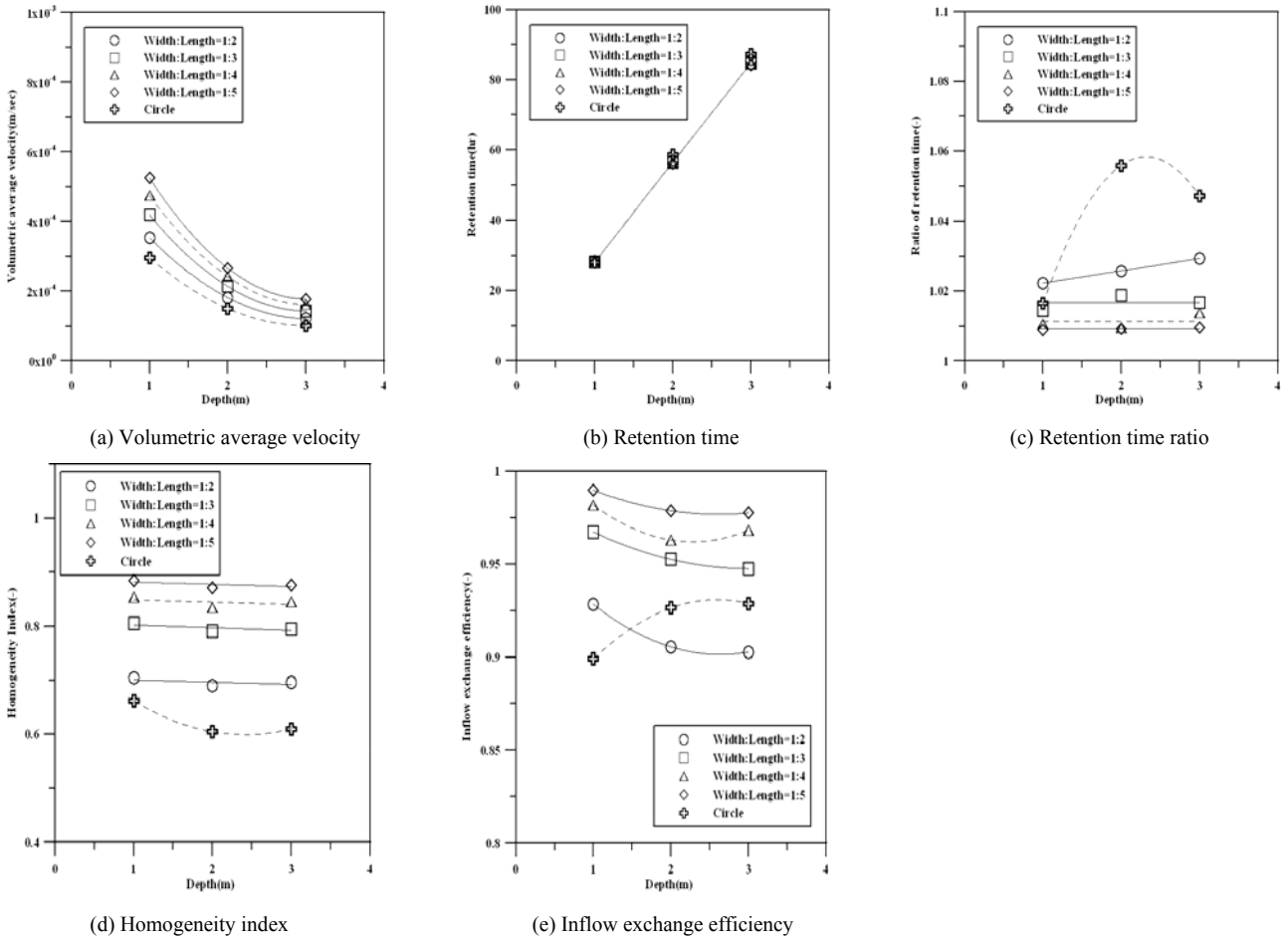

(a) Volumetric average velocity (b) Retention time (c) Retention time ratio

(d) Homogeneity index (e) Inflow exchange efficiency

Figure 7. Flow characteristics by depth of settling pond.

CONCLUSIONS

1) To estimate the retention time for settling pond design a computational analysis method was proposed using the concept of the inflow age And, the retention time, the stagnant level, the distribution level and the exchange level of the mine drainage in a settling pond were also proposed by defining the concept of retention time, retention time ratio, homogeneity index and inflow exchange efficiency, respectively. Therefore, the basis to find out the optimum conditions needed for designing a settling pond was established.

2) The flow characteristics for the flow rate in the rectangular pond with the area of 500 m^2, the width:length of 1:3 and the depth of 3 m were analyzed. It was confirmed that the maximum proper inflow rate is 15 ℓ/sec by analyzing the estimating indices suggested for settling pond design.

3) The retention time was identical regardless of the shape of the settling pond, and as the length become larger than the width, the stagnant level get lowered, more homogeneous distribution get appeared and therefore it is more appropriate as an settling pond. However, the round pond was revealed to be the worst settling pond.

4) To predict the depth of the pond or the time that the sediments in the pond need to be cleaned, the relation between the retention time and the depth of the rectangular pond was proposed on figure. The effect on the retention time ratio and the homogeneity index was negligible and only the inflow exchange efficiency tended to be decreased by increasing the depth.

ACKNOWLEDGMENTS

This research was supported by the Research Project of the Korea Institute of Geoscience and Mineral Resources(KIGAM) funded by the Ministry of Knowledge Economy of Korea.

REFERENCES

1. Banks, S.B., 2003, The UK Coal Authority Minewater-Treatment Scheme Programme: Performance of Operational Systems, Journal of the Chartered Institution of Water and Environmental Management, Vol. 17, No 2, pp. 117-122.
2. Laine, D.M. and Jarvis, A.P., 2003, Engineering design aspects of passive in situ remediation of mining effluents, Land Contamination & Reclamation, Vol. 11, No. 2, pp. 113-125
3. NCB, 1982, *Technical management of water in the coal mining industry*. Mining Department, National Coal Board, London, pp. 129.
4. Parker, K., 2003, Mine water management on a national scale - experiences from the Coal Authority, Land Contamination and Reclamation, Vol. 11, No. 2, pp. 181-190.
5. PRAMID Consortium, 2003, Engineering Guidelines For the Passive Remediation of Acid and/or Metalliferous Mine Drainage and Similar Wastewaters, Passive In-situ Remediation of Acidic Mine/Industrial Drainage, pp. 61-64.

NUMERICAL MODEL OF PULVERIZED COAL COMBUSTION IN FURNACE

R. Straka[1,*], J. Makovička[2], M. Beneš[2], V. Havlena[2]

[1] AGH University of Science and Technology, Cracow, Poland
[2]Czech Technical University, Prague, Czech Republic

ABSTRACT. We describe behaviour of the air-coal mixture using the Navier-Stokes equations for gas and particle phases, accompanied by a turbulence model. The undergoing chemical reactions are described by the Arrhenian kinetics. We also consider the heat transfer via conduction and radiation. Moreover we use improved turbulence-chemistry interactions for reaction terms. The system of PDEs is discretized using the finite volume method (FVM) and an advection upstream splitting method as the Riemann solver. The resulting ODEs are solved using the 4th-order Runge-Kutta method. Sample simulation results for typical power production levels are presented.

Keywords: *Turbulence, heat transfer, combustion, NO_x*

INTRODUCTION

Our main motivation of the combustion model research is its use for design of the combustion chamber geometry and other important parameters needed for the boiler operation. In this paper we compare experimental and simulated values of the temperature fields and present other simulated properties of a boiler, mainly NO production. Production of the nitrogen oxides, which strongly depends on the temperature distribution, can be controlled by intelligent distribution of fuel and oxygen into the burners. Because the experiments on a real device are prohibitively cumbersome and expensive, in extreme cases even hazardous, the only way to test the behaviour of the furnace is mathematical modelling.

An industrial pulverized coal furnace is basically a vertical channel with square cross-section. The dimensions are determined by the power generation requirements from the order of meters to tens of meters. In the case we model, the furnace has 35 meters in height and 7 meters in width and depth. Power production of such a furnace is about 90 MW, and the furnace coupled with a steam generator is capable of producing about 100 tons of pressurized superheated steam per hour.

In the bottom of the channel walls, there are several burners, jets where the mixture of the air and coal powder is injected. The mixture then flows up and burns, while it transfers some of the combustion heat to the walls containing the water pipes.

At the top, the heated flue gas continues to flow to the superheater channel where further heat exchange occurs, and this has already been covered by [3].Our main concern is now modelling of the processes in the area, where the coal gets burnt and nitric oxides are produced. We numerically investigated influence of different setups of the burners on the production of NO and total heat production and utilization by the boiler walls. We also compared numerical results with experimentally measured values from real coal power plant.

* Corresponding author: R. Straka
Phone: + (48)-12-6172637
E-mail address: straka@metal.agh.edu.pl

$$\frac{\partial \rho}{\partial t} + \frac{\partial (\rho u_j)}{\partial x_j} = 0$$

$$\frac{\partial}{\partial t}(\rho u_i) + \frac{\partial}{\partial x_j}(\rho u_i u_j) = -\frac{\partial p}{\partial x_i} + \frac{\partial}{\partial x_j}\left[\mu_{\text{eff}}\left(\frac{\partial u_i}{\partial x_j} + \frac{\partial u_j}{\partial x_i} - \frac{2}{3}\delta_{ij}\frac{\partial u_l}{\partial x_l}\right)\right] + g_i$$

$$\frac{\partial}{\partial t}(\rho h) + \frac{\partial}{\partial x_j}(\rho u_j h) = -n_{\text{coal}}\frac{\mathrm{d}m_{\text{coal}}}{\mathrm{d}t}h_{\text{comb}} + q_r + q_c + q_s$$

$$\frac{\partial}{\partial t}(\rho Y_i) + \frac{\partial}{\partial x_j}(\rho Y_i u_j) = \nabla \vec{J}_i + R_i$$

$$\vec{J}_i = -\left(\rho D_{i,m} + \frac{\mu_t}{\text{Sc}_t}\right)\nabla Y_i, \quad \mu_{\text{eff}} = \mu + \mu_t = \mu + \rho C_\mu \frac{k^2}{\epsilon}$$

$$-q_c = \nabla \cdot (\lambda \nabla T), \quad q_r = \nabla \cdot \left(cT^3 \nabla T\right), \quad q_s = -A(T_{\text{gas}} - T_{\text{wall}}) - B(T_{\text{gas}}^4 - T_{\text{wall}}^4)$$

Figure 1. Navier-Stokes equations

MATHEMATICAL MODEL

The mathematical model of combustion is based on the Navier-Stokes equations for a mixture of multiple components where the coal particles are treated as one of the phases. Unlike e.g. in [2], where the gas particles are treated separately and use separate equations of momentum, we chose to use this approach, as it simplifies the model especially when dealing with turbulence, and also removes several empirical relations and constants.

Currently, the following components of the mixture are considered:

- chemical compounds engaged in major thermal and fuel NO reactions (nitrogen, oxygen, nitric oxide, hydrogen cyanide, ammonia, carbon dioxide and water
- char and volatile part of the coal particle

The gas phase is described by the equations which can be seen from Figure 1.

The particle mass change rate is currently described by the one-step Arrhenian kinetics, which is used separately for the char and volatile coal components - combustion of the volatiles is more rapid than combustion of the char

$$\frac{dm}{dt} = -Am^a \left[O_2\right]^b \exp\left(\frac{\Delta E}{\overline{R}T}\right) \tag{1}$$

These equations are accompanied by the equation of state, as usual

$$p = (\gamma - 1)\rho\left(u - \frac{1}{2}u^2\right) \tag{2}$$

For the turbulence modelling, we use the standard $k-\varepsilon$ model, which describes the evolution of turbulence using two equations (see Figure 2).

SIMPLIFIED MODEL OF NO CHEMISTRY

$$\frac{\partial}{\partial t}(\rho k) + \frac{\partial}{\partial x_j}(\rho k u_j) = \frac{\partial}{\partial x_j}\left[\left(\mu + \frac{\mu_t}{\sigma_k}\right)\frac{\partial k}{\partial x_j}\right] + G_k - \rho\epsilon$$

$$\frac{\partial}{\partial t}(\rho\epsilon) + \frac{\partial}{\partial x_j}(\rho\epsilon u_j) = \frac{\partial}{\partial x_j}\left[\left(\mu + \frac{\mu_t}{\sigma_\epsilon}\right)\frac{\partial \epsilon}{\partial x_j}\right] + C_{1\epsilon}\frac{\epsilon}{k}G_k - C_{2\epsilon}\rho\frac{\epsilon^2}{k}$$

$$S_{ij} = \frac{1}{2}\left(\frac{\partial u_i}{\partial x_j} + \frac{\partial u_j}{\partial x_i}\right), \quad G_k = \mu_t S^2, \quad S = (2S_{jl}S_{jl})^{1/2}$$

$$C_{1\epsilon} = 1.44, \quad C_{2\epsilon} = 1.92, \quad \sigma_k = 1.0, \quad \sigma_\epsilon = 1.3, \quad \mathrm{Sc}_t = 0.7$$

Figure 2. Turbulence model

This model has been developed to approximately describe the amounts of NO emissions leaving a coal combustion furnace. The real mechanism of coal flue gas production seems to be very complicated, so that just the most important phenomena and reaction paths were considered to provide maximum possibility of using this model in real-time control and operation systems.
There are two major processes attributing to the total NO. The former is known as Thermal NO or Zeldovich and simply consists of oxidation of atmospheric nitrogen at high temperature conditions. The latter is called Fuel NO and describes NO creation from nitrogen, which is chemically bounded in coal fuel. Fuel NO is usually the major source of NO emissions, when the thermal way is suppressed. These are the only mechanisms involved, although a few more could be considered (such as Prompt NO (Fenimore) or Nitrous oxide intermediate mechanisms).

Thermal NO
Thermal NO generation mechanism attributes only at high temperature conditions and is represented by a set of three equations, introduced by Zeldovich [4] and extended by Bowman [5]

$$\begin{aligned} O + N_2 &\overset{k_1}{\leftrightarrow} N + NO \\ N + O_2 &\overset{k_2}{\leftrightarrow} O + NO \\ N + OH &\overset{k_3}{\leftrightarrow} H + NO \end{aligned} \tag{3}$$

All these reactions are considered to be reversible. Rate constants can be found in [8].
In order to compute the NO concentration, concentrations of nitrogen radical, oxygen radical and hydroxyl radical must be known. It is useful to assume that N is in a quasi-steady state according to its nearly immediate conservation after creation. In fact, this N radical formation is the rate limiting factor for thermal NO production, due to extremely high activation energy of nitrogen molecule, which is caused by a triple bond between two nitrogen atoms. Hence, the NO formation rate can be stated as

$$\frac{d[NO]}{dt} = 2k_{+1}[O][N_2]\frac{1 - \dfrac{k_{-1}k_{-2}[NO]^2}{k_{+1}[N_2]k_{+2}[O_2]}}{1 + \dfrac{k_{-1}[NO]}{k_{+2}[O_2] + k_{+3}[OH]}} \tag{4}$$

Under certain conditions, the oxygen molecule splits and recombines cyclically

$$O_2 \overset{K_1}{\leftrightarrow} O + O \tag{5}$$

which can be profitably described by following partial equilibrium approach [6]

$$[O] = K_1 [O_2]^{1/2} T^{1/2} \tag{6}$$

As for OH radical, a similar partial equilibrium approach can be made, according to next reaction

$$O + H_2O \overset{K_2}{\leftrightarrow} OH + OH \tag{7}$$

and the approach is [7]

$$[OH] = K_2 [O]^{1/2} [H_2O]^{1/2} T^{-0,57} \tag{8}$$

Equilibrium constants K_1 and K_2 are as follows

$$K_1 = 36{,}64 \exp\left(\frac{-27123}{T}\right)$$
$$K_2 = 2{,}129 \cdot 10^2 \exp\left(\frac{-4595}{T}\right) \tag{9}$$

Fuel NO

Composition analysis show, that nitrogen-based species are more or less present in coal, usually in amounts of tenths to units of percent by weight. When the coal is heated, these species are transformed into certain intermediates and then into NO. Fuel itself is therefore a significant source of NO pollutants. When a coal particle is heated, it is presumed, that nitrogen compounds are distributed into volatiles and char. In several studies (e.g. [9]) it is unreasonably told, that half of the coal-bounded nitrogen is distributed to volatiles and half into the char. Since there is no reason for a presupposition like this, a parameter α is introduced to describe the distribution of the coal-bounded nitrogen between the volatiles and char part of the coal particle.

$$m_{vol}^N = \alpha m_{tot}^N$$
$$m_{char}^N = (1-\alpha) m_{tot}^N \tag{10}$$

where $\alpha \in [0,1]$.As already mentioned, nitrogen transforms to pollutants via intermediates, which usually are ammonia NH_3 and hydrocyanide HCN. To proceed further, we must define four parameters to describe complex partitioning of the fuel bound nitrogen.

- β is amount of volatile bounded nitrogen which converts to HCN
- δ_1 is distribution of char bounded nitrogen which converts to HCN
- δ_2 is distribution of char bounded nitrogen which converts to NH_3
- δ_3 is distribution of char bounded nitrogen which converts to NO
- $\beta \in [0,1], \delta_1 + \delta_2 + \delta_3 = 1$

Different parametric studies should be carried out to find the best values of these parameters suitable for specific type of coal. Five overall reactions of either NO formation or depletion were incorporated in the combustion part of the numerical code.

<u>*NO, HCN, NH_3 reactions.*</u> According to [10], formation of Fuel NO is given by reactions

$$HCN + O_2 \overset{k_4}{\rightarrow} NO + Z$$
$$NH_3 + O_2 \overset{k_5}{\rightarrow} NO + Z$$
$$HCN + NO \overset{k_6}{\rightarrow} N_2 + Z \tag{11}$$
$$NH_3 + NO \overset{k_7}{\rightarrow} N_2 + Z$$

where k_* are reaction rates taken from [10] and Z are the other products we simply neglect.

Table 1
Air distribution among the burners.

Air setup	Burner 1	Burner 2	Burner 3	Burner 4	OFA
Normal	25%	25%	25%	25%	0%
Air staging 1	50%	20%	20%	10%	0%
Air staging 2	10%	20%	20%	50%	0%
Over-fire air	20%	20%	20%	20%	20%

Heterogeneous reduction of NO. Present char allows following adsorption process to occur (12)

$$Char + NO \xrightarrow{k_8} N_2 + Z$$

Levy [11] uses surface area of pore (BET) to define NO source term (13)

$$R_{NO} = k_8 c_s A_{BET} \overline{M}_{NO} p_{NO}$$

$$k_8 = 2{,}27 \cdot 10^3 \exp\left(\frac{-17168{,}33}{T}\right)$$

In order to evaluate overall NO source term, single source terms have to be summarized. This overall source term can be further used in transport equations. As for HCN and NH_3 source terms, it is possible to determine them from coal burnout rate. It is assumed, that nitrogen from both char and volatiles transforms to intermediate species quickly and totally.

NUMERICAL ALGORITHM

For numerical solution of the equations, finite volume method (FVM) is used. For left and right hand sides the advection upstream splitting method [1] is used to approximate fluxes in the FVM formulation, and edge dual-volume approximation is used to approximate the second order derivatives respectively. For detailed description of the solution procedure, see [3].

RESULTS

Here we will present computed profiles of the interesting parameters of the boiler. Properties of the coal and boiler setup used in simulations are given in the Table 2. Those parameters are consistent with lignite, with medium volume of volatile matter. Operating parameters for studied cases are given in Table 1. We investigated numerically four cases. The first case is the normal operation with air distributed equally among burners, see Figure 3. In the second case the part of total air is fetched to the over-fire-air (OFA) slot. In third and fourth case, air-staging method is used and air is distributed among burners as indicated in Table 2. Comparison of the studied cases is depicted at Figure 4. The comparison of measured data, [13], with numerically obtained is at Figure 5.

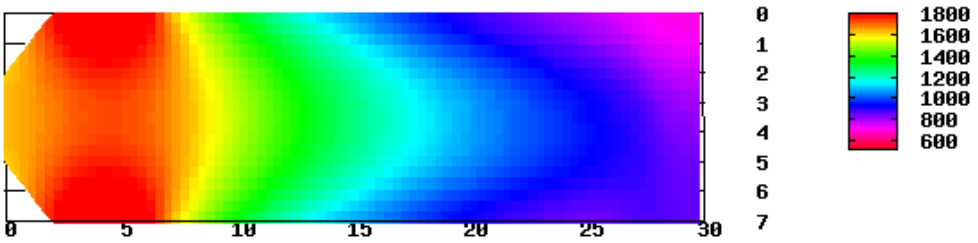

Figure 3. Temperature profile in Kelvins for the normal operation condition

Table 2
Coal properties and inlet conditions.

Parameter	Value	Unit
Ultimate analysis:		
Ash	0,095	-
Moisture	0,3	-
Carbon	0,4572	-
Hydrogen	0,0369	-
Sulfur	0,0116	-
Nitrogen	0,0051	-
Oxygen	0,0942	-
Volatile matter	0,54	-
LHV	17,922	MJ/kg
Oxygen per 1kgf	0,999	m^3/kg
Air excess coef.	1,3	-
Inlet temperature	400	K
Inlet coal mass flux	16,4	kg/s

CONCLUSION

We have developed a mathematical model, which approximates the combustion process in an industrial furnace, while being affordable from the computational complexity standpoint. We show the effects of air-staging and OFA on the most important parameters of the boiler as heat production, heat transfer to the walls and NO concentration at the outlet of the boiler. It can be seen at the figures that the NO concentrations are severely affected by the air-staging techniques. Such results are in good agreement with an experimentally observed reduction of the concentration of NO by air-staging [12]. At the Figure 4, one can see that maximum heat is transferred to the walls for the Normal operation mode and for Air-staging 2 mode (which is consistent with creating fuel-rich and fuel-lean zones in order to decrease NO concentration and make the char burnout complete). In every case the char burnout was complete. We can conclude that OFA technique is the best possible for reduction of the NO concentration even if some heat transfer to the water-wall is lost (due to lower temperature of the region above the OFA slots), but the overall heat escaping with flue gases can be utilised in other parts of the flue-gas duct which are not modelled here.

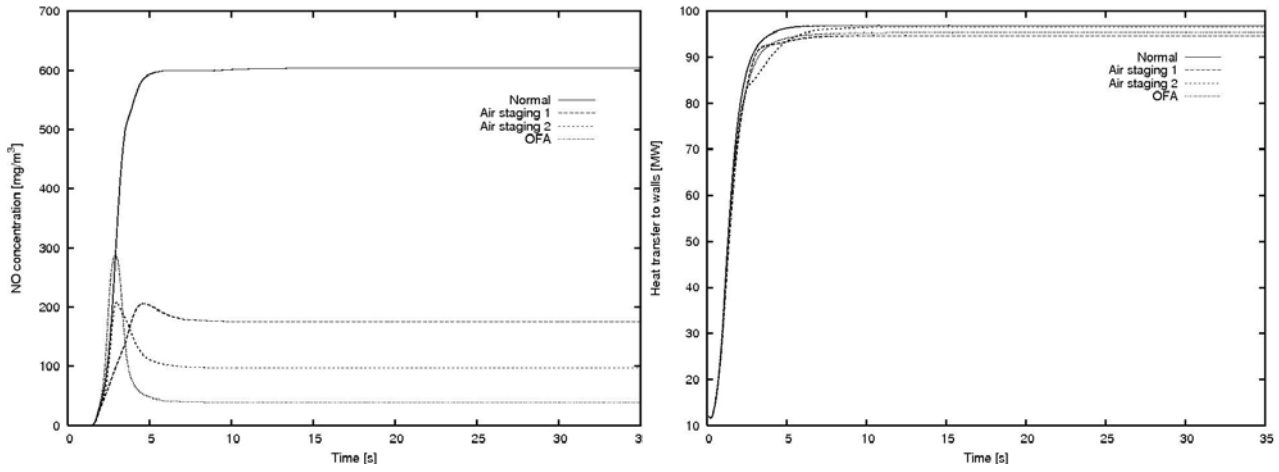

Figure 4. NO concentration and heat transferred to the water-wall

NOMENCLATURE

A	frequency factor
A_{BET}	surface area of coal pores
A,B	heat conduction to walls coefficients
a,b	reaction orders
$C_{\mu,1\varepsilon,2\varepsilon}$	turbulence model constants
c	radiation heat transfer coefficient
c_s	coal particles concentration
G_k	turbulent energy production
k_i	reaction rate constant
k	turbulent kinetic energy
LHV	lower heating value
n	number of particles
R_i	source term of species i
S_{ij}	strain rate tensor
Y_i	mass fraction of species i
δ_{ij}	Kronecker delta
ε	turbulent energy dissipation
λ	thermal conductivity
$\sigma_{k,\varepsilon}$	turbulent Prandtl numbers

c	conduction
comb	related to combustion
eff	effective
gas	related to gas
i,j,l	vector/tensor components
i	species
m	air-coal mixture
r	radiation
s	gas-wall radiation coefficient
t	turbulent
+	forward reaction
-	backward reaction

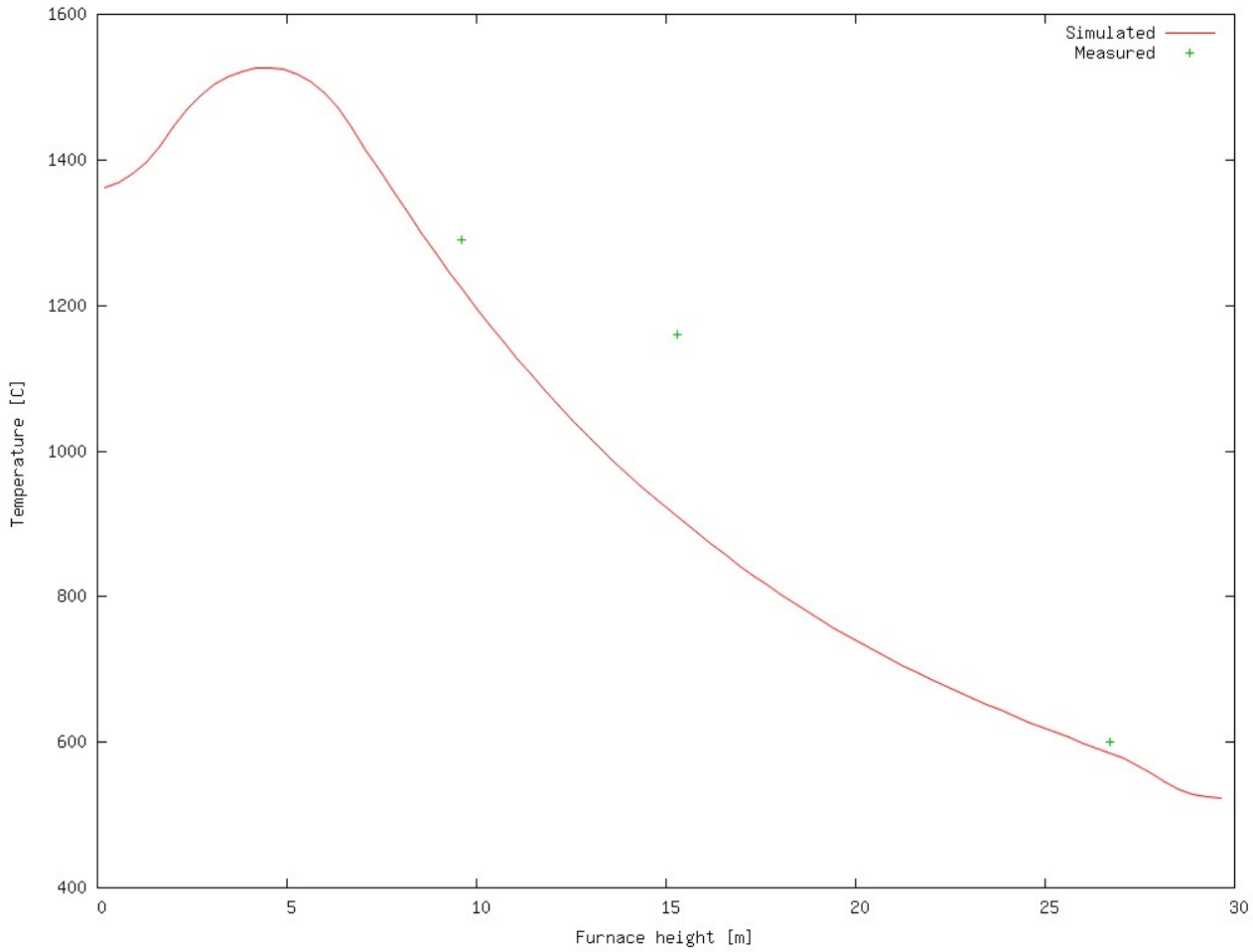

Figure 5. Comparison of the measured and computed temperatures

ACKNOWLEDGMENTS

This work has been partly supported by the project "Applied Mathematics in Physical and Technical Sciences" MSM 6840770010 of the Ministry of Education of the Czech Republic, by the project "Advanced Control and Optimization for Power Generation" No.1H-PK/22 of the Ministry of Industry and Trade of the Czech Republic and by the project "Jindřich Nečas Center for Mathematical Modelling" of the Czech Ministry of Education, Youth and Sport.

REFERENCES

1. Liou, M. S. and Steffen Jr., C., A New Flux Splitting Scheme, J. Comp. Phys., Vol. 107, pp 23-29, 1993.
2. Guo, Y. C. and Chan, C.K., A Multi-Fluid Model for Simulating Turbulent Gas-Particle Flow and Pulverized Coal Combustion, Fuel, Vol. 79, pp 1467-1476, 2000.
3. Makovička, J., Havlena, V. and Beneš, M., Mathematical Modelling of Steam and Flue Gas Flow in a Heat Exchanger of a Steam Boiler, *ALGORITMY 2002 Proceedings of contributed papers*, Publication House of STU, pp 171-178, 2002.
4. Zeldovich, J. B., The Oxidation of Nitrogen in Combustion and Explosion, Acta Physicochimica, Vol. 21, pp 577-628, 1946.
5. Bowman, C. T. and Seery, D. J., *Emissions from Continuous Combustion Systems*, Plenum Press, New York, 1972.
6. Warnatz, J., *NO_x Formation in High Temperature Processes*, University of Stuttgart, Germany, 2001.
7. Baulch, D. L., et al., Evaluated Kinetic Data for Combustion Modelling, Journal of Physical and Chemical Reference Data, Vol. 21, pp 411-750, 1992.
8. NIST, Chemical Kinetics Database on the Web, National Institute of Standards and Technology, 2000, http://www.kinetics.nist.gov
9. Kim, C. and Lior, N., A Numerical Analysis of NO_x Formation and Control in Radiatively-Conductively-Stabilized Pulverized Coal Combustor, Chemical Engineering Journal, Vol. 71, pp 221-231, 1998.
10. De Soete, G. G., Overall Reaction Rates of NO and N Formation from Fuel Nitrogen, *Proceedings of the 15th Symposium (International) on Combustion*, The Combustion Institute, pp 1093-1102, 1975.
11. Levy, J. M., Chen, L. K., Sarofim, A. F. and Beer, J. M., NO/Char Reactions at Pulverized Coal Flame Conditions, *Proceedings of the 18th Symposium (International) on Combustion*, The Combustion Institute, pp 111-120, 1981.
12. Wilk, R. K., *Low-Emission Combustion*, Wydawnictwo Politechniki Śląskiej, Gliwice, 2002.
13. Makovička, J., Mathematical Model of Pulverized Coal Combustion, *PhD Thesis*, CTU-FNEPS, Department of Mathematics, Prague, 2009.

OPERATING CHARACTERISTIC OF STEAM EJECTOR BASED ON THE HARTLEY'S EXPERIMENTAL SCHEME DETERMINED BY NUMERICAL MODELING OF FLOW

J. Kasperski, S.Pietrowicz*
Wroclaw University of Technology, Institute of Power Engineering and Fluid Dynamics,
Wrocław, Poland

ABSTRACT. The phenomena occurring in an ejector are complicated, especially if they concern non typical geometry and configuration of the nozzles. Nowadays numerical techniques permit modeling of thermal-flow processes occurring in steam refrigeration ejectors. The obtained numerical results show good conformity with experimental data. The numerical calculations were carried out for the fixed steam parameters on the inlets of the ejector nozzles according to the correct turbulence model. Determining of a more complete operating characteristic requires to consider changes of the steam parameters on ejector inlets. The characteristic was based on scheme`s arrangements called Hartley`s scheme, which allows to limit the number of calculation experiments. Conduction of the numerical calculations using the Hartley's scheme permits to determine polynomial coefficients of searched characteristic, especially concerning square relations and linear interaction of two or three parameters simultaneously.

Keywords: *planned experiment, steam ejector, FEM*

INTRODUCTION

The analytical relations for ejector are known for the long time, but they do not consider all phenomena occurring in a device. The phenomena are complicated, especially if they concern non typical geometry and configuration of the nozzles. Recently, in literature on ejectors one can find many theoretical models in respect of the selected flow processes. These models are based on analytical relations taking into consideration the shock wave and non isentropic processes, mixing of the streams, flow losses etc. These types of models are usually one dimensional calculated on the assumption of axisymetrical construction and stationary position of ejector.
One of the modern research methods is using the numerical techniques based on the finite element method (FEM), which allows to analyze the multidimensional phenomena considering the specific construction of nozzles, rotation and processes occurring in wet steam region. In the earlier researches the authors successfully used the numerical modeling techniques joined with ANSYS CFX in order to calculate the thermal flow processes in ejector with saturated steam as a cooling medium.
In previous work [1,2] the numerical results were compared with the experimental data achieving very satisfying correlations of the effects for suction pressure in function of entrainment ratio $p_e = f(U)$.

* Corresponding author: Dr Sławomir Pietrowicz
Phone: + (48)-71 -320 36 17, Fax: + (48)-71-328 38 18
E-mail address: slawomir.pietrowicz@pwr.wroc.pl

NUMERICAL MODELING

The physical processes occurring in ejector can be described using the continuity, momentum and energy equations [3,4]. The system of these three equations was solved by the authors using the finite element method technique in ANSYS CFX 11.0 software. The device which was subjected to the numerical analysis is shown in Figure 1a. Assuming that the flows occurring in the ejector are axisymmetric the numerical calculations were simplified to the ejector`s sector shown in Figure 1b.

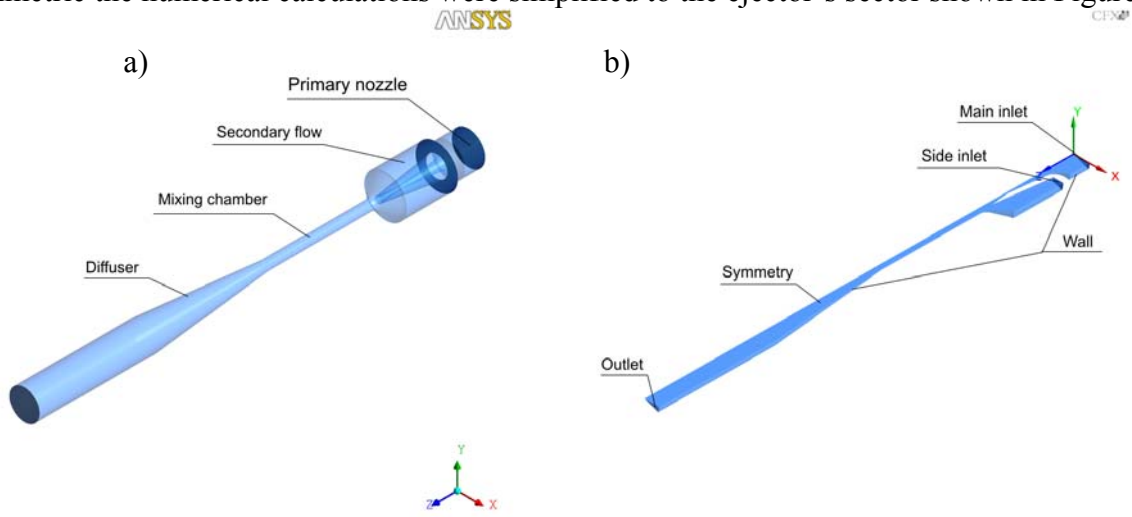

Figure 1. The main elements of the analyzed ejector; a) the physical model, b) the simplified numerical model with the applied boundary conditions

The analyzed domain of calculations was meshed using the 4986 elements: 245 elements of wedge type and 4741 elements of hexahedra type. The mesh was generated in ANSYS ICEM 11.0 software. Additionally, in the places where the high pressure and temperature gradients were expected - very near the walls and in the outlet surrounding of the primary nozzle - the mesh was thickened. The details of the structured mesh are shown in Figure 2.

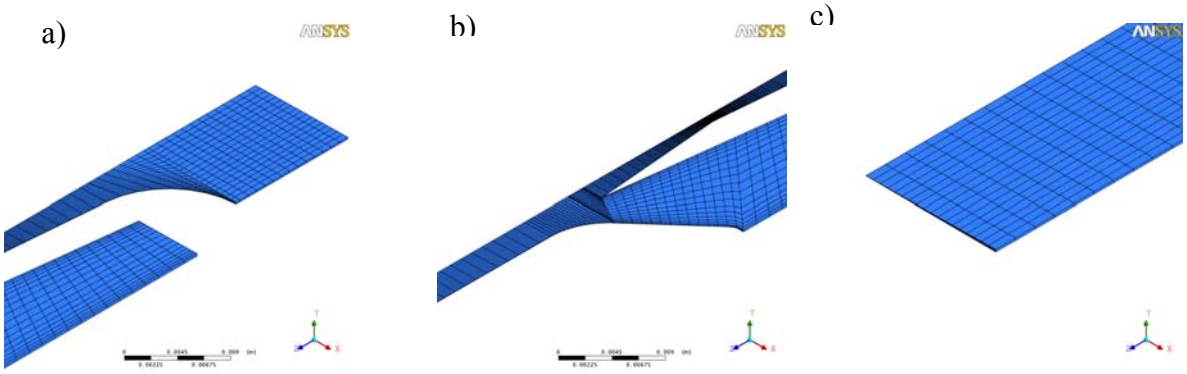

Figure 2. The details of the mesh applied in numerical calculations; a) the motive nozzle with part of the induced nozzle, b) the middle part of the ejector – the mixing region of the two streams, c) the outlet of the ejector

In the numerical domain the following boundary conditions were assumed (Fig. 1b):

- the main inlet is the *inlet* type condition at given saturated temperature of steam and the value of mass flow rate;

- the side inlet is the *inlet* type condition at given saturated temperature of steam and the value of mass flow rate;
- the outlet is the *outlet* type condition at given average absolute pressure;
- at the walls of ejector - the *adiabatic wall without slip* type condition;
- at the side-surfaces in respect of axisymmetric form of the fluid flow the *symmetry* type of conditions were applied.

The working medium was the steam (R718), whose properties were calculated on the basis of the model of steam called IAPWS-IF97 [5] proposed in ANSYS CFX 11.0 software. It was assumed that the steam supplied to primary and secondary nozzle was saturated and the quality of steam equaled x = 1.

Very important for the flow processes is using the correct turbulence model. Comparing the numerical results with the experimental data proved that one of the best models of turbulence is model called *SST - the shear stress transport*.

The examples of numerical calculations of temperature, pressure, Mach number, quality and Mach number of steam at the same entrainment ratio equaled 0.3 are shown in Figure 3.

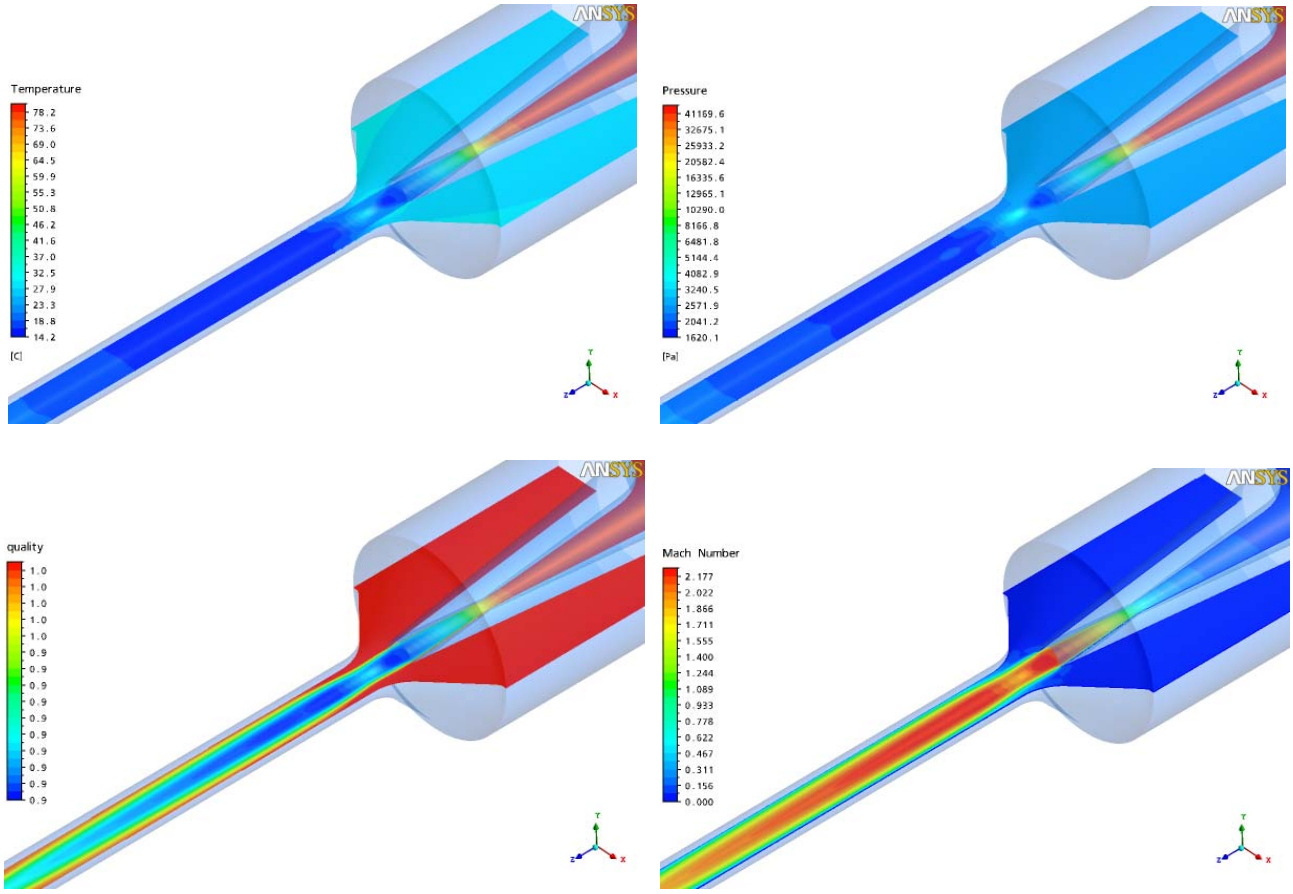

Figure 3. Example o the numerical results: a) temperature, b) pressure (in logarithm scale), c) quality, d) Mach number

OPERATIONAL CHARACTERISTIC OF THE EJECTOR

Application of the ejector in refrigeration cycle demands the knowledge about the operating characteristic taking into account the limited changes of the parameters (pressure/temperature) of motive steam from generator, induced steam from evaporator and steam flowing into condenser. The numerical procedures of thermal flow processes require an appropriate definition of operating

characteristic. One of its form is a relation of induced pressure as a function of entrainment ratio and motive pressure

$$p_e = f(U, p_g) \tag{1}$$

partly shown in the previous research. While determining the operating characteristic of the ejector for the independent variables it is important to respect non-linear relations and interaction of the input parameters. Consideration of logarithmic relation between saturated temperature and pressure permits to reduce the influence of approximation errors. In the proposed variant that relation is described by formula

$$t_e = f(U, t_g) \tag{2}$$

which improves the operating usefulness of characteristic. Determination of non-linear relation (2) demands an experiment scheme and matching the input values for all scheme`s arrangements.

NUMERICAL EXPERIMENT PLAN

In case of using the Hartley`s [6] scheme while performing the experimental tests for the two input variables (Fig. 4), the scheme can be limited to 6 from among 9 experiments of the full scheme keeping nonlinear description.

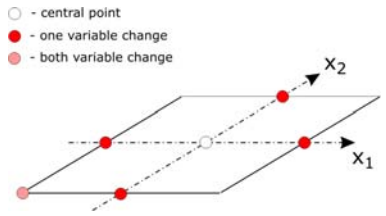

Figure 4. The value of main variables on the Hartley's scheme for two variables.

This scheme allows to calculate 6 polynomial coefficients of the relation (2) including square relations and interaction of the input parameters. According to the Hartley's plan value relation (2) can be described as follows:

$$y = a_1 + a_2 \cdot x_1 + a_3 \cdot x_1^{\,2} + a_4 \cdot x_2 + a_5 \cdot x_2^{\,2} + a_6 \cdot x_1 \cdot x_2 \tag{3}$$

For the variables t_e, U, t_g :

$$t_e = a_1 + a_2 \cdot U + a_3 \cdot U^2 + a_4 \cdot t_g + a_5 \cdot t_g^2 + a_6 \cdot U \cdot t_g \tag{4}$$

Generating of input data set for all six scheme configurations requires establishing of three levels for each input variable. After consideration of technically realistic values of variables the authors assumed the following values of variables: minimum (-1), central (0) and maximum (1) (Table 1).

Table 1
The range of input variables

variable	value		
	-1	0	+1
U (-)	0.0	0.15	0.3
t_n (^{o}C)	70	80	90

The whole scheme of calculations of the experiments were shown in the table 2, 3 and the results of time-consuming calculations were presented graphically on the figure 5.

Table 2
The plan value of the input and output variables

scheme num.	Hartley's plan value		numerical procedure data input					numerical results	
			ejection	generator		condenser		evaporator	
	x_1	x_2	U -	t_g (°C)	p_g (kPa)	t_c (°C)	p_c (kPa)	t_e (°C)	p_e (kPa)
1	-1	-1	0	70	31.2	35	5.63	24.10	3.003
2	1	0	0.3	80	47.4			21.7	2.603
3	-1	0	0	80	47.4			6.4	0.963
4	0	-1	0.15	70	31.2			25.54	3.274
5	0	1	0.15	90	70.2			19.55	2.275
6	0	0	0.15	80	47.4			14.2	1.623

Table 3
The calculated coefficients

coefficient	calculated value
a_1	615.4709509
a_2	-14.29154333
a_3	0.083476956
a_4	-285.9878087
a_5	-6.666666667
a_6	4.237347609

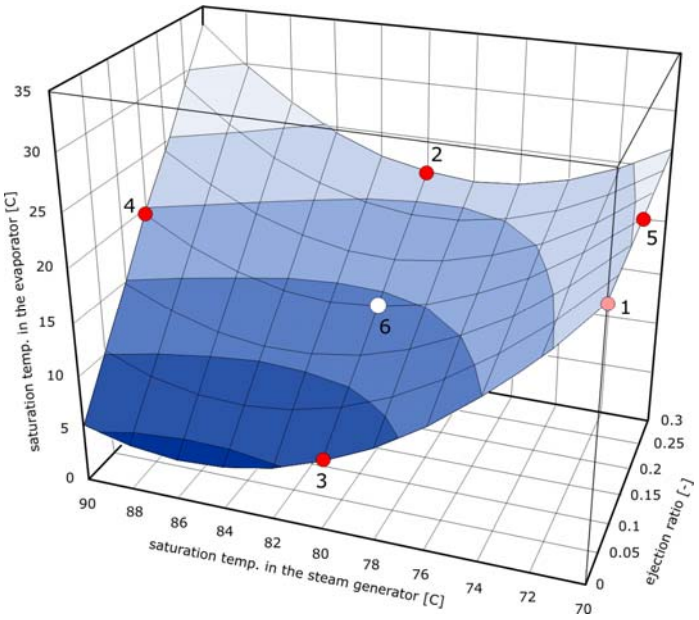

Figure 5. The relations between main parameters of analyzed ejector. The points from 1 to 6 are accordance with the position on the Hartley's scheme.

On the basis of the obtained values of induced pressure and applying standard matrix calculations the values of polynomial coefficients of equations (4) were determined. The received characteristic (4) can be transformed to more useful formula by employing numerical procedures.

$$U = f(t_g, t_e) \tag{5}$$

The graphic form of characteristic (5) is presented in Fig. 5.

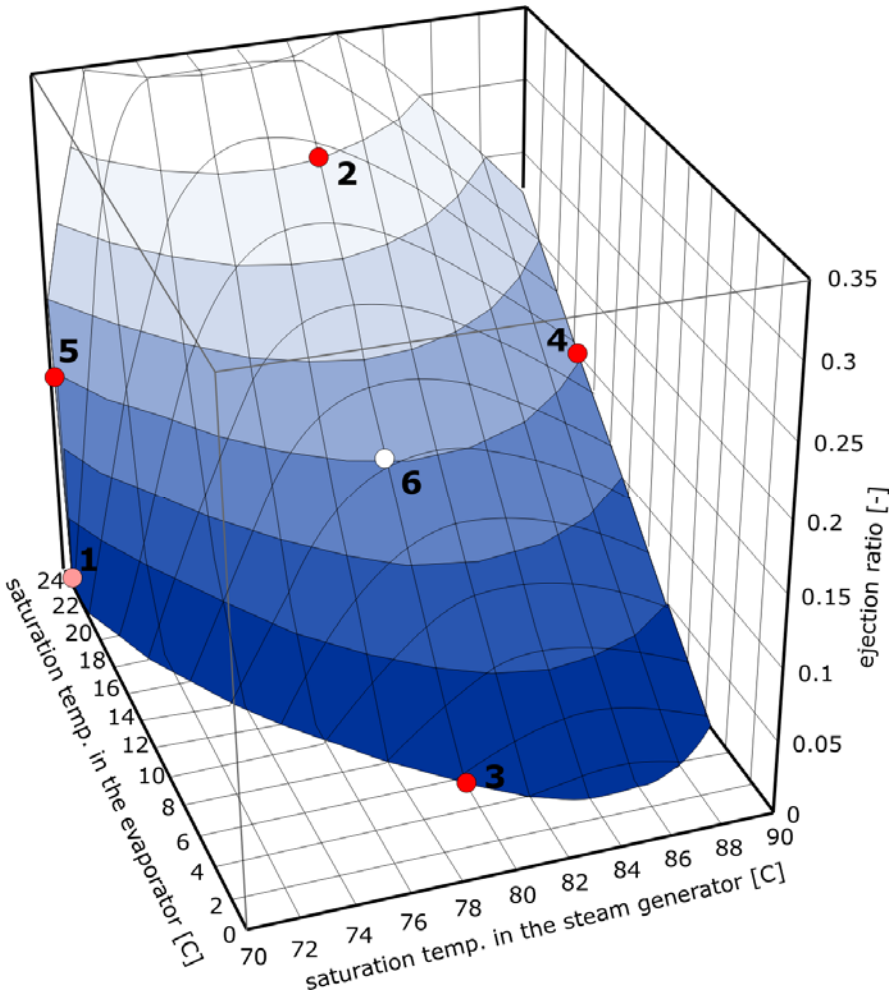

Figure 6. The inverted relations between main parameters of analyzed ejector.

CONCLUSIONS

Nowadays numerical techniques permit modeling of thermal-flow processes occurring in steam refrigeration ejectors. The obtained numerical results show good conformity with experimental data. The numerical calculations were carried out for the fixed steam parameters on the inlets of the ejector nozzles. Determining of a more complete operating characteristic requires to consider changes of the steam parameters on ejector inlets. The characteristic was based on scheme`s arrangements called Hartley`s scheme, which allows to limit the number of calculation experiments. Conduction of the numerical calculations using the Hartley's scheme permits to determine

polynomial coefficients of searched characteristic, especially concerning square relations and linear interaction of two or three parameters simultaneously.

REFERENCES

1. Pietrowicz S., Kasperski J., The thermo-flow processes proceeding during the two – phase flow in supersonic ejector applied in low power solar air conditioning systems, 2007, The 22nd International Congress of Refrigeration, China, ICR07-B1-1073
2. Pietrowicz S., Kasperski J., The numerical modeling of thermo – flow processes in high – speed rotation ejector used in refrigerating system, 2007, The 22nd International Congress of Refrigeration, China, ICR07-B1-1076
3. Alexis G.K., Rogdakis E.D., 2003, A verification study of steam-ejector refrigeration model, *Applied Thermal Engineering* 23
4. Bartosiewicz Y., Aidoun Z., Desevaux P., Mercadier Y., 2005, Numerical and experimental investigations on supersonic ejectors, *International Journal of Heat and Fluid Flow* 26, 56-70;
5. Wagner W., Kruse A., 1998,The Industrial Standard IAPWS-IF97, *Properties of Water and Steam*, Springer, Berlin;
6. Korzynski M., The methodology of experiment, *WNT*, Warszawa, 2006 (in Polish)

NUMERICAL-EXPERIMENTAL METHODOLOGY TO DETERMINE FIN EFFECTIVENESS AND HEAT FLUX DISTIBUTION

A. Willockx*, C. T'Joen, H. Canière, H. Huisseune, M. De Paepe
University of Ghent - UGENT, Gent, Belgium

ABSTRACT. The goal of this study is to determine the fin effectiveness and local convection coefficients of longitudinal fins with a coupled experimental-numerical method. Therefore the conductive heat fluxes through the cooling fin need to be known. Fin temperatures are measured experimentally with infrared thermography and these measurement data are used as boundary conditions for a 3D numerical fin model. In order to determine the heat fluxes through the cooling fin from surface temperatures, a 3D inverse heat conduction problem (IHCP) has to be solved. Results from a numerical and experimental test case give accurate fin effectiveness, but still show significant fluctuations on the heat fluxes.

Keywords: *inverse conduction, fin effectiveness, infrared measurement, conjugate gradient*

INTRODUCTION

Fins are widely used in heat exchangers, for cooling of electronics,… A good fin performance indicator is important for the design. Two potential indicators are fin efficiency and fin effectiveness. Fin efficiency is the commonly used parameter, but has the big disadvantage that the real performance of the fin is compared to the performance of an ideal non-existing fin of the same shape but with infinitely high thermal conductance. This makes it difficult to compare the thermal performance of different fin forms. Fin efficiency is an idealization and has physically no meaning. On the other hand, fin effectiveness measures the heat transfer gain obtained by placement of the fin and gives an idea of its real performance. It gives the ratio of the heat transferred by the fin to the heat transferred from the surface covered by the fin's base under the same thermal conditions, in the absence of the fin. Fin effectiveness makes it possible to compare the performance of different types of fins and thus is a better performance indicator [1]. This can be used to develop a decision system to choose a fin type in order to remove a certain amount of heat from a surface for a given free surface area.
Geometrical variations of longitudinal fins for heat transfer enhancement have previously been researched [2-4]. Matrices of flat plate fins [2], perforated fins [3] and dimpled channels [4] have been considered. However the effectiveness of these fin types is not determined. The local convective heat transfer coefficients were determined but only for specific arrangements. The matrix of the flat plate fins had a significant influence on the convective heat transfer. Unlike the test cases in this paper, the fins investigated in the mentioned papers [2-4] were exposed to a perpendicular air stream. In this paper, the air flow is parallel to the longitudinal fins.
The objective of this paper is to identify the fin effectiveness as well as the variation of the local convective heat transfer coefficient on the fin surface. Therefore the heat fluxes through the fin model and the primary surface need to be known. It is very difficult to do accurate heat flux measurements or measure a heat flux distribution on a surface, especially for large surfaces. Therefore preference is given to temperature measurements, which are more accurate and easier to perform. Complete surface

* Corresponding author: A . Willockx
Phone: + (32)-9-2643289, Fax: + (32)-9-2643355
E-mail address: arnout.willockx@ugent.be

temperature profiles can be measured with an infrared camera. The use of infrared thermography to measure surface temperatures from which heat flux distributions are determined is not uncommon [5,6]. Heat flux distributions [6] or convection coefficient profiles [5] can be calculated from surface temperatures by solving an inverse heat conduction problem (IHCP), which is a mathematically ill-posed problem and cannot be solved directly with CFD. There exist various solution methods for inverse heat conduction problems. The description and solution of IHCP's is highly mathematical and falls out of the scope of this paper.
In this study, a procedure is developed in which experimental measurements are coupled with an inverse numerical algorithm in order to determine fin effectiveness and local convection coefficient distribution for different fin forms. The experimental setup and measurements are described thoroughly, with special attention to the use of infrared thermography. The solution methodology of the IHCP is described, but for the detailed numerical solution method of the IHCP is referred to [7]. An example case is illustrated.

EXPERIMENTAL SETUP

Test rig

A test rig is designed in which both fin effectiveness and local heat transfer coefficients for different fin forms can be determined. In order to experimentally determine fin effectiveness, heat fluxes through the primary surface and the fin need to be measured. However, heat flux measurements are very delicate, have relatively large measurement errors and the heat flux distribution is disturbed by the measurement. Moreover, it is not possible with the current techniques to measure the heat flux distribution on a surface at one moment. This would require many sensors on the surface, which should influence the heat flux distribution and the air flow on the surface. Therefore it was chosen to measure temperatures and calculate heat fluxes from these measurements, which means that an IHCP needs to be solved. Thus the experimental measurements are processed by a numerical procedure to obtain the heat fluxes, so actually this is a coupled experimental-numerical study. This procedure has the advantage that the measurements are more accurate, easier and faster. The surface temperatures are measured with an infrared camera, which has two big advantages: it gives a temperature distribution on a surface with one measurement. and it is a non-intrusive measurement technique. Air flow, temperature and heat flux distribution are not disturbed by the temperature measurement, which increases the accuracy. The biggest error in the heat flux determination depends on the accuracy of the IHCP solution, not the experimental measurements.
The definition of fin effectiveness is the ratio of heat exchange by the fin (=Q_f) to that of the primary surface that is covered by the fin's base in absence of the fin (=Q_b), thus:

$$\eta = \frac{Q_f}{Q_b} \tag{1}$$

So in order to experimentally determine fin effectiveness, a primary surface has to be heated and the heat flux through this surface has to be known. In a second phase, a fin is placed on a part of this heated primary surface and the heat flux through the fin is determined. The setup is built as follows. A rectangular aluminum reference block is heated at the bottom. The upper surface of the block is the primary surface. A second aluminum block of the same dimensions is made, but with an aluminum cooling fin on top. Aluminum is used because of its high thermal conductivity (k = 200 W/mK). A flexible isoflux heat foil is placed at the bottom of the reference block in order to induce a heat flux through the primary surface. The heat losses sideways and especially downwards need to be minimized in order to force all heat flux upwards through the aluminum block and fin. Therefore a guard heater assembly is constructed around the primary surface. The guard heater is set at the same temperature as the bottom and side walls of the aluminum block, which are measured with thermocouples. So there are almost no conduction heat losses at the bottom of the upper heat foil and from the side walls of the block due to a lack of temperature difference. The aluminum block with cooling fin and the guard heater assembly are set in a slab of polyurethane and placed in a wind tunnel with a rectangular test

section (figure 1). The wind tunnel is used to examine the influence of Re-number on the local convective heat transfer coefficient and fin effectiveness. The Reynolds number (based on fin length as reference length) can be varied from 12750 to 63750. The base of the fin is at the same height as the bottom of the wind tunnel (figure 1) to avoid disturbance of the air flow at the test section. The temperature profiles on the fin surface and top of the reference block (primary surface) are measured by infrared thermography. Some adjustments were made to the test rig in order to use this measurement technique.

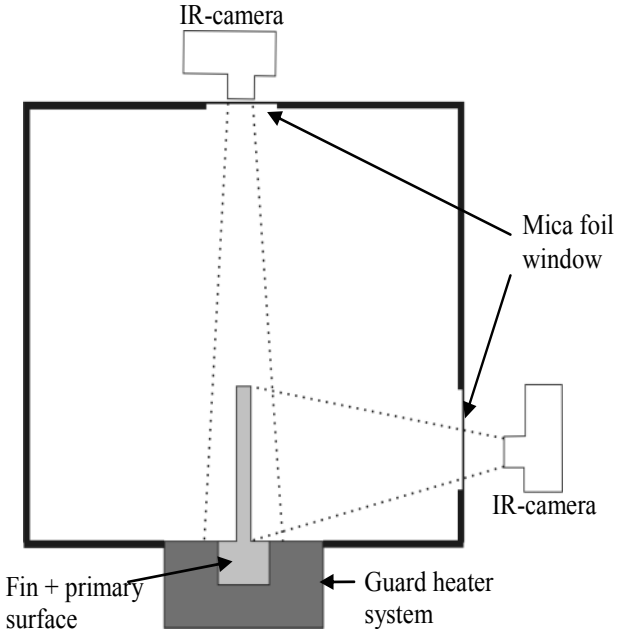

Figure 1. Experimental setup in wind tunnel

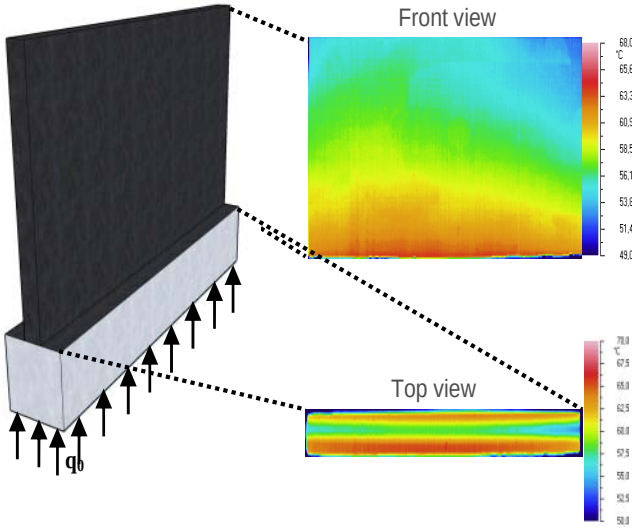

Figure 2. Infrared temperature measurements

Infrared thermography as measurement technique

The goal of this research is to study longitudinal fins of heat sinks to cool electronics; which have dimensions of the order of magnitude of 60mm long, 40mm high and 1 mm thick. It was chosen to upscale the fin dimensions 4 times. This improves the temperature resolution, especially at the sides of the fin where there is interference with the surrounding temperatures of the colder wind tunnel wall. This influence is bigger for temperature measurements of small objects, so scaling improves the accuracy of the temperature measurement and thus on the determination of the local convection coefficient. The scaling of the fin dimensions also eases the general design of the test rig.

Thermography has the big advantage that it is a non-intrusive measurement technique and a complete temperature distribution is obtained with one measurement. However, the front and back of the wind tunnel are made out of Plexiglas. As most common solid materials, Plexiglas is not transparent for infrared radiation, which would make it impossible to measure the fin temperature with the infrared camera placed outside the wind tunnel. Therefore infrared transparent windows are necessary. The temperature image of the front side is the same as the rear side due to the symmetry and the isoflux heat flux at the bottom of the block, so only one side of the fin needs to be measured. The temperatures at the upper side of the fin and the primary surface are also measured (figure 2). Thus two windows need to be placed: one at the top and one at the side of the wind tunnel test section (figure 1). A Midas long wave (LW) infrared camera, which has a spectral response from 8 µm to 14 µm, is used. HDPE foil is very thin and has a relatively high transmittance (91%) for IR-radiation in the LW spectrum. Compared to most materials used for infrared transparent windows, HDPE is a very cheap material.

However, it can not withstand high pressure differences, both it is strong enough for the pressure differences in the low speed wind tunnel. Therefore both windows were made of HDPE foil.
An object with a high emissivity has a low reflectivity, so there is less influence of the surroundings on the temperature measurement. The fin and primary surface are made out of aluminum, which has a relatively low emissivity. Therefore they are painted with a matt white paint, which has a high emissivity and will increase the accuracy of the measurements.

MEASUREMENT DATA

First the camera was calibrated in order to do accurate measurements. The calibration techniques used are not discussed in this paper, only the results are given. The two most important parameters that need to be calibrated are the emissivity ε of the matt white paint and the transmittance of the HDPE foil window. Emissivity of the paint was determined at 94% in a temperature range of 50°C to 80°C (which is the temperature range the test fins attain in during the experiment). The transmittance of the HDPE foil is determined at 91%.
An example of the obtained temperature measurement data is shown in figure 3 for a longitudinal plate fin. In these infrared images, each pixel represents a temperature measurement.

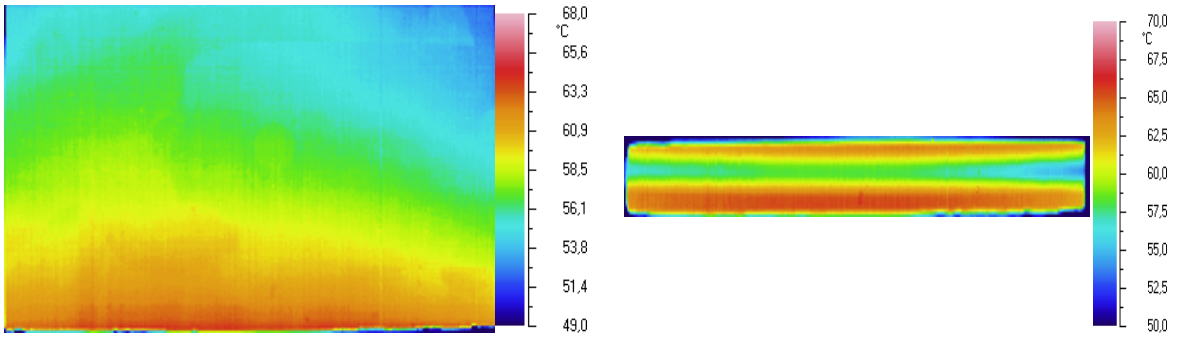

a. Front view of fin b. Top view of fin

Figure 3. Infrared temperature measurement of a longitudinal plate fin

INVERSE CONDUCTION PROBLEM

These temperature measurement data are used as boundary conditions for a 3D numerical model of the fin and the primary surface (figure 4). In a direct heat conduction problem, the internal and surface temperatures of a body are determined for given boundary conditions. On the other hand, if temperature measurements are done on its boundary and the boundary conditions [6] have to be derived from these measurements, one has to solve an inverse heat conduction problem (IHCP). An IHCP is mathematically ill-posed, because the uniqueness, existence and stability of the solution cannot be assured [8]. This makes it difficult to solve an IHCP. There exist various solution methods for inverse heat conduction problems. Most methods are implemented for one or two-dimensional inverse problems [8]. The IHCP in this study is three dimensional and there is only limited literature on 3-D inverse problems, especially for determining local convection coefficients. A 3-D IHCP is difficult to solve due to the complexity and high computational cost [9].
The scaled numerical model of the fin and primary surface is shown in figure 4. The boundary conditions imposed on the fin model are inherent with those of the experiment, which gives the following three-dimensional IHCP (figure 4). The temperatures are measured on all fin surface (S1-S5) and on top of the primary surface (S6-S7). A constant heat flux q_0 is induced at the bottom of the primary surface (S8) and the side walls are set adiabatic (S9-S12), which was experimentally imposed by using a guard heater. There is a thermal resistance between the primary surface and the fin, as

shown in figure 4. This thermal resistance is also considered into the inverse heat conduction problem because it causes a temperature drop between the primary surface and the fin, and thus between surfaces S6-S7 and S4-S5, which could otherwise cause problems in the accuracy of the IHCP solution. The primary surface and fin are both made out of aluminium with thermal conductivity k=200W/mK.

The local convection coefficients $h(S_i)$ on S_1-S_7 have to be determined, from which the heat flux distribution can also be determined. The experimental temperature measurements on these surfaces are denoted as $Y_m(S_i)$ (m=1-M) where M is the total amount of measurement points, thus the number of pixels on the infrared image of the fin and primary surface as in figure 4. The convection coefficients $h(S_i)$ can be estimated based on these temperature measurements $Y_m(S_i)$, by minimizing the functional:

$$J[h(S_i)] = \sum_{m=1}^{M} [T_m(S_i) - Y_m(S_i)]^2 \text{ for i=1-7} \quad (2)$$

in which $T_m(S_i)$ are the computed temperatures at the measurement locations from the direct problem solution with the estimated convection coefficients $h(S_i)$. A conjugate gradient method (CGM) is used to minimize the functional J in equation (2). The CGM is coupled with the finite volume code FLUENT [10]. However, the heat fluxes on the fin surface obtained with this numerical algorithm still show significant fluctuations which are not physical but inherent to ill-posed problems. In order to dampen these fluctuations, a first order Tikhonov regularization is added to the numerical algorithm. A detailed description of the numerical algorithm is given in [7].

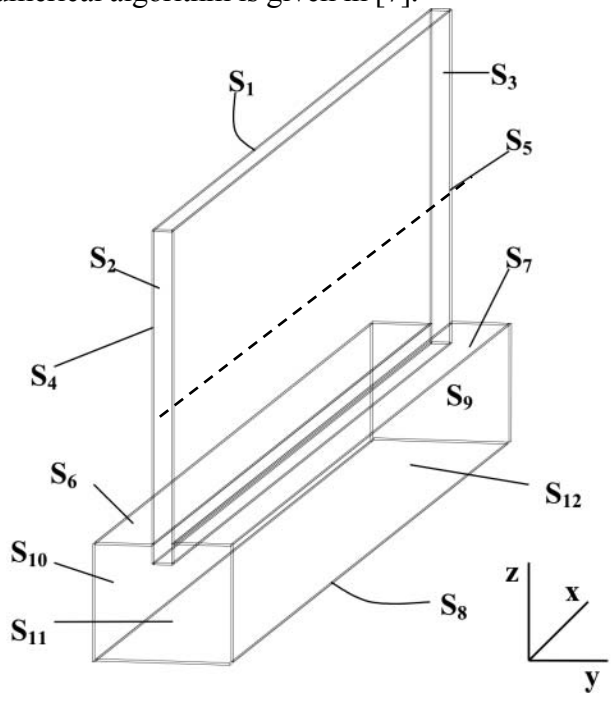

Figure 4. Fin model for inverse conduction problem

RESULTS

Numerical test cases

The accuracy of the numerical algorithm to solve the IHCP first has to be checked for the described model of a longitudinal fin (figure 4). Therefore some numerical test cases are developed: the temperature profiles on boundaries S_1-S_7 are numerically simulated by solving a direct heat conduction problem with imposed convection coefficient profiles on surfaces S_1-S_7. It is assumed that there are no measurement errors on these simulated temperatures. These simulated temperatures on S_1-S_7 are

denoted $Y_m(S_i)$. The grid of the fin model consists of 303057 cells. The number of cells on the fin side is equal to the number of pixels (thus measurement points) of the thermographic measurement. This means that each cell corresponds with a pixel or measurement point. On the seven surfaces S_1-S_7 there are 63477 measurement points (=M in equation (2)). This large amount of measurement points can cause long calculation times before convergence is obtained. Several test cases were simulated, two of which will be discussed

First case: Linear convection coefficient profile. In the first case a linear convection coefficient profile is imposed on S_1,S_4,S_5,S_6,S_7 over the length of the fin (x-direction in figure 4) from h=10W/m^{2}K at S_2 till 40W/m^{2}K at S_3. There is no change of the profile over the height of the fin. The convection coefficient profile is shown in figure 5a for the front side of the fin (S_5) over the length of the fin (thus along x-axis) at the middle of the fin height. (dashed line in figure 4). The simulated temperatures on S_1-S_7 are the measured temperatures $Y_m(S_i)$ of equation (2) and have to be reconstructed by solving the IHCP. The solution of the IHCP with the numerical algorithm gives the estimated convection coefficient profiles on these surfaces and is compared with the imposed convection coefficient profile. In figure 6a, the relative error between the calculated and imposed convection coefficients over the fin length of the fin at the middle of the fin height is set out. The largest error is 2.5%., so the measured and estimated temperature profiles are almost identical.

Second case:Exponential convection coefficient profile. In this case, the convection coefficient profiles on surfaces S_1-S_7 are based on the boundary layer thickness for a given wind speed along the fin. Such a convection coefficient profile has an exponential form. The convection coefficient profile is shown in figure 5b for the front side of the fin (S_5) over the length of the fin at the middle of the fin height. In figure 6b, the relative error on the estimated $h(S_i)$ is set out.

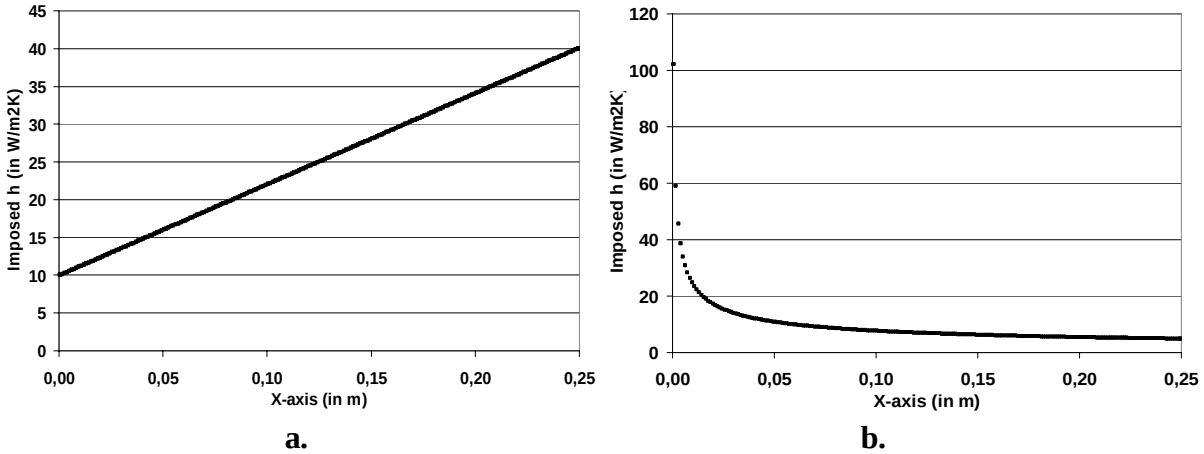

a. **b.**

Figure 5. Imposed h-profile on the fin surface halfway the fin height: a. Linear; b. Exponential

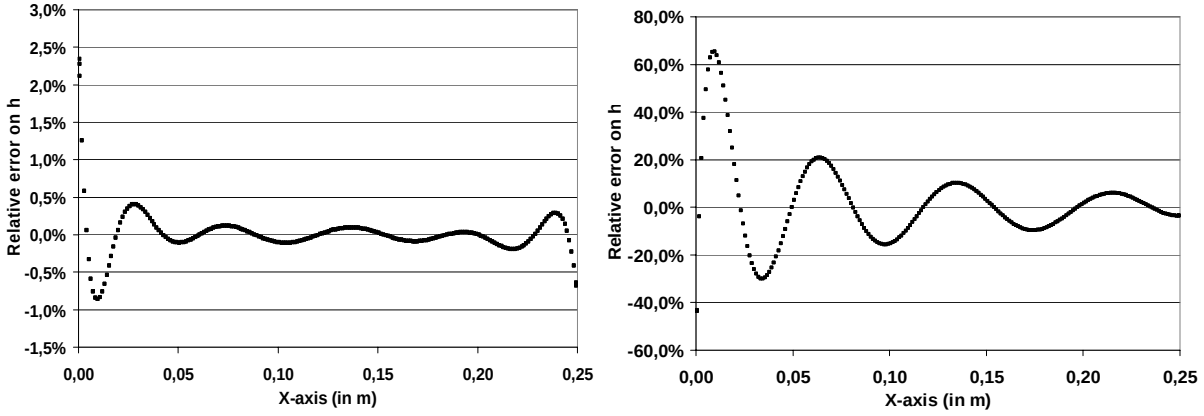

a. **b.**

Figure 6. Relative error on IHCP solution halfway the fin height. a. linear h-profile; b. exponential h-profile

Fin effectiveness. From the solution of the IHCP it is possible to determine fin effectiveness. In Table 1, the fin effectiveness is determined with the IHCP solution and with a direct conduction calculation. The results show that the solution of the IHCP with the numerical algorithm gives accurate results for the fin effectiveness. So the IHCP algorithm can be used to determine the fin effectiveness from experimental temperature measurements.

Table 1: Accuracy of numerical algorithm for fin effectiveness

	Effectiveness direct conduction	Effectiveness IHCP	Error
Case a	4.580	4.580	0.0024%
Case b	4.663	4.662	0.01%

Discussion. In the first case, the J-functional of equation (2) drops below $8*10^{-5}$ after 300 iterations of the IHCP algorithm, which means a maximum error of $3*10^{-5}$K on each temperature measurement. In the second case, the J-functional drops below 1.6 after 340 iterations, which corresponds with a maximum error of 0.003K on each temperature measurement. Although the obtained temperature profiles on S_1-S_7 are correct, there is an error on the estimated $h(S_i)$. There is a wiggle in the estimated convection coefficient profile with alternating areas of positive and relative errors (Figs.5a and 5b). In the first case, these errors are small (<1%). In the second case, they become much bigger: up to 60% on the left side of the fin (figure 6b) where the imposed exponential profile has the biggest value i.e. 100W/m^{2}K.
The big error in the second case is induced by the large $h(S_i)$ values in these first cells at the left side of S_5 and on S_2. After the first few cells, $h(S_i)$ drops quickly to values below 20 W/m^{2}K and remains between 15 and 10 W/m^{2}K for the largest part of the fin. It is seen on figure 6b that $h(S_i)$ is largely overestimated (>60%) in the first cells, followed by a larger region of underestimation (>30%), then again a zone of overestimated $h(S_i)$ (±20%), and finally a region of small over- and underestimation. So the relative errors decrease over the length of the fin, and the area of positive and negative relative error zones is inverse proportional with the absolute value of the error. The results of case a show that the algorithm gives better results if there is no large peak in the imposed h-profiles.
Thus it seems that the algorithm still has difficulties to capture peaks in convection coefficient profiles and still needs to be adjusted to improve the accuracy. These numerical test cases show that it is not possible yet to use the algorithm to determine the local convection coefficient profile from experimental temperature measurements. However, the calculated profiles fluctuate around the correct solution and the global flux distribution over the different temperature surfaces seems to be correct. The results in Table 1 confirm this: although the local convection coefficient profiles cannot be determined accurately, the fin effectiveness is calculated precisely (only 0.01% error). Therefore it is already possible to use the numerical IHCP algorithm to determine the fin effectiveness from the experimental temperature measurements.

Experimental results
Results are already obtained for the simplest longitudinal fin form: a straight rectangular longitudinal fin. It can be seen in figure 7 that there is a small drop in the fin effectiveness with increasing Re-number (2.7% drop for Re from 12500 to 62500). This drop is mainly due to measurement errors and thus the error on the fin effectiveness. So fin effectiveness remains nearly constant for varying Re in the obtained range of Re-numbers

CONCLUSION

A coupled experimental-numerical method is developed to determine fin effectiveness and local convection coefficients for longitudinal fins. Therefore a 3-D IHCP has to be solved. With the developed algorithm the 3D IHCP can be solved but still lacks accuracy for the real, more complex h-profiles. This still needs to be improved. Fin effectiveness can already be determined accurately, and results are shown for a straight rectangular fin.

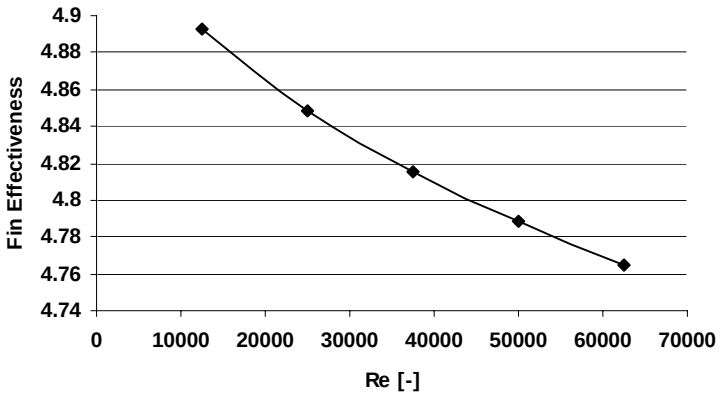

Figure 7. Fin effectiveness at different Re-numbers for a straight longitudinal fin

REFERENCES

1. Heggs, P. J., Fin Effectiveness Is a Better Performance Indicator Than Fin Efficiency, *Impeche Conference Transactions*, Vol. 1999-7, pp.3, 1999
2. Guglielmini, G., Nannei, E., Tanda, G., Natural Convection and Radiation Heat Transfer From Staggered Vertical Fins, *International Journal Heat and Mass Transfer,* Vol. 30, No. 9, pp. 1941-1948, 1987
3. Buchlin, J-M., Convective Heat Transfer in a Channel with Perforated Ribs, *International Journal of Thermal Sciences*, Vol. 41, No. 4, pp. 332-340, 2002
4. Mahmood, G.I., Ligrani, P. M., Heat Transfer in a Dimpled Channel: Combined Influences of Aspect Ratio, Temperature Ratio, Reynolds Number and Flow Structure, *International Journal of Heat and Mass Transfer*, Vol. 45, No. 10, pp. 2011-2020, 2002
5. Huang, C.H., Yuan, I. C, Ay, A three-dimensional inverse problem in imaging the local heat transfer coefficients for plate finned-tube heat exchangers, *International Journal of Heat and Mass Transfer*, Vol. 46, pp.3629-3638, 2003
6. C.H. Huang, S.P. Wang, A three-dimensional inverse heat conduction problem in estimating surface heat flux by conjugate gradient method, *International Journal of Heat and Mass Transfer*, Vol. 42, pp.3387-3403, 1999
7. Willockx, A., T'Joen, C., Steeman, H.-J., Canière, H., De Paepe, M., Fin Effectiveness in Longitudinal Fins: Solving the Inverse Heat Conduction Problem, *The 19th International Symposium on Transport Phenomena,* 17-20 August, Reykjavik, Iceland, 2008
8. Beck, J.V. , Blackwell, B. and St. Clair jr., C.R., Inverse Heat Conduction, Wiley, New York,1985
9. Kim, S.K., Lee, J.S, Lee, W.I., A solution method for a nonlinear three-dimensional inverse heat conduction problem using the sequential gradient method combined with cubic-spline function specification, *Numerical Heat Transfer, Part B,* Vol. 43, pp.43-61, 2003
10. FLUENT User's Guide, Version 6.1, Fluent Incorporated

AIRFOIL'S COOLING OPTIMIZATION BASED ON CHT SOLUTION

G. Nowak*, W. Wróblewski

Silesian University of Technology
Institute of Power Engineering and Turbomachinery
ul. Konarskiego 18, 44-100 Gliwice, Poland

ABSTRACT. Optimization of cooling system configuration within a gas turbine airfoil requires specification of thermal boundary conditions in each passage. For this purpose either empirical formulae for fluid temperature distribution along a passage or one dimensional fluid flow coupled with thermal calculations in the solid have been usually used. Imperfection of such a simplified approach is based on the fact that some effects are lost, i.e. the circumferential distribution of temperature and turbulence level. Significant improvement can be achieved with of Conjugate Heat Transfer (CHT) application for the interior of the airfoil (solid and cooling channels). A disadvantage of such an approach in connection with evolutionary search results in high computational costs. To overcome the drawbacks some computational strategy has to be worked out. This paper presents an automatic optimization process, which uses CHT analysis solved with Ansys CFX software. Numerical grid for both the solid and cooling passages is generated with ICEM CFD. The task is solved for fixed, once calculated, boundary conditions at the external wall. In this paper authors give some outlook for such a computations. Features of application of CHT for cooling optimization is assessed. The optimization results are compared to those obtained for the simplified method with empirical boundary condition evaluation.

Keywords: optimization, *evolutionary algorithm, Conjugate Heat Transfer (CHT), airfoil cooling*

INTRODUCTION

The main goal of gas turbine development is to increase its thermodynamic efficiency which depends on several factors, where the most significant are the turbine inlet temperature. Hot gas temperature raise affects the level of both the specific power and thermal efficiency of the cycle. In consequence, it improves weight/power ratio of the engine, which is one of the major goals of aerospace propulsion design (Lakshminarayana, 1996). The development in this area is possible due to the progress in material engineering as well as the prevention of high temperature effects within the materials. Modern materials additionally covered with Thermal Barrier Coatings (TBC) should meet the requirements concerning the operation regime of hot gas path components. The temperatures however are nowadays so high, that the material engineering activity is not sufficient and the application of cooling for the hot components is necessary.

Taking into account different aspects of airfoil manufacturing and the turbine performance, the most convenient way of component temperature reduction is internal convective cooling. It is based on the coolant flow, mainly air, extracted from the compressor bleed, via internal cooling passages. In the most simple form a passage is cylindrical and is supplied with air at the blade root. Coolant flows out into the hot gas at the blade tip. To enhance the heat transfer in the internal passages some turbulators in a form of ribs and pin-fins are applied, which also enlarge the heat transfer area. This paper deals with internal convective cooling realized with smooth, circular passages.

* Corresponding author: Dr Grzegorz Nowak
Phone: + (48)-32-2372822, Fax: + (48)-32-2372680
E-mail address: Grzegorz.nowak@polsl.pl

An accurate computational analysis of the processes that take place during the convective cooling is very challenging. The main difficulty emerges from the determination of boundary conditions in the passages, especially the assessment of convective heat transfer coefficient and the coolant bulk temperature. This problem can be resolved with coupled field analyses. Some attempts especially in the field of Conjugate Heat Transfer (CHT) solution for cooled geometries, were recently presented by Facchini et al. (2004), Montomoli et al. (2004) and a similar task but for the case of rib-roughened cooling channels, is discussed by Fedruzzi and Arts (2004) or Kusterer et al. (2004) for the film cooled blade. Recently Verstraete et al. (2008) presented a technique which implements a meta model of CHT based on Artificial Neural Network and Radial Base Functions. This meta model is a substitute for full CHT analysis for the optimization problem. It is however iteratively fed and improved with CHT solution data.

An internal cooling system, due to its discrete nature (local cooling with a number of passages), is a source of enhanced thermal gradients within the component, which in consequence produce higher thermal stresses and decrease the component's lifetime. So, a great care should be taken to keep the temperature variations as low as possible.

The problem of cooling system optimization seems to be quite new and has been the point of interest only in the last several years. This is due to the high computational costs of such problems, especially if accurate models need to be involved. Scientific research undertaken so far which has aimed to find the optimal cooling system has dealt with the internal passage convective cooling only. It seems to be the only cooling technique that can be, at the moment, analysed as a whole. Dulikravich with his team (Martin and Dulikravich, 2001, Jeong et al., 2003, Dennis et al., 2003a, b) for several years have studied different problems concerning blade optimization from the point of view of flow, thermal and structural criteria. They dealt mainly with optimization of internal cooling passages (Dennis et al., 2003, Martin and Dulikravich, 2001) and possible coolant outflow at the trailing edge of the blade (Dulikravich et al., 1999). The works mentioned reveal that although they operate on many design variables, the search process was significantly restrained in terms of the geometry changes (i.e. optimization undergone passage fillets or passage distance from the wall etc.). In 2003 Dennis et al. (2003a) showed a work dealing with optimization of a large number of cylindrical cooling passages. All the passages were located close to the external wall and they could move only within a narrow strap along the wall. The aim of the research was to find such a passage distribution that would, by keeping the blade temperature at an allowable limit, minimize the heat flux and also the coolant usage. Very interesting seems to be another work of Dennis et al. (2003b), where the optimization of serpentine-like cooling passage was presented. This task was realized in 3D with the thermo-mechanical criteria involved. The results showed large potential hidden in a cooling system; appropriate size and location of channels had a great influence on the coolant usage, thermal stress level and in consequence lifetime of the component. Nowak and Wroblewski (2007) presented the optimization of location and side of internal cooling passages whose shape was circular and their number was fixed. In this research the passages could freely move within the domain by satisfying the thermo-mechanical criteria for a 3D configuration.

All of the papers dealing with optimization problem used fixed thermal boundary conditions for the external surface of the blade. In the case of internal passages the heat transfer conditions were assessed on the basis of experimental relationships (usually Dittus-Bolter equation). Such estimation of thermal boundary conditions seemed to be very approximate but good enough to demonstrate the optimization techniques themselves. However, accuracy of heat transfer determination has a critical influence on the heat amount transmitted from the working medium to the coolant, which in turn determines temperature distribution within the cooled airfoil. If so, more precise estimation of thermal boundary conditions, both on the external surface of the blade and the cooling passages will influence the optimization as well. This paper demonstrates a possibility to implement the CHT analysis for the cooling system optimization, which is a step forward comparing to the approach used so far.

The optimization problems dealing with turbine blade cooling systems usually involved quite a high number of design variables as well as a complex, implicit and susceptible to slight

parameter changes, response (function) of the system in question. This response in a form of temperature, stress or other parameters was not monotonic but usually included a large number of local extremes, which was a significant problem for many gradient-based optimization methods (Mueller, 2002). In such cases, the stochastic methods were preferred, which was observed in almost all works mentioned before.

The most common was the evolutionary approach which apart from some disadvantages, was suitable to solve complex technical problems.

EVOLUTIONARY OPTIMIZATION

The optimization based on the evolutionary algorithm imitates real life with its evolution process of living organism. This method, which is based on a probabilistic search and an imitation of biological evolution, is able to overcome the settlement in local extremes, where many traditional optimization methods would finish their running.

The evolution process in a population comprised of abstract individuals, prepared for the optimization problem needs, takes place to produce better individuals in the successive populations till the optimal solution (best fitted individual) is reached. So the first step in the evolutionary search is the adequate preparation of the individual, which should include all the design parameters. In the optimization of a cooling structure the design parameters define all the variables which describe a specific configuration. The design variables in the evolutionary algorithm are usually binary or real coded to compose the chromosome of a single individual. In the case of binary coding the chromosome is structured as a string of bits, whereas while using floating point numbers it has a form of a vector built of the design parameters:

$$I = \left[a_1, a_2, a_3, \ldots a_n\right] \quad \left(a_i \rightarrow \Re\right) \tag{1}$$

Similar to biology, each individual reacts somehow to the external (surroundings) conditions. This reaction is quantified and represents the level of adoption to the conditions. This value is called fitness. In other words it shows to what extent the particular individuals fulfill the optimization criteria.

The population composed of a number of individuals, where the size of the population depends on the problem in question, is then subject to the evolutionary operations. Such operations change the genotype (some of the design parameters) of the members, which in consequence changes their fitness.

For the purpose of this research, the Single Objective Evolutionary Algorithm (SOEA) is used for the optimization search. This process is automatically coupled with the ICEM CFD and Ansys CFX software utilized for the computation of each cooling configuration.

CALCULATION PROCEDURE

The aim of the present optimization process is to find optimal size and location of circular cooling passages. The optimization is to be approached with objectives formulated on the basis of an airfoil's thermal field. This requires specification of boundary conditions both on the external profile and the cooling passages. Since the optimization changes the cooling structure and in consequence the cooling conditions it would be necessary to adjust the boundary conditions to current cooling configuration. To take the changes into consideration a CHT problem should be involved. However full CHT is computationally expensive from the point of view of the optimization where usually many cooling candidates need to be analyzed. This paper tries to implement the CHT problem into the optimization task.

Model for CHT problem

The problem is solved for a 3D model of the well known C3X profile taken from literature (Hylton et al., 1983) , which was extensively investigated by NASA. The vane profile is assumed to be aerodynamically optimal and fixed during the computation process. The report of the NASA

research has been the source of basic information for the purpose of this work. The vane in question is originally a convectively cooled one with ten internal passages as presented in Fig. 1. The airfoil was investigated within a linear 3-vane cascade supplied with exhaust gases from a burner. Cooling of the 76.2 mm high vane was provided with air. The air is flowing radially through ten circular channels.

The whole computational domain is 3D and consists of a periodic domain with one vane. It is divided into three sub domains: hot gas domain, solid domain of the vane and cooling air domain. The hot gas domain was extended in the axial direction upstream of the blade leading edge and downstream of the trailing edge to specify the uniform boundary conditions.

The vane material is stainless steel, which has a low, constant thermal conductivity of *k=16* W/m/K, a constant density of ρ=7900 kg/m^3, a molar mass of 55.85 kg/kmol and a specific heat capacity of *c=585.2* J/kg/K.

The flow conditions were assumed from the run 158, following the Hylton et al., (1983) nomenclature. The total pressure and total temperature were specified at the inlet, with the static pressure derived using p_{t1}=0.2435MPa and M_2 =0.91 specified at the exit. For the hot gas flow at the inlet, the turbulence intensity T_{u1} = 8.3% was specified to be the experimental value.
The inlet turbulence length scale L_{t1} was specified to be 0.4 mm (0.5% of the vane axial chord) as proposed by Luo and Razinsky (2007). Both the molecular viscosity and conductivity were specified as a function of static temperature using Sutherland's law. The specific heat is assumed as a constant value.

The flow conditions for the coolant flow in the passages were not taken from the experiment exactly. It was necessary to specify boundary conditions independently on the hole position and diameter. For all cooling channels the equal boundary conditions were assumed. At the inlet the total pressure p_{tc}=0.3 MPa and total temperature T_{tc}=375 K were taken. The flow at the inlet had a high turbulence level Tu_{1c}=10%. At the outlet the static pressure was p_{2c}=0.28 MPa. The coolant flow conditions ensured that the level of the blade temperature was similar to the experiment.
The end walls at hub and shroud were assumed as symmetry. Simplification of the model enabled to avoid a boundary layer modelling in those regions.

Numerical solution and turbulence model

The flow solver was the commercial CFD package ANSYS CFX. It solves 3D RANS equations on unstructured meshes of different cell types and a mixed structure. The solution strategy is based on the algebraic multi-grid method. For Conjugate Heat Transfer analysis, the energy equations for the fluid and solid are solved simultaneously. The energy equation for the solid is a degenerate form of the energy equation for fluids and is solved using the same numerical algorithm.

The turbulent eddy viscosity was obtained from the SST turbulence model. The Gamma-theta transition model is used to simulate boundary layer transition, which is one of the key features of blade heat transfer. In the Gamma-theta model two additional equations for the intermittency and transition onset Reynolds number are solved.

Mesh

The model geometry was created and meshed using the ICEM CFD package. Since the C3X vane had a constant cross section, a 2D mesh for all domains was generated first. For the external gas path region the quad dominated mesh was chosen with elements evenly distributed in the layers near the wall boundary. It ensures nearly orthogonality of the mesh near the vane surface. In the solid region the unstructured quad dominated mesh was also used. The holes were discretized using an O-type grids. The merged 2D mesh was then stretched up to form the 3D mesh. The 3D grid had only 10 layers to reduce the total mesh size, because the reduction in time consumption was strongly preferred in the optimization process. Totally, the mesh consisted of about 131000 cells for the entire domain, with about 80000 cells for the hot gas domain, 11000 for the solid domain and 40000 for the ten cooling passages.

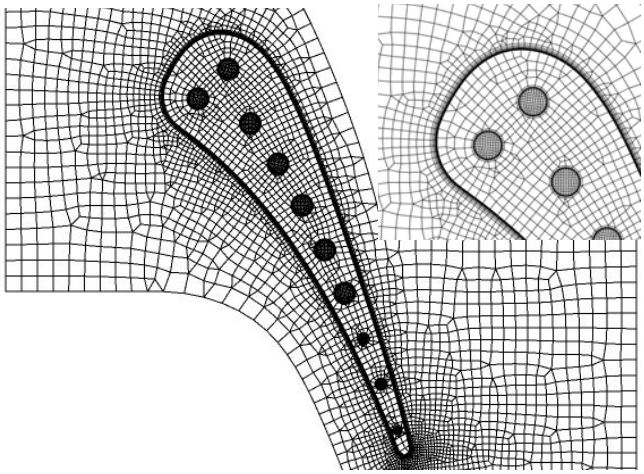

Fig 1. Computational meshes for all domains

The computational grids on the one layer are shown in Fig. 1. The near-wall spacing of the gas path mesh is about y+=1.

CHT solver protocol

The optimization procedure calls the CHT solver many times. Implementation of the full CHT problem for the optimization seems to be irrational in terms of computational cost. In order to make the problem feasible to be considered it was decided to reduce its size. There assumed that instead of full CHT solution it would do, at this stage, to take into account the CHT problem within the airfoil only (airfoil material and cooling passages), with fixed boundary conditions at the blade wall. Those boundary conditions are obtained from the full CHT prediction for the original configuration. The algorithm for the CHT solution consists of three steps. In the first step the cooling passages generated by the evolutionary algorithm are automatically meshed using a script file for ICEM CFD. Next, new meshes for the solid and the cooling channels are reloaded into the simulation file in the pre-processing of the ANSYS CFX and the solver is started. When the solver reaches the prescribed residual level (set to 1e-4 for the maximum residual) results in the third step are loaded to the postprocessor and necessary data for optimization procedure are exported. All steps are controlled by user defined procedures and proceed automatically.

Cooling structure coding

Each individual of the genetic population represented the cooling system configuration, which was equipped with ten channels and during the optimization the number was fixed. A circular passage definition requires 3 variables: 2 space coordinates and a radius. Taking into account the whole cooling system it made the optimization problem formulated in 30 dimensional design space. All the design parameters were stored within a design vector:

$$I = \left[x_1, y_1, r_1, ..., x_{10}, y_{10}, r_{10}\right] \tag{2}$$

The objective function was defined in the domain of the blade cross-section, so the constraints needed to be properly determined. The cooling passages might freely move within the blade domain, but care should be taken to prevent passages from overlapping and crossing the boundary. Even a single passage which violated the boundaries made the individual discredited for further calculations. This was because of an automatic model generation for CHT computations. To meet the modeling requirements both minimum mutual distance between neighboring passages and wall distance was restrained to 5mm and 1mm, respectively. Additionally, the minimum (1mm) and maximum (6mm) passage radius were specified.

Evolutionary search

At the beginning of the calculation process the base (initial) population was sampled with the constraint criteria being satisfied. So the whole base population was composed of a set of feasible cooling configurations. To determine the fitness function value for each cooling system candidate the chromosome was decoded (specific values were transferred from local to global system) in order to build the computational model. Then a command file for ICEM software was prepared for the flow and thermal model grid generation. In the next step the CHT computations, which involved the blade domain with cooling channels were performed giving as a result the temperature distribution within the airfoil and the flow field in the passages. On the basis of the results obtained the fitness of the specific solution was calculated. This process was repeated for each population member.

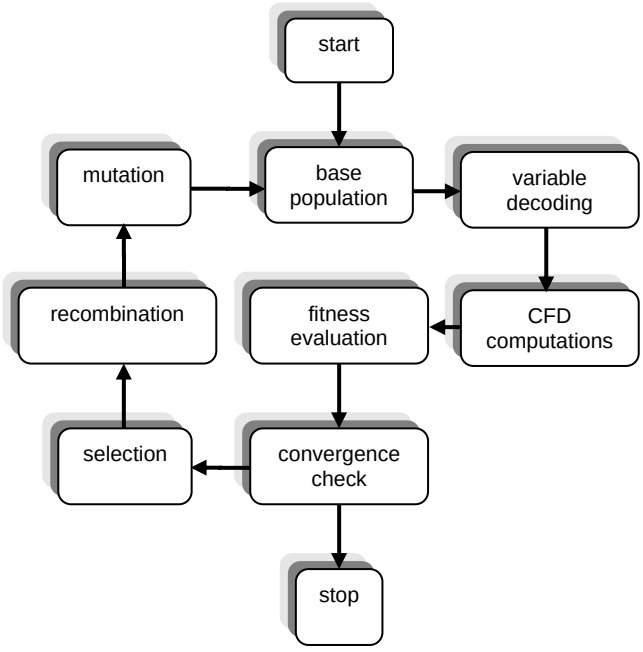

Fig. 2 Evolutionary algorithm flow chart

After that, the population was subject to the genetic operations and in consequence a new offspring population was obtained. Then the constraints for each individual of the children population were checked and the process was repeated (Fig. 2).

NUMERICAL INVESTIGATIONS

Objective Function

Turbine component cooling was provided in order to keep its temperature below the allowable limit. This was because of the safety and reliability reasons. On the other hand, the presence of cooling introduced a negative impact on airfoil thermal load and eventually durability, as well as the turbine efficiency. So, in order to meet the requirements mentioned the following objective function in a form of weighted sum of particular criteria was proposed:

$$f = w_1\left(\frac{\max_i(T_i)}{T_t}\right)^2 + w_2\left(\frac{1}{n}\sum_{i=1}^{n}\left(\frac{T_i}{T_{av}}\right)^2\right) + w_3\left(\frac{\dot{m}}{\dot{m}_t}\right)^2 \tag{3}$$

where T_i stood for temperature at node i, T_{av}, and T_t, represented the average and target temperature, respectively. Actual and target coolant mass flow was denoted with $\dot{m}$ and $\dot{m}_t$, respectively. Weight coefficients w_i are responsible for adjusting the influence of each factor on the objective function value. Function (3) tended to reduce all of its parameters to their desired values indexed with t.

Since the evolutionary algorithm searched for the best fitted (maximum fitness value) solution, the fitness function (F) was elaborated with the formula:

$$F = \frac{W}{\sqrt{f}} \tag{4}$$

where W was a constant value multiplier and f stood for the objective function (3).

Results

Before the optimization problem was approached, it was necessary to solve the full CHT problem for the entire domain and as a result the boundary conditions for the reduced CHT problem (solid and cooling passages) were obtained. As the boundary condition the HTC distribution at the blade surface was chosen assuming constant reference fluid temperature T_f=*808 K*. Fig 3 shows the distribution of the HTC at the vane midspan. On the suction side of the airfoil for the x/C_x=0.65 a sudden increase of HTC is observed, which represents the laminar-turbulent transition. From the experimental research (Hylton et al., 1983) it is known that the transition process appears earlier, and some additional work to calibrate the transition model and/or inlet boundary turbulence level could be done. At this stage of the analysis it was decided to skip the additional problem emerged and to assume that at that design level, approximation with assumed turbulence level and standard values for transition model was sufficiently accurate.

As mentioned before, the airfoil in question was originally equipped with ten cylindrical cooling passages and that number was fixed during the optimization. The original cooling configuration was the reference case for the analysis done. Since the CHT analysis for each cooling candidate required several minutes to get the solution, the computations were performed in parallel on a single PC with Quad CPU and 8 GB RAM. It was possible to run four analyses at once.

Calculations were performed for the weighted single objective function given by (3) with the following target values: T_t = 600K and m_t=0.025kg/s. The results, obtained both for air and steam cooling, showed about 40% growth of the fitness value compared to the original cooling system of the airfoil regarding to the criteria posed. It is mainly because of significantly lower coolant usage whose consumption dropped by about 60%, although the airfoil maximum temperature raised by 4% in the case of air cooling and 5% for steam cooling. There is also a growth in the mean temperature by about 11%. This however resulted in more isothermal material, which in turn would reduce thermal load and increase lifetime.

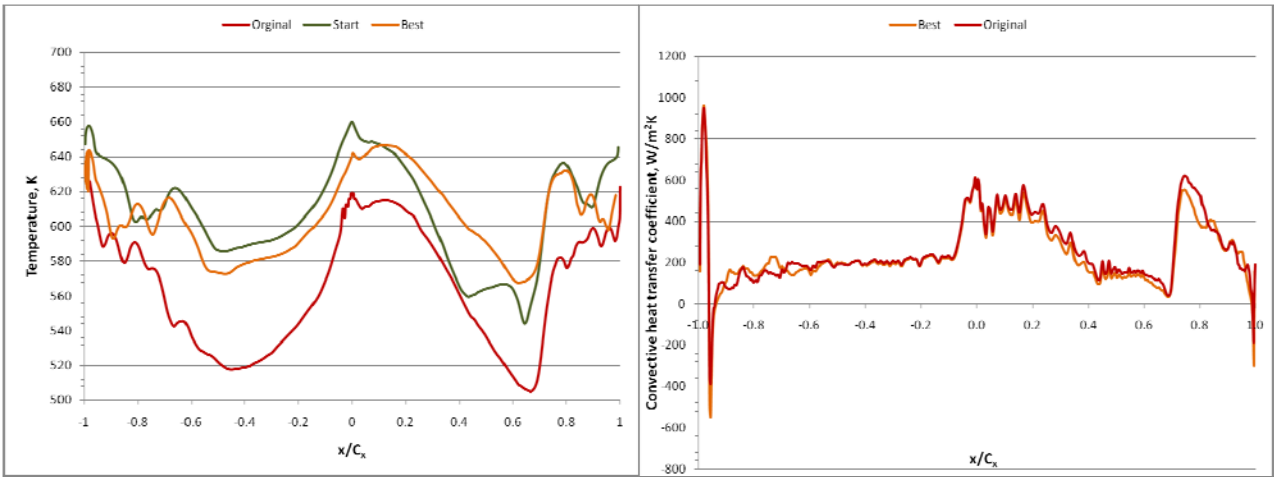

Fig. 3 Temperature distribution for the original, start and best configuration at the midspan (left) and HTC distribution for the original and best configurations (T_f=808 K) – results for the air cooling.

The results were obtained for the objective function weight coefficients: w_1=0.5, w_2=0.25 and w_3=0.25. Although the highest weight coefficient is connected with the maximum temperature factor, the most influential was the mass flow objective, which forced the design into coolant usage reduction. Of course, by weights modifications the user is able to favor specific objectives. There is also another way to keep particular objective parameters within a specified range by application of penalty for the solutions that do not meet the limitations.

Fig. 3 presents the temperature in the solid. In the original configuration the temperature level is changing strongly between the middle region of the blade and both the leading and the trailing edge region. The spanwise difference is visible especially on the rear part of the vane. The best configuration of the holes with the predicted temperature is shown in Fig.3b and 3d for air and steam cooling, respectively. The channels obtained for air cooling are visibly smaller than in the original case, whereas steam cooling required, in this particular calculations, passages of size comparable to the original ones. This was due to the cooling steam parameters, considerably lower than in the case of the air.

Comparison of the temperature distribution along the blade surface at the midsection of the vane for the original, initial and the best configuration is presented in Fig. 3. The temperature level for the original solution is lower than for the other configurations in consideration, but the difference between the minimum and maximum is greater by about 120 K. For the best solution obtained from the optimization this difference is about 80 K.

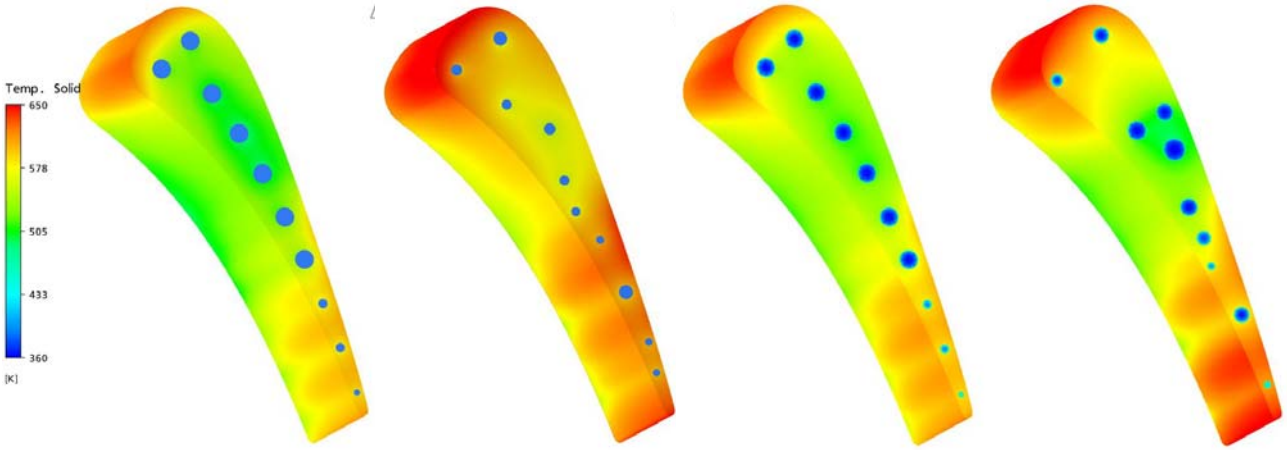

Fig. 4 Vane metal temperature a) original configuration – air cooling, b) optimized configuration – air cooling, c) original configuration – steam cooling, d) optimized configuration – steam cooling.

The best cooling candidate resulting from the optimization was analysed using the full CHT algorithm as used for the original vane. The HTC on the blade obtained for the optimized blade were compared with the original case at the midspan in Fig. 4. The position of the transition on the suction side is the same as for the original case. It enables to deduce that the change in cooling passage position does not influence the transition. The difference in the front of the blade is lower than in the rear part. The distribution is very similar. A relatively small difference in the HTC could cause the changes in the heat flux balance for the blade. From this point of view in the further research full CHT problem should be taken into account.

The optimization revealed that relocation of cooling channels could improve performance of the system both from the point of view of a cooled component's lifetime and turbine efficiency by reduction of coolant usage.

CONCLUSIONS

The paper presents the application of Conjugate Heat Transfer prediction for optimization of a cooling system configuration. The search procedure utilized the evolutionary algorithm. The evaluation of a particular solution was done on the basis of CHT analyses within a cooled airfoil. For the purpose of this research a convectively cooled airfoil was assumed and the optimization consisted in the relocation and diameter changes of the cooling passages. The search procedure was run as a Single Objective Algorithm but the fitness function entailed three different criteria: one was to minimize the blade maximum temperature, the next tended indirectly to reduce the thermal loading by providing more isothermal material and the last tried to lower down coolant usage.

Results of the optimization were juxtaposed to the original C3X airfoil. Changes in the cooling structure resulted in a significant advantage coming from more isothermal material of the blade. Also a much lower coolant usage was observed (60% reduction) with the maximum airfoil temperature only slightly higher (about 4%) than in the reference case. Applied optimization strategy is said to be one of the best tools for the global optimum search especially in the case of problems with complex geometries and a large number of design variables.
The main improvement worked out in the area of airfoil cooling optimization was the inclusion of CHT analysis for the blade interior, instead of empirical formulae for heat transfer conditions, which were widely used in such problems. This project showed the direction which should be followed to obtain more reliable designs.

One of the most painful disadvantages of the evolutionary algorithm together with the CHT analysis is their high computational cost, so a parallel computing is required while using this approach.

The next step in the development of a cooling system optimization should be the application of the full CHT prediction, which would make the whole process more reliable. Also in the future work the flow should be considered more precisely: including more layers in the spanwise direction and hub and tip boundary layer, using finer grids in the holes, analyzing the different turbulence models, calibrating a transition model. Nowadays it is a task for the single case CHT analysis and therefore extension of the optimization procedure could be done stepwise, depending on the computer power.

REFERENCES

Bohn D., Krüger U., Kusterer K. (2001): *Conjugate Heat Transfer: An Advanced Computational Method for the Cooling Design of Modern Gas Turbine Blades and Vanes. Heat Transfer in Gas Turbines* (Eds. B.Sunden, M.Faghri) WIT Press, Southampton, 2001, pp 58-108.

Dennis B., Egorov I., Dulikravich G., Yoshimura S., (2003a): *Optimization of a Large Number Coolant Passages Located Close to the Surface of a Turbine Blade*, ASME Paper GT2003-38051

Dennis B., Egorov I., Sobieczky H., Yoshimura S., Dulikravich G., (2003b) *Thermoelasticity Optimization of 3-D Serpentine Cooling Passages in Turbine Blades*, ASME Paper GT2003-38180

Dulikravich G., Martin T., Dennis B., Foster N., (1999): *Multidisciplinary Hybrid Constrained GA Optimization*, Evolutionary Algorithms in Engineering and Computer Science: Recent Advances and Industrial Applications, Editors: K. Miettinen, M. M. Makela, P. Neittaanmaki and J. Periaux, Wiley & Sons

Facchini B., Magi A., Scotti Del Greco A. (2004): *Conjugate Heat Transfer Simulation of Radially Cooled Gas Turbine Vane*, ASME Paper GT 2004-54213.

Favoretto C., Funazaki K. (2003): *Application of Genetic Algorithms to Design of an Internal Turbine Cooling System*, ASME Paper GT2003-38408

Fedrizzi, R., Arts, T. (2004): *Investigation of the conjugate convective-conductive thermal behavior of a rib-roughened internal cooling channel*, ASME Paper GT2004-53046

Goldberg D. (1989): *Genetic Algorithms in Search, Optimization, and Machine Learning,* Addison-Wesley, Reading

Hylton L., Mihelc M., Turner E., Nealy D., York R. (1983),: *Analytical and Experimental Evaluation of the Heat Transfer Distribution Over the Surfaces of Turbine Vanes*, NASA Lewis Research Centre

Jeong M., Dennis B., Yoshimura S. (2003): *Multidimensional Solution Clustering and Its Application to the Coolant Passage Optimization of a Turbine Blade,* Int. Design Engineering Technical Conference (DETC'03), Chicago

Kusterer K., Bohn D., Sugimoto T., Tanaka R. (2004): *Conjugate Calculation for a Film-Cooled Blade Under Different Operating Conditions*, ASME Paper GT 2004-53719

Luo J, Razinsky E.H. (2007): *Conjugate Heat Transfer Analysis of a Cooled Turbine Vane Using the V2F Turbulence Model,* Trans. of. ASME, Journal of Turbomachinery, Vol.129,, pp. 773-781

Martin T.J., Dulikravich G.S. (2001): *Aero-Thermo-Elastic Concurrent Optimization of Internally Cooled Turbine Blades*, in Coupled Field Problems, Series of Advances in Boundary Elements (eds. Kassab A., Aliabadi M.), WIT Press, Boston, MA, pp. 137-184

Michalewicz Z. (1996): Genetic Algorithms + Data Structures = Evolution Programs, Springer Verlag

Montomoli F., Della Gatta S., Adami S., Martelli F.(2004): *Conjugate Heat Transfer Modeling in Film Cooled Blades,* ASME Paper GT 2004-53177

Mueller S. (2002): *Bio-Inspired Optimization Algorithms for Engineering Application*, PhD Thesis, Swiss Federal Institute of Technology, Zurich

Nowak G., Wróblewski W. (2007): *Thermo-mechanical Optimization of Turbine Vane*, ASME Paper GT2007-28169

Shoko I., Saeki H., Inomata A., Ootomo F., Yamashita K., Fukuyama Y., Koda E., Takehashi T., Sato M., Koyama M., Ninomiya-T. (2005): *Conceptual design and cooling blade development of 1700 degrees C class high-temperature gas turbine*, Trans. of ASME J. Engineering for Gas Turbines and Power, 127(2) pp. 358-68

Zecchi S., Arcangeli L., Facchini B., Coutandin D. (2004): *Features of Cooling Systems Simulation Tool Used in Industrial Preliminary Design Stage,* ASME Paper GT 2004-53547

Verstraete, T., et al., (2008): *Design And Optimization Of The Internal Cooling Channels Of A HP Turbine Blade — Part II, Optimization,* ASME Paper GT2008-51080

Experimental Methodology

EXPERIMENTAL INVESTIGATION OF EVAPORATIVE HEAT TRANSFER CHARACTERISTICS AT THE 3-PHASE CONTACT LINE

K. Ibrahem[1], M. F. Abd Rabbo[2], T. Gambaryan-Roisman[1], P. Stephan[1,*]
[1]Darmstadt University of Technology, Department of Mechanical Engineering, Chair of Technical Thermodynamics. Petersenstr. 30, D-64287 Darmstadt, Germany
[2]Benha University, Shoubra faculty of Engineering, Department of Mechanical Engineering. 108 Shoubra street, Cairo, Egypt.

ABSTRACT. An experimental study is conducted to investigate the local heat flow at a solid-liquid-vapor contact line. A vertical channel of 600 μm width is built using two parallel flat plates; a 10 μm thick stainless steel heating foil forms a part of one of the flat plates. A liquid-vapor meniscus is formed between the plates due to capillary forces. In this study the fluid HFE7100 is evaporated inside the channel under steady state conditions. Two-dimensional microscale temperature fields at the back side of the heating foil are observed with a infrared camera with a spatial resolution of 14.8 μm ×14.8 μm. An in-situ calibration procedure is applied. The measured local wall temperature difference between the contact line area and the bulk liquid is up to 12 K. The local heat fluxes from the heater to the evaporating meniscus are calculated from the measured wall temperatures using an energy balance for each pixel element. The local heat fluxes at the contact line area are found to be about 5.4-6.5 times higher than the mean input heat fluxes at the foil.

Keywords: *3-phase contact line, meniscus, micro-region, heat transfer*

INTRODUCTION

The increasing power dissipation and miniaturization of microelectronic circuits drive extensive studies on high performance cooling systems. Such systems are often based on evaporative cooling processes in micro heat pipes, capillary pumped loops and spray cooling devices. In most of these systems the wall is only partly flooded with a macroscopic liquid layer, and the flow pattern is characterized by the presence of 3-phase contact lines. A common and important heat transfer mechanism in these cooling systems is evaporation of ultrathin liquid films in the vicinity of 3-phase contact line accompanied by extremely high heat fluxes. Understanding the phase change phenomena in the 3-phase contact line region is important for optimizing the evaporative cooling processes [1].

The thermodynamic and hydrodynamic interactions near the 3-phase contact line, or in other words the interaction between a thin film of liquid, its vapor, and a solid surface have been extensively studied. Fundamentally, most of the studies are based on a thin film evaporation concept introduced by group of Wayner [2] and first applied to macroscopic systems by Stephan and Busse [3]. Renk and Wayner [2] modelled evaporation of a tiny liquid film (later referred to as a “micro-region” [3]) between the adsorbed, non-evaporating film covering an apparently dry area and the macro-region with a high conductive heat resistance (see Fig. 1). The model has predicted that the local evaporative flux reaches a maximum value in the micro-region.

* Corresponding author: Prof. P. Stephan
Phone: + (49)-06151-16-3159, Fax: + (49)-06151-16-6561
E-mail address: pstephan@ttd.tu-darmstadt.de

Therefore, in spite of small geometrical dimensions (typically around 1 μm), a considerable amount of the heat supplied to a macroscopic system may flow through the micro-region. Under steady conditions the liquid is constantly supplied from the macro region to the micro-region. The liquid flow is governed by the gradients of the capillary pressure and the disjoining pressure in the micro region, both of them determined by the film thickness profile. Differential equations were formulated for predicting the distribution of the film thickness and local heat flux in the micro region and shown that the film thickness profile and the apparent contact angle depend on the wall superheat.

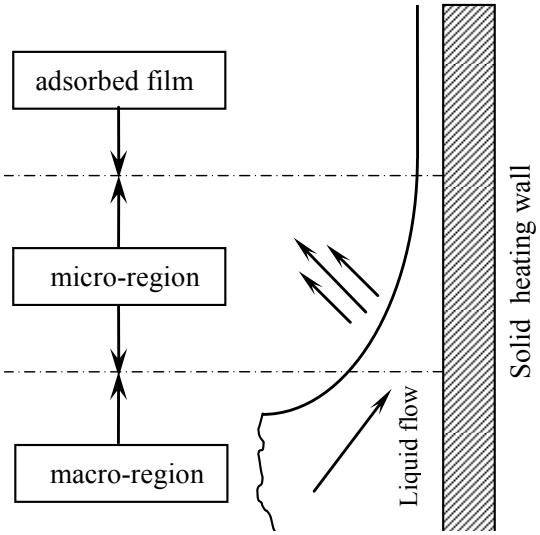

Figure 1. Micro -region model [1]

Stephan and Busse [3] have extended the micro-region evaporation theory to description of macroscopic systems and applied it to computation of temperature field and evaporation rate in a heat pipe. They have combined the solution of the equation describing the shape of the liquid-vapor interface and heat flux distribution in the micro-region with the solution of a macroscopic heat transfer problem in a heat pipe with open grooves. Stephan and Busse have found that the heat transfer in the 3-phase contact line area could have a significant influence on the overall macroscopic heat transfer.

Thin film evaporation in the micro-region has been studied experimentally [4]-[7]. The meniscus profile and the adsorbed layer thickness have been measured using interferometry technique. It has been found that the meniscus shape depends on the applied heat flux. The authors have experimentally confirmed the theoretical prediction concerning the strong influence of disjoining pressure on the flow field in the micro-region [5]. A good agreement between the experimental data and the results of theoretical models has been demonstrated.

Höhmann and Stephan [1] used a high resolution temperature measurement technique to monitor the microscale wall temperature distribution in the vicinity of evaporating liquid meniscus. This technique is based on Thermochromic Liquid Crystals (TLC), which are characterized by a temperature dependence of spectral reflective properties. The color play of TLCs has been recorded by a CCD camera in conjunction with a microscope. The pixel color values (or hue-values) have been translated into temperatures. As a result, two-dimensional temperature distribution underneath the evaporating meniscus has been determined with a spatial resolution of 1 μm. The authors have registered a local wall temperature drop in the vicinity of the 3-phase contact line which has been attributed to strong evaporative cooling in the micro-region. However, the TLC measuring technique is only applicable to relatively low input heat fluxes due to a narrow temperature range of TLCs. Therefore, the measured local temperature drop due to the micro-region evaporation was limited to 0.2 K.

The TLC technique and infrared thermography have been applied for investigation of the micro-region evaporation effect on nucleate boiling [8]-[10]. The authors have measured the non-stationary wall temperature distribution underneath a single growing bubble and a sequence of growing, departing and ascending bubbles under terrestrial and reduced gravity conditions. The measured temperature distribution has been used for computation of the wall heat flux distribution

[10]. A ring-shaped region of the wall temperature drop has been observed close to the 3-phase contact line at the bubble foot, corresponding to a ring-shaped region of high heat flux. The influence of the gravity level on the bubble frequency and the departure diameter has been evaluated with the same technique. Kandlikar *et al.* [11] and [12] have studied heat transfer from a stable evaporating meniscus formed between a needle dispensing water over a heated circular face of a rotating copper block. It has been found that the heat flux increases in direct proportion to the surface velocity and the water flow rate. The study provided an important insight into the role of the evaporating liquid-vapor interface and transient heat conduction around a nucleating bubble in pool boiling. In these experiments the wall temperature in the vicinity of evaporating 3-phase contact line has not been measured. The measurements have been performed in the air environment and not at saturation conditions.

Although numerous experimental and theoretical works on the thin film evaporation near the 3-phase contact line have been conducted, a full understanding of the relevant microscale heat and mass transport phenomena has not been yet achieved. Additional high resolution experimental investigations are needed for accurate determination of the temperature and heat and mass flux distributions in micro-region in a wide range of thermodynamic conditions and applied heat fluxes. The present investigation is focused on measurements of the wall temperature distribution near the 3-phase contact line at evaporation conditions. This temperature distribution is used to evaluate the distribution of the wall heat flux.

EXPERIMENTAL SETUP AND PROCEDURE

The schematic of the experimental setup is shown in Fig. 2. The setup contains a working fluid cell made of copper which is flooded with tempered water to guarantee isothermal conditions The temperature of the working fluid is kept near the saturation temperature at the system pressure. The control of the tempered water bath is carried out with a thermostat system. Inlet and outlet temperatures of the tempered water bath are measured and used for the temperature control. Additionally, the temperatures of the working fluid in the copper container and of the vapor entering the condenser are measured. A stainless steel vertical test channel is attached to the copper container. The 600 μm width test channel is formed by two parallel plates. A liquid column with a single liquid-vapor meniscus rises and accepts a steady position in this channel due to capillary forces. One of the two parallel plates is equipped with a 10 μm thick 22mm×14mm electrically heated stainless steel foil (see Fig. 3). The other side of the channel is formed by an unheated copper plate equipped with 5 thermocouples fixed in holes at a 0.5 mm distance from the front surface. These thermocouples are placed in front of the heating foil and used for the calibration of the infrared camera readings as well as for measurement of the average working fluid temperature in front of the heating foil. The pressure of the test cell is measured using calibrated pressure transducer. The vapor produced in the channel flows to the condenser which is located in a pressure chamber. The condenser and the pressure chamber with compensation bellow are connected with a vacuum pump controlling the pressure in the whole system. The working fluid is a methoxy-nonafluorobutane ($C_4F_9OCH_3$) fluid HFE-7100 with a normal boiling temperature of 61°C at atmospheric pressure. The back side of the foil is coated with a black paint by an airbrush.

The temperature field at the back side of the heater is observed with a high-speed infrared camera with a spatial resolution of 14.8 μm ×14.8 μm per pixel, a format of 320 × 256 pixels, and a temporal resolution of 244Hz. Thermocouples are calibrated against standard calibrated and certified temperature measurement device PT100 in the temperature range from 10°C to 90°C. The maximal error of thermocouple reading after calibration is kept within ±0.1°C.

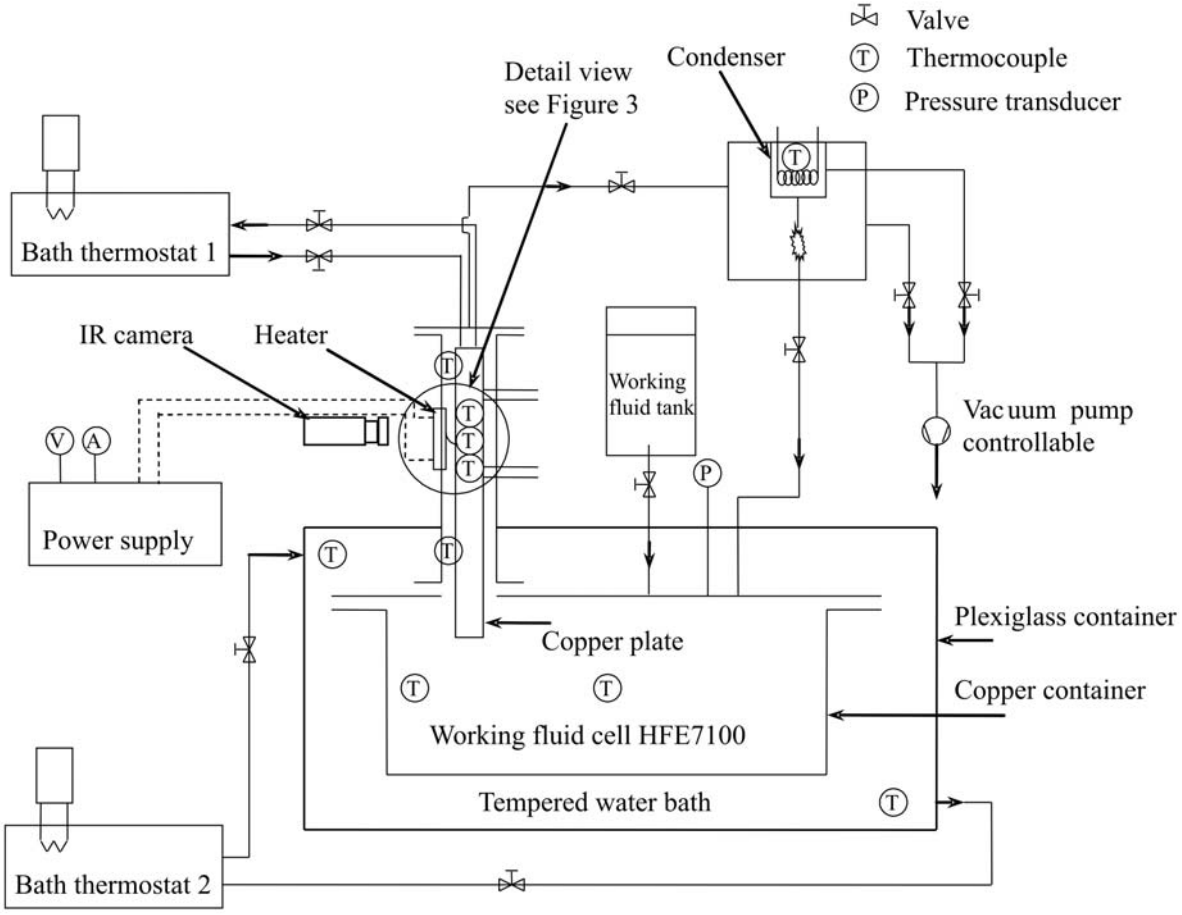

Figure 2. Flow chart of the experimental setup

The calibration of the infrared camera measurements is performed as follows. The unheated side of the channel (the copper plate of 10mm thickness) is moved toward the heating foil until a good thermal contact with the heating foil is reached. A uniform temperature of the copper plate is maintained by pumping heated water through internal heating passages manufactured within this plate. The infrared radiation from the back side of the heating foil is calibrated in the range from 10°C to 90°C.

The working fluid is carefully degassed before each experiment. The experiment is conducted at pressure of 510 mbar corresponding to saturation temperature of 41.6 °C, while the subcooling of the working fluid varies in different experiments from 3 to 6.5 K. The input heat flux to the heating foil varies from 183W/m^2 to 12.170 kW/m^2.

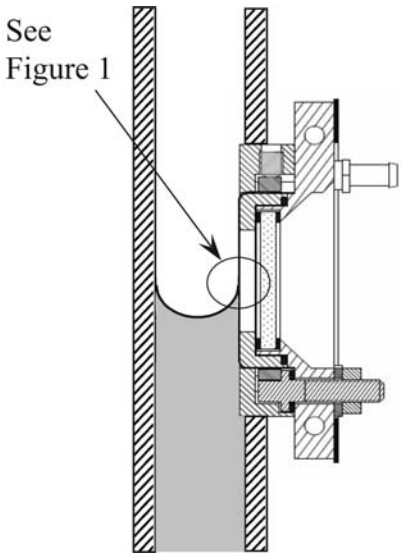

Figure 3. Channel detailed view

EXPERIMENTAL RESULTS

Local wall temperature and heat flux distributions underneath evaporating meniscus are presented in this section.

Figure 4 shows the two-dimensional wall temperature distributions underneath the evaporating meniscus at different input heat fluxes. It is observed that the temperature of the apparently dry region (or a region covered with adsorbed layer) is much higher than the temperature of the liquid bulk. The difference between these temperatures depends on the input heat flux. The temperature at the adsorbed layer region is high due to the very slow heat transfer in the vapor. The temperature distribution clearly shows a local minimum just underneath the 3-phase contact line separating the bulk liquid area from the apparently dry wall area. This temperature minimum is caused by strong evaporation near the contact line which is represented in Fig. 4 by horizontal dashed lines.

The difference between the minimal temperature near the 3-phase contact line and the mean bulk fluid temperature ranges from ~0.4 K to ~12 K depending on the input heat flux. The difference between the minimal temperature at the contact line and the wall temperature in the adsorbed layer region ranges from ~1.4 K to ~70 K depending on the input heat flux and on the position of the contact line which affects the percentage of wetted area of the heater. The temperature in the apparently dry adsorbed layer region increases with increasing of the dry area.

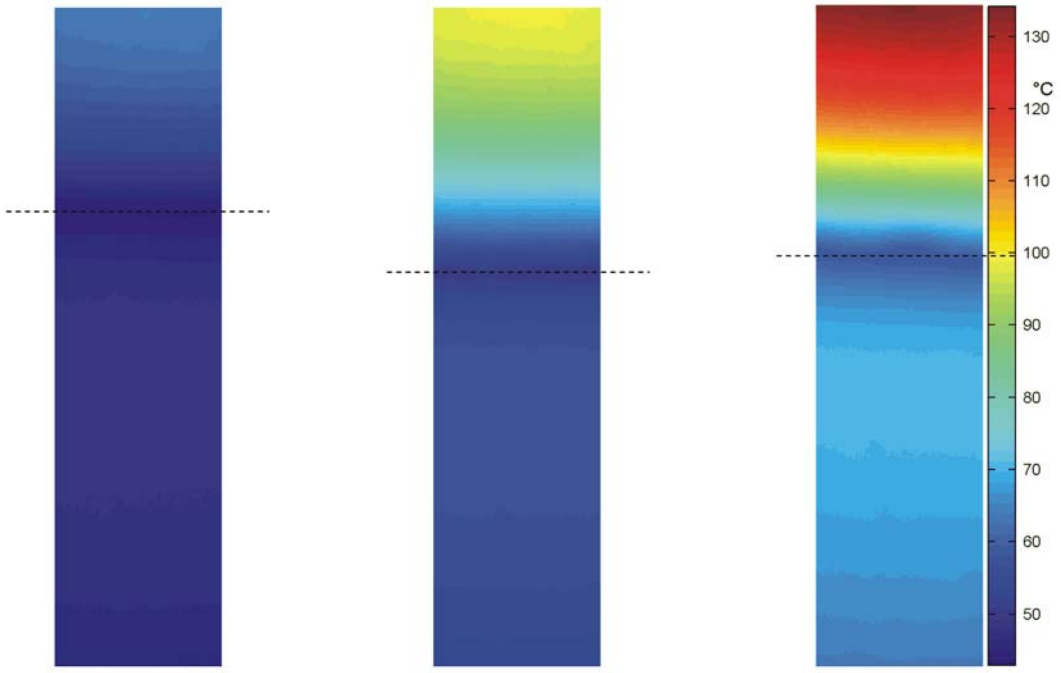

a) q= 3.425kW/m^2 b) q= 6.510kW/m^2 c) q= 10.645kW/m^2

Figure 4. Two dimensional local wall temperature distribution underneath the meniscus at different input heat fluxes (dashed line at the location of contact line area)

Figure 5 shows local wall temperature distribution along a vertical line underneath the meniscus at different input heat fluxes. The zero position on the *x*-axis coincides with the position of the contact line area defined as the location of the local temperature minimum. Negative *x*-values correspond to the liquid bulk region, and positive *x*-values correspond to the adsorbed layer region or the vapor

region where the temperature raises to high values. It has been observed that at high heat fluxes (above 9.5 kW/m^2) the liquid front is not stable, and some bubbles are formed and disturb the meniscus. At lower heat fluxes (3.4 to 9.5 kW/m^2) the liquid front seams to undergo a slow oscillatory motion which can be attributed to the instability of evaporating 3-phase contact line.

The local heat flux from the heater to the meniscus is calculated from the temperature distribution using the energy balance for each pixel element and two successive temperature images [10]. The heating foil is discretized in elements of the infrared camera pixels of 14.8µm × 14.8µm using a Matlab procedure. It is assumed that the back side of the heating foil is adiabatic thanks to the good thermal insulation provided by an air chamber at reduced pressure at the back of the heating foil. It is also assumed that there is no temperature difference between the front and the back side of the heating foil due to the small thickness of the heater.

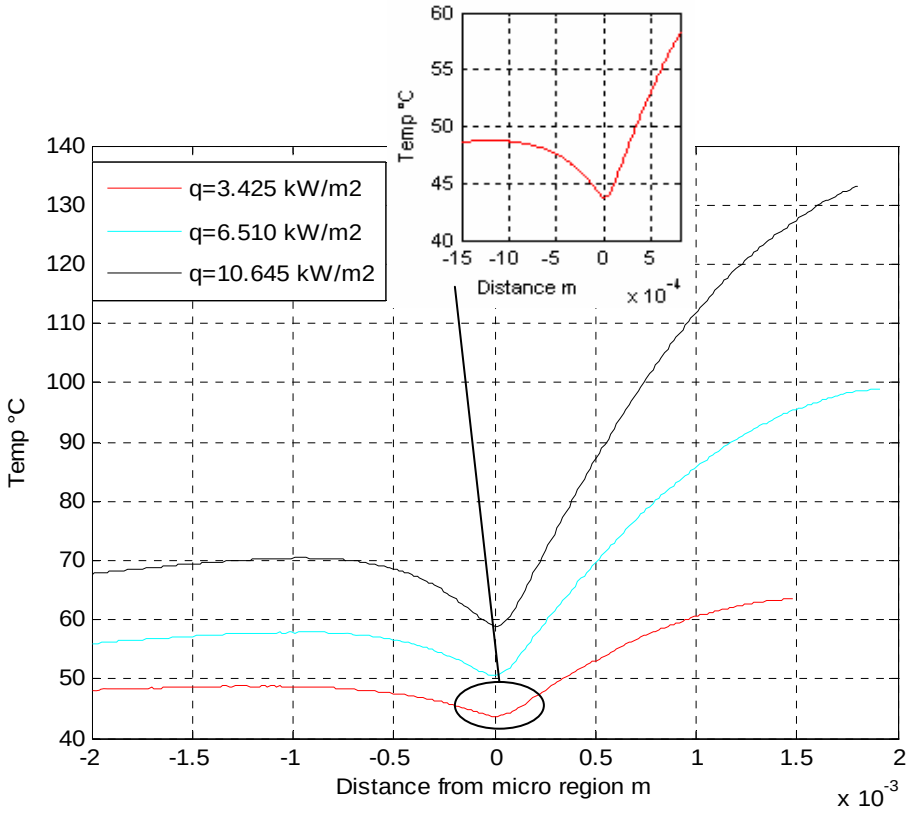

Figure 5. Linear local wall temperature distribution underneath the meniscus at different input heat fluxes

Figure 6 shows calculated two-dimensional heat flux distributions. It can be observed from this figure that the heat flux reaches a maximal value near the 3-phase contact line, even so the power input to the foil is constant and the heat generation is uniform in the heating foil. The local maximum of the heat flux is due to the high evaporation rate predicted for the contact line region, and due to conduction in the foil from neighbouring zones where the temperature is high. These phenomena are affected dramatically by the heating foil thickness, thermal conductivity, density, and heat capacity. Therefore, these properties of the heating foil are important for the modelling of the transport processes at the micro-region. Figure 7 shows the local heat flux distribution along a vertical line for different input heat fluxes. It can be observed that the heat flux in the liquid bulk decreases slightly due to heat conduction in the heating foil and due to the decreasing of the liquid

film thickness in the liquid bulk. The heat flux strongly increases at the contact line area, corresponding to the high evaporation region. The maximal heat fluxes at the contact line area exceed the mean heat fluxes by a factor of 5.4 to 6.5. The heat fluxes in the adsorbed layer region are lower than that in the bulk liquid.

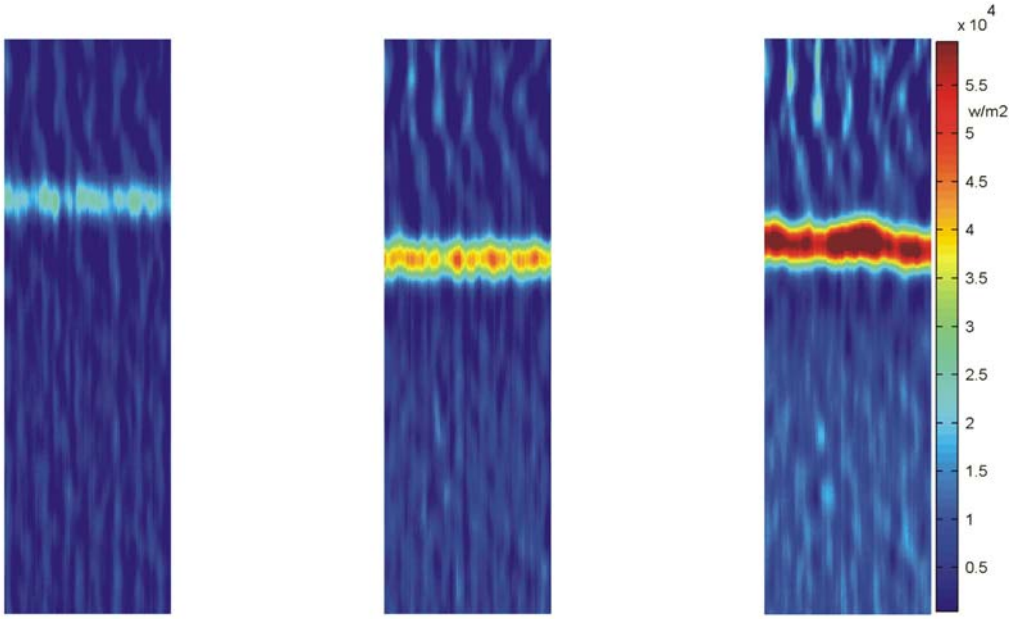

a) q= 3.425kW/m^2 b) q= 6.510kW/m^2 c) q= 10.645kW/m^2

Figure 6. Two dimensional local calculated heat flux distribution to the meniscus for different input heat fluxes

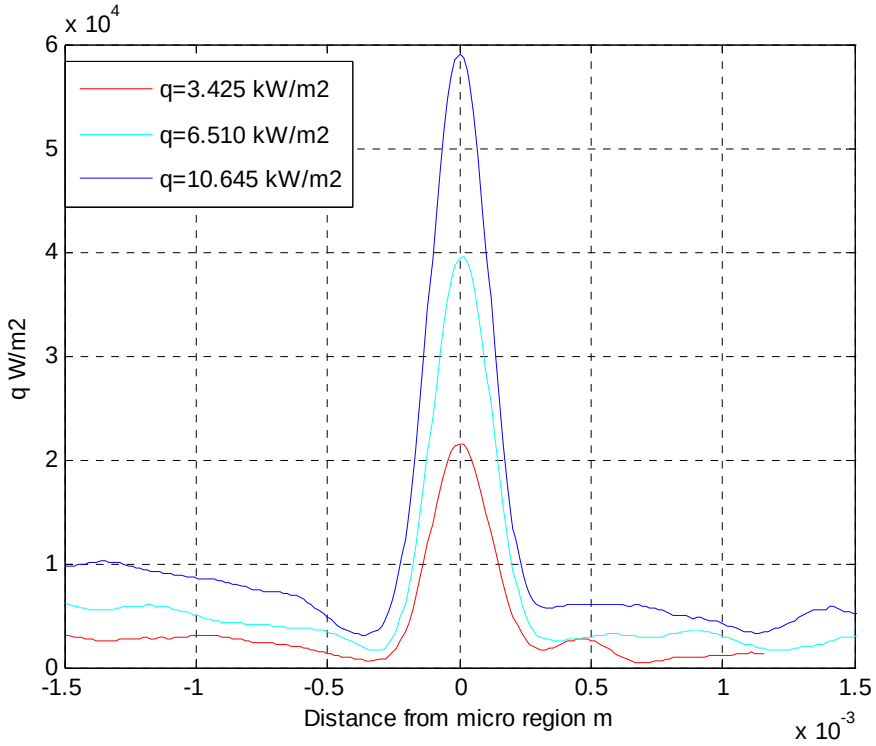

Figure 7. Linear local heat flux distribution for different input heat fluxes

CONCLUSIONS

An infrared thermography system was used to measure two-dimensional temperature distribution underneath a single evaporating meniscus in the contact line area with a high spatial resolution of 14.8 μm × 14.8 μm. Due to extremely high local evaporation rate in this area a temperature difference up to 12 K between the wall temperatures at the contact line area and the bulk liquid has been observed. The local heat flux distribution from the heater to the fluid has been calculated from the measured wall temperature distributions for constant uniform input heat fluxes.

High local heat fluxes could be observed at contact line area with values up to 5.4-6.5 times higher than the mean input heat fluxes. The experimental observations confirm the results of theoretical and numerical studies predicting strong local temperature gradients in the contact line area due to locally high evaporation rates.

REFERENCES

1. Höhmann, C., and Stephan, P., Microscale Temperature Measurement at an Evaporating Liquid Meniscus, *Experimental Thermal and Fluid Science*, Vol. 26, pp 157-162, June 2002.
2. Renk, F. J., and Wayner, P. C., An Evaporating Ethanol Meniscus Part 2: Analytical Studies, *J. Heat Transfer*, Vol. 101, pp 59-62, 1979.
3. Stephan, P., and Busse, C., Analysis of The Heat Transfer Coefficient of Grooved Heat Pipe Evaporator Walls, *Int. J. Heat Mass Transfer*, Vol. 35, No. 2, pp 383-391, 1992.
4. Renk, F. J., and Wayner, P. C., An Evaporating Ethanol Meniscus Part 1: Experimental studies, *J. Heat Transfer*, vol. 101, pp 55-58, 1979.
5. Panchamgam, S. S., Gokhale, S. J., Plawsky, J. L., DasGupta, S., and Wayner, P. C., Experimental Determination of The Effect of Disjoining Pressure on Shear in The Contact Line Region of a Moving Evaporating Thin Film, *J. Heat Transfer*, Vol. 127, pp 231-243, 2005.
6. Zheng, L., Wang, Y.-X., Plawsky, J. L., and Wayner, P. C., Accuracy of Measurements of Curvature and Apparent Contact Angle in a Constrained Vapor Bubble Heat Exchanger, *Int. J. Heat Mass Transfer*, Vol. 45, No.10, pp 2021-2030, 2002.
7. Panchamgam, S. S., Chatterjee, A., Plawsky, J. L., and Wayner, P. C., Comprehensive Experimental and Theoretical Study of Fluid Flow and Heat Transfer in a Microscopic Evaporating Meniscus in a Miniature Heat Exchanger, *Int. J. Heat Mass Transfer*, Vol. 51, No. 21-22, pp 5368-5379, October 2008.
8. Wagner, E., Sodtke, C., Schweizer, N., and Stephan, P., Experimental Study of Nucleate Boiling Heat Transfer Under Low Gravity Conditions Using TLCs for High Resolution Temperature Measurements, *Int. J. Heat Mass Transfer*, Vol. 42, pp 875–883, 2006.
9. Sodtke, C., Kern, J., Schweizer, N., and Stephan, P., High Resolution Measurements of Wall Temperature Distribution Underneath a Single Vapour Bubble Under Low Gravity Conditions, *Int. J. Heat Mass Transfer*, Vol. 49, pp 1100-1106, 2006.
10. Wagner, E., Stephan, P., Koeppen, O., and Auracher, H., High Resolution Temperature Measurements at Moving Vapor/Liquid and Vapor/Liquid/Solid Interfaces During Bubble Growth in Nucleate Boiling, *4th International Berlin Workshop on Transport Phenomena with Moving Boundaries*, Berlin, Germany, September 27-28, 2007.
11. Kandlikar, S. G., Kuan, W. K., and Mukherjee, A., Experimental Study of Heat Transfer in an Evaporating Meniscus on a Moving Heated Surface, *J. Heat transfer*, Vol.127, No.3, pp 244-252, 2005.
12. Kandlikar, S. G., and Kuan, W. K., Circular Evaporating Meniscus-A New Way to Study Heat Transfer Mechanism During Nucleate Boiling, *5th International Conference on Boiling Heat Transfer*, Jamaica, May 4–8, 2003.

EXPERIMENTAL INVESTIGATIONS ON AIR ENTRAINMENT BY MEANS OF IMPINGING JETS

D. V. Danciu*, M. J. da Silva, M. Schmidtke, D. Lucas
Institute of Safety Research, Forschungszentrum Dresden-Rossendorf e.V., Germany

ABSTRACT. The phenomenon of air entrainment as a result of an impinging water jet was experimentally studied by means of videometry and image processing methods. A series of experiments at different conditions was performed and evaluated. Each experiment consisted of a 10s recorded sequence with a frequency of 200Hz. Jet lengths varied between 0.01m and 0.2m and jet exit velocities ranged between 0.8m/s and 2.5m/s. Image processing algorithms were applied to extract information about jet penetration depth, width of the bubble plume and bubble size distribution. Therefore, images were subdued to background subtraction, binarization and averaging. Bubble sizes were estimated from single images by subsequent background subtraction, cell segmentation, bubble detection and bubble size calculation by means of a Hough-transform based algorithm. It was found that the bubble sizes were in accordance to the data present in the literature. The penetration depth of the plume was compared to an empirical formula presented by Bin in the literature. It was established that in addition to the impact velocity, the amount of entrained gas has a significant effect on the penetration depth.

Keywords: *air entrainment, impinging jet, image processing, penetration depth, bubble size*

INTRODUCTION

A water jet impinging on a free surface of a pool causes air entrainment as soon as the jet velocity is high enough (inception velocity). A swarm of bubbles appears as result of the impingement. Impinging jets may be applied in several industrial processes and also in different situations related to reactor safety analysis. The primary example for the application of impinging jets in reactor safety systems is the emergency core cooling (ECC) injection into a partially filled cold leg, which takes place in some scenarios of loss of coolant accidents. In this case, the injected cold water impinges as a jet on the surface of the hot water inside the cold leg. Depending on the velocity of the jet, steam bubbles may be entrained below the surface by the impinging jet. These bubbles contribute to heat exchange and mixing of the fluids. Heat transfer between cold and hot water and mixing in the cold leg play an important role since the mixed water enters the reactor pressure vessel and may cause high temperature gradients at the wall of the vessel (pressurized thermal shock).
The mechanism of air entrainment has been studied over the past years. Recent works in this area are those of Chirichella et al and Cummings and Chanson. The experiments described in [6] studied air entrainment produced by a translating axisymmetric laminar water jet and established three boundaries between the entrainment regimes. In [7] air entrainment was studied by means of visualization experiments. The inception conditions of air-water flows were found to depend critically upon the jet turbulence. Even though many studies have been made regarding air

* Corresponding author: D. V. Danciu
Phone: + (49)-351-2602170, Fax: + (49)-351-2602383
E-mail address: d.danciu@fzd.de

entrainment caused by means of impinging jets, there is a certain lack of systematic data in the literature with regard to the penetration depth of the bubbles and the gas void fraction.
Our experimental setup was developed so that it allows studying the air entrainment phenomenon under different velocity and jet length conditions and to validate the models implemented in the CFD codes against the experimental data.

EXPERIMENTAL SETUP

Figure 1 shows a schematic of the experimental setup. The experiments were carried out in a 0.3m x 0.3m x 0.5m water tank constructed with transparent acrylic walls for visualization purposes. The water level in the tank was kept constant at 0.28 m throughout the experiments. Water was pumped out of the tank and re-injected through a smooth 6 mm diameter, 50 mm long steel pipe used as nozzle to produce a vertical falling round jet. A rotameter was used for the measurement of the flow rate. Images of the impact between the jet and the water pool were captured by a high-speed camera (DRS Technologies). For each experimental condition, a sequence of images of the region below the surface was taken. The camera was operated with a frame rate of 200 frames per second. Backlighting with high luminosity LED panels was used during the experiments in order to have a proper exposure at the required filming rate.
Experiments were realized for different nozzle heights (L_j in Figure 1) and volumetric flow rates, with both tap- and de-ionized water.
The experiments consisted in a vertical liquid jet of different lengths and velocities impinging on the calm surface of the water pool at an angle of 90°. The velocity of the jet ranged between 0.9 m/s and 2.5 m/s at the nozzle exit and the jet length was varied between 0.01 m and 0.2 m.

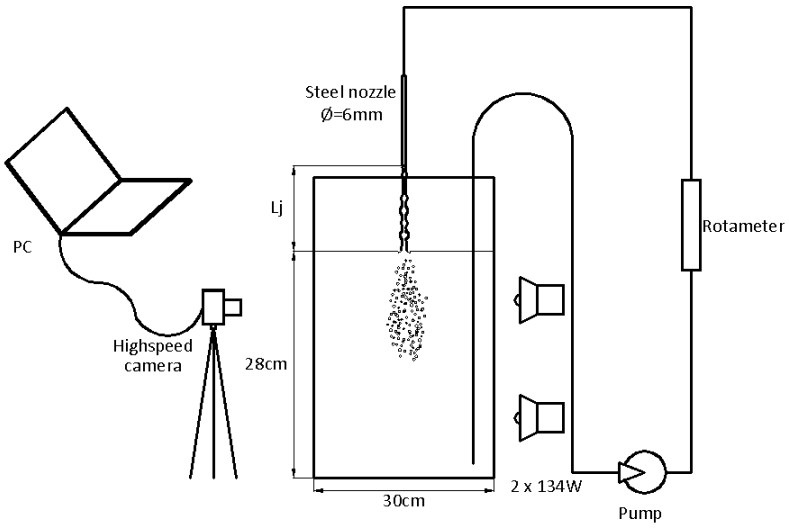

Figure 1. Schematic of the experimental setup

The velocity of the jet at the plunge point is calculated as:

$$v_j = \sqrt{v_0^2 + 2gL_j} \tag{1}$$

where v_0 is the velocity of the jet at the nozzle exit, L_j is the jet length and g the earth acceleration. In (1) free falling is assumed for the water after leaving the nozzle.

OBSERVATIONS

In some cases it is difficult to determine the conditions for the inception of air entrainment. Air entrainment can also occur for a very short period of time immediately after the impact, regardless of the nozzle height and the velocity of the jet. However, our discussion regards only cases of fully established flow.

Similar to [6], where it was stated that the incipient air entrainment takes place with the appearance of at least one bubble, in the absence of other bubbles in the water pool, which lasts longer than 2s beneath the surface of the pool, we also observed three distinct entrainment regimes during our experiments.

- The first regime is the one where during the impingement no bubbles appear; although for all our experimental conditions we had a fully turbulent flow developed in the nozzle (Re > 2300).
- The second one is the medium entrainment regime, where either only one or two bubbles appear after a period of time, remain trapped under the surface for a short time and disappear after a few seconds (incipient entrainment), or a swarm of bubbles is being entrained from time to time (intermittent entrainment).
- The last regime is that of continuous air entrainment, when large air pockets and bubble swarms are continuously being entrained.

Figure 2 illustrates the distribution of the entrainment regimes dependent on impact velocity and jet length for all experimental conditions. Both tap- and de-ionized water exhibit the same behavior.

The velocity of the jet and its diameter are affected by the gravity. According to [1], the jet diameter, d_j, can be calculated as a dependence on a reference diameter which was experimentally calculated for L_j = 3cm. However, if we consider the conservation of the mass flow rate, we can also calculate the jet diameter at the impact as a function of the jet diameter at the nozzle, d_0, and of the jet impact velocity as:

$$d_j = d_0 \sqrt{\frac{v_0}{v_j}} \tag{2}$$

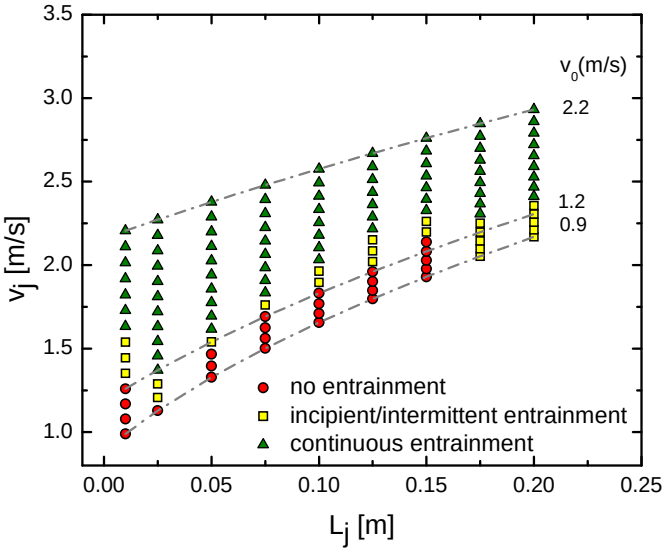

Figure 2. Entrainment regimes as a function of v_j, the jet impact velocity and the jet length, L_j.

Applying equation (2) the jet diameter at the impact with the pool surface suffers a change, especially for the higher jet lengths, when the jet diameter at the impact with the pool represents only ca 75-85% of the initial jet diameter.
An important role in the occurrence of air entrainment is played by the roughness of the jet. To prove the importance of the jet surface disturbances in the entrainment process, our experiments include tests where a 7.5 cm long jet which did not entrain air was disturbed with a thin needle. Due to the appearance of waves and thus an increase of the surface roughness of the jet, air entrainment takes place. The number of the entrained bubbles is proportional to the duration of the disturbance. We also observed that if the tip of the needle barely touches the jet, only a small number of bubbles appears and the bubble sizes are smaller than in the case of a deeper disturbance, when the bubbles are larger and present in a larger number. Figure 3 presents such an example.

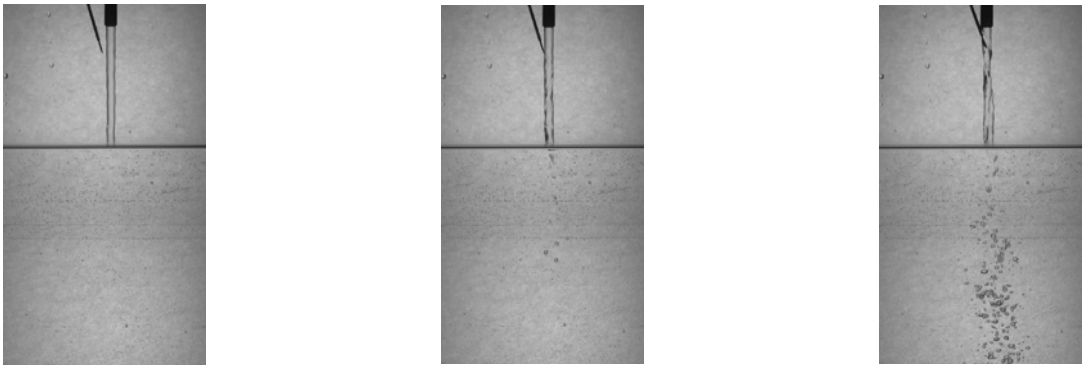

a. b. c.

Figure 3. Sequence presenting the influence of jet surface disturbances on air entrainment
a. no entrainment (undisturbed jet); b. superficial disturbance; c. deep disturbance

The length of the jet along with the gravitational acceleration plays an important role in the inception of air entrainment. For different flow rates, air entrainment does not occur. As soon as the length of the jet is being increased even with just a few millimeters, air entrainment occurs.
A distinctive and interesting situation takes place for v_0=1.2 m/s (for both tap- and de-ionized water), where all entrainment regimes are present. They vary with the jet length, starting with no entrainment, then jumping directly to the continuous entrainment regime, switching to incipient/intermittent entrainment followed by no entrainment for several jet lengths, returning to intermittent entrainment and continuous entrainment. Figure 4 presents the pictures corresponding to the jet lengths for which air entrainment takes place. It is important to mention that our experiments are reproducible.

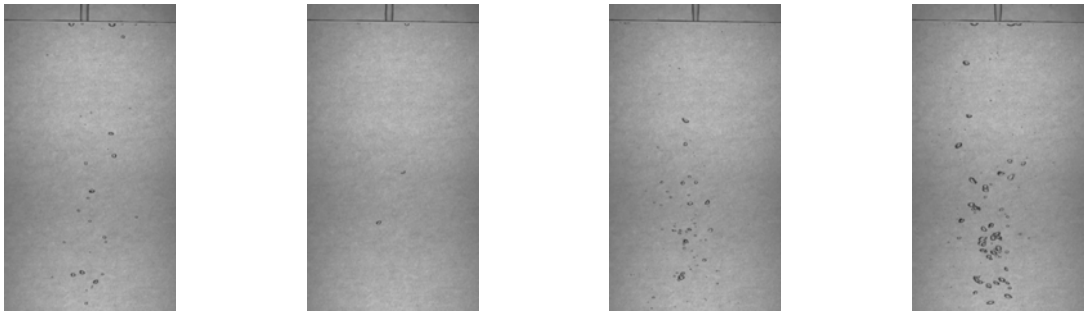

L_j = 0.025 m L_j = 0.05 m L_j = 0.175 m L_j = 0.2 m

Figure 4. Air entrainment at v_0 = 1.2 m/s

METHODOLOGY AND ANALYSIS

The objective of our experiments was to gather information about the bubble size distribution, the penetration depth of the plume, the width of the plume and their variation in time.
In each experiment a sequence of 2000 frames was recorded. The flow rate and length of the jet were varied for each experiment. Image processing algorithms were applied to extract the sought information. The experiments involved two types of water: tap water and de-ionized water.

Penetration depth

During the experiments, we observed that the length of the jet plays an important role in the entrainment process. We determined the variation of the penetration depth in time for different experimental conditions. Due to the fact that the plume fluctuates, one cannot refer to the penetration depth at a distinct moment. The variation of the penetration depth is shown in Figure 5 for three different nozzle exit velocities, but equal impact velocity. The penetration depth was calculated as the deepest point toward which bubbles travel, for each single frame of the respective recorded sequences. Therefore, considering the temporal fluctuation of the penetration depth, the best way to find it for a set of experimental conditions is to average it over the entire sequence.

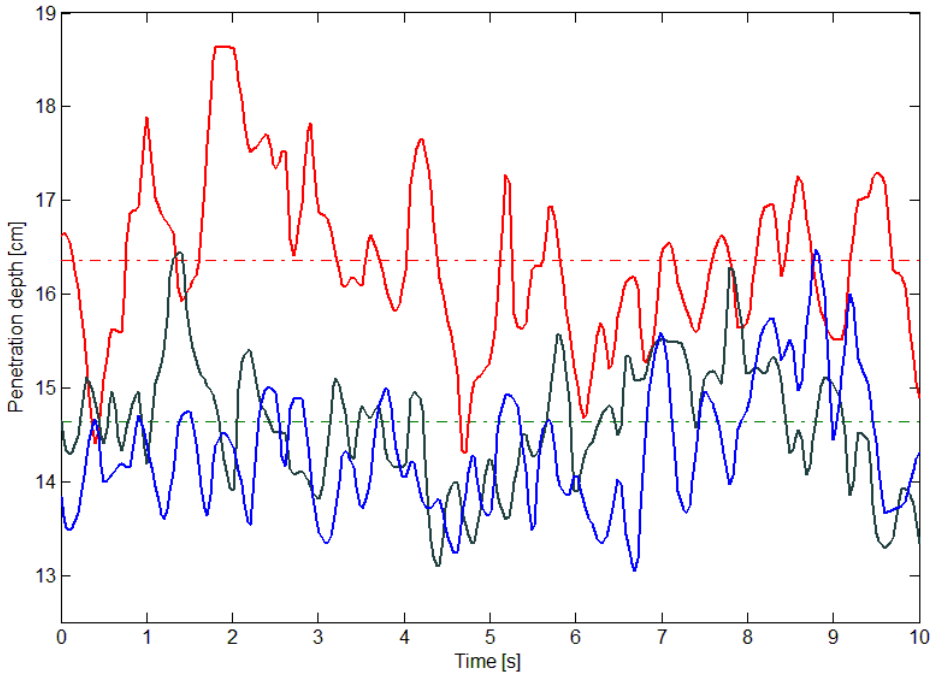

Figure 5. Penetration depth variation in time for v_0=1.8 m/s (red), v_0=2 m/s (green) and v_0=2.2 m/s (blue)

The mean penetration depth obtained with the above described method is in concordance with the values obtained by applying the averaging method described below.
Images were subdued to background subtraction, removal of the small air bubbles at the walls and averaging. Our algorithm averages over the entire 2000 frames sequence. It is noticeable in the averaged imagine (Figure 6, bottom) that, at the tip, the plume is rarefied, meaning that only a small amount of bubbles travels that deep. Therefore, we have chosen to consider as penetration depth the first grey level value from the bottom of the plume which represents only ten percent of the maximum grey level value of the averaged plume, found usually in the core of the plume.

Figure 6 shows an example of the penetration depth variation for three different nozzle exit velocities, but identical impact velocity, v_j = 2.5 m/s. The penetration depth of the air bubbles decreases with the increase of the impact velocity, most of the time. The difference between the first two cases is obvious and, although between the next two cases the penetration depth only varies with ca. 0.5 cm, one can easily note the difference in the volume of entrained air for all three examples. The plume becomes denser with the velocity and, due to the fact that the buoyancy forces surpass the viscous drag exerted by the downward moving jet, the plume retracts towards the surface of the water.

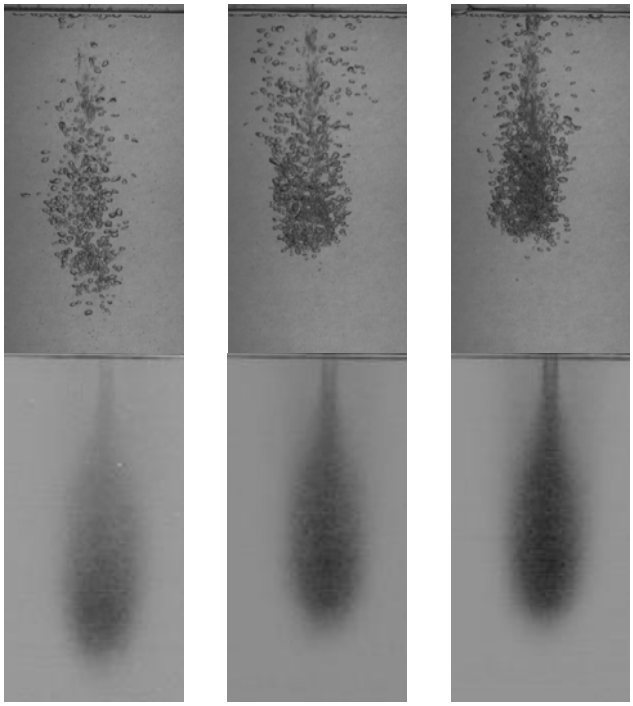

v_0=1.8 m/s L_j=15 cm | v_0=2 m/s L_j=12.5 cm | v_0=2.2 m/s L_j=7.5 cm

Figure 6. Example of the penetration depth variation for constant impact velocity v_j=2.5 m/s, for the three different nozzle exit velocities and jet lengths: snapshots (top) and processed sequences (bottom) for tap water

According to Bin [1], the penetration depth can be calculated as:

$$H_p = 2.1 v_j^{0.775} d_0^{0.67}$$

which means that for constant impact velocity, the penetration depth should be constant. The penetration depth as a result of equation 3 is found between 12 cm and 16 cm for impact velocities between 2 m/s and 3 m/s. Figure 6 shows the variation of the penetration depth for three different nozzle exit velocities and different jet lengths for tap water, as a result of our image processing algorithms. We observe that the behavior of the penetration depth is not monotonous with the impact velocity, opposite to equation 3. The values of the penetration depth for the de-ionized water experiments are found in the same range and follow the same trend as in the case of tap water. They slightly vary from the values obtained for tap water and this might be due to the difference between the surface tensions of the two fluids, induced by the bipolar molecules and unipolar ions present in the tap water which increase its surface tension. However, the values of the penetration depth are

found in the range given by Bins' formula, although we get different penetration depths for the same impact velocity and nozzle diameter (but different nozzle velocities and jet lengths). In our experiments we vary the impact velocity by modifying the length of the jet and the nozzle exit velocity. We can observe that for v_0 = 2 m/s and v_0 = 2.2 m/s, the penetration depth has a downward trend (see Figure 6). It first decreases with the jet length and then fluctuates slightly between 13 and 14 cm. By increasing the jet length for a constant nozzle exit velocity, we increase the impact velocity and the jet momentum transport into the pool. This should lead to a higher penetration depth, as predicted by equation 2. The penetration depth does not increase, though, with the impact velocity. This might be caused by the fact that for higher jet lengths the gas void fraction inside the plume increases, thus counteracting the jet momentum by buoyancy driven friction. Hence, the two opposite effects are responsible for the behavior of the penetration depth. In the case of v_0 = 1.8 m/s the penetration depth behaves non-monotonously, similar to the entrainment behavior in Figure 4. In Figure 4 (v_0 = 1.2 m/s) the amount of entrained gas varies not monotonous with the jet length. This indicates that the jet surface instabilities which trigger gas entrainment do not increase monotonous with the jet length. Maybe different kinds of surface instabilities play a role here: surface instabilities triggered by the nozzle edge and surface instabilities which grow with the jet length, such as Rayleigh instabilities.

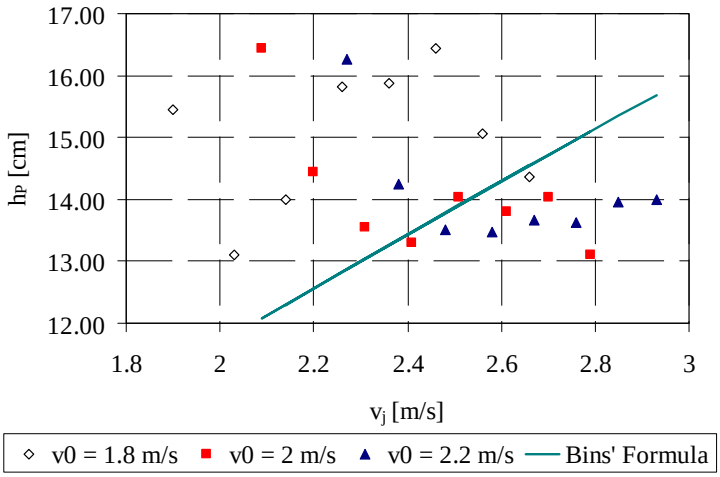

Figure 7. Processed penetration depth variation for three different nozzle exit velocities and jet length ranging between 0.025m and 0.2m (tap water)

Bubbles size distribution / estimation

Bubble sizes were estimated from single images by means of image processing through subsequent background subtraction, cell segmentation, bubble detection and bubble size calculation by means of a Hough transform based algorithm. It was found that the latter algorithm could only be used for experiments with a small number of bubbles in the plume. Otherwise, bubbles sizes could only be estimated at the edge of the plume where the bubbles do not overlap. Figure 7 shows an example of detected bubbles in a thin plume.

The Sauter mean diameter in the region of the rising bubbles was about 3 - 4mm, in agreement with previous data from the literature [1]. The smallest measurable bubbles were found to range between 0.3mm and 1.5mm. Some of the largest bubbles had diameters around the value of 7mm.

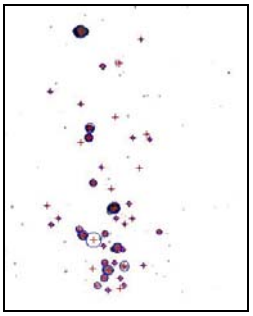

Figure 8. Image with bubbles detected (centre positions and radii marked)

CONCLUSIONS

To study the phenomenon of air entrainment by means of impinging circular jets, a video observation technique was used. Experiments have been carried out in a square tank for various jet exit velocities and jet lengths. The experimental data was processed and will be further used to validate the models implemented in CFD.

Some key parameters in air entrainment occurrence are: the velocity of the jet, the physical properties of the liquid, the length of the jet (falling height) and the turbulence of the jet. The penetration depth of the plume was measured and compared with an empirical formula by Bin. It has been found that in addition to the impact velocity, the amount of entrained gas has a significant effect on the penetration depth.

Further experiments are planned at FZD for a better observation of the liquid field velocities by means of PIV methods and quantitative void fraction measurements with x-ray radiography.

REFERENCES

1. Bin A. K., Gas entrainment by plunging liquid jets, Chem. Eng. Sci., Vol. 48, No. 21, pp. 3585-3630, 1993.
2. Bonetto F. & Lahey Jr. R.T., An experimental study on air carryunder due to a plunging liquid jet, Int. J. Multiphase Flow, Vol. 19, No. 2, pp. 281-294, 1993.
3. Chanson H., Aoki S. & Hoque A., Physical modelling and similitude of air bubble entrainment at vertical circular plunging jets, Chem. Eng. Sci., Vol. 59, pp. 747-758, 2004.
4. Chanson H. & Brattberg T., Experimental investigations of air bubble entrainment in developing shear layers, Univ. of Queensland, Dep. of Civil Eng., Report CH48/97, 1997.
5. Chanson H. & Manasseh R., Air entrainment processes in a circular plunging jet: void-fraction and acoustic measurements, J. of Fluids Eng., Vol. 125, pp. 910-921, 2003.
6. Chirichella D., Ledesma R. Gomez, Kiger K. T. & Duncan J. H., Incipient air entrainment in a translating axisymmetric plunging laminar jet, Physics of Fluids, Vol. 14, pp. 781-790, 2002.
7. Cummings P. D. & Chanson H., An experimental study of individual air bubble entrainment at a planar plunging jet, Trans. I. Ch. E., Vol. 76, pp. 159-164, 1999.
8. Davoust L., Achard J. L. & El Hammoumi M., Air entrainment by a plunging jet: the dynamical roughness concept and its estimation by a light absorption technique, Int. Journal of Multiphase Flow, Vol. 28, pp. 1541-1564, 2002.
9. El Hammoumi M., Achard J. L. & Davoust L., Measurements of air entrainment by vertical plunging liquid jets, Experiments in Fluids, Vol. 32, pp. 624-638, 2002.
10. Oguz H. N., The role of surface disturbances in the entrainment of bubbles by a liquid jet, J. Fluid Mech., Vol.372, pp. 189-212, 1998.

THE EFFECT OF CROSS FLOW ON MULTIPLE JET IMPINGEMENT HEAT TRANSFER ON A CONCAVE WALL

N. Yoshida[1], K. Takeishi[1,*], Y. Oda[1], H. Maeda[1]
[1]Department of Mechanical Engineering, Osaka University, Osaka, Japan

ABSTRACT. Multiple jet impingement heat transfer on a concave surface was investigated by naphthalene sublimation techniques for one-row jets and three-row jets with cross flows. The experiments were conducted for Re = 5000 at cross-flow/jet velocity ratios of 0.15, 0.2, 0.25, 0.3, and 0.4, at the nozzle to plate distance of 3.75d. The location of the maximum local Nusselt number was found to move downstream as the cross-flow rate increases. When the cross-flow/jet velocity ratio increases from 0.25 to 0.35 in one-row jets (and 0.3 to 0.4 in three-row jets), the maximum Nusselt number decreases dramatically. In addition, locally high Nusselt number regions were observed between the neighbouring jets and show streaky distributions due to the collisions of wall jets, while they gradually disappear as the cross flow rate increases.

Keywords: *Gas turbine, Heat transfer, Jet impingement cooling, Concave surfaces*

INTRODUCTION

The demand for higher efficiency in combined cycle power plants is to be met by raising the turbine inlet temperature of gas turbines. High temperature heavy-duty gas turbines have been actively developed and the turbine inlet temperature of the latest one reaches a level of 1770 K. As the turbine inlet temperature increases further, the turbine first vane and blade will be exposed to a higher temperature gas stream and will be subjected to severer thermal conditions. Thus, sophisticated cooling schemes such as impingement cooling, film cooling and pin fin cooling have been adopted to maintain the turbine vane and blade under the allowable metallurgical temperature limit. Especially, the effective removal of locally concentrated heat by impingement jets has been utilized to cool the inner surface of the vane's leading edge, which is exposed to high temperature and subjected to high heat flux. Since the high heat transfer rate at the stagnation region decays rapidly in the wall jet region, multiple jet impingement cooling has been employed in real gas turbines to eliminate the excessive thermal load on the leading edge of gas turbine vanes.

Since the leading edge of the turbine vanes has concave surfaces, it is important to investigate the effect of the curvature on the multiple jet impingement heat transfer. Chupp et al. [1] and Metzger et al. [2] investigated the effects of jet-to-jet spacing and the nozzle to plate distance for impingement cooling with a row of circular jets on a semi-circular surface. Bunker and Metzger [3], Metzger and Bunker [4] suggested that the major influencing parameters are Reynolds number, leading edge shape, jet spacing and size, jet arrangement, the number of jet holes and the distance between jet exit and inner surface of leading edge. Gau and Chung [5] visualized the jet flow impinging on both convex and concave semi-circular surfaces and showed the distinctive characteristics of flow and heat transfer on these surfaces. They also showed that Nusselt number increased as the curvature increased due to the vigorous vortex motion in the jet mixing region.

* Corresponding author: Prof. K. Takeishi
Phone: + (81)-6-6879-7311, Fax: + (81)-6-6879-7313
E-mail address: takeishi@mech.eng.osaka-u.ac.jp

Hrycak [6] studied heat transfer from a row of impinging jets to concave cylindrical surfaces. Choi et al. [7] studied the impinging jet flow and heat transfer on a semi-circular concave surface. However, earlier studies [8] on multiple impinging jet on concave walls employed thermocouples embedded in heated target plates. Thus, the resolution of Nusselt number profiles has been limited and heat conduction loss along the target walls was inevitable. In addition, there are few studies on multiple impinging jet heat transfer including cross flow effect, which is important in real gas turbines.

Therefore, in this study, local Nusselt number distributions of multiple impinging jets on a concave target wall were measured in high resolution using the naphthalene sublimation technique, which is enhanced by a high-precision laser displacement gauge and a *x*-*y* automatic traverse with a stepping motor to control the angle of the laser gauge. The effect of curvature and cross flow on heat transfer was investigated. In addition, corresponding numerical simulations were conducted to investigate the capability to predict local Nusselt number distributions and the complex flow structures induced by the multiple jets on a concave wall with and without cross flow.

EXPERIMENTAL METHOD

Figures 1 and 2 show a schematic layout of experimental apparatus and the test section, respectively, for the naphthalene sublimation technique based on the analogy between heat/mass transfer. Dry air for generating multiple jets and cross flow was separately supplied to the test section by two air compressors with controlled flow rates. The test section consists of a half-cylindrical nozzle plate, a jet-supply chamber, a concave target plate, and sidewalls. The nozzle plate is 1 mm in thickness and has one row ($\theta = 0°$) or three rows ($\theta = -40.5°$, 0°, 40.5°) of in-line jet holes. Each row of jet holes on the nozzle plate has seven round holes of 2 mm in diameter with a pitch of 14 mm in *x* direction. Thus, the nozzle plate generates multiple impinging jets on the concave target surface covered with a naphthalene layer. Upstream of the nozzle plate, there was a flow-settling section equipped with mesh screens, in order to reduce the turbulence intensity and to form a uniform air flow at the exit. The air velocities at the exit of each hole on the nozzle plate were measured with a total pressure tube, and the non-uniformity of the velocity distribution was confirmed to be within 3%. The volume flow rate of air was carefully measured with a rotameter to maintain the nozzle exit velocity. Cross flow was supplied from an end of the flow channel, which is in between the nozzle plate and the concave wall, through a mesh screen located upstream.

The concave target surface was covered with a naphthalene molding, which has a half-cylindrical shape of 40 mm in diameter and 110 mm in width. To make the concave surface of solidified naphthalene smooth, following manufacturing steps has been conducted. Firstly, reagent grade

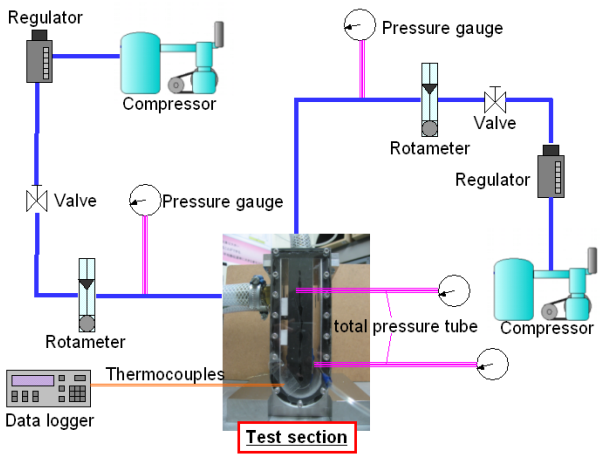

Figure. 1 Experimental apparatus

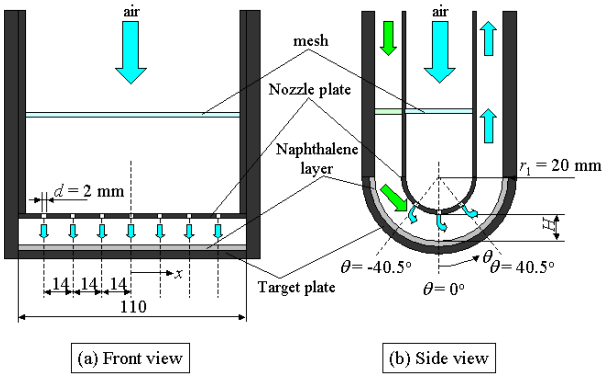

Figure. 2 Cross sectional view of test section

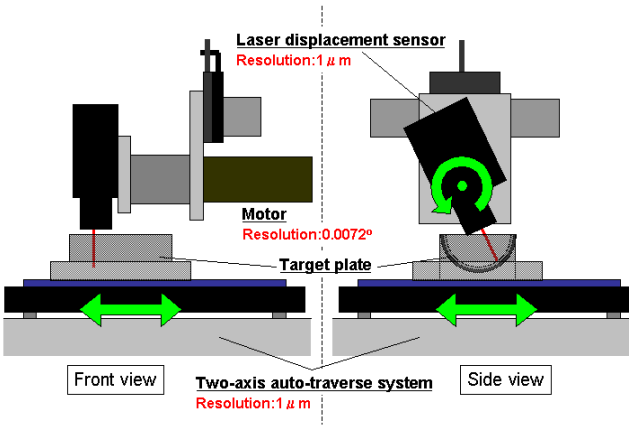

Figure. 3 Laser displacement sensing system

(98% pure) naphthalene crystals were melted on an induction heater until they boiled. After the naphthalene temperature became about 380 K, secondly, they were poured into the mold, which was preheated at about 330 K. After the mold was cooled to room temperature and naphthalene was solidified, thirdly, a cover plate of the mold was struck to be removed.

The naphthalene sublimation depth was measured with the apparatus shown schematically in Figure 3. It consists of a two-axis precision auto-traverse system, a laser displacement sensor, a stepping motor to control the angle of the laser gauge, a micrometer, a data logger, and a personal computer. Displacement was measured by the laser displacement sensor, which has the range of ±1 mm, with resolution of 0.1 μm and linearity error of 0.3%. The two-axis auto-traverse system has a resolution of 1 μm in each direction, and the stepping motor has a resolution of 0.0072°. Before air impinges on the naphthalene plates, the laser displacement sensor scanned the initial surface profile. The measurement range in the x direction was 50 mm and the scanning interval was 0.2 mm, whereas that in the θ direction was ±60° and the interval was 1°. The total scanning time was about 120 minutes. After the air impingement lasting for 20 minutes, the surface profile was scanned again. Then, the local naphthalene sublimation depth δ was calculated as the local change of surface position from the initial values. The local mass transfer coefficient at each location is calculated from the following relation:

$$h_D = \frac{RT_W}{P_W} \cdot \frac{\rho_S \delta}{t_e} \tag{1}$$

where R is the gas constant, T_w is the naphthalene surface temperature, p_w is the saturated vapor pressure of naphthalene in air, ρ_s is the density of solid naphthalene, δ is the depth of naphthalene sublimation, and t_e is the impinging time. The thermophysical properties of naphthalene were obtained from Goldstein and Cho [9]. The local mass transfer coefficient can be converted to the local heat transfer coefficient by using the analogy between heat and mass transfer:

$$h = h_D \rho C_p \left(S_c / P_r\right)^{1-n} \tag{2}$$

where ρ is the density of air, C_p is the specific heat at constant pressure, Sc is the Schmidt number, Pr is the Prandtl number, and n is the empirical constant being 0.4 in this experiment. Nusselt number is defined as $Nu = hd/\lambda$. The experiments were conducted at the nozzle to plate distance of $3.75d$ and Re = 5000, 10000, and 15000 without cross flow using one-row jets, and for Re = 5000 with cross flows at cross-flow/jet velocity ratios of V_c/V_i = 0.15, 0.2, 0.25, 0.3, and 0.4, using one-row jets and three-row jets.

NUMERICAL METHOD

In this study, numerical simulations using FLUENT 6.3 were also conducted to compare the predicted results with measured data obtained by naphthalene sublimation technique, for the case of three row jets at Re = 5000 and V_c/V_i = 0, 0.15, 0.2, 0.3, and 0.4. Figure 4 (a) shows an overall view of the computational domain, which includes a jet-supply chamber before nozzle exits to ensure appropriate profiles of velocity and turbulent quantities at the nozzle exit. Assuming periodic flows

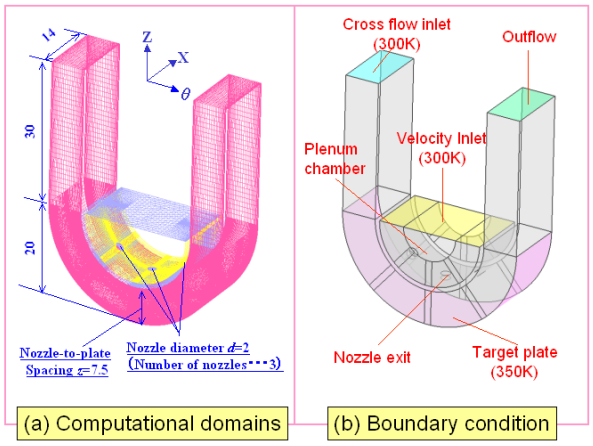

Figure. 4 Computational domains

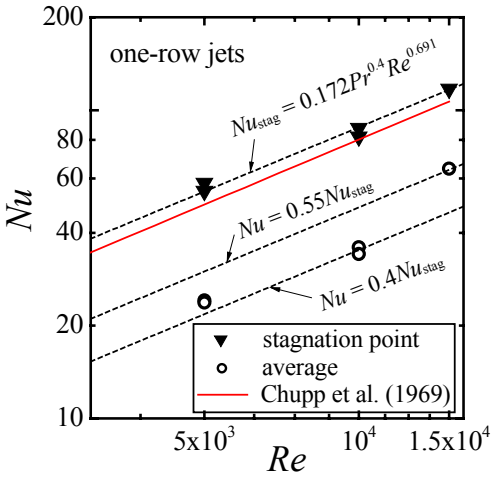

Figure. 5 Nusselt number at stagnation point

in x direction, only a single array of nozzles in the mid-plane (x = 0) was included in the domain. The number of total cells was 1,400,000. The grid spacing in the wall normal direction on the target surfaces satisfies $y^+ < 2$.

For a turbulence model, a realizable k-ε model was used with an option of the enhanced wall treatment, which is a near-wall modeling method that combines a two-layer model with enhanced wall functions and can consider the pressure gradient effect near the wall [10]. For the prediction of turbulent heat fluxes, a constant turbulent Prandtl number, Pr_t = 0.85, was used assuming the direct analogy between the turbulent heat transport and momentum transport. For stable computations, a first-order upwind differential scheme was employed to discretize the convection terms of momentum, turbulent kinetic energy and its dissipation rate. For the convective term of energy equations, a 2nd-order upwind scheme was employed.

Figure 4 (b) shows boundary conditions applied to each boundary. An appropriate magnitude of uniform velocities and temperature were applied to the top surfaces of the jet-supply chamber to achieve Re = 5000 at 300 K in the nozzles. Turbulent intensity of 0.5% was assumed at the inlet based on measurements by a hotwire anemometer. A uniform temperature of 350 K was applied to the target surfaces for a concave case to simulate the condition of naphthalene wall in the experiment.

RESULTS AND DISCUSSION

Figure 5 shows experimentally obtained relations between Reynolds number and the local Nusselt number at the stagnation point in the case of one-row jets for Re = 5000, 10000, and 15000 without cross flow, together with the averaged Nusselt number over $-20.25° \le \theta \le 20.25°$. By fitting these data using the least square method, the following empirical correlation was obtained.

$$Nu_{stag} = 0.172 Pr^{0.4} Re^{0.691} \quad (3)$$

$$0.4 \le Nu_{ave} / Nu_{stag} \le 0.55 \quad (4)$$

As shown in the figure, the present experimental data show a good agreement with the empirical relation by Chupp et al. [1].

Figures 6 and 7 show the experimentally obtained local Nusselt number distributions in one-row jets and three-row jets, respectively, for the cross-flow/jet velocity ratios of V_c/V_i = 0, 0.2, and 0.4. It is to be noted that the figures show normally-projected views of contours on concave target surfaces having a curvature, and thus the contour maps are scaled non-linearly in θ direction as indicated by

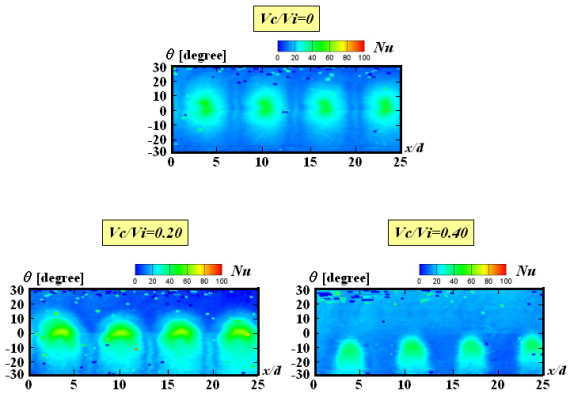

Figure. 6 Local *Nu* for one-row jets cases

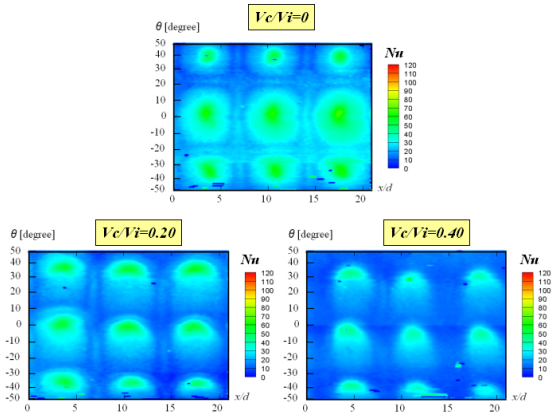

Figure. 7 Local *Nu* for three-row jets cases.

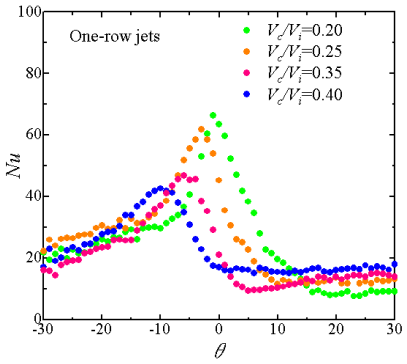

Figure. 8 *Nu* at x = const. on stagnation points for one-row jets cases

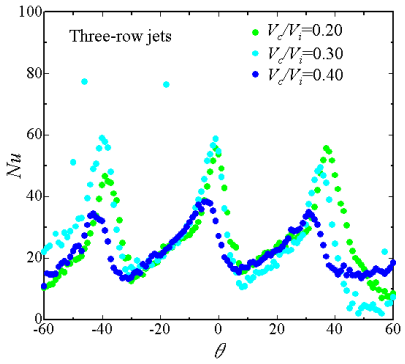

Figure. 9 *Nu* at x = const. on stagnation points for three-row jets cases

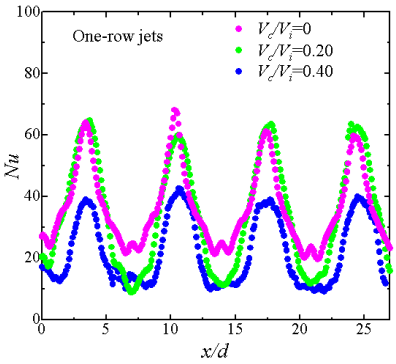

Figure. 10 *Nu* at θ = const. on stagnation points for one-row jets cases

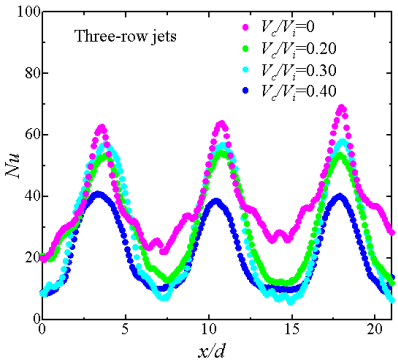

Figure. 11 *Nu* at θ = const. on stagnation points for three-row jets cases

non-uniform intervals of the ticks. Figures 6 and 7 clearly indicate that the location of the maximum local Nusselt number moves downstream from the geometrical center of each jet as the velocity ratio V_c/V_i increases. Therefore, heat transfer coefficient is lowered upstream the stagnation region of each jet and enhanced in the downstream region. The drift distance of local maximum Nusselt number in three-row jets is shorter than that in one-row jets, because the blocking of cross flow by the upstream jets occurs in the three-row jets case. In addition, locally high Nusselt number regions were observed between the neighboring jets and show streaky distributions in the θ direction at $V_c/V_i = 0$ in the one-row jets case. This indicates that collisions of wall jets occur there and affect the local heat transfer. In the three-row jets case, the locally high *Nu* region was found to surround each jet at $V_c/V_i = 0$. As the cross flow rate increases, the jet interacting regions begin to be drifted

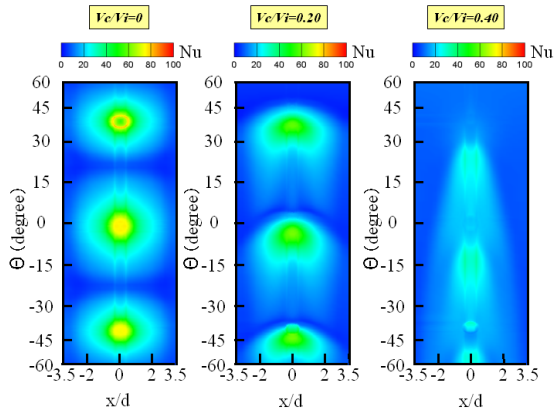

Figure. 12 Local Nusselt number on concave surface by numerical simulation

downstream and finally vanish away. This indicates that the strong cross flow weakens the impingement of jet on the target wall, which leads to weaker wall jets and their interactions, and finally results in the washout of wall jets.

Figures 8 and 9 shows the local Nusselt number distribution in a constant x line, which passes through the stagnation point, for the cases of one-row jets and three-row jets, respectively. It can be quantitatively confirmed that the cross flow rate has a strong effect on the local Nu distribution. As can be seen in Figures 6 and 7, an increase of cross flow rate decreases the maximum Nusselt number and washes out the peak position downstream. Especially, when V_c/V_i increases from 0.25 to 0.35 in one-row jets (and 0.3 to 0.4 in three-row jets), the maximum Nusselt number decreases dramatically. On the other hand, in case of one-row jets, Nusselt number increases at $15° < \theta < 30°$ when V_c/V_i changes from 0.2 to 0.4. This indicates that heat transfer augmentation by cross flows becomes larger than that by impinging jets at the region when V_c/V_i is large.

Figures 10 and 11 show the experimental results of local Nusselt number distributions in constant θ lines, where the maximum Nu were observed, for the cases of one-row jets and three-row jets, respectively. For all cross flow rates, Nu distributions of the one-row jets and three-row jets show similar values. Without cross flows, locally high heat transfer region, i.e. wall-jet interaction regions, can be clearly observed in between the impinging jets both for one-row and three-row jets cases. As the cross flow rate increases from $V_c/V_i = 0$ to 0.2, the wall-jet interaction region disappears, while the maximum Nu at the stagnation point is not affected much by cross flows. This indicates that the cross flow circumvents the impinging jets and flows through between the impinging jets, washing out the wall-jets downstream. As the cross flow rate further increases from $V_c/V_i = 0.2$ to 0.4, the maximum Nu decreases dramatically, as seen in Figures 8 and 9. This is because the strong cross flow bends the impinging jets in the cross flow direction and the potential core region of the jet cannot reach the target plate, as seen later in the numerical simulations.

Figure 12 shows the local Nusselt number distributions by numerical simulations corresponding to the experiments for three-row jets cases at $V_c/V_i = 0$, 0.2, and 0.4. Figure 13 also shows the comparison of the predicted Nu distributions at $x/d = 0$ with those in the experiments for the three-

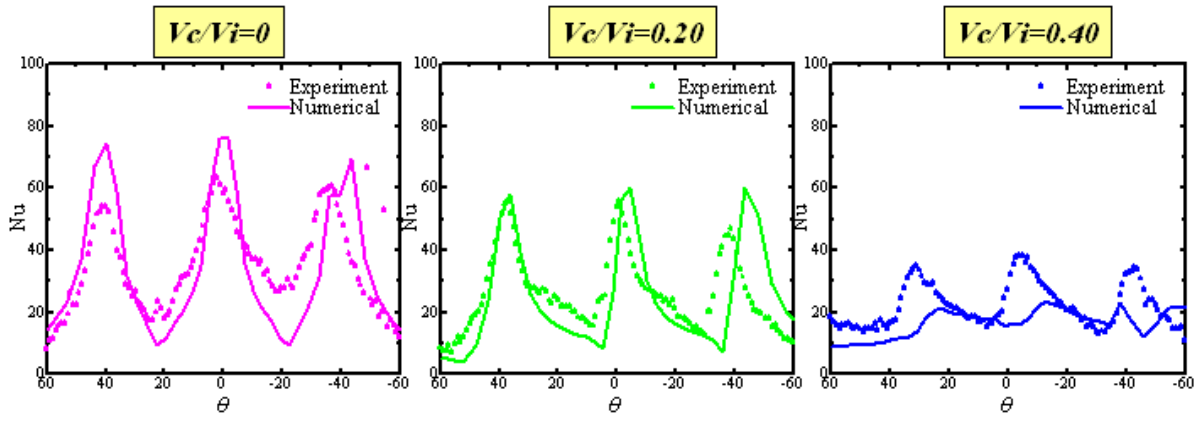

Figure. 13 Comparison of Nu at x = const. on stagnation points

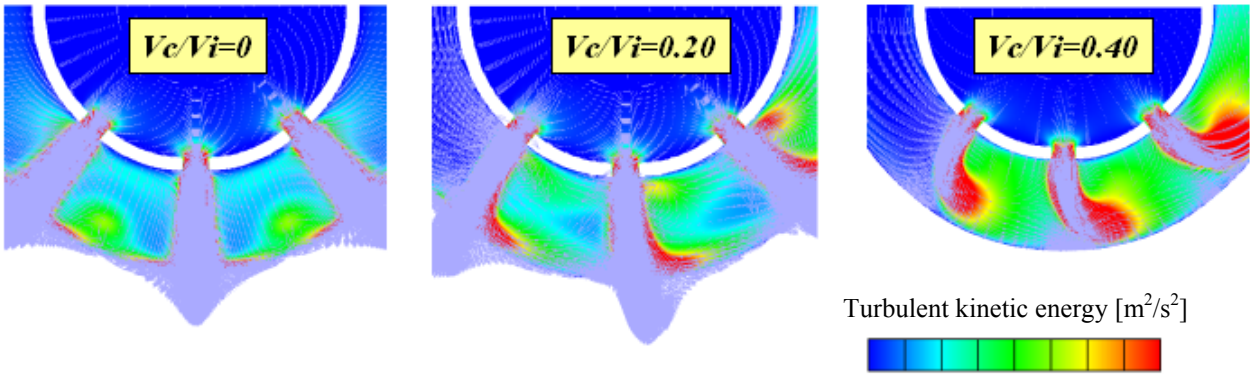

Figure. 14 Velocity vector fields with a contour of turbulent kinetic energy at $x/d = 0$

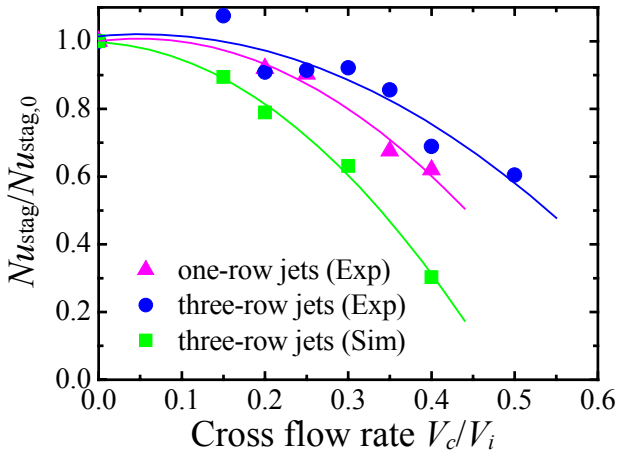

Figure. 15 Cross flow effect on stagnation Nusselt number

row jets case. The values of Nusselt number at V_c/V_i = 0 and 0.2 show similar profiles in acceptable agreement with experiments, while at $V_c/V_i = 0.40$ the present numerical simulation using a realizable k-ε model cannot predict the Nu distribution both qualitatively and quantitatively. In addition, it was found that the present simulation could not reproduce the wall jet interaction regions between the impinging jets. This indicates the limited capability of linear eddy viscosity models to predict such complex three-dimensional turbulent flows. Thus, other sophisticated turbulence models, such as non-linear eddy viscosity models, second moment closure models, hybrid RANS/LES, or LES, is required to capture the physical mechanism underlying this characteristic phenomena. In this sense, the present experimental observation gives interesting data to evaluate the prediction capability of turbulence models.

Figure 14 shows numerically predicted velocity vector fields of y and z components with contours of turbulent kinetic energy fields at $x/d = 0$ plane for the case of $Re = 5000$ at $V_c/V_i = 0$, 0.2, and 0.4. This figure clearly shows that the impinging jet from a nozzle plate is curved when a cross flow exists. Especially, at $V_c/V_i = 0.4$, impinging jet cannot reach the target plate, and a wall jet region seems to disappear at the upstream side of a cross flow. For V_c/V_i = 0 and 0.2, there are high turbulent kinetic energy regions above the stagnation regions, while no such region exists for V_c/V_i = 0.4. The high turbulent kinetic energy regions correspond well to the high Nusselt number regions around the stagnation points shown in Figure 13. In addition, low turbulent kinetic energy regions also correspond well to low Nusselt number regions. Thus, it can be concluded that turbulent kinetic energy plays an important role in heat transfer enhancement by impinging jets with cross flows.

Figure 15 shows the experimental and numerical relations between the cross flow rate and the stagnation point Nusselt number, Nu_{stag}, which is defined as the locally maximum Nu. Note that Nu_{stag} is normalized by Nu_{stag} in no cross flow. It is clear that the cross flow effect becomes remarkable when the cross flow rates exceed 0.35, where Nu_{stag}/Nu_{stag0} becomes less than 0.9 in the three-row jets case. The heat transfer coefficient of the three row jets is more weakly affected by the cross flow than that of one row jets, because the blocking of cross flow by upstream jets occurs in three-row jets cases. The present numerical simulations using k-ε realizable model can predict the tendency of cross flow effects but tend to overestimate the cross flow effects on Nu_{stag}.

CONCLUSIONS

Local Nusselt number distributions were measured by the naphthalene sublimation technique for one-row impinging jets and three row impinging jets on a concave surface with cross flow. In addition, numerical simulations using a realizable k-ε model were conducted to further investigate the heat transfer characteristics of the three-row jets impinging on a concave surface, and to clarify the detail of the complex flow structure. Consequently, the following conclusions were obtained.

1. The location of the maximum local Nusselt number moves downstream as the cross-flow/jet-velocity ratio increases. The drift distance in three-row jets is shorter than that in one-row jets, because the blocking of cross flow by the upstream jets occurs in the three-row jets case.

2. Locally high Nusselt number regions were observed between the neighboring jets and show streaky distributions due to the collisions of wall jets. As the cross flow rate increases, the wall-jet interacting regions begin to be drifted downstream and finally vanish away, because the strong cross flow weakens the wall jets and finally washes out them.

3. When the cross-flow/jet-velocity ratio increases from 0.25 to 0.35 in one-row jets (and 0.3 to 0.4 in three-row jets), the maximum Nusselt number decreases dramatically. This is because the strong cross flow bends the impinging jets in the cross flow direction and the potential core region of the jet cannot reach the target plate.

REFERENCES

1. Chupp, R.E., Helms, H.E., Mcfadden, P.W. and Brown, T.R., Evaluation of internal heat-transfer coefficients for impingement-cooled turbine airfoils, *J. AIRCRAFT*, Vol. 6 No. 3, pp. 203-208, 1969.
2. Metzger, D.E., Yamashita, T. and Jenkins, C.W., Impingement cooling of concave surfaces with lines of circular air jets, *ASME J. of Engineering for Power,* Vol. 91, pp. 149-158, 1969.
3. Bunker, R.S. and Metzger, D.E., Local heat transfer in internally cooled turbine airfoil leading edge regions. Part 1: impingement cooling without film coolant extraction, *ASME J. of Turbomachinery*, Vol. 112, pp. 451-458, 1990.
4. Metzger, D.E. and Bunker, R.S., Local heat transfer in internally cooled turbine airfoil leading edge regions. Part 2: impingement cooling with film coolant extraction, *ASME J. of Turbomachinery*, Vol. 112, pp. 459-466, 1990.
5. Gau, C. and Chung, C.M., Surface curvature effect on slot air-jet impingement cooling flow and heat transfer process, *ASME J. of Heat Transfer*, Vol. 113, pp. 858-864, 1991.
6. Hrycak, P., Heat transfer from a row of impinging jets to concave cylindrical surfaces, *Int. J. Heat Mass Transfer*, Vol. 24, pp. 407-419, 1981.
7. Choi, M., Yoo, H.S., Yang, G. and Lee, J.S., Measurements of impinging jet flow and flow and heat transfer on a semi-circular concave surface, *Int. J. Heat Mass Transfer*, Vol. 43, pp. 1811-1822, 2000.
8. Takeishi, K., Matsuura, M. and Sato, T., Heat transfer coefficient of impingement cooling on a flat and concave target plate, *Proc. of International Symposium on Heat and Mass Transfer*, pp. 207-212, 1994.
9. Goldstein, R.J., Cho, H.H., A review of mass transfer measurements using naphthalene sublimation, *Experimental Thermal and Fluid Sci.*, Vol. 10, pp. 416-434, 1995.
10. Fluent Inc., *Fluent 6.2 User's Guide*, Fluent Inc., Lebanon, NH, USA, 2005.

HEAT AND MASS TRANSFER BETWEEN AIR AND POROUS MATERIALS: A BENCHMARK EXPERIMENT

M. Van Belleghem[1,*], H.-J. Steeman[1], Henk Huisseune[1], Christophe T'Joen[1], Arnold Janssens[2], Michel De Paepe[1]
[1]Ghent University, Department of Flow, Heat and Combustion Mechanics, Ghent, Belgium
[2]Ghent University, Department of Architecture and Urban Planning, Ghent, Belgium

ABSTRACT. CFD (Computational Fluid Dynamics) can be used to calculate air flows in and around buildings. By linking CFD with a HAM-model (Heat, Air and Moisture), heat and mass transfer between air and porous materials is incorporated into the calculations. This paper presents experimental data for the validation of these newly developed CFD-HAM models.
To conduct the experiments, a climate chamber representing a small room of 1.8 meter high, 1.8 meter wide and 1.89 meter long was built. Air enters the room as a jet of which the temperature and relative humidity are closely controlled. A sample of calcium silicate was placed in one of the walls of the chamber. During the experiment the relative humidity of the jet was altered from 50% during 16 hours to 70% during 8 hours. This cycle was repeated several times. Meanwhile temperature and relative humidity in the chamber and in the calcium silicate sample were monitored.

Keywords: *experiment, hygroscopic material, moist air, heat and mass transfer*

INTRODUCTION

Temperature and relative humidity are two very important parameters in the building interior. First of all they determine to a great extent the comfort level of a building. For example temperature inside an office or a house is kept between certain levels, not to cold and not to hot. Once the temperature deviates from these levels, occupants experience discomfort. The same counts for the relative humidity in a room. Both too dry and too humid air is unpleasant for building occupants and studies have shown that relative humidity has a severe impact on the perceived indoor air quality [1].
Next, temperature and relative humidity also play an important role in the durability of a building. A lot of damage mechanisms in buildings are triggered by temperature or relative humidity or a combination of both. For example too high relative humidity can cause mould growth or even condensation. An other example is damage caused by temperature and humidity fluctuations. Materials shrink and expand as temperature drops and rises alternately. Hygroscopic materials adsorb or desorb water vapour when relative humidity changes, causing again expansion or shrinkage. This expanding or shrinking resolves into stresses in the material which lead to cracks and damage [2].

Often large, expansive and energy consuming equipment is needed to keep temperature and relative humidity at an acceptable level. For many decades researchers have looked for ways to improve the energy efficiency of buildings without reducing the comfort level. Simonson et al. [3] found that using hygroscopic building materials can reduce relative humidity and temperature fluctuations and increase the perceived indoor air quality and occupant comfort level. An other study showed that using hygroscopic materials in a building can reduce the energy use of that building [4].

* Corresponding author: Marnix Van Belleghem
Phone: + (32)-9-2643289, Fax: + (32)-9-2643575
E-mail address: Marnix.vanbelleghem@ugent.be

Due to rapid development in computer memory and speed, it has become popular to perform computer simulations to evaluate the hygrothermal behaviour of a building. These simulations also help in improving the design of buildings. Chen [5] gives a short overview of some of the current modelling techniques. Here a distinction is made between zonal models and CFD models to calculate air distributions in buildings. In zonal or lumped models a building is divided into zones, mostly one zone for every room. The parameters of interest (temperature, ventilation rate, relative humidity) are considered constant for every zone. These strong simplifications limit the computational time to minutes or even seconds. In reality however air in a room is not well mixed and research has shown that local temperature and relative humidity in a room can differ a lot [6, 7]. By using CFD models (Computational Fluid Dynamics) local effects can be studied. CFD can calculate air distributions in rooms in detail. Often a model for heat and species transport is added so temperature and relative humidity distributions are calculated as well.

However, to incorporate vapour transport in building materials an extra model has to be added. Two approaches can be found in literature namely the directly coupled models and the indirectly coupled models. Directly coupled models solve both the fluid domain and the porous material domain with one solver. Examples of such models can be found in [6] where steady state calculations are performed and [8] for transient simulations. Indirectly coupled models solve the fluid and porous domain in different solvers and exchange the information. An example of this approach can be found in [9].

Because these computer models have different levels of approximations, the results will also have different levels of uncertainty. Consequently, CFD results can not be trusted without proper validation. However, finding the necessary validation data in literature is not so evident.
Belardi et al. [10] developed a model for evaluating the non-isothermal moisture migration in porous building materials. To evaluate this model, one- and two-dimensional experiments were performed using lime-cement mortar and Gotland sandstone. However, these experiments were designed to create a constant temperature and relative humidity at the boundaries of the material. So they are not useful to validate coupled CFD-HAM models where air movement is simulated as well.
Talukdar et al. [11] discus the design of an experimental facility, the transient moisture transfer (TMT) facility. This facility is designed to measure 1-D heat and moisture transfer between a flowing air stream and a porous material. The experimental data generated with this facility is excellent to validate CFD-HAM model. Nevertheless the question still remains whether or not the model performs well for full scale environments with more complex airflow. Therefore a new test setup has been designed and built for more complex flows.

CLIMATE CHAMBER DESIGN

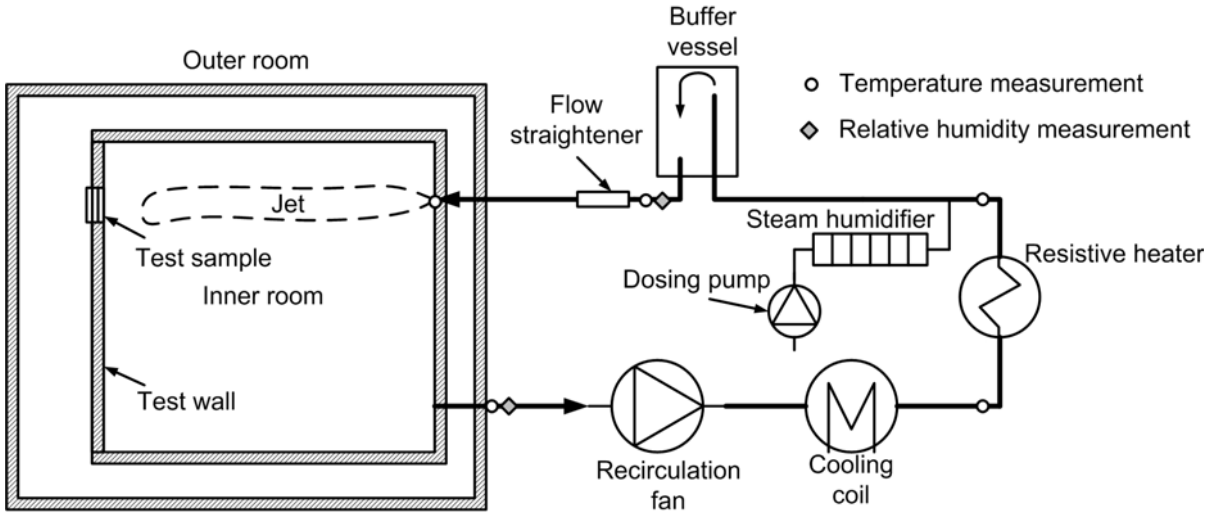

Figure 1. Schematic representation of the test facility.

The purpose of the experimental setup is to measure temperature and relative humidity distributions in a porous material sample together with the air flow patterns around the material. Contrary to the TMT-facility of Talukdar et al. [11], the new setup is used to generate more realistic flow patterns typical for buildings. A schematic representation of the new test facility is shown in Figure 1.

The test facility can be divided into two parts namely the climate chamber shown on the left of Figure 1 and the climate control group shown on the right of Figure 1.
The climate chamber is made up of an inner and an outer room. The inner room measures 1.8m wide, 1.8m high and 1.89m deep. Here an air jet enters and hits a test sample of calcium silicate installed in the opposite wall. The outer room is merely there to reduce the influences of the outside temperature fluctuations. The wall panels of the inner and outer room consist of 6 cm rigid high density polyurethane foam (λ=0.0223W/mK) sprayed in between two skins of white polyester lacquered, galvanized steel plate, 0.63mm in thickness. The floor panels consist of multiplex panels with phenol anti-slip surface reinforced with glass fibre.
Temperature, relative humidity and velocity of the entering air jet are closely controlled with a dedicated air conditioning system. This system draws air from the inner room with a recirculation fan. This air is than cooled below the dewpoint by a cooling coil and thus dehumidified. The dehumidified air is then reheated to the desired temperature and a specially designed steam humidifier humidifies the air to the desired relative humidity. The air then passes through a buffer vessel to dampen out some fluctuations. Finally a flow straightener ensures a fully developed flow pattern when the air enters the climate chamber.

TEST SAMPLE

A test sample of calcium silicate is placed in a test wall as shown on Figure 1. This samples measures 200mm by 200mm and has a thickness of 100mm. The sample is sliced in four layers of various depths. Figure 2 shows the details of the test sample. The first layer of calcium silicate has a thickness of 10mm, the second a thickness of 15mm, the third measures 25mm and the last 50mm.

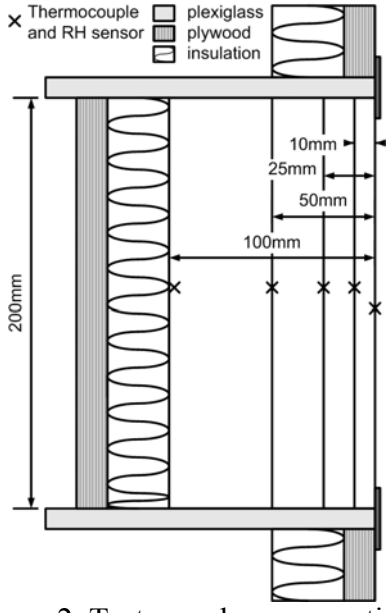

Figure 2. Test sample cross section.

In between the different layers, thermocouples and relative humidity sensors are placed. These sensors measure the temperature and relative humidity distribution in the sample. Thermocouples type K are used for this setup and calibrated with a dry block calibrator. This results in an accuracy of ±0.1°C.

Small capacitance relative humidity sensors made by Honeywell are used for the relative humidity measurements in the sample. These sensors relate the electrical capacitance of the sensor material with the relative humidity of the surrounding air. A chilled mirror with an uncertainty 0.2°C for the dew point is used as a transfer standard for calibrating the relative humidity sensors. This results in a total uncertainty on the relative humidity sensors of 1.4%.
The test sample is placed in a box of Plexiglas. The sample side walls and back wall are sealed with paraffin to avoid moisture penetration. At the same time insulation around the sample should avoid heat losses to the surroundings.

For validation purposes it is very important to have a good knowledge of the material properties. The properties of the calcium silicate used here were measured during the HAMSTAD-project (Heat, Air and Moisture Standards Development). More details on this project funded by the European Commission can be found in [12]. An overview of the material properties is shown in Table 1. The governing equation for moisture transport using a permeability approach is given by

$$-\frac{\partial w}{\partial t} = C\frac{\partial p_c}{\partial t} = \Delta\cdot(K\nabla p_c)$$
$$C = \left|\frac{\partial w}{\partial p_c}\right| \tag{1}$$

To properly describe the capillary pressure curve in the hygroscopic as well as the overhygroscopic range, a multimodal function of the "van Genuchten" type is used.

$$w(p_c) = w(p_{c,0})\sum_{i=1}^{3}\gamma_i(1+(c_i p_c)^{n_i})^{-[1-1/n_i]} \tag{2}$$

Here $w(p_{c,0})$ stands for the water content at zero capillary pressure, γ_i are the weighting factors ($0<\gamma_i\le 1, \Sigma\gamma_i = 1$), c_i and n_i are model parameters. The appropriate values of these parameters are also tabulated in Table 1.

Table 1
Material properties of calcium silicate

Property	**Value**	**Unit**	
Bulk density ρ	270	kg/m³	
Thermal capacity c_p	1000	J/kgK	
Thermal conductivity λ	$0.06+5.6.10^{-4}w$	W/mK	
Capillary moisture content w_{sat}	894	kg/m³	
Moisture content w			
Index i	1	2	3
Weight factor γ_i	0.05	0.1	0.85
Parameter c_i	$-2.46x10^{-6}$	$-2x10^{-6}$	$-2.47x10^{-6}$
Exponent n_i	3	1.85	2.44

The moisture permeability K is given by

$$K = \frac{2.61\times10^{-5}}{5.6R_vT}\left(1-\frac{w}{w_{sat}}\right)\Bigg/\left(0.8\left(1-\frac{w}{w_{sat}}\right)^2+0.2\right) \tag{3}$$

CLIMATE CONTROL

During the experiment the boundary conditions have to be well known. Therefore the climate chamber is well insulated and made air tight. To increase the insulation effect an outer room is built around the inner room which reduces the effect of outdoor temperature fluctuations. All these measures should result in adiabatic and moisture impermeable boundary conditions.
Not only the boundary conditions but also the inlet conditions have to be closely controlled. The inlet velocity is kept constant by setting the fan at a constant rotation speed. Temperature and relative humidity are controlled by a dedicated air conditioning unit. The control strategy for temperature and relative humidity is shown on Figure 3. Two approaches can be used. Figure 3a shows the first approach. In this control strategy two control loops can be distinguished namely one for temperature and one for relative humidity. Temperature and relative humidity are measured at the chamber inlet. These values are then compared with the corresponding setpoints. The difference between setpoint and measured value then serves as an input for the PID controller which steers the resistive heater for temperature control and the humidifier for humidity control. G11, G12 and G22 on Figure 3a represent the transfer functions of the system. The two control loops are not entirely separated. Changes in temperature change the relative humidity when the absolute humidity stays the same. This is represented by G12.
To avoid this effect a second approach based on the humidity ratio ω can be implemented as shown on Figure 3b. At a constant temperature a change in the humidity ratio will alter the relative humidity in accordance with equation 4. On the other hand, a change in temperature will not alter the humidity ratio as long as the water vapour pressure is lower than the saturation pressure. This means that the two control loops on Figure 3b no longer interact with each other which allows a smoother control.

$$\varphi = \frac{\omega p}{\omega p_{sat} + 0.622\, p_{sat}} \tag{4}$$

The relative humidity is measured with capacitive sensors. These sensors are used not only for humidity measurements in the test sample as mentioned earlier, but also for humidity control. However, therefore a fast response of the sensors is essential. To check the response time of the sensors two small tests were conducted. During the first test the humidity ratio is kept constant while the temperature alters. In the second test, temperature is kept constant while the humidity ratio is altered. The response of the humidity sensor is then measured. Results of these measurements showed that when temperature stays constant, the response of the sensors is in the order of seconds or even less. However the response time grows tremendously when temperature changes. A response time up to ten minutes is measured. This is in correspondence with Dooley et al.[13] who came to the same conclusions.

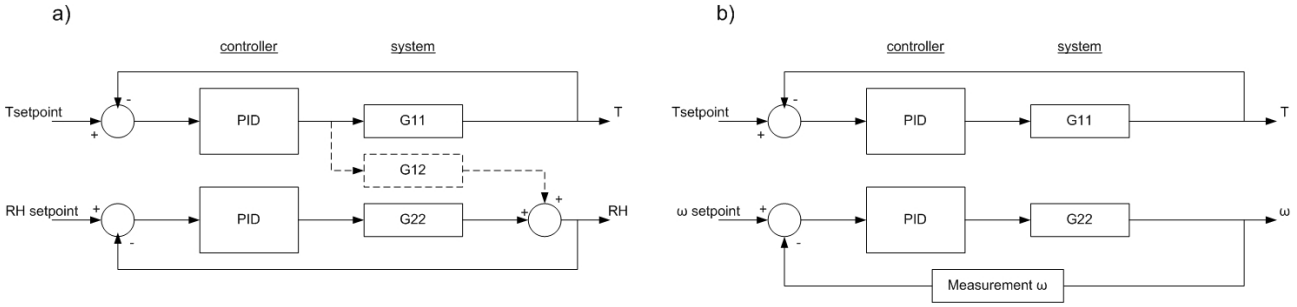

Figure 3. Control algorithms, (a) controlling relative humidity RH[%],
(b) controlling humidity ratio ω[kg/m³]

TEST PROCEDURE

The test sample is first preconditioned in the climate chamber. Therefore the chamber inlet temperature is set at 25°C and the inlet relative humidity to 50%. The jet blows with a mass flow rate of 68 ± 2 kg/hr on the test sample. The sample is preconditioned until fluctuations in temperature and relative humidity in the sample over one day are smaller than the measurement error. For the temperature this error is 0.1°C, for the relative humidity 1.4%.
Once the test sample and climate chamber can be considered at steady state, step changes in relative humidity are performed while temperature at the chamber inlet is kept constant. First the relative humidity is augmented from 50% to 70% during 8 hours and then it is lowered again to 50% during 16 hours thus covering a whole day. This cycle is repeated for several times and the response of the temperature and relative humidity in the test sample is measured. The results of these measurements are discussed in the next paragraph.

MEASUREMENT RESULTS

Moist air at constant temperature hits the test sample. At first the test sample is preconditioned so that the temperature and humidity inside the sample can be considered constant. Figure 4 and Figure 5 show the temperature and relative humidity inside the test sample at various depths. At the start of the measurements, temperature and relative humidity are almost the same for all three measurement depths. Temperature at 50mm is slightly lower than at the other depths probably because of a bad insulation of the back wall of the sample. A cycle of eight hours high relative humidity (70%) and 16 hours of low relative humidity (50%) is then performed. When the air relative humidity changes from 50% to 70% the porous test sample start to take up moisture and the relative humidity in the test sample starts to rise. Part of the water vapour entering the porous material condenses and releases latent heat. This latent heat results in a temperature increase in the test sample even if the supply air temperature is kept constant. The farther away from the surface of the sample, the less pronounced the temperature and relative humidity changes are. The opposite effects are seen when the relative humidity of the air changes from 70% back to 50%. The relative humidity in the sample drops as well as the temperature because moisture in liquid form evaporates from the sample using latent heat for the phase change. These measurements seem to correspond well with the expectations and can now be used for validation purposes.

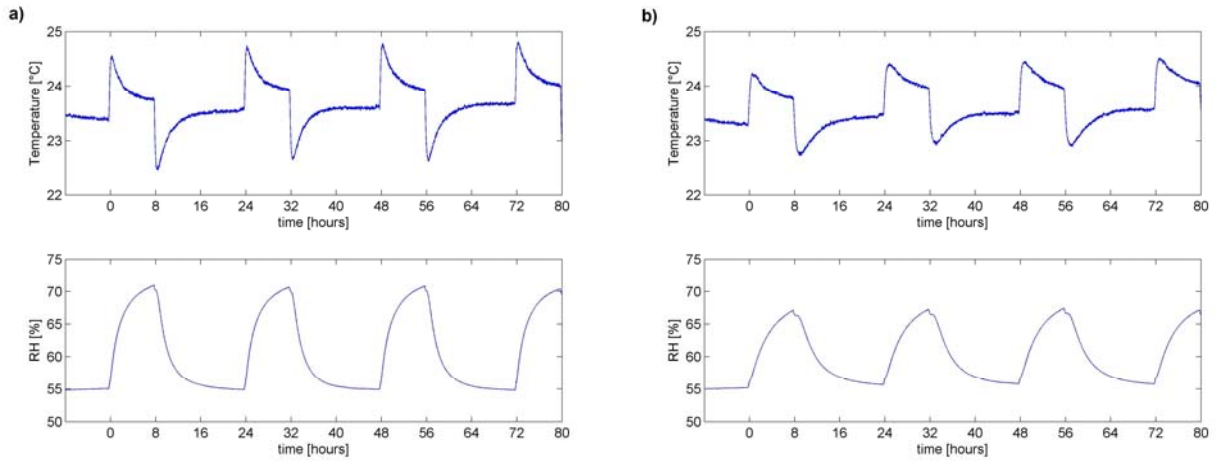

Figure 4. Temperature and relative humidity inside the test sample at 10mm depth (a) and 25mm (b)

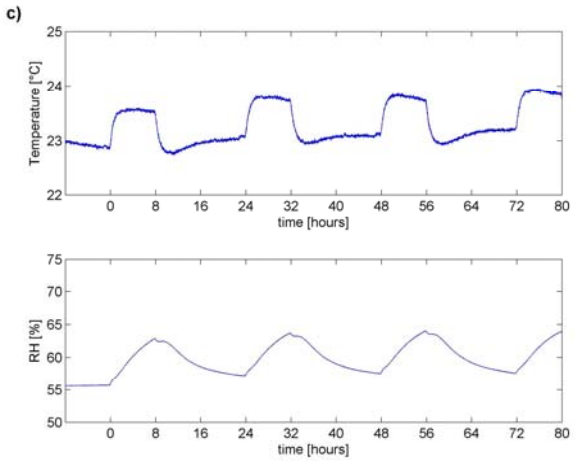

Figure 5. Temperature and relative humidity inside the test sample at 50mm depth (c)

CONCLUSIONS

CFD is becoming increasingly popular to investigate local heat, air and moisture transfer problems in buildings. New models are being developed but there is still a lack of well documented experimental data for validation. In this paper the design of a climate chamber is discussed together with some measurement results.
Inside the climate chamber a sample of calcium silicate was placed. The material properties of this sample were measured during an earlier research project. Temperature and relative humidity were measured inside the sample at 10mm, 25mm and 50mm depth. The sample was first preconditioned at 50% RH and 25°C and then exposed to cycles of 8 hours high humidity and 16 hours low humidity. The resulting measurements of temperature and relative humidity are presented in this paper. The measurements correspond well with the expectations. These measurements can now be used to validate new CFD-HAM models.

NOMENCLATURE

Quantity	Symbol	SI unit
Moisture capacity	C	m^2/s^2
Moisture permeability	K	s
Capillary pressure	p_c	Pa
Ideal gas constant water vapour	R_v	J/kgK
Moisture content	w	kg/m^3
Saturation moisture content	w_{sat}	kg/m^3

ACKNOWLEDGEMENT

The results presented in this paper have been obtained within the frame of the FWO project B/05836/02 funded by the FWO-Flanders (Research Fund Flanders) and the IWT SBO-050451 project heat, air and moisture performance engineering a whole building approach funded by the IWT (Institute for Science and Technology in Flanders). There financial support is gratefully acknowledged.

REFERENCES

1. Fang L., Clausen G., and Fanger P.O., Impact of temperature and humidity on the perception of indoor air quality, *Indoor Air-International Journal of Indoor Air Quality and Climate*,Vol. 8, 1998, pp. 80-90
2. Roels S., Moonen P., De Proft K., and Carmeliet J., A coupled discrete-continuum approach to simulate moisture effects on damage processes in porous materials, *Computer Methods in Applied Mechanics and Engineering*,Vol. 195, 2006, pp. 7139-7153
3. Simonson C.J., Salonvaara M., and Ojanen T., The effect of structures on indoor humidity - possibility to improve comfort and perceived air quality, *Indoor Air*,Vol. 12, 2002, pp. 243-251
4. Osanyintola O.F. and Simonson C.J., Moisture buffering capacity of hygroscopic building materials: Experimental facilities and energy impact, *Energy and Buildings*,Vol. 38, 2006, pp. 1270-1282
5. Chen Q., Computer Simulations and experimental measurements of air distribution. in buildings: Past, present, and future, *Hvac&R Research*,Vol. 13, 2007, pp. 849-851
6. Mortensen L.H., Woloszyn M., Rode C., and Peuhkuri R., Investigation of microclimate by CFD modeling of moisture interactions between air and constructions, *Journal of Building Physics*,Vol. 30, 2007, pp. 279-315
7. Steeman H.J., Janssens A., Carmeliet J., and De Paepe M., Modelling indoor air and hygrothermal wall interaction in building simulation: Comparison between CFD and a well-mixed zonal model, *Building and Environment*,Vol. 44, 2009, pp. 572-583
8. Steeman H.-J., Janssens A., and De Paepe M., Coupling moisture transport in air flows and porous materials using CFD, *8th Symposium on Building Physics in the Nordic Countries*, 2008, pp.
9. Neale A., Derome D., Blocken B., and Carmeliet J., Coupled simulation of vapour flow between air and a porous material, *Performance of exterior envelopes of whole buildings X conference* 2007, pp.
10. Belarbi R., Qin M., Aït-Mokhtar A., and Nilsson L.-O., Experimental and theoretical investigation of non-isothermal transfer in hygroscopic building materials, *Building and Environment*,Vol. 43, 2008, pp. 2154-2162
11. Talukdar P., Olutmayin S.O., Osanyintola O.F., and Simonson C.J., An experimental data set for benchmarking 1-D, transient heat and moisture transfer models of hygroscopic building materials. Part I: Experimental facility and material property data, *International Journal of Heat and Mass Transfer*,Vol. 50, 2007, pp. 4527-4539
12. Adan O., Brocken H., Carmeliet J., Hens H., Roels S., and Hagentoft C.E., Determination of Liquid Water Transfer Properties of Porous Building Materials and Development of Numerical Assessment Methods: Introduction to the EC HAMSTAD Project, *Journal of Thermal Envelope and Building Science*,Vol. 27, 2004, pp. 253-260
13. Dooley J.B. and O'Neal D.L., The transient response of capacitive thin-film polymer humidity sensors, *Hvac&R Research*,Vol. 14, 2008, pp. 663-682

COMPARISON OF DIFFERENT TOOLS TO STUDY GAS-LIQUID FLOW

L.A. Abdulkareem[1], V. Hernandez-Perez[1], B.J. Azzopardi[1,*], S. Sharaf[1], S. Thiele[2], M.J. Da Silva[2]

[1] Process and Environmental Engineering Research Division
Faculty of Engineering, University of Nottingham, Nottingham, UK
[2]Institute of Safety Research, Forschungszentrum Dresden-Rossendorf, Germany

ABSTRACT. In an effort to obtain a comprehensive knowledge of gas-liquid flows, in this paper the use of different tools available at the University of Nottingham to study gas-liquid flow in pipes is presented, followed by a comparison of the instrumentation performance. Air-silicone oil is used as the working mixture. The tools are capacitance wire mesh sensor (WMS), electrical capacitance tomography (ECT), capacitance probes and computational fluid dynamics (CFD) modelling. This is supplemented by illustrations of the sort of information that have been obtained. In general the agreement in the comparison is fairly good. However, it is observed that the WMS provides a better spatial resolution than ECT (with a first order reconstruction method) and is excellent for measurement of bubbly flow parameters.

Keywords: *Wire-mesh, ECT, capacitance, CFD*

INTRODUCTION

The flow of gas-liquid mixtures is of paramount importance to a number of operations in industry. A recent example is the flows of oil and natural gas from sea bed completions to the floating production/storage facilities. The flows are made complex by the very flexible nature of the interface between gases and liquid. Not surprisingly, considerable efforts have been put into measuring the distribution of the phases about the pipe and on methods from predicting that. This includes a wide range of tomographic sensors that are able to produce a graphical representation of the cross sectional flow inside the pipe, such as, x-ray tomography, gamma-densitometry tomography, positron emission tomography, magnetic resonance imaging, ultrasonic system, infrared tomography and electrical based tomography. The requirement in most work is to supply a relatively low cost imaging of industrial processes for control purposes, which is known as process tomography, while maintaining at the same time a fast time resolution with the consequence of much lower, but sufficient, image resolution. Consequently it is expected that only two systems can be considered to fall within this criterion, namely, ultrasound and electrical tomography, which have eventually developed into powerful experimental instruments capable of flow pattern identification due to the improvement of digital technology.

The field of electrical tomography can be separated into two distinct regions based on the method by which the electrical field is produced, either resistance or capacitance. Each individual measurement technique will have unique advantages and disadvantages in relation to the accuracy, frequency and resolution of the measured images produced. The choice will be based primarily on the electrical properties of the fluids, whether they conduct or not. Electrical capacitance

* Corresponding author: Prof. B.J. Azzopardi
Phone: + (44)- 0115 951 4160, Fax: + (44)- 0115 951 4115
E-mail address: Barry.Azzopardi@nottingham.ac.uk

tomography (ECT) is a truly non-invasive technique since the sensing electrodes are usually not in contact with the medium under consideration but are positioned peripherally around the pipe exterior. Most of the work reported in the literature which involves ECT has been carried out with gas-solid flows such as fluidised beds and pneumatic conveying, for example Azzopardi et al. [2]. However, recently the range of applications is growing fast.

A tomography technique based on electrical resistance measurement is the conductivity wire mesh sensor, which although intrusive, allows the study of two-phase flows with high spatial and temporal resolution. As a result recently an increasing number of applications of this technique have been reported, for gas-liquid flow in different flow regimes, for instance, Azzopardi et al. [1]. However this sensor is not able to detect flows where no conductive phase is present. In order to tackle the study of nonconductive flows, more recently this sensor has been improved by Da Silva et al. [3] at Forschungszentrum Dresden-Rossendorf, resulting in what is known as capacitance wire mesh sensor, whose main structure is similar to the conductivity wire mesh sensor. Early results obtained with this instrument at Nottingham were introduced by Thiele et al. [4].

On the other hand, attempts have also been made to achieve the prediction of multiphase flow behaviour in terms of the phase distribution, interface location and velocity field using the approach of computational fluid dynamics. Several multiphase flow models for computational fluid dynamics are being implemented in commercial packages, making it possible to study the flow behaviour. It is important however to compare this predictions with experimental data in order to increase confidence in its applicability and overcome shortcomings.

In an effort to extract as much information as possible on the complex behaviour of two-phase flows, in this paper a comparison of the performance of different tools available at the University of Nottingham to study gas-liquid flow in pipes is done. The comparison is made based on several two-phase flow parameters such as phase distribution and structures frequency. This is supplemented by illustrations of the sort of information that have been obtained. The tools are capacitance wire mesh sensor (WMS), electrical capacitance tomography (ECT), capacitance probes and computational fluid dynamics (CFD) modelling.

DESCRIPTION OF TOOLS

All the work hereby reported is based on the flows that were created on an inclinable facility, which has been kept vertical for this particular task. This facility has a test pipe of 6 m length and of 67 mm internal diameter with the two-phase flow being fed at the bottom. More details can be found in Hernández Pérez et al. [8]. Conditions studied were superficial velocities: air - from 0.05 to 4.7 m/s and for liquid - from 0.0 m/s to 0.7 m/s. The two-phase mixture under investigation is air-silicone oil, where silicone oil is an excellent insulator and has a viscosity ~5cp. The measurements were carried out simultaneously with the instruments located along the pipe as shown in Table 1.

Table 1
Location of instrumentation on the test section of the rig

	Cap probe 1	ECT Plane 1	ECT Plane 2	Cap probe 2	Wire mesh
Location from the mixing section (m)	4.15	4.40	4.49	4.75	4.92

The first capacitance probe was located at 4.15 m from the inlet, followed shortly by the ECT; this gives a flow development length of approximately 62 pipe diameters to the first capacitance sensor and a total of approximately 67 pipe diameters to the ECT. The two capacitance sensors are

separated by a distance of 0.35 m and placed directly on the outside wall of the pipe. The wire mesh sensor was located at 4.92 m from the mixing or inlet section, i.e. at the top, in order to avoid any possible intrusive effects to impinge on the measurements from the other probes. A brief description of the instrumentation is provided below. This was supplemented with high speed footage to capture the flow behaviour after the wire mesh sensor.

Capacitance probes

The capacitance probes were used earlier by Hernandez-Perez and Azzopardi [5]. It consists of a pair of electrodes mounted around the pipe. This arrangement provides values of the cross section averaged liquid holdup (or void fraction).

Capacitance wire mesh sensor

The capacitance wire mesh sensor consists of two planes of 24 stainless steel wires with 0.12 mm diameter, 2.8 mm wire separation within each plane and 2 mm axial plane distance. The sensor is built into an acrylic resin frame supports which allows it to be mounted in the test pipe. Figure 1 shows a photograph of the sensor. A detailed description of this instrument can be found in Da Silva et al. [3].

Electrical Capacitance Tomography (ECT)

Electrical Capacitance Tomography is a non-intrusive measurement technique that exploits the difference in relative permittivity of the two phases present in the pipe. The ECT system (Tomoflow R100) utilised consists of a capacitance sensor, measurement circuitry and a data acquisition computer; it has been described and used previously by Hassan and Azzopardi [6] for liquid-liquid flow and also been applied successfully to gas-solid flows by Azzopardi et al. [1]. The capacitance sensor comprises a set of equal sized electrodes. They are made using flexible Printed Circuit Board (PCB) technology. It is easy to adapt the instrument to pipes of different diameter. Here, an 8 electrode capacitance sensor has been mounted externally around the pipe, as the pipe wall material is non-conducting. The measurement electrodes are 35 mm long and 26.43 mm wide each. The distance between centres of two measuring planes is 89 mm. Guard electrodes are placed on either side of the measurement electrodes. The probes were calibrated by taking readings with the pipe empty (gas only) and full of silicone oil.

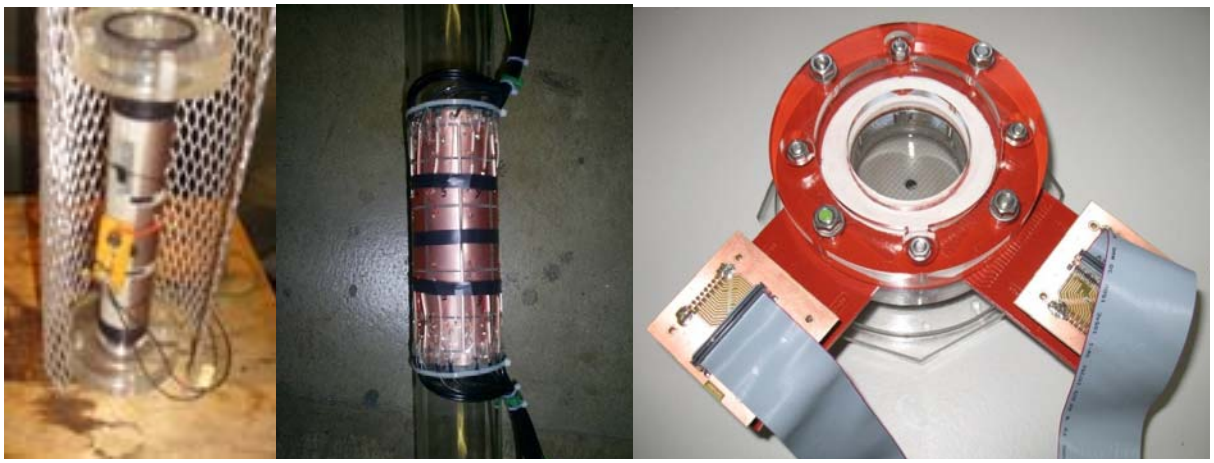

Capacitance probe | **Electrical Capacitance Tomography (ECT)** | **Wire Mesh Sensor (WMS)**

Figure 1. Instrumentation employed in this work

Computational Fluid Dynamics (CFD)

In addition to the measurement instruments above, CFD modelling is being used to predict the flow behaviour, particularly the velocity field. The velocity field is important because it determines the interaction among bubbles. In this case a particular condition has been chosen to suit the applicability of the Volume Of Fluid (VOF) approach of Hirt and Nichols [7] as employed in earlier work, Hernández Pérez et al. [8], on a vertical pipe of 67 mm diameter. As in the experimental work, the air and silicone oil flow is supplied at the inlet section of the computational flow domain (pipe), then the two-phase mixture flows along the pipe and is finally discharged through the outlet at atmospheric pressure. Here a different commercial CFD package is has been employed from the earlier work [8]. This implies a few differences, mainly in the solution algorithm utilised; the Semi-Implicit Method for Pressure-Linked Equations (SIMPLE) has been used in Star-CD. A mesh with 300,000 cells has been used, meaning a similar spatial resolution to that of the WMS.

RESULTS AND DISCUSSION

Example results are shown in Figure 2. The images on the left side display the wire mesh sensor output of the instantaneous cross sectional phase distribution. This particular version has 24x24 wires and so a spatial resolution of 2.75 mm. It can sample entire the plain at frequencies of up to 5000 Hz. However, most of the results obtained were taken at 1000 Hz. The measurements are confined to a single plain. In contrast, ECT output, also illustrated in Figure 2 (on the right), shows the cross-sectional distribution of the two-phase mixture averaged over the length of the sensor electrodes, which must be sufficiently large to give a measureable change in capacitance. Furthermore due to the so called soft-field nature of this tomographic modality, it has a lower cross sectional resolution. It was also taken at a lower sampling frequency (200 Hz); however, ECT has capabilities for higher sampling frequencies at the cost of a spatial resolution. It can be appreciated that he Taylor bubble observed at the lower part of Figure 2 is off-centre, due to flow instabilities.

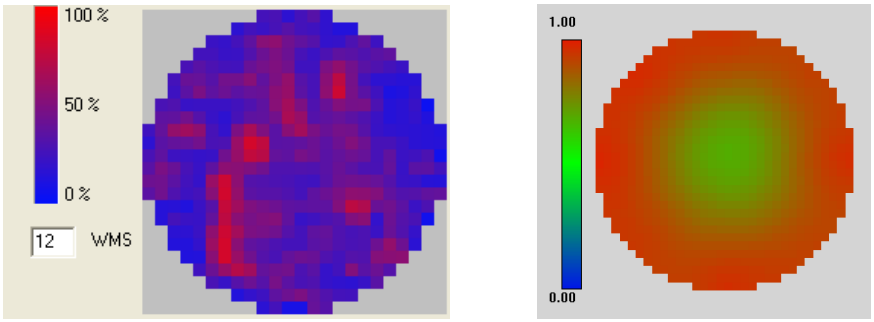

Liquid slug body above; Taylor bubble below

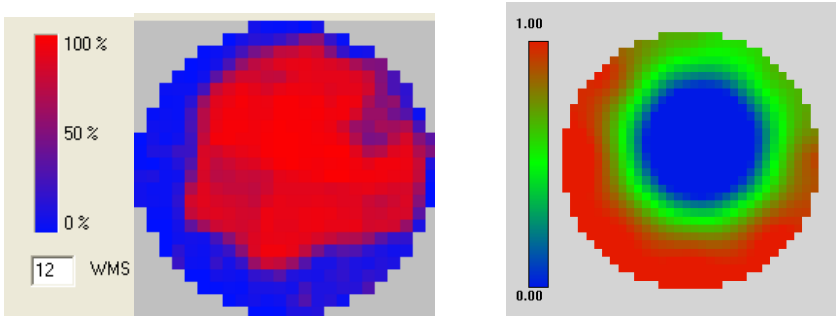

Wire mesh sensor **Electrical Capacitance tomography**

Figure 2. Comparison between contours of phase distribution taken simultaneously with both wire-mesh sensor and electrical capacitance tomography. Screenshots taken at a liquid superficial velocity of 0 m/s and a gas superficial velocity of 1.4 m/s

An advantage of ECT is that measurements are made simultaneously at two plains and therefore information can be obtained on structure velocities.

If the representation of the gas-liquid interface is considered, it can be observed that the wire mesh sensor produces a sharper interface together with a better spatial resolution than ECT as shown in Figure 2. These differences are more noticeable in the bubbly flow region. In fact the WMS has been widely used as a tool for the measurement of bubble size, which is a very important parameter to describe dispersed bubble flows, Prasser et al. [9], as well as the liquid slug body in slug flow regime. Visual observations in the transparent section of the pipe show that the gas entrainment consists of a considerable amount of bubbles smaller than the resolution of the wire mesh sensor, which might not be captured. It is noted that the ECT images presented here have been obtained utilising a first level reconstruction algorithm. Data is also being examined using the methodology of Warsito and Fan [10], which is known to give sharper, more detailed images.

It is important to note that the relevance of this work is that, the combination of the high resolution of the WMS with measurements at two positions of the ECT provides a more detailed understanding of the flow structure over a wide range of flow conditions. In addition, the measurements at five axial positions allow structures to be tracked as they progress downstream. Particular attention has been paid to the detection of structures such as liquid slugs and Taylor bubbles by means of the time series of void fraction, as in Figure 3, where the time series for WMS, ECT and capacitance probe are presented. The time series are similar with small differences that show the structure development when moving along the pipe.

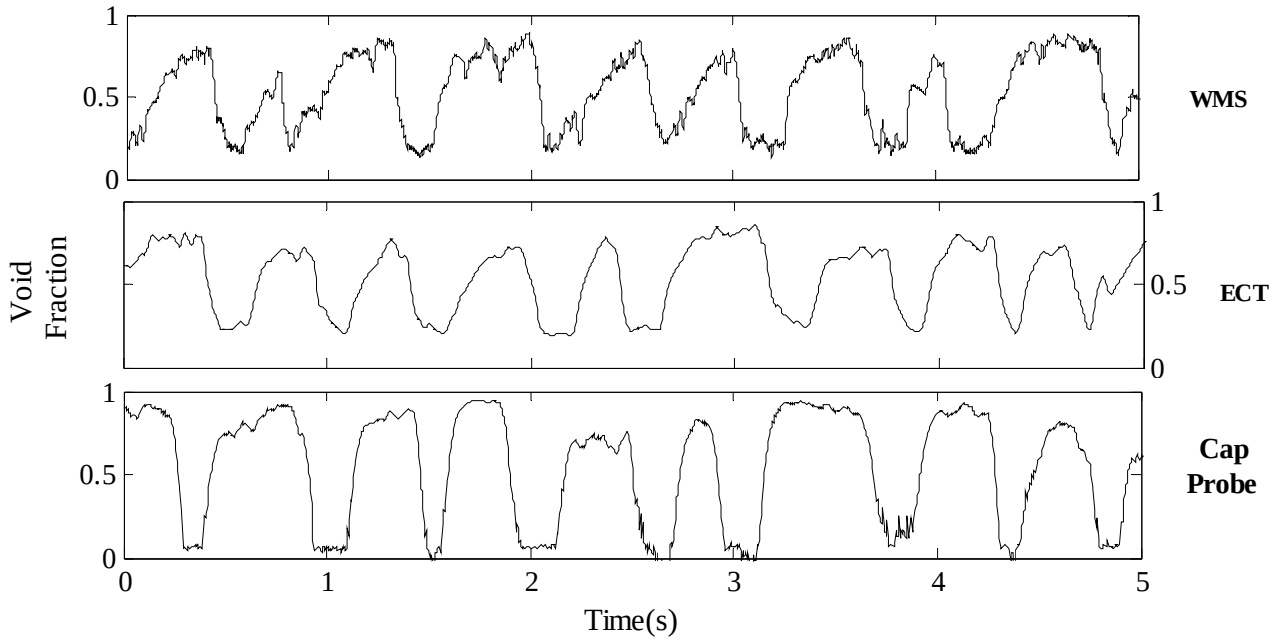

Figure 3. Comparison of time series of cross sectional average void fraction. Superficial velocities are 0 m/s and 0.56 m/s for gas and liquid respectively

Most studies of two-phase flow using ECT or wire mesh sensor are focused on the phase distribution, however, more information can be obtained. In many situations it is necessary to know the mean value of the gas or liquid volume fraction. Average void fraction has been calculated for several runs at different flow conditions. A typical example of the average void faction comparison is presented in Figure 4. The results of all of these instruments are shown to agree on the overall (averaged over time and cross-section) void fraction. However some differences are found which are under investigation, as they could be due to the instruments positions and flow development or calibration problem.

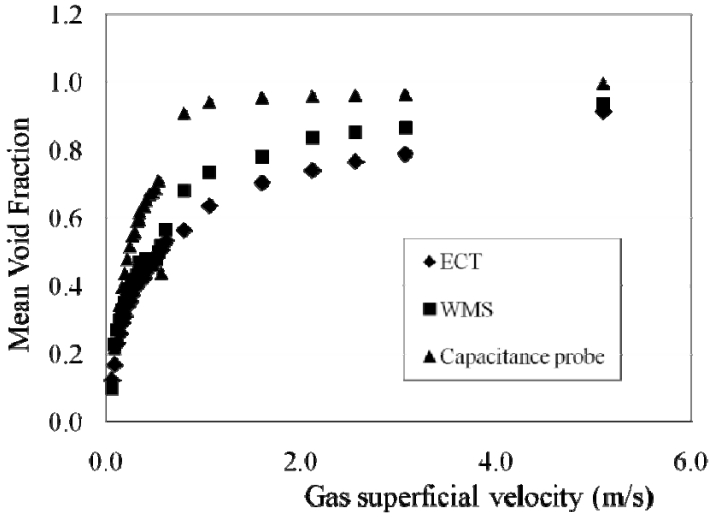

Figure 4. Comparison of mean void fraction: liquid superficial velocity = 0 m/s

Flow pattern identification shown by means of the Probability Density Function (PDF) of the cross-sectional averaged data of WMS and ECT along with capacitance probe readings has been carried out. A typical example is presented in Figure 5. All three instruments predict slug flow, as demonstrated by the double peak shape of the plots.

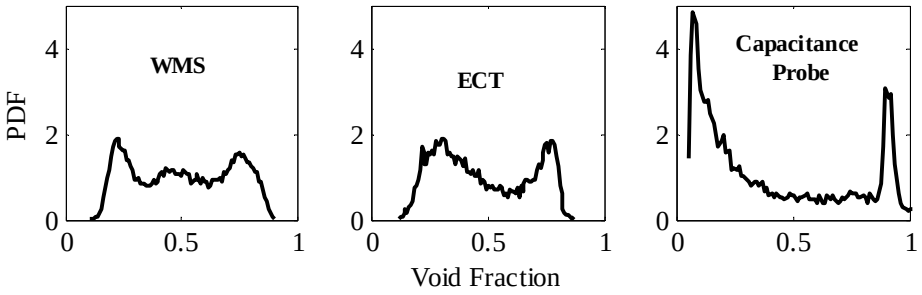

Figure 5. Comparison flow pattern prediction by Probability Density Function. The PDFs correspond to the time series presented in Figure 3

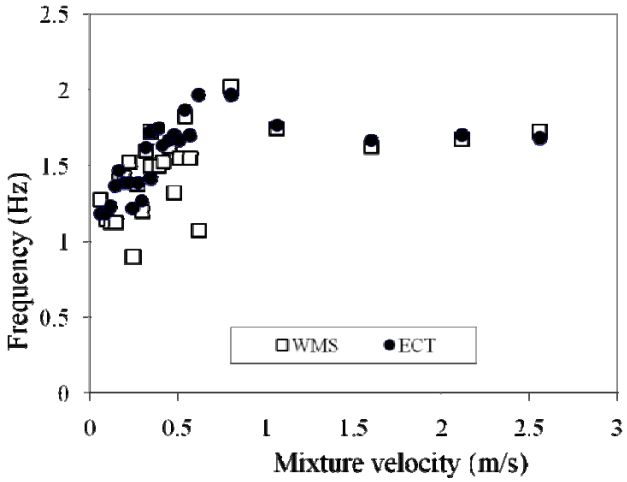

Figure 6. Comparison of structure frequency: liquid superficial velocity: 0 m/s

Structure frequency has been obtained applying Power Spectral Density (PSD) method and the results are presented in Figure 6 for the case of liquid superficial velocity of 0 m/s. The agreement is fairly good, particularly for the conditions of mixture velocity above 1 m/s. As expected, scatter

in the frequencies at mixture velocity lower than 1 m/s is observed and could be associated with bubbly flow where the structures such as small bubbles and void waves are not so easily identified. In addition, structure velocity has been obtained by applying cross correlation corresponding to two signals at two measurement stations. As expected, a fairly linear relation is obtained with the mixture velocity, Figure 7, which is in agreement with the correlation of Nicklin et al. [11].

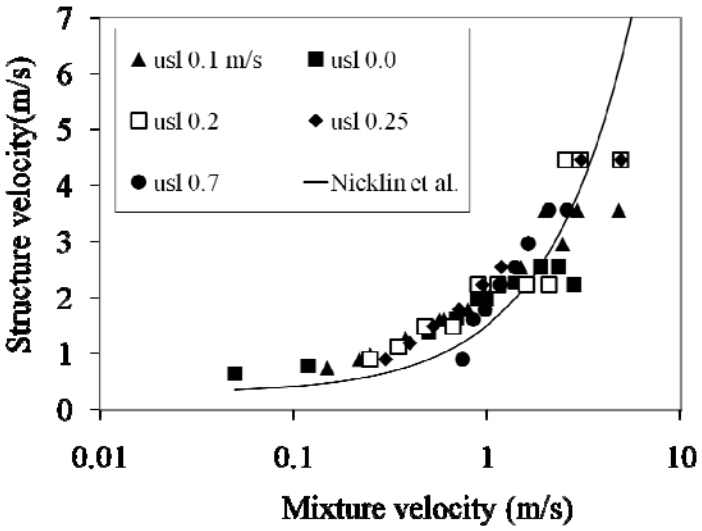

Figure 7. Structure velocity obtained using ECT

The CFD output shows characteristics similar to those observed visually and from the instrumentation. The flow is rather complicated, as can be seen in Figure 8, heterogeneous gas hold-up distribution within the pipe induces density fluctuations that originate circulation currents influencing strongly phase mixing. A cluster of small bubbles is observed by both ECT and CFD as a single bigger bubble. Hernández Pérez et al. [8], observed that the agreement is both qualitative but also quantitative, i.e., in the Probability Density Function plots and in the Power Spectral Densities obtained from experiment and computational results. Those parameters will be extracted from the present computations.

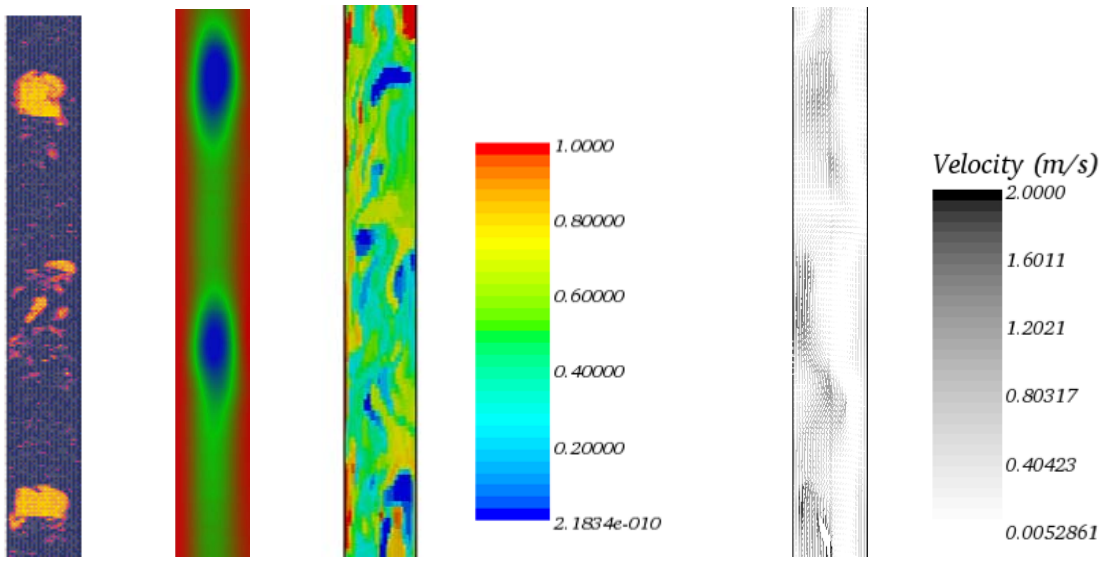

WMS ECT CFD contours of liquid and velocity field

Figure 8. Comparison of phase distribution obtained with WMS, ECT and CFD respectively, CFD velocity field is also included. Superficial velocities: liquid 0m/s and gas 0.15 m/s.

CONCLUSIONS

Different tools have been used to study gas-liquid flows and a comparison has carried out of the outputs. The combination has resulted in a comprehensive characterisation of the flow by gathering several flow parameters, which include flow pattern identification, structure frequency and velocity, void fraction and velocity field. By placing different sensors along the pipe flow structures have been tracked. In general the agreement in the comparison is fairly good. However, it is observed that the WMS currently provides a better spatial resolution than ECT and is excellent for measurement of bubbly flow parameters. Some differences have been found in the measured average void fraction values.

ACKNOWLEDGEMENTS

This work has been undertaken within the Joint Project on Transient Multiphase Flows and Flow Assurance. The Authors wish to acknowledge the contributions made to this project by the UK Engineering and Physical Sciences Research Council (EPSRC) and the following: - Advantica; BP Exploration; CD-adapco; Chevron; ConocoPhillips; ENI; ExxonMobil; FEESA; IFP; Institutt for Energiteknikk; Norsk Hydro; PDVSA (INTERVEP); Petrobras; PETRONAS; Scandpower PT; Shell; SINTEF; Statoil and TOTAL. The Authors wish to express their sincere gratitude for this support.

L. Abdulkareem would like to thank The Kurdish Government for supporting his PhD study

REFERENCES

1. Azzopardi B.J., Hernandez Perez, V., Kaji R., Da Silva M.J., Beyer M., and Hampel U., (2008), Wire mesh sensor studies in a vertical pipe, HEAT 2008, Fifth International Conference on Transport Phenomena in Multiphase Systems, Bialystok, Poland.
2. Azzopardi, B.J., Jackson, K., Robinson, J.P., Kaji, R., Byars, M., Hunt, A., (2008), Fluctuations in dense phase pneumatic conveying of pulverised coal measured using electrical capacitance tomography, Chemical Engineering Science, Vol. 63, pp 2548-2558.
3. Da Silva M.J., Schleicher E., Hampel U., (2007), Capacitance wire-mesh sensor for fast measurement of phase fraction distributions. Measurement Science and Technology, Vol. 18, pp. 2245-2251.
4. Thiele, S., Da Silva, M.J., Hampel, U., Abdulkareem, L. and Azzopardi, B.J., (2008), High resolution oil-gas two-phase flow measurement with a new wire mesh capacitance tomography, 5th international symposium on process tomography, 25-26 August 2008, Zakopane Poland
5. Hernández Pérez, V., and Azzopardi, B.J., (2006), Effect of inclination on gas-liquid flows. 10th Int. Conf. Multiphase Flow in Industrial Plant, Tropea, Italy 20 to 22 September, pp 207-220.
6. Hasan, N.M. and Azzopardi, B.J., (2007), Imaging stratifying liquid-liquid flow by capacitance tomography, Flow Measurement and Instrumentation, 18, 241-246.
7. Hirt, C.W. and Nichols, B.D., (1981), Volume of Fluid (VOF) Method for the Dynamics of Free Boundaries, J. Comp. Phys. 39, 201.
8. Hernández Pérez, V., Azzopardi, B.J. and Morvan, H., (2007), Slug flow in inclined pipes. 6th Int. Conf. Multiphase Flow, Leipzig, Germany 5 to 9.
9. Prasser, H.-M., Scholz, D. and Zippe, C., (2001), Bubble size measurement using wire-mesh sensors, Flow Measurement and Instrumentation Vol. 12, pp 299-312
10. Warsito, W. and Fan, L.S. (2001), Measurement of real-time flow structures in gas–liquid and gas–liquid–solid flow systems using electrical capacitance tomography (ECT), *Chem. Eng. Sci.*, Vol. 56, pp 6455–6462.
11. Nicklin, O. J., Wilkes, J. O., and Davison, J. F., (1962), Two-phase flow in vertical tubes, Transactions of the institute of Chemical Engineers, Vol. 40, pp. 61-68.

WAVY STRUCTURE OF LIQUID FILMS IN ANNULAR GAS-LIQUID FLOW

S. Alekseenko[1,2 *], V. Antipin[2], A. Cherdantsev[1,2], S. Kharlamov[2], D. Markovich[1,2]

[1] Novosibirsk State University, Novosibirsk, Russia
[2] Institute of Thermophysics, Novosibirsk, Russia

ABSTRACT. High-speed modification of LIF technique was used to study spatio-temporal evolution of waves on liquid film in annular gas-liquid flow with and without entrainment. It was shown that in both flow regimes wavy structure is represented by two types of waves: primary and secondary waves; all the secondary waves are generated at the back fronts of primary ones. In entrainment regimes primary waves are known as disturbance waves, and secondary waves are known as ripples, although regularities of ripples generation were not clarified in earlier works. Separation of waves in regimes without entrainment into primary and secondary ones, and, consequently, similarity of liquid film wavy structure in regimes with and without entrainment, is shown for the first time.
Keywords: *annular flow, disturbance wave, ripple wave*

INTRODUCTION

The joint flow of liquid film along channel wall and high-velocity gas stream along the center of the channel is called annular two-phase flow. The case of high gas and liquid flowrates when liquid droplets are entrained from film surface into the core of gas stream is called annular-dispersed flow. Heat and mass transfer of annular-dispersed flow are essentially influenced by the liquid entrainment, and physically based modeling of this process is very important but still unsolved problem. According to the commonly accepted opinion, two types of waves exist on film surface in presence of entrainment: disturbance waves with high (several times higher than average thickness of the film) amplitude and short-length ripple waves. Woodmansee & Hanratty [1] observed that ripples travelling on disturbance waves crests are ruptured by the gas flow and considered this phenomenon as the main source of entrainment.

The quantitative information on appearance and evolution of these two types of waves and on their interrelations is necessary for creating the physically based models of entrainment phenomenon. In the most part of experimental works where wavy structure in annular flow is studied, investigators separate all the waves into disturbance waves and ripples (normally the amplitude-based criteria are used for this purpose) and then study these two types separately as if they are totally independent on each other [2-4]. The disturbance waves seem to be the most interesting type of waves for the investigators, and huge amount of works is devoted to measuring their characteristics like frequency, velocity, spacing, amplitude, etc. (see, e.g., review [5]). The disturbance waves properties usually keep constant values along large (several meters) downstream distances [6], whereas ripples have short lifetime [2, 7-9].

The characteristic feature of entrainment phenomenon which must be taken into account in all entrainment models is the existence of so-called critical Reynolds number. When liquid Reynolds number is lesser than this critical value, there is no entrainment at any gas stream velocity. The commonly accepted explanation of this feature is that the disturbance waves do not appear in regimes without entrainment. Thereby, film surface in no-entrainment regimes is considered to be covered by

* Corresponding author: Prof. S. Alekseenko
Phone: +7 (383) 330-70-50, Fax: +7 (383) 330-84-80
E-mail address: aleks@itp.nsc.ru

the ripples only; the transition to entrainment is considered to occur when disturbance waves appear due to increasing of liquid flowrate [5, 10-11].
Ripples that present on liquid film surface in regimes without entrainment are considered to belong to the same type as the ripples that present in regimes with entrainment. Properties of ripples in regimes without entrainment were studied in works [3, 12-13]. The amplitudes, velocities and wavelengths were shown not to change with downstream distance and slightly depend on gas and liquid flowrates. Asali and Hanratty [14] have shown that experimentally measured spatial wavelength of ripples exceeds theoretically predicted wavelength of maximum growth nearly twice.
Some works, devoted to studying the wavy structure of annular flow, were based on different approaches. Thus, Sekoguchi and coauthors [15-17] used a multiple-electrode conductivity system to resolute the spatio-temporal evolution of liquid film thickness. In particular, they found "ephemeral waves", which sometimes appear on back fronts of disturbance waves and move slower than the latter. Another type of waves was observed by Ohba and Nagae [18] in upward flow near the transition to entrainment. These waves, that were named "ring waves" were found to be shorter than disturbance waves and wider than ripples; this difference was observed in longitudinal as well in transverse direction.
Nevertheless, the literature lacks systematic information on the regularities of waves appearance and evolution in annular and annular-dispersed flows. The aim of our work is to obtain the detailed and systematic information on waves appearance and interrelation in annular flows in regimes with and without entrainment.

EXPERIMENTAL SETUP AND MEASUREMENTS TECHNIQUE

The downward annular flow was organized in vertical Plexiglas cylindrical tube with inner diameter d=15 mm and 1 meter length. Measurements were performed 8-20 cm downstream the inlet. The ring slot distributor with the gap width of 0.5 mm was used to introduce the liquid film into the tube; the gas flow entered the channel through a smaller diameter tube, co-axial to the channel.
Liquid Reynolds numbers Re=142, 220 and 350 were chosen for regimes with entrainment, and Re=40 and 60 – for regimes without entrainment. Re was defined as $q/\pi d\nu$, where q is volumetric liquid flowrate and ν is kinematic viscosity of liquid. The range of average gas velocities Vg was 22-58 m/s (gas Reynolds numbers 22000-58000, respectively). Distilled water was used as the liquid, air was used as the gas.
Laser induced fluorescence technique was used to recover the instantaneous distribution of film thickness along the longitudinal section of the channel. To ensure high sampling rate, the CCD-camera with linear (one-pixel width) sensor was used for registration the local brightness of the re-emitted light. This camera allowed working frequency of 2 kHz. The investigated section was enlightened by the continuous green (532 nm) laser; the beam was optically transformed into vertical sheet with width about 1 mm. The fluorescent dye was Rhodamin-6G (concentration was 30 mg/l).
Spatial resolution was 0.1 mm per pixel. Exposition time of the measuring system was 250 μs and registration frame rate was 2000 fps. The dependency of local intensity of re-emitted light on local film thickness was obtained by organizing a set of gaps of certain thickness. The detailed description of registration system can be found in [19].
The most convenient form of presentation of experimentally obtained data on film thickness evolution in space and time are the spatio-temporal fields of film thickness (see Figs. 1, 2, 4). The waves move across this surface along characteristic lines, and velocity of a wave is characterized by the slope of this line.

EXPERIMENTAL RESULTS

Regimes with entrainment

An example of spatio-temporal evolution of film thickness for flow with entrainment is shown in Figure 1. The disturbance waves move along high-slope characteristic lines. Flow direction is from lower values of x to higher values. Disturbance waves are separated by thin substrate of approximately constant thickness. It can be seen that surface of substrate is covered by ripples, and that all the ripples traveling on substrate appear at the back slopes of disturbance waves.

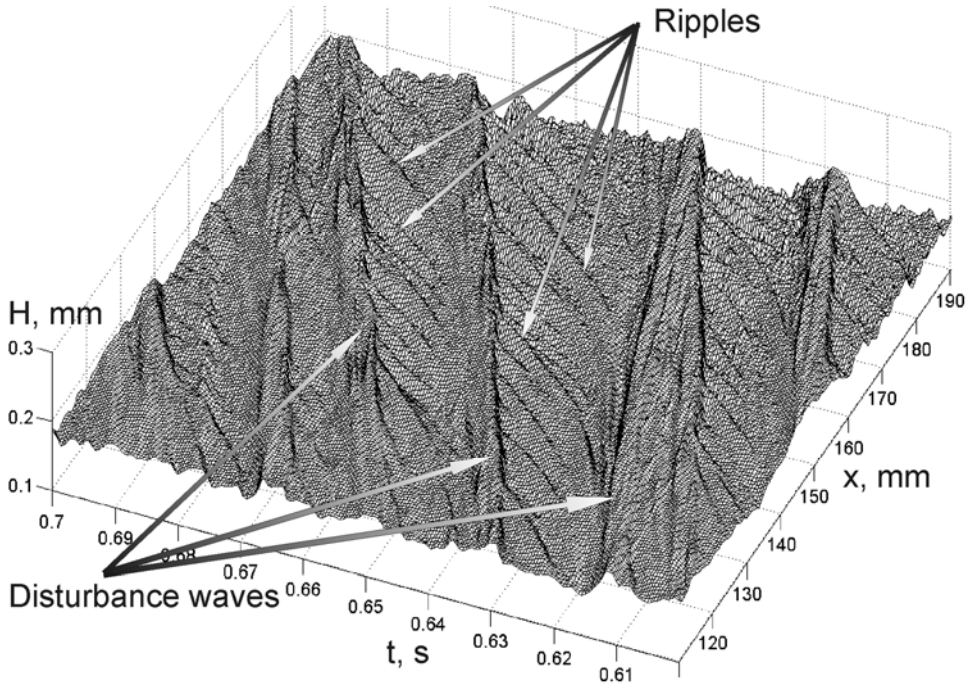

Figure 1. Disturbance waves and ripples on substrate in entrainment regime. Heights of disturbance waves are decreased to make ripples on substrate more distinguishable. Re=350, Vg=27 m/s.

The velocity of a ripple right after inception is close to that of disturbance wave, but afterwards it slowly decelerates and finally reaches some constant value of velocity. When the following disturbance wave overtakes the ripple on substrate, the latter is being absorbed by the former without essential influence on the disturbance wave's characteristics. The described picture explains short lifetime of such ripples, that was revealed in earlier works (e.g., [2]) using cross-correlation analysis.
Figure 2 shows a higher-scale picture of spatio-temporal evolution of disturbance wave. It can be seen that crest of disturbance wave is also covered by ripples. Similar to ripples on substrate, these ripples do also appear at the back slope of disturbance wave, but the inception point in this case is located closer to front of disturbance wave. Ripples on disturbance waves crests move faster than parent disturbance waves, and, after reaching the disturbance wave's front, they gradually disappear. This disappearance corresponds to mentioned above description of entrainment, made in [1] – the disappearing ripples are evidently disrupted by the gas flow and the resulting droplets are entrained into the core of gas stream.

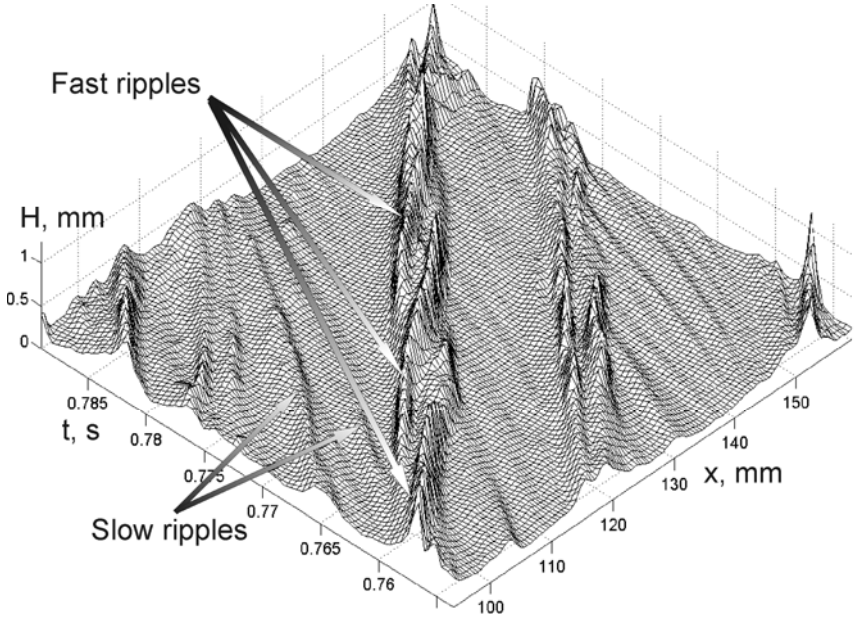

Figure 2. Ripples on disturbance wave. Re=350, Vg=27 m/s.

Figure 3 shows the average velocity of disturbance waves and ripples depending on gas stream velocity. Solid circles correspond to the average velocity of "fast" ripples travelling on disturbance waves crests, squares mark the average velocity of disturbance waves, crosses mark the velocity of "slow" ripples travelling on substrate, and the empty circles indicate the difference between velocity of the "fast" ripples and velocity of disturbance waves. It can be seen that this relative velocity is rather close to the velocity of "slow" ripples on substrate. All the velocities linearly depend on gas stream velocity.

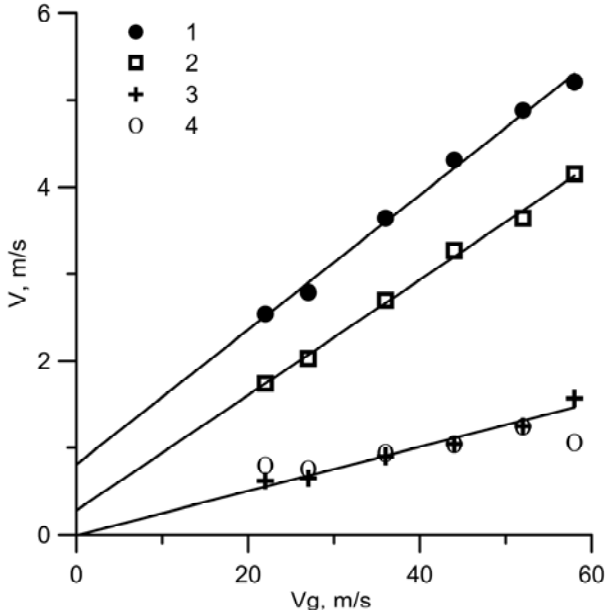

Figure 3. Average velocities of "fast" ripples (1), disturbance waves (2) and "slow" ripples (3). The velocity of "fast" ripples relatively to disturbance waves is also shown (4.)

Regimes without entrainment

Below certain value of liquid Reynolds number (Re~70 for downward air-water flow [5]), called critical Reynolds number, no entrainment was observed even for very high gas velocities. This is usually explained by absence of disturbance waves in regimes without entrainment. Thus, on liquid film surface in such regimes one could expect to observe only one type of waves - the ripples.

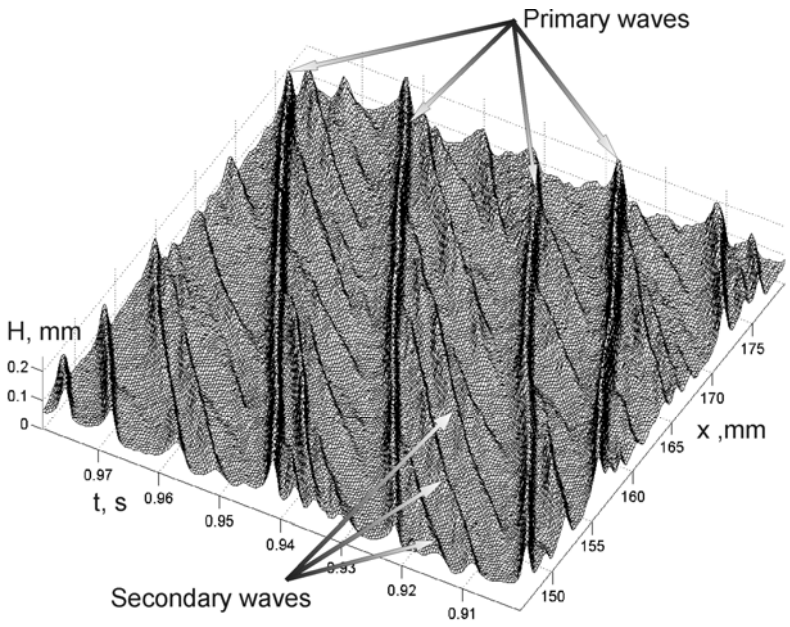

Figure 4. Primary and secondary waves in regimes without entrainment. Re=40, Vg=27 m/s.

Our experiments unexpectedly showed that in regimes without entrainment wavy structure also consists of two types of waves (see Figure 4). Waves, belonging to one of these types, are generated at the back fronts of waves of the other type, that's why we have called these two types "primary waves" and "secondary waves". The primary waves are characterized by high velocity and long life. The secondary waves appear at the back fronts of primary ones; they move essentially slower and are thus short-living, since any of them is promptly absorbed by the following primary wave. The described picture is very similar to that of regimes with entrainment: primary waves resemble disturbance waves, and secondary waves are similar to "slow" ripples, traveling on substrate.

The two main differences are observed between wavy structure in regimes with and without entrainment. First one consists in fact that in regimes without entrainment the secondary waves can move only slower than primary ones, while in regimes with entrainment secondary waves (usually called "ripples") may move either slower or faster than primary waves (usually called "disturbance waves"), as it was shown in Figures 1 and 2.

The second difference, that possibly explains the first one, is the fact that disturbance waves in regimes with entrainment are much higher than primary waves in regimes without entrainment; the sharp change in amplitude of primary waves occurs near the critical Reynolds number. The amplitudes of primary and secondary waves in regimes without entrainment are rather close to each other. That is the reason why the two types of waves in such regimes were not identified in earlier works where standard methods of waves separation with amplitude-based criteria were used.

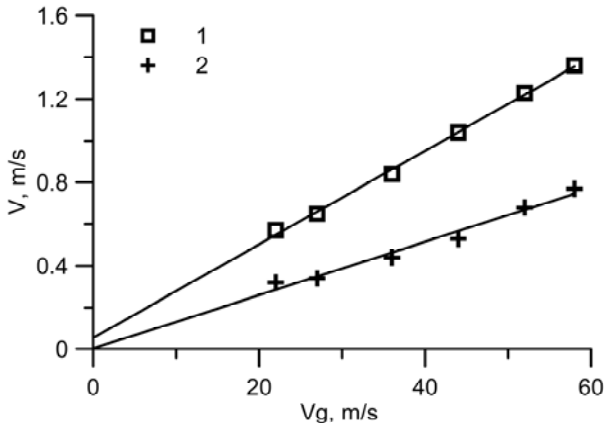

Fig. 5. Average velocities of primary (1) and secondary (2) waves in regime without entrainment. Re=40.

Figure 5 shows the average velocities of primary and secondary waves in regime without entrainment. Squares mark the average velocity of primary waves, crosses mark the velocity of secondary waves. The velocities of both types linearly grow with gas stream velocity and velocity of primary waves is about twice higher than that of secondary waves. The separation criterion, based on velocities of individual waves, allows effective separation the two types of waves in regimes without entrainment.

CONCLUSIONS

Experimental observations revealed that wavy structure in regimes with and without entrainment consists of two types of waves: long-living and short-living waves. Short-living waves are always generated at the back fronts of long-living waves, that's why we prefer to refer long-living waves as "primary waves" and the short-living waves as "secondary waves". The short life of secondary waves is explained by the scenario of their evolution: in a short time after appearance they are either being absorbed by the following primary wave (case of "slow" secondary waves) or being disrupted by the gas shear at the crest of primary wave (case of "fast" secondary waves). "Fast" secondary waves are observed only in regimes with entrainment that is possibly explained by the high amplitude of primary waves in such regimes. Primary waves and "slow" secondary waves exist in both regimes (with and without entrainment). In regimes with entrainment the primary waves are known as "disturbance waves", the secondary waves are known as "ripples". In regimes without entrainment the existence of primary and secondary waves was found for the first time.

The described similarity gives essentially different understanding of the transition to entrainment. It was commonly accepted that with increasing of liquid flowrate the transition to entrainment occurs due to appearance of the new type of waves – disturbance waves. Our observations allow the supposition that the primary waves in regimes without entrainment belong to the same type of waves as the disturbance waves in regimes with entrainment do. In other words, the wavy structure in regimes with and without entrainment is represented by the same two types of waves. The transition to entrainment, in our opinion, occurs due to abrupt growth of primary waves amplitude, and this growth leads to appearance of "fast" primary waves. The disruption of the latter by the gas shear is the reason of entrainment. Thus, these experimental observations allow development of the fundamentally new theoretical approaches to modeling of entrainment phenomenon.

AKNOWLEDGEMENTS

This work was supported by RF President grant NSh-4366.2008.8.

REFERENCES

1. Woodmansee, D.E. and Hanratty, T.J., Mechanism for the removal of droplets from a liquid surface by a parallel air flow, *Chem. Engng. Sci.*, Vol. 24, pp. 299-307, 1969.
2. K.J. Chu and A.E. Dukler, Statistical characteristics of thin, wavy liquid film. III. Structure of large waves and their resistance to gas flow, *AIChE J.*, Vol. 21, pp. 583-593, 1975.
3. Suzuki, K., Hagiwara, Y. and Sato, T., Heat transfer and flow characteristics of two-phase two-component annular flow, *Int. J. Heat Mass Transfer*, Vol. 26, pp. 597-605, 1983.
4. Bontozoglou, V. and Hanratty, T.J., Wave height estimation in stratified gas-liquid flows, *AIChE J.*, Vol. 35, pp. 1346-1350, 1989.
5. Azzopardi, B.J., Drops in annular two-phase flow, *Int. J. Mult. Flow,* Vol. 23, pp. 1-53, 1997.
6. Hall Taylor, N.S., Hewitt, G.F. and Lacey, P.M.C., The motion and frequency of large disturbance waves in annular two-phase flow in air-water mixture, *Chem. Engng. Sci.*, Vol. 18, pp. 537-552, 1963.
7. Hall Taylor, N.S. and Nedderman, R.M., The coalescence of disturbance waves in annular two-phase flow, *Chem. Engng. Sci., Vol.* 23, pp. 551-564, 1968.
8. Thwaites, G.R., Kulov, N.N. and Nedderman, R.M., Liquid film properties in two-phase annular flow, *Chem. Engng. Sci.*, Vol. 31, pp. 481-486, 1976.
9. Wolf, A., Jayanti, S. and Hewitt, G.F., Flow development in vertical annular flow, *Chem. Engng. Sci.*, Vol. 56, pp. 3221-3235, 2001.
10. Hewitt, G.F. and Hall Taylor, N.S., *Annular two-phase flow,* Pergamon press, Oxford, 1970.
11. Ishii, M. and Grolmes, M.A., Inception criteria for droplet entrainment in two-phase concurrent film flow, *AIChE J.,* Vol. 21, pp. 308-318, 1975.
12. Hagiwara, Y., Miwada, T. and Suzuki, K., Heat transfer and wave structure in the developing region of two-component two-phase annular flow, *Phys.-Chem. Hydrodyn.*, Vol. 6, pp. 141-156, 1985.
13. Alekseenko, S.V., Cherdantsev, A.V., Kharlamov, S.M. and Markovich, D.M. Experimental study of liquid film wavy structure in annular two-phase flow, *DVD-ROM Proceedings 6th Int. Conf. Mult. Flow*, Leipzig, Germany, July 9 – 13 2007, PS5_2.
14. Asali, J.C. and Hanratty, T.J., Ripples generated on a liquid film at high gas velocities, *Int. J. Mult. Flow*, Vol. 19, pp. 229-243, 1993.
15. Sekoguchi, K., Takeishi, M. and Ishimatsu, T., Interfacial structure in vertical upward annular flow, *Phys.-Chem. Hydrodyn.,* Vol. 6, pp. 239-255, 1985.
16. Sekoguchi, K. and Takeishi, M., Interfacial structures in upward huge wave flow and annular flow regimes, *Int. J. Mult. Flow,* 15, pp. 295-305, 1989.
17. Sekoguchi, K. and Mori, K., New development of experimental study on interfacial structure on gas-liquid two-phase flow, *Exp. Heat Transfer Fluid Mech. Thermodyn. Ed. Ets,* Vol. 2, pp. 1177-1188, 1997.
18. Ohba, K. and Nagae, K., Characteristics and behavior of the interfacial wave on the liquid film in a vertically upward air-water two-phase annular flow, *Nucl. Engng. Des,* Vol. 141, pp. 17-25, 1993.
19. Alekseenko, S.V., Antipin, V.A., Cherdantsev, A.V., Kharlamov, S.M. and Markovich, D.M., Investigation of waves interaction in annular gas-liquid flow using high-speed fluorescent visualization technique, *Microgravity – Sci. Technol.*, Vol. 20, pp. 271-275, 2008.

INFRARED THERMOGRAPHY OF FLUIDIC MUSCLES

E. Ravina[1] *

[1] University of Genoa, Dept. of Mechanics and Machine Design, Genoa, Italy

ABSTRACT. The paper describes the results of a research activity, still under development, oriented to the characterization of pneumatic muscles and based on infrared thermography monitoring. Fluidic muscles are innovative pneumatic components able to mimic human muscular contractions and extensions. On the contrary of many other pneumatic and fluidic devices, the working conditions of muscles are characterized by significant fluid temperature variations: this suggest an interdisciplinary approach, researching correlations between mechanical and thermal variables.

Keywords: *fluidics, muscles, thermography*

INTRODUCTION

The concept of fluidic muscle has been patented in fifties. It is related to the contraction/extension of animal muscles and often it is realized through cylindrical elastomers operating under internal pressure variation (Fig. 1).
The muscle uses membrane expansion to achieve its stroke length. The proprietary membrane consists of a collection of woven fibres; the weave is a three-dimensional rhomboidal form, which helps give the tube its flexibility and the ability to expand. Two woven layers of the high-tensile supporting material enclose the muscle's polymer core.
Applying either pneumatic or hydraulic pressure to the muscle causes radial expansion. This action produces tensile force in the axial direction, which shortens the muscle and generates an initial pulling force that is more than ten times that of a pneumatic cylinder at the same pressure and diameter. Acting much like a spring, the force exerted by the pneumatic muscle varies as a function of its elongation. Maximum force is produced at the neutral position.

Figure 1. Fluidic muscle (by FESTO)

* Corresponding author: Prof. E. Ravina
Phone: + (39)-10-3532848, Fax: + (39)-10-3532834
E-mail address: enrico.ravina@unige.it

Although fluidic muscles are used as a substitute for pneumatic cylinders, they cannot be used as a one-to-one replacement in a given application. That's because they are typically twice as long as conventional cylinders for a given stroke length. Various couplings and attachments facilitate use of the fluidic muscle in a wide range of applications, including assembly tables, presses, lifting equipment, and medical equipment. This device used as actuator or spring is characterized by:

- low cost;
- high power/weigh ratio;
- good efficiency;
- no relative motions;
- no lubrication;
- use of cheap and ecological fluids (air, water,..);
- possibility of application in extreme environments (vacuum, high gradients of temperature, magnetic fields, radioactivity,..).

The muscle assemblies three main components:

- deformable body realized in elastomer, with high axial deformability;
- external undeformable fibres;
- metallic terminals.

Attractive features of this type of pneumatic actuator concern arising generated forces (up to 10 times higher than a conventional cylinder of the same diameter), good mechanical responses (velocities from 0.001 mm/s up to 3 m/s, accelerations up to 100 m/s^2, forces up to 6 kN), zero leakage (any mechanical parts in relative motion), simple control technology both for high (up to 100 Hz) and very low actuation frequencies. In addition, its lightness and compactness allow versatile and innovative applications.

However dynamic behaviour, optimal performances and life cycle are strongly influenced by environmental parameters, by mechanical and thermal stresses related to the operating conditions and by air fluid dynamics. Phenomena of interest concern hysteresis cycles under different pressure loads, repeatability position errors, reproducibility conditions, and relationships between contraction phases or frequency and air temperature distribution.

In particular the actual temperature distribution along the muscle strongly influences its mechanical response: it depends on the techniques of air supply and drain, on the muscle length, and on the inside pressure levels. The versatility of use of this fluidic component in very different applications and working conditions suggests the development of not invasive monitoring procedures, in order to identify the role of the temperature distribution on its mechanical performances.

TEST BENCH

The experimental investigation is developed through an original test bench (Fig. 2), expressly designed and realized by the author for monitoring and diagnosis of fluidic muscles.

Different sizes of muscles can be tested, simulating variable external loads by means an antagonist pneumatic actuator. The muscle can be actuated with timed on-off pneumatic valve or by a proportional flow control valve. The test bench is equipped with a load cell located between muscle and antagonist cylinder, while pressure transducers detect the inside pneumatic conditions. Muscle terminals can be misaligned in different way, simulating actual operating conditions.

The variable geometry of the muscle surface, continuously submitted to contractions and stretching, doesn't allow the temperature measurement by means contact conventional sensors (thermocouples or thermometers): infrared thermography is successfully applied. The heat produced within the muscle is conducted, through the composite layers forming the muscle, on the outside surface, where can be detected by a thermo camera: in this experience an IR Flex Cam T camera (by Infrared Solution, inc.) is used.

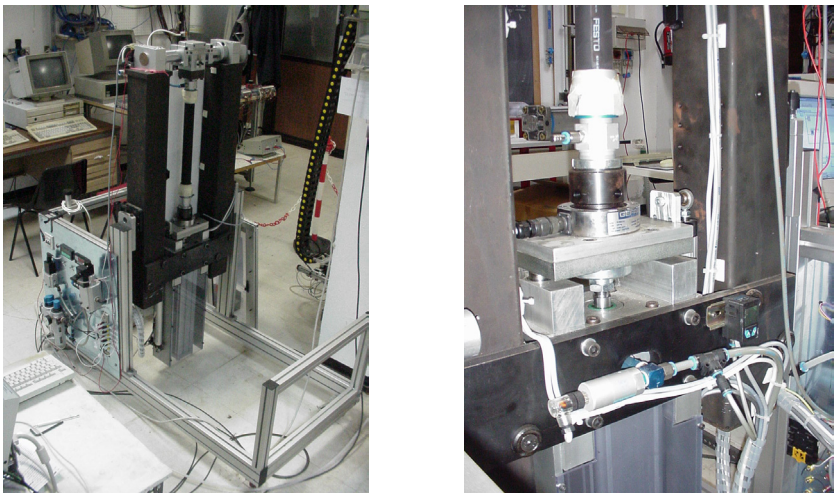

Figure 2. Overall view and details of the experimental test bench

The basic theoretical reference (Stephan – Boltzmann law) correlates the emitted power to the absolute temperature of the surface through the emissivity; the general relationship relating the effective radiance to the surface temperature is:

$$L = \tau\,\varepsilon\,L^0(T) + \tau\,(1-\varepsilon)\,L^0(T_a) + (1-\tau)\,L^0(T_{atm})$$

where L is the radiance, L^0 the total radiance of a reference black body, τ the effective atmospheric transmissivity, ε the emissivity, T the absolute temperature the body under test, T_{atm} the temperature of the non-scattering isothermal atmosphere and T_a the temperature of the isothermal surroundings.
The correct evaluation of the muscle surface temperature detected by thermo-cameras must takes into account of the shape of the emitting body: the pneumatic muscle is assumed as a body having a cylindrical symmetry and the detected temperature is corrected taking into account the shot angle Φ between muscle and camera: compensation functions proposed in literature are applied.
Finally the environment temperature must be considered: in the present research activity the muscle surroundings temperature is monitored in real time and used as parameter for the correct evaluation of the muscle temperature distribution.
All the test bench mechanical and thermal variables are managed to an acquisition and control unit operating with virtual instrumentation software (Labview, by National Instruments inc.), originally implemented on PC. Mechanical actions and programmed thermo- pictures are automatically integrated.

SOME EXPERIMENTAL TESTS

The aim of the study is to find all possible correlations between cinematic and dynamic performances of fluidic muscles and their temperature distributions: in particular correspondences between actual position errors and temperature may be a significant monitoring reference on correct working conditions.
An original set of experimental tests, fully automatic, are implemented on different sizes of muscles; key parameters are:

- input air pressures at the muscle and at the antagonist cylinder;
- maximum contraction factor (up to 25% of the muscle length);
- excitation frequency;
- digital t_{ON}/t_{OFF} sequences;
- programmed opening laws to flow control proportional valves;

- fluid dynamic air conditions inside the muscle;
- thermal environmental conditions.

Reasons of space force to select the aspects analysed in this paper. In particular, results concerning the effects on the temperature distribution along the muscle in correlation with muscle length, working frequency and supply pressure are focussed and discussed.
Standard tests are organized programming sets of 500 continuous contraction/extension cycles on muscles having different size: here muscles having 40 mm of diameter and length from 120 to 360 mm are compared. The pressure supply is variable from 1 to 6 bars: the same metallic terminal of the muscle is involved in inlet and outlet fluid flow. Tests aren't implemented in thermostatic chamber, but the environmental temperature variation is in the range 25.5 ÷ 26.5 °C, acceptable for compared experiments oriented to detect different thermal distributions.
The emissivity is chosen equal to 0.95, approximating the composite material of the muscle surface to rubber. Particular care has been kept to effects of reflection generated by the metallic terminals: screens of special adhesive paper are successfully used.
Significant gradients of temperature and inverted distributions are surprising results of this integrated analysis.

Effect of the muscle length

Muscles of different length (from 120 mm, named hereafter "short" muscle, up to 360 mm, named "long" muscle) are compared all things being equal: diameter (40 mm), working frequency (0.5 Hz), contraction factor (20% of the nominal length) and inlet pressure (4 bar).
Figs. 3 and 4 refers on temperature distribution at the end of the working cycle: an overview shows that the temperature is more uniformly distributed in the "short" than in the "long" muscle.

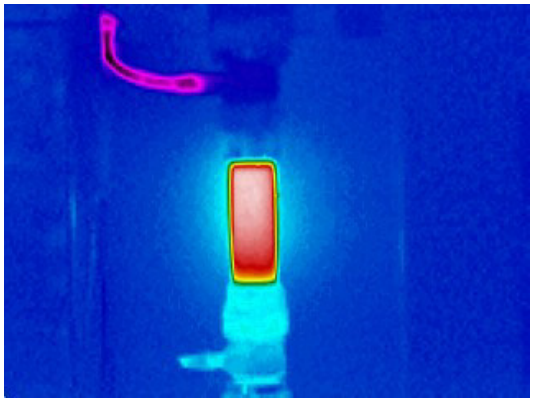

Figure 3. "Short" muscle infrared view

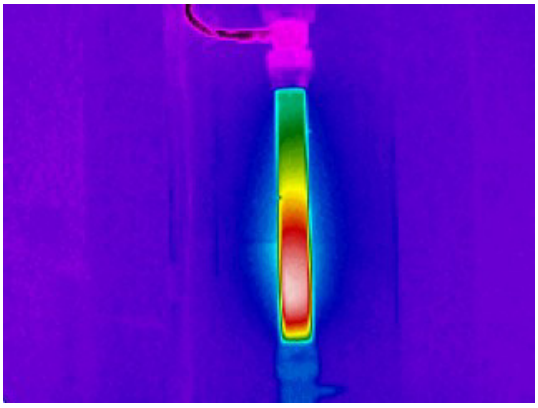

Figure 4. "Long" muscle infrared view

Figs. 5 and 6 report the longitudinal (axial) temperature distribution: minimum and maximum values are very similar, while average values and functions of axial distribution are very different. Short muscle shows a more uniform temperature, while into long muscle the heat is concentrated at the opposite side with respect to the pneumatic connection.

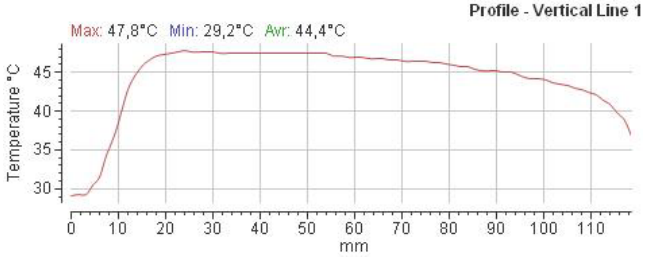

Figure 5. Axial distribution ("short" muscle)

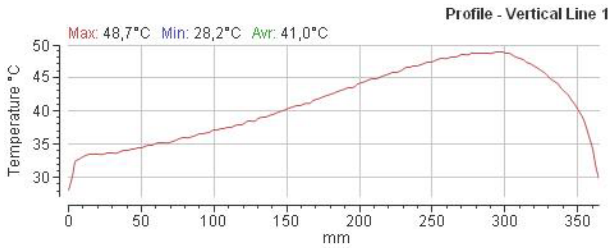

Figure 6. Axial distribution ("long" muscle)

This phenomenon increases reducing the contraction factor and the internal air pressure: for instance Figs. 7 and 8 show the corresponding results at 15% of contraction factor and air pressure at 3 bar.

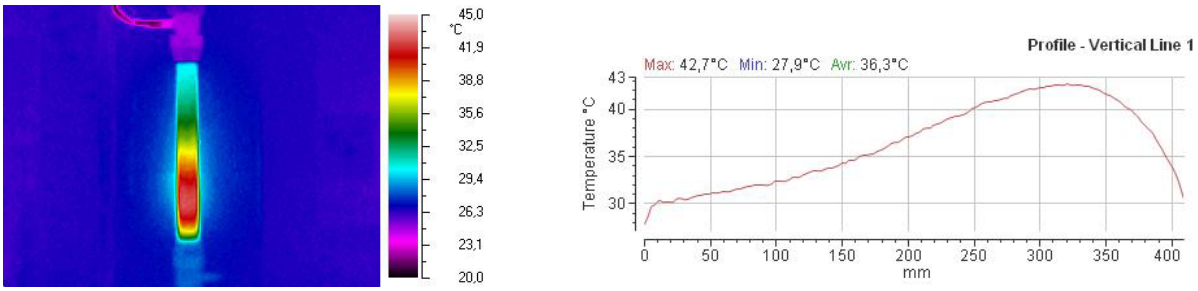

Figure 7. “Long” muscle at 3 bar and 15% of contraction factor

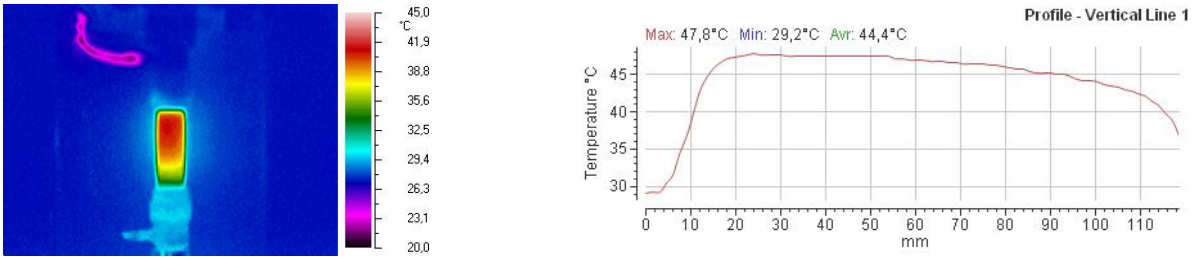

Figure 8. “Short” muscle at 3 bar and 15% of contraction factor

Minimum and maximum temperatures of 120 and 360 length muscles are reported in Figs. 9 and 10. Contraction factor is selected at 10%, 15% and 20% (codes c10, c12 and c20) and the air pressure is changed from 2 to 6 bar (codes from p20 to p60); an identification contraction-pressure code is used. For example, c10p50 code concerns a test with contraction factor of 10% and pressure of 5 bars. All the pneumatic parts of the muscle are monitored, including metallic terminal, fittings and hoses.

Figure 9. Minimum and maximum temperatures on a “short muscle”

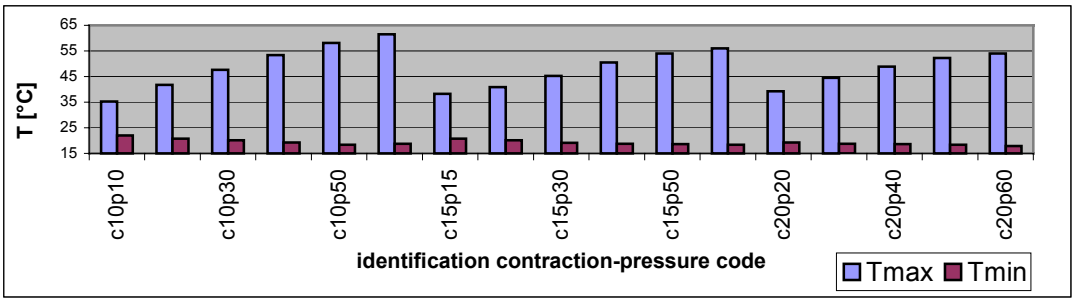

Figure 10. Minimum and maximum temperature on a “long” muscle

An overall comparison on hot and cold spots shows differences of temperature up to 45 °C: coldest points are typically located on the air hose.

Effect of the working frequency

Fluidic muscles are able to cover a wide range of working frequency, satisfying both very slow and very fast motion conditions. Frequency variation influences the local temperature of the muscle, in different way with the length. An example of results is reported in Fig. 11. Temperatures of "long" and "short" muscles (length codes L360 and L120) are compared on four frequency values: 0.25, 0.50, 0.75 and 1 Hz (frequency codes from F025 to F100). Contraction factor is fixed to 10% and the air pressure to 6 bars. Long muscle reaches higher temperatures: this trend is also confirmed to higher frequencies, but maximum and minimum temperatures trend to a stabilization.

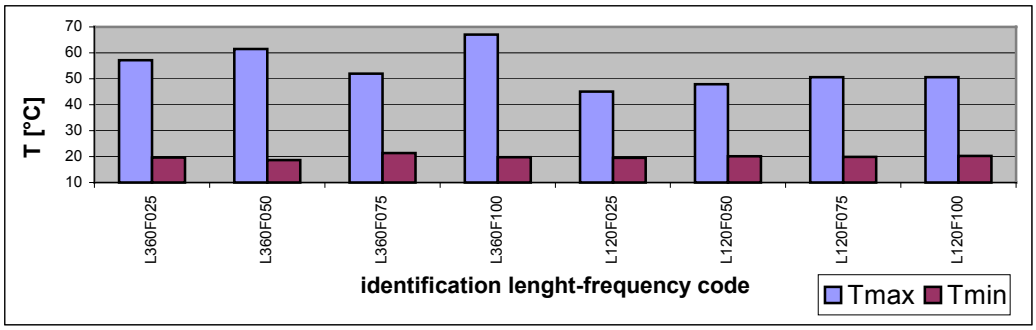

Figure 11. Effects of the working frequency

The effect of the frequency on the thermal distribution is shown in Figs. 12 and 13 (a and b), respectively at frequencies of 0.25 Hz and 1 Hz. Fig. 12 concerns a "short" muscle and compares, practically at the same number of pixels, the density vs. temperature on a rectangular area selecting hot and cold points of its flexible surface. Peaks of density are detected to high temperatures and this effect is enhanced at higher frequencies.

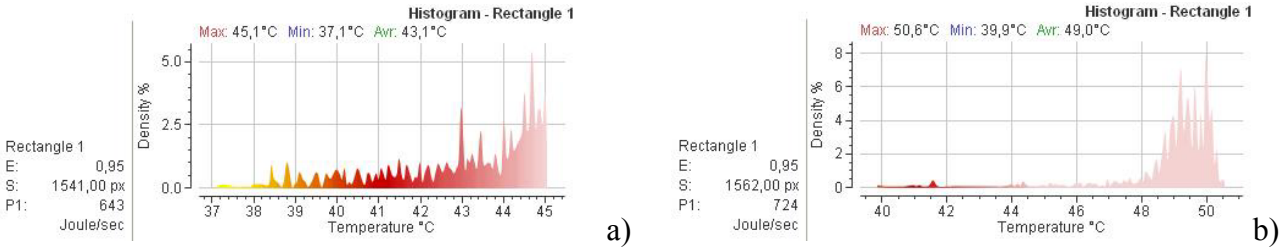

Figure 12 (a and b). Density vs. temperature for "short" muscle working at different frequencies

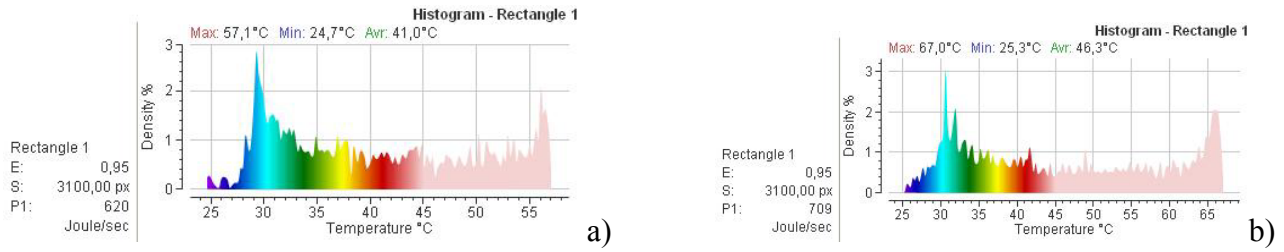

Figure 13 (a and b). Density vs. temperature for "long" muscle working at different frequencies

The detected density distribution for "long" muscles is very different. Relevant concentrations are detected to low temperatures (Fig. 13) and the dependence to the frequency values seems to be less significant. The maximum temperatures are higher (58 ÷ 68 °C against 45 ÷ 52 °C); P_1 represents the corresponding absolute radiation power.
In all the different case studies the absolute radiation power $[P_1 = \sigma \varepsilon T^4]$, the radiation energy $[P_2 = \sigma \varepsilon (T^4 - T_0^4)]$ and the radiation energy + the energy loss by convention $[P_3 = \sigma \varepsilon (T^4 - T_0^4) + h_m (T-T_0)^{3/4}]$ can be evaluated and compared.

Effect of the supply pressure
Inside pressure level plays a role of position stabilization of the muscle, especially when it is used as actuator. For example in Fig. 14 temperature distributions on the same "short" muscle supplied at 2 and 6 bar, are compared: maximum temperature increases with pressure, while the density distributions are very similar.

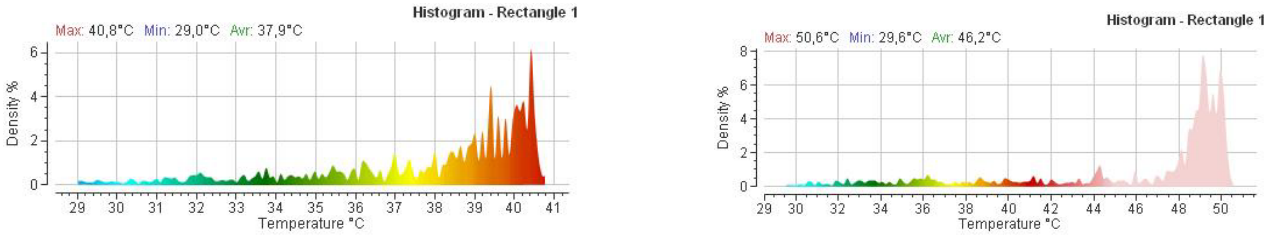

Figure 14. Density distribution for a "short" muscle supplied at 2 and 6 bar

MECHANICAL FALLOUT

Thermal phenomena are interlaced to muscles cinematic and dynamic performances: on this aspect the research activity is still under development. In particular it is oriented to monitoring the position errors generated by muscles applied in automatic sequences, under different working conditions and to the definition of relationships between the corresponding variables. Hereafter some example of results deduced from the experimentation on the cited test bench are reported.
Fig. 15 compares the error position of a "long" muscle under three different contraction factors (10, 15 and 20%), powered on 20 automatic cycles at pressure of 2 and 6 bar. Increasing pressure the error decreases. Finally, Fig. 16 synthesizes analogous trends for a "short" muscle, powered at pressure of 4 and 6 bar. The error distribution is very different with respect to the previous case, while the effect of the contraction factor on the position accuracy seems to be not particularly significant. These tests have been initially implemented on 200 automatic cycles: moreover, the observed characteristic distribution of the position error is stabilized within the initial 20 cycles.

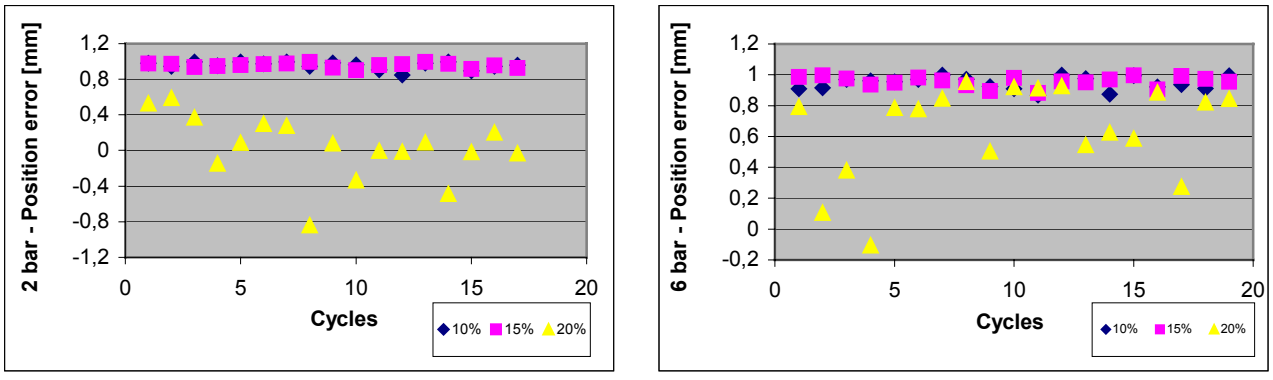

Figure 15. Position error of a "long" muscle, actuated at 2 and 6 bar

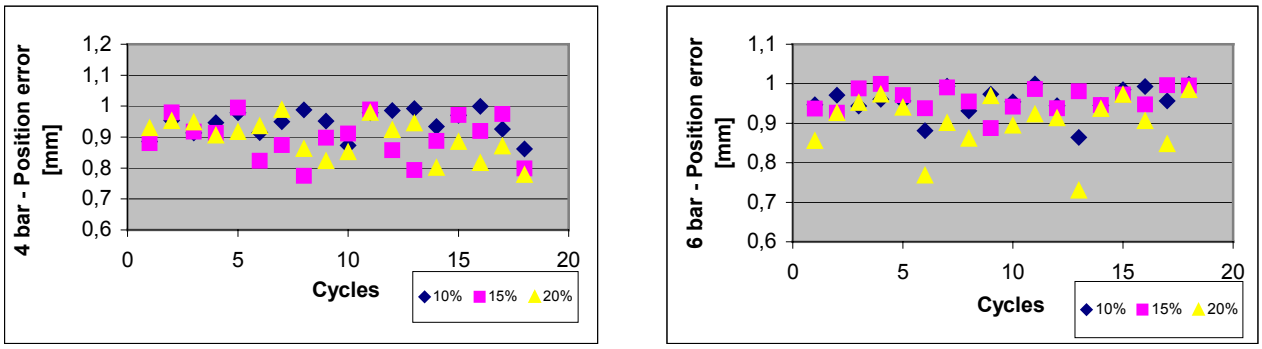

Figure 16. Position error of a "short" muscle, actuated at 4 and 6 bar

CONCLUDING REMARKS

The fluidic muscle is a mechanical device working under variable temperature: that is one of its peculiar operating aspects, very different with respect to other pneumatic components, usually working in quasi-isothermal conditions. A methodical analysis of the thermal behaviour of fluidic muscles has been implemented: monitoring based on not intrusive temperature detection is proposed. Under asymmetrical supply and exhaust "short" and "long" muscles are compared.
The final goal of the present research is the correlation between thermodynamic phenomena and mechanical performances: in this paper only some problems related to the thermodynamics of fluidic muscles have been focussed and described. Comparisons between standard and anomalous thermal distributions seem to be also significant in order to predict equipment troubleshooting and anomalous or failure conditions.

REFERENCES

1. Amon, J.S., Muscling in manufacturing, *Engineer*, Vol. 292, No. 7624, p. 40, 2003.
2. Caldwell, D.G., Natural and artificial muscle elements as robot actuators, *Mechatronics*, Vol. 3, No. 3, pp. 269-283, 1993.
3. Maldague, X.P. and Moore, P.O., Non destructive thermal testing handbook. Vol. 3: Infrared and thermal testing, *ASNT*, Washington, U.S.A.
4. Tanaka, Y., Study on artificial rubber muscle, *Mechatronics*, Vol. 3, No. 1, pp. 59-75, 2000.
5. Tuijthof, G.J.M. and Herder, J.L., Design, actuation and control of an anthropomorphic robot arm, *Mechanism and Machine Theory*, Vol. 35, pp. 945-962, 2000.
6. Wiebusch, B., Fluidic muscles flex in three diverse applications, *Design News*, May 6, 2002.
7. Strobach, D., Kecskemethy, A., An analysis of simplified muscle activation parameterization, *in Proc. Of the 77th Annual Scientific Conference of GAMM*, Berlin, Germany, march 27-31, 2006.
8. Klute, G.K., Hannaford, B., Modelling pneumatic McKibben artificial muscle actuators: approaches and experimental results, *ASME Journal of Dynamic Systems, Measurements and Control*, 1999.

DETERMINATION OF THE INSTANTANEOUS HEAT FLUX IN A RAPID COMPRESSION MACHINE

T. Roestenberg[1, *], M.J. Glushenkov[2], A.E. Kronberg[2], Th.H. vd Meer[1]
[1] University of Twente, Faculty of Engineering Technology, Laboratory of Thermal Engineering, Enschede, The Netherlands
[2] Energy Conversion Technologies BV, Enschede, The Netherlands

ABSTRACT. Experimental data obtained in a free piston rapid compression machine is presented in this article. The goal of the experiments was to find a relation between the compression pressure in the device and the heat flux out of the compressed gas in order to ultimately provide insight in the energy efficiency of the Pulsed Compression Reactor. A sophisticated surface thermocouple was used to measure the temperature of the cover of a single shot experimental setup. Calculating the heat flux and coupling this result to the measured pressure, a linear, reproducible relation between the pressure and heat flux was found.
From the measurements it could be concluded that as far as the measurement technique is concerned, the data shows that the experimental sensor as well as the analysis method used gives insightful information about the device under investigation. The formation of a cold boundary layer during compression could be observed.

Keywords: *Adiabatic compression, Chemical reactors, Heat transfer, Pulsed Compression Reactor*

INTRODUCTION

Background

To cope with the tremendous world wide energy losses in the chemical industry, the Pulsed Compression Reactor (PCR) is under development. The principals of this reactor were developed over fifty years ago as can be seen from patents by Brutzkus [1] and the book by Kolbanovskii [2]. Further developments have been achieved by Glushenkov [3]. It promises to be a very compact, economical and energy efficient alternative to conventional chemical reactors used for the most energy consuming high temperature processes. Though it is expected that the PCR is much more efficient than conventional reactors, no real research has been done to ascertain the energy efficiency qualitatively. Two main energy losses from the PCR can be identified: heat losses to the surrounding and pressure losses through the gap along the reactor wall. This article focuses on obtaining a relationship between the heat flux from the hot compressed zone and pressure in the reactor, thus giving some insight into the quantitative heat losses from the reactor.
The PCR is a free piston impulse compression device. It rapidly compresses the reactants by a free piston. Due to the compression the reactants are heated and spontaneously react, similar to a homogeneous charge compression ignition engine. The expansion of the compressed gasses release energy to the piston, which is immediately used to compress the next batch of reactants in a continuous process. The experiments under discussion in this article mimic a single pulse of

* Corresponding author: Ir. T. Roestenberg
Phone: + (31)-53-4892507, Fax: + (31)-53-4893663
E-mail address: t.roestenberg@utwente.nl

compression, investigating the heat transfer effects during this single stroke of compression, without chemical reactions.

Goal of the experiments

Research in the past on heat losses from internal combustion engines has yielded many different empirical relations, relating various parameters, such as temperature, pressure and compression ratio to heat transfer rate [4-11]. This experiment attempts to find such a relation for a free piston compressor, capable of attaining compression ratios well beyond those reached in internal combustion engines. Specifically the relation between the pressure of the compressed gas and the heat flux to the wall is sought after. This relation gives an indication of the deviation of the process from ideal-, adiabatic assumptions. It is also a start to find the quantitative energy efficiency of the pulsed compression reactor. Previous research on the Pulsed Compression Reactor performed by Roestenberg et al. [12], focussed on finding the heat flux from a similar but continuous reactor. The results found here were averaged results over a large series of cycles. This research attempts to find the instantaneous heat transfer during one pulse.

EXPERIMENTAL SETUP

The experimental setup is comprised of a stainless steel cylinder, containing a free-, graphite piston. The cylinder and piston is machined to have a very tight clearance. The motion of the piston is initiated by injecting compressed air into the cylinder below the piston. This is done through an especially designed fast acting valve. This valve, as well as the cylinder with piston is shown schematically in Figure 1. The figure shows the three valve chambers: the lower-, trigger- and launch chamber, the valve shoe, the cylinder, the piston, the upper chamber and the top cover. The lower chamber of the valve is pre-charged with a counter pressure, to push the valve shoe up and hold the valve closed. The launch chamber is then charged with the launch gas. To initiate the process, compressed air is injected into the trigger chamber. The combined pressure of the launch gas and the trigger gas forces the valve down, enabling the launch gas to escape into the cylinder. Immediately as the launch gas escapes, the piston starts to move up, and the valve closes again. As the piston moves up, the gas above the piston is compressed and the temperature and pressure in the upper chamber rise. As the piston passes the outlet ports, the remaining launch gas escapes. During the descent of the piston, the pressure reached below the piston is limited by the presence of a small hole, to dampen the reciprocation of the piston. During the cycle, which lasts in the order of 10ms (depending of the pressures used), the pressures in the different valve chambers as well as in the top chamber are recorded. Also a fast thermocouple integrated in the surface of the upper cover measures and records the temperature of the surface of the top cover.

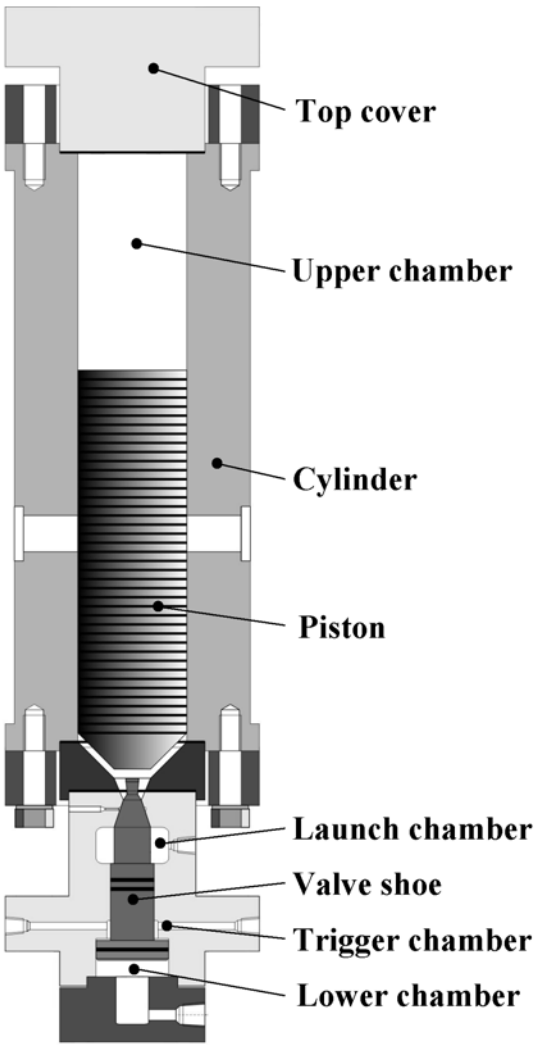

Figure 1. Schematic drawing of the single shot reactor

Measurement techniques

The parameters of interest to be measured are the pressure of the gas and the temperature of the surface of the top cover. The pressure is measured using a fibre optic high temperature dynamic pressure sensor. This sensor, produced by Optrand Inc., measures the pressure by optically monitoring the deflection of a flexing metal diaphragm. The type used was a 20kHz AutoPSI sensor.

To measure the temperature of the surface of the reactor cover, no readily available sensor was found. Instead a thermocouple, designed especially for this purpose, was manufactured. The technique was used before by Oude Nijeweme [13] and Gatowski et al. [14]. The thermocouple consisted of a chromel and a constantane ribbon, each 25µm thick. These were sandwiched between two sheets of mica and separated by a third sheet, each 5µm thick. This sandwich, 1mm wide, was embedded in the material of the reactor cover, running vertically through the cover and protruding on both sides. This is schematically shown in Figure 2. Before use, the inner surface of the thermocouple was grinded with fine sanding paper. This formed micro junctions across the mica between the chromel and constantane sheets, completing the thermocouple circuit. The temperature of the micro junctions could now be measured by measuring the potential difference between the two protruding sheets on the outside of the reactor.

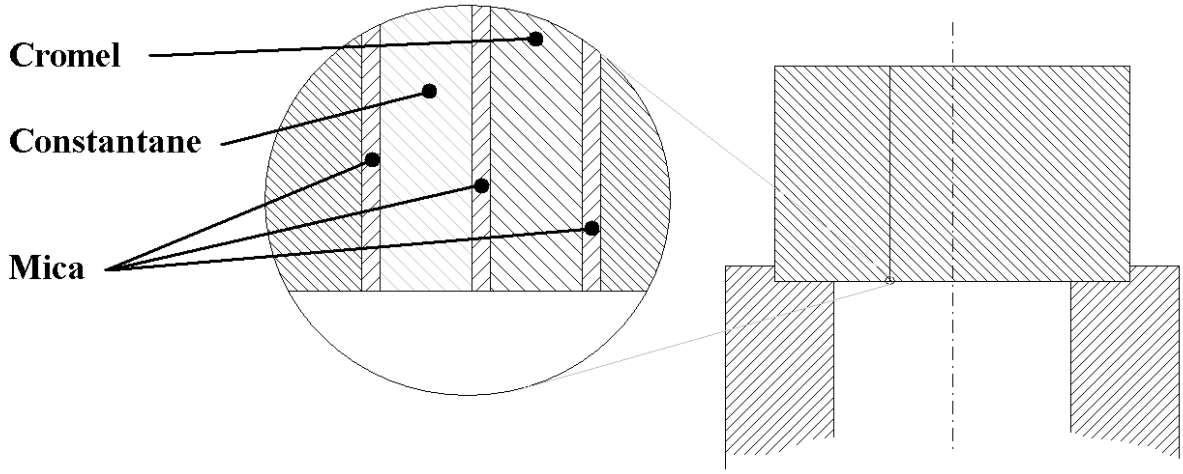

Figure 2. Schematic view of the temperature sensor

DATA ANALYSIS METHOD

The data obtained by the experiment contains some degree of electronic noise. In order to make the data more suitable for data analysis, the data is filtered by means of a fifth order Butterworth low-pass filter, with a cut off frequency equal to one tenth of the sample frequency (for most experiments the sample frequency was 150kHz). This reduced the amplitude of the noise in the measurements significantly enough to make further analysis of the results possible and meaningful.

To analyse the data obtained, and find the heat flux from the compressed gas into the reactor cover, the analytical solution was the solution to the penetration problem into a semi infinite domain with a non constant surface temperature, taken from Hoogendoorn et al. [15], was applied. This solution is shown in equation (1).

$$T(x,t) = \int_0^t \frac{dT_0}{dt'} erfc\left(\frac{x}{\sqrt{4\alpha(t-t')}}\right) dt' \tag{1}$$

The solution is a function of the wall surface temperature T_0. The heat flux into the wall is a function of the gradient of the temperature at the surface.

$$q(t) = -k\frac{\partial T}{\partial x}\bigg|_{x=0} = -\frac{k}{\sqrt{\alpha}}\int_0^t \frac{dT_0}{dt'}\frac{\partial}{\partial x} erfc\left(\frac{x}{\sqrt{4\alpha(t-t')}}\right)\bigg|_{x=0} dt' \tag{2}$$

The derivative of the surface temperature with respect to time that occurs in the equation should somehow be extracted from the measurement data. To apply this equation to the measurement data obtained, the integral in equation (2) is written as a summation of discrete integrals, each over the length of one measurement time step. In this equation, N is the number of samples taken in the measurement, up to time t.

$$q(t) = -\frac{k}{\sqrt{\pi\alpha}}\sum_{i=1}^{N-1}\int_{t_i}^{t_{i+1}} \frac{dT_0}{dt'}\frac{1}{\sqrt{t-t'}}dt' \tag{3}$$

The smaller integrals are chosen such that, from t_i to t_{i+1}, the temperature at the wall is known at the bounds of the integral from the measurement. The gradient of this temperature with respect to time can therefore be estimated for the period within the integral, by linear approximation. This can be solved exact for any time in the measurement, by evaluating all the separate integrals, and carrying out the summation.

$$q(t) = -\frac{k}{\sqrt{\pi\alpha}}\sum_{i=1}^{N-1}\int_{t_i}^{t_{i+1}} \frac{T_{i+1}-T_i}{\Delta t}\frac{1}{\sqrt{t-t'}}dt' \tag{4}$$

By evaluating equation (4) for all measurement times, the heat flux, as a function of time, is calculated for the whole measurement.

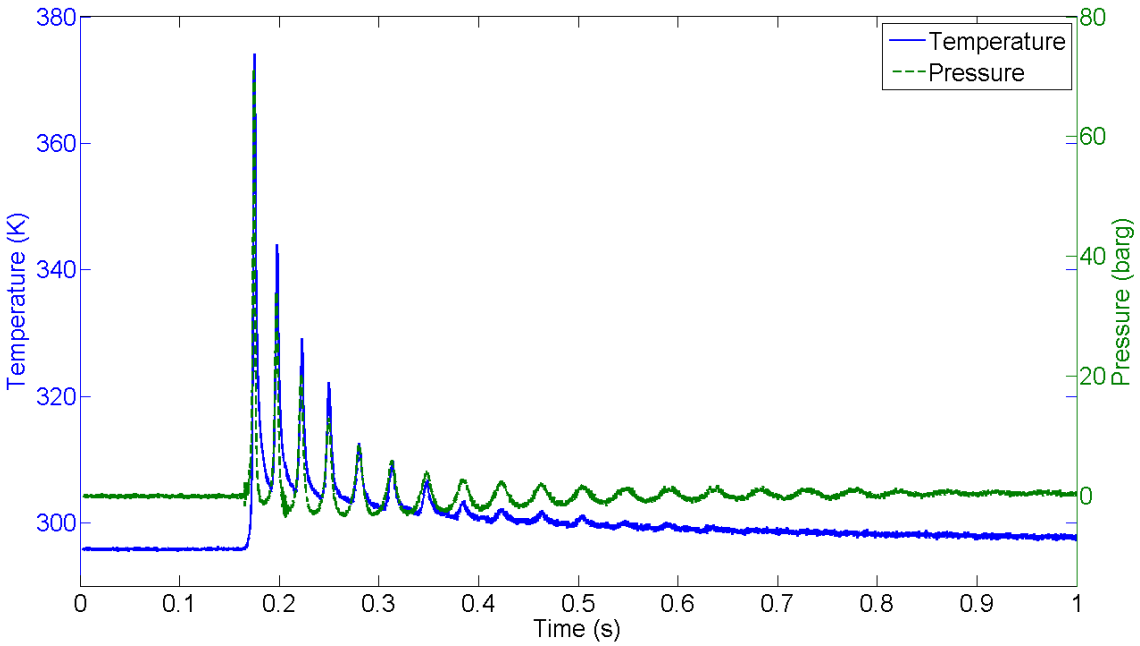

Figure 3. Example of measured pressure and temperature

RESULTS

Data obtained

A series of experiments was performed, at various launch pressures. Experiments were carried out several times for each launch pressure. In Table 1 the different launch pressures used, their respective average peak pressure and temperature are indicated. Additionally the maximum deviation from the measured average is shown. The result of the measured pressure and the measured surface temperature of one of the experiments is shown in Figure 3. It is clear that though real "single shot" behaviour is not attained, the reciprocations of the piston are heavily dampened. In Figure 4 the first peak of the experiment is zoomed in upon. There is a small phase shift between the pressure peak, and the temperature peak. Because of the walls thermal inertia, the surface temperature does not follow the gas temperature directly. When the gas is already cooling down, it's temperature is still higher than that of the wall, and heat is still flowing to the wall. Thus the peak wall temperature is reached as the gas is already cooling.

Table 1
Experimental results

Launch pressure (barg)	Average peak pressure (barg)	Max. deviation from average (bar)	Peak wall temperature (K)	Max. deviation from average (K)
40	71	1.0	373	1.4
60	144	2.0	417	7.1
80	230	6.5	471	9.1

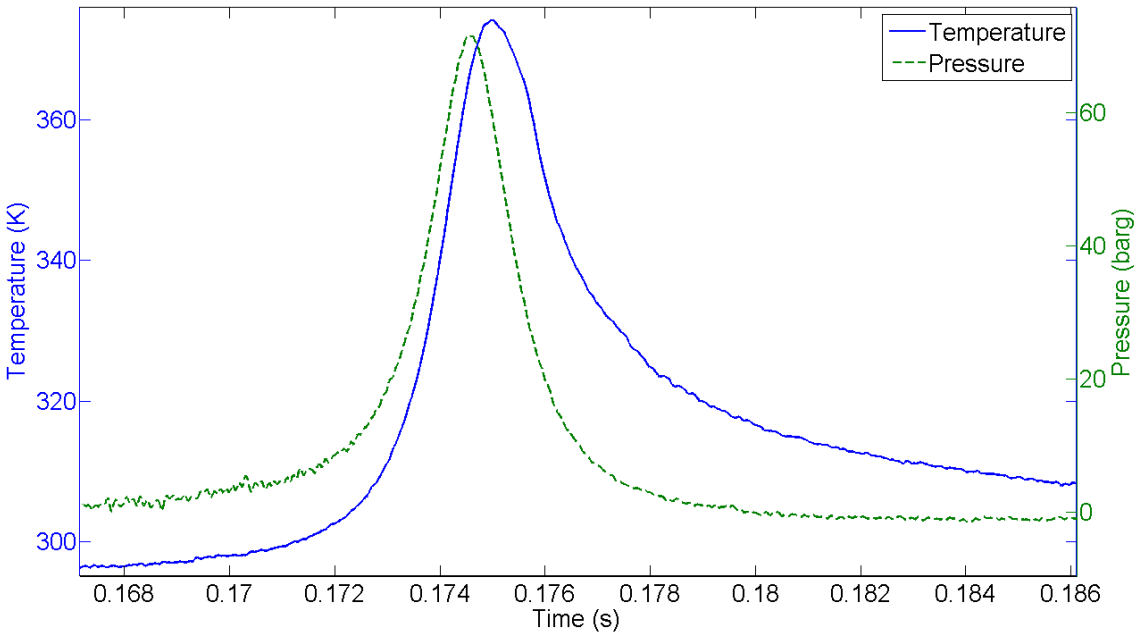

Figure 4. Example zoomed in on first peak

Results by post-processing

When the analysis method described earlier is applied to the data obtained, the heat flux can be calculated. In Figure 5 the calculated heat flux is plotted against the measured pressure, for the same experiment as in Figure 3 and Figure 4. From this plot a linear relation between the pressure and the

heat flux becomes visible. The heat flux during the compression of the gas is somewhat higher than the heat flux during expansion. The fluctuations that are visible in the result can be made to disappear by using a filter with a lower pass frequency. The downside is that the height of the peaks of the experiment, which are quite sharp, is reduced significantly, influencing the results.
The results of one entire series are shown in Figure 6. It is visible that the same gradient of the P-Q line is found, irrespective of the pressure reached. From this figure, also another interesting feature appears. During the down stroke, all measurements show a sudden dip in the heat flux, to the negative side, around 30 barg. While when looking at a single measurement one might think that this is caused by noise or calculation error, it becomes clear looking at Figure 6, that it does in fact occur every experiment, and for experiments with the same peak pressure, also around the same point during expansion.

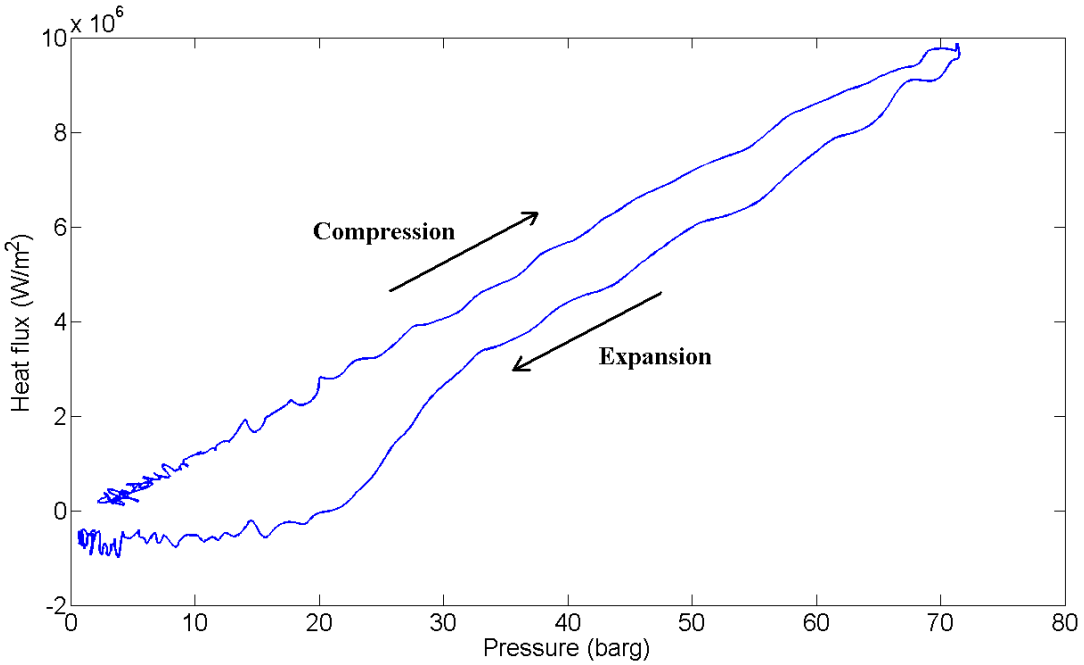

Figure 5. Plot of calculated heat flux against measured pressure

CONCLUSIONS AND DISCUSSION

From the data obtained several conclusions can be drawn. Firstly, as far as the measurement technique is concerned, the data shows that the experimental sensor as well as the analysis method used gives insightful information about the device under investigation. Though one question one might ask is whether the sensor does indeed measure the temperature of the surface fast enough to justify the analysis technique. Though this question remains partially unanswered, the following can be reported. During one series of experiments the data produced by the sensor after one test to very high pressure (360 barg, sensor surface temperature over 600 K), the shape of the temperature curves recorded was different than previous experiments. Also subsequent experiments to lower pressures, gave different results than expected and obtained before (measured temperatures were lower, with a larger phase shift, and less of a determined spike). This was attributed to oxidation of the sensor surface during the brief high temperatures, and indeed regrinding of the sensor solved the problem. This might lead one to conclude that, if a minute layer of oxidation does already influence the results so gravely, the sensor does indeed, when in good condition, measure the surface temperature.
Perhaps the most striking feature of the results found is the linearity of the heat flux-pressure relation during the compression stroke. Though the linearity diminishes somewhat for higher launch pressures,

the similarity in results for different pressures is still striking. Since the goal of the experiments was to find a relation between pressure and heat flux, one could argue that the results could hardly have been better. Future research will have to determine the nature of this relation.
The formation and progression of a boundary layer is visible in that the heat flux is slightly lower for the expansion stroke than the compression stroke. This effect becomes more pronounced as higher pressures and, as a result, higher temperatures are reached. This seems logical, since for a bigger temperature difference between the core gas and the wall, the formed boundary layer is more likely to have a more pronounced effect on the heat flux.

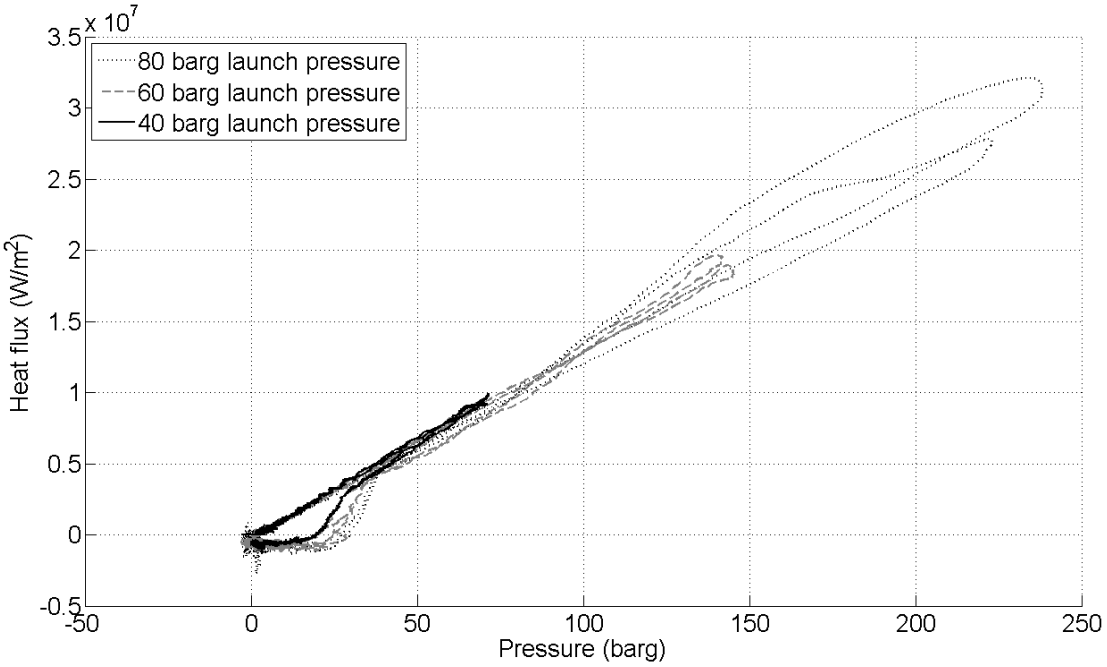

Figure 6. Plot of the results of one series of experiments

The observed sudden dip is also an interesting result for discussions. One possible explanation may be offered (among others) by the work of Annand et al. [5]. In their experiments, which were similar to these, but with a lower pressure, also a rapid drop of the heat flux to below zero was found during the expansion, at a moment where the temperature difference was still positive. This was explained by the following thought experiment. If one considers a compressed gas at 800 K, surrounded by a wall at 400 K, a relatively cool boundary layer, with a temperature between that of the gas and the wall, will rapidly be established. As the gas is then expanded to ambient pressure, the core of the gas will cool to a temperature close to the temperature it had before compression (assuming no chemical reactions took place, and not too much heat was lost). However, the boundary layer will cool to a temperature much lower than that, even lower than that of the wall. This super-cooled boundary layer will introduce negative heat flux towards the wall, well before the core gas temperature is lower, or even equal, to the wall temperature. Since the likelihood of the presence of a boundary layer was already discussed, there is also a very clear possibility of this boundary layer to become super-cooled. Of course, a super-cooled boundary layer occurs only when a high rate of cooling (due to expansion) is present. The occurrence of the sudden dip in heat flux is reasonably near the end of expansion, a moment when cooling rate is highest. Whether this explains the sudden dip in the heat flux remains to be proven.

ACKNOWLEGDEMENTS

This project is sponsored by Senter-Novem EOS-LT, project number 03025.

REFERENCES

[1] Brutzkus, M. *Apparatus for chemical production and research*, US Patent 1586508, 1926.

[2] Kolbanovskii, Y. A., et al. *Impulsnoe sgatie gasov v chimii i technologii*, Moskva, Nauka, 1982. (Pulsed compression of gases in chemistry and technology, Moskow, Nauka, 1982.)

[3] Glushenkov M. Y. Russian Pat., No 2097121, 29.01.1997; No 2115467, 02.12.1997; No 2142844, 05.04.1999.

[4] Adair et al., 1972, Instantaneous heat transfer to the cylinder wall in reciprocating compressors, *Proceedings of the 1972 Purdue Compressor Technology Conference*, Purdue University.

[5] Annand, W.J.D. and Pinfold, D., 1980, Heat Transfer in the Cylinder of a Motored Reciprocating Engine, *SAE Paper 800457*, Society of Automotive Engineers.

[6] Borman, G. and Nishiwaki, K., 1987, Internal Combustion Engine Heat Transfer, *Progress in Energy and Combustions Science*, Vol 13, No 1, pp 1-46.

[7] Kornhauser, A.A., 1989, Gas-Wall Heat Transfer during Compression and Expansion, *PhD Thesis*, Massachusetts Institute of Technology.

[8] Lawton, B., 1987, Effect of compression and expansion on instantaneous heat transfer in reciprocating internal combustion engines, *MIMechE Paper Vol 201*, No. A3.

[9] Lee, K.P., 1983, A Simplistic Model of Cyclic Heat Transfer Phenomena in Closed Spaces, *Proc. 18th IECEC*, pp. 720-730.

[10] Lyford-Pike, E.J. and Heywood, J.B., 1984, Thermal Boundary Layer Thicknesses in the cylinder of a Spark Ignition Engine, *M.S. Thesis*, Dept. of Mech. Eng., Massachusetts Institute of Technology.

[11] Pfriem, H., 1943, Periodic Heat Transfer at Small Pressure Fluctuations, NACA TM-1048

[12] Roestenberg, T. et al., Heat transfer study of the Pulsed Compression Reactor, *Chemical Engineering Science* (in press).

[13] Oude Nijeweme, D.J., 2000, Unsteady in-cylinder heat transfer in a spark ignition engine: experiments and modelling, *M.Sc.Thesis*, University of Twente.

[14] Gatowski, J.A. et al., An experimental Investigation of Surface Thermometry and Heat Flux, *Experimental Thermal and Fluid Science*, Vol. 2, 1989, pp 280-292.

[15] C.J. Hoogendoorn en T.H. van der Meer, *Fysische transportverschijnselen II* (Physical Transport Phenomena), 1991 (reprint 2007) / 214 p. / ISBN 978-90-6562-059-0

YIELD STRESS DROPS: CREATION, FREE-FALL AND IMPACT ON A SOLID SURFACE

G. German, V. Bertola*
University of Edinburgh, Edinburgh, United Kingdom

ABSTRACT. The process of drop formation from a capillary needle and its subsequent impact on a solid surface is studied experimentally by high-speed imaging, with focus on drops of viscoplastic or yield stress fluids (i.e., those materials which exhibit a fluid behaviour only when the applied stress exceeds a certain threshold value, called yield stress), and compared to the behaviour observed in Newtonian drops. The yield stress of the fluid is shown to alter significantly the detachment process, the drop shape during free-fall, and the impact morphology. The results can be interpreted in terms of a dimensionless number comparing the yield stress magnitude and the capillary pressure.

Keywords: *Drops, Yield stress, Bingham fluid, Capillary break-up, Drop impact*

INTRODUCTION

The creation of a liquid drop falling by gravity, and the subsequent impact on a solid surface, are common phenomena in Nature as well as in several industrial applications, and extensive literature can be found about them [1,2]. Examples of applications are spray painting and cleaning, inkjet printing, pesticide distribution, spray cooling and firefighting devices, fuel atomisation in internal combustion engines, fabrication of micro-lenses, and many others [3].

As it is well known, the behaviour of a drop after collision with the surface is complex, and depends both on the characteristics of the drop and on those of the surface. In all cases, during the first few milliseconds after making contact with the surface, the drop spreads creating a disc-shaped liquid layer called lamella. Subsequently, the lamella retracts, and its behaviour is essentially determined by the competition between inertial forces (depending on the drop kinetic energy) and capillary forces (depending on the surface tension). The relevant dimensionless numbers during the impact and the expansion phase are the Weber number, defined as $We = \rho D_0 u^2 / \sigma$, and the Reynolds number, $Re = \rho D_0 u / \eta$, where ρ is the fluid density, D_0 the drop equilibrium diameter, u the impact velocity, η the fluid viscosity, and σ its surface tension. These numbers express the ratios between inertia and capillarity and between inertia and viscous dissipation, respectively. Sometimes, viscous dissipation is taken into account using the Ohnesorge number, $Oh = \sqrt{We} / Re$. During the retraction phase there is a competition between viscous dissipation and capillarity, expressed by the capillary number, $Ca = u_R \eta / \sigma$, where the impact velocity is replaced by the retraction velocity of the lamella, u_R.

Although most applications involve Newtonian fluids, in the past decade the study of non-Newtonian drops has been attracting a growing interest [4-7]. While these works focus on the effect of viscoelasticity on impacting drops, obtained by dissolving small amounts (of the order of 100 ppm) of flexible polymers into a Newtonian solvent, the study of the so-called viscoplastic or yield stress fluids has received a comparatively little attention [8]. Such fluids respond like elastic solids for applied

* Corresponding author: Dr. V. Bertola
Phone: + (44)-131-6508697, Fax: + (44)-131-6506551
E-mail address: V.Bertola@ed.ac.uk

stresses lower than a certain threshold value, which is called the yield stress, and flow only when the yield stress is overcome. A well-known constitutive equation for yield stress fluids is provided by the Herschel-Bulkley model [9], which can be written in the form:

$$\tau = \tau_0 + C\dot{\gamma}^n \tag{1}$$

where $\dot{\gamma}$ is the shear rate, τ_0 is the yield stress, and C and n are constants. For $n = 1$ equation (1) reduces to the Bingham model [10]. A more accurate description of the yield stress fluid phenomenology can be achieved through advanced rheophysical models [11].

The aim of this work is to investigate the morphology of drops of a model yield stress fluid detaching by gravity from a capillary needle and impacting onto a solid surface. A previous study on vaseline drops impacting on a plexiglass surface [8] shows that the fluid yield stress can prevent the formation of spherical drops, and relates the maximum spreading diameter of the lamella to the yield stress magnitude through the Bingham number, $Bm = \tau_0 D_0 / \eta u$. However, this analysis remains somewhat qualitative, and completely neglects capillarity. Here, the whole process of drop formation by capillary instability, free fall, and impact on surfaces of different wettability is studied, attempting at isolating the effects of the yield stress from those of viscosity and shear-thinning. The results can be interpreted by introducing a dimensionless number that compares the yield stress and the capillary pressure, which was previously introduced to characterise the flow of a gel in capillary tubes [12].

EXPERIMENTS

Fluid characterisation

Model yield stress fluids were prepared using a water-based polymer gel (commercial hairdressing gel). The typical composition of these gels includes a blend of water, alcohol, silicones, glycerine, surfactants, and other polymers. In order to change the value of the yield stress in a continuous fashion, the gel was diluted into de-ionized water at different concentrations (five solutions with mass fractions of 0.2, 0.25, 0.3, 0.35 and 0.4). The solutions were mixed slowly in a container to avoid the formation of bubbles, left to settle for 24 hours and then thoroughly mixed to ensure homogeneity using a magnetic stirrer.

The yield stress of these model fluids was measured by means of a Haake MARS rotational rheometer, equipped with a plate–plate sensor having a diameter of 35 mm and a gap of 1 mm. Sandpaper was glued on both the rotating an the fixed surface in order to avoid wall slip effects. The yield point of each solution was determined by imposing a stress ramp (100 points in 300 s) on the fluid sample, and measuring the angular displacement of the rotating plate.

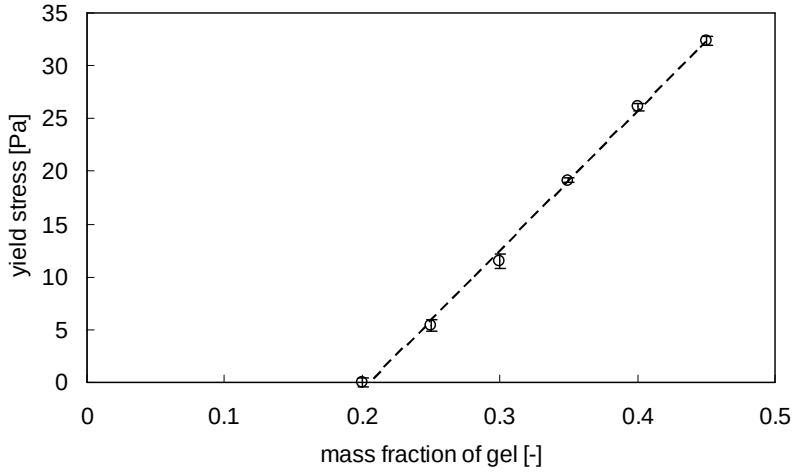

Figure 1. Measured yield stress of the model fluid as a function of the gel concentration.

For small values of the stress, the sample behaves like a solid and has a little deformation; when the stress grows beyond a critical value, the sample starts flowing and therefore the angular displacement of the disk grows indefinitely at a faster rate. The crossover of the two straight lines interpolating the deformation-stress curve in a log–log scale before and after its bending point defined the yield point. The results are reported in figure 1, which shows that the yield stress is a linear function of the hair-gel mass fraction. Apparent viscosity measurements obtained by controlled shear rate tests in the shear rate range $0 < \dot{\gamma} < 100$ s^{-1} reveal a shear-thinning behaviour, which was fitted using the Herschel-Bulkley model (equation 1).

The equilibrium surface tension of the fluids was measured with a Kruss EasyDyne tensiometer equipped with a De Nouy ring. Since the sensor displacement is imposed, this method is not affected by the yield stress of the fluid: in fact, the measured surface tension was 34 ± 2 mJ/m^2 for all solutions, in good agreement with the value measured for aqueous solutions of polysorbate 20 surfactant (which is a component of the gel) above the critical micellar concentration (c.m.c. = 36 mJ/m^2) [13]. Dynamic surface tension effects, which may be important due to the short timescale of drop impacts (typically ~5 ms), were not considered because at concentrations above the c.m.c. several surfactant molecules are available in the bulk fluid, so that the migration time for the surfactant molecules to reach the newly created surface during the lamella spreading can be neglected.

Experimental setup and procedure

The experimental setup is schematically shown in figure 2. Drops were created at the tip of a 0.838 mm i.d. (gauge 18) hypodermic needle with flattened bevel by a screw-driven syringe dispenser, and detached under their own weight. In order to change the impact velocity, the dropping height was adjusted using a Vernier height gauge with a precision of ±0.01 mm. The needle was centered over an aluminium square block (40 mm x 40 mm) upon which different substrates could be placed. In particular, impacts on a hydrophilic clean glass surface were compared to impacts on a hydrophobic Parafilm-M surface (equilibrium contact angle with water $\theta_e = 95^o \pm 2^o$).

A high-frame rate CMOS camera (Mikrotron MC1311) equipped with a 18-108/2.5 macro zoom lens (Navitar Zoom 7000) and horizontally aligned with the surface recorded the impacts of single drops. Back-to-front illumination was provided by a fluorescent lamp equipped with light diffuser, which ensured a uniform illumination intensity, and images with a resolution of 720×512 pixels were captured at 1000 frames per second. Magnification was kept constant throughout all experiments and lengths on the image could be calculated by comparison with a reference length (maximum spatial resolution: 33 μm). To ensure a fine optical alignment, the camera, the heated surface and the backlight were fixed to an optical breadboard.

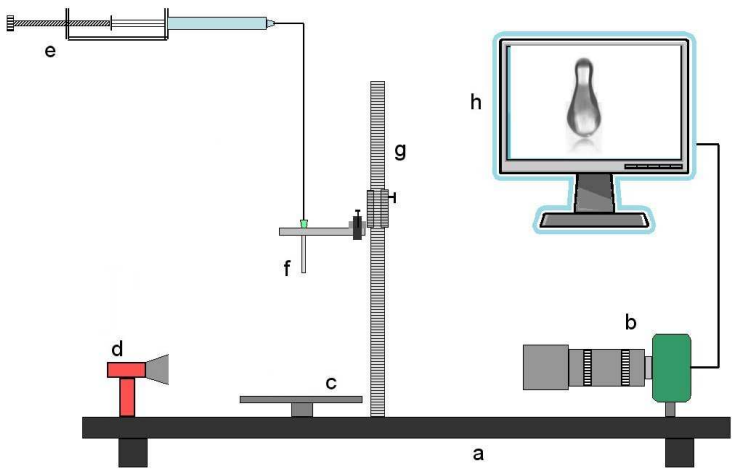

Figure 2. Experimental apparatus: (a) optical breadboard; (b) high-speed camera with zoom lens; (c) impact surface; (d) LED light; (e) dispenser; (f) needle; (g) height gauge; (h) data acquisition system.

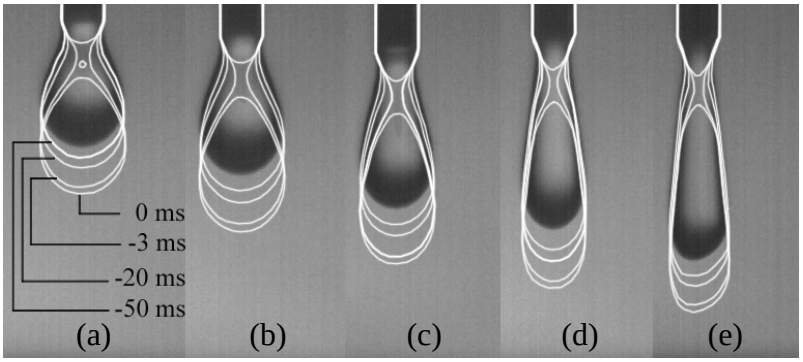

Figure 3. Shape of viscoplastic drops during detachment, for τ_0 = 0 Pa (a), τ_0 = 5.4 Pa (b), τ_0 = 11.5 Pa (c), τ_0 = 19.1 Pa (d) and τ_0 = 26.1 Pa (e). The origin of times corresponds to the drop pinch-off.

Drop weight measurements made with a precision balance (Mettler Toledo MT100) allowed calculation of the equivalent drop diameter at equilibrium, $D_0 = \sqrt[3]{6m/\pi\rho}$. Statistical measurements over 50 samples showed that the diameter is a linear function of the gel concentration in the fluid, x:

$$D_0 = 3.059 - 1.222x \tag{2}$$

The impact velocity was measured from digital images of falling drops. For small distances of the dispensing needle above the impact surface ($H \leq 15$ cm), it was found to be identical to the theoretical free-fall velocity, $u = \sqrt{2g(H - D_0)}$. Drop impacts were studied for fall heights between 7.5 and 200 mm, corresponding to a range of Weber numbers between 1 and 350.

RESULTS

Drop creation and free-fall

The process of drop formation when the fluid is released very slowly from a nozzle is well understood for Newtonian fluids (see e.g. [14]), and depends on the balance between capillarity and gravity. Drops take a spherical shape to minimise the surface energy, and fall by gravity when the liquid filament that connects them to the nozzle becomes unstable and breaks up. The pinch-off causes free oscillations of the drop during free-fall, which are dampened down by viscosity until the equilibrium spherical shape is retrieved.

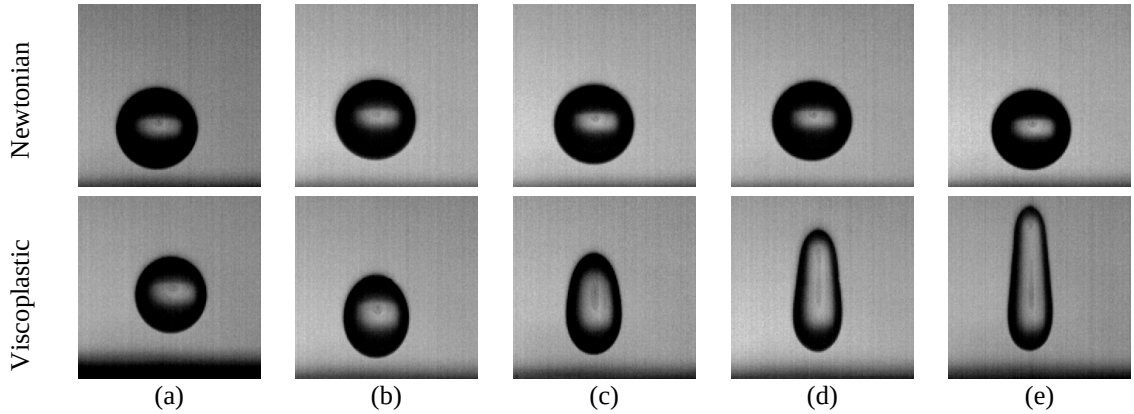

Figure 4. Comparison of Newtonian drops (glycerol solutions) with viscoplastic drops of increasing yield stress during free-fall. (a) η = 0.056 Pa·s, τ_0 = 0 Pa; (b) η = 0.213 Pa·s, τ_0 = 5.4 Pa; (c) η = 0.428 Pa·s, τ_0 = 11.5 Pa; (d) η = 0.631 Pa·s, τ_0 = 19.1 Pa; (e) η = 0.925 Pa·s, τ_0 = 26.1 Pa.

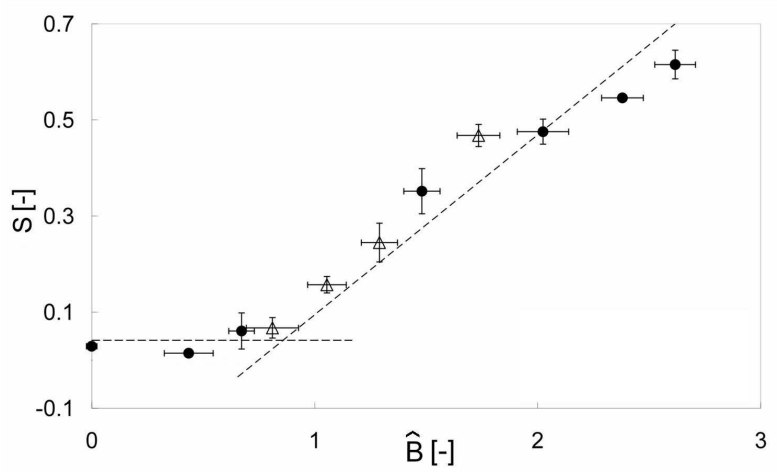

Figure 5. Shape factor as a function of the Bingham-capillary number.

The morphology of viscoplastic drops differs significantly from that of Newtonian drops. In particular, drops of yield stress fluids take a prolate shape as they are released from the nozzle, as shown in figure 3. This behaviour can be observed when the yield stress magnitude is greater than a certain value (in this case 11.5 Pa), which however may vary [8,15].
The prolate shape is conserved during free-fall as shown in figure 4, which compares Newtonian drops of different viscosities (obtained from water-glycerol solutions of different concentrations) and viscoplastic drops of increasing yield stress. While Newtonian drops always reach a spherical shape to minimise surface energy irrespective of the fluid viscosity, this does not happen in viscoplastic drops when the fluid yield stress overcomes the Laplace pressure.
To characterise the drop shape during free-fall one can introduce the following shape parameter:

$$S = \frac{H - D}{H + D} \tag{3}$$

where H and D are the drop dimensions in the vertical and the horizontal directions, respectively. Thus, $S = 0$ corresponds to spherical drops, while prolate shapes are characterised by $S > 0$. The competition between the capillary pressure and the yield stress can be represented in terms of the product of the Bingham and the capillary numbers, where the characteristic length scale is the equivalent diameter D_0:

$$\hat{B} = \frac{\tau_0 D_0}{\sigma} \tag{4}$$

This dimensionless group arises naturally, for example, from the analysis of the flow of a yield stress liquid inside capillary tubes [12].
Figure 5 displays the shape factor S as a function of the Bingham-capillary number, $\hat{B}$, showing a transition around $\hat{B} \approx 1$, where surface tension forces equal those arising from fluid-yield stress. For values of $\hat{B} < 1$, representative of drops whose capillary pressure exceeds the fluid yield-stress, the equilibrium free-fall shapes are spherical. For values of $\hat{B} > 1$, representative of fluid drops in which the yield-stress is higher than the capillary pressure, the equilibrium drop shape will be non-spherical, with a shape factor increasing as a linear function of the Bingham-capillary number.

Drop impact
Figure 6 shows image sequences describing the impact of viscoplastic drops on a Parafilm-M surface, for different values of the yield stress. Upon impact, drops take the shape of a disk spreading on the substrate. However, for the higher values of the yield stress, a peak can be observed in the centre of the lamella even at maximum spreading. This feature is enhanced at low Weber numbers.

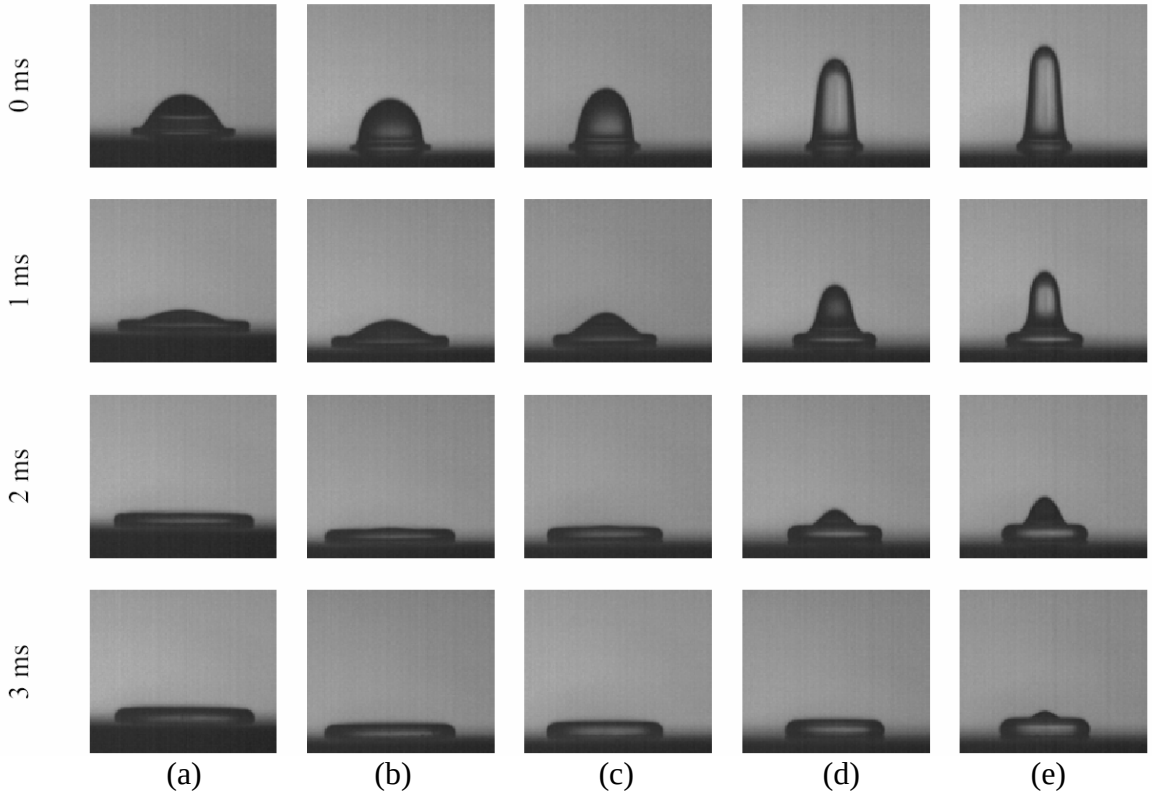

Figure 6. Impact morphology of viscoplastic drops (falling height: 100 mm), for τ_0 = 0 Pa (a), τ_0 = 5.4 Pa (b), τ_0 = 11.5 Pa (c), τ_0 = 19.1 Pa (d) and τ_0 = 26.1 Pa (e).

To study the influence of the surface wettability on the inertial spreading of viscoplastic drops, the maximum spreading diameter, D_{Max}, was measured for drops impacting on parafilm and glass substrates, which have different surface energies. Over the range 0 < We < 350, the results closely agree, with differences that fall within the experimental error, as shown in figure 7.

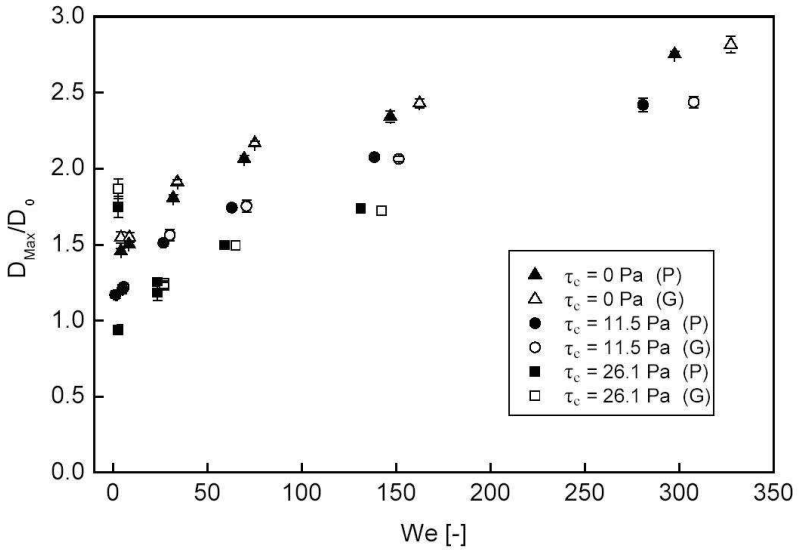

Figure 7. Maximum spreading diameter of viscoplastic drops impacting on glass (filled symbols) and Parafilm-M (open symbols) substrates, for different values of the yield stress.

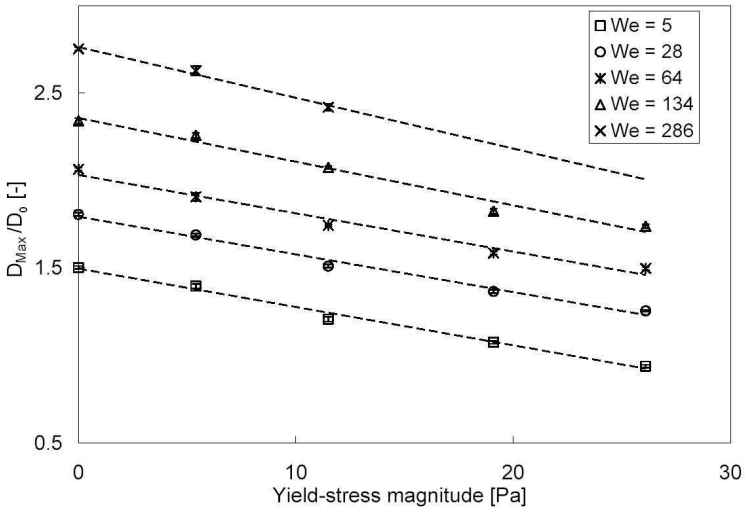

Figure 8. Maximum spreading diameter of viscoplastic drops impacting on a Parafilm-M substrate as a function of the fluid yield stress. The dashed lines correspond to the linear least square best-fit.

The maximum spreading diameter of viscoplastic drops is plotted in figure 8 with respect to the yield stress magnitude, for different Weber numbers. These values are systematically lower than those obtained with Newtonian fluids of the same apparent viscosity in the same range of Weber numbers [16]. The maximum spreading diameter decreases linearly with the yield stress; however, these results may include potential effects of shear-thinning, which have not been taken into account. It is not possible to establish the independent influence of yield-stress on impact dynamics directly from the experimental results because the viscometric behaviour of the shear-thinning and yield-stress solutions differ, therefore a like-with-like comparison cannot be made.

CONCLUSIONS

Systematic experiments show that drops of viscoplastic fluids exhibit peculiar behaviour during free-fall after detachment and when impacting on solid surfaces. Unlike Newtonian, viscoelastic and shear-thinning fluids, which assume a spherical equilibrium drop shape during free-fall, viscoplastic fluid drops may have a non-spherical equilibrium shape, with an aspect ratio that varies as a function of the yield stress. This relationship could be characterised by a dimensionless number which is the product of the Bingham and the capillary numbers, and represents the ratio of the Laplace pressure (which acts to minimise the surface energy) to the yield-stress. In drops where the Laplace pressure exceeds the yield-stress a spherical equilibrium drop shape is obtained; otherwise drops are prolate, and their aspect ratio grows linearly with the yield stress in the explored range of experimental parameters.
The inertial spreading of drops after impacting on a solid surface does not seem to be affected significantly by the surface wettability. The maximum spreading diameter appears to be smaller than that of Newtonian drops of the same viscosity and Weber number, however a direct quantitative comparison is difficult because one should also take into account the potential effects of shear thinning.
At the end of the expansion phase, the fluids with the higher yield stresses exhibit peaks at the centre of the lamella. This suggests that the drop deformation is localised in the external part, while the central part remains undeformed because the stress is smaller than the yield point of the fluid.

ACKNOWLEDGMENTS

G. German gratefully acknowledges a DTA studentship from the EPSRC.

REFERENCES

1. Rein, M., Phenomena of liquid drop impact on solid and liquid surfaces. *Fluid Dynam. Res.*, Vol. 12, pp. 61-93, 1993.
2. Rein, M., *Drop-surface interaction*, Springer, New York, 2003.
3. Bertola, V., Some applications of controlled drop deposition on solid surfaces, *Recent Patents on Mechanical Engineering*, Vol. 1, pp. 167-174, 2008.
4. Crooks, R., Boger, D.V., Influence of fluid elasticity on drops impacting on dry surfaces, *J. Rheol.*, Vol. 44, pp. 973-996, 2000.
5. Bergeron, V., Designing Intelligent Fluids for Controlling Spray Applications, *C.R. Physique*, Vol. 4, pp. 211-219, 2003.
6. A. Rozhkov, B. Prunet-Foch, M. Vignes-Adler, Impact of drops of polymer solutions on small targets, *Phys. Fluids*, Vol. 15, pp. 2006-2019, 2003.
7. Bertola, V., Drop impact on a hot surface: effect of a polymer additive, *Exp. Fluids*, Vol. 37, pp. 653-664, 2004.
8. Nigen, S., Experimental investigation of the impact of an (apparent) yield-stress material, *Atom. Sprays*, Vol. 15, pp. 103-, 2005.
9. Bird R.B., Gance, D. and Yarusso, B.J. The rheology and flow of viscoplastic materials, *Rev. Chem. Eng.*, Vol. 1, pp. 1-70, 1982.
10. Bingham, E.C., An investigation of the laws of plastic flow, *U.S. Bureau of Standards Bulletin*, Vol. 13, pp. 309 (1916).
11. Coussot, P., Rheophysics of pastes: a review of microscopic modelling approaches, *Soft Matter*, Vol. 3, pp. 528-540, 2007.
12. Bertola, V., Wicking with a yield-stress fluid, *Journal of Physics: Condensed Matter*, Vol. 21, article 035107, 2009.
13. Mittal, K. L., Determination of CMC of polysorbate 20 in aqueous solution by surface tension method, *J. Pharm. Sci.*, Vol. 61, pp. 1334–1335, 1972.
14. Eggers, J., Nonlinear dynamics and breakup of free-surface flows, *Rev. Mod. Phys.*, Vol. 69, pp. 865-929, 1997.
15. Davidson, M.R., Cooper-White, J.J., Pendant drop formation of shear-thinning and yield stress fluids, *Appl. Math. Mod.*, Vol. 30, pp. 1392-1405, 2006.
16. German, G., Bertola, V., A review of drop impact models and validation with high-viscosity Newtonian fluids, *Atomization and Sprays*, in press, 2009.

THREE DIMENSIONAL EFFECTS IN INCLINED FILM FLOWS

V. Leontidis[1], M. Vlachogiannis[2], N. Andritsos[1], V. Bontozoglou[1,*]
[1]University of Thessaly, Department of Mechanical & Industrial Engineering, Volos, Greece
[2]Technological Educational Institute of Larissa, Greece

ABSTRACT. The characteristics and spatiotemporal evolution of free surface structures in inclined film flows are studied using the fluorescence imaging technique. Particular emphasis is placed on the effect of channel width, a parameter that has not previously been considered. Nominally two-dimensional solitary humps are observed to develop a curved crestline and a transverse variation of wave height. The relation between height and phase speed is shown to be always linear and to depend strongly on channel inclination and width. The critical Re for transition to a fully three-dimensional free surface is determined, and two alternative transition scenarios are identified, one active for small inclinations and low viscosity liquids and the other active for higher inclinations and/or viscous liquids.

Keywords: *inclined film flow, wall effect, three-dimensional waves, curved solitary waves*

INTRODUCTION

Today there is large amount of experimental and theoretical/numerical evidence that the spatiotemporal dynamics of gravity-driven film flows at low and intermediate Reynolds number is dominated by localized free surface structures separated by relatively long stretches of substrate, known as solitary waves [1]. Solitary waves consist of an asymmetric hump, with steep front and gently sloping tail, preceded by capillary, front-running ripples. These waves can occur either naturally, if the film is triggered only by random noise, or artificially by imposing a constant-frequency disturbance. The wave characteristics are the same in both cases; only in the latter the wave-train is more regular.

Theoretical/computational efforts treat this first nonlinear stage of development as a two-dimensional phenomenon, and focus on: (a) the prediction of the relation between wave height and phase velocity [2], and (b) the understanding of the interaction between neighboring humps [3]. A subsequent stage of flow development with increasing Re is the deformation and break-up of the crestline by three-dimensional effects.

Concerning problem (a), the relation between wave height and phase velocity, it is well known from the theoretical literature that the proper scaling involves the substrate thickness, h_{sub}, and the mean substrate velocity, u_{sub}. Using this scaling, Tihon et al. [4] confirmed experimentally the linear relation given in Equation (1). The constant term, which is equal to 3, corresponds to the linear phase velocity, i.e. the velocity of waves of infinitesimal height.

$$\frac{c}{u_{sub}} - 3 \approx 1.8 \frac{h_{max} - h_{sub}}{h_{sub}} \qquad (1)$$

* Corresponding author: Prof. V. Bontozoglou
Phone: + (30)-2421074069, Fax: + (30)-2421074085
E-mail address: bont@mie.uth.gr

Concerning problem (b), hump interaction and three-dimensional evolution, an overview has recently been provided by Demekhin and coworkers [5]. More specifically, these authors proposed that for vertically falling liquid films five possible wave regimes exist, depending on Re. The first regime is dominated from linear stability theory, which predicts that the primary instability occurs at zero Re, but for $Re<Re^{(1)}$=3-5 the instability is too week and the film appears visibly flat. The second regime, $Re^{(1)}<Re<Re^{(2)}$=40, is characterized as two dimensional and the waves are almost sinusoidal in the beginning and solitary at the end of the interval. They can be disturbed by transverse perturbations resulting in solitary waves with curved fronts, but they retain the main properties of 2D solitary waves and the film height across the crest-line is constant. In the third interval, $Re^{(2)}<Re<Re^{(3)}$=400, the 2D solitary waves become unstable to spanwise disturbances and brake-up into 3D structures. The main shape of the waves is horseshoe-like solitons ('Λ waves') with round fronts at the begging and pointed structures at end of the regime. The fourth interval, $Re^{(3)}<Re<Re^{(4)}$=800-1500, consists of large 2D roll waves, which have arise from the coalescence of the 3D waves. Finally, for $Re>Re^{(5)}$ the usual turbulence occurs. It is expected that for inclined film flows the observed flow regimes to be the same, but the transitions to occur in different Reynolds numbers depending on inclination angle.

Despite the above idealized transition sequence, experiments indicate that solitary waves in channels of finite width are always 3D in the sense that their crestlines are curved in the transverse direction [6]. Though this characteristic has been blamed as responsible for discrepancies between wave height measurements and predictions [5], it appears not to have been systematically investigated. Furthermore, the mechanism of the subsequent break-up of the crestline is not fully understood, neither is the effect of liquid properties and channel inclination angle. Last but not least, the possible dependence of the above phenomena on the width of the channel has not been questioned. Thus, the present work focuses on the experimental investigation of the detailed characteristics of waves -starting from the nominally 2D regime- with particular emphasis on the effect of channel width.

EXPERIMENTAL DESCRIPTION

Experimental apparatus

The facility where the experiments were carried out is represented in Figure 1. The main parts of the apparatus (flat wall and side walls) are made of glass. The length, L, of the channel is 3 m and the maximum width, W, 0.45 m. Installing long stripes of glass on top of the wall the channel width could be reduced. In the present work the studied widths were 0.25, 0.35 and 0.45 m. The inclination angle, φ, was varying between 3^o and 15^o. In order to disturb the liquid film and impose a disturbance of certain frequency, f, a timer-controlled on/off electro-valve was used. The frequency of the imposed disturbance was 0.5, 1 and 2 Hz. The working fluids were tap water and aqueous solutions of glycerol, with concentrations of 20-40% by weight. The viscosity of the water-glycerol solutions was determined by measuring the refractive index with a refractometer.

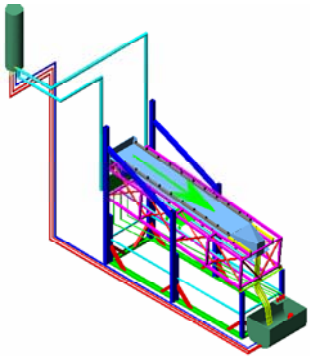

Figure 1. Sketch of the experimental apparatus

Fluorescence imaging method and image analysis

In order to obtain spatiotemporal measurements of the film thickness the fluorescence imaging technique was used, which has been developed by Liu and coworkers [8]. This method has been applied in a similar but smaller channel and has been described in details in a previous work [9]. The working fluid is being doped with a small concentration of dye (200-300 ppm of sodium salt of fluorescein-$C_{20}H_{10}O_5Na_2$) and the film fluoresces under ultraviolet illumination. Using a shuttered high-resolution black and white CCD camera and a monochrome frame grabber board we acquire and digitize images (576×768 pixels with 8-bit of resolution). In all experiments each frame corresponds to a 110 mm×147 mm window of channel area, with the 110 mm to be in the transverse direction. The CCD camera has been placed under the channel approximately 2.5 m from the inlet. Image processing is accomplished using the MATLAB® software. Generally, each photo frame is being transformed into a two dimensional matrix (576×768 elements) contained the film height in the streamwise and transverse direction.

EXPERIMENTAL RESULTS

Flow regimes

Three distinct flow regimes have been observed during the experiments, and these are depicted in Figure 2. For small Reynolds numbers the flow is stable to any disturbances. Figure 2 includes both the classical theoretical prediction, $Re_{cr,th}=5/6\cot\varphi$, and the experimentally determined critical Re. It is noted that prediction and experiment disagree, and the deviation increases at smaller inclinations. As we show in a different study [10], the deviation is the effect of finite channel width. Thus, narrow channels and small inclinations significantly stabilize the flow.

Beyond the critical Re, the flow develops travelling waves. This should ideally be a two-dimensional (2D) regime, but the waves actually observed are not rigorously 2D because their crestlines are symmetrically curved around the channel center plane and because the wave height varies in the transverse direction. The last curve in Figure 2 corresponds to the transition to fully three-dimensional (3D) flow. The 3D transition may proceed through the development of small-scale structures and/or the disintegration of the main crestlines. The eventual outcome of the 3D transition is the establishment of a chaotic distribution of 'horse-shoe' waves. The rest of the paper describes the main characteristics of the curved 2D solitary waves and the evolving 3D structures.

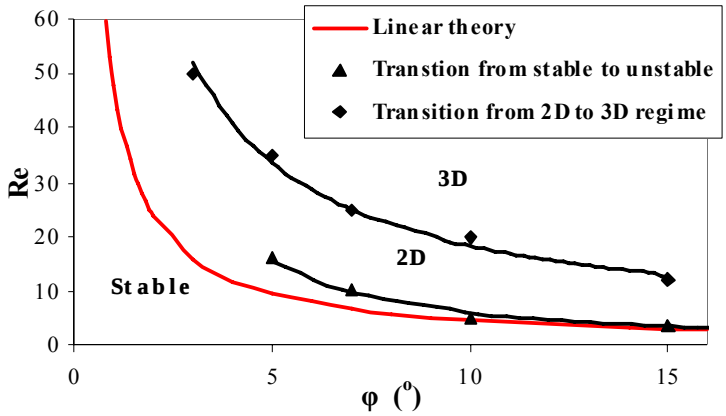

Figure 2. Flow regimes for W=250 mm

Curved 2D solitary waves

As already mentioned, the solitary waves are not fully two-dimensional. Measurements of the maximum local wave height across the crestline are shown in Figure 3, and indicate that the film thickness varies in the transverse direction, with maximum in the channel center plane and minimum near the side walls. With increasing Re, the difference in wave height between walls and center plane increases and the variation becomes steeper and is located closer to the walls. It is also observed that the wave height near the walls appears to be independent of Reynolds number.

The shape of the crestline of these nominally 2D solitary waves is symmetrically curved around the channel center plane. A typical example is shown in Figure 4, where colors represent iso-elevation contours. It is also observed from the figure that the wavelength of capillary ripples varies across the channel, and as expected is smaller at the center where the solitary hump is steeper.

Our observations indicate that the shape of fully-developed waves is always satisfactorily approximated by a parabola. Thus, the deviation from straight-crested dynamics is presently characterized by the curvature, k, at the apex of the parabola. The variation of curvature with Re is shown in Figure 5 for a large number of experiments corresponding to different liquid viscosities, and channel inclinations and widths. A universal trend is the decrease in curvature with Re, i.e. the higher the Re the flatter the wave. A similar effect is observed with channel width (open and filled triangles), indicating that the genuine 2D limit is approached by wide channels and high Re. Additionally, a comparison of the filled symbols shows that, at constant Re, curvature decreases with the increase in viscosity. This can be attributed to the second dimensionless number characterizing the flow, which also includes the effect of surface tension, σ. A popular choice that is only function of physical properties is the Kapitsa number, $Ka=\sigma/\rho g^{1/3}\nu^{4/3}$. Finally, higher inclinations are also observed to lead to sharper waves (compare open triangles and squares).

The above characteristics of fully-developed waves are better understood by observing their evolution with fetch. Indeed, at short distance from the entrance, disturbances appear as 2D. The subsequent change in shape may be explained by noting that the side walls locally provide resistance to wave growth, both because of viscous effects and contact-line hysteresis. Given the well-documented direct relation between wave height and phase velocity, it is expected that this side-part of the wave crest will tend to be left behind, leading gradually to a curved wave. The transverse curvature contributes a capillary force that decelerates the central part of the wave, eventually resulting in a fully-developed profile.

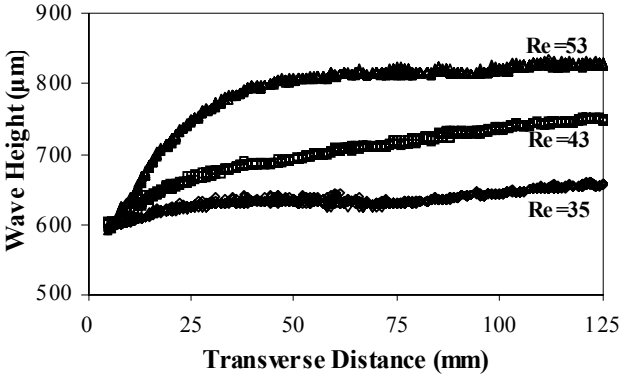

Figure 3. Variation of local film thickness across the crest-line of 2D waves ($\varphi=3^o$, W=250 mm)

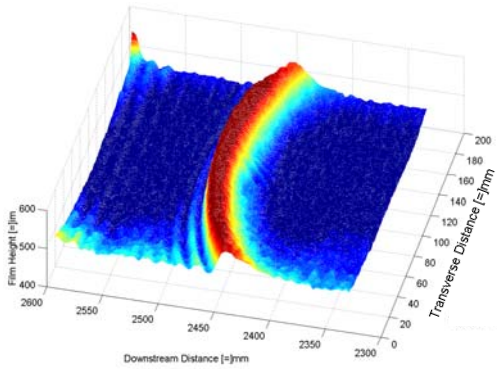

Figure 4. Representation of a curved 2D solitary wave (φ=5°, W=350 mm, Re=37, 1 Hz)

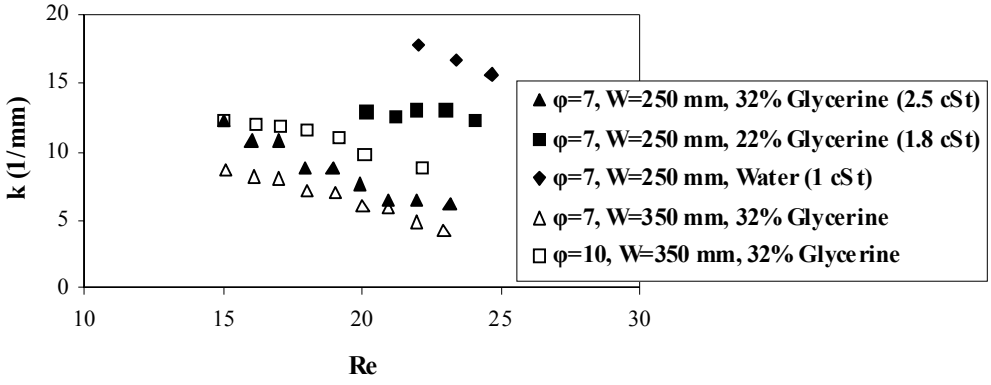

Figure 5. Effect of Re, channel width, inclination angle and fluid viscosity on wave shape

The above tentative explanation of wave evolution relies on the repeatedly observed strong correlation between wave phase speed and height. Thus, it is of interest to examine if such a correlation is also confirmed by the present data. More specifically, using the appropriate scaling based on substrate properties, it is always observed that the following linear relation is obeyed:

$$\frac{c}{u_{sub}} \approx S\frac{h_{max}-h_{sub}}{h_{sub}} + C_o \qquad (2)$$

Figure 6 provides a representative example of relevant data. The slope, S, is mainly a function of inclination angle, with steeper channels leading to faster waves (Figure 7a). It also increases slightly with channel width. On the other hand, the constant term (which corresponds to the linear phase speed and is theoretically predicted as equal to 3), C_o, shows a strong dependence on channel width and inclination, and approaches the theoretical limit only for wide enough channels (Figure 7b).

Three-dimensional transition

The first manifestation of 3D phenomena is characterized by a critical Re. Relevant data are shown in Figure 8, and demonstrate not only the expected inverse effect of inclination angle, but also a similar effect of channel width. More specifically, narrow channels postpone the 3D transition to higher Re, as they also do with the primary instability of the flat film. On the other hand, the fluid properties have no impact on transition, indicating that the second dimensionless number (e.g. Ka) is presently irrelevant.

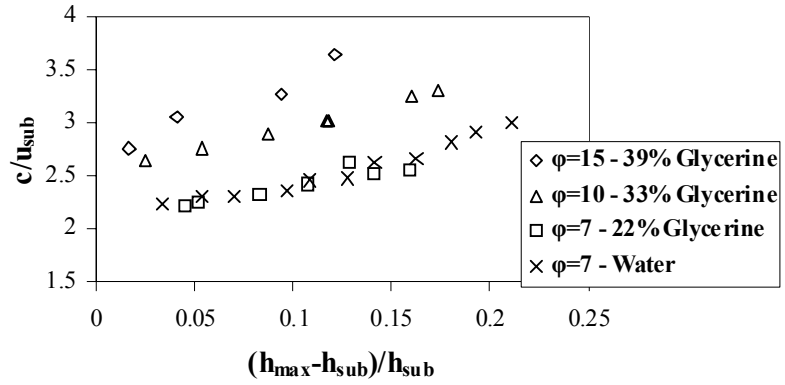

Figure 6. Normalization of the maximum wave height and phase velocity (W=250 mm)

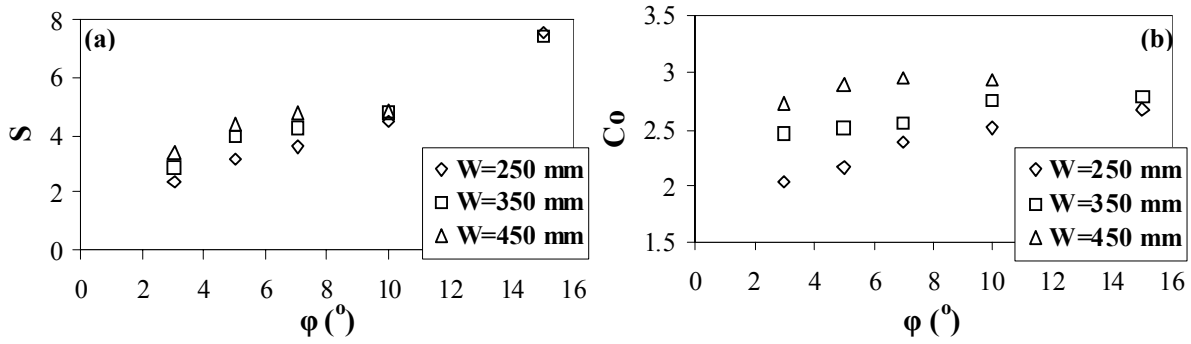

Figure 7. Effect of W and φ on slope and constant term of linear equation

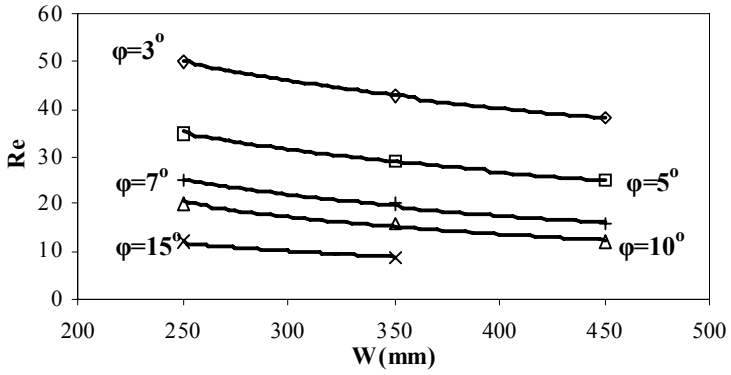

Figure 8. Transition from 2D to 3D flow regime

The phenomenology differs for nearly horizontal and for more inclined channes. More specifically, at inclinations up to 5°, solitary waves in water develop a front-running 3D structure that consists of a transversely periodic array of small depressions (Figure 9). Line profiles along the curved wave indicate that the 3D structure is sinusoidal with roughly constant height, A_d, and transverse wavelength, L_d, that decreases with Re (Figure 10). For larger inclinations (5-15°) either the solitary wave crest becomes skewed (Figure 11a) or 3D parasitic waves develop behind the major humps (Figure 11b). Finally, a combination of the above structures has been observed is some experiments.

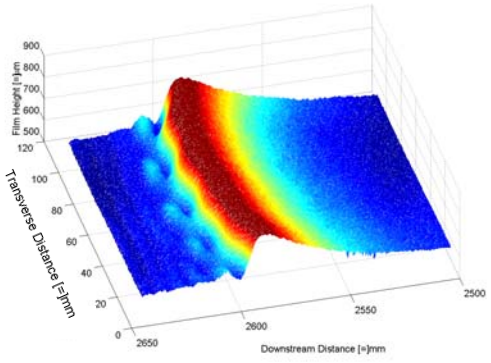

Figure 9. Representation of 3D periodic depressions (φ=3°, W=250 mm, Re=55, f=1 Hz)

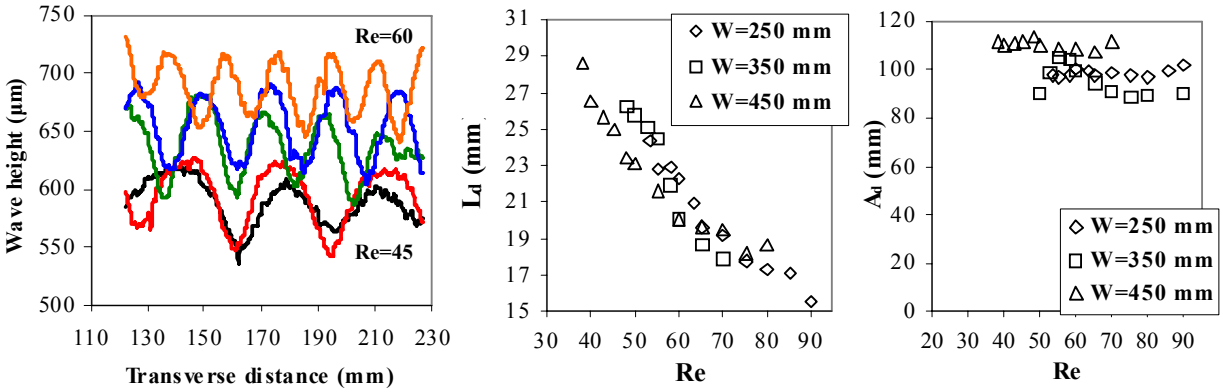

Figure 10. Sinusoidal line profile of depressions and effect of Re on transverse wavelength and amplitude of depressions

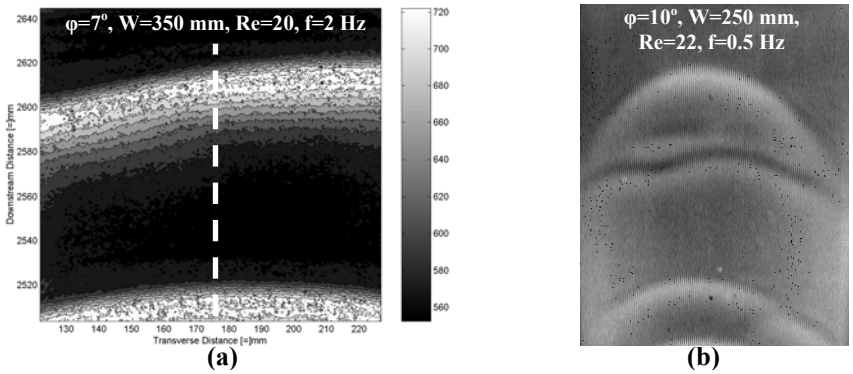

Figure 11. a) Representation of 3D oblique solitary wave and b) photo of 3D parasitic waves

CONCLUDING REMARKS

The fluorescence method was used in order to study experimentally the spatio-temporal evolution of the free surface of inclined liquid film flows at small and intermediate inclination angles. Experiments were done in a 3 meter long channel of variable width, and particular emphasis was placed on the effect of channel width on the observed transitions and on the characteristics of the waves. Three distinct flow regimes were identified: (i) the stable flat free surface, (ii) the disturbed

free surface with nominally 2D waves and (iii) the disturbed free surface with fully 3D waves. Both transitions (i)-(ii) and (ii)-(iii) were significantly influenced by the width of the channel, and in particular were postponed to higher Re for narrow channels.

The first travelling waves observed are not truly 2D, because their crestlines are symmetrically curved around the channel center plane and their height varies in the transverse direction. The curvature of the crestlines varies inversely with Re and also depends on channel inclination and width. For fully-developed waves, the wave height at the center plane and the wave speed are always linearly correlated when nondimensionalized with the respective substrate thickness and velocity. The slope and intercept of the linear relation have been systematically measured. The former depends mainly on channel inclination, with steeper channels producing faster waves. The latter corresponds to the phase speed of zero-amplitude waves and is theoretically predicted as equal to 3. Our data indicate that the intercept actually depends strongly on channel width and the theoretical limit is asymptotically attained only for wide enough channels.

Two alternative scenarios were identified for transition to a fully three-dimensional free surface. At small inclinations and with low viscosity liquids, the curved 2D solitary wave persists, but a small-scale 3D instability develops ahead of it. The instability consists of a regular series of periodic depressions with constant amplitude and with length inversely proportional to Re. This structure is believed to be the result of a capillary instability triggered by the high streamwise curvature in front of the solitary hump. The second scenario of 3D transition occurs at higher inclinations and for viscous liquids, and involves a disintegration of the main wave crest with concomitant generation of parasitic 3D waves behind it.

REFERENCES

1. Chang, H.-C. and Demekhin, E. A., *Complex Wave Dynamics on Thin Films*, Elsevier, Amsterdam, 2002.
2. Mudunuri, R. R. and Balakotaiah, V., Solitary Waves on Thin Failing Films in the Very Low Forcing Frequency Limit, *AIChE J.*, Vol. 52, pp 3995-4003, 2006.
3. Malamataris, N., Vlachogiannis, M. and Bontozoglou, V., Solitary Waves on Inclined Films: Flow Structure and Binary Interactions, *Phys. Fluids*, Vol. 14, pp 1082-1094, 2002.
4. Tihon, J., Serifi, K., Argyriadi, K. and Bontozoglou, V., Solitary Waves on Inclined Films: Their Characteristics and the Effects on Wall Shear Stress, *Exp. Fluids*, Vol. 41, pp 79-89, 2006.
5. Demekhin, E. A., Kalaidin, E. N., Kalliadasis, S. and Vlaskin, S. Yu., Three-Dimensional Localized Coherent Structures of Surface Turbulence. I. Scenarios of Two-Dimensional-Three-Dimensional Transition, *Phys. Fluids*, Vol. 19, art. no. 114103, 2007.
6. Liu, J. and Gollub, J. P., Solitary Wave Dynamics of Film Flows, *Phys. Fluids*, Vol. 6, pp 1702–1712, 1994.
7. Scheid, B., Ruyer-Quil, C. and Manneville, P., Wave Patterns in Film Flows: Modeling and Three-Dimensional Waves, *J. Fluid Mech.*, Vol. 562, pp 183–222, 2006.
8. Liu, J., Paul, J. D. and Gollub, J. P., Measurements of the Primary Instabilities of Film Flows. *J. Fluid Mech*., Vol. 250, pp 69-101, 1993.
9. Vlachogiannis, M. and Bontozoglou, V., Observations of Solitary Wave Dynamics of Film Flows. *J. Fluid Mech.*, Vol. 435, pp 191-215, 2001.
10. Vlachogiannis, M., Samandas, A., Leontidis, V. and Bontozoglou V., Effect of Channel Width on the Instability of Inclined Film Flow, *Under preparation*.

TIME RESOLVED HEAT TRANSFER TO AN IMPINGING SYNTHETIC AIR JET

D. I. Rylatt*, T.S. O'Donovan
Heriot-Watt University, Edinburgh, United Kingdom

ABSTRACT. Heat transfer to an impinging synthetic air jet is investigated experimentally. This investigation presents heat transfer data for a synthetic air jet at orifice to impingement surface distances of *1* to *8* jet diameters, and jet excitation frequencies of *45* to *85Hz*. The jet impinges on an ohmically heated constantan foil surface and a thermal imaging camera is used to acquire high spatial and temporal resolution surface temperature measurements. For the full range of heights studied, the heat transfer peaks at the stagnation point and decreases with increasing radial distance. At low H/D values (≤ 2) however secondary peaks are evident in the far wall jet region. These peaks have been attributed to the vortices which pass over the heated surface and do not occur at larger values of H/D as the vortices have broken down prior to impingement. The influence of the vortices of the time-averaged and time-varying surface heat transfer is reported.

Keywords: *synthetic jet, jet impingement heat transfer, vortices, infrared thermography*

INTRODUCTION

Continuous or steady air jet impingement has many applications in cooling due to the high localised and area averaged heat transfer coefficients they can achieve. Applications include, but are not limited to, the cooling of turbine blades, grinding processes and electronics. Synthetic air jet impingement is a promising new technology that can outperform continuous air jet impingement cooling. Both Smith and Swift [1] and Pavlova and Amitay [2] have shown that synthetic air jets can provide up to three times the cooling of continuous air jet impingement for a similar range of Reynolds numbers. Kercher [3] have shown that a synthetic air jet can provide twice the cooling of standard commercial electronics cooling technology. Synthetic air jets are compact, require no external plumbing and are therefore more easily integrated into various cooling applications.

The main variables to be considered in any study of continuous air jet impingement are the height of the nozzle above the impingement surface, the jet Reynolds number and angle of impingement. These parameters together with several others such as nozzle geometry, confinement, arrays, swirl etc are comprehensively reviewed by Martin [4]. It is, by now well established that the heat transfer to an impinging air jet is a maximum at the geometric centre where the flow is considered stagnant on a time-average basis. In general, the rate of heat transfer decreases monotonically with increasing radial distance from the stagnation point. At low nozzle to surface spacings however secondary peaks occur at a radial location and these have been attributed to an abrupt increase wall jet turbulence by Goldstein et al. [5]

More recently the effect of vortices in an impinging jet flow on the surface heat transfer has been investigated. Vortices occur naturally in a jet flow and are due to Kelvin Helmholtz instabilities in

* Corresponding author: D. I. Rylatt
Phone: + (44)-131-4514737, Fax: + (44)-131-4513129
E-mail address: dir1@hw.ac.uk

the shear layer. They form at the jet exit, detach and flow downstream periodically. O'Donovan and Murray [6, 7] have shown that naturally occurring vortices in a continuous impinging air jet influence the magnitude of the secondary peaks that occur in the heat transfer distribution. Both Liu and Sullivan [8] and O'Donovan and Murray [9] have shown that acoustic excitation of an continuous air jet can be used to control the passing frequency of the vortices in the flow and this, in turn, can influence the shape and magnitude of the secondary peak in the heat transfer distribution. Hoffman et al. [10] have shown that pulsating a continuous impinging jet can also influence the overall magnitude of the surface heat transfer by increasing the mixing in the flow.

Synthetic air jet comprise almost entirely of successive vortex rings. A jet is formed by the periodic oscillation of a diaphragm bounded to a cavity containing an orifice; air is drawn into the cavity then ejected cyclically, thus generating a zero net mass flux jet flow that consists of chains of vortices. The ability of synthetic air jets to effectively remove heat is attributed to the high turbulence of the flow relative to continuous air jets. The current investigation is concerned with measuring the surface heat flux to an impinging synthetic air jet with high spatial and temporal resolution. The effect of successive impinging vortices is investigated at low H/D and compared to the heat transfer at high H/D where the vortices have broken down and are the flow is more uniform. The motivation for the current work is to better understand the mechanisms by which synthetic air jets transfer heat with a view to optimising jet design and operation.

EXPERIMENTAL SETUP

The experimental setup (figure 1) consists of two main components: a synthetic air jet, and a heated impingement surface. The synthetic jet is mounted directly above the heated surface with the jet flow directly perpendicular to it.

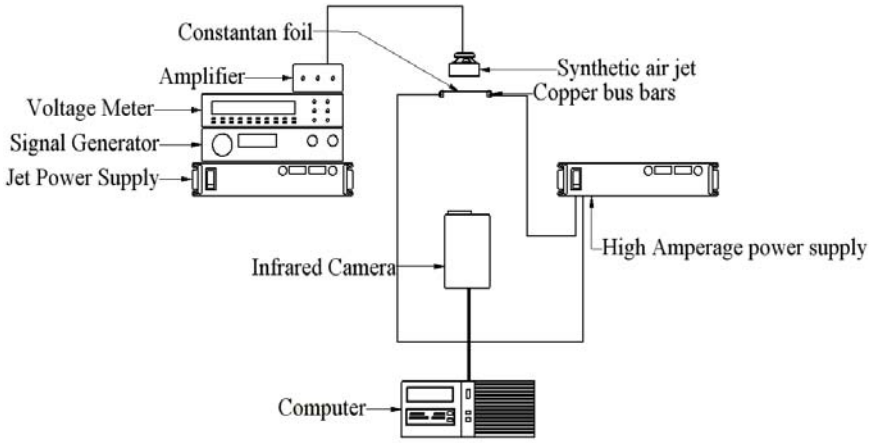

Figure 1: schematic diagram of the experimental set up

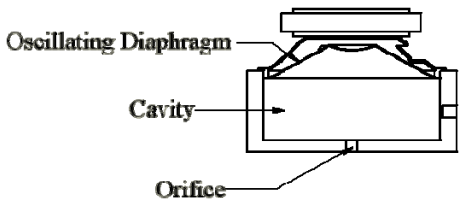

Figure 2: cross sectional view of a synthetic air jet

As indicated in figure 1, the synthetic air jet consists of a cavity with an oscillating diaphragm or actuator on one end and the jet orifice opposite it. The cavity diameter is *76mm* and has a depth of 30 mm and the circular orifice is *5mm* in diameter and *5mm* in length. The whole assembly is fabricated from a *90mm* by *90mm* by *35mm* aluminium block. All dimensions are accurate to within *0.1mm*. The synthetic jet actuator is a Visaton© FR8 *8Ω* acoustic speaker with a power rating of *10W*, a frequency range up to *20kHz*, a resonant frequency of *150Hz* and a maximum cone displacement of *4mm*. The actuator is powered by a sinusoidal voltage signal generated by a Thurlby Thandar instruments, TG315, *3MHz* function and sweep generator and amplified by a Kemo® MO 034 *40W* power amplifier which has a frequency range from *20* to *25kHz*, and a sensitivity of *~500mV*. The jet assembly is attached to a Manfrotto 454 micro positioning plate, to allow for fine adjustment of the distance between the synthetic air jet and the impingement surface.

The impingement surface consists of a thin resistance heater foil that has a surface area of *150mm* by *100mm* and approximates a uniform wall flux thermal boundary condition. Three different thicknesses of Constantan® Resistance Alloy (Cu55/Ni45) foil were used in this research; these thicknesses were *10*, *25* and *50μm* and were fabricated by Goodfellows Cambridge Limited. The undersides of the foils were lightly coated with a mat black paint to increase the surface emissivity value to approximately 0.98; this was necessary to ensure accurate surface temperature measurements with an infrared thermal imaging camera. The foils are clamped between two copper bus bars, with nominal electrical conductivity of $58.47Sm^{-1}$. The bus bars are held in place by two electrically insulating nylon struts, one of which is attached to two linear bearings to allow for positioning and tensioning of the foils. A direct current voltage is applied across the foil via the bus bars by a Farnel AP 20 - 80 regulated power supply which is capable of supplying up to *80Amps*. To ensure minimum losses in transmission a *35mm* core copper welding cable was used to connect the bus bars to the power supply.

All the components of the experimental setup are contained within a frame constructed of *45mm* by *45mm* extruded aluminium profile. The rig was enclosed on all sides by Perspex shielding to ensure that ambient air temperatures and velocities has minimal effect on the measurements.

As indicated in the diagram, a FLIR SC3000 high speed thermal imaging camera is mounted directly beneath the heated surface. The camera was used to measure the surface temperature of the foil with high spatial and temporal resolution. The maximum frame rate is *750Hz* which yields an image of *320 x 19* pixels. The field measured by the camera at this resolution was *100* by *6.3mm* which yields an image resolution of *3 pixels per mm*. The camera has a temperature sensitivity of *20mK* at *30°C* and a range of *-20* to *1500°C* with an accuracy of *±1%*. The minimum focal length is *300mm* with a plane lens, to allow for fine adjustments in the focus which is not easily achieved with the internal stepping motor focusing system; the camera is also attached to a Manfrotto 454 micro positioning plate. For all tests conducted the maximum operating temperature of the foils was less than *100°C*.

Heat transfer data are presented in the form of the time-average and time-varying Nusselt number which uses the diameter of the jet to normalise the surface convective heat transfer coefficient. This can be calculated as follows:

$$h = \frac{q''_{gen}}{\left(T_{surf} - T_{jet}\right)} \tag{1}$$

$$q''_{gen} = \frac{VI}{A_{surf}} \tag{2}$$

and V is the applied voltage, I is the current drawn by the foil resistance, A_{surf} is the surface area of the foil and T_{jet} is the jet temperature which is measured independently by a T-type thermocouple in the synthetic air jet cavity. This analysis assumes one dimensional heat conduction through the foil before convection to the impinging air jet. It is, however, well established that even for thin foils heat conducted laterally is significant. A correction for both lateral conduction and heat capacitance as used by Golobic et al. [11] was also used in this study to calculate the mean and time-varying surface heat transfer coefficient.

RESULTS & DISCUSSION

Time-average Nusselt number distributions to impinging synthetic air jets for a range of parameters are presented in this section. Time-varying heat transfer measurements are also presented and are used to discuss the differences between the time averaged data.

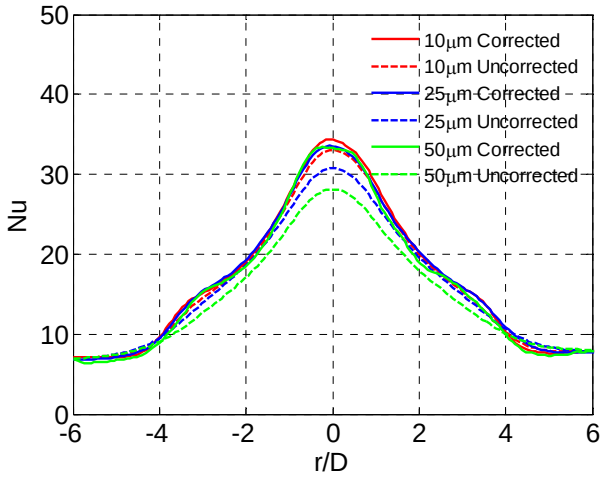

Figure 3: Corrected & Uncorrected Nusselt No. Distributions; $H/D = 2, f_e=45Hz$

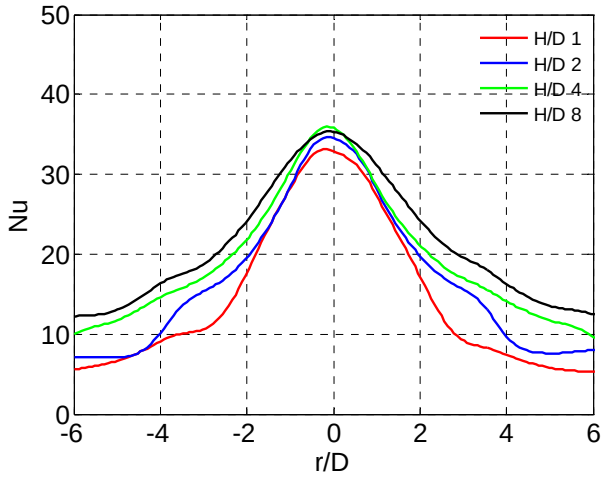

Figure 4: Nusselt No. Distributions; $f_e=45Hz$

As discussed in the experimental rig section, lateral conduction in the foil must be accounted for to accurately calculate the surface heat transfer coefficient. This has been done by using a finite difference technique which was also used by Golobic et al. [11]. In order to verify the correction technique, three foil thicknesses were used in the study (*10*, *25* and *50μm*). Figure 3 demonstrates that, for all foil thicknesses, the same heat transfer distribution results after the correction is applied. Before the correction is applied, both the peak in the heat transfer distribution and the rate at which the heat transfer decreases with increasing radial distance is lower for the thicker foils. Once the correction is applied all three distributions merge to give the same result irrespective of the foil thickness.

For the full range of heights studied, the heat transfer peaks at the stagnation point and decreases with increasing radial distance. The shape and magnitude of the heat transfer distribution changes significantly for different *H/D* values as illustrated in figure 4. At a certain radial location the rate at which the heat transfer decay which indicates the presence of a secondary peak as investigated by O'Donovan and Murray [7] who have shown that vortices in steady impinging jets contribute to the magnitude of secondary peaks. The distributions in figure 4 indicate that vortices in an impinging synthetic air jet may also results in a change of slope in the heat transfer decay; this is most evident for H/D $\leq$ 2 as the magnitude of these peaks decrease with increasing *H/D*.

Figure 5 presents the fluctuating heat transfer distribution which is an indication of instabilities in the flow along the impingent surface. As with the mean Nusselt number distributions, fluctuations in the surface heat transfer (*Nu'*) peak at the stagnation point and decrease with increasing radial distance. By comparing figures 4 and 5, it can be seen that areas of increased fluctuations in the heat transfer correspond to area of increased mean heat transfer. In particular, the change in slope in the mean heat transfer distributions at r/D ≈ 3 correspond to an increase in turbulence in the wall jet flow. This is similar to the observations of O'Donovan and Murray [7] for a steady impinging air jet where the abrupt increase in turbulence results from the breakdown of vortices in the jet flow. To further understand the convective heat transfer to a synthetic air jet the time varying heat transfer coefficient was examined.

Surface temperature measurements for each test setup were captured at *250Hz* for *20* seconds; the data were phase locked to convert the *5000* images to *50* averages of 100 images each at a distinct point in the jet cycle. An example of a surface Nusselt number distribution is presented in figure 6 and x's indicate the locations where the time-resolved heat transfer signals are examined.

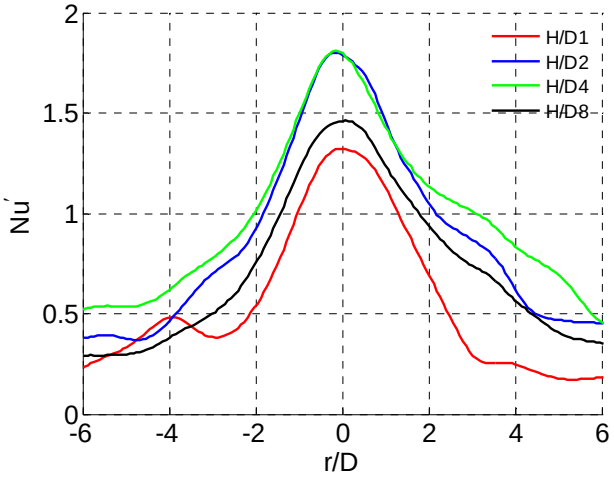

Figure 5: Fluctuating Nusselt No. Distributions; *H/D*=2; f_e=*45Hz*

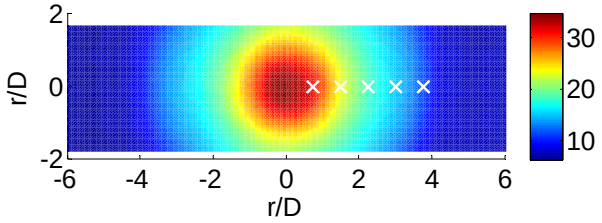

Figure 6: Nusselt No. distribution *H/D=2,* f_e*=45Hz*

Figure 7 shows the phase averaged Nusselt number timeline at a distance of *0.8* diameters from the stagnation point. It is clear that the heat transfer signal fluctuates sinusoidally at this location and this is true for all locations in up to secondary peak at *r/D=4*. This radial location corresponds to location of the secondary peak in the mean heat transfer distribution. Beyond this radial location however, at *r/D=4.5,* the heat transfer fluctuations are more random; this is clearly evident in figure 8. This supports the findings of O'Donovan and Murray that the secondary peak in the heat transfer distribution results from the break down of vortices in the wall jet. The heat transfer fluctuates sinusoidally before the secondary peak because the synthetic air jet vortices are strong and coherent structures which pass in the wall jet. The vortices break down in the wall jet which increases the turbulence and the results in a slight increase in heat transfer locally. The random fluctuations of the heat transfer signals beyond the radial location of the peak location indicate the vortices have been broken down into random turbulence.

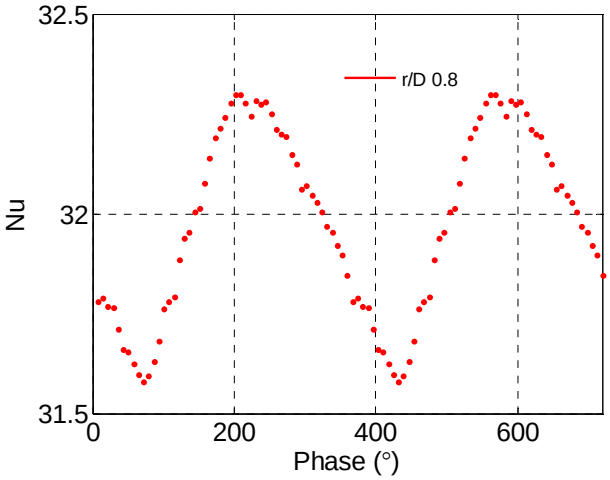

Figure 7: phase averaged Nusselt number f_e=45Hz, H/D = 2, r/D=0.8

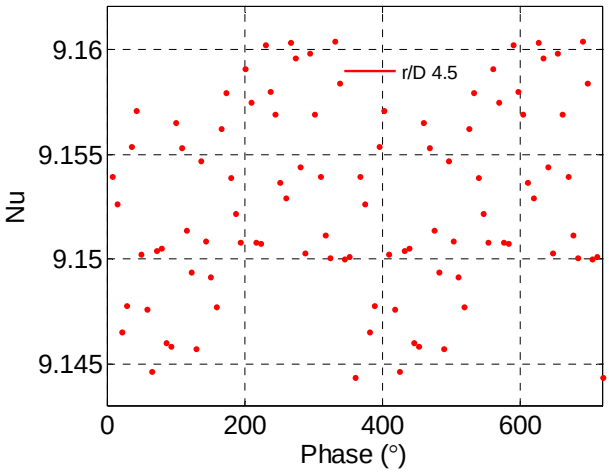

Figure 8: Phase Averaged Heat Transfer Signals; f_e=45Hz, H/D=2, r/D=4.5

In the following results only radial locations les *4.5* diameters have been examined. Figures 9 to 12 present normalised phase averaged signals for 4 different nozzle to impingement surface spacings and a single excitation frequency of *45Hz*. It can be seen that the heat transfer fluctuates sinusoidally at each radial location. Close to the stagnation region the heat transfer fluctuates in phase however at greater radial distances fluctuations occur further out of phase. For all frequencies studied the phase spread increases for *H/D=1* to *4* and has began to converge again at *H/D=8*.

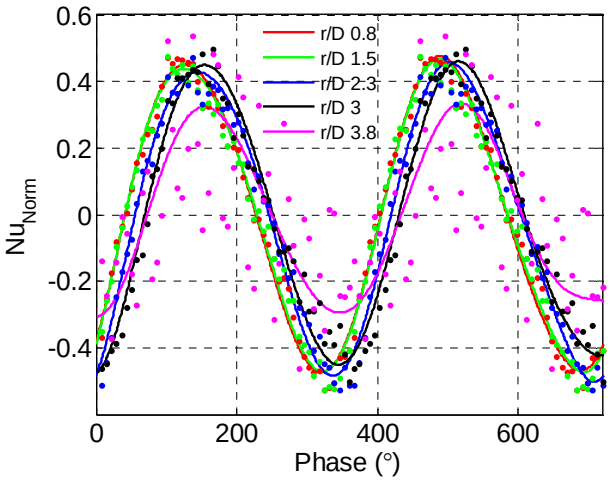

Figure 9: Normalised Phase Averaged Heat Transfer Signals; f_e=45Hz, H/D = 1

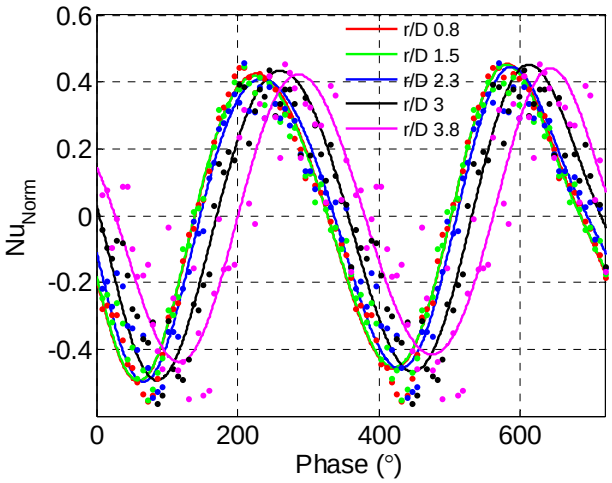

Figure 10: Normalised Phase Averaged Heat Transfer Signals; f_e=45Hz, H/D = 2

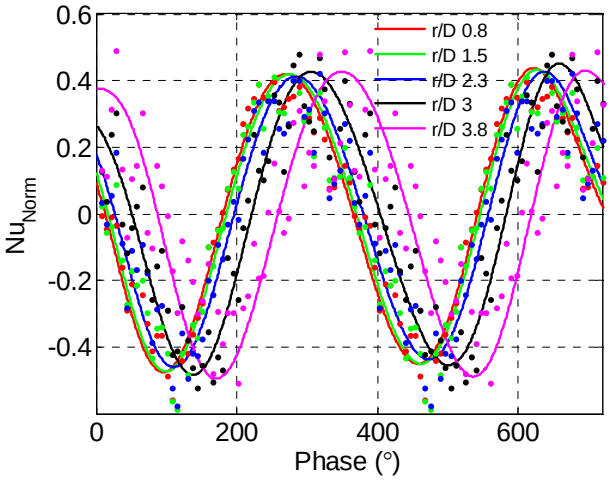

Figure 11: Normalised Phase Averaged Heat Transfer Signals; f_e=45Hz, H/D = 4

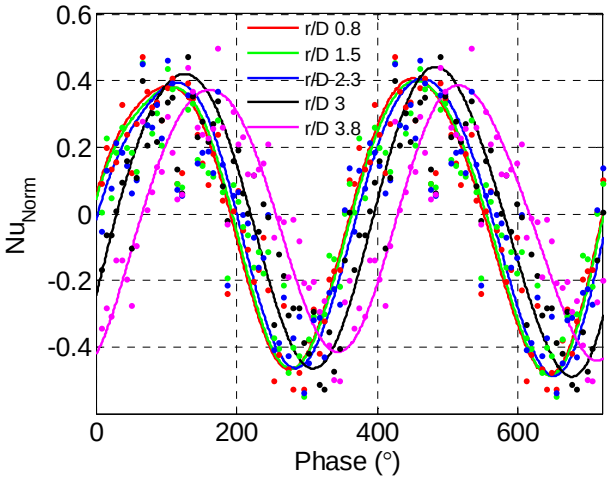

Figure 12: Normalised Phase Averaged Heat Transfer Signals; f_e=45Hz, H/D = 8

For *H/D=1* low fluctuations in the heat transfer imply that the flow is less turbulent than at higher *H/D*, which leads to relatively low heat transfer. As can be seen from figure 9 the flow across the impingement surface is quite closely in phase and remains strongly sinusoidal until *r/D=3.8* where it begins to break down this corresponds with a slight increase heat transfer and instabilities in the flow which can be seen in figures 4 and 5 respectively.

At *H/D=2* high *Nu* and *Nu'* indicates a more turbulent flow; this flow stays in phase up to a radial location of approximately *2* diameters from the stagnation point. Beyond this radial location, the heat transfer signals move radically out of phase but stay coherent/sinusoidal until *r/D=3.8* and by *r/D=4.5* it has all but lost remanence of a sinusoid. Again this corresponds with areas of increased heat transfer and instabilities in the flow which can be seen as of secondary peaks in figures 4 and 5 respectively. This is attributed to successive vortices impinging upon the surface and travelling out radially then breaking down into turbulence.

At *H/D=4*, similar to *H/D=2* high *Nu* and *Nu'* indicates a turbulent flow but the absence of secondary peaks implies that the vortices present in the flow at lower *H/D* values have begun to break down before impingement but have not fully broken down. The phase data is in general less coherent than at lower *H/D* values and moves out of phase more rapidly. For *H/D=8* the reduction in the *Nu'* is because the vortices has broken down the high *Nu* is because the jet is less confined and has entrained more and cooler air than at higher *H/D*.

CONCLUSIONS

Both mean and fluctuating heat transfer distributions to an impinging synthetic air jet have been presented for a range of experimental parameters. Phase locked time-traces of the heat transfer signals have been used to understand the convective heat transfer mechanisms in such a flow. It has been shown that the surface heat transfer fluctuates sinusoidally in the near wall jet region for low nozzle to impingement surface spacings. With increasing radial location however the fluctuations occur out of phase with each other indicting the passing of a vortex in the wall jet flow. At large *r/D*, beyond the secondary peak in the mean heat transfer distribution the sinusoidal nature of the heat transfer no longer exists indicating that the vortex has broken down into random turbulence. This is thought to have contributed to the magnitude/existence of a secondary peak in the mean heat transfer distribution.

From the phase information, it is apparent that at large values of *H/D* the vortex is broken down before impingement with the surface and this could explain why there is no secondary peak at larger *H/D*.

REFERENCES

1. Smith, B.L. and G.W. Swift, *A comparison between synthetic jets and continuous jets.* Experiments in Fluids, 2003. **34**: p. 467 - 472.
2. Pavlova, A. and M. Amitay, *Electronic cooling using synthetic jet impingement.* ASME Journal of Heat Transfer, 2006. **128**: p. 897 - 907.
3. Kercher, D.S., J.B. Lee, O. Brand, M.G. Allen, and A. Glezer, *Microjet cooling devices for thermal management of electronics.* IEEE Transactions on Components and Packaging Technologies, 2003. **26**: p. 359 - 366.
4. Martin, H., *Heat and mass transfer between impinging gas jets and solid surfaces.* Advances in Heat Transfer, 1977. **13**: p. 1 - 60.
5. Goldstein, R.J., A.I. Behbahani, and K. Heppelmann, *Streamwise distribution of the recovery factor and the local heat transfer coefficient to an impinging circular air jet.* International Journal of Heat and Mass Transfer, 1986. **29**: p. 1227 - 1235.
6. O'Donovan, T.S. and D.B. Murray, *Jet impingement heat transfer - Part I: Mean and root-mean-square heat transfer and velocity distributions.* International Journal of Heat and Mass Transfer, 2007. **50**(17-18): p. 3291-3301.
7. O'Donovan, T.S. and D.B. Murray, *Jet impingement heat transfer - Part II: A temporal investigation of heat transfer and local fluid velocities.* International Journal of Heat and Mass Transfer, 2007. **50**(17-18): p. 3302-3314.
8. Liu, T. and J.P. Sullivan, *Heat transfer and flow structures in an excited circular impinging jet.* International Journal of Heat and Mass Transfer, 1996. **39**: p. 3695 - 3706.
9. O'Donovan, T.S. and D.B. Murray. *Effect of acoustic excitation on the heat transfer to an impinging air jet*. in *ASME-JSME Thermal Engineering Summer Heat Transfer Conference*. 2007. Vancouver.
10. Hofmann, H.M., D.L. Movileanu, M. Kind, and H. Martin, *Influence of a pulsation on heat transfer and flow structure in submerged impinging jets.* International Journal of Heat and Mass Transfer, 2007. **50**(17-18): p. 3638-3648.
11. Golobic, I., J. Petkovsek, M. Baselj, A. Papez, and D. Kenning, *Experimental determination of transient wall temperature distributions close to growing vapor bubbles.* Heat and Mass Transfer, 2007.

EFFECT OF FLUID PROPERTIES AND PIPE INCLINATION ON FLOW PATTERN IN TWO-PHASE GAS-LIQUID FLOW

Ch. Tzotzi[1], M. Vlachogiannis[2] and N. Andritsos[1,*]
[1]Department of Mechanical & Industrial Engineering, University of Thessaly, Volos, Greece
[2]Technological Educational Institute of Larissa, Greece

ABSTRACT. The present study investigates the effect of several fluid properties on flow pattern transitions in horizontal and near-horizontal pipes over a wide velocity range. The fluids chosen for the experiments were selected so as to allow changes in one property, without affecting significantly other properties. Experiments have been conducted using a 12.75-m long test loop with and i.d. of 24 mm and pipe inclinations of $\pm 0.25^o$ $+0.5^o$ and $\pm 1^o$. Apart from air, two other gases (CO_2 and He) were employed to vary gas density, while the effect of surface tension was examined using an aqueous solution of n-butanol. The various transitions were identified visually, coupled with a statistical analysis of film height and pressure drop measurements.

Keywords: *two-phase flow, physical properties, pipe inclination, flow regime transitions*

INTRODUCTION

The prediction of pressure drop and liquid holdup occurring during two-phase gas-liquid flow in pipes is of particular interest to the petroleum, chemical and nuclear industries. These design parameters are strongly dependent on the flow pattern that prevails in the pipe. To occurrence of a specific flow pattern depends upon the flow rates, the physical properties of the two phases and the geometrical characteristics of the pipe. Generally, the transition from one flow pattern to another is not abrupt, except for the transition to intermittent from stratified flow. Within the transitional zones, the flow behavior exhibits characteristics of the flow patterns on both sides of the transition.

The effect of fluids properties on two-phase flow phenomena has been a subject for study by a number of investigators over the past 50 years. Weisman et al. (1979) examined the effect of physical properties (liquid viscosity, gas density and surface tension) on flow patterns in horizontal lines. They also proposed semi-empirical corrections for the transitions to account for the fluid properties and pipe diameter. A systematic experimental investigation of the effect of liquid viscosity (in the range 1-80 cP) on flow characteristics was carried out by Andritsos and Hanratty (1987). Recently, Funada and Joseph (2001) studied the stability of stratified gas-liquid flow in a rectangular channel taking into consideration the liquid viscosity and surface tension effect. The effect of surface tension on the stability of the interface was also investigated by Guo et al. (2002). They concluded that the increase of surface tension "stabilizes" the interface.

The effect of pipe inclination on flow patterns for gas-liquid flow was investigated experimentally by Barnea et al. (1980). It was observed that in downflow the stratified region is considerably expanded as the angle of inclination increases and higher liquid flow rates are required for the transition to intermittent flow. Conversely, upward inclination results in the expansion of

* Corresponding author: Associate Prof. N. Andritsos
Phone: + (30)-24210-74072, Fax: + (30)-24210-74085
E-mail address: nandrits@mie.uth.gr

intermittent flow region and stratified flow shrinks in a small bell-shaped region. Experimental investigations in slightly inclined pipes were also carried out by Andreussi and Bendiksen (1989) and Kokal and Stanislav (1989). Recently, Woods et al. (2000) and Simmons and Hanratty (2001) focused on the transition to intermittent flow in downward and upward inclined pipes, respectively, both experimentally and theoretically.

EXPERIMENTAL FACILITY AND TECHNIQUES

Experiments were carried out in a smooth, transparent Plexiglas pipe with an internal diameter of 24 mm and a total length of 12.35 m. A schematic of the experimental setup is shown in Figure 1. The carefully levelled pipe is placed on a steel frame that can be inclined slightly, up to ±3°. The liquid and gas phases were introduced into the pipe with a vertically placed Y-section, with water flowing in the lower branch. The two-phase mixture is emptied in plastic separator open to the atmosphere. Water is usually circulated through the system in a closed loop using a centrifugal pump. The air flow is supplied by an AIRCO M529 (4 HP) reciprocating compressor. The CO_2 flow is supplied by a bank of commercial CO_2 cylinders (Air Liquide), while the commercial-type He was provided by a single cylinder (Air Liquide) which limited the duration and the number of water-He runs. The volumetric flow rates of both phases were measured with a bank of three rotamerers for each phase. All three gas rotameters were calibrated using a Ritter BG 40 gas meter (minimum flow rate 0.4 m^3/h and maximum flow rate 65 m^3/h) for the three gas phases.

The liquid height and the wave velocity were measured at two locations in the pipeline (namely at 88D and 336D) using pairs of parallel wire conductance probes that extended in the vertical direction over the entire cross section of the pipe. The wires were 0.4 mm dia. chromel and their separation was 3 mm. An oscillating signal was sent to the probes and an analyser converted the response to an analogue signal. A HAMEG HM 8030 5-MHz function generator was used to provide the input sine signal at a frequency of 25 kHz. A demodulation circuit provided the peaks of the output signal synchronously using the square wave output of the function generator as a reference. The output voltage was found to vary linearly with the conductance only at very high resistances (R > 50,000 Ohm).

Pressure drops were measured in the gas phase at relatively low gas velocities with an inclined U-tube glass manometer. Most pressure drops data were taken in the liquid phase and were measured by a diaphragm-type ABB 2600T series differential pressure transmitter. The measuring range of the transmitter was 50-1000 Pa. Care was taken to keep air out of the connection lines, which were frequently purged of gas bubbles. The length over which the pressure drop was measured was varied depending on the phase flow rates.

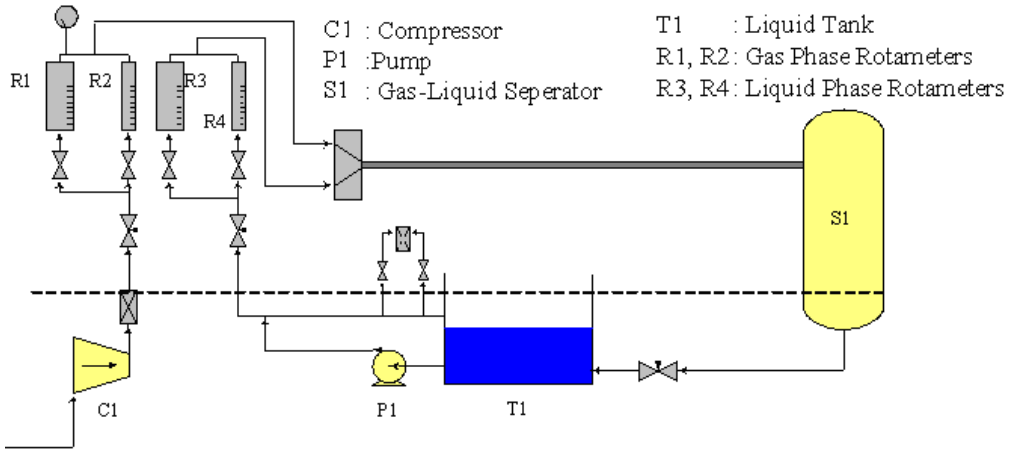

Figure 1. Schematic of the experimental apparatus

EFFECT OF FLUID PROPERTIES IN HORIZONTAL FLOW

The flow pattern that occurs in a pipe is affected not only by the flow rates, but also by the fluid properties and the system characteristics (diameter, roughness, inclination angle). In the present study CO_2 (ρ=1.81 kg/m^3 at 25ºC and 1 atm) and He (ρ=0.167 kg/m^3) were used as gas phases in order to explore the effect of gas density on the flow patterns. The effect of surface tension was examined using a n-butanol-water solution (measured value σ=0.04 N/m).

The effect of increasing the gas density is to decrease (at a constant liquid velocity) the gas velocity required for transition to 2-D (two-dimensional) and K-H (Kelvin-Helmholtz or large-amplitude) waves. This behaviour is clearly illustrated in Fig. 2a for the CO_2-water system. It is of interest that the only transition that remains unchanged is the transition from stratified to slug flow, although the slug-to-pseudo slug transition is affected by gas density.

The effect of surface tension is depicted in Figure 2b. The transitions to 2-D and to K-H waves are shifted to lower superficial gas velocities with decreasing surface tension (from 0.072 N/m to 0.04 N/m). The effect is stronger for 2-D waves, since for superficial gas velocities higher than 1 m/s employed in this study no smooth stratified region has been observed. As before, the transition to slug flow is not affected by a change in surface tension.

The transitions to 2-D and K-H waves for all the systems examined in this work can be described reasonably well by the semi-theoretical equations proposed in a previous work (Andritsos et al. 2008), as shown in Figures 3a and 3b.

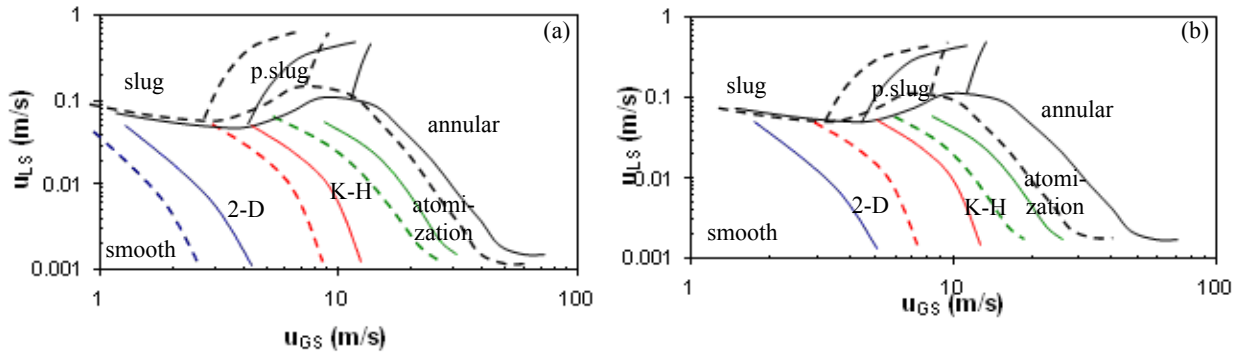

Figure 2. Comparison between air-water (continuous lines) and CO_2-water flow maps (left figure, dashed lines) and air-butanol+water flow map (right figure, dashed lines)

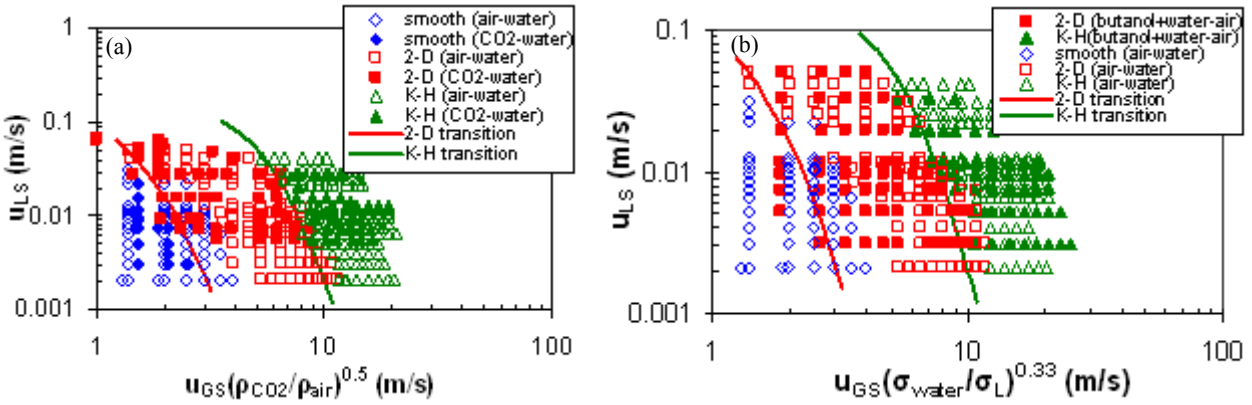

Figure 3. Comparison of semi-theoretical wave pattern transitions with CO_2-water (left) and n-butanol+water-air data (right)

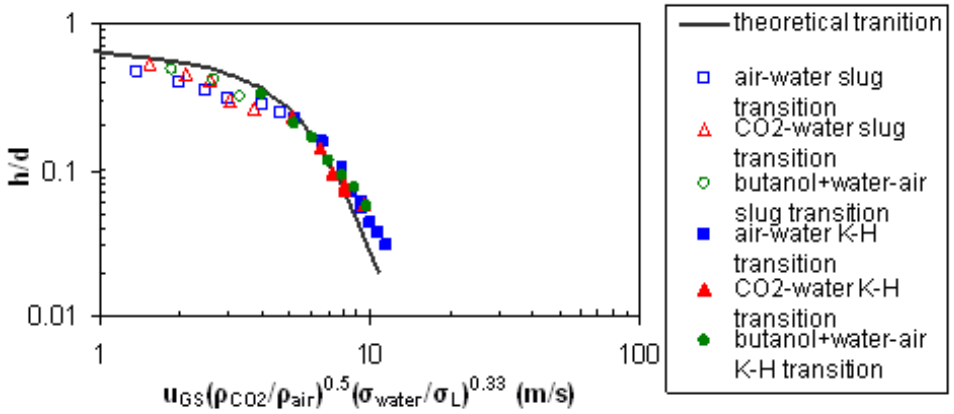

Figure 4. Comparison between experimental transition to slug flow and K-H waves with the proposed equations

The so-called K-H waves are irregular, large amplitude waves, which appear to be initiated by gas-phase pressure variations 180° out of phase with the wave height, i.e. due to Kelvin-Helmholtz mechanism, the same mechanism responsible for slug formation, when the height of liquid phase is high enough for these waves to grow and block the pipe cross-section (Andritsos et al. 1989). It was observed in this study (Figure 4) that the experimental transition to K-H waves and slug flow for systems with different physical properties agree quite well with the equation proposed in a previous work (Andritsos et al. 2008) with suitable modification of the system's co-ordinates.

As it is stated in the introduction, transition from one flow pattern to another does not take place abruptly, but a transitional zone exists, where the flow exhibits characteristics of the flow patterns on both sides of the transition. It is observed that transitional zone in the butanol+water-air system is wider than that of air-water and CO_2-water systems. Moreover, wave characteristics in this transitional zone are quite different for butanol solution compared to those for water.

At a liquid superficial velocity of 0.011 m/s the required gas velocity for the transition to K-H waves is ~9.4 m/s for the air-water system and ~7 m/s for butanol+water-air system, as can be seen in the film height traces presented in Figure 5. It can be also seen that for the butanol solution the transition zone is wider than that encountered for water. In addition, just before transition, some kind of "single" waves are observed with the butanol solution, but absent in the water. With increasing gas velocity these "single" waves coalesce and large amplitude waves are formed (u_{GS}=9.4 m/s). Finally, with further increasing gas velocity K-H waves are formed (u_{GS}=12.4 m/s). For air-water system (Figure 5b) at the beginning of the transition zone large amplitude small wavelength waves are observed (u_{GS}=9.4 m/s). With an increase in gas velocity (u_{GS}=10.2 m/s) the waves start to acquire K-H waves characteristics, as the amplitude of these waves become larger and their crests become steep. Finally, K-H waves are formed at u_{GS}=11.8 m/s. It is noted that this kind of "single" waves are not observed during the runs in the air-water and CO_2-water systems.

EFFECT OF DOWNWARD INCLINATION

In downflow the liquid moves obviously more rapidly and has a lower height in the pipe owing to downward gravity forces. As a result stratified flow region is considerable expanded as the angle of inclination increases. Figure 6 illustrates the shifting of the transition boundaries in flow maps as the inclination angle increases. In addition, for φ=1° the stratified smooth region was not observed even for zero gas velocity, obviously due to the effect of gravity.

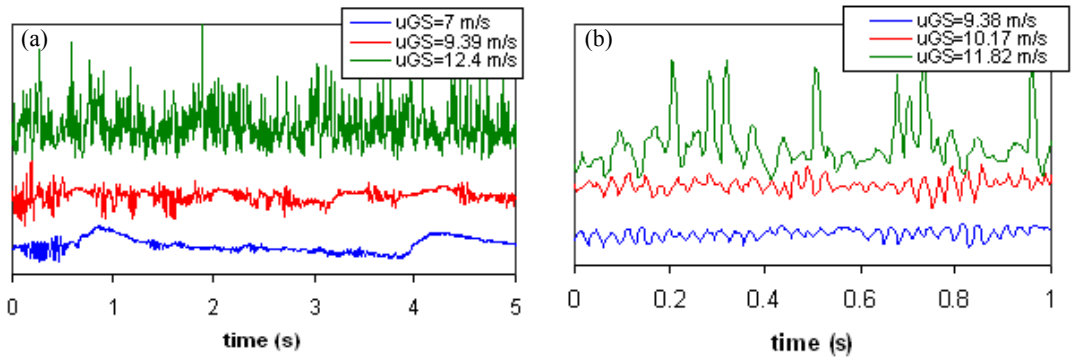

Figure 5. Wave evolution for and butanol+water-air (left) air-water system (right), u_{LS}=0.011 m/s

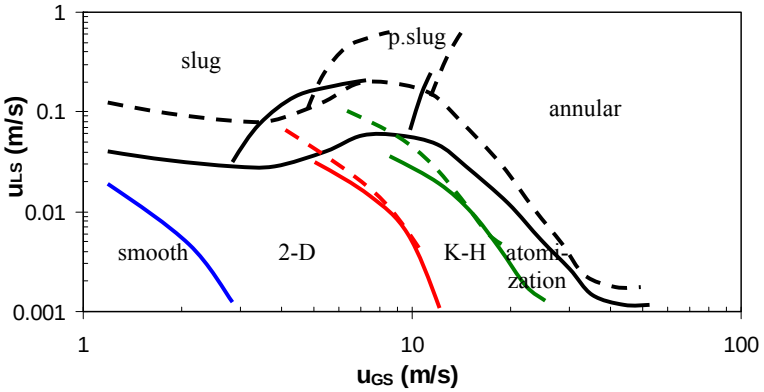

Figure 6. Comparison of air-water flow maps at φ=0.25º (continuous lines) and φ=1º (dashed lines)

Two different types of waves (2-D and K-H) were again identified in the stratified region and it turns out that, although the transition to 2-D waves is shifted to lower superficial gas velocities, the transition to K-H wave region remains rather unaffected by the inclination angle. As in horizontal flow, lowering the surface tension alters the appearance of waves in the "2-D" region. In the butanol+water-air system 2-D waves are not observed; instead some type of saturated periodic waves are formed, as can be seen in Figure 7b (for u_{GS}=3.97 m/s). On the other hand, K-H waves sustain their characteristics for all the systems examined in this study

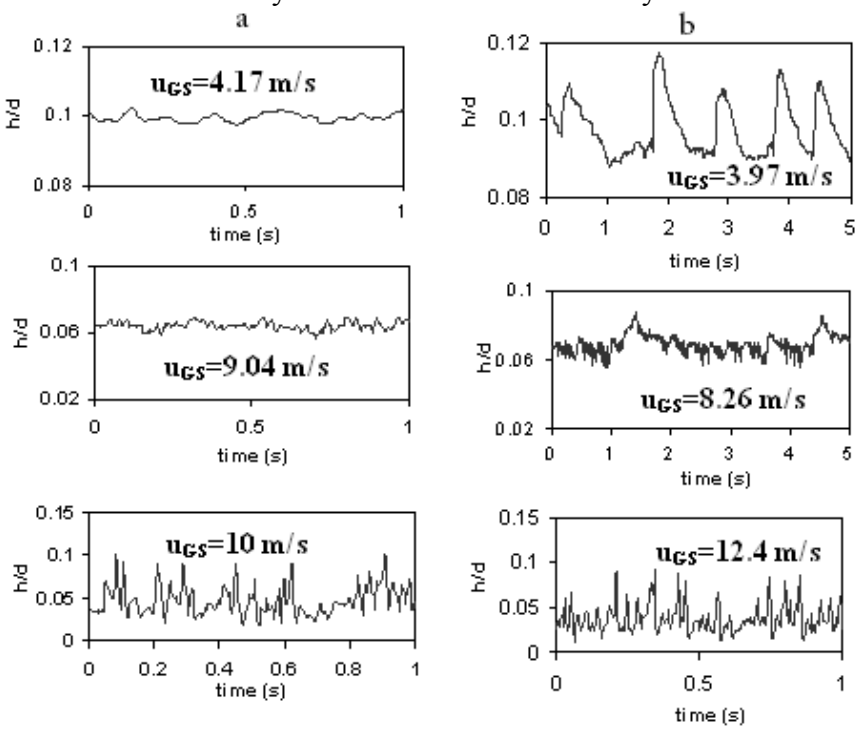

Figure 7. Film height traces in a CO_2-water system (left) and butanol+water-air system (right), u_{LS}=0.011 m/s

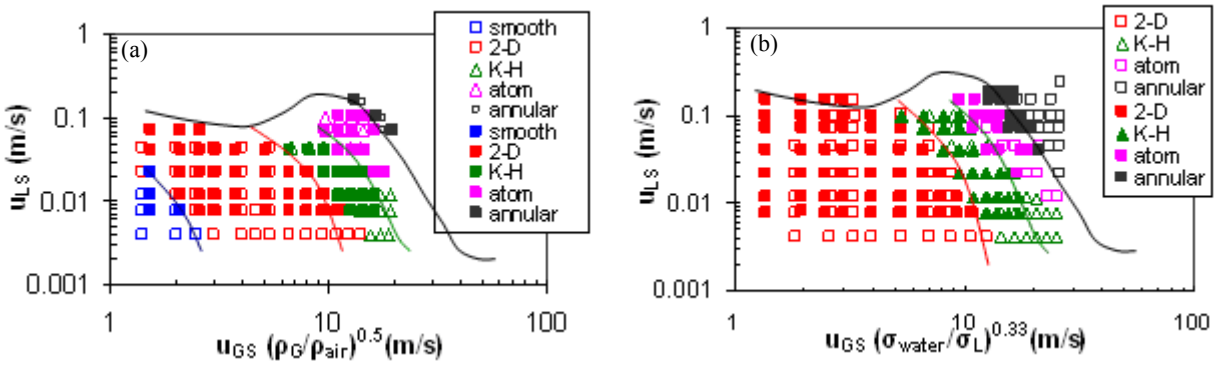

Figure 8. Comparison of flow maps at φ=0.25° (left, filled symbols air-water, open symbols CO_2-water) and at φ=1° (right, filled symbols air-water, open symbols butanol+water-air)

Both the gas density and the surface tension affect the various transitions in downflow in a similar manner with that found in horizontal flow. CO_2 and butanol solution were used in order to examine the effect of gas density and surface tension, respectively. It can be also shown that with proper modification of flow map axes the transitions to various subregimes of stratified flow almost coincide for the two systems, as depicted in Figure 8.

EFFECT OF UPWARD INCLINATION

For upward flows, even a small pipe inclination can cause severe slugging, even at low liquid velocities, while the stratified flow region takes the form of a bell-shaped area, as illustrated in Figure 9 for two pipe inclinations. In our study, a pseudo-slug flow is also considered, which is defined in a similar way as in horizontal flow, i.e. using as criterion the ratio of the slug velocity to the gas phase velocity. Following the above consideration, the pseudo-slug flow region precedes the transition from slug to stratified flow with increasing gas velocity at a constant liquid velocity.

Moreover, in the stratified flow region in upward flow two different types of waves were also identified, which retain 2-D and K-H wave characteristics. Both the transitions to 2-D and K-H waves were shifted to higher gas velocities as the inclination angle increases. Wave traces in stratified flow are presented in Figures 10 and 11. Following the transition from pseudo-slug to stratified flow, 2-D waves were first observed (illustrated in Figure 10a), while with an increase in gas velocity small amplitude irregular waves are formed (Figure 10b). Finally, at even higher gas velocities waves resembling the K-H one in horizontal flow appear in the pipe.

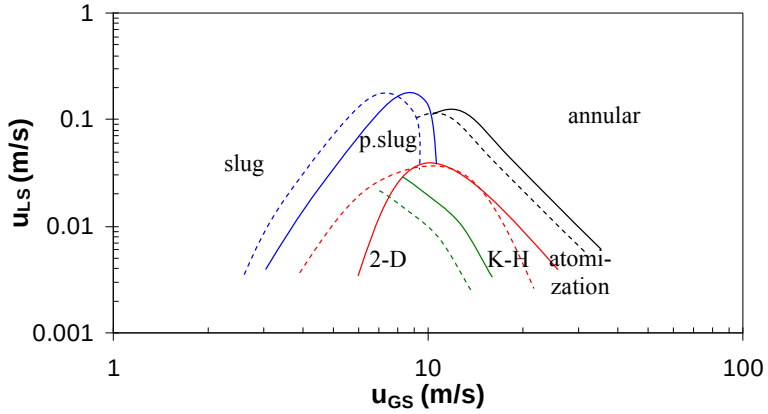

Figure 9. Comparison of air-water flow maps for two inclinations (φ=1° continuous lines, φ=0.25° dashed lines)

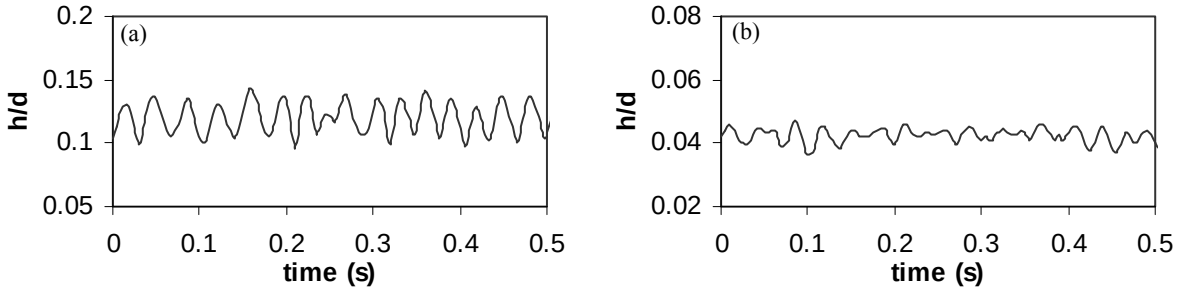

Figure 10. 2-D waves in stratified flow for air-water system at φ=0.25º in increasing superficial gas velocity

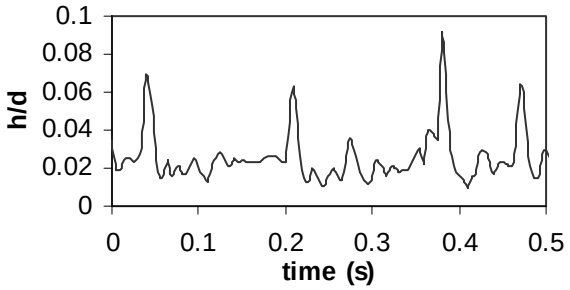

Figure 11. K-H waves in stratified flow for air-water system at φ=0.25º

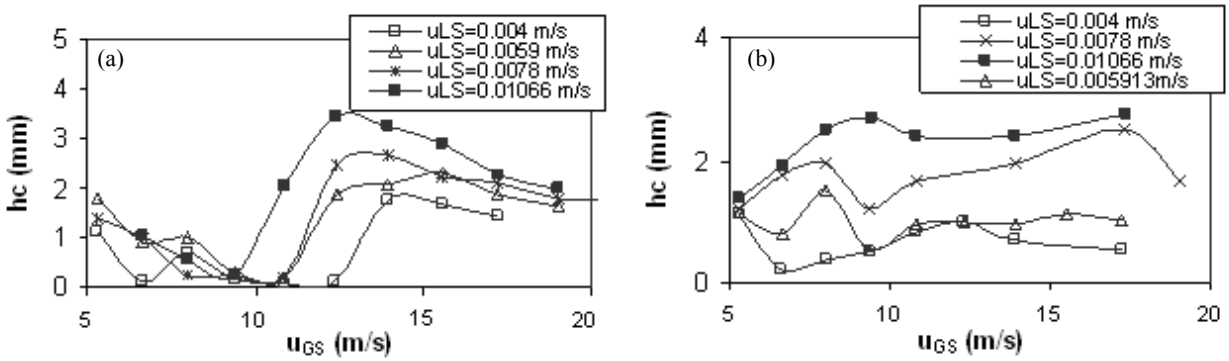

Figure 12. Wave amplitude in stratified region with increasing superficial gas velocity for air-water system (left figure) and butanol+water-air system (right figure) at φ=0.55º.

The wave amplitude decreases with increasing superficial gas velocity and the waves become steeper as shown in Figure 11. The two wave types are not distinct only from their appearance (which is also reflected in the large value of autocorrelation coefficient of the wave trace), but also from their amplitude as shown in Figure 12. It is evident that for the air-water system the transition from 2-D to K-H waves is rather abrupt, while the use of a low surface tension liquid results in roughly uniform wave amplitudes regardless of the wave type (Figure 12b).

CONCLUDING REMARKS

Experimental data are provided regarding the effect of fluid properties and pipe inclination for two-phase gas-liquid flow in a 0.024 i.d. pipe. Flow patterns were identified by a combination of visual and video observations and analysis of liquid height and pressure drop measurements.

In a horizontal pipe the transitions to the various flow patterns (bubbly flow has not been considered) are affected by changes in gas density and surface tension, apart from the transition between stratified and slug/plug flow. A decrease of the surface tension by using an aqueous solution of n-butanol results in the shifting of the transitions to the two main types of waves to

lower gas velocities. The transitions to 2-D and K-H wave regions can be predicted quite well by the semi-theoretical correlations (Andritsos et al. 2008).

For small downward inclination of the pipe, the stratified flow region is considerable expanded whereas for even a small upward pipe inclination the stratified flow regime shrinks to a bell-shaped area. Two different types of waves (2-D and K-H) can be identified for upward and downward inclinations for all the systems examined, exhibiting characteristics similar to those found in horizontal flow.

REFERENCES

1. Weisman, J., Duncan, D., Gibson, J. and Crawford, T., Effects of Fluid Properties and Pipe Diameter on Two-Phase Flow Patterns in Horizontal Lines, *Int. J. Multiphase Flow*, Vol 5, p.p. 437-462, 1979.
2. Andritsos, N. and Hanratty, T.J., Interfacial Instabilities for Horizontal Gas-Liquid Flows in Pipelines, *Int. J. Multiphase Flow*, Vol 13, pp. 583-603, 1987.
3. Funada, T. and Joseph, D.D., Viscous Potential Flow Analysis of Kelvin-Helmholtz Instability in a Channel, *J. Fluid Mech.*, Vol 445, p.p. 263-283, 2001.
4. Guo, L.J., Li, G.J. and Chen X.J., A Linear and Non-Linear Analysis on Interfacial Instability Of Gas-Liquid Two-Phase Flow Through a Circular Pipe, *Int. J. Heat Mass Transfer*, Vol 45, p.p. 1525-1534, 2002.
5. Barnea, D., Shoham, O., Taitel, Y. and Dukler, A.E., Flow Pattern Transition for Gas-Liquid Flow in Horizontal and Inclined Pipes, *Int. J. Multiphase Flow*, Vol 6, p.p. 217-225, 1980.
6. Andreussi, P. and Bendiksen, K., An Investigation of Void Fraction in Liquid Slugs for Horizontal and Inclined Gas-Liquid Pipe flow, *Int. J. Multiphase Flow*, Vol 15, p.p. 937-946, 1989.
7. Kokal, S.L. and Stanislav, J.F., An Experimental Study of Two-Phase in Slightly Inclined Pipes-I.Flow Patterns, *Chem. Eng. Sci.*, Vol 44, p.p. 665-679, 1989.
8. Woods, B.D., Hulburt, E.T. and Hanratty, T.J., Mechanism of Slug Formation in Downwardly Inclined Pipes, *Int. J. Multiphase Flow*, Vol 26, p.p. 977-998, 2000.
9. Simmons, M.J.H. and Hanratty, T.J., Transition from Stratified to Intermittent Flows in Small Angle Upflows, *Int. J. Multiphase Flow*, Vol 27, p.p. 599-616, 2001.
10. Andritsos, N., Tzotzi, C. and Hanratty, T.J., Interfacial Shear Stress in Wavy Stratified Gas-Liquid Two-Phase Flow, *Proceedings of 5th European Thermal-Sciences Conference*, The Netherlands, May 2008.

STUDY OF CHARACTERISTICS OF EXPLOSION BOILING-UP OF SUBCOOLED LIQUID ON A HOT SURFACE

Yu. Zeigarnik[1], Yu. Ivochkin[1], A. Oksman[1], K. Belov[1], A. Kryukov[2], Yu. Puzina[2]
[1]Joint Institute for High Temperatures of the Russian Academy of Sciences, Moscow, Russia
[2]Moscow Power Engineering Institute, Moscow, Russia

ABSTRACT. The technique for estimating the contact area between a cold water and a hot hemispheric surface is described. Synchronized measurements of pressure pulses in a liquid phase, those of a temperature in a solid body, and parameters of a contact of the superheated body with a coolant under the conditions of a sharp change of boiling regimes (from a film to nucleate one) are conducted. Specific features of the processes under study, which to a considerable extent are determined by the hemisphere temperature, its thermophysical properties, and the presence of surface oxides are determined. It is revealed that the maximum amplitude of pressure pulses of up to approximately 1 MPa are obtained in the range of the superheated body temperatures, which are close to the temperature of ultimate superheating of water. The dependences of the velocity of water spreading along the heated surface and the time lag of its boiling-up (flashing) on the hemisphere temperature are obtained. Interpretation of the results obtained using the methods of fluid dynamics and molecular-kinetic theory is made. An attempt to describe transfer processes and evolution of inter-phase surfaces at the initial contact of water with a hot hemispherical surface is done.

Keywords: *boiling, pressure pulses, boiling-up, wettability*

INTRODUCTION

The knowledge of regularities of transition from the film boiling regime to the nucleate one is very important for many technological processes [1]. Certain specific features of this process are of great importance while triggering steam explosion in the course of spontaneous fragmentation of hot-coolant droplets falling into a cold liquid. It is generally accepted that fragmentation of these droplets is connected with explosion-type destruction of vapor envelopes surrounding superheated droplets. In the literature, there are more than ten original ideas that describe fragmentation process [2]. At the same time, details of physical processes that accompany the vapor-cavity collapse are studied insufficiently thoroughly. In particular, in the past, rather small attention was paid to the problem of contact of the hot and cold media, as well as to studying specific methodological questions that appear while studying detail characteristics of pressure pulses. In our paper we describe and analyze new experimental data concerning these problems.

THE EXPERIMENTAL INSTALLATION AND MEASUREMENT TECHNIQUE

On the basis of our experiments conducted earlier [3] one can suppose that the destruction of the vapor envelope, including the first contact between hot and cold media, takes place similarly on the

*Corresponding authors: Ph.D. Yu. Yu. Puzina
Phone: +7(495)3627841, Fax: +7(495)3628643
e-mail address: Puzina2006@rambler.ru
Postgraduate student K. I. Belov
Phone: +7(495)36116873
e-mail address: vortex@iht.mpei.ac.ru

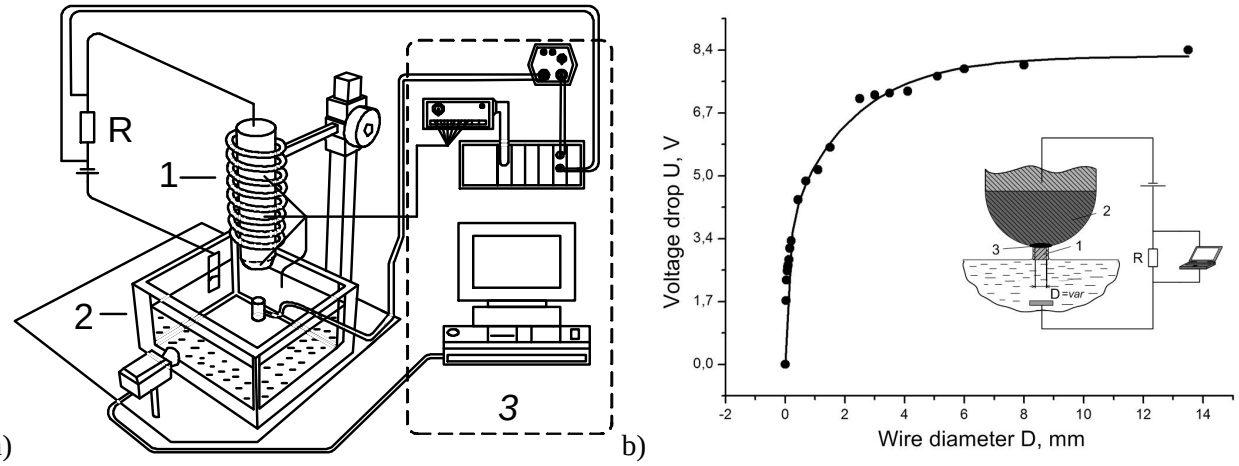

Figure 1. The layout of the experimental installation (a) and calibration curve of the electric-contact probe. *1*- working specimen; *2*- tank with water; *3*- measurement complex.

superheated solid and liquid-metal surfaces. Since to conduct experiments with solid metal specimens is considerably simpler and possibilities of the latter, as to physical properties variation and surface-condition control, are significantly larger, most experiments simulating the initial stage of the vapor film destruction were carried out with hemispherical highly heated surfaces immersed into cold water.

Figure 1a shows the layout of the experimental installation and the scheme of measurements. The test section was a cylindrical copper rod, at the end of which a changeable tip was mounted. Cylindrical rod of 10 mm in diameter with hemispherical end was used as a tip. Tips made of grade Kh18N10T stainless steel were used in the experiments. Electric current passed through the spiral wound on the copper rod was applied for heating the test section.

The experiments were carried out as follows. In the initial (taken from water) position the tip was heated by a propane jet for several tens of seconds. This led to formation of oxide film on the tip surface. After oxidation, the tip was cooled and heated again to the desired temperature by the electric heater in argon atmosphere. After this, the electric heater was switched-off and the heated test section with the use of special coordinate spacer was immersed into the vessel filled with distilled water at a depth equal to the hemisphere radius. The immersion velocity was several mm/s. The initial hemisphere temperature was approximately 500^{o}C. This value was chosen to ensure stable film-boiling regime. The technique applied made it possible to accomplish explosion-like vapor film collapse on the heated surface by a simple way. In experiments, distilled water at a room (~18^{o}C) temperature was used. Preliminarily boiling for two hours provided water degassing.

Monitoring of the processses under study was conducted with the use of microscopes and video cameras. Temperature measurements carried out by Chromel-Alumel thermocouples imbedded into stainless steel capillary tubes, along with monitoring temperatures in the hemisphere center and other pints of the test section, made it possible to determine heat flux value on the hemisphere surface under film boiling conditions. Kistler 601A piezo-sensors operated in combination with Kistler 5015 charge amplifiers were used as pressure gages. Measuring and treating the signals from different sensors were conducted with the use of Labview software and the National Instruments devices. A typical sampling rate was 5 10^{5} s^{-1}.

Characteristics of the process of water coming into with the hot surfaces were determined by measuring a voltage drop at the reference resistor, which was part of closed electric circuit

comprised direct-current source, two electrodes (the test section functioned as one electrode and the copper plate immersed into water pool, as another), connecting wires, water and steam volumes. When there was no contact between the water and the test-section surface, the total resistance of the circuit was determined by electric resistance of the steam layer and has the maximum value, respectively, the current and voltage drop on the reference resistor were minimal. At an instant of water contact with the test-section surface the electric current in the circuit increased sharply. When this happened, the voltage drop on the reference resistor changed depending on an area of the contact surface.

The calibration curve of the voltage drop on the reference resistor as a function of equivalent contact area (Fig. 1b) was obtained in the course of special experiment, when a contact spot was simulated by the end surface of the copper wire isolated from side surfaces (see the insert in Fig. 1b). The tip of the wire, whose diameter in the experiments was varied from 30 μm to 15 mm, was soldered to hemispherical surface of the test section, while the other was immersed into water by several millimeters. The trustworthiness of the technique proposed was confirmed by a good agreement of the contact-area value determined with the use of calibration curve with the total hemisphere-surface area in the case, when nucleate boiling occurred at the entire surface of the specimen.

An important methodological problem that arises in the course of pressure measurements with the use of piezo-electric gages is the influence of the pulse temperature impact on their readings. In our experiments, the gages were located in water at different distances from the lower part of the hemisphere; in so doing, the minimal distance was 5 mm. Under these conditions, in addition to the pressure action proper, the gage's reading can experience a temperature impact. In particular, these effects can be caused by a short-term entry of the transducer's sensitive element, which is usually located in a cold liquid, into relatively hot "vapor cloud", that is formed under explosion-like destruction of the vapor layer. According to the manufacturer's specifications, the temperature-sensitivity coefficient of the gage is $k = 0.0001\ K^{-1}$. Numerical estimates based on this value attest weak effect of the temperature factor should be anticipated. These specified characteristics, however, are valid under conditions, when all parts of the gage (membranes, casing, piezo-element, etc.) are equally heated and have one and the same constant temperature. In our case these conditions are not met. Therefore, special experiments were conducted to investigate possible effect of temperature pulses on piezo-electric gages readings. In these experiments, during relatively short time interval (~0.5 to 10 s) the sensitive element of the transducer experienced the impact of the hot air moved with a velocity of several m/s. The air temperature was within a range of 100-300^{o}C. The results obtained showed the existence of rather strong response of the gage to a sharp raise in a temperature (apparently, due to temperature distortions). The effect recognized generates false signals, such as incomprehensible recordings of low-frequency intense rarefaction pulsations that accompany the process of transition boiling after vapor-cavity collapse [3, 4]. This fact shows certain caution should be given when interpreting experimental data on pressure pulses.

RESULTS OF EXPERIMENTAL STUDIES

The experiments conducted made it possible to reveal that pressure oscillations accompanying explosion-like destruction of the vapor film constitute a pack of pressure pulses, the amplitude and typical shape of which are to a considerable extent determined by a temperature of the heated hemisphere (see Fig. 2 and the inserts in it). The explosion-like vapor film destruction is not observed (there are no significant pressure pulses) at relatively low ($T < 180^{o}$C) and high values ($T > 410^{o}$C) of the hemisphere temperature. Between these two values of a temperature, a pack of pressure pulses is formed, which is characterized by two (microsecond and millisecond) time scales. An amplitude of the pressure pulse can be as high as ~1 MPa, which is sufficient to trigger vapor explosion [5]. It is important to point out that, as it can be seen from Fig. 2, maximum pressure

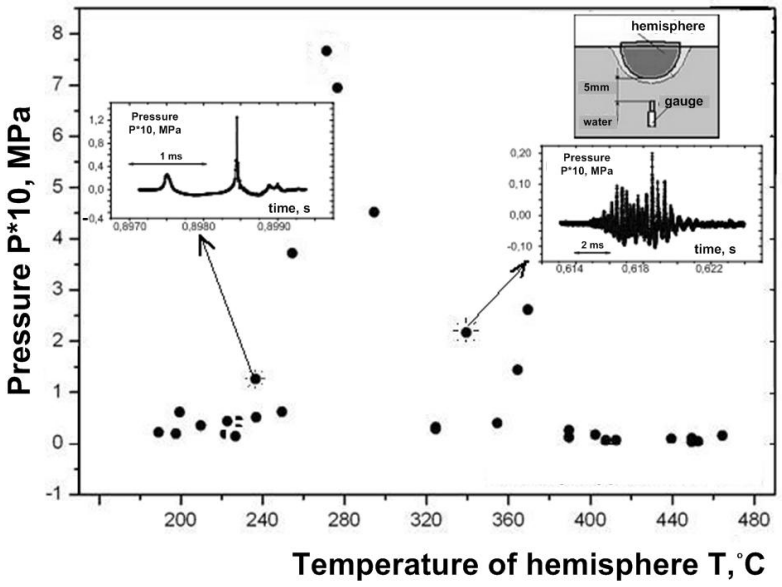

Figure 2. Dependence of the maximum amplitude of pressure pulses on the heated hemisphere temperature. Specimens are made of stainless steel. Water temperature is 20°C.

pulses are observed within a range a temperature of the heated-surface that is close to the temperature of the ultimate superheating of water. According to different experimental estimates, at atmospheric pressure, the latter is equal to about 250-280°C [6].

Along with the amplitude of the pressure pulse, a temperature of the heated surface considerably affects the frequency of pulsations and the number of them in the pack; they both increase with an increase in the temperature by an exponent law.

Detailed investigations into the phenomena under study can be accomplished by conducting finer comprehensive experiments. In particular, interesting additional information can be obtained from measuring pressure pulses, which is carried out simultaneously with determination of the degree of the cold liquid contact with the heated body (equivalent radius or the contact area) with the use of electro contact probe. Figures 3a – 3c shows typical results from such investigations obtained with specimens made of stainless steel.

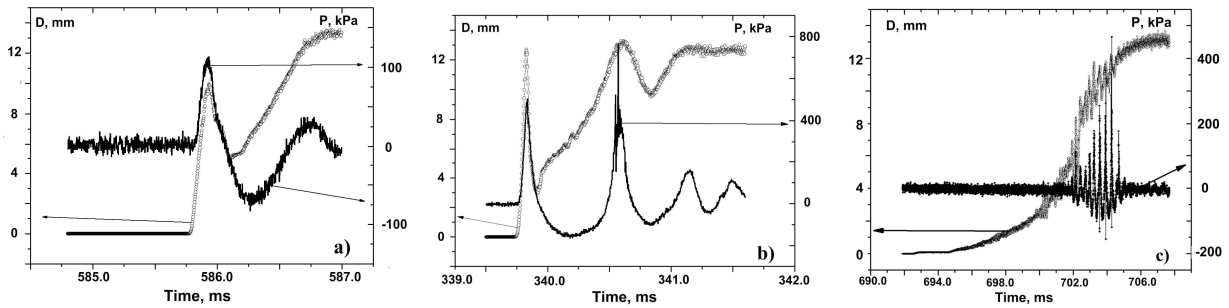

Figure 3. Simultaneous oscillograms of pressure and equivalent diameter of the contact spot. Specimens are made of stainless steel. Hemisphere temperature at a moment of explosion-like collapse (destruction) of the vapor film: (a) 219; (b) 279; (c) 315°C.

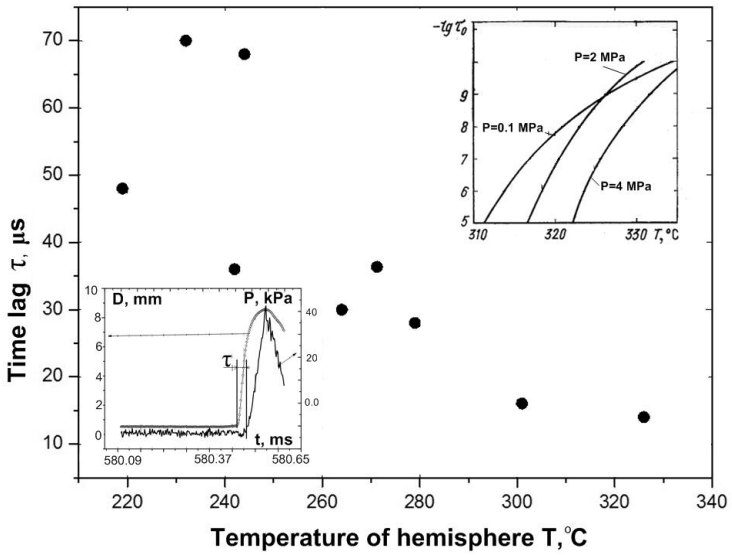

Figure 4. Dependence of the time necessary for heating cold water (water temperature is 20°C) till its boiling-up during water coming into contact with the heated surface on the hemisphere temperature. The insert in the right upper angle shows the calculated data from [6].

It is necessary to point out the fact that the cold liquid comes into contact with a hot surface, the temperature of which is higher than the ultimate temperature of the liquid superheating. The processes occurred on the specimens made of stainless steel and copper differ each other. In addition, we should point out the following. First, as it is seen from the curves in Fig. 3, the behavior of pressure pulses, at least at the initial stage of the contact, follows a change in the contact spot in time, i.e., the signals from the electric-contact and pressure sensors are correlated. Second, in all tests conducted, after coming the water into contact with the hot surface, an increase in pressure did not take place simultaneously with this event; certain time lag caused by the necessity of heating the cold liquid before its spontaneous boiling-up (flashing) was observed. The magnitude of this time lag in the tests conducted was tens of microseconds and it decreased with an increase in the hemisphere temperature (Fig. 4). We should note that the experimental data obtained well agree with the theoretical estimates of the time of contacting of cold water (T=20°C) and a hot surface under flashing in [6].

Finally, from the curves given in Fig. 3 we can assess the velocity of wetting the hot surface by water (the ratio of a change in the contact spot radius to the duration of this process), which, as it follows from the data presented, depends on the hemisphere temperature and can be rather high, of about 70 m/s.

INTERPRETATION OF EXPERIMENTAL DATA

Heat and mass transfer processes that occur in the case of coming into contact of a hot heater and cold liquid qualitatively can be described as follows. At the initial instant, one or some vapor bubbles are formed on a solid surface (Fig. 5a). A considerable increase in a volume of a liquid "tongue" due to evaporation leads to propagation of the latter along the heater surface (Fig. 5b). Condensation of the superheated vapor from the vapor film surrounding the hot surface accelerates contact spot expansion. Motion of liquid pulls away the vapor bubble from the nucleation cite and it begins to collapse inside the cold liquid (Fig. 5c). At the final stage of the collapse, the pressure in the liquid near the interface increases considerably. Single or cumulative bubble-collapse effects bring to the appearance of a pressure pulse in the liquid and subsequent explosion-like destruction of the vapor film. Contact spot expansion is completed by the transition to the developed nucleate

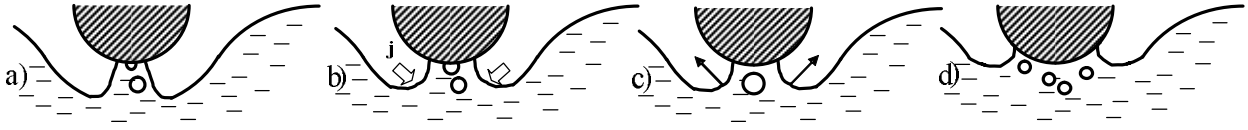

Figure 5. Qualitative description of the process

boiling (Fig. 5d). The velocity of propagation of the interface front is about 100 m/s, which is rather high for such type of problem.

Numerical results that we have obtained earlier on the basis of our technique for calculating characteristics of a smooth stationary axisymmetric interface formed during immersion of a hemispherical heater into cold water are in a good agreement with experimental data [7]. When so doing, the mathematical description of the problem included a set of equations that represent general and special compatibility conditions at the interface. Thus, to describe the problem under consideration, three equations of conservation, i.e., those of mass, momentum, and energy, are stated at the interface, which correlate respective characteristics of the liquid and vapor phases. Linear Labuntsov-Muratova correlation is used as a special compatibility condition (nonequilibrium boundary condition). This formula was obtained [8] with the use of principles of molecular-kinetic theory and makes it possible to calculate mass flow rate during evaporation and condensation, with an interface temperature and vapor pressure being known.

The model that describes vapor-bubble collapse near the interface shows a good agreement with experimental data as to a magnitude of the pressure jump [3]. Therefore, it was proposed to use this model to describe the propagation of the liquid "tongue" along the heater surface.

At the first step, the formation and collapse of a single vapor bubble in a liquid was analyzed. According to the known solutions to the traditional problems of the mechanics of two-phase systems [9] the time of the vapor bubble growth up to the departure diameter of 0.3 mm is not less than $8.2\ 10^{-4}$ s. In this case, the velocity of motion of the interface due to vapor-bubble expansion will be of about 0.1 m/s.

If we suppose that at the beginning of the vapor bubble collapse the temperature in the bubble is 100^{o}C and the corresponding pressure at the saturation line is 10^5 Pa, the bubble collapses due to action of hydrostatic pressure difference between the lower point of the heating surface and the free liquid surface, which is equal to approximately 50 Pa. The analysis of the vapor bubble dynamics with the use of the model based on Rayleigh's equation shows that under such conditions the bubble-collapse time is $6.1\ 10^{-4}$s. When this happens, the value of pressure in the liquid reaches 1 MPa, which is an agreement with experiments [3].

Another possibility of bubbles formation is their appearance not on heater surface but in liquid near this surface. Collapse of these bubbles can give corresponding addition to pressure pulse.

A rate of vapor condensation from the film on the cold-liquid surface is assessed with the use of the correlation following from the solution of the Boltzmann kinetic equation [8]; where P is the pressure of the gas removed, Pa; T_s is the interface temperature, K; P_s is the equilibrium vapor pressure at the saturation line corresponding to T_s; and T is the gas temperature far from the interface, K.

$$j = 1.67 \frac{P - P_s}{\sqrt{2\pi R T_\infty}} \qquad (1)$$

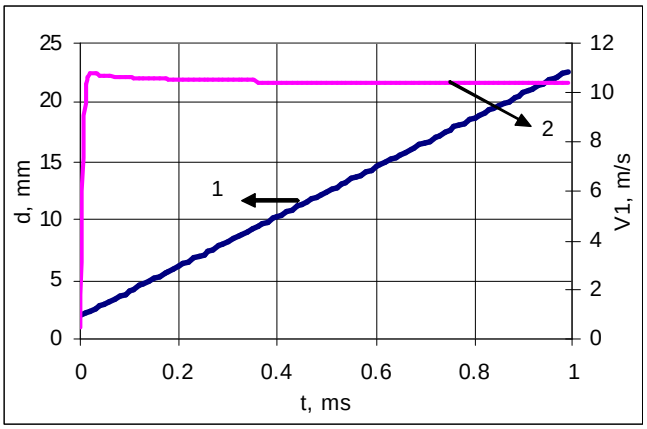

Fig. 6. Dimension of the contact spot (*1*) and corresponding velocity of the vapor-liquid interface motion (*2*) as functions of time.

With the pressure difference at the interface of 50 Pa the mass flow rate is 5.75 10^{-2} kg/(m^2 s) and the corresponding interface velocity is 5.75 10^{-5} m/s. We see from these calculations that, with the above parameters of the two-phase medium, condensation does not affect considerably the liquid-vapor interface motion.

The final stage of the process is as follows. Due to pressure pulse impact the liquid moves in lateral directions, with depth layers being included in this motion. The velocity of liquid propagation at the initial stage of the process and an increase in the contact spot dimension are estimated using the non-steady solution of Gromeko's problem about the motion of viscous liquid plug in the duct [10]. The duration of the pressure pulse is 10 μs; the initial dimension of the contact spot is 2 mm.

Comparison of the calculation results with experimental data shows that characteristic times of heat and mass transfer processes agree, at least by an order of magnitude (see table).

Table.
Comparison of characteristic values

Characteristic values	Experiment	Calculations
Time from coming into contact till a pressure pulse, μs	10-100	100-1000
Pressure pulse in a liquid, MPa	1	1
Velocity of liquid front propagation, m/s	10-100	11
Averaged time of contact spot spreading after pressure pulse, ms	1-5	-

The differences between the experimental and calculation data are caused, first of all, by the fact that a behavior of only a single bubble was analyzed, while, in reality, several bubbles can be formed. Nonisothermal condition of the heater and certain dynamic effects connected with surface wettability were not accounted for also. Collective phenomena lead to noise appearance and to changing liquid-front velocity. When this happens, both acceleration and deceleration of the front motion can take place.

Hence, the dynamics of the interface during vapor-bubble collapse in a cold liquid determines expansion of the contact spot and it is favorable for explosion-like vapor film destruction. The speed of the dynamic effects motion on the interface is comparable with a sound velocity.

CONCLUSIONS

1. A simple technique was developed, which made it possible to recognize the existence of contact and determine contact area during interaction of the cold water and hot surface.

2. Synchronized measurements of pressure pulses, solid body temperature, and contact area were carried out. It was found that depending on the velocity of water spreading over the heated surface single pressure pulse or a pack of successive pulses can occur.

3. Pressure pulses of up to 1 MPa were seen in the regimes with single pulses. They took place at a heating surface temperature close the temperature of ultimate superheating of water. Attempt to calculate the value of pressure pulse can give same order of these characteristic as in measurements.

4. The time lag, which is necessary to heat liquid before explosion-like boiling-up is about 10 μs, which is in agreement with corresponding theoretical estimates.

The authors gave their appreciations to V. V. Glazkov, V. G. Zhilin, O. A. Sinkevich, and V. V.Yagov for fruitful discussion and comments of the results of this work.

The work was supported by the Russian Foundation of Basic Research (Projects nos. 08-08-00792 and 08-08-00638) and grant of the President of the Russian Federation for state support of the young Russian scientist MK-1672.2008.8.

REFERENCES

1. Ametistov E. V., Klimenko V. V., and Pavlov Yu. M., *Boiling of Cryogenic Liquids*, Energoatomizdat, Moscow, 1995 [in Russian].
2. El-Genk M. S., Mathwest R. B., and Bankoff S. G., Molten Fuel-Coolant Interaction Phenomena with Application to Fuel Safety, *Progress in Nuclear Energy*, 1987, vol.1, pp. 151-198.
3. Zeigarnik Yu. A., Ivochkin Yu. P., Kryukov A. P., et al., Pressure Pulsations During the Growth and Collapse of Vapor Cavities in a Subcooled Liquid, *Proc. of 5th European Thermal Science Conf.*, 18-22 May, Eindhoven, The Netherlands, paper TPF-16.
4. Zyszkowski W., Study of the Thermal Explosion Phenomenon in Molten Copper-Water System, *Int. Journal Heat and Mass Transfer*, 1976, vol. 19, p. 849.
5. Nelson L. S. and Duda P. M., Steam Explosion Experiments with Single Drops of Iron Oxide Melted with CO_2-Laser, *High Temperature-High Pressure*, 1982, vol. 14, p. 259.
6. Skripov V. P., Sinitsyn E. N., Pavlov P. A., et al., Thermophysical Proprties of liquids in Metastable State, *Handbook*, Atomizdat, 1980 [in Russian].
7. Puzina Yu. Yu. and Ivochkin Yu. P., Curvature Change of Vapor-Liquid Interface under the Affect of Heat Flux, *XVI School-Seminar of Young Scientists under the direction of Academician A. I. Leont'ev*, MEI Publishing, 2007, vol. 1, pp. 486-489 [in Russian].
8. Muratova T. M. and Labuntsov D. A., Kinetic Analysis of the Processes of Evaporation and Condensation, *Teplof. Vys. Temp.*, vol. 7, No. 5, pp. 959-967 [in Russian].
9. Labuntsov D. A. and Yagov V. V., *Mechanics of Two-Phase Systems*, MEI Publishing, Moscow, 2000 [in Russian].
10. Slezkin N. A., *Dynamics of Viscous Incompressible Liquid*, Gostekhizdat, Moscow, 1955 [in Russian].

EXPERIMENTAL ANALYSIS OF DROPLET GENERATION

G. Wojciechowski*, P. Domagała, S. Drobniak

Czestochowa University of Technology,
Institute of Thermal Machinery, Czestochowa Poland

ABSTRACT. The paper presents results of experimental analysis concerning the primary breakup of liquid jet. The experiment was carried out for two test conditions with and without excitation with the injector based on Rayleigh phenomenon. The breakup process was investigated by optical methods based on fast micro photography. The results obtained constitute the data base for verification of numerical modelling of liquid jet breakup.

Keywords: *liquid jet primary breakup, atomization*

INTRODUCTION

The atomization of liquid jets is of great importance for several industrial processes, such as generation of sprays, fuel injection in internal combustion (IC) and jet engines and combustion of liquid fuels. The dominant trend in liquid fuel combustion systems is the increase of fuel injection pressure (in IC engines) or injection to high shear stress environment (in aeroengines) that leads to the decrease of mean diameter of generated droplets. In most combustion systems reduction of fuel droplets diameter provides easier ignition, a wider range of burning conditions and lower concentrations of pollutants in exhaust gases as well as the improvement of engine efficiency.
Disintegration of a liquid jet emerging from simple cylindrical nozzle may be affected by several factors i.e. the turbulence in the liquid jet and in the surrounding air, cavitation in the nozzle atomizer, and the interferential friction between emerging liquid jet and surrounding medium, which were identified as the most important ones [1], [2]. It should also be stated that atomization and jet breakup are the instability – driven processes and therefore they are highly unsteady. Most of the research concerning the atomization problem was performed experimentally, the numerical modelling encounters severe difficulties resulting from the presence of two separate phases with discontinuous change of phase properties and from the unsteady nature of jet breakup processes, which can not be properly accounted for with the use of RANS methods. That is why it is only recently that the first successful attempts of jet primary breakup numerical modeling could be performed [3]. One should notice however, that this solution was obtained with low order solver, while the proper capturing of interaction between turbulence and jet breakup processes will require higher order accuracy solver, especially when application of LES is considered [4].
The interest of industry in the problem stated above was the reason for establishing EU STREP project TIMECOP [5], devoted to experimental and numerical investigations on atomization and evaporation of liquid fuels in jet engines. Within TIMECOP project the researchers from Institute of Thermal Machinery CzuT are responsible for LES modelling of liquid jet primary breakup and generation of high quality experimental data needed for verification of numerical modelling.

* Corresponding author: mgr inż. G. Wojciechowski
Phone: + (48)-34-3250507, Fax: + (48)-34-32505555
E-mail address: wojciechowski@imc.pcz.czest.pl

The motivation for the present study is twofold. First reason is, that the existing knowledge concerning disintegration of liquid jets and evaporation of droplets was obtained for comparatively large diameters of jets and droplets [1], while currently designed aircraft engines utilize much smaller fuel nozzle diameters [6]. Second motivation is, that most of experimental results concerning the jet primary breakup have been obtained in the first part of last century [1] and even if these results are very accurate and reliable, they contain at most the basic statistics like mean and variance of analyzed quantities.. The above statement outlines the main motivation for the present study which is devoted to the experimental analysis of liquid jet primary breakup in the range of jet diameters of the order of ~ 100μm.

The phenomenon of uniform liquid – jet breakup was theoretically studied by Rayleigh [7]. A more general theory for disintegration of jet at low speed was developed by Weber [8] who extended Rayleigh's analysis to include viscosity and the effect of air resistance on the disintegration of jet into drops. Typing level headings.

APARATUS AND MEASUREMENTS TECHNIQUES

Injector used in current study shown in Figure 1. was designed by T. Kowalewski and used at IPPT PAN [9]. This injector is based on Rayleigh instability phenomenon. The plenum chamber of this injector is made of copper, while nozzle and bottom plate are fabricated of stainless steel. Piezoelectric transducer fixed to bottom plate introduced controlled disturbances to the liquid jet (for non excited case this feature was not used).

Injector is equipped with replaceable nozzles with different exit diameters in the range from 50μm to 2mm. During the present research the 100μm nozzle was used.

The schematic diagram of the test rig is shown in Figure 2. This test facility consists of two main parts. The first part serves for the droplet generation and the second part of this facility serves for recording of generated droplets. The main components of the test facility are as follows

- Atomiser (1) equipped with replaceable nozzles
- Digital camera (2) Canon 400D placed on micromanipulator (13),
- LED lamp (4) with (3), driven by impulse generator (5),
- Synchronisation unit (6),
- Harmonic Generator (7) with controlled amplitude and frequency of excitation,
- Amplifier (8) exciting piezoelectric transducer of atomizer (1)
- Oscilloscopes (9) i (10) and frequency meter (11),
- High pressure tank manometer (15) and flow meter (14).

Figure 1. Injector based on Rayleigh instability from IPPT PAN

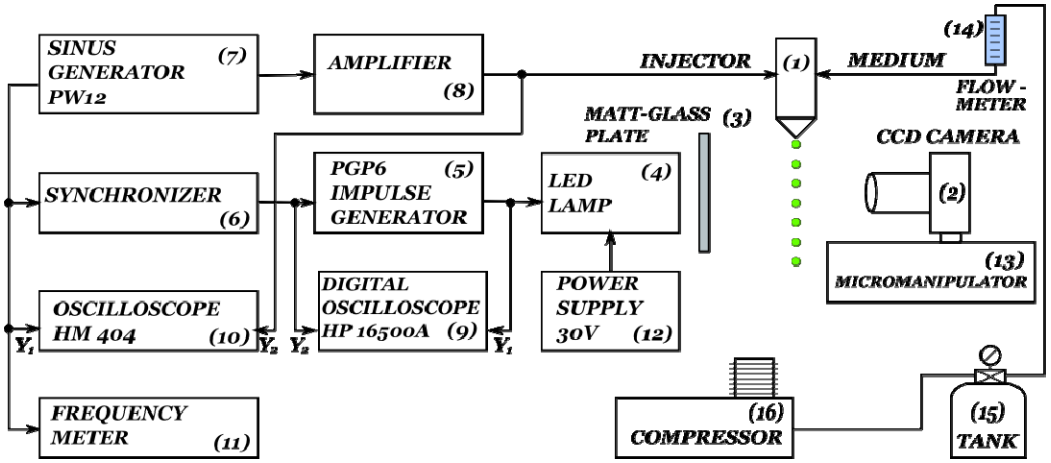

Figure 2. Scheme of equipment used for experimental investigation of atomisation process.

The atomised liquid was supplied to atomizer (1), from the pressure stabilising in tank (15). Determination of flow velocity was based on flow meter (14).
The part of test facility responsible for recording of generated droplets is composed of:

- CCD camera (2)
- LED lamp (4),
- Flash synchronizer (6),
- Impulse generator (5),

Synchronizer (6) and impulse generator (5) allow for precise adjustment of flash duration and delay with respect to driving signal of piezoelectric transducer. The measurements of flash duration and delay was done by digital oscilloscope HP16500A (9). The duration and the delay of flash was achieved by impulse generator PGP6. Amplitude and frequency of driving signal of piezoelectric transducer was determined by generator of harmonic signal (7), those parameters were measured by oscilloscope HM 404 (10) and frequency meter (11). The details of experimental setup and measuring techniques may be found in [10]
As a liquid chemically clean water was supplied to injector. The temperature of liquid and ambient temperature were recorded and controlled during the measurements.
Recorded images were analysed with ImageJ software [11]. Recorded images had uniform brightness and there was no need for image equalisation.

RESULTS

Non excited case

The first quantity needed for verification of numerical modeling was the length of liquid jet column before its disintegration into droplets. It is a non-stationary process and not only the mean value of disintegration length but also the range of variation of this parameter had to be determined. Figure 3 presents the variation of jet column length for four test cases analyzed, mean values are presented together with bars corresponding to minimum and maximum values of jet disintegration length recorded for particular test cases.
Jet length is presented in Figure 3a while sample images of jet disintegration process have been shown in Figure 3b. One may notice (Figure 3a), that the linear growth of mean disintegration length was obtained for first three test cases, which was accompanied by the gradual increase of the range of L/d_0 variation as it is indicated by the width of bars. It must be noticed however, that the data for Re=346 deviate from this tendency, because not only mean value is above linear fit but also the width of bars is

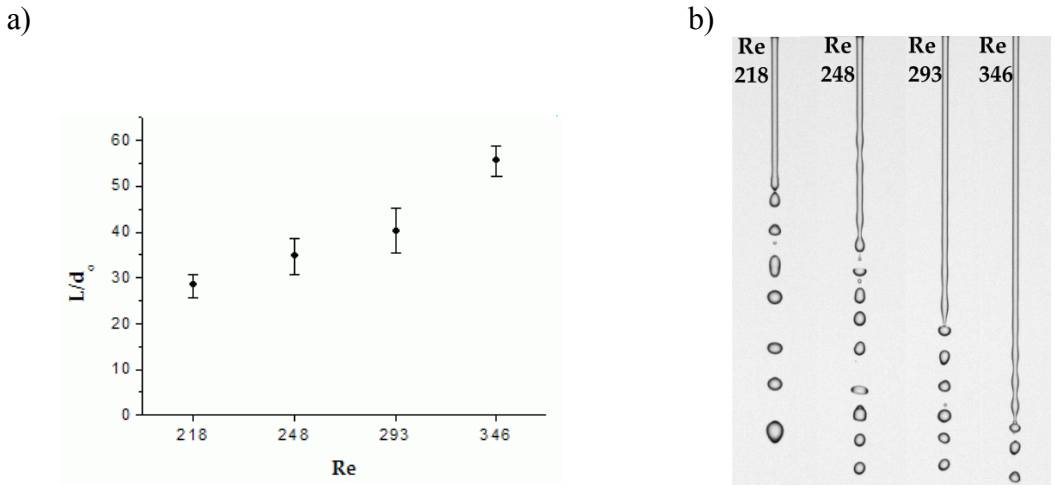

Figure 3. Distribution of jet length a) versus Re number, and b) sample images.

smaller then for Re=293. It should also be stated that results obtained for non excited case in low range of Reynolds number confirm the theoretical predictions of Weber, more information about this problem may be found in [10].

The next stage of present investigations concerned the pdf distributions of droplets generated as a result of liquid jet breakup. Particular distributions for all test cases analyzed have been shown in Figures 4 to 7. All pdf distributions reveal three characteristic peaks. First peak of all pdf distributions obtained for smallest values of d/d_0 confirms the presence of pilot droplets. On the average the diameter of pilot droplets is 4 to 5 times smaller then the diameter of "main" droplets. The second peak corresponds to the appearance of droplets generated as a result of jet breakup. For comparison the line corresponding to theoretical value obtained by Rayleigh

$$d_R = 1.89Dj \tag{1}$$

has also been plotted at this figure and one may notice the perfect agreement of experimental results with equation (1). The third peak corresponds to the presence of droplets resulting from amalgamation of neighbouring droplets and also in this case the line corresponding to droplet diameter d_a resulting from amalgamation of two identical droplets with diameter d, i.e.

$$d_a = \sqrt[3]{2}d \tag{2}$$

has been marked at pdf distributions. One may notice that for the lowest Reynolds numbers applied Re=218-293 (see Figures 5-7), the peak corresponding to droplets resulting from primary jet breakup is dominant in pdf distributions. It is interesting to note, that the average size of amalgamated droplets is greater then the value calculated as a simple connection of two neighbouring droplets, it may be caused by participation of pilots which become amalgamated with neighbouring large droplets, that leads to the increase of diameter of the resulting droplets. The Re=346 test case differs considerably, because the probabilities of primary and amalgamated droplets appearance are almost equal. It is interesting to note that the third peak of pdf for Re=346 indicates the value lower then the average diameter of amalgamated droplets. It may result from the possible breakup of amalgamated droplets which is due to their large diameters, which in turn makes them more susceptible to aerodynamic forces.

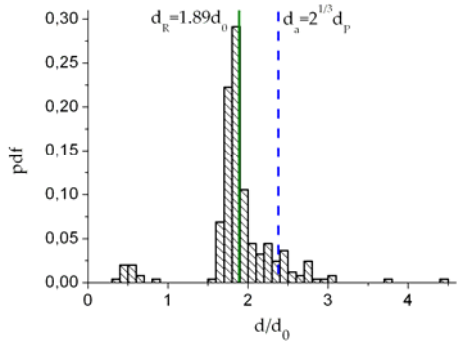

Figure 4. Pdf distributions of droplet size for Re=218

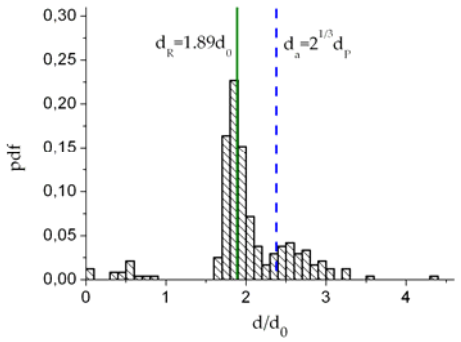

Figure 5. Pdf distributions of droplet size for Re=248

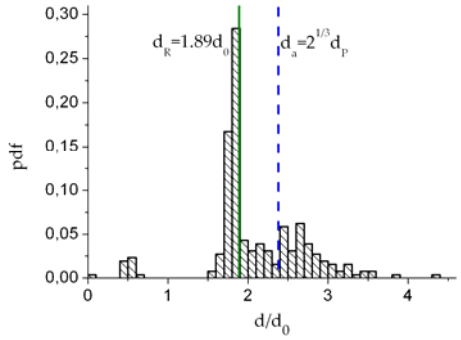

Figure 6. Pdf distributions of droplet size for Re=293

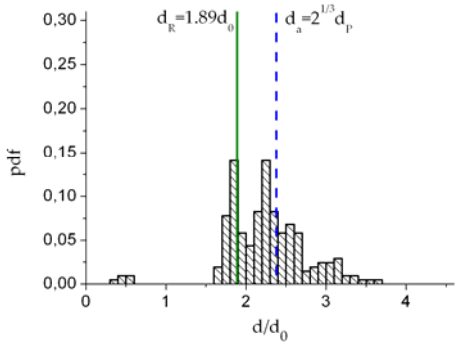

Figure 7. Pdf distributions of droplet size for Re=346

Excited case

For the selected Reynolds numbers the influence of frequency of excitation was investigated in order to find out the most sensitive frequencies of the liquid jet column, this information was also needed for numerical experiments. Investigations were performed for the Reynolds number Re=250, the excitation frequency was supplied to piezoelectric element mounted in the plenum chamber of the injector. Again the instantaneous pictures were recorded and processed with the use of techniques described in [10]. Figure 8 presents the variation of jet column length for sample Reynolds number equal Re=250 for different frequencies of excitation. The jet length was normalized by nozzle exit diameter denoted as d_0, the frequency of excitation was normalized by Rayleigh frequency (denoted as f_R) defined as:

$$f_R = \frac{U_L}{\lambda_{opt}} \tag{3}$$

where:

$$\lambda_{opt} = 4.508 D_j \tag{4}$$

For illustration, sample of recorded images of jet disintegration process have been shown in Figure 8b for frequencies marked at the plot.

One may notice the appearance of the minimum of the jet length for a range of excitation frequencies and good agreement of present experiment with literature data [1], with give the following range:

$$3.5 D_j < \lambda < 7 D_j \tag{5}$$

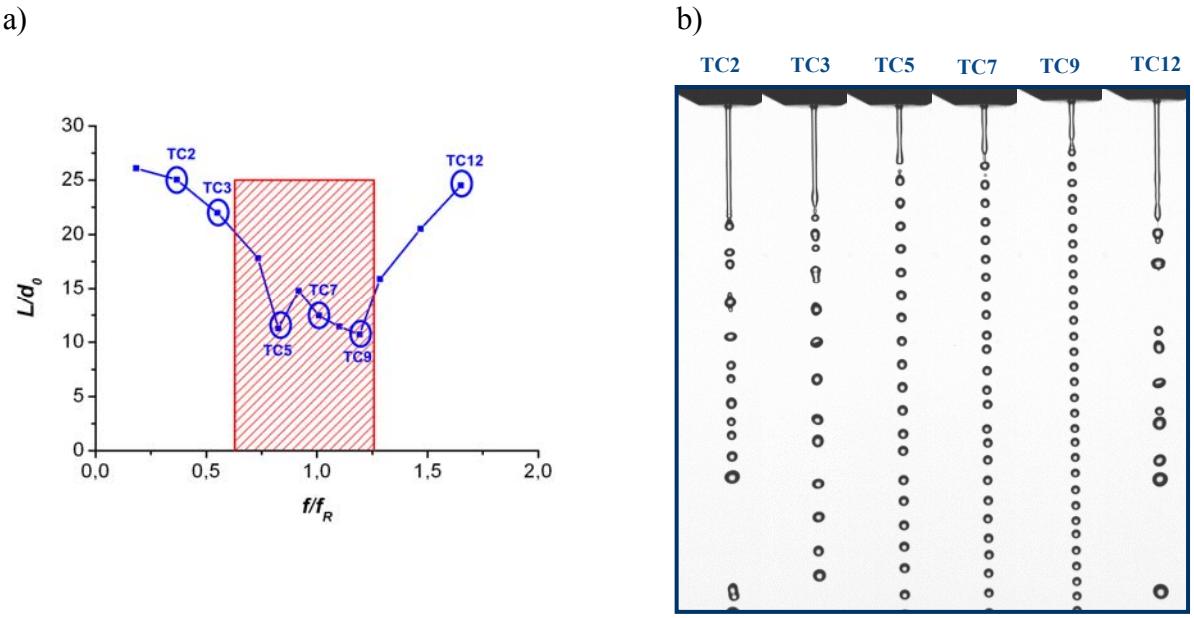

Figure 8. Distribution of jet length a) versus frequency of excitation, and b) sample images for sample test cases.

For comparison the hatched area corresponding to theoretical data defined by equation (5), was plotted in this graph. It should be noticed that the reaction of the jet to excitation frequency is not monotonous, in particular two neighboring minima may be observed in the picture (the reason for this behaviour are currently investigated)

The next stage of investigations concerned the determination of pdf distributions of droplet sizes generated as a result of liquid jet breakup due to excitation. Particular distributions for test cases analyzed have been shown in Figures 9 to 14. Table 1 presents all test conditions and test cases investigated, which were collected as a data base for comparison with the results of numerical simulations.

Table 1
Summary of investigated test cases for excited test case Re = 250

Test Case	TC1	TC2	TC3	TC4	TC5	TC6	TC7	TC8	TC9	TC10	TC11	TC12
f [Hz]	1000	2000	3000	4000	4500	5000	5500	6000	6500	7000	8000	9000
f/f_R	0,18	0,37	0,55	0,73	0,83	0.92	1,0	1,1	1,19	1.28	1,46	1,65
L [mm]	x	x	x	x	x	x	x	x	x	x	x	x
d [mm]		x			x	x	x		x			x

All pdf distributions have been normalized by the injector nozzle diameter d_0, also for comparison the line corresponding to theoretical Rayleigh value denoted as d_R and line corresponding to amalgamated droplets denoted as d_a were plotted at these figures. One may notice that for the lowest value of frequency of excitation the pdf distribution of droplet size is quite flat, that means that injector is producing wide range of droplets sizes, what is undesirable from future work point of view. But as the frequency of excitation is increased the pdf distributions reveal more selective distribution of droplets frequencies, especially for frequencies close to the theoretical value of Rayleigh frequency equal for this case f_R=5.45 kHz. As we move to TC9 (second minimum of jet length see Figure 8) one may notice that the mean diameter of generated droplets shown in Figure 13 is smaller than defined by

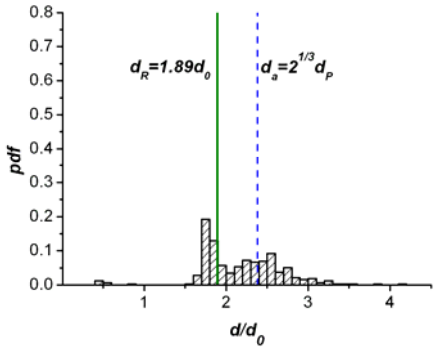

Figure 9. Pdf distributions of droplet size for TC2

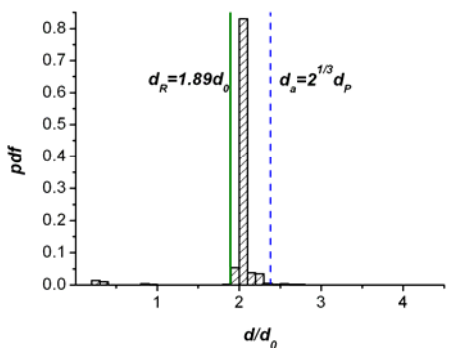

Figure 10. Pdf distributions of droplet size for TC5

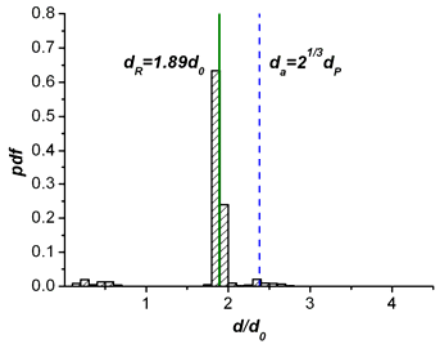

Figure 11. Pdf distributions of droplet size for TC6

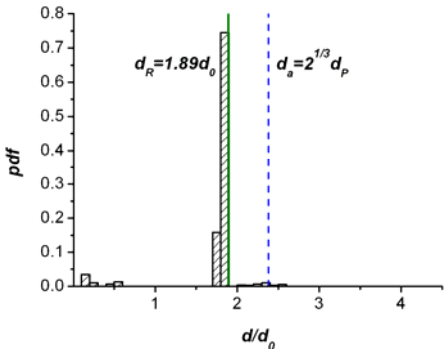

Figure 12. Pdf distributions of droplet size for TC7

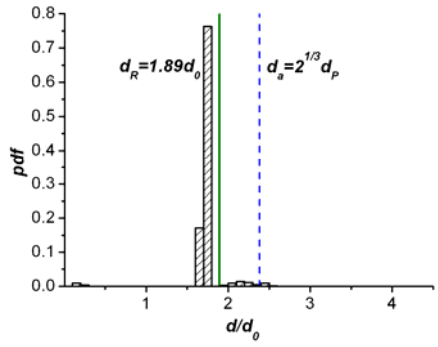

Figure 13. Pdf distributions of droplet size for TC9

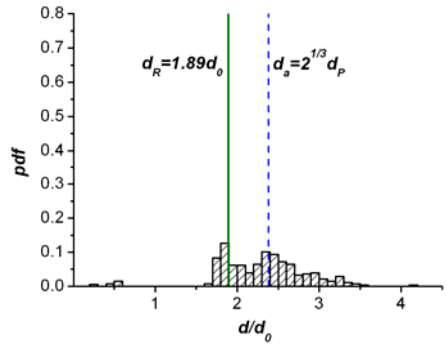

Figure 14. Pdf distributions of droplet size for TC12

Rayleigh. And finally for the last test case TC12 (Figure 14) one may notice similar pdf distribution of droplets like for first pdf distribution for the lowest frequency of excitation (compare Figures 14 and 9). Even if the pdf distributions in Figures 9 and 14 are rather flat one may still notice two characteristic peaks corresponding to droplets generated due to primary jet breakup and due to amalgamation of two neighboring droplets.

SUMMARY

For the injector based on Rayleigh injector two test cases were investigated i.e. with and without excitation. For both cases the length of the liquid jet column before disintegration and the size

distributions of resulting droplets were investigated. The histograms of droplet size distributions reveal three peaks corresponding to presence of pilots droplets, to droplets generated due to jet breakup, and to droplets resulting from amalgamation of neighboring droplets. It was also found that dominant peaks correspond to droplets generated due to primary jet breakup for Reynolds numbers below Re=300, while for the largest Re number investigated the probability of primary and amalgamated droplets were found equal.

Experimental investigations for the case with excitation show the appearance of the minimum of the liquid jet length for certain range of frequency of excitation. These results are in good agreement with literature data. Again the histograms of droplet size distributions reveal three peaks corresponding to presence of pilots droplets, droplets generated due to primary jet breakup, and droplets resulting from amalgamation of neighboring droplets with dominant peak corresponding to droplets generated due to primary jet breakup.

NOMENCLATURE

d – droplet diameter, m
d_a – amalgamated droplet diameter, m
d_P – primary droplet diameter, m
d_R – droplet diameter defined by Rayleigh, m
d_0 – injector nozzle diameter, m
D_j – liquid jet diameter, m
f – frequency of excitation, Hz
f_R - frequency of excitation defined by Rayleigh, Hz
L – breakup length, m
U_L – velocity of liquid, m/s
Re – Reynolds number
λ – wavelength, m
λopt – optimal wavelength, m

ACKNOWLEDGEMENTS

The research was performed under the TIMECOP EU project (contract No STREP 030828) and SPB TIMECOP funded by MNiSzW.

This work received funding from the European Community through the project TIMECOP-AE (Project #AST5-CT-2006-030828). It reflects only the author's views and the Community is not liable for any use that may be made of the information contained therein.

REFERENCES

1. Lefebvre, A. H., *Atomization and Sprays* Hemisphere Publishing Corporation, New York 1989
2. Eggers, J. Villermaux, E., Physics of liquid jets, *Rep. Prog. Phys*. 71 2008
3. Menard, T. Tanguy, S. Berlemont, A., Validation and application to 3D simulation of the primary break-up of a liquid jet *Int. J. Multiphase Flow*, Vol. 33, pp. 510-524 2007.
4. Marek, M. Tyliszczak, A. Bogusławski, A., Modeling of Liquid Jet Breakeup With Level Set and Ghost Fluid, *ETMM7 ERCOFTAC Conf*., Cyprus, 4 – 6 June, 2008
5. http://timecop-ae.com
6. Eggels R., *Rolls – Royce Deutschland*, Germany, private communication
7. Rayleigh, Lord On the instability of Jets Proc. London Math. Soc 110:4 1878 (quoted after [1])
8. Weber, C., Disintegration of Liquid Jets *Z. Angew. Math. Mech*. Vol. 11, No 2, 1931 136 – 139 (quoted after [1])
9. Kowalewski, T., *IPPT PAN Warsaw*, private communication
10. Wojciechowski, G. Drobniak, S. Domagała, P., Experimental Analysis of Droplet Generation *Archives of Thermodynamic* Vol. 29 No 3 2008
11. http://rsb.info.nih.gov/ij/

DOE SCHARDIN'S SCHLIEREN #2 IN INVESTIGATING FREE CONVECTION IN VERTICAL CHANNELS

D. Ambrosini[1,*], D. Paoletti[1], G. Galli[2]
[1]University of L'Aquila, L'Aquila, Italy
[2]University of Roma "La Sapienza", Roma, Italy

ABSTRACT. Recently flow visualization by fringe projection, through a test section with non-uniform refractive index distribution, was proposed using a diffractive optical element (DOE) to generate fringes. Information about temperature gradient, encoded in the deformed fringe pattern, is obtained by correlation algorithms or by Fourier Transform algorithms. The main feature of this proposed procedure is the flexibility in suiting to different heat transfer phenomena.
The aim of this paper is to evaluate the performance of this system and consider the sensitivity problems that can arise when working fluid is air. Some experimental results are given for a particular case study: free convection in vertical channels in air, which is encountered in many technological applications. It was found that this technique can work in air but its sensitivity should be increased. Some possible ways to increase sensitivity are suggested.

Keywords: *heat transfer, free convection, flow visualization, Schlieren, holographic interferometry*

INTRODUCTION

Flows having a variable fluid density can be visualized by optical methods [1, 2].
Practical investigations frequently involve operation under less than ideal condition. In particular, operating conditions may include vibration, difficult optical access and short data sampling times when studying transient processes. Therefore, key features of a successful optical method for studying convection in transparent media include: low sensitivity to external disturbance in comparison with traditional interferometric techniques; good measurement sensitivity; low cost and simplicity of the system; possibility of use by non-optically skilled operators; full digital data elaboration, to take advantage of the current progress of computer hardware and software.
Recently [3], a fringe projection technique was proposed to study the refractive index variation in fluid and hence to measure the convective heat transfer. This method, which can be considered a type of Schardin's schlieren #2 [4], uses a simple and cheap fringe generator, realized with a diffractive optical element (DOE) illuminated by a spherical wave [3].
The idea of mapping refractive fields through a distortion of an otherwise regular pattern is old, simple and effective. It was fully exploited and developed in the correct context by schlieren pioneer Hubert Schardin [4, 5].
The technique discussed in this paper is similar to "synthetic schlieren" [6, 7] and to "Background Oriented Schlieren" (BOS) [8].

* Corresponding author: Prof. D . Ambrosini
Phone: + (39)-862-434336, Fax: + (39)-862-434303
E-mail address: dario.ambrosini@univaq.it

Synthetic Schlieren [6, 7] involves the study of the deformations induced by the test section in a regular (lines, dots) or random dots pattern. Similar methods, based on grid pattern distortions, were almost simultaneously proposed [9-11], not always realizing they can mostly be traced back to Schardin's schlieren # 2 [5].
BOS [8] used background artificially generated by splashing tiny droplets of white wall paint or background naturally presents (i.e. grass).
The main features of both synthetic schlieren and BOS are present in the early pioneering work of Giglio et al. [12]
In DOE Schardin's schlieren #2 the fringe patterns, generated by the DOE, are projected on a ground glass plate. The phase object (test section) is placed in front of the ground glass (in other words, in front of the fringe pattern), which is imaged by a digital video camera. Grating patterns, during the evolution of heat transfer phenomena, are captured by a TV camera and stored in a computer. The images can then be processed, for instance with the aid of Fast Fourier Transform (FFT) and signal demodulating techniques, to obtain a visualization of temperature gradient and the heat transfer coefficient.
All data processing that follows the acquisition is accomplished inside the PC, and there is no need for a skilled technician, since no special operations are to be performed to handle the system. The inherent simplicity and the fact that only readily available and unsophisticated equipment is required, characterize the method.
Unfortunately, this system may exhibit poor performances when working fluid is air. Therefore, the aim of this paper is to evaluate the system performance in this case and search for possible ways to improve it.
In the next section, the principles and some details of the proposed system are described. Furthermore, we present a discussion of system performances and some experiments on free convection in vertical channels in air, which is encountered in many technological applications.

BASIC THEORY

The optical scheme of DOE Schardin's schlieren method #2 is shown in Figure 1.
The fringe generator (see [3] for details) is a phase saw-tooth grating, illuminated by a laser diode (Lasiris by StockerYale, wavelength 638.5 nm, output power 5 mW) pigtailed to a single-mode optical fiber.

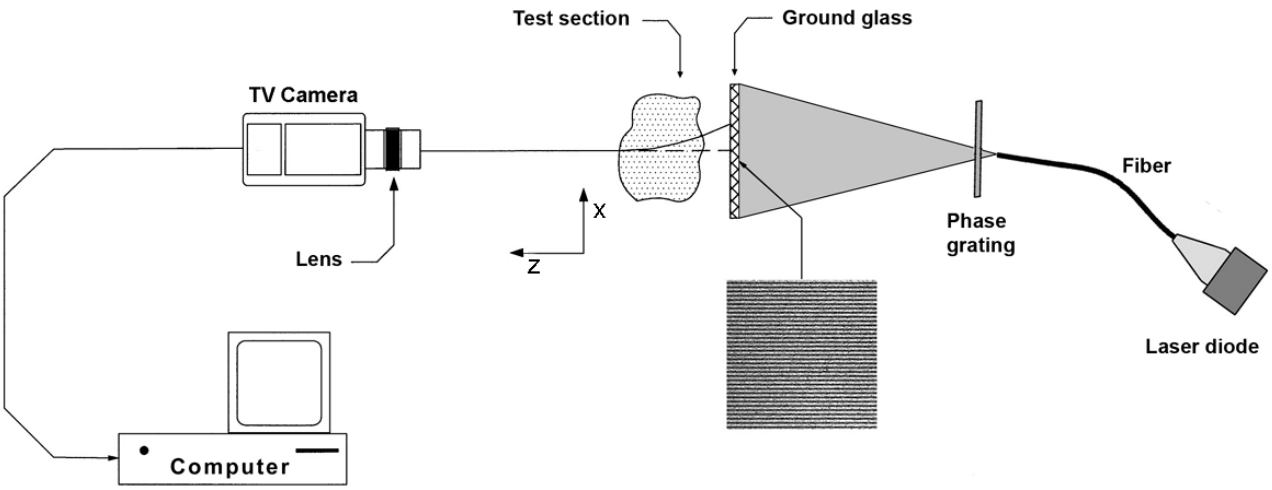

Figure 1. Schematic layout of experimental setup.

The fiber end acts as a point source. Therefore, a spherical wave comes out from the fiber. This light impinges on the grating, which acts as a beam divider. In the superposition region of the two exiting beams, interference fringes are formed.
The DOE should concentrate most of the output energy on two diffraction orders, thus behaving as a beam splitter. The performance of a DOE can be evaluated by its diffraction efficiency, which is the ratio between the power of the desired order and the power of the incident beam. If the maximum phase shift introduced by the saw-tooth grating is π we obtain a zero order and a +1 order with the same ideal diffraction efficiency of about 0.405 and a total diffraction efficiency (ratio of the power exiting in the desired orders and the incident power) of 0.81.
In practice, the diffraction efficiency of the used DOE is lower: 0.4 for the zero order and 0.31 for the +1 order; however the diffraction efficiency, relatively to the interesting orders, remains reasonably good (about 0.71). Because the two beams have comparable intensity, good quality fringes are obtained. The key feature of this fringe generator is the ability to change fringe period by simply changing the distance between fiber end and grating (see [12] for details).
The DOE is a blazed grating (with a saw-tooth profile) realized on index-matched epoxy. The grating size is 25×25 mm^2 and its period is 70 grooves mm^{-1}.
The fringe pattern obtained with the DOE-based fringe generator is projected on a ground glass plate. The test section is placed just in front of the ground glass (i.e., no distance between test section and screen), which is imaged by a TV camera, through a narrow bandpass filter matched to the laser diode wavelength.
The TV camera was a Silicon Video® 9T001C with PIXCI® D2X imaging board by EPIX Inc., with a resolution of 2048 × 1536 pixels. The camera was equipped with a TEC-55 55mm F/2.8 Telecentric Computar Lens and connected to a PC.

DATA PROCESSING AND DISCUSSION

If refractive index n in the test section is non-uniform, the rays through the test object will be deflected. In other words, if the refractive index changes, the deflection angle will also change. The change of the deflection angle can be regarded as a local translation of the fringe pattern [3]. In strict analogy with speckle photography [14], this displacement is proportional to the temperature gradient [3]. It can be shown [3] that, for a simple geometry allowing 1D refraction, the deflection angle of a ray, entering the test section in $x = x_0$ and passing through the test section can be written as

$$\beta = \frac{dx}{dz} \cong \frac{\ell}{n(x_0)} \left. \frac{\partial n}{\partial x} \right|_{x_0} \tag{1}$$

where ℓ represents the thickness of the test cell (measured along the propagation axis) and the relative apparent translation of the fringe pattern is

$$\xi(x_0) = \ell \tan\beta \cong \frac{\ell^2}{n(x_0)} \left. \frac{\partial n}{\partial x} \right|_{x_0} \tag{2}$$

Assuming temperature as a function of only one space variable (say x), equation (2) can be rewritten as

$$\xi(x_0) \cong \frac{\ell^2}{n(x_0)} \left. \frac{\partial n(T)}{\partial T} \frac{\partial T(x)}{\partial x} \right|_{x_0} \tag{3}$$

In literature are available several relations for calculating n and its derivative for different wavelengths and fluids [1].
The intensity of the projected fringe pattern, as seen from the TV camera on the ground glass through the non-uniform refractive index field is

$$I(x,y) = 2A^2\left\{1+\cos\left[2\pi f_x x + \varphi + \phi_\xi(x)\right]\right\} \tag{4}$$

where A is a real amplitude term, fringe frequency f_x and phase φ depend on geometric parameters, laser wavelength λ and the period of the saw-tooth grating [3] and $\phi_\xi(x) = 2\pi f_x \xi$ is the phase modulation introduced by local translation.
A qualitative visualization of the temperature gradient field can be obtained by subtracting the image recorded with a refractive index gradient, equation (4), from a reference image (no temperature gradient in the test field) and performing some image filtering [10, 11]. No complicated numerical calculations are required; therefore visualization can be recorded in quasi-real time (25 frames/s).

Quantitative data processing

PIV-mode. Considering equation (3), the temperature gradient field can be obtained calculating the pattern displacement $\xi(x_0)$ by using a cross-correlation approach of the PIV (Particle Image Velocimetry) type: sub-images are extracted from the reference image (thermal equilibrium in the test section) and the deformed image (temperature gradient in the test field), then the correlation surface is obtained using suitable correlation filters. The peak location in the correlation surface gives the relative displacement between the two sub-images.

Phase analysis-mode. Considering equation (4), quantitative data processing can be performed using a demodulation algorithm based on the Fourier transform and unwrapping procedures [3, 15-16] to obtain the phase term ϕ_ξ and then the pattern displacement $\xi(x_0)$.

Discussion

PIV-mode is the simplest quantitative data processing, due to the possibility of using existing PIV software with only minor modifications. However, it may exhibit some loss of resolution, due to the dimension of the sub-images.
Some problems may arise when working fluid is air. Water refractivity (defined as n - 1) is about 1125 times air refractivity. Water refractivity change, per 1 K temperature change, is about 129 times greater than air refractivity change [5]. Considering beam deflection, the difference is more evident: 1 K temperature change in water gives rise to a deflection of 47 arcseconds (1 rad = 206264.8 arcseconds); in air 10 K give rise to a deflection of 3.6 arcseconds [5].
To alleviate these problems when working in air, methods are needed to increase the sensitivity.
The sensitivity of the method can be defined as the amount of change of the measured quantity for a given refractive index (or temperature) gradient.
Considering equation (2) and the definition of ϕ_ξ, for both PIV-mode and Phase analysis-mode the sensitivity increases with ℓ; in other words, in analogy with conventional schlieren [5], extensive test sections along the propagation axis z are easiest to see.
Sensitivity can be increased, for both PIV-mode and Phase analysis-mode, by introducing a distance between the ground glass and the test section (say W). In fact, reconsidering its derivation [3], equation (2) can be rewritten as

$$\xi(x_0) \cong \frac{\ell(\ell+W)}{n(x_0)}\left.\frac{\partial n}{\partial x}\right|_{x_0} \tag{5}$$

In other words, image displacement (and thus sensitivity) can be increased if the screen is moved away from the test section; this added distance practically acts as an amplification factor. However, this usually lead to problems in proper focusing and should be adopted moderately.
A further way to improve sensitivity can be devised by considering Phase analysis-mode [3]: from previous relations, its sensitivity increases with fringe frequency f_x, which can be modified in the system by simply changing the distance between fiber end and DOE (see Figure 1).
However, about 10-15 pixels per fringe are needed to correctly process the fringes, thus limiting the maximum number of fringes (i.e. maximum frequency) that can be used.
A final way to improve sensitivity is to use more sophisticated phase extraction techniques [17].
To gain further insight about the combination of these improving strategies, let us consider an example. The deflection angle β can be rewritten as

$$\beta = \frac{\phi_\xi(x)}{2\pi f_x(\ell + W)} \tag{6}$$

The numerical value of β, in radians, in conventional schlieren analysis is routinely converted to arcseconds. Now, we can estimate the minimum detectable deflection angle, which, as said, depends on measured phase, fringe frequency, test section dimension ℓ and amplification factor W.

Table 1
Minimum detectable deflection angle (β) for a combination of improving strategies.

	W = 0 65 fringes	W = 0 85 fringes	W = 0.1 m 65 fringes	W = 0.1 m 85 fringes
Takeda method [18]	159 arcseconds 0.8 mrad	121 arcseconds 0.6 mrad	53 arcseconds 0.25 mrad	40 arcseconds 0.2 mrad
"Takeda improved"	80 arcseconds 0.4 mrad	60 arcseconds 0.29 mrad	26 arcseconds 0.13 mrad	20 arcseconds 0.1 mrad

Table 1 shows examples of minimum β combining different improving strategies: for all cases the test object had a length ℓ = 0.05 *m* and the field of view was 0.05 x 0.05 m^2, TV camera had 1024 x 1024 pixels, thus limiting maximum number of fringes at about 100. In Takeda method [18], used in [3], phase values can be obtained with a resolution of about π / 10. We consider as "Takeda improved" a phase extraction technique capable of a resolution of about π / 20 [17]. Sensitivity can be further increased using a higher resolution TV camera and/or reduced field of view and/or different phase extraction techniques.

EXPERIMENTAL RESULTS

The test section consisted of a vertical heated plate, made up of two aluminium sheets with a plane electrical resistance in between, and two shrouding vertical walls. The shrouding walls were smooth, unheated and placed so as to form two adjacent, symmetrical, vertical channels.
The heated plate had five transverse, square-cross-sectioned ribs on each side. The ribs were made integral with the baseplate to guarantee the absence of contact resistance. The dimensions of the heated plate were: overall thickness (without ribs) 0.012 *m*, height H = 0.175 *m*, length L =0.3 *m*. The length was set much greater than the other dimensions in order to favor a two-dimensional thermal field in the channels. The square ribs had a height of 0.00485 *m* and were regularly spaced at an interval of 0.035 *m*.

The spacing *S* between each unheated wall and the heated plate, set equal on both sides, was chosen in order to yield a channel aspect ratio *S/H* equal to 0.2. The plate was instrumented with fine-gauge, chromel-alumel thermocouples, calibrated to ± 0.1 K.
In the following, pattern displacements are evaluated using correlation algorithms (PIV-mode) based on the package MatPIV 1.6.1 by J.K. Sveen [19]. This package has the distinctive feature of being Open Source and of working in the MATLAB environment, thus sharing its capabilities of technical calculations and data visualizations.
This same test section was investigated in past years using holographic interferometry and schlieren [20, 21]. It was found that for all the S/H values, *h* starts from a high value at the leading edge and then sharply decreases, reaching a very low value at the junction between the baseplate and the first rib. From this point on, the h variations along the vertical coordinate are periodic in nature and the periodicity is equal to the rib pitch P. Two regions showing different thermal behavior can be identified: the rib and the inter-rib regions. Vertical sides of ribs show highly efficient heat transfer conditions. Along the inter-rib regions, *h* distributions are characterized by very low values close to the ribs (since they act as obstacles to the natural convection currents) and by relative maxima approximately at the midpoint of each inter-rib region.
A double exposed hologram is shown, for comparison, in Figure 2, right, for S/H = 0.2 and a temperature difference of 11 K: fringes are isotherm lines [20, 21]. The yellow rectangle shows the region of the channel depicted in DOE Schardin's schlieren #2 results.
Preliminary experimental measurements were performed taking two images, one with the plate at thermal equilibrium with ambient air (293 K) and the second with the heated plate at constant temperature (304 K). To increase sensitivity an amplification factor $W = 0.2$ *m* was used.
Then the two images were processed according to the PIV-mode data reduction previously outlined.

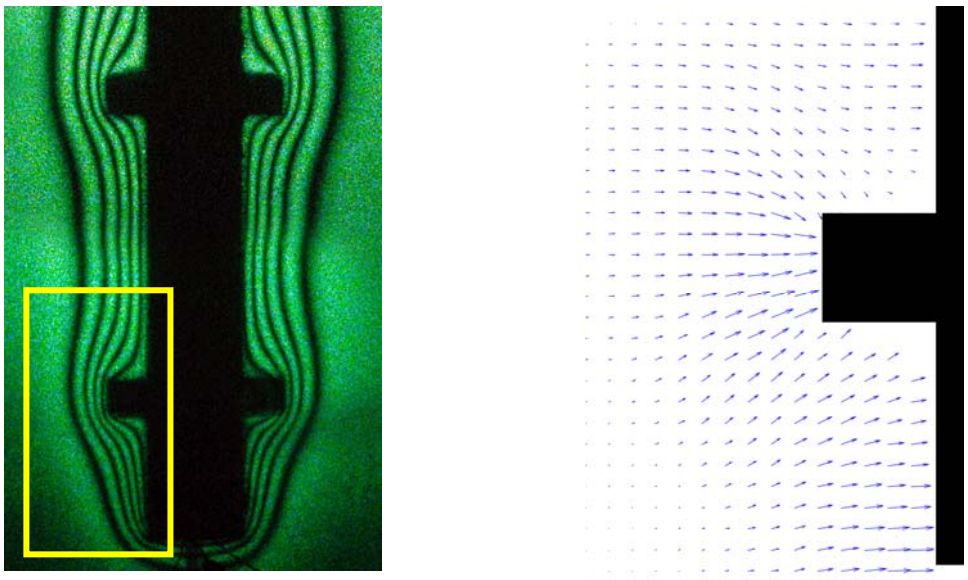

Figure 2. Holographic interferometry (left) and displacement field (right), proportional to the temperature gradient. S/H = 0.2, wall-to-fluid temperature difference 11 K.

The displacement field (Figure 2, right) was obtained in the simplest way, with a single iteration through the images and a 50% overlap of the interrogation windows.
The displacement field (proportional to the temperature gradient field) clearly identifies a laminar region: temperature gradients are not negligible (i.e. different from deep blue) only near the plate. Furthermore, minimum displacements (i.e. minimum temperature gradient) can be observed close to the ribs, while high displacements occur at the leading edge as well as at ribs vertical side.

This behavior can be appreciated more clearly from Figure 3, left, where the displacement magnitude is shown.
Finally, Figure 3, right, shows the lines of iso-displacement magnitude. This map agrees very well with the "equal light shift" lines obtained by the focal filament method traditional schlieren on the same test section [21].

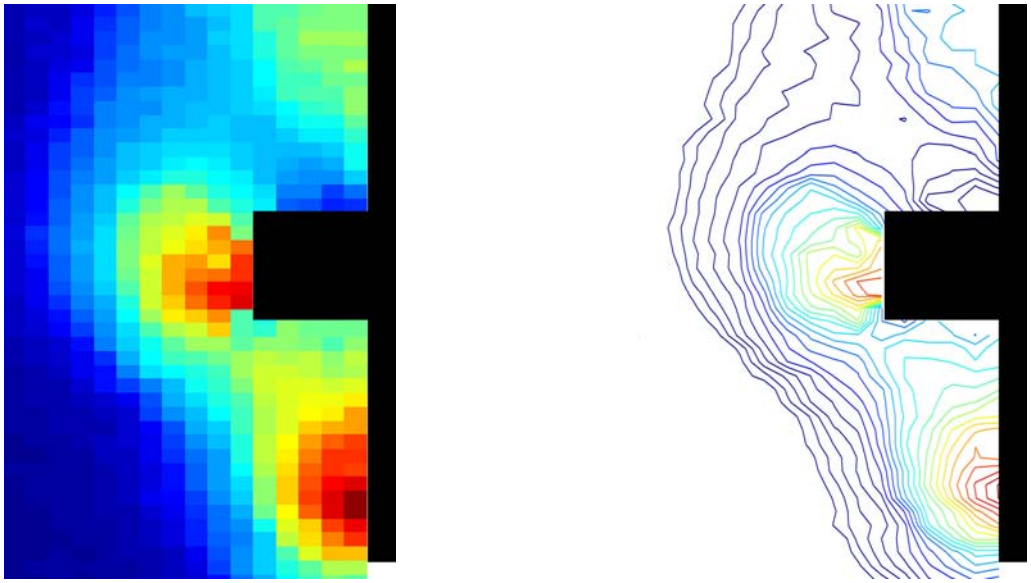

Figure 3. Displacement magnitude (left) and iso-displacement magnitude lines (right). S/H = 0.2, wall-to-fluid temperature difference 11 K.

CONCLUSIONS

In this paper we consider the DOE Schardin's schlieren #2 technique to investigate free convection in air. It was found that the application in air may give rise to sensitivity problems. As a solution was proposed a combination of strategies for improving sensitivity, such as modifying the experimental setup (introducing a distance between test section and ground glass), increasing the frequency of the projected pattern and/or using a different data processing.
Preliminary experiments, conducted using the MatPIV package in a MATLAB® environment, were performed in a vertical channel with an aspect ratio S/H = 0.2.
The technique was able to work in air and to give detailed information about many flow field features identified by holographic interferometry and traditional schlieren.

NOMENCLATURE

f_x	pattern frequency
ℓ	thickness of test section
A	Amplitude term
I	light intensity
S	spacing between heated plate and lateral wall
S/H	aspect ratio of the channel
W	geometric parameter

Greek Letters

ϕ_ξ	phase term introduced by local shift

φ phase term
λ laser wavelength
ξ local translation

REFERENCES

1. Merzkirch, W., *Flow Visualization*, Academic Press, Orlando, 1987.
2. Ambrosini, D. and Rastogi, P.K. (Eds.), Special Issue on "Optical methods in heat transfer and fluid flow", *Opt. Lasers Engin*., vol. 44, pp. 155-350, 2006.
3. Ambrosini, D. and Paoletti, D., Heat transfer measurements by a diffractive optical element fringe projection, *Opt. Eng*., vol. 46, paper n. 093606, 2007.
4. Schardin, H., Die Schlierenverfahren und ihre Anwendungen, *Ergebnisse der Exakten Naturwissenschaften*, Vol. 20, pp. 303-439, 1942.
5. Settles, G.S., *Schlieren and Shadowgraph Techniques*, Springer, Berlin, 2001.
6. Dalziel, S.B., Hughes, G.O., Sutherland, B.R., Synthetic Schlieren, *Proceedings of 8th Int. Symposium on Flow Visualization,* Sorrento (Italy), September 1-4, 1998, paper # 62.
7. Dalziel, S.B., Hughes, G.O., Sutherland, B.R., Whole-field density measurements by 'synthetic schlieren', *Exp. Fluids*, Vol. 28, pp. 322-335, 2001.
8. Richard, H. and Raffel, M., Principle and applications of the background oriented schlieren (BOS) method, *Meas. Sci. Tehnol.,* Vol. 12, pp. 1576-1585, 2001.
9. Massig, J.H., Measurement of phase object by simple means, *Appl. Opt.*, Vol. 38, pp. 4103-4105, 1999.
10. Perciante, C.D., Ferrari, J.A., Visualization of two-dimensional phase gradients by subtraction of a reference periodic pattern, *Appl. Opt.*, Vol. 39, pp. 2081-2083, 2000.
11. Ambrosini, D., Guattari, G., Sapia, C., Schirripa Spagnolo, G., Flow visualization via fringe projection, *Proceedings of 9th Int. Symposium on Flow Visualization,* Edinburgh (UK), August 22-25, 2000, paper # 117.
12. Schirripa Spagnolo, G. and Ambrosini, D., Diffractive optical element-based profilometer for surface inspection, *Opt. Eng*., vol. 40, pp. 44-52, 2001.
13. Giglio, M., Musazzi, S., Perini, U., A white light speckle schlieren technique, *Opt. Comm.*, Vol. 36, pp. 117-120, 1981.
14. Fomin, N.A., *Speckle photography for fluid mechanics measurements*, Springer-Verlag, Berlin, 1998.
15. Kreis, T., *Holographic Interferometry*, Akademie Verlag, Berlin, 1996.
16. Ghiglia, D.C., Pritt, M.D., *Two-dimensional Phase Unwrapping*, Wiley, New York, 1998.
17. Huntley, J.M., Automated analysis of speckle interferograms, in Rastogi P.K. (Ed.), *Digital speckle pattern interferometry and related techniques,* Wiley, Chichester, 2001.
18. Takeda, M., Ina, H., Kobayashi, S., Fourier-transform method of fringe-pattern analysis for computer-based topography and interferometry, *J. Opt. Soc. Am.*, Vol. 72, pp. 156-160, 1982.
19. The MatPIV Home: http://www.math.uio.no/~jks/matpiv, accessed February 19, 2009.
20. Ambrosini, D., Paoletti, D., Tanda, G., Measurement of Free Convection Heat Transfer Coefficients along a Rib-Roughened Vertical Surface, *Proceedings of 16th Int. Symposium on Transport Phenomena*, Prague (Czech Republic), August 29-September 1, 2005.
21. Ambrosini D., Tanda G., Comparative measurements of natural convection heat transfer in channels by holographic interferometry and schlieren. *Eur. J. Phys*., Vol. 27, pp. 159-172, 2006.

INFLUENCE OF POLLUTIONS ON THE THERMAL CHARACTERISTICS, HEAT EFFICIENCY AND OPTIMAL DIMENSIONS OF TUBES WITH LONDITUDINAL FINS

V. Gorobets*, A. Dolinsky, V. Mendeleyev
Institute of engineering thermophysics NAS of Ukraine, Kiev

ABSTRACT. In this report the results of experimental investigation the influence of polluting on heat characteristics of tube with longitudinal fins are presented. The thickness of polluting on the finned surface in the different time moments is measured. The dynamic of growth for polluted thickness is determined. As follow from experiments the profile of polluting along the height of fins is near to trapezoidal . The temperature distributions in fins and total heat flux leading by finned wall for the different time moments are found. The presence of pollution on the finned surface leads to change of temperature distribution in fins which substantially differ from the similar distributions for "clean" fins. The questions connected with the choice of the optimum dimensions of fins having the polluting are discussed. It is showed that optimum dimensions of fin are depended from the value Biot number of polluting.

Keywords: *polluting, fin, tube, temperature*

INTRODUCTION

In the process of exploitation of finned heat exchanges, which work in polluted environment there is aggravated of their heat efficiency. It is caused by precipitation of pollution on the extended surface. The profile of this polluting along the fin height may be complicated and the influence of pollution on the thermal characteristics of finned surface can be considerable.

Modelling of heat transfer processes in the fins with polluting or coating which possess a low heat conductivity was showed [1, 2], that in this case the thermal characteristics of finned surface have a considerable distinction from characteristics of "clean" surfaces. For example, the temperature distributions in fins with polluting have the great differences from the similar distributions for fins without polluting. Besides, the presence of polluting on the finned surface lead to necessary to take into account the influence of polluting on the choice the optimum dimensions of fins [1,2].

In this report there are presented the results of experimental investigation in which the processes of growth the polluting on the finned surface and influence of pollution on the temperature distributions, heat efficiency of fins and summary heat flux from tubes with the longitudinal fins were studied. Also, there are studied the questions connected with the calculated heat transfer methods and the choice of fin optimum dimensions for conditions of pollution of the extended surface.

EXPERIMENTAL APPARATUS AND PROCEDURES

There was created the experimental set up for investigation of influence the polluting on heat transfer conditions in tubes with longitudinal fins (Figure 1). As a source for producing of the waste gases with the polluted components was used the diesel-generated engine having power 48 kWt

*Corresponding author: Dr. V. Gorobets
Phone:(38 044) 4532858 Fax: (38 044) 4566091
E-meil address: gorobetsv@ukr.net

which work using the fuel-oil. The experimental test section consists of the finned tube, which is concluded within the outside tube (system “tube in tube”). The heating surfaces of this section had the next dimensions: outside tube diameter – 89 mm, inside tube diameter – 30 mm, length of tube – 2500 mm; fin height – 20 mm; fin thickness – 1 mm; number fins on the tube – 12.

The experiments were carried out in three directions:

1) Carrying out of balance tests
2) Measuring the temperature of heat carriers in an interpipe channel and into a pipe, in the wall of pipe and along the fin height in the differentsections of test section.
3) Determination the thickness, and thermophysical properties of polluting.

In balance tests the expenditure of exhaust-gas and water, and output temperatures of gas and water were determined. Also the aerodynamic resistance in gas highway was determined.

For realisation of the works to second and third direction of finned pipe was prepared in three sections for the distances L_1=200, L_2=1250 and L_3=2300 from the beginning of fins (Figure 2). In these sections for measuring of temperatures in finned pipe were set thermocouples - in the pipe under a fin, in a middle part of pipe between the fins and also few thermocouples along the height of fin with distance 5 mm between them (Figure 2a).

With the purpose of determination the thickness, and thermophysical properties of polluting on the fin were made the insertions of type «swallow tail» with toothed base (Figure 2b). For each from three sections on the length of pipe were made three insertions. It gives the enable to take out of insertions in different time moments. For providing of reliable contact between insertions and fin an aluminium foil was . In different moments of time the measuring of expenditures, pressures, temperatures were conducted and the collection of insertions were . Further the thickness of polluting on the different height of fin was measured, weighing the insertions with polluting and measuring the coefficient of heat conductivity for the samples of polluting was made.

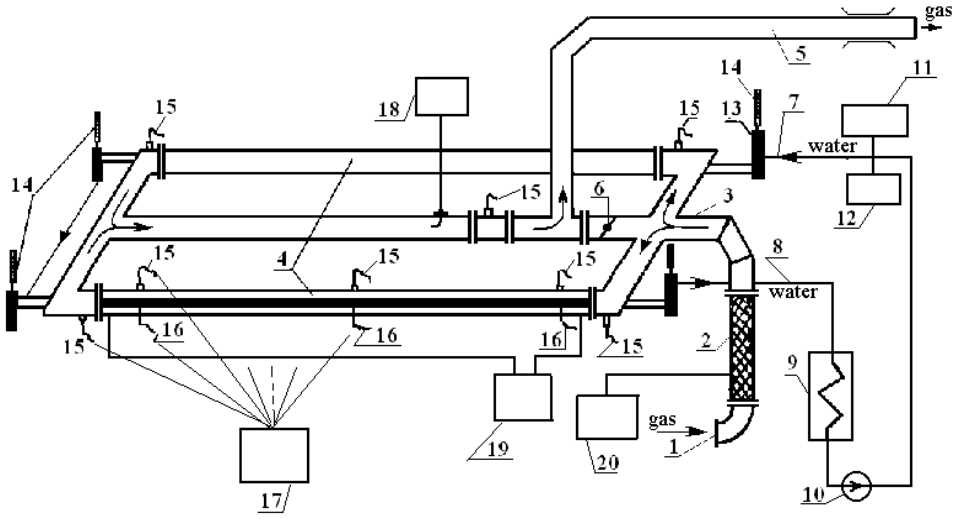

Figure 1. Scheme of the experimental set up: 1 - inlet tube; 2 - flexible junction; 3 - gas collector; 4 - experimental sections; 5 - outlet tube; 6 - regulation valve; 7 - arrangement for bring up of cold water; 8 - arrangement for leading of hot water; 9 - system for cooling of hot water; 10 - circular pump; 11 – device for measuring of water expenditure; 12 – device for measuring the pressure of water; 13 – thermometer for measuring the temperature of water; 14 – cartridge-case of thermometer; 15 - 16 – thermocouples; 17 – device for measuring of temperatures; 18 - device for measuring of gas expenditure; 19 - device for measuring the change of gas pressure in the experimental section; 20 - device for measuring of gas pressure.

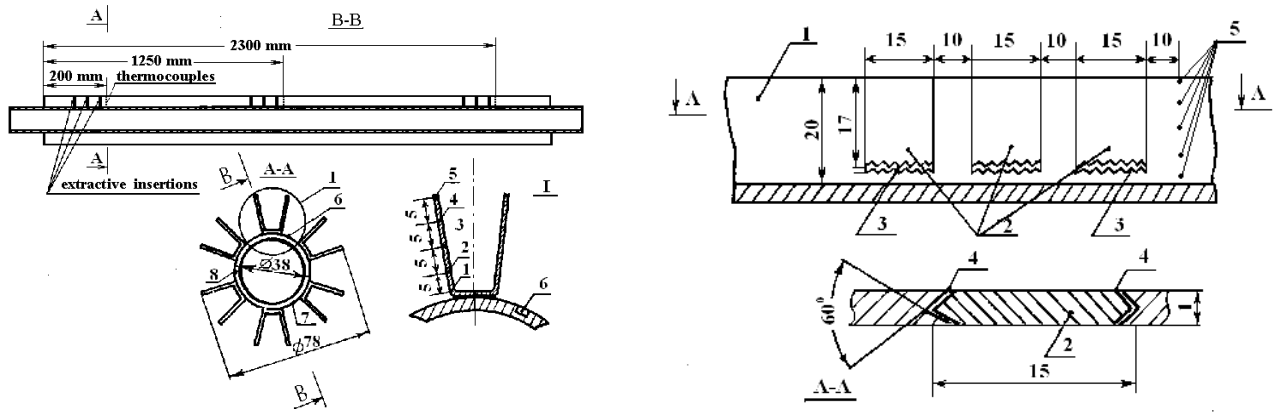

a) b)

Figure 2. Experimental section: a) longitudinal and cross section of finned tube, 1-8 – thermocouples along of fin height and on the tube; b) area of fin with insertions for determine the thickness and profile of polluting, 1 – fin; 2 – insertions of type «swallow tail»; 3 - toothed base of insertions; 4 – junction the insertion with fin; 5 - thermocouples.

There are conducted the measuring for the time period right up to complete stabilising of thickness of polluted layer. Such measuring are conducted in a few stages:

I. tests with a clean surface period of time);
II. in 72 hours (3 days) the work of setting;
III. in 144 hours (6 days) the work of setting;
IV. in 216 hours (9 days) the work of setting;
V. in 288 hours (12 days) the work of setting.

RESULTS AND DISCUSSIONS

As the conducted measuring have showed after expiration of 216-220 hours (9 days) the thickness of pollution on the surface of finned pipe is stabilised. The results of measuring of expenditure for gas and heat carriers, their temperatures on and of experimental section for different time periods are presented in a Table 1.

In a Table 2 the results of measuring the thickness of pollution are presented for different sections

Table 1
Expenditure and temperature of heat carriers

Name of	Dimension	Stage I	Stage II	Stage III	Stage IV
Time	hour	4	72	144	216
Gas expenditure	kg/hour	215	207	206	205
Temperature of gas input output	$^{\circ}C$	 294.9 91.6	 294.2 110.3	 295.0 124.4	 296,5 128,5
Water expenditure	kg/hour	3670	3700	3470	3710
Temperature of water input output	$^{\circ}C$	 57.6 60.3	 56.6 58.6	 50.7 53.1	 54,0 56,2

Table 2
Thickness of polluting on the surface along the fin height for the different sections

Name of	Dimen-sion	Stage II			Stage III			Stage IV		
		L_1	L_2	L_3	L_1	L_2	L_3	L_1	L_2	L_3
Gas expenditure	Kg/hour	207			206			205		
Temperature of gas	$^{\circ}C$	288	190	124	290	204	129	291	205	131
Thickness of polluting along the height of fin	mm									
0,15h		0.88	0.60	0.22	1.35	1.12	0.53	1.65	1.45	0.90
0,25h		0.82	0.5	0.22	1.25	1.08		1.60		0.88
0,5h		0.67	0.35	0.18	1.08	0.89	0.35	1.35	1.25	0.78
0,75h		0.54	0.26	0.12	0.95	0.74	0.30	1.25	1.10	0.72
h		0.49	0.23	0.08	0.87	0.60	0.25	1.15	1.00	0.67
Average thickness of polluting along the height of fin	mm	0.75	0.40	0.17	1.13	0.90	0.38	1.40	1.26	0.80
Average increase of polluting	mm	0.75	0.40	0.17	0.38	0.50	0.21	0.27	0.36	0.42

along the length of finned pipe and along the height of fin for the different distances from fin base. Besides in a Table 2 the average thickness and average increase of thickness of pollution along the height of fin are presented for the different sections of pipe. As follows from the measuring, the thickness of polluting increases on a measure approaching to fin base, and of pollution along the height of fin for all sections is near to trapezoidal (Figure 3). The thickness of polluting is decreased along the length of fin (Figure 4). The dynamics of change the polluted thickness on the fin in time is presented on a Figure 5. From a figure ensues, that for the initial periods of time

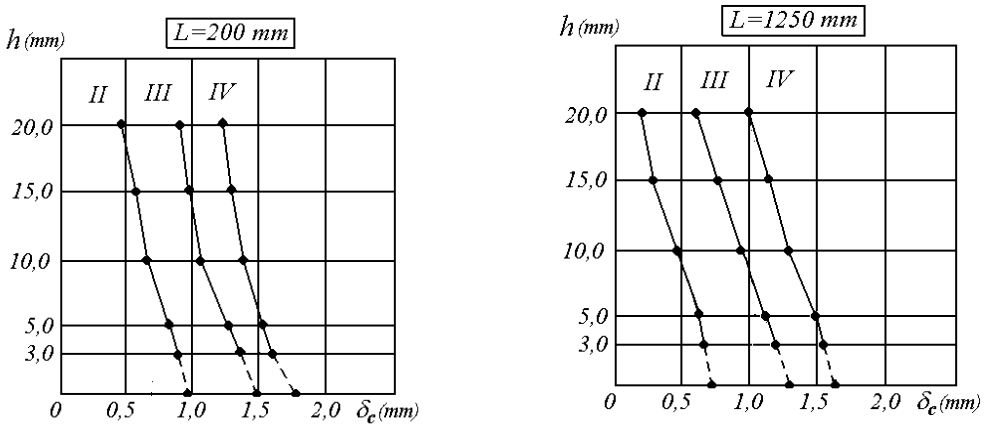

Figure 3. The distribution of thickness of polluting along the fin height in the different cross-section of fin: a) L =200 mm; b) L =1250 mm

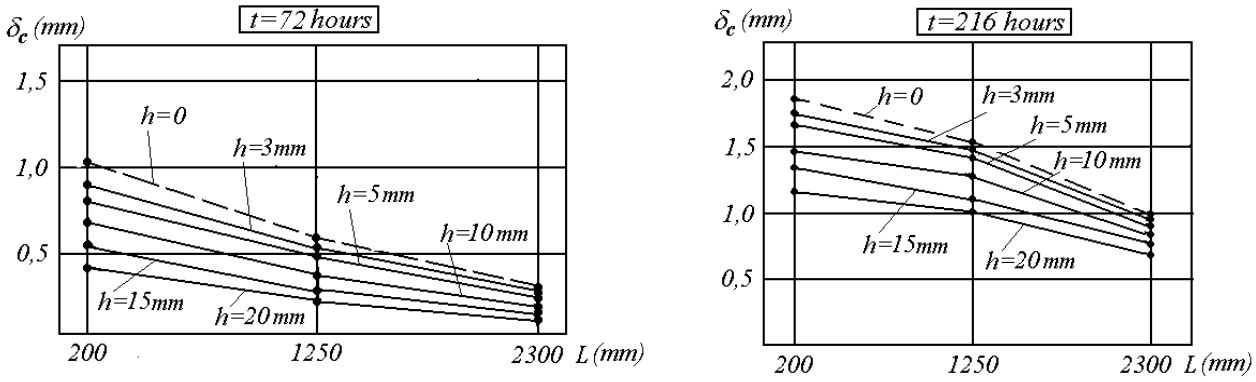

a) b)

Figure 4. Distribution of thickness of polluting along the fin length in the different cross-section on the height of fin: a) t =72 hours; b) t =216 hours

the growth of deposit takes a place most intensively. In time a speedof increase falls not increased in future, therefore there is stabilising of deposit thicknessThis process is typicalfor all sections along length of pipe. However, the processes of stabilisation of pollution have some displacement at times (late of process) as far as approaching to areas of finned surface. Characteristically, that on the initial areas of finned pipe the increase of depositsis substantially greater, than on the areas.

Measuring the coefficientof heat conductivity for material of polluting is conducted. It is received, that this value near $\lambda_c = 0.11$ Wt/m ^{0}C. Some deviations from this value are caused the different structure of pollution as far as their growth on the finned surface in the different time moments. In the initial periods of time they have more dense structure, and in time soot pollution have more friable structure, and its thermophysical properties are changed. Measuring was showed that maximal deviations from the middle value 0.11 Wt/m ^{0}C no exceed 10%.

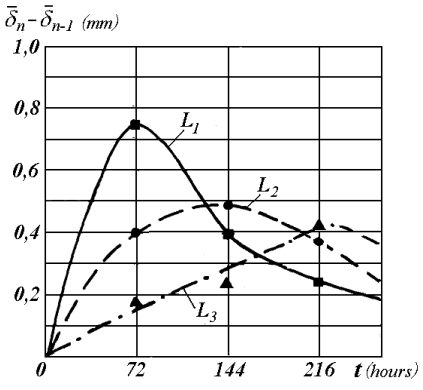

Figure 5. The dynamics of change of average polluting thickness on a fin (n =II, III, IV – number stage)

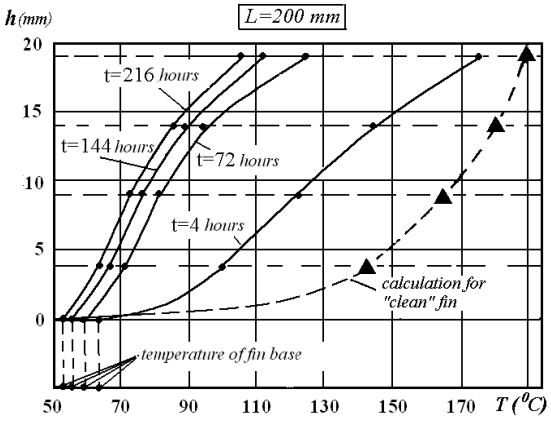

Figure 6. The temperature distributions along the height of fin for the section L =200 mm in the different time periods

Table 3
Temperature of fin along the height for the different sections along the lengthof pipe

Name of	Stage I			Stage II			Stage III			Stage IV		
	L_1	L_2	L_3	L_1	L_2	L_3	L_1	L_2	L_3	L_1	L_2	L_3
Gas expenditure, kg/hour	215			207			206			205		
Temperature of gas, $^{\circ}C$	282	154	91	288	190	124	290	204	129	291	205	131
Temperature of tube, $^{\circ}C$	65	62	60	59	59	58	54	54	52	57	56	55
Temperature of fin along the height, $^{\circ}C$												
0,15h	65	62	60	59	59	58	54	54	52	57	56	55
0,25h	102	87	64	67	64	60	65	60	53	67	60	57
0,5h	117	93	65	82	69	62	76	64	57	78	66	60
0,75h	140	98	66	95	77	64	92	74	60	99	75	63
h	187	122	76	126	93	72	118	86	86	120	89	70

The results of measuring the temperature of pipeand fins, in the differentpoints on height for the different sections along the length of finned pipe, are presented in a Table 3. The typical temperature distributions along the height of fin, in one of sections for different time moments are showed on a Figure 6. As follows from a figure, the temperature distributing in the fins at presence of polluting substantially differ from the distributing for fins without polluting. The presence of deposits on the finned surface leads to more uniform distribution of temperature along the height of fins the more, the greater a thickness of deposits.

On a Figure 7 the distributing of temperatures along the length of fins in the different sections on the height of fin for the initial moment of time, when t =4 hours and for the terms of stabilising of deposit thickness at t =216 hours are shown.

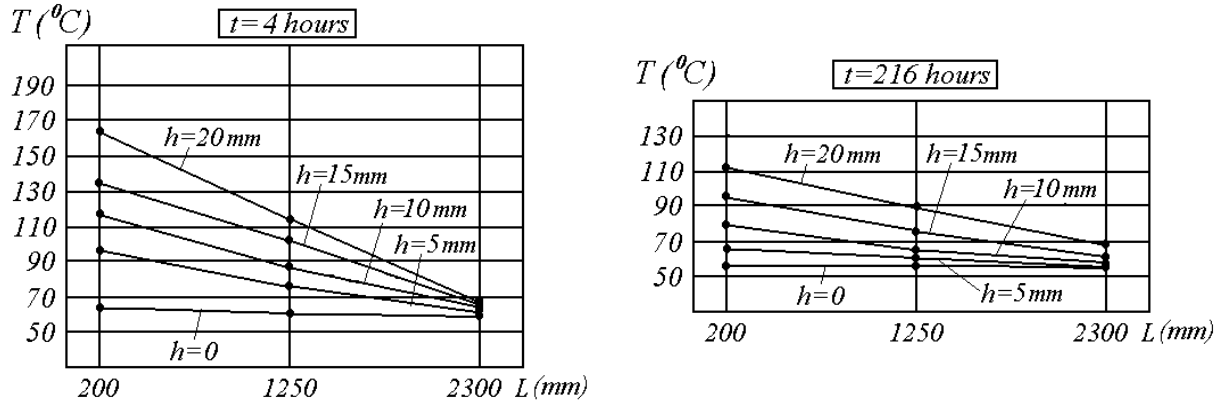

a) b)

Figure 7. The temperature distributions along the length of fin for the different sections on the fin height: a) t =4 hours; b) t =216 hours

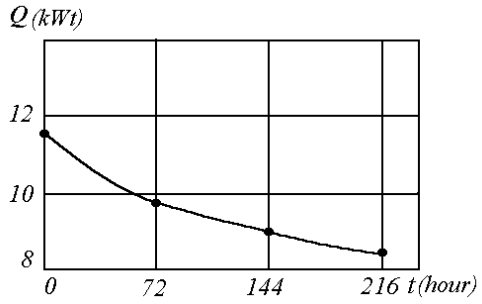

Figure 8. The total heat flux leading from finned tube in the different periods of time

Using the balance measurement of the expenditures and temperatures for gas and water heat carriers the total heat flux leading from finned tube in the different moments of time were calculated. The results of calculation are presented on a Figure 8. As follow from the figure a presence of polluting on the surface of finned tube leads to considerable decreasing of total heat flux which consists of nearly 30%.

The numeral modelling of heat transfer in pipes with longitudinal fins at presence of polluting on an external surface is conducted. Decisions are for the temperature distributing and heat efficiency of finned tubes with deposits at using the simplified, two-dimensional and conjugated model for this task. The comparison of results, which are found in these models, with experimental data is showed the satisfactory their coincidence. Maximal errors, which are in the calculations, consist of about 15%.

By an important question at design of heat-exchanges, which work in polluted environment is question of choice the optimum of fins. In paper [2] are the formulas for calculation of optimum thickness and height of longitudinal fins with polluting or coating

$$\delta_{f,opt} = 0{,}632\frac{1+Bi_c}{\alpha\lambda_c}\left(\frac{Q_f}{T_0 - T_g}\right)^2, \quad (1)$$

$$h_{f,opt} = 0{,}7979\frac{1+Bi_c}{\alpha}\left(\frac{Q_f}{T_0 - T_g}\right), \quad (2)$$

where α is heat transfer coefficient, h_f, δ_f - accordingly, height and thickness of fin, δ_c is a thickness of polluting or coating, T_0 is a temperature of fin base, T_g is a temperature of external heat carrier, $Bi_c = \alpha\delta_c / \lambda_c$ is Biot number of polluting, Q_f - heat flux leading by fin.

As follows from the expressions (1), (2) an optimum heightand thickness of fins depends on Biot number of polluting. These are increased with growth of Biot number. If to conduct the of Biot number value for the middle thickness of deposit after stabilising of process than the of Biot number consist of about 0,5. With such conditon the optimum thickness and height of fins in 1,5 time exceed as compared with optimum of «clean» fins. Influence of nonuniformity of polluting along the fin height on the optimum fin dimensions may be take into account using the correct coefficients [2].

The correct choice of optimum of fins for heat exchanges with extended surfaces which subject to pollution enables to improve the mass and dimensional characteristics of such heat exchanges.

CONCLUSIONS

1) Dynamic of change the thickness of pollution on the surface of finned tube is determined. It is found that maximal speed of growth the thickness of polluting takes place on the initial section of finned surface. In the course of time the thickness of pollution is stabilised and besides the process of stabilisation is late as far as approach to end of the finned tube. Profile of polluting along the height of fins is near to trapezoidal profile for all sections along the length of longitudinal fin.
2) The temperature distributions in finned tube for the different moments of time are measured. It is found that the presence of pollution on the finned surface leads to more uniform distribution of temperature along the height of fins if to compare with the temperature distribution of

"clean" finned surface. This uniformity of the temperature distribution the more, the greater a thickness of polluting. Presence of polluting on the surface of finned tube leads for considerable decreasing of total leaded heat flux.

3) The optimum dimensions of polluted fins depend on the Biot number of polluting and increase with the growth of this value. For the studied condition the optimum height and thickness of longitudinal fins may exceed in 1,5 time the optimum dimensions of "clean" fins.

REFERENCES

1. Gorobets, V., Thermal efficiency and the optimum sizes of finned surfaces with coating, *Proceeding of 13th Intern. Heat Transfer Conference*. Sydney. Australia. Aug. 13-18, 2006, HTE-14, 13p.
2. Gorobets, V., Influence of coating on thermal characteristics and optimal sizes of fins, *Journ. of Enhanced Heat Transfer,*. Vol. 15, No. 1, pp. 65-80, 2008.

EMPIRICAL INVESTIGATION ON HEAT TRANSFER AND PRESSURE DROP DURING FLOW BOILING OF R-134a INSIDE MICROFIN FLATTENED TUBES

M.A. Akhavan-Behabadi*, M. Nasr and S.E. Marashi
Faculty of Mechanical Engineering, University College of Engineering, University of Tehran, Tehran, Iran

ABSTRACT. In this study, pressure drop and heat transfer characteristics of R-134a under convective boiling conditions in horizontal microfinned flattened tubes were investigated. The test set-up was a well instrumented vapor compression refrigeration system. Microfinned copper tubes with internal diameter of 8.92 mm and thickness of 0.3 mm were flattened into oblong shape with different internal heights of 6.6 mm, 5.5 mm, 3.8 mm and 2.8 mm. Refrigerant R-134a flowing inside the flattened tube was heated by an electrical heating coil wrapped around it. The experiments were carried out for mass velocities from 74 $kgm^{-2}s^{-1}$ to 106 $kgm^{-2}s^{-1}$ and vapor qualities from approximately 25% to 95%. The results shows that the heat transfer coefficient and the pressure drop increase for a given mass velocity and vapor quality, as the tube profile is flattened. The maximum heat transfer enhancement and pressure drop increasing relative to the round tube values was achieved by the flattened tube with the lowest internal height of 2.8 mm. For the tube with lowest inside height, the highest heat transfer coefficient enhancement of 239% was achieved at mass velocity of 85 kg m^{-2} s^{-1} and vapor quality of 85%. , while the highest pressure drop increasing of 400% was gained at mass velocity of 74 kg m^{-2} s^{-1} and vapor quality of 30%. Also, the heat transfer coefficient and pressure drop increase by increase of mass velocity and vapor quality for all the tube profiles.

Keywords: *Boiling, Heat Transfer, Pressure Drop, Microfin, Flattened Tube*

INTRODUCTION

The heat transfer equipments like evaporators and condensers have an important role to play in different industries such as refrigeration, air-conditioning, power plant, and chemical industries. To save the limited available energy resources, design and manufacturing of efficient heat transfer equipments is essential. Different methods have been used by numerous investigators to increase the heat transfer rate in these equipments. The methods of increasing heat transfer coefficients are divided into two categories; active techniques and passive techniques. In passive methods, enhanced tubes with specific geometry or adding fluids are used for increasing the heat transfer rates. On the other hand, in active methods, external forces like electrical or acoustic field or surface vibrations are used. Although these methods increase the heat transfer rates, they also usually increase the pressure drop .

One of the passive techniques to enhance the heat transfer rates in heat exchangers is using of flattened tubes instead of round tubes. A study conducted by Wilson et al. [1] investigated refrigerant behaviour (pressure drop, heat transfer coefficient and void fraction) in flattened copper passageways in a condenser. They reported the enhancement of condensation heat transfer coefficient and pressure drop as the tube was flattened.

*Corresponding author: Prof. M.A. Akhavan-Behabadi
Phone: +98 (21)88337123, Fax: +98 (21)88337123
E-mail address: akhavan@ut.ac.ir

Another method to augment the heat transfer coefficients is using of extended surfaces. Bandarra Filho and Saiz Jabardo [2] performed a study on convective boiling of R-134a in herringbone and standard microfin copper tubes. The ranges of vapor quality was from 5% to 90% and mass velocity from 100 to 500 kg m^{-2} s^{-1}. Experimental results indicated that the herringbone tube has a distinct heat transfer performance for the mass velocity ranges considered in their study. Thermal performance of the herringbone tube has been found better than that of the standard microfin tube at high mass velocities, while at the lowest mass velocity (G=100 kg s^{-1} m^{-2}), for vapor qualities higher than 50%, the performance of the herringbone tube was worse than that of the standard microfin tube.

In the present research, an experimental investigation has been carried out to study the enhancement of heat transfer coefficient and pressure drop increment in an evaporator with micro fin flattened tubes.

EXPERIMENTAL FACILITY AND PROCEDURE

The test apparatus was a well instrumented vapor compression refrigeration system. The schematic diagram of experimental set-up has been shown in figure 1. The test apparatus included a pre-evaporator, a test-evaporator, and an after-evaporator. Refrigerant R-134a flowing inside the tube of these three evaporators was heated by the electrical coil heaters wrapped around the tubes. The input power to each heater was controlled by a dimmer.

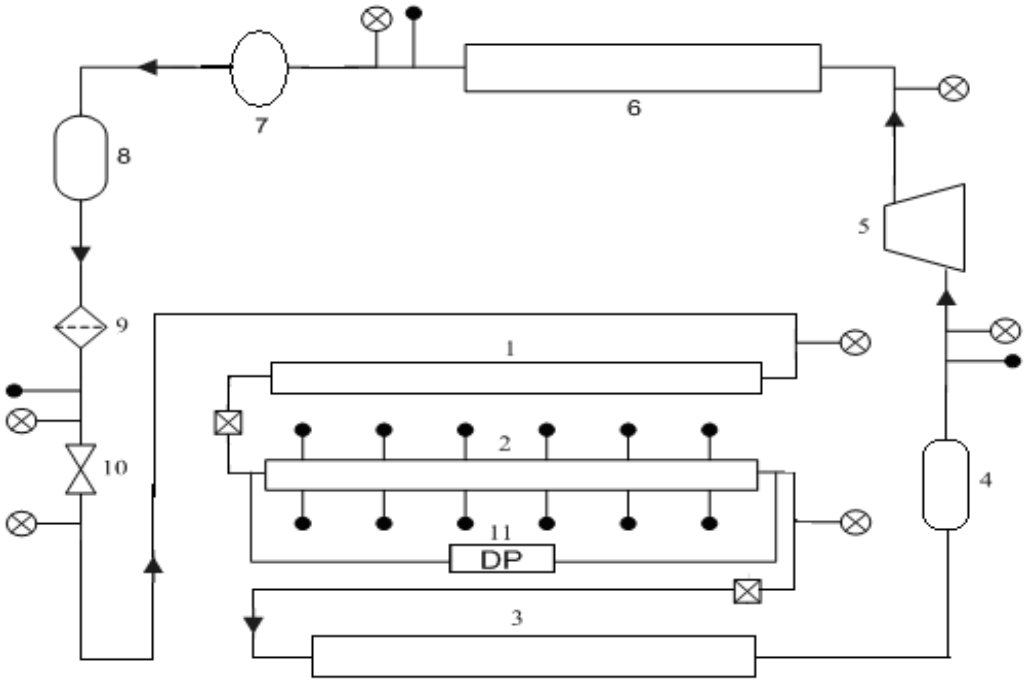

1- Pre Evaporator	7- Rotameter
2-Test Evaporator	8-Receiver
3-After Evaporator	9- filter-drier
4-Accumulator	10-Expansion Valve
5-Compressor	11-Differential Pressure Transducer
6-Condenser	
Thermocouple - ●—	Shut off - ⧅ ⁄ Valve
Flow Direction - ←—	Pressure Gauge ⊗—

Figure 1. Schematic diagram of experimental apparatus

The pre-evaporator was used to achieve the desired vapor qualities at the inlet of test-evaporator by heating the refrigerant which enters the pre-evaporator after expansion valve. The after-evaporator was used to ensure that the vapor leaving the test-evaporator has been changed to superheated vapor before entering the compressor.

The test-evaporator was a horizontal copper tube with 1.2 m long which 1.1 m of it, is wrapped with electrical coil heater to heat Refrigerant R-134a flowing inside the tube. Microfinned tubes which were used in this study were helical (Standard) type. Figure 2 shows the shape and dimensions of microfinned tubes used in this study.

For determining the effect of flattening the tubes on increasing heat transfer and pressure drop, round tubes flattened into oblong shapes with inside heights of 6.6 mm, 5.5 mm, 3.8 mm, and 2.8 mm.

To measure the outside tube wall temperatures, wall-mounted T-type (cu-con.) thermocouples were placed at four stations along the test-evaporator tube length with 22 cm distance from each other. At each station, four thermocouples were mounted on the top, bottom, and two sides in the middle of the tube. The refrigerant pressures and temperatures at the inlet and outlet of the test-evaporator were also measured. The provisions were also made to measure the other necessary parameters.

In this study, R-134a was used as refrigerant, because of its non-destructive effects on environment. The mass fluxes varied from 74 to 106 kg $m^{-2}s^{-1}$.The test-evaporator inlet vapor quality ranges varied from approximately 25% to 95%. During each test run, the difference between the inlet and outlet vapor qualities of test-evaporator was about 10%. The mean vapor quality of test section was taken as the average of its inlet and outlet vapor qualities.

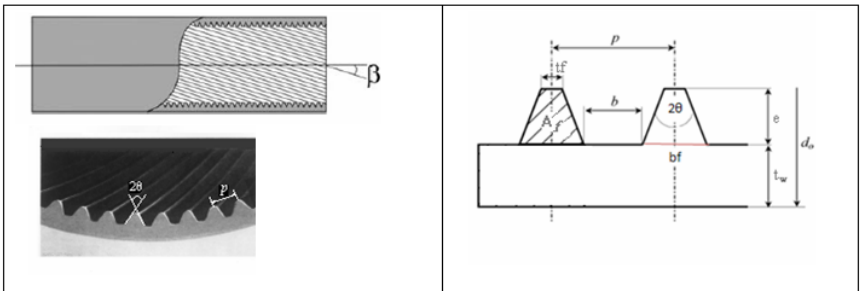

Outside diameter	$d_o = 9.52mm$	Fin tip	$tf = 0.096mm$
Wall thickness	$t_w = 0.3mm$	Fin pitch	$p = 0.48mm$
Fin height	$e = 0.25mm$	Helix angle	$\beta = 15^\circ$
Number of fin	$n = 55$	Fin tip angle	$2\theta = 15^\circ$
Fin base	$bf = 0.207mm$	Fin area	$A_f = 0.379$
Pipe length	L= 1200 mm	Area enhancement	$\varepsilon_a = 1.63$

Figure 2**.** Dimensions of microfinned tubes.

The heat transfer coefficient of test-evaporator was determined using the heat gain from electrical heater and the temperature difference between the evaporator inside wall surface and the boiling refrigerant. The temperature of tube outside wall was taken as the average of temperatures reading by thermocouples. The temperature of refrigerant was the saturation temperature corresponding to the average pressure of the inlet and outlet of test evaporator. The thermo-physical properties of R-134a were taken from [3].For reading the pressure drop in the evaporator, PMD-75, which is an equipment for measurement of pressure drop with a calibrated accuracy of 0.075*SPN% (SPN is pressure in the evaporator), is used in a by-pass line between inlet and outlet of test evaporator.

PRESSURE DROP RESULTS

Figure 3 shows the variation of pressure drop gradient versus vapor quality for flattened tubes at mass velocity of 85 kg/m^{2}s. The results for round tube is also presented here for comparison.

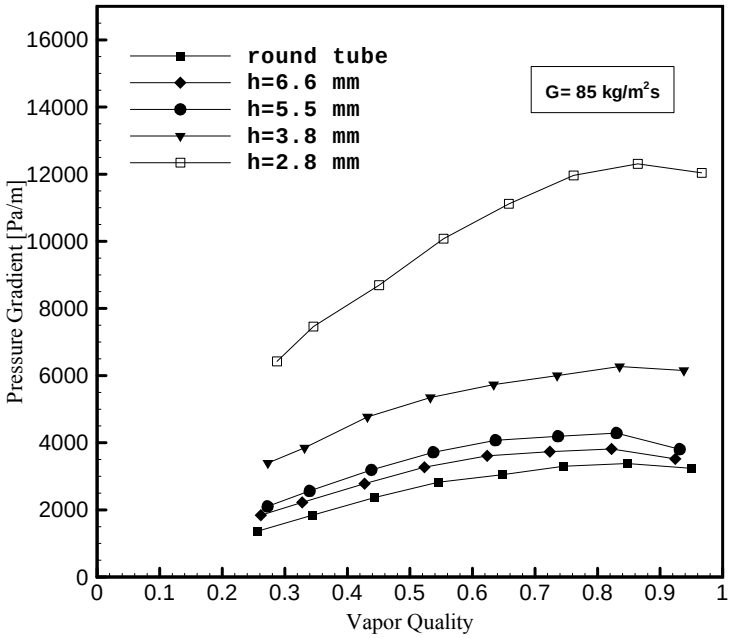

Figure 3. Pressure drop gradient versus vapor quality for different tubes at G=85 kgm^{-2}s^{-1}

From figure 3 it is evident that, the pressure drop increases by increase of vapor quality in flattened tube similar to the round tube. Moreover, pressure drop increases at a given mass velocity, as the tube profile is flattened. The main effect of flattening tube profile at a constant mass velocity is the increased vapor velocity. As an illustration, when a tube cross section is reduced in half, the velocity essentially doubled which is a quadrupling of the vapor's kinetic energy. This increase in vapor kinetic energy results in a higher shearing of the liquid layer, thinning the liquid phase, which reduces the mass in the tube and increase the pressure drop.

Flattened tubes results shows that the pressure drop ratio, respect to round tube decreases with the increase of vapor quality, especially in flattened tubes with high internal heights. This is due the fact that, flattening the tube profile causes changing of flow pattern from stratify-wavy to annular flow pattern mostly in low vapor quality region, while at high vapor quality region, the flow pattern inside the round tube is mostly annular flow. Moreover, the pressure drop ratio increases, as the tube profile is flattened. The minimum pressure drop ratio of 1.006 is achieved in flattened tube with the highest internal height of 6.6 mm, while the maximum pressure drop ratio of 5 is obtained in the flattened tube with the lowest internal height of 2.8 mm.

In order to predict pressure drop during flow boiling of R-134a inside microfinned flattened tubes, ΔP_{fri}, the following correlation was developed using the present experimental data.

$$\Delta P_{fri} = \Delta P_f \varphi^2 \tag{1}$$

Where, ΔP_f is the liquid single phase pressure gradient calculated with the assume that all the refrigerant flows as liquid phase in the tube. φ^2 is the two phase correction multiplier obtained as below:

$$\varphi^2 = 12.80 X_{tt}^{-1.5} (1-x)^{1.8} G^{*0.06} h^{*0.26} \tag{2}$$

In which, X_{tt} is Martinelli parameter, $\overset{*}{h}$ and $\overset{*}{G}$ are the dimensionless internal height and mass velocity calculated as below:

$$\overset{*}{G} = \frac{G}{G_0} \qquad \overset{*}{h} = \frac{h}{h_0} \tag{3}$$

h_0 is reference internal height and is equal to 2.8 mm and G_0 is reference mass velocity and is equal to 74 $kgm^{-2}s^{-1}$.

Figure 4 compare the flattened tubes empirical pressure drop data with the values predicted by Eq. (1). As we can see, Eq.(1) predicts the present experimental data within an error band of ± 20%.

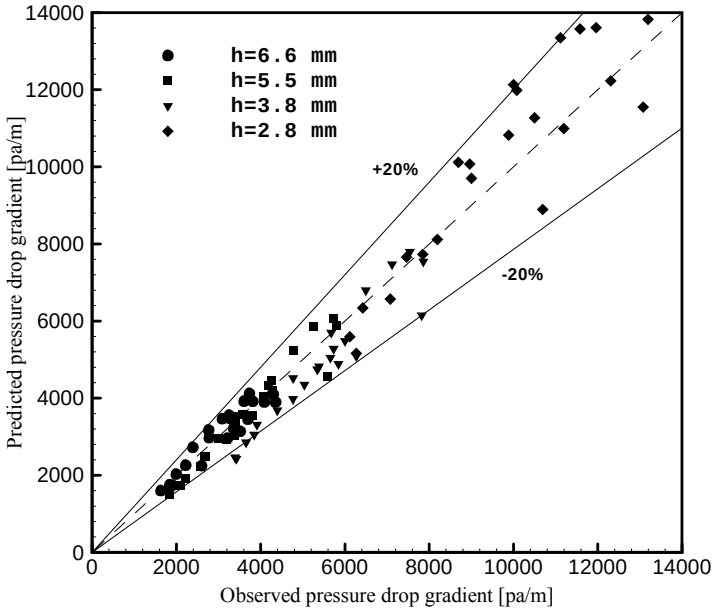

Figure 4. Comparison of observed pressure drop gradient with equation (1)

HEAT TRANSFER RESULTS

The variation of heat transfer coefficient with vapor quality has been shown in Figures 5-6. Figure 5 is for round tube, while figure 6 has been drawn for the flattened tube with inside height of 3.8 mm.

Nearly a similar trend can be seen from figures 5-6. Heat transfer coefficient elevates when vapor quality increases until it gets to a maximum value, then it falls. The reason for this phenomenon is the fact that by increasing of the vapor quality, the thickness of liquid film on the tube inside wall decreases, as a result, the thermal resistance decreases. Finally, at the top of the tube inside wall, the partial dryness will be happened and the film of liquid is disappeared. Then, with the progress of increasing of vapor quality, the wet surface area of the tube is reduced and the heat transfer coefficient decreases.

Moreover, as we can see from figures 5-6, by increasing the mass velocity, heat transfer coefficient is increased. This is due the fact that, at high mass velocities, the flow pattern will be changed from stratified flow to annular flow earlier than low mass velocities. The annular flow has higher rate of heat transfer rather than stratified flow. Actually in the annular flow, the liquid film around the tube inside wall increases the turbulent interaction between the vapor and liquid phases through the roughness of the liquid-vapor interface.

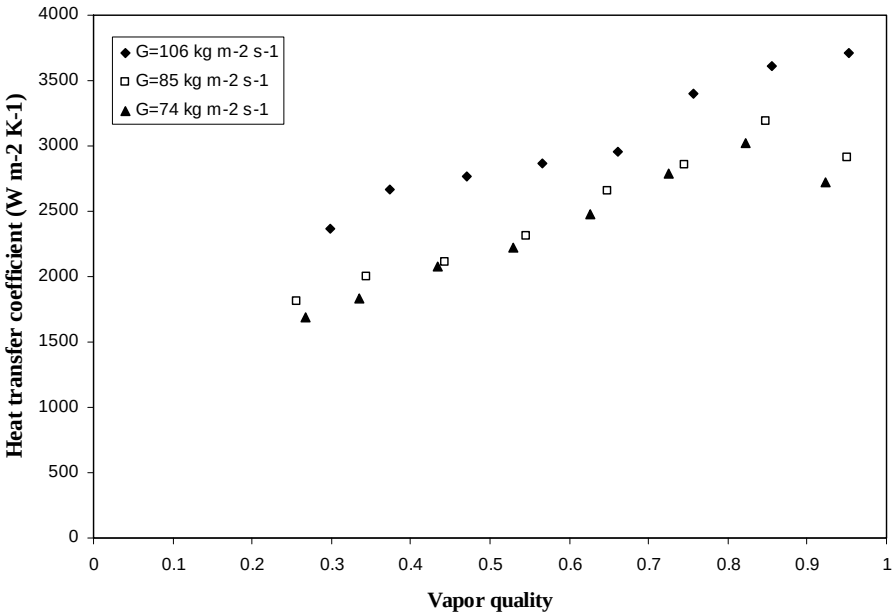

Figure 5. Heat transfer coefficient versus vapor quality for microfin round tube

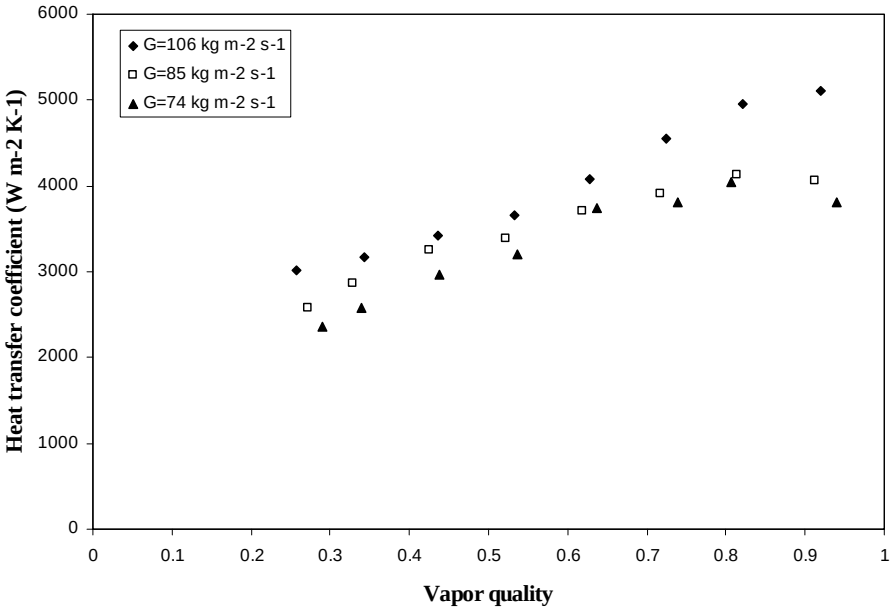

Figure 6. Heat transfer coefficient for microfin flattened tube with inside height of 3.8 mm

The variation of heat transfer coefficient with vapor quality for round tube and the flattened tube with internal height of 2.8 mm at mass velocity of 106 kg/s.m^2 has been shown in figure 7. We can study the effect of both flattening the tube and existence of microfinsfin in figure 7. As we can see, heat transfer coefficients increases by using of micro finned tube instead of smooth tube and also by flattening the tube.

Reasons for increasing the heat transfer rates due to using microfin tube are as follows:
First, helical fins by increasing turbulence in flow and tangential velocity near the wall, and also producing of vortex flow, increase the coefficients of heat transfer. Second, existence of fins increases the surface of heat transfer. Third, microfins by decreasing the flow cross sectional area, increase the velocity of flow and as a result ,the coefficient of heat transfer is enhanced.

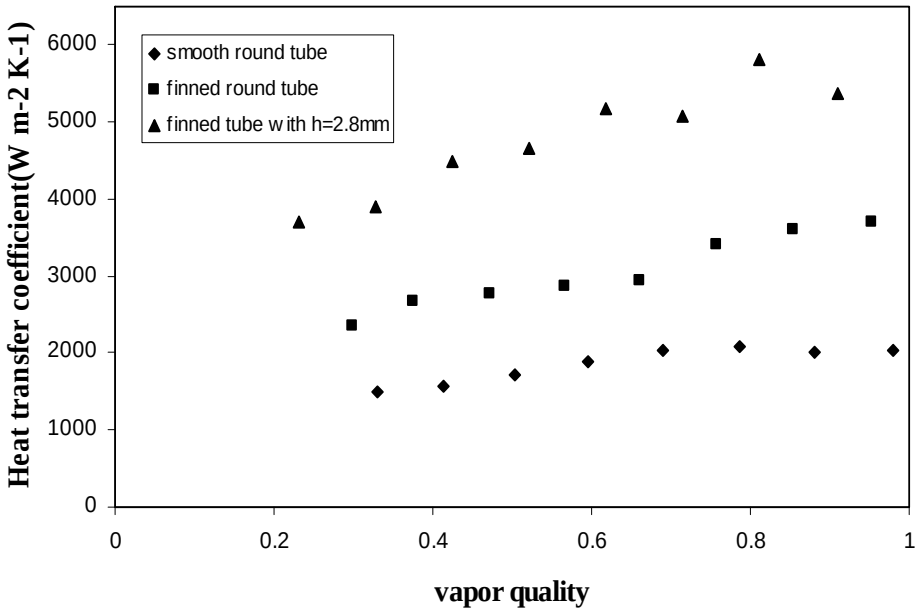

Figure 7. Heat transfer coefficient versus vapor quality at mass velocity of 106 kg m-2 s-1

In figure 8, the variation of heat transfer coefficient for different tubes at mass velocity of 85 kg m^{-2} s^{-1} were depicted. It is observed that, the heat transfer coefficient increases by flattening the tube. At a same mass velocity and vapour quality, the highest heat transfer coefficient enhancement obtained in the flattened tube with the lowest internal height of 2.8 mm. The same trend was also seen in other mass velocities.

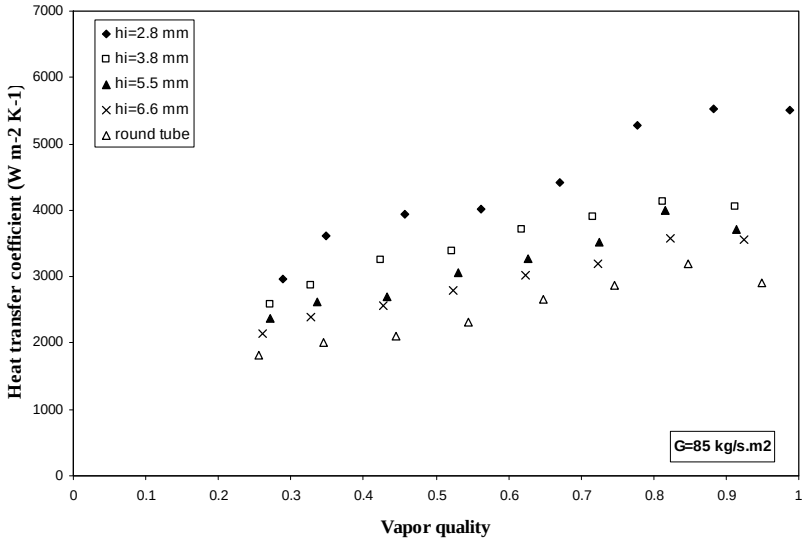

Figure 8. Variation of heat transfer coefficient with vapor quality for different tubes at constant mass velocity of 85 kg m^{-2} s^{-1}

The reasons for elevated heat transfer in flattened tube are unknown, but Wilson et al [1] made some speculation for condensing heat transfer coefficient. First, transition from stratified flow to annular flow is earlier, as the lowered height of the tube reduces the energy needed to wet upper tube surface. Annular flow tends to have higher rates of heat transfer because the film around the tube increases the turbulent interaction between the vapor and liquid phases through the roughness of the liquid film. Second, the flattened tube may alter the flow field in a manner that increase the heat transfer without changing the flow field configuration. That is, the flow field may be unaltered

from a stratified or annular flow configuration, but the flow field within that configuration may be affected. For example, some annular flows have “disturbance wave” or “ring wave” structures while others do not. Third possibility is the formation of a different flow field configuration from that commonly observed in round tubes.

CONCLUSIONS

The following conclusions have been drawn from the present study:

1- As it was expected, the heat transfer coefficient and pressure drop were elevated by increasing the mass velocity and vapor quality in flattened tube like round tube.
2- The flow boiling heat transfer coefficient and pressure drop are increased when the flattened tube is used instead of the round tube.
3- In the tube with lowest inside height The highest heat transfer coefficient enhancement of 239% was achieved at mass velocity of 85 kg m^{-2} s^{-1} and vapor quality of 85% and, the highest pressure drop increase of 400% was achieved at mass velocity of 74 kg m^{-2} s^{-1} and vapor quality of 30%
4- Pressure drop ratio respect to round tube in flattened tubes decreased by increment of vapor quality when mass velocity is fixed.

REFERENCES

1. Wilson, M.J., Newell, T.A., Chato, J.C., Infante Ferreira, C.A., "Refrigerant charge, pressure drop, and condensation heat transfer in flattened tubes", International Journal of Refrigeration, Vol. 26, pp. 442-451, 2003.
2. Bandarra Filho, Enio P., Jabardo, José M. Saiz, "Convective boiling performance of refrigerant R-134a in herringbone and microfin copper tubes", International Journal of Refrigerantion, Vol. 29, pp. 81-91, 2006.
3. Sonntag, R., Borgnakke, C., Van Wylen, G., Fundamentals of classical thermodynamics, Sixth Edition, John Wiley & Sons, New York, 2003.
4. Wolverine Tube, Inc., Engineering Data Book III, Chapter 13, 2007.

TEST PROCEDURE BASED ON A MASS BALANCE TO EVALUATE STEAM TRAP LOSSES OPERATING UNDER NO LOAD CONDITIONS: EXPERIMENTAL VALIDATION

B. Beauchamp[1], S. Kajl[1,*], L. Lamarche[1]
[11]Ecole de technologie supérieure, Montreal, Canada

ABSTRACT. This paper presents the experimental validation of a test procedure based on a mass balance to evaluate steam trap losses under no-load (live steam) conditions. The evaluated method is a modified version of an initial test procedure proposed by the authors. The validity of the method was accomplished by realizing several series of steam loss tests and comparing the results with the energy balance proposed per *ASTM* performance test code *PTC39.1, Condensate removal devices for steam system.*

Keywords: *steam trap, steam loss test, energy balance, mass balance, energy efficiency*

INTRODUCTION

Steam is a widely used heat transport medium. In any steam system, steam traps are used to improve the overall efficiency of the system. One of the main tasks of a steam trap is to evacuate condensate and non-condensable gas as they accumulate. To maximize the efficiency of the system, steam traps must also minimize steam losses as these losses are generally quite costly and thus undesirable. It is therefore important to identify and quantify steam trap losses in order to reduce energy waste and operating costs. On-site accurate quantification of steam trap losses is currently not realizable. However, to quantify steam trap losses it is possible to proceed as per performance test code ASTM PTC39.1, *condensate removal devices for steam system* [1] by using a test rig. Test code ASTM PTC39.1 describes a procedure to quantify the steam trap losses for two kinds of operating conditions: load conditions and no-load conditions. The procedure is based on an energy balance conducted in a calorimetric tank that collects condensate downstream of the steam trap. This procedure, established for tests done under load conditions, is conclusive based on the authors' experience by conducting multiple steam loss tests. However, for tests done under no-load conditions where steam trap losses are low or non-existent, this method often fails. This paper proposes a test procedure based on a mass balance to evaluate steam trap losses operating under no-load conditions. The method is a modified version of an initial test procedure proposed by the authors.

* Corresponding author: Dr Stanislaw Kajl
Phone: + 514 396-8517, Fax: + 514 396-8530
E-mail address: stanislaw.kajl@etsmtl.ca

TEST CODE PROCEDURE AS PER ASTM PTC39.1

The test code ASTM PTC39.1 for quantifying steam trap losses is based on an energy balance. Figure 1 presents the schematic representation of the testing bench respecting test code ASTM PTC39.1. To conduct tests under no-load conditions it is possible to empty the cooling water from the heat exchanger. The main steps for the test are:

- Warm up the installation to achieve the desired steady state conditions. Position valve 3 in order to send condensate to the drain device.
- Fill the calorimetric tank approximately half full with water that is at least 8 Kelvin below ambient temperature.
- Once the setup is completed, start test by positioning valve 3 to send condensate to the calorimetric tank. Note all initial parameters: time, temperatures, pressure, mass, etc.
- When the temperature of the water in the calorimetric tank is as many degrees above ambient temperature as the initial temperature was below, position valve 3 to send condensate to the drain device. Note all final parameters: time, temperatures, pressure, mass, etc.

For tests under no-load conditions involving low or non-existent steam losses, the required increase in water temperature in the calorimetric tank is usually not achievable. In order to achieve the required increase in water temperature, the tests would need to be conducted with either (i) different size of calorimetric tank according to the range of expected steam losses or (ii) for a long test period.

- Using different sizes of calorimetric tank is not an interesting solution. For each test, the size of the calorimetric tank to be used to insure an appropriate increase in water temperature depends of the steam losses which are unknown a priori. Preliminary tests would therefore need to be conducted to select the appropriate size of calorimetric tank.

- Conducting the test for a sufficient long test period to achieve the required increase in water temperature using a unique calorimetric tank is not considered an appropriate solution. The calorimetric tank needs to be large enough for tests where high steam losses are expected. This results in an oversized calorimetric tank for tests where low steam losses are expected. To achieve the required increase in water temperature when steam losses are low the tests would need to be conducted over an extended time period. Although the required increase in water temperature could be achieve in such conditions, the uncertainty of the tests results would be greatly penalized. The calorimetric tank is insulated but heat losses from its walls are unavoidable and would alter the results over extended time period especially when steam losses are low.

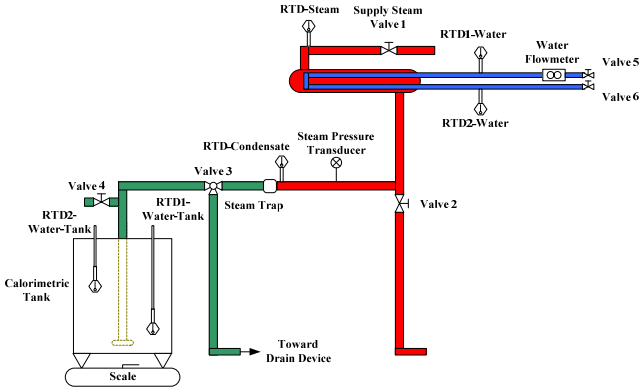

Figure 1. Testing bench respecting test code ASTM PTC39.1

TEST PROCEDURE BASED ON A MASS BALANCE

Initial test procedure proposed by the authors

The test procedure proposed in this paper is a modified version of an initial test procedure proposed by the authors [2] to quantify steam trap losses under no-load conditions based on a mass balance. The initial version of the procedure did not imply any modifications to the test rig. Its limitations mainly concerned the fact that the unavoidable condensation of operation, occurring in the steam line upstream of the steam trap and resulting from the heat losses through convection and radiation from the piping, has to be evaluated for each required operating pressures. This test procedure is presented for clarity purposes.

It is important to note that although tests are considered to be conducted under no-load conditions, there is always a small load that results from radiative and convective heat exchange between the test bench and the surrounding environment. The main steps for the test procedure based on a mass balance are:

- Warm up the installation to achieve the desired steady state conditions. Position valve 3 in order to send condensate to the drain device.
- Quantify the small load that results from testing bench radiative and convective heat losses (referred to here as the condensation of operation)
- Fill the calorimetric tank approximately half full with water that is at least 8 Kelvin below ambient temperature.
- Once the setup is completed, start test by positioning valve 3 to send condensate to the calorimetric tank. Note all initial parameters: time, temperatures, pressure, mass, etc.
- Two cases can occur:
    - Water temperature in the calorimetric tank increases quickly which indicates that steam losses are relatively high. Therefore, total steam loss can be evaluated from an energy balance as per test code ASTM PTC39.1
    - Water temperature in the calorimetric tank increases very slowly or not at all which indicates that steam loss is relatively low or non-existent. Here, steam loss can be evaluated from a mass balance as proposed.
- Tests must be conducted over a significant period of time to allow a reasonable amount of condensate to be collected in the tank. A test time of one hour has been used.
- Once the test time is completed, position valve 3 to send condensate to the drain device. Note all final parameters: time, temperatures, pressure, mass, etc.

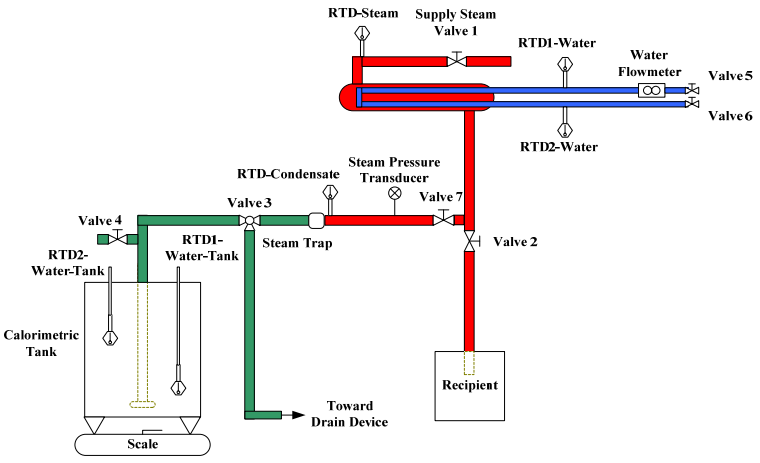

Figure 2. Testing bench used for the initial mass balance procedure

As mentioned above, in order to evaluate steam loss based on a mass balance, the small load, called condensation of operation, must be evaluated for each operating pressure. Valve 7 is installed, on our test bench (figure 2), just upstream of the steam trap to allow accumulation of condensate in the line. The condensation of operation represents the condensation that occurs in the steam line upstream of the steam trap. In operation, the steam trap will therefore have to evacuate this condensation. The main steps of the proposed procedure are:

- Determine the amount of condensate resulting from the steam pressure setting of the installation at the required operating pressure ($W_{setting}$).
- Determine the amount of condensate resulting from the testing bench condensation during no-load conditions at the required operating pressure ($W_{operation}$).

From the time interval, the condensation of operation can be expressed as a flow rate of condensation. This steady state condensation of operation represents the small load resulting from heat losses due to radiation and convection.

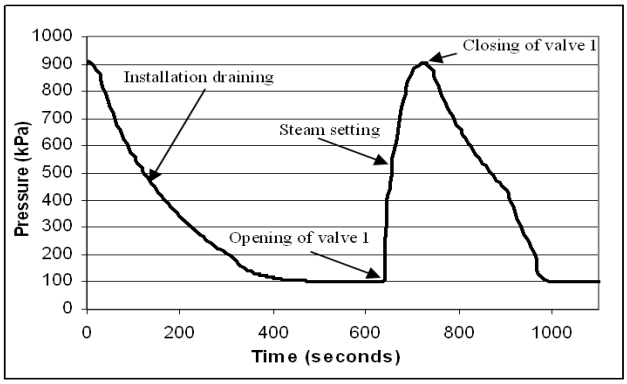

Figure 3. Steam setting of the installation

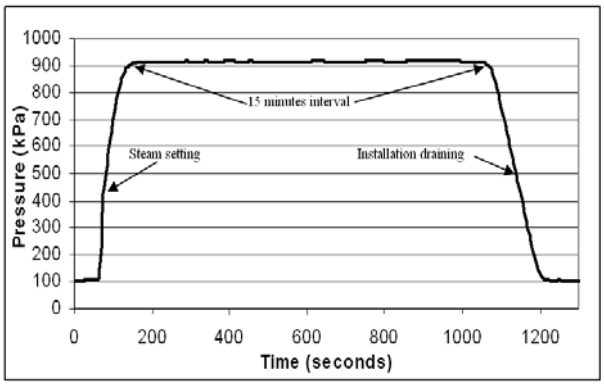

Figure 4. Operation under no load conditions

Table 1
Procedure to determine the condensation of operation and steam pressure setting condensation

Operation step n°.	**Steam pressure setting of the installation (See figure 3)**	**Operation under no-load conditions (See figure 4)**
1.	Warm up installation (valve 1 open, valve 2 closed, valve 3 to drain device, valve 7 open)	
2.	Fill a recipient (about 20 L) half full with water and note its weight (W_{beg})	
3.	Close steam valve 1	
4.	Drain the installation by opening drain valve 2 and closing valve 7 until the installation pressure is null	
5.	Close valve 2 and open steam valve 1 in order to build required pressure	
6.	When required operation pressure is reached, close steam valve 1	When required operation pressure is reached start timing interval, wait for 15 minutes and close steam valve 1
7.	Open valve 2 to accumulate condensate in the recipient filled with cold water	
8.	When installation pressure is null, close valve 2	
9.	Measure final mass of recipient ($W_{end,\ setting}$)	Measure final mass of recipient ($W_{end,\ operation}$)
10.	Condensation resulting from the steam setting of the installation $W_{setting} = W_{beg} - W_{end,\ setting}$	Condensation resulting from the operation under no load conditions $W_{operation} = W_{beg} - W_{end,\ operation} - W_{setting}$

Modified version of the test procedure

The modified version of the initial test procedure based on a mass balance required minor modifications of the initial test rig. The main advantage of the modified test procedure is that it applies for every required operating pressure without the necessity to pre-evaluate the condensation of operation.

The modified version of the test procedure required the installation of an additional steam trap downstream of valve 2 to ensure that the tested steam trap is fed with live steam. Furthermore, fluid flow downstream of the steam trap is collected in an additional tank and scale assembly using drain device through valve 3. The additional tank must be filled with an initial known mass of cold water in order to condensate any steam collected in the tank. Since tested steam trap is fed with live steam, the evaluation of the condensation of operation, occurring in the steam line upstream of the tested steam trap and resulting from the heat losses through convection and radiation from the piping, is not required. We note that the additional tank and scale assembly is not necessarily essential but greatly facilitates and improves in some ways the uncertainty of the results. Steam leakage from steam traps in good working condition fed with live steam is expected to be low. Therefore, the use of a large calorimetric tank and scale to collect a small amount of fluid downstream of the traps combined with the possibility of fluid being trapped in the piping between the tested trap and the calorimetric tank increases the uncertainty of the results. To conduct our tests, we selected the dimensions of the additional tank and scale assembly so that they would suit the possible range of the expected results and positioned that assembly as close to the trap as possible (through valve 3).

The main steps for the modified test procedure based on a mass balance are:

- Warm up the installation to achieve the desired steady state conditions. Position valve 3 in order to send condensate to the calorimetric tank.
- Once the setup is completed, start test by positioning valve 3 to send condensate to additional tank. Note all initial parameters: time, temperatures, pressure, mass, etc.
- Two cases can occur:
    - Water temperature in the calorimetric tank increases quickly which indicates that steam losses are relatively high. Therefore, total steam loss can be evaluated from an energy balance as per test code ASTM PTC39.1
    - Water temperature in the calorimetric tank increases very slowly or not at all which indicates that steam loss is relatively low or non-existent. Here, steam loss can be evaluated from a mass balance as proposed.
- Tests must be conducted over a significant period of time to allow a reasonable amount of condensate to be collected in the tank. A test time of one hour has been used.
- Once the test time is completed, open valve 3 to send condensate to the calorimetric tank. Note all final parameters: time, temperatures, pressure, mass, etc.

It is important to note that the modified test procedure based on a mass balance for traps fed with live steam considers convection and radiation heat losses from the body of the trap as steam losses. In order not to include those heat losses as steam losses it would be necessary to estimate or experimentally evaluate the heat losses from the body of each tested trap. The mass balance principle applied under no-load (live steam) condition considers all the fluid discharge through the trap as steam. For some particular needs, this way of measuring fluid discharge through a trap can be interesting. Even though fluid discharge through a trap resulting from its body heat losses is not a steam leakage, it nevertheless represents live steam that must be supplied to the trap.

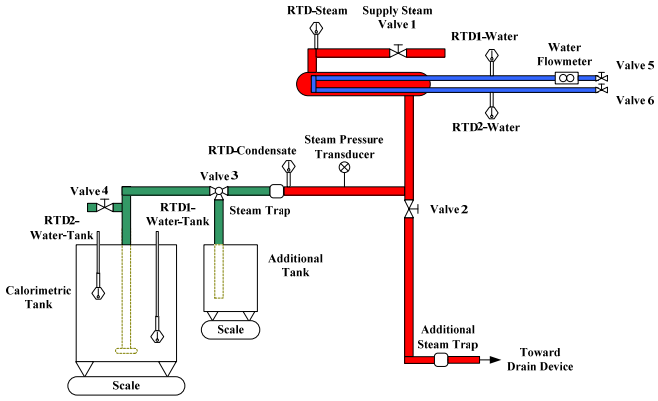

Figure 5. Modified test bench to conduct steam loss test using mass balance

The energy balance, proposed in ASTM PTC39.1, does not consider convection and radiation heat losses from the body of the trap as steam losses. The energy balance only considers fluid that is collected in the calorimetric tank in steam phase as steam losses. Furthermore, the unavoidable convective and radiative heat losses from the piping and other equipment between the tested trap and the calorimetric tank are also not considered by using the energy balance. Even though efforts are made to keep the piping and other equipment heat losses as low as possible, the steam losses evaluated with the energy balance are considered lightly underestimated.

EXPERIMENTAL RESULTS

Tests results for live steam feeding of the steam traps

Over 81 individual tests for operating pressures of 204 and 791 kPa have been conducted to ensure steam traps were fed with live steam. Such measurements were conducted with new steam traps installed on the test rig. These steam traps were considered in good working condition. Heat losses (by radiation and convection) from the steam traps' body are unavoidable for most tested steam traps. Such heat losses either condense the steam or cool the condensate and therefore cause the closing mechanism of the steam trap to open. Condensate (and possibly live steam) is discharge and is then replaced by steam. Therefore, even if a steam trap is fed with live steam and is in good operating condition (not leaking), some condensate could be discharge by this trap. Laboratory test conducted by Spirax Sarco [3] stated that energy loss from different steam traps could approximately vary from 0.25 to 1.40 kg/hr for a 500 kPa operating pressures. As noted in their results these energy losses are referred as a guide since heat losses will vary according to operating conditions, ambient environment conditions, steam trap size and steam trap type.

In our laboratory, for different types of traps, the measured amount of mass accumulated downstream of the traps varied between 0.0 to 1.3 kg/hr for an operating pressure of 204 kPa (figure 6) and between 0.0 to 2.6 kg/hr for an operating pressure of 791 kPa (figure 7). Some small thermostatic and balanced pressure & thermostatic (BP&T) steam traps were reported with zero (0) mass accumulation as could be expected from good operating conditions of such type of steam traps. Other type of steam traps (inverted bucket, float & thermostatic (F&T), thermodynamic and bi-metallic) were reported with mass accumulations varying from 0.1 to 2.6 kg/hr. Those measured mass accumulations were considered as normal condensation caused by heat losses through convection and radiation from the body of the steam trap. It is part of a subsequent research project to evaluate those heat losses for different steam traps.

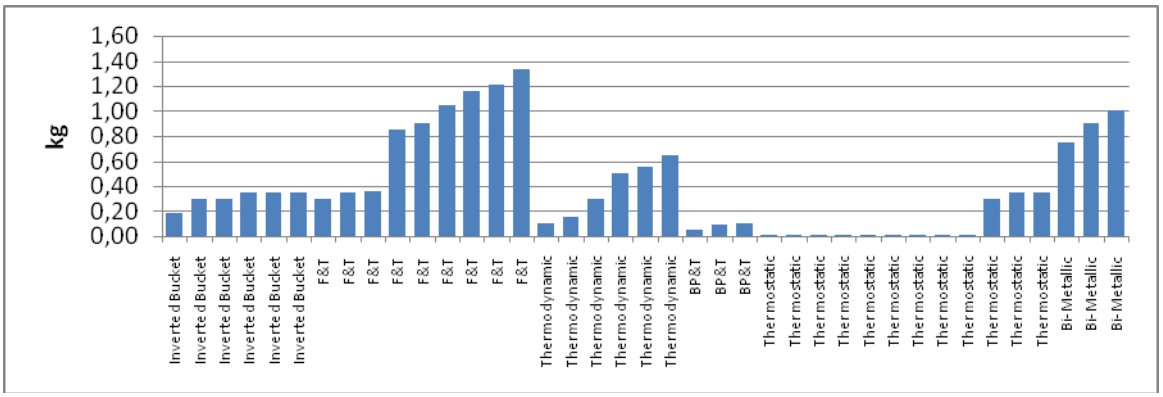

Figure 6. Mass accumulation for one hour for different traps (204 kPa)

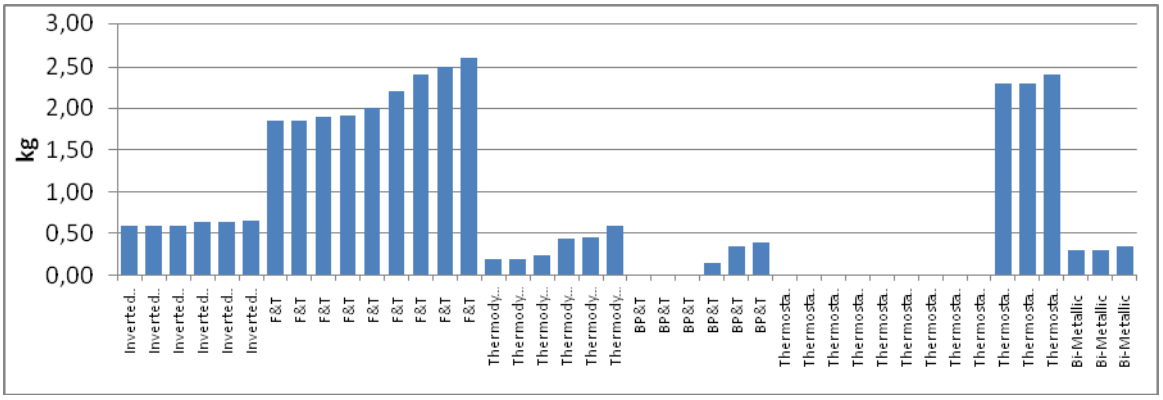

Figure 7. Mass accumulation for one hour for different trap (791 kPa)

Steam loss test results for defective steam traps

Over 78 individual tests for operating pressures of 204 and 791 kPa have been conducted to measure steam losses from defective steam traps fed with live steam. The defective steam traps had their valve intentionally held open by different means depending on their type. Since the traps' valves were held open, live steam was expected to blow through. Steam leakage measurements were therefore conducted using both the energy balance method proposed in ASTM PTC39.1 and the mass balance method presented in this paper. In order to compare the results of both methods, the mass balance is conducted in the initial calorimetric tank instead of the additional tank and scale assembly installed.

As presented in figures 8 and 9 the energy and mass balance methods give comparable results for both tested operating pressures and all type of traps tested. For an operating pressure of 204 kPa, the absolute difference between the steam losses evaluated using both method varies between 0.0 to 1.8 kg/hr. The relative error using the energy balance results as the reference varies between 0.0 to 7.0%. For an operating pressure of 791 kPa, the absolute difference between the steam losses evaluated using both method varies between 0.0 to 6.4 kg/hr. The relative error using the energy balance results as the reference varies between 0.0 to 11.0%.

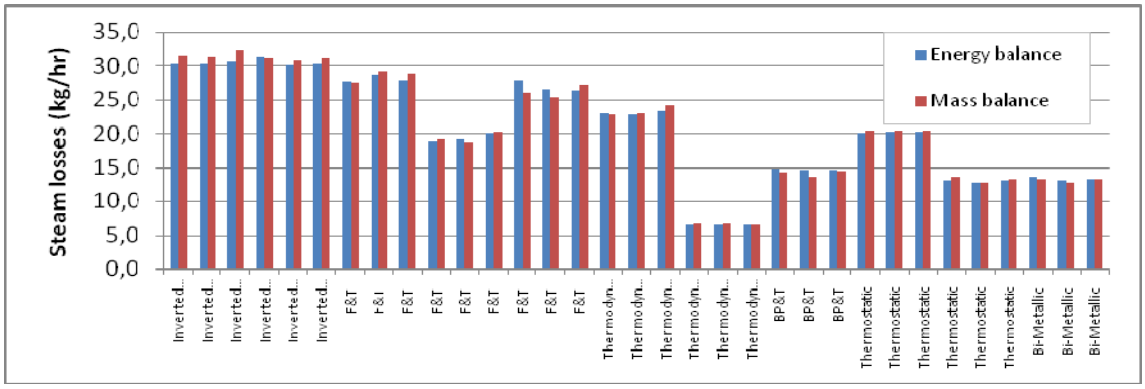

Figure 8. Steam losses results for defective traps fed with live steam (204 kPa)

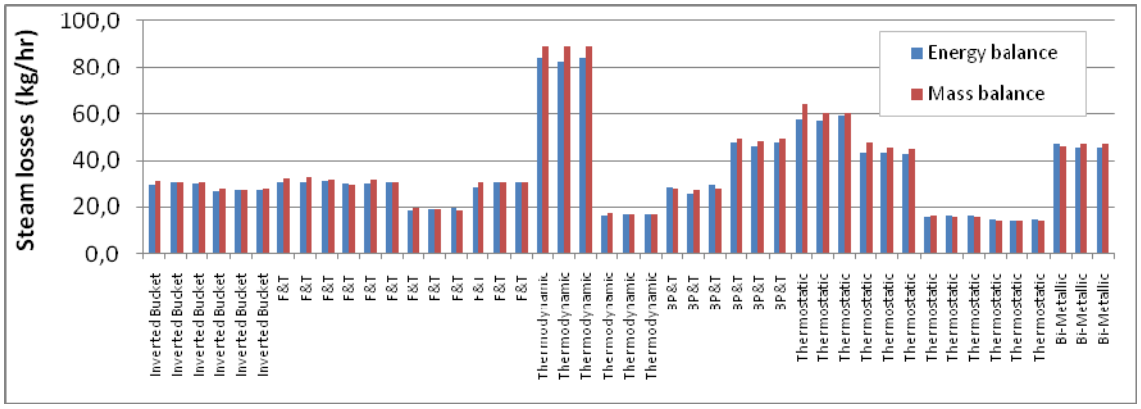

Figure 9. Steam losses results for defective traps fed with live steam (791 kPa)

CONCLUSIONS

A test procedure based on a mass balance to evaluate steam trap losses under no-load (live steam) conditions has been developed and experimentally validated. This procedure has been developed to be able to evaluate steam losses for steam traps fed with live steam when the proposed energy balance in ASTM PTC39.1 fails. From the authors' experience, the energy balance fails when steam losses are low or non-existent. Only minor modifications are necessary to the proposed test rig in ASTM PTC39.1 standard. Experiments conducted by the authors for moderate to high steam losses revealed that steam losses evaluated using the mass balance are in agreement with those from the energy balance. For over 78 tests, the relative error for the results obtained using the mass balance varies between 0.0 to 11.0% which is considered acceptable. Care must nevertheless be taken when interpreting the results because the mass balance method does consider traps' body heat losses as steam losses while energy balance doesn't. However, piping and equipment heat losses between the trap and the calorimetric tanks influence the energy balance method but not the mass balance method. The experimental evaluation of steam traps' body heat losses would allow a better comparison between the energy and the mass balance methods.

REFERENCES

1. ANSI/ASME PTC39.1 Condensate Removal Devices for Steam Systems.
2. **Beauchamp, B.** et Kajl, S., (2005) Test procedure based on a mass balance to evaluate steam trap losses operating under no load conditions. XI International conference of air conditioning, air protection & district heating 2005. 247-252.
3. The Steam and Condensate Loop book, Spirax Sarco Publisher Limited, 2005.

PREDICTION OF FLUIDIZATION BEHAVIOUR AND A QUASI-STATIONARY APPROACH TO DRYING KINETICS OF IRREGULAR PARTICULATE FOOD MATERIALS

Wijitha Senadeera*
School of Engineering Systems, Queensland University of Technology
2 George Street GPO Box 2434, Brisbane QLD 4001, Australia

ABSTRACT**.** Changes in fluidization behaviour behaviour was characterised for parallelepiped particles with three aspect ratios, 1:1, 2:1 and 3:1 and spherical particles. All drying experiments were conducted at 50^0C and 15 % RH using a heat pump dehumidifier system. Fluidization experiments were undertaken for the bed heights of 100, 80, 60 and 40 mm and at 10 moisture content levels. Due to irregularities in shape minimum fluidisation velocity of parallelepiped particulates (potato) could not fitted to any empirical model. Also a generalized equation was used to predict minimum fluidization velocity. The modified quasi-stationary method (MQSM) has been proposed to describe drying kinetics of parallelepiped particulates at 30^o C, 40^o C and 50^o C that dry mostly in the falling rate period in a batch type fluid bed dryer.

Keywords: *Fluidization, Generalised model, Quasi-stationary approach, irregular particulate*

INTRODUCTION

The minimum fluidisation velocity of a material is the superficial velocity at which material bed starts to fluidise The Ergun equation (Ergun, 1952) is the widely accepted model to determine *minimum fluidization velocity* of a fluid to fluidize the particle (Kunii and Levenspiel, 1969; Zenz and Harbor, 1971; Michelis and Calvelo, 1994).The Ergun equation (Equation 1) is used to calculate minimum fluidization velocity of baker's yeast (Egerer et al., 1985), peas (Rios et al., 1984) and diced potato and potato strips (Vazquez and Calvelo, 1980; Vazquez and Calvelo, 1983). An equation similar to Ergun is valid for peas (Michelis and Calvelo, 1994). The values for velocity obtained by the Ergun equation are mostly reliable for spherical and relatively small particles. Most agro-food particulates however comprise of various shapes and sizes, and consist of larger particles. Therefore, the minimum fluidization values obtained from Ergun equation do not conform to the experimental values (Mclain and McKay, 1980, 1981a, 1981b; McKay et al., 1987)

$$(1-\varepsilon_{mf})(\rho_s-\rho_f)g = 150\frac{(1-\varepsilon_{mf})^2}{\varepsilon_{mf}^3}\frac{\mu u_{mf}}{(\phi d_p)^2} + 1.75\frac{(1-\varepsilon_{mf})}{\varepsilon_{mf}^3}\frac{\rho_f u_{mf}^2}{\phi d_p} \qquad (1)$$

where ε_{mf} – bed porosity at minimum fluidization velocity, ρ_s – particle density (kg/m^3), ρ_f – fluid density (kg/m^3), μ - viscosity (N s/m^2), u_{mf} – minimum fluidization velocity (m/s), d_p – particle equivalent diameter (m), ϕ - sphericity

* Corresponding author: Wijitha Senadeera
Phone: +61-7-31386887,Fax: +61-7-31381516
E-mail: w3.senadeera@qut.edu.au

The Ergun equation consists of *viscous* and *kinetic energy* terms. In the case of larger particles at higher Reynolds numbers (Re > 1000) the fluidization behaviour is mainly governed by the kinetic energy term in the Ergun equation. Hence the Ergun equation can be simplified for (Kunii and Levenspiel, 1969) a wide variety of systems and a generalized equation can be applied to predict minimum fludisation velocity for larger particles when Reynolds number > 1000 using some modification.

$$u_{mf}{}^2 = \frac{\phi d_p}{1.75}\frac{(\rho_s - \rho_f)}{\rho_f} g \varepsilon_{mf}{}^3 \quad (2)$$

where, ε_{mf} – bed porosity at minimum fluidization velocity, ρ_s – particle density (kg/m^3), ρ_f – fluid density (kg/m^3), u_{mf} – minimum fluidization velocity (m/s), d_p – particle equivalent diameter (m), ϕ - sphericity, g - acceleration due to gravity (m/s^2)

For wide variety of systems it was found that value $\frac{1}{\phi\, \varepsilon_{mf}{}^3} \cong 14$ (Wen and Yu, 1966) and a generalized equation can be applied to predict u_{mf} for larger particles when Re > 1000.

$$u_{mf}{}^2 = \frac{d_p(\rho_s - \rho_f)}{24.5\rho_f} g \quad (3)$$

where, ρ_s – particle density (kg/m^3), ρ_f – fluid density (kg/m^3), u_{mf} – minimum fluidization velocity (m/s), d_p – particle equivalent diameter (m), Re – Reynolds number

There is a continuous change in physical properties of the particulates during drying, which also changes the fluidization behaviour of the particles. It is very important to understand these changes, so that the air-flow during drying can be controlled to achieve an optimum fluidization.

Some limitations of the empirical models derived to describe drying characteristics could be eliminated by using a semi-empirical approach. Such a method is the modified quasi-stationary method (Efremov, 1999). This method has been proposed to describe drying kinetics of parallelepiped particulates at three drying temperatures where particles dry mostly in the falling rate period in a batch type fluid bed dryer. The model is based on mass conduction of solid materials in bulk, given in terms of effective moisture diffusivity, resulting in the following semi-theoretical equation for drying kinetics;

$$MR = \frac{m - m_e}{m_i - m_e} = \frac{1}{1 + \left(\frac{t}{\sigma}\right)^p} \quad (4)$$

Where, MR – dimensionless moisture, m – moisture at given time (kg/kg db), m_e – equilibrium moisture (kg/kg db), m_i – initial moisture content, t-drying time (h), σ – characteristic time (h) and p – dimensionless parameter

The objective of this study is to understand changes in minimum fluidization velocity for a parallelepiped food material during drying and relate this to moisture content by a suitable model, and compare the experimental minimum fluidization velocity with the generalized model predictions. Also a modified quasi-stationary method (MQSM) has been proposed to describe drying kinetics of parallelepiped particulates at 30^{o}C, 40^{o}C, and 50^o C in a batch type fluid bed dryer.

MATERIAL AND METHODS

Material preparation

Potato *Solanum tuberosum* of the variety Sebago was purchased from the same supplier in 50 kg bags. Parallelepipeds were made in a Dicing Machine (Hobart, Australia), by incorporating a cutter which makes 6.5mm X 6.5mm square cross-section. According to the required aspect ratios of 3:1, 2:1 and 1:1, the particles were cut carefully to lengths of 19.5, 13 and 6.5 mm respectively using a cutting blade. Immediately after cutting, all the samples were immersed in a sodium metabisulphite solution (0.1 % w/w) for 15 minutes to prevent browning during drying. The samples were drained on a mesh tray. Then samples were placed in a plastic bag and kept it in a cold room for 24 hours at 4^{o} C in order to produce uniform moisture distribution within the sample.

Particle density determination. To determine the particle density, a known number of particles were weighed by an electronic balance (Sartorius), and the volume was measured by the difference in meniscus levels before and after immersion of particles in liquid paraffin in a measuring cylinder. The difference in meniscus levels was measured by a vernier caliper (accuracy 0.05mm). This value was used to calculate the equivalent diameter of the particle, which was used in the generalized equation (Equation 3).

Moisture content determination. Moisture content was determined by measuring the loss in weight of finely chopped samples held at 70^{0} C and 13.3 Kpa vacuum for 24 hours (AOAC, 1995).

Experimental method for fluidisation experiment

First, fluidisation characteristics of the un-dried samples were measured in the fluidizing column with the prepared samples. After that samples were dried on a fixed bed in a heat pump dehumidifier system and samples were withdrawn at nine pre-determined time intervals during drying and used for measurement of fluidisation characteristics at different moisture contents. Fluidisation characteristics measured were minimum fluidisation velocity at four bed heights of 100, 80, 60, and 40 mm in a fluidized bed column (Figure 1).

Figure 1. Fluidisation column connected to the heat pump dryer

Drying in a fixed bed. Samples for studying fluidisation behaviour were dried in a heat pump dehumidifier system (Baleden Pty Ltd, Brisbane, Australia) in Food Science and Technology, School of Land and Food Sciences, University of Queensland, Gatton, Australia (Figure 1). The drying was undertaken at an air temperature of 50^{o} C (which is a common drying temperature) and

relative humidity of 15 %. Before materials were loaded in the dryer, the dryer was run for 2 hours to achieve steady state conditions. Materials were placed into the drying system on mesh trays as thin layers, and stacked vertically to achieve maximum exposure to the air-flow. Samples were removed at nine pre-determined time intervals. They were placed into a sealed container and immediately used for fluidizing experiments. For moisture determination, samples were stored immediately in a pre-dried sample bottle.

Determination of minimum fluidisation velocity All fluidisation trials were conducted in a batch type flexi-glass fluidizing column of 185 mm inside diameter and length 1 m (Figure 1). The hot air was taken from a heat pump dehumidifier system (Intertherm P/L, Brisbane, Australia) coupled to the fluidizing column by flexible ducts. Bed height was measured from a scale attached to the column. The change of bed pressure drop was measured while increasing the velocity through the bed for each height. In order to determine the optimum bed height for improved fluidisation bed heights of 100, 80, 60 and 40 mm were used. Measurements of pressure drop for each bed height took less than 3 min.

Visual observation of the bed at an instance of fluidization after bed expansion was the criteria considered to categorise minimum fluidization. Also this value was compared with graphical variation of the pressure drop of the bed with velocity. Both observed and graphical values were identical.

Drying in a fluidised bed One batch stored in the cold room was taken for fluidised bed drying experimentation. Fluidised bed dryer was connected to the heat pump dehumidifier system (Figure 1). The drying conditions of 30^0 C, 40^0 C and 50^0 C were set by the temperature controller in the heat pump dehumidifier system, and the drying set up was run for 2 hours to achieve steady state conditions of drying before material introduction. Initial bed height of 150 mm was used. The hot air velocity passing through the material bed was kept at a constant value of 2.2 m/s for all drying experiments. This velocity was selected, because it was within the limit of fluidisation and terminal velocity of the material concerned and within the capability of the fan. The air-flow entering the dryer was controlled by flow control valves. Samples were collected from the dryer at 30 minutes intervals through the sample outlet. Each time they were collected in a sealable container and immediately used for moisture determination and volume measurements.

ANALYSIS OF EXPERIMENTAL DATA AND MODELLING PROCEDURE

Fluidisation data were analysed for the analysis of variance (ANOVA) to evaluate differences, and, linear and non-linear regression to obtain suitable models. The coefficients of Equation 4 were estimated using Matlab (2008) Curve Fitting Tool Box on a personal computer. Model validity was tested using measures of coefficient of determination (R^2) and mean absolute error percentage (MAE%). Mean absolute error percentage (MAE%) (Equation 5) was calculated according to the methods given by Mayer and Butler (1993) for different L:D ratios and are given in Table 1.

$$\mathrm{MAE\%} = 100\left[\Sigma\left(\left|y_i - \hat{y}_i\right| / \left|\hat{y}_i\right|\right)\right] / n \quad (5)$$

RESULTS AND DISCUSSION

Fluidisation behaviour

For aspect ratio 1:1, minimum fluidization occurred together with slugging and channeling at the moisture 560 % db for all bed heights. Reduction in minimum fluidization velocity was fairly linear down to 300 % db moisture. Between moisture contents values 220~260 % db, there existed a sudden change of minimum fluidization value for all bed heights (which described as the transition region in Figure 3). The magnitude of this change in minimum fluidization velocity decreased as bed height decreased. At low moisture values irregular behaviour in fluidization velocity was observed due to uneven shrinkage and interlocking of particles. Figure 2 shows fluidization behaviour of potato with aspect ratio 1:1, which shows some what regular fluidization behaviour.

In the case of aspect ratio 2:1 (graph not shown), when moisture content of particles was initially 570 % db, fluidization did not start until 310 % db moisture for the bed height of 100 mm, and at 340 % db moisture for the remainder of the bed heights. Sudden changes in minimum fluidization velocity were observed between moisture values of 140 % and 160 % db, a very narrow moisture range. This may be due to change in bed porosity. Below 140 % db moisture content minimum fluidization velocity was reduced showing irregular behaviour below 40 % db moisture, similar effect as 1:1.

For aspect ratio 3:1 at 100 mm bed height particles tend to fluidise after they have been dried too a moisture content of 300 % db from initial moisture of 540 %. In all other bed heights, fluidization started when moisture content was less than 326 % db. Suden change in minimum fluidization velocity was observed in the middle ranges of moisture content (60% - 70 % db). As moisture reduced during drying also resulted in increasing sphericity value (which was not measured) could have been contributed to better fluidization.

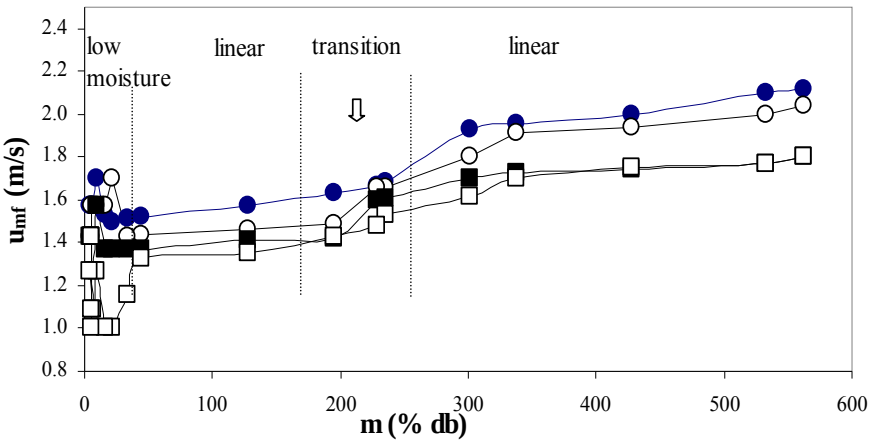

• 100 mm o 80 mm ■ 60 mm □ 40 mm

Figure 2. Fluidisation behaviour of potato aspect ratio = 1:1

Modelling of minimum fluidisation velocity with change in moisture content. Fluidisation behaviour of potato particles could not be modelled due to the irregular trend of change of minimum fluidisation velocity with moisture content for all aspect ratios. The change of minimum fluidization velocity with moisture reduction was less for lower bed heights. The change of minimum fluidization velocity with the moisture reduction was less for lower bed heights. For aspect ratio of 1:1 u_{mf} ($m \sim 0$) increased from 1.1 m/s to 1.6 m/s when bed height increased from 40 mm to 100 mm. For aspect ratio of 2:1, u_{mf} ($m \sim 0$) increased with increased bed heights and changed from 1.3 m/s to 1.7 m/s for the bed heights of 40 mm to 100 mm respectively. This change for aspect ratio 3: was in the range 1.8 m/s to 2.1 m/s.

Minimum fluidisation velocity calculation based on the generalized equation. The Generalized model was used to calculate the predicted values of minimum fluidisation velocity. For all three aspect ratios, this generalized model value was compared with the experimental value. The mean absolute error percentage value is more than 10% for the aspect ratio 3:1, for the bed heights of 100, 80 and 60 mm (Table 1).

Table 1
Mean absolute error percentage (MAE %) of observed and predicted values

Aspect ratio	**MAE%**			
	100mm	**80mm**	**60mm**	**40mm**
1:1	8.83	4.09	2.75	2.03
2:1	7.55	6.26	1.03	1.02
3:1	13.46	12.98	10.80	3.68

The generalized model predicted minimum fluidization velocity changes from 1.30 m/s (5 % db moisture) to 1.68 m/s (562 % db moisture) for the aspect ratio 1:1. The predicted minimum fluidization velocity for the aspect ratio 2:1 varied from 1.45 m/s (4.3 % db moisture) to 1.76 m/s (338 % db moisture). The variation in predicted minimum fluidization velocity for the aspect ratio 3:1 was 1.58 m/s (4.7 % db moisture) to 2.12 m/s (326 % db moisture). (Predicted and observed plots are not shown).

Quasi-stationary approach to drying kinetics

Table 2 shows the value p (Index of Hydrodynamic Intensity) in equation 4, which is a representation of hydrodynamic condition of the bed during drying experimentation for different aspect ratios.

Table 2
Index of hydrodynamic intensity (p) for different aspect ratios

L:D Ratio	**p**
1:1	1.81
2:1	1.69
3:1	1.67

From the values given in Table 2 it was observed that Hydrodynamic intensity (p) of the fluidized bed is vary with the size. The slight variations observed among sizes, may be attributed to channeling and slugging behaviour of the particles at higher initial moisture contents. Also it can be both material shape and aerodynamic of the bed dependent. Table 3 shows the characteristic times (σ) for different aspect ratios and drying conditions.

Table 3

Characteristic time for different aspect ratios at drying temperatures

	30°C	**40°C**	**50°C**
1:1	0.9268	0.7814	0.5797
2:1	1.059	0.9392	0.7720
3:1	1.122	1.038	0.7920

Good agreement of experimental data with predicted values indicate that the parameters obtained for hydrodynamic intensity and characteristic time (For all the cases coefficient of determination R^2 was above 0.99). It was also observed that characteristic time was proportional to the drying air temperatures and decreased with increased temperature.

CONCLUSION

Fluidisation behaviour with moisture could not be modelled for parallelepiped (potato) particles due to its irregular nature. But generalised equation predicts the minimum fluidisation with a reasonable accuracy for the particles. If sphericity changes during drying is measured an accurate predictions of minimum fluidisation velocity could be obtained using Ergun Equation. Onset of fluidisation of particles depended on bed height, sphericity and moisture content. Good fluidisation was observed only at low moisture levels. The magnitude of the minimum fluidisation velocity decreased with the decreased bed height and with decreased moisture content. The modified quasi stationary could be used to describe drying kinetics of the fluid bed drying accurately and characteristic drying time decreased with increased drying temperature.

NOMENCLATURE

d	equivalent diameter	(m)
D	diameter	(m)
g	acceleration due to gravity	(m/s^2)
L	length	(m)
m	moisture content (dry basis)	(kg/kg db)
MR	dimensionless moisture	
p	hydrodynamic intensity	
Re	Reynolds number	
t	drying time	(h)
u	velocity	(m/s)
y	value	
σ	characteristic time	(h)
ϕ	sphericity	
ε	porosity	
ρ	density	(kg/m^3)
μ	viscosity	($N\ s/m^2$)

Superscripts

$\wedge$	predicted value

Subscripts

e	equilibrium
f	fluid
i	integer
mf	minimum fluidization
n	no of observations
o	initial
p	particle
s	solid

REFERENCES

1. AOAC, (1995). *Official Methods of Analysis*, 16th edition, Association of Official analytical Chemists, Washington DC.
2. Efremov, G. I. (1999), A Modified Quasistationary Method of Describing The Kinetics of Drying of Hygroscopic Materials, *Journal of Engineering Physics and Thermophysics*, 72(3), 396-400.
3. Ergun, S. (1952). Fluid flow through packed columns. *Chemical Engineering Progresses*. 48(2), 89 110.
4. Kunii, D. and Levenspiel, O. (1977). *Fluidization Engineering*. (Second Edition) Butterworth - Heinemann, Sydney, Australia.
5. Mathworks (2008), Matlab 7.6.0. *The Language of Technical Computing*, The Mathworks Inc., USA
6. Mayer, D. G. and Butler, D. G. (1993). Statistical validation. *Ecological modeling*, 68: 21 - 32.
7. McLain, H. D. and McKay, G. (1980). The fluidization of cuboid particles, *Trans.I ChemE*. 58(4), 107 - 115.
8. McLain, H. D. and McKay, G. (1981). The fluidization of potato chips. *Journal of Food Technology*. 16, 59 - 66.
9. McKay, G., Murphy, W. R. and Jodieri-Dabbaghzadeh, S. (1987). Fluidisation and hydraulic transport of carrot pieces. *Journal of Food Engineering*. 6, 377 - 399.
10. Rios, G. M., Marin, M. and Gibert, H. (1984). New developments of fluidization in the IQF food area. In *Engineering and Food*, Vol 2: Processing Applications. B. M. McKenna eds) pp. 669 - 667, Elsevier Applied Science Publishers. London.
11. Vazquez, A. and Calvelo, A. (1983). Gas-particle heat transfer coefficient for the fluidization of different shaped foods, *Journal of Food Science*. 48, 114 - 118.
12. Vazquez, A. and Calvelo, A. (1980). Gas particle heat transfer coefficient in fluidized pea beds, *Journal of Food Process Engineering*, 4, 53 - 70.
13. Wen, C. Y. and Hu Y. H. (1966). A generalized method for predicting the minimum fluidization velocity. *AIchE Journal*. 12, 610- 612.

THE EFFECT OF IMPELLER-VOLUTE GAP ON PRESSURE FLUCTUATIONS INSIDE A DOUBLE-VOLUTE CENTRIFUGAL PUMP OPERATING AT REDUCED FLOW RATES

Attia E. Khalifa*, Amro M. Al-Qutub
King Fahd University of Petroleum & Minerals, Dhahran 31261, Saudi Arabia

ABSTRACT**.** One of the main causes of flow-induced vibration at blade passing frequencies in centrifugal diffuser pumps is the inappropriate radial gap between impeller and volute vanes. A small gap may be preferable for pump performance, head and efficiency. However, it may initiate strong impeller/volute interaction, resulting in high pressure pulsation inside the pump and consequent high vibrations to the pump components. In the present study, the effect of the radial gap and flow rate on pressure fluctuations due to impeller-volute interaction has been investigated experimentally on a double volute boiler feed pump stage. Results showed that pressure fluctuations inside the pump are sensitive to the radial gap as well as the flow capacity. Increasing the gap from 2.5% to 4.25% of impeller diameter gave the maximum reduction in pressure fluctuations and their energies, especially at reduced flow rates. The reduction in amplitude and energy of the fluctuations (from 20 to 06% depending on flow rate and measuring location) was achieved at the expense of 0.92% loss in pump head and 0.5% in efficiency for the rated capacity.

Keywords*: Radial gap, impeller-volute interaction, reduced flow rate, pressure fluctuations, double volute centrifugal pump.*

INTRODUCTION

Optimization of the gap selection depends on the pump design and expected dynamic operating conditions. In high-pressure high-speed pumps, the minimum radial gap is an important design parameter that controls the pressure pulsation resulting from the impeller-volute interaction. Under off-design conditions, the pressure fluctuations are excited around the impeller due to this interaction, leading to additional radial loads on the pump shaft and general vibration behaviour of the pump. Reducing the impeller/volute interaction by increasing the radial gap can reduce the pressure fluctuations. However, the performance of the pump is degraded with the increasing gap. Experimental testing is needed in order to determine the suitable gap design for the pump under consideration. Pressure fluctuations due to this interaction occur mainly at blade passing frequency (BPF) and its higher harmonics. Khalifa et al. [1] studied a high vibration problem in a double volute Boiler Feed Pump (BFP) operating at reduced flow rates. Vibration spikes appeared mainly at 5xRPM frequency, which corresponds to the first blade passing frequency. The energy content of these fluctuations was found to be sensitive to the flow rate and is location-dependent. It becomes more significant at partial flow rates.

* Corresponding author: Dr. Attia Khalifa
Phone: + (966)-3-8604967; Fax: + (966)-3-8602949
E-mail address: attia@kfupm.edu.sa

Unsteady pressure signals measured at suction and discharge pipes do not reflect properly the behaviour of fluctuations inside the pump. The impeller/volute interaction results in circumferential unevenness of fluctuations around the impeller and the unevenness become more significant at off-design flow rates [2]. The pump geometry and impeller/volute combination play an important role in the severity of the pressure pulsation inside the pump [3]. Large high-head pumps are usually available only in the double (split) volute design to minimize the net radial force on the pump shaft when a pump has to operate away from the BEP. Studies on the effect of flow rate on pressure fluctuation at the blade pass frequency at different axial planes in the pump showed that it is maximum at the central impeller plane [4]. The flow-induced vibration in high-pressure pumps has specific characteristics that can be clearly observed in the frequency domain [5]. Harmonics of the blade passing frequency dominate the spectrum, and there is a particular relation among their amplitudes. The rise in the amplitudes is not equal for all harmonics. The time variant and spatial nature of these pressure distributions (pressure mode shapes) can be visualized [6].

Increasing the impeller to diffuser clearance, or changing the number of impeller blades, is a common solution for the high-pressure pulsation problems in high pressure centrifugal pumps. The pressure pulsations arising from the interaction of the impeller and vaned diffuser were measured at 2 times the impeller blade pass frequency in the discharge pipe [7]. The gap was increased from 3% to 12% of the impeller diameter. A reduction of 10 % in the flow capacity, at the rated head, resulted from this modification while the efficiency remained almost the same. The effect of radial gap between impeller and diffuser on vibration, noise, and performance was examined, under different flow rate conditions, by trimming the impeller to achieve different gaps [8]. At the maximum radial gap between the impeller and diffuser, the overall levels of vibration and noise were minimum. The present study continues the experimental investigation on flow-induced vibration problem presented by Khalifa et al. [1] for a boiler feed pump at SEC power plant. It aims to study the effect of increasing the radial gap between the impeller and volute vanes on pressure fluctuations at different flow rates and pump performance.

EXPERIMENTAL SETUP

The model pump has a speed of 3540 rpm, actually measured at 60 Hz. The flow rate is measured by an orifice meter; which has a discharge coefficient of 0.618. Orifice pressure taps are connected to a PDCR 4170, 700 mbar differential pressure transducer which has ±0.08% FS accuracy. Balance on the flow rate is checked using a U-tube manometer. The flow rate is controlled by a gate valve in the discharge pipe. A schematic diagram for the test loop is shown in the Figure 1. Reverse engineering was done to produce the model single-stage volute and impeller. Collected geometrical data from the original boiler feed pump were used to generate CAD files and then the impeller and volute were produced by CNC machines. A scale factor of 0.4 for the model pump was selected, taking into consideration similarity laws and practicality of the experimental setup. The impeller was balanced dynamically on a two-plane balancing machine to minimize the effect of rotor imbalance as a source of vibration. A shaft-like extension was attached to the impeller to simulate the actual flow characteristics at the suction of the original boiler feed pump. Locations of the static and dynamic pressure transducers were arranged in geometrical symmetry positions around the impeller as shown in Figure 2. The coordinates of these locations relative to the volute horizontal centreline are given in reference [1].

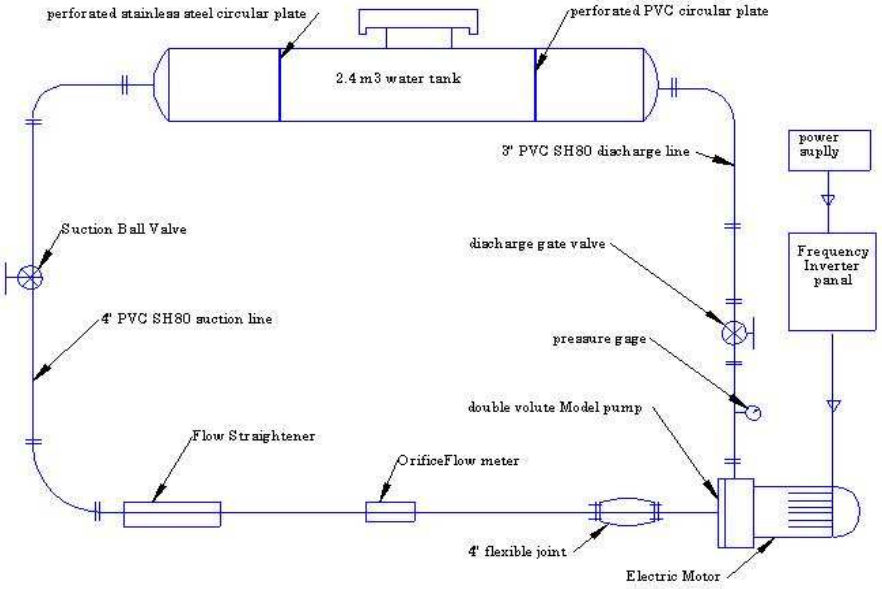

Figure 1. Schematic diagram for the test loop

Nine pressure transducers were placed flush within the volute plexiglass cover plate at the impeller discharge. One pressure transducer was placed at the discharge pipe, and another one at suction pipe. OMEGA's DPX101-250 high-responses dynamic pressure transducers were used to measure the pressure fluctuations. Figure 3 shows the model pump components and assembly.

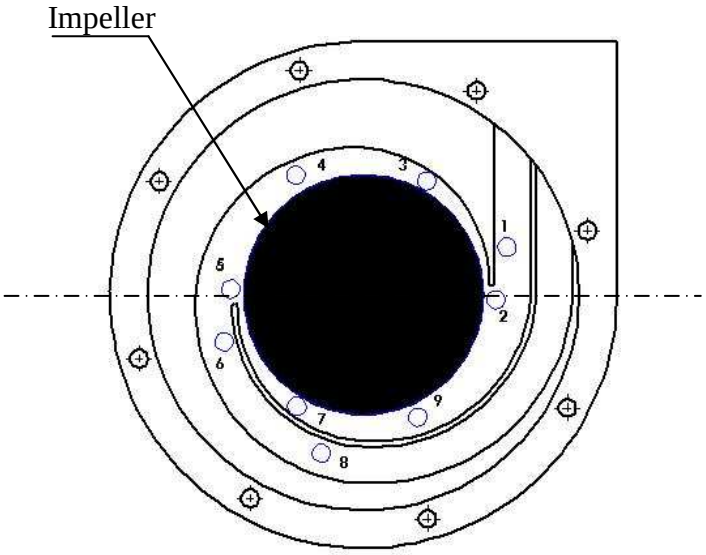

Figure 2. Model pump design and measuring locations

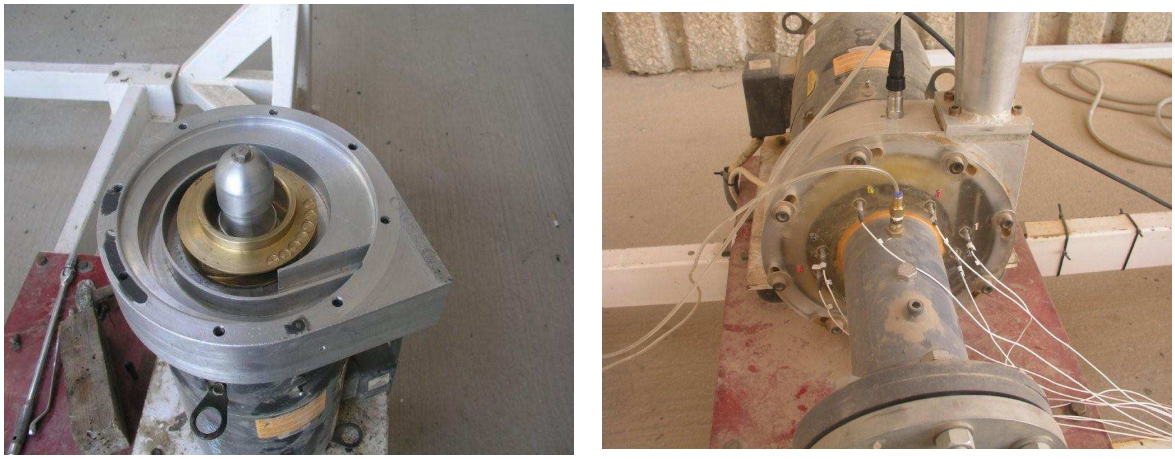

Figure 3. Model pump components and assembly

RESULTS

The original gap design for the scaled model pump is 3.6 mm, which is equivalent to 2.5 % of the impeller diameter. The experimental matrix was designed to test gaps of 3.6, 4.85, 6, and 7 mm at different flow rates ratios (Q/Qn) of 1, 0.75, 0.5, and 0.25. Qn represents the nominal flow rate corresponding to best efficiency point for the original gap design of 3.6 mm, and it was measured to be 12 l/s. The pressure distribution, the fluctuations inside the pump, and the pump performance, were examined. The consecutive gaps were achieved by cutting back 10 mm from the volute vanes each time. For example; figure 4 shows the original gap design (3.6 mm, a) and the maximum gap (7 mm, b), achieved by cutting back the volute vanes 30 mm in the vertical direction. This is equivalent to increasing the gap from 2.5% to 5% of impeller diameter. The measuring locations were fixed for all gaps. Uncertainty analysis for the measured and calculated variables showed that the uncertainty values at the best efficiency point are limited to 1% for the total head, 1.5% for the flow rate, and 2% for the efficiency. Pump specific speed is 1620.

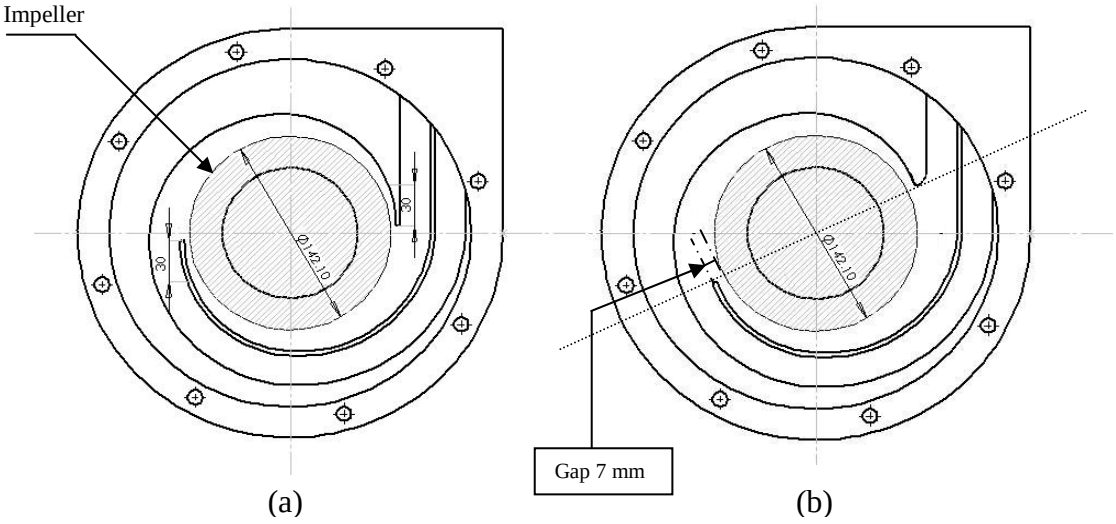

Figure 4. (a) Original gap (3.6mm); and (b) the max gap (7 mm), dim. in mm

As an illustration, Figure 5 displays a typical fluctuation time history (for two shaft revolutions time, 0.034 sec) and the frequency spectrum (FFT) for location # 3 and gap 3.6 mm, at two different flow ratios of 1 and 0.5. Dominant peak occurred at a frequency of 295 Hz which corresponds to 5xRPM or the first blade passing (1st BPF). Smaller peaks appeared at 10xRPM (2nd BPF) and 15xRPM (3rd BPF). The amplitude and strength of these fluctuations were found to be sensitive to the flow rate. All other locations inside the pump experienced similar behaviour [1].

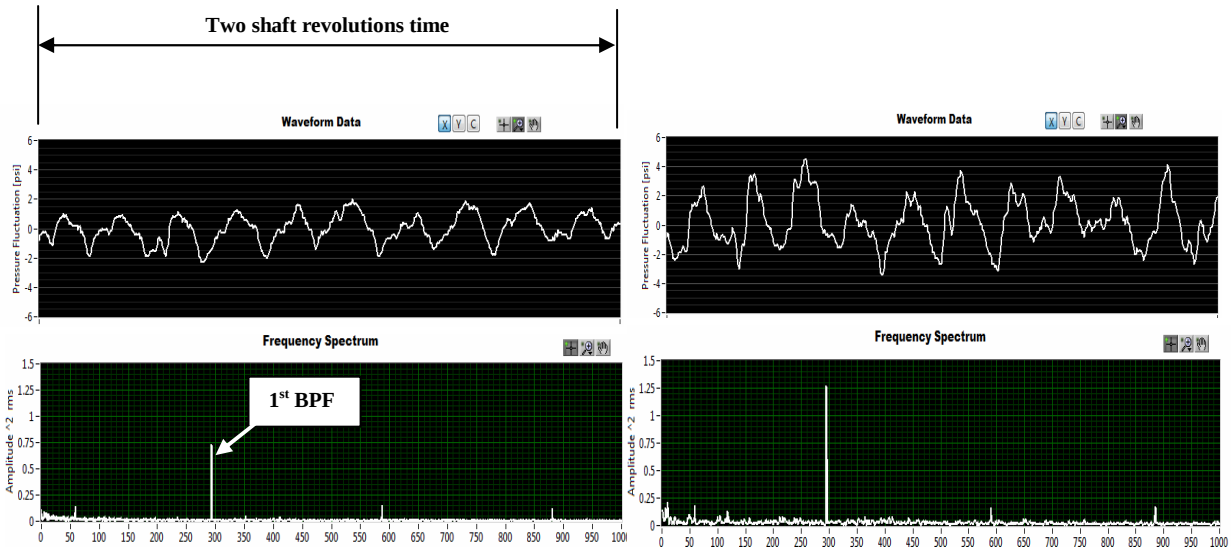

(a) Q/Qn=1 (b) Q/Qn=0.5

Figure 5. Real time pressure fluctuations and frequency spectrum at location 3: gap 3.6 mm

The combined effect of gap and flow rate on pressure fluctuations (peak-to-peak) inside the pump, at two different flow ratios of 1 and 0.5, is shown in Figure 6. When the pump operates at the designed flow rate, figure 6-a, the gap of 6 mm gives the lower fluctuations at almost all measuring locations, but it is still comparable to fluctuations resulting from other gaps. If the flow rate is reduced to 50% of the nominal value, figure 6-b, pressure fluctuations become higher (by 50% to 90% according to the location) and are not uniform around the impeller. Points 3 and 7 show remarkable peaks at reduced flow rates; they are the closest points to the interactions zone which is the source of pressure pulsation.

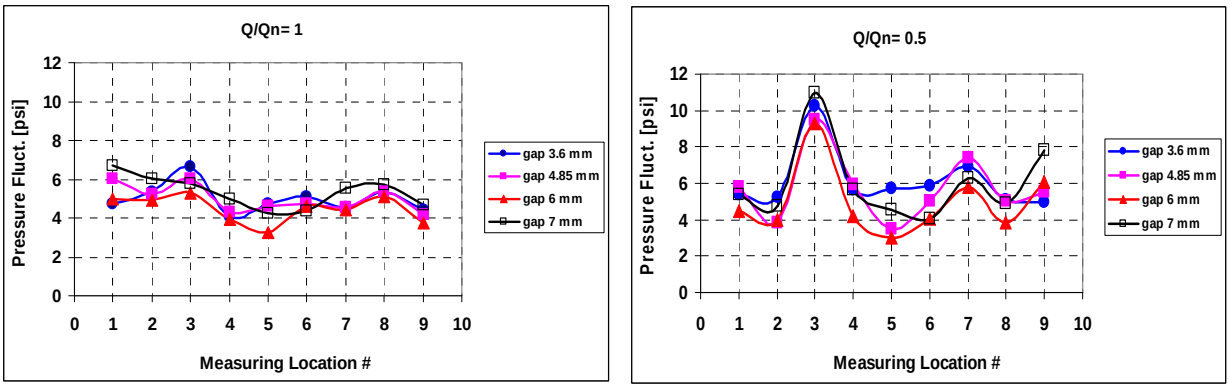

(a) Q/Qn=1 (b) Q/Qn=0.5

Figure 6. Effect of gap on pressure fluctuations (peak-to-peak) inside the pump

The gap of 6 mm still performs well, giving lower pressure fluctuations for all measuring locations. Since the measuring locations are fixed, cutting back the volute vanes brings the interactions source closer to points 3, 4, 7, and 9 around the impeller. The effect of gap and flow rate on fluctuation and FFT measured at location # 4 is given in Figure 7 for deeper investigation. As the flow is reduced, the fluctuations amplitude increases. Gap 6 mm always gives the lower fluctuation for all flow rates, and it is more effective at lower flow rates. In contrast to the original gap of 3.6 mm, the FFT magnitude (which was shown to increase with reducing the flow rate [1]) decreased with the reducing flow rate if the gap of 6 mm is used. The behaviour of measuring point # 4 is not typical, but it is quite general inside the pump.

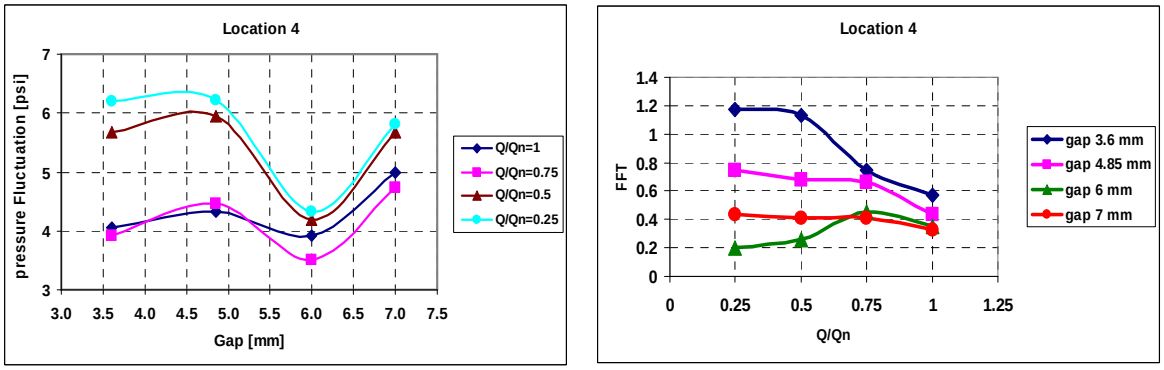

(a) Pressure fluctuation (b) FFT magnitude

Figure 7. Gap/flow rate effect on fluctuations amplitudes and FFT Mag. at location # 4

Since increasing the gap has a positive effect on the fluctuations, the gap of 7 mm was expected to perform better. However, cutting back the volute vanes more than a certain limit produces unsuitable flow angle at the leading edges of volute vanes, and it has a negative effect on the symmetry of the pressure distribution around the impeller. Figure 8 is a comparison between pressure distributions at geometrically similar pairs of locations around the impeller for the gaps of 3.6 mm and 7 mm. At the rated capacity, pressure values are equivalent for all measuring locations inside the pump. For the original 3.6 mm gap, the double volute design keeps the pressure distribution symmetry around the impeller, at all flow rates. When the larger gap of 7 mm is implemented, the pressure around the impeller becomes asymmetric, particularly at reduced flow rates. This gives rise to higher amplitudes of local fluctuations, and it produces a net radial force on the impeller.

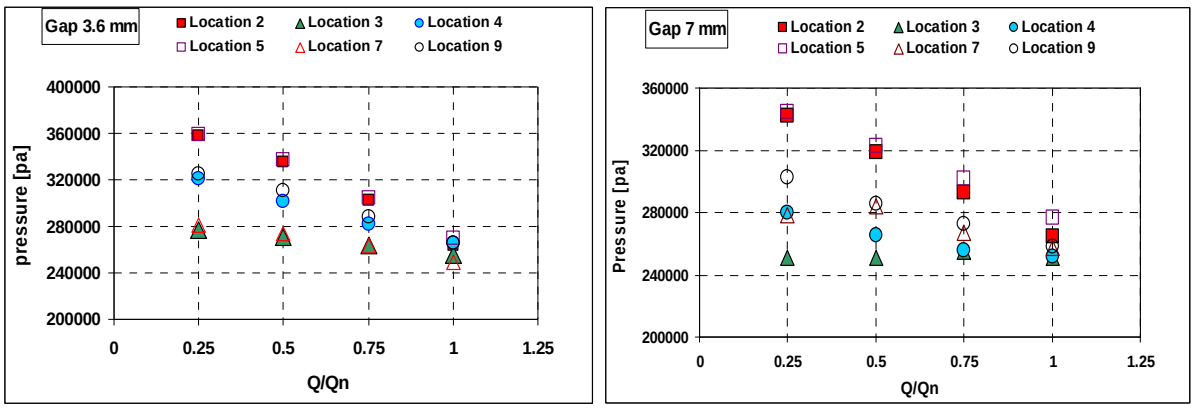

(a) Gap 3.6 mm (b) Gap 7mm

Figure 8. Static pressures at geometrically similar points around the impeller

Pumps are designed to operate at their best efficiency. Changing the gap design shifts the operating point, usually to a lower head when the gap is increased. The exact effect of changing the gap between the impeller and volute vanes is a matter of experimentation. The effect of different gaps on pump performance is shown in Figure 9. Considering the 6 mm gap to be optimum for the pump design under study, a reduction of 0.5% in efficiency and 0.92% in head was recorded at a constant flow rate of 12 l/s. This reduction falls within the uncertainty limits of the measurements. However, if the pump operates at flow rate above 125% (above 15 l/s), increasing the gap has a significant negative effect on the pump performance.

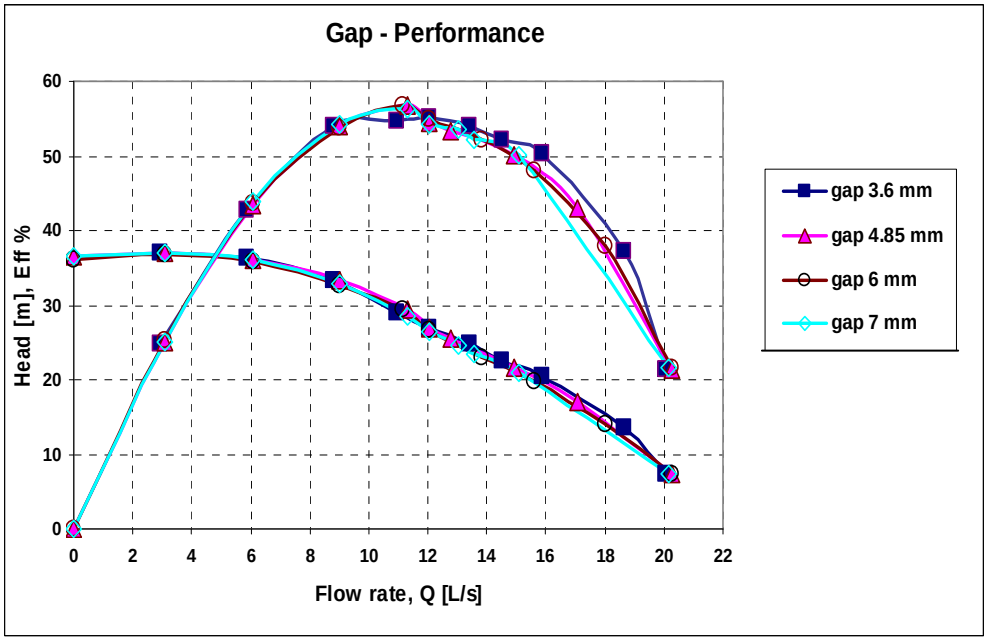

Figure 9. Effect of gap on pump performance at 3540 rpm

CONCLUSION

Experiments were carried out on a high-pressure double-volute model pump stage to study the effect of increasing the radial gap on pressure fluctuations due to impeller-volute interaction at different flow rates. The effect of different gaps on pump performance is also examined. The impeller/volute interaction is an important design parameter in developing high-energy pumps like the double-volute boiler feed pumps. The optimum gap is selected by experimentation based on the pump design and operating conditions. For the present pump, it is desirable to increase the radial gap from 3.6 mm to 6 mm (from 2.5% to 4.25% of the impeller diameter). This gap serves very well in reducing the pressure fluctuations at part-load conditions as well as at design conditions. Gaps larger than this optimum value may produce reverse effects. The improvement in fluctuations amplitude was achieved at the expense of 0.92% loss in pump head and 0.5% in efficiency for the rated capacity.

ACKNOWLEDGMENT

The authors acknowledge the Saudi Electricity Company (SEC) and King Fahd University of Petroleum & Minerals (KFUPM) for the sponsorship of this research.

REFERENCES

1. Khalifa A., Al-Qutub A., Ben-Mansour R., Experiments on Pressure Fluctuations in a High Pressure-Double Volute Centrifugal Pump under Part Load Conditions, *Proceedings of the Fourth International Conference on Thermal Energy: Theory and Applications*, January 12-14, 2009 Abu Dhabi, UAE.
2. Guo S., Maruta Y., Experimental Investigation on Pressure Fluctuations and Vibration of the Impeller in a Centrifugal Pump with Vaned Diffusers, *JSME International Journal*, series B, Vol. 48, No. 1, 2005
3. Baun D., Flack R., Effect of Volute Design and Number of Impeller Blades on Lateral Impeller Forces and Hydraulic Performance, *International Journal of Rotating Machinery*, 9(2): 145-152, 2003.
4. Gonzalez J. and Santolaria C., Unsteady Flow Structure and Global Variables in a Centrifugal Pump, *Journal of Fluid Engineering, Transactions of the ASME*, September 2006, Vol. 128, 937-946.
5. Rodrigues, C., Egusquiza, E., Santos I., Frequencies in the vibration induced by rotor stator interaction in a centrifugal pump turbine, *J Fluids Eng Trans ASME*, Vol. 129, n 11, pp 1428-1435, Nov 2007
6. Franke G., Fisher R., Powell C., Seidel U., Koutnik J., On Pressure Mode Shapes Arising from Rotor/Stator Interaction, *Sound and Vibration*, pp 14-18, March 2005.
7. Makay E., Cooper P., Sloteman D., Gibson R., Investigation of Pressure Pulsations Arising from Impeller Diffuser Interaction in a Large Centrifugal Pump, *Proceedings: Rotating machinery conference and Exposition, ASME*, Vol. 1, 1993.
8. Srivastav, O. P., Pandu K. R., and Gupta K., Effect of Radial Gap Between Impeller And Diffuser on Vibration and Noise in a Centrifugal Pump, *IE(I) Journal- MC*, Vol. 84, April 2003.
9. Atkins, K. and Tison, J., Solving Pulsation Induced Vibration Problem in Centrifugal Pumps, *Pumps And Systems Magazine*, January 1993.
10. Zhang M. and Tsukamoto H., Unsteady hydrodynamic Forces Due to Rotor-Stator Interaction on a Diffuser pump with Identical Number of Vanes on the Impeller and Diffuser, *Journal Of Fluid Engineering, Transactions Of The ASME*, July 2005, Vol. 127, 743-751.
11. Wang H. and Tsukamoto H., Experimental and Numerical Study of Unsteady Flow in A Diffuser Pump at off Design Conditions, *Journal of Fluid Engineering, Transactions of the ASME*, September 2003, Vol. 125, 767-773.
12. Choi J. S., McLaughlin D. K., and Thompson D. E., Experiments on The Unsteady Flow Field and Noise Generation In A Centrifugal Pump Impeller, *Journal of Sound and Vibration* 263, 2003, 493-514.
13. Qin W. and Tsukamoto H., Theoretical Study of Pressure Fluctuations Downstream of Diffuser Pump Impeller- Part 1: Fundamental Analysis on Rotor-Stator Interaction, *Journal of Fluid Engineering*, September 1997, Vol. 119, pp. 647-652.
14. Qin W. and Tsukamoto H., Theoretical Study of Pressure Fluctuations Downstream of Diffuser Pump Impeller- Part 2: Effect of Volute, Flow Rate and Radial Gap, *Journal of Fluid Engineering*, September 1997, Vol. 119, pp. 653-658.

DEVELOPMENT OF AN ULTRASONIC APPARATUS FOR THE STUDY OF THE STRUCTURE OF AIR-WATER BUBBLY FLOWS AND THE DETERMINATION OF THE VOID FRACTION

E. I., Tanahashi[1], J. R., Abud-Jr[1], R. D. M., Carvalho[1*], O. J., Venturini[1], F., Neves-Jr[2], and F. A., França[3]

[1]Universidade Federal de Itajubá (UNIFEI), Itajubá, MG, Brazil
[2]Universidade Tecnológica Federal do Paraná (UTFPR), Curitiba, PR, Brazil
[3]Universidade Estadual de Campinas (UNICAMP), Campinas, SP, Brazil

ABSTRACT. This paper presents experimental data on the axial flow topology of vertical, upward, air-water bubbly flows. The flow structure was investigated using an ultrasonic apparatus consisting of one emitter transducer and three receivers at different positions along the pipe circumference; in addition, high-speed motion pictures of the flow patterns were made. The ultrasonic signals from all sensors were cross-analyzed so that meaningful information about the two-phase flow could be sorted out. Upon analyzing mean values of the acoustic energy attenuation as a function of the void fraction for all sensors, a clear correlation was obtained. Investigation of instantaneous values of the acoustic attenuation allowed for identification of specific gas structures, which was corroborated by the high-speed filming. As the paper main result, the potential of the ultrasonic technique for void fraction and flow structure determination was further established.

Keywords: ultrasonic technique, high-speed filming, air-water flow, void fraction, flow patterns

INTRODUCTION

Multiphase flows are very common in the petroleum industry, oftentimes involving harsh media, strict safety restrictions, access difficulties, long distances, and aggressive surroundings. Accordingly, there is a growing interest in the use of non-invasive techniques for measuring basic variables in multiphase flows such as the concentration of dispersed phases. In addition, knowledge of the flow structure is essential for a better understanding and assessment of the transport processes involved. The ultrasonic technique apparently can fulfill these requirements; the main ultrasonic parameters normally used are sound pressure intensity, energy attenuation and the wave transit time. As the concentration and size distribution of the dispersed media (bubbles, oil droplets or solid particles) change these signal properties vary due to the combined effect of acoustic attenuation and transmission phenomena — reflection, refraction, and scattering of the sound beam by the dispersed phases and acoustic attenuation by the continuous phase.

The ultrasonic technique has been used for the characterization of flow patterns in horizontal gas-liquid flows [1]. The authors presented and discussed the general features of the waveforms obtained, but signal processing was not discussed. A detailed discussion of the acoustic signals and the computation of the signals amplitude and energy from the waveforms were presented in [2]; these acoustic parameters correlated closely with the void fraction. Ultrasound computerized tomography (UCT) has been studied by many researchers since the early 1980s. The authors in [3]

*Corresponding author: Ricardo Dias Martins de Carvalho
Phone: + (55)-35-36291304, Fax: + (55)-35-36291148
E-mail address: martins@unifei.edu.br

were able to successfully reconstruct the distribution of simulated and actual gas-liquid two-phase flows over the cross-section of a pipe using the UCT technique. The reconstructed image resolution was 0.6% of the cross-sectional area, but the image reconstruction time was much longer than the data acquisition time and could only be done off-line.

For many years, visual techniques have been an important tool for the study of the structure of two-phase flows. Particle image velocimetry (PIV) was used to investigate the flow field in a bubbly gas-liquid system [4]. As discussed by the authors, digital cameras and automatic image analysis have made quantitative optical measurements easier; however, the success of bubble identification depends on image quality and lighting conditions.

The main goal of the present paper is demonstrate the use of the ultrasonic technique to measure the void fraction and to identify specific gas structures present in an air-water bubbly flow. The ultrasonic instrumentation used is much simpler than UCT instrumentation and the ultrasonic identification of gas structures was corroborated by a careful analysis of the high-speed filming.

EXPERIMENTAL APPARATUS AND PROCEDURE

An experimental apparatus was designed and built specifically for the study of the ultrasonic measurement of the void fraction in vertical, upward air-water flows (Figure 1a). This apparatus is described in detail in [2]. The air-water mixer consists of a water-filled tank where the lower end of a 54-mm inner diameter acrylic pipe is inserted. Inside this pipe there is a cylindrical porous medium through which compressed air is injected into the water flow. The ultrasonic test section is actually a 10-cm long segment of the same 54-mm diameter acrylic pipe onto which the ultrasonic probes are attached. A 1.6-m long segment of the acrylic pipe then discharges the air-water two-phase flow into a phase separator; the air is vented into the atmosphere while the gravity driven water flow returns to the liquid reservoir. A centrifugal pump driven by a frequency inverter then forces the water back to the air-water mixer, thus closing the flow loop.

The main reasoning behind the transducers arrangement in Figure 1b was that there should be one ultrasonic sensor in each quadrant of the pipe circumference; however, assuming the bubbly flow to be radially symmetrical from a statistical point of view only half the circumference was instrumented. Due to limitations in the equipment available, the emitter transducer at $\theta = 0^o$ was not set to operate in the pulse-echo mode; however, this will be done in the near future in order to capture the acoustic energy reflected backwards off the gas structures. The direct transmission receiver ($\theta = 180^o$) was expected to get the energy transmitted through the bubbly flow; the side sensors ($\theta = 45^o$ and 135^o) were expected to receive at least part of the energy scattered off the acoustic beam. It is expected that a cross-analysis of the signals from all receiver transducers will disclose features of the instantaneous bubbly flow topology as well as the main aspects of the phase distribution over the pipe cross-section. The ultrasonic sensors used were Panametrics Videoscan 2.25 MHz, 13 mm diameter ultrasonic transducers. The filming station located just downstream of the test section allowed for high speed motion pictures (1000 fps) of the gas-liquid flow. The camera used was a REDLAKE Motion Pro X3 with 1280 x 1024 resolution.

In view of the limitations of the acquisition equipment used, two different experimental procedures were adopted. The first procedure referred to data acquisition from the 180° receiver only in conjuction with the high-speed filming; the second procedure consisted of simultaneous data acquisition from all receivers. In the first procedure the emitter transducer was excited at 8.45 kHz, the maximum allowed by the ultrasonic pulser, and the sampling period was set to 5.0 sec. In the second procedure, the sampling period was set to 2.98 sec in view of data storage limitations and the emitter transducer was excited at 1.72 kHz. In this case, no synchronized filming was made. Data were acquired at 20 MHz sampling frequency in both procedures. Ultrasonic data were obtained for the entire bubbly flow regime, i.e. zero to 15% void fraction range, in 1% steps. The ultrasonic wave sound intensity and energy were calculated by an independent MatLab signal processing algorithm. The energy ratios were referenced to the value at the same sensor for single-

phase water flow. In order to correlate these acoustic attenuation results with the void fraction, data from [5], collected at this same test section, were used.

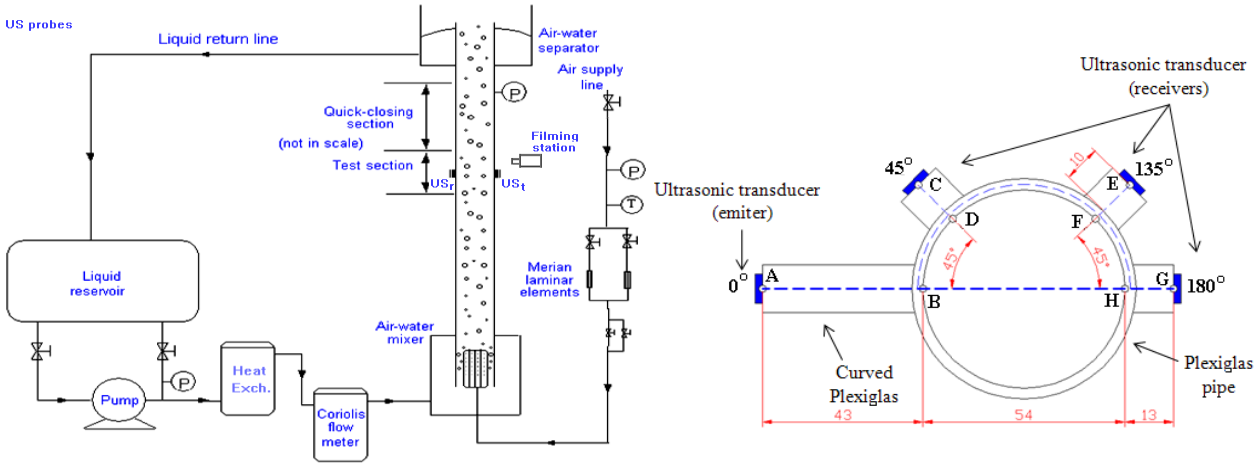

Figure 1. Schematic view of: (a) air-water bubbly flow test rig, (b) ultrasonic instrumentation.

ANALYSIS OF THE HIGH-SPEED FILMS

The fast pictures were analyzed for different flow patterns as the void fraction increased within the so-called bubbly flow regime. In broad terms, lower void fractions produced discrete bubbles; their distribution seemed to be the most uniform over the pipe cross section for 4 ~ 6% void fraction. Clustering then appeared and coalescence started taking place at 8%, at which point small mushrooms were clearly seen. For slightly higher void fractions, cap bubbles were already present. Incipient Taylor bubbles first appeared at 12%; they grew longer and appeared regularly at 14%. For this void fraction, the flow pattern was the well known axial intermittent topology of Taylor bubbles and aerated liquid slugs. Referring to Figure 4, on the basis of these visual analysis alone the bubbly flow regime was broken down into three sub-regimes [2]: (1) the discrete and clustering bubble sub-regime ($\alpha < 8\%$), when both spherical-ellipsoid discrete bubbles and larger distorted discrete bubbles would flow separately or in bubble clusters; (2) the cap bubbles sub-regime ($8 \leq \alpha < 12\%$), when coalescence took place to form small mushrooms and cap-bubbles; (3) the transition to slug flow ($\alpha \geq 12\%$), when incipient Taylor bubbles first appear.

As will be discussed shortly, these sub-regimes boundaries were superimposed to ultrasonic data from all sensors and very consistent trends were found; the main focus now was to identify very specific gas structures to be matched to the ultrasonic data. Some of these images are shown in Table 2. The main contention here is that these same gas structures occur not only for the indicated void fractions, but as a specific feature of the axial flow topology for other void fractions as well. If so, they can be interpreted as the letters of an alphabet whereby the axial flow topology is written and can be unequivocally detected by the ultrasound.

ANALYSIS OF THE ACOUSTIC SIGNALS

Preliminary Data Reduction

The acoustic trace signals captured by the ultrasonic apparatus are made up of longitudinal and shear waves and base noise. However, not all waves carry meaningful information about the two-phase flow. Hence, the meaningless waves and the base noise should be filtered out of the trace signals so as to eliminate systematic errors from the calculations of the acoustic parameters. In this regard, in a preliminary study it was verified that all captured waves displayed very similar

frequency makeup, thus precluding the application of the usual frequency domain filtering techniques. Therefore, a time domain filtering approach was tried.

Figure 2 depicts average ultrasonic paths for longitudinal and shear waves in the ultrasonic assembly shown previously in Figure 1b; Table 1 provides further details on the acoustic waves likely to propagate in this apparatus. It can be seen that only LW1 and SW3 are affected by and carry information about the two-phase flow. In addition, LW1 is the only wave that can be reflected and diffracted to the side sensors by the gas structures.

The approximate transit times associated with these waves as shown in Table 1 allowed for their identification in the acoustic signals from each sensor. As shown in Figure 2, only LW1 and SW3 are unmistakably identified in the trace signals from the 180° receiver. For the 45° sensor, only LW2 shows up very clearly. For the last sensor, none of the waves could be identified.

The overall conclusion seems to be that only LW1 and SW3, the waves that carry information about the two-phase, have a clear direct imprint on the 180° sensor trace signals. For the remaining sensors, they are either too weak or could not be unmistakably identified so as to be of any use for measurement purposes. Moreover, SW3 carries very little energy relative to LW1 and is rapidly attenuated by increasing void fraction. Therefore, SW3 was dropped as a measurement tool and attention was focused on LW1 only.

Table 1
Main features of the acoustic waves likely to occur in the ultrasonic assembly.

Acoustic Wave	**Acoustic Path**	**Propagation Velocity (water / acryl.)** [m/s]	**Average Length of Acoustic Path [mm]**	**Transit Time [μs]**	**Ultrasonic Transducer**	**Remarks**
LW 1	A-B-H-G	1,480 / 2,730	110.0	57.0	180º	Longitudinal wave generated in A that goes through the two-phase flow
	A-B-H-F-E		120.8	64.6	135º	
	A-B-H-F-D-C		165.5	81.3	45º	
LW 2	A-B-D-C	0 / 2,730	75.4	27.6	45º	Longitudinal wave generated in A that travels through the acrylic only
	A-B-D-F-E		120.0	44.0	135º	
	A-B-D-F-H-G		142.2	52.2	180º	
SW 1	A-B-D-C	0 / 1,430	75.4	52.7	45º	Shear wave generated in A that travels through the acrylic only
	A-B-D-F-E		120.0	83.9	135º	
	A-B-D-F-H-G		142.2	99.4	180º	
SW 2	A-B-D-C		75.4	40.5	45º	Shear wave generated in B that travels through the acrylic only
	A-B-D-F-E		120.0	70.1	135º	
	A-B-D-F-H-G		142.2	85.9	180º	
SW 3	A-B-H-G		110.0	61.3	180º	Shear wave generated in H from LW 1; it travels through the acrylic only
	A-B-H-F-E		120.8	67.9	135º	
	A-B-H-F-D-C		165.5	100.1	45º	

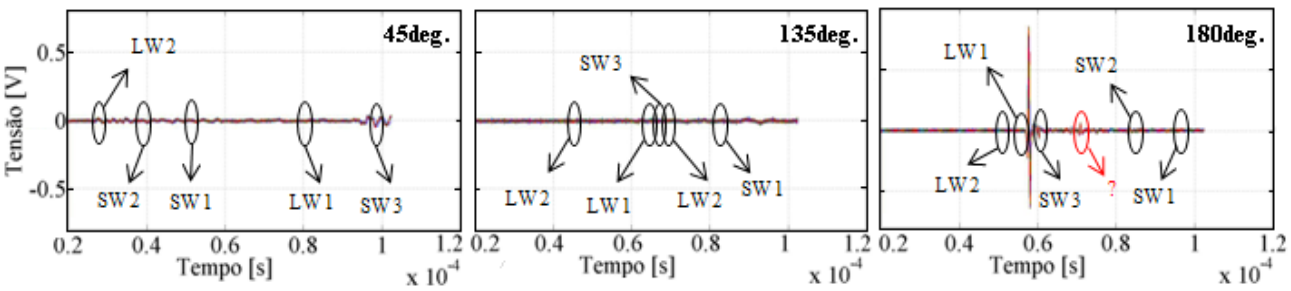

Figure 2. Identification of the likely acoustic waves (single-phase water flow).

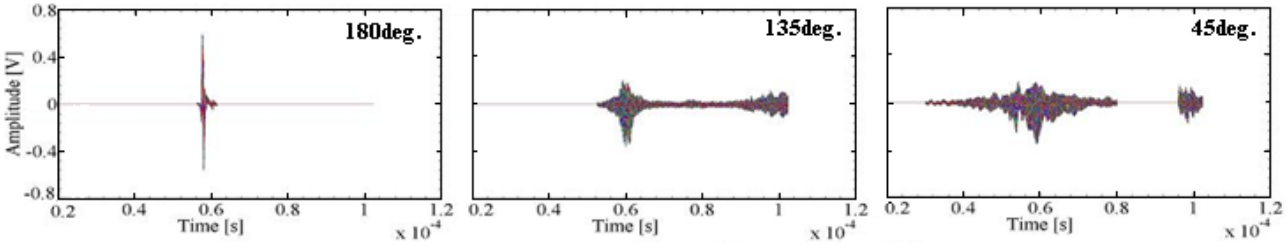

Figure 3. Data reduction windows for the sensors (1% void fraction).

In this connection, the trace signals for all receivers were analyzed as a function of void fraction so as to corroborate the conclusions drawn for the acoustic waves detailed in Figure 2. For the 180° sensor, it was a fairly straightforward matter to cross out time intervals of the acquisition window that were not related to LW1 and SW3. The remaining "data reduction window" is shown in Figure 3. For the 45° and 135° sensor, random reflection and diffraction of LW1 by gas structures made this task more difficult. Imprints of these acoustic phenomena in the trace signals spread out through most of the acquisition window, the only restriction being that it can only happen after the 15.75μs time instant. This corresponds to the time LW1 hits point B in Figure 1b and thereupon starts crossing the two-phase flow.

From this consideration and from observations of which regions of the acquisition window were sensitive to void fraction variations, the selected data reduction windows for the 45° and 135° sensors are as shown in Figure 3. It is believed that by using the data reduction windows systematic errors are greatly diminished in the calculations of acoustic parameters and, hence, the resulting numerical values become more meaningful.

Main Results

As can be seen in Figure 4, the average energy ratios revealed clear trends for all receivers. Whereas the energy received by the 180° sensor continually decreased with void fraction, an eleven-fold increase in the energy received by 135° sensor can be observed; meanwhile, the energy increase for the 45° sensor is about three-fold only for the entire void fraction span. In trying to associate the acoustic behavior with the flow patterns, one verifies a rapid increase in the energy received at the 135° sensor up to 4% void fraction. Keeping in mind that $\alpha = 5\%$ corresponds approximately to the most uniform discrete bubbles distribution, one could say that the rapid orderly increase in bubble population throughout the pipe cross-section causes a substantial increase in the amount of acoustic energy diverted to the 135° sensor. It is noteworthy that the data for this sensor started leveling off at 5% and not at 8% void fraction, which is when coalescence started taking place; this indicates that energy diversion to the 135° sensor by discrete bubbles reaches an asymptotic limit irrespective of any possible hindering action by coalesced gas structures. In fact, the data leveling off in the 5 to 11% void fraction range suggests that relatively small coalesced gas structures such as mushrooms and cap bubbles neither hinder nor contribute significantly to energy diversion to the 135° sensor. The behavior observed for $\alpha \geq 12\%$, which corresponds to the first appearances of Taylor bubbles, can be explained in terms of the flow pattern intermittence. It is conceivable that Taylor bubbles either greatly attenuate or effectively block the acoustic path to the 180° and 135° sensors. However, discrete bubbles in the liquid aerated slugs can freely divert the acoustic energy from the former to the latter sensor. The step increase observed in Figure 4 for the 135° sensor at 12% void fraction can then be explained on the assumption that the effect of liquid aerated slugs is far greater than that of Taylor bubbles. For the 45° sensor, clear trends can be identified as shown in Figure 4. A systematic increase can be observed up to 8%; the data then level off for the remaining void fraction range tested. It could thus be said that discrete bubbles increasingly reflect or otherwise direct acoustic energy to the 45° sensor, a process that is hindered by randomly occurring and randomly positioned coalesced gas structures in the cap bubbles sub-regime.

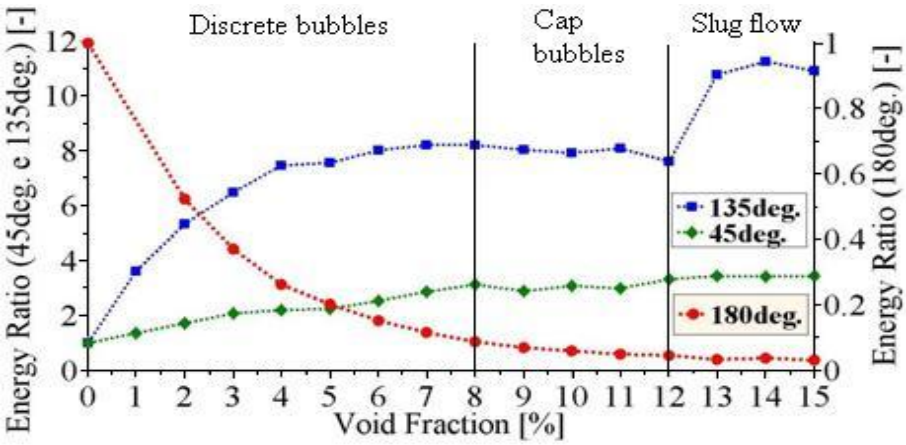

Figure 4. Average energy ratios as a function of void fraction for all receivers (j_{water} = 25.5 cm/s).

It is once again speculated that the onset of the slug flow with the intermittence between Taylor bubbles and liquid aerated slugs precludes the interference in their acoustic action by one another; however, their effects cancel each other out in the overall balance and energy diversion to the 45° sensor remains essentially constant.

The energy ratios of the individual ultrasonic pulses were analyzed in an attempt to identify specific gas structures imprinted in the ultrasonic signals. Due to limitations of the ultrasonic apparatus, it was only possible to synchronize data acquisition from two sensors at a time. Hence, data were simultaneously obtained from the 180° and 135° sensors; then for the same operating conditions, data were once again obtained for the 180° and 45° sensors. The 180° sensor was selected as reference due to its clear-cut behavior, thoroughly discussed in previous studies [2]. This procedure was repeated for all void fractions in the bubbly flow regime (0 to 15%). Figure 6 shows the resulting energy ratio distributions at the 180º, 135º, and 45º transducers whereas Figure 5 illustrates the instantaneous energy ratios at the 45° and 135° sensor corresponding to instantaneous energy ratios at the 180° sensor.

Upon analyzing similar plots for all void fractions tested, the energy ratios for the 45° sensor were observed to remain within a very limited range throughout the entire bubbly flow regime. Apparently, the amount of acoustic energy diverted to this sensor changes very little despite great variations in the gas structures at the pipe cross-section. The 135° sensor, on the other hand, displayed significant variations with the nominal void fraction and with the instantaneous energy ratio as measured by the 180° sensor; moreover, there seemed to be a split in its behavior at about 0.7 energy ratio. Up to this value, which indicates the presence of large gas structures in the cross-section or denser bubble populations, the 135°sensor exhibited repeatable trends. For energy ratios above 0.7, which indicates smaller gas structures or less dense bubble populations, great variability in the 135° sensor response was observed. This was checked by comparing plots like these in Figure 5 for different acoustic samples for the same operating conditions.

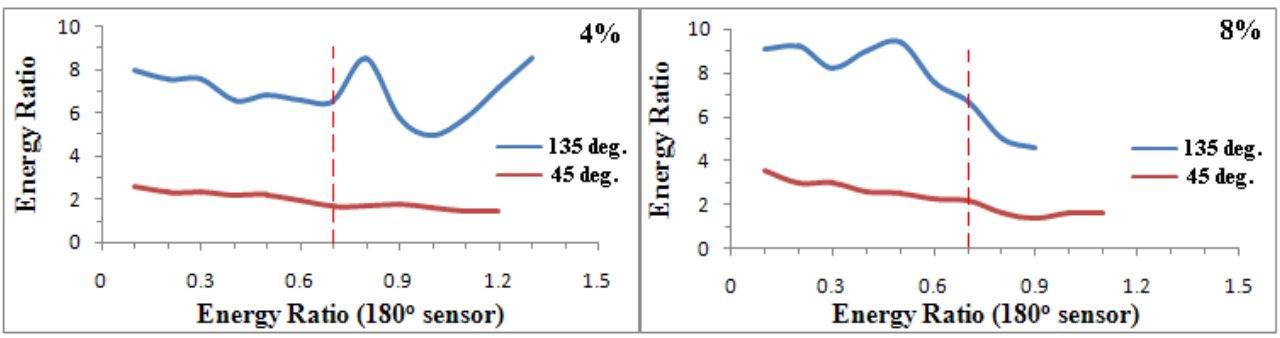

Figure 5. Individual pulses energy ratios for 4% and 8% void fraction.

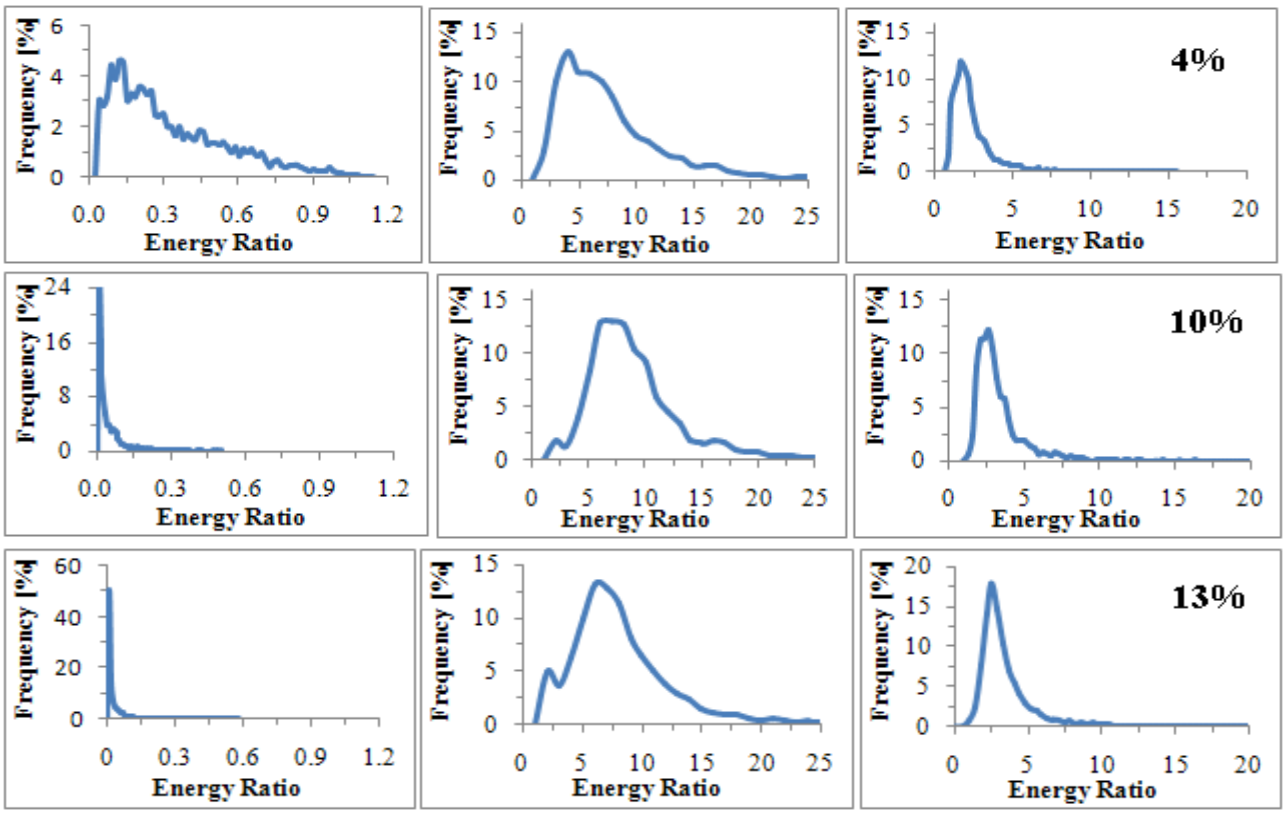

Figure 6. Energy ratio distributions at the 180º, 135º and 45º for different void fraction.

Table 2
Energy ratios corresponding to the specific gas structures.

Gas Structure		Small bubbles very near the wall	Scattered discrete bubbles	Sparsely populated discrete bubbles	Denser bubble population	Cap bubbles	Taylor bubbles
$\frac{E_{2\emptyset}}{E_{1\emptyset}}$	**180º**	0.0-0.3	0.3-0.6	0.0-0.3	0.3-0.6	0.0-0.03	0.0-0.03
	135º	4.0-5.5	3.5-4.5	7.5-9.0	8.0-12.0	6.0-8.0	8.0-12.0
	45º	0.9-1.0	0.9-1.0	0.9-2.5	2.0-2.5	2.0-4.0	2.0-4.0
Figure		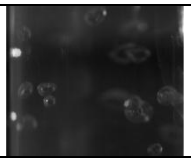	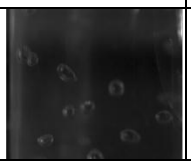	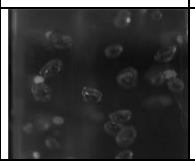	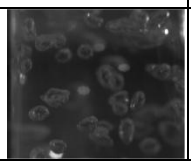	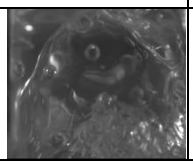	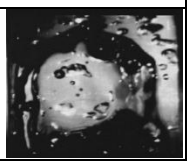

The conclusion is drawn that the main pieces of information about specific gas structures come from the 180º sensor followed by the 135º sensor; information from the 45º sensor can be used as fine tuning. Unfortunately, no information is available at the present time from the 0º sensor in pulse-echo mode; backward reflections should be a more recurrent, less random phenomena than side reflections to the 45º and 135º sensors. Once available, simultaneous information from all four sensors combined will make for unmistakable identification of specific gas structures. For the time being, an extensive analysis was made to identify combinations of the energy ratios from the 180º, 135º and 45º sensors that could be associated with specific aspects of the flow axial topology (Table 2). Each three-digit combination in ranges as shown in Table 2 is expected to always indicate the presence of a particular gas structure in the pipe cross section regardless of the nominal void fraction. For instance, the distribution called *scattered discrete bubbles*, which is typical of very low

void fractions, was associated with the (0.3-0.6; 2.5-4.0; 0.9-1.0) triad. These energy ratios combination occurs fairly often for 4% nominal void fraction, less so for 10% (the first and third ranges are almost absent from the corresponding sensor distribution), and does not occur at all for 13% void fraction (the 0.3 to 0.6 range is not covered by the 180° sensor). The (0.0-0.03; 6.0- 8.0; 2.0-4.0) and (0.0-0.03; 8.0- 12.0; 2.0-4.0) triads were observed to be associated with cap bubbles and Taylor bubbles; respectively; accordingly, they do not occur at 4% void fraction. Even though they are both present in the distributions in Figure 6 for 8% and 13%, the frequency of occurrence is consistent with the fact that cap bubbles evolve into Taylor bubbles. In addition, inspection of plots similar to those in Figure 5 reveals that on an instantaneous time basis the 135º sensor does allow for a clear distinction between cap bubbles and Taylor bubbles.

From these empirical observations summarized in Table 2, one could conjecture that energy diversion to the 45º sensor is mainly associated with backward acoustic reflections regardless of the specific gas structures at the pipe cross-section. This backward reflection would be more evenly distributed along the pipe circumference in the 45º quadrant and thus would not change much at the 45º sensor. Conversely, energy diversion to the 135º sensor would be due to forward scattering and multiple reflections off large gas structures and denser bubble populations (energy ratios below 0.7 as measured by the 180º sensor); this would lead to the repeatable trends mentioned previously. For scattered bubbles and smaller gas structures energy would hit the 135º sensor due to diffraction of the acoustic beam. The amount of energy diverted would be very much dependent upon the exact position of the gas phase, hence the great variability observed.

CONCLUSIONS

Acoustic attenuation and high-speed filming data have been presented on the axial flow topology of vertical, upward, air-water bubbly flows. Time average attenuation data correlated very closely with the void fraction; instantaneous data were shown to be a promising tool for detection of specific gas structures. The potential of the ultrasonic technique for void fraction and flow structure determination then seems further established.

ACKNOWLEDGMENTS

The authors gratefully acknowledge the financial support received from PETROBRAS, the *Brazilian National Petroleum Company*, and FINEP, the *Brazilian National Research and Development Funding Agency*, which made this work possible.

REFERENCES

1. Chang, J. S., Ichikawa, Y., Irons, G. A., 1982, Flow Regime Characterization and Liquid Film Thickness Measurement in Horizontal Gas-Liquid Two-Phase Flow by an Ultrasonic Method, AIAA/ASME Joint Plasma Thermophysics HTC.
2. Carvalho, R. D. M., Venturini, O. J. Neves Jr., F., Arruda, L. V. R., and Franca, F. A., 2007b, Experimental Study of Ultrasonic Signals Characteristics in Air-Water Bubbly Flows, Proc. 5th Int. Conf. Heat Transfer, Fluid Mech., and Therm. (HEFAT 2007), Sun City, South Africa.
3. Xu, L. J., and Xu, L. A. Gas/Liquid Two-Phase Flow Regime Identification by Ultrasonic Tomography. Flow Measurement and Instrumentation. 1997, Vol. 8, 3/4, p. 145-155.
4. Laakonen, M., Honkanen, M., Saarenrinne, P., and Aittamaa, J. Local Bubble Size Distributions, Gas-Liquid Interfacial Areas and Gas Holdups in a Stirred Vessel with Particle Image Velocimetry. Chemical Engineering Journal. 2005, Vol. 109, p. 37-47.
5. Dias, S., Franca, F. A., Rosa, E. S., 2000, Statistical Method to Calculate Local Interfacial Variables in Two-Phase Bubbly Flows Using Intrusive Crossing Probes. Int. J. Multiphase Flow. 2000, Vol. 26, 11, pp. 1797-1830.

HEAT TRANSFER AND FRICTION CHARACTERISTIC OF A SINGLE ROW HELICALLY FINNED COMPACT HEAT EXCHANGER

H. Huisseune*, C. T'Joen and M. De Paepe
Department of Flow, Heat and Combustion Mechanics,
Ghent University – UGent, Gent, Belgium

ABSTRACT. Single row heat exchangers with individually finned tubes are widely used in applications where a rugged configuration and low pressure drop are desirable. However, experimental data in open literature are rare. In this study, the heat transfer and friction correlation of a single row heat exchanger with helically finned tubes are experimentally determined in an open air wind tunnel. During the experiments the geometry of the tubes was fixed, but the transversal tube pitch was parametrically varied. The experimental data show that a decrease in transversal tube pitch results in higher Nusselt numbers (due to higher velocities in the minimum cross section) and higher friction factors (due to increasing blockage). The proposed heat transfer correlation can describe 95% of the data within ±12% and shows a 4.24% mean deviation. The friction correlation predicts 95% of the data within ±19% and gives a mean deviation of 6.84%. Comparison with literature illustrates that none of the existing literature correlations can accurately predict the results of this study.

Keywords: *helical fin, single row, heat exchanger, heat transfer, friction*

INTRODUCTION

When exchanging heat with air, the main thermal resistance is located on the airside of the heat exchanger (more than 85%). To improve the heat transfer rate, the heat transfer surface is increased by adding fins. However, these fins also result in a significant pressure drop penalty.
Tubes can be individually finned, or multiple tubes can pass through each fin (these are the so called continuous fins). This study focuses on individually finned tubes for compressed air cooling using water. These tubes are more rugged than the continuous fin designs, but also less compact.
Heat exchangers consisting of individually finned tubes have been studied extensively in the past. Jameson and Schenectady [1] tested various tube arrangements. The values of the proportionality constants, which are needed to evaluate the suggested pressure drop relations, were tabulated. Further, they deduced a relation of the form of the fanning equation which correlates the data for all the tube sizes and arrangements tested. A pressure drop correlation applicable to both bare and finned tube bundles was established by Gunter and Shaw [2]. In the discussion accompanying their article, Jameson validated this correlation with his own test data and suggested a revised expression. Also other authors have questioned the Gunter and Shaw relationship [3,4,5]. Two widely cited correlations for a staggered tube layout are the Briggs and Young [6] (heat transfer) and Robinson and Briggs [5] (pressure drop) correlation. These relations were recommended by Webb [3].
Mirkovic [7] performed tests on heat exchangers with helically finned tubes in a staggered eight row configuration to determine the thermal and hydraulic characteristics. Correction factors for other numbers of tube rows were reported. The heat transfer and pressure drop correlations suggested by the ESDU [8] are based on data for bundles containing four or more tube rows. For bundles less than four rows deep, the ESDU [8] advises to multiply the Nusselt number with a

* Corresponding author: H. Huisseune
Phone: + (32)-9-2643355 Fax: + (32)-9-2643575
E-mail address: Henk.Huisseune@UGent.be

correction factor as recommended by Huber and Rabas [9] and to calculate the pressure loss coefficient of a single row bundle as about 80% of that of a deep bundle (Eckels and Rabas [10]). Using experimental data from open literature, Genic et al. [11] established new pressure drop correlations for in-line and staggered helically finned tube bundles. The correction factors of Brauer [12,13], Yudin [14] or Weierman [15] were suggested to calculate the pressure drop for a one row heat exchanger. Eckels and Rabas [10] demonstrated that the effect of the row number on heat transfer in finned tube bundles is dependent on the Reynolds number, a point which is not considered in the previously mentioned correction factors. They also discussed the row effect on pressure drop: comparing the data of several authors, they concluded that the friction factor can increase or decrease with the row number. In contrast to the heat transfer row effect, the influence of the number of rows on the pressure drop is not only dependent on the Reynolds number, but also on the tube diameter, tube pitch and fin density. Consequently, correcting the correlation of a multiple row tube bank to obtain the heat transfer coefficient or pressure drop of a single row heat exchanger (as studied in this work) does not result in accurate predictions. However, research on the thermal hydraulic behaviour of heat exchangers with one row of tubes is little. Jameson and Schenectady [1] reported pressure drop data for a single row bundle. Lapin and Schurig [16] experimentally determined the effect of the number of staggered rows on the airside convective heat transfer coefficient. They studied finned tube banks from one to eight rows deep. Schmidt [17] established a Nusselt correlation for one tube row of a multi row heat exchanger. Sparrow and Samie [18] determined the heat transfer and pressure drop characteristics for one and two row tube bundles. For the one row tube bundle, the transversal tube pitch was parametrically varied. They concluded that the Nusselt numbers increase with decreasing transversal pitch. This is explained by the higher velocities in the minimum cross section for smaller transversal tube pitches at a fixed free stream velocity. The same trend is found in the ESDU correlation [8]. However, Mirkovic [7] observed that the Nusselt numbers increase when the transversal tube pitch is enlarged. This result of Mirkovic [7] is questionable. By correlating the Nusselt numbers using the Reynolds number Re_c based on the maximum velocity in the heat exchanger instead of the free stream Reynolds number Re_∞ based on the inlet velocity, Sparrow and Samie [18] established a heat transfer expression independent of the transversal tube pitch. Most authors reported similar results [1,6,10,17]. The transversal tube pitch also has an important influence on the pressure drop over the bundle: the pressure drop increases with decreasing pitch, due to the increasing blockage [1,5,6,8,18]. Again Mirkovic [7] observed the opposite effect: an increase in pressure drop with transversal pitch.

The above discussion reveals the need for more experimental data of single row annular finned tubes. These heat exchangers are used in applications where a rugged configuration and low pressure drop are desirable, e.g. compressed air cooling. To the authors' knowledge, only two heat transfer correlations [16,18] and one pressure drop correlation [1], deduced from data of single row heat exchangers, are available in open literature for design purposes. In this study, the heat transfer and friction characteristic of a single row heat exchanger with helically finned tubes were experimentally determined. The transversal tube pitch was parametrically varied.

METHODOLOGY

Experimental equipment

The test rig consisted of an open air wind tunnel and a closed water cycle. Measurements were performed on the airside as well as the waterside of the heat exchanger. A radial fan sucked air through a calibrated nozzle (ISO5167). To determine the air mass flow rate, the pressure drop over the nozzle was measured using a differential pressure transducer. The fan was driven by a frequency controller which allowed setting an air mass flow rate between 0.1 and 1 kg/s. The air passed through the diffuser, the settling chamber and the sinusoidal contraction section, before entering the test section. The honeycomb and screen flow straightener in the settling chamber as well as the sinusoidal contraction ensured a uniform air flow at the inlet of the test section.

A single row heat exchanger with helicoidally finned tubes was placed in the test section. The helical fins were extruded out of the aluminum base tube, eliminating the contact resistance. The

Table 1
Dimensions of the Helicoidally Finned Tubes Used in This Work

d_{ext} (mm)	13
t_{fin} (mm)	0.65
D_{fin} (mm)	24.8
F_p (mm)	2.4

geometry of the tubes is listed in Table 1. During the experiments these dimensions were fixed. Only the transversal tube pitch X_t was varied, yielding the dimensionless values:

$$X_t / d_{ext} = 1.92;\ 2.27;\ 2.45;\ 2.84;\ 3.27$$

Depending on the transversal tube pitch, 8 or 10 tubes were positioned. The remaining gap was filled to $X_t/2$ to avoid bypass flow.

The closed water cycle consisted of an electric boiler with a power limit of 6 kW, several valves and a circulation pump. The water temperature was controlled with a PID controller. The pump was driven by a frequency controlled engine. The water mass flow rate was measured with a calibrated electromagnetic flow meter. The tubes and distributors bringing the hot water to the heat exchanger were well insulated. The water flew through the heat exchanger in two passes (4 by 4 or 5 by 5 depending on the transversal tube pitch).

All temperatures were measured using calibrated K type thermocouples and read with a Keithley 2700 Multimeter/Data Acquisition System. The measurements were performed at steady state conditions for different Reynolds numbers.

Data reduction

The air mass flow rate and temperature measurements were used to determine the overall heat balance on the water and air side of the single row bundle. The difference between both heat transfer rates was for all measurements smaller than 5%. Next, the overall heat transfer resistance $(UA)^{-1}$ was calculated using the effectiveness-NTU relationships for the given configuration [19]. As is clear from equation (1), the overall heat transfer resistance $(UA)^{-1}$ consists of convection and fouling on the airside, contact resistance between the fins and tube, conduction through the tube wall and fouling and convection on the waterside. The contact resistance of the tested heat exchanger was zero, because the fins were extruded out of the base tube, and clean air and filtered water were used during the experiments resulting in negligible fouling. Taking this into account and using the Gnielinski correlation [20] on the waterside, the airside convection coefficient h_{ext} was determined from equation (1).

$$\frac{1}{UA} = \frac{1}{\eta_{ext} h_{ext} A_{ext}} + R_{f,ext} + R_c + \frac{\ln\left(\frac{d_{ext}}{d_{in}}\right)}{2\pi\lambda_T L_T} + R_{f,in} + \frac{1}{h_{in} A_{in}} \tag{1}$$

The dimensionless airside convection coefficient is defined by the Nusselt number (equation (2)).

$$Nu = \frac{h_{ext} \cdot d_{ext}}{\lambda_{air}} \tag{2}$$

The pressure measurements were performed under isothermal conditions and the friction factor was calculated according to equation (3) [21].

$$f = \frac{A_c}{A_{ext}} \cdot \left[\frac{2\Delta p \cdot \rho_{air,in}}{G_c^2} \right] \tag{3}$$

RESULTS AND DISCUSSION

Heat transfer

The Nusselt numbers for the tested single row heat exchangers are plotted versus the freestream Reynolds number Re_∞ (based on the inlet velocity and external tube diameter) in Figure 1. The

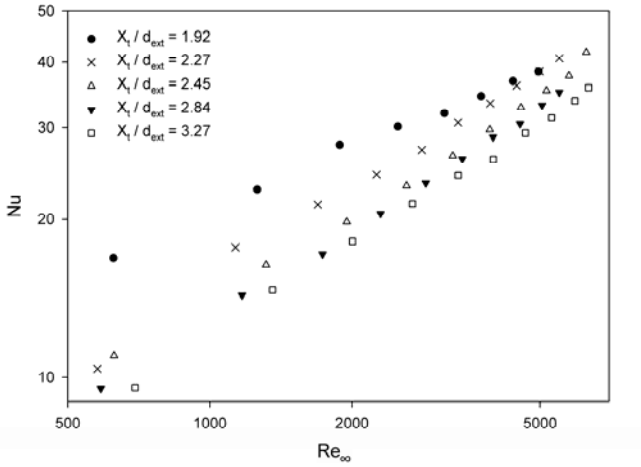

Figure 1. Experimental Nusselt numbers plotted versus the freestream Reynolds number Re_∞ for different transversal tube pitches

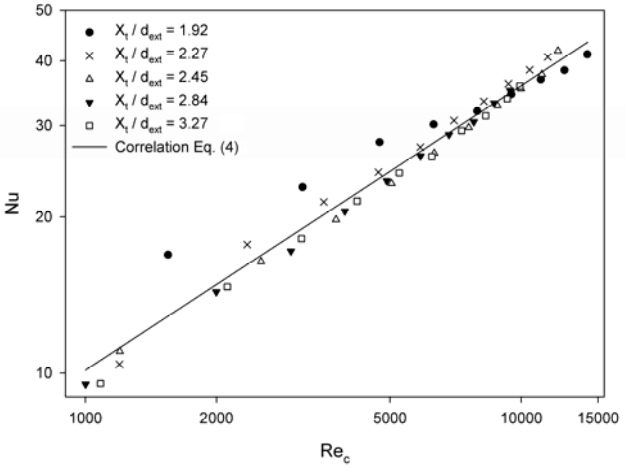

Figure 2. Experimental data and Nu correlation independent of X_t/d_{ext} (equation (4)) plotted versus the minimum-area Reynolds number Re_c

results are parameterized by the dimensionless transversal tube pitch X_t/d_{ext}. Mirkovic [7] reported that a decrease in transversal tube pitch results in a heat transfer rate decrease. However, most authors state that a decrease in X_t results in an increase of the Nusselt number, because of the higher local velocities in the minimum cross sectional area [8,18]. This is also seen in our measurements, see Figure 1. To take the effect of X_t into account, Sparrow and Samie [18] suggested correlating the Nusselt number results by using the minimum-area Reynolds number Re_c (based on the external tube diameter and the air velocity at the minimal cross-sectional area), instead of the freestream Reynolds number Re_∞. Figure 2 shows the experimental data as function of Re_c.

A correlation independent of the transversal tube pitch was determined via a least-mean-squares fit:

$$Nu = 0.2290 \cdot Re_c^{0.5486} \tag{4}$$

This correlation, also plotted in Figure 2, is able to predict 95% of the experimental data within ± 15% and gives a mean deviation of 4.76%. The prediction capability of the correlation is poorer for small values of Re and X_t. To obtain a better match with the experimental data, a dimensionless group dependent on the transversal tube pitch X_t is added to the correlation in addition to using the minimum-area Reynolds number Re_c. The regression analysis resulted in:

$$Nu = 0.2995 \cdot Re_c^{0.5396} \cdot \left(\frac{X_t}{d_{ext}} \right)^{-0.2068} \tag{5}$$

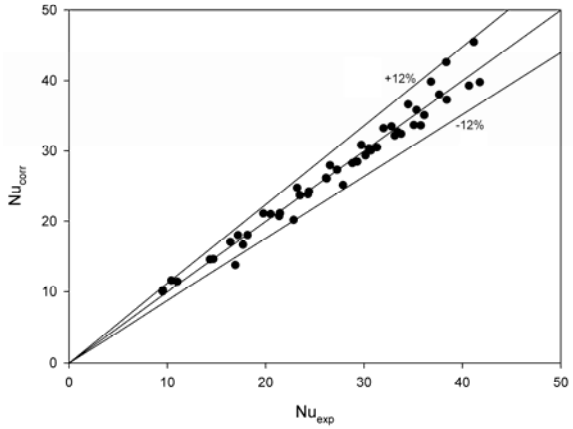

Figure 3. Comparison of the heat transfer correlation (equation (5)) with the experimental data

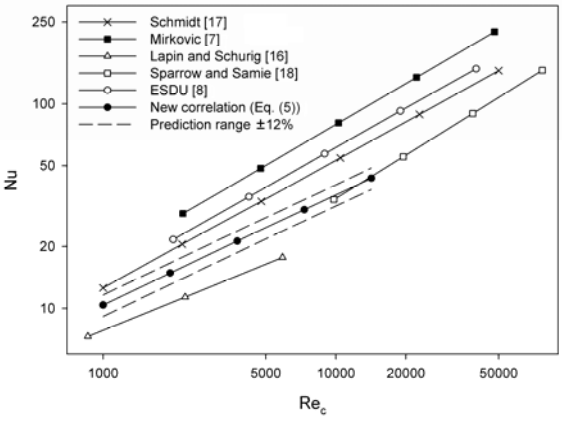

Figure 4. Comparison of equation (5) with heat transfer characteristics from open literature

Table 2
Application Ranges of Heat Transfer Correlations from Open Literature

Authors	**Re_c**	**d_{ext} (mm)**	**X_t / d_{ext}**	**D_{fin} / d_{ext}**	**s / d_{ext}**
Mirkovic [7]	2200 - 48000	25.4 - 50.8	1.969 - 4.724	1.375 - 1.75	0.053 - 0.142
ESDU [8]	2000 - 40000	9.5 - 51	$1.15<X_t/X_l<1.72$	1.220 - 4.474	0.014 - 0.990
Lapin and Schurig [16]	960 - 4800	15.875	2.4	2.4	0.1712
Schmidt [17]	1000 - 50000	9.7 - 27.9	1.72 - 3.83	1.8 - 2.6	0.07 - 0.36
Sparrow and Samie [18]	9800 - 77000	31.75	1.926 - 6.408	1.8	0.1
New correlation (equation (5))	1000 - 14200	13	1.92 - 3.27	1.91	0.135

Table 3
Heat Exchanger Geometry Used for Comparison with Literature Correlations

d_{ext} (mm)	13
D_{fin} / d_{ext}	1.91
t_{fin} / d_{ext}	0.05
F_p / d_{ext}	0.185
X_t / d_{ext}	2.4
X_l / d_{ext}	1.91

Figure 3 compares equation (5) with the experimental data. The proposed heat transfer correlation can describe 95% of the data within ± 12% and shows a 4.24% mean deviation.
Figure 4 compares the new correlation with correlations for a single row heat exchanger with annular finned tubes found in literature. Table 2 shows the data ranges used in the correlations. Data from open literature were recalculated to Reynolds numbers based on the external tube diameter and the air velocity at the minimal cross-sectional area. The Nusselt numbers are evaluated for the heat exchanger geometry of Table 3. The transversal tube pitch is set to the value of Lapin and Schurig's tests [16]. Mirkovic [7] and the ESDU [8] predict the highest Nusselt numbers. However, these are multiple tube row correlations corrected with a constant factor to apply them on a single row heat exchanger. Figure 4 shows that correcting multiple row correlations for single row arrays does not result in reliable predictions. Moreover, Eckels and Rabas [10] showed that the influence of the number of rows on the heat transfer in finned tube bundles is dependent on the Reynolds number, a point which is not considered in the correction diagram of Mirkovic [7] and by the ESDU [8]. Schmidt presented a Nusselt correlation for one tube row of a multi-row tube bundle. It was expected that the average Nusselt number of one tube row in a multi-row bundle is lower than the Nusselt number of a single row heat exchanger, because the first row in a multi row heat exchanger transfers more heat than the subsequent rows. However, this is not seen in Figure 4: even

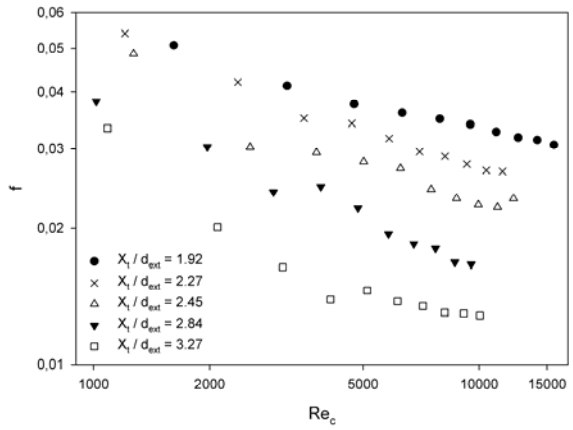

Figure 5. Experimental friction factors plotted versus the minimum-area Reynolds number Re_c for different transversal tube pitches

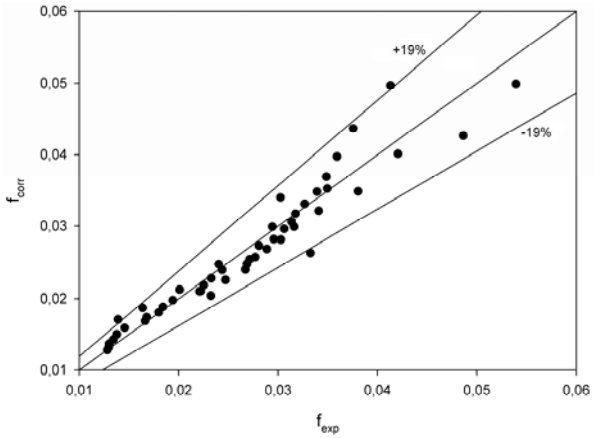

Figure 6. Comparison of the friction correlation (equation (6)) with the experimental data

though the geometry of our heat exchanger is within the application range of Schmidt [17], his correlation lies above our equation (5). The correlations of Lapin and Schurig [16] and Sparrow and Samie [18] are correlations for single row heat exchangers. The expression of Lapin and Schurig [16] underestimates our correlation (equation (5)). A possible explanation is that their tests were performed on a heat exchanger with larger fin spacing. The correlation of Sparrow and Samie [18] is only applicable for higher Reynolds numbers (which were not reached in our tests because of fan restrictions). In the overlapping Reynolds range the correlation well corresponds to our relation.

Pressure drop

The friction factors, calculated according to equation (3), are presented in Figure 5. They are plotted as function of Re_c for the different values of the transversal tube pitch. Unlike the heat transfer data, the use of the minimum-area velocity does not bring the pressure drop data together (compare Figure 5 with Figure 2). This is due to the vena contracta effect: the geometrically minimum free flow area is not the actual minimum free flow area [18].

For a given X_t, the friction factor decreases with increasing Reynolds number. For a fixed Re_c, the pressure drop across the heat exchanger increases with decreasing transversal tube pitch (i.e. increasing blockage). This is in accordance with the results of most authors [1,5,6,8,18]. The finding of Mirkovic [7] – the pressure drop increases with the transversal tube pitch – should be questioned.

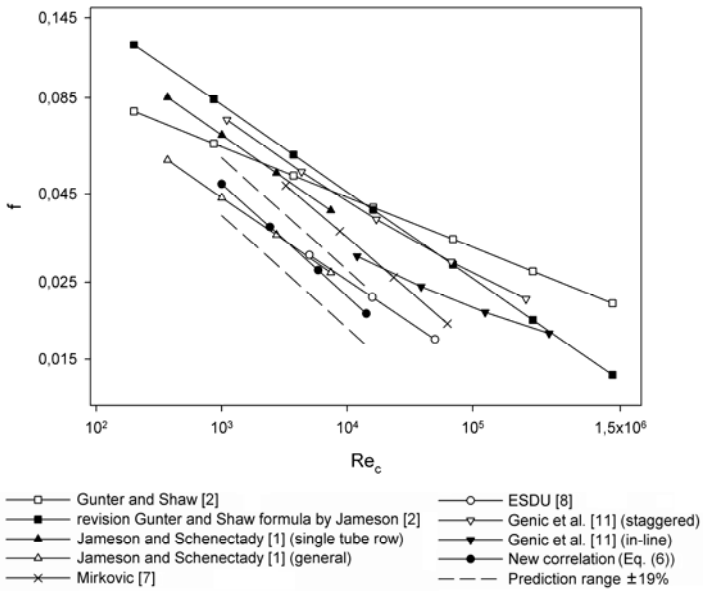

Figure 7. Comparison of equation (6) with friction characteristics from open literature

Table 4
Application Ranges of Friction Correlations from Open Literature

Authors		**Re_c**	**d_{ext} (mm)**	**X_t / d_{ext}**	**D_{fin} / d_{ext}**	**s / d_{ext}**
Gunter and Shaw [2]		200 - 1300000	25.4	1.313	1.5	0.113
Jameson [2]		200 - 1300000	15.875 - 25.4	1.959 - 3.633	1.737 - 1.951	0.102 - 0.213
Jameson and Schenectady [1] (single tube row)		370 - 7400	15.875	1.971	1.794	0.168
Jameson and Schenectady [1] (general correlation)		370 - 7400	15.875 - 25.4	1.959 - 3.633	1.737 - 1.951	0.102 - 0.213
Mirkovic [7]		3250 - 63000	25.4 - 50.8	1.969 - 4.724	1.375 - 1.75	0.053 - 0.142
ESDU [8]		5000 - 50000	9.5 - 51	1.85 - 4.75	1.220 - 4.474	0.014 - 0.990
Genic et al. [11]	Staggered	1100 - 265000	9.65 - 32	0.952 - 3.5	0.841 - 4.572	0.068 - 0.350
	Inline	12000 - 406000	32	2 - 4	1.563	0.147
New correlation (equation (6))		1000 - 14200	13	1.92 - 3.27	1.91	0.135

These experimental data were correlated via a least-mean-squares fit, resulting in:

$$f = 2.271 \cdot Re_c^{-0.3245} \cdot \left(\frac{X_t}{d_{ext}} \right)^{-1.8486} \quad (6)$$

Figure 6 compares equation (6) with the experimental data. This friction correlation predicts 95% of the data within ± 19% and gives a mean deviation of 6.84%.

In Figure 7 the new friction characteristic equation (6) is compared with correlations from literature. Their application ranges are listed in Table 4. Data from open literature were recalculated to friction factors as defined by equation (3) and Reynolds numbers based on the external tube diameter and the air velocity at the minimal cross-sectional area. The correlations are plotted for the heat exchanger geometry of Table 3. Jameson and Schenectady [1] reported data to calculate the friction factors of a single row heat exchanger. The higher values compared with the results of this paper are probably due to the fact that their correlation is not applicable to the heat exchanger geometry of Table 3. Their general expression, which correlates the data for all the tube sizes and arrangements tested (ranging from 1 to 8 tube rows), shows better agreement. The Gunter and Shaw relationship [2] predicts friction values which are much too high. This was also observed by other authors [2,3,4,5]. The slope differs from most other correlations and shows similarity with the in-line configuration of Genic et al. [11]. In the discussion accompanying their article, Jameson suggested a revised version of the Gunter and Shaw equation [2]. The slope of this revised correlation is consistent with our results, but the friction factors are still overestimated. Mirkovic [7] and the ESDU [8] presented a per row pressure drop correlation for staggered, multi-row arrays. Mirkovic' correlation [7] is based on heat exchangers with large tube diameters. This may explain the higher friction values. The ESDU [8] suggests a correction factor of 0.8 for a single row bundle, which results in a better match with the correlation developed in this study. Genic et al. [11] considered staggered and in-line multiple row tube bundles. They advised the correction factors of Brauer [12,13], Yudin [14] or Weierman [15] for a heat exchanger with one tube row. Similar to the heat transfer results, correcting multi-row pressure drop expressions for a single row heat exchanger does not lead to accurate predictions.

UNCERTAINTY ANALYSIS

In order to be able to indicate the quality of the measurements a thorough error analysis was performed. The error of the manometer (pocket manometer of Furness Controls) used to measure the pressure drop across the nozzle was 0.5 Pa. This resulted in a maximum relative error of 0.9% on the air mass flow rate. The maximum relative error of the electromagnetic water flow meter (Kent Veriflux VSC) was found to be 3.0%. The K type thermocouples had an accuracy of 0.1°C. The error on the thermodynamic properties of water and air can be found in literature [22-24].

For each measurement, the relative error was determined. An average was then taken from all the results. The average relative error on the Nusselt number was 7.5% and on the friction factor 5.8%.

CONCLUSIONS

In this study the heat transfer and friction characteristic of a single row heat exchanger with helically finned tubes were determined. The transversal tube pitch was parametrically varied. A thorough error analysis was performed to validate the results. The measurements show that a decrease in transversal tube pitch results in larger heat transfer coefficients (due to higher velocities in the minimum cross sectional area) and larger pressure drops (due to increasing blockage). The Nusselt numbers and friction factors were correlated using the minimum-area Reynolds numbers. The heat transfer correlation can describe 95% of the data within ± 12% and shows a 4.24% mean deviation. The friction correlation predicts 95% of the data within ± 19% and gives a mean deviation of 6.84%. Both equations are dependent on the transversal tube pitch. These new correlations were compared with correlations from open literature. Experimental data on single row heat exchangers are rare. It is concluded that correcting multi-row expressions to apply on single row heat exchangers does not lead to reliable predictions. In general, the new correlations show the

same trend as most literature correlations, but none of the literature correlations can accurately predict the results of this study.

ACKNOWLEDGEMENTS

The first author works as doctoral fellow of the Flemish Research Foundation (FWO Vlaanderen). The second author is a doctoral fellow supported by the Special Research Fund of Ghent University (BOF).

REFERENCES

1. Jameson, S.L., and Schenectady, N.Y., Tube spacing in finned-tube banks, Transaction of the ASME, Vol. 67, pp. 633 – 642, 1945.
2. Gunter, A.Y., and Shaw, W.A., A General Correlation of Friction Factors for Various Types of Surfaces in Crossflow, Transactions of the ASME, Vol. 67, pp. 643-660, 1945.
3. Webb, R.L., Air-side Heat Transfer in Finned Tube Heat Exchangers, Heat Transfer Engineering, Vol. 1, No. 3, pp. 33-49, 1980.
4. Ward, D.J., and Young, E.H., Heat Transfer and Pressure Drop of Air in Forced Convection Across Triangular Pitch Banks of Finned Tubes, Chemical Engineering Progress Symposium, Vol. 59, No. 41, pp. 37-44, 1963.
5. Robinson, K.K., and Briggs, D.E., Pressure Drop of Air Flowing Across Triangular Pitch Banks of Finned Tubes, Chemical Engineering Progress Symposium Series, Vol. 62, No. 64, pp. 177-184, 1966.
6. Briggs, D.E., and Young, E.H., Convection Heat Transfer and Pressure Drop of Air Flowing Across Triangular Pitch Banks of Finned Tubes, Chemical Engineering Progress Symposium Series, Vol. 59, No. 41, pp. 1-10, 1963.
7. Mirkovic, Z., Heat transfer and flow resistance correlation for helically finned and staggered tube banks in crossflow, Heat Exchangers: Design and Theory Source Book, edited by N.H. Afgan and E.U. Schlunder, pp. 559 – 584, 1974.
8. ESDU 86022, High-fin staggered tube banks: heat transfer and pressure drop for turbulent single phase gas flow, 1986.
9. Huber, F.V., and Rabas, T.J., The Effect of Geometry on the Heat Transfer Row Correction for Typical Finned Tube Bundles, AIChE National Heat Transfer Conference, Denver, Co, 1985.
10. Eckels, P.W., and Rabas, T.J., Heat Transfer and Pressure Drop of Typical Air Cooler Finned Tubes, Journal of Heat Transfer - Transactions of the ASME, Vol. 107, pp. 198-204, 1985.
11. Genic, S.B., Jacimovic, B.M., and Latinovic B.R., Research on air pressure drop in helically-finned tube heat exchangers, Applied Thermal Engineering, Vol. 26, pp. 478-485, 2006.
12. Brauer, H., Wärme- und Strömungstechnische Untersuchungen an Quer Angeströmten Rippenrohrbündeln, Teil 1: Versuchsanlagen und Meβergebnisse bei Höheren Drücken, pp.327-335, Teil 2: Einfluβ der Rippen- und der Rohranordnung, pp. 431-438, Chemie Ingenieur Technik, Vol. 33, 1961.
13. Brauer, H., Wärmeubertragung und Strömungswiderstand bei Fluchtend und Versetztargeordneten Rippenrohren, Dechema Monograpic, Band 40, 1962.
14. Yudin, V.F., Teploobmen Poperechno Orebrennykh Trub, Mashinostroenie, Leningrad, 1982.
15. Weierman, C., Pressure Drop Data for Heavy-Duty Finned Tubes, Chemical Engineering Progress, Vol. 73, No. 2, pp. 69-72, 1977.
16. Lapin, A., and Schurig, F., Heat Transfer Coefficients for finned Exchangers, Industrial and Engineering Chemistry, Vol. 51, No. 8, pp. 941-944, 1959.
17. Schmidt, E., Der Wärmeübergang an Rippenrohren und die Berechnung von Rohrbündel-Wärmeaustauschern, Kältetechnik, Vol. 15, No. 4, pp. 370-378, 1963.
18. Sparrow, E.M., and Samie, F., Heat Transfer and Pressure Drop Results for One- and Two-Row Arrays of Finned Tubes, International Journal of Heat and Mass Transfer, Vol. 28, No. 12, pp. 2247-2259, 1985.
19. Shah, R.K., and Sekulic, D.P., Fundamentals of Heat Exchanger Design, John Wiley & Sons, Inc., Hoboken, New Jersey, 2003.
20. Gnielinski, V., New Equations for Heat and Mass Transfer in Turbulent Tube and Channel Flow, International Chemical Engineering, Vol. 29, pp. 359-368, 1976.
21. Kays, W.M., and London, A.L., Compact Heat Exchangers, third ed., McGraw-Hill, New York, 1984.
22. Kadoya, K., Matsunaga, N., and Nagashima, A., Viscosity and Thermal-Conductivity of Dry Air in the Gaseous-Phase, Journal of Physical and Chemical Reference Data, Vol. 14, No. 4, pp. 947-970, 1985.
23. IAPWS Release on the IAPWS Formulation 1995 for the Thermodynamic Properties of Ordinary Water Substance for General and Scientific Use (IAPWS-95), 1996. Available at http://www.iapws.org.
24. Revised release on the IAPWS industrial formulation 1997 for the thermodynamic properties of water and steam (IAPWS-IF97), 2007. Available at http://www.iapws.org.

Fluid Mechanics

ExHFT-7
28 June – 03 July 2009, Krakow, Poland

OSCILLATIONS INDUCED BY A FIN ON THE SIDEWALL OF A DIFFERENTIALLY HEATED CAVITY

F. Xu*, J. Patterson, C. Lei, T. Bednarz
James Cook University, Townsville, QLD 4811, Australia

ABSTRACT Temperature measurements of the thermal flow around a fin placed on the heated sidewall of a differentially heated cavity were performed. The oscillations of the thermal flow around the fin in the transition from sudden start-up to a quasi-steady state were observed based on the temperature time series. Spectral analyses of the temperature signals reveal the frequency characteristics of the oscillations. The temperature measurements also show that the oscillations of the thermal flow around the fin depend on the Rayleigh number. Furthermore, the temperature time series were compared with those obtained in the cases without a fin.

Keywords: *Oscillations, thermal flow, fin, differentially heated cavity*

INTRODUCTION

Natural convection flows in a differentially heated cavity are of significance in many industrial systems such as solar collectors and nuclear reactors. Previous studies [1-3] demonstrated that following sudden heating, perturbations on the thermal boundary layer, which are referred to as the leading edge effect (LEE), arise in the vicinity of the leading edge of a vertical wall and propagate downstream. The LEE plays a fundamental role in the early development of the thermal boundary layer, and its propagation speed is therefore of interest. Initial views on the propagation speed of the LEE suggested that the LEE travelled at the boundary layer flow velocity [1], but it was demonstrated that this propagation speed lags behind the experimental results [2, 3]. Armfield and Patterson [4] showed that a better model for estimating the LEE propagation is to use the maximum speed of the travelling waves in the thermal boundary layer, which was confirmed by experiments [3]. Previous studies (e.g. [5-7]) also showed that the ceiling of the cavity forces a horizontal intrusion into the interior, which separates from and then reattaches to the ceiling, resulting in a series of trailing waves. The intrusion may develop a cavity-scale oscillation after it reaches the opposing wall. As the flow approaches a steady or quasi-steady state, the interior fluid in the cavity is stratified, and a double-layer structure of the vertical thermal boundary layer is formed [8].

Apart from understanding the basic flows in a differentially heated cavity, enhancing or depressing the heat transfer through the cavity is of practical significance in numerous industrial applications. Placing a fin on the sidewall of the cavity provides a simple way to change the thermal flow adjacent to the sidewall and in turn enhance or depress the heat transfer [9]. Studies of the thermal flow induced by a fin on a heated or cooled sidewall of a cavity have also been extensively reported in the literature, most of which examined the effects of the material properties, geometry and position of the fin. Clearly, the fin may be either conducting or adiabatic. It is expected that a conducting fin attached to the sidewall increases the surface area for heat transfer, and in turn increases the overall heat transfer through the cavity. Accordingly, the effect of the thermal

* Corresponding author: Dr. F. Xu
Phone: + (61)-7-47814420, Fax: + (61)-7-47816788
E-mail address: feng.xu@jcu.edu.au

conductivity of different fin materials on heat transfer through the finned sidewall was investigated extensively [10-14].

An adiabatic or poorly conducting fin may also have a significant impact on the natural convection flows in a differentially heated cavity and the heat transfer through the cavity, and in particular the geometry and the location of the fin may play an important role. The study in [9] demonstrated that, as the thickness of a fin which has a poor thermal conductivity and is located at the mid height of the hot sidewall is reduced, the heat transfer through the cavity initially decreases until a critical thickness is reached. If the thickness is reduced further below the critical thickness, the heat transfer through the cavity increases again. The fin length is another factor affecting natural convection flows in the cavity. If the length of the adiabatic fin is sufficiently large, secondary circulations arise at the upper and lower base corners of the fin [14]. The heat transfer through the finned sidewall is reduced as the fin length increases since natural convection flows adjacent to the finned sidewall are depressed. Furthermore, comprehensive investigations of the effect of the position of a fin on natural convection flows in the cavity may be found in [14].

Steady natural convection flows induced by an adiabatic fin have been the focus of previous studies (see e.g. [14]). However, since unsteady natural convection in the cavity has many applications in industry, experimental investigations of the transient thermal flow around an adiabatic fin have been performed by the present authors [15, 16]. The flow visualizations in [15, 16] show that, following sudden heating, the fin on the sidewall blocks the upstream boundary layer flow and forces an intrusion front beneath the fin which eventually reattaches to the downstream sidewall after it bypasses the fin. Indeed, the fin significantly changes the transient thermal boundary layer flow.

It was demonstrated that for different Rayleigh numbers the adiabatic fin may play different roles in the thermal flow adjacent to the finned wall [14, 17]. For low Rayleigh numbers, the thermal flow around the adiabatic fin is laminar and the heat transfer through the finned wall is depressed (see e.g. [14]). On the other hand, for high Rayleigh numbers, the adiabatic fin may trigger instabilities of the thermal flow, and thus enhance the heat transfer through the finned wall, in comparison with that through a wall without a fin [17]. However, understanding of the instabilities induced by the adiabatic fin is still incomplete, and thus further temperature measurements were performed in this study. The oscillations of the thermal flow around the fin were observed and the frequency features of the oscillations were characterized.

EXPERIMENTAL SETUP

In this study, temperature measurements were carried out in the model cavity shown in Figure 1. Briefly, the cavity, containing water as the working fluid, is 1-m long (L), 0.24-m high (H) and 0.5-m wide (W) with a fin of cross-section 0.04-m × 0.002-m attached at the mid height of the hot

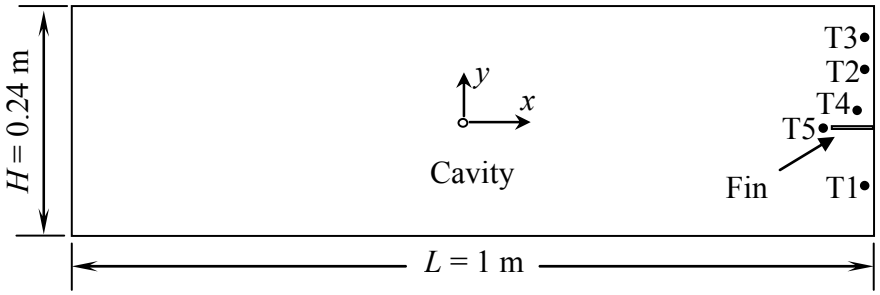

Figure 1. Schematic of the experimental model: Points T1 to T5 denote Thermistor locations, which are corresponding to Thermistor 1 (0.4983 m, -0.0624 m), Thermistor 2 (0.4978 m, 0.0628 m), Thermistor 3 (0.4974 m, 0.0866 m), Thermistor 4 (0.4956 m, 0.007 m), and Thermistor 5 (0.4572 m, -0.0013 m) respectively.

sidewall. The cavity walls and the fin are all made from Perspex sheets except the cooled and heated sidewalls, which are made of 0.00113-m thick gold-coated copper plates (note that due to the poor thermal conductivity of Perspex compared with the thermal conductivity of the copper plate, the Perspex fin may be considered approximately adiabatic).

The sidewall with the fin is heated by the hot water in a water bath, and the opposing sidewall without a fin cooled by the cold water in another water bath. Each water bath is initially separated from the sidewall by a pneumatically operated gate with an air gap between the gate and the sidewall. When the experiment starts, the gates are rapidly lifted, and the hot and cold water in the two water baths flushes against the copper sidewalls. An approximately instantaneous isothermal boundary condition is established at each end of the cavity because this process is completed within a second. During the experiments, the temperatures of the water in the water baths, connected to two separate refrigerated/heating circulators, are kept constant with a temperature stability of ± 0.01 K.

In the experiments, Thermometrics FP07 thermistors were employed. The body of the thermistor has a maximum diameter of 2.2 mm and a length of 12.6 mm, and is mounted in an insulated tube in order to minimize thermal disturbances to the flow field. Since the thermal flow around the fin is the focus of this paper, all five thermistors were placed in the vicinity of the fin and the hot sidewall. Three of the thermistors were placed along the sidewall at different heights, with the other two located around the fin, as shown in Figure 1. Note that for the description of the physical locations, the origin of the coordinates is at the center of the cavity.

The runtime of each experiment is dependent on the development of natural convection flows in the cavity, which is determined by three dimensionless parameters governing the flow: the Rayleigh number (Ra), the Prandtl number (Pr) and the aspect ratio (A). They are defined as follows,

$$Ra = \frac{g\beta\Delta T H^3}{\nu\alpha}, \tag{1}$$

$$Pr = \frac{\nu}{\alpha}, \tag{2}$$

$$A = \frac{H}{L}. \tag{3}$$

Note that the fin length is also a dimensional parameter controlling the thermal flow around the fin on the sidewall. However, a fix fin length is considered in this study.

Table 1. Experimental parameters for temperature measurements

Experiment	Initial temperature of water in cavity (T_0, K)	Temperature difference between sidewalls (ΔT, K)	Ra ($\times 10^9$)	Pr
1	296.65	4	1.01	6.45
2	296.55	8	2.00	6.47
3	295.55	16	3.77	6.63
4	295.55	32	7.54	6.63

RESULTS AND DISCUSSION

Four experiments with temperature differences between the two sidewalls ranging from 4 to 32 K were performed, and the corresponding ranges of Ra and Pr are $1.01 \sim 7.54 \times 10^9$ and $6.45 \sim 6.63$ respectively. All experimental conditions are listed in Table 1. In this section, the results of the

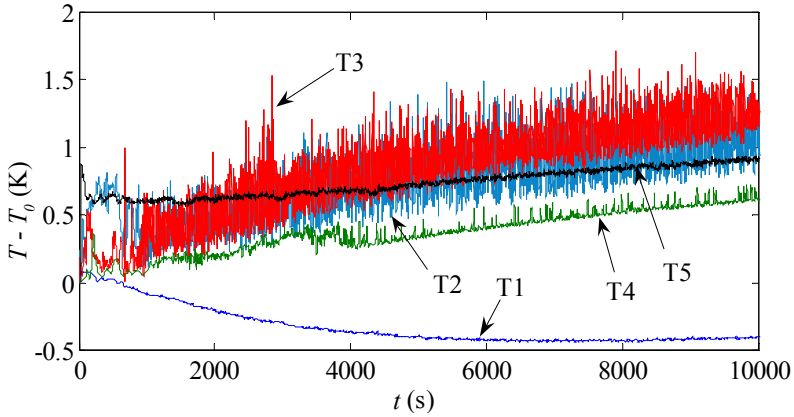

Figure 2. Temperatures measured at the locations shown in Figure 1.

temperature measurements are described based on $Ra = 2 \times 10^9$ (Experiment 2) unless specified otherwise.

Figure 2 shows the time series of the temperatures measured at the five locations. Clearly, the temperature time series are oscillatory and eventually approach respective quasi-steady states. Furthermore, the temperatures in the upper part of the cavity increase with time and the temperature measured by Thermistor 1 in the lower part of the cavity decreases with time. This indicates that a stable stratification of the fluid in the cavity is continuously reinforced [8].

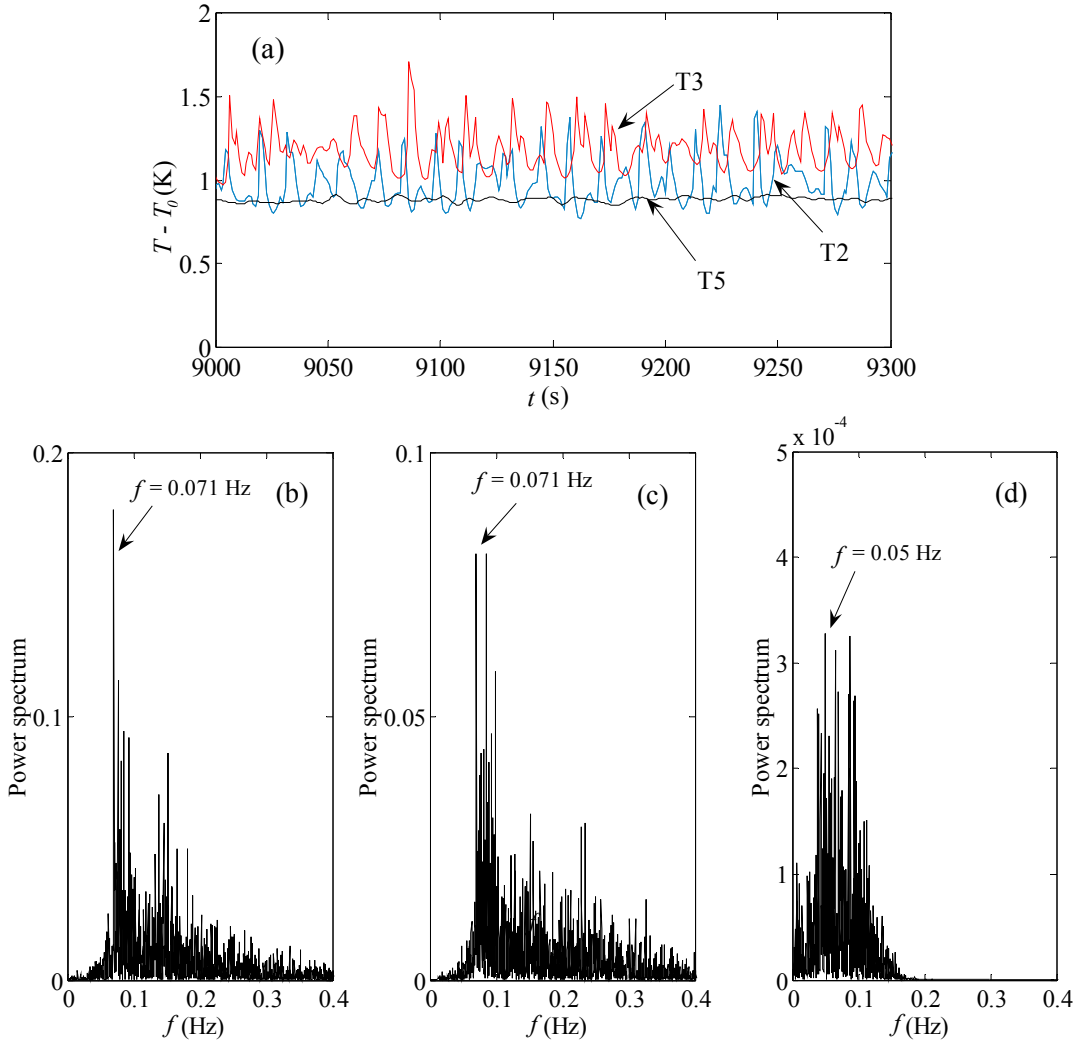

Figure 3. Temperatures and power spectra from Thermistors 2, 3 and 5 in the quasi-stage stage. (a) Temperature time series from Thermistors 2, 3 and 5. (b) Spectrum for Thermistor 2. (c) Spectrum for Thermistor 3. (d) Spectrum for Thermistor 5.

For the purpose of displaying the wave features of the thermal flow around the fin at the quasi-steady state, Figure 3(a) replots the temperature time series from Thermistors 2, 3 and 5 over a period of 300 s in this stage. It is seen in this figure that the amplitude of the temperature waves at this stage is strongly dependent on the spatial location but less dependent on time. The temperature time series from Thermistor 5 shows the oscillations of the thermal flow around the fin, that from Thermistor 2 shows the travelling waves in the vertical boundary layer induced by these oscillations, and that from Thermistor 3 shows the travelling waves in the further downstream boundary layer.

Figures 3(b), 3(c) and 3(d) show the power spectra for Thermistors 2, 3 and 5 respectively. It is clear that the frequency characteristics of the temperature waves are different at these locations. However, it is seen in Figures 3(b) and 3(c) that both the dominant frequencies of the temperature time series from Thermistors 2 and 3 are around 0.071 Hz; that is, the dominant frequencies do not change when the oscillations in the thermal boundary layer propagate downstream of the fin. Figure 3(d) shows that the peak of the spectrum for Thermistor 5 (upstream of Thermistors 2 and 3, refer to Figure 1) is around 0.05 Hz, lower than those for Thermistors 2 and 3. The above results indicate that for the present Rayleigh number ($Ra = 2 \times 10^9$), the oscillations within a narrow band of frequencies around 0.071 Hz are selectively amplified in the downstream side of the fin, which could be caused by the unstable thermal layer above the fin which has an adverse temperature gradient with warmer fluid underneath colder fluid [17].

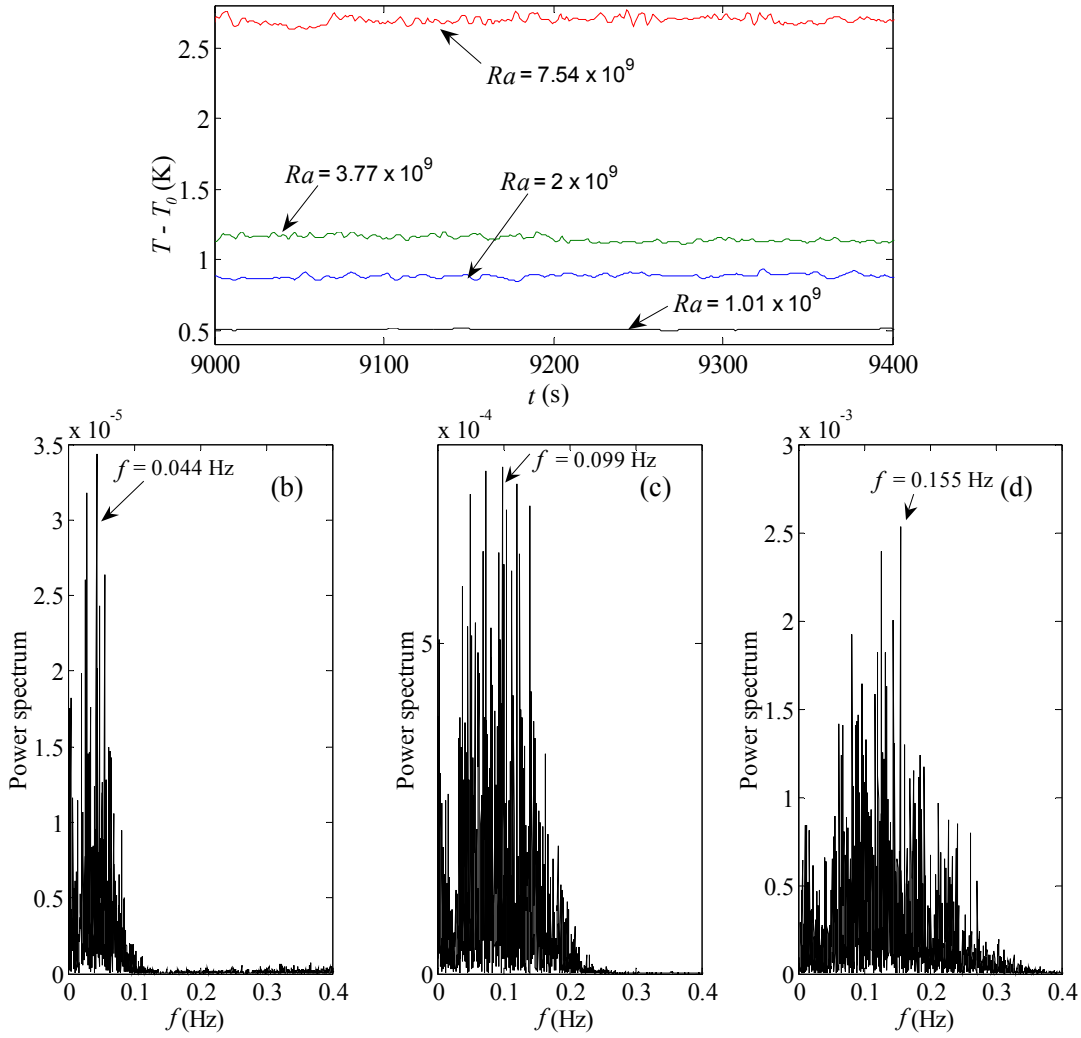

Figure 4. Temperatures and spectra from Thermistor 5 (0.4572 m, -0.0013 m) in the quasi-steady stage for different Rayleigh numbers. (a) Temperature time series. (b) Spectrum for $Ra = 1.01 \times 10^9$. (c) Spectrum for $Ra = 3.77 \times 10^9$. (d) Spectrum for $Ra = 7.54 \times 10^9$.

Indeed, the oscillations of the thermal flow around the fin depend on the Rayleigh number. Figure 4(a) shows the temperature time series from Thermistor 5 in the quasi-steady stage for different Rayleigh numbers. It is clear that the average temperature from Thermistor 5 increases with the temperature difference between the two sidewalls (see Table 1). Furthermore, both the amplitude and dominant frequency of the oscillations change with the Rayleigh number. The power spectra of the temperature time series in Figures 4(b), 4(c) and 4(d) show that the dominant frequency of the oscillations increases as the Rayleigh number increases.

Figure 5 shows the comparisons of the temperature time series in the downstream thermal boundary layer in the cases with and without a fin (note that the temperature measurements for the case without a fin are reported separately in [18]). It is seen in this figure that the fin apparently changes the character of the oscillations in the thermal boundary layer on the downstream side of the fin. For instance, Figures 5(a) and 5(b) show that due to the presence of the fin, the thermal flow at the downstream side of the fin is more unstable; that is, the amplitudes of the oscillations are larger than those in the cases without a fin. This is consistent with the numerical results reported in [17] which also demonstrated that these unstable flows at the downstream side of the fin may in turn enhance heat transfer through the finned sidewall. Further comparisons of the temperature measurements between the cases with and without a fin are currently being conducted.

CONCLUSIONS

In this paper, the temperatures of the thermal flow around a fin placed at the mid height of the hot sidewall of a differentially heated cavity were measured by a set of fast-response thermistors. The transient and quasi-steady state flow features were characterized based on the temperature

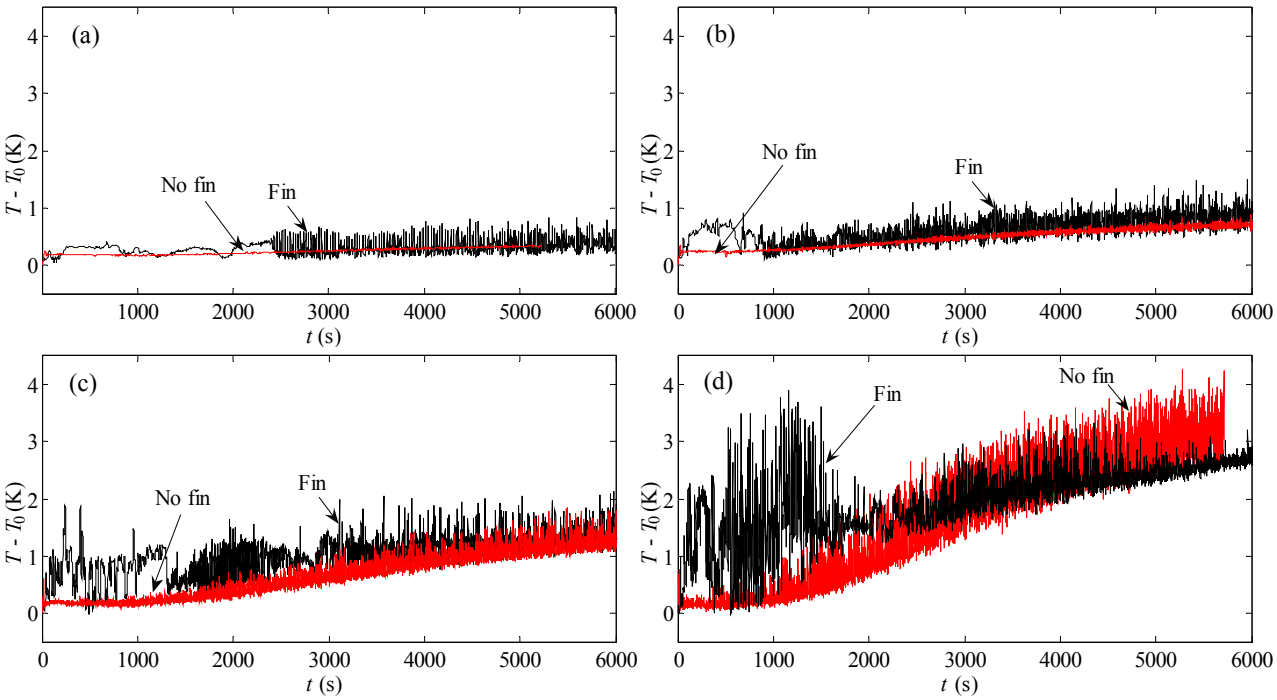

Figure 5. Temperatures in the cases with a fin at (0.4978 m, 0.0628 m) and without a fin at (0.4974 m, 0.0624 m) for different Rayleigh numbers. (a) Cases with a fin for $Ra = 1.01 \times 10^9$ and without a fin for $Ra = 0.88 \times 10^9$. (b) Cases with a fin for $Ra = 2 \times 10^9$ and without a fin for $Ra = 1.75 \times 10^9$. (c) Cases with and without a fin for $Ra = 3.77 \times 10^9$. (d) Cases with a fin for $Ra = 7.54 \times 10^9$ and without a fin for $Ra = 6.87 \times 10^9$.

measurements.

The temperature measurements clearly show the stratification of the fluid in the cavity and the oscillations of the thermal flow around the fin. Furthermore, the spectral analyses of the temperature time series in the quasi-steady stage have revealed the dominant frequencies of the oscillations of the thermal flow around the fin and its dependence on the Rayleigh number.

Nomenclature

A	aspect ratio
f	frequency (Hz)
g	acceleration due to gravity (m/s^2)
H, L, W	height, length and width of the cavity (m)
Pr	Prandtl number
Ra	Rayleigh number
t	time **(**s**)**
T_0	initial temperature of the fluid (K)
ΔT	temperature difference between sidewalls (K)
x, y	horizontal and vertical coordinates (m)
β	coefficient of thermal expansion (1/K)
α	thermal diffusivity (m^2/s)
ν	kinematic viscosity (m^2/s)

Acknowledgement
The Authers would like to thank the Australian Research Council for its financial support.

REFERENCES

1. Goldstein, R. J. and Briggs, D. G., Transient free convection about vertical plates and cylinders, *J. Heat Transfer*, Vol. 86, pp 490-500, 1964.
2. Mahajan, R. L. and Gebhart, B., Leading edge effects in transient natural convection flow adjacent to a vertical surface, *J. Heat Transfer*, Vol. 100, pp 731-733, 1978.
3. Patterson, J. C., Graham, T., Schöpf, W. and Armfield, S. W., Boundary layer development on a semi-infinite suddenly heated vertical plate, *J. Fluid Mech*., Vol. 453, pp 39-55, 2002.
4. Armfield, S. W. and Patterson, J. C., Wave properties of natural convection boundary layers, *J. Fluid Mech*., Vol. 239, pp 195-212, 1992.
5. Ivey, G. N., Experiment on transient natural convection in a cavity, *J. Fluid Mech.*, Vol. 144, pp 389-401, 1984.
6. Patterson, J. C. and Armfield, S. W., Transient features of natural convection in a cavity, *J. Fluid Mech.*, Vol. 219, pp 469-497, 1990.
7. Ravi, M. R. R., Henkes, R. A. W. M. and Hoogendoorn, C. J., On the high-Rayleigh-number structure of steady laminar natural-convection flow in a square enclosure, *J. Fluid Mech*., Vol. 262, pp 325-351, 1994.
8. Xu, F., Patterson, J. C. and Lei, C., Shadowgraph observations of the transition of the thermal boundary layer in a side-heated cavity, *Exp. Fluids*, Vol. 38, pp 770-779, 2005.
9. Nag, A., Sarkar, A. and Sastri, V. M. K., Effect of thick horizontal partial partition attached to one of the active walls of a differentially heated square cavity, *Numer. Heat Transfer*, Part A 25, 611-625, 1994.
10. Frederick, R. L., Natural convection in an inclined square enclosure with a partition attached to its cold wall, *Int. J. Heat Mass Transfer*, Vol. 32, pp 87-94, 1989.

11. Nag, A., Sarkar, A. and Sastri, V. M. K., Natural convection in a differentially heated square cavity with a horizontal partition plate on the hot wall, *Comput. Method Appl. M.*, Vol. 110, pp 143-156, 1993.
12. Shi, X. and Khodadadi, J. M., Laminar natural convection heat transfer in a differentially heated square cavity due to a thin fin on the hot wall, *J. Heat Transfer*, Vol. 125, pp 624-634, 2003.
13. Tasnim, S. H. and Collins, M. R., Numerical analysis of heat transfer in a square cavity with a baffle on the hot wall, *Int. Comm. Heat Mass Transfer*, Vol. 31, pp 639-650, 2004.
14. Bilgen, E., Natural convection in cavities with a thin fin on the hot wall, *Int. J. Heat Mass Transfer*, Vol. 48, pp 3493-3505, 2005..
15. Xu, F., Patterson, J. C. and Lei, C., Experimental observations of the thermal flow around a square obstruction on a vertical wall in a differentially heated cavity, *Exp. Fluids*, Vol. 40, pp 363-371, 2006.
16. Xu, F., Patterson, J. C. and Lei, C., An experimental study of the unsteady thermal flow around a thin fin on a sidewall of a differentially heated cavity, *Int. J. Heat Fluid Flow*, Vol. 29, pp 1139-1153, 2008.
17. Xu, F., Patterson, J. C. and Lei, C., Transition to a periodic flow induced by a thin fin on the sidewall of a differentially heated cavity, *Int. J. Heat Mass Transfer*, Vol. 52, pp 620-628, 2009.
18. Xu, F., Patterson, J. C., Lei, C. and Benardz, T., Travelling waves in the thermal boundary layer adjacent to the sidewall of a differentially heated cavity, *7th World Conference on Experimental Heat Transfer, Fluid Mechanics and Thermodynamics*, Krakow, Poland June 28 - July 03, 2009 (submitted).

T.

TRANSITION OF FLOW IN FREE LIQUID FILM EXPOSED TO TEMPERATURE GRADIENT

I. Ueno[1,*], T. Watanabe[2] & T. Matsuya[2,]
[1]Tokyo University of Science, Chiba, Japan
[2]Graduate School at Tokyo University of Science, Chiba, Japan

ABSTRACT. Flow transition in a thin free liquid film exposed to a temperature difference is concerned. A free liquid film of O(1 mm) in width and length is formed in a rectangular hole in a thin plate of O(0.1 – 1 mm) in thickness. A designated temperature difference is added between the both end walls to realize a thermocapillary-driven flow on the both free surfaces. One can realize several flow patterns in the film by varying the temperature difference imposed. The authors focus on the formations and occurring conditions of such unique flows in the free liquid film.

Keywords: *free liquid film, flow pattern, transition, thermocapillary effect, particle*

INTRODUCTION

The authors have been inspired by a series of scientific performances by Dr. Donald Pettit, a NASA astronaut, on The International Space Station during his stay in 2003. Among his invaluable performances, one can see a unique behavior of free liquid film of O(10 cm) in diameter sustained in a metal ring [1]. A microgravity condition would enable a liquid film to be sustained stably with its surface tension and wettability of the sustainer against the liquid concerned. This unique system is a potential way to realize a new kind of crystallization process of materials. A free liquid film has a great feature that a contact area with a solid sustainer can be minimized. This is a vigorous advantage to avoid the liquid contaminated by impurities supplied from the solid. It is of great importance to accumulate knowledge on a thermal-fluid dynamics of a free film of a liquid with a non-zero temperature coefficient of the surface tension exposed to a non-uniform temperature field.
In the case of a thin liquid film form in a rectangular cavity (i.e., a liquid film with a single free surface) with a temperature difference between both-end walls, Smith & Davis [2] predicted that a new type of thermal-fluid instability would arise in the film beyond a critical temperature difference. Under a temperature difference smaller than the critical value, a two-dimensional steady flow parallel to the imposed temperature gradient is induced in the film. After the onset of the transition, roll structure emerges in the film and propagate in a direction inclined to the imposed temperature gradient. This unique instability was named as 'hydrothermal wave instability,' and was revealed by an experimental approach by Riley & Neitzel [3]. After their beautiful experimental work, a number of experimental and numerical works have been carried out with a liquid film with a single free surface for a decade [4].
In the case of free liquid films, on the other hand, little knowledge has been accumulated on a flow dynamics in such a thin film with two free surfaces; one can easily imagine that a long-lasted stable free liquid film is hardly formed in a terrestrial experiment.
In the present study, the authors carry out a three-dimensional numerical simulation and a series of experiments with their special attention to a flow field inside the free surface under non-uniform

* Corresponding author: Dr. I. Ueno
Phone: + (81)-4-71241501, Fax: + (81)-4-71239814
E-mail address: ich@rs.noda.tus.ac.jp

temperature distribution; that is, a thermocapillary-driven flow induced in a free thin liquid film under a temperature gradient parallel to the free surfaces.

TARGET GEOMETRY

Target geometry is shown in Fig. 1. A thin liquid film with two free surfaces parallel to x-z plain is concerned. Length in the direction of the temperature gradient is defined as L_x, and that in the span-wise direction L_z. The thickness of the film is presented as d. In the present geometry, two kinds of aspect ratios are defined; that is, $\Gamma_x = L_z/L_x$ and $\Gamma_y = L_x/d$. One end wall is maintained at a temperature of T_h, and the other at T_c ($T_h > T_c$). Thus the film is exposed to a temperature difference $\Delta T = T_h - T_c$. Intensity of the thermocapillary effect imposed to the film is described by non-dimensional Marangoni number;

$$\mathrm{Ma} = \frac{\sigma_T \Delta T \cdot d^2}{\rho \nu \kappa L_x} = \frac{\sigma_T \Delta T \cdot d^2}{\rho \nu^2 L_x} \cdot \frac{\nu}{\kappa} = \mathrm{Re}_\sigma \cdot \mathrm{Pr}$$

where σ_T is the absolute value of the temperature coefficient of the surface tension ($\equiv |\partial\sigma/\partial T|$), ρ the density, ν the kinematic viscosity, κ the thermal diffusivity. The Marangoni number can be described as the product of the thermocapillary Reynolds number Re_σ and Prandtl number Pr.

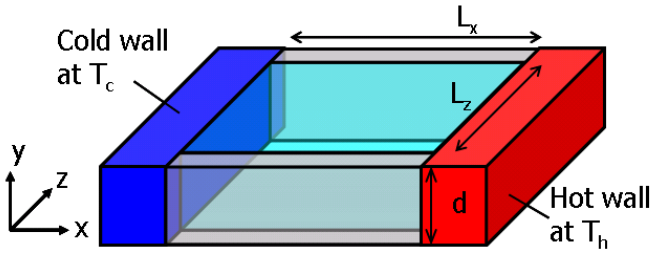

Figure 1. Target geometry: a free liquid film exposed to a temperature gradient.

NUMERICAL SIMULATION

In the numerical simulation, the authors solve following non-dimensional equations of continuity, momentum and energy by a finite differential method.

$$\nabla \cdot \mathbf{u} = 0$$

$$\frac{\partial \mathbf{u}}{\partial t} + (\mathbf{u} \cdot \nabla)\mathbf{u} = -\nabla \mathbf{P} + \frac{\mathrm{Pr}}{\mathrm{Ma}} \nabla^2 \mathbf{u}$$

$$\mathrm{Ma}\left(\frac{\partial T}{\partial t} + (\mathbf{u} \cdot \nabla) T \right) = \nabla^2 T$$

Free surfaces are assumed to be flat without any dynamical deformation. Stress balance on the free surface leads so-called 'Marangoni' boundary conditions. Non-slip condition is applied to the both of hot and cold walls. The Prandtl number is fixed at 10.0 through the simulation. The present numerical code is validated under the condition of the single-free-surface thin film by comparing the incident angle, the wave number and the travelling velocity of the HW with the theoretical prediction by Smith & Davis [3].

EXPERIMENT

In order to realize a stable free liquid film in a series of experiments under the normal gravity, the authors prepared a rectangular hole in aluminium plates of 0.2 mm and 0.6 mm in thickness, and the one of iron of 1.0 mm in thickness as the liquid film holder. A liquid film is formed and sustained inside the rectangular hole. Figure 2 shows one example of the prepared holders; one side of the plate is heated, and the other cooled to expose the hole to a designated temperature difference. Silicone oils of 2 and 5 cSt were employed as the examined fluids. Temperature near the end walls sustaining the free liquid film was measured with thermocouples to evaluate the temperature difference ΔT.

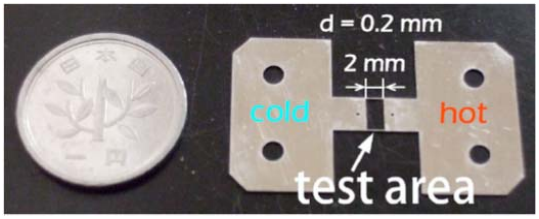

Figure 2. Example of liquid film holder (right). Liquid film is formed in a square region indicated by a circle. Thickness of the holder in the figure is of 0.2 mm.

Induced flow was visualized by suspending silver-coated hollow glass particles of 10 μm in diameter. The visualized flow was detected by a CCD camera whose frame rate was 30 frame/s. Shutter speed was 1/60 s. Temperature variation over the top free surface was measured by use of an infrared camera.

RESULTS & DISCUSSION

Three dimensional numerical simulation indicates a two-dimensional flow inside the film is realized in which the fluid returns in the middle region of the film under a small temperature gradient. By increasing the temperature difference between the end walls, instability takes place to realize a three-dimensional flow. Figure 3 indicates (1) top view of the deviation of the temperature over the top free surface and (2) cross-sectional view in x-y plane of 'oscillatory' flows. Case (a) indicates a single free surface (top surface is free) and case (b) two free surfaces under the same intensity of the thermocapillary effect. In the figure right wall is hot, and left wall cold. Lines in the film in the frames (2) indicate the isotherms. In the case of (b) free liquid film, one can clearly observe a typical inclined thermal wave propagating with a certain angle. There exists a slight difference in the propagating angle, the speed of the hydrothermal wave between the cases (a) and (b). Clear difference is emerged in the cross-sectional view; the free film has a double-layered structure of rolls with a constant phase shift. That is, an effective thickness of the liquid film to realize the hydrothermal wave instability must be different for the free liquid film case.

Typical examples of the induced flow field observed from above are shown in Fig. 4. Under small-enough temperature difference, a similar basic flow is realized inside the film (Fig. 4-(a)). That is, thermocapillary effect drives the free surfaces towards the cold wall, and the fluid returned towards the hot wall in the middle region of the film between the free surfaces. By increasing the temperature difference between the walls, a three-dimensional oscillatory flow emerged in the film (Fig. 4-(b)). The oscillatory flow, however, never exhibits an ordered hydrothermal wave instability with a certain wavelength and propagation speed as predicted by the simulation aforementioned, but a span-wise cellular pattern (Fig. 4-(b)). That is, the film is divided into two cells in a span-wise direction, and the flow indicates a three dimensional pattern. The particles in one cell seldom penetrate into another cell. This span-wise cellar pattern has not been indicated by the present

numerical simulation. and could be a unique flow structure in the case of the free liquid film. Such a pattern has not been reported in the case of the thin liquid film in the cavity.

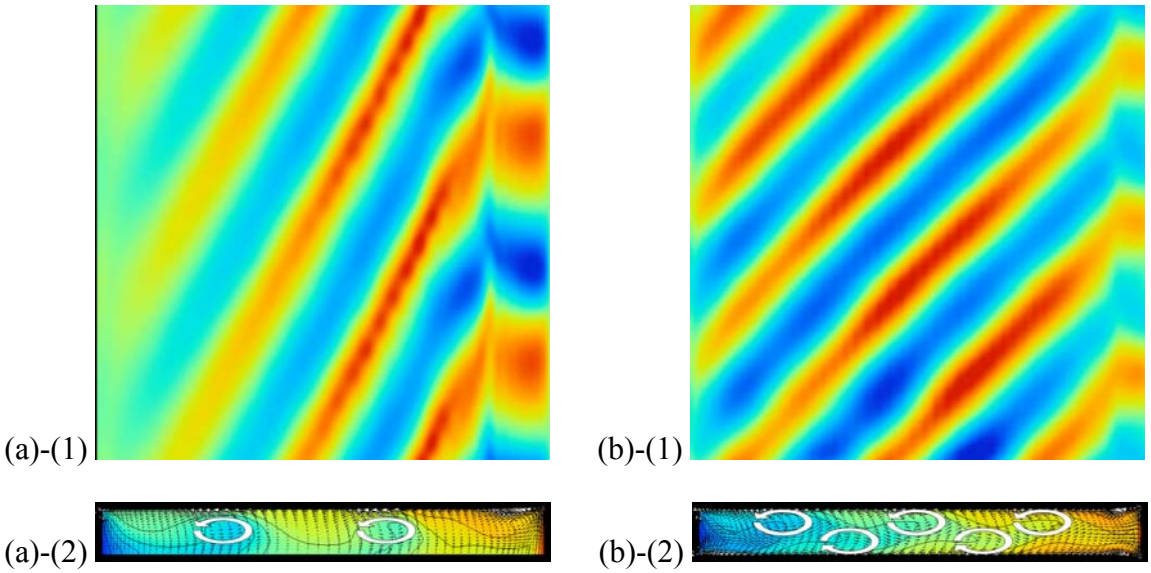

Figure 3. Typical example of 'oscillatory' flow; (1) top view of the deviation of the temperature over the top free surface and (2) cross-sectional view in x-y plane in the cases of (a) a thin liquid film in the cavity (a single free surface (top surface is free)) and (b) two free surfaces under the same intensity of the thermo- capillary effect. Right-hand side is the hot wall, and the opposite is the cold wall for each frame. Marangoni number Ma is kept constant at 1×10^3.

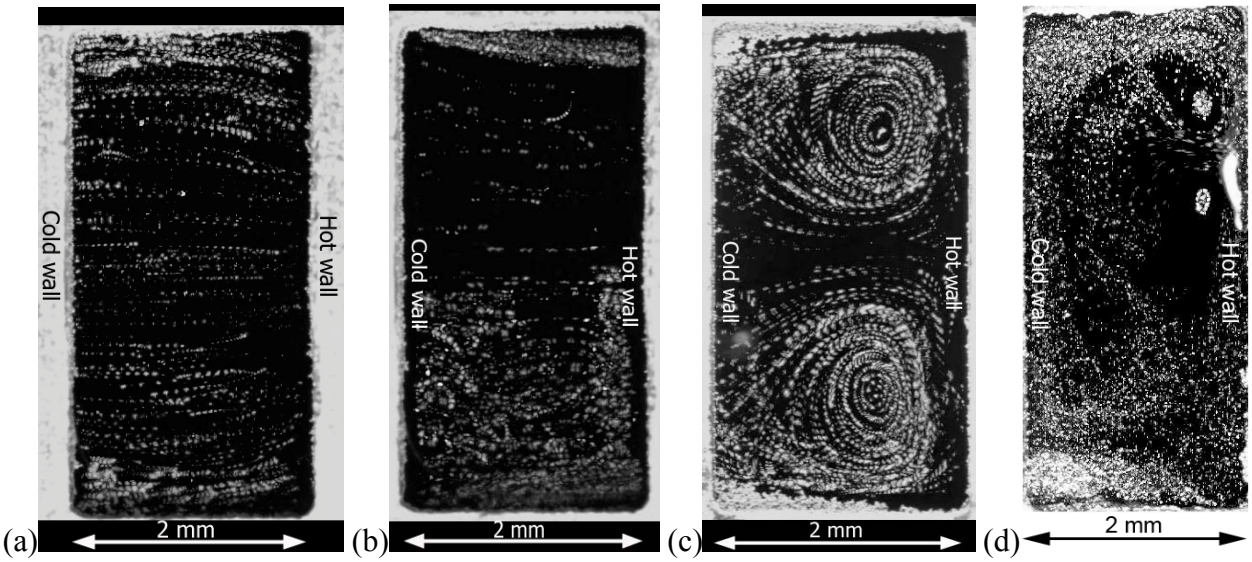

Figure 4. Typical examples of the induced flow in the free liquid film of (L_x, L_y) = (2.0 mm, 4.0 mm) observed from above; (a) ΔT = 4.7 K (Ma = 2.2×10^2) and (b) ΔT = 31.5 K (Ma = 1.5×10^3) in the case of d = 0.6 mm, and (c) ΔT = 6.8 K (Ma = 26) and (d) ΔT = 17.8 K (Ma = 68) in the case of d = 0.2 mm. These images are obtained by integrating the obtained frames for 1.0 s.

In the case of thin liquid film of 0.2 mm in thickness, two-dimensional basic flow is hardly realized; even under a small thermocapillary effect, or at small Marangoni number, a single-layered span-wise cellular pattern emerges in the film shown in Fig. 4 (c). Further increasing ΔT, the flow exhibits a chaotic behavior as shown in Fig. 4 (d). This could be the first capture of the route to the chaotic flow in a free liquid film by the present authors' group, to the best of their knowledge.
Nonetheless, a double-layered hydrothermal wave instability as predicted by the numerical simulation (Fig. 3-(b)) hardly emerges in the film in the experimental runs so far. The authors continue further investigation on occurring conditions of induced flow patterns and mechanism of these instabilities by both of numerical and experimental approaches.

CONCLUSIONS

Thermocapillary-driven flow induced in a free thin liquid film under a temperature gradient parallel to the free surfaces is investigated. By a series of three-dimensional numerical simulations, a double-layered return flow emerges as a basic flow at a small thermocapillary effect, and then a double-layered hydrothermal wave instability arises in the film as increasing the thermocapillary effect. By an experimental approach, the authors realize to form a stable free liquid film under a designated temperature gradient between the end walls. A double-layered basic flow appears at a small thermocapillary effect as the prediction by the simulation. A stable hydrothermal wave instability, however, is never realized in the film so far, but a single-layered span-wise cellular flow emerges.

REFERENCES

1. http://science.nasa.gov/headlines/ y2003/25feb_nosoap.htm
2. Smith, M. K. & Davis, S. H., Instabilities of dynamic thermocapillary liquid layers. Part 1. Convective instabilities, *J. Fluid Mech.* 132, pp.119-144, 1983.
3. Riley, R. J. & Neitzel, G. P., Instability of thermocapillary–buoyancy convection in shallow layers. Part 1. Characterization of steady and oscillatory instabilities, *J. Fluid Mech.* 359, pp.143-164, 1998.
4. *e.g.*, Kawamura, H., Tagaya, E. & Hoshino, Y., A consideration on the relation between the oscillatory thermocapillary flow in a liquid bridge and the hydrothermal wave in a thin liquid layerInt. *J. Heat Mass Trans.* 50, pp. 1263-1268, 2007.

EXPERIMENTAL INVESTIGATION OF SHEDDING MODE II BEHIND A ROTATING CYLINDER

I. Yildirim[1], C.C.M. Rindt[1,*], A.A. van Steenhoven[1]
[1] Eindhoven University of Technology, Mechanical Engineering Department, Energy Technology Section, Eindhoven, the Netherlands

ABSTRACT. The transition of the flow behind a circular rotating cylinder is investigated experimentally. In literature it has been shown numerically that for a rotating cylinder there exist two instability areas where the vortex shedding is not suppressed [1, 2, 3]. Shedding mode I is predicted to appear and also measured experimentally at low rotation rates whereas shedding mode II is predicted to occur around rotation rates of about $\alpha \approx 5$, where α is defined as the ratio between the circumferential velocity at the cylinder surface and the incoming free-stream velocity. Shedding mode II is numerically associated with one-order-of-magnitude lower shedding frequencies and is found only in a narrow range of the parameter α. With the use of the tin-precipitation method, we were able to visualize and quantify Shedding Mode II. The experimentally found Strouhal numbers associated with the second instability mode are 0.017 for $\alpha = 4.96$ and 0.011 for $\alpha = 5.1$

Keywords: rotating cylinder, shedding mode II, tin precipitation method, experimental fluid mechanics

INTRODUCTION

The two-dimensional flow passing a rotating cylinder has been an interesting subject for research for long time. The interest in this type of flow not only comes from understanding of the wake dynamics but also from the flow control applications. The flow around a rotating cylinder is categorized according to two non-dimensional parameters; the Reynolds number and the rotation rate:

$$\mathrm{Re} = \frac{U_\infty D}{\nu} \tag{1}$$

$$\alpha = \frac{D\omega}{2U_\infty} \tag{2}$$

Here D is the cylinder diameter, ω the angular velocity of the rotating cylinder, U_∞ the free-stream velocity and ν the kinematic viscosity.

Previously, it has been shown numerically and for low rotation rates also experimentally that for a rotating cylinder there exist two instability areas where the vortex shedding is not suppressed. These areas are indicated as mode I and II in a sketch of the instability diagram, Figure 1 [1]. In between these areas the flow is steady.

* Corresponding author: Dr. Ir. C.C.M. Rindt
Phone: +(31)-40-2472978, Fax: +(31)-40-2475399
E-mail address: c.c.m.rindt@tue.nl

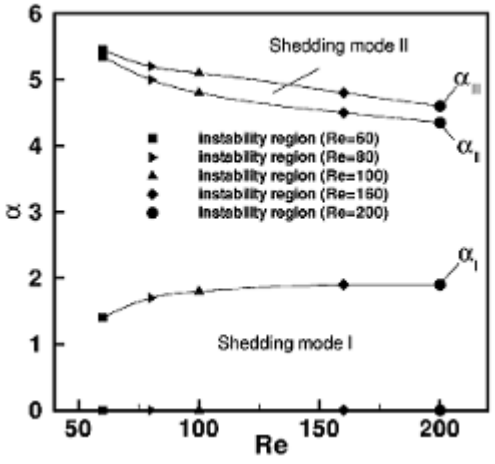

Figure 1. Stability diagram for different Reynolds numbers and rotation rates [1].

Shedding mode I is appearing at low rotation rates whereas shedding mode II is observed around rotation rates of about $\alpha \approx 5$. Mode I corresponds to the classic von Karman vortex street, which becomes asymmetric when the cylinder is rotating and is eventually quenched for values $\alpha \approx 2$. Mode II, conversely, is associated with one-order-of-magnitude lower shedding frequencies and is found only in a narrow range of the parameter α, which can be found in numerical studies of Stojkovic et. al. [1], Mittal and Kumar [2] and Elkoury et. al. [3].

In this work the transition of the flow behind a circular rotating cylinder is investigated experimentally. Therefore, the aim of the present work is to experimentally verify the existence of shedding mode II and to compare its main features with those obtained in the numerical studies [1-3]. To the best of our knowledge mode II has never been identified experimentally.

After the brief description of the experimental method and the set-up the results from the experiments are summarized. The final section consists of the discussion of the experiments and possible future work about the rotating case.

EXPERIMENTAL SET-UP

Experiments were done in a towing tank [4]. It has dimensions $L \times W \times H = 500cm \times 50cm \times 75cm$. Reynolds number is fixed to 100 during the experiments and the rotation rate of the cylinder is changed only. The diameter of the circular cylinder is $D = 10mm$ and it is placed between two square shaped plexiglass end plates. The rotation rate α was changed from 0 to 5.1 by an electric motor. Information about the flow physics is obtained from flow visualization experiments which are performed in a towing tank using the electrochemical tin-precipitation method. Flow visualizations are performed in a two-dimensional configuration where the tin sheet is oriented vertically with respect to the cylinder, Figure 2.

In this method tin-ions are separated from a tin-anode by applying a voltage difference. This voltage difference causes very small tin-hydroxide particle to form. Since those tin-hydroxide particles do not dissolve in water, they can be used to visualize the flow [5].

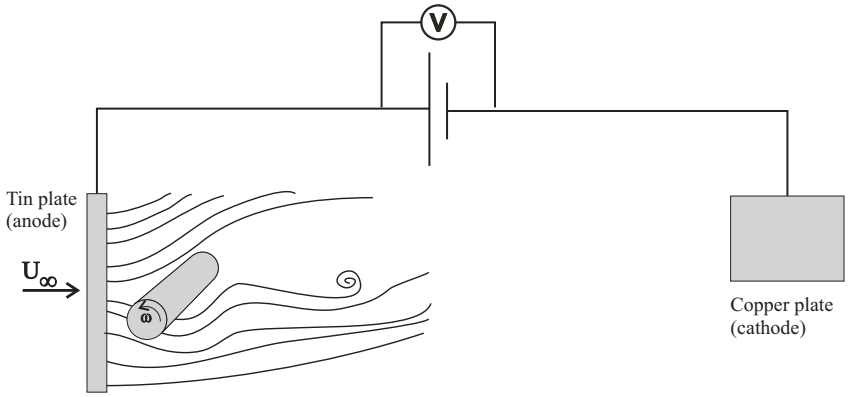

Figure 2. Sketch of the tin-precipitation method set-up.

RESULTS

Verification of the experimental method

As the first step the reliability of the experiments was assessed, in order to do these different $\mathrm{Re}-\alpha$ combinations are chosen for evaluation.

α=0, Re=100. For this parameter set the flow is expected to be two-dimensional with von Karman vortex shedding patterns. The results from the experiments can be seen in Figure 3. The flow in the image is from the left to the right and the vertical structures behind can easily be seen. The calculated shedding frequency from the image sequence is $St = 0.166$, which is in good agreement with the values from the literature [6, 7]. Based on this comparison, it can be concluded that the results of this experiment is consistent with the results of the literature and the method produces reliable results.

α=1.6, Re=100. Shedding Mode I can be seen at this parameter set. From Figure 4 it can be noted that the vortex shedding is not suppressed completely but changed due to the rotation. The strength of the upper shed vortices seems to be reduced since they are not distinctive as in the non rotating case. On the other hand the lower shed vortices are clearly visible.

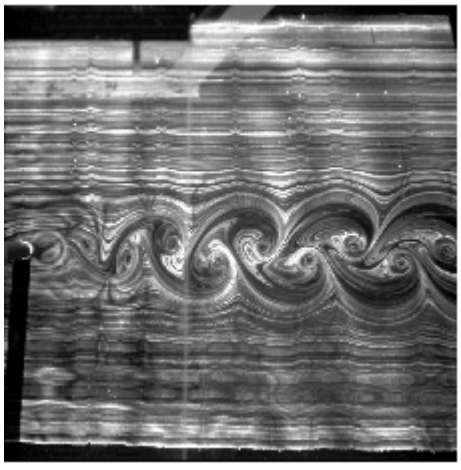

Figure 3. Flow visualization of von Karman vortex street, $\mathrm{Re} = 100, \alpha = 0$.

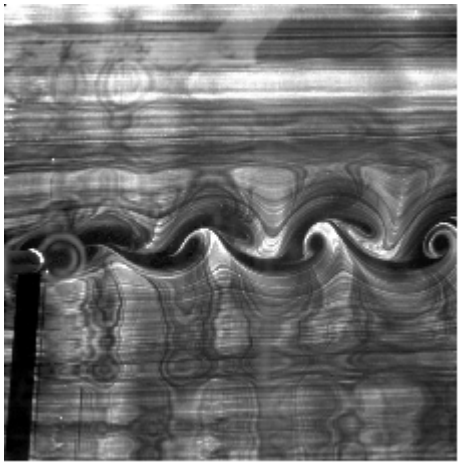

Figure 4. Vortex shedding in first instability region, $\mathrm{Re} = 100, \alpha = 1.6$.

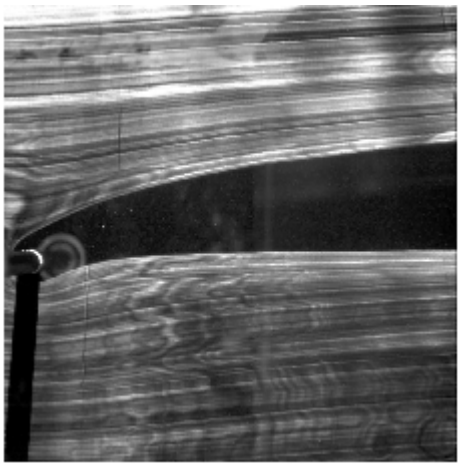

Figure 5. Suppressed vortex shedding by rotation, $\mathrm{Re} = 100, \alpha = 3$

α=3, Re=100. In the stability diagram $\alpha = 3$ is between the two shedding modes. In this rotation rate the vortex shedding is completely suppressed and there is no vortex shedding from the cylinder. This can be clearly seen from the visualization results in Figure 5.

As the result of these initial experiments, it can be concluded that the tin-precipitation method gives reliable results about the nature of the flow and about some quantitative properties of the flow.

Shedding mode II

Further increase of the rotation rate of the cylinder puts the flow regime into another instability region which is denoted as *second instability mode* or *shedding mode II*. In this mode, shedding of a single vortex exhibits itself. The period of the shedding is quite large when compared to the shedding period of von Karman vortices and it requires large experiment time in order to see the phenomenon.

α=4.96, Re=100. The experiments at this parameter set made it possible to identify four single vortices which can be seen in Figure 6. At this stage the wake behind the rotating cylinder is not as stable at it was at $\alpha = 3$. This feature can be realized form the behaviour of the tin sheet. On the other hand, on the lower part of the wake four distinct and counter clockwise rotating vortices are easily seen. The period between the vortices is calculated using the image sequence. The resulting Strouhal

number of the vortex shedding is $St \approx 0.017$. This value of the non-dimensional shedding frequency is of the same order-of-magnitude as of the numerical simulations in the literature [1]. From this similarity it can be concluded that those vortices are likely to be shedding mode II vortices.

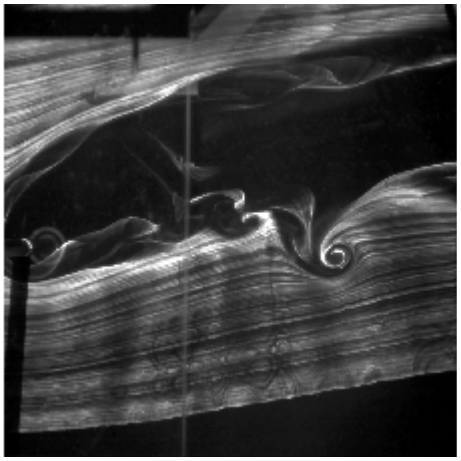

Figure 6. Captured vortex of shedding mode II at Re=100 and α=4.96.

α=5.1, Re=100. When the angular velocity of the cylinder is slightly increased the wake behind the cylinder becomes more organized and the shedding vortices are detected easily. The three shed vortices and the wake are shown in Figure 7. Again the counter clockwise rotating vortices are located at the lower portion of the wake. However, in this case the calculated mean Strouhal number from the image sequences is 0.011. This Strouhal number is again consistent with the numerical results that were obtained by Stojkovic et. al.[1].

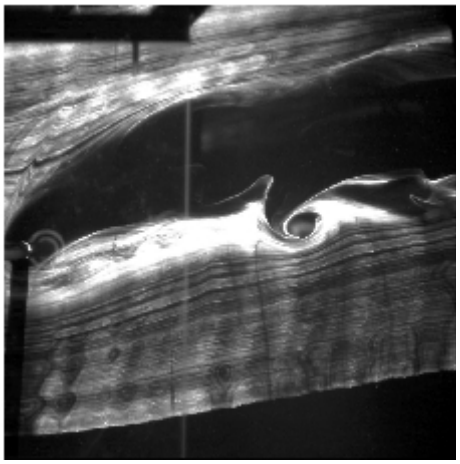

Figure 7. Captured vortex of shedding mode II at Re=100 and α=5.1.

CONCLUSIONS

In this research flow visualizations are performed in a two-dimensional configuration where the tin sheet is oriented vertically with respect to the cylinder. In order to reduce the number of experiments and to avoid the three-dimensional effects of the cylinder flow, the experiments were done at a fixed Reynolds number of $\mathrm{Re} = 100$. At two different rotation rates $\alpha = 4.96$ and $\alpha = 5.1$ single vortices with large shedding periods were observed. The analysis of pictures revealed that for α=4.96 there are four distinct vortices shed from the rotating cylinder. The calculated mean Strouhal number from the image sequences is 0.017. For the slightly higher rotation rate, α=5.1, the experiment showed three distinct vortices. The calculated mean Strouhal number in this case was 0.017. These Strouhal numbers are consistent with the numerical results that were obtained with the results that can be found in literature [1, 2, 3].

Based on the results and observations during the experiments, it can be concluded that those vortices actually proves the existence of Shedding Mode II. However, due to the large shedding period of the vortices and physical limitation of the towing tank, the analysis till so far is limited. A more quantitative analysis and detailed comparison with numerical results will be the topic of future study.

REFERENCES

1. Stojkovic, D., Schon, P., Breuer, M. and Durst, F., On the New vortex Shedding Mode Past a Rotating Circular Cylinder, *Physics of Fluid*., Vol. 15, No. 5, pp 1257-1260, 2003.
2. Mittal, S. and Kumar, B., Flow Past a Rotating Cylinder, *Journal of Fluid Mechanics*, Vol. 476, pp 303-334, 2003.
3. Elakoury, R., Martinat, G., Braza, M., Perrin, R., Hoarau, Y., Harran, G. and Ruiz, D., Succesive Steps of 2-D and 3-D Transition in the Flow Past a Rotating Cylinder at Moderate Reynolds Numbers, *Proceedings of IUTAM Symposium on Unsteady Separated Flows and Their Control*, Corfu, Greece, June 18-22, 2007.
4. Kieft, R.N., Rindt, C.C.M., van Steenhoven, A.A., and van Heist, G.J.F., On the Wake Structure behind a Heated Horizontal Cylinder in Cross-flow, *Journal of Fluid Mechanics*, Vol. 486, pp 189-211, 2003.
5. Maas, W., Rindt, C. and van Steenhoven, A., The Influence of Heat on the 3D-transition of the von Karman Vortex Street, *International Journal of Heat and Mass Transfer*, Vol. 16, No. 46, pp.3069–3081, 2003.
6. Williamson, C.H.K. and Brown, G.L., A Series in $1/\sqrt{\mathrm{Re}}$ to Represent the Strouhal-Reynolds Number Relationship of the Cylinder Wake, *Journal of Fluids and Structures*, Vol. 12, pp.1073–1085, 1998.
7. Fey, U., Konig, M. and Eckelmann, H., A new Strouhal-Reynolds Number Relationship for the Circular Cylinder in the Range $47<\mathrm{Re}<2\times10^5$, *Physics of Fluids*, Vol. 10, No. 7, pp.1547–1549, 1998.

PHASE DISTRIBUTION MEASUREMENTS BY CONDUCTANCE PROBES AND PRESSURE DROP IN GAS-LIQUID FLOWS

G.P. van der Meulen, M. Zangana, D. Zhao and B.J. Azzopardi*
Process and Environmental Engineering Research Division
Faculty of Engineering, University of Nottingham
University Park, Nottingham, NG7 2RD, United Kingdom.

ABSTRACT. The performance and accuracy of conductance probes, employed in phase distribution measurements in gas-liquid flow, was addressed. The conventional calibration method for annular-type flows was extended for a 127mm vertical pipe to allow for gas entrainment into the liquid film travelling at the pipe wall. Glass beads with different diameters were placed between the non-conductive insert and the pipe wall to simulate the gas bubbles entrained in the liquid film. Furthermore, an experimental campaign was executed in order to investigate the transition boundaries for two-phase air-water flow between churn and annular patterns in large diameter pipes. A direct relation between phase distribution and pressure drop was found. High fluctuations in the film thickness amplitude led to an increase in pressure drop. With an increasing gas superficial velocity, both film thickness and pressure drop decreased dramatically into the transition area. In this area features of flow-reversal were found. Approaching annular flow, both parameters decreased gradually.

Keywords: *gas-liquid flows, conductance probes, pressure drop, film thickness, measurement techniques.*

INTRODUCTION

Multiphase flows are encountered in the petroleum, power generation, chemical and process industries [1]. Given that the majority of studies in vertical gas-liquid flows are carried out in relatively small diameter tubes, the existing literature shows no common consensus with regard to phase distributions in large diameter pipes. For instance, the absence of typical slug flow in large diameter pipes has been reported [2-4]. In addition, other fundamental differences have also been observed. Wave mechanisms in vertical annular-type two phase for a large 125mm pipe diameter have been characterised [5]. This showed that the waves are circumferentially localized around the pipe periphery. In contrast, for small pipe diameters (32mm), the waves show a reasonable coherence [6]. Transitions between flow patterns is one of the complicated features in two phase flow, especially those between slug and churn to annular flow. Work was carried out in this particular area for small pipe diameter previously by some researchers. For instance, it was suggested that the transition to annular flow can be related to the superficial gas velocity at which flow-reversal takes place [7]. They also showed that the pressure gradient passes through a minimum as the gas velocity is reduced and therefore the liquid film thickness increases. The present study addresses vertical two-phase air-water flows in a large diameter (127mm) vertical pipe. An intensive experimental campaign was devised to understand the flow behaviour at the transition boundary from the annular to churn flow through analysing the time series of the measured liquid film thickness and pressure drop signals.

EXPERIMENTAL FACILITY

The experiments conducted in the present study are primarily carried out on a closed loop facility, containing a 127mm id, 11 m tall riser (Figure 1). Liquid is stored in the main separator and pumped into the riser base. The gas phase is compressed by two liquid ring vacuum pumps operated

* Corresponding author: B.J. Azzopardi
Phone: + (44) (0) 115 951 4160
E-mail address: barry.azzopardi@nottingham.ac.uk

in parallel and delivered to the riser base. The phases come together in the mixer and from this point the flow develops along the tall riser. The flow is then directed horizontally into the downcomer and back into the separator. Here the gas is separated from the liquid and the fluids are fed to the compressors and pump. The flow of both fluids can be regulated by valves and the flow rates monitored by flow meters. System pressure can be up to 5 barg. Gas and liquid superficial velocities of up to 17 m/s and 1.5 m/s, respectively, can be achieved. Temperatures and pressures are measured at various points throughout the experimental facility. The vertical pipe is equipped with a transparent acrylic resin section (Figure 1 Insert) wherein pressure drop and void fraction measurements are acquired and which is 11.8 pipe diameters long. The conductance probe rings, used for phase distribution measurements in the present study, are located at 62.7, 63.5 and 65.5 pipe diameters from the riser base, respectively. The stainless steel rings are flush mounted with the pipe wall. They were located using cylindrical dowels placed at either side of wall sections

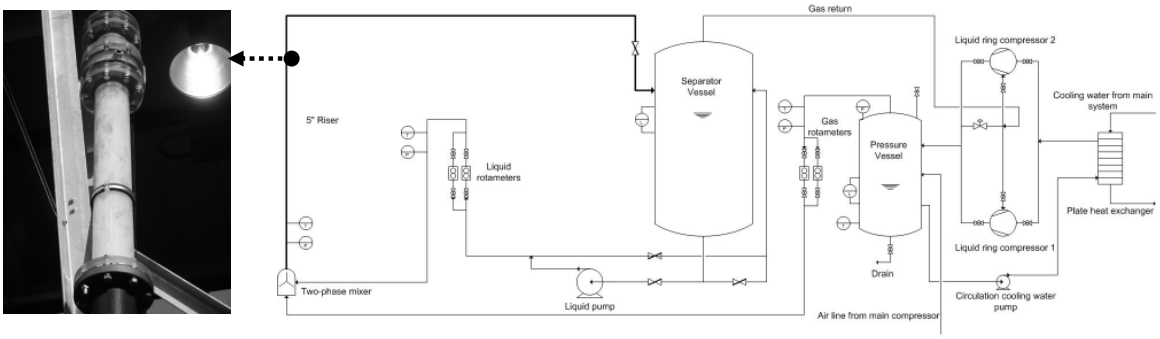

Figure 1. Closed loop facility. (Insert - Transparent Riser Section)

The thickness s of the rings is 3mm and the distance D_e between the probes is 25 mm, insulated by non-conducting acrylic resin. This is a electrode separation distance to pipe diameter ratio, D_e/D_t, of 0.20. The total, time averaged, pressure drop is being measured by an electronic differential pressure detector/transmitter (Rosemount 1151 smart model), with a range of 0- 37.4 kPa and an output voltage from 1 to 5 V, i.e. a resolution of 9.35 kPa per volt. Two pressure tappings, separated by an axial distance of 12.9 pipe diameters, across the transparent section, are connected to the differential pressure device via stainless steel tubes. The tubes were filled with water to keep the density constant. This was assured by an efficient purging procedure which eliminated the risk of gas fractions in the pressure lines. The latter procedure was repeated at the start of each set of the experiments. Data acquisition was performed through a PC equipped with a National Instrument (NI) DAQ card. An existing data acquisition programme in Labview [9] was adapted to convert the voltage output of the probes into a cross section averaged void fraction. The data acquisition rate was 1 kHz

CONDUCTANCE PROBE THEORY

In gas-liquid annular-type flow, the instantaneous wall film thickness can be determined by measurements of the electrical conductance between two electrodes in contact with the liquid film. Different types of electrodes such as parallel wires, flush-wires, flush-mounted pins and flush-mounted rings have been adopted [10,11,12,13,14,15,16,17,18]. Among these probes, the flush-mounted parallel ring probe is attractive to researchers because it provides non-intrusive measurements, can pick up small impedance and allows electric field to be efficiently confined. It was proposed that the apparent conductance K_{app} for two parallel strips embedded flush onto a flat surface can be defined as [19];

$$K_{app} = K^*_{app} L\gamma \tag{1}$$

with

$$K_{app}^{*} = \frac{k(m)}{k(1-m)} \tag{2}$$

and

$$m = \frac{\sinh^2(\pi s/2h)}{\sinh^2[\pi(s+De)/2h]} \tag{3}$$

Where, K_{app}^{*} is the dimensionless apparent conductance, L electrode length, s electrode width, γ liquid conductivity h liquid film thickness and Function k the complete elliptic integral of the first kind,

$$k(m) = \int_0^{\pi/2} \left(1 - m\sin^2\theta\right)^{-0.5} d\theta \tag{4}$$

Furthermore, it was proposed that the conductance of annular liquid film can be quantified by above equations by replacing h to a liquid equivalent thickness h_E [19].

$$h_E = -\frac{D}{D_E}\ln(1-2h/D) \tag{5}$$

h_E can also be defined as $h_E = A_L / P_L$ [16], where A_L is the cross-sectional area occupied by liquid and P_L the wetted length of electrode for the application of the annular and stratified flow [19]. The analytical solution to the apparent conductance of the ring probe is according [17],

$$K_{app}^{*} = \frac{\pi^3}{32}\left(\frac{2s}{L}\right)^2\left[\sum_{i=0}^{\infty}(2i+1)^{-3} b_i^2 f_i\right] \tag{6}$$

With

$$b_i = \cos[(De+s)\theta] - \cos[(De-s)\theta] \tag{7}$$

and f_i is the product of modified Bessel functions I_0, I_1, K_0, K_1,

$$f_i = \frac{I_0(D\theta)}{I_1(D\theta)}\left[\frac{1+\dfrac{I_1[(D-2h)\theta]K_0(D\theta)}{K_1[(D-2h)\theta]I_0(D\theta)}}{1-\dfrac{I_1[(D-2h)\theta]K_1(D\theta)}{K_1[(D-2h)\theta]I_1(D\theta)}}\right] \tag{8}$$

Where

$$\theta = \frac{(2i+1)\pi}{2L} \tag{9}$$

A different expression for b_i was adopted by [18],

$$b_i = \cos[(De-2s)\theta] - \cos[(De)\theta] \tag{10}$$

CONVENTIONAL CONDUCTANCE PROBE CALIBRATION

The unique resistive characteristics of the individual conductance probes need to be identified. When the probe pair is subject to an electrical current, the relationship between the dimensionless resistivity E of the probe ring and its voltage output V_{out} should be linear in the form of;

$$E = aV_{out} + b \tag{11}$$

Gradients a and b can be obtained from this relationship. The resistance R_x of the two phase flow is being simulated by a variable resistor in between each of the probe pairs. Hence, the probe resistance R_{probe} is the product of the applied voltage V_{app}, the voltage measured subject to the applied variable resistor V_x and R_{ref}, the internal circuit variable resistance, by using;

$$R_{probe} = \frac{V_x}{(V_{app} - V_x)} R_{ref} \tag{12}$$

By plotting the expression;

$$E^{*} = \frac{(R_x/R_{ref} - 1)}{(R_x/R_{ref} + 1)} \tag{13}$$

against V_{out} , Equation 11 was deduced. The regression data for the relationship was $a = 3.21$, $b = 0.042$ and $R^2 = 0.99$. Equation 11 can then be substituted into the expression for the dimensionless conductance G_e^* of the two phase flow

$$G_e^* = \frac{(1+E_{full})/(1-E_{full})}{(1+E_{TP})/(1-E_{TP})} \tag{14}$$

In which E_{full} is the dimensionless resistance for the flow domain fully occupied by liquid ($\varepsilon_l = 1$) and E_{TP} the dimensionless resistance for two-phase flow. Ultimately, by decreasing the diameter of the insert and subsequently repetition of a significant number of calibration steps, one can relate the phase distribution at each probe to the dimensionless conductance. The relationship of the calibration curve can be mathematically expressed in the form;

$$\varepsilon_l = c(G_e^*)^3 + b(G_e^*)^2 + a(G_e^*) + d \tag{15}$$

NEW APPROACH TO CONDUCTANCE PROBE CALIBRATION

The conductance probes need calibration before it can be employed for measurements. Annular-type flow is usually simulated by placing a non-conductive rod inside the pipe and the conductive liquid is filled in the annulus between the rod and pipe wall. This is an "ideal" situation that no bubbles exist in the liquid film. In contrast, in gas-liquid annular-type flow, the continuous trapping and folding actions of the disturbance waves transport gas bubbles into the liquid film. The presence of a considerable amount of bubbles in the liquid film was reported in air/water horizontal and vertical annular-type flow systems [20,21,4]. More recently, the bubble size distribution, bubble mean diameter and bubble number concentration in the wall film of a horizontal annular flow in a pipe of 15.1 mm diameter was quantified [22]. Bubble size has an exponential distribution with the average of diameters between 15% and 45% of the film thickness at the gas superficial velocity ranging from 28 to 65 m/s and the liquid superficial velocity from 0.019 m/s to 0.14 m/s. Around 100 bubbles/cm^2 exist in the wall film at the gas superficial velocity 28 m/s. Therefore, a new approach for probe calibration was devised. In order to simulate gas bubbles in the liquid film during annular-type flows, packing of spherical glass beads was used. While the diameter of the insert decreased with calibration steps, beads with a larger diameter were used to occupy a fraction of the annulus between the insert and pipe wall. The diameter of beads used was 3, 4 and 6mm. The procedure, carried out off-line, of calibration was performed according the following steps; (1) a conventional void fraction measurement was first done with the single insert only; (2) the test section was then emptied, dried and the insert re-installed; (3) a known theoretical volumetric amount of beads were added to the annulus; (4) in order to verify the theoretical bead voidage, the height of beads in the annulus was returned to a water volume. The annulus was then filled with water until the level of water was equal to the level of beads. The water left was then weighted and the in situ bead voidage calculated (5) a void fraction measurement was then performed. The difference between the void fraction measured with the single insert and the single insert-beads combination was verified by repeating the calibration with an additional cylindrical insert which represented a volumetric fraction equal to the sum of the initial insert-beads combination. (6) the final step in the calibration procedure, for one particular single insert diameter, single insert-bead combination and the additional insert, was taken the void fraction measurement of the latter. Annular flow calibration data obtained from the 127mm pipe was plotted and comparison was made between a theoretical 70mm flow arrangement, solved by using the model derived by [17]. In addition, also other models proposed were solved and plotted for the 127mm pipe [17,18,19]. The results are shown in Figure 2. The data obtained with the new calibration approach shows deviations from the initial calibration points by using the single insert for ideal annular-type flows. The error was determined using Equation 15. This returned the void fraction as theoretically responded by the probes according the calibration curve and thus for an "ideal" annular-type flow regime. These results were plotted against

the experimental G_e^* obtained during calibration with single insert-bead combination. Figure 3 shows the absolute error. It can be noted that this not directly explains the effect of bead diameter. Therefore the relative error between the bead diameters was determined, shown by Table 1.

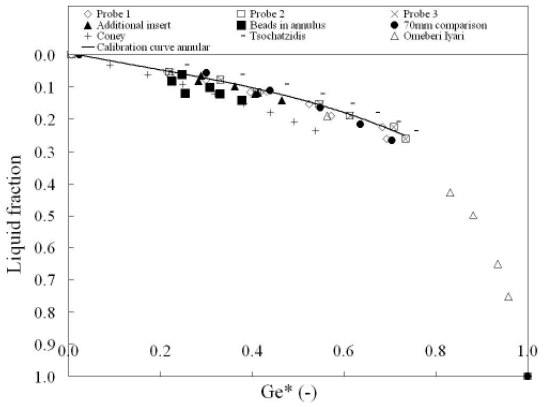

Figure 2. Annular flow calibration curve

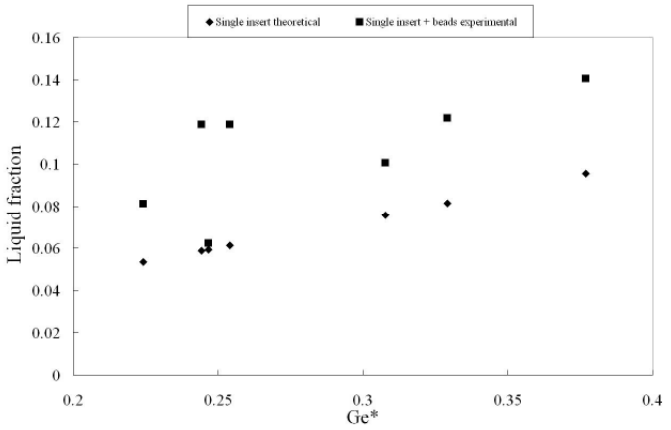

Figure 3. Error between calibration procedures.

Table 1. Relative error between beads

Bead diameter (mm)	Change in bead voidage (%)	Change in Error (%)
3	20	624.9
4	23.2	48.8
6	12.9	3.5

RESULTS AND DISCUSSION

Experiments were carried out at two liquid superficial velocities of 0.014 and 0.04 m/s and gas superficial velocities from 3.8 to 15.8 m/s. The system pressure was set at 2 barg. Figures 4 and 5 show how the film thickness and pressure drop vary with gas superficial velocity.

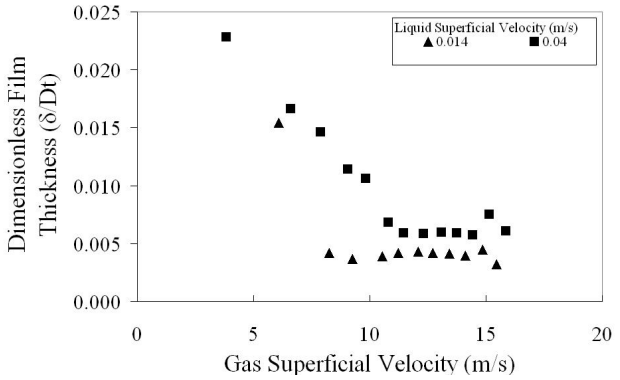

Figure 4. Dimensionless film thickness as function of superficial gas velocity.

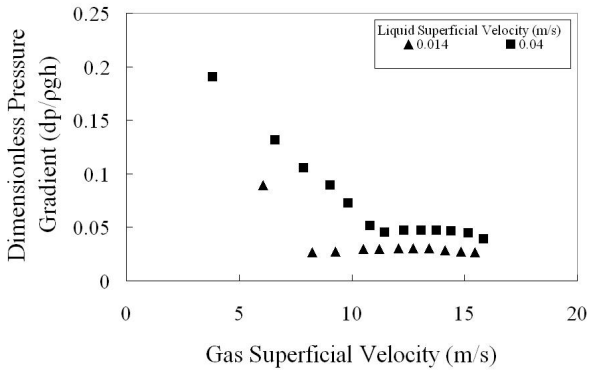

Figure 5. Dimensionless pressure gradient as function of superficial gas velocity.

From Figures 4 and 5 it is apparent that there is a very obvious and systematic effect of the superficial gas velocity on the film thickness and the pressure drop. There is a steep decrease of both film thickness and pressure drop over gas velocities of 3.82 to 10.86 m/s and from 6.07 to 8.25 m/s for liquid superficial velocities of 0.04 and 0.014 m/s respectively. At higher gas superficial velocities there is a gradual increase. It is suggested that the change of slope is linked to a transition of flow pattern from churn to annular flow. In contrast to the smaller diameter cases [7], the pressure gradient in annular flow for this larger pipe increases only slowly with gas velocity. Therefore the expected minimum is not very clear. Further statistical analysis of the data was carried out for both the film thickness and pressure drop at a liquid superficial velocity of 0.04 m/s. Three regions of Figures 4 and 5 were of particular interest. These are tentatively identified as being from: the churn flow area, the transition area and the annular flow area. The gas superficial

velocities are 6.6, 10.8 and 15.8 m/s respectively. The analysis employed Probability Density Function, autocorrelation/Power Spectral Density (for most probable frequency) and cross correlation (for time delay and thence structure velocity). The results are shown in Figure 6 and 7. The time series of the film thickness in the churn flow area show clearly the presence of waves, these are believed to result in the larger pressure gradient. However, the waves decrease in amplitude with increasing gas superficial velocity, with correspondingly lower pressure gradient as can be seen from the time series of pressure drop in the annular flow area. The Power Spectral Density curves all show clear peaks which occur in both the film thickness and pressure gradient data with the frequencies at which those peaks occur having equivalent values for both signals. In addition, cross correlation was performed between two successive conductance probe signals. The distance between the first and the third conductance probe is 2.8 pipe diameters. As can be seen from Figure 6, the majority of the time lag for the churn flow area and annular flow area is positive. However, for the transition area, the time lag shows a peak with a negative value. This indicates that at the transition from churn to annular flow in the present study, there are waves which move up and those which move down.

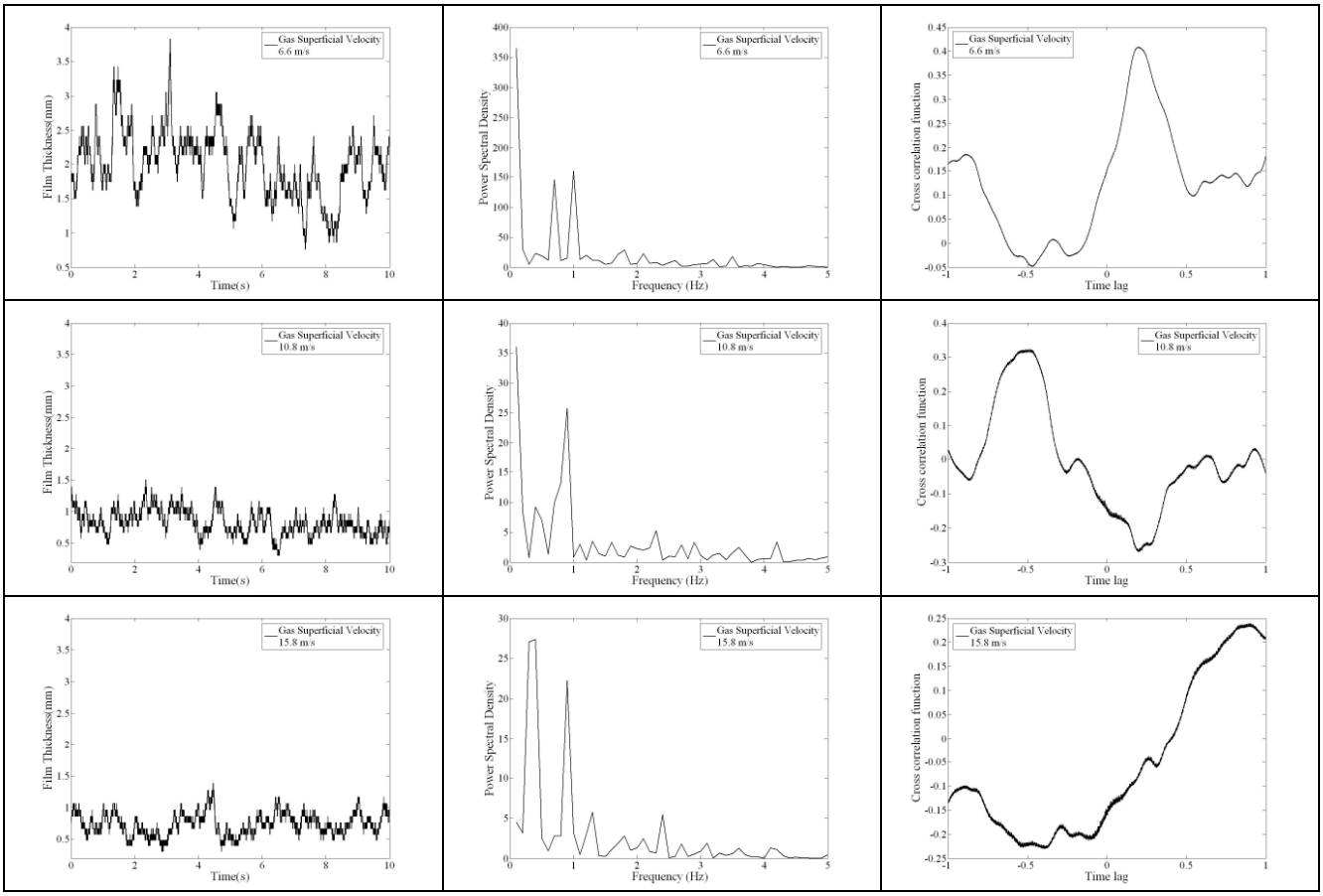

Figure 6. Film thickness time series, Power Spectral Density (PSD) and cross correlation .

CONCLUSION

The results of the present study show that the calibration of conductance ring probes needs to be approached carefully. The performance and accuracy of these probe types is strongly dependant on the calibration procedures. In churn and annular-type gas-liquid flows one may encounter gas bubbles entrained in the liquid film, particularly in the waves. The comparison between the new approaches suggested in the present study for the calibration of conductance probes in annular-type flows to the conventional method shows that the gas bubbles entrained in the liquid film can cause erroneous results. The inappropriate calibration of the conductance probes can lead to an unrealistic view of the phase distributions in annular-type flow and the transition to churn flow. Simultaneous

phase distribution measurements and visual observation (e.g. high speed photography) may therefore reduce the risk of experimental errors. However, it may be concluded that conductance probes, calibrated for a specific flow regime, are producing invalid results when used otherwise. The current experimental results of liquid film thickness and pressure drop show that there are similar trends for each. At lower gas superficial velocity there are larger liquid fractions and the pressure drop decreases significantly. This feature may therefore be directly related to the amplitude of the liquid film thickness and thus the existence of disturbance waves. Three important features in the film thickness and pressure drop can be noted; (1) there is a relatively large shift in the transition region between the two liquid conditions; (2) after a dramatic decrease of pressure drop, there is not a very clear minimum in the pressure drop, as previously reported by various workers for smaller pipe diameters; (3) in the transition region between churn and annular flow, as evidenced by the negative structure velocity obtained from cross correlation, flow reversal is occurring.

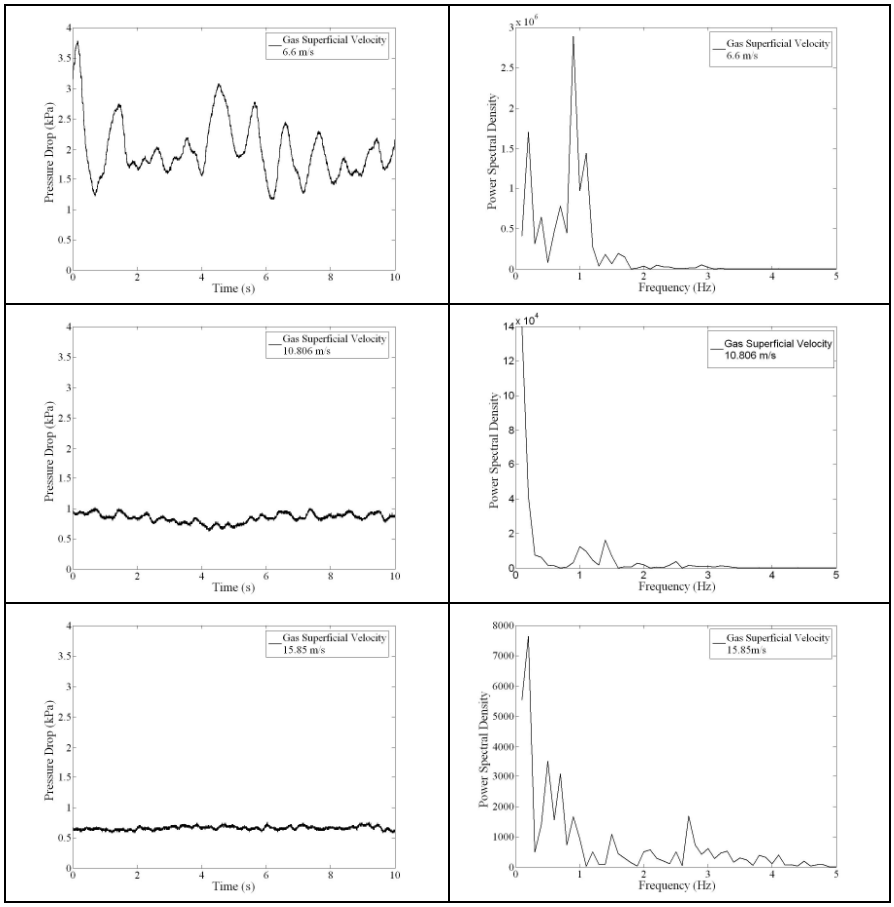

Figure 7 Pressure drop time series and Power Spectral Density (PSD).

ACKNOWLEDGEMENT

This work has been undertaken within the Joint Project on Transient Multiphase Flows and Flow Assurance. The Authors wish to acknowledge the contributions made to this project by the UK Engineering and Physical Sciences Research Council (EPSRC) and the following: - Advantica; BP Exploration; CD-adapco; Chevron; ConocoPhillips; ENI; ExxonMobil; FEESA; IFP; Institutt for Energiteknikk; Norsk Hydro; PDVSA (INTERVEP); Petrobras; PETRONAS; Scandpower PT; Shell; SINTEF; Statoil and TOTAL. The Authors wish to express their sincere gratitude for this support. The Ministry of Higher Education in the Kurdistan Regional Government and Koya University are highly acknowledged for their contribution to PhD candidate M. Zangana.

REFERENCES

1. Shoham, O., Mechanistic Modeling of Gas-Liquid Two-Phase Flow in Pipes, ISBN 978-1-55563-107-9, Society of Petroleum Engineers, USA. 2006.
2. Cheng.H, Hills, .J.H. and Azzopardi.B.J A study of the bubble to slug transition in vertical gas liquid flow in columns of different diameter. Int.J.Multiphase Flow ,vol. 24, No, 3, pp.431-452. 1998.
3. Ohnuki, A. and Akimoto, H. Experimental study on transition of flow pattern and phase distribution in upward air water two phase flow along a large vertical pipe. Int. J. Multiphase Flow, vol 26, pp367-386. 2000.
4. Omebere-Iyari, N.K., The effect of pipe diameter and pressure in vertical two-phase flow, PhD Thesis, University of Nottingham, UK. 2006.
5. Azzopardi, B.J.,Taylor S.,and Gibbons, D.B. Annular two phase flow in a large diameter tube.,Int. conference on the physical modeling of multiphase flow, Coventry, UK. 1983.
6. Hewitt, G.F. and Lovergrove, P.C. Frequency and velocity measurements of disturbance waves in annular two-phase flow. UKAEA Report AERE R4304. 1969.
7. Hewitt G.F.,Lacy P.M.C.,Nicholls B. Transition in film flow in a vertical tube symposium on two phase flow, Exeter, 2 pp. B401-B429. 1965.
8. Azzopardi, B.J. Drops in annular two-phase flow, Int J Multiphase Flow 23, pp.1-53. 1997.
9. Guglielmini, G. Carratterizzazione sperimentale del moto bifase intermittente in presenza di singolarita mediante sonde ad impedenza, Laurea Thesis, Universita degli studi di Genova, Italia. 2002.
10. Miya, M., Woodmansee, D. E. and Hanratty, T. J. A model for roll waves in gas-liquid flows, Chem. Eng. Sci., 26, 1915-1931. 1971.
11. Brown, R.C., Andreussi P. and Zanelli, S. The use of wire probes for the measurement of liquid thickness in annular gas-liquid flows. Can J Chem Eng 56, 754–757. 1978.
12. Koskie, J.E., Mudawar,I. and Tiederman, W.G. Parallel wire probes for measurements of thick liquid films. Int J Multiphase Flow 15, 521–530. 1989.
13. Kang H. C. and Kim, M. H. The development of a flush-wire probe and calibration method for measuring liquid film thickness, Int. J. Multiphase Flow 18, 423-437.1992
14. Conte, G., Azzopardi, B.J. Film thickness variation about a T-junction, International Journal of Multiphase Flow 29, 305–328. 2003
15. Asali, J. C. and Hanratty, T. J. Interfacial drag and film height for vertical annular flow. AIChE J. 31 895–902. 1985.
16. Andreussi, P. Di Donfrancesco, A.and Messia, M.. An impedance method for the measurement of liquid hold-up in two phase flow. Int J Multiphase Flow 14 777–785. 1988.
17. Tsochatzidis, N. A., Karapantsios, T. D., Kostoglou, M. V. and Karabelas, A. J. A conductivity probe for measuring liquid fraction in pipes and packed beds. Int. J. Multiphase Flow 18 653–67. 1992.
18. Fossa, M. Design and performance of a conductivity probe for measuring the liquid fraction in two-phase gas–liquid flows. Flow Meas. Instrum. 9 103–109. 1998.
19. Coney, M.W.E. The theory and application of conductance probes for the measurement of liquid film thickness in two-phase flow. J. Phys. E: Scient. Instrum. 6: 903-10. 1973.
20. Jacowitz, L.A., Brodkey R.S. An analysis of geometry and pressure drop for the horizontal, annular, two-phase flow of water and air in the entrance region of a pipe. Chem. Eng. Sci. 19, 261–274. 1964.
21. Hewitt, G.F., Jayanti, S., Hope, C.B. Structure of thin liquid films in gas–liquid horizontal flow. Int. J. Multiphase Flow 16, 951–957. 1990.
22. Rodriguez, D. J. and Shedd, T. A. Entrainment of gas in the liquid film of horizontal annular, two-phase flow, International Journal of Multiphase Flow, 30, 565–583. 2004.

PARTICLE- AND FLUID-LIKE BEHAVIORS ON SEDIMENTATION OF A STRATIFIED SUSPENSION

K. Sato[1*], T. Mitsui[1], S. Harada[1,]
[1]Hokkaido University, Sapporo, Japan

ABSTRACT. The sedimentation of partially suspended particles in fluid is studied experimentally. The settling behavior of particles in a stratified suspension, which has both the upper and lower interfaces, is observed in various conditions. We examine whether the macroscopic or the microscopic natures of suspension is dominant during sedimentation, *i.e.*, whether the particles settle as a particle assembly relative to surrounding fluid or as a continuous suspension. The experimental observation shows that the gravity-induced instability of suspension-fluid interface governs the particle motion for high concentration and small particle size. However, the microscopic nature of suspension comes out in case of large particles with low concentration. In this study, the dependency of sedimentation behavior of stratified suspension on concentration and constituent particle size is discussed quantitatively.

Keywords: *Sedimentation, Suspension, Rayleigh-Taylor Instability, Linear Stability Analysis*

INTRODUCTION

Sedimentation of suspended particles in liquid is an important phenomenon in the field of environmental, chemical and material engineering and is related to various processes such as coating, accumulation, separation, filtration of particulate materials. It is already known that the mean settling velocity of particles in a stationary fluid changes with concentration due to their hydrodynamic interactions [1]. The hydrodynamic interaction of suspended particles affects not only the mean settling velocity but also their relative motions. The resultant fluctuating motion brings about the diffusion of settling particles, which is called hydrodynamic diffusion [2]-[8]. Generally, the hydrodynamic interactions between particles are long-ranged under conditions of low particle Reynolds number, since the disturbed flow by the motion of individual particles decays inversely proportional to the interparticle distance [9]. Consequently it is more influential with the settling motion of fine particles in viscous fluid.

The relative motion of particle in suspensions is also caused by macroscopic hydrodynamic effect. In case of sedimentation of homogeneous suspensions, the variation of the concentration evolves almost one-dimensionally in the vertical direction [10]. On the other hand, if the suspension is not uniform and the positive concentration gradient exists against gravity, the lateral variation of concentration will develop during the sedimentation [11]-[15]. This lateral variation of concentration is similar to the gravity-induced instability of pure fluid and can be explained from the viewpoint of continuous fluid.

The purpose of this study is to investigate the hydrodynamic effect on the sedimentation of inhomogeneous suspension. We have investigated the settling of a stratified suspension which has both the upper and lower interfaces of concentration in quasi-two dimensional vessel. We observed the settling behavior of particles in the suspension and measured the settling velocity of particles

Corresponding author: K. Sato
Phone/Fax: + (81)-11-7066310
E-mail address: kodai@trans-er.eng.hokudai.ac.jp

near the interfaces. Especially we examine the effect of constituent particle size on the sedimenting suspension in order to know whether the macroscopic or the microscopic natures of suspension is dominant during sedimentation, *i.e.*, the particles settle as a particle assembly relative to surrounding fluid or as a continuous suspension.

EXPERIMENTAL SETUP

Figure 1 shows the schematic diagram of the experimental apparatus. The test cell is quasi-two dimensional vessel with a height L =240mm, a width W =100mm. The vessel depth D is adjustable from 3mm to 12mm. In order to stratify the suspension, we used two slits in back side of vessel so as to put stainless steel blades into them. The thickness of the blade is 0.5mm and the distance between two blades L_s is 19.5mm. The blades divide the test cell into three parts in vertical direction. The lower blade separates the lower pure fluid and suspension, while the upper blade separates the upper fluid-suspension. Therefore the distance between blades L_s corresponds to the initial height of the stratified suspension.

The procedure of our experiment is as follows. At first pure fluid is filled into the lower part of the vessel and then the lower part is closed by the lower blade. Next the suspension is poured into the vessel above the lower blade until the surface reaches the position of the upper blade. Finally the upper blade is put into the vessel and the pure fluid is filled above it. Consequently, stratified suspension is held between the two blades. After these settings, the blades are removed backward simultaneously. The settling behavior of the suspended particles by gravity is recorded by a digital video camera. The suspension contains silicone oil and glass particles with diameter in d_p=30μm and 100μm or polystyrene particles in d_p=550μm and 800μm. Mass density of glass and polystyrene are ρ_p=2500 kg/m^3 and 1050 kg/m^3, respectively. The suspension is mixed by stirring for several hours and is deaerated well in constant temperature (22±1C˚). The silicone oil which has the different property (density ρ_f=970–972 kg/m^3, viscosity μ_f = 971–1944 mPa·s) is used for making suspension. The pure fluid which is used to fill the upper and lower part of the vessel has the same property as the suspension. Therefore the initial condition can be interpreted as *partially suspended particles in a static pure fluid*.

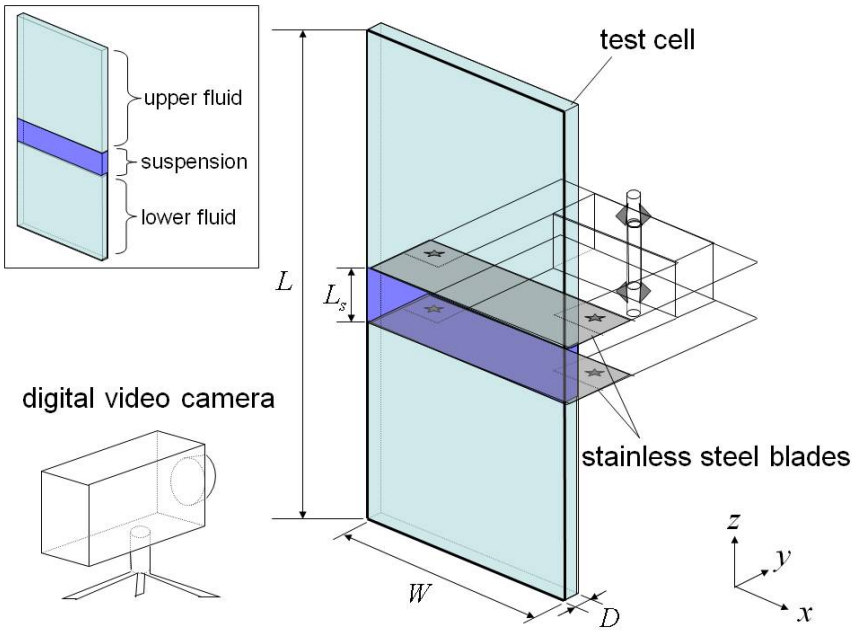

Figure 1. Schematic diagram of experimental system

LINEAR STABILITY ANALYSIS

When two immiscible fluids are separated by a horizontal boundary with positive density gradient in the vertical direction, it is known that the gravity-induced instability occurs at the interface (Rayleigh-Taylor instability). Rayleigh-Taylor instability is caused by the balance between gravity force and interfacial tension, and is influenced by density and viscosity of both fluids. In case of two inviscid fluids, the condition for instability is as follows [16];

$$gk\left[\frac{\overline{\rho}_2-\overline{\rho}_1}{\overline{\rho}_2+\overline{\rho}_1}-\frac{k^2T}{g\left(\overline{\rho}_2+\overline{\rho}_1\right)}\right]>0\,, \tag{1}$$

where $\overline{\rho}_1$ and $\overline{\rho}_2$ are the density of the lower and the upper fluid, k is the wave number of the disturbance and T is the coefficient of interfacial tension. In case of viscous fluids, the equation of instability condition is more complicated and is a function of the viscosity $\overline{\mu}_1$ and $\overline{\mu}_2$.

The similar gravity-induced instability can be observed at the suspension-fluid boundary even though there is no distinct interface between them. Völtz *et al.* [11-13] has been studied systematically the sedimentation of suspension in a vessel which has narrow width. They reported that the instability of a suspension-fluid interface could be predicted from a similar analysis to immiscible viscous fluids on the assumption that the suspension is pure fluid having apparent density ρ_s and viscosity μ_s as;

$$\rho_s=(1-\phi)\rho_f+\phi\rho_p\,, \tag{2}$$

$$\mu_s=(1+2.5\phi)\mu_f\,, \tag{3}$$

where ϕ is the concentration of suspended particles. Equation (3) is known as Einstein's apparent viscosity.

In order to understand the macroscopic nature of sedimenting suspension, we examine Rayleigh-Taylor instability of two viscous fluids in quasi-two dimensional vessel by linear stability analysis. Since most part of analytical procedure is similar to the well-known linear analysis of hydrodynamic stability [16], the different point from three dimensional analysis is described here. On the assumption that the vessel has narrow depth, the velocity in y direction is set to zero and the velocity and density fluctuation has parabolic Poiseuille profiles [12,17].

$$u_i(x,y,z,t)=\hat{u}_i(z)\exp(ikx+nt)\zeta(y)\,, \tag{4}$$

$$\rho(x,y,z,t)=\overline{\rho}(z)+\hat{\rho}(z)\exp(ikx+nt)\zeta(y)\,, \tag{5}$$

where k is the wave number of disturbance in x direction, n is the growth rate of disturbance, and $\zeta(y)$ indicates a parabolic function in y direction defined by

$$\zeta(y)=\frac{6}{D^2}\left(\frac{D^2}{4}-y^2\right), \tag{6}$$

where D is the vessel depth. Substituting equations (4) and (5) to Stokes equation and continuity equation for viscous fluid and averaging over y direction, we finally obtain the relationship between the wave number k and the growth rate n

$$\begin{aligned}&-\left[\frac{gk}{n^2}(\alpha_1-\alpha_2)+\beta_1+\beta_2\right]\left[\beta_2q_1+\beta_1q_2-k(\beta_1+\beta_2)\right]-4k\beta_1\beta_2\\&\quad+\frac{4k^2}{n}(\alpha_1\overline{\nu}_1-\alpha_2\overline{\nu}_2)\left[\beta_2q_1-\beta_1q_2+k(\beta_1-\beta_2)\right]+\frac{4k^3}{n^2}(\alpha_1\overline{\nu}_1-\alpha_2\overline{\nu}_2)^2(q_1-k)(q_2-k)=0,\end{aligned} \tag{7}$$

where $\bar{\nu}$ is kinematic viscosity ($=\bar{\mu}/\bar{\rho}$) and subscripts 1 and 2 indicate the lower and the upper fluid respectively. α, β and q are defined as follows;

$$\alpha_1 = \frac{\bar{\rho}_1}{\bar{\rho}_1 + \bar{\rho}_2}, \qquad \alpha_2 = \frac{\bar{\rho}_2}{\bar{\rho}_1 + \bar{\rho}_2}, \qquad \beta_1 = \alpha_1\left(1 + \frac{\bar{\nu}_1\eta}{n}\right), \qquad \beta_2 = \alpha_2\left(1 + \frac{\bar{\nu}_2\eta}{n}\right),$$

$$q_1 = \sqrt{\frac{n}{\bar{\nu}_1} + k^2 + \eta}, \qquad q_2 = \sqrt{\frac{n}{\bar{\nu}_2} + k^2 + \eta},$$

where $\eta = \partial^2\zeta/\partial y^2 = 12/D^2$.

For stratified suspension, we set $\bar{\rho}_1$, $\bar{\nu}_1$ (lower fluid) to properties of pure fluid ρ_f, ν_f and set $\bar{\rho}_2, \bar{\nu}_2$ (upper fluid) to apparent properties of suspension ρ_s, ν_s which are defined by equations (2) and (3).

RESULTS AND DISCUSSION

Sedimentation behaviour of suspension

Figure 2 shows the observation results of settling behavior of suspension with different particle and fluid. As described in Table 1, We changed the particle density ρ_p, diameter d_p, concentration ϕ, fluid viscosity μ_f and vessel depth D. The Stokes settling velocity for a single particle $U_0 = (\rho_p - \rho_f)gd_p^2/18\mu_f$ is also shown in the Table 1. The corresponding particle Reynolds number $Re_p = \rho_f U_0 d_p/\mu_f$ is less than 0.01 for all conditions.

As shown in Figure 2, while the suspension keeps its upper interface almost flat, a perturbation of the lower interface develops. The flat upper interfaces are due to a self-sharpening effect which results from the dependency of the settling velocity on the local particle concentration [10]. The instability at the lower interface is obviously the gravity-induced instability described in the previous section. For small particles and dense concentration (Figure 2a), the suspension behaves like immiscible fluid, and therefore finger-like perturbation (finger) can be found clearly. It should be emphasized again that the system considered here is *partially suspended particles in a static pure fluid* because the suspension is made of the same fluid as the upper and lower ones. Therefore there is no defined border between the suspension and the fluid. Here we call this settling behavior as *fluid-like settling* of suspension.

On the other hand, in case of large particle and dilute concentration (Figure 2c), the suspended particles seem to settle individually. For hindered settling of particle in fluid, it is known that the mean velocity of the particles is expressed as $f(\phi)U_0$, where $f(\phi)$ is a decreasing function of the particle volumetric ratio. A well-known empirical relation for $f(\phi)$ is as follows;

$$f(\phi) = (1-\phi)^n, \tag{8}$$

where n is a constant and is generally 5 to 5.5 [1]. Another factor of the settling velocity is the wall effect. The settling velocity of particle is influenced by the presence of the wall and, for our experimental condition, it decreases around ten percent of the Stokes velocity [9]. At all events, if we consider that the particle settles individually, the settling velocity will be the same order of magnitude as the Stokes settling velocity U_0. We call this kind of settling behavior as *particle-like settling*.

Table 1
Physical properties of particle and fluid

	ρ_p (kg/m^3)	d_p (μm)	ϕ	μ_f (mPa·s)	D (mm)	U_0 (mm/s)
(a) glass particle	2500	30	0.03	1944	8	3.85×10^{-4}
(b) polystyrene particle	1050	550	0.1	971	8	1.34×10^{-2}
(c) polystyrene particle	1050	800	0.01	1944	12	1.40×10^{-2}

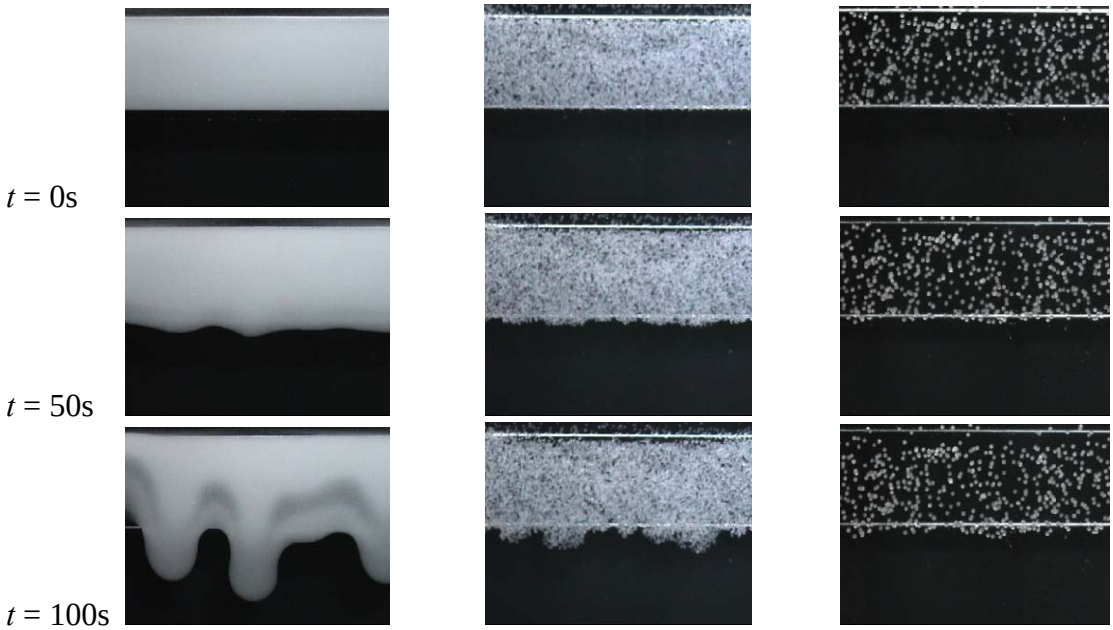

(a) d_p=30μm, ϕ=0.03, D=8mm (b) d_p=550μm, ϕ=0.1, D=8mm (c) d_p=800μm, ϕ=0.01, D=12mm

Figure 2. Settling behaviors of stratified suspension

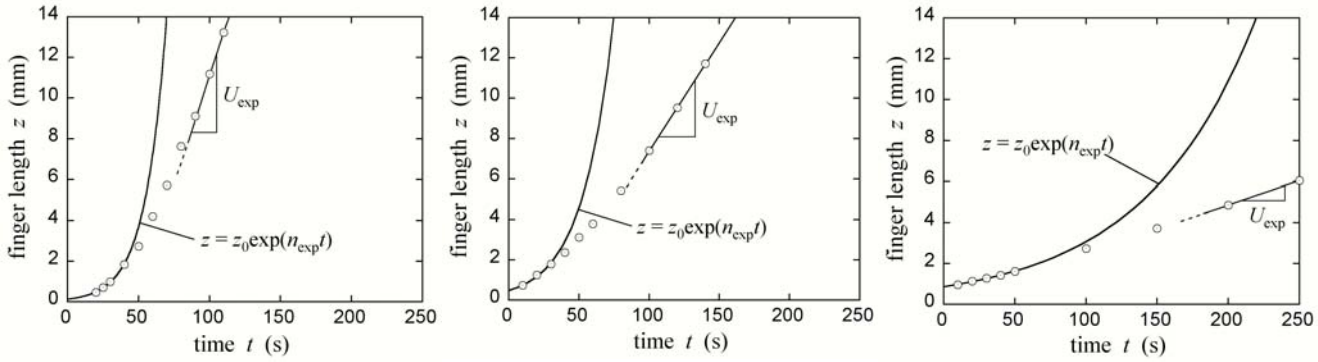

(a) d_p=30μm, ϕ=0.03, D=8mm (b) d_p=550μm, ϕ=0.1, D=8mm (c) d_p=800μm, ϕ=0.01, D=12mm

Figure 3. Change in average length of fingers with time

Figure 3 shows the change in the average length of fingers with time. For all conditions, the fingers grow exponentially at the beginning and then their growth speed becomes constant. The exponential growth of fingers can be seen in the Rayleigh-Taylor instability of immiscible fluids and the finger length z can be calculated by linear stability analysis as the following form,

$$z = z_0 \exp(nt), \tag{9}$$

where n is the growth rate. We define two experimental values which express the settling speed of particles. As shown in Figure 3, we calculated the exponential growth rate n_{exp} and the succeeding settling velocity U_{exp} from experimental results.

If the suspension behavior is perfectly fluid-like, the experimental growth rate n_{exp} will be close to the growth rate calculated by linear stability analysis n_{theo}. On the other hand, if the suspension behavior is perfectly particle-like, the change in the finger length with time will become almost linear and the succeeding growth velocity U_{exp} will be the same order of magnitude as the Stokes settling velocity U_0. Comparing the experimental results from this point of view, we finally found the settling velocity U_{exp} of condition (a) is the largest although it has the smallest Stokes velocity (see Table 1). The detailed comparisons of these values are given later.

Instabilities on Fluid-like Settling of Suspension

In order to understand the fluid-like settling of suspension, the experimental results for small particle are compared to the theoretical results for immiscible fluids. Figure 4 shows the results of the growth rate n for given wave number k calculated by equation 7 under the experimental conditions of d_p = 30μm, ϕ = 0.03, μ_f =1944mPa·s. We set $\overline{\rho}_1$, $\overline{\nu}_1$ (lower fluid) to properties of pure fluid ρ_f, ν_f and set $\overline{\rho}_2$, $\overline{\nu}_2$ (upper fluid) to apparent properties of suspension ρ_s, ν_s which are defined by equations (2) and (3). The theoretical analysis shows that the growth rate of disturbance is larger for larger vessel depth D and the wave number of maximum growth of disturbance k_{max} also depends on D.

Figure 4 (a)-(c) are the experimental pictures for same conditions as theoretical analysis. It is found that the width of finger is larger for larger vessel depth D. Yellow line in each picture indicates the wave length of maximum growth of disturbance λ (=$2\pi/k_{max}$) predicted by theoretical results. They are in quantitative agreement with wave length of disturbance (finger width) observed in experiment. Such perfectly fluid-like behaviors of suspension have been studied by Völtz *et al.* [11-13]. The main purpose of our study is investigating the transition from fluid-like settling to particle-like settling of suspension as explained below.

Transition from Fluid-like to Particle-like Settling

We consider the parameter which describes the transition from fluid-like to particle-like settling of suspension as shown in Figure 2. The parameter would be a function of particle density ρ_p, particle diameter d_p, liquid density ρ_f, liquid viscosity μ_f, particle concentration ϕ and vessel depth D. We propose a new dimensionless parameter $H = H(\rho_p, d_p, \rho_f, \mu_f, \phi, D)$ as follows:

$$H = \frac{l}{\lambda} \tag{10}$$

where l is average distance between particles in suspension and is function of d_p and ϕ. $\lambda = \lambda(\phi, \rho_p, \rho_f, \mu_f, D)$ is the wave length of interfacial perturbation (finger) which can be obtained from the linear stability analysis.

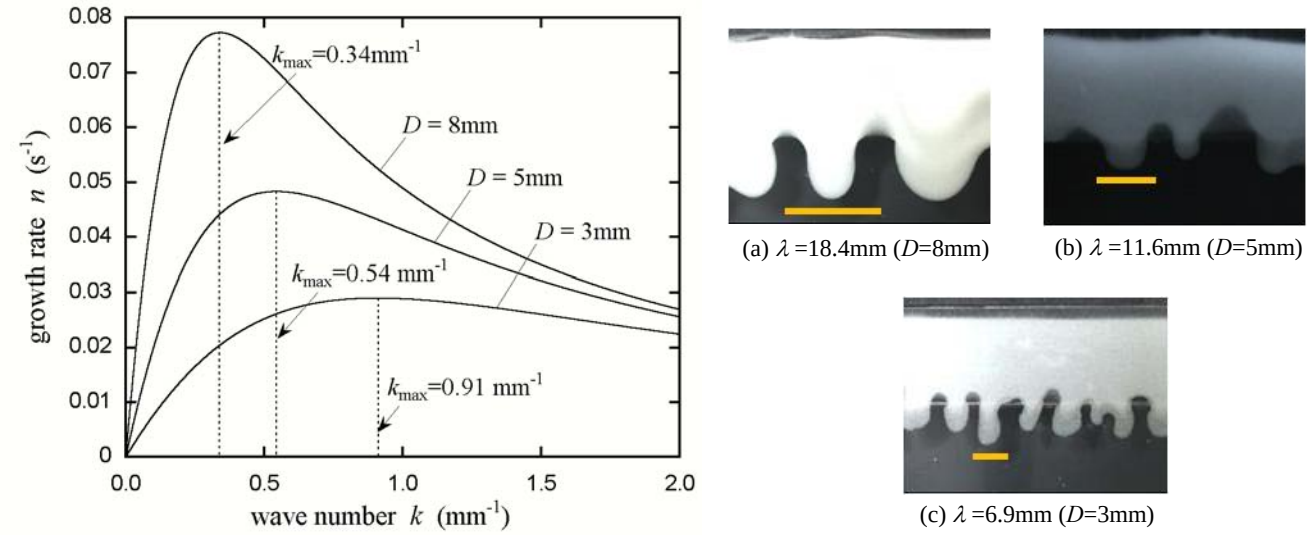

Figure 4. Maximum wave number k_{max} calculated by linear stability analysis and corresponding wave length $\lambda = 2\pi/k_{max}$ for glass particle suspension (d_p = 30μm, ϕ = 0.03, μ_f =1944mPa·s)

Figure 5 indicates the physical meaning of equation (10). It can be found that the parameter H expresses the border resolution of the density interface. That is, when H is large, the particles in suspension cannot form the finger clearly. By a simple assumption, the average distance between particles is calculated as $l \sim d_p \phi^{-1/3}$ and consequently H is as follows.

$$H = \frac{d_p}{\lambda \phi^{1/3}}. \tag{11}$$

As explained above, if suspension behaves perfectly fluid-like, the growth rate obtained experimentally n_{exp} is close to that by linear stability analysis n_{theo}. On the other hand, if it behaves particle-like, the measured velocity U_{exp} is close to the Stokes settling velocity U_0. Figure 6 shows $n_{\mathrm{exp}}/n_{\mathrm{theo}}$ and U_{exp}/U_0 obtained by 14 experiments with variation in fluid and particle properties and also the vessel depth. The horizontal axis is set to the parameter H given by equation (11). As can be seen in Figure 6, we could classify the settling behaviors of suspension as fluid-like, particle-like settlings and their transition by new parameter H.

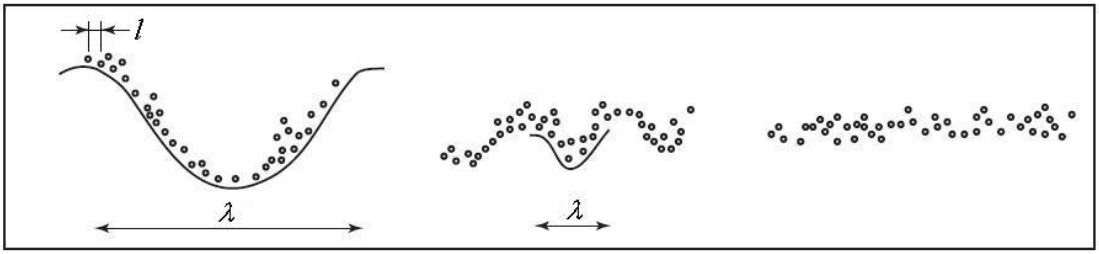

(a) $\lambda > l$ (b) $\lambda \sim l$ (c) $\lambda < l$

Figure 5. Relation between wave length of interfacial pertuabation and average distance between particles

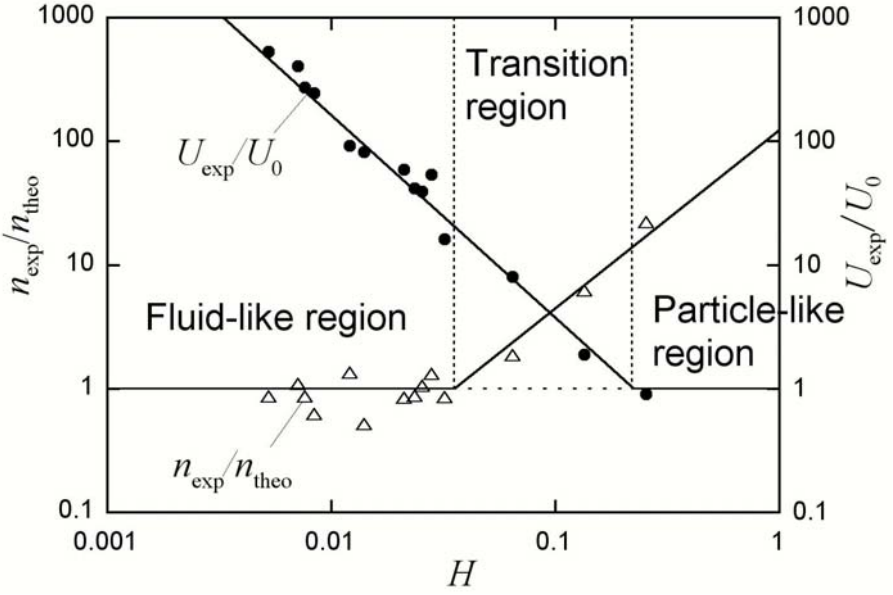

Figure 6 Transition from fluid-like to particle-like behaviors of suspension ($n_{\mathrm{exp}} / n_{\mathrm{theo}}$ and U_{exp} / U_0 represent the index of fluid-like and particle-like settling respectively)

CONCLUSIONS

The sedimentation of inhomogeneous suspensions in quasi two-dimensional vessel was investigated experimentally. We have examined whether the particles behave as a particle assembly (particle-like settling) or as a continuous suspension (fluid-like settling). If the suspended particles are adequately small, the settling behavior is completely fluid-like and the settling velocity is dominated by downstream flow due to the gravity-induced instability. The experimental results showed that the settling velocity of particles is influenced not only by the physical properties of particle and fluid but the size of the vessel. The transition of fluid-like to particle-like behaviors can be predicted quantitatively by a new parameter which expresses the border resolution of the density interface.

REFERENCES

1. Davis, R. H. and Acrivos, A., Sedimentation of noncolloidal particles at low Reynolds numbers, *Ann. Rev. Fluid Mech.*, Vol.17, pp 91-118, 1985.
2. Lee, S., Jang, Y., Choi, C. and Lee, T., Combined effect of sedimentation velocity fluctuation and self-sharpening on interface broadening, *Phys. Fluids A*, Vol. 4, No. 12, pp 2601-2606, 1992.
3. Xue, J.-Z., Herbolzheimer, E., Rutgers, M. A., Russel, W. B. and Chaikin, P. M., Diffusion, dispersion, and settling of hard spheres, *Phys. Rev. Lett.*, Vol.69, No.11, pp 1715-1718, 1992.
4. Nicolai, H. and Guazzelli, E., Effect of the vessel size on the hydrodynamic diffusion of sedimenting spheres, *Phys. Fluids*, Vol.7, No.1, pp 3-5, 1995.
5. Nicolai, H., Herzhaft, B., Hinch, E. J., Oger, L. and Guazzelli, E., Particle velocity fluctuations and hydrodynamic self-diffusion of sedimenting non-Brownian spheres, *Phys. Fluids*, Vol.7, No.1, pp 12-23, 1995.
6. Martin, J., Rakotomalala, N. and Salin, D., Hydrodynamic dispersion of noncolloidal suspensions: measurement from Einstein's Argument, *Phys. Rev. Lett.*, Vol.74, No. 8, pp 1347-1350, 1995.
7. Davis, R. H., Hydrodynamic diffusion of suspended particles: a symposium, *J. Fluid Mech.*, Vol.310, pp 325-335, 1996.
8. Mucha, P. J. and Brenner, M. P., Diffusivities and front propagation in sedimentation, *Phys. Fluids*, Vol.15, No.5, pp 1305-1313, 2003.
9. Happel J. and Brenner H., *Low Reynolds number hydrodynamics: with special applications to particulate media*, Kluwer Academic Publishers, 1973.
10. Kynch, G. J., A theory of sedimentation, *Trans. Faraday Soc.*, Vol.48, pp 166-176, 1952.
11. Völtz, C., Schröter, M., Iori, G., Betat, A., Lange, A., Engel, A. and Rehberg, I., Finger-like patterns in sedimenting water-sand suspensions, *Phys. Rep.*, Vol.337, pp117-138, 2000.
12. Völtz, C., Pesch, W. and Rehberg, I., Rayleigh-Taylor instability in a sedimenting suspension, *Phys. Rev. E*, Vol.65, 011404, 2001.
13. Völtz, C., Granular dynamics of density profiles in a suspension interface, *Phys. Rev. E*, Vol.68, 021408, 2003.
14. Blanchette, F. and Bush, J. W. M., Particle concentration evolution and sedimentation-induced instabilities in a stably stratified environment, *Phys. Fluids*, Vol.17, 073302, 2005.
15. Michioka, H. And Sumita, I., Reyleigh-Taylor instability of a particle packed viscous fluid: Implications for a solidifying magma, *Geophys. Res. Lett*., Vol.32, L03309, 2005.
16. Chandrasekhar, S., *Hydrodynamic and Hydromagnetic Stability*, Clarendon Press, 1961.
17. Huang, J. and Edwards, B.F., Pattern formation and evolution near autocatalytic reaction fronts in a narrow vertical slab, *Phys. Rev. E*, Vol.54, pp 2620-2627, 1996.

A LAMINAR CHANNEL FLOW EFFECTED BY SYNTHETIC JETS – EXPERIMENTAL AND NUMERICAL STUDIES

P. Dančová[1,2], H.C. de Lange[3], T. Vít[1,2], D. Šponiar[1,4], Z. Trávníček[1,*]
[1]Institute of Thermomechanics AS CR, v.v.i., Prague, Czech Republic
[2]Technical University of Liberec, Czech Republic
[3]Eindhoven University of Technology, The Netherlands
[4]Czech Technical University, Prague, Czech Republic

ABSTRACT. This study deals with a laminar channel flow interacting with a synthetic jet, with emphasis on low Reynolds numbers. The study is predominantly experimental, with supporting numerical simulations. The experiments were performed with water as the working fluids, and two methods were used: Laser Doppler Vibrometry for measurement of membrane oscillations, and PIV. The experimental and numerical results confirmed that the channel flow can be effectively controlled by means of the synthetic jet. As a result of the synthetic jet propagation through the channel flow, two significant effects were found: an oblique jet impingement and an overall modification on the channel flow more downstream the impingement area. Based on these local and overall effects, a possibility of heat/mass transfer enhancement was deduced. The authors suggest that this technique can be used for desirable augmentation of various applications.

Keywords: *Synthetic jet, flow control, flow visualization, Particle Image Velocimetry*

INTRODUCTION

A synthetic jet (SJ) is generated by the periodic motion of an actuator oscillating membrane. It is synthesized by the interactions within a train of vortices. The time-mean mass flux in SJ orifice is zero; hence the other common expression is zero-net-mass-flux (ZNMF) jet [1–3]. This study focuses on the interaction of a SJ with a laminar channel flow, with emphasis on low Reynolds numbers. This arrangement can be useful in many micro-scale applications, such as cooling of micro-electronics or the detection of various (biological, biomedical or chemical) species. The flow regime in micro-scale is usually laminar with very small Reynolds numbers. Therefore, the transfer processes such as mixing and cooling are typically based on gradient diffusion. Despite the present Reynolds numbers (in order 10^2) are too low for transition to turbulence, an actuation can essentially enhance the transport mixing creating the so-called "quasi-turbulent" flow character [4].

EXPERIMENTAL AND NUMERICAL INVESTIGATION

Problem parameterization

The "stroke length" is defined as $L_0 = U_0 T$, where U_0 is the time-mean orifice velocity relevant to the extrusion stroke [1], T is the time period ($T=1/f$), and f is the frequency. The Reynolds number of SJ is $Re_{SJ} = U_0 D/\nu$, where D is the diameter of the actuator orifice. The Reynolds number of 2D channel flow is $Re_C = U_C(2H)/\nu$, where U_C is the time-mean velocity through the channel, i.e. $U_C = (2/3)U_{max}$, where U_{max} is the maximum velocity and H is the channel width.

* Corresponding author: Z. Trávníček, Ph.D.
Phone: +(420)-266-053 302, Fax: + (420)-286-584695
E-mail address: tr@it.cas.cz

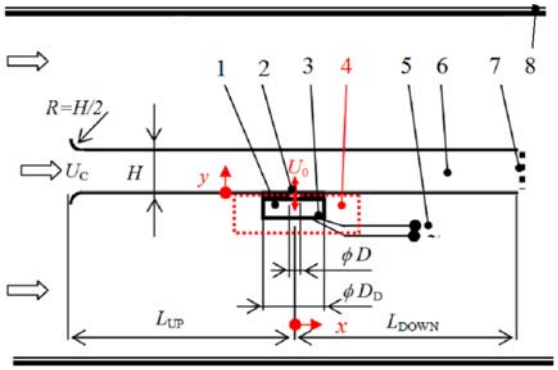

Figure 1. Schematic view of the present configuration. 1 – SJ cavity, 2 – SJ orifice, 3 – SJ membrane, 4 – SJ actuator, 5 – AC supply, 6 – tested channel, 7 – grid, 8 – water channel

Experimental setup and methods

Experimental setup. Figure 1 shows a schematic view of the present configuration - the tested channel inside the closed-loop circulation water channel (at TU Eindhoven). The tested channel was made out of Plexiglas. The inlet was carefully rounded to prevent inlet flow separation, and the outlet was equipped with a grid to control the flow velocity through the channel. The channel length, height and width were L_{UP}+L_{DOWN} = 1020mm, H = 40mm, and B = 200mm, respectively. The SJ-actuator (pos. 4) consists of a sealed cavity with an emitting orifice (diameter D = 3.0mm) and with an actuating piezoelectric membrane (D_D = 36mm). The actuator orifice is oriented vertically upwards to the exposed channel of cross section dimensions *H x width* = 40mm x 200mm.

Laser Doppler Vibrometry measurement. The piezoelectric membrane (piezoceramic transducer - PCT) is composed of two basic layers – a piezoceramic layer and a metallic membrane. Measurement of the oscillating PCT membrane is based on the Doppler effect, and the portable digital vibrometer Ometron VQ-1000-D B&K 8338 was used. The main parameters: frequency range 0.5 Hz ÷ 22 kHz; measurement ranges (full scale (peak-peak)) 20mm/s, 100mm/s, 500mm/s; spurious free dynamic range (SFDR): > 90dB; and best resolution: 0.02 μm/s/Hz$^{0.5}$.

Particle Image Velocimetry experiments (PIV). Seeding particles were polyamide balls of 20μm in diameter (DANTEC). The particles were illuminated by a double pulse laser with maximum 200mJ per 5ns pulse, and repetition rate 2 x 15Hz. A typical delay time 30ms was used. The laser beam was expanded by a cylindrical lens into a light sheet about 1mm in thickness. The image pairs were acquired using a 10 Bit CCD camera Kodac ES 1.0 with a spatial resolution of 1008 x 1018 pixels and the maximum frequency of 30 frames/s. The resulting vector maps were averaged over 54 double pulses in sequence. Velocity vectors were determined by adaptive correlation over interrogation windows 32 x 32 pixels at a 50% overlap and by cross-correlation over interrogation windows 64 x 32 pixels at a 50% overlap, respectively. Adaptive correlation was used on the images which show the SJ flow in the direct vicinity of the actuator, cross correlation was used on the images far from the SJ actuator. Data processing used software FlowManager 4.71 (DANTEC).

Numerical simulation

The flow is assumed to be three-dimensional, laminar, incompressible, and isothermal. Both stationary and non-stationary (periodical) problems are studied. The flow fields are computed with the finite-volume method using the commercial solver FLUENT; two governing equations are the mass and momentum conservations. Discretization of the domain uses hexahedron cells. The SJ cavity and SJ orifice contain a fine grid with hexahedrons of a typical size (0.2–0.5) mm and 0.2 mm, respectively. Further from the SJ, the size of the hexahedrons gradually increases

(the maximum of the aspect ration of cell sides is about 70) up to 2.0 mm. The total number of control volumes is about $2.2 \cdot 10^6$. The length of time step of the unsteady problem was chosen about t/T = 1/120. The computation process was highly time-consuming – a typical time for computation of an unsteady task under 16 CPU computer was 150 hours.

The boundary conditions follow the experimental conditions and the working fluid is water at temperature 20°C and pressure 10^5 Pa. The density and dynamic viscosity of water is $\rho = 998$ kg/m^3 and $\mu = 0{,}977\ 10^{-3}$ kg/(m·s), (i.e., the kinematic viscosity $\nu = \mu/\rho = 0{,}979\ 10^{-6}$ m^2/s). Three tasks were studied: (A) Main laminar channel flow without SJ; the boundary conditions were the uniform velocity profile at the channel inlet ($U_C = 0.006$ m/s) and the static pressure 10^5 Pa at the channel outlet. (B) Single round SJ directing across the channel without the main channel flow; the boundary conditions were the (uniform in space and harmonic in time) velocity profile on the diaphragm, $V = V_{max} \sin(\omega t)$, where the max. diaphragm velocity is V_{max}=0.0013m/s, $\omega = 2\pi f$, and f=15.0Hz. (C) Complex flow field A+B, i.e. an interaction of the main laminar channel flow with the single round SJ.

RESULTS AND DISCUSSION

Experimental results

The actuating frequency of the SJ actuator was chosen f = 15.0Hz – to match the present PIV laser repetition rate. It was near the actuator resonance frequency (about 18Hz, as was found during an auxiliary measurement by using Hot Wire Anemometry). The actuator was fed with sinusoidal current, and the electrical voltage and current were about 48V (peak-peak) and 0.076A (rms).

Laser Doppler Vibrometry measurement. The sampling rate for this measurement was 3000Hz. The period starts in zero position of the driving signal. From the membrane velocity and continuity equation, the velocity in the orifice $u_0(t)$ was evaluated; then the time-mean orifice velocity and Reynolds number were evaluated as U_0=0.059m/s and Re_{SJ}=177.

Figures 2(a) and 2(b) show the comparison of measured and theoretical sinusoidal displacement of the membrane centre in time, and the comparison of measured and theoretical cosinusoidal velocity in time, respectively. The sinusoidal displacement is described as $\Delta y(t)=\Delta y_{max}\sin(2\pi ft)$, and the relevant cosinusoidal velocity as $v(t)=v_{max}\cos(2\pi ft)$. The least squares fitting gives Δy_{max}=0.0274mm – see Figure 2(a). The relevant maximum of the membrane velocity is $v_{max}=2\pi f\Delta y_{max}$ = 0.00255m/s.

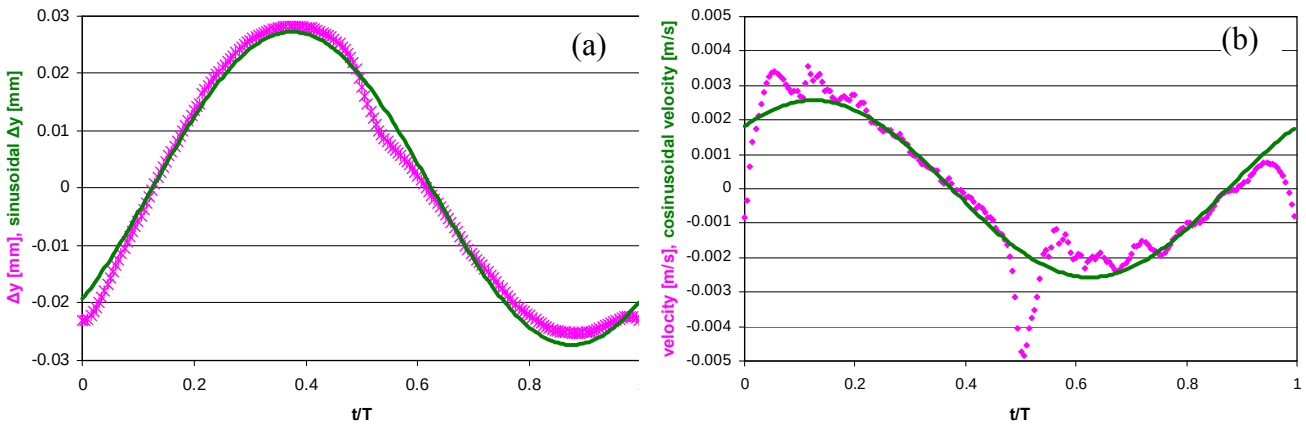

Figure 2. Oscillating membrane: (a) displacement, (b) velocity

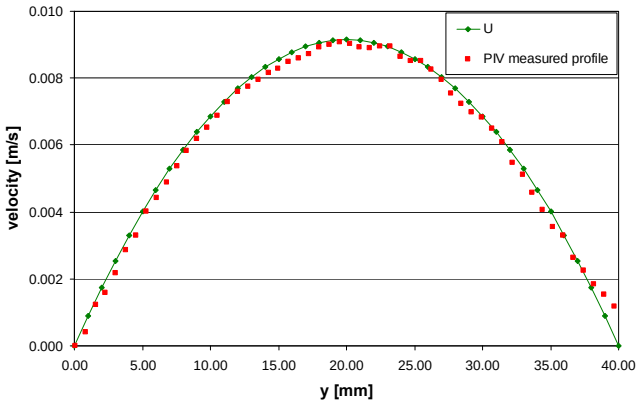

Figure 3. Velocity profile of a channel flow without SJ

Considering continuity, the plug flow model of an extruded fluid column, and the parabolic shape of the membrane deflection, the maximum of the velocity in the actuator orifice can be evaluated as $U_{max}=0.5(D_D/D)^2 v_{max} = 0.183$m/s. Finally, the sinusoidal character gives $U_0=U_{max}/\pi = 0.0583$m/s. Obviously, this sinusoidal approximation of the membrane displacement gives practically the same velocity U_0 as was written above (0.059m/s).

PIV measurement. Figure 3 shows that the time-mean velocity profile for the channel flow without SJ interaction (measured at $x = 0$) compares very well with the parabolic Poiseuille profile (denoted by U): $U = 6\,U_C[y/H–(y/H)^2]$. The time-mean velocity through the channel cross section was evaluated from the parabolic profile (Figure 3), $U_C = 0.006$m/s; the Reynolds number is $Re_C = 480$.

The interaction of the channel flow with a SJ is shown in Figure 4 in a form of contours of time-mean velocity magnitude. This experiment clearly demonstrates the SJ bending and its propagation downstream in the main channel flow. Moreover, SJ reaches the opposite wall (y=40mm), where an oblique jet impingement can be identified (at x = 30–40mm, see the ellipse mark in Figure 4). Obviously, heat/mass transfer enhancement can be expected in the impingement area – this effect is desirable in various applications. Nevertheless, even more important than this local effect could be an overall modification on the channel flow more downstream the impingement area. To explain this effect, the following text discusses profiles of the time-mean velocity at x=12–115mm.

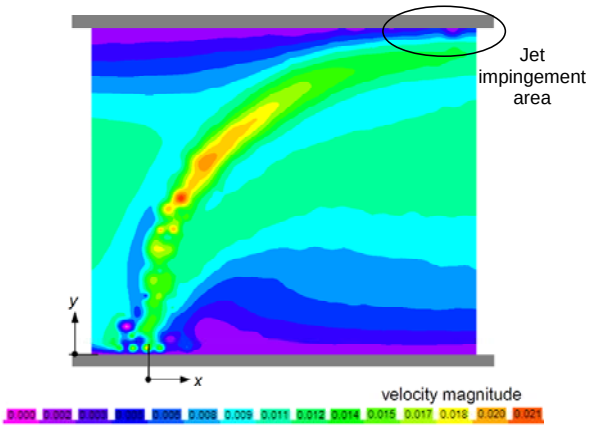

Figure 4. Velocity magnitude of the channel flow interacting with SJ. The presented PIV experiment covers area x from –7mm to 40mm, and y from 0 to 40mm.

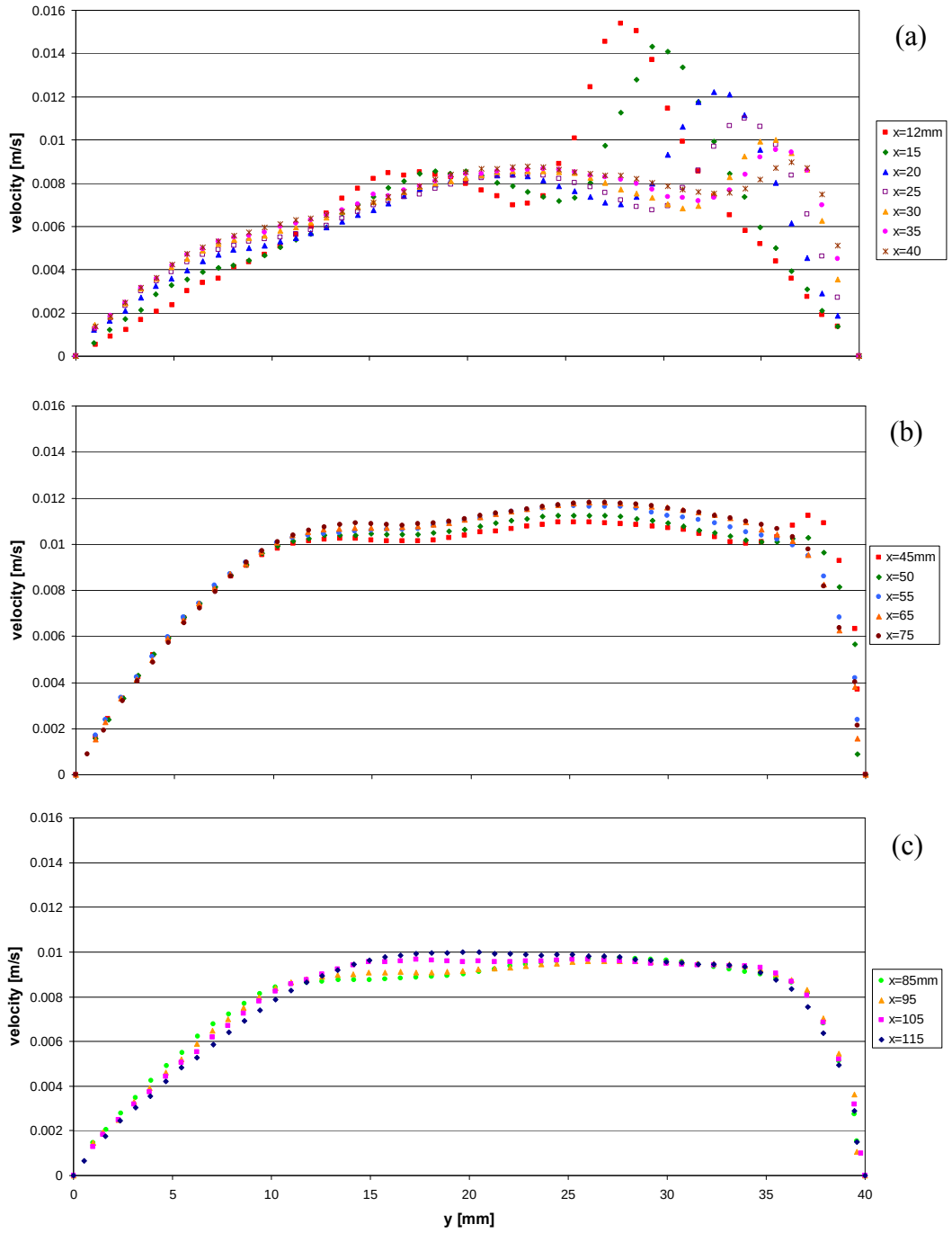

Figure 5. Velocity profile of the channel flow affected with SJ; $t/T = 0.5$

Figure 5 shows results from PIV measurements of the channel flow interacting with a SJ. Figure 5a shows that the velocity profile is influenced first on the top of the channel – i.e. on the wall opposite of the SJ actuator – the velocity there is nearly 0.016m/s. Obviously, it is caused by rather high velocity of SJ – the velocity U_0 was one order higher than U_C, as is evaluated below. More downstream, the flow development is propagated downwards to the bottom channel wall – Figures 5(b and c). The flow profile again redistributes towards a parabolic profile, however at x=115mm this profile is not yet achieved.

Results of numerical simulations

Main laminar channel flow without actuations. Figure 6a shows velocity profiles, which were

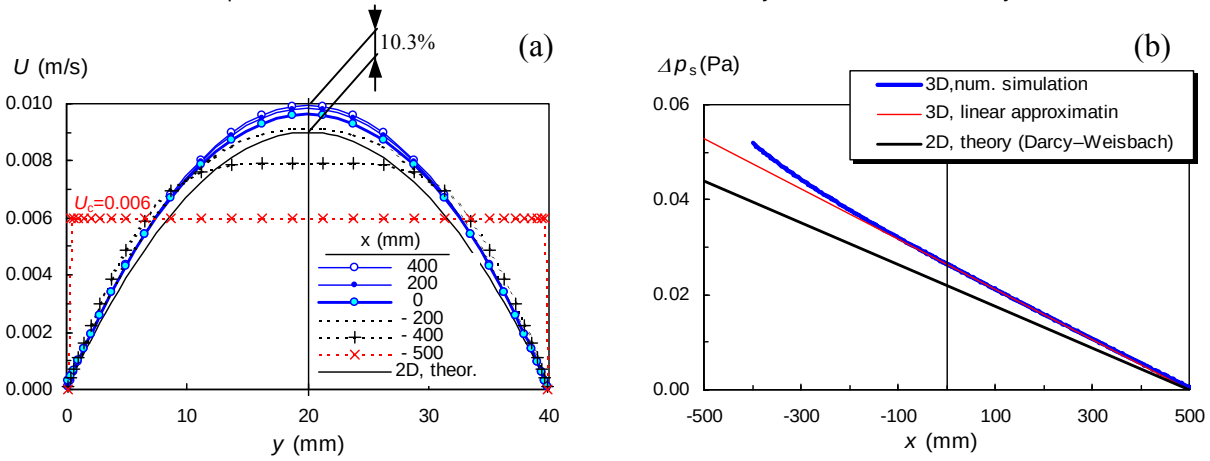

Figure 6. Numerical simulation of the channel flow; (a) velocity profile across the channel, (b) pressure drop along the channel center

computed from the channel inlet $x = -500$mm, where constant velocity $U_C = 0.006$ m/s is prescribed across the channel. According to our expectations, the uniform inlet flow develops into the parabolic channel flow profile, and this process takes place mainly in the first half of the channel (approximately x = from –500mm to -200mm). The increase of the velocity maximum in the second half of the channel ($x > 0$), relating to the final stage of developing is rather small, only 3.7%. For comparison purposes, 2D theoretical laminar parabolic profile of developed channel flow is plotted in Figure 6a, too. Obviously, 2D flow reaches smaller maximum velocity than 3D flow under identical time-mean velocity through channel U_C. This is due to the 3D effect of the boundary layer on the channel side walls $z = \pm B/2$. The difference between velocity profiles of 2D and 3D flows is plotted in Figure 6a, too: 2D flow reaches $U_{max} = 1.5\ U_c$, and the present 3D flow reaches 10.3% higher $U_{max,3D} = 1.654\ U_c$.

It is worthwhile to mention here that consideration of the 3D effect slightly decreases the experimental time-mean channel flow velocity U_c and the Reynolds number Re_c, which was discussed earlier. Taking into account the 3D channel flow character, the velocity and Reynolds number are $U_{c,3D}$ = 0.0054m/s and 435, respectively. Moreover, accounting for the hydraulic diameter of 3D channel, instead of the 2D simplification leads to a decrease of the Reynolds number $Re_{C,3D} = D_h\, U_{C,3D}\, /\nu$, where D_h is the hydraulic diameter of the channel, $D_h = 2H/(1+H/B)$, i.e. $D_h = (5/3)H$ for the present geometry. This 3D evaluation gives the resultant value $Re_{c,3D} = 363$.

Figure 6b shows the static pressure drop computed along the channel center (x = from –500mm to 500mm, $y = H/2$, $z = 0$). For comparison purposes, the pressure drop resulting from the theoretical 2D solution given by the Darcy–Weisbach equation is shown also in Figure 6b. Understandably, the 3D effects from the channel side walls imply that 3D channel flow needs higher pressure drop to reach the same volume flow (i.e. the same channel velocity U_C) as 2D flow. Figure 6b shows, that 2D simplification implies a pressure drop decrease by 17% against the computed 3D flow. The linear approximation of the pressure drop related to the 3D fully developed flow is plotted in Figure 6 too. It well correlates the numerical results in the range from $x = -100$mm to $x = 500$mm. For this approximation, the Darcy–Weisbach friction factor of the present channel was concluded to be $f = 80/Re_{C,3D}$. These characteristics show that the main channel flow is well-captured in these simulations with the set numerical parameters and resolution.

Synthetic jet without channel flow. Figure 7(a) shows the SJ period in a form of contours of velocity magnitude. The images were evaluated at 4 equal time intervals during the actuating period (t/T = 0, 0.25, 0.50 and 0.75). The period origin is defined at the moment of zero velocity in the actuator

orifice, at the beginning of the extrusion stroke. The main visible feature is that the generated SJ crosses the channel width *H*, and it reaches the opposite channel wall where SJ impingement is formed. Moreover, Figure 7(a) for $t/T = 0.75$ shows "the range of the actuator suction" – a spot of small velocity located on the axis at x= approximately $0.35D$; further downstream only the positive orientation of the vertical velocity component exist during the actuation cycle.

An interaction of the channel flow with synthetic jet. Figure 7(b) shows an interaction of the channel flow with SJ in a form of contours of velocity during the actuation period. The numerical simulation shows SJ bending and propagation downstream the main channel flow – cf. Figure 4 showing PIV experiment for the same case. Despite numerical simulation predicts smaller SJ bending (impingement area is predicted at x~15mm in Figure 7(b), and experimental Figure 4 shows x~(30–40)mm) the character of the results is comparable.

Moreover, Figure 7(b) demonstrates another effect: the channel flow exhibits two areas of low velocities at the leading and trailing parts of SJ. This effect is known from steady jets in cross flows, and it resembles front stagnation area and rear separation bubble of bluff bodies in cross flows.

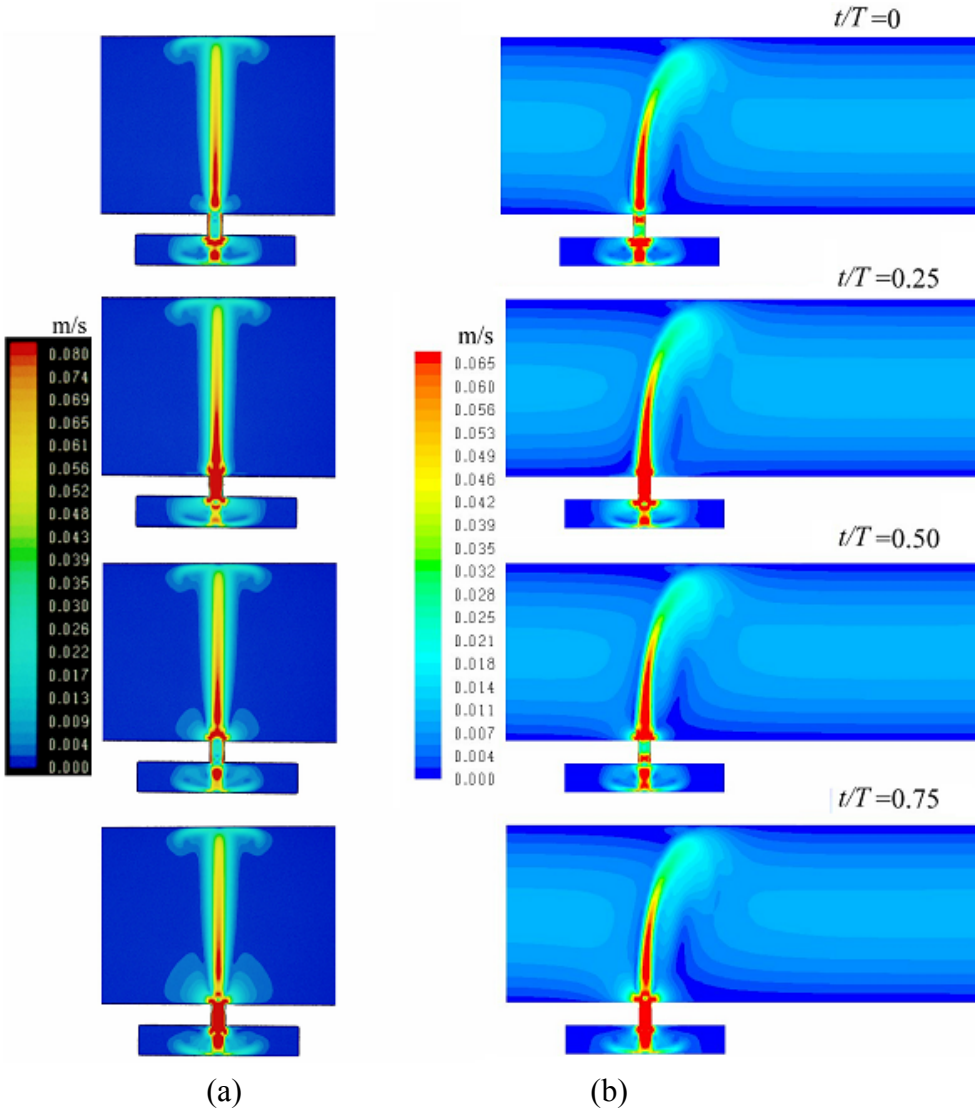

Figure 7. Numerical simulation of SJ period – contours of velocity magnitude during the actuation period; (a) SJ without a channel flow, (b) SJ interacting with the channel flow

CONCLUSIONS

The present study deals with a laminar channel flow interacting with a synthetic jet, with emphasis on low Reynolds numbers. The study consists of experimental and numerical parts. The experimental part of this study used two methods: measurement of oscillations of the actuating membrane using Laser Doppler Vibrometry, and PIV experiment. Laser Doppler Vibrometry evaluated the local displacement and velocity of the membrane. Based on the continuity equation and considering plug flow model of fluid column, data were transformed into the approximation of the orifice velocity in time $u_0(t)$, the time-mean orifice velocity relevant to the extrusion stroke U_0, and the Reynolds number $Re_{SJ} = 177$.

PIV experiment with the channel flow alone (without synthetic jet) confirmed laminar character of flow, and the velocity profile agreed very well with the parabolic Poiseuille profile. The Reynolds number of the channel flow was adjusted $Re_C = 480$. Sequentially, PIV experiment was performed with the same channel flow under the synthetic jet actuation. The experiment demonstrates bending of the synthetic jet and its propagation through the channel flow. The synthetic jet crossed entire channel width, and an oblique jet impingement was identified on the opposite channel wall. An overall modification on the flow more downstream the impingement area was identified too.

Numerical simulations were performed under identical conditions as the experiments. Three tasks were systematically studied: (A) the main laminar channel flow without actuations, (B) the single round synthetic jet directing across the channel in quiescent fluid, (C) an interaction of the main laminar channel flow with the round synthetic jet. The simulation predicted quite well (A) the channel flow development into the parabolic Poiseuille profile, (B) synthetic jet formation, and (C) the character of the synthetic jet propagation into the flow field. A reasonable agreement with experiments was concluded.

The present experiments and numerical simulation confirmed that the laminar channel flow at low Reynolds numbers can be effectively controlled by means of the synthetic jet. An oblique jet impingement and an overall modification on the channel flow more downstream the impingement area was found. Based on these local and overall effects, a possibility of heat/mass transfer enhancement was deduced. The authors suggest that this technique can be used for desirable augmentation of various (typically micro-scale) applications such as cooling of micro-electronics, micro-mixing, and detection of various (biological, biomedical or chemical) matters.

Acknowledgement. We gratefully acknowledge the support of the GAASCR (IAA200760801) and TU Eindhoven (the provider of the experimental facility).

REFERENCES

1. Smith, B.L., Glezer, A., The formation and evolution of synthetic jets, *Phys. Fluids*, Vol. 10, pp 2281-2297, 1998.
2. Cater J.E. and Soria J., The evolution of round zero-net-mass-flux jets, *J. Fluid Mech.,* Vol. 472, pp 167-200, 2002.
3. Tesař, V. and Zhong, S., Efficiency of synthetic jets generation, *Transactions of the Aeronautical and Astronautical Society of the Republic of China*, Vol. 35, No. 1, pp 45–53, 2003.
4. Timchenko, V., Reizes, J.A., and Leonardi, E., An evaluation of synthetic jets for heat transfer enhancement in air cooled micro-channels, *Int. J. Numer. Methods Heat Fluid Flow*, Vol. 17, No. 3, pp 263-283, 2007.

VISUALIZATION TECHNIQUES FOR ESTIMATING THERMAL BOUNDARY LAYERS OF NATURAL CONVECTION FLOWS

Tomasz P. Bednarz*, Feng Xu, Chengwang Lei, John C. Patterson
School of Engineering, James Cook University, Townsville QLD 4811, Australia

ABSTRACT. Particle Image Thermometry (PIT) and shadowgraph methods can be successfully used for estimating thermal boundary layer thickness in transient natural convection flows. PIT is a technique by which temperature fields are extracted by post-processing true-colour photographs of the flow patterns obtained with the application of thermo-chromic liquid crystals added to the working fluid. This is usually done using a calibration curve (hue versus temperature). With such calibration data, every pixel of the colour photograph is transformed to a temperature value, and thus accurate experimental temperature maps can be obtained. In this paper, the general PIT image processing techniques are presented, and new image processing procedures to determine the post-processing window size based on the visible particle size are described.

Shadowgraph is another technique that is used to visualize thermal flow fields. It is known that the intensity variation of shadowgraph images is approximately sensitive to the second derivative of temperature, and a bright strip in a shadowgraph image corresponds to the minima or maxima of the second derivative of temperature in the direction normal to the strip. The present paper describes the advantages and limitations of this technique. Also working examples of the shadowgraph technique used in natural convection flows are presented.

Keywords: *Particle Image Thermometry*, *shadowgraph*, *image processing, thermal boundary layer*

INTRODUCTION

Accurate temperature field data and proper visualization techniques are essential for heat transfer and fluid flow analyses, for example in evaluation of convective heat transfer coefficients in complex geometries or in dynamic fluid flows, as well as for estimating thermal-boundary layers, etc. Traditional temperature sensors such as thermocouples or thermistors can only provide temperature information at discrete points. Moreover, the presence of these sensors in the flow domain may disturb the original flow or physical phenomena. In many thermal flow problems such as the transient growth of thermal boundary layers in natural convection experiments, our interest is mainly in the overall flow field rather than discrete locations in the flow. For this purpose *Particle Image Thermometry* (PIT) and *Shadowgraph* methods can be successfully utilized, as it will be shown in the present work by several examples.

The PIT technique makes use of the special optical properties of TLCs (Thermo-chromic Liquid Crystals), which are widely used in science and engineering to map temperature distributions in fluids or on rigid surfaces. TLCs usually exist in smectic, nematic or cholersteric (also chiral nematic) phases [1, 2]. When a white light source shines on the chiral nematic TLC, light of only one particular wavelength corresponding to the temperature of the TLC is reflected. Thus, this property is used to measure accurately the temperature by observing the reflected wavelengths (or colours). The visible

* Corresponding author: Dr Tomasz P Bednarz
Phone: + (61)-7-47815218, Fax: + (61)-7-47816788
E-mail address: tomasz.bednarz@jcu.edu.au

colour of TLCs turns from colourless (black against a black background) to red over a certain temperature range. As the temperature increases, the TLCs' colour passes through the visible colour spectrum in sequence (orange, yellow, green, blue, violet) before turning colourless again at a higher temperature [3, 4]. These colour changes are repeatable and reversible, as long as the TLCs are not chemically degraded or physically damaged. TLCs therefore can be calibrated accurately against known temperatures and used as temperature indicators. The response time of TLCs is only 3 ms, which is short enough for typical thermal fluid problems. TLCs are normally clear or slightly milky in appearance and change their colour over a narrow range of temperatures. Their colour-temperature play range depends on the TLC composition prepared during the manufacturing process, and can be selected for bands of about 0.5ºC to 20ºC with working temperatures ranging from -30 ºC to above 100 ºC [5]. The suspension of thermo-chromic liquid crystals can be used not only for temperature visualization but also for concurrent velocity estimations through the method of Particle Image Velocimetry [1, 6], as seen in Figure 1.

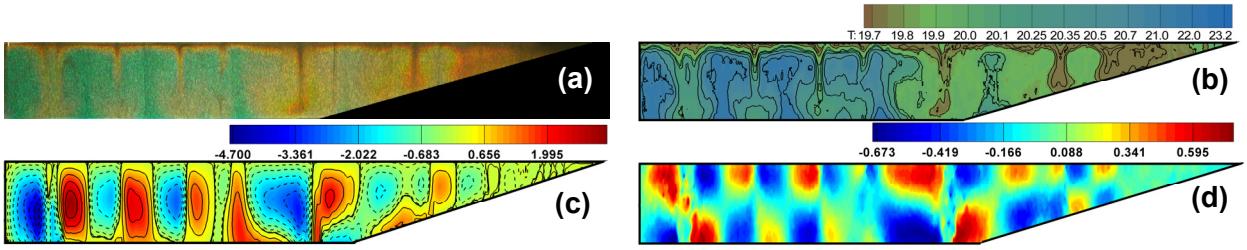

Figure 1. Example of concurrent temperature and velocity extraction in a reservoir model subject to diurnal temperature changes at the water surface [6]; (a) raw image; (b) isotherms extracted through PIT technique; (c) streamline contours and (b) contours of the horizontal velocity extracted using the PIV technique.

Due to its relative simplicity, the shadowgraph technique has also been extensively applied to the observation of various flows. The shadowgraph technique is based on the principle that the refractive index of light depends on the density of the fluid through which it passes; a non uniform temperature field, and therefore density field, will deflect parallel light non-uniformly, and thus an interference pattern will be observed on a distant screen [7]. Therefore, this technique is usually employed to visualize natural convection flows [8, 9]. Various shadowgraph methods can be divided into two categories: direct and focused (see e.g. [10]). The direct shadowgraph means that, in the simplest case, only a bright light source, an object and a suitable surface (on which to cast the shadowgraph image) are required. However, the focused shadowgraph, which will be described in the following section, has been more extensively applied because it enables easy adjustment of the imaging plane through adjusting the camera settings despite that its optical setup is more complex than the direct one.

It is well known that the boundary layer adjacent to a thermal wall has a large temperature gradient in the direction normal to the wall surface, which in turn results in the density variation of the fluid adjacent to the thermal wall. Accordingly, the shadowgraph technique can be used to visualize the transient development of the thermal boundary layer and measure its thickness [11]. In this paper, the shadowgraph technique is employed to estimate the thickness of the thermal boundary layer adjacent to the sidewall of a differentially heated cavity.

PARTICLE IMAGE THERMOMETRY

Calibration

The colour-to-temperature calibration of the liquid crystals was carried out using the experimental model presented in Figure 2. The colour images at a uniform temperature were taken by a digital camera and were digitised in RGB colour space. For calibration purpose, every pixel in the RGB colour space was transformed to another trichromic decomposition called HSI (Hue, Saturation, and

Intensity) according to the methodology presented in [12, 13]. The most important value for colour-to-temperature calibration is the hue value which represents the dominant colour related directly to a specific spectral wavelength. The value of hue is independent of light intensity, so minor variations of the light intensity across the illuminated plane do not affect the calibration. A simple spatial mean filter based on a sliding-window analysis that calculates the mean value of each colour component in the window and replaces the centre pixel value with the calculated mean value was additionally applied. In preliminary tests it was found that the optimal value of the window size is 9×9 pixels, which approximately corresponds to the size of a single particle of the liquid crystal visible in the photograph.

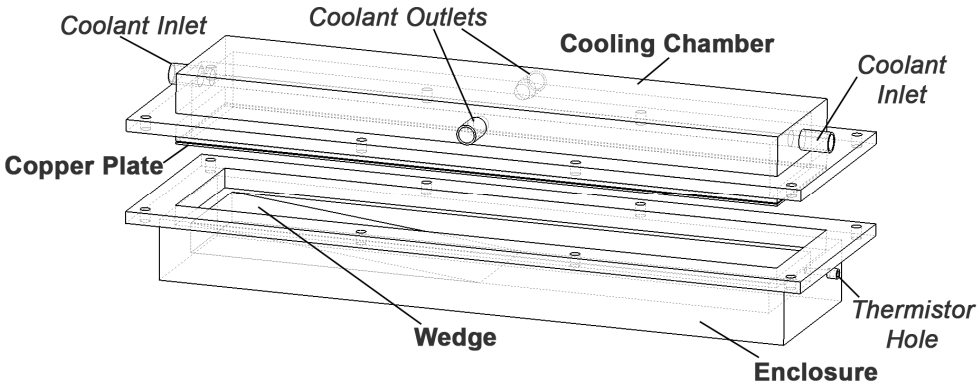

Figure 2. Experimental model of reservoir [6, 13].

For calibration, the water body was cooled to a constant temperature in the range from 24.2ºC to 18.9ºC in 26 steps. At every step, the water was kept at the specified temperature for about 20-25 minutes, and then an experimental photograph was taken (Figure 3a). After that, the temperature was set to the next calibration step, and the above procedure was repeated. In the region with steep increase of the hue value, the number of calibration points was increased since a very small change in the temperature caused a relatively large change in the colour response (hue value). A sixth-order polynomial regression was used to fit the known temperatures with the corresponding hue values calculated from the RGB colour components. The polynomial fit was only applied to points within the monotonic region (i.e. for temperatures between 19.7-23.7ºC in Fig. 3b). Although the nominal temperature indicating range of KWN-20/30 is between 20 and 30ºC, only part of this region (i.e. the monotonic region mentioned above) can be used with confidence for accurate temperature estimation. Above 23.7ºC, the TLCs hue response was almost constant and it was not considered for further analysis. The error bars in Figure 3b represent one standard deviation in the calculated hue from the region of interest within the measured colour bandwidth of the KXN-20/30 liquid crystals used here. As seen in Fig. 3b, there were some variations of the reflected wavelength from the TLC particles at the same temperature. The highest uncertainty occurs at higher temperatures, at which the colour response of the TLCs is entering a transparent regime. The departure of the TLC indicated temperature (obtained using the sixth-order polynomial calibration curve) from the actual temperature (the reference temperature for calibration) is indicated by the coefficient of determination R^2 and the mean absolute error of the linear correlation between the indicated and actual temperatures, which are 0.9953 and 0.059ºC respectively from the present calibration.

Estimation of the Thermal Boundary Layer

Figure 4(a) presents a set of experimental photographs showing the transient response of the thermal boundary layer immediately below the water surface in the initial growth stage in a cooling experiment. The numbers in the lower-left corner of each photograph indicate the relative time measured in seconds after the initiation of cooling. Initially, the fluid was stationary and isothermal, and there was no heat conduction in the enclosure. As soon as the surface cooling started, a thermal boundary layer started to grow downwards underneath the water surface. By comparing the images shown in Figure 4(a), it is seen that a horizontal strip of red/brown colour expanded downwards along

the entire top surface. This red/brown strip met the sloping bottom near the tip. Therefore, a local temperature gradient is created along the sloping bottom in the tip region. This temperature gradient is responsible for the development of a convective flow (to be described later) with relatively colder fluid flowing down along the slope into the deeper regions, resulting in a convective circulation in the enclosure [14].

The presented photographs show clearly the transient growth of the thermal boundary layer and allow an estimation of the boundary layer thickness at different times. Here, the thermal boundary layer thickness can be determined as the distance between the top of the enclosure and the mid height of a very narrow band with distinct colour transition between brown (representing the relatively colder fluid in the thermal boundary layer) and blue colours (representing the relatively warmer fluid in the interior). The lower boundary of the thermal boundary layer is indicated by overdrawn white horizontal lines in Figure 4(a).

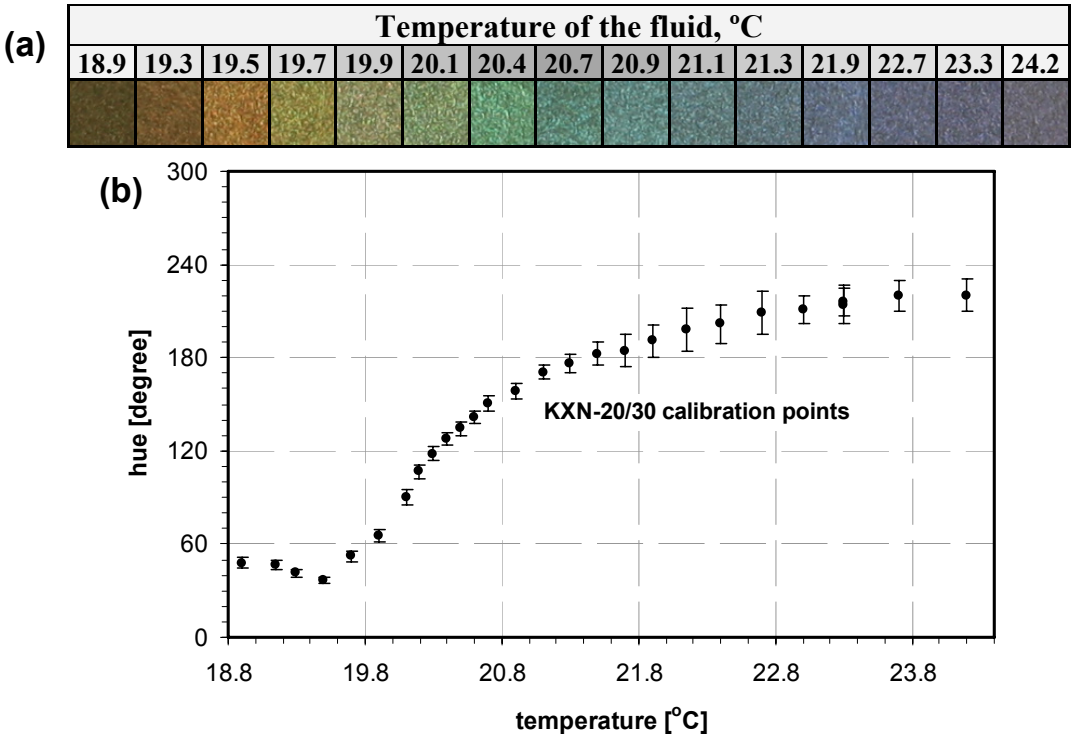

Figure 3. (a) Colour responses of the TLC used in the present experiment. (b) Calibration data points for the KXN-20/30 slurry (temperature versus hue).

Figure 4(b) shows temperature profiles in the thermal boundary layer at three different times in the early stage of the flow development before the convective instabilities were initiated. The profiles are extracted using the PIT technique along a vertical line at a horizontal location of 0.15 m from the tip, and are plotted against the distance below the surface. The figure clearly shows the growth of the thermal boundary layer with time. It is worth noting in Figure 4(b) that the temperature at the water surface is not constant. Instead, it decreases with time. This is a direct result of the present experimental setup, in which a copper plate of a finite thickness is used to conduct heat between the cooling water in the cooling chamber and the water body in the reservoir model. The temperature at the upper surface of the copper plate is maintained approximately constant by the circulating cooling water. In order to maintain a continuous temperature change from the copper plate to the expanding cooling thermal boundary layer under the water surface, a decreasing temperature with time at the lower surface of the copper plate (which is the same as the water surface temperature) is necessary. The result shown in Figure 4(b) implies that the cooling rate at the water surface also decreases with time at this stage.

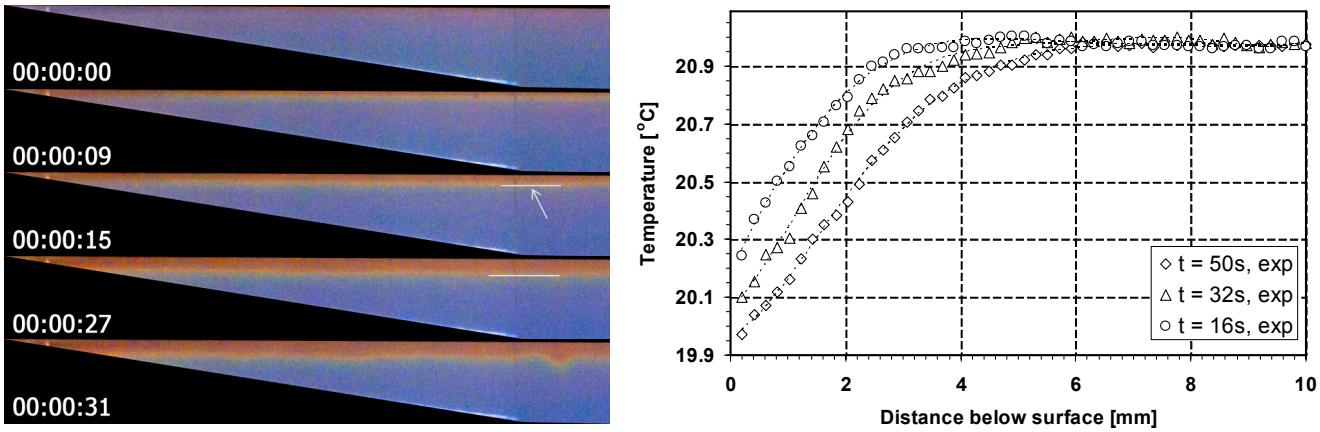

Figure 4. (a) Transient growth of the thermal boundary layer in the initial stage of cooling, (b) temperature profiles in the thermal boundary layer extracted using PIT technique.

A thermal boundary layer started to grow downwards underneath the water surface immediately after the surface cooling started, and the growth of the thickness of the thermal boundary layer with time in the early stage can be described by a simple scaling relation $\delta_T \sim (\kappa t)^{1/2}$ [13-15]. It is worth noting that this scaling law holds only for the initial development of the thermal boundary layer when heat transfer is dominated by conduction. Figure 5 plots the thicknesses of the thermal boundary layer measured in two separate experiments at $Gr = 2.04\times10^4$ and $Pr = 8.05$, in 2 runs and at $Gr = 7.82\times10^3$ and $Pr = 6.91$, against time t during the early growth stage of the thermal boundary layer. The thermal boundary layer thickness was measured at a horizontal location of 0.15 m from the tip, and was determined for the first case as described above, and for the second case where the hue value was 160 (corresponding to a temperature of 20.95 ºC). In Figure 5, the circles, crosses and triangles represent the experimental data, and the dashed lines represent the trend-line fitted to the experimental data. This demonstrates that thermo-chromic liquid crystals can be successfully used for estimating thermal boundary layers in convective flows.

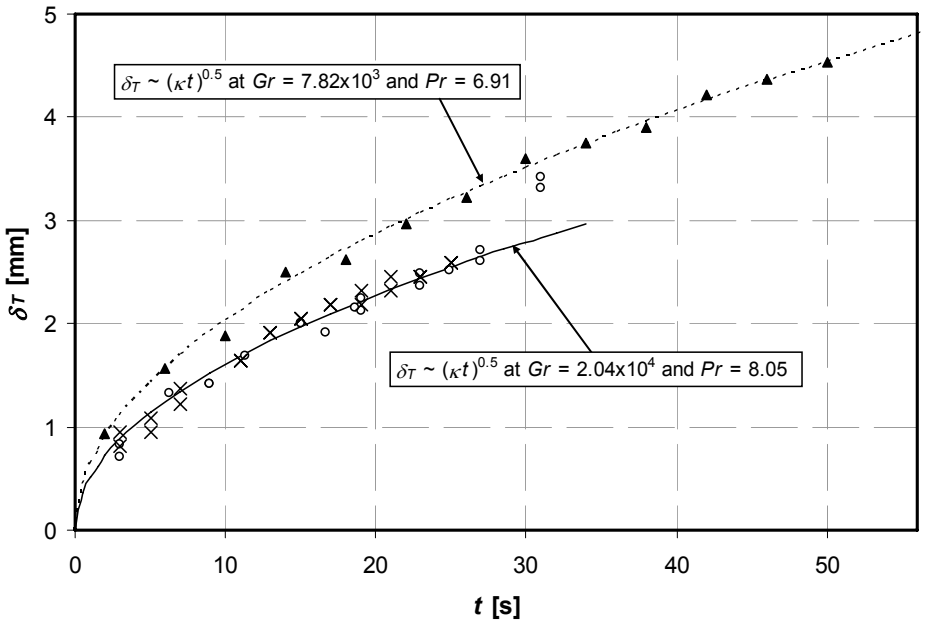

Figure 5. Sample growths of the thickness of thermal boundary layers (TBL is plotted against time). The circles/crosses are the experimental data from two experiments; the solid and dashed lines are scaling predictions.

SHADOWGRAPH

We consider the vertical thermal boundary layer adjacent to the sidewall of a differentially heated cavity. For the purpose of shadowgraph visualization, a Z-shaped focused shadowgraph setup is employed in this paper. Figure 6 sketches a top view of the shadowgraph optical setup, in which a point light source (a 12-W bulb in a small black box with a pin hole covered by a piece of ground glass) is placed at the focal point of a silver-coated spherical mirror with a diameter of 0.3 m and a focal length of 2.4 m. Such an optical setup results in a parallel light beam leaving the spherical mirror. When the parallel light beam passes through the model cavity filled with fluid of non-uniform temperatures, it is deflected by the fluid due to variations of the refractive index of the fluid. In fact, the refractive index depends on the fluid density, and in turn on the temperature. Therefore, a non-uniform pattern with varying light intensity is formed after the originally parallel light beam exits from the cavity. The distance from the mirror to the light-entering sidewall of the cavity is 2.6 m.

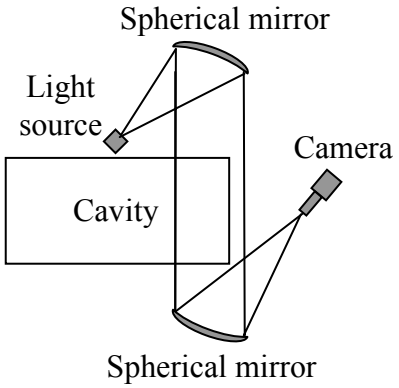

Figure 6. Schematic of the optical setup of the focused shadowgraph.

The exiting light beam is projected onto another identical spherical mirror, and refocused to a black-and-white CCD camera (Pulnix TM-6CN) at the focal point of this mirror. The distance from the light-exiting sidewall to the mirror is 1.8 m, shorter than that on the other side of the cavity (in order to reduce the loss of the intensity of the light beam), but that from the mirror to the camera is still 2.4 m, which is the focal length of the spherical mirror. The CCD camera is connected to a frame-grabber board installed in a computer. As a consequence, a time series of the recorded shadowgraph images displays the development of the temperature field of the fluid adjacent to the sidewall of the cavity.

Figure 7(a) presents a series of shadowgraph images showing the growth of the thermal boundary layer adjacent to the hot sidewall following sudden heating. In the shadowgraph images, the thermal boundary layer is approximately represented by the vertical dark regions, bonded by a clear bright strip. These bright strips are associated with the extrema of the second derivative of the temperature in approximately the horizontal direction. This position may be used as a measure of the boundary layer thickness [11]. It is clear in Figure 7(a) that the thickness of the thermal boundary layer increases from upstream to downstream, and also grows with time. The shadowgraph images in Figure 7(a) have been processed by subtracting a background image recorded immediately before the start of the experiments in order to display more clearly the thickness variations of the thermal boundary layer.

As previously described (also refer to [15]), a scaling relation ($\delta_T \sim (\kappa \cdot t)^{1/2}$) may be used to characterize the thickness growth of the thermal boundary layer with time in the initial stage. Figure 7(b) plots the time series of the thicknesses measured at three different locations along the sidewall. The thickness is determined as the width of the dark strips, typically shown in Figure 7(a), and the measurements have been taken from the full time series of images. The thickness values in Figure

7(b) show step changes with time. This is because the resolution of the imaging system is 0.44 mm per pixel in the present experimental set-up, and any variations of less than 0.44 mm cannot be detected by the imaging system. Note that Figure 7(b) plots the measured thickness of the thermal boundary layer against the scaling prediction, and reveals that the experimental measurements are consistent with the theoretical prediction of $(\kappa t)^{1/2}$ for the initial 10 seconds although the slopes of the fitting lines are not equal to unity. As time increases, the measurements deviate from the scaling (the deviating times at heights -0.052, 0.015 and 0.089 m are about 10 s, 14 s and 20 s, respectively), suggesting that convection effects become important. After approximately 20 seconds, the thickness at the height of 0.089 m starts to fluctuate and eventually approaches a constant value. Indeed, the waves at the height of 0.089 m are caused by the leading edge effect (see [16]).

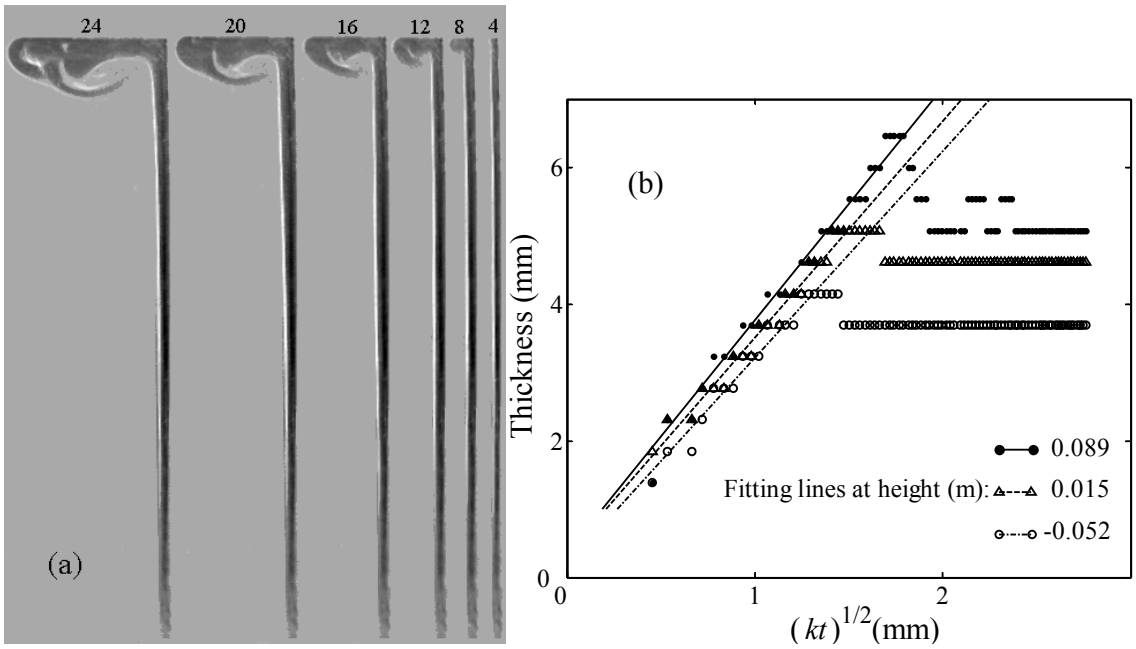

Figure 7. (a) Shadowgraph images of the thermal boundary layer adjacent to the hot sidewall at different times (from 4s to 24s) for $Ra = 3.9 \times 10^9$. (b) Thickness of the thermal boundary layer vs time.

CONCLUSIONS

The present paper has presented examples of application of the PIT and shadowgraph visualization methods for the estimation of thermal boundary layer thickness in natural convection flows.

The first example shows the application of the PIT technique for the estimation of the thermal boundary layer growth carried out in a reservoir model subject to sudden cooling at the water surface. Two equivalent methods of measuring boundary layer thickness were presented, and both produced results consistent with the scaling prediction reported in [15].

The second example shows the application of the shadowgraph technique for measuring the early development of the thermal boundary layer adjacent to the sidewall of a differentially heated cavity following sudden heating. Based on shadowgraph images, the thicknesses of the thermal boundary layer at different heights were measured. The measurements are also consistent with the scaling relation reported in [15].

ACKNOWLEGMENT

The authors are grateful for the financial support of the Australian Research Council.

REFERENCES

1. Park, H. G, Dabiri, D. and Gharib, M., Digital particle image velocimetry / thermometry and application to the wake of a heated circular cylinder, *Experiments in Fluids*, Vol. 30, pp 327-338, 2001.
2. Pigon, K. and Ruziewicz, Z., Chemical Physics - Volume 1, Wydawnictwo Naukowo Techniczne PWN, 1993, in Polish.
3. Smith, C. R., Sabatino, D. R. and Praisner, T. J., Temperature sensing with thermochromic liquid crystals, *Experiments in Fluids*, Vol. 30, pp 190-201, 2001.
4. Fujisawa, N. and Funatani, S., Simultaneous measurement of temperature and velocity in a turbulent thermal convection by the extended range scanning liquid crystal visualization technique, *Experiments in Fluids*, Suppl., pp 158-165, 2000.
5. Stasiek, J.A. and Kowalewski, T.A., TLCs applied for heat transfer research, *Opto-Electronics Review*, Vol. 10, pp 1-10, 2002.
6. Bednarz, T. P., Lei, C. and Patterson, J. C., An experimental study of unsteady natural convection in a reservoir model subject to periodic thermal forcing using combined PIV and PIT techniques, *Experiments in Fluids*, 2009, in press.
7. Merzkirch, W., Flow Visualization, Academic Press, New York, 1974.
8. Schöpf, W. and Patterson, J. C., Natural convection in a side-heated cavity: visualization of the initial flow features, *Journal of Fluid Mechanics*, Vol. 295, pp 357-279, 1995.
9. Schöpf, W. and Patterson, J. C., Visualization of natural convection in a side-heated cavity: transition to the final steady state, *International Journal of Heat and Mass Transfer*, Vol. 39, pp 3497-3509, 1996.
10. Settles, G. S., Schlieren and Shadowgraph Techniques, Springer-Verlag, New York, 2001.
11. Lei, C. and Patterson, J. C., Natural convection in a reservoir sidearm subject to solar radiation: experimental observations, *Exp. Fluids*, Vol. 32, pp 590-599, 2002.
12. Bednarz, T. P., Lei, C. and Patterson, J. C., Particle image thermometry for natural convection flows, *16th Australasian Fluid Mechanics Conference*, Gold Coast, December 2-7.
13. Bednarz, T. P., Lei, C. and Patterson, J. C., An experimental study of unsteady natural convection in a reservoir model cooled from the water surface, *Experimental Thermal and Fluid Science*, Vol. 32, pp 844-856, 2008.
14. Bednarz, T. P., Lei, C. and Patterson, J. C., A numerical study of unsteady natural convection induced by iso-flux surface cooling in a reservoir model, *International Journal of Heat and Mass Transfer*, Vol. 52, pp 56-66, 2009.
15. Patterson, J. C. and Imberger, J., Unsteady natural convection in a rectangular cavity, *J. Fluid Mech*., Vol. 100, pp 65-86, 1980.
16. Patterson, J. C., Graham, T., Schöpf, W. and Armfield, S. W., Boundary layer development on a semi-infinite suddenly heated vertical plate, *J. Fluid Mech*., Vol. 453, pp 39-55, 2002.

ExHFT-7
28 June – 03 July 2009, Krakow, Poland

SPANWISE VORTEX STRUCTURE FROM AN IN-LINE FORCED OSCILLATING CIRCULAR CYLINDER

Y. Yokoi[1, *], K. Hirao[2]
[1]The National Defense Academy, Yokosuka, Japan
[2]Japan Air Self-Defense Force, Kakamigahara, Japan

ABSTRACT. In this study, the flow features of vortex shedding from a circular cylinder oscillating along the direction of the flow were observed by visualizing water flow experiment at the ranges of the frequency ratio f/f_K=0 ~ 5, amplitude ratio $2a/d$ = 0.4 and Reynolds number Re = 1700. As a result of the experiments, the structure of the vortex flow which depends on the frequency ratio was clarified by observing flow from both to the axial direction and the direction of span. In the case of lock-in state f_{VK}/f = 1/1, two kinds of vortex structure were obtained. One of which was three-dimensional on the side of low oscillation frequency, and the other was two-dimensional on the side of high oscillation frequency. In the case of lock-in state f_{VK}/f = 1/2, even if the lock-in had occurred, it was shown that the time difference sometimes occurred to the direction of the span in vortex shedding.

Keywords: *vortex, lock-in, in-line oscillation, flow visualization*

INTRODUCTION

The flow induced vibration problem is very important problem for engineering field so that there are many reports and useful knowledge has been accumulated by many researchers [1]. The 'lock-in' is the phenomenon which the vortex shedding frequency from a cylinder synchronizes with the frequency of cylinder vibration. And it is one of most interesting phenomenon in the field of flow induced vibration. In recent years, the review and the view about the flow-induced vibration including the lock-in phenomenon were reported by Griffin and Hall [2] and Okajima [3] [4]. Although there are many studies about the lock-in and its flow pattern, there are few reports which example to have examined to use a lock-in phenomenon effectively industrially. In order to examine the industrial use of the lock-in phenomenon, the lock-in range and the state of the flow at the time of lock-in must be more widely known in detail. Therefore, the systematically and scrupulous investigation by which the range of oscillation frequency and amplitude expanded becomes necessary, and database which accumulated the results is required. Yokoi and Hirao [5] investigated the effect of cylinder oscillation on vortex shedding and they show the flow pattern distribution in the lock-in region by flow visualization. In general, many of studies that observe the flow pattern from an oscillating cylinder and the range of the lock-in are observed from the plane including the cylinder section and there are few studies which observe from the direction of the cylinder span. It is important to understand the vortex structure with a three-dimensional aspect to understand the flow induced vibration problem. In this study, the flow features of vortex shedding from a circular cylinder oscillating along the direction of the flow were investigated from the direction of cylinder span by visualizing water flow experiment.

* Corresponding author: Dr. Y . Yokoi
Phone: + (81)-46-8413810 Ext. 3416, Fax: + (81)-46-8445900
E-mail address: yokoi@nda.ac.jp

EXPERIMENTAL APPARATUS AND METHOD

Experimental apparatus

The experimental apparatus consists of a closed circuit water channel, a cylinder oscillator, a set of visual apparatus and set of data record equipment. Figure 1 shows the cover shot and the drawing of the closed circuit water channel. The closed circuit water channel is a vertical circulation type of 5.8m in length, 1.2m in width, and 2.5m in height, and the volume of water is 4 tons. The water channel is consisted of water flow generation equipment (2 axial flow type pumps), rectification device, test section and 4 corner parts with guide vanes. The test section is 2m in length, 0.8m in width, 0.4m in depth, and the flume structure with the surface of the water. In the test section, the window made of the glass of 1.5m in length and 0.4m in width has been installed in the both sides wall and the bottom for the observation. The velocity distribution in the test section was ±1.5% against main flow velocity 0.4m/s from depth 50mm-350mm and the test section center in the direction of width within the range of ±300mm. There is a set of rail orbit on the flume flange and a carriage is set up. The oscillator which installed CCD (charge-coupled device) camera and circular

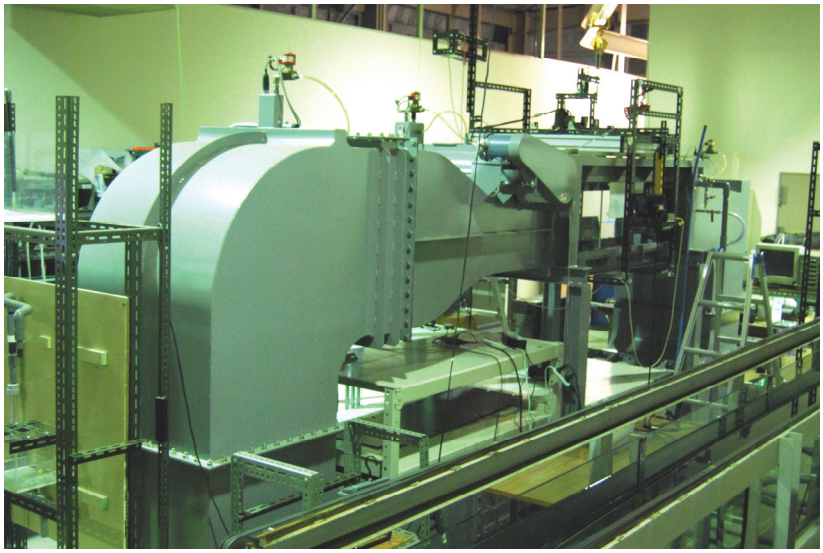

(a) Aspect of closed circuit water channel

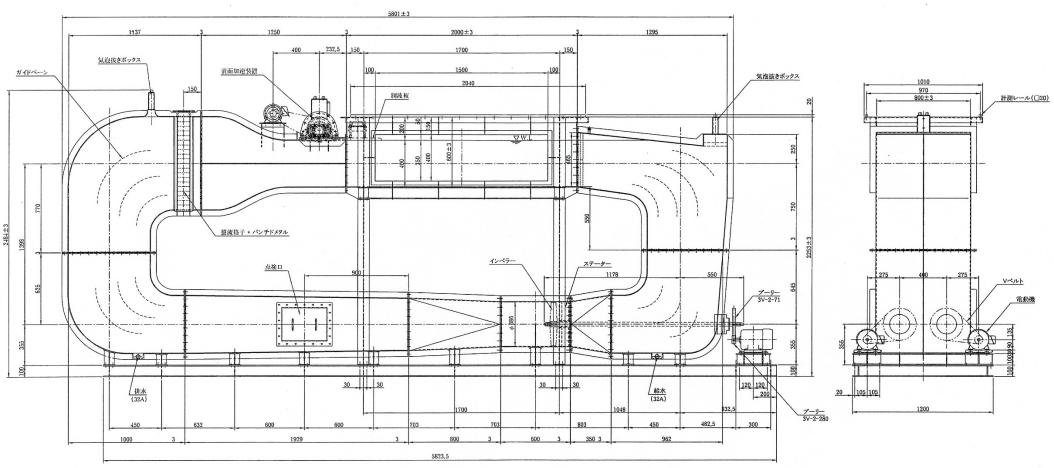

(b) Schematic diagram (the carriage and the equipment on the carriage are not written here)

Fig. 1 The cover shot and the drawing of the closed circuit water channel

cylinder, the visualization apparatus are loaded into the carriage. Figure 2 shows the schematic diagram of the cylinder oscillator. The cylinder oscillator is using a Scotch-yoke mechanism and the oscillator consists of a small-sized variable DC motor with a controller, a turn disk and a connecting rod. The amplitude of oscillation is set by changing the rotation radius of connecting edge on the turn disk, while the frequency of oscillation is controlled by changing the revolution speed of the turn disk.

Test circular cylinder and flow visualization method

The test circular cylinder is made from acrylic resin with 20mm of outside diameter, 16mm caliber, 440mm length. As shown in Figure 3, dye ooze ports (φ1mm) for the flow visual observation are arranged from a front stagnation point to the position of ±60° on the surface of the circular cylinder by two rows, and 50 and 51 ports are made respectively at intervals of 4mm. The row of the dye port becomes independent respectively, and can use the color of the tracer properly. An acrylic disk of 200mm in the diameter with 30° sharp edge is set up respectively at both ends of the circular

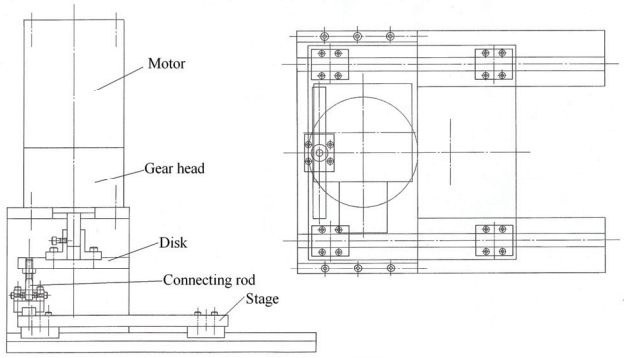

Fig. 2 Schematic diagram of the cylinder oscillator

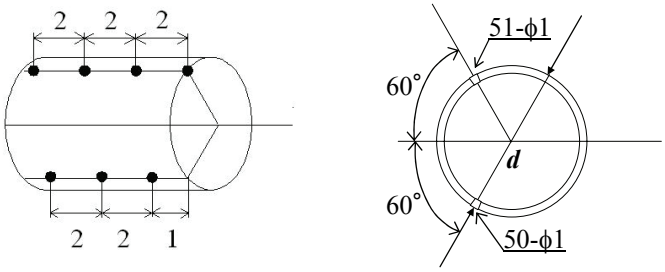

Fig. 3 Arrangement of dye ports on a surface of circular cylinder

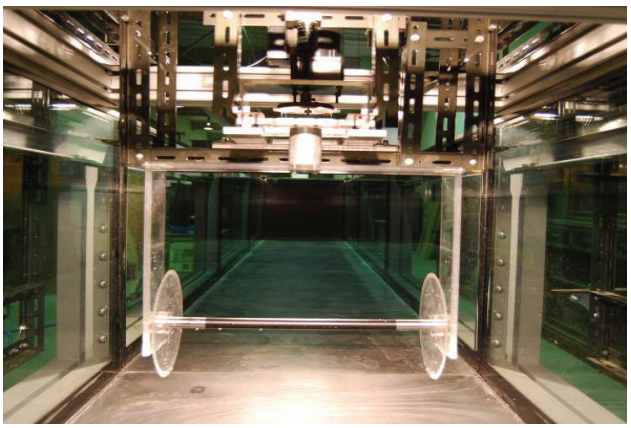

Fig. 4 Circular cylinder installation situation

cylinder span 400mm. As shown in Figure 4, the circular cylinder is installed in the oscillator by the horizontal posture through the holder arm to become 250mm under the surface of the water when the water level in the test section of closed circuit water channel is assumed to be 400mm, and oscillates periodically to the direction of the flow.

The flow visualization was performed with the aid of dye injection method. The tracer inks of two colors that the specific gravity is adjusted ('Color-fan': turquoise and fluorescent pink) are oozed from the dye ports on the surface of cylinder. Two halogen lamps (white light 500W) were used for the lighting, and it was applied from the observation window of both sides of the test section of water channel. Two CCD video cameras were used to take a picture of the aspect of the flow. One was set up to look about the direction of the span, and other one was set up as seen axially. The visualized flow patterns were monitored by the CCD video cameras and recorded on video tapes

Experimental parameters

The main experimental parameters given by the oscillation frequency ratio f/f_K (the ratio of circular cylinder oscillation frequency f to natural Karman vortex's frequency f_K), the amplitude ratio $2a/d$ (the ratio of half amplitude of cylinder motion a to the outside diameter of cylinder d) and the mean flow velocity U in the test section. The mean flow velocity U was 0.085 m/s which correspond to Reynolds number Re about 1700 ($Re=Ud/v$, where v is the kinematic viscosity of water. The amplitude ratio $2a/d$ was set 0.4, and the oscillation frequency ratio f/f_K was varied from 0.0 to 5.0.

Experimental procedure

The experiment was performed by the following procedures. The flow velocity of the test section is set by inputting the operating frequency to the operating control board. The oscillation amplitude of the circular cylinder is set with the cylinder oscillator. And, circular cylinder oscillation frequency f is gradually set based on the natural Karman vortex shedding frequency f_K which is shed from stationary cylinder. Two kinds of tracer ink for the flow visualization are oozed from the surface of the oscillating circular cylinder. The arrangement of colors of the tracer inks is assumed that the surface of the water side is fluorescent pink, and the bottom of the water side is a turquoise (blue). The visualized flow features were monitored with two CCD video cameras, and recorded in video tapes. Here, in this experiment, the observation point of vortex shedding frequency was $2.5d$ and $5.5d$ behind the cylinder. The vortex shedding frequency was obtained from the number and the measurement time of past vortex at the observation point. The cylinder oscillation frequency was measured by frequency analyzer.

EXPERIMENTAL RESULTS AND DISCUSSION

The visualized flow experiment that observed the direction of the circular cylinder span was performed based on a previous experimental result [5]. The variation of mean vortex shedding frequency ratio f_{VK}/f_K with oscillation ratio f/f_K is shown in Figure 5, in which the abscissa is the oscillation frequency ratio f/f_K and the ordinate is the vortex shedding frequency ratio f_{VK}/f_K. Two solid lines in the figure have the ratio of the vortex shedding frequency in case of the cylinder oscillation f_{VK} and the circular cylinder oscillating frequency f and mean the 'lock-in' status. Therefore, the occurrence of lock-in can be assumed when experimental data are shown on the line. It is noteworthy that if the vortex shedding frequency ratio f_{VK}/f_K is close to unity, the effect of the circular cylinder oscillation frequency on the vortex shedding frequency seems to be small. If there is no difference between f_{VK} and f_K, it means that the vortex shedding frequency f_{VK} is independent of the oscillation frequency f. It is shown to begin to receive the influence of the cylinder oscillation as the oscillation frequency increases, to enter the state of the lock-in of $f_{VK}/f=1/1$, the state of the lock-in of $f_{VK}/f=1/2$, and the state of the lock-in of $f_{VK}/f=1/1$, and to come off from the state of the lock-in. Here, the symbols from "A" to "H" in the figure show the observation points in this experiment.

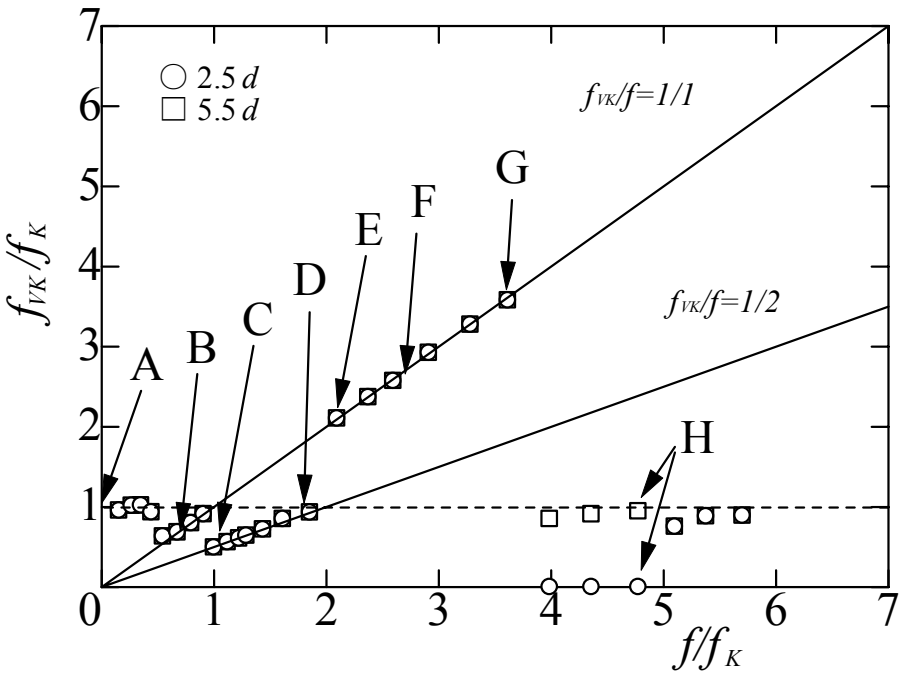

Fig. 5 Variation of mean vortex shedding frequency ratio f_{VK}/f_K with oscillation frequency ratio f/f_K

Figure 6 shows the flow visualization photographs of the vortex flow around a stationary or oscillating circular cylinder seen from the direction of the span. In order to facilitate the visual understanding of the vortex structure, the flow pattern seen from the direction of the cylinder axis is shown together in figure. Figure 6(a) shows the feature of the vortex shedding from a stationary circular cylinder in the direction of the span. The flow seems two dimensional when seeing axially because the vortex is alternately shed and Karman vortex street is formed. However, the tracer streak line swings when the flow feature is seen from the direction of the span. Therefore, it is surmisable that the flow around stationary circular cylinder is a three-dimensional flow. The characteristic of a three-dimensional separation flow on a stationary circular cylinder is reported by references [6] and [7]. It is one of the most interesting experiments of this study to examine how the characteristic of a three-dimensional separation flow on the oscillating circular cylinder changes.

Figure 6(b) shows the flow feature of the low frequency side of the f_{VK}/f=1/1 lock-in. The vortex structure of the direction of the span is three-dimensional though vortices are shed simultaneously from both sides of the circular cylinder.

Figures 6(c) and 6(d) show the flow feature of the f_{VK}/f=1/2 lock-in state. Figure 6(c) shows the flow feature on the low frequency side of the f_{VK}/f=1/2 lock-in. Although vortices are shed simultaneously from both sides of the circular cylinder, an alternate vortex street is formed because the direction of vortex shedding has changed. A complex flow feature can be seen by seeing from the direction of the span. As for the roll of the separated shear layer, it is seen not two dimensional because there is locally a time difference. The direction of the vortex shedding will change in an arbitrary circular cylinder section because the roll of the lower side separated shear layer that a blue tracer shows and the roll of the upper side separated shear layer that a pink tracer shows exist simultaneously attended with the time difference. When the cylinder oscillation frequency f is increased further, the vortex of the mushroom section shape is formed as shown in

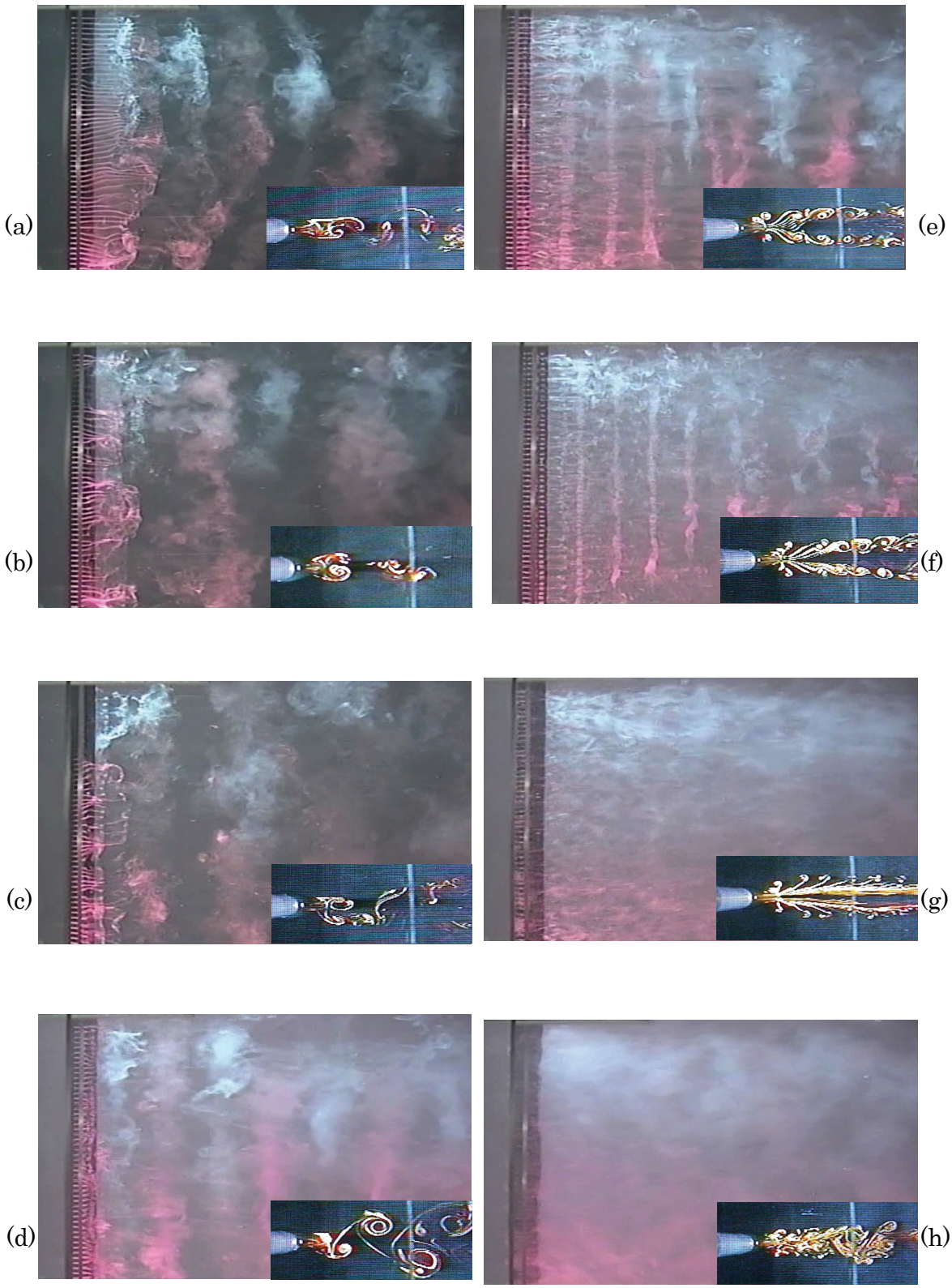

Fig. 6 Representative flow patterns, (every points correspond to Fig. 5)
(a) f/f_K=0.00, (b) f/f_K=0.71, (c) f/f_K=1.09,
(d) f/f_K=1.94, (e) f/f_K=2.06, (f) f/f_K=2.85,
(g) f/f_K=3.59, (h) f/f_K=4.85,

Figure 6(d). It shows the flow feature on the high frequency side of the f_{VK}/f=1/2 lock-in. It was observed to become a two dimensional vortex structure though there was no time difference in the roll of the separated shear layer in the direction of the span in such a case. It was obtained that the structure of the vortex flow was different because of the existence of the time difference of the roll of the vortex in the direction of the span even if it was the same state of the f_{VK}/f=1/2 lock-in.

It becomes the lock-in of f_{VK}/f=1/1 on the high frequency side when the vibration frequency is increased, and the symmetry vortex street is formed as shown in Figure 6(e). In this case, the roll of the vortex in the direction of the span is two dimensional, and it is understood that the union of the vortex in the same direction of the rotation is shown in the cylinder wake. Vortices of the mushroom section shape are shed as shown in Figure 6(f) when the cylinder oscillation frequency f is further increased and the stagnation area where an unstable wave like as Kelvin-Helmholtz's instability was accompanied is formed. In this case, the vortex structure of the direction of the span seems to be two dimensional, and it is observed that the character is kept long. Figure 6(g) shows the flow feature when the oscillation frequency is increased more than the state of Figure 6(f). Small vortices of the mushroom section shape are shed from both sides of the circular cylinder and a long stagnation area is formed. However, remarkable horizontal vortexes are not seen in this case in the vortex structure of the direction of the span.

Figure 6(h) shows the flow feature in the state of non lock-in. It is shown that the discharge of the vortex becomes massive, unites some of that, and forms the oscillation flow. However, the vortex structure of the direction of the span cannot be clearly captured by this flow visualization technique.

These photographs show that the discharged vortex structure depends on a three dimensional character in the direction of the span. In order to clarify such a correlation, the simultaneous observation from axially and the direction of the span becomes important. And, it is likely to become a research topic in the future. In the vortex shedding from the circular cylinder that oscillating in the direction of the flow, it was clarified that the vortex structure was different depending on the oscillation frequency ratio f/f_K in the same state of the lock-in as a result of investigating the span-wise vortex structure. For the case of f_{VK}/f=1/1 lock-in, there are two lock-in areas. Figure 6(b) shows the state of the lock-in caused on the low frequency side, and the span-wise characteristic is not two dimensional. On the other hand, Figures 6(e) and 6(f) show the state of the lock-in caused on the high frequency side, and the span-wise characteristic is two dimensional. Moreover, for the lock-in of f_{VK}/f=1/2, the characteristic is different because it depends on the oscillation frequency ratio f/f_K in the lock-in area though the lock-in area is one. As shown in Figures 6(c) and 6(d), it has been understood that there is the time difference (time delay) is in the roll of the vortex in the direction of the span on the low frequency side and there is no time difference on the high frequency side.

CONCLUSIONS

Focusing on the appearance of the three-dimensional instability in separated flow, a flow visualization study on features of boundary layer separation over an oscillating circular cylinder was performed. The following conclusions were obtained.

(1) In the vortex shedding from an oscillating circular cylinder in the direction of the flow, the appearance of the flow feature of the direction of the span corresponding to the flow pattern of the vortex flow seen axially was obtained.

(2) As for the same state of the f_{VK}/f=1/1 lock-in, the structure of the direction of the span was observed to differ on the low frequency side and the high frequency side. Two kinds of vortex

structure were obtained. One of which was three dimensional on the side of low oscillation frequency, and the other was two dimensional on the side of high oscillation frequency.

(3) In the case of lock-in state f_{VK}/f=1/2, even if the lock-in had occurred, it was shown that the time delay sometimes occurred to the direction of the span in time of vortex shedding. It has been understood that the time delay decides the characteristic of the flow. That is, when there is no time difference in the direction of cylinder span at the roll of the vortex, the characteristic of vortex structure becomes two dimensional, and when there is a time difference in the direction of cylinder span at the roll of the vortex, the characteristic of vortex structure becomes three dimensional.

REFERENCES

1. The Japan Society of Mechanical Engineers ed., *Guideline for Evaluation of Flow-Induced Vibration of a Cylindrical Structure in a Pipe*, The Japan Society of Mechanical Engineers, 1998, pp. B1-B88.
2. Griffin, O.M. and Hall, M.S., Review-Vortex Shedding Lock-on and Flow Control in Bluff Body Wakes, *Trans. ASME J. Fluids Eng*., Vol.113, pp. 526-537, 1991.
3. Okajima, A., Flow-Induced Vibration of Bluff Body, *Transaction of Japan Society of Mechanical Engineers, Series B*, Vol.65, No.635, pp.2190-2195, 1999.
4. Okajima, A., Vortical Flow and Fluiddynamic Characteristics of an Oscillating Bluff Body, *Transaction of Japan Society of Mechanical Engineers, Series B*, Vol.66, No.644, pp.948-953, 2000.
5. Yokoi, Y. and Hirao, K., Vortex Flow Around an In-Line Forced Oscillating Circular Cylinder, *Transaction of Japan Society of Mechanical Engineers, Series B*, Vol.74, No.746, pp.2099-2108, 2008.
6. Yokoi, Y. and Kamemoto, K., Initial Stage of a Three-Dimensional Vortex Structure Existing in a Two-Dimensional Boundary Layer Separation Flow (Observation of Laminar Boundary Layer Separation over a Circular Cylinder by Flow Visualization), *JSME International Journal, Series II*, Vol.35, No.2, pp.189-195, 1992.
7. Yokoi, Y. and Kamemoto, K., Initial Stage of a Three-Dimensional Vortex Structure Existing in a Two-Dimensional Boundary Layer Separation Flow (Visual Observation of Laminar Boundary Layer Separation over a Circular Cylinder from the Side of a Separated Region), *JSME International Journal, Series B*, Vol.36, No.2, pp.201-206, 1993.

VELOCITY AND CONCENTRATION FIELD OF DISCHARGE FROM A BOAT PROPELLER

R. Situ*, R. J. Brown, A. Loberto
School of Engineering Systems, Queensland University of Technology, Brisbane, Australia

ABSTRACT. Two-stroke outboard boat engines using total loss lubrication deposit a significant proportion of their lubricant and fuel directly into the water. The purpose of this work is to document the velocity and concentration field characteristics of a submerged swirling water jet emanating from a propeller in order to provide information on its fundamental characteristics. Measurements of the velocity and concentration field were performed in a turbulent jet generated by a model boat propeller (0.02 m diameter) operating at 1500 rpm and 3000 rpm. The measurements were carried out in the Zone of Established Flow up to 50 propeller diameters downstream of the propeller. Both the mean axial velocity profile and the mean concentration profile showed self-similarity. Further, the stand deviation growth curve was linear. The effects of propeller speed and dye release location were also investigated.

Keywords: *propeller, swirl jet, turbulence, concentration field, self-similarity*

INTRODUCTION

Boats and ships release approximately 1.0 million tonnes of oil into the marine environment worldwide each year [1]. In addition, significant quantities of unburned fuel, toxic combustion by-products and well over 14 million tonnes of antifouling agents (tri-butyl tin) are directly released into the water and dispersed by the vessels' propeller annular. In all situations, propellers create considerable turbulence, which thoroughly mixes pollutants and chemicals into the water. While there has been considerable research on propellers for ship propulsion, very little research has been done on the dispersing action of the propeller. Nevertheless, to estimate the effective contaminant concentrations emitted by vessels, it is of great importance to quantify flow field in the jet region.

Turbulent jet flow issued from an orifice has been investigated for more than fifty years. Albertson [2] classified the jet diffusion into two zones: the Zone of Flow Establishment (ZFE), and the Zone of Established Flow (ZEF). The ZFE starts from the outlet of the orifice and ends where mixing with surrounding fluid reaches the centreline of the jet. In the follow-up ZEF, the cross-sectional mean axial velocity profiles exhibit a Gaussian normal distribution and dynamic self-similarity. Furthermore, the velocity profile is independent of the details of the generating source of the jet [3]. Hence, this self-similarity can also be found in a swirling jet and an impeller jet. A swirling jet is characterised by the presence of the centrifugal effect that produces transverse and longitudinal pressure gradients. It is widely used in different technological processes and in engineering. The swirling flow may be generated by: i) mixing of tangential flow with axial through-flow [4, 5]; ii) rotating long pipe [6–8], and iii) vanes for turbines, compressors, or propellers [3, 9, and 10].

* Corresponding author: Dr. Rong Situ
Phone: + (61)-7-31382452, Fax: + (61)-7-31388381
E-mail address: situ@qut.edu.au

Although many investigations have been attempted on air swirling jets, only a few workers have studied the limited range of a water jet emanating from a propeller [11]. The purpose of this paper is to document the velocity and scalar field characteristics of a water swirling jet, and to provide information on the fundamental characteristics of such a jet far enough downstream to make it relevant to the eventual modelling of this mixing problem.

EXPERIMENTAL FACILITY AND PROCEDURES

The experimental setup comprised a three-bladed propeller, powered by a variable speed electric motor with flexible cable transmission, held in space by an aerofoil-shaped frame where the long axis coincides with direction of flow. A schematic showing the major experimental spatial parameters can be seen in Figure 1. The axial coordinate referred to throughout this paper is the *x*-axis shown, while the tangential coordinate is perpendicular to the page in Figure 1 as it is tangential to the propeller blade rotational plane. The source of the jet used in this experiment was a commercialised scale-model boat propeller made of three brass blades. The propeller tip diameter, D_p, was 20 mm. Dye was released at a constant volume flow rate for each profile from two point locations, namely: i) upstream of the propeller by 4 mm along the centreline and 8 mm above the axis of rotation, ii) downstream, symmetric in the *x-y* plane with above. The internal diameter of the injection pipe was 1 mm. The flow of dye was constant maintained by a syringe pump driven from a feed screw running at a constant rotational speed.

The tests were conducted in the closed loop flume at the Department of Mechanical Engineering at Kyoto University, Japan. The flume had dimensions of 12 m (L) × 0.4 m (W) × 0.2 m (H). The water level and also the volume flow rate in the flume were controlled with a straight edged weir at the exit and a header tank. The water level was held at 150 mm for all experiments. The Reynolds numbers for the jet flow in these experiments were 1.4×10^4 and 6.2×10^4 respectively, corresponding to propeller speeds of 1500 rpm and 3000 rpm. The ambient velocity and characteristic length for the flume is 0.04 m/s and 0.086 m respectively. The maximum error in the alignment of the test rig was less than 0.25%. The error in velocity measurements was mainly due to refractive index fluctuations, and was estimated to be 0.3%.

Instantaneous stream-wise and vertical water velocities were simultaneously measured by using a two-colour laser-Doppler velocimeter (LDV, DANTEC 55X) [12]. The turbulent intensity and Reynolds stress were also measured. The mean and fluctuations in the concentration were measured with a Komori concentration probe, held in place by an adjustable frame. The Komori probe has a frequency response of up to 100 Hz sampled at rate of 1 kHz. The average maximum variation in back to back mean concentration measurements across a vertical array of data was found to be around 300% [12].

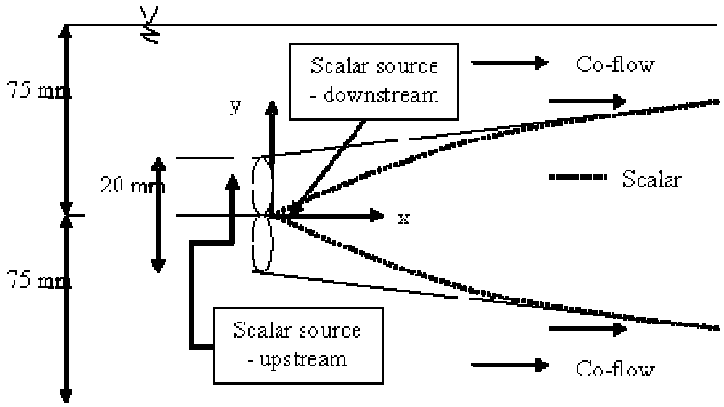

Figure 1. Schematic diagram of experimental setup.

EXPERIMENTAL RESULTS AND DISCUSSIONS

Radial profile of velocity distribution

In current study, velocity measurements were taken from $2.5D_p$ downstream. This means that the jet flow was already established and measurements in the ZFE were not possible. It has been shown in experiments with similar experimental conditions that the mean velocity profiles for a propeller becomes self-similar between approximately $2D_p$ and $3D_p$ [3] and thus the measurements were taken in the ZEF. The practical outcome of this is that from this point further downstream the radial distribution of the mean axial velocity will take on the shape of a Gaussian profile [11].

Mean axial velocity. The full radial fields of mean axial velocity data are displayed for two propeller speeds, N, 1500 rpm and 3000 rpm in Figure 2. The normalisation constant is the tangential tip velocity of the propeller, $U_p = 2\pi NR_p$. Each figure contains five series, representing different axial downstream locations from $2.5D_p$ to $50D_p$. Both figures illustrate the tendency for a slight drift toward the free surface at both speeds. At $x/D_p = 2.5$, within the radial band of $+/-1D_p$, there is some evidence of the local peak velocities from the blades still remaining with the peak velocities occurring either side of the centreline. Inside the ZFE, the axial velocity will vary with radial position along the blade. The position of maximum velocity coincides with the position of maximum thrust and this is taken to be located between $0.5R$ to $0.7R$ [3, 10, 11]. The results here appear to lie approximately in this zone, and they are similar to those described by Petersson et al. [10] where a three-bladed mixer operated in weak co-flow at 1800 rpm. His particular experiment showed a peak of 0.19 at about $r/D_p = 0.25$ at $x/D_p = 2$, whereas here a peak of about 0.35 at around $-0.5D_p$ from the axis at $x/D_p = 2.5$ was observed. Both 1500 rpm and 3000 rpm results show very similar peak magnitudes and location and asymmetric pattern, with good internal consistency. Also, note the small areas of low amplitude negative velocity around $y/D_p = -1$ to -3 at this close proximity to the propeller due to recirculation flow.

Between $x/D_p = 4$ and 6 the peak normalised axial velocity was 0.13–0.10 and the off-axis peak eroded away [10]. Figure 2(a) shows a centred peak of 0.25 at 1500 rpm, while Figure 2(b) shows a broad peak around 1.5 D_p wide (radial) with a magnitude of about 0.21 (both were at $x/D_p = 5$). At $x/D_p = 10$, Figures 2(a) and 2(b) both exhibit a peak of 0.17 while the result of Petersson et al. [10] was approximately 0.08. Their result at $x/D_p = 12$ is similar and those results cease at that point. At $x/D_p = 20$, both figures show similar peaks and distribution, although both are becoming less consistent by this stage. Further downstream at $x/D_p = 50$, both jets are degraded badly and, interestingly, 3000 rpm has half the relative velocity of 1500 rpm. In general, the experiment with

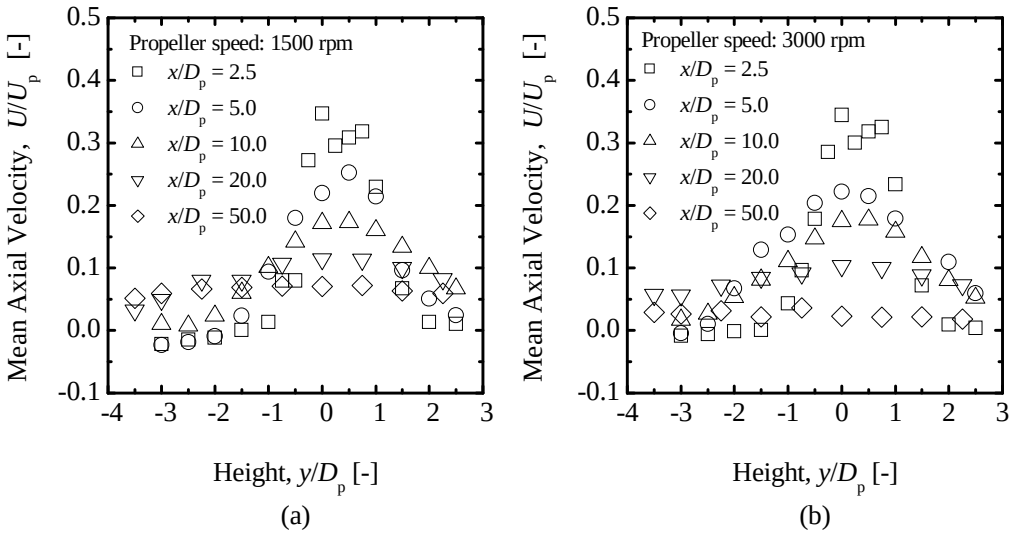

Figure 2. Mean axial velocity profiles.

the small propeller showed relative velocities greater than 1.5–2.0 times those of the three-bladed mixer of Petersson et al. [10], possibly due to the blade profile variations and the emphasis on thrust versus mixing in the case of the smaller 20 mm propeller.

Self-similarity. The mean axial velocities shown in Figure 2 are normalised in Figure 3 with the fitting Gaussian function expressed as:

$$U = U_{\mathrm{m}} \exp\left[-\frac{1}{2}\left(\frac{y-\delta}{\sigma} \right)^2 \right] \tag{1}$$

where U_{m}, δ, σ are local maximum mean axial velocity, vertical offset, and standard deviation, respectively. The vertical offset is determined as the vertical position of the jet maximum velocity relative to the geometric centreline. Since the jet is fully developed into the ZEF by the first measuring position, the evidence of local maximum velocities along the blade vanished and the jet only displays a single maximum. This equation was used by Brown and Bilger [13] for the study of reactive plumes. In contrast to other forms, such as that used by Petersson [10], all the key parameters of magnitude, width, and position are stated explicitly and thus can be exclusively fitted to record physically meaningful statistics about the flow. Figure 3 shows that the data is self-similar at 1500 rpm for all measured locations from $2.5D_{\mathrm{p}}$ to $50D_{\mathrm{p}}$. However, at 3000 rpm the $50D_{\mathrm{p}}$ location failed to allow for a Gaussian profile to be fitted. At this condition the relative mean axial velocity was consistently half what it was at 1500 rpm, right across the whole radial distribution.

Mean tangential velocity. Figure 4 shows the mean tangential velocity distribution at 1500 rpm and 3000 rpm. At both speeds there is a common pronounced peak near the radial position of y/D_{p} = 0.5; this indicates a solid body rotation of water that quickly dissipates downstream [10]. Only at the 3000 rpm condition this structure is maintained to $5D_{\mathrm{p}}$ downstream. This peak at $5D_{\mathrm{p}}$ also moves radially outward from the propeller axis as the swirling jet begins to spread.

A tangential velocity plot where all the data series tend to zero at the axis would indicate good alignment of the measuring apparatus and experimental rig. There is evidence of this trend in Figure 4, but it is not as strong as that exhibited in other similar experiments [10]. Along with a lack of symmetry, this might also be due to the misalignment, which may have even contributed to the far field collapse of the jet at the 3000 rpm condition since the jet edges were being affected by the boundaries and the tolerance for misalignment would be low in these circumstances.

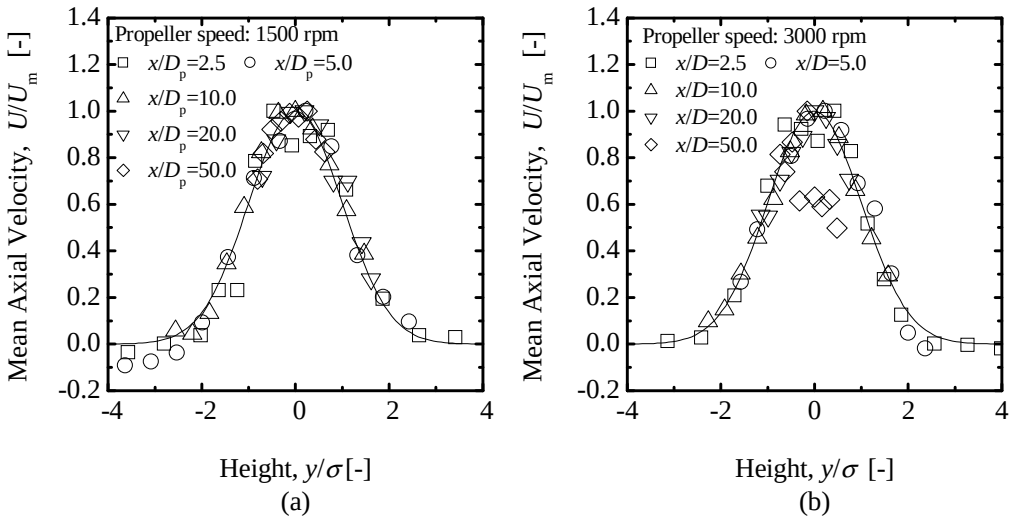

Figure 3. Normalised mean velocity profiles.

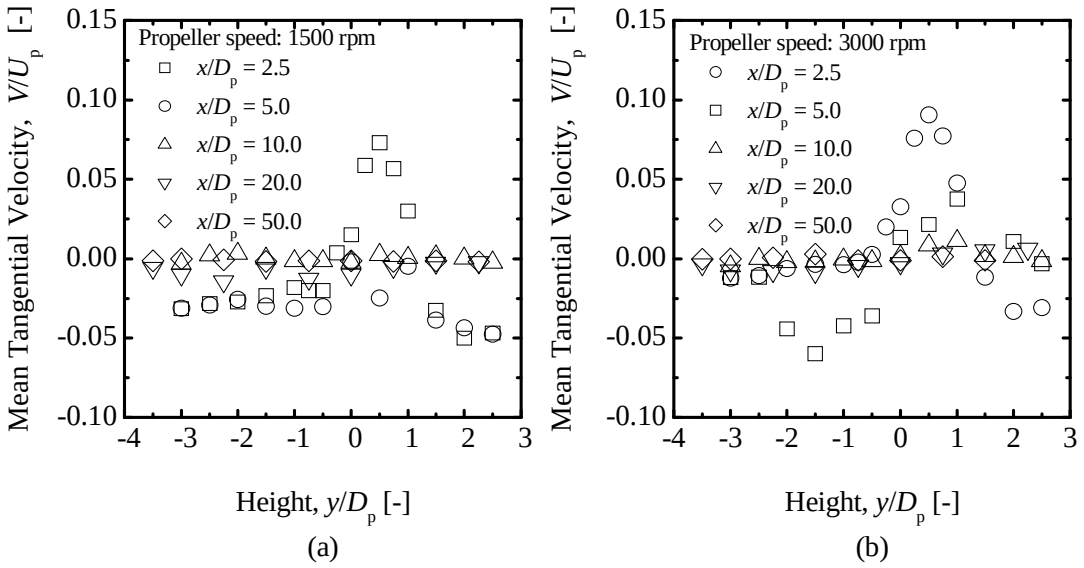

Figure 4. Mean tangential velocity profiles.

Mean axial flow field

Standard deviation growth. As explained earlier, the flow structure in the ZEF shows self-similarity, and the standard deviation of the fitted Gaussian function grows along the flow. Figure 5(a) displays the growth trend of the standard deviation of the water swirling jets for the current study and Petersson et al.'s study [10]. Both datasets displays linear growth with the axial direction. The similar growth trend of standard deviation for air jets are shown in Figure 5(b), where D_0 is the diameter of the orifice or nozzle from which air is issued. The degree of swirling jet is described by a dimensionless swirl number [4] as:

$$S \equiv G_\theta / RG_x = 2\pi\rho \int_{r=0}^{\infty} r^2 UV dr \Big/ R \cdot 2\pi\rho \int_{r=0}^{\infty} r\left(U^2 - \frac{V^2}{2}\right) dr \qquad (2)$$

where R is the radius of the orifice or nozzle, and ρ is fluid density. According to this definition, the swirl numbers for the current study are 0.23 for 1500 rpm and 0.33 for 3000 rpm, respectively.

Volume flux and entrainment. The volume flux, Q, was calculated by integrating the mean velocity profile at each downstream station as:

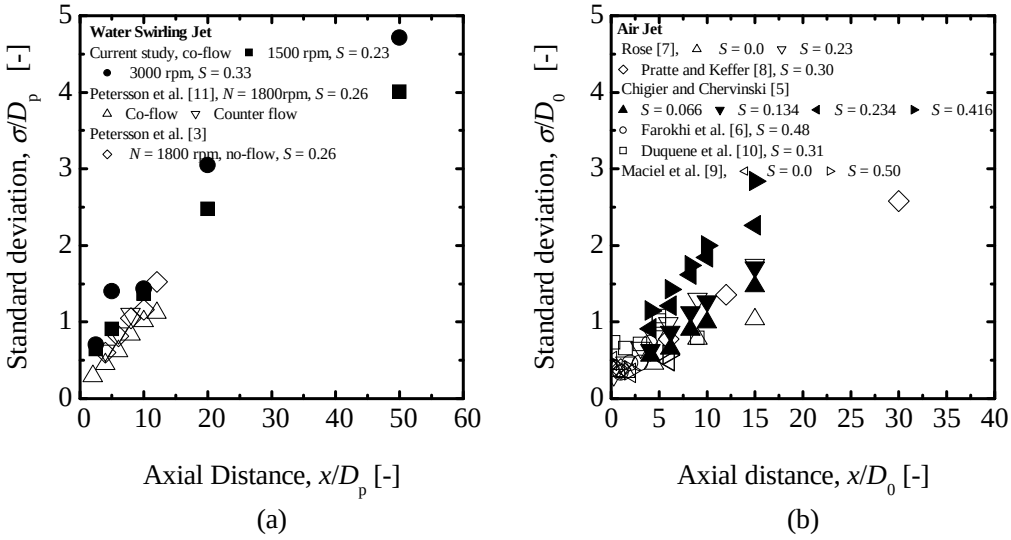

Figure 5. Standard deviation of the mean velocity profile.

$$Q = 2\pi \int_{r=0}^{\infty} rUdr \tag{3}$$

and is normalised against the source momentum $Q_0 = \pi R^2 U_p$. The normalised volume fluxes for both water and air jets display a growth trend along the axial distance in Figure 6. The volume flux at $x = 50D_p$ is not shown for two reasons. First, the self-similarity breaks down most downstream from the propeller, and the flow is more dependent on the ambient flow. Second, the walls of the flume are seemingly affecting the entrainment; this was also pointed out by Petersson et al. [3].

Figure 6 (a) shows that the normalised volume flux of the current data is about four times higher than those obtained by Petersson et al. [10]. The standard deviations of the two datasets are similar, as shown in Figure 6(a). This large difference is mostly due to the difference in the amplitudes of axial velocity. Figure 6(b) plots the normalised volume flux for air jets by Rose [6] and Chigier and Chervinsky [4]. It clearly shows that in an unconstrained jet one would expect to see continual steady growth with increasing distance downstream. Furthermore, the volume flux increases with increasing swirl number, which tends to entrain more ambient fluid into the jet. In addition, the correlation proposed by Albertson [2] agrees well with the data for non-swirl flow ($S = 0$).

Concentration field

Mean concentration field. The mean concentration field was recorded at five measuring stations, i.e., $x/D_p = 2.0$, 2.5, 5, 10, and 20, with the source both upstream and downstream of the propeller. The downstream source experiment was only conducted at a propeller speed of 3000 rpm, and the upstream experiment was conducted at both 1500 rpm and 3000 rpm. The collection of data sets is collapsed using self-similarity as shown in Figure 7 The full suite of data is displayed in subsequent sections relating to the individual parametric trends of C_{max}, r' and σ. Comparison between upstream release data, shown in Figure 7(a) and 7(b) indicated that the plume takes longer to establish self-similar behaviour at 3000 rpm. The data points at measuring stations closer to the source tend to fit less well to a best-fit Gaussian curve. On the other hand, the effect of dye release location can be found by examining Figure 7(b) and 7(c). The figures show that placing the scalar source upstream of the propeller would superimpose a more complex and varied mixing regime.

Mean concentration plume standard deviation growth. The rate of spread of the plume was similar in general for all three experimental conditions. This is shown in Figure 8(a): the standard

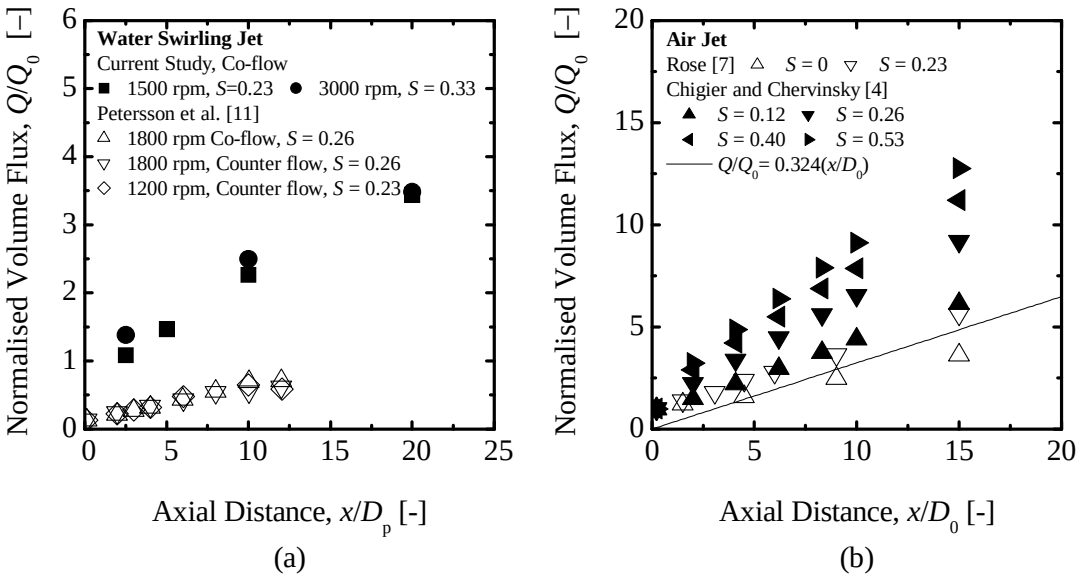

Figure 6. Nomalised volume flux development for water and air jets.

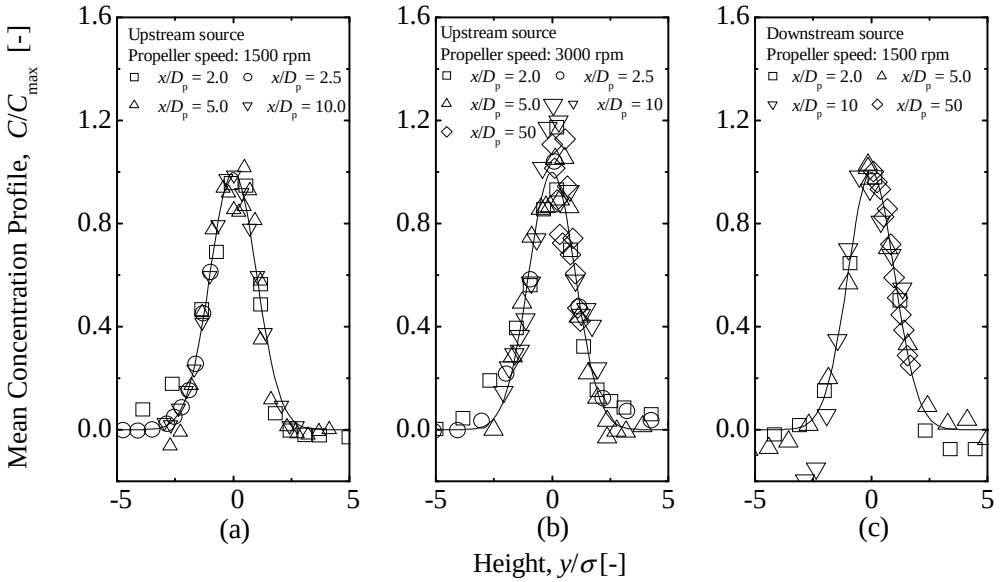

Figure 7. Normalised mean concentration profiles.

deviation of the mean concentration profile. Comparison between these three conditions shows that higher propeller speeds push the virtual origin further upstream (from 2.1 D_p for 1500 rpm to 3.6D_p for 3000 rpm; both for upstream release), and upstream source produces a higher concentration flux spread (7.2° for 3000rpm) than for a downstream source (5.6°).

Concentration Flux Integral. A concentration flux can be calculated in the same way that the velocity field was integrated to calculate volume fluxes:

$$F = \pi \int_{r=0}^{\infty} rUCdr \tag{4}$$

Equation (4) shows that this calculation integrates the products of the instantaneous mean velocity and concentration to give a quantity in the units: ppm.m^{3}s^{-1}. This integral flux trend is displayed in Figure 8(b), normalised against the known source flux, F_s. Figure 8(b) indicates that concentration flux was mainly preserved up to 50 D_p downstream, and the source location has a larger affect than rpm. The decay of mean Gaussian concentrations were dependent on velocity but the radial spreading was dependent on the source condition. The concentration flux integral should be affected to some extent by both of those phenomena because they collectively define the radial concentration

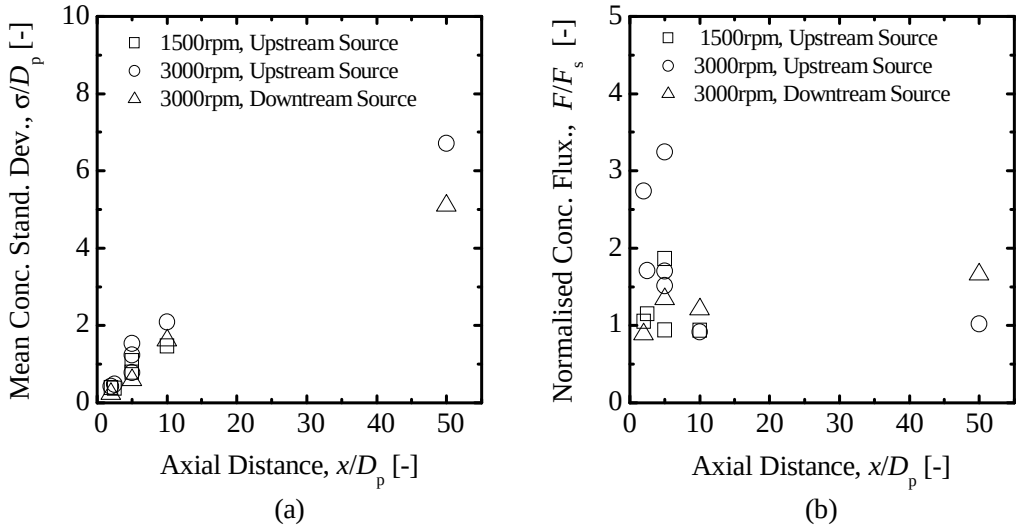

Figure 8. Axial concentration profiles.

profile that has been integrated here. However, at two different speeds, the two upstream source experiments exhibit a similar integral trend, decaying to 10 D_p then settling at a normalised flux of unity. The downstream sourced integral starts around unity and climbs toward 1.5 by $50D_p$.

CONCLUSIONS

Two-stroke outboard boat engines using total loss lubrication deposit a significant proportion of their lubricant and fuel directly into the water. Emissions of outboard motors are largely unaddressed in the literature and could be critical because the exhaust of most outboard engines is released below the water and mixed by the action of the propeller. The purpose of this work is to document the velocity and concentration field characteristics of a submerged swirling jet emanating from a propeller. Measurements of the velocity field (axial and tangential) and concentration field were performed in a turbulent jet generated by a model boat propeller (0.02 m diameter) operating at 1500 rpm and 3000 rpm in a weak co-flow of 0.04 m/s. The measurements were carried out in the ZEF up to 50 propeller diameters downstream of the propeller that was placed in a glass-walled flume, 0.4 m wide with a free surface depth of 0.15 m. Mean velocity and concentration distribution results are presented. Self-similarity of the mean axial velocity and concentration is preserved up to 20 propeller diameters from the propeller. The standard deviation of the fitting Gaussion profile of mean axial velocity and mean concentration shows linear growth along the axial distance. Furthermore, the volume flux shows linear growth while axial momentum flux is mainly preserved for the current data. The effects of propeller speed and dye release location on the velocity and scalar field were also investigated.

REFERENCES

1. Kelly C. A., Ayoki G. A., Brown R. J. and Swarrop C. R., Underwater Emissions from a Two-Stroke Outboard Engine: A Comparison Between An EAL And An Equivalent Mineral, *Mater. Des.*, 26, 609–617, 2005.
2. Albertson M. L., Dai Y. B., Jensen R. A. and Rouse H., Diffusion of Submerged Jets, *ASCE Trans.*, Paper No. 2409, 115, 639–664, 1950.
3. Petersson P., Larson M. and Jonsson L., Measurments of the Velocity Field Downstream of an Impeller, *J. Fluids Eng.-Trans. ASME*, 118, 602–610, 1996.
4. Chigier N. A. and Chervinsky A., Experimental Investigations of Swirling Vortex Motion in Jets, *J. Appl. Mech.*, 34, 443–451, 1967.
5. Farokhi S., Taghavi R. and Rice E. J., Effect of Initial Swirl Distribution on the Evolution of a Turbulent Jet, *AIAA J.*, 27, 700–706, 1989.
6. Rose W. G., A swirling round turbulent jet, 1: Mean flow measurements, *J. App. Mech.*, 29, 615–625, 1962.
7. Pratte B. D. and Keffer J. F., The Swirling Turbulent Jet, *J. Basic Eng.-Trans. ASME*, 93, 739–748, 1972.
8. Maciel Y., Facciolo L., Duwig C., Fuchs L. and Alfredsson P. H., Near-Field Dynamics Of A Turbulent Round Jet With Moderate Swirl, *Int. J. Heat Fluid Flow*, 29, 675–686, 2008.
9. Duquenne A. M., Guiraud P. and Bertrand J., Swirl-Induced Improvement Of Turbulent Mixing: Laser Study In A Jet-Stirred Turbular Reactor, *Chem. Eng. Sci.*, 48, 3805–3812, 1993.
10. Petersson P., Larson M. and Jonsson L., Development of a Turbulent Jet Generated by a Mixer in Weak Co-Flow and Counter-Flow, *Int. J. Heat Fluid Flow*, 21, 1–10, 2000.
11. Hamill G. A. and Johnston H. T., Decay of Maximum Velocity Within the Initial Stages of a Propeller Wash, *J. Hydraul. Res.*, 31, 605–613, 1993.
12. Komiri S. and Nagata K., Effect of Molecular Diffusivities on Counter-Gradient Scalar and Momentum Transfer in Strongly Stable Stratification, *J. Fluid Mech.*, 326, 208–237, 1996.
13. Brown R. J. and Bilger R. W., An Experimental Study of a Reactive Plume in Grid Turbulence, *J. Fluid Mech.*, 312, 373–407, 1996.

THERMAL AND HYDRODYNAMIC STUDY OF A FLAT PLATE HEAT PIPE

S. Lips, F. Lefèvre [*], J. Bonjour
Université de Lyon, CNRS
INSA-Lyon, CETHIL, UMR5008, F-69621, Villeurbanne, France

ABSTRACT. An experimental study of a flat plate heat pipe having a capillary structure made of rectangular grooves is presented. Its thermal performance and hydrodynamic behaviour is analysed for two different filling ratios and for different heat fluxes. A confocal microscope is used to determine the shape of the liquid-vapour interface, and particularly, the value of the meniscus curvature radius along the grooves. The uncertainties associated to this experimental method are discussed. The importance of coupling both thermal performance and pressure drop determination in order to validate numerical models is shown. A good agreement is found between numerical and experimental results.

Keywords: *Flat heat pipe, meniscus curvature, thermal resistance, micro-grooves, confocal microscope*

INTRODUCTION

Flat plate heat pipes (FPHP) are micro-fluidic devices that are usually designed for thermal management of electronic components [1]. They can also be used in others applications, such as the cooling of proton exchange membrane fuel cells [2]. They are used for their heat transfer capacity as well as their capacity of homogenizing the temperature of the heat source.
A FPHP is a cavity of small thickness filled with a two-phase working fluid. Heat sources and heat sinks are located anywhere on the cavity with the other parts being insulated. Heat is transported from heat sources to heat sinks by vaporization of the liquid and condensation of the vapour. The parts of the system where evaporation and condensation occur are the evaporator and the condenser, respectively. The liquid returns from the evaporator to the condenser through a capillary structure made of micro-grooves, meshes or sintered powder wicks.
A lot of works have been published on flat heat pipes and several numerical models have been proposed in order to predict the thermal performance and/or the capillary limit of FPHP or micro heat pipes [2-10]. These models are based on hydrodynamic and thermal governing equations for fluid flow that are solved numerically or analytically. Hydrodynamic and thermal behaviours of a FPHP are highly correlated to the liquid/vapour interfacial shape, and especially the meniscus curvature radius. The major part of the heat flux is transferred through thin films at both the evaporator and condenser locations. Thus, heat transfer phenomena are highly linked to hydrodynamic parameters and to interfacial properties. Although a lot of works have been published on flat plate heat pipes, the literature is poor in experimental papers. Furthermore, the provided measurements are not sufficient to describe the behaviour of these systems, but only to estimate their overall thermal performance. The physical phenomena that drive a heat pipe are complex and cannot be understood only with temperature sensors. Indeed, measurements of the location and the shape of liquid films

* Corresponding author: F. Lefèvre
Phone: + (33)-4 7243 8251, Fax: + (33)-4 7243 8811,
E-mail address: frederic.lefevre@insa-lyon.fr

inside a heat pipe are required in association with temperature measurements to understand the physical mechanisms that drive the system.
In this communication, we present an experimental study of the thermal and hydrodynamic behaviour of a FPHP with micro-grooved as its capillary structure. A confocal microscope is used to measure the meniscus curvature radii in the grooves. The uncertainties due to this experimental method are discussed. The importance of coupling both thermal and hydrodynamic measurements is shown.

EXPERIMENTAL SET-UP

The flat plate heat pipe test apparatus

The flat heat pipe under investigation is shown in figure 1. Its capillary structure, of dimensions 70×90 mm², is made of 88 longitudinal micro-grooves machined in a copper plate. Each groove has a rectangular cross-section of height and width equal to 400 µm. The distance between two grooves is equal to 400 µm. The wall thickness under the grooves and the vapour space are equal to 3 mm and 2 mm respectively. The FPHP is hermetically sealed on its upper face with a transparent plate, which allows the liquid-vapour meniscus observation in the grooves. A filling copper pipe closed by a valve is sealed on the grooved plate at the extremity of the condenser. The heat source is located on the copper wall (Figure 2). It is a heated copper block of dimensions 70 × 20 mm^2 supplied by a 0 - 220 V AC power supply. Electric power is obtained by measuring the voltage drop across the heating resistor and the current, thanks to a calibrated resistance. The heat sink is a water heat exchanger of dimensions 30 × 70 mm^2. The water flow rate is constant and the inlet temperature is controlled by means of a thermostatic bath in order to have a constant working temperature when the heat input increases. The heat source and the heat sink are separated by an adiabatic area of length equal to 40 mm. Two series of nine calibrated thermistors are located symmetrically along the FPHP wall. They are fixed thanks to silver lacquer in small grooves that were machined in the wall in order to reduce the contact resistance (figure 1). The value of their resistance is recorded by a Keithley 2700 multimeter. The working temperature of the FPHP is the saturation temperature T_{sat}, which is determined as the mean temperature of the six thermistors located in the middle of the adiabatic zone. The FPHP is thermally insulated during the thermal tests. Before the thermal tests, the FPHP is degassed and filled carefully [2].

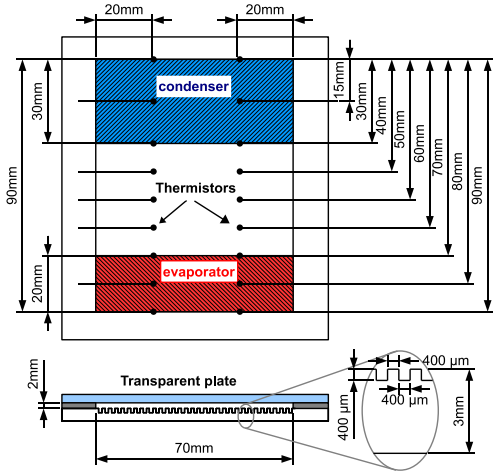

Figure 1: Schematic of the FPHP

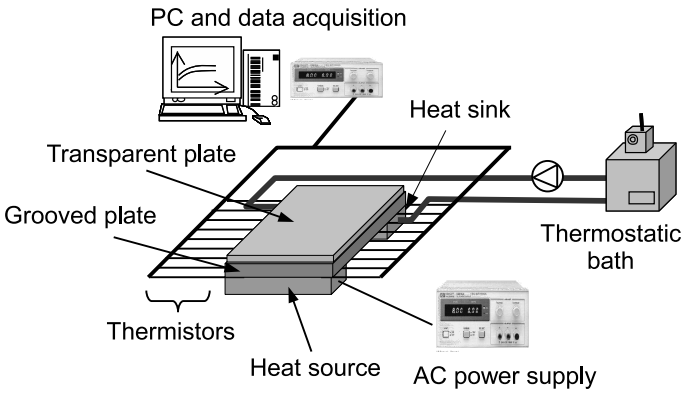

Figure 2: Schematic of the flat heat pipe test apparatus

Confocal microscopy

Measurements of hydrodynamic parameters in a FPHP are difficult: most of non intrusive standard methods are not useful in such an application. For example, the process of insemination used in micro PIV is not appropriate. Indeed, particles introduced in the liquid would be blocked at the evaporator because of their non evaporative properties. Measurements by means of a camera or image-analyzing interferometry through a transparent system are not feasible. Indeed heat sources and heat sinks have to be located on the system, which prevents any optical system to pass through the FPHP. As a result, the liquid film has to be measured from above and not from under. Furthermore, the experimental bench should sustain high pressure variations that occur in working conditions. Among non intrusive methods, confocal microscopy is well adapted to characterization of the liquid/vapour interfacial shape in the capillary structure. The FPHP must be tightly sealed thanks to a transparent plate in order to realize measurements in saturated atmosphere.
Optical principles of confocal microscopy are described in figure 3. A white light point source is decomposed by a chromatic aberration lens into a series of monochromatic point images in the measurement space. The reflected light passes back through the lens and is directed towards a spectral detector by a semi-transparent beam. The spectral analysis of the collected lights that are separated by a spatial filter allows the location of the surface to be measured. The monochromatic light having the highest intensity corresponds to the surface to be measured.
The confocal microscope is a STIL Micromesure 2 system. The chromatic aberration lens is fixed on a motorized system in the *z* direction. The optical sensor has a nominal measuring range of 350 µm and the working distance is about 13 mm. The diameter of the spot is equal to 3 µm. As the measurement is punctual, the FPHP is fixed on a micrometric motorized table in *x* and *y* directions, which allows to achieve profile and surface measurements. The uncertainty in z direction is equal to 60 nm. The optical system has been calibrated to take into account the characteristics of the transparent sealing plate.
The visualisation of profiles or surfaces is limited to steady state configurations. Indeed, the scanning time can vary from few seconds for a small profile to several hours for a surface measurement in high resolution. As a result, the use of confocal microscopy for the study of transient phenomena is difficult and is limited to punctual measurements or to small profile measurements.

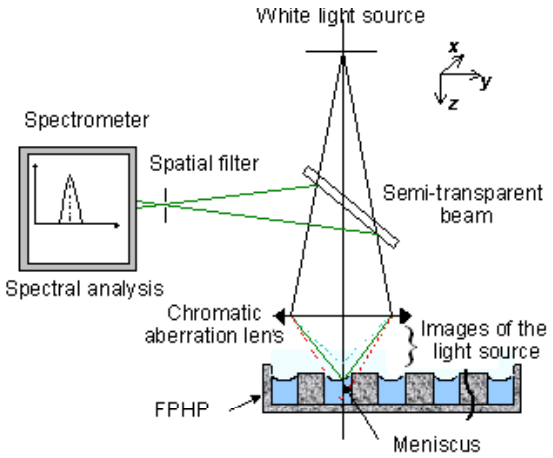

Figure 3: Confocal microscopy principles

EXPERIMENTAL RESULTS

Measurement of the meniscus curvature radius

The thermal and hydrodynamic performance of the FPHP has been characterized for different heat fluxes from 0 W to 88 W and for two different filling ratios f_r. For higher heat fluxes, measurements by confocal microscopy are not possible because of boiling phenomena at the evaporator [11]. Figure 4 presents an example of two profiles obtained at the condenser and at the evaporator of the FPHP. The menisci and the top of the fins are visible. At the evaporator, the junction between the menisci and the top of the fins can not be measured because the slope of the liquid/vapour interface is too stiff and thus, the light is reflected out of the measurement space. However, circles fitting at best the experimental data show that menisci are circular and always attached to the fins top even for small curvature radii. Figure 5 (a) and (b) present the mean curvature radii along the FPHP for different heat fluxes and for filling ratios of 9% and 13%, respectively. The standard deviation of the measurements is indicated for each point under the form of a vertical bar. This uncertainty is not due to the confocal microscope, but to the dispersion of the curvature radius measurements in different grooves at the same position along the FPHP. As a consequence, the radius of curvature has been measured in several grooves and the mean value is retained. The level of meniscus curvature radii increases with the increase of the filling ratio. In non working conditions, the meniscus curvature radius is about 1.5 mm for f_r = 9% and it reaches 2.5 mm for f_r = 13%. Thus, the filling ratio has to be taken into account to model meniscus curvature variations along the grooves and the resulting temperature field. For a fixed filling ratio, it appears that there is a location in the FPHP where the meniscus curvature radius is constant whatever the heat flux. This particular position is closed to the middle of the condenser in this experiment. In [2], Rulliere *et al.* found a similar particular position that was located in the adiabatic zone.

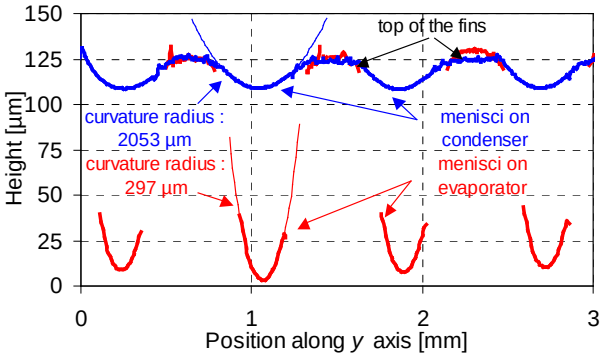

Figure 4: Menisci visualization at the condenser and the evaporator

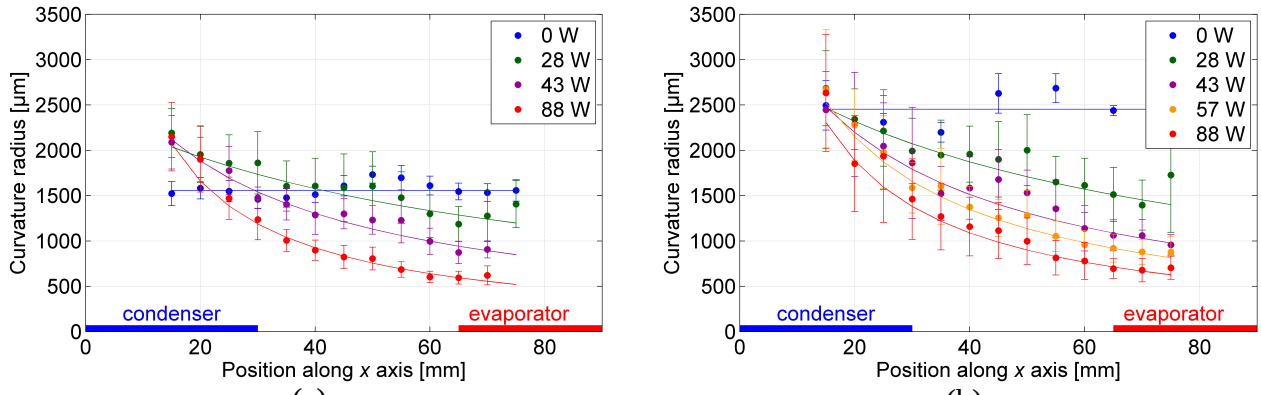

Figure 5: Meniscus curvature radius along the FPHP (f_r = 9% (a) and f_r = 13 % (b))

Pressure drop measurements in the FPHP

The meniscus curvature radius is directly linked to the capillary pressure (i.e. the difference between vapour pressure and liquid pressure) by the Laplace-Young law:

$$P_{cap} = P_v - P_l = \frac{\sigma}{r} \tag{1}$$

The capillary pressure along the FPHP for different heat fluxes and for two filling ratios is presented in figure 6 (a) and (b). Assuming that the capillary pressure is linear with the position along the grooves in the adiabatic zone, it is possible to determine the mean total pressure drop (i.e. the sum of the mean liquid and vapour pressure drops) along the FPHP by measuring the slope of the fitting line. A particular attention is given to the uncertainty of this mean total pressure drop. Figure 7 presents the capillary pressure along the FPHP in several grooves for Q = 88 W and f_r = 13%. Although the measurement dispersion in different grooves is important, the slopes of the fitting lines are close one to the other. Thus, the mean pressure drop in the FPHP and its standard deviation is the mean of the fitting line slopes in each groove and their corresponding standard deviation. In that example, the mean pressure drop is equal to 266 Pa/m and its standard deviation is equal to 52 Pa/m.
These measurements are compared to numerical results in next sections. However, the mass flow in the grooves has to be estimated to calculate the induced pressure drop. Indeed, one part of the heat flux is directly transferred by heat conduction in the wall from the heat source to the heat sink.

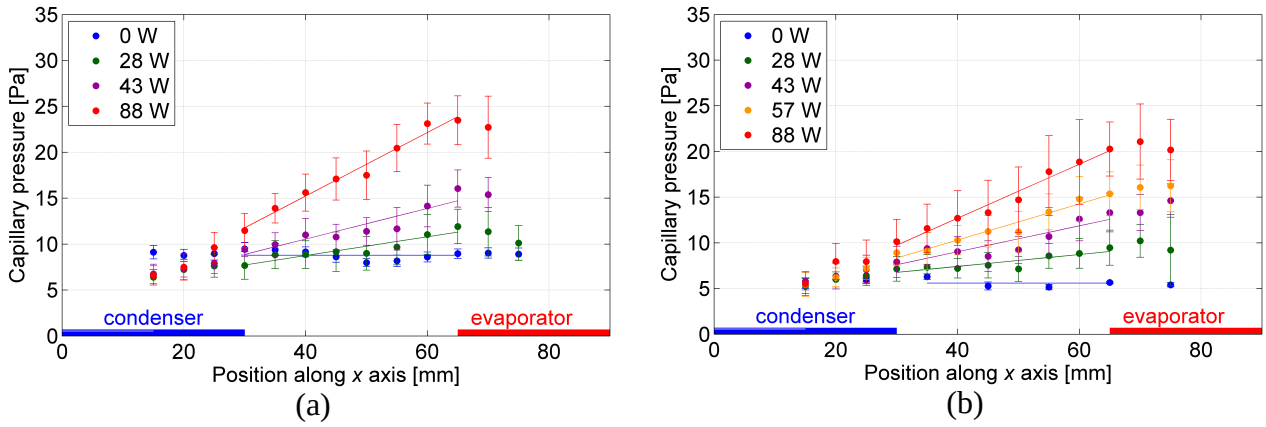

Figure 6: Capillary pressure along the FPHP (f_r = 9% (a) and f_r = 13% (b))

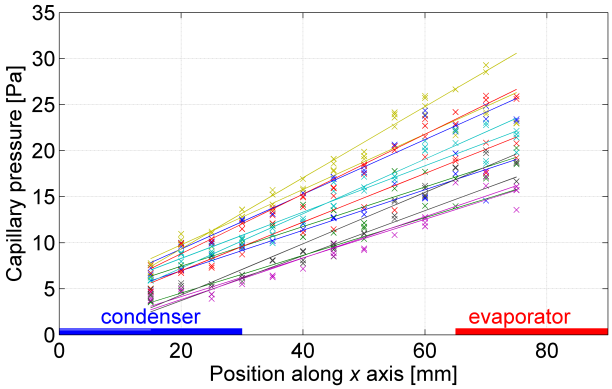

Figure 7: Capillary pressure dispersion in the grooves (Q = 88 W ; f_r = 13 %)

Estimation of the mass flow in the grooves

Liquid and vapour pressure drops depend on geometric parameters of the FPHP (width and height of the grooves, vapour space height, etc.), on thermophysical properties (viscosity, latent heat of vaporization, …) and on hydrodynamic parameters (interfacial shear stress, effect of the phase change on streamlines, effect of the meniscus on the fluid flows, etc.), but it depends primarily on the mass flow in the grooves and in the vapour space. Indeed, for laminar flows, pressure drops are proportional to the fluid velocity and hence to the mass flow in the channel. In a FPHP, the heat flux imposed at the heat source is transferred to the condenser by both heat conduction and phase change.
The mass flow in the grooves in the adiabatic zone is equal to:

$$\dot{m}_{l,v} = \alpha \frac{Q_{tot}}{h_{lv}} \quad \text{with} \quad \alpha = \frac{Q_{\text{phase change}}}{Q_{tot}} \tag{2}$$

Experimentally, it is possible to estimate α by considering both the total thermal resistance R_{tot} and the conduction thermal resistance R_{cond} of the FPHP:

$$\alpha = 1 - \frac{R_{tot}}{R_{cond}} \tag{3}$$

R_{tot} can be calculated with the temperatures measured for a given fluid charge in working conditions and R_{cond} is the thermal resistance calculated when the FPHP is empty:

$$R_{tot} = \frac{T_{\max} - T_{\min}}{Q_{tot}} \quad ; \quad R_{cond} = \left(\frac{T_{\max} - T_{\min}}{Q_{tot}} \right)_{FPHP\ \ empty} \tag{4}$$

Figure 8 presents the temperature profile along the FPHP for different heat fluxes and for two filling ratios. The thermal resistance of the FPHP as a function of the heat flux is plotted in figure 9 for filling ratios of 0%, 9% and 13%. Thermal resistances obtained for filling ratios of 9% and 13% are sensibly equal. Moreover, thermal resistances are almost constant with the heat flux. Thus, the part α of heat fluxed transferred by phase change is hence almost constant with the heat flux too. For filling ratios of 9% and 13%, α is equal to 45 +/- 5% of the total heat flux imposed at the heat source.

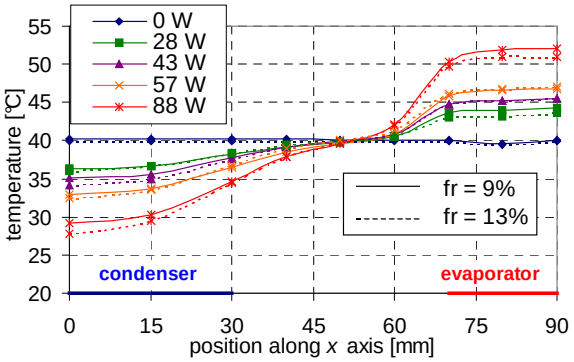

Figure 8: Temperature field along the FPHP

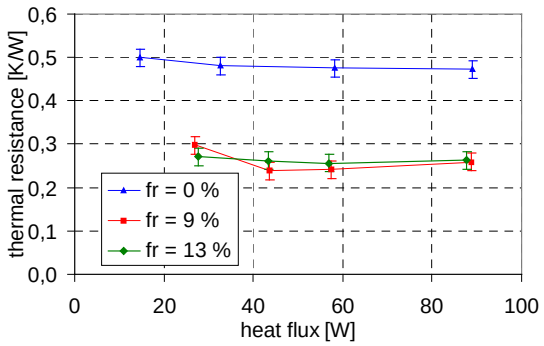

Figure 9: Thermal resistance of the FPHP

Comparison with numerical model

A hydrodynamic model has been developed under the finite elements based commercial software Comsol Multiphysics. Liquid and vapour flows in a groove section and in the vapour space have been simulated assuming laminar flow. The geometrical characteristics are those presented in figure 1 and the meniscus curvature radius is imposed. The liquid-vapour interface has been taken into account assuming the continuity of the shear stress at the liquid-vapour interface. A non-slip boundary condition is imposed at the walls. The mass flow in the channels is calculated with equation (2). Figure 10 summarizes the boundary conditions of the model and figure 11 presents the velocity fields in the channels for Q = 88 W and r = 0.5 mm.

The mean pressure drop in the grooves is presented in figure 12 as a function of the heat flux. Experimental results are presented for two filling ratios (f_r = 9% and f_r = 13%) and numerical results (in solid lines) are presented for three different meniscus curvature radii. As α is constant in the experiments, the mass flow in the grooves is proportional to the heat flux. Hence, pressure drops vary linearly with the imposed heat flux. Pressure drops are smaller for a filling ratio of 13 % than for a filling ratio of 9%. This difference can be explained by the reduction of the liquid cross section when the filling ratio decreases. Indeed, a decrease of the filling ratio induces a decrease of the meniscus curvature radius in the grooves, as seen in figure 5 (a) and (b). The influence of the curvature radius on pressure drops is shown by numerical results. The measurements obtained by confocal microscopy are in good agreement with the calculated pressure drops.

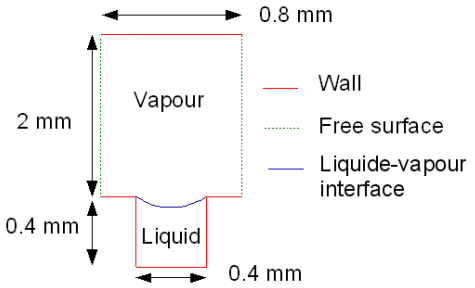

Figure 10: Boundary conditions of the model

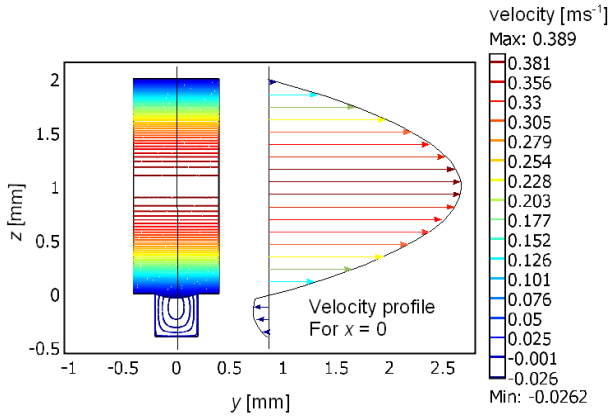

Figure 11: Velocity fields in the channels

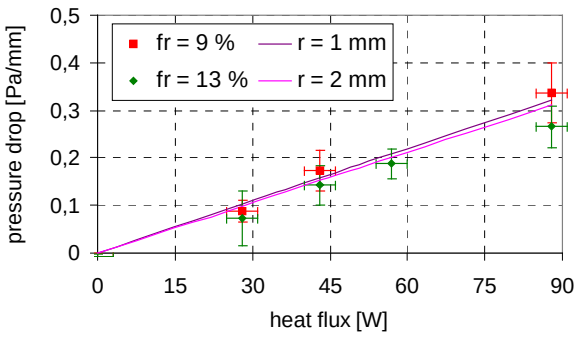

Figure 12: Experimental and numerical mean pressure drop

CONCLUSION

The physical phenomena that drive a heat pipe are complex and cannot be understood only with temperature sensors. Measurements of the location and the shape of liquid films inside the system are required in association with temperature measurements to understand the physical mechanisms that drive a heat pipe. Thermal data are available in the literature, but hydrodynamic data are rare. In this study, a confocal microscope was used to measure the meniscus curvature radii in the grooves of a FPHP. Temperature measurements are used to calculate the part of the heat flux transferred from the evaporator to the condenser by phase change. Both measurements are necessary to compare theoretical and experimental pressure drops.

NOMENCLATURE

f_r	filling ratio, -	cond	condenser
h_{lv}	latent heat of vaporization, J kg^{-1}	l	liquid
m	mass flow, kg s^{-1}	max	maximum
P	pressure, Pa	min	minimum
Q	heat power, W	tot	total
r	radius of curvature, m	v	vapour
R	thermal resistance, K W^{-1}		
T	Temperature, K	*Greek symbols*	
		α	ratio , -
Subscripts		σ	surface tension, Nm^{-1}
Cap	capillary		

REFERENCES

1. M. Lallemand, F. Lefèvre, Micro/mini heat pipes for the cooling of electronic devices, 13th *International Heat Pipe Conference*, Shanghaï, China, 2004, pp. 12-22.
2. R. Rullière, F. Lefèvre, M. Lallemand, Prediction of the maximum heat transfer capability of two-phase heat spreaders - Experimental validation, *Int. J. Heat Mass Transfer*, Vol 50., pp. 1255-1262, 2007.
3. F. Lefèvre, R. Rullière, Guillaume Pandraud, M. Lallemand, Prediction of the temperature field in flat heat pipes with micro-grooves - Experimental validation, *Int. J. Heat Mass Transfer*, Vol 51., pp. 4083-4094, 2008.
4. R. Revellin, R. Rullière, F. Lefèvre, J. Bonjour, Experimental validation of an analytical model for predicting the thermal and hydrodynamic capabilities of flat micro heat pipes, *Appl. Therm. Eng.*, Vol 29., pp. 1114-1122, 2008.
5. R. Hopkins, A. Faghri, D. Khrustalev, Flat miniature heat pipes with micro capillary grooves, *J. Heat Transfer*, Vol. 121, pp. 102-109, 1999.
6. B. Suman, P. Kumar, An analytical model for fluid flow and heat transfer in a micro-heat pipe of plygonal shape. *Int. J. Heat Mass Transfer*, Vol. 48, pp. 4498-4509, 2005.
7. M. Ivanova, A. Lai, C. Gillot, N. Sillon, C. Shaeffer, F. Lefèvre, M. Lallemand, E. Fournier, Design, fabrication and test of silicon heat pipes with radial microcapillary grooves. *ITHERM'2006*, San Diego, 30 mai - 2 Juin, 2006.
8. S. Launay, V. Sartre, M. B. H. Mantelli, K. V. de Paiva, M. Lallemand, Investigation of a wire plate micro heat pipe array, *Int. J. Therm. Sci.*, Vol. 43, pp. 499-507, 2003.
9. Y. X. Wang, G. P. Peterson, Analysis of wire-bonded micro heat pipe arrays. *J. Thermophysics Heat Transfer*, Vol. 16, No 3, pp. 346-355, 2002.
10. J. P. Longtin, B. Badran, F. M. Gerner, A one-dimensional model of a micro heat pipe during steady-state operation, *J. Heat Transfer*, Vol. 116, pp. 709-715, 1994.
11. S. Lips, F. Lefèvre, J. Bonjour, Nucleate boiling in a flat grooved heat pipe, *Int. J. Therm. Sci.*, in press, doi:10.1016/j.ijthermalsci.2008.11.011.

ANALYSIS OF TWO-PHASE FLOWS IN PIPES AND SUBCHANNELS UNDER HIGH PRESSURE

N. Alleborn[1,*], R. Reinders[1], S. Lo[2], A. Splawski[2]
[1] AREVA, AREVA NP GmbH, Paul-Gossen Str. 100, 91052 Erlangen, Germany
[2] CD-adapco, G3, Trident House, Trident Park, Basil Hill Road, Didcot, OX11 7HJ, UK

ABSTRACT. A major goal of fuel assembly design for nuclear power plants is a reliable prediction of the critical heat flux. Development and validation of computational fluid dynamics (CFD) methods for predicting two-phase flows and critical heat flux (CHF) conditions is subject of ongoing research at AREVA-NP. This paper deals with numerical modelling of subcooled flow boiling of water in pipes and subchannels at flow conditions corresponding to the range of pressurized water reactor operation conditions. As simulation tool the commercial CFD software Star-CD is used in conjunction with its Extended Boiling Framework (EBF), a software package providing modelling tools for two-phase flow boiling. Substantial progress towards a CFD prediction of thermal hydraulic phenomena relevant for fuel assembly design could be achieved. In the future, modelling will be needed to be complemented by experimental validation data with sufficient local resolution, to validate CFD models for high pressure thermal hydraulic operating conditions.

Keywords: *Two-phase flow, CFD, validation experiments, nuclear power plant, fuel assembly*

INTRODUCTION

The thermal-hydraulic design of fuel assemblies for nuclear power plants nowadays relies strongly on theoretical and numerical design tools. A fuel assembly contains a bundle of several fuel rods containing the nuclear fuel, see sketch in Figure 1 (a). The heat released in the fuel rods by nuclear fission is transferred to water flowing parallel to the rods in the interstices, the so called subchannels. Heat transfer is enhanced by spacer grids, which generate fluid mixing and give additional mechanical stability. In order to improve the performance of fuel assemblies, e.g. by an optimized spacer grid design, numerical simulation of two-phase boiling flows by computational fluid dynamics (CFD) becomes increasingly important to assess geometric variants prior to costly experiments. An important goal for modelling is finally the prediction of critical heat flux (CHF), which poses an operating limit for the fuel assembly. To provide an efficient heat transfer from the fuel rods to the coolant, the fuel element requires an optimized design, with appropriately shaped mixing devices, as e.g. vanes, at the spacer grids. When the heat flux reaches a critical value at given flow conditions, the vapor generation at the rod surface prevents sufficient cooling. As a consequence of the reduced heat removal, the rod temperature rises rapidly and the rod may become jeopardized. The onset of this critical heat flux depends on the flow conditions (flow rate, subcooling, pressure) and the geometry.

While single phase flow CFD is meanwhile an established tool in industrial design, numerical modelling of two-phase flows coupled with phase change (boiling/condensation) is still subject of ongoing research efforts worldwide see [1],[2] for a review. For modelling and validation, experimental data on two-phase flows are particularly important.

* Corresponding author: Dr.-Ing. N. Alleborn
Phone: + (49)-9131-9005741, Fax: + (49)-9131-9004082

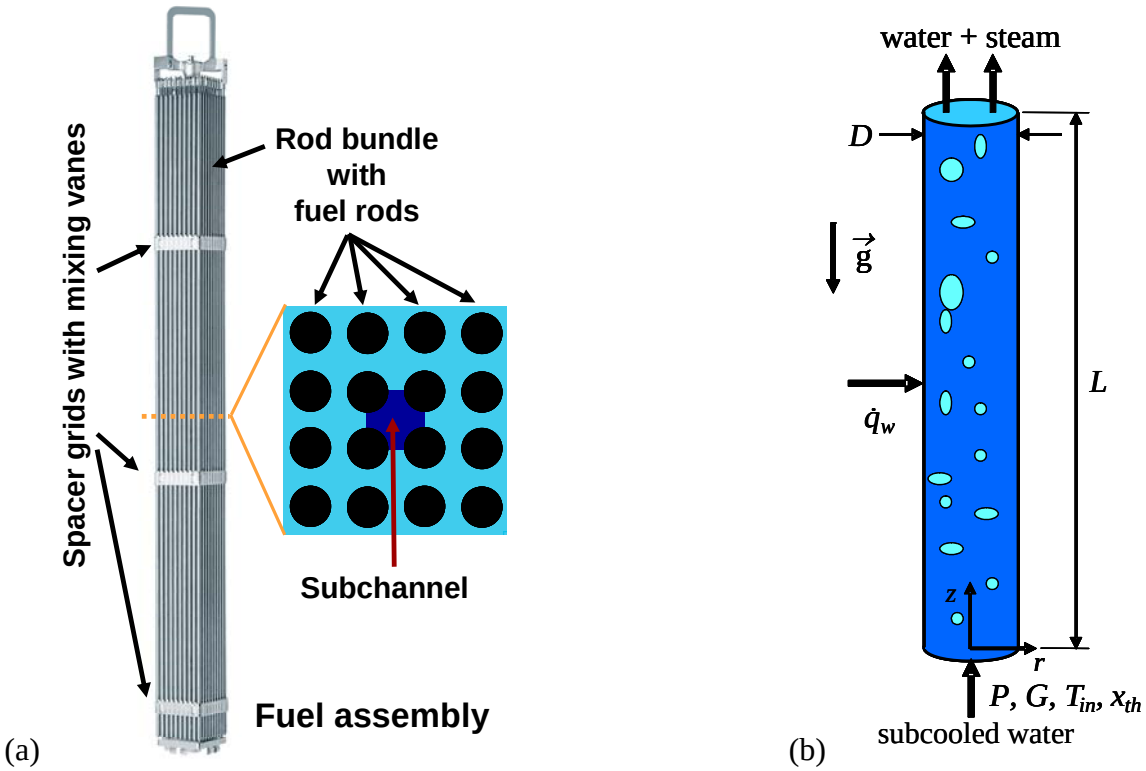

Figure 1. (a) Sketch of a fuel assembly for nuclear power plants. Enlarged bundle cross section: fuel rod array with subchannels for coolant flow. (b) Sketch of a laboratory scale flow boiling experiment for generating CFD validation data in simple geometries (here: circular pipe).

A requirement for application in nuclear industry is the availability of experimental validation data for CFD under realistic thermal hydraulic conditions occurring in boiling and pressurized water reactors (BWR and PWR, resp.), in a pressure range up to 200 bar. A comprehensive review of the available literature on experimental validation data for local flow boiling models for CFD software revealed gaps in this range of operating conditions, see e.g. [1]. There is a need in nuclear industry to close these gaps by appropriate experiments using advanced experimental techniques, such as fast X-ray tomography, digital image analysis, etc., to obtain *local* data of void fraction, liquid and vapour velocities [3]. This data is needed to get a fundamental insight into two-phase flow physics and to validate numerical models. Although integral measurements (e.g. average axial void fraction or CHF determination) provide a base to evaluate plausibility and quantitative results, they do not in general allow conclusive distinguishing between CFD flow boiling models, giving e.g. different local void distribution but same average. Model fluid experiments at low pressure, like refrigerants, are useful for fundamental studies, but accurate scaling to realistic thermal-hydraulic conditions is a matter of ongoing scientific debate. The particular challenge for two-phase flow experiments is the limited access of the flow domain at pressure occurring in thermal hydraulics applications.

For modelling two-phase flow on the scale of sub-channels and fuel assemblies, the Eulerian two-fluid approach is most common [1],[2],[4],[5] where the two phases are treated as interpenetrating continua, with conservation equations obtained by an averaging procedure. This approach requires appropriate closure equations for describing the inter-phase mass, momentum and energy transport. Setting up such closure models requires both a thorough theoretical background and detailed experimental data to describe inter-phase transfer. For developing such models, simple flow geometries as sketched in Figure 1 (b), like pipes, channels or annuli, proved to be convenient test cases to obtain experimental data on the flow configuration, such as local temperatures or void fraction [6],[7], and to tune models and validate numerical codes cf. e.g. [1],[5],[8]. The application

of two-phase CFD to sub-channels and to fuel assemblies has been tackled by numerous groups in the past, see e.g. [7],[9],[10],[11]. Recently, intense research has been also devoted to flows near or at CHF conditions [11],[12],[13]. Although the main physical phenomena could be reproduced, an improvement of the physical models underlying the two-phase CFD software is necessary and also improved experiments to provide local validation data for CFD are required, in order to clarify the complex interplay of the underlying physical submodels.

The present paper deals with numerical modelling of subcooled flow boiling of water in circular pipes and subchannels of fuel assemblies. As simulation tool the commercial CFD software Star-CD is used in conjunction with its Extended Boiling Framework (EBF), a software package providing tools (user routines) for modelling Eulerian two-phase flows with boiling in the bubbly flow regime. The package has been applied to reference experiments on flow boiling for conditions near or at critical heat flux from literature, such as e.g. [6]. In the framework of this paper the status of ongoing research and development work towards a more reliable prediction of critical heat flux is presented, but also the demands for experimental validation data are expressed.

NUMERICAL MODEL

Governing Equations

Subcooled flow boiling in pipes is described in the frame of an Eulerian approach, where the two phases are treated as interpenetrating continua which coexist in the flow domain. Each phase has its own physical properties and its own velocity and temperature fields, $\vec{u}_k$ and T_k, respectively, with $k=l,v$ denoting the liquid and vapour phase, respectively. The local fraction of a phase is characterized by its void fraction ε_k, for which $\varepsilon_l + \varepsilon_v = 1$ holds by definition. Both phases are assumed to have the same pressure field p. The governing equations of the flow problem are mass, momentum and enthalpy balances for each phase k, resulting in the classical six-equation two-fluid model. The interaction between the two phases is described by inter-phase transfer terms which enter the transport equations as source or sink terms. Following [4], the governing equations implemented in Star-CD are given as

- mass balances

$$\frac{\partial}{\partial t}\left(\varepsilon_k \rho_k\right) + \nabla \cdot \left(\varepsilon_k \rho_k \vec{u}_k\right) = \dot{m}_k \,, \tag{1}$$

- momentum balances

$$\begin{aligned} \frac{\partial}{\partial t}\left(\varepsilon_k \rho_k \vec{u}_k\right) + \nabla \cdot \left(\varepsilon_k \rho_k \vec{u}_k \vec{u}_k\right) = \\ -\varepsilon_k \nabla p + \nabla \cdot \left(\varepsilon_k \left(\tau_k + \tau_k^t\right)\right) + \varepsilon_k \rho_k \vec{g} + \vec{F}_k \end{aligned} \,, \tag{2}$$

- enthalpy balances

$$\begin{aligned} \frac{\partial}{\partial t}\left(\varepsilon_k \rho_k \hat{H}_k\right) + \nabla \cdot \left(\varepsilon_k \rho_k \vec{u}_k \hat{H}_k\right) = \\ \nabla \cdot \left(\varepsilon_k \lambda_k \nabla T_k + \frac{\mu_k^t}{\sigma_h^t} \nabla \hat{H}_k \right) + Q_k \end{aligned} \,. \tag{3}$$

In equations (1)-(3), $\hat{H}_k = \hat{H}_k(T_k, P)$ denotes the enthalpy at system pressure P, ρ_k is the density, μ_k viscosity, λ_k thermal conductivity and σ_h^t the turbulent thermal diffusion Prandtl number. For the mass, momentum and energy inter-phase terms conservation requires $\mathrm{I}_v = -\mathrm{I}_l$, with $\mathrm{I}_k = \dot{m}_k, \vec{F}_k,$ and Q_k, respectively. In order to calculate the turbulent stresses τ^t for the liquid and vapour phase in Equation (3) above, an extended k-ε turbulence model is used, containing extra

source terms which account for the effect of the vapour phase on the turbulence field, cf. [4] for details.

Interfacial forces

Due to the averaging process for the two-fluid formulation, inter-phase interaction terms between the two phases occur for which appropriate models have to be provided to close the system of equations. Between the two phases, drag, lift, virtual mass, turbulent drag, wall lubrication and convective momentum transfer act as interfacial forces [4]:

$$\vec{F}_v = \vec{F}_D + \vec{F}_L + \vec{F}_M + \vec{F}_T + \vec{F}_W + \left(\dot{m}_{vl}\vec{u}_v - \dot{m}_{lv}\vec{u}_l\right). \quad (4)$$

Bulk boiling model

The heat and mass transfer between the liquid and the vapour phase for bubbly flow is described in the frame of an energy balance as described in [4]. Liquid and vapour side heat fluxes to the interface are modelled using heat transfer coefficients, the mass flux through the interface then results from the difference between the liquid and gas side heat fluxes, divided by the latent heat. The local bubble diameter is assumed for simplicity to be a function of the local subcooling in the fluid, using an empirical model of Kurul and Podowski [4].

Wall heat partitioning model

The total heat flux through the wall q''_w is split up into several parts, determined by a wall heat partitioning model [4], extended in the spirit of [11],[12],[13] for modelling CHF. In subcooled flow heat is transferred in part directly to the liquid and the vapour which are in contact with the heated surface by convective transfer, using single phase heat transfer coefficients (convective part). Evaporation starts from nucleation sites at the heated surface, creating bubbles adjacent to the wall, which leave the surface when reaching their departure diameter (evaporative part). The nucleation site density and the departure diameter determine the fraction of the wall area covered by nucleation sites, empirical models are adopted here, cf. [4]. After bubble detachment, cooler water replenishes the space occupied by the bubble, which has to be heated again (quenching part).

PROBLEM DESCRIPTION

In order to investigate subcooled flow boiling, two-phase flow through uniformly heated vertical circular pipes of diameter D and length L is considered in the present work. Figure 1 (b) shows a sketch of the problem under consideration. Subcooled water enters the pipe with inlet temperature T_{in}, thermodynamic quality $x_{th,in}$, and mass flow rate density G. The water is heated by a uniform wall heat flux q''_w at the wall. For this configuration, experimental data on flow, temperature and average void fraction is available in the literature, cf. e.g. [6] and also databases on CHF experiments for circular pipes, cf. e.g. [14]. For circular pipes, steady, axisymmetric flow configurations are considered for the numerical computations. A fully 3D CFD simulation has been carried out for subchannel geometries.

NUMERICAL RESULTS

Two-phase flow under CHF conditions were investigated at PWR conditions, using parameters derived from an experimental set of Weatherhead (1963), see [14], with P=138 bar, G=940-2650 kg/m^{2}s and outlet qualities $x_{th,o}$= -0.05 in a pipe with L=0.457 m and D=7.7 mm. As flow regime, bubbly flow with the liquid phase being the continuous phase is assumed, in addition allowing for a regime change in the wall layer at high void fraction. Lift and wall lubrication forces are switched off. Profiles of void fraction, liquid and vapour temperatures are shown in Figure 2 for illustration, for a particular set of parameters. The heat flux was increased, until the wall temperature T_w

increase reached outlet region of the experiment (at $z \approx 0.45$ m), where CHF is observed. The computational domain has been chosen longer to get more detailed insight into the flow behaviour. The contour plot of the void fraction (Figure 2, left) shows a rather pronounced layer of high void content near the wall.

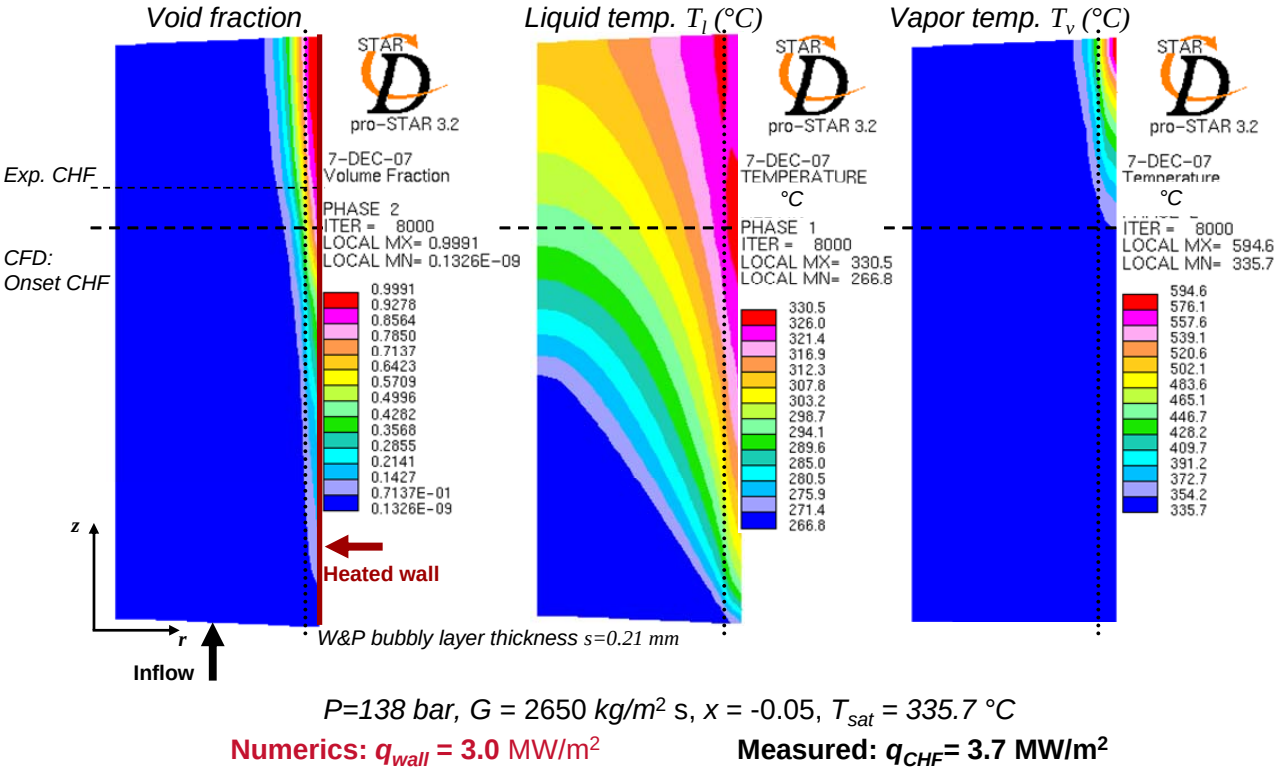

Figure 2. Numerical computation of critical heat flux for the Weatherhead experiment.

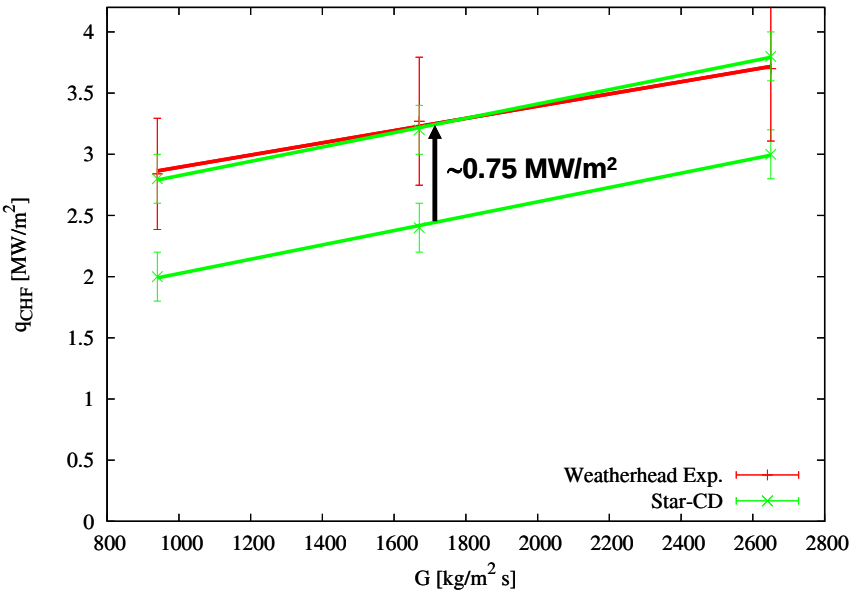

Figure 3. Comparison of computed CHF values with Weatherhead experiments (before and after shifting by a single additive constant).

The thickness of the layer with $\varepsilon >> 0.7$ matches qualitatively well with the prediction of the Weisman-Pei one-dimensional correlation (vertical dotted line) [15]. The CHF results obtained by using the modified heat partitioning model are summarized in their dependence on the mass flux

in Figure 3. It is interesting to note that the qualitative dependence of the CHF value on mass flux is very well captured by the model, however, the critical heat flux is under-predicted. Shifting the values by a *single* additive constant allows matching of CFD and experimental results very well.

Subchannel with vaned spacers – Influence of swirl on CHF

Results for two-phase flow simulations in a subchannel with vanes are presented for a generic spacer configuration with a four-fold symmetry, allowing to exploit the symmetry and to reduce the size of the computational domain to a ¼ subchannel with cyclic boundary conditions. In Figure 4 results for void distribution and lateral velocity components are shown in two horizontal sections at different distances from the vane tips.

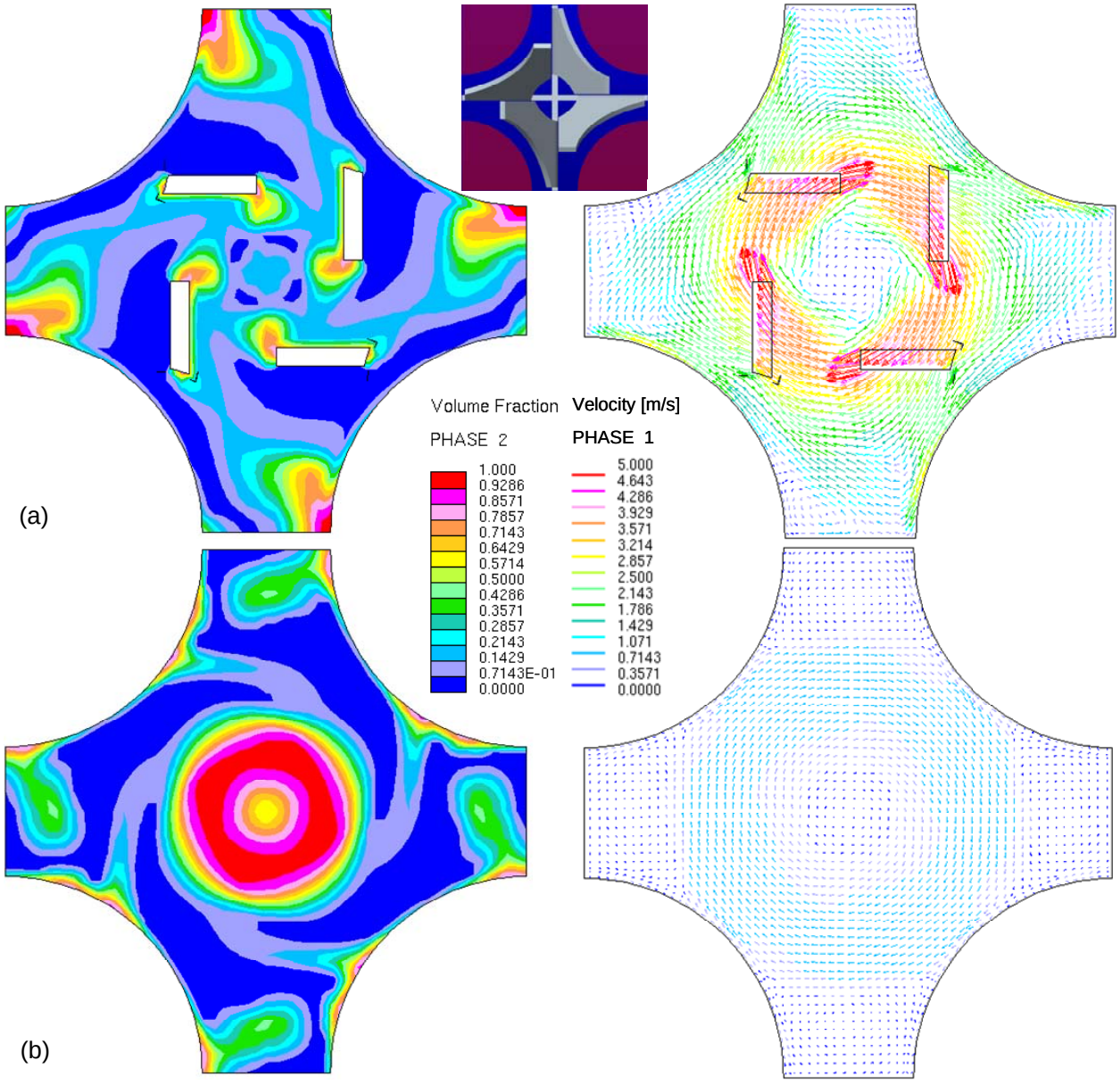

Figure 4. Subchannel geometry with vanes: Horizontal cuts, void fraction (left), horizontal components of velocity (right), (a) 1 mm before vane tip, (b) 150 mm downstream of vane tip.

The vanes generate swirl and cause a redistribution of the void fraction, with liquid gathering preferentially on the lower side of the vane (low void, blue colour) due to local centrifugal forces resulting from the local curvature of stream lines, while on the upper side vapour is accumulating, cf. Figure 4 (a). The centrifugal forces in the swirl flow are dominant downstream of the vanes and

cause a separation of the vapour and the liquid, with a vapour core developing in the centre of the channel, see Figure 4 (b). Bubble pockets with high void fraction develop on the rod surface, which may cause the onset of CHF. In a next step, the investigation of the influence of swirl has been extended towards the development of CHF in a subchannel section with several spacer spans 4-vane grids. In order to reduce the complexity of the model and to speed up computation time, only two spans of the subchannel, with inlet and outlet sections, are considered.

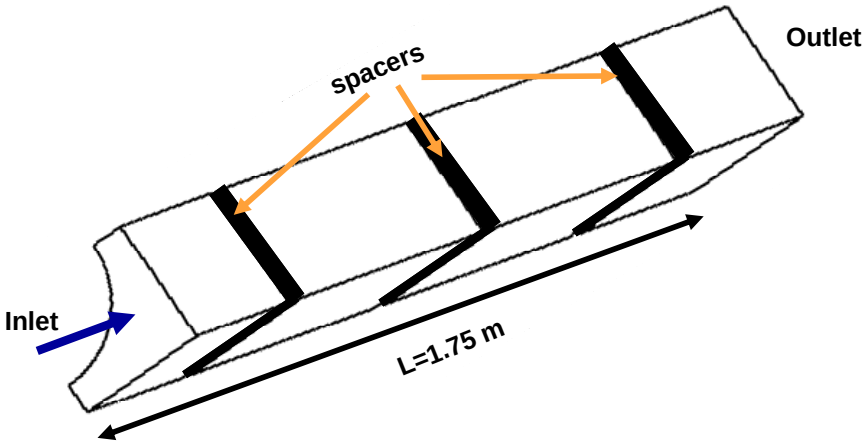

Figure 5. Sketch of the computational domain (one quarter of channel, exploiting symmetries) of the subchannel section with three spacers.

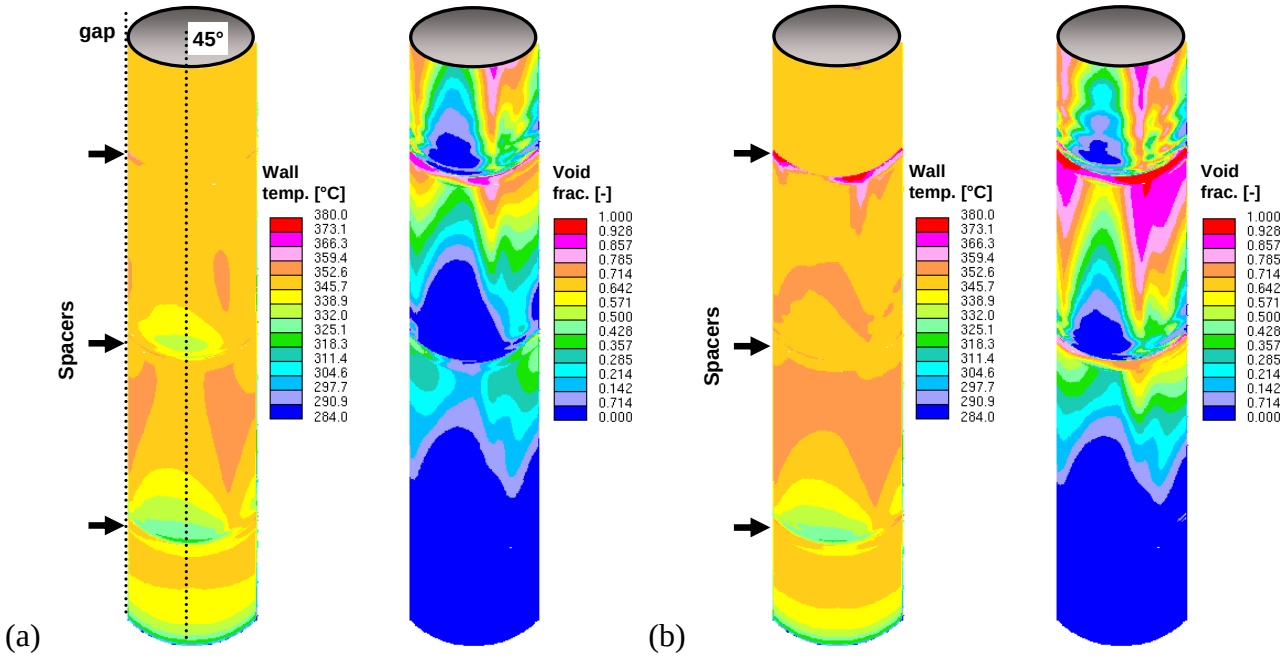

Figure 6. Rod temperature T_w (left) and void fraction ε near rod surface (right) for (a) q''_w=2.0 MW/m^2 and (b) q''_w=2.1 MW/m^2 (plotted on one quarter of rod surface).

Figure 5 shows a sketch of the configuration. The operation conditions investigated here correspond to G=3000 kg/m^2 s and T_{in} = 195 °C. In Figure 6 contour plots of the wall temperature T_w (surface temperature of the rod) and for the void fraction ε adjacent to the rod surface are plotted for a wall heat flux q''_w = 2.0 MW/m^2 (a) and for q''_w = 2.1 MW/m^2 (b). For the lower heat flux, a wall temperature increase, causing CHF, was already observed in the outlet section of the subchannel *without spacers*, which was computed for comparison. Figure 6 (a) shows, that due to the swirl generated by the spacer vanes, the rod surface is significantly cooled even below saturation temperature (T_{sat} =339.5°C) downstream of the first and second spacer, in an area around the 45°

position. The effect of the spacers on the wall temperature becomes clear in Figure 7, where the wall temperature along the 45° line and along the gap is plotted for both the subchannel *with spacers* and *without spacers*. The improved heat transfer by the swirling motion causes a steep drop of the wall temperature along the 45° line downstream of the first two spacers (red line in Figure 7). The wall temperature increases and reaches the level of the subchannel *without spacers* (green line in Figure 7) just before the next spacer, in the last third of the span. The effect of the third spacer on T_w appears much less pronounced, apparently due the higher void content of the flow towards end of heated length, the wall temperature downstream of the third spacer is hardly influenced. Along the gap of the subchannel, the effect of the spacers on T_w is also significantly smaller. Figure 6 shows also contour plots of the local void fraction adjacent to the rod surface. Significant void production sets in the first span (before the second spacer), up to this point the flow is essentially single phase. The swirl generated by the second spacer causes a redistribution of the void, especially before the 3rd spacer and in the outlet section the formation of bubble pockets appear, which may lead to CHF, cf. Figure 6 (b). It should be noted here, that the increase of the CHF value by the action of vanes is in the range observed by measurements.

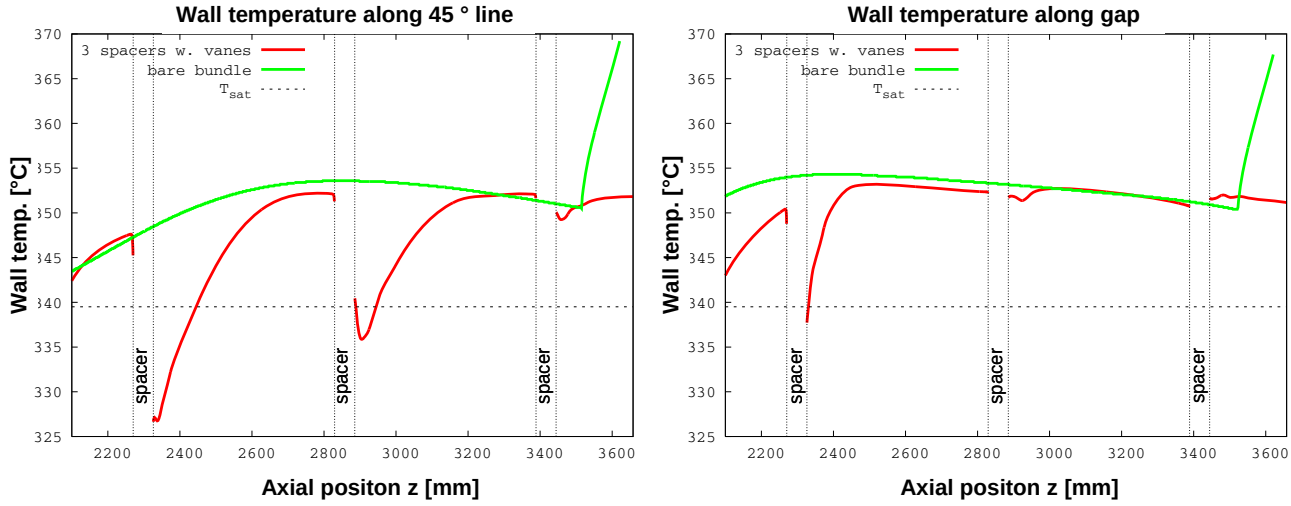

Figure 7. Rod temperature at 45° position (left) and in the bundle gap (right) for $q"_w$=2.0 MW/m^2. Comparison between vaned spacer (red line) and subchannel *without spacers* (‘bare bundle’) (green line).

CONCLUSIONS

In this paper numerical modelling of subcooled flow boiling at CHF conditions has been investigated using the software package Star-CD with its extended boiling framework (EBF). Goal of the ongoing research is to use two-phase CFD methods for the prediction of critical heat flux (CHF) in subchannels of fuel assemblies. The numerical results show for the investigated parameters, that the two-phase CFD model is capable to produce quantitative results, which reproduce trends of the parameter dependence very well. In addition, two-phase CFD provides a valuable qualitative insight into regions in the subchannel, which are otherwise not accessible by experimental methods. Still, deeper insight into the underlying physical mechanisms of two-phase boiling flows at high pressures is required, to significantly improve the accuracy of the models. Experimental data on void, velocity and temperature distribution with a high spatial, down to the sub-millimetre scale as the results presented in Figure 2 and Figure 4 imply, are desirable. The development of non-intrusive measurement methods, for instance, is considered an attractive prospective for obtaining validation data in the future.

The authors would like to thank J. Bigot, F. Burtak, M. Leberig, T. Kehely, T. Salnikova, and J.-P. Simoneau for fruitful discussions.

REFERENCES

[1] Bestion, D., Anglart, H., Peturaud, P., Smith, B., Krepper, E., Moretti, F. and Macek, J., Review of Available Data for Validation of NURESIM Two-Phase CFD Software Applied to CHF Investigations., *12th International Topical Meeting on Nuclear Reactor Thermal Hydraulics (NURETH-12)*, Pittsburgh, USA, Paper No. 43, 2007.

[2] Yadigaroglu, G., Computational Fluid Dynamics for Nuclear Applications: From CFD to Multi-Scale CMFD, *Nucl. Eng. Des.*, Vol. 235, pp. 153-164, 2005.

[3] Fischer, F. and Hampel, U., Ultra Fast Electron Beam X-Ray Computed Tomography for Two-Phase Flow Measurement, *XCFD4NRS – Experiments and CFD Code Applications to Nuclear Reactor Safety, OECD/NEA & IAEA Workshop*, Grenoble, 10-12.9.2008, Paper BOI-08, 2008.

[4] Lo, S., Modelling Multiphase Flow with an Eulerian Approach, *VKI-Lecture Series – Industrial Two-Phase Flow CFD*, von Karman Institute, Brussels, 2005.

[5] Krepper, E., Koncar, B. and Egorov, Y., CFD Modelling of Subcooled Boiling – Concept, Validation and Application to Fuel Assembly Design, *Nucl. Eng. Des.*, Vol. 237, pp. 716-731, 2007.

[6] Bartolomei, C.G. and Chanturiya, V.M., Experimental Study of True Void Fraction When Boiling Subcooled Water in Vertical Tubes, *Teploenergetika*, Vol. 14, No. 2, pp. 80-83, 1967.

[7] Boucker, M., Guelfi, A., Mimouni, S., Peturaud, P., Bestion, D. and Hervieu, E., Towards the Prediction of Local Thermal-Hydraulics in Real PWR Core Conditions using NEPTUNE-CFD Software, *Workshop on Modeling and Measurements of Two-Phase Flows and Heat Transfer in Nuclear Fuel Assemblies*, KTH Stockholm, Sweden, 2006.

[8] Montout, M., Haynes, P.-A. and Colin, C., Bubble Diameter Models at a Heated Wall for Subcooled Boiling Flow and Numerical CFD Simulations of the Impact of the Bubble Sliding on the Heat Flux Repartition, *6th Int. Conf. Multiphase Flow – ICMF 2007*, Leipzig, Germany, Paper No. 288, 2007.

[9] Anglart, H. and Nylund, O., CFD Application to Prediction of Void Distribution in Two-Phase Bubbly Flows in Rod Bundles, *Nucl. Eng. Des.*, Vol. 163, pp. 81-98, 1996.

[10] Salnikova, T., Progress in CFD Analyses Applied to Subchannel Conditions, *15th Int. Conf. on Nucl. Eng.*, Nagoya, Japan, Paper-No. ICONE15-10418, 2007.

[11] Salnikova, T., Two-phase CFD Analysis in Subchannel Flow under Swirl Conditions, *Ph.D. Thesis*, Technical University of Dresden, Dresden, Germany, submitted, 2008.

[12] Rao, Y.F., Hori, K. and Tsuge, A., Numerical Simulation of Two-Phase Boiling Flows and Prediction of DNB under PWR Conditions with a Multidimensional Two-Fluid Model, *JSME Int. J.*, Vol. 43, No. 4, pp. 608-613, 2000.

[13] Macek, J. and Vyskocil, L., Simulation of critical heat flux experiments in NEPTUNE_CFD code, *XCFD4NRS – Experiments and CFD Code Applications to Nuclear Reactor Safety, OECD/NEA & IAEA Workshop*, Grenoble, 10-12.9.2008, Paper BOI-11, 2008.

[14] Collier, J.G. and Thome, J.R., *Convective Boiling and Condensation*, Oxford, 1994.

[15] Weisman, J. and Pei, B.S., Prediction of Critical Heat Flux in Flow Boiling at Low Qualities, *Int. J. Heat Mass Transf.*, Vol. 26, No. 10, pp. 1463-1477, 1983.

PREDICTION OF ASYMMETRIC AIR BUBBLE OSCILLATIONS

C. W.M. van der Geld*, J.G.M. Kuerten
Eindhoven University of Technology, Eindhoven, The Netherlans

ABSTRACT. Production of sound by asymmetric air bubble oscillations in water is enhanced when the parameter $\{p_L R_0 / \sigma\}$ approaches a resonance value that depends on $\gamma = c_p/c_v$. With an Euler-Lagrange approach a new, extended Rayleigh-Plesset equation is derived that takes account of arbitrary axisymmetric interface deformation. A solution of this equation for the isotropic 'breathing mode' is presented that is shown to predict the amplitude well over long periods of time. This breathing mode causes monopole emission of sound. The solution behaves properly also at resonance. The parameters p_L and σ have been varied in a broad range and in all cases the dimensionless equation (15) was found to be valid. The radian frequency ω_3 defined by equation (9) is found to change gradually in time. This is related to the well-known experience [5] that ω_3 appears to depend on initial amplitude β for nonlinear deformation of bubbles and spheres of liquid. At resonance, the fluid properties and the pressure are such that energy is quickly converted from the driving anisotropic deformation mode to the breathing mode. But also far from resonance, each deforming air bubble produces sound, be it with smaller amplitude.

Keywords: *bubble deformation, large amplitude oscillation, resonance, sound production*

INTRODUCTION

Sound in water can be produced by a water surface ruffled by the wind, by jets impinging at a free surface, by air bubbles emerging from an underwater nozzle and by imploding steam bubbles (cavitation). Fully nonlinear theories for sound production by bubble pulsations were given by many researchers but merely for cavitation phenomena. See the review of Plesset & Prosperetti [1]. However, sound is also produced by air bubbles, as partly explained by Minnaert [2] who showed that the frequency of the sound is close to that of the radial mode of isotropic bubble oscillation, the so-called 'breathing mode'. A nonlinear theory for air bubbles was given by Longuet-Higgins [3]. He performed a perturbation analysis of three sets of parameters (velocity potential, interface, pressure) simultaneously with an equation of state that pertains to air bubbles:

$$p_b V^{\gamma} \equiv \text{constant}, \tag{1}$$

with $\gamma = c_p/c_v$, V the bubble volume and p_b the pressure in the bubble. Let P_n denote the n^{th}-Legendre polynomials. Longuet-Higgins showed that each oscillation with amplitude β at the frequency of the linear fundamental mode corresponding to P_n produces oscillations that behave at a distance just as those of the breathing mode, but at twice the frequency of the fundamental mode (ω_n) and with an amplitude proportional to β^2. Longuet-Higgins derived a $\cos(2\omega_n t)$-component in solving his equation (6.23) with a velocity potential Φ given by $Z R_0 \sin(2\omega_n t)/r$. Here R_0 denotes the initial bubble radius, ω_n the frequency of a normal mode with order n, t is time and r the radial distance from the

* Corresponding author: Dr. C.W.M. van der Geld
Phone: + (31)-40-2472923, Fax: + (31)-40-2475399
E-mail address: c.w.m.v.d.geld@tue.nl

bubble. This leads to amplitude of the breathing mode, b_1, that is inversely proportional to $\{\omega_{RP}^2 - 4\omega_n^2\}$, with

$$\omega_{RP}^2 = 3\,\gamma p_L/(\rho_L R_0^2) + (3\gamma - 1)2\sigma/(\rho_L R_0^3). \tag{2}$$

Selecting ω_{RP}^2 close to $4\omega_n^2$ obviously causes large amplitudes which enhances the generation of sound. However, this solution leaves the questions unanswered what precisely will happen close to resonance, how the full analytical solution of the breathing mode amplitude reads and what the level of accuracy is of the truncated expressions at time scales that are a multitude of $2\pi/\omega_n$. These are the questions addressed in this paper. It will be shown that next to the above potential $Z\,R_0 \sin(2\omega_n t)\,/r$ a second solution, $Q\,R_0 \cos(2\omega_n t)\,/r$, of the Laplace equation exists that needs to be taken into account in order to predict the breathing mode well.

APPROACH

Consider an axisymmetric, freely deforming air bubble in an ideal, infinite liquid for which $p_b V^\gamma$ is constant. Viscous effects are neglected. Our approach is threefold. The first method is based on the Euler-Lagrange approach in which the coefficients $b_m(t)$ in the expansion of the function $R(\theta,t)$ that describes the interface:

$$R(\theta,t) = \sum_m b_m(t)\, P_{m-1}(\cos\theta) \tag{3}$$

are generalized coordinates. Here θ is polar angle in a spherical coordinate system. An analytical solution for arbitrary axisymmetric deformation of convex shapes is obtained that needs to be integrated in time, the only numerical step. This method, named BEL for sake of convenience, is compared with boundary element method (BEM) solutions for validation purposes. These are the full solutions that coincide if sufficient coordinates (BEL) and sufficient wall point (BEM) are employed. Without loss of generality only initial shapes will be considered for which b_1 and b_3 are nonzero. For excitation of normal modes other than b_3 similar results hold since the extended Rayleigh-Plesset equation that accounts for general deformation reads [4]

$$2\psi_{11}\mathrm{d}^2b_1/\mathrm{d}t^2 + 2\sum_k \psi_{k1}\mathrm{d}^2b_k/\mathrm{d}t^2 = 2\,Q_1/\rho_L - (\mathrm{d}b_1/\mathrm{d}t)^2\,\partial\psi_{11}/\partial b_1 - 2\mathrm{d}b_1/\mathrm{d}t\,\sum_{k=3}\mathrm{d}b_k/\mathrm{d}t\,\partial\psi_{11}/\partial b_k$$
$$+ \sum_{k=3}\mathrm{d}b_k/\mathrm{d}t\;\mathrm{d}b_m/\mathrm{d}t\,\partial\psi_{mk}/\partial b_1 - 2\sum_{k=3}\mathrm{d}b_k/\mathrm{d}t\;\mathrm{d}b_m/\mathrm{d}t\,\partial\psi_{m1}/\partial b_k \tag{4}$$

Here each ψ_{mk} denotes an added mass coefficient that depends on all generalized coordinates. The Q_1 is the generalized force that is given by

$$Q_1 = (p_b - p_L)\,\partial V/\partial b_1 - \sigma\,\partial A/\partial b_1 \tag{5}$$

with A the surface area of the bubble. An equation similar to (4) exists for b_3. Details of this approach are given in a previous paper [4] that also summarizes the main features of the BEM.

The third method is based on the BEL solution and constitutes a perturbation analysis that produces approximate solutions. Note that only a single set of parameters, the generalized coordinates, needs to be perturbed which lead to a consistent and coherent solution of which the accuracy is readily assessed. This approach is explained in the next section.

RESULTS AND ANALYSIS

Let β denote $b_3(t=0)/R_0$, with $R_0 = b_1(t=0)$. A perturbation calculation of b_1 and b_3 simultaneously:

$$b_1 = b_{1,0} + \beta\, b_{1,1} + \beta^2\, b_{1,2} + \ldots; \tag{6}$$

$$b_3 = b_{3,0} + \beta\, b_{3,1} + \beta^2\, b_{3,2} + \ldots \tag{7}$$

yields

$$b_3 = \beta\cos(\omega_L\, t) + \beta^2\, \mathrm{C}\cos(2\,\omega_L\, \mathrm{t}) + \ldots \tag{8}$$

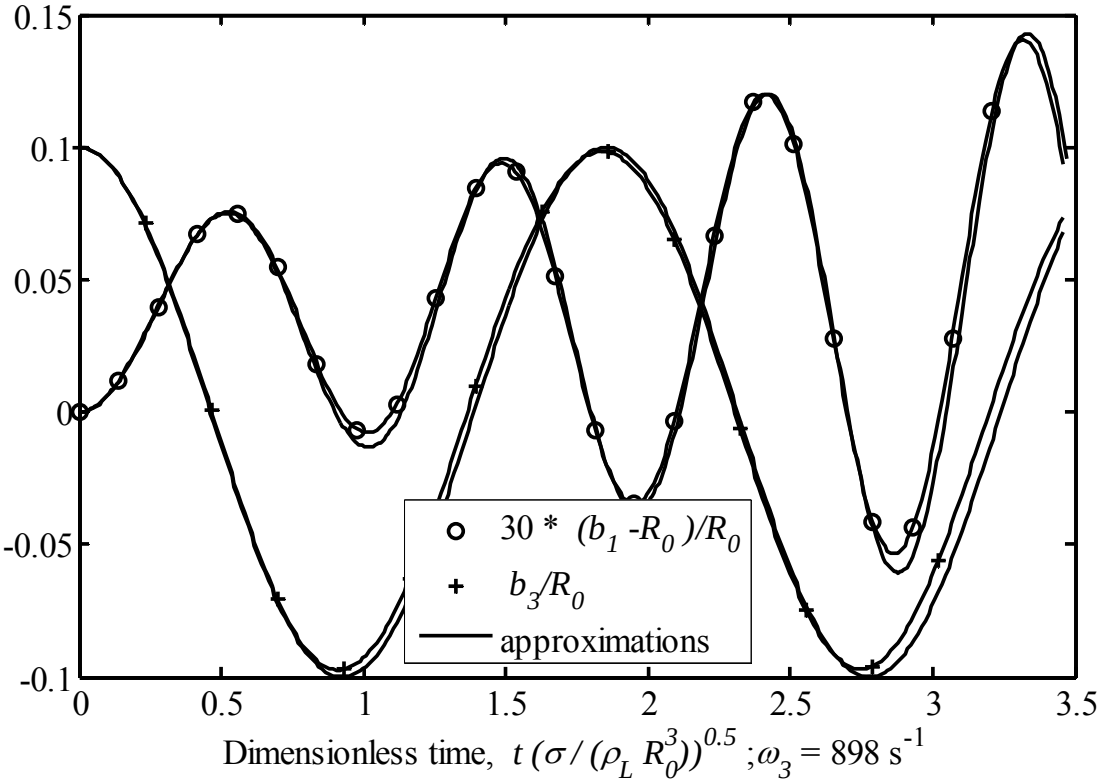

Figure 1 Shape coefficient histories at early times for b_3-excitation with $\beta = 0.1$, $\gamma = 1.4$ and $p_L R_0/\sigma = 10.89$, *i.e.* $k = 1.1$.

with $\omega_L^2 = 12\ \sigma/(\rho_L R_0^3)$ and C a constant. This shows that if b_3 is approximated by

$$b_3 \approx \beta \cos(\omega_3 t), \tag{9}$$

ω_3 becomes dependent on amplitude β. This is in agreement with the findings of both experiments and previous analysis, see the summarizing figure 4 of Tsamopoulos & Brown (1983, page 535). It also explains why the approximation for b_3 given by equation (9) in figure 1 deviates from the full BEL and BEM solutions; the value of ω_3, given in the caption, is obtained by fitting to the first cycle of the full solution of b_3. If ω_L would have been used, the agreement would have been slightly worse.

For the perturbation calculation ω_3 does not exist. In the remainder of this paper, ω_3 is assumed to be equal to ω_L unless specified explicitly otherwise. The symbol ω_3 is kept for reasons that will become clear shortly. The perturbation analysis shows that the breathing mode is described by

$$(b_1 - 1) / R_0 = \mathrm{A}\ \beta^2\ \{\cos(2\ \omega_3 t) - \cos(\omega_{RP} t)\} + \mathrm{B}\ \beta^2 \{\cos(\omega_{RP} t) - 1\} \tag{10}$$

with $\omega_{RP}^2 = 3\ \gamma p_L/(\rho_L R_0^2) + (3\gamma - 1) 2\sigma/(\rho_L R_0^3)$ and

$$\mathrm{A} = 0.2\{\omega_{RP}^2 - (17/6)\omega_3^2\} / (4\omega_3^2 - \omega_{RP}^2)\ ; \quad \mathrm{B} = -0.2\{\omega_{RP}^2 + \omega_3^2/2 + \omega_L^2/3\} / \omega_3^2 \tag{11}$$

The occurrence of the term with ω_L in B stems from the initial condition of the pressure in the bubble, p_b. Despite the initial deformation, prescribed by $\beta = 0.1$, the initial value of p_b has been chosen to be $p_L + 2\sigma/R_0$, *i.e.* the equilibrium value of a sphere with radius R_0. The actual equilibrium pressure, minus p_L, is given by 2σ divided by the radius of the volume-equivalent sphere of the initial bubble. Since this radius is larger, the mean value of b_1/R_0 is found to exceed 1, see figure 1. The physics of an initial offset in pressure leads to an extra ω_L-term in the generalized b_1-force, Q_1:

$$Q_1/(4\pi\,\rho_L\,\beta^2) = -\,\omega_{RP}^2\,b_{1,2} + \omega_{RP}^2\,0.2\,\sin(\omega_3\,t)^2 + 0.2\,\omega_L^2/6 \qquad (12)$$

Equation (12) is accurate up to order β^2. The governing equation of b_1, an extension of the Rayleigh-Plesset equation, reads

$$b_1^3\,\mathrm{d}^2b_1/\mathrm{d}t^2 + b_1^2\,b_3\,\mathrm{d}^2b_3/\mathrm{d}t^2\,((1/3) + (b_3/b_1)/7) + b_1^2\,(\mathrm{d}b_3/\mathrm{d}t)^2\,((7/30) - (b_3/b_1)/105) = Q_1/(4\pi\,\rho_L) \qquad (13)$$

The terms with the ratio (b_3/b_1) in equation (13) are insignificant to the present level of approximation, but contribute to $b_{1,3}$. equations (7), (12) and (13) lead to the solution given by equation (10), and the last term on the RHS of equation (12) for Q_1 leads directly to the ω_L-term in B.

If the solution for b_1 given by equation (10) with $\omega_3 = \omega_L$ would have been drawn in figure 1, the agreement with the full solution would have been slightly worse than the solid line actually drawn for b_1 in figure 1. This latter line has been obtained by fitting ω_3 to the first part of the full solution of b_3 and using the value thus obtained for ω_3 in equation (10). This is formally improper since higher orders of β would need to be taken into account, but it turns out to be an easy way to obtain better agreement between estimations of b_3 based on equation (10) and full solutions for b_3 obtained with BEL and BEM, during a certain interval of time. In the sequel of this paper, this procedure will be named the approximating of b_3 with equation (9) and equation (10). This approximation is the main reason to maintain the symbol ω_3 in the equations. The agreement for b_1 shown in figure 1 is actually quite good considering the b_3-accuracy of the approximation (9), also drawn as a solid line in this figure. Other computations have been performed with $\beta = 0.001$ and smaller, which yielded very good agreement between equation (10), $b_3 = \beta\,\cos(\omega_L\,t)$, and full BEL and BEM solutions. This shows that discrepancies in figure 1 are due to higher order terms in β.

In order to study the characteristics of the breathing mode close to resonance it is advantageous to define λ, k and ψ, as follows, and to rewrite equation (10). Let

$$\lambda \equiv \omega_3/\omega_L,\quad k \equiv \{p_L R_0/\sigma\}/\{16/\gamma - 2 + 2/(3\gamma)\},\quad \psi \equiv (\mathrm{k}-1)(25-3\gamma) + 24 \qquad (14)$$

In the definition of λ, ω_3 stems from fitting and equation (9). With dimensionless time τ given by $t\,\sqrt{\{\sigma/(\rho_L\,R_0^3)\}}$, equation (10) is written as follows:

$$b_1/R_0 = 1 - 0.2\,\beta^2\{1 + 7\lambda^2/(\psi - 24\,\lambda^2)\}\sin(\tau\,\{\sqrt{(\psi/2)} - \lambda\sqrt{12}\})\,\sin(\tau\,\{\sqrt{(\psi/2)} + \lambda\sqrt{12}\}) + -\,0.1\beta^2\,\{1 + 3\,\lambda^2/\psi + 2/\psi\}\,\{\cos(\tau\,\sqrt{(2\psi)}) - 1\} \qquad (15)$$

The amplitude of the double sinus-term in equation (15) clearly increases for ψ approaching 24, which is equivalent to k approaching 1 (equation 14). Full 'resonance' occurs for k equal to $\{1 - 24(1-\lambda^2)/(25 - 3\gamma)\}$, in which case the double sine term changes into a term that increases linearly with dimensionless time τ. The predictive capacity of equation (15) for a time comprising a multitude of cycles with duration $2\pi/\omega_L$ is investigated in figure 2.

Figure 2 shows that the amplitude of the double sinus-prediction of equation (15) is in very good agreement with the full solutions of BEL and BEM. The main radian oscillation frequency of b_3, the fitted ω_3 from (9), is found to be changing continuously with time. If the period of oscillation is made dimensionless as in the definition of t, the dimensionless radian frequency is at early times about 3.4135, which is less than the dimensionless frequency of ω_L, $\sqrt{12} \approx 3.4641$. At later times it decreases even more.

The even coefficients b_2, b_4, …, are zero for reasons of symmetry. The first nonzero coefficient, b_5/R_0, has no contribution to $b_{1,2}$ and $b_{3,1}$ and consequently no influence on the time history of b_1 in figure 2. In each b_3-cycle of duration of about $2\pi/\omega_L$ where the maximum amplitude of b_1 reaches its maximum (at dimensionless times 8 and 23 in figure 2, for example), the maximum amplitude of b_3 is somewhat lower than in other such b_3-cycles. Part of the surface energy of the driving mode, b_3, is apparently

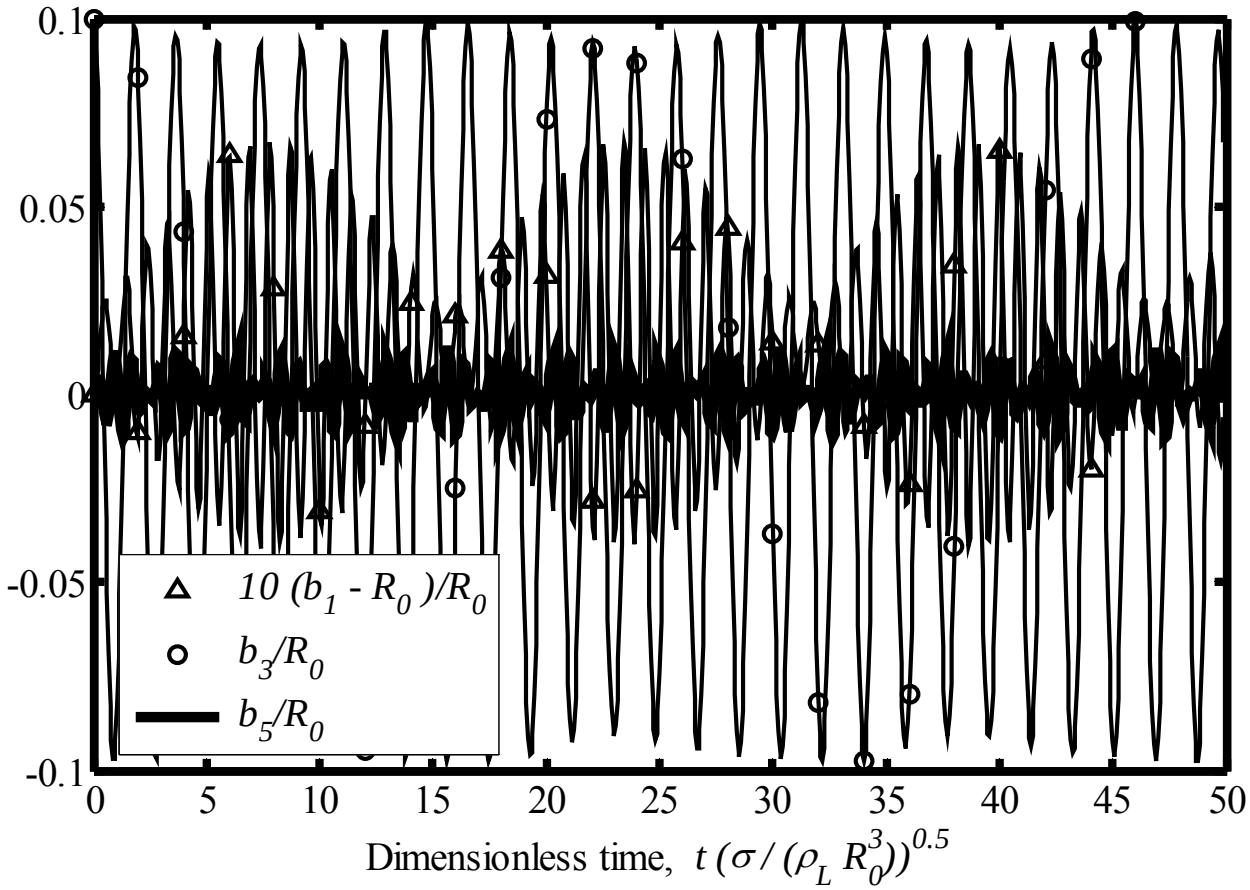

Figure 2. Shape coefficient histories for b_3-excitation with $\beta = 0.1$, $\gamma = 1.4$ and $p_L R_0/\sigma = 10.89$, *i.e.* $k = 1.1$. This condition is for example obtained with water with $\sigma = 0.07$ N/m and $\rho_L = 1000$ kg/m^3 at a pressure of 762.3 Pa, if $R_0 = 1$ mm. Values of $|b_5/b_1|$ are about 0.01 at maximum; values of $(b_1–1)/R_0$ vary between about –0.04 and 0.07.

converted into sound-making isotropic vibrations of the bubble, the so-called breathing mode of b_1. As compared to cases when k is far from 1, the amplitudes this breathing mode attains are quite high. The conditions of figure 2, for k =1.1, are beneficial for sustained generation of sound at a reasonable level at the two frequencies of the sine-terms in equation (15). This condition can be obtained for $R_0 = 1$ mm, as in figure 2, but also for other pressures and surface tension coefficients as long as $p_L R_0/\sigma =$ 10.89 equals 1.1.

The closer to resonance the value of k is chosen, the higher the amplitude of b_1 gets, see figure 3. The corresponding shapes of the bubble are all in the range from spherical to slightly ellipsoidal, still.

The higher the maximum amplitude of b_1 during a period of dimensionless time $\pi/\{\sqrt{(\psi/2)} - \lambda\sqrt{12}\}$, about the time-span shown in figure 3, the lower the corresponding maximum of b_3, as is clearly observed in figure 3. In this case of $k = 1$, the main radian frequency of b_3 (ω_3 from equation 9) hardly varies in time since it is close to $\omega_{RP}/2$.

Although the amplitude of b_1 has been blown up considerably by selecting $k = 1$, and that of b_3 decreased considerably, the periodicity on the time scale $\pi/\{\sqrt{(\psi/2)} - \lambda\sqrt{12}\}$ is not lost for the above cases with initial shape deformation given by $\beta = 0.1$. Shapes remain not far from spherical, and for example b_5 is unimportant for the b_1-history. All this is not true anymore for $\beta = 0.4$, see figure's 4 and 5. The shape changes considerably in this case of $k = 12$, $\sigma = 0.05$ N/m, $\rho_L = 1000$ kg/m^3, $R_0 = 1$ mm, $\gamma = 0.1$, $p_L R_0 / \sigma = 2000$ (resonance value close to 164.7). Other conditions for $\beta = 0.4$ resulted in even stronger deformations. Not only the value of b_5 becomes significant, see figure 5, also the amplitude of

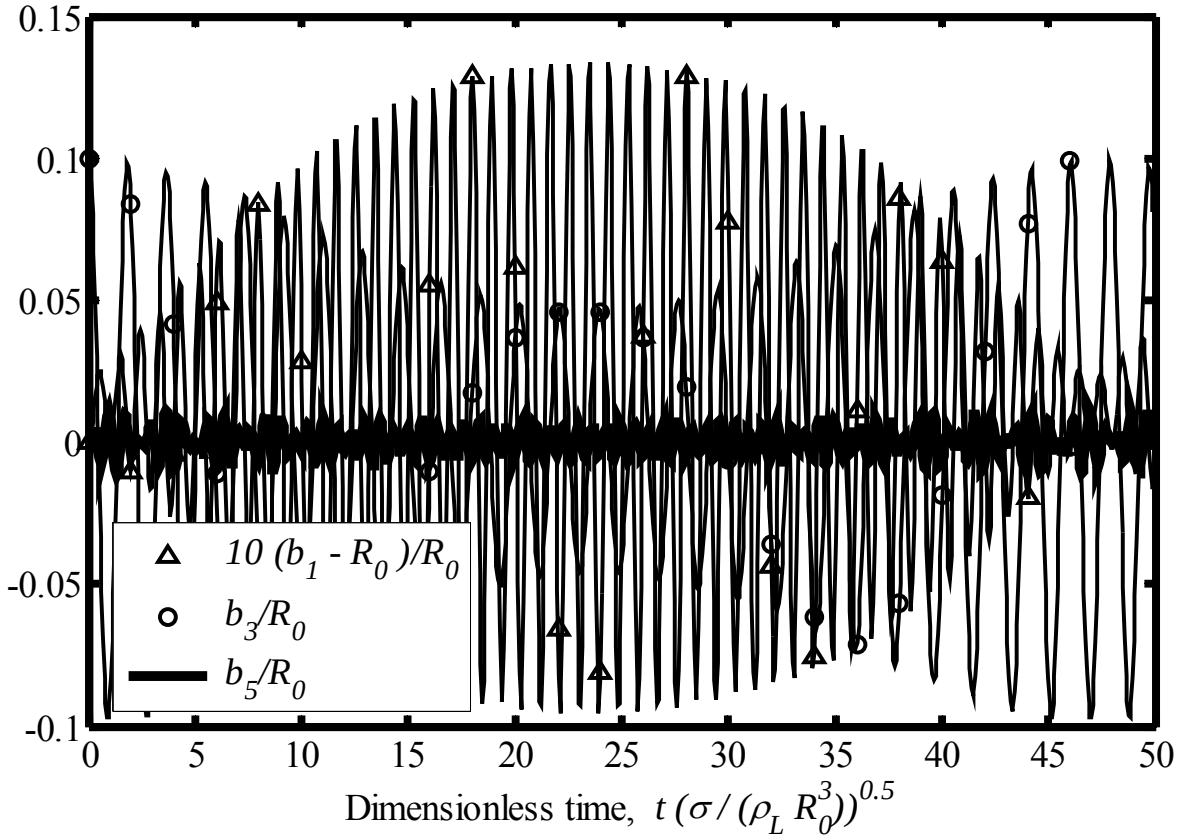

Figure 3. Shape coefficient histories for b_3-excitation with $\beta = 0.1$, $\gamma = 1.4$ and $p_L R_0/\sigma = 9.9048$, *i.e.* $k = 1.0$.

b_1 is not well predicted by equation (15) anymore. The radian frequency ω_3, fitted with equation (9), deviates by as much as 18 % of ω_L already in the first b_3-cycle.

These violent interface deformations are well described by both BEL and BEM, but not by the approximations given in the above. It will be investigated in a future study whether the inclusion of higher order terms in β leads to a better approximation.

CONCLUSIONS

An Euler-Lagrange approach has been followed to derive a new, extended Rayleigh-Plesset equation that takes account of the interaction between a fundamental anisotropic deformation mode and the isotropic expansion-compression mode, the so-called breathing mode. The latter mode is connected to parameter b_1, usually written as R in the context of Rayleigh-Plesset bubble dynamics. As fundamental mode the one related to Legendre polynomial P_3 has been chosen since this constitutes the most important anisotropic deformation mode and since the procedure for higher modes is essentially the same. The amplitude of this mode is given by b_3 and is not restricted to small values, *i.e.* nonlinear interaction has been studied. Deformation of gas bubbles for which the constitutive equation is given by $p_L V^\gamma \equiv$ constant is studied. For moderate deformation with initial amplitude $b_3(t=0) = \beta$ about 0.1 it has been found that the extended Rayleigh-Plesset equation (15), or its equivalent equation (10), yields good predictions of the amplitudes that b_1 attains in the course of time. Comparison has been made with full solutions of the complete Euler-Lagrange equations and with computations with the boundary element method. Interesting features of equation (15) are the occurrence of an amplitude that is inversely proportional to $(4\omega_3^2 - \omega_{RP}^2)$, a finding first derived by Longuet-Higgins [3], a proper behaviour in the limit $(4\omega_3^2 - \omega_{RP}^2)$ going to zero, and the occurrence of a low dimensionless frequency $\{\sqrt{(\psi/2)} - \lambda\sqrt{12}\}$ and the high radian frequency $\{\sqrt{(\psi/2)} + \lambda\sqrt{12}\}$. The latter frequencies are

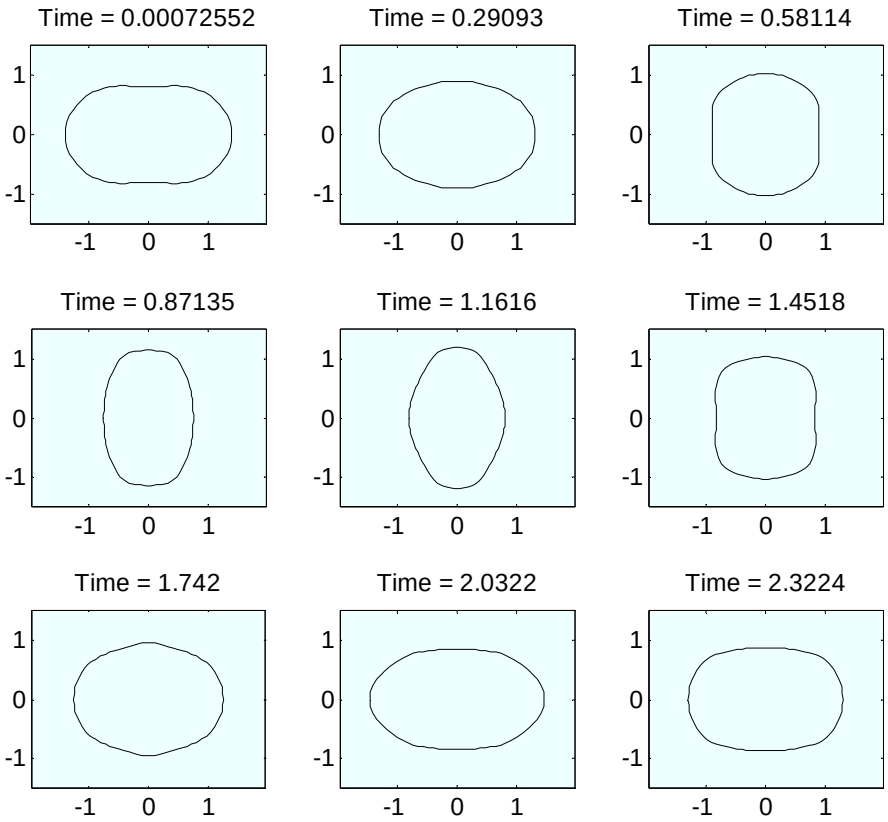

Figure 4. Shapes at various characteristic times, for b_3-excitation with $\beta = 0.1$, $\gamma = 0.1$ and $p_L R_0/\sigma = 2000$, *i.e.* $k = 12$. See figure 5 for corresponding histories of deformation coefficients at corresponding dimensionless times.

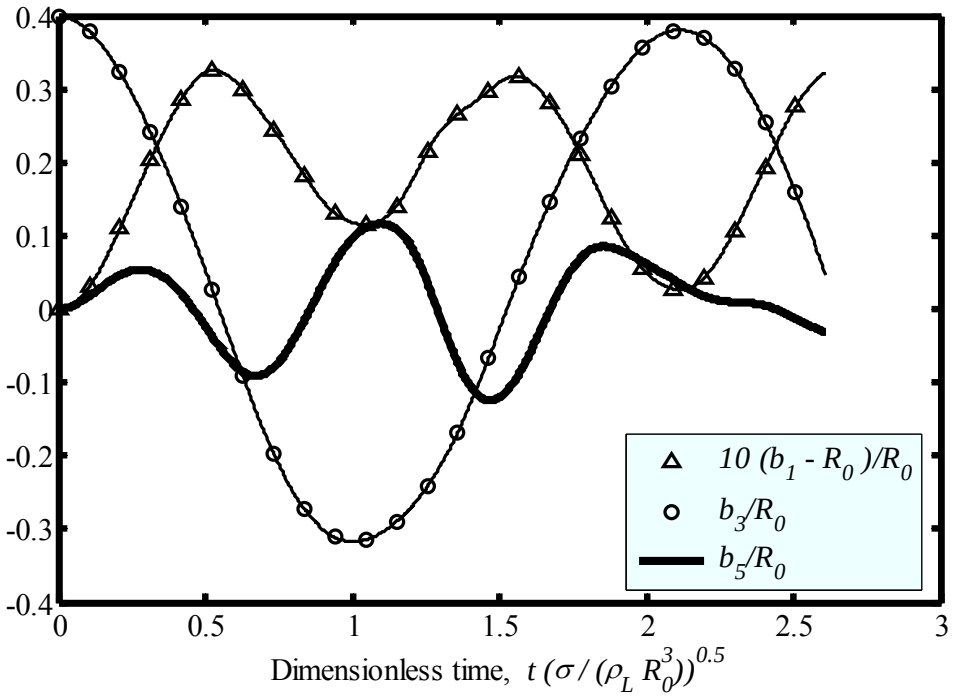

Figure 5. Shape coefficient histories for b_3-excitation with $\beta = 0.4$, $\gamma = 0.1$ and $p_L R_0/\sigma = 2000$, *i.e.* $k = 12$. See figure 4 for corresponding shapes.

clearly observed in actual deformation cases, see for example figure 3. The case of resonance depends on the parameter $\{p_L R_0/\sigma\}$ and the parameter k defined in equation (14); at resonance k is close to 1.

The parameters p_L and σ have been varied in a broad range and in all cases the dimensionless equation (15) was found to hold. The radian frequency ω_3 defined by equation (9) is found to change gradually in the course of time for k-values far from resonance.The reason is that b_3 depends on terms that are second order in β (equation 8) and is only fairly well described by equation (9) during periods of time of about $2\pi/\omega_L$. This explains the well-known experience [5] that ω_3 appears to depend on initial amplitude β for nonlinear deformation of bubbles and spheres of liquid. Practical cases are not close to resonance and ω_3 then changes in time; for times exceeding the dimensionless time $\pi/\{\sqrt{(\psi/2)} - \lambda\sqrt{12}\}$ equation (15) predicts the amplitudes well, but not the times at which the amplitudes are reached. We expect that this will be solved by predicting b_3 more accurately and intend to investigate this in a future study.

For a certain type of fluid a pressure-dependent initial b_1-value, R_0, may exist for which resonance occurs. At resonance, the fluid properties and the pressure are such that energy is quickly converted from the driving fundamental deformation mode to the breathing mode and much sound is produced. Far from resonance, each deforming bubble produces sound, be it with smaller amplitude, since each fundamental mode of oscillation is strongly coupled to the breathing mode (as in equation 13). The nonlinear production of sound by deforming gas-liquid interfaces created by sea waves or underwater nozzles may be better predicted with the results of this paper, in particular with the extended Rayleigh-Plesset equation (13) and its solution (15).

NOMENCLATURE

A	area of bubble surface
k	resonance indicator: $\{p_L R_0/\sigma\}$ / { 16/ γ – 2 + 2/(3γ) }
R_0	initial amplitude of the isotropic breathing mode: $b_1(t = 0)$
Q_1	generalized force, defined by equation 5.
V	bubble volume
β	initial dimensionless amplitude of the anisotropic deformation mode: $b_3(t = 0)/R_0$
γ	ratio of specific heats, c_p/c_v
λ	ratio of observed radian frequency, ω_3 (equation 9), to ω_L: ω_3 / ω_L
ψ	(k – 1)(25 – 3γ) + 24
ω	radian frequency. $\omega_L^2 = 12\ \sigma/(\rho_L R_0^3)$; ω_{RP} is defined in equation 2; ω_3 by equation 9.

REFERENCES

1. Plesset, M.S. & Prosperetti, A. Bubble dynamics and cavitation. *Ann. Rev. Fluid Mech.,* Vol. 9, pp. 145-185, 1977.
2. Minnaert, M., On musical air bubbles and the sounds of running water. *Phil. Mag.*, Vol. 16, pp. 235-248, 1933.
3. Longuet-Higgins, M.S., Monopole emission of sound by asymmetric bubble oscillations. Part 1, normal modes, *J. Fluid Mechanics*, Vol. 201, pp 525-541, 1989.
4. Geld, C.W.M. van der & Kuerten, J.G.M., Axisymmetric dynamics of a bubble near a plane wall. Submitted for publication, *J. Fluid Mechanics*, 2008.
5 Tsamopoulos, J.A. & Brown, R.A., Nonlinear oscillations of inviscid drops and bubbles. *J. Fluid Mechanics*, Vol. 127, pp. 519-537, 1983.

EXPERIMENTAL STUDY ON SPACIAL STRUCTURE IN THE DRAG REDUCING CHANNEL FLOW OF VISCOELASTIC FLUID - BEHAVIOUR OF UNSTABLE LAYER

W. Gu[1], A. Saito[2], M. Motozawa[2], D. Wang[1], Y. Kawaguchi[2]*
[1]Shanghai Jiao Tong University, Shanghai, China
[2]Tokyo University of Science, Chiba, Japan

ABSTRACT. In this paper, drag reducing flow of dilute surfactant solution in a two dimensional channel has been investigated. We paid attention to the effects of Reynolds number ranging from 10000 to 40000 and concentration of additives CTAC from 25ppm to 100ppm in the flow. To measure the instantaneous velocity *u*-*v* in *x*-*y* plane, Particle Image Velocimetry (PIV) was employed. Turbulent statistics was calculated from the velocity data of few hundreds of PIV images. As a result of this study, we found that there appeared a train of inclined fluid lumps having high streamwise velocity fluctuation at the fixed *y*-position. We named this region "unstable layer". It was also found that the distribution of turbulent statistics has multiple peaks corresponding to the position where unstable layer exists. This characteristic structure of the drag reducing flow was discussed in the comparison of turbulent intensity and local mean velocity gradient.

Keywords: *Non-Newtonian fluid, Drag-reduction, PIV*

INTRODUCTION

The dilute solution of some kind of surfactant or polymer show obvious drag reduction (DR) comparatively with the water at the high Reynolds number[1]. This characteristic is useful for saving pumping power in a water-circulating device such as a district heating/cooling (DHC) system. For such applications, the surfactant additives are more advantageous than polymers because surfactant has self-repairing ability and as a result less affected to the mechanical degradation caused by the pump in the circulation system. Therefore, research in drag-reducing flow has received great attentions for the past several decades. Because the slight viscoelasticity of solution affects to the energy dissipation process of the flow, the flow with drag reduction exhibits special flow pattern which is different from laminar flow or turbulent one of Newtonian fluid. Therefore it is important to investigate the detailed structure in the drag reducing flow.

Many researches on the drag reducing flow have proceeded. Kawaguchi et al.[2] carried out the investigation of turbulent statistics in a two dimensional channel by LDV or PIV. They found that two components of velocity fluctuation were suppressed and Reynolds shear stress almost disappeared in the drag reducing flow. Li et al.[3] investigated the Reynolds number dependence of the turbulent structures in a drag-reducing flow by using relatively low-resolution PIV. They examined relationship between the dynamic process of the Shear-Induced Structure in the solution and turbulence. Thus the investigation of turbulent statistics and turbulent structures in the drag reducing flow is under the progress in the recent years[4,5].

In this paper, drag reducing flow of dilute surfactant solution in a two dimensional channel has been investigated experimentally by using high resolution CCD camera. We pay attention to the

* Corresponding author: Prof. Y.Kawaguchi
Phone: + (81)-4-7124-1501(Ext.3903), Fax: + (81)-4-7123-9814
E-mail address: yasuo@rs.noda.tus.ac.jp

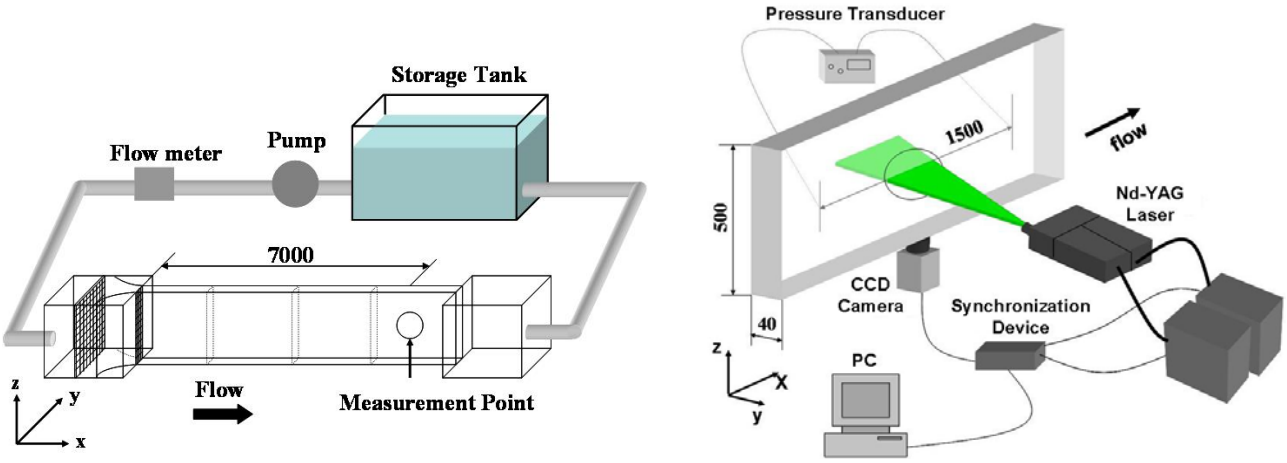

(a) Flow System (b) PIV Arrangement

Figure 1. Experimental Facility.

effects of surfactant concentration and Reynolds number on the fine turbulent structure near the wall. We employed PIV to measure the instantaneous velocity *u*-*v* in the *x*-*y* plane. The turbulent structure was discussed based on the instantaneous velocity distribution in *x*-*y* plane. Turbulent statistics was calculated from the measured velocity data, and mean velocity profiles, distribution of root mean square (RMS) of velocity fluctuation components *u* and *v*, and Reynolds shear stress were obtained. Based on these measurements, the characteristic turbulent structure in the drag reducing flow was discussed.

EXPERIMENTAL SET-UP

Figure 1 shows (a)flow system and (b)PIV arrangement. Flow system consists of closed-circuit water loop with two dimensional channel test section. The channel was made of transparent acrylic resin having a length of 8m, inner height (*H*) of 0.04m, and spanwise width (*W*) of 0.5m. A honeycomb rectifier with length of 0.15m was set at the channel entrance for removing large eddies. An electromagnetic flow meter with an uncertainty of ±0.01 m^3/min was installed upstream of the channel for measuring flow rate *Q*. Bulk mean velocity U_b can be calculated by this flow rate, it represents $U_b=Q/A$, where *A* is the cross section area in the channel. Storage tank in the flow loop contained a heater and an agitator to adjust a temperature of fluid. The temperature of fluid maintained at 25°C with an uncertainty of ±0.1°C. The wall shear stress was estimated from pressure drop of the channel, which was measured with pressure tabs located on the wall of channel over a distance of 1.5m with an uncertainty of ±0.1Pa.

The PIV system consists of a double-pulsed laser, laser sheet optics, charge-coupled device (CCD) camera, synchronization device, image-sampling computer and image processing software (Dantec Dynamics studio ver. 1.45). The double-pulsed laser (New Wave Research Co. Ltd., MiniLase-Ⅱ /30Hz) is a combination of a pair of Nd-YAG lasers, each having an output of 30mJ/pulse and maximum repetition rate of 30Hz. The synchronization device communicates with the CCD camera and computer, and generates pulses to control the double-pulse laser. The CCD camera used in this experiment has a resolution of 2048×2048 pixels. The laser sheets were aligned at *z*=250mm (*z*=0 at the side-wall) for the *x*-*y* plane measurements. The measurement point is located at 7m downstream from the channel entrance. At the location of the measurements, the channel was equipped with two circular glass windows having a diameter of 0.15m on both sides of the channel. PIV images were acquired for 500 dual frames for all the measurements. The photograph acquisition rate was 4Hz. The picture were taken to cover the full height of the channel (the PIV image covered an area of about 60×60 mm^2). The interrogation area was set to be 64×64 pixels with 75% overlap in each

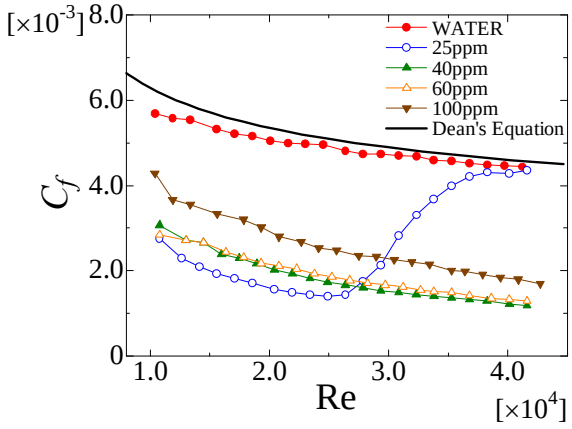

Figure 2. Friction coefficient versus Re.

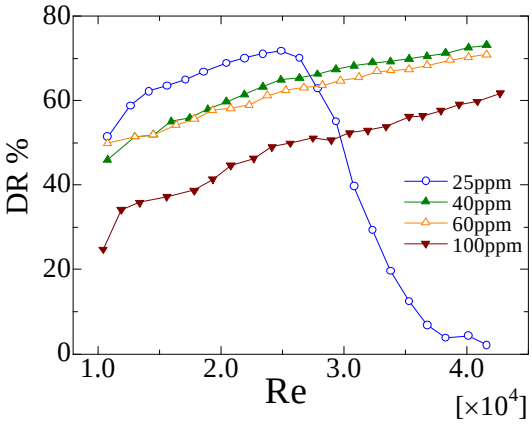

Figure 3. Drag reduction rate versus Re.

direction. The spacing between adjacent vectors in both directions was around 0.45mm. The tracer particles used to seed the flow were acrylic colloid. The particle concentration was adjusted so that on average at least ten particle pairs were observed in an interrogation window for each case.

The surfactant tested in this measurement was the cationic surfactant, cetyltrimethyl ammonium chloride (CTAC : $C_{16}H_{33}N(CH_3)_3Cl$). Local tap water was used as the solvent. Sodium salicylate (NaSal) was added to the solution with the same weight concentration as that of CTAC for providing counterions. The molar ratio of Sodium salicylate to the CTAC was about 2. The CTAC solution with concentration of 25ppm, 40ppm, 60ppm, and 100ppm was selected as drag-reducing fluid. Tap water was also used as the tested fluid for comparison. In this paper, Reynolds number was defined as $\mathrm{Re}=U_bH/v$, where U_b is the bulk mean velocity, H is the height of the channel and v is kinematic viscosity of the solvent. Re was ranged from 10000 to 40000 for each concentration.

RESULTS AND DISCUSSION

In this section, the instantaneous velocity maps and the results of turbulent statistics were analysed in the water and surfactant solution flows based on the PIV measurements in the x-y plane. Turbulent statistics was calculated from the instantaneous velocity data of 500 PIV images for each condition.

Friction coefficient and drag reduction rate

The friction coefficient was obtained from the pressure drop of the channel. Based on this measurement, drag reduction rate (DR) can be calculated. The drag reduction rate was defined as

$$\mathrm{DR} = (C_{f,w}-C_{f,s})/C_{f,w} \times 100\ \% \qquad (1)$$

where C_f is the friction coefficient $C_f = \tau_w / (1/2\rho U_b^2)$, and the subscript w and s represent water and surfactant solution, respectively. τ_w is the wall shear stress and ρ is the density of the solvent.

Figures 2 and 3 show the friction coefficient distribution and the DR distribution versus Reynolds number, respectively. The solid line in Figure 2 is the friction coefficient of water flow in a two dimensional channel obtained by Dean[6]. This line represents following equation.

$$\mathrm{Re} = \sqrt{2/C_f}\,\exp[0.41(\sqrt{2/C_f} - 2.4)] \qquad (2)$$

The friction coefficient of drag reducing flow is much smaller than that of water flow. Especially, in case of 40ppm, 60ppm and 100ppm, drag was reduced largely in the wide range of Reynolds number. Maximum DR in this study was about 73%. On the contrary, in case of 25ppm, DR has a maximum at critical Reynolds number, and DR starts to decrease with increasing Reynolds number beyond the critical Reynolds number, and finally disappeared. This seems to be explained that the network structure of micelles is destroyed with high shear rate and viscoelasticity effect of fluid

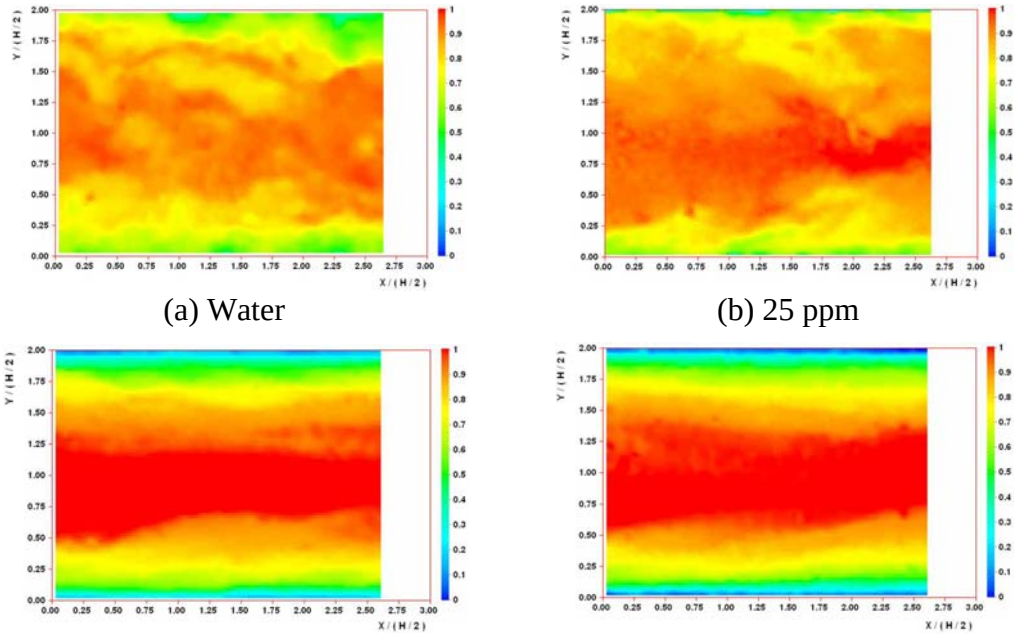

(a) Water (b) 25 ppm

(c) 40 ppm (d) 60 ppm

Figure 4. Instantaneous distributions of streamwise velocity (Re=40000).

also disappears. This rheological property depends on the surfactant concentration and temperature of fluid. It is worth noting that the friction coefficient changes according to the Reynolds number at 25ppm but not in the other concentrations. This suggests that in this Reynolds number range, surfactants suppress the turbulence at the concentration of 40ppm. Surplus of surfactant gives no effects to the suppressed turbulence. Under the lower concentration condition such as 25ppm, the drag reduction rate has a complicated relation with Reynolds number. It suggests that the turbulent eddies which have different scale in different Reynolds number are interacting to the turbulent suppression at this concentration range.

Instantaneous distribution of streamwise velocity and velocity fluctuation

Figure 4 shows instantaneous distributions of streamwise velocity u for Re=40000 in the x-y plane. Main flow direction is from left to right. The contour of these maps shows the streamwise velocity. In the water flow, it is seen that there are many eddies with different size and intensity coexists, by this motion, momentum transportation of fluid is occurring actively. This is the common idea for the Newtonian fluid turbulence and was confirmed from the cloud like pattern seen in the present PIV picture. In contrast with water flow, the turbulent structure in the drag reducing flow at high reduction rate is very different as shown in Figure4(c), (d). It is observed that smaller eddies disappears and fluctuation in larger size survives. There remains “wavy structure” along the streamwise direction. The wavy structure seems regular and detailed discussion on this regularity will be given in the next section. This structure is far from the normal turbulence but it is not also the same with the laminar flow of Newtonian fluid. Therefore, the drag reducing flow is not simply the suppression of turbulence.

Figure 5 shows the distributions of instantaneous streamwise velocity fluctuation u' for Re=40000. The velocity fluctuation was defined as the instantaneous local velocity subtracted the local mean velocity averaged by 500 velocity fields from the instantaneous local velocity. As shown in Figure 5, streamwise velocity fluctuation was observed in the drag reducing flow. In the water flow, velocity fluctuation occurs irregularly. However, we found that there appeared a train of inclined fluid lumps having a different velocity at the fixed y-position in the drag reducing flow, as shown Figure5(c), (d). This alternating behaviour relates to the wavy fashion of instantaneous velocity distribution in Figure4(c), (d). When the RMS of turbulent fluctuation is calculated at this position, the value of

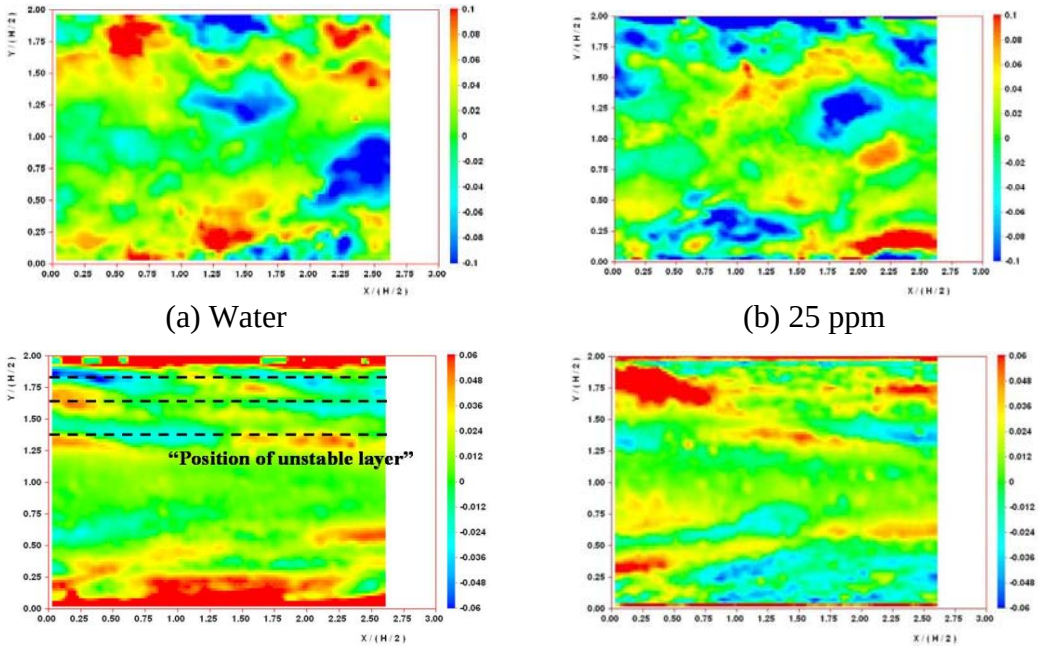

(a) Water (b) 25 ppm

(c) 40 ppm (d) 60 ppm

Figure 5. Instantaneous distributions of streamwise velocity fluctuation *u'* (Re=40000).

velocity fluctuation becomes high. Through the detailed investigation of numbers of PIV map, it was observed that this layer spreads to the *x*-direction, parallel to the wall surface and has relatively thin in *y*-direction, but the value of velocity fluctuation is relatively small out of this layer. Therefore, we named this region as "unstable layer". Another interesting characteristic is that the unstable layer can be found in multiple places. This means that the "wavy structure" exists at different y-position which forms a group of waves. Surprisingly, the positions of the unstable layer were almost unchanged for the number of PIV maps. This feature is also very different from normal turbulent fluctuation which spreads in irregular position, frequency and intensity.

Turbulent statistics results

Figure 6 shows the streamwise mean velocity profiles normalized by the friction velocity u_τ which is estimated from the pressure drop of the channel. This figure shows the case of Re=40000. The log-law profiles of streamwise mean velocity for Newtonian turbulent flow and drag-reducing flow are defined as follows,

$$U^+=2.4\ln y^+ +5.5 \quad (3)$$

$$U^+=11.7\ln y^+ -17 \quad (4)$$

Mean velocity profile of water flow is in good agreement with equation (3). In drag reducing flow, mean velocity profiles are upshifted in the log-law layer with a larger gradient compared with that in water flow, and close to equation (4). Equation (4) was suggested by Virk for the ultimate velocity profile of polymer solution flow[7]. This upshift of mean velocity directly indicates the large drag reduction existence in this condition. On the contrary, in case of 25ppm where drag reduction disappeared, mean velocity profile is almost same as that in water flow.

Figure 7 shows the distribution of RMS of streamwise velocity fluctuation *u'* normalized by U_b. Horizontal axis is normalized by the half of the channel height *h* (=*H*/2). Figure 7(a) and (b) show the effects on the surfactant concentration and Reynolds number, respectively. In the drag reducing flow, u_{rms} decreases throughout the channel height than that in water flow. The value of u_{rms} decreases with increasing drag reduction rate. The turbulent fluctuation normalized by the bulk mean velocity is suppressed by drag reduction additives. Although u_{rms} has a peak with low DR as Re=10000 for 40ppm, u_{rms} has multiple peaks in the case with high DR as Re=30000 and 40000 for 40ppm. The position

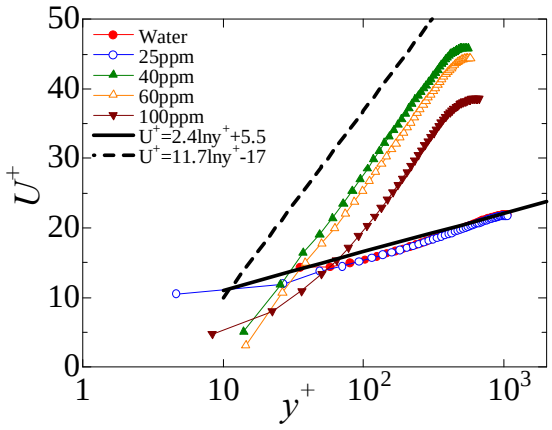

Figure 6. Streamwise mean velocity profiles (Re=40000).

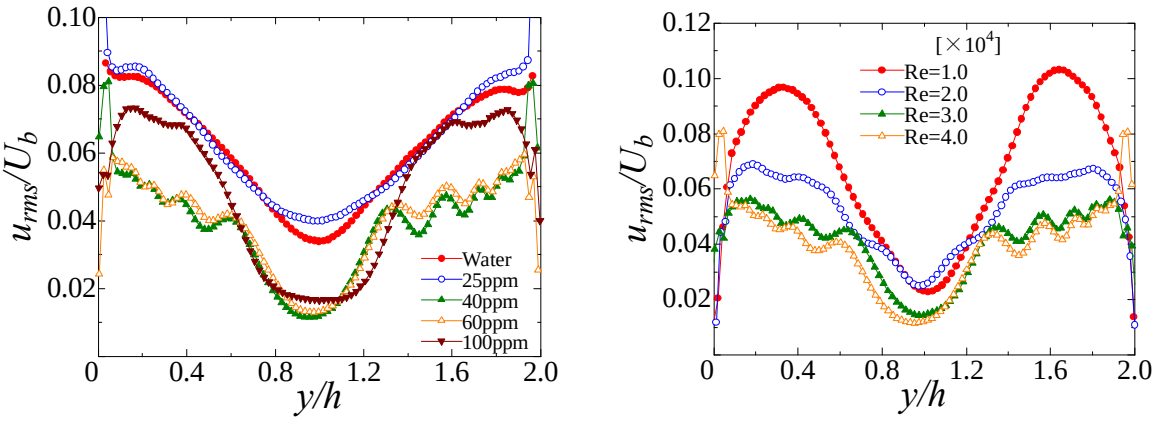

(a) Effect of surfactant concentration (Re=40000) (b) Effect of Reynolds number (40ppm)

Figure 7. Distribution of RMS of streamwise velocity fluctuation.

where appeared multiple peaks is the same position where the unstable layer appeared in the instantaneous velocity fluctuation map. The local statistical value at the location of the unstable layer will be summarized in the last part of this chapter. Similar characteristic to these multiple peaks in the drag reducing flow was observed in other studies in turbulent boundary layer[8]. It is interesting that the similar characteristics have been found in the other type of shear flow but detailed discussion will be the task in the future.

Figure 8 shows the distribution of RMS of wall normal velocity fluctuation v' normalized by U_b for Re=40000. In the drag reducing flow, v_{rms} largely decreases throughout the channel height than that in water flow. The amount of decrease of v_{rms} is much higher than that of u_{rms}. This fact suggests that the turbulent energy transport between the different directional components is inhibited by the effect of additives. Therefore, the directional components becomes to anisotropic in the drag reducing flow. In the distribution of v_{rms}, there did not appear the multiple peaks seen in the distribution of u_{rms}.

Figure 9 shows the distribution of Reynolds shear stress uv normalized by $u_\tau{}^2$ for Re=40000. In the turbulent water flow, Reynolds shear stress has the large value near the wall, and this corresponds to the larger frictional drag. In the drag reducing flow, Reynolds shear stress largely decreases and the value is almost zero throughout the channel height. This is the typical characteristics accompanied with high drag reduction. When examining carefully, the value has the multiple peaks at similar position of peaks in the distribution of u_{rms}.

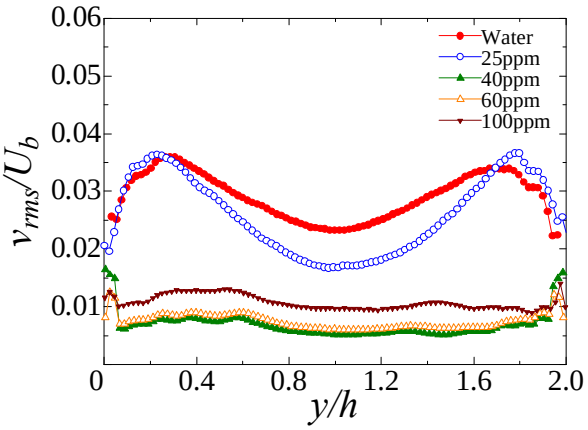

Figure 8. Distribution of RMS of the wall normal velocity fluctuation (Re=40000).

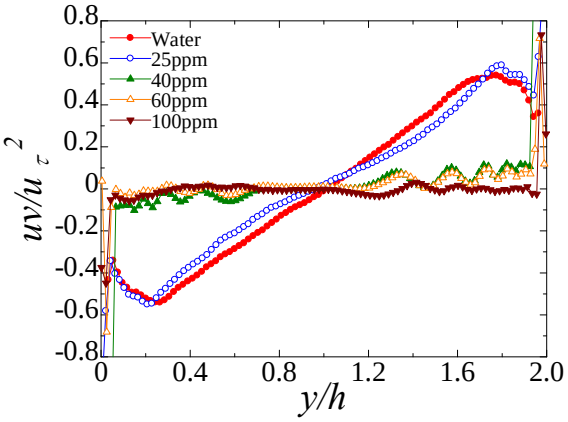

Figure 9. Distribution of Reynolds shear stress (Re=40000).

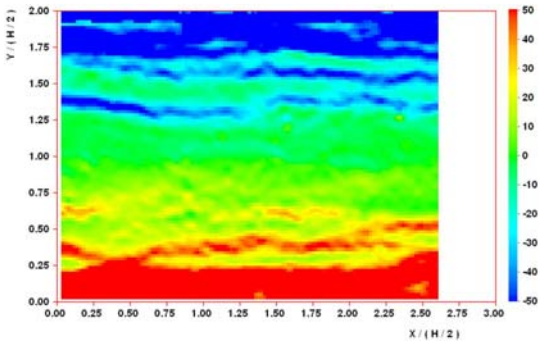

Figure 10. Distribution of instantaneous velocity gradient (40ppm, Re=40000).

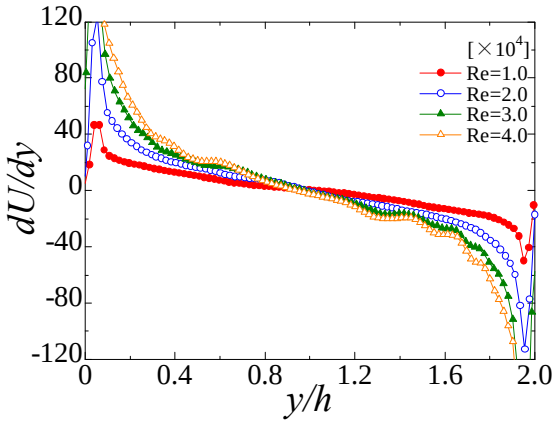

Figure 11. Distribution of mean velocity gradient (40ppm).

To see the relation of unstable layer and local shear rate, examining the instantaneous velocity gradient map is useful. Figure 10 shows the distribution of instantaneous local velocity gradient *du/dy* in the drag reducing flow. It can be seen that the high velocity gradient appears in location of the unstable layer. This coincidence was observed at each of PIV map.

Figure 11 shows the distribution of the mean velocity gradient *dU/dy* for Re=40000. In the case with low DR as Re=10000, the value of *dU/dy* decreases gradually toward to the center of the channel. On the contrary, in the case of Re=40000, the value of *dU/dy* is high in the unstable layer. Because the mean velocity differs for different Reynolds number, the mean velocity gradient also differs for each case. One interesting finding is that even the local value of velocity gradient is different, the unstable layers appear at same y-positions. This fact suggests that the local value of velocity gradient itself does not matter to produce the unstable layer.

Presently, we cannot declare the full mechanism of the unstable layer, but we can summarize the observation in Table 1. From this summary, the unstable layer has “turbulence-like” characteristics. But just outside of this layer, the character disappears. Therefore, the layered structure of “unstable layer” and “stable layer” are locally and temporally stable. The velocity fluctuation found in the unstable layer is regular in space. These characteristics are far from the normal turbulence found in Newtonian fluid. The reason we call the layer as “turbulent-like” comes from this findings.

One possible explanation for existence of the unstable layer may be related to the instability phenomena appearing in the viscoelastic fluid. The fluid has intrinsic time scale and in certain shear condition, the flow becomes unstable. One typical observation in laminar flow is “shear induced

Table 1
Statistical property of at the position of unstable layer

Statistical property	Value
RMS of Streamwise velocity component u_{rms}	Peak
RMS of wall-normal velocity component v_{rms}	Vague peak
Reynolds shear stress	Peak
Mean velocity gradient	Peak

state" which is the formation of large molecular structure under the steady shear. When this phenomenon appears, the cross-talk between the shear and viscosity change occurs and the flow becomes unstable. Presently, we cannot claim the unstable layer is caused by the "shear induced state", further investigation on the idea of viscoelastic instability may be fruitful.

CONCLUSION

The characteristic structure of the drag reducing flow with surfactant additives was investigated experimentally. We employed PIV to measure instantaneous velocity in *x*-*y* plane, instantaneous velocity distribution and turbulent statistics was obtained. As a result of this study, the following conclusions in the drag reducing flow were obtained.

In the instantaneous velocity fluctuation map, there appeared a train of inclined fluid lumps having high velocity fluctuation at the fixed *y*-position. The distributions of u_{rms} and Reynolds shear stress have multiple peaks at this position. The position where unstable layer exists is unaffected by the Reynolds number and the surfactant concentration. Although further analysis is necessary, it is speculated that this ordered motion is taking important role in the momentum transfer in a viscoelastic fluid turbulence.

REFERENCES

1. Toms, B. A., Some observations on the flow of linear polymer solutions through straight tubes at large Reynolds numbers, *Proceedings of 1st International Congress on Rheology*, Amsterdam, 1948, pp. 135-141.
2. Kawaguchi, Y., Tawaraya, Y., Yabe, A., Hishida, K. and Maeda, M., Turbulent Transport Mechanism in a Drag Reducing Flow with Surfactant Additive Investigated by Two Component LDV, *Proceedings of 8th International Symposium on Application of Laser Techniques to Fluid Mechanics*, Lisbon, July 8-11, 1996, pp.29.4.1-29.4.7.
3. Li, F-Ch., Kawaguchi, Y., Segawa, T. and Hishida, K., Reynolds-number dependence of turbulence structures in a drag-reducing surfactant solution channel flow investigated by PIV, *Physics of Fluids,* Vol.17, 075104, pp. 1-13, 2005.
4. White, C.M. and Mungal, M.G., Mecahnics and Prediction of Turbulent Drag Reduction with Additives, *Annu. Rev. Fluid Mech.*, Vol.40, pp. 235-56, 2008.
5. Li, F.-Ch., Kawaguchi, Y., Hishida, K., and Oshima, M., Investigation of turbulence structures in a drag-reduced turbulent channel flow with surfactant additive by stereoscopic particle image velocimetry, *Experiments in Fluids*, Vol.40, pp. 218-230, 2006.
6. Dean, R.B., Reynolds Number Dependence of Skin Friction and other Bulk Flow Variables in Two-Dimensional Rectangular Duct Flow, *J. Fluid Eng.*, Vol.100, pp.215-223, 1978.
7. Virk, P., Mickley, H., and Smith, H., The ultimate asymptote and mean flow structure in Toms' phenomenon, *ASME J. Appl. Mech.*, Vol.37, pp.480-493, 1970.
8. Itoh, M. and Tamano, S., Drag reduction of turbulent flows of surfactant solutions, *Proceedings of the 7th JSME-KSME Thermal and Fluids Engineering Conference,* Sapporo, 2008, CD-Rom.

SYSTEM AIR – GLYCERIN: TOTAL VOLUMETRIC AIR FLOW RATE USING PICTURES OF THE FLOW

M.A.T. Talaia[1 *]
[1]Physics Department, University of Aveiro, Aveiro, Portugal

ABSTRACT. Usually the flow of gas is measured or controlled using a rotameter or a flow measurer.
In this work, for a system air - glycerin the flow of air injected into the base of a vertical and transparent column of quadrangle section, for flow regime with Reynolds number very low (dominate forces of viscosity) produce air bubbles that rise with a spherical geometric shape, can be obtained through pictures.
A theoretical and experimental model was developed based on a dimensional analysis.
The results obtained are very interesting and shows that the model developed predicts, with excellent agreement, the flow of air injected into the base of the column and the number of bubbles of air that arrives to the free surface of the glycerin with Reynolds number from 0.10 to 0.16, terminal velocity from 0.023 m/s to 0.035 m/s and diameter of the bubble air from 0.006 m to 0.007 m.

Keywords: *two phase – flow, gas bubble, terminal velocity, air / glycerin system e, volumetric air flow rate*

INTRODUCTION

Terminal velocity of a single bubble rising through an infinite stagnant liquid is of fundamental importance in the field of gas liquid two phase flow.
As is known, the single isolated gas bubble rising velocity in a liquid large column depends on buoyancy and drag forces. Interactions between forces happen due to surface tension, viscosity, inertia and buoyancy produce a various effects which are quite often evidenced by different bubble shapes and trajectories. Many industrial processes include bubble columns for promoting mass transfer, high pressure evaporators and so on.
The dependence of the velocity on the rising bubble volume for air bubbles in liquid has been determined experimentally by numerous investigators; our team [1-10] and another team [11-23] among the others.
In the present study, for a air - glycerin system the flow of gas injected into the base of a vertical and transparent column of quadrangle section, for flow regime with the Reynolds number very low produce air bubbles that rise with a spherical geometric shape, can be obtained through picture. For a constant flow of air is possible to observe that the air bubbles produced near the injector (centered at the base of the column) rise and when they reach terminal velocity they move maintaining a constant distance between them. If a picture can be obtained it is possible to determinate through its interpretation and of the terminal velocity of the air bubble the total volumetric air flow rate. The velocity of the air bubble will depend on the fluid proprieties, acceleration due gravity and the size of the bubble.

* Corresponding author: Prof. M.A.R. Talaia
Phone: + (351)-234370823, Fax: + (351)-234378197
E-mail address: mart@ua.pt

EXPERIMENTAL METHOD

The experimental technique adopted in the present paper to study the behaviour of air bubbles which rise in the interior of a viscid liquid (in this particular case is glycerin), when the volume of injected gas is altered, by an appropriated system placed in the base of a vertical column, is easily understood through the scheme in Figure 1.

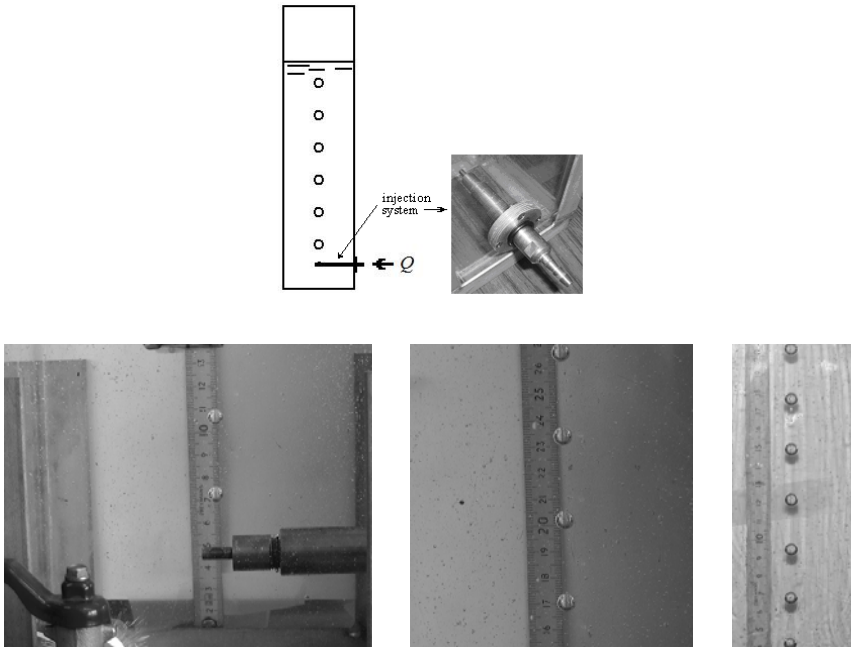

Figure 1 – Schematic of the experimental apparatus; injection system and pictures with the movement of air bubbles

The device used is made of a transparent acrylic glass column, with a height of 1.5 m and a squared section with a 0.15 m ridge. The column is open on the top of the superior part which allows the surface of the liquid to be in contact with the atmosphere.
In the base of the column was installed a tap which allows the exit of the liquid. The height of the liquid determines the pressure of the air bubbles injection and consequently the size of the bubbles, distance between bubbles and terminal velocity of the air bubbles. An injection system is also placed in the base of the column. The exit of the air occurs in the middle (axis longitudinal) to eliminate the wall effects, when the isolated and separated bubbles rise in the interior of the liquid. As the Figure 1 shows, the air exit in the injection system happens through a 0.001 m hole. This can be easily replaced by other exit diameters. The size of the air bubbles depends of the pressure due to the height of the liquid column, the diameter of the injection hole and the superficial tension.
In this work we care about developing experimental techniques of observation and collect of data. Thus, there will be introduced only data referring to the air bubbles which rose with a spherical shape in the glycerin interior. By being a viscid liquid, the glycerin has a great advantage instead of water, in which the techniques are harder to implement and control.
The injection system is connected to the compressed air net. The compressed air passes through a “box / lung” to eliminate the small pressure variations in the alimentation net. A system of air flow measure was installed to control the registered and observed data.
The size of the air bubbles which form inside the glycerin is controlled by one manometer of pressure and by the height of the liquid inside the column.

A tape measure placed in the lateral side of the column allows, by picture and a video system, the determination of the terminal velocity of the air bubbles. Knowing the distance in a certain time and considering the uniform movement (no acceleration) the velocity is easily determined.
The air flow was also measured using two different processes: counting the number of bubbles that get to the surface of the liquid or that pass a level during a determined amount of time and/or collecting the air bubbles in a volume graduated collector during a certain time. To the same air flow, the diameter of the air bubbles was also determined by photo and/or calculation. Also, each bubble was collected in a graduated cylinder at the top of the column in order to determine its volume. In order to minimize the error of the air bubble diameter, and for the same bubble size, the gathered bubbles inside a cylinder graduated were counted. The total volume was divided later by the number of air bubbles gathered
The physical properties of the glycerin (dynamic density and viscosity) were determined.
During the experimental work there was the concern to maintain the constant temperature, because the glycerin viscosity is very much influenced by it.

DEVELOPED MODEL

Pictures of the rising movement of the air bubbles inside the glycerin allowed the development of a simple model to preview the flow of air which is injected in the base of the column.
The air flow was considered to air bubbles that move inside the glycerin with the same terminal velocity, therefore with the same distance between the air bubbles.
As the Figure 2 shows, the volume of the sphere of air of each bubble was considered as a circular column of air between spheres. Therefore, the air bubbles rising system with the same distance between air bubbles is equal to an air column system which moves in the interior of the glycerine, with the same terminal velocity of each isolated air bubble. In this situation the continuity equation was used.
The dimensional analysis allowed the development of two equations which constants are determined by the experimental conditions.

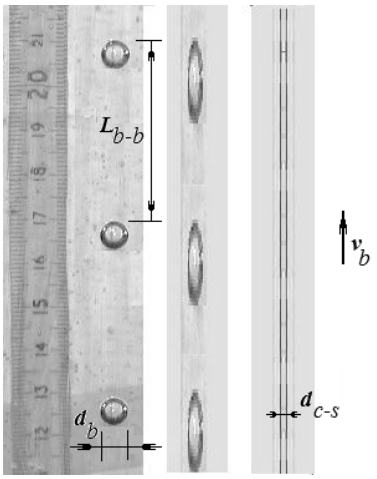

Figure 2 – Theoretical model: air column system

THEORY

In this work we applied dimensional analysis to determine dimensionless groups governing the total volumetric air flow rate of gas bubbles in stagnant liquid, rising in long vertical tubes filled with liquid viscosity.
Physically, we expect the volumetric air flow rate of gas bubbles Q should depend on eight variables

$$Q = Q\left(\rho_l, \Delta\rho, \mu_l, \sigma_{l/g}, g, L_{b-b}, v_b, d_b\right) \tag{1}$$

where ρ_l is the density of liquid, $\Delta\rho = \rho_l - \rho_g$ the apparent density, ρ_g the density of gas, μ_l the dynamic viscosity of liquid, $\rho_{l/g}$ the surface tension of liquid/gas, g the acceleration due gravity, L_{b-b} the distance between gas bubbles, v_b the terminal velocity of one single isolated gas bubble and d_b the equivalent bubble diameter (diameter of a sphere with same volume as the bubble).
The dimensional analysis of equation (1) can be obtained through traditional techniques [24]. The independent variable chosen were g, ρ_l and d_e.
Thus, the six dimensionless groups are:

$$\Pi_1 = \frac{Q}{\sqrt{gd_e^5}} \qquad \Pi_2 = \frac{\Delta\rho}{\rho_l} \tag{2}$$

$$\Pi_3 = \frac{\mu_l}{\sqrt{\rho_l^2 g d_e^3}} \qquad \Pi_4 = \frac{\rho_{l/g}}{\rho_l g d_b^2} \tag{3}$$

$$\Pi_5 = \frac{L_{b-b}}{d_b} \qquad \Pi_6 = \frac{v_b}{\sqrt{gd_e}} \tag{4}$$

Algebraic manipulation leads to

$$Z = \frac{\sigma_{l/g}\Delta\rho}{\rho_l g^{1/2} d_b^{1/2} \mu_l} \tag{5}$$

$$\mathrm{Re}_b = \frac{\rho_l v_b d_b}{\mu_l} \tag{6}$$

For values of $\Pi_1 = \phi\left(\Pi_6\Pi_5^{-1} = \Pi_7\right)$ may be written

$$Q = k\frac{v_b d_b^3}{L_{b-b}} \tag{7}$$

where *k* is a experimental constant.
Also, according Figure 2,

$$\pi\frac{d_{c-s}^2}{4} = \pi\frac{d_b^3}{6L_{b-b}} \qquad d_{c-s} = \left(\frac{2d_b^3}{3L_{b-b}}\right)^{1/2} \tag{8}$$

where d_{c-s} is the gas column with terminal velocity v_b.
Then, also

$$Q = k' d_{c-s}^2 v_b \Leftrightarrow k' d_{c-s}^2 \frac{d}{\Delta t} \tag{9}$$

being $k' = 1{,}5k$.

If we take a time interval $\Delta t\left(=t_f - t_i\right)$, between two marks which define the referential distance d [all measurements were made from the top (nose) of the gas bubble],we can calculate the experimental terminal velocity, being $v_b = \dfrac{d}{\Delta t}$.

By other hand, it is possible to obtain

$$Q = n\frac{\pi d_b^3}{6\Delta t'} \tag{10}$$

where n is a number of gas bubbles considered during a time interval $\Delta t'$.
So,

$$n = \frac{d}{L_{b-b}}\left(\frac{\Delta t'}{\Delta t}\right) \tag{11}$$

RESULTS AND DISCUSSION

The Figure 3 show for the air glycerin system the experimental data, experimental straight line where $k = \left(0.5246 \pm 0.0258\right)$ and theoretical straight line where $k = \pi/6$.
The experimental data allowed the determination of the constants value and its uncertainty or associated error.
So, the experimental equation will be

$$Q = \left(0.5249 \pm 0.0258\right)\frac{v_b d_b^3}{L_{b-b}} \tag{12}$$

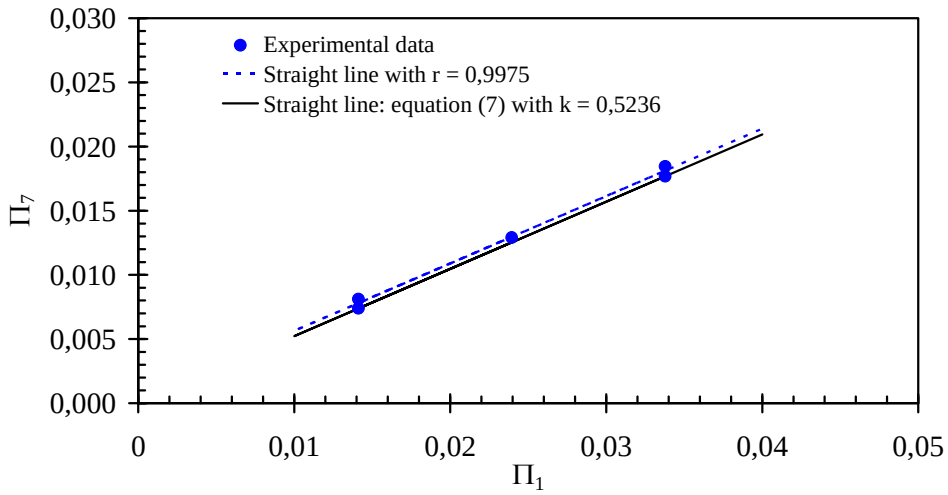

Figure 3 – Experimental data considering $\Pi_1 = \phi\left(\Pi_7\right)$: air glycerin system

So, the equation (12) that can be used to the air / glycerin system with *Z* number from 0.15 to 0.16, terminal velocity from 0.023 m/s to 0.035 m/s and Reynolds number from 0.10 to 0.16.
The results obtained are very interesting and shows that the model developed predicts, with excellent agreement.

with Reynolds number, terminal velocity from and diameter of the bubble air from 0.006 m to 0.007 m.

RESEARCH IN COURSE

It is being studied a injection system which allows the decreasing of the air bubbles size. The superficial tension between fluids (gas / liquid) is important to the formation of the size of the air bubble. At this moment are also being made essays with low viscid liquids, like water. In this stage can be recognized the difficulty of the air / water system in the variables control. The research is in course and it is expected, in a near future, to have an amount of very interesting data. It is being considered the replacement of the picture technique by the use of a transducer differential pressure column.

CONCLUDING REMARKS

During the research, all experiments were carried out at constant temperature.
A method based in the dimensional analysis is presented to preview the air flow by some data read and photograph technique.
Adimensional parameters allowed the presentation of expressions that let preview the constant air flow which is injected in the vase of a column filled with glycerin.
The expression constants were determined by experimental data and the developed and showed expression is in concordance with the theoretical model.
The obtained results are interesting to limit values defined by equivalents air bubbles diameters, terminal velocity of air bubble and where fluids physical properties are known.
Experimental data show that it is possible to work out expression to accurately predict total volumetric air flow rate in air glycerine system.

NOMENCLATURE

Roman Letters

d	distance control
d_b	equivalent air bubble diameter
d_{c-s}	diameter of column of the air
g	gravitational acceleration
k	constant
i	indices
L_{b-b}	distance between air bubble
n	number of the air bubble during $\Delta t'$
Q	volumetric flow rate
Re_b	Reynolds number
t_i	initial time
t_f	final time
v_b	terminal velocity of the air bubble
Z	adimensional parameter

Greek Letters

$\Delta\rho$	apparent density $\left(=\rho_l-\rho_g\right)$
Δt	time interval to distance d

$\Delta t'$ time interval to total controlled of the air bubble

ρ_g density of the gas

ρ_l density of the liquid

μ_l viscosity of the liquid

$\sigma_{l/g}$ surface tension

Π_i adimensional parameter

REFERENCES

1. Talaia, M. A. R., Terminal Velocity of a Bubble Rise in a Liquid Column. *Proceedings of WASET - World Academy of Science, Engineering and Technology*, Vol. 22, ISBN: 978-975-01752-1-3, pp 264-269, 2007.
2. Talaia, M. A. R., Ferreira, C. S. G. e Sá, T. M. B. B., Velocity of Single Gas Bubble in Stagnant Water. *Proceedings of the 4º Simpósio de Meteorologia e Geofísica da APMG e 6º Encontro Luso-espanhol de Meteorologia*, ISBN 972-9083-13-4, Instituto de Meteorologia, Lisboa 2005, pp 140-143, 2006.
3. Talaia, M. A. R., Film flow down vertical surfaces with appreciable shear stress on the interface gas – liquid. *Proceedings of the NURETH 11 Conference – Eleven International Topical Meeting on Nuclear Reactor Thermal Hydraulics*, Edited by Hervé Lemonnier in cooperation with the session organizers of the technical program committee, ISBN 2-9516195-0-2, Avignon, France, Paper 292, 13 pages, 2005.
4. Talaia, M. A. R., Predicting the Rise Velocity of Single Gas Slugs in Stagnant Liquid: Influence of Liquid Viscosity and Tube Diameter, *Proceedings of the 3rd International Symposium on Two-Phase Flow Modelling and Experimentation, Edizioni ET*S, ISBN 88-467-1075-4, Pisa, Italy, paper JMC-MTA-1, 5 pages, 2004.
5. Talaia, M. A. R., Movement of Single Gas Slugs Rising in Vertical Columns Filled With Water. Effect of High Density and Diameter in its Velocity, *Proceedings of* 39th *European Two-Phase Flow Group Meeting*, CDROM, paper E-2, Aveiro, 6 pages, 2001.
6. Talaia, M. A. R., Uma Análise Dimensional: Ascensão de uma Bolha num Líquido Parado, *Gazeta de Física*, Vol. 23, Fasc. 2, pp 9-12, 2000.
7. Guedes de Carvalho, J. R. F. Talaia, M. A. R. and Ferreira, M. J. F., Flooding Instability of High Density Gas Slugs Rising in Vertical Tubes Filled with Water, *Chem. Eng. Sci*., Vol. 55, pp 3785-3802, 2000..
8. Guedes de Carvalho, J. R. F. Talaia, M. A. R. and Ferreira, M. J. F., Flooding of High Density Gas Slugs Rising in Viscous Liquids". *Proceedings of the Second International Symposium on Two-Phase Flow Modelling and Experimentation, Celata, G.P., Marco, P. and Shah, R.K. (editors), Edizioni ETS*, Pisa, Italy, Vol. 2, pp 771-778, 1999.
9. Guedes de Carvalho, J. R. F. and Talaia, M. A. R., Interfacial Shear Stress as a Criterion for Flooding in Counter - Current Film Flow along Vertical Surfaces. *Chem. Eng. Sci*., Vol. 53, pp 2041-2051, 1998.
10. Talaia, M. A. R., Estabilidade de Bolhas em Líquidos e Encharcamento em Colunas de Parede Molhada, *PhD Thesis* apresentada à Faculdade de Engenharia da Universidade do Porto, Setembro, Porto, 1997.
11. Bhaga, D., and Weber, M. E., Bubbles in viscous liquids: shape, wakes and velocities, *J. Fluid Mech.*, 105, 1981.
12. Celata, G. P., Cumo, M., D'Annibale, F., and Tomiyama, A., Terminal bubble rising velocity in one-component systems. *Proceedings of* 39th *European Two-Phase Flow Group Meeting*, CDROM, paper F-3, Aveiro, 10 pages, 2001.

13. Collins, R., The effect of a containing cylindrical boundary on the velocity of a large gas bubble in a liquid. *J. Fluid Mech.*, 28, part 1, 97-112, 1967.
14. Davies, R. M., and Taylor, G. I., The mechanics of large bubbles rising through liquids in tubes. *Proc. of Roy. Soc.*, London, 200, Ser. A, pp 375-390, 1950.
15. Garner, F. H., and Hammerton, D., Circulation inside gas bubbles. *Chem. Eng. Science*, 3, Nº 1, pp 1-11, 1954.
16. Grace, J. R., Wairegi, T., and Nguyen, T. H., Shapes and velocities of single drops and bubbles moving freely Through Immiscible Liquids. *Inst. Chem. Eng.*, 54, 176, 1976.
17. Hamerman, W. L., and Morton, R. K., David W. Taylor Model Basin. Rept. 802, 1953.
18. Harmathy, T. Z., Velocity of large drops and bubbles in media of infinite or restricted extent. *A. I. Ch. E. Journal*, 6, pp 281-288, 1960.
19. Peebles, F., and Garber, H., Studies on the motion of gas bubbles in liquid. *Chem. Eng. Prog.*, 49, n. 2, pp 88-97, 1953.
20. Tomiyama, A., Grag, lift and virtual mass forces acting on a single bubble. *Proceedings of the 3rd International Symposium on Two-Phase Flow Modelling and Experimentation, Edizioni ET*S, CDROM, Pisa, Italy, 10 pages, 2004.
21. Tomiyama, A., Celata, G. P., Hosokawa, S., and Yoshida, S., Terminal velocity of single bubbles in surface tension force dominant regime. *Proceedings of* 39th *European Two-Phase Flow Group Meeting*, CDROM, paper F-2, Aveiro, 8 pages, 2001.
22. Wallis, G. B., *One-dimensional Two-phase Flow*, Bubbly Flow, Chap. 9, McGraw-Hill, New York, pp 243-281, 1969.
23. White, E. T., and Beardmore, R. H., The velocity of rise of single cylindrical air bubbles through liquids contained in vertical tubes. *Chem. Engng. Sci*., 17, pp 351-361, 1962.
24. Kay, J. M., and Nedderman, R. M., *Fluid mechanics and transfer processes*, London, Cambridge University Press, 1985.

TRAVELLING WAVES IN A NATURAL CONVECTION BOUNDARY LAYER ADJACENT TO A SIDEWALL OF A DIFFERENTIALLY HEATED CAVITY

F. Xu*, J. Patterson, C. Lei, T. Bednarz
James Cook University, Townsville, QLD 4811, Australia

ABSTRACT Travelling waves in a natural convection boundary layer adjacent to a sidewall of a differentially heated cavity are investigated experimentally. The travelling waves in the transition from an initially isothermal interior fluid ambient to an eventually stratified interior fluid ambient are described based on temperature measurements. The temperature time series at discrete points in the natural convection boundary layer show features consistent with previous visualizations, and the wave features of the fully developed natural convection boundary layer are discussed.

Keywords: *Travelling waves, natural convection boundary layer, differentially heated cavity*

INTRODUCTION

Natural convection induced by a horizontal temperature difference is one of the major flow phenomena of the oceans and atmosphere, and also is of significance in many industrial processes such as electronic cooling systems, heat exchangers, and solar collectors. Accordingly, the study of natural convection flows in a differentially heated cavity was the initial impetus for modelling the above flow phenomena. Considerable studies have revealed important mechanisms of the complex flows in the differentially heated cavity. In particular, the work by Patterson and Imberger [1] characterized the physical features of natural convection flows in the cavity with suddenly heated and cooled sidewalls respectively, and classified them into different flow regimes through detailed scaling analyses. Furthermore, it has also been demonstrated by experimental measurements [2-6] and numerical simulations [7, 8] that a transition of the interior fluid in the cavity from an initially isothermal to finally stratified state occurs.

One of the important flow phenomena in a differentially heated cavity is the evolution of the natural convection boundary layer flow adjacent to the sidewall. Studies (see e.g. [1]) show that when a sidewall of the cavity is abruptly heated or cooled, heat is first transferred in the direction normal to the sidewall surface, resulting in the growth of a natural convection boundary layer with time. Associated with this natural convection boundary layer growth, a one-dimensional (1D) vertical flow driven by buoyancy forces develops. This 1D response lasts only for a short time near a finite length surface. Perturbations from the leading edge effect (hereinafter referred to as LEE) quickly lead to an unstable flow downstream, which eventually develops into a steady two-dimensional (2D) flow [9] as long as the Rayleigh number is sufficiently small. Goldstein and Briggs [10] gave an estimate for this transition time, however, their prediction lagged behind the experimental measurements [11]. Subsequently, Armfield and Patterson [12] suggested that the LEE arrival time is determined from the velocity of the travelling waves triggered by the start-up perturbation, rather than the maximum convection velocity. This suggestion was supported by the experimental

* Corresponding author: Dr. F. Xu
Phone: + (61)-7-47814420, Fax: + (61)-7-47816788
E-mail address: feng.xu@jcu.edu.au

measurements [5]. Indeed, the LEE not only induces the transition from 1D to 2D laminar flows but also is a potential source of turbulence if the Rayleigh number is larger than a critical value.

The horizontal intrusion, discharged from the downstream end of the vertical natural convection boundary layer, is also an important flow phenomenon in a differentially heated cavity. Experiments (e.g. [2-4]) have demonstrated that the separation of the intrusion from the ceiling always appears at the upstream end of the intrusion. The mechanisms responsible for the separation have also been extensively investigated (see e.g. [2, 4, 13]).

Although considerable attention has been paid to the initial transient response of the unsteady natural convection flows in the differentially heated cavity following sudden heating, there have been few investigations of the transition of the natural convection boundary layer to a quasi-steady state except for the visualizations reported in [5, 14]. In order to obtain further understanding of the full transition of the natural convection boundary layer adjacent to the sidewall, particularly the temperature features during the full transition, in this study, thermistors are employed to measure the temperatures of the natural convection boundary layer, and the travelling waves in the natural convection boundary layer are described.

EXPERIMENTAL SETUP

The temperature measurements were carried out near the hot sidewall of a differentially heated cavity sketched in Figure 1, which is similar to that described in [5]. The cavity, containing water as the working fluid, is 1-m long (L), 0.24-m high (H) and 0.5-m wide (W). The cavity walls are made from Perspex sheets except the cooled and heated sidewalls, which are made of 0.00113-m thick gold-coated copper plates.

In the experiments, one sidewall is heated by the hot water in a water bath and the opposing sidewall cooled by the cold water in another water bath. Each water bath, connected to a refrigerated/heating circulator, is initially separated from the sidewall by a pneumatically operated gate with an air gap between the gate and the sidewall. At the start of the experiments, the gates are rapidly lifted, allowing the hot and cold water respectively in the two water baths to flush against the copper sidewalls. This process is completed within a fraction of a second, and thus a close to instantaneous isothermal boundary condition is established at each end of the cavity [5]. During the experiments, the temperatures of the water in the water baths are kept constant by the circulators with a temperature stability of ± 0.01 K.

Thermometrics FP07 thermistors with a time constant of 0.007 s in water are used to measure the temperature of the flows adjacent to the sidewall. The body of the thermistor has a maximum diameter of 2.2 mm and a length of 12.6 mm, and is mounted in an insulated tube in order to minimize thermal disturbances. All four thermistors were placed in the vicinity of the hot sidewall,

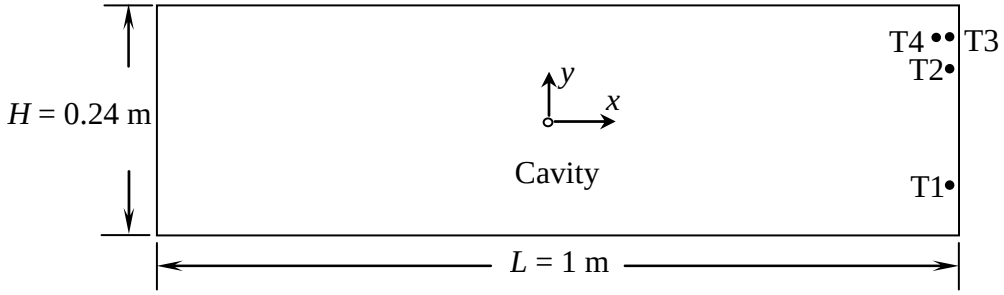

Figure 1. Schematic of the experimental cavity: Points T1 to T4 denote Thermistor locations, which are corresponding to Thermistor 1 (0.4978 m, -0.048 m), Thermistor 2 (0.4974 m, 0.0624 m), Thermistor 3 (0.497 m, 0.0899 m) and Thermistor 4 (0.4869 m, 0.0868 m) respectively.

as seen in Figure 1, three of which (T1 – T3) are close to the sidewall but at different heights with the fourth (T4) located further from the sidewall but at approximately the same height as T3. For the description of physical locations, the origin of the coordinates is at the center of the cavity.

The dimensionless controlling parameters in the experiments are the Rayleigh number (*Ra*), the Prandtl number (*Pr*) and the aspect ratio (*A*), defined respectively as follows,

$$Ra = \frac{g\beta\Delta T H^3}{\nu\alpha} \tag{1}$$

$$Pr = \frac{\nu}{\alpha} \tag{2}$$

$$A = \frac{H}{L} \tag{3}$$

Table 1. Experimental parameters for temperature measurements

Experiment	Initial temperature of water in cavity (T_0, K)	Temperature difference between sidewalls (ΔT, K)	Ra ($\times 10^9$)	Pr
1	294.45	4	0.88	6.83
2	294.45	8	1.75	6.83
3	295.55	16	3.77	6.63
4	294.15	32	6.87	6.81

RESULTS AND DISCUSSION

It is clear that the experimental conditions may be varied by changing the temperature difference between the two sidewalls. Four experiments with temperature differences between the two sidewalls ranging from 4 to 32 K were performed, and the corresponding ranges of *Ra* and *Pr* are $0.877 \sim 6.87 \times 10^9$ and $6.63 \sim 6.83$ respectively. Table 1 lists all experimental parameters. The results of the temperature measurements will be described based on $Ra = 1.75 \times 10^9$ (Experiment 2) in this section unless specified otherwise.

Figure 2 shows the time series of the temperatures measured at the four locations. The temperature fluctuations of the natural convection flows adjacent to the sidewall are clear and the time series of

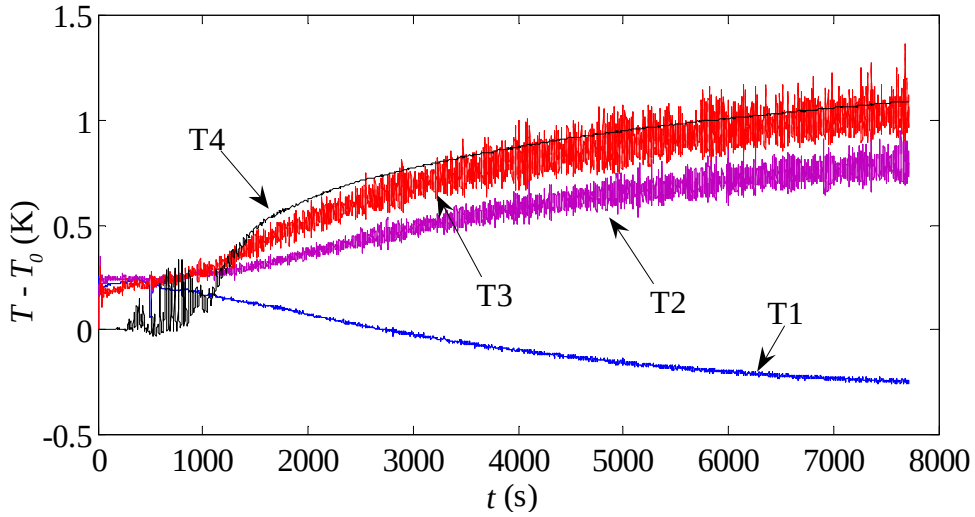

Figure 2. Time series of the temperatures at different locations (shown in Figure 1) for the Rayleigh number of 1.75×10^9.

the temperatures at all the four locations eventually approach quasi-steady states respectively. It is seen in this figure that the temperatures measured by Thermistors 2 - 4 in the upper part of the cavity increase with time and the temperature measured by Thermistor 1 in the lower part of the cavity decreases with time. As a consequence, the difference between the two time series of the temperatures by Thermistors 1 and 3 increases with time. This implies that a stable stratification of the fluid in the cavity is continuously reinforced [15]; that is, the transition of the interior fluid in the cavity from an initially isothermal state to an eventually stratified state occurs.

The transient features of the natural convection boundary layer flow will be demonstrated with a closer examination of these time series, as described in the following sections.

Temperatures in the early stage

Figure 3(a) replots the temperature time series measured by Thermistors 1, 2 and 3 in the early stage (up to 100 s). It is seen in this figure that the features of the LEE are clear, which are characterized by an overshoot (also see [5]) followed by an oscillatory signal. Furthermore, there are distinct differences in the initial temperature growth recorded by Thermistors 1 and 2 and 3; that is, the temperature by Thermistor 1 increases more quickly than those by Thermistors 2 and 3. This is because the location of Thermistor 1 is closer to the hot sidewall than those of Thermisters 2 and 3, as shown in Figure 1.

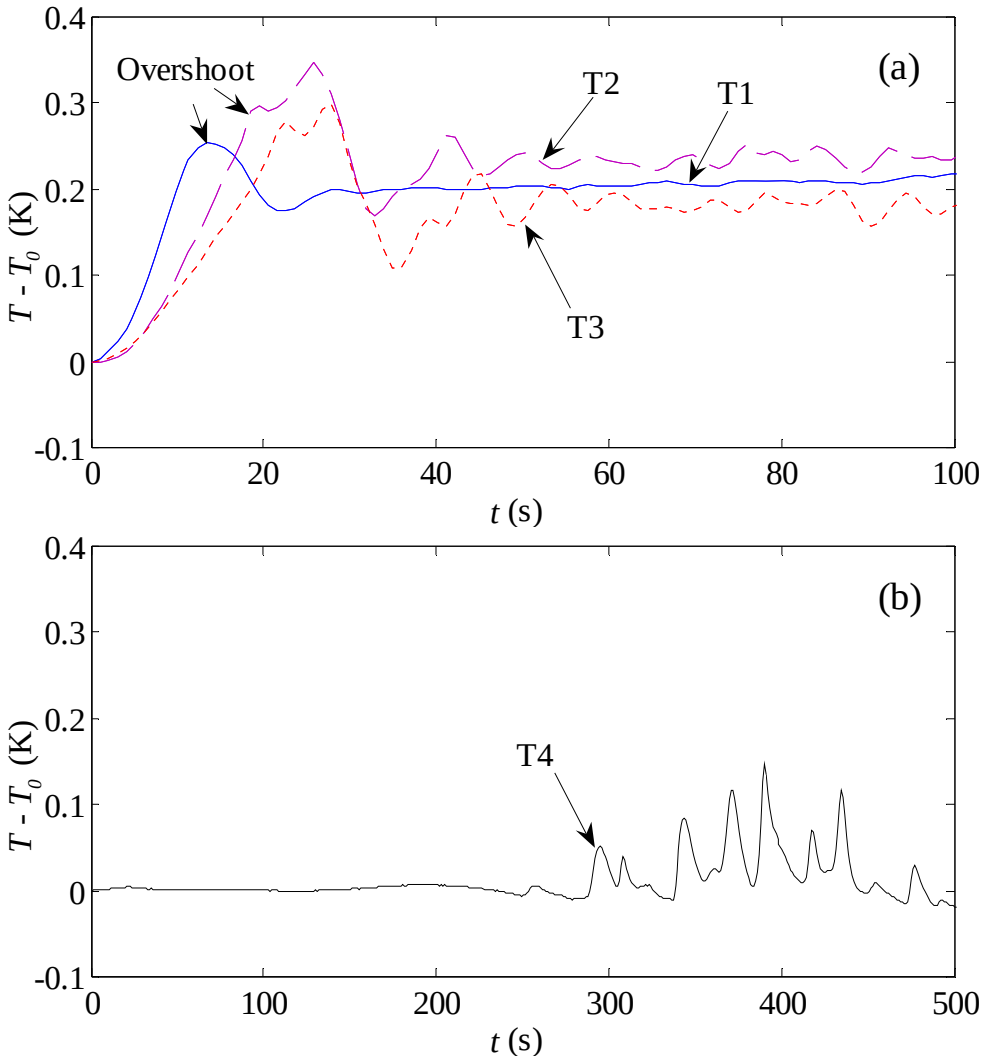

Figure 3. Time series of the temperatures at different locations in the early stage. (a) Temperatures measured by Thermistors 1, 2 and 3. (b) Temperature measured by Thermistor 4.

Figure 3(a) also shows that following the overshoot, the temperature measured by Thermistor 1 approaches an approximate constant, whereas the temperatures measured by Thermistors 2 and 3 remain oscillatory. This means that the travelling waves (convective instabilities [16]) in the natural convection boundary layer grow as they propagate downstream (also see Figure 2).

The temperature in the early stage measured by Thermistor 4 is replotted in Figure 3(b). It is clear that, differently from those measured by Thermistors 1, 2 and 3, the temperature by Thermistor 4 changes little in the early stage (until about 250 s). This is because the location of Thermistor 4 is far from the hot sidewall and the LEE is not recorded by Thermistor 4. However, after approximately 250 s at which time the cold intrusion flow from the opposite sidewall has arrived at the upstream end of the boundary layer and triggered additional waves in the boundary layer (refer to visualizations in [6]), the horizontal intrusion flow, discharged from the end of the natural convection boundary layer, becomes unstable, and thus these waves are recorded by Thermistor 4 located under the horizontal intrusion flow. Furthermore, it is worth noting that the frequency (around 0.05 Hz) of the temperature waves recorded by Thermistor 4 is much lower than those by Thermistors 1, 2 and 3 (around 0.12 Hz). This confirms that this signal is an instability of the intrusion rather than the vertical boundary layer.

The early transient features of the temperature time series are dependent on the Rayleigh number. Figure 4 shows the temperature time series measured by Thermistor 1 for two different Rayleigh numbers, relative to the initial temperature (T_0) in each case. Clearly, as the Rayleigh number increases, the temperature in the natural convection boundary layer grows more rapidly during the early stage and the overshoot is also larger, as seen in Figure 4.

Travelling waves in the quasi-steady stage

Following a slow transitional stage, the amplitudes of the temperature waves recorded by all thermistors approach constant values (refer to Figure 2). In order to display further the wave features of the boundary layer, Figure 5(a) shows the temperature time series from Thermistors 1 to 3 for a short time period in the quasi-steady stage. It is seen in this figure that the amplitude of the temperature waves at this time is strongly dependent on the spatial location but less dependent on time. The temperature time series from Thermistor 1 displays the upstream waves, and those from Thermistors 2 and 3 display the travelling waves in the downstream natural convection boundary layer. Similar to the results in the early stage (see Figure 3a), the travelling waves grow significantly in the quasi-steady stage as they propagate downstream.

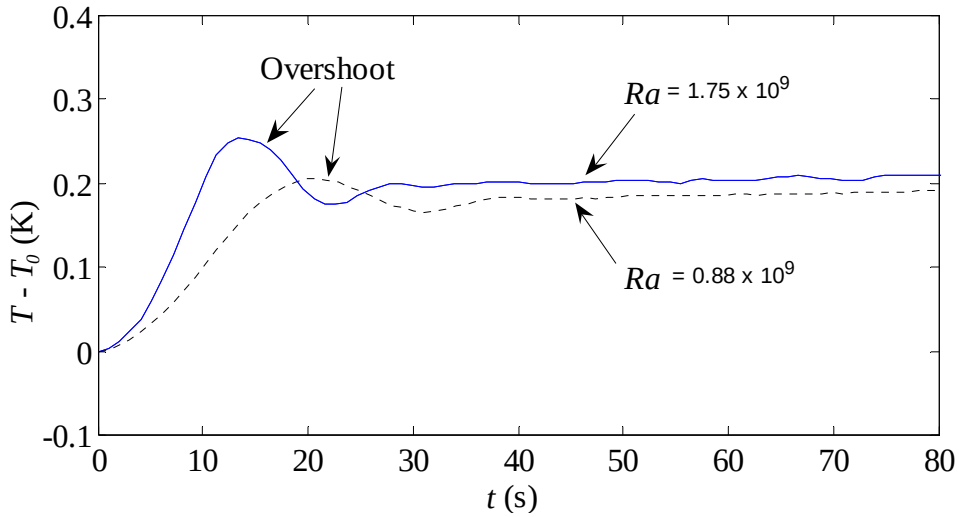

Figure 4. Temperature time series at the point (0.4978, -0.048, Thermister 1) for two different Rayleigh numbers.

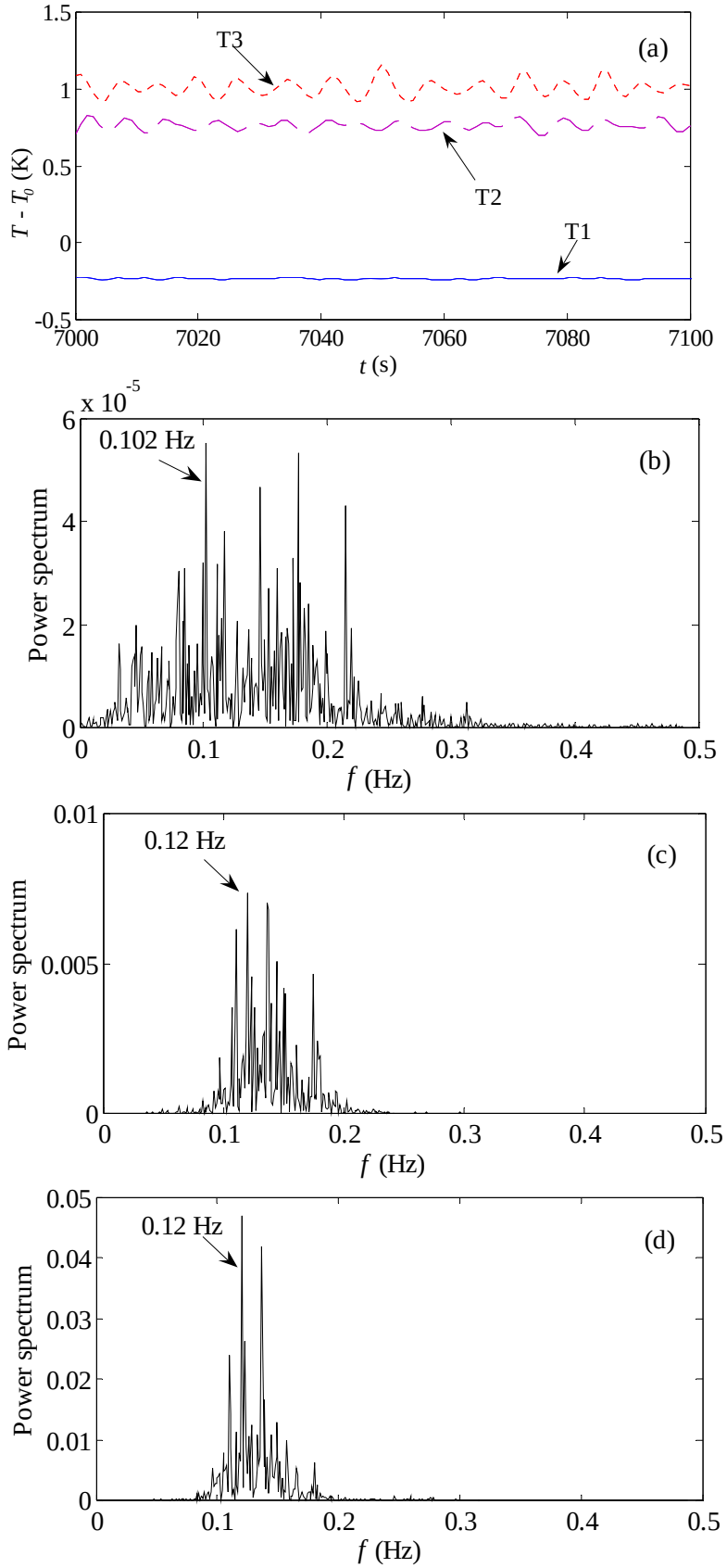

Figure 5. Temperatures and power spectra in the quasi-stage stage. (a) Temperature time series from Thermistors 1 to 3. (b) Spectrum for Thermistor 1. (c) Spectrum for Thermistor 2. (d) Spectrum for Thermistor 3.

The corresponding power spectra of the temperature signals from Thermistors 1, 2 and 3 are shown in Figures 5(b), 5(c) and 5(d), respectively. Clearly, the frequency characteristics of the temperature

waves are different at these locations. For example, at the Thermistor 1 location, the peak of the spectrum is around 0.102 Hz, but the dominant frequencies of the temperature waves at the Thermistors 2 and 3 locations are around 0.12 Hz. That is, the dominant frequencies of the temperature waves change with the locations at which the temperature signals are recorded.

CONCLUSIONS

In this paper, the temperatures of the unsteady natural convection flows adjacent to the sidewall of a differentially heated cavity are measured by fast-response thermistors. The travelling wave features in the natural convection boundary layer are characterized.

The present temperature measurements show features consistent with the flow visualizations in [6]. The temperature time series from thermistors at different locations clearly characterize the LEE and other transient features of the natural convection boundary layer in the transition from an initially isothermal interior fluid ambient to an eventually stratified interior fluid ambient. Furthermore, the spectral analysis of the temperature time series has revealed the dominant frequency of the travelling waves in the natural convection boundary layer. The travelling waves in the natural convection boundary layer are indeed convective instabilities.

NOMENCLATURE

A	aspect ratio
T_0	initial temperature of the fluid (K)
ΔT	temperature difference between sidewalls (K)

ACKNOWLEDGEMENTS

The Authers would like to thank the Australian Research Council for its financial support.

REFERENCES

1. Patterson, J. C. and Imberger, J., Unsteady natural convection in a rectangular cavity, *J. Fluid Mech*., Vol. 100, pp 65-86, 1980.
2. Ivey, G. N., Experiment on transient natural convection in a cavity, *J. Fluid Mech.*, Vol. 144, pp 389-401, 1984.
3. Patterson, J. C. and Armfield, S. W., Transient features of natural convection in a cavity, *J. Fluid Mech.*, Vol. 219, pp 469-497, 1990.
4. Schöpf, W. and Patterson, J. C., Natural convection in a side-heated cavity: visualization of the initial flow features, *J. Fluid Mech*., Vol. 295, pp 357-279, 1995.
5. Patterson, J. C., Graham, T., Schöpf, W. and Armfield, S. W., Boundary layer development on a semi-infinite suddenly heated vertical plate, *J. Fluid Mech*., Vol. 453, pp 39-55, 2002.
6. Xu, F., Patterson, J. C. and Lei, C., Shadowgraph observations of the transition of the thermal boundary layer in a side-heated cavity, *Exp. Fluids*, Vol. 38, pp 770-779, 2005.
7. Paolucci, S. and Chenoweth, D. R., Transition to chaos in a differentially heated vertical cavity, *J. Fluid Mech*., Vol. 201, pp 379-410, 1989.
8. Schladow S. G., Patterson, J. C. and Street, R. L., Transient flow in a side-heated cavity at high Rayleigh number: a numerical study, *J Fluid Mech*., Vol. 200, pp 121-148, 1989.
9. Ostrach, S., *Theory of laminar flows*, Princeton Univ Press, Princeton, 1964.
10. Goldstein, R. J. and Briggs, D. G., Transient free convection about vertical plates and cylinders, *J. Heat Transfer*, Vol. 86, pp 490-500, 1964.
11. Mahajan, R. L. and Gebhart, B., Leading edge effects in transient natural convection flow adjacent to a vertical surface, *J. Heat Transfer*, Vol. 100, pp 731-733, 1978.
12. Armfield, S. W. and Patterson, J. C., Wave properties of natural convection boundary layers, *J. Fluid Mech*., Vol. 239, pp 195-212, 1992.

13. Ravi, M. R. R., Henkes, R. A. W. M. and Hoogendoorn, C. J., On the high-Rayleigh-number structure of steady laminar natural-convection flow in a square enclosure, *J. Fluid Mech.*, Vol. 262, pp 325-351, 1994.
14. Schöpf, W. and Patterson, J. C., Visualization of natural convection in a side-heated cavity: transition to the final steady state, *Int. J. Heat Mass Transfer*, Vol. 39, pp 3497-3509, 1996.
15. Eckert, E. R. G. and Carlson, W. O., Natural convection in an air layer enclosed between two vertical plates at different temperatures, *Int. J. Heat Mass Transfer*, Vol. 2, pp 106-120, 1961.
16. Le Quere, P. and Behnia, M., From onset of unsteadiness to chaos in a differentially heated square cavity, *J. Fluid Mech.*, Vol. 359, pp 81-107, 1998.

DUAL INVESTIGATIONS ON THE IMPROVEMENT OF EFFUSION COOLING BY SHAPED HOLES

B. Boust[1, *], G. Lalizel[1], M. Fénot[1], C. Bianchini[2], A. Ceccherini[2], G. Cinque[3], S. Colantuoni[3]
[1] Laboratoire de Combustion et de Détonique, Poitiers, France
[2] Dipartimento di Energetica "S. Stecco", Università degli Studi di Firenze, Italy
[3] Avio S.P.A., Pomigliano d'Arco, Napoli, Italy

ABSTRACT. This work is dedicated to the improvement of effusion cooling efficiency on combustion liners, by using an innovative multiperforation made of shaped holes of elliptical cross-section. Low-temperature experiments provided a spatial characterization of cooling efficiency in a suction-type wind tunnel, whereas discrete measurements were performed in the engine-like conditions of THALIE facility. A RANS computational study was also performed to give a detailed insight on the aerothermodynamics of the complex flow created by effusion holes. Experimental and numerical data confirm the enhancement of effusion cooling by shaped holes, thanks to a better coverage of the first rows of the plate, and a better individual efficiency of each hole.

Keywords: *combustor liner, effusion cooling, adiabatic efficiency, thermochromic liquid crystals*

INTRODUCTION

Due to the increasing need to reduce the emissions of aero-engines, it is necessary to optimize the design and integration of engine components. Among them, the combustion chamber focuses many of the challenges encountered. Indeed, it is the very place at which combustion and thermal phenomena pilot the emissions and efficiency of the engine. Therefore, the combustion liner faces important mechanical and thermal stresses. Moreover, the need for higher engine efficiency leads to increasing combustion temperature and pressure that emphasize stresses on the liner.
This statement points out the importance of an adapted cooling of combustion liners. For this, the use of multiperforation is a common way to create a full-coverage cooling of the liner, which is referred to as effusion cooling. However, this technique requires a significant mass flow of fresh air taken from the compressor. Thus, an adapted design is required so that the air passing through effusion holes does not affect locally the combustion rate and globally the engine efficiency.
In terms of multiperforation design, many aspects of hole geometry can be varied. The spacing, the angle, or the length to diameter ratio can be optimized by simple variation, whereas the shape of the hole itself is much harder to study due to practical difficulties in machining and controlling the shape, for instance. Former studies have pointed out experimentally the influence of the transverse dimension of the holes on cooling efficiency, either with converging slot holes called "consoles" [1] or laterally diffused holes [2]. The common feature of these design solutions is a greater extension of the hole perpendicularly to the flow, inducing a better coverage of the multiperforated wall.
This work focuses on an innovative design of multiperforation, using holes of elliptical cross-section that can be processed through laser drilling. Experiments were carried out on cooled plates to compare the efficiency of shaped to conventional holes. A RANS simulation was also carried out to give a detailed insight on the aerothermodynamics of the complex flow of the jets in crossflow.

* Corresponding author: Dr. B. Boust
Phone: + (33)549366090, Fax: + (33)549366064
E-mail address: bastien.boust@lcd.ensma.fr

EXPERIMENTAL SETUP AND MEASUREMENTS

Experiments were carried out to compare the cooling efficiency of conventional and shaped holes, using two experimental devices. The first one allows a fine spatial characterization of cooling efficiency at low temperature, whereas the second one allows a discrete measurement of cooling efficiency in engine-like conditions. Such experiments aim at quantifying the thermal behaviour of each hole geometry in terms of cooling efficiency. Practically, each hole geometry is studied using flat plates drilled with arrays of holes.

Suction-type wind tunnel

The first experiments consist of low-temperature measurements in a suction type wind tunnel.

Experimental facility. The test rig is an open-loop suction-type wind tunnel allowing the measurement of heat transfer, cooling efficiency and pressure loss on multiperforated plates, by controlling completely the mainstream flow and the coolant flow.
The mainstream air flow, at atmospheric pressure and ambient temperature, passes first through a 24 kW controlled electric heater, where desired temperature is reached and kept constant, before entering the PolyMethyl-MethAcrylate test section depicted in Figure 1, through a setting valve.
The coolant flow temperature is controlled by mixing heated air and cool air. Four rotary vane vacuum pumps (total power installed 59 kW) provide the suction for a maximum mass flow rate of 0.50 kg/s. Both flow rates are set up by guiding the motor speeds between 300 and 1200 rpm, and throttling the remote controlled motorized valves. The air temperature exiting from the heater is controlled by means of a four wire resistance temperature detector (RTD Pt-100).
The rig allows performing measurements on test samples made of adiabatic (stereolithography resin, STL) and conductive material (stainless steel, AISI 321), see Table 1.

Table 1
Geometric features of the multiperforated plates

Multiperforated plate	with circular holes	with shaped holes
Plate thickness (mm)	12.7	12.7
Number of holes	38	28
Number of rows	8	5
Streamwise to spanwise pitch ratio	2.3	2.0
Porosity	0.036	0.0375
Angle of the holes (°)	17.0	17.0
Hydraulic diameter of the holes (mm)	2.65	3.385
Length to diameter ratio L/D	16.39	12.8

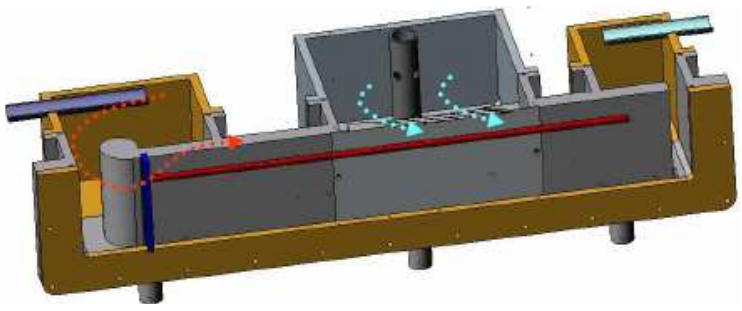

Figure 1. Suction-type wind tunnel

Diagnostics. Tests are run once flow rates, pressures and temperatures have reached steady conditions. Adiabatic and overall cooling efficiencies, denoted resp. as η_{aw} and η_{ov} (see equations (1) and (2)), are evaluated resp. on adiabatic and conductive plate using thermochromic liquid crystals that provide surface temperature T_w. Efficiencies are computed starting from the measured wall temperature values by means of different post-processing procedures accurately described by [3]. The final result of such procedures is the achievement of η_{aw} values once the plate heat loss due to holes heat sink effect is evaluated.

$$\eta_{aw} = \frac{T_{main} - T_{aw}}{T_{main} - T_c} \tag{1}$$

$$\eta_{ov} = \frac{T_{main} - T_w}{T_{main} - T_c} \tag{2}$$

Conditions investigated. All tests have been carried out setting approximately the coolant temperature at 306 K and the mainstream temperature at 317 K and 322 K, resp. for adiabatic and conductive tests. Experimental survey has been performed setting jet Reynolds number at 12500, and imposing three values of blowing ratio close to engine operating conditions (BR = 5–7–9). Blowing ratio is commonly defined from flow momentum in the holes and in the mainstream.

$$BR = \frac{(\rho V)_{hole}}{(\rho V)_{main}} \tag{3}$$

High-temperature wind tunnel THALIE

In the second set of experiments, conductive plates are exposed to realistic engine conditions.

Experimental facility. Experiments are carried out using THALIE, that is a high-temperature wind tunnel designed to study THermal and Aerodynamic features of Experimental Liners, see Figure 2. THALIE generates experimental conditions close to those encountered in the vicinity of combustor liners, in terms of gas velocity, temperature, pressure, and pressure drop across the liner. The test section is equipped with apertures, allowing optical measurements (PIV, LDV, visualization, fluorescence, thermography), as well as intrusive measurements (gas sampling, thermocouples).

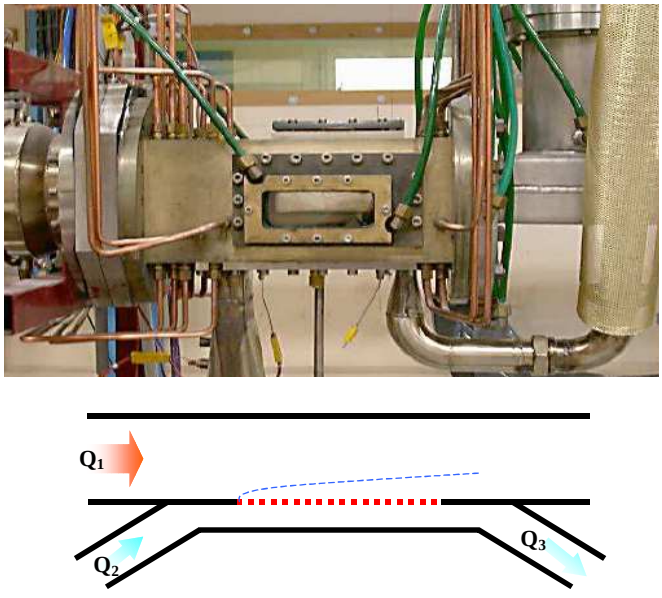

Figure 2. High-temperature wind tunnel THALIE

During an experiment, a multiperforated plate is submitted to a hot gas flow and a coolant flow. The hot flow, Q_1, is made of combustion products supplied by a tubular combustor fuelled with kerosene. The cooling air flow, Q_2, can be heated electrically. The temperatures of both the hot and cooling flows are P.I.D. controlled, ensuring the stability and reliability of experiments. The flow passing through the multiperforated plate, Q_h, is only a fraction of the cooling flow. It is driven by controlling the pressure drop across the plate, ΔP. Q_h is evaluated as the difference between the incoming (Q_2) and outgoing (Q_3) coolant flows. The controlled mass flow rates (Q_1, Q_2 and Q_3) are measured using vortex-type flowmeters. T_1 and T_2 are measured by K-type thermocouples.
Experiments are carried out twice, i.e. once using a plate with conventional holes, and once using a plate with shaped holes. The multiperforated plates are manufactured by AVIO S.p.A. with thermal coating and laser drilling technology (see Table 2). Overall, both plates have similar properties, and similitude rules have been applied to scale the multiperforation. The experimental conditions summarized in Table 3 provide a wide range of blowing ratio, BR = 1–10.

Table 2
Geometric features of the multiperforated plates

Multiperforated plate	with circular holes	with shaped holes
Plate thickness (mm)	2.5	2.5
Number of holes	569	234
Number of rows	17	12
Streamwise to spanwise pitch ratio	2.1	2.0
Total cross-section of the holes (mm²)	149	149
Angle of the holes (°)	18.5	17.3
Hydraulic diameter of the holes (mm)	0.58	0.76
Length to diameter ratio	13.6	11.1

Table 3
Operating conditions of the experiments

	Hot flow	Cooling flow	Hole flow
Subscript	1	2	h
Reynolds number	60,000 – 80,000	10,000 – 100,000	0 – 20,000
Cross-section (mm)	126×72	100×20	
Mass flow rate (kg/s)	0.4	0 – 0.2	
Temperature (K)	1000	288	
Pressure (bar)	3.0	3.0 – 3.5	

Diagnostics. The cooling efficiency of the multiperforated plate is evaluated by means of adiabatic and overall efficiency. Overall efficiency, η_{ov}, takes into account convection as well as conduction and radiation. Evaluating η_{ov} requires the measurement of wall temperature, T_w, see equation (4). Thus, the multiperforated zone is instrumented with K-type thermocouples of diameter 0.5 mm, sheathed with stainless steel. They provide the wall temperature on the cold side of the plate.

$$\eta_{ov} = \frac{T_1 - T_w}{T_1 - T_2} \tag{4}$$

Adiabatic efficiency, η_{ad}, is the cooling efficiency of an equivalent adiabatic plate. It is evaluated by assuming the analogy between heat and mass transfer, which consists of equal molecular and thermal diffusivities, i.e. a unity Lewis number. Measuring adiabatic efficiency requires the local concentration of a reference gaseous species at the wall surface on the hot side, C_w, as well as inside the primary and secondary flows, respectively C_1 and C_2, see equation (5).

$$\eta_{ad} = \frac{C_1 - C_w}{C_1 - C_2} \tag{5}$$

For this, a water-cooled sampling probe of diameter 6.0 mm is set inside the hot flow by the top aperture and fixed to a displacement system driven by a computer. The sampling orifice of diameter 0.7 mm is located at the conical tip of the probe. The reference gaseous species selected for sampling is CO_2, which concentration is constant in the hot flow and null in the cool flow, i.e. C_2=0. CO_2 is probed by an inline gas analyser (COSMA) based on the absorption of infrared radiation.

NUMERICAL SIMULATION

This numerical study was performed using a solver developed into the open-source environment for continuum mechanics analysis named OpenFOAM® [4]. The toolkit implements operator-based implicit and explicit 2nd-order and 4th-order finite volume discretization in 3-dimensional space.
These simulations were run using the steady-state compressible SIMPLE-like solver developed at University of Florence and validated in [5]. The energy equation is solved in terms of total-enthalpy in order to avoid energy losses in high acceleration regions namely the coolant flow into the ducts. The two-layer turbulence model by Rodi was used to model turbulent behavior with Norris and Reynolds closure formulas [6]. Even though the gain compared to standard two-equation eddy viscosity models is considerable in terms of well reproducing near-wall behavior, this model, further referred to as isotropic, suffers the well-known deficiency of the eddy viscosity models to correctly predict the lateral spreading of the jet in crossflow. The same model was thus tested implementing an algebraic correction to increase the lateral diffusion of momentum, energy and turbulence as proposed by [7]. This corrected version is later referred to as the anisotropic model.
For conductive tests, the coupling between solid and fluid was achieved in an explicit manner: at each iteration step a new value of total temperature on the boundary is calculated imposing the continuity of the thermal flux across the interface. A weighted average based on face overlapping area allows the use of non-conformal interfaces between fluid and solid domain. More details on the coupling procedure and the treatment of generic grid interfaces can be found in [8].
The meshes used to perform such calculations finely discretize boundary layer reaching y^+ values up to 1 for all walls of interest, namely the two sides of the plate and the hole ducts. In order to save computational cost all other walls were treated as inviscid wall (symmetry planes) thus avoiding the clustering. Moreover two symmetry planes were inserted at the center of holes, and only one spanwise pitch was simulated in order to save computational cost and to better impose stationary behavior, see Figure 3. The total grid size is around 3 million cells for both the conventional and the shaped geometries. Apart from the different dimensions, the numerical setup to reproduce the two experimental rigs only differs in the boundary conditions for the abduction of coolant. For the suction-type tunnel, constant pressure plenum is simulated imposing no cross-flow and a large low-speed inlet area, see Figure 3. As for THALIE, the same conditions as for the mainstream are applied to the coolant. The boundary conditions were extracted from the experimental ones. For the low-speed wind tunnel, the blowing ratio could be imposed and the pressure drop between plenum and mainstream taken as results. For the THALIE rig, the procedure was inverse, thus it was not possible to investigate numerically the two rig configurations exactly at the same blowing ratio.

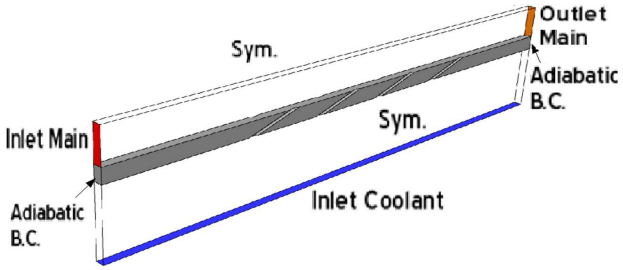

Figure 3. Overview of numerical boundary conditions

RESULTS AND DISCUSSION

In this section, the results of experiments reported along with the results of numerical simulation are expected to determine whether shaped holes actually improve the efficiency of effusion cooling.

Suction-type wind tunnel

On such rig, the fine resolution of temperature measurements allows investigating the spatial distribution of efficiency. Results are reported in terms of spanwise averaged efficiency. However, efficiency is so uniform for conductive tests that only spanwise averaged profiles are reported.

Adiabatic efficiency maps. In conventional geometry, experimental results at BR=5–7 are reported together with numerical simulations at BR=6, see Figure 4a. Firstly, experimental maps (Exp) exhibit a cold zone upstream of the holes due to the effect of the coolant ducts inside the plate, meaning that the hypothesis of adiabatic behaviour is not completely respected. Secondly, both turbulence models fail in predicting the downstream film development. While the isotropic model (TL) under-predicts the lateral diffusion of jets, the anisotropic correction (TLA) emphasizes this effect too much. In shaped configuration, the shape of coolant wake is better simulated by the anisotropic model, see Figure 4b. By comparing both geometries, the spanwise profile of conventional geometry is obviously more uniform. Shaped geometry should therefore be studied carefully as far as thermal stresses are concerned.

Spanwise averaged efficiency. The profiles of adiabatic and overall efficiency at BR=5 are shown in Figure 5. The anisotropic model simulates well the efficiency of shaped geometry, but overestimates that of conventional geometry. This result is confuting the findings on conventional geometry for higher angles and lower blowing ratios [9]. As for overall efficiency, the conventional plate is better cooled due to a higher heat sink effect connected with a higher L/D. As can be seen comparing experiments with computations, the different modeling of solid plate far form the drilled part modifies strongly the profile of overall efficiency. Although conventional geometry behaves better in terms of cooling performance, this is only related to the specific test conditions. A deeper survey points out that shaped configuration is better performing at higher blowing ratios [10].

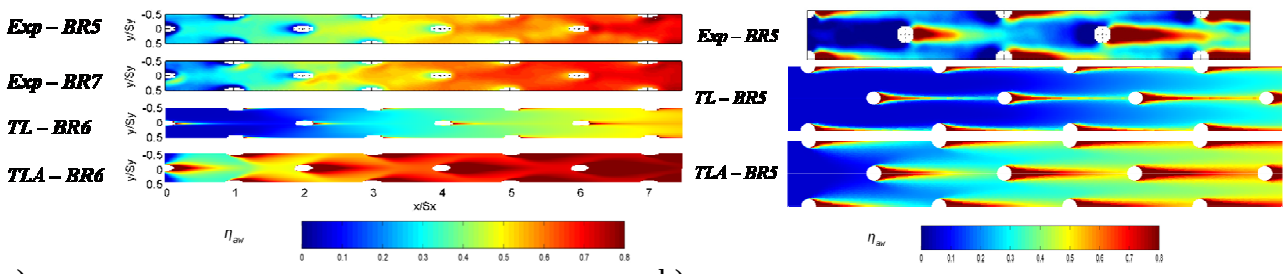

a) b)

Figure 4. Adiabatic efficiency maps (low temperature) – a) Conventional case, b) Shaped case

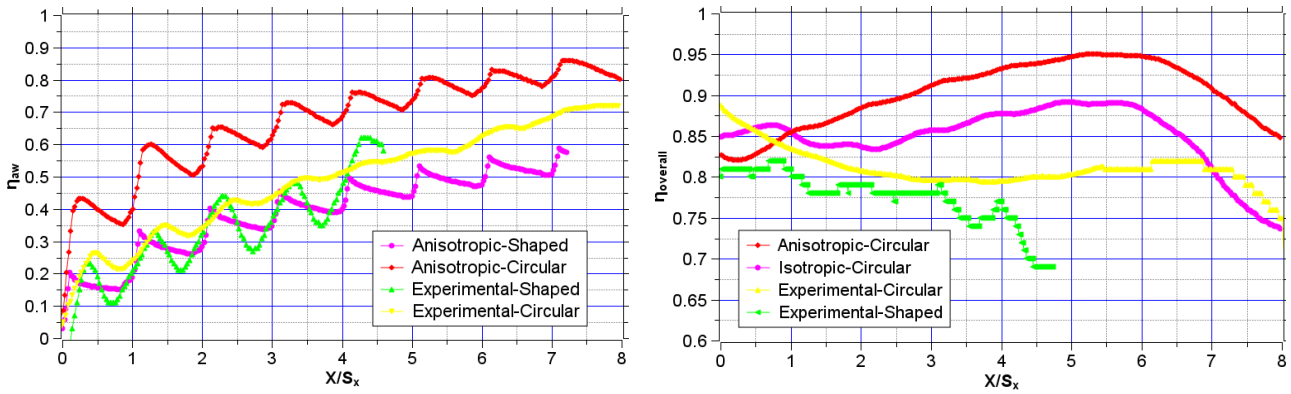

a) b)

Figure 5. Spanwise averaged efficiency (BR=5, low temperature) – a) Adiabatic, b) Overall

High temperature wind tunnel THALIE

Measurements of adiabatic and overall cooling efficiency allow the comparison between the two multiperforation geometries, i.e. with conventional or shaped holes.

Adiabatic efficiency quantifies the ability of the plate to perform effusion cooling through the holes, regardless of conduction and radiation phenomena. The streamwise profile of adiabatic efficiency along the plate is presented for experimental and numerical data (see Figure 6a). As usual, adiabatic efficiency increases with increasing blowing ratio. Experimental data show a high uncertainty at low BR, but converge quickly towards an asymptotic curve near BR=5. The experimental and numerical profiles of adiabatic efficiency indicate that cooling is enhanced by shaped holes. The benefit in efficiency decreases along the plate, from 0.08 at 5th row to 0.02 at 10th row. Especially, this benefit exceeds 0.15 at the first two rows due to a strong increase in efficiency in the wake of shaped holes.

The evolution of overall efficiency versus BR is similar to that of adiabatic efficiency, because increasing BR improves effusion cooling (see Figure 6b). Experimental curves confirm that shaped holes enhance overall cooling in the first rows, compared to conventional geometry. Cooling efficiency is similar for both geometries between 3rd and 6th rows. Then, conventional holes have better cooling performance downstream of the 7th row. These results are confirmed by a satisfactory agreement between simulation and experimental data at BR=3.3.

Finally, shaped holes lead to improved wall cooling, even though the higher L/D in conventional geometry enhances the heat sink effect due to a greater inner surface of the conventional holes.

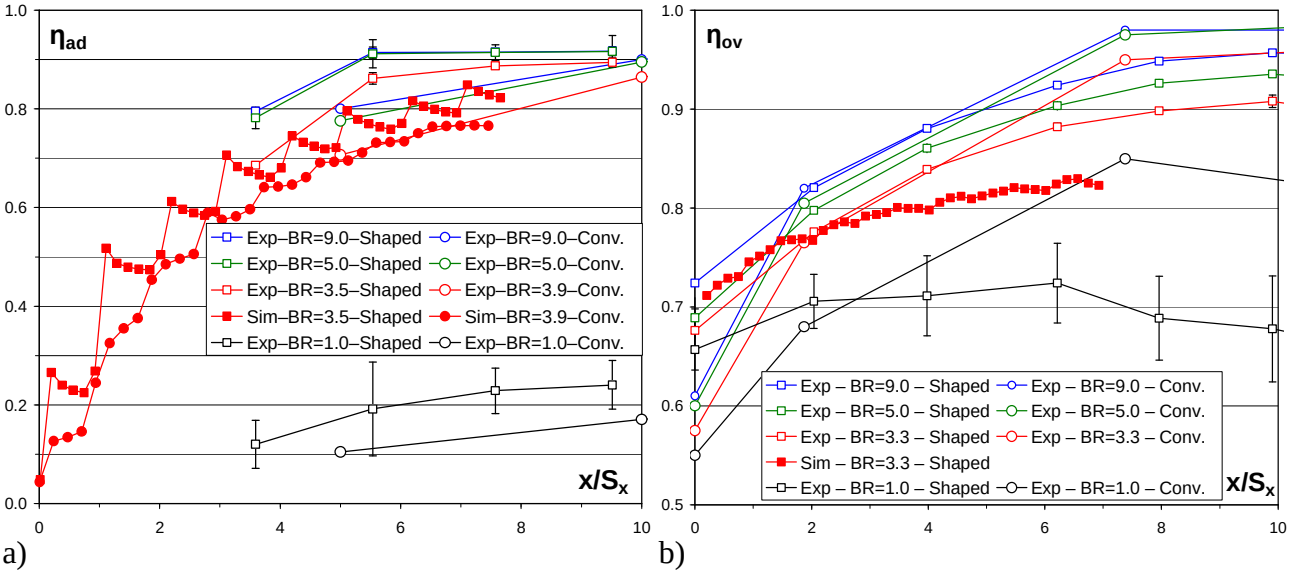

a) b)

Figure 6. Streamwise profile of cooling efficiency (high temperature) – a) Adiabatic, b) Overall

CONCLUSIONS

Experiments and simulations have been carried out on two geometries of effusion cooling, involving conventional holes and holes of elliptical cross-section. Two configurations have been addressed, providing high blowing ratios in either low-temperature or realistic engine conditions.
This survey points out many features of effusion cooling by shaped holes. Experiments and simulation show that they have a better individual cooling behaviour inducing higher efficiency in the first rows (up to 15%), but conventional holes lead to a better film formation that provides superior thermal protection after several rows of holes. Additionally, this improvement in cooling efficiency is proved to depend strongly on physical conditions, such as blowing ratio and length to diameter ratio [10].
Finally, shaped holes of elliptical cross-section provide a promising way for improving effusion cooling. Indeed, this design recalls not only the shape but also the high thermal efficiency of "consoles" [1]. Further studies should check that such cooling improvement is obtained without penalty to the mechanical strength requirements induced by thermal stresses of combustion liners.

ACKNOWLEDGEMENTS

The present work was supported by the European Commission as part of FP6 STREP INTELLECT D.M., which is gratefully acknowledged together with consortium partners.

REFERENCES

1. Sargison, J. E., Guo, S. M., Oldfield, M. L. G., Lock, G. D., Rawlinson, A. J., A converging slot-hole film cooling geometry – Part 1: Low-speed flat plat heat transfer and loss, *ASME J. Turbomachinery*, Vol. 124, No. 3, pp 453-460, 2002.
2. Hyams, D. G., Leylek, J. H., A detailed analysis of film cooling physics: Part III – Streamwise injection with shaped holes, *ASME J. Turbomachinery*, Vol. 122, No. 1, pp 122-132, 2000.
3. Facchini, B., Tarchi, L., Toni, L., A post processing procedure for the evaluation of adiabatic and overall effectiveness of effusion cooling geometries, *Proceedings of the 19th Symposium on measurement techniques*, Rhode S. Genèse, 2008.
4. Jasak, H., Weller, H. G., Nordin, N., In-cylinder CFD simulation using a c++ object-oriented toolkit, *SAE techincal paper* 2004-01-0110, 2004.
5. Mangani, L., Bianchini, C., Andreini, A., Facchini, B., Development and validation of a c++ object oriented CFD code for heat transfer analysis, *ASME-JSME Summer Heat Transfer Conference, Vancouver*, 2007.
6. Rodi, W., Experience with two-layer models combining k-epsilon model with a one-equation model near the wall, *29th Aerospace Sciences Meeting*, AIAA 91-0216, 1991.
7. Lakehal, D., Theodoris, G. S., Rodi, W., Three-dimensional flow and heat transfer calculations of film cooling at the leading edge of a symmetrical turbine blade model, *International journal of heat and fluid flow*, Vol. 22, No. 5, pp 113-122, 2001.
8. Bianchini, C., Facchini, B., Mangani, L., Conjugate heat transfer analysis of an internally cooled turbine blade with an object oriented CFD code, *European Turbomachinery Congress*, Graz, 2009.
9. Andreini, A., Mangani, L., Application of an object-oriented CFD code to heat transfer analysis, *ASME paper* GT 2008-51118, 2008.
10. Facchini, B., Tarchi, L., Toni, L., Cinque, G., Colantuoni, S., Investigation of circular and shaped effusion cooling arrays for combustor liner application – Part 1: Experimental analysis, *ASME paper* GT 2009-60037, 2009.

TORNADO-LIKE FLOWS: EXPERIMENTS ON GENESIS, STABILITY AND PREVENTION

A.Y. Varaksin*, M.E. Romash, V.N. Kopeitsev
Joint Institute of High Temperatures, Russian Academy of Sciences, Moscow, Russia

ABSTRACT. The fundamental possibility of physical simulation of wall-free concentrated air vortices (called as tornado-like flows) under laboratory conditions was demonstrated. These vortices were generated over a heated underlying surface due to unstable air stratification. The heating rates of underlying surface and air temporal and spatial temperature shear, which lead to the stable genesis of wall-free vortices have been defined. The influence of operation mode parameters on the characteristics (the time of appearance, the place of appearance, the length of the trajectory, the velocity of travel, the lifetime, the height, the diameter, and others) of generated air vortices was observed. High efficiency of influence of obstacles in the form of vertical grids of different height and cells on vortex characteristics (up to vortex breakdown) was clearly detected. The received fundamental results are useful for the increase of effectiveness of the tornado shelters and for finding the new ways of tornado prevention.

Keywords: *tornado-like flow, wall-free concentrated vortices, unstable air stratification*

INTRODUCTION

Vortex (swirling) flows are widely occurring in nature (atmospheric cyclones, sand storms, air tornadoes, typhoons, forest fires) and find numerous engineering applications (vortex tubes, cyclone separators, centrifugal nozzles, vortex cells, various turbulence simulators, and the like).
So the tornadoes occur frequently in North America and other parts of the world. They destroy everything on its path and lead to the human fatalities [1, 2]. The aim of this paper is to study the characteristic of the wall-free gas-solid concentrated vortices (called here as tornado-like flows) under laboratory conditions.
Vortex flows bounded by the walls are formed by way of tangential nozzle delivery of medium, application of mechanical swirling devices (guide swirl vanes, screws, internal spiral ribbing, and the like), and intensive rotation of body elements of channels (rotating tubes). The thus obtained vortex flows are convenient for detailed experimental description; however, their characteristics may significantly differ from the parameters of real vortex structures observed in the Earth atmosphere.
The study of free (not bounded by the walls) concentrated (the vorticity is localized in space) vortices is complicated by a number of reasons such as spontaneity of formation, space-time instability, practical impossibility of controlling the characteristics and so on. Therefore, even in view of the dynamics of development of direct simulation techniques (DNS method, LES method, and others), the solution of three-dimensional unsteady-state Navier-Stokes equations for a complex hydrodynamic and thermophysical object such as free concentrated vortex may hardly be accomplished in the immediate future because of complexity of formulating the boundary and initial conditions. The difficulties identified above account for the apparent absence of experimental

* Corresponding author: Prof. A.Y. Varaksin
Phone: + (7)-495-4858090, Fax: + (7)-495-4842683
E-mail address: varaksin_a@mail.ru

studies producing results in stability and dynamics of free concentrated vortices, which could be used for verifying mathematical models (see for example [3, 4]).
There are a number of works where the authors try to measure the parameters of the real tornadoes (for example, [5, 6]).
Therefore, an urgent need appears to exist in the arrangement of dedicated experimental investigations of wall-free concentrated air vortices which are similar to the real air tornadoes. It is important to note, that the most hurricanes are accompanied by the tornadoes, and the hydro-dynamical structure of tornadoes and hurricanes is approximately the same. One can assume that the good result in the tornado studying may be used for human defence from hurricanes. Thus the tornado-like flows research in laboratory conditions is very actual.
The aim of this paper is to study the questions of generation, stability and prevention of the wall-free concentrated vortices (called here as tornado-like flows) in the laboratory conditions.

EXPERIMENTAL SETUP AND PROCEDURE

The experimental setup is schematically shown in Figure 1. It was located in a room with floor *1* 6 by 6 m^2 in area and ceiling *2* 3.3 m high at a distance of 0.5 m from one of walls *3*. The experimental setup included a deck *4* 0.35 m high with three legs *5*. The horizontal surface of the deck *4* was a sheet of aluminum (grade D16AM) 1100 mm in diameter and 1.5 mm thick. The top (underlying) surface of the aluminum sheet was blackened with heat-resistant paint. Placed under the deck was an electrically ignited gas burner *6* of maximal thermal power of 3.5 kW. The diameter of flame *7* of the burner was varied (for different modes of thermal power) from 200 to 300 mm. A liquefied propane-butane mixture required for the operation of the gas burner was placed in a 27-liter vessel *8*.
The experimental setup makes possible the controlled heating of the underlying surface of aluminum sheet, which leads to the generation of unsteady vortex structures *9* as a result of development of unsteady stratification of air [7, 8]. The vortex structures being formed were visualized using tracer particles (micrometer-sized particles of magnesia) which were applied in a thin layer onto the underlying surface prior to experiments.

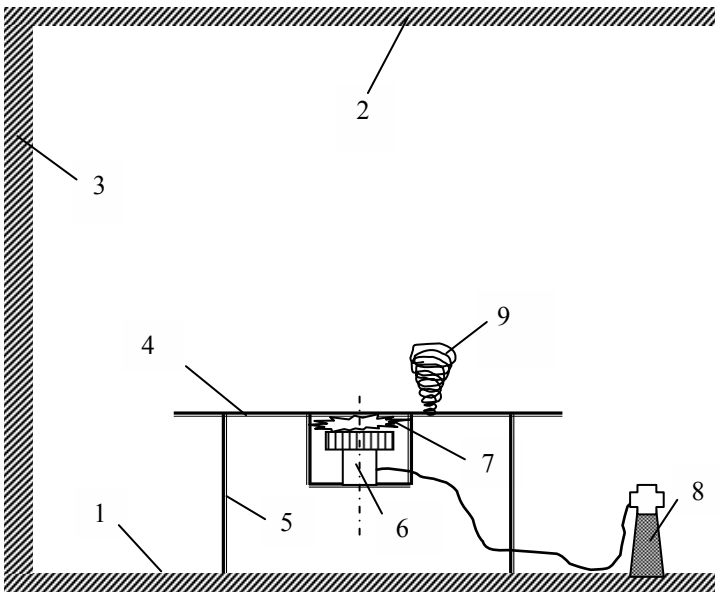

Figure 1. Schematic of the experimental setup

Table 1
Characteristics of the operating (thermal) modes

Mode	Heating	τ_h, s	τ_c, s	$T_{c\max}$, K
1		60	600	420
2	Weak	120	900	470
3		180	1200	500
4		60	600	500
5	Strong	120	900	580
6		180	1200	610

A digital video camera (Sanyo VCC-6572P) was used for video filming of vortices being generated. The wakes of vortex structures were photographed by a camera (Casio Exilim EX-S500). An infrared thermometer (AZ8868) was used for measuring the temperature of the underlying surface of the sheet. The temperature measurements (along the radius) were performed at six points with coordinates r =0, 100, 200, 300, 400 and 500 mm (r is the distance from the sheet centre).
Also monitored in the course of experiments was the air temperature in the room. The initial (prior to experiments) difference between the air temperature on the level of underlying surface T_1 and in the vicinity of the room ceiling T_2 was $\Delta T = T_2 - T_1 \approx 1$ ^{0}C. The maximal increase in the air temperature in the vicinity of the ceiling after a single experiment in one thermal mode (see below) reached a value of ΔT_2 =3-4 ^{0}C. Further experiments were performed after complete "cooling off" of the room to initial values of temperature.
The Table 1 gives the principal parameters of thermal modes employed for generation and study of the characteristics of air vortices. Here τ_h - heating time; τ_c - cooling time; $T_{c\max}$ - maximum temperature of the underlying surface centre. Thus, in the present study we used six different operation modes of underlying surface heating which are characterized by the time of heating (gas burner working time), time of cooling (time after gas burner switching off) and maximum temperature in the centre of underlying surface.

RESULTS AND DISCUSSION

The results concerning tornado genesis, stability and prevention will be discussed below.

Tornado genesis

A stable generation of vortices was observed in all modes except for mode no.1 (see Table 1). The temporal and spatial temperature distributions for the underlying surface and air for all operation modes have been determined. The typical measured temperature distributions for mode no.6 are shown in Figures 2-4.
Figure 2 gives the dependences of temperature of underlying surface centre and air at the point $y = 50$ mm above underlying surface for mode no.6. One can see that this mode is characterized by the following values of maximum temperature: $T_{c\max} = 610$ K (for underlying surface) and $T_{a\max} = 334$ K (for air) at $\tau_h = 180$ s.
The temperature distributions along the radius of underlying surface for mode no.6 under heating for underlying surface and air are given in Figure 3 and Figure 4, respectively. Some decrease in temperature in the central region of underlying surface ($r < 100$ mm), observed for short times of heating ($\tau_h \le 120$ s), is attributed to the structural features of the employed gas burner.

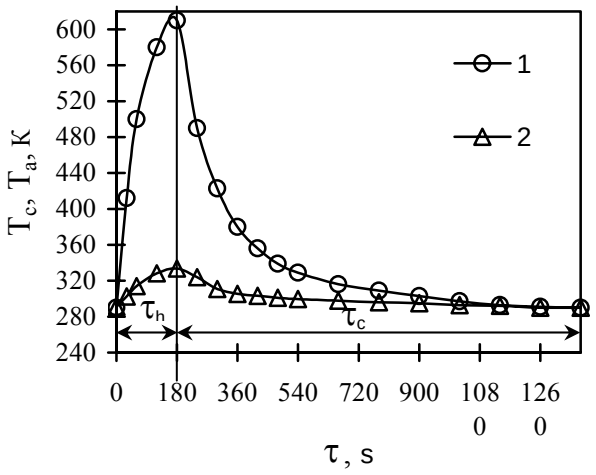

Figure 2. The temperature of underlying surface and air ($y = 50$ mm) as a function of time (mode no.6); $r = 0$: (1) underlying surface, (2) air

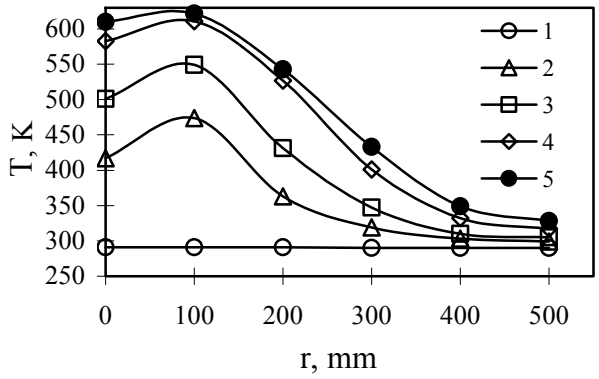

Figure 3. The temperature of underlying surface as a function of the radius and of time under heating (mode no.6): (1) $\tau_h = 0$, (2) 30 s, (3) 60 s, (4) 120 s, (5) 180 s

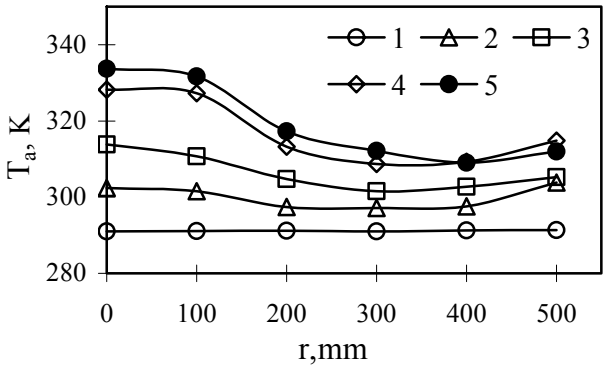

Figure 4. The temperature of air as a function of the radius and of time under heating (mode no.6), $y = 50$ mm: (1) $\tau_h = 0$, (2) 30 s, (3) 60 s, (4) 120 s, (5) 180 s

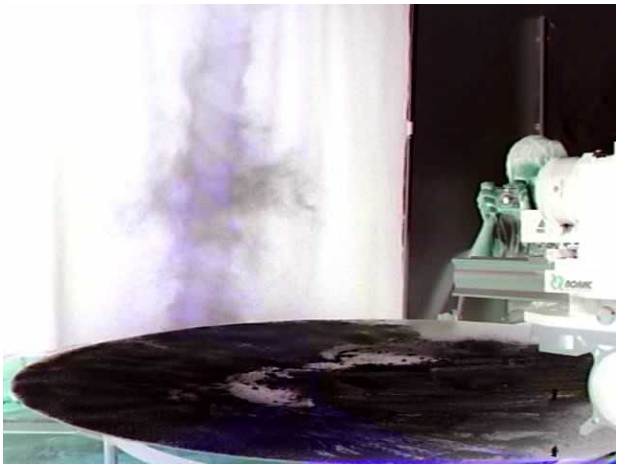

Figure 5. Photograph of tornado-like vortex (negative colours)

The video filming and the use of magnesia particles made it possible to visualize the vortex structures arising above the underlying surface. Frame-by-frame analysis of video records in different thermal modes (see Table 1) enables one to obtain information about the following parameters of the process of generation of vortices and their characteristics: (1) the values of temperature, at which the vortices are generated; (2) the region of underlying surface, where the vortices are generated; (3) the direction of rotation of vortex structure; (4) the number of vortices observed per experiments; (5) the trajectory of travel of the vortex base; (6) the length of the trajectory of the vortex base; (7) the velocity of the vortex base; (8) the lifetime of vortex structure; (9) the height of vortices; (10) the diameter of vortices, and others.

(a) (b)

Figure 6. Photographs of vortex structures: (a) frame with recorded wall-free concentrated vortex (negative colours); (b) air tornado in North America

Repeated experiments in different modes gave rise to the following inferences. Vortex structure began to form in the mode of heating of the underlying surface after the temperature at its centre reached a value of $T_c = 470\,\mathrm{K}$. The largest vortices were generated at temperatures at the surface centre $T_c > 570\,\mathrm{K}$. Vortex structures were largely generated in a circular region (150 mm $< r <$ 250 mm), i.e., in the region of abrupt rise of temperature gradient. The direction of rotation of all vortices being observed was counterclockwise (if the underlying surface is viewed from above). Up to ten vortex structures were observed per experiment. Three types of trajectories (wakes) of motion of vortex base were identified (see below). The maximal length of trajectory of the base of vortex structures was 100-200 cm with the velocity of travel of 5-20 cm/s. The limiting lifetime of observed vortices was about 40 s. The maximal height of generated vortex structures could be 1.5 m, and their maximal diameter – 0.3 m. An example of observed large-scale (visible height about 1.5 m) vortex with long (about 40 s) lifetime is shown in Figure 5.

The example of experimentally observed vortex structure is given on a large scale in Figure 6a for the purpose of detailing its basic parts (vortex core, peripheral region, vortex cascade). Given in Figure 6b for comparison is a photograph of a real air tornado in North America.

Tornado stability

The received distributions of air temperature allowed to find the values of dimensionless number, i.e. Rayleigh number for different thermal modes. This Rayleigh number has the form

$$Ra = \frac{g\,h^3 \beta\,\Delta T}{\nu\,a} \tag{1}$$

Here, g is acceleration of gravity, h is the characteristic distance in vertical direction where the temperature difference exists, β is the coefficient of volume expansion, ΔT is the temperature difference causing the convection, ν is the coefficient of kinematic viscosity, a is the thermal diffusivity.

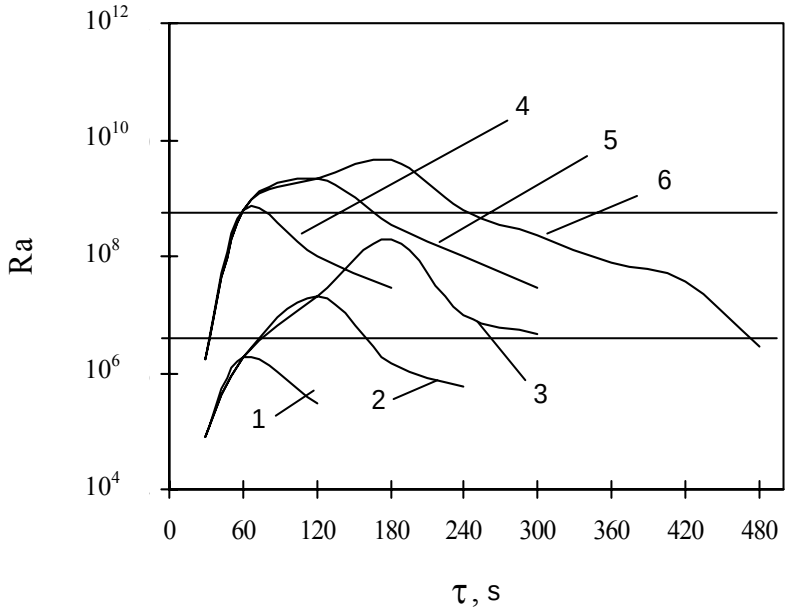

Figure 7. Rayleigh numbers as a function of time for different thermal modes; $r = 0$: (1) mode no.1, (2) no.2, (3) no.3, (4) no.4, (5) no.5, (6) no.6

For the estimations, we take h, as the distance from underlying surface in vertical direction to the place where the air temperature exceeds the surrounding temperature only for 10 K. The values of β, ν and a were taken for parameters of surrounding air.

Figure 7 gives the time dependence of Rayleigh number at the centre of underlying surface for all six operating modes. A stable generation of vortices was observed in all modes except for mode no.1. Therefore, the Rayleigh number $Ra \approx 10^7$ may be taken as a minimal value at which the vortex structures began to form. The largest vortices were generated in case of operation in modes no.5 and no.6, which correspond to $Ra \geq 10^9$. There are two horizontal lines in Figure 7, which correspond to $Ra = 10^7$ and $Ra = 10^9$ respectively. By using these lines it is easy to define the time of existence of relatively small ($10^7 < Ra < 10^9$) and large vortices ($Ra > 10^9$) for the different operation modes. Received ranges of Rayleigh number are in good agreement with the experimental data on vortices generation on modes of heating and cooling of underlying surface.

Tornado prevention

In the present work the method of tornado prevention was developed and verified experimentally. The method consists of the creation of obstacles on the vortex path in the form of vertical grids with different height and size of cells. It was supposed, that this method may become an effective means of vortex characteristics control which leads to its weakening and/or destruction. Probably such grid defence constructions will be beyond comparison among another ways of tornado prevention due to simplicity of manufacturing and low price.

The height of grids used in experiments was chosen by realization of geometric similarity between real tornadoes (actual obstacles) and experimental vortices (model grids).

The main six variants of vortex behaviour during its interaction with grid were detected. They are: 1) vortex motion to the grid and its breakdown without grid intersection; 2) vortex destruction in the time of grid crossing (see Figure 8a); 3) vortex deceleration near the grid (up to full stop) and following breakdown (see Figure 8b); 4) change direction of vortex motion near the grid, then motion along the grid with following destruction; 5) vortex breakdown during grid crossing with second generation of vortex after grid; 6) intersection of grid by vortex accompanied of change of motion direction and its characteristics (vortex weakening).

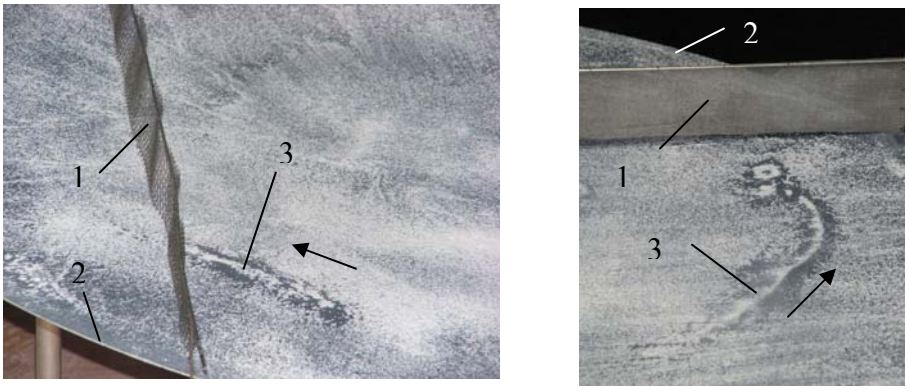

(a) (b)

Figure 8. Photographs of vortex tracks during their interaction with vertical grids: (a) case of vortex breakdown due to collision with grid; (b) case of vortex breakdown after stop before grid.
Digits refer: (1) grid, (2) edge of underlying surface, (3) vortex track.
The arrow shows the direction of vortex motion

Probably, there exist several physical mechanisms of grid-vortex interaction. The generation of small-scale turbulence near the grid which leads to the disturbance of vortex structure symmetry [9], acoustical oscillations generated by grid and running towards to the vortex are among these mechanisms together with some others.

CONCLUSIONS

The fundamental possibility of physical simulation of tornado-like air vortices under laboratory conditions was demonstrated. The influence of operation thermal mode parameters on the characteristics of generated air vortices was observed. The efficiency of the proposed method of tornado prevention was verified under laboratory conditions by means of study of vertical grids influence on behaviour of wall-free vortices with structure which is similar to the structure of real tornadoes. The received fundamental results are useful for the increase of effectiveness of the tornado prevention.

ACKNOWLEDGMENTS

This study was supported in part by the Program for basic research of the Division of Energetics, Machinery, Mechanics, and Control Systems of the Russian Academy of Sciences on "The investigation of fundamental problems of burning and detonation in energetics", by the Russian Foundation for Basic Research (grant no. 08-08-00743), and by the grant of the President of Russian Federation (MD-4995.2007.8).

REFERENCES

1. Ashley, W. S., Spatial and Temporal Analysis of Tornado Fatalities in the United States: 1880-2005, *Weather and Forecasting*, Vol. 22, No. 6, pp 1214-1228, 2007.
2. Simmons, K. M. and Sutter, D., Tornado Shelters and the Manufactured Home Parks Market, *Natural Hazards*, Vol. 43, No. 3, pp 365-378, 2007.
3. Shtern, V., Borissov, A. and Hussain, F., Vortex-Sinks with Axial Flows: Solution and Applications, *Phys. of Fluids*, Vol. 9, No. 10, pp 2941-2959, 1997.
4. Yih, C.-S., Tornado-Like Flows, *Phys. of Fluids*, Vol. 19, No. 7, pp 076601-1-076601-6, 2007.
5. Wurman, J., Richardson, Y., Alexander, C. et al., Dual-Doppler Analysis of Winds and Vorticity Budget Terms near a Tornado, *Monthly Weather Review*, Vol. 135, No. 6, pp 2392-2405, 2007.
6. Wurman, J., Alexander, C., Robinson, P. et al., Low-Level Winds in Tornadoes and Potential Catastrophic Tornado Impacts in Urban Areas Reply, *Bull. Amer. Meteor. Soc.*, Vol. 89, No. 10, pp 1580-1581, 2008.
7. Varaksin, A. Yu., Romash, M. E., Kopeitsev, V. N. and Taekin, S. I., The Possibility of Physical Simulation of Air Tornados under Laboratory Conditions, *High Temperature*, Vol. 46, No. 6, pp 888-891, 2008.
8. Varaksin, A. Yu., Romash, M. E., Taekin, S. I. and Kopeitsev, V. N., The Generation of Free Concentrated Air Vortexes under Laboratory Conditions, *High Temperature*, Vol. 47, No. 1, pp 78-82, 2009.
9. Varaksin, A. Y., *Turbulent Particle-Laden Flows*, Springer, Berlin, 2007.

GRANULAR BED LIFTING IN SHOCK WAVE BY THE MECHANISM OF INTRAPHASE INTERACTION OF PARTICLES

S. Poplavski
Cristianovich Institute of Theoretical and Applied Mechanics,
SB RAS, Novosibirsk, Russia

ABSTRACT. Dynamics of lifting of the coal dust bed in the flow behind shock wave is experimentally investigated. On the base of the observations and quantitative data the physical mechanism of the process is suggested which supposes the existence of intermediate state of dust among the dense granular bed and the suspended state. This intermediate stratum is characterized by high concentration and mobility of the particles, and their collisions cause to further lifting. For this mechanism the ballistic model is suggested. In the frames of the model the dependence of vertical velocity and height are found. The comparison of this dependences with the experimental data demonstrate well agreement.

Keywords: *shock waves, multiphase flows*

INTRODUCTION

Mixing behind a shock wave (SW) gliding above a dust layer is an important issue within the framework of the dust explosion problem. There are many experimental and theoretical publications on this topic, but there is no unified model of the process [1]. The available models of bed lifting can be divided into two groups. The first one includes models that take into account the effect of the SW front and the flow behind it on the dust layer. These models consider a granular material as a continuous medium and the interface between the gas and the layer of particles as a contact surface between two fluids. Mostly advanced model in the frames of this approach was represented in the article [2]. Detail consideration of the wave dynamics in granular medium speaks well of this approach. The second group includes models that take into account only the effect of the flow behind the SW and the physical forces acting on the particles from the flow. These are the following forces: 1) the force generated by difference in velocity on the particle scale in the shear flow (Saffman effect) [3, 4]; 2) the force induced by rotation of a sphere in the flow (Magnus effect) [5]. The validity of these models is supported by the fact that bed lifting is also observed in the flows without shock waves.

Each mechanism is realized within its own physical constraints, but they all are possible if the interface between the phases and the particles possess certain mobility. This state of a granular medium, which is conventionally called a fluidized bed, is possible in the case of external energy supply, for instance, from a tangential flow and in the case of intraphase exchange of momentum in the bed through particle collisions. The role of collisions was noted in [5], but this effect was not quantified.

The analysis of the granular bed interaction is not complete without consideration of the papers, which are devoted to some special cases of the particles transition from the state of dense layer to suspended state. First of all these are the investigations of dust lifting behind reflected shock [6, 7].

* Corresponding author: S. Poplavski
Phone: + (7)-383-330-7855, Fax: + (7)-383-330-7268
E-mail address: s.poplav@itam.nsc.ru

It is known that behind reflected shock the gas is in the quiescent state and all mentioned mechanisms cease to be actual. However the experiments demonstrate that layer of dust being lifted in the incident shock continues to rise in the reflected wave and in addition - more rapidly [6]. It was shown by numerical simulation that behind the reflected shock propagating over the dust layer the large scale vortex appears in the vertical plane unlike the case of a channel with the smooth wall [7]. Velocity field of the particles confirms the influence of the ascending vortex part on the particles lifting in the reflected shock. The nature of the vortex they explain by the shock front curvature near the dust layer surface. This effect in it's turn connected with the flow non-uniformity in the incident wave because of the losses of the gas flow momentum in two phase mixture above the dense particles layer.

One more paper on the stability of granular bed has to be mentioned, which suggested the important effect far back in 1940 [8]. In the paper the particles takeoff from the bed was considered irrespective of the shock wave but only as a result of flow action just as the Saffman and Magnus effects is connected with the flow behind the shock wave.

However it is need the presence of particle in the flow for the action of Saffman and Magnus forces, but those mechanisms does not explain proper particles takeoff like other effects though. The value of the article is the fact that it experimentally proves and substantiates the quantitative criterions of the particles takeoff solely under the action of the flow sliding above the dusty layer.

In the proposed model the particles on the layer surface were considered untied, but each of them lies in surface irregularities formed with chaotic layout of the particles of lower layer. On average half of midship area of the upper particles is located in the gas flow. On the Figure 1 from paper [8] diagram of the forces is shown which influence on the particle of upper layer in sliding flow.

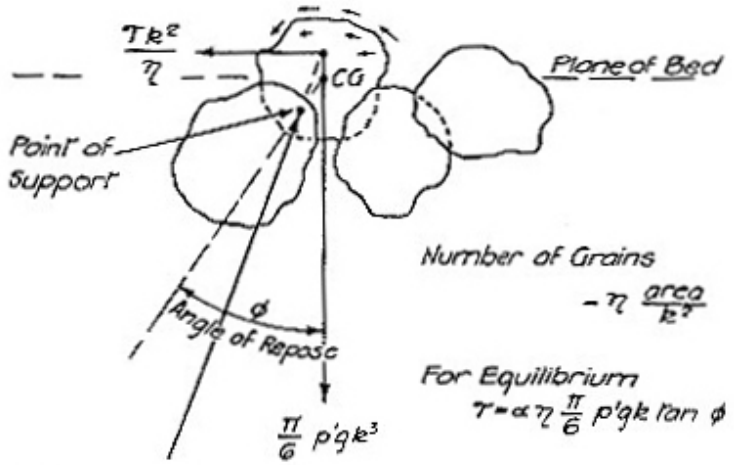

Figure 1. Frame of forces for the upper particle on the granular bed from [8], here k – is average particle size, η - coefficient of bed density, τ- tangential tension.

It is shown in the paper that dusty bed becomes instability when aerodynamics force is enough to "roll out" the particle along inclined trajectory at an angle ("angle of response" φ) on the height of radius. If the aerodynamics force exceeds the particle weight too much then the particles leave the bed at an "angle of response" φ relatively to bed surface. In the proposed model takeoff velocity is not defined, but it can be shown that this velocity is small. In fact at known average acceleration A on the length $\sim d$ particle get velocity $V \sim \sqrt{Ad}$. Acceleration of spherical particle at large Re number can be expressed from the motion equation:

$$A = \frac{s\rho u^2 C_d}{4m} = \frac{3}{8}\frac{\rho}{\rho_p}\frac{u^2 C_d}{d} \quad \text{then} \quad V = u\sqrt{\frac{3}{8}C_d\frac{\rho}{\rho_p}} \cong 10^{-2}u$$

It is clear that initial particles velocity is not large because the critical flow velocity u is small when dusty bed loses stability. According to experimental data [8] angle φ is about 30°- 45° for different types of dust, then the velocity vertical component is ~ 0.5-0.7V. In view of it this mechanism can not provide the lifting of small particles on the big height on the other hand it explains proper appearance of free and moving particles over the dense bed surface. Small thickness of an intermediate stratum between the particles bed and particles suspension is evidence of high concentration of particles inside the stratum. In this state the particles can be lifted by any mechanisms above mentioned.

The existence of such intermediate stratum produces conditions for multiple collisions of the particles with further flight along the ballistic trajectories. In the present paper the lifting of granular bed behind the shock wave is studied. An attempt to study the contribution of the particle collision mechanism to bed lifting behind the SW is made in the present work. The influence of the mechanism is investigated coupled with the particles ballistic flight model.

EXPERIMENTS AND DATA ANALYSIS.

Experiments with single particles

The experiments were performed in the shock tube with the particles of different size and shape, with different type of bed and with individual particles as well. Single particles on the channel floor behind shock wave behave ambiguously. Preliminary tests have shown that individual spherical particle does not lift from the smooth wall at least during observation time up to 0.5 ms. Single particle with an irregular shape is lifted by the flow at the same conditions. On the Figure 2 shadow picture of state of the rear monolayer of the irregular particles is shown after 250 μs of the SW front passing.

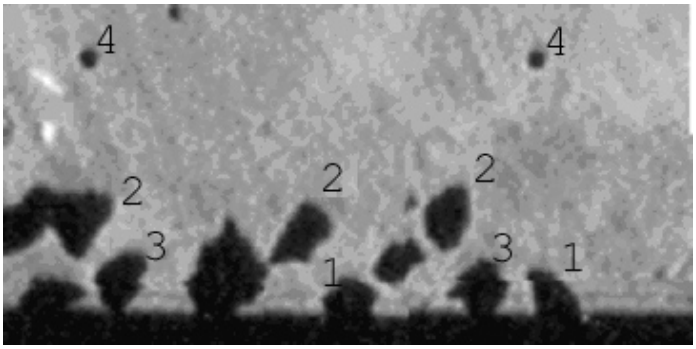

Figure 2. The lifting of the rear monolayer of the irregular particles after 250 μs of the SW front passing; 1 – the particles at rest, 2 – takeoff the particles, 3 – rolling particles, 4 – points of scale on glass window of the shock tube channel (distance 10 mm), particles size 1.5-2 mm.

The analysis of such series of the frames shows that the particles is lifted on reaching critical rolling velocity with different delay depending on a peculiarity of shape: the number of verges and the difference between maximum and minimum size. This mechanism, which has not been yet described, to all appearance involves forced vertical oscillations of the center of mass of the particle during its rolling. In the present paper the following criterion of the particles takeoff is suggested by this mechanism. When the acceleration of oscillations is higher than g (constant of gravitation), the particle separates from the wall or from the bed surface. A parametric analysis shows that lifting of

a particle of size d by this mechanism occurs at a rolling velocity $u_x \geq \sqrt{10dg}$, and the initial vertical velocity is $u_0 \approx \sqrt{dg}$. Comparison of those estimations with the experimental observations shows well agreement and the lifting delay is connecting with achievement of the critical velocity u_x. The lifting of the spherical particles from the rough wall or from the bed surface by the flow is explained in a similar way. The velocity u_0 is too small to be responsible for the lifting height observed, but it indicates that there exists an intermediate state between the bed and the suspension, where the particles possess significant mobility at a high concentration. This state of dust more appropriately known as liquefied state.

Experiments with granular bed in shock wave

In the experiments with dusty layers the particles of different size was used and different types of layer location and roughness were investigated. The multiframe shadow method was used for the visualization of dust lifting [5]. Figure 3 shows typical series of shadow pictures obtained in the experiments with the coal dusts for two kind of layer surface. Figure 3***a*** shows dusty bed with natural roughness, and Figure 3***b*** shows the surface with an artificial transverse grooves for addition flow whirl. The height of image darkening over an initial dusty bed surface and further height evolution because of suspended layer appearance were recorded.

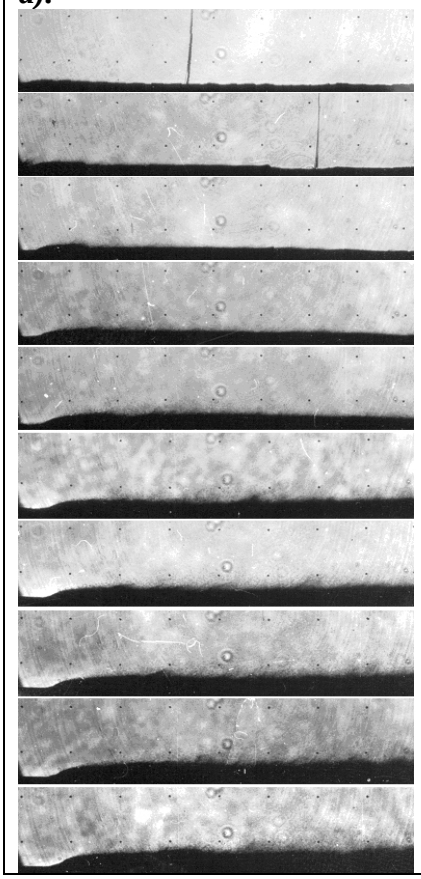

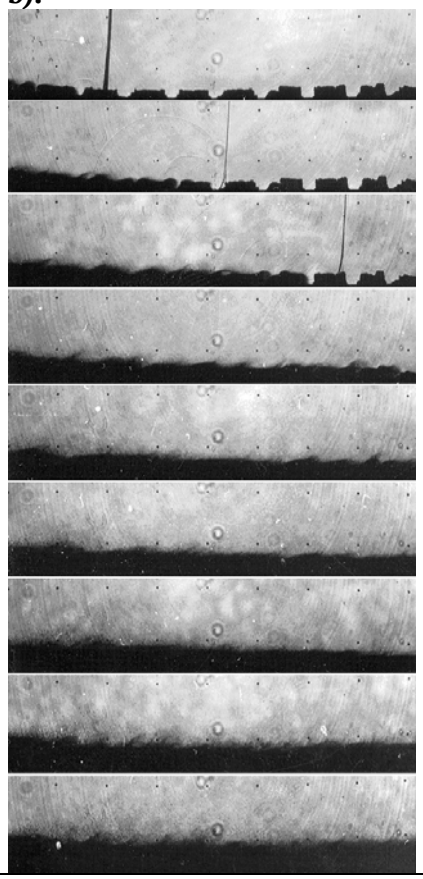

Figure 3.

a). Coal dust layer behind SW; SW Mach number $M_S = 1.54$; gas velocity $u_2 = 258$ m/s; particles size $d < 100$ μm, layer thicness 3-4 mm;

b). Coal dust layer with artificial transverse grooves behind SW; SW Mach number $M_S = 1.35$; gas velocity $u_2 = 175$ m/s; particles size $d < 100$ μm, layer thicness 3-4 mm;

time interval among the frams 50 μs

For the quantitative study the dynamics of a border of absolute darkening of the layer image was chosen. The volume concentration of particles on this border β_{tr}, is estimated at the approach of line optics as

$$\beta_{tr} = \frac{2}{3}\frac{d}{l},$$

here d - an average particles size, l - the optical thickness of tow phase area inside the shock tube channel. For the characteristic value $l \sim 10^{-2}$ m at $d \sim 100$ μm the volume concentration of particles is $\beta_{tr} \approx 10^{-2}$. At such a concentration an average distance among particles is small and comes to

~ 3*d*, but under the border of transparency is even less. In these conditions the collisions of the particles are very probable in view of chaotic component of their velocity because of mutual influence. Figure 4 shows the collision parameters for the case of equal spheres. In the present model it is adopted that collision velocity *V* particles get from the main flow on the length of free path.

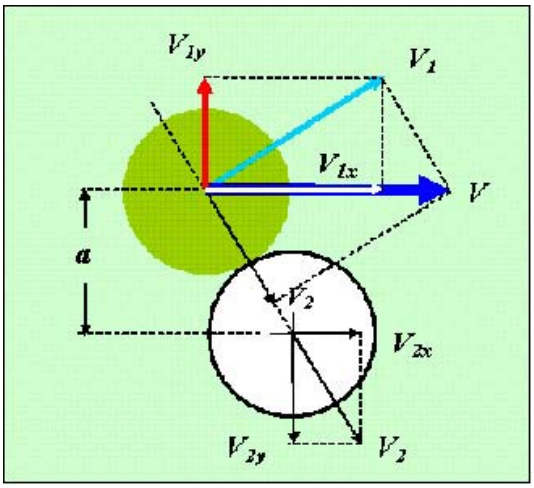

Figure 4. Collision parameters for the case of equal spheres.

Experiencing collisions with each other and with the rough bed surface, they acquire transverse (including vertical) velocity and leave the fluidized bed. In the elementary case of spherical particles of an identical size, their vertical velocity is

$$V_y(\delta,\alpha) = V\delta\sqrt{1-\delta^2}\,\sin\alpha, \quad 0 \le \delta \le 1,\ 0 \le \alpha \le \pi, \tag{1}$$

where *V* is the impact velocity, δ is the impact parameter of the collision *a/d*, and α is the angle of inclination of the impact plane to the bed plane. It is clear that averaging of Eq. (1) with respect to δ and α yields $V_0=V(2k/\pi)$. The impact velocity of particles at the early stage of acceleration can be expressed in terms of the mean free path L_f in the fluidized bed $V \cong u\left(\sqrt{2L_f/\lambda_ч} - 2L_f/\lambda_ч\right)$, where $\lambda_ч = 2\rho_p d/\rho C_x$, $L_f \cong 0.9d/\sqrt[3]{\beta_{tr}}$, $\beta_{tr} \sim d/l$ is the concentration of particles on the visible boundary of the bed. Assuming the particle to be lifted only owing to the momentum induced by the collision, there constructed a mathematical tool that allows predicting the basic parameters of the process, such as the maximum height of particle lifting and the concentration of the suspension.

Hovering of a particle. A process of hovering or a particle deposition in the presence of gravitational forces is not determinant but competitive to the lifting process. However we consider it here in the first place since its parameters are turned to be universal and are used for description of other relaxation processes taking place at a motion of solid particles in gas. We define the hovering as a stage of the particle deposition when the particle has reached a steady vertical velocity, i.e. the gravitational force becomes equal to the aerodynamical one.
We consider quantitatively dynamics of a particle in the gravitation field taking into account drag forces. The particle motion equation is given by

$$\frac{dV_y}{dt} = g - C_x\frac{s}{m}\frac{\rho V_y^{\,2}}{2}, \quad (t=0, \quad V=0). \tag{2}$$

Here the V_y is the vertical component of the particle velocity in coordinate system connected with the gas phase, *s, m,* C_x – midsection area, mass and drag coefficient of the particle, ρ is the gas density, *g* is the gravitational acceleration. It is obvious that behavior of the function V_y has an

asymptotical character, and the asymptote includes all basic physical parameters of the process. Therefore prior to integration of the equation we set the left hand side of the formula equal to zero. So we determine the asymptote as the steady fall velocity at the moment when the forces achieve the balance state. This asymptote value is the hovering velocity evaluated as

$$v = \sqrt{\frac{m}{s}\frac{2g}{C_x \rho}} \ . \tag{3}$$

In particular, a particle of irregular shape (cubic, for instance) with size d and the material density ρ_p has the hovering velocity as following

$$v = \sqrt{2\frac{\rho_p}{\rho}\frac{dg}{C_x}}\ , \text{ and sphere of diameter } d \text{ has } v = \sqrt{\frac{4}{3}\frac{\rho_p}{\rho}\frac{dg}{C_x}}\ .$$

For a coal particle this estimation gives $v \approx 30\sqrt{dg}$ at the gas density 2.2 kg/m^3 for a weak enough SW of Mach number M_s=1.4. Therefore the coal particle of size $d \approx 10$ μm has the hovering velocity of $v \approx 0.3$ m/s, and for $d \approx 1$ μm the velocity is $v \approx 0.1$ m/s. These unexpectedly big values are obtained for the drag coefficient $C_x \sim 1$, which has been chosen from those considerations that the flow regime in vicinity of the particle corresponds to relatively big Reynolds numbers. This regime is determined by the main (lengthwise) stream behind the SW. However in still gas the hovering corresponds to Stokes regime with $C_x \sim 20$ and higher. In this case the hovering velocity is $v \sim 10^{-2}$ m/s and even smaller.

It is obvious that choice of the C_x value depends totally on a level of completeness of the lengthwise velocity relaxation on moment of the hovering balancing achievement. In other words it depends on ratio of lengthwise relaxation time scale to the hovering balancing time. Bit it is correct for cases when scale time of the problem is bigger then both these scales. In other cases the most important parameter influencing the choice of C_x value is the problem time scale.

Besides determining the steady particle fall velocity the hovering velocity is a criterion of the particle lifting in an ascending stream. Indeed if the gas velocity has the vertical component u_y in the laboratory coordinate system and the velocity is higher than the hovering velocity, then according to (2) and (3) the particles within the given coordinate system will elevate with the velocity equal to

$$V_y = u_y - \sqrt{\frac{m}{s}\frac{2g}{C_x \rho}}\ .$$

Then even for weak SWs (M_s=1.4) at the stream velocity ~200 m/s a fluctuation of the velocity vector higher than 0.1% has to evoke lifting of the particles bigger then 10 μm. In angle expression it corresponds to a negligible flow deviation about ~0.06°. Such flow fluctuation can appear first due to weak oblique shocks and in the second place due to surface roughness and even the layer roughness.

The particle lifting height and velocity. In order to validate the model in the frame of experimental data a dependency of thickness of the dust-gas mixture over the layer vs. time of the flow impact has been found taking into account size and density of the particles, collision elasticity and flow parameters. Let us estimate the maximal lifting height of the particle of size d, thrown up with the initial velocity V_0 under the action of gravity and aerodynamical drag. We integrate the equation of motion

$$-\frac{dV}{dt} = g + C_y \frac{s}{m}\frac{\rho V^2}{2} \text{ with the initial condition } V = V_0 \text{ at } t = 0. \tag{4}$$

Using the notations $\Psi = V/v$ and $\theta = t/\tau_y$ determined earlier, where

$$v = \sqrt{\frac{m}{s}\frac{2g}{C_x\rho}} = \sqrt{2\frac{\rho_p}{\rho}\frac{dg}{C_x}}, \qquad \tau_y = \frac{v}{g} = \sqrt{\frac{m}{s}\frac{2}{C_x\rho g}} = \sqrt{2\frac{\rho_p}{\rho}\frac{d}{C_x g}}$$

we rewrite the equation (4) as

$$-\frac{d\Psi}{d\theta} = 1 + \Psi^2 \text{ with initial condition } \Psi = \Psi_0 = V_0/v \text{ for } \theta = 0. \tag{5}$$

The solution of this equation $\Psi(\theta) = tg(\theta^* - \theta)$ includes upper time limit of integration which equals to time period which needs for a particle to be lifted to the maximal height θ^*:

$$\theta^* = \frac{t^*}{\tau} = arctg\left(\frac{V_0}{v}\right) \quad (0 < t^*/\tau < \pi/2), \tag{6}$$

and the solution is given by

$$V(t) = v * tg\left(\frac{t^* - t}{\tau_y}\right) \tag{7}$$

Integrating (7) in the limits defined in (6) we get the required function of the particle lifting height depending on time and the relaxation parameters v and τ_y.

$$H(t) = v\tau_y \ln\frac{\cos\left(\theta^* - t/\tau_y\right)}{\cos\theta^*}. \tag{8}$$

This function is used in the paper for the comparison with the experimental data on dynamics of the layer lifting behind the SW. The value $v\tau_y$ is constant of relaxation length which within the Stokes approach is proportional to Reynolds number:

$$\lambda_y = 2\frac{\rho_p}{\rho}\frac{d}{C_y} = \frac{1}{12}\frac{\rho_p}{\rho}d\,\mathrm{Re} = \frac{1}{12}\frac{\rho_p}{\rho}\frac{d^2 v}{\nu}$$

Therefore we can estimate the maximal particle (layer) lifting height as following

$$H_{\max} = \lambda_y \ln\frac{1}{\cos\left[arctg\left(V_0/v\right)\right]}. \tag{9}$$

At small particle collision velocities when $V_0/v < 1$, the aerodynamical force influence on dynamical process and the height of lifting decreases. So we able to consider only two terms of decomposition one

$$\varphi = arctg\left(V_0/v\right) \cong V_0/v - \left(V_0/v\right)^3 + \ldots \text{, and also } \ln\frac{1}{\cos\varphi} \cong \frac{\varphi^2}{2} + \frac{\varphi^4}{12} + \ldots$$

Finally we get

$$H_{\max} \cong \frac{V_0^2}{2g}\left[1 - \frac{1}{2}\left(V_0/v\right)^2 - \frac{7}{9}\left(V_0/v\right)^4 + \ldots\right]. \tag{10}$$

Dependence (8) was compared with experimental data, and their good agreement was demonstrated (see Fig.6).

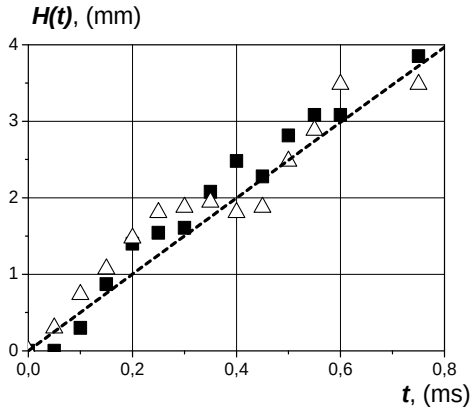

Figure 5. Dynamics of lifting of a coal-dust layer behind a shock wave; the points are the experimental data, and the curve is calculated by Eq. (8).

CONCLUSIONS

Dynamics of lifting of the coal dust bed in the flow behind shock wave is experimentally investigated. On the base of the observations and quantitative data the physical mechanism of the process is suggested which supposes the existence of intermediate state of dust among the dense granular bed and the suspended state. This intermediate stratum is characterized by high concentration and mobility of the particles, and their collisions cause to further lifting. For this mechanism the ballistic model is suggested. In the frames of the model the dependence of vertical velocity and height are found. The comparison of that dependence with the experimental data demonstrates well agreement.

This work was supported by the Russian Foundation for Basic Research (Grant No. 08 – 01 – 92010-NNS a).

REFERENCES

1. Fedorov, A.V., Mixing in wave processes propagating in gas mix, *Overview. Combustion, Explosion and Shock Wave,* Vol. 40, No. 1, pp 17-31, 2004.
2. Fedorov A.V., Fedorova N.N., Numerical simulations of dust lifting under the action of shock wave propagating along the near-wall layer, *J. Phys. IV*, Vol. 12, pp 97-104, 2002.
3. Merzkirch W., Bracht K., The erosion of dust by a shock wave in air: initial studies with laminar flow, *Int. J. Multiphase Flow*, Vol. 4, No. 1, pp 89-95, 1978.
4. Saffman P.G., The lift on a small sphere in a slow shear flow, *J. Fluid Mech.,* Vol. 22, part 2, pp 385-400, 1965.
5. Boiko V.M., Papyrin A.N., Dynamics of the formation of a gas suspension behind a shock wave sliding over the surface of a loose material, *Combustion, Explosion and Shock Wave,* Vol. 23, No. 2, pp 231-235, 1987.
6. Boiko V.M., Laser diagnostic of micro processes at the interaction of shock waves with liquid and solid particles, *Doc. Dissert. Novosibirsk*, 1995. (in Russia)
7. Kiselev S.P., Kiselev V.P., Duct lifting behind reflected shock wave sliding over the dust layer, *Applied Mechanics and Technical Physics*, Vol. 42, No. 5, pp 8-15, 2001. (in Russia)
8. White C.M., The equilibrium of grains on the bed of a stream, *Proceedings The Royal Society,* Vol. 174, No. 958, pp 322-338, 1940.

ON THE DROP DYNAMIC AT AN EARLY STAGE OF THE VELOCITY RELAXATION IN SHOCK WAVE

V. Boiko, S. Poplavski
Cristianovich Institute of Theoretical and Applied Mechanics,
SB RAS, Novosibirsk, Russia

ABSTRACT. An experimental study of motion of droplets in the flow behind incident shock waves is presented. The aim of the present work was to investigate the velocity relocation and to measure the aerodynamic drag of drop in wide parameters range in the frames of a unified approach. The drops of water, alcohol, acetone, hexane and tridecane of 2 – 3 mm in diameter were tested in the flow behind shock wave with Mach number M = 0.15-0.55. Special attention was given to an early stage of the velocity relaxation, when the influence of deformation was significant. Data on the drops aerodynamic drag was obtained taking into account deformation and mass erosion. The influence of the drop deformation and mass erosion on the aerodynamic drag C_x was studied. Clear temporal correlation of C_x with the processes of deformation and breakup was shown. The influence of shock wave intensity on the value and dynamic of C_x was shown. These results enable to explain the C_x data dispersion of different authors with differences of time observation and Weber number. The value of real aerodynamic drag for the centre of mass of the drop C_x was found. It was shown that on an early stage of the velocity relaxation C_x for centre of mass is comparable with C_D of solid sphere.

Keywords: *shock waves, gas-drops mixtures, velocity relaxation, aerodynamic drag*

INTRODUCTION

The behavior of fuel drops at sudden penetration in gas flow (in particular in the flow behind shock wave) is important for multiples applications in the chemistry technology, power engineering, aircraft and rocket propulsion engineering [1]. Inert interaction of shock wave with the water drops is of interest from the point of view of the flight of high velocity aircrafts in rainy region.

The problem involves large group of complicated and interrelated processes, which run simultaneously. These are the acceleration of drop as a unit, evolution of the surface wave disturbance, deformation, and breakup. All available knowledge on these processes and determinative parameters by now were found experimentally and are reviewed in a number of articles [1 - 3].

Deformation of the drop and mass erosion are the determinatives in the problem of drop dynamic in the steady flow behind incident shock wave. There are known six modes of the drop behavior at sudden penetration to the gas flow depending on Weber number $We = \rho u^2 d/\sigma$, where $\rho u^2/2$ – is dynamic pressure, d – is the drop diameter, σ - is surface tension. Many authors suggest critical values of the Weber number which correspond to the main modes [1, 3]. So according to [3], following kinds of deformation and breakup (and the corresponding critical Weber number We_{cr}) are mostly typical for the low-viscosity liquids (water, alcohol, kerosene and so on):

* Corresponding author: S. Poplavski
Phone: + (7)-383-330-7855, Fax: + (7)-383-330-7268
E-mail address: s.poplav@itam.nsc.ru

1. vibrational breakup We = 8 ÷ 12,
2. bag breakup 12< We < 50,
3. bag-and-stamen breakup 50< We < 100,
4. sheet stripping 100< We < 350 ,
5. wave crest stripping We ≥ 350,
6. catastrophic breakup We ≥ 350.

The first mode is realized in the narrow Weber number range, has a large time delay of breakup and is not practically realized in the shock waves. The second and third modes looks like a soap bubble and are not observed in the experiments with shock waves as in the case of the first mode [4].
Following three modes are observed at large Weber number and cardinally differ from the above mentioned modes [5, 6]. Breakup of the drop at such conditions happens by means mass erosion from the liquid surface with the action of different mechanisms.
First of them is an entrainment of liquid boundary layer from the drop equator (sheet stripping) as a shroud with subsequent fragmentation (mode 4) [6].
The second one is the entrainment of droplets from the crests of micro-waves on the windward side of parental drop (wave crest stripping). This kind of waves is the result of evolution of Kelvin-Helmholtz instability, which is the characteristic feature of the shear streams [7] (mode 5).
One more sort of the instability of liquid surface (Rayleigh-Taylor instability [7]) provokes the drop breakup into several large parts (mode 6). Further breakup of the secondary droplets happens by the mode 4 or 5.
In incident shock waves with the flow velocity behind front u ≥ 50 m/s both stripping mechanisms in general take place, namely - sheet stripping mode and wave crest stripping mode [5, 6]. Our last experiments show that stripping mechanisms of drops breakup are observed in the wide range of Weber number 200 ≤ We ≤ 8000. Change of Weber number of the drop-shock interaction produces only the changes of duration of typical stages of the process. The observation of different stages of the velocity relaxation in the experiments can be reason of large differences of data on the drops aerodynamic drag obtained by various authors. The aim of the present work was to investigate the drops dynamic in incident shock waves and to measure the drop aerodynamic drag in wide range of main parameters in the frames of a unified approach taking into account the deformation and mass erosion.

EXPERIMENTS AND DATA ANALYSIS.

The experimental investigations of the acceleration of drops in the flow behind shock waves are confronted with considerable difficulties. It concerned with the registration of extremely small displacement *S(t)* especially on early stage of the velocity relaxation at $S(t) < d/50$ when the influence of the measurement error is considerably. This procedure requires both perfect diagnostic methods for the maximum spatial and time resolution during registration and modern approaches at the image treating.
The experiments were performed in the shock tube which was outlined in paper [8]. The low pressure channel of the 5 meters length has the square cross section 52x52 mm in the test chamber. Drop generator in the top wall of the channel was equipped by synchronization with the triggering system of the shock tube. It permits to place the descending drop on the centre of test chamber at moment of the shock front arrival.
The shock tube was equipped with fast-acting multi-frame shadowgraph registration on the base of laser stroboscope as a light source. Typical shadow picture of the process is shown on Fig.1. The exposition time ($30 – 50 \times 10^{-9}$ c), number of the frames (15-20) and intervals (10-50 μs) were setting by the laser stroboscope. Spatial separation of the frames was performed by high speed photographic camera with the rotating mirror prism.

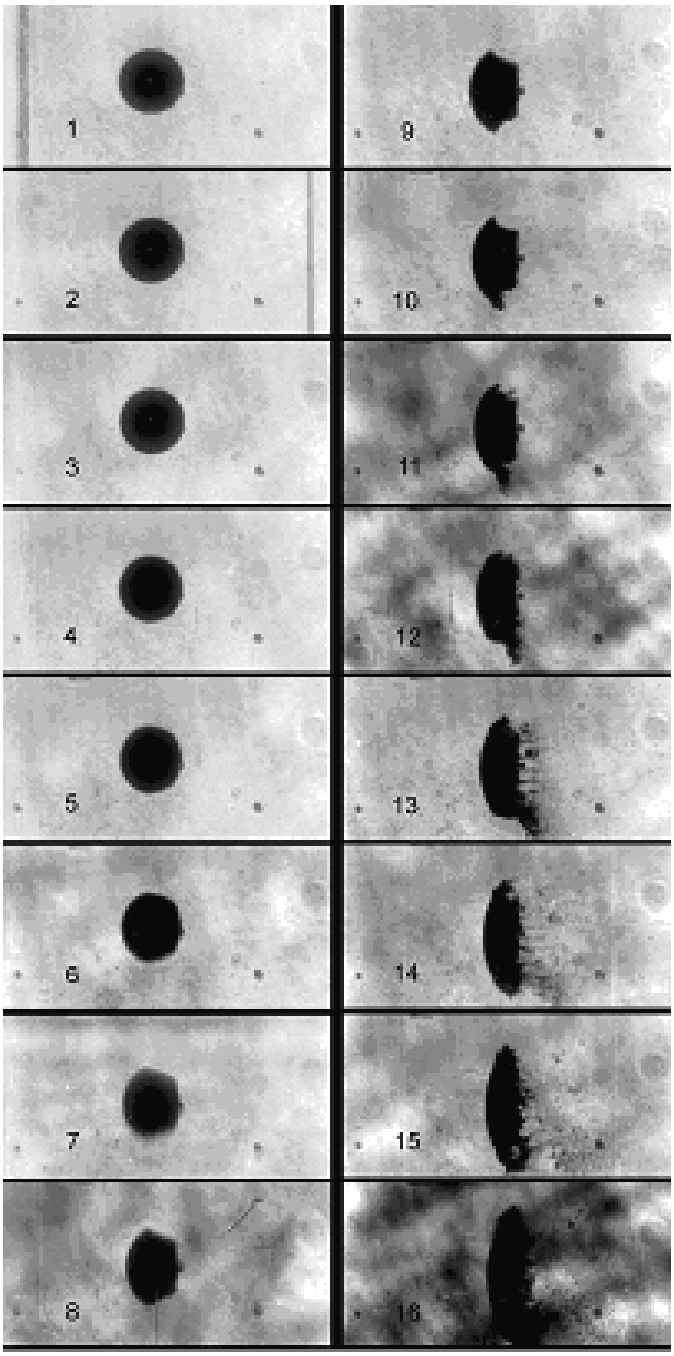

Figure 1. Water drop in the flow behind incident shock wave; M = 0.22; u = 79 м/с; d = 2.8 мм; We = 400; time intervals between the frames $\Delta t = 30 \pm 0.2$ μs

The dimensions of the frame were 18x24 mm and spatial resolution of the optic system was about 20 μm at the subject plane. Precision of time intervals was ~ 0.2 μs. The obtained photos were scanned without loss of the spatial resolution for the further treatment in the digital form.

Series of shadow pictures of the process of drop interaction with shock wave was obtained in every from 50 experiments. Total duration of the series amounts about 600 μs with the interval 30 μs between the frames.

The drops of water, alcohol, acetone, hexane and tridecane of 2 – 3 mm in diameter were tested in the flow behind shock wave with Mach number M = 0.15-0.55. Relatively low shock wave intensity was chosen to provide enough high Weber number We ≥ 300 but extend in time all characteristic effects to study in details.

The influence of deformation on the aerodynamic drag

The measurements of lateral size of the drops have shown that the rate of increase of the midship diameter usually has an unstable mode, but it is close to linear in the time interval at an early stage before mass erosion. Then we can use an empirical value t_{2d} (time of twice increase of the midship diameter) for the dependence of the midship diameter

$$d = d_0\left(1 + t/t_{2d}\right) \tag{1}$$

in the motion equation of the drop in the flow behind shock wave

$$\frac{\pi d_0^3}{6}\rho_l \frac{dV}{dt} = \frac{\pi d_0^2}{4}\left(1 + t/t_{2d}\right)^2 C_D \frac{\rho(u-V)^2}{2} \tag{2}$$

This equation with the initial condition ($t = 0$ then $V = 0$) has the exact solution

$$\frac{V}{u} = 1 - \frac{1}{1 + \frac{t}{\tau}\left[1 + \frac{t}{t_{2d}} + \frac{1}{3}\left(\frac{t}{t_{2d}}\right)^2\right]}, \tag{3}$$

where $\tau = \frac{4}{3}\frac{\rho_l}{\rho}\frac{d_0}{uC_D}$ is the constant of the velocity relaxation, ρ and ρ_l - are the gas and liquid density, d_0 – is the initial drop diameter, u – is the gas velocity, C_D – is aerodynamic drag of a sphere at the same conditions. Comparison of the solution (3) with the velocity function for the solid sphere from [9]

$$\frac{V}{u} = \frac{t/\tau}{1 + t/\tau} = 1 - \frac{1}{1 + \frac{t}{\tau}} \tag{4}$$

shows that these expressions are differ by factor in the square brackets in (3). Introducing new value τ^*

$$\tau^* = \frac{\tau}{1 + \frac{t}{t_{2d}} + \frac{1}{3}\left(\frac{t}{t_{2d}}\right)^2} = \frac{4}{3}\frac{\rho_P}{\rho}\frac{d_0}{uC_X\left[1 + \frac{t}{t_{2d}} + \frac{1}{3}\left(\frac{t}{t_{2d}}\right)^2\right]} = \frac{4}{3}\frac{\rho_P}{\rho}\frac{d_0}{uC^*} \tag{5}$$

where

$$C^*(t) = C_X\left[1 + \frac{t}{t_{2d}} + \frac{1}{3}\left(\frac{t}{t_{2d}}\right)^2\right] \tag{6}$$

we will find usual expression for drop velocity $\frac{V}{u} = 1 - \frac{1}{1 + \frac{t}{\tau^*}}$ similar to (4) with the variable aerodynamic drag (6) in the expression for τ^* (5). From the expression (6) it is evidently that at the moment $t \approx t_{2d}$ (stage of the intense mass erosion), aerodynamic drag of the drop C^* amounts to $\sim 2.3C_X$. This estimation satisfactorily agrees with the experimental measurements from the papers

[1, 2]. The comparison of the expression (3) with the experiment is shown on the Figure 2. Data on drop velocity is obtained by numerical differentiation of measurements of drop displacement depending on time.

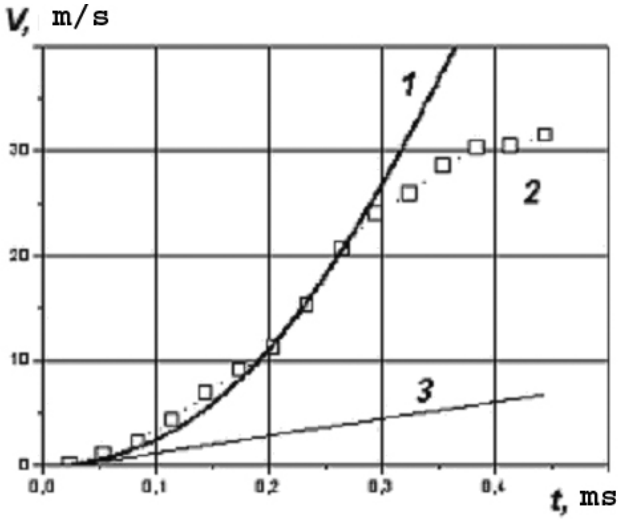

Figure 2. Velocity of the drop (alcohol) in the flow behind shock wave;
the curves: *1* – formula (3), *2* – numerical differentiation of drop displacement depending on time, *3* – velocity of solid sphere according to (4), u = 157 m/s, We = $5*10^3$.

Time delay of drop breakup

The expressions (1)-(6) are very effective for the fast engineering estimations of dynamical parameters of the drop in shock waves and in other cases of sudden acceleration in the flow. But application of them is limited by the time of mass erosion. Time delay of drop breakup was registered on the shadow pictures by appearance of the shroud of micro-droplets in the aerodynamic trail of drop. Figure 3 shows the shape of drop at the moment of mass erosion, place of mass erosion, and delay of the breakup beginning at different Weber number with an example of water.

All investigated liquids reveal the same basic tendencies of the shape evolution before the mass erosion. Distinctive peculiarity of the drop shape is the formation of two sharp curves of the generatrix, which separate tree sort of shape with different geometry. Windward side is part of sphere and is confined by first curves of the generatrix, lateral surface is the truncated cone, and the bottom of the drop is almost flat.

To all appearance the sharp curves of the generatrix are a recall of free liquid surface on the discontinuity of outside pressure distribution of the gas flow at the streamline with the gas flow separation. Outflow of liquid to the low pressure zone of flow separation is the main cause of ring-shaped waves which are observed as sharp curves of the generatrix. From the Figure 3 it is seen that both crests of these waves later will become the mass erosion points as a mostly unstable section of the liquid surface.

Those comprehensive data about the shape of drop in shock wave is found for the first time. This phenomenological picture of drop breakup rather changes the conventional conception of drop breakup by the "sheet stripping" mode. Apparently time delay of drop breakup t_{br} is not determined by delay of boundary layer formation inside the drop but for the most part - by the time of recall of liquid surface on the outside pressure discontinuity.

The experiments show that time delay of drop breakup t_{br} for all investigated liquids well described with hyperbolic expression from Mach number of the flow but more general form is the dependence from Weber number: $t_{br} \approx k \cdot We^{-0.5}$ with moderate change of coefficient k for different liquids. For the water $k = 7.8 \cdot 10^{-3}$ s, for the alcohol $k = 7.7 \cdot 10^{-3}$ s, for the hexane $k = 8{,}1 \cdot 10^{-3}$ s, for the tridecane $k = 8.5 \cdot 10^{-3}$ s, for the acetone $k = 8.8 \cdot 10^{-3}$ s.

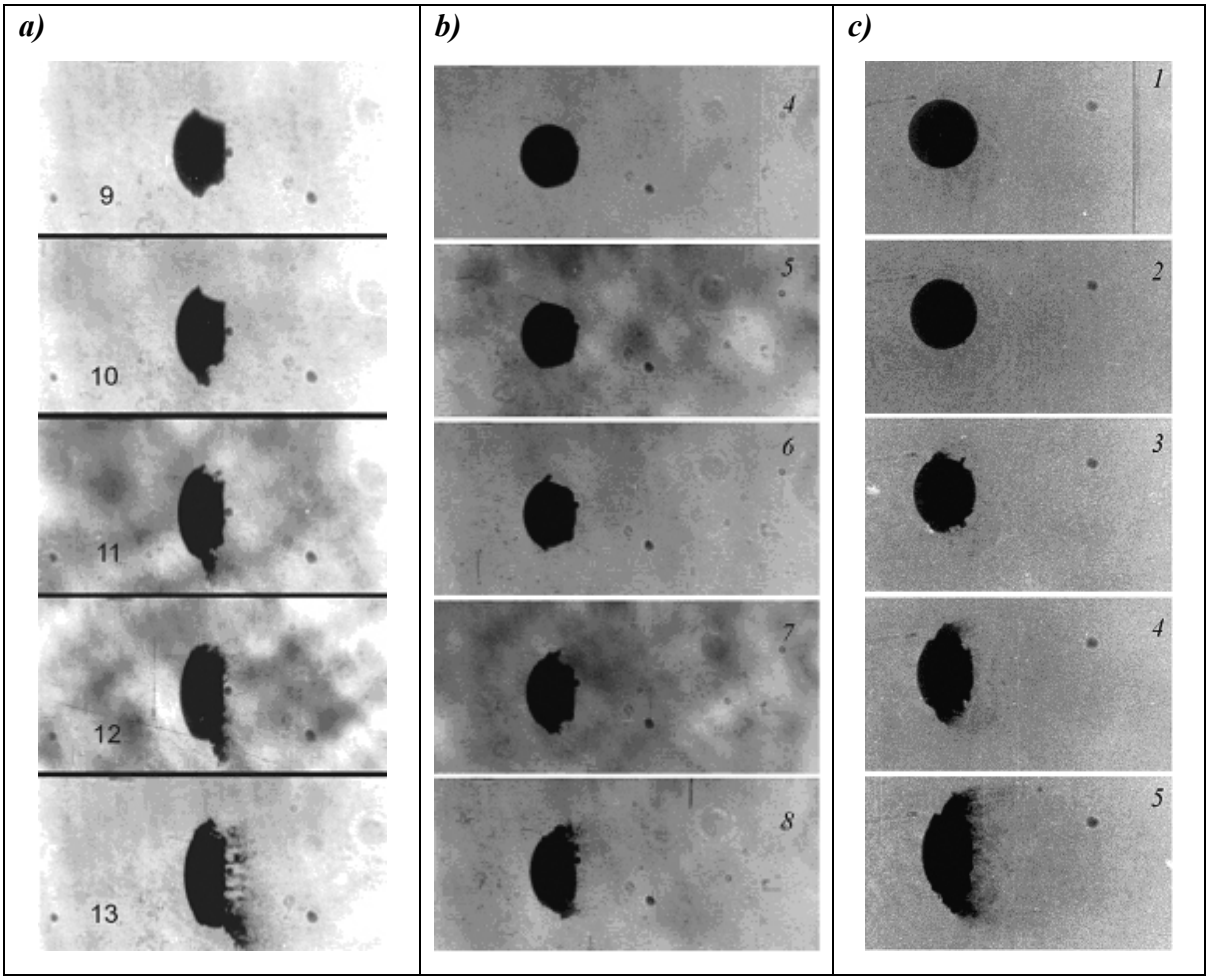

Figure 3. Fragments of shadow series of the water drop evolution by the time of breakup beginning; ***a)*** We = 400, ***b)*** We = 950, ***c)*** We = 2100,

The aerodynamic drag measurement of drop in shock wave

In the present work we follow of the conventional approach when the aerodynamic drag C_x of the drop as a liquid deformable body is calculated from approximation of "x-t" trajectory of the leading edge as for a solid sphere with initial drop diameter d [1]. The approximation can be carried out using the expression (7)

$$X = kT^2,\ X = x/d,\ T = \frac{t}{\tau_d},\ \tau_d = \frac{d}{u}\sqrt{\frac{\rho_p}{\rho}},\ k = const = \frac{3}{8}C_x \qquad (7)$$

Here d and ρ_p are size and density of drop, u and ρ are velocity and density of gas. In the paper [9] it is shown that displacement of solid sphere can be described by expression (8) It is an alternative way to approximate data on the drop displacement with the help of approximate function for solid sphere where for the drop one can use only the first term of the polynomial

$$S(t;u,\tau) \cong \frac{1}{2}\frac{u}{\tau}t^2 - \frac{1}{3}\frac{u}{\tau^2}t^3 + \frac{1}{4}\frac{u}{\tau^3}t^4 - ...; \tau = \frac{4}{3}\frac{\rho_p}{\rho}\frac{d}{C_D u} \tag{8}$$

As it clear from the Fig.1 aerodynamic drag can not be constant in time for such sharp evolution of the drop shape. The aerodynamic drag is not constant even for a free accelerated solid sphere in the flow because of fast change of the streamline mode. Since the measurement of C_x is an averaging on observation time, then one can use a set of data from whole data array.
Procedure of treatment of limited data samples (data sampling) permitted to obtain the quantitative dependence of the drop aerodynamic drag C_x as a function of the observation time of velocity relaxation process at different Weber number We (see Figure. 4). The maximums on curves correspond to the maximum deformation and the mass erosion start. The absence of maximum for large We number just means that mass erosion begins much earlier and prevents considerable increase of lateral droplet size.

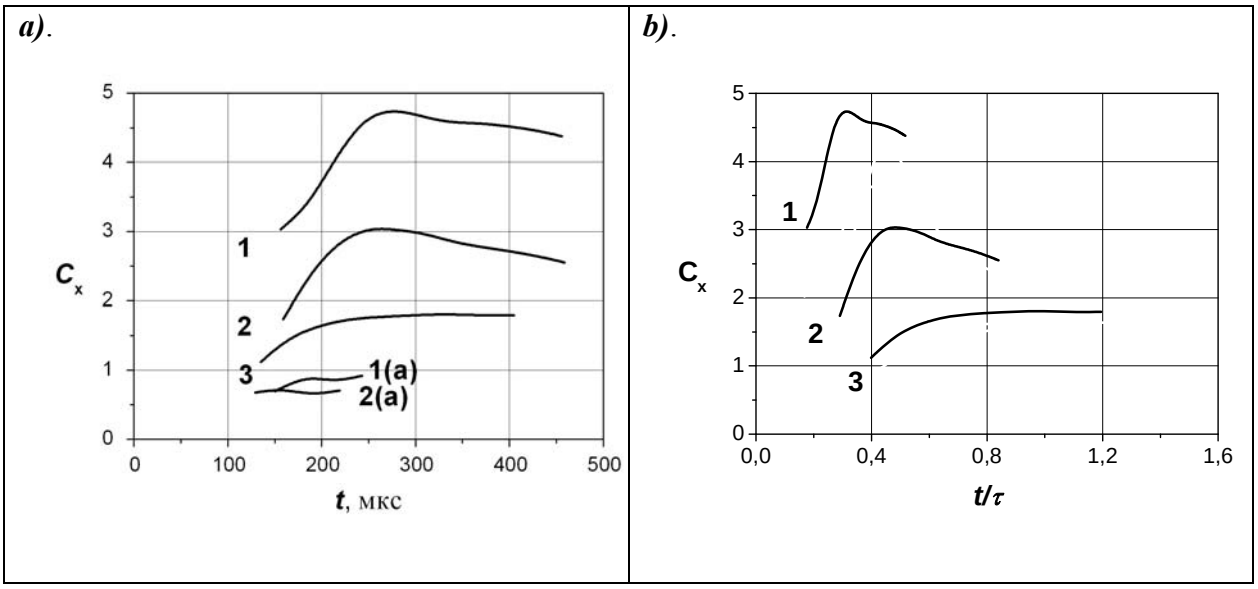

Figure 4. C_x of water drop as a function of the duration of stay in shock wave: a) – from physical time; b) – from nondimensional time; 1 – We = 400, 2 - We = 1010, 3 - We = 2250 for the leading edge; 1(a), 2(a) – for the centre of mass.

Similar dependences were found for othres 4 investigated liquids. It was sugested that nonstationarity of drag at early stage of the velocity relaxation effects on the everaging during larger duration of observation. It coud be reason of large differences of data on the drops aerodynamic drag obtained by various authors.
The measurements of drag for centre of mass were performed for the first time. It was found that the last is considerably less then for leading edge and close to solid sphere drag.

CONCLUSIONS

The drops of water, alcohol, acetone, hexane and tridecane of 2 – 3 mm in diameter were tested in the flow behind shock wave with Mach number M = 0.15-0.55. Data on the drops aerodynamic drag was obtained taking into account the deformation and mass erosion. The influence of the drop deformation and mass erosion on the aerodynamic drag C_x was studied. Clear temporal correlation of C_x with the processes of deformation and breakup was shown. The influence of shock wave intensity on the value and dynamic of C_x was found. These results enable to explain the C_x data dispersion of different authors with differences of time observation and Weber number. The value of real aerodynamic drag for the centre of mass of the drop C_x was measured. It was shown that on an early stage of the velocity relaxation C_x for the centre of mass is comparable with C_D of solid sphere.

This work was supported by the Russian Foundation for Basic Research (Grants No. 04-01-00235, № 07-01-00318).

REFERENCES

1. Gelfand, B.E., Droplet breakup phenomena in flows velocity lag, *Prog. Energy Combust. Sci.*. Vol. 22, pp 201-265, 1996.
2. Wierzba, A., Takayama, K., Experimental investigation on liquid droplet breakup in a gas stream, *Rept. Inst. High Speed Mech. (Tohoku Univ.),* Vol. 53, No. 382, pp 1-99, 1987.
3. Pilch, M., Erdman, C., Use of break-up time data and velocity history data to predict the maximum size of stable fragments for acceleration-induced break-up of a liquid drop, *Int. J. Multiphase Flow*, Vol.13, pp 741-757, 1987.
4. Dai, Z., Faeth, G.M., Temporal properties of secondary drop breakup in the multimode breakup regime, *Int. J. of Multiphase Flow*, Vol. 27, pp 217-236, 2001.
5. Joseph, D.D., Belanger, J., Beavers, G.S., Breakup of a liquid drop suddenly exposed to a high speed air stream, *Int. J. Multiphase Flow*, Vol. 25. pp 1263-1303, 1999.
6. Ranger, A.A., Nicholls, J.A., Aerodynamics shattering of liquid drops, *AIAA J.,* Vol. 7, No. 2, pp 285-290, 1969.
7. Engel, O.G., Fragmentation of wavedrops in the zone behind on air shock, *J. Rev. Nat. Bur. Stand.*, Vol. 60, No. 3, pp 245-280, 1958.
8. Boiko, V.M., Kiselyov, V.P., Kiselyov, S.P., Papyrin, A.N., Fomin, V.M., Poplavski, S.V., Shock wave interaction with a cloud of particles, *Shock Waves*, Vol. 7, No. 5, pp 117-125, 1997.
9. Boiko, V.M., Poplavski, S.V., Dynamics of irregularly shaped bodies in a flow behind a shock wave, *Comptes rendus de l'Academie des Sciences Mechanics, Paris*, Vol. 332, pp 181-187, 2004.

SIZING OF SAFETY VALVES FOR VERY VISCOUS SHEAR-THINNING LIQUIDS

D. Moncalvo[1,2,*], L. Friedel[2], B. Jörgensen[1]
[1] LESER GmbH & Co. KG, Hamburg, Germany
[2] TU Hamburg-Harburg, Hamburg, Germany

ABSTRACT. The extension of the actual sizing standards for safety valves from Newtonian liquids to shear-thinning polymers is impeded by the lack of measurements. Here, liquid and two-phase flows of aqueous solutions of polyvinylpyrrolidone are discussed on behalf of new experimental data. In liquid flows the mass flow rate is weakly affected by an increment in the polymer weight in the solution. This result suggests that the rate of viscosity increment with the polymer concentration between the seat and the disk is very slow. In support of this theory the distributions of the shear rates and of the viscosities are calculated computationally and that effect is evinced. In two-phase flows the total mass flow rate at constant relieving pressure and quality increases notably with the polymer weight in the liquid. A possible explanation considers both that air entrapment strains shear-thinning liquids to very large shear rates and that a reduction in the void fraction following a redistribution of the phases occurs, when the viscosity of the medium increases.

Keywords: *shear-thinning, non-Newtonian, viscous flow, two-phase flow, safety valve*

INTRODUCTION AND STATE OF THE ART

Safety valves are employed for the protection of reactors and pressurized units from overpressure caused by malfunction, run-away reactions, external fire, etc. If the medium is a very viscous Newtonian liquid the sizing standards ISO 4126 Part 1 [1] and API RP 520 [2] introduce a viscosity correction factor to estimate the reduction in the flow capacity of the safety valve when the viscosity of the liquid is increased. Darby [3] proposed to extend the viscosity correction factor to shear-thinning liquids assuming the power-law rheological model but he could not validate this suggestion, since there are no published measurements on the flows of non-Newtonian media.

The topic of this paper is a description of liquid and two-phase flows of shear-thinning media in safety valves and the final purpose is to find some hints for a future extension of the actual sizing standards.

* Corresponding author: M. Sc. Davide Moncalvo
Phone: + (49)-40-25165162, Fax: + (49)-40-25165562
E-mail address: moncalvo.d@leser.com

Table 1
Experimental Test Conditions

Liquids (Single and two-phase flows)	Aqueous solutions of polyvinylpyrrolidone
Gas (Two-phase flows)	Air
Relieving temperature	18 – 25 [°C]
Back pressure	1 [bar]
Liquid flows	
Relieving pressure	1 – 7 [bar]
Mass flow	0.75 – 6 [kg/s]
Two-phase flows	
Relieving pressure	6 and 7 [bar]
Total mass flow	1.0 – 3.2 [kg/s]
Quality	0.01 – 0.10 [--]
Safety valve LESER Type 441 DN 25/40	
Seat diameter	23 [mm]
Disk Lift	2.2 [mm]

EXPERIMENTAL PROGRAM AND SET-UP

Three aqueous solutions of polyvinylpyrrolidone (PVP) K90 with a polymer weight of 4 ± 0.3, 12 ± 0.4 and 16.5 ± 0.6%-weight are the test liquids. In two-phase flows this liquid phase is mixed with dried ambient air.

The experimental conditions of the liquid and the two-phase flows are written in Table 1. The relieving pressure in liquid flows is increased from 1 to 7 bar, while in two-phase flows it is maintained at the constant values of either 6 or 7 bar. The relieving temperature and the back pressure are ambient. The mass flow increases between 0.75 and 6 kg/s in liquid flows and between 1 and 3.2 kg/s in two-phase flows. The quality in two-phase flows changes from 0.01 to 0.10.

The safety valve is a LESER Type 441 DN 25/40 with a seat diameter of 23 mm and a lift of 2.2 mm, which is mounted without the spring load in agreement to the requirements in ISO 4126-1 [1] for the measurement of the flow characteristics.

Description of the test facility and of the sensors

The measurements have been carried out with the facility in Figure 1 at the *Institut für Strömungsmechanik* of the T.U. Hamburg-Harburg [4]. This facility contains a closed loop for the liquid phase and a piping for the injection of dried ambient air. The liquid is pumped from the feeding reservoir into the relief vessel, on whose top the safety valve is mounted. From the valve the medium is discharged into a collection tank, which is connected to the feeding vessel so that the liquid circulates. The collection vessel acts also like an open gravity separator of viscous two-phase mixtures. The mass flow rates of the components determine the relieving condition in the relief vessel. The liquid mass flow rate is adjusted by the user at the pump and eventually with the bypass line, which sends the capacity in excess back into the collection vessel. The mass flow rate of air is manually controlled by a ball valve in position H103 and the exceeding air feed is released to the ambience throughout the butterfly valve in position H101. In two-phase flows both mass flow rates

must be simultaneously regulated in order to record measurements at different qualities but at the same relieving pressure.

The list of the sensors, which have been inserted in this facility, is given in Table 2. This table contains the main product characteristics, the position of the sensors in the test-rig, the measurement range and the calibration errors. Calibration details can be found in Moncalvo and Friedel [4].

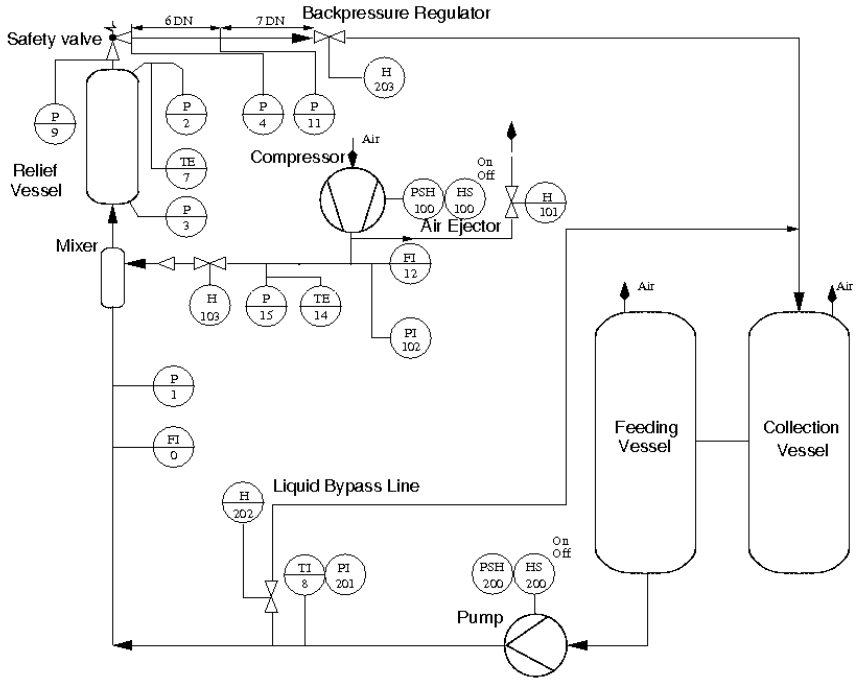

Figure 1. Test facility

Table 2
List of the Sensors installed in the Test Facility of Figure 1

Location	Type	Measuring range	Calibration accuracy
P1, P2, P3, P4 P9, P11, P15	Piezoelectric pressure sensor	1 – 16 bar	0.04 bar
T7 , T8	Temperature sensor Pt 100	15 – 37°C	0.15 °C
T14	Thermocouple NiCr-Ni		1.0°C
FI 0	Electromagnetic flowmeter	0 – 60 m³/h	0.3 m³/h
FI 12	Thermal flowmeter	0 – 2000 Nm³/h	10 Nm³/h

The measurement of the volume flow rates and of the densities determines the mass flow rate of each component, which is necessary to calculate the total mass flow rate of the mixture and the quality, respectively on the base of equation (1) and equation (2).

$$\dot{M}_{TOT} = \dot{M}_G + \dot{M}_L \quad (1)$$

$$\dot{x} = \dot{M}_G / \dot{M}_{TOT} \quad (2)$$

PHYSICAL PROPERTIES

The density, the dynamic viscosity and the surface tension of the aqueous solutions of polyvinyl-pyrrolidone at ambient temperature are listed in Table 3. Own measurements of the density agree with those of Carlfors and Rymdén [5] as well as with those of Renz [6]. The zero-shear viscosity increases remarkably with the polymer concentration from about 0.2 Pa s to 2 Pa s and all the aqueous solutions are clearly shear-thinning, see Figure 2. A shear-thinning behavior is also proven by Bell [6] for the solutions he tested, which had a polymer content above 10 %-weight. This figure shows that the curvature of the flow curves increases with the polymer weight of the liquid, which means that the difference in the viscosity of two solutions at the same temperature remarkably diminishes when the shear rate increases. An analytical expression for the flow curves is the shear-thinning model of Yasuda et al. [8] in equation (3).

$$\mu = \mu_0 + \left(\mu_0 - \mu_\infty\right)\left[1 + \left(\lambda\dot{\gamma}\right)^a\right]^{(n-1)/a} \quad \text{with} \quad 0 \le n \le 1 \tag{3}$$

Pahl et al. [9] reported a simplification of this model under the assumption that the viscosity at very high shear rates, μ_∞, comes close to zero, see equation (4).

$$\mu = \mu_0\left[1 + \lambda\dot{\gamma}\right]^{-c} \quad c = 1 - n \tag{4}$$

Table 3
Physical Properties of the Aqueous Solutions of Polyvinylpyrrolidone at Ambient Temperature

	Density (kg/m³)	Viscosity (Pa s) at shear rate (1/s)				Surface tension with Air (mN/m)
water	998.2	0.001				72.4
PVP 4 %-weight	1007.1	0.25	0.24	0.23	0.16	72.0
PVP 12 %-weight	1020.9	1.00	0.95	0.73	0.37	69.8
PVP 16 %-weight	1029.7	2.89	2.86	1.88	0.83	70.0

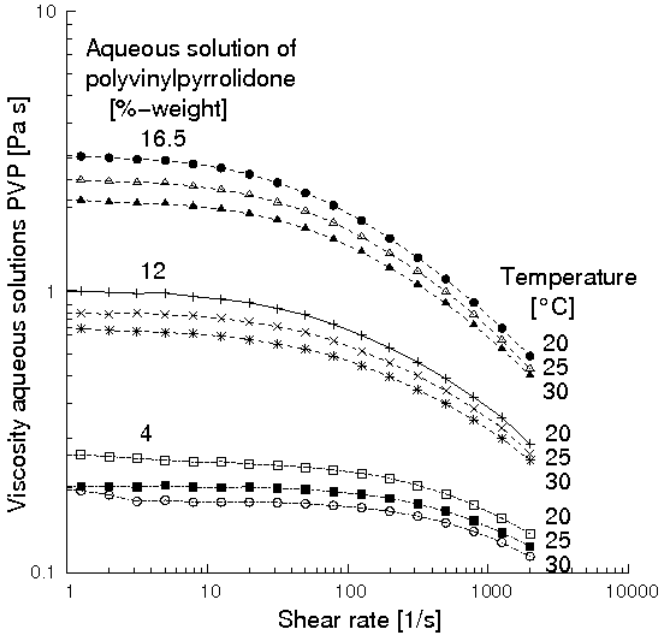

Figure 2. Rheological behavior of the aqueous solutions of polyvinylpyrrolidone

Table 4
Empirical Coefficients for the Viscosity of the Aqueous Solutions of Polyvinylpyrrolidone

	Shear-thinning media - Yasuda model -			Ubbelohde – Walter temperature dependence of μ_0		
	μ_0 (Pa s)	c (--)	λ (s)	υ_0 (mm²/s)	T_* (K)	m (--)
water	0.001	0	0	0.995	230.82	-5.026
PVP 4 %-weight	0.27	0.236	0.00843	268.1	240.69	-6.134
PVP 12 %-weight	1.03	0.386	0.01319	1008.7	252.70	-8.327
PVP 16 %-weight	3.09	0.457	0.01842	3086.6	252.50	-8.086

In equation (4) μ_0 is the zero-shear viscosity , c represents the degree of pseudoplasticity of the solution, which indicates the rate of viscosity reduction with the shear rate and λ is the Carreau time constant. On behalf of Figure 2 the shape of the flow curves is assumed to be unvaried between 20 and 30°C. Therefore, the dependence of the viscosity from temperature is given by that of the zero-shear viscosity, which follows an Ubbelohde-Walther relationship [9], like that in equation (5).

$$\log_{10}\log_{10}(\upsilon/\upsilon_0+1)=m\ \log_{10}(T/T_*) \tag{5}$$

In equation (5) υ_0 and T_* are a fictitious kinematic viscosity and temperature and m is the rate of the logarithmic reduction. The values for these parameters in Table 4 are empirical under the assumption that υ_0 is equal to the zero-shear kinematic viscosity at 20°C.

The surface tension of the aqueous solutions of polyvinylpyrrolidone in Table 3 shows little changes in function of the polymer weight of the solution.

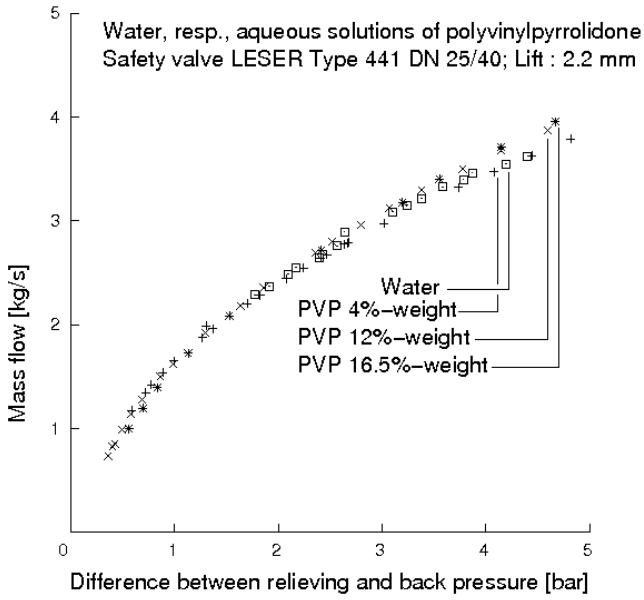

Figure 3. Mass flow rates of the aqueous solutions of polyvinylpyrrolidone for increasing differences between the relieving and the back pressure

RESULTS AND DISCUSSION

The mass flow rates of the aqueous solutions of polyvinylpyrrolidone present small deviations among each other in a wide range of relieving pressures, see Figure 3. This fact suggests that the viscous losses and therefore the viscosities in the region between the seat and the disk, where most of the pressure drop in the safety valve occurs, must increase very weakly with the polymer weight in the aqueous solutions. On behalf of the experienced increase in the pseudoplasticity of the solutions with the polymer weight it seems reasonable that the shear rates in that region must be very large in all aqueous solutions and they must increase with the polymer weight. This explanation sounds a priori plausible, considering that large velocity gradients due to the acceleration of the liquid must be present between the seat and the disk.

In order to support this theory, at least qualitatively, the flow of the aqueous solutions is calculated in the whole range of relieving pressures using the CFD software ANSYS CFX. A grid is generated in the flow volume of the valve, of the relief vessel and of the outlet pipe on the base of the criteria recommended by Moncalvo et al. [10]. The flows are assumed steady-state and adiabatic at the metal walls. Since it is not possible to establish a priori if the flow in the valve is laminar or turbulent for a given reliving scenario, two series of calculations are done, once assuming laminar flows and then using the SST turbulence model. The criterion for the choice between the flow regimes is the minimization of the error in the calculation of the mass flow rate; which ranges for all aqueous solutions between 1 and 8 %. The impact of the different sources of errors on the calculations is currently under study.

The computational distribution of the shear rates and that of the viscosities in the region between the seat and the disk are displayed in Figure 4 for the solution with 16 % polymer weight at a relieving pressure of 2.1 bar (SST). According to this figure the shear rates between the seat and the disk, which are well above one thousand, are the largest in the safety valve and therefore viscosities as low as one tenth of the zero-shear value are evinced for that aqueous solution. No substantially qualitative divergence is found in the distributions, which are calculated using the laminar and the turbulent flow assumption.

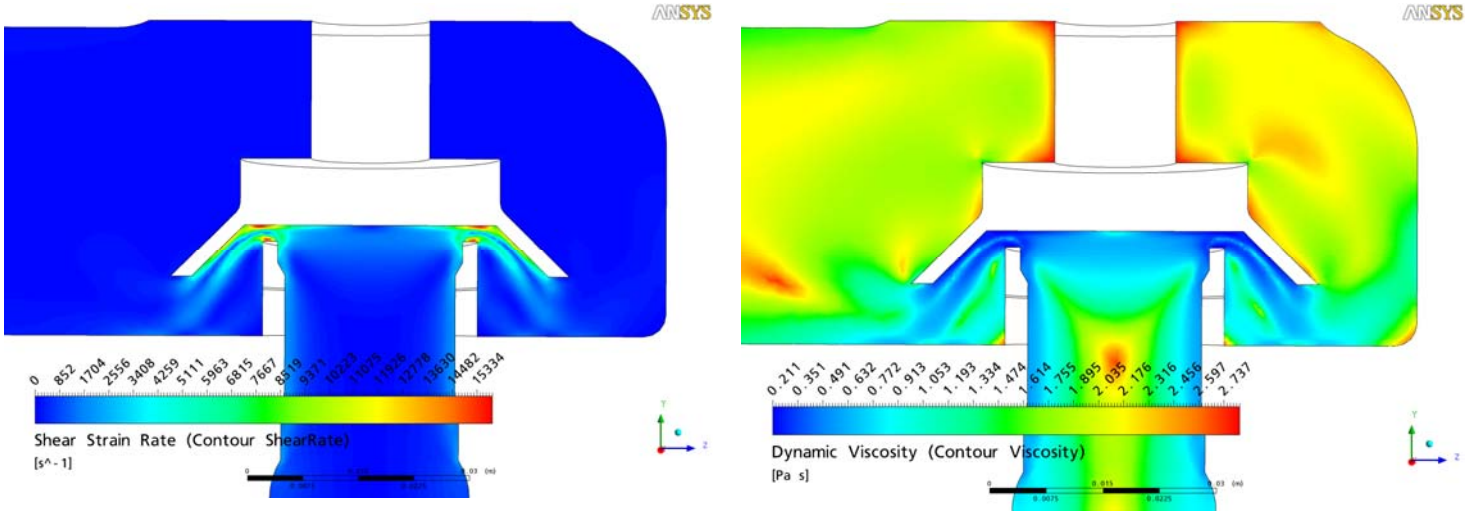

Figure 4. Shear rate and viscosity of the aqueous solution PVP 16 %-weight at the relieving condition of 2.1 bar and 22°C calculated by the software ANSYS CFX with the SST turbulence model

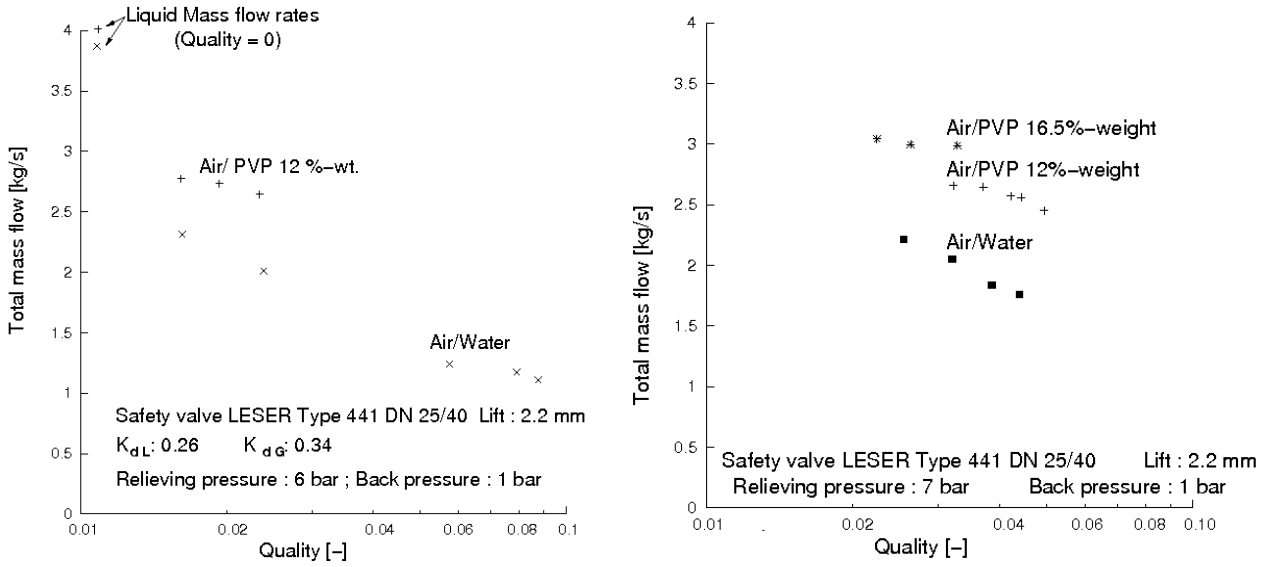

Figure 5. Total mass flow rate of the aqueous solutions of polyvinylpyrrolidone and air in function of quality at the relieving pressure of 6 (left) and 7 bar (right)

For the two-phase flows of air and aqueous solutions of polyvinylpyrrolidone Figure 5 shows that an increment of the polymer weight in the liquid causes an increase in the total mass flow rate of the mixture at constant relieving pressures in the whole range of qualities. A similar behavior was evinced in co-current pipe flows [11, 12]. Shu [13] explained it suggesting that the entrapment of air in the liquid causes large velocity gradients and therefore strains it to very high shear rates.

However, the effect of high shear strains on the reduction of the viscous losses would lead to a far marginal - if any - increment of the total mass flow rate when the polymer weight of the solution is increased. This implies that some additional phenomenon must be considered in order to explain the results. The analogy with co-current pipe flows suggests that the phases redistribute in new structures when the viscosity of the liquid in the safety valve is increased in consequence of the larger liquid drag on the gas. In order to win this resistance, the gas needs to have a higher pressure than the surrounding liquid and therefore it compresses itself, leading to a reduction in the void fraction in the mixture, see Mukherjee [14]. If the total mass flow rate and the quality are unchanged, a reduction of the void fraction leads to a loss in the momentum of the mixture, which determines the pressure in the relief vessel. Since the measurements are here taken at constant relieving pressure at any quality, the total mass flow rate must increase with the polymer weight.

CONCLUSIONS

No reduction in the flow capacity of the safety valves is observed in both liquid and two-phase flows of aqueous solutions of polyvinylpyrrolidone when the polymer content is increased up to 16 %-weight. The authors showed that the pseudoplasticity of these solutions has a paramount role in the reduction of the viscous losses in the region between the seat and the disk of the safety valve. This effect must be accounted for in a possible extension of the viscosity correction factor to this type of media. In fact, the conclusions evinced with polyvinylpyrrolidone are in principle expectable also with other shear-thinning polymers in other types of safety valves for non-cavitating flows.

NOMENCLATURE

$\dot{x}$	Quality	[-]
$\dot{\gamma}$	Shear rate	[1/s]
λ	Carreau time constant	[s]
μ_0	Zero-shear viscosity	[Pa s]
μ_∞	Infinite-shear viscosity	[Pa s]

ACKNOWLEDGEMENTS

The authors wish to thank the Laboratory of Rheology at Baiersdorf AG, Hamburg and in particular Mr. R. Brummer and Mr. M. Griebenow for letting them use the torsional viscometer. Special recognition deserves the Laboratory of Ceramics at T.U. Hamburg-Harburg, namely Mrs. B. Brinkmann for the friendly support and guidance with the rotational viscometer. The authors are also very grateful to BASF SE, Ludwigshafen for the delivery of polyvinylpyrrolidone.

REFERENCES

1. ISO 4126-1 Safety devices for protection against excessive pressure – Part 1: Safety valves, 2004.
2. API RP 520 Sizing, selection and installation of pressure-relieving devices in refineries. Part-I-Sizing and selection, 2000.
3. Darby, R. Size safety relief valves for any condition, *Chem. Eng.*, Vol. 16, No. 2, pp 42-50, 2005.
4. Moncalvo, D. and Friedel, L. Influence of the liquid phase physical properties on the void fraction at the inlet of a full-lift safety valve, *Chem. Eng. Technol.*, Vol. 32, No. 2, pp 273-282, 2009
5. Carlfors, J. and Rymdén, R. Partial specific volume and refractive index increment of polyvinylpyrrolidone in aqueous solutions: temperature, concentration and wavelength dependence, *Eur. Polym. J.*, Vol. 18, No. 11, pp 933-937, 1982.
6. Renz, R. Das diskontinuierliche Vermischen von Flüssigkeiten in zylindrischen Behältern, *PhD Thesis*, Universität Hannover, 1992.
7. Bell, K.I. Top venting of low and high viscosity fluids during vessel depressurisation, *PhD Thesis*, University of London, 1994.
8. Yasuda, K. and Armstrong, R.C. and Cohen, R.E., Shear flow properties of concentrated solutions of linear and star branched polystyrenes, *Rheol. Acta*, Vol. 20, pp 168-178, 1981.
9. Pahl, M. and Geißle, W. and Laun H.-M., *Praktische Rheologie der Kunststoffe und Elastomere*, VDI Verlag, Düsseldorf, 1991.
10. Moncalvo, D. and Friedel, L. and Jörgensen, B. and Höhne, T. Sizing of safety valves using ANSYS CFX-Flo, *Chem. Eng. Technol.*, Vol. 32, No. 2, pp 247-251, 2009
11. Farooqi, S.I. and Richardson, J.R., Horizontal flow of air and liquid (Newtonian and non-Newtonian) in a smooth pipe, *Trans. Inst. Chem. Eng.*, Vol. 60, pp 292-305, 1982.
12. Mahalingham, R. and Valle, R.A., Momentum transfer in two-phase flow of gas-pseudoplastic liquid mixtures, *Ind. Eng. Chem. Fundam.*, Vol. 11, No. 4, pp 470-477, 1972.
13. Shu, M.T., Horizontal two-phase flow. Gas and non-Newtonian liquids, *PhD Thesis*, Drexel University, 1981.
14. Mukherjee, H., An experimental study of inclined two-phase flow, *PhD Thesis*, University of Tulsa, 1979.

CHARACTERISTICS OF VORTEX STRUCTURE INDUCED BY A SOLITARY WAVE PROPAGATING OVER A RECTANGULAR CAVITY

C. Lin[1,*], T. C. Ho[2], C. S. Chang[3]
[1]Professor, National Chung Hsing University, Taichung, Taiwan, R.O.C.
[2]Ph.D. Candidate, National Chung Hsing University, Taichung, Taiwan, R.O.C.
[3]Master, National Chung Hsing University, Taichung, Taiwan, R.O.C.

ABSTRACT. The vortex shedding induced by a solitary wave propagating over a rectangular cavity is studied experimentally, using particle image velocimetry (PIV) and a flow visualization technique. The aspect ratio of rectangular cavity (i.e., ratio of the length to the depth of a cavity, A_r) ranges from 0.33 to infinity in this paper. The ratio of wave height to water depth in the experiment is kept at 0.2. Detailed vortical structures for $A_r = 0.33 \sim \infty$ were observed using particle trajectory photography and measured by PIV. Quantitative characteristics of the primary vortex generated in the cavity, such as trajectories of the jet flow and circulation of the vortex, are investigated in detail.

Keywords: *wave-cavity interaction, solitary waves, aspect ratio, vortices, flow visualization*

INTRODUCTION

The propagation of water waves over a submerged obstacle has received much attention for decades. In physical applications, it relates not only to coastal and ocean engineering problems, but also to the sustainable development for near-shore environment. A submerged obstacle can be regarded as a submerged dike used to prevent coast erosion caused by surging waves. To have a better understanding of the complex flow field generated by wave-obstacle interaction, many researchers used rectangular shape to simplify the geometry of submerged dike.

On the other hand, there is a natural disaster 'tsunami' which has tremendous energy, and may cause huge damage in the near shore region. On December 26, 2004, an earthquake with an intensity of 8.9 on the Richter scale taking place near the Island of Sumatra generated a tsunami which severely impacted the shores of the Indian Ocean, particularly from Indonesia to Sri Lanka. The tsunami washed away long reaches of the coast. In the disaster, the base of American Navy located in the Indian Ocean, Diego Garcia, was not damaged by the tsunami. The reason might be attributed to the coral reef near the base, and the existence of the trench 'Chagos' which is 5,400 km deep, 740 m long outside of the coral reef. Coral reef and Chagos trench may act as an obstruction which decreases the energy of the tsunami. Hence, the topic concerning a tsunami propagating over a trench needs to be further investigated.

Few studies concern about a solitary wave propagating over a cavity. Tang and Chang [1] studied the wave deformation numerically under such a condition. The influences of water depth, cavity number, and aspect ratio of the cavity were discussed. Nakoulima et al. [2] discussed the problem of a solitary wave propagating over periodic cavities. They found that wave dispersion was more obvious with the increase of the cavity length, and the wave amplitude varied suddenly in the location where bottom elevation changed substantially. The cavity also decreased the amplitude of

* Corresponding author: Prof. C. Lin
Phone: + (886)-4-22855182, Fax: + (886)-4-22862857
E-mail address: clin@mail.ce.nchu.edu.tw

incident solitary wave, but the topography of the bottom in the downstream side of the cavity determined the final wave height of a solitary wave.

The main concerns of most existing investigations have been focused on the establishment of numerical model and the spatial variation of the wave profile. Therefore, the flow phenomenon while a solitary wave propagating over a cavity has not been investigated experimentally. The objective of this study is to elucidate the characteristics of flow structure induced by a solitary water wave propagating over the rectangular cavity. Flow visualization techniques and particle image velocimetry (PIV) were both used in the study.

EXPERIMENTATION

Experiments are conducted in a glass-walled wave flume located at Hydraulic Laboratory, National Chung Hsing University. A wave maker, equipped with a piston-type wave paddle which is driven by a variable-speed motor, is installed at one end of the wave flume. The wave maker was designed originally for producing monochromatic waves with periods ranging from 0.4 to 2.0 sec and with wave heights (H) up to 3.5 cm. An electromagnetic clutch particularly installed inside the wave maker allows rapid starting and stopping of the piston-type wave paddle. Two capacitance-type wave gauges are used to detect the water surface elevations in the experiments.

A submerged rectangular cavity made of acrylic material is set upon the bottom of the wave flume and has the same spanwise width as the wave flume. The depth of the cavity, D, is 3.0 cm, while the length L varies from 1.0 cm to infinity (see Fig. 1). The aspect ratio of rectangular cavity (i.e., ratio of the length to the depth of a cavity, A_r) ranges from 0.33 to infinity in the present study. The still water depth, h, used in the experiments is 7.0 cm and the wave height of incident solitary wave is kept at about 1.2 cm.

Particle tracing photography is employed to observe the vortex structure generated by a solitary wave propagating over a rectangular cavity. A Phantom camera is used to obtain images at a rate up to 1000 frame/sec. A high-resolution particle image velocimetry (PIV) system is also used to measure the velocity field of the flow structure on the plane of symmetry. The light source for the PIV system is the Continuum Surelite Nd: YAG dual lasers, which contained a crystal harmonic generator to produce the frequency-doubled (532 nm) green light from the original (1064 nm) invisible infrared light. In the experiments, successive frame-pairs were captured in the rate of 10 fps and then analyzed using the TSI Insight 3.0 Software.

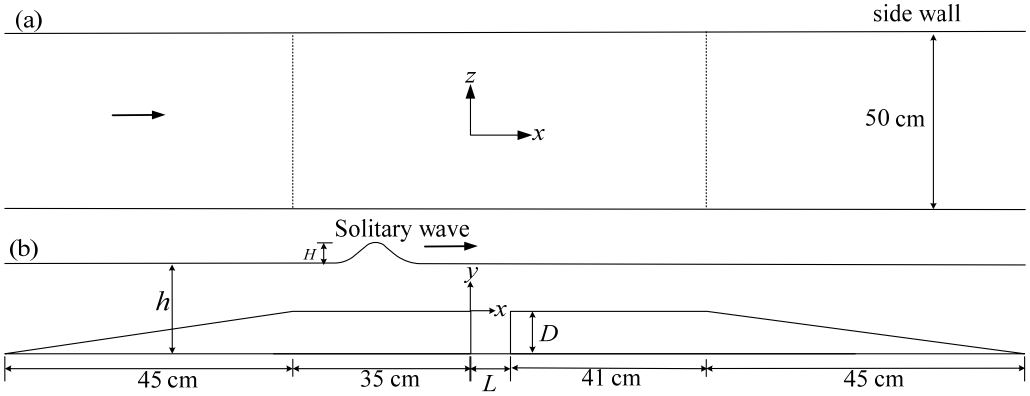

Fig. 1 Diagram of the experimental set up: (a) top view, (b) side view

RESULTS AND CONCLUSIONS

Since the generation of a solitary wave in the present study followed the traditional method, the generated waves may contain certain discrepancies as compared with the theoretical wave form of

$$\eta(x,t) = H \sec h^2 \left[\sqrt{\frac{3H}{4h^3}} (x - ct) \right] \tag{1}$$

where η denotes the free surface elevation, x and t the streamwise direction and time, H the wave height, h the water depth, and c the wave celerity that can be calculated as $c = \sqrt{g(h+H)}$.

Validation for the generated waves was performed by comparing not only the free surface displacement but also the velocity profile along the entire depth as well as the wave celerity. The free surface comparison for the target solitary wave (H = 1.4 cm, h = 7.0 cm) is shown in Fig. 2 Very good agreement is obtained from the comparison. A series of repeatability tests for generating a solitary wave in the flume was also performed. It was found that the generated solitary waves are highly repeatable.

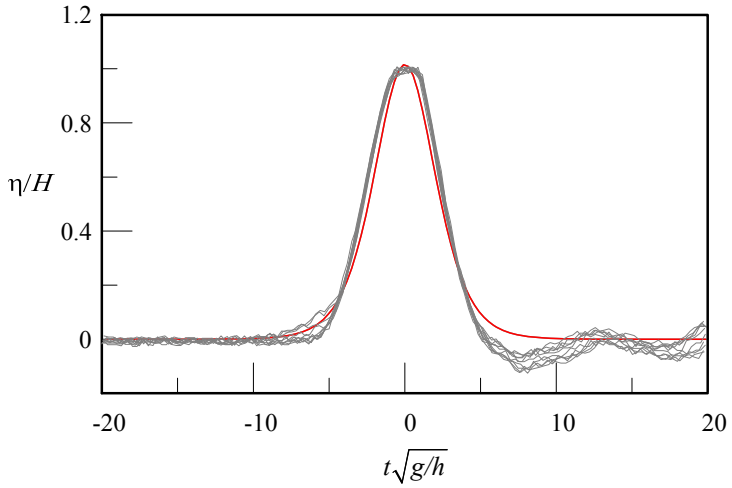

Fig. 2 Free surface elevation of the solitary wave versus non-dimensional time (gray line: experimental data, bold line: theory)

Flow visualization

First, the length of the cavity was first set at infinity. In this case, the condition in the frontal edge of the cavity is similar to the lee side of the rectangular dike (Lin et al. [3]). The flow pattern of this original situation is used to compare with those of cases for A_r = 0.33 ~ 1.0. From the comparisons of qualitative flow visualization pictures and quantitative property of the primary vortex, the influence of A_r can be easily observed.

The images taken using particle trajectory photography are shown in Fig. 3. Note that the frontal edge of the cavity is located at x = 0, and the free surface elevation at each instance can be found in Fig. 2. It shows the beginning of vortex generation process when the wave crest is very close to and just reaches the frontal edge of the cavity. One clockwise vortex is generated at the frontal edge of the cavity due to flow separation. This primary vortex is defined as vortex A_v. The primary vortex grows larger due to formation of the shear layer (Lin et al. [3]) and moves downstream because of the inertia force caused by incident solitary wave. As the wave crest passes, the size of the primary vortex A_v grows in the beginning as shown in Fig. 3(a).

After the passage of the wave crest, the downward velocity of the solitary wave decreases on the lee side of frontal edge of the cavity, thus causing the increase of the upward inertia and in turn forcing the primary vortex to move up rapidly, as demonstrated in Figs. 4(c) and 4(d). In addition, the near-wall upward velocity gradient causes the flow to separate, and in turn creates a counterclockwise vortex near the top of frontal edge (see Fig. 4(c)).

Fig. 5 shows the vortex shedding processes for A_r = 0.75. The vortex starts to shed out when the wave crest just passes the cavity in Fig. 5(a). At the instance, the vortex D_v was generated at the top of the end wall of the cavity. It is relatively small but the number of vortex D_v increases with time. The primary vortex A_v grew larger and rotated continuously, and size of the vortex also increased. The vortex A_v moves toward to the end wall and impinges it (see Fig. 5(a)). At this instance, the vortex D_v separated to two pairs of vorticies. Then a strong adverse velocity is observed to push the group of vortex D_v upstream In Fig. 5(b), The primary vortex A_v touch the end wall of the cavity,

and the vortex E_v and F_v induced by the viscous boundary layer between primary vortex A_v and end wall are discovered. Then primary vortex A_v deformed to an elliptic shape due to the impingement of adverse velocity. In the instance, the minor secondary vortex D_v` induced by the adverse velocity was also formed. Due to the influence of the adverse velocity profile, the direction of the vertical jet skewed to the downstream side. In Fig. 5, the direction of the vertical jet is different from that in the case of $A_r = \infty$, in which vertical jet almost towards to the water surface.

The images for $A_r = 0.33$ and 0.5 are shown in Figs. 6 and 7. Fig. 6(a) shows that the vortex starts to shed out when the wave crest is just close to the cavity. This clockwise vortex is generated at the edge due to flow separation. At the instance, vortex D_v is generated at the top of end wall of the cavity. The size of vortex D_v is relatively tiny. It is smaller than that of the case for $A_r = 1.0$. It may be due to the small separation region caused by small A_r.

The primary vortex A_v grows larger and rotates continuously, but the size of the vortex is confined by the length of the cavity as shown in Fig. 6(b). The vortex A_v touches the end wall and the vortex E_v and F_v are produced (see Fig. 6(c)). They are also secondary vortices caused by the boundary layer between the primary vortex A_v and the end wall. The same result is also observed in the Fig. 7. The size of vortex A_v is smaller than that in the case of $A_r = 0.5$.

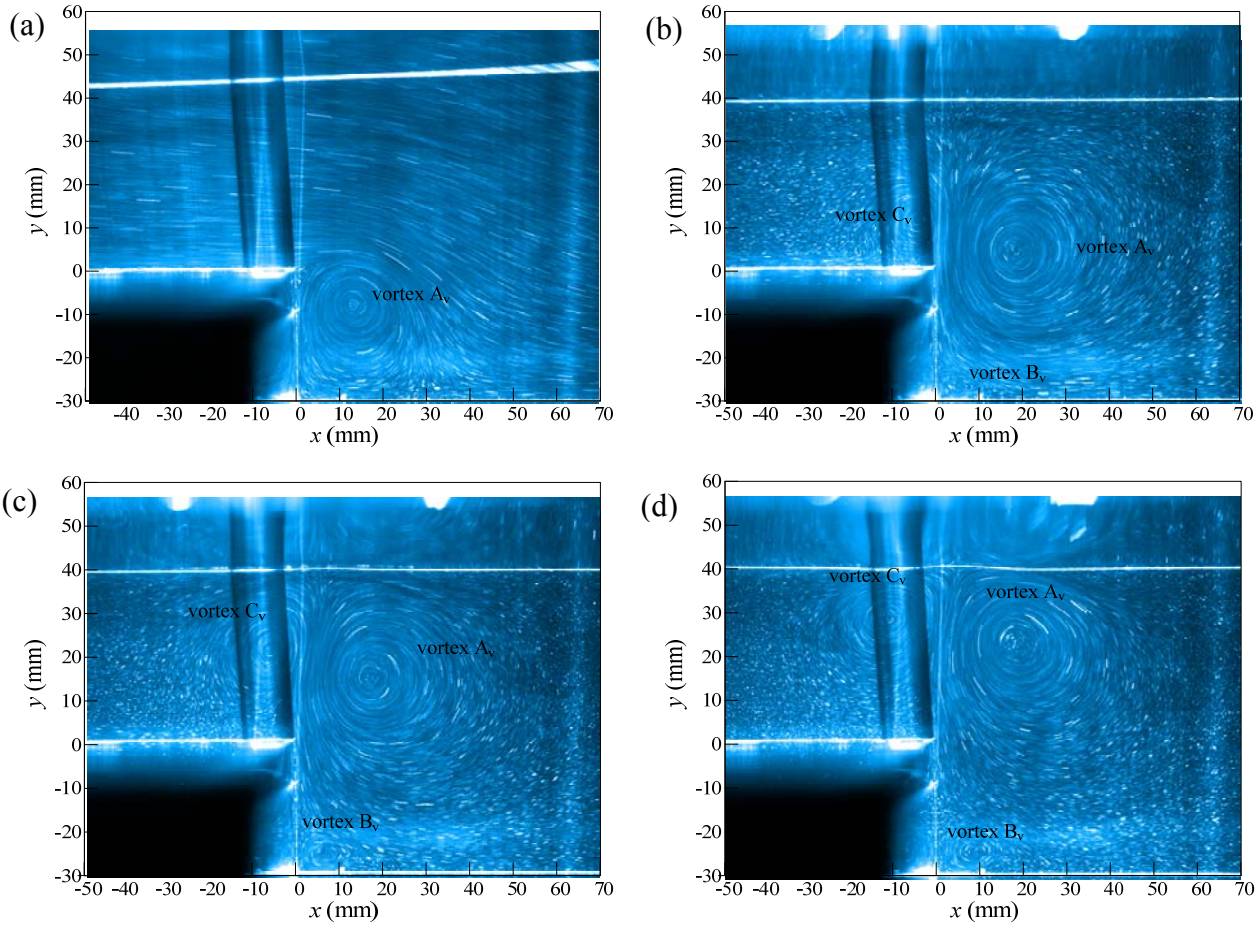

Fig. 3 Flow visualization taken at $t\sqrt{g/h}$ = (a) 0; (b) 10; (c) 14 and (d) 18 for H/h = 0.2 and $A_r = \infty$)

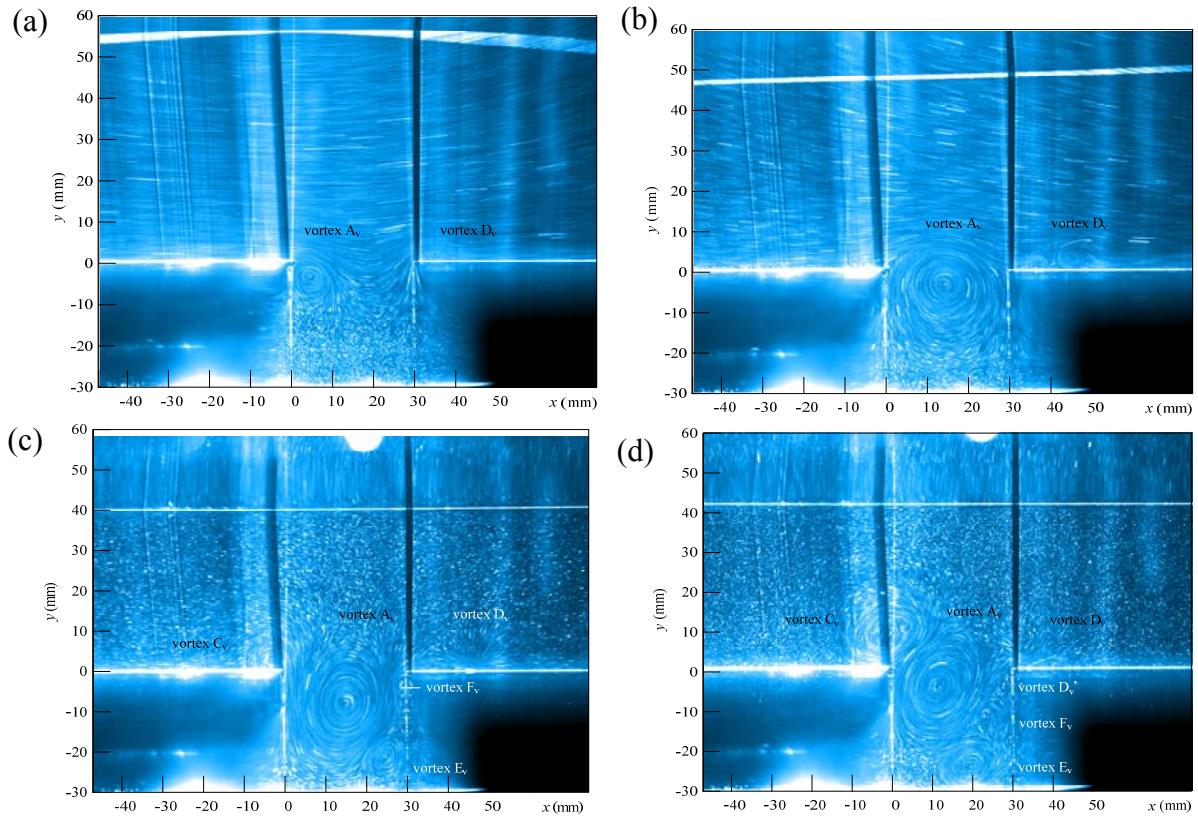

Fig. 4 Images taken using particle trajectory photography at $t\sqrt{g/h}$ = (a) 0, (b) 2, (c) 8, and (d) 12 for A_r = 1.0

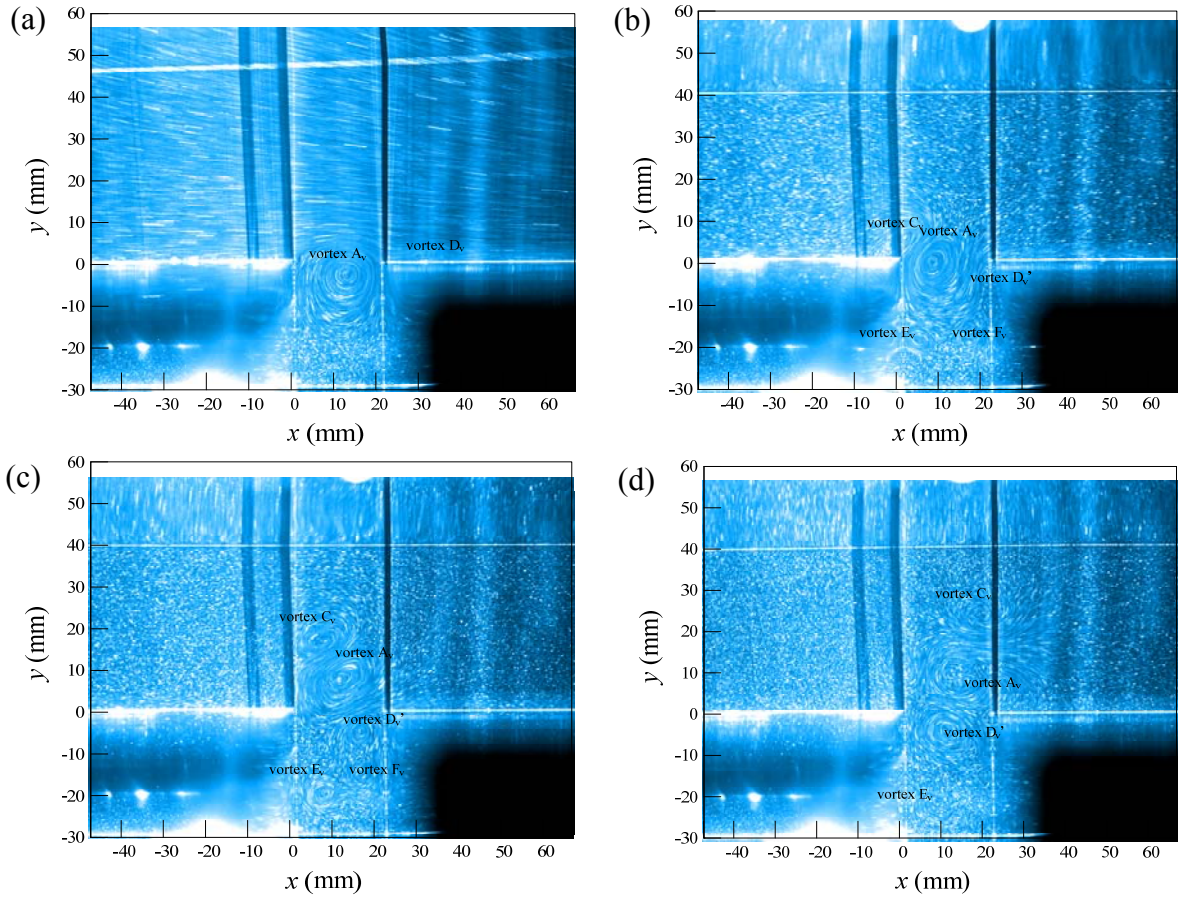

Fig. 5 Flow visualization taken at $t\sqrt{g/h}$ = (a) 0; (b) 10; (c) 14 and (d) 18 for H/h = 0.2 and A_r = 0.75)

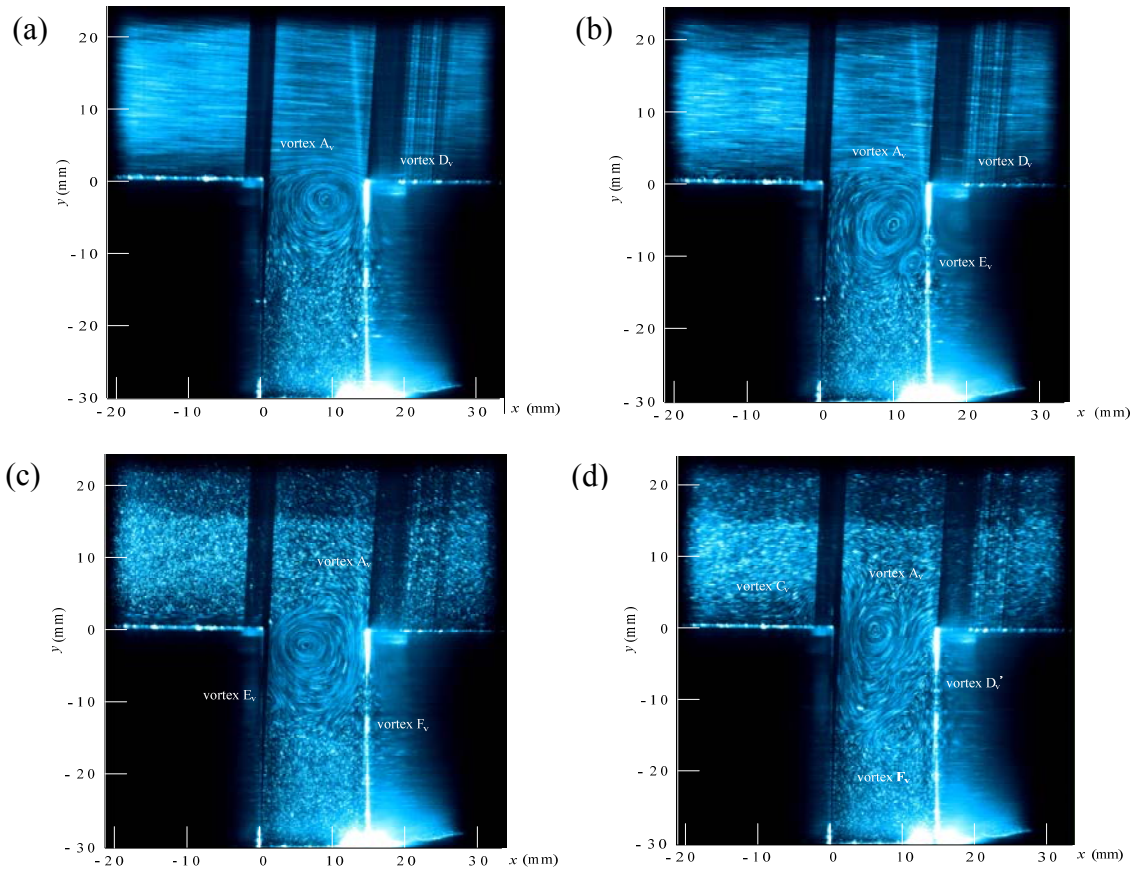

Fig. 6 Images taken using particle trajectory photography at $t\sqrt{g/h}$ = (a) 0, (b) 2, (c) 8, and (d) 12 for $A_r = 0.5$

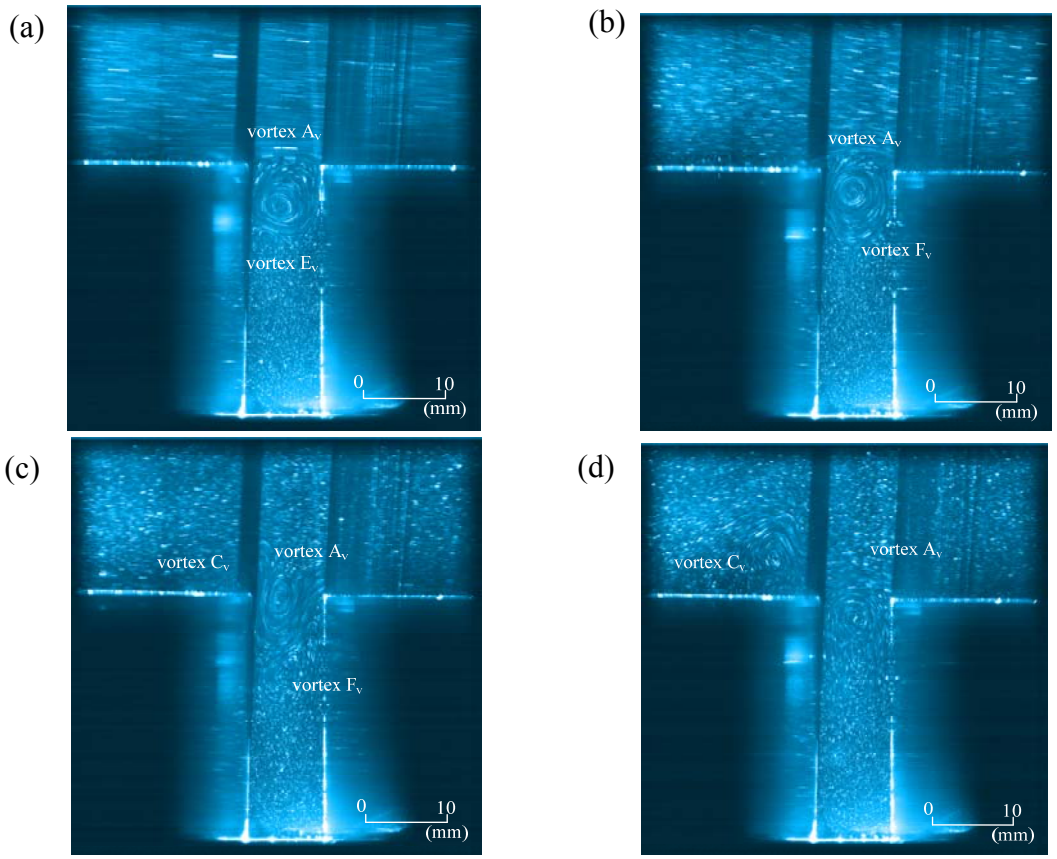

Fig. 7 Images taken using particle trajectory photography at $t\sqrt{g/h}$ = (a) 0, (b) 4, (c) 8, and (d) 12 for $A_r = 0.33$

Characteristics of vortex A_v and jet like flow in the cavity

Fig. 8 demonstrates the trajectory of vertical jet at different A_r. The trajectories were obtained by drawing the path of jet like flow from flow visualization picture. The trajectories are nearly the same for A_r = 2.0 ~ ∞. But the characteristic of jet like flow is quite different at A_r = 0.75 and 1.0. This is because that the primary vortex was pushed by the adverse velocity. The other reason is the scale of the jet is relatively small for A_r < 1.0 due to the size of the primary vortex was confined by length of the cavity.

The circulation of the primary vortex (Γ) can thus be determined using the Stokes theorem shown below to integrate the vorticity of the primary vortex A_v within the region while vorticity (ω) is less than - 2.

$$\Gamma = \oint_c \vec{V} d\vec{s} = \iint_A \omega dA \tag{2}$$

where $\vec{V}$ is the velocity vector ($\vec{V} = u\vec{i} + v\vec{j}$).

As illustrated in Fig. 9, the circulation increases at $t\sqrt{g/h}$ ranging from -4 to 2, and it keeps almost in the same value at $t\sqrt{g/h}$ ranging from 2 to 16. Finally, it decreases because of vortex dissipation at $t\sqrt{g/h}$ ranging from 16 to 40 for aspect ratio varying from 1.0 to ∞. But the circulation does not keep constant for aspect ratio ranging from 0.33 to 0.75 at $t\sqrt{g/h}$ varying from 2 to 16. It decreases obviously while $t\sqrt{g/h}$ varies from 0 to 20. The circulation also decreases with decrease of the aspect ratio at the same non-dimensional time. The circulation of primary vortex highly decreases at low aspect ratio for A_r varying from 0.33 to 0.75 due to the viscous effect of boundary layer induced by the end wall of the cavity. Many vortices such as vortex E_v and F_v are induced by the flow separation, and in turn a part of the kinetic energy of the primary vortex A_v is broken down by these two vortices. The critical aspect ratio of flow pattern can be determined as A_r = 1.0. All the characteristics change obviously while A_r is less than 1.0.

CONCLUSION

The flow pattern of vortex generation process induced by a solitary wave propagating over a cavity has been investigated experimentally. The wave height of the solitary wave is 1.4 cm and water depth is equal to 7 cm. The depth of the cavity is 3 cm for A_r = 0.33 ~ ∞. Particle trajectories photography was used to observe the vortex generation process qualitatively while PIV was used to measure the velocity distribution in the cavity quantitatively.

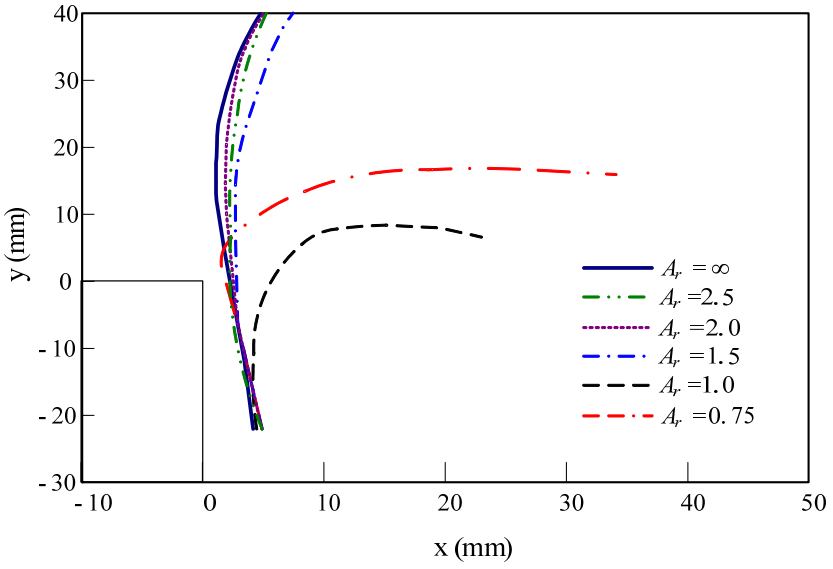

Fig. 8 Trajectory of vertical jet at different A_r

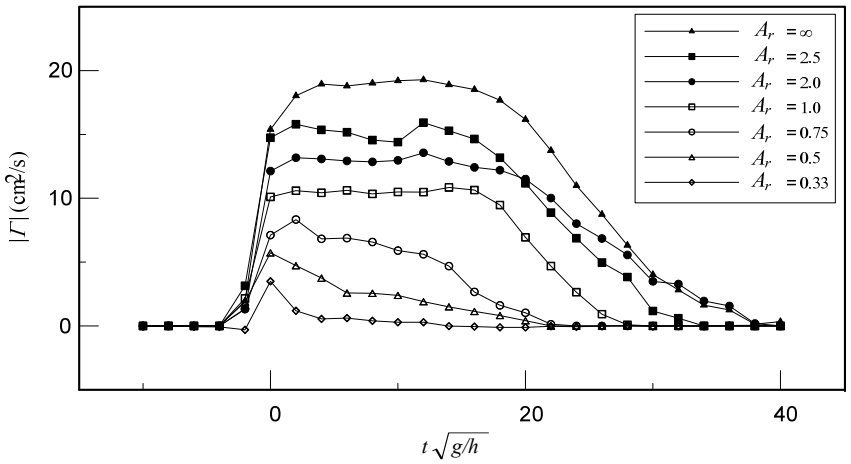

Fig. 9 Variation of the circulation of the primary vortex calculating by a low limit of vorticity equal to -2 (1/s) for different aspect ratios of a cavity

In the case $A_r = \infty$, the result is similar to the flow pattern in the lee side of the rectangular dike while a solitary wave propagates over it. The corresponding figures show a jet-like upward velocity in between the vortex pair that impinged the water surface directly. Due to the influence of the adverse velocity in the case $A_r = 0.75$, the direction of the vertical jet induced by the primary vortex A_v skewed to the downstream side.

In addition, quantitative results are listed as follows: The vorticity increases rapidly at $t\sqrt{g/h}$ ranging from -6 to 2, and then decreases gradually after the solitary wave crest passing at $t\sqrt{g/h}$ ranging from 2 to 40. This indicates that primary vortex A_v obtains the energy from incident solitary wave, and it decays while the solitary wave moves far away.

REFERENCES

1. Chang, C. H. and Tang, C. J., Simulation of tsunami passing over a trench, *Symposium on Applications of Computer Science for Civil and Hydraulic Engineering*, 2005, pp 136-140.
2. Nakoulima, O., Zahibo, N., Pelinovsky, E., Talipova, T., Kurkin, A., Solitary wave dynamics in shallow water over periodic topography, *Chaos*, Vol. 15, pp 0371071-0371078, 2005.
3. Lin, C., Ho, T. C., Chang, S. C., Hsieh, S. C., and Chang, K. A., Vortex shedding induced by a solitary wave propagating over a submerged vertical plate, *International Journal of Heat and Fluid Flow*, Vol. 26, pp 894-904, 2005.

A STUDY ON THE HELICAL ANNULAR FLOW WITH ROTATING INNER CYLINDER

Y.J. Kim[1, *], D.K. Lee[1], S.M. Han[2], N.S. Woo[3] and Y.K. Hwang[2]
[1] Korea Institute of Geoscience and Mineral Resources, Daejeon, S. Korea
[2] School of Mechanical Engineering, Sungkyunkwan University, Suwon, S. Korea
[3]Korea Institute of Construction and Technology, Goyang, S. Korea

ABSTRACT. An experimental and numerical investigation was done in order to study the appearance of hydrodynamic instabilities at low bulk axial Reynolds number in the gap between two coaxial cylinders with a diameter ratio of 0.52, 0.8 and 0.9, whose outer cylinders are stationary and inner one is rotating. Skin friction coefficient and wall shear stress have been measured for fully developed laminar flows of water when the inner cylinder rotates at the speed of 0~600 rpm. They point to the existence of a flow instability mechanism. The rotation of the inner cylinder promotes the onset of transition due to the excitation of Taylor vortices.

Keywords: *Wall shear stress, Skin friction coefficient, Vortex flow, Slimhole annulus*

INTRODCUTION

Wall shear stress is of great importance in fluid mechanics research, as it represents the local tangential force by the fluid on a surface in contact with it. By integrating the wall shear stress along the surface, one can compute its contribution to the lift and drag on immersed objects and the pressure drop in pipes and other internal flows.

Rotating flows in annular passages are important, since they have many engineering applications in bearings, rotating-tube heat exchangers and, especially, annulus flows of mud in case of slim hole drilling of oil well.

Shear stresses close to the wall of the borehole can erode it, and cause to cave. This phenomenon can be very dangerous in case of the rotating rods are not supported anymore by the wall and can break. It strongly depends on the velocity gradients. A laminar flow regime induces lower velocity gradients than a turbulent flow and thus lower shear stresses[1].

Vibration and shock data along with torque and weight on bit can be used to modify drilling parameters for increased bit and bottom hole assembly reliability and performance. Successful drilling requires that the drilling fluid pressure stay within a tight mud-weight window defined by the pressure limits for wellbore stability. The lower pressure limit is either the pore pressure in the formation or the limit for avoiding wellbore collapse. The upper pressure limit for the drilling fluid is the minimum that will fracture the formation.

Diprima[2] applied the non-linear theory to investigate the relation between the Taylor number, *Ta*

* Corresponding author: PhD. Y.J. Kim
Phone: + (82)-42-868-3090, Fax: + (82)-42-868-3418
E-mail address: kyjp7272@kigam.re.kr

and the stability in a rotating annulus with a bulk flow. Obi *et al*.[3] measured local wall shear stress using the wall velocity gradient in turbulent channel flows. They evaluated the wall shear stress with the fluid viscosity and velocity gradient as Newton's viscosity law.

Dumont *et al*.[4] investigated wall shear stress experimentally in the Taylor-Couette flow at a low Reynolds number. That is, they studied the appearance of hydrodynamic instabilities at a low *Re* in the gap between two coaxial cylinders. Escudier *et al*.[5] carried out numerical and experimental study of fully developed laminar flow of a Newtonian liquid through an eccentric annulus. The results are reported for calculations of the flow field, wall shear stress and friction factor for a range of values of eccentricity and Taylor number.

This paper concerns an experimental and computational study of fully developed laminar flows of a Newtonian fluid through a concentric and eccentric annulus with combined bulk axial flow and inner cylinder rotation. The results are reported for calculations of the flow field, wall shear stress distribution and friction factor for a range of values of eccentricity, radius ratio and Taylor number.

DATA REDUCTION

The skin friction coefficient C_f can be obtained as Eq. (1),

$$C_f = \frac{dp}{dz} \cdot \frac{D_h}{2\rho \bar{v}_z^2} \tag{1}$$

where, the pressure loss dp/dz was measured in experiment, D_h (=2($R_2 - R_1$)) is the hydraulic diameter and ρ is the fluid density. For laminar boundary layers of Newtonian fluids, the wall shear stress τ_w can be determined from the velocity derivative normal to the wall as Eq. (2),

$$\tau_w = \mu \cdot \frac{\partial v_z}{\partial y} \tag{2}$$

where, μ is the fluid viscosity.

EXPERIMENTAL AND MUMERICAL METHODS

Experimental apparatus

The experimental equipment consists of a cylinder part, supporting part, fluid-providing and rotating part and measuring part which measure the flow rate, pressure loss and the temperature. The flow configuration and instrumentation are described detailed by Kim and Hwang[6]. To ensure fully developed flow in the measuring section, the length of straight pipe upstream of the test section is 2.32m, corresponding to 126 hydraulic diameters, in order to produce an artificially thickened boundary layer.

The flow rate has been measured with a magnetic flow meter whose accuracy is within the limit of ± 0.5 %. The temperature of the working fluid has been measured by a digital multi-meter. The inner cylinder may be rotated at any speed up to a maximum of 1000rpm by means of an A.C. motor. The temperature of the fluid within the pipe rig is maintained at 25±0.5°C. The maximum uncertainties are less than ±6 for the flow of water.

Numerical simulation

In a numerical study, a laminar flow of water in an eccentric annulus has been calculated. A control volume based finite volume method is used to solve the equations of motion. The problem reduced to the solution of the conservation of mass and momentum equations along with the appropriate boundary and initial conditions.

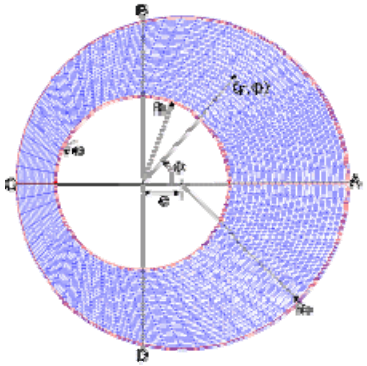

Figure 1**.** Configuration of grid used for numerical calculations.

A typical mesh of the discretised borehole domain in the horizontal plain is shown in Fig. 2. The inner cylinder radius is R_1 =10 mm, the outer cylinder R_2 =19.2 mm (diameter ratio of 0.52) and the eccentricity, e is varied from 0.2 to 0.7.

Since the fully developed flow condition was of concern here, only one row of cell was needed in the axial direction. That is, stream wise fully developed periodic condition is used. The distortions of the axial velocity distribution and the movements of the peak axial velocity are calculated to understand the effect of rotation, eccentricity and flow rate on flow field.

The constant velocity of fluid and the Neumann boundary conditions are imposed on inlet and outlet of an annulus, respectively. No slip boundary conditions are used at the inner and outer cylinders

RESULTS AND DISCUSSION

Experimental results

The influence of the inner cylinder rotation for fluids is apparent from the skin friction coefficient versus the Reynolds number. The skin friction coefficient is obtained from pressure loss measurements by using Eq. 2. The skin friction coefficient decreases linearly as the Reynolds number is increased in laminar flow regime. The fact that the skin friction coefficient drops off with increasing the Reynolds number should not mislead us into thinking that shear stress decreases with velocity.

In the case of water as shown in Fig.3, the skin friction coefficient in non-rotating decreases linearly as the Reynolds number is increased and it increases as the radius ratios and the rotational speed of the inner cylinder are increased. The correlation between the skin friction coefficient and the Reynolds number is $C_f = 23.8/Re$ in the radius ratio of 0.52 as shown in Fig. 3(a) and the numerator approaches to 24 as the radius ratio reaches to one.

The effect of axial flow on the skin friction coefficient becomes more prevalent with increasing radius ratios. So the effect of rotation on the skin friction coefficient becomes weak as the radius ratios increase. There is no reliable skin friction coefficient in the transitional flow regime. For turbulent flow of fluid, the skin friction coefficient decreases gradually with the Reynolds number.

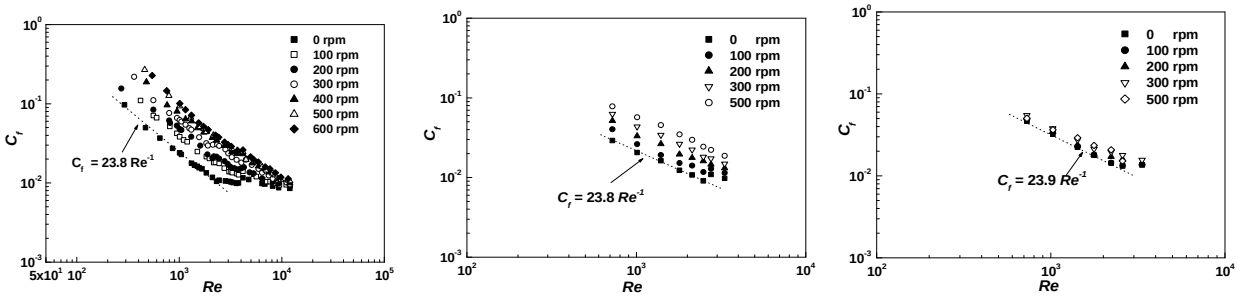

(a) η = 0.52 (b) η = 0.8 (c) η = 0.9

Figure 2**.** Skin friction coefficient of water as a function of *Re* at 0~600 rpm.

When the rotational speed of the inner cylinder is increased from 0 rpm to 500 rpm, the increasing rate of the pressure loss is 50%, 45%, and 30% for the radius ratios of 0.52, 0.8, and 0.9, respectively. Also for the same flow rate and rotational speed, the pressure losses are increased up to 80% and 95% when the radius ratios are increased from 0.52 to 0.8 and 0.9, respectively. That is, pressure loss increased significantly with decreasing annular gap.

Numerical results

To obtain a more realistic representation of the drilling operation, the helical flow of water in an eccentric annulus was considered. Numerical calculations have been extended for the case where the inner cylinder rotates about its own axis at a constant rotational speed. Detailed calculations have been carried out for radius ratio of 0.52 covering eccentricities up to 0.7 and Taylor numbers up to 50,000.

Contour of axial velocity for the radius ratio, η = 0.52 and *Ta* = 5,000~25,000 covering eccentricities of 0.2, 0.5 and 0.7 are shown in Fig. 3. The corresponding distributions of the axial and tangential component of the shear stress are shown in Figs. 4~5.

For a fixed rotation speed at low eccentricity (e=0.2) in Fig. 3 (a), the tangential flow around the annulus is slightly reduced by the blockage effect associated with the eccentricity. So the axial velocity peak is moved in the sense of rotation into a narrow gap. As the eccentricity is increased (e=0.5, 0.7), recirculation of the cross flow develops adjacent to the surface of the outer cylinder and the axial velocity peak is roughly centered in the wide gap as shown in Fig. 3 (b). An unexpected feature of the calculations for eccentricity of 0.7, but not seen for e=0.2 and 0.5 is the appearance of a second peak in the axial velocity, located in the narrowing gap, for combinations of very high eccentricities and Taylor number (Fig. 3 (c)).

The distortion of the axial velocity distribution and the movement of the peak axial velocity, due to the combined effects of eccentricity and rotation result in the distributions of the axial component of the surface shear stress shown in Figs. 4~5 for η=0.52 and *Re*=1050. In order to reveal the relative contributions to the skin friction coefficient, the shear stress on the surface of the outer cylinder τ has been weighted by R_2. As shown in Fig. 4 (a), axial component of the shear stress initially has a maximum in the narrowing gap and a minimum in the widening gap. With increasing eccentricity the value of axial shear stress increases apparently as the rotational speed of the inner cylinder increases. However, in the case of ε=0.7 the location of the maximum shear stress is moved according to the change of the maximum axial velocity as shown in Fig. 4(c).

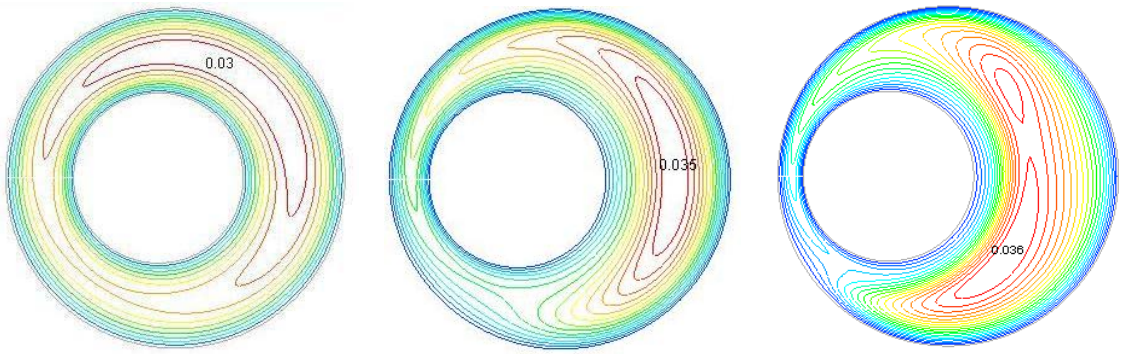

(a) ε =0.2 (b) ε =0.5 (c) ε =0.7

Figure 3**.** Contours of axial velocity of water for *Re*=1050 and *Ta*=25,000.

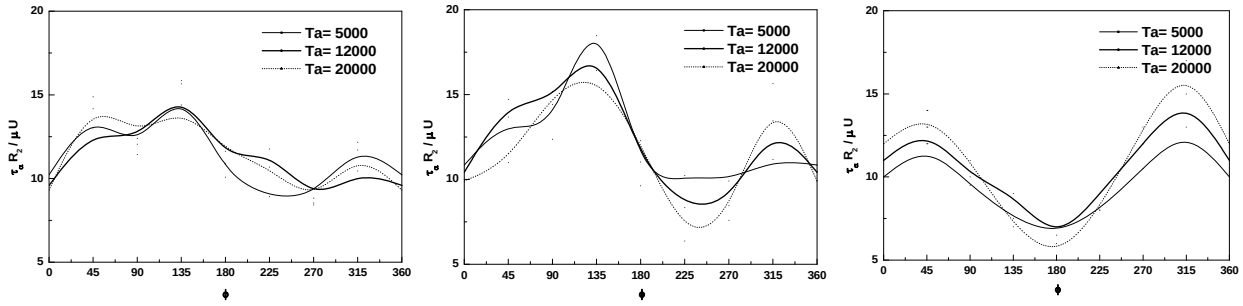

(a) ε=0.2 (b) ε=0.5 (c) ε=0.7

Figure 4**.** Azimuthal distribution of the axial surface shear stress of water for *Re*=1050.

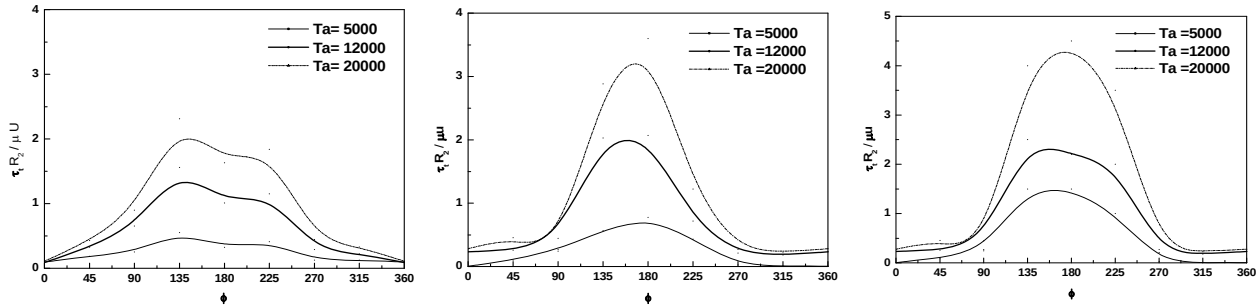

(a) ε=0.2 (b) ε=0.5 (c) ε=0.7

Figure 5**.** Azimuthal distribution of the tangential surface shear stress of water for *Re*=1050.

CONCLUSIONS

In this study the effect of the rotational speeds, radius ratio and eccentricity on the skin friction coefficients and wall shear stress in concentric and eccentric annuli has been investigated experimentally and numerically.

The skin friction coefficient in non-rotating decreases linearly as the Reynolds number is increased and it increases as the radius ratios and the rotational speed of the inner cylinder are increased. The effect of axial flow on the skin friction coefficient becomes more prevalent with increasing radius ratios. So the effect of rotation on the skin friction coefficient becomes weak as the radius ratios increase.

A numerical analysis considered mainly the effect of annular eccentricity and inner cylinder rotation. The present analysis has demonstrated the importance of the drill pipe rotation and eccentricity. In eccentricity of 0.7, the flow field is recirculation dominated and unexpected

behavior is observed. For high Taylor number the axial velocity peak is so strongly advected towards the lower side of the inner cylinder that two opposing effects act to create two local peaks of the axial velocity.

ACKNOWLEDGMENTS

This work was supported by the Development of Coiled Tubing Drilling System Project (Energy Technology Innovation) of the Korea Institute of Geoscience & Mineral Resources (KIGAM) funded by Korea Energy Management Corporation. This support is gratefully acknowledged.

REFERENCES

1. Delwiche, R.A., Slimhole Drillihng Hydraulics, *Society of Petroleum Engineering Inc., SPE 24596,* pp. 521-541, 1992.
2. Diprima, R.C., The Stability of a Viscous Fluid between Rotating Cylinder with a Bulk Flow., *J. Fluid Mech.,* Vol.366, pp.621-631,1960.
3. Obi,S., Inoue, K., Furukawa, T. and Masuda, S., Experimental Study on the Statistics of Wall Shear Stress in Turbulent Channel Flows, *Int. J. Heat and Fluid Flow*, Vol. 17, pp. 187-192, 1996.
4. Dumont, E., Fayoll, F., Sobolik, V. and Legrand, J., Wall Shear Rate in the Taylor-Couette, *Proceedings of ICHMT Seminar*, Cesme, July 4-8, 1994, pp 1-14.
5. Escudier, M.P., Gouldson, I. and Legrand, J., Effects of Inner Cylinder Rotation on Laminar Flow of a Newtonian Fluid Through an Eccentric Annulus, *I. J. Heat and Fluid Flow*, Vol. 21, pp. 92-103, 2002.
6. Kim, Y. J. and Hwang, Y.K., Experimental Study on the Vortex Flow in a Concentric Annulus with a Rotating Inner Cylinder, *KSME International Journal,* Vol. 17, No. 4, pp.562-570, 2003.

HYDRODYNAMIC CHARACTERISTICS OF WEIS-FOGH TYPE SHIP'S PROPULSION MECHANISM HAVING ELASTIC WING

K. D. Ro[1, *], J. T. Park[1] and J. H. Kim[1]
[1]Gyeongsang National University, Tongyeong, Republic of Korea

ABSTRACT. This experiment was conducted in attempt of improving hydrodynamic efficiency of the propulsion mechanism by installing a spring to the wing so that the opening angle of the wing in one stroke can be changed automatically, compared to the existing method of fixed maximum opening angle in Weis-Fogh type ship propulsion mechanism. Average thrust coefficient was almost fixed with all velocity ratio with the prototype, but with the spring type, thrust coefficient increased sharply as velocity ratio increased. Average propulsive efficiency was larger with bigger opening angle in the prototype, but in the spring type, the one with smaller spring coefficient had larger value. In the range over 1.0 in velocity ratio where big thrust can be generated, spring type had more than twice of propulsive efficiency increase compared to the prototype.

Keywords: *Hydraulic Machine, Propulsion Mechanism, Fluid Force, Elastic Wing*

INTRODUCTION

The Weis-Fogh mechanism[1,2], which was discovered by the hovering flight of a small bee(Encarsia Formosa), is gathering attention of many scientists studying hydrodynamics for the unique and efficient lift generation mechanism[3~7]. Recently, engineering application of the mechanism is actively attempted as well[8~12]. Some scientists proposed a propulsion model that applied the principle of the mechanism, and conducted experiments on dynamic characteristics and driving test of a model ship, which showed that this propulsion mechanism worked very effectively as a new ship propulsion system[9]. Also, Some scientists visualized the unsteady flow field that was created around the wings when the propulsion mechanism was being operated[13], and verified the time variation of the thrust and the drag on the wing[14]. The weakest point of this mechanism is that while the efficiency of propulsion is high, the range of the velocity ratio that generates maximum propulsive efficiency is narrow, and the velocity ratio is under 1, which means the thrust is relatively small. To put to practical use of this propulsion mechanism, supplementing this weak point is most important. To generate high thrust in the high velocity ratio range, changing the wing of propulsion mechanism from a hard, flat-plate to elastic body would make it possible. In fact, the wings of a small bee and the body of a fish are elastic, and there is enough possibility that elastic body contributes to the improvement in thrust. Therefore, in this study, we will attempt to improve the thrust, drag, and efficiency characteristics of the propulsion mechanism by using an elastic wing with attached spring which automatically adjusts the opening angle in one stroke.

* Corresponding author: Prof. K. D. Ro
Phone: + (82)-55-640-3123, Fax: + (82)-55-640-3128
E-mail address: rokid@gaechuk.gsnu.ac.kr

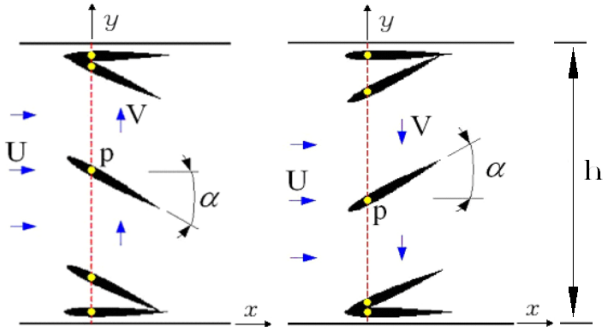

(a) Up stroke (b) Down stroke

Figure 1. A model of propulsion mechanism

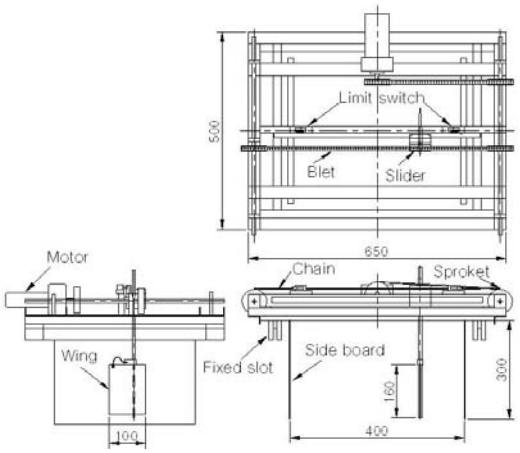

Figure 2. Driving unit of the wing (unit:mm)

EXOERIMENTAL METHOD

Model of a propulsion mechanism

First, the model of the propulsion mechanism that will be used in this experiment is shown in Figure 1.

The figure shows the model from upper perpendicular side; as one flat-plate wing works in a certain motion in the water channel, thrust is generated toward the left of the figure, which is the direction of the ship. As point P, which corresponds to the center shaft of the wing, oscillates perpendicular to uniform flow U and in the velocity of V, the wing first opens from the lower surface, then maintaining an opening angle of α, it moves translationally in parallel, and finally rotates and closes on the upper surface. Then, the wing repeats the motion by opening at the upper surface in rotation, moves in translation, and finally rotates and closes on the lower surface. Originally in the Weis-Fogh mechanism, one pair of wings open at a certain angle, and while maintaining the angle, each wing moves to the opposite direction of each other. But when seen from the body, the movement of the each wing can be considered as reciprocals. Therefore, by installing channel walls at the symmetrical line and executing the motion with a single wing as in Figure 1, by the mirror effect, the identical effects can be achieved as the Weis-Fogh mechanism.

Measurement of the thrust and drag acting on the wing

The experiment is conducted by making a wing driving system that gives the same wing movement as the propulsion mechanism in Figure 1, which is installed in the circulating water channel where uniform flow runs, and measuring thrust and drag on the wing. The schematic diagram of driving unit of the wing is shown in Figure 2. The main structure of the system is made with acrylic board and aluminum angle bar, and the dimensions are 500mm in length and 650mm in width to fit into the circulating water channel. In the wing driving system, the shaft is fixed onto the slider and the slider is attached to one side of the belt so that when the motor(DC 30W) spins forth or backwards, the wing moves in an oscillating motion. The front and back spin of the motor is operated by a limit switch and a relay circuit installed at the ends of the slider rail, and the velocity of the wing movement is controlled with adjusting the spin speed of the motor. The wing used in this experiment was made in the shape of NACA0010; as shown in Figure 3, the size of the wing is chord C=100mm, and its span 160mm. The shaft was penetrated at the point of 0.75C away from trailing edge of the wing through a hole of 3mm in diameter.

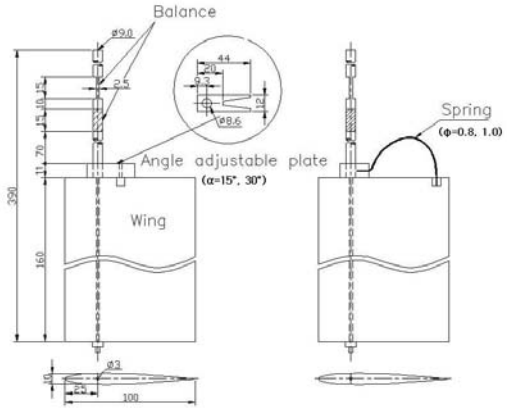

(a) Prototype wing (b) Spring type wing

Figure 3. Structure of the wing and shaft (unit:mm)

Table 1
The Spring coefficients of each elastic wing

The diameter of spring (ø)	ø =0.8mm	ø =1.0mm
Spring coefficient (N·m/rad)	0.0884	0.1185

The shaft was made with a titanium bar, 9mm in diameter. The wing is inserted in the shaft of the wing so that when the slider moves in a reciprocating motion, a momentum around the shaft works toward the wing to open it, and in the closing stage, the leading edge of the wing collides with the side board, forcing it to close. In this experiment, two types of wings were used as shown in Figure 3 (a) and (b). Maximum opening angle α is fixed in (a), and α=15°, 30° angle adjustment plate was made. (b) was made so that opening angle α was automatically adjusted by the water resistance applied on the wing when it moved; in other words, two kinds of steel line, diameter of ø =0.8, 1.0, were bent to function as springs as shown in Figure 3 (b). The ultimate point of this experiment is to improve propulsive efficiency by adjusting opening angle with the water resistance, instead of prototype's fixed opening angle in Weis-Fogh type propulsion mechanism. The measurement of the spring coefficient of each spring is shown in Table 1.

Thrust and drag was measured by cutting the balance, or top of the shaft, evenly in front, back, right and left, as shown in Figure 3, and by attaching 4 strain gauges, thrust and drag was measured by deformation of these gauges. In other words, the voltage waveforms from the strain gauge comes out as the value of thrust and drag by pre-compensated coefficient on a personal computer, through a bridge circuit, strain amplifier and A/D converter in each channel(2 channels in total).

The experiment fixed maximum opening angle α at 15° and 30°, changed uniform flow U(U=0.049~ 0.349m/s) and wing movement velocity V(V=0.055~ 0.246m/s) at regular intervals to prototype wing and spring type which automatically adjusts opening angle, measured the time variation of thrust and drag, and yielded average thrust coefficient, average drag coefficient, and average propulsive efficiency by averaging the values in one cycle. The range of Reynolds number is Re=7.2×10^3~3.9×10^4 when wing chord was fixed as unit length and yielded by uniform flow U.

Definition of the characteristic coefficients

Each coefficient that shows the hydrodynamic characteristic of this propulsion mechanism, that is, thrust coefficient C_T and drag coefficient C_D is defined as follows, by wing movement velocity V.

$$C_T = \frac{T}{\frac{1}{2}\rho V^2 S} \tag{1}$$

$$C_D = \frac{D}{\frac{1}{2}\rho V^2 S} \tag{2}$$

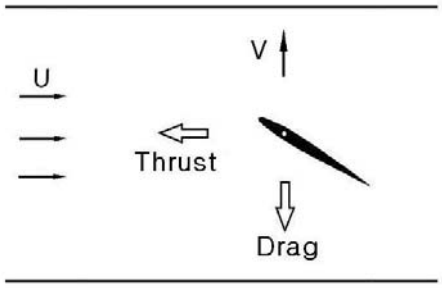

Figure 4. Definitions of thrust and drag

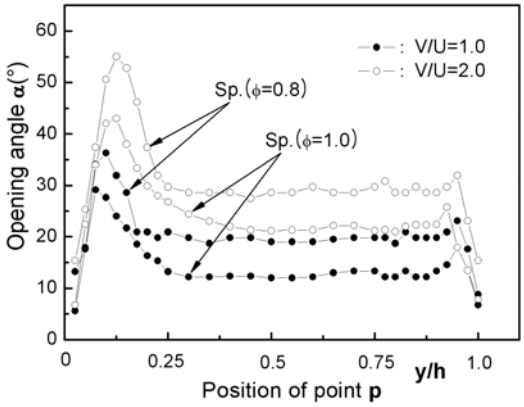

Figure 5. Variations for opening angle according to the wing position in a stroke for each spring type elastic wing

T represents thrust, D for drag, ρ for the density of the fluid, and S for the wing area below the water surface. As defined in Figure 4, thrust T is in the direction of the progress of the ship, which is the opposite direction of uniform flow U. Drag D is the opposite direction of wing movement velocity V.

Also, the average propulsive efficiency of the mechanism $\bar{\eta}$ is the power applied to the wing, namely the percentage of the net output generated from the wing to input, and is calculated as follows.

$$\bar{\eta} = \frac{\int_0^{T_C} C_T U dt}{\int_0^{T_C} C_D V dt} \times 100 \tag{3}$$

Here T_C represents the period of one cycle of wing movement.

RESULTS AND DISCUSSIONS

First, in one stroke of each spring type elastic wing illustrated in Table 1, the change of opening angle according to wing position change is shown in Figure 5. Here, x-axis expresses the dimensionless value of wing moving distance y to the width of the channel h; as shown in the figure, although there are some differences according to the velocity ratio V/U and the spring coefficient, the change of opening angle according to the wing position change in the channel is very big when the wing leaves from the channel surface, then the opening angle decreases until it comes to a certain angle where it stabilizes and moves translationally, then finally, when the wing approaches the other side of the channel, it opens up a little bit before it closes. The change of thrust coefficient C_T and drag coefficient C_D over 2 reciprocating movements of the wing at velocity ratio V/U=1.0 is shown in Figure 6.

The dotted line in the figure expresses the prototype flat-plate wing with maximum fixed angle at α=15°, and the solid line expresses the spring type elastic wing that adjusts opening angle by using steel line of ø =1.0 used as spring. In the figure, the x-axis expresses the traveling distance of wing shaft normalized by the channel width; this value means the number of strokes. First, looking at the

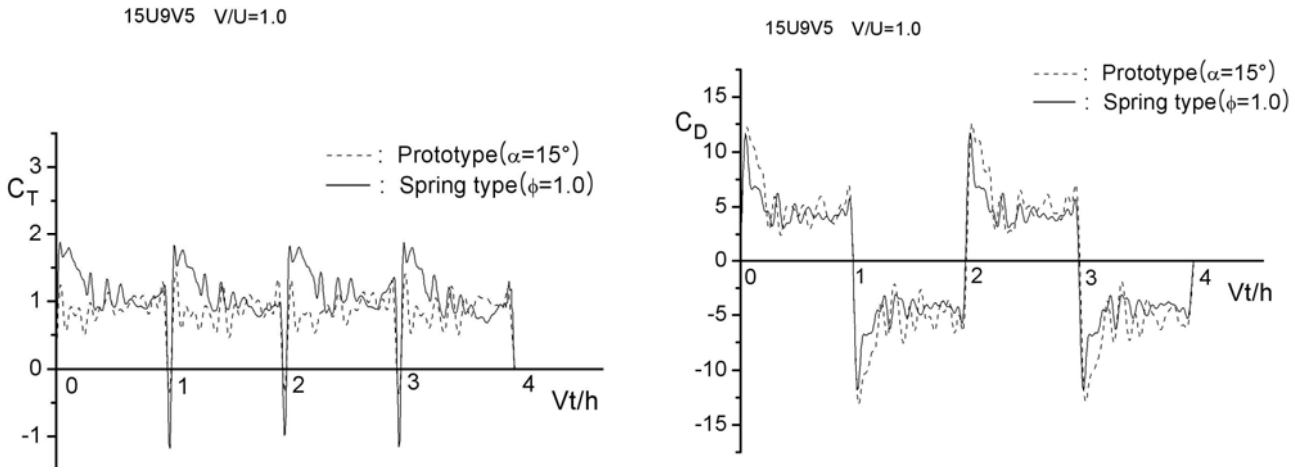

(a) Thrust coefficients (b) Drag coefficients

Figure 6. Time variations for thrust and drag coefficients(V/U=1.0)

change of thrust coefficient, the value is + through the whole stroke except for the opening stages, which means regardless of the wing's reciprocating motion, thrust occurs toward the direction of the progress of the ship. However, when comparing the dotted and solid lines, in dotted line, there are some fluctuations but have relatively constant value, whereas solid line decreases after having a large value at the beginning of the stroke. This is because when the wing moves from opening stage to translational stage, during opening, the negative pressure side of the wing, that is, the wing takes off from the wall where the pressure between the wing and the channel wall is much lower than the pressure toward the moving direction. As a result, a vortex is released from the trailing edge of the wing. In fact, in the prototype case, during the opening in visualization experiment [13] of the flow field, fluid is inhaled because of the negative pressure between the wing and the wall, and through numerical calculation [14], we confirmed that vortex was released from the trailing edge of the wing in translational stage. But in the spring type case, a momentum is applied because of the spring; therefore before it takes off, the wing has to open up to a larger angle as the trailing edge of the wing touches the wall, which we can assume that right before take off, the pressure difference of both sides of the wing should be smaller than in the prototype. Therefore in the spring type case, the wing can shift over to translational stage with effective Weis-Fogh mechanism.

Meanwhile, when looking at the change of drag coefficient (b), in each stroke, the value is reversed with x-axis; this is because each stroke of wing movement is in opposite direction. Solid line of the drag coefficient is smaller than dotted line, but the difference is very small. This is because with elastic wing, the opening angle increases little bit because of water resistance during wing movement. Especially water resistance increases in the closing stage, but as shown in Figure 5, opening angle opens automatically by spring, which prevents decrease of propulsive efficiency that occur with drag increase.

(a) Average thrust coefficient and (b) Average drag coefficient with the change in velocity ratio V/U of prototype wing with the maximum opening angle of α=15° and spring type elastic wing with ø =1.0 spring is shown in Figure 7. Each point in (a) and (b) in the figure corresponds with the average value of 1 cycle in Figure 6 of (a) and (b). First, when looking at the distribution of average thrust coefficient, with the prototype(α=15°), the values are almost constant regardless of the velocity ratio. Compared to this, with spring type(ø =1.0), the value increases sharply as the velocity ratio increases. In the former type, the opening angle does not change even though the velocity ratio increases; but in the latter, as explained before in Figure 6, as velocity ratio increases, the opening angle right before the translational stage increases sharply as shown in Figure 5 to have impressive Weis-Fogh effect. Also, when looking at the distribution of average drag coefficient,

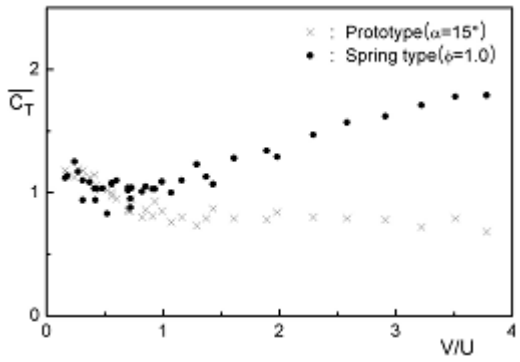

(a) Average thrust coefficients

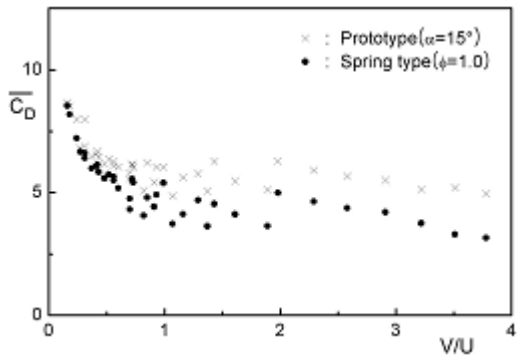

(b) Average drag coefficients

Figure 7. Average thrust and drag coefficients with velocity

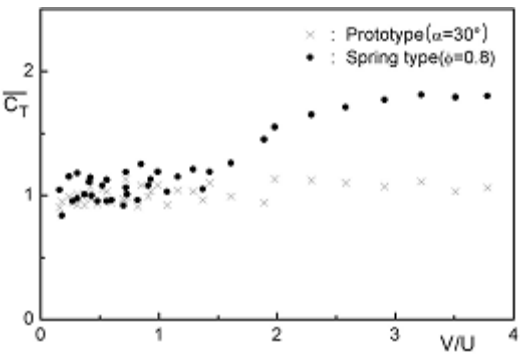

(a) Average thrust coefficients

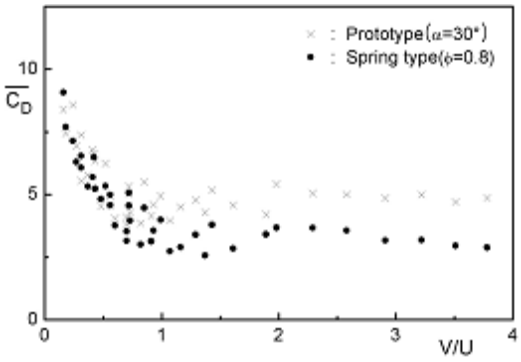

(b) Average drag coefficients

Figure 8. Average thrust and drag coefficients with velocity ratio

over velocity ratio of 1, the differences between the values are increasing little bit as velocity ratio increases; this is because in the spring type case, opening angle increases as velocity ratio increases, which led to decrease in average drag. On the other hand, where the velocity ratio is small, especially under 0.5, as velocity ratio decreases, average thrust coefficient is similar in both types, whereas the average drag coefficient increases in both. This is because in this range, water resistance is small which makes the opening angle to be small.

(a) Average thrust coefficient and (b) Average drag coefficient with the change in velocity ratio V/U of prototype wing with the maximum opening angle of α=30° and spring type elastic wing with ø =0.8 spring is shown in Figure 8. The spring coefficient is smaller than the one in Figure 7; therefore at the same velocity ratio, even if the opening angle is big, the tendency in change of average thrust coefficient and average drag coefficient according to the velocity ratio is same. The average thrust coefficient of prototype(α=30°) is 1.0, which is constant regardless of the velocity ratio. However, with the spring type(ø =0.8), the value increases sharply as the velocity ratio increases. Only it did not increase in a straight line because the spring coefficient was too small, so that the increase in opening angle with velocity ratio exceeded the range of elasticity. Meanwhile, the distribution of the average drag coefficient was both similar in tendency with velocity ratio as Figure 7, but the absolute value was smaller in the spring type than the prototype. This is because in the spring type, as velocity ratio increases, the opening angle increased also, which led to the decrease of average drag.

Average propulsive efficiency of various types of wings with the change in velocity ratio V/U is shown in Figure 9. When the velocity ratio is over 1, with the prototype where the maximum opening angle is constant, the one with big opening angle has larger average propulsive efficiency; with the spring type where the opening angle changes, the one with small spring coefficient has

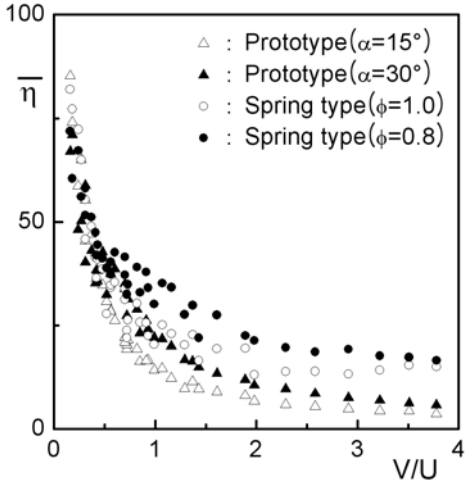

Figure 9. Average propulsive efficiency with velocity ratio for wings of various type

larger value. Especially over the velocity ratio of 1.5 where large thrust can be generated, by automatically adjusting the opening angle with a spring, propulsive efficiency can be increased over twice of the existing fixed angle type. Therefore, practical application of the propulsion mechanism is anticipated, which can greatly complement the weakness of low propulsive efficiency of the prototype in the large velocity ratio range.

CONCLUSIONS

This study was conducted in attempt of improving hydrodynamic efficiency of the propulsion mechanism by installing a spring to the wing so that the opening angle of the wing in one stroke can be changed automatically, compared to the existing method of fixed maximum opening angle in Weis-Fogh type ship propulsion mechanism. There were 2 prototypes of wing with the maximum opening angle of α=15° and α=30°, and 2 types of elastic wing with different spring coefficients. By changing the velocity ratio V/U, thrust, drag, and propulsive efficiency were examined experimentally. The summaries of results are as follows:

(1) With the spring type, the opening angle has large value when moving from opening stage to the translational stage, and moving from translational stage to closing stage.

(2) Average thrust coefficient was constant with the prototype with all velocity ratio, but it increased sharply with the spring type as velocity ratio increased.

(3) Average drag coefficient with velocity ratio was similar in the tendency with each other, but the absolute value was smaller in the spring type than the prototype.

(4) Average propulsive efficiency was larger with the bigger opening angle of the prototype, and with the smaller spring coefficient of the spring type.

(5) In the range of velocity ratio over 1.5 where large thrust can be generated, the spring type showed over twice of the propulsive efficiency than the prototype.

ACKNOWLEDGMENTS

This work was supported by the Korea Science and Engineering Foundation(KOSEF) grant funded by the Korea government (MOST) (No. R01-2007-000-10038-0) and by the NURI

REFERENCES

1. Weis-Fogh, T., Quick Estimates of Flight Fitness in Hovering Animals, Including Novel Mechanism for Lift Production, *Journal of Experimental Biology*, Vol.59, pp.169-230, 1973.
2. Lighthill, M. J., On the Weis-Fogh Mechanism of Lift Generation, *Journal of Fluid Mechanics*, Vol.60, Part 1, pp.1-17, 1973.
3. Maxworthy, T., Experiments on the Weis-Fogh Mechanism of Lift Generation by Insects in Hovering Flight. Part 1. Dynamics of the 'Fling', *Journal of Fluid Mechanics*, Vol.93, pp.47-63, 1979.
4. Edwards, R. H. and Cheng, H. K., The Separation Vortex in the Weis-Fogh Circulation-Generation Mechanism, *Journal of Fluid Mechanics*, Vol.120, pp. 463-473, 1982.
5. Spedding, G. R. and Maxworthy, T., The Generation of Circulation and Lift in a Rigid Two-Dimensional Fling, *Journal of Fluid Mechanics*, Vol.165, pp.247-272, 1986.
6. Ro, K. D. and Tsutahara. M., Numerical Analysis of Unsteady Flow in the Weis-Fogh Mechanism by the 3D Discrete Vortex Method with GRAPE3A, *Transactions of the ASME*, *Journal of Fluids Engineering*, Vol.119 pp.96-102, 1997.
7. Zhang Shesheng, et, Research and progress of Weis-Fogh mechanism hydrodynamics, *Journal of Hydrodynamics*, Vol.3, pp.55-60, 1999.
8. Furber, S. B. and Ffowcs Williams, J. E., Is the Weis-Fogh Principle Exploitable in Turbomachinary*?, Journal of Fluid Mechanics*, Vol.94, Part 3, pp.519-540, 1979.
9. Tsutahara, M. and Kimura, T., An Application of the Weis-Fogh Mechanism to Ship Propulsion, *Transactions of the ASME, Journal of Fluids Engineering*, Vol. 109, pp. 107-113, 1987.
10. Tsutahara, M. and Kimura, T., A Pilot Pump using the Weis-Fogh Mechanism and its Characteristics, *Transactions of the JSME,* Vol.54, No.498, pp.393-397, 1987.
11. Tsutahara, M. and Kimura, T., Study of a Fan Using the Weis-Fogh Mechanism (An Experimental Fan and Its Characteristics), *Transactions of the JSME*, Vol.60, No.571, pp.910-915, 1994.
12. Zhang S. S., Hydrodynamic model of Weis-Fogh mechanism hydrofoil, *Journal of Hydrodynamics*, Vol.4. pp.35-39, 1996.
13. Ro, K. D., Kim, K. S. and Kim, J. H., The Flow Characteristics around Airfoil Moving Reciprocally in a Channel, *Transactions of the KSME*, Vol.32, No.7, pp. 536-541, 2008(in Korean).
14. K. D. Ro, B. S. Zhu and H. K. Kang, Numerical Analysis of Unsteady Viscous Flow Through a Weis-Fogh Type Ship Propulsion Mechanism Using the Advanced Vortex Method, *Transactions of the ASME*, *Journal of Fluids Engineering*, Vol. 128, pp. 481-487, 2006.

A STUDY FOR CONVEYING SOLID PARTICLES ON THE TWO-PHASE FLOW IN AN ANNULUS

S. M. Han[1], Y. J. Kim[2], N. S. Woo[3], Y. K. Hwang[1*]
[1] School of Mechanical Engineering, Sungkyunkwan University, Suwon, S. Korea
[2] Korea Institute of Geoscience and Mineral Resources, Daejeon, S. Korea
[3]Korea Institute of Construction and Technology, Goyang, S. Korea

ABSTRACT. An investigation is conducted to study a 2-phase vertically upward hydraulic transport of solid particles in slim hole concentric annulus with rotation of the inner cylinder. Lift forces acting on a fluidized particle plays a central role in many importance applications, such as the removal of drill cuttings in horizontal drill holes, sand transport in fractured reservoirs, sediment transport and cleaning of particles from surfaces. In this study a clear acrylic pipe was used in order to observe the movement of solid particles. Annular velocities varied from 0.3 m/s to 2.0 m/s. Main parameters considered in the study were inner-pipe rotary speed, fluid flow regime and particle injection rate. Pressure drops and average flow rates were measured in the Reynolds number range of $10^2 < Re < 10^4$. For both water and CMC solutions, the higher the concentration of the solid particles is, the larger the pressure gradients become.

Keywords: *Liquid-solid two-phase flow, Drilling fluid, Slim hole annulus flow, Solid concentration*

INTRODUCTION

Rotating flows in annular passages are important, since they have many engineering applications in bearings, rotating-tube heat exchangers and, especially, annulus flows of mud in case of slim hole drilling of oil well.

When an oil well is drilled, it is necessary to transport the cuttings up to the surface. To this end, fluid is pumped through the center of drill pipe and back up to the surface through the annular gap between the drill pipe and the drilled hole. The fluid is viscous, non-Newtonian, and will typically have gel strength. The flow up to the annulus might be laminar or it might be turbulent, depending on the situation.

Therefore, numerous mathematical and empirical models for the prediction of cuttings transport in horizontal and directional wells have been developed by several researchers. A detailed reveals that the cuttings transport characteristics change with an increase in wellbore angle. Tomren et al. [1] and Ford et al. [2] carried out experimental study on cuttings transport in inclined annulus and observed the existence of different layers that might occur during the mud flow and cuttings in an annulus.

Interest has been growing in the interaction between particle and local flow structure in particulate two-phase flow. Pigott [3] discussed the application of Stoke's law for laminar flow and Rittinger's formula for turbulent flow to drilled particle settling velocity calculation. He concluded that high fluid viscosity was not necessary and suggested that laminar flow in the annulus would lead to more efficient

* Corresponding author: Prof. Y. K. Hwang
Phone: + (82)- 31-290-7437, Fax: + (82)- 31-290-5889
E-mail address: ykhwang@skku.edu

cleaning. For trouble-free operation, he also recommended that the volumetric cuttings concentration in the annulus be kept less than 5%.

Sifferman et al. [4] found that annular velocity and fluid rheological properties are the most important factors influencing the transport ability of a fluid. Other variables such as particle size, drill pipe rotation, drill pipe eccentricity have only moderate effects on carrying capacity in their study.

Sellgren [5] and Ozbelge et al. [6] discussed the pressure drop and the choice of operating velocities in the vertical upward pipe flows of solid-liquid mixtures. He reported that additional turbulence was created due to the relative velocity between the solid and fluid phases.

This paper concerns an experimental and numerical study of fully developed solid-liquid mixture flow of Newtonian fluid, water and non-Newtonian fluid, CMC solutions through concentric and eccentric annuli with combined bulk axial flow and inner cylinder rotation.

The flow characteristics of solid-liquid mixtures, flowing upward through a vertical annulus in a closed loop system, is determined by measuring the concentration profiles of solids and the axial pressure drops in the test section. It is expected that the results of this study will be useful to explain the effect of solids on solid-liquid mixture transport phenomena in the annular geometry.

EXPERIMENTAL METHOD

The objective of the solid-liquid mixture flow experiments was to provide high quality data on the effects of pipe rotation, flow regime, fluid properties, solid concentration on pressure loss in slim hole annuli. The set-up used in the experiments is a closed-loop system consisting of a centrifugal slurry pump with a by-pass line, a vertical annulus and a feed slurry tank as shown in Fig. 1(a). The flow configuration and instrumentation are described by Kim and Hwang [7].

The outside diameter of the inner pipe (D_i) and the inside diameter of the outer pipe (D_o) being 30 mm and 44 mm, respectively, yield a radius ratio of 0.7 for the annulus. To ensure fully developed flow in the measuring section, the length of straight pipe upstream of the test section is 1.8 m, corresponding to 126 hydraulic diameters, in order to produce an artificially thickened boundary layer.

A cylindrical head tank was used for the preparation of the feed particles. The tank having a conical bottom in order to avoid the settling of the solids and it is connected from its bottom to a centrifugal pump with a vertical pipe.

Pressure drops and averaged flow rates were measured in the Reynolds number ranger of $500 < Re < 3000$. The flow rate has been measured with a magnetic flow meter whose accuracy is within the limit of $\pm$ 0.5 percent. The inner cylinder may be rotated at any speed up to a maximum of 600rpm by means of an A.C. motor. And the axial velocity of solid particle was measured by using high speed camera installed outside of the cylinder. The outer cylinder was made of transparent acryl pipe.

Static pressures are measured with holes of 0.5 mm diameter distributed longitudinally in the outer cylinder. 2 static pressure taps are installed along the flow direction in measuring part. The static pressures are read from a calibrated manometer bank with 1 mm resolution. The specific gravity of the manometer fluid CCl_4 is 1.88, and it gives a height in the range of 20~600 mm.

The head tank was filled with water up to a marked level and the pump was started. Particles, at a desired feed solid concentration were prepared in the head tank by adding the uniformly sized sand

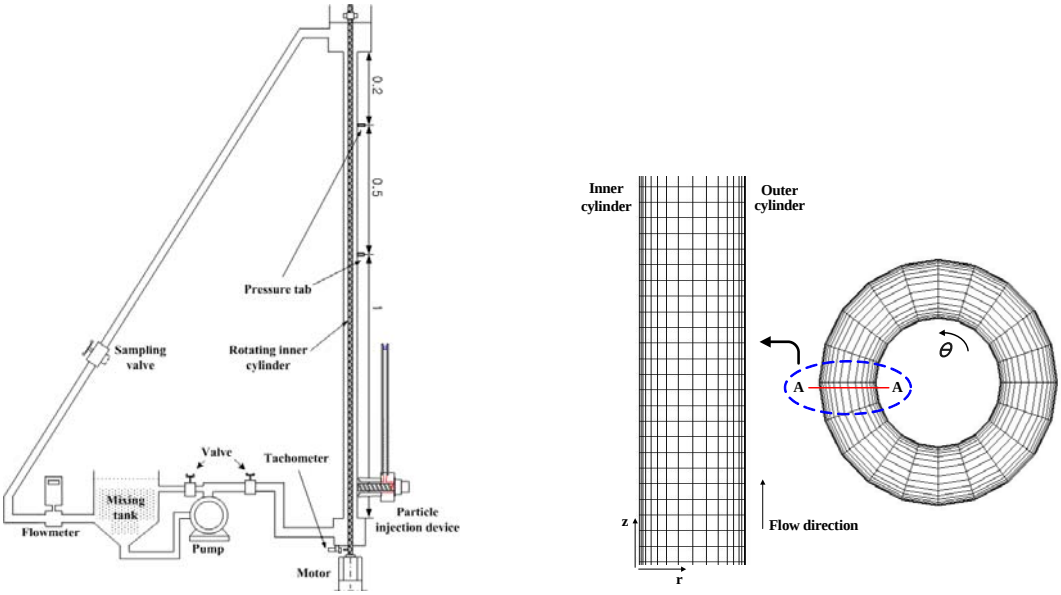

(a) Experimental set-up (b) Computational grid

Figure 1. Experimental set-up and computational grid

particle. The mixture flow rate was adjusted manually by the by-pass valve installed after the outlet of the pump. When the mixture flow reaches steady state, the axial pressure drops and velocity of solid particle were measured simultaneously. The mean diameter of particles was 0.1 cm and a material density of 2.55 g/cm^3 were used in the experiments.

NUMERICAL METHOD

Traditionally, the annulus between drill pipe and the borehole has been represented as a concentric annulus as shown in Fig. 1(b). There are two main approaches to modeling multi phase flows that account for the interaction between the phases. These are the Eulerian-Eulerian and the Eulerian-Lagrangian approaches. The former is based on the concept of interpenetrating continua, for which all the phases are treated as continuous media with properties analogous to those of a fluid. The Eulerian-Lagrangian approach adopts a continuum description for the liquid phase and tracks the discrete phases using Lagrangian particle trajectory analysis.

In the numerical study, the Eulerian-Eulerian approach for granular flow is used that allows the determination of the pressure and viscosity of the solids phase instead of empirical correlations.

In a numerical study of solid-liquid mixture, a laminar flow of water in an eccentric annulus has been calculated. A control volume based finite volume method is used to solve the equations of motion. The problem reduced to the solution of the conservation of mass and momentum equations along with the appropriate boundary and initial conditions.

The governing set of partial differential equations was discretized using a finite volume technique. The discretized equations along with the initial and boundary conditions were solved using FLUENT. Particle-particle interactions via friction were also included.

The solids volume fraction in a domain of known volume was specified at the beginning of each simulation to correspond to the desired solids loading. The particles used in the simulation were solid spheres with a density of 2.55 g/cm^3. Values of the coefficient of restitution and the friction coefficients for these particles were assumed to be 0.9 and 0.09, respectively. The same coefficient of friction was also assumed for interactions between the walls and the particles.

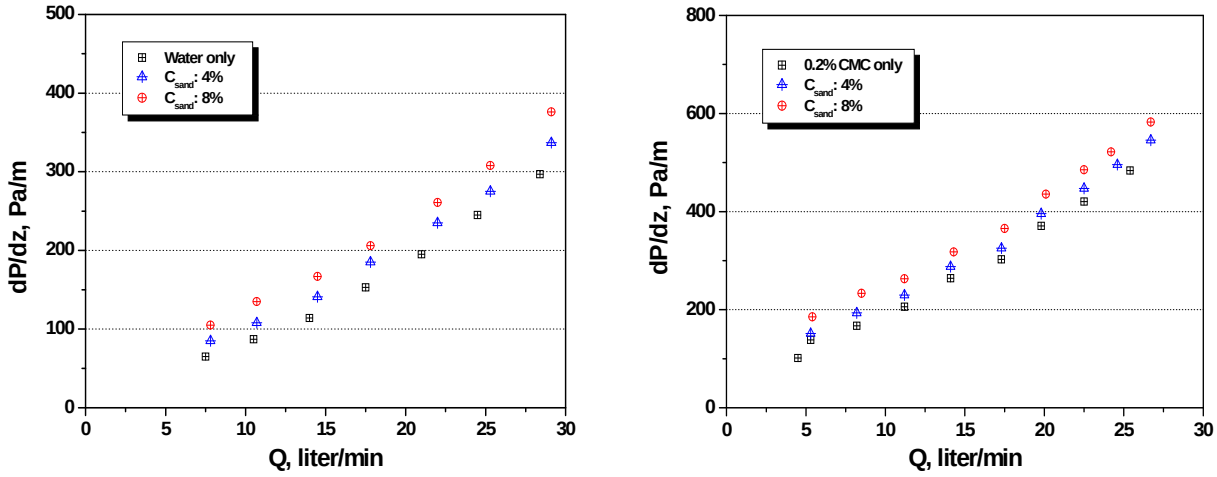

(a) Water (b) 0.2% CMC solution

Figure 2. Pressure drop as a function of fluid velocity and solid concentration

No-slip boundary conditions are imposed on all the solid surfaces for the continuous phase. The same conditions are also applied to the discrete phase and imposed in the corresponding momentum equations. The inlet liquid velocity and the outlet pressure were specified. No-slip boundary conditions were assumed at the walls for the liquid phase. Interactions of particles with the walls were modeled with the same formulation used for solids pressure and granular viscosity for the particle-particle interactions.

RESULT AND DISCUSSION

Hydrodynamic characteristics of single phase flows are known well, but the same is not valid for solid-liquid mixture and multi phase flows. In this study, the flow characteristics of solid-liquid mixture flows are investigated experimentally at different operating conditions.

For solid-liquid mixture flows at different operating conditions, the experimental and numerical parameters are the feed solid concentration, mixture velocity in the annulus, rotational speed of inner cylinder, inclination of annulus, and eccentricity of inner cylinder. The important characteristics of solid-liquid flows are the pressure drop versus mixture velocity relationship and solid particle transport velocity.

The pressure drop versus mixture velocity and annular inclination are shown in Fig. 2, for the mean particle size of 0.1 cm. In Fig. 2(a), the total pressure drop increases with along the increase of volume concentration of solid particles and mixture velocity. For higher volume fraction, the hydraulic pressure drop of two-phase mixture increases due to the friction between the wall and solids or among solids. Results of experiments and numerical simulation shows good agreement, but numerical results are slightly lower than experimental values.

The pressure drop versus mixture velocity and annular inclination are shown in Fig. 3 (a), for the mean particle size of 0.2 cm and sand volume fraction of 4% and 8%. The carrier fluids are water. The pressure drop increases along the increase of annulus inclination. Also, the pressure drop of solid-liquid mixture flow is largely increased compared to the single phase fluid flow. The pressure drop of solid-liquid mixture flow increases due to the friction between the wall and solids or among solids.

As shown in Fig. 3 (b). the total pressure drop increases with along the increase of volume concentration of solid particles and mixture velocity. For higher volume fraction, the hydraulic

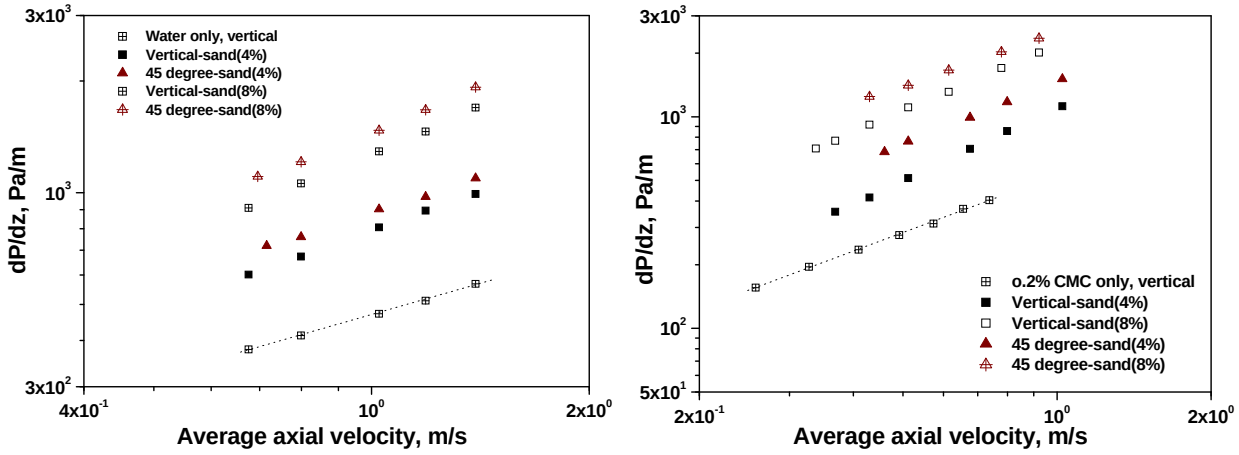

(a) Water (b) 0.2% CMC solution

Figure 3. Comparison of pressure loss in fluid with sand concentration at 0 rpm.

pressure drop of two-phase mixture increases due to the friction between the wall and solids or among solids.

Averaged velocity of solid particles with mixture velocity, rotational speed of inner cylinder, and inclination of annulus is shown in Figs. 4 (a) and (b). At very low mixture velocities, some of the particles may settle down in the annulus. The velocity of solid particles is gradually increased with the

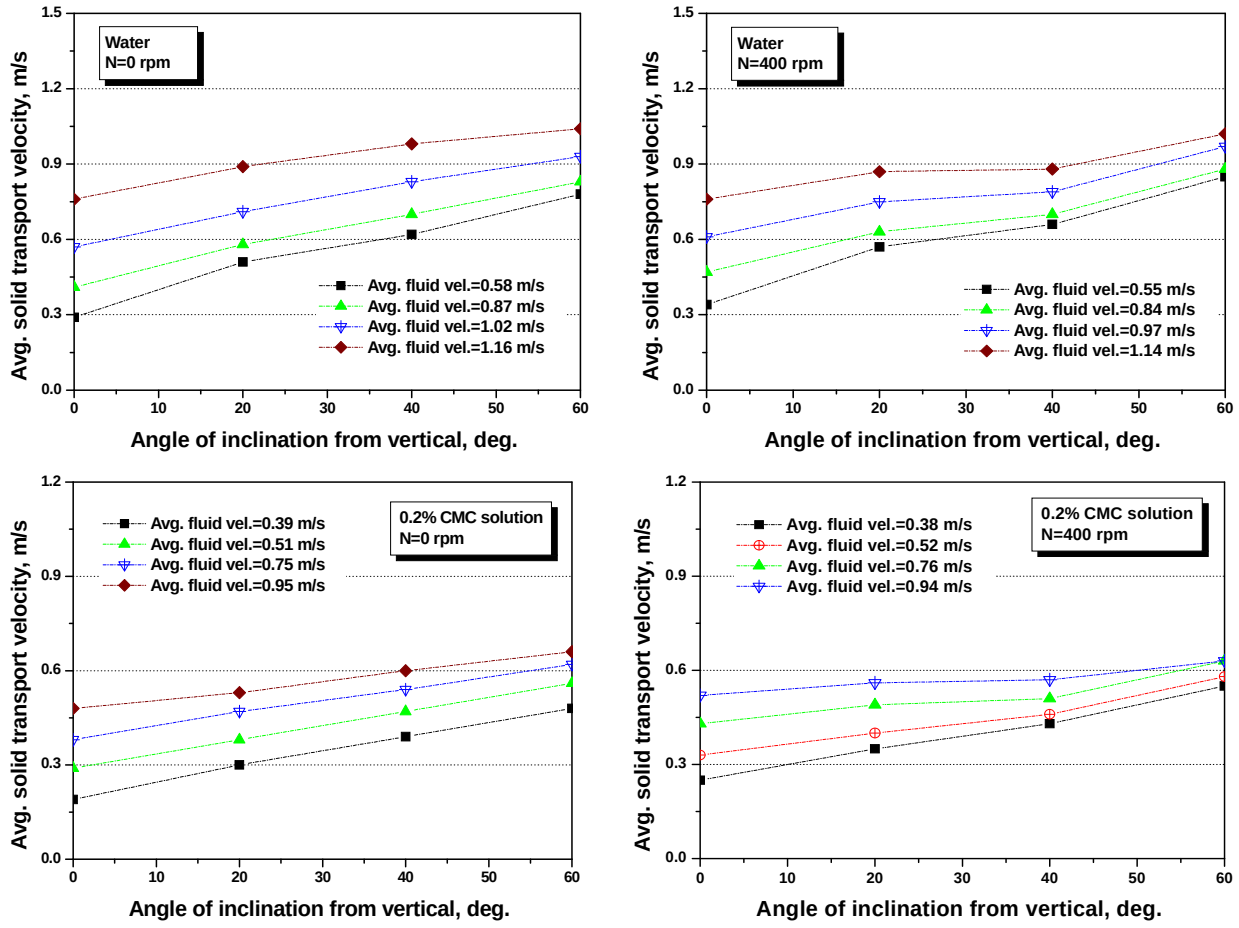

(a) Solid velocity (0 rpm) (b) Solid velocity (400 rpm)

Figure 4. Solid transport velocity as a function of fluid velocity and inclination of annulus

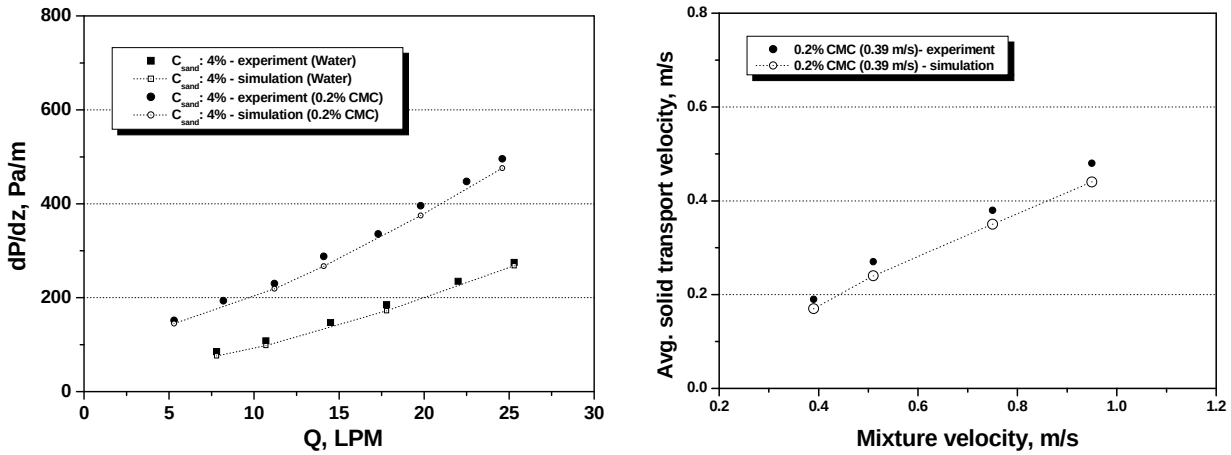

(a) Pressure drop (b) Solid transport velocity

Figure 5**.** Comparison of pressure drop and solid velocity with mixture flow rate in vertical annulus

increasing mixture velocity and inclination of annuls form the vertical. As a result, the amount of solids carried to the annulus is also gradually increased. Rotation of the inner cylinder generally improves the transport of solid particles and it is more pronounced at lower mixture velocities and appears to be negligible at high rotational speeds of 300 rpm. One explanation for this may be that at high flow rate, the mixture velocity is the dominating factor on the particle transportation, with rotational speed having marginal effects.

Viscoelastic fluids have been observed to provide better capability to mobilize and transport particles. As shown in Fig. 2, 0.2% CMC solution transports solid particles at lower mixture velocities compared with water. The effective viscosity of 0.2% CMC solution shows a shear-thinning behavior. The repeated experiments show that ±3% error in the solid particle velocity measurements and ±3.5% error in the pressure drop measurements.

To obtain a more realistic representation of the drilling operation, the solid-liquid mixture flow in concentric and eccentric annuli for a Newtonian fluid and then for a power law fluid was considered. Numerical calculations have been extended for the case where the inner cylinder rotates about its own axis at a constant rotational speed. Detailed calculations have been carried out for radius ratio of 0.7 covering eccentricities up to 0.2 and rotational speed of the inner cylinder up to 100 rpm.

The computational domain consists of 15, 96, and 500 nodes in the radial, azimuthal and axial directions respectively. And the calculation results were compared with experimental data in terms of pressure drop.

Calculation results were compared to experimental data in order to validate from the numerical model results. The calculation results showed a good agreement with experimental data for the pressure drop and particle transport velocity in solid-liquid mixture flow as shown in Fig. 5. Results of experiments and numerical simulation shows good agreement, but numerical results are slightly lower than experimental values.

Volume fraction contours of solid particle in the z-section for 30° inclined concentric annulus are shown in Fig. 6. The carrier fluid water and the fluid velocity is 0.6 m/s. So the flow regime is turbulent. The annulus is inclined 30 degree from vertical. In the case of non-rotation in Fig. 6(a), the profile of particle volume fraction is axisymmetric and the particles are located in the bottom side of annulus because of the gravitational effect. The particle volume fraction is decreased as the rotational speed of inner cylinder is increased up to 400 rpm as shown in Figs. 6(b) and (c). From the Fig. 6,

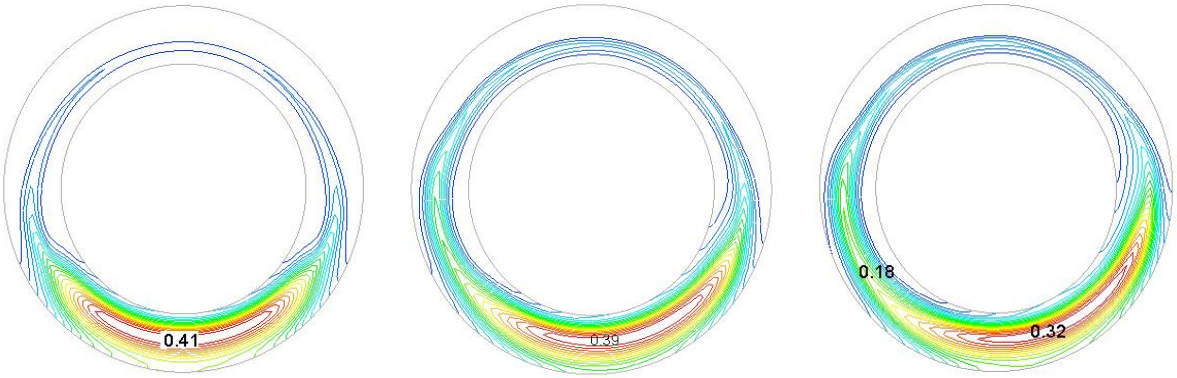

(a) 0 rpm (b) 200 rpm (c) 400 rpm

Figure 6. Contour of solid volume fraction in 30° inclined annulus (water velocity=0.6 m/s, initial C_{VT}=8%)

rotation of the inner cylinder disturbs the formation of bed. Generally this effect is profitable for the cuttings transport in an inclined annulus.

Calculation results were compared to experimental data in order to validate from the numerical model results. The calculation results showed a good agreement with experimental data for the pressure drop and particle transport velocity in solid-liquid mixture flow as shown in Fig. 7.

CONCLUSION

In this study the steady laminar and turbulent upward flows of solid-liquid mixtures through a concentric annulus has been investigated experimental and numerical methods.

The two-phase pressure drop increases with the feed concentration and the flow rate. For higher volume fraction, the hydraulic pressure drop of two-phase mixture increases due to the friction between the wall and solids or among solids.

Generally, 0.2% CMC solution is observed to provide better transport than water. The main reason for this is uniform velocity profile of shear-thinning fluid. And Rotation of the inner cylinder generally improves the transport of solid particles and it is more pronounced at lower mixture velocities and appears to be weakened at high flow rate.

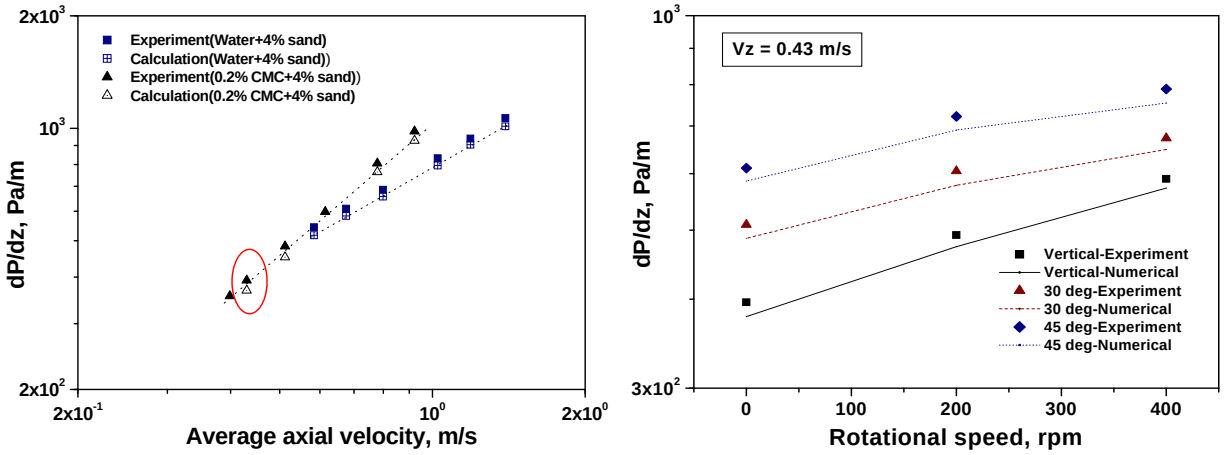

(a) 0rpm (b) 0.2% CMC +4% Sand

Figure 7. Comparison of pressure loss in water and 0.2% CMC solution as a function of flow rate.

Numerical calculations were run for 0.2% CMC solution as carrier fluid and the calculation results showed a good agreement with experimental data for the pressure drop, but numerical results are slightly lower than experimental values.

For small excursions from a concentric annulus, the axial pressure drop falls with the increase of eccentricity as the shear-thinning effects will have ample opportunity to dominate inertial effects.

Numerical calculation predicted that almost all sand particles settle down to the lower part of the annulus and some particles were suspended in the upper part of the annulus. As the hole inclination is increased from vertical, the volume fraction of sand is increased.

ACKNOWLEDGEMENT

This work was supported by the Brain Korea 21 Project in 2008

REFERENCES

1. Tomren, P. H., Iyoho, A. W. and Azar, J. J., An experimental study of cuttings transport in directional wells, *SPE Drilling Engineering*, SPE 121, 1986.
2. Ford, J. T., Peden, J. M., Oyeneyin, E. G., & Zarrough, R., Experimental investigation of drilled cuttings transport in inclined boreholes, *SPE Annual Technical Conference*, New Orleans, Sept.23-26, SPE 20421, 1991.
3. Pigott, R. J. S., Mud Flow in Drilling, Drilling and Production Practice, *API*, pp. 91-103, 1941.
4. Sifferman, T. R., et al., Drill-Cuttings Transport in Full-Scale Vertical Annulus, *J. Pet. Tech.*, pp. 1295-1302, 1974.
5. Sellgren, A., The choice of operating velocity in vertical solid-water pipeline systems, *BHRA Fluid Eng.*, Paper D3, pp. 211-226, 1982.
6. Ozbelge, T. A., & Beyaz, A., Dilute solid-liquid upward flows through a vertical annulus in a closed loop system, *Int. J. of Multiphase flow*, Vol. 27, pp. 737-752, 2001.
7. Kim, Y. J., & Hwang, Y, K., Experimental Study on the Vortex Flow in a Concentric Annulus with Rotating Inner Cylinder, *KSME Int. Journal*, Vol. 17, No. 4, pp. 562-570, 2003.

FLOW AROUND A CYLINDER SWIMMING IN A QUIESCENT FLUID

M. Nazarinia*, D. Lo Jacono, M. C. Thompson and J. Sheridan
Department of Mechanical & Aerospace Engineering, Monash University, Australia

ABSTRACT. The flow structures around a circular cylinder undergoing combined oscillatory translation and rotation in a quiescent fluid have been investigated experimentally and numerically. Experiments were performed for the set of parameters that was shown previously to result in a net thrust i.e. the *swimming cylinder* case. The range of Reynolds number covered in this study was $141 \leq Re \leq 628$. The velocity fields were measured in multiple planes using particle image velocimetry. The experimental setup was such that the cylinder was mounted vertically to an actuator to create the horizontal translation. The circular cylinder used has an outer diameter of 20mm and length of 800mm. Experimental results confirmed that at certain phase differences between the two motions, i.e. out-of-phase or in phase, the cylinder is capable of generating thrust in a perpendicular direction to the translational oscillation. Experiments were also undertaken to investigate the three-dimensional nature of the flow. Additional analysis on the stability of such flow has been carried out with numerical simulation and confirmed the experimental measurements.

Keywords: *wake, cylinder, quiescent, instability*

INTRODUCTION

A circular cylinder undergoing a combination of translation and rotation oscillatory motions in quiescent fluid has not received much attention until now. It is well known that when a bluff body is oscillating translationally in a quiescent fluid, secondary streaming is generated around the body owing to the influence of nonlinear effects [1]. However, the combination of the two oscillatory forcing mechanisms can, under specific conditions, result in a net thrust being experienced by the circular cylinder in a direction normal to the translational axis [2]. The cylinder experiencing thrust and undergoing a series of pitch and plunge motions has been labeled the *swimming cylinder*. Numerous studies of flow over bodies undergoing pure oscillatory motions exist in the literature. These oscillatory motions include pure translation [3-8] and pure rotation [9-11].

So far, to the best knowledge of the authors, only the investigation by Blackburn et al. [2] and several more recent ones [12-14] have been reported on the combined oscillatory motion. However, the work by Blackburn et al. [2] is the only one on the swimming cylinder (e.g. the quiescent case) and to date no experiments have confirmed this phenomenon. A number of interesting features have been shown to occur as a result of combining the two motions. Blackburn et al. [2] found out that a jet flow will be produced by the cylinder when the two imposed motions are in phase or of opposite phases, i.e. $\Phi = (0, \pi)$. The propulsive force produced by the cylinder caused it to accelerate until eventually reaching a terminal speed of 33% of the peak translational speed.

* Corresponding author: Mr. M. Nazarinia
Phone: + (61)-3-99053537, Fax: + (61)-3-99051825
E-mail address: mehdi.nazarinia@monash.edu.au

The purpose of the present study is to investigate not only the near wake structures arising from this combination of forcing mechanisms, but also their associated three-dimensional nature, which has not received attention so far. The present study incorporates experimental and numerical results. To characterise the experiments, the authors employed particle image velocimetry (PIV) technique. A direct numerical simulation and Floquet analysis are also used to support and extend the present investigation. After defining the problem and the methods and techniques used, the results and discussion will be presented below.

PROBLEM DEFINITION

The flow over a cylinder undergoing combined translation and rotation oscillations depends on five independent parameters. The equations of the forcing motions are defined as:

$$y(t) = A_t \sin(2\pi f_t t), \tag{1}$$

$$\theta(t) = A_\theta \sin(2\pi f_\theta t + \Phi), \tag{2}$$

where A_t (A_θ) is the amplitude of translational (rotational) motion, f_t (f_θ) is the frequency of translational (rotational) oscillation, and Φ is the phase difference between rotational and translational motions ***(refer to Figure 1)***. The five independent parameters can be written as translational and rotational Keulegan-Carpenter numbers:

$$KC_{[t,\theta]} = \frac{U_{\max_{[t,\theta]}}}{f_{[t,\theta]} D} = \frac{2\pi A_{[t,\theta]}}{D} \tag{3}$$

and as the translational and rotational Stokes number:

$$\beta_{[t,\theta]} = \frac{f_{[t,\theta]} D^2}{\nu} \tag{4}$$

where D is the diameter of the cylinder, U_{maxt} ($U_{max\theta}$) is the maximum translational (rotational) velocity of the cylinder motion and ν is the kinematic viscosity of the fluid. A Reynolds number can also be defined as a combination of two of the above dimensionless parameters. The associated translational Reynolds number, Re_t, is then:

$$Re_t = \frac{U_{\max} D}{\nu} = KC_t \beta_t. \tag{5}$$

METHODS AND TECHNIQUES

Experimental setup

The experiments were conducted in the FLAIR free-surface closed-loop water channel at the Department of Mechanical and Aerospace Engineering, Monash University. The model used for these experiments was a ***rigid*** hollow carbon fibre circular cylinder with a length of 800mm and outer diameter of 20mm, giving an aspect ratio of 40. The cylinder was suspended vertically from an actuator that was controlled by a micro-stepping stepper motor. The cylinder was fitted with an end plate to reduce the end effects. The end plate was designed following recommendations by Stansby [15], and consisted of a circular plate with a diameter of 9D. The Cartesian coordinate system in use is defined such that the origin is located at the centre of the circular cylinder (at $t = 0$) at the window shown in Figure 1 with x, y and z representing the streamwise, transverse, and spanwise directions, respectively. ***The window is located at a depth of 620mm under the water surface.*** The cylinder was

also oscillated rotationally by using another high-resolution stepper motor. The stepper motors were controlled using a two-axis indexer and two high-resolution drivers (running at 50800 steps/rev). A pure sinusoidal profile, as defined in equations (1) and (2), was used throughout the experiments. During each set of experiments the fluid was *initially* at rest, i.e. quiescent flow. Special care was always taken to ensure the quiescency of the flow. Prior to each set of experiment a honeycomb device was used to break large-scale structures into small-scale, minimising the background noise. Typically, the amplitude of the background noise, measured with the norm of velocity magnitude, was kept below 1.41% of the U_{maxt}, for β = 45. Experiments were performed for a particular set of parameters which has been shown previously to be that of a swimming cylinder [2]: the frequency ratios were held the same $\beta_t = \beta_\theta = \beta$, the amplitude of rotational motion $A_\theta = 1$ radian and the phase difference between the two motions $\Phi = \pi$. With these values the associated translational and rotational Keulegan-Carpenter number are $KC_t = KC_\theta = \pi$. The nondimensional frequency chosen ranged from $45 < \beta < 200$, consequently the range of Re_t covered $141 < Re_t < 628$.

Experimental technique: particle image velocimetry (PIV)

The PIV technique was used to measure the flow fields around the combined oscillating circular cylinder. The PIV set-up, illustrated in Figure 1, was based on that originally described by Adrian [16]. For this purpose, the flow was seeded with spherical polyamide particles having a mean diameter of 20 μm and specific gravity of 1.016. In this system, the particles were illuminated using two miniature Nd:YAG laser sources. The planes of interest for these experiments were the *yz*- and *xy*-plane, being the spanwise and streamwise perpendicular to the cylinder planes respectively, as shown in Figure 1. Pairs of images were captured on a high resolution CCD camera system with a maximum resolution of 4008×2672 pixels. The camera was equipped with a 105mm lens and was triggered by a TTL-signal, which was delivered from the stepper motor. At a particular phase in the oscillation cycle, a number of image pairs over successive cycles were stored for further processing, ***producing phase-locked velocity fields.***

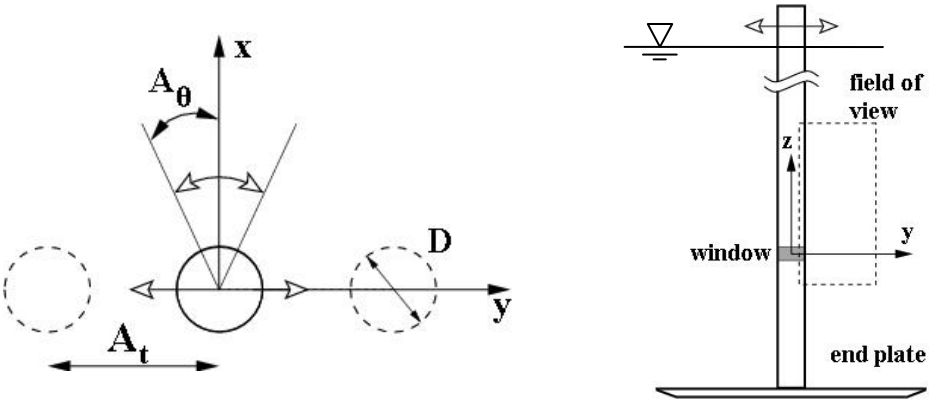

Figure 1. Schematic showing the problem geometry and important parameters relevant to the combined forced oscillation and the circular cylinder model. The green lines show the laser sheet in the streamwise plane (left) and spanwise plane (right).

Each image pair was processed using in-house PIV software ([17, 18]). This software uses a double-frame, cross-correlation multi-window algorithm to extract a grid of displacement vectors from the PIV images. An interrogation window of 32×32 (with an initial window size of 64×64) pixels was found to give satisfactory results with 50% overlap. More than 98% of the vectors were valid for all experiments. This window size corresponds to an average interrogation window of $0.064D \times 0.064D$ and measurement resolution of 249×166 (total of 41334) vectors in each field of view. The overall field of view was $8.0D \times 5.3D$. The displacement fields from these analyses are

presented using phase-averaged vorticity and velocity fields, where the phase-averages were calculated from 30 or more instantaneous velocity fields.

Numerical formulation

The base flows for the present study were calculated by solving the incompressible, time-dependent Navier-Stokes equations. The discretisation method employed was a spectral-element method, using seventh-order Lagrange polynomials associated with Gauss-Lobatto-Legendre quadrature points. A three-step time-splitting scheme is employed [19-21]. A computational domain extending $30D \times 30D$ was split into 518 elements, the majority of which were concentrated in the boundary layer. The resolution, element distribution and domain size are consistent with those used successfully in previous similar studies [20, 22 , 23]. At the cylinder surface, a time-dependent Dirichlet condition was utilized that varied sinusoidally in time according to the driven translational and rotational oscillation. The code employed a power method to resolve the most dominant Floquet mode (and the magnitude of the largest Floquet multiplier). Further details of the method in general can be found in [19], and details of the implementation used here in [20]; the formulation of Floquet stability analysis can also be found elsewhere [24].

RESULTS AND DISCUSSION

Figure 2 shows a comparison of the velocity at y/D=0.6 behind a purely translational oscillating circular cylinder in a quiescent flow. The measurements are taken at KC_t=5 and β=20, similar to previous numerical and experimental results of Dütsch et al. [8]. Figure 2 shows that the present experiment and the numerical simulations match the experimental results of Dütsch et al. [8] very closely. As can be seen, the present experimental results match more closely to the numerical results compared with the experimental results of Dütsch et al. [8]. Also excellent agreement was found with the results of Dütsch et al. [8] at different locations behind the cylinder which further validates our experimental setup.

Figure 3 shows the agreement between the present numerical simulation and the experiments for the ω_z vorticity contours around the cylinder undergoing combined translational and rotational oscillation at $KC=\Phi=\pi$ and $\beta=90$. On the left the present phase averaged experimental results are shown while on the right are the numerical simulations. The cylinder is at the middle of the oscillation cycle starting the motion towards the top of the page, in the vertical direction and rotating clockwise in the negative direction at the instant shown. These experiments confirm the earlier results of the numerical simulations of Blackburn et al. [2]. Figure 3 clearly shows the vorticity transport to one side of the cylinder as well as comparing the same flow between the present experimental and numerical investigation. Figure 3 also shows the excellent qualitative agreement between the experimental and numerical results.

Figure 4 shows the sequence of one complete cycle of translational and rotational oscillations in eight different consecutive snapshots, from t=0 to t=7T/8, where T is the period of oscillations. The cylinder, based on equations (1) and (2), starts the motion from the centre to the top of the page, the positive direction of y, and at the same time starts rotating clockwise, the negative direction of rotation angle, θ. Figure 4c shows the instant where the cylinder is at its maximum vertical position and the most negative angular displacement. As the oscillations are 180° out-of-phase, the maximum surface-tangential component of cylinder acceleration is located on the left hand side of the cylinder, i.e. it is where the accelerations are additive rather than in opposition. Morton [25] has shown that this combination of accelerations will result in the generation of vorticity on that side of the cylinder while the cancellation of accelerations on the other side results in a cross-annihilation of vorticity. The direction of rotation of the vortices will result in their being stretched and directed to only one side of the cylinder and perpendicular to its translation axis will necessarily result in thrust generation in this direction. Only in certain cases does the motion of the cylinder thus act to

produce vorticity more strongly from one side of the cylinder while retaining an overall zero production of vorticity from the cylinder. As reported by Blackburn at al. [2], for this to occur a threshold amplitude of oscillation is required. The phase angle between the motions seems to influence the degree to which cross-annihilation of vorticity occurs and the distance from the cylinder at which vorticity persists.

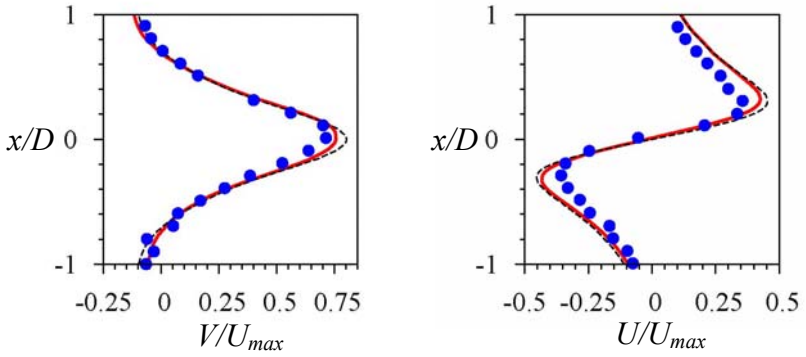

Figure 2. Comparison of the velocity components at y/D=0.6 behind the purely translationally oscillating cylinder in a quiescent flow (at KC_t=5 and β=20). solid (red) lines: present experiment; the dashed (black) lines: present numerical simulation; filled circle (blue) points: the experimental results of [8].

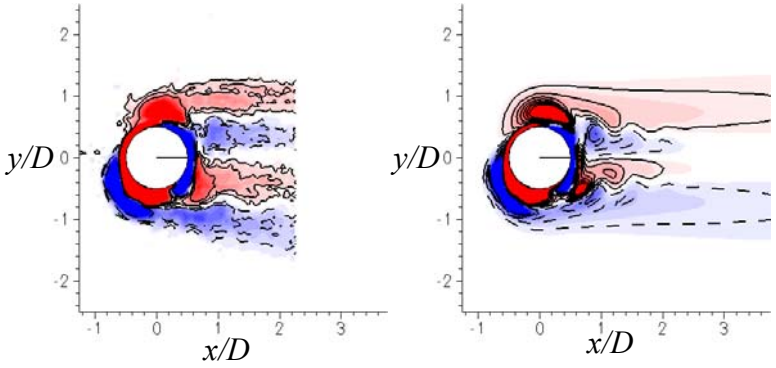

Figure 3. Vorticity contours, ω_z, around the cylinder undergoing combined translational and rotational oscillation at KC=Φ=π and β=90. The dashed lines (blue) are showing the clockwise direction of vorticities, negative, where the solid lines (red) are showing the counter-clockwise direction, positive. Left: present experiments; Right: numerical simulations.

Experiments were also undertaken to investigate the three-dimensional nature of the flow. The onset of three-dimensionality was measured and calculated to occur at β_c=32. Figure 5 shows the spanwise distribution of ω_x vorticity. Figure 5a shows the two-dimensionality of the flow for $\beta < \beta_c$ while at the higher β values shown in Figure 5b and c the flow displays a characteristic spanwise wavelength λ. The wavelength of the spanwise structures was found to be in the range $1.8 < \lambda/D < 2.0$. Numerical simulations with Floquet analysis have been performed and confirmed this wavelength; the comparison is shown in Figure 6.

CONCLUSIONS

The research reported here extends the study of Blackburn et al. [2] both experimentally and numerically. The study is restricted to the case with the phase angle set to Φ=π, and large amplitude oscillations-corresponding to a *swimming cylinder*. For the first time flow around a cylinder

undergoing a combined translation and rotation oscillatory motion has been measured experimentally. The development of wake three-dimensionality has also been examined experimentally. The stability of the wake to the growth of three-dimensional flow through Floquet stability analysis has also been determined. In particular, the experimental results along with our numerical simulations show and confirm how a cylinder at certain phase difference between the combined motions can generate thrust. Because of the phase difference, the oscillation velocities at the cylinder surface cancel on one side and reinforce on the other. This leads to preferential vorticity generation and transport on one side, and the cylinder rotational motion sweeps this vorticity around to the other side producing a thrust wake. We also find that the wake undergoes three-dimensional transition at low Reynolds numbers (Re ≈ 100) to an instability mode with a wavelength of about two cylinder diameters. The experimental results also indicate that the development of three-dimensionality in the wake leads to significant distortion of the previously two-dimensional wake.

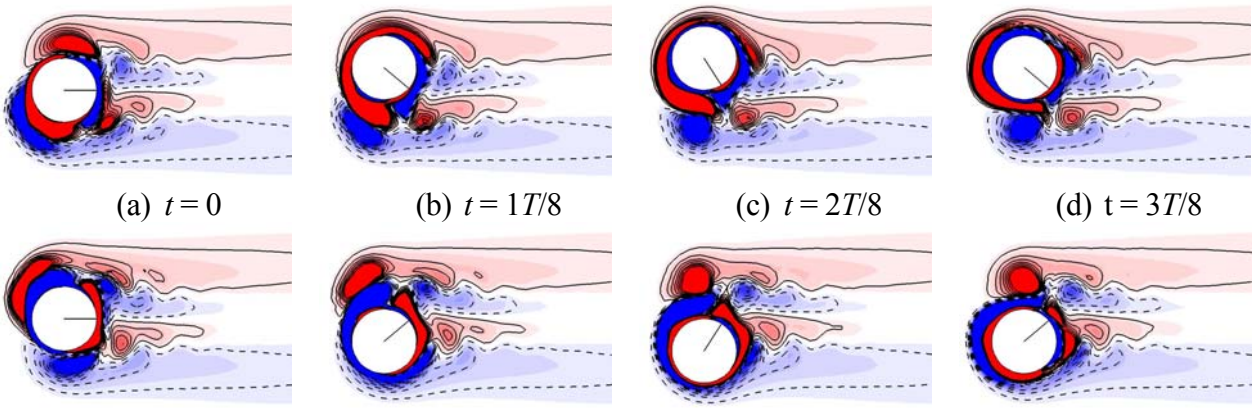

Figure 4. Flow produced by cylinder with combined oscillatory translation and rotation. This figure shows the sequence and development of the ω_z vorticity for one complete cycle, (a) $t = 0$ to (h) $t = 7T/8$ at $KC=\Phi=\pi$ and $\beta=90$ where T is the period of oscillation. The radial line shows the rotational displacement of the cylinder. The dashed lines (blue) are showing the clockwise direction of vorticities, negative, where the solid lines (red) are showing the counter clockwise direction, positive.

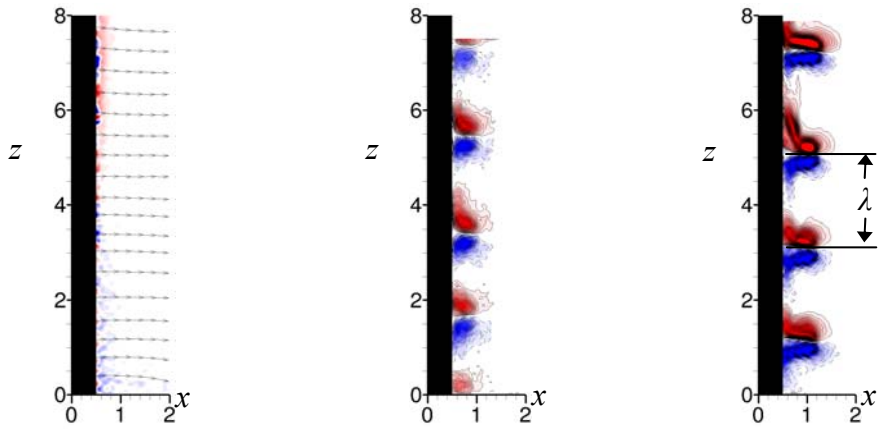

Figure 5. Spanwise distribution of flow for three values of β at $KC=\Phi=\pi$: (a) $\beta=20$: streamlines showing parallel and therefore two-dimensional vortex shedding; (b) and (c) β =45, 90, respectively: ω_x out-of-plane vorticity contours showing the mush-room structures along the span.

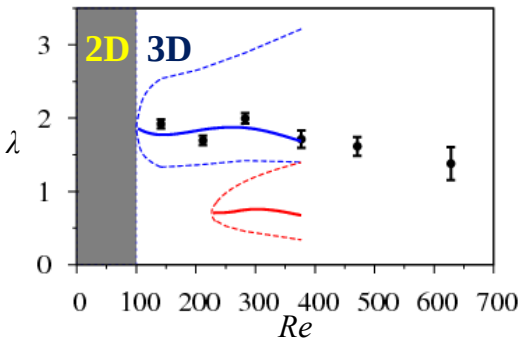

Figure 6. Comparison of the Floquet analysis predicted values for the wavelengths as a function of Reynolds number with experimental measurements for $KC=\Phi=\pi$.

ACKNOWLEDGEMENTS

MN would like to acknowledge the support of a Monash Graduate Scholarship (MGS) and a Monash International Postgraduate Research Scholarship (MIPRS). DLJ acknowledges support from ARC Discovery grant DP0774525 and computing time from the Australian Partnership for Advanced Computing (APAC).

REFERENCES

1. Bearman, P. W., Graham, J. M. R., Naylor, P., and Obasaju, E. D., *The role of vortices in oscillatory flow about bluff cylinders*, in *International Symposium on Hydrodynamics in Ocean Engineering*. 1981: Trondheim, Norway. p. 621-635.
2. Blackburn, H. M., Sheridan, J., and Elston, J. R., Bluff-body propulsion produced by combined rotary and translational oscillation. *Physics of Fluids*, Vol. 11, No.1, pp 4-6, 1999.
3. Honji, H., Streaked flow around an oscillating cylinder. *J. Fluid Mech.*, Vol. 107, pp 509-520, 1981.
4. Williamson, C. H. K., Sinusoidal flow relative to circular cylinders. *J. Fluid Mech.*, Vol. 155, pp 141-174, 1985.
5. Tatsuno, M. and Bearman, P. W., A visual study of the flow around an oscillating circular cylinder at low Keulegan-Carpenter numbers and low Stokes numbers. *J. Fluid Mech.*, Vol. 211, pp 157-182, 1990.
6. Justesen, P., A numerical study of oscillating flow around a circular cylinder. *J. Fluid Mech.*, Vol. 222, pp 157-196, 1991.
7. Iliadis, G. and Anagnostopoulos, G., Viscous oscillatory flow around a circular cylinder at low Keulegan-Carpenter numbers and frequency parameters. *International Journal for Numerical Methods in Fluids*, Vol. 26, pp 403-442, 1998.
8. Dütsch, H., Dusrt, F., Becker, S., and Lienhart, H., Low-Reynolds-number flow around an oscillating circular cylinder at low Keulegan-Carpenter numbers. *J. Fluid Mech.*, Vol. 360, pp 249-271, 1998.
9. Tokumaru, P. T. and Dimotakis, P. E., Rotary oscillation control of a cylinder wake. *J. Fluid Mech.*, Vol. 224, pp 77-90, 1991.
10. Poncet, P., Topological aspects of three-dimensional wakes behind rotary oscillating cylinders. *J. Fluid Mech.*, Vol. 517, pp 27-53, 2004.
11. Thiria, B., Goujon-Durand, S., and Wesfreid, J. E., The wake of a cylinder performing rotary oscillSations. *J. Fluid Mech.*, Vol. 560, pp 123-147, 2006.

12. Al-Mdallal, Q. M., Analysis and computation of the cross-flow past an oscillating cylinder with two degrees of freedom, Memorial University of Newfoundland Department of Mathematics and Statistics, 2004.
13. Lo Jacono, D., Nazarinia, M., Thompson, M. C., and Sheridan, J. Flow behind a cylinder forced by a combination of oscillatory translational and rotational motions. *Proceedings of XXII International Congress of Theoretical and Applied Mechanics*, Adelaide, Australia, University of Adelaide, August 24-29, 2008, pp 349.
14. Elston, J. R., The structures and instabilities of flow generated by an oscillating circular cylinder, *PhD Thesis*, Monash University Mech. Eng. Dept., Melbourne, 2005.
15. Stansby, P. K., The effect of end plates on the base pressure coefficient of a circular cylinder. *R. Aeronaut.*, Vol. 78, pp 36-37, 1974.
16. Adrian, R. J., Particle-imaging techniques for experimental fluid mechanics. *Annual Review Fluid Mechanics*, Vol. 23, pp 261-304, 1991.
17. Fouras, A., Lo Jacono, D., and Hourigan, K., Target-free stereo PIV: A novel technique with inherent error estimation and improved accuracy. *Experiments in Fluids*, Vol. 44, No.2, pp 317-329, 2008.
18. Fouras, A. and Soria, J., Accuracy of out-of-plane vorticity measurements derived from in-plane velocity field data. *Experiments in Fluids*, Vol. 25, pp 409-430, 1998.
19. Karniadakis, G. E. and Sherwin, S. J., *Spectral/hp methods for computational fluid dynamics*, Oxford Universoty Press, Oxford, 2005.
20. Thompson, M. C., Hourigan, K., and Sheridan, J., Three-dimensional instabilities in the wake of a circular cylinder. *Exp. Therm. Fluid Sci.*, Vol. 12, pp 190-196, 1996.
21. Canuto, C., Hussaini, M., Quarteroni, A., and Zang, T., *Spectral Methods in Fluid Dynamics*, Springer Verlag, 2nd ed, Berlin and New York, 1990.
22. Leontini, J. S., Thompson, M. C., and Hourigan, K., Three-dimensional transition in the wake of a transversely oscillating cylinder. *J. Fluid Mech.*, Vol. 577, pp 79-104, 2007.
23. Thompson, M. C., Leweke, T., and Williamson, C. H. K., The physical mechanism of transition in bluff body wakes. *J. Fluids & Structures*, Vol. 15, pp 607-616, 2001.
24. Barkley, D. and Henderson, R. D., Three-dimensional Floquet stability analysis of the wake of a circular cylinder. *J. Fluid Mech.*, Vol. 322, pp 215-241, 1996.
25. Morton, B. R., The generation and decay of vorticity. *Geophysical & Astrophysical Fluid Dynamics*, Vol. 28, No.3, pp 277-308, 1984.

FLOW PROFILES ON THE FIN SIDE OF A PLATE FIN-AND-TUBE HEAT EXCHANGER EXPERIENCING GROSS FLOW MALDISTRIBUTION

J. Hoffmann-Vocke*, J. Neale, M. Walmsley
Energy Research Group, The University of Waikato, Hamilton, New Zealand

ABSTRACT. Flow profile measurement using thermal anemometry has been carried out for various conditions in a plate fin-and-tube airside inlet header. Commonly applied inlet header geometries, with an area ratio of 9:1 are used with results from wide-angle square diffusers compared with a sudden expansion. All geometries provided poor flow distribution leading to gross flow maldistribution at the outlet of the header. Considerably higher magnitudes of flow maldistribution were measured in an open header than with the test plate fin-and tube heat exchanger in place. Gross flow maldistribution entering a plate fin-and- tube heat exchanger results in a complex inlet profile that can only be accurately determined by the measurement of all three velocity components. Significant differences exist between magnitude of flow maldistribution entering and leaving the test plate fin-and-tube heat exchanger. Flow profile changes are caused by the spreading of the flow as it passes through the heat exchanger. Internal flow spreading occurs only in the axis perpendicular to the orientation of the tubes. Therefore it is concluded that using the unmixed fin side assumption in plate fin-and-tube heat exchangers is not valid in cases of inlet flow maldistribution.

Keywords: *heat exchanger, gross flow maldistribution, plate fin-and-tube, unmixed flow*

INTRODUCTION

Compact heat exchangers such as plate fin-and-tube geometries are widely used in various chemical and process industries for applications such as; process gas heaters and coolers. In order to increase compactness and overcome the low density and thermal conductivity of gases, a secondary heat transfer area in the form of fins are commonly employed. The secondary heat transfer area to primary area ratio is commonly as large as 30 or 50. The hydraulic flow resistance on the fin side (gas side) can become a significant factor due to the large number of small passages created between the fins. The gas side pressure drop is approximately proportional to the velocity squared, and as a result in most cases velocities are kept low to minimize the required pumping power, since this can be a major operating expense [1]. The large air side surface area and desire for low pressure drop, results in a heat exchanger geometry consisting of a large frontal surface area and a short flow length.

Typically the gas side design is based on the assumption of a uniform mass flow distribution through the fin-and-tube bundles [2, 3]. In industrial applications such as in process gas heaters, this is typically not the case [4, 5]. Non uniform distribution (maldistribution) of gas flow on the fin side of fin-and-tube heat exchangers can be caused by a variety of factors. Common variables causing flow maldistribution are; entry conditions, bypass, fabrication tolerances, shallow bundle effects, and general equipment and exchanger system effects [6]. One of the most common causes

* Corresponding author: J.Hoffmann-Vocke
Phone: + (64)-7-8384937, Fax: + (64)-7-8384835
E-mail address: jh63@waikato.ac.nz

of flow maldistribution in large industrial gas heat exchangers is the design of entry conditions, such as headers and inlet ducts [7]. The gas side header transitions between the higher velocity transport ducting and the much larger heat exchanger inlet face. Typical industrial applications usually exhibit an area ratio of 8 to 10 between the ducting and heat exchanger inlet. This inlet header is typically some form of 3D compound angle diffuser, providing a sudden uncontrolled transition from the ducting to the heat exchanger inlet face. Expanding fluid flow under an adverse pressure gradient as experienced in any diffusing geometry, leads to significant boundary layer growth. In most industrial applications the rate of uncontrolled expansion is very high, leading to separation of the flow. As a result the uniformity of the mass flow leaving the header and entering the fin-and-tube heat exchanger in an industrial setting is typically quite low.

The effect of flow maldistribution on the gas side of a fin-and-tube heat exchanger can vary considerably depending on the specific case. Generally the effects can be classified into two groups; performance, such as duty and pressure drop, and mechanical; such as increased wear or reduced service life. There are a considerable number of variables involved in determining the effect of flow maldistribution on the performance and mechanical integrity. The complexity and multitude of variables associated with flow maldistribution in heat exchangers have contributed to the lack of systematic effort to predict the occurrence and effects of flow maldistribution. A contributing factor has been the difficulty in actually identifying flow maldistribution within a heat exchanger. Past research has shown that heat exchangers with high effectiveness, or low temperature differences such as fin-and-tube heat exchangers are especially prone to a reduction in thermal performance from flow maldistribution [6].

Various researchers [2, 3, 8-11], have investigated the effects of flow maldistribution on fin- and-tube heat exchangers using experimental and numerical methods. Investigations commonly involve the exposure of particular heat exchanger geometry to a specific magnitude of flow maldistribution. In the experimental investigations the specific heat exchanger geometry, pass arrangement, tube bundle depth, and fin and tube materials mean that each case is exclusively relevant to those conditions. The researchers do not have a sufficient variety of test results to allow trends and performance relations to be attained. Most of the past work has focused on fin-tube heat exchangers used in air conditioning and heat shedding applications. These types of applications utilise axial fans to force air through the heat exchanger. The diameter of the axial fan outlet is typically quite similar to that of the heat exchanger face, meaning that only small magnitudes of flow maldistribution are typically experienced. The effects of flow maldistribution of the magnitude possible in industrial process gas heaters utilising centrifugal fans and small diameter higher velocity ducting have had little investigation. Typically past numerical work on flow maldistribution is not limited to a specific case by case basis. However, the common shortfall is the simplifications made regarding the fin side flow profile. The most common and questionable assumption is the unmixed fin-side flow assumption [12, 13] that are used in fin-and-tube heat exchanger design and performance evaluation. Simplifications of this order are typically used to make the numerical simulation manageable, however this trivialises the complexity of the flow behaviour encountered in flow maldistribution within a heat exchanger. The past research provided results for specific cases; however this limited amount of work does not provide a relevant and comprehensive foundation for assessing the effects on fin-and-tube heat exchangers used as industrial process gas heaters and coolers.

Accurately assessing the performance changes associated with flow maldistribution in fin-and tube heat exchangers requires first; a detailed understanding of the gas flow profile, and how it evolves throughout the heat exchanger system. The current investigation aims at providing a valuable contribution to this point. Experimental measurements quantifying the magnitude and direction of flow maldistribution entering and leaving the heat exchanger are presented.

EXPERIMENTAL SETUP

Experimental investigations of air flow profiles and hydraulic performance of a plate fin-and tube heat exchanger have been carried out on a laboratory scale forced draught air heater model. The air heater model consists of modular sections that can easily be interchanged to allow the investigation of multiple configurations. Figure 1 below shows the inlet configuration starting with a 4.0 kW FlexLine D634DD centrifugal fan (A). This is followed by an outlet contraction (B) which adapts the rectangular fan exit to the square inlet ducting (D_h = 0.3 m). The initial 3.3 hydraulic diameters of inlet ducting (C) are then followed by a circular honeycomb matrix (D) consisting of plastic drinking straws. The matrix has an aspect ratio (x/D_h) of 12 and is used for flow conditioning and bulk flow measurement. The circular straw matrix is then followed by a further 5 hydraulic diameters of inlet ducting (E). Figure 1 shows the sudden 180° expansion (F) in place following the inlet ducting. Various square expansion sections all with an area ratio of 9:1 can be placed in location F, to provide different inlet conditions to the heat exchanger. The expansion section is then followed by various lengths of square straight ducting (G) comprising of a hydraulic diameter of 0.9 m.

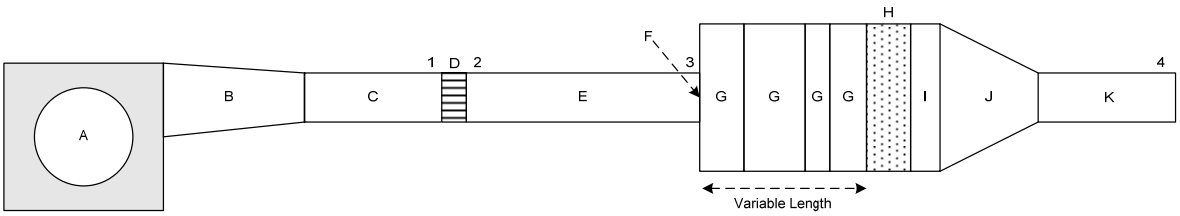

Figure 1. Schematic showing the main aspects of the experimental rig

Various lengths of large (D_h = 0.9 m) inlet ducting are available and allow the variation of the distance between the expansion and heat exchanger inlet face. A four row staggered plate-fin and tube heat exchanger (H) has been used as the test heat exchanger geometry. The 13.3 mm OD copper tubes are arranged with a 31.75 mm transalation and 28 mm longitudinal spacing. The aluminium continuous plate fins have a pitch of 310 fins per meter with an average thickness of 0.2 mm. The overall dimension of the heat exchanger is 0.9 m in height by 0.88 m in width and a 0.11 m in depth. The exit of the heat exchanger is followed by further straight ducting (I), giving a development length after the heat exchanger exit face. The development length is important in smoothing out some of the non-uniformities associated with the flow exiting the tube bundle. The straight exit ducts are followed by a 60° contraction diffuser (J) with an area ratio of 9:1. This is then followed by an outlet duct identical to inlet duct C. The numbers detailed on Figure 1 show the location of important pressure tap points for measuring system performance (3 & 4) and bulk flow rate (1& 2).

Point wise air velocity measurement is carried out using a calibrated TSI VelociCalc Plus thermal anemometer. This film thermal anemometer provides averaged readings over a time interval of 2 seconds or greater. Each 2 second average is compromised of 20 individual readings taken at a frequency of 10 Hz. Multiple time-averaged velocities where taken at each point in the line or plane of interest. In most locations, 25 individual two-second averaged measurements provided a stable average of the local velocity. The draw back of thermal anemometry using a single hot-film sensor is that only the velocity magnitude is attained. Flow direction cannot be determined with positive and negative velocities giving the same result. To overcome this problem, a tuft of fine

yarn made from bamboo fibres was located near the hotwire probe to allow the visual estimation of flow direction. This method is most accurate in steady flows, where the yarn tuft provides a stable direction indicator. In fluctuating flows the error of this method becomes higher; however, it still provides important additional information on the state of the local flow field. Through the use of the yarn tuft, the velocity readings can be more accurately interpreted.

Measurement of the bulk inlet velocity is carried out by determining the pressure drop across the circular straw honeycomb screen. The screen pressure drop has been calibrated to flow velocity using thermal anemometry measurements. Static pressure measurements were taken at wall mounted pressure taps.

Velocity measurements at the inlet and outlet of the test heat exchanger where measured 0.03 m and 0.212 m from the inlet and outlet face respectively. Measurements in front and behind the heat exchanger were carried out along lines corresponding to the vertical and horizontal axis of symmetry. Where visual flow direction measurements are made using the yarn tuft, the x-axis corresponds to the main flow direction, normal to the heat exchanger. For vertical profiles, the y-axis runs from the bottom to the top of the heat exchanger. Correspondingly, the z-axis flow direction for horizontal profiles corresponds to running from right to left of the heat exchanger inlet face. Distance locations of the velocity measurements are taken from bottom to top and right to left of the heat exchanger inlet face.

RESULTS

Characterisation of potential flow maldistribution

Initial investigations involved the measurement of air flow profiles exiting 3D square diffusers similar to those used as transition headers in process gas heat exchangers. In industrial process gas heat exchangers such as the air heaters used in milk powder plants, the minimisation of space and capital cost is the main driving force for the gas side header and ducting design. The area ratio of 8-10:1 between the transport ducting and heat exchanger inlet face requires a significant angle of expansion to achieve the transition within limited space. The common range of total included expansion angles is typically between 25° and 90°. Uncontrolled expansion rates of this magnitude in a diffusing passage lead to excessive boundary layer growth and then flow separation. Figure 2 below displays the exit velocity profiles of two different square diffusers each with and area ratio (outlet to inlet) of 9:1. Each diffuser has an equal mass flux. Due to the unsteady nature of the fluctuating flow in the square diffusers the contours are a time averaged representation of the steady flow. As illustrated by the profiles, significant non-uniformity exists and the majority of the flow is confined to a separated jet. The magnitude of the flow maldistribution can be summarised numerically by the use of a mass weighted average velocity. For the ideal case of a uniform distribution of the same mass flux the mass weighted velocity would be 2.67 m/s. In comparison the exit mass weighted velocity for the 30° case is 11.37 m/s, while for the 90° case a further increase to 16.60 m/s is achieved. It is thus apparent that under flow conditions common in industrial process gas heat exchanger headers there is potential for significant flow maldistribution to occur. While the potential for flow maldistribution is clear, the effect of the downstream heat exchanger on the upstream flow profile needs to be characterised.

Wide angle diffuser simulation by sudden expansion

The flow profiles shown in Figure 2 illustrate the flow maldistribution possible in a wide angle square diffuser. As mentioned previously the nature of the flow in these diffusers is quite unstable and in the case of the 30° diffuser highly non-symmetrical.

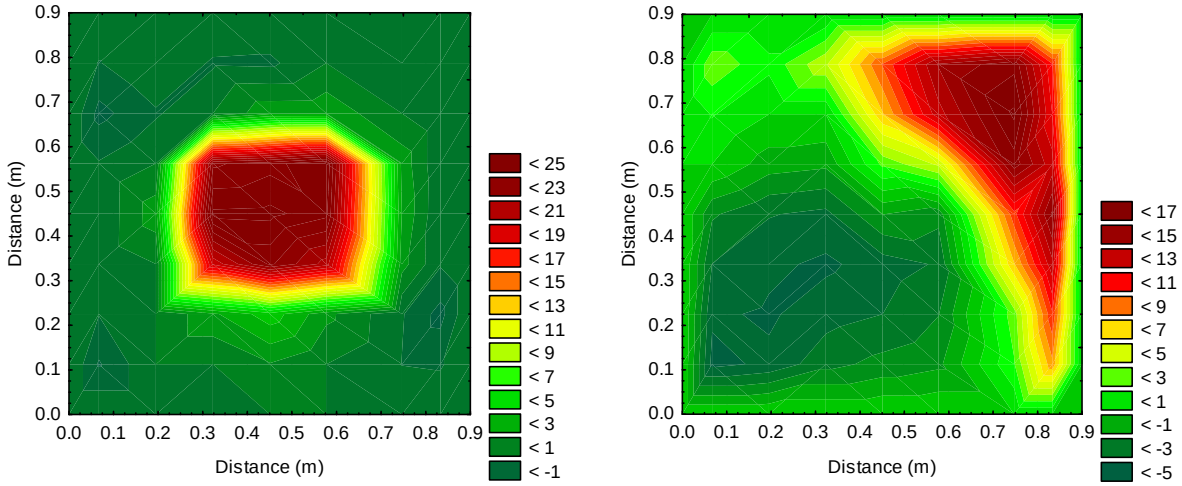

Figure 2. Square diffuser exit velocity (m/s) profiles for (left) 90° diffuser and (right) 30° diffuser

In order to simplify the maldistribution profile and reduce the fluctuations a sudden expansion with an identical area ratio (9:1) has been used to generate the flow maldistribution for the subsequent heat exchanger investigation. The sudden expansion provides a comparatively stable maldistribution with reliable lines of symmetry. This allows a reduction in measurements from a full plain traverse to just two line traverses along the vertical and horizontal lines of symmetry. Figure 3(A) shows the velocity profile comparison between the vertical and horizontal centre lines of the 90° diffuser and sudden expansion. These profiles show the velocity magnitudes of the different geometries at similar distances from the expansion entrance. As expected the sudden expansion provides a more symmetric and consistent profile. In order to further simplify the number of variables, the effect of Reynolds number on the jet profile has been investigated for the sudden expansion geometry. The jet profiles are in the so called development region ($0 \leq x/d \leq 25$) for common self-similar free shear flows such as the round jet. The self-similar behaviour (within a reasonable approximation) is commonly exhibited for a range, but not all x [14]. As confirmed by Figure 3(B) the mean jet profiles exhibit Reynolds number independence for the range tested. Due to the wall and downstream blockage effects, it is unlikely that the jets exhibit any of the self-similar behaviour as seen with the true free shear flows. As part of the experiments carried out with the sudden expansion geometry, the Reynolds number independence has been checked for each configuration.

Plate-fin and tube inlet velocity profiles following sudden expansion

Velocity measurements before and after the test heat exchanger have been carried out for two different inlet velocity profiles. Both profiles were formed by the sudden expansion inlet condition but, differed in the number of duct diameters from the expansion to the heat exchanger inlet face. Configuration A1 placed the heat exchanger inlet face 0.35 hydraulic diameters (D_h = 0.9m) after the sudden expansion. Configuration B1 provided a longer inlet length giving 2.13 hydraulic diameters for the jet profile to develop prior to entering the heat exchanger. Figure 4 shows the velocity magnitude of the vertical and horizontal centre lines for flow entering and exiting the heat exchanger. Figure 4A illustrates the smoothing effect the extra development length provides to configuration B1. Comparison between plots A and B shows the evidence for some form of flow spreading occurring as there is a significant reduction in velocity magnitude

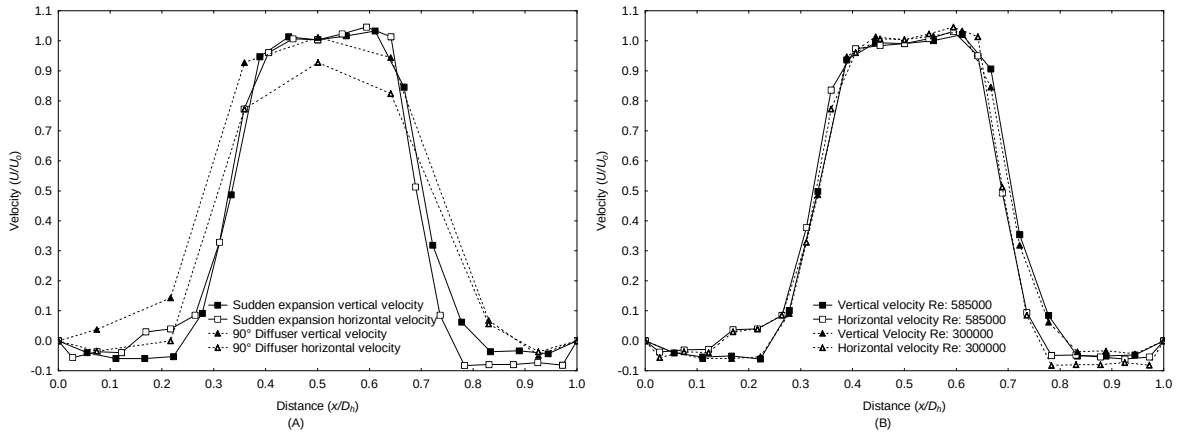

Figure 3. (A) Comparison between 90° diffuser and sudden expansion exit velocity magnitude, (B) Reynolds number independence of jet profile for sudden expansion geometry

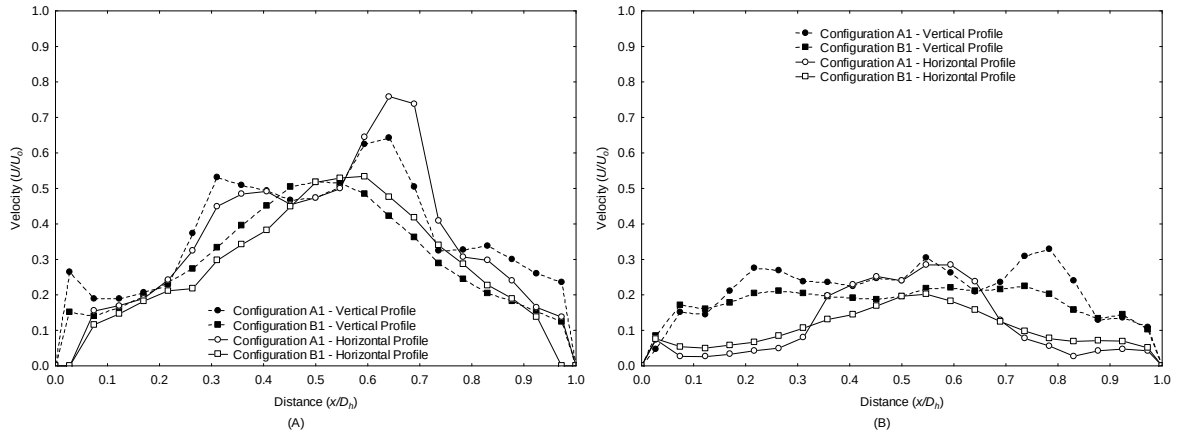

Figure 4 (A) Inlet velocity magnitude, (B) outlet velocity magnitude

While Figure 4 clearly shows that some form of flow spreading is occurring as the flow travels through the heat exchanger, it is difficult to determine any further detail in relation to the direction of the flow as it passes through the heat exchanger. By measuring the inlet flow direction and determining the individual velocity components, a more accurate representation of the flow field can be made. Figure 5 below splits the inlet velocity magnitude into individual components. It becomes clear from Figure 5 that the inlet velocity profile is a lot less uniform, and that only the central region contains significant amounts of flow perpendicular to the inlet face. Significant amounts of air flow are moving in the y and z axis parallel to the heat exchanger face. A proportion of the parallel flow then recirculates at the sides and vertical extremities of the heat exchanger as shown by the negative x-velocities and decay of the Y and Z velocity components. It is clear from the magnitude of the negative x-velocities found at the heat exchanger extremities that the majority of the flow does not recirculate. Instead, the slope of the y and z velocity profiles suggests that a portion of the flow is continuously bled off, passing through the heat exchanger. The resulting outlet profile becomes a combination of flow spreading before and through the heat exchanger. Flow spreading within the heat exchanger is predominantly associated with the dissipation of the x-velocity jet. Comparison of the vertical and horizontal outlet profile indicates that the flow spreading in each direction is not equal. The outer regions of the horizontal exit profile indicate a reduction of flow through these sections of the heat exchanger.

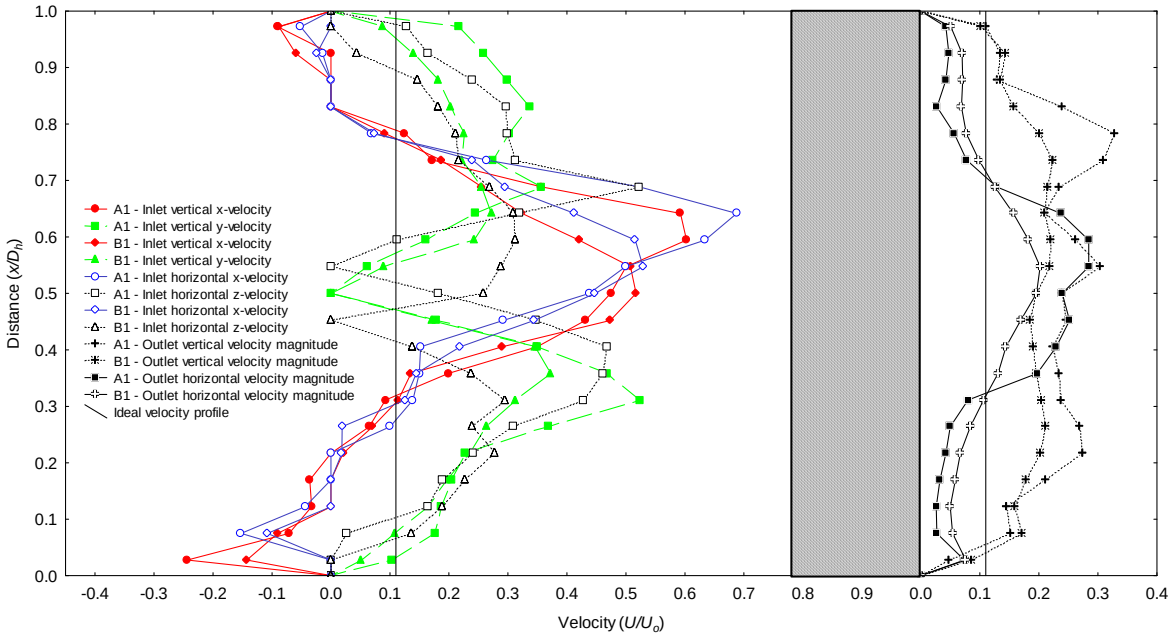

Figure 5. Inlet velocity component profiles and outlet velocity magnitude profiles

This can be explained by vertical orientation of the continuous plate fins. The reduction of flow spreading in the horizontal axis increases the magnitude of the vertical outlet velocity profile. The average vertical outlet velocity magnitude is over twice the ideal value (0.111); corresponding to a uniform flow distribution. Further insight into the extent of flow spreading can be attained by comparing the jet width on the inlet and outlet of the heat exchanger. The jet width is commonly determined by the spacing of the points corresponding to a velocity half the magnitude of the central velocity. Using this methodology, there is no significant horizontal spreading, while spreading in the vertical axis approximately doubles the width of the jet.

Dividing the heat exchanger entry and exit faces both into three by three square grid segments (300 mm square) the following flow conditions are experienced. On the inlet face, the central segment contains the majority of the high velocity jet at approximately five times the ideal flow velocity. The other eight remaining segments have a majority of the flow parallel to the heat exchanger, gradually reducing in velocity and resulting in a negative recirculation at the edges. On the outlet face the three segments corresponding to the vertical line of symmetry contain an average velocity two times the ideal. The remaining segments all contain velocities equal or below the ideal.

CONCLUSIONS

Experimental results using square wide angle diffusers confirm that exit flow conditions are highly non-uniform. As the expansion rate is increased, the non-uniformity of the exit flow condition increases, reaching a maximum corresponding to a sudden expansion. Significant differences exist between the sudden expansion jet profile in an empty duct and that entering the face of the test heat exchanger. Accurate measurement of the inlet flow profile requires the determination of flow direction, not only magnitude. Actual flow measurements 0.03 m before the heat exchanger inlet face reveal a complex flow profile containing flow normal and parallel to the heat exchanger. Only

the central jet region contains high velocities normal to the heat exchanger inlet face. The magnitude of the central jet entering the heat exchanger is approximately halved compared to that of a jet in an unobstructed duct. Flow measurement into, and out of the plate fin-and-tube heat exchanger illustrates changes in the flow profile, resulting in a more uniform exit flow distribution. The flow spreading is most significant in the vertical direction, normal to the orientation of the tubes. Due to the continuous vertical fins, flow spreading in the horizontal axis only occurs before the heat exchanger. Accurate calculation of heat exchanger performance variables such as pressure drop and heat transfer need to take into account inlet maldistribution and flow spreading through the heat exchanger. Performance calculations using the inlet profile throughout the whole depth of the heat exchanger, as commonly used in the unmixed fin-side flow assumption will result in significant error.

REFERENCES

1. Sahin, H.M., A.R. Dal, and E. Baysal, 3-D Numerical study on the correlation between variable inclined fin angles and thermal behaviour in plate fin-tube heat exchanger. *Applied Thermal Engineering*, 2007. **27**(11-12): p. 1806-1816.
2. Rabas, T.J. Effect of nonuniform inlet flow and temperature distributions on the thermal performance of air-cooled condensers. 1987. Pittsburgh, PA, USA: ASME, New York, NY, USA.
3. Ranganayakulu, C., K.N. Seetharamu, and K.V. Sreevatsan, The Effects of inlet fluid flow nonuniformity on thermal performance and pressure drops in crossflow plate-fin compact heat exchangers. *International Journal of Heat and Mass Transfer*, 1997. **40**(1): p. 27-38.
4. Chiou, J.P., The advancement of compact heat exchanger theory considering the effects of longitudinal heat conduction and flow nonuniformity. *American Society of Mechanical Engineers, Heat Transfer Division, (Publication) HTD*, 1979. **10**: p. 101-121.
5. Ranganayakulu, C. and K.N. Seetharamu, Combined effects of longitudinal heat conduction, flow nonuniformity and temperature nonuniformity in crossflow plate-fin heat exchangers. *International Communications in Heat and Mass Transfer*, 1999. **26**(5): p. 669-678.
6. Kitto, J.B. and J.M. Robertson, Effects of Maldistribution of Flow on Heat Transfer Equipment Performance. *Heat Transfer Engineering*, 1989. **10**(1): p. 18 - 25.
7. Hoffmann-Vocke, J., J.R. Neale, and M. Walmsley. Fin Side Flow Maldistribution And Its Effects On Multi-Row Plate Fin-And-Tube Heat Exchangers. *in SCENZ 2008*. 2008. Hamilton, New Zealand.
8. Fagan, T., The effect of air flow maldistribution on air-to refrigerant heat exchanger performance. *ASHRAE Transactions*, 1980. **80**(7).
9. Soler, A.I. and K.P. Singh. Effect of Nonuniform Inlet Air Flow on Air Cooler Heat Exchanger Performance. 1983.
10. Beiler, M.G. and D.G. Kroger, Thermal Performance Reduction in Air-Cooled Heat Exchangers Due to Non uniform Flow and Temperature Distributions. *Heat Transfer Engineering*, 1996. **17**(1): p. 82 - 92.
11. T'Joen, C., et al., Performance Prediction of Compact Fin-and-Tube Heat Exchangers in Maldistributed Airflow. *Heat Transfer Engineering*, 2007. **28**(12): p. 986 - 996.
12. Cengel, Y., A., and R. Turner, H.,, *Fundamentals of Thermal-Fluid Sciences*. 2001, Singapore: McGraw-Hill Book Co.
13. Kakac, S., A.E. Bergles, and F. Mayinger, *Heat Exchangers, Thermal-Hydraulic Fundamentals and Design*. 1981: Hemisphere Publishing Corporation.
14. Pope, S.B., *Turbulent Flows*. 2000, Cambridge: Cambridge University Press.

AEROSOL PARTICLE FOCUSING IN AN ACOUSTIC CHANNEL

P. Vainshtein* and M. Shapiro

Laboratory of Transport Processes in Porous Materials, Faculty of Mechanical Engineering, Technion - Israel Institute of Technology, Haifa 32000, Israel

ABSTRACT. We investigate analytically and numerically focusing of aerosol micron-and-submicron size particles in the incompressible laminar flow in a three-dimensional quadrupole acoustic channel of hyperbolic cross-section. The fluid-particle interaction of micron-size non-diffusive particles is described by a linear drag force. Considering motion of diffusive submicron particles, we account for their random displacements. It is shown that acoustic oscillations with frequency of about 1 kHz focus micron size particles on axial distance comparable to channel cross-sectional size. Submicron diffusive particles cannot be focused exactly at the channel axis owing to the adverse effect of Brownian motion leading to the diffusion broadening. It is shown that the achievable focusing width decreases with increasing the strength of the acoustic field.

Keywords: *focusing, acoustics, channel, aerosol*

INTRODUCTION

Lens arrays used for aerodynamic particle focusing in aerosol instrumentation [1] have disadvantages related to early flow separation adversely affecting focusing efficiency. In work, [2] we proposed and investigated focusing scheme in a model planar channel with oscillating walls free from this shortcoming. However, in the planner channel the axial oscillatory pressure growth takes place. This precludes possibility of its practical implementation. Here we develop that study and consider aerosol particle focusing in a three-dimensional channel of hyperbolic cross-section (Figure 1). The channel walls undergo acoustic excitation resulting in quadrupole pressure disturbances.

Previously such a quadrupole channel with hyperbolic electrodes was employed for ions focusing by means of an ac electric field [3].

ANALYSIS OF FLUID MOTION

We consider wavelength, λ satisfying condition $\lambda >> r_0$. Here r_0 is the distance shown in Figure 1. Cross-sectional acoustic field is generated at the channel walls (1) and (2) by pressure disturbances described by Eqs. (1) and (2).

$$p' - p_0 = -p_s \cos \omega t' \quad \text{at} \quad z'^2 - y'^2 = r_0^2 \tag{1}$$

$$p' - p_0 = p_s \cos \omega t' \quad \text{at} \quad y'^2 - z'^2 = r_0^2 \tag{2}$$

here and below primed variables are dimensional, $\omega = 2\pi f$ is the angular frequency of pressure

*Corresponding author: Dr P. Vainshtein
Phone: 972 4 8293266, Fax: 972 4 295711
E-mail address: merpeva@tx.technion.ac.il

oscillations, f is the corresponding frequency, p_s is the amplitude of the pressure oscillations. Under condition $\lambda >> r_0$ and assumption on small oscillations amplitude, $\varepsilon = p_s / p_0 << 1$ (here p_0 is the undisturbed gas pressure), the flow velocity field within the channel may be considered incompressible and creeping. It is described by Navier-Stokes and continuity equations (3).

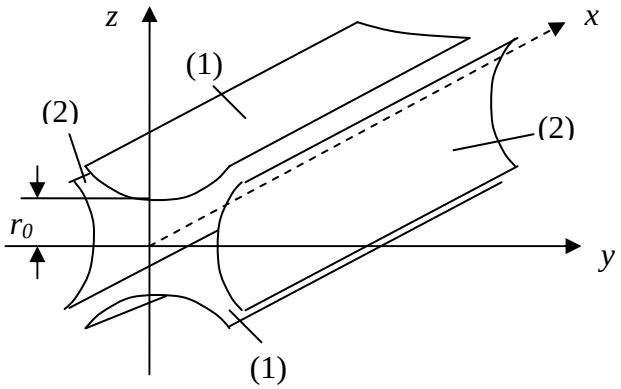

Figure 1. Quadrupole acoustic channel.

$$\frac{\partial \mathbf{u}'}{\partial t'} = -\frac{1}{\rho_f}\nabla p' + \nu\nabla^2\mathbf{u}', \ \nabla\mathbf{u}' = 0 \tag{3}$$

where $\mathbf{u}' = (u', \mathrm{v}', \mathrm{w}')$ is the velocity vector, ρ_f is the fluid density, ν is the fluid kinematic viscosity. According to (3), the pressure distributions satisfy the Laplace equation.

We assume flow velocities in a channel cross-section to be *x*-independent. Let the channel have a length *L*. The imposed pressure drop leads to the axial flow with maximal velocity *U*, say. The obtained solution for the pressure is

$$p' - p_0 = x'\frac{\partial p'}{\partial x'} + \frac{p_s \cos\omega t'}{r_0^2}\left(y'^2 - z'^2\right), \ \frac{\partial p'}{\partial x'} = \text{const} \tag{4}$$

In (4), the first hydraulic term is assumed much smaller than the second acoustic one. This restriction is fulfilled in a wide range of flow and acoustic parameters. Let us set for instance $r_0 = 0.5\,\text{cm}$, U=5 cm/sec, L=1 cm, SPL=140 dB. Then in air where $\rho_f = 1.29\,\text{kg/m}^3$, $\nu = 1.5\times10^{-5}\,\text{m}^2/\text{sec}$, one has $-L\partial p'/\partial x' = 10^{-3}\,\text{Pa}$ while $p_s = 300\,\text{Pa}$. Under this restriction pressure distribution (4) satisfies boundary conditions (1) and (2).

According to (4) the axial pressure does not contain oscillatory components. This situation is different from that occurring in the planner channel [2]. The axial velocity component is independent of time and axial coordinate. It may be approximated in the near-axis region by Poiseuille formula

$$u' = \frac{r_0^2\partial p'/\partial x'}{4\rho_f\nu}\left(1 - \frac{r'^2}{r_0^2}\right) = U\left(1 - \frac{r'^2}{r_0^2}\right) \tag{5}$$

here $r' = \left(y'^2 + z'^2\right)^{1/2}$ is a magnitude of the radius-vector.

The cross-sectional velocity components are

$$\mathrm{v}' = -\mathrm{v}_s\frac{y'}{r_0}\sin\omega t', \quad w' = \mathrm{v}_s\frac{z'}{r_0}\sin\omega t' \tag{6}$$

where

$$\mathrm{v}_s = 2\frac{p_s}{\rho_f \omega r_0} = 2\varepsilon \frac{p_0}{\rho_f \omega r_0} \tag{7}$$

is the characteristic amplitude of fluid velocity oscillations occurring in the channel. For a given channel half-size, r_0, this amplitude is determined by the frequency of acoustic field and sound pressure level (SPL).

According to (6) the channel walls perform oscillations perpendicular to the channel axis. Opposite walls of the channel contract and expand aerosol-filled channel interior in phase. On the contrary, adjacent walls act in counter-phase. By such a way quadrupole excitation of fluid oscillations inside the channel is accomplished.

The fluid velocity (6) is independent of viscosity; however it satisfies the equations of the viscous flow and no-slip boundary condition. This is because the cross-sectional velocity vector on the walls is normal to the walls (Figure 2). Moreover, this vector is normal to the surfaces equidistant to channel walls. Indeed, cross-sectional vectors tangent to the surfaces equidistant to (1) and (2) are $\mathbf{T} = (2z', 2y')$ and $\mathbf{T} = (-2z', -2y')$, respectively. The scalar product of these vectors and that given by (6) is equal to zero. Thus no velocity oscillations in directions parallel to the channel walls take place. Moreover the *z'-y'* shear stress components in any channel's cross-section are identically zero everywhere and hence no secondary streaming is present.

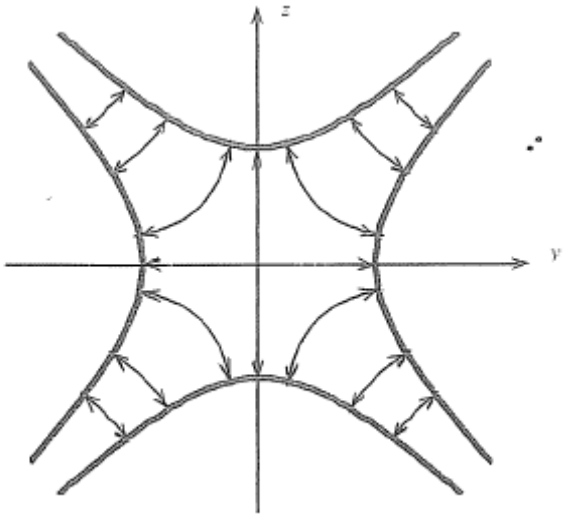

Figure 2. Sketch of cross-sectional fluid streamlines. Arrows show directions of fluid oscillations.

Then the fluid velocity oscillates along the streamlines (Figure 2). It is linearly distributed and vanishing at the channel axis. This leads to particles drifting motion towards the axis and their focusing there. We describe this effect below.

ANALYSIS OF PARTICLE MOTION

We assume a dilute aerosol of rigid particles so that particle-particle interactions are negligible and the presence of particles does not affect the fluid flow. Consider trajectories of a diffusive particle of radius *a* in flow field (5), (6). The fluid-particle interaction is described by the Langevin equation

$$\frac{\mathrm{d}\mathbf{v}_p'}{\mathrm{d}t'} = \frac{\mathbf{u}' - \mathbf{v}_p'}{\tau} + \Xi_{\mathbf{Br}}, \tag{8}$$

where $\mathbf{v}_p^{'}$ is the particle velocity vector, $\tau = 2a^2 C(Kn)/9\nu\Pi_\rho$ is the Stokes relaxation time, Π_ρ is the fluid-to particle-density ratio and $C(Kn)$ is the Cunningham correction factor expressed via the Knudsen number, $Kn = \ell / 2a$ where $C(Kn) = 1 + Kn\left[A + Q\exp(-B/Kn)\right]$ with A=2.51, Q=0.8, B=0.55. Here ℓ is the molecular free path which under normal atmospheric conditions is equal to 65 nm. This approximation is valid for aerosol applications when $\omega\tau\Pi_\rho << 1$. In Eq. (8) $\Xi_{\mathbf{Br}}$ is the Brownian acceleration which describes the effect of Brownian diffusion, important for submicron and nanometer particles [1].

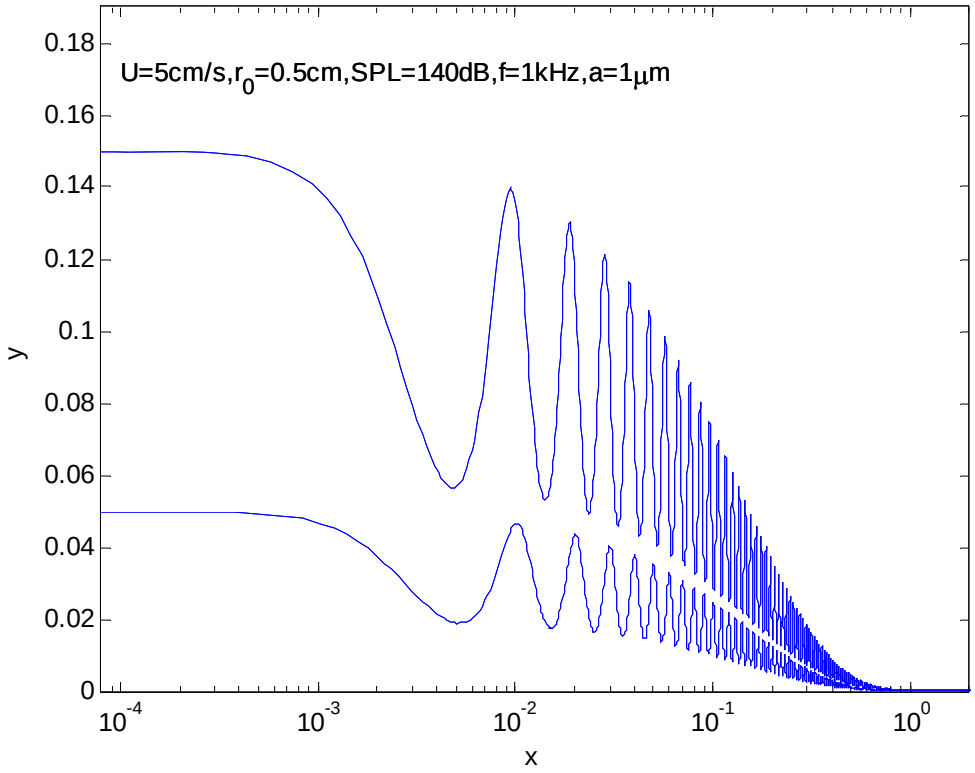

Figure 3. Particle trajectories in the quadrupole acoustic channel.

We define the following dimensionless variables

$$t = \omega t^{'},\ x = \frac{x^{'}}{r_0}, y = \frac{y^{'}}{r_0},\ \ z = \frac{z^{'}}{r_0},\ \ r = \frac{r^{'}}{r_0}, \mathbf{u}_p = \frac{\mathbf{u}_p^{'}}{\omega r_0},\ \mathbf{u} = \frac{\mathbf{u}^{'}}{\omega r_0} \tag{9}$$

Focusing efficiency is investigated for variety of flow and particle parameters expressed in terms of the dimensionless group, namely

$$\beta = \frac{\mathrm{v}_s}{\omega r_0} = 2\frac{p_s}{\rho_f (\omega r_0)^2},\ \ \Pi_U = \frac{U}{\omega r_0}, \Pi_D = \sqrt{\frac{D}{\omega r_0^2}},\ \ \omega\tau \tag{10}$$

Here $\omega\tau$ is the frequency parameter, representing the particle Stokes number of the problem, β is the acoustic strength parameter, Π_U is the axial flow velocity parameter, Π_D is the particle diffusion parameter, D is the particle diffusion coefficient.

Equations of particle motion represent a special case of the damped Mathieu equations. Their stability is governed by parameters $\omega\tau$ and β. The analysis shows that practically interesting cases of acoustic field intensities and frequencies and particle sizes lie well in the stability region.

To characterize the focusing efficiency we consider 10-fold focusing when particle ordinate

decays by a factor of 10 [2]. It is found that there exists a critical value of the Stokes number $\omega\tau$, namely $(\omega\tau)_1 = 1$ determining the maximal focusing efficiency.

In calculations we seed the particles at $x_0 = 0$, at various values of $y_0 = z_0$, and with initial velocities coinciding with those of fluid.

Figure 3 shows trajectories of 1μm non-diffusive particles in the acoustic channel. Particles are seeded at $x_0 = 0$ and $y_0 = z_0 = 0.15$ and $y_0 = z_0 = 0.05$. All particles approach steadily the channel axis in about one radius distance. This happens due to particle drifting motion towards the channel axis and downstream axial motion.

Considering small diffusive particles, we assume $\omega\tau << 1$. Such particles can be regarded inertialess. Computer simulations of Brownian walks can be made by adding at each time-step of $\Delta t^{'}$ a random displacement $\mathbf{A}^{'}G_n$ to the systematic displacement $\mathbf{u}^{'}_{ps}\Delta t^{'}$ [4]

$$\mathbf{R}^{'}_{n+1} = \mathbf{R}^{'}_{n} + \mathbf{u}^{'}_{ps}\Delta t^{'} + \mathbf{A}^{'}G_n \tag{11}$$

where $\mathbf{R}^{'}_{n}$ is the vector of particle displacement at previous time steps, G_n is the zero-mean, unite-variance, independent Gaussian random numbers and $\mathbf{A}^{'}$ is the vector of the random displacement amplitude, each component of which is given by

$$A^{'} = \sqrt{2D\Delta t^{'}} = \sqrt{\frac{2k_B T\tau}{m_p}\Delta t^{'}} \tag{12}$$

here k_B is the Boltzmann constant, T is the local absolute temperature, and m_p is the particle mass. For determination of the systematic particle velocity we consider separately axial and cross-sectional particle motion. Steady axial component of drag will produce a steady axial particle velocity coinciding with that of fluid (see (5)). To describe the cross-sectional systematic velocity we use the smallness of the frequency parameter, $\omega\tau << 1$. Under this condition, the cross-sectional particle velocity can be expressed as a power series of $\omega\tau$ [2]

$$\mathbf{u}_p(y,z) = \mathbf{u}(y,z) - \omega\tau\frac{\mathrm{d}\mathbf{u}(y,z)}{\mathrm{d}t} + O((\omega\tau)^2) \tag{13}$$

Substituting Eq. (6) into Eqs. (13), one obtains for cross-sectional particle velocity the expression which contains periodic and also non-periodic terms. The latter give rise to the steady part of the velocity about which the oscillations proceed. This steady part is said to be a systematic cross-sectional particle velocity. Then, one can rewrite (11) in the following dimensionless form

$$x_{n+1} = x_n + \Pi_U(1 - r_n^2)\Delta t + \Pi_B G_n \tag{14}$$

$$y_{n+1} = y_n - \frac{1}{2}\omega\tau\beta^2 y_n\Delta t + \Pi_B G_n \tag{15}$$

$$z_{n+1} = z_n - \frac{1}{2}\omega\tau\beta^2 z_n\Delta t + \Pi_B G_n \tag{16}$$

here

$$\Pi_B = \sqrt{\frac{2k_B T\tau}{m_p r_0^2\omega}\Delta t} \tag{17}$$

is the dimensionless amplitude of the random displacement. In (14)-(16), the second terms on the r.h.s stands for the systematic velocity.

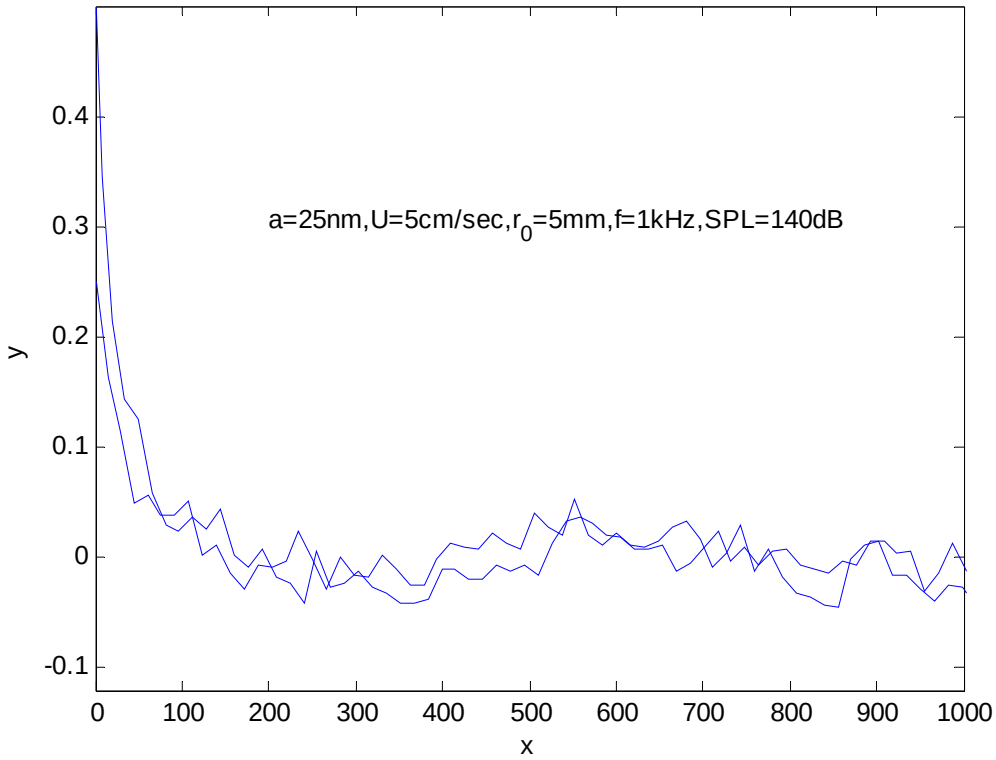

Figure 4. Simulated diffusion particle trajectories $y(x)$ starting from x=0, $y_0 = z_0 = 0.5$ and $y_0 = z_0 = 0.25$.

Figure 4 shows such simulated particle trajectories $y(x)$ starting from x=0, $y_0 = z_0 = 0.5$ and $y_0 = z_0 = 0.25$ for a=25 nm. It is seen that particles move towards the axis and reach it, i.e. they focus. This occurs in about one hundred radius distance.

The acoustic force does not affect the particles arrived at the axis. In the absence of Brownian motion particles moving along the axis will stay on it. However, Brownian motion causes the particles to walk randomly about the channel axis. These random walks lead to diffusion broadening of the stream of the moving along the axis particles. Thus, the diffusion broadening prevents forming narrower particles stream. We note that intensity of the diffusion broadening increases with decreasing particle size.

Besides, it is seen from Figure 4 that the width of particle stream does not grow with increasing x but is on average unchangeable. This is explained by the balance between velocities related to the random and systematic particle displacements occurring while particles continue to walk randomly about the axis. The achievable focusing half-width, $y_B^{'}$, can be estimated proceeding from this velocity balance. Differentiating the expression for the average free random particle displacement $(2Dt)^{1/2}$, one obtains for the corresponding velocity the following equation

$$v_{pB}^{'} = \sqrt{D/2t^{'}} = D/y^{'} \tag{18}$$

For the systematic velocity one has, from Eqs. (15), (16)

$$v_{ps}^{'} = -\frac{1}{2}\beta^2\omega^2\tau y^{'} \tag{19}$$

Equating magnitudes of the velocities given by (18) and (19), one obtains

$$y_B^{'} = \frac{1}{\beta}\sqrt{\frac{2D}{\omega^2 \tau}} \tag{20}$$

Figure 5 shows the dependence of $y_B^{'}$ on particle size in the acoustic channel at SPL=140 dB and *f*=1 kHz. Calculated values of $y_B^{'}$ are in agreement with diffusion broadening seen in Figure 4.

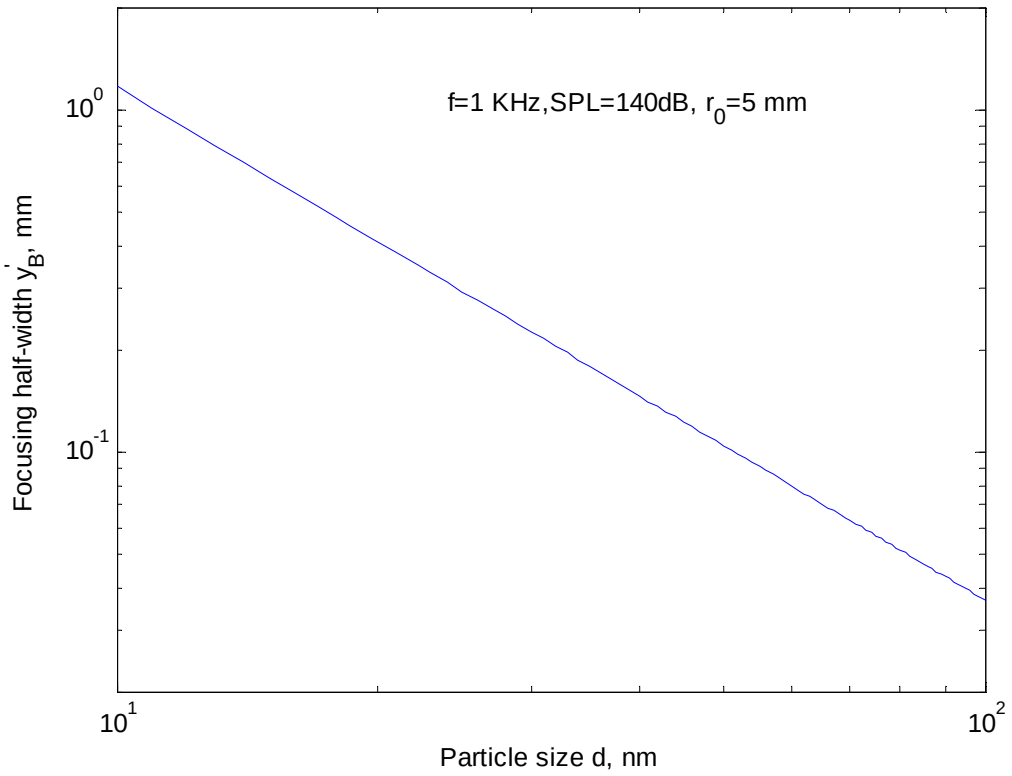

Figure 5. Dependence of focusing half-width on particle size in the acoustic channels

It is seen in Figure 5, for instance, that for a particle of $d = 50$ nm and $d = 30$ nm one has $y_B^{'} = 0.1\text{mm}$ and $y_B^{'} = 0.2\,\text{mm}$, respectively (see also Figure 4).

It is also seen in Figure 5 that a particle of $d = 10$ nm cannot in fact be concentrated in the considered channel of $r_0 = 5\text{mm}$, because focusing half-width for such particles (~1 mm) is comparable with the channel half-size.

At the same time, nanometer particles can in principle be concentrated in narrower channels.

Recall that acoustic strength parameter grows with decreasing channel size as $\beta \sim r_0^{-2}$ (see Eq. (10)). Thus the diminution of the channel size is equivalent to the increase the acoustic field intensity. Such a diminution would result in the increase of the focusing rate: the particles would reach the channel axis by a shorter time. Besides, $y_B^{'}$ diminishes with decreasing channel size as $y_B^{'} \sim r_0^2$ (see (20) and (10)).

CONCLUSIONS

An exploration of acoustic focusing of micron-and-submicron size aerosol particles in a three-dimensional quadrupole acoustic channel of hyperbolic cross-section has been carried out. Acoustic wavelength is considered much larger than the channel cross-sectional size, $\lambda >> 2r_0$.

The channel walls undergo acoustic excitation resulting in pressure disturbances leading to a linearly distributed oscillating cross-sectional fluid velocity vanishing at the axis. This results in particles drifting motion towards the axis. At the same time, the imposed axial flow drives particles downstream. As a result the particles focus along the channel axis.

The drifting particle motion is described by the damped Mathieu equation, solutions of which can, generally, be stable or unstable. The stability is governed by the frequency parameter $\omega\tau$ (the Stokes number of the problem) and acoustic strength parameter β. It is shown that the practically interesting values of these parameters lie well the stability region.

It is found that there exists a critical value of $\omega\tau$, namely $(\omega\tau)_1 = 1$ determining the maximal focusing efficiency of non-diffusive particles.

The motion of diffusive particles is studied under condition $\omega\tau << 1$. It is shown that acoustic focusing of submicron diffusive particles is possible: they reach the channel axis. The focusing rate increases with increasing acoustic strength parameter β. However, the focusing is degraded by the adverse influence of Brownian motion. This motion leads to diffusion broadening of stream of particles while they move along the channel axis. The broadening increases with decreasing particle size. The achievable focusing width is determined by the balance of random and systematic particle velocities. Its estimate shows that this width diminishes with increasing acoustic strength parameter β. Hence acoustic field controls the diffusive particle broadening.

Thus a quadrupole acoustic channel has attractive characteristics and can be applied in the development of new systems of aerosol particles focusing. The ideas developed in this paper were used in the rational design of the acoustic channel capable of generating a focused beam of micron-and-submicron size aerosol particles [5].

ACKOWLEGMENT

This research has been supported by the Technion V.P.R. Fund.

REFERENCES

1. Wang, X., Gidwani, A., Girshick, S.L. and McMurry, P.H., Aerodynamic focusing of nanoparticles: II Numerical simulation of particle motion through aerodynamic lenses, *Aerosol Sci. Techn.*, Vol. 39, pp 624-636, 2005.
2. Vainshtein, P. and Shapiro, M., Aerodynamic focusing in a channel with oscillating walls, *J. Aerosol Science*, Vol. 39, pp 929-939, 2008.
3. Paul, W., and Raether, M., Das elektrische massenfilter, *Z Phys.*, Vol. 140, pp. 262-273, 1955.
4. Grassia, P.S., Hinch, E.J., and Nitsche, L.C., Computer simulations of Brownian motion of complex systems, *J. Fluid Mech.*, Vol. 282, pp 373-403, 1995.
5. Vainshtein, P. and Shapiro, M., An acoustic channel for aerosol particle focusing. *U.S. Provisional patent application*, #61/149,061, 2009.

COMBINED PIV AND SCHLIEREN INVESTIGATION OF SEPARATED BUOYANT JET MIXING: INFLUENCE OF AXIAL SEPARATION

Ankur Deep Bordoloi[1], P. K. Panigrahi[2, *]
[1]Masters student, of Mechanical Engineering, IIT Kanpur, U.P., India
[2]Professor, Department of Mechanical Engineering, IIT Kanpur, U.P., India

ABSTRACT

The flow field and the mixing of two inclined separated jets inside a tubular reactor have been experimentally investigated using stereo Particle Image Velocimetry and schlieren deflectometry technique. Effect of axial separation distance between the two jet exit planes is examined by keeping the O_2 nozzle exit plane at two different downstream locations (L/d_1 = 4.8 and 6.7, d_1 is the diameter of the O_2 nozzle). The velocity field, stream traces, turbulent kinetic energy, vorticity and coherent structure identifier results are used to explain the flow field responsible for jet mixing. Due to the opposition between the buoyancy force and the inertia force, flow reversal takes place in He-jet and recirculation structures appear in the neighbourhood of the jet exit. Depending on the relative buoyancy strength (Richardson number, Ri_2), the flow reversal takes place at different axial locations of the He-jet. At high Richardson number (Ri_2 = 1.8), the recirculation zone is almost symmetric about the He-jet axis and there is no interaction between the two jets. On the other hand, when the Richardson number is low (Ri_2 = 1.0), the He-jet penetration depth increases. Schlieren deflectometry has been used to obtain qualitative visualization of the mixing at different flow conditions. At the low Richardson number and low jet axial separation distance, the He-jet and O_2-jet mixing is highest due to the direct interaction between the two jets due to turbulence. The extent of mixing between the two jets depends on the axial separation and jet mixing is higher for smaller axial separation between the two separated jets.

Keywords: *jet mixing, buoyant jet, stereo PIV, Schlieren, recirculation*

INTRODUCTION

The proper mixing of jets has critical influence on the performance of many industrial applications i.e. burners, chemical reactors, combustion chambers etc. Separated jet is an important jet-mixing configuration where two jets are vertically inclined to each other at particular angle. If there is a significant difference of density between the jet and the ambient air, the buoyancy effects play a significant role in the mixing. A buoyant jet can either be positively or negatively buoyant depending on whether the buoyancy force is supported or opposed by the jet's inertia force. The relative magnitude of buoyancy and inertia force determine the evolution and growth of buoyancy dominated jets.

Literature on mixing of separated jets is surprisingly less. Bordoloi and Panigrahi [1] have recently studied the importance of buoyancy in mixing of He-jet with non-buoyant O_2 jet. They reported that the Richardson number of the buoyant jet plays a crucial role to control mixing in the near exit region of the O_2 jet. Turner [2] and Mizushina et al. [3] investigated negatively buoyant jets and reported some important fundamental observations. In a negatively buoyant upward jet, the

* Corresponding author: Prof. P. K. Panigrahi
Phone: + (91)-512-2597686, Fax: + (91)-512-2597408
E-mail address: panig@iitk.ac.in

buoyancy force always acts downwards and there should be sufficient momentum for the jet in order to reach a steady height. The jet spreads axially with a constant slope. They observed that the penetration height of a negatively buoyant jet depends only on the discharge Froude number of the jet. Subbarao and Cantwell [4] observed that buoyant jets undergo transition to turbulence at Richardson number above unity exhibiting highly structured and repeatable breakdown while intermixing with the co-flowing stream. He et al. [5] observed in case of negatively buoyant wall jets, the influence of buoyancy to have stabilizing effect on the jet with increase in Richardson number, which restricted the jet's penetration depth and its lateral spread. This gives rise to a strong shear layer in the interface between the jet and the ambient fluid with large amount of turbulence in the flow. Kikkert et al. [6] presented the analytical solution for negatively buoyant jets and compared it with results from experiments. Pantzlaff and Lueptow [7] studied positively and negatively buoyant jets separately in order to understand the transient behaviour of buoyancy driven jets using PIV technique. They suggested that a negatively upward buoyant jet is an optimal mixing strategy in designing systems for jet mixing of different densities. Pham et al. [8] have investigated three dimensional behaviour of thermal plume and mass entrainment rate of the ambient fluid into the plume using 3D PIV technique.

The present study is an extension of the work done by Bordoloi and Panigrahi [1]. The potential benefit of using separated nozzle geometry is the controllability of mixing zones by adjusting the separation distance between the exit planes of the two nozzles. This paper experimentally examines the influence of axial separation distance between the exit planes of two jets on mixing of two variable density separated jets inclined at ±3º to the vertical axis. The laser schlieren deflectometry technique has been used to investigate the mixing between two jets. The stereo-Particle Image Velocimetry technique has been used to obtain the velocity field for explanation of jet mixing.

EXPERIMENTAL SETUP

The experiments are conducted in a vertical tubular reactor of octagonal cross-section with 1 m length and having distance between two parallel faces as 21.67 cm. The geometrical details of the separated nozzle can be seen in Figure 1. The two nozzles are mounted on the top of a reactor. The Helium nozzle has a perforated circular plate with 21 randomly distributed perforations of uniform size (diameter = 1 mm) at the end of a circular pipe (outer diameter = 12.5 mm). The special Oxygen nozzle configuration is adopted for increasing the jet mixing. The exit plane of the He – nozzle is located at 100 mm below the top wall of the reactor.

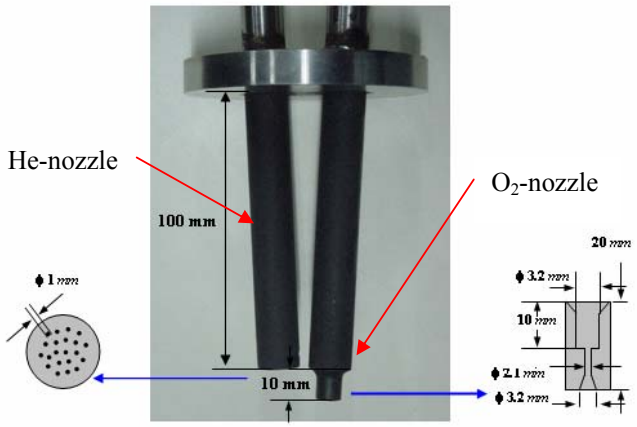

Figure 1. Schematic of the separated nozzle geometry

The axial separation distance between the two nozzles are varied between L/d_1 = 4.8 and 6.7 where d_1 is the diameter of the O_2 nozzle. Relevant notes on the detail of the experimental setup can be found in [1].

The PIV measurements are carried out in the central plane of the jets. The central region of interest is illuminated with a thin laser sheet. A double pulsed Nd: YAG laser (New Wave) of wavelength 532 nm and 15 mJ/pulse with maximum repetition rate 15 Hz has been used. The laser sheet has a maximum span area of 10 x 10 cm^2 and the sheet thickness is about 0.8 mm. Two Peltier-cooled 12 bit CCD cameras (PCO, Sensicam: 1280 x 1024 pixels) in stereo settings were used for acquisition of PIV images.

Both the cameras and the laser are synchronized with a synchronizer controlled by a dual processor PC. The cameras are oriented at a fixed angle with respect to the normal of the measurement plane. The PIV image calibration has been carried out using a fixed three dimensional grid with marker points located in alternate planes. The two planes are separated by a distance of 2 mm. The calibration target is placed at the image plane for calibration image and this image is used for mapping the camera plane to the object plane. The laser light sheet is carefully aligned with the calibration grid to ensure same measurement and calibration locations. The time of separation between two successive pulses is between 205 - 312 μs depending on the flow conditions. The time-averaged velocity field is obtained by averaging a sequence of 800 velocity vector images. The 2D to 3D conversion of velocity is done by using VidPIV 4.6XP software. The unwanted part of a PIV image is annotated before performing PIV cross-correlation calculations. For present analysis, multi-pass interrogation technique, with local median filtering followed by outlier interpolation, has been used. The percentages of valid vectors were about 97%.

Table 1: Experimental Details.

	Helium Jet	Oxygen Jet
Nozzle Index	1	2
Nozzle Pipe Diameter (mm)	9.5	9.5
Perforation Diameter (mm)	1.0	--
Throat diameter (mm)	--	2.1
Volume flow rates (lpm)	1.25, 2.25	0.25
Reynolds number (*R*e)	47, 63	170
Richardson number (*Ri*)	1.8, 1.0	8.65×10^{-05}
Axial separation distance (L/d_1)	4.8, 6.7	

The Richardson number (*Ri*) is calculated individually for two gas jets considering the ambient air to be at rest using the relation, $Ri = \dfrac{|\rho_g - \rho_a| gd}{\rho_g U_g^2}$ [Favre-Marinet *et al.* [9]]. Here subscript '*g*' indicates the dominant gas jet (i.e. Helium or Oxygen) and '*a*' indicates the ambient fluid. For the same O_2-jet velocity, the Richardson number of the He-jet is kept at Ri_2 = 1.8 and 1.0. These two experimental sets were repeated for two different axial separation distance between the exit planes of the Helium and the Oxygen jets. The details of experimental conditions, i.e. the volume flow rates, Reynolds number and Richardson number for both gases are summarized in Table 1.

RESULTS AND DISCUSSIONS

The controllability for jet-mixing, that separated jet configuration may offer in terms of relative buoyancy strength and axial separation distance, is examined in the present study. The effect of relative buoyancy strength has been studied for two different axial separation distances. The smoke visualization, mean velocity, turbulence kinetic energy, coherent structure identifier and Schlieren results are systematically discussed in the following sections.

Visualization

Figure 2 shows the instantaneous visualization images for two different Richardson numbers (Ri_2 = 1.8 and 1.0) of the Helium jet. Figure 2 also shows the effect of axial separation (L/d_1 = 4.8, 6.7) between the exit planes of the two jets. At high Richardson

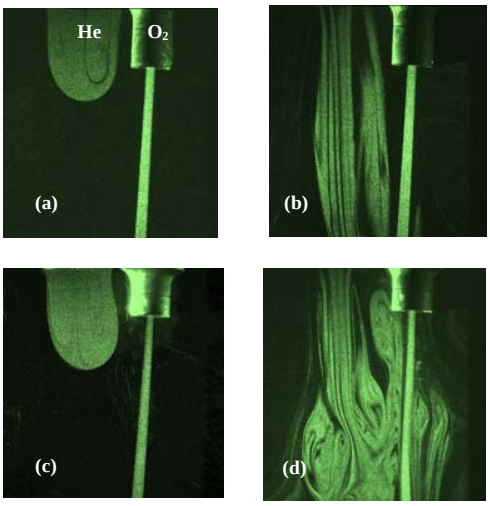

Figure 2. Instantaneous flow visualization images for (a) L /d_1 = 6.7, Ri_2 = 1.8, (b) L /d_1 = 6.7, Ri_2 = 1.0, (c) L /d_1 = 4.8, Ri_2 = 1.8 and (d) L /d_1 = 4.8, Ri_2 = 1.0

number (Ri_2 = 1.8) the flow reversal takes place in the neighbourhood of the He-nozzle exit without interacting with the O_2-jet due to the dominance of buoyancy (Figure 2(a), (c)). The presence of O_2-jet generates a low pressure zone in the inter-jet region. Depending on the axial separation distance, the intensity of the low pressure region varies. This leads to variation in the shape of the recirculation bubble near the jet exit region at high Richardson number. When the axial separation distance is high (L/d_1 = 6.7, Figure 2(a)) the recirculation bubble is almost symmetric about the nozzle axis. However, when the axial distance between the two jets is low (L/d_1 = 4.8), the low pressure region intensifies and distorts the recirculation bubble. Figure 2(c) shows that the recirculation bubble bulges asymmetrically from its jet axis towards the inter-jet region at L/d_1 = 4.8. At low Richardson number (Ri_2 = 1.0), the He-jet penetrates deeper into the ambient air due to higher strength of inertia and the two jets interact in the downstream of the flow. It can be seen that the extent of interaction is inversely dependent on the axial separation between the two nozzles. Figure 2 (b) and (d) show that when the axial separation is high (L/d_1 = 6.7), the interaction between the two jets is less as compared to when the axial separation between the two jet is low (L/d_1 = 4.8). Overall, qualitative information on the effect of Richardson number and axial separation distance between the two nozzles could be obtained from the visualization pictures of the flow field.

Mean velocity field

The time averaged normalized radial velocity (v/u_{max}) field super-imposed with time-averaged stream traces is shown in Figure 3 for two different Richardson numbers of the He-jet and for two different axial separation distances between the jets. Here u_{max} is the corresponding maximum local O_2 jet velocity. The radial velocity field is important for radial mixing problem of jets as it gives a clear picture on the radial entrainment of the jet into the ambient. The stream-traces provide an understanding of the recirculation patterns if flow-reversibility is prevalent in the flow field. At Ri_2 = 1.8 and L/d_1 = 6.7 (Figure 3(a)), there are two strong and opposite radial velocity regions in the neighbourhood of the two recirculation bubbles of the He-jet. Due to the low pressure region generated, the strength of radial velocity is more in the inter-jet region as compared to the opposite side. When the Richardson number is decreased to Ri_2 = 1.0 (Figure 3(b)), keeping all the other conditions the same, the inertia force dominates and the strong radial velocity region is extended

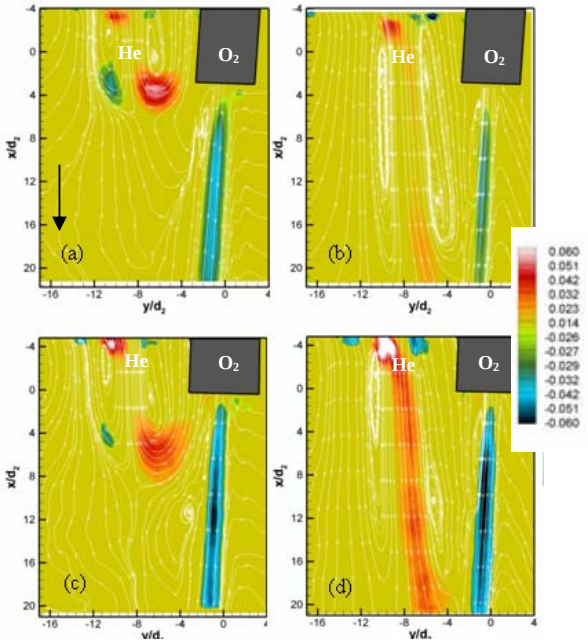

Figure 3. Time averaged radial velocity (v/u_{max}) contours superimposed with stream traces for (a) L/d_1 = 6.7, Ri_2 = 1.8, (b) L/d_1 = 6.7, Ri_2 = 1.0, (c) L/d_1 = 4.8, Ri_2 = 1.8 and (d) L/d_1 = 4.8, Ri_2 = 1.0

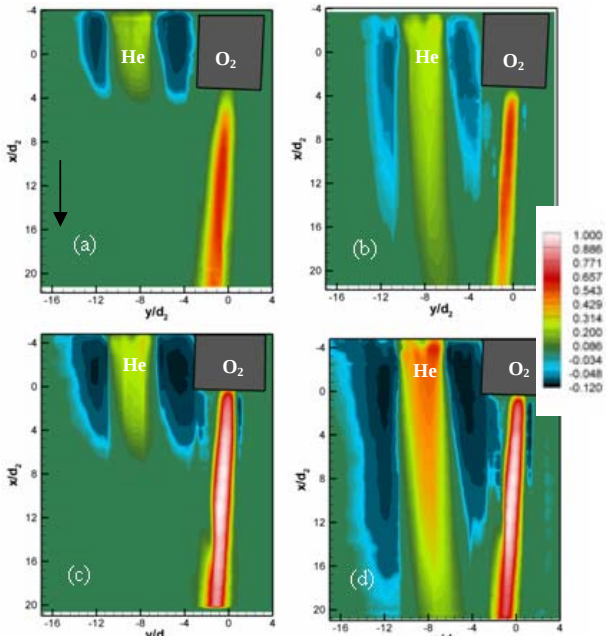

Figure 4. Time averaged axial velocity (u/u_{max}) contours for (a) L/d_1 = 6.7, Ri_2 = 1.8, (b) L/d_1 = 6.7, Ri_2 = 1.0, (c) L/d_1 = 4.8, Ri_2 = 1.8 and (d) L/d_1 = 4.8, Ri_2 = 1.0

downstream. This also gives rise to stretching of the two recirculation bubbles along the downstream direction as can be seen. The influence of axial separation on radial velocity distribution can easily be distinguished by comparing Figure 3(a) and 3 (c) for Ri_2 = 1.8 and 3(b) and 3(d) for Ri_2 = 1.0. When the axial separation distance is more (L/d_1 = 6.7), the effect of low pressure region in the inter-jet region is not as pronounced as when this distance is less (L/d_1 = 4.8). In Figure 3(c), the radial velocity in the inter-jet region becomes stronger and that in the opposite side almost insignificant. At lower Richardson number (Ri_2 = 1.0), the effect of axial separation can more prominently be seen. As a combined effect of low axial separation and buoyancy force, the He-jet strongly drifts towards the O_2-jet. Moreover, the recirculation bubbles become largely asymmetric about the jet axis. Figure 3(d) shows that the strong radial velocity in the inter-jet region extends further downstream when the axial separation distance is low (L/d_1 = 4.8). This is the case where the two jet interacts vigorously with each other (refer to Figure 2(d)).

Figure 4 shows the time averaged normalized axial velocity field (u/u_{max}) for the above four conditions. The individual Helium jet through the pores interacts with each other at downstream region and merges as a single jet flow. For all the four cases, the merged Helium jet is having a core positive axial velocity region. Due to the flow reversal taking place in the shear region of the jet, negative axial velocity regions also appear around the core, after a balance between the buoyancy and inertia takes place. The length of the positive axial velocity core gives an estimate of the extent of axial penetration of the jet into the ambient air and is dependent on the relative strength of buoyancy with respect to inertia force. At Ri_2 = 1.0 and L/d_1 = 6.7 (Figure 4(a)), the extent of axial velocity penetration is the lowest. Moreover, the negative velocity region is more or less symmetrically distributed around the core without influencing the O_2 jet. When the axial separation distance is decreased (L/d_1 = 4.8) at Ri_2 = 1.0, the penetration distance increases and the reversing flow with negative velocity intrudes the inter-jet region (Figure 4 (c)). When the axial separation distance is less, the presence of negatively buoyant He-jet also influences the growth of O_2 jet even at high Richardson number (Ri_2 = 1.8) of He-jet. The shear layer of O_2 jet, facing the He-jet, is distorted by the reverse flow of Helium and there is subsequent increase of velocity magnitude in the central core region of the O_2-jet. At low Richardson number (Ri_2 = 1.0) and high axial separation distance (L/d_1 = 6.7), the penetration distance increases but the negative velocity region is more or less symmetrically distributed around the positive velocity core (Figure 4(b)). On the other hand, at low axial separation (L/d_1 = 4.8) and low Richardson number (Ri_2 = 1.0), the reversing flow with negative velocity engulfs the interj-et region substantially influencing the growth of the O_2 jet (Figure 4(d)).

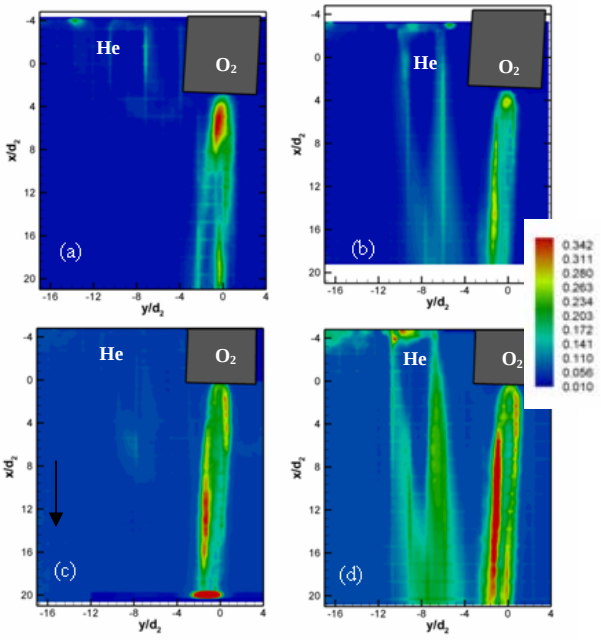

Figure 5. Turbulent kinetic energy (e_k) contours for (a) L /d_1 = 6.7, Ri_2 = 1.8, (b) L /d_1 = 6.7, Ri_2 = 1.0, (c) L /d_1 = 4.8, Ri_2 = 1.8 and (d) L /d_1 = 4.8, Ri_2 = 1.0

Turbulent kinetic energy

The overall fluctuating nature of a flow field can be understood by the total turbulent kinetic energy (e_k) of the flow. It is important for understanding the effective mixing and interaction between the two jets. The normalized total kinetic energy is calculated as

$$e_K = \frac{1}{2}\left(\frac{\langle u'u'\rangle + \langle v'v'\rangle + \langle w'w'\rangle}{U^2}\right) \quad (1)$$

Where, u', v' and w' are the fluctuating velocity in streamwise (x), radial (y) and transverse (z) directions respectively. The turbulent kinetic energy of the O_2 jet depends both on jet inertia and its interaction with the He-jet. At Ri_2 = 1.8 and L/d_1 = 6.7, a region of strong turbulent kinetic energy (e_k) appears in the near exit region of the O_2 jet. Further downstream, contours of e_k appear along the two shear layers of the O_2 jet with almost zero e_k in the central core of the O_2 jet (Figure 5 (a)). When the axial separation distance is low (L/d_1 = 4.8), the shear layer in the O_2 jet facing the He-jet encounters large fluctuations giving rise to strong turbulent kinetic energy. Figure 5 (c) shows that the distribution of e_k is uneven in the two shear layers of the O_2 jet. Due to entrainment of He-jet, the e_k concentration is much higher in the inter-jet region as compared to the opposite side. The influence of He-jet entrainment into the O_2 jet is stronger when the Richardson number is low. At Ri_2 = 1.0 the fluctuating field also becomes prominent in the He-jet (Figure 5 (b) and 5(d)) due to greater penetration depth of the jet. When both axial separation distance and Richardson number are low, there is the maximum turbulent kinetic energy appears in the mixing region of the O_2 jet. In Figure 5 (d), a very strong concentration of e_k appears in the O_2 jet along the side of the inter-jet region giving indication of maximum mixing taking place between the two jets.

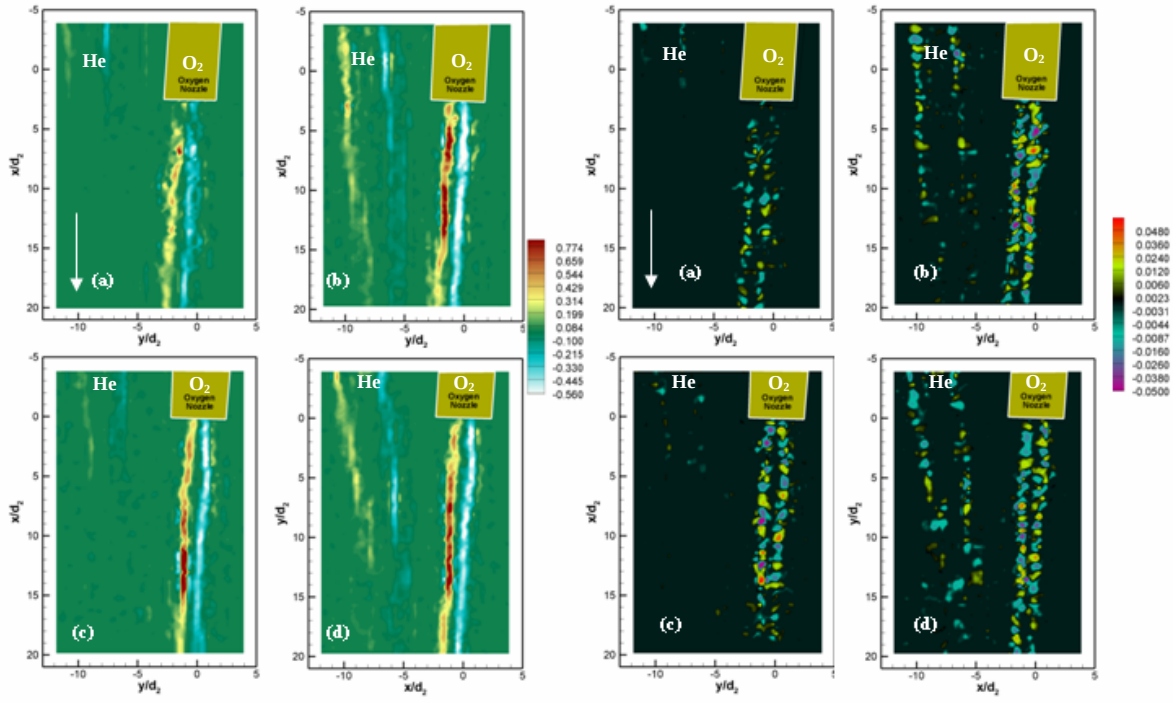

Figure 6. Instantaneous vorticity contours for (a) L /d_1 = 6.7, Ri_2 = 1.8, (b) L /d_1 = 6.7, Ri_2 = 1.0, (c) L /d_1 = 4.8, Ri_2 = 1.8 and (d) L /d_1 = 4.8, Ri_2 = 1.0

Figure 7. Instantaneous coherent structure identifiers (second invariant of velocity gradient tensor) contours for (a) L /d_1 = 6.7, Ri_2 = 1.8, (b) L /d_1 = 6.7, Ri_2 = 1.0, (c) L /d_1 = 4.8, Ri_2 = 1.8 and (d) L /d_1 = 4.8, Ri_2 = 1.0

Vortical structure identifiers

The instantaneous vorticity distribution can be used to get a picture of the behaviour of velocity shear and rotation of the fluid in motion. But vorticity distribution can not distinguish between

rotational motion associated with a vortex and shear due to velocity difference between a pair of fluid element. In jet mixing problems it is useful to find the second invariant of velocity gradient tensor ($Q = 0.5\left(tr\left(\Omega\Omega^t\right) - tr\left(SS^t\right)\right)$, where S and Ω are symmetric and anti-symmetric components of velocity gradient tensor) in order to identify the region of vortex and shear.

For the 2-dimensional flow in x–y plane, the z-component of vorticity (ω_z) is expressed as,

$$\omega_z = \left(\frac{\partial v}{\partial x} - \frac{\partial u}{\partial y}\right) \qquad (2)$$

The 2-D simplification of quantity (Q_{2D-z}) has been calculated using:

$$Q_{2D-z} = -\left(\frac{\partial v}{\partial x}\right)\left(\frac{\partial u}{\partial y}\right) \qquad (3)$$

Implementing Richardson's finite difference method the velocity gradient field has been obtained from the PIV data. The proper implementation of vorticity (ω_z) and second invariant of velocity gradient tensor (Q_{2D-z}) calculation has been verified using a numerically generated velocity field consisting of two Oseen vortices superposed on shearing motion with tan h profile.

Figure 6 shows the instantaneous vorticity (ω_z) contours for (a) Ri_2 = 1.8, L/d_1 = 6.7, (b) Ri_2 = 1.0, L/d_1 = 4.8, (c) Ri_2 = 1.8, L/d_1 = 4.8 and (d) Ri_2 = 1.0, L/d_1 = 4.8. Figure 7 shows the second invariant of velocity gradient tensor (Q_{2D-z}) for the above four conditions. Large positive Q_{2D-z} indicates vortex core and negative values indicate straining regions. When the Richardson number is high and axial separation distance is low (Figure 6 (a)), the shear layer strength of the He-jet is not significant. As a result, the vorticity distribution in the He-jet is relatively weak. The O_2-jet shows strong shearing motions with only negative values of Q_{2D-z} without powerful vortex core zones (Figure 7(a)). At lower Richardson number and for the same axial separation between two jets, strong concentrated vorticity distribution is observed in the downstream region of the He- jet (Figure 6 (b)). The O_2-jet also shows intertwined positive and negative Q_{2D-z} regions indicating presence of both straining and rotation (Figure 7 (b)). The axial separation also has influence on the evolution and merging of vortical structures. At the same Richardson number (Ri_2 = 1.8) as that in case (a), the small scale vorticity distribution is extended further downstream for the lower axial separation distance (Figure 6 (c)). Moreover, the rotational contribution of the He-jet is prominent when the axial separation distance is less (Figure 7 (c)). At low Richardson number (Ri_2 = 1.0) and low axial separation distance (L/d_1 = 4.8), the small scale structures merge leading to extended vorticity distribution in the inter-jet region with orderly positive and negative flow structures in both the jet (Figure 6 (d) and 7(d)). This is responsible for increasing the mixing between the two jets.

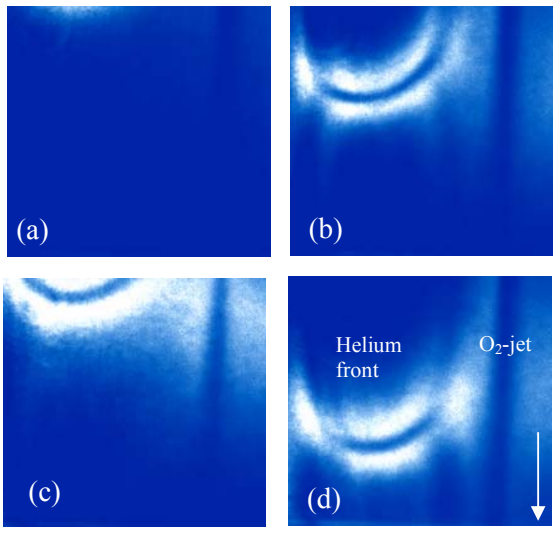

Figure 8. Instantaneous Schlieren visualization images for (a) L /d_1 = 14, Ri_2 = 0.2, (b) L /d_1 = 14, Ri_2 = 0.02, (c) L /d_1 = 10, Ri_2 = 0.2 and (d) L /d_1 = 10 Ri_2 = 0 02

Schlieren Deflectometry

Laser Schlieren deflectometry has been used to obtain the qualitative concentration distribution of mixing between He and O_2 jets in the inter-jet

region. Figure 8 shows the qualitative Schlieren visualization images in the inter-jet region for (a) Ri_2 = 1.8, L/d_1 = 6.7 (b) Ri_2 = 1.0, L/d_1 = 4.8 (c) Ri_2 = 1.8, L/d_1 = 4.8 and (d) Ri_2 = 1.0, L/d_1 = 4.8. The white region of Figure 8 is the interface between the He-jet and ambient air. The mixing between two streams leads to density gradient and hence a clear contrast in the schlieren images. When both axial separation and Richardson number are high (Figure 8 (a)), the He-jet front does not penetrate significantly into the inter-jet region. Therefore, the He-jet is visible only near the jet exit region. However, at low Richardson number and low axial separation distance (Figure 8 (d)) the front penetrates into the inter-jet region indicating higher possibility of interaction between the two jets. For all the other cases (Figure 8(b) and 8(c)), the jet front penetrates to an intermediate depth. The schlieren images in Figure 8 show similar evolution of jet boundary as that of the smoke visualization images in Figure 2. The large interaction between the two jets observed in Figure 2 (d) manifests as stronger mixing zone in the inter-jet region of Figure 8 (d).

CONCLUSION

The mixing of two separated inclined jets has been investigated using stereo PIV and laser schlieren technique. The combined effect of buoyancy and axial separation distance between the exit planes of two jets has been studied using time averaged velocity field, stream traces, total turbulent kinetic energy, instantaneous vorticity and coherent structure identifiers The Schlieren deflectometry technique has shown used for presenting both penetration depth and the mixing between two jets. It has been observed that both strength of buoyancy and axial separation distance between the exit planes of two jets are important control parameters for mixing enhancement between the two jets. Maximum mixing is observed at low Richardson number and low axial separation distance between the exit planes of two jets.

REFERENCES

1. Bordoloi, A. D. and Panigrahi, P. K.: Buoyancy Dominated He-O2 Separated Jet Mixing in a Tubular Reactor, Trans. ASME Journal of Fluids Engineering, Vol. 130 (9), pp. 0912031-13 (2008).
2. Turner J. S, Jets and Plumes with Negative and Reversing Buoyancy, Journal of Fluid Mechanics, Vol. 26**,** pp. 779-792 (1966).
3. Mizushina T., Ogino H., Takeuchi H., Ikawa H., An Experimental Study of Vertical Turbulent Jet with Negative Buoyancy, Wärme-und Stoffübertragung (Thermo- and fluid dynamics), Vol. 16, pp. 15-21 (1982).
4. Subbarao E. R., Cantwell B. J., Investigation of a Co-flowing Buoyant Jet: Experiments on the Effect of Reynolds Number and Richardson Number, Journal of Fluid Mechanics, Vol. 245, pp. 69-90 (1992).
5. He S., Xu Z., Jackson J.D., An experimental investigation of buoyancy opposed wall jet flow, International Journal of Heat and Fluid Flow, Vol. 23, pp. 487-496 (2002).
6. Kikkert G. A., Davidson M. J., Nokes R. I., Inclined negatively buoyant discharges, Journal of hydraulic engineering, Vol. 133 (5), pp. 545-554 (2007).
7. Pantzlaff L., Lueptow R. M., Transient Positively and Negatively Buoyant Turbulent Round Jets, Experiments in Fluids, Vol. 27, pp. 117-125 (1999).
8. Pham M. V., Plourde F., Kim S. D., Three-dimensional Characterization of a Pure Thermal Plume, Journal of Heat Transfer, Vol. 127, (6), pp. 624-636 (2005).
9. Favre-Marinet M., Camano E. B., Sarboch J., Near Field of Coaxial Jets with Large Density Differences, Experiments in Fluids, Vol. 26, pp. 97 -106 (1999).

NON-STEADY FLOW IN PIPES

R. Tosato*
Department of Mechanical Engineering, University of Padua , Padova, Italy

ABSTRACT. Here the problem of a correct prediction of transient pressures and pulsations in pipes and in reciprocating compressors is considered, with a particular approach to connecting pipes and their specific boundary conditions (valves, closed and open ends, cylinder, etc.).
The possibility of employing the method of characteristics for gas flow is well known for ideal flows. We are using for real flows a numerical solution method which, in comparison with other mesh methods, decreases the mathematical errors of smearing because the influence of linearizations is much less than these mesh methods.
We suggest dividing pipes in three sections:
- the sections at the right and left ends have to be very short (only one cell) and mesh methods are used to apply the boundary conditions;
- the intermediate section is the longest part (more cells) and uses a modified inverse method which makes linear interpolations to determine $\Delta\lambda$, $\Delta\beta$ and ΔAA along characteristic lines. Linear interpolations are not used to determine λ, β and AA at initial points of characteristic lines.

Keywords: *Pipes, unsteady flow, numerical method*

INTRODUCTION

It is possible to get waves in liquids which are nominally incompressible, and these can have major effects on the behaviour of the plant in which they occur. Waterhammer, which occurs when a valve in a pipeline is closed rapidly, can generate pressures that are high enough to burst the pipe.
Unsteady gas flow occurs in many engineering fields and can have an important influence on the performances and on the design of devices if they are driven by unsteady gas dynamics. Pulsating combustion boilers are devices consistent of a constant volume combustion chamber fitted with automatic spring-loaded valves. The charge of air and gas is induced into the chamber at low pressure and then ignited by a spark. The pressure gas open the second valve and exhausted onto heat exchangers.
Pressure exchange engines is an alternative to the centrifugal compressor. The concept was to compress the air, by the direct action of another fluid, exhaust gas. The dynamic pressure exchanger has been applied as a `supercharger' for reciprocating engines.
A correct predicting of transient pressures inside the cylinder and inside the connection pipes in reciprocating compressors mainly depend from lengths of pipes and it is important because the vibrations and the life of valves are dependent from them.
The non-steady gas flow in pips is assumed to be one-dimensional with a good correspondance to the reality and two kinds of flows are usually considered:

a) the homentropic flow of a perfect gas;
b) the non-homentropic flow with area changes, friction, heat transfer and entropy gradients.

Many publications have fully described non-steady compressible flow basic equations and their solutions /1,2,3,4/.

* Prof. R . Tosato
Phone: + (39)-049-8276769, Fax: + (39)-049-8276785
E-mail address: renzo.tosato@unipd.it

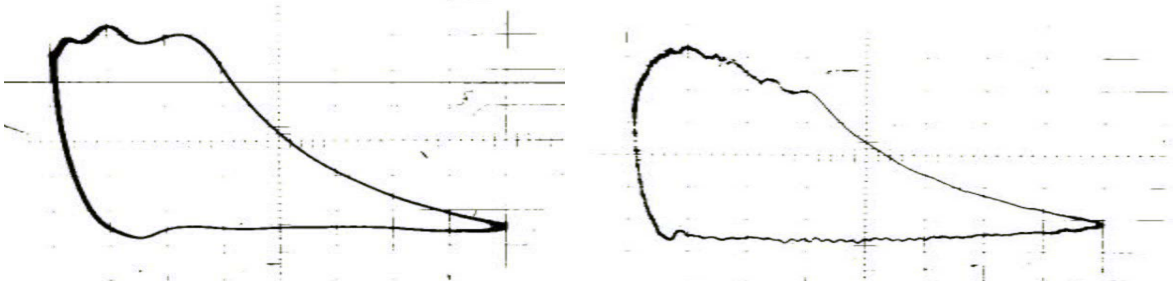

Figure 1. Experimental pressure pulsations of a compressor with long or short connecting pipes

By the method of characteristics continuity, momentum and energy conservation partial differential equations are transformed into three total differential equations (compatibility equations) along three characteristic directions:

- the path line characteristic U, - the λ characteristic U+A, - the β characteristic U-A.

The Riemann variables λ and β and the entropy level AA are used to define all physical parameters and the fluid velocity **u** in the pipe.

Non-homoentropic flow (area change, friction , heat transfer and entropy gradients):

I) <u>along a λ characteristic line</u>

a) direction condition dX/dZ = U+A = K1*λ - K2*β (1)

b) compatibility condition dA+(k-1)/2*dU = dλ = -(k-1)/2*A*U/F*dF/dX*dZ+A*dAA/AA-
-(k-1)/2*2*f*xref/D*U**3/|U|*(1-(k-1)*U/A)*dZ+(k-1)**2/2*q*xref/aref**3/A*dZ (2)

II) <u>along a β characteristic line</u>

a) direction condition dX/dZ = U-A = K2*λ - K1*β (3)

b) compatibility condition dA-(k-1)/2*dU= dβ = -(k-1)/2*A*U/F*dF/dX*dZ+A*dAA/AA+
+(k-1)/2*2*f*xref/D*U**3/|U|*(1+(k-1)*U/A)*dZ+(k-1)**2/2*q*xref/aref**3/A*dZ (4)

III) <u>along a path line U</u>

a) direction condition dX/dZ = U = (λ-β)/(k-1) (5)

b) compatibility condition dAA=(k-1)/2*AA/A**2*(q*xref/aref**3+2*f*xref/D*|U**3|)*dZ (6)

Pressure p and velocity **u** at every point are evaluated from the values of λ, β and AA at this point, by the relationships between pressures, velocity and speeds of sound:

(p/pref)**((k-1)/(2*k)) = a/aA = A/AA = (λ+β)/AA/2 (7)

u/aref=U= (λ-β)/(k-1) (8)

H**omentropic flow** (ideal gas)

Only two characteristic lines are used (λ and β) and equations (2) and (4) are simpler and reduced to dλ = dβ = 0 when the cross area F is constant.

I) <u>along a λ characteristic line</u>

a) direction condition dX/dZ = U+A = K1•λ - K2*β, (1')

b) compatibility condition dA + (k-1)/2*dU = dλ = 0 (2')

<u>II) along a β characteristic line</u>

a) direction condition dX/dZ = U-A = K2*λ - Kl*β (3')

b) compatibility condition dA-(k-1)/2*dU= dβ = 0 (4')

The graphical solution of the characteristic equations is precise, but it is only simple for homentropic flow and very complex for the non-homentropic one.

In the Example 1 in Benson's book /4/.a sudden opening of valve in pipe and discharge from a very large receiver is illustrated.

NUMERICAL SOLUTION OF EQUATIONS

Numerical solution is always preferred. It is based on the direct transformation of total differential equations (1) ... (6) into finite difference equations and on their integration advancing the solution for a series of time steps DZ and space steps DX, starting from initial conditions at time Z=0.
For non-homentropic flow, according to Zucrow and Hoffman /3/, three methods are usually employed to construct a finite difference grid and for marching through a flow field (X,Z) with a numerical algorithm:
a) the direct marching methods locate the solution point at the intersection of two characteristics (U+C, U-C or U) extending from two known initial data points; the values of flow properties at the third initial data point are evaluated by interpolation;
b) the inverse marching methods specify a priori the locations of the solution points (on lines of constant Z+ΔZ time and constant X coordinate for mesh method) and three characteristics are extended from the solution point to three initial points; three interpolations are used to determine flow properties at these initial data points;
c) the modified inverse marching methods only locate a priori the Z+ΔZ coordinate of the solution point and determine its X coordinate along a characteristic passing through one known initial point (non mesh method); two interpolations need to calculate properties at a further two initial points.

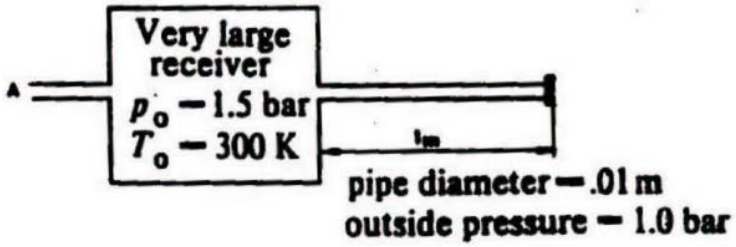

Figure 2. Example 1 (Benson's book /4/.)

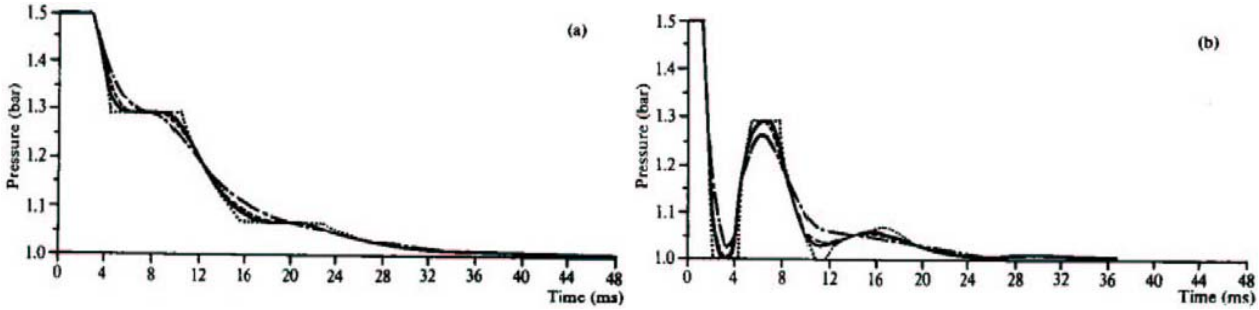

Figure 3. graphical and numerical results solving Example 1, at pipe entry a) and at mid-point b), as a function of the time T (Benson's book /4/.)

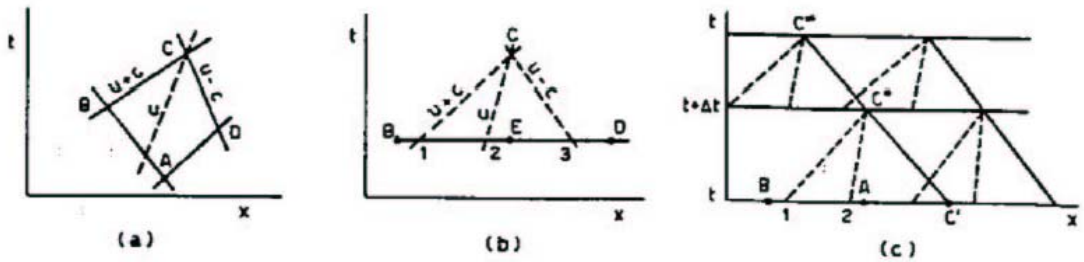

Figure 4. a) direct method, b) inverse method, .c) inverse modified method

Linear interpolations and other simplified assumptions, introduced to achieve an acceptable solution with a reasonable computing time, reduce the accuracy of the solution, in comparison with the graphical solution proposed by Jenny /5/ and experimental results. The solution is smeared and this mathematical damping prevents the model from predicting higher frequency pressure pulsations usually experimentally observed in reciprocating compressors. These pulsations have to be accounted for to simulate the dynamics of the valves.
The mesh method introduces the greatest smearing of the solution because of the amount of interpolations and because the interpolations are based on flow properties at points outside the domain of dependence.
Usual simplified assumptions are:
- the values of variables appearing in the equations are those existing at time Z;
- the characteristics connecting times Z and Z+ΔZ are straight and the slope is equal to the value at the beginning of the step;
- the pipe length is divided into a low number of elements.
- no iteration is carried out to account for the changes of variables during the step;
- a low number of characteristics is used and the total amount of old and new ones introduced at complex boundary conditions is controlled to avoid it becoming too large.
For non-homentropic flow, Pajri, Corberan and Boada /6/, discovered that the linear interpolations of λ and β along the grid interval may introduce errors and sharp pressure gradients. To improve the accuracy of numerical results, they used a modified non-mesh method along pathlines and a mesh method for λ and β calculations with linearizations made on the pressure values.
Also, the numerical solution mesh method for homentropic flow uses linear interpolations in such a way that smearing errors are still present and Benson /3/ plotted the difference of results comparing them with graphical solution results

EXPERIMENTAL AND NUMERICA RESULTS FOR SIMPLE BOUNDARY

Sudden opening of valve to the atmosphere, at total open end, different pipes are considered.
Pressure of the air in the pipe, at the closed end is plotted as function of the time, for the following test conditions:

Pipe lengths	TM =	3.20	m		Pipe diameter	DH =	2,2 1,2 0.4	cm
Initial pressare	P	=	2 bar		External pressure		=	1 bar

In Fig.4 Experimental results are compared with numerical calculations. It is possible to reduce the errors only by a high number of X points in the pipe and DZ steps near to the compatibility limit.

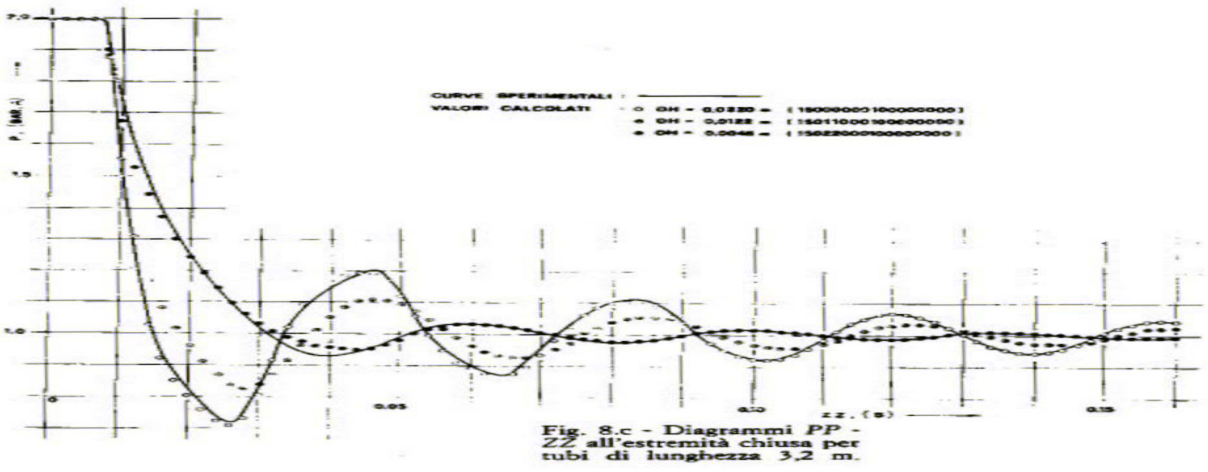

Figure 4. Experimental (------) and numerical results (…….)

CALCULATION METHOD

For pipes with the complex boundary conditions characteristic of compressors (the cylinder, valves, nozzles, junctions of pipes, sudden enlargements and contractions), the number of characteristics λ and β increases rapidly, those of the same family intersect. Algorithms become more complex and computing time longer, especially because of boundary conditions.

Internal of pipe

To reduce this problem we prefer to adopt:

- a non-mesh method, over the entire length of the pipe, to calculate AA along the U characteristics,
- a mesh method, in the cells near the boundaries, to calculate λ and β in the fixed nodes;
- a non-mesh modified method, in the interior part of the pipe, to calculate λ, and β along the corresponding characteristics;

By this method λ and β lines pass from the interior part of the pipe to the cells near the boundaries, and vice-versa, without any reflections and then without any number rise. All linearizations are avoided in the internal part of the pipe and only one characteristic, at the end of each time step, arrives at each boundary end of the pipe.

This method is also applicable in the homentropic case, without any integration of the equations along the pathlines U. Fig. 1 considers this kind of flow.

Therefore, referring to Fig. 5, we consider a pipe whose length L has been divided into a number N of equal elements. Initial conditions (λ, β and AA), at the time Z=0 and at the fixed points 1, 2, ... N+1, are known. The U characteristics start from these points, the λ characteristics from 1, 2, ... N points and the β ones from 2, 3, ... N+1 points. The same number marks a characteristic line and its intersection points with lines of Z and Z+ΔZ times.

We divided the pipe into:

I section between 1 and 2 mesh points,
II section between 2 and N mesh points,
III section between N and N+1 mesh points.

At the generic instant Z, the values of variables β, λ ed AA are known at corresponding moving points as results of previous steps. To determine flow conditions at Z+ΔZ time it is necessary to limit the value of ΔZ by the Courant-Friedrich-Lewy condition.

For all three sections we determine, at Z+ΔZ time, the positions of pathlines U (new points 1', 2', ... N+1') and the values of the variable AA (eq.6) by a non-mesh method, in these moving points, using values at old points.

Inside the I section, a mesh method is used to calculate λ at the fixed point 2, at time Z+ΔZ, using variables at points 1 and 2 at time Z.

Inside the section II we first locate the positions of new points 2", 3", ... N-1" and then, by linear interpolation, the values here of AA and of the variable ΔAA of eq. 2. The values of λ at these new moving points are calculated by eq. 2, using the variables of initial points 2", 3", ... N-1".

Inside the III section the values of λ at mesh points N and N+1 are evaluated by a mesh method using the variables at initial points N-1, N and N+1.

The calculation of β values at mesh points 1, 2 and N, inside I and III section, and at new points 3"', 4"', ... N"' inside the II section, is obviously made in the same manner and therefore we haven't described it.

The λ value in the left boundary (point 1) and β value at the right end (point N+1) are easily obtained by the well known boundary condition equations.

To increase the accuracy, an iterative procedure can be introduced using values still obtained at solution moving points at Z+ΔZ time.

Values of λ ,β and AA at mesh points, at time Z+ΔZ, are evaluated by linear interpolation.

The total number of U characteristics is maintained equal to N+1 introducing a new U line when a U line intersects the boundary ends and eliminating a U line when another U line enters from a pipe connected at the boundary end.
Also the number of λ e β lines is maintained equal to N-1 inside the II section of the pipe. When two lines of the same family intersect, they are substituted by only one or by two close and parallel characteristics.
For the first time step, the method is the same, the difference being that at the initial time all moving points are coincident with fixed mesh points.

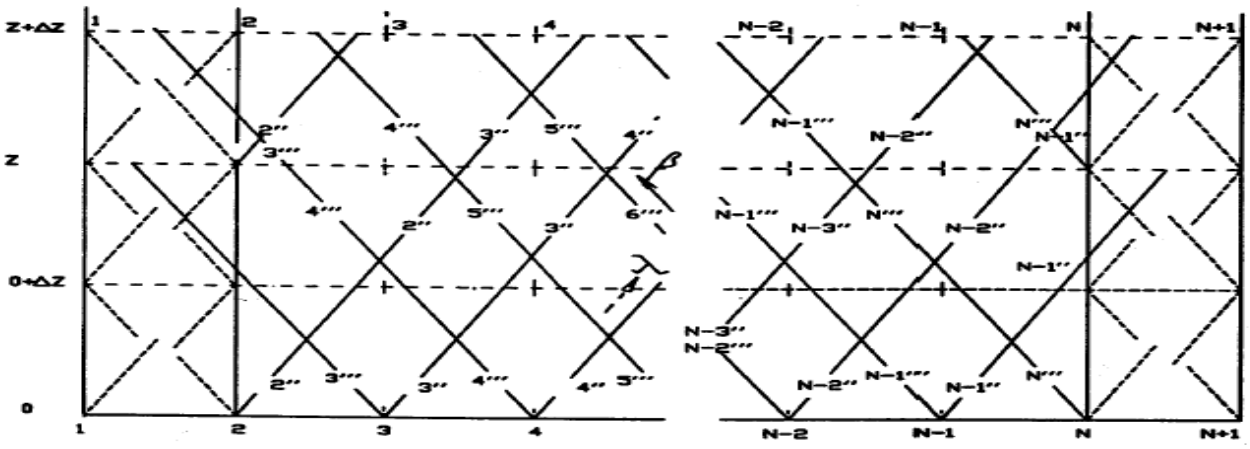

fig. 5. Characteristics λ and moving points 2", 3", N-1", characteristics β and moving points 3"', 4"', ..., N"', fixed points in the position diagram, for a homentropic flow, in a pipe with N intervals.

Boundary Conditions
Only one characteristic arrives at the pipe-end at the end of the time step and this is the simplest way to solve boundary condition calculations. The use of specific equations is done at the end of the time step.

TEST OF NUMERICAL METHOD FOR HOMENTROPIC FLOW
The proposed method can be adopted to simulate non-steady flow in reciprocating compressors and their piping systems. To show the accuracy of results Example 1 of homentropic flow is simulated and compared with graphical solution. illustrated in Benson's book /4/.
In order to test the numerical method, a Fortran program was written to simulate homentropic flow. Two subroutines allow to evaluate the positions of Riemann characteristics and the values of λ e β at moving and mesh points. Other subroutines simulate the normal boundary conditions of compressor pipes. The program considers the total number N of elements of three sections as a variable and it is possible to vary, from 2 to N, the number of cells of external sectors I and II in order to evaluate the influence of linearizations. No iteration procedure is used.
In this example a pipe connects an infinite reservoir, at the pressure of 1.5 bar and temperature of 300 K, to the atmosphere. The air (k=1.4) flows through the pipe, 1 m long, when the atmospheric end of the pipe is suddenly opened. Waves which start from the atmospheric end propagate as rarefaction to the reservoir side and reflect as compression waves which travel to the atmospheric end.
Pressures P1 at the open end, P3 at pipe entry and P2 at mid-point, when N=40, 30, 20 (continuous lines) and N=10 (dotted line) and only for one mesh in section I and III, are plotted against the time T, in fig. 6.

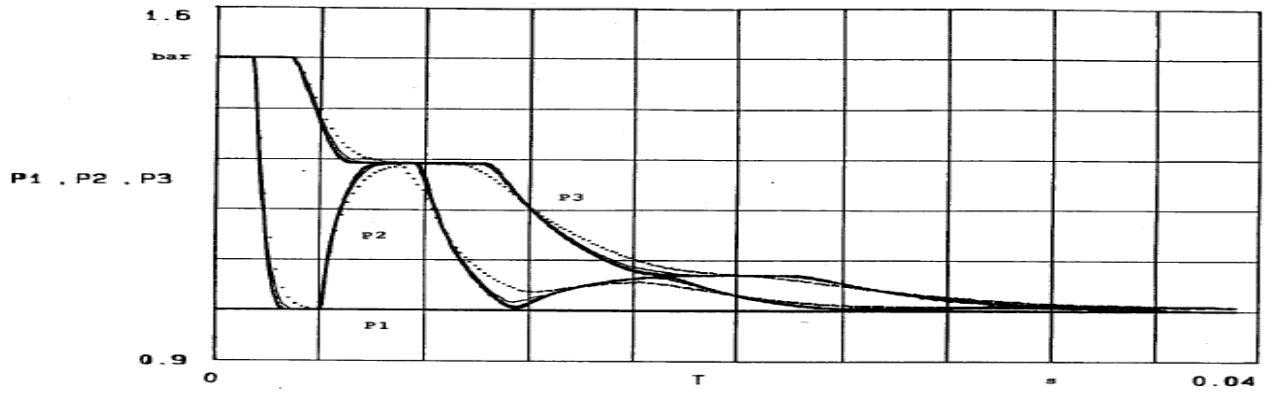

Figure. 6. Pressures at the open end P1, at pipe entry P3 and at mid-point P2, as a function of the time T. Effect of the number N of meshes on the accuracy.

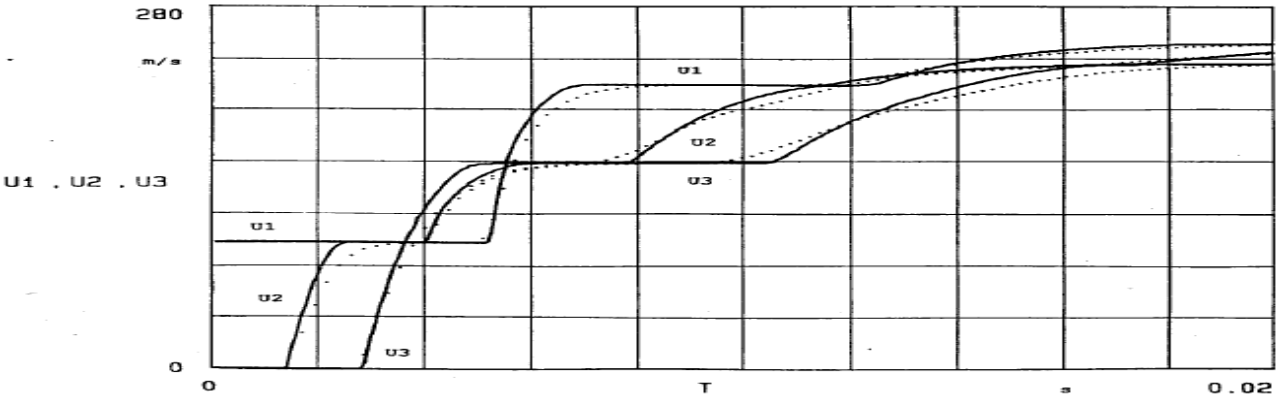

fig. 7. Velocity U1, U2 and U3 curves.

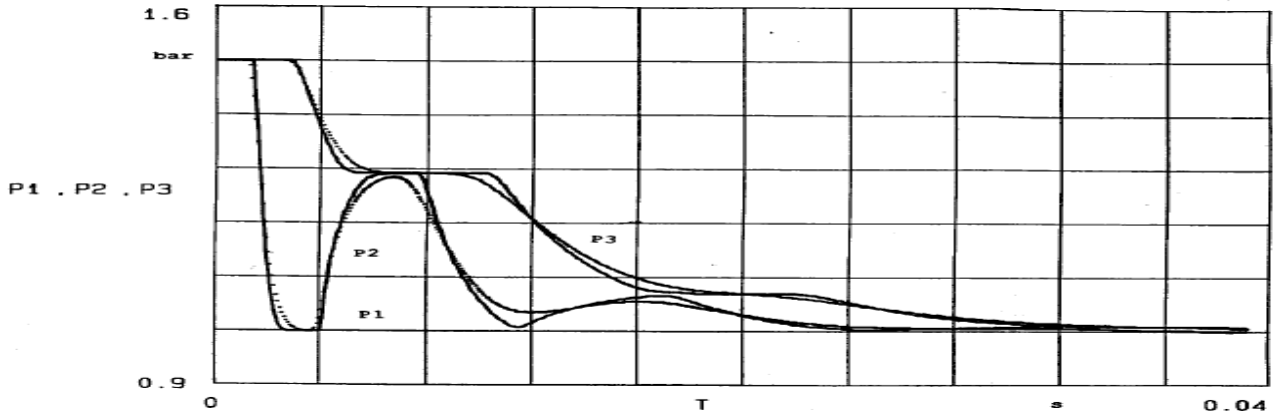

fig. 8. Comparison between mesh method (dotted lines) and the proposed method (continuous line) for N=30. Effect of linearizations.

Velocity diagrams of the same points are plotted in fig. 7.
For N=40, 30 and 20 these diagrams are very close to results obtained by graphical method. The shapes of the curves are not smoothed out and for this reason the method is able to simulate high frequency pressure pulsations.
Pressure diagrams calculated by the proposed method (continuous line) and by mesh-method (dotted line) are plotted in Fig. 8, with N=30.

CONCLUSIONS

Theoretical analysis has been carried on for homentropic flow in a pipe and compared with results obtained by graphical solution. Information on the possibility for the model to represent the flow with a high degree of accuracy is positive. The influence of residual linearizations still present in the proposed method is negligible, if the pipe is divided into a number of finite elements higher than 20. The method here described for homentropic and non-homentropic flow achieves, in this condition, the same accuracy as the graphical method of characteristics.

ACKNOWLEDGMENT

This work has been supported by MURST funds. Their contribution is gratefully acknowledged.

NOMENCLATURE

a	sonic velocity			aref		sonic velocity at reference conditions	
aA			sonic velocity at reference pressure				
A	=	a/aref	non dimensional sonic velocity				
AA	=	aA/aref	entropy level of non-homentropic flow				
Cp, Cv			specific heats of gas				
K	=	Cp/Cv	ratio of specific heats (ideal gas is considered)				
K1	=	(k+1)/(k-1)/2	constant				
K2	=	(3-k)/(k-1)/2	constant				
D			diameter				
F			area of cross section				
f			friction factor				
p	gas pressure			pref		pressure at reference conditions	
q			heat transfer rate per unit mass				
T	time			Z	=	aref*T/xref	non-dimensional time
u			gas velocity				
U	=	u/aref	non-dimensional gas velocity				
x	distance from the left end of the pipe			xref		reference length	
X	=	x/xref	non dimensional distance				
β	=	A-U*(k-1)/2	Riemann variable of characteristic				
λ	=	A+U*(k-1)/2	Riemann variable of characteristic				

REFERENCES

1. Shapiro A. H., The Dynamics and Thermodynamics of compressible fluid flow, *The Ronald Press,* Vols. 1 and 2, , 1954.
2. Zucrow, Hoffman. Gas Dynamics: multidimensional flow. *J. Wiley and S.*, Vol. II, pag. 332, 1977.
3. Benson R.S., The Thermodynamics and Gas Dynamics of Internal Combustion Engines, *I,Horlock J.H. and Winterbone D.E*, Vol..,1982.
4. F.Pajri, J.M. Corberan, F. Boada, Modifications of the Method of Characteristics for the Analysis of the Gas Exchange Process in Internal Combustion Engines, *Proc. of the Institution of Mech. Eng.*, Vol. 200 n.4, 1986.
5. Jenny E., L'ècoulement transitoire unidimensionnel et l'influence du frottement, des apports de chaleur e des variations de section, *Revue Brown Boveri*, November 1950.
6. F.Pajri, J.M. Corberan, F. Boada, Modifications of the Method of Characteristics for the Analysis of the Gas Exchange Process in Internal Combustion Engines, *Proc. of the Institution of Mech. Eng.*, Vol. 200 n.4, 1986.

DEVELOPMENT OF CAPILLARY MOTION AT THE FREE SURFACE OF A FLUID

M.O. Denisova*, K.G. Kostarev
Institute of Continuous Media Mechanics UB RAS, 614013 Perm, Russia

ABSTRACT. The experiments on studying the solutal flows near the gas bubbles and liquid drops in narrow channels filled with inhomogeneous solutions of surfactants have shown that the development of capillary motion occurs with a considerable time delay with respect to the time of formation of the surfactant concentration gradient at the interface. To ascertain the reason of this phenomenon we investigated the development of the Marangoni convection in the vertical Hele-Shaw cells of varying thickness partially filled with water. The capillary motion was initiated by local injection of the droplet of surfactant solution of onto the free surface of water. The resulting distribution of the surfactant in the near-surface volume of water was visualized by the interference method.
The conducted experiment has provided supporting evidence for the view that the development of the capillary motion at the horizontal free surface is also of the threshold nature. It has been found that the value of the surfactant concentration threshold abruptly increases with the increase of the cuvette thickness and the initial concentration of the alcohol in water (in case when the alcohol solutions are used instead of water).

Keywords: surfactant, free surface, Marangoni convection

INTRODUCTION

It is well known that the Marangoni convection is a fluid motion driven by the capillary forces at the interface. These forces carry the fluid toward the regions with higher surface tension. In general, these are the regions with lower temperature and/or the regions with lower concentration of a surface-active substance (surfactant).
Since Newtonian fluids have zero force of rest friction, it is generally assumed that their free surface begins to move even at an arbitrary small difference in surface tension. On the other hand, in some cases for example in the case of surfactant diffusion from a drop of binary mixture into the surrounding homogeneous fluid the development of the Marangoni effects begins only at a certain proportion of liquid components in a drop[1]. A delay in the development of capillary motion is also observed in experiments investigating inhomogeneous surfactant solutions with gas and liquid inclusions [2,3] and buoyancy of higher concentration jets from the submerged surfactant sources [4,5]. The use of interferometry in these experiments provides visual evidence that interface motion begins only after formation of a marked (up to several percents) difference in the surfactant concentration. Moreover, in the case of a drop, initiation of the capillary motion is observed just after penetration of a surfactant through the interface and formation of its initial distribution in the drop. The analysis of the obtained results shows that it would seem more reasonable to relate the appearance of the surfactant concentration threshold in the observed phenomena to the existence of the original adsorption layer at the surface of a Newtonian fluid, owing to which the fluid acquires

* M.O Denisova
Phone: + (7)-342-2378314, Fax: + (7)-342-2378487
E-mail address: Maria.Denisova@icmm.ru

rheological properties. The source of the layer is a group of surfactants non-removable by standard purification methods

The objective of this study is to determine experimentally the conditions favorable for development of the solutal Marangoni convection. Consideration was given to the process of initiation of a capillary motion due to local injection of a droplet of a controllable surfactant with concentration C_d onto the free surface of distillate or a water solution of this surfactant with lower concentration C_s.

In the experiment, the role of the controllable surfactant was played by isopropyl alcohol diluted with water to weight concentration of 0.5 to 15%. To generate a droplet of such a solution with a volume of 5 μL we used a mechanical pipettor with accuracy of 0.1 μL. manufactured by BIOHIT company. Then the formed drop smoothly came into contact with a free surface of a basic fluid or was injected into the fluid near its free surface.

The cuvette filled with a basic fluid had the form of a vertical rectangular cavity with dimensions of 90×40 mm and thickness b ranging from 1.2 to 20 mm. The walls of the cuvette were formed by parallel glass plates covered with a semi-transparent mirror film which with appropriate adjustment allowed us to create a working cell of the Fiseau interferometer for making observation of the concentration fields on the side of a wide face.

In view of the supposition that a certain amount of uncontrollable surfactant always exists on the fluid surface one could infer that the amount of such surfactants is specified both by the degree of purification of the fluid and by quality of cuvette preparation. In our experiments, for the zero level of preparation we adopted the threshold for initiation of the solutal Marangoni convection in distillate or in a water solution of isopropyl alcohol in the cuvette, which was washed three times by isopropyl alcohol, then, during 15 minutes, by running water and finally by distillate. Such cleaning procedure was widely used in investigations described in works [2,3] because it allowed us to get clear of the “traces” of fluids used for creation of drops insoluble in water.

The improvements in preparation of the cuvette led to development of a new technique according to which a cuvette after each series of tests was filled with 10% solution of a detergent “7X Serva” for a long period of time (~12 hours) and then was washed several times with concentrated detergent “Fairy” accompanied with mechanical cleaning of the cuvette walls after which it was washed for an hour with running water and a liter of distillate.

The next step toward improvement of the process of water purification was the use of deionizer “Vodoley” manufactured by Khimelectronika company (Moscow, Russia). The distilled water was passed three times through the device until its electrical conductivity was reduced by an order of magnitude (from 2.4 to 0.15 μS/cm). Deionized water was used in the experiments as a basic fluid and for final washing of the cuvette (repeated several times).

The result of such careful preparation of the cuvette was high purity of the free surface of the fluid filling the cuvette. A need for preliminary cleaning of the cuvette was supported by a number of tests with alcohol solutions, in which a noticeable evaporation of the alcohol and the resulting surface motion began already at $C_s = 4\%$ (in solutions prepared on the basis of a standard distillate the alcohol evaporation could be observed at $C_s > 10\%$ and only due to a sweat appeared on the glass walls) In view of these circumstances, an equilibrium distribution of the alcohol, at which the free surface of the working fluid remained stationary, could be obtained only by isolating the cuvette from the environment by means of a special cover with a hole for drop injections.

The interference patterns formed in the cuvette were recorded by a video camera. In thin cuvettes, such as the Hele-Shaw cells the majority of flows and concentration fields had a two-dimensional structure. Therefore, the optical path of the interferometer transmitted beam was dependent only on the cuvette thickness and the content of admixture in a fluid in the plane of wide cuvette faces. Thus, for cuvette of thickness $b = 3.8$ mm a transition from one interference band to another corresponded to a change in concentration of isopropyl alcohol in water by 0.085%.

During tests the ambient temperature and the fluid temperature was (24±1)°C.

RESULTS

At first, the development of convective motion was investigated in the situation, in which a drop of the surfactant solution was injected onto the free surface on the side of a gas phase. In this case, a drop hanging at the end of the needle was put slowly to the surface of the fluid. As soon as the drop touched the surface it was sucked into the bulk of water under the action of capillary forces minimizing the arising total surface (Figure 1*a*). As a result, the surfactant lying on the drop surface immediately landed up on the surface of the fluid.

When a drop of the surfactant solution was introduced on the side of the liquid phase it didn't deform the free surface of the fluid, although the time the drop took to reach the interface as a buoyant jet (Figure 1*e*) was rather long. Despite the fact that the whole bulk of the surfactant solution rose to the surface as a single portion it did not have its own surface. Therefore the processes of mixing and dissolution began well before the surfactant reached the fluid surface and caused a decrease in concentration of the solution coming into contact with the fluid surface.

The experiments showed that the initiation of a capillary motion on a horizontal free surface of the working fluid occurs in a threshold manner like in the case of curved interfaces [2.3]. An example is given in Figure 1, which shows a series of interferograms of the concentration field in the case when surfactant concentration in the drop is higher than the threshold value for a given thickness of the cuvette. Therefore, as soon as the drop reaches the fluid surface, there appears an intensive but rapidly damping capillary motion in the form of two cells (Figure 1b – 1c) or two convective cell trains (Figure 1f – 1g) [4].

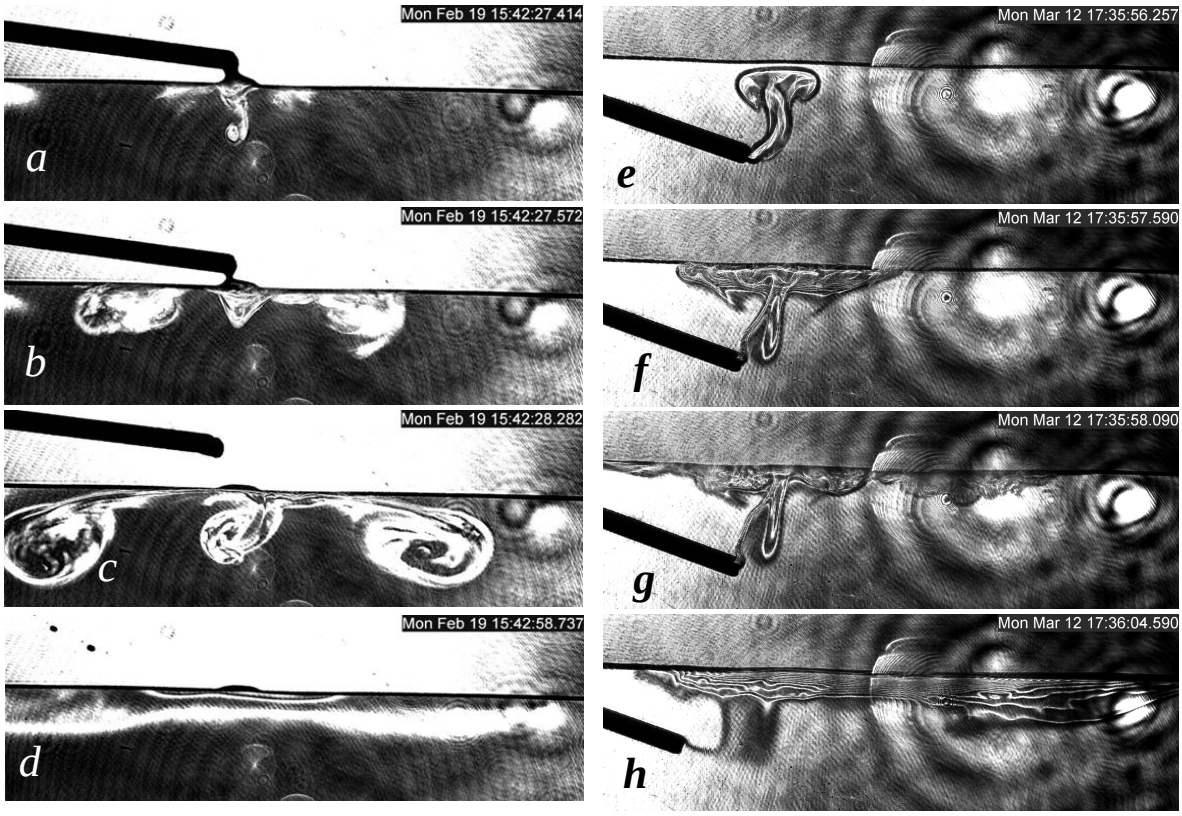

Figure 1. Injection of a drop of the surfactant solution onto the free surface of water in cuvette b = 1.2 mm on the side of gas phase(the elapsed time t, s: a – 0.2; b – 0.4; c– 0.9; d – 31.4), C_d = 6%; on the side of liquid phase (the elapsed time t, s: e – 0.8; f – 2.1, g – 2.6, h – 9.1) C_d = 12%

As it might be expected, the value of the surfactant concentration threshold decreases with increasing the degree of preliminary water purification and cleaning of the cuvette walls. Figure 2 shows the dependence of the threshold difference ΔC in the initial alcohol concentration between the droplet and the basic fluid on its content in the fluid and the degree of purification. It is seen that the use of a new procedure for preparation of the cuvette and deionization of water reduces the value of the threshold by 50%, yet a non-threshold development of solutal-capillary convection has not been achieved. Note that a similar behavior of the water surface is observed after injection of a microdrop of the surfactant on the side of the gas phase: a threshold value of the concentration difference is 7.0% for distillate, 5.0%- for distillate in the cuvette prepared in accordance with the new purification procedure and 3.0% - for deionized water and cleaned cuvette (cuvette thickness b = 3.8 mm).

As it is evident from Figure 2, the value of the threshold essentially depends on the content of an alcohol in water reaching a maximal value at minimal concentration of the surfactant in the solution. The obtained results confirm the supposition as to a complicated composition of the group of surfactants forming the initial adsorption layer at the free surface of the fluid. Most of the have the boiling point lower than 100°C and therefore survive during water distillation. Half of the surfactants (group *A*) can be removed by means of ion-exchange filter and cleaning of cuvette walls. The second half (group *B*) do not have electrical charges and therefore stay in the solution. Co-linearity of curves *1* and *2* in Figure 2 means that the surfactants of the group *A* are not sensitive to changes in the concentration of the alcohol in water and are held on the fluid surface as separate molecules. By contrast, the surfactants of the group *B* form the so-called hard film [6]. An increase of the alcohol concentration in a basic fluid gradually destroys the film but does not remove molecules of the surfactants from the surface which preserves conditions for delay of motion.

The assumption concerning the properties of the film formed by surfactants of the group *B* is supported by its poor deformability in thin cuvettes which is the reason for adding a greater amount of the alcohol for sustaining of capillary convection (Figure 3). Moreover, convergence of curves *1* and *2* in the region of small thickness of the cuvette cavity suggests that for thinner cuvettes the degree of purification is less important than for cuvettes with relatively large area of the free surface.

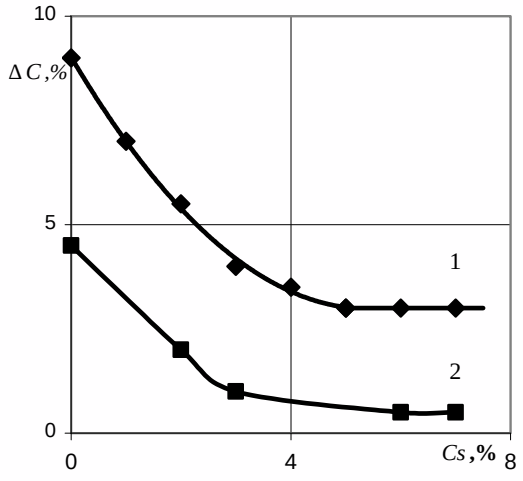

Figure 2. Threshold difference of alcohol concentration *versus* alcohol concentration in the basic fluid for different degrees of water purification: 1- distillate, 2 –deionized water Injection of the surfactant on the side of liquid phase (b =3.8 mm)

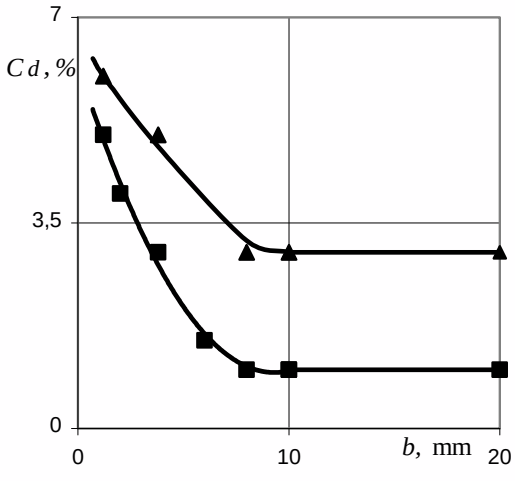

Figure 3. Threshold concentration of alcohol *versus* cuvette thickness for different degrees of water purification: 1- distillate, 2 –deionized water. Injection of the surfactant on the side of gas phase

Of no less importance for overcoming the threshold and development of the capillary motion is the direction in which the drop of the alcohol solution is injected onto the surface of the basic fluid. Figure 4 shows that for deionized water the value of the threshold decreases by 1.5 times in the case when the alcohol is introduced on the side of the gas phase (then, initial rupture of the film of non-controllable surfactants is realized mechanically). With the growth of alcohol concentration in the basic solution the threshold concentration difference rapidly decreases, and curves for different directions of surfactant injection converge until they coincide at C_s~ 4 – 6% and then tend to an asymptotic value, which in the examined interval C_s remains non-zero (ΔC ~0.5%). It should be noted that an increase in the surfactant concentration reduces the surface tension of the basic solution which provides explanation for the fact that the observed tendency to reducing the concentration threshold with increase of C_s agrees well with the results of investigations concerning development of capillary convection on the free surface of gas bubbles in vertically stratified solutions of some surfactants [2].

In cuvettes of different thickness and, accordingly, with different characteristic dimensions of the free surface, the direction of surfactant injection has a much greater effect on the development of capillary motion (Figure 5) Thus after injection of a droplet on the side of the gas phase the resulting local rupture of the adsorption layer accompanied by formation of longitudinal gradient of alcohol concentration at the surface of deionized water reduces the concentration threshold for initiation of the solutal Marangoni convection approximately by 3 times for all cuvettes used in the tests.

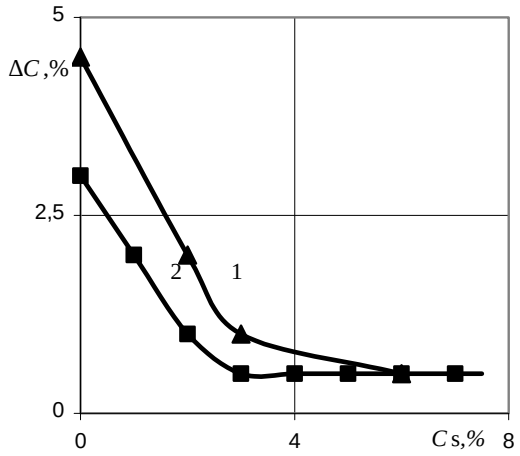

Figure 4.Threshold difference of alcohol concentration *versus* alcohol content in the basic fluid in the case of drop injection on the side of liquid*(1)* and gas *(2)* phase (b =3.8 mm)

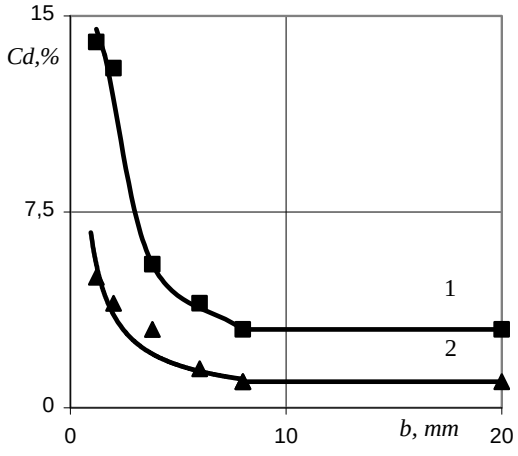

Figure 5. Threshold alcohol concentration *versus* cuvette thickness in the case of drop injection on the side of liquid *(1)* and gas *(2)* phase

An abrupt decrease of the concentration threshold in cuvettes of thickness more than 10mm accounts for the fact that retardation of the Marangoni motion is not discussed in most of the problems considering stability of shallow layers and films. It is also of interest to analyze the results of tests in which the boundary of the free surface of the basic fluid (water) coincides with the edge of the cuvette which allows us to change the curvature of the free surface and, respectively, the length of the arc connecting the walls of the cuvette, keeping the characteristic dimensions of the

cavity unchanged. The tests showed that in the absence of meniscus (the length of the arc is minimal) the concentration threshold increases markedly *(*ΔC =7%), whereas in the presence of the meniscus (no matter whether it is convex or concave) the concentration threshold decreases (ΔC = 5% at the meniscus deflection of 1.1-1.3 mm beneath or above the horizontal plane for cuvette with b =3.8 mm).

CONCLUSIONS

The performed experiments support the view that the reason for the observed delay in the development of the capillary motion at the surface of water and water solutions is the adsorption layer which is formed on the basis of surfactants showing different properties. Some of the surfactants can be removed by preliminary purification of water with the aid of ion –exchange filters. However even the remaining part of surfactants will suffice for generation of a rather high concentration threshold especially in the case of a free surface or interface with small characteristic dimensions. The observed effect may exert an essential influence on the mass transfer processes which occur in technological setups using drops and gas bubbles and are the object of investigations in chemistry, cellular biology and in microfluidics problems.

The work was supported by the project of RFBR № 09-01-00484 and the Integration project of SB, UB and F-E B of RAS №116.

REFERENCES

1. Lewis J. B., Pratt H. R. C., Instabilities induced by mass transfer and deformable fluid interfaces, *Nature*, Vol. 171, pp. 1155-1161, 1953.
2. Birikh R. V., Zuev A. L., Kostarev K. G., Rudakov R. N., Convective self-oscillations near air-bubble surface in horizontal rectangular channel, *Fluid Dynamics*, Vol. 41, No. 4, pp. 514-520, 2006.
3. Bushueva K. A., Denisova M. O., Zuev A. L., Kostarev K.G., Flow development at the surfaces of bubbles and droplets in gradient solutions of liquid surfactants, *Colloid J.*, Vol. 70, No. 4,pp. 416-422, 2008.
4. Kovalchuk V. I., Kamusewitz H., Vollhardt D., Kovalchuk N. M., Auto-oscillation of surface tension, *Phys. Rev. E*., Vol. 60, No. 3, pp 2029–2036, 1999.
5. Kovalchuk N. M. and Vollhardt D., Effect of substance properties on the appearance and characteristics of repeated surface tension auto-oscillation driven by Marangoni force, *Phys. Rev. E*., Vol. 69, No. 016307, pp. 1–13, 2004.
6. Abramzon A. A., Surface-active substances. Properties and application., *L.: Chemistry*, pp. 246, 1975.

EXPERIMENTAL EVALUATION OF THE INJECTION RATIO IMPACT ON THE DYNAMICS OF TWIN TANDEM INCLINED JETS INTERACTING WITH AN ONCOMING CROSSFLOW

A. Radhouane[1*], N. Mahjoub[1], H. Mhiri[1], G. Le Palec[2], P. Bournot[2]
[1]National Engineering School of Monastir, Route of Ouardanine, Monastir, Tunisia
[2] IUSTI, UMR 6595, Technopôle Château-Gombert, 5 rue Enrico Fermi, 13013 Marseille Cedex 20, France

ABSTRACT. The present work deals with the common "twin jets in crossflow" configuration due to its wide presence in different applications and to its tight relationship with different domains. The jets handled in this experimental study are inclined, arranged inline with the oncoming crossflow and emitted according to different jet to mainstream velocity rates. Our main goal is to determine the influence of this parameter on the different characterizing features of the resulting flowfield and more particularly on the dynamic ones. The developed vortical structures as well as the velocity fields are some of these features and if they raise such an increasing interest; it is due to their close relation with various environmental problems and technical constraints. The examined data are experimentally depicted by means of the Particle Image Velocimetry (PIV) technique and the flow visualizations are realized by means of a CCD camera.

Keywords: *twin jets, crossflow, injection ratio, velocity field, vortical structures*

INTRODUCTION

Several industrial and/or academic applications make use of the common "Twin jets in crossflow" configuration. The most familiar industrial application making use of this configuration is without any doubt the chimney stacks exhaust. It is however found in further applications like the VSTOL aircrafts, the discharge of the liquid effluents through piping systems, the film cooling of turbine blades, the combustor wall cooling, the injection of gas in combustion or any other chemical chambers; etc...These various applications state of the wide applicability of the twin jets in crossflow configuration in several domains, of the different technical constraints to which it may be confronted, of the various environmental drawbacks it may engender, etc… These factors and others have largely enhanced the research on this particular theme.

Ziegler et al. [1] are pioneers in the domain since they considered the question since the early seventies by simulating the behavior of both side-by-side and tandem twin jets exhausting normally into a Crossflow. The elaborated physical model was based upon experimental data and allowed the description of the resulting flowfield mechanisms like the shielding effect provided by the upstream jet on the following one, the influence of the presence of the jets on each others, etc… It also justified the deflection of each of the jets in terms of the entrainment of the mainstream fluid and of the pressure forces acting on the jets' boundaries.

Schwendemann [2] considered the same arrangements but proceeded exclusively experimentally. The jets were also considered at different initial inclination angles in order to compare their trajectories. A further experimental consideration of both arrangements has been performed by

* A. Radhouane
Phone: + (216)-97-557269, Fax: + (216)-73-500514
E-mail address: radhouane_amina@yahoo.fr

DiMicco et al. [3]. It was particularly dedicated to the different interactions taking place both between the emitted jets, and between the jets and the mainstream. The experiments captured by means of flow visualization; tested the impact of both the jet centerline-to-centerline spacing and the momentum flux ratio on the penetration of the jets. It was shown that the reduction of these parameters decreases the penetration of the jets among the main stream. In a second part, DiMicco et al. [4] demonstrated the insignificance of the effect of the momentum flux ratio on the depth penetration under different angular orientations and over a jet-spacing/diameter range contained between 2.7 and 12.1. This statement seems however no longer true under the largest spacing and at the lowest momentum ratio. Structurally speaking, constructive and destructive interferences take place as both the angular orientation and the jet spacing are changed. In a try to extend previous results, Kolar et al. [5] chose to consider experimentally the same arrangements (tandem and side by side) to explore a further feature: the distribution of the developed vortical structures and their overall circulation that was quite similar to the contrarotating vortex pair relatively to the single jet case.

Further authors restrained their attention to the twin inline jets in crossflow and confronted their behavior to that of the single jets in crossflow. This is the case of Disimile et al.[6] whose experimentations resulted in a relation between the jets development and some of their geometric parameters such as the jet-nozzle spacing and the jet to mainstream velocity ratio. The video digitization allowed also the determination of the average penetration of the jets within the crossflow and proved the similarity of the twin and single jets in crossflow characteristics.

The PIV experiments of Ibrahim and Gutmark [7] evaluated the impact of a further parameter; the injection ratio; on both single and double jets' evolutions. This impact was explored on different dynamic features such as the jets trajectories and penetration, the deflection of the jets trajectories, the mass entrainment approximation based on the jets trajectories, the windward and leeward jets spread, the size, location and magnitude of the reverse flow regions, etc…the turbulent kinetic energy proved that the behavior of a double jet in a tandem setup follows the same trend as that of a higher blowing ratio single jet in crossflow.

More recent works elaborated numerically by Radhouane et al. [8, 9] were exclusively devoted to the twin inline jets in Crossflow. The first one ([8]) examined rather the global behavior of the twin jets while progressing within the environing flow and gave even an overall idea about the influence of the injection ratio on the temperature distribution. The second ([9]) focused more deeply on the thermal distributions and cartographies and on their variation under a changing injection ratio.

In the present work, we propose to evaluate the influence of this same parameter (the injection ratio) but on the dynamic features of the resulting flowfield. The latter enclose the different velocity distributions as well as the established vortical structures whose understanding is as already said of a great relevance.

EXPERIMENTAL SET-UP

Consideration was given to two tandem inclined jets inline with the oncoming crossflow; both interacting flows are fed with air. In spite of its simplicity, the geometric configuration is however delicate to build due to the inclination of the jets and to the feeding of their corresponding nozzles by the same main air supply. For the matter, a 10 mm diameter cylindrical pipe is inclined and then connected to two further similar ones that are inclined according to the same angle. The nozzles are then razed at the level of the injection plate that is actually the ground of the experimental wind tunnel (figure 1). This operation generates two identical elliptic exit sections characterized by a small and a grand diameter respectively equivalent to d and $d/\sin\alpha$. The inclination angle of the jets is maintained constant in the present experimentations and equivalent to 60° with reference to the longitudinal leading direction (x coordinate). The centers of the jet nozzles are separated by a distance of D=3d and the emitted jets together with the oncoming crossflow are finally discharged to the atmosphere outside the laboratory through an exit cross section whose dimensions are 0.2m in width and 0.3 m in height.

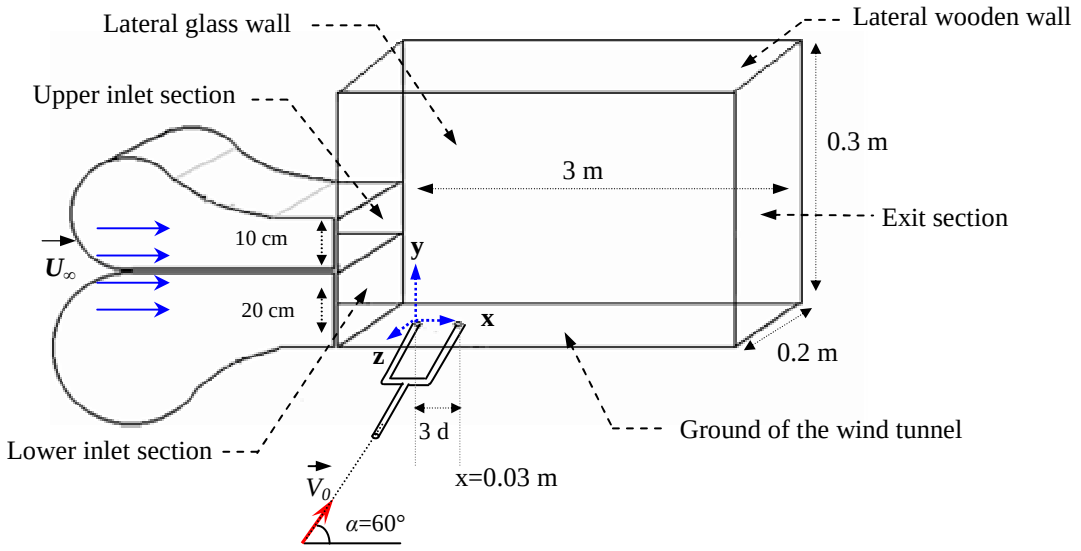

Figure 1. Description of the experimental set-up

The whole tunnel is characterized by an open top wall. The ground is made of wood and covered with plastic for the particle image velocimetry (PIV) technique and the visualizations requirements. One of the lateral sides is made of wood and painted black in order to reduce the possible light reflection. As to the second side, it is made of Pyrex to allow the optical access and then the observation of the interacting flows' progression.

A diffuser initially present at the entrance of the tunnel is removed during the experiments only for more commodities. The engendered sudden diameter change is likely to affect the flow dynamics, that's why we placed the jet nozzles approximately 2.5 m farther from the tunnel entrance. This disposition proved to be efficient. In fact, the mainstream velocities depicted by means of the hot wire anemometry technique showed a 10 mm width shear layer (figure 2) and a global turbulence intensity level that did not go beyond the percentage of 0.2%.

The velocity of the oncoming crossflow is actually generated by engines implanted at the entrance of the tunnel. The one relative to the lower inlet section generates velocities ranging between 0 and 16 m/s whereas the upper inlet section introduces velocities varying between 0 and 42 m/s. In our work, velocities will not go beyond 10 m/s that's why we will only use the lower inlet section.

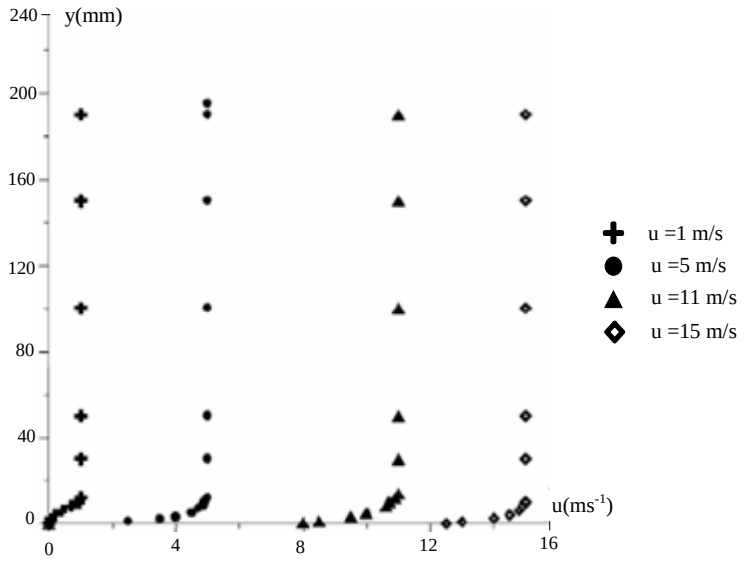

Figure 2. Velocity Profiles of the mainstream at the entrance of the test cross section (at x=0.2 m)

As already said, both jets are fed with the same main air supply. To detect the flows' progression, we added seeding particles. The jets are seeded with glycerin particles whose diameter is approximately equivalent to 1 µm (the seeding density is approximately 30 particles per ml of pure jet fluid). As to the main air flow, it is seeded with oil droplets of approximately 0.8 µm diameter, and is introduced into the tunnel at the ambient temperature (T_∞)

To be able to characterize well and locate the different flow features, we chose a Cartesian coordinate system whose origin is located at the upstream jet nozzle center. This choice is motivated by the possible asymmetry of the resulting flowfield in spite of the symmetry of the geometry as stated in the literature by several authors like Smith et al.[10], Muppidi et al.[11], Yuan et al. [12], etc…

Once the geometry built and the jets and the main air flow emitted; we proceed to the different two dimensional measurements by means of the particle image velocimetry (PIV) technique together with a CCD camera; the lateral behavior having been kept for a later exploration in future works.

The adopted technique (PIV) is essentially based upon a TSI PowerView system, including a 50 mJ dual YAG laser producing two flat pulses, the duration of one ranging from 5×10^{-9} to 10^{-8} seconds, a PowerView 4M high resolution cross-correlation camera (2 k × 2 k resolution, 12 bits), a synchronizer and "Insight" Windows-based software for acquisition, processing and post-processing. This software allows the synchronization of pulsations according to the observed phenomena, and the adjustment of the time step between two images. The final fields are averages performed on 100 successive acquisitions. For each point, experimental uncertainties were estimated as follows: $\frac{V_{\max} - V_{\min}}{V_{av}}$ where V_{max}, V_{min} and V_{av} are, respectively, the maximum velocity, the minimum velocity and the average velocity measured over the whole process. These uncertainties were about 5%.

Now that we defined the geometry and measurements technique, we propose to begin with the examination of the global structural evolution of the jets under a variable injection ratio. The images of the resulting flowfield are taken at the symmetry plane (z=0) and in the vicinity of the jet nozzles where the most significant interactions take place (figure 3). We even confronted them to the infinite injection ratio case (free jets in absence of crossflow) in order to find out the impact of its existence on the emitted jets. The variation of the ratio between the jets velocity and the one relative to the mainstream proved to highly affect the whole resulting flowfield structures. Figure 3 represents only the leading edge and the wake vortices as only theses can be observed on the symmetry plane (z=0). The first type vortices, also called jet shear layer vortices or ring vortices, develop on the upper periphery of the evolving jets and result from the direct interaction of the jets with the environing flow. They are quasi-steady and are a consequence of the Kelvin-Helmholtz instability established at the annular shear layer that separates from the edges of the injectors.

The second, the wake vortices, are also known as upright vortices, zipper vortices, tornado like vortices or Fric's vortices since they were first identified by Fric and Roshko [13]. They develop rather between the lower side of the jets and the injection plate. The upright vortices appellation comes from the fact that one side of the vortex string is connected to the jets and follows their trajectories whereas the other end stays close to the cross flow wall, positioning the vortex in an upright orientation.

The impact of the injection ratio on these two main features is summed up in the three following major points. The first one consists in the farther emission of the jets from the injection plate under an increasing velocity ratio thanks to the greater initial impulse brought to the jets. When on the contrary the injection ratio declines, the jets are rapidly confined against the injection plate. This shows the close relationship existing between the different flows interactions and progression and the imposed velocity ratio. It is like a duel between the emitted jets and the oncoming crossflow that is won by the flow characterized by the more significant velocity. The flow detaining the higher velocity is then more likely to impose itself: its trajectory, its magnitude, etc…

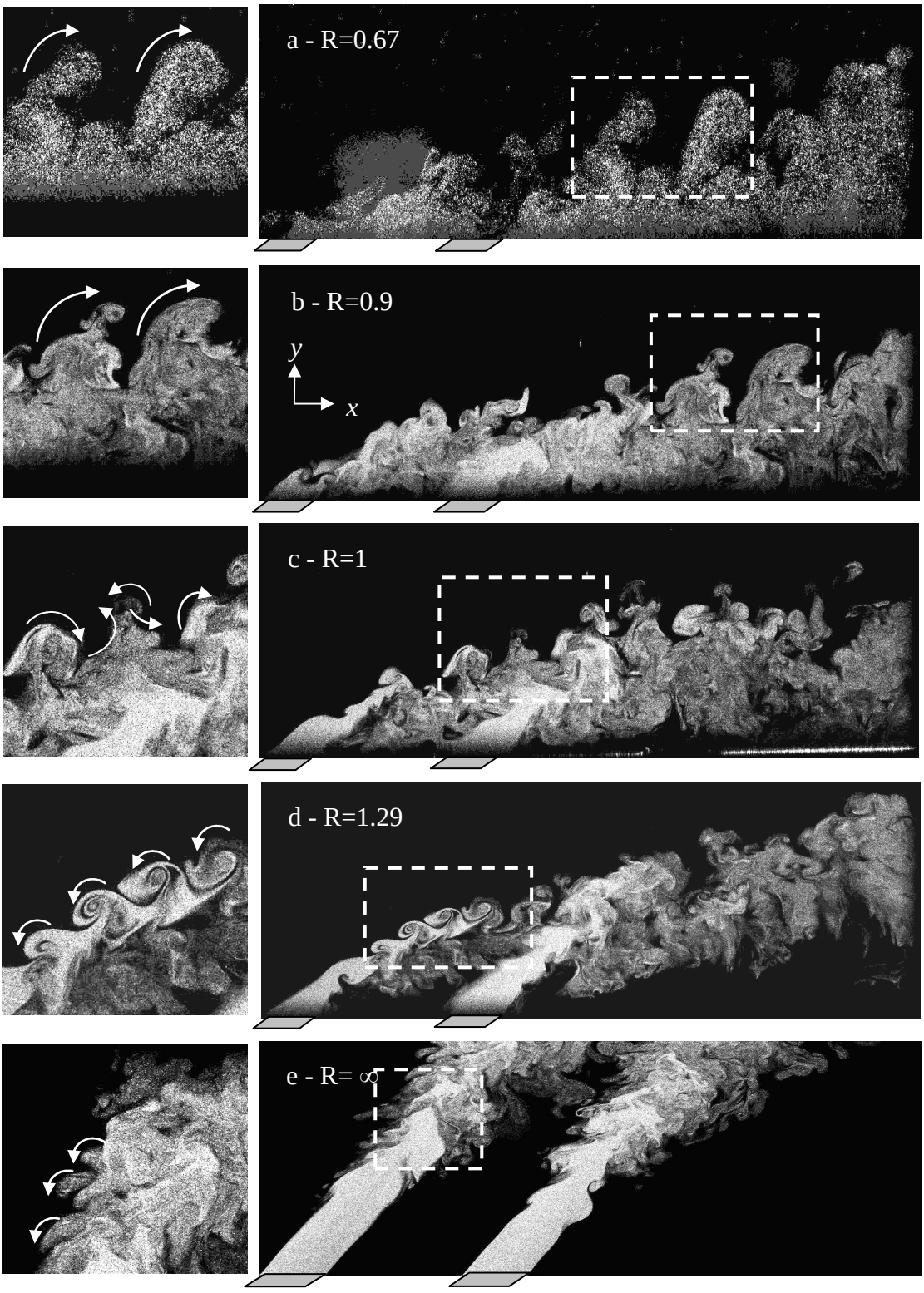

Figure 3. Impact of the injection ratio on the development and orientation of the resulting flow vortical structures on the symmetry plane (z=0)

So if the jets are confined against the injection plate under the weaker velocity ratios (fig. 3-a and b) it's due to the larger scale of the environing flow with reference to the emitted jets. The latter are consequently immediately deflected by the crossflow and flattened against the injection plate preventing them from fleeing it freely as it is the case in absence of crossflow when R=∞ (fig. 3-e). The flattening and deflecting processes are more manifest on the upstream jet due to its prior

confrontation with the oncoming mainstream. It is on the other hand sensibly reduced on the downstream jet thanks to the shielding effect brought to it by the rear jet.
When on the contrary the injection rate rises, the jets gain in strength with reference to the mainstream. They are consequently more likely to confront it and even to resist to its flattening effect. Of course this resistance is not total as soon as the crossflow exists, but it is proportional to the injection ratio. As already aid, it is total only in absence of mainstream (fig. 3- e) where the jets are not bent any more; but follow a straight trajectory imposed by the initial injection streamwise angle. The intermediate case relative to R=1 (fig. 3-c) contains both phenomena since the jets are bent in the direction of the environing flow initiating the confinement of the combined jets. The confinement is however neither immediate nor total. The jets are henceforth dynamically equivalent which justifies the confinement delay and its weaker impact. The latter is perceived through the detachment of the combined jets from the injection plate. This detachment is total is absence of crossflow.
We move now to the second feature affected by the variation of velocity ratio: the existence and the orientation of the developed vortical structures; we mean here rather the leading edge vortices whose sense of orientation may be clockwise, anticlockwise or both of them in particular cases. The vortices rotate clockwise under the weaker velocity ratios and this sense is imposed by the crossflow as shown in fig. 3-a and b. It is not clear on the figure but that must be the sense of rotation of the wake vortices too which may justify the attachment of the emitted jets to the injection wall. When the velocity ratio reaches the unity, we already said that both interacting flows are dynamically equivalent which is at the origin of the presence of double sensed vortices as shown in figure 3.c. Under R=1.29, we've just went beyond the critical ratio, that's why in addition to the anticlockwise vortices we note the existence of sparse clockwise ones (inside the dashed line in fig. 3-d). The latter are totally vanished in absence of the crossing flow (fig. 3-e) and even at the periphery of the downstream jet. In fact under this injection condition, the jets no longer interact together; maybe a closer distance between the jet nozzles would generate this interaction.
The third observation to make is precisely concerning what happens between the jet columns and its variation under a changing injection ratio. In fact, the jets are immediately flattened against the injection plate under the weakest values due to their quasi absent resistance towards the oncoming crossflow. This process generates pronounced interactions between the jets while evolving. These interactions are however less significant and take place progressively higher and then farther from the injection plate. This is actually due to the fact that the jets are progressively are strong (with reference to the crossflow) and then more likely to maintain their trajectories before expanding and generating mutual interactions; of course in addition to the interactions with the mainstream.

We propose now to check the above mentioned observations concerning the developed disturbances but in terms of mean velocity magnitudes and vectors. Both features are gathered on the mean velocity cartographies of the resulting flowfield; on which we also delimited the main characterizing zones of the domain; always in terms of the velocity feature (figure 4). Of course the cartographies were plotted under the different injection ratios apart from the R=0.9 case that is approximately identical to the R=0.67 one.
The first observation to make concerns the vertical domain extent of the plotted cartographies that translates well the impact of the injection ratio on the flow dynamics. In fact the major flow interactions are contained within a domain height of approximately 20 mm under the weakest ratio, to progressively become 25 mm, 45 mm and finally 60 mm respectively under R=1, R=1.29 and R=∞. This is the best way to comfort the jets' confinement reduction as their velocity is reinforced with reference to the oncoming crossflow. This confinement decrease is accompanied by a new dividing of the mean velocity field that is initially divided into three then four distinct zones to finally become a single zone. Under the weakest injection ratio; R=0.67; (fig. 4-a) three main zones develop. The first one contains the emitted jets that were immediately bent and entered in mutual interaction. The following zone contains the expanded jets that have combined. As to the upper layer, it contains the crossflow remained out of any interaction due to the limited extent of the

emitted jets. Scarce disturbances are present at the peripheral side of the jets which could be induced by too many light reflections in spite of all the adopted precautions.
When the injection rate attains the unity, the first zone contains always the emitted jets but this time they are still separate. They inter in interaction only in the following zone where they expand and generate a wake region close to the wall. The two following layers contain always the same phenomena: the combined jet streams and then the free crossflow. The extent of the different zones is however larger due to the further impulsion brought to the jets and then to their deeper crossing of the environing flow before bending and dispersing. The same partition of the domain is maintained for the next injection case relative to R=1.29. Only the height of these zones varies since the first zone extent changes from 4 to 10 mm, the second from 7 to 14 mm, the third from 10 to 17 mm (fig. 4-b and c). When the injection ratio becomes infinite, there is no longer a need nor a reason to divide the domain as there are no longer any interactions in absence of the crossflow.
It comes then from the abovementioned observations that the injection ratio is responsible for the organization of the established resulting flowfield.

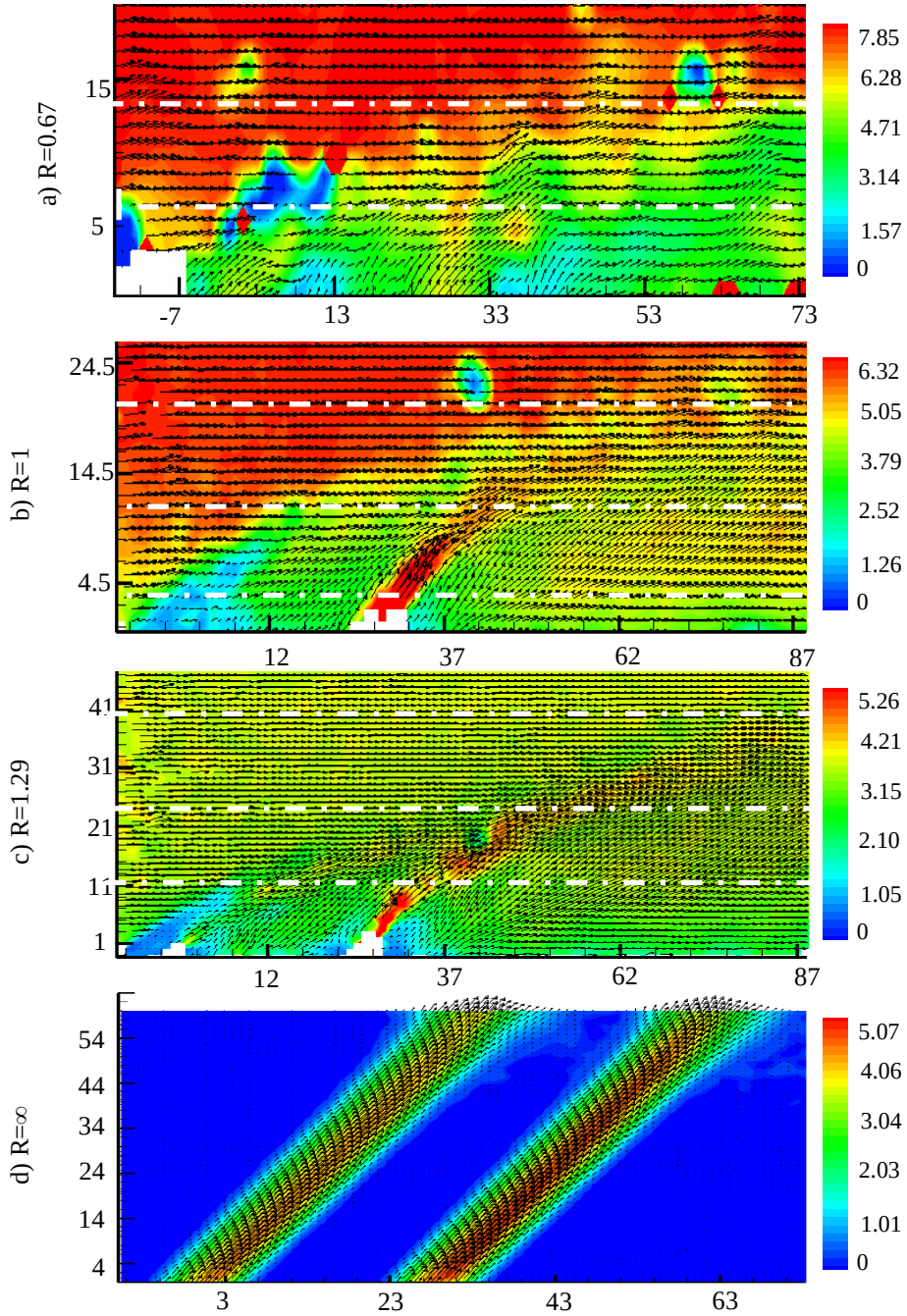

Figure 4. Mean velocity cartographies on the symmetry plane and under the different velocity ratios

When it is too low, the jets are unable to oppose any resistance to the oncoming crossflow which justifies their immediate flattening against the injection plate. At the vicinity of the critical R=1 case; the jets oppose a slight resistance to the mainstream which enables them to flee freely the injection plate before tilting. If the velocity ratio rises further, the jets are reinforced and cross more deeply the domain before sloping. The tilting process actually disappears when the ratio becomes infinite: when the crossflow no longer exists.

CONCLUSIONS

The present experimental consideration of twin inclined jets within a crossflow showed the complexity of the established resulting flowfield in spite of the simplicity of the configuration geometry. This complexity is expressed through the change in the sense of orientation of the developed vortical structures that change from clockwise to anticlockwise as the injection rate climbs… It is also manifest in the change of the whole flowfield organization in terms of the mean velocity cartographies; the borders were decided by the jets behavior that are initially emitted straight, then interact before combining and finally completely dispersing.

REFERENCES

1. Ziegler, H., Wooler, P.T., "Multiple Jets Exhausted into a Crossflow," *J. Aircrafl*, 8(6), pp. 414-420, 1970
2. Schwendemann, M.F., "A Wind Tunnel Investigation of Stratified Jets and Closely Spaced Jets Exhausting into a Cross Flow", *Rept. NOR* 73-98, Northrop Aircraft Division, Hawthorne, CA, 1973.
3. DiMicco, R.G., Fabris, D. Disimile, P.J., "The effect of constructive and destructive interface on the downstream development of twin jets in a crossflow. Part1: destructive interference of laterally spaced jets". *AIAA-90-1623*, 1990
4. DiMicco, R.G., Fabris, D., Disimile, P.J., "The effect of constructive and destructive interface on the downstream development of twin jets in a crossflow. Part2: Interference effects of angularly displaced jets". *AIAA, SAE: 26th ASME and ASEE, Joint Propulsion Conference*, Orlando, FL, 12p, 1990
5. Kolar, V., Savory, E., Takao H., Todoroki, T., Okamoto, S., Toy, N., "Vorticity and Circulation Aspects of Twin Jets in Cross-Flow for an Oblique Nozzle Arrangement", *Proceedings of the Institution of Mechanical Engineers*, Part G: Journal of Aerospace Engineering, 220(4), pp.247-252, 2006
6. Disimile, P.J., Dimicco, R.G., Toy, N., Savory, E, "The development of twin-jets issuing into a crossflow", *12th Symposium on Turbulence, A91-54251* 23-34, Rolla, MO, University of Missouri-Rolla, 1990
7. Ibrahim, I.M., Gutmark, E.J., "Dynamics of single and twin circular jets in crossflow". *44th AIAA Aerospace Sciences Meeting and Exhibit*, Reno, Nevada, 2006
8. Radhouane, A., Mahjoub Saïd, N., Mhiri, H., Lepalec, G., Bournot, P., "Etude numérique d'une interaction de deux jets inclinés avec un écoulement transversal"; *Congrès français de thermique (SFT 2007)*, Iles des Embiez – Var (83), France, 29 mai-1 juin 2007, pp. 307-312, 2007
9. Radhouane, A., Mahjoub Saïd, N., Mhiri, H., Lepalec, G., Bournot, P., "Contribution à la modélisation de l'interaction entre deux jets inclinés et un écoulement transversal: refroidissement par jets, *13èmes journées internationales de thermique (JITH 07)*, Albi (France), 28-30 août 2007
10. Smith S.H, Mungal M.G., "Mixing, structure and scaling of the jet in crossflow". *J Fluid Mech* 357, pp. 83-122, 1998
11. Muppidi, S., Mahesh, K. , "Two-dimensional model problem to explain counter-rotating vortex pair formation in a transverse jet", *Physics of Fluids J*. 18(8), 2006
12. Yuan, L.L., Street, R.L., "Trajectory and entrainment of a round jet in crossflow". Physics of fluids, 10(9), pp. 2323-2335, 1998
13. Fric, T.F., Roshko, A., "Vortical Structure in the Wake of a Transverse Jet", *Journal of Fluid Mechanics*, 279, pp. 1-47, 1994.

Heat and Mass Transfer

EXPERIMENTAL ANALYSIS OF VACUUM DRYING OF THE HIGH VOLTAGE BUSHING

A.J. Nowak[1,*], Z.P. Buliński[1], K. Kasza[2], Ł. Matysiak[2]
[1]Silesian University of Technology, Gliwice, Poland
[2]ABB Research Centre, Kraków, Poland

ABSTRACT. This paper deals with the computational model and its experimental validation of the paper vacuum drying process. Proposed numerical approach is based on the commercial CFD software package, FLUENT. Complex vacuum drying multi-physics includes air flow, heat transfer, water evaporation, moisture diffusion, etc. For validation purpose small scale vacuum chamber and paper bushing were built. During vacuum experiment inside the paper bushing temperatures were measured, obtained experimental results demonstrated fairly good agreement computation results.

Keywords: *validation experiment, paper vacuum drying, bushing, computer simulations*.

INTRODUCTION

A crepe paper is one of the best insulation material which is commonly used in the electro-technology for instance, in the high voltage bushings (schematically shown in Figure 1). Bushings are parts of any high voltage electrical transformer they allow to carry current at high potential (by means of capacity-controlled electric field) through a grounded barrier [1] e.g. metal transformer casing. Working principle of the bushing made of conductor and insulator is schematically shown in Figure 1. Conducting core is carefully wrapped with the crepe paper (Figure 2), which is then impregnated with the epoxy resin and eventually cured. Such technology is widely known as the resin-impregnated paper (RIP) technology [1].

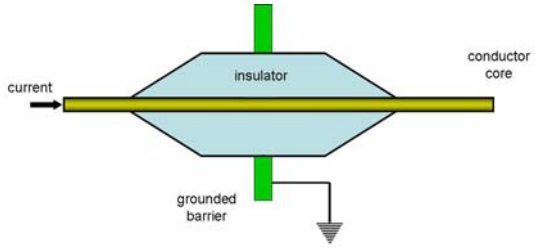

Figure 1. Bushing principle of working

Figure 2. Structure of the crepe paper

* Corresponding author: Prof. A.J. Nowak
Phone: + (48)-32-237 1025, Fax: + (48)-32-237 2872
E-mail address: andrzej.j.nowak@polsl.pl

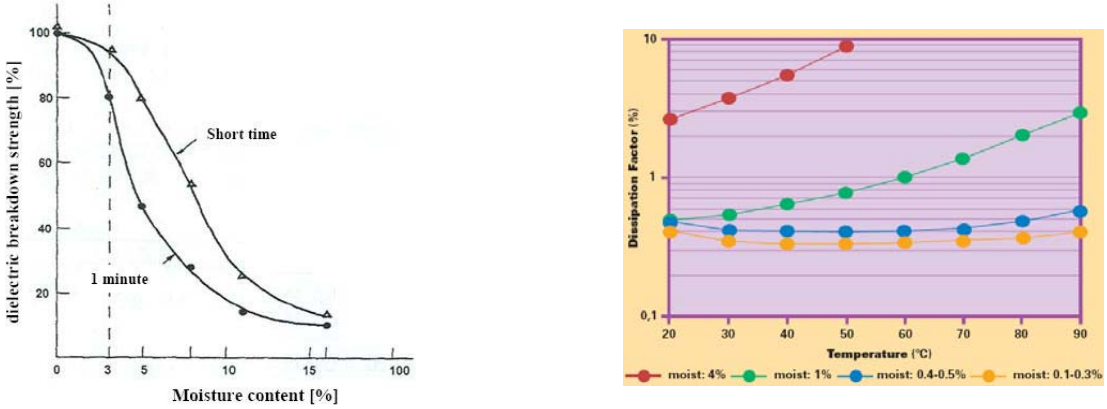

a) Dielectric breakdown strength b) Dissipation factor

Figure 3. Dependence of the paper insulation properties on moisture content

Unfortunately insulating properties of the crepe depend strongly on the moisture content. When the moisture content within the paper exceeds the value of 3% the paper dielectric breakdown strength weakens drastically. On the other hand the dissipation factor increases rapidly when the moisture content within the paper exceeds the value of 0.5%. Both these behaviours [2] are documented in Figure 3.

Considering above discussed paper properties it is strongly recommended to decrease the water content in the insulation material below 1% or even lower if possible. That is why a special attention should be paid to the proper planning and carrying out the drying stage of the production process. Production of the bushing begins in specialized computer-controlled winding machine where crepe paper together with conduction inserts is wrapped onto a solid mandrel rod or a central tube. Once the paper coil is precisely formed on the conductor the series of heating and vacuum cycles are applied. During each heating cycle buoyancy flow of hot air increases temperature of the paper. After that stage vacuum is applied to speed up of water evaporation and its evacuation. This process is often characterized by the significant temperature drop within the paper (up to 30^{o}C -50^{o}C) caused by very intense evaporation process and high value of the water latent heat of evaporation being equal to 2270 kJ/kg at room temperature.

The vacuum drying is generally time-consuming and consequently energy-consuming technology. One can even say that the drying stage is often the most significant part of the bushing manufacturing process. Although it is certain that the drying time is dependent on the product geometry, initial water content within the paper and process parameters, it is still not obvious how this relationships look like. Therefore it would be very desirable to possess precise mathematical model of the process, capable of improving it or even optimise it. Preliminary version of such a model was presented in [3, 4]. Model is built up utilising a commercial Computational Fluid Dynamic (CFD) software *Fluent* [4]. Some important effective quantities occurring in the model are measured experimentally. Unknown and/or uncertain fields required for the model are determined through inverse analysis described in details in other papers. Finally, the whole model is validated by comparison of computational results with measurements obtained in the specially designed experiment.

GOVERNING EQUATIONS OF THE MATHEMATICAL MODEL

Formulated mathematical model of the vacuum paper drying process utilises the concept of porous medium, which is in thermodynamic equilibrium with a humid air. As a consequence only one energy equation, common for both phases, is solved. Water is treated as a one phase regardless it state, i.e. no matter it is free or bounded water. Its distribution within the paper is resolved by considering so-called lumped diffusion equation containing the effective diffusion coefficient of water D within porous material (crepe paper). This coefficient, dependent on the water content and temperature, is calculated based on the sorption/desorption curves. Such curves have been determined experimentally within the course of the project as will be discussed further. The governing equations of the model consist:
Continuity equation

$$\frac{\partial \rho_a}{\partial t} + \nabla \cdot \left(\rho_a \mathbf{w}\right) = \dot{m}_{H_2O} \tag{1}$$

Diffusion equations of humid air constituents

$$\begin{aligned} &\left(\rho_a Y^a_{H_2O} \mathbf{w}\right) = -\nabla \cdot \left(\mathbf{J}^a_{H_2O}\right) + \dot{m}_{H_2O} \\ &\frac{\partial\left(\rho_a Y^a_{O_2}\right)}{\partial t} + \nabla \cdot \left(\rho_a Y^a_{O_2} \mathbf{w}\right) = -\nabla \cdot \left(\mathbf{J}^a_{O_2}\right) \\ &\sum_{i=H_2O,O_2,N_2} Y^a_i = 1, \qquad \mathbf{J}^a_i = \rho_a D_{i,a} \nabla Y^a_i \end{aligned} \tag{2}$$

Momentum equation

$$\frac{\partial(\rho_a \boldsymbol{w})}{\partial t} + \nabla \cdot (\rho_a \boldsymbol{w}\boldsymbol{w}) = -\nabla p + \nabla \tau_i + \rho_a \boldsymbol{g} + \mathbf{S}_i \tag{3}$$

Energy equation

$$\begin{aligned} &\frac{\partial\left[\gamma \rho_a h_a + (1-\gamma)\rho_s h_s\right]}{\partial t} + \nabla \cdot \left[\boldsymbol{w}_a \left(\rho_a h_a + p\right)\right] = \\ &= \nabla \cdot \left(\tau \cdot \boldsymbol{w}_a + k_{eff} \nabla T\right) + \dot{m}_{H_2O} \Delta h \\ &k_{eff} = \gamma k_a + (1-\gamma) k_s \end{aligned} \tag{4}$$

Porous media model

$$\mathbf{S} = -\left(\mu \, \boldsymbol{D} \cdot \boldsymbol{w} + \frac{\rho_i |\boldsymbol{w}|}{2} \mathbf{C} \cdot \boldsymbol{w}_i \right) \tag{5}$$

Lumped diffusion model of moisture transport through porous material

$$\frac{\partial X}{\partial t} = \nabla \cdot \left(D_{eff} \nabla X\right) + \frac{\dot{m}_{H_2O}}{(1-\gamma)\rho_s} \tag{6}$$

Turbulence model – standard κ–ε

$$\frac{\mathrm{D}(\rho_a \kappa)}{\mathrm{D}t} = \nabla \cdot \left[\left(\mu_a + \frac{\mu_t}{\sigma_t} \right) \nabla \kappa \right] + G_\kappa - \rho \varepsilon$$
$$\frac{\mathrm{D}(\rho \varepsilon)}{\mathrm{D}t} = \nabla \cdot \left[\left(\mu_a + \frac{\mu_t}{\sigma_t} \right) \nabla \varepsilon \right] + C_{\varepsilon 1} \frac{\varepsilon}{\kappa} G_\kappa - \rho C_{\varepsilon 2} \frac{\varepsilon^2}{\kappa} \tag{7}$$

Model of mass transfer between porous medium and air – Herz-Knudsen equation together with Henderson sorption isotherm formulation

$$\dot{m}_{H_2O} = -\frac{2 C_{mt} (1-\gamma)}{r_f} \sqrt{\frac{M_{H_2O}}{2\pi R}} \frac{p_{eq} - p_v}{\sqrt{T}}$$
$$p_{eq} = p_{sat}\, \varphi(X,T) \tag{8}$$
$$\varphi(X,T) = 1 - \exp\left[-(AT + B) X^n \right]$$

In the above equations ρ represents density, T is the temperature, $\boldsymbol{w}$ stands for the velocity vector and h is the enthalpy. Chemical composition of the humid air is defined using mole fractions Y_i while water content in the paper is described by symbol X. Equilibrium relationship between these two quantities should be found experimentally determining so called sorption isotherm. Practically they define equilibrium between wet paper and humid air at a given temperature and pressure. Index a in the governing equations identifies humid air while index s refers to solid part of the porous material (paper). Symbol τ represents stress tensor, $\boldsymbol{S}$ is the source term in momentum equation and k stands for the thermal conductivity.

It should also be stressed that in the proposed model both the mass flux of the water steam in the gaseous phase and the moisture transport within the wet paper are proportional to the water diffusion coefficients D. Although relevant value in the gaseous phase can be get from the subject literature, e.g. [1], its effective value in the porous material, specific heat of the paper as well as constants A and B describing sorption isotherms (equation (8)) should rather be found experimentally.

SELECTED MEASUREMENTS

As already mentioned the numerous of measurements have been carried out within the course of the project. The first experiment referred to determining sorption isotherms. It consisted of drying of the paper sample within the particular environment (temperature and relative humidity of the air) managed inside a desiccator. Investigated sample was hung using tiny thread on the balance pan and placed inside above mentioned desiccator filled with saturated salt solution. Temperature sensor PT100 was also placed inside the desiccator and connected to the regulator which controlled operation of the heating lamps. When temperature inside the desiccator decreased below the preset temperature minus threshold, regulator turned on heating lamps and causing increase of the temperature. When it rose above the preset value plus threshold, regulator turned off lamps. Threshold was equal to 0.2 K, what gave regulation tolerance equal to 0.4 K. The desiccator and heating lamps were placed inside glass tank which walls were covered with an aluminium foil to minimize ambient influence. Balance was connected to the computer for online reading acquisition. Balance reading was printed to the text file for further utilization. General view of the experimental stand together with the character of the obtained sorption isotherm are shown in Figure 4 and 5.

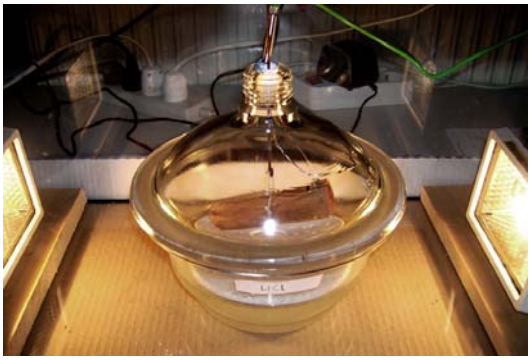

Figure 4. Experimental stand for determining of sorption isotherms

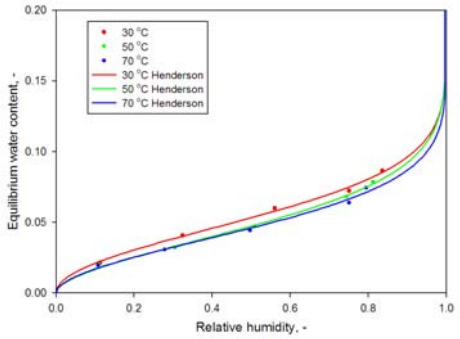

Figure 5. Exemplary sorption isotherms

Paper samples were prepared as rolls with mass equal to around 20 grams. At the beginning of the experimental procedure the sample was being dried for about 24 hours in temperature 110°C inside an electrical dryer. Then the dried sample was placed on the balance pan inside the desiccator and acquisition software was started. Measurements were carried out until equilibrium state between surrounding air and the moisture entrapped in the paper sample was established. Usually each measurement lasted between 12 and 30 hours. Humidity of the air inside the desiccator was not measured during experiment, since it was assumed that salt solution was saturated and therefore it was determined by the actual air temperature.

Measurements of the specific heat of the paper was carried out with Simultaneous Thermal Analysis instrument STA 409 PG Luxx produced by Netzsch. This instrument offers TG measurements resolution of 2µg and DSC resolution below 1µV. All specific heat measurements were carried out in the range from 30 to 170°C in dry air atmosphere with protective gas flow rate 20 ml/min. After calibration was preformed each sample underwent four-stage measurement procedure: moist sample run, vacuum, drying, dried sample run. Exemplary DSC and TG results for moist sample are shown in Figure 6 and 7.

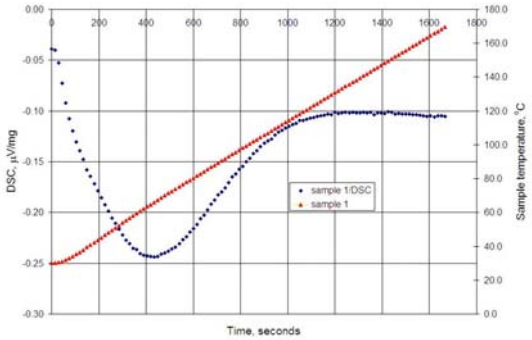

Figure 6. Exemplary DSC results

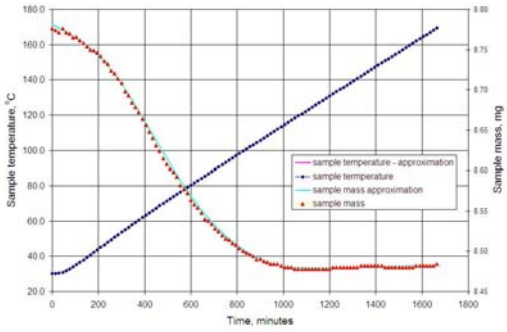

Figure 7. Exemplary TG results

The mean value of diffusion coefficient D_{eff} was in this work calculated with half equilibrium time method and its dependence on the water content was determined with the slope method. Exemplary results obtained for temperature 50°C is shown in Figure 8. It should be stressed that although curves show the diffusion coefficient dependent on the water content these values are actually averaged over the sample thickness for a given time instance. It explains to some extent dramatic increase and fall down of the diffusion coefficient values at the beginning and the end of a curve.

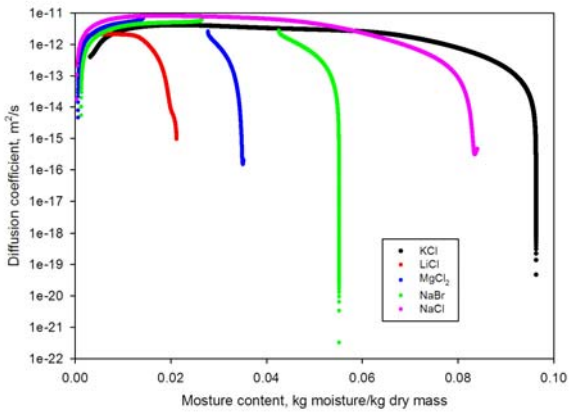

Figure 8. Water content dependent effective diffusion coefficient at temperature 50°C.

VALIDATION EXPERIMENT

To validate experimentally the developed mathematical model a special experimental rig has been prepared. It consisted of the vacuum chamber inside which paper coil on an aluminium rod (playing a role of the high voltage bushing) was placed. The paper coil has dimensions: height 200mm, external diameter 110mm, diameter of internal aluminium conductor 30mm. Chamber interior was connected through rubber hose with the vacuum pump. Part of the hose was coiled up and dipped in the vessel filed with a cold brine forming something like condenser of the vapour removed from the bushing. The vacuum chamber and the whole experimental rig are shown in Figure 9 and 10.

Figure 9. The vacuum chamber

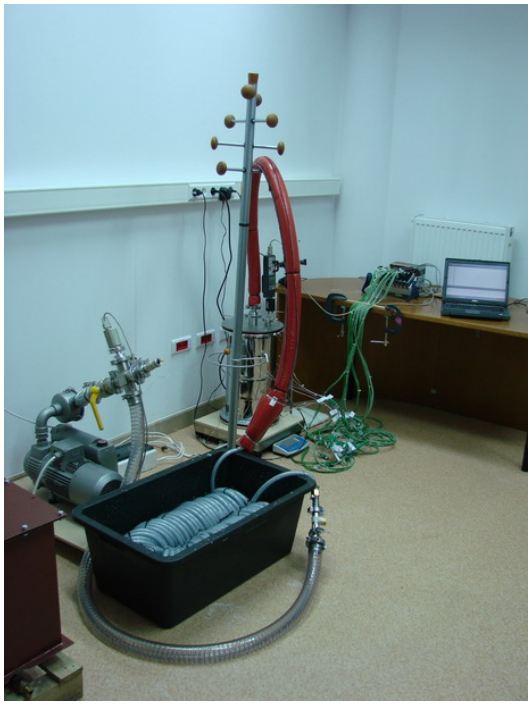

Figure 10. The whole experimental rig

Figure 11. The paper coil equipped with thermocouples

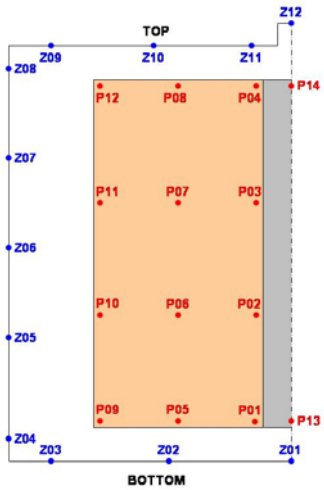

Figure 12. Location of the thermocouples

The paper coil has been equipped with 12 thermocouples as it is shown in Figure 11. These twelve thermocouples, marked in Figure 12 as (P1 - P12), were used for validation purposes. Because of axial symmetry of the object, Figure 12 contains only half of the coil cross-section. Additional twelve thermocouples marked (Z1 - Z12), were positioned on the inside walls, and were all used to establish boundary conditions. The last two thermocouples (Z13 and Z14) have been located inside the aluminium rod to measure its temperature.

At the chamber inlet/outlet static pressure was measured. These measurements were prescribed as a pressure type boundary condition. Temperature recordings are plotted in Figure 13.

To determine the changes of the water content within the experimental bushing it was weighted before and after experiment and after long drying in an oven in temperature over 100^{o}C. Recorded masses showed that approximate mass of water removed from the bushing in experiment was equal to 40 grams.

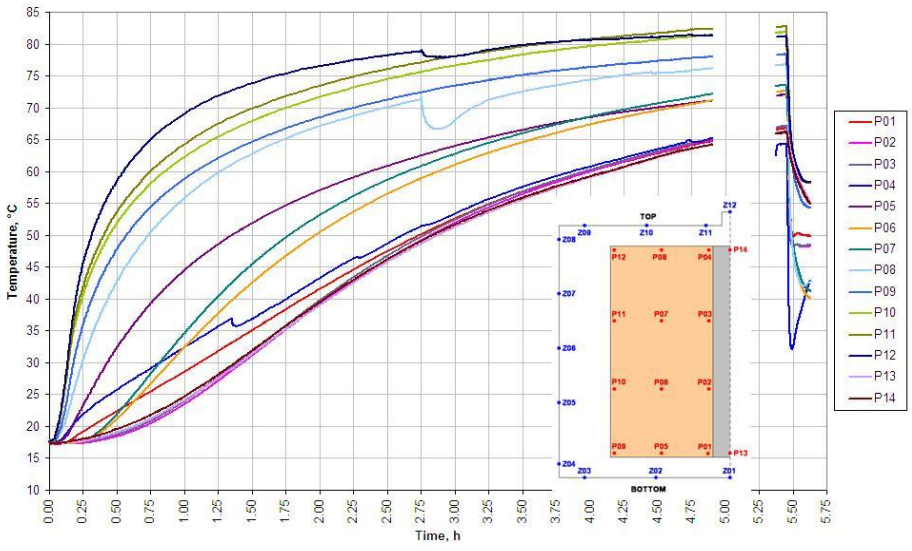

Figure 13. Temperature recordings within the paper coil.

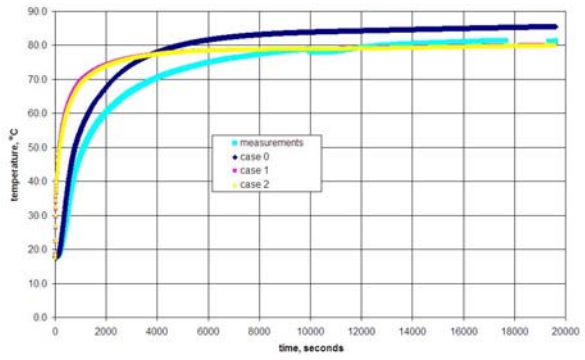

Figure 14. Temperature at point P12 with respect to heating time – comparison of calculated cases with measurement data.

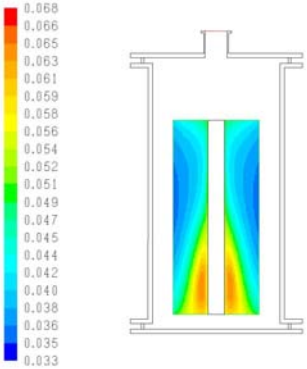

Figure 15. Water distribution inside the paper coil after heating period for one of the computational cases.

Heating period lasted about 6 hours and than vacuum was applied for about half an hour. Comparison between calculated temperatures at location of the thermocouple P12 and measurements at the same point for heating cycle are shown in Figure 14. Water distribution inside the paper coil after heating period for one of the computational cases is demonstrated in Figure 15. Many more results will be demonstrated during the conference.

CONCLUSIONS

Analysing carefully results of the carried out analysis the following general conclusions can be drawn:

- Developed model can successfully describe vacuum drying process,
- Presented model appears to be appropriate for engineering applications,
- Temperature and water content fields within computational domain are mainly influenced by the evaporation constant in Eq. (8),
- Cellulose thermal conductivity coefficient moderately influence temperature and water content fields,
- Lumped water diffusivity reveals almost no influence on temperature and water content. Its value has been measured experimentally,
- Preliminary research show the influence of anisotropy of porous material and shows its meaning influence on both temperature and water content fields.

REFERENCES

1. Getson D.M., *High Voltage Bushings*, ABB Materials, 2002.
2. Russek R.M., Drying and Impregnation of Paper-Insulated Power Cables, *IEEE Transactions on Power Apparatus and Systems*, pp 34 - 52, 1967.
3. Kasza K., Saj P., Sekuła R., Bulinski Z., Nowak A.J., Analysis and Optimization of Paper Vacuum Drying Process by Application of Advanced Numerical Modelling Approach. *Proc. of the Int. Conf. on Computational Methods ICCM 2007*, Hiroshima, Japan, April 4 - 6, 2007.
4. Bulinski Z., Kasza K., Sekuła R., Nowak A.J., Computational Model of Vacuum Drying Process. *Proc. of the Int. Conf. on Computational Methods for Coupled Problems in Science and Engineering*, Coupled Problems 2007, Santa Eulalia, Ibiza, Spain, May 21 - 23, 2007.

EXPERIMENTAL INVESTIGATION OF HEAT AND MASS TRANSFER FROM A FALLING FILM

Džana Kadrić[1], Šefko Šikalo[1] and Ejup N. Ganić [2,*]
[1]Faculty of Mechanical Engineering, University of Sarajevo, www.unsa.ba
[2]Sarajevo School of Science and Technology, Sarajevo, Bosnia and Herzegovina, www.ssst.edu.ba

ABSTRACT. Results of an experimental investigation of heat and mass transfer from the falling wall film to humid air are presented in this paper. Falling film is formed on the top of vertical flat plates. Air of known humidity was blown along the plates in the counter-flow mode. Heat and mass transfer occurred between unsaturated air in direct contact with the falling film.
The influence of inlet film temperature and mass flow rates of film and air on the heat and mass transfer are investigated.
Results of three sets of measurements are presented: case A – film flow rate 0.019 kgs^{-1}, t_{in}=45°C; case B – film flow rate 0.029 kgs^{-1}, t_{in}=45°C and case C – film flow rate 0.019 kgs^{-1}, t_{in}=30°C. The air flow rate was varied in the range from 0.055 to 0.093 kgs^{-1}.
Experimental results of heat and mass transfer are analysed. Some of them are given as a function of dimensionless groups.

Keywords: *Falling film, heat transfer, evaporation*

INTRODUCTION

During the direct contact of the wall falling film and humid air the simultaneous heat and mass transfer occurs. This process is often found in industrial applications such as cooling towers, film cooling, drying, desalination etc. Therefore it has been a subject of investigations in many theoretical, experimental and numerical studies. There are a number of phenomena which could be investigated. Among them, we would like to emphasise the following:
Heat and mass transfer between the film and humid air and influence of different parameters on the film cooling. Some of the parameters which are studied are film flow rate, inlet film temperature, inlet air humidity, inlet air temperature, etc. [1, 2, 3, as well as references therein].
Values of latent and sensitive heat transferred and their ratio in a total heat exchanged. According to our experimental results the latent component of heat transfer has a dominant role in a total heat transferred. Some investigators have reported that the latent component could reach up to 95 % of the total heat transfer. As a result, the amount of evaporated water vapour is an important parameter. The water temperature decrease is mostly influenced by rate of water film evaporation [3, 4, 5, 6].
We experimentally studied the influence of inlet water film temperature, film flow rate and air flow rate on heat and mass transfer coefficient. Some results of the study are shown as a ratio of latent heat to total heat transfer rate.

* Corresponding author: Prof. Ejup N. Ganic
Phone: + (387)-33-563 035 , Fax: + (387)-33-563 033
E-mail address: ejup.ganic@ssst.edu.ba

APPARATUS AND EXPERIMENTAL TECHNIQUES

An experimental setup consists of water and air supply lines, and a test section. Simultaneous heat and mass transfer occur in direct contact between water and air, in a counter flow mode, as Figure 1 shows. Air is supplied from compressor and flows through a dust and moisture separator and a pressure regulator. To control and measure air flow easily, the air supply line separates in two branches. Compressed air flows through flow control valves, flowmeters and enters the test section. Two air flow meters provide more flexible and precise measurements. The flowmeters with measuring range from 0.85 to 4.25 m^3/min are used. A hygrometer and thermometer are built in the air line.
Distilled water is pumped from a storage vessel by a variable speed pump though a flowmeter to a large volume heater. A small volume heater with fine temperature regulation provided to control temperature of water at the inlet of test section. A water flowmeter with measuring range from 28 to 171 l/h is used. Temperature of water is measured at the inlet of test section and in a water drainage pipe.

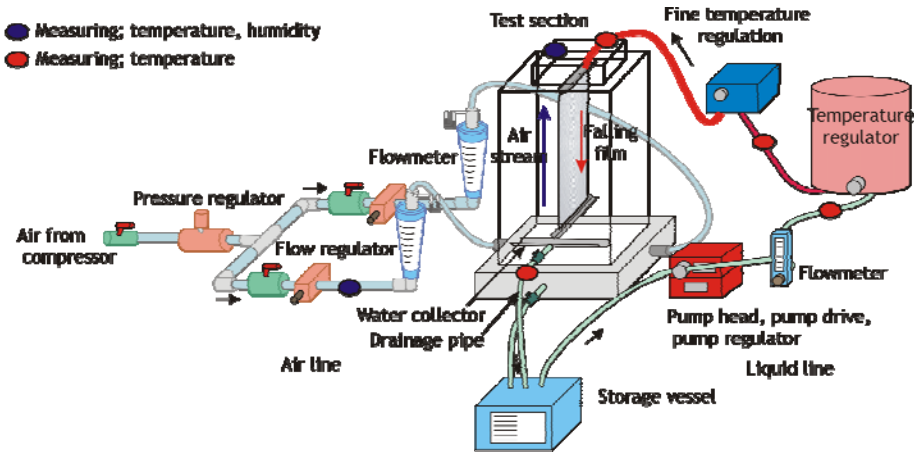

Figure 1. Schematic of the experimental setup

Test section consists of transparent Plexiglas wall. It is 0.61 m high, and has a square cross section area of 0.3 x 0.3 m^2. A set of five vertical flat plates are used as a packing to spread and cool falling water film. Salonite (concrete asbestos) plates, dimensions of L=250 mm width, H=500 mm height, t=6 mm thickness are used, where plates spacing were 40 mm. Salonite is a highly wettable material and allows highly equal distribution of liquid across the plates. A water distribution system equally spreads water flow rate from the top of the plates. A thin wall liquid film is formed on both sides of the plates. Water collects on the bottom of the plates and then drains out of the test section. A stainless steal segment supports the section, and distributes air flow cross over to the test section.

Experimental procedure

Heated distilled water spreads over the plates forming laminar falling film. Turbulent air flow cools the liquid film. Experimental setup and position of measuring points are shown in Figure 2.
Humidity and temperature of air is measured in five points at the section outlet.

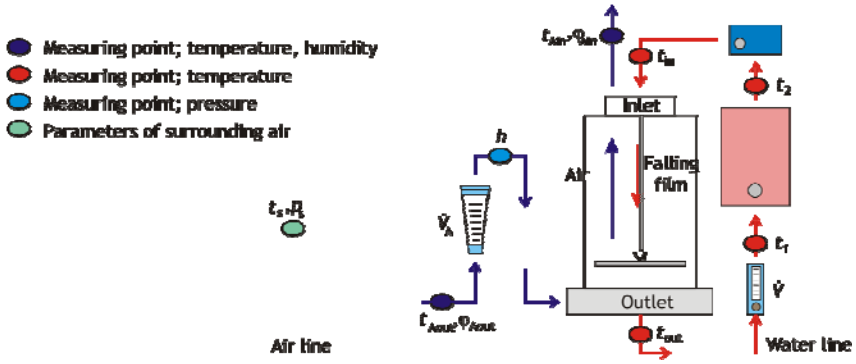

Figure 2. Measuring points

A number of measurements are performed and they are as follows: case A – film flow rate 0.019 kgs^{-1}, t_{in}=45°C; case B – film flow rate 0.029 kgs^{-1}, t_{in}=45°C and case C – film flow rate 0.019 kgs^{-1}, t_{in}=30°C. The air flow rate was varied in the range from 0.055 to 0.093 kgs^{-1}. One of the parameters is varied; others were constant to determine its influence on the transfer coefficients.

ENERGY BALANCES

In direct contact of laminar falling film and turbulent air stream, process of simultaneous heat and mass exchange occurs. Water temperature decreases, air temperature and humidity increases. Energy balance of falling film and air flow are analyzed.

Energy balance for the air flow

Total amount of heat transferred to the air flow consists of sensible heat, which is defined by change of temperature of dry thermometer, and latent heat, which is defined by change of absolute humidity of air. Energy balance for the air flow gives:

$$Q_{air}=Q_{sen}+Q_{lat}=\dot{m}_{air}c_p(t_{air,in}-t_{air,out})+\dot{m}_{air}(x_{air,in}-x_{air,out})h_{fg} \quad (1)$$

where: $\dot{m}_{air}$ is mass flow rate of air, kg/s, h_{fg} is latent heat of phase change at the average water temperature, J/kg.

Energy balance for the falling film

From the energy balance of the falling film, one could calculate the total heat exchanged in the process as:

$$Q=\dot{m}_{in}c_{p,in}t_{in}-c_{p,out}(\dot{m}_{in}-E)t_{out} \quad (2)$$

The water evaporation rate E, kg/s, could be calculated from the total change of the absolute air humidity:

$$E=\dot{m}_{air}(x_{air,in}-x_{air,out}) \quad (3)$$

Heat and mass transfer coefficients

Heat and mass transfer coefficients for air are calculated under the assumption that heat and mass exchange take place between the two layers of air. The first one is thin, saturated air layer in

proximity of falling film and the second one is a bulk air flow. The first layer has the temperature of the falling film.
Heat and mass coefficients are:

$$\alpha_{\text{air}} = \frac{Q_{\text{sen}}}{A\Delta t_{\text{air,lm}}}, \text{ W/m}^2\text{K and} \quad \beta_{\text{air}} = \frac{Q_{\text{lat}}}{A\Delta x_{\text{air,lm}} h_{fg}}, \text{ kg/m}^2\text{s} \tag{4}$$

where $\Delta t_{\text{air,lm}}$ is a logarithmic mean temperature difference, °C, and $\Delta x_{\text{air,lm}}$ is a logarithmic mean absolute humidity difference, kg/kg$_{\text{dry_air}}$.
Heat transfer coefficient for falling film is calculated as:

$$\alpha = \frac{Q}{A\Delta t_{\text{lm}}}, \text{ W/m}^2\text{K} \tag{5}$$

Dimensionless numbers

Dimensionless numbers for the air flow and for the falling film are calculated as follows.

Air flow
The Reynolds number, defined as for forced-convection heat transfer, for air is calculated as:

$$\text{Re}_{\text{air}} = \frac{(\dot{m}_{\text{air}}/\text{A}_{\text{c,air}})D_{\text{h,air}}}{\mu_{\text{air}}} \tag{6}$$

where: $\dot{m}_{\text{air}}$ is mass flow rate of air, kg/s, $A_{\text{c,air}}$ cross section of a flow, m^2, and $D_{\text{h,air}}$ is characteristic hydrodynamic length, m, given in Table 1.
The Nusselt number is defined as a dimensionless heat transfer coefficient, based on sensible heat of air flow,

$$\text{Nu}_{\text{air}} = \frac{\alpha_{\text{air}} D_{\text{t,air}}}{\lambda_{\text{air}}} \tag{7}$$

where λ_{air} is air conductivity, W/mK, and $D_{\text{t,air}}$ is characteristic thermal length, m.
The Sherwood number is defined as a dimensionless mass transfer coefficient, based on latent heat of air flow,

$$\text{Sh} = \frac{\beta_M D_{\text{t,air}}}{c\boldsymbol{D}} \tag{8}$$

where β_M mass transfer coefficient, mol/m^{2}s, c is molar concentration of water vapour, mol/m^3, and $\boldsymbol{D}$ is the mass diffusivity of water vapour into air.

Table 1
Characteristic lengths

Falling film	Air flow
Characteristic thermal length, $D_t = 4\,A_p/O_t$	
$A_p = 2{\cdot}5L\delta$; $O_t = 2{\cdot}5L$; $D_t = 4\delta$	$A_{p,air} = 0.3^2 - 5(t+2\delta)L$; $O_{t,air} = 2{\cdot}5L$; $D_{t,air} = 2{\cdot}0.3^2/(5L) - 2(t+2\delta)$
Characteristic hydrodynamic length, $D_t = 4\,A_p/O_h$	
$A_p = 2{\cdot}5L\delta$; $O_h = 2{\cdot}5L$; $D_h = 4\delta$	$A_{p,air} = 0.3^2 - 5(t+2\delta)L$; $O_{h,air} = 2{\cdot}5\,(L+t+2\delta)+4{\cdot}0.3$

Falling film

The Reynolds number of falling film is calculated as:

$$\mathrm{Re} = \frac{4\Gamma}{\mu} \tag{9}$$

where Γ is mass flow rate per unit perimeter L, kg/sm^2. The Nusselt number of falling film is calculated as:

$$\mathrm{Nu} = \frac{\alpha \mathrm{D_h}}{\lambda} = \frac{\alpha 4\delta}{\lambda} \tag{10}$$

RESULTS AND DISCUSSION

In this section, the results of direct measurements of an overall heat and mass transfer coefficients are presented and discussed.

The air flow results

The highest values of total heat transfer we had for case B (2.07 kW< Q_B < 2.52 kW). The lowest values of total heat transfer we had for the case C (0.97 kW< Q_C < 1.17 kW). For the case A (1.68 kW< Q_A < 2.07 kW) we had a total heat transfer between that for case B and C. Ratio of latent heat component to the total heat transfer is higher than 80 %, as Figure 3 shows. The highest ratio is obtained for case C.

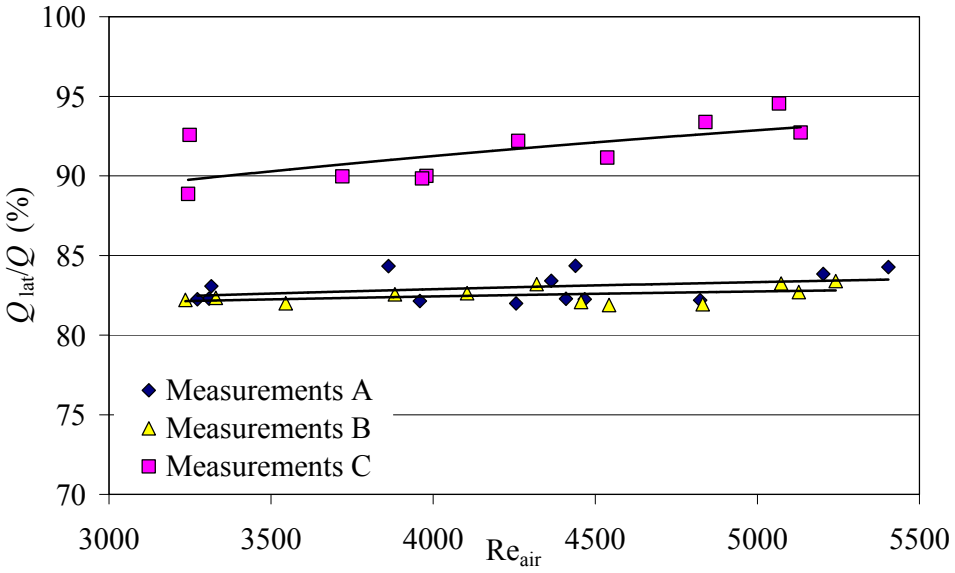

Figure 3. Ratio of latent and total heat transfer rates

Film temperature at the inlet of test section for the case C has the lowest value; as a result, the sensible heat transfer is the lowest, and the component of latent heat is the highest. Comparing the results for case A and case B shows that increase in the mass rate flow does not significantly affect this ratio. An increase of the air Reynolds number slightly increases the ratio of Q_{lat}/Q. These results are in agreement with other authors [1, 2, 4, 5, 6]. Thus, heat transfer between the falling film and air flow is controlled by mass transfer (vaporization of liquid film).

The Nusselt and Sherwood numbers for the air flow for case A and B are equal about one, as Figure 4 shows. For the case C (lower inlet film temperature) this ratio is about 0.6. For this case mass transfer is larger then in case A and B.

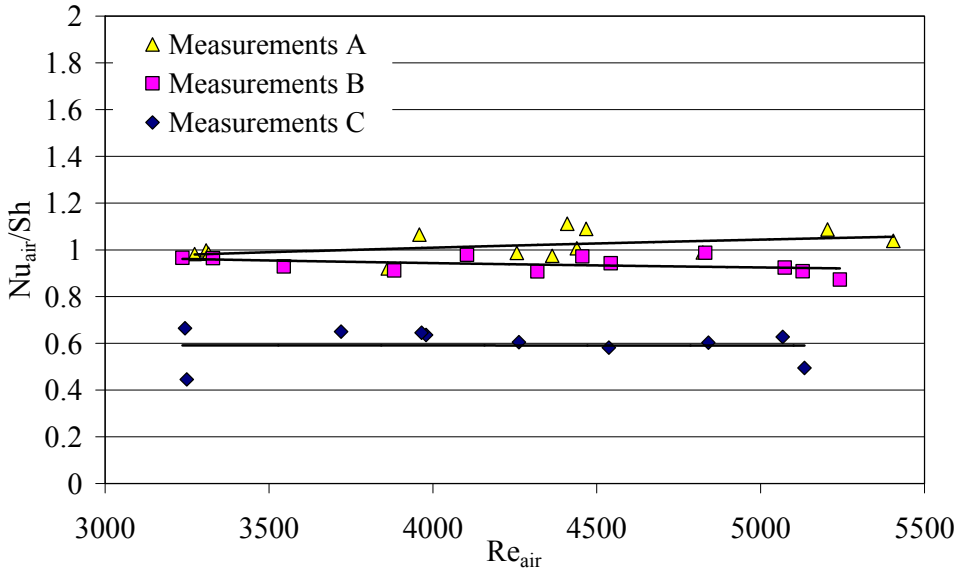

Figure 4. Ratio of Nusselt and Sherwood numbers for air

As a result of experimental investigation [7] of the simultaneous heat and mass transfer between the humid air and the moving water film, the following correlation is proposed for the Sherwood number:

$$\mathrm{Sh}=1.622\ \mathrm{Re}^{0.412}\mathrm{Sc}^{0.34}(1+\beta^{0.3}) \tag{11}$$

where Sc is Scmidt number and β is velocity ratio u_{air}/u.

Experimental results presented as Sherwood number in a function of Reynolds number is shown in Figure 5. Comparison of values calculated by equation (11) and obtained experimentally shows a good agreement. Some deviation in results is due to the experimental setup. Equation (11) is proposed for the heat and mass transfer between the horizontal moving water film and the flow of humid air while our experiment investigates the falling film formed on the vertical flat plates.

The percentage of liquid film evaporation is compared to the equation presented by Qureshi and Zubair [3]:

$$\frac{E}{\dot{m}} = -0.00849 + 0.1544(t_{\mathrm{in}} - t_{\mathrm{out}}) \tag{12}$$

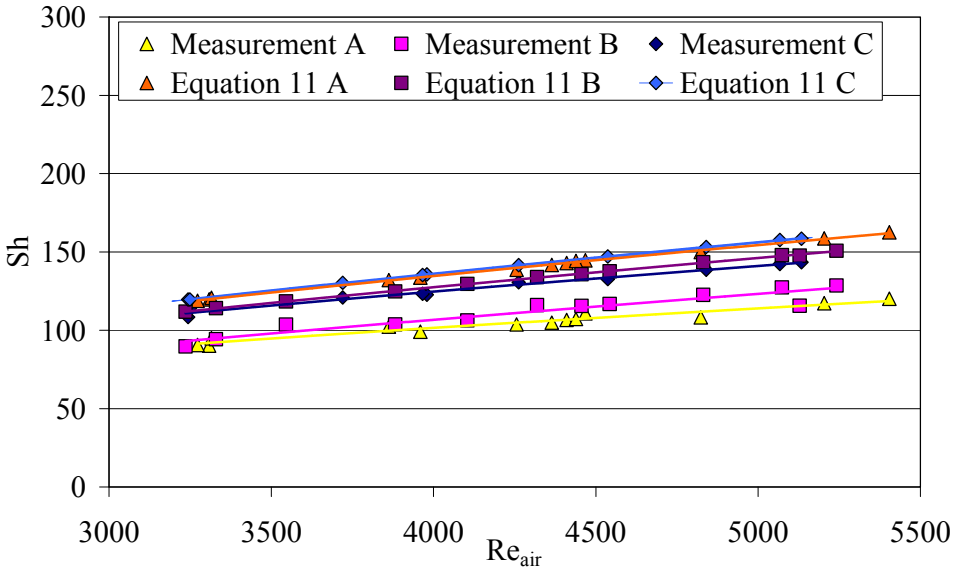

Figure 5. Sherwood number

For the case A good agreement is obtained, while for the cases B and C, the equation (12) slightly underpredicts the evaporation rate as it is shown in Figure 6.

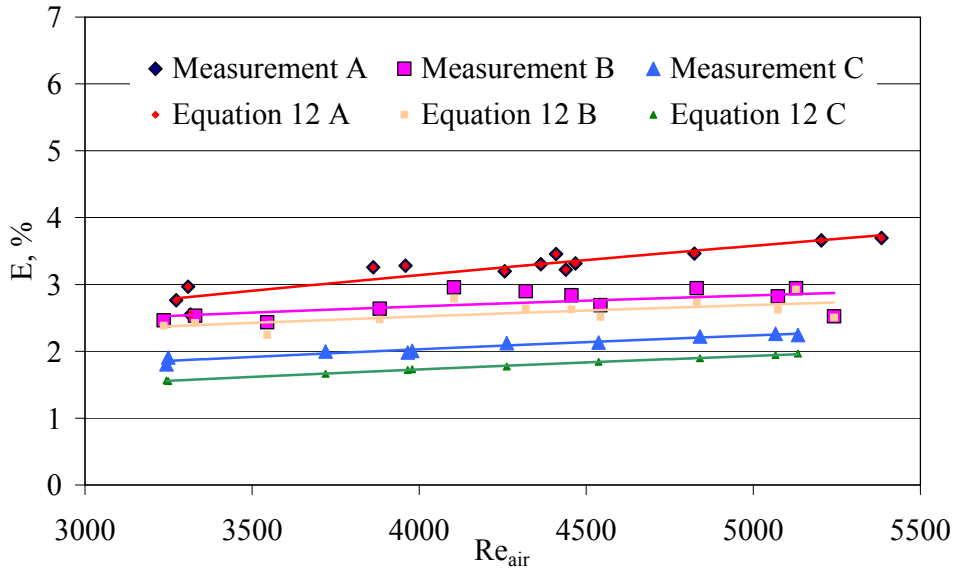

Figure 6. Comparison of measured and calculated vales of percentage evaporation loss

The falling film results

The overall film temperature drop is shown in Figure 7. Comparing the results of the cases A (0.019 kgs^{-1}, t_{in}=45°C) and B (0.029 kgs^{-1}, t_{in}=45°C), it is obvious that an increase of the film mass flow decreases the overall temperature drop. While comparison of the results for the cases A and C (0.019 kgs^{-1}, t_{in}=30°C) shows that increase of the inlet film temperature results in a larger temperature drop, these results completely coincide with the results [1, 2, 4, 5, 6]. The influence of

the air Reynolds number on the overall temperature drop is also obvious from Figure 7. The film temperature drop increases with increase of the air Reynolds number.

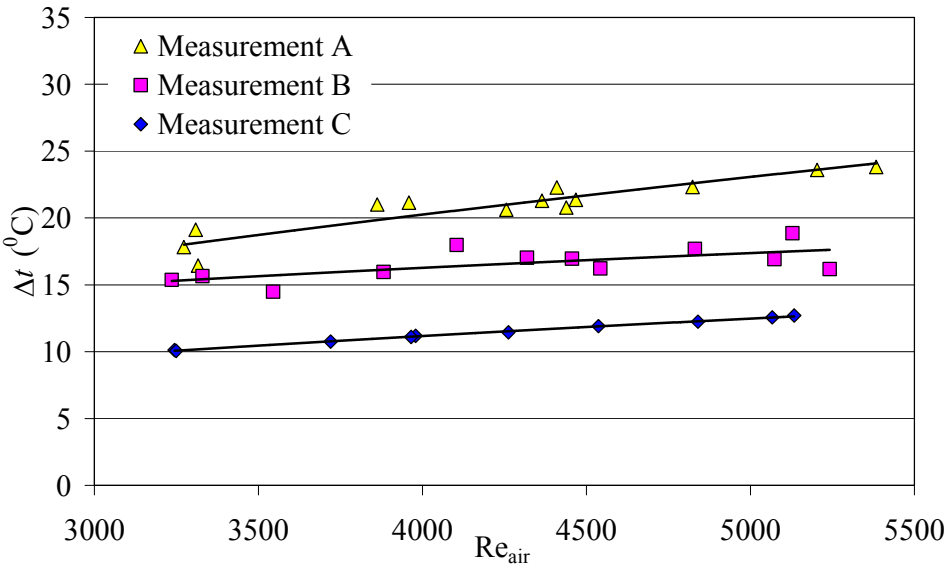

Figure 7. Overall film temperature drop ($\Delta t = t_{in} - t_{out}$)

FINAL REMARKS

Results of experimental investigation of simultaneous heat and mass transfer between wavy laminar wall falling film and a turbulent stream of humid air flow are presented in this paper. The effects of inlet water film temperature and its mass flow rates and cooling air flow on the heat and mass transfer are investigated. Latent heat component from the liquid film vaporization prevail in the total heat transferred. An increase of inlet film temperature and a decrease of film mass flow rates resulted in an increase of overall film temperature drop. An increase of the air mass flow rate results in an increase in more intensive water film cooling.

REFERENCES

1. W. M. Yan, Binary diffusion and heat transfer in mixed convection pipe flows with film evaporation, *Int. J. Heat and Mass Transfer,* Vol. 36, 2115 - 2123, (1993)
2. W. M. Yan, Effects of film vaporization on turbulent mixed convection heat and mass transfer in vertical channel, *Int. J. Heat and Mass Transfer,* Vol. 38, 713 - 722, (1995)
3. B. A. Qureishi and S. M. Zubair, Prediction of evaporation loses in wet cooling towers, *Heat transfer engineering*, 27:9, 86-92, (2006)
4. G. V. Sesha and A. Mani, Analysis of forced convective evaporation system for tannery effluent (soak liquor), *Int. Comm. Heat Transfer*, Vol. 30, No. 5, pp. 727 - 736, (2003)
5. W. M. Yan, T. F. Lin and Y. L. Tsay, Evaporative cooling of liquid film through interfacial heat and mass transfer in a vertical channel-I. Experimental study, *Int. J. Heat and Mass Transfer,* Vol. 34, 1105 -1111, (1991)
6. W. M. Yan, Convective heat and mass transfer from a falling film to a laminar gas stream. *Wärme-und Stoffübertragung* 29, 79 - 87, (1993)
7. M.G.Mousa, Heat and mass transfer from moist air flowing over moving water film II – experimental study, *Mansoura Engineering Journal*, Vol. 30, No. 2, pp.M65 – M74, (2005)

NUCLEATE BOILING OF NATURAL REFRIGERANTS IN A WIDE PRESSURE RANGE

Andrea Luke*, Björn Müller
Institute of Thermodynamics, Leibniz University Hannover, 30167, Hannover, Germany

ABSTRACT. Experiments with propane boiling on a horizontal mild steel tube (19 mm O.D.) with different surface structures have recently been started in a wide pressure range, in which the local heat transfer along the circumference of the tube, the roughness topography of the tube surface, and bubble formation and motion are measured in order to study the convective and evaporative contributions to heat transfer in nucleate boiling. First results show the variation of convective effects with heat flux, pressure and azimuthal position. The heat transfer measurements with propane are represented in a wide range of saturation pressure and heat flux and are compared with corresponding results of the literature. Large cavities within the drawn surface promote the activation of bubble nuclei for very small superheat and in consequence enhancement effects.

Keywords: *Pool boiling, surface roughness, natural refrigerants, heat transfer*

INTRODUCTION

Heat exchangers become more and more miniaturized to save energy and to take care of the natural ressources. High heat flux densities can be transfered by small temperature gradients in evaporators. This high transfer capability is now used even on fields, where two phase systems were avoided by reason of their complexity. New prediction methods for the heat and mass transfer in boiling will be therefore required in future to succeed the empirical correlations used until now. The calculation methods for the design of evaporators are based on more or less acurate heat transfer measurements. They are often not attended by equally accurate studies of the roughness of the heated surface and of the bubble formation, especially data for a large pressure range are rare in literature.
In order to provide experimental material that meets the above mentioned criteria, measurements with a horizontal plain mild steel tube (19 mm O.D.) have recently been started, because data for mild steel tubes are often not avaible in literature. In these experiments the local and the average heat transfer is measured by a great number of miniaturized thermocouples, the topography of the microstructure is analysed by means of a new stylus instrument and bubble formation and motion is investigated by a high speed video system. The microstructure of the originally drawn surface is prepared in a differently manner first a very smooth polished one and in future a uniformly fine sandblasted surface will be applied. In this paper heat transfer measurements with propane are represented in a wide range of saturation pressure and heat flux and are compared with corresponding results of the literature. Propane is a natural refrigerant and is discussed to replace refrigerants with high global warming potential.

DESIGN OF THE TEST TUBES AND EXPERIMENTAL PROCEDURE

The heat transfer measurements and the investigation of the bubble formation are carried out in a standard apparatus for pool boiling suggested by Gorenflo and Goetz [1]. The apparatus is modified by Kaupmann et al. [2] and recently by Kruck and Luke [3]. A new apparatus for pool boiling is now designed to investigate the heat transfer for boiling fluids like carbon dioxide with high pressures and for fluids in supercritical state. The main features of the apparatus are:

* Corresponding author: Prof. Dr.-Ing. habil. A. Luke
Phone: + (49)-511-762-2877, Fax: + (49)-511-762-3857
E-mail address: ift@ift.uni-hannover.de

- A natural circulation loop of the test fluid between evaporator and condenser both are situated in a PID temperature controlled chamber,
- the dc-heated horizontal test tube in the evaporator,
- the superheat of the tube wall is directly measured by miniature thermocouples (Ø 0,25mm) with one junction located in the boiling liquid below the test tube and the other junction in the test tube,
- Bubble formation on the different sections of the tube is observed through sight glasses in the evaporator, photographs and high speed video frames are taken.

Propane is used as boiling liquid on the outside of the test tubes. The saturation pressure is varied in a large range from p* = 0.03 to p* = 0.5 and the heat flux is varied from q = 50 W/m² up to 10^5 W / m^2, see Table 1. The electrically heated test tube is horizontally located inside the evaporator. The test tube consists of three coaxial tubes. The center tube is a round copper bar with one helix groove for the resistance heater element. This is inserted into an inner tube with 12 grooves on the outer surface to fix the thermocouples at their azimuthal and axial position. This tube is enclosed by the test tube itself and a cap at the end of the tube. In a special process all parts of the tube are soft soldered together under reduced conditions for an optimal heat conduction. The mild steel tubes and the copper tubes are designed similarly, for the details see [3].

SURFACE ANALYSIS

The material of the horizontal test tube is mild steel and copper. The outer surface with the diameter D = 19 mm is taken with the originally drawn surface provided by the manufacturing process. The outer diameter is varied slightly after the surface preparation, see Table 2. The drawn surface is the same basic surface for further procedure for enhancement (e.g. [4]). The surface is polished after the investigation of the heat transfer measurements. The polishing procedure results in a very smooth deterministic microstructure but the surface is more or less without real technical relevance. To provide a regularly structured more technical smooth surface in future, the surface will be fine sandblasted acc. to [5].
The heating surfaces are analyzed by a contactless stylus instrument [5]. A diamond tip swinging by ultrasound is driven slowly over the surface by special forward feeds. The movements of the tip correspond to the surface roughness and they are digitalized and amplified. One scan represents a conventional roughness profile (see Figure 2), where the standard parameters acc. to DIN EN ISO 4287 (10.98) can be applied. Measurements of more than 1000 scans in an axial direction with of the tube Δy = 0.5 µm represents a topography of the area 0.5 x 0.5 mm. The 2-dimensional standardized roughness parameters have equivalent counterparts in 3-dimensional characterization S_i [8] added to Table 2. The area and the profiles investigated are shorter than standardized due to the long measuring time [5]. Several scans are provided near each thermocouple and topographies at selected positions.

Table 1: Parameter of the heat transfer measurements

Tube	roughness P_a	fluid	Pressure p* [-]	Heat flux [W/m²]
R1, polished, ∅ = 18.85 mm	P_a = 0.04 µm	Propane	0.5, 0.2, 0.1, 0.07	50 - 80k 50 - 60k
R5, drawn, ∅ = 19.0 mm	P_a = 0.5 µm	Propane	0.5, 0.2, 0.1, 0.07, 0.05, 0.03	50 - 100k 50 - 80k
R5, polished, ∅ = 18.82 mm	P_a = 0.5 µm	Propane	0.5, 0.2, 0.1, 0.07, 0.05, 0.03	50 - 100k 50 - 80k
R9, polished, ∅ = 18.85 mm	P_a = 0.02 µm	Propane		

Table 2
Roughness parameters of the polished and drawn test tubes acc. to DIN EN ISO 4287 (10.98) with the gauge length of x = 0.5mm, without cut-off ($\lambda_c = \infty$)

Diameter (code number) Treatment	Azimuthal position		P_a [µm]	P_q [µm]	P_p [µm]	P_{pm} [µm]	P_t [µm]	P_z [µm]	runs
D = 18.85 mm	near 4	average	0.04	0.06	0.21	0.42	0.24	0.11	
mild steel, polished	thermocouples	max.	0.13	0.20	2.15	2.58	1.10	0.85	
R1SP1		min.	0.02	0.03	0.07	0.17	0.14	0.06	4275
		σ	0.01	0.02	0.19	0.23	0.08	0.06	
		S_i 1)	0.41	0.52	1.77		3.81	3.21	
D = 18.85 mm	near	average	0.1	0.15	0.41	1.13	0.54	0.23	
mild steel , polished with cavities	1 cavity	max.	1.07	1.99	1.93	11.96	3.16	0.78	
R1SP2		min.	0.03	0.04	0.12	0.27	0.21	0.09	2687
		σ	0.12	0.24	0.32	1.57	0.40	0.13	
		S_i 1)	0.22	0.38	1.65		8.34	4.68	
D = 19.00 mm	near	average	0.66	0.94	1.51	5.99	3.49	0.97	
mild steel,	10 thermocouples	max.	1.95	3.02	7.36	16.88	8.70	3.53	
drawn		min.	0.17	0.23	0.34	1.41	0.87	0.28	13305
R5SZ1 & Z2		σ	0.30	0.41	0.88	2.55	1.42	0.46	
		S_i 1)	0.81	1.16	4.24		13.99	11.32	
D = 18.82 mm	near 2	average	0.03	0.05	0.16	0.4	0.24	0.11	
mild steel, polished	thermocouples	max.	0.13	0.16	0.58	1.09	0.69	0.32	
before heat transfer measurements		min.	0.02	0.02	0.06	0.12	0.1	0.05	2192
R5SP1		σ	0.01	0.02	0.08	0.16	0.08	0.05	
		S_i 1)	0.22	0.28	1.11		2.32	2.09	
D = 18.82 mm	near 2	average	0.03	0.04	0.09	0.3	0.19	0.07	
mild steel, polished	thermocouples	max.	0.06	0.13	0.27	1.56	0.44	0.11	
after heat transfer measurements		min.	0.02	0.02	0.05	0.15	0.13	0.05	1439
R5SP1N		σ	0.01	0.01	0.02	0.15	0.05	0.01	
		S_i 1)	0.18	0.24	0.74		2.12	1.89	
D = 18.85 mm	near 12	average	0.02	0.03	0.10	0.31	0.17	0.07	
copper, polished	thermocouples	max.	0.23	0.48	1.00	3.05	1.01	0.37	
R9CP1		min.	0.01	0.01	0.04	0.08	0.07	0.03	7550
		σ	0.01	0.01	0.03	0.10	0.03	0.01	
		S_i 1)	0.08	0.12	0.35		1.36	1.10	

1) The three-dimensional parameters S_a, S_q, S_p, S_t, S_z correspond to the two-dimensional // gauge length = 0.5mm, without cut-off ($\lambda_c = \infty$)

The results of the roughness measurements in form of the standardized parameters acc. to DIN EN ISO 4287 (10.98) are listed in Table 2 for the polished and the drawn surfaces. Characteristic profiles with the typical enlargement z/x are shown in Figure 2, bottom, for the drawn (left) and the polished mild steel tube (right). Each profile represents a profile with the average mean roughness P_a of Table 2 of the surface investigated. The photorealistic and isometric representations of the topography are shown in Figure 2 (top) to demonstrate the 3-dimensional impression of the surface and the size and the local distribution of real cavities on the heated surface. The topography of the very irregularly drawn surface shows a typical structure due to the manufacturing process. Very large cavities – including several re-entrant ones – vary with small cavities, see the profiles in Figure 2. The result is a large scatter in the average values as the mean roughness P_a. The mean roughness – taken normal to the main roughness structure e.g. the grooves in the polished surface - represents the reference value in the empirical correlations for the heat transfer acc. to [6]. P_a scatters from values near the reference value of $P_a = 0.66$µm up to values three times larger $P_{a,max} = 1.95$ µm or to values four times smaller $P_{a,min} = 0.17$µm, see Table 2. This variation is reflected by high values of standard deviation and the wide distribution of the mean roughness value, s. Figure 3. The differences of the P_a-values within one topography is also visualized by Figure 3 considering the scattering in a very small distances ($\Delta y = 0.5$µm). The scattering of the mean roughness would result in a local variation of the heat transfer coefficient of ca. ± 16 % acc. to Stephan [7] or to the VDI-heat atlas [6]. The few large very deep cavities will be the favoured sites for beginning nucleation for small superheats and low pressures and the small cavities between the large ones will be only activated for high pressures and very high superheats.
The polished surface is prepared by the same devices as the emery ground surfaces investigated before [5], but with another emery paper (2000#). The result should be a mean roughness of $P_a = 0.02$ µm – 0.04 µm with a regular surface structure. The 3-dimensional mean roughness is always higher than the 2-dimensional value because a superimposed waviness for the topography has to be considered,

this is especially the case for the polished surfaces. The polished steel surface is in average somewhat rougher than the carefully polished copper tube because of the very rough original drawn surface, while the copper surface has some rougher grooves, see Figure 6 and Table 2. The first polishing procedure of the steel tube was not as successful as assumed, some of the deep cavities were not removed, s. Figure 5. The mean roughness is increasing ten times in the area of the cavity, see Figure, the heat transfer augments locally by more than 50% acc. to [6].

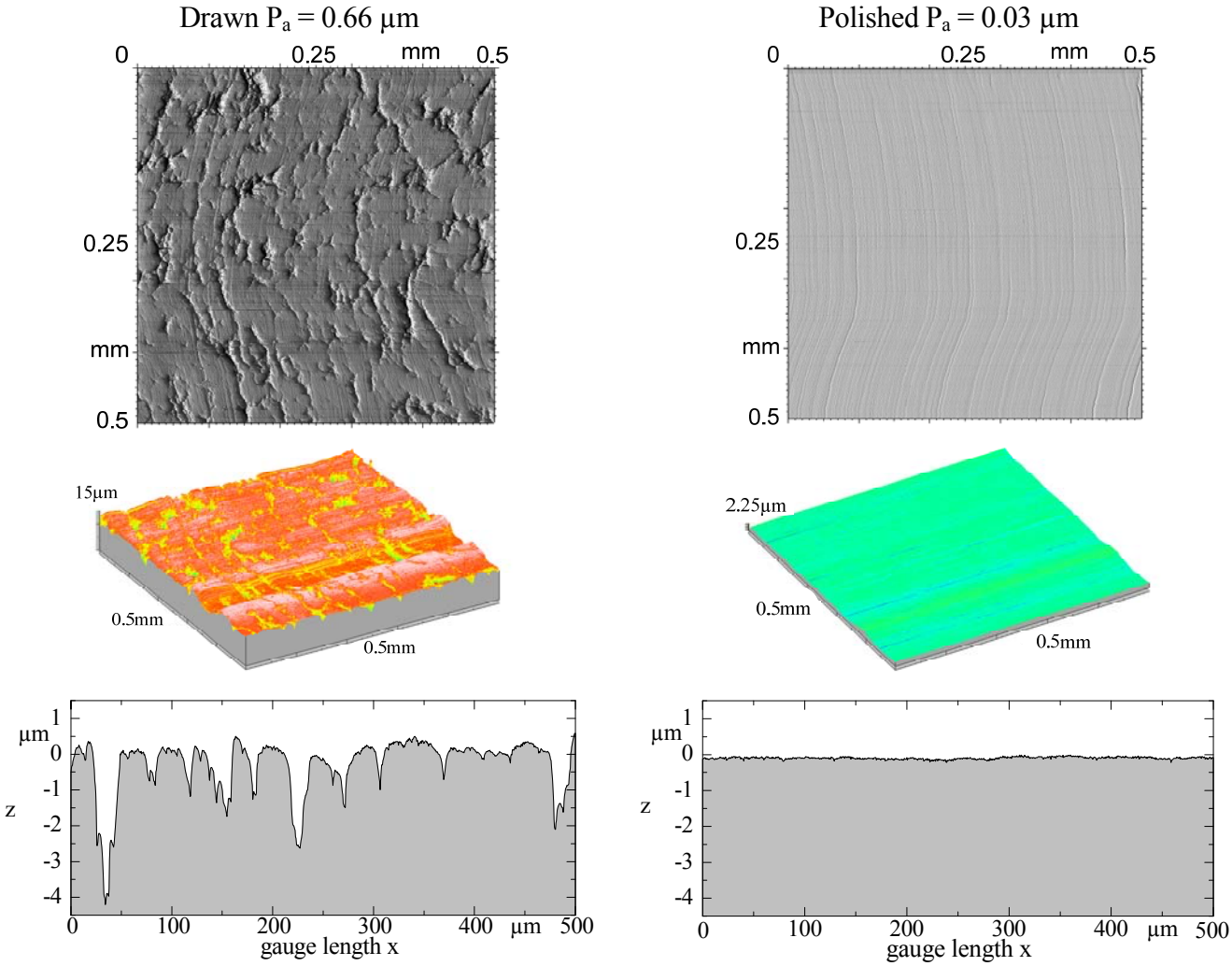

Figure 1. Top Photorealistic representations of the drawn (left) and polished (right) Profiles in azimuthal (x-) direction (bottom) with the common enlargement (z/x = 36) and isometric topography with the common enlargement (z/x = 5) of the drawn (left) and the polished (right) mild steel tube

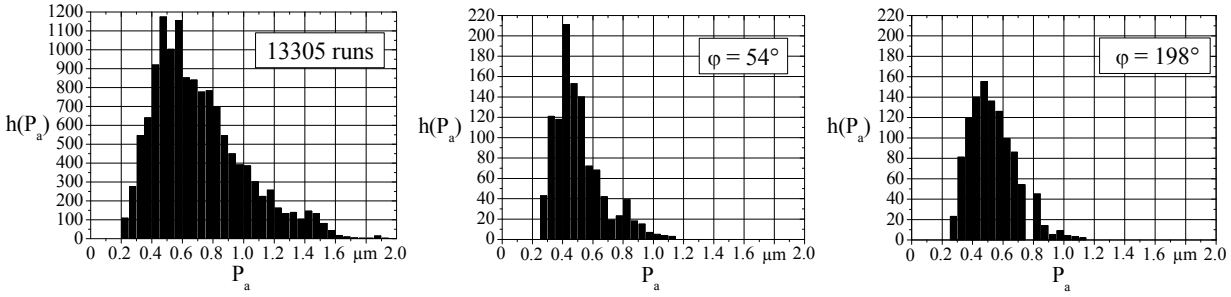

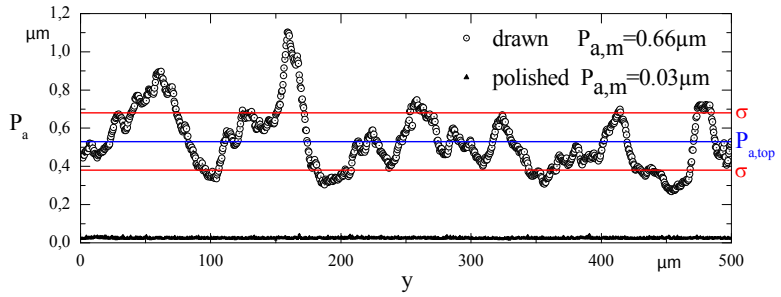

Figure 2. Overall and local size distributions of the mean roughness parameters P_a for the drawn mild steel tube (top) and Representation of the P_a-values for 1001 consecutive runs, each with 0.5 µm lateral distance, at one location on the drawn surface with comparison to the polished one (bottom).

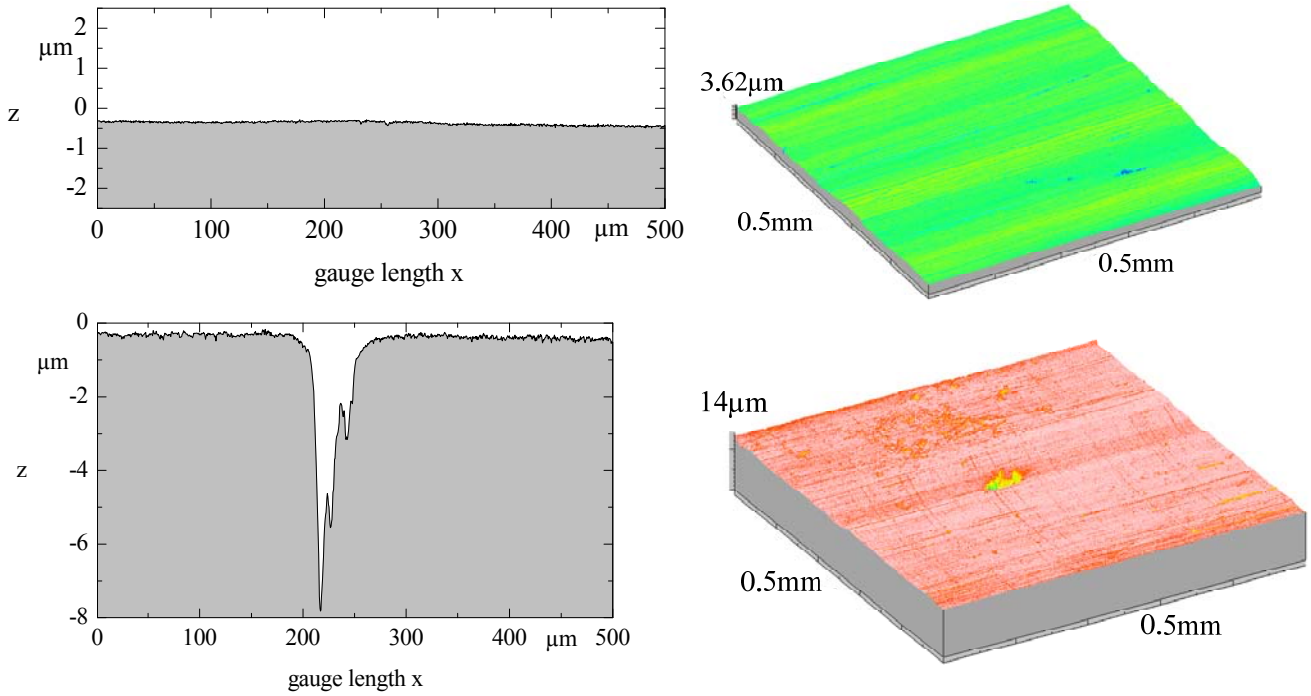

Figure 3. Characteristic profile and isometric representation of the polished copper tube (top) and the polished mild steel tube with cavities (bottom) (enlargement: left z/x: 36, right: z/x: 5)

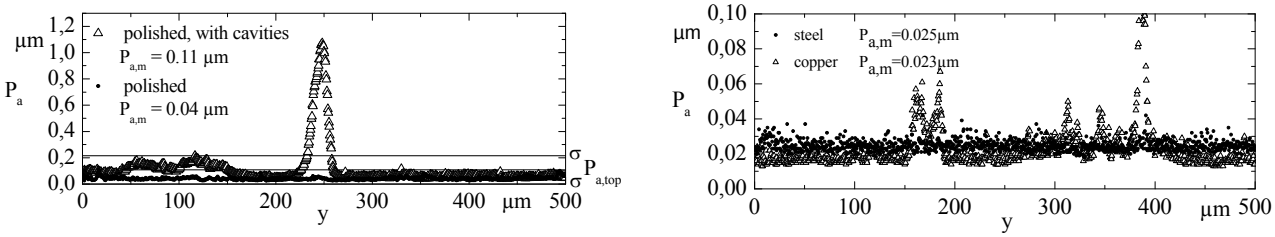

Figure 4. The mean roughness P_a of each scan of one measured topography of the drawn and the polished mild steel tube (left) and the polished surface with remaining cavities of the former structure (right).

AVERAGE HEAT TRANSFER PERFORMANCE

The heat transfer coefficient α is defined by the ratio of the heat flux q and the superheat ΔT

$$\alpha = \frac{q}{\Delta T} = \frac{q}{T_W - T_S} \qquad (1)$$

T_s is the saturation temperature of the boiling liquid in the pool and T_w is the wall temperature of the tube surface taking into account the heat conduction from the thermocouples to the surface. The

experimental error limits of α depend on the measured superheat from 2.5 % for low pressures and low heat fluxes up to nearly 7 % of high pressures and low heat fluxes.
The results of the average heat transfer performance of the mild steel tube for the three different surface structures are represented in form of the double logarithmic plot of α as function of q in Figure 4 for the drawn and the polished surface of Figure 2. Natural convective heat transfer without bubble formation on the heated surface and with smaller relative increase of the heat transfer coefficient occurs for low heat fluxes and pressures. The experimental results are in the transition area of $10^7 \leq \mathrm{GrPr} \leq 10^8$. The correlation for the laminar flow [6]

$$Nu \approx (Gr \cdot \mathrm{Pr})^{1/4} \tag{2}$$

describes quite well the data for lower pressures of the drawn surface and the polished one and the correlation for turbulent flow [6]

$$Nu \approx (Gr \cdot \mathrm{Pr})^{0.33} \tag{3}$$

the values for the higher pressure on the drawn surface. The well known strong increase of the heat transfer coefficient α with the heat flux and pressure in the range of fully developed nucleate boiling is demonstrated for all surfaces. The experimental values are interpolated by straight lines of the α-values acc. to

$$\alpha \propto q^n \tag{4}$$

for constant pressures. α increases with very uniform slope and reduced saturation pressure p* within the range of nucleate boiling for the polished surface, see Figure 5 right. The lines of the different pressures are quite separated for high pressures, while there is nearly no differences between the experimental results for the two lowest pressures investigated p* = 0.05 and 0.03, see Figure 4. The slope for the drawn surface is no longer constant for the whole pressure range. For low to intermediate heat fluxes the α-q relationship is similar to those of the polished surface, only the slope is smaller. For high heat fluxes the increase of α with q and p_s vanishes for pressures between p* = 0.5 and p* = 0.2. The α-values for the highest pressure are nearly parallel to those of p* = 0.2.

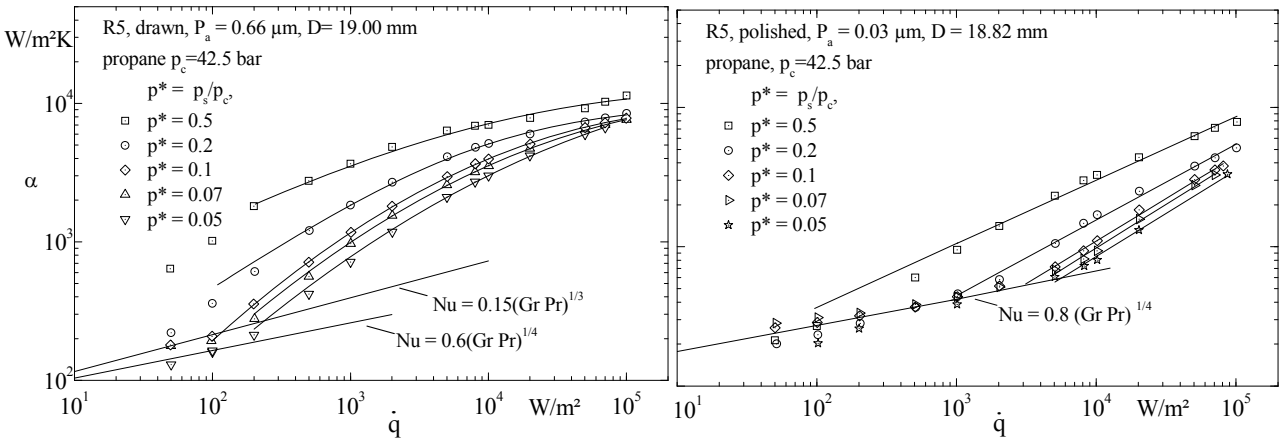

Figure 5. Average heat transfer performance of the mild steel tubes, propane boiling at different heat fluxes and pressures, left: drawn surface, right: polished surface (without cavities)

This behaviour may be explained by the bubble formation on the irregularly structured heated surface. Almost all large cavities within the topographies of Figure 2 are activated and the surface is covered with bubbles. The augmentation of the heat flux effects no more in higher heat transfer rates. For very high pressure as p* = 0.5, more and very small bubbles are activated, see Figure5. The main effect of the surface roughness is within the range of beginning nucleation, see Figure 5. The superheat for a stable bubble nuclei on the drawn surface is with ΔT = 0.85K ten times lower than on the polished surface with ΔT = 9 K for p* = 0.05 see Figure 6, left. For high to intermediate

pressures, the differences in the superheat for beginning nucleation are reduced to $\Delta T = 1.8$ K and $\Delta T = 0.2$ K for $p^* = 0.2$, see Figure 6.

The comparison with the measurements of propane boiling on a horizontal mild steel tube with different surface finishes demonstrates the well known effect, that the heat transfer coefficient augments with increasing mean surface roughness $P_{a,}$, figure 7.

The differences between the two polished surfaces is due to various deep re-entrant like cavities distributed equally over the surface, see the topography of figure 1 and 3. These cavities are the remains of the previous original drawn surface, not removed by the polishing procedure. They evoke very active stable nucleation sites especially for low heat fluxes or low superheats, respectively. This is also observed by the comparison of the bubble formation on emery ground and sandblasted surfaces, see [9]. For high heat fluxes the α-values of the two smooth surfaces are equal at $p^* = 0.1$. The comparison of the new data of Mertz et al. [11] for the same original surface and for the same diameter shows that the heat transfer coefficient is slightly higher and the slope is nearly the same. The decrease for high heat fluxes and the stronger increase of α for small heat fluxes is not observed by Mertz [11]. On the other hand, the values of Mertz correspond well with the recalculated data of the polished surface, see figure 7. The data of the drawn surface are similar to the rough sandblasted surface of [10], see figure 7. The data of the emery ground surface have the same superheat for beginning nucleation, while the slope of the α - q relationship is quite different. The increase of the α-values for Propane at constant intermediate heat flux q = 20 kW/m² with the reduced saturation pressure $p^* = p_s/p_c$ is shown in the lower diagram of Figure. The values of former investigations with a mild steel tube of smaller O.D. (D = 7.6 mm) and three different surface finishes [10] are added. The relative pressure dependence of α according to the correlation for organic fluids in the VDI Heat Atlas [6] predicts the experimental pressure dependence quite well at low to intermediate pressures after fitting to the pertaining experimental α-values at $p^* = 0.1$, cf. also figure 8. At high reduced pressures, the increase of the new experimental heat transfer coefficient for propane with p* is less pronounced acc. to eq. (5), cf. the curve and the symbols in the lower diagram.

$$F(p^*) = 1.2p^{*0.27} + \left(2.5 + \frac{1}{1-p^*}\right)p^* \qquad (5)$$

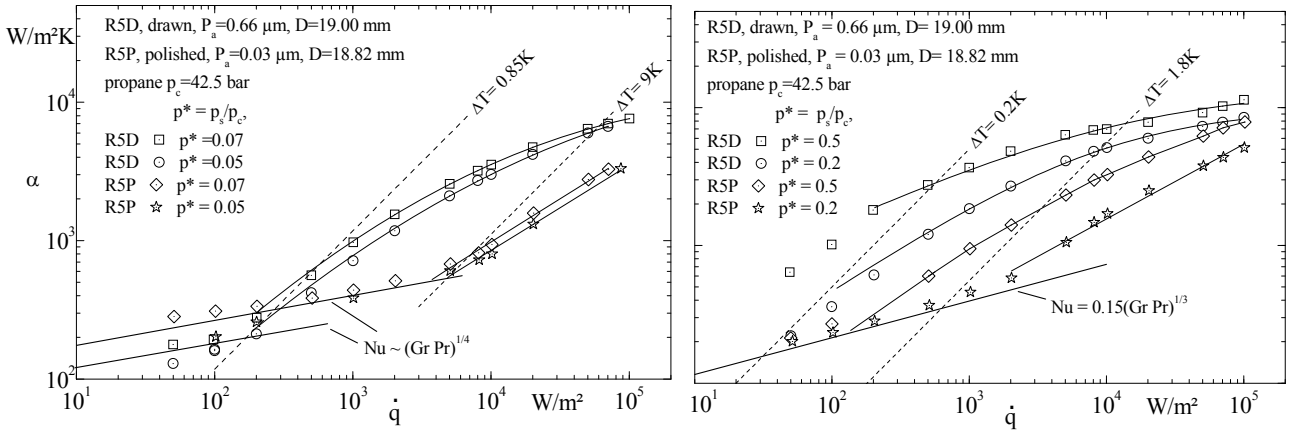

Figure 6. Comparison of the heat transfer coefficient α as function of the heat flux q for the drawn and polished mild tube for high pressures (right) and low pressures (left).

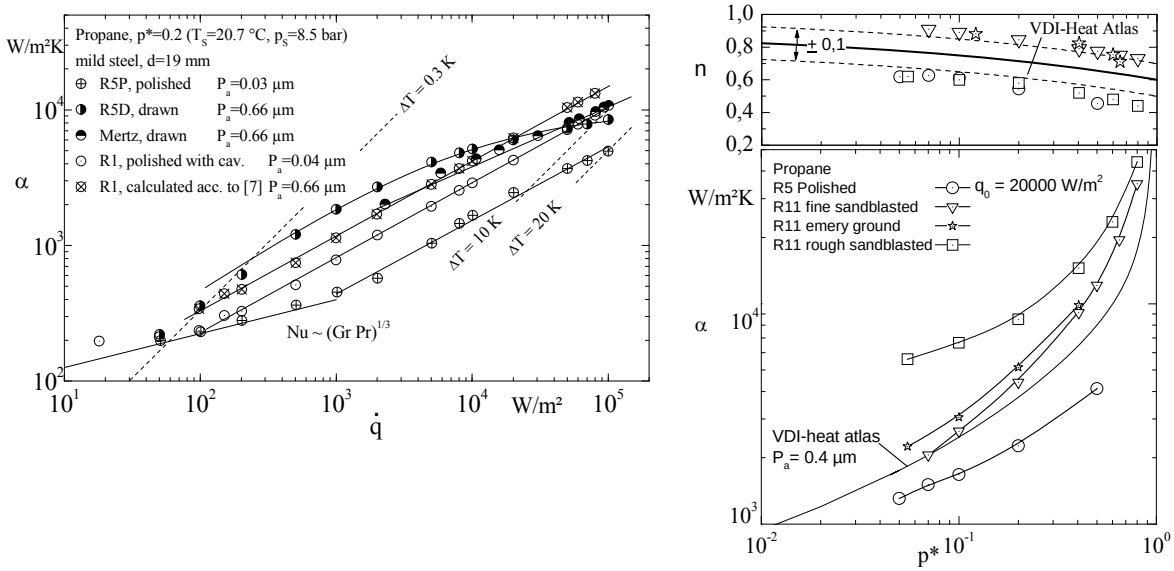

Figure 7. left: Comparison of the heat transfer coefficient α as function of the heat flux q for polished with and without cavities and drawn mild tube for p* = 0.1 and data of literature. right: pressure dependence of α interpolated for q = 20000 W/m^2 (bottom) and of the slope of the interpolation lines (top) for propane on the polished tube and three surfaces of literature.

$$n = 0.9 - 0.3p^{*0.3} \tag{6}$$

The same holds the increase of α with q over the entire pressure range, as can be conclude from the comparison between the experimental data for the exponent n with the correlation of [6] given as solid line in the upper diagram of figure 8. Similar deviations of the calculation method of the VDI Heat Atlas[6] also from new experimental results have been found in recent investigations [4].

REFERENCES

1. Gorenflo, D., Goetz J., Proposal of a Standard Apparatus for the Measurement of Pool Boiling Heat Transfer, Heat and Mass Transfer, 16(2), 69-78, 1982
2. Kaupmann, P., Gorenflo, D., Luke, A., Pool Boiling Heat Transfer on horizontal Steel Tubes with Different Diameters; Multiphase Science and Technology, 12 No.2, 14-26, 2001
3. Luke, A., Kruck, O., Heat transfer measurement of R134a and propane boiling at evaporator tubes with plain and enhanced finned surfaces; Proc. 12th Int. Refrig. and A.C. Conf., Purdue (USA) 2008
4. Kruck, O., Luke, A., Pool boiling of R134a and propane on horizontal mild steel tubes with plain and enhanced surfaces; Proc. 7th Conf. on Boiling Heat Transfer, Florianapolis (Brazil) 2009
5. Luke, A., Preparation, Measurement and Analysis of the Microstructure of evaporator surfaces;
   Int. J. Therm. Sci. 45, 237-256, 2006
6. Gorenflo, D., Pool boiling. Chapt. Ha. VDI-Heat Atlas, VDI-Verlag, Düsseldorf 1993.
7. Stephan, K., Beitrag zur Thermodynamik des Wärmeüberganges beim Sieden; Abhandlung des D. Kältetech. Vereins Nr.18, C.F. Müller-Verlag, Karlsruhe 1964.
8. Stout KJ., Sullivan PJ., Dong WP., Mainsah E., Luo N., Zahouani H. 1993, The Development of Methods for the Characterisation of Roughness in Three Dimensions; Publ. No. EUR 15178 EN
9. Luke, A., Active and Potential Bubble Nucleation Sites on Different Structured Heated Surfaces;
   Chem. Eng. Research and Design, 82, 462 – 470, 2004
10. Luke, A., Pool boiling heat transfer from horizontal tubes with different surface roughness, Int. J. Refrig. 20, 561-574, 1997
11. Mertz, R., Groll, M. Evaporation heat transfer from enhanced industrial heat exchanger tubes using hydrocarbons, Heat and Technology, 17 No.2, 3-11,1999

ANALYSIS OF THE EFFECT OF OPERATING PARAMETERS ON THE EFFECTIVENESS OF INTERMITTENT SPRAY COOLING

S. Fest*, J. Schmidt
Otto-von-Guericke University Magdeburg, Magdeburg, Germany

ABSTRACT. An experimental study is reported on intermittent spray cooling in the film boiling regime. The presented measurements are obtained using the infrared measuring techniques and are conducted to quantify the effects of injection frequency and pulse duration on mean surface temperature, whereby, the coolant quantity is kept constant. Calculating the mean surface temperature, an area of 30 x 30 mm² is analysed, which conforms to the main impact area of the spray. It is observed that the lowest tested pulse duration of 5 ms yield intensified cooling in terms of maximum heat removal at predetermined cooling quantity. The effect of pulse duration on heat transfer is reduced with increasing injection frequency. All studied pulse duration features a maximum of heat removal at injection frequency of less than10 Hz.

Keywords: *spray cooling, intermittent spray, film boiling*

INTRODUCTION

Spray cooling heat transfer in the film boiling regime is of great importance to attain stable and uniform cooling. At this, spray cooling using intermittent sprays has been suggested as a technological concept in terms of effectiveness and controlling of the cooling potential [1]. A suitable combination of pulse duration and injection frequency promises a reduction of thermal stresses and distortion in components as well as a reduction of coolant.

The spray cooling process possesses a complex nature and depends on spray parameters, such as droplet size, velocity and mass flux, but also on liquid and surface properties. Previous works [1][2] have shown that neither the injection frequency nor pulse duration changes significantly the droplet diameter and axial velocity distribution in wide range of operating parameters. Thereby, changing in heat transfer can not be ascribed to changing of spray characteristics. A research program is being conducted aimed at characterising the effect of injection frequency and pulse duration on the mean surface temperature, whereby, the cooling quantity is kept constant. The effectiveness of the operating parameters is evaluated based on the approach of maximal heat removal at predetermined cooling quantity.

METHODS AND MATERIALS

The experimental configuration consists of a BOSCH multiple-orifice injector directed perpendicular to a sheet made of Inconel 600 (100 x 60 x 0.3 mm), which is directly electrical heated. A schematic of the experimental setup is shown in Figure 1. Using a self-build triggering system, the injection frequency f_{inj}, the pulse duration Δt_{inj} and the number of injections N are

* Corresponding author: Stephanie Fest
Phone: + (49)-391-6712559, Fax: + (49)-391-6712762
E-mail address: stephanie.fest@st.ovgu.de

controlled. The pulse duration is varied from 5 ms to 15 ms and the injection frequency is adapted to realise duty cycles, defined as $DC = (\Delta t_{inj} \cdot f_{inj}) \times 100\,\%$ [3], from 2.5 % to 40 %. All studied cases and their conditions are summarised in Table 1. During these experiments, the impinging distance is kept constant and equal to 150 mm and the injection pressure is set to 7 bar. The produced water spray features under these working condition a mean diameter of about 50µm as well as a mean velocity of about 5 m/s and the total spray angle is about 25 deg.

Table 1

Working Conditions

Cases	Δt_{inj} [ms]	DC [%]	N [-]
1-16	5	2.5, 5, 7.5, 10, 12.5, 15, 17.5, 20, 22.5, 25, 27.5, 30, 32.5, 35, 37.5, 40	40
17-32	7.5		27
33-48	10		20
49-64	15		13

An infrared camera (Flir ThermaCam Sc 3000) records the surface temperature with a sampling rate up to 750 Hz. Hereby, one camera image corresponds to a certain time, and surface temperatures are obtained for the whole impact area of the spray. The temperature information of each camera image is converted to a 2-dimensional Matlab matrix, whereby, the matrix size amounts to the number pixel for the length and the width of the Inconel 600 sheet. The data are further processed in Matlab to a 3-dimensional matrix, whereas the third component is the time. As infrared measurements depend strongly on the emissivity of the surface, the camera facing sheet side is coated with a black painting called Senotherm UHT 600 with a thickness of about 20 µm. Since the emissivity is temperature-dependent, all temperature data of the 3-dimensional matrix needs to be subsequently corrected (see [4] for further details).

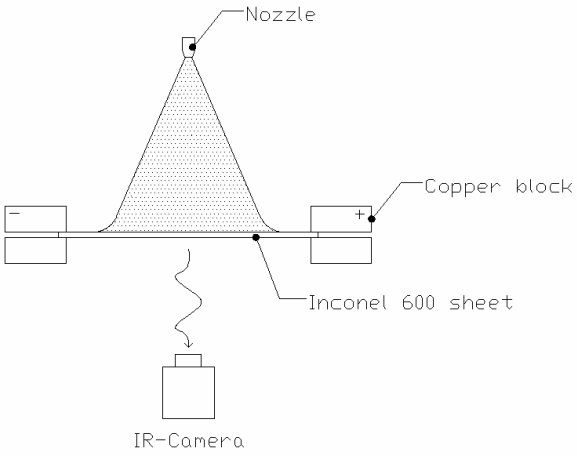

Figure 1: Schematic of the experimental apparatus

RESULTS AND DISCUSSION

Intermittent sprays are characterised by injection frequency and pulse duration. Both parameters are related with the variable duty cycle which is often used as influence parameter on heat transfer. Figure 2 illustrates the mass flux distribution and the corresponding decrease in surface temperature

after 40 consecutive injection cycles for pulse duration of 5 ms and duty cycles of 5 % and 15 %, respectively. The spray characteristic of the multiple-orifice injector is developed with local intensified mass fluxes in the centre of each single jet. A duty cycle of 5 % leads to relatively uniform cooling. In contrast, a duty cycle of 15 % yield strong surface temperature distribution and the local cooling depends on the local mass flux. Thereby, the mean surface temperature is used to evaluate cooling processes for various combination of pulse duration and injection frequency. Calculating the mean surface temperature along a serious of injection cycles, an area of 30 x 30 mm² is analysed, which conforms to the main impact area of the spray.
Studying the effect of pulse duration on mean surface temperature is based on a constant cooling quantity. Doubling the pulse duration, approximately, the double amount of liquid is atomised. Hence, changing of pulse duration requires an altering of injection numbers according Table 1.

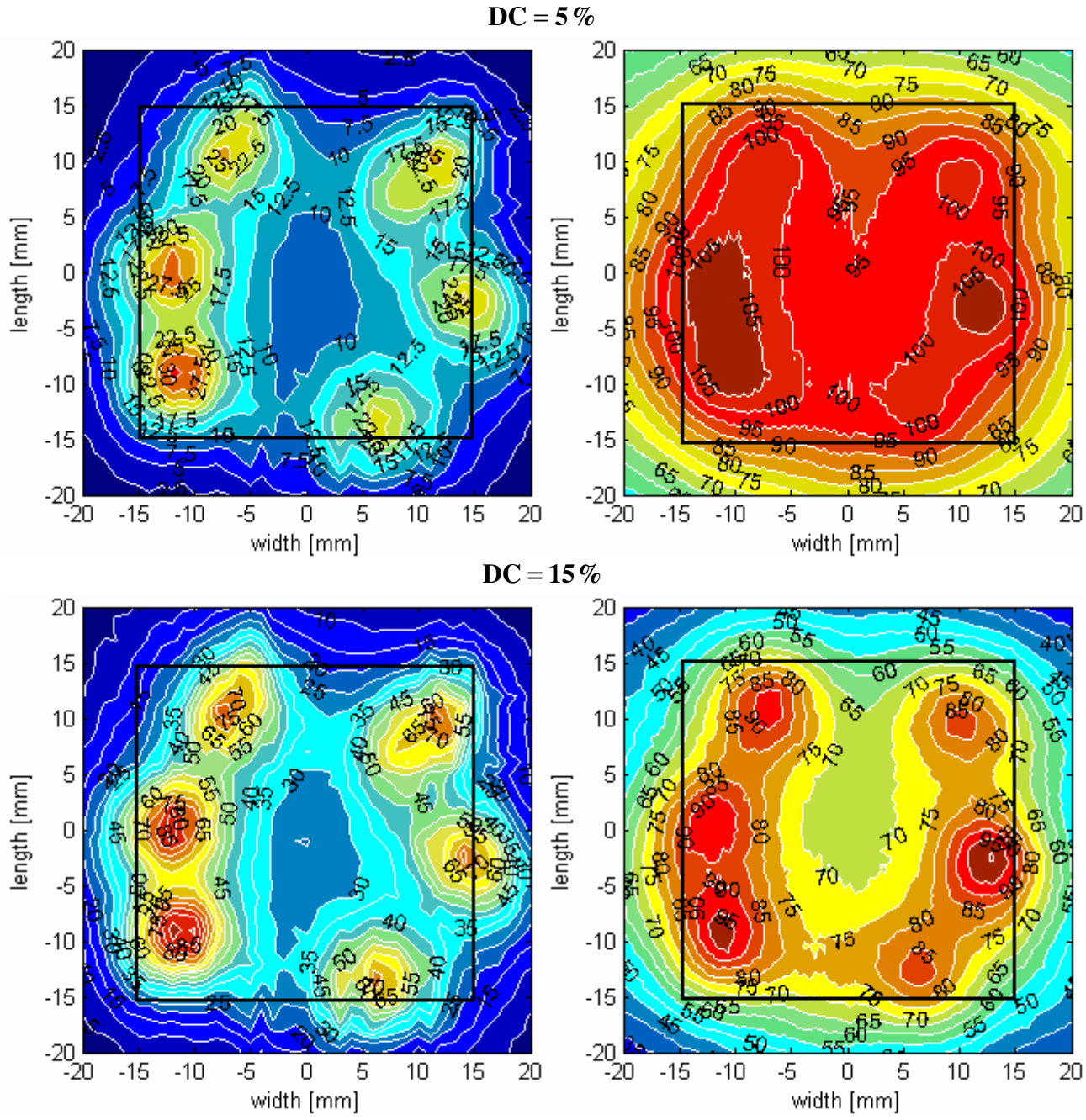

Figure 2. Mass flux [mg/(cm² s)] (left) and decrease in surface temperature [K] (right)

Figure 3 shows the initial mean surface temperature decays along a serious of consecutive injection cycles at a duty cycles of 5 %and illustrates the effect of pulse duration. The results indicate that the lowest tested pulse duration of 5 ms yields intensified cooling. In general, the cooling potential decreases with increasing pulse duration. The difference in mean surface temperature between the lowest and highest tested pulse duration amounts to 30 K. Obtaining a mean surface temperature of about 340°C, 13 injection cycles are approximately necessitated for pulse duration of 15 ms, and 26 injection cycles are only required for a pulse duration of 5 ms. This corresponds to a reduction of coolant of about 30 %.

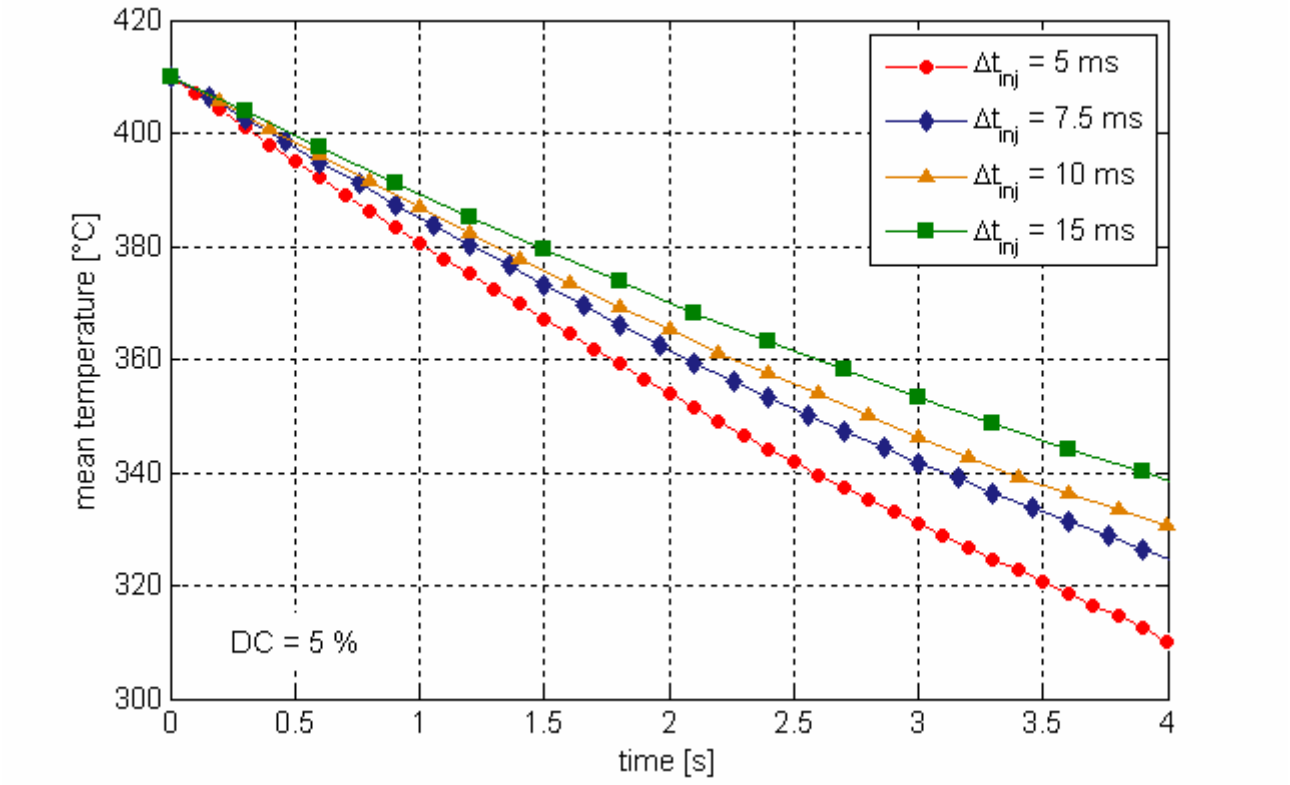

Figure 3. Mean surface temperature decays along a serious of consecutive injection cycles for duty cycle of 5 %

Figure 4 shows the transient surface temperature for pulse duration of 15 ms and a duty cycle of 5 %. Each injection features two periods: a period of direct liquid-solid contact during the initial phase of spray impact and a period, where a vapour layer is formed. The heat transferred from the wall in this first phase is in order of magnitude higher than the amount of heat through the subsequent formed vapour layer [5]. The length of the second period depends on the injections frequency, and the surface temperature drop depends on the initial surface temperature and on the corresponding boiling regime as well as the amount of injected cooling liquid. In the film boiling regime, the surface temperature drop decreases with decreasing surface temperature. At an initial surface temperature of about 400°C, the surface temperature drop is about 5 K for pulse duration of 15 ms. Decreases the surface temperature to about 300°C, the temperature drop amounts about 3 K. Hence, the development of the mean surface temperature, as shown in Figure 3, features a non-linearity, which is specially pronounced for pulse duration of 5 ms due to the intensified cooling.

Figure 4 illustrates that the surface temperature can also reheat during the period with formation of vapour layer. The experimental results are obtained by a non-stationary measurement method with

continuous electrical heating source. At this, the Inconel 600 sheet is directly electrical heated up to the steady state temperature, and heat is removed by natural convection and radiation. The heat flux by convection as well as radiation is a function of surface temperature and reduces with decreasing surface temperature (see [4] for further details). Hence, during the cooling process the ratio of heat flux by radiation and convection decreases and the surface temperature reheats during one injection cycles for low injection frequencies when the coolant is completely vaporised. However, the cooling efficiency can be improved by adapting the injection frequency.

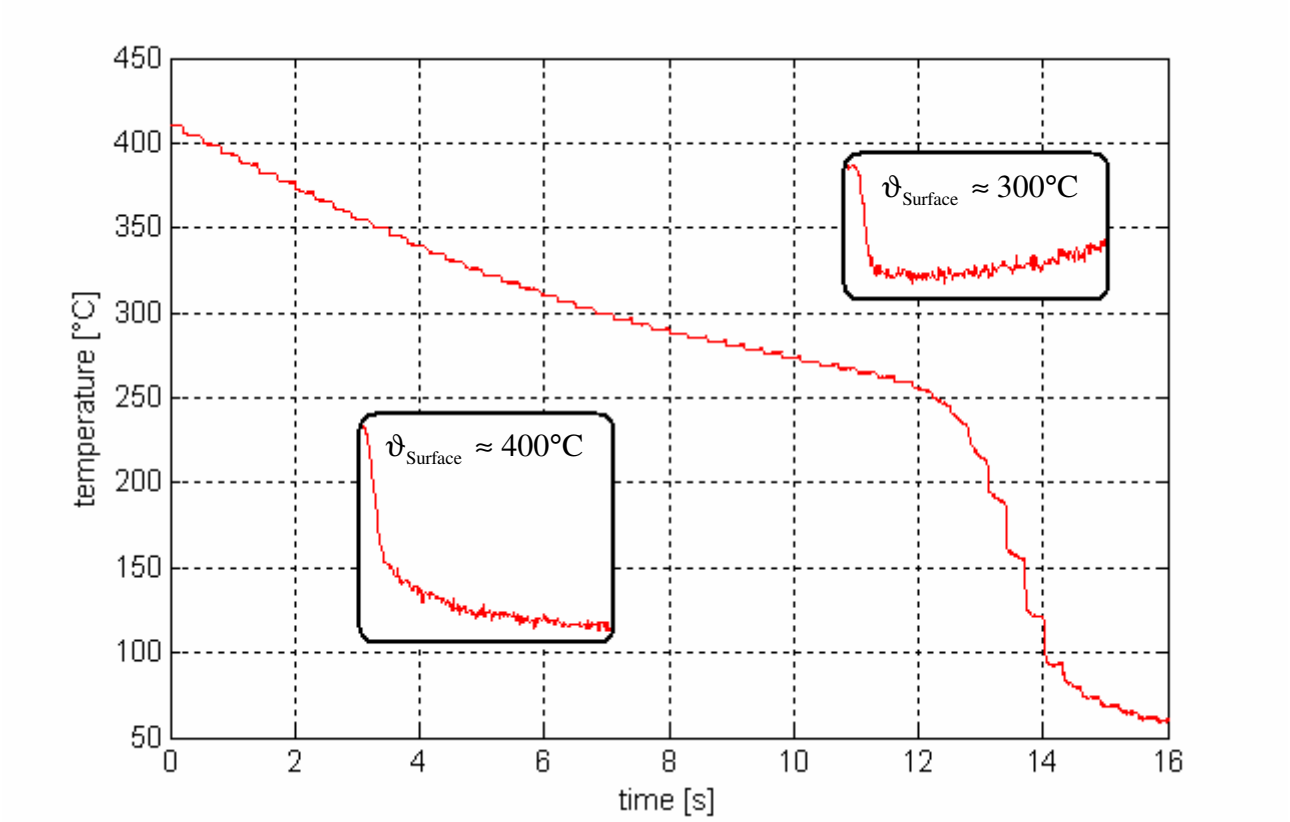

Figure 4. Temperature development for pulse duration of 15 ms and duty cycle of 5 %

The influence of the injection frequency on the cooling process is shown in Figure 5, where the mean surface temperature drop after N injection cycles is plotted versus the variable duty cycle. If the pulse duration is fixed and the injection frequency increases, the variable duty cycle increases, and the cooling process becomes faster. The lower mean surface temperature drop with increasing duty cycle points that the coolant does not completely vaporise during two subsequent pulses, and a liquid film is formed above the characteristic vapour layer of the film boiling regime. Local limited chilling effects (compare Figure 2) could result in thermal stresses and distortion in components at higher injection frequencies. However, the lowest tested pulse duration yields intensified cooling for all studied duty cycles. But, the effect of pulse duration on the cooling process is reduced with increasing duty cycles, and the surface temperature drop features an asymptotic behaviour. All studied pulse durations offer an optimum duty cycle, which is lower than 15 %, which correspond to an injection frequency of less than 10 Hz.

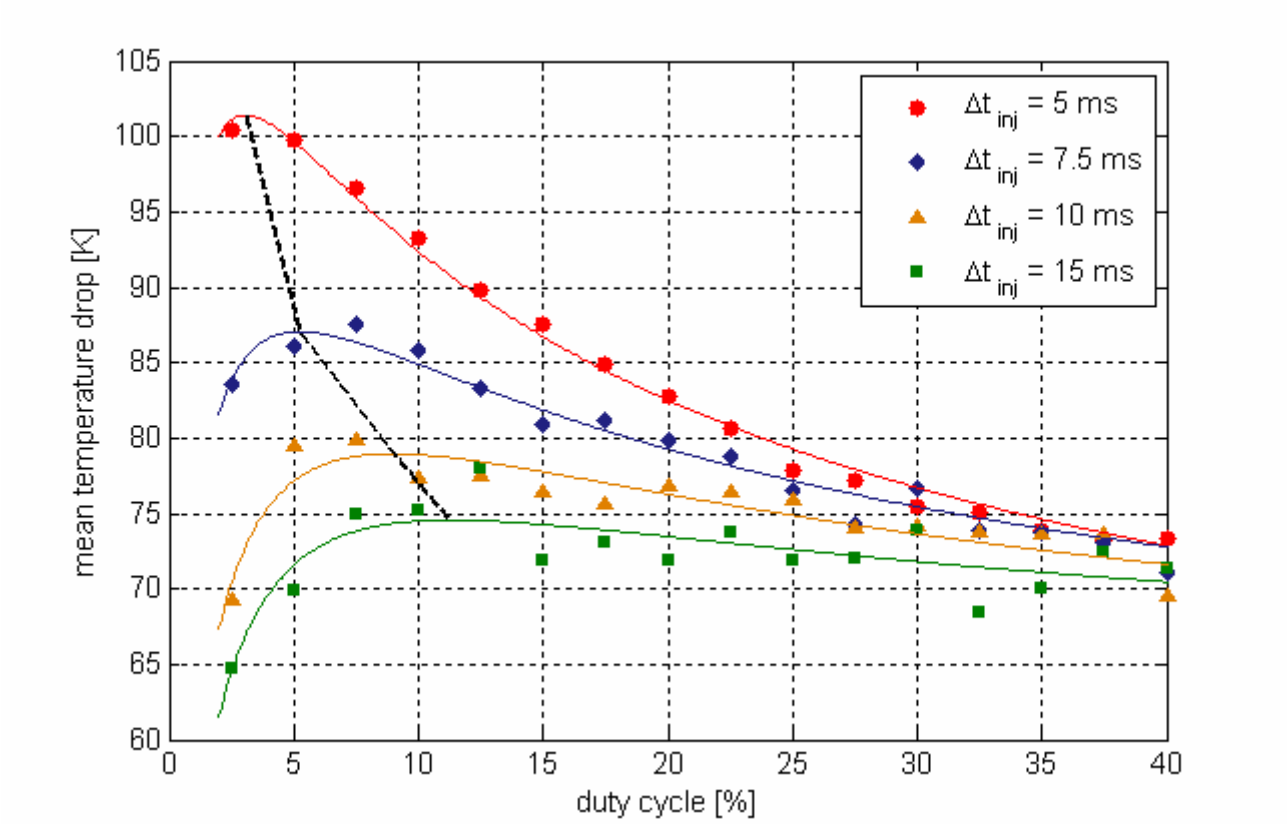

Figure 5. Mean surface temperature drop after a serious of consecutive injection cycles

CONCLUSIONS

An experimental study is carried out in the range of film boiling aimed characterising the effect of pulse duration and injection frequency on heat flow during intermittent spray cooling processes. The injection frequency has not only an impact on the cooling rate but also on the uniformity of the cooling process. In general, low injection frequencies lead to a relatively uniform cooling. High injection frequencies yield strong surface temperature distribution and the local cooling depends on the local mass flux. Thereby, the mean surface temperature is chosen as evaluating parameter on heat flow, whereby; the main impact area of the spray is used calculating the mean surface temperature.

The lowest tested pulse duration of 5 ms features the best heat flow behaviour at a predetermined coolant quantity for all studied injection frequencies. But, the influence of pulse duration on the cooling process is reduced with increasing duty cycles. All studied pulse durations offer a maximum of heat flow, which corresponds to a maximum of the mean surface temperature drop, for injection frequencies less than 10 Hz. At higher injection frequency and consequently higher duty cycles, the heat flow is limited, which points that the coolant does not completely vaporise during two subsequent pulses, and a liquid film is formed above the characteristic vapour layer of the film boiling regime.

ACKNOWLEDGEMENT

The financial support of the German Research Foundation (DFG-Graduiertenkolleg 828 “Micro-Macro-Interactions in Structured Media and Particle Systems”) is gratefully acknowledged.

REFERENCES

1. Panão, M.R.O., Moeira, A.L.N., 6th International Conference on Multiphase Flow, Leipzig, Germany, July 9-13, 2007, S4_Thu_A_48.
2. Fest, S., Schmidt, J., 7th International Symposium on Heat Transfer, Peking, China, October 26-29, 2009.
3. Majaron, B., Svaasand, L.S., Aguilar, G., Nelson, J.S., Physics in Medicine and Biology., Vol. 47, No. 18, pp 3275-3288, 2002.
4. Fest, S., Schmidt, J., 22nd European Conference on Liquid Atomization and Spray Systems, Como Lake, Italy, September 7-10, 2008, A018.
5. Wruck, N., 1999, "Transientes Sieden von Tropfen beim Wandaufprall", *PhD Thesis*, RWTH Aachen, 1999.

HEAT LOSS AND EVAPORATION RATE FROM AN AGITATED WATER TANK

H. Alonso Martín, A. Revel, B. P. Huynh*
University of Technology, Sydney, NSW, Australia

ABSTRACT. Experiments have been performed to investigate the heat loss and evaporation rate from an open-top tank of heated water that is also agitated vigorously by air bubbling through it. High consumption of electrical energy in heating the solutions for an electroplating process prompted this study; and the experimental set-up thus serves as a model for an electroplating tank in this process. Air is injected from the tank's floor, and an electrical heater is used to maintain water at a constant, elevated temperature, compensating the heat being lost to the surroundings. A heat transfer model is developed for the process and is seen to agree well with measurements. Water's evaporation rate is found to be proportional to the injected air flow rate, and that most of the supplied energy goes into evaporating the water.

Keywords: *heat loss, evaporation rate, agitation, air injection*

INTRODUCTION

In some industrial processes like electroplating, air is bubbled through the liquid solutions to make them highly agitated, well-mixed and uniform to enhance the process. Often, the solutions are maintained at an elevated temperature, and the bubbling air increases significantly evaporation from the solutions. As a result, energy is spent on evaporating the liquid, in addition to the need to replace the lost liquid, as key properties like correct chemical compositions have to be maintained in the solutions.

High consumption of electrical energy in heating the solutions in an electroplating process provided the initial impetus for this work. This paper thus reports on an experimental study of the heat loss and evaporation rate from an open-top tank of heated water that is also agitated vigorously by air bubbling through it. The experimental set-up serves as a model for an electroplating tank.

Evaporation from bodies of water has been considered by a number of authors, but with water in a calm state or only mildly agitated (similar to a used swimming pool) [1-9]. Bubbling a gas through liquid solutions is also used in direct-contact evaporation process, for example, for concentrating aqueous solutions. In a typical such process, the equipment is basically constituted of a liquid column through which a superheated gas is bubbled [10-12]. However, the conditions and energy-flow paths pertaining to such evaporation process are different to those of the present work. The emphasis is also different. Here, the main aim of air injection is to create a highly agitated, well-mixed, homogeneous solution that is beneficial to a process like electroplating, and evaporation and its concomitant consumption of energy are by-products that have to be dealt with. In an evaporation process, on the other hand, evaporation is the aim itself.

* Corresponding author: B. P. Huynh
Phone: + (61)-2-95142675, Fax: + (61)-2-95142655
E-mail address: Phuoc.Huynh@uts.edu.au

A heat transfer model is also developed in this work to help predict energy consumption. Calculations based on this model, which is rather straightforward and robust, will be seen to compare well with measurements. It will also be seen that evaporation increases linearly with the rate of injected air for agitation, and that most of the supplied energy goes into evaporating the water.

EXPERIMENTS

The initial impetus for this work was to mimic an industrial electroplating process, and investigate the effects of air injection on the energy consumption and evaporation water loss. Thus an experimental set-up was developed in the Heat Transfer laboratory of the University of Technology, Sydney, Australia, for the investigation, and experiments were performed during the second half of 2008, using heated water as the solution, in an open-top small tank which serves as model for an electroplating tank. The set-up is shown in Figure 1. The main components are

- Stainless steel tank of dimensions Length×Width×Height = 900×300×280 mm; wall thickness 1.6 mm; open at the top
- Tank's walls and underside are insulated with expanded poly-styrene (EPS) sheet, 20 mm thick
- 3-kW electrical immersion-element heater, 275 mm long, with built-in rod-thermostat of range 10 − 80 ºC
- Power clamp meter to 600 V, 200 A rms
- Two analogue-to-digital converters to log the temperature and power signals into a laptop
- Air receiver with regulator (0 − 690 kPa) and 0.75 kW air compressor delivery (ambient air supply to the compressor)
- Calibrated rotameter for air-flow measurement (0 to 2.50 g/s)
- 2-m-long perforated plastic tube laid on the floor of the tank in a figure-8 shape, which distributes the injected air uniformly from the compressor to the water surface via 10 equi-spaced 3-mm-diameter holes serving as air nozzles. The tube free end was blocked
- Six type-T thermocouples for measuring temperatures
- An assembly of siphon and measuring cylinder for recording water level in the tank
- A laptop computer for data logging and processing

A measuring cylinder connected by a siphon tube to the tank shows the drop in water surface level from which evaporative mass loss is deduced. Temperatures within the liquid, on tank's internal and external walls and inside one of the holes of the perforated plastic tube are recorded using six type-T thermocouples. Approximate locations of the thermocouples are shown in Figure 2. Air required for agitation is supplied from a compressor. Air's mass flow rate is measured with a previously calibrated rotameter.

Water temperature is controlled by a thermostat switching an electrical immersion-heater on and off. The thermostat's temperature control band is within ± 1 K, so an average bulk temperature is assumed. When steady state is reached, thermal loss is balanced by the electrical energy supplied to the heating element. This energy is measured with an electrical power meter coupled to a data acquisition device and logging to a computer. Thus the energy required to maintain the water's temperature is obtained by summing the power meter's recorded square-wave inputs over an extended period. Figure 3 shows an example of a series of 2.79 kW inputs with "element-on" periods recorded over a duration of 30000 seconds. By integrating the instantaneous power reading over time, the electrical energy supplied to the heater is obtained. This energy maintains a steady

water temperature as required, and the derived averaged power is thus equal to the heat loss from the tank's water to the surroundings.

Thanks to strong convection resulting from the heating element being located at the tank's bottom, water temperature is fairly uniform throughout the tank. This is similar to measurements presented in [13]. Figure 4 thus shows a representative set of temperature records from an experiment without air injection, conducted on 15-09-2008. When there is air injection, this well-mixed condition is further enhanced by the strong agitation resulting from air bubbling through the water. Note that since the injected air's temperature is measured with a thermocouple inserted inside the figure-8-shaped plastic tube, when there is no air-injection (like the case shown in Figure 4), this temperature is close to that of the heated water. With air injection, on the other hand, as there is a continuous supply of cooler air from the compressor, air temperature is substantially lower than the water temperature. Air temperature, however, is not among the test parameters considered in this work.

Temperatures were recorded with an accuracy of ± 0.5 K, whereas measurement of air mass flow rate per unit tank's surface area is estimated to be accurate to ± 0.17 g/s·m^2. Uncertainties associated with the measured electrical power provided by the heater is ± 0.4 %, while water evaporation rate was measured with an accuracy better than about ± 10 %. Repeatability of the measurements was also good. Thus, in one set of 5 experiments to measure a water evaporation rate under similar conditions, the mean value obtained was 2510 g/h.m^2, with a standard deviation of only 125 g/h.m^2.

In the rest of this work, however, only mean values are shown.

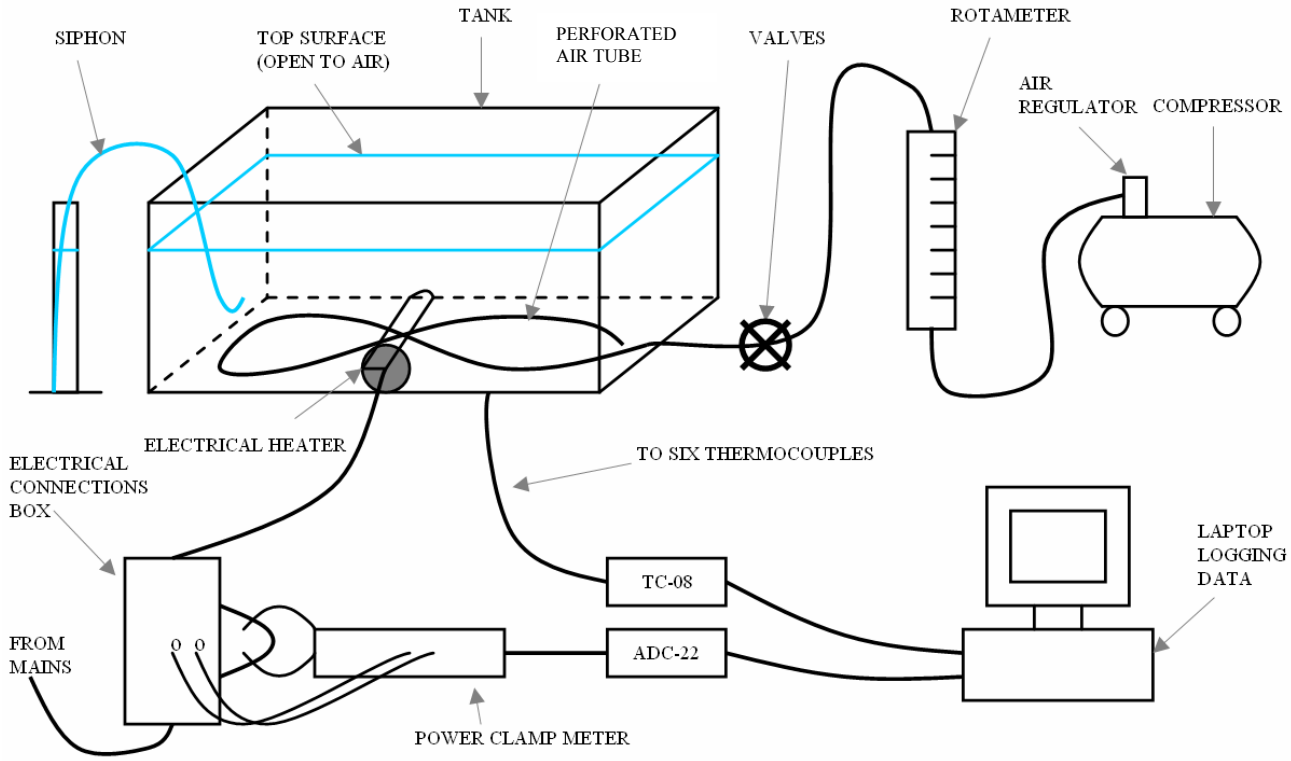

Figure 1. Experimental tank and instruments

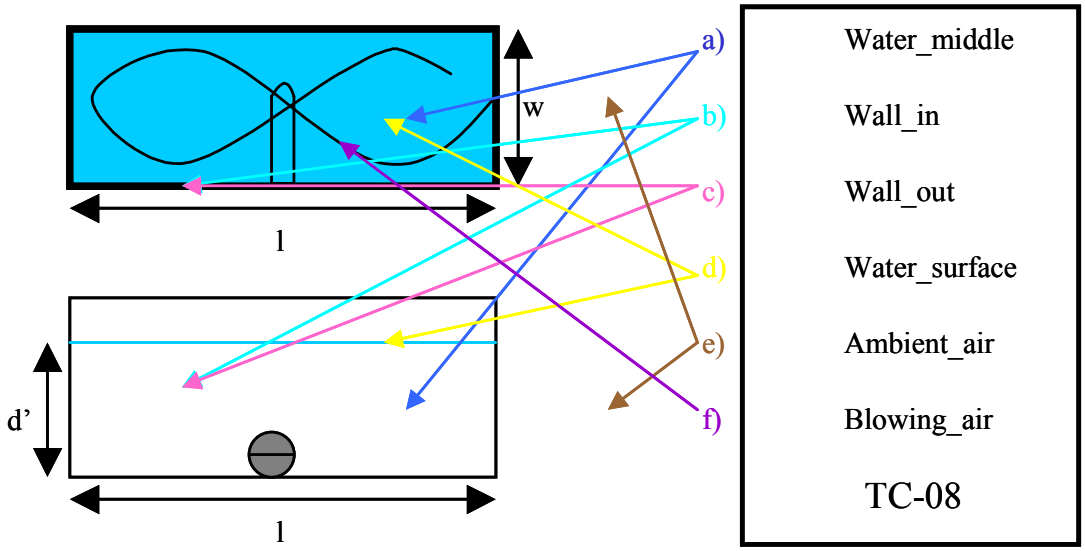

Figure 2. Approximate locations of the six thermocouples (top view above, side view below); l is tank's length, w tank's width, d' water depth

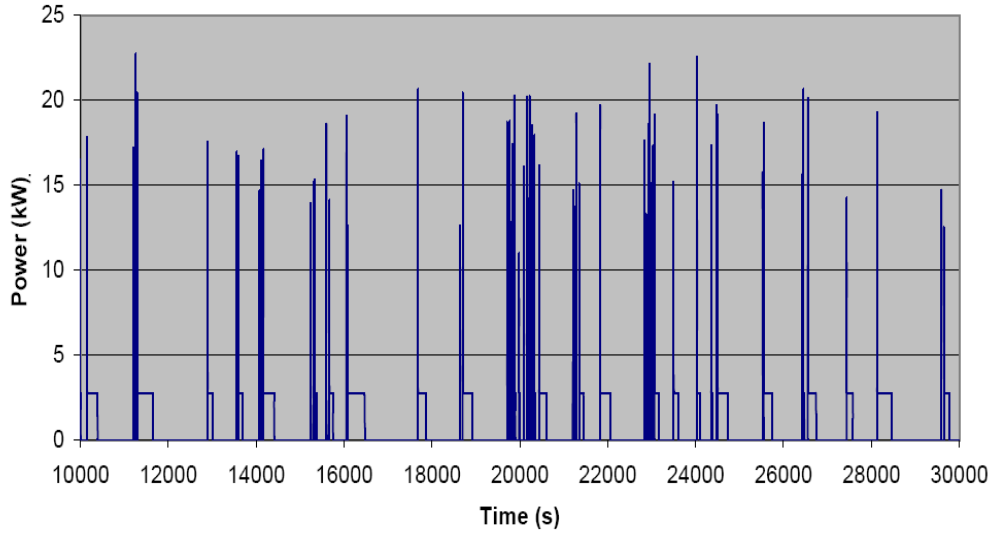

Figure 3. Power signals from ADC-22; these electrical records showing "on/off" durations that are used to estimate energy input (test conducted on 15-09-08)

RESULTS AND DISCUSSION

Experiments were performed for different air-injection rates. First, however, evaporation rate without air agitation was measured and compared with the correlation developed by Boelter et al. [9] and also used by Paulken [6]. This correlation for evaporation into still air is

$$J = 74.0\ (P_w - P_a)^{1.22} \quad (1)$$

where J is evaporation rate per unit surface area in g/h.m^2, P_w vapour pressure at the water surface in kPa, and P_a partial pressure of water vapour in the ambient air in kPa. The comparison shows very good agreement. Thus, from the experiment conducted on 15-09-2008, the following values

were obtained: surface temperature 59.7 °C, ambient temperature 24.6 °C, relative humidity 55 %, measured evaporation rate 2520 g/h.m^2. On the other hand, using thermophysical data of saturated water corresponding to the above condition [14], Boelter et al.'s formula gives 2500 g/h.m^2, differing from measured value by less than 1%.

Figure 5 shows the increase of evaporation ΔJ above that corresponding to non-agitation (zero air-injection) in terms of air-injection rate per unit surface area m. ΔJ is seen to be proportional to m according to

$$\Delta J = 22.7\ m\ ;\quad m \text{ in } g/s.m^2,\ \Delta J \text{ in } \% \tag{2}$$

Results of Figure 5 have been obtained with water temperature and the ambience maintained at fairly constant conditions, pertaining to this work as described above. Note also that the measured evaporation rate corresponding to zero air-injection is J =2520 g/h.m^2, from above.

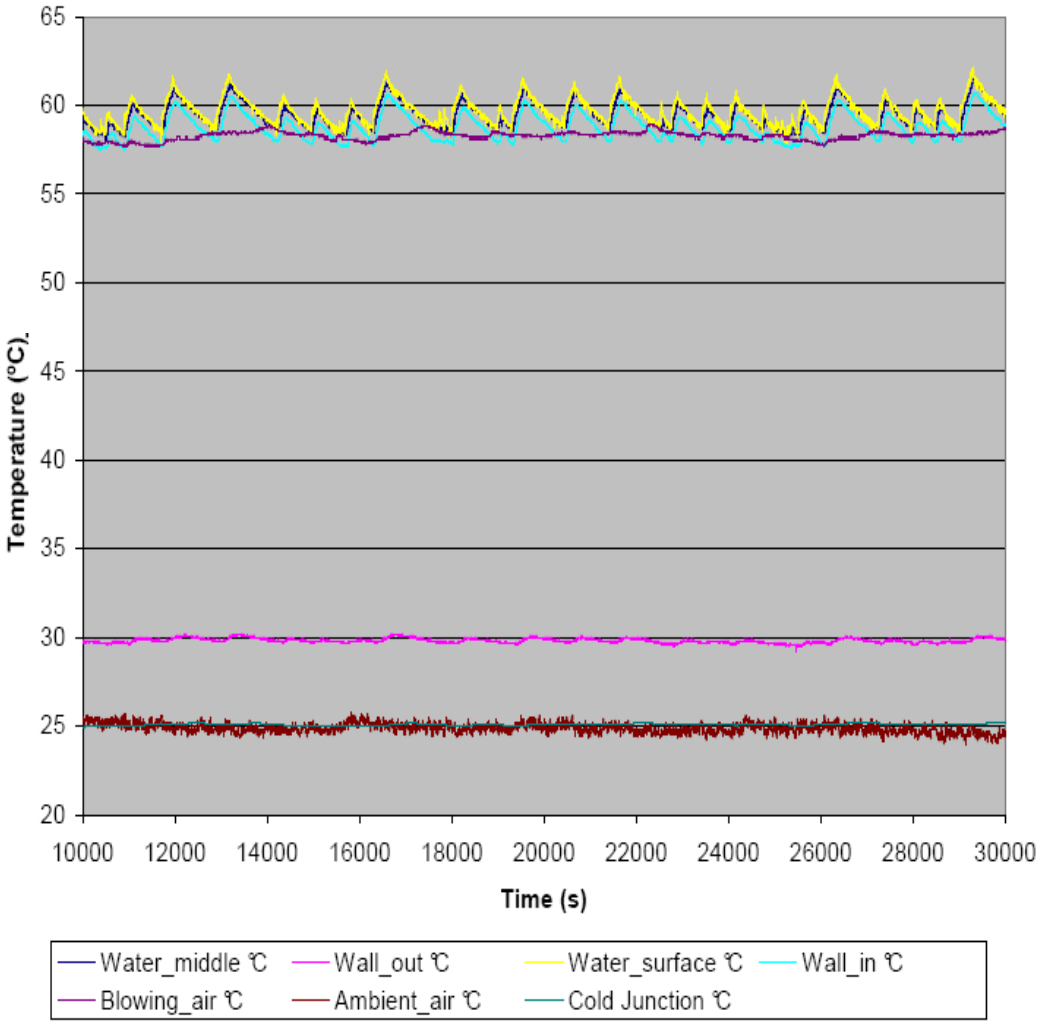

Figure 4. Temperature records from an experiment without air injection, conducted on 15-09-2008. The saw-tooth traces at the top are water temperatures at mid-tank and at surface, and internal wall temperature; they show that the tank is well mixed

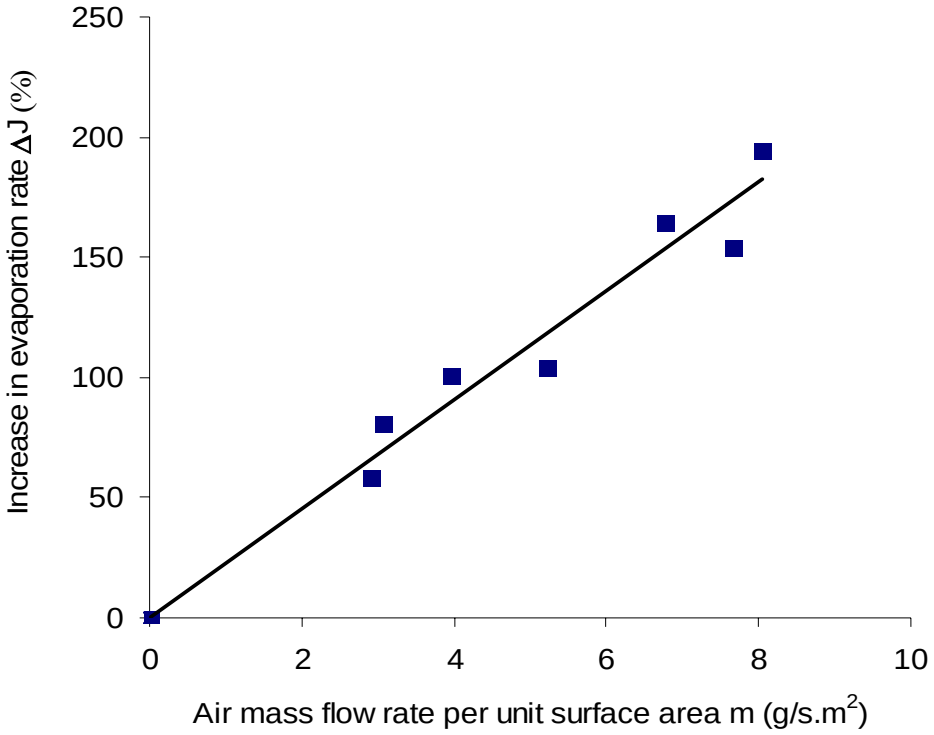

Figure 5. Increase in evaporation rate in terms of air-injection rate; correlation is $\Delta J = 22.7$ m.

The electrical power consumed by the heating element and measured with the power clamp meter (see Figure 3) is also seen to agree well with calculations based on a heat transfer model. In this model, total heat loss from the tank's water is due to (1) evaporation, (2) conduction through the tank's walls, (3) radiation from water surface, and (4) convective loss from the hot water surface to the air above. Taking 13.85 W/m.K for steel wall's thermal conductivity, 0.040 W/m.K for EPS wall cover's, 0.96 for water surface's emissivity [14], using the above measurements of 15-09-2008 which now also include internal wall temperature 58.9 °C, external wall (cover surface) temperature 29.7 °C, and using the convective heat transfer relation $Nu = 0.54Ra^{1/4}$ for water surface [14] where Nu is the Nusselt number and Ra Rayleigh number, both based on ambient air's properties, total heat loss from the tank's water has been calculated to be 616 W. On the other hand, consumed electrical power was measured to be 647 W, giving a difference of only 5 % between the two values.

The ratio of Heat-Loss-by-Evaporation over Total-Power-Consumed $Q_{evap}/Q_{total\text{-}elect}$ is of special interest. For the non-agitation case, using latent heat of evaporation 2.37×10^6 J/kg [14] heat loss due to evaporation has been calculated to be $Q_{evap} = 448$ W, thus representing 69 % (= 448/647) of the total power consumed.

When air is bubbled through the water, this ratio is higher. Thus, from another set of measurements (of experiment conducted on 17-09-2008) air-injection rate was 3.05 g/s.m^2 and evaporation rate 4560 g/h.m^2 (3.42×10^{-4} kg/s from a surface area of 0.27 m^2), therefore requiring an evaporation heat $Q_{evap} = 810$ W. The measured electrical power was 987 W. This gives a ratio of $Q_{evap}/Q_{total\text{-}elect}$ of 82 %. That $Q_{evap}/Q_{total\text{-}elect}$ increases with air-injection rate m agrees with expectation. For,

$$\text{Total heat loss (approximately equal to electrical power consumed } Q_{total\text{-}elect}) = \text{conduction loss } Q_{cond} + \text{radiation loss } Q_{rad} + \text{convection loss } Q_{conv} + \text{evaporation heat } Q_{evap} \quad (3)$$

As air-injection increases, Q_{evap} increases as a result of increasing ΔJ, while Q_{conv} and Q_{rad} stay unchanged, and Q_{conv} expected to increase only slightly (mainly due to water surface being more agitated). The ratio $Q_{total\text{-}elect}/Q_{evap}$ thus decreases, or $Q_{evap}/Q_{total\text{-}elect}$ increases.

In fact, this ratio can readily be calculated, as in the following example. Using above data from the experiment conducted on 17-09-2008, the following values have been obtained Q_{cond} = 55 W, Q_{rad} = 65 W, $Q_{conv} \approx$ 50 W, and Q_{evap} = 810 W. These then give a total heat loss of 980 W, in good agreement with the measured electrical power of 987 W above.

Using this procedure, at the highest evaporation rate measured in this work (ΔJ = 194.5 % or J = 7420 g/h.m^2) the ratio $Q_{evap}/Q_{total\text{-}elect}$ can be estimated to be 89 %. The concern of high energy consumption in industrial processes like electroplating where air bubbling is used is thus clear.

Figure 6 shows a comparison of the tank's surface region when there is no air injection versus when there is a significant injection. In the latter case, the much agitated water surface and high vapour concentration are evident. It should, however, be also pointed out that size and shape of the injected air that issues from the equi-spaced holes of about the same diameter on the plastic tube, causing strong mixing and stirring of the water, are not among the test parameters in this work.

Figure 6. Comparison of evaporation and agitation states on tank's surface when there is no air injection (left) versus when there is a significant injection (right)

CONCLUSIONS

Experiments have been performed using a heated water tank to investigate the effects of water agitation on evaporation rate and power consumption. Agitation was achieved by having air bubbling through the water. Evaporation rate has been found to increase linearly with higher rate of

injected air. A model developed for the heat loss from the tank's water agrees well with measured total energy consumed by the heating element. Most of the heat loss is due to evaporation. The ratio of evaporation heat over total energy consumed is seen to increase with air injection, starting from around 69 % at zero injection, for the conditions pertaining to this work. Calculation of this ratio agrees well with measurements; and this ratio has been shown to grow to 89 % at the highest air injection rate used in this work. Also, very good agreement has been obtained for evaporation rate between this work's measurements and the correlation developed by Boelter et al. when there is no air agitation.

ACKNOWLEDGMENT

The authors gratefully acknowledge the precious support provided by laboratory and workshop staff Messrs Richard Dibbs, Chris Chapman, Russell Nicholson, and Harold Myer, during the course of this work.

REFERENCES

1. Asdrubali, F., A Scale Model to Evaluate Water Evaporation From Indoor Swimming Pools, *Energy and Buildings*, Vol. 41(3), pp 311-319, 2009.
2. Shah, M. M., Calculating Evaporation From Indoor Water Pools, *HPAC Engineering*, Vol, 76, pp 21-23, March 2004.
3. Shah, M. M., Prediction of Evaporation From Indoor Swimming Pools, *Energy and Buildings*, Vol. 35, pp 707-713, 2003.
4. El-Dessouky, H., Ettouney, H., Alatiqi, I. and Al-Shamari, M., Evaporation Rates From Fresh and Saline Water Into Moving Air, *Industrial & Engineering Chemistry Research*, Vol. 41(3), pp 642-650, 2002.
5. Smith, C. C, Löf, G. and Jones, R., Rates of Evaporation From Swimming Pools in Active Use, *ASHRAE Transactions*, Vol. 104, pp 514-523, 1998.
6. Paulken, M. T., Farley, B., Jeter, S. and Abdel-Khalik, S., Experimental Investigation of Water Evaporation Into Low-velocity Air Currents, *ASHRAE Transactions*, Vol. 101(1), pp 90-96, 1995.
7. Jones, R., Smith, C. C. and Löf, G., Measurement and Analysis of Evaporation From an Inactive Outdoor Swimming Pool, *Solar Energy*, Vol. 53(1), pp 3-7, 1994.
8. Smith, C. C., Jones, R. and Löf, G., Energy Requirements and Potential Savings for Heated Indoor Swimming Pools, *ASHRAE Transactions*, Vol. 99(2), pp 864-874, 1993.
9. Boelter, L. M., Gordon, H. S. and Griffin, J. R., Free Evaporation Into Air of Water From a Free Horizontal Quiet Surface, *Industrial and Engineering Chemistry*, Vol. 38(6), pp 596-600, 1946.
10. Ribeiro Jr., C. P. and Lage, P. L. C., Gas-Liquid Direct-Contact Evaporation: A Review, *Chemical Engineering and Technology*, Vol. 28(10), pp 1081-1107, 2005.
11. Ribeiro Jr., C. P. and Lage, P. L. C., Direct-Contact Evaporation in the Homogeneous and Heterogeneous Bubbling Regimes. Part I: Experimental Analysis, *International Journal of Heat and Mass Transfer*, Vol. 47, pp 3825-3840, 2004.
12. Ribeiro Jr., C. P. and Lage, P. L. C., Direct-Contact Evaporation in the Homogeneous and Heterogeneous Bubbling Regimes. Part II: Dynamic Simulation, *International Journal of Heat and Mass Transfer*, Vol. 47, pp 3841-3854, 2004.
13. Marshall, J. and Plumb, R. A., *Atmosphere, Ocean, and Climate Dynamics*, Elsevier, San Diego, California, 2008.
14. Incropera, F. P. and De Witt, D. P., *Fundamentals of Heat and Mass Transfer, 6th Ed.*, Wiley, New York, 2007.

ESTIMATION OF THERMAL CONDUCTIVITY AND EMISSIVITY USING CONJUGATE HEAT TRANSFER EXPERIMENTS

R. Krishna Sabareesh[1], S. Prasanna[1], S.P. Venkateshan[1,*]
[1]Heat Transfer and Thermal Power Laboratory, IIT Madras, Chennai, India

ABSTRACT. Steady state experiments on the basic aspects of conjugate heat transfer occurring from a vertical flat plate made of different materials (Aluminium, Titanium alloy and Bakelite), in quiescent air, with an embedded heater have been explored in the present work. Numerical studies are also conducted and the simulated temperature profiles are then compared with the experimentally obtained temperature distribution to obtain the residual, the minimization of which using, the Least Square Method, retrieves the parameters, surface emissivity and plate material thermal conductivity. The experiments have been carried out for various power inputs and the consistency of the proposed method is tested. The values of emissivity and thermal conductivity obtained by the present method are in good agreement with the previously reported values.

Keywords: *Conjugate heat transfer, thermal conductivity, emissivity, inverse problem, Interferometer*

INTRODUCTION

Conjugate heat transfer problems occur in many practical applications. Several studies have been made in the area of conduction-convection coupling. The heat transfer enhancement by extended surfaces such as fins, is an example that falls in this category. Vynnycky and Kimura [1] investigated analytically and numerically two dimensional conjugate free convection from a vertical plate adjacent to a semi-infinite fluid region. Córdova and Treviño [2] studied the effect of longitudinal heat conduction in the cooling of a vertical thin plate in natural convective flow, using both numerical and asymptotic techniques. Recently Nouanegue et al [3] investigated numerically the conjugate heat transfer by natural convection, conduction and radiation in open cavities. Despite a large number of publications available in the area of conjugate heat transfer, only very few experimental studies are found in literature. Miyamoto et al [4] performed both experimental and numerical studies on a vertical plate subjected to a uniform heat flux and identified the criteria for assuming, basically a constant heat flux situation as an isothermal one. Kimura et al [5] investigated experimentally and analytically conjugate heat transfer and proposed a simple expression for average heat transfer.

The determination of thermo-physical properties from the measured temperature profiles is essentially a parameter retrieval problem in heat conduction. Any parameter retrieval problem involves two stages, forward model and inverse problem. Forward model in the parlance of heat transfer refers to the determination of temperature profile in a material whose thermo-physical properties are known. The inverse problem refers to the determination of these properties by knowing the temperature distribution in the body. An accurate knowledge of the thermo-physical properties like emissivity and thermal conductivity is important in accurately modelling and simulating many engineering applications. Most

* Corresponding author: Prof. S.P.Venkateshan
Phone: + 91-44-2257 4686, Fax: +91-44-2257 4652
E-mail address: profspv@gmail.com

of the conventional methods used for the determination of emissivity require a vacuum environment to avoid other modes of heat transfer. Krishnan et al [6] proposed a novel method for the estimation of emissivity, by conducting transient cooling experiments on a vertical heated plate in quiescent air. Following that, Venugopal et al [7] proposed a new method for the simultaneous estimation of emissivity and specific heat by carrying out transient cooling experiments.

The main purpose of the present work is to estimate emissivity and thermal conductivity, by carrying out steady state conjugate heat transfer experiments.

EXPERIMENTAL SETUP AND PROCEDURE

Since the experimental setup has been described in detail in [7], only a brief review will be presented here. The setup consists of a vertical plate assembly suspended freely from two parallel stainless steel rods using two Teflon rods as depicted in figure 1. The test plate assembly consists of two plates of dimensions 150 × 250 × 3 mm with a flat heater sandwiched between them. The flat heater is formed by winding a Nichrome wire over a mica sheet and the same is electrically insulated from the unexposed side of the test plates by using mica sheets. The two halves of the test plate are fastened together using screws and nuts which are seated in countersunk holes to avoid disturbances to flow due to protrusion. The temperatures at different locations (as shown in figure 2) are recorded using calibrated K- type (36AWG) stainless steel sheathed thermocouples which are fixed to the plate by means of highly conducting copper cement. A separate K- type thermocouple is kept inside the test section to measure the ambient temperature. All thermocouples are connected to a personal computer based data acquisition system (Model No. 34970A, Agilent Technologies Ltd.) through compensating wires. The power input to the heater is supplied from a regulated dc power source (Aplab Systems Ltd., India, Model No. H0615).

Steady state experiments, simulating natural convection environment inside the test section, are carried out for various power inputs. Steady state is assumed to be reached when the variation in the temperature readings of all the thermocouples is within ±0.1 °C in 10 minutes. The experiments are carried out for three different materials of the test plate (aluminium, titanium alloy, and bakelite [supplied by M/S Bakelite Hylam, Hyderabad, India]) The experiments on aluminium and titanium test plate are conducted for three different surface conditions viz. ‘no coating’, aluminium paint and blackboard paint, while the experiments on bakelite are conducted only for the ‘no coating’ condition.

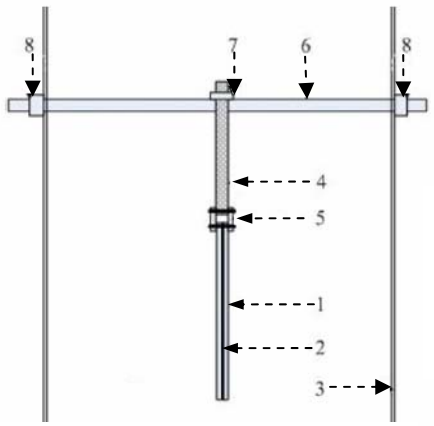

Figure 1. Schematic of experimental setup
1-heated vertical plate; 2- electric heater; 3- side wall of test section (wood) ; 4-Teflon rod; 5-Steel strip; 6-Stainless steel rod; 7,8-adjusting nut

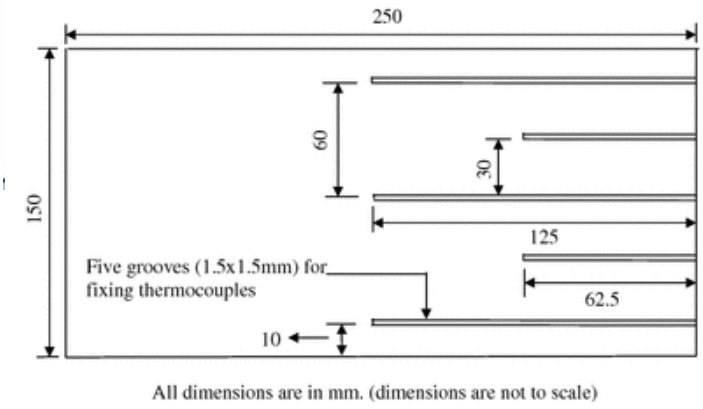

Figure 2. Arrangement of the thermocouples in the plate

NUMERICAL SIMULATIONS

The experimental conditions have been simulated numerically using the commercially available CFD package FLUENT 6.3. Extensive grid independence study has been carried out and proper mesh has been selected. The result that is obtained from the numerical simulations is used as the forward model. The forward model involves obtaining the temperature distribution along the plate for different combinations of emissivity and thermal conductivity and for various heat inputs. The important observations from the numerical study are as follows.

Figure 3 represents the temperature profiles obtained for different values of thermal conductivity, for a fixed heat input and emissivity. It is seen that as the thermal conductivity of the material increases, the temperature gradient along the plate decreases. Therefore, the isothermal assumption is strictly valid for materials having high thermal conductivity, such as aluminium. Figure 4 shows the variation of local heat transfer coefficient along the plate for different values of thermal conductivity. It is seen that the heat transfer coefficient is *independent* of the thermal conductivity of the plate**.**

Table 1 shows the variation of the average temperature of the plate for a thermal conductivity of 200 W/m K, for different values of emissivity. It is seen that the average temperature of the plate decreases with increase in emissivity. It is also seen that the average heat transfer coefficient decreases with increase in emissivity which is in accordance with the observations made by Rammohan et al. [8]. Table 2 shows the dependence of the average temperature of the plate on the thermal conductivity for a given emissivity and power input. It is clear that for a given emissivity, the average plate temperature is *independent* of thermal conductivity.

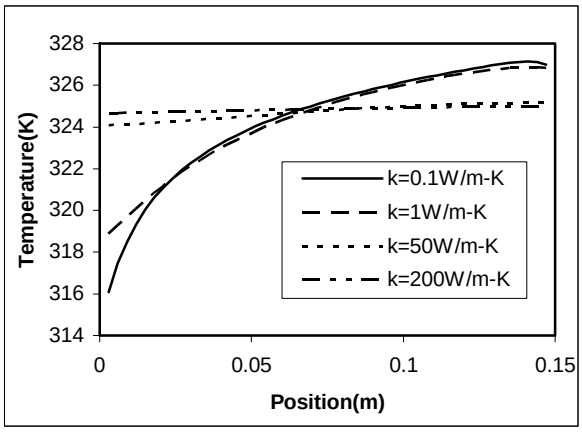

Figure 3. Temperature profiles for different thermal conductivities

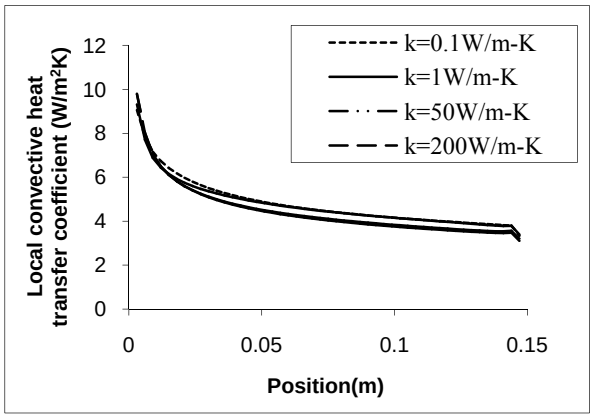

Figure 4. Local convective heat transfer coefficient for different thermal conductivities

Table 1
Average plate temperature and heat transfer coefficient variation with emissivity

k (W/m-K)	ε	T_{avg}(K)	h_{avg} (W/m^{2}K)
200	0	338.8124	5.0321
	0.5	324.8486	4.5414
	1	318.2963	4.1994

Table 2
Dependence of average plate temperature on thermal conductivity

ε	k(W/m-K)	T_{avg}(K)
0.5	0.1	324.3798
	1	324.4856
	50	324.7282
	200	324.8486

Interferometric results

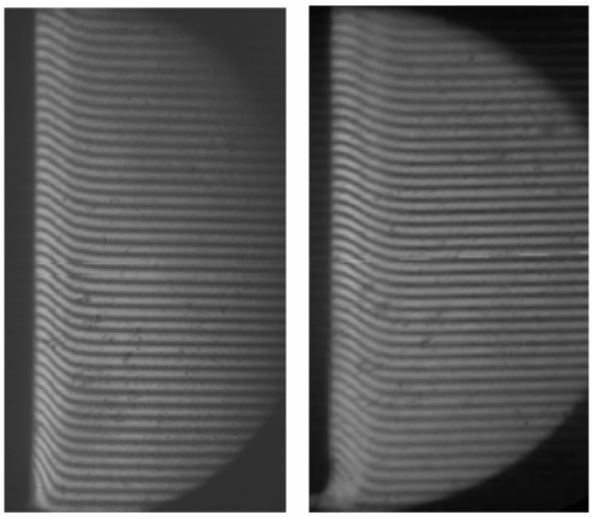

(a) (b)

Figure 5. Interferogram for (a) aluminium and (b) titanium plates coated with aluminium paint

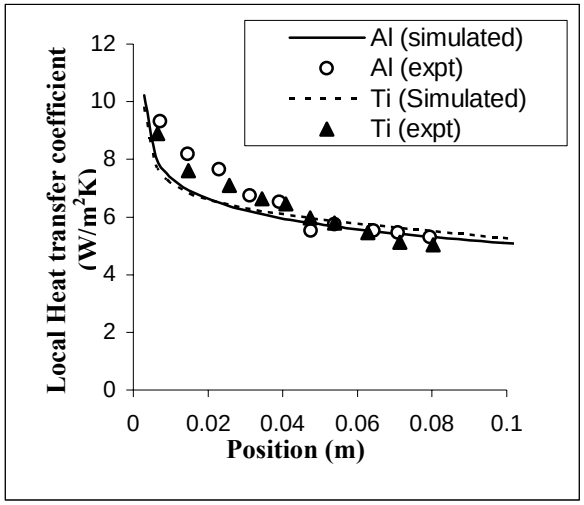

Figure 6. Local convective heat transfer coefficient for aluminium and titanium alloy coated with aluminium paint.

Local heat transfer measurements by a Differential interferometer (DI) have been further used to validate the numerical observation. The principle of operation of the DI has been explained in [9]. The optical setup used in the present study is same as that of [10]. The main advantage of the DI is that the convective heat transfer coefficient at the wall can be directly determined from the interferograms. Figure 5 shows the interferograms corresponding to aluminium and titanium plates coated with aluminium paint, for the same heat input. The field of view available for the interferometer used in the present study is only 9.5 cm and hence the studies have been restricted to that length of the plate starting from its leading edge. Figure 6 shows the comparison between the numerically simulated and experimentally obtained local convective heat transfer coefficient for both aluminium and titanium plates for the same experimental conditions. It is seen that the results from the interferograms corroborate very well with the numerical study far away from the leading edge. Close to the leading edge, the temperature gradients are very high and the fringes obtained are very steep. Hence the variation could be attributed to the errors in the calculation of fringe shift and other experimental uncertainties. Inspite of this, it is found that the local heat transfer coefficient obtained is more or less independent of the thermal conductivity of the material, justifying the use of the numerical scheme as the forward model for parameter retrieval.

INVERSE PROBLEM

From the experiments, the temperature distribution along the plate for a particular surface condition and thermal conductivity is obtained. The forward model gives the temperature distribution for known values of emissivity and thermal conductivity. So the inverse problem is to retrieve the unknown parameters, emissivity and thermal conductivity, by minimizing the sum of the squares of the differences between the numerically simulated and the experimentally obtained temperatures, which is called as the Least Square Residual (LSR), *R.* Mathematically, which can be represented as

$$R = \sum_{i=1}^{n} \left(T_i^{sim} - T_i^{\exp} \right)^2 \tag{1}$$

Table 3
Database for emissivity retrieval

ε	T_{avg} (K)
0	360.2877
0.1	354.5516
0.2	349.9143
0.3	346.068
0.4	342.8107
0.5	340.0091
0.6	337.5683
0.7	335.4196
0.8	333.511
0.9	331.8035
1	330.2659

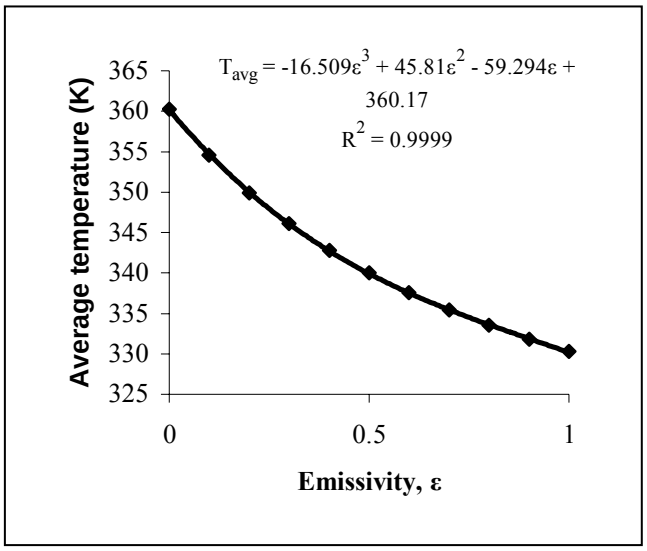

Figure 7. Cubic fit for the database

Retrieval of emissivity

From the numerical study, it is clear that for a given heat input, the average temperature of the plate as well as the average heat transfer coefficient are independent of the thermal conductivity, but depend only on the emissivity of the plate. A database of simulated average plate temperatures is created for different values of emissivity for a fixed value of heat input. The thermal conductivity independence ensures that even if a paint, whose emissivity is to be retrieved, is applied on a material of unknown thermal conductivity; the database can be generated using any value of thermal conductivity in the forward model. A cubic polynomial is then fit for that particular database. One typical example of such a database is shown table 3 and figure 7. The cubic equation is then solved by substituting the experimentally obtained average plate temperature in the equation. The root of the cubic equation gives the value of the emissivity which we are trying to retrieve. Thus this method of retrieving the emissivity of the coating is superior to other methods [6, 7] as it does not require the knowledge of any other thermo- physical property.

Retrieval of thermal conductivity

Once the emissivity and heat input are fixed, the temperature distribution along the plate depends only on the thermal conductivity. So the forward model is run with the retrieved value of the emissivity obtained by the previous method, for different values of thermal conductivity. The temperature distribution that is obtained for each value of thermal conductivity is given a cubic fit. Figure 8 represents one such fit for a certain thermal conductivity value. The temperatures at the positions where the thermocouples are located in the plate are then calculated using the fit polynomial. This is then compared with the experimentally obtained temperatures at the corresponding positions, to obtain the residual. The LSR for each value of thermal conductivity is calculated and then plotted against thermal conductivity. The minimum value of this curve corresponds to the value of the thermal conductivity which we are trying to retrieve.

Table 4 represents a typical database for a particular value of emissivity. The simulated temperatures for four different thermal conductivities are also shown. LSR, which is obtained by squaring the difference between the numerical and experimental temperatures at each point, is then plotted. Figure 9 represents one such typical graph where the LSR plots are shown for a power input of 60 W for the titanium plate and 15 W for the bakelite plate. The minimum corresponding to each curve represents the thermal conductivity for that power input.

Table 4
Database for the estimation of thermal conductivity of titanium alloy

Position(m)	Expt(K)	k=5W/mK	k=10W/mK	k=15W/mK	k=20W/mK
0.02	363.621	361.531	363.942	365.256	366.097
0.05	367.41	369.288	369.163	369.223	369.307
0.08	372.631	374.031	372.547	371.874	371.493
0.11	373.239	375.214	373.632	372.823	372.326
0.14	373.027	372.289	371.955	371.683	371.473

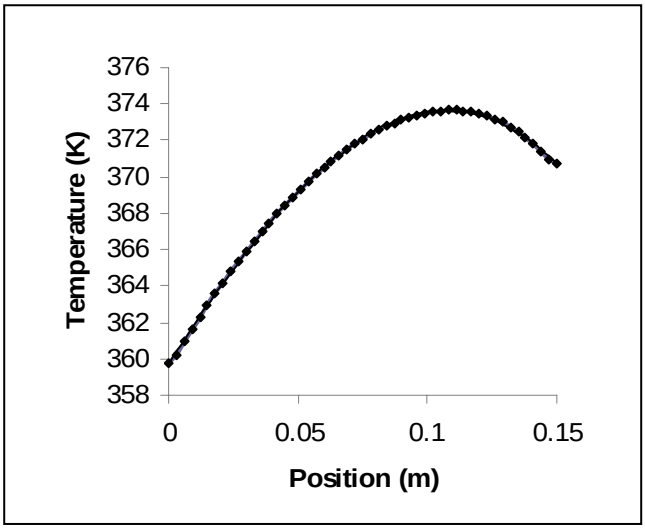

Figure 8.Numerically simulated temperature profile used in the estimation of thermal conductivity of titanium

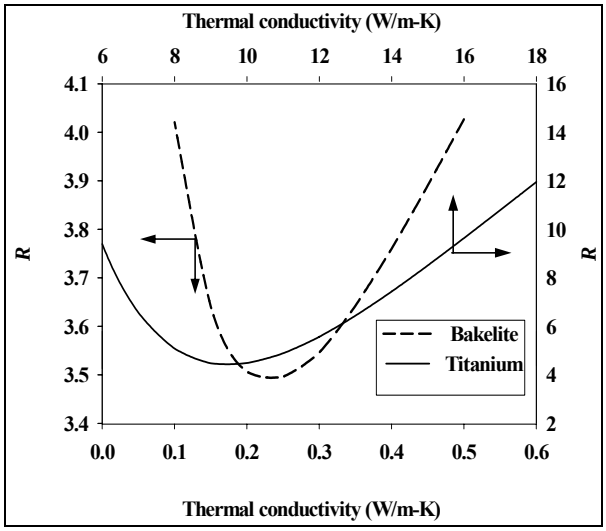

Figure 9. Least Square Residual plots for determining the thermal conductivity of titanium and bakelite

RESULTS AND DISCUSSIONS

The experiments are conducted for various power inputs ranging from 30W to 90W at an interval of 10 W for both aluminium and titanium plates. As bakelite is having very low thermal conductivity, the experiments are conducted for lower power inputs only (10W, 15W and 20W). This is to ensure that the independence of heat transfer coefficient on thermal conductivity is still valid and that the method proposed for determining both emissivity and thermal conductivity can be used without any modification. The mean value of the parameters, emissivity and thermal conductivity, along with the standard deviations, obtained from the present study are summarized in the tables presented below. The metallurgical compositions of the materials, Aluminium and Titanium, observed using scanning electron microscope (Make: FEI-Czech Republic, Model: QUANTA 200) are as follows. Aluminium: Al 92.48%, O 7.52%; Titanium: Ti 59.4%, O 15.31%, N 25.29 %(All in mole fraction).

Estimation of emissivity

Table 5 represents the results of the emissivity measurements done for three different materials of the test plate, with different surface conditions viz. with blackboard paint and aluminium paint (Manufacturer: Agsar Paints Private Ltd., Tutucorin, India) coating for Titanium and Aluminium test plates and with no coating for bakelite. From the present study it is found that the emissivity is a weak function of temperature in the range considered, which is in agreement with the observations made by Venugopal et al. [7]. The emissivity of blackboard paint coating was reported as 0.85 [9]

Table 5
Retrieved values of emissivity for different materials of the test plate with different surface conditions

Material	Paint Applied	Mean value	Standard Deviation *
Titanium alloy	Blackboard paint	0.859	0.010
	Aluminium paint	0.397	0.005
Aluminium	Blackboard paint	0.879	0.010
	Aluminium paint	0.411	0.018
Bakelite	No coating	0.725	0.002

Table 6
Retrieved values of thermal conductivity for titanium alloy and commercial bakelite

Material	Mean value (W/mK)	Standard Deviation * (W/mK)
Titanium alloy	9.95	0.840
Bakelite	0.22	0.011

* Standard deviation values quoted in Table 5 and 6 are based on repeated measurements.

and that of the aluminium paint was reported as 0.457 [11]. The very slight difference in the results obtained in the present study and that found in [9, 11] could be due to the difference in the surface condition of the plate, make of the paints and thickness of the coating applied. The emissivity of bakelite is obtained as 0.725 which is used as an *input* in the determination of thermal conductivity of bakelite. It is also observed that the emissivity of the plate is independent of the test plate material.

Estimation of thermal conductivity

Table 6 indicates the mean values of thermal conductivity obtained for titanium alloy and bakelite. The thermal conductivity of titanium alloy is reported as 9 W/m-K [12] while that of bakelite is reported as 0.233 W/m-K. [13]. As the proposed method requires a reasonable temperature gradient along the plate for determining the thermal conductivity, it cannot be used for materials with high thermal conductivity like aluminium, which will be having more or less uniform temperature profile throughout the plate.

CONCLUSIONS

A novel method which involves a judicious combination of both experiments and numerical simulations has been proposed to estimate the parameters, emissivity and thermal conductivity. The present experimental setup is simple to construct and does not demand vacuum for the estimation of emissivity. The thermal conductivity retrieval proposed here can be applied over a wide range starting from insulators to materials having moderate thermal conductivities, though it cannot be extended to materials having very high thermal conductivity due to the absence of appreciable temperature variation along the plate. Moreover the present inverse methodology for parameter retrieval does not require any sophisticated optimization technique. The consistency of the above method has been tested extensively for a wide range of operating conditions. The retrieval of the parameters depends only on the temperature measurements and is independent of any other thermo-physical property of the test material.

REFERENCES

1. Vynnycky, M. and Kimura, S., Conjugate free convection due to a heated vertical plate, *Int.J.Heat Mass Transfer.,* Vol. 39, No. 5, pp 1067-1080, 1996.
2. Córdova, J. and Treviño,C., Effects of longitudinal heat conduction of a vertical thin plate in a natural convective cooling process, *Wärme- und Stoffübertragung* **,** Vol. 29, pp. 195–204, 1994.
3. Nouanegue, H., Muftuoglu, A. and Bilgen,E., Conjugate heat transfer by natural convection, conduction and radiation in open cavities, *Int.J.Heat Mass Transfer.,* Vol. 51, pp 6054-6062, 2008.
4. Miyamoto, M., Sumikawa, J., Akiyoshi, T. and Nakamura,T. ,Effects of axial heat conduction in a vertical flat plate on free convection heat transfer, *Int.J.Heat Mass Transfer.,* Vol. 23, pp 1545-1553, 1980.
5. Shigeo Kimura, Atsushi Okajima and Takahiro Kiwata, Conjuagate natural convection from a vertical heated slab, *Int.J.Heat Mass Transfer.,* Vol. 41, pp 3203-3211, 1998.
6. Krishnan, A.S., Balaji, C. and Venkateshan, S.P., A synergistic approach to parameter estimation in multimode heat transfer, *Int.Comm.Heat Mass Transfer.,* Vol. 30, No. 4, pp 515-524, 2003.
7. Venugopal, G., Deiveegan, M., Balaji, C. and Venkateshan, S.P., Simultaneous Retrieval of Total Hemispherical Emissivity and Specific Heat From Transient Multimode Heat Transfer Experiments, *Journal of Heat Transfer, ASME,* 2008, *130*, 061601
8. Rammohan Rao, V., Balaji, C. and Venkateshan, S.P., Interferometric study of interaction of free convection with surface radiation in an L corner, *Int.J.Heat Mass Transfer.,* Vol. 40, pp 2941-2947, 1997.
9. Rammohan Rao, V., Interferometric study of interaction between radiation and free convection in fins and fin arrays, *PhD Thesis*, Mechanical Engineering Department., IIT Madras, 1992.
10. Ramesh, N., Experimental study of interaction of natural convection with surface radiation, *PhD Thesis*, Mechanical Engineering Department., IIT Madras, 1999.
11. Especel, D. and Matteï, S. Total emissivity measurements without use of an absolute reference, *Infrared Physics and Technology*, Vol. 37, pp 777-784, 1996.
12. Thermo-physical property database: http://tpsx.arc.nasa.gov/
13. Ren-Tsung Huang, Wen-Junn Sheu and Chi-Chuan Wang, Orientation effect on natural convective performance of square pin fin heat sinks, *Int.J.Heat Mass Transfer,* Vol. 51, pp 2368-2376, 2008.

MATHEMATICAL MODELLING OF LOW TEMPERATURE CONDENSATION COUPLED WITH ADSORPTION

A. Rotkegel *
Institute of Chemical Engineering Polish Academy of Sciences, Gliwice, Poland

ABSTRACT. The mathematical model of Volatile Organic Compound (VOC) removal from air in the integrated system of low temperature condensation followed by adsorption is presented. Mathematical model of the integrated system consists of two different calculation steps: low temperature condensation of vapors in the presence of inert gas, and low temperature adsorption of vapors. Due to the character of two mentioned processes, each of them must be calculated otherwise. The removal of VOC from gases in the integrated process of low temperature condensation followed by adsorption enables to remove VOC from gases almost completely at relatively high condensation temperatures (240K). The sorption capacity increases with the lower of adsorption temperature, but gives smaller values of diffusional time constant. This fact leads to the increase of mass transfer zone in the adsorber, breakthrough curves become more flat, and in final result utilization of adsorber capacity is lower.

Keywords: *VOC removal, adsorption, condensation, low temperature*

INTRODUCTION

Volatile Organic Compounds (VOCs) are emitted into the atmosphere in the considerable amount by the chemical industry, as a result of the production, storing, transportation and the distribution of colors, varnishes, solvents and liquid fuels. The considerable growth of the consumption of volatile organic compounds in the industry will cause enlargement of the threat for natural environment and the health of the population, because about 80% of VOCs are emitted into the atmosphere [1-3]. To limit the harmful influence of emitted VOC on the natural environment it is necessary to reduce considerably the emission of these substances.

This requires lowering the concentration of VOCs in gases exhausted into the atmosphere to a very low concentrations, of a ppm range. The achievement of this aim needs further development and improvement of existing techniques of VOCs removal, such as: the catalytic or thermal oxidation [4], absorption, cryogenic condensation and adsorption [5, 6].

According to literature reports [5], the use of cryogenic condensation in the process of VOCs removal from gases is more frequently used in industrial installations.

The achievement of the high degree of the cleaning gas in the process of cryogenic condensation requires cooling down the gas mixture to the temperature of about 170 K, which can be realized practically by using the liquid nitrogen, as a cooling medium.

The alternative way to the cryogenic condensation, allowing to achieve the low concentrations of VOCs in gas mixtures emitted to the atmosphere, is the use of hybrid process of condensation followed by adsorption [7-8]. Applying such a hybrid arrangement is more effective than the application of each process separately [7-8]. The process of VOCs condensation can be realized in the considerably higher temperatures than in the process of the cryogenic condensation alone (240 to 250 K), using other cooling media such as: refrigerating brine, ammonia or glycols. The process of VOCs adsorption is done in the temperatures in which gas mixtures leave the condenser, and the

* Corresponding author: PhD A. Rotkegel
Phone: + (48)-32-2310811, Fax: + (48)-32-2310318
E-mail address: arot@iich.gliwice.pl

desorption process in the temperature insignificantly higher than 273 K. The gas mixture from the desorber is led to the condenser, which allows to recover the whole quantity of volatile organic compounds as condensates. This way of carrying of the process allows to avoid additional costs connected with the utilization of gases after desorption process.

EXPERIMENTAL SET-UP

The experimental studies of integrated process of low-temperature condensation coupled with adsorption, was described in detail in [9]. The experimental set-up was composed of: the condenser plus two working adsorbers running alternately in the cycles adsorption – desorption. Such settings of apparatuses allows continuous work of the installation of gas mixtures cleaning. As a cleaning gas the mixture of 2-propanol and nitrogen was used. The concentration of 2-propanol was changed in the range from 4 to 25 g/Nm^3. The active carbon AP3-60 made by Chemviron-Carbon was applied as the packing of adsorbers. The experimental set-up is presented in Fig. 1

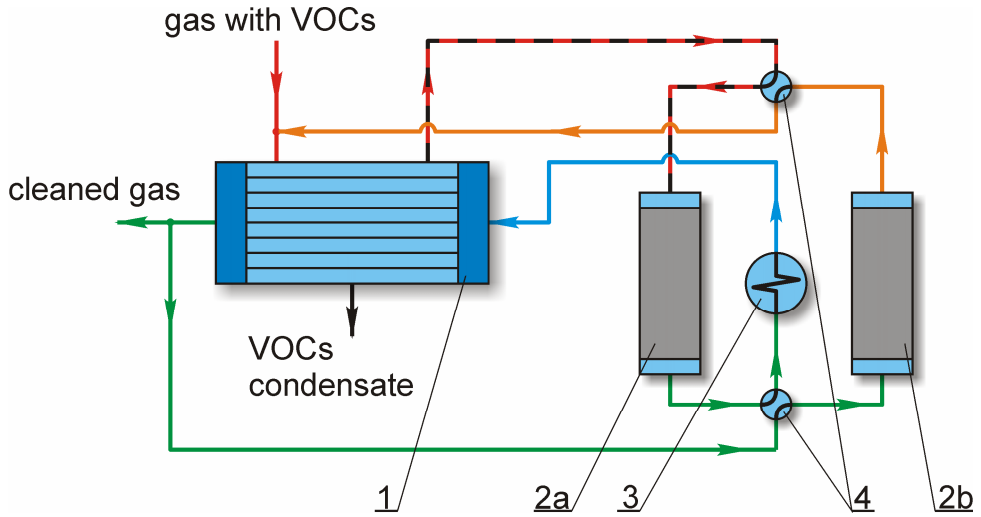

Figure 1. Experimental setup: 1 – condenser, 2a,2b – adsorbers, 3 – heat exchanger, 4 – 4-way valves

MATHEMATICAL MODEL

Mathematical model of the integrated system consists of two different calculation steps: low temperature condensation of vapors in the presence of inert gas, and low temperature adsorption of vapors. Due to the character of two mentioned processes, each of them must be calculated otherwise. The model of low temperature condensation was described using a system of ordinary differential equations with boundary conditions. The model of adsorption was described using the system of partial differential equations with initial and boundary conditions.

Mathematical model of low temperature condensation

The process of condensation is described using the set of four ordinary differential equations with the boundary conditions, together with the following assumptions:

- the process occurs under steady state, isothermal and adiabatic conditions,
- heat and mass transfer resistances in liquid film are neglected,
- on the interfacial surface of the condensate - vapor mixture a thermodynamic liquid-gas equilibrium exists,
- according to film theory, heat and mass transfer resistances occur only in the gas phase near the interface; these resistances can be determined by the respective heat and mass transfer coefficients.

To calculate the temperature and concentration profiles along the condenser it is necessary to set and solve the system of differential equations of mass and heat balances. Assuming that the mass flow of vapour to the liquid phase has a positive sign, the corresponding system of equations for one dimensional model can be presented as follow; mass balances in gas and liquid phase:

$$\frac{dG_k}{dl} = -nN_k \pi d \tag{1}$$

$$\frac{dG_c}{dl} = nN_k \pi d \tag{2}$$

heat balances in gas and liquid phase:

$$G\,\bar{c}_{pA}\frac{dT_A}{dl} = \pi\, nd\,(T_A - T_w)\,(N_k\,\bar{c}_{pA} - \alpha_A) \tag{3}$$

$$G\,\bar{c}_{pB}\frac{dT_B}{dl} = -\pi\, nd\,\alpha_B (T_w - T_B) \tag{4}$$

The wall temperature was calculated from the equation of continuity of heat flux, where the heat resistance in the liquid film was omitted :

$$N_k\,\Delta H_k + \alpha_A (T_A - T_w) = \alpha_B (T_w - T_B) \tag{5}$$

The heat and mass transfer coefficients were determined experimentally

Mathematical model of adsorption

The process of adsorption is described by the set of partial differential equations with the initial and boundary conditions and the following assumptions:

- the process is isothermal,
- thermal equilibrium occurs between gas and adsorbent grains,
- the gas flow rate by the adsorbent bed is fixed,
- in the adsorbent bed gas plug flow profile with axial dispersion exists,
- mass transport between gas phase and the liquid layer on adsorbent surface is described by a linear equation of mass transfer,
- the concentration profile in adsorbent pore is parabolic,
- the pressure drop through the adsorber bed is neglected,
- gas mixture flowing through the adsorber is treated as an ideal one,
- mass transport velocity given by linear driving force (LDF) equation.

With the above assumptions, the adsorption process of VOC on the adsorber bed can be described with the following equations [10][11]:

$$-D_L\frac{\partial^2 c}{\partial z^2} + w\frac{\partial c}{\partial z} + \frac{\partial c}{\partial \tau} + k_l\left(\frac{1-\varepsilon}{\varepsilon}\right)\left(q^* - \bar{q}\right) = 0 \tag{6}$$

At a parabolic concentration profile in the sorbent pore the value coefficient k_l can be calculated [12], [13] from:

$$k_l = 15\frac{D}{r_p^2} \tag{7}$$

Diffusion coefficient D_L for the axial dispersion can be calculated from relationship by Wakao and Funazkri [14]

$$\frac{\varepsilon D_L}{D_m} = 20 + 0.5 Re_L\, Sc_L \tag{8}$$

where binary diffusion coefficient was calculated from Schettler-Giddings [15] correlation:

$$D_m = 1.013\times10^{-2} T^{1.75} \frac{\sqrt{1/M_i + 1/M_I}}{P\left(\sqrt[3]{V_i} + \sqrt[3]{V_I}\right)^2} \tag{9}$$

To solve the partial differential equation (6) the following initial and boundary conditions were assumed:

$$\begin{aligned} c\big|_{\tau=0} &= 0 \\ q\big|_{\tau=0} &= q^*(t_{ads}, c) = 0 \end{aligned} \tag{10}$$

and

$$\begin{aligned} c\big|_{z=0} &= C_1 \\ \left.\frac{\partial c}{\partial z}\right|_{z=z} &= 0 \end{aligned} \tag{11}$$

NUMERICAL CALCULATIONS

Numerical calculations were carried out separately for the low-temperature condensation and adsorption process. For the low temperature condensation calculations the system of ordinary differential equations was integrated using the DE/STEP procedure of Shampine-Gordon [16]. Integration of the differential equations was carried out according with the direction of flow of gas-vapour mixture. In each integration step the physical and thermodynamical parameters of components were calculated.

For low temperature adsorption the system of partial differential equations (6) with initial (10) and boundary (11) conditions were solved using finite differences method with implicit scheme. In our calculations the QUICK method described by Leonard [17] was used. In this method the finite dfference $\Delta c_i/\Delta z$ in the i-node is described as:

$$\frac{\Delta c_i}{\Delta z} = \frac{1}{8\Delta z}\left(c_{i-2} - 7c_{i-1} + 3c_i + 3c_{i+1}\right) \tag{12}$$

With the above assumption the equation (6) can be presented in the form of finite differences in the i-node and the n-time step as:

$$\begin{aligned} \frac{c_i^{n+1} - c_i^n}{\Delta\tau} = \frac{D_L}{2\Delta z^2}\left(c_{i-1}^n - 2c_i^n + c_{i+1}^n + c_{i-1}^{n+1} - 2c_i^{n+1} + c_{i+1}^{n+1}\right) - \\ \frac{w}{16\Delta z}\left(c_{i-2}^n - 7c_{i-1}^n + 3c_i^n + 3c_{i+1}^n + c_{i-2}^{n+1} - 7c_{i-1}^{n+1} + 3c_i^{n+1} + 3c_{i+1}^{n+1}\right) - \left(\frac{1-\varepsilon}{\varepsilon}\right) k_l\left(q^*(c_i^n) - \overline{q_i^n}\right) \end{aligned} \tag{13}$$

and

$$\frac{\overline{q_i^{n+1}} - \overline{q_i^n}}{\Delta\tau} = k_l\left(q^*(c_i^n) - \overline{q_i^n}\right) \tag{14}$$

To solve such formulated problem the system of n equations should be solved in each time step (where n is equal to the amount of the calculation nodes in the adsorbent bed). Good calculation accuracy was achieved for n equal to 80 and time step equal to 10^{-2} sec.

COMPARISON OF CALCULATION RESULTS WITH EXPERIMENTAL DATA

To compare calculation results of low temperature condensation with experimental data the graph of calculated condensation efficiency vs. experimental one was done. The condensation efficiency was defined as:

$$\eta = \frac{C_0 - C_1}{C_0} \tag{15}$$

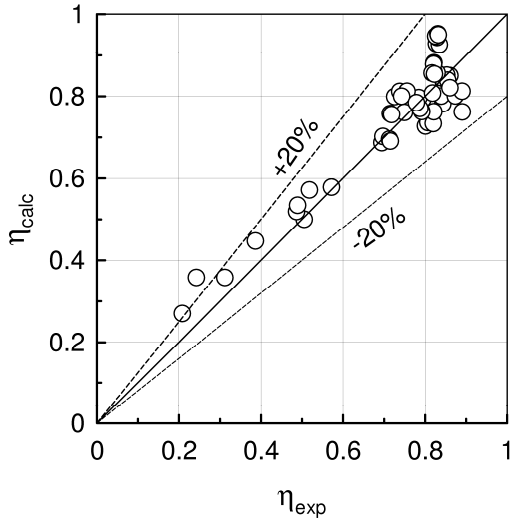

Figure 2. Calculated efficiency of condensation vs. experimental ones

Figure 2 shows that the calculated efficiency of the condensation process is consistent with experimental data within the range of about 20%. Average error of calculation of exhausted gas temperatures, concentration and condensation efficiency and their standard deviations, was given in the table 1.

Table 1. Standard deviation and average error of condensation process calculations

Parametr	Average error	Standard deviation
T_{A1} [K]	1.97	0.55
T_{B1} [K]	1.05	0.81
C_1 [g/Nm^3]	0.50	0.50
η	0.049	0.060

The comparison of calculated adsorption breakthrough time vs. experimental one was given in figure 3. Notation τ_{01}, τ_{05}, τ_{10} describes times at which the concentration of VOC in the outlet of the adsorber reached the value of 1%, 5% and 10% of inlet concentration respectively. Figure 3 shows that error of calculated breakthrough times was less than 25%. Absolute mean error of calculated breakthrough time was equal to 10.68 min, relative error was 8.77% and standard deviation was equal to 6.61 min.

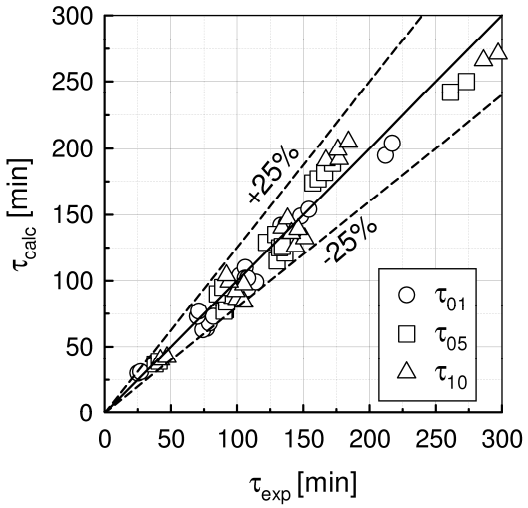

Figure 3. Calculated breakthrough times vs. experimental ones.

TEMPERATURE EFFECT ON THE ADSORPTION PROCESS

Adsorption isotherms of 2-propanol on activated carbon AP3-60 is presented in figure 4. As can be seen the maximum sorption capacity of adsorbent bed increases with the decrease of adsorption temperature, especially for small concentrations of propanol-2 in the inlet gas to the adsorber.

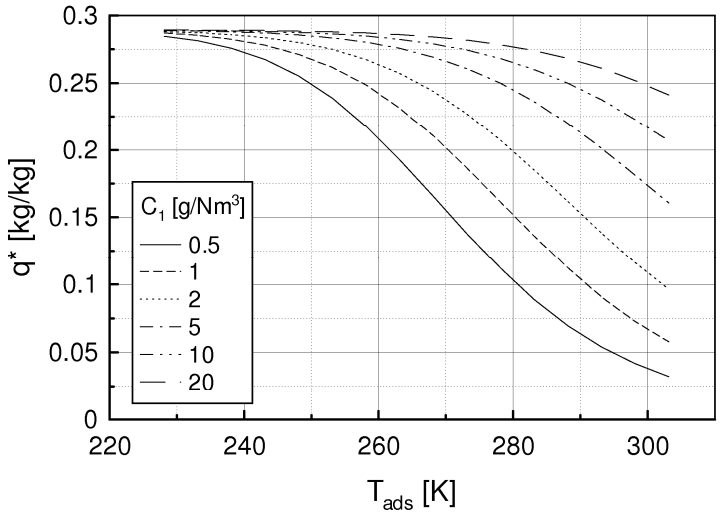

Figure 4. The dependence of the maximum sorption capacity of the adsorption temperature for different concentrations of 2-propanol at the inlet to the adsorber.

But with the reduction of the adsorption temperature the diffusional time constant decreases, which leads to a reduction of diffusion rate in the adsorbent pores and as a result the mass transfer zone in adsorber increases and breakthrough time decreases.

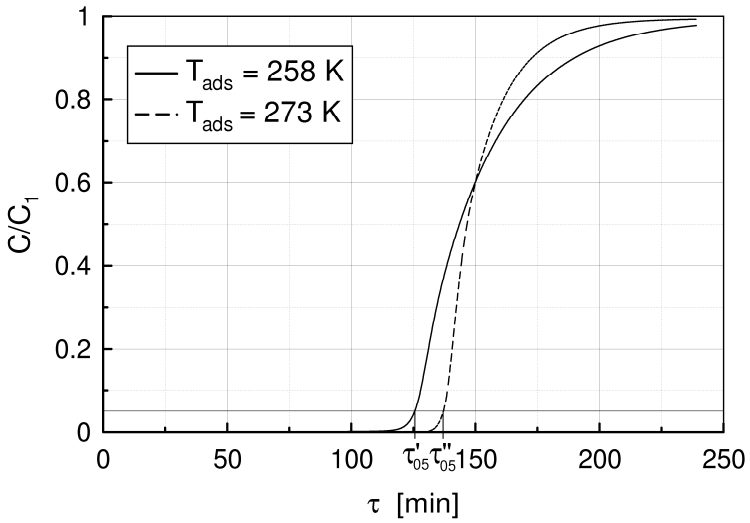

Figure 5. Calculated adsorber breakthrough curves for two different adsorption temperatures.

CONCLUSIONS

Based on the developed mathematical models of condensation and adsorption processes the numerical calculations were performed and compared with experimental data. Analysis of the numerical calculations all w to formulate the following conclusions:

- VOCs removal from gaseous mixtures in the integrated system of condensation and adsorption enables to remove almost completely VOCs from gaseous mixtures. High degree gas purification is possible in condensation temperatures higher than 235 K

- The purification of gaseous mixtures from VOCs in the integrated system of condensation and adsorption is especially useful when the concentration of VOCs in gases is relatively high. In this case the advantage of the two used processes increases:
  - condensation is a process of low sensitivities to the oscillation of inlet concentration of VOCs, in which the relatively low and stable concentration of VOCs in gases introduced to the adsorber can be achieved
  - adsorption of low concentration component from gases leads to the extension of adsorption cycle time and allows to limit the financial cost of apparatus.
- Numerical results, obtained by developed mathematical model, show good accuracy with experimental data
- Adsorber sorption capacity increase with decrease of adsorption temperature. On the other hand, lowering the adsorption temperature leads to decrease of the diffusional time constant, the mass transfer zone in adsorber increases and in final effect the utilization of adserber bed capacity decreases. For this reason, together with a decrease of adsorption temperature the "long" adsorber bed should be used, ie, those in which the ratio of the mass transfer zone length to the total length of the adsorber bed will be relatively small.

NOTATION

C – VOC concentration in the gas mixture , $g\ Nm^{-3}$
C_0 – VOC concentration on the inlet to the condenser, $g\ Nm^{-3}$
C_1 – VOC concentration on the outlet from the condenser, $g\ Nm^{-3}$
c – VOC concentration in the gas phase in the adsorber, $kg\ m^{-3}$
c_p – specific heat, $J\ kg^{-1}K^{-1}$
D/r_p^2 – diffusional time constant, s^{-1}
D_L – diffusion coefficient in the adsorbent bed, m^2s^{-1}
D_m – binary diffusion coefficient, m^2s^{-1}
d – condenser tube diameter, *m*
G – flow rate of gas mixture in the condenser, $kg\ s^{-1}$
G_k – flow rate of cooling medium, $kg\ s^{-1}$
G_c – condensate flow rate, $kg\ s^{-1}$
ΔH – heat of vaporisation, $J\ kg^{-1}$
k_l – effective adsorption rate constatnt $k_l=15D_e/r_p^2$, s^{-1}
l – condensator tube length, *m*
n – amount of tubes in the condenser
q – concentration in the adsorbed phase, $kg\ kg^{-1}$
r_p – microporous particle radius, *m*
T – temperature, *K*
w – velocity, $m\ s^{-1}$
z – length of adsorbent bed, *m*
α – heat transfer coefficient, $Wm^{-2}K^{-1}$
ε - porosity
η- efficiency of condensation process
τ – time, *min*
τ_{przeb} – adsorber breakthrough time, *min*
τ_{01} – time, at which the concentration at the outlet of the adsorber reaches the 1% of inlet one, *min*
τ_{05} – time, at which the concentration at the outlet of the adsorber reaches the 5% of inlet one, *min*
τ_{10} – time, at which the concentration at the outlet of the adsorber reaches the 10% of inlet one, *min*

Subscripts

0 – inlet

1 – outlet
A – refers to medium in the condenser tubes
ads – adsorption
B – refers to medium in shell space of the codenser
exp –experimental value
calc – calculated value
w – refers to wall

Superscripts

* equilibrium conditions
- mean value
n – n-th time step

REFERENCES

1. Bräutingen M., Kruse D., Ermittlung der Emissionen organischer Lösemittel in der Bundesrepublik Deutschland, *Forschungsbericht 10404116/01*, Umweltbundesamt, April 1992 (in german)
2. Malte B., Emissionen organischer Lösemittel in Österreich, *Mengeanalyse und Vermindungspotentiale*, T. U. Wien, 1993 (in german)
3. Zubilewicz M., Zmiany w branży farb i lakierów w kierunku wyrobów przyjaznych środowisku. I konferencja „Nowoczesne programy ekologiczne", *Chemik*, 12, pp. 56-60, 2000 (in polish)
4. Ruddy E. N., Carroll L. A., Selected the best VOC control strategy, *Chem. Eng. Progress*, 89, 28, 1993
5. Zesis R. F., Ibbetson C., Cryogenic condensation puts a chill on VOCs, *Pollution Engineering*, 29 (9), 56-61, 1997.
6. Bontemps A., *Heat Exchangers in Enviromental systems. Theoretical and Practical Aspects Heat Transfer in Condensation and Evaporation*, EUROTHERM 62, 17-18 Nov. (1998), 382-392
7. Gupta V. K., Verma N.; Removal of volatile organic compounds by cryogenic condensation followed by adsorption, *Chem. Eng. Sci.*, 57, 2679-2696, 2002
8. Dwivedi P., Saur V., Sharma A., Verma N., Comparative study of removal of volatile organic compounds by cryogenic condensation and adsorption by activated carbon fiber, *Separation and Purification Technology*, 39, 23-27, 2004
9. Rotkegel A., Experimental study of low temperature condensation coupled with adsorption, *Chem. and Proc. Engineering*, 29, 639-650, 2008
10. Ruthven D.M., *Principles of adsorption and adsorption processes*, John Willey and Sons, New York, 1992
11. Yang R.T., *Gas separation by adsorption processes*, Imperial College Press, London,1997
12. Rice R.G., Aproximate solution for batch, packed tube and radialflow adsorbers – comparison with experiment, *Chem.Eng.Sci.*, 37, 83, 1982
13. Liaw C.H,. Wang J.S.P,. Greenkorn R.A,. Chao K.C, Kinetics of fixed-bed adsorption: A new solution, *AIChE J*. 25, 376, 1979
14. Wakao N., Funazkri T., Effect of fluid dispersion coefficients on particle-to-fluid mass transfer coefficients in packed beds, *Chem. Eng.Sci.*, 33, 1375, 1978
15. Reid R.C., Prausnitz J.M., Sherwood T.K., *The Properties of Gases and Liquids*, McGraw-Hill, New York, 1977
16. Shampine L.F., Gordon M.K., *Solution of Ordinary Differential Equations, The Initial Value Problem*, W.H. Freeman & Co, San Francisco, 1975
17. Leonard B.P., A Stable and Accurate Convective Modelling Procedure Based on Quadratic Upstream Interpolation, *Comp.Method.Appl.Mech.Eng.*, 29, 59, 1979

THERMAL CHARACTERISTICS IN A LAYER OF CORRODING IRON POWDER

K. Murata[1,*], H. Nakahata[1], K. Araga[1] and Y. Komatsu[2]
[1]Kinki University Technical College, Kumano, Japan
[2]FJ Tech Kumano Laboratory, Kumano, Japan

ABSTRACT. This paper presents an experimental investigation of the thermal characteristics in a layer of an exothermic powder mixture that is utilized in body warmers, hot compresses, etc. The research objective is to develop a manufacturing method that enables the exothermic temperature to be controlled in order to prevent cases of low-temperature burns. The exothermic powder mixture generally comprises metal powder, catalyst powder, and vermiculite particle absorbing some saline solution. The measurements of the oxygen volume consumed by corrosion of iron powder show that the reaction velocity depends on the reaction temperature, the volume of the saline solution, and the reaction rate of the iron, in addition to the ambient oxygen density; a correlation is suggested for the reaction velocity. The variation over time of the temperature distribution and the generated heat in a layer of the exothermic powder mixture is examined using a porous film to control the oxygen volume flowing into the layer.

Keywords: *corrosion, iron powder, chemical reaction, heat transfer, mass transfer, porous media*

INTRODUCTION

It is well known that reaction heat generated from the corrosion of metal is utilized in body warmers, hot compresses, etc. These products generally comprise an exothermic mixture of metal powder, a metal chloride, a water-absorbing agent, and a catalyst; the mixture is enclosed in a porous bag or spread on a sheet coated with a therapeutic agent. This exothermic powder mixture is in great demand worldwide, especially in the medical field; therefore, safety is an essential requirement for utilizing this mixture continuously while the patient is asleep. However, many cases of low-temperature burns have occurred recently because the temperature of the exothermic powder increased to a value greater than the estimated value. Research by the authors concluded that low-temperature burns are caused by variation in the maximum temperature of the exothermic powder; thus, it is necessary to comprehend the thermo chemical characteristics of the corrosive reaction of metal and to develop the manufacturing process in order to precisely control the temperature and its variation in the exothermic powder. This paper is an experimental investigation of the thermal characteristics in a layer of the exothermic powder mixture. The reaction velocity of corrosion and the time variation in temperature and heat generation in a layer of the exothermic powder mixture are reported.

OUTLINE OF IRON CORROSION

From the perspective of electrochemistry, corrosion occurs due to the presence of many local-action short-circuited cells with a small volume of water solution on the surface of the metal, as shown in

* Corresponding author: Prof. K. Murata
Phone: + (81)-597-89-2011, Fax: + (81)-597-89-1018
E-mail address: murata@ktc.ac.jp

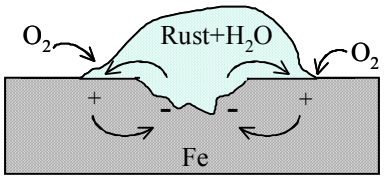

Figure 1. Oxygen concentration cells on an iron surface [1]

Figure 1. Metal ions are precipitated in the anode regions according to equation (1). This reaction is rapid in general environment.

$$Fe \rightarrow Fe^{2+} + 2e^{-} \tag{1}$$

In the general corrosion of iron, the reaction velocity in the cathode is much lower than that in the anode, so corrosion is controlled by the reaction in the cathode. The reaction in the cathode is promoted by equation (2) when oxygen is dissolved in the water solution.

$$2H^{+} + \frac{1}{2}O_2 \rightarrow H_2O - 2e^{-} \tag{2}$$

The dissolved oxygen reacts with the hydrogen atom adsorbed on the iron surface. This reaction velocity is rate-determined by the diffusion velocity of dissolved oxygen as it diffuses to the iron surface through the water solution. By adding equations (1) and (2) and using $H_2O \rightarrow H^{+}+OH^{-}$, equation (3) is obtained.

$$Fe + H_2O + \frac{1}{2}O_2 \rightarrow Fe(OH)_2 \tag{3}$$

A hydrate of ferrous oxide, FeO/nH_2O, or ferrous hydroxide, $Fe(OH)_2$, forms the barrier layer on the iron surface, through which the dissolved oxygen must diffuse to the iron surface. As it comes into contact with the dissolved oxygen on the outer surface of the barrier layer, the hydrate of ferrous oxide changes into a hydrate of ferric oxide, Fe_2O_3/nH_2O, or ferric hydroxide, $Fe(OH)_3$, as seen in equation (4). Iron rust generally comprises orange or reddish brown hydrates of ferric oxide, Fe_2O_3/nH_2O.

$$Fe(OH)_2 + \frac{1}{2}H_2O + \frac{1}{4}O_2 \rightarrow Fe(OH)_3 \tag{4}$$

By adding equations (3) and (4), equation (5) can be obtained. The reaction heat is 403kJ/mol-Fe.

$$Fe + \frac{3}{2}H_2O + \frac{3}{4}O_2 \rightarrow Fe(OH)_3 + 403kJ/mol \tag{5}$$

The reaction velocity depends on the solution film thickness, the pH and the concentration of dissolved oxygen and salt in the saline solution, in addition to the reaction temperature. However, it is known that the reaction velocity is independent of pH at pH 4-10, and reaches its maximum value at a salt concentration of 3 wt% [1].

MASS TRANSFER MODEL FOR OXYGEN IN IRON POWDER CORROSION

Figure 2 shows the distribution of the oxygen concentration in the region of the gas–liquid–solid phase reaction. In this model, it is assumed that the reaction velocity of equations (1) and (2) is significantly high, and equation (3) is rate-determined by the velocity at which the dissolved oxygen diffuses through the water solution and reaches the iron surface (in the cathode region).
The mole flux of oxygen that passes through the gas–liquid interface and reaches the iron surface, *N*, is represented by equations (6) and (7) in the gas and liquid phases, respectively.

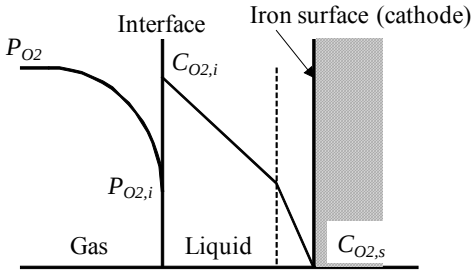

Figure 2. Concentration distribution in the reaction region

$$N = k_G\left(P_{O2} - P_{O2,i}\right) \tag{6}$$

$$N = k_L\left(C_{O2,i} - C_{O2,s}\right) \tag{7}$$

Here, k_G and k_L are the mass transfer coefficients in the gas and liquid phases, P_{O2} and $P_{O2,i}$ are the partial pressures of oxygen in the atmosphere and the gas–liquid interface, and $C_{O2,i}$ and $C_{O2,s}$ are the oxygen concentrations in the gas–liquid interface and the iron surface of the water solution, respectively. The reaction velocity of equation (2) is so high that the oxygen concentration in the iron surface, $C_{O2,s}$, is negligible (i.e., $C_{O2,s} = 0$). By equating (6) and (7), and eliminating $P_{O2,i}$ and $C_{O2,i}$ using Henry's equation for gas–liquid equilibrium, equation (8) is obtained.

$$N = \frac{1}{1/k_G + H/k_L} P_{O2} \tag{8}$$

Here, H is Henry's constant, and $P_{O2,i} = HC_{O2,i}$. Accordingly, it is considered that the apparent reaction velocity in iron corrosion is proportional to the oxygen pressure; further, the apparent velocity is rate-determined by the mass transfer resistances in the gas and liquid phases.

MEASUREMENTS OF THE APPARENT REACTION VELOCITY

Experimental apparatus and method

Figure 3 shows the apparatus used for the reaction velocity measurements. A mixture containing specified weights of iron powder, activated carbon powder, and vermiculite particle absorbing saline solution is introduced into a mini-autoclave, and then placed in a constant temperature bath after the atmosphere inside the mini-autoclave has been replaced with pure oxygen. The apparent reaction

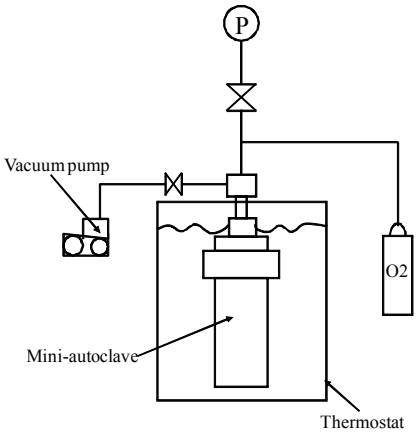

(a) Photograph (b) Schematic diagram

Figure 3. Apparatus for reaction velocity measurements

Table 1
Range of experimental parameters

Iron powder (mean powder size = 100μm)	2.0g
Activated carbon (powder size < 150μm)	0.4g
Saline solution (salinity = 3wt%)	0.5-1.1cc
Vermiculite (mean particle size = 1mm)	0.256g
Temperature	35-70degC
Initial oxygen pressure	about100kPa

velocity is obtained from the degradation of oxygen pressure in the mini-autoclave. Its volume is 47 cc. The weights of the iron powder, activated carbon powder, and vermiculite particle are 2.0, 0.4, and 0.256 g, respectively. However, the volume ratio is approximately 1:2.1:3.3 since their apparent densities are 3.08, 0.29 and 0.12 g/cm^3, respectively. The salinity in the saline solution is 3 wt%. Ranges of the experimental parameters are listed in Table 1.
The degradation rate of the oxygen pressure in the mini-autoclave is considered to be proportional to the oxygen pressure, so equation (9) is obtained.

$$\frac{dP_{O2}}{dt} = -aP_{O2} \tag{9}$$

Here, t is the elapsed time, and a is the reaction velocity constant. Integrating equation (9) leads to

$$\ln\left(\frac{P_{O2}}{P_{O2,0}}\right) = -at \quad \text{or} \quad \frac{P_{O2}}{P_{O2,0}} = \exp(-at) \tag{10}$$

The mass transfer resistance in the gas phase is low compared with that in the liquid phase when the volume of the powder mixture is small and it is surrounded by pure oxygen, as in this experiment.

Experimental results and discussion

Figure 4(a) shows an example of the experimental results, where the vertical and horizontal axes correspond to the pressure in the mini-autoclave P^* and the elapsed time t, respectively. The amount of saline solution is constant at 0.967 cc, and this value is the stoichiometric volume of water needed for the complete reaction of all the iron powder. The amount of vermiculite is determined to be 0.256 g, so the saturation rate of water content in the vermiculite particle is 80%. In the preliminary experiments, it is found that the reaction rate increases gradually with the saturation rate of water content in the vermiculite particle when the amount of saline solution is constant, but the dependence is small. The reaction temperature is 35, 40, 50, 60, and 70°C. First, the inner pressure rises drastically due to the increased supply of oxygen after evacuation; then, the inner pressure falls gradually with elapsed time.

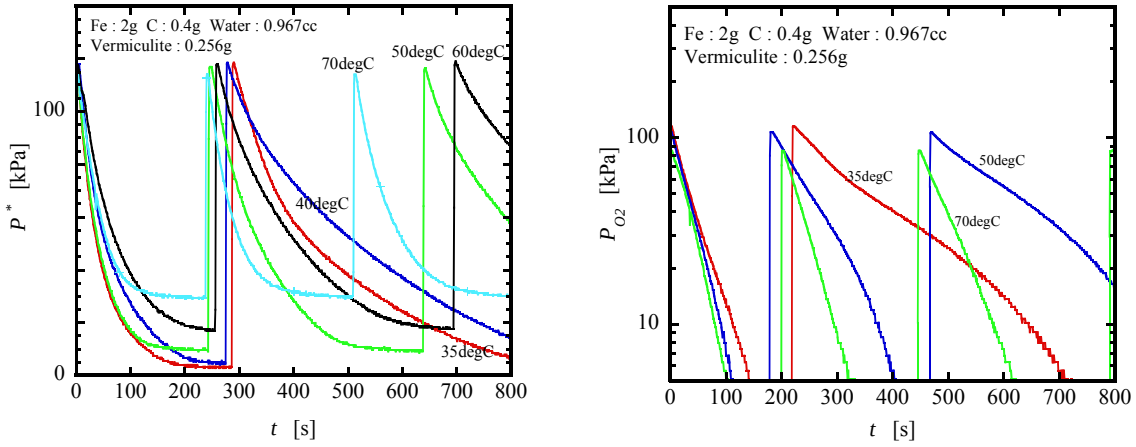

(a) The inner pressure P^* (b) The oxygen partial pressure P_{O2}

Figure 4. Variation in the inner pressure and the oxygen partial pressure with time

This degradation of the inner pressure indicates that oxygen is consumed due to iron corrosion. With time, the inner pressure approaches a constant non-zero value. This asymptotic value seems to correspond to the saturation vapor pressure of water since it increases with temperature. In order to examine the effect of the reaction rate of iron powder on the reaction velocity, oxygen is newly supplied several times after all the oxygen in the mini-autoclave has been consumed. Figure 4(b) shows the variation in the oxygen partial pressures at 35, 50, and 70°C; these partial pressures are obtained by subtracting the saturation steam pressure from the inner pressure in the mini-autoclave. The degradation rate of oxygen partial pressure corresponds to the reaction velocity constant, and the number of times oxygen is newly supplied corresponds to the reaction rate of the iron powder. Accordingly, it is found that the reaction velocity constant increases with temperature and decreases with the reaction rate of iron powder.

Figure 5 (a) and (b) indicate the variation in the reaction velocity constant with reaction temperature T and with the non-dimensional quantity of water absorbed in vermiculite particle Y_{W0}, respectively. Here, Y_{w0} is the initial volume of water absorbed in the vermiculite particle divided by the stoichiometric volume of water needed for the complete reaction of all iron powder. In addition, X is the reaction rate of the iron powder and represents the ratio of the reacted iron mass to the total iron mass. The reaction velocity constant a increases with the reaction temperature T, although the dependence is small. The reaction velocity constant a increases with Y_{w0}, i.e., water volume, but decreases when Y_{w0} is over 1.0. This can be explained as follows. The reaction velocity increases with the wet area of the iron surface, i.e., with water volume. However, the liquid film on the iron surface becomes thick and the mass transfer resistance also increases with water volume. Reaction velocity data are often plotted against $1/T$ to yield the well-known Arrhenius plot; however, it is not appropriate here because the rate-determining factor in the corrosion reaction, which is the mass transfer resistance through the liquid film on the iron surface, is different from that in general chemical reactions.

Figure 6 shows variations in the reaction velocity constant a with the rate of unreacted iron $1 - X$. The reaction velocity constant decreases rapidly as the reaction progresses. This is because the mass transfer coefficient in the liquid phase decreases due to the diffusion barrier layer of ferrous hydroxide, $Fe(OH)_2$, formed by the corrosion reaction. In addition, this layer is also considered to be one of the reasons why the mass transfer resistance in the gas phase increases, due to aggregation of the iron powder with the progress of the corrosion reaction. The reaction velocity constant data were correlated with equation (11) as a function of the volume of saline solution Y_{w0}, the reaction temperature T, and the reaction rate of iron powder X.

$$a = 9.7 \times 10^{-42} Y_{w0}^{3.48} T^{15.7} (1 - X)^{14.6} \tag{11}$$

The solid lines indicate equation (11) in Figure 6. If the reaction velocity r is defined as the reacted iron

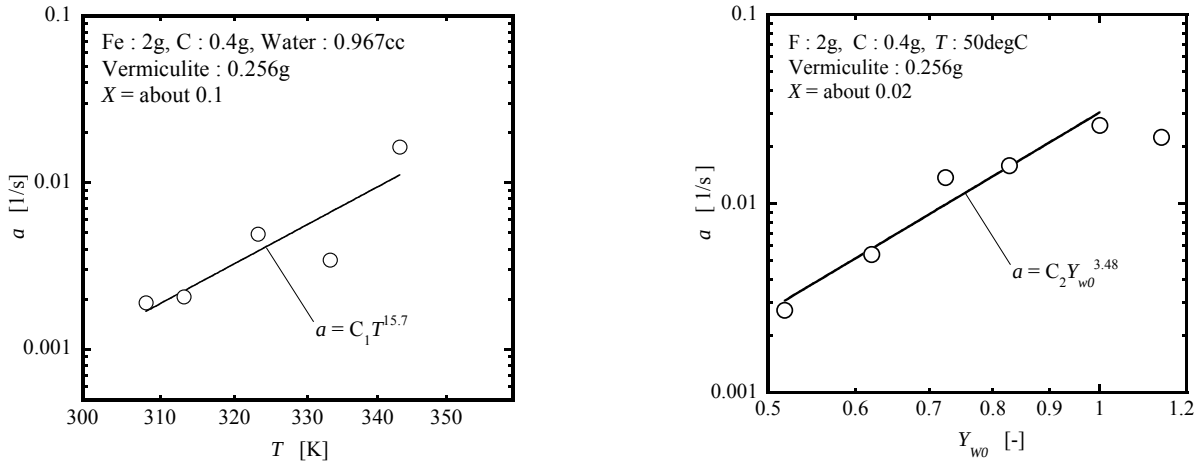

(a) Variation with the reaction temperature T (b) Variation with the water volume Y_{w0}

Figure 5. Variation in the reaction velocity constant a

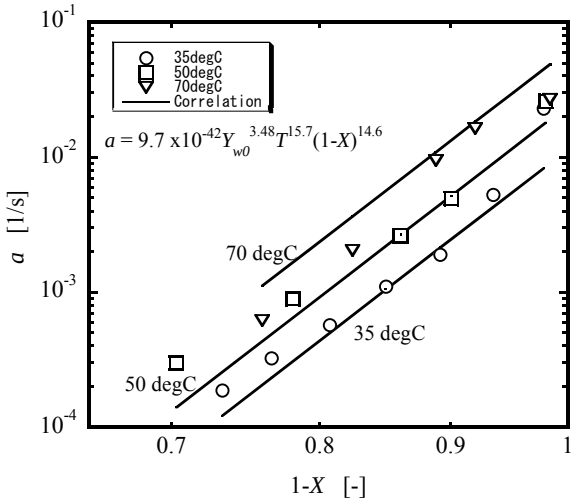

Figure 6. Variation in the reaction velocity constant a with the reaction rate of iron powder X

per unit volume of the powder mixture layer per second, it is represented by equation (12).

$$r = \frac{4}{3} a \frac{V_{aut}}{V_{lay}} C_{O2} = 9.6 \times 10^{-41} Y_{w0}{}^{3.48} T^{15.7} (1 - X)^{14.6} C_{O2} \qquad [\frac{kmol}{m^3 s}] \tag{12}$$

Here, V_{aut} is the volume of the mini-autoclave (=47cc), V_{lay} is the volume of the powder mixture used in this experiment (=6.3cc), and C_{O2} is the molar density of oxygen. This equation for reaction velocity will be used for thermal analysis in a layer of the exothermic powder mixture.

THERMAL CHARACTERISTICS IN A LAYER OF THE POWDER MIXTURE

Experimental apparatus and prodedure

Figure 7 (a) and (b) show a schematic diagram of the experimental apparatus and a photograph of the experimental chamber. The experimental apparatus comprises a 100 mm × 100 mm × 30 mm rectangular vessel made of polycarbonate resin. A copper plate, which is kept at a constant temperature (approximately 34°C) by cooling water, is installed at the bottom of the vessel. A heat flux sensor sheet (0.4 mm in thickness) is adhered to the cooling plate to measure the dissipated heat. A small amount of silicone compound is applied between the sensor sheet and the cooling plate so that the contact thermal resistance may be suppressed. The powder mixture is packed on the sensor sheet to a depth of 10 mm; this mixture is composed of 31.5 g of iron powder, 6.2 g of activated carbon powder, and 4.0 g of vermiculite particle absorbing 15.2 cc of saline solution (the salinity is 3 wt%). The volume of saline solution and vermiculite particle is determined so that Y_{w0} is equal to 1 and the saturation rate of water content in the vermiculite particle is 80%. The temperature distribution in a layer of the powder mixture is measured by C-A thermocouples (ϕ0.5 mm OD). The locations for temperature measurements are (measured in terms of the height from the surface of the sensor sheet) 0 mm (i.e., on the surface), 3 mm, 6 mm, 9 mm, and the inside of the sensor sheet, and the temperatures at these locations are denoted by T_1, T_2, T_3, T_4, and T_0, respectively. The experimental apparatus is installed in an acrylic chamber, which is indicated in Figure 7(b), and is operated from outside with vinyl gloves. The experimental procedure is as follows.

First, some activated carbon powder and vermiculite particle are dried at 100°C in an electric drier for 2 h and allowed to cool to the ambient temperature. This vermiculite particle absorbing a specified volume of saline solution is mixed sufficiently with the activated carbon powder. Second, the iron powder and the mixture of the activated carbon powder and the vermiculite particle are placed in the experimental chamber; then, the door is closed. Enough nitrogen gas is supplied into the chamber from the upper inlet so that the air inside the chamber is completely replaced with nitrogen. At the same time, cooling water is supplied to the cooling plate to keep it at a specified temperature (approximately

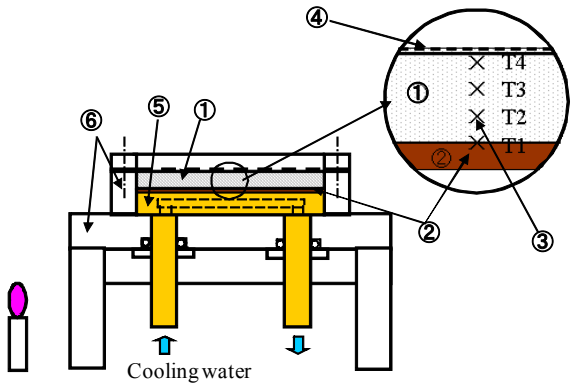

1. Exothermic powder mixture 2. Heat flux sensor
3. Thermocouples 4. Porous film 5. Cooling plate
6. Polycarbonate materials

(a) Schematic diagram of the experimental apparatus

(b) Photograph of the experimental chamber

Figure 7. Experimental equipment

34°C). Next, the iron powder is sufficiently mixed with the mixture of vermiculite and activated carbon in the chamber to produce the powder mixture for the experiment. The powder mixture is packed on the heat flux sensor sheet to a depth of 10 mm, and the thermocouples T_2, T_3, and T_4 are placed in the specified positions inside the powder mixture layer. Finally, the door of the chamber is opened so that the chamber inside may be quickly replaced with air. The temperature distribution in the powder mixture layer and the heat flux dissipated to the cooling plate are measured over a time span of a few hours. Some experiments are conducted with a porous film fixed on the powder mixture layer to control the oxygen volume flowing into the layer. In the other experiments without a porous film, a piece of tissue paper is placed on the powder mixture layer to avoid the effect of air currents.

Experimental results and discussion

Figure 8 (a) and (b) are examples of the experimental result and show the variation over time of the temperatures T_0, T_1, T_2, T_3, and T_4 and the heat flux dissipated to the cooling plate q. Here, T_5 is the ambient temperature inside the experimental chamber, and T_0 is the inside temperature of the sensor sheet, which is nearly constant. First, the experimental result without a porous film (Figure 7(a)) is explained, where the volume of oxygen flowing into the exothermic powder mixture is not controlled. The abrupt increase in the temperatures T_2, T_3, and T_4 at the elapsed time t ~100 s indicates that these thermocouples are placed in the specified positions inside the powder mixture layer, so these temperature data make sense after this time. A small increase in the heat flux q is recognized at t ~180 s, although the door of the chamber is closed. This shows that the corrosion reaction begins gradually, with a small volume of oxygen remaining in the chamber, immediately after mixing the iron powder with the activated carbon and vermiculite particle. The temperatures T_2, T_3, T_4, and the heat flux q again increase drastically at t ~350 s when the door of the chamber is opened, but decrease rapidly after reaching the maximum at t ~550 s. The maximum T_2 is approximately 48°C. These variations show that the reaction occurs abruptly due to the large amount of oxygen present, but the reaction velocity decreases rapidly with the reaction rate of the iron powder. Thereafter, the temperatures T_2, T_3, and T_4 are lower than T_1. This occurs because the ambient temperature, T_5, is lower than the surface temperature of the cooling plate, so more heat is dissipated from the upper surface of the powder mixture layer. In addition, it is observed that some steam flows out to the tissue paper placed on the powder mixture layer.

Next, the experimental result with a porous film fixed on the powder mixture layer (Figure 7(b)) is explained, where the volume of oxygen flowing into the exothermic powder mixture is controlled. The abrupt increase in the temperatures T_2, T_3, and T_4 at the elapsed time t ~200 s indicates that the

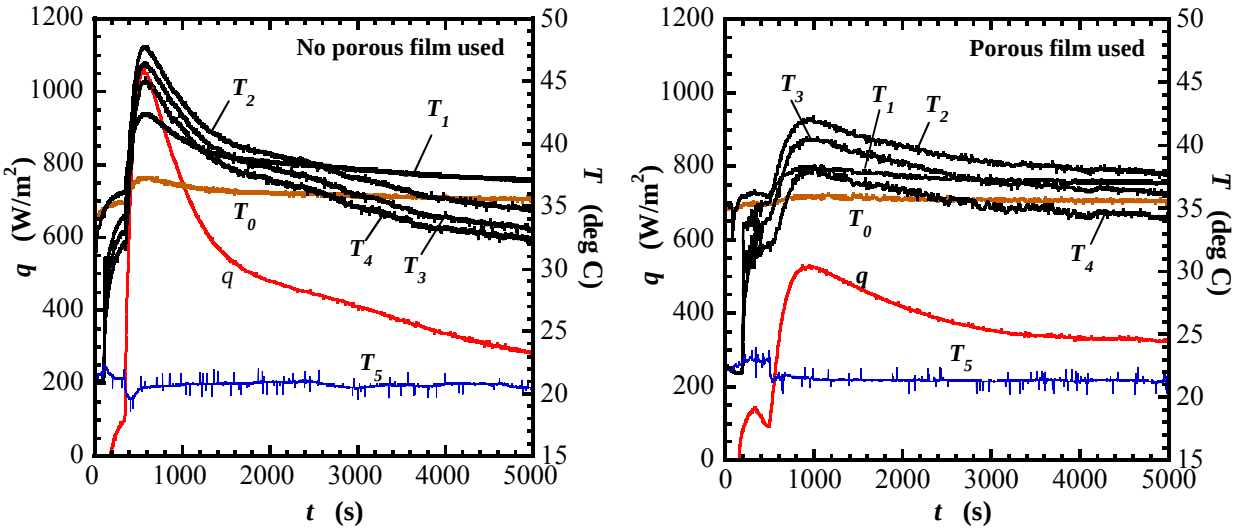

(a) Without a porous film (b) With a porous film

Figure 8. Experimental results in a layer of exothermic powder mixture

thermocouples are placed in the specified positions inside the powder mixture layer, so these temperature data make sense after this time. The small increase and decrease in the heat flux q at t ~150 to 500 s shows that the corrosion reaction begins gradually with the oxygen remaining in the chamber, but the oxygen inside the layer of powder mixture is exhausted since the oxygen volume flowing into the powder layer is suppressed by the porous film. The temperatures T_2, T_3, and T_4 and the heat flux q again increase rapidly at t ~500 s when the door is opened, reach the maximum at t ~900 s, and decrease gradually thereafter. Although the variation in the temperature and heat flux observed in Figure 7(b) is similar to that observed in Figure 7(a), the variation in the latter case is more gradual. The maximum of the temperature and heat flux is also lower, which shows that the oxygen volume flowing into the powder layer is suppressed by the porous film. The steam and heat dissipated from the upper surface also decrease.

CONCLUDING REMARKS

1. Thermal characteristics in the exothermic powder mixture composed of iron, activated carbon, and vermiculite particle absorbing saline solution were examined experimentally.
2. The reaction velocity in the exothermic powder mixture is particularly dependent on the partial pressure of oxygen (or the molar density of oxygen) and the reaction rate of iron, in addition to the volume of saline solution and the reaction temperature. A correlation for the reaction velocity is proposed as a function of these parameters. In a future study, a numerical analysis using this correlation will be conducted on flow and heat transfer in a layer of the exothermic powder mixture.
3. It is important to adjust the volume of supplied oxygen for temperature control in a layer of the exothermic powder mixture.

ACKNOWLEDGMENTS

The authors would like to express their gratitude for the considerable support of this research from Minoru Kan-no, President of Kinki University Technical College.

REFERENCES

1. Uhlig, H. H., *Corrosion and Corrosion Control*, John Wiley & Sons, Inc., New York, 1983.

EXPERIMENTAL STUDY OF DRYING FRESH PEPPER BERRIES IN A SOLAR DRYER

A. Vakhguelt*, C. J. Chong, T. B. Luk
Swinburne University of Technology, Sarawak Campus, Kuching, 93550 Sarawak, Malaysia

ABSTRACT. The Sarawak State of Malaysia is one of the main suppliers of white and black pepper to the world. Rural areas of the state do not always have a proper energy supply especially in the farming fields. The traditional method of drying pepper employed by farmers is outdoor drying, which is not effective especially in this area where the yearly rainfall level is about 4 m. The aim of this study was to develop a mobile drying device which can be easily relocated where the harvest is collected. The authors of this paper have proposed drying of the pepper using a natural-convection based solar dryer. At the initial stage a series of experiments was conducted to study the drying characteristics of fresh pepper berries with the aim of finding the optimal conditions for obtaining a high quality product as well as assessing productivity of the proposed solar dryer. The data obtained from experimental study has shown that the highest temperature of a drying process should not exceed 55° C for quality final product. At the same time it was found that the higher the temperature achieved in the dryer, the faster the drying happened. The drying characteristics obtained were used to design and study a solar drying device to achieve optimal conditions for the process of drying pepper berries. The experiments have shown the advantage of using the proposed solar dryer with natural convection driven process compared to traditional outdoor drying. This device reduces the time of drying and improves the quality of product as well as gives the opportunity for continuous process regardless of weather conditions. The limitation of the moisture content of the final product depends on external humidity of the surrounding air. The device does not use any external source of energy and can be used in any location.

Keywords: *pepper berries, drying, solar dryer, temperature, airflow*

INTRODUCTION

The drying of the agricultural products is a very important problem faced by many industries. It is an especially big problem for tropical countries with intensive rainfall level. During the rainy season with very high humidity levels, the drying of agricultural products becomes a major problem. Difficulty also comes when these agricultural products are located far away from the urban areas usually without electricity supply. This paper addresses these problems by investigating an alternative way to traditional drying of the white and black pepper, that is by introducing the solar dryer which uses the natural convection concept (see Figures 1 and 2). The main idea is to use a drying chamber with a transparent top surface for the penetration of the sun rays connected to a chimney of flexible height. The air flow through this chamber due to the pressure difference at the bottom and top end of the chimney is meant to remove the moisture from inside the pepper berries during the drying process. By varying the height of the chimney we may change the airflow rate which also helps to maintain the favourable temperature inside the solar drying chamber during high temperature time due to high solar radiation. Change of the height of chimney may also help to

* Corresponding author: Prof. A. Vakhguelt
Phone: + (60)-82-260665, Fax: + (60)-82-423594
E-mail address: avakhguelt@swinburne.edu.my

maintain a certain level of the moisture content in the chamber at different times of the drying process.

Figure 1. Drying of white pepper by spreading evenly on mats [1].

The study of the solar dryer operation was carried out initially by studying the drying characteristics of the fresh pepper berries in a lab scale dryer at the different temperatures. It was done to find the optimal regime of drying to address in the drying chamber of the proposed solar dryer. The next step of this study was to study airflow rate variations as a function of the height of the chimney and its diameter. Experimental investigations were carried out in the conditions when air was still. In this case the airflow rate is minimal in contrast to the case when we have windy conditions and the airflow rate will be increased through the chimney. Some of the experimental results are presented below.

EXPERIMENTAL STUDY OF THE FRESH PEPPER BERRIES DRYING

In order to study the drying characteristics of pepper berries, drying experiments partially based on investigation method adopted by A. Lopez et al. [2] were conducted to find out the effect of air temperature on the drying rate. To find out the drying characteristics of pepper berries, a number of the experiments were carried out at different temperatures using a lab scale dryer. During drying the weight of the berries portion was monitored by sensible scale to observe the change of weight of pepper berries with respect to time. The relationship between the moisture content of pepper berries with time was monitored at six different air temperature points which ranged from 30^{o}C to 55^{o}C at 5^{o}C intervals. Pepper berries were left in a gravity convection oven at constant temperatures. Weight loss was measured using load cell and was recorded at 30 minute interval. The study was carried out with pepper berries grown in Sarawak [1]. Samples of pepper brought in were divided into smaller samples for experiments and each sample was sealed in a plastic package and stored in the fridge at low temperature to prevent changing of initial moisture content. Before starting each package of pepper used was weighed prior to each drying experiment.

Each drying experiment was running until three constant readings of the weight of pepper berries were obtained consecutively. After each experiment, the moisture content of the dried pepper berries was determined using the AOAC Official Method 935.29 at temperature between 100-150^{o}C [11]. From literature [3-10], it was expected that the weight of pepper berries reduced exponentially with respect to time. As the air temperature increased, the moisture content lost faster during the

initial period of drying. Obtained results of the drying of the fresh pepper berries are presented in Figure 2. We can see that weight of the berries portion during real drying is reduced nearly exponentially with some variations which could be considered as error of the measurements. From these experiments the optimal regime of the pepper berries was found and used for design of the solar dryer. At initial stage of the solar dryer design, a number of experiments were carried out to find appropriate variation of the airflow rate as the function of height of a chimney.

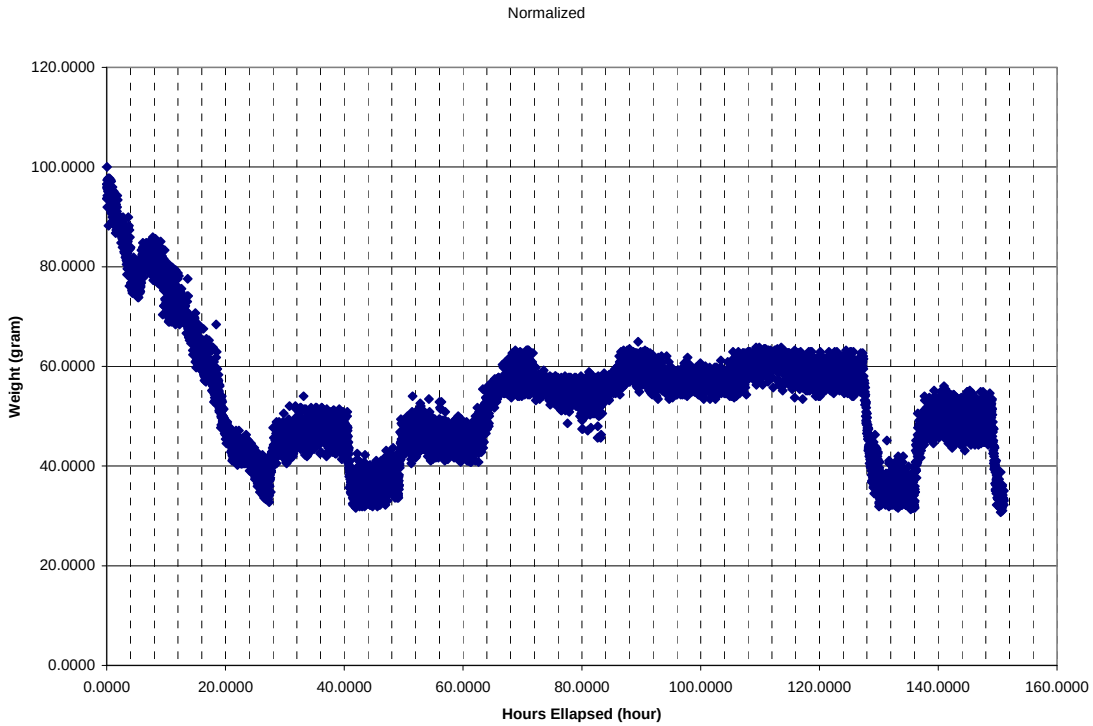

Figure 2. Drying of the pepper berries in the gravity convection oven at $50^{\circ}C$.

EXPERIMENTAL STUDY OF AIRFLOW CONTROL

It is known that in the solar dryer, the airflow is generated due to pressure difference at the lower and upper levels of the chimney. Airflow generated by this type of device is very important especially for the areas with the high relative humidity and heavy rainfall [12]. This airflow will be able to transport away excess moisture content which is delivered from the berries by diffusion during the drying process. Buoyancy also helps to increase airflow in addition to pressure difference during day time operation of the solar dryer in the transparent drying compartment. For the dryer equipped with a chimney, stack induced ventilation can be achieved. Our system utilizes the atmospheric pressure difference as well as the variation in air density across the height at different openings in vertical slope due to temperature difference. For a second part contribution we can consider that a vertical air velocity is approximately proportional to the air temperature rise in the heat collector and the stack height [13]. Using Boussinesq approximation we may expect that maximum free convection current could be:

$$V_{tower,\max} = \sqrt{2gH_{tower}\frac{\Delta T}{T_0}} \tag{1}$$

Here ΔT is temperature difference between ambient and the collector outlet and H_{tower} is the height of the chimney. Using this formula we are able to estimate airflow rate through the system which consists of the chimney and the drying compartment [14].

Conceptual Framework

The flow rate through the drying compartment can be changed by adjusting the pressure difference between two ends of the chimney or adjusting its height. If the pressure head loss along the chimney can be neglected, this is applied to the large diameters; infinite height may lead to infinite boost of airflow in the chimney and also the drying compartment. The variation of chimney height can be achieved by multiple-section telescopic constructions. Each section shall be air-tight sealed to prevent reduction of ultimate pressure difference due to leakage at any connecting joints; yet, at the same time, the chimney should maintain the flexibility of the telescoping action.

To check how temperature can affect the mass flow rate through drying compartment, we can monitor the temperatures at three points: at the inlet section of the chimney; at the outlet section of the chimney; and, at the surface of the mesh where the raw bits are to be dried. The temperature measurements at the top of the chimney will provide effective ambient operating temperature to the control system; and it is to be compared to the measurement obtainable at the bottom of the chimney. In this case, the driving force due to free convection in the chimney can be approximately measured, where from equation 1 the higher the differences, the higher the flow rates. When the drying compartment is properly sealed with only one inlet at the far end from the chimney, then mass flow rate can be predicted by relating the cross-sectional area of the drying compartment to the cross-sectional area of the chimney; provided it is longitudinal equal-width along the flow path.

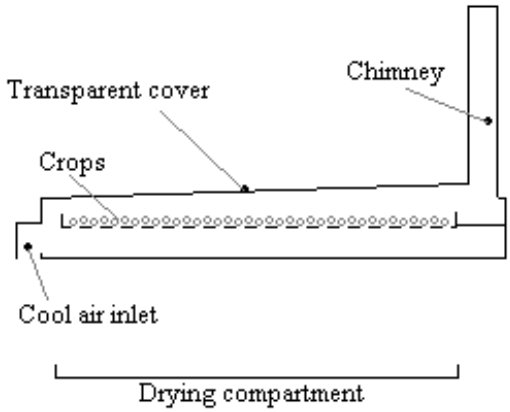

Figure 3. Proposed solar dryer mechanical outline.

Monitoring the temperatures at the different points gives the opportunity to control the height of the chimney which will be changed to create optimal airflow rate. This circumstance enables the controller to make decisions based on real-time difference in temperature captured, since drying force is the fraction of the temperature difference between both ends of the chimney. We know that the mass flow rate will have direct influence on the temperature profile inside the drying compartment. To achieve the shortest possible drying period while maintaining the quality of the final product, a stable supply of heat flux and controlling the efficiency of moisture transportation is extremely crucial. Fluctuation in heat flux would bring a negative effect to the transportation of the moisture content from inside to the surface of the crops. High flow rate may lead to case hardening especially for those crops which have high sugar content. The system to monitor the temperatures at three points is managed by a microcontroller based single board computer in which high resolution temperature sensors are utilized. The microcontroller compares the temperature values and makes the decision whether to lower down or pull up the chimney to obtain the most suitable temperature and flow rate.

Proposed outline of the solar dryer

The proposed solar dryer is based on direct heating mode where the raw bits of the agriculture product to be dried are placed inside the dryer facing upward directly to the sunlight (Figure 3). The upper part of the drying compartment is transparent, so it allows the sun radiation to access the internal area of the dryer and heat up both the air and the crop. The chimney is made of uPVC pipe

to make it light and strong with reasonably good thermal insulation properties. Each section of the pipe is sealed with PVC flexible pipe connecting two adjacent parts to prevent air leakage and heat losses. The "telescopic chimney" is supported by two supporting poles to provide a vertical arrangement as well as the mechanism for height adjustment (Figure 4a). The mechanism is connected to motor by tension-run driving system which converts rotational motion to linear motion. To protect the sensors and the drying compartment from direct contact with the water due to rain on the top of chimney, a cap is installed.

Free convection operation and control mechanism

As mentioned above the basic idea of the solar dryer operation is based on the necessity to move away the high moisture containing air from the drying compartment providing optimal conditions to deliver moist from inside of the pepper berries to their surface. The higher temperature in the drying compartment and the higher air velocity increases the diffusion and removal of moisture from the berries. To control the air velocity the mechanism of chimney height change is introduced. This also helps to control the air velocity during weather changes as well as to address it to the night conditions. In our case automation of the control is introduced.

The control system primarily depends on the readings from three temperature sensors (Figure 4b) and it is also assisted by two limit switches (Figure 4a) as well as preset flow rate and temperature setting to position the height of the chimney periodically. Temperature sensors placed at three different locations are used to observe the drying conditions inside the solar dryer. The control architecture is graphically illustrated in the block diagram shown in Figure 5.

Let the reading of temperature sensor 1 be represented by TS1, Limit switch 1 be LS1 and so on; and preset temperature and flow rate be PT and PF respectively. Note that PF means the maximum range of temperature difference between the projected TS2 and TS3. The control logic is illustrated with the following conditions:

- When TS2 <= TS3, Chimney rise to maximum height (until triggering the LS1)
- When (TS2 – TS3) > PF, Chimney retract and vice versa (until touching either LS1 or LS2)
- When TS1 > PT, Chimney rise to increase airflow

In normal conditions, TS2 should have higher value than the TS3; yet if it is reversed and the resistance of the chimney is low enough (at minimum height) reverse flow may lock up the proper transportation of moist air from the crops and thus slow down the drying process. On the other hand, when the value difference between the TS2 and TS3 is too far from PF, it would mean the airflow rate is far beyond the acceptable flow rate and could result in case hardening. In this case, lowering down the chimney would lead to a drop in the air flow and vice versa.

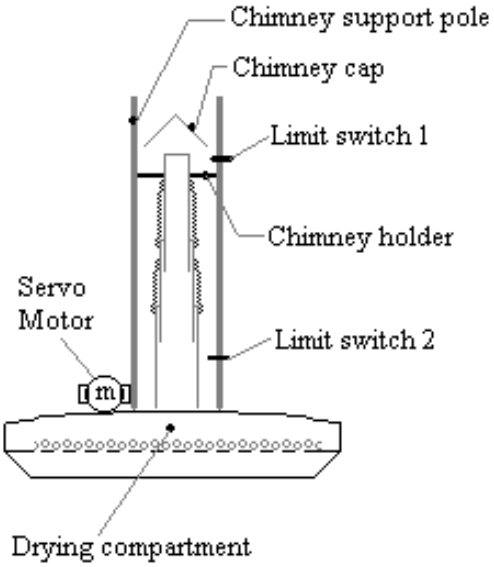

Figure 4a. Mechanical and electrical feedback system.

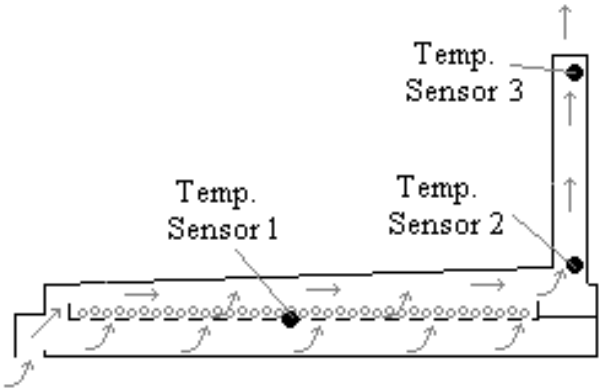

Figure 4b. Placement of the feedback sensors

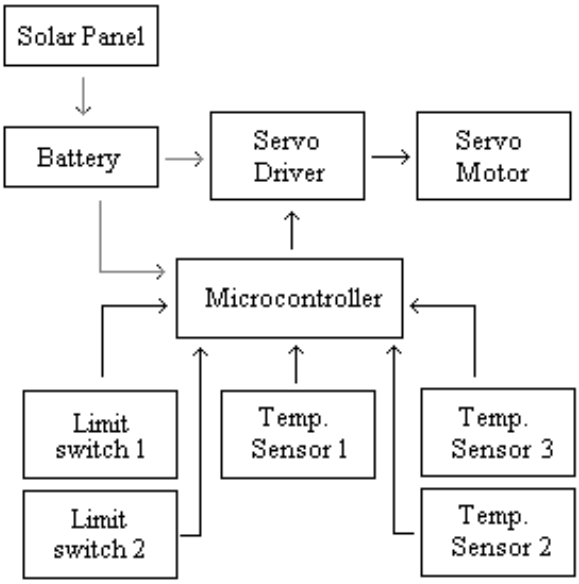

Figure 5. Mass flow control System Block Diagram

The last case explains that the surface temperature TS1 should be controlled by adjusting the flow rate as it indicates the drying temperature which will directly influence the
drying rate of the crops. The proposed outline will enable the alternative flow path above the tray. By boosting the horizontal flow, this will induce negative pressure to encourage bottom-up mass flow from the tray to decrease the heating temperature to desired level.
To cater for head loss due to changes in air properties and aging of pipe wall in dynamic environment over time, TS1 will be monitored against the time rather than solely comparing to PT. In conditions when the raising of chimney causes the TS1 to be elevated too fast, it is necessary to put an exception instruction to lower down the chimney until TS1 is stabilized. Although the surface temperature might still be higher than PT, yet optimum mass flow rate can be reached to achieve least possible overheat range and this will lead to warning being signalled to the operator.

CONCLUSION

The proposed solar dryer provides an efficient tool for drying any agricultural products in the fast changing environment of the tropical climate. This solar dryer could be used in any rural location as it does not need to have a power supply and can be operated as a mobile unit. Automation of this solar dryer helps to increase its efficiency for the crops drying in dynamic weather conditions as it can maintain the quality and boost the product throughput due to a consistent drying environment as

well as a shorter period of drying time. The system also utilizes active control over a passive system and thus makes room for utilization of green energy (solar panel) in an active control structure.

REFERENCES

1 A.D. Paulus, G. Megir and L. Eng, "Pepper Technology Package.", Department of Agricultural Sarawak, 24 – 25.

2 A. Lopez, M.T. Piqué, J. Boatella, A. Ferrán, J. Garcia and A. Romero, "Drying Characteristics of the Hazelnut.", *Drying Technology*, 16(3-5), 627-649 (1998).

3 M.C. Garau, S. Simal, A. Femenia and C. Rosselló, "Drying of Orange Skin: Drying Kinetics modeling and Functional Properties.", *Journal of Food Engineering* 75 (2006) 288-295.

4 R.P.F. Guiné and R.M.C. Fernandes, "Analysis of the Drying Kinetics of Chestnuts.", *Journal of Food Engineering* 76 (2006) 460-467.

5 A. Kaya, O. Aydin, C. Demirtas and M. Akgün, "An Experimental Study on the Drying Kinetics of Quince.", *Desalination* 212 (2007) 328-343.

6 A. Kaya, O. Aydin and C. Demirtas, "Drying Kinetics of Red Delicious Apple.", *Biosystems Engineering* (2007) 96(4), 517-524, doi:10.1016/j.biosystemseng.2006.12.009 PH – Postharvest Technology.

7 Nourhène, B., Mohammed, K. and Nabil K., "Experimental and Mathematical Investigations of Convective Solar Drying of Four Varieties of Olive Leaves.", *Food and Bioproducts Processing* (2008), doi:10.1016/j.fbp.2007.10.001

8 C.T. Kiranoudis, E. Tsami, Z.B. Maroulis and D. Marinos-Kouris, "Drying Kinetics of Some Fruits.", *Drying Technology,* 15(5), 1399-1418 (1997).

9 T. Gunhan, V. Demir, E. Hancioglu and A. Hepbasli, "Mathematical Modelling of Drying of Bay Leaves." *Energy Conservations and Management* 46(2005) 1667 – 1679.

10 V. Demir, T.Gunhan and A.K. Yagcioglu, "Mathematical Modelling of Convection Drying of Green Table Olives.", *Biosystems Engineering* (2007)98, 47–53.

11 Official Methods of Analysis of AOAC International, 16th Edition, 4th Revision, 1998.

12 Turhan Koyuncu, (2005), "An Investigation on the Performance Improvement of Greenhouse-type Agricultural Dryers", Renewable Energy, 31, 2006, pp.1055-1071.

13 Jörg Schlaich, Rudolf Bergermann, Wolfgang Schiel and Gerhard Weinrebe (2005), "Design of Commercial Solar Updraft Tower Systems – Utilization of Solar Induced Convective Flows for Power Generation", In Journal of Solar Energy Engineering 127 (1), pp.117-124.

14 Unger, J. (1988). Konvektionsströmungen, Teubner, Stuttgart.

EXPERIMENTAL INVESTIGATION OF NUCLEATE POOL BOILING HEAT TRANSFER FROM SMALL HORIZONTAL TUBE BUNDLES

J.T. Cieslinski [1*], K. Krasowski [2]
[1] Gdansk University of Technology, Narutowicza 11/12, 80952 Gdansk, Poland
[2] Elblag Power Plant, Elektryczna 20a, 82300 Elblag, Poland

ABSTRACT. Measurements of boiling heat transfer coefficients in water, methanol and refrigerant R141b are reported for the bundles of smooth tubes that represent a portion of a flooded-type evaporator. Each bundle contained 19 instrumented, electrically heated tubes in a staggered triangular-pitch layout. The effect of heat flux density, tube pitch and operating pressure is studied in the paper. Bundle factor and bundle effect are discussed as well. A correlation for prediction a bundle average heat transfer coefficient is proposed.

Keywords: *boiling heat transfer, tube bundle, flooded-type evaporator*

NOMENCLATURE

D - diameter [m],
g - acceleration due to gravity [m/s^2],
I - current [A],
L – active tube length [m],
p - pressure [N/m^2],
q - heat flux density [W/m^2],
r - latent heat of vaporization [J/kg],
s - pitch [m],
t – temperature [°],
U – voltage drop [V]

Greek symbols
$\overline{\alpha}$ - average heat transfer coefficient [W/m^{2}K],
λ - thermal conductivity [W/mK],
ρ - density [kg/m^3],
μ - viscosity [Ns/m^2],
σ - surface tension [N/m].

Subscripts
cr - critical,
i – inner,
l – liquid,
o – outer,
v - vapour

INTRODUCTION

Flooded-type evaporators are widely applied in industrial heat exchange systems. Numerous studies were performed to understand bundle boiling heat transfer. In particular, the effect of tube position within a bundle, operating conditions, bundle layouts and tube spacing was examined [1-4]. Several correlations for the prediction of heat transfer coefficient of individual tube as well as tube bundle were proposed [5-8].

Marto and Anderson [2] made measurements of boiling heat transfer coefficients in R-113 for a bundle of 15 electrically heated, smooth copper tubes arranged in an equilateral triangular pitch with s/D=2. It has been reported that lower tubes within a bundle can significantly increase

* Corresponding author: Prof. Janusz T. Cieslinski
Phone: + (48)-58-3471622, Fax: + (48)-58-3471807
E-mail address: jcieslin@pg.gda.pl

nucleate boiling heat transfer from the upper tubes at low heat fluxes. This is referred to as *bundle effect*.

Qiu and Liu [4] investigated experimentally the effects of tube spacing, positions of tubes and test pressures on the boiling heat transfer of water in restricted spaces of the compact staggered bundles consisting of smooth horizontal tubes. A compact staggered bundle with a tube spacing of a 0.3 mm displayed a maximum heat transfer enhancement in the range of the low and moderate heat fluxes. For boiling in compact bundles, the position of the heated tubes within the bundle has some effect on the heat transfer for the tube spacings of 1.0 and 0.5 mm. However, the position of the heated tubes has hardly any effect on the heat transfer for a tube spacing of 0.3 mm. For the case where the tube spacing is equal to or larger than 1.0 mm, the effect of the pressure on the heat transfer enhancement was insignificant.

Gupta et al. [6] conducted experiments with water boiling at atmospheric pressure on a smooth stainless steel tube arrangements: two or three tubes placed one above the other at different pitch distances (s/d=1.5-6.0) of commercial finish having a 19.05 mm outside diameter heated directly by means of a high alternating current. Heat transfer characteristics of the lowermost tubes in a tube bundle have been found to be independent of the presence of the bundle. Besides, the maximum enhancement of the order of 100% was observed for the top tube of a 1x3 tube bundle under low heat flux conditions.

Kumar et al. [7] studied boiling of water at sub-atmospheric pressure on twin tube arrangement. Two copper, electrically heated, tubes having 32 mm outer diameter were placed one over another. Negligible influence of the tube materials on heat transfer coefficients was reported.

Leong and Cornwell [9] performed experimental study with large, 241-tube arrangement that simulated slice of the reboiler. Experiments have been conducted with refrigerant R113 at atmospheric pressure. The local heat transfer coefficients for bottom row tubes in the tube bundle were almost the same as for a single tube, whilst for the top row tubes were considerably higher.

Gupta [10] investigated nucleate boiling heat transfer in an electrically heated 5 x 3 in line horizontal tube bundle under pool and low cross-flow conditions of saturated water near atmospheric pressure. For configuration tested as well as for single column tube bundles heat transfer coefficients were nearly the same as that on a single tube. The maximum heat transfer coefficient on top tube of central column was about seven times higher than that on the bottom tube at the same heat flux of 23 kW/m^2 under pool boiling conditions.

Two-phase interactions that occur in tube bundles during boiling are very complex and can vary with heat flux density, operating pressure, fluid properties, tube surface, pool height and bundle layout. It is a known fact that heat transfer coefficients for a tube bundle are usually larger than those for nucleate pool boiling on a single tube under the same conditions. This is referred to as *bundle factor*.

In [11] it is pointed out that the boiling mechanism in a flooded refrigerant evaporator is different from that which occurs in a kettle reboiler used in the process industry. As a result it is difficult to use information from one type of bundle and fluid combination, and apply it to another situation.

The purpose of the present paper is to provide a comprehensive nucleate boiling database for water, methanol and refrigerant R141b from a small bundle of smooth tubes that represents a portion of a flooded-type evaporator. The effect of heat flux density, tube pitch and operating pressure is studied in the paper. Bundle factor and bundle effect are discussed as well. A correlation for prediction of a bundle average heat transfer coefficient is proposed.

EXPERIMENTAL APPARATUS AND PROCEDURE

Figure 1 shows a schematic diagram of the experimental apparatus. Essentially, it is consisted of a cylindrical test vessel made of stainless steel having a diameter and length of 0.3 m, a horizontal smooth tube bundle, a condenser, a measuring system, a visualization system and an electric power supply system. The vessel is equipped with three inspection windows for direct observation and visualization of the boiling process. Vapour from the test vessel flows through a stainless steel tube having an inside diameter 50 mm and gets to the condenser, installed above the vessel. The flowrate of cooling water through the condenser was regulated by manual valve and measured by a flowmeter. Test liquid entering the vessel is at the saturated state and its temperature is controlled by a heating element placed in the preheater.

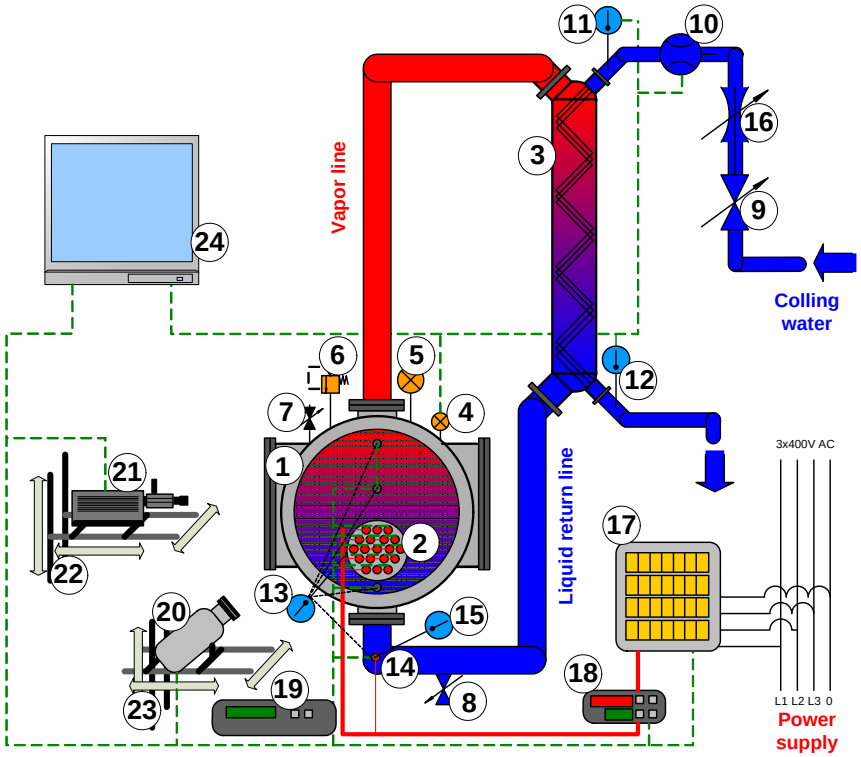

Figure 1. Schematic diagram of the experimental apparatus; 1 – test vessel, 2 – tube bundle, 3 – condenser, 4 – pressure transducer, 5 – pressure gauge, 6 – safety-valve, 7 – valve to setting of pressure in test vessel, 8 – drain valve of test liquid, 9 – drain valve of cooling water, 10 – flowmeter, 11, 12, 13, 15 – thermocouples, 14 – preheater, 16 – manual valve of flow control, 17 – wattmeter, 18 – regulators, 19 – multiplexer, 20 – high speed camera, 21 – CCD camera, 22 – mobile support (3d) of CCD camera, 23 – mobile support (3d) of high speed camera, 24 – computer aided data acquisition system

The evaporator was designed to simulate a slice of a flooded-type evaporator. The bundle consists of 19 electrically-heated smooth tubes which are arranged in a staggered triangular-pitch layout with a pitch-to-diameter ratio of 1.7 and 2.0. The bundles were cantilever-mounted from the back wall of the evaporator to permit in-bundle visualization. A stainless steel tube of R_a = 0.40 μm having 10 mm OD and 0.6 mm wall thickness formed single test heater. Electrical energy supplied to heating elements is controlled by electronic regulators. Each cartridge heater is equipped with a separate regulator.

Each tube was 180 mm long and effective length was 155 mm. The liquid level was maintained at ca. 15 mm above top row of tubes in the bundle.

As pointed out in [12,13] great care must be exercised with the cartridge heater and temperature measuring instrumentation to ensure good accuracy of the measurement of the inside temperature of the heating cylinder. In the open literature descriptions of very sophisticated temperature measuring instrumentation can be found [14].

Each tube was equipped with four thermocouples evenly spaced at 90° on the inner wall and midway between the heated length of a tube. The wall temperature t_w was calculated from the formula [15]

$$t_w = t_i - UI\frac{\ln(D_o / D_i)}{2\pi\lambda L}$$

where t_i was calculated as the arithmetic mean of four measured inside wall temperatures.

RESULTS AND DISCUSSION

Independently on pitch and operating pressure the highest bundle average heat transfer coefficients were obtained for boiling water. As an example Fig. 2 shows experimental results for three tested boiling liquids and bundle pitch-to-diameter ratio of 1.7 recorded at atmospheric pressure.

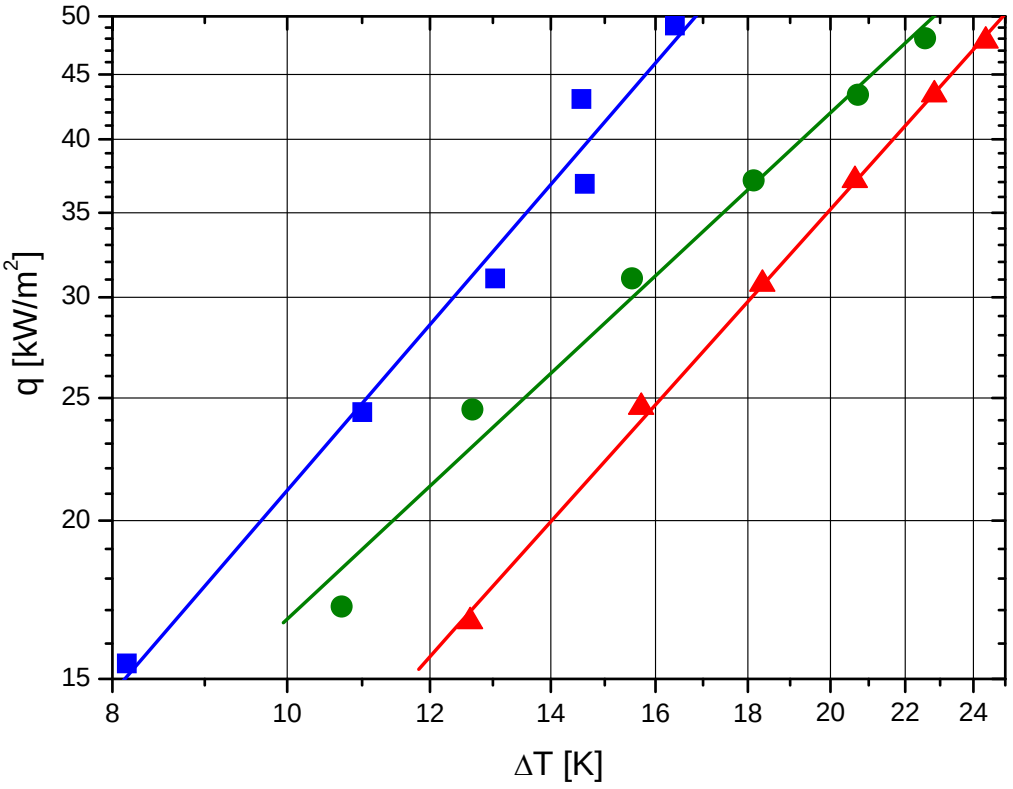

Figure 2. Boiling curves for three tested liquids at atmospheric pressure and bundle pitch-to-diameter ratio of 1.7; ■ - water, ● – methanol, ▲ - R141b

For all tested liquids, both atmospheric and sub-atmospheric pressure, higher heat transfer coefficients were obtained for greater pitch-to-diameter ratio examined, i.e. 2.0. Exemplarily, Fig. 3 illustrates influence of pitch-to-diameter ratio for refrigerant R141b boiling at atmospheric pressure.

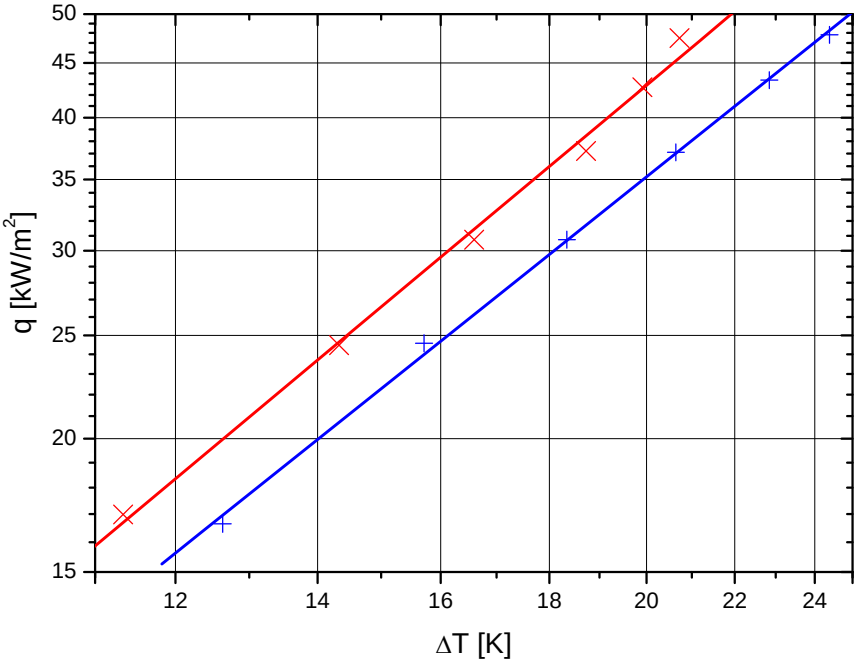

Figure 3. Influence of pitch-to-diameter ratio for R141b boiling at atmospheric pressure; pitch-to-diameter ratio: + 1.7, × - 2.0

Independently on pitch and kind of liquid tested higher heat transfer coefficients were obtained for atmospheric pressure. As an example Fig. 4 displays boiling curves for methanol boiling at atmospheric and sub-atmospheric pressure and bundle pitch-to-diameter ratio of 2.0.

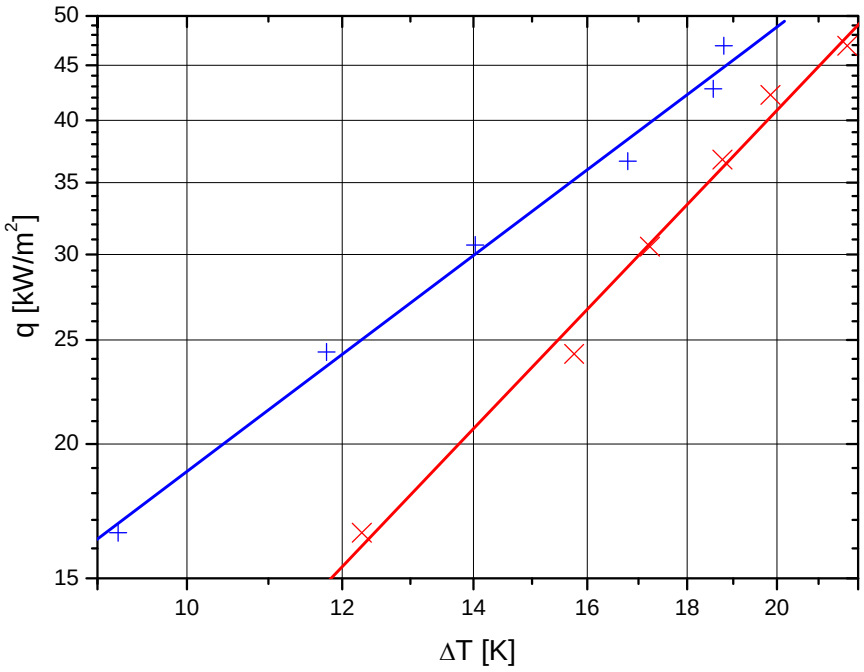

Figure 4. Influence of pressure for methanol boiling on smooth tube bundle with pitch-to-diameter ratio 2.0; × - sub-atmospheric pressure, + - atmospheric pressure

Figure 5 illustrates average heat transfer coefficients for row of tubes and selected heat flux densities in the case of water boiling at atmospheric pressure on tube bundle with pitch-to-diameter ratio 1.7. The higher was heat flux density the higher was heat transfer coefficient for all rows of tubes and simultaneously average heat transfer coefficient increases from bottom to the top row of tubes.

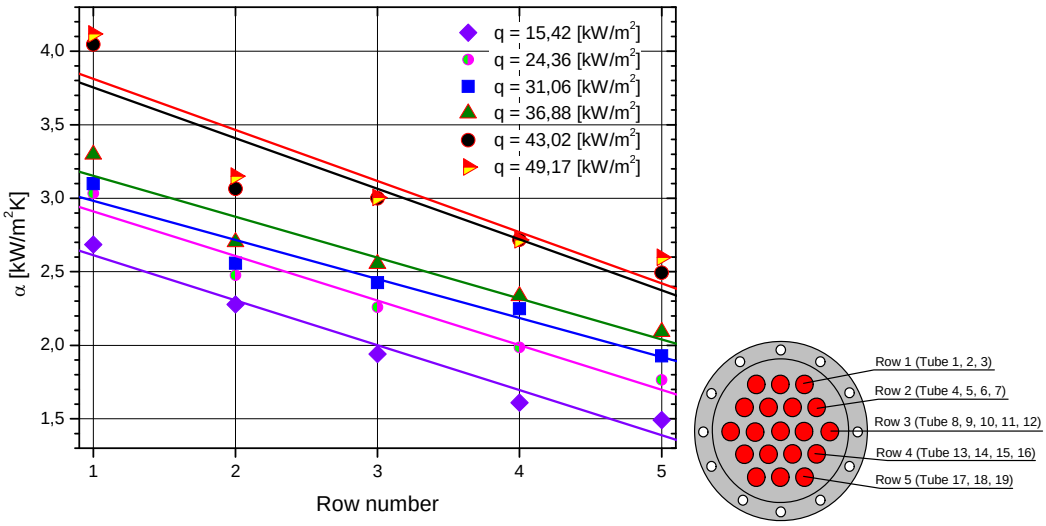

Figure 5. Row average heat transfer coefficient against row position in a tube bundle

Bundle factor and bundle effect (Fig. 6) decrease with heat flux density increase. Likewise literature data [16] bundle effect is slightly higher than bundle factor.

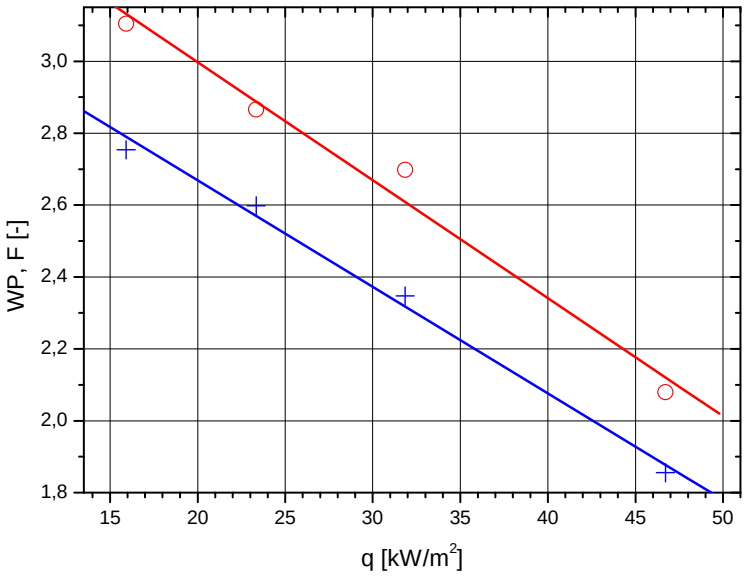

Figure 6. Bundle factor (F - +) and bundle effect (WP – ○) for methanol boiling at atmospheric pressure on smooth bundle with pitch-to-diameter ratio of 2.0

A multidimensional regression analysis using the least squares method was used to establish correlation equation for prediction of bundle average heat transfer coefficient

$$Nu = 61.392 Bo^{0.316} \left(\ln\left(\frac{p}{p_{cr}} \right)^2 \right)^{-1.55} \left(\frac{s}{D} \right)^{0.73} \tag{1}$$

where:

$Nu = \frac{\overline{\alpha} D_o}{\lambda_l}$ - Nusselt number,

$Bo = \frac{qLa\rho_l}{\rho_v r \mu_l}$ - boiling number,

$La = \sqrt{\frac{\sigma}{g(\rho_l - \rho_v)}}$ - characteristic length.

A comparison of predicted data against the experimentally obtained under the present investigation is displayed in Fig. 7. For about 96% of experimental points the discrepancy between experimental data and values calculated from proposed correlation is lower than ±40%.

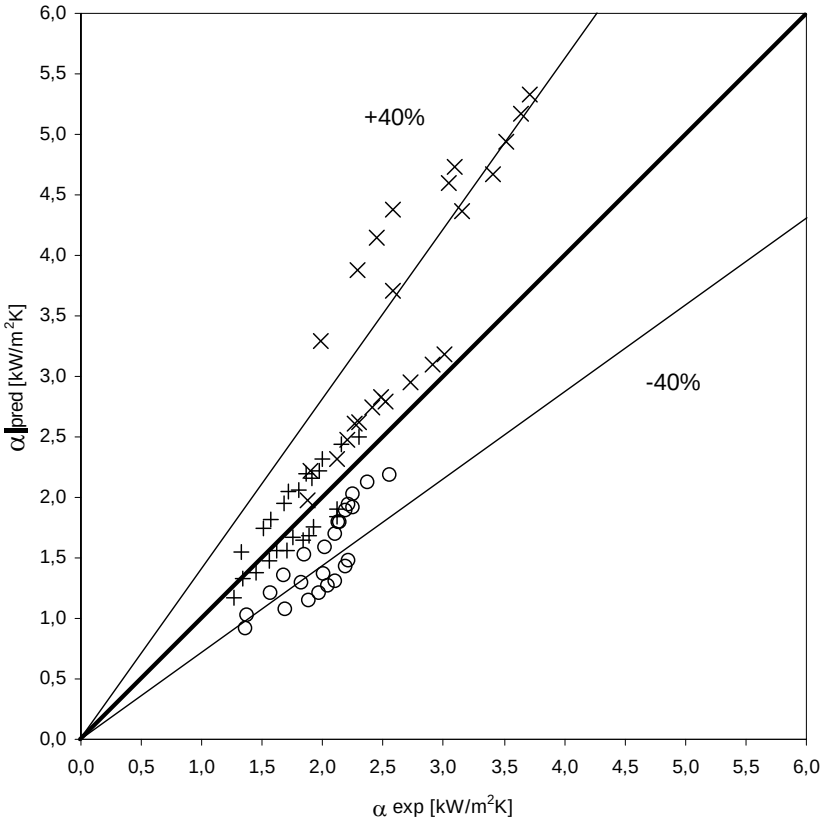

Figure 7. Predicted vs. experimental average heat transfer coefficients in smooth tube bundle; × - water, ○ – methanol, + - R141b

CONCLUSIONS

The following conclusions can be made from the present investigation on boiling heat transfer in smooth tube bundles under atmospheric and sub-atmospheric pressures:

1. Distilled water has an evident superiority over methanol and refrigerant R141b for each tested tube bundle.

2. For atmospheric pressure higher heat transfer coefficients were recorded than for sub-atmospheric pressure.
3. Increase in pitch-to-diameter ratio results in average heat transfer coefficient increase for all three liquid tested as well as atmospheric- and sub-atmospheric pressure.
4. Row average heat transfer coefficient increases from bottom to top row of tubes.
5. A Nusselt-type relation has been proposed to predict the heat transfer coefficient and the predicted values correlate satisfactory with the experimental data related to water, methanol and refrigerant R141b over some range of pressure.

REFERENCES

1. Palen J.W., Yarden A., Taborek J.: Characteristics of boiling outside large-scale horizontal multitube bundles. AIChE Symp. Ser.,68, s. 50-61, 1972.
2. Marto P.J., Anderson C.L.: Nucleate boiling characteristics of R-113 in small tube bundle. ASME J. Heat Transfer, vol. 114, s. 425-433, 1992
3. Browne M.W., Bansal P.K.: Heat transfer characteristics of boiling phenomenon in flooded refrigerant evaporators. Applied Thermal Engng, vol. 19, 595-624, 1999
4. Qiu Y.H., Liu Z.H.: Boiling heat transfer of water on smooth tubes in a compact staggered tube bundle. Applied Thermal Engineering, vol. 24, s. 1431-1441, 2004.
5. Rebrov P.N., Bukin V.G., Danilova G.N.: A correlation for local coefficients of heat transfer in boiling of R12 and R22 refrigerants on multirow bundles of smooth tubes. Heat Transfer – Soviet Research, vol. 21, no. 4, 543-548, 1989.
6. Gupta A., Saini J.S., Varma H.K.: Boiling heat transfer in small horizontal tube bundles at low cross-flow velocities. Int. Journal of Heat and Mass Transfer, Vol. 38, Nr 4, s. 599-605, 1995.
7. Kumar S., Mohanty B., Gupta S.C.: Boiling heat transfer from vertical row of horizontal tubes. Int. Journal of Heat and Mass Transfer, vol. 45, s. 3857-3864, 2002.
8. Da Silva E.F., Ribtatski G., Saiz-Jabardo J.M.: Experimental study on the nucleate boiling heat transfer coefficients on a vertical array of horizontal smooth tubes. Proc. 5th Int. Conf. On Transport Phenomena in Multiphase Systems HEAT2008, Białystok, 2008, vol. 2, 139-146
9. Leong L.S., Cornwell K.: Heat transfer coefficients in a reboiler tube bundle. The Chemical Engineer, 343, s. 219-221, 1979.
10. Gupta A.: Enhancement of boiling heat transfer in a 3x5 tube bundle. Int. Journal of Heat and Mass Transfer, vol. 48, s. 3763-3772, 2005.
11. Webb R.L., Choi K.D., Apparao T.R.: A theoretical model for prediction of the heat load in flooded refrigerant evaporator. ASHRAE Trans., vol. 95, Pt. 1, 326-338, 1989.
12. Marto P.J., Anderson C.L.: Nucleate boiling characteristics of R-113 in small tube bundle. Transactions ASME J. Heat Transfer, vol. 114, 1992, pp. 425-433.
13. Cieśliński J.T.: Modelling of temperature field of cylindrical pool boiling heating section. Developments in mechanical engineering, vol. 3, GUT Publishers, 2009.
14. Bier K., Goetz J., Gorenflo D.: Zum Einfluß des Umfangwinkels auf den Wärmeübergang beim Blasensieden an Horizontalen Rohren. Wärme-Stoffübertragung, Vol. 15, 1981, pp. 159-169.
15. Chiou Ch.B., Lu D.Ch., Wang Ch.Ch.: Pool boiling of R-22, R124 and R-134a on a plain tube. Int. J. Heat Mass Transfer, Vol. 40, No. 7, 1997, pp. 1657-1666.
16. Memory S.B., Akcasayar N., Erydin H., Marto P.J.: Nucleate pool boiling of R-114 and R-114-oil mixtures from smooth and enhanced surfaces – II. Tube bundles. Int. Journal of Heat and Mass Transfer, vol. 38, Nr 8, s. 1363-1374, 1995.

Heat Transfer

FEATURES OF CONVECTION FLOWS AND HEAT TRANSFER IN MAGNETIC COLLOIDS

S.A. Suslov[1, *], A.A. Bozhko[2], G.F. Putin[2]

[1] Swinburne University of Technology, Hawthorn, Victoria, Australia
[2] Perm State University, Perm, Russia

ABSTRACT. Undertaken experimental observations and stability analysis have shown that a simple parallel buoyancy-induced flow in a differentially heated vertical layer of ferrofluid that is placed in an external uniform horizontal magnetic field is subject to a number of instabilities leading to the appearance of various convection patterns. Depending on the values of the governing parameters, the instability patterns are found to consist of vertical stationary magneto-convection rolls and/or vertically or obliquely counter-propagating thermo-gravitational or thermo-magnetic waves. Vertical rolls are the most prominent feature of the thermo-magnetic convection while inclined rolls and waves result from the interaction of the magnetic and gravitational mechanisms. Convective flow patterns are characterized by significantly increased heat transfer rates in comparison to pure conduction states. In particular, a significant intensification of an integral heat transfer was observed in convection regimes corresponding to vertical stationary rolls. It is found that these patterns are caused completely by a thermo-magnetic mechanism and are the consequence of an internal magnetic field gradient induced by the temperature dependence of fluid magnetization. These were not detected in earlier experiments and computations.

Keywords: *magneto-convection, thermo-magnetic waves, ferrocolloid, magnetic field*

INTRODUCTION

Common non-conducting artificial magnetic colloids (ferrofluids) consist of stable dispersions of single-domain ferromagnetic nano-particles in a liquid carrier. Such magnetic fluids respond to an external magnetic field similarly to natural paramagnetic and diamagnetic fluids (e.g. water, protein solutions, paramagnetic melts) and gases (e.g. oxygen). However the degree of magnetization in ferrofluids is many orders of magnitude higher than that in natural magnetic fluids. Therefore noticeable magnetic effects on fluid flows can be observed in magnetic fields created by ordinary permanent or electro-magnets which make these fluids suitable for a wide range of applications such as heat career in powerful loud speakers, controllable sealants in bearings, targeted drug delivery in cancer treatments etc.

Non-uniform heating results in non-uniform magnetization of ferrofluid that is placed in an external magnetic field. Subsequently, a ponderomotive force arises which drives stronger magnetized fluid particles to the regions with a stronger magnetic field. This phenomenon known as magneto-convection is different from convection caused by gravitational buoyancy forces. In fact, magneto-convection can be induced even if gravity is not present e.g. in outer space. Therefore it is potentially possible to use ferrofluids as a heat carrier in heat exchangers operating in reduced gravity conditions at orbital stations where adequate cooling by natural gravitational convection

* Corresponding author: Dr Sergey A. Suslov
Phone: + (61)-3-9214-5952, Fax: + (61)-3-9214-8264
E-mail address: ssuslov@swin.edu.au

cannot be achieved. The study of combined convection caused by the competing gravitational and magnetic mechanisms is undertaken in the current work with the emphasis on effects caused by fluid magnetization.

EXPERIMENTAL APPARATUS

A kerosene-based magnetic fluid used in experiments contained magnetite particles with the average size of 10 nm. The magnetic phase concentration was around 10%. Such a fluid is non-transparent for layers thicker than a few tenths of a millimeter. Therefore the only possible direct investigation of the arising convection patterns is via the measurements of thermal fields and heat fluxes. The focus of the undertaken study was on magneto-convection caused by ponderomotive forces arising in a fluid placed in an external uniform magnetic field. Thus the experimental conditions were chosen in such a way that magnetic effects were stronger or at least comparable with gravitational ones. Quantitatively, this meant that the ratio Gr_m/Gr exceeded the unity, where $Gr_m = \frac{\rho\mu_0 K^2\Theta^2 d^2}{\eta(1+\chi)}$ and $Gr = \frac{\rho^2\beta\,\Theta g\, d^3}{\eta^2}$ are the magnetic and gravitational Grashof numbers, respectively. Here $\rho = 1.25\cdot10^3$ kg/m^3 is the density of the fluid, $\mu_0 = 4\pi\times10^{-7}$ H/m is the magnetic constant, $\eta = 0.006$ kg/(m·s) is its dynamic viscosity, $\beta = 0.86\cdot10^{-3}$ is the coefficient of thermal expansion, $K\sim10^2$ A/(m K) is the pyromagnetic coefficient, $\chi = 5$ is the differential magnetic susceptibility, $2d$ is the thickness of a fluid layer and 2Θ is the temperature difference between the enclosure walls. Since $Gr_m / Gr \sim K^2\Theta / d$, in order to emphasize the magnetic convection mechanism thin layers of a strongly magnetizeable fluid subject to large temperature differences were used in experiments. Flows in three narrow cylindrical chambers with the diameter of 75mm and thicknesses of $2d$=2± 0.05, $2d$=3.5± 0.03 and $2d$=5± 0.05 mm were studied. A 3.5 mm vertical layer was used in order to investigate the evolution of convection patterns visualized by means of a liquid crystal thermo-indicator. The 2 mm and 5 mm layers were used to measure the integral heat flux across the chamber. The narrow cylindrical shape of the experimental cavities was chosen since it preserves the uniformity of the internal magnetic field when the apparatus is placed in an external uniform field generated by Helmholtz coils or an electromagnet [1]. Magnetic fields up to 200 kA/m were used in experiments.

Two experimental chamber designs are schematically shown in Figure 1. The 3.5 mm chamber intended for visual observations of convection patterns using a thermo-sensitive liquid crystal sheet is shown in the left diagram in Figure 1. One of the walls of this chamber was formed by a copper heater (2). Its temperature was determined by the water that was pumped through the channels drilled in the body of a heat exchanger. The opposite wall of this chamber was connected to a transparent heat exchanger (3) made of Plexiglas parallel plates separated by a gap filled with cool water. A circular Plexiglas frame (4) ensured the uniformity of the fluid layer thickness. The temperature variation of water pumped through both heat exchangers did not exceed 0.05 K. A 0.1 mm thick thermo-sensitive liquid crystal sheet (5) was glued to the outer side of a Plexiglas heat exchanger. In the absence of convection, a uniform temperature gradient establishes across the test fluid layer so that a liquid crystal sheet remains isothermal and thus is uniformly colored. When convection is present the heat flux across the fluid layer is non-uniform and the color of a liquid crystal changes from brown at approximately 24 °C to blue at approximately 27 °C. A 1 mm thick glass plate (6) protected the liquid crystal from direct exposure to the chemically aggressive ferrofluid. Even though the presence of such a “sandwich” structure reduced the thermal sensitivity and spatial resolution of the sensor it was still possible to reliably register surface temperature variations of several tenths of a degree. When the flow is relatively slow the relationship between the transverse velocity component and the convective distortion of the thermal field is approximately linear so that the color variations in the liquid-crystal thermo-indicator directly show

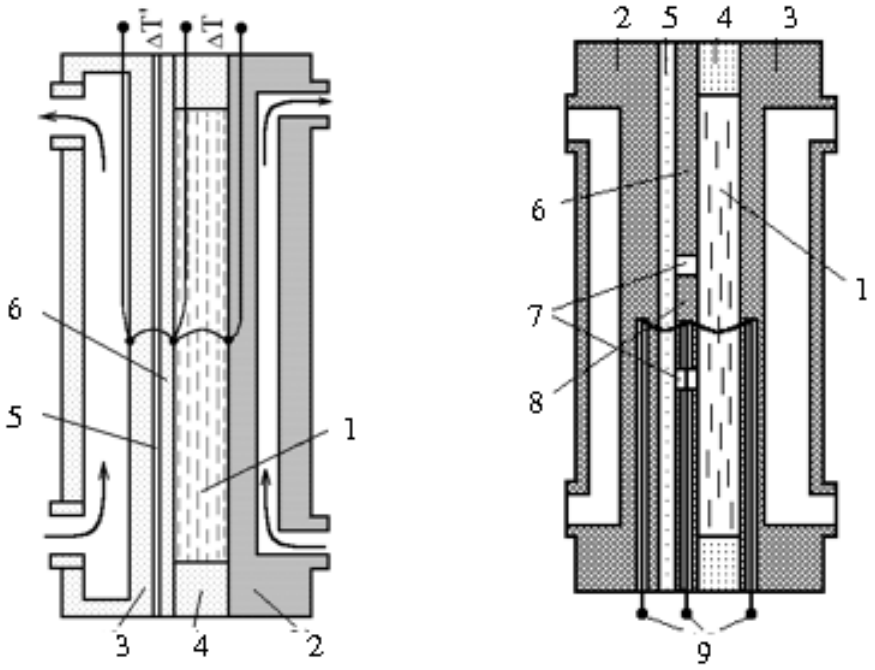

Figure 1. Cross-sectional view of test enclosures with thicknesses of (left) 3.50 mm: 1 – ferrofluid layer; 2 and 3 – copper or Plexiglas heat exchangers; 4 – circular Plexiglas frame; 5 – liquid crystal sheet; 6 – protective organic glass plate; (right) 2.00 and 5 mm: 1– ferrofluid layer; 2, 3 – copper heat exchangers; 4 – circular Plexiglass frame; 5 – fluoroplastic layer; 6 – copper plate; 7 – circular heat-insulating groove; 8 – copper bush; 9 – thermocouples.

the structure of the arising convective patterns. Their intensity is then estimated by comparing the local coloration with that observed in the non-convective state.

The schematic cross-sectional view of enclosures used to measure integral transverse heat flux is shown in the right diagram in Figure 1. A fluid layer (1) with the thickness of 2.00 (or 5.00) ± 0.05 mm was confined by two copper heat exchangers (2) and (3). The circular sidewall of the layer (4) was made of Plexiglas. In order to minimize the influence of the boundary effects on the heat flux measurements, the copper plate (6) was separated from the centrally located 17 mm circular integral sensor (8) by a groove (7) filled with a heat-insulating material. Thus the heat flux was measured only in the centre of the cavity. The use of such a design enabled us to significantly improve the accuracy of the convection threshold measurements in comparison with the other experimental designs in which a sensor occupies the entire sidewall.

The intensities of the integral heat transfer across the ferrofluid layer (1) were determined using Schmidt-Milverton method [2] i.e. by comparing the temperature difference ΔT between the layer boundaries and the temperature difference $\Delta T'$ across the fluoroplastic layer (5). Temperature differences were measured using differential copper-constantan thermo-couples with a wire diameter of 0.1 mm. In steady and slowly varying states, when the temperature profile across the fluoroplastic layer is linear, Nusselt number Nu (the ratio of the total heat flux to purely conductive heat flux component) is determined from the expression: $Nu = k\Delta T'/\Delta T$. Here k is an empirical constant characterizing the ratio of the effective thermal diffusivities of fluid and fluoroplastic. In the absence of convection this constant is computed from the conductive heat flux balance condition $k = \Delta T / \Delta T'$.

When estimating the numerical values of the relevant nondimensional parameters such as gravitational and magnetic Grashof numbers it is important to keep in mind that the properties of ferrofluid, which in fact is a magnetic colloid, depend strongly on the way the fluid was prepared. In

particular, they are strongly influenced by the size distribution of solid phase particles, the interaction between these particles, the presence of a surfactant such as oleic acid, the composition of a base fluid (kerosene) and other factors [3]. In the context of the current investigation it is important that aggregates containing between a few tens up to a thousand magnetite particles are formed in an experimental fluid [4]. The number and sizes of such aggregates, and subsequently the rotational and magnetic viscosities of the ferrofluid, are determined by the history and type of experimental measurements [3, 5]. The value of a magnetic susceptibility χ, which is typically assumed constant, actually depends on the concentration of the formed aggregates [6]. In addition, the definition of the magnetic Grashof number Gr_{m} contains the pyromagnetic coefficient K, which is a function of the fluid's magnetization M. Even in an ideal situation the magnetization grows with the applied magnetic field H according to the linear law $M = \chi H$. Therefore strictly speaking the pyromagnetic coefficient K, which is a linear function of magnetization $K = \beta_M M$, where $\beta_M = 5 \cdot 10^{-3}$ 1/K is the relative pyromagnetic coefficient for the used ferrofluid, cannot be considered as constant in experimental conditions. These inevitable properties variations of magnetic colloids typically do not have a qualitative effect on the observed convection characteristics. However they may lead to noticeable quantitative deviations of the reported experimental values of parameters such as magnetic Grashof numbers from those assumed or found in the analysis and computations. To minimize possible confusion caused by this uncertainty in evaluating the experimental parameters the comparisons between experimental and analytical results given below use relative (to critical value) rather than absolute values of the governing flow parameters.

THERMO-MAGNETIC CONVECTION IN A VERTICAL LAYER

The liquid crystal temperature distribution on the lateral wide surface of the enclosure for the basic and secondary flows is shown in Figure 2. Figure 2(a) shows the schematic and the liquid crystal image corresponding to a shear flow arising in a pure conduction state when no magnetic field is applied. The blue upper and brown lower regions in the left photo show that the temperature stratification along the vertical layer exists so that the average temperature of the fluid increases upward. This is due to the finite vertical size of the enclosure. The thermal stratification effect is less pronounced in enclosures with larger aspect ratio (i.e. with a thinner gap width) and thus it is neglected in the analysis of infinitely tall layer presented below. Despite the presence of the thermal stratification, the resolution of a liquid crystal sensor was sufficiently high to detect the qualitative change in the flow behaviour after a magnetic field of sufficient strength was applied perpendicular to the fluid layer as shown in Figure 2(b). The applied external magnetic field causes magnetization of a ferrofluid. The degree of magnetization depends on the local fluid temperature: colder fluid magnetizes stronger. In turn, the fluid magnetization reduces the local magnetic field. In the considered geometry its magnitude decreases from hot to cold wall as discussed in [7]. As a result the arising ponderomotive force drives stronger magnetized colder fluid into the regions of stronger magnetic field near the hot wall. This is a physical reason for a change in the flow behaviour: once the ponderomotive force becomes sufficiently strong, the pure conduction state becomes unstable and magneto-convection begins. Experimentally this is detected by a characteristic change in the colour pattern of the liquid crystal sensor, see the photo in Figure 2(b). The observed patterns suggest that at the onset magnetic convection takes the form of stationary vertical rolls aligned with the direction of the base shear flow. This is in contrast to gravitational convection, which takes the form of horizontal rolls or thermo-gravitational waves propagating vertically in the considered configuration. Note that thermo-magnetic convection mechanism is completely independent of the direction of the gravity vector, but as discussed in [7] it is most pronounced in the absence of gravity. For this reason the analytical magneto-convection results, which are compared with experimental observations, below are obtained in the limit of $Gr \to 0$. The non-zero gravity, which is inevitably present in laboratory experiments, introduces a secondary effect leading to the inclination of convection rolls and their unsteadiness for larger values of the gravitational Grashof number. Such patterns have been observed experimentally and are illustrated in Figure 3.

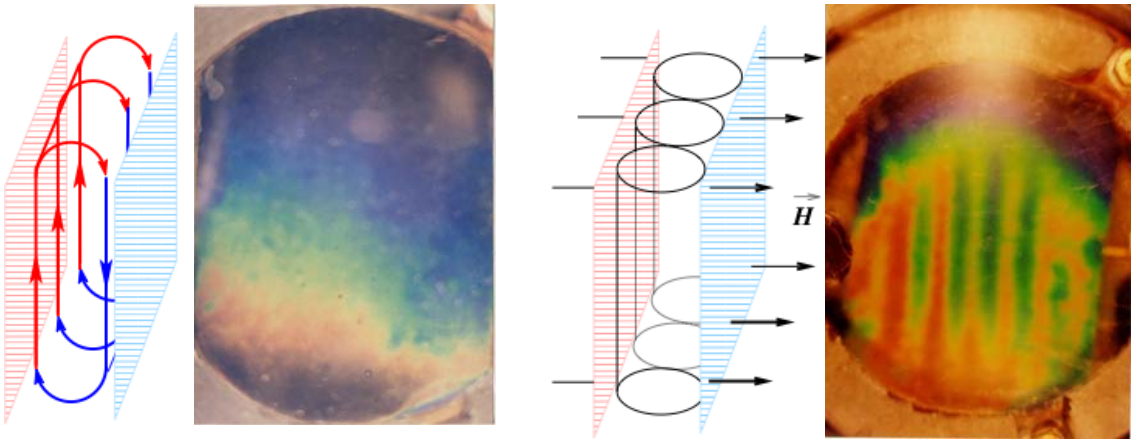

(a) (b)

Figure 2. Qualitative diagrams and liquid crystal surface photographs of flows at Θ= 10 K: (a) H = 0; (b) H = 15 kA/m. The temperature variation from cool (brown) to warm (blue) liquid is approximately 3 K. The red/brown strips in photograph (b) correspond to a convective flow of a cool fluid away from the transparent enclosure wall while the blue/green strips show the location where warm fluid impinges the photographed surface. Magnetic field is perpendicular to the plane of photographs.

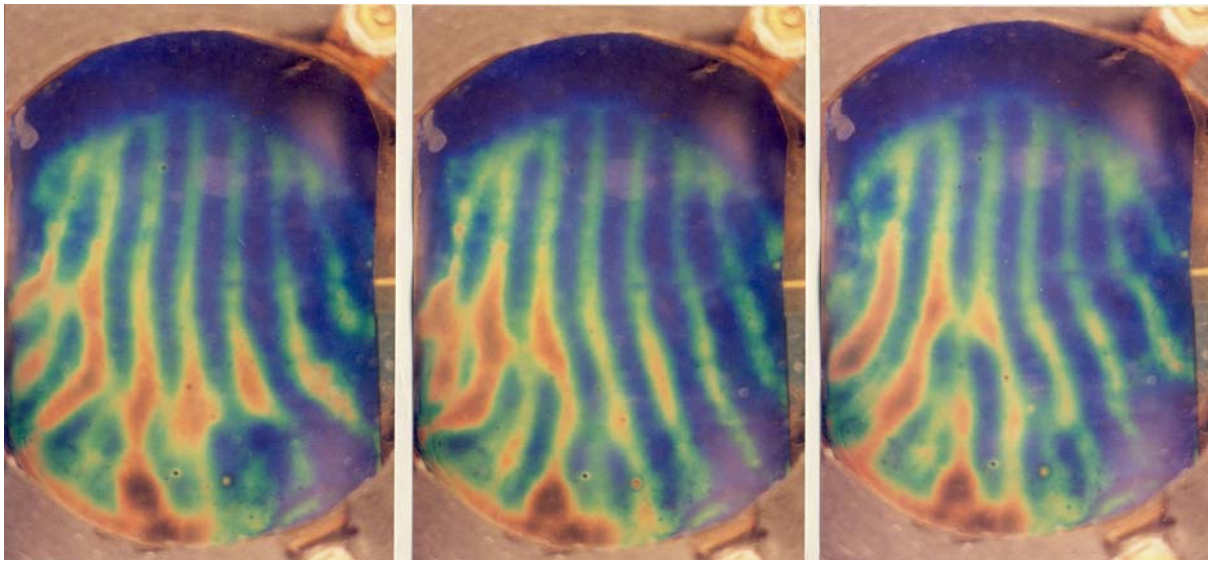

Figure 3. Inclined unsteady patterns in mixed thermo-magnetic and thermo-gravitational convection at $(Gr_m, Gr) \approx (15,8)$. The time interval between snapshots is 1 min.

The observed convection patterns are generally consistent with the pattern classification given in [7] for an infinitely wide and tall vertical layer of ferrofluid. It was shown there via comprehensive linear stability analysis of the basic shear flow that depending on the values of gravitational and magnetic Grashof numbers (with the other governing parameters being fixed, e.g. the fluids Prandtl number is taken to be 130 consistently with the current experiments) there are four major parametric regions summarized in Figure 4 (with up to 16 fine subregions which have been identified in [7]) distinguished by the dominant convection patterns and mechanisms. At low to

moderate values of the gravitational Grashof numbers (i.e. for thin fluid layers) vertical stationary thermo-magnetic rolls dominate the flow. The range of magnetic Grashof numbers for this regime is

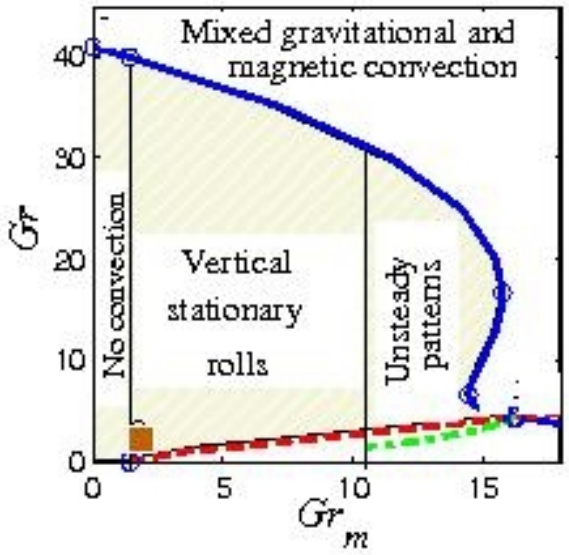

Figure 4. Convection pattern diagram for an infinite ferrofluid layer. See [7] for a detailed discussion.

the widest among all identified patterns, see the region between the two vertical lines in Figure 4. Since the gravitational buoyancy force is secondary in this regime, for the purpose of the initial weakly nonlinear analysis we disregard the buoyancy effects and only take into account magneto-convection. The mathematical details of this analysis are quite involved (see [8], for example) and will be reported elsewhere. Here we will only mention that the eigenfunctions of a linearised stability problem which are horizontally periodic with wavenumber β along the layer, and which represent vertical convection rolls, are taken as the basis of an asymptotic expansion carried out up to the third order in time-dependent roll amplitude $A(t)$. Consistently agreeing with experimental observations the analysis shows that the transition to a magneto-convection state occurs via a supercritical bifurcation. Therefore for the values of the magnetic Grashof number above critical (see the left vertical line in Figure 4) the roll amplitude grows until it reaches its saturation value A_s. Subsequently, the flow Nusselt number is computed at the enclosure wall as $Nu = 1 - A_s^2 \frac{d}{\Theta} \frac{d\Theta_{20}}{dx}$, where Θ_{20} is the average deviation of the temperature field from that corresponding to a pure conduction state, and x is the coordinate across the layer. The left plot in Figure 5 shows that the experimental and computed values of the Nusselt number are in reasonable agreement near the convection threshold. Yet the difference between the analytical and experimental values obtained for different enclosures is noticeable. While this discrepancy may be attributed to the difficulties with estimating the values of experimental parameters which were discussed above there appears to exist an experimentally observed trend: the Nusselt number values found for a thicker layer characterised by larger gravitational Grashof numbers are somewhat lower than those for a thin enclosure. This is consistent with the analytical conclusions of [7] where it was shown that the buoyancy effects characterised by the gravitational Grashof number tend to suppress magneto-convection. It was also found in experiments that the effective heat flux across the layer rapidly increases once convection sets, reaches its maximum and then starts decreasing for larger supercritical values of the magnetic Grashof number. Similar behaviour is predicted by our analysis, see the line in the left plot in Figure 5, even though strictly speaking the accuracy of weakly nonlinear approach is only guaranteed in the vicinity of a convection threshold. The right plot in

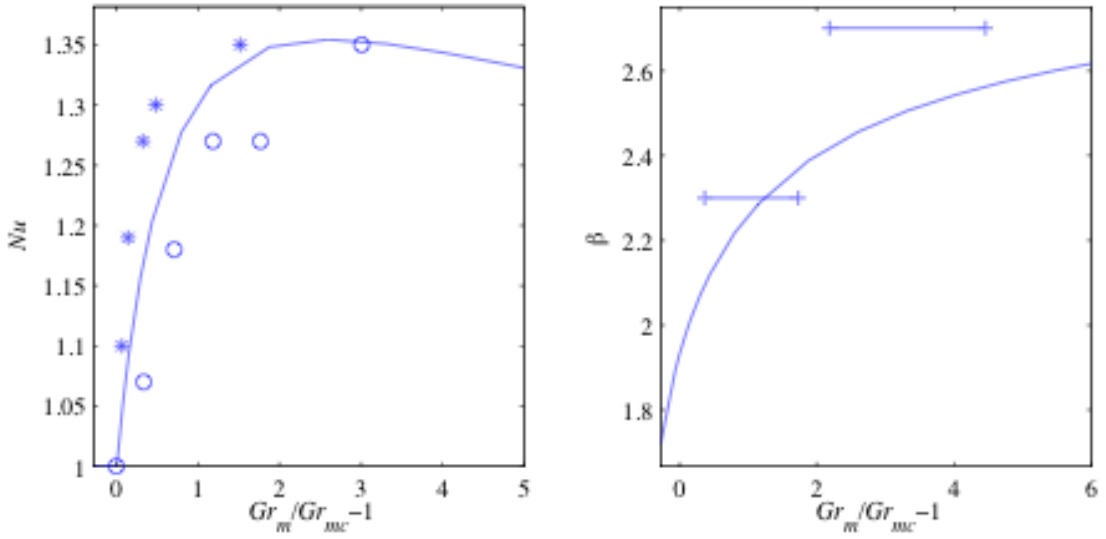

Figure 5. Experimental (symbols) and analytical (lines) results for Nusselt number and the dominant wavenumber for thermomagnetic convection taking the form of vertical stationary rolls. The star and circle symbols show experimental results for 2 mm and 5 mm thick enclosures, respectively. Convection roll wavenumbers experimentally observed in 3.5 mm enclosure over a range of magnetic Grashof numbers are shown by the connected plus symbols in the right plot.

Figure 5 presents the values of a dominant convection roll wavenumber as a function of the supercriticality parameter. According to the analysis it grows with magnetic Grashof number. The available experimentally measured wavenumbers are also shown in this plot. The agreement is very good near the criticality, but the analytical values are somewhat lower than experimental in far supercritical regimes. This is expected since in reality the unstable wavenumbers spectrum widens away from a bifurcation point so that a spatial modulation of periodic instability patterns brought about by the enclosure boundaries occurs. This may lead to the deviation of the dominant wavenumber predicted for an infinite layer from that observed in finite geometry.

Regimes qualitatively different from stationary vertical rolls are detected experimentally and predicted analytically for the larger values of magnetic Grashof number (to the right of the second vertical line in Figure 4). The analysis shows that waves counter-propagating along the hot and cold enclosure walls in the vertical or inclined direction appear in these regimes. Despite their relative weakness in comparison with stationary rolls they are nevertheless visible in experiments as they cause slow drift or blinking of the flow patterns. Disturbance energy analysis performed by the authors in [9] shows that such waves are caused by a magnetic mechanism which is different from that found in gravitational convection occurring in large Prandtl number fluids. In contrast to pure thermo-gravitational waves thermo-magnetic waves can propagate obliquely to the direction of gravity, which indeed was observed in experiments.

CONCLUSIONS

The performed linear and weakly nonlinear analyses of thermo-magneto convection flows in a vertical ferrofluid layer confirm and clarify the major features and characteristics of such flows observed experimentally. The qualitative agreement between analytical and experimental results is good. Both provide evidence of the dominant role of magneto-convection over gravitational convection in thin vertical layers of ferrofluid and demonstrate the existence of steady as well as unsteady convection patterns geometrically different from those observed in gravitational convection. However further analytical and experimental efforts are required before it can be concluded as to whether a consistent

quantitative agreement can be achieved. In particular, experiments in an enclosure of a larger aspect ratio are required to eliminate the enclosure boundary influence on magnetic field and flow patterns, and more accurate methods of estimating fluid properties and experimental flow parameters need to be developed. Further analytical development needs to incorporate the effects of gravitational convection competing with magneto-convection, the effects of spatial modulation and of three-dimensionality of the observed patterns. This work is currently underway.

ACKNOWLEDGEMENTS

The work of AAB and GFP was partially supported by the Russian Foundation for Basic Research and Government of Perm Region, Russia, under grant № 07-08-96039.

REFERENCES

1. D.V. Sivuhin, *Electricity.* Science. Moscow, 1983 (in Russian).
2. R.J. Schmidt and S.W. Milverton, On the instability of a fluid when heated from below, *Proc. Roy. Soc. London. Ser. A.,* 152, pp. 586-594, 1935.
3. E.Y. Blums, M.M. Maiorov and A.O. Tsebers, *Magnetic Fluids*/Zinatne, Riga, Latvia (in Russian), 1989.
4. V.M. Buzmakov and A.F. Pshenichnikov, On the structure of microaggregates in magnetite colloids, *J. Colloid and Interface Sci.*, 182(1), pp. 63-70, 1996.
5. L.M. Pop, S. Odenbach and A. Wiedenmann, The microscopic mechanisms of the magnetoviscous effect in ferrofluids investigated by small angle neutron scattering, *Proceedings of the 15th Riga and 6th PAMIR Conference on Fundamental and Applied MHD*, pp. 321–324, Riga, Latvia, June 27–July 1, 2005.
6. A.F. Pshenichnikov and V.V. Mekhonoshin, Equilibrium magnetization and microstructure of the system of superparamagnetic interacting particles: numerical simulation, *J. Magnetism and Magnetic Materials,* 213, pp. 357-369, 2000.
7. S.A. Suslov, Thermomagnetic convection in a vertical layer of ferromagnetic fluid, *Phys. Fluids*, 20, 084101, 2008.
8. S.A. Suslov and S. Paolucci, Nonlinear analysis of convection flow in a tall vertical enclosure under non-Boussinesq conditions, *J. Fluid Mech.,* 344, pp. 1-41, 1997.
9. S.A. Suslov, A.A. Bozhko and G.F. Putin, Thermo-magneto-convective instabilities in a vertical layer of a ferro-magnetic fluid, *Proceedings of the APM2008: XXXVI Summer School on "Advanced Problems in Mechanics"*, pp. 644—651, St. Petersburg (Repino), Russia. 6-10 July 2008.

PRESSURE DROP INSIDE A SMOOTH TUBE WITH DIFFERENT INLET GEOMETRIES IN THE TRANSITIONAL FLOW REGIME FOR WATER COOLED AT A CONSTANT WALL TEMPERATURE

J.P. Meyer*, L. Liebenberg and J.A. Olivier
Department of Mechanical and Aeronautical Engineering, University of Pretoria,
Pretoria, 0002, South Africa

ABSTRACT. Due to design constraints or changes in operating conditions, heat exchangers are often forced to operate in the transitional flow regime. However, there is not much design information available in this regime. It is also well known that the entrance has an influence on the transition position, exacerbating the absence of available design information in the transitional flow regime. The purpose of this study is thus to obtain pressure drop data for water inside smooth tubes, while the wall temperature is maintained constant. Adiabatic as well as diabatic experiments were conducted on water inside a smooth tube with an inner diameter of 15.88 mm. For diabatic experiments, water was cooled in the tube with chilled water in the annulus. Testing conditions were similar to those that can be expected in commercial chillers with Reynolds numbers in the transitional flow regime ranging between 1 000 and 20 000, Prandtl numbers between 4 and 6, and Grashof numbers in the order of 10^5. Four inlet profiles were investigated, namely hydrodynamically fully developed, square-edged, re-entrant and bellmouth. Adiabatic results confirmed that transition from laminar to turbulent flow was strongly dependent on the inlet profile, with transition being delayed to Reynolds numbers as high as 7 000. However, diabatic friction factor results confirmed that transition was independent of the inlet, with transition occurring at a Reynolds number of approximately 2 100. This was attributed to the buoyancy-induced secondary flows in the tube, interfering with the natural growth of the boundary layer.

Keywords: *smooth tubes, inlet, geometries, transitional, pressure drop*

INTRODUCTION

It is common practice to design heat exchangers of water chillers in such a way that they do not operate in the transition region. This is mainly due to the perceived chaotic behaviour as well as the paucity of information in this region. Due to design constraints or changes in operating conditions, heat exchangers are often forced to operate in this region. This is even worse for enhanced tubes as much less information in this region is available. It is also well known that the entrance has an influence on where transition occurs, adding to the scarcity of available information.

It is accepted in literature that transition from laminar to turbulent flow inside tubes occurs at a Reynolds number of approximately 2 300 [1]. Although this is an accepted value, transition in reality occurs in the range of Reynolds numbers between 2 300 and 10 000 [2]. It is normally advised when designing heat exchangers to remain outside these limits due to the uncertainty and flow instability of this region. For this reason, little design information is available with specific reference to heat transfer and pressure drop data in the transitional flow regime.

* Corresponding author: Prof. J.P. Meyer
Phone: + (27)-12-420 3104, Fax: +(27)-12-362 5124
E-mail address: josua.meyer@up.ac.za

Furthermore, inlet profiles were found to have a profound influence on the transition Reynolds number. Ghajar and co-workers [2-10] performed extensive studies into the effect of three different types of inlets on the critical Reynolds number. However, Ghajar and co-workers used a constant heat flux boundary condition, which heats and does not cool fluids in a tube and does not ensure a constant wall temperature as would occur with water flowing in the inside of the tubes of a shell-and-tube heat exchanger (as is the case in the current work), where refrigerant boiling occurs on the outside.

Heat transfer also had an effect on the laminar friction factor, increasing with the amount of heat added [8]. This effect was also observed by Nunner [11], who performed similar heat transfer experiments. The increase (as much as 100%) was attributed to the buoyancy-induced secondary flow.

The main objective of this paper is to obtain pressure drop data in the transitional flow regime for water flowing through a horizontal smooth tube, while the temperature of the wall is kept constant. The constant wall temperature is the same condition experienced in water chillers where water is cooled in the inner tubes of a shell-and-tube heat exchanger with refrigerant boiling on the outside of the water tubes.

EXPERIMENTAL SET-UP

The experimental test section consisted of a tube-in-tube heat exchanger in a counterflow configuration. Water was used as the working fluid for both streams, with the inner fluid being hot and the annulus fluid being cold. The inlet tube temperature of the inner tube was 40-45ºC and the annulus inlet temperature was 20 ºC. Heating of the test fluid for the inner tube was done by means of a secondary flow loop containing water from a large reservoir. The temperature in this reservoir was maintained at approximately 60ºC by means of an electric heater, while the reservoir for the annulus water was cooled with a chiller.

The test fluid was pumped through the system with two electronically controlled positive displacement pumps. The two pumps were installed in parallel and were used in accordance with the flow rate requirements. The cold water loop was connected to a second large reservoir, which again was connected to a chiller. The water was circulated through the system via an electronically controlled positive displacement pump. Coriolis flow meters were used to measure the mass flow rates.

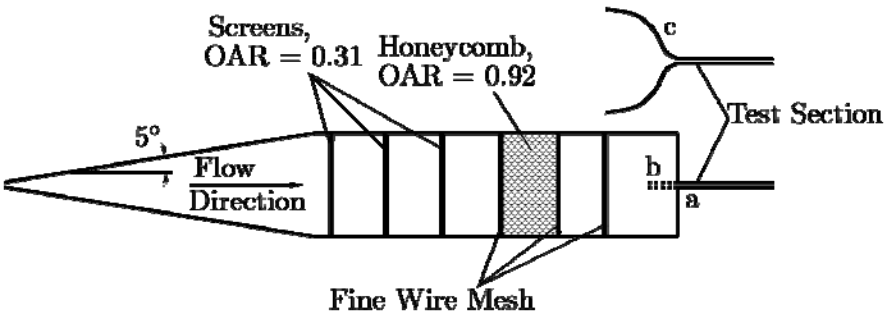

Figure 1. Calming section with the different types of inlet configurations: a) square-edged, b) re-entrant and c) bellmouth.

Prior to the flow entering the test section, for three of the four different types of test sections, the flow first went through a calming section as shown schematically in Figure 1. The purpose of the calming section was two-fold; first, to remove any unsteadiness in the flow and to ensure a uniform velocity distribution and, second, to house three of the four different types of inlets to be investigated. The calming section geometry was based on work conducted by Ghajar and Tam [10]

and consisted of a 5º diffuser, which increased from a diameter of 15 mm to 140 mm. This angle was chosen such to prevent flow separation from the diffuser wall. Three screens were placed after the diffuser with an *open-area ratio* (OAR) of 0.31. The OAR is the ratio of the area occupied by the holes to the total area occupied by the whole screen. A honeycomb section, which had an OAR of 0.92, followed the screens. Prior to and after the honeycomb, a wire mesh was placed with the wires having a diameter of 0.8 mm and the OAR being 0.54. Another fine wire mesh was inserted between the last honeycomb mesh and the test inlet. This mesh had a wire diameter of 0.3 mm and an OAR of 0.17.

Three different inlets could be housed on the calming section, namely a *square-edged*, *re-entrant* and a *bellmouth* inlet. These inlets are also shown in Figure 1 as items a, b and c, respectively. The calming section was designed such that the inlets could easily be interchanged. The square-edged inlet is characterised by a sudden contraction of the flow. This is a typical situation encountered in the header of a shell-and-tube exchanger.

The re-entrant inlet makes use of the square-edged inlet except that the tube slides into the inlet by one tube diameter. This would simulate a floating header in a shell-and-tube heat exchanger.

The third type of inlet is the bellmouth. The bellmouth is characterised by a smooth contraction, having a contraction ratio of 8.8. The shape of the bellmouth was calculated with the method suggested by Morel [12]. The use of a bellmouth is thought to help in the reduction of fouling, although practical application thereof is uncommon in heat exchangers.

The fourth type of inlet used was a fully developed inlet, which did not make use of the calming section. This inlet had an inner diameter being the same as that of the test section. The length of the fully developed inlet was determined in terms of the suggestion by Durst et al. [13], who required a minimum length of 120-tube diameters. To ensure this minimum was met, the length of the inlet was chosen as 160-tube diameters. Cooling started, in the case of adiabatic tests, after this inlet section, while for the other inlets, cooling started after the calming section.

All the insulated test sections were operated in a counterflow configuration and were manufactured from hard-drawn copper tubes. The total length of each test section was approximately 5 m. The tubes tested had a nominal outside diameter of 15.88 mm and inner diameter of 14.482 mm. A constant wall temperature boundary condition for the inner tube was enforced by having a high annulus flow rate. The annulus inner diameter of 20.7 mm was chosen such that the space between the annulus and the inner tube was small, ensuring high flow velocities and thus turbulent flow in the annulus, which further ensured that the annulus had a small thermal resistance compared with that of the inner tube. To prevent sagging and the outer tube touching the inner tube, a capillary tube was wound around the outer surface of the inner tube at a constant pitch of approximately 60º. This also further promoted a rotational flow velocity inside the annulus, producing a higher heat transfer coefficient and thus low thermal resistance.

Differential pressure measurements were made possible by means of two pressure taps inserted at the inlet and outlet of the inner tube. A full experimental uncertainty analysis was performed on the system using the method suggested by Kline and McClintock [14]. Uncertainties for the calculated heat transfer coefficient and friction factors were less than 5% and 18%, respectively.

DATA REDUCTION

The inner tube's average heat transfer coefficient was obtained by making use of the overall heat transfer coefficient and the sum of the thermal resistances, given by

$$\alpha_i = \frac{1}{A_i}\left[\frac{1}{UA} - R_w - \frac{1}{\alpha_o A_o}\right]^{-1} \tag{1}$$

where α is the heat transfer coefficient, A the heat transfer surface area, R the thermal resistance and the footnotes i and o denote inner and outer, respectively. UA is the overall heat transfer coefficient, which can be obtained by means of the overall heat transferred and the log-mean temperature difference T_{lmtd}, that is

$$UA = \frac{\dot{Q}_i}{T_{lmtd}} \tag{2}$$

$\dot{Q}_i$ is the heat transferred in the inner tube, calculated as

$$\dot{Q}_i = \dot{m}_i C_p \Delta T \tag{3}$$

where $\dot{m}$ is the inner-tube mass flow rate, C_p the average specific heat at constant pressure, and ΔT the temperature difference between the in- and outlet of the inner tube. The annulus heat transfer coefficient was calculated by means of the outer-annulus mean wall temperature T_a and inner-tube outer-wall temperature measurements T_{wo}:

$$\alpha_o = \frac{\dot{Q}_i}{A(T_{wo} - T_a)} \tag{4}$$

The inner-tube heat transfer rate was used for all the calculations since it had the lowest uncertainty. Throughout the tests the annulus flow rate was kept as high as possible as this reduced the thermal resistance of the annulus, reducing its influence in Equation (1) and hence decreasing the equation's overall uncertainty. Experimental data were only captured once an energy balance of less than 1% was achieved and steady-state conditions were reached. This entailed that the flow and temperatures did not vary over a period of 10 minutes. At low inner-tube Reynolds numbers (<6 000), this requirement was not met due to the high annulus flow rate and its uncertainty. Validation tests were, however, conducted by substantially lowering the annulus flow rate. These tests proved that the heat transfer error in the inner tube at low Reynolds numbers was indeed less than 1%.

The friction factor of the tube was determined by

$$f = \frac{2D\Delta p}{\rho u^2 L_{\Delta p}} \tag{5}$$

where f is the friction factor, D the tube diameter, Δp the pressure drop, ρ the density, u the average velocity, and $L_{\Delta p}$ the pressure drop length. Since it was not possible to measure inside the inner tube, as it would disturb the laminar velocity distribution and stability, the fluid properties were calculated at the average inner-tube fluid temperature, which, in turn, was determined by the resulting heat transfer coefficient, which was determined from Equation (1), as

$$T_i = \frac{\dot{Q}_i}{A\alpha_i} + T_{wi} \tag{6}$$

where T_{wi} is the inner tube inside wall temperature.

RESULTS

Adiabatic friction factors

Figure 2 shows the adiabatic friction factor results with various inlet profiles. This figure shows how the transition region is manipulated by the use of different types of inlets. The square-edged inlet delays transition to Reynolds numbers of around 2 600, while the bellmouth inlet delays it to about 7 000. Transition for the re-entrant inlet did not differ much from the fully developed inlet. Thus, the smoother the inlet, the more transition is delayed.

Laminar flow results for the various inlets, unlike the fully developed results, are slightly higher than the laminar friction factor obtained from the Poiseuille relation.

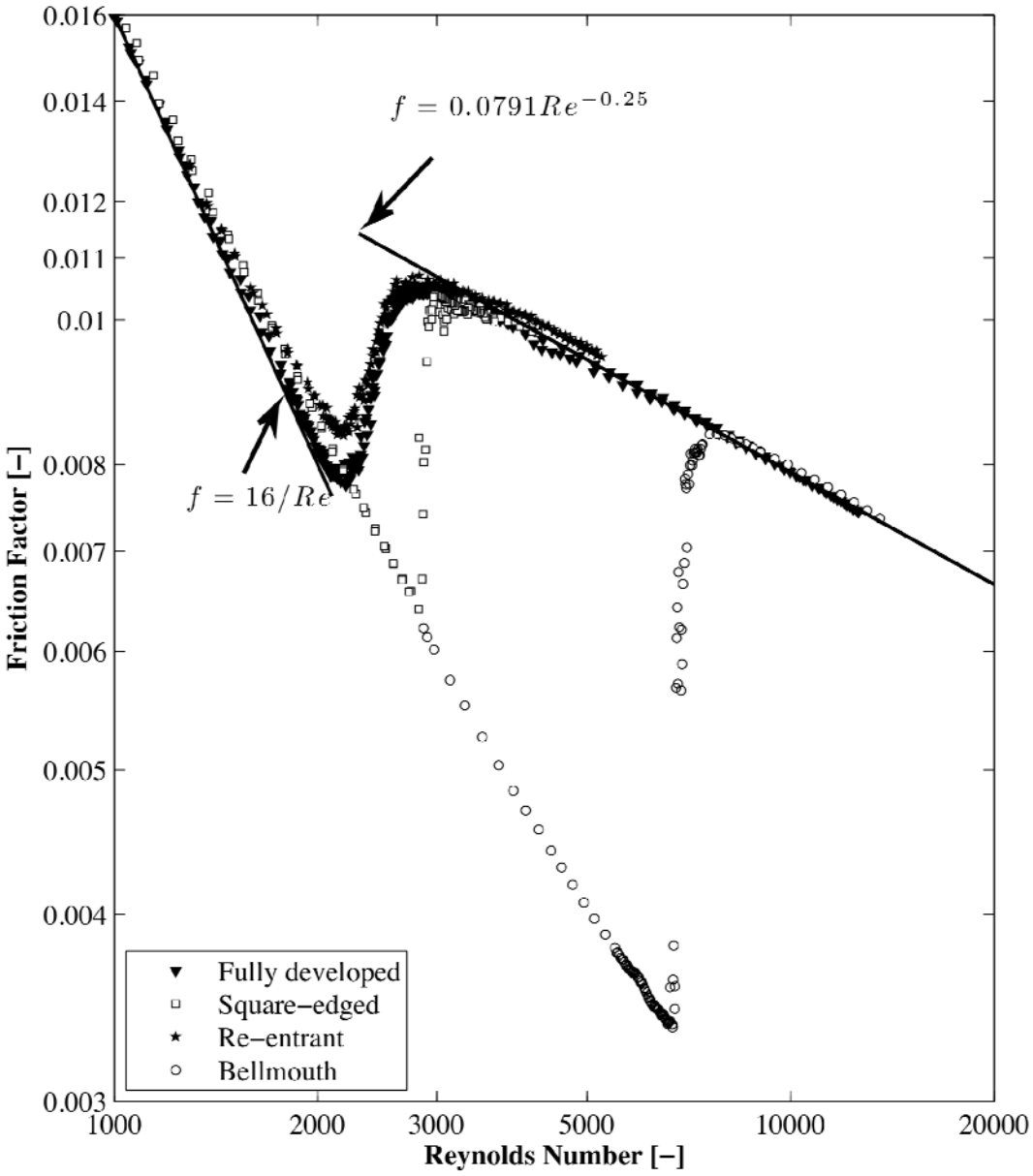

Figure 2. Adiabatic friction factors for the smooth tube with various inlets.

Diabatic friction factor

Since it has been shown that viscosity differences between the bulk of the fluid and the fluid at the wall have an effect on friction factors [15], it is of importance to report on the diabatic friction factors as well. This is further substantiated by the fact that there is a secondary flow component present [8]. The presence of this secondary flow is shown in Figure 3 with regard to the laminar and transition regions for all the different inlets of the two diameter tubes. Plotted on the graph are the experimental friction factors for the smooth tube during fully developed flow, the laminar Poiseuille relation, the turbulent Blasius equation and the Blasius equation with a viscosity ratio correction, $(\mu/\mu_w)^{-0.2}$, as suggested by Allen and Eckert [16].

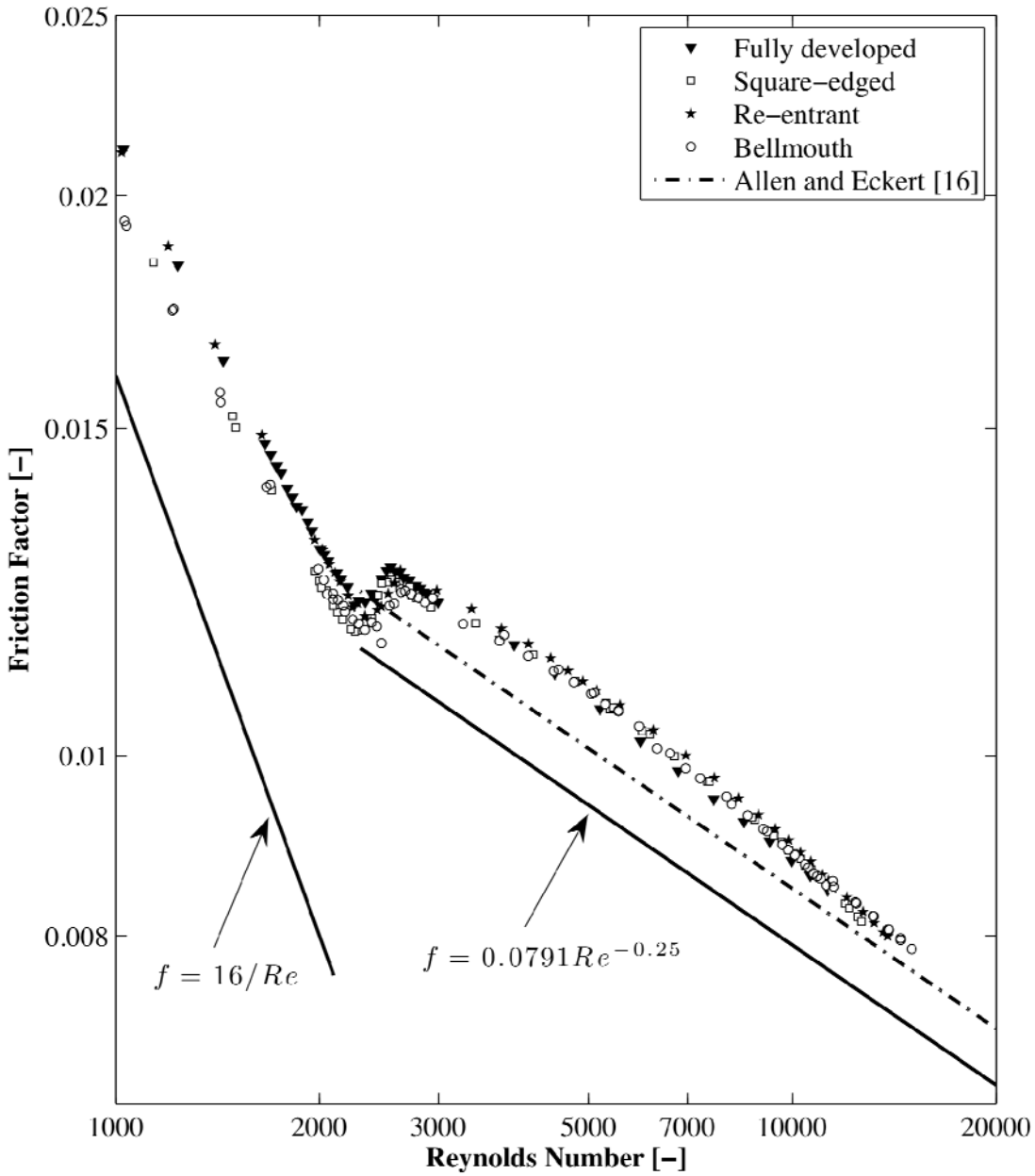

Figure 3. Diabatic friction factors for the smooth tubes with various inlets.

Turbulent flow results correlated fairly well with the viscosity ratio correction, although it would seem as if full turbulence is only reached at Reynolds numbers above 15 000. Unfortunately, the range of data was limited such that this could not be confirmed by taking measurements at Reynolds

numbers greater than 15 000. For the laminar flow region, friction factors were on average 35% higher than predicted by the Poiseuille relation. Even with a viscosity correction, the prediction only improved by 4%. This increase in friction factor can be attributed to the secondary flow effects, with data from Nunner [11] showing similar results. Tam and Ghajar [8] also noted this increase and found that it was dependent on the heating rate. This implies that since the friction factor is proportional to the wall shear stress, which in turn is proportional to the velocity gradient at the wall, secondary flows distort the velocity profile in such a way that the velocity gradient near the wall is much greater. This would then give rise to the higher friction factors. Many numerical and experimental studies have been performed showing this distortion [17-19].

CONCLUSIONS

Adiabatic friction factors showed that transition from laminar to turbulent flow was strongly dependent on the type of inlet used. The smoother the inlet, the more transition was delayed. Results for the bellmouth inlet showed the largest delay, with transition only occurring at a Reynolds number of approximately 7 000.

On the contrary, diabatic friction factor results also showed that transition was independent of the type of inlet. Laminar friction factors were, however, much higher than the values predicted by the Poiseuille relation. This was also attributed to the natural convection flows influencing the boundary layer to such a degree that the shear stress at the tube wall is higher than normal.

ACKNOWLEDGEMENTS

The following organisations are thanked for their support: the American Society of Heating, Refrigerating and Air-Conditioning Engineers (ASHRAE), which was the main sponsor of this project (RP-1280), the University of Pretoria, the Technology and Human Resources for Industry Programme (THRIP) - AL631, the Tertiary Education Support Programme (TESP) of Eskom, the National Research Foundation (NRF), CSIR, SANERI, and the National Aerospace Centre of Excellence (NACoE).

REFERENCES

1. ASHRAE, Fluid Flow, *ASHRAE Handbook – Fundamentals*, American Society of Heating, Refrigerating and Air-Conditioning Engineers, Inc., Atlanta, 2005.
2. Tam, L.M. and Ghajar, A.J., Effect of Inlet Geometry and Heating on the Fully Developed Friction Factor in the Transition Region of a Horizontal Tube, *Experimental Thermal and Fluid Science*, Vol. 15, pp. 52-64, 1997.
3. Ghajar, A.J. and Madon, K.F., Pressure Drop Measurements in the Transition Region for a Circular Tube with Three Different Inlet Configurations, *Experimental Thermal and Fluid Science*, Vol. 5, pp. 129-135, 1992.
4. Ghajar, A.J. and Tam, L.M., Heat Transfer Measurements and Correlations in the Transition Region for a Circular Tube with Three Different Inlet Configurations, *Experimental Thermal and Fluid Science*, Vol. 8, pp. 79-90, 1994.
5. Tam, L.M. and Ghajar, A. J., The Unusual Behavior of Local Heat Transfer Coefficient in a Circular Tube with a Bell-Mouth Inlet, *Experimental Thermal and Fluid Science*, Vol. 16, No. 3, pp. 187-194, 1998.
6. Tam, L.M. and Ghajar, A. J., Transitional Heat Transfer in Plain Horizontal Tubes, *Heat Transfer Engineering*, Vol. 27, No. 5, pp. 23-38, 2006.
7. Ghajar, A.J. and Zurigat, Y.H., Microcomputer-Assisted Heat Transfer Measurement/Analysis of a Circular Tube, *International Journal of Applied Engineering Education*, Vol. 7, No. 2, pp. 125-134, 1991.

8. Tam, L.M. and Ghajar, A.J., Effect of Inlet Geometry and Heating on the Fully Developed Friction Factor in the Transition Region of a Horizontal Tube, *Experimental Thermal and Fluid Science*, Vol. 15, pp. 52-64, 1997.
9. Ghajar, A.J. and Tam, L.M., Flow Regime Maps for a Horizontal Pipe with Uniform Wall Heat Flux and Three Inlet Configurations, *Experimental Thermal and Fluid Science*, Vol. 10, pp. 287-297, 1995.
10. Ghajar, A.J. and Tam, L.M., Laminar-Transition-Turbulent Forced and Mixed Convective Heat Transfer Correlations for Pipe Flows with Different Inlet Configurations, *HTD, Fundamentals of Forced Convective Heat Transfer*, ASME, Vol. 181, pp. 15-23, 1990.
11. Nunner, W., Heat Transfer and Pressure Drop in Rough Tubes, *VDI-Forschungsheft*, 455-B5-39, 1956.
12. Morel, T., Comprehensive Design of Axisymmetric Wind Tunnel Contractions, *Journal of Fluids Engineering*, Vol. 97, No. 2, pp. 225-233, 1975.
13. Durst, F., Ray, S., Ünsal, B. and Bayoumi, O.A., The Development Lengths of Laminar Pipe and Channel Flows, *Journal of Fluids Engineering,* Vol. 127, pp. 1154-1160, 2005.
14. Kline, S.J. and McClintock, F.A., Describing Uncertainties in Single-Sample Experiments, *Mechanical Engineering*, Vol. 75, pp. 3-8, 1953.
15. Sieder, E.N. and Tate, G.E., Heat Transfer and Pressure Drop in Liquids in Tubes, *Industrial and Engineering Chemistry*, Vol. 28, No. 12, pp. 1429-1435, 1936.
16. Allen, R.W. and Eckert, E.R.G., Friction and Heat-Transfer Measurements to Turbulent Pipe Flow of Water (Pr=7 and 8) at Uniform Wall Heat Flux, *Journal of Heat Transfer*, Vol. 86, pp. 301-310, 1964.
17. Mikesell, R.D., *The Effects of Heat Transfer on the Flow in a Horizontal Pipe,* Ph.D. thesis, Chemical Engineering Department, University of Illinois, 1963.
18. Faris, G.N. and Viskanta, R., An Analysis of Laminar Combined Forced and Free Convection Heat Transfer in a Horizontal Tube, *International Journal of Heat and Mass Transfer*, Vol. 12, pp. 1295-1309, 1969.
19. Hishida, M., Nagano, Y. and Montesclaros, M.S., Combined Forced and Free Convection in the Entrance Region of an Isothermally Heated Horizontal Pipe, *Journal of Heat Transfer*, Vol. 104, pp. 153-159, 1982.

FLOW PATTERN PREDICTION OF CO_2 AT HIGH PRESSURE BY DISCRETE BUBBLE MODEL

T. Ami[1,*], H. Umekawa[1], M. Ozawa[1], M. Shoji[2]
[1]Kansai University, Osaka, Japan
[2]Kanagawa University, Kanagawa, Japan

ABSTRACT. Spatio-temporal fluctuation of void fraction fluctuation is one of the typical and inherent characteristics of two-phase flow. So far conducted modellings are based on a time-averaging concept for making use of conventional hydrodynamic theory, which brings, on one hand, about the a substantial conflict in simulating such inherent thermal-flow fluctuations including flow pattern transition, void fraction, pressure drop and heat transfer. This paper describes alternative approach for two-phase flow dynamics in a horizontal flow. The developed model successfully simulated the void fraction fluctuation and thus the PDF, so that the flow pattern map was well reconstructed.

Keywords: *discrete bubble model, horizontal flow, flow pattern, void propagation*

INTRODUCTION

Two-phase flow is a very complex system due to an existence of interface between gas and liquid phases. In addition, the interface structures are spatio-temporally deformable, because break-up, coalescence and expansion of bubbles are always encountered while flowing downstream. In this field of study, this instantaneous geometrical configuration is referred to as a flow pattern. The thermal-flow characteristics of two-phase flow are greatly dependent on the combination of two phases, and thus the flow pattern is a very important planning and/or design factor of two-phase flow systems, such as boilers, boiling water reactors, steam generators of pressurized water reactors and other heat exchangers. At high heat flux condition in these boiling two-phase flow systems, a critical heat flux (CHF) may occur by the inherent fluctuations of two-phase flow. However, in the conventional two-phase flow modellings such as drift-flux model and two-fluid model, a spatio-temporally irregular two-phase flow, e.g. slug flow shows two peaks of probability density function (PDF) of void fraction fluctuation, is formulated as a continuous two-phase flow having a uniform distribution of void fraction. That is caused by a time-averaging process in the two-phase flow modelling, otherwise the conventional hydrodynamics theory is hardy applied. Thus, these conventional modellings fail to simulate the void fraction fluctuation, the flow pattern transition and the critical heat flux due to inherent fluctuation.

An alternative approach to solve the current problem, the discrete bubble model [1, 2] has been developed by the authors in the framework of a pattern dynamics approach. In the discrete bubble model, two-phase flow is simulated with the void propagation equation as a global rule applied over the whole flow filed and a few local rules corresponding to momentum effect, i.e. the wake effect of preceding bubbles, the compressibility of gas phase and the phase re-distribution causing by geometrical constraint. This discrete bubble model successfully realized void fraction fluctuation as well as the specific statistical nature of each flow pattern in vertical upward flow. In the present

* Corresponding author: Prof. M. Ozawa
Phone: + (81)-6-63680807, Fax: + (81)-6-63680807
E-mail address: ozawa@ipcku.kansai-u.ac.jp

investigation, the discrete bubble model is extended so as to be applicable to horizontal flow, which is a prime interest in this paper.

DISCRETE BUBBLE MODEL

The fundamental concept of the newly developed discrete bubble model for isothermal horizontal flow is the same as the previous one for vertical upward flow [1, 2]. The newly introduced and/or replaced relationships for local rules are the pressure jump condition and slip relationship suitable to horizontal flow, and the rest are unchanged.

Calculation model

Figure 1 shows the flow field considered. A one-dimensional horizontal flow is provided together with the isothermal assumption. A liquid phase is supplied at the left end and a gas phase is injected through a mixing chamber of length L_M. The two-phase mixture from the mixing chamber flows through the channel toward the right end, where the mixture flows out freely at the system pressure.

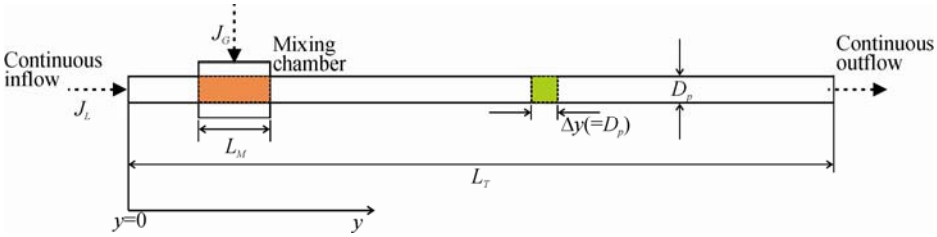

Figure 1. Flow model

The flow field is segmented into the cylindrical cells with the same length as the tube diameter D_p, and this cylindrical cell is used as the frame of reference. The representative bubble is defined as a single gas volume in the cell integrated over the frame of reference and having a geometrical similarity to the unit cell as shown in Figure 2.

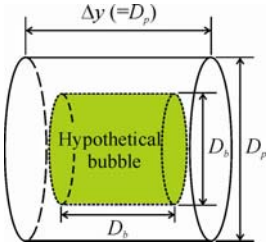

Figure 2. Single hypothetical bubble

Then the void fraction ε in the cell is simply given by

$$\varepsilon = \left(D_b / D_p\right)^3 \tag{1}$$

where D_b is the diameter and length of the single hypothetical bubble. The void propagation equation, as a global rule, is given by equation (2).

$$\frac{\partial \varepsilon}{\partial t} + \frac{\partial\left(\varepsilon U_G\right)}{\partial y} = q\left(= \frac{j_G}{L_M}\right) \tag{2}$$

where U_G is a velocity of gas phase, q is a source term of gas phase, j_G is a volumetric flux of gas phase. In the adiabatic section other than the mixing section, this source term is set at $q = 0$. The local rules which control the behaviour of each hypothetical bubble are needed to represent the two-phase flow dynamics, such as bubble coalescence, breakup, expansion and/or compression leading to the flow pattern transition. The following discussion covers newly introduced and/or replaced local rules together with the other rules applied consistently regardless of the flow direction.

Relative velocity between gas and liquid phases

The velocity of gas phase U_G is the sum of the total volumetric flux j_T (= a volumetric flux of gas phase j_G + a volumetric flux of liquid phase j_L) and the drift velocity of gas phase v_{Gj} which is a function of a void fraction and a slip velocity u_r (= U_G - the velocity of liquid phase U_L). In the vertical flow modelling, the slip velocity was estimated by the force balance acting on a single bubble, i.e. the buoyancy and the drag force. In this horizontal flow model, the following equation is used as the slip relationship.

$$Fr = 0.542 - 1.76Bd^{-0.56} \tag{3}$$

where Fr is the Froude number (= $u_r/(gD_p(\rho_L - \rho_G)/\rho_L)^{0.5}$), Bd is the Bond number (= $(\rho_L - \rho_G)gD_p^2/\sigma$), g is the gravitational acceleration, ρ_L and ρ_G are densities of liquid and gas phases, respectively. σ is the surface tension. This equation was derived from the analytical and experimental investigation on the gas cavity velocity in emptying process from a liquid-filled horizontal channel [3, 4].

Wake effect of the preceding bubble

The wake effect is one of very important factors of the flow pattern transition. When two bubbles moves successively, a succeeding bubble is affected by the wake due to a preceding bubble. The succeeding bubble is pulled by the preceding bubble, and these two bubbles coalesce into a single large bubble. The maximum wake velocity induced by the preceding bubble is given by equation (4), which is the same relationship as the previous vertical upward flow.

$$u_{w,\max,i} = c_1 u_{r,i+1}\left(C_D D_{b,i+1}^2 / \Delta y^2\right)^{1/3} \quad (\varepsilon_{i+1} \geq \varepsilon_i) \tag{4}$$

where $u_{w,max}$ is the maximum wake velocity, c_1 (= 0.715) is a constant, C_D (= 0.44) is a drag coefficient, Δy is a length of unit cell, i is a cell number from the inlet. In the case of $\varepsilon_{i+1} < \varepsilon_i$, $u_{w,max,i}$ is set 0. This wake effect is assumed to have an exponential decay and the local wake velocity u_w of the subjected bubble is given by the summation of the respective wake effects of the preceding bubbles.

$$u_{w,i} = u_{w,\max,i} + \sum_{j=1}^{c3} u_{w,\max,i+j} \exp\{-c_2(j+1)\} \tag{5}$$

where c_2 (= 0.14) and c_3 (= 20) are constant in this simulation. Finally, the substitution of this wake velocity into the following equation gives the ship velocity.

$$u_{r,i+1} = u_{w,i}\left\{\left(C_D D_{b,i+1}^2 / \Delta y^2\right)^{1/3}\right\}^{-1} \quad (u_{w,i} > 0) \tag{6}$$

Compressibility of gas phase

The flowing bubble is expanded or compressed due to the local pressure fluctuations. Isothermal state change of gas phase is assumed. In a horizontal flow, the gravity term plays only a minor role in the total pressure, while a dominant factor in a vertical flow. Then the pressure jump conditions across the cells are given by the regime-based modelling of slug flow [5].

$$p_i - p_{i+1} = \Delta p_f - \rho_L g\left(\varepsilon_{L,i} H_{eq,i} - \varepsilon_{L,i+1} H_{eq,i+1}\right)/2 + \varepsilon_{L,i+1}\rho_L U_{L,i+1}\left(U_{L,i+1} - U_{G,i+1}\right) - \varepsilon_{L,i}\rho_L U_{L,i}\left(U_{L,i} - U_{G,i}\right) \quad (6)$$

where p is a pressure, H_{eq} is the equivalent liquid height, ε_L is a liquid holdup. Each term of the R.H.S. in equation (6) represents the frictional pressure drop, the static pressure difference caused by liquid height difference, the scooped and shed momentum at the tail and the nose of the bubble. The frictional pressure drop is calculated as the sum of the part of liquid phase and the part of bubble. The wall friction factor of liquid phase is a function of Reynolds number similar to single phase flow based on hydrodynamics, while the wall friction factor around the bubble is 0.005 [6]. The equivalent liquid height in equation (7) is calculated by using the separated flow model as shown in Figure 3 [4, 5].

$$\varepsilon_L H_{eq}/2 = \frac{1}{A}\int_0^h y C_i dy \quad (7)$$

where A is the area of cross section, h is the height of gas-liquid interface, y is the distance from a gas-liquid interface and C_i is the chord length at y. The third and fourth terms in equation (6) are not limited in a horizontal flow, but are insignificant in a vertical flow relative to the gravity term.

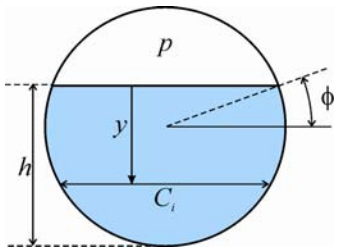

Figure 3. Equivalent liquid height based on separate flow model

Phase re-distribution due to geometrical construction

The large bubble is expanded due to the compressibility of gas phase in this model. In the course of simulation the diameter of hypothetical bubble becomes larger beyond the tube diameter. In order to avoid this inconsistency, the limiting void fraction ε_{cr} is set, and the excess amount ($\Delta\varepsilon_i = \varepsilon_i - \varepsilon_{cr}$) beyond the limiting void fraction is compensated through the re-distribution process to the downstream cell. On the other hand, a surplus liquid holdup pushed out of the downstream cell $\delta\varepsilon_L$ is uniformly re-distributed to upstream cells as shown in Figure 4.

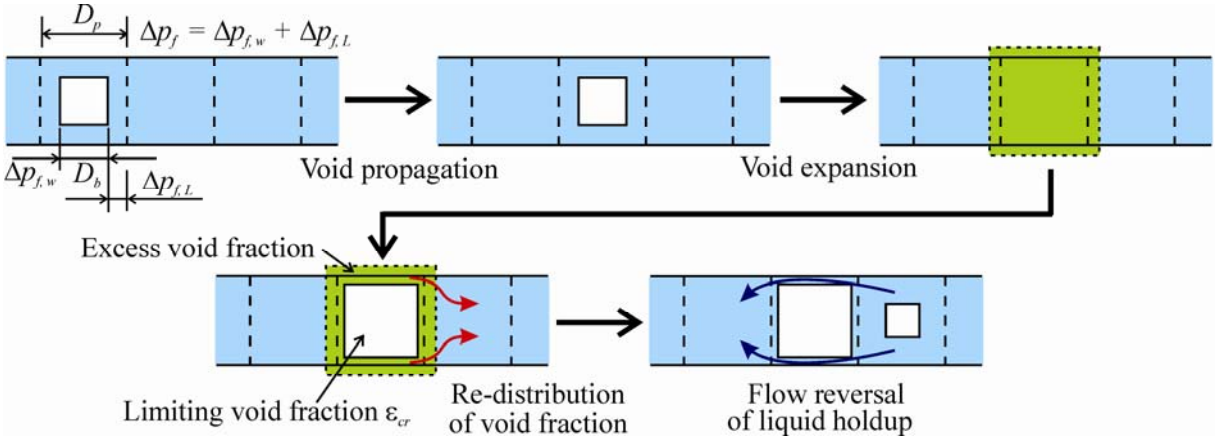

Figure 4. Sequence of simulation

The re-distributed liquid holdup is assumed to be a function of the limiting void fraction as follows:

$$\delta\varepsilon_{L,i} = \Delta\varepsilon_{L,i}/i = \left\{-\Delta\varepsilon_L \exp\left(-c_4\varepsilon_{cr}\right)\right\}/i \tag{8}$$

where c_4 (= 5) is a constant. The limiting void fraction is 0.95, by considering the thickness of liquid film in an annular flow.

NUMERICAL SIMULATION

The numerical simulation was conducted with a finite-difference method. The time derivative and the convective term were expressed by a forward difference and an upwind difference, respectively. To compare with simulation results, the experiment was conducted by using a one-through forced convective boiling system of CO_2 [7, 8]. The simulation conditions and the system configurations are set so as to meet the experimental condition list in Table 1.

Table 1
Simulation conditions and system configurations

Parameter	Set data
Working fluid	CO_2
System pressure	6.5 MPa
Mass flux G	50 to 800 kg/m^{2}s
Quality x	0.01 to 0.9
Length of the test section L_T	400 mm
Length of the mixing section L_M	20 mm
Pressure tap distance L_P	200 mm
Tube diameter D_p	2.0 mm
Number of mesh GN	200
Mesh length Δy	2.0 mm
Time step Δt	0.01 ms

Void fraction fluctuation and flow pattern map

Typical snapshots of the void fraction distribution along the tube are shown in Figure 5 (1) together with the corresponding PDF in Figure 5 (2) detected at the middle position, y = 222 mm, along the tube. Two vertical lines in the snapshot represent the mixing section.

The first group of simulation results is similar to those in a vertical upward flow [1, 2, 9]. In Figure 5 (1)-1 (G = 300 kg/m^{2}s, x = 0.01), there are ripple-like void fraction fluctuation, i.e. void wave, travelling along the tube. The corresponding PDF has a single peak at low void fraction as shown in Figure 5 (2)-1. The flow pattern is considered as a bubbly flow. Increased vapour quality as shown in Figure 5 (1)-2 (G = 50 kg/m^{2}s, x = 0.1), relatively large void waves, corresponding to large bubbles, are intermittently formed along the tube. The PDF has two peaks at both low and high void fractions. The flow pattern is recognized as a slug flow. At the highest quality shown in Figure 5 (1)-3 (G = 300 kg/m^{2}s, x = 0.9), the void fraction becomes rather uniform, keeping almost constant value close to the pre-determinant limiting value. The PDF has a single peak at high void fraction as shown in Figure 5 (2)-3. This flow pattern corresponds to an annular flow.

The next two flow patterns are uniquely appeared in this horizontal flow simulation. In Figure 5 (1)-4 (G = 300 kg/m^{2}s, x = 0.5), there are the sinuous wave-like distribution of void fraction. This wave

fluctuates within a moderate range of void fraction. The corresponding PDF has still two peaks as in Figure 5 (2)-4, while the amplitude is relatively small compared with the slug flow. This type of flow seems a transitional flow pattern from the slug to the annular flow, and is quite similar to the slug-annular flow observed in the experiment. In the last case, Figure 5 (1)-5 (G = 50 kg/m^{2}s, x = 0.8), the void fraction is rather high at wave crest, however, with quite low void fraction at wave trough. Such flow behaviour is similar to the annular flow but with large amplitude waves on the liquid flow. Then the PDF shows two peaks, and this last flow pattern is quite similar to the wavy-annular flow observed in the experiment.

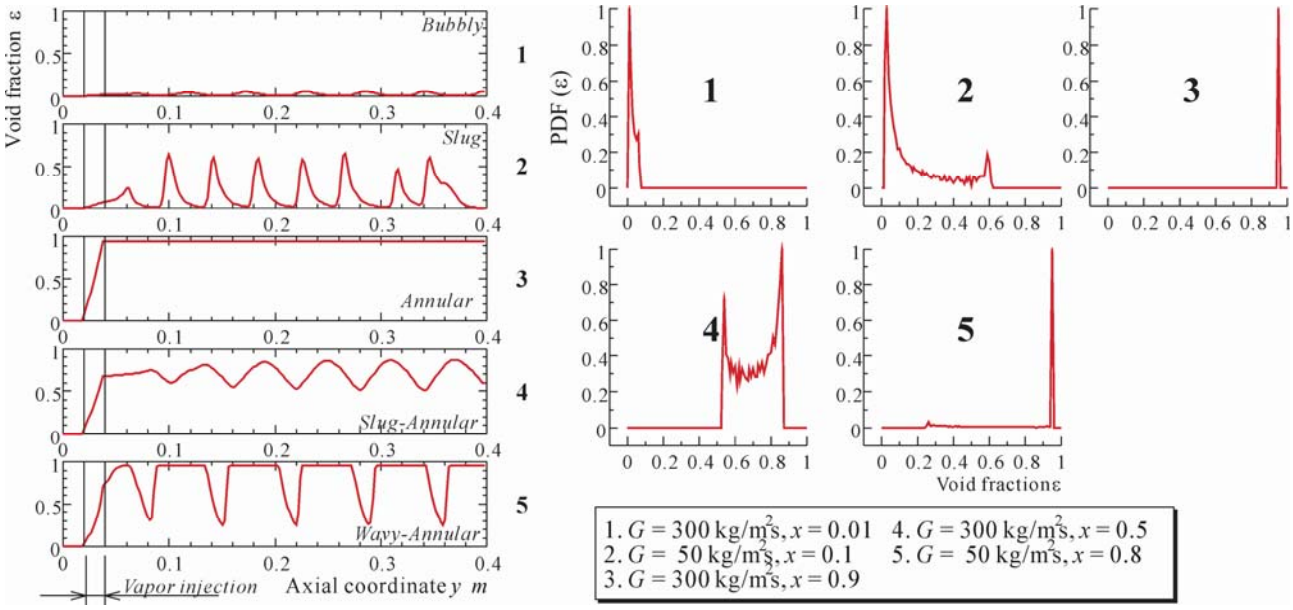

(1) Snapshot (2) PDF

Figure 5. Characteristics of void fraction

The flow pattern identification are conducted with the simulation data, when the identification is, at the first step, based on the above-mentioned typical feature together with the simulation results of discrete bubble model for vertical upward flow [1, 2, 9]. Threshold conditions are listed as a function of a maximum ε_{max} and a minimum ε_{min} void fraction:

Bubbly flow:	$\varepsilon_{min} < 0.1$, $\varepsilon_{max} < 0.6$
Slug flow:	$\varepsilon_{min} < 0.1$, $\varepsilon_{max} \geq 0.6$
Slug-Annular flow:	$0.1 < \varepsilon_{min} < 0.8$, $\varepsilon_{max} < 0.9$
Wavy-Annular flow:	$0.1 < \varepsilon_{min} < 0.6$, $\varepsilon_{max} \geq 0.9$
Annular flow:	$\varepsilon_{min} \geq 0.9$

The flow patterns are potted as a function of x - G in Figure 6 (1)-(a) together with Weisman's diagram [10] for conventional size channel, and the j_G - j_L system in Figure 6 (2)-(a) with Mandhane et al. [11]. The flow pattern map developed for CO_2 or micro-channel, e.g. Cheng et al. [12] and Revellin-Thome [13], does not agree with this experimental results. As a reference, the experimental flow pattern map and photographs of typical flow pattern are shown in Figure 6 (1)-(b), (2)-(b) and Figure 7, respectively.

The flow pattern map with numerical simulation approximately coincides with the experimental observation. The feature that the slug-annular flow penetrates into the annular flow regime predicted with the Weisman's threshold criteria is similar to the experiments. The slug flow has not been observed in the experiment owing to the limitation of pump system, while the comparison with experimental results [8] at 5.0 MPa verifies the relevance of the present model in predicting flow

pattern, including slug flow. Both the simulation and experimental results approximately agree, except the existence of the slug-annular flow, with the Weisman's flow pattern maps. On the other hand, Mandhane's flow pattern map does not agree with the experimental and simulation results, because the flow pattern map of Mandhane was developed based on the data of air-water system.

These results suggest the flow pattern in the mini-channel of CO_2 at high pressure to be similar in conventional channel. In the case of CO_2 at high pressure, a density ratio of liquid to vapour is small, but the effect of surface tension is much more weak. This leads to the applicability of the conventional these threshold criteria as well as the present discrete bubble model to rather small-bore channel, e.g. 2mm.

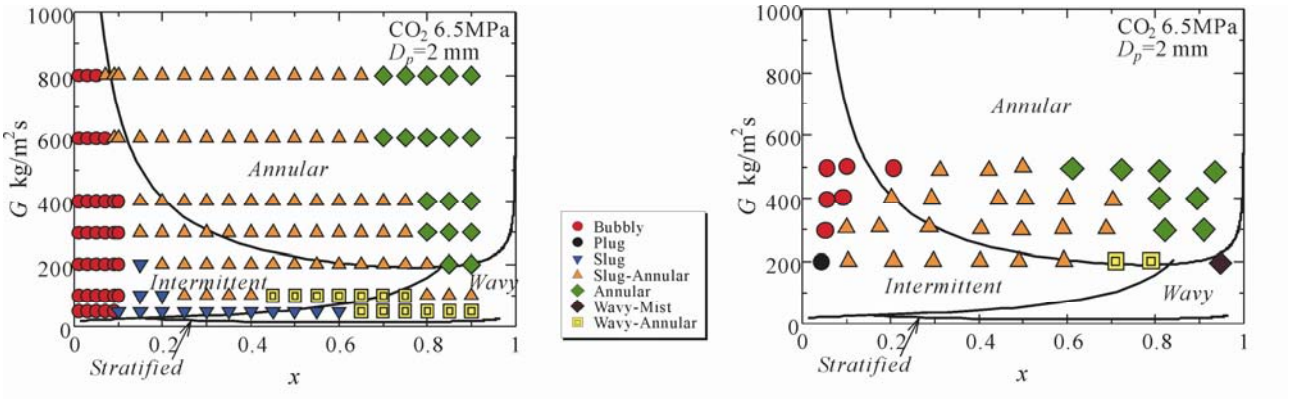

(a) Simulation (b) Experiment

(1) x - G system with Weisman's flow pattern transition

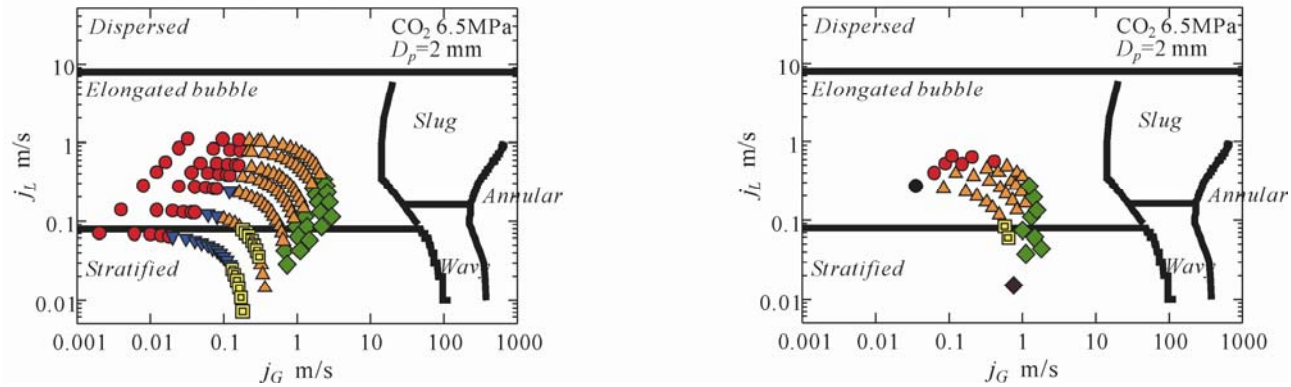

(a) Simulation (b) Experiment

(2) j_G - j_L system with Mandhane's flow pattern transition

Figure 6. Comparison of simulation and experimental results

Figure 7. Photograph of flow patterns

CONCLUSIONS

The discrete bubble model for a vertical flow was successfully modified so as to include horizontal flow mechanisms and the inherent void fraction and flow fluctuation in a horizontal flow of two-phase mixture. The numerical simulation with this model properly realized PDF of void fraction which was available for flow pattern identification. The flow patterns appeared in the simulation were bubbly, slug, slug-annular, wavy-annular and annular flows. The resulting flow pattern maps were in good agreement with the experimental results of CO_2 two-phase flow at high pressure.

ACKNOWLEDGMENTS

This work was supported by JSPS. KAKENHI (19360104). T. Ami is JSPS Research Fellow.

REFERENCES

1. Ozawa, M., Ami, T., Umekawa, H. and Shoji, M., Pattern Dynamics Simulation of Void Wave Propagation, *Multiphase Science and Technology*, Vol. 19, No. 4, pp. 343-361, 2007.
2. Ami, T., Umekawa, H., Ozawa, M. and Shoji, M., Investigation on Two-Phase Flow Dynamics with Discrete Bubble Model, *Thermal Science and Engineering*, Vol. 15, No. 4, pp. 197-209, 2007, in Japanese.
3. Weber, M. E., Drift in Intermittent Two-Phase Flow in Horizontal Pipe, *Can. J. Chem. Eng.*, Vol. 59, No. 3, pp. 1891-1898, 1981.
4. Sakaguchi, T., Ozawa, M., Hamaguchi, H. and Fukunaga, T., Behavior of a Large Bubble in a Horizontal Channel (2nd Report, Large Bubble Penetrating into Running Liquid), *Trans. JSME Ser.B*, Vol. 56, No. 527, pp.1891-1898, 1990, in Japanese.
5. Ozawa, M., Sakaguchi, T. and Hamaguchi, H., Gas-Liquid Two-Phase Transient Slug Flow Modeling, *Memories of the Faculty of Engineering*, Kobe University, No. 32, 1985, pp. 1-23.
6. Wallis, G.B., *One-dimensional Two-Phase Flow*, McGraw-Hill, New York, 1969, pp. 323-324.
7. Ozawa, M., Ami, T., Ishihara, H., Umekawa, H., Matsumoto, R., Tanaka, T., Yamamoto, T. and Ueda, Y., Flow Pattern and Boiling Heat Transfer of CO_2 in Horizontal Small-Bore Tubes, *Proceeding of the US-Japan Seminar on Two-Phase Flow Dynamics*, Santa Monica, CA, 2008.
8. Yamamoto, T., Ueda, Y., Ishihara, I., Ozawa, M., Umekawa, H. and Matsumoto, R., Flow Boiling Heat Transfer of Carbon Dioxie at High Pressure in Horizontal Mini-Channels, *Proceeding of 6th International Conference on Multiphase Flow*, Leipzig, S7_Web_D_44, 2007.
9. Jones Jr., O.C. and Zuber, N., The Interrelation between Void Fraction Fluctuations and Flow Patterns in Two-Phase Flow, *Int. J. Multiphase Flow*, Vol. 2, pp. 273-306, 1975.
10. Weisman, J., Duncan, D., Gibson, J. and Crawford, T., Effects of Fluid Properties and Pipe Diameter on Two-Phase Flow Patterns in Horizontal Lines, *Int. J. Multiphase Flow*, Vol. 5, pp. 437-462, 1979.
11. Mandhane, J. M., Gregory, G. A. and Aziz, K., A Flow Pattern Map for Gas-Liquid Flow in Horizontal Pipes, *Int. J. Multiphase Flow*, Vol. 1, pp.537-553, 1974.
12. Cheng, L., Ribatski, G., Quibén, J. M. and Thome, J. R., New Prediction Methods for CO_2 Evaporation inside Tubes: Part I- A Two-Phase Flow Pattern Map and a Flow Pattern Based Phenomenological Model for Two-Phase Flow Frictional Pressure Drop, *Int. J. Heat and Mass Transfer*, Vol. 51, pp. 111-124, 2008.
13. Revellin, R. and Thome, J. R., A New Type of Diabatic Flow Pattern Map for Boiling Heat Transfer in Microchannels, *J. Micromech. Microeng.*, Vol. 17, pp. 788-796, 2007.

ANALYSIS OF MELTING IN VERTICAL TUBES

H. Shmueli[1], L. Katsman[1], L. Fraiman[1], E. Benisti[1], G. Ziskind[1,*], R. Letan[1]
[1]Heat Transfer Laboratory, Department of Mechanical Engineering,
Ben-Gurion University of the Negev, Beer-Sheva, Israel

ABSTRACT. Melting of a phase change material (PCM) in vertical circular tubes is analyzed based on experimental results obtained in our previous studies. The total initial height of the PCM is divided into horizontal slices. As the melting process advances, the relative share of the solid phase inside each slice decreases. The images taken throughout the melting process are used to determine the volume of the solid phase in each slice at various instants. For each slice, the dependence of the volume on time is approximated by a polynomial function. Then, the melt fraction as a function of time is calculated for each slice separately. The time derivative of the polynomial function is calculated, yielding the heat transfer rate as a function of time for each slice. Based on the results, it is possible to observe the different heat transfer mechanisms that affect the melting process. In particular, at the initial stage of melting the heat transfer rate to the solid PCM is rather uniform along the whole height of the solid phase, corresponding to conduction from the wall to the solid through a gradually increasing liquid layer. As the process advances, heat to the upper part of the solid is brought by convection in the liquid phase. A sharp increase in the convective heat transfer to a certain slice is accompanied, however, by a reduction of the remaining solid volume in that slice. As a result, the heat transfer rate to a slice starts to decrease sharply at some instant, and reaches effectively zero when the melting process in the slice is complete.

Keywords: *melting, vertical tube, melt fraction, local heat transfer, convection*

INTRODUCTION

Phase-change materials (PCMs) are suggested for use in various thermal energy storage systems where their latent heat can be utilized. Vertical tubes are frequently cited as suitable PCM containers. A number of detailed experimental investigations of melting in vertical tubes are reported in the literature. Sparrow and Broadbent [1] studied melting of paraffin in a thin wall copper tube. Visualization was done by interrupting the melting process at various stages and observation of the solid taken outside the tube. Various temperature differences between the wall and the paraffin were explored. Sparrow and Broadbent [1] analyzed the role of convection and established the characteristic conical shape of the remaining solid, widely cited in the literature. Also, they established that the process of melting is governed by both conduction and convection. Menon et al. [2] studied melting of a commercial paraffin wax in vertical copper tubes. Various PCM heights were explored. Visual studies of melting were performed separately, in a glass tube. The observed patterns were similar to those reported by Sparrow and Broadbent [1]. More recently, Jones et al. [3] studied melting of in a vertical cylindrical enclosure heated from the side. The objective was to provide benchmark experimental measurements for validation of numerical codes, using rather sophisticated techniques for monitoring the melting front and image analysis. The melt volume fraction was determined experimentally from the reconstructed interface locations.

* Corresponding author: Dr. G. Ziskind
Phone: + (972)-8-6477089, Fax: + (972)-8-6472813
E-mail address: gziskind@bgu.ac.il

In our previous studies, Katsman et al. [4] explored experimentally the process of melting of a phase change material (PCM) in cylindrical geometry. The material used was a commercially available paraffin-type substance. The experiments were conducted using vertical tubes of four different nominal diameters, namely 1, 2, 3, and 4cm, filled with the PCM and immersed in a water bath. In each tube the experiments were performed at the water bath temperatures of 10, 20 and 30°C above the melting point of the paraffin. The experiments provided detailed phase fields inside the system which were compared with the experimental results from the literature. As the study was done for the same PCM height of 17cm inside the tubes, it was not possible to analyze the effects of the height on the process of melting. Using the same experimental set-up, Fraiman et al. [5] investigated melting at two additional initial PCM heights of 12cm and 6cm inside the tubes. Shmueli et al [6] compared experimental pictures, obtained in previous investigations, with simulation results, providing a detailed heat flux distribution on the inner wall of the tube.

The images of the melting solid, photographically recorded by Katsman [4] and Fraiman et al. [5], reflected transformation of shapes from a cylinder to a cone, which in the process changed in shape and size. Following these observations, the present study attempts to reach an insight into the physical phenomena, which govern this process, by focusing on the local heat transfer to the melting solid inside a vertical tube.

ANALYSIS

The objective of the present study is to obtain the melt fraction and heat transfer rate via determining the volume of the solid phase at various instants during the melting process, based on the experimentally recorded images. An example of image sequence is shown in Figure 1 for the entire melting process in tube with inner diameter of D=4cm, initial PCM height of H=12cm, and temperature difference of ΔT=10 degrees between the outside wall and the PCM melting temperature. The initial height of the solid PCM has been now divided into 12 horizontal "slices", each H_{sl} =1 cm high. The slices, as shown in Figure 1, were denoted from 00-01 at the bottom, to 11-12 at the top. A schematic description of slice definition and evolution is given in Figure 2.

One can see from Figs. 1 and 2 that as the process of melting advances, each of the slices shrinks in volume at rates that vary with time and slice location. Therefore, the image of each slice was measured at the recorded time, and the instantaneous volume was calculated, assuming axis-symmetry of the image. Figure 2 gives a detailed description of that procedure at two sequential instants, t and $t+\Delta t$: the given slice, k to k+1, where k runs from 0 to H/H_{sl}, is characterized by its maximum and minimum diameters, D_k and D_{k+1}. For instance, for the case shown in Figure 1, the maximum number of slices is 12. As can be seen from Figs. 1 and 2, the diameter of the same slice at different instants decreases, until the whole solid slice vanishes completely due to phase change. Thus, as the melting process advances, the number of remaining slices decreases due to the solid shrinkage. Once the maximum and minimum diameters of the slices are measured from the recorded images, the mean diameter is calculated for every slice as

$$D_m(t) = \frac{D_k(t) + D_{k+1}(t)}{2} \tag{1}$$

Then, the time-dependent diameter for each slice is plotted and approximated by a polynomial function using the MATLAB software.

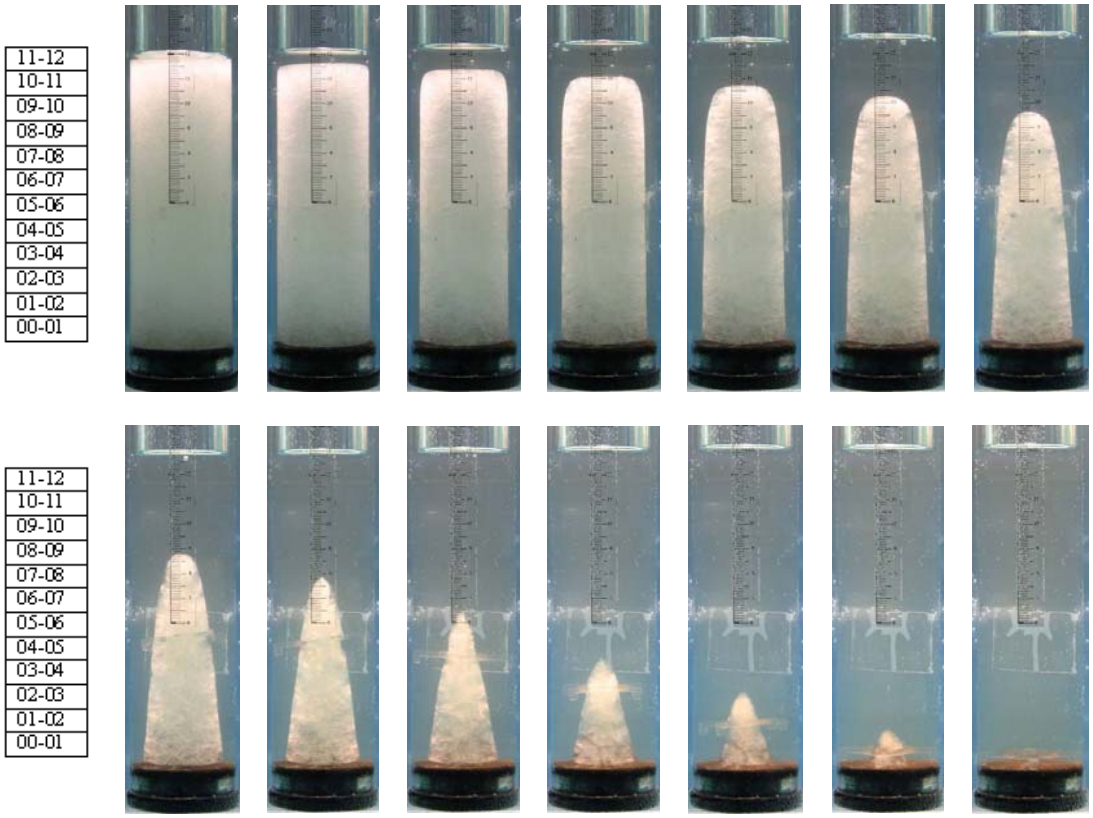

Figure 1. The entire melting process recorded D=4cm, H=12cm, and ΔT=10.

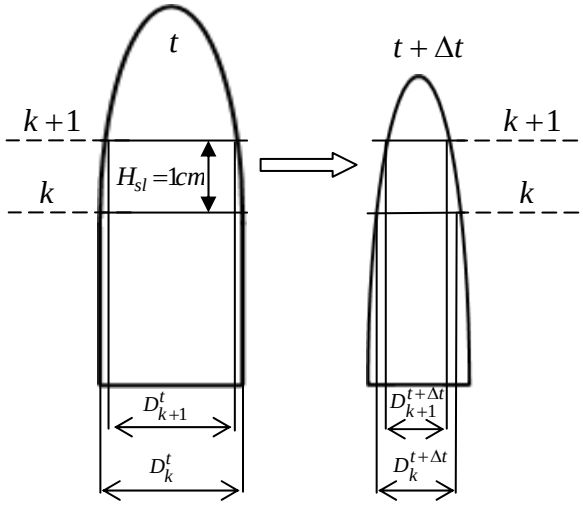

Figure 2. Schematics of slice definition and evolution.

Further, it is assumed that the volume of each slice can be calculated as that of a cylinder which diameter equals D_m, i.e.

$$V_{slice}(t) = \frac{\pi D_m^2(t)}{4} H_{sl} \tag{2}$$

Figure 3 shows the time-dependent volume for each slice of Figure 1 by a separate curve. One can see that at the initial stage of melting the volume of the solid PCM is rather uniform along the whole height of the solid phase, indicating that the dominant heat transfer mechanism during that time is conduction. At some point, the volume starts to deviate from the combined curve, reflecting the development of convective flow at various heights.

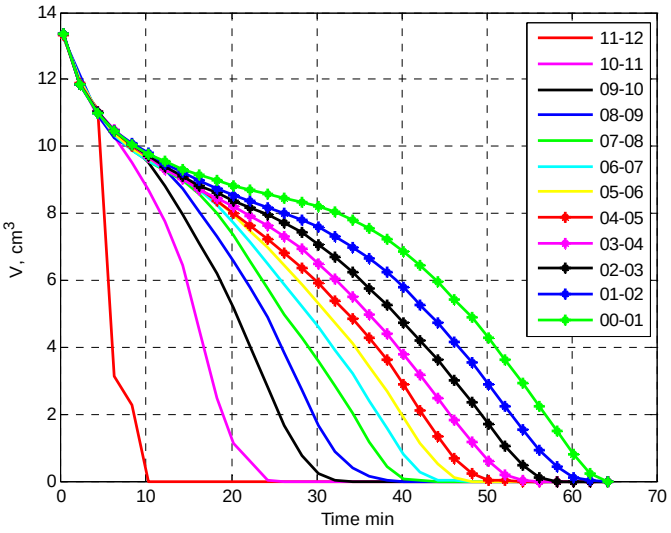

Figure 3. Volume of various solid slices as a function of time.

Having the solid volume, the melt fraction of each slice can be computed as follows:

$$mf_{slice}(t) = 1 - \frac{V_{slice}(t)}{V_{slice}(t=0)} \tag{3}$$

The melt fraction reflects the relative share of material mass which has already become liquid for the time t elapsed since the process has started. This share must be proportional to the heat stored in the PCM due to the phase change. Therefore, the heat stored in the PCM expresses itself in the change of the volume with time. Thus, the heat transfer rate is proportional to the time derivative of the volume:

$$q_{slice}(t) = -\rho L \cdot \frac{dV_{slice}}{dt} \tag{4}$$

where L is the specific latent heat of the PCM. We note that integration of the above expression over a period of time gives the amount of heat stored in the PCM during that period.

RESULTS AND DISCUSSION

In the present paper, six different cases of melting in a cylindrical tube are examined. The cases vary with PCM height, namely 17, 12 and 6cm, in tube with inner diameter, 3 and 4cm and with the temperature differences of 10 and 30 degrees. Figure 4 shows the calculated melt fraction (a) and heat transfer rate (b) for melting with the inner tube diameter of D=3cm, initial PCM height of H=17cm and temperature differences of ΔT=10 degrees between the outside wall and the PCM melting temperature. For each slice, the melt fraction and heat transfer rate are shown by a separate

curve, as a function of time. One can see that at the initial stage of melting the heat transfer rate to the solid PCM is rather uniform along the whole height of the solid phase, causing the initial uniform melting, see Figure 1. Moreover, the lines reflecting the rates in different slices practically coincide during the initial stage. This combined curve shows a monotonic decrease in the heat transfer rate, which corresponds to conduction from the wall to the solid through a liquid layer. The layer width increases with time, thus leading to a gradual increase in the thermal resistance to conduction.

As the process advances, very high heat transfer rates are encountered in the upper slices. This result indicates that heat to the upper part of the solid is already brought by convection in the liquid phase, while conduction dominates the heat transfer to the solid outside the upper region. Gradually, the heat transfer rates for other slices, from the upper to the lower, starts to deviate from the combined curve, reflecting the development of convective flow at various heights. An increase in the convective heat transfer to a certain slice is accompanied, however, by a reduction of the remaining solid volume in that slice. As a result, the heat transfer rate to a slice starts to decrease sharply at some instant, and reaches effectively zero when the melting process in the slice is complete.

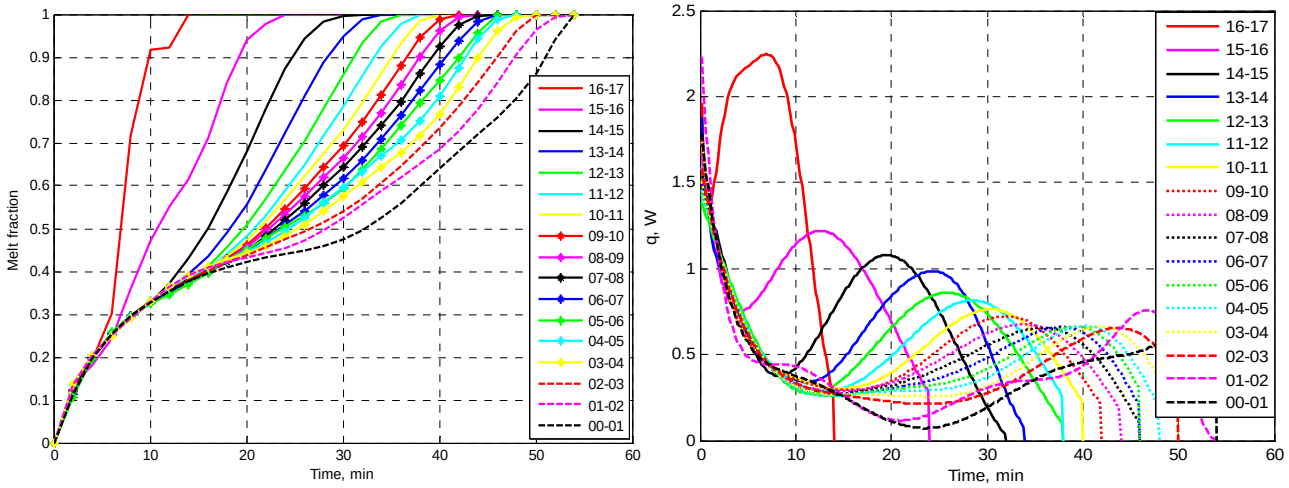

a. melt fraction b. local heat transfer rate

Figure 4. H=17 cm, D=3 cm, ΔT=10 ºC

Similar patterns are shown in Figure 5 for the same tube diameter and PCM height, but with the higher temperature difference of ΔT=30 degrees. Obviously, the complete melting time is now much shorter, namely 19 minutes instead of 54 minutes. Due to the higher temperature difference between the wall and the PCM, the local heat transfer rates reach higher values. However, their behaviour is similar for both cases.

Figure 6 shows the melt fractions and heat transfer rates for a case with a larger tube diameter, but smaller initial PCM height, namely H=12cm, D=4cm, for ΔT=10ºC. Again, the behaviour of the melt fraction and the local heat transfer rates follows the patterns described above. One can also see that while the temperature difference is identical to that of the case of Figure 4, the slice heat transfer rates here are higher. This result can be attributed to a stronger convective flow.

In Figure 7, the results are shown for the same tube diameter and initial PCM height, but with the higher temperature difference of ΔT=30 degrees. As expected, the melting time is much shorter than for the case of Figure 6. One can also note that, similarly to the difference between the results of

Figure 6 and 4, the local heat transfer rates here are typically higher than those in Figure 5 for the same temperature difference.

Figure 8 shows the melt fractions and heat transfer rates for a case with a larger tube diameter, but smaller initial PCM height, namely H=6cm, D=4cm, for ΔT=10ºC. In Figure 9, the results are shown for the same tube diameter and initial PCM height, but with the higher temperature difference of ΔT=30 degrees. The results here are generally similar to those discussed for other initial PCM heights. However, comparing Figures 4a-9a, one can see that the smaller the PCM height, the earlier the divergence of melt fraction curves for different slices appears. This result indicates on the increasing role of convection at the early stages of melting for smaller initial PCM heights.

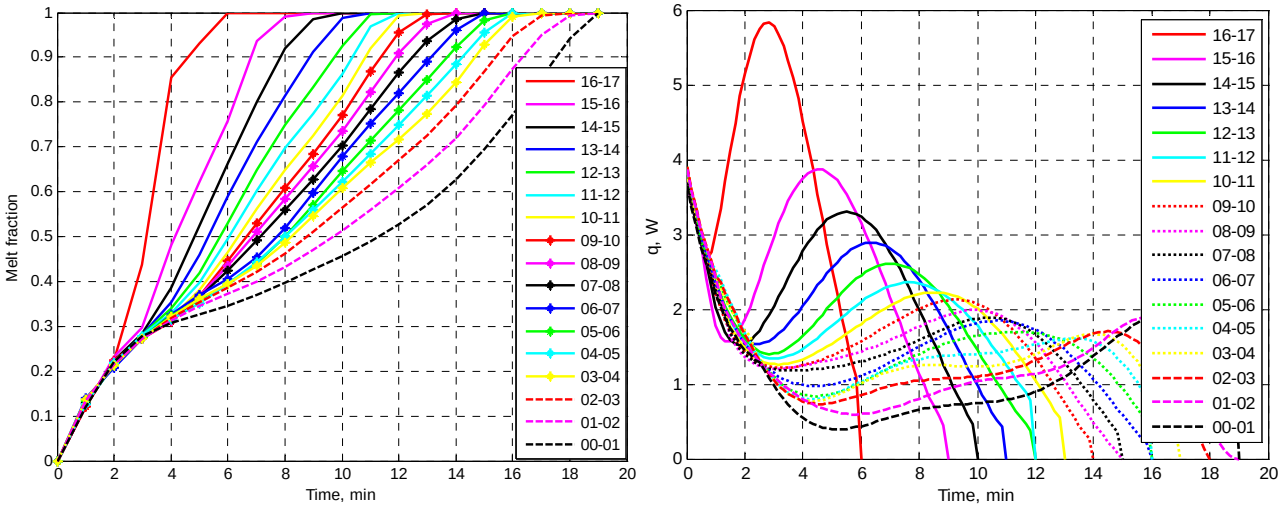

a. melt fraction b. local heat transfer rate

Figure 5. H=17 cm, D=3 cm, ΔT=30 ºC

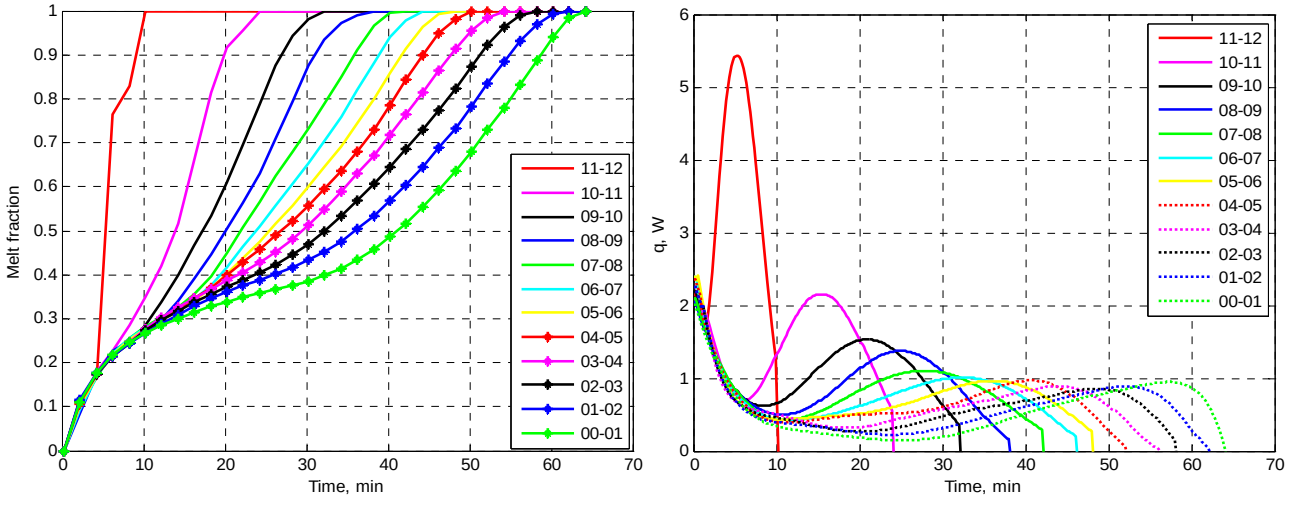

a. melt fraction b. local heat transfer rate

Figure 6. H=12cm, D=4cm, ΔT=10ºC

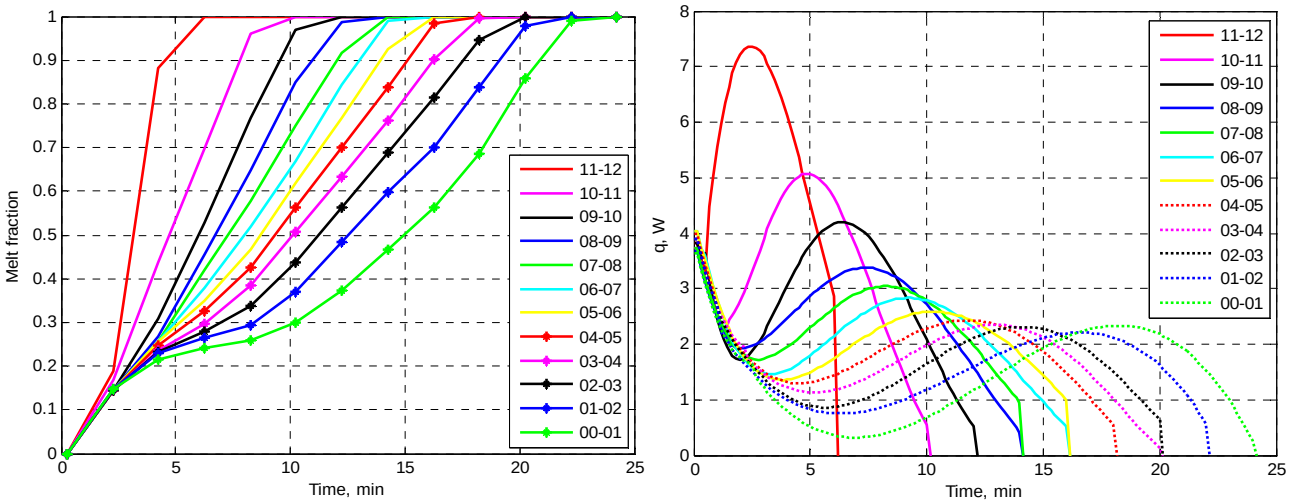

a. melt fraction b. local heat transfer rate

Figure 7. H=12 cm, D=4 cm, ΔT=30 ºC

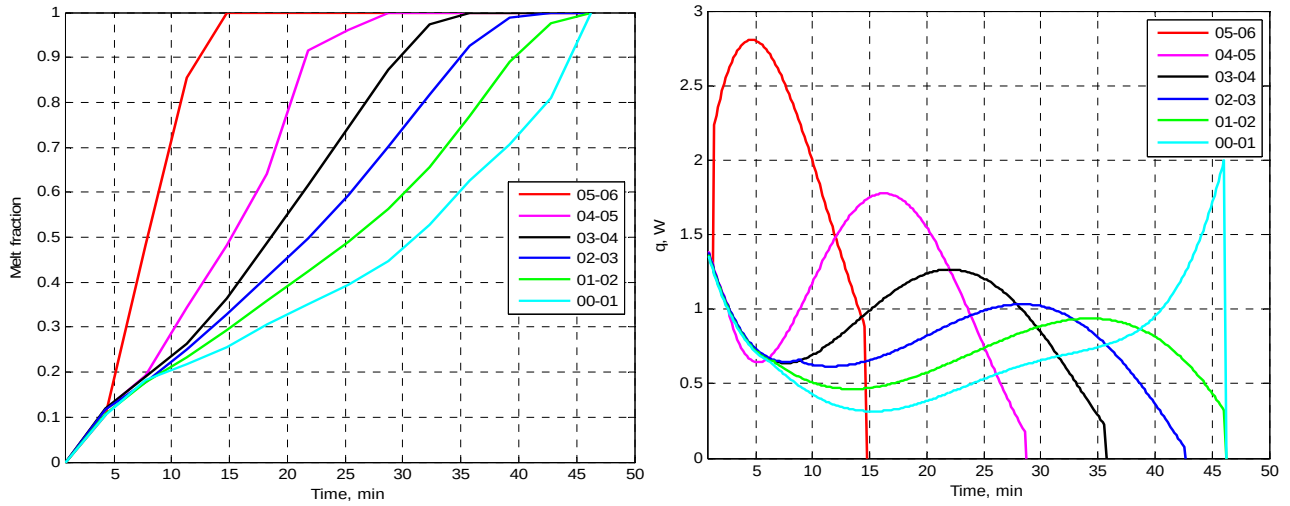

a. melt fraction b. local heat transfer rate

Figure 8. H=6 cm, D=4 cm, ΔT=10 ºC

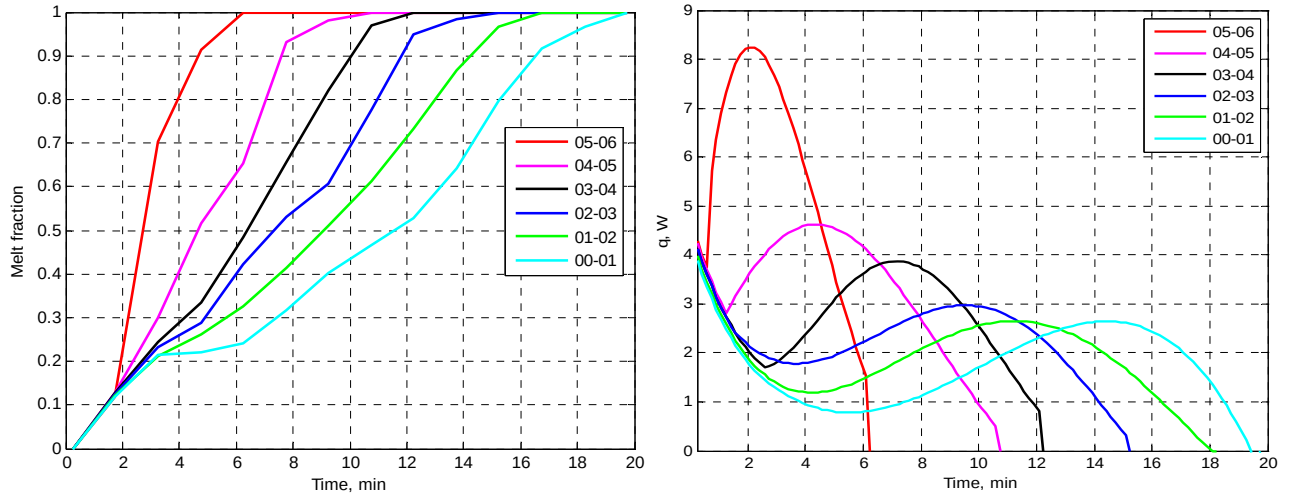

a. melt fraction b. local heat transfer rate

Figure 9. H=6cm, D=4 cm, ΔT=30 ºC

Figure 10 shows the vector flow fields in the upper part of the tube for relatively early and advanced stages of melting, obtained numerically as discussed by Shmueli et al. [6]. One can see that at the initial stages, the solid shape is almost cylindrical, whereas later on the shape becomes more conical due to convection in the liquid phase. This result supports the analysis presented above.

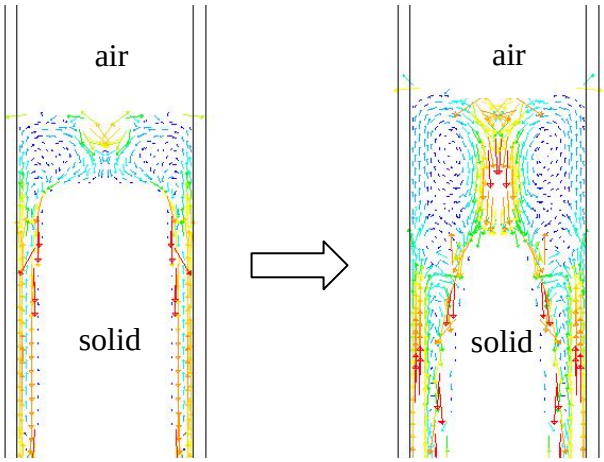

Figure 10. Examples of simulated flow fields.

CONCLUSIONS

Melting of a phase change material (PCM) in vertical circular tubes has been analyzed. The experimental images taken throughout the melting process have been used to determine the volume of the solid phase at various instants. The dependence of the local volume on time has been used to calculate the local melt fraction and heat transfer rate as a function of time. The results make it possible to observe the different heat transfer mechanisms that affect the melting process: at the initial stage of melting the heat transfer rate to the solid PCM is rather uniform, corresponding to conduction from the wall to the solid through a liquid layer. At the more advanced stages, heat to the upper part of the solid is brought by convection in the liquid phase, causing reduction and eventually disappearance of the remaining solid from the top to the bottom of the tube.

REFERENCES

1. Sparrow, E.M. and Broadbent, J.A., Inward Melting in a Vertical Tube which Allows Free Expansion of the Phase-Change Medium, *ASME J. Heat Transfer* Vol. 104, pp. 309-315, 1982.
2. Menon, A.S., Weber, M.E. and Mujumdar, A.S., The Dynamics of Energy Storage for Paraffin Wax in Cylindrical Containers, *The Canadian Journal of Chemical Engineering* Vol. 61, pp. 647-653, 1983.
3. Jones, B.J., Sun, D., Krishnan, S. and Garimella, S.V., Experimental and Numerical Study of Melting in a Cylinder, *Int. J. Heat and Mass Transfer* Vol. 49, pp. 2724-2738, 2006.
4. Katsman, L., Dubovsky, V., Ziskind, G., and Letan, R., Experimental Investigation of Solid-Liquid Phase Change in Cylindrical Geometry, *Proceedings of the 2007 ASME-JSME Thermal Engineering Conference*, Vancouver, Canada, July 2007.
5. Fraiman, L., Benisti, E., Ziskind, G., and Letan, R., Experimental Investigation of Melting in Vertical Circular Tubes, *Proceedings of 9th Biennial ASME Conference on Engineering Systems Design and Analysis*, Haifa, Israel, 7-9 July 2008.
6. Shmueli, H., Ziskind, G. and Letan, R., Numerical and Experimental Investigation of Melting in Vertical Circular Tubes, *Proceedings of the ASME 2008 Summer Heat Transfer Conference*, Jacksonville, Florida, USA, 10-14 August 2008.

EXPERIMENTAL STUDY ON MELTING HEAT TRANSFER OF PHASE CHANGE MATERIALS IN OPEN CELL METAL FOAMS EMBEDDED IN HEAT SINK

J.L. Wang[1], Z. G. Qu[1]*, W. Q. Li[1] , W. Q. Tao[1] , C.Y. Zhao[1,2] , T. J Lu. [1,3]
[1] State Key Laboratory of Multiphase Flow in Power Engineering, Xi'an Jiaotong University, China
[2]University of Warwick, Coventry, England
[3]MOE Key Laboratory for Strength and Vibration, Xi'an Jiaotong University, China

ABSTRACT. Phase change materials (PCM) have high latent heat of fusion with controllable temperature stability and have been used in thermal management for high power electronic device working in intermittent condition. Due to low thermal resistance of PCM, high porosity open-cell metal foams can be embedded in the PCM to improve the thermal conductivity to enhance solid-liquid phase change heat transfer. In this work, a hybrid heat sink whose substrate is hollow is proposed and cooper metal foams filled with paraffin wax are sintered inside the hollow space. The heat sink is heated by film heater attached to the heat sink to simulate the electric chip. The heater surface temperature variations are tested. The influence of metal foam porosity, pore diameter and PCM thermal property on total thermal resistance is studied. The finding is expected to provide guideline for thermal design of high power electronics working on transient condition.

Key words: *Phase change materials, metal foams, melting, solidification, thermal resistance*

INTRODUCTION

Thermal management of electronic device has encounter a great challenge due to the increasing power and decreasing size. Therefore, the traditional positive cooling systems sometimes can't accomplish the cooling task very well considering their economic cost, complex degree, operating conditions and so on [1]. Among the various methods of the thermal control technologies, the passive cooling method using phase change materials (PCM) is receiving considerable attention in recent years.

When PCM is used in the cooling system of electronic device, the latent heat of solid-liquid phase change absorbs heat released from the working electronic chip, keeping chip temperature at allowable range. When electronic device stops working, PCM just melt totally, then the molten PCM solidfies for reuse during the idle time. Therefore, passive thermal management using PCM is suitable for applications working on intermittent or transient conditions [2].

According to Shatikian et al. [3], PCM can be divided into three kinds：organic , inorganic like metals, alloys，and hydrated salts. Paraffin wax which belong to the organic group is the most promising PCM for electronic device cooling system due to its obvious advantages：high latent heat, easy availability, temperature and chemical stability, non-toxicity and so on. PCM cooling systems have proven to be effective in small volume applications with little paraffin wax [2,4]. However, the low conductivity (0.21-0.24W/mK) has become its fatal defect when it's used in larger volume. When the

*Corresponding author, Dr. Z.G Qu
Phone:+(086)-29-82668036, Fax:+(086)-29-82668036
E-mail address: zgqu@mail.xjtu.edu.cn

PCM-based cooling system is used for high power applications, heat dissipated from heat source can not enter into the whole mass effectively, then the melting zone just appears near the heat source, whereas for higher conductivity, heat can be distributed throughout the whole block more effectively [5]. Therefore, heat transfer enhancement techniques is necessary in PCM-based cooling systems for high power electronic applications.

In order to overcome this problems, various methods to improve conductivity of paraffin have been proposed in decades, such as internal fins embedded in paraffin [3,6,7,8,9], inserting metal and graphite-compound matrices in paraffin [1], dispersing high-conductivity particles in the paraffin [10,11,5]. Akhilesh et al. [6] and Wang et al. [7] conducted numerical simulations about PCM-based heat sink with internal fins embedded in the paraffin for cooling portable electronic device, exploring the proper parameters such as sizes, PCM volume fraction, aspect ratio, PCM properties and so on to improve performance of the cooling system. Employing aluminium foams impregnated with PCM as heat sinks for cooling electronics applications, Lafdi et al. [12] implemented experiment to investigate how parameters such as foam properties, heat sink shape, heat sink orientation influencing cooling performance. The numerical simulation [1] they carried out later showed a good agreement of experimental results. Kim and Drzal [10] and Weinstein et al. [5] incorporated graphite nanofibers into paraffin and have a remarkable effects on enhancing paraffin conductivity in the heat storage and electronic device cooling systems.

It can be seen that there are few works exploring PCM melting in cooper porous foams. In the present work, a composite heat sink with paraffin embedded with cooper metal foams encapsulated in its substrate cavity is proposed for electronic device cooling system. The objective of the experiment is to investigate the effects of heat sink parameters such as paraffin property, cooper foam properties(porosity, pore size) on performance of the composite heat sink.

EXPERIMENTAL APPARATUS AND METHOD

Experimental apparatus

The schematic of the aluminium heat sink is shown in Figure 1 and its length is 110 mm, width is 110 mm and the height is 120 mm, and 12 fins is evenly distributed on the top part of heat sink whose height is 30 mm. The substrate of the heat sink is hollow in which the open cell copper metal foam (100×100×80 mm) is fixed compactly inside hollow cavity embedded with paraffin. and then contact thermal resistance between cooper foam and heat sink wall can be alleviated. Four heaters of dimensions 20×20mm are pasted tightly to the bottom of the heat sink to simulate electronic chips with highly conductive silicon paste (heat conductivity =2.5W/m^{2}K). A total of six T-type thermocouples are used, five of which are arranged between heater and bottom wall, the left one for measuring environment temperature and an OMEGA HFS-3 type thin film heat flux sensor is attached between heater and bottom wall of heat sink aiming to test the heat power accurately shown in Figure 2. Since the four heater is distributed symmetrically, so one film heat flux sensor can meet the test requirement. A 2700-multimeter/data acquisition system is used for temperature and heat flux tracking. The data is acquainted every five minutes. The melted liquid paraffin is injected into the open cell cooper metal foam and solidified in advanced before the experiment. With above methods, the heat conductivity of paraffin can be improved to great extend and the heat generated from chips passes through the wall into the cavity and then absorbed by the paraffin. The melting process for PCM will occur conjugated with metal foam matrix heat conduction and melted paraffin natural convection.

(a) Diagram (b) whole view (c) cooper metal foam in substrate hollow cavity

Figure 1. The tested composite heat sink

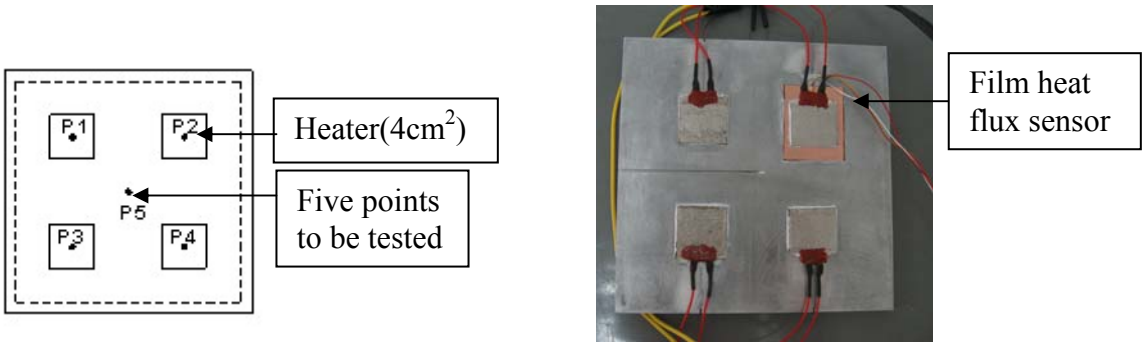

(a) location of heat heaters (b) location of film heat flux sensor

Figure 2. The heaters and film heat flux sensor

Data reduction

There are two kinds of paraffin used in this experiment and the thermal properties of the applied paraffin including latent heat of fusion and melting point are tested with DSC of TA-Q200 with liquid nitrogen cooling system. The DSC results are shown in Figure 3 and 4 for two kinds of paraffin respectively. It can be found that for two tested paraffin, the melting points are 52℃-54℃and 60℃-62℃; the latent heat are 129kJ/kg and 113kJ/kg respectively. The geometric structure parameters of cooper foams used in the experiment are shown in Table 1.

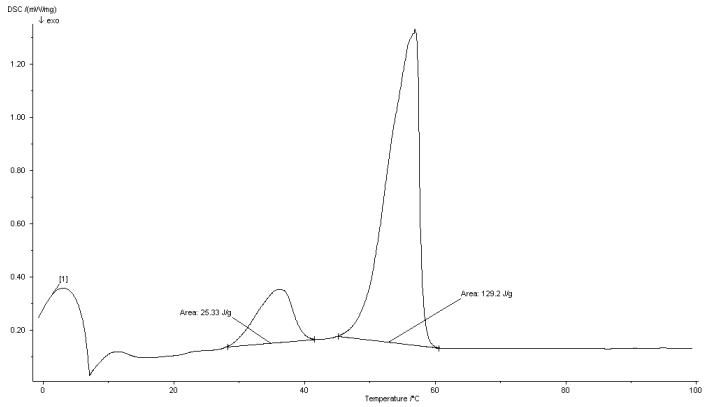

Figure3 DSC results of paraffin type 1

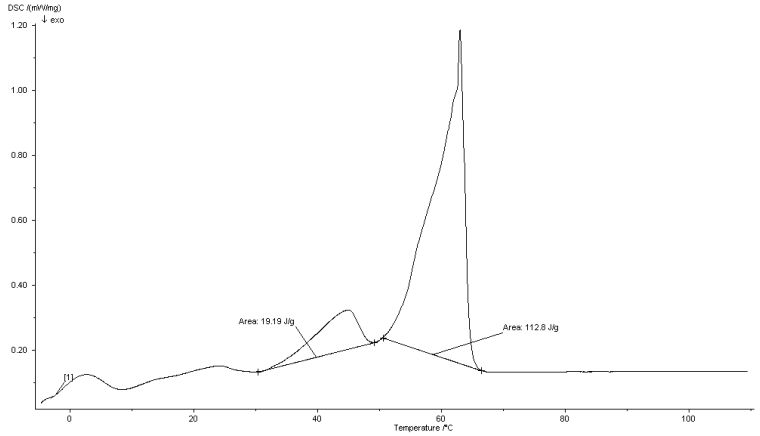

Figure4 DSC results of paraffin type 2

Table 1
Properties of Cooper Foams

Samples No.	Porosity ε	Pores per inch PPI	Size (length*width*height) (mm)
1	0.90	10	100*100*80
2	0.90	20	100*100*80
3	0.90	40	100*100*80
4	0.95	10	100*100*80
5	0.95	20	100*100*80
6	0.95	40	100*100*80

In order to remove the influence of variations of environment temperature and input power, junction temperature variation was tracked and transferred into thermal resistance which is defined as the temperature rise per unit input power. The relation of the two is as shown in equation (1).

$$R = \frac{T_j - T_a}{q * A} \quad (1)$$

Where R represents total thermal resistance of the heat sink (K/W); T_j represents junction temperature (℃); T_a represents the ambient temperature (℃); q represents heat flux of heater $\left(\mathrm{W/m^2}\right)$ which is $1.75\times10^4\mathrm{W/m^2}$; A represents area of heater (m^2). In order to compare the performance with metal foam embedded in PCM, the thermal resistance of heat sink with only metal foam is also studied as comparison reference.

RESULTS AND DISCUSSION

The experimental results are extracted in terms of above total thermal resistance-time. Here only the results of point 1 is only presented since the four heaters are completely identical and is located symetrically. The four key factors including paraffin kind, paraffin property, porosity and PPI on heat

sink thermal resistance are presented respectively. In the following presentation, when one factor is discussed, the other two are kept constant.

The effects of paraffin property

Fig.5 shows thermal resistance as a function of time for two kinds of paraffin wax saturated in the metal foam, with the same porosity of 0.9 and PPI (pore number per inch) of 40. The studied two kinds of paraffin with two different melting points, 52 to 54 and 60 to 62 are respectively and another pure metal foam are introduced to the experiment for comparison. It can be seen that thermal resistance for the pure metal is quite a little higher compared with those with filled with paraffin at the beginning and reaches to the steady state with least time. This phenomenon is mainly attributed to that the temperature has not exceed to the paraffin melting point, the heat condition mechanism dominates and the air heat conductivity is lower to one order than the PCM to create relative larger air thermal resistance in the foam pores which has a dramatically negative effect on heat transfer through the medium, in contrast, the other two porous media saturated with solid paraffin present a relatively less increasing trend in temperature before onset of melting since the equivalent heat conductivity of paraffin is enhanced to some extent by the metal solid matrix.

When the time continues, It is revealed that the paraffin begins to melt to absorb the heat to store as its latent heat in the melting process to lead that the thermal resistance is almost kept constanct and much lower than those with only metal foams. It is to noted that the average thermal resistance for the paraffin with fusion point between 52 and 54 is smaller than that between 60 and 62 due to lower melting temperature and the former medium starts melting earlier than the latter, However, the time duration of the melting process for the latter medium is longer than the former, 80min versus 70min respectively shown as melting zone 1 and melting zone 2 in Figure 5. The most significant discrepancy on thermal resistance (about 1℃/W) appears at the time of the 80thmin. After the melting process , the temperatures for both foams with wax go up sharply until the whole heat transfer process reaches to a steady state and the corresponding thermal resistance at phase change process is narrowed in a very small range.

From the above analysis, if the chip of electronic device works on transient condition, we can choose PCM with proper melting point, latent heat mass quantity based on the chip working interval to make the working time transient interval of chip is less than the melting duration time, the chip can be cooled effectively.

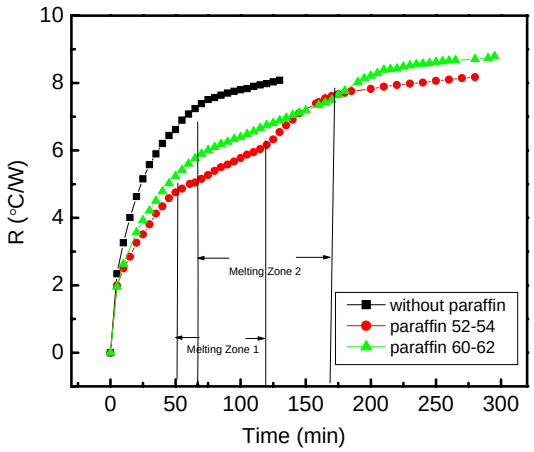

Figure 5 Thermal resistance variation with time for PCM with different melting point

The effects of pore density

The performance of heat sink under three PPI(10, 20 ,40) are studied and the comparison results are displayed in Figure 6. In the present part of study, the paraffin is employed as the type 1 with melting point between 52 to 54 degree and the foam porosity ε is fixed as 0.95. but different PPI(s) (PPI=10, 20, 40) have been chosen for the experiment. It is found that the thermal resistance has dramatically increased and the final steady-state temperature is reached quickly for foams without PCM.For the foams with PCM and the whole thermal resistance is much reduced during the melting process compared with the pure metal foam. It is also found that PPI has relatively mild impact on the performance in heat transfer during phase change process since the thermal resistance is mainly influenced by PCM mass quantity in the foam and in this case the porosity is fixed. It is noted that metal foam with higher PPI can provide more heat transfer surface areas when the porosity is fixed. Hence the thermal resistance of 40 PPI is the lowest while the value for 10 PPI is the highest in the melting duration. In the final steady state, although the foam of 40 PPI has the largest surface area, but it can create more flow resistance to make the heat conduction dominates the heat transfer process and the natural convection is very weak to lead that the thermal resistance is the highest. On the other hand, the foam with 20 PPI has relative larger heat transfer area than the foam with 10 PPI and has relative flow resistance to make natural convection is significant to lead to the smallest thermal resistance of the three PPI.

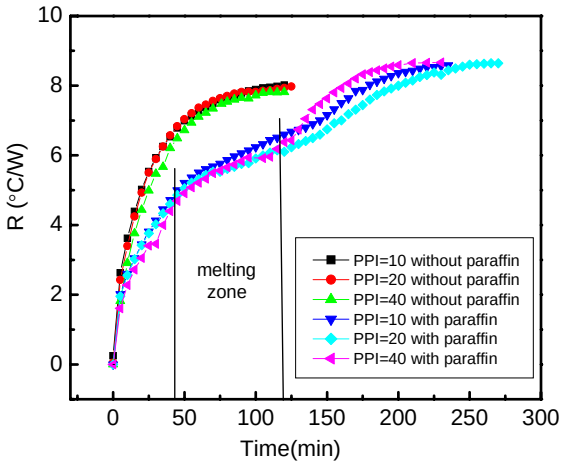

Figure 6 Thermal resistance variation with time for PCM with different PPI

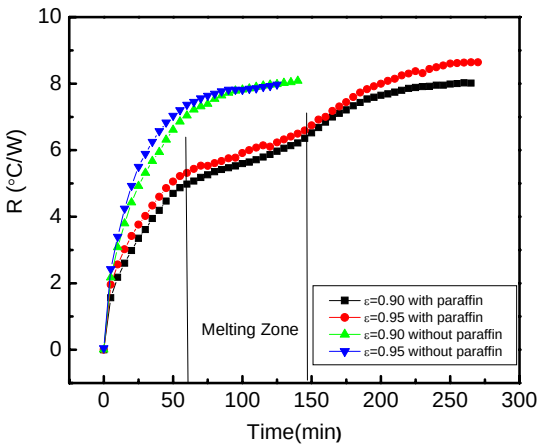

Figure 7 Thermal resistance varation with time for PCM with different porosity

The effects of porosity

The thermal resistance for two studied porosity ε=0.90 and ε=0.95 under the conduit on that the PPI equals 20 with melting point between 52 to 54 degree ia studied. The comparison results are shown in Figure 7. It is found that the thermal resistance is much lower than those with pure metal foam For the two metal foams with different porosity, the porosity plays important role to the thermal resistance and the higher the porosity is, the more thermal resistance it can be achieved in this experimental range. This is attributed that when the PPI is fixed, higher porosity means the metal matrix diameter is smaller that means the function of the metal matrix is more weak. However, the porosity can not be too small to achieve low thermal resistance, otherwise the PCM mass quantity will be reduced greatly and its function will be lost.

CONCLUSIONS

An experimental study on melting heat transfer of phase change materials in open cell cooper foams embedded in heat sink for electronic device has been carried out in this paper. Paraffin wax is introduced as PCM embedded in cooper foam in this experiment. The influencing parameters such as paraffin property, foam porosity and foam pore size are discussed. The major conclusions are as follows:

(1) The proposed campsite heat sink has much lower thermal resit ace for thermal management for higher power electronic devices working on transient condition. The chip surface temperature can be controlled by employing proper PCM thermal property and mass quantity.
(2) During the melting process, the effects of PPI has relative mild effect on thermal resistance and higher PPI can provide positive effect on thermal resistance due to the relative large heat transfer surface when the porosity is fixed.
(3) During the melting process, the effects of porosity has significant effect on thermal resistance and higher lower porosity can provide positive effect on thermal resistance when the porosity is greater than 0.9 due to the relative low heat conductivity resistance when the pore density is fixed. However , it can be predicted that the porosity can not be two small, otherwise, the mass quantity of PCM will reduced significantly.

ACKNOWLEDGEMENT

The authors want to give thanks to National Basic Research Programme of China(No.2006CB601203) and National Natural Science Foundation of China(No.50806057) for support.

REFERENCE

1. Lafdi, K., Mesalhy, O. and Elgafy, A., Merits of employing foam encapsulated phase change materials for pulsed power electronics cooling applications, ASME J. Electrn. Packag., Vol. 130, No. 2, pp 0210041 – 0210048, 2008.
2. Kandasamy, R., Wang, X. Q. and Mujumdar, A. S., Application of phase cahnge materials in thermal management of electronics, Appl. Therm. Eng., Vol. 27, No. 17-18, pp 2822–2832, 2007.
3. Shatikian, V., Ziskind, G. and Letan, R., Numerical investigation of a PCM-based heat sink with internal fins, Int. J. Heat Mass Transfer, Vol. 48, pp 3689-3706, 2005.

4. Tan, F. L. and Tso, C. P., Cooling of mobile electronic devices using phase change materials, Appl. Therm. Eng., Vol. 24, pp 159–169, 2004.
5. Weinstein, R. D., Kopec, T. C., Fleischer, A. S., D'Addio, E. and Bessel, C. A., The experimental exploration of embedding phase change materials with graphite nanofibers for the thermal management of electronics, J. Heat Transfer, Vol. 130, pp 0424051-0424058, 2008.
6. Akhilesh, R., Narasimhan, A. and Balaji, C., Method to improve geometry for heat transfer enhancement in PCM composite heat sinks, International Journal of Heat and Mass Transfer, Vol. 48, pp 2759-2770, 2005.
7. Wang, X. Q., Yap, C. and Mujumdar, A. S., A parametric study of phase change material(PCM)-based heat sinks, International Journal of Thermal Sciences, Vol. 47, pp 1055-1068, 2008.
8. Bugaje, I. M., Enhacing the thermal response of latent heat storage systems, Int. J. Energy Res., Vol. 21, pp 759-766, 1997.
9. Leland, J. and Recktenwald, G., Optimization of a phase change heat sink for extreme environments, Proc SEMITHERM, pp 351-356, 2003.
10. Kim, S. and Drazal, L. T., High latent heat storage and high thermal conductive phase change materials using exfoliated graphite nanoplatelets, Solar Energy Materials & Solar cells, Vol. 93, pp 136-142, 2009.
11. Wang, W., Yang, X. X., Fang, Y. T., Ding, J. and Yan, J. Y., Enhanced thermal conductivity and thermal performance of form-stable composite phase change materials by using β-Aluminum nitride, Applied Energy, 2008.
12. Lafdi, K., Mesalhy, O. and Shikh, S., Experimental study on the influence of foam porosity and pore size on the melting of phase change materials, J. Appl. Phys., Vol. 102, pp 0835491-0835496, 2007.

WATER MIST HEAT TRANSFER FROM GLASS SURFACE

R. Karvinen*, O. Ovaskainen, A. Aronen
Tampere University of Technology, Tampere, Finland

ABSTRACT. The aim of the research is to study the possibility of increasing convection heat transfer from a glass surface using an air–water droplet mist instead of air jets when the glass surface temperature is over 500 ºC. This type of problem is met in tempering thin glasses where very high convection is needed in the cooling phase in order to create a compression stress in the surface and a tensile one in the centre. By using the mist cooling, energy consumption could be reduced and the optical quality of the glass improved.

The idea of using a mist is to utilize phase change when droplets hit the surface. However, it can happen that a vapour layer is formed between the surface and the droplet, and the convection heat transfer is very low. The surface temperature below which phase change occurs is determined by the Leidenfrost temperature, which must be obtained experimentally. The main parameters affecting the Leidenfrost temperature are the thermal properties of the liquid and the surface material to be cooled.

In experiments a hot glass plate with a known thickness was cooled from the upper surface by a mist jet and the lower surface temperature was measured. From the measured temperature the start of the phase change can be obtained, but determining the upper surface temperature requires the solution of an inverse heat conduction problem. In order to test the reliability of an experimental approach also the Leidenfrost temperatures of some metallic materials were measured and the results were compared with those in the literature. For glass the existing data is very sparse. In addition to water, also a mixture of water and ethanol was used. It was noted that the Leidenfrost temperature for glass is slightly more than 500 ºC.

Keywords: *water mist, Leidenfrost temperature, heat transfer, glass tempering*

INTRODUCTION

In glass tempering we want a compression stress in the surface of a glass plate and tension in the middle. This is achieved if cooling is efficient enough. The demand for thin low-cost tempered glass has raised the question of using a water mist in a glass tempering process. Traditionally, glass tempering is done by high- velocity impinging air jets, which can cause undesirable effects on glass flatness. Also air compressing requires lots of energy. By using a water mist, we could lower the energy consumption of the process and make it more cost-efficient. Water mist has been used extensively in the metallurgical industry for cooling and there is a great amount of knowledge concerning heat transfer between metal surfaces and a water mist [4-11]. Different kinds of heat transfer correlations exist, but they are insufficient to predict heat transfer from glass plates.

Water boiling on a hot surface can be divided into three regimes: film boiling, transition boiling and boiling regime. In our study, interest focuses on water mist changing from the film boiling regime to transition boiling, and what the critical heat flux (CHF) is, i.e. the highest value of the cooling

* Corresponding author: Prof. Reijo Karvinen . Tampere University of Technology
Phone: +358 3 31152021, Fax: + 358 3 31153751
E-mail address: reijo.karvinen@tut.fi

heat flux. For a film boiling region Sözbir et al. have suggested that the mist heat transfer and air convection can be treated separately and they presented a correlation for the mist heat transfer from a stainless steel plate [7]. Glass has not been studied properly yet. One correlation in a film boiling region has been presented for glass, but the authors presenting it suspect its reliability [5].

There are only a few articles dealing with glass tempering using a water mist [5, 6]. According to these articles, tempered glass has been made successfully in laboratory conditions with very short spraying times. In order to obtain the required stress field in glass, cooling should occur between 500–700 ºC. In our research, the main interest has been in determining the Leidenfrost (LF) temperature for a water mist with different mist properties and materials, especially glass. Above the LF temperature a thin vapour layer forms between water drops, i.e. we have a film boiling regime, which prevents efficient heat transfer. Below the LF temperature the vapour layer disappears and water is in contact with the surface and wets it. The transition boiling starts and the critical heat transfer occurs. If the glass temperature is low at this point, brittle glass usually breaks. For pyrex glass the LF temperature for saturated water drops has been about 500 ºC, and for drops at 26 ºC over 700 ºC [1,2]. Baumeister et al. and Bernardin et al. have investigated the LF phenomenon and reported factors affecting the LF temperature [1-3]. In the studies above, drops have been carefully located on the surface which is totally different as is the mist cooling. Different materials and liquids were used to determine the LF temperature.

In the case of metal plates the LF phenomenon and heat transfer depend on many characteristics of the mist and the drops in it. Maybe the most important property is the mist mass flux (kg/m^2s), which separates dilute and dense mists. According to Deb and Yao, the drops of a dilute mist do not interact with each other and can be viewed separately [10]. Thus, heat transfer can be modelled as one drop impinging on the surface. Drops of a dense mist start to influence each other by disturbing their hydrodynamic and thermal zones on a solid surface. For both cases Deb and Yao have developed correlations for heat transfer and they have found regimes of mass flux where a dilute mist changes to a dense one. Deb and Yao arrived at a value of about 2 kg/m^2s for the separation point for stainless steel plate. For glass the effect of mist properties has not been investigated.

Hoogendoorn and Den Hond suggested that the LF temperature for stainless steel increases with an increase in the water flux in a mist and in the drop velocity [4]. Also Sözbir and Yao confirmed the same phenomenon and reported that by increasing air velocity in a water mist also the LF point becomes higher [7]. In our study the aim was to investigate the same phenomenon for ROBAX® glass and aluminium plate. Also the effect of different fluid properties on the LF temperature was investigated.

EXPERIMENTAL SETUP

An experimental study was carried out with the setup shown in Figures 1 and 2, in which a full-cone atomizing nozzle was controlled by compressed air (AB Sibe). Also another atomizing nozzle (paint sprayer) with almost the same characteristics as AB Sibe was used for ethanol. Steel, copper, aluminium, brass and ROBAX® glass were used as materials in the experiments. The dimensions of plates were 50 x 50 mm. The thickness of ROBAX® glass plate was 4 mm and that of other materials equal to10 mm. Plates were located inside an insulation during heating. When the plate temperature was over the LF point, for metals 350–400 ºC and for glass 750–850 ºC, the plates were taken out of the oven and positioned under the mist. A shutter was displaced from the upper surface of the tested surface and quenching started. Cooling continued until strong evaporation had ceased. The metal plates were cleaned and polished after cooling. The liquids used in experiments were water, a mixture of ethanol and water and pure ethanol. Measurements were done mainly with plates in a horizontal positions, except in the case of ethanol, when plates were in a vertical position.

Figure 1. Photo of experimental setup.

Table 1
Properties of mists used.

Mists # 1-7	*# 1 Ethano L=200 mm*	*# 2 Water L=200mm; p=2.2•10^5 Pa*	*# 3 Water L=150mm; p=2.2•10^5 Pa*	*# 4 Water L=200mm; p=1.7•10^5 Pa*	*# 5 Water L=150mm; p=1.7•10^5 Pa*	*# 6 Water L=200mm; p=1.3•10^5 Pa*	*# 7 Water L=150mm; p=1.3•10^5 Pa*
Dia, μm	14.5	12.5	10.8	12.6	10.2	4.4	4.0
V, m/s	8.8	12.8	16.2	11.7	15.1	8.1	10.9
Q, (kg/m^{2}s)•10^{-1}	12.2	14.5	18.5	11.4	17.0	0.2	0.3

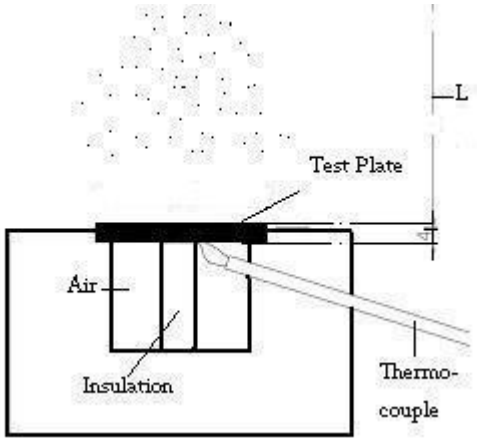

Figure 2. Schematic of experimental setup.

In the case of metal plates, temperature was measured in the middle and at the bottom. The temperature of ROBAX® glass was measured only from the bottom surface. K-type thermocouples were used and temperature was recorded at 0.1 s intervals. The distance between an impinging point and the nozzle could be adjusted and the water flux of the mist was adjusted with an air pressure valve. Distances used were from 150 mm to 300 mm and air pressure was 1.3- 6.0 • 10^5 Pa. Water temperature in the mist was 17 ºC.

Droplet sizes of water mists were measured with a laser Doppler anemometer. The results of different mists are shown in Table 1. Measurements of mist properties were done at the distances of 200 mm and 150 mm from the nozzle and atomizing air pressures were 1.3 - 2.2 • 10^5 Pa. 20000 drop samples were taken from the mist in every measurement.

Mostly aluminium and ROBAX® glass plates were tested. Aluminium was used because it is easy to handle and there are data from previous studies that can be compared with our results [3, 9]. The main interest was in glass. ROBAX® glass was chosen in experiments for its thermal endurance and its small thermal expansion (α (20–700 ºC) = 0.0±0.3•10^{-6} K^{-1}) which allow it to withstand severe stresses during quenching. Its properties are close to those of soda glass, which is usually the material in a tempering process. The properties of ROBAX® glass are: thermal conductivity k (90 ºC) = 1.6 W/mK, density ρ = 2.56 g/cm^3 and mean specific heat capacity c_p (20–100 °C) = 0.8 J/kgK.

EXPERIMENTAL UNCERTAINTY

Temperature measurements of metal plates are exact because the thermocouple was located in a hole inside the plate. In the case of a glass plate, the thermocouple head is in contact with the bottom of the plate and a piece of insulation presses the thermocouple against the plate. Because the thermal conductivity of glass was about 1.6 W/mK and that of insulation material 0.1 W/mK, heat transfer from insulation to the thermocouple can have an effect which cannot be taken into account in data treatment. High temperatures of glass can also contaminate the thermocouple and cause an

error. It is difficult to predict the error because there is no data on the temperature distribution in insulation. As to the properties of the mist the smallest drops could be ignored by the instrument.

MEASURED RESULTS

In Figure 3 a clear drop in the time-temperature curve for aluminium can be seen. Also the difference in the LF point with different mist properties is shown. In Figure 3, L is the distance between the nozzle and surface and p is the air pressure in the nozzle. However, the difference in the LF temperature is quite small for different mists. This is due to the fact that mass fluxes of mists were almost the same and they were probably in a dilute spray region for aluminium. The transition of the LF point is very clearly seen in Figure 4, when different fluids, i.e. water, ethanol and their mixture, are used. The effectiveness of cooling can be seen on the basis of the cooling curve and cooling time. The fluid properties change the LF point significantly. A change of almost 50 ºC is noted when use is made of a 50 % mixture compared with pure water. In reference [3] the LF temperature of the water drop for wiped aluminium is 171 ºC, which is lower than the mist results shown in Figures 3 and 4. The roughness of aluminium, which can have an effect, is unknown in our study. For ethanol the LF temperature in reference [3] is 157 ºC, which is very close to the result shown in Figure 4.

Time-temperature curves for glass are shown in Figures 5 and 6. In the figures for instance the parameter (250, 1.7) means that the distance from the nozzle to the surface is 250 mm and the air pressure in the nozzle is $1.7 \bullet 10^5$ Pa. The change in fluid and mist properties affects the LF point, but the change is not as great as with metals. The start in the boiling regime was difficult to see visually or hear in the case of glass. The greatest clear change can be seen at about 800 ºC in Figure 6 and the lowest is slightly over 500 ºC in Figure 5. Differences in LF temperatures for different mists are higher for glass than for aluminium. This can be seen by comparing the results for glass in Figures 5 and 6 with those for aluminium in Figures 3 and 4.

The measured LF point of 50 % ethanol mist is about 550 ºC. In our measurements with glass it was not possible to see any change in the cooling curve for 100 % ethanol. The amount of water in the mixture seems to control the LF temperature

The top surface temperature cannot be directly obtained from measured ones at the bottom surface.

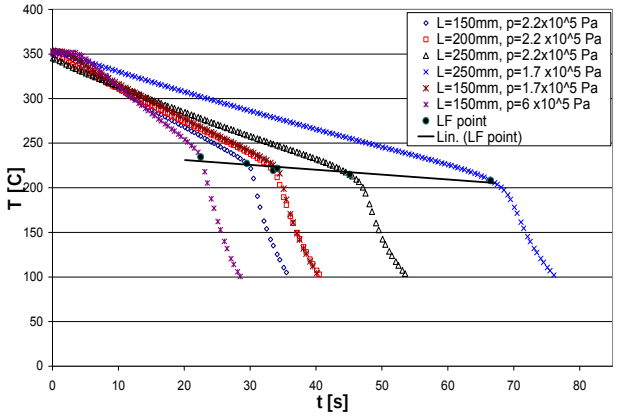

Figure 3. Effect of water mist on LF temperature for aluminium plate.

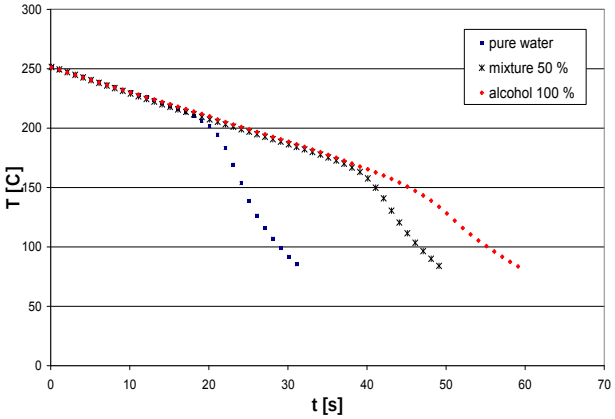

Figure 4. Effect of liquid mixture on LF temperature for aluminium. L = 200 mm, horizontal mist.

It is very difficult to get measurement data from the glass surface when it has been cooled by the mist. In that case it must be calculated from the measured temperature of the lower surface temperature

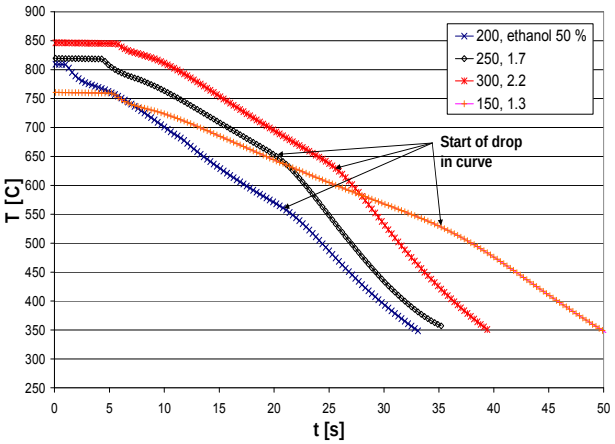

Figure 5. Time-temperature data for glass with 50 % ethanol mist and dilute water mists.

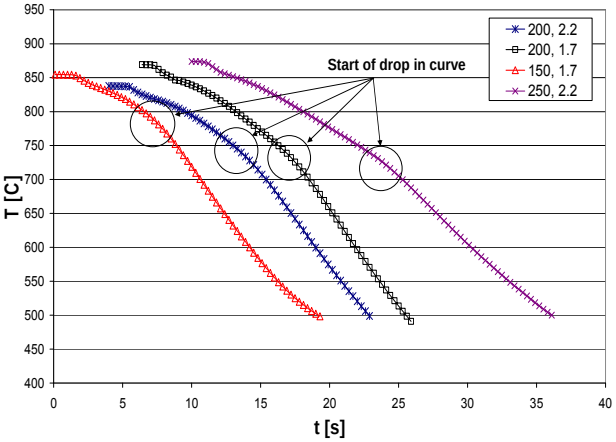

Figure 6. Time-temperature data for glass with dense mists.

SOLUTION OF INVERSE HEAT CONDUCTION PROBLEM

In order to obtain the surface temperature of the plate, an inverse heat conduction problem must be solved. The calculation is based on the basic equation of heat conduction. Mathematically, the inverse heat conduction problem belongs to so-called ill-posed problems, i.e. small changes in measured data can lead to large errors in calculated values. Soti et al. explain that the physical reason of ill-posed problem in heat transfer is that the variations of surface conditions are damped in moving towards the interior of a solid body [12]. Here, all material properties are assumed to be constant in the solution of the inverse problem, governed by the heat conduction equation(1) with the initial and boundary conditions (2) - (4):

$$\frac{\partial T}{\partial t} = \frac{\partial}{\partial x}\alpha\frac{\partial T}{\partial x} \tag{1}$$

$$T(0,x) = T_o \tag{2}$$

$$-k\frac{\partial T(t,l)}{\partial x} = q_s \tag{3}$$

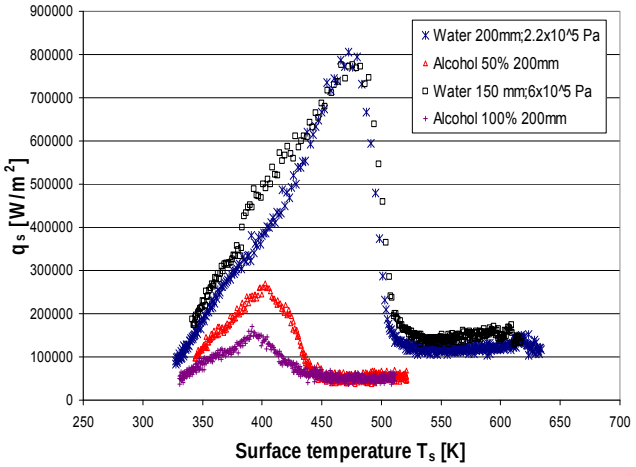

Figure 7. Calculated cooling heat flux at upper surface of aluminium.

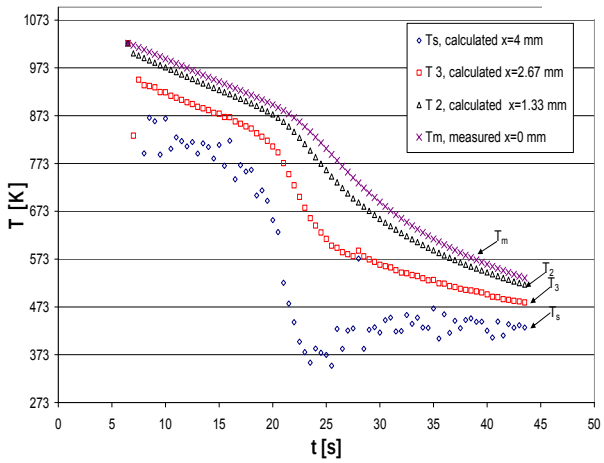

Figure 8. Calculated temperature field in 4 mm glass. Water mist #2 in Table 1.

$$T(t,0) = T_m\,,\quad k\frac{\partial T(t,0)}{\partial x} = 0 \tag{4}$$

Heat flux at the upper surface has to be solved when the temperature of the lower surface is known. In the equations above and below, α is the thermal diffusivity, τ is the conductive time constant of a solid, k is the heat conductivity, ρ is the density, l is the plate thickness and c_p the specific heat. T_0 is the initial plate temperature, T_m is the measured lower surface temperature, T_s is the surface temperature to be solved together with heat q_s flux from the upper surface.

A one- dimensional implicit difference method was used for equation (1). The method guesses the boundary values and starts to iterate until the result converges to the measured temperature. No optimization algorithm for solving temperatures and heat transfer was adopted.

Calculations for aluminium were reliable, because aluminium is almost isothermal and there is just a small difference between the measured temperature in the middle of the plate and the surface temperature. Results are shown in Figure 7. On the other hand, calculations for a glass plate, as can be seen in Figures 8 and 10, are not exact due to the low conductivity of glass, which causes oscillations in the surface temperature. To make calculations more reliable for glas, a more sophisticated solution method for an inverse problem is required [9,12].

An analytical method for solving the inverse problem is presented for the symmetrical configuration in [9] and is what we have used in our experiments. The solution of heat conduction equation (1) for the surface temperature and heat flux gives:

$$T_s = T_m(t) + \frac{1}{2}\tau\frac{dT_m}{dt} + \frac{1}{24}\tau^2\frac{d^2T_m}{dt^2} + \ldots \tag{5}$$

$$q_s = -\frac{k}{l}\left[\tau\frac{dT_m}{dt} + \frac{1}{6}\tau^2\frac{d^2T_m}{dt^2} + \ldots\right] \tag{6}$$

$$\tau = \frac{l^2}{\alpha},\quad \alpha = \frac{k}{\rho c_p}$$

The results of this method are shown in Figures 9 and 10. From Figure 10 it can be seen that the finite difference method gives almost the same result as equations (5) and(6). However, the result is oscillating due to uncertainties in measured data.

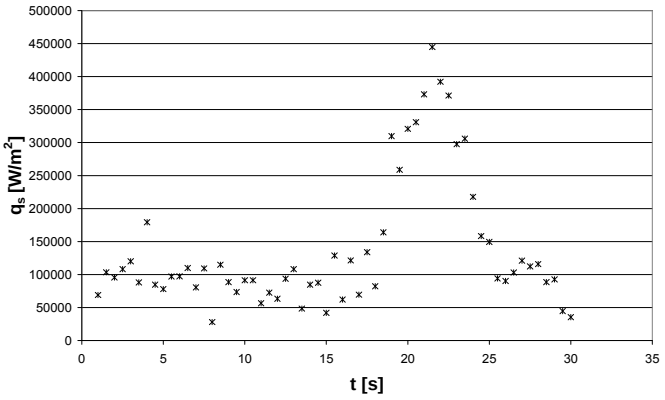

Figure 9. Calculated heat flux in surface using Eq. (6) for glass. L = 300 mm, p = 2.2 • 10^5 Pa.

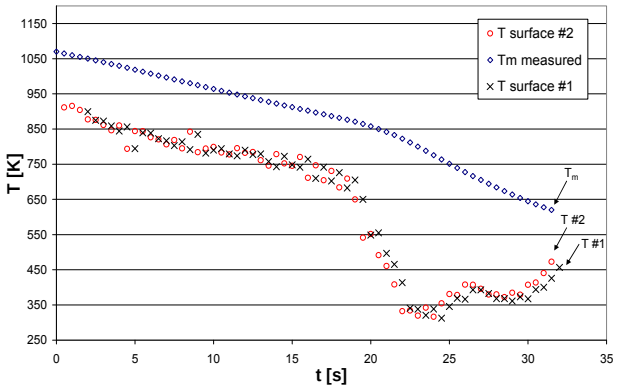

Figure 10. Measured data and calculated surface temperature in glass. #1 calculated with Eq. (5). #2 calculated with finite difference method. L =300 mm, p = 2.2 • 10^5 Pa.

CONCLUSIONS

The main aim of the study was to measure heat transfer of a water-air mist impinging on a hot surface of glass. The research was conducted by measuring the lower surface temperature of a plate when it was cooled by the mist from the upper surface. A practical application in which this type of heat transfer is of interest, is the tempering process for thin glasses. Metal surfaces and mixtures of water and ethanol as a fluid were also used in order to compare the reliability of our test facility, because results for these can be found in the literature.

The results for an aluminium plate showed that the difference between the Leidenfrost temperature (LF), i.e. the temperature below which heat transfer is essentially increased, for water mists with different properties is small, but a 50 % ethanol mixture decreases it by almost 90 ºC. The LF temperature was not measured directly, but was based on the solution of an inverse heat conduction problem. In the case of metal surfaces this type of approach is reliable, but for glass with a low heat conductivity it can give an erroneous result, because small changes in measured data can result in a difference of tens of degrees centigrade of calculated LF temperatures.

According to the measurements, when mist properties were changed, the denser ones gave a higher temperature where the increase in heat transfer occurs. This gives also a clear indication of the transition of the LF temperature. The change in a cooling curve for glass started at about 500 ºC and finished at almost 800 ºC with different mist properties. With the densest mists the change in the curve was not clearly observed. According to our measurements and calculations it seems that the LT temperature for glass, when water mist is used , is slightly higher than 500 ^{o} C.

REFERENCES

1. Baumeister, K.J., Simon, F.F. Leidenfrost temperature—its correlation for liquid metals, cryogens, hydrocarbons, and water. *Journal of Heat Transfer,* Vol. 95, No. 2, pp 166-173, 1973.

2. Baumeister K.J., Henry R.E., Simon F.F. Role of the surface in the measurement of the Leidenfrost temperature. *Augmentation of Convective Heat and Mass Transfer, ASME, New York*, pp 91–101, 1970.

3. Bernardin J. D. Mudawar I. The Leidenfrost point: Experimental study and assessment of existing models. *Journal of heat transfer*, Vol. 121, No. 4, pp 894-903, 1999.

4. Hoogendoorn, C. J., Den Hond, R. Leidenfrost temperature and heat-transfer coefficients for water sprays impinging on a hot surface. *Heat transfer 1974; Proceedings of the Fifth International Conference*, Vol. 4, Society of Heat Transfer of Japan, pp 135-138, 1974.

5. Ohkubo H., Nishio S. Mist Cooling for Thermal Tempering of Glass. *JSME international journal*, Vol. 31, No. 3, pp 444-450, 1988.

6. Sözbir N., Yao S. C. Experimental investigation of water mist cooling for glass tempering. *Atomization and Spays*, Vol. 14, pp 191-210, 2004.

7. Sözbir N., Chang Y. W., Yao S. C. Heat transfer of impacting water mist on high temperature metal surfaces. *Journal of heat transfer,* Vol. 125, pp 70-74, 2003.

8. Choi K. J., Yao S. C. Mechanisms of film boiling heat transfer of normally impacting spray *International Journal of Heat and Mass Transfer*, Vol. 30, Issue 2, pp 311-318, 1987.

9. Ciofalo M., Caronia A., Di Liberto M., Puleo S. The Nukiyama curve in water spray cooling: Its derivation from temperature–time histories and its dependence on the quantities that characterize drop impact. *International Journal of Heat and Mass Transfer*, Vol. 50, Issues 25-26, pp 4948-4966, 2007.

10. Deb S., Yao S. C. Analysis on film boiling heat transfer of impacting sprays. *International Journal of Heat and Mass Transfer*, Vol. 32, No. 11, pp 2099-2112, 1989.

11. Fujimoto H., Hatta N., Asakawa H., Hashimoto T. Predictable modelling of heat transfer coefficient between spraying water and a hot surface above the Leidenfrost temperature. *ISIJ international*, Vol. 37, No. 5, pp 492-497, 1997.

12. Soti V., Ahmadizadeh Y., Pourgholi R., Ebrahimi M. Estimation of heat flux in one-dimensional inverse heat conduction problem. *International Mathematical Forum*, No. 10, pp 455-464, 2007.

HEAT TRANSFER CHARACTERISTICS OF A COUPLE OF ARGON JET IMPINGEMENT WITH SMALL JET TO TARGET SPACING

J. Aharon*[1,2], I. Hochbaum[1], M. Corengold[1], A. Marzuk[1], O. Ben Yehuda[1]
[1] N.R.C.N, P.O.Box 9001, Be'er Sheva, 84190, Israel
[2]Ben Gurion University of the Negev, P.O.Box , Be'er Sheva, Israel

ABSTRACT. In the present work a couple of Argon jets were investigated as a heat source for temperature controlled brazing process. Local convective heat transfer coefficients were measured for a couple of Argon jets with a constant jet to jet spacing and jet to target spacing of 0.5 and 1 mm. The configurations were a couple of circular 4 mm diameter jets with a space of 10 mm between their centers. The target was two copper cylinders 6 mm diameter and 13 mm in high which were heated by the hot jets. The gas temperature was about 350 ^{o}C and Reynolds number was in the range of 3500 to 10000. The convective heat transfer coefficient was obtained from the calculation of the transient heating of copper cylinders and the assumption of lumped heat capacity and constant heat transfer coefficient during the process. The heat transfer coefficient values were calculated from the experimental time constant of the heating process.

It was found that the Nusselt number which was measured is much higher than reported value in the literature (about one order of magnitude at the same Reynolds number) due to the small jet to jet spacing (x/d=2.5) and the small target dimensions. A small effect was found of the jet to target spacing for the same Reynolds number. The experimental results were correlated to the next correlation:

$$Nu = 0.72\,\mathrm{Re}^{0.74}\,\mathrm{Pr}^{1/3}$$

Keywords: *jet impingement, brazing, heat transfer, Argon*

INTRODUCTION

Impinging fluid jets are widely used for heating or cooling in engineering systems and processes. Those applications include the turbine blades cooling, cooling of electronic systems, metallurgic treatments of metals and drying systems. The use of jet impingement is due to the high convective heat transfer that can be achieved without increasing of the flow rate or the target surface.

Several investigators have measured the heat transfer characteristics of a single jet or jet array focusing on the heat transfer coefficient that obtained by that mechanism. In most of the works such as Friedman and Mueller [1], Gardon and Cobonpue [2] and Chance [3] the investigators tried to determine the influence of the cooling flow rate, fluid properties and system geometry on the convective heat transfer.

The metallurgic limitation of the gas turbine blade temperature motivate the investigators to focus their works on cooling the turbine blades in order to increase the maximum working temperature of the engine and the thermodynamic efficiency. Many works (experimental and/or numerical) focus on the prediction of jet impingement onto concave surface, a situation typically employed for the

* Corresponding author: Dr. J. Aharon
Phone: +972-8-6567827, fax: +972-8-6567593
E-mail address: jaharon@bgumail.bgu.ac.il

internal cooling of the leading edge of a blade. Measurements of the relevant flow have been reported by Kounadis [4] and Iacovides et al. [5] using an array of jets impinging onto the curved wall of semi-circular passage. Most of those works use air as the cooling fluid because of its availability in gas turbine. In studies which are investigating the quenching process of metals usually the cooling fluid is water (such as the work of Aharon et al. [6]) oil or any other inert gas in order to avoid oxidation of the quenched surface during the cooling process.

In the electronic industry the brazing process of circuit components is very common and the usual way to apply that process is by using a hot iron which heats the electronic component's terminals to the required temperature to get the melting of the solder. At that process the temperature of the component and the solder is usually uncontrolled which may cause damage to the component. It is also important to control the melting and solidification duration to get the required metallurgical structure of the solder for better brazing results. The use of hot inert gas jet for brazing process may result a more controlled temperature profile of the melting and solidification of the braze and a minimum heating of the electric component.

The purpose of the present study is to measure the local convective heat transfer coefficients for a couple of Argon jets with a constant jet to jet spacing and two values of the jet to target spacing. The measurement conducted during a heating of the target as a simulation of the brazing process

.

THE EXPERIMENTAL SET UP

The test system is shown in Figure 1 (a) where detailed Figure of the nozzles and the target is presented in Figure 1 (b). The heating gas supplied from a gas vessel (1) thought a flow meter (2) to the system. At the inlet of the system the gas heated to the required temperature by using an electrical 1.5 kW heater (3). The power to the heater was controlled by AC transformer. The outlet temperature of the gas was measured by a thermocouple which was located at the exit of the heater. The hot gas flow from the heater to the jets plenum (5) and exit through two circular jets nozzles (6) to the target. The nozzles diameter was 4 mm and the space between them was 10 mm. Two other thermocouples measured the gas temperature at the plenum and at the nozzle for accurate evaluation of the exit gas temperature.

The heated target was two cupper cylinders 6 mm diameter and 13 mm in high which were heated by the hot gas. The target temperature was measured continuously during the heating process by a thermocouple which located inside a hole which was drilled in one of the cylinders. The using of cupper cylinder ensures an isotherm temperature profile in the target and a lumped heating process. The target was insolated from the surrounding to avoid heat losses. The spacing between the target and the nozzle outlet obtained by using suitable spacers (7) and locate them under the target block (8). Because of the high thermal capacity of the system, the initial heating of the nozzles and the plenum was done by using air as heating fluid.

EXPERIMENTAL PROCEDURE

The experimental procedure consists of the following steps. In the first step the system was heating to a required temperature by using air as a heating fluid. The air valve opened and electric power was supplied to the heater. When the required outlet temperature of the air was achieved, the air valve was closed and the Argon valve was opened to get the required flow rate through the nozzles. The electric power to the heater was adjusted to keep the outlet Argon temperature. The required spacers were located above the nozzles plenum and the target block was placed above the spacers. Three leading rods were connected to the nozzles plenum to lead the target block and the

cupper cylinders above the nozzles exit A continuous measurement of the target temperature was made as well as the outlet gas temperature until reaching an asymptotical measured temperature value. The experiments matrix is presented in table 1. As it can be seen the outlet velocity and temperature were changed as a parameter for each jet to target spacing.

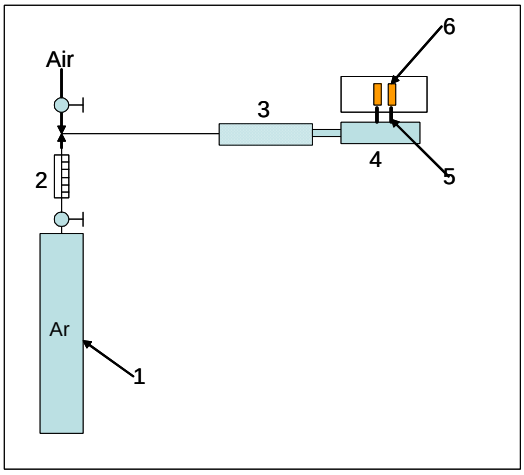

(a)

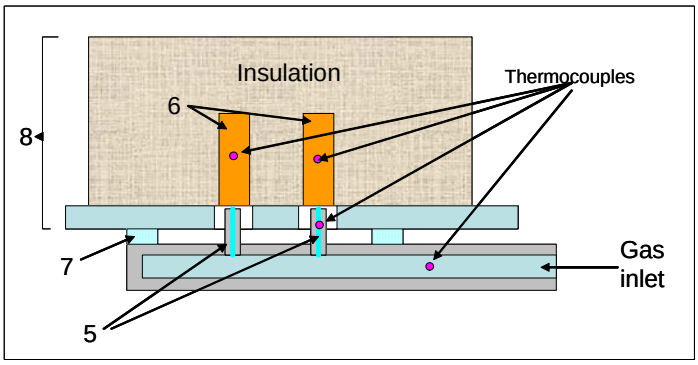

(b)

Figure 1. (a) The test system, (b) The nozzles and the target.

Table 1
Experiments matrix

Jet to target spacing [mm]	0.5	1
Outlet velocity [m/sec]	47	47
	70	70
	94	94
	117	117
	140	140

RESULTS AND DISCUSSION

Each run was terminated when an asymptotical measured target temperature value was achieved. A typical target temperature measurement is presented in Figure 2. That experiment was conducted with outlet Argon velocity of 47 m/sec and exit temperature of 350 ^{o}C. The volumetric measured flow rate increases at the outlet of the heater and the nozzles due to the heating of the gas. To

calculate the outlet velocity it was assumed that there is pressure drop between the flow meter and the nozzle and that the Argon acts as an ideal gas.

The normalized target temperature is presented for various jets velocities in Figure 3 and 4 for jet to target spacing of 0.5 and 1 mm respectively. It can be seen that the time to reach the asymptotic temperature value decreases with the jet velocity. In Figure 5 a comparison of the results from the experiments with the two jet to target spacing values is presented for jet velocity of 47, 70 and 94 m/sec. In that figure it can be seen that the cooling rate with the smallest spacing is lower than with the higher value.

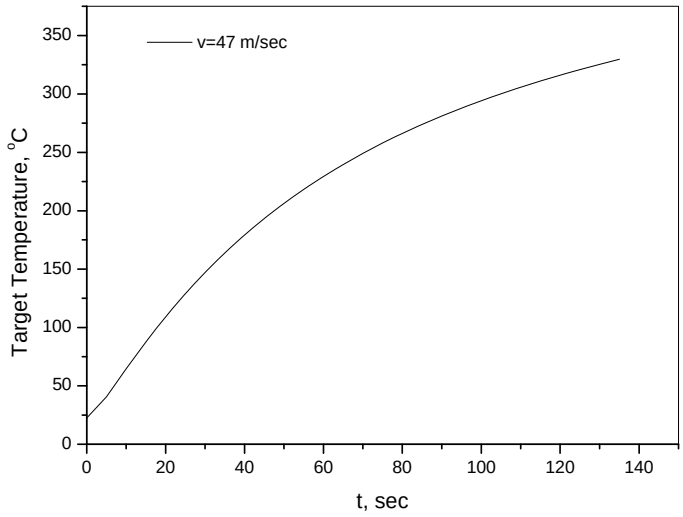

Figure 2. Typical target measured temperature during the experiment (v=47 m/sec).

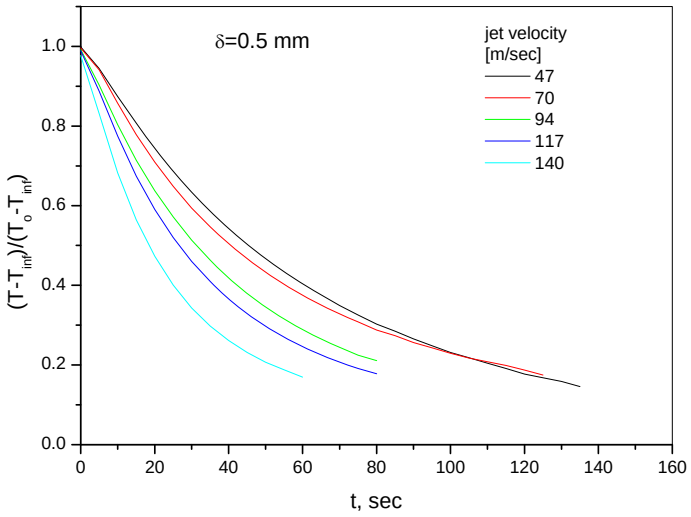

Figure 3. The normalized target temperature for various jets velocities (jet to target spacing of 0.5 mm).

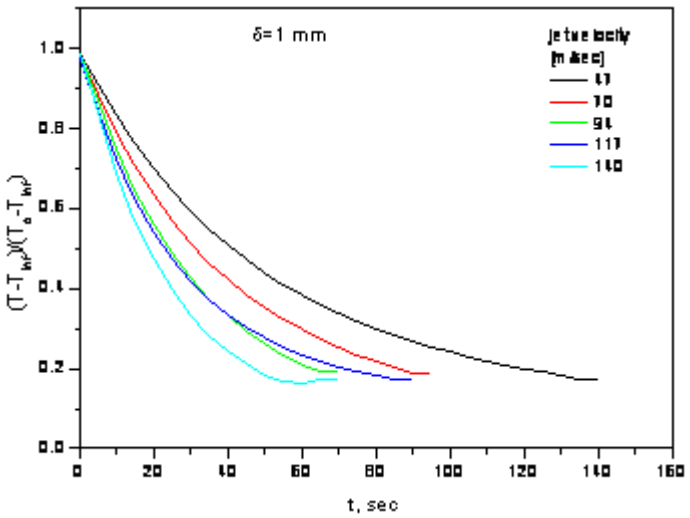

Figure 4. The normalized target temperature for various jets velocities (jet to target spacing of 1 mm).

The convective heat transfer coefficient was obtained by using the assumption of lumped heat capacity and constant heat transfer coefficient during the process. In that model the temperature change during the heating process can be presented by equation (1).

$$T(t) = (T_o - T_\infty) \cdot \exp(-hA/(\rho CV)_{Cu}) + T_o \qquad (1)$$

The time constant of the system at that process is $\tau = (\rho CV)_{Cu}/hA$ in which the system temperature difference ($T-T_\infty$) reaches a value of 36.8 percent of the initial difference (T_o-T_∞). The heat transfer coefficient values were calculated by using the experimental measured values of τ and the time constant definition.

The Nusselt number values which obtained from the experimental heat transfer coefficient results are presented in Figure 6 versus the Reynolds number. Bothe the Nusselt and the Reynolds numbers are based on the nozzle diameter and velocity and gas properties at 350 ^oC. The best fit for the experimental results can be presented by the correlation in equation (2).

$$Nu = 0.72\,\mathrm{Re}^{0.74}\,\mathrm{Pr}^{1/3} \qquad (2)$$

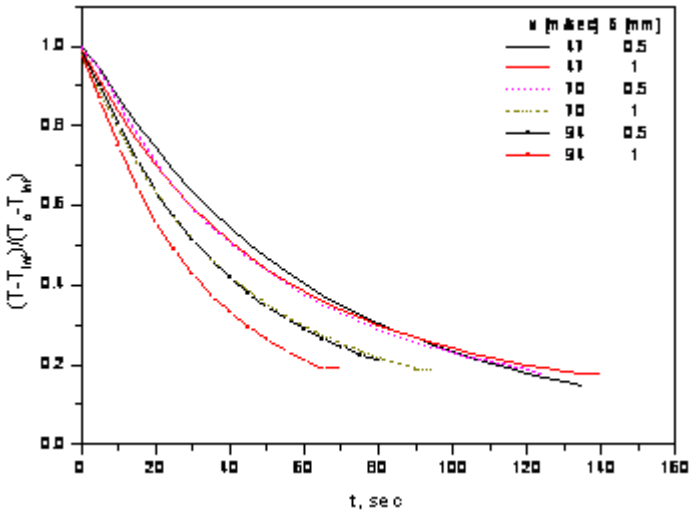

Figure 5: A comparison between the two jet to target spacing values results.

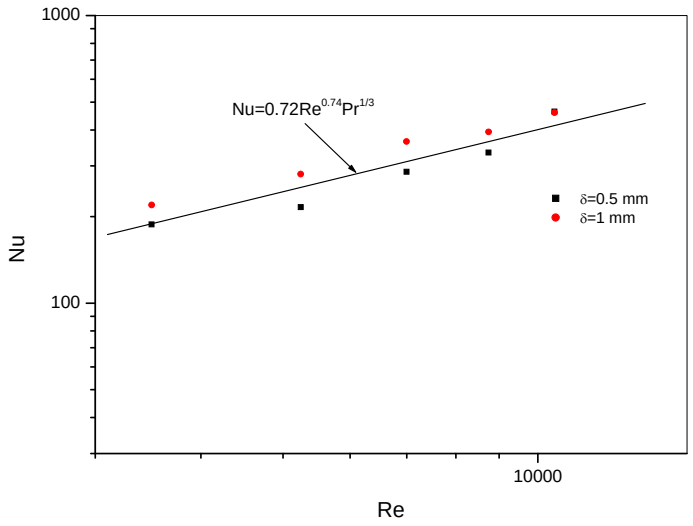

Figure 6: Experimental Nusselt number vs. Reynolds number.

CONCLUSIONS

1. The local convective heat transfer coefficient which was obtained from the experiments is much higher than the average values which are reported in the literature. That result is because of the small spacing between the jet and the target and the dimensions of the target.
2. The heat transfer coefficient increases with the spacing between the jet and the target. However the effect of the jet to target spacing is small.
3. The experimental results for the both jet to target spacing were correlated with the Reynolds number based on the exit velocity and the jets diameter.

REFERENCES

1. Fridman, S. J., and Mueller, A. C., Heat Transfer to Flat Surfaces, Proceedings, General Discussion on Heat Transfer, the Institute of Mechanical Engineers, London, England, pp. 138-142, 1951
2. Gordon, R., and Cobonpuo, J., Heat Transfer Between a Flat Plate and Jet of Air Impinging on it, International Developments in Heat Transfer, Proceedings of 2ed International Heat Transfer Conf., ASME, New York, N.Y., pp. 454-460, 1962
3. Chance, J. L., Experimental Investigation of Air Impingement Heat Transfer Under an Array of Round Jets, Tappi, vol. 57, No. 6, pp. 108-112, 1974
4. Kouna, D., Flow and local Thermal Measurements in Stationary and Rotating Gas Turbine Cooling Passages, Ph.D. Thesis, University of Manchester, 2005
5. Iacovides, H., Kpunadis, D., Launder, B. E., Li, J. K., Xu, Z. Y., Experimental Study of the Flow and Thermal Development of a Row of Cooling Jets Impinging on a Rotating Concave Surface, ASME J. Turbomach. 127, pp 222-229, 2005
6. Aharon, J., Harari, R., Weiss, Y., Haim, M., and Katz, M., Cooling of High Temperature Cylindrical Surface using an Array of Water Impingement Jets, Proceedings of 11th International Heat Transfer Conf. Korea August, 1998

MICRO STEAM GENERATOR USING TUBULAR FLAME

H. Funagoshi[1,*], R. Matsumoto[1], M. Ozawa[1], M. Katsuki[2]
[1]Kansai University, Osaka, Japan
[2]Emeritus Professor at Osaka University, Osaka, Japan

ABSTRACT. The purpose of this study is to develop a micro steam generator using a tubular flame. The tubular flame is formed in a swirl flow field induced by injecting the air-fuel mixture tangentially into the cylindrical chamber. The tubular flame consists of an inner hot gas core of burning gas and an outer region of unburned mixture. By installing a water tube into the hot gas core of the tubular flame, the water tube is heated by the surrounding high-temperature burning gas with very low heat loss. The combustion test was carried out using 13A city gas. The vortex structure was weakly affected by the installed water tube, while the tubular flame becomes unstable by the excess cooling with the water tube at high air ratio. This paper focuses on the stability of the tubular flame with the heat absorption and related heat transfer characteristics of the water tube.

Keywords: *Tubular flame, Heat transfer, Flame stability, Steam generator*

INTRODUCTION

The tubular flame is formed in a swirl flow field induced by injecting the air-fuel mixture tangentially into the cylindrical chamber. Figure 1 shows the structure of the tubular flame. The circular luminous flame exists in the combustion chamber. The burning reaction occurs in radial direction, then, the outer region of the tubular flame remains unburned. The high-temperature burning gas flows through the center of the cylindrical chamber. This flame has some constructional advantages. First, the tubular flame is covered with the unburned low-temperature gas, thus the heat loss is extremely suppressed at low level. Second, the tubular flame is stable and suitable to achieve the lean combustion in a stretched and swirl flow field.

The tubular flame has been studied widely by S. Ishizuka et al [1-9]. They developed the tubular flame burner from 4 mm to 300 mm in inner diameter, and reported combustion characteristics on a variety of fuels such as methane, propane, bunker C and biomass [1-6]. These reports presented the structure of the tubular flame, effects of flame stretch, fuel concentration, temperature distribution and extinction limit. The flow field in the combustion chamber was reported in recent years [7-9]. They

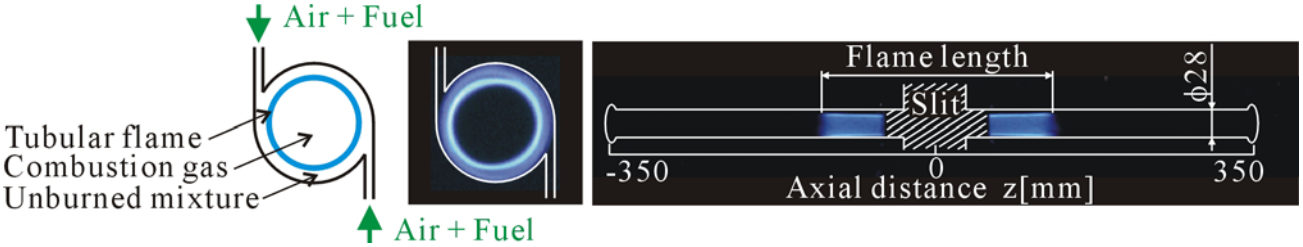

Figure 1 Tubular flame (Q =7 kW, λ =1.4).

* Corresponding author: H. Funagoshi
Phone: + (81)-6-6368-0942, Fax: + (81)-6368-0942
E-mail address: matumoto@kansai-u.ac.jp

developed the tubular flame burner with 150 kW output for industrial boiler and heating furnace applications.

By the way, increasing attentions has been given to a cooking method using superheated steam in considering the health maintenance through foods of good quality. The superheated steam generator (S-SG) for the cooking instruments should be compact for the household use. Considering a limitation of electric capacity of domestic use, the heat source for S-SG is preferably supplied through combustion of city gas. The combustion in the narrow space causes an incomplete combustion, thus the combustion technology suppressing the carbon monoxide CO is essential in the development of the S-SG for the household use. Iio et al. [10] developed the micro superheated steam generator using the partially-premixed burner with the internal exhaust-gas recirculation. Further miniaturization S-SG keeping the high output and the low-CO concentration, the new combustion technology should be developed for the S-SG.

In this study, the tubular flame is applied to the micro superheated steam generator. The conventional burner needs a relatively large space for the complete combustion. However, the tubular flame can be achieved stable and lean combustion in a small bore tube. By installing a water tube into the hot gas core of the tubular flame, the water tube is heated by the surrounding high-temperature burning gas. This concept means that the S-SG is constructed by integration of the heat exchanger into the tubular flame burner. The compact S-SG is thus achieved, and at the same time effective heat transfer is performed on the water tube by surrounding high-temperature gas. However, the excess cooling by the water tube brings the tubular flame unstable. Therefore, the heat transfer on the water tube is important to develop the efficient S-SG.

This report describes the first step of the research aiming at the development of the tubular-flame steam generator. The combustion test was carried out using 13A city gas, and the stability of the tubular flame is examined. The heat transfer characteristics on the water tube are investigated.

EXPERIMENTAL APPARATUS

The experimental apparatus is shown in Figure 2. The combustion chamber is a cylindrical tube with D=28 mm in inner diameter and L=700 mm in length. The middle position of the combustion chamber, the gas injection unit made of SUS304, was installed. The gas injection unit has two slits of 2 mm in thickness and 50 mm in width, through which fuel and air mixture was injected tangentially into the chamber. To observe the tubular flame, quartz glass tubes were used as the combustion chamber. To ensure the uniform velocity in the slits, the cylindrical plenum chambers were equipped at the slit inlets.

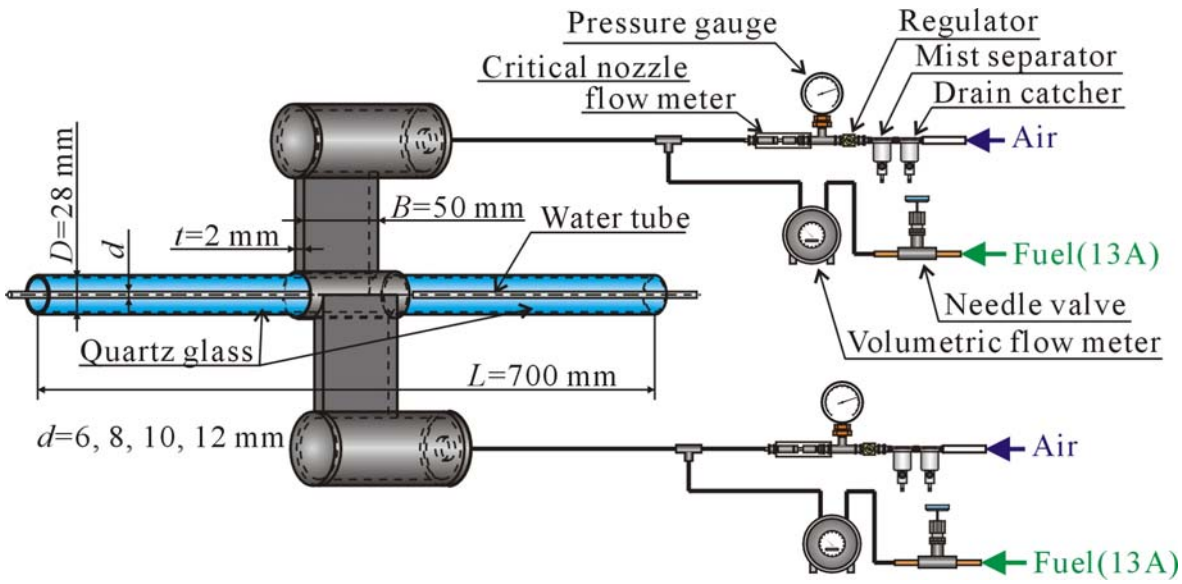

Figure 2 Experimental apparatus.

Each of the water tube of 6, 8, 10 and 12 mm in outer diameter of SUS304 tube, is inserted into the center of the combustion chamber. The wall thickness of the SUS tube is 0.5 mm. The flow rate of the water was measured by a rotameter and the bulk temperature was measured by K-type sheathed thermocouples of 1 mm in diameter. The water flow rate was kept enough high so as to avoid boiling in the water tube. The combustion chamber is set at 30 degree inclined from the horizon for smooth removal of bubbles, if any.

Fuel is 13A city gas consisting of 89 % of methane, 7 % of ethane, 3 % of propane and 1 % of butane. The low heating value is 40.4 MJ/m^3_N. The flow rate of the fuel gas was measured by a wet-type volumetric flow meter. Combustion air is supplied from the compressor, and the flow rate was regulated by means of the critical flow nozzle. Fuel and air were well-mixed and supplied to the combustor. The combustion rate was from 2 to 7 kW.

The combustion gas was sampled at the exit of the combustion chamber by using a water-cooled sampling probe, and was analyzed with the gas analyzer (Horiba Corp. PG-235). The CO, NOx and O_2 concentrations were measured by infrared adsorption, chemiluminescence, and zirconia oxygen sensor, respectively.

The swirl number, which represent the angler momentum relating to the axial momentum, is defined as follows [7];

$$S = \frac{G_w}{G_z \cdot R} = \frac{\int_0^R (u_\theta r)(\rho u_z)(2\pi r)\,dr}{\int_0^R \left(\rho u_z{}^2 + p\right)(2\pi r)\,dr \cdot R} \tag{1}$$

where G_w is the angular momentum, G_z is the axial momentum and R is the radius of the combustion chamber. The angular momentum G_w is assumed to be constant in the combustion chamber, $G_w = 2\{\rho(Btu_s)\,u_s\,D/2\}$, where u_s is the tangential velocity at the slit exit. The axial momentum is given by the mean axial velocity as $G_z = 2\left[\rho\left\{\left(\pi D^2/4\right)u_{z,ave}\right\}u_{z,ave}\right]$. The axial mean velocity $u_{z,ave}$ is a function of the velocity at the slit u_s, $Btu_s = \left(\pi D^2/4\right)u_{z,ave}$. Thus, the swirl number is simply expressed by Equation (2) when the axial pressure drop is neglected.

$$S = \frac{\pi D^2/4}{Bt} \tag{2}$$

Then the swirl number is determined from the dimensions of the combustion chamber. In the present experiment, the swirl number was 6.

COMBUSTION CHARACTERISTICS OF TUBULAR FLAME WITH WATER TUBE

Figure 3 shows the flame pattern at the combustion rate Q=7 kW without the water tube. The flame was recorded with a digital video camera. Experiments were carried out for various air ratio λ at the constant heat release rate Q. The air ratio λ is defined as the ratio of air volume relative to the stoichiometric volume of air, i.e. the inverse of the equivalence ratio. In these figures, the center of the flame cannot be observed due to the gas injecting unit. As shown in Figure 3, the stable tubular flame was formed in the combustion chamber. The diameter of the flame is almost constant along the axis of the tubular flame. An increase in the air ratio λ results in an increase in the flame length. Shiraga et al. [11] reported that the burning velocity becomes lower with a decrease in the fuel concentration. To ensure the complete combustion, the long flame length, i.e. the large flame surface, is needed at high air ratio and high injecting velocity.

Even inserting the water tube into the tubular flame, the stable tubular flame was formed in the combustion chamber at the air ratio λ=1.3 and 1.4, as shown in Figure 4 (a) and (b). The shape of

(a) Q=7 kW, λ=1.3, u_s=14.1 m/s

(b) Q=7 kW, λ=1.4, u_s=15.1 m/s

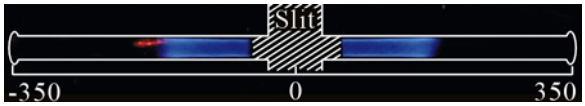

(c) Q=7 kW, λ=1.5, u_s=16.1 m/s

Figure 3 Flame pattern without water tube.

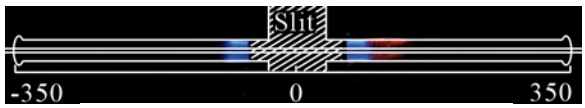

(a) Q=7 kW, λ=1.3, d=6 mm

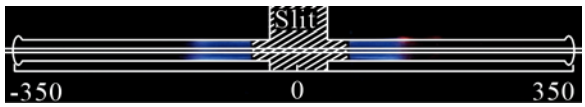

(b) Q=7 kW, λ=1.4, d=6 mm

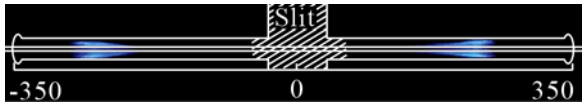

(c) Q=7 kW, λ=1.5, d=6 mm

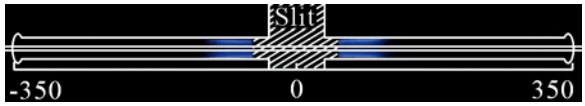

(d) Q=7 kW, λ=1.5, d=6 mm

Figure 4 Flame pattern with water tube.

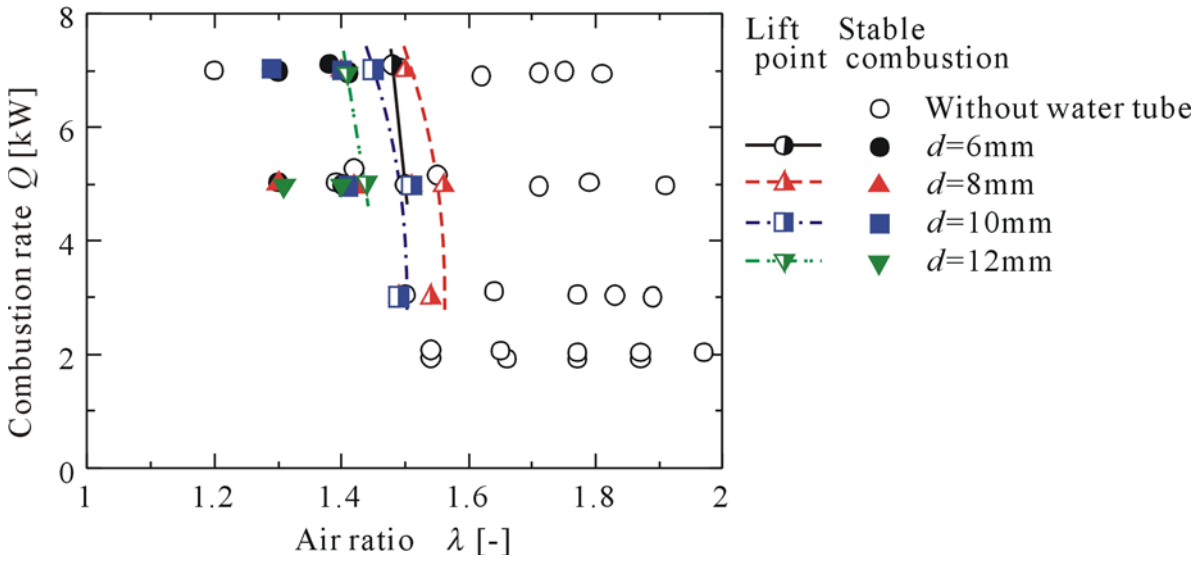

Figure 5 Flame lift point.

the tubular flame is almost the same with the case without water tube. At the air ratio λ =1.5, however, the tubular flame flickers, which is equivalent to the state of alternation flame lifting and holding, as shown in Figure 4 (c) and (d). When the air ratio is higher than λ =1.5, the tubular flame becomes extinct. In the case of Figure 4 (b), the water tube absorbs the heat from the hot burning gas about 1.6 kW, which corresponds to about 23 % of the heat release rate. The tubular flame becomes unstable combustion due to the excess cooling by the water tube. Thus the heat absorption rate, i.e. heat transfer characteristics is a key issue in achieving a stable combustion.

The stable combustion map and the equivalent flame lifting point are plotted in Figure 5. The open circles show the stable tubular flame without water tube. When the water tube is not equipped in the combustion chamber, the flame extinction is not observed even at high air ratio. At low combustion rate and low air ratio, the tubular flame cannot be observed due to the short flame. By applying the water tube into the combustion chamber, the stable combustion region is limited in the

region represented by the solid plots in Figure 5. The equivalent flame lifting occurs at around the air ratio λ=1.5. An increase in the water tube diameter d brings about the flame lifting point to be shifted toward low air ratio, except the water tube of 6 mm. An increase in the heat transfer area results in an increase in the heat absorption rate, which induces the unstable combustion. Thus, the stable combustion area becomes narrower with an increase in the water tube diameter.

HEAT TRANSFER CHARACTERISTICS ON THE WATER TUBE

To achieve the stable tubular flame with the heat absorption by the water tube, the heat transfer characteristics on the water tube is important. The local heat transfer coefficient on the water tube is evaluated from the temperature profiles of water and burning gas.

The heat exchange process in the combustion chamber with the water tube is considered as a double-tube type heat exchanger. The local heat flux q from the high temperature burning gas to the water tube is estimated by the sensible heat of water calculating from the temperature gradient of the water along the flow direction, as follow;

$$q = \frac{m_w c_w}{\pi d} \cdot \frac{dT_w}{dz}, \tag{3}$$

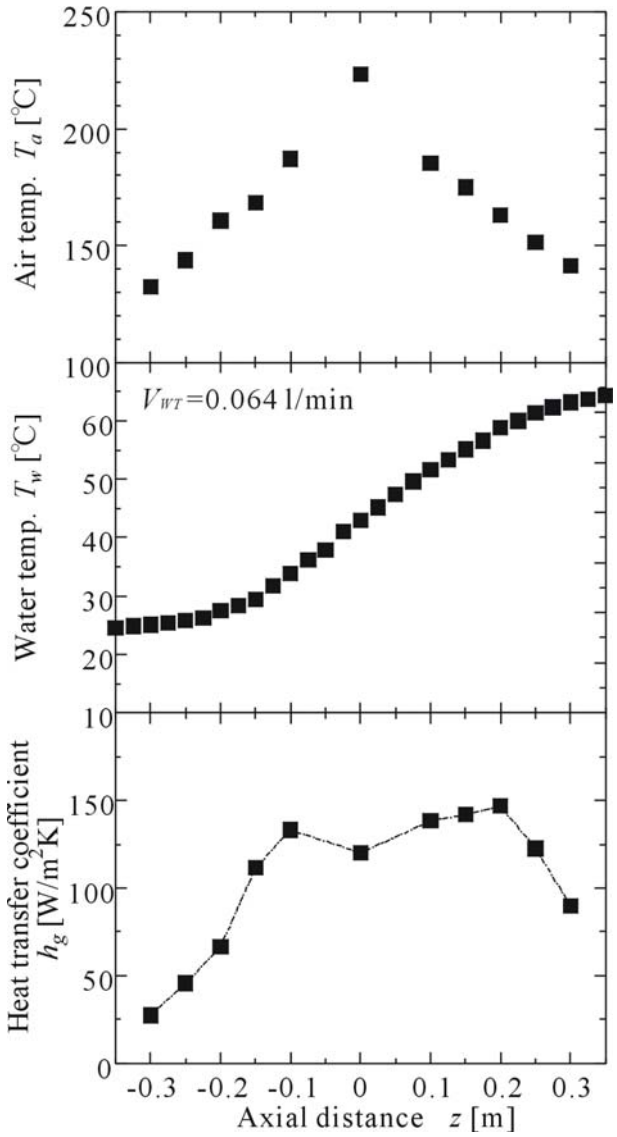

Figure 6 Distributions of temperature and heat transfer coefficient in the non-combustion case (D=28 mm, d=6 mm).

where m_w and c_w are mass flow rate and the specific heat of water, respectively. The thermal resistances of the SUS tube wall and the heat transfer on the water side are sufficiently low. Therefore, the local heat transfer coefficient h_g outside the water tube is calculated by Equation (4).

$$h_g = \frac{q}{T_g - T_w} \tag{4}$$

To ensure the measurement of heat transfer, the preliminary test was carried out in the non-combustion case. The electrically preheated air is used as the working fluid to simulate the combustion flow field. The preheated air flow rate is adjusted to as the combustion experiment (Q =7 kW, λ =1.4) of 9.94 m^3_N/h.

The temperature profiles of the non-combustion case are shown in Figure 6. The air temperature is 503 K at the inlet and decreases with the axial direction. The water temperature increases along the water flow direction from 298 K to 338 K, which corresponds to 178 W of heat absorption rate. The local temperature gradient of water is determined from the neighboring five temperature measurement points. Local heat transfer coefficient is shown in Figure 6 calculated by Equation (4). Relatively high heat transfer coefficient appears at z<±150 mm even in the low mean axial velocity of 4.3 m/s. The swirl flow induces the heat transfer enhancement in the middle of the combustion chamber. On the downstream, however, the heat transfer coefficient decreases due to the attenuation of the swirl effect. On the non-combustion test, the heat transfer coefficient can be estimated from the temperature profiles.

The measurement of the heat transfer coefficient on the combustion tests are carried out at the 5 and 7 kW with the water tube of 6 mm in outer diameter.

The combustion gas temperature was measured by a silica-coated R-type thermocouple of 200 μm in diameter. The representative temperature distributions in the radial direction of the combustion gas are shown in Figure 7 at 5 kW. r is the radial direction from the center of the combustion chamber. At z=0 mm, the temperature of the outside of the tubular flame is low due to the unburned gas mixture. The temperature increases rapidly at r=8 mm, reaches its maximum at of 1653 K at r=4 mm. The luminous flame zone is expected to be around at r=8 mm. At the combustion rate 5 kW with λ=1.4, the tubular flame has 140 mm in length, thus the combustion is completed at around z=±70 mm. Outside the combustion zone, the temperature distribution becomes flat as typically shown in the data at z=-100, -200 and -300 mm. Therefore, the bulk gas temperature T_g in Equation (4) can be estimated as the radial-averaged temperature of the combustion gas. At z=0 mm, T_g is averaged from r=4 to 8 mm of the burning gas temperature.

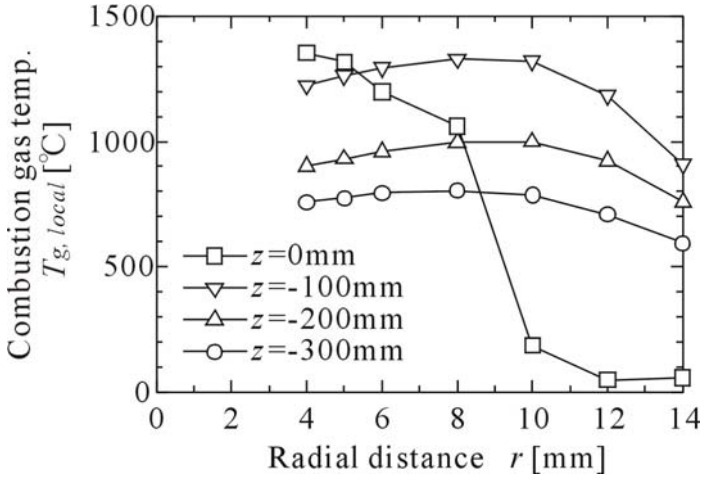

Figure 7 Temperature distributions of the burning gas in the radial direction (Q =5 kW, λ =1.4, d =6 mm).

Figure 8 shows temperature distributions of the radial-averaged combustion gas and the water at the combustion rate of 5 and 7 kW with air ratio λ=1.4. The gas temperature at z=0 mm is lower than the adiabatic flame temperature plotted by the cross plot, and the gas temperature at the end of the tubular flame shows almost the same with that at z=0 mm. In the combustion zone, the bulk temperature of the combustion gas is considered as an almost uniform profile in the axial direction, because the combustion reaction takes place together with the heat transfer inside of the tubular flame. Outside of the tubular flame, the gas temperature decreases along the axial direction.

Figure 8 also shows distributions of the local heat transfer coefficient. On the combustion experiments, the heat transfer coefficient reaches maximum at both ends of reaction zone, and is slightly lower at the center (z=0 mm). The combustion gas flow rate increases along the flow direction due to the combustion reaction. This causes the heat transfer maximum at the both ends of reaction zone. The heat transfer coefficient shows almost the same with distribution at the non-combustion case. This suggests that the radiant heat transfer is weak than the convective heat transfer in such a narrow flow area. Therefore, the heat absorption rate on the water tube in the tubular flame can be evaluated by the convective heat transfer of the combustion gas.

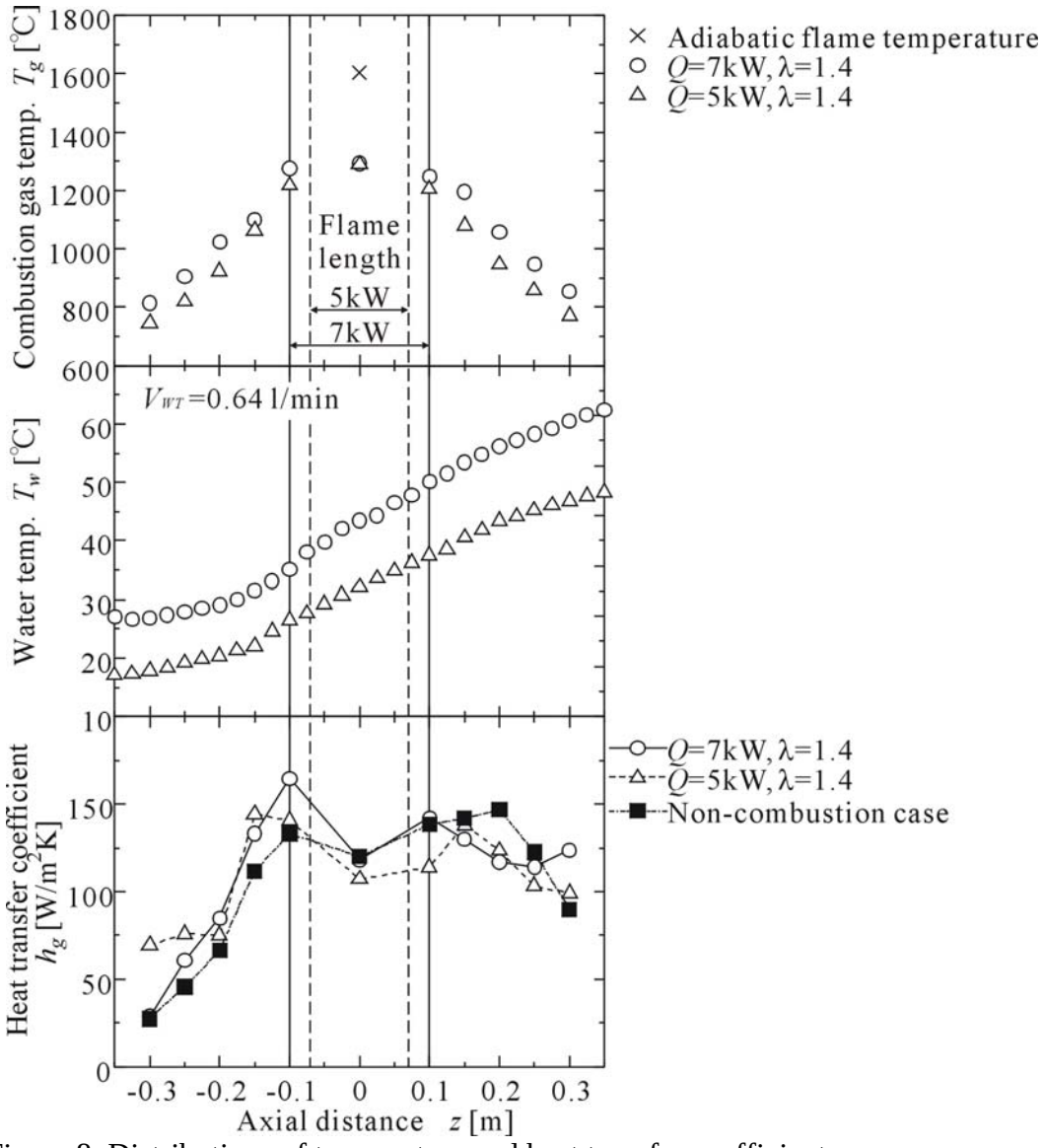

Figure 8 Distributions of temperature and heat transfer coefficient in the combustion case (D=28 mm, d=6 mm).

CONCLUSION

This study was conducted aiming at the development of the compact steam generator using the tubular flame. This paper describes the fundamental combustion characteristics of the tubular flame with water tube inserted into the center. Then, the heat transfer characteristics on the water tube surface was investigated. The results are summarized as follows:

(1) The stable tubular flame is formed even with the water tube in the hot gas core. By increasing the air ratio, however, the tubular flame becomes unstable due to the excess cooling by the water tube.

(2) The local heat transfer coefficient on the water tube surface is estimated. The heat transfer coefficient shows almost the same with distribution at the non-combustion case. The heat absorption rate on the water tube can be evaluated by the convective heat transfer of the combustion gas.

ACKNOWLEDGMENTS

This research was financially supported by the Kansai University Research Grants: Grant-in-Aid for Encouragement of Scientists, 2008, “Development of micro steam generator using tubular flame”

REFERENCES

1. Sakai, Y. and Ishizuka, S., 1st Report, Structures of the Tubular Flames of Lean Methane/Air Mixtures in a Rotating Stretched-Flow Field, *JSME Journal, Series B*, Vol. 56, No. 524, pp 292-299, 1990.
2. Zhang, Y., Ishizuka, S., Zhu, H. and Kee, R. J., Effects of stretch rate, pressure, and pressure diffusion on combustion characteristics of a premixed tubular flame, *Proceedings of the 45th Symposium (Japanese) on Combustion*, pp 34-35, 2007.
3. Nishihara, K., Nagatomo, S., Ishizuka, S., Akiyama, S. and Suzukawa, Y., The Development of a Tubular Flame Burner for Kerosene and Heavy Oil, *Proceedings of the 41th Symposium (Japanese) on Combustion*, pp 217-218, 2003.
4. Uekawa, Y., Shimokuri, D., Ishizuka, S., Nishihara, K., Akiyama, S. and Suzukawa, Y., The Development of a Tubular Flame Burner for Kerosene and Heavy Oil (2nd Report), *Proceedings of the 42th Symposium (Japanese) on Combustion*, pp 459-460, 2004.
5. Kumagai, K., Ishizuka, S., Taketomi, H., Nakajima, Y. and Iino, Y., Development of a Portable Tubular Flame Burner, *Proceedings of the 45th Symposium (Japanese) on Combustion*, pp 220-221, 2007.
6. Nakamura, T., Shimokuri, D., Ishizuka, S., Ishii, K. and Toh, H., Research of Oscillatory Combustion in a Tubular Flame Burner (2nd Report), *Proceedings of the 46th Symposium (Japanese) on Combustion*, pp 324-325, 2008.
7. Mukae, Y., Shimokuri, D., Zhang, Y. and Ishizuka, S., Flow Field in Swirl-Type Tubular Flame Burners, *Proceedings of the 43th Symposium (Japanese) on Combustion*, pp 6-7, 2005.
8. Mukae, Y., Shimokuri, D., Zhang, Y. and Ishizuka, S., Flow Field in Swirl-Type Tubular Flame Burners 2nd report, *Proceedings of the 44th Symposium (Japanese) on Combustion*, pp 318-319, 2006.
9. Shimokuri, D., Mukae, Y., Zhang, Y. and Ishizuka, S., Flow Field in Swirl-Type Tubular Flame Burners 3nd report, *Proceedings of the 44th Symposium (Japanese) on Combustion*, pp 202-203, 2006.
10. Iio, T., Matsumoto, R., Ozawa, M., Takemori, T., Hisazumi, Y. and Kegasa, A., Development of Micro Superheated-Steam Generator, *Proceedings of the Seventh JSME-KSME Thermal and Fluids Engineering Conference*, CD-ROM, M122, 2008.
11. Shiraga, Y., Shimokuri, D. and Ishizuka, S., Effects of Scale on the Combustion Characteristics of Tubular Flame Burner, *Proceedings of the 44th Symposium (Japanese) on Combustion*, pp 24-25, 2006.

EXPERIMENTAL RESEARCH ON A SCRAPED SURFACE HEAT EXCHANGER

G.Boccardi[1,*], G.P.Celata[1], R.Lazzarini[2], L.Saraceno[1], R.Trinchieri[1]
[1]Institute of Thermal-Fluid Dynamics, ENEA, Rome, Italy
[2]Carpigiani, Bologna, Italy

ABSTRACT. Scraped Surface Heat Exchangers (SSHE) are usually employed in presence of high viscosity fluids; the scraping is generally obtained by a mechanical agitation system. In this work results of an experimental campaign on a SSHE, used in a commercial machine for ice-cream production, are presented. The ice-cream mix, after the mixing with the air, goes into the SSHE, working as evaporator, where is cooled to obtain soft ice-cream. A particular difficulty in SSHE performance analysis arises from the non-Newtonian behaviour of the ice-cream mixture; for this reasons, some assumptions on rheological properties of ice-cream mix have been accepted. Experimental tests are carried out by varying ice-cream mass flowrate, liquid mix inlet temperature and agitator speed. Starting from correlations available in literature, dimensionless analysis has been applied to the experimental evidences to develop a heat transfer correlation. The predictions of proposed correlation show a good agreement with the experimental data.

Keywords: *SSHE, scraped, agitator, non-Newtonian.*

INTRODUCTION

Heat exchangers with mechanical systems of agitation and scraping (SSHE, Scraped-Surface Heat Exchangers) are widely used (many constructive geometries are available [1]) in presence of viscous or partially solid fluids. Agitators ensure the constant removal and replacement of stagnant fluid from exchanger surfaces that is very important when working temperatures are close to fluid solidification or evaporation conditions. Moreover, it is useful for heat transfer improvement, in order to reduce possible fouling problems and to induce a mixing improvement and, consequently, a rapid balance in the mass fluid temperature as well.
In this paper, starting from experimental test data and correlations available in literature, a heat transfer correlation for a particular SSHE, used as evaporator, has been developed.
The SSHE tested works in a soft ice-cream machine; the liquid ice-cream mixture, containing a variable quantity of air, goes into the heat exchanger where is whipped and cooled and, finally, goes out as ice-cream. This mixture behaves as a non-Newtonian fluid and is made up of various components (milkfat, water, sugar, egg yolk solids, flavor). Moreover, because some of those components may also change state or characteristics during the process, mixture physical quantities may strongly depend by temperature. In particular, the tested mixture shows a pseudoplastic behavior for temperatures higher than -2°C, whereas for lower temperatures (range of liquid-solid phase transition), it behaves as a plastic fluid, involving considerable problems of physical representation.
In a previous step of this activity, that aims to obtain a SSHE simulation tool useful for sizing and design purposes, we have already carried out some preliminary test sets using a mixture of water and propylene-glycol, instead of ice-cream mixture, to define some aspects of the machine behaviour [2].

* Corresponding author: Dr. G. Boccardi
Phone: + (39)-06-30483664, Fax: + (39)-06-30483026
E-mail address: boccardi@casaccia.enea.it

In this paper, to estimate the overall heat transfer coefficient, all test data have been processed with a methodology proposed from Skelland [3, 4] and based on the dimensional analysis application. To conclude, the predictions of the achieved heat transfer correlation have been compared with experimental data.

EXPERIMENTAL FACILITY

Ice cream flows inside a cylindrical tube where the agitator (type "helical ribbon" and named beater for this application) is located; the cooling fluid (R404A) runs in counter-current flow inside a rectangular section coil that is helically wrapped on the cylinder external surface. Due to an industrial patent protection, below we can only provide its main geometrical characteristics (Table 1).

Table 1
SSHE geometrical characteristics

Exchanger tube i.d., D mm	85
Tube exchange length, L mm	250
Heat transfer area thickness, s mm	2.25
Rectangular coil size a×b, mm	10x6.5
Coil pitch, mm	12
Total coil lenght l, m	6.03

The experimental setup is a commercial soft ice-cream machine (figure 1) that is modified and instrumented in order to achieve the planned experimental test conditions. The use of two inverters, connected to the compressor and the agitator electric motors, allows a wider range of tests. All circuit points of interest in the process study are instrumented with pressure gauges and thermocouples; refrigerant mass flow-rate is detected using a Coriolis mass flow-meter, while some electrical power consumptions are also recorded.

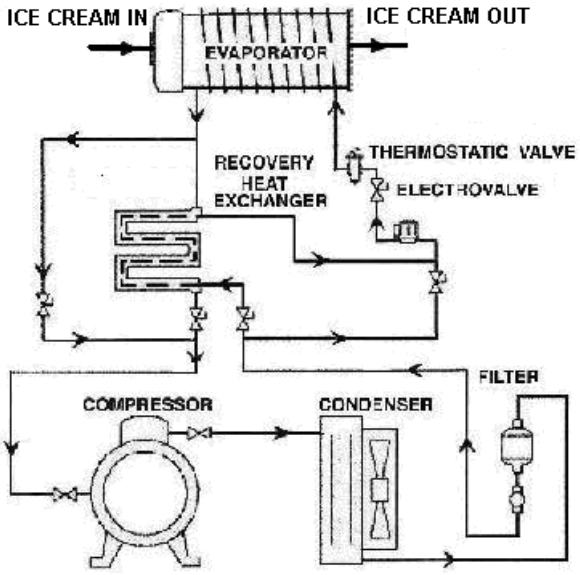

Figure 1. The experimental setup

The ice-cream mass flow-rate is calculated by the ratio between produced ice-cream weight and corresponding time of extraction. A specific and very important parameter to have comparable tests

is the ice-cream quality that stands for the "goodness" of ice-cream production; this is directly evaluated by soft ice-cream machine and shown by a number on the display (afterwards called ICQN).

TEST MATRIX

Five series of tests with different agitator speeds on the SSHE have been carried out, for a total of 152 runs. For each set, fixing the evaporator inlet ice cream temperature between -1 °C and +6 °C and accepting an ICQN range of 6 ÷ 9, the ice mass flow rate $\dot{M}$ (with a range of 8 ÷ 32 kg/h) and the agitator engine power consumption W_{agit} have been measured. Using a recovery heat exchanger with appropriate adjustments on the thermostatic valve, refrigerant conditions close to complete evaporation have been obtained; this test condition is essential to have useful tests for a further analysis on heat transfer coefficient [2]. Ranges of significant controlled parameters along with corresponding number of performed tests are indicated in Table 2.

Table 2
Test matrix

	Inlet Temperature ranges [°C]					
N [rps]	*-1÷1*	*1÷2*	*2÷3*	*3÷4*	*4÷5*	*5÷6*
1.906	5	4	7	4	6	5
2.145	5	3	4	3	4	-
2.383	5	3	4	7	4	4
2.62	6	7	10	9	4	-
2.86	5	10	5	6	10	3

EXPERIMENTAL INVESTIGATIONS

Experimental heat transfer coefficient

The evaporator overall heat transfer coefficient, U, can be obtained from the general equation

$$Q = U\ A\ \Delta T_{lm} \tag{1}$$

where A is the scraped surface area and ΔT_{lm} is logarithmic mean temperature difference; the amount of heat transferred per unit of time Q is given by

$$\dot{Q} = \dot{M}\left\{\frac{y}{100}\left[c_{pl}(T_{in} - T_{cc}) + \lambda + c_{ps}(T_{cc} - T_{ic})\right] + \left(\frac{100 - y}{100}\right)\left[c_{pl}(T_{in} - T_{ic})\right]\right\} + W_{agit} \tag{2}$$

where W_{agit} is a frictional thermal power transferred to the fluid by the agitator. The amount Q is determined experimentally since we are able to measure all involved quantities, including the power absorbed by agitator engine. On the other hand, the theoretical expression of the global coefficient U for a cylindrical surface yields:

$$\frac{1}{U} = \frac{1}{h_i} + \frac{\ln\left(\phi_e / \phi_i\right)\phi_i}{2k} + \frac{\phi_i}{\phi_e h_e} \tag{3}$$

where h_i and h_e are the ice-cream and two-phase refrigerant adduction heat transfer coefficients, respectively, k is the thermal conductivity of tube wall and ϕ_i , ϕ_e are inner and outer tube diameters, respectively. The coefficient h_e is calculated using the Schrock-Grossman's correlation [5] as modified by Nariai et al. [6], for predicting boiling heat transfer coefficient in a helically coiled tube. This correlation, modified with the introduction of a corrective factor, Fc, proposed by Kattan et al. [7] for the non-azeotropic behaviour of a refrigerant mixture (R404a), is defined as:

$$h_e = h_l \left[1.1 \left(\frac{1}{\chi_{tt}} \right)^{0.66} + 7400\, Bo \right] F_c \tag{4}$$

where χ_{tt} is the Martinelli parameter [7] and h_l represents the liquid heat transfer coefficient calculated with the well-known Dittus-Boelter correlation [8]. From previous correlations we can calculate the h_i coefficient, hereunder denoted with h_{iexp}, once evaporator geometry and conductivity of the material used are known.

Dimensional analysis to determine h_i

To describe thermal exchange in the SSHE, considering its particular working characteristics, we identified four meaningful dimensionless groups: Prandtl number (Pr), the ratio between the rotating device speed and fluid axial velocity, rotational Reynolds number (Re_r), and a group that defines the geometry of the heat exchanger. In our tests this last group is constant because we have tested only a SSHE so the functional relationship between the Nusselt number and the main dimensionless groups can be given in the form:

$$Nu = h_{i\,ad} \frac{D}{k} = \alpha \left(\frac{c_p \mu}{k} \right)^{\beta} \left(\frac{ND}{\nu} \right)^{\gamma} \left(\frac{\rho N D^2}{\mu} \right)^{\delta} \tag{5}$$

where α contains the constant value of geometrical group as well.

<u>*Method development.*</u> For a non-Newtonian fluid is more complex to calculate some physical properties, in particular the density (that is a temperature function) and viscosity (that depends on temperature and average shear rate γ_a).

In these tests, the mixture density has been calculated by experimental measures while the relationship between viscosity μ and shear rate γ_a is available thanks to laboratory rheological tests (fig 2). For helical ribbon agitators with low clearance "c", the average shear rate γ_a can be evaluated from the following equation [9,10]:

$$\gamma_a = \left[34 - 144 \left(c/D \right) \right] N \tag{6}$$

For the SSHE, having clearance ≈ 0, the term in square bracket in (6) reduce to 34. With the average shear rate so calculated and fig.2 data, it is possible to estimate ice-cream mixture viscosity.

To calculate the coefficients α, β, γ and δ in (5), we have carried out test series at constant values of Re_r and Pr. In this way it is possible to highlight a relationship between Nu and the dimensionless second group in (5) and, therefore, calculate its exponent γ. By way similar subsequent analysis we are able to define the other parameters. Physical properties have been evaluated at average bulk fluid temperature.

Hereafter, the various steps of the procedure are briefly described (some figures are not presented for paper length problems).

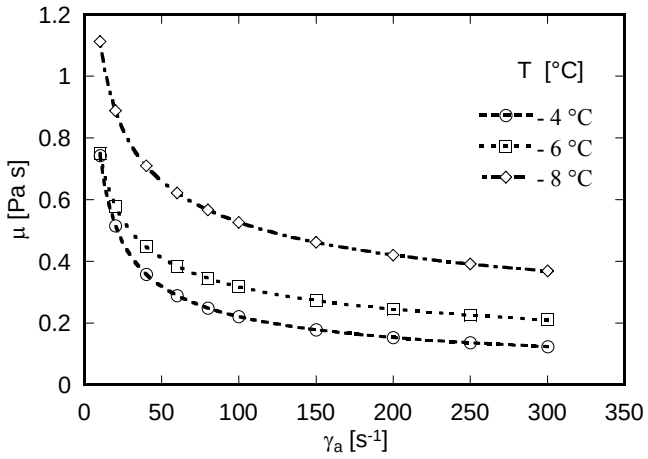

Figure 2. Viscosity vs shear rate, parameter temperature

γ exponent evaluation. Exponent γ is calculated using all test data that are reported in the log-log plot of $Nu_{exp} = h_{exp}D/k$ vs. DN/v dimensionless group, fig. 3. For better clarity, fig. 3 shows only some tests among those elaborated.

We can observe that the points at constant Re_r (in this step Pr is considered constant for all the tests even if, depending on the test execution difficulty, its values are in a short range) practically lay along straight lines. All the lines are almost parallel thus the mean slope, which is about -0.329, can be considered the exponent γ□□ value. This value will be revised later in a final plot. The calculated exponent is used in the following steps.

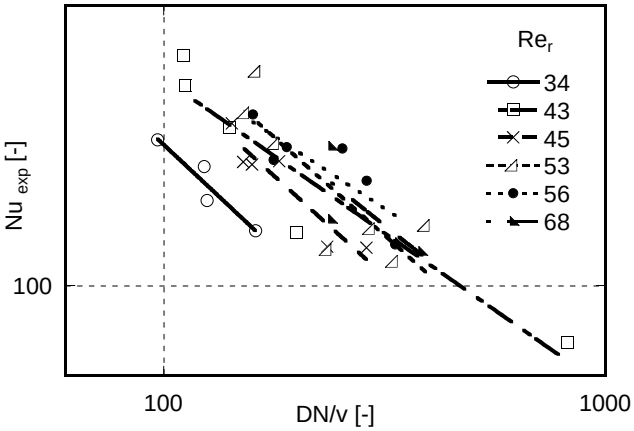

Figure 3. γ exponent evaluation

δ □exponent evaluation. In a preliminary assessment of this exponent, all tests are still used in the log-log plot of

$$Nu\left(\frac{ND}{\nu}\right)^{0.329} \; vs. \quad \frac{\rho ND^2}{\mu}$$

obtaining a situation similar to the previous one; δ value obtained is about 0.497.

β exponent evaluation. In this step, all data tests are used. In a log-log plot we compare

$$Nu\left(\frac{\rho ND^2}{\mu}\right)^{-0.497}\left(\frac{ND}{\nu}\right)^{0.329} vs.\ Pr$$

The slope for all data fits is about 0.546 and corresponds to the exponent β.

coefficient α evaluation and revised value for all exponents. A final plot of all the data against the *DN/v* dimensionless group is drawn to assess the coefficient α. Figure 4 shows a log-log plot of

$$Nu\left(\frac{c_p\mu}{k}\right)^{-0.546}\left(\frac{\rho N D^2}{\mu}\right)^{-0.497} \quad vs. \quad \frac{DN}{v}$$

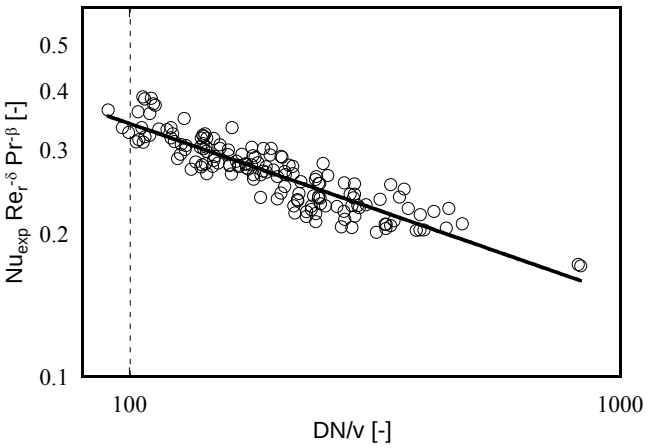

Figure 4. Coefficient α and new γ exponent evaluation

The intercept has a value of 4.55 and the slope of the line gives a revised value for γ equal to -0.344, which is slightly different to the first value calculated γ (-0.329). On the basis of previous experiences, we consider the convergence process acceptable when the difference between two consecutive γ values is less than 0.01, therefore we have repeated the procedure introducing this γ value in the second step *("δ exponent evaluation"*). Finally, at whole process convergence, the final correlation is:

$$Nu = h_{iad}\frac{D}{k} = 1.8\left(\frac{c_p\,\mu}{k}\right)^{0.671}\left(\frac{N\,D}{v}\right)^{-0.36}\left(\frac{\rho\,N\,D^2}{\mu}\right)^{0.568} \qquad (7)$$

Result evaluation

Differences between coefficient values h_{iad} obtained by (7) and experimental values h_{iexp} are shown in Fig. 5. Predictions are on average centred with errors between -14.8 and +17.5 % but a large part of points has lower error.

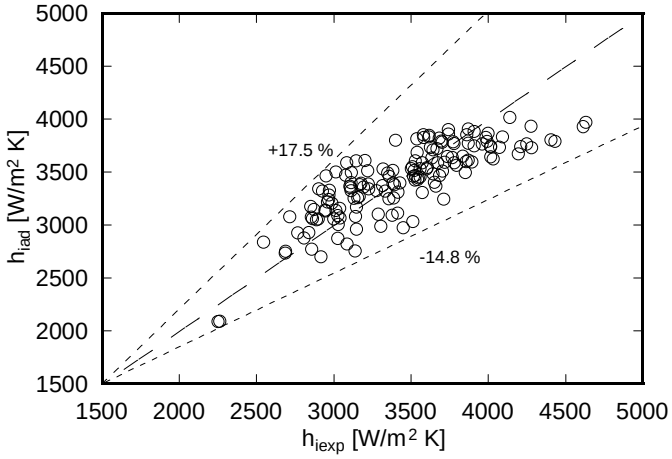

Figure 5. Correlation predictions h_{iad} vs h_{iexp}

If R_h and Δ indicate, respectively:

$$R_h = \frac{h_{iad}}{h_{i\,exp}} \qquad \Delta = R_h - R_m \tag{8}$$

with R_m all data mean (ideally equal to unit), it is possible to obtain normal distributions of such variables in terms of absolute errors, Δ [11]. The normal distribution is represented by a probability density function $P(\Delta)$

$$P(\Delta) = \frac{1}{\sqrt{2\pi}\ \sigma}\ e^{-\frac{\Delta^2}{2\sigma^2}} \tag{9}$$

where σ is the standard deviation of the same distribution. For current experimental data, σ is 0.0743. It is worthy pointing out here that the integral

$$\int_{-\Delta_1}^{+\Delta_1} P(\Delta)\, d\Delta = \int_{-\Delta_1}^{+\Delta_1} \frac{1}{\sqrt{2\pi}\ \sigma}\ e^{-\frac{\Delta^2}{2\sigma^2}}\, d\Delta \tag{10}$$

is the probability that result of a measurement, R_h, is affected by an error between $-\Delta$ and $+\Delta$.
Table 3 shows the probability that data obtained fall within some special ranges; we can note that there is a probability of approximately 70% that the submitted correlations predictions are affected by an error lower than ± 7.4%, and that only about 16% of data have an error greater than ±10.5%.

Table 3
Statistics values

Δ	$\int$	**probability**	$\Delta_{\%}$
0.674σ	0.5	50 %	±5
σ	0.684	68.4 %	±7.43
$\sigma\sqrt{2}$	0.842	84.2 %	±10.51
2σ	0.95	95%	±14.86

CONCLUSIONS

Before reading any conclusion it is necessary to premise some difficulties that are associated with tests.
The first one is the achievement of the same ice cream quality in every test (ICQN control). If the machine is operated under conditions far from commercial production, we noted that the torque-resistant might loose the simple relationship and be affected by test conditions.
Another problem depends on rheologic characteristics of process fluid and on difficulty to express physical properties by an average bulk fluid temperature only.
Finally, we have to remind the complexity to obtain refrigerant conditions close to complete evaporation that might involve little errors.
The main aim of the present study is the development of a heat transfer correlation for the SSHEs installed in the soft ice cream machine under consideration. We have developed a correlation based on Skelland [3, 4], looking for different dimensionless groups that allow a better representation of the SSHE design.
The results obtained allow thinking that the used methodology and the chosen dimensionless groups look appropriated for the development of a heat transfer correlation for the SSHE tested. This step is

crucial for the research planning therefore other geometries and different heat transfer conditions which will be considered.
As far as the correlation performance is concerned, despite unavoidable procedural difficulties, the results are encouraging, since most of its predictions have an acceptable error (Table 3).
Finally, this experimental research has confirmed, as on the other hand reported by many authors [1], the importance of the impeller geometrical characteristics for the research of a SSHE heat transfer correlation.

Nomenclature

c	clearance [m]
N	agitator revolution speed [s^{-1}]
U	overall heat transfer coeff [$Wm^{-2}K^{-1}$]
y	frozen water fraction in the final product [-]
λ	latent heat of evaporation [J kg^{-1}]
ϕ	diameter [m]
Re_r	rotational Reynolds number $\rho ND^2/\mu$ [-]

Subscripts

ad	adimensional
agit	agitator
cc	freezing start
e	external
exc	exchanged
exp	experimental
i	internal
ic	ice cream
s	shaft

REFERENCES

1. Gray J. B., Uhl V. W, *Mixing – Theory and Practice*, Academy Press, 1966.
2. Boccardi G., Celata G.P., Lazzarini R., Saraceno L., Trinchieri R., Development of a heat exchange correlation in the presence of an agitator, *5th European Thermal-Sciences Conference*, 18-22 May 2008, Eindhoven, the Netherlands.
3. Skelland A.H.P., Correlation of Scraped-Film Heat Transfer in the Votator, *Chemical Engineering Science*,vol.7, 1958.
4. Skelland A.H.P., Oliver D.R. and Tooke S., Heat Transfer in a Water-Cooled Scraped Surface Heat Exchanger, *British Chemical Engineering*, vol. 7 ,1962.
5. Schrock V.E. and Grossman L.M., Forced Convection Boiling in Tubes, *Nuclear Science and Engineering*, vol. 12, 1962.
6. Nariai H., Kobayashi M. and Matsuoka T., Friction pressure drop and heat transfer coefficient of two-phase flow in helically coiled tube once-hrough steam generator for integrated type marine water reactor, *J.Nucl.Sci.Technol.*, vol. 109, No.11, 1982.
7. Kattan N., Thome J.R. and Favrat D., R-502 and two near-azeotropic alternatives: Part I – In tube Flow-Boiling Tests, *ASHRAE Transactions*, 1995.
8. Dittus F.W. and Boelter L.M.K., *University of California Publications on Engineering*, Berkeley, Vol.2, p.443, 1930.
9. Ayazi Shamlou P. and Edwards M.F., Power consumption of helical ribbon mixers in viscous newtonian and non newtonian fluids, *Chemical Engineering Science*, vol.40, No.9, pp 1773-1781, 1985
10. Ayazi Shamlou P. and Edwards M.F., Heat transfer to viscous newtonian and non newtonian fluids for helical ribbon mixers, *Chemical Engineering Science*, vol.41, No.8, pp 1957-1967, 1986
11. Box G.E.P., Hunter W.G., Hunter J.S., Statistics for Experimenters, Wiley-Interscience, 1978.

BUBBLE FORMATION IN POOL BOILING OF NATURAL REFRIGERANTS ON HORIZONTAL TUBES

Andrea Luke*, Björn Müller, Yabai Wang
Institute of Thermodynamics, Leibniz University Hannover, 30167, Hannover, Germany

ABSTRACT. A general theory for boiling heat transfer could be developed in the future, if the heat transfer of a single bubble and the interaction between neighbouring bubbles are integrated in the evaluation modeling. The influence of microstructure of a heating surface and of the bubble formation on nucleate boiling heat transfer is investigated. The aim is to develop a correlation of the local and temporal activation of the potential nucleation sites, which can be statistically determined by the envelope area method based on the roughness measurements of the heating surface before the heat transfer measurements. The activation of nucleation sites, the bubble growth and departure and the sliding along the superheated wall of the test tube are observed by high speed video sequences.
The video sequences of nucleate boiling of natural refrigerants on a differently structured copper tube and a mild steel tube, respectively, are evaluated using a special evaluation program. The raw-data of the evaluation of the video sequences will be sorted and converted for the statistical analysis. The bubble departure diameter and frequency will be compared to existing empirical and semi-empirical correlations of literature. The bubbles are tracked along their way sliding in the superheated liquid. The characteristic behaviour of nucleation sites during nucleate boiling, for example the local and temporal distribution of the nucleation sites and frequency distribution of the distance to the next active nucleation site, will be also analyzed for different pressures.

Keywords: *pool boiling, natural refrigerants, active nucleation sites, bubble formation*

INTRODUCTION

The long term aim in design of modern evaporators is to find a correlation based on the phenomena of vapour bubble formation within the cavities of the microstructure of the heated surface. The essential thing to be found out is the activation and deactivation criteria for nucleation sites in which the micro and macro topography of the heated surface, material properties of wall and liquid, and operating conditions enter. This implies for the experimental studies of nucleate boiling heat transfer that detailed and precise information on the topography of the heated surface and of the bubble formation and motion are as important as the heat transfer results, and that all kind of data originate from the same experiment.
High speed video technique offers the possibility to get more detailed information of the bubble formation. The density of active nucleation sites is determined with semi-automatical evaluation methods of the high speed image sequencies. The paper will focus on the bubbble formation for an intermediate pressure from low to high heat fluxes of boiling propane on an horizontal copper tube with fine sandblasted surface and on an horizontal steel tube with drawn and polished surface (for the heat transfer results, cf also Luke and Müller [6]). The cavities within the measured topographies acting as potential nucleation sites are determined additionally and are discussed in form of standardized parameters and statistical ones [3],[9].

* Corresponding author: Prof. Dr.-Ing. habil. A. Luke
Phone: + (49)-511-762-2877, Fax: + (49)-511-762-3857
E-mail address: ift@ift.uni-hannover.de

EXPERIMENTAL PROCEDURE FOR HEAT TRANSFER AND BUBBLE FORMATION

The heat transfer and the bubble formation are investigated during the same experiment in a so-called Standard Apparatus, [1], [2]. The main parts of the apparatus are

- the dc-heated hoziontal test tubes in the evaporator,
- evaporator and condenser combined to a natural circulation loop for the test fluid and placed in a conditioned chamber whose air temperature is adjusted to the saturation temperature T_S of the liquid in the evaporator.

The measurements are performed for boiling propane boiling on a horizontal copper tube with an outer diameter of D = 25.4 mm with a fine sandblasted surface and on a mild steel tube (D =19 mm) for a wide pressure and heat flux range [3]. Parallel to the heat transfer measurements, the bubble formation is examined by photographs and by high speed video technique with 1000 images/s for a resolution of 512x512pixel. The evaluation is performed by special semiautomatical programms to determine number, local position of the active nucleation sites and the size of the growing bubbles in each ms. The local distribution of the nucleation sites and of the bubble departure diameter and frequency on the entire heating surface and their total number are measured at a constant spatial resolution, by investigating several overlapping camera settings for one boiling condition (e.g. from the upper to the lower surface, s. Figure 1).The number of active sites have been counted on the area examinated and presented true to scale in Figure 2, by two typical examples of the bubble formation within ca. 5x5mm² of the test tube surface near the horizontal median line of the copper tube. The images represent two succeeding video images with "momentary", simultaneously active nucleation sites during 1ms, indicated by horizontal arrows in Figure 2, left. The result varies from ms to ms, demonstrated by two new dashed angular arrows in Figure 2 right, these sites are activated between the two images. The average number of momentary sites is approximately $N/A_M = 9$ /mm² during the total session of 500 ms (as seen in the right image in Figure 2).

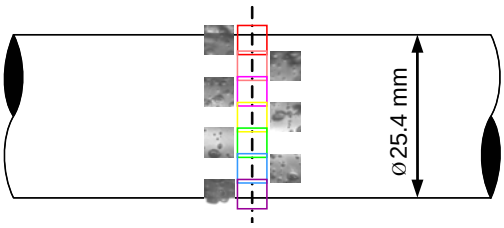

Figure 1. Sketch of the overlapping settings for one boiling condition on the fine sandblasted copper tube with D = 25.4 mm

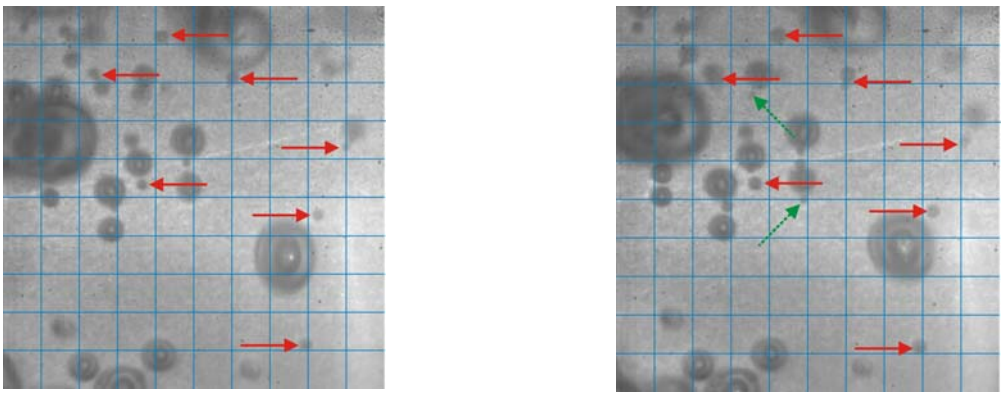

Figure 2. Bubble formation on the median line of the test tube for propane boiling at p* = 0.1, q = 20kW/m²: Selected images with typical momentary active nucleation sites (horizontal arrows) and activated one ms later, see the dashed angular arrows, right.

HEAT TRANSFER AND LOCAL ANALYSIS OF THE WALL SUPERHEAT

The results for the heat transfer are presented in Figure 3 (left) and for the steel tube in Figure 3 (right) as double logarithmic diagram of the heat transfer coefficient α versus the heat flux q with the saturation pressure reduced to the critical pressure, $p^* = p_s / p_c$ as parameter. α increases strongly in the regime of boiling with increasing pressure and heat flux and achieves values of 10^5 W/m²K. The variation of the local wall superheat ΔT with the azimuthal angle φ and heat flux q is represented in Fig. 4 for propane boiling $p^* = 0.1$ (top) and for the intermediate heat flux $q = 20$ kW/m² with the pressure as parameter (bottom). As known from recent experiments, the superheat of the tube wall varies significantly with the azimuthal position φ. The maximum variation of the superheat ΔT occurs at the intermediate heat flux $q = 20$kW/m² (or for superheats greater than 20 K). Similar variations of ΔT with φ are observed with differing pressures, see Figure 4 bottom. The relative effect is most pronounced at intermediate pressure $p^* = 0.1$ and it decreases to lower pressures and to higher ones, respectively. The local effect is on the rough surface the same as on the smooth one, the curves are only shifted to smaller superheats. These results may be explained by the corresponding variation of bubble formation and the roughness [5]. The heat transfer in the lower parts of the tube surface is enhanced at intermediate heat flux by the bubbles sliding along the superheated tube surface improving heat transfer by convective effects and additional evaporation. At high heat fluxes and pressures, i.e. high superheats, the importance of the sliding bubbles diminishes because the tube is entirely covered by bubbles growing at their nucleation sites. At very low heat fluxes only very few potential nucleation sites become active, so that only very few bubbles exist. The same explanation holds for the variation of $\Delta T(\varphi)$ with the reduced pressure p^*, because the active nucleation site density is much smaller at low and much greater at high reduced pressures than at intermediate. Further reasons are the smaller difference between the densities of vapour and liquid at high reduced pressures and the large bubble departure diameter at very low reduced pressures.

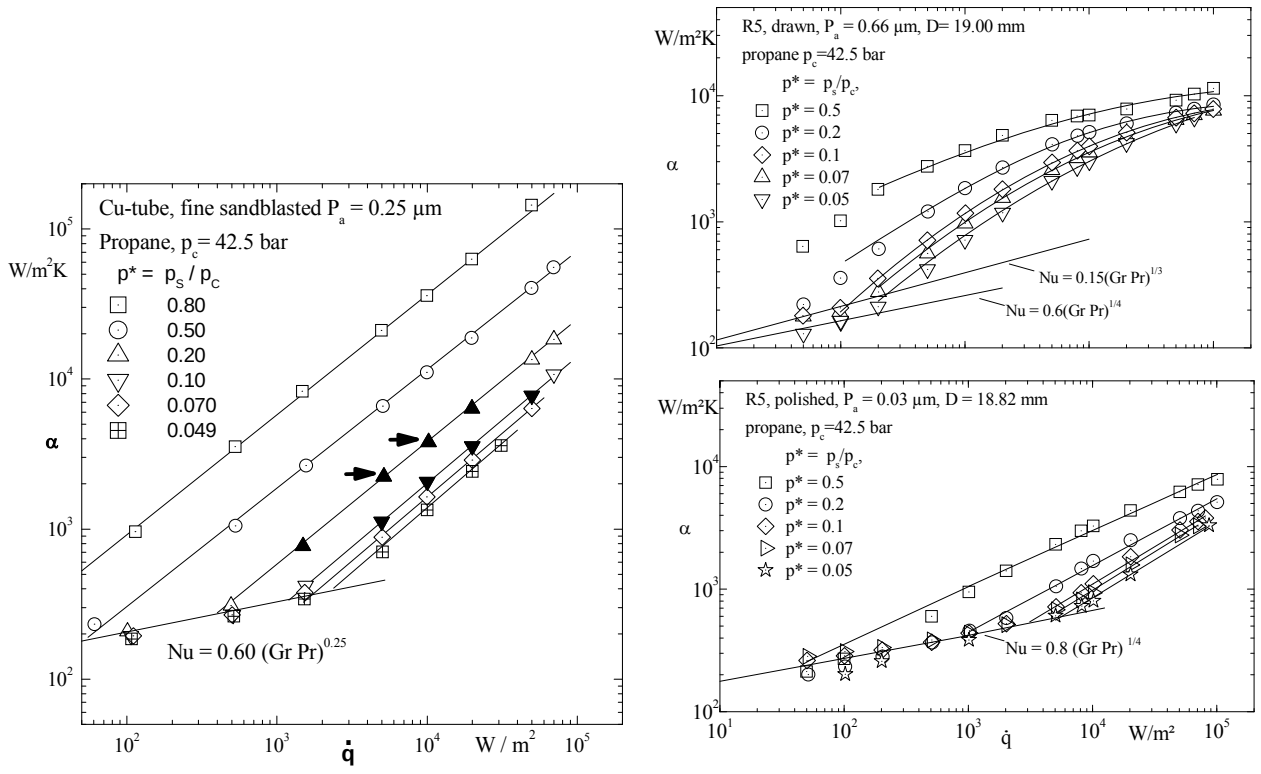

Figure 3: left: The heat transfer coefficient α as function of the heat flux q. Open symbols: Heat transfer measurements investigated. Closed symbols: parallel evaluation of bubble formation;
right: Average heat transfer performance of the mild steel tubes; propane boiling at different heat fluxes and pressures on the drawn surface (top) and on the polished surface without cavities (bottom)

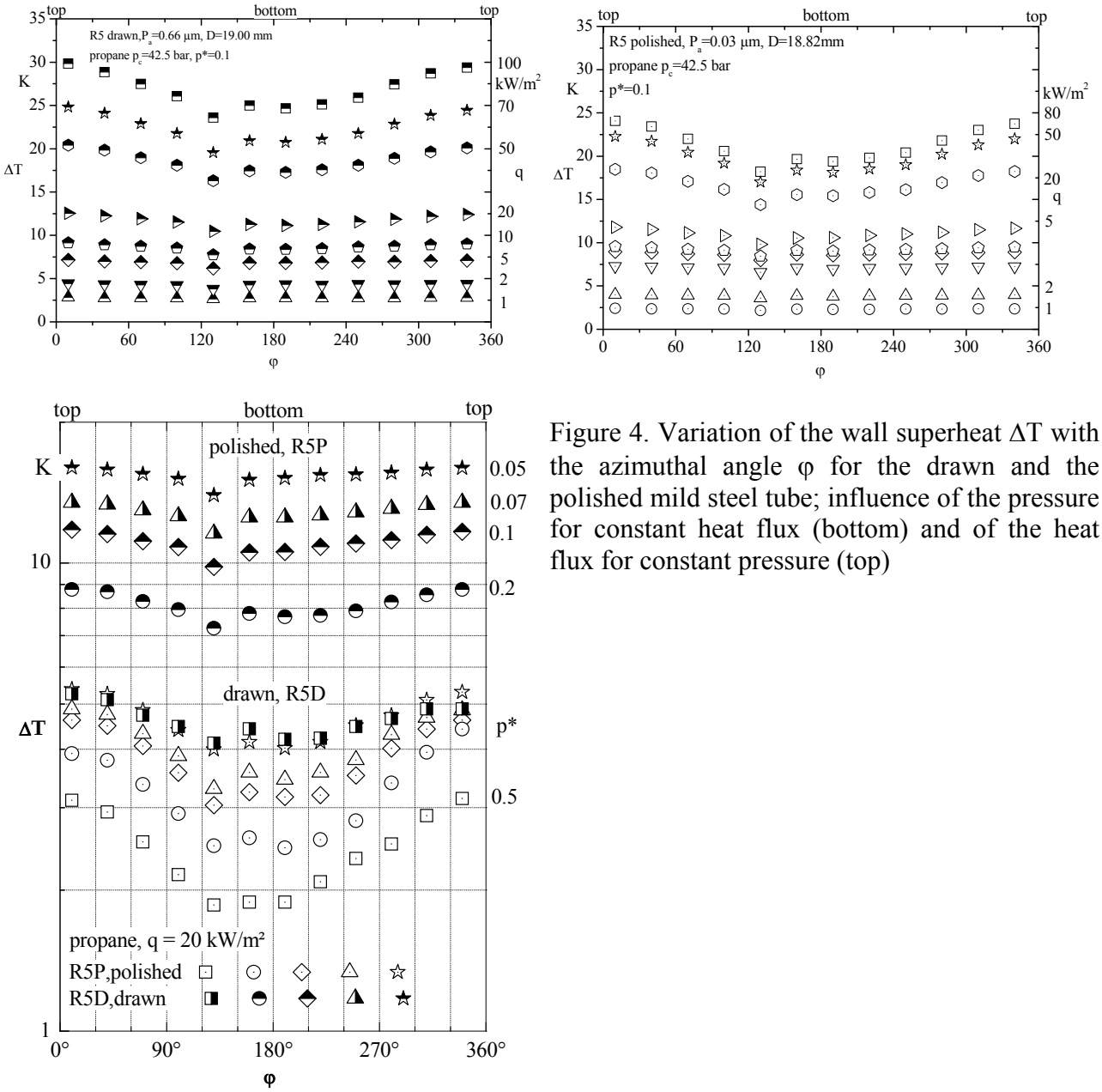

Figure 4. Variation of the wall superheat ΔT with the azimuthal angle φ for the drawn and the polished mild steel tube; influence of the pressure for constant heat flux (bottom) and of the heat flux for constant pressure (top)

RESULTS FOR THE BUBBLE FORMATION

The average numbers of cumulative and momentary sites for all image sequences of video investigated for two pressures are shown in Figure 6 as function of the heat flux (left) and of the critical radius r_c for stable bubble nuclei (right). There is a large difference between the cumulative and momentary numbers of sites, e.g. the cumulative numbers of sites are for a factor 70 higher than the momentary for p* = 0.2 and q = 20 kW/m². The decreasing effect for the highest heat fluxes may be due to the difficulty to properly distinguish the single active sites for intensive boiling with turbulent bubble movement, and with interaction of the growing bubbles with those upstreaming along the heated surface. The local distributions of the cumulative nucleation sites near the flank of the horizontal tube are shown in Fig. 6, left, for a selected boiling condition (intermediate heat flux q = 10 kW/m²) and a selected sequence near the flank of the copper tube. Each area is subdivided in cells for better comparison with the size of the topographies investigated for the roughness analysis. The active sites show in some parts some agglomerations on the fine sandblasted surface, but mainly the tube surface is uniformly covered by active nucleation sites, see Fig. 7, left.

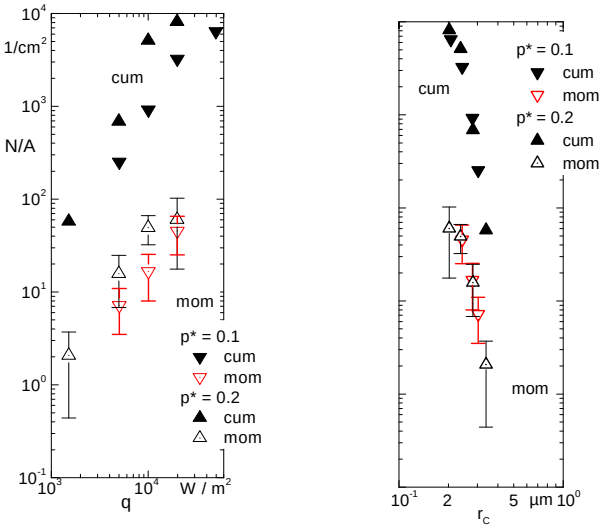

Figure 5. The number of active sites as function of q (left) and of the critical radius of a stable nucleus (right)

The contribution by upstreaming bubbles may be observed in the left and right part of the diagram in Fig. 6. An indication of the interaction between adjacent sites is the statistical analysis of their nearest distances such as the size distributions in Fig. 6, right. The histograms may be described by a modified Weibull function. The smallest distances are far away from the value of the critical radius of ca. $r_c \approx 0.25$ µm, but it is expected that the bubbles will coalesce during their growth, especially near the departure moment ($d_A \approx 0.25$mm on the flank of the test tube, see Figure 10) - if they are activated simultaneously. The numbers of momentary nucleation sites are not constant during the sequence of about 500 images = 500 ms. The temporal resolution of the activation is shown in Figure 7 for the same boiling conditions as in Figure 6. A cycle of activation is succeeded by one of deactivation with a regular fluctuation to the average value of $N/A_{M,m}$. The momentary active nucleation sites are distributed irregularly over the surface, see the crosses in Fig and the symbols in Figure. There are more active sites in this ms as in average, see Fig 7 and 8. In consequence, the model assumption of stable nucleation sites with constant frequence have to be checked. For fine sandblasted surfaces, the most of the nucleation sites are activated once during the entire sequence.

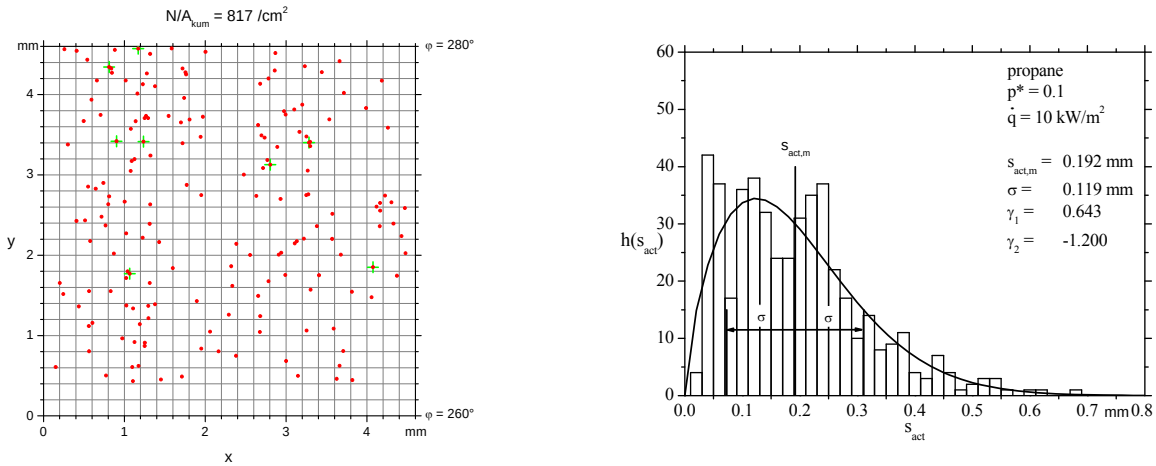

Figure 6. local distribution size of the nearest distances (left) and of all active cumulative nucleation sites for propane boiling on an horizontal copper tube at p* = 0.1, q = 10kW/m² (right)

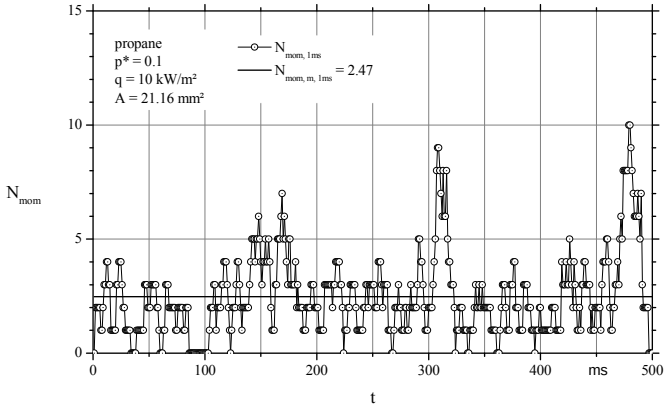

Figure 7. Temporal resolution of the activation with N/A_M as function of the evaluation time of the video sequence by different evaluation times

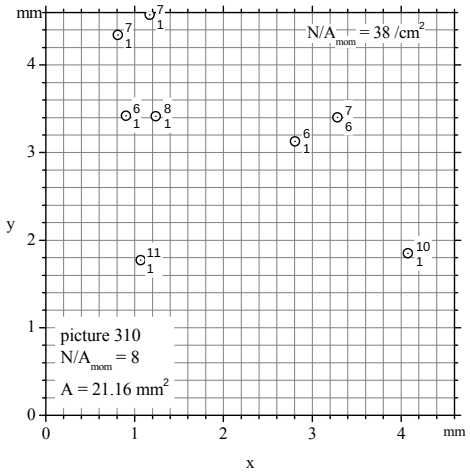

Figure 8. Local distribution of the active nucleation sites for p* = 0.1 and q = 10 kW/m² on the fine sandblasted surface of the copper tube

Most frequently bubbles are measured manually. Shortly after departing from the surface the bubbles are usually not spherical, but rather elliptical. In this case the largest horizontal and vertical diameter, d_x and d_y, is measured at this point in time. The departure diameter d_A is computed as an effective diameter according to

$$d_A = (d_x^2\, d_y)^{1/3} \qquad (4.1)$$

The bubble departure diameter is a function of the position of the active nucleation sites on the horizontal tubes, which is demonstrated in Figure 9 at p* = 0.1 and two different heat fluxes. The flank of the tube corresponds to 270° (s. also Fig). The size distribution of the bubble departure diameter is quite large, see the scatter of the data in Figure 9, right, while d_A seems to be influenced by the heat flux due to the increasing influence of the interaction of the bubbles. The measured values of d_A increase systematically from the flank of the tube (φ = 270) to the top or the bottom. This effect has also been found by Luke and Gorenflo [8] for propane on a smaller steel tube. The data $d_{A,min}$ at φ = 270° are characteristic for this part of the tube and are lower than acc. to calculation methods like those of Weckesser [7]. The relative increase of the calculation method of [8] are in good agreement with the new experimental data. The bubbles are larger at the bottom of the tube, where only a component of the gravitational acceleration is effective, and the larger bubbles on the top are caused by a higher superheat of the up streaming liquid and by separation and recirculation. This discussion shows that applying results on horizontal plates to horizontal tubes is questionable.

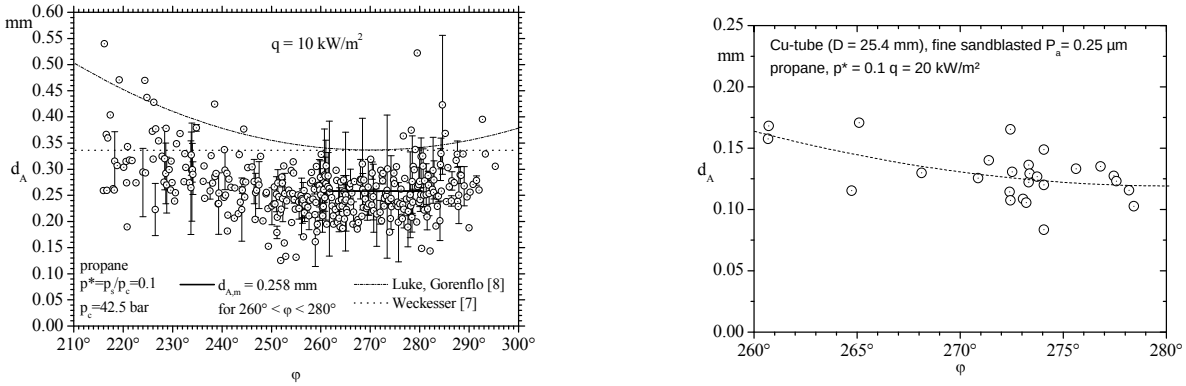

Figure 9. Bubble departure diameter as function of the azimuthal position and comparison with calculation methods of the literature for p* = 0.1 and two heat fluxes for boiling propane on a horizontal fine sandblasted copper tube (φ = 270° is near the flank of the tube).

The results of the evaluation of one sequence for propane boiling on a fine sandblasted copper tube surface with p* = 0.1 and a heat flux of q = 10 kW/m² near the median line of the tube is represented in Figure 11. The bubble No 707 is identified and tracked until it vanishes from the image (squares), cf also Figure 10. Bubbles smaller than d_B = 0.05 mm cannot be detected by this method due to the insufficient resolution in pixels. Shortly after activation the bubble is growing on its nucleation site to the departure diameter (d_A = 0.30 mm; closed squares). After departure, it still grows while it is streaming up along the superheated tube surface (open squares). The scatter within the data for the bubble diameter is due to the variation of the visible two-dimensional shape (the projection area) of the bubble, while the third dimension in direction of the tube surface cannot be evaluated. The bubble is only analysed from its top. The variation of the shape follows the influences caused by the movements of the liquid and the up-sliding bubbles. The uncertainties can be estimated to be in the order of 7% to 12% of the values of the bubble diameter. The growth of a bubble situated on another nucleation site (circles in Figure 11) is stronger and it departs with larger diameter from its site (d_A = 0.45 mm).

The sliding path of the bubbles No 707 and 748 along the tube surface is shown in Figure 11. The bubble No. 707 is drifted due to convective effects to the left side, while the way of No. 748 is quite irregular (Compare also the variation in the bubble diameter in Figure 9).

The sliding bubbles can be separated in different types: the first one still grows by contact with the superheated boundary layer during its movement upwards, see Figure 12. The diameter of the second type remains more or less constant because it is obviously far away from the superheated surface. The way of the bubble No. 60 is strictly upwards and undisturbed, see Fig 12, while the bubbles closer to the superheated surface as No 498 drift to the left side, see Figure 12.

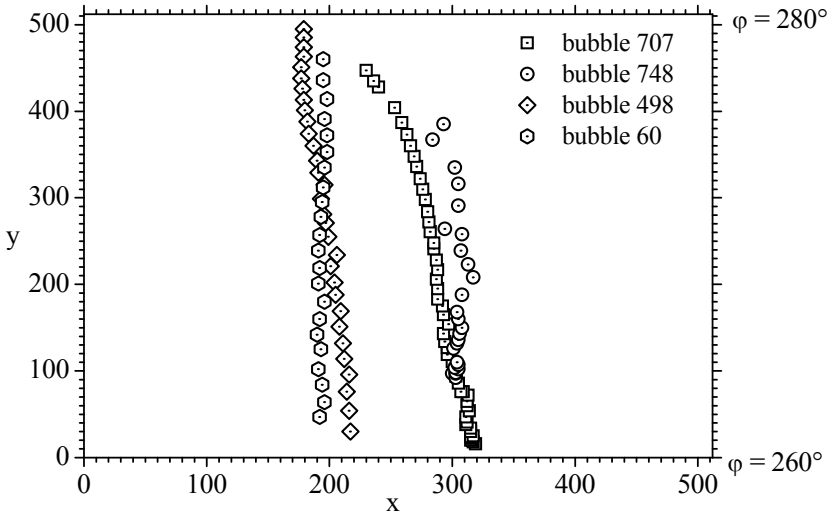

Figure 10. The sliding path of selected up streaming bubbles along the superheated boundary layer of the fine sandblasted copper tube for boiling propane (p* = 0.1 and q = 10 kW/m²).

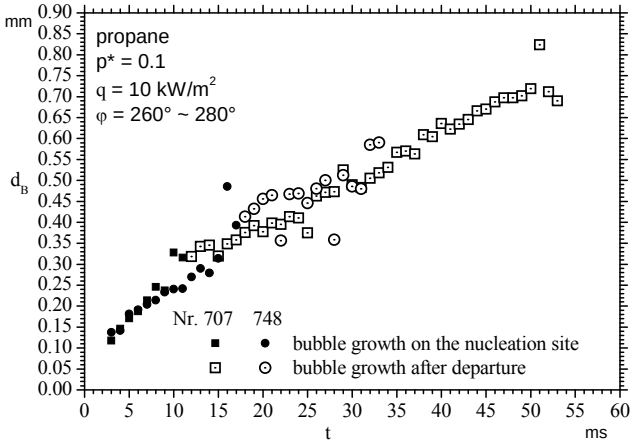

Figure 11. Two examples of bubbles growing on their nucleation sites and then sliding along the superheated surface

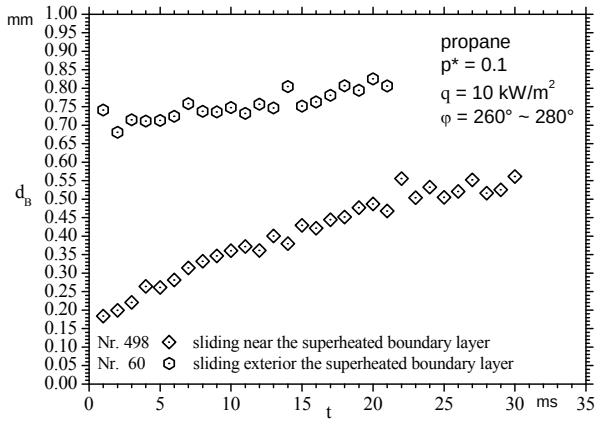

Figure 12. Examples of bubbles moving upwards and growing or which do not grow (bottom) by sliding along the superheated surface

CONCLUSIONS

The coherent new data of heat transfer, bubble formation and roughness from the same heated surface gives new idea for the activation of bubbles on the surface, their growth on the site and by sliding up and the manifold interaction between them. The evaluation of high speed video images offers the possibility to receive much more detailed information about the activation of bubbles and of the heated surface and its cavities, but it was very time consuming. Semi-automatic and automatic programs are developed to identify and track the individual bubbles. Some video sequences have been analysed previously for a few examples because of the large amount of data. The cumulative active nucleation sites are distributed statistically, especially for low heat fluxes agglomerations are observed over the median line of the horizontal test tube. The density distribution of the nearest distances between the adjacent sites shows that interaction of bubbles growing at their sites is possible if they are active simultaneously. The growth of the bubbles sliding-up along the superheated tube surface results in values nearly twice the bubble departure diameter. Their contribution to the vapour production in model assumptions has to be considered in future. The long-term aim is that the new results shall enable to interpret the fundamentals in boiling heat transfer and to establish new calculation methods using them.

REFERENCES

1. Gorenflo, D., Goetz J., Proposal of a Standard Apparatus for the Measurement of Pool Boiling Heat Transfer, Heat and Mass Transfer, 16(2), 69-78, 1982
2. Luke, A., Kruck, O., Heat transfer measurement of R134a and propane boiling at evaporator tubes with plain and enhanced finned surfaces; Proc. 12th Int. Refrig. and A.C. Conf., Purdue (USA) 2008
3. Luke, A., Preparation, Measurement and Analysis of the Microstructure of evaporator surfaces; Int. J. Therm. Sci. 45, 237-256, 2006
4. Gorenflo, D., Pool boiling. Chapt. Ha. VDI-Heat Atlas, VDI-Verlag, Düsseldorf 1993
5. Luke, A., Active and Potential Bubble Nucleation Sites on Different Structured Heated Surfaces; Chem. Eng. Research and Design, 82, 462-470, 2004
6. Luke, A., Müller, B.C.F., Nucleate Boiling of Natural Refrigerants in a wide Pressure Range; Proc. 7th Experimental Heat Transfer, Fluid Mechanics and Thermodynamics (ExHFT-7), Krakow (Poland) 2009
7. Weckesser, M., Untersuchungen zur Blasenbildung beim Sieden in freier Konvektion. Diss. Universität Karlsruhe (TH), 1990
8. Luke, A., Gorenflo D., Heat Transfer and Size Distribution of Active Nucleation Sites in Boiling Propane outside a Tube; Int. J. Therm. Sci., 39, 919-930, 2000
9. Luke, A., Interactions between bubble formation and heating surface in nucleate boiling; Proc. 7th Conf. on Boiling Heat Transfer, Florianapolis (Brazil),2009

MEAN FLOW AND THERMO-HYDRAULIC BEHAVIOUR IN INCLINED LOUVERED FINS

C. T'Joen[1,*], H. Huisseune[1], M. De Paepe[1]
[1]Department of Flow, Heat and Combustion Mechanics, Ghent University, Belgium

ABSTRACT. In this study a hybrid fin design, the inclined louvered fin, is considered. The aim of the design is to increase heat transfer at low Reynolds numbers compared to louvered fins. To study the flow field behaviour a series of flow visualisation experiments have been performed to measure the mean flow angle and to observe the transition to unsteady flow. The mean flow angle was determined using validated CFD simulations. Parallel a series of wind tunnel measurements were performed to determine the thermo-hydraulic characteristics. The impact of the fin pitch, fin angle and louver thickness were studied. A strong coupling was found between the flow behaviour and the thermo-hydraulics showing clear boundary layer driven flow.

Keywords: *compact heat exchanger, inclined louvered fins, flow behaviour*

INTRODUCTION

When exchanging heat with air, the main thermal resistance in a heat exchanger is located on the air-side. To increase the heat transfer rate, the exterior surface area is enlarged by adding fins. Manufacturers continuously seek to increase the fin performance in order to reduce the heat exchanger size and cost. Today, highly interrupted surfaces are widely used to enhance the thermal performance of compact heat exchangers. These interrupted fins exploit two mechanisms to provide a performance improvement compared to continuous fins: (1) interrupted surfaces restart the thermal boundary layer, and because the resulting average thermal boundary layer thickness is smaller for several short plates than for one long plate, the average convective heat transfer coefficient is higher for the interrupted surfaces; and (2) above a critical Reynolds number, interrupted surfaces can cause vortex shedding and the resulting mixing and flow unsteadiness result in an increased heat transfer. Two widely used interrupted fin designs are the offset strip or slit fin and the louvered fin. Both consist of arrays of flat plates. In slit fins these plates are aligned to the main flow, while in louvered fins the plates are set at an angle to the flow. The inclined louvered fin is a hybrid design of louvered and offset strip fins, as described by Shah *et al.* [1]. The plates are aligned with the main flow (Fig. 1) but are set out in a staggered layout, forming a stair like deflecting channel. In Fig. 1 the main geometric parameters are indicated: the fin pitch F_p, the louver pitch L_p, the fin thickness t, the fin angle φ and the number of louvers. Just as in louvered fins there are distinct inlet-, turnaround- and exit-louvers. Usually air-side heat transfer and pressure drop characteristics of a new fin type are determined from experimental data (using the Wilson plot measurement technique, see e.g. Rose [2]) on full scale heat exchangers. This method requires the manufacturing of complete exchangers and thus is expensive. An alternative is to study a scaled model of the novel fin type. This approach was selected at UGent to study the inclined louvered fin.

* Corresponding author: dr. C. T'Joen
Phone: + (32)-9-2543355 Fax: + (32)-9-2643575
E-mail address: christophe.tjoen@ugent.be

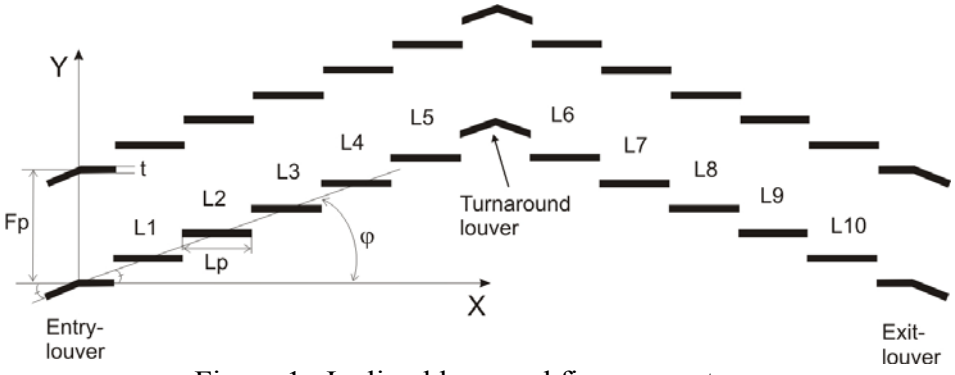

Figure 1. Inclined louvered fin: parameters.

Tanaka *et al.* [3] used a simple analytical model to study the flow in inclined louvered fins (with a nonzero louver angle – in this study the louver angle is kept constant at 0°) and concluded that a high average heat transfer coefficient could be realized provided that (1) the minimum traverse space to the adjacent louver is wide enough to include the boundary layers and (2) the longitudinal distance between the stream-wise louvers is wide enough to eliminate wakes. After a series of visualizations using large scale models, a single heat exchanger was built, tested and compared to a standard louvered fin. In the considered velocity range (1-5 m/s) the average heat transfer coefficient of the inclined louvered fin core was 16% higher and the pressure drop 21-27% lower compared to the standard louvered fin heat exchanger. This example clearly indicates the potential of this fin type.

MEAN FLOW BEHAVIOUR IN INCLINED LOUVERED FINS

Both in louvered fins and slit fins previous studies have shown a strong link between the thermo-hydraulic behaviour and the flow characteristics (slit fins: DeJong and Jacobi [4] – louvered fins: DeJong and Jacobi [5] and Achaichia and Cowell [6]). The interrupted surface breaks up the thermal boundary layer increasing the heat transfer coefficient, and the accumulation of flow perturbations due to the louvers results in a gradual transition to unsteady flow, as shown by Tafti and Zhang [7]. Using mass transfer measurements DeJong and Jacobi [4] showed that unsteady flow results in increased (local) heat transfer coefficients. In louvered fins an additional flow characteristic arises: at high Reynolds numbers the flow is deflected. Louvered fins show two different flow profiles, as shown by Cowell *et al.* [8]. At low Reynolds numbers the thick boundary layers block the passage between the louvers, forcing the flow between the different fins. This is referred to as 'duct oriented flow' in Fig. 2. As the Reynolds number increases the flow passages open up and 'louvered oriented flow' is created. This is indicated in Fig. 2. As is shown, the flow is deflected at high Reynolds numbers; extending its flow path throughout the fin array (the right side of Fig. 2 gives an impression of the modified flow path). For high Reynolds numbers the flow angle approaches the louver angle. This increases the heat transfer rate. But as the flow path is extended so is the frictional pressure drop. The degree of flow deflection is usually quantified using the concept 'flow efficiency' η. This is the ratio of the mean flow angle α to louver angle θ, Eq. (1). Achaichia and Cowell [6] found a strong link between the heat transfer rate of flat tube louvered fin heat exchangers and the mean flow behaviour, relating the Stanton number to η (Eq. (2)).

$$\eta = \frac{\alpha}{\vartheta} \tag{1}$$

$$St = 1.18 \cdot \eta \cdot \mathrm{Re}_{Lp}^{-0.58} \tag{2}$$

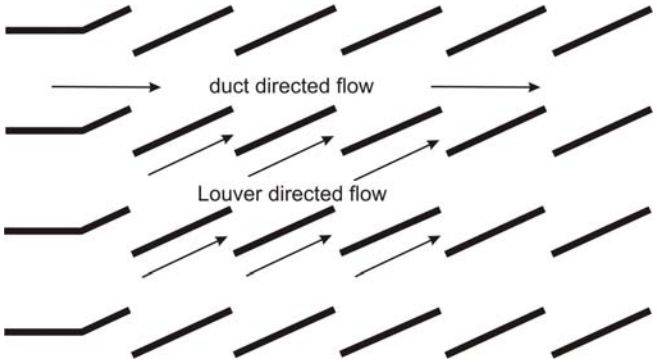

Figure 2. Duct directed flow versus louver directed flow.

Using a large database of validated two dimensional numerical CFD-simulations, Zhang and Tafti [9] determined a correlation for the flow efficiency of louvered fins. Results show that η is strongly dependent on geometrical parameters, especially at low Reynolds numbers. Flow efficiency increases with Re and louver angle, while decreasing with fin pitch and thickness ratio.

If the geometry of the inclined louvered fin (Fig. 1) is considered, *a priori* it is clear that similar phenomena as in louvered fins will occur. At low Re_{Lp} the thick boundary layers will block the passages between the louvers, forcing the flow to wind up and down. As Re_{Lp} increases, the flow passages will open up and the flow becomes more slit fin like, aligned with the louvers. To study the flow behaviour through the fin array and to determine at which Reynolds number the flow becomes unsteady, a series of water tunnel experiments were performed. In the closed loop water tunnel (located at the University of Illinois), the water is circulated using a frequency controlled pump through a plenum, followed by a contraction section, the test section and then finally a reservoir. To ensure a uniform flow at the inlet of the test section, two honeycomb flow straighteners are used in the contraction. The test section has a length of 0.4 m, a width of 0.3 m, a height of 0.3 m and is made of transparent plexiglass. A digital camera was used to record the images. The water temperature is measured using an E-type thermocouple. To determine the water velocity the time required for a single streakline to travel a given distance (0.25 m) was measured using a chronometer. To visualise the flow, dye is injected at a specific point just upstream of the test section, highlighting a single streakline. Scaled models (20:1) of the inclined louvered fin were placed in the test section. Six configurations with varying geometric parameters were studied (Table 1, L_p = 0.02 m). The scaling factor was selected in order to obtain sufficient spatial resolution, while maintaining a sufficiently large number of fin rows to ensure periodic flow behaviour. DeJong and Jacobi [10] showed that wall effects can result in a strong distortion of the measured mean flow angle. More details on the measurement setup and procedure can be found in T'Joen *et al.* [11].

Table 1. Geometric parameters of the studied inclined louvered fins

Fin parameters	Configuration 1	Configuration 2	Configuration 3
F_p	0.0340 m	0.0225 m	0.0340 m
φ	12.64°	12.64°	30.96°
t	0.002 m	0.002 m	0.002 m
Fin parameters	Configuration 4	Configuration 5	Configuration 6
F_p	0.0225 m	0.0276 m	0.0276 m
φ	30.96°	19.78°	19.78°
t	0.002 m	0.002 m	0.004 m

In order to quantify the flow behaviour in the inclined louvered fins, the 'fin angle alignment factor' ζ (defined in Eq. (3) as the ratio of the mean flow angle α to the fin angle φ) is introduced. Note that the definition is identical to that of the 'flow efficiency' η for standard louvered fins. For louvered fins, a high value of η corresponds to a flow almost parallel to the louvers, resulting in large heat transfer coefficients due to thin boundary layers. Thus high values of η are good from a heat transfer perspective, resulting in the term flow '*efficiency*' for η. For the inclined louvered fin array, high values of ζ indicate that the flow along the louver surface is dramatically reduced, and the local heat transfer coefficient can be expected to be reduced. This would make the term 'flow efficiency' misleading for inclined louvered fins, thus an alternate term is used, the 'fin angle alignment factor'.

$$\varsigma = \frac{\alpha}{\varphi} \approx \frac{\tan\alpha}{\tan\varphi} \tag{3}$$

For each of the six configurations images of the flow field were recorded at various Reynolds numbers. At each Re_{Lp} the dye injection point was varied over the channel width. This resulted in a series of images of various streaklines which, once combined, provide an overview of the total flow field at a given Reynolds number. For each of the images ζ can be determined graphically by using the approximation in Eq. (3). The images were imported into a graphical software package. The mean flow angle was determined between the point where the streakline enters the fin array and the midpoint of the turnaround louver. For each configuration a series of graphs can then be produced, one per Reynolds number, showing the local values of ζ set out against the injection location. This value represents the position of the injector relative to the fin passage and is scaled with the fin pitch, so it ranges from 0 (top of the fin passage) to 1 (bottom of the fin passage). An example is shown in Fig. 3 (filled symbols). The error bars are indicated. A detailed description of the uncertainty analysis can be found in T'Joen *et al.* [11]. There is clearly a strong variation depending on the injection location.

To determine a correct average value the gaps between the data points should be filled with additional data. To this end, a series of numerical simulations were undertaken. The flow through the fin configurations was simulated using Fluent©. Two dimensional cases were studied using unstructured quadrilateral meshes. A single louver row was simulated with an entry region (two fin pitches) and exit region (five fin pitches). The height of the computational domain is set to one fin pitch with periodic boundary conditions on the top and bottom of the domain. The double precision segregated solver was used with convergence criteria of 1e-8 for continuity and velocity components and 1e-6 for energy. A grid independence study was performed.

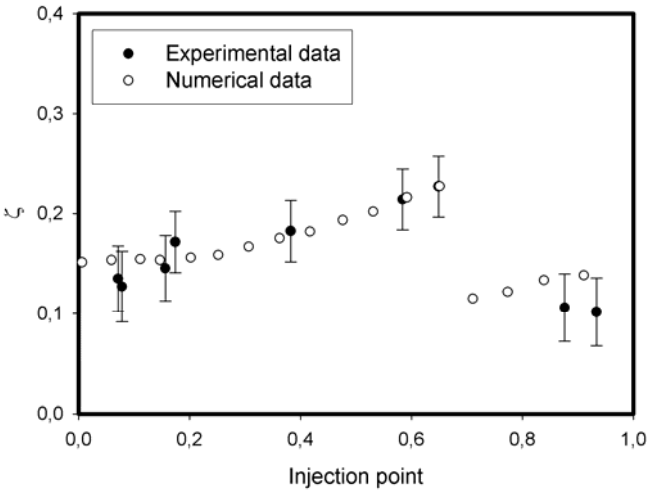

Figure 3. Comparison of the experimentally and numerically determined local ζ values set out against the injection point, configuration 5 - Re_{Lp} = 402.

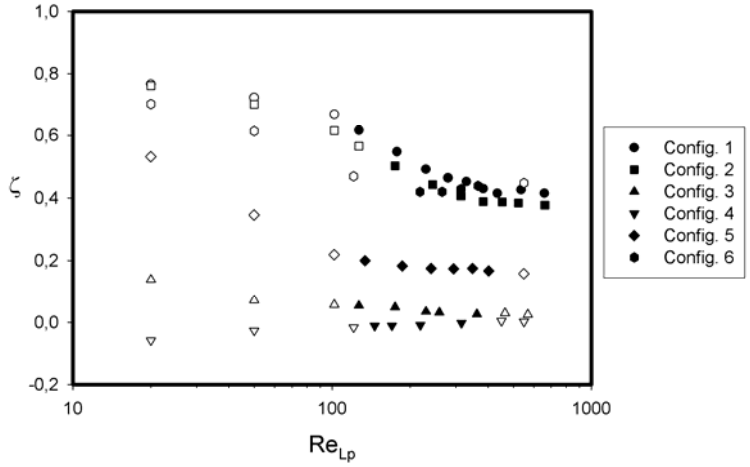

Figure 4. Averaged ζ values for the 6 different configurations over the studied Reynolds number range. The filled symbols represent validated numerical simulations. The open symbols are purely numerical cases without accompanying experimental data.

In order to determine ζ from the simulations, the same procedure was used as for the water tunnel experiments. The streamlines were visualized using the 'path lines' option and the resulting image was exported to the graphical software. This resulted in a set of numerical data points, spread out evenly over the fin spacing, as can be seen in Fig. 3. The agreement between the simulations and the experimental data is very good. Using the validated numerical data it is possible to determine a well defined average value for ζ. These values are shown in Fig. 4 for the different configurations. Compared to flow efficiency data of louvered fins, two key differences can be seen:

- The flow deflection is considerably lower than those found in standard louvered fins, Zhang and Tafti [9] reported η values between 0.5 and 0.95 in the same Re_{Lp} range. So it is clear that inclined louvered fins generate flow deflection, but that it is less pronounced.
- Figure 5 also shows that for most configurations (3 - 4 - 5 - 6) the flow deflection is nearly constant in the considered Reynolds range. This is a large difference with standard louvered fins, which show a sharp reduction in η (and thus become less effective) once Re_{Lp} drops below 300. The flow deflection also shows an opposite trend in inclined louvered fins, increasing as the Reynolds number decreases.

UNSTEADY FLOW IN INCLINED LOUVERED FINS

During the flow visualization experiments the transition from steady laminar flow to unsteady flow was studied as well. It was found that the initial instability appears in the wake of the exit louver. As the Reynolds number increases the flow instabilities move upstream into the fin array. The onset of unsteady flow occurred at low Reynolds numbers (200-300). The transition was triggered geometrically due to the recirculation zones present on top and underneath of the inlet, turnaround and exit louver. Figure 5 shows the Reynolds numbers at which the first unsteady flow patterns were detected at the inlet-, turnaround- and exit-louver for configurations 1-5. It can be seen that the fin pitch and fin angle both impact the transition to unsteady flow. The louver pitch L_p was used to make other length scales non dimensional. This is expressed by a superscript *, so the ratio of the fin pitch and louver pitch is noted as F_p^*. For comparison the transitional behaviour in 2 louvered fins (Tafti and Zhang [7]) and 1 slit fin (DeJong and Jacobi [4]) are shown as well. As can be seen the transition in inclined louvered fins occurs at much lower Reynolds numbers and also moves upstream much faster than in the louvered fin or slit fin. This is consistent with a transition that is purely geometrically triggered rather than due to the accumulation of flow disturbances.

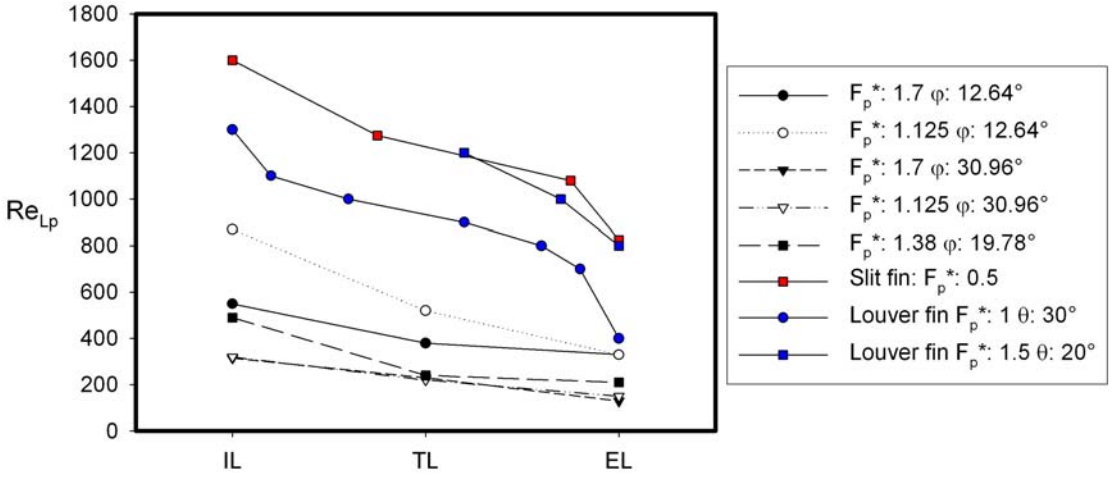

Figure 5. Reynolds number of the onset of unsteady flow at three locations in the inclined louvered fin configurations compared with similar data for louvered fins [7] and a slit fin [4].

THERMO-HYDRAULIC BEHAVIOUR OF INCLINED LOUVERED FINS

To determine the thermo-hydraulic characteristics of the inclined louvered fin, a series of wind tunnel experiments was performed on the scaled models. The air mass flow rate is measured using a calibrated orifice plate (ISO 5167). The fin parts are made out of printed circuit board material coated with a thin copper layer on both sides (2 mm thick). To provide heating (a uniform heat flux) a current is sent through the copper layer. The different louvers are connected in series to each other electrically using wires, ensuring the same heat flux is dissipated throughout the fin array. The test section and the downstream settling channel are insulated using 5 cm thick PUR foam in order to reduce the heat loss to the environment. The pressure drop over the test section is measured using a differential pressure transducer. These measurements were done without heating. The pressure taps were set along the sides of the channel. The air inlet temperature was measured using a thermocouple. To determine the heat transfer coefficient the local surface temperatures are measured using K-type thermocouples. A measurement louver was made using balsa wood. Nineteen thermocouples were inserted in the centre along the flow direction in order to measure the surface temperature change along the flow path. In the experiments the local heat flux q is imposed, and the local surface temperature is measured. Thus only a reference temperature T_{ref} is required to determine the local heat transfer coefficient, Eq. (4). To allow for easy comparison with other fin types the inlet temperature was used as a reference value. The resulting local heat transfer coefficients are averaged out over the fin surface area to determine the Colburn j factor. During the experiments it was found that a temperature difference was present between the top and the bottom of the measurement louver, due to the finite conduction of this louver. By measuring the thermal conductivity of the balsa wood (0.045 W/mK) the conductive flux q_{cond} could be determined. This flux through the louver is then added to or subtracted from the imposed heat flux boundary during the data reduction (Eq. (4)).

$$h = \frac{q \pm q_{cond}}{T_w - T_{ref}} \tag{4}$$

Figure 6 shows the parallels between ζ, the friction factor f and the Colburn j-factor for different configurations. As can be seen, there is a strong link between the mean flow behaviour and the resulting thermo-hydraulics: a strong change in ζ results in a transition in the friction factor curves away from the laminar flow solution (solid line). The same trends were found in the heat transfer

data. Increasing F_p^* lowers the friction factor. For the small fin angle cases the Colburn factor increases as F_p^* decreases due to increased fin compactness, while for the larger fin angle cases the reverse occurred. This is probably due to thermal wake interference. The small fin angle cases show two distinct transition points, one due to the change in ζ and the other due to the onset of unsteady flow. For the cases with a large fin angle only the transition due to unsteady flow can be found as the fin angle values are already low and extremely low Reynolds numbers would be required to detect the transition due to the sudden shift in ζ.

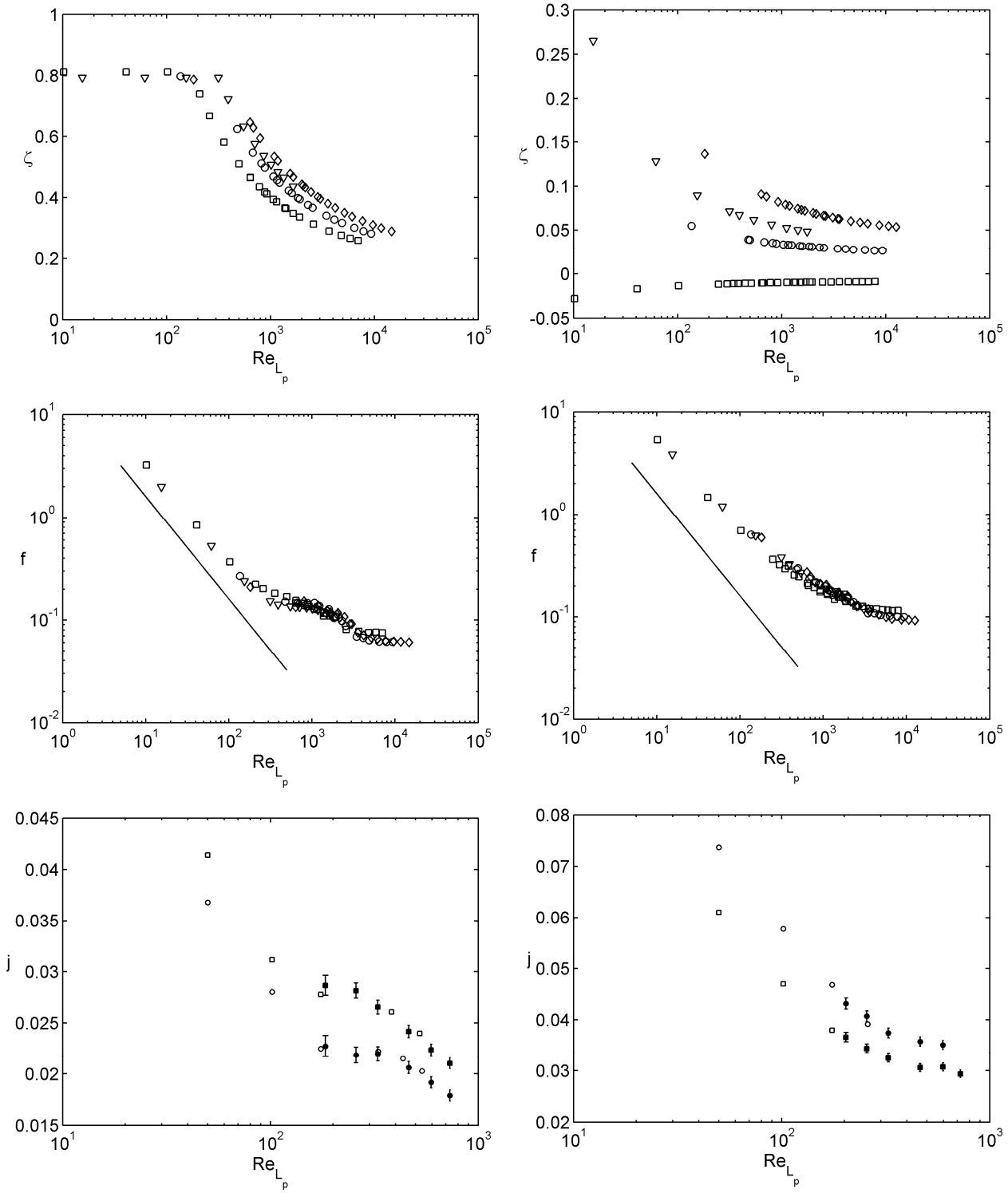

Figure 6. Fin angle alignment factor (top row), friction factor (middle row) and Colburn factor (bottom row) set out against Re_{Lp}. Left column: φ = 12.64°, right column: φ = 30.96°. Filled symbols: experimental data – open symbols: numerical data. Square symbols: $F_p^* = 1.125$, circle symbols: $F_p^* = 1.5$, triangle symbols: $F_p^* = 1.7$, diamond symbols: $F_p^* = 2$.

NOMENCLATURE

F_p	fin pitch [m]
L_p	louver pitch [m]
Re_{Lp}	Reynolds number based on the inlet velocity and the louver pitch [-]
q	heat flux [W/m²]
t	fin thickness [m]
α	mean flow angle [°]
ζ	fin angle alignment factor [-]
θ	louver angle [°]
φ	fin angle [°]

CONCLUSIONS

In this study the flow behaviour and thermo-hydraulic characteristics of a hybrid fin design, the inclined louvered fin, have been reported. Using a combination of experimental (water tunnel visualization) and numerical (CFD simulation) data the flow behaviour was quantified through the fin angle alignment factor ζ. At low Reynolds numbers the flow is deflected due to boundary layer growth. Comparison of the ζ curves with the j and f data set out against Re, revealed the strong link between the flow and j – f. A sharp decrease in ζ results in a rise of both j and f, as the flow becomes better aligned with the louvers. The onset of unsteady flow further increases j and f. During the visualization it was shown that unsteady flow occurs at low Reynolds numbers (~200-300) and that this transition is geometrically driven by recirculation zones on the inclined sections of the fin array. These findings could have significant impact for low Reynolds number applications.

REFERENCES

1. Shah, R.K., Heikal, M.R., Thonon, B. and Tochon, P., Progress in the numerical analysis of compact heat exchangers, *Advances of heat transfer*, Vol. 34, pp. 363-443, 2001.
2. Rose, J.W., Heat transfer coefficients, Wilson plots and accuracy of thermal measurements, *Experimental Thermal and Fluid Science*, vol. 28, pp. 77-86, 2004.
3. Tanaka, T., Itoh, M., Kudoh, M. and Tomita, A., Improvement of compact heat exchangers with inclined louvered fins, *Bulletin of JSME*, Vol. 27, pp. 219-226, 1984.
4. DeJong, N.C. and Jacobi, A.M., An experimental study of flow and heat transfer in parallel-plate arrays: local, row-by-row and surface average behaviour, *International Journal of Heat and Mass Transfer*, Vol. 40, pp. 1365-1378, 1997.
5. DeJong, N.C. and Jacobi, A.M., Localised flow and heat transfer interactions in louvered fins, *International Journal of Heat and Mass Transfer*, Vol. 46, pp. 443-455, 2003.
6. Achaichia, A. and Cowell, T.A., Heat transfer and pressure drop characteristics of flat tube and louvered plate fin surfaces, *Experimental Thermal and Fluid Science*, Vol. 1, pp. 147-157, 1988.
7. Tafti, D.K. and Zhang, X., Geometry effects on flow transition in multilouvered fins – onset, propagation and characteristic frequencies, *International Journal of Heat and Mass Transfer*, Vol. 44, pp. 4195-4210, 2001.
8. Cowell, T.A., Heikal, M.R. and Achaichia, A., 1995, Flow and heat transfer in compact louvered fin surfaces, *Experimental Thermal and Fluid Science*, Vol. 10, pp. 192-199.
9. Zhang, X. and Tafti, D.K., Flow efficiency in multi-louvered fins, *International Journal of Heat and Mass Transfer*, Vol. 46, pp. 1737-1750, 2003.
10. DeJong, N. and Jacobi, A., Flow, heat transfer and pressure drop in the near-wall region of louvered-fin arrays, *Exp. Thermal Fluid Science*, Vol. 27, pp. 237-250, 2003.
11. T'Joen, C., Jacobi, A.M. and De Paepe, M., Flow visualization in inclined louvered fins, *Experimental and Thermal Fluid Science* (accepted for publication)

HEAT TRANSFER FROM A HEMISPHERCAL CAVITY TO A SWIRL IMPINGING JET

V.I. Terekhov, Yu.M. Mshvidobadze
Kutateladze Institute of Thermophysics SB RAS, Novosibirsk, Russia

ABSTRACT. Experimental results on investigation of heat transfer at interaction of an air impact jet with a semi-spherical cavity are presented in this work. This research is continuation of investigations of turbulent jet interaction with complex surfaces and search for the method of heat transfer control. Experiments were carried out with fixed geometry of a semi-spherical cavity (D_C = 46 mm) and swirl parameter (R = 0; 0.58; 1.0; 2.74). The distance between the axisymmetrical nozzle and obstacle was 2÷10 sizes over the nozzle diameter, and the Reynolds number varied within $Re_0 = (1÷6)\cdot10^4$. It was found out that with an increase in swirling heat transfer intensity decreases because of fast mixing of the jet with ambient medium. In general, the pattern of swirl jet interaction with a concave surface is complex and multifactor

Keywords: *semi-spherical cavity, impinging swirl jet, heat transfer*

INTRODUCTION

Jets impinging onto heat-exchanging surfaces can be used in many technical apparatuses as very efficient heat-transfer intensifiers. Interest in this field was initiated many years ago, and since then ample data concerning this problem have been accumulated [1, 2]. Nonetheless, jets of interest still attract considerable attention, and extensive studies aimed at searching for new methods to control heat and mass transfer in such systems are presently under way. One strategy here implies modification of the surface onto which the jets impinge with obstacles. The authors of [3-5] examined heat transfer in narrow channels in which a system of jets impinging onto a surface modified with cavities was organized. It was shown that such systems exhibit good performance characteristics and can be used, in particular, for cooling turbine blades from inside. Yet, the physical reasons underlying the observed intensification of heat-transfer processes in the systems of interest have remained unveiled.

Cavities used as obstacles modifying the streamlined surfaces attract considerable interest as they proved capable of generating exotic self-oscillatory flow modes and intensifying heat transfer [6 - 9]. In the case of jets impinging onto heat-exchanging surfaces the interaction pattern of the jet flow with the surface is much more complicated compared to a flat surface. For instance, vortex formation processes and local flow separations induced by obstacles prepared in the form of cavities may give rise to a complex, unstable flow involving large-scale low-frequency oscillations, Taylor-Görtler vortices, etc. Under such conditions, accurate prediction of heat-transfer processes becomes problematic, although this problem was addressed in several publications.

The aerodynamic structure of the flow and the heat transfer from hemispherical cavity versus the jet Reynolds number and as functions of the distance from the nozzle exit to the heat-exchanging surface were examined in [10]. The jet flow was not swirling, and the cavity-to-nozzle diameter ratio was D_c/d_0 =5.4. The average heat transfer from the cavity surface was found to be decreased twice compared to the case of a flat surface, all other conditions being identical. With decreasing the nozzle diameter, the heat transfer grows in value and, according to [11], at D_c/d_0 = 44 its

* Corresponding author: Prof. V.I.Terekhov
Phone: + (7)-383-3306736, Fax: + (7)-383-3308480
E-mail address: Terekhov@itp.nsc.ru

intensity may become exceeding the same quantity for flat surface. Moreover, in the region outside the cavity the thermal interaction between the lateral flow and the jet rapidly degenerates, making the heat transfer almost vanishing here [10]. In the cavity, pronounced vortex formations arise. These formations, resembling Taylor-Görtler vortices, give rise to coherent structures that can be easily registered by heat flow microsensors.

In [12], local heat transfer in hemispherical cavity was examined as a function of cavity-to-nozzle diameter ratio in the range $D_C/d_0 = 11 \div 30$. Here, unlike in [11], increase in the nozzle diameter was found to suppress heat transfer throughout the whole examined range of Reynolds numbers, $Re_0 \sim 10^4$ to $5 \cdot 10^4$. Thus, the experimental data concerning the interaction of jet flows with curvilinear surfaces are still few in number and contradictory.

The problem becomes even more complicated if the jet flow impinging onto an obstacle has a rotational velocity component. So far, the heat transfer and the structure of flow between a swirling jet and a surface onto which this jet impinges remain poorly understood. Reported studies [13-17], also few in number, show the interaction of a swirling jet with an obstacle to be a complex many-factor process. An increase in jet pre-rotation intensity enhances mixing processes in the system; as a result, the heat transfer of the surface interacting with the jet at large nozzle-to-surface separations ($L/d_0 > 6$) turns out to be substantially reduced in comparison with non-swirling jets. At small nozzle-to-surface separations, $L/d_0 < 6$, the picture may be opposite, with additional maxima emerging in the radial distribution of heat-transfer intensity due to specific formation pattern of swirling jets with different pre-rotations, Reynolds numbers, and separations between the jet turning point and the surface onto which the jet impinges.

Expectedly, pre-rotation of the jet approaching a surface modified with a spherical cavity will complicate the problem. The fluid leaving the cavity will interact with the rotational jet flow impinging onto the obstacle, thus causing the formation of unsteady three-dimensional flows hard to predict numerically.

The purpose of the present study was to experimentally examine the time-average heat transfer from a surface with spherical cavity during impingement of a swirling jet onto this surface. Such flows are often encountered in low-temperature plasma generators and in power-plant cooling systems.

EXPERIMENTAL FACILITY AND PROCEDURE

The experiments were carried out on an experimental setup whose schematic diagram is shown in Fig. 1. This setup was described in detail elsewhere [18]. A room-temperature axisymmetric swirling air jet emanated out of the nozzle whose diameter was $d_0 = 8.5$ mm. The cavity diameter was fixed, equal to $D_C = 46$ mm, and the cavity depth was either $\Delta = 0$, 12, or 23 mm. The gas-flow velocity U_0 at the nozzle exit plane was varied in the range from 20 to 100 m/s, corresponding to Reynolds numbers $Re_0 = U_0 d_0/\nu = 10^4 \div 5 \cdot 10^4$.

The distribution of flow velocity over the nozzle outlet was almost uniform, the turbulence number being $Tu \cong 0.3\%$. The jet approached the obstacle normally, and the nozzle-to-surface separation S was varied from 0 to $10d_C$.

The jet flow was made swirling by pre-rotating it with a flat swirler with variable slit inclination angle. The jet pre-rotation parameter, defined as the momentum ratio between the circumferential component of the jet flow and the jet flow along the jet axis, was R = 0, 0.58, 1, or 2.74.

The test section, 50-mm thick and 190-mm in diameter, was prepared from copper. The desired temperature difference between the jet and the obstacle, about 40^0 in the majority of tests, was achieved with the help of an ohmic heater installed over the obstacle. The choice of copper, having a high value of thermal conductivity, as the obstacle material was motivated by the desire to organize the boundary condition $T_w \cong$ const at the obstacle surface. The temperature of the streamlined surface and the flow temperature were measured by chromel-copel thermocouples.

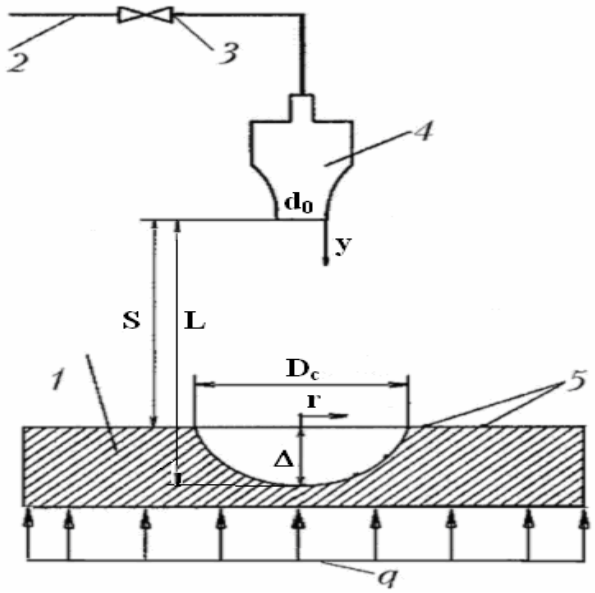

Figure 1. Experimental setup 1 – obstacle; 2 – air line; 3 – regulating valve; 4 - nozzle; 5 – heat-flux meters.

The heat fluxes were measured by gradient-type heat flow sensors glued onto the obstacle [19]. The characteristics of the sensors were as follows: in-plane dimensions - 2.5x2.5 mm (these dimensions were much smaller than the characteristic spatial scale of the flow under study), thickness - 0.2 mm, volt-watt sensitivity ≈ 10 mV/W, response time - 0.05 ms. In the course of measurements the arrays of instantaneous values of heat-flux densities were used to calculate the time-average heat fluxes, and also the heat-flow pulsations and spectra. The total number of realizations in one measurement was chosen to equal 10^4. The time in which one measurement was taken was varied from 10 to 90 s; it was found experimentally that this time affected measured data insignificantly. A tailored multi-channel unit was used to amplify the signals from the thermocouples and heat-flow sensors; then, the signals were fed to a computer to be processed there. The coefficient of heat transfer was defined as $\alpha_i = q_i / (T_w - T_0)$, where q_i is the local heat-flux density measured by sensor, and T_w and T_0 are respectively the temperature of the surface and the temperature of the air at the nozzle exit. An error analysis showed that the measurement inaccuracy for heat fluxes in our experiments was within 0.3÷10%. Simultaneously, the measurement inaccuracy for square-mean pulsations of heat fluxes was much greater, amounting to 30% for the obstacle with cavity. In processing the experimental data, experimentally determined losses of heat by radiation and free convection were taken into account.

Normally to the cavity surface and to the flat surface adjacent to the cavity, holes 0.5 mm in diameter were drilled; these holes were used to measure the radial distributions of pressure. In the tests, the average component of pressure was registered, and estimates of the intensity of pressure pulsations were made.

INTERACTION OF SWIRLING JET WITH A FLAT OBSTACLE

At the first stage of the study, we experimentally examined the heat transfer of flat obstacles interacting with eddying jets. A specific feature of such jets is their high ejective capacity due to which the jet divergence angle grew in value with increasing jet pre-rotation [14-16]. As a result, the heat-transfer maximum got displaced off the center (see Fig. 2). Depending on pre-rotation and nozzle-to-obstacle separation, this maximum could be either distinctly pronounced (Fig. 2a, $L/d_0 = 2$) or smooth (Fig. 2b, $L/d_0 = 10$). A similar tendency was also observed at other jet pre-rotations.

Importantly, in the majority of our experiments the radial distributions of local heat transfer behaved similarly, the heat transfer increasing with increasing the Reynolds number (see Fig. 2a).

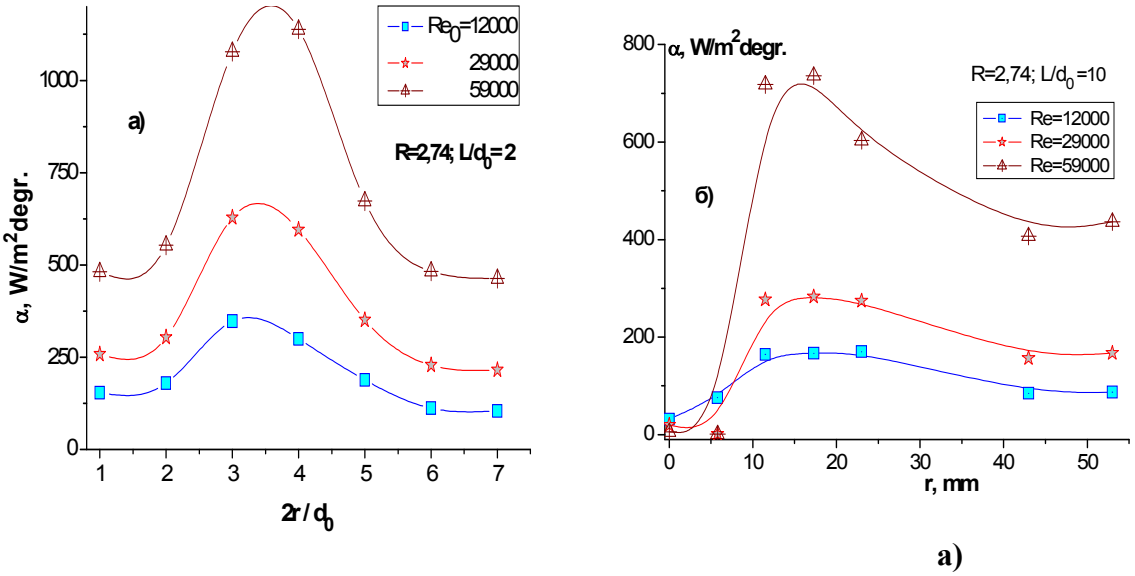

a)

b)

Figure 2. Distributions of heat-transfer coefficients over the flat surface interacting with a swirling jet.

Effect of a swirling angle of a impinging jet on a local heat transfer is shown on Fig. 3. It is visible, that with increase swirling parameter of a jets intensity of heat transfer is considerably reduced. At large parameter (R = 2,74) external region of flow heat transfer practically is absent, that speaks about intensive mixing impinging jets with an environment media.

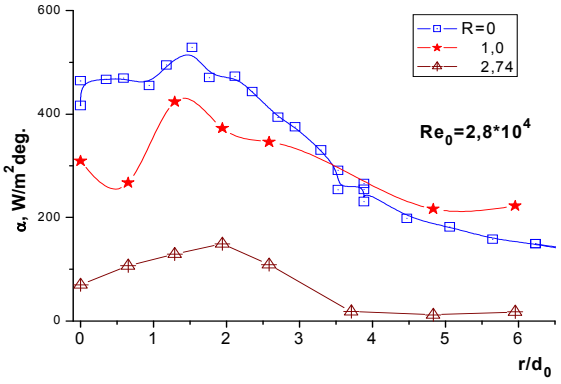

Figure 3. Effect of jet pre-rotation on the heat transfer from flat surface, $L/d_0 = 10$

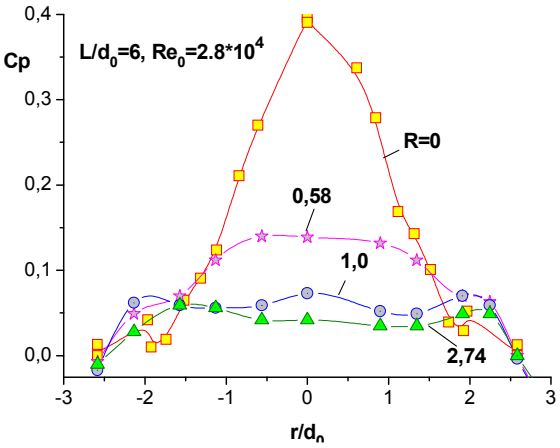

Figure.4. Pressure coefficient in the cavity onto which a swirling jet impinges

INTERACTION OF SWIRLING JET WITH HEMISPHERICAL CAVITY

PRESSURE PATTERN

The value of the pressure coefficient was found as the pressure drop between the surface and the atmosphere normalized to the dynamic pressure of the jet flow at the nozzle exit plane, $cp=2(p_i-p_a)/\rho_0 u_0^2$. A typical distribution of pressure coefficient over the radius of spherical cavity is exemplified in Fig. 4. Without pre-rotation (R=0) the pressure profile exhibits a distinct axial maximum. At the periphery, an inflection point brought about by the separation of the flow in this region is observed. The mechanism underlying the formation of flow in a cavity impinged by non-swirling jet was discussed in more detail in [10, 18].

With increasing the jet pre-rotation parameter the pressure level notably diminished due to the rapid expansion of the jet flow and the reduction of the jet momentum in the axial region. For instance, at R=2.74 the pressure coefficient is one order of magnitude smaller in comparison with non-swirling jet.

Another characteristic feature in the behavior of cavity pressure deserves mention. With swirling jets, the distributions of pressure in the peripheral region display no inflections. Moreover, a growth of pressure is observed in this zone due to the absence of flow separation and the action of centrifugal forces pressurizing the fluid here, as well as due to the influence of the surface curvature. Apparently, these factors will have influence on the formation of the temperature field in the system and on the heat- and mass-transfer processes proceeding there.

LOCAL AND AVERAGE HEAT TRANSFER IN CAVITY

The distribution of local heat-transfer coefficients in the radial direction is shown in Fig. 5. The rate of heat transfer is maximal in the absence of jet pre-rotation. As the jet pre-rotation parameter R grows in value, the Nusselt number starts exhibiting a non-monotonic behavior both along the radius, with the formation of additional maxima, and versus R. In the vicinity of the cavity the heat-transfer intensity for swirling jets turns out to be more than twice decreased. On the contrary, in the cavity the heat transfer from the swirling jet turns out to be enhanced in comparison with the case of non-swirling jets, the radial distribution of the heat-transfer coefficient being more uniform here.

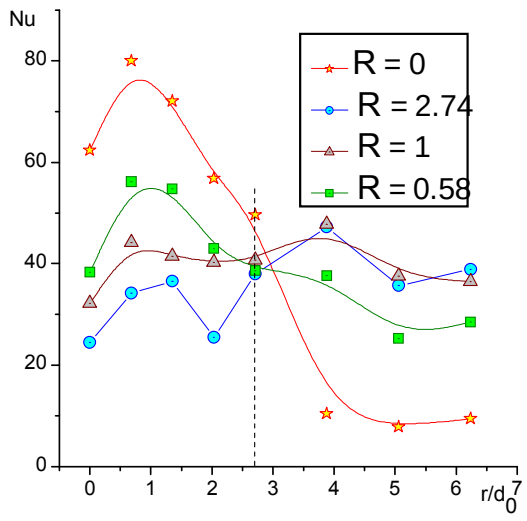

Figure 5. Local heat transfer for an obstacle with spherical cavity impinged by a jet. $Re_0=2.8\ 10^4$, $L/d_0 = 10$. The dashed line shows the cavity boundary.

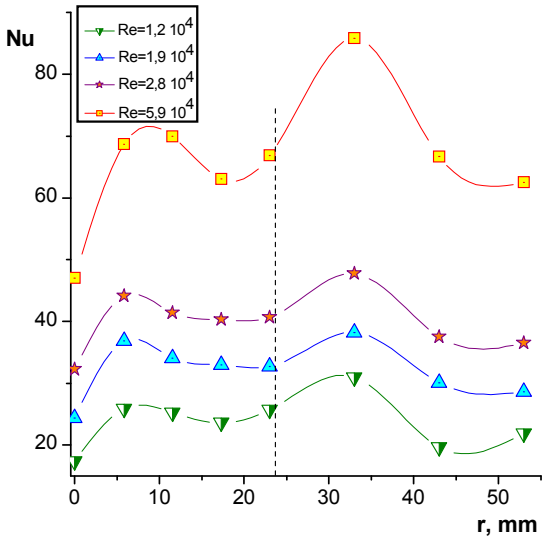

Figure 6 Effect of Reynolds number on the heat transfer of swirling jet. R =1, $L/d_0 = 10$

The latter points to a greater expansion angle of swirling jets, resulting in a growth of heat transfer in the region outside the cavity.

At fixed jet pre-rotation the heat-transfer data for different Reynolds numbers proved to be self-similar. This is evident from Fig. 6. Only at large Re_d numbers the heat-transfer maxima are pronounced more distinctly, with their position over the radius being quite stable.

An important characteristic of jets impinging onto surfaces is the heat transfer at the stagnation point. The experimental data $Nu_0 = f(Re_0)$ for various jet pre-rotations are shown in Fig. 7. Here, the most intense heat transfer is observed in the absence of pre-rotation (R=0), whereas the increase in the pre-rotation results in that the rate of heat transfer at the center of the cavity decreases. First of all, it is the formation of a complex aerodynamic structure during the interaction of jet with hemispherical cavity that underlies the complex behavior displayed by heat transfer.

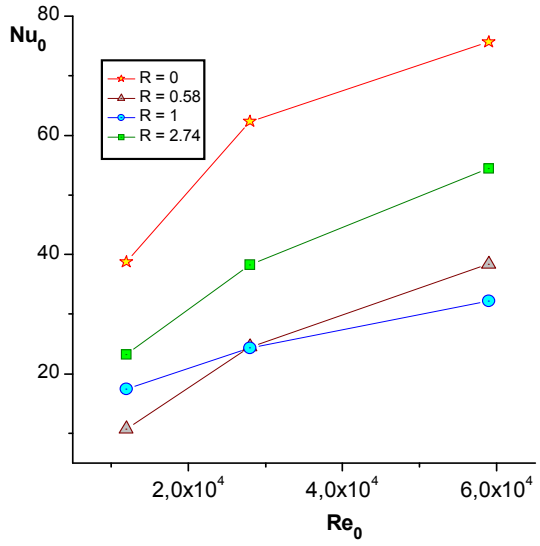

Figure 7. Distribution of Nusselt number Nu_0 at the stagnant point of the flow, $L/d_0 = 10$

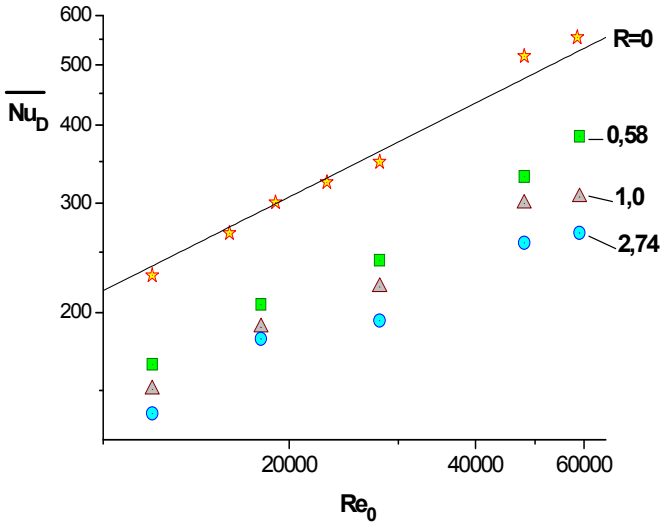

Figure 8. The Nusselt number $\overline{Nu}_D$ averaged over the cavity surface versus jet pre-rotation. $L/d_0 = 6.0$.

From the viewpoint of applications, a most important point in such complex problems is the deduction of correlation dependences for the average heat transfer versus Reynolds number and other governing parameters. In view of axial symmetry, in the present study the average value of the heat-transfer coefficient over the entire surface of cavity was obtained by integrating the local distributions over the radius. The average number $\overline{Nu}_D$ versus Re_0 at $L/d_c = 6$ for various jet pre-rotations is shown in Fig. 8. Here, the Nusselt number was calculated from the cavity diameter and from the mean value of the heat-transfer coefficient, $\overline{Nu}_D = \overline{\alpha} D_C/\lambda$. With increasing the jet pre-rotation at all other conditions kept unchanged the heat-transfer intensity decreases in value. For a non-swirling jet the experimental data obtained at $L/d_0 = 6$ can be fitted with the empirical relation

$$\overline{Nu}_D = 2.17 \cdot Re_0^{0.5}, \qquad (1)$$

typical of laminar heat-transfer mode. As a matter of fact, the flow in the cavity is turbulent; yet, the specific character of the formed flow pattern, namely, the involvement of reverse flows, curved flow streamlines, large-scale structures, etc., has resulted in the above relation for heat transfer. Apparently, relations of type (1) will undergo changes with distance to the heat-exchanging surface,

and for this evolution to be clarified additional tests or numerical experiments are required. Although the rate of heat transfer in the cavity proper decreases in the case of swirling jets, the total heat transfer, including the area adjacent to the cavity may be increased. For this possibility to check, here again additional studies are required.

SUMMARY

An experimental study of heat transfer during impingement of swirling jet onto hemispherical cavity was performed. It is shown that, following jet pre-rotation, additional maxima appear in the radial distribution of heat transfer, brought about by specific features of mixing processes of eddying jets with ambient air.

The intensity of heat transfer in cavity for swirling jets is substantially, by a factor of 2-3, reduced in comparison with non-swirling jets. On the contrary, outside the cavity the heat transfer for swirling jets is more intense. During variation of jet pre-rotation parameter the local Nusselt numbers vary non-monotonically both at the stagnant point and at different points over the radius, pointing to a complex mechanism of hydrodynamic and thermal processes in swirling jets impinging onto spherical cavities. At fixed distance to the plate and at jet pre-rotation parameter kept unchanged the distributions of heat transfer are self-similar if considered versus the Reynolds number.

This work was supported by the Russian Foundation for Basic Research (Grant No. 07-08-00025). The authors are grateful to S.V. Kalinina for fruitful discussions.

REFERENCES

1. Yudaev B.N., Mikhailov M.S., and Savin V.K, Heat transfer in jet flows impinging on obstacles, Mashinostroenie, Moscow, 1977, (in Russian).
2. Martin H., Heat and mass transfer between impinging gas jet and solid surface, Advances in Heat Transfer, 13, Academic Press, New York, 1977.
3. Kanokjaruvijit K., Martinez-Botas R. F., Parametric effects on heat transfer of impingement on dimpled surface, *J. of Turbomashinery of ASME,* Vol. 127, pp. 287-296, 2005.
4. Kanokjaruvijit K., Martinez-Botas R. F. Jet impingement on a dimpled surface with different crossflow schemes, *Int. J. of Heat and Mass Transfer,* Vol. 48, pp. 16-170, 2005.
5. Ekkad S.V., Kontrovitz D., Jet impingement heat transfer on dimpled target surfaces, *Int. J. of Heat and Fluid Flow*, Vol. 23, pp. 22-28, 2002.
6. Terekhov V.I., Kalinina S.V, Flow and heat transfer in a single spherical cavity: state of the problem and unanswered questions. (Review), *Thermophysics and Aeromechanics,* Vol. 9, pp. 497-520, 2002.
7. Afanasyev V.N., Chudnovsky Y.P., Leontiev A.I., Roganov P.S., Turbulent flow, friction and heat transfer characteristics for spherical cavities on a flat plate, *Experimental Thermal and Fluid Science*, Vol. 7, pp. 1-8, 1993.
8. Terekhov V.I., Kalinina S.V., Mshvidobadze Yu.M., Heat-transfer coefficient and aerodynamic resistance on a surface with a single dimple, *Enhanced Heat Transfer,* Vol. 4, pp. 131-145, 1997.
9. Mahmood G.I., Ligrani P.M., Heat transfer in a dimpled channel: combined influences of aspect ratio, temperature ratio, Reynolds number, and flow structure, *Int. J. Heat Mass Transfer*, Vol. 45, No.10, pp. 2011-2020, 2002.
10. Terekhov V.I., Barsanov V.L., Kalinina S.V., Mshvidobadze Yu.M., Experimental study of flow structure and heat transfer under a jet flow past a spherical-cavity obstacle, J. of *Engineering Physics and Thermophysics,* Vol. 79 pp.657-665, 2006.

11. Hrycak P. Heat transfer and flow characteristics of jets impinging on a concave hemispherical plate. *Proc. 7th Int. Heat Trans. Conf.,* Munchen Hemisphere Publ. Corp., Wash., N-York, London, 1982, Vol. 3. pp. 357-362.
12. Lee D.H., Chung Y.S., Won S.Y., The effect of concave surface curvature on heat transfer from a fully developed round impinging jet, *Int. J. of Heat and Mass Transfer*., Vol. 42, pp. 2489-2497, 1999.
13. Ward J., Mahmood M., Heat transfer from a turbulent swirling, impinging jet, *Proc. 7th Int. Heat Trans. Conf.* Munchen Hemisphere Publ. Corp., Wash., N-York, 1982, Vol. 3. pp. 401-406.
14. Lukashov V.V., Popov S.V., Semenov S.V., The analysis of research results of heat transfer swirled and non- swirled impinging jets*, Izv. SO AN USSR*,.Vol.6, pp. 133-142, 1989, (in Russian).
15. Volchkov E.P., Lukashov V.V., Semenov S.V., Terekhov V.I., Friction and heat transfer in a spatial boundary layer forming by interaction of a swirling flow on a plane, *Proc. 2nd World Conf. on Experimental Heat Transfer, Fluid Mech. and Thermodynamics,* Dubrovnik. pp.112-117, 1991.
16. Huang B., Douglas W., Mujumdar A., Heat transfer under a laminar, swirling, impinging jet – a numerical study, *Proc. 6th Int. Heat Transfer Conf.,* Toronto. 1978, Vol. 5. pp.311-316.
17. Wen M.-Y., Jang K.-J., An impingiment cooling on a flat surface by using circular jet with longitudinal swirling strips, *Int. J. Heat and Mass Transfer*., Vol. 46. pp. 4657- 4667, 2003.
18. Terekhov V.I., Barsanov V.L., Kalinina S.V., Mshvidobadze Yu.M., Investigation into the flow structure and heat transfer of a jet flow impinging perpendicularly on a complex-geometry obstacle, *Proc. of the XXVII Siberian Thermophysical Seminar,* Novosibirsk, Inst. of Thermophys., CD-publication: ISBN-5-89017-027-9, No.143, 2004.
19. Sapozhnikov S.Z.,. Mityakov V.Yu, Mityakov A.V., Gradient heat-flux probes, St.-Petersburg, SPTU Press, 2003, (in Russian).

HEAT CONVECTION AND FLOW REVERSALS IN A VERTICAL CHANNEL

J.-C. Tisserand[1,*], M. Creyssels[1], M. Gibert[2], B. Castaing[1], F. Chillà[1]
[1]Ecole Normale Supérieure-Université de Lyon, Lyon, France
[2] Max Planck Institut, Göttingen, Germany

ABSTRACT. The main heat transport mechanism is convection. Convection occurs in many situations such as for example in natural situations : stars, planet's atmosphere or in half-natural situations : vertical access pit of an underground quarry [1]. The most popular configuration studied in laboratory is the Rayleigh-Benard one [2, 3, 4, 5]. However, the behaviour of a Rayleigh-Bénard's cell is mainly controlled by the neighbourhood of the horizontal plates, where convection vanishes. However for example in stars there are no such plates.

In order to understand how heat fluxes are carried in these situations [6, 7, 8, 9], we study it in a channel which links two chambers, the hot one at the lower end, and the cold one at the upper end. The channel is vertical. In this configuration, the flow in the channel is either globally ascending in the left part, and descending in the right one, or the opposite. Thus, flow reversals appear and they can be described by a characteristic time τ". It is worth noticing that reversals can be found in other situations such as for example with earth magnetic field [10]. In this study, we look at the dependence between τ" and the difference of temperature δT between the hot plate and the cold plate.

Keywords: *Convection, Channel, Flow, Reversals*

EXPERIMENTAL SET-UP

In order to do the experiments, the cell is filled with water, and is constituted of a classical Rayleigh-Bénard's cell with two horizontal plates : the upper is cold and the other is hot. The height of the cell is 40 cm and the section is 40×10 cm^2. The walls of the cell, twenty millimetres thick, are made with PMMA. As we can see on the figure 1, two honeycomb structures allow to prevent convection from appearing in about 50% of the cell. Between these structures, the channel has a cross section which is 10×10 cm^2 and his height is 20 cm. This channel is the zone of interest. Besides, a regulated water bath controls the temperature of the upper plate. The hot chamber is closed with a bottom plate which is heated by Joule effect thanks to resistors. Therefore, the difference of temperature δT is imposed by at once a power supply which heats the hot plate and a thermal bath which colds the upper plate.

* Corresponding author: J.-C. Tisserand
Phone: + (33)-472728491, Fax: + (33)-472728950
E-mail address: jean-christophe.tisserand@ens-lyon.fr

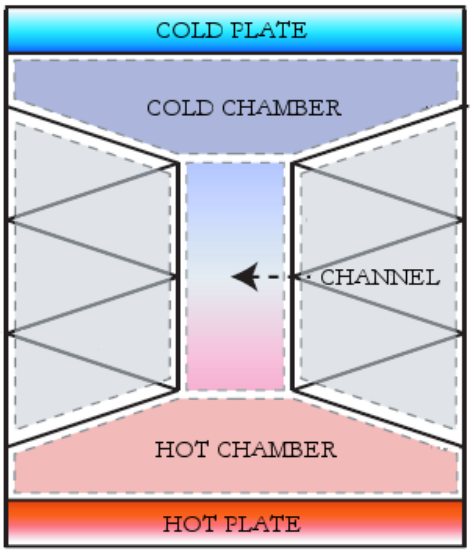

Figure 1. Picture of the cell

RESULTS

For our measurements, we use two resistive thermometers R_1 and R_2 inserted in the channel. Both thermometers are positioned on the same vertical line, each at the bottom end of a "L" structure. Moreover the vertical bars being made of two tubes, one sliding inside the other which allow to change the distance δz between the two thermistors. Resistances R_1 and R_2 are measured with two different Wheatstone bridges and we record both tension S_1 and S_2 thanks to an acquisition card. On each channel, signals S_1 and S_2 are turbulent time-correlated. We increase the space δz between R_1 and R_2 and for each time lag τ, we calculate the correlation C between S_1 and S_2 defined by

$$C(\delta z,\tau)=\frac{\left\langle \delta S_1(t+\tau)\delta S_2(t)\right\rangle}{\sqrt{\left\langle \delta S_1^2\right\rangle\left\langle \delta S_2^2\right\rangle}}$$

Where $\delta S_1(t)=S_1(t)-\langle S_1\rangle$ and $\delta S_2(t)=S_2(t)-\langle S_2\rangle$. As we can see on the Figure 2, except for the smallest distance, each curve presents two peaks. These peaks figure a delay between the two signals, the temperature perturbations travelling from one thermistor to the other.

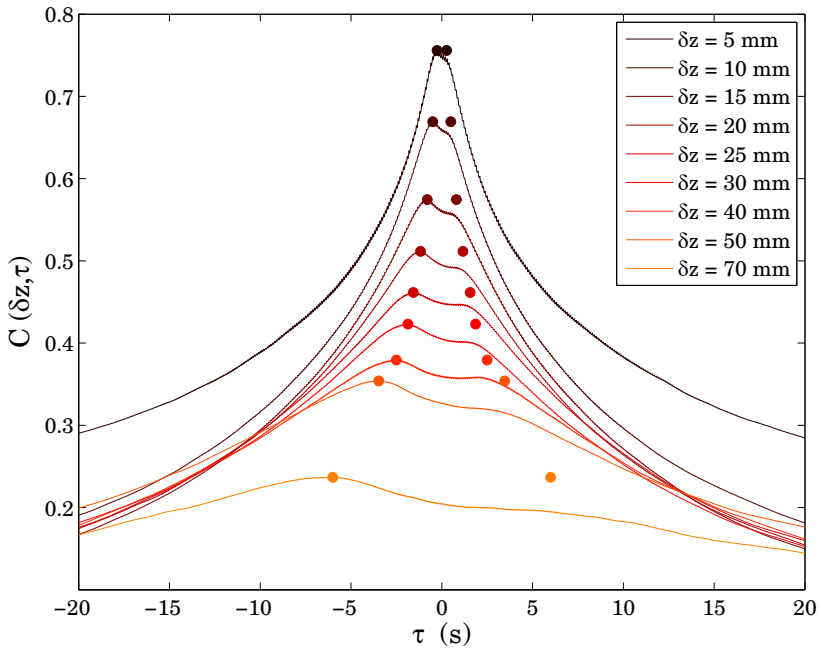

Figure 2. Correlation *C* versus time lag τ

On this figure, the presence of two maxima, approximately at symmetric times ±τ', seems to indicate that the flow undergoes reversals. Thanks to this maximum time lag τ', we can define a velocity *V*=δz/τ'. For instance, if the difference of temperature δT between the hot plate and the cold plate is 18°C and if the mean temperature in the channel is about 30°C, we can plot in the figure 3, the distance δz between the two thermistors versus τ'.

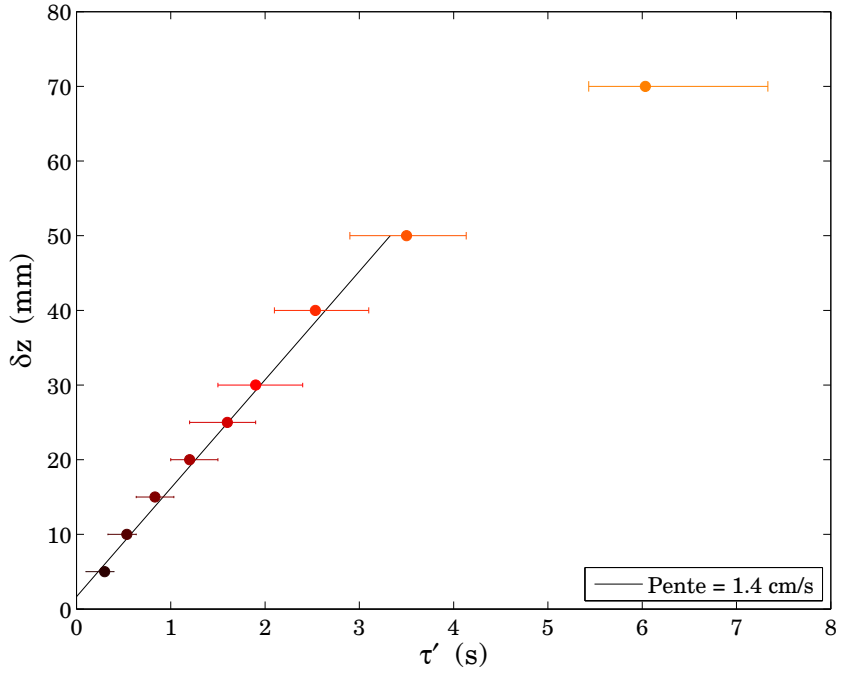

Figure 3. Distance δz versus maximum time lag τ'

In the Figure 3, the slope of the straight line, which stands for the velocity *V*, is about 1,4 cm.s^{-1}. It's worth noticing that the velocity *V* is close to the rms velocity V_{rms} measured with Particle Image Velocimetry in a previous study [11]. For example, with the same power, we obtained V_{rms}=1,23 cm/s. Furthermore, in the Figure 4, we plot, at once, the autocorrelation ϕ converted in distance and the correlation function *C*(δz,0) versus δz.

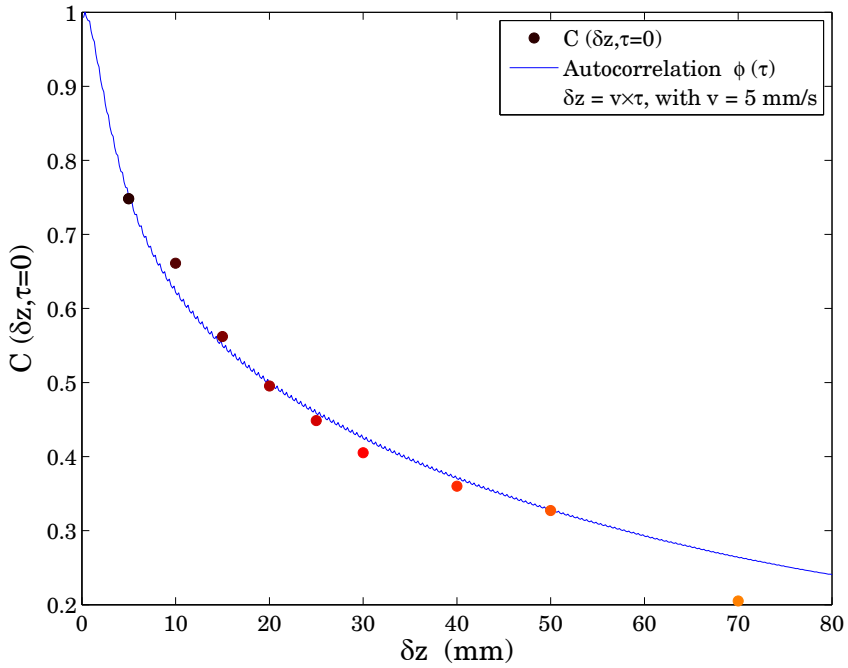

Figure 4. ϕ(δz) and *C*(δz,0) versus δz

We can notice that the ratio between the correlation length obtained with *C*(δz,0) and the correlation time obtained with the autocorrelation function ϕ give us a velocity v which is much smaller than the velocity *V*. This suggests a peculiar organisation for the coherent structures carrying the heat. Their travelling velocity as a whole is much smaller than the velocity occurring within the structure.

At last, with shadowgraph and thanks to a camera, we record image of the channel with a frequency of 1 Hz for three weeks for each measurements. Looking at the correlation between two successive images, we can deduce in real time if the flow in the channel is globally ascending in the left part, and descending in the right one, or the opposite. Therefore from then on, we can plot on the Figure 5 the characteristic time τ" versus the difference of temperature δT.

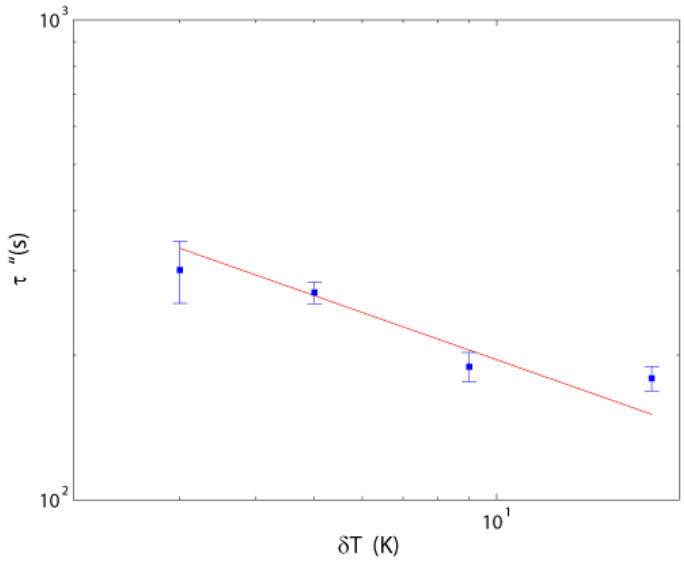

Figure 5. Characteristic time of flow reversals versus the difference of temperature

A simple model based on a previous experiment [11] is also developed and it predicts the relation between τ" and the difference of temperature δT.

REFERENCES

1. Perrier, F. Morat, P. Le Mouel, JL. [2002] Dynamics of Air Avalanches in the Access Pit of an Underground Quarry, *Phys. Rev. Letters*, Vol 89, 134501
2. Kraichnan, R. H. [1962] Turbulent Thermal Convection at Arbitrary Prandtl Number, *Phys. Fluids*, Vol 5, 1374.
3. Chavanne, X. Chillà, F. Chabaud, B. Castaing, B. Hébral, B. [2001] Turbulent Rayleigh-Bénard convection in gaseous and liquid He, *Phys. Fluids*, Vol 13, 1300.
4. Shang, X.D. Qiu, X.L. Tong, P. Xia, K.Q. [2003] Measured local heat transport in turbulent Rayleigh-Bénard convection, *Phys.Rev. Letters*, Vol 90, 074501
5. Grossmann, S. Lohse, D. [2004] Fluctuations in Rayleigh-Bénard convection: The role of plumes, *Phys. Fluids*, Vol 16, 4462
6. Siggia, E., [1994], High Rayleigh number convection, *Annu. Rev. Fluid Mech.*, Vol 26, 137
7. Calzavarini, E. Lohse, D. Toschi, F. Tripiccione, R. [2005] Rayleigh and Prandtl number scaling in the bulk of Rayleigh-Bénard turbulence, *Phys. Fluids*, Vol 17, 055107.
8. Lohse, D. Toschi, F. [2003], Ultimate State of Thermal Convection, *Phys. Rev. Letters*, Vol 90, 034502.
9. Niemela, J. J. Skrbek, L. Sreenivasan, K. R. Donnelly, R. J. [2000] Turbulent convection at very high Rayleigh numbers, *Nature*, Vol 404, 837
10. Berhanu & al. [2007], Magnetic field reversals in an experimental turbulent dynamo, *Europhys. Lett.*, Vol. 77, 59001
11. Gibert, M. Pabiou, H. Chillà, F. and Castaing, B. [2006], High-Rayleigh-Number Convection in a Vertical Channel, *Phys.Rev. Letters*, Vol. 96, 084501.

AN EXPERIMENTAL INVESTIGATION OF THE INFLUENCE OF THERMAL EFFECTS ON INCEPTION OF CAVITATION IN SHARP-EDGED ORIFICES

M.G. De Giorgi [*], M. Tarantino, A. Ficarella
[2]University of Salento, Dep. Of Engineering for Innovation, Lecce, Italy

ABSTRACT. Cavitation remains a persistent problem for internal flow devices due to both performance reduction and the ability of cavitation bubbles to cause significant component surface damage during bubble collapse. The focus of this study is the experimental characterization of cavitation in a sharp-edged orifice in presence of thermal effects, considering water at different temperatures and cryogenic fluid, in particular nitrogen. The flow is investigated by means of visual observations and pressure signals. By means of high-frequency response pressure transducers strategically placed in the orifice cavitation could be sensed by the correlation of the power spectrum of the pressure signal measured with a cavitation index.

Keywords: *cavitation, two-phase flow , cryogenic, sharp-edged orifice, spectral analysis*

INTRODUCTION

Cavitation and boiling are very similar in the effects, but they are different in the mechanism of generation. These two processes can be distinguished by the fact that cavitation is the process of nucleation in a liquid when the pressure falls below the saturated vapor pressure, while the boiling is the process of nucleation that occurs when the temperature is higher than the saturated vapor temperature.
High performance hydraulic systems can operate at cavitating conditions leading to decreasing in the mass flow rate, and increased levels of dynamical structural loading in addition to the potential danger of cavitation erosion. Cavitation in hydraulic machinery can limit performance, lower efficiency, introduce severe structural vibration, generate acoustic noise, choke flow, and cause catastrophic damage. Any fluid handling device is vulnerable to cavitation once apposite hydrodynamic conditions are encountered. Cavitation in conventional orifices has been investigated by many researchers [1,2,3,4,5]. When the pressure downstream of the mechanical constriction such as venturi or orifice falls below the vapour pressure of the liquid a number of cavities are generated, which subsequently collapse with the recovery of pressure downstream of the mechanical constriction.
The nozzle discharge of cold fluid has been studied extensively over past several years, the main emphasis of the research in this area has been given to a variety of applications, such as fuel injector nozzles or high speed cutting jets [6,7,8,9,10]. In contrast the studies of hot and cryogenic fluid in orifice have been few. The discharge of a high-pressure hot fluid involves flashing of the liquid, while studies on the discharge of a cool fluid may focus on cavitation of the high-speed liquid flow within the nozzle. Clearly, there are similarities between these two-phase change processes. Cavitation is usually driven by the inertial growth of the vapour phase, while flash boiling can be thermally driven at the vapor–liquid interface. In the former case, the vapour pressure is quite low compared to the driving pressure and ample superheat is available in the liquid. In the latter case, the vapor pressure is

* Corresponding author: Prof. M.G. De Giorgi
Phone: + (39)-0832-297759, Fax: + (39)-0832-297777
E-mail address: mariagrazia.degiorgi@unisalento.it

comparable to the driving pressure and the rate of mass transfer may be limited by the temperature of the surrounding liquid and possibly heat transport to the interface.
Acoustical noise, pressure fluctuations, and accelerometer readings have been interested to mostly mechanical engineers, who wish to understand investigators over a span of years to detect cavitation inception and to correlate developed cavitation with the cavitation number. The effect of cavitation on the energy spectra measured by various instruments are reported in [11,12,13,14]. In the past researchers [15, 16,17] used the accelerometer output as a criterion of defining cavitation inception and development in orifices and water valves.
In the present study visual observations and spectral analysis have been used to characterize of cavitation in flow through a sharp-edged orifice in presence of thermal effects, considering water at different temperatures and thermo-sensible fluid, in particular a cryogenic fluid, as nitrogen.

EXPERIMENTAL SETUP

Liquid nitrogen cavitation

A schematic illustration of the experimental set-up, used to investigate the internal nozzle flow, is shown in figure 1. The liquid nitrogen has been chosen as the cryogenic working fluid.
The set-up consists of a nitrogen supply tank, at a temperature of 82 K, two on-off valves and a flow visualization test section. The test section is an assembly of a central internal nozzle, in which the fluid flows; two vacuum chambers, for the thermal isolation and two flanges. In order to perform the continuous monitoring of cavitation phenomenon, four plexiglass plates are fitted between the assembly components. The supply tank is connected to the visualization chamber by a 2 m long pipe. The test section is a 15 mm-long rectangular orifice nozzle with a throat cross section 2 mm by 8 mm. After the visualization chamber, the nitrogen liquid is ejected in atmosphere as gas. The line is filled with pressurized cryogenic liquid at a pressure of 2 bar and flow immediately occurred when the first on-off valve after the nitrogen pressure tank is opened.
The cavitation phenomenon can be observed within the flow, at a certain flow rate, in the throat section. If the pressure is below the vapor pressure at the flow temperature, cavitation occurs.
The acquisition and data elaboration system is based on: three KULITE CT-190 cryogenic ruggedized pressure sensors, with a sensibility of 14.31 mV/bar and a temperature range of -195.5/120°C; a NI-4472 Dynamic Signal Acquisition Device for PCI up to 102.4 ks/s with two pole anti-alias lowpass filter for each input channel; a KISTLER 8702B100 accelerometer; a silicone diode temperature sensor (model 430, Scientific Instruments) coupled with cryogenic temperature monitor.
Observation of cavitation behavior has been made using a high-speed video camera system (CCD Kodak Motion Corder Analyzer FASTCAM-Super 10k). The imagines have been acquired at 2000 fps and then have been downloaded and stored on a pc to be subsequently processed digitally.
For the different test cases, the pressure and accelerometer signals have been acquired at a frequency of 102 kHz and 65000 samples, for a total data period of 0.637 s.
The acquisition programs were developed in-situ using the software Labview and the signal processing code was developed using Labview too.

Water cavitation

The experimental setup for water cavitation is showed in figure 1. The water flow is driven by a 1.10 kW centrifugal pump, capable of a maximum flow rate of $1.67 \cdot 10^{-3}$ m^3/s, located 1 m below the test section, in order to prevent cavitation in the pump. The mass flow rate through the test section, and then the pressure drop, has been varied by means of two calibrated control valves (control valve 1 and 2 in 5). In particular, a variable portion of the water flow was by-passed from the test section directly at the intake of the pump by means of the control valve 1; the control valve

2 was used to modify the inlet pressure further and therefore the pressure drop across the test section. The water was heated and maintained at the desired temperature by an electrical water heater, under the control of a thermostat.
Both circular and rectangular orifices were studied. The circular sharp-edge orifice is has an internal diameter of 3.5 mm and a length of 7.5 mm placed in a duct with an internal diameter of 11.2 mm. The rectangular orifice is the same used in nitrogen experiments.
The acquisition and data elaboration system is based on: two Kistler 4045A piezoresistive pressure sensors (for the upstream and downstream signals); a KISTLER 701A pressure quartz sensor (for the throath signal); a NI-4472 Dynamic Signal Acquisition Device for PCI up to 102.4 ks/s with two pole anti-alias lowpass filter for each input channel; a KISTLER 8702B100 accelerometer; a silicone diode temperature sensor (model 430, Scientific Instruments) coupled with cryogenic temperature monitor. The high speed video camera, the acquiring method and the software used for data elaboration are the same of nitrogen cavitation. For both, water and nitrogen fluids, the cavitation number is defined as follows:

$$\sigma = \frac{(P_u - P_v)}{(P_u - P_d)} \qquad (1)$$

where P_u, P_d and P_v are respectively the upstream, downstream and vapor pressures of the fluid.

Set-up for nitrogen cavitation

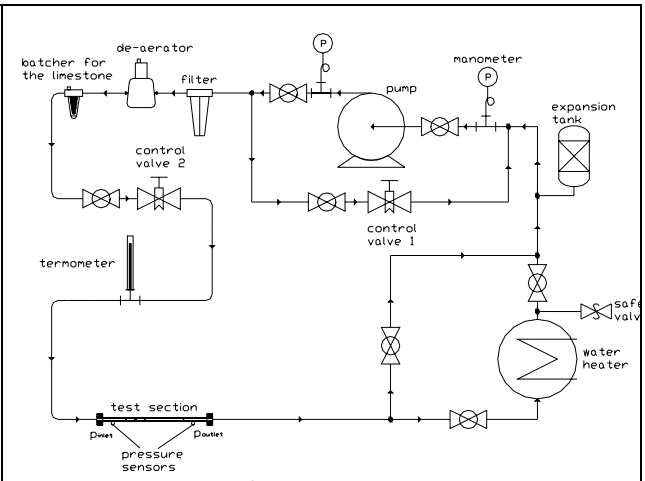

Set-up for water cavitation

Figure 1. Experimental set-up.

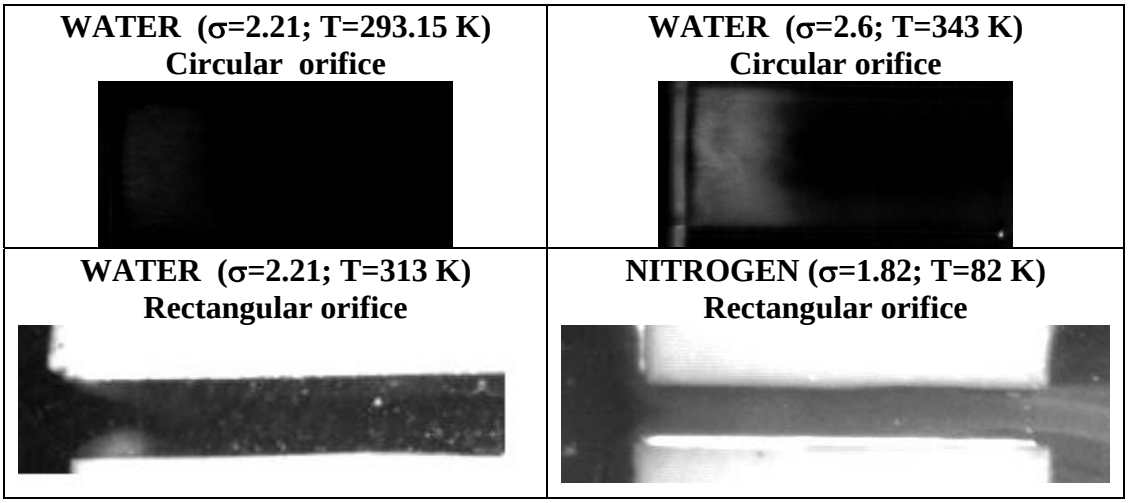

Figure 2. Visualization pictures of incipient cavitation in nitrogen and in water in the restricted area.

EXPERIMENTAL RESULTS AND DISCUSSION

Visual observations

The general visualization pictures of incipient cavitation are shown in figure 2 in the case of water at different temperature and nitrogen at 82 K. Looking to water experiments it is clear that cavitation appears at high cavitation number if the temperature increases. This is due to the fact that at high temperature smaller pressure variations are necessary to reach the phase change curve, due to the increase in vapour pressure. Comparing circular and rectangular orifices, it seems that the value of the cavitation number at the inception of the two-phase flow is not influenced by the cross section geometry. However the cross section influences the cavity shape.
The appearance of the cavitation structures is different for water and nitrogen. In the case of water a vapour cavity forms when cavitation starts, although the cavitation zone does not reach the outlet of the orifice, while in cryogenic fluids cavitation grows rapidly at the moment of the incipience.
Then in the case of nitrogen the cavitation starts at lower cavitation number than in water. An explanation is that the ratio between the liquid density and the vapour density of nitrogen is ten times smaller than the same ratio for water, so a greater mass transfer and a greater heat transfer are necessary to obtain the same vapour cavities, for the nitrogen than the water. As show in figure 3, in the case of water cavitation and circular orifice, cavitation starts at the upstream corner of the orifice restricted area. First, the length of cavitating zone keeps almost constant or slightly increases at higher cavitation number (subcavitation stage). Next the length begins to increase with the decrease in cavitation number (transition-cavitation stage). Then, it finally rapidly increases to occupy the whole part of the orifice throat (supercavitation stage). After this stage, as cavitation is further developed, the main cavitating area exceeds the orifice throat and a vapor pocket is created in the jet region (supercavitation regime). It appears that the length of the vapor pocket increases quickly with flow velocity. This is found also in the rectangular orifice (see figure 4 and figure 5). Comparing water and nitrogen experiments (figure 6) , a different cavitating behaviour is found. Looking to the fully developed cavitation in the case of cryogenic fluid, it presents a frothy appearance due to a much finer structure than in water under ambient conditions. The flow separation takes place at the exit of the restricted area. In this flow situation, the flow contains bubbles highly concentrate in the the separation shear layer, between the central core and near wall regions.
This behaviour is in accordance with previous observations of cavitation in helium, by Ishii [18].
The difference between water and cryogenic cavitation suggests that researchers must be careful to use experiments in hot water to study cryogenic cavitation by similarity.

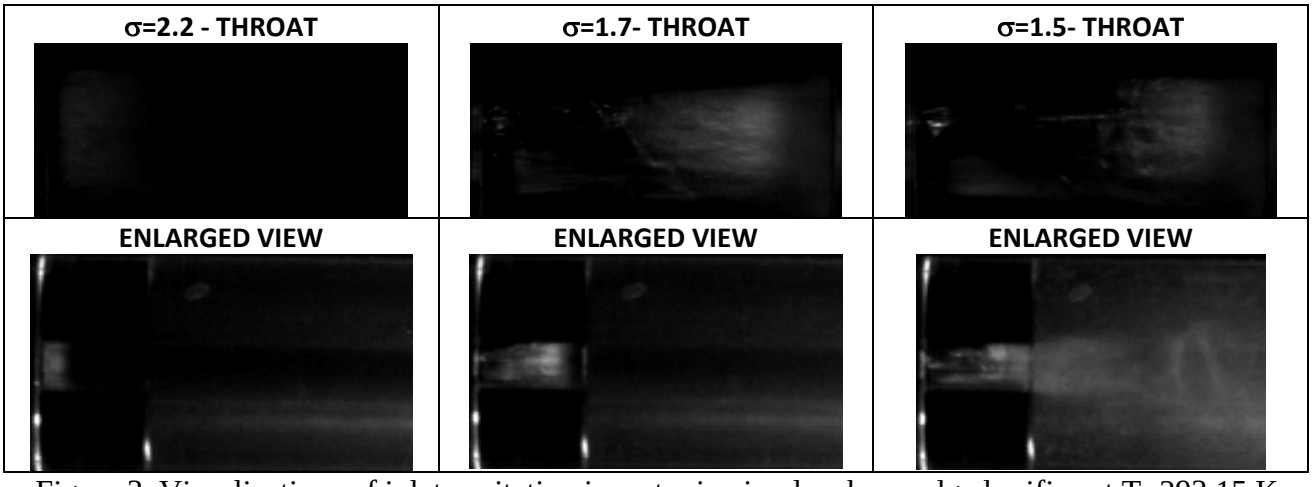

Figure 3. Visualizations of inlet cavitation in water in circular sharp-edged orifice at T=293.15 K.

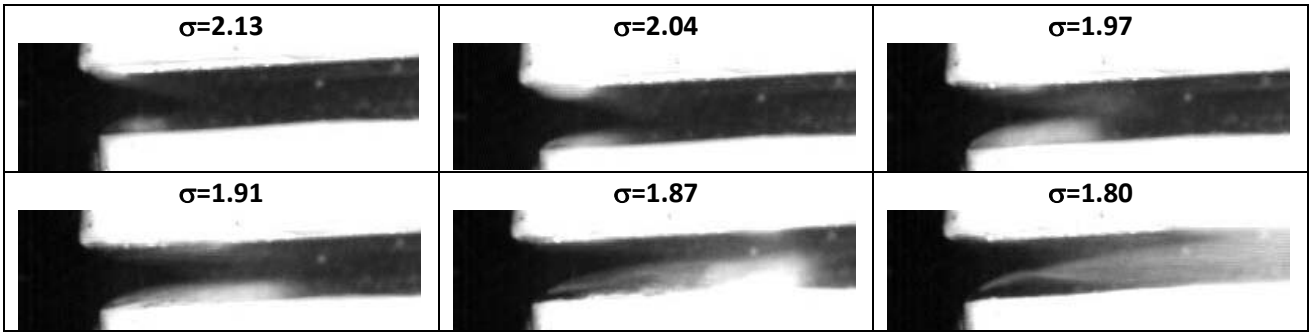

Figure 4. Visualizations of inlet cavitation in water in rectangular sharp-edged orifice , T=293.15 K.

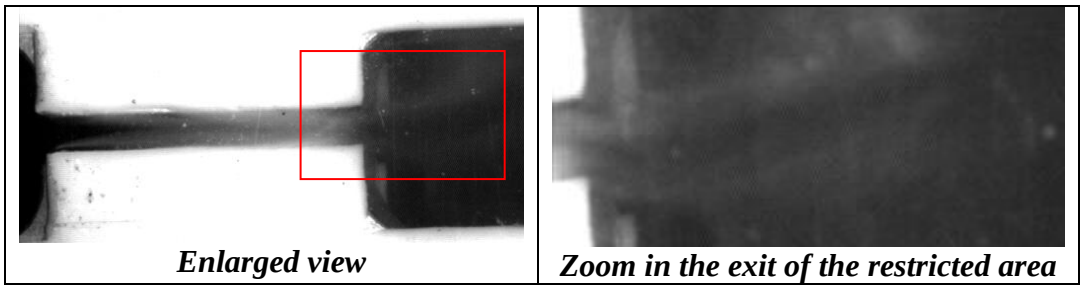

Figure 5. Visualization of water cavitation in the rectangular sharp-edged orifice (σ=1.80, T=293.15) K.

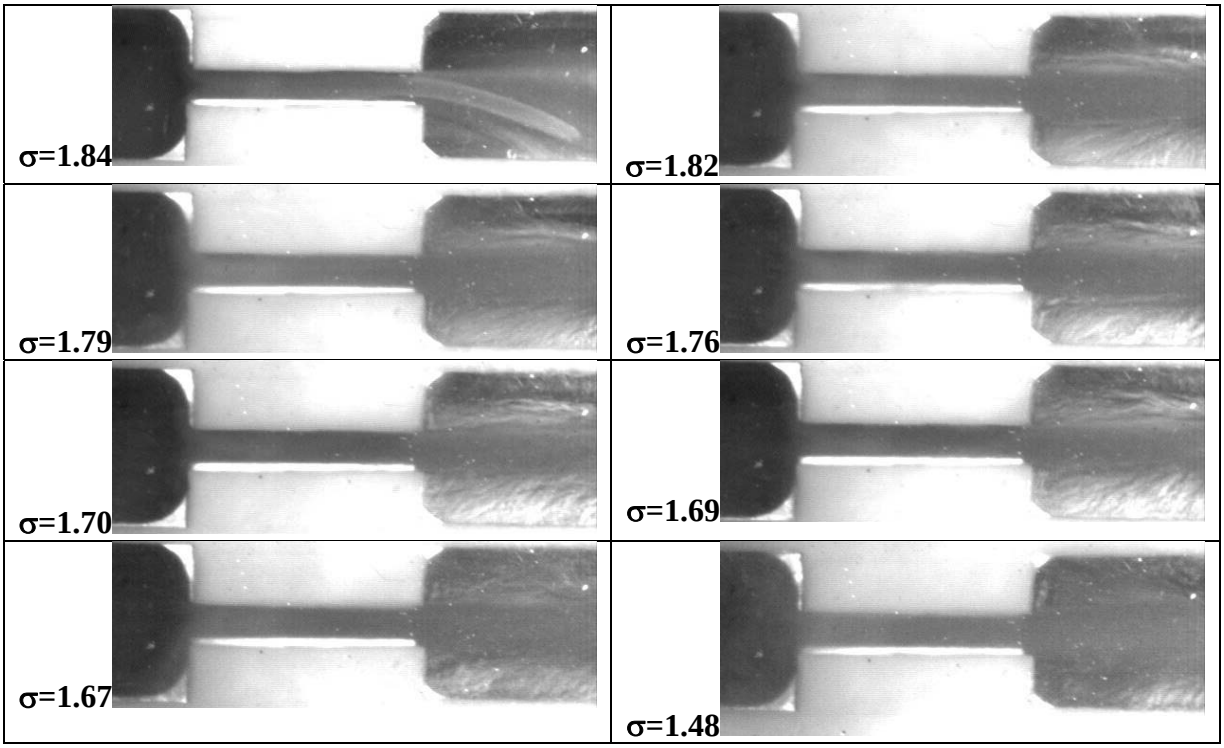

Figure 6. Visualization pictures of cavitation in liquid nitrogen.

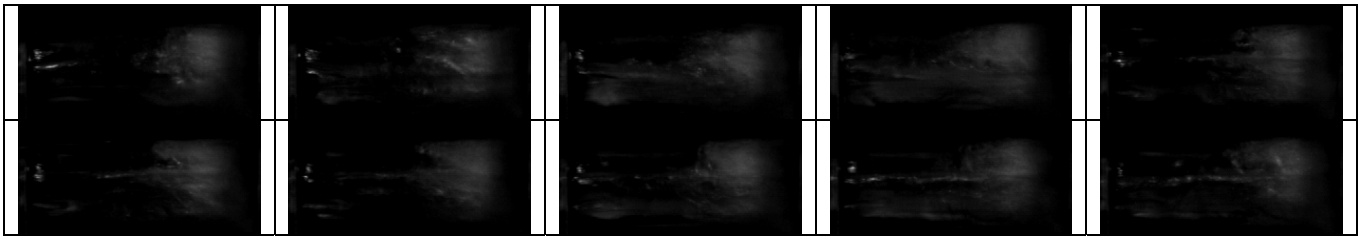

Figure 7. Temporal cavity shedding behaviour in the throat of the circular cylindrical orifice at T=293.15 K and σ=1.7.

The spectral analysis of cavitation

Flow observations show a more or less regular growth and shedding of vapour clouds that are convected downstream and take the form of horseshoe vortices before they collapse (see figure 7). Previous works have shown similar behaviour. In [19] periodic unsteady motion of separated vortex cavitation was experimentally investigated in a cylindrical orifice flow. A characteristic frequency, corresponding to the cavitation development as cloud shedding, can be observed in the power spectrum of the pressure. So in order to cope with many of the phenomena encountered in the study a number of signal analysis tools are employed. Of special interest is the ability to observe signal evolution in both time and frequency. Spectral analysis is one of the methods of examining the cavitation threshold. It enables observing the spectrum of the signal emitted from the cavitation area. The appearance of cavitation is manifested in the spectrum in the form of increasing of some frequency amplitude. In the process of cavitation inception, development and collapse, the bubble will experience volume expansion, compression, until collapse and vanishing. The pressure oscillations due to bubble growth and collapse can be identify by the power spectrum of the pressure signal measured at different nozzle positions. As in the visual observation, also the spectral analysis shows different cavitation regimes in water cavitation. In figure 8 the amplitude spectrum of the Fourier Transform of the downstream pressure is showed in the case of the circular orifice for water at different temperature are shown.
The first cavitation regime (no cavitating flow), occurs in the range of σ between the highest value tested and 2.2 at T = 293.15 K, and σ = 2.5 at T = 343.15 K. At the cavitation inception an evident increase of the peak amplitude of the first frequency components can be observed. A further reduction of the cavitation number brings to a sharp increase in the length of the cavitating zone (2nd regime). This cavitation regime is characterized by a sharp increase of the amplitude of the frequency spectrum, observed in the range from the critical values to σ = 1.7 at T = 308.15 K, and to σ = 2.1 at T = 343.15 K. As well as the cavitation volume increases to the outlet of the orifice (3rd cavitation regime), first a noticeable reduction of the amplitudes of the frequency spectrum can be noticed and then an increase in the amplitudes. These amplitudes tend to a rapid increase with a further reduction of the cavitation number below the cavitation number σ = 1.5 at T = 308.15 K, and σ = 1.9 at T = 343.15 K
The fourth stage of the cavitation phenomenon, that is revealed as the smallest values of the cavitation number are achieved, can be directly related to an evident increase of the amplitude of the first frequency component. This is confirmed by visual observations.

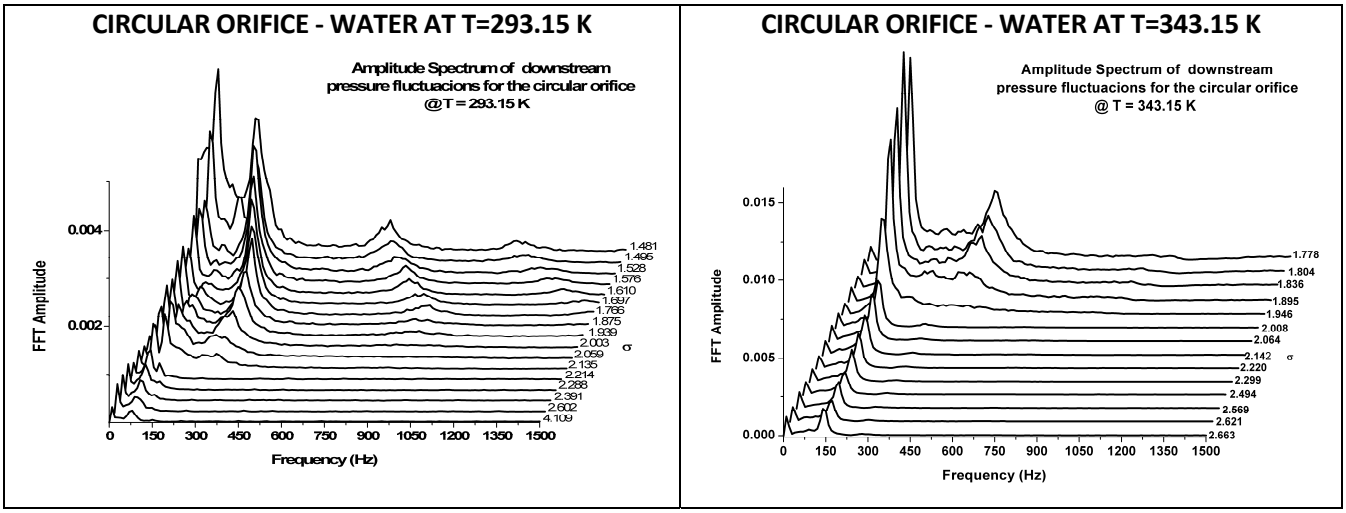

Figure 8. Amplitude Spectrum of the pressure oscillations measured in the case of circular sharp-edge orifice for water at T=293.15 K and at T=343.15K.

Figure 8 shows also that increasing the flow temperature the amplitudes of the spectrum in the range of low frequency increases. In figure 9 the amplitude spectra of the pressure oscillations measured in the case of nitrogen and of water in the rectangular orifice are shown. It is notable that the main pressure frequency content is in the range of lower frequencies for nitrogen, up to 70 Hz, especially for low cavitation number. Then the amplitude of the spectrum is highest in the downstream pressure fluctuations for water. The different between water and nitrogen is also evident looking to the temporal signals. In particular the standard deviation of the pressure vibration signals (figure 10) shows a higher oscillation for lower cavitation numbers in water cavitation. This is correlated to an increase in the activated nuclei density at low pressure and in water, that allows the bubble growing and collapsing, as confirmed by the increase of the standard deviation also for accelerometer signals.

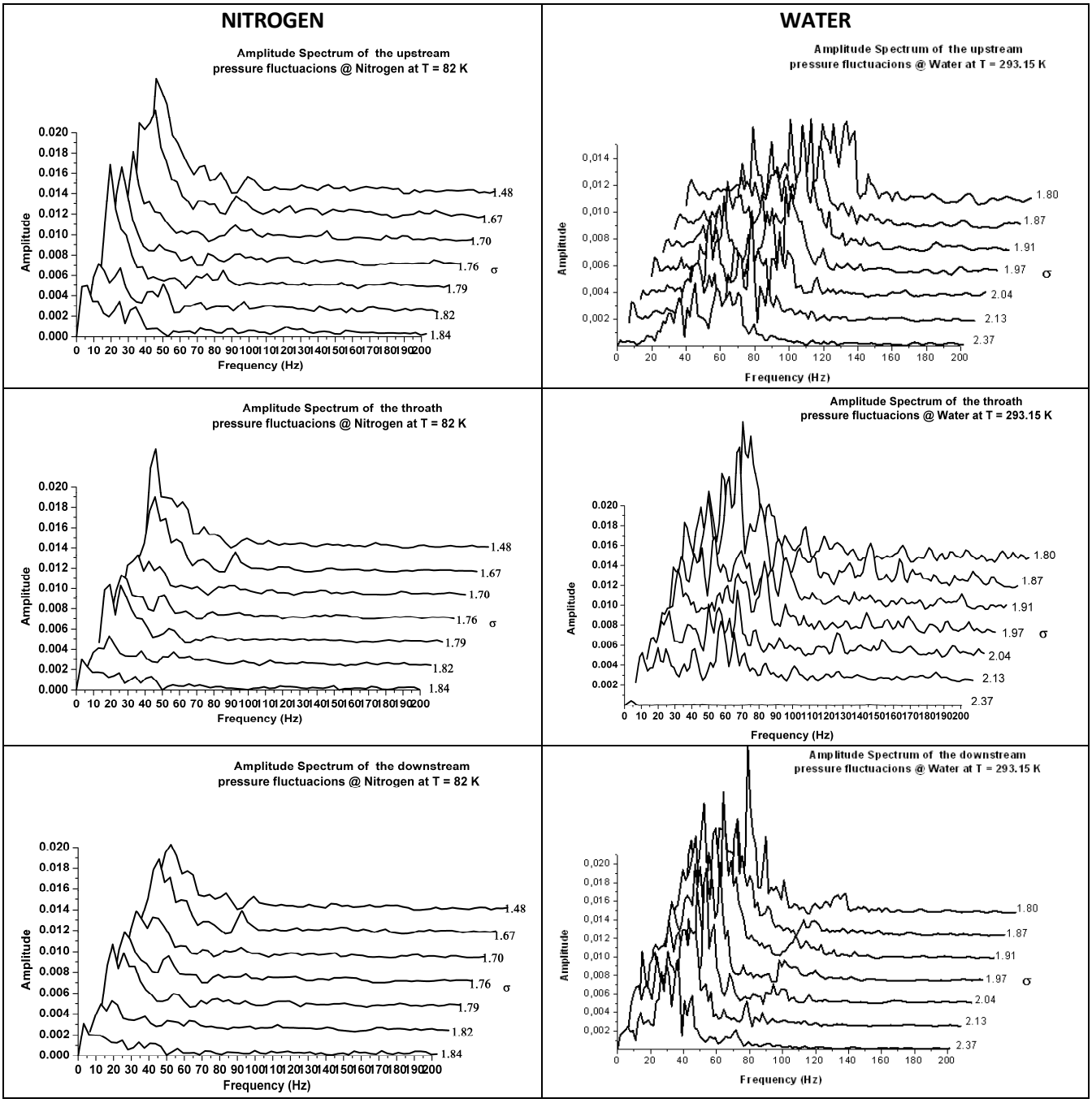

Figure 9. Amplitude Spectrum of the pressure oscillations in the rectangular sharp-edge orifice, nitrogen at constant temperature T = 82 K and water at T=293.15 K

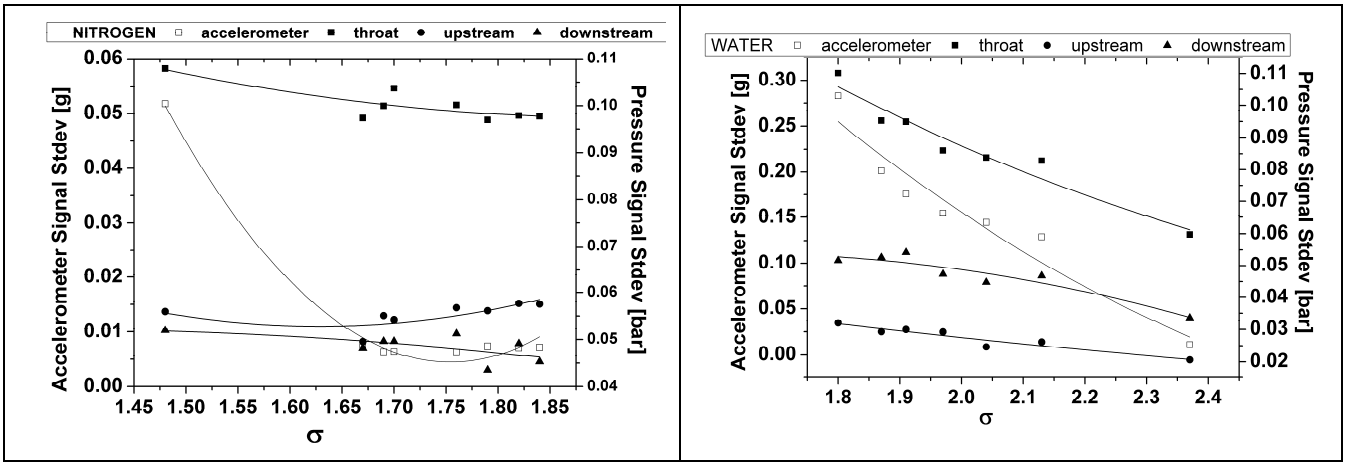

Figure 10. Standard deviation of the pressure signals measured in the case of the rectangular sharp-edge orifice for nitrogen at T=82 K and water at constant temperature T = 293.15 K

CONCLUSIONS

Some experimental studies on cavitation phenomena in both nitrogen and water flows at different temperature have been conducted by visual observation and pressure measurements. The conclusions are summarized as follows. Water cavitation appears at highest cavitation number if the temperature increases. This is due to the fact that at high temperature smaller pressure variations are necessary to reach the phase change curve, due to the increase in vapour pressure. Comparing circular and rectangular orifices, it seems that the value of the cavitation number at the inception of the two-phase flow is not influenced by the cross section geometry. However the cross section influences the cavity shape. The development of the cavitation structures is different for water and nitrogen. In the case of water a vapour cavity forms when cavitation starts, although the cavitation zone does not reach the outlet of the orifice, then as cavitation is further developed, the main cavitating area increases to occupy the whole part of the orifice throat (supercavitation stage). After this stage, as cavitation is further developed, the main cavitating area exceeds the orifice throat and a vapor pocket is created in the core of the jet region (supercavitation regime). In cryogenic fluids cavitation grows rapidly at the moment of the incipience and two-phase flow reaches the outlet, with bubbles highly concentrate in the separation shear layer, between the central core and near wall regions. Finally a good correlation is evident between the visual observations and the spectral analysis.

REFERENCES

1. Yan, Y. and Thorpe, R. B., Flow regime transitions due to cavitation in the flow through an orifice *Int. J. Multiphase Flow*, vol. 16, 1023, 1990.
2. Ramamurthi, K. and Nandakumar, K. Characteristics of flow through small sharp-edged cylindrical orifices, *Flow Meas. Instrum.* Vol.10, 133, 1999.
3. Bikai, Z. Yan, H., Zhang, T. and Zhuangyun, L., Experimental investigation of the flow characteristics of small orifices and valves in water hydraulics, *J. Process Mech. Engg.* 216, 235 2002.
4. Ramamurthi K. and Patnaik,, S. R. Influence of periodic disturbances on inception of cavitation in sharp-edged orifices, *Exp. Fluids* 33, 720, 2002.
5. Tafreshi, H. and Pourdeyhimi, B., Simulating cavitation and hydraulic flip inside hydroentangling nozzles, *Textile Research Journal*, Vol. 74, No. 4, pp. 359-364, 2004.
6. He, L. and Ruiz, F., Effect of cavitation on flow and turbulence in plain orifices for high-speed atomization, *Atomization and Sprays* , Vol. 5, pp. 569–584, 1995.

7. Nurick, N. H., Orifice cavitation and its effect on spray mixing, *J. Fluid Eng.*, Vol. 98, pp. 681-687 , 1976.
8. Tamaki, N., Shimizu, M. Nishida, K. and Hiroyasu, H., Effects of cavitation and internal flow on atomization of a liquid jet, *Atomization and Sprays*, Vol. 2, pp. 179- 197 , 1998.
9. N. Tamaki, M. Shimizu, and H. Hiroyasu, Enhancement of the atomization of a liquid jet by cavitation in a nozzle hole, *Atomization and Sprays* , Vol. 11, No.2, 2001.
10. K. Ahn, J. Kim, and Y yoon, Effects of orifice internal flow on transverse injection into subsonic crossflows: Cavitation and hydraulic flip," Atomization and Sprays 16 (1) (2006) 15- 34.
11. Jorgensen, D. W., Noise from Cavitating Submerged Water Jets, *Journal of the Acoustical Society of America*, Vol. 33, pp.1334-1338, 1961.
12. Deeprose, W. M., King, N. W., McNulty, P. J., and Pearsall, I. S., Cavitation Noise, Flow Noise and Erosion, *Cavitation Conference, Institution Mechanical Engineers*, Sept. 3-5, 1974, Edinburgh, pp. 373-381.
13. Oba, R., and It, Y., Cavitation Shock Pressures in a Venturi, *ASME Cavitation and polyphase Flow Forum*, 1975, pp. 2-6.
14. Blake, W. K., Wolpert, M. J., and Geib, F. E., "Cavitation Noise and Inception as Influenced by Boundary-Layer Development on a Hydrofoil," Journal ofFluidMechanics, Vol. 80, 1977, pp. 617-640.
15. Tullis, J. P., and Govindarajan, R., "Cavitation and Size Scale Effects for Orifices," Journal of the Hydraulics Division, ASCE, Vol. 99, Mar. 1973, pp. 417-430.
16. Ball, J. W., and Tullis, J. P., "Cavitation in Butterfly Valves," Journal of the HydraulicsDivision, ASCE, Vol. 99, Sept. 1973, pp. 1303-1318.
17. Tullis, J. P., "Testing Valves for Cavitation," Cavitation Conference, Institution Mechanical Engineers, Sept. 3-5, 1974, Edinburgh, pp. 47-55.
18. Ishii T.; Murakami M., “Comparison of cavitation flows in He I and He II”, *Cryogenics*, Vol. 43, No 9, pp. 507-514, 2003.
19. Sato, K. ; Saito, Y., Unstable cavitation behavior in a circular-cylindrical orifice flow, *JSME international journal. Series B, fluids and thermal engineering*, Vol. 45, No.3, pp. 638-645, 2002.

HYDRAULIC CHARACTERISTICS OF FLOW BOILING OF HYDROCARBON FLUIDS: EFFECT OF SUBCOOLED BOILING

V. V. Wadekar
HTFS, AspenTech Ltd, Reading, United Kingdom

ABSTRACT. Two-phase hydraulic characteristics, in terms of pressure drop and void fraction data, are reported for boiling of hydrocarbon fluids in vertical upflow. These data were obtained simultaneously with the boiling heat transfer measurements. The systematic trends of the measured pressure gradient with respect to vapour quality, mass flux and pressure are examined. This provides useful information in terms of the relative importance of the constituent parts of the two-phase pressure gradients and confirms the internal consistency of the measured data. These two-phase pressure drop data under flow boiling conditions are then compared with various correlations from the open literature and also with the HTFS correlation. Typical results of these comparisons are presented. It is noted that in the near zero vapour quality region the measured pressure gradient data may be lower than expected because of the effect of subcooled boiling. This effect is taken into account by the HTFS method when pressure drop is calculated for flow boiling.

Keywords: *two-phase, pressure drop, boiling, hydrocarbon, void fraction*

INTRODUCTION

The amount of information that exists in the published literature on flow boiling heat transfer to hydrocarbon fluids is rather limited. Even more limited is the information on two-phase pressure drop for boiling of hydrocarbon fluids. In previous papers some data were reported (Wadekar *et al*, 2008) for boiling of hydrocarbons, along with detailed analysis dealing with some apparently anomalous trends of void fraction at near dryout vapour qualities (Wadekar et al, 2007). The current paper carries forward this work by examining large amount of pressure drop data for single component hydrocarbon fluids, *n*-pentane and *iso*-octane and examines the possible effect of subcooled boiling.

Two-phase pressure drop can be measured for gas-liquid adiabatic flow or it can also be measured for vapour-liquid non-adiabatic, boiling or condensing flow. Because of ease and low cost of operation, laboratory measurements tend to be made with adiabatic gas-liquid flow e.g. air-water flow, rather than vapour-liquid flow with phase change. Two-phase pressure drop correlations are largely based on data for such adiabatic gas-liquid two-phase flow. On the other hand, two-phase heat transfer equipment, by default, will have boiling or condensing flows. It is generally accepted that the two-phase pressure drop and flow pattern characteristics for non-adiabatic flow could be similar to adiabatic gas-liquid flow. For example, Frankum et al (1997) have reported that the two-phase flow patterns for evaporating flows are similar to gas-liquid adiabatic two-phase flow. However, it is still desirable to carry out validation of pressure drop correlations for boiling hydrocarbons; such validation is especially relevant to oil and gas, and petroleum industry where a large number of process reboilers and vaporisers are used for hydrocarbon duties. Therefore, the paper also reports the results of validation of the proprietary HTFS pressure drop correlation used in the commercial heat exchanger design and simulation software.

State of the art thermal-hydraulic methods and correlations are developed by the Aspen HTFS Research Network, run by the Aspen Technology company, for modelling process heat exchange

* Corresponding author: Dr V.V. Wadekar
Phone: + (44) 0118-92 26414, Fax: + (44) 0118 92 26401
E-mail address: vishwas.wadekar@aspentech.com

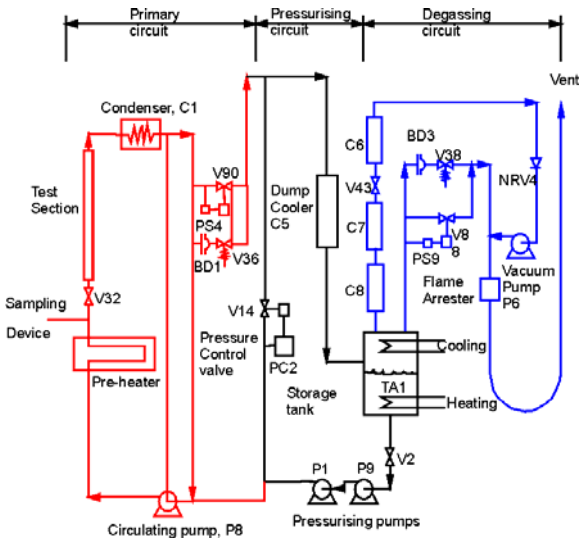

Figure 1. Rig circuit diagram for the HTFS HPBR facility

equipment. Methods and correlations developed by the HTFS Research Network are proprietary and are known as the HTFS methods or correlations.

EXPERIMENTAL DETAILS

The HTFS High Pressure Boiling Rig (HPBR) was used to obtain the heat transfer and pressure drop measurements. As shown in Figure 1, the HPBR had three distinct circuits: the primary circuit, the pressurising circuit and the de-gassing circuit. The primary circuit contained the test section, through which the test fluid was circulated at a fixed flow rate, inlet temperature and pressure. It also contained a circulating pump and condenser. The pressurising circuit generated a constant pressure in the primary circuit, with two pressurising pumps, arranged in series, and pumping against a partially closed valve, V14. Finally, the de-gassing circuit was used to remove dissolved gases from the test fluid, since these may affect its boiling characteristics. The circuit contained a fluid storage tank, TA1, to which vacuum could be applied to reduce the dissolved gas content.

The test section was a 8.68 m long 321 stainless steel tube, with an internal diameter of 25.4 mm and an outer diameter of 38.0 mm (a thickness of 6.3 mm). The long length of the test-section allowed a large number of simultaneous pressure drop measurements to be made, over a wide range of vapour qualities and flow regimes, as the flow passed from the single phase liquid inlet condition, through subcooled and saturated boiling to two-phase flow at the outlet. The test section was directly heated by passing electrical current (up to 4000 Ampere) at low voltage (up to 30 Volts), through the test-section wall. Heat transfer and pressure measurements were carried out along the test section. Details of the bulk fluid and wall temperature measurements are given by Urso et al (2002).

For each experimental run a total of 11 local pressure drop measurements were recorded along the test-section length, together with three absolute pressure measurements, at inlet, middle and outlet of the test-section, Figure 2. Each pressure drop measurement was across 0.75 m test-section length. Further details of pressure drop measurements are given by Kandlbinder (1997).

Test Procedure

After initial start-up of the rig, for each experimental test-run, the flowrate, pressure, inlet temperature etc. were set to the desired values and electric power was applied to the test section. Subsequently, the test conditions were monitored until steady state condition was achieved, and only then five consecutive scans of all measurements including temperatures, pressures and

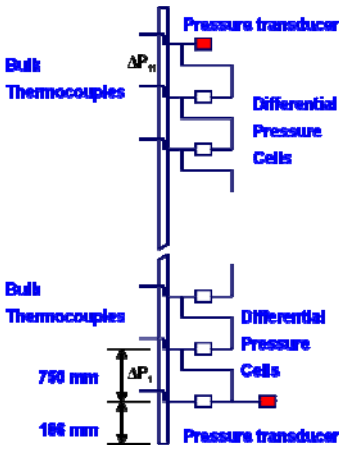

Figure 2. Details of test-section showing positions of pressure tapings

pressure drops were recorded. The experimental conditions were then altered and the process repeated. Each pressure drop measurement reported here, thus, corresponds to average of five consecutive scans.

Local vapour qualities along the length of the test-section were calculated from heat balance, assuming thermodynamic equilibrium between the vapour and liquid phases. As stated earlier, each pressure drop measurement was carried out across a 0.75 m test-section length. The vapour quality over this length would vary depending on the applied heat flux and flowrate. It was assumed that the measured pressure drop corresponded to the vapour quality occurring at the mid point between the differential pressure tapings. Single phase experiments were performed to check the heat balance accuracy. The typical errors associated with heat balance were less than 5%. The calibrations carried out for differential pressure cells indicated that typical errors associated with pressure drop measurements were around 5%.

MEASURED DATA

The pressure drop data, reported here, encompass a range of mass fluxes varying from 35 to 500 kg/m^{2}s, heat fluxes from 10 to 100 kW/m^2 (generally in increments of 10 kW/m^2), and pressures from 1.5 to 20 bar. These data were recorded simultaneously to the heat transfer measurements for flow boiling. In order to check the internal consistency of the data, they are plotted in Figures 3 to 5 as pressure gradient against vapour quality. In these graphs the experimental data are shown by various symbols and solid curves are, unless stated otherwise, predictions of the HTFS methods. These curves also highlight and illustrate the trends exhibited by the experimental data.

Effect of mass flux

Figure 3 shows the pressure gradient data at a fixed nominal pressure and heat flux, but varying mass fluxes, ranging from 70 to 410 kg/m²s. In addition to the data points, trend lines are also shown at different mass fluxes. The data at low mass fluxes, i.e. less than 210 kg/m²s, appear to be grouped together, and are reasonably well represented by a single monotonically decreasing curve. Here the contribution of the frictional component is small and the data are dominated by the gravitational component, and hence the apparent lack of mass flux dependence. These data, as discussed later, are useful in back calculating the void fraction. At high mass fluxes, however, the frictional component makes increasing contribution with increasing vapour quality and the data require different trend lines at three higher mass fluxes of 210, 310 and 410 kg/m²s.

Furthermore, at a given mass flux, the data also exhibit a characteristic minimum because, with increasing vapour quality, the two-phase gravity component decreases and the frictional component

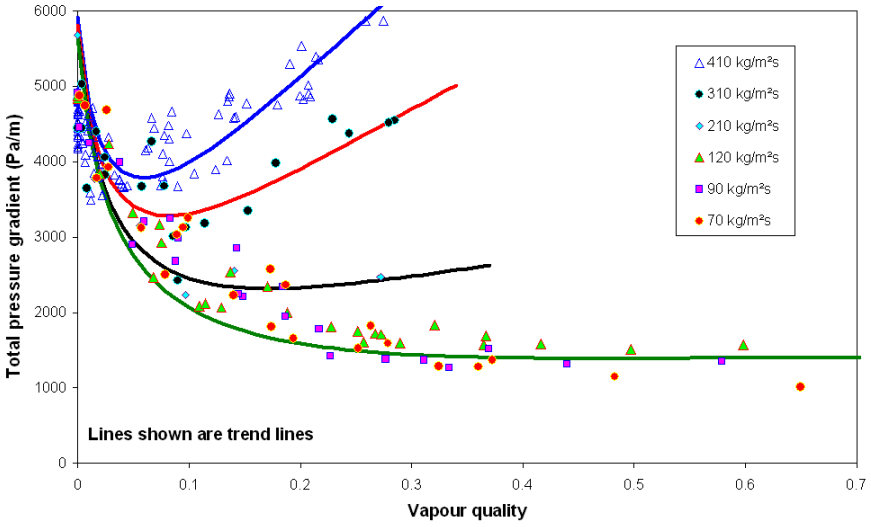

Figure 3. Effect of mass flux and vapour quality on measured pressure gradient

increases. The trend lines are rather difficult to draw in this area; they are shown to tentatively illustrate the trends. At low mass fluxes the frictional component increases with vapour quality rather slowly and, as a result, the characteristic minimum, seen at higher mass flux, is not exhibited in the range of vapour qualities covered here.

Effect of pressure

Figure 4 shows the measured pressure gradient data at a fixed mass flux and heat flux but varying pressures, ranging from 2.3 to 10 bar. With increasing pressure the vapour density increases. Therefore, at a given vapour quality, the two-phase frictional component decreases and the two-phase gravitational component increases with pressure. This is reflected in the data in two ways. At lower pressures of 2.3 and 3 bar the pressure gradient against vapour quality curve goes through a well defined minimum. At higher pressure of 10 bar, however, there is a monotonic decrease of the pressure gradient with the vapour quality.

Effect of heat flux

The effect of heat flux on the pressure gradient is examined in Figure 5 which shows some typical measured data. These data are plotted as the pressure gradient against the vapour quality at a fixed nominal mass flux and pressure. It can be seen that, there is some systematic variation of the

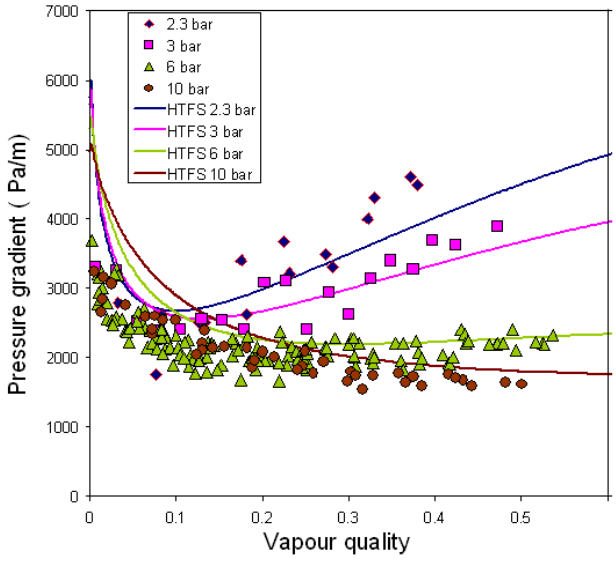

Figure 4. Systematic effect of pressure

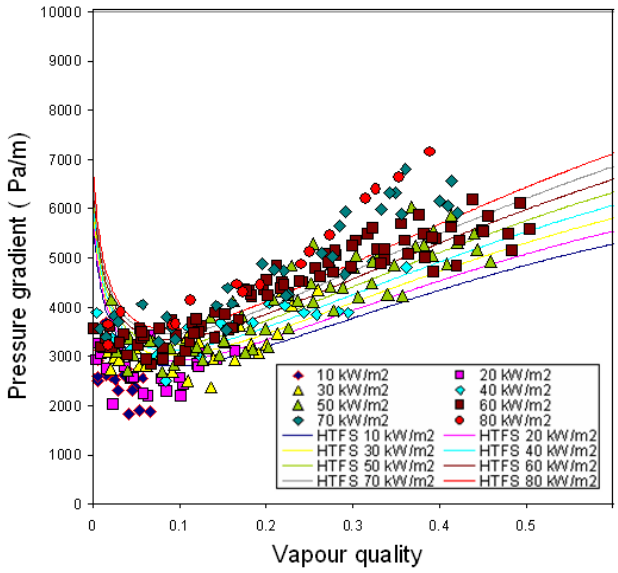

Figure 5. Systematic effect of heat flux

gradient with the applied heat flux. The calculations carried out using the HTFS method show that at the highest heat flux the contribution due to the acceleration component was around than 36%. Figure 5 appears to indicate that, in general, there is overprediction of the measured data at low vapour qualities and underprediction at high vapour qualities. Both these trends are examined in further detail after the brief discussion on void fraction.

Void fraction

Figure 6 shows the void fraction data that were back calculated from the measured pressure gradients. This back calculation was achieved by focussing on the pressure drop data dominated by the gravitational component, and relating that component to the void fraction. More details of the procedure followed are given by Wadekar et al (2007). Figure 6 confirms that the void fraction data are predicted reasonably well by the HTFS void fraction correlation; this is also corroborated by the average and RMS deviations shown in Table 1.

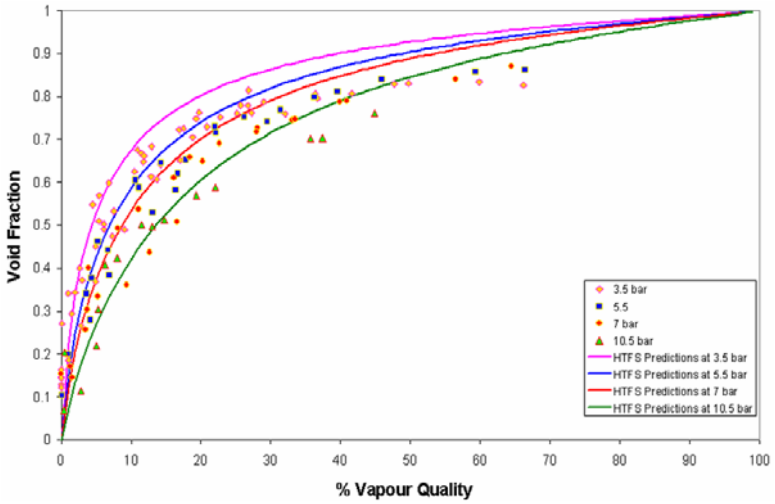

Figure 6. Comparison of experimental void fraction with HTFS predictions.

Table 1
Comparison of different predictive methods for void fraction data (115 points)

Void Fraction Method	RMS Deviation (%)	Average Deviation (%)
Chisholm (1973)	33.3	-12.8
Homogeneous	42.4	-32.1
HTFS	35.0	-6.3
Schrage *at al* (1998)	192.4	20.6
Zivi (1964)	42.4	-32.1

DATA AND PRESSURE DROP CORRELATIONS

The pressure drop data were compared with various correlations. Here comparison of the data with the Chisholm correlation and HTFS correlation are presented. Because the measured data contains the three components of the pressure gradient, namely, friction, gravity and acceleration, the predictions also consist of the sum total of all three components.

The gravitational pressure gradient is calculated from the following equation.

$$\frac{dp_g}{dz} = g\left[(1-\varepsilon)\rho_l + \varepsilon\rho_v\right] \tag{1}$$

The acceleration pressure gradient is calculated by the following equation.

$$\frac{dp_a}{dz} = \dot{m}^2 \frac{\left[\frac{x^2}{\varepsilon\rho_v} + \frac{(1-x)^2}{(1-\varepsilon)\rho_l}\right]_{in} - \left[\frac{x^2}{\varepsilon\rho_v} + \frac{(1-x)^2}{(1-\varepsilon)\rho_l}\right]_{out}}{\Delta z} \tag{2}$$

The length Δz is over which the calculations are carried out. As mentioned earlier the HTFS void fraction correlation was confirmed to perform well in predicting the measured void fraction data and therefore it was used to calculate the void fraction, ε, needed in Equations (1) and (2).

Chisholm correlation

Chisholm and co-workers (see, for example, Chisholm, 1973) formulated a two-phase frictional pressure drop correlation using the following ratio, Γ , similar to the Lokhart-Martinelli parameter

$$\Gamma^2 = \left(\frac{dp_f}{dz}\right)_{GO} \Big/ \left(\frac{dp_f}{dz}\right)_{LO} \tag{3}$$

Equation (3) shows that Γ^2 is the ratio of single phase gas (or vapour) to liquid phase frictional pressure gradient when the total flow is flowing as the respective phase.

The Chisholm correlation is one of the successful and well established two-phase pressure drop correlations. Figure 7 shows the results for the Chisholm correlation. Figure 7 and the subsequent Figure 8 also show the RMS and average errors. In general there appears to be a degree of overprediction of the data, reflected in the correspondingly high values of RMS and average errors.

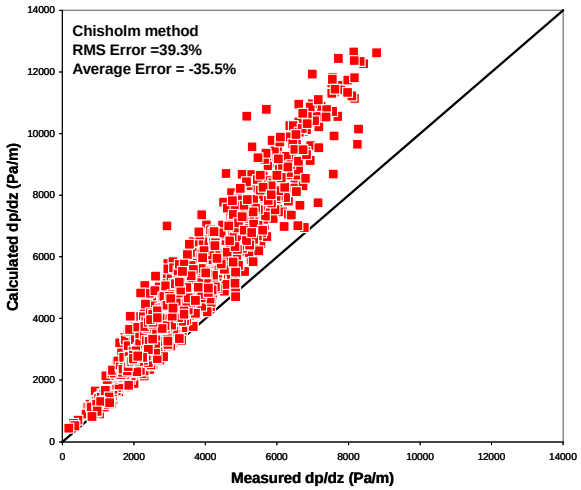

Figure 7. Comparison of measured data with the Chisholm correlation

HTFS correlation

The HTFS two-phase pressure drop correlation is a complex proprietary correlation developed using a large amount of measured data. In general Figures 4 and 5 show that the HTFS predictions largely follow the trends of the data over a range of parameters. Some instances of either over or underprediction of the data are, at least, partly due to the use of nominal rather than the actual

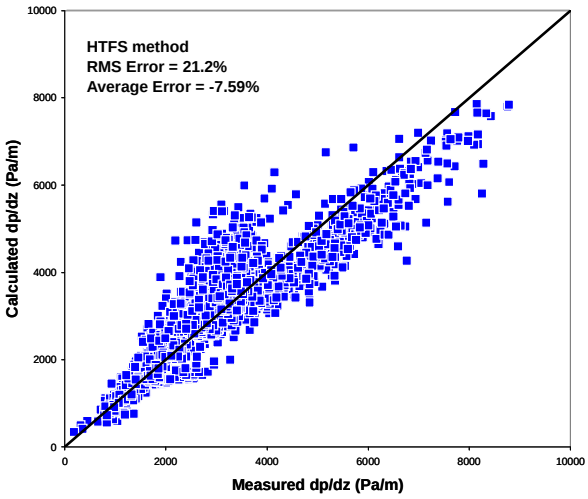

Figure 8. Comparison of measured data with HTFS correlation

conditions. In order to fully address this for all the data points, Figure 8 was prepared; it shows the entire data set of more than 2000 data points. Similar to Figure 7, the measured pressure drop data are compared with the sum total of the gravity, friction and acceleration components using the actual conditions of mass flux, heat flux, pressure and vapour quality. It can be seen from Figure 8 that the HTFS correlation predicts the data well with the RMS error of 21.2 % and the average error of -7.59%. This is particularly good considering that the data were obtained over a wide range of mass fluxes, pressures and vapour qualities for boiling hydrocarbon fluids.

EFFECT OF SUBCOOLED BOILING

It would be appropriate to make some observations about the possible effect of subcooled boiling on two-phase pressure drop. Further analysis indicated that subcooled boiling could indeed affect the pressure drop characteristics in the near zero vapour quality region. This is because of the higher void fraction (than expected from the thermodynamic equilibrium quality) in the subcooled boiling region. In addition to this direct effect, there is also carryover of increased actual, non-equilibrium vapour quality in the positive, near zero vapour quality region. Together, these two effects could cause lower than expected gravitational component, resulting in a total pressure gradient which is less than the calculated gradient in the low quality region. Comparison of measured data and the

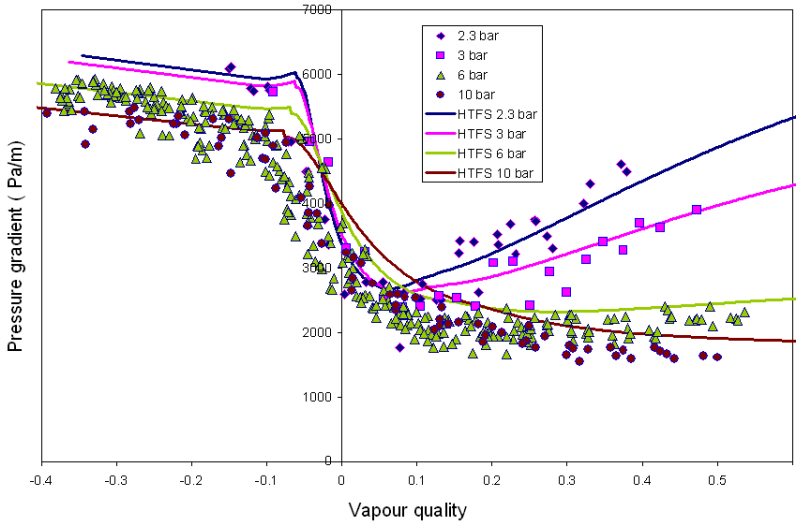

Figure 9. HTFS predictions of data including subcooled boiling effect

full HTFS correlation for flow boiling, which includes the effect of subcooled boiling, is shown in Figure 9. Note that Figure 9 uses the same data, as shown in Figure 4, in the positive quality region. A comparison of Figure 4 and 9 shows the improvement in predictions obtained by considering the effect of subcooled boiling in the positive, near zero quality region. Further results showing the detailed effect of subcooled boiling will be presented in a subsequent paper.

CONCLUSIONS AND FUTURE WORK

The HTFS correlation for calculation of pressure gradient, including two-phase friction, gravity and acceleration components, is validated for boiling hydrocarbon flow. It is demonstrated that the HTFS correlation performs, at least as well, and in some cases better, than other correlations, such as the Chisholm correlation in the open literature. The back calculated void fraction data, using the measured pressure drop data dominated by gravity component, confirm that the HTFS correlation for void fraction also performs well and also effect of subcooled boiling is taken into account appropriately.

An area of further work would be the boiling of mixtures. It is well known that boiling heat transfer for mixtures is affected by the mass transfer effects and this is confirmed by the data reported by Kandlbinder (1997). In general hydrodynamics of two-phase flow would not be affected by these effects. Nevertheless, it would be interesting to compare two-phase pressure gradients for mixtures and single component hydrocarbons.

ACKNOWLEDGEMENTS

The experimental work was performed by Drs M E D Urso and T. Kandlbinder using the HTFS High Pressure Boiling Rig Facility, as part of joint research projects between HTFS and Imperial College, London. Mr P Stepney provided the technician support. Thanks are due to Drs Y.S. Tian and K M Miller for the valuable assistance provided in data analysis. Author is grateful to HTFS, Aspen Technology for the permission given to publish the paper.

REFERENCES

Chisholm, D., 1973, "Pressure gradients due to friction during the flow evaporating two-phase mixtures in smooth tubes and channels," *Intl. J. Heat and Mass Transfer*, Vol.16, pp. 347-358.

Frankum, D. P., Wadekar, V. V. and Azzopardi, B. J., 1997, "Two-phase flow patterns for evaporating flow," *Experimental Thermal and Fluid Science*, Vol 15, pp. 183-192.

Kandlbinder, T., 1997, "Experimental investigation of forced convective boiling of hydrocarbons and their mixtures," PhD Thesis, Imperial College of Science Technology and Medicine, London.

Schrage, D. S., Hsu J. T. and Jensen M. K., 1998, Two-phase pressure drop in vertical crossflow across a horizontal tube bundle, *AIChE Journal*, 34, pp. 107-115.

Urso, M. E. D., Wadekar, V. V. and Hewitt, G. F., 2002, Heat transfer at the dryout and near-dryout regions in flow boiling, *Proc.12th International Heat Transfer Conference 2002*, pp. 701-706.

Wadekar, V. V, Miller, K. M. and Urso M. E. D., 2007, "Two-phase pressure drop and void fraction during flow boiling of iso-octane", *Multiphase Science and Technology*, Vol. 19, pp. 211-223.

Wadekar V.V., Tian Y.S. and Kandlbinder T., Two-phase pressure drop during flow boiling of hydrocarbon fluids, *Proceedings of 5th European Thermal-Science Conference*, The Netherlands, 2008.

Zivi, S. M., 1964, "Estimation of steady-state steam void fraction by means of the principle of minimum entropy production", *Journal of Heat Transfer*, 86, pp. 247-252.

STUDIES OF FLOW PATTERNS OVER HORIZONTAL TUBES OF FALLING FILM HEAT EXCHANGERS

A.T. Pise [*1], S B. Patole[1] and N. U. Korde[2]

[1] Department of Mechanical Engg. Govt. College of Engineering. Karad 415124, M.S. (India)
[2] Department of Mechanical Engg,G.H.Raisoni Institute of Engg. & Tech.,Pune 412207 MS India)

ABSTRACT**.** When a liquid falls from one horizontal tube to another below it, the flow may take the form of discrete droplets, jets, or a continuous sheet; the mode plays an important role in the wetting and heat transfer characteristics of the film. Experiments were carried to explore the effects of thermo physical properties like viscosity, surface tension, inertial, and gravitational effects and geometrical parameters on falling film mode transitions. Water, distilled water + n-heptanol (200 ppm) and SAE40 oil served as test liquids. Parameters like tube diameter, tube spacing, flow rate of the liquid were varied systematically. Depending on these parameters, the observed modes were droplet, droplet/column, column, column/sheet, and partial sheet. The complete sheet mode was not observed for SAE40 Oil. Based on experimental data flow charts were developed showing range of parameter for each flow pattern. The mode transitions for droplet- jet, droplet to column were in good agreement with reported literature, while the column/sheet to sheet mode occurs at higher values of Re_f. The regions of different flow patterns are shown in flow maps. The flow map indicates that when inertia effects dominate, the flow take the sheet mode. Gravity or surface tension effect dominated flows result in droplet mode. The formation of jets is apparently related to a complicated competition between these effects and viscous forces. Transitional Reynolds numbers can be correlated to modified Galileo numbers with reasonable accuracy in the current experimental range for all the transitions. Experimental correlations are suggested for the prediction of different flow patterns.

Keywords: *Falling film heat exchangers, Horizontal tube, Flow Pattern, Tube banks*

INTRODUCTION

Falling film heat exchangers with horizontal tube are used in the chemical, refrigeration, and petroleum and desalinization industries because they provide higher heat transfer coefficient and operate with smaller liquid inventories than flooded heat exchangers. When a liquid film flows from one horizontal tube to another below it, according to an increasing flow rate order, the flow may takes the form of droplets, circular jets or continuous sheet as shown in Figure 1.

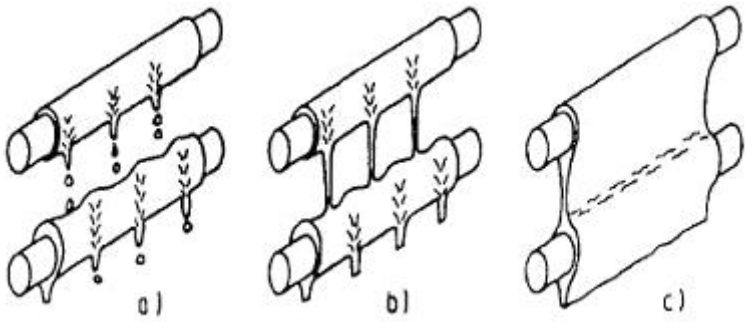

Figure 1. Schematic of three mode a) Droplet mode b) Column mode and c) Sheet mode [1].

* Corresponding author: Prof. Dr. A.T. Pise
Phone: +(91)-2164-271711/271712, Fax: +(91)-2164-271713
E-mail address: ashokpise@yahoo.com

Then, it tends to spread along the tube it flows in layer form around the periphery and falls off the bottom. As a result of this spreading tendency of the impinging columns or droplets along the tube overlapping waves are generated between adjacent columns. When inertia effects dominate, the flow will take the sheet mode. Gravity or surface tension dominated flows result in a droplet pattern. The formation of jets is apparently related to a complicated competition between these effects and viscous forces. Mixed modes representing combinations of two idealized modes existed at the intermediate flow rates so called droplet-jet and jet-sheet modes.

Based on the experimental results, Mitrovic [1] pointed out that the transition of flow modes depend on the flow rate, fluid thermo physical properties and the tube spacing. When liquid flow between adjacent tubes in the form of droplet trains or stationary columns. Ganic and Getachew [2], suggest that primary factor for changing the physical form of the liquid is the mass flow rate. Experimental observations by Ganic and Roppo [3] indicated that apart from the mass flow rate, the tube spacing and liquid viscosity also contribute to the physical form of the liquid. At low flow rate the liquid is usually in the form of droplets that are generated at a discrete point along the underside of a horizontal tube. As the flow rate increases the transition from droplet to column occur slowly over a range of flow rates. They observed that the droplet to column mode occur over a relatively large Reynolds number around 180, and it was affected by the tube spacing. While studying film condensation, Kutateladze et al., [4], suggested that the transition of flow mode was controlled by the modified Archimedes number based on the capillary constant. Armbruster and Mitrovic [5], modeled the mode transition among the droplet, jet and sheet modes, according to $Re = A\ Ga^{1/4}$, where A is an empirical constant. Re is Reynolds number and Ga is Galileo number. For sufficiently high stagnation pressure, they observed that the radial flows from adjacent jet collide and film surface is raised between the jets. The crests created at the top of the tube remain nearly unchanged around the tube, and forms the departure sites for jets leaving the tube. This flow mode is called staggered mode. In addition they found that the transition solely dependent on the liquid flow rate. Hu and Jacobi [6,7], suggested the flow modes, based on the observation of flow transition as droplet mode, droplet jet mode, an unsteady jet mode, the inline jet mode, the staggered jet mode, the jet sheet mode and the sheet mode. They found that, the flow modes are independent of geometric effect. The effect of gravitational, inertial, viscous and surface tension forces are correlated by using Reynolds number and modified Galileo number in $Re = AGa^{b}$, where A and b are empirical constant.

Researchers observed flow patterns and their transitions for different fluids and there is no agreements of dependency of flow transitions influenced by the diameter of the tube and its, spacing, surface roughness, mass flow rate of the fluid. Also empirical correlations proposed are different [5,6,7]. So there is need to verify the effects of these parameters on the mode of transitions.

So proposed work is to investigate the mode of transition and effects of parameters like wettability of tube, considering the effect of contact angle, departure site spacing, thermo-physical properties of fluid like water, distilled water + n-heptanol and SAE 40 oil.

EXPERIMENTAL METHOD

Test Rig

The test facility as is provided with a closed circuit forced circulation loop of test liquid its construction is explained in earlier paper on departure site spacing [ExHFT-7].

Experimental Procedure

Before starting a test, tubes with desired diameter were aligned in the test section at prescribed tube spacing. Since the falling film flow is gravity driven, a tube inclination would cause a non-uniform distribution of the flow. Therefore, the tubes were carefully leveled before test, and leveling was checked again after the liquid started circulating in the system. The test liquid was circulated

through the system for 15 to 30 minutes to ensure that the tubes were fully wetted and the piping system was free of air. Then the fluid flow rate was adjusted for different flow rates and the flow pattern and mode of transitions were observed by naked eye for increasing as well as decreasing flow rates. At each flow mode transition, flow rate was recorded. Similar test are carried for water, distilled water with n-heptanol (200 ppm) and SAE40 oil fluids with varying tube diameter and spacing. Some clipping and photographs were taken for different flow rates. All the experiments reported were conducted over adiabatic tubes at atmospheric pressure having temperature of the liquids were room temperature.

RESULTS AND DISCUSSION

Flow Patterns

Flow modes observed during increased and decreased flow rates of test liquids with varying tube diameter and its spacing are discussed. Also some images of the flow modes observed during testing these liquids are shown in Figures 2- 4. For each of these working fluids, the three modes were observed. Mixed modes representing combinations of two idealized modes were also observed: the droplet-jet and jet-sheet modes. Furthermore three distinct jet mode patterns were manifested, a distinction very rarely found in the literature. Because of these observations, and for other related reasons, a careful classification of the falling-film flow patterns was undertaken. At low flow rates, liquid dripped from regularly spaced sites along the bottom of the horizontal tubes, exhibiting the so-called droplet mode. The sites were not simultaneously active; droplets alternately fall from neighboring sites.

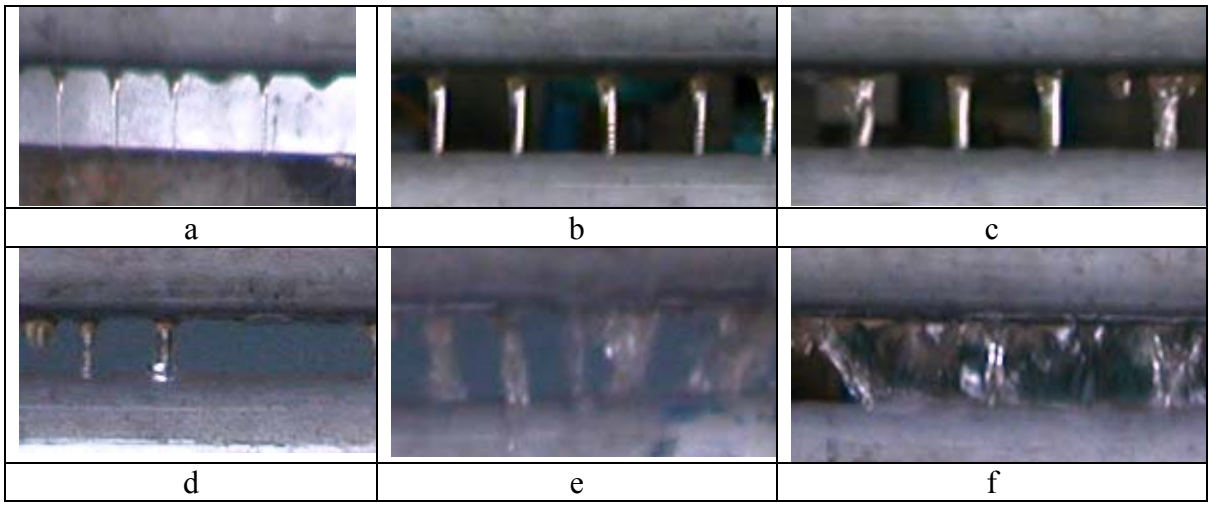

Figure 2. Photographs of observed flow modes for water are a) droplet b) droplet jet c) inline jet d) staggered jet e) jet sheet and f) sheet

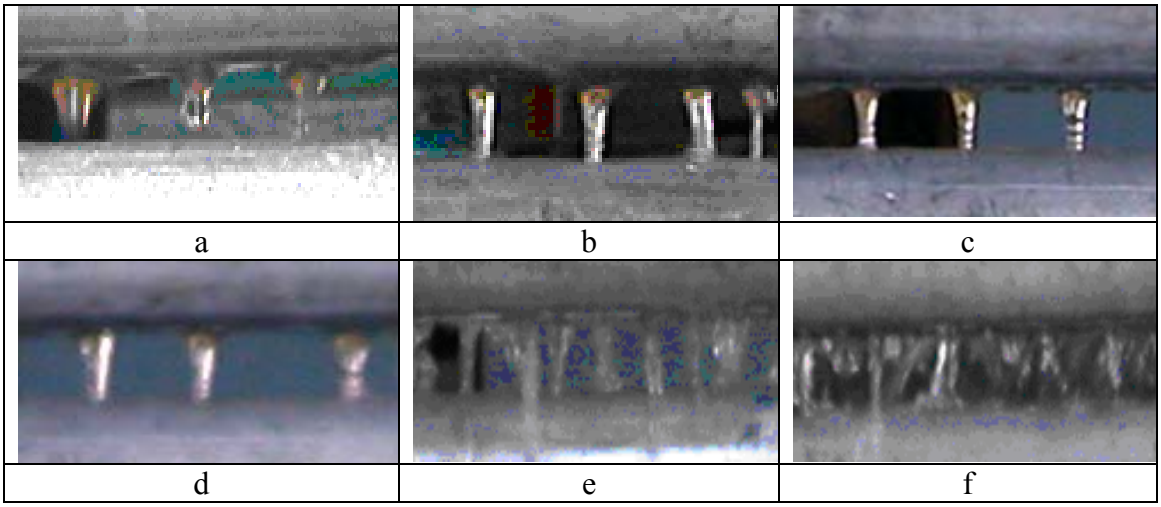

Figure 3. Photographs of flow modes for distilled water with n-heptanol a) droplet b) droplet jet

c) inline jet d) staggered jet e) jet sheet and f) sheet

The dripping frequency increased with an increase in flow rate, and all the sites became active simultaneously at a certain flow rate. A further increase in the flow rate eventually resulted in liquid departing from at least one site as a continuous jet. A flow with droplets and jets is called a droplet-jet mode, and such a transition is a droplet / droplet-jet transitions, in the reverse direction these conditions represent a droplet-jet / droplet transition (all backward transitions will be denoted in this way). From the droplet -jet mode, a sufficient increase in liquid flow rate caused liquid to falls continuously from every departure site on the bottom of the tube. The complete establishment of this flow pattern represents a droplet – jet / jet transition. Under some conditions the jet mode was established with departure sites directly beneath impingement sites; this pattern is inline jet mode.

a b c

Figure 4. Photographs of flow modes for SAE 40 oil are a) droplet jet b) inline jet c) Staggered jet

The diameter of the liquid jets increased with the flow rate and, eventually, the jets moved closer together and another discrete jet was added to the quasi-steady jet pattern. For some test conditions, a further increase in flow rate resulted in unsteadiness in the location of the jet departure sites. When the jet departure sites exhibited unsteady behavior, the flow was classified as an unsteady jet mode. From inline jet, staggered jets, or unsteady jets, a sufficient increase in the flow rate eventually resulted in jets merging to form a partial sheet. This flow pattern is called a jet-sheet mode and the transition with an increasing flow rate is denoted as jet/ jet sheet transition. Finally the flow exhibited a jet-sheet/sheet transition. When the final discrete jet merged to form a complete sheet of liquid the flow was said to be in the sheet mode under these conditions. Similar modes observed by Hu and Jacobi [9, 10].

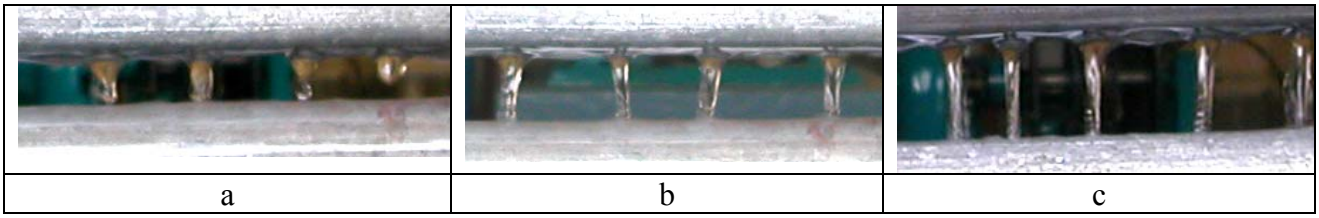

a b c

Figure 5. The observed flow modes for distilled water at constant flow rate for same diameter of tube with different spacing.

Also there was no considerable effect of tube spacing on flow patterns were observed (Figure 5) Mode of Transitions : Armbruster and Mitrovic [5] and Hu and Jacobi [6] proposed flow pattern maps where the film modes were presented as functions of Re_f and of a modified Galileo number, Ga.

$$\mathrm{Re}_f = A.(Ga)^n \quad (1)$$

Where Reynolds number $\mathrm{Re}_f = 4\Gamma/\mu$ (2)

$$Ga = \sigma^3 \rho/(g\eta^4) \quad (3)$$

Based on the experimental data the following correlations were suggested for the mode transitions.

Transition Mode	Transition Criteria	RMS Deviation	
Droplet/Droplet-Jet	$Re_f = 0.276\ Ga^{0.389}$	1.98	(4)
Droplet-Jet/ Jet	$Re_f = 0.286\ Ga^{0.3093}$	2.04	(5)
Jet / Jet – sheet	$Re_f = 1.0956\ Ga^{0.2807}$	1.72	(6)
Jet-Sheet/Sheet	$Re_f = 2.68\ Ga^{0.2628}$	5.7	(7)

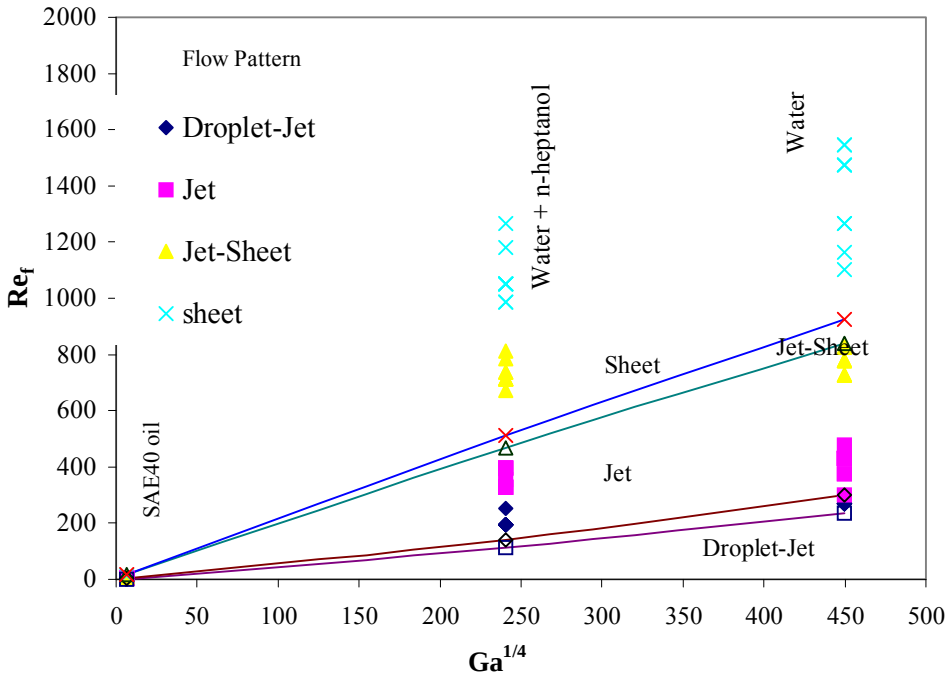

Figure 6. Flow regime map for the falling film mode transitions, comparison [6]

The straight lines indicate the correlation presented by Hu and Jacobi [6] and the points represents the experimental values. It is observed that for the same diameter flow transition changes as the spacing between tube increases.

Reynolds number represents ratio of inertia forces to viscous forces, a high Reynolds number flow is inertial dominated. The flow map provides a clear interpretation of physics of flow; Inertia dominated flows (Re tends to ∞) will results in the sheet modes. Modified Galileo number can be interpreted as ratio of gravitational force to viscous force. The flow map demonstrates that gravity dominated flows will takes the droplet mode.
The flow map implies that droplet mode occurs when surface tension effect dominates. The modified Galileo number reflects both gravitational and surface tension effects; both of the interpretations are intuitive, and there is more valid interpretation of physics reflected by flow regime map.

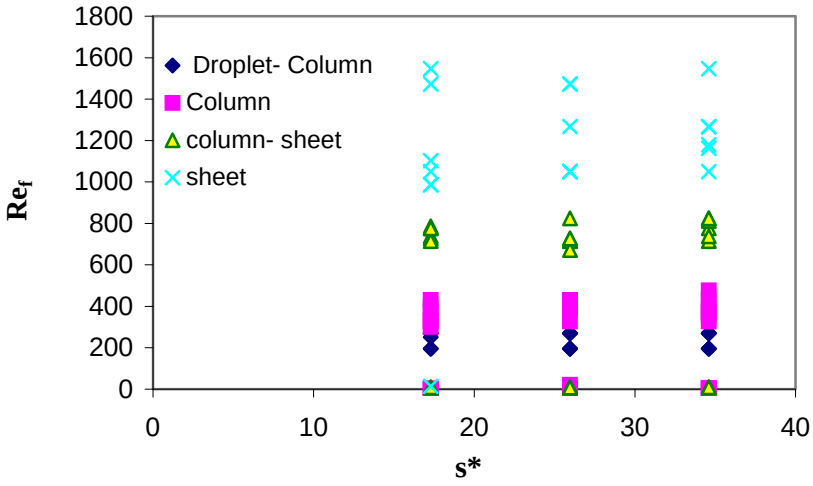

Figure 7. Effects of Tube Spacing on Transitional Reynolds Number

Tube Spacing

Figure 7 shows effects of tube spacing on transitional film Reynolds number. There is no considerable effect of tube spacing on transitional Film Reynolds number.

CONCLUSIONS

From the results of this study the following major conclusions are drawn.

The observed patterns were same as reported in literature like droplet, droplet/column, column, column/sheet, and sheet. The complete sheet mode was not observed for SAE40 Oil. The mode transitions for droplet- jet, droplet to column were in good agreement with Hu and Jacobi [9] (1998), while the column/sheet to sheet mode occurs at higher values of Re_f. The flow map indicates that when inertia effects dominate, the flow will take the sheet mode. Gravity or surface tension effect dominated flows result in droplet mode. The formation of jets is apparently related to a complicated competition between these effects and viscous forces. Transitional Reynolds numbers can be correlated to modified Galileo numbers with reasonable accuracy in the current experimental range for all the transitions. Equations 4 to 7 are suggested for the prediction of different flow patterns. There is no considerable effect of tube spacing on transitional Film Reynolds number.

These results provide deeper understanding of the falling film mode transitions and a useful tool for designing and modeling heat exchangers. Comparisons with existing models suggest that further work in this area is needed. Because falling film heat exchangers uses a range of fluids with concurrent and counter-current vapor flows, future work in this area should include vapor-shear effects with a wide range of fluid properties.

NOMENCLATURE

d - Diameter, mm
d* - Normalized tube diameter, d/a, dimensionless
Ga - Modified Galileo number, dimensionless
g - Gravitational acceleration, m /s^2
Re_f - Film Reynolds number, dimensionless
s - Tube spacing, mm
s* - Normalised tube spacing s/a dimensinless
Γ - Total liquid mass flow rate per unit length of tube, kg /ms
μ - Dynamic viscosity, N –s/m^2
ρ - Mass density, kg/m^3
σ - Surface tension at gas/liquid interface, N/m

REFERENCES

1. Mitrovic J., "Influence of tube spacing and flow rate on heat transfer from a horizontal tube to a falling liquid film", Proceedings of the eighth international heat transfer conference, SanFrancisco, vol.4, 1986, pp.1949–56.
2. Ganic E.N., Getachew D., "Effects of surface condition and working fluid on fluid breakdown during heat transfer", proceeding of Eighth Heat transfer Conference, San Francisco, Vol. 4, 1986 pp 1931-36.
3. Ganic E.N., Roppo M.N., "An experimental study of falling liquid breakdown on a horizontal cylinder during heat transfer", Journal of Heat Transfer, 102, 1980, pp - 1593-99.
4. Kutateladze S.S., Gogonin I.I., "Heat Transfer in film condensation of slowly moving vapour", International Journal of Heat and Mass Transfer, Vol. 22, pp 1949- 56.
5. Armbruster R., Mitrovic J.,"Evaporative Cooling of a Falling Water Film on Horizontal Tubes". Experimental Thermal and Fluid Science 18, Elsevier, pp. 183-194 (1998).
6. Hu X., Jacobi A.M., "The Intertube Falling Film Part 1- Flow Characteristics, Mode Transition and Hysteresis," ASME Journal of Heat Transfer, 118 pp. 616-625 (1996).
7. Hu X., Jacobi A.M., "The Intertube Falling Film Part 2- Mode Effects on Sensible Heat Transfer to a Falling Liquid Film," ASME Journal of Heat Transfer, 118 pp. 626-633 (1996).
8. Pise, A., Kant, K., Devotta, K., "Effect of additives on flow patterns in horizontal tube falling film absorber of a LiBr-H_2O refrigeration system," 2nd International conference on Heat Transfer, Fluid Mechanics and Thermodynamics, 24-26 June, Victoria falls, Zambia, pp 1-7
9. Hu X., Jacobi A.M., "Departure Site Spacing for Liquid Droplets and Jets Falling Between Horizontal Circular Tubes", Experimental Thermal and fluid Science pp. 322-331, (1998).
10. Jacobi A.M., Ribatski G., "Falling Film Evaporation on Horizontal Tubes – A Critical Review", International Journal of Refrigeration pp. 635- 653, (2005).

STUDIES OF DEPARTURE-SITE SPACING FOR LIQUID DROPLETS AND JETS FALLING BETWEEN ON HORIZONTAL CIRCULAR TUBES

A.T. Pise [*1], S B. Patole[1] and N. U. Korde[2]

[1] Department of Mechanical Engg. Govt. College of Engineering. Karad M.S. 415124 (India)
[2] Department of Mechanical Engg. G.H.Raisoni Inst. of Engg. & Tech., Pune M.S. 412207 (India)

ABSTRACT**.** The heat and mass transfer of the horizontal falling film heat exchangers are mainly depends on the wetting characteristics of the flow and the flow patterns between the tubes. The wetting characteristics of the flow over the tube are closely related to the departure-site spacing between the adjacent droplets/columns mode. Experiments were conducted exploring the effects of thermo physical properties like viscosity, surface tension, inertial, and gravitational effects and geometrical parameters on departure site spacing between the adjacent droplets/columns mode. Water, Distilled water with n-heptanol as surfactants and SAE40 oil served as test liquids. The effect of geometrical parameters like tube diameter and spacings between the consecutive tubes on the departure-site spacing was investigated for the smooth tubes. The flow modes and its behaviour over the tubes were observed visually and photographed with clippings by digital video camera. Measurements of departure-site spacing between the adjacent droplets/jets were reported for the test liquids. For the conditions of this study, departure-site spacing increased with decreasing Re_f for high - Ga fluids and was nearly independent of Re_f for low-Ga fluids. Departure site spacings increased slightly with tube diameters.

This paper aims to find the effect of various parameters on departure site spacing between the adjacent droplets/jets.

Keywords: *Falling film heat exchangers, Horizontal tube, Departures site spacing, Tube banks*

INTRODUCTION

Falling film heat exchangers with horizontal tubes, arranged one upon the other, thus forming a bundle have been used in chemical, refrigeration, petroleum, refining, desalination, and food industries. They provide higher heat transfer coefficients and operate with smaller liquid inventories than flooded heat exchangers. Also they offer advantages in dealing with liquid distribution, noncondensable gases, fouling and other problems. In a typical falling film heat exchanger, the liquid film is introduced at the top of the tube bank through nozzles or drip-tray distribution system. The liquid flows as a film around the tubes. It begins to extend from the underside of the tube and eventually detaches and falls freely until it impacts the top of the next tube. This process is repeated through the entire tube bank. The behavior of real films involves many complex interactions such as the waves and ripples generated by an impacting drop. When a liquid film falls from one horizontal tube to another below it, the flow may take the form of discrete droplets, jets, or a continuous sheet [1]. The mode plays an important role in the heat transfer. The flow pattern and wetting characteristics in the falling film heat exchangers have significant impact on the sensible and latent heat transfer.

* Corresponding author: Prof. Dr. A.T. Pise
Phone: +(91)-2164-271711/271712, Fax: +(91)-2164-271713
E-mail address: ashokpise@yahoo.com

The wetting characteristics and film complex over the tube depends upon distance between adjacent droplets/jets is so called departure site spacing λ (see Figure 1). The departure site spacing is considered to be an important parameter to understand the falling film flow behavior. This paper is aimed to analyze the effects of thermo physical properties like viscosity, surface tension, inertial, and gravitational effects and geometrical parameters on departure site spacing between the adjacent droplets/columns mode.

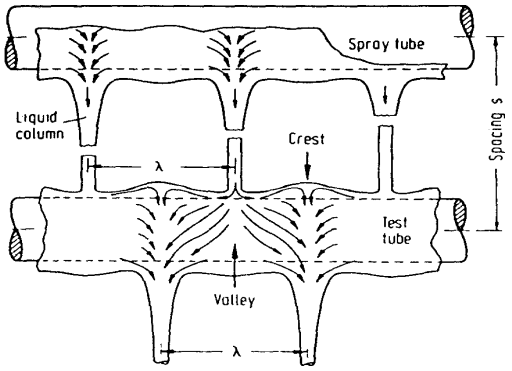

Figure 1. Stationary columns and flow of liquid on the tube.[2]

Departure Site Spacing

The average distance between the two adjacent droplets/columns can be explained with the Taylor instability theory

$$\lambda = 2\pi\sqrt{\frac{n\sigma}{\rho g}} \tag{1}$$

Where n is a factor ≥ 2. n was taken equal to 3, assumed to be thick films, n was taken equal to 2, assumed to be thin film.

The influence of inter tube spacing and flow rate on falling film heat transfer on horizontal plain tube bundles for subcooled liquid without evaporation was investigated by Mitrovic [2], for isopropanol and water. He measured the distance between the two adjacent columns from still photographs, obtaining a value of 22 mm for water at 25°C and 13.5 mm for iso propanol at 21.5°C. These values fall between the critical wavelength λ_{crit} and most dangerous wavelength λ_d. The departure site spacing can be calculated according to equations given by the Lienhard and Wang [3].

$$\lambda_c = 2\pi\sqrt{\left(\frac{g\left(\rho_L-\rho_g\right)}{\sigma}+\frac{2}{D^2}\right)^{-1}} \tag{2}$$

$$\lambda_d = \lambda_{cric}\sqrt{3} \tag{3}$$

Hu and Jacobi [4] experimentally investigated the effects of parameters like tube diameters, tube spacing and liquid flow rate on the film wavelength using four working fluids. They reported that the wavelength depends on flow rate and decreases for an increase in Re. A weak dependence on tube diameter was observed, with wavelength increasing with tube diameter. The dependence of wavelength on the tube spacing was also observed to be the weakest. They correlate the wavelength with Re, $Ga^{1/4}$ and tube diameter and provide a new widely applicable correlation.

$$\lambda = \left(0.863\frac{2\pi\sqrt{3}}{\sqrt{1+2\left(a/d_o\right)^2}} - 0.863\frac{\mathrm{Re}_f}{Ga^{1/4}}\right)a \tag{4}$$

Yung et al. [5], developed an equation to estimate the wavelength of low viscosity liquids like water, ethyl alcohol and ammonia. Ganic and Roppo [6], observed wavelength to be lower than predicted by the Taylor instability and unaffected by the flow rate and tube spacing for the jet mode. Armbruster and Mitrovic [7] provided a correlation for jet spacing; which was based on data with two fluids namely water and isopropyl alcohol. Using current nomenclature, the correlation can be written as

$$\lambda = \frac{2\pi\sqrt{2}}{\sqrt{\frac{g(\rho-\rho_v)}{\sigma}\left(1+\left(\frac{Re_f/2}{Ga^{1/4}}\right)^{0.8}\right)+\frac{2}{d^2}}} \tag{5}$$

This expression is somewhat unique, in that it explicitly accounts for a flow rate effects on the jet spacing. Siyoung et al [9], reported that, the departure site spacing is closer as the flow rate increases and the tube diameter decreases for smooth tube. They proposed a non dimensionalized departure site spacing relation with Reynolds number as

$$\lambda^* = \left(\frac{2\Pi\sqrt{3}}{\sqrt{1+\frac{3}{d^{*2}}}}\right)^{1.1} - 1.62\,Re^{0.22} \tag{6}$$

EXPERIMENTAL METHOD

Experimental Setup

The test facility as shown in Figure 2, is provided with a closed circuit forced circulation loop of test liquid. The purpose of liquid loop was to supply liquid medium to test section. The liquid circulation loop consisted of distributor, reservoir, flow pump and flow meter. The test liquid in reservoir was delivered by pump to distributor via flow meter then passed over the tubes assembly. In the experimental set up to damp the vibrations in the distributor, flow through the flow meter first passed to a circular tube having 2.5 mm diameter holes along its periphery.

At the bottom of distributor small holes of 1.57 mm diameter were drilled at 4 mm apart. The distance between bottom of distributor & top of first tube is kept 5 mm. Commercially available tubes of different diameters viz. 27, 32 and 42 mm with intertube spacing of 10, 15 and 20 mm were kept in the experiment. The arrangement of the tube side stands is made such that the spacing between the tubes can be changed easily.

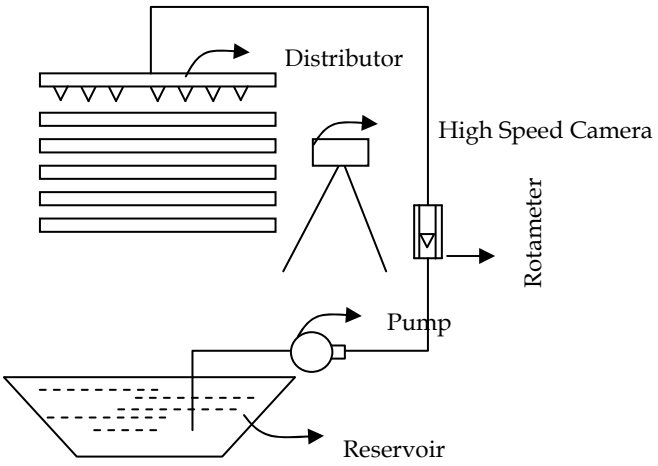

Figure 2. Schematic of experimental setup

Experimental Procedure

Before test, tubes with desired diameter were aligned horizontally in the test section at prescribed tube spacing. As the falling film flow is gravity driven, a tube inclination would cause a non-uniform distribution of the flow. Also leveling was checked after the liquid started circulating in the system. The liquid flow rate was adjusted to obtain a jet mode, and the tubes were considered leveled if the jets fell at fixed sites without drifting toward either end of the test tube. The test liquid was circulated through the system for 15 to 30 minutes to ensure that the tubes were fully wetted and the piping system was free of air. Then the fluid flow rate was adjusted, mode existed was droplets/columns. Similar tests were carried for water, distilled water with n-heptanol (200 ppm) and SAE40 oil fluids with varying tube diameter and spacing. Some clippings and images were taken for different flow rates. All the experiments reported were conducted over adiabatic tubes at atmospheric pressure having temperature of the liquids were room 25°C.

RESULTS & DISCUSSION

Departure Site Spacing

The measurement of departure site spacing was carried out from the frames, which were excerpted from the Digital video camera for three different fluids viz. water, distilled water with n-heptanol and SAE40 oil. Software Adobe Photoshop 7.0 was used to measure the distance between the two adjacent droplets or columns.

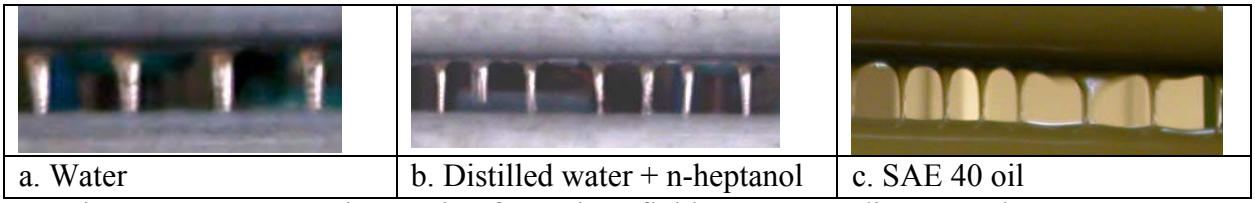

a. Water	b. Distilled water + n-heptanol	c. SAE 40 oil

Figure 3. Departure site spacing for various fluids on 27 mm diameter tube

Figure 3 show the images of departure site spacing of test liquids. It shows that λ^* is higher for water and jets are higher diameter as compared to other test liquids. It might be due to higher surface tension of water as compared to others. Surface tension reduced due to presence of additive (n-heptanol) in water reduces jet diameter, film thickness and λ^*. Viscosity effect is more pronounced for oil film becomes thick and jet is thin and broader at the bottom of the tube. The decreased in Re results in increased in λ^*. Effect of tube diameter are more pronounced and λ^* increases with diameter.

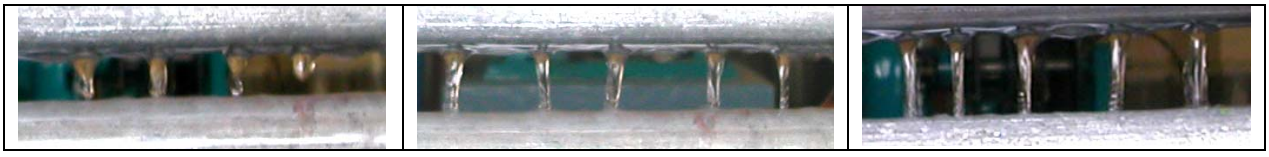

Figure 4. Liquid jet shapes for distilled water at 10mm, 15mm and 20 mm spacing

Figure 4 shows shapes of jet at different spacing between the tubes. For small values of spacing the jet appears to take a shape of pendent drop as increase in spacing, the jet becomes elongated, taking the shape of an inverted bell. For further increase in tube spacing results in jet shape like the upper frustum of cone.

Figures 5-7 show the dimensionless departure site spacing λ^* plotted against Re_f for varying tube diameter and intertube spacing for water, distilled water with n-heptanol and oil respectively.

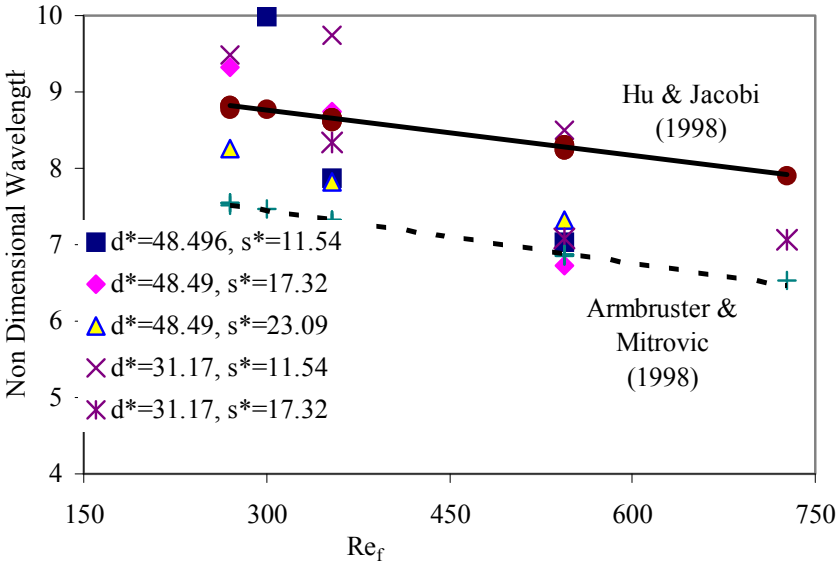

Figure 5. Departure site Spacing (Water)

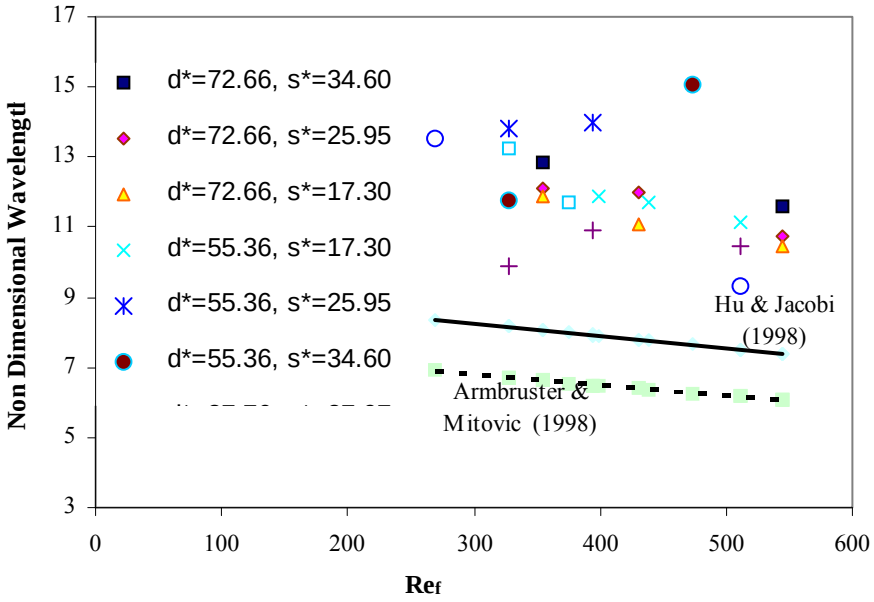

Figure 6. Departure site Spacing (Water + n-heptanol)

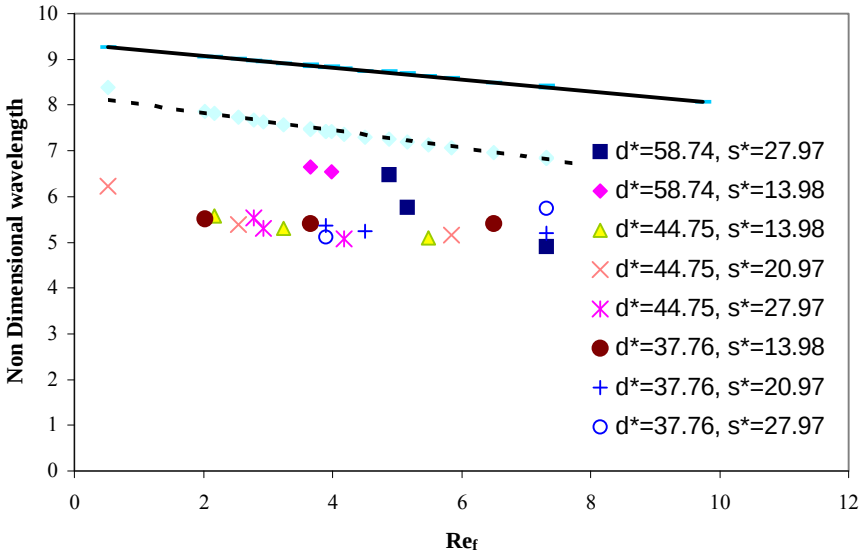

Figure 7. Departure site spacing (SAE 40 Oil)

Measured λ* are compared with Hu & Jacobi [4] and Armbruster & Mitrovic [7]. Figures 5-7 showed, for water results are good agreement with Hu & Jacobi [4] and Armbruster & Mitrovic [7] while water + n-heptanol it is higher side and SAE oil lower side for all test diameter and spacing. The data clearly show that λ^* depends on Re_f especially at low Re_f and high $Ga^{1/4}$. A decrease in Re_f is accompanied by increase in λ^*. At low $Ga^{1/4}$, λ^* appears to be insensitive to Re_f over a wide range. Irrespective of fluid, departure site spacing slightly increased with the increased in diameter of tube. Also it is observed that departure site spacing slightly decreased for water and SAE 40 oil with the increased in tube spacing.

CONCLUSIONS

From the results of this study the following major conclusions are drawn.
Departure-site depends on mass flow rate and decreases for increase in Re_f; this dependence is higher for fluids with a large $Ga^{1/4}$. Using Taylor's instability theory, departure-site spacing was under predicted for thick films and over predicted for thick films. In the experimental data, a weak dependence on tube diameter was observed, with λ^* increasing with tube diameter. The dependence of λ on tube spacing was observed to be the weakest. These results provide deeper understanding of the falling film mode transitions and a useful tool for designing and modeling heat exchangers. Comparisons with existing models suggest that further work in this area is needed.

NOMENCLATURE

d - Diameter, mm
d* - Normalized tube diameter, d/a, dimensionless
Ga - Modified Galileo number, dimensionless
g - Gravitational acceleration, m /s^2
Re_f - Film Reynolds number, dimensionless
s - Tube spacing, mm
λ - Departure-site Spacing
Γ - Total liquid mass flow rate per unit length of tube, kg /ms
λ* - Normalized departure-site spacing, dimensionless
μ - Dynamic viscosity, N –s/m^2
ρ - Mass density, kg/m^3
σ - Surface tension at gas/liquid interface, N/m

REFERENCES

1. Hu X., Jacobi A.M., "The Intertube Falling Film Part 2- Mode Effects on Sensible Heat Transfer to a Falling Liquid Film," ASME Journal of Heat Transfer, 118 pp. 626-633 (1996)
2. Mitrovic J., "Influence of tube spacing and flow rate on heat transfer from a horizontal tube to a falling liquid film", Proceedings of the eighth international heat transfer conference, SanFrancisco, vol.41986, pp.1949–56.
3. Lienhard, J. H., and Wong, P. T. Y., "The Dominant Unstable Wavelength and Minimum Heat Flux during Film Boiling on a Horizontal Cylinder, Transactions of ASME, J. of Heat Transfer, 86, 1964,pp. 220-226.
4. Hu X., Jacobi A.M., "Departure Site Spacing for Liquid Droplets and Jets Falling Between Horizontal Circular Tubes", Experimental Thermal and fluid Science pp. 322-331, (1998).
5. Yung D, Lorenz J.J.Ganic E.N., "Vapor/liquid interaction and entrainment in falling film evaporators", J. Heat Transfer, 102(1980) pp. 20–25.
6. Ganic E.N., Roppo M.N., "An experimental study of falling liquid breakdown on a horizontal cylinder during heat transfer", Journal of Heat Transfer, 102, 1980, pp - 1593-99.
7. Armbruster R., Mitrovic J.,"Evaporative Cooling of a Falling Water Film on Horizontal Tubes". Experimental Thermal and Fluid Science 18, Elsevier, pp. 183-194 (1998).
8. Hu X., Jacobi A.M., "The Intertube Falling Film Part 1- Flow Characteristics, Mode Transition and Hysteresis," ASME Journal of Heat Transfer, 118 pp. 616-625 (1996).
9. Siyoung J., Kyung H.K., Kyongmin K., Eun S.J., "Effect of Surface Roughness on The Wetting of a Horizontal Tube Falling Film Heat Exchanger", ISHPC 02, Proceeding of the International Sorption Heat Pump Conference, Shangai, China, September 24-27, 2002. pp. 305-309.

EXPERIMENTAL ANALYSIS OF BOILING IN SATURATED FC72 CONFINED POOLS:PRELIMINARY RESULTS

S. Filippeschi[1]
[1] Department of Energy,University of Pisa, Pisa, Italy

ABSTRACT. This paper deals with the analysis of the nucleate pool boiling regime in the case of a copper plate surface immersed in a FC72 fluid at saturation condition. The apparatus has been tested and calibrated by using water and by comparing the experimental data with four correlations. The minimum prediction error is 12,25%. After that the effect of the lateral confinement with FC72 has been studied by reducing the diameter of the vessel which contains the pool. The investigated diameters have been (72, 64, 52, 42, 34 mm). Besides for each diameter the effect of the immersion depth on the heat transfer coefficient has been evaluated. These first preliminary data shows that an enhancement of the theoretically expected heat transfer coefficient have been measured for each diameter except for the diameter 42 mm, where a drastic deterioration of the heat transfer has been observed. A dependence of the CHF on the immersion depth has been observed for little diameters.

Keywords: *Pool boiling, FC72, confined boiling, small liquid pools, immersion depth.*

INTRODUCTION

Boiling heat transfer regime aroused a great interest in the past since the 1900s. For the great number of its possible applications, the natural convective boiling or pool boiling, has been studied by a lot of researchers. Different fluids, different surfaces and materials, different orientations with respect to the gravity and low-gravity conditions have been analysed and experimented [1], [2]. Pool boiling regimes have found a large employment in a large number of technical fields.
The pool boiling regime, which had been studied in the past, is usually characterised by a surface immersed in a large pool of liquid where the sidewalls are far enough from the boiling surface. In compact two-phase devices with small pools of liquid when the boiling is employed as the main thermal control mechanism of a surface in a confined space, its behaviour can be very different to that of the boiling in a large liquid pool, [3],[4].
In 1986 Westwater et al. [5] presented a lot of experimental boiling data of circular flat surfaces (9 diameters from 6.4 to 304.8 mm) at atmospheric pressure with liquid nitrogen, Freon 116, and ethane.
They noted that boiling data depended strongly on the plate diameter when the diameter was small. They found a critical diameter, which made the heat transfer abruptly fall, and in the case of nucleate boiling it was about $2.5\lambda_D$, where λ_D is the most dangerous wavelength for Taylor instability, given by equation (1):

$$\lambda_D = 2\pi \cdot \sqrt{3} \cdot \sqrt{\frac{\sigma}{g \cdot (\rho_f - \rho_g)}}. \qquad (1)$$

In 1987 Elkassabgi and Lienhard [6] studied the effects of the sidewall and of the immersion depth on the critical heat flux (CHF) with methanol. They noted that the CHF decreased with a linear dependence on the ratio of the distance between the sidewall confinement and the diameter of the

* Corresponding author: Dr. S. Filippeschi
Phone: + (39)-50-2217153, Fax: + (39)-50-2217150
E-mail address: s.filippeschil@ing.unipi.it

heater. They showed that the effect of the immersion depth on the CHF was negligible for ratios higher than 14.78.
In 1998 Bonjour and Lallemand [7] experimentally studied the natural convective boiling of R-113 in a narrow rectangular vertical channel (confined space). The channel height was 120 mm and the gap-size ranges was from 0.5 to 2 mm. They observed, with a hot wire anemometer, three boiling regimes: nucleate boiling with isolated deformed bubbles, nucleate boiling with coalesced bubbles and partial dry-out. Both first two regimes result in a heat transfer enhancement whereas the latter implies a heat transfer deterioration.
In 1998 El Genk and Sauber [8] tested different correlations for uniformly-heated small liquid pools of water, ethanol, methanol, Dowtherm-A, R-11 and R-113 in small cylindrical enclosures. All correlations were within ±15% of most experimental data. The data covered a wide range of pool diameters (6÷37 mm) and heated pool heights (50÷800 mm).
In 2003 Zhao et al. [9] studied the confinement effect of a mesh screen on a horizontal surface. The gap range experimentally studied was 1-5.9 mm. A weak enhancement of the heat transfer coefficient was observed as the nucleate boiling is fully developed.
In 2004 Passos et al. [10] presented results for FC72 and FC87 on a downward facing surface and in confined spaces between a heated copper disk (diameter 12 mm and thickness 2 mm) and an unheated surface, for distances varying between 0.2 and 13 mm. They noted that a decrease in the distance between the plates causes an enhancement of the boiling. In 2008 Kang et al. [11] presented the last of several papers on the pool boiling heat transfer in a vertical annulus. They noted that there was a heat transfer deterioration as the gap size decreased.
This literature review shows that there are a wide number of vague statements and discrepant results in the study of confined boiling. If the gap space effect seem to enhance the heat transfer in particular configurations, in the other cases a deterioration has been observed. Especially in the case of small boiling pools of liquid the effect of the confinement is, at the moment, not so clear.
This paper presents a preliminary study on the small pools of boiling liquid. In particular it deals with the combined effect of the lateral sidewall (D_E) and of the immersion depth on the heat transfer coefficient of a circular plate surface (D_S=18.8 mm).The surface material is copper, the fluid is FC72 at saturation conditions. The investigated ratio D_S/D_E are within the range 1.8÷3.8. Preliminary results of these effects are shown.

EXPERIMENTAL ACTIVITY

Experimental facility

The experimental facility consists of a gravity assisted loop two-phase thermosyphon and a set of instruments and control systems. A photo of the two-phase thermosyphon is shown in Figure 1.a. The thermosyphon consists of an evaporator and a condenser which are connected between them with two flexible pipes. A mechanical sketch of the evaporator is shown in Figure 1.b. It consists of a glass tube closed at the bottom and at the top by two plates. The glass tube is 85 mm high, but it has different internal diameters D_E. (72, 64, 52, 42, 34 mm). The bottom plate is made of a phenolic resin named kite brand Tufnol (ρ= 1440 kg/m^3, k= 0.26 W/m K, c=1.5 kJ/kg K). The bottom plate holds the copper dissipator heated from the bottom by a mica thermofoil heater. The particular shape of the dissipator allows to enhance the heat flux up to 500 kW/m^2 about. The top circular surface of the dissipator (D_S=18.8 mm) is wetted by the working fluid.
A metallic stand for the thermocouples is anchored to the bottom plate. This rigid stand prevents the thermocouples from changing their positions during the tests, because of the convective motions of the working fluid. The 6 thermocouples, all K-type, are located at 6 different distances from the bottom plate 2, 5, 10, 20, 30 and 80 mm. These thermocouples are used to monitor a possible thermal stratification inside the pool. A further thermocouple has been located within the copper dissipater 1.5 mm under the upper surface of dissipator, in order to calculate the temperature of the wall T_W.

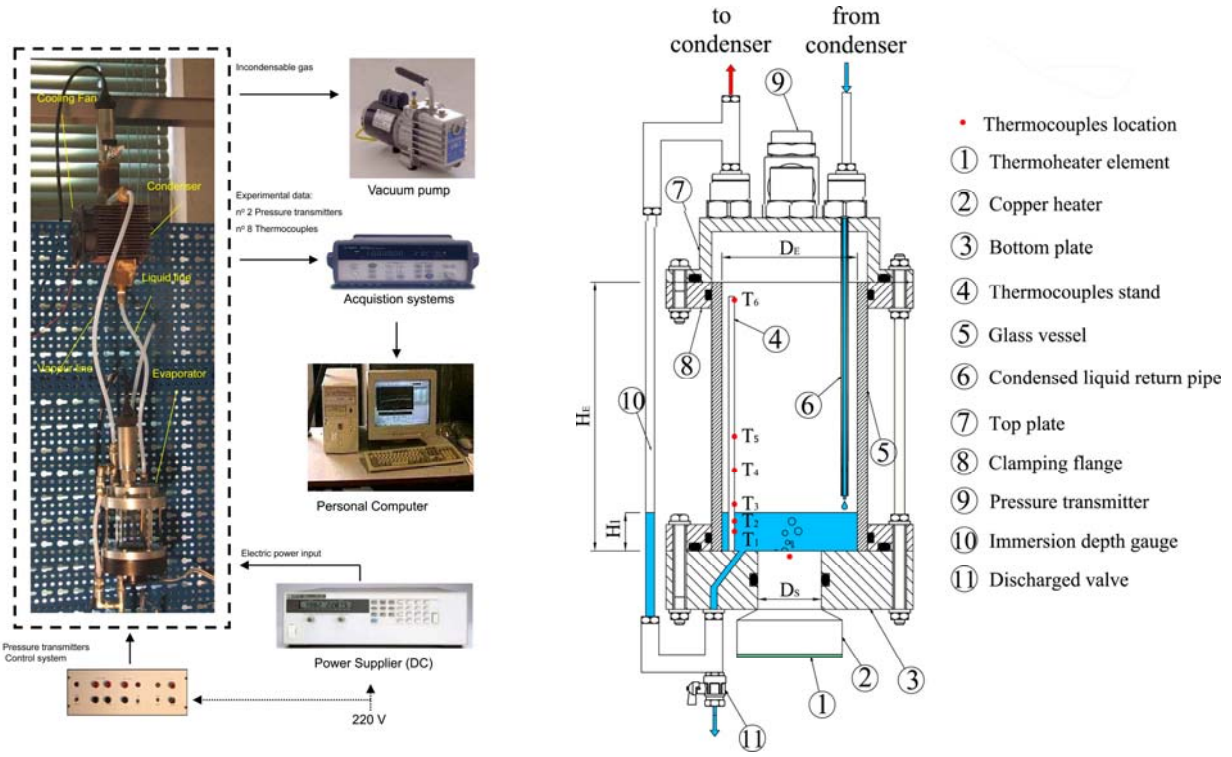

(a) (b)

Figure 1. The experimental facility and a scheme of the evaporation section

The top plate is made of aluminium. On the top plate have been placed: the connection with the vapour line, the connection with the return of the condensed liquid, a pressure transmitter and a valve connected with a vacuum pump. The return of the condensed liquid inside the evaporator is realised by a metallic pipe with an internal diameter of 2 mm. The position of this tube remains the same during all the tests. The outlet ending of the tube is locate at 16 mm over the heating surface in a lateral position and does not directly influence the fluid-dynamic close to the heating surface.

The remote condenser is made of copper. It consists of 4 copper tubes, 90 mm high, with an external diameter of 10 mm, which are connected with an inlet and an outlet manifold and which are covered with 16 copper fins interspaced by 5 mm. These fins are 0.5 mm thick and have a squared form of a side of 80 mm. The condenser is cooled by a centrifugal fan with an air flow rate of 50 m^3/h. The condenser has been designed to remove up to 150 W. In the upper part of the condenser has been place a vessel, to collect all the incondensable gases, and a pressure transmitter. In the upper vessel has been placed a valve connected with a vacuum pump. The condenser has been placed 0.6 m above the evaporator.

Instruments and procedures

The experimental apparatus which has been previously described, is equipped with some instruments and control systems. All the thermocouples used during the tests are K-type thermocouples, 0.5 mm thick, which are connected with a data acquisition switch unit Agilent 34970A. The accuracy specification is ±0.2 K on the differential measurement of two thermocouples. All the readings have been logged in a personal computer. The two pressure measurements are got with two absolutely pressure transmitters Druck PTX75/11 (±0.1% FS (±250 Pa)). The input power is supplied by a thermofoil heater which is electrically connected with a high performance DC power supplies Agilent 6574A.

For each test both the immersion depth and the diameter can change. The diameters D_E which are tested are 72, 64, 52, 42, 34 mm. For each diameter are carried out 5 tests at different immersion depths H_l (80, 60, 20, 10, 7 mm).

The procedure of a single test is here briefly described. The evaporation section is assembled with the glass cylinder of diameter D_E, the vacuum is realised within the loop and the evaporator is charged with a fixed volume of liquid. As soon as the wished immersion depth is reached, the vacuum pump is used again to drain off the incondensable gases.

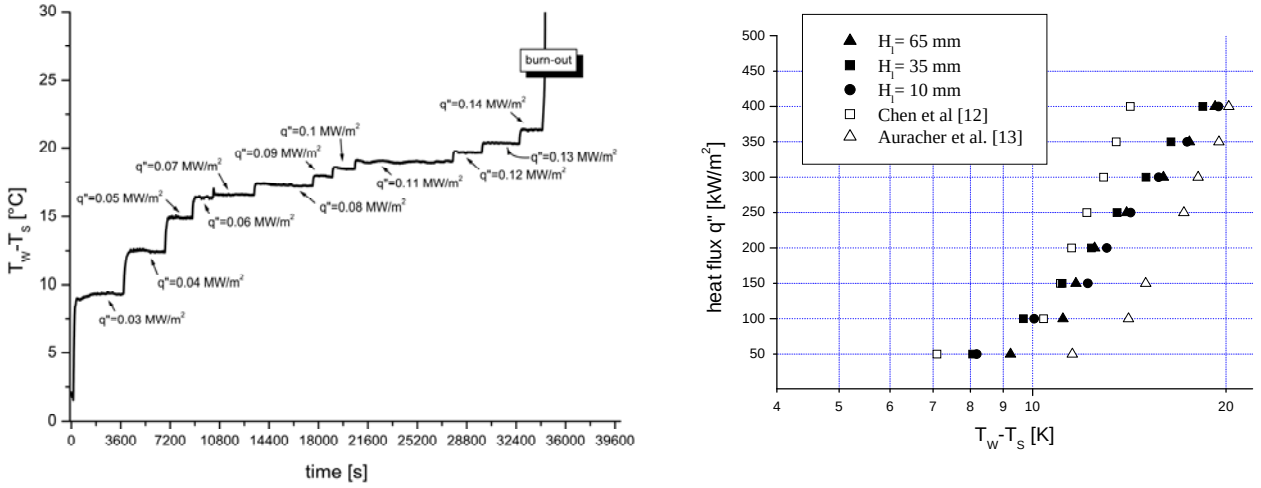

(a) (b)

Figure 2. (a) Power increasing steps over time (b) Experimental data: water (D_E=72 mm; P=1 atm)

After that the input power is supplied to the thermo-heater starting from a heat flux of 30 kW/m^2 up to the CHF with a increasing step of 10 kW/m^2. For each power step a time necessary to reach the regime heat transfer conditions is waited. An example of the evolution over time of the wall superheat T_W-T_S in dependence on the power input step, is shown in Figure 2.a. Each test is repeated three times without discharge the liquid from the apparatus.

During the tests two different fluids are used: water and FC72. During the test with FC72 a further precaution is kept: an input power is supplied to the thermo-heater and a boiling regime is reached. The apparatus has been carried out for one hour at least and after all the incondensable gases, collected in the upper reservoir of the condenser, are removed with the vacuum pump. In such a way that a degassing of the FC72 is made.

Calibration tests and uncertainties -Water

Water has been used to calibrate the apparatus and to define the uncertainties, because there are a wide literature on the nucleate boiling of a copper plate surface with water at atmospheric pressure.

Figure 2.b shows the wall superheat measured during the experiments for each imposed heat flux for 3 different immersion depths (H_l= 10, 35 and 65 mm). The diameter D_E has been of 72 mm, in order to avoid any effect of the sidewall confinement. These data have been compared with the experimental data available in the literature. All the data in the literature are included within the range of data reported in [12] and [13]. The average wall superheat, experimentally obtained, show errors of about 25% with respect to the data in [12] and [13] for high heat fluxes, whereas they show errors lower than 15% for heat fluxes lower than 200 kW/m^2.

The same data have been compared with the most used nucleate boiling correlations. The first correlation which has been used is that of Stephan and Abdelsalam [14]. They reported, in the case of water, a correlation obtained with a mean absolute deviation between the predictions of the correlation and experimental data of about 11.3%. The applicable correlation for water is the equation (2):

$$\frac{h_{SA}\cdot D_b}{k_f} = 0.246\cdot 10^7 \cdot \left(\frac{q''\cdot D_b}{k_f}\right)^{0.673} \cdot \left(\frac{h_{fg}\cdot {D_b}^2}{{k_f}^2}\right)^{-1.58} \cdot \left(\frac{c\cdot T_s\cdot D_b}{\alpha_f}\right)^{1.26} \qquad (2)$$

where D_b is the bubble diameter expressed by the Fritz correlation by using a contact angle of 45° in the case of water [2]. The second correlation which has been used is that of Rosenhow et al. [1] reported in equation (3):

$$\frac{c \cdot \Delta T_{WS}}{h_{fg}} = C_{sf} \cdot \left[\frac{q''}{\mu \cdot h_{fg}} \sqrt{\frac{\sigma}{g(\rho_f - \rho_g)}} \right]^{0.33} \cdot \left(\frac{c \cdot \mu_f}{k_f} \right)^n \tag{3}$$

In [15] Rosenhow et al compared the accuracy of six well-known nucleate pool-boiling correlations against the reliable experimental databases. They noted that in the case of water and copper surface the correlation with the highest accuracy is that of Rosenhow [1] with a root mean square accuracy of 14% if C_{sf}=0.17 and n=0.76.

In addition to these two classic correlations has been used the Kutateladze correlation [15] which has been developed for predicting the pool boiling regime in two-phase thermosyphons. It is reported in equation (4):

$$h_{Ku} = 6.95 \cdot 10^{-4} \cdot \frac{k_l}{\sqrt{\frac{\sigma}{g \cdot (\rho_f - \rho_g)}}} \cdot \mathrm{Pr}^{0.35} \cdot \left(\frac{q'' \cdot L^*}{\rho_g h_{fg} \nu_f} \right)^{0.7} \cdot \left(\frac{p \cdot L^*}{\sigma} \right)^{0.7} . \tag{4}$$

The Kutateladze correlation has been corrected in the case of small pool liquid uniformly heated, by El-Genk and Saber [8] The El Genk and Sauber correlation is expressed by equation (5)

$$h_{EL} = (1.0 + 4.95) \cdot \psi) \cdot h_{Ku} ; \tag{5}$$

where the term ψ is the mixing coefficient which is given by the equation (6)

$$\psi = \left(\frac{\rho_g}{\rho_f} \right)^{0.4} \cdot \left[\frac{p \cdot \nu_f}{\sigma} \cdot \left(\frac{\rho_f^2}{\sigma \cdot g \cdot (\rho_f - \rho_g)} \right)^{0.25} \right]^{0.25} ; \tag{6}$$

it reflects for the contribution of mixing by sliding and rising bubbles to the nucleate boiling heat transfer in small liquid pools.

Figure 3 shows the comparison between the correlations (2)÷(6) and the experimental data which has been got with water and large diameter liquid pools (D_E=72 mm) at three different immersion depths. Table 1 shows the comparison between the average value of the experimental heat transfer coefficient and those theoretically calculated together to their relative prediction errors.

Figure 3 and Table 1 shows that the Rosenhow correlation has the best accordance with the presented experimental data for heat fluxes lower than 250 kW/m^2. For high heat fluxes the best accordance is given by the El Genk and Sauber correlation. The maximum prediction error is 13.16% and 12.25% for Rosenhow and El Genk and Sauber correlations, respectively.

RESULTS

Sidewall confinement effect

The experimental activity has been carried out with FC72 (C6F14) in saturation condition at atmospheric pressure. As described above, for each experimental condition (diameter and immersion depth) the test have been repeated three times, both without change the fluid and by changing the fluid every time. Every time which the fluid was changed, the boiling copper surface was cleaned with acetone. All the results have shown a good repeatability, except for the case of 42 mm where a sensible difference between the test with a clean or a dirty surface has been observed.

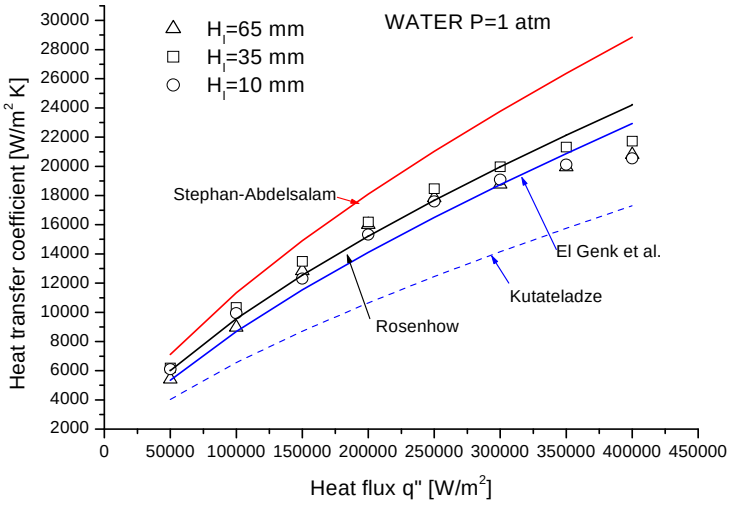

Figure 3. Different pool boiling correlations and the experimental data (D_E=72 mm, water)

Table 1
Comparison between the theory and the experiments

q" (kW/m^2)	h_{Ex} (W/m^{2}K)	h_R (W/m^{2}K)	e_R (%)	h_{SA} (W/m^{2}K)	e_{SA} (%)	h_{Ku} (W/m^{2}K)	e_{Ku} (%)	h_{EL} (W/m^{2}K)	e_{EL} (%)
50	5904	6011	1.78	7119	17.07	4036	46.28	5348	10.39
150	12879	12550	2.62	14912	13.63	8709	47.88	11540	11.60
250	17967	17672	1.67	21030	14.56	12452	44.29	16500	8.88
350	20462	22140	7.58	26374	22.42	15759	29.84	20882	2.01
400	21024	24212	13.16	28854	27.14	17303	21.50	22929	8.30

Figure 4 shows the boiling curves in the cases of different confinement diameters and different immersion depths. The bold black line represents the Rosenhow correlation by using the coefficients suggested by Pioro et al. in [15] for the refrigerant fluids and copper surfaces.

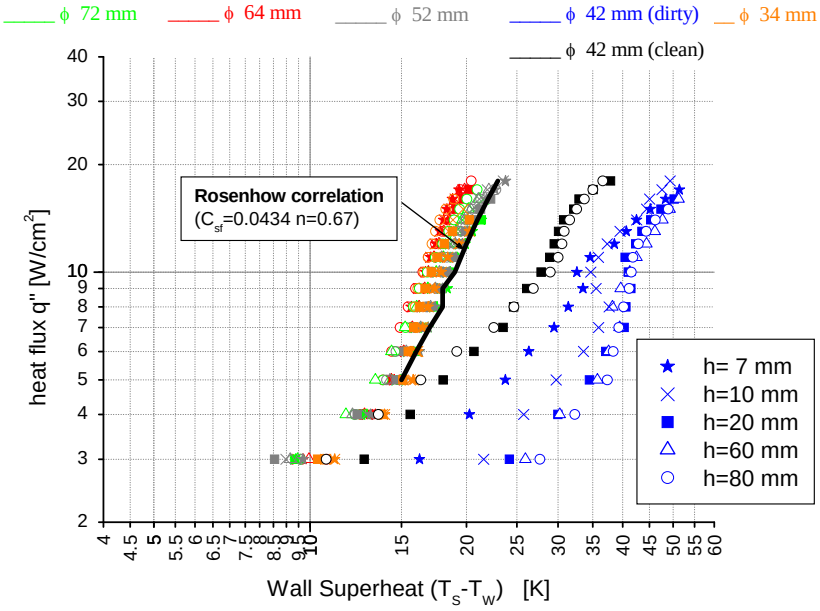

Figure 4: Boiling data of FC72 for different parameters D_E and H_l

An enhancement of the heat transfer coefficient is observed with respect to that theoretically expected for all the diameters except for the case of 42 mm. In this case a wide spread of experimental data has been observed, but a drastic deterioration of the heat transfer coefficient has been however measured for each test. The results of this diameter are very influenced by the fluid and the surface cleanness, especially for low heat fluxes.This kind of behaviour is very strange and hardly predictable. In 1986 Westwater et al. [5] found that boiling data depended strongly on the plate and vessel diameter when the diameter is small and a critical value of this parameter was determined. For diameter lower than the critical one the heat transfer coefficient abruptly falls.

For nucleate boiling the critical plate diameter was judged to be about $2.5\lambda_D$. In the case of FC72 the Taylor instability length λ_D, given by equation (1), is approximately 8.62 mm, so that the critical diameter should be 21.55 mm about. These data shows that the critical diameter has been found in the value of 42 mm ($4.8\lambda_D$ about), but in the case of diameters (34 mm) lower than the critical value, the heat transfer coefficient increases and not decreases. In the case of very small pools of liquid or very little gap space sizes, an enhancement of the heat transfer coefficient has been reported in the literature[8]-[11]. The behaviour observed during the test could not be in contrast with the literature. Besides Westwater et al. did not present experimental data for diameter lower than the critical one and therefore, a further increase in the heat transfer coefficient, could be measured in that experiment also. Another possible explanation could be provide by the roughness effect.

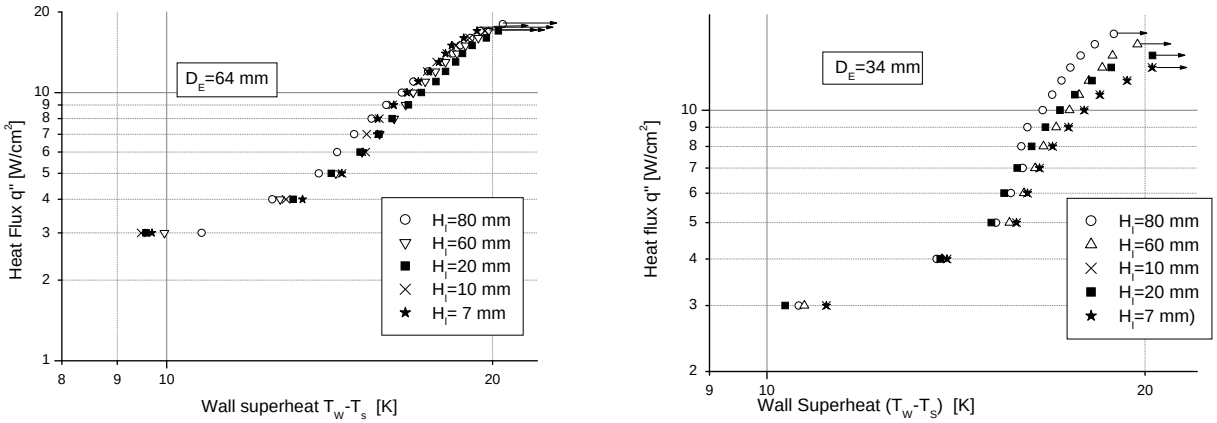

(a) (b)

Figure 5. Experimental data at different H_l in the case of (a) 64 mm and (b) 34 mm

An excessive cleaning of the surface could have made a real coating of oxidation dust over the boiling surface, by decreasing the nucleation sites number. A further experimental activity focus on the fouling effect of the long time tests could explain this behaviour.

Immersion depth effect

The experiments have been carried out by changing the immersion depth of the small pool of liquid for each diameter. Figure 4 shows that the influence of the immersion depth on the boiling regime is very little. For diameters higher than 34 mm, the influence of the immersion depth on the heat transfer coefficient is low (±5%) as show the case of 64 mm reported in Figure 5.a.

As shown in Figure 5.b, in the case of D_E=34 mm, the immersion depth does not influence the heat transfer during a natural convective regime but in a fully developed regime. The heat transfer coefficient decreases as the immersion depth decreases for heat fluxes close to the CHF above all.

Besides Figure 5.b shows that a linear decrease in CHF value is observed as the immersion depth decrease. These preliminary results seems to confirm the results presented in [6], but a more accurate analysis must be made. A major effect of the immersion depth has been observed in the case of dirty surface. A further experimental activity can better explain this preliminary observation.

CONCLUSIONS

This paper deals with the experimental analysis of the boiling heat transfer regime in case of small pools of liquid. A new experimentally facility has been presented and tested by using water as working fluid. The experimental boiling data are in accordance with the data and the pool boiling correlations reported in the literature. In particular the El Genk and Sauber correlation has shown the best agreement with the experimental data with a maximum prediction error measured of 12%.

By using the new apparatus the effect of the lateral confinement and the effect of the immersion depth on the boiling regimes have been investigated, by observing the phenomena in small pools of FC72 in saturation condition. These preliminary results have shown that an enhancement of the heat transfer coefficient with respect of that predicted by Rosenhow correlation has been observed for all the tube diameters tested (72, 64, 52 and 34 mm) and for each immersion depth (80, 60, 20 ,10 and 7 mm). Just only in the case of the 42 mm diameter the heat transfer coefficient abruptly falls. Some preliminary results on the effect of the immersion depth on CHF have been presented.

REFERENCES

1. Rosenhow W.M., Hartnett J.P., *Handbook of Heat Transfer*, Mc Graw Hill Inc., ISBN 0070535760, 1973, chapter 13.
2. Lienhard J.H IV,. Lienhard J.H V, *A Heat Transfer Textbook*, Phlogiston Press, 3rd edition, 2003, chapter 9.
3. Latrofa E., Filippeschi S., Salvadori G., On the Possibility of Evaporator Drastic Scale Reduction in a Periodically Operating Two-Phase Thermosyphon, *Proceedings of 3rd Intern. Symp. on Two-Phase Flow Mod. and Exp.* Pisa, 2004.
4. Filippeschi S., Salvadori G., Transient analysis of boiling heat transfer in periodic drying out miniature pools, *Int. Journal of Multiphase Flow*, vol. 34, iss. 11, pp. 1088-1095, 2008.
5. Westwater J.W., Hwalek J.J., Irving M.E., Suggested standard Method for Obtaining Boiling Curves by Quenching, *American Chem. Society, Ind. Eng. Chem. Fundam.*, pp.685-692, 1986.
6. Elkassabgi Y., Lienhard J.H., Sidewall and immersion depth effects on pool boiling burnout for horizontal cylindrical heaters, *Trans. ASME, J. of Heat Transfer*, vol. 109, pp.1055-1057, 1987.
7. Bonjour L, Lallemand M., Flow patterns during boiling in a narrow space between two vertical surfaces, *Int. Journal of Multiphase Flow,* vol. 24, pp. 947-960, 1998.
8. El-Genk M. S.and Saber H. H., Heat transfer correlations for small, heated liquid pools, *Int. J. Heat Mass Transfer,* vol. 41, is. 2, pp. 261-274, 1998.
9. Zhao Y., Tsuruta T., Ji C., Experimental study of nucleate boiling heat transfer enhancement in confined space, *Experimental Thermal and Fluid Science*, vol. 28, pp. 9–16, 2003.
10. Passos J.C., Hirata F.R., Possamai L.F.B., Balsamo M., Misale M., Confined boiling of FC72 and FC87 on a downward facing heating copper disk, *International Journal of Heat and Fluid Flow*, vol. 25, pp.313–319, 2004.
11. Kang M. G., Pool boiling heat transfer in a vertical annulus as the bottom inflow area changes, *International Journal of Heat and Mass Transfer,* vol. 51, pp. 3369–3377, 2008.
12. Chen Li, Evaporation from microstructured surfaces, *Rensselaer Polytechnic Institute* http://www.rpi.edu/~petersb/research/scms/scms1.html, 2005
13. Auracher, H., Marquardt, W., Buchholz, M., Hohl, R., Luttich, Blum, T.J., New Experimental Results on Steady-state and Transient Pool Boiling Heat Transfer, *Thermal Science and Engineering*, vol. 9, iss. 5, pp. 29-39., 2001.
14. Stephan K., Abdelsalam M., Heat transfer correlation for natural convection boiling, *International Journal of Heat and Mass Transfer*, vol. 23, pp. 73-87,1980.
15. Pioro I.L., Rohsenow W., Doerffer S.S., Nucleate pool-boiling heat transfer. II: assessment of prediction methods, *Int. Journal of Heat and Mass Transfe*r, vol. 47, pp.5045–5057, 2004.

CONSTRUCTAL HEAT TRANSFER IN THE ENTRANCE REGION OF PARALLEL PLATE CHANNELS AND DUCTS

T. Bello-Ochende[1*], J. P. Meyer[1] and A. Bejan[2]

[1]Department of Mechanical and Aeronautical Engineering, University of Pretoria, Pretoria, 0002, South Africa
[2]Department of Mechanical Engineering and Materials Sciences, Duke University Box 90300, Durham, NC, 27708-300, USA

ABSTRACT. This paper reports an increase in the heat transfer rate density by using the entrance regions in parallel plate channel and ducts with laminar flow. The heat transfer rate density is increased by taking advantage of the presence of relatively isothermal fluid at the entrance regions, in order to stimulate a more complete thermal interaction between walls and fluid. Two new methods are studied; the first part of this work consists of numerical simulation in a large number of flow configurations, one differing slightly from the next to determine the optimum plate spacing, and the maximum heat transfer rate density. In the subsequent stages, smaller plates are inserted in the centre plane between two adjacent (optimized space) longer plates in the entranced region where the boundary layer is thin and a core of unused fluid exists. The heat transfer rate density is further increased by progressively inserting shorter plates between the longer plates and then optimizing the whole structure. The resulting structures are optimized multi-scale structures with horizontal equidistant heated plates of decreasing length scales. In the second parts of this report, the ducts square entrances are wrinkled on the perimeter, at the one-third and the two-third positions. The new structure has two degrees of freedom. The fluid flow through the ducts is by the imposed pressure difference across the ducts. Numerical simulations were conducted studying the effects of the dimensionless pressure drop on the optimized configurations which show an increase of between eight to seventeen percent enhancement in heat transfer rate density.

Keywords: *Constructal, Maximum heat transfer density, Multi-scale, Entrance region, Optimal*

INTRODUCTION

Compactness and miniaturisation are driven by the need to remove more and more heat transfer from a given volume. The figure of merit is the heat transfer density. A recent trend in heat transfer research has been the focus on the generation of optimal flow architecture, as a mechanism by which the system achieves its maximal heat transfer density objective under certain constraints [1-3].The strategy is to endow the flow configuration with the freedom to morph, and to examine systematically many of the eligible design configurations. Strategy and systematic search mean that architectural features that have been found to be beneficial in the past can be refined and incorporated into more complex systems of the present. A similar idea has also been pursued and implemented by Dirker and co-workers [4-6] in the cooling of power electronics by embedded solids.

One class of flow features that aid the achievement of high-heat transfer density is the optimal spacings that have been reported for forced convection [7-9]. The progress in this area has been reviewed in [10-14]. Optimal spacings have been determined for parallel plate channels, cylinders in cross-flow, staggered parallel plates, and pin fin arrays with impinging flow. In each configuration, the optimal spacing is a single-length scale that is distributed throughout the available volume.

The optimal spacing idea was taken theoretically and numerically one step further in [1, 7, 15], where the flow structure had not one but several optimal-length scales. These were distributed non-uniformly through the flow space with more and smaller plates in the entrance region of the available volume. The

* Corresponding author: Dr Tunde Bello-Ochende
Phone: + (27)-12-420-3105, Fax: + (27)-12-362-5124
E-mail address: tbochende@up.ac.za

reason is that the boundary layers were thinner at the entrance and more plates could be fitted together optimally.

In this paper, we evaluated this design approach numerically, by considering forced convection cooling of a volume filled by stacks of parallel plates that generate heat. The plates are modelled three dimensionally which represents the actual geometry in space and the limitations of the result obtained using two-dimensional parallel plates [1] are eliminated. The flow and heat transfer are simulated numerically for a wide range of flow configurations. Each numerical simulation shows that the entrance region of every parallel plate channel has a core of unused (isothermal) fluid. In this wedge-shaped region, we progressively inserted smaller heat-generating plates, and then we optimised the multi-scale assembly. The maximisation of heat transfer density is pursued geometrically, by varying more and more degrees of freedom. The result is a class of progressively better flow structures with multiple-length scales that are distributed non-uniformly through the flow**.**

In the second part of this paper we propose a new concept to improve the constructal design for the cooling of a duct. We start with a square packing of channels, Fig 1. The size of the square ducts is to be selected numerically subject by fixing the pressure drop across the packing. The entranced regions of the duct do not participate fully in the heat transfer enterprise, because of the presence of relatively isothermal (cold) fluid that has not interacted thermally with the walls. Next, the duct entrance is wrinkled to stimulate a more complete thermal interaction between walls and fluid. The new structure has two degrees of freedom: the length of the wrinkled entrance, and the length or the spacing of the square ducts. These geometric features are optimized for maximum volumetric heat transfer density.

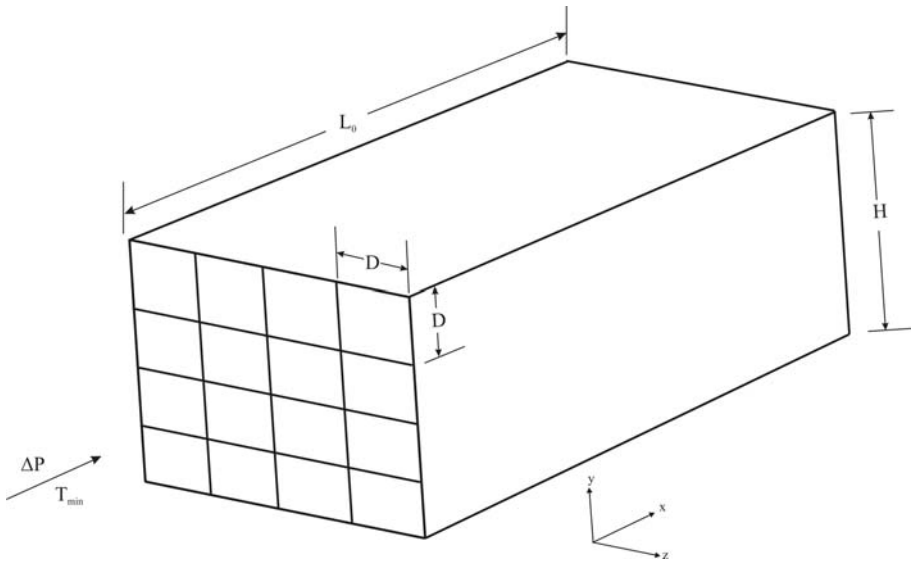

Figure 1. Packing of channels with square cross-sections

ENTRANCE REGIONS WITH WRINKLED ENTRANCES

Consider the three dimensional configuration of a channel with a wrinkled perimeter around a square cross-section. Figure 2 shows the entrance of one square channel after each side was wrinkled at the one-third and two-thirds positions. The walls of the channels (including the wrinkled portions) are maintained at the temperature T_{max}. The channel is cooled by a single-phase fluid at T_{min}, which is forced into the channel by a specified pressure difference (ΔP). The coolant is modelled as a Newtonian fluid with constant properties. The dimensionless equations for the steady-state flow of mass, momentum and energy are

$$\frac{\partial \tilde{u}}{\partial \tilde{x}} + \frac{\partial \tilde{v}}{\partial \tilde{y}} + \frac{\partial \tilde{w}}{\partial \tilde{z}} = 0 \tag{1}$$

$$\frac{Be}{Pr}\left(\tilde{u}\frac{\partial \tilde{u}}{\partial \tilde{x}} + \tilde{v}\frac{\partial \tilde{u}}{\partial \tilde{y}} + \tilde{w}\frac{\partial \tilde{u}}{\partial \tilde{z}} \right) = -\frac{\partial \tilde{P}}{\partial \tilde{x}} + \nabla^2 \tilde{u} \tag{2}$$

$$\frac{Be}{Pr}\left(\tilde{u}\frac{\partial\tilde{v}}{\partial\tilde{x}}+\tilde{v}\frac{\partial\tilde{v}}{\partial\tilde{y}}+\tilde{w}\frac{\partial\tilde{v}}{\partial\tilde{z}}\right)=-\frac{\partial\tilde{P}}{\partial\tilde{y}}+\nabla^2\tilde{v} \tag{3}$$

$$\frac{Be}{Pr}\left(\tilde{u}\frac{\partial\tilde{w}}{\partial\tilde{x}}+\tilde{v}\frac{\partial\tilde{w}}{\partial\tilde{y}}+\tilde{w}\frac{\partial\tilde{w}}{\partial\tilde{z}}\right)=-\frac{d\tilde{P}}{d\tilde{z}}+\nabla^2\tilde{w} \tag{4}$$

$$Be\left(\tilde{u}\frac{\partial\tilde{T}}{\partial\tilde{x}}+\tilde{v}\frac{\partial\tilde{T}}{\partial\tilde{y}}+\tilde{w}\frac{\partial\tilde{T}}{\partial\tilde{z}}\right)=\nabla^2\tilde{T} \tag{5}$$

where $\nabla^2=\partial^2/\partial\tilde{x}^2+\partial^2/\partial\tilde{y}^2+\partial^2/\partial\tilde{z}^2$, and the dimensionless pressure difference is defined as [16, 17]:

$$Be=\frac{\Delta P L_0^2}{\mu\alpha} \tag{6}$$

The non-dimensionalization of the governing equations is based on defining the variables

$$\tilde{x},\tilde{y},\tilde{z}=\frac{(x,y,z)}{L_0},\quad \tilde{P}=\frac{P}{\Delta P} \tag{7}$$

$$(\tilde{u},\tilde{v},\tilde{w},\tilde{U})=\frac{(u,v,w,U)}{\Delta P L_0/\mu},\quad \tilde{T}=\frac{T-T_{min}}{T_{wall}-T_{min}} \tag{8}$$

The boundary conditions are

$$\tilde{P}=1,\quad \tilde{v}=\tilde{w}=0,\quad \tilde{T}=0 \text{ at } \tilde{x}=0 \tag{9}$$

$$\tilde{u}=\tilde{v}=\tilde{w}=0,\quad \tilde{T}=1 \text{ on the walls} \tag{10}$$

$$\tilde{P}=\frac{\partial\tilde{u}}{\partial\tilde{x}}=\frac{\partial\tilde{v}}{\partial\tilde{x}}=\frac{\partial\tilde{w}}{\partial\tilde{x}}=\frac{\partial\tilde{T}}{\partial\tilde{x}}=0 \text{ at } \tilde{x}=\tilde{L}_0 \tag{11}$$

$$\tilde{D}=\frac{D}{L_0},\quad \tilde{L}_1=\frac{L_1}{L_0} \tag{12}$$

We are interested in the geometric arrangement of the wrinkled packing for which the overall heat transfer rate per unit of flow volume is a maximum:

$$q'''=\frac{\text{total heat transfer rate from walls to stream}}{\text{volume of one duct}}=\frac{q}{L_0D^2} \tag{13}$$

In dimensionless form, the above definition can be rewritten as

$$\tilde{q}=\frac{qL_0}{k(T_w-T_\infty)D^2} \tag{14}$$

Numerical method

We solved Eqs. (2) - (5) by using a commercial finite volume code [18, 19]. The domain was discretized using tetrahedral elements, and the governing equations were integrated on every control volume. Second order schemes were used for the diffusive terms. The pressure-velocity coupling was performed with the SIMPLE procedure. Convergence was obtained when the normalized residuals for the mass and momentum equations were smaller than 10^{-4}, and the residual of the energy equation became smaller than 10^{-8}. To obtain accurate numerical results, several mesh refinement tests were conducted. The monitored quantity was the overall heat transfer rate density, which was computed with Eq. (14). Convergence was established based on the criterion

$$\gamma=\left|\tilde{q}_j-\tilde{q}_{j-1}\right|\Big/\left|\tilde{q}_j\right|\le 0.02 \tag{15}$$

where j is the mesh iteration index, such that j increases when the mesh is more refined. When the criterion is satisfied, the j −1 mesh is selected as the converged mesh. A mesh size of 0.005 per unit length in the y and z directions, and a mesh size of 0.01 per unit length in the axial direction were found to satisfy the criterion chosen in Eq. (15).

Packing of wrinkled ducts

We started the optimization procedure by considering the case in which the mouth of the square channel is smooth, without wrinkles. In this case the only degree of freedom is the duct size, $\tilde{D}$. Figure 2 shows the selection of the channel size and the heat transfer rate density, and indicates that an optimal size exists for a channel with a square packing. In the second phase of this study we considered a modified type of wrinkling which allows us to pack the wrinkled entrances into a larger assembly, as shown in figures 2 and 3. The number of degrees of freedom of the geometry is two.

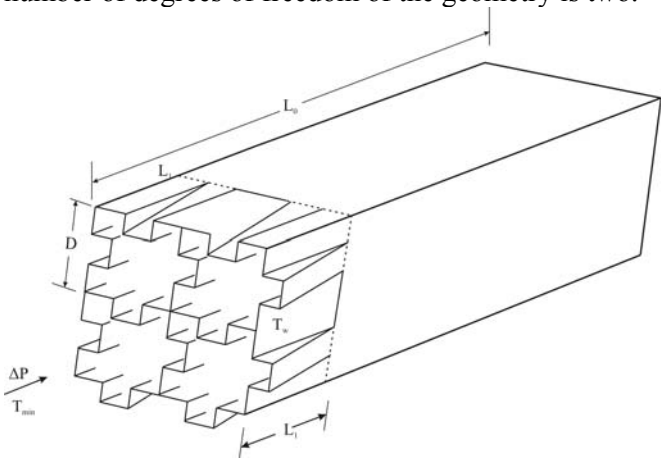

Figure 2. Packing of channels with wrinkled square cross-sections

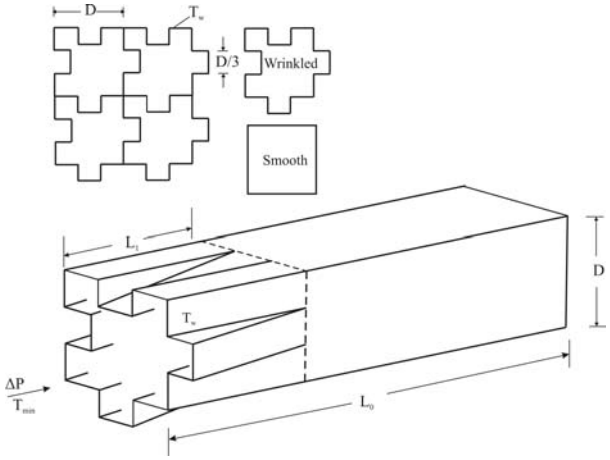

Figure 3. Packing of wrinkled square entrances showing an elemental computational unit of a square channel with wrinkled entrances

The depth of the wrinkled section is kept fixed at $\tilde{D}/6$, in order for the total volume of the new design to be same as that of smooth ducts, and to prevent the wrinkled walls from touching. These modifications prevent numerical instabilities and allow the flow to fill the entrance. Any changes in the position ($\tilde{D}/6$) results in increases or decreases in the total volume when compared with the total volume of a smooth tube of comparable size. The numerical procedure for flow simulation and geometry optimization was the same as the procedure describe in numerical method. As shown in the example of Figure 4, the Be number was fixed, and many configurations of ($\tilde{D}$, $\tilde{L}_1$) were simulated in search of the configuration with the highest heat transfer density $\tilde{q}$. This procedure was then repeated over the range $10^5 \leq$ Be $\leq 10^8$. The results for the new wrinkled duct are reported in Figore 5. Its shows how the new optimized square cross-section, the optimized length of the fold and the maximized performances vary with the dimensionless pressure difference. The optimal length of the fold ($\tilde{L}_{1,opt}$) shows little variation with Be. The optimal duct size decreases as Be increases which is consistence with other constructal studies.

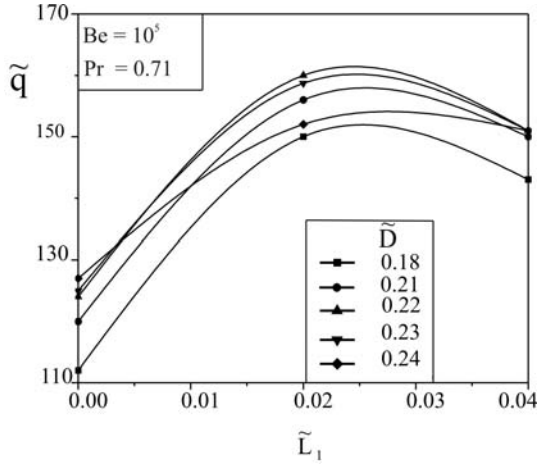

Figure 4. The effect of $\tilde{L}_1$ and $\tilde{D}$ (wrinkled) on the heat transfer density in the assembly of Fig. 3

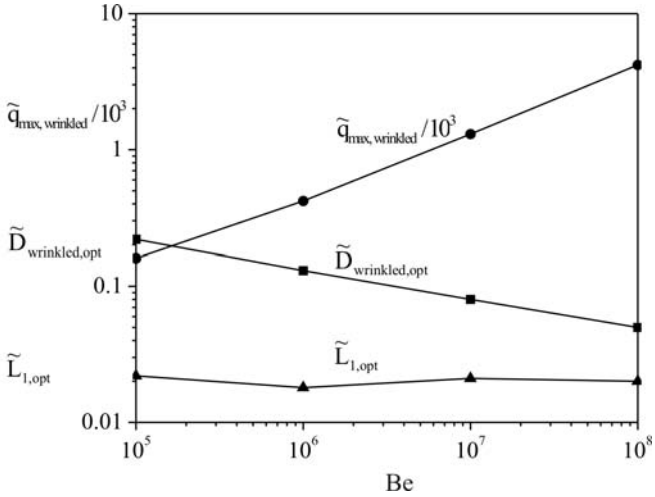

Figure 5. The effect of dimensionless pressure difference on the optimized length scales and on the heat transfer rate density on the assembly of Fig. 3.

ENTRANCE REGIONS WITH PLATE INSERT

Consider a stack of three-dimensional heat-generating parallel plates that form a channel in space as shown in Figures 6, 8 and 9. The plates are modelled as isothermal with temperature $T = T_w$. A stream of coolant with temperature $T = T_{min}$ is forced through the channels that is formed by the plates. The problem consists of maximising the heat transfer rate between the coolant and the heat-generating plates. The governing equations are the continuity, momentum and energy equations (1-5). The assumptions are the same as those of the wrinkled ducts, the boundary conditions are:

$$\tilde{P} = 1, \quad \tilde{v} = \tilde{w} = 0, \text{ and } \tilde{T} = 0 \text{ at } \tilde{x} = 0 \tag{16}$$

$$\tilde{u} = \tilde{v} = \tilde{w} = \frac{\partial \tilde{T}}{\partial \tilde{z}} = 0, \text{ at } \tilde{z} = 0 \text{ and } \tilde{z} = \tilde{W} \tag{17}$$

$$\frac{\partial \tilde{u}}{\partial \tilde{y}} = \frac{\partial \tilde{w}}{\partial \tilde{y}} = v = 0 \quad \text{at } \tilde{y} = 0 \text{ and } \tilde{y} = \tilde{D}_0 + \tilde{t} \tag{18}$$

$$\tilde{u} = \tilde{v} = \tilde{w} = 0, \quad \tilde{T} = 1 \text{ on the surface of the plates} \tag{19}$$

$$\tilde{P} = \frac{\partial \tilde{u}}{\partial \tilde{x}} = \frac{\partial \tilde{v}}{\partial \tilde{x}} = \frac{\partial \tilde{w}}{\partial \tilde{x}} = \frac{\partial \tilde{T}}{\partial \tilde{x}} = 0 \quad \text{at } \tilde{x} = (\tilde{L}_0 + \tilde{L}_u + \tilde{L}_d) \tag{20}$$

The dimensionless overall heat transfer density based on the total fluid volume is

$$\tilde{q} = \frac{qL_0}{k(T_w - T_\infty)WD_0} \tag{21}$$

Channels with plates insert

In the first phase of this study, we simulated numerically the heat and fluid flow fields for Figure 6 in the laminar range represented by $10^5 \leq Be \leq 10^7$, plate thickness $0.01 \leq \tilde{t} \leq 0.05$ and width $\tilde{W} = 1$, for several geometries in search of the optimal spacing. The optimisation of the stack of parallel plate channels has one degree of freedom, the spacing between the plates. This was optimised for a given Be and Pr and a fixed plate thickness. The results are shown in Figure 7. Comparison between the theoretical results, $\tilde{D}_0 = 2.7 Be_{L_0}^{-1/4}$ and numerical results shows the same trend.

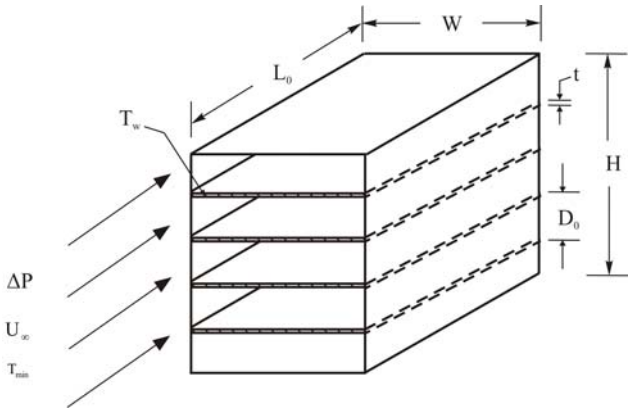

Figure 6. Stack of parallel plate channels

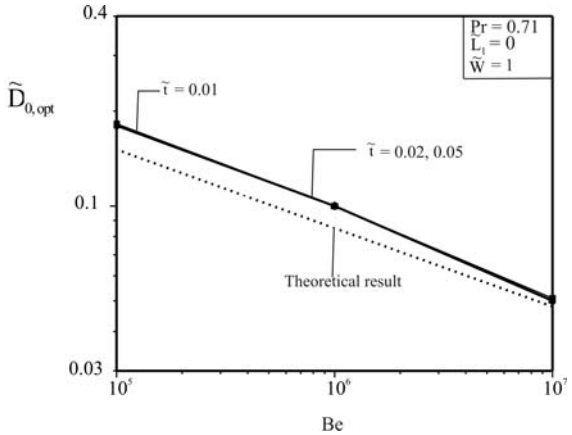

Figure 7. The maximised total heat transfer rate from a plate with finite thickness as a function of dimensionless pressure drop number.

In the sequence of increasing more complex structures and utilising the fluid wedge between two parallel plates, a small $\tilde{L}_1$-long plate with plate thickness $0.5\tilde{t}$ was inserted between the plates with thickness $\tilde{t}$ as shown in Figure 8.

To determine the contribution of the $\tilde{L}_1$-long plate, we fixed $\tilde{D}_{0,\,opt}$ at the values determined previously (Figure 7) so that the already optimised structure stays the same. The spacing between the plates becomes $\tilde{D}_{opt} = 2\,\tilde{D}_{1,opt}$. The thickness of the plates was set at $\tilde{t} = 0.01$, as the maximised $\tilde{q}$ is insensitive to changes in $\tilde{t}$ as previously determined. We now optimized $\tilde{L}_1$ by varying its length until we obtained an optimal length that corresponded to the new maximised $\tilde{q}$. The procedure stated above was repeated for several Bejan number in the range $10^5 \le Be \le 10^7$ and Pr = 0.71, for the ratio of $\tilde{D}_{0,opt}/\tilde{D}_{1,opt} = 2$. The results are shown in Figure 10.

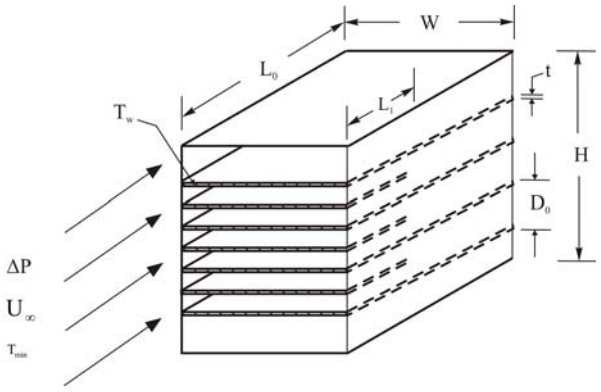

Figure 8. Stacks of parallel plates, with small plate insert

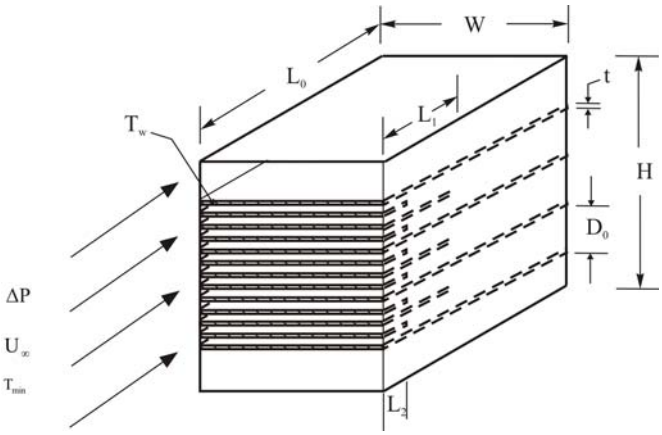

Figure 9. Three-dimensional stacks of parallel plate channels with smaller plate inserts

In the sequence of constructing a multi-scale assembly, and determining the contribution brought about by enduring the flow structure with more degrees of freedom, we inserted a second plate, $\tilde{L}_2$ (see Figure 9) in the channels formed between the L_0 and $\tilde{L}_{1,opt}$ channel, while still retaining the optimal spacing $D_{0,opt}$ obtained without plate insert. We now varied the length of the second plate until an optimal length, $\tilde{L}_{2,opt}$ of the plate that maximises the heat transfer rate density is obtained.

Figure 10 show the contribution of the second plate inserts to the heat transfer rate density is not significant. So inserting more plate to the structure is not beneficial to the heat transfer rate density. It was therefore decided to keep the number of plate inserts to two. Figure 11 shows that as the pressure number increases, the plate length increases. This is due to the fact that the slenderness of the plates also increases with the pressure drop number. Note that $\tilde{D}_{opt} = 2\,\tilde{D}_{1,opt} = 4\,\tilde{D}_{2,opt}$.

Figure 12 shows the comparisons of the theoretical heat transfer prediction, Eq. (22) and the results obtained from numerical analysis. It was observed that the general trend is the same and the agreement is acceptable. Figure 12 shows that the maximised heat transfer rate density increases in proportion to $Be^{1/2}$. This confirms the analytical result Bejan and Fautrelle [20] which can be rewritten in the notation employed in this paper for asymmetric plate inserts:

$$\tilde{q} = 0.36 Be^{1/2}\left(1+\frac{m}{2}\right)^{1/2} \qquad (22)$$

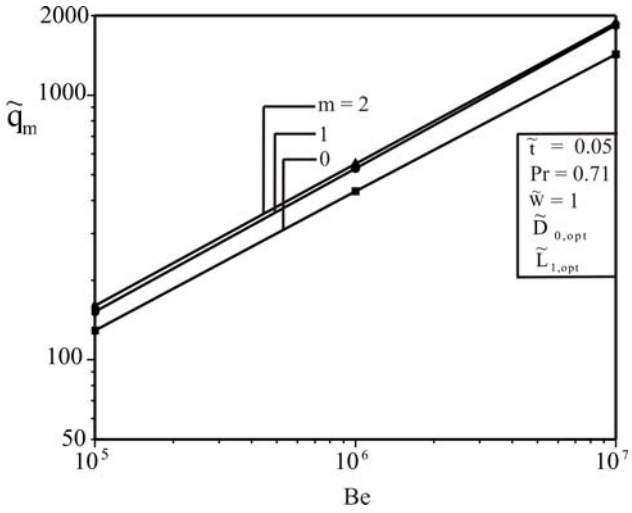

Figure 10. The maximized heat transfer density of the flow structure with three plates

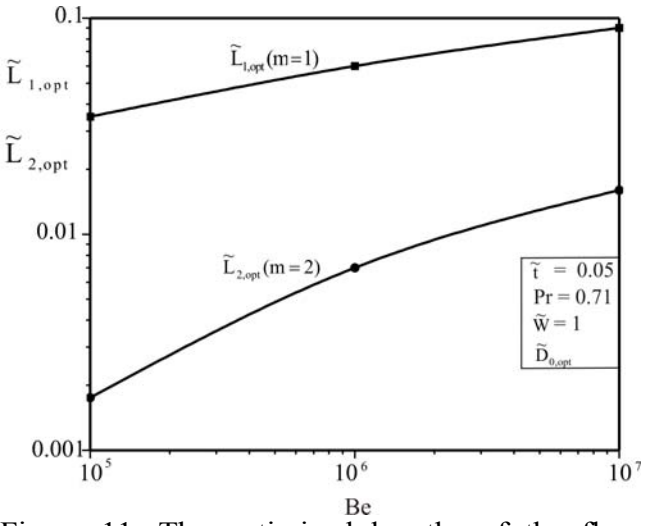

Figure 11. The optimized lengths of the flow structure with two length scales for the ratio $\tilde{D}_{o,opt}=2\tilde{D}_{1,opt}=4\tilde{D}_{2,opt}$.

Parameter m is the number of new (inserted) plate lengths, for example when m = 1, 2 as in Figure 12. The prediction is that the heat transfer rate density increases in progressively smaller steps as the number of length scales increases. This is confirmed by the numerical result shown in Fig. 12. Using the relationship obtained from Bejan and Fautrelle [20].

$$2^{4m}\left(1+\frac{m}{2}\right) = \frac{Be}{10^3} \tag{23}$$

and solving for m for Be in the range 10^5 to 10^8, one find that the realistic cut off (smallest) length scales below which the boundary layer are no longer distinct and where the sequence of generating optimal length scale ends is approximately m = 2, which also correspond to our numerical results.

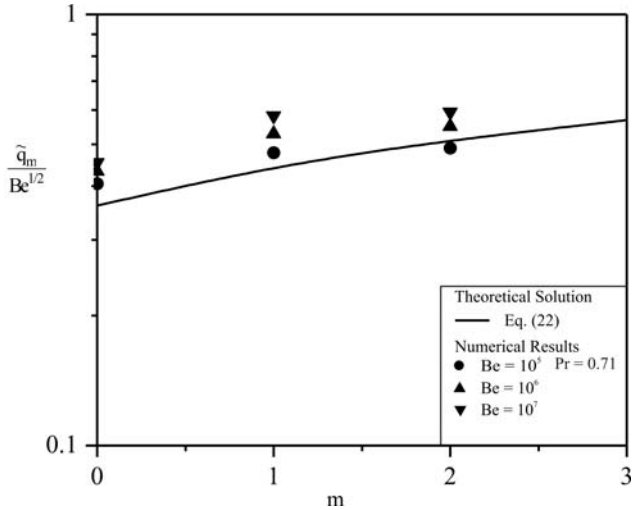

Figure 12. Comparison between the theoretical maximum heat transfer and the numerical results obtained from this study versus number of plates inserted.

CONCLUSION

In the first part of this paper, we described a new design for increasing the heat transfer rate density by using wrinkled entrance regions in ducts with laminar forced convection. The method consists of wrinkling the perimeter of square entrances, and by extending these deformations gradually downstream to a length ($\tilde{L}_1$) that is optimized. This new geometry allows a more complete heat transfer interaction between the walls and the fluid. The results show that the heat transfer rate density increases with the imposed pressure difference. In the second part of the paper, we illustrated the emergence of a multi-scale forced convection flow

structure for maximal heat transfer rate density for three-dimensional parallel plates installed in a fixed volume, and ducts wrinkled at the entrances. The objective was achieved by inserting smaller plates in the entrance region formed between successive plates. This technique utilises to the fullest the fluid surrounding the two tips of two neighbourhood plates where the boundary layers are the thinnest. The optimised spacing was fixed with each new (smaller) plate that is inserted into the entrance region of each channel. Optimal spacings were found numerically for structures with one length scale. Performance increases as complexity increases. The number of plate-length scales is limited by the validity of the boundary layer assumption. The smallest plate is the one where the plate length is comparable with the boundary layer thickness. The fundamental value of this study is that multi-scale flow structures are applicable to every sector of heat exchanger design. This approach promises the development of new and unconventional internal flow structures for heat exchangers and cooled electronic.

NOMENCLATURE

Be	dimensionless pressure number,
d	spacing between two-dimensional parallel plates, m
D	sides of duct cross-section, m
D_0	spacing between two plates, m
D_1	spacing between the L_0 and L_1 plates when L_1 plate is inserted, m
H	stack height, m
j	mesh interation index
k	thermal conductivity, W/mK
L_u	length of control volume before the plate, m
L_0	plate length in the flow direction, m
L_1	flow length of the first plate insert and flow length of the wrinkled section, m
L_2	flow length of the second plate insert, m
L_d	length of control volume downstream after the plate, m
m	number of new inserted plates
n	number of plates
P	pressure, Pa
Pr	Prandtl number
Re	Reynold number
q	heat transfer, W
$\widetilde{q}$	dimensionless heat transfer
t	plate thickness, m
T	temperature, K
T_w	wall temperature, K
T_∞	free-stream temperature, K
u	velocity component in the x-direction, m/s
v	velocity component, in the y-direction, m/s
w	velocity component, in the z-direction, m/s
U_∞	free-stream velocity, m/s
U	mean velocity, m/s
W	plate width, m
x	Cartesian axis direction, m
y	Cartesian axis direction, m
z	Cartesian axis direction, m
Greek	
α	thermal diffusivity, m^2/s
μ	viscosity, kg/s m
ν	kinematic viscosity, m^2/s
γ	convergence criterion
δ	boundary layer thickness, m
φ	porosity
Subscripts	
0, 1, 2	no plate insert, first plate inserts, second plate insert
max	maximum

opt optimum
u upstream
W wall

REFERENCES

1. Bello-Ochende T and Bejan, W., Maximal heat transfer density: Plates with multiple lengths in forced convection, *Int. J. of Thermal Sciences,* Vol. 43, pp 1181 – 1186, 2004.
2. Bello-Ochende, T., Liebenberg, L., and Meyer, J. P., Constructal cooling channels for micro-channel heat sinks, *Int. J. Heat Mass Transfer*, Vol 50, pp 4141-4150, 2007.
3. Bello-Ochende, T., Liebenberg, L., Malan, A. G., Bejan, A., and Meyer, J. P., Constructal conjugate heat transfer in three-dimensional cooling channels*, J. Enhanced Heat Transfer* Vol. 14 (4) pp 279-293, 2007 .
4. Dirker, J., Liu, W., Van Wyk, J. D., Meyer, J. P., and Malan, A. G., Embedded solid state heat extraction in integrated power electronic modules*, IEEE Transactions on Power Electronics,* Vol 20 No. 3, 694 – 703, 2005.
5. Dirker, J., Malan, A. G., and Meyer, J. P., Thermal characterization of rectangular cooling shapes in heat generating mediums-a three dimensional investigation, *Stonjniski Vesnik – Journal of Mechanical Engineering*, Vol 51 No 7-8, pp 391-398, 2005.
6. Dirker, J., Van Wyk, J. D., and Meyer, J. P., Cooling of power electronics by embedded solids, *ASME Journals of Electronic Packaging*, Vol 128, pp, 388-387, 2006.
7. Bejan, A., *Shape and Structure, from Engineering to Nature*, Cambridge University Press, Cambridge, UK, 2000.
8. Bejan, A., and Fautrelle, Y., Constructal multi-scale structure for maximal heat transfer density, *Acta Mechanica* Vol. 163, pp 39-49, 2003.
9. Bejan, A., and Sciubba, E., The optimal spacing for parallel plates cooled by forced convection*, International Journal of Heat and Mass Transfer*, Vol. 35, pp 3259-3264, 1992.
10. Aihara, T., Ohara, T., Sasaco, A., Akaku, M., and Gori, F., Augmentation of free-convection of heat transfer between vertical parallel plates by inserting an auxiliaryplate*, 2nd European Thermal-Sciences and 14th UIT National Heat Transfer Conference*, Rome, Italy, 2006.
11. Kim, S. J., and Lee, S. W., eds., Air cooling technology for electronic equipment, CRC Press, Boca Raton, FL, 1996, Chapter 1.
12. Koo, J.-M., Im, S., Jiang, L., and Goodson, K. E., Integrated micro channel cooling for three-dimensional electronic architectures, *J. Heat Transfer,* Vol. 127, pp 49- 58, 2005.
13. Matos, R. S., Laursen, T. A., Vargas, J. V. C., and Bejan, A, Three-dimensional optimization of staggard finned circular and elliptic tubes in forced convection, *Int. J. Thermal Sciences* 43 (2004) 447 – 487.
14. Morega, A. M., Bejan, A., and Lee, S. W., Free stream cooling of a stack of parallel plates, *Int. J. Heat and Mass Transfer*, Vol. 38, pp 519 – 531, 1995.
15. da Silva, A. K., and Bejan, A., Constructal multi-scale structure for maximal heat transfer density in natural convenction, *Int. J. Heat Fluid Flow,* Vol. 26, pp 34-44, 2005.
16. Bhattacharjee, S., and Grosshandler, W. L., The formation of a wall jet near a high temperature wall under microgravity environment, *ASME HTD*, Vol. 96, pp 711-716, 1988.
17. Petrescu, S., Comments on the optimal spacing of parallel plates cooled by forced convection, *Int. J. Heat Mass Transfer*, Vol. 37. pp 1283, 1994.
18. www.fluent.com
19. Patankar, S. V.*, Numerical Heat Transfer and Fluid flow*, Hemisphere, Washington DC, 1980.
20. Bejan A., and Fautrelle, Y., Constructal multi-scale structure for maximal heat transfer density, Acta Mechanica, Vol. 163, pp 39-49, 2003.

HT-20

ExHFT-7
28 June – 03 July 2009, Krakow, Poland

LOCAL HEAT TRANSFER FROM MICRO IMPINGING JET ARRAYS

T. Lupton[1], A. Robinson[1], D. Murray[1]
[1]CTVR (Centre for Telecommunications Value-Chain Research)
Department of Mechanical and Manufacturing Engineering, Trinity College Dublin, Ireland

ABSTRACT. Much research has been carried out into the area of large scale impinging jet heat transfer but smaller scale jets are relatively unexplored in comparison. In this study 620 μm diameter confined air jets impinge normally onto an ohmically heated flat surface. The resulting surface temperature distributions, from a 3 x 3 in-line jet array, are recorded with an infrared camera with a spatial resolution of 47.5 μm. The inter jet spacing was kept constant at 4 jet diameters and the jet-to-target spacing was varied from 0.42 to 3.35 jet diameters. Tests were carried out at jet Reynolds numbers of 3000 and 6300 corresponding to Mach numbers of approximately 0.21 and 0.43. Results are presented in terms of local heat transfer coefficient distribution. The results indicate that small scale jet impingement heat transfer is fundamentally different than its larger scale counterpart. The effects of entraining warm fluid into the pre-impact jet are thought to considerably affect the heat transfer behaviour of the jets.

Keywords: *microscale, jet impinging, convective heat transfer, heated thin foil method, infrared thermography*

INTRODUCTION

Impinging jet flows are capable of achieving high heat transfer due to the very thin boundary layers resulting from them. A comprehensive literature review exists for macro scale impinging jet heat transfer, Martin [1], Webb and Ma [2] and Garimella [3]. However, the potential use of jets in thermal management of electronic devices has generated an interest in micro scale jet heat transfer. Garimella and Rice [4] noted that the effect of nozzle diameter on heat transfer is not always captured by conventional Nusselt number correlations. San et al. [5] noted similar effects for jet diameters smaller than 6 mm. Pence et al. [6] noted that direct scaling of macro scale heat transfer equations, as correlated by Martin [1], to the micro scale is improper as the fluid flow is dynamically different. Moderate Reynolds number jet flows can correspond to high Mach numbers in micro scale jets since the small characteristic lengths result in high jet velocities. The goal of this study is to investigate how parameters such as Reynolds number and nozzle-to-impingement surface spacing influence the heat transfer mechanisms for multiple micro-sized jets.

EXPERIMENTAL SET-UP

This study looks at a 3 x 3 in-line jet array with 620 μm diameter orifices, as depicted in figure 1. Several geometric and flow parameters are known to affect the local heat transfer resulting from such an array. Tests were carried out at a fixed inter jet spacing of S/D = 4, two Reynolds numbers were tested, Re = 3000 and Re = 6300 and the nozzle-to-impingement surface spacing was varied in increments from 0.42 to 3.35 jet diameters.

* Corresponding author: T. Lupton
Phone: + (353)-1-8961061, Fax: + (353)-1-6795554
E-mail address: tlupton@tcd.ie

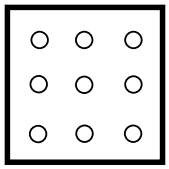

Figure 1. Test nozzle configuration for the 3 x 3 in-line array

The experimental facility used is illustrated in figure 2. The air flow to the test section was controlled with a MKS type 1179A mass flow controller (0-20 LPM ± 1% F.S). Air enters a plenum chamber where the stagnation temperature is monitored with a 1.5 mm diameter type-K thermocouple. The air inside the plenum then passes through a pipe nozzle with a development length, L_{dev}, of 20 jet diameters. This is sufficiently long to ensure a fully developed velocity profile at the exit of the nozzle, Incropera [7]. The nozzle surface is subject to heating from the foil beneath it. In order to maintain both the temperature of the air in the plenum and the temperature of the nozzle surface at ambient conditions, cooling channels were embedded into the nozzle plate. The coolant, water, is maintained at ambient temperature by passing it through a cross flow heat exchanger. Both the heated foil and nozzle plate had widths greater than 40 jet diameters as San et al. [5] demonstrated that stagnation Nusselt numbers varied with the width of the heated surface for $W/D < 40$. The heater assembly consisted of a 25 μm thick stainless steel foil (AISI 321 - Fe/Cr18/Ni9/Ti) which was heated ohmically by a Lambda DC power supply capable of supplying 200 A at 6V. The potential difference across the foil was measured from voltage taps attached to the foil. Construction of the impingement surface involved bonding the 80 mm by 28 mm foil to two copper bus bars with an electrically conductive, silver loaded epoxy. One bus bar was then fixed to a rigid stand whilst the other was mounted to a section of the stand which could traverse linearly along a pair of guidance rods. After the foil was cured, springs, located along the guidance rod, were adjusted to tension the foil. This tensioning system ensured that the foil remained continuously taut with varying system temperature.

The jets impinged onto the upper surface of the foil, however, as the metallic foil is so thin, calculations of the Biot number showed that the temperature drop across the thickness of the foil was negligible. Therefore, by cooling the upper surface with impinging jets it is possible to indirectly and non-intrusively record the resulting upper surface temperature distribution from the lower surface of the foil via infra red thermography. To facilitate accurate temperature measurement, the exposed underside area of the foil was covered with a thin layer of matt black paint with an emissivity $\varepsilon = 0.95$. Utilizing a FLIR ThermoCam A40 fitted with a close focus lens, IR thermal images were captured to record the temperature distribution of the foil. The total camera viewing area was 15.2 mm by 11.4 mm with a spatial resolution of 47.5 μm and a frame rate up to 50 Hz. The nozzle exit to impingement surface spacing, H, was set by zeroing the system through placing the jet exit surface in contact with the impinging surface. Subsequent to zeroing a traversing stage fitted with micrometers was used to accurately position the plenum relative to the foil.

DATA REDUCTION AND EXPERIMENTAL UNCERTAINTY

As some tests were carried out at large Mach numbers, $M = 0.43$, for which compressibility effects were significant, Re and M were calculate from an iterative approach outlined by Goodro et al. [8]. Goldstein et al. [9] determined that impinging high speed jets caused non-uniform temperature profiles on the adiabatic surface. This variation in temperature was accounted for by using the adiabatic wall temperature as the reference temperature in the calculation of the local heat transfer coefficients, equation 1.

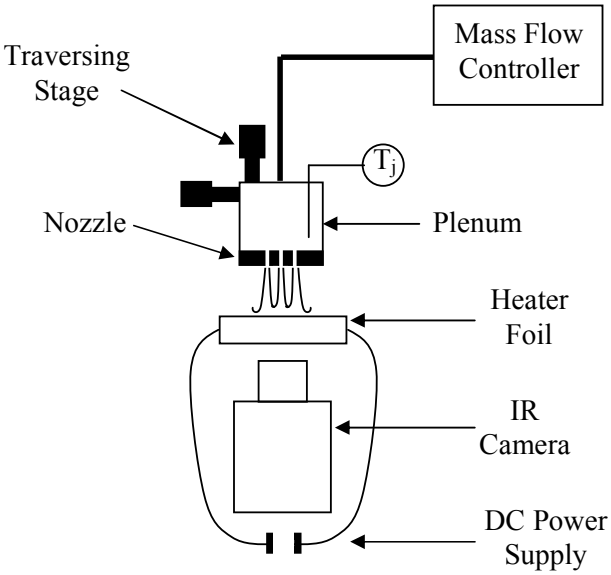

Figure 2. Experimental facility.

$$h = \frac{q''_{conv,jet}}{(T_{h,w} - T_{a,w})} \tag{1}$$

The adiabatic wall temperature, $T_{a,w}$, and the heated wall temperature, $T_{h,w}$, were obtained by recording the temperature distribution resulting from the 9 jets impinging onto first an unheated and subsequently a heated impingement surface, figure 3. The heat flux due to forced convection, $q''_{conv,jet}$, was calculated from an energy balance, equation 2.

$$q''_{conv,jet} = q''_{gen} - q''_{rad} + q''_{lc} \tag{2}$$

The largest term on the r.h.s. of equation 2 is q''_{gen}, the heat flux generated in the foil. The heat flux due to radiation, q''_{rad}, is relatively small however the heat flux due to lateral conduction, q''_{lc}, which is negligible in a macro scale system, is of the same order of magnitude as the generated heat flux. Calculating q''_{lc} required numerically approximating the 2nd spatial derivatives of heated temperature distribution. These derivatives were achieved by using finite difference approximations, however spatial fluctuations in the temperature field have a severe impact on numerical approximations of the 2nd spatial derivatives of temperature. To overcome this, a Wiener filter is used to smooth the data, Rainieri et al. [10].

In order to quantify the level of uncertainty in the lateral conduction component a Monte Carlo technique was implemented for each Reynolds number tested. For the purpose of uncertainty calculation, each measurement is denoted by x_i and the uncertainty in the measurement w_i. The result of a calculation using these measurements is denoted Z and the uncertainty in the calculated result is denoted by w_z. The uncertainty w_z is calculated from the method of Kline and McClintock [11] using the following equation:

$$w_z = \sqrt{\left(\sum_{i=1}^{n} \left[\frac{\partial Z}{\partial x_i} w_i \right]^2 \right)} \tag{3}$$

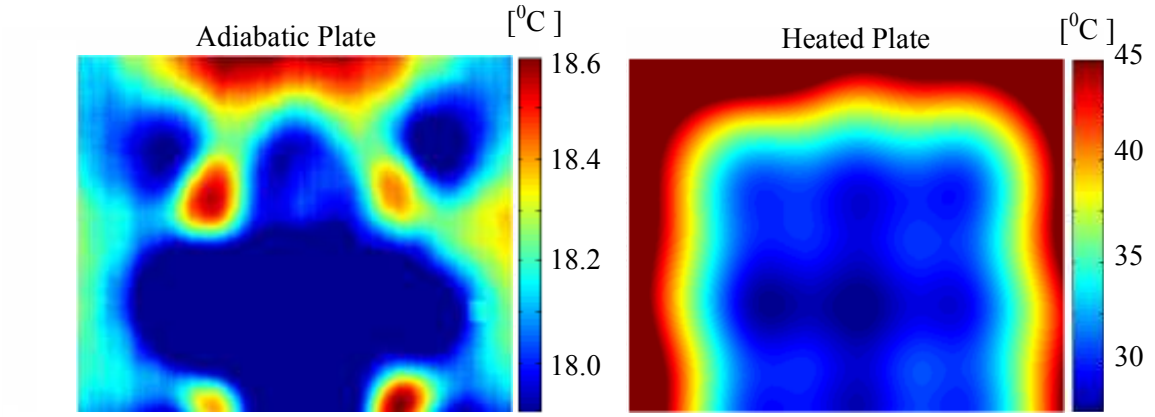

Figure 3. Temperature distributions resulting from a 3 by 3 inline jet array impinging onto a cold and a hot surface at H/D = 2.1 & Re = 6300.

The maximum experimental uncertainties are summarized in table 1.

Table 1
Calculated uncertainty

		Re		q''_{lc} (W/m^2)		h (W/m^2 K)	
S/D (mm)	**H/D (mm)**	3000	6300	Re=3000	Re=6300	Re=3000	Re=6300
±7%	±10%	±4%	±8%	±12%	±9%	±12.5%	±9.5%

RESULTS AND DISCUSSION

Hubar and Viskanta [12] studied a 6.35 mm diameter 3 by 3 square jet array and found varying nozzle to target spacing from 1 to 6 jet diameters has little effect on the resulting Nusselt Numbers. However Garimella and Schroeder [13] later showed, for a similar shaped 1.59 mm diameter array, that decreasing nozzle to target spacing increased heat transfer. Similar results were seen for the tests carried out in this investigation, as illustrated in figure 4. Behbahani and Goldstein [14] attributed these findings to increasing turbulent intensity found at decreasing H/D values due to increased mixing caused by spent fluid from neighbouring jets. Another phenomenon that affects heat transfer and depends on nozzle to impingement spacing is entrainment. Azar et. al. [15] describes how entrainment can modify a jet's pre-impact temperature and Striegl and Diller [15] showed that the entrainment of warm air decreases with decreasing H/D.

In all test for H/D < 3, the central jet of a nine-jet array had considerable larger stagnation region heat transfer than its peripheral jets, figure 4, which is consistent with findings of Garimella and Schroeder [13]. This could be caused by the effects of turbulence intensity and entrainment. The central jet is surrounded by eight jets so it is expected that the temperature of the entrained fluid is lower in the central jet than in the fluid entrained by the peripheral jets. The increase in the stagnation heat transfer for the central jet compared to the peripheral jets is more pronounced at large Reynolds numbers which can be clearly seen at the bottom of figure 4.

Figure 5 shows the local heat transfer at values of H/D = 0.42, 1.68 & 2.94 and Re = 3000 & 6300. The images show the heat transfer between the stagnation zones. The central zone between any 4 adjacent jets demonstrates local minima in heat transfer. However, the linear zones located between

2 adjacent jets demonstrated relatively high heat transfer which has been associated with inter jet interaction. The interaction zones between the centre jet and adjacent peripheral jets demonstrated higher heat transfer than the interaction zones between purely peripheral jets.

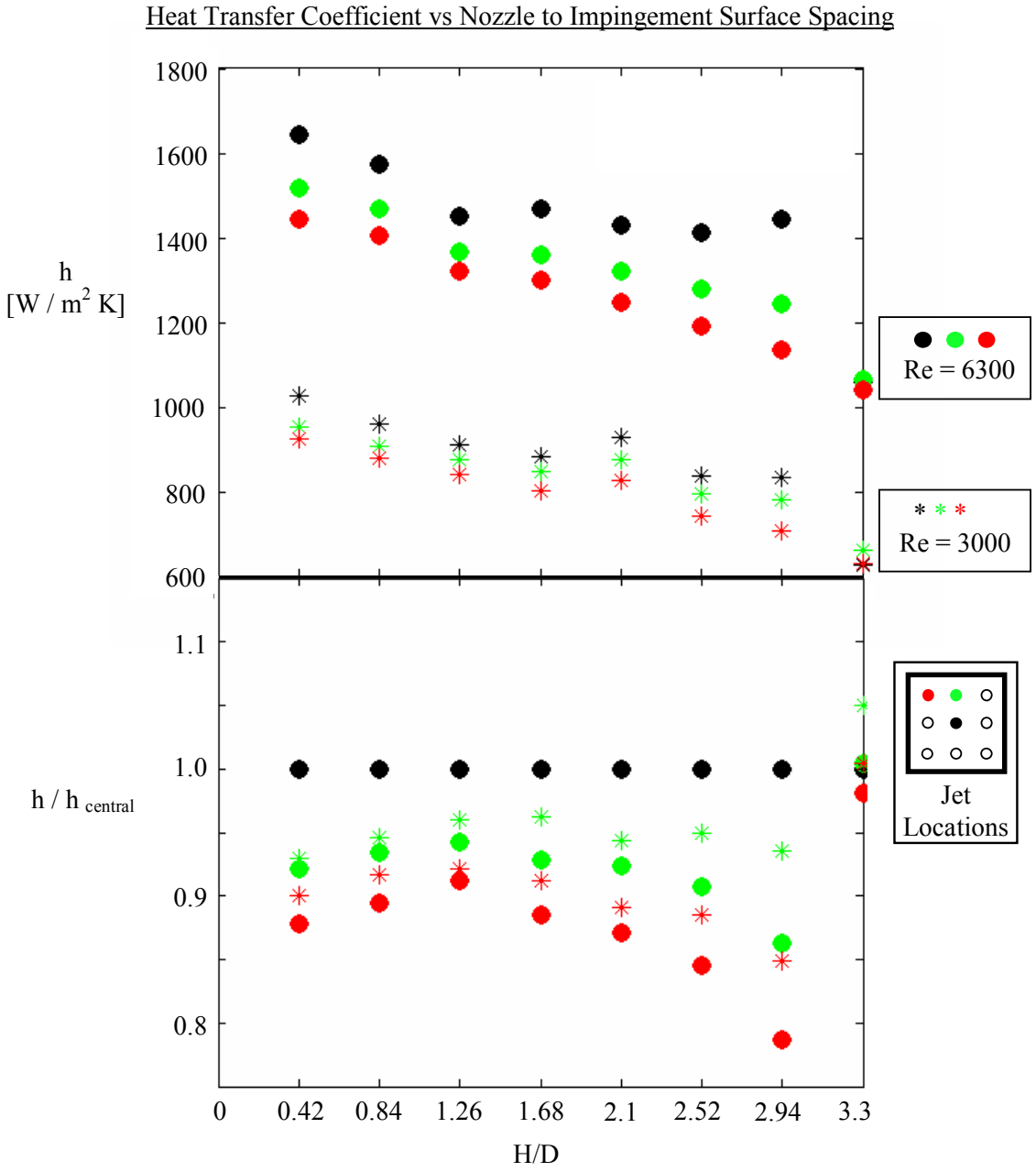

Figure 4. Stagnation point heat transfer coefficients at different nozzle to impingement surface spacings, for 3 individual jets found in a 3 x 3 inline jet array.

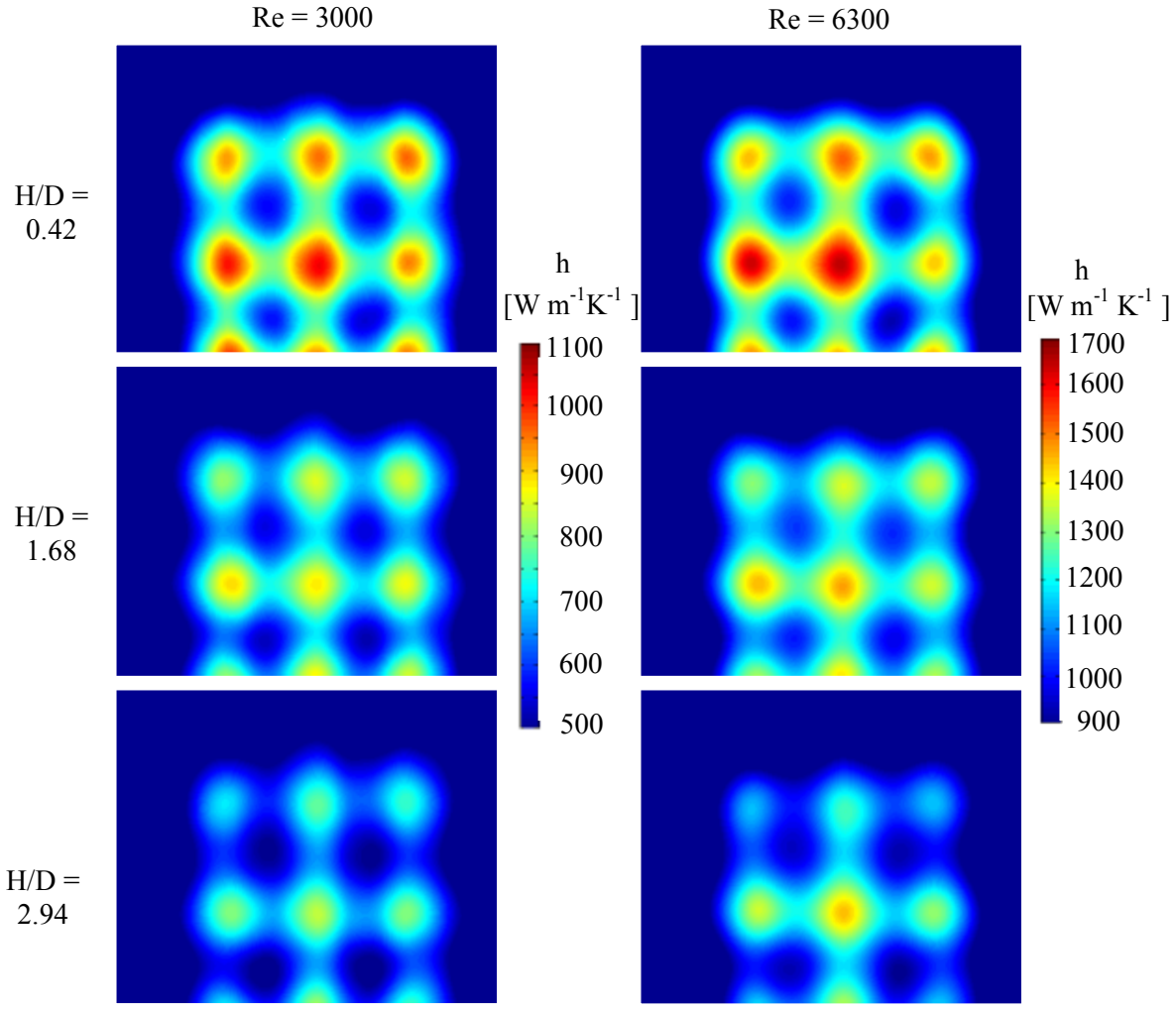

Figure 5. Local heat transfer distributions resulting from a 3 x 3 inline jet array impinging at H/D values of 0.42, 1.68 & 2.94 and at Reynolds numbers of 3000 & 6300.
Each image is 10 mm by 13 mm.

CONCLUSIONS

Micro jet heat transfer for a 3 x 3 array of 620 μm diameter jets was investigated experimentally. Experiments were performed using a heated thin foil and infrared thermography at a interjet spacing, S/D, of 4 and Reynolds number of 3000 & 6300; nozzle to impingement surface spacing was varied from 0.42 to 3.35 jet diameters.

The small length scale associated with micro jets suggests that Reynolds number scaling from the macroscale to the microscale is inappropriate, due to the high velocities associated with relatively low Reynolds numbers. These velocities result in high subsonic Mach numbers making compressibility a factor. It is thought that entrainment effects and turbulence intensity are vastly more significant at smaller scale.

The microjets studied demonstrated increasing heat transfer, both local and area averaged, with an increased Reynolds number. Heat transfer was also found to increase with decreasing nozzle to impingement surface spacings. Post-impact jet interactions lead to increased heat transfer in regions found between adjacent jets. The highest heat transfer was found to be in the stagnation zone associated with the central jet.

NOMENCLATURE

D	Jet diameter, (m)
H	Distance between the nozzle exit and the impingement plate, (m)
S	Inter jet spacing, (m)
T	Temperature, (K)
W	Width of the heated foil, (m)
q''	Heat flux, (W m^{-2})

Subscripts

a	Adiabatic
conv	Convection
dev	Development (length)
gen	Generated
h	Heated
lc	Lateral conduction
rad	Radiation
stg	Stagnation
w	Impingement surface (wall)

ACKNOWLEDGMENTS

The authors gratefully acknowledge the technical support staff of the Mechanical and Manufacturing Engineering Department of Trinity College. The project is funded by SFI through the Centre for Telecommunications Value-Chain Research (CTVR).

REFERENCES

1 H. Martin, Heat and mass transfer between impinging gas jets and solid surfaces, *Adv. Heat Transfer,* Vol. 13, pp. 1-60, 1977

2 Webb, B.W. and Ma, C.F., Single phase liquid jet impingement heat transfer, *Adv. Heat Transfer*, Vol. 26, pp. 105–217, 1995

3 Garimella, S.V., Heat transfer and flow fields in confined jet impingement, *Annual Review of Heat Transfer*, Vol. 11, pp. 413-494, 1999

4 Garimella, S.V., and Rice, R.A., Confined and submerged liquid jet impingement heat transfer, *ASME J. Heat Transfer*, Vol. 117, pp.871-877, 1995

5 San, J.Y., Huang, C.H., and Shu, M.H., Impingement cooling of a confined circular air jet, *Int. J. Heat Mass Transfer*, Vol. 40, pp. 1355–1364, 1997

6 Pence, D.V., Boeschoten, P.A., and Liburdy, J.A., Simulation of compressible micro-scale jet impingement heat transfer, *Journal of Heat Transfer*, Vol. 125, No. 3, pp. 447-453, 2003

7 Incropera, F.P., Liquid Cooling of Electronic Devices by Single-Phase Convection, ISBN 0-471-15986-7 publisher Wiley Interscience, 1999

8 Goodro, M., Park, J., Ligrani, P., Fox, M. and Moon, H., Effects of Mach Number on Jet Array Impingement Heat Transfer, *Heat Mass Transfer*, Vol. 50, iss. 1-2, pp. 367–380, 2007

9 Goldstein, R. J., Behbahani, A.I., and Heppelmann, K.K., Streamwise Distribution of the Recovery Factor and the Local Heat Transfer Coefficient to an Impinging Circular Air Jet, *Int. J. Heat Mass Transfer*, Vol. 29 No. 8, pp. 1227–1235, 1986

10 Rainieri, S., Bozzoli F., and Pagliarini, G., Wiener filtering technique applied to thermographic data reduction intended for the estimation of plate fins performance, *Experimental Thermal and Fluid Science*, Vol. 28, Iss. 2-3, pp. 179-183, 2004

11 Kline, S.J. and McClintock, F.A., Describing Uncertainties in Single Sample Experiments, *Mechanical Engineering*, Vol. 75, January, pp. 3-8, 1953

15 Azar, K., Benson, J.R., and Manno, V.P., An Experimental Investigation of Microjet Impingement Cooling, *Heat transfer in electronic equipment*, Vol. 171, 1991

12 Huber, A. M., and Viskanta, R., Convective Heat Transfer to a Confined Impinging Array of Air Jets With Spent Air Exits," *ASME J. Heat Transfer*, Vol. 116, pp. 570-576, 1994

13 Garimella, S.V., and Schroeder, V.P., Local heat transfer distributions in confined multiple air jet impingement, *ASME Journal of Electronic Packaging*, Vol. 123, pp. 165–172, 2001

14 Behbahani, A.I., and Goldstein, R.J., Local heat transfer to staggered arrays of impinging circular air jets. *J. Eng. Power,* Vol. 105, pp. 354–360, 1983

15 Striegl, S. A., and Diller, T. E., The effect of entrainment temperature on jet impingement heat transfer, *ASME J. Heat Transfer*, Vol. 106, pp. 27–33, 1984

PERFORMANCE OF THREE DIFFERENT EVAPORATIVE COOLING SYSTEMS

E. Velasco[1] *, F. J. Rey[1] , A. Tejero[1], F. E. Flores.[2]
[1]University of Valladolid, Valladolid, Spain
[2]University of Quintana Roo, Quintana Roo, Mexico

ABSTRACT. This paper aims to describe three different evaporative cooling systems. The first is an indirect evaporative cooling system, which operates as an aluminium plate exchanger. It has two independent air streams. The supply air stream needs to be cooled, while the exhaust air is in direct contact with a water flow in order to improve heat transfer to the primary air. The second case is a semi-indirect evaporative cooling system which consists of a bank of porous ceramic pipes arranged vertically. The supply air circulates outside the pipes, while the return air is in contact with the water which circulates inside to allow heat and mass transfer and thus cool the primary air flow. The third system is also semi-indirect and has been manufactured with hollow bricks. It is fed by the primary air stream used for cooling, which comes into direct contact with the porous humid surface of the outer walls of the bricks, thus facilitating heat and mass transfer. This work compares the performance of these systems, considering heat transfer surfaces of approximately $2m^2$.

Keywords: Evaporative cooling, heat recovery, cooling capacity

INTRODUCTION

Nowadays, the availability of energy is essential for everyday life and welfare all over the world, even though energy consumption in wealthy countries is much higher. Therefore, population and economic growth is expected to involve a faster increase in energy consumption, despite the rise in fossil fuel prices.

Taking this into account, many problems such as dependency on sources, increased cost or the environmental impact of energy use and transformation are to be faced. Thus, new legislation to ensure sustainable energy provision at an affordable price is needed. In this context, evaporative cooling systems are of increasing interest to reduce thermal energy demand in buildings, since it is easier to cool with cold water than with hot air [1]. In fact, it has been demonstrated that these systems are more efficient and profitable than those cooled by air. Moreover, this technology can be both mechanical and healthy (Legionnaire's disease) if due maintenance is provided.

In this paper, an indirect evaporative cooling system and two different semi-indirect evaporative cooling systems are analysed. The comparative study has been developed in terms of effectiveness and cooling capacity considering heat transfer surfaces of $2m^2$ in every case. When designing the two semi-indirect systems, some technological criteria have been taken into account to avoid the risks of aerosols which might disperse legionnaire's bacteria [2] or other pathogen elements [3]. This objective has been achieved because humidification is produced through a porous surface, thus avoiding generating aerosols, whose pore diameter is too small to allow it to act as a filter for the

* Corresponding author: Prof. E. Velasco
Phone: + (34)-98-3423684, Fax: + (34)-98-3423363
E-mail address: eloy@eis.uva.es

bacteria [4]. Moreover, working with relative air humidity below 70% reduces the risk of this kind of disease.

DESCRIPTION OF THE THREE EVAPORATIVE COOLING SYSTEMS

Three systems were designed and constructed in the thermal engineering department of the University of Valladolid. An experimental study was then performed to characterise their behaviour. As mentioned previously, these systems were an indirect evaporative cooler (IEC), a semi-indirect evaporative cooler made with ceramic pipes (SIECCP) and a semi-indirect evaporative cooler made with hollow bricks (SIECHB).

The first equipment, shown in figure 1, is made of aluminium plates. The supply air which we are to cool circulates on one side of the plates, while the other is in contact with water previously cooled with air from the room, which has a higher cooling capacity than that of the outside air.

The main characteristic of this system is that it consists of a plate heat exchanger, so that the water does not come into contact with the supply air. Thus, it avoids the proliferation of legionnaire's bacteria on the primary air. However, it also implies a lower effect of the evaporative cooling in the supply air.

The geometric characteristics of this equipment are shown in table 1.

Figure 1. Indirect Evaporative Cooler (IEC)

Table 1
Geometric Characteristics of the IEC

Thickness	3×10^{-3} m
Length	0.3 m
Number of plates	25
Geometry	Flat plates
Area	2.25 m^2

The second equipment consists of a bank of tubes arranged vertically [5], which can behave either as an indirect or direct cooler depending on the outside air temperature and relative humidity. In the first case, it works in a heat-recovery mode, using the pipes as a heat exchanger. In the other, humidification of the outside air is permitted, as water is capillary transported through the ceramic

wall. The supply air that has to be cooled circulates outside the pipes, while the return air and the cooled water circulate inside.

The pores of the ceramic pipes have such a small diameter that they act as a filter between the two streams of air, avoiding contamination of the supply air from the contaminants in the return air. Furthermore, this material shows a high corrosion and oxidization resistance, as well as high porosity. The geometric characteristics of the SIECCP are shown in table 2.

The left image shown in figure 2 is a detail of one of the pipes that make up the system. The one in the middle provides a vertical pipe arrangement, while the one on the right is a general view of the equipment installation.

The evaporative cooling system designed and constructed with hollow bricks is semi-indirect so that it is made with porous material. It has been installed in a heat-recovery system to cool a climate chamber equipped with an extra heat pump which helps it to reach thermal comfort conditions [6].

Table 2
Geometric Characteristics of the SECCP

Inside diameter	15 mm
Outside diameter	25 mm
Wall thickness	5 mm
Length	30 mm
Length L	25 mm
Length D	29.15 mm
Pipe length	600 mm
Area	2.3 m2
Arrangement	Herringbone
Number of columns	7
Number of rows	7
Number of pipes	49

Figure 2. Different views of the installation of the SECCP.

The SIECHB works with a primary air stream cooled when coming into direct contact with the humid porous surface of the bricks, allowing heat and mass exchange.

Depending on the permeability of the surface, there is a higher or lower diffusion of water from the pores to the air stream, the specific humidity of the supply air being the parameter which controls this mass exchange process. For this reason, the process is called semi-indirect.

Figure 3 shows, from left to right, a detail of a hollow brick similar to the ones used, a view of the evaporative cooler and the system installed in a heat-recovery mode. The dimensions of the hollow bricks are shown in table 3.

Since humidification occurs through a porous surface, as with the system previously described, the presence of aerosols that might disperse the legionnaire bacteria is prevented.

All the phenomenon described can be observed in any semi-indirect system. For that reason, there is a combined heat and mass exchange, increasing the cooling effect and optimizing the thermal process [7].

Figure 3. Semi-indirect Ceramic Evaporative Cooler (hollow bricks).

Table 3.
Dimensions of a Hollow Brick.

Length (m)	Height (m)	Thickness (m)	Hollow section (m2)	Side area (m2)	Number of bricks
0.198	0.41	0.043	7.92E-04	0.201	12

EXPERIMENTAL RESULTS OF SOME TESTS

Due to the limits established by each experimental device, it has only been possible to compare tests setting a 120 m^3/h volume flow for the indirect cooler, while 140 m^3/h and 240 m^3/h have been set for the semi-indirect evaporative ceramic pipe and hollow brick coolers respectively. All the tests

have been developed for the minimum level of relative humidity given by the outdoor air conditions. The entire process has been developed maintaining the comfort conditions inside the climate chamber.

Different levels of temperature have been tested in each case ranging from 24ºC to 44ºC for the level of inlet air volume flow fixed, corresponding to summer conditions. Inlet and return air temperature and relative humidity were subsequently measured to calculate specific humidity, wet bulb temperature, thermal and wet-bulb thermal efficiency, as well as cooling capacity.

The thermal efficiency is defined by equation (1).

$$\varepsilon_T = \frac{T_1 - T_2}{T_1 - T_3} \tag{1}$$

whereas wet bulb thermal efficiency [8] is given by the equation (2).

$$\varepsilon_{WBT} = \frac{T_1 - T_2}{T_1 - T_{3WB}} \tag{2}$$

The cooling capacity is defined by equation (3).

$$E_{CC} = \dot{m} \cdot (h_1 - h_2) \tag{3}$$

The results and graphs of some tests performed on the evaporative cooling systems are shown in tables 4 - 6, and graphs of figures 4 - 6.

Table 4
Results for the IEC for the Lowest Airflow and Water Flow.

x_1 (g/kg)	T_1 (ºC)	T_2 (ºC)	T_3 (ºC)	T_{3WB} (ºC)	ε_{WBT}	ε_T	E_{CC} (W)
3.9	24.5	17.3	20.6	15.0	0.76	1.85	322.3
5.1	28.2	19.2	21.3	15.9	0.73	1.30	384.2
5.5	31.9	20.0	21.3	15.3	0.71	1.13	500.0
6.2	36.6	21.3	21.4	15.0	0.71	1.01	630.6
6.5	37.7	21.8	21.4	15.3	0.71	0.98	663.6

Table 5
Results for the SIECCP for the Lowest Airflow and Water Flow.

x_1 (g/kg)	T_1 (ºC)	T_2 (ºC)	T_3 (ºC)	T_{3WB} (ºC)	ε_{WBT}	ε_T	E_{CC} (W)
7.0	25.5	20.8	23.8	15.0	0.45	2.76	202.0
7.0	30.1	22.6	25.7	15.7	0.52	1.73	313.8
9.8	35.6	25.4	25.6	17.9	0.58	1.02	441.8
12.3	39.9	27.2	24.8	19.6	0.63	0.84	520.3
13.0	43.4	28.9	24.8	20.1	0.62	0.78	588.7

Table 6
Results for the SIECHB for the Lowest Airflow and Water Flow.

x_1 (g/kg)	T_1 (ºC)	T_2 (ºC)	T_3 (ºC)	T_{3WB} (ºC)	ε_{WBT}	ε_T	E_{CC} (W)
8.0	25.0	19.1	21.9	16.3	0.68	1.93	308.5
10.4	30.0	23.5	23.7	19.4	0.61	1.03	332.1
9.9	35.0	26.0	23.4	19.4	0.58	0.77	660.4
9.9	39.9	28.5	23.3	19.4	0.56	0.69	935.9

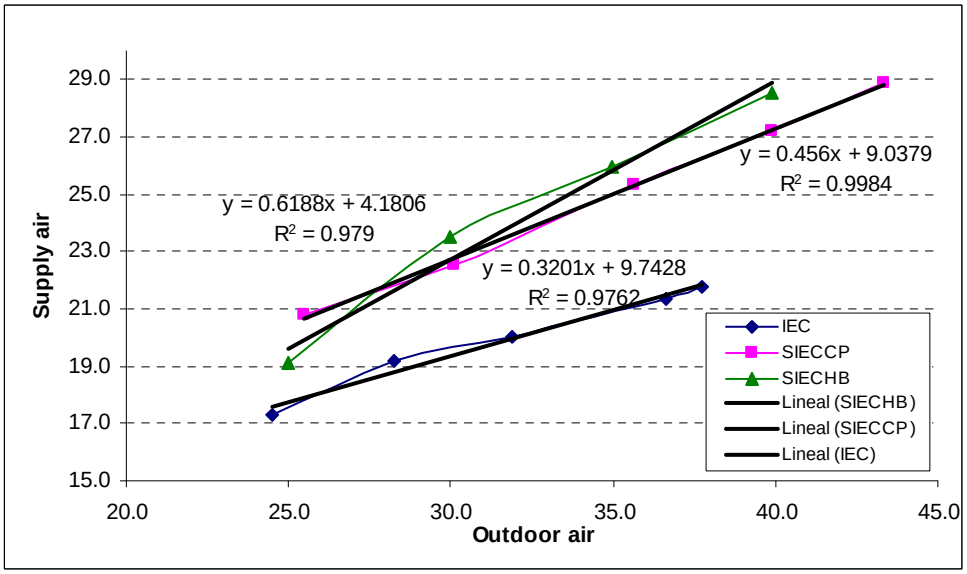

Figure 4. Output temperature vs. inlet temperature.

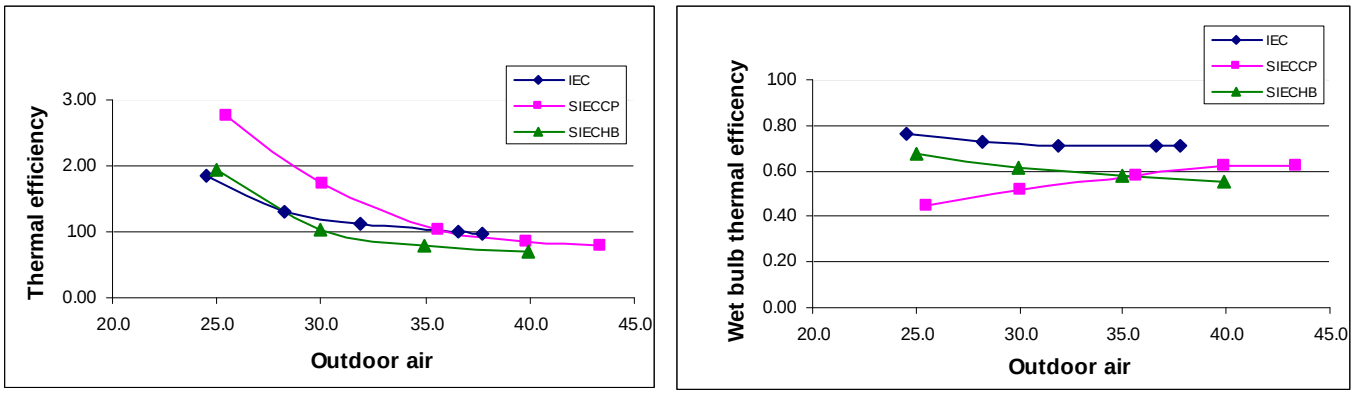

Figure 5. Thermal efficiency and wet bulb thermal efficiency vs. inlet temperature.

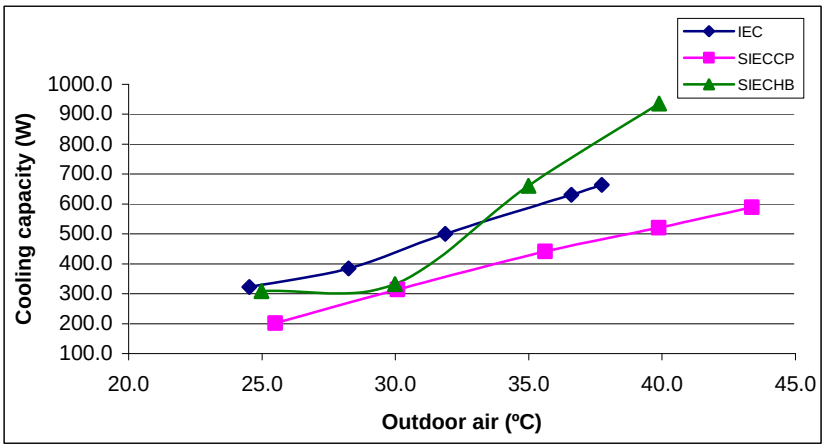

Figure 6. Cooling capacity vs. inlet temperature.

CONCLUSIONS

For the air volume flow levels permitted by the experimental device and low relative air humidity, results evidence that every system could be properly used for cooling outdoor air.

However, the efficiency of these systems is especially interesting in those climates characterised by a high outside air temperature and low relative humidity. This fact is validated by the experimental results, which show an increase in the evaporative capacity of the air, and thus a higher cooling capacity, associated to the increase in supply air temperature.

As can be seen in figure 4, inlet air temperature is proportionally related to return air temperature in the three cases, the indirect system providing the lowest temperatures. This is due both to the use of a lower air volume flow and the characteristics of the material with which it was constructed, as aluminium has a higher conductivity than the ceramic materials used in the other two systems.

By contrast, thermal efficiency diminishes as temperature increases. However, the phenomenon of evaporative cooling allows a lower cooling temperature than that of the output air, values given thus being over 1 in many cases, which would be the maximum obtainable by using a conventional heat-recovery system. Evaporative cooling systems can thus improve cooling capacity in conventional heat-recovery systems working in dry climates.

As the air volume flow is smaller in the case of the indirect system, wet-bulb thermal efficiency obtained in this case is over 60%, while for the semi-indirect systems this efficiency is around 60%, which is enough to ensure that the supply air from the systems is not saturated.

Moreover, the semi-indirect systems, which take advantage of the evaporative cooling capacity of outdoor air, allow supply air temperatures below 30ºC when working with inlet air temperatures of 40ºC. Therefore, this kind of device also provides high cooling power for high levels of air volume flow.

Of the three systems, the SIECHB provides a better cooling capacity for high temperatures. Furthermore, the materials used for its construction are hollow bricks, very common in the building sector, meaning the system has the highest porosity and is the cheapest, an advantage for its use as a commercial system. It can also be combined easily with passive cooling systems.

An increase in the level of the air volume flow involves a lower thermal leap as well as lower levels of relative humidity output when working with evaporative systems. It is possible, therefore, to vary the air volume flow which circulates through these systems in order to control the relative humidity in the supply air so that it is low enough to avoid problems such as the risk of producing aerosols or condensations in the coldest areas of the premises.

Improvements in semi-indirect evaporative cooling systems focus on the use of thinner walls, which might not only increase water flow through the ceramic material but also reduce thermal resistance to heat exchange, as this kind of material is characterised by low thermal conductivity. This would entail an increase in the cooling capacity of the system, although it should be taken into account that such a reduction in wall thickness must not weaken the system's frame.

NOMENCLATURE

ε_T	thermal efficiency	T_{3WB}	return air wet bulb temperature (ºC).
ε_{WBT}	wet bulb thermal efficiency	$\dot{m}$	primary airflow (kg/s).
E_{CC}	cooling capacity (W)	h_1	enthalpy (primary airflow) at the entrance of the device (kJ/kg).
x_1	absolute humidity (g/kg)		
T_1	outdoor air dry temperature (ºC).	h_2	enthalpy (primary airflow) outside the device (kJ/kg).
T_2	inlet air dry temperature (ºC).		
T_3	return air dry temperature (ºC).		

ACKNOWLEDGEMENTS

This work forms part of the research being carried out within the framework of the "Reduction of energy consumption and carbon dioxide emission in buildings combining evaporative cooling, free cooling and energy recovery in all-air systems", project supported by the Ministry of Science and Technology through the call for scientific research and technological development research projects. Reference number ENE 2008-02274/CON.

REFERENCES

1. Velasco Gómez, E. and Rey Martínez, F. J., Beneficios del Enfriamiento Evaporativo, *Montajes e instalaciones*, No. 401, pp 47 – 51, January 2006.
2. Xiao Ping, W., Johnson, P. and Akbarzadeh, A., Application of Heat Pipe Heat Exchanger to Humidity Control in Air Conditioning Systems, *Applied Thermal Engineering,* Vol. 17 (6), pp 561-568, 1997.
3. ASHRAE Standard 62-1989. *ASHRAE*, Washington, DC., 1989.
4. Velasco Gómez, E., Rey Martínez, F. J., Varela Díez, F., Flores Murrieta, F. and Dapena Echeverría, M., La Utilización del Enfriamiento Evaporativo como Alternativa Energética Eficiente, *Ecoconstrucción*, No. 4, pp 44 – 49, January – February 2007.
5. Rey Martínez, F. J., Velasco Gómez, E., Varela Díez, F., Herrero Martín, R., and Martínez Gutiérrez, J., Comparative Study of Two Different Evaporative Systems: an Indirect Evaporative Cooler and a Semi-Indirect Ceramic Evaporative Cooler, *Energy and Buildings*, 2004, No. 36, pp 696-708.
6. Flores Murrieta, F.E., Velasco Gómez, E. and Rey Martínez, F.J., Enfriamiento Evaporativo Cerámico: una Tecnología Eficiente en Edificios, *Montajes e instalaciones*, No. 427, pp 77-86, 2008.
7. Kaviany, M., *Principles of Heat Transfer in Porous Media,* Springer-Verlag Publ. Co., ISBN 0-387-94550-4, New York., 1999.
8. Wang Shan, K., *Handbook of Air Conditioning and Refrigeration*, 2nd edition, McGraw Hill Publ. Co., ISBN: 0-07-068-167-8, New York, 2001.

Experimental Investigation of Flow and Forced Convection Heat Transfer, in Fully Filled Rectangular Duct Using Porous Media

H. Shokouhmand[1, *], S. M. Emami[2]
Tehran, Iran
University of TEHRAN, Faculty of Engineering
Mechanical Engineering Dep.

ABSTRACT. An experimental study was performed to investigate the heat transfer characteristics of the convection flow through a rectangular air duct with aspect ratio of 10 (a/b=10) which is filled with metallic porous materials. All four walls of the duct are subjected to a constant and uniform heat flux. The Reynolds number based on the hydraulic diameter has been kept between 500-2000 in order to ensure the laminar flow through the duct. The effect of different parameters such as variable porosity and density of porous layers have been investigated. For different porous layers configuration, heat flux at the walls, wall temperatures and air mass flow rate has been measured and the Nusselt number has been calculated. The results are compared with the clear flow case where no porous material was used. it can be concluded that higher heat transfer rates can be achieved in porous media flow case at the expense of a reasonable pressure drop. Based on the experimental data new empirical correlations for both Nusselt number and friction factor have also been developed for such air duct, which gives a good agreement between predicted values and experimental values of Nusselt number and friction factor.

Keywords: *Heat transfer enhancement, Pressure drop, Porous media*

INTRODUCTION

Theoretical and applied research in flow and heat transfer in porous media has received more attention during the past three decades. This is due to the importance of this research area in many engineering applications such as solid matrix heat exchangers, heat pipes, drying efficiency, electronic cooling, enhanced heat transfer by surface modification, nuclear reactors using gaseous coolants flowing through radioactive pellets, dehumidifying, Porous preheaters and flame stabilizers, oil and gas flow in reservoirs, catalytic converter for air pollution reduction of combustion products, etc.
Kays and London [1] pointed out that an effective way to increase the performance of a heat exchanger is to increase its surface area to volume ratio. Kim et al. [2] established correlations for friction factor and overall heat transfer coefficient for metal foam channel heat exchangers via experimental techniques. Hsu et al. [3] and Hsu and Fu [4] measured the velocity and the pressure drop for both steady and oscillating flows across porous columns packed from wire screens. Varshney and Saini [5] have experimentally investigated the heat transfer and the fluid flow characteristics of a solar air heater having its duct packed with wire mesh screen matrices (air flowing parallel to matrix planes). Lee and Vafai [6] developed an analytical solution for temperature distribution within a channel filled with a porous medium and subject to a constant heat flux boundary condition. They established an analytical relationship for Nusselt number as a function of solid and fluid effective thermal conductivities and solid–fluid interfacial characteristics utilizing local thermal non-equilibrium model.

* Corresponding author: Prof. H. Shokouhmand
Phone: + (98)-21-820814829, Fax: + (98)-21-820814829
E-mail address: hshokoh@me.ut.ac.ir
m.emammi@me.ut.ac.ir

Open cell porous matrix such as an unconsolidated bed of small particles, woven metal screens, or foam matrixes provides excellent heat-transfer characteristics due to its large surface area to volume ratio. Woven metal screens have other advantages include easy arrangement, high permeability and relatively small deviation of the pore size from the mean value.

Present experimental study includes the heat transfer and pressure drop investigations of the flow passing through a rectangular channel in which different porous media are located. All four walls of the channel are heated by uniform heat flux about 174 W/m². The experiments were carried out for Reynolds numbers (based on the hydraulic diameter) between 500-2000, and 3 different porous media, which their porosities varied between 95.0% and 97.9%, were examined. The maximum increase in the length-averaged value of the Nusselt number of about 4.9 times in comparison with the clear flow case was achieved with a porous medium fully filled the duct (porosity 97.9% and a Reynolds number of about 2000). Using experimental data, two correlations have been developed for predicting the Nusselt number and friction factor for such rectangular air ducts. Comparison of the empirical correlations with experimental data in open literature validated the empirical correlations.

EXPERIMENTAL STUDY

Setup and procedure

The schematic diagram of test setup is shown in Figure 1. The setup includes the test section, flat heater, centrifugal fan and instrumentations for measuring mass flow rate of air, pressure drop, temperature and voltage for heating the test section. Air from the quiescent laboratory room is driven into the operators by means of a downstream-positioned fan (8). The air enters a long hydrodynamic development length (1.2 m), (1) and (2), in order to establish a well-defined velocity profile at its downstream end. The downstream end of the development section is mated to the inlet of the test section (3). The test section is a rectangular duct with cross-sectional aspect ratio of 10, filled with a metallic porous matrix. The length of the test section in the flow direction is 0.5 m. The downstream end of the test section is mated to the exit section (4) that is an extension of the test section walls, but without the porous medium. The inlet of the exit section was equipped with honeycomb straighter for uniforming the flow field. The exit section was followed by a mixing ...

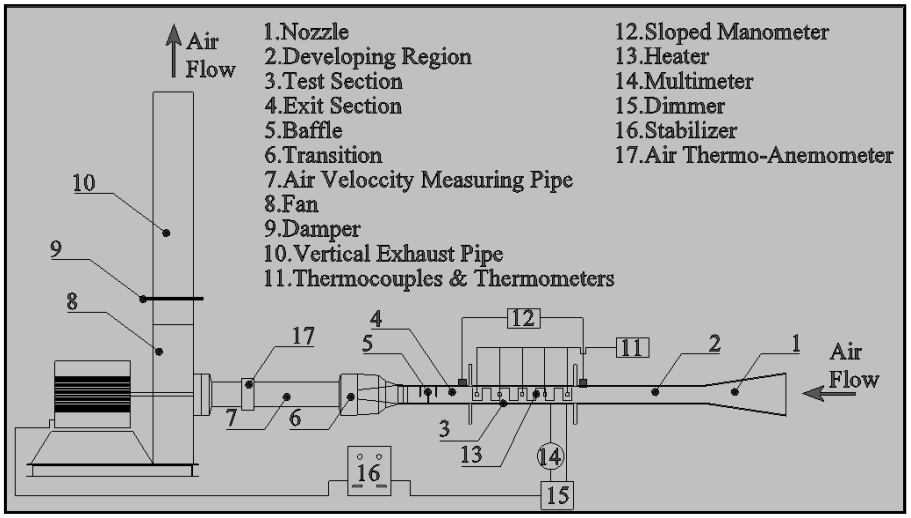

Figure 1. Experimental setup

device (5), namely baffles for mixing the air. The mixing device enabled measurement of the bulk mean temperature at the outlet of the test section. The length of the exit section was 0.35 m and its cross section area matched with that of the test duct. Three equally spaced baffle plates which spread over 0.0425 m length beyond the exit section were provided for the purpose of mixing the hot air coming out of the test section to obtain a uniform temperature of the air at the outlet. The mixing section was connected to the pipe fitting (7) through a transition piece and flexible pipes (6). At the far end of the air velocity measurement pipe, an isolation device was installed to decouple any possible blower-motor vibration.

Heating of test section was accomplished on all of its bounding surfaces by means of a flat heater. The heater plates consist of asbestos sheet, mica and nichrome wires. The wires were fixed on asbestos sheet covered with strips of mica to keep the uniform distance between the wires. The heater was fabricated to produce about 2000 W/m^2 heat energy. With the help of a voltage regulator, a voltage of 65 V across the wires having total resistance of 54 Ω was maintained. Corresponding to this voltage of 65 V and resistance of 54 Ω, about 78 W of energy over a surface area of 0.45 m^2 was obtained. All of the outer bounding surfaces of heater and exit section were carefully wrapped with a 0.038 m thick rock wool (k = 0.03 W/m K) as insulating material to minimize the extraneous heat losses.

Temperatures were measured by thermocouples deployed along the centre span of the walls of the test section and its upstream and downstream extensions. The thermocouples (Type J, 0.3-mm-diameter) had been specifically calibrated after their installation (±0.1℃). At all thermocouple locations, the thermocouple junctions were pressed tightly against the outer surface of the respective walls. Using 20 thermocouples, temperatures of all four surfaces of the test section, at five axial positions (0.020, 0.135, 0.250, 0.365 and 0.480 m) were measured. In addition, three thermocouples were used to measure the fluid bulk temperature, respectively positioned upstream and (among the baffles of) downstream of the heated test section. The thermocouples out puts were displayed in ℃, by Hanyoung- ED6 temperature meters.

The pressure drop across the test section has been measured by a sloped manometer having 0.01 mm accuracy. The liquid having density of 784 kg/m^3 at 29℃ has been used in manometer to increase the accuracy further.

For the measurement of the mass flow rate, a dedicated instrumented section (7), situated downstream of the exit section, was used. The instrumented section had been previously calibrated against a rotameter.

The porous media used for experiments were manufactured from commercial steel screens (wire diameter 0.45×10^{-3} m, density 7830 kg/m^3, thermal conductivity 64 W/mK) which cut into a rectangular shape with dimension of 0.4×0.04 m^2 are packed layer by layer in the 0.5 m long test section. Three different porous media, whose properties are presented in Table 1, were obtained by varying the distance between two adjacent screens L.

Table 1
Porous medium characteristics

Porous medium	Screen Dimension (mm)²	L (mm)	ε (%)	K (m²)	F	D_p	$Da = \frac{K}{(H/2)^2}$
(1)	40×400	2	95.0	2.88×10^{-7}	4.69×10^{-2}	2.45×10^{-3}	7.20×10^{-4}
(2)	40×400	4	97.0	3.23×10^{-7}	2.81×10^{-2}	2.45×10^{-3}	8.07×10^{-4}
(3)	40×400	6	97.9	4.13×10^{-7}	2.01×10^{-2}	2.45×10^{-3}	1.03×10^{-4}

All joints of duct, inlet section, test section, exit section, transition and pipes are thoroughly checked up for any leakage before starting the experiment every time. All the measuring equipments were checked up before starting the experiment. Usually an initial period of approximately 3–4 h was required before reaching steady-state conditions (considered to be attained, when the temperatures indicated by the thermocouples did not vary with more than ±0.3°C within a period of about 20 min). Following parameters were measured for each set of readings: pressure drop across the test section, temperatures of the test section walls, the fluid bulk temperature at inlet and outlet of the test section, voltage and electric current supplied to heater, air velocity and temperature at the air velocity measurement pipe, to measure the air flow rates. After collecting a set of data at steady-state conditions, the mass flow rate of air was increased so that the next value of the Re number differed from the previous one by about 250 units. A new set of data was collected when steady-state conditions were reached again, usually within a period of approximately 40 min. That is, the mass flow rate of air was increased progressively until a maximum value of Re ~ 2000 was reached.

In order to verify the validity of the experimental setup the values of Nusselt number and friction factor were compared with the values obtained from correlations available in the literature for smooth duct namely Shah and London set of equations [7] and modified Blasius equation [7]. The Nusselt numbers have a maximum deviation of 5.86% while the maximum deviation of the friction factor is 2.63% from the predicted values by the Shah and London and Blasius equations, respectively.

Data reduction

The experimental data was used to determine the desired parameters as given below. All the properties of air, viz. density, viscosity, specific heat used in the calculation, were evaluated at the arithmetic mean of the inlet and the outlet temperature of air. The heat transfer rate, Q_{air} to the air can be determined as:

$$Q_{air} = \dot{m} c_p (T_{out} - T_{in}) \tag{1}$$

The local heat flux from the wall to the flowing fluid, q (assumed uniform on all surfaces which bound the porous medium) obtained from:

$$q = Q_{air} / A_s \tag{2}$$

where A_s is the heat transfer area m^2.

The average Nusselt number based on the hydraulic diameter $\overline{Nu}_{D_h}$ was evaluated in accordance with the following equation:

$$\overline{Nu}_{D_h} = \frac{qD_h}{(\overline{T}_s - T_m)k_{air}} \tag{3}$$

where hydraulic diameter D_h is,

$$D_h = \frac{4A_c}{P} \tag{4}$$

and the average surface temperature $\overline{T}_s$ can be calculated from the 20 points of the local surface temperatures, which can be expressed as

$$\overline{T_s} = \frac{\sum T_s}{20} \tag{5}$$

and the average air temperature T_m is given by,

$$T_m = \frac{T_{out} + T_{in}}{2} \tag{6}$$

The modified fanning friction factor f_{D_p} (the ratio of the wall shear stress at channel to the flow kinetic energy) and the modified Reynolds number Re_{D_p} [8] are defined as

$$f_{D_p} = \frac{\Delta p}{L_0}\frac{D_p}{\rho u^2}\frac{\varepsilon^3}{(1-\varepsilon)} \tag{7}$$

$$\frac{\mathrm{Re}_{D_p}}{1-\varepsilon} = \frac{D_p \rho u}{\mu} \tag{8}$$

where the equivalent spherical diameter D_p, is the characteristic length of woven metal screens (shown in table 1) and defined as $D_p = 6/S_V$ (S_V, is the surface area per unit volume of solid phase).

RESULT AND DISCUSSION

Average Nusselt number results

The variation of the average Nusselt number ($\overline{Nu}_{D_h}$) versus the Reynolds number (Re_{D_h}) for three studied porous medium, is shown in Figure 2. It was observed that the value of average Nusselt number increased with the increase in Reynolds number. It can also be observed that the effect of ...

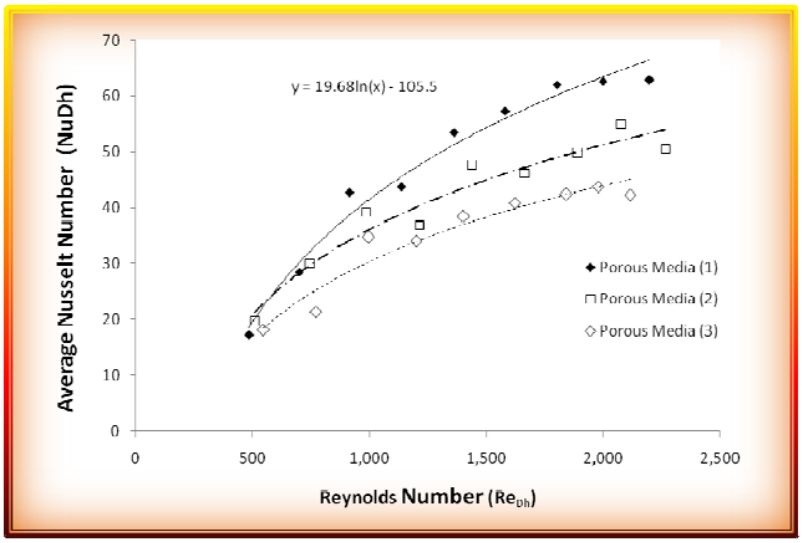

Figure 2. Effects of Reynolds number on average Nusselt number for 3 studied porous medium.

Reynolds number on Nusselt number decreases, at higher Reynolds numbers. As seen in the Figure 2, the effect of Reynolds number (Re_{D_h}) on average Nusselt number decreases for third porous medium when Re reaches the value of 2100, and a similar trend occurs for second and first porous medium when Re reaches the value of 1900. Another aspect demonstrated in Figure 2 is that the porosity has an important influence on the average Nusselt number. If the porosity decreases from 0.98 to 0.97, the average Nusselt number increases between 13% and 37% depending on Reynolds number. However, average Nusselt number increases up to 70% when the porosity is decreased from 0.98 to 0.95. This appears to be due to a higher level of turbulence created in the flow as the porosity decreased and the flow passages become more tortuous and narrower with a higher solidity of such matrices.

Pressure drop results

The variation of the pressure drop (Δp) versus the Reynolds number (Re_{D_h}) for three studied porous medium, is shown in Figure 3. It was observed that the higher the Reynolds number, the higher the pressure drop. It can also be observed from Figure 3 that the value of pressure drop increased monotonically with a decrease in porosity. If the porosity decreases from 0.98 to 0.97, the pressure drop (Δp) increases between 50% and 150% depending on Reynolds number. However, pressure drop (Δp) increases up to 200% when the porosity is decreased from 0.98 to 0.95.

Development of correlation

The modified fanning friction factors f_{D_p} of the three porous medium used in this study were determined following the definition given in equation (7) and plotted as functions of $Re/(1-\varepsilon)$ in Figure 4. In this figure, it is noted that f_{D_p} decreases with the increase of $Re/(1-\varepsilon)$. It should also be noted that the data for the three porous medium fell well into a single curve.

Jones et al. [9] analyzed the pressure drop characteristics of granular porous materials. The equation is given below:

$$f_{D_p} = 150\frac{1-\varepsilon}{Re_{D_p}} + 3.89\left(\frac{1-\varepsilon}{Re_{D_p}}\right)^{0.13} \tag{9}$$

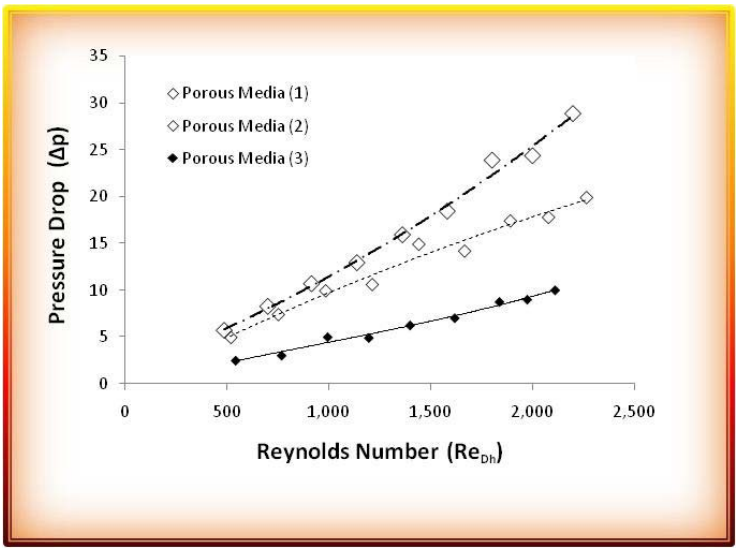

Figure 3. Effects of Reynolds number on pressure drop for 3 studied porous medium.

Table 2
Properties of metal screens

Dimension of screen (m)	Mass of a single screen (kg)	Thickness of a single screen (m)	Diameter of warp wire (m)	D_P (m)	Woven density (wires/in.)
0.4×0.04	23.77×10^{-3}	0.85×10^{-3}	0.45×10^{-3}	2.45×10^{-3}	17

In order to develop a correlation for pressure drop characteristic of flow through woven metal screens (Table 2), this study adopts a general equation in the form of equation (9), given below in equation (10).

$$f_{D_p} = \alpha \frac{1-\varepsilon}{Re_{D_p}} + \beta \left(\frac{1-\varepsilon}{Re_{D_p}}\right)^{\gamma} \tag{10}$$

A series of experiments were conducted to determine the coefficients α, β, and γ of equation (10). Based on the measured pressure drops of three woven metal matrices, present study developed an empirical equation of friction characteristic for woven metal screens. As shown in Figure 4, the correlation for the three porous medium was determined to be

$$f_{D_p} = 0.006 \frac{1-\varepsilon}{Re_{D_p}} + 0.39 \left(\frac{1-\varepsilon}{Re_{D_p}}\right)^{0.81} \tag{11}$$

Figure 5 shows the comparison of equation (11) with the experimental data (obtained from this study) of the metal screens of the plain square type. Figure 5 shows that data from present study all fall within ±25% of equation (11).

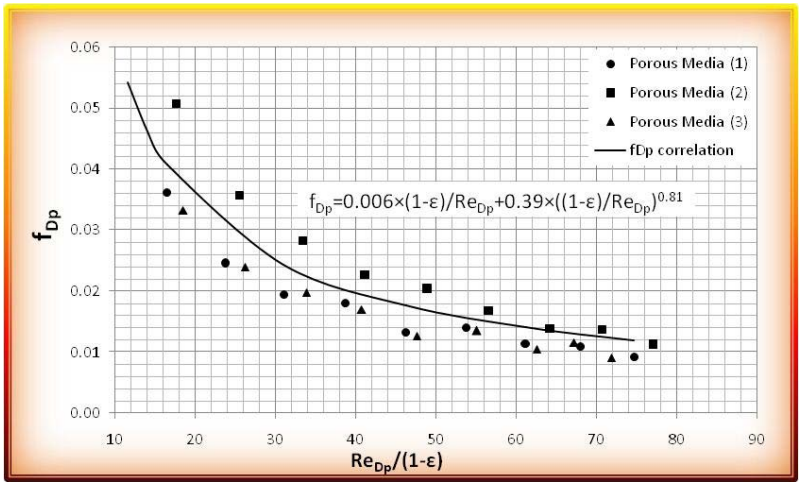

Figure 4. Correlation between f_{D_p} and $Re_{D_p}/(1-\varepsilon)$.

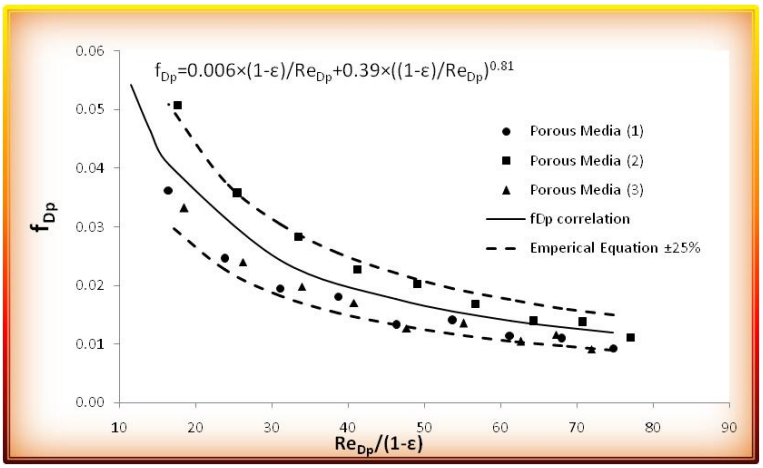

Figure 5. Deviation between experimental data and the correlation.

CONCLUSIONS

In this study, an experimental setup was established for data collection on heat transfer and fluid flow characteristics of air through woven metal screens. It is shown that higher heat transfer rates are achieved when using porous inserts at the expense of a reasonable pressure drop, which depends on the permeability of the porous media.

Based on the measured pressure drops of three porous matrices, this study developed an empirical equation of friction characteristic for plain-square-type metal screens. The empirical equation is:

$$f_{D_p} = 0.006\frac{1-\varepsilon}{Re_{D_p}} + 0.39\left(\frac{1-\varepsilon}{Re_{D_p}}\right)^{0.81}$$

where

$$f_{D_p} = \frac{\Delta p}{L_0}\frac{D_p}{\rho u^2}\frac{\varepsilon^3}{(1-\varepsilon)}, \qquad \frac{\mathrm{Re}_{D_p}}{1-\varepsilon} = \frac{D_p \rho u}{\mu} \qquad \text{and} \qquad D_p = 6/S_V$$

REFERENCES

1. Kays, W.M. and London, A.L., Compact Heat Exchangers, McGraw-Hill, 1964.
2. S.Y. Kim, J.W. Paek, B.H. Kang, Flow and heat transfer correlations for porous fin in a plate-fin heat exchanger, ASME J. Heat Transfer 122 (2000) 572–578.
3. C.T.Hsu, H.L.Fu, and P.Cheng. On pressure-velocity correlation of steady and oscillating flows in regenerators made of wire-screens. *ASME J. Fluids Eng.*121:52–56, 1999.
4. C.T.Hsu and H.Fu. Measurements of pressure drop of high frequency oscillating flows through a packed column made of wire-screens, 2004 (in manuscript).
5. D.Y. Lee, K. Vafai, Analytical characterization and conceptual assessment of solid and fluid temperature differentials in porous media, Int. J. Heat Mass Transfer 42 (1999) 423–435.
6. Varshney, L., Saini, J.S., 1998. Heat transfer and friction factor correlations for rectangular solar air heater duct packed with wire mesh screen matrices. Solar Energy 62 (4), 255–262.
7. Rohsenow, W. M., and Hartnett, J. P. (1973).Handbook of Heat Transfer, McGraw-Hill.
8. Ergun S., Fluid flow through packed columns, Chem. Eng.Prog. 48 (1952) 89–94.
9. Jones D.P., Krier H., Gas flow resistance measurements through packed beds at high Reynolds numbers, J. Fluids Eng. 105 (1983) 168–173.

DISTRIBUTION AND HEAT TRANSFER CHARACTERISTICS OF CO_2 IN A MULTI MICRO-CHANNEL TUBE EVAPORATOR

Siyoung Jeong *, Dae-hwan Kim
Dept. of Mechanical Engineering, Sogang Univ., Seoul, Republic of Korea

ABSTRACT. In this study, the distribution and heat transfer characteristics of CO_2 are experimentally investigated for an evaporator composed of 10 extruded aluminum tubes. The 1000 mm long tube has six micro-channels with a diameter of 0.8 mm. The distribution of CO_2 into each tube and the heat transfer characteristics are investigated by measuring the wall temperature along the tubes. The temperature differences are greater at upper tubes (pass #9 and 10) and at longer distance from the inlet. It is thought that less refrigerant is supplied to upper tubes because of the mal-distribution due to the gravity. Further investigation is required on these phenomena with more experimental data.

Keywords: *Refrigerant distribution, Evaporator, Carbon dioxide, Micro-channel tube*

INTRODUCTION

Because of the restriction on using ozone depleting substances, a natural working fluid CO_2 is a good candidate for a refrigerant of vapour compression refrigeration systems. Because of high operating pressure of CO_2 refrigeration systems, micro-channel tubes made of extruded aluminum are suitable for evaporators. In designing the micro-channel evaporator of a CO_2 refrigeration system, one of the issues is the refrigerant distribution in evaporators as Pettersen et al. [1] pointed out.

Some studies [2, 3] have been carried out for various micro-channel evaporators. However, since the properties of CO_2 is quite different from those of conventional refrigerants, two-phase flow pattern and heat transfer characteristics of CO_2 is quite different from other refrigerants. Moreover, researches on CO_2 are very limited [4, 5]. Therefore, the refrigerant distribution characteristics studies on CO_2 are needed to be investigated extensively considering the geometry of the evaporators and various operating conditions such as mass flux and heat flux.

In our research, the flow distribution characteristics of a parallel-flow micro-channel evaporator will be investigated considering the evaporator position, inlet and exit location, and various operating conditions. Some preliminary experimental results are presented in this paper.

EXPERIMENT

Experimental apparatus

Since direct measurement of liquid distribution is difficult, heat transfer tube wall temperatures were used as an indirect indicator. Regions with little or no liquid will have poor internal heat transfer, resulting in high tube -wall temperatures.

Figure 1 shows the schematic diagram of the experimental apparatus. The sub-cooled liquid state CO_2 is circulated by a magnetic gear pump, and the mass flow rate is measured by a mass flow meter using Coriolis' effect. A pre-heater is installed to make CO_2 at the test section inlet a saturated liquid state. The state of the refrigerant flow is observed at two sight glasses installed at the inlet and exit of the test section. The inlet refrigerant pressure is detected by an absolute

* Corresponding author
Phone: + (82)-2-705-8633, Fax: + (82)-2-712-0799
E-mail address: syjeong@sogang.ac.kr

pressure transmitter (A.P.T.). A differential pressure transmitter (D.P.T.) measures the pressure difference between the inlet and outlet of the test section. In the test section consisting of ten parallel extruded aluminium tubes (Figure 2), liquid state carbon dioxide is heated and evaporated by the Joule heat of the heating wire winding the micro-channel tube. The inlet and exit header have three connecting pipes respectively to test the effect of the inlet and exit location. In the present study, the inlet is the bottom of the header and the exit is the top of the header. The length of the tube is 1000mm, and it has 6 circular micro-channels of which the diameter is 0.8mm (Figure 3). Figure 4 shows a cross section of header and the tube arrangement. The inner diameter of header is 15mm, and ten tubes are installed at the interval of 15mm. The tubes are inserted 5 mm into the header.

Calibrated T-type thermocouples were attached at the tube wall to measure the outer wall temperature. The thermocouples are checked to have the accuracy of 0.2K by flowing liquid-phase CO_2. Temperatures were measured at 5 locations per tube (6, 248, 490, 732, and 974 mm from the inlet of the test section). The details of the heating wire and the thermocouple arrangement are shown in Figure 5. The temperature and pressure data were recorded in a data acquisition board. In order to condense the evaporated CO_2, a thermostat and a counter flow heat exchanger was installed. The liquefied CO_2 refrigerant, which is separated in the accumulator, is supplied to the gear pump. A relief valve was installed to secure the system from overpressure. The entire system including the test section is well insulated. Before charging the system with CO_2 refrigerant, the system was evacuated by a vacuum pump. The charging amount was measured with an electronic scale. For each experimental condition, the data were collected for 2 minutes when the system reached steady state.

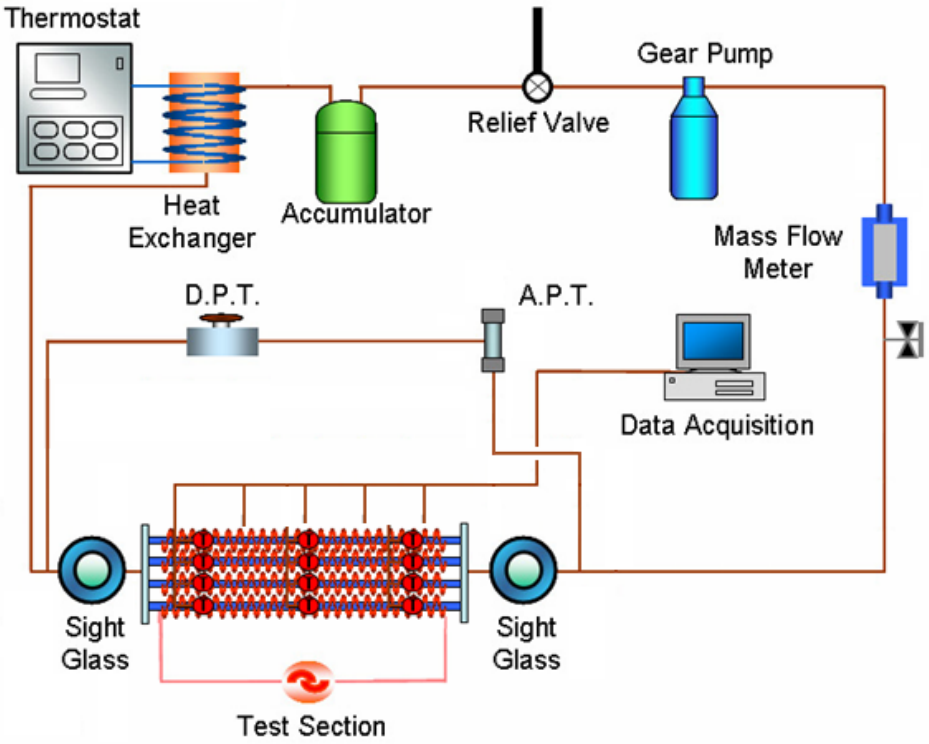

Figure 1. Experimental apparatus

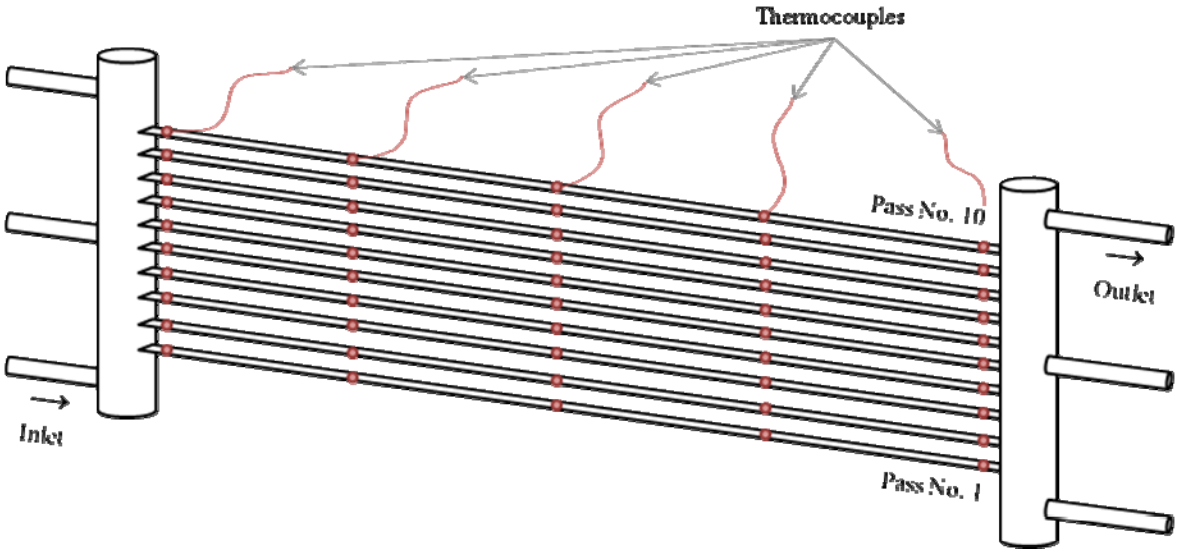

Figure 2. Test section

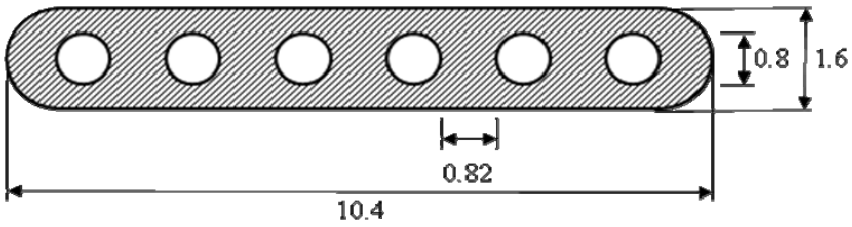

Figure 3. Cross section of the micro-channel tube (unit: mm)

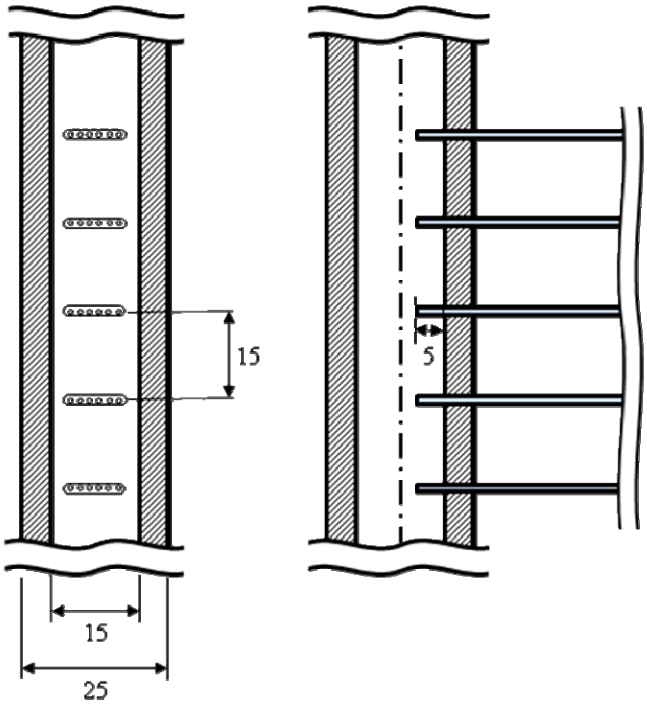

Figure 4. Cross section of the header (unit: mm)

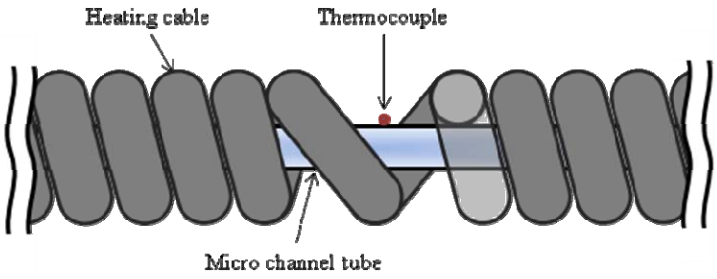

Figure 5. Arrangement of the heating wire and the thermocouple

The heat flux is calculated by the electric current and resistance of the test section.

$$q'' = \frac{I^2 R}{A} \tag{1}$$

The saturation temperature of CO_2 is determined from the property relation of CO_2. The properties of CO_2 were calculated with REFPROP version 6.01.

$$P_{sat} = P_{sat.in} - \Delta P \frac{l}{L} \tag{2}$$

$$T_{sat} = f\left(P_{sat}\right) \tag{3}$$

Temperature difference between the outer wall temperature and the saturation temperature of is an indirect indicator of the flow distribution.

$$\Delta T = T_{wo} - T_{sat} \tag{4}$$

RESULT AND DISCUSSION

Figure 6 shows the temperature difference at the mass flow rates of the refrigerant were 160, 200, and 400 kg/m^{2}s. All of them are under the same heat flux condition of 8kW/m^2. The evaporation temperature of the refrigerant is 5^{o}C. Because of its similarity, the temperatures at pass 2, 3, 4 and 6 are not plotted on the graph.

In spite of the mass flow variation, the temperature distribution of other passes than pass #10, do not change considerably. Temperature differences are about 10 K regardless of the mass flux and the distance from the inlet. The difference among the passes becomes remarkable at lower mass fluxes. At the mass flux of 200 kg/m^{2}s it is observed that the temperature differences are higher at upper tubes (pass #9 and10). Especially, the top pass (pass #10) shows much higher temperature difference at the distance of 732 and 974 mm. It is thought that less refrigerant is supplied to upper tubes because of the mal-distribution due to the gravity. It seems that the dry-out of CO_2 causes a high temperature difference. It implies that the mal-distribution of the refrigerant can be a serious problem for upper tubes at lower mass fluxes.

Figure 7 shows the pressure drop across the test section. If the tubes are not heated, the pressure drop is increased almost in proportion to the mass flow rate. At the heat flux of 8kW/m^2, the pressure drop increases by about 30 % comparing with no heat flux condition.

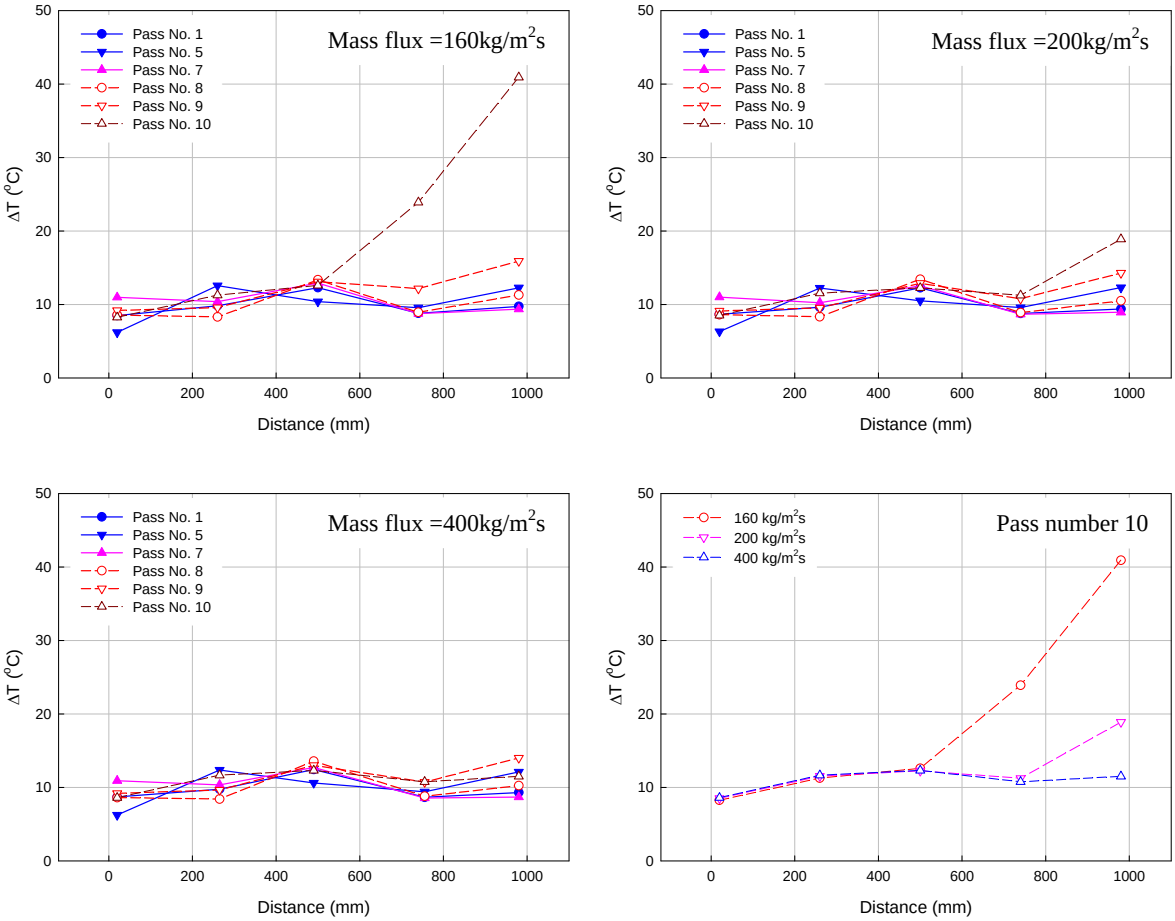

Figure 6 Effect of mass flux on temperature difference (T=5°C, q'' =8kW/m^2)

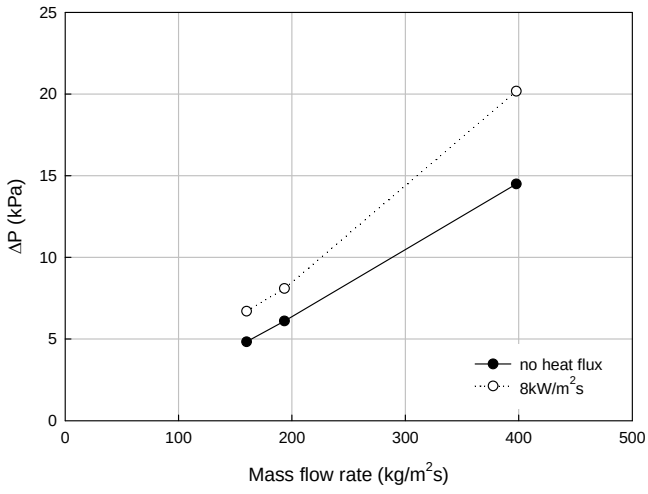

Figure 7 Effect of mass flux on pressure drop (T=5°C, q'' =8kW/m^2)

CONCLUSION

In this paper, the flow distribution characteristics of a multi-port parallel-flow CO_2 evaporator using micro-channel tubes are studied, and the following preliminary results are obtained.

- The inlet and exit part of the tube indicate higher temperature difference than the middle of the tube.
- The temperature differences are higher at upper tubes (pass #9 and10). Especially, the top pass (pass #10) shows much higher temperature difference than other passes. It is thought that less refrigerant is supplied to upper tubes because of the mal-distribution due to the gravity.
- Especially at the top pass(pass #10), this tendency is observed more clearly at the end of the channel, if the mass flux is lower,.

Further investigation is required on these phenomena with more experimental data.

NOMENCLATURE

A	Inner wall area (m^2)
L	Length of test tube (m)
l	Distance from the inlet (m)
ΔP	Pressure drop between inlet and exit (kPa)

Subscripts

in	inlet
sat	Saturated state
wo	Outer wall

ACKNOWLEDGEMENTS

This study was supported by the Ministry of Commerce, Industry, and Energy of Korea (No. 00014863: Development of CO_2 heat exchangers for cooling, heating and hot water supply system).

REFERENCES

1. J. Pettersen, A. Hafner and G. Skaugen, Development of compact heat exchangers for CO_2 air-conditioning systems, *International Journal of Refrigeration*, Vol. 21 No. 3 pp. 180-193, 1998.
2. Tushar Kulkarni, Clark W. Bullard, Keumnam Cho, Header design tradeoffs in microchannel evaporators, *Applied Thermal Engineering*, Vol. 24, pp 759-776, 2004.
3. Honggi Cho and Keumnam Cho, Performance comparison of microchannel evaporators with refrigerant R-22, *Journal of Mechanical Science and Technology*, Vol. 21, pp. 1926-1934, 2007.
4. Rin Yun, Yongchan Kim, Min Soo Kim, Convective boiling heat transfer characteristics of CO_2 in microchannels, *International Journal of Heat and Mass Transfer*, Vol. 48, pp. 235-242, 2005.
5. Siyoung Jeong, Dongho Park, Evaporating heat transfer and pressure drop of CO_2 in a multi-channel micro-tube, Submitted to the *22nd IIR international congress of refrigeration*, Beijing, China, August 21-26, 2007.

HEAT TRANSFER HYSTERESIS FOR SUDDEN GROWTH HEAT FLUX

T.M. Wójcik
Kielce University of Technology, Kielce, Poland

ABSTRACT. The paper presents results of experimental investigations of boiling heat transfer in metal, fibrous capillary porous structures. Boiling curves were determined in terms of dynamic changes of heat flux. The measurements in these terms confirmed the existence of type II hysteresis. All the ranges of boiling curve designated for slow changes of the heat flux are shown at the curve in terms of dynamic changes of heat flux. The phenomenon of hysteresis type II is independent of the supply of heat, and models developed for type II hysteresis can be transferred to the actual conditions of acceptance of electronic systems in the heat.

Keywords: porous covering, boiling, hysteresis

INTRODUCTION

Capillary porous structures (CPSs) intensify heat transfer in boiling. Boiling heat transfer on surfaces with CPSs is a complex thermodynamic process combining phase change, heat transfer as well as the motion of liquid and vapor. Due to incomplete understanding of the boiling process inside the porous structures, the formulae defining the heat flux or heat transfer coefficients are mostly empirical or based on the similarity theory. Until now, no general view has been formed on the causes behind the increase in the heat transfer coefficient and the decrease in superheating of the heating surface which initiates the boiling process on porous surfaces.

Heat transfer hysteresis manifests much more clearly when the heating surface is covered with CPS than in boiling on a smooth surface.

One of the least frequently presented types of boiling heat transfer hysteresis is *II type hysteresis*, also called *simple hysteresis loop*. It is characterized by the heat transfer coefficient increase at the heat flux diminishing, prior to the heat flux reaching the maximum value. Hysteresis of this type was only presented by Tehver [1] - Figure 1, Kravčenko [2] - Figure 2, Wójcik and Poniewski [3,4]. Figure 3 presents the characteristic experimental boiling curve for *type II hysteresis* observed by Wójcik and Poniewski. The heat transfer coefficient increases as the heat flux diminishes, prior to the latter reaching the maximum density. The change in the value of the heat transfer coefficient is attributed to the change in the number of active boiling centres. *II type hysteresis* might be caused by the fact that the centres once activated remain so when the heat flux decreases.

Corresponding author: Dr. T.M. Wójcik
Phone: + (48)-41-3424458,
E-mail address: tmptw@tu.kielce.pl

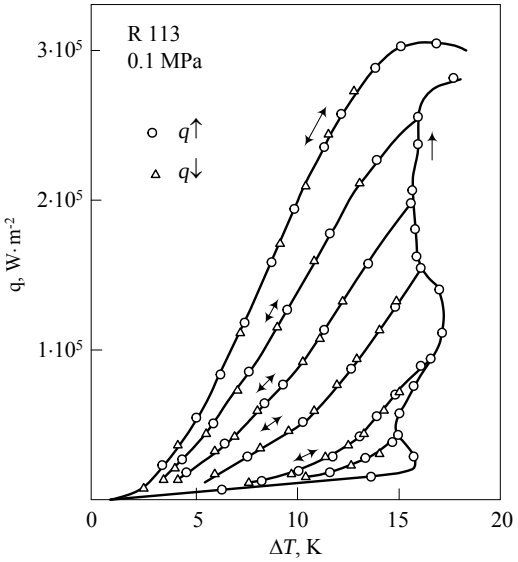

Figure 1. II type hysteresis presented by Tehver [1], plasma-sprayed surface.

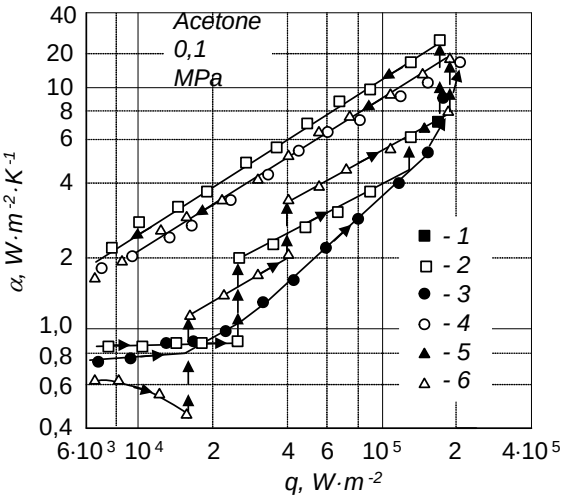

Figure 2. II type hysteresis presented by Kravčenko [2], gas-thermally porous surfaces.

Hysteresis is observed after the heat flux is decreased in range ***b***, Fig.3. Phenomenon was determined for the liquids of the contact angle smaller than that of water, i.e. R-113, R-123, ethanol and for copper, fibrous coverings of small thickness ($\delta \leq 0.6$ mm). The typical phenomena presented in this figure were also observed for ethanol or refrigerants, for other coverings. At boiling of ethanol, refrigerants R 113 and R 123, for samples of small covering thickness, the II type hysteresis phenomena were observed in the whole range of porosity changes.

MECHANISMS OF BOILING HYSTERESIS

The analysis of experimental results for type II hysteresis helped to determine the characteristic ranges of boiling curves.

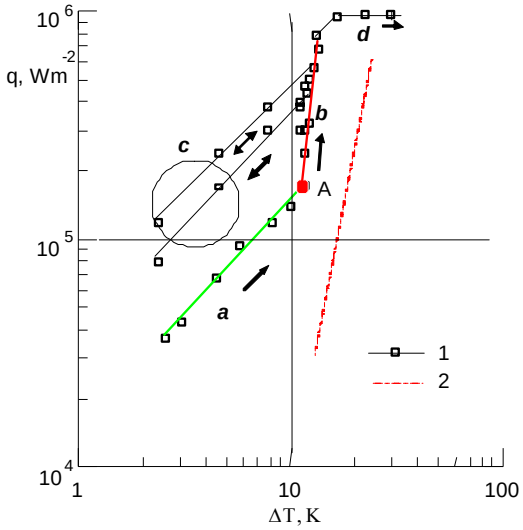

Figure 3. II type hysteresis observed by Wójcik and Poniewski [3,4].

An explicit nucleate boiling was observed in range ***a,*** Fig.3. It was assumed that the boiling initiates on the porous covering external surface. The character of the boiling curve, - $q \sim \Delta T^{1...2}$, in part ***a*** indicates a constant or slightly increasing value of a heat transfer coefficient. The number of active nucleation sites is either constant or slightly increasing. The occurrence of such a mechanism is fostered by porous covering characteristics. High value of skeleton heat conductivity of the structure ($\lambda_s \sim 70$ $Wm^{-1}K^{-1}$) and its small thickness result in slight temperature drops on the covering thickness.

In the structure of non-homogeneous pore size distribution, gradual activation of nuclei of smaller and smaller diameter D_a takes place, when the heating surface temperature increases.

The heat transfer mechanism in the range ***a*** is presented in Figure 4.

Along with increasing the heat flux, in point ***"A"*** (Fig.3) there is a change in boiling curve slope into - $q \sim \Delta T^{4...9}$, which confirms a change in heat transfer mechanism. In point ***"A"*** pores activation inside the structure takes place, and it is a delayed activation (in terms of higher superheating value ΔT than this coming from nucleation superheating dependence, formula (1)). The phenomena is fostered by physical parameters of heat-carrying agent, specially a low value of contact angle, causing the "flooding" of potential nucleation sites inside the structure.

A sudden change in the boiling curve in range ***b*** indicates that along with the increasing heat flux, the number of nucleation sites also increases. Activation of new sites is more violent than for technically smooth surface, for which $q \sim \Delta T^{3.3}$.

Hysteresis occurs after the heat flux has been diminished in range ***b.*** It means that after the activation of nucleation sites inside the structure and after diminishing the heat flux they are still active. The heat transfer mechanism in the range ***b*** is presented in Figure 5.

Boiling curve segments in range ***c*** are stable in temperature ranges presented in Fig.3, with increasing and diminishing heat flux. In range ***c*** moving to the curve located above is possible through curve ***b.*** A lower heat flux value for the same temperature difference (lower curve from ranges ***c*** or curve ***a***) is possible to obtain only when the boiling is stopped.

Ranges ***b*** and ***c*** are especially important for the mechanism of type II hysteresis forming.

EXPERIMENTAL SET-UP AND METHODOLOGY OF INVESTIGATIONS

The objective of the present study was to investigate whether the heat flux supply has an impact on the hysteresis phenomenon and determine the shape of the curve with boiling hysteresis in terms of dynamic changes of heat flux. The diagram of the measurement stand and its basic module is presented in Figure 6.

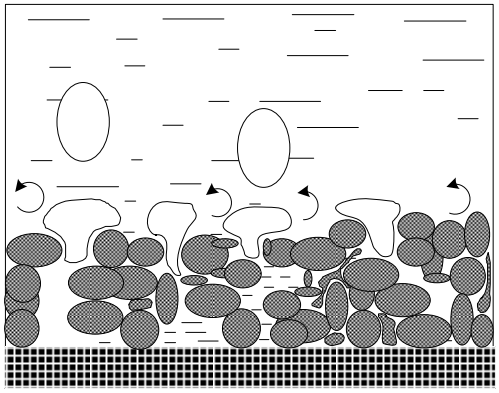

Figure 4. Heat transfer mechanism in range **a** boiling curve with type II hysteresis.

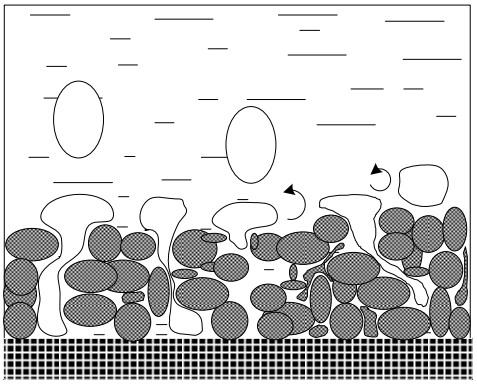

Figure 5. Heat transfer mechanism in range **b** boiling curve with type II hysteresis.

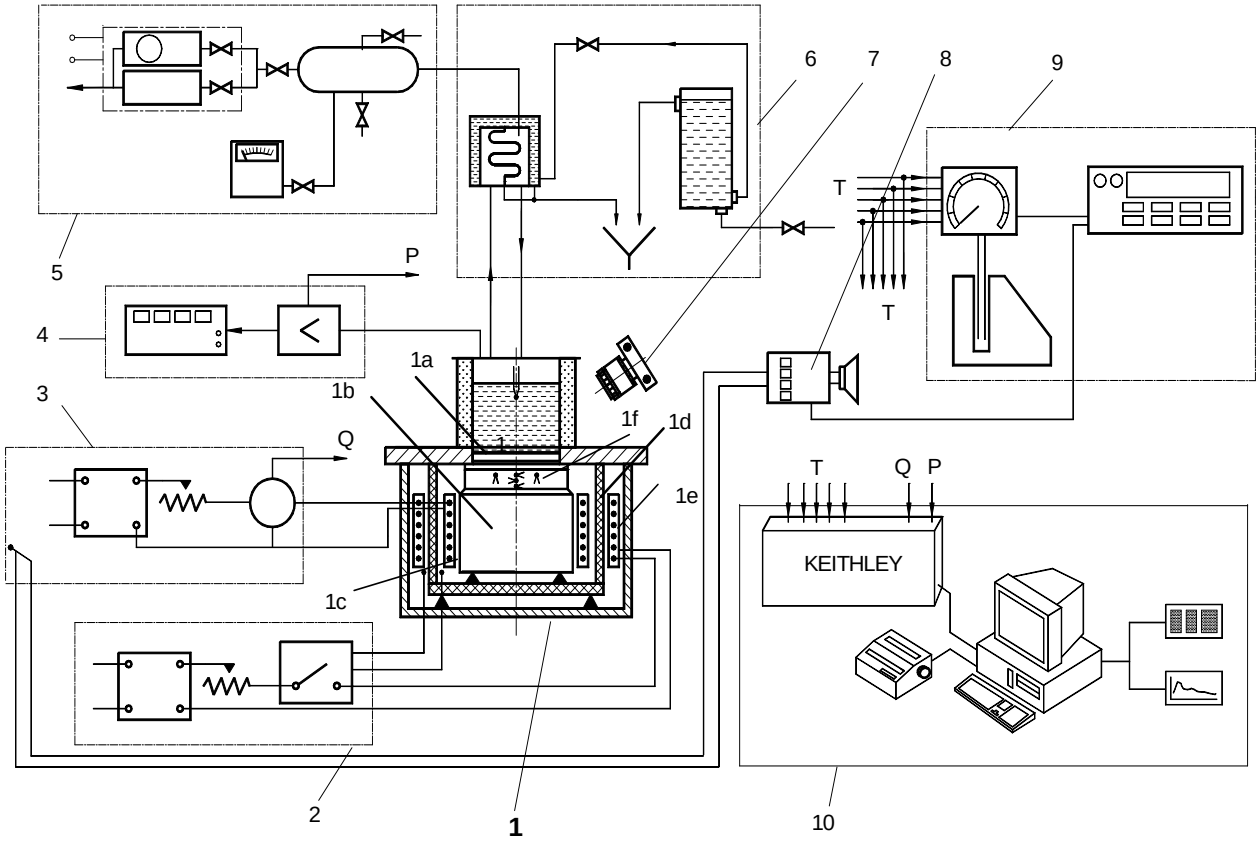

Figure 6. Diagram of the experimental stand and auxiliary systems: 1 - basic module; 2- heat loss compensation system; 3 - heating module with input power reading ; 4 - measurement of pressure in liquid tank; 5 - low pressure generating and measuring module; 6 - vapor cooling and condensate recovering module; 7 - digital high speed camera; 8 - excessive temperature signaling module; 9 - temperature measuring module; 10 - data collecting and processing module; p - pressure; Q- electric power; T- temperature.

A specimen (1a, Fig. 6) with a porous covering was mounted on a copper cylinder (1b). A heater wound around the cylinder (1c) was charged via autotransformer. The cylinder was thermally isolated with a ceramic pipe (1d) and insulation fillings. A compensation heater (1e) mounted on the exterior of the ceramic pipe (1d) provided additional protection against heat loss. Type K thermocouples (1f) were mounted underneath the specimen, on the axis of the cylinder and in the boiling liquid. The temperature of the heating surface was determined by extrapolating to it temperatures measured along the axis of the cylinder.

The measurement error was 9% for temperature differences and 12% for the heat flux.

Metal, fibrous capillary-porous covering of the heating surface is a layer of sprinkled wires, sintered to one another and to the heating surface, Fig. 8. The main structural parameters of the covering, made most often of copper or steel, are as follows: wire diameter d_w, wire length l_w , layer porosity Π, layer thickness δ. They range: d_w = 10 - 100 μm, l_w = 1 - 10 mm, Π = 40 – 85%, δ = 0.2 – 2 mm. For metal, fibrous coverings, unlike in other methods, e.g. thermal spray technique, we can plan the parameters that want to obtain.

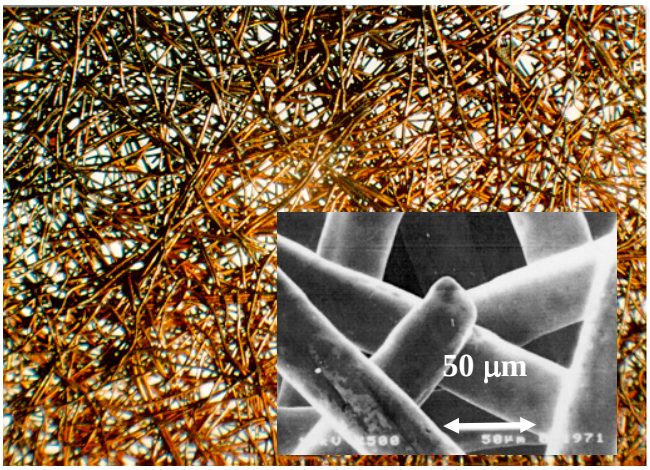

Figure 8. Metal, fibrous porous structure.

The advantages fibrous, porous coverings have over structures manufactured with other methods have been well recognised. Those coverings are characterised by high skeleton conductivity as well as only open porosity and simple manufacturing. Other advantages include the possibility of porous coverings deposition over the base surfaces of complex shapes and, which is the most important, a high value of the heat transfer coefficient. The latter was confirmed by many experimental investigations.

The basic investigation of boiling heat transfer on a heating surface covered with a porous layer was preceded by testing measurements of the stand. The test consisted in determining the boiling curve for the smooth reference surface and comparing it with data provided in literature. The results of heat transfer measurements for nucleate boiling on a copper reference surface were in the range of results obtained by other authors.

The investigation of heat transfer on horizontal heating surfaces covered with porous layers was carried out for ethanol, R – 113 and R - 123 boiling, at atmospheric pressure.

Prior to the experiment, the CPSs were submitted to a preparatory procedure that included wiping them with acetone, rinsing in ethanol, and drying. Specimens mounted to the heating cylinder were left in the liquid for approximately 24 hours. The proper experiments were preceded by intense nucleate

boiling for approximately half an hour. The power of the main heater was then decreased, until boiling subsided.

The applied experimental procedure, Figure 9, was as follows: first, the heater power was increased. Once the target heat flux q_1, Fig. 9a, was attained, it was reduced to a value at which nucleate boiling did not subside. The procedure was repeated by increasing the heat flux to the new value of q_2, Fig. 9b, which was bigger than the previous one, and once more decreased. These steps were repeated until the maximum heat flux q_{max} was reached, Fig. 9c. It was not always possible to obtain the maximum heat flux for a certain porous structure. Figure 3 presents the characteristic experimental boiling curve obtained for this procedure.

The aim of this study was to investigate whether the heat flux supply has an impact on the hysteresis phenomenon and determine the shape of the curve with boiling hysteresis in terms of dynamic changes of heat flux. The procedure was as follows: after the system has reached the balance, under the conditions of stable nucleate heating (q_{min}), the heater power increased to q_{max}, Fig. 9d (1), which resulted in a systematic increase specimen temperature. Once the maximum allowed temperature measured inside the heating cylinder was attained, the heat flux was decreased until boiling subsided, Fig. 9d (1).

Thermocouples were mounted underneath the specimen, on the axis of the heating cylinder and in the boiling liquid. Temperatures were recorded every 0.5 seconds through a data acquisition system. The heat flux density was determined by a gradient method. The temperature of the heating surface was determined by extrapolating to it the temperatures measured along the axis of the cylinder.

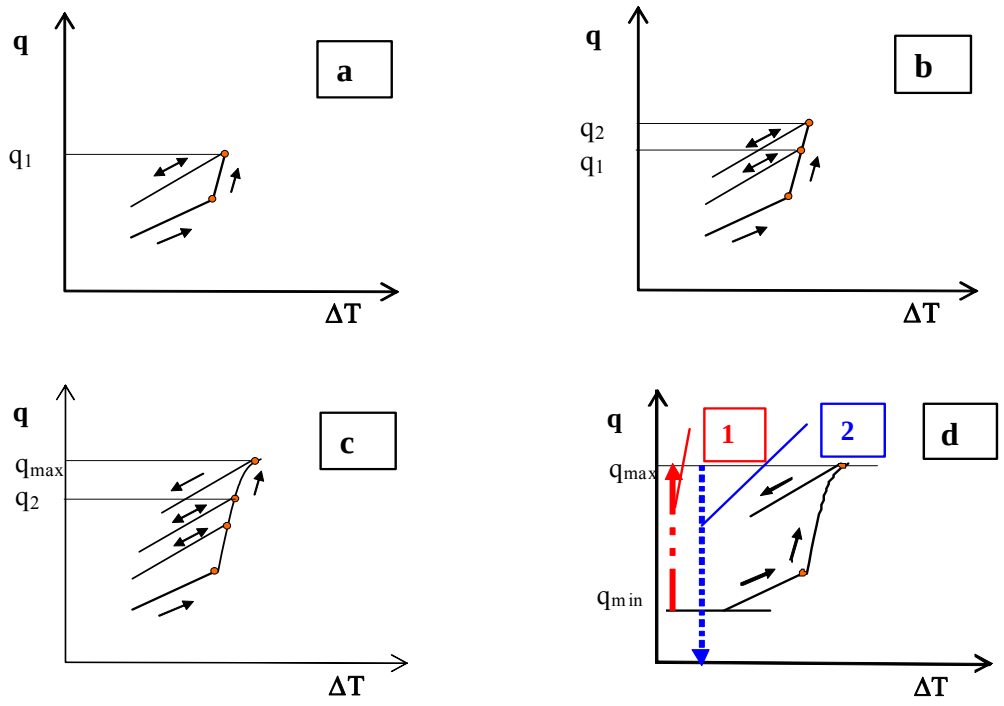

Figure 9. Procedure of determining the boiling curve *(curves **a**, **b** and **c** apply to hysteresis occurring before q_{max} is attained, and curve **d** hysteresis for sudden growth heat flux)*

RESULTS

Figure 10 shows the results of the measurements for the thin-layer covering of copper, fibrous CPS. The measurements and calculations confirmed the existence of *type II hysteresis* in terms of dynamic changes of heat flux. The ranges of *a, b, c* and *d* are shown at boiling curve, just as in Figure 3. As planned, the method of the heat flux supply does not affect the type II heat transfer hysteresis, confirms the physical mechanisms of the phenomenon.

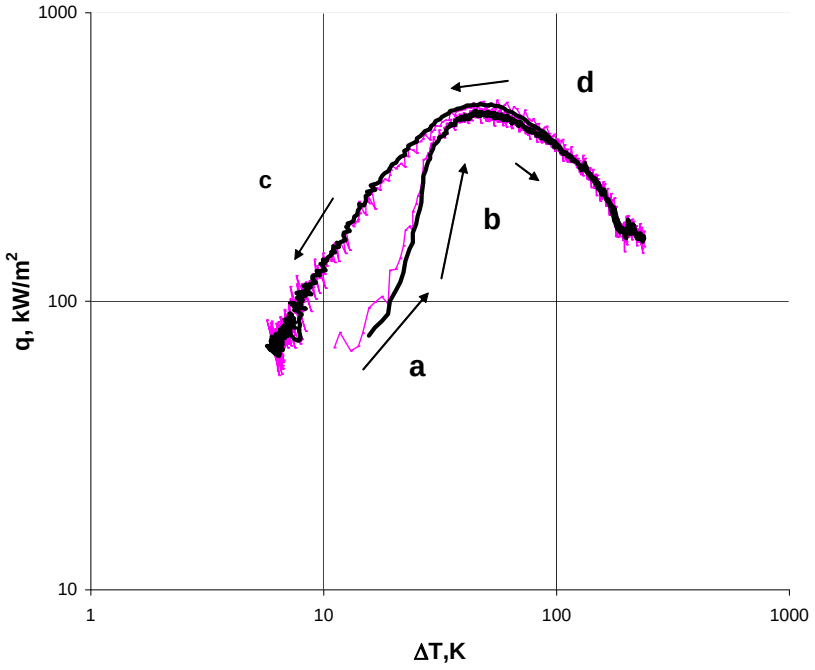

Figure 10. Results of experimental research for R - 123, copper, fibrous, CPS, δ = 0.6 mm, Π= 85%, atmospheric pressure

CONCLUSIONS

The aim of this paper was to investigate whether the heat flux supply has an impact on the hysteresis phenomenon and to determine the shape of the curve with boiling hysteresis in terms of dynamic changes of heat flux.

The measurements and calculations confirmed the existence of type II hysteresis in these terms.

All the ranges shown of boiling curve designated for slow changes of the feat flux are shown at curve in terms of dynamic changes of heat flux.

This means that the type II hysteresis phenomenon is independent of the supply of heat and models developed for type II hysteresis can be transferred to the actual conditions of reception of heat, for example rapid changes in the load of electronic circuits.

REFERENCES

1. Tehver Ja.Ch., Sui Ch.N., Temkina V.S., Heat Transfer and Hysteresis Phenomenon in Boiling on Porous Plasma - Sprayed Surface, *Experimental Thermal and Fluid Science,* Vol. 5, pp. 714-727, 1992.
2. Kravčenko V.A., Ostrovskij N.Ju., Boiling hysteresis and transient phenomena for pure and mixed liquids on sprayed surfaces (in Russian), *Teploenergetika*, No. 6, pp. 61-63, 1988.
3. Poniewski M.E., Wojcik T.M., Experimental Investigation of Boiling Heat Transfer Hysteresis on Metal Fibrous Porous Coverings, *Archives of Thermodynamics*, Vol. 20, No. 1-2, pp. 93-118, 1999.
4. Wojcik T.M., Poniewski M.E., Experimental Investigations and Modeling of Boiling Heat Transfer Hysteresis on Porous Surfaces, *Journal of Enhanced Heat Transfer*, Vol. 15 (4), pp. 1–13, 2008.

Acknowledgment

This paper was supported by The Polish State Committee for Scientific Research, Grant No R0602602

AN EXPERIMENTAL STUDY ON PERFORMANCE OF POLYMER HEAT EXCHANGER FOR EXHAUST HEAT RECOVERY IN VENTILATION SYSTEM

S. Y. Yoo, K. H. Han*, J. H. Kim
BK21 Mechatronics Group in Chungnam National University, Daejeon, Korea

ABSTRACT. The purpose of this research is to develop high efficiency polymer plate heat exchangers which can be substituted for aluminium plate heat exchangers and applied directly to the conventional ventilation system. Since thermal conductivity of polymer is much smaller than that of aluminium, enhancement techniques for convective heat transfer are adopted to compensate conduction resistance. Square dimple type and hexagon dimple type heat exchangers are developed and compared with square plate type and hexagon plate type heat exchangers used as reference model. Thermal performance and pressure drop for each polymer heat exchanger are measured in various operation conditions and compared each other. From the experimental results, correlations for the heat transfer coefficient and friction factor are obtained. Effectiveness of the square dimple type and hexagon dimple type is improved about 100% and 50% at air velocity of 2.5m/sec compared to the square plate type and the hexagon plate type, respectively.

Keywords: *polymer heat exchanger, ventilation system, heat transfer enhancement, pressure drop, effectiveness*

INTRODUCTION

Heat recovery units have been widely used for energy saving and it usually recovers around 60~80% of wasted thermal energy which improves about 20~30% of total system efficiency. Conventional HVAC systems have commonly adopted the rotary-wheel type, and the aluminium plate type heat exchangers. However, they have been used only for limited industrial applications such as buildings because of high cost and lack of concern of people in practical fields like HVAC systems in housing. An integrated unit that consists of air filters, heat exchangers, and an air-conditioning system not only makes a pleasant environment also saves lots of energy in cooling and heating.

The aluminium plate heat exchangers have been used widely for ventilation heat recovery in the air-conditioning system, and various non-metallic materials such as pulp, Teflon, and polymer have been adopted as a material of heat exchangers for the same usage. Among those non-metallic materials, polymer is one of the most promised materials because of its competitive mechanical advantages: low cost, light weight, easy processing, high corrosion-resistance, and so forth. [1]

The principal aim of this research is to develop high efficiency polymer plate heat exchangers which can be substituted for aluminium plate heat exchangers. Typical plate type heat exchangers have smooth flat-plate surfaces or finned-flat-plate surfaces. Since these kinds of surface structures demonstrate a low heat transfer coefficient, typically passive ways, which are to increase surface area or the number of plates per unit volume, have been applied for heat exchanger designs.[2] Thus, these heat exchangers have a bigger volume and a low efficiency. In order to obtain competitive polymer

* Corresponding author: K. H. Han
Phone: + (82)-42-821-8901, Fax: + (82)-42-821-8894
E-mail address: khhan@cnu.ac.kr

plate heat exchangers, various heat transfer enhancement techniques should be studied and applied to overcome the extremely low thermal conductivity.

Heat transfer enhancement techniques can be classified as passive, which manipulate the plate surface, and active which manage working fluid inside of heat exchangers. In this research, various passive enhancement techniques are applied to develop polymer plate heat exchangers. Since thermal conductivity of polymer is far smaller than that of aluminium, various heat transfer enhancement techniques are applied to design the surface of polymer plates.

DESIGN OF POLYMER HEAT EXCHANGERS

Existing polymer heat exchangers for exhaust heat recovery have a plate-fin-type structure which has great manufacturing advantages by being pressed in the forming process. In this study, four different prototypes of heat exchangers are designed and manufactured.(dimple square type, dimple hexagon type, square plate type and hexagon plate type) PP and PVC that have thickness 4mm are chosen for material of polymer heat exchanger because of its competitive mechanical characteristics. Both show high resistance to heat and chemical elements. Moreover, it is easy to fabricate on any complex surface geometry.

Heat exchangers have been initially developed using square flat, and the hexagon flat type heat exchanger can be used as of reference model to evaluate how much heat transfer performance increases. As shown in Figure 1, square and hexagon plate type heat exchangers are fabricated without manipulation of heat transfer area. The square plate type heat exchanger has a 4mm height and 230mm width of inflow. The flame to divide the flow is constructed with acrylic that has a 5mm width of both side, 2mm width of central side. The hexagon flat type is fabricated with hexagonal heat transfer area that satisfies the structure of flow of cross and counter in both. It has a 160mm width of inflow, and 4mm height of each channel.

In this study, enhanced heat transfer techniques are applied to develop the square dimple type and hexagon dimple type. Figure 2 depicts the surface and configuration of plates. Two different sizes of dimples, a hemisphere shape of a 4mm diameter and a 1mm diameter, are placed alternately with 25mm distance in between each of them. The bigger dimples not only increase the heat transfer area and generate vortexes and turbulence but also support the plates. Thus, any supporting frame is not required between plates. The outside of the dimples act as vortex generators, and secondary flows inside of the dimples promote heat transfer. The square dimple and hexagon dimple type heat exchangers are expected to produce higher overall heat transfer performance and pressure drop than simple plate type since it has a complex surface geometry compared to that of the simple plate type. The inflow width of each type is 210mm in dimple square type and 160mm in dimple hexagon type.

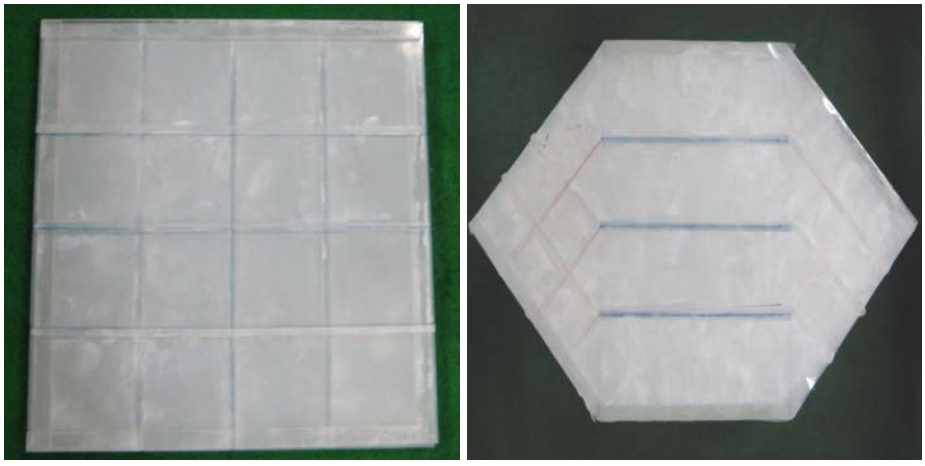

Figure 1. (a) Square plate type and (b) hexagon plate type polymer heat exchanger

Figure 2. (a) Square dimple type and (b) hexagon dimple type polymer heat exchanger

EXPERIMENTAL APPARATUS AND METHODS

Experimental apparatus

A test apparatus for polymer plate heat exchanger is designed, and Figure 3 shows the schematic of the performance test facility. In order to minimize heat loss to surroundings, whole ducts are well insulated. Each fan is set up at the end of both outlets of a heat exchanger, and they operate as suction pumps which can eliminate disturbances in measuring. Nozzles are used as flow meters and placed at the outlets of fans. A hot water bath and a cold water bath are used for maintaining constant inlet air temperature. Inflow airs to cold side and hot side pass fin-tube-type heat exchangers in which hot water

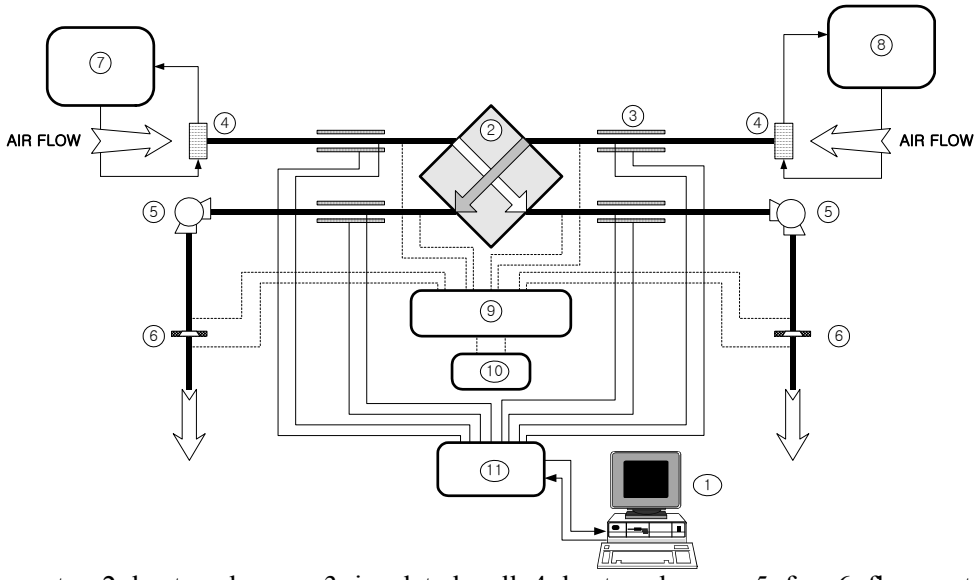

1: computer, 2: heat exchanger, 3: insulated wall, 4: heat exchanger, 5: fan, 6: flow meter,

7: hot water bath, 8: cool water bath, 9: scanning box, 10: micro-manometer, 11: data acquisition system

…: pressure measuring, —: temperature measuring

Figure 3. Schematic of performance test facility

and cold water are circulated. Pressure drop in heat exchanger and flow rate are measured using micro-manometer and scanning box simultaneously. Because multi-sampling provides high precision results 14 pressure-measuring tabs are installed at inlet/outlet of heat exchanger and nozzles: two tabs are located at the upper side and the lower side of duct for each inlet/outlet of heat exchanger, and three tabs are set at each nozzle. In order to eliminate the influence of dynamic pressure on measuring flow rate, pressure-measuring tabs have a 2mm diameter less than recommended 3.2mm in ASHRAE standards. Calibrated T-type thermocouples are inserted on the duct wall for monitoring interaction between the duct sides and surroundings.[3]

Experimental methods

System performance can be described by heat transfer efficiency and pressure loss. Thus, in this study, performance tests are carried out on both of them. Pressure losses between the inlet and outlet of the heat exchanger are measured according to different flow rates, 0.3 ~ 3 m/sec. Heat transfer performance tests and pressure loss tests are performed under the same condition simultaneously. It is required to eliminate heat interaction between the flow air and duct wall before the performance test. Therefore, 1 hour pre-running at the initial condition of the test keeps all conditions a steady state inside of the apparatus. After the system reaches a steady state, another pre-running period is necessary to obtain steady state at given flow rate and it takes around 5 minutes to come to the steady state. The results of the last two minutes are taken from the 10 minutes running at given operation conditions.

RESULTS AND DISCUSSION

Pressure loss

Figure 4 provides the measured pressure loss of each heat exchanger model at various air velocities. Pressure loss tends to increase with the square of the velocity. The square plate type which has the simplest structure of flow channels shows the lowest pressure loss compared to other heat exchangers. Both dimple type has the similar pressure drop and show higher results than both plate type. In the case of hexagon plate type, there is no manipulation of heat transfer area like square plate type, but pressure loss is higher than square plate type because of existing separation zone of flow.

The friction factor f is a dimensionless number that is used for the quantitative comparison of the pressure losses of heat exchangers, and Reynolds number is used as a dimensionless number for air velocity. Figure 5 shows friction factors of each heat exchanger model according to various Reynolds number. Friction factor and Reynolds number are defined in equation (1) and (2)

$$f = \frac{\Delta P}{\frac{1}{2}\rho V^2} \cdot \frac{D_h}{L} \tag{1}$$

$$\mathrm{Re} = \frac{VD_h}{\upsilon} \tag{2}$$

Here, the parameter L is the channel length of heat exchanger V is the face velocity and D_h is the hydraulic diameter of a channel. Both dimple type show higher friction factors than both plate type. Friction factors of the square dimple type are prone to decrease gradually with increasing Reynolds number, while friction factors of the square plate type drop rapidly. The principle reason of this trend is that main pressure loss is occurring inside of the channels of former heat exchangers, but it happens at the face of heat exchanger for the latter model. This indicates that pressure loss in the low Reynolds number range, and pressure loss inside of channels increases as flow rate increases. Thus, Figure 5 illustrates well about this phenomenon nicely. Unlikely, friction factors of hexagon type heat exchangers decrease with similar tenderness. Since, the hexagon type is less number of

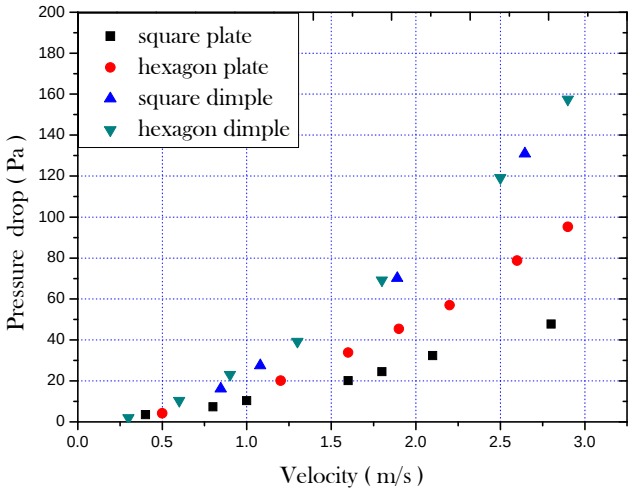

Figure 4. Comparison of pressure loss at various air velocities

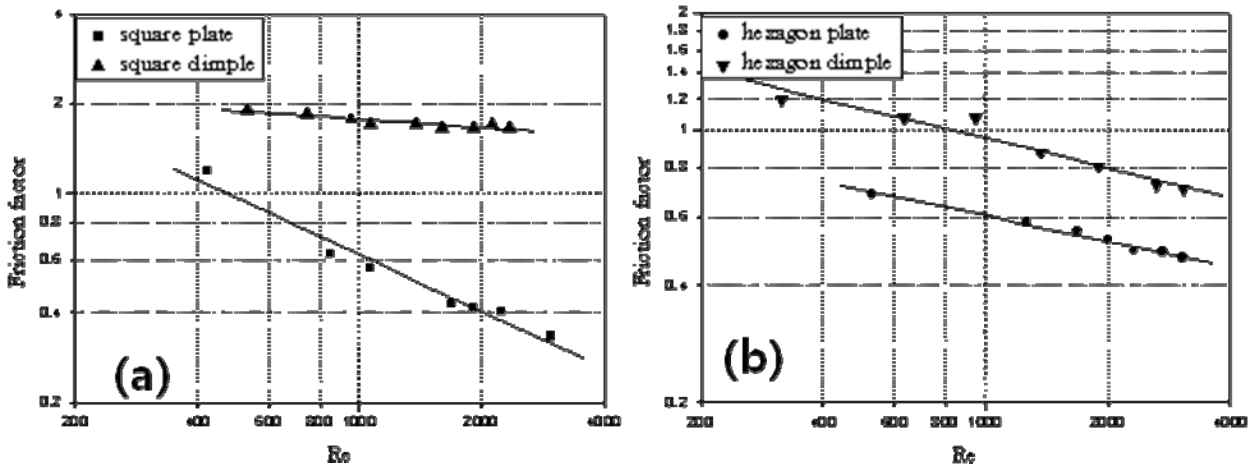

Figure 5. Comparison of dependence of friction factor on Reynolds number of (a) square shape (b) hexagon shape.

dimple than square dimple type, the rate of pressure losses of both hexagon type heat exchanger are considered as similar.

As a result, the correlation equation that need to calculate the power of heat exchanger in ventilation system can be obtained from Figure 5.

$$\text{Square plate type} : \quad f = 47.6\,\mathrm{Re}^{-0.627} \tag{3}$$

$$\text{Hexagon plate type} : \quad f = 2.71\,\mathrm{Re}^{-0.217} \tag{4}$$

$$\text{Square dimple type} : \quad f = 3.38\,\mathrm{Re}^{-0.093} \tag{5}$$

$$\text{Hexagon dimple type} : \quad f = 5.41\,\mathrm{Re}^{-0.261} \tag{6}$$

Heat transfer performance

If there are no heat losses, the heat transfer rate in heat exchangers from the hot air should be equal to the heat transfer rate to the cold air based on the first law of thermodynamics. The overall heat transfer rate for an air-to-air heat exchanger can be expressed as by Newton's law of cooling, and it can be modified for cross-flow heat exchangers, adopting the correlation factors as

$$\dot{Q} = UAF\Delta T_m \tag{7}$$

where $\dot{Q}$ is the heat transfer rate, U is the overall heat transfer rate, A is the heat transfer area, F is the correction factor, and ΔT_m is the log mean temperature difference. The maximum error of the heat transfer rate balance between the cold side and the hot side is less than 5%, and the error becomes less than 2% over the air velocity 1.5 m/sec. Thus, average values of two heat transfer rates are taken as the representative heat transfer rate. Heat transfer capacity of heat exchangers can be expressed in terms of the value of UAF, and Figure 6 provides the value of UAF of each model at various velocities. Both dimple type also has higher value of UAF than that of both models as in the pressure loss comparison, but the square dimple type shows higher values of UAF than the values of the dimple hexagon model.

The average heat transfer coefficient can be obtained using the value of UAF based on energy balance equations. Nusselt number is used as a dimensionless number of the heat transfer coefficient. Figure 7 shows the comparison of the dependence of Nusselt number on Reynolds number of each model. The correlation equations about Nusselt number on Reynolds number of each models represent as

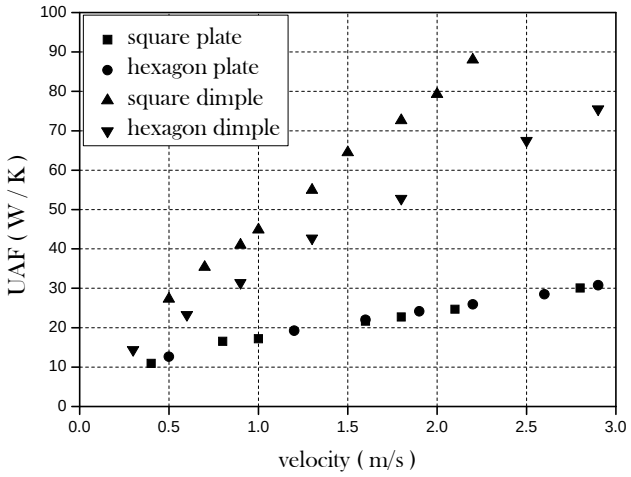

Figure 6. Comparison of UAF at various air velocities

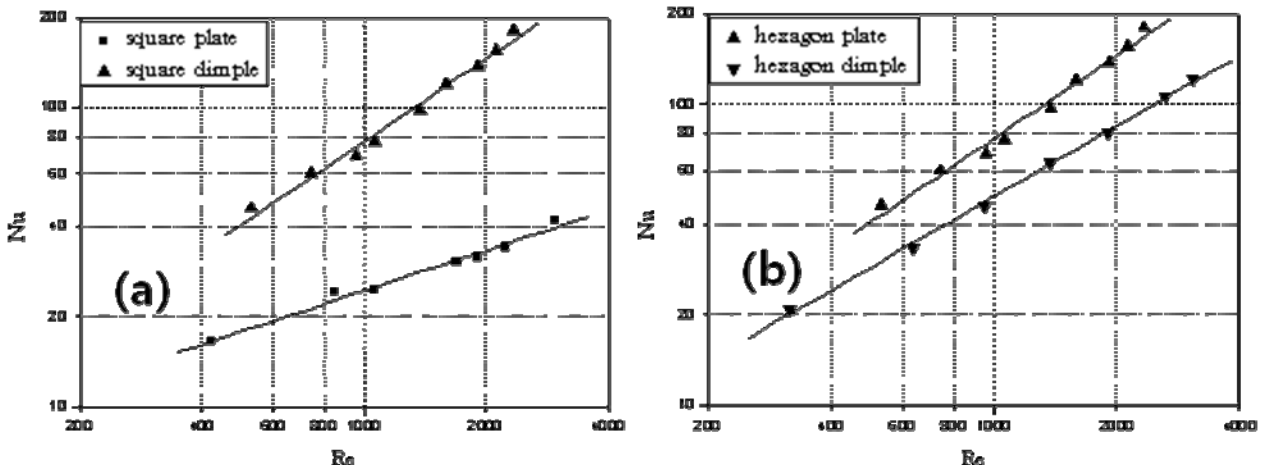

Figure 7. Comparison of dependence of Nusselt number on Reynolds number of (a) square shape (b) hexagon shape.

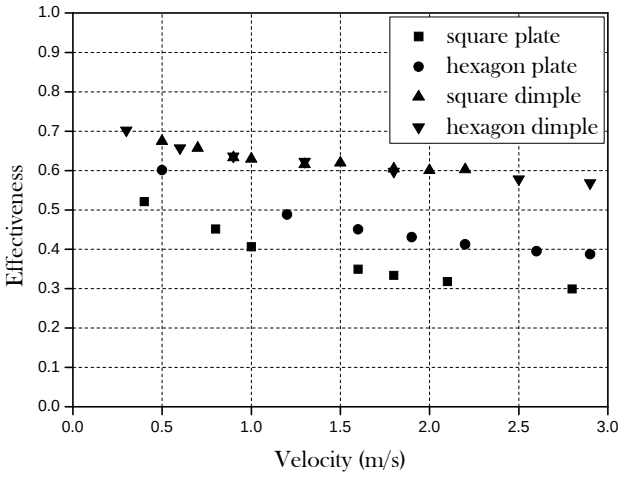

Figure 8. Comparison of effectiveness at various air velocities

$$\text{Square plate type} \quad : \quad Nu = 0.478\,\mathrm{Re}^{0.971} \tag{8}$$

$$\text{Hexagon plate type} \quad : \quad Nu = 0.512\,\mathrm{Re}^{0.928} \tag{9}$$

$$\text{Square dimple type} \quad : \quad Nu = 0.389\,\mathrm{Re}^{1.435} \tag{10}$$

$$\text{Hexagon dimple type} \quad : \quad Nu = 0.368\,\mathrm{Re}^{1.384} \tag{11}$$

Another way to investigate the performance of heat exchangers is based on a dimensionless value called the heat transfer effectiveness ε defined as

$$\varepsilon = \frac{\dot{Q}_{actual}}{\dot{Q}_{\max}} \tag{12}$$

Figure 8 provides the comparison of effectiveness at various velocities. The square dimple and hexagon dimple type show very similar results through whole ranges of velocity, and hexagon plate type is somewhat better than the square plate type. The effectiveness of the square dimple type and the hexagon dimple type are improved about 100% and 50% at air velocity 2.5m/sec. Effectiveness tends to decrease as velocity increases

Performance at equivalent fan power

The allowed fan capacity and the pressure loss should be considered in heat exchanger design. Pressure losses inside of heat exchangers can be converted to electrical input power to the fans. Enhanced overall performance of heat exchangers is obtained by the difference in the amount of improved heat transfer rate as a gain and pressure loss as a loss under same condition. Figure 9 shows possible heat transfer capacities of each model at the same fan power, and this comparison allows evaluating overall performance improvement and input power simultaneously. The square dimple type shows slightly higher overall performance than the hexagon dimple type.

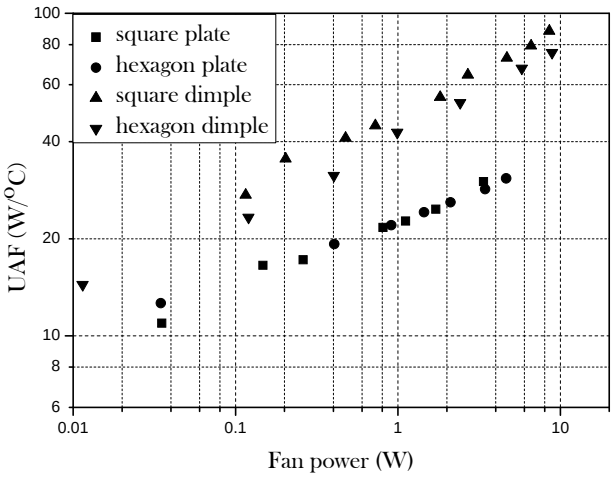

Figure 9. Comparison of UAF at equivalent fan power

CONCLUSION

Four types of the polymer plate heat exchanger are designed and manufactured, that is, the square plate type, hexagon plate type, square dimple type, hexagon dimple type. Thermal performance and pressure loss of the polymer plate heat exchanger are measured and compared in various operating conditions. The major results of this study are as follows.

[1] Friction factor of the square dimple type and hexagon dimple type increase about 350%, 60% respectively compare to the square plate type and the hexagon plate type heat exchanger at Reynolds number 2,000

[2] Effectiveness of the square dimple type and hexagon dimple type is improved about 100% and 50% at air velocity of 2.5m/sec compared to the square plate type and the hexagon plate type, respectively.

ACKNOWLEDGEMENT

This research was partially supported by the Korea Energy Management Corporation and by the Program for the Training of Graduate Students in Regional Innovation.

REFERENCES

1. Chung, M. H., A Study on the Heat Recovery Performance of Plastic and Paper Heat Exchanger, PhD thesis, Chungnam National University, Daejeon, Korea, 2003.
2. Fehle, R., Klas, J., and Mayinger, F., Investigation of Local Heat Transfer in Compact Heat Exchangers by Holographic Interferometry, Experimental Thermal and Fluid Science, Vol 10., pp181-194, 1995.
3. Method of Testing Air-to-air Heat Exchanger, ASHRAE Standard-84, 1991

NATURAL CONVECTION REGIME WITHIN A WING LEADING EDGE ENCLOSURE. PART 1: EFFECTS OF VENTILATION CONFIGURATION

D. Moore[1*], V. Egan[1], D. Newport[1], V. Lacarac[2]
[1]Department of Mechanical & Aeronautical Engineering, University of Limerick, Limerick, Ireland
[2]Airbus, Filton, Bristol BS99, 7AR, United Kingdom

ABSTRACT. The natural convection regime present within a simulated aircraft wing leading edge enclosure containing a horizontal isothermal cylinder is presented in this paper. A number of different ventilation configurations are investigated and compared to an unventilated case. A mixing ventilation regime with a single vent located on the lower surface of the enclosure exhibited very little difference in the thermal distribution within the enclosure compared to the unventilated case. This highlights the poor performance of mixing ventilation in such a configuration. Moving to a displacement ventilation configuration showed a significant reduction in the enclosure temperatures, with the greatest reduction seen with the vent openings placed on the upper and lower enclosure surfaces respectively. Placing the two ventilation openings on the lower enclosure surface saw a reduction of 70% in the mass flow rate across the vent boundary compared to the vents located on the upper and lower surfaces. As a result a significant increase in the average enclosure temperature was recorded.

Keywords: *Natural convection, Enclosure, Ventilation.*

INTRODUCTION

Natural convection plays an important role in many engineering disciplines such as electronics cooling, nuclear reactors and aircraft heat transfer. The convective regime present depends on enclosure geometry, the position and type of thermal boundary conditions along with the material and fluid properties within the enclosure. In natural convection, a coupling of the thermal and velocity fields is present within an enclosure. This means that a slight change in the operating conditions may have a significant impact on the enclosure thermal distribution, altering the convective regime considerably. This effect needs top be fully appreciated in order to limit the exposure of thermally sensitive equipment operating within to high heat loads.

During normal operations, particularly in high ambient temperature environments during turnaround, an aircraft stationary on the tarmac may be subjected to significant heating effects. Solar loading on the upper skin surface coupled with ground reflection heating the lower surface can result in an aggressive thermal environment for the aircraft to operate in. This is especially true in the wing leading edge where the presence of an engine bleed duct transporting high temperature fluid to the main fuselage through the leading edge also contributes to this thermal environment. The overall influence of both these contributions to heat transfer in a wing leading edge must be understood for effective thermal management.

Differentially heated enclosures have been the subject of numerous investigations in the literature including studies on the effect of aspect ratio [1-3], thermal boundary conditions [4,5], and enclosure geometries [6-8]. The convective regime present within is found to be highly sensitive to enclosure

* Corresponding author: Mr. D. Moore
Phone: + (353)-61-202471, Fax: + (353)-61-202393
E-mail address: daithi.moore@ul.ie

conditions often with complex flow patterns induced, even for simple geometrical and thermal boundary conditions. Convective instabilities may also be increased when deviating away from a simple square or rectangular enclosure to a more complex shape [7]

The introduction of a discrete source into such an enclosure has a marked effect on natural convection within. For a heated object within an isothermal or adiabatic enclosure, the flow regime is driven solely by the heat source and is primarily determined by position [9] and Rayleigh number. A much more complex system is present when the heat source is coupled with external boundary conditions (e.g. a differentially heated enclosure). In this case the interaction between the two systems produce a regime that is much more complex than for each contribution seen separately, which may be difficult to predict without some insight into the flow phenomenon present. To the best of the authors' knowledge, research in this area has not received considerable attention compared to the previous cases, especially in non-standard geometries.

In many engineering applications however, simple natural convection alone may not be enough to provide adequate enclosure cooling, especially if subjected to a high thermal load. In such cases, effective enclosure ventilation is required with a view to reducing the aggressive thermal environment. Typical enclosure ventilation consists of one of two mechanisms: mixing ventilation and displacement ventilation. Mixing ventilation occurs when both the inlet and outlet ventilation flow pass through the same opening in an enclosure. A transfer to displacement ventilation occurs when a second ventilation opening exists in an enclosure, allowing for a separate opening for inlet and outlet ventilation flow. Haslavsky *et al* [10] study the effect of changing from mixing to displacement ventilation on a heated surface within an enclosure. They found that a significant reduction in ΔT between the component and its surroundings is possible, highlighting the effectiveness of displacement over mixing ventilation. Enclosure aspect ratio is also important with respect to enclosure ventilation. Bilgen & Yanange [11] found that a tall or wide enclosure can tend to choke the natural convection flow within, reducing the ventilation performance. This lead to a 50% drop in the Nusselt No. compared to the optimum configuration with an aspect ratio of 1.

This paper details an investigation into the effect of enclosure geometrical configuration upon the ventilation of a simulated aircraft wing leading edge compartment. The configuration and boundary conditions represent a stationary aircraft subjected to direct solar loading from above and ground reflection from below. A horizontal heated cylinder representing an engine bleed duct is also present within the enclosure. In order to reduce any aggressive thermal environment which may be present in the enclosure, ventilation openings are placed on the upper and lower wing skin surfaces. Different ventilation regimes are investigated, both mixing and displacement types and are compared to an unventilated enclosure to assess their performance.

DATA REDUCTION

The temperature, horizontal and vertical positioning were non-dimensionalised using the following transformations:

$$T^* = \frac{T - T_C}{T_H - T_C}, \quad X^* = \frac{x}{L}, \quad Y^* = \frac{y}{H}$$

where the subscripts C and H denote the coldest and hottest surface temperature respectively. The Rayleigh number based on cylinder diameter (d) is defined as:

$$Ra = \frac{g\beta(\Delta T)d^3}{\nu\alpha}$$

The fluid velocity normal to the vent boundaries are obtained from the expression

$$N = U_i Cos\theta + V_j Sin\theta$$

where θ is the angle of inclination of the vent. The mass flow rate is defined as

$$\dot{m} = \int \rho NA$$

where A is the unit area taken across the vent surface.

EXPERIMENTATION

Experimental temperature and velocity measurements were recorded within a ventilated leading edge enclosure. The enclosure dimensions are 300mm (H) x 550mm (L) x 600mm (D). The rear wall and leading edge surfaces were constructed from 10mm and 3mm thick respictively. An aluminium horizontal cylinder of diameter 50mm, length 580mm and wall thickness 3mm is present at location A of Figure 1. A glass window is present at the front of the enclosure for optical access, with the back of the enclosure sealed with a polycarbonate sheet. A polycarbonate window is also present in the rear wall of the enclosure to allow for laser sheet illumination in the enclosure.

Thermal boundary conditions are applied to the enclosure surfaces using Elemex thin film rubber backed heater mat with a 500W mat attached to the upper and lower surfaces of the enclosure and a 250W mat attached to the cylinder surface. Each heater mat is connected to a Eurotherm 2216e PID controller, which provided isothermal conditions on the enclosure surfaces, verified by thermocouples in contact with the enclosure surfaces. All other surfaces of the enclosure are assumed to be adiabatic with approximately 50mm of fibreglass insulation placed over the exterior surfaces to eliminate any heat loss to the environment. Ventilation openings 1 – 3 are placed in the enclosure as shown in Figure 1. These are 50mm in width and have a wire mesh placed over the openings, which constitute a 60% open ventilation area.

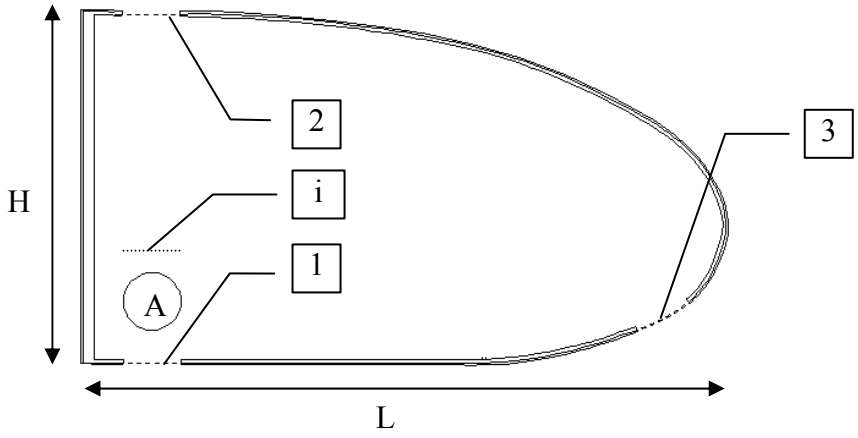

Figure 1 Enclosure Configuration Parameters

A number of different configurations within the leading edge enclosure are investigated. The enclosure geometrical configurations for Cases 1 – 4 are outlined in Table 1 in conjunction with Figure 1. Cases 1-4 represent the different ventilation configurations; an unventilated enclosure (Case 1), mixing ventilation (Case 2) and displacement ventilation (Case 3 & 4). All cases are subjected to identical

thermal boundary conditions, with the upper surface, lower surface and cylinder heated to 373K, 343K and 408K respectively. This results in a Rayleigh number based on the cylinder diameter of 6.5×10^5. All fluid properties are taken at the film temperature.

Table 1
Enclosure Geometrical Configurations Case 1 - 4

	Case 1	Case 2	Case 3	Case 4
Vent Openings	-	1	1 & 2	1 & 3

Temperature measurements are taken within the enclosure using calibrated K-type thermocouples placed along the interior surfaces and the horizontal and vertical centreline within the enclosure. The temperatures are recorded using a Stanford Research Systems SR630 16 Channel Thermocouple Reader. All temperature measurements are recorded at steady-state conditions which are defined as no greater than ±0.5°C change per hour. A maximum uncertainty in T* is found to be 1.3% during experimentation.

Velocity measurements within the enclosure are obtained by employing Particle Image Velocimetery (PIV). The flow was seeded using incense smoke, its particle diameter of typically 0.1-0.5μm [13, 14] deemed sufficiently small to accurately follow the flow field within the enclosure. In order to allow the seeding particles to reach neutral buoyancy, an external enclosure of 1.2m (H) x 1.2m (W) x 0.6m (D) was constructed, with the leading edge placed centrally within the enclosure. The incense smoke was then introduced into the outer enclosure with testing commencing after 30 minutes. Image acquisition was controlled by the TSI Insight 3G software package connected to a 2 Megapixel Powerview 2M Plus CCD Camera. The camera has a resolution of 1600 x 1200 and records at 30Hz. A AF Micro Nikkor 50mm f/1.2 D lens was attached to the camera which operated at an aperture of 1/2.8. The flow field was illuminated using a double pulsed 400mJ Nd-Yag laser (532nm) with a maximum operating frequency of 90Hz. Laser optics produce a 1.5mm laser sheet focused 500mm from the lens. The time between pulses is based upon a calculation of

$$t \leq \frac{8Sd_{pixel}}{v_{\max}}$$

where S is the image scale factor, d_{pixel} is the camera pixel pitch and v_{max} is the maximum fluid velocity expected in the test region.

RESULTS

For a simple heated ventilated enclosure, the external temperature boundary conditions are the sole drivers of the convective flow within. The presence of an isothermal cylinder adds complexity to the system with interaction between the enclosure and the buoyant cylinder plume significantly changing the resultant velocity and thermal distribution within the enclosure. Entrained exterior air will also interact with the enclosure flow and so the position and sizing of ventilation openings will be important with regard to the final enclosure conditions.

With these factors in mind, this section will describe the effect of different enclosure configurations, as outlined in Table 1, on the natural convection regime within the leading edge. The effect of ventilation orientation is also analysed, with unventilated, mixing and displacement ventilation systems investigated.

Ventilation configuration

The enclosure temperature distributions for Cases 1 – 4 are presented in Figure 2. A marked difference in the thermal environment within the leading edge can be seen depending on the ventilation configuration. As expected, the highest enclosure temperatures are seen for the unventilated enclosure in Case 1. A constant T* of 0.6 is seen along the horizontal centreline in Figure 2 (a), with a slight increase to 0.67 at X* = 0.1 due to the presence of the heated cylinder plume in this region. An approximately linear increase in T* from 0.54 to 0.61 along the vertical centreline in Figure 2 (b) suggesting a stably stratified fluid is present within the enclosure for this configuration. The mixing ventilation configuration in Case 2 exhibits an almost identical temperature distribution in the enclosure to that seen for Case 1. This demonstrates the ineffectiveness of a single vent located at the bottom surface of an enclosure. There is very little influx of cooler exterior air into the enclosure to aid in reducing the interior temperatures. This is mainly attributed to the choking of the ventilation flow at the vent boundary as for a mixing ventilation scenario, both the inflow and outflow must occur at the same opening in the enclosure. In Case 2 the opening is relatively small (50mm) and this severely reduces the ability of cooler exterior air to be entrained into the enclosure. A small recirculation zone is present at the vent boundary, with very little penetration into the enclosure. The rear wall temperatures seen in Figure 2 (c) are also almost identical between Case 1 and Case 2, again illustrating the ineffectiveness of this ventilation regime for the system under investigation.

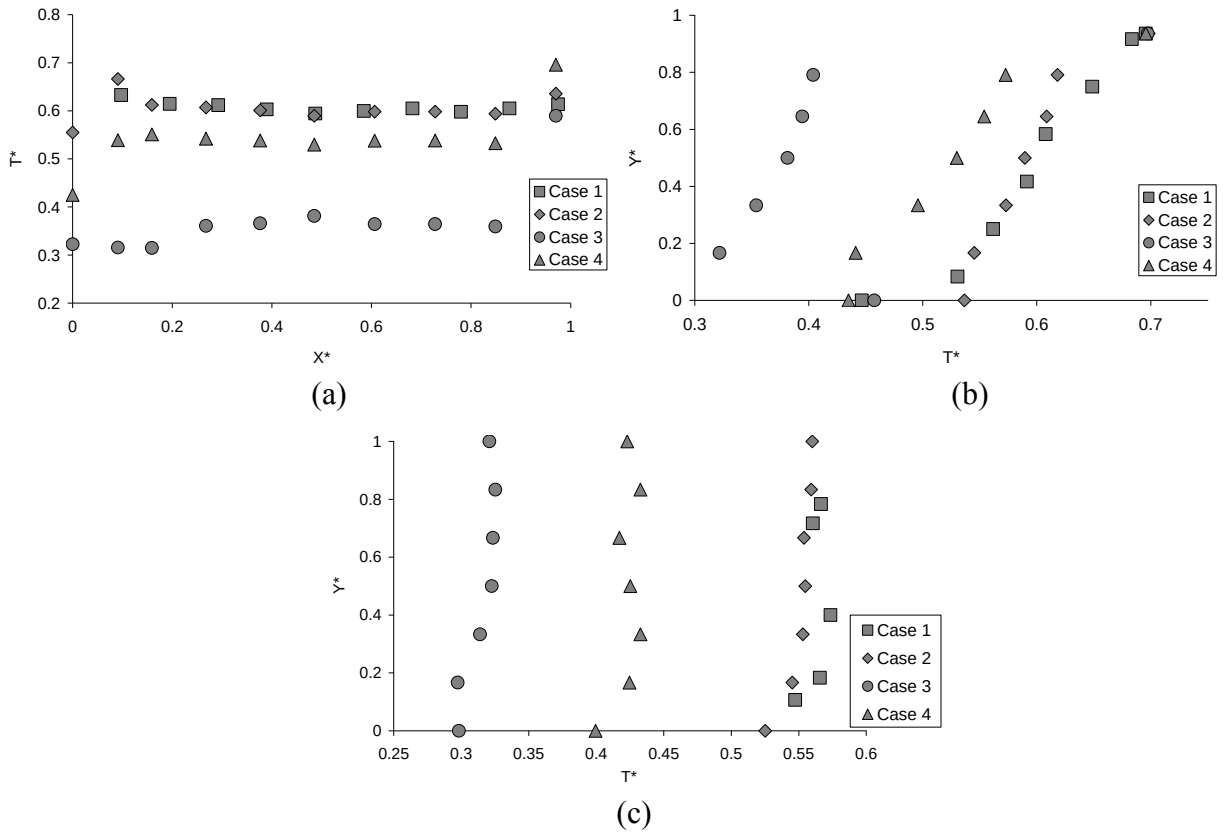

Figure 2 Enclosure Temperature Distributions for the Different Ventilation configurations in Cases 1 – 4 : (a) profile along horizontal centreline, (b) profile taken along vertical centreline, (c) profile taken along vertical centreline

Transferring to a displacement ventilation regime in Case 3 & Case 4 shows a significant reduction in both the interior fluid and rear wall temperatures compared to the previous cases. The lowest enclosure

temperatures are seen in Case 3 with the vent openings located on the upper and lower enclosure surfaces. An approximate T* of 0.35 along the horizontal centreline is 40% lower than Case 2 and 35% lower than for Case 4. A similar trend in seen along the vertical centreline in Figure 2 (b), with the temperatures seen in Case 3 40% and 30% lower than Case 2 & Case 4 respectively. The temperature distribution along vertical centreline in Figure 2 (b) suggests the presence of large thermal gradients along both the upper and lower surface of the enclosure ($0<Y^*<0.19$ and $0.8<Y^*<1$). This indicates regions of high heat transfer along the interior enclosure surfaces in Case 3. This effect is not seen to the same extent for the other cases presented, particularly along the lower enclosure surface. This phenomenon may be present, but the spatial resolution of the thermocouple distribution used may not be sufficiently fine to capture any such effect.

The temperature profiles along the rear wall of the enclosure again show a large variation depending on the ventilation configuration. As noted previously, T* is identical along the wall height for the unventilated and mixing ventilation regimes in Case 1 & Case 2. The lowest wall temperatures are again seen in Case 3, which are up to 40% lower than Case 1 & Case 2. This occurs due to the ventilation path passing adjacent to the rear wall as it travels from the inlet to exit vent, helping to reduce the temperatures along the enclosure rear wall. The rear wall temperature reduction is much greater compared to the reduction in the interior fluid temperatures within the enclosure in Case 4. This is primarily as a result of a change in the cylinder plume orientation. For Case 1 & Case 2, the plume was found to attach to the rear wall surface with its heating effect contributing significantly to the temperature of the surface. In Case 4, the plume is found not to attach to the rear wall of the enclosure, but is orientated towards the centre of the compartment. This sets up an anticlockwise recirculation in the rear of the enclosure, resulting in a negative buoyant flow along the rear wall, producing the decrease in T* of 25% in Case 4 compared to Case 1 & Case 2. All of the T* profiles for the four cases under investigation show an approximately constant temperature along the rear wall height. This suggests that the rear wall is thermally isolated from the rest of the enclosure, with conduction between the rear wall and upper and lower enclosure surfaces inhibited.

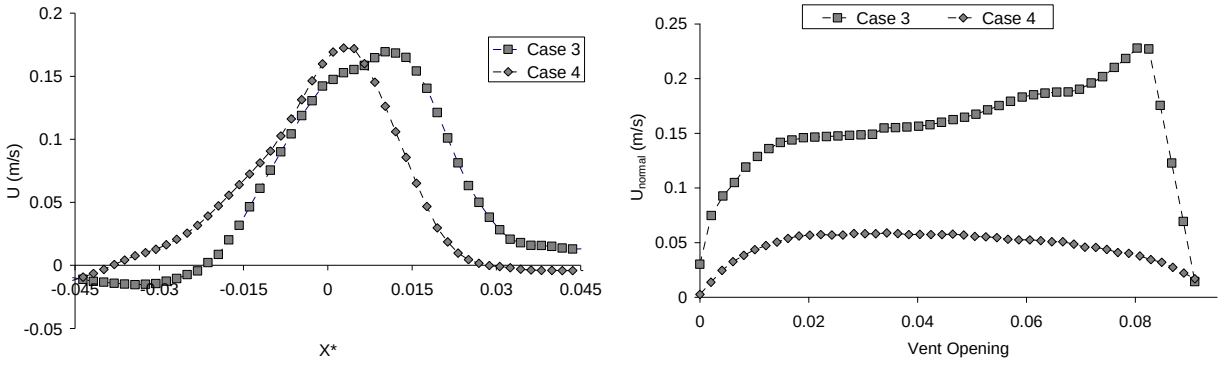

(a) (b)

Figure 3 Velocity profile comparison between the two displacement ventilation regimes under investigation: (a) Cylinder plume structure taken along line (i) in Figure 1, (b) Exit vent flow taken normal to opening (2) for Case 3 and opening (3) for Case 4

The ventilation strategy used in Case 3 is found to be optimal as it allows for the entrainment of cool exterior air to be entrained into the enclosure from below and the hotter, more buoyant fluid to exit through the vent opening in the upper surface of the enclosure. This allows a direct path for the ventilation flow to enter the enclosure, interact within, and then exit through the upper vent. Case 4 show a moderate reduction in the horizontal centreline temperature from 0.6 to 0.55, with the largest

influence seen in the vertical centreline, particularly along the lower enclosure surface in this configuration. This suggests that the ventilation path in Case 4 is mainly limited to the lower surface of the enclosure, as it is entrained into the enclosure at the rear vent and passes towards the front vent opening with very little interaction with the remainder of the enclosure. All the temperature profiles exhibit a similar trend along both centrelines, with approximately constant temperatures along the horizontal centreline and linearly increasing temperatures along the vertical centreline. Very little difference in the cylinder plume structures in Figure 3 (a) is noted between Case 3 and Case 4, with Case 4 deflecting towards the centre of the enclosure to a greater degree, with its point of maximum velocity found at X* = 0.011 compared to X* = 0.003 in Case 4.

Table 2
Mass Flow Rates (kg/m) along the Vent Boundary & Average enclosure temperature

	Case 3	Case 4
Exit Vent	0.0184	0.00559
Average Enclosure T*	0.356	0.53

A large difference can be seen in the velocity profile at the exit vent of the enclosure in Figure 3 (b), with Case 3 showing a maximum velocity of 0.23 m/s whilst Case 4 has a maximum velocity at the outlet of 0.056 m/s. This results in a significant reduction in the mass flow rate of air exiting the enclosure from 0.0184 kg/s to 0.00559 kg/s with a corresponding increase in the average enclosure temperature as shown in Table 2. The main benefit of the ventilation regime in Case 3 is that both the buoyant cylinder plume and the enclosure surface flow can exit at the upper surface enclosure opening. In Case 4, the exit flow is comprised mainly of the air travelling along the lower surface of the enclosure, with very little contribution from the cylinder plume.

Whilst Case 3 is found to be the most effective method of reducing the temperature distributions within the enclosure, it may be very impractical from a wing design perspective, with the introduction of a ventilation opening on the upper skin surface incurring a significant drag penalty onto the wing. A more practical solution may be the configuration presented in Case 4 due to possible ventilation locations already present along the lower wing skin surface.

CONCLUSIONS

A comparison between a number of different ventilation configurations is presented in this paper. It was found that a single vent located on the lower surface of the enclosure in Case 2 is highly inefficient at reducing the enclosure temperatures, with an identical thermal distribution present to an unventilated enclosure seen in Case 1. This is primarily due to the choking of the ventilation flow at the vent boundary with little overall entrainment into the enclosure due to the small vent size.

Moving to a displacement ventilation regime in Case 3 shows a significant reduction in the interior temperature distributions with the provision of a separate opening for both the inlet and exit flow. This allowed for more effective removal of heat from the enclosure and an elimination of any recirculation at the vent boundary restricting entrainment into the enclosure. This however, does not represent an adequate ventilation solution as due to design constraints in the leading edge ventilation openings are limited to the lower enclosure surface.

Restricting the ventilation openings to the lower surface in Case 4 saw a rise in the temperatures in the enclosure compared to Case 3. In this case the ventilation path is restricted to the lower enclosure surface as air is entrained into the enclosure at the rear vent and exits the enclosure at the front vent, with little interaction with the core fluid.

Case 4 shows a significant drop of approximately 70% in the mass flow rate of air crossing the exit vent boundary compared to Case 3. In Case 3 there is a contribution from both the buoyant cylinder plume as well as the heated surface flow combining to cross the vent boundary, whereas in Case 4 this is reduced to the flow traveling along the heated lower surface only exiting at the front vent, with little contribution from the cylinder plume.

In Case 4 the rear wall temperatures exhibit a larger drop than the enclosure fluid temperatures when comparing them to the unventilated and mixing ventilated enclosure. This is as a result in a change in the cylinder plume orientation. For Case 1 and Case 2, the cylinder plume is attached to the enclosure rear wall, helping to increase is temperature whereas in Case 4, the plume travels towards the centre of the enclosure. This reduces its heating effect upon the rear wall, whilst at the same time helping to increase the overall enclosure fluid temperature due to strong mixing of the plume flow within the core region.

REFERENCES

[1] Cesini, G., et al., 1999, "Natural convection from a horizontal cylinder in a rectangular cavity." *International Journal of Heat and Mass Transfer*, 42, pp. 1801-1811.

[2] De, A. K. and Dalal, A., 2006, "A numerical study of natural convection around a square, horizontal, heated cylinder placed in an enclosure." *International Journal of Heat and Mass Transfer*, 49, pp. 4608-4623

[3] Cacagni, B., Marsili, F., and Paroncini, M., 2005, "Natural convective heat transfer in square enclosures heated from below." *Applied Thermal Engineering*, 25, pp. 2522-2531

[4] Ben Cheikh, N., Ben Beya, B., and Lili, T., 2007, "Influence of thermal boundary conditions on natural convection in a square enclosure partially heated from below." *International Communications in Heat and Mass Transfer*, 34, pp. 369-379.

[5] Chen, T.-H. and Chen, L.-Y., 2007, "Study of buoyancy induced flows subjected to partially heated sources on the left and bottom walls in a square enclosure." *International Journal of Thermal Sciences*, 46, pp. 1219-1231.

[6] Cianfrini, C., Corcione, M., and Dell'omo, P. P., 2005, "Natural convection in tilted square cavities with differentially heated opposite walls." *International Journal of Thermal Sciences*, 44, pp. 441-451.

[7] Natarajan, E., Basak, T., and Roy, S., 2008, "Natural convection flows in a trapezoidal enclosure with uniform and non-uniform heating of bottom wall." *International Journal of Heat and Mass Transfer*, 51, pp. 747-756.

[8] Lei, C., Armfield, S., and Patterson, J., 2007, "Unsteady natural convection in a waterfilled isosceles triangular enclosure heated from below." *International Journal of Heat and Mass Transfer*, 51, pp. 2637-2650.

[14] Koizumi, H. and Hosokawa, I., 1996, "Chaotic behaviour and heat transfer performance of the natural convection around a hot horizontal cylinder affected by a flat ceiling." *International Journal of Heat and Mass Transfer*, 39(5), pp. 1081-1091

[10] Haslavsky, V., Tanny, J., Teitel, M., 2006, "Interaction between the mixing and displacement modes in a naturally ventilated enclosure", *Building and Environment*, 41, 1755-1761

[11] Bilgen, E., Yamane, T., 2004, "Conjugate heat transfer in enclosures with openings for ventilation", *Heat and Mass Transfer*, 40, pp 401-411.

NATURAL CONVECTION REGIME WITHIN A WING LEADING EDGE ENCLOSURE. PART 2: EFFECTS OF ENCLOSURE PARTITIONING

D. Moore[1*], V. Egan[1], D. Newport[1], V. Lacarac[2]
[1]Department of Mechanical & Aeronautical Engineering, University of Limerick, Limerick, Ireland
[2]Airbus, Filton, Bristol BS99, 7AR, United Kingdom

ABSTRACT. The natural convection regime present within a ventilated enclosure containing a horizontal isothermal cylinder is investigated in this paper. The introduction of a dividing partition into the enclosure saw a marked change in the flow structure present, with the ventilation path between inlet and outlet vent blocked by the partition. Cylinder positioning within the partitioned enclosure is investigated, with a large difference noted the temperature profiles within the interior enclosure fluid and along the enclosure rear wall. The natural convection regime is found to be highly sensitive to the effect of cylinder positioning within the enclosure. A significant reduction in the mass flow rate of air leaving the enclosure is found upon partitioning the enclosure with a pure displacement ventilation regime no longer present for the partitioned cases. This is due to the presence of a region of backflow into the enclosure at the exit vent boundary reducing the overall ventilation effectiveness.

Keywords: *Natural convection, Enclosure, Ventilation, Partitioning*

INTRODUCTION

An understanding of the natural convection regime present within an enclosure is vital in order to provide sufficient provision for component cooling within the enclosure. As the resultant thermal and flow structures are a product of the external boundary conditions, they can be sensitive to the enclosure geometry, orientation and location of heat sources within the enclosure along with the fluid and material properties. In many scenarios, the resultant regime may be highly complex with a strong interaction between the thermal and velocity fields, where a slight change in one can have a marked effect on the other. This means that it can be difficult to quantify the enclosure conditions present without extensive investigation beforehand. One such scenario occurs in the leading edge enclosure of aircraft wings.

As aircraft operations have spread through the world, the range of thermal environments which they encounter varies can vary from arctic to hot dry desert conditions. In these high ambient temperature environments, there may be significant thermal loading present on the leading edge enclosure. This is as a result of direct solar radiation onto the upper enclosure skin and reflection from the ground tarmac heating the lower surface of the enclosure. This differentially heated enclosure is coupled with the presence of a heated horizontal cylinder travelling through the leading edge. This represents an engine bleed duct which transports high temperature fluid from the turbine high stage compressor to the main fuselage where it's used to power various aircraft systems. The combination of both effects can again be very complex and proper understanding of the flow characteristics is vital to provide effective thermal management within the enclosure.

* Corresponding author: Mr. D. Moore
Phone: + (353)-61-202471, Fax: + (353)-61-20
E-mail address: daithi.moore@ul.ie

Significant research has been carried out in the field of differentially heated enclosures, with the effect of enclosure geometry [1-3], thermal boundary conditions [4,5] and aspect ratio [6-8] highly influential on the final enclosure thermal distribution. The introduction of a discrete source into such an enclosure has a marked effect on natural convection within. For a heated object within an isothermal or adiabatic enclosure, the flow regime is driven solely by the heat source and is primarily determined by position [9] and Rayleigh number. A much more complex system is present when the heat source is coupled with external boundary conditions (e.g. a differentially heated enclosure). In this case the interaction between the two systems produce a regime that is much more complex than for each contribution seen separately, which may be difficult to predict without some insight into the flow phenomenon present. To the best of the authors' knowledge, research in this area has not received considerable attention compared to the previous cases, especially in non-standard geometries.

Partitioning an enclosure can have a marked effect on natural convection [11] and can be detrimental to ventilation flow by inhibiting the transport of high temperature fluid from one region to another. Khalifa & Abdullah [12] investigated the effect of different partition configurations on the enclosure Nusselt No. Partitioning, regardless of configuration reduces the Nusselt No. due to the confining of high temperature fluid to a certain region of the enclosure. In extreme cases a large partition to enclosure height can reduce the enclosure Nusselt No by up to 75% [12].

This paper describes the effect of introducing a partitioning structure into the ventilated leading edge enclosure previously investigated in Part 1 [14]. The objectives of this research is to investigate the impact of enclosure partitioning on the ventilation performance and the enclosure thermal distribution. For the current enclosure configuration, the cylinder plume is the main driving force of the convective regime present within. As such the effect of cylinder placement is important with regards to the final enclosure conditions. An investigation into cylinder location within the partitioned ventilated enclosure is carried out in order to determine its impact on the ventilation efficiency and enclosure conditions.

DATA REDUCTION

The temperature, horizontal and vertical positioning were non-dimensionalised using the following transformations:

$$T^* = \frac{T - T_C}{T_H - T_C}, \quad X^* = \frac{x}{L}, \quad Y^* = \frac{y}{H}$$

where the subscripts C and H denote the coldest and hottest surface temperature respectively. The Rayleigh number is defined as:

$$Ra = \frac{g\beta(\Delta T)d^3}{\nu\alpha}$$

The fluid velocity normal to the vent boundaries are obtained from the expression

$$N = U_i Cos\theta + V_j Sin\theta$$

where θ is the angle of inclination of the vent. The mass flow rate is defined as

$$\dot{m} = \int \rho NA$$

where A is the unit area taken across the vent surface.

EXPERIMENTATION

Experimental temperature and velocity measurements were recorded within a ventilated leading edge enclosure. A detailed description of the experimental apparatus is outlined in Part 1 [14].

A number of different configurations within the leading edge enclosure are investigated. The enclosure geometrical configurations for Cases 1 – 4 are outlined in Table 1 in conjunction with Figure 1. Case 4 is the original unpartitioned enclosure subjected to displacement ventilation with two vent openings on the lower surface. Case 2 introduces a partition into the enclosure, with the effect of cylinder position determined from Cases 2-4. All cases are subjected to identical thermal boundary conditions, with the upper surface, lower surface and cylinder heated to 373K, 343K and 408K respectively. This results in a Rayleigh number based on the cylinder diameter of 6.5×10^5. All fluid properties are taken at the film temperature. A description of the methods used to obtain the temperature and velocity distributions are outlined in Part 1 [14].

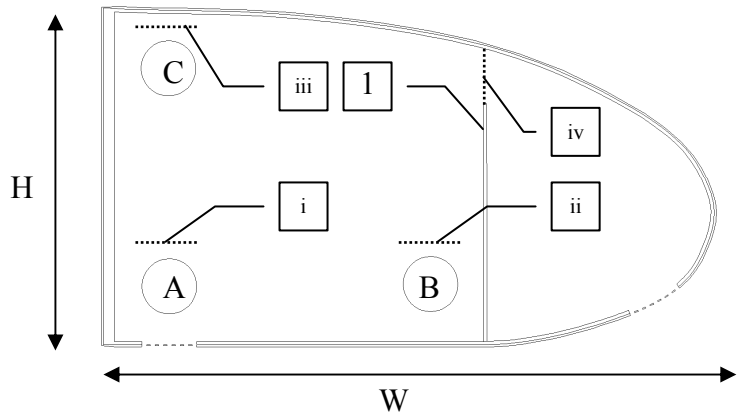

Figure 1 Enclosure Configuration Parameters

Table 1
Enclosure Geometrical Configurations Case 1 - 4

	Case 1	Case 2	Case 3	Case 4
Cylinder Position	A	A	B	C
Partition	No	Yes	Yes	Yes

RESULTS

In this section the effect of enclosure partitioning through the introduction of a leading edge sub-spar is investigated. The results are compared to the unpartitioned enclosure analysed in Part 1 [14]. In order to determine the sensitivity of natural convection regime to bleed duct placement within the partitioned enclosure, three cylinder positions are investigated and the subsequent effect on enclosure ventilation discussed.

Enclosure Partitioning

The impact of introducing a partitioning structure into the leading edge enclosure is examined in this section. From the literature, partitioning is seen to have a detrimental effect upon the natural convection regime present within an enclosure. This results in a restriction in the flow path which can

confine higher temperature fluid to a smaller region, reducing the overall Nusselt number within. A partition is placed in the enclosure as shown in Figure 1. To allow laser access into the front partitioned space, the partition is constructed from transparent glass, with conduction from the heated enclosure surface to the partition assumed negligible due to the low thermal conductivity of the material.

The partitioned and unpartitioned temperature distributions are presented in Figure 2. In the rear partitioned section of the enclosure, both temperature profiles show a constant T* along the horizontal centreline in Figure 2 (a), with T* = 0.54 for Case 1 and T* = 0.51 for Case 2. Upon reaching the partition, there is an increase in T* from 0.51 to 0.55 between the rear and front partitioned sections in Case 2, whilst Case 1 remains at 0.54. This illustrates that the front and rear sections are at significantly different temperatures in Case 2 and that higher temperature fluid will exit through the vent in the front partitioned region. Along the vertical centreline in Figure 2 (b), three distinct regions are present in the enclosure for Cases 1 & 2. Both profiles indicate an linear gradient in T* from 0.5 to 0.56 in the centre region of the enclosure between $0.34 < Y^* < 0.8$. Below Y* = 0.34, an increase in the thermal gradient is noted, primarily due to the cooler entrained air entering the enclosure and passing over the lower surface. A significant increase in the thermal gradient is also present above Y* = 0.8, which is also greater than that recorded below Y* = 0.34. This suggests that a higher temperature gradient and hence enhanced heat transfer is present in this region. This is contrary to the expected result, with the cooler ventilation flow passing over the lower enclosure surface, producing a sharper temperature gradient here compared to the upper surface. This further reduction in T* along the lower surface may be present in experimentation, with the spacing used between adjacent thermocouples not sufficiently small to capture such a temperature profile close to the surface.

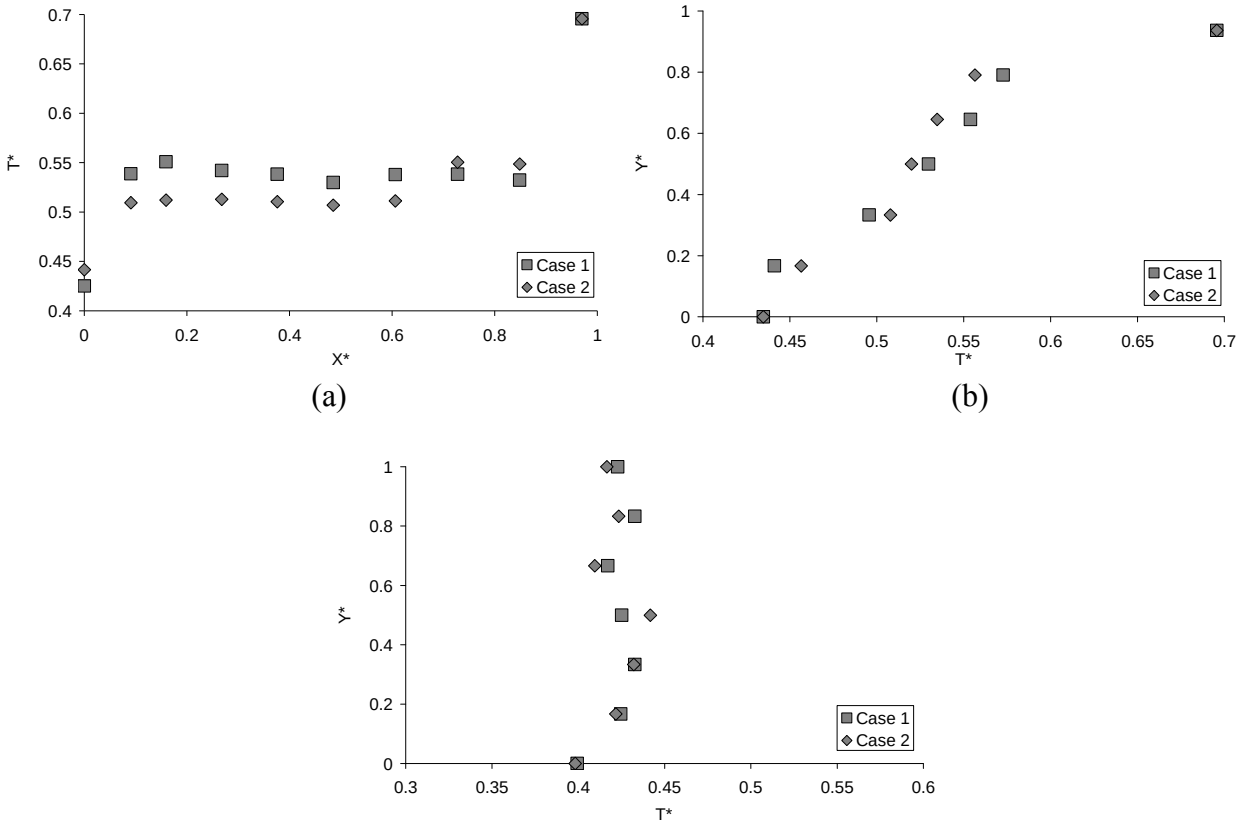

Figure 2 Partitioning effects upon the enclosure temperature distributions: (a) profile along horizontal centreline, (b) profile taken along vertical centreline, (c) profile taken along vertical centreline

Very little difference is seen in the rear wall temperatures of the enclosure after the introduction of the partition. T* along the wall height remains within the range of 0.42 – 0.44, highlighting the thermal isolation of the rear wall within the enclosure. A slight reduction in T* is seen in the region between Y* = 0.5 – 0.8 due an anticlockwise recirculation present in the upper left corner of the enclosure in both cases, enhancing mixing in this region and reducing T*. This recirculation is present even with the marked differences noted in the cylinder plume orientation for Case 1 & Case 2. In Case 1, the plume is deflected towards the centre of the enclosure, at an angle of approximately 75° to the horizontal. In Case 2, the plume is found to attach to the rear wall of the enclosure, but only for a maximum distance of 40mm. It then detaches and dissipates into the centre of the enclosure, minimising its influence on the rear wall temperatures. This is the opposite effect to that seen in Part 1 [14] where the plume orientation can have a large influence on the magnitude of rear wall temperatures, depending on ventilation configuration.

Cylinder positioning

Previous investigations into an unventilated leading edge [15] have shown the influence of cylinder position on the velocity and thermal distributions within the enclosure. In order to determine if cylinder positioning plays an important role in a ventilated and partitioned enclosure, a number of cylinder positions are investigated in Cases 2-4.

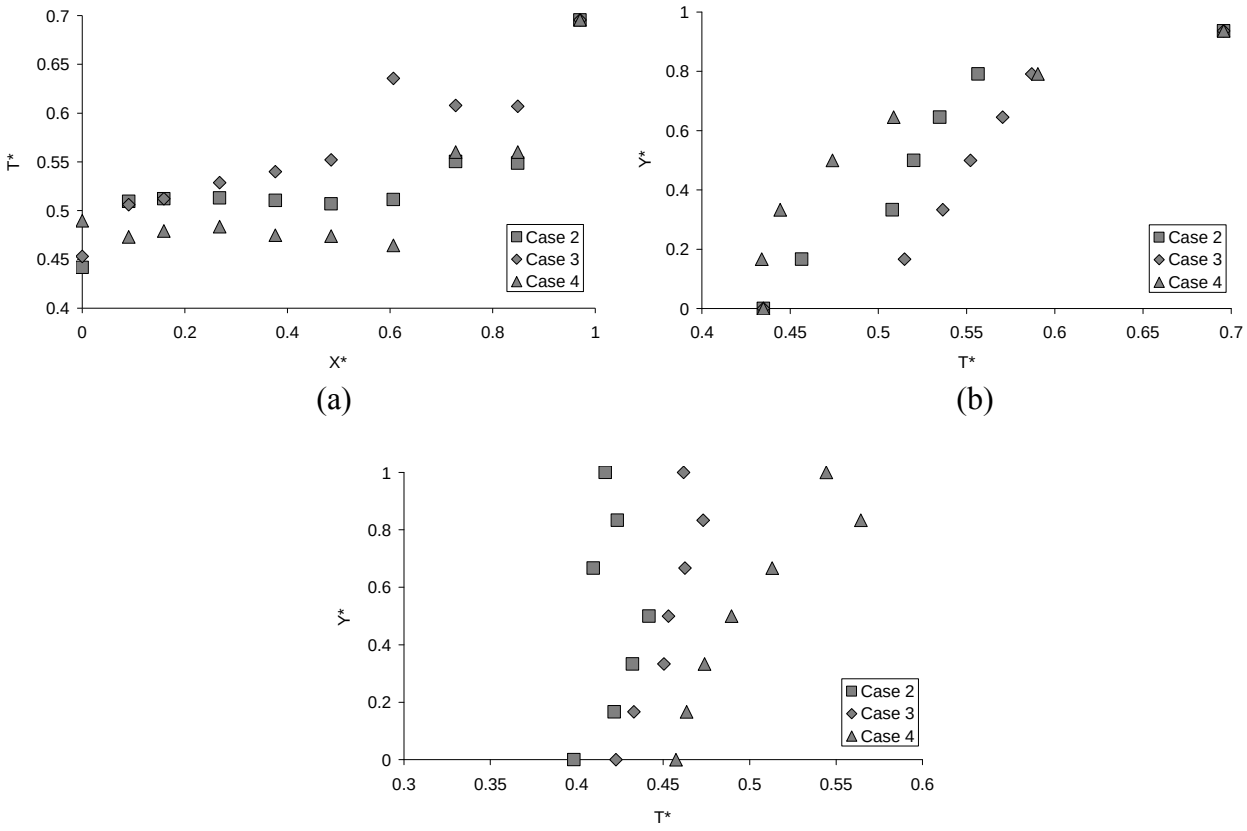

Figure 3 The effect of cylinder placement on the thermal distributions within the partitioned enclosure: (a) profile along horizontal centreline, (b) profile taken along vertical centreline, (c) profile taken along vertical centreline

Figure 3 (a) – (c) presents the enclosure temperature distributions for the various cylinder positions. Along the horizontal centreline, the lowest enclosure temperatures are found for the cylinder located in the upper left corner of the enclosure in Case 4. This is due to the confinement of the high temperature plume flow to the upper region of the enclosure, with minimal mixing below the cylinder and strong thermal stratification present in the rear partitioned space. A similar result was found for the

unventilated enclosure [15]. T* increases from 0.46 in the rear section to 0.55 beyond the partition, indication that the higher temperature plume flow travels along the upper surface of the enclosure before entering the front partitioned space. This is beneficial as it means the bulk of the high temperature fluid within the enclosure will enter the front section of the enclosure, when it can then be removed at the forward vent. This is also seen in Case 2 and Case 3, with a smaller difference recorded between front and rear temperatures in these cases compared to Case 4. Case 2 shows a constant T* of 0.51 along the centreline, increasing to 0.54 beyond the partition. Case 3 exhibits an increasing T* in the rear of the enclosure from 0.49 to 0.55, with a maximum of 0.65 due to the presence of the cylinder plume at this measurement location. A decrease in T* to 0.61 occurs in the front partitioned case.

Along the vertical centreline, three distinct temperature profiles are evident along the enclosure height for the varying cylinder positions. Case 2 consists of three separate fluid regions; adjacent to the lower surface, the core region of the enclosure and the upper surface as outlined in the previous section. Case 3 shows a region of increasing T* from 0.51 to 0.57 between $0.18<Y^*<0.8$, with large gradients present along the upper and lower enclosure surfaces, suggesting high heat transfer in these regions. Case 4 shows an increasing temperature gradient along the vertical height, due to the dominance of the cylinder plume in the upper region of the enclosure leading to the large increases in T* in Figure 3 (b).

The enclosure rear wall temperatures presented in Figure 3 (c) also show three different profiles present depending on cylinder positioning. Case 2 has two separate regions, an increasing temperature in the lower half of the enclosure $Y^* < 0.5$ with a reduction in T* seen above this region. This is attributed to the presence of the heated cylinder increasing the temperatures locally in the lower region, with an anticlockwise recirculation in the upper left corner of the enclosure. This recirculation zone enhances mixing and helps reduce T* in this region. With the cylinder positioned away from the rear wall in Case 3, a much shallower thermal gradient is present along the rear wall. T* increases slightly from 0.43 to 0.45 along the wall height. Case 4 shows a constantly increasing gradient along the rear wall surface reaching a maximum of 0.56 at $Y^* = 0.8$ due to the presence of the heated cylinder in the upper left corner of the enclosure. This then reduces to 0.54 at the uppermost point of the rear wall.

Comparing the effects of different ventilation configurations in Part 1 [14] to those seen in Cases 2 – 4 shows the large influence that cylinder positioning has on the resultant interior fluid and enclosure surface temperatures. In the different ventilation scenarios, the temperature profiles remained similar for all configurations, with only a change in magnitude noted between the different cases. Such a trend was not evident in the cylinder placement investigation, with the location of the cylinder having a marked effect on the final temperature distribution. This demonstrates that the natural convective regime within the leading edge enclosure is much more sensitive to partitioning and cylinder location than to the ventilation configuration alone and that these two geometrical effects are important parameter to be understood when dealing with natural convection ventilation in such an enclosure.

Enclosure flow comparisons

The cylinder plume velocity profiles recorded using PIV for Case 1 – 4 are presented in Figure 4. There is little difference between the plume magnitudes for Case 1 – 3, with a maximum of 0.2 m/s seen in Case 2 with Case 1 & 3 at 0.17 m/s. Different plume orientations however are noted, with Case 1 & 3 deflect slightly towards the centre of the enclosure. Case 2 veers towards the rear wall of the enclosure, where it will attach at approximately two-thirds of the enclosure height and Case 4 impinges on the upper enclosure surface. Due to the confinement effect of the upper enclosure surface on the plume, Case 4 exhibits a significantly lower velocity magnitude of 0.07 m/s, and is symmetrical about the cylinder centreline.

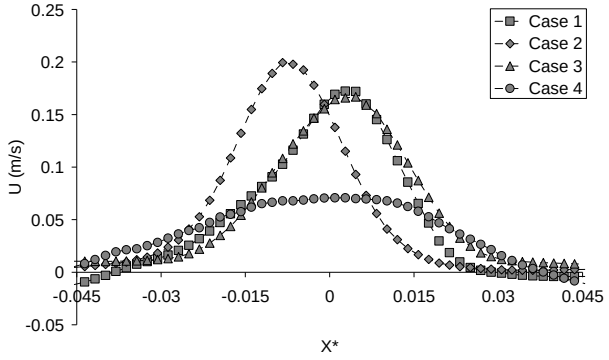

Figure 4 Horizontal cylinder plume velocity profiles, Case 1 – 4. Case 1 & 2 taken at location (i) in Figure 1, Case 3 taken at (ii), Case 4 taken at (iii)

The velocity profiles shown in Figure 5 are recorded above the partition and highlights shows the influence of cylinder positioning on the flow entering the front section of the leading edge. Depending on cylinder position there can be two opposing flows travelling in this region as in Case 2 and Case 4 or a single flow direction as in Case 3. This has a large impact of the overall mass flow entering the front section of the enclosure, which is then removed from the enclosure through the front vent. Case 2 & Case 3 have flow rates of 2.64×10^{-3} kg/s and 4.56×10^{-3} kg/s respectively. Case 4 has a mass flow of 3.59×10^{-4} kg/s entering the front of the enclosure, 92% lower that Case 3.

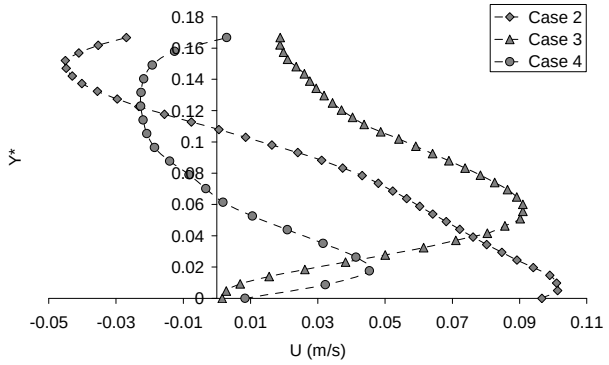

Figure 5 Velocity profile between the top of the partition and the upper enclosure surface taken along position (iv) in Figure 1

The velocity profiles normal to the exit vent boundaries in Figure 6 illustrate the effect partitioning and bleed duct positioning has on the ventilation flow in the enclosure. Partitioning the enclosure severely reduces the velocity and mass flow at the exit vent boundary for Case 2 – 4. A change from a pure displacement ventilation mechanism to a mixing/displacement combination is seen, with some back flow present along the vent boundary. This reaches a maximum of 33% of the vent opening in Case 4, which reduces the enclosure ventilation effectiveness as the overall mass flow out of the exit vent reduces to 8.9×10^{-4} kg/s in Case 4 from 5.59 $\times 10^{-3}$ kg/sin Case 1.

Partitioning the enclosure also severely reduces the amount of air exiting the enclosure compared to the unpartitioned enclosure in Case 1 as shown in Table 2. The introduction of the partition in Case 2 reduces the mass flow at the exit vent by 58% compared to Case 1. Case 2 and Case 3 show similar flow rates across the vent boundaries, even though the amount of air entering the front of the enclosure over the top of the partition is 73% higher in Case 3 A significant amount of recirculation occurs in the front partitioned section for this case, reducing the amount of air exiting the enclosure at the front vent. The temperature of the flow exiting the enclosure in Case 3 is higher compared to Case 2. This is beneficial from a ventilation perspective as the removal of higher temperature fluid at equal or lower magnitudes is seen to be more efficient than lower temperature fluid at higher velocities [16].

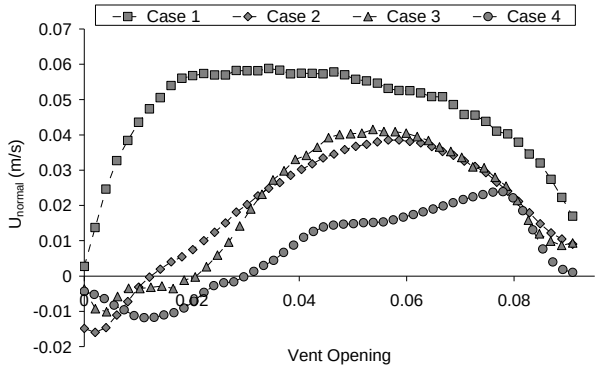

Figure 6 Velocity Profiles normal to the exit vent boundary

Table 2
Mass Flow Rates (kg/m) above the Enclosure Partition and along the Vent Boundary

	Case 1	Case 2	Case 3	Case 4
Top of Partition	-	2.64×10^{-3}	4.56×10^{-3}	3.59×10^{-4}
Exit Vent	5.59×10^{-3}	2.32×10^{-3}	2.26×10^{-3}	8.9×10^{-4}
T* in Front Partitioned Area	-	0.5495	0.6074	0.56

CONCLUSIONS

The introduction of a partition into the leading edge enclosure has a significant effect on the natural convection regime present. It forms a direct block in the ventilation path between the front and rear vent openings. This produces two distinct regions in the enclosure, the rear partitioned space, where the cylinder plume dominates and the front partitioned space, where the high temperature fluid is removed. Due to the partition gap located near the upper enclosure surface, only the higher temperature fluid from the rear partitioned space can travel towards the front exit vent. As a result the front partitioned space is at a noticeably higher temperature than the rear of the enclosure in Case 2.

In the partitioned enclosure, the dominance of the cylinder plume means that its flow path must be understood and optomised in order to ensure adequate ventilation. When the plume is orientated such that it travels towards the outlet vent of the enclosure as in Case 2 & 3, most of the high temperature fluid can be removed from the enclosure. When it does not travel directly towards the exit vent as in Case 4, the plume flow is recirculated within the enclosure, increasing the local wall and air temperaures. Its effect must be fully understood when considering the design of a leading edge enclosure.

Partitioning severely reduces the velocity magnitude across the exit vent boundary and can introduce a region of backflow into the enclosure, which moves away from a pure displacement ventilation regime and reduces the ventilation efficiency.

Cylinder positioning is found to have a larger influence upon the temperature profiles within the leading edge compared to ventilation configuration. The different ventilation orientations analysed in Part 1 [14] produced similar profiles with varying magnitudes, whereas the different cylinder positions investigated here produced distinct profiles for each of the three cases investigated. This suggests that the convective regime within the leading edge is more sensitive to cylinder placement than ventilation configuration, and cylinder placement effects need to be understood.

REFERENCES

[1] Basak, T. and Roy, S., 2008, "Role of 'Bejan's heatlines' in heat flow visualisation and optimal thermal mixing for differentially heated square enclosures." *International Journal of Heat and Mass Transfer*, 51, pp. 3486-3503

[2] Cianfrini, C., Corcione, M., and Dell'omo, P. P., 2005, "Natural convection in tilted square cavities with differentially heated opposite walls." *International Journal of Thermal Sciences*, 44, pp. 441-451.

[3] Hsieh, K. J. and Lien, F. S., 2004, "Numerical modelling of buoyancy-driven turbulent flows in enclosures." *International Journal of Heat and Fluid Flow*, 25, pp. 659-670.

[4] Cacagni, B., Marsili, F., and Paroncini, M., 2005, "Natural convective heat transfer in square enclosures heated from below." *Applied Thermal Engineering*, 25, pp. 2522-2531.

[5] Sharma, A. K., Velusamy, K., and Balaji, C., 2007, "Turbulent natural convection in an enclosure with localised heating from below." *International Journal of Thermal Sciences*, 46, pp. 1232-1421.

[6] Cesini, G., et al., 1999, "Natural convection from a horizontal cylinder in a rectangular cavity." *International Journal of Heat and Mass Transfer*, 42, pp. 1801-1811.

[7] De, A. K. and Dalal, A., 2006, "A numerical study of natural convection around a square, horizontal, heated cylinder placed in an enclosure." *International Journal of Heat and Mass Transfer*, 49, pp. 4608-4623

[8] Cacagni, B., Marsili, F., and Paroncini, M., 2005, "Natural convective heat transfer in square enclosures heated from below." *Applied Thermal Engineering*, 25, pp. 2522-2531

[9] Sadeghipour, M. S. and Razi, Y. P., 2001, "Natural convection from a confined horizontal cylinder: the optimum distance between confining walls." *International Journal of Heat and Mass Transfer*, 44, pp. 367-374.

[10] Ekundayo, C. O., Probert, S. D., and Newborough, M., 1998, "Heat transfers from a horizontal cylinder in a rectangular enclosure." Applied Energy, 61, pp. 57-78.

[11] Bilgen, E., 2002, "Natural convection in enclosures with partial partitions", *Renewable Energy*, 26, 257-270

[12] Khalifa, A.N., Abdullah, S.E., 1999, "Buoyancy driven convection in undivided and partially divided enclosures", *Energy Conversion and Management*, 40, 717-727.

[13] Mahapatra, S.K., Sarkar, A.., Sarkar, A., 2007, "Numerical simulation of opposing mixed convection in differentially heated square enclosure with partition", *International Journal of Thermal Sciences*, 46, 970-979.

[14] Moore, D., Egan, V., Newport, D., Lacarac, V., 2009, " Natural convection regime within a wing leading edge enclosure. Part 1: Effects of ventilation configuration" in *ExHFT-7 7th World Conference on Experimental Heat Transfer, Fluid Mechanics and Thermodynamics*, Krakow, Poland.

[15] Egan, V., HT2008-56321 "Velocity Field Measurements in Leading Edge Wing Compartments." in *ASME Summer Heat Transfer Conference 2008*. 2008: Jacksonville, Florida, USA.

[16] Bilgen, E., Yamane, T., 2004, "Conjugate heat transfer in enclosures with openings for ventilation", *Heat and Mass Transfer*, 40, 401-411.

THE EFFECT OF VELOCITY RATIO ON THE THERMAL-HYDRAULIC PERFORMANCE OF RECIPROCATING SCRAPED SURFACE HEAT EXCHANGERS AT LOW REYNOLDS NUMBER

J. P. Solano[1,*], A. García[1], P.G. Vicente[2], A. Viedma[1]
[1]Universidad Politécnica de Cartagena, Murcia, Spain
[2]Universidad Miguel Hernández, Elche, Spain

ABSTRACT. The thermal-hydraulic performance of a reciprocating scraper inserted in a round tube at low Reynolds number is studied. Pressure drop and heat transfer characteristics have been experimentally determined in static conditions in laminar regime (Re_h=30), and results are contrasted with dynamic performance at several velocity ratios (ω=0.1 - 1). Maximum increases of Fanning friction factor of the order of 1.2 have been found, together with increases in Nusselt number of the order of 2, using propylene-glycol as working fluid.

Keywords: *heat transfer enhancement, pressure drop, SSHE, fouling*

INTRODUCTION

Heat transfer processes in the food and chemical industries frequently deal with highly viscous liquids. The performance of heat exchangers working under these conditions is usually low, as a result of the characteristics of the encountered laminar regime [1]. Moreover, the heat transfer surfaces may become coated with a deposit of solid material after a period of operation. This phenomenon, known as fouling, causes a reduced overall heat transfer coefficient [2]. Heat exchangers are generally over-designed to compensate for the anticipated fouling [1]. Moreover, cleaning operations decrease equipment availability, which causes as well a considerable economic impact.

Among the several technical solutions for fouling cleaning and prevention [3], mechanically assisted heat exchangers, where a heat transfer surface is periodically scraped by a moving element, constitute a suitable solution for applications with severe tendency to fouling and low heat transfer rates. Dynamic heat exchangers with rotating scraping blades are found in commercial practice (SSHE): they prevent fouling and promote mixing and heat transfer. Many investigations have focused on these anti-fouling devices, studying flow pattern characteristics [4], their thermo-hydraulic performance [5] or scraping efficiency [6].

This work presents the study of a dynamic insert device moved alternatively along the axial direction by a hydraulic cylinder. The active insert device is made up of several semi-circular elements, which are mounted on a shaft with a pitch of 5D (Fig. 1). When inserted inside the tube,

* Corresponding author: Juan Pedro Solano
Phone: + (34)-325938, Fax: + (34)-325999
E-mail address: juanp.solano@upct.es

the device produces a double effect: the induced flow generates macroscopic displacements from the boundary layer region to the axis of the tube, increasing heat transfer, and the elements with reciprocating movement scrape the inner tube-wall, avoiding fouling. The industrial version of this device is manufactured and market by the Spanish company HRS-Spiratube.

There is empirical evidence of the heat transfer enhancement and fouling prevention of this kind of active devices. However, the authors have not found in the open literature previous works related to this type of mechanically-assisted heat exchangers.

This work presents an experimental study on the pressure drop and heat transfer characteristics of the active insert device depicted in Fig. 1. Experimental results of Fanning friction factor *f* and Nusselt number *Nu* as functions of scraping frequency are provided for Re_{Dh}=30 (laminar flow).

EXPERIMENTAL SET-UP

A schematic diagram of the experimental setup is shown in Fig. 2. It consists of two independent circuits: the main circuit, where the dynamic insert device was installed, and the secondary circuit which was used for regulating the tank temperature to a desirable value. The reciprocating movement of the inserted scraper is achieved by means of a hydraulic unit. This unit moves a double-effect cylinder over which the shaft of the insert device is mounted. Mechanical arrangement of the end-stroke connections provides the system with a movement amplitude of 10D (180 mm). All the instrumentation was connected to a HP 34970A Data Acquisition Unit.

Pressure drop tests were carried out in the hydro-dynamically developed region under isothermal conditions. The hydraulic diameter $D_h = D - d$ was used as the reference diameter to calculate all friction factors. It takes account of the presence of the shaft inside the tube, but does not consider the effect of the plugs mounted on it. Fanning coefficients f_{Dh} were determined from fluid mass flow rate and mean pressure drop measurements by means of

$$f_{Dh} = \frac{D_h}{L_p} \frac{\overline{\Delta P}}{2 \rho \, \overline{u}_f^{\,2}} \tag{1}$$

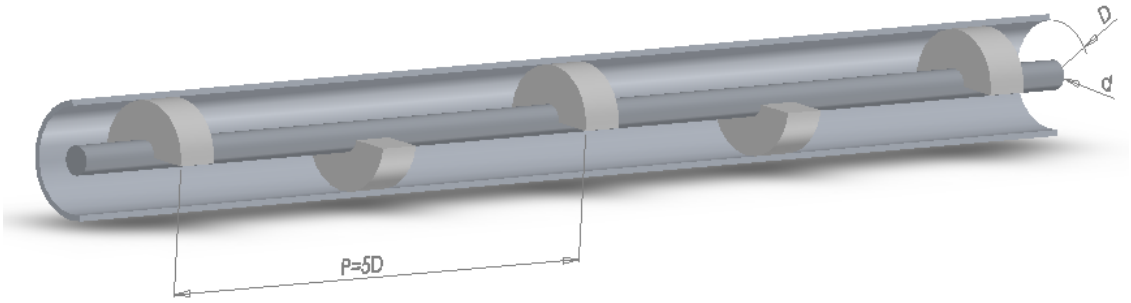

Figure 1. Sketch of the active device

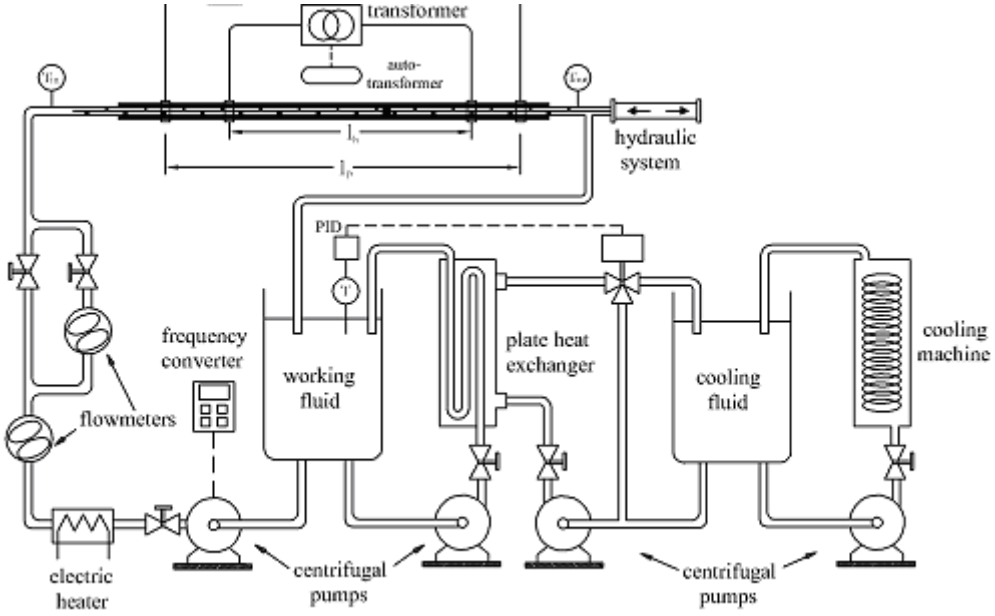

Figure 2. Experimental setup

Time-dependent pressure during the scraping process was measured in two sections of the tube separated by a distance L_p=1.8 m. Two piezorresistive pressure sensors (Kistler K-Line) were connected to each tube section with four pressure taps separated by 90º. Mean pressure drop in the tube over the scraping cycle, $\overline{\Delta P}$, was computed by integration of the instantaneous signal over 50 cycles.

Heat transfer experiments were carried out under uniform heat flux conditions, where energy was added to the working fluid by Joule effect heating. A 6 kVA transformer was connected to the smooth tube by copper electrodes and power supply was regulated by means of an auto-transformer. The length between electrodes defined the heat transfer test section (L_h = 1 m). To reduce heat losses, this section was coated with a thermal insulation of 20 mm thickness and thermal conductivity 0.04 W/mK. The overall electrical power added to the heating section, Q, was calculated by measuring the voltage between electrodes (0-15 V) and the electrical current (0-600A).

Fluid inlet and outlet temperatures, T_{in} and T_{out} were measured by submerged type resistance temperature detectors (RTDs). Since heat was added uniformly along the tube length, the bulk temperature of the fluid at the measuring section, $T_b(x_p)$, was calculated by considering a linear variation with the axial direction. Average outside surface temperature of the wall $\overline{T}_{wo}$ was measured at six different axial positions along a scraper pitch, located at 30 diameters from the upstream electrode, that ensure fully developed flow. The value of $\overline{T}_{wo}$ at each axial position was calculated by averaging the temperatures measured with eight surface type RTDs peripherally spaced by every 45º at each axial position.

The RTD naked sensors were wrapped with ultra-thin plastic films, which assured electrical isolation. The low thickness of the film makes its thermal resistance negligible. A highly thermal-

conductive paste was spread between the tube wall and the wrapped RTD sensor. Each temperature value used for data reduction was averaged over 30 data sampled every 9 seconds.

Two calibration tests with no electrical heating were done: the first test was performed to determine heat losses in the test section Q_1 by measuring $(T_{in} - T_{out})$ at low flow rates, and the second test at high flow rates to calculate the lay-out resistances of the surface type RTDs $(T_{in} \approx T_{out} \approx \overline{T}_{wo})$.

Heat flux added to the test fluid q'' is calculated by subtracting heat losses to the overall electrical power added in the test section. The power factor was 1.0, as the copper electrodes were directly connected to the metallic tube, which is a pure resistive load. The inner wall temperature $\overline{T}_{wi}$ for each experimental point, was determined by using a numerical model that solves the steady-state, one dimensional, radial, heat conduction equation in the tube wall and insulation from the following input data: $\overline{T}_{wo}$, Q, Q_1 and $T_b(x_p)$. The local Nusselt number was calculated by means of

$$Nu_x = \frac{D_h}{k} \frac{q''}{\overline{T}_{wi} - T_b(x_p)} \tag{2}$$

Visualization experiments [7] allow to state that the flow is fully developed at few pitches (2-3 p). Thus, local Nusselt number computed with Equation (2) is a periodic value. Nusselt number results at the six axial positions were corrected by the factor $(\mu_w / \mu_b)^{0.14}$ to obtain correlations free of variable properties effects [8]. Pitch-averaged Nusselt number was obtained by averaging the six local values computed with the presented methodology.

The experimental uncertainty was calculated by following the "*Guide to the expression of uncertainty in measurement*", published by ISO [9]. Details of the uncertainty assignation to the experimental data are given by the authors in [10]. Uncertainty calculations based on a 95% confidence level showed maximum values of 4% for Reynolds number, 3.5% for Prandtl number, 6% for Nusselt number and 8% for friction factor.

RESULTS

An experimental research was carried out to assess the effect of the scraping frequency on the thermal-hydraulic behaviour of the dynamic insert device sketched in Fig. 1. Experiments were carried out employing propylene-glycol at 15ºC, with a flow rate of 150 l/h, yielding to Reynolds number Re_{Dh}=30. The scraping frequencies ranged from 0.1 to 1 Hz. The velocity ratio ω, defined as $\omega = u_{scraping}/u_{fluid,}$ was found to be an excellent non-dimensional parameter to evaluate dynamic effects. The range of velocity ratios tested was ω=[0.1 0.3 0.5 0.75 1].

Pressure drop results

Pressure drop tests were carried out under isothermal conditions, covering the wide range of velocity ratios presented above, for constant Reynolds number Re_{Dh}=30. A test in static conditions (ω=0) was also performed. Time-averaged pressure drop results were employed for computing the mean Fanning friction factor as a function of ω.

Unsteady pressure signal. Figure 3 (left) shows a detail of the pressure signals over two scraping cycles, for working conditions Re_{Dh}=30 and ω=0.3. The scraper movement in the opposite direction of the flow is called "counter-current", and the scraper movement in the same direction of the flow

is called "co-current". The signals $p_1(t)$ and $p_2(t)$ can be substracted to obtain the unsteady pressure drop in the tube section (see Figure 4, right). Resulting mean pressure drop is also depicted in this graph.

The low, constant scraping velocity generates quasi-steady flow conditions in each semi-cycle, which can allow to assess the separate performance of the dynamic device in counter-current and co-current movement.

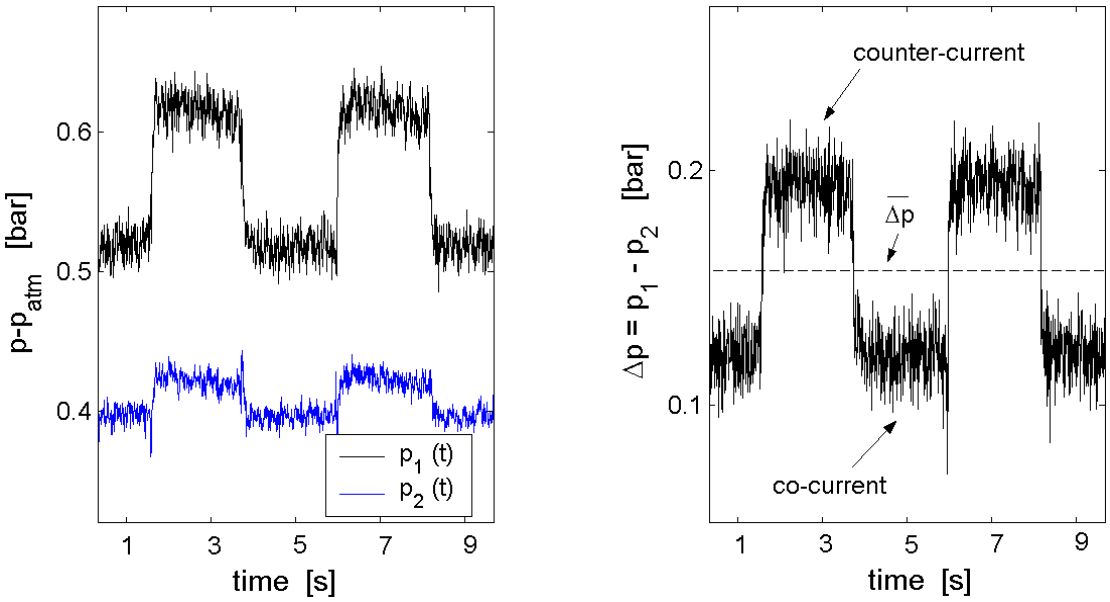

Figure 3. Unsteady pressure signal in the tube section, Re_h=30, ω=0.3

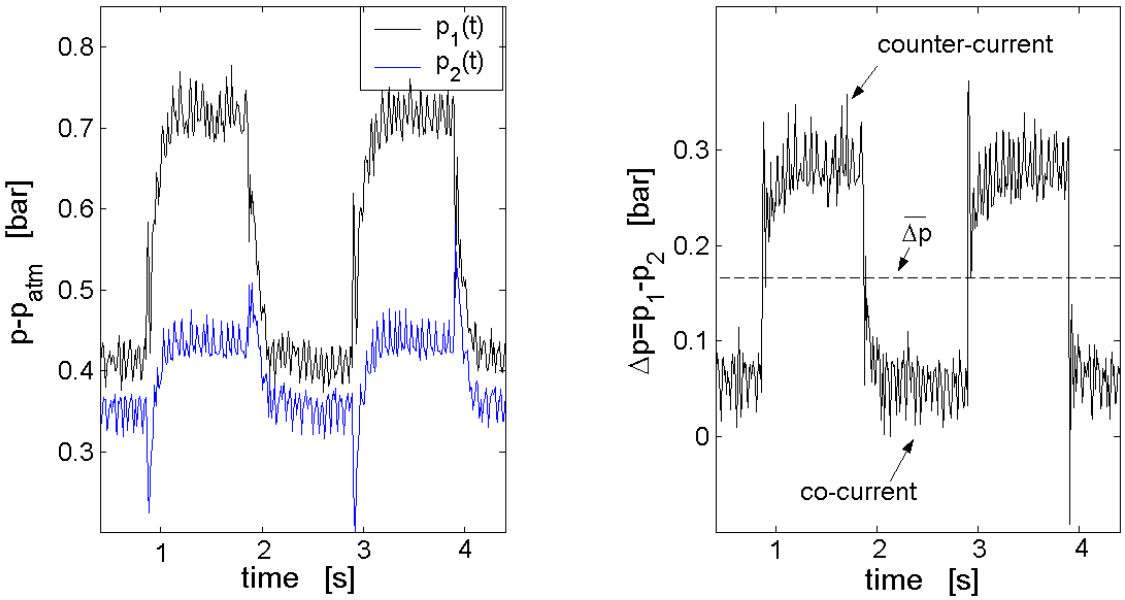

Figure 4. Unsteady pressure signal in the tube section, Re_h=30, ω=1

Counter-current performance yields to high pressure drops in the tube, as expected from the blockage effect generated by the scraper during its movement against the flow [7]. However, when the device

moves co-current, pressure drop decreases dramatically. This result reveals the lower blockage of the scraper when it moves within the flow direction.

Figure 4 shows the unsteady pressure evolution measured for the working condition Re_{Dh}=30 and ω=1. In this situation, the scraper velocity is 3.3 times higher than the velocity with ω=0.3, whereas flow rate in the tube is kept constant. Pressure drop across the tube shows transient evolutions at the commencement of each semi-cycle, as a result of the higher velocity of the scraper and the sudden movement reversal imposed by the hydraulic unit.

Pressure drop in the counter-current semi-cycle is 50% higher than for ω=0.3. Thus, scraper velocity can be stated as a remarkable factor in the increase of the blockage effect in counter-current performance. Conversely, pressure drop in the co-current semi-cycle is much lower than the equivalent result for ω=0.3. The velocity of the device in the flow direction generates a low pressure field downwards, yielding to lower pressure drops. Mean pressure drop for velocity ratio ω=1 is still higher than the corresponding value found for ω=0.3. Considering than, for higher scraping frequencies, counter-current pressure drop increases while co-current pressure drop decreases, the major influence of the counter-current characteristics in the global performance of the dynamic device can be assessed.

Fanning friction factor. The value of $\overline{\Delta P}$ for each velocity ratio can be employed to compute the mean Fanning friction factor, as explained in Equation 1. Experimental results for the range of interest are presented in Figure 5. Fanning friction factor results can be employed to estimate the pressure drop augmentation due to the insertion of the scraping device in a smooth tube with similar mass flow rate. This augmentation can be computed in laminar regime as follows:

$$\frac{\Delta P_{scraping}}{\Delta P_{smooth}} = f_{Dh} \times \frac{\mathrm{Re}_{Dh}}{16} \times \frac{D^4}{D_h{}^3 (D+d)} \tag{3}$$

According to this expression, pressure drop increases of 5.7 have been found in static conditions, referred to the smooth tube $(\Delta P_{\omega=0}/\Delta P_{smooth})$. In dynamic conditions, mean Fanning friction factor increases for higher velocity ratios. Pressure drop augmentation in the inserted tube due to the movement of the scraper with ω=0.1 is $\Delta P_{\omega=0.1}/\Delta P_{\omega=0}$ =1.06, while the increase due to the movement of the scraper at a velocity ten times higher (ω=1) is $\Delta P_{\omega=1}/\Delta P_{\omega=0}$ =1.21.

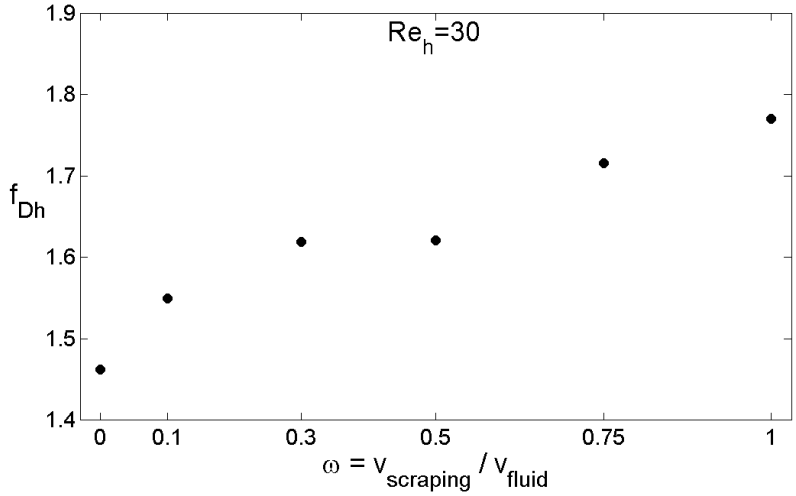

Figure 5. Mean Fanning friction factor as a function of velocity ratio (Re_{Dh}=30)

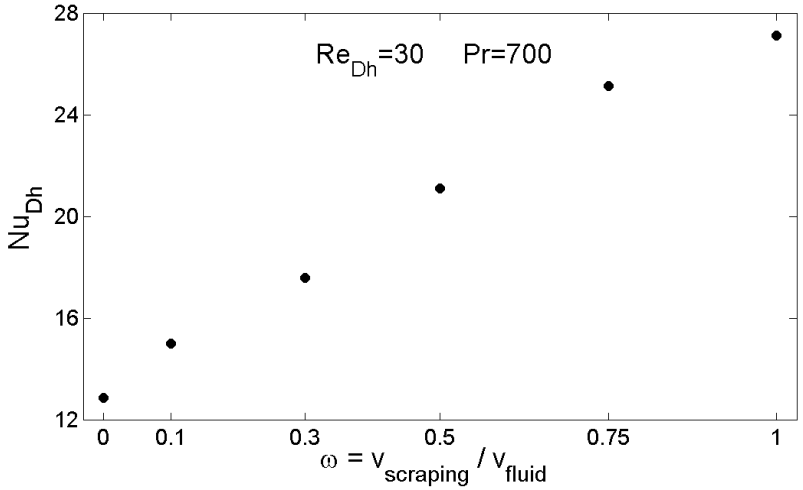

Figure 6. Mean Nusselt number as a function of velocity ratio (Re_{Dh}=30)

Heat transfer results

Heat transfer tests were performed under uniform heat flux conditions, for Re_{Dh}=30 and similar velocity ratios than in the previous section. Prandtl number was Pr=700, using propylene-glycol as working fluid at T=15ºC.

The insertion of the scraper in a smooth tube, working in static conditions, yields to heat transfer augmentations of 4.1 (referred to the asymptotic solution $Nu_{D,\infty}$=4.36). The mixing promoted by the insert device plays an essential role in this result. The effect of scraping movement increases heat transfer characteristics. For velocity ratio ω=0.1, heat transfer augments 1.35 times with respect to the static conditions. The continuous removal of the boundary layer, and the enhanced radial mixing between peripheral and core flows justify this result [11]. If scraping velocity increases ten times (ω=1), heat transfer augments only $Nu_{\omega=1}/Nu_{\omega=0.1}=1.55$. It reveals the fact that oscillatory flow mixing presents a saturation behaviour, owing to two opposite phenomena: during the counter-current semi-cycle, the flow structures that appear in the tube may promote intensive heat and mass transfer, and this effect should be as much important as the higher is the scraping velocity. However, during the co-current semi-cycle, the flow configuration may present low levels of enhanced heat transfer, according to the pressure drop signal (Figure 4) and the heat and momentum analogy [12]: the scraper movement in the flow direction generates low shear stress rates in the tube wall.

CONCLUSIONS

1. A comprehensive experimental research has been carried out to obtain the influence of scraping velocity on the thermal-hydraulic behaviour of a dynamic insert device, for low Reynolds number. The velocity ratio, ranging from 0.1 to 1, was found to be an excellent parameter to evaluate dynamic effects

2. The unsteady pressure evolution in the tube during the scraping cycle was assessed. Pressure drop in counter-current semi-cycle increases with scraping velocity, while it decreases during the co-current semi-cycle for higher scraping velocities.

3. Augmentations of pressure drop of 5.7 times were found for the device in static conditions, referred to a smooth tube with similar mass flow rate. Maximum increases of pressure drop of 1.2 times were found for ω=1, with respect to the static performance (ω=0).

4. Heat transfer increases of 4.1 times with respect to the smooth tube were found for the static device. The movement of the device promotes intensive heat and mass transfer, with augmentations of the order of 2 for ω=1, with respect to the static performance (ω=0).

ACKNOWLEDGMENTS

This research has been partially financed by the DPI2007-66551-C02-01 grant of the "Dirección General de Investigación del Ministerio de Educación y Ciencia de España" and the “HRS Spiratube” company.

REFERENCES

1. Webb, R.L., *Principles of Enhanced Heat Transfer,* Wiley Interscience, New York, 1994
2. Bergles, A.E., ExHFT for fourth generation heat transfer technology, *Experimental Thermal an Fluid Science,* Vol. 26, pp 335-344, 2002.
3. Müller-Steinhagen, H., *Handbook of Heat Exchanger Fouling – Mitigation and Cleaning Technologies*, Publico Publications, 2000.
4. Wang, W., Walt, J.H., McCarthy, K.L., Flow profiles of power law fluids in scraped surface heat exchanger geometry using MRI, *Journal of Food Process Engineering,* Vol. 22, pp 11-27, 1999.
5. De Goede, R., De Jong, E.J., Heat transfer properties of a scraped-surface heat exchanger in the turbulent flow regime, *Chemical Engineering Science,* Vol. 48, No. 8, pp.1393-1404, 1993.
6. Sun, K.-H., Pyle, D.L., Fitt, A.D., Please, C.P., Baines, M.J., Hall-Taylor, N., Numerical study of 2D heat transfer in a scraped surface heat exchanger, *Computers & Fluids,* Vol. 33 pp 869-880, 2004.
7. Solano, J.P., García, A., Pedrero, J.M., Vicente, P.G., Viedma, A., Experimental Investigation of flow pattern in enhanced heat exchangers with active insert devices, *Proceedings of ASME-ATI Conference,* Milan, Italy, May 2006, pp 252-260
8. Sieder, E.N., y Tate, E.G., Heat transfer and pressure drop of liquids in tubes, *Ind. Eng. Chem.,* Vol. 28, p. 1429. 1936.
9. Guide to the Expression of Uncertainty in Measurement, first ed., ISBN 92-67-10-188-9, *International Organization for Standardization,* Switzerland, 1995.
10. Vicente, P.G., García, A., Viedma, A., Experimental study of mixed convection and pressure drop in helically dimpled tubes for laminar and transition flow, *International Journal of Heat and Mass Transfer,* Vol. 45, pp 5091–5105, 2002.
11. Mackley, M.R., Stonestreet, P., Heat transfer and associated energy dissipation for oscillatory flow in baffled tubes, *Chemical Engineering Science,* Vol. 50 (14), pp 2211-2224, 1995.
12. Colburn, A.P., A method of correlating forced convection heat transfer data and a comparison with fluid friction, *Trans. AIChE,* Vol. 29, 174-210, 1933.

EFFECT OF RIB SPACING ON HEAT TRANSFER IN RECTANGULAR CHANNELS WITH 45 DEG RIBS ON ONE WALL

G. Tanda*, R. Abram
DIPTEM/TEC, University of Genova,
via all'Opera Pia 15a
I-16145 Genova, Italy

ABSTRACT. An experimental investigation of heat transfer in a rectangular channel with angled rib turbulators, inclined at 45 deg, is presented. The angled ribs were deployed with parallel orientations on one wall of the channel. The aim of the work was to study the effect of the rib spacing on the thermal performance of the ribbed channel. Experiments were based on the use of heating foils and the steady-state, liquid crystal thermography. From the processing of liquid crystal images, the maps of local heat transfer coefficient (and local Nusselt number) have been reconstructed. The thermal performance of each ribbed channel is identified by the average Nusselt number and by the friction factor obtained from the measured pressure drop across the ribbed test section. The optimal rib pitch-to-height ratio giving the best heat transfer performance was identified, for the explored range of Reynolds number, under the constraints of constant mass flow rate or pumping power.

Keywords: *heat transfer, forced convection, rectangular channel, angled ribs*

INTRODUCTION

Modern high-performance gas turbine engines operate at high entry gas temperature, well above the allowable metal temperature. Therefore, highly efficient cooling technologies (film cooling, impingement cooling, internal cooling) are required for vanes and blades of advanced gas turbines [1]. Internal cooling is achieved by passing the coolant through passages inside the blades. The specific technology has developed from simple smooth cooling passages to very complex geometries, involving a great number of different circuit designs and flow path surfaces. Rib turbulators, periodically deployed along the main direction of flow, were one of the first improvements of blade internal cooling.

The inclination of ribs can lead to superior heat transfer performance because of the secondary flow induced by the rib angle. This secondary flow has the form of two counter-rotating vortices, aligned with the inclined ribs, which carry cold fluid from the central core region towards the ribbed walls. These cells, interacting with the main flow, affect the flow reattachment and recirculation between ribs, and interrupt boundary layer growth downstream of the reattachment regions.

Since the 45 deg orientation of rib turbulators (relative to the main flow direction) appears to be the most common in practice today, the majority of recent research papers are focused (mainly or only) on this geometry. Despite the large mass of studies dealing with channels with 45 deg angled ribs, some issues still remain unresolved. For instance, whereas the ideal rib pitch-to-height ratio *p/e* for channels with transverse ribs is approximately equal to 10, irrespective of the value of the channel aspect ratio AR [2-4], angling the ribs (by 45 deg) gives the best thermal performance again at

* Corresponding author: Prof. G.Tanda
Phone: + (39)-010-3532881, Fax: + (39)-010-311870
E-mail address: giovanni.tanda@unige.it

p/e=10 for AR=1 ([5], only heat transfer from ribs considered, ribs in a staggered arrangement). As AR is reduced, the ideal *p/e* is still equal to 10 if the performance comparison with the smooth channel is based on the total heat transfer area; conversely, the optimum *p/e* is lowered to 3 and 2.5 (for AR = 0.5 and 0.25, respectively) when the comparison is based on the projected area ([6-7], heat transfer from ribs and inter-rib regions, ribs arranged in-line). These studies also indicated that the optimum rib spacing is very sensitive to other parameters, such as the rib height-to-hydraulic diameter ratio *e*/*D*, and the thermal conductivity of ribs (i.e., if the ribs exchange heat with convective fluid or not). Seemingly, no systematic studies on the effect of the rib spacing on heat transfer for AR values larger than one are available in the literature. A further, less investigated, aspect concerns the effect of the number of ribbed walls on heat transfer and friction characteristics in a channel. Most literature papers consider square or rectangular channels with ribs on two opposite walls, the other walls remaining smooth. In refs. [8-9] both the heat transfer coefficient and the friction factor were found to increase with an increasing number of ribbed walls, but the relative increase in heat transfer is lower that the relative increase in friction factor. This result seems to suggest that the heat transfer performance of one-ribbed wall channels (per unit pumping power) could be potentially similar or superior to the two-ribbed wall channels (with less manufacturing efforts).

In this paper, local and average heat transfer coefficients in a rib-roughened rectangular channel (aspect ratio AR=5, hydraulic diameter *D*=0.033 m) are presented. Configurations include sequences of continuous, 45 deg angled ribs, having square cross-sections (rib height *e* = 3 mm, *e/D* = 0.09). Ribs were regularly spaced over one side of the channel (the wider one), heated at uniform heat flux (the other sides remaining smooth and unheated). Four values of the rib pitch *p* were considered (*p*= 20,30,40, and 60 mm), so as to yield four values of the rib pitch-to-height (*p/e*= 6.66, 10, 13.33 and 20), the Reynolds number Re ranging from 9000 to 35500. Ribs, made of balsa wood, were considered to be nearly adiabatic for the thermal boundary condition; therefore attention was focused on local and average heat transfer coefficients on the inter-rib regions of the heated plate. The study was performed by using the steady-state liquid crystal technique.

EXPERIMENTAL APPARATUS AND PROCEDURE

Experimental setup

The description of the experimental apparatus is facilitated by reference to Figure 1. The main components are the wind tunnel, the test section, the heating arrangement, and the instrumentation.

An open-circuit suction-type wind tunnel was used for this study. Air, drawn at room temperature, passed through a filter and entered a rectangular channel (width *W*=0.1 m, height *H*=0.02 m, aspect ratio AR=5, hydraulic diameter *D*= 0.033 m) in which the test section was fitted.

The test section was a rectangular channel, as wide and high as the entry and exit sections and delimited by a thin heated plate (width *W*=0.1 m, length *L*=0.28 m) and lateral and frontal unheated Plexiglas walls. The plate was made of 0.5 mm thick stainless steel to which a plane heater had been attached to provide a controllable uniform heat flux. A thin liquid crystal (LC) sheet was applied on the side opposite to the heater to measure local wall temperature. Pressure taps, connected to a common alcohol manometer, were located at the inlet and outlet of the test section in the streamwise direction. A Venturi flowmeter was used for the measurement of mass flow rate.

Thermosensitive, cholesteric liquid crystals were used to measure temperature distributions on the heated surface. The pre-packaged LC sheet (0.15 mm thick) consisted of a thermochromic liquid crystal layer on a black background applied onto a mylar film and backed with a pressure-sensitive adhesive. The color distribution of the liquid crystals was observed by a CCD videocamera through the Plexiglas wall opposite to the heated surface and stored in a PC via an IEEE 1394 interface. The relationship between the color (hue) and the temperature of the thermosensitive liquid crystals was found by a calibration experiment. The calibration test was carried out by gradually heating a 5mm thick aluminum plate (calibration plate) covered by a LC film identical to that used in the experiments. LCs here employed had a red start temperature of 30°C with a bandwidth of 4°C. The

hue-temperature correlation was found to be fairly linear and repeatable in the range from 31.5 to 32.5 °C (hue in the 70-140 range): this field of hue was therefore selected for the quantitative analysis of each LC image. The corresponding calibration line has an uncertainty band (at the 95% confidence interval) of ±0.2 K.
Additional details of the experimental setup are available in refs. [10,11].

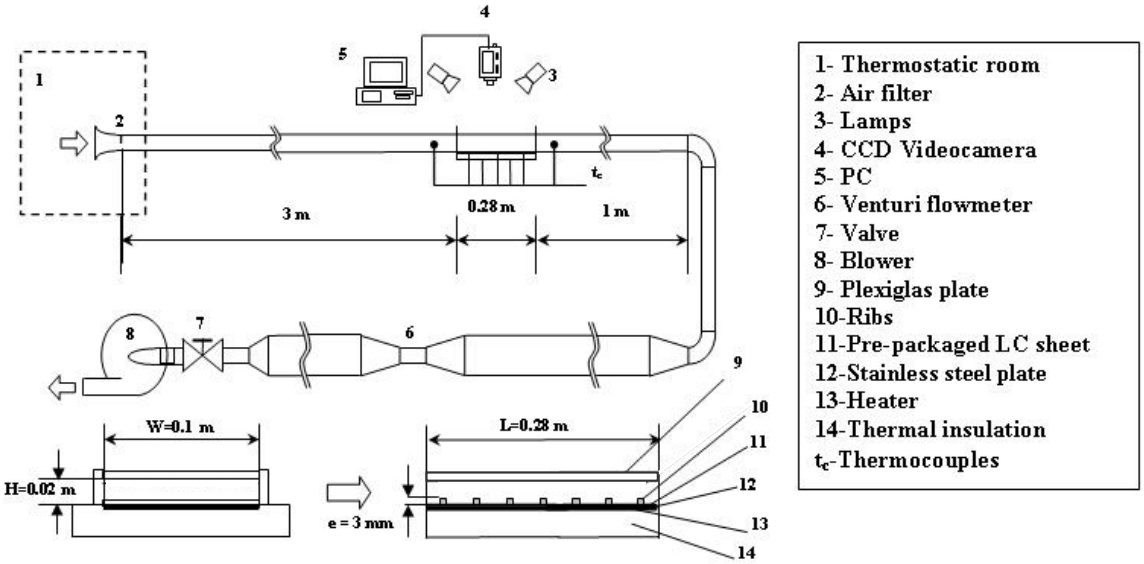

Figure 1. Schematic layout of experimental setup and test section

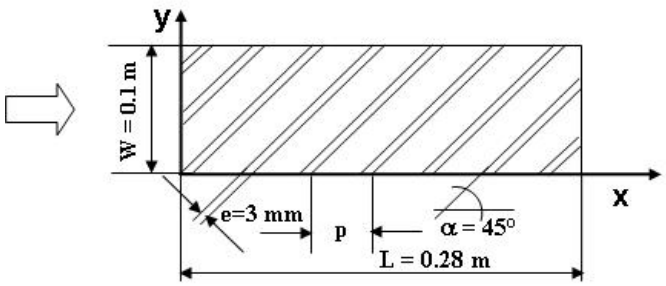

Figure 2. Geometry of the rib-roughened heated surface

Rib configurations
Ribs, made of balsa wood, had a square section (side *e* is equal to 3 mm) and a blockage ratio *e/H* = 0.15 (*e/D* =0.09). Owing to their low thermal conductivity, ribs were considered to be virtually adiabatic and their function was to generate turbulence in the airflow in order to increase the inter-rib heat transfer. They were glued at periodic streamwise stations (longitudinal rib pitch *p* from 20 to 60 mm, giving rib pitch-to-height values *p/e* from 6.66 to 20) as shown in Fig.2.

Operating procedure and data reduction
After the rib array had been set and the airflow had been adjusted to a prescribed velocity, the DC current was supplied to the heater. The surface temperature was maintained within the thermosensitivity region of the liquid crystals by controlling the input power delivered to the heater. Once steady-state conditions were reached, input power, thermocouple readings and the LC images were recorded. The image of the colored pattern of LCs, taken by the CCD were processed by using a custom-made software to convert the hue into the surface temperature in order to extract the local heat transfer coefficient according to the following relationship:

$$h = q_{conv}/(T_{LC}-T_{air,x}) \quad (1)$$

where q_{conv} is the convective heat flux, assumed to be uniformly distributed over the heated plate, T_{LC} is the surface temperature detected by the LCs, and $T_{air,x}$ is the bulk temperature of the air at the x position along the streamwise direction.
The convective heat flux was evaluated as follows:

$$q_{conv} = (Q_{el} - Q_{rad} - Q_{dis} - Q_{ribs})/A \quad (2)$$

where Q_{el} is the measured input power to the heater, Q_{rad} is the calculated radiative heat transfer rate to the surroundings, Q_{dis} is the calculated heat transfer rate dissipated through the insulation on the rear face of the heater, and A is the area of the plate surface exposed to the airflow. The term Q_{ribs} takes into account the heat dissipation from the ribs. Even though the ribs were deemed to be adiabatic owing to their low thermal conductance, the conventional one-dimensional fin model was applied to estimate (by an iterative procedure, assuming the heat transfer coefficient along the rib to be equal to the average heat transfer coefficient over the baseplate) the amount of heat transfer rate delivered to the airflow from their sides.
The bulk temperature of air at the x-position was calculated by the following equation:

$$T_{air,x} = T_{air,0} + (Q_{el} - Q_{dis} - Q_{rad})(x/L)/(m' c_p) \quad (3)$$

where $T_{air,0}$ is the air temperature measured at the entrance of the test section (where the flow is isothermal), c_p is the air specific heat, m' is the mass flow rate and L is the heated surface length.
As previously explained, only points with the hue within the 70-140 range were processed; outside the selected hue interval, no information is gained. Therefore, in those cases, tests were repeated at the same air flow rate and for 7-15 different values of the input power, so as to move the color pattern toward the regions not previously monitored and locally extract the values of the heat transfer coefficient.
Experimental data were recast in dimensionless form, introducing the Nusselt number Nu and the Reynolds number Re as follows:

$$\mathrm{Nu} = h D/k \quad (4)$$

$$\mathrm{Re} = G D/\mu \quad (5)$$

where $G = m'/(W H)$ is the air mass velocity in the channel (air mass flow rate per unit area) and $D = 2 W H/(W+H)$ is the channel hydraulic diameter.
To obtain a dimensionless representation of the pressure drop ΔP due to the ribs, the friction factor f, based on adiabatic conditions (i.e., test without heating), was introduced according to the Fanning definition:

$$f = (\Delta P/L') D \rho/(2 G^2) \quad (6)$$

where L' is the axial distance between the two pressure taps, approximately equal to the test section length L. Thermal conductivity k, dynamic viscosity μ and density ρ of air were evaluated at the film temperature.

RESULTS AND DISCUSSION

Local heat transfer coefficient

The flow pattern generated by the 45 deg angled ribs is typically three-dimensional owing to the interactions of the oblique secondary flows with the main flow over the ribbed wall. This can lead to significant spanwise variations of the local heat transfer coefficient, especially for channels having a low aspect ratio.
A typical liquid crystal image, recorded for the one-ribbed-wall channel, is presented in Fig.3: the main flow is from the left to the right. The color changes in each inter-rib region as one moves along the direction parallel to the ribs reflect the 3-D character of the flow and thermal fields. From

the processing of a set of LC images, the map of the heat transfer coefficient on the heated wall is recovered, as shown in Fig.4 for *p/e* = 13.33 and Re = 29000. Inspection of the figure shows a higher heat transfer performance in the upstream acute angle region, where the secondary flow brings core air to the wall and low heat transfer coefficients in the downstream, opposite, acute angle corner. This behaviour has been typically encountered for each rib configuration and Reynolds number explored.

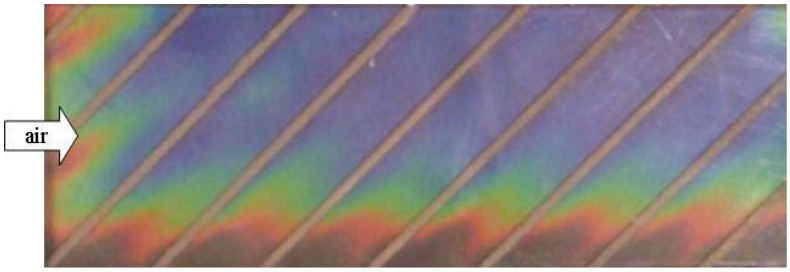

Figure 3. Typical liquid crystal image for the ribbed heated plate

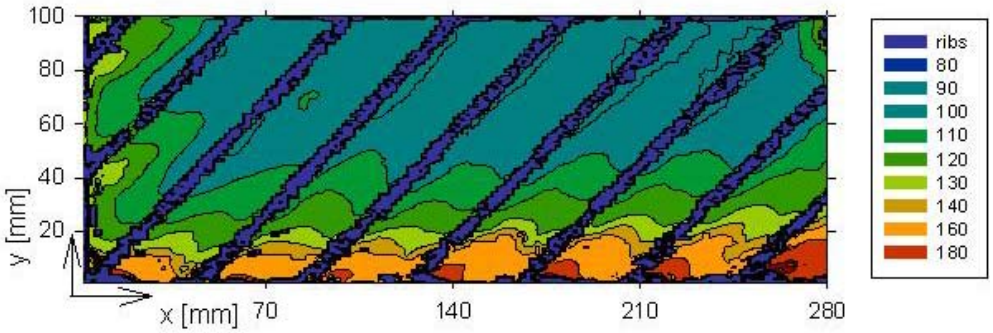

Figure 4. Local heat transfer coefficient *h* [W/m^{2}K] along the ribbed heated surface for *p/e*=13.33, Re=29000

Generally speaking, a development region is observed from the entrance up to about 3-4 diameters in the streamwise direction. Beyond the entrance region, the local, inter-rib h (and Nu) numbers exhibit a nearly periodic distribution whose features are strongly related to the rib pitch-to-height ratio and to the spanwise coordinate.

Local values of the heat transfer coefficient were spatially averaged over each wall region between two consecutive ribs (module) and presented, in dimensionless form, in Figure 5. The distributions of the per-module mean Nu value is reported as a function of the streamwise coordinate, identified by the module number N_x. Owing to the specific features of the rib installations, the geometry repeats itself identically from the 5th to the 13th module for *p/e*=6.66, from the 3rd to the 8th module for *p/e*=10, from the 3rd to the 6th module for *p/e* = 13.33 and from the 2nd to the 4th for *p/e*=20.0. Within these intervals, the per-module mean Nu appears to be only slightly affected by the streamwise coordinate for any experimental condition. The integration of local Nu values over the whole heat transfer area (the area of the heated wall not covered by the ribs) gives the full-surface Nusselt number that allows a direct comparison of heat transfer performance to be performed. To quantify the degree of heat transfer enhancement relative to the smooth channel, the full-surface Nusselt number was normalized by the Nusselt number Nu_0 given by the Dittus-Boelter correlation for fully developed turbulent flow in smooth circular tubes (Eq.7)

$$Nu_0 = 0.023\ Re^{0.8}\ Pr^{0.4} \qquad (7)$$

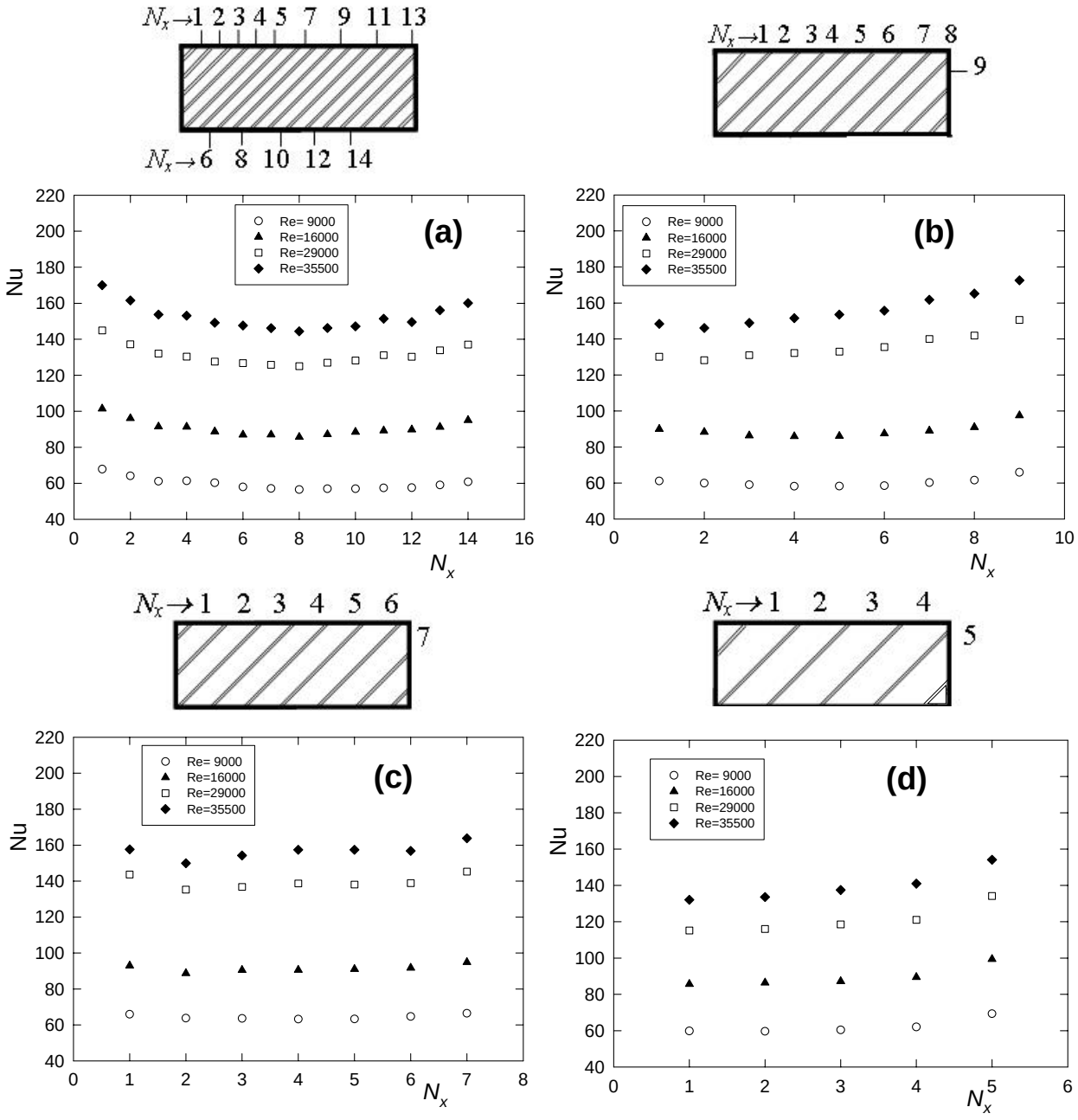

Figure 5. Per-module Nusselt number for *p/e* = 6.66 (a), 10.0 (b), 13.33 (c), 20.0 (d).

Figure 6 shows the normalized Nusselt number versus the Reynolds number, for all the investigated geometries. This figure serves as a comparison of the thermal performance among the different configurations for the constraint of constant mass flow rate. The heat transfer augmentation is in the 1.6-2.4 range and decreases with Re, as typically occurs in rib-roughened channels. It is conjectured that the secondary flow features are affected the rib pitch; in particular, the rib pitch-to-height ratio which accommodates the maximum heat transfer is *p/e*=13.33 at the lowest mass flow rates and *p/e*=10.0-13.33 at the highest mass flow rates. For the optimum value *p/e*=13.33, the ribbed wall with transverse ribs (data from [10]) performs slightly better than that with angled ribs, as found also in [12] for ribbed channels with high aspect ratio. This is ascribed to the fact that, for high channel aspect ratios, the secondary flows induced by angled ribs have a reduced impact on heat transfer levels.

Fanning friction factor of the ribbed channels, calculated according to Eq.(6), was normalized by the friction factor f_0 for fully developed turbulent flow in smooth circular tubes proposed by Blasius:

$$f_0 = 0.046\ \mathrm{Re}^{-0.2} \quad (8)$$

As expected, the normalized friction factor, shown in Fig.7, increases with increasing Reynolds number. Relative to the smooth channel, the degree of enhancement of the friction factor is between 2.6 and 4.3. A criterion to evaluate the performance of the rib-roughened channels is to estimate the quantity Nu/Nu_0 according to the same power required to pump the convective fluid inside the ribbed (enhanced) and the smooth (reference) channels. In order to comply with this constraint, the mass flow rates passing through the enhanced and reference channels cannot be the same; the assumption of constant pumping power leads to

$$f_0\,\mathrm{Re}_0^3 = f\,\mathrm{Re}^3 \quad (9)$$

where Re_0 is the value of the Reynolds number for the reference channel. If Eq.(8) is used to correlate f_0 and Re_0, it follows that:

$$\mathrm{Re}_0 = (21.74\, f\mathrm{Re}^3)^{0.357} \quad (10)$$

with Re_0 representing the value to be used in Eq.(7) to evaluate Nu_0.
The value of Nu/Nu_0 reported in Figure 8 (where the abscissa Re_0 was chosen as a convenient reference for all the ribbed channels) can determine whether or not a given geometry is potentially advantageous under the requirement that the pumping power must be the same. Again, the surface with angled ribs having *p/e*=13.33 performs better than the other surfaces, including that having transverse ribs of same dimensions and pitch (data from [10]).

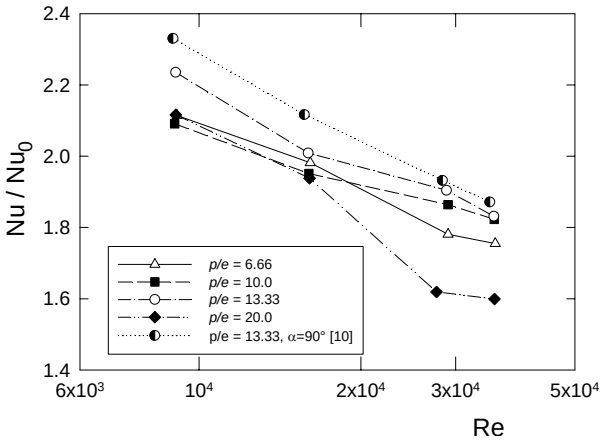

Figure 6. Normalized full-surface Nu vs. Re for angled (α=45°) and transverse (α=90°,[10]) ribs.

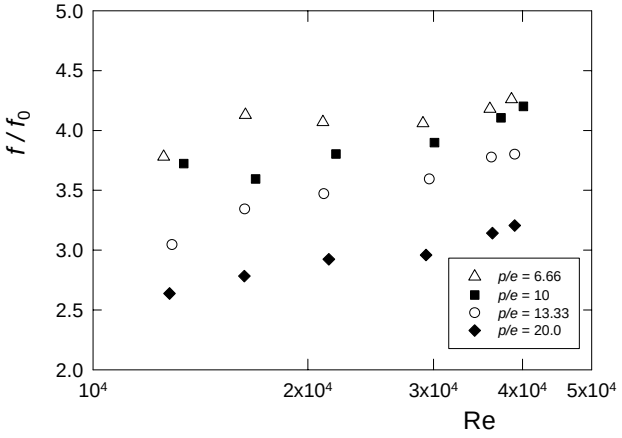

Figure 7. Normalized friction factor f vs. Re

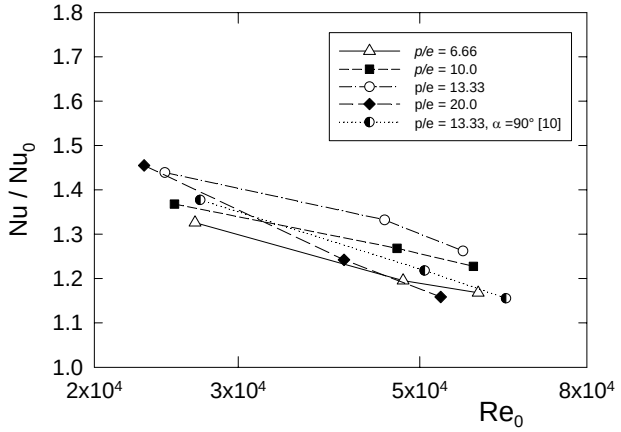

Figure 8. Normalized full-surface Nu vs. the smooth-channel Reynolds number Re_0 for angled (α=45°) and transverse (α=90°,[10]) ribs and the constraint of constant pumping power.

CONCLUSIONS

Heat transfer characteristics of rectangular channels (AR=5) with 45 deg angled, parallel ribs with different values of the rib pitch, have been experimentally investigated by means of the steady-state liquid crystal thermography. The parallel ribs have been installed either onto one wall of the channel. Based on the results, the following conclusions are drawn.

After a relatively short entrance region, local Nusselt number attains a nearly periodic distribution along the streamwise direction, with features markedly affected by the rib pitch and the spanwise coordinate; in particular, spanwise Nusselt number values decrease along the rib direction, from the acute upstream angle to the acute downstream angle.

The per-module mean Nu values appear to be only slightly affected by the streamwise coordinate for any experimental condition.

The full-surface averaged Nu values have been compared to those for a reference condition (a smooth channel with the same hydraulic diameter). Heat transfer augmentations relative to the smooth channel, for the constant mass flow rate criterion, are in the 1.6-2.4 range and decrease with Re, as typically occurs in rib-roughened channels. Heat transfer performance, relative to a smooth channel under the constraint of constant pumping power, is generally better for the higher rib pitch-to-height ratio (p/e=13.33), regardless of the value of the Reynolds number.

ACKNOWLEDGEMENTS

This research has been financially supported by company Ansaldo Energia, Genoa, Italy.

REFERENCES

1. Han, J.C., Dutta, S., and Ekkad, S.V., *Gas Turbine Heat Transfer and Cooling Technology*, Taylor and Francis, New York, 2000.

2. Han, J.C., Glickmann, L.R., and Rohsenow, W.M., An Investigation of Heat Transfer and Friction for Rib-Roughened Surfaces, *Int.J. Heat Mass Transfer*, Vol.21, pp.1143-1156, 1978.

3. Han, J.C., Heat Transfer and Friction in Channels with Two Opposite Rib-Roughened Walls, *ASME J. Heat Transfer*, Vol.106, pp.774-781, 1984.

4. Han, J.C., and Park, J.S., Developing Heat Transfer in Rectangular Channels with Rib Turbulators, *Int. J. Heat Mass Transfer*, Vol.31 pp.183-195, 1988.

5. Taslim, M.E., and Lengkong, A., 45 deg Staggered Rib Heat Transfer Coefficient Measurements in a Square Channel, *ASME J.of Turbomachinery,* Vol.120, pp.571-580, 1988.

6. Liu, Y.H., Wright, L.M., Fu, W.L., and Han, J.C., Rib Spacing Effect on Heat Transfer in Rotating Two-Pass Ribbed Channels (AR=1:2), *J. of Thermophysics and Heat Transfer*, Vol.21**,** pp. 582-595, 2007.

7. Huh, M., Liu, Y.H., Han, J.C., and Chopra, S., Effect of Rib Spacing on Heat Transfer in a Two-Pass Rectangular Channel (AR=1:4) with a Sharp Entrance at High Rotation Number, *Proceedings of ASME Turbo Expo 2008 for Land, Sea and Air,* Berlin, Germany, June 9-13, 2008.

8. Chandra, P.R., Niland, M.E., and Han, J.C., Turbulent Flow Heat Transfer and Friction in a Rectangular Channel with Varying Numbers of Ribbed Walls, *ASME J. of Turbomachinery*, Vol.119, pp.374-380, 1997.

9. Chandra, P.R., Alexander, C.R., and Han, J.C., Heat Transfer and Friction Behaviours in Rectangular Channels with Varying Number of Ribbed Walls, *Int. J. Heat Mass Transfer*, Vol.46, pp.481-495, 2003.

10. Tanda, G., Heat Transfer in Rectangular Channels with Transverse and V-Shaped Broken Ribs, *Int. J. Heat Mass Transfer*, Vol.47, pp.229-243, 2004.

11. Tanda G., Abram R., Forced Convection Heat Transfer in Channels with Rib Turbulators Inclined at 45 deg, *ASME J. of Turbomachinery*, Vol.131, pp. (021021)1-9, 2009.

12. Han, J.C., Heat Transfer and Friction Characteristics in Rectangular Channels with Rib Turbulators, *ASME J. of Heat Transfer*, Vol.110, pp. 321-328, 1988.

THERMAL ANALYSIS OF CAR AIR COOLER UNIT

D. Trzebinski*, I. Szczygiel*
*Institute of Thermal Technology, Gliwice, Poland

ABSTRACT. In the paper thermodynamic analysis of car air cooler is presented. Typical refrigerator cycles are studied. One with uncontrolled orifice and non controlled compressor, second with thermostatic controlled expansion valve and externally controlled compressor. The influence of refrigerant charge and the inlet air temperature on the coefficient of performance, exergy efficiency, heat flux and temperature in evaporator and compressor net power was investigated. The impact of improper refrigerant charge on the performance of A/C systems was also checked. The simplified CFD model of car interior is also provided.

Keywords: *thermal comfort, air conditioning, COP, cooling systems*

THERMAL COMFORT IN CAR CABIN

The problem of proper thermal comfort inside the compartments is seriously treated nowadays. The techniques of achieving quite good effects of thermal comfort are well recognized in the habitats, but in mobile spaces, like cars, trains and buses are still under development. Temperature in an vehicle cabin is closely related with the occurrence of traffic accidents [1]. Zlatoper has created the ranking list of the factors which affect the traffic accidents in United States and placed the temperature on the third position [2]. In hot summer days internal temperature often exceeds +40°C. So it is obvious, that the thermal conditions in the vehicles' cabins directly influences on the driver's and passengers safety.

Both too high and too low ambient temperature influences human physical and mental state. Driver`s efficiency researches indicate that it can be even 35% higher at +20°C than at +35°C. Decrease of efficiency at +5°C can be the same as that at +35°C [3, 4].
There are also additional parameters, which influences on the thermal comfort: air flow speed, air humidity, outer wall temperature and, what is important in vehicles cabins, sun radiation. In many cases thermal parameters are controlled only by regulating air temperature and mass flow rate. Due to that, air flow speed can locally exceeds its reasonable value.
It is hard to strictly define the thermal comfort. Usually thermal comfort means that temperature is between 20°C and 22°C, humidity is about 50% and air velocity is under 0,5 m/s. This can be called independent factors.

There is also second group of factors affecting thermal comfort – individual human feelings which are much harder to define, because each person has their own preferences for thermal comfort. One can say there is thermal comfort when amount of people saying “I fell bad here” is the lowest. [5].
The symptoms of thermal discomfort are intensive sweat production, increment of heart beat frequency, and as a result , the decrease of driver concentration and efficiency.

* Corresponding author: D. Trzebinski, MSc
Phone: + (48)-32-2372974, Fax: + (48)-32-2372872
E-mail address: daniel.trzebinski@polsl.pl

The investigations presented in this paper are the part of larger project, which assumes complex modelling of thermal state of car interior. First part assumes creation of CFD model of car interior.

This part should should answer the question how the air mass flow rate distribution at the inflow to the cabin influences the temperature and air flow inside the cabin, especially in the passengers surroundings. The full numerical model of cabin and the numerical simulations will be helpful in optimization of air inlets, air mass flow rate, humidity conditions etc. with the respect to the thermal comfort. In the paper the very first results of the simplified model are presented. Second part is thermodynamic modelling of air cooling unit in order to estimate the influence of basic cabin parameters on the A/C unit COP, power consumption of the unit and fuel consumption of the vehicle. Different types of working fluid will be checked. In the paper the initial results of this part are shown. The A/C unit model and CFD model are assumed to be coupled. In the third part of the project the experimental verification of both models will be performed.

NUMERICAL MODEL OF CAR INTERIOR

The numerical model was built within the Gambit/Fluent environment. In the paper simplified (rough grid with 800000 cells), 3D model is presented. At this stage of investigations the flow is isothermal: only the air flow in the cabin is investigated and presented. Contours of velocity in the model are shown in figures 2 and 3. Full 3D CFD model including sun radiation and internal heat generation with more detailed geometry is under construction now.

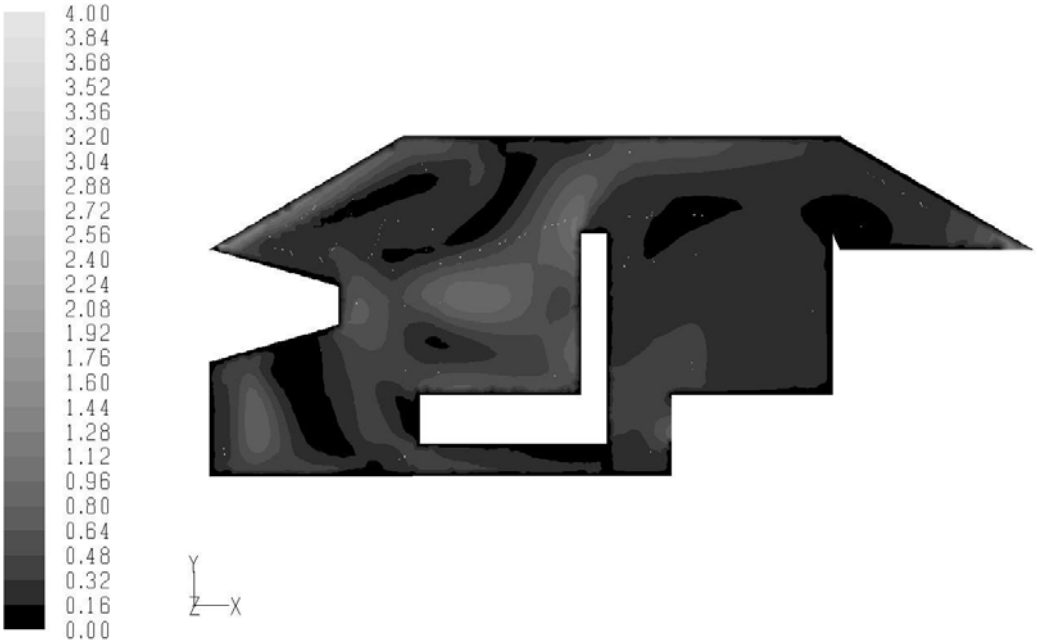

Figure 1. Contours of velocity [m/s]

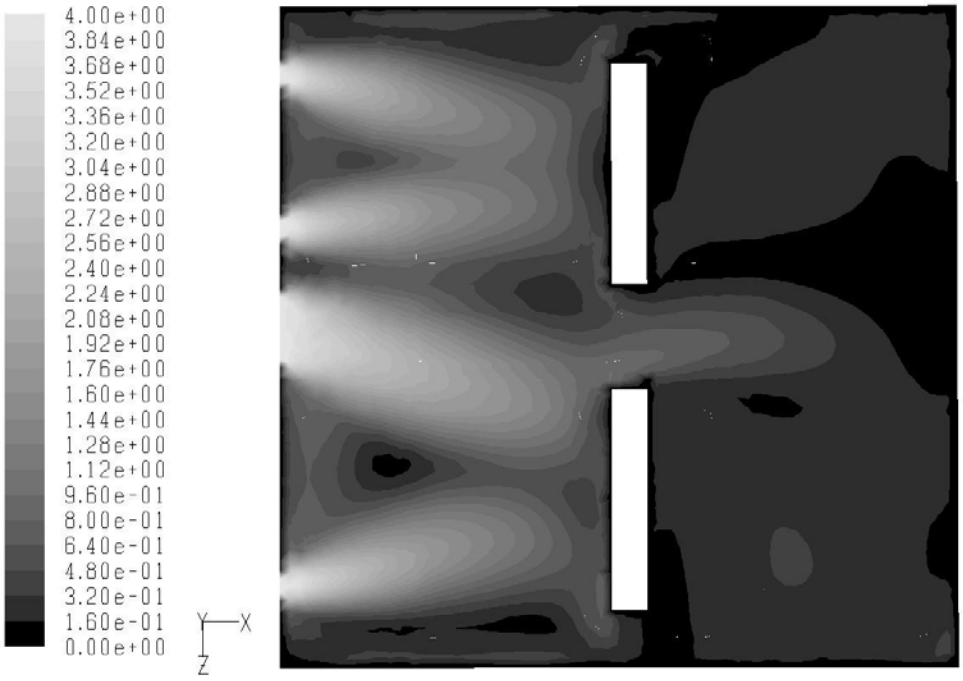

Figure 2. Contours of velocity [m/s]

THERMAL ANALYSIS OF REFRIGERATOR CYCLE

The heat flux which should be transfered out of the car cabin is about 2 kW [6, 7]. Heat balance of car cabin is shown in figure 1.

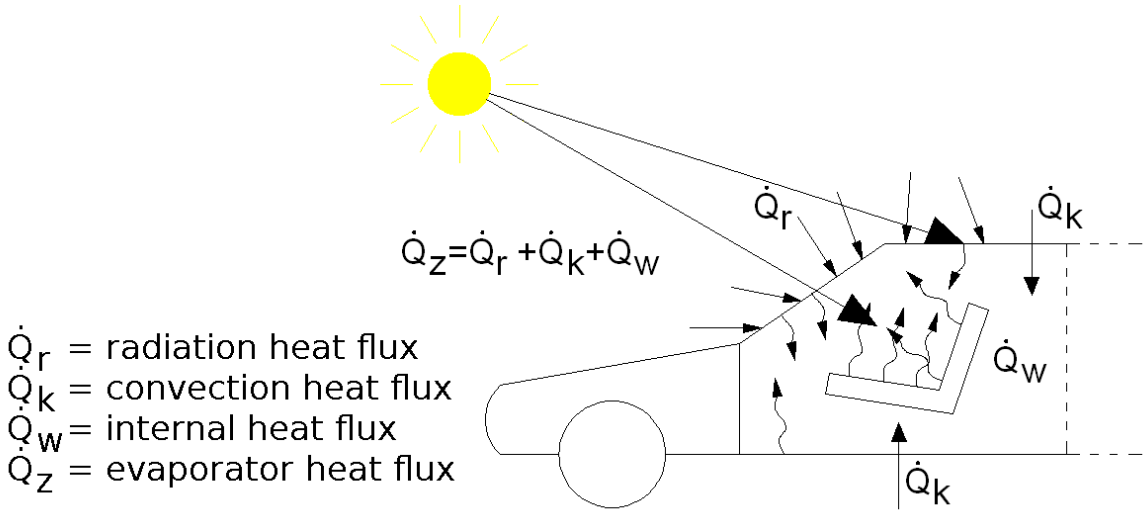

Figure 3. Car cabin heat balance.

An optimum A/C unit should assure thermal comfort under time varying thermal loads with minimal energy consumption. Compressor in the unit is driven by the vehicle engine and therefore considerably increases the fuel consumption. In the paper two types of unit are considered. First with uncontrolled orifice and non controlled compressor (fixed piston displacement), second with thermostatic controlled expansion valve assuring 1K superheating of refrigerant at compressor inlet

and externally controlled compressor (piston displacement from 60 to 120 cm^3). Both cases work with compressor speed 1000 and 3000 rev/min. Nominally refrigerant charge (medium – R134a) is 0,44 kg. The charges 0,22 kg (50% nominal) and 0,055 kg (12% nominal) were also considered. Air temperature changes from 20°C to 45°C. The refrigerator scheme is shown in figure 4. For the simulations commercial Kuli software was used [8].

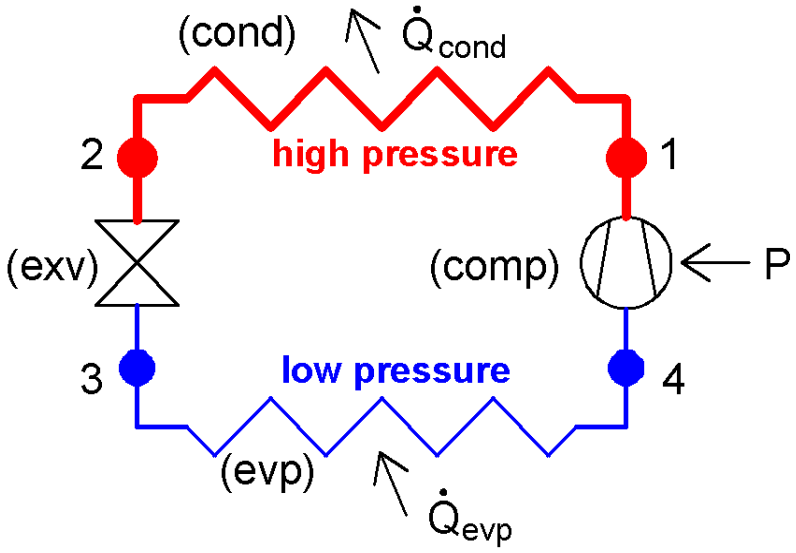

Figure 4. Scheme of refrigerator cycle.

As it was mentioned, the aim of the investigations was the influence of refrigerant charge and inlet air temperature on the air A/C unit parameters: COP, exergy efficiency (η_{carnot}), heat transfer in evaporator (Q_{evap}), refrigerant temperature inside evaporator and compressor driving power. The parameters are defined in the following way:

$$COP = \frac{\dot{Q}_{evap}}{\dot{Q}_{comp}} \tag{1}$$

$$\eta_{carnot} = COP \frac{T_{cond} - T_{evap}}{T_{evap}} \tag{2}$$

$$\dot{Q}_{evap} = \dot{M}(h_4 - h_3) \tag{3}$$

where:
T_{cond} – condenser temperature
T_{evap} – evaporator temperature
h_4 – refrigerant enthalpy after evaporator
h_3 – refrigerant enthalpy before evaporator
$\dot{M}$ – refrigerant factor mass flow rate

Non controlled cycle

In this case as expansion valve is orifice and everything depends on orifice effective throttle area.
If the area is too high the compressor works properly (without fluid droplets) only in some range. If effective throttle area is too low the refrigerant at evaporator outlet is always superheated but the temperature at compressor outlet can be very high. That high temperature involves two another problems. First is higher compressor material durability, second is a problem with liquid phase at condenser outlet, especially with higher ambient air temperature. When the refrigerant is not liquid, or what is better, subcooled, efficiency of all system decreases significantly.

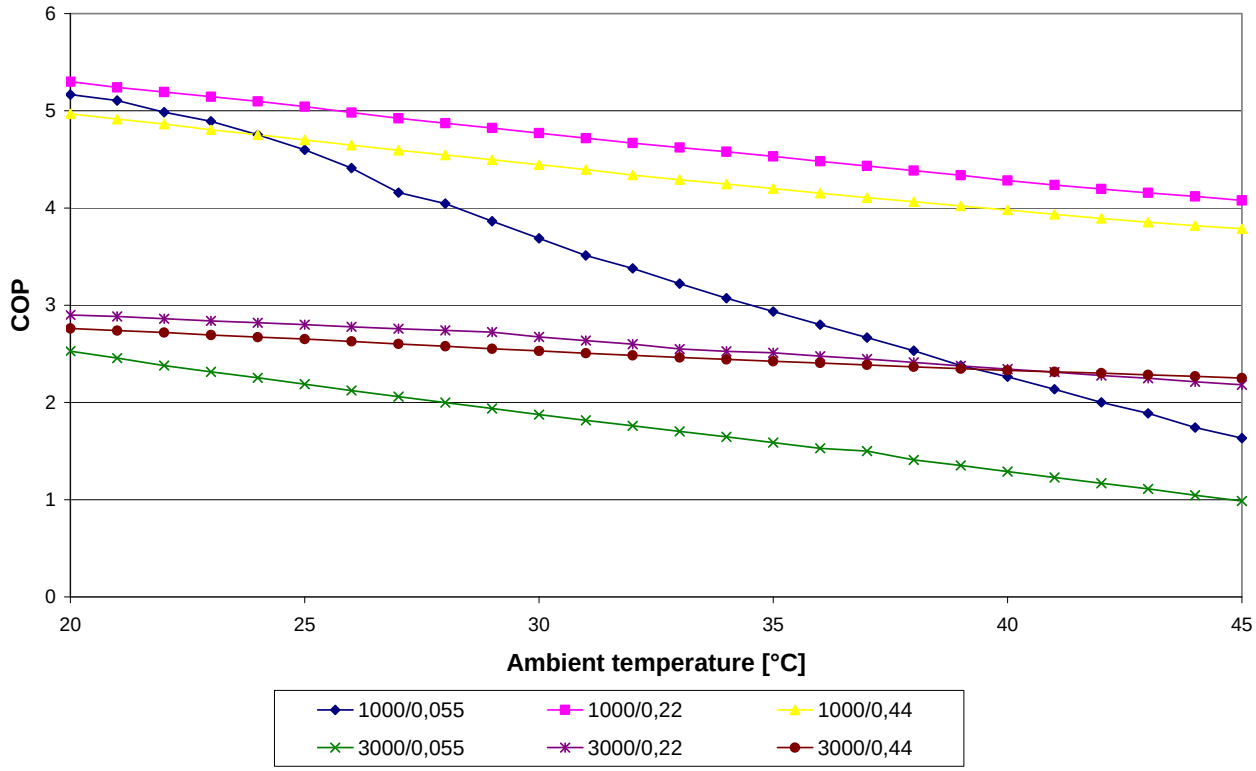

Figure 5. COP as a function of ambient temperature.

In this case, at 20°C irrespectively of refrigerant charge, COP is about 5 for 3000 rev/min and 3 for 1000 rev/min and decreases of 1 at 45°C air temperature. For 0,055 kg charge the drop is about 3 for 1000 rev/min and 2 for 3000 rev/min (figure 5).

Similarly behaves heat transferred in the evaporator. For the charge 0,44 kg and 0,22 kg, the heat flux increases with air temperature. It is shown in figure 6. For 45°C the heat flux is two times higher than for 20°C. For the charge 0,055 kg the situation is opposite – heat flux decreases with air temperature.

There is one advantage of 0,055 kg charge case: compressor power is low: at 3000 rev/min is below 1 kW while for 0,44 kg is twice higher. But here is almost impossible to achieve required temperature inside car cabin in this case. Heat transferred in the evaporator is just too low.

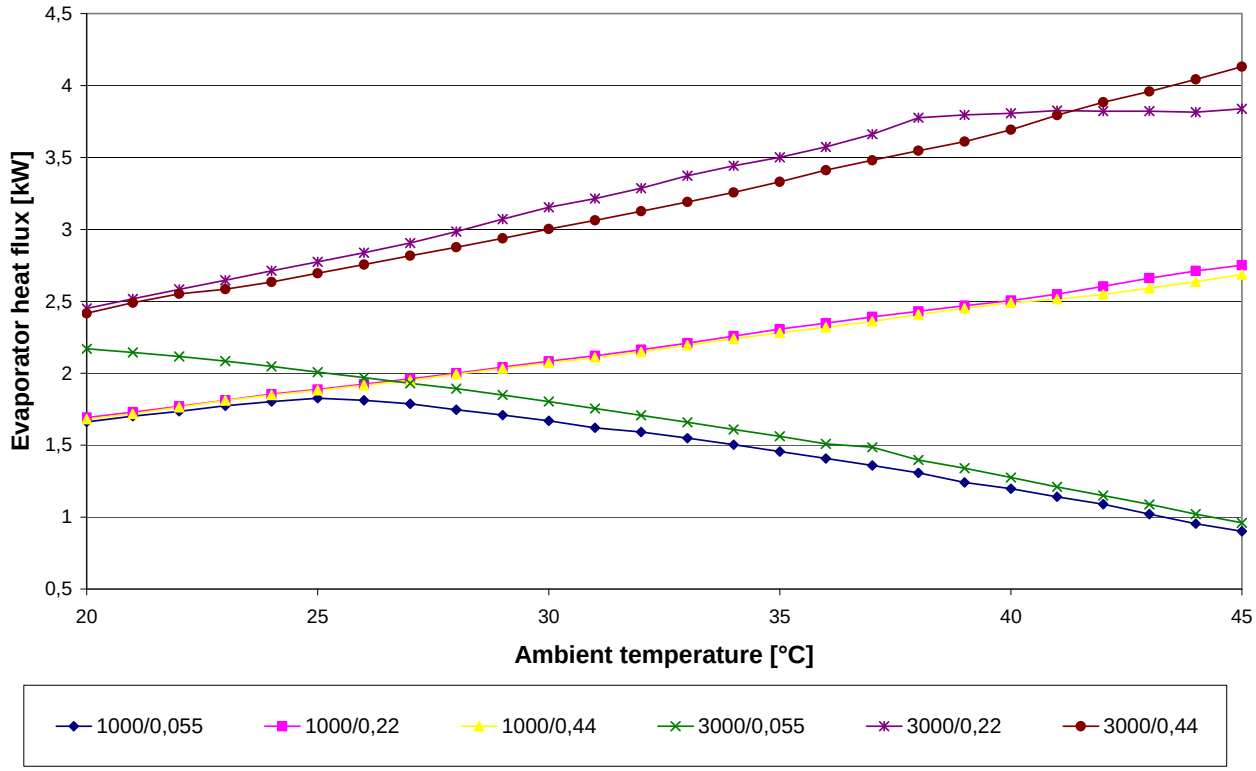

Figure 6. Evaporator heat flux as a function of ambient temperature.

Controlled cycle

In this case there is no problem with too high temperature, because expansion valve always assures 1K of superheating. So there is no problem with high temperature material durability, because temperature at compressor outlet is lower too. If the temperature at compressor outlet is lower it is also easier to obtain liquid phase at condenser outlet.

One can say the controlled cycle is more "flexible". In this case heat flux in evaporator can be about 1,5 kW higher than in non controlled one, which means that we can reject 1,5 kW of heat flux more from car compartment. For 0,055 kg charge, compressor inlet (evaporator outlet) temperature is about 40°C at 45°C air temperature. It means that temperature at compressor outlet can be about 100°C.

For other charges inlet temperatures are similar and always below 15°C.

COP tendency is similar to non controlled cycle but the values are a little bit lower (figure 7). The compressor power is always higher than in non controlled cycle. There is also higher heat flux in evaporator for both 1000 and 3000 rev/min cases (figure 8). For the charge 0,055 kg COP is equal to 0,25 at 45°C air temperature.

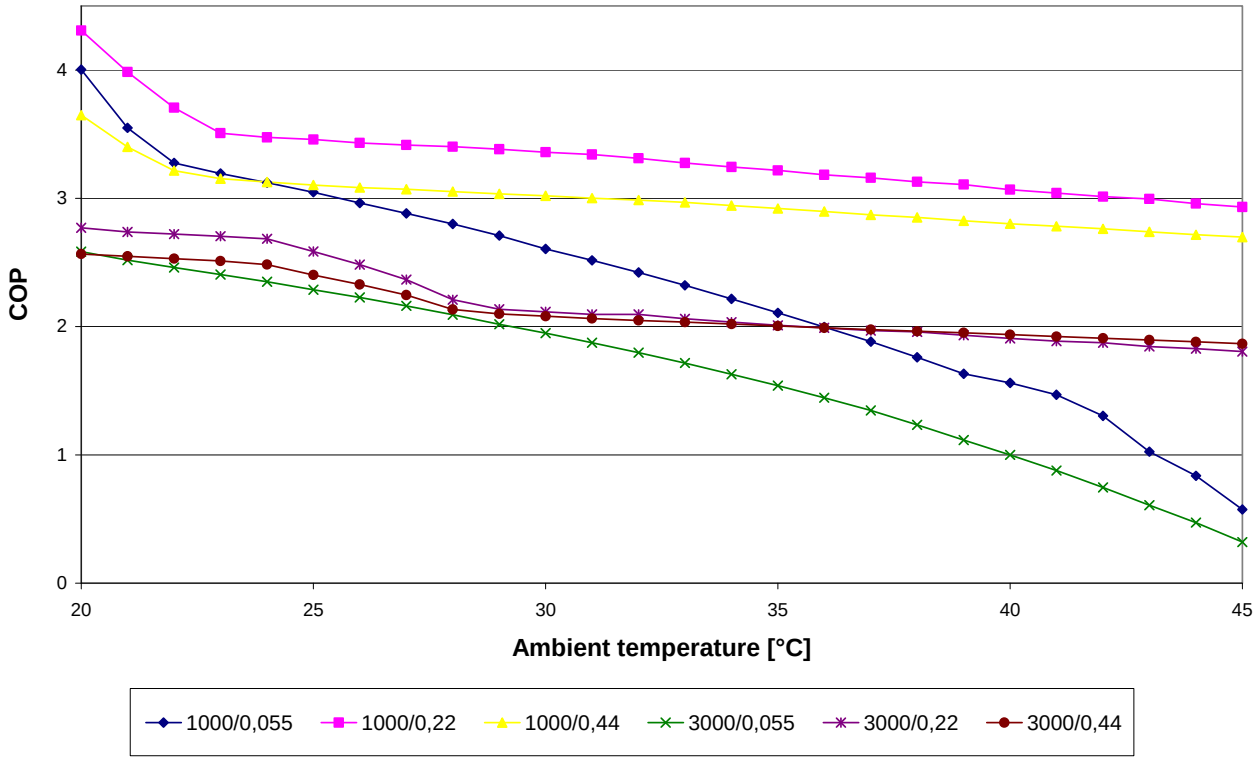

Figure 7. COP as a function of ambient temperature.

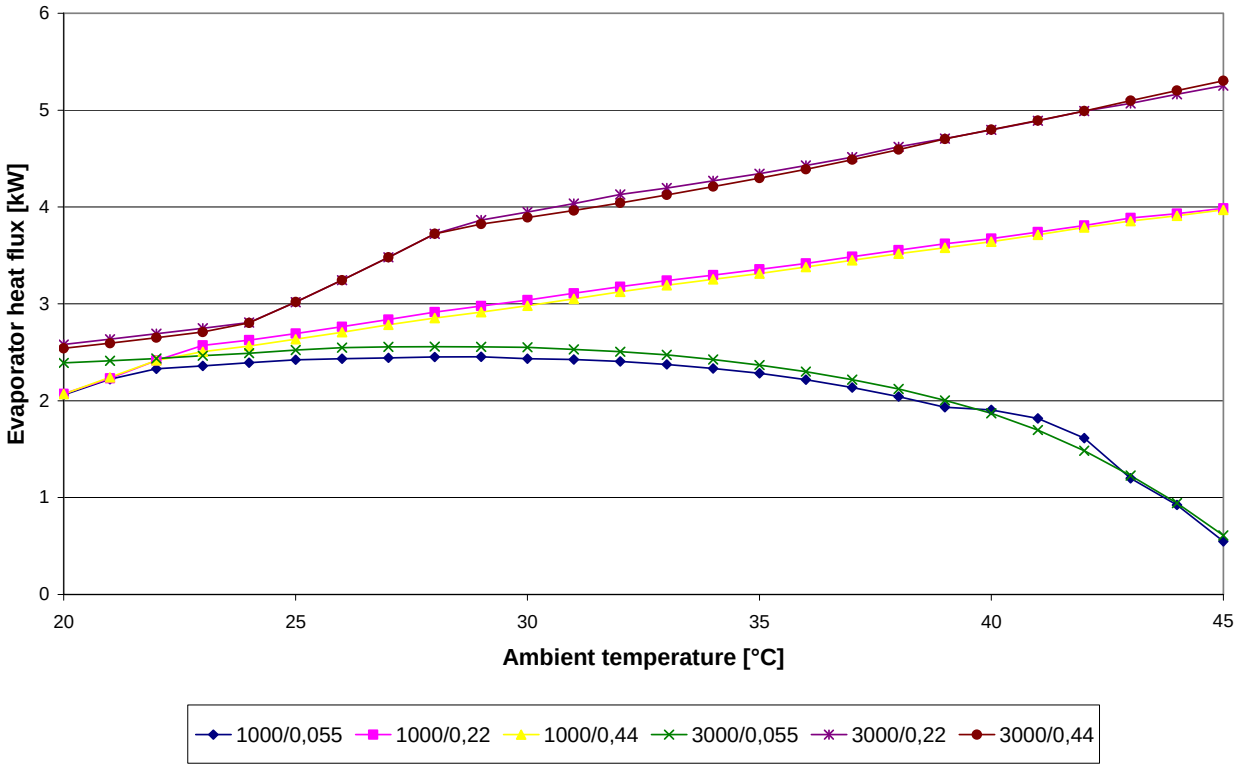

Figure 8. Evaporator heat flux as a function of ambient temperature.

Comparing the cases one can say that non controlled case is better than controlled. COP values are higher for non controlled, compressor power is lower (lower fuel consumption) but from the other side heat flux in evaporator is lower and refrigerant temperature is higher.

Additionally it should be stressed out, that for the charge 0,055 kg compressor works only with vapour phase refrigerant. For the charge 0,11 kg it works with vapour phase above 35°C air temperature. For the charge 0,44 kg liquid always appears in compressor.

All the simulations show how important is proper refrigerant charge in A/C systems. It is impossible to estimate the amount of refrigerant in the cycle without special measuring instruments. There is only one symptom to say that refrigerant charge is too low – the outlet air temperature from A/C is too high.

CONCLUSIONS

In the paper, the initial, simplified numerical model of the car interior as well as the thermal analysis of A/C unit cycle are presented. The plans for future investigations assume the full 3D, temperature dependent numerical model coupled with thermal model of A/C unit. Experimental verification of the model is also planned.
Basing on the simulations to date, it can be noticed that the decrease of the refrigerant charge decreases COP. Decrease is higher in controlled cycle because the temperature in evaporator is higher which causes lower heat flux in evaporator and higher compressor power. Beneficial is that compressor works always with refrigerant in gas phase. For non controlled cycle efficiency is higher but the hazard of compressor work with liquid appears.
In both cases COP is lower when refrigerant charge is below its nominal value. This is the reason why refrigerant charge control is so important, especially in car air conditioning units, which are not so hermetic like home air conditioning units.

REFERENCES

1. H.A.M. Daanen, E. Vliert, X. Huang: *Driving performance in cold, warm and thermoneutral environments.* Appl. Ergon. 34 (2003), 597-602
2. Zlatoper T.: *Determinants of motor vehicle deaths in the United States: a cross-sectional analysis, special issue: theoretical models for traffic safety*, Accid. Anal. Prev. 23 (5) (1991(431-436
3. Cengiz T.G., Babalik F. C.: *An on-the-road experiment into the thermal comfort of car seats*, Applied Ergonomics Volume: 38, Issue: 3, May, 2007, pp. 337-347
4. Daanen Hein A.M., van de Vliert Evert, Huang, Xu: *Driving performance in cold, warm and thermoneutral environments*, Applied Ergonomics Volume: 34, Issue: 6, November, 2003, pp. 597-602
5. Trzebinski D., Szczygiel I.: *Analiza komfortu cieplnego kabiny pasażerskiej samochodu osobowego*, Systems 2008, Volume 13, Special Issue 1/2
6. Kwasniowski S. (red): *Ogrzewnictwo, wentylacja i klimatyzacja w pojazdach mechanicznych*, Wrocław, Nawigator, 1995
7. Zhang Y., Zhao R.: Overall thermal sensation, acceptability and comfort, Building and environment 43 (2008) 44-50
8. Farzaneh Y., Tootoonchi A.A.: *Controlling automobile thermal komfort Rusing optimized fuzzy controller*, Applied Thermal Engineering 28 (2008) 1906-1917
9. http://www.kuli.at

HEAT TRANSFER ENHANCEMENT IN DUCTS DUE TO ACOUSTIC EXCITATION

G. Bennett*, J. Mahon, D. Murray, T. Persoons, I. Davis
University of Dublin, Trinity College, Dublin 2, Ireland

ABSTRACT. The thermoacoustic effect that results from the interaction of a sound wave in a compressible fluid in contact with solid boundaries is known to be capable of removing heat from power dissipating systems. In this paper the standing wave acoustic field that is generated in an open ended duct, a section of which is heated, and how it interacts with the aerodynamic flow field is examined by an experimental study. Specifically, the effect the fluctuating acoustic pressure and associated particle velocity have on the internal fluid dynamics is investigated. The ultimate goal is to fully understand and optimize the interaction mechanisms in order to enhance the overall convective heat transfer from a heated duct to internal flow. An experimental rig which has been designed and built allows the fundamental fluid dynamic, acoustic and heat transfer mechanisms to be studied. The rig consists of a circular duct with a central copper isothermally heated section which is instrumented with thermocouples, a heat flux sensor, microphones and a cross-wire probe. The cross wire is used to measure both time varying temperature and velocity at a high frequency and spatial resolution and a calibration procedure which allows the sensor to measure fluctuating velocity at elevated temperatures is reported. Results from the current investigation demonstrate how convective heat transfer from the heated duct section to the internal flow is enhanced due to acoustic excitation. In this preliminary, investigative study, it is suggested that two different heat transfer mechanisms are identified: one associated with the increased turbulent mixing due to the added particle velocity; the second associated with acoustic streaming. The results show significant increases in flow temperature and heat transfer coefficients for free and forced convection regimes.

Keywords: *Convective Heat Transfer, Duct Acoustics, Standing Wave*

INTRODUCTION

Thermal management remains today one of the most important bottlenecks in the further development of electronic devices. Whilst new approaches, such as heat pipes and thermoelectric cooling technologies, are being developed, forced convection is still a necessary technique. As acoustic power is approximately proportional to (flow velocity)^6 to (flow velocity)^8 it is crucial that fan performance be optimised. The acoustic penalty for an increase in flow velocity is addressed in this paper, as an effective means to reduce the noise created by the fan would facilitate increased heat transfer. The long term goal of this exploratory work aims to address the following question ***"To what extent can the existing noise from fans in electronics' thermal management systems be optimized to enhance convective cooling?"***

The 2006 market report by the European Electronic Component Manufacturers Association (EECA) shows [1, 2] that the European market for electronic components is worth in excess of €45 billion. The global semiconductor market grew by over 11.5% in the first half of 2006, covering the areas of power transmission, telecommunications, computers and peripherals, automotive and

* Corresponding author: Dr. Gareth Bennett
Phone: + (353)-1-8961383, Fax: + (353)-1-6795554
E-mail address: gareth.bennett@tcd.ie

aerospace [3]. The industry supports over 207,000 direct jobs in the EU [1], and many more indirect jobs.

Current fan-based forced convection techniques[4] with high performance heat sinks are capable of cooling up to 13 W/cm^2. For microprocessors, the heat dissipation is still increasing exponentially, while current processor designs are around the limit of 15 W/cm^2 corresponding to the forced air cooling bottleneck[5]. Since the current integrated circuits are pushing the power boundary, new cooling technologies are being examined. In telecommunications, the maximum power density is currently around 24 W/cm^2, requiring heat pipes to spread the heat to a larger surface area[6]. Present thermoelectric cooling technology[7] is limited to a power density of about 10 W/cm^2, although more advanced materials are being developed to increase the power density to beyond 500 W/cm^2. However, this is an expensive solution with a limited relevance for broad range applications.

The substantial research effort going into removing the heat generated by the electronic circuitry, using advanced methods such as heat pipes or liquid cooling provides an effective way of transporting the heat away from the confined chip geometry to a larger heat-sink with fan, where the heat is more easily transferred to the surrounding air. Crucially, the use of advanced high heat flux cooling methods does not eliminate the need for fan-based air cooling. This is the framework for the proposed research, which aims to use fan noise in a constructive way, to enhance convective heat transfer in thermal systems.

The thermoacoustic streaming theory initiated by Lord Rayleigh[8] has excited researchers and engineers for over one hundred years. The thermoacoustic instability observation of Rijke's Tube that Rayleigh's theory was able to explain, is found today in pulse combustor engines and low NOx aero-engine multi-stage annular combustors, and attempts to computationally model the phenomenon continue[9, 10]. Since Rayleigh, more recent fundamental theoretical studies have been carried out by Karimi et al.[11], and Swift[12, 13] and Garrett[14] in the area of thermoacoustics applied to refrigeration. The theoretical acoustic enhancement of heat transfer to particles and droplets such as pulverized coal particles and coal-water slurry fuel droplets[15, 16] has been examined as have experimental studies for configurations such as enclosures[17], parallel plates[18], flow over cylinders[19], heated wires[20] and impinging jet flows[21, 22]. Recently, the phenomenon has been applied to cooling of products within the electronics industry by Komarov and Hirasawa[20], and Lee and Loh[23] and to plasma screens by Kim at al.[24].

A fundamental experimental study on the heat transfer enhancement in ducts due to the acoustic excitation of axial fans is proposed in this project. The results of the work will find application in thermoacoustic refrigeration, heat transfer in ducts and in the electronics sector.

EXPERIMENTAL SETUP

General rig layout

The principal element of the experimental rig is a vertically oriented circular duct of an overall length equal to 2.944m and an internal diameter of approximately 0.1m. The duct, as shown in figure 1, consists of three parts: lower and upper sections of PMMA (Polymethyl Methacrylate) and a central section of copper. The transparent PMMA was chosen for its low thermal conductivity and for its suitability for future PIV measurements. The wall thickness is 10mm with an internal diameter of 100mm. The central copper section of 0.520m length and 1.5mm wall thickness was chosen for its high thermal conductivity and is mounted to a support frame via an Ertalon 6 PLA flange of 10mm thickness clamped at each end. The copper section thus butts against the PMMA at both ends and is in contact with just the two low conductivity 10mm thick Ertalon flanges. This mounting arrangement was designed to reduce conductive heat loss from the copper section which is heated on its external

surface by a Holroyd 1.5 kW H/SR-PA silicon heater mat over the length between the flanges of 0.5m. The mat is powered by a RegaVolt Variac, and the current to the mat is monitored via a multi-meter which allows the power input to be measured. The schematic also shows the copper pipe to be instrumented with two T-type thermocouples, which are mounted, at either end, flush with the inside of the pipe surface. Three 6mm holes were cut through the heater mat and copper piping along its length to allow for access of the cross-wire anemometer and for microphone pressure measurements, with any unused holes blocked during testing. A type 27036 RdF Micro-foil heat-flux sensor with integral T-type thermocouple is placed mid-point of the total length of the pipe which is 9.1mm below the top cross-wire hole. As a right-angled cross wire was employed to ensure no disturbance to the flow field by the hot wire support, the 9.1mm length corresponds to the extension of the cross-wire normal to the probe. This set up allows for temperature and velocity profiles to be measured at the same mid-point axial location as the heat flux sensor.

A D.C. tube-axial fan is mounted at the top of the duct and is used to control the fluid velocity through the pipe. In addition to the cross-wire velocity measurements, a pitot-static tube was used to monitor average flow velocities. A 600W JBL 2206 H speaker is located at the lower end of the duct and is used to introduce pressure fluctuations at set frequencies. A gap between the speaker and the duct allows air to be drawn up through the duct for forced convection tests.

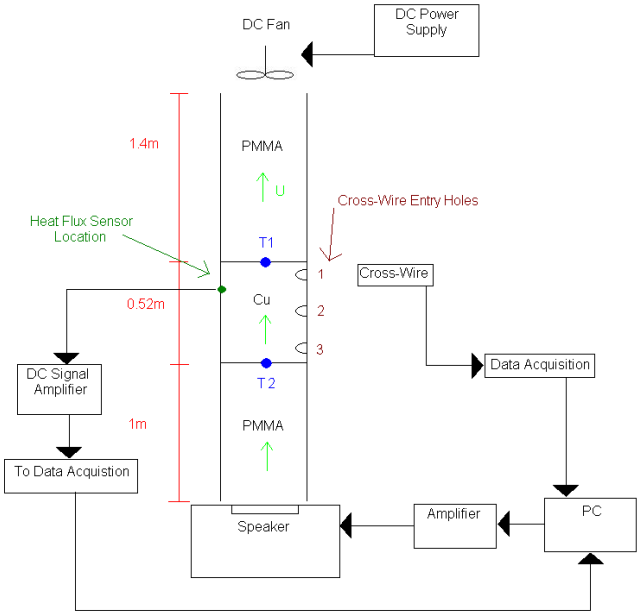

Figure 1. Experimental test rig

Instrumentation

A Dantec X-probe type 55P63, with a right angle between the sensor and the probe holder, is used to obtain velocity and temperature measurements. One of the wires of the cross-probe is used to measure fluctuating velocity obtained using a Dantec StreamLine Constant Temperature Anemometer (CTA). The other 'cold-wire' is configured to act as a resistance thermometer using constant-current anemometry (CCA) the temperature of which is determined by an accurate measure of its resistance.
The radial position of the cross-wire is accurately controlled by a linear actuator attached to a stepper motor which was calibrated to ensure spatial precision. The micro-foil sensor signal, of the order of μV, is amplified x1000 using an Omega Omni-Amp III DC Signal Amplifier. The thermocouples are connected to an Omega Toggler device which displays the temperature on-screen. The DC fan used is powered by a Thurlby 30V-1A DC power source. The speaker used to introduce the standing wave receives a signal from a QSC Power amplifier, which in turn receives a signal from .wav files

generated in Matlab and output via LabView through a National Instruments D/A converter. All data from the heat-flux sensor, the cross-wire and the microphones are acquired by a National Instruments data acquisition system, using N.I.'s LabView and and Dantec's StreamWare software on a Dell Precision T3400 PC. A LabView programme was written to automate control of the speaker frequency, the cross-wire location via the stepper motor and data acquisition of the heat flux sensor and cross-wire measurements.

Cross-Wire Calibration

Hotwire anemometry is based on convective heat transfer from a heated wire. However, in this test setup the temperature of the fluid may vary with time and/or is at a different temperature to nominal ambient temperature at which the hotwire was calibrated. As the principle underlying the measurement of flow velocity is based on heat transfer it is necessary to measure the actual temperature of the flow and hence correct for the temperature difference.

There are a number of approaches to correct the velocity for elevated temperature. The simplest method is based on the assumption that heat transfer from the probe is proportional to the temperature difference (between the wire and ambient temperature) and the relationship is shown in equation 1

$$E_{corr} = \left(\frac{T_w - T_0}{T_w - T_a} \right)^{\frac{1 \pm m}{2}} E_a \tag{1}$$

where E_a = acquired voltage, E_{corr}= temperature corrected voltage, T_w=hotwire measurement, T_0= ambient reference temperature, T_a= fluid temperature during calibration and m = temperature loading factor, which is a dimensionless physical material property (for air, m = 0.16).

A more accurate approach for calibrating the hotwire is direct calibration of the hotwire at the ambient temperature of the fluid under test. In the current study both the fluid velocity and temperature vary significantly, hence direct calibration was the most accurate and appropriate method. A discussion of this approach can be found in Bearman[2].

The accuracy of the results from the hotwire anemometry system is dependent on both the acquired voltage (velocity) and temperature of the fluid. Hence, it is important to measure both simultaneously. Both quantities were measured using a cross wire probe, type 55P63. The method of temperature measurement used in this paper is based on a resistance thermometer. The temperature measurements were obtained from the resistance measurement of wire 1. Wire 2 was used to measure flow velocity using a standard constant temperature anemometer.

The resistance wire was calibrated by exposing the wire with flow at a known temperature and fitting a curve between temperature and measured resistance. A linear relationship was measured between the two quantities. Equation 2 shows the relationship between wire resistance and temperature. This was the basis for the temperature measurement.

$$R = R_0 \left[1 + \alpha \left(T - T_0 \right) \right] \tag{2}$$

where R is the wire resistance at temperature T, R_0 is the wire resistance at the reference temperature T_0 and α is the temperature coefficient of resistance.

The velocity and temperature sensitivity of the hotwire were obtained by operating the hotwire at a fixed overheat ratio of 1 and hence a fixed wire resistance. The hotwire system was balanced at an ambient temperature of *20.1°C*. The output voltage was recorded as a function of velocity and fluid

temperature by using a specially designed calibration rig as shown in figure 2. The calibration was performed at a range of flow velocities ranging from 1m/s to 7m/s at four ambient temperatures of 20, 30.1, 39.8 and 50.1°*C*. The set of calibration data are shown in figure 3. A fourth order polynomial was used to fit the data as per equation 3.

$$U = C_0 + C_2 E + C_2 E^2 + C_3 E^3 + C_4 E^4 \tag{3}$$

where C_0 to C_4 are the calibration constants and E is the anemometer voltage.

The cross-wire as a sensor was chosen as an attractive solution for temperature and velocity measurement as high spatial and frequency resolutions could be achieved at almost coincident positions. In addition, as both wires were contained within the one holder, a good aerodynamic seal could be obtained at the sensor/copper duct interface. However, due to these proximate locations, tests had to be conducted to ensure that the "cold-wire" was not influenced by the presence of the hot wire, i.e. the "cold-wire" measured the fluid temperature independently of the hot-wire temperature. Tests were conducted to determine the influence of operating the hot-wire (*286°C*) on the resistance wire for a range of ambient temperatures (*20*, *40* and *60°C)* and for two flow velocities of 2m/s and 3m/s. The values chosen are comparable to the parameters under test. It was found that the temperature fluctuated about a mean value and that the variation in measurement with and without the hot-wire operating was consistent with random experimental error.

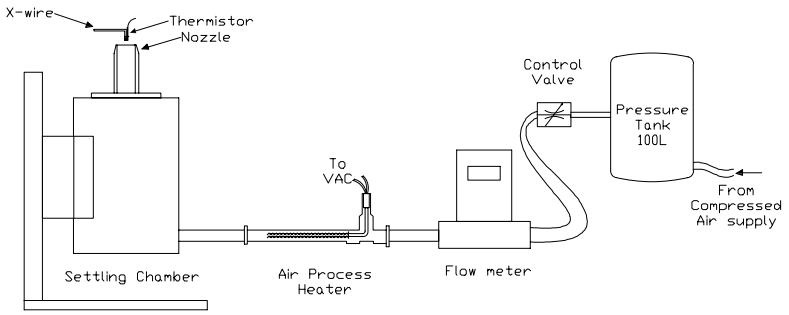

Figure 2. Rig to calibrate "cold-wire" for temperature measurement and the hot-wire for temperature corrected velocity measurement.

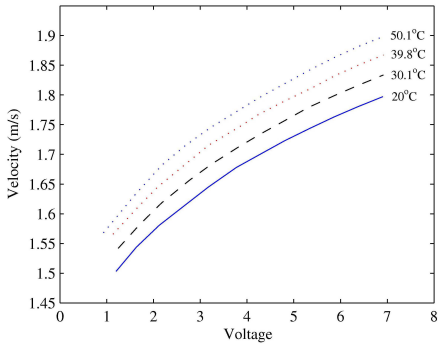

Figure 3. The dependence of hot-wire voltage on flow velocity at a number of ambient temperatures

Hydrodynamic, Thermal and Acoustic Considerations

For the forced convection tests discussed in this paper the mean velocity was measured to be 1.93m/s which for air in a duct of diameter 0.1m results in a Reynolds number of 12,841. Being greater than 10,000, the flow is considered to be fully turbulent. The axial measurement position of the heatflux

sensor and cross-wire was located at the downstream end of the heated section. This results in x/D≈15 from the entrance of the duct and x/D≈5 from the beginning of the heated section.

The upper section of the duct was thus increased in length so that the heatflux sensor was located at exactly the midpoint of the total duct length. Fixing the measurement plane at the centre of the pipe allowed acoustic pressure or particle velocity nodes and anti-nodes to be easily aligned at this plane. By exciting the duct with random noise, and measuring its response with a microphone located flush with the inside of the duct wall, the duct resonant modes could be measured. These frequencies agreed closely with the theoretical resonant modes for an open ended duct according to the equation

$$f_n = n\left(\frac{c}{2(L+\Delta)}\right) \tag{4}$$

where Δ is an end correction to account for the radiation impedance at the end of an open duct. Δ =(D/2)*z, where z is a function of the flange size at the termination. For our rig z is approximately equal to 0.61. Figure 4 shows an illustration of the first four resonant frequencies examined in our duct and how the normalised pressure distribution, in blue and normalised particle velocity distribution, in red, vary along its length. The heat flux sensor is indicated by a small black square towards the end of the heated section at the midway point. Frequencies 63Hz and 167Hz result in particle velocity nodes at the measurement plane, whereas 113Hz and 223Hz result in particle velocity antinodes.

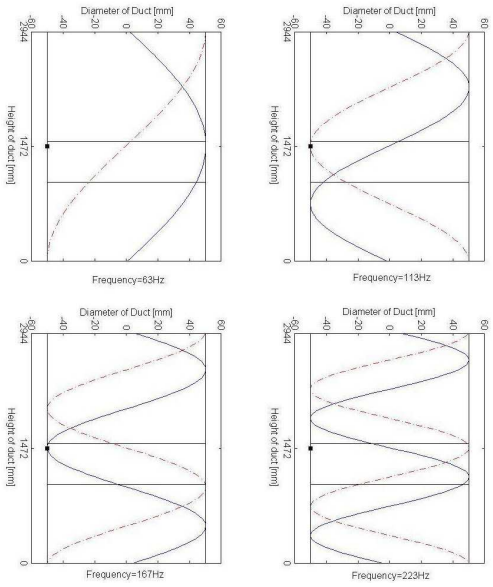

Figure 4. Acoustic pressure (blue) and particle velocity (red) distributions along the length of the duct for the first four resonant modes of the duct.

RESULTS AND DISCUSSION

Temperature, velocity and heat flux measurements were taken at the mid point of the duct (the measurement plane) for a series of experimental configurations. The main variables were: wall temperature [ambient, hot]; flow [free convection, forced convection]; frequency [0Hz, 63Hz, 113Hz, 167Hz, 223Hz]. For free convection the wall temperature was 78.8°*C* whereas for forced convection the temperature was 60.4°*C*. As both 63Hz and 167Hz result in particle velocity nodes at the

measurement plane, these shall be referred to as N1 and N2 where as frequencies 113Hz and 223Hz will be referred to as A1 and A2, due to the fact that particle velocity is a maximum at this location. Figure 4 shows the effect that the standing wave has on the time averaged temperature profile for both free and forced convection configurations. For the free convection situation, the added sound serves to reduce the temperature near the duct wall (8-4mm from the wall) whereas the temperature in the main body of the flow increases significantly. A2 differs in a band centred at 10mm from the wall where the temperature is particularly elevated - an increase of 50-80%. For the forced convection case, an increase in mean temperature is again to be seen but this time the effect is localised to bands near the wall, the centre distance of which changes with frequency. Again, the temperatures decreases very close to the wall for all frequencies.

Figure 5 plots temperature corrected mean and fluctuating velocity readings for hot and cold wall temperatures for forced convection. These results show that N1 and N2 behave similarly to each other as do A1 and A2 and, at least qualitatively, for most positions there is little difference between the cold and hot wall conditions. From observation of the fluctuating velocity of frequencies A1 and A2, the particle velocity can be quantified as approximately 0.4m/s at the measurement plane. As the plane wave cut-off frequency for this diameter duct is approximately 2kHz, all four frequencies considered generate plane wave standing waves and thus the particle velocity should increase uniformly across the diameter. This is clearly seen for frequencies A1 and A2, as expected with a slight difference close to the wall for the heated wall condition. In contrast for frequencies N1 and N2 the fluctuating velocity should be expected to remain unchanged as the location is at a velocity node. This is the case except, surprisingly, at banded distances from the wall where large increases in fluctuating velocity are measured. In the same bands for the same two N1 and N2 frequencies, the mean velocity is also seen to increase significantly. For all frequencies, the mean velocity also increases, to a varying extent, outside of these bands.

Qualitatively, the unusual banded behaviour is suggested to be caused by acoustic streaming where two different types of circulatory flow structures may be generated: “Rayleigh” structures generated outside viscous boundary layers and a second streaming “Schlichting” structure generated in the immediate vicinity of the viscous boundaries. In the results presented in this paper, the Rayleigh structure is thought to be identifiable for the N1 and N2 frequencies. Some qualitative differences between the hot and cold wall conditions close to the wall might be attributed to Schlichting structures but further testing needs to be done to verify this. If this is the case, these circulatory structures serve to remove heat from the wall surface and to circulate this heat into the flow where it is exhausted with the mean flow. Whereas acoustic streaming is normally restricted in the literature to closed ended ducts, the experimental setup described here benefits from the fact that standing waves can be generated in open ended ducts at low frequencies.

Figure 6 summarises these results for the hot wall case from the point of view of heat transfer. For the no flow case the mean temperature is plotted as a function of frequency whereas for the forced convection case both the mean temperature and a mass-flow rate averaged temperature (bulk temperature) is presented. The bulk temperature is calculated according to equation (5)

$$T_b = \frac{\sum_{j=1}^{N}\left(T_j \times U_j\right)}{\sum_{j=1}^{N} U_j} \tag{5}$$

where j is a measurement location. For the free convection case, the average temperature increases due to acoustic excitation, markedly at A1, whereas for forced convection only N1 and N2 result in a temperature increase.

Availing of the heat flux measurement, the convective heat transfer coefficient can be calculated according to equation 6.

$$h = \frac{q^{"}}{(T_s - T_m)} \tag{6}$$

where Ts is a surface temperature and Tm is mean fluid temperature. In figure 6, results using both the mean temperature and the bulk temperature are used for comparison. However, unfortunately, due to an instrumentation error, the heat flux thermocouple failed. This means that an accurate measure of the surface temperature at the heat flux sensor as a function of frequency was not available. To overcome this, the "cold-wire" temperature closest to the heat flux sensor, which was approximately 1mm away was used. Using this approach, the heat transfer coefficients are presented relative to the 0Hz benchmark. Despite the erroneous surface temperature, qualitative similarities are apparent with the other data which give credence to the results. For the free convection case, remarkable increases in heat transfer coefficient are measured for all frequencies. For higher velocities again the N1 and N2 frequencies pair off as do the A1 and A2 frequencies, with the velocity node frequencies giving the greatest increase in heat transfer coefficient.

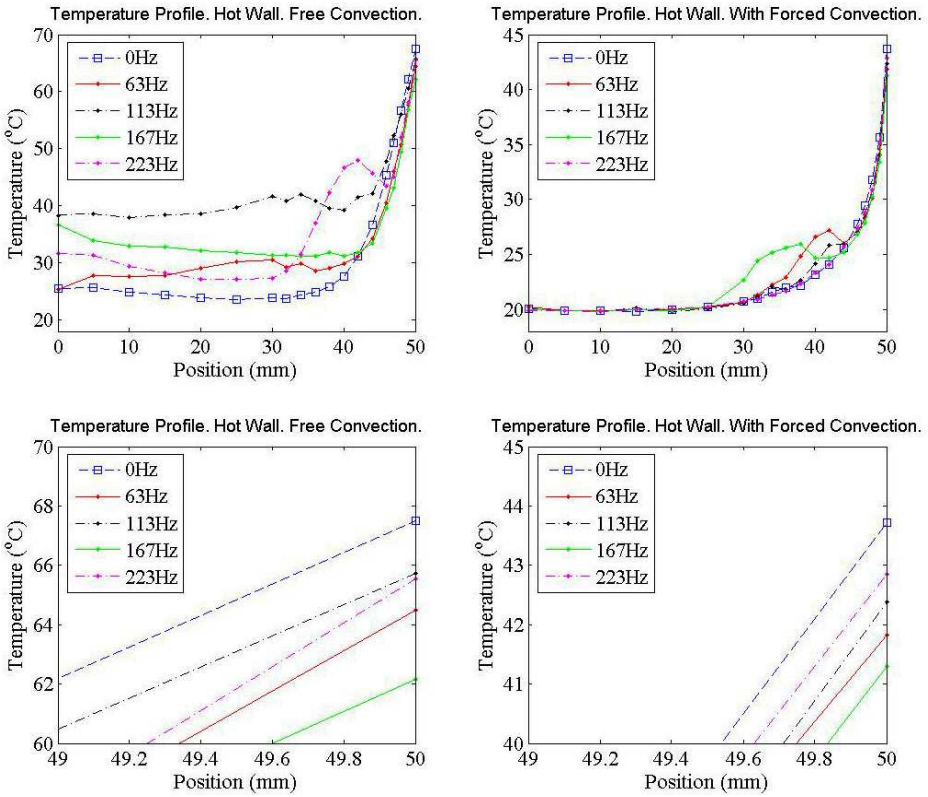

Figure 4. Time averaged temperature profiles over a radius of the duct at the measurement plane as a function of resonant mode frequency. The first figure is for a free convection condition with a wall temperature of *78.8°C.* The second plot is for forced convection with mean velocity of 1.94m/s and a wall temperature of *60.4°C.* The bottom two figures are close ups at the wall surface. The centre line of the duct corresponds to 0mm.

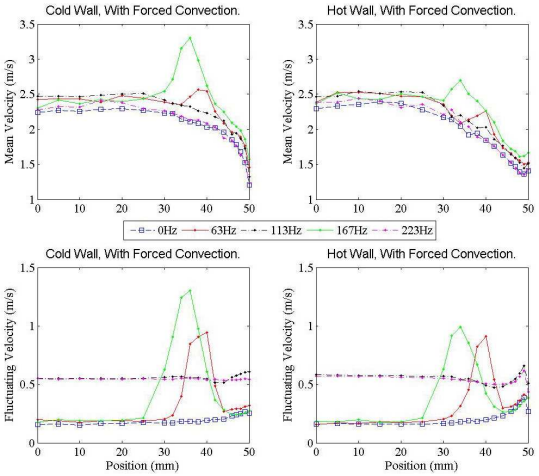

Figure 5. Mean and fluctuating velocity profiles as a function of frequency and wall temperature in the direction of flow.

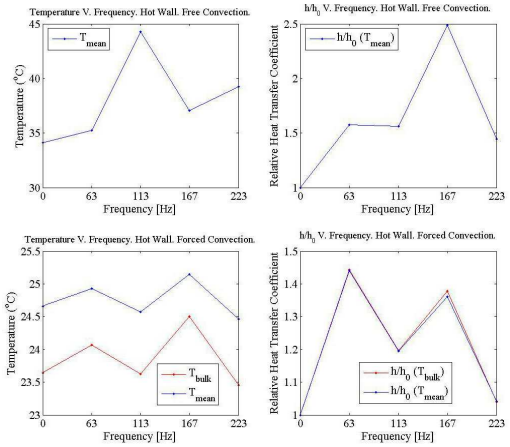

Figure 6. Averaged temperature and relative heat transfer coefficient as a function of standing wave frequency.

CONCLUSIONS

Temperature, mean velocity and fluctuating velocity distributions across the radius of a vertical heated open ended duct subject to acoustic excitation have been presented for forced and free convection cases. By exciting the duct at different standing wave resonant modes, the influence a particle velocity anti-node (pressure node) versus a particle velocity node (pressure anti-node) has on measurements at the same plane could be isolated. From the velocity results two principal heat transfer mechanisms are suggested. The first is due to an increase in particle velocity associated with the anti-node. This increase in fluctuation is aligned with an increase in turbulence and the resultant increase in turbulent mixing is seen to increase the heat transfer. The second mechanism is suggested, in this investigative work, to be attributed to acoustic streaming where two different types of circulatory flow structures may be generated. These sound induced heat transfer mechanisms coupled with free convection are seen to combine efficiently, serving to transport heat into the flow to be exhausted from the duct.

REFERENCES

1. *EECA Market Report 2006, European Electronic Component Manufacturers Association, 2006.*
2. Bearman, P.W., *Correction for the effect of ambient temperature drift on hotwire measurements in incompressible flow.* . DISA Information. 1971.

3. *World UPS Market Records Double-Digit Growth, 2006.*
4. Janssen, G., Kole, A., Leroux, A., *Trends in cooling of electronics: The use of thermal roadmaps*, in *Electronics Cooling*. Aug 2004.
5. M. J. Ellsworth, R.E.S., *High powered chip cooling: Air and beyond,* in *Electronics Cooling*. Aug 2005.
6. A. Vukovic, E.C., in *Communication network power efficiency: Assessment, limitations and directions*. Aug 2004.
7. K. Fukutani, Y.Z., A. Shakouri,, *Solid-state microrefrigerator on a chip*, in *Electronics Cooling*. Aug 2006.
8. Strutt, J.W.r.B.R., *The theory of sound*. 2nd ed. rev. and enl. ed. 1945, New York: Dover.
9. B. Entezam, W.K.V.M., J. Majdalanit, *MODELING OF A RIJKE-TUBE PULSE COMBUSTOR USING COMPUTATIONAL FLUID DYNAMICS*, in *33rd AIAA/ASME/SAE/ASEE Joint Propulsion Conference and Exhibit, AIAA-1997-2718* 1997: Seattle, WA.
10. hantschk c.-c., v.d., *Numerical simulation of self-excited thermoacoustic instabilities in a Rijke Tube.* Journal of Sound and Vibration, 1999. **227**(3): p. 511-522.
11. Karimi, N., M.J. Brear, and W.H. Moase, *Acoustic and disturbance energy analysis of a flow with heat communication.* Journal of Fluid Mechanics, 2008. **597**: p. 67-89.
12. Swift, G.W., *Thermoacoustic Engines.* Journal of the Acoustical Society of America, 1988. **84**(4): p. 1145-1180.
13. Swift, G.W., *Thermoacoustic Engines and Refrigerators.* Physics Today, 1995. **48**(7): p. 22-28.
14. Garrett, S.L., *Resource letter: TA-1: Thermoacoustic engines and refrigerators.* American Journal of Physics, 2004. **72**(1): p. 11-17.
15. Ha, M.Y. and S. Yavuzkurt, *A Theoretical Investigation of Acoustic Enhancement of Heat and Mass-Transfer .1. Pure Oscillating Flow.* International Journal of Heat and Mass Transfer, 1993. **36**(8): p. 2183-2192.
16. Ha, M.Y. and S. Yavuzkurt, *A Theoretical Investigation of Acoustic Enhancement of Heat and Mass-Transfer .2. Oscillating Flow with a Steady Velocity Component.* International Journal of Heat and Mass Transfer, 1993. **36**(8): p. 2193-2202.
17. Aktas, M.K., B. Farouk, and Y.Q. Lin, *Heat transfer enhancement by acoustic streaming in an enclosure.* Journal of Heat Transfer-Transactions of the Asme, 2005. **127**(12): p. 1313-1321.
18. Vainshtein, P., M. Fichman, and C. Gutfinger, *Acoustic Enhancement of Heat-Transfer between 2 Parallel Plates.* International Journal of Heat and Mass Transfer, 1995. **38**(10): p. 1893-1899.
19. Su, J.H., C. Gau, and C.S. Yang, *Enhancement of heat transfer over a cylinder by acoustic excitation.* Journal of Thermophysics and Heat Transfer, 2006. **20**(2): p. 256-266.
20. Komarov, S. and M. Hirasawa, *Enhancement of gas phase heat transfer by acoustic field application.* Ultrasonics, 2003. **41**(4): p. 289-293.
21. O'Donovan, T.S. and D.B. Murray. *Effect of acoustic excitation on the heat transfer to an impinging air jet (HT2007-32800).* in *ASME-JSME Thermal Engineering Summer Heat Transfer Conference*. 2007. Vancouver.
22. O'Donovan, T.S. and D.B. Murray. *Heat transfer to an acoustical excited impinging air jet.* in *Proceedings of the 5th European Thermal-Sciences Conference*. 2008. Eindhoven.
23. Lee, D.R. and B.G. Loh, *Smart cooling technology utilizing acoustic streaming.* Ieee Transactions on Components and Packaging Technologies, 2007. **30**(4): p. 691-699.
24. KIM, S.K., W.N. KIM, and S.Y. KIM, *Plasma display panel cooling by an acoustic pulsating flow device*, in *ITherm 2004 : (Ninth Intersociety Conference on Thermal and Thermomechanical Phenomena in Electronic Systems)* 2004, IEEE: Mirage Hotel & Casino, Las Vegas, NV, June 1-June 4, 2004

PLATE HEAT EXCHANGER - INERTIA FLYWHEEL PERFORMANCE IN LOSS OF FLOW ACCIDENT

A. Talal*, A. Amr
Reactors Department, Atomic Energy Authority, Egypt

ABSTRACT**.** One of the most wide used heat exchangers in process plants is the plate heat exchanger (PHE) for its wide advantages. Its plates are assembled or disassembled easily; hence, it has a high availability for altering its heat transfer characteristics. Egypt second research reactor uses the PHE on its primary core cooling circuit (11MWatt/PHE). So, modeling and simulation for PHE is acquired a great attention where the changing in its mass flow rate or its number of plates are worthy to be studied due to their effects on reactor core performance. An inertia flywheel is mounted on the core cooling system pump to feed the core and hence the PHE with a coolant flow during the loss of electrical power supply transients to protect the core against overheating. Accordingly, the PHE is played a strong role in the case of Loss of Flow (LOF) transients; it continues in transferring the core decay power to the cooling tower until the forced core cooling mode is valueless hence the natural convection core cooling is a matter of must. The PHE performance during the LOF transient is one of the parameters that determine the time of transition from forced to natural mode. The developed model is validated in two ways, first by a set of Alfa Laval available data for M30-FG PHE and secondly by comparing the developed model results with that obtained by A. D. WRIGHT model. The validation showed that the developed model can be used for simulating the PHE with a good accuracy. From the simulation of M30-FG PHE, it is concluded that, the heat exchanger primary flow can be increased by 20% over its nominal value without exceeding the permissible pressure limit (100KPa) and hence its power is increased to 12.4 MWatt. This type of PHE can withstand a decrease in its nominal number of plates up to 15%, with nominal flow fixed, without exceeding the pressure limit and give a performance near the designed performance. Increasing the number of plates over its nominal value, with nominal flow fixed, could not produce a noticeable enhancement as could be expected. After a 62 sec from the initiation of loss of flow transient, the primary side outlet temperature is equaled to the secondary side inlet temperature (30 ^{o}C), this time is adequate to change the core cooling mode from forced to natural by opening a passive device (flapper valve) to establish it. During this time the PHE with the aid of inertia flywheel are dissipated energy of 207.917 MJ through the cooling tower and protected the core from over heating.

Keywords: *Plate Heat Exchanger, Performance prediction, Heat transfer coefficient*

INTRODUCTION

The steady state and transient behavior of heat exchangers have been a constant topic of investigation for the heat transfer community. With the many innovations in computational machinery the challenge of predicting the thermal

* Corresponding author: Associate Prof. Talal Abou El Maaty
Phone: (002) 0113212358
E-mail address: talal22969@yahoo.com

Figure 1. Plate type Heat exchanger

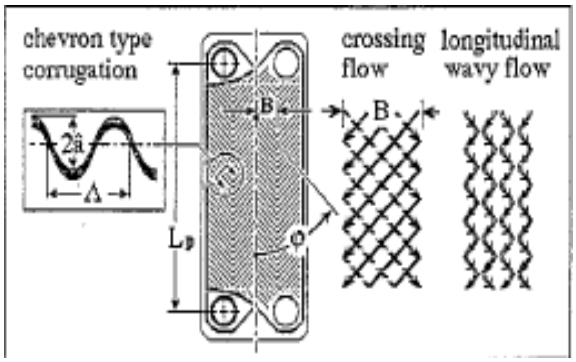

Figure 2. Two flow types at gap

behavior of heat exchangers accurately and at the same time using simpler modeling concepts has been taken up in different ways by different investigators. Plate and frame heat exchangers are offered by a large number of manufactures as standard series production equipment over a wide range of sizes. They consist of a number of gasket metal plates clamped between a stationary head and a follower plate by tie bolts as shown in Figure 1. A number of detailed experiments studies have been focused on that type of heat exchangers. Theses studies incorporated in addition to the fundamental nature of the corrugation patterns some important parameters like the corrugation amplitude, corrugation wave length, corrugation inclination angle and flow rate [1, 2, 3, 4]. The inclination angle of the crests and furrows of the sinusoidal corrugation heat exchanger pattern relative to the main flow direction has been shown to be the most important design parameter with respect to fluid friction and heat transfer. Two kinds of flow may exist in the gap between two plates [5]: The crossing flow of small sub-streams following the furrows of the first and the second plate, respectively, over the whole width of the corrugation pattern, dominating at lower inclination angles (lower pressure drop); and the wavy longitudinal flow between two vertical rows of contact points, prevailing at high inclination angles (high pressure drop), as shown in Figure 2. A better method has been developed for calculating the effectiveness and the pressure drop of two streams PHE after plate's rearrangement, based on its existing performance [6], this therefore means that, complete Knowledge of the friction factor and heat transfer correlations is not needed and a full rating calculation is unnecessary. The methodology in its present form, however only works for systems in which true counter-currency can be assumed and the number of channels per pass is the same on both sides; this methodology is adopted in the present work to determine the worth from increasing or decreasing the number of plates for M30-FG PHE used in Egypt Second Reactor (ETRR 2) cooling system. A mathematical model is developed in algorithmic form for the steady state simulation of gasket heat exchangers with generalized configurations [7]; the configuration is defined by the number of channels, the number of passes at each side, fluid locations, feed connection locations and type of channel flow. The main purposes of this model are to study the configuration influence on the exchanger performance and to further develop a method for configuration optimization. A thermal modeling of a PHE on steady state assuming constant fluid physical properties and uniform flow distribution inside the PHE was presented [8], leading to two approaches for obtaining the log-mean temperature difference correction factor: approach 1, that assumes pure counter current flow conditions and approach 2, that accounts for different configurations and requires the solution of the differential thermal model of the PHE. An optimal design of PHE has been carried out [9]; this design consists of two catalogues: the design with fixed allowable pressure drops and the complete optimal design without pressure drop specifications. Compared the traditional design methods, the current approach does not contain many trials [9]. In the design with fixed allowable pressure drops, full utilization of allowable pressure drops is taken

as the design objective. In the complete optimal design without pressure drop specifications, pressure drops are economically optimized during the design [9].

EFFECTIVNESS AND HEAT TRANSFER CALCULATIONS

The following model has been developed to study the PHE performance during the change in primary side flow rate, the change in the number of plates and also it is used for the evaluation of PHE performance in loss of flow (LOF) transient. The NTU method is the one adopted in PHE calculations, and it's therefore explained as follows; the effectiveness of the heat exchanger is the ratio of the actual heat transfer rate to the maximum possible heat transfer rate.

Effectiveness calculations

$Q = E\, C_{min}\, (T_{hi}-T_{ci})$ (1)

$C_h = W_h\, c_{p,h}$ (2)

$C_c = W_c\, c_{p,c}$ (3)

$C_{max} = C_h$ and $C_{min} = C_c$ if $C_h > C_c$ (4)

$C_{max} = C_c$ and $C_{min} = C_h$ if $C_c > C_h$ (5)

For counter currency flow:-

$E1 = 1-\exp(-NTU\,(1-C_{min}/C_{max}))$

$E2 = 1-(C_{min}/C_{max})\exp(-NTU\,(1-C_{min}/C_{max}))$

$E = E1 / E2$ (6)

$NTU = UA/C_{min}$ (7)

$U = 1/(1/h_h + x_p/k_p + 1/h_c)$ (8)

Heat transfer calculations

Turbulent flow mode. Dittus Boelter's correlation is used for calculating the heat transfer coefficient in turbulent flow regime.

$$Nu = 0.023\ \mathrm{Re}^{0.8}\ pr^{0.4} \times Fac \qquad \mathrm{Re} \succ 10000 \qquad (9)$$

Where; $\mathrm{Re} = G \times D_e / \mu$, $D_e = 4\hat{a}$ and $d = 2\hat{a}$

The dimensions D_e, $\hat{\mathbf{a}}$ and d are as shown in Figure 2. The coolant mass flux, G, has the following definitions in both sides of PHE.

$G = \dot{M} / N \times d \times W$, (primary side) and $G = \dot{M} / (N+1) \times d \times W$ (secondary side)

Laminar flow mode. With the aim of calculating the heat transfer coefficient for forced laminar regime, the H. Martin [5] recommended correlation for obtaining the heat transfer coefficient as a

function of the corrugation inclination angle φ, the Reynolds number Re, and the friction factor is used.

$$Nu = Nu^* \,\mathrm{Pr}^{1/3}\left(\frac{\mu}{\mu_w}\right)^{1/6} \qquad \mathrm{Re} \le 2000 \tag{10-a}$$

$$Nu^* = c_q\left[\zeta.\mathrm{Re}^2\,\sin(2\varphi)\right]^q \tag{10-b}$$

The parameters c_q, q and ζ are functions in the corrugation inclination angle φ [5] and the value of ζ is equal 4 times the Fanning friction factor (f)

$$\frac{1}{\sqrt{f}} = \frac{\cos\varphi}{\sqrt{a_1\,\tan\varphi + a_2\sin\varphi + f_o/\cos\varphi}} + \frac{1-\cos\varphi}{\sqrt{a_3\,f_1}} \tag{10-c}$$

Where; $f_o = 16/\mathrm{Re}$ and $f_1 = (149/\mathrm{Re}) + 0.9625$

The value of the constants a_1, a_2 and a_3 are calculated as defined in the H. Martin [5]

Transition flow mode. To evaluate the heat transfer coefficient in the transition regime the interpolation between Laminar and turbulent is used.

PRESSURE DROP CALCULATIONS

A similar procedure to that used in A. D. Wright [6] work is adopted here for calculating the pressure drop in both the primary and secondary side of the PHE. The fanning friction factor used in [6] is corrected in this study according to H. Martin work [5] because the constants K (φ) and n (φ) depend on the corrugation inclination angle φ .

$$\mathbf{f = K(\varphi) / Re^{n(\varphi)}} \tag{11}$$

Channel pressure drop:-

$$\Delta P_{ch} = \frac{2\,L\,K(\varphi)(G)^2}{\rho\,D_e}(\mathrm{Re})^{-n(\varphi)} \tag{12}$$

Port pressure drop:-

$$\Delta P_{po} = 1.3\left(G_{po}\right)^2\frac{1}{2\rho_{po}} \tag{13}$$

Where; $G_{po} = 4\dot{M}\ /\pi D_p^2$

$$\Delta P_{tot} = \Delta P_{ch} + \Delta P_{po} \tag{14}$$

A. D. Wright [6] has developed a method for calculating the effectiveness and pressure drop of PHE based on its existing performance. This method therefore, means that complete Knowledge of the friction factor and heat transfer correlations is not needed and a full rating calculation unnecessary.

$$\Omega = \left(\frac{1 - E_{old}}{1 - E_{old}\, C_{\min}} \right) \tag{15}$$

$$\psi = \frac{q_1 \left(2N_{new} - 1\right) N_{old}^{b1}}{n_1 \left(2N_{old} - 1\right) N_{new}^{b1}} \tag{16}$$

$$E_{new} = \frac{1 - \Omega^{\psi}}{1 - C_{\min}\, \Omega^{\psi}} \tag{17}$$

$$\Delta P_{new} = \Delta P_{old} \left(\frac{N_{new}}{N_{old}} \right)^{n(\varphi)-2} \tag{18}$$

LOSS OF FLOW SIMULATION

The transient behavior of ETRR-2 core in case of loss of flow (LOF) transient is simulated by a PARET code [10]. The code was validated by the actual experimental measured transient response in various SPERT cores [11]. A one core cooling channel (average channel) is represented the reactor core in this simulation. It is required to calculate the core average exit temperature variation with the flow cost down caused by the inertia flywheel after the reactor is scrammed. Both the decay power generated after scram, that is neutronically calculated [12], and the flywheel flow coast down, that is measured experimentally, were feed to PARET code as a function of time to calculate the average core exit temperature with time. Hence, the average core exit temperature and the flywheel flow coast down were introduced to the PHE developed program to calculate the PHE performance during the LOF transient.

HEX. MODEL VALIDATION

A set of Alfa Laval data [13], for the PHE M30-FG, were used for the developed model validation. Different PHE primary side flow rates ranging from 10^6 Kg/h to 5×10^4 Kg/h, with a fixed secondary side flow rate of 1.35×10^6 Kg/h were used in the validation. Both the PHE primary side inlet temperature and the secondary side inlet temperatures were fixed to 49.5 ^{o}C and 30 ^{o}C respectively during the validation. With these conditions, the model were used to calculate the primary side outlet temperature, the secondary side outlet temperature, the PHE transferred power, the effectiveness and primary side pressure drop. The model results were compared with the available data as shown through Figure 3 to Figure 5. A reasonable consistence was existed between the developed model results and the Alfa Laval data. Based on these comparisons, the developed model is reliable to simulate the PHE.

RESULTS AND DISCUSSION

Variation of the primary side mass flow:-

The PHE performance were studied during the variation of the primary side flow rate around its designed value (10^6 Kg/h) , by steps equaled ± 5 % each. The PHE inlet temperatures for both the primary and the secondary sides were fixed to 49.5 ^{o}C and 30 ^{o}C respectively in all

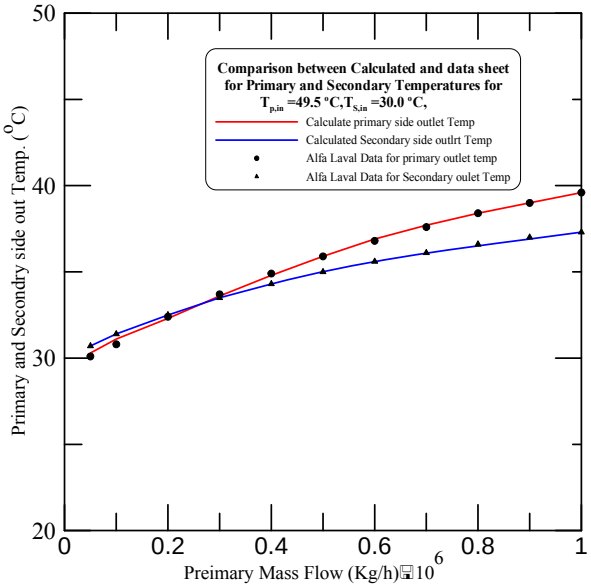

Figure 3. PHE primary and secondary outlet temperatures variation with flow rate

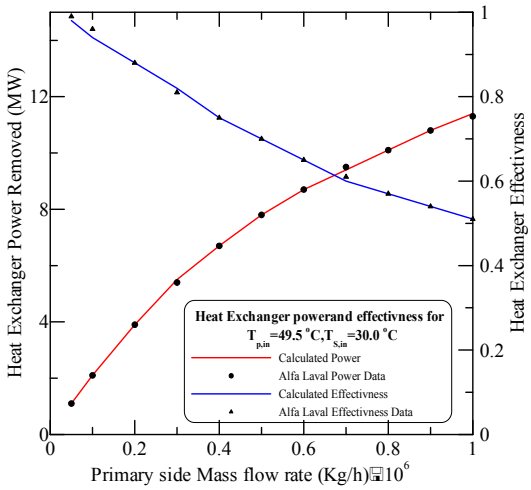

Figure 4. PHE power and effectiveness variation with flow rate

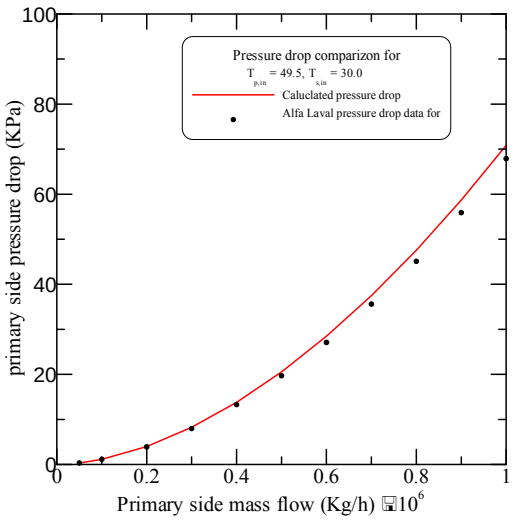

Figure 5. PHE primary side channel pressure drop variation with flow rate

the simulated steps. This study has a complete illustration in both Table 1 and Figure 6, where the following parameters were recorded, the PHE power, the primary side pressure drop, the primary side outlet temperature and the effectiveness. A gradual increase in the PHE power was recorded as the primary side mass flow rate was increased. The increase in the primary side pressure drop was limited the increase in mass flow at +20% from the designed value. The calculated pressure drop at +20% increments in primary flow was 98.1 KPa and the maximum permissible value for this type of PHE is 100 Kpa, so, the maximum permissible power for this PHE was limited to 12.4 MW. The primary side outlet temperature at this limit condition was increased from 39.6 ^{o}C (nominal design value) to 40.5 ^{o}C while the effectiveness was reduced from 0.51 to 0.46. Decreasing the primary side flow rate enhanced the PHE effectiveness and reduced the pressure drop but the transferred power was reduced as a result.

Variation in PHE plates:-

The PHE performance studied here was incorporated the variation in its nominal plates with fixed nominal flow rates (10^6 Kg/h in primary, 1.35×10^6 Kg/h in secondary), fixed inlet temperatures in both the primary and secondary sides. The simulation was carried out at steps each of ± 5 % of the nominal value (161/159 Pl). The results of this study was represented in both Table 2 and Figure 7, where the following parameters were calculated, the PHE power, the primary side pressure drop, the secondary side pressure drop, the primary side outlet temperature and the effectiveness. The results were showed that, slight changes from the nominal values were occurred during the reduction steps except for those occurred in the pressure drop values in both the PHE sides. The primary side pressure drop was increased from 70 KPa at nominal condition to 105.63 KPa at -20% reductions in the nominal plates. While, the secondary side pressure drop was increased from 123.5 KPa to 183.1 KPa for the same condition. So, the maximum permissible reduction in plates without a great change in PHE performance was limited to –15% of the nominal value, where the primary side pressure drop was less than 100 Kpa. Form this simulation; one can be expected that a reasonable PHE performance is attained if a number of its plates are lost in maintenance. Increasing the number of PHE plates could not cause a great performance enhancement as could be expected, where most of the thermal parameters still around its designed values, while the pressure drops in both sides were recorded a high decrease due to the increase in the number of channels with fixed flow rates. For more conservative, this study was performed again by A. D. WRIGHT [6] model that described through equations (15) to (18).

Table 1, Heat exchanger performance for varying the primary mass flow

%ΔQ(Kg/h)	$T_{p,o}$(^{o}C)	$T_{s,o}$(^{o}C)	P(MW)	EFF.	ΔP_p(Kpa)	ΔP_s(Kpa)
.00	39.6	37.3	11.4	.51	70.84	123.3
-5.00	39.3	37.1	11.1	.52	64.64	123.4
-10.00	39.0	36.9	10.8	.54	58.69	123.4
-15.00	38.7	36.7	10.4	.55	52.99	123.5
-20.00	38.4	36.5	10.1	.57	47.56	123.5
5.00	39.8	37.5	11.6	.5	77.29	123.3
10.00	40.0	37.7	11.9	.49	83.98	123.2
15.00	40.3	37.8	12.1	.47	90.92	123.2
20.00	40.5	38.0	12.4	.46	98.1	123.2

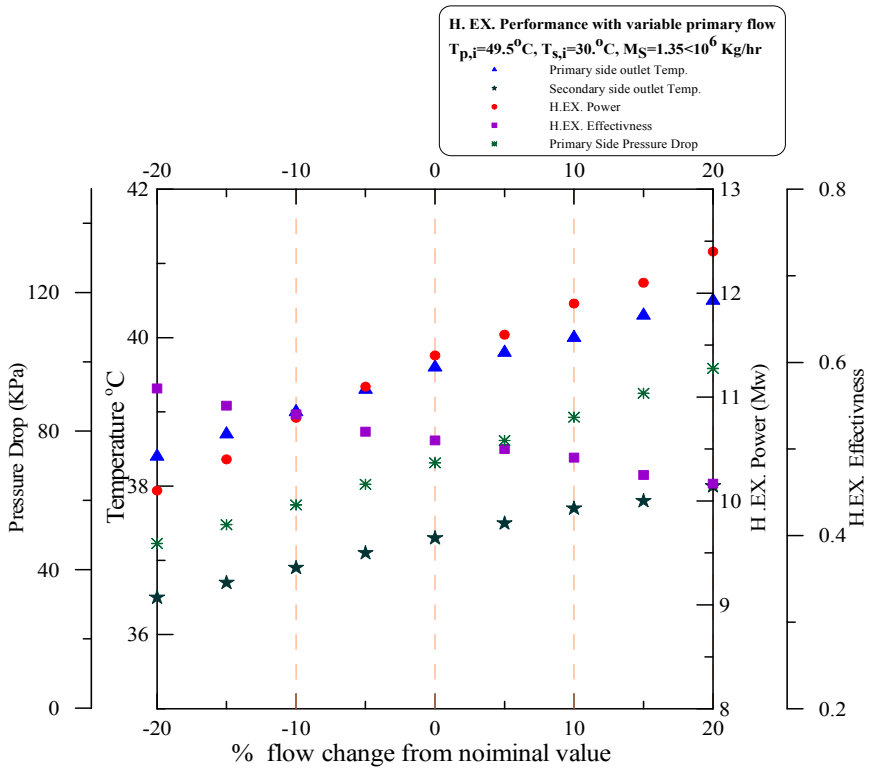

Figure 6. Heat exchanger performance for varying the primary mass flow

The results obtained by A. D. WRIGHT model were represented between brackets in Table 2, to compare them with the developed model results. The comparisons were indicated a good degree of consistency, but A. D. Wright model has a limited using for the cases with fixed flow and only the variations in the HEX plates. Also, it is required the known of the previous PHE performance to make a new study by A. D. Wright model.

PHE performance for loss of flow transient:-

A trip in the primary core cooling system pump, while the reactor was operated at full power (22MW), is one of the probable events that cause loss of flow transient. Figure 8 shows the experimental values of the total core flow cost down (two primary pumps) and the neutronic core decay power [12] that were feed to the PARET code to calculate the average core outlet temperature variation with time; hence this temperature was feed to the PHE developed model, as an inlet temperature to the PHE primary side, to calculate both the PHE power and the removed energy variation with time as shown in Figure 9. The calculated thermal power through the PHE was followed the flow cost down trend and did not follow the core power trend, where the core power is related to neutronic calculations that are based on fission fragments decay. After a 62 sec from the initiation of loss of flow transient, the PHE primary side outlet temperature was equaled to the secondary side inlet temperature (30 ^{o}C), this time is adequate to change the core cooling mode from forced to natural by opening a passive device (flapper valve) to establish it. During this time the PHE with the aid of inertia flywheel were dissipated energy of 207.917 MJ through the cooling tower and protected the reactor core over heating.

Table 2 Heat exchanger performances for varying the number of plates

% Plate Change	$T_{p,o}$(°C)	$T_{s,o}$(°C)	P(MW)	EFF.	ΔP_p(Kpa)	ΔP_s(Kpa)
.00	39.6 (39.6)	37.3 (37.3)	11.4 (11.4)	.51 (.51)	70.84 (70.84)	123.5 (123.5)
-5.00	39.6 (39.6)	37.3 (37.3)	11.3 (11.3)	.51 (.507)	77.66 (77.667)	135.1 (135.216)
-10.00	39.7 (39.7)	37.2 (37.2)	11.2 (11.2)	.50 (.504)	85.55 (85.577)	148.7 (148.989)
-15.00	39.8 (39.7)	37.1 (37.2)	11.0 (11.2)	.50 (.501)	94.78 (94.818)	164.5 (165.077)
-20.00	39.9 (39.8)	37.0 (37.1)	10.9 (11.1)	.49 (.497)	105.65 (105.713)	183.1 (184.044)
5.00	39.5 (39.5)	37.4 (37.4)	11.5 (11.4)	.51 (.513)	64.91 (64.902)	113.1 (112.993)
10.00	39.4 (39.4)	37.4 (37.4)	11.5 (11.5)	.52 (.516)	59.72 (59.705)	104.1 (103.946)
15.00	39.3 (39.4)	37.5 (37.4)	11.5 (11.5)	.52 (.518)	55.15 (55.129)	96.2 (95.978)
20.00	39.3 (39.3)	37.5 (37.5)	11.7 (11.6)	.53 (.521)	51.1 (51.076)	89.2 (88.923)

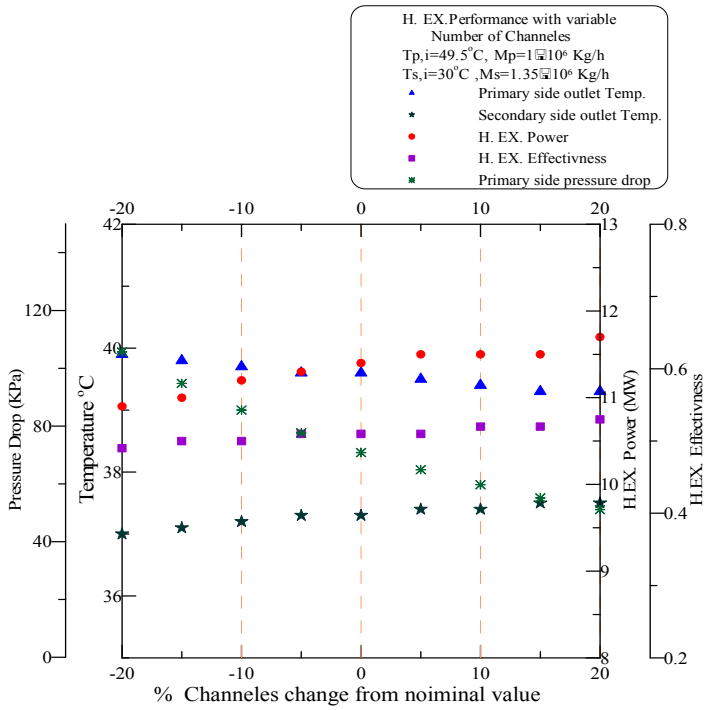

Figure 7. Heat exchanger performances for varying the number of plates

The power at which the PHE flow was cut of is 1.781 MW, it a reasonable value where the reactor main pool has the capability to remove up to 2 MW through the natural convection cooling. If there was no flywheel the PHE flow is cut of at the moment of scram, hence energy of 207.917 MJ will be dissipated in the core zone before the establishment of the natural convection cooling mode, the matter that will cause core over heating, local boiling and voids. The PHE temperature responses, effectiveness and pressure drops during the LOF transients were illustrated in Figure 10 and Figure 11. The primary side outlet temperature and the secondary side outlet temperature approximately

reached each other after 62.0 sec; hence the effectiveness was reached its maximum value at this time (0.9). By this time a nearly stable HEX. Performance was obtained where the PHE primary flow and hence primary side pressure drop were reached their lower values.

CONCLUSION

A M30-FG PHE with 161 plates, a total heat transfer area of 292 m^2, nominal primary side flow of 10^6 Kg/h and nominal secondary side flow of 1.35×10^6 Kg/h, can withstand the increase in flow through its primary side by a 20% of its nominal value without exceeding the pressure drop limit (100 Kpa) and can transfer a thermal power up to 12.4 MW to the cooling tower, where both the PHE primary side inlet temperature and the secondary side inlet temperature are fixed to 49.5 ^oC and 30 ^oC respectively. This type of PHE can withstand a reduction in its nominal number plates by -15% without affecting its thermal performance. While increasing the number of its plates with the same nominal flow does not produce a significant effect. The inertia flywheel with the PHE plays a strong turn during the first few

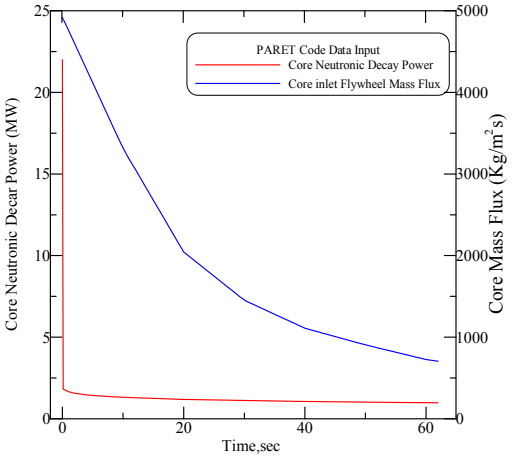

Figure 8. Core decay power with flow cost down after SCRAM

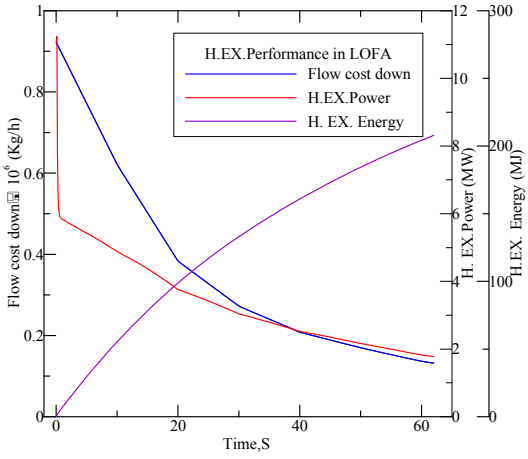

Figure 9. HEX. Power, flow and energy after SCRAM trip

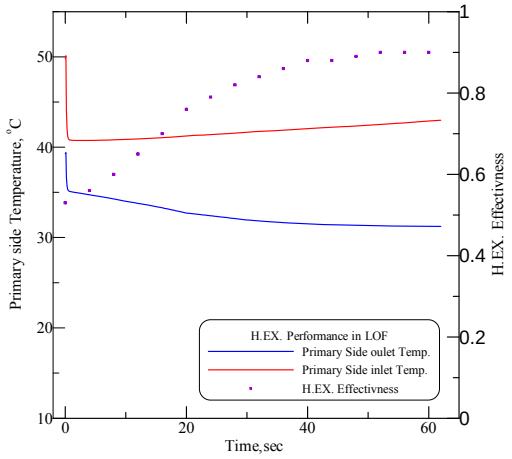

Figure 10. HEX. Effectiveness, primary and secondary out temperatures

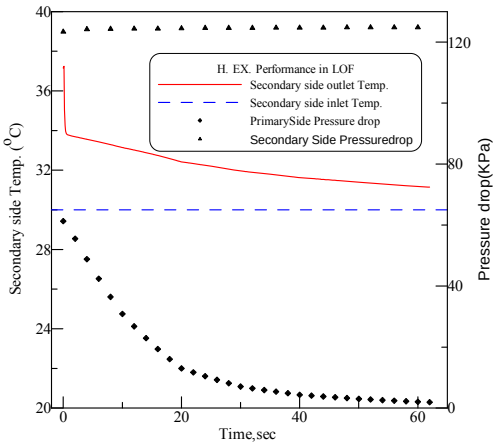

Figure 11. HEX. Primary and secondary inlet temperatures and pressure drops

seconds after (62 sec) SCRAM trip, where they protect the core from over heating and hence from local boiling. During this time a dissipated energy of 207.917 MJ through the cooling tower is achieved. The power at which the PHE flow is cut of is 1.781 MW, hence the flapper valve open to change the cooling mode from forced to natural. This transition ensures the reactor safety criteria; the maximum removed power by natural convection is 2 MW.

NOMENCLTURE

A	Total heat transfer area, m^2	N_{old}	The old number of cooling channels, related to equation (16)
â	Amplitude of the sinusoidal corrugation, m	NTU	The number of heat transfer units
a_1,a_2,a_3	Constants related to equation (10-c)	n	Constant related to equation (11)
b_1	Reynolds number exponent in equation (9) or in equation (10-a) or combination between them.	n_1	The number of cooling channels per path
C	Fluid total heat capacity, W/K	Q	Heat transfer, Watt
c_p	Fluid specific heat, J/Kg K	q_1	The number of HEX. Pathes
c_q	Parameter related to equation (10-b)	T	Temperature, k
D_e	HEX. Channel equivalent diameter, m	U	Overall heat transfer coefficient, W/m^2 k
d	Gap width between two plates, m	W	HEX. Plate width, m
D_p	HEX. Port diameter, m	X_p	HEX. Plate thickness, m
E	HEX. Effectiveness		**Greek symbols**
E_{old}	HEX. Old effectiveness related to equation (15)	φ	HEX. Corrugation inclination angle
E_{new}	HEX. New effectiveness related to equation (15)	ρ	Fluid density, Kg/m^3
Fac	HEX. Area corrugation factor	ζ	Friction factor related to equation (10-b)
f	Fanning friction factor	μ	Fluid viscosity, N s/m^2
G	Fluid mass flux in channel, Kg/m^2 s	Δp	Pressure drop, Pa
G_{po}	HEX. Port mass flux, Kg/m^2 s		**Subscripts**
h	Heat transfer coefficient, W/m^2 k	h	Hot fluid
K	Constant related to equation (11)	c	Cold fluid
k_p	HEX. Plate thermal conductivity, W/m.K	hi	Hot fluid inlet
L	HEX. Effective plate length, m	ci	Cold fluid inlet
$\dot{M}$	Fluid flow rate, Kg/s	ch	Related to channel
N	Number of primary side cooling channels	p,po	Related to port
N_{new}	The new number of cooling channels, related to equation (16)	old	HEX. Old configuration
		new	HEX. New configuration

REFERENCEES

1. K. Okada, M. Ono, T. Tomimura, T. Okuma, H. Konno and S. Ohtani, Design and heat transfer characteristics of new plate heat exchanger, *Heat Transfer-Jpn. Res., I (1972) 90-95*
2. G. Rosenblad and A. Kullendorff, Estimating heat transfer rates from mass transfer studies on plate heat exchanger surfaces, Warme Stoffubertrag., 8(1975) 187-191.
3. W. W. Focke, J. Zachariades and I. Olivier, the effect of corrugation angle on the thermo hydraulic performance of plate heat exchangers, Int. J. Heat Transfer, 28 (1985) 1469-1479.
4. G. Gaiser, Stomungs- und Transportvorgange in gewellten Strukturen , Dissertation, Universitat Stuttgrat, 1990.
5. H. Martin, A theoretical approach to predict the performance of chevron-type Plate heat exchangers, Chemical Engineering and Processing 35 (1996) 301-310
6. A. D. Wright and P. J. Heggs, Rating calculation for Plate heat exchanger effectiveness and pressure drop using existing performance data, Trans IchemE, Vol 80, Part A, April 2002.
7. Jorge A. W. Gut, Jose M. Pinto, Modeling of plate heat exchangers with generalized configurations, International Journal of Heat and Mass Transfer 46 (2003) 2571-2585.
8. Jorge A. W. Gut, Renato Fernandes, Jose M. Pinto, Carmen C. Tadini, Thermal model validation of plate heat exchangers with generalized configurations, Chemical Engineering Science 59 (2004) 4591-4600.
9. Lieke Wang, Bngt Sunden, Optimal design of plate heat exchangers with and without pressure drop specifications, Applied Thermal Engineering 23 (2003) 295-311.
10. Obenchain, C.F., “PARET-A program for the analysis of reactor transients”. IDO-17282, 1969.
11. The PARET and the analysis of the SPERT I transients. W. Woodruff. ANL/RERTR/TM-4, Conf-821155, sept 1982.
12. Proposed ANS Standard Decay Energy Release Rates Following shutdown of Uranium-Fueled Thermal Reactors ANSI 5-1, 1971.
13. Alfa Laval Report for M30 PHEX, Nov.-1994.

ENHANCEMENT, SUPPRESSION AND INVERSION OF THE CONVECTIVE MODES OF A PARAMAGNETIC FLUID IN A DIFFERENTIALLY HEATED CUBICAL CAVITY PLACED UNDER A STRONG MAGNETIC FIELD

T.P. Bednarz[1,*], E. Fornalik[2], J.S. Szmyd[2], C. Lei[1], J.C. Patterson[1], F. Xu[1], H. Ozoe[3]
[1]School of Engineering & Physical Sciences, JCU, Townsville QLD 4811, Australia
[2]AGH University of Science and Technology, 30 Mickiewicz Ave, Krakow, Poland
[3]Interdisciplinary Graduate School of Engineering Sciences, Kyushu University, Japan

ABSTRACT. This report is concerned with the influence of a strong magnetic field generated by a 5-Tesla and 10-Tesla super-conducting magnet respectively on natural convection of a paramagnetic fluid in a differentially heated cubic enclosure. The working fluid is prepared to be a mixture of an aqueous solution of glycerol (80% in mass) and gadolinium nitrate hexahydrate of 0.8 mol/kg. A small quantity of thermo-chromic liquid crystals is added to the working fluid for visualisation purpose. The cube of side 0.032 m is heated and cooled from two opposing vertical walls and placed under different configurations of the magnetic field. Flow visualization and heat transfer measurements are carried out to show a full picture of the flow phenomena. Three different cases are described here in order to show how to enhance, suppress or invert the convective motion and heat transfer.
It should be emphasized that knowing how to control the magnetic force makes it possible, for instance, to suppress the influence of the gravity and to study particular low gravity convection phenomena under terrestrial conditions. It is far more economical to conduct preliminary experiments on earth before sending a space-craft to the outer space to do the experiments. Moreover, magnetic convection finds applications in crystal growth, mixing, material processing, etc, where the effects of convection may be undesirable.

Keywords: *thermo-magnetic convection*, *paramagnetic fluid*, *heat transfer rate, super-conducting magnet*

INTRODUCTION

The phenomenon of natural convection is present everywhere in nature and is ubiquitous in our daily experience. In many scientific and industrial applications, it is often necessary to control convective flows induced by natural convection in order to achieve specific outcomes. This work presents a novel method for controlling convective flows in terrestrial conditions, i.e., enhancing, suppressing, or inverting convection with the application of a magnetic field acting on a common paramagnetic fluid. More specifically, the focus here is on understanding the relation between an applied magnetic field and the resulting flow and the corresponding heat transfer rate for a particular thermal system configuration. The present work is also a step forward in understanding the complex processes that may occur in microgravity environments in space where natural convection has no place. Moreover, conducting experiments in terrestrial conditions as though they were occurring in the Cosmos provides an economical way to investigate processes relevant to microgravity environments. Acting along with

* Corresponding author: Dr Tomasz P Bednarz
Phone: + (61)-7-47815218, Fax: + (61)-7-47816788
E-mail address: tomasz.bednarz@jcu.edu.au

the gravitational force, the magnetic force has great potential for applications ranging from quasi-non-gravitational or enhanced gravitational acceleration at a scale comparable with the bore of a super-conducting magnet to micro-scale magnetic effects in atomic level processes.
It is well known that a magnetic field acts not only on ferrous materials but also on ordinary substances such as water, air, wood, etc. The atomic configuration of materials with a very small value of magnetic susceptibility determines whether a specific material is paramagnetic or diamagnetic, that is, whether it is attracted to or repelled by the magnetic field. Paramagnetic materials have positive magnetic susceptibility which is a function of the absolute temperature. In contrast, the magnetic susceptibility of diamagnetic materials is negative and independent of the temperature.
The present experiments are pertinent to the thermal magnetic convection in a cubic cavity filled with a paramagnetic fluid. Magnetic convection is driven by the magnetic buoyancy force, which is proportional to the gradient of the square of the magnetic induction and also depends on the temperature field [1-3].
A number of examples of application of a magnetic force on the convection of paramagnetic or diamagnetic fluids have been reported in the past, after the discovery in 1986 of high-temperature super-conducting materials for producing super-conducting magnets for laboratory use. In 1991, Braithwaite et al. [4] described the enhancement or cancellation of gravitational convection due to a magnetic field for a solution of gadolinium nitrate in a shallow layer heated from below and cooled from above. Subsequently many research works have been conducted in this area. Ikezoe et al. [5] has succeeded in droplet levitation for diamagnetic and paramagnetic fluids. The group of Wakayama investigated the behaviour of air in a strong magnetic field, and a new magneto-aerodynamic airflow generation [6] and the promotion of combustion [7] were reported. Also, Kitazawa and co-workers [8, 9] have reported many new findings and applications of the magnetic force. Most of the early works on magnetic convection are summarized in a recent book by Ozoe [2].
The present work shows that, by applying a magnetic field, the convective motion can be suppressed, enhanced or inverted, and the heat transfer rate can be controlled accordingly.

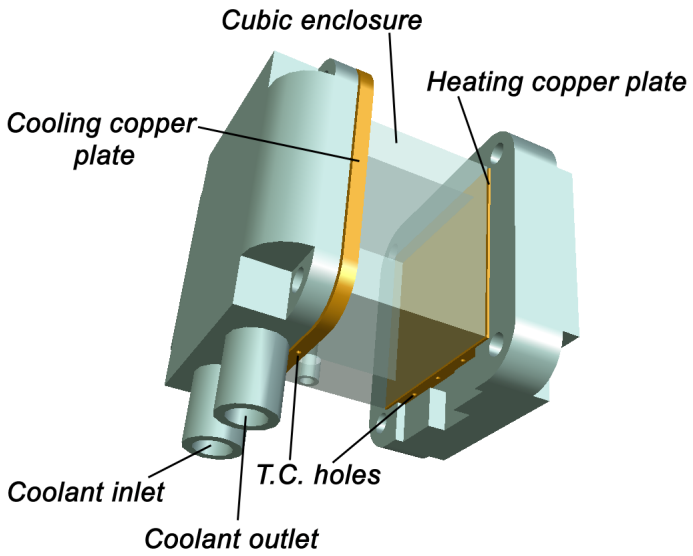

Figure 1. Experimental apparatus. Internal dimensions of the cube are 0.032m × 0.032m × 0.032m.

EXPERIMENTAL APPARATUS

The experimental apparatus is comprised of five separate elements and is shown in Figure 1. These include two copper plates (one for the cooling side, the other for the heating side), a cubical cavity of internal dimensions of l = 32 mm on each side made of transparent Plexiglas, and the cooling and heating chambers, also made of Plexiglas. The experimental system was set up in a way so that both copper plates were vertical. One copper plate was heated with rubber-coated nichrome wire located in

the heating chamber and connected to a DC power supply Kikusui PAK 60-12A, and the other copper plate was cooled by running cold water from a constant temperature circulator LAUDA RK20 KS. The electric voltage and current of the nichrome wire were measured with two multi-meters Keithley 2000 respectively. The temperatures of the two copper plates were measured with six T-type thermocouples inserted into small and deep T.C. holes, three in each plate for averaging purpose.

WORKING FLUID AND EXPERIMENTAL PARAMETERS

The enclosure was filled with an 80% mass aqueous solution of glycerol in which gadolinium nitrate hexahydrate $Gd(NO_3)_3{\cdot}6H_2O$ was dissolved to a concentration of 0.8 mol/kg in order to make the working fluid paramagnetic. The magnetic susceptibility of the working fluid was measured with a magnetic susceptibility balance by Evan's method (MSB Mk1) [12], the density ρ with a pycnometer (Brand 25 ml), the viscosity μ with an Ostwald's viscometer and the thermal expansion coefficient was estimated using $\beta = -\rho^{-1}\left(\partial\rho/\partial T\right)$. The other properties were estimated for the 80% mass aqueous solution of glycerol [13]. The major properties of the working fluid are listed in Table 1.
The present experiments may be characterized by dimensionless parameters such as the Rayleigh number *Ra* which is based on the temperature difference obtained in convection experiments and is defined as follows:

$$Ra = \frac{g\beta l^3\left(\theta_{hot} - \theta_{cold}\right)}{\alpha\nu} \tag{1}$$

and the Prandl number computed at the reference temperature:

$$Pr = \frac{\nu}{\alpha} \tag{2}$$

where θ_{hot} and θ_{cold} are the hot and cold wall temperatures respectively measured as the average of the three thermistor readings from each plate, α is the thermal diffusivity. The dimensional values of magnetic induction measured in the centre of the solenoid system are used to characterize the strength of the magnetic field.

Table 1
Important properties of the working fluid

Property	α [13]	β	λ [13]	μ	ν	ρ	χ	Pr
Value	1.01×10^{-7}	0.52×10^{-3}	0.397	86.9×10^{-3}	5.9×10^{-5}	1463	23.1×10^{-8}	584
Unit	m^2/s	1/K	W/(m·K)	Pa·s	m^2/s	kg/m^3	m^3/kg	–

FLOW VISUALISATION

In order to visualize and measure the temperature field, a very small amount of thermo-chromic liquid crystal slurry (KWN-20/25, Japan Capsular Products) was added to the working fluid. The colour response of the liquid crystal slurry is presented in Figure 2. The concentration of the slurry was adjusted for each experiment, and was in general less than 0.1 ml per litre of the working fluid. Quantitative temperature information was extracted non-invasively from the experimental photographs using the Particle Image Thermometry (PIT) technique [14]. This was done using a calibrated hue versus temperature curve. With the calibration data, every pixel of the colour photograph was transformed to a temperature value, and thus accurate experimental temperature maps were obtained. More details about this method can be found in [14-17].

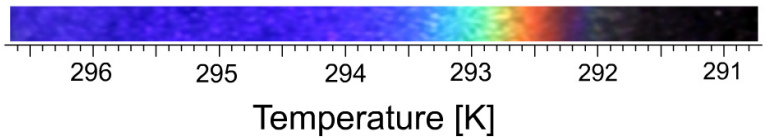

Figure 2. Relation between temperature and color indicated by the TLCs used in the experiment.

For visualization purpose, the 10-Tesla super-conducting magnet was used. The cube was placed outside of the bore for clear view of the flow field. The centre of the cube was always placed at a distance of 0.233 m from the centre of the solenoids and depending on the case investigated the magnet could be oriented vertically or horizontally. A light sheet coming from a projector lamp located at a distance of 3 m was used to illuminate a middle cross-section of the cube giving a colour map of the temperature field. All experimental images were taken by a Canon EOS 10D digital camera with a Canon EF 70-200mm f2.8 IS lens after a steady state was attained for each case.

HEAT TRANSFER MEASUREMENTS

For the purpose of heat transfer measurements, the method developed by Ozoe and Churchill [18] was used. At first, a conduction experiment was carried out. The cubic enclosure was placed in a position to be heated from above and cooled from below. Then, the temperature difference was measured between the hot and cold walls at various heating rates with the cold plate held at a fixed temperature and controlled by the thermostatic water bath and the opposite plate heated by the nichrome wire. The net conduction heat flux through the working fluid layer was then estimated theoretically using Fourier's law:

$$Q_{cond\_net} = \frac{\lambda A(\theta_{hot} - \theta_{cold})}{l} \tag{3}$$

where A is the area of the cross section.
The power input $Q_{cond} = UI$ [W] to the heated cooper plate, where U is the measured voltage and I is the measured current, allowed an estimate of the heat loss which is given by:

$$Q_{loss} = Q_{cond} - Q_{cond\_net} = Q_{cond} - \frac{\lambda A(\theta_{hot} - \theta_{cold})}{l} \tag{4}$$

The net convection heat flux could be then calculated from a specific convection experiment carried out with the same experimental apparatus. The measured value of the heat supply from the heated plate ($Q_{conv} = UI$) can be directly used to calculate Q_{conv_net} as follows:

$$Q_{conv\_net} = Q_{conv} - Q_{loss} \tag{5}$$

with the assumption that the heat loss (Q_{loss}) for a specified temperature difference ΔT depends only on the temperature difference and does not depend on the heat transfer mode inside the enclosure (whether it is in conduction or convection mode) [18]. Therefore, the estimated values of Q_{loss} from the conduction experiment are also used in the convection experiments.
After the two quantities Q_{cond_net} and Q_{conv_net} are determined, the average Nusselt number can be easily obtained for A= ℓ^2 as follows:

$$Nu = \frac{Q_{conv\_net}}{Q_{cond\_net}} = \frac{Q_{conv} - Q_{loss}}{l\,\lambda(\theta_{hot} - \theta_{cold})} \tag{5}$$

It should be pointed out that all heat transfer measurements were carried out using the 5-Tesla super-conducting magnet instead of the 10-Tesla super-conducting magnet. For these measurements the experimental apparatus was placed inside the bore of the magnet and thermally insulated to minimise the heat loss. Readers can refer to [2-3, 10-11, 14] for further details.

RESULTS

The results presented in this paper are for the cases of natural convection resulted in a differentially heated cube subject to a strong magnetic field, and three different configurations are considered. The purpose here is to demonstrate how to enhance, suppress or invert the convective motion using a strong magnetic field. Also heat transfer measurement results are described here for each of the case.

Enhancement of the convection

Enhancement of the convection using a strong magnetic field is presented for the case in which the super-conducting magnet was oriented horizontally and the hot wall was close to the solenoid. The gravitational and magnetic buoyancy forces acting on the fluid for this case are depicted in Figure 3a. Figure 3a also plots the average Nusselt numbers versus the magnetic induction measured at the centre of the solenoid. As seen in this figure, the average Nusselt number at the magnetic induction of 0 T was around 5 as the convective flow was present in the enclosure without the magnetic field. As the strength of the magnetic field was increased, the heat transfer rate also increased. Therefore, the results clearly indicate the enhancement of the convection with the increasing strength of the magnetic field in this case.
Figures 3b and 3c show vertical cross-sections of the temperature fields at 0 T and 10 T respectively. In these figures, the experimental images along with the isotherms obtained using the PIT method are shown. At the magnetic induction of 0 T, the usual natural convection temperature structures can be observed. The cold fluid close to the cooled wall moves down the wall and then along the bottom toward the right-hand side hot wall. Being heated up there, the fluid climbs up the heated wall and then moves along the top ceiling toward the left-hand side cooled wall. A convective circulation was established. An increase in the strength of the magnetic field causes stronger convection in this case as indicated by the increase of the heat transfer rate. It is seen in Figure 3b that the thicknesses of the thermal layers above the floor and under the ceiling are reduced at 10 T, suggesting a stronger circulation. At the magnetic induction of 10 T, clear thermal tongues are observed close to the cold and hot walls. They are caused by strong attraction of the relatively colder fluid towards the solenoid and repulsion of the warmer fluid. In fact, paramagnetic fluids are always attracted toward the magnet, however to obey Curie and continuity laws in the enclosed cavity, the warmer fluid appears to be repelled, i.e., is pushed or squizzed by the colder fluid which is always attracted more than the warmer fluid.

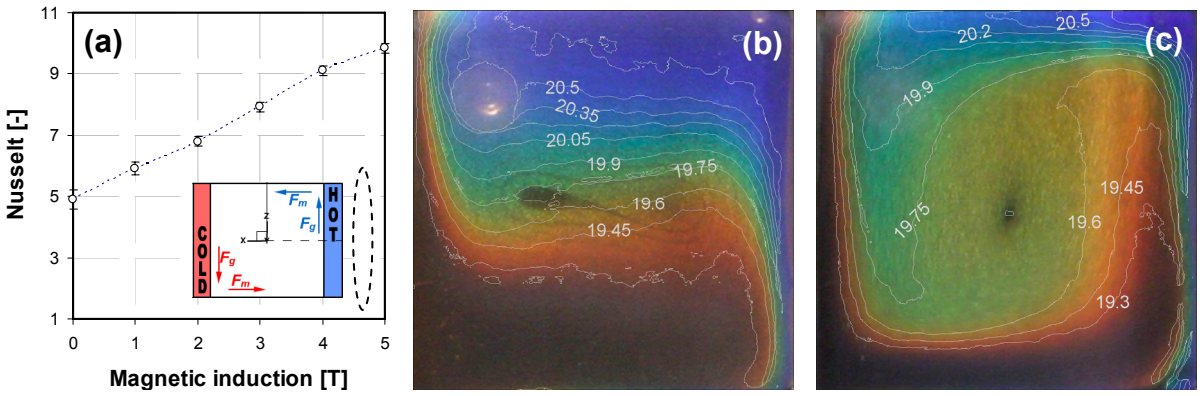

Figure 3 Enhancement of the convection. (a) Nusselt numbers at various magnetic inductions (obtained with *Ra* ranging from 1.49×10^5 to 9.93×10^4); (b) and (c) TLC color images and temperature profiles at (b) 0 T; (c) 10 T.

Suppression of the convection

Suppression of the convection using a strong magnetic field is presented for the case in which the super-conducting magnet was oriented horizontally and the cold wall was close to the solenoid. The gravitational and magnetic buoyancy forces acting on the fluid for this case are depicted in Figure 4a. Figure 4a also plots the average Nusselt numbers versus the magnetic induction measured at the centre of the solenoid. As seen in this figure, the average Nusselt number at the magnetic induction of 0 T was around 3.7 as the convective flow was present in the enclosure without the magnetic field. It is worth noting that reported average Nusselt numbers at the 0-T magnetic induction are not the same for different experiments (refer to Figures 3a and 4a). This is due to some adjustment of the experimental conditions from one experiment to another. The adjustment is necessary to ensure the observed temperature field is always within the visible range of the TLCs over the full range of the magnetic induction. It is seen in Figure 4a that, as the strength of the magnetic field was increased, the heat transfer rate decreased. Therefore, the results clearly indicate the suppression of the convection with the increasing strength of the magnetic field in this case.
Figure 4b shows the isotherms at a mid-vertical plane of the enclosure at the magnetic induction of 0 T. The left side wall is heated and the right side wall is cooled. Since the walls are made of copper plate, the isothermal condition is well satisfied. These isotherms are typical for pure natural convection with a clockwise circulation and a thermal stratification in the core region. Figure 4c shows the results obtained at the magnetic induction of 10 T. The isotherms become approximately vertical, indicating a conduction-like temperature structure. In this case, the cold fluid is trapped close to the cooled vertical wall by the strong magnetic field, and as seen the convection in the enclosure is suppressed.

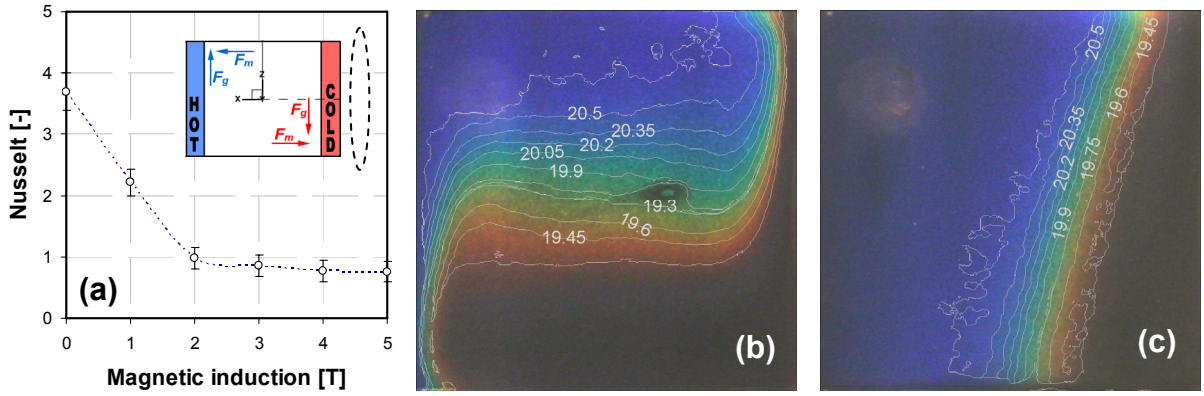

Figure 4 Suppression of the convection. (a) Nusselt numbers at various magnetic inductions (obtained with *Ra* ranging from 1.49×10^5 to 9.93×10^4); (b) and (c) TLC color images and temperature profiles at (b) 0 T; (c) 10 T.

Inversion of the convection

Inversion of the convective motion using a strong magnetic field is presented for the case in which the super-conducting magnet is placed vertically with the cube located below the solenoid. The Nusselt numbers were estimated from equation (5) and are presented in Figure 5a. The Nusselt numbers are plotted versus the maximum magnetic induction. Also, as shown in Figure 5a, the magnetic and gravitational buoyancy forces act in the opposite direction and when the strength of the magnetic field is relatively weak, they compensate each other. The Nusselt number reaches its minimum at around 1 T. For higher strengths of the magnetic induction, the Nusselt number increases with the increasing magnetic induction. Therefore, it can be said, that when the magnetic field strength increases, the magnetic buoyancy force becomes dominant and the convection is inverted.
At 0 T (Figure 5b) the usual gravitational convection occurred. However, when the magnetic field is imposed, the magnetic buoyancy force is expected to cancel or overcome the gravity effect. At 8 T, the

magnetic force is already dominant and the convection is reversed in comparison with that at 0 T. As seen in Figure 5c, relatively colder fluid is attracted to the solenoid's location. The cold fluid moves up along the left-hand side cooled wall, and then along the top ceiling toward the heated wall. After being heated by the hot wall, the relatively warmer fluid falls down along the heated wall.

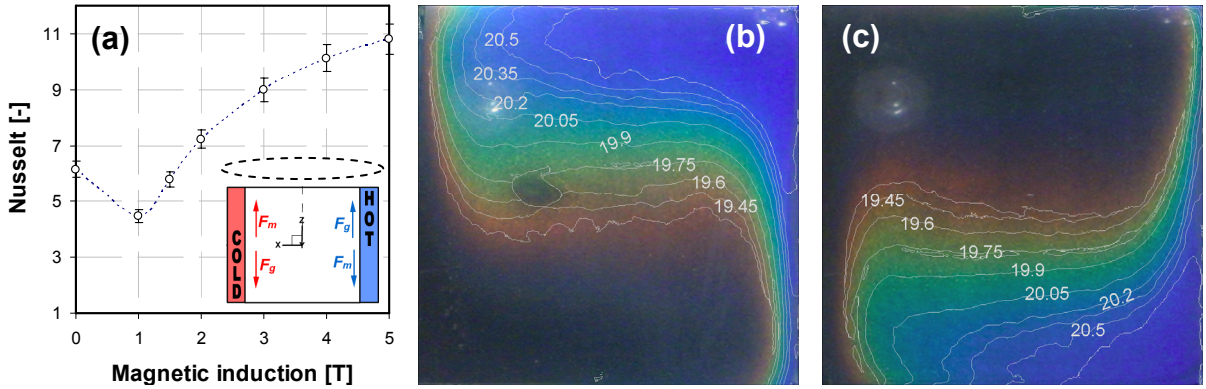

Figure 5 Inversion of the convection. (a) Nusselt numbers at various magnetic inductions (obtained with *Ra* ranging from 1.62×10^5 to 9.51×10^4); (b) and (c) TLC color images and temperature profiles at (b) 0 T; (c) 8 T.

CONCLUSIONS

In this paper, convection of a paramagnetic fluid in a differentially heated cubical enclosure subject to a magnetic field has been investigated experimentally. The enclosure was placed in different configurations relative to the magnetic field. As demonstrated above, using a strong magnetic field we can either enhance, suppress or invert the usual gravitational convection with different combinations of the two forms of body forces (gravitational and magnetic buoyancy forces) that act together to drive thermo-magnetic convection of a paramagnetic fluid. For instance, a suppression of the convection to an almost conduction-like state was presented. The cold fluid was trapped by the magnetic buoyancy force acting in a horizontal direction along the cold vertical wall situated close to the solenoid system. Another example presents an inversion of the usual gravitational convection when the magnet is located above the enclosure. The purpose of this study is to demonstrate that gravitational convection can be controlled in terrestrial conditions with the application of a sufficiently strong magnetic field. This finds applications in many industrial processes such as crystal growth procedures, in which gravitational convection is undesirable.

REFERENCES

1. Tagawa, T., Shigemitsu, R. and Ozoe, H., Magnetizing force modelled and numerically solved for natural convection of air in a cubic enclosure: effect of the direction of the magnetic field, *International Journal of Heat and Mass Transfer*, Vol. 45, pp 267-277, 2002.
2. Ozoe, H., Magnetizing convection, Imperial College Press, 2005.
3. Bednarz, T., Fornalik, E., Tagawa, T., Ozoe, H., Szmyd, J. S., Convection of paramagnetic fluid in a cube heated and cooled from side walls and placed below a superconducting magnet - comparison between experiment and numerical computations, *Thermal Science & Engineering*, Vol. 14, pp 107-114, 2006.
4. Braithwaite, D., Beaungnon, R. and Tournier, R., *Nature*, Vol. 354, pp 134-136, 1991.
5. Ikezoe, Y., Hirota, N, Nakagawa, J. and Kitazawa, K., Making water levitate, *Nature*, Vol. 393, pp 749-750, 1998.
6. Wakayama, M. and Wakayama, N. I., Magnetic acceleration of inhaled and exhaled flows in breathing, *Japanese Journal of Applied Physics*, Vol. 39 pp 262-264, 2000.

7. Wakayama, N. I., Magnetic promotion of combustion in diffusion flames, *Combustion and Flame*, Vol. 93, pp 207-214, 1993.
8. Uetake, H., Nakagawa, J., Hirota, N. and Kitazawa, K., Nonmechanical magnetothermal wind blower by superconducting magnet, *Journal of Applied Physics*, Vol. 85, pp 5735-5737, 1999.
9. Nakagawa, J., Hirota, N. and Kitazawa, K., Magnetic field enhancement of water vaporization, *Journal of Applied Physics*, Vol. 86, pp 2923-2925, 1999.
10. Bednarz, T., Fornalik, E., Ozoe, H., Szmyd, J. S., Patterson, J. C. and Lei, C., Influence of a horizontal magnetic field on the natural convection of paramagnetic fluid in a cube heated and cooled from two vertical side walls, *International Journal of Thermal Sciences*, Vol. 47, pp 668-689, 2007.
11. Bednarz, T., Lei, C., Patterson, J. C. and Ozoe, H., Effect of a transverse, horizontal magnetic field on natural convection of a paramagnetic fluid in a cube, *International Journal of Thermal Sciences*, Vol. 48, pp 26-33, 2009.
12. Sherwood Scientific Ltd., Magnetic susceptibility balance instruction manual 2nd Edition, Cambridge, 2001.
13. Lide, D.R., Handbook of Chemistry and Physics, Chemical Rubber Company Press, Baca Raton, FL, 2001-2002.
14. Bednarz, T., Lei, C. and Patterson, J. C., Particle Image Thermometry for natural convection flows, Proceedings of the 16th Austrlasian Fluid Mechanics Conference, Gold Coast Australia, pp 1165-1170, December 2007.
15. Park, H. G., Dabiri, D., Gharib, M., Digital particle image velocimetry / thermometry and application to the wake of a heated circular cylinder, *Experiments in Fluids*, Vol. 30, pp 327-338, 2001.
16. Kowalewski, T. A., Experimental methods for quantitative analysis of thermally driven flow, experimental benchmarks for code validations", 5 lectures from Advanced School on Phase Change with Convection - modelling and validation: coordinated by Prof. Kowalewski and Prof. Gobin, CISM, Udine/Italy 2002.
17. Stasiek J. A., Thermochrmomic liquid crystals and true colour image processing in heat transfer and fluid-flow research, *Heat and Mass Transfer*, Vol. 33, pp 27-39, 1997.
18. Ozoe, H., Churchill, S. W., Hydrodynamic stability and natural convection in Newtonian and non-Newtonian fluids heated from below, AIChE Symposium Series Heat Transfer, Vol. 69, pp 126-133, 1993.

FLUCTUATING AND TIME AVERAGED HEAT TRANSFER CHARACTERISTICS OF A STEADY JET AT LOW REYNOLDS NUMBERS.

R. Farrelly *, A. McGuinn, T. Persoons, D. B. Murray

Trinity College Dublin, Dublin, Ireland

ABSTRACT**.** A study has been carried out to compare fluctuating and time averaged heat transfer measurements of a steady impinging air jet at low Reynolds numbers. The steady jet issued from a 5mm diameter orifice plate with air being supplied by a compressor via a plenum chamber, and being controlled by a mass flow controller. Tests were conducted for Reynolds numbers ranging from 1000 to 4000, and for non-dimensional surface to jet exit spacings (H/D) from 1 to 6. Initial studies have shown a distinct difference between trends in time-averaged and fluctuating Nusselt number profiles. Whereas the time-averaged profiles show a uniform/linear increase with Re from 1000 to 4000, the fluctuating Nu profiles seem to indicate a transition from a nearly laminar jet at Re=1000 to turbulent jets at Re = 3000, 4000.'

Keywords: *Steady Jet, Fluctuating, Nusselt Number, Reynolds number, Impinging, Velocity, PIV*

INTRODUCTION

Steady impinging jet heat transfer has received considerable attention over the last few decades particularly in many industrial and engineering applications (e.g. manufacturing, material processing and electronics cooling). This is largely due to the fact that an impinging air jet is known to yield relatively high local and area averaged convective heat transfer coefficients, O'Donovan et al. [1]. Hollworth and Durbin [2] investigated the impingement cooling of electronics and Babic et al. [3] used jet impingement for the cooling of a grinding process. In these, and in other cases research has been conducted with a specific application as the focus but there has also been many investigations into the fluid flow and heat transfer characteristics. These have led to the identification of several parameters which influence heat transfer on the impingement surface.

The flow and heat transfer characteristics of an impinging jet are affected by numerous parameters like confinement and impingement angle but the two parameters with greatest influence are the jet Reynolds number, and the surface to jet exit spacing (H/D). Impinging jets are commonly divided into three regions on the basis of the flow structure (i) the free jet region, (ii) the stagnation region and (iii) the wall-jet region, as illustrated in figure 1. Numerical modelling and theoretical studies have also formed part of the extensive research into jet impingement heat transfer; a theoretical study by Shadlesky [4] developed a solution for heat transfer at the stagnation point. More fundamental research has been conducted into the effects of turbulence on heat transfer. Jet turbulence intensity has been augmented by Gardon and Akfirat [5] by the use of turbulence grids at the jet exit. The flow along the plate from the geometric centre through the stagnation zone and the eventual formation of the wall jet are investigated by Lytle and Webb [6]. Although jet impingement heat transfer has been studied extensively by many researchers including O'Donovan

* Corresponding author: Rayhaan Farrelly
Phone: + (353)-1-8961061, Fax: + (353)-1-6795554
E-mail: farrelra@tcd.ie

et al [7], the amount of information available for low Reynolds number jet flows, in the laminar to turbulent transition range, is more limited. In particular the approach of examining both the fluctuating and time averaged heat transfer characteristics at low Reynolds numbers has yet to be explored fully.

The purpose of this study is to acquire an understanding of how steady impinging air jets behave at low H/D values and low Reynolds numbers, by comparing time averaged and fluctuating heat transfer data, with the use of Particle Image Velocimetry (PIV) to elucidate the heat transfer results.

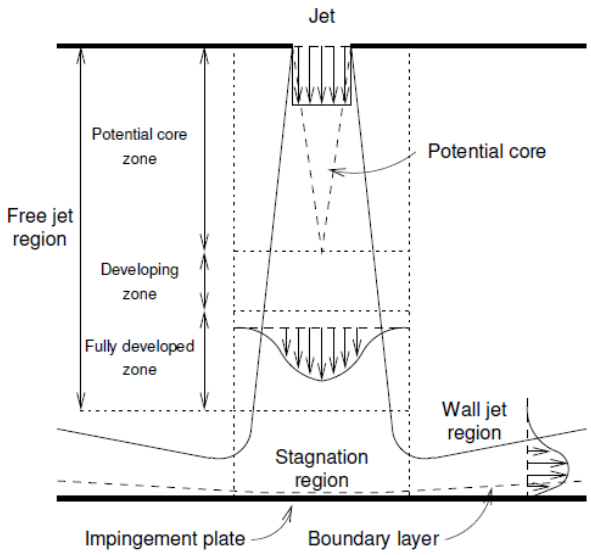

Figure 1. impinging jet flow regimes [8]

EXPERIMENTAL SETUP

There are three main elements that make up the experimental rig, these being the steady jet, heated, instrumented impingement surface and the particle image velocimetry (PIV) system. The impingement surface and the jet are mounted on independent carriages that travel on orthogonal tracks; the carriage for the impingement surface is moved using a computer controlled traverse, whereas the carriage for the jets is moved using a manually operated lead screw actuator. The instruments associated with the heated impingement surface are two single point heat flux sensors and two thermocouples. The rig design is presented in figure 2.

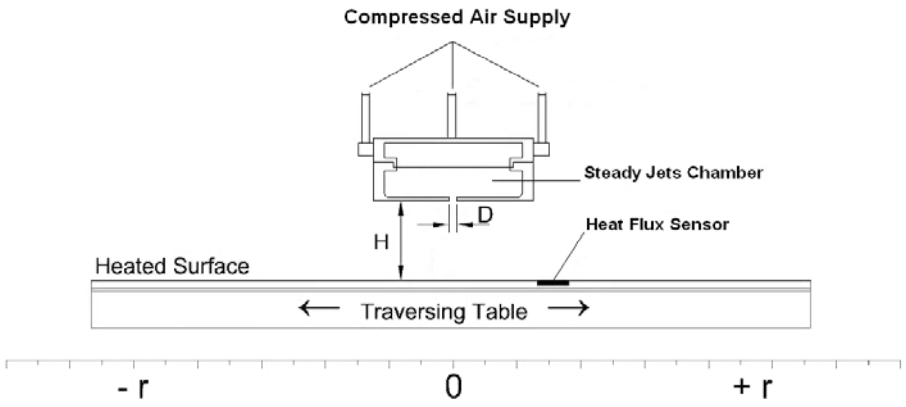

Figure 2. Schematic of the steady jet apparatus

The cavity body and orifice plate are constructed from a thermoplastic and were fabricated using a method of rapid prototyping called fused deposition modelling. The cavity has an approximate volume of 100cm^3 with an orifice diameter of 5mm. Care was taken to ensure a well defined outlet velocity profile with the use of a flow straightener. The steady jet is clamped onto a carriage, which allows for height adjustment from 1 to 6 diameters above the impingement surface. The jet is fixed at a normal angle of impingement (90°).

The steady jet was formed from a constant compressed air source that was maintained at flow rates corresponding to jet Reynolds numbers ranging from 1000 to 4000 by an MKS® Instruments 1579A Digital Mass Flow Controller, which has an accuracy of 1% of full scale and a repeatability of ± 0.2% of full scale (300 slm). The jet impinges onto a surface that consists of a 5mm thick flat copper plate measuring 425mm x 550mm. To the underside of the plate a silicon rubber heater mat is glued with a thin layer of adhesive. The mat is approximately 1.1mm thick. The underside of the plate and mat assembly is insulated from the surroundings. The entire assembly is such that it approximates a uniform wall temperature boundary condition. The system is typically operated at a surface temperature of 40°C.

Two sensors were utilised in this study (i) an RdF Micro-Foil® heat flux sensor, and (ii) a Senflex® hot film sensor. The first sensor measures the temperature differential across a known thermal barrier using a differential thermopile. The heat flux through the sensor is based on the following equation:

$$\ddot{q} = k_s \frac{\Delta T}{\delta} \tag{1}$$

where ΔT is the temperature difference across the thickness (δ) of the barrier and k_s is the thermal conductivity of the barrier (kapton). A single pole T-type thermocouple is also embedded in this sensor to measure the local temperature.

Both sensors are positioned centrally on the plate, and together with the jet and plate carriage arrangement, allow for heat transfer measurements beyond 20 diameters from the geometric centre of the jet. In this study, testing has only been concerned within the region of 1 to 6 diameters from the geometric centre of the jet.

The Senflex® hot film sensor operates in conjunction with a Constant Temperature Anemometer (CTA) to measure the fluctuating heat flux to the impinging jet. This sensor consists of a nickel sensor element that has been electron beam deposited onto a 0.051mm thick Upilex S polyimide film. The hot film element has a physical area of approximately 0.1mm x 1.44mm and is less than 0.2μm thick. The sensor has a typical cold resistance of between 6 and 8 Ohms. Two copper strips are also deposited on the film; these provide terminals for connection to the CTA. These strips have a resistance of approximately 0.002 Ω /mm. The hot film is maintained at a slight overheat (≈1°C) above that of the copper plate using a Dantec StreamLine CTA. The power required to maintain the film at this overheat is equal to the heat actively being dissipated from the film. The CTA essentially acts as a Wheatstone bridge where the hot film acts as one resistor in the bridge. The resistance of the film varies with temperature and therefore, this film temperature can be controlled by varying a decade resistance which forms one arm of the Wheatstone bridge. The square of the voltage required to maintain the film at a constant temperature is proportional to the heat transferred to the air as described in equation (2):

$$q_{dissipated} \propto \frac{V_{out}^2}{R} \tag{2}$$

Time averaged velocity measurements have been performed using time resolved Particle image velocimetry (PIV). PIV has provided insight into both velocity and fluctuating nature of the jet flow at different Reynolds numbers.

The PIV system comprises of a Quantronix Darwin-Duo Nd:YLF twin cavity laser and a LaVision HighSpeedStar6 CCD camera.(1024x1024 pixels, 12 bit) with a 105mm lens. A glycol-water aerosol is used for seeding, with particle diameters between 0.2 and 0.3 µm. The velocity fields have been processed with LaVision's Davis 7 software using multi-pass cross-correlation with an interrogation window size decreasing from 64x64 to 16x16 pixels at 50% overlap.

RESULTS AND DISCUSSION

Results have been obtained for a jet that impinges perpendicularly to a flat plate. Four Reynolds numbers have been considered (1000, 2000, 3000, and 4000) and four surface to jet exit spacings (H/D = 1, 2, 4, and 6) were selected as this range provided a clear indication of the effects on impinging jets at low Reynolds numbers and low H/D values.

The results are presented as time averaged heat transfer distributions and fluctuating heat transfer distributions for each H/D from 1 to 6. A direct comparison between the time averaged and fluctuating heat transfer profiles of the jet will be made, with reference to corresponding PIV data where available.

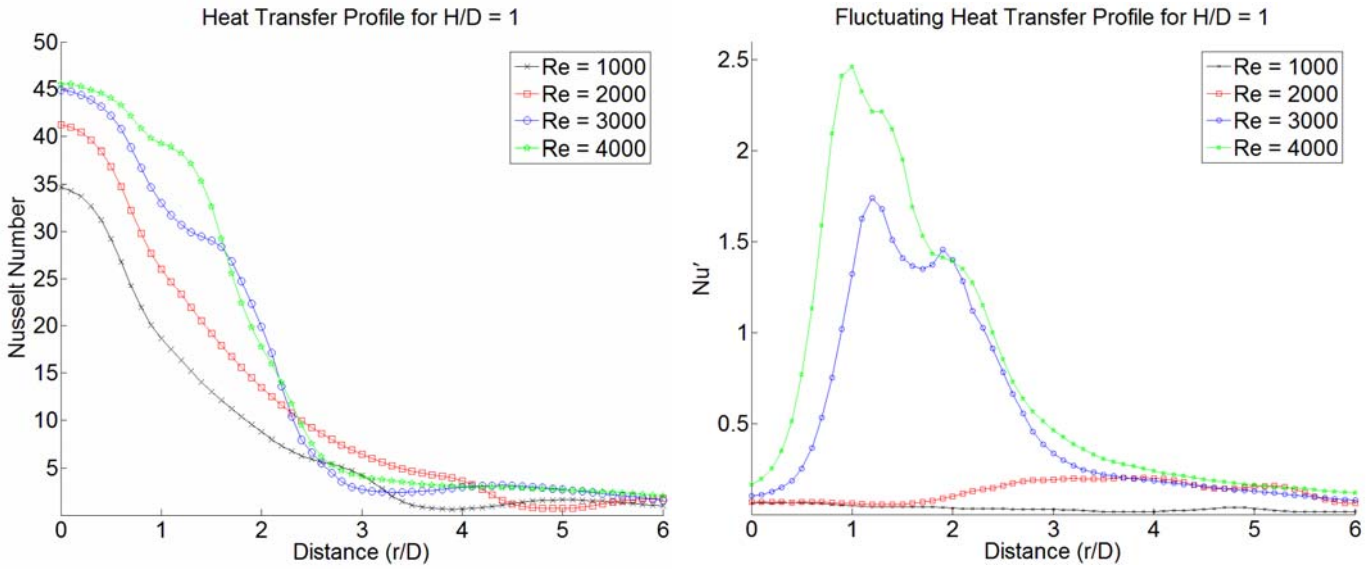

(a) Time averaged heat transfer distribution (b) Fluctuating heat transfer distribution

Figure 3. Time averaged and fluctuating heat transfer profiles H/D=1

Figures 3a and 3b illustrate the heat transfer profiles for the steady impinging jet at matching Reynolds numbers and jet exit to plate spacings (H/D). the presence of secondary peaks at a radial distance of approximately $1 < r/D < 2$ for the time averaged heat transfer distribution there appears

to be a transition to turbulence at Reynolds numbers 3000, 4000. This is clearly evident in the fluctuating heat transfer distribution (figure 3b) at Re = 3000 and 4000. There is quite a large fluctuation in heat transfer present between Re = 3000 and 4000 in figure 3b.

It is worth noting that at this H/D the orifice plate imposes a strong degree of confinement on the jet. As the height of the jet above the impingement surface is increased there is less likelihood of confinement occurring, therefore allowing the jet to fully propagate, and maximum heat transfer to take place.

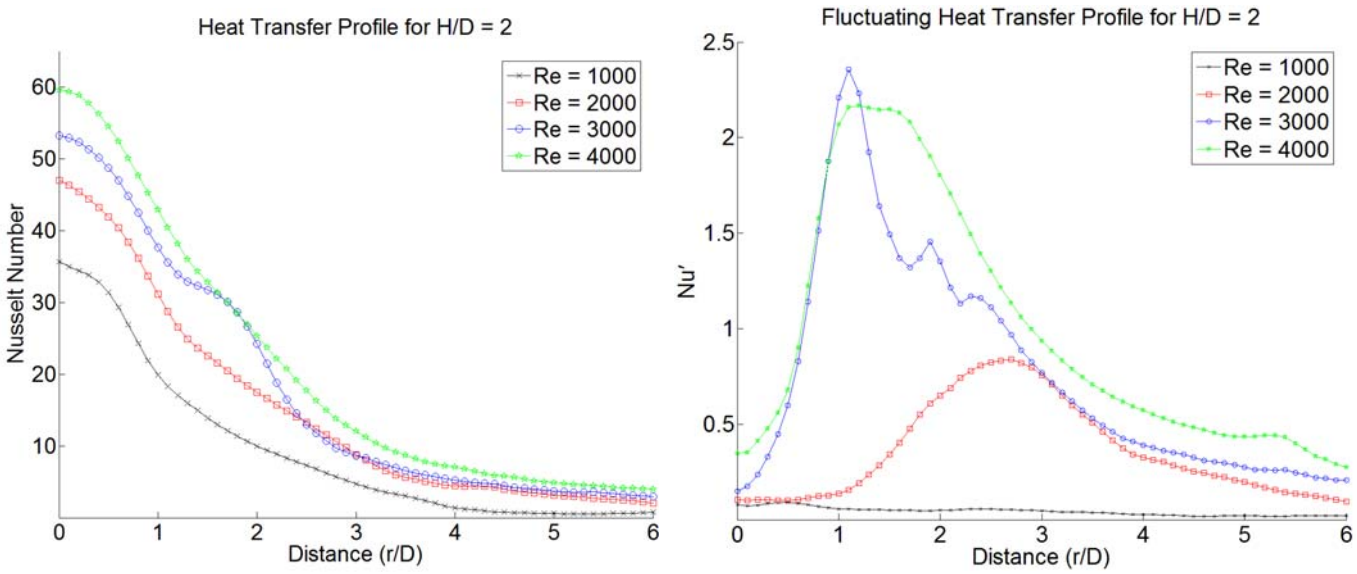

(a) Time averaged heat transfer distribution (b) Fluctuating heat transfer distribution

Figure 4. Time averaged and fluctuating heat transfer profiles H/D=2

Figure 4 shows the heat transfer results for H/D = 2. From figure 4b, at a Reynolds number of 3000 there is what appears to be a laminar core which results in a transition to turbulence at r/D of approximately 1.5. This is reflected in a local increase in time averaged heat transfer, as shown in figure 4a.

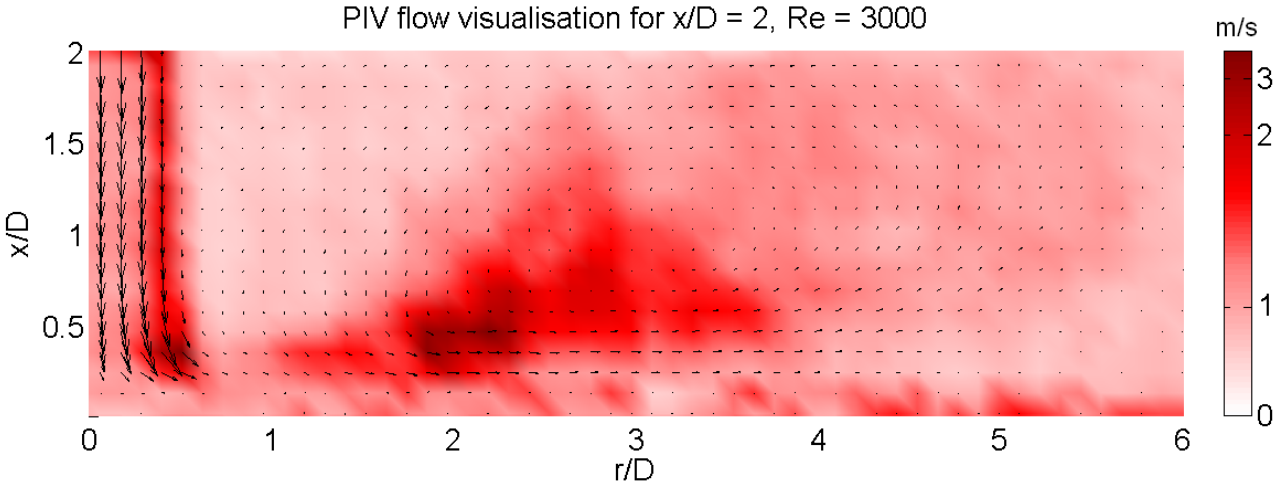

Figure 5. PIV fluctuating velocity plot x/D=2, Re=3000

The PIV fluctuating velocity plot is a combination of the mean velocity vectors and the root mean square velocity colour map. The PIV fluctuating velocity scale is defined using a custom colour map where deep red signifies large fluctuations and white represents zero fluctuation. This scale was defined by using the mean and root mean square velocity maps that were outputted from DaVis 7. The R.M.S. velocity scale is defined using the colour bar on each PIV image. The mean velocity scale is from 0 – 17 m/s.

Figure 5 shows the PIV time average velocity plot for x/D = 2 and Re = 3000. It can be seen that there are very large fluctuations in the shear layer before impingement and subsequently a transition to turbulence. Since the jet is laminar at the parameters shown, transition to turbulence after impact and this can be seen in the fluctuating heat transfer and PIV data at $0.5 < x/D < 4$. The core is maintained right up until impingement; there are relatively low velocity fluctuations in the core, a coherent core which results in low fluctuating heat transfer. Where the jet impinges an area of high fluctuation are evident. Areas of recirculation can be clearly seen in the figure 5. The heat transfer fluctuations are caused by vortices in the shear layer impacting upon the plate, this can be seen at $0.5 < x/D < 2$ for both the PIV data and fluctuating heat transfer.

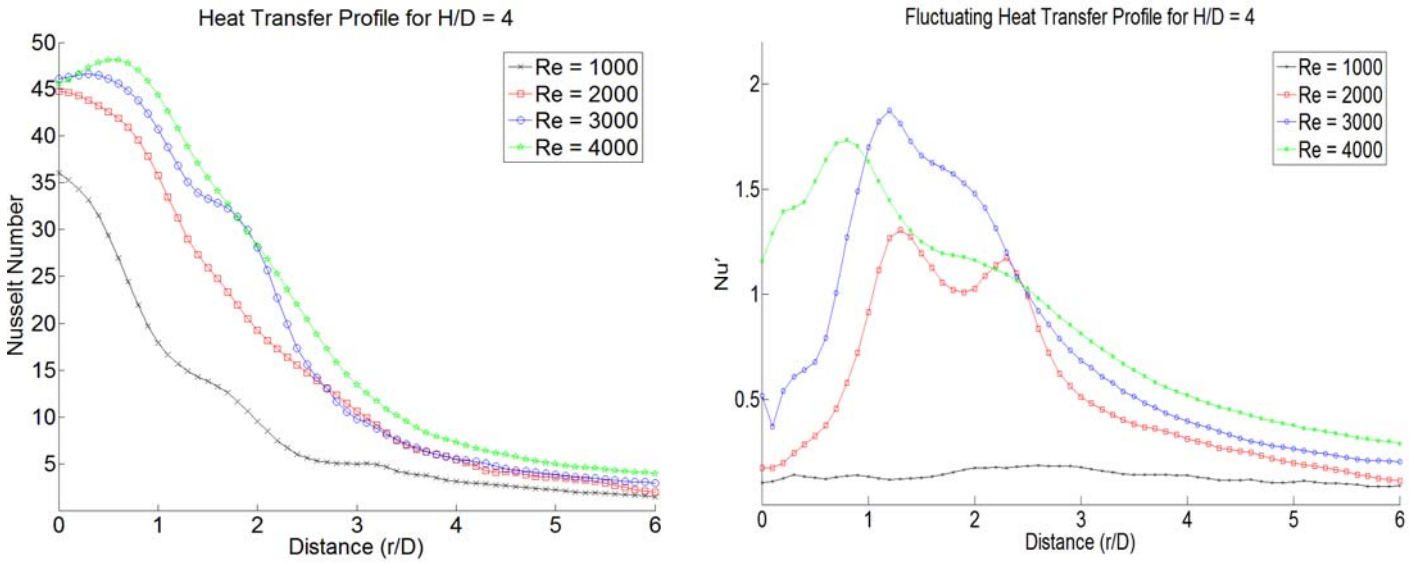

(a) Time averaged heat transfer distribution (b) Fluctuating heat transfer distribution

Figure 6. Time averaged and fluctuating heat transfer profiles

In figure 6 for H/D of 4, there is what appears to be a local minimum at a Reynolds number equal to 4000 on the time averaged heat transfer distribution which correlates with the fluctuating heat transfer distribution. Overall the fluctuations in heat transfer are higher in the stagnation zone, which could mean turbulence starts earlier in the jet due to the higher Reynolds number. There appears to be a loss of momentum in the jet at this H/D, which could be due to a diminished potential core.

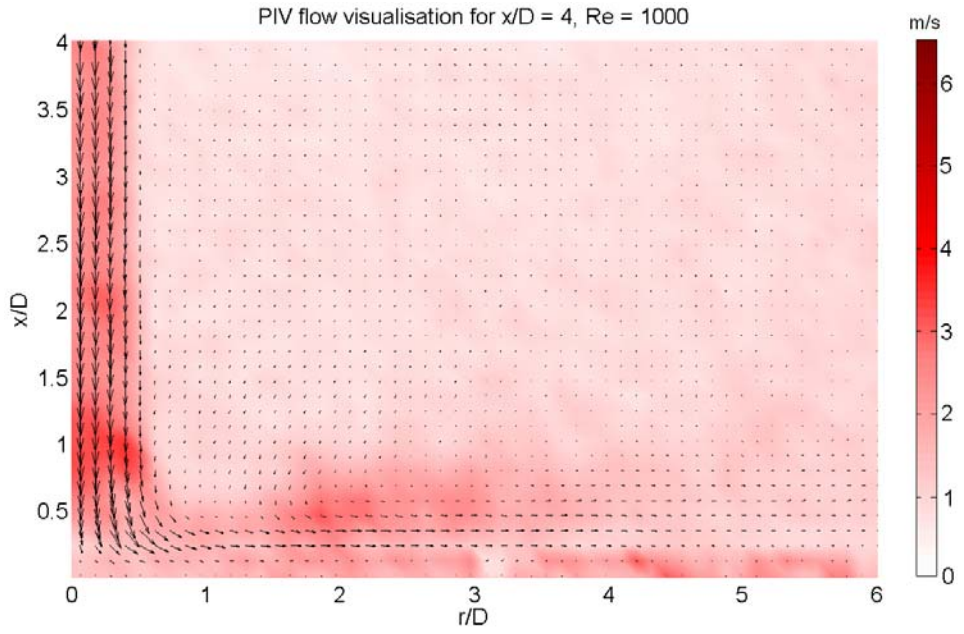

Figure 7. PIV fluctuating velocity plot x/D=4, Re=1000

Figure 7 shows very slight fluctuation in velocity in the core, this is due to a reduced potential core from a loss of momentum at H/D = 4 and low Reynolds number.

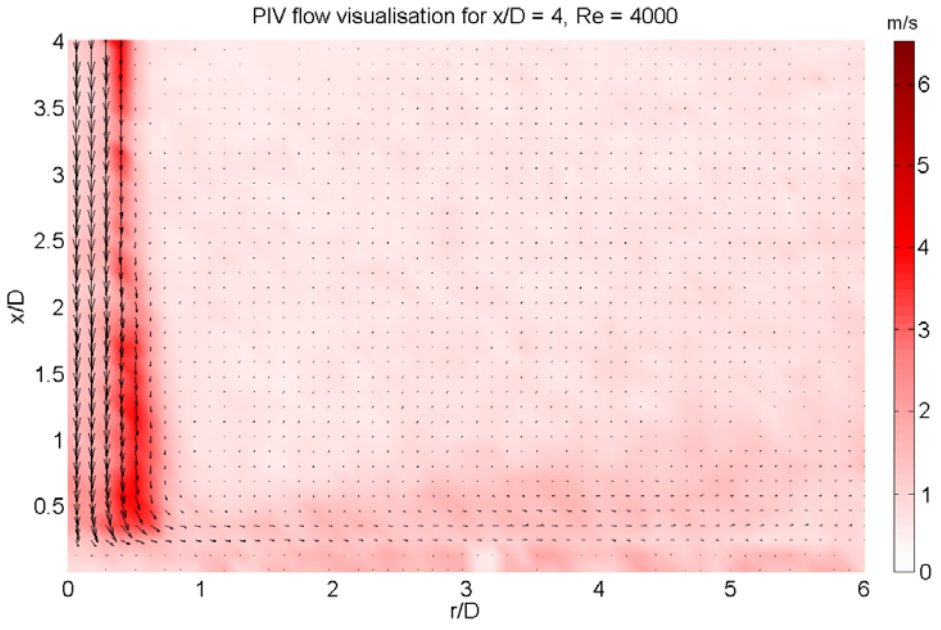

Figure 8. PIV fluctuating velocity plot x/D=4, Re=4000

The potential core is maintained at a greater height above the surface due to increased flow momentum, the lower fluctuating velocity in the core corresponds with the low local fluctuating heat transfer (figure 6b) observed at this jet exit to plate spacing and Reynolds number. A turbulent shear layer is observed at this height

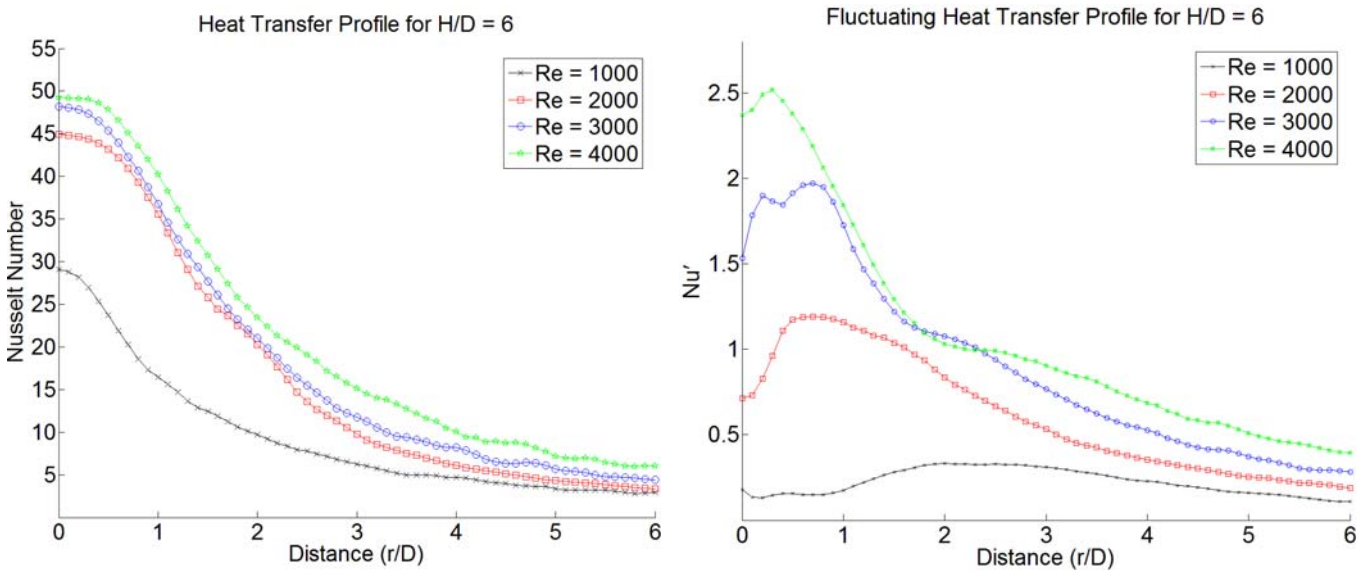

(a) Time averaged heat transfer distribution (b) Fluctuating heat transfer distribution

Figure 9. Time averaged and fluctuating heat transfer profiles

Comparison of figures 6a and 9a helps to illustrate the effects that jet exit to plate spacing have on the jet. A loss of momentum for Reynolds number of 1000 is apparent at H/D of 6, as the Nusselt numbers for this Reynolds number are lower than observed in figure 6a at the H/D = 4. The distributions in figure 9a show no evidence of secondary peaks and the Nusselt numbers reduce uniformly with increasing r/D, which indicates that the jet has been able to fully propagate; this is due to the higher jet to plate spacing allowing there to be a more fully developed flow. In figure 9b the Reynolds number of 2000 shows low levels of heat transfer fluctuation upon impingement. It is noted that Re = 1000 remains laminar throughout the H/D values tested (1, 2, 4 and 6)

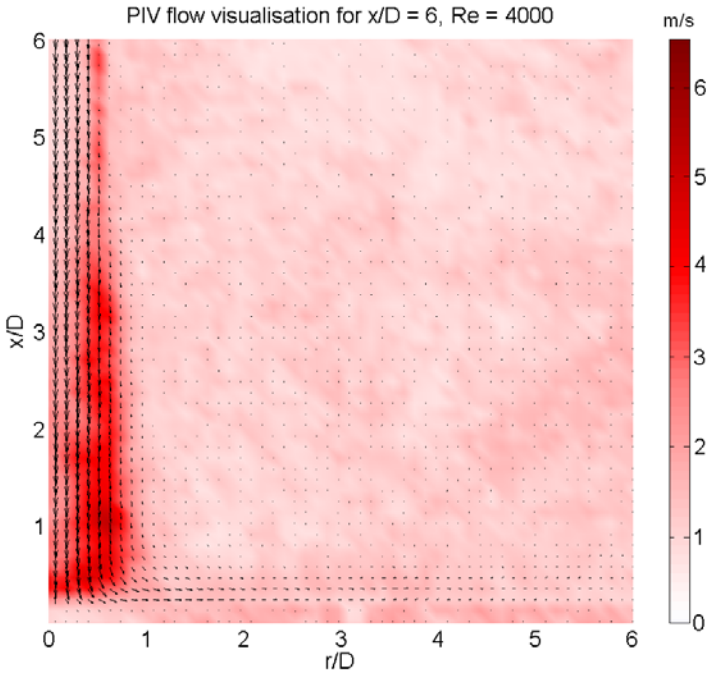

Figure 10. PIV fluctuating velocity plot H/D=6

Figure 10 shows a core that is almost diminished by the time it impinges on the surface and has greater fluctuating velocities. Less momentum in the potential core means that the core is less coherent and more turbulent before impingement, this is indicated by the intensity of the colours and this is also indicated in figure 9b for the fluctuating heat transfer profile. It is worth noting that there are lower fluctuations in the wall jet region for all PIV fluctuating velocity plots.

CONCLUSIONS

Results have been presented for time averaged heat transfer, fluctuating heat transfer and PIV fluctuating velocity plots relating to an axially symmetric impinging air jet. It has been shown that at low jet exit to plate spacing the time averaged heat transfer distribution in the radial direction shows evidence of secondary peaks. These peaks have been reported by several investigators including Farrelly et al [9] and have been attributed, in general, to an abrupt increase in turbulence in the wall jet boundary layer.

The fact that the peaks occur at approximately the same location for both Nu and Nu' distributions indicates a correlation between the heat transfer fluctuations and the mean heat transfer. Increasing Nusselt numbers for the time averaged heat transfer plots can be seen with increasing H/D at large r/D values, due to less confinement.

Peak Nusselt numbers recorded for the range of jet exit to plate spacings occur at an H/D = 2. An increase in H/D results in a loss of momentum and the onset of turbulent flow is reflected in the fluctuating heat transfer distributions at H/D = 4 and above. It is noted from the PIV data presented that there are lower fluctuations in the wall jet region.

NOMENCLATURE

Nu' – Fluctuating heat transfer

REFERENCES

1. T.S. O'Donovan, Jet impingement heat transfer – Part I: Mean and root-mean-square heat transfer and velocity distributions. *Int. J. heat and mass transfer* Vol. 50, (2007) 3291-3301
2. B.R. Hollworth, M. Durbin, Impingement cooling of electronics, ASME J. Heat Transfer 114 (1992) 607–613.
3. D.M. Babic, D.B. Murray, A.A. Torrance, Mist jet cooling of grinding processes, *Int. J. Mach. Tools Manuf.* 45 (2005) 1171-1177.
4. P.S. Shadlesky, Stagnation point heat transfer for jet impingement to a plane surface, *AIAA J. 21* (1983) 1214–1215.
5. R.J. Gardon, J.C. Akfirat, The role of turbulence in determining the heat transfer characteristics of impinging jets, *Int. J. Heat Mass Transfer* 8 (1965) 1261–1272.
6. D. Lytle, B.W. Webb, Air jet impingement heat transfer at low nozzle-plate spacings, *Int. J. Heat Mass Transfer* 37 (1994) 1687-1697.
7. T.S. O'Donovan, Jet impingement heat transfer – Part I: Mean and root-mean-square heat transfer and velocity distributions. *Int. J. heat and mass transfer* Vol. 50, (2007) 3291-3301
8. Incropera, F.P., *Liquid Cooling of Electronic Devices by Single-Phase Convection,* Publ. Wiley Interscience, 1999
9. R. Farrelly, A. McGuinn, T. Persoons, D.B. Murray, A heat transfer comparison between a synthetic jet and a steady jet at low Reynolds number. *ASME IMECE2008*, IMECE2008-68726

A COMBINED EXPERIMENTAL-NUMERICAL APPROACH TO INVESTIGATE HEAT TRANSFER COEFFICIENT IN A TUBE-IN-TUBE HEAT EXCHANGER

F. M. Shemirani, M. A. Akhavan-Behabadi* , H.Aria
Faculty of Mechanical Engineering, University College of Engineering,
University of Tehran, Iran

ABSTRACT. In the present study, the flow boiling heat transfer coefficient of R-134a in a vertical and a horizontal helically coiled tube-in-tube heat exchanger have been investigated experimentally. The refrigerant flow inside the inner copper tube was heated by hot water flows in the annulus in opposite direction. The average vapor quality of R134a in the test section varies from 0.1 to 0.8. The refrigerant mass fluxes are 112, 132, and 152 kg/m^{2}s. A commercial Computational Fluid Dynamics package [FLUENT 6.0] was used to predict water-side heat transfer coefficient to find the best results for our special case. Furthermore, the variation of heat transfer coefficient with vapor quality and the mass flux is studied experimentally.

Keywords: *experimental, numerical, heat transfer, augmentation, helicoidal.*

INTRODUCTION

The heat transfer equipments like evaporators and condensers have an important role to play in different industries such as refrigeration, air-conditioning, power plant, and chemical industries. To save the limited available energy resources, design and manufacturing of efficient heat transfer equipments is essential. Different methods have been used by numerous investigators to increase the heat transfer rates in these equipments.

One of the techniques to enhance the heat transfer coefficients in two phase flow is to use helical pipes instead of straight ones. The modification of the flow in the helically coiled tubes is due to the centrifugal forces[1]. The curvature of the tube produces a secondary flow field with a circulatory motion in the gas core, which pushes the liquid particles toward the center of curvature of the coil [2]. Thus the application of curved tubes in heat exchange process can be highly beneficial in comparison with the straight tube. These applications can arise in the food processing industry for heating and cooling of highly viscous liquid food, such as pastes, or for products that are sensitive to high shear stresses.

Garimella et al. [3] reported an experimental investigation on forced convection heat transfer in coiled annular ducts. They found that the heat transfer coefficients obtained from the coiled annular ducts were higher than those obtained from a straight annulus, especially in the laminar region.

Yang et al. [4] carried out a numerical-experimental study on flow boiling of R-141B in a horizontal coiled tube. They conducted their tests in two flow rates of 10 and 15 l/hr and three different heat fluxes, and observed that flow velocity predicted in the simulations showed a strongly dependence on the phase distribution. Moreover, they depicted the evolution of flow pattern inside the tube.

An investigation was done to study the boiling process in a horizontal coiled tube by Wu et al. [5]. They applied the Eulerian multiphase flow model and paid special interests in flow mode. They

* Corresponding Author: M.A. Akhavan-Behabadi
Email: akhavan@ut.ac.ir
Fax: +98 21 88337123

found that the phase distributions showed a continuous stratification in the horizontal tubes and were influenced by both buoyancy force and centrifugal force in the tube bends.
D. G. Prabhanjan et al. [6] reported comparison of heat transfer rates between a straight tube heat exchanger and a helically coiled heat exchanger during heating in single phase and with water bath. Their results show that helical pipes have greater heat transfer coefficients rather than straight pipes. Also, the increasing of water bath temperature increases the heat transfer coefficient, but changing of mass fluxes has no significant effect on heat transfer coefficient.
In the present study, a numerical-experimental investigation has been carried out on flow boiling heat transfer coefficient of R-134a inside horizontal and vertical helically coiled tube-in-tube heat exchangers. A numerical method is employed to calculate the water-side heat transfer coefficient. The refrigerant side heat transfer coefficient is obtained by applying an energy balance between the water and refrigerant (heat rejected by water = heat absorbed by refrigerant).
The effect of different parameters such as vapor quality and mass velocity on water site heat transfer coefficient and also refrigerant side heat transfer coefficient are discussed.

EXPERIMENTAL FACILITY

The experimental set-up which was used in this investigation is a well instrumented vapor compression refrigeration cycle. The schematic diagram of experimental apparatus has been shown in figure 1. It is consisted of: 1- compressor, 2-condenser, 3-rotameter, 4-accumulator, 5-filter-dryer, 6-expansion valve, 7-sight glass, 8-pre-evaporator, 9-pressure transmitter, 10-test section, 11-after-evaporator, and 12-accumulator.
The schematic diagram of test section is shown in figure 2. It is a helically coiled tube-in-tube counter flow heat exchanger. Refrigerant R-134a flow inside the inner tube is heated by the warm water flowing in the annulus. The outer diameter of the inner tube is 9.52 mm and its thickness is 0.62 mm. The inner diameter of the outer tube is 29 mm. The diameter and pitch of the coil are 305 mm and 45 mm, respectively.

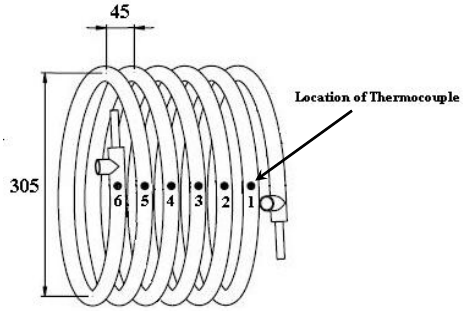

Figure 2. Schematic diagram of horizontal test section

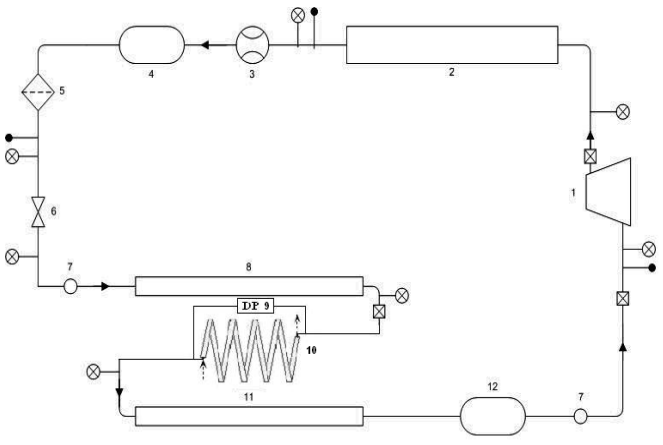

Figure 1. Schematic diagram of experimental apparatus (with horizontal test section)

In addition, there was a pre-evaporator used before the test-evaporator in order to achieve the required vapor qualities at the entrance of test-evaporator. Also, an after-evaporator was employed to ensure that the vapor will be superheated before entering the compressor. Refrigerant which flows inside the inner tube of pre-evaporator and after-evaporator is electrically heated by the coils wrapped around them. All the three evaporators were completely insulated.

NUMERICAL-EXPERIMENTAL APPROACH

Based on the definition of overall heat transfer coefficient, U_o, and using the energy balance equation, we have:

$$Q = U_o A_o . \Delta T_{lm} = \dot{m}_w C_{p_w} \left(T_{w,out} - T_{w,in} \right) \tag{1}$$

Then, the refrigerant-side heat transfer coefficient, H_f is obtained from equation (2).

$$H_f = \left(\frac{A_i}{U_o A_o} - \frac{A_i}{H_w A_o} - R_t A_i \right)^{-1} \tag{2}$$

where, R_t is the tube wall heat resistance. To calculate water-side heat transfer coefficient, H_w, there are some empirical correlations, however, using such correlations in the ranges of the operating parameters of the present study, is accompanied with a considerable error. Therefore, in the present work, we calculated H_w numerically using exact boundary conditions.

The critical Reynolds number for the transition from laminar flow to turbulent flow in a curved pipe or helical coiled tube is important for adoption of different formulas. Two criteria have been suggested. The first one is [7]:

$$Re_{cr} = 20000 \left(\frac{d}{D} \right)^{0.32} \tag{3}$$

and the second one is [8]:

$$Re_{cr} = 2100 \left[1 + 12 \left(\frac{d}{D} \right)^{0.5} \right] \tag{4}$$

Critical Reynolds numbers calculated by both of above mentioned equations are more than 8000, which is much higher than the Reynolds numbers of the present study, therefore, the flow regime is considered as laminar.

Using a commercial software, FLUENT, a finite volume method has been invoked to discretize and solve the governing equations of mass, momentum, and energy conservations.

A second-order upwind method has been employed throughout the domain to compute the heat and momentum fluxes. Also, SIMPLE method was used to calculate and correct the pressure and velocity fields.

As the convergence criteria, the residuals resulting from the integration of different equations were used. For this purpose, the computation was stopped when the residuals of all the governing equations were less than 10^{-6}.

RESULTS AND DISCUSSION

The numerical results for water-side heat transfer coefficient of the vertical and horizontal tube-in-tube heat exchanger versus water Reynolds number for different Prandtl numbers are depicted in figures 3 and 4, respectively.

It is obvious from these figures that water-side heat transfer coefficient increases by increment of water Reynolds number. The major cause of this phenomenon is that by increasing the Reynolds

number, the turbulence of the flow is promoted. Moreover, increasing the water Pr enhances water-side heat transfer coefficient.

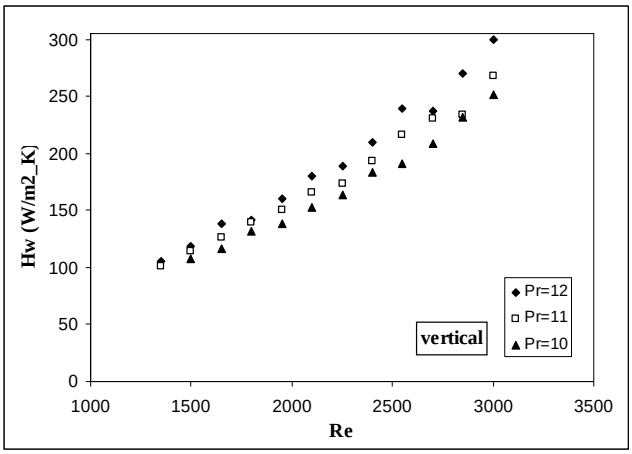

Figure 3. Water-side heat transfer coefficient versus water Reynolds number for vertical helically coiled tube

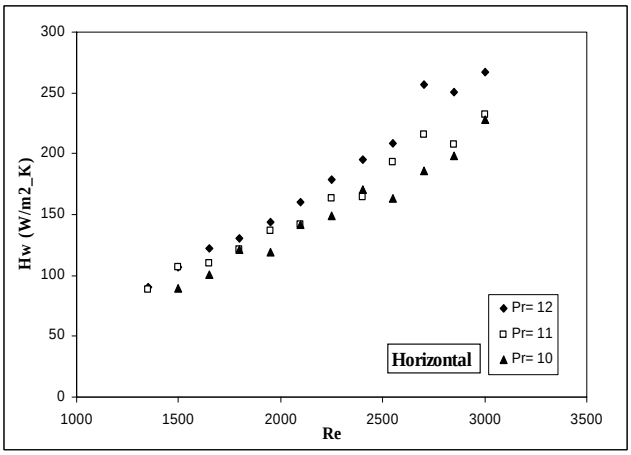

Figure 4. Water-side heat transfer coefficient versus water Reynolds number for horizontal helically coiled tube

The variation of refrigerant-side heat transfer coefficient h_f for vertical and horizontal heat exchangers versus average vapor quality at different mass fluxes are shown in figures 5 and 6.
It is seen from these figures that refrigerant-side heat transfer coefficient reduces with the decrease of vapor quality, continuously. This reduction is due to the lower specific volume of gas which based on the continuity causes the velocity of fluid decreases, which in turn leads to lower heat transfer coefficients. It is also because of the increment of the liquid film thickness and therefore more thermal resistance.
It can be seen that the mass flux has a strong effect on the heat transfer performance, especially at high average vapor qualities. This effect may be explained by the previous studies by Berthoud and Jayanti [1] in that the interfacial vapor liquid shear stress and the intensity of the secondary flow was augmented with increasing mass flux, which resulted in the enhancement of droplet entrainment and redeposition. This enhancement induced the increased numbers and larger sizes of waves on the liquid film surface, which increased the heat transfer area. In addition, at higher velocities, which were due to the raised mass flux, the degree of turbulence of the fluid was intensified, and hence, the heat transfer coefficients were augmented [9].

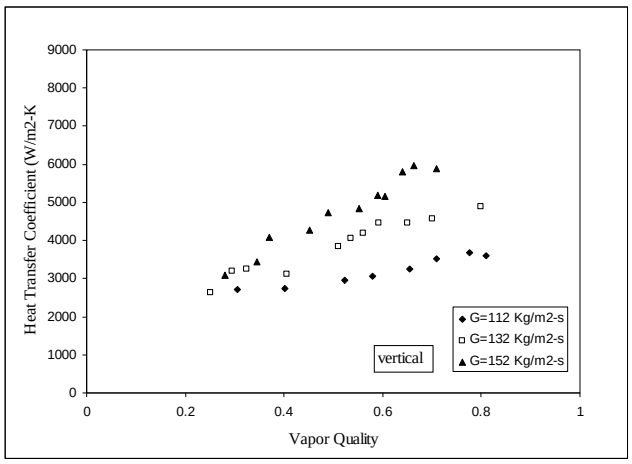

Figure 5. Refrigerant-side heat transfer coefficient versus average vapor quality for vertical helically coiled tube

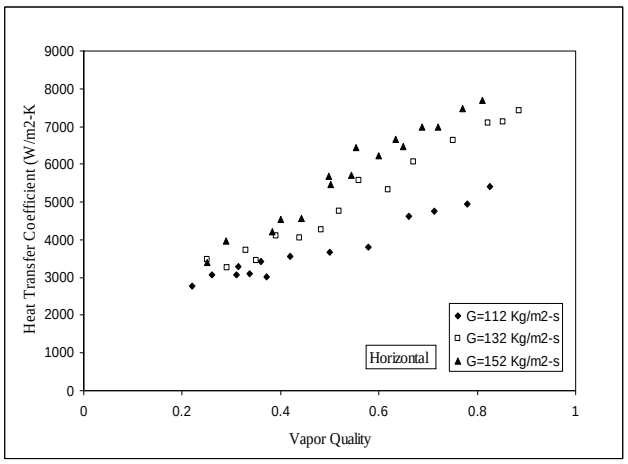

Figure 6. Refrigerant-side heat transfer coefficient versus average vapor quality for horizontal helically coiled tube

In figures7-9, the comparison of h_f for different mass velocities at different vapor qualities is illustrated. It can be seen from these figures that horizontal helically coiled tubes always have greater refrigerant-side heat transfer coefficients. It may be because of greater mixings in horizontally orientated heat exchangers.

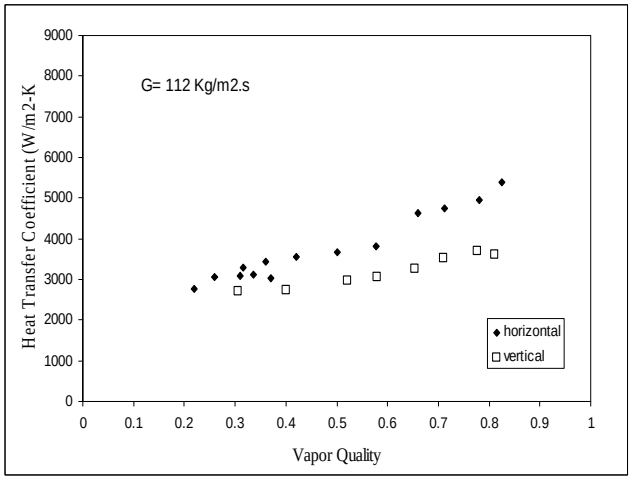

Figure 7. Comparison of horizontal and vertical helically coiled tube refrigerant-side heat transfer coefficients at G=112 kg/m^{2}s

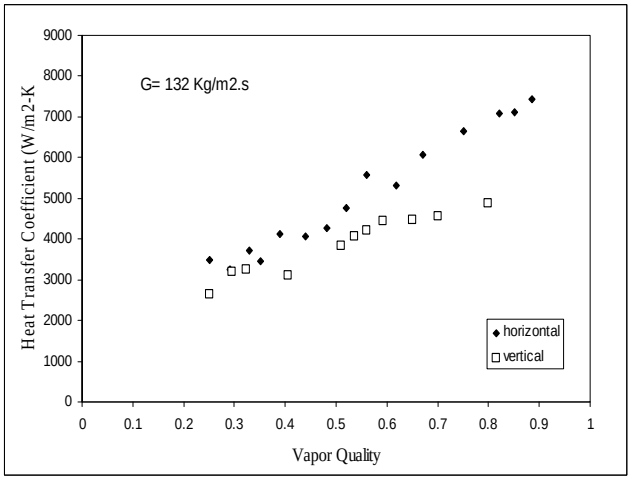

Figure 8. Comparison of horizontal and vertical helically coiled tube refrigerant-side heat transfer coefficients at G=132 kg/m^{2}s

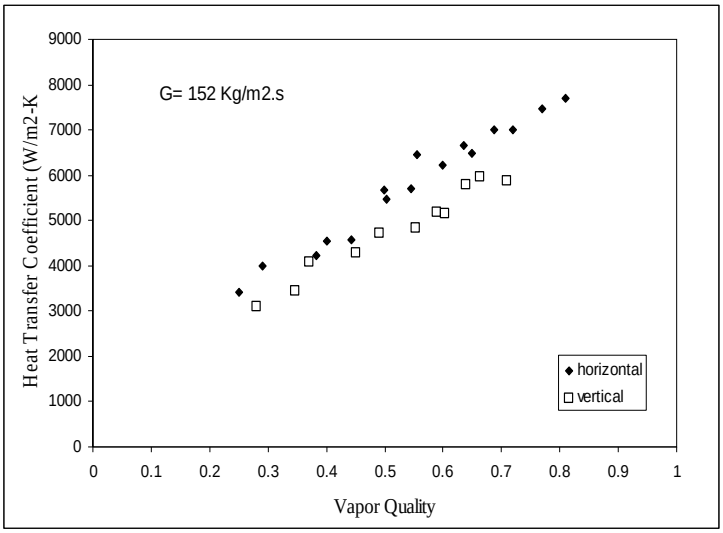

Figure 9. Comparison of horizontal and vertical helically coiled tube refrigerant-side heat transfer coefficients at G=152 kg/m^{2}s

CONCLUSIONS

1. Water-side heat transfer coefficient increases by increasing the water-side Reynolds number.
2. Increment of the water Prandtl number increases water-side heat transfer coefficient.
3. Refrigerant-side heat transfer coefficient reduces with the decrease of vapor quality, continuously.
4. Increase in mass velocity enhances the refrigerant-side heat transfer coefficient.
5. Horizontal helically coiled tubes have greater refrigerant-side heat transfer coefficients than vertical helically coiled tubes.

REFERENECES

[1] Berthoud, G., Jayanti, S., "Characterization of dryout in helical coils", International Journal of Heat and Mass Transfer, Vol. 33, No. 7, 1990, PP. 1451-1463.

[2] Collier, J., and Thome, J., "Convective Boiling and Condensation", Oxford University Press, 1994.

[3] Garimella, S., Richards, D.E., Christensen, R.N., "Experimental investigation of heat transfer in coiled annular ducts", ASME Journal of Heat transfer, Vol. 110, 1988, PP. 329-336.

[4] Yang, Z., Peng, X.F., Ye, P., "Numerical and experimental investigation of two phase flow during boiling in a coiled tube" , International Journal of Heat and Mass Transfer, Vol. 51, 2008, PP. 1003–1016.

[5] Wu, H.L., Peng, X.F., Gong, P. Ye, Y., "Simulation of refrigerant flow boiling in serpentine tubes", Int. Journal of Heat and Mass Transfer, Vol. 50, 2007, PP. 1186–1195.

[6] Prabhanjan, D. G., Raghavan, G. S. V., "Comparison of heat transfer rates between a straight tube heat exchanger and a helically coiled heat exchanger", International Communications in Heat and Mass Transfer, Vol. 29, Issue 2, February 2002, PP.185-191.

[7] Ito, H., "Frictional factors for turbulent flow in curved pipes", ASME Journal of Basic Engineering, Vol. 81, 1959, PP. 123–134.

[8] Srinivansan, P.S., Nandapurkar, S.S., Holland, F.A., "Pressure drop and heat transfer in coils", The Chem. Eng., Vol. 218, 1968, PP.113–119.

[9] Wongwises, S., and Polsongkram, M., "Evaporation heat transfer and pressure drop of HFC-134a in a helically coiled concentric tube-in-tube heat exchanger", International Journal of Heat and Mass Transfer, Vol. 49, 2006, PP. 658-670.

EXPERIMENTAL INVESTIGATION OF THERMO-AERODYNAMIC CHARACTERISTICS OF FINING FLAT-OVAL TUBE BANKS

Ye. Pysmennyy[1], A. Terekh[1], P. Bagriy[1] and G. Polupan[2]
[1]National Technical University of Ukraine, Kyiv, Ukraine
[2]National Polytechnic Institute of Mexico, Mexico DF, Mexico

ABSTRACT. In this work the experimental results of heat exchange and hydrodynamics researches of flat-oval tubes with plate rectangular fins are presented. Results of comparative tests of the heat exchangers fabricated from flat-oval tubes with plate rectangular fins, from round steel tubes with welding spiral fins, from oval tubes with oval fins and from round bimetallic tubes with spiral aluminium fins are resulted also. It is shown that flat-oval tubes have advantages on heat exchange and hydraulic resistance in comparison with existing types of fining tubes.

Keywords: *flat-oval tube, plate rectangular fins, thermo-aerodynamic efficiency*

The considerable increase in the price of materials and power resources stimulates the research in areas of power and material saving. Important decisions in these areas relate to the design of new type developed convective heat exchange surfaces and the equipment on their base, which is characterized by high heat power efficiency, adaptability to manufacture and by a low manufacture cost. Convective heat exchange surfaces with cross-section-fining tubes are widely used in the power industry as elements of boiler-recuperators for gas turbines, in dry-type cooling towers and in air condensers, in waste heat recuperators of industrial installations, at gas cooling in gas compression stations etc. However, the type of fining tubes actually applied in such devices possesses a number of essential flaws. Those are weak thermal contacts between the fins and tube surfaces, high cost of materials for bimetallic tubes, rather low degree of developed surfaces, the big complexity and process cost for fabrication of steel tubes with spiral fins. These disadvantages limit the wide application of fining tubes. Taking into account the large necessity in heat transfer equipments for the different industries the design of fining tubes with the smaller material consumption and low production cost leads to essential material and power saving.

The complex investigation of heat and mass flows for fining surfaces has been done [1] and the new kind of fining tubs with flat-oval cross-sections and with plate rectangular fins [2] has been designed (Figure 1). The flat-oval tubes have plate rectangular fins on flat lateral sites only. This design allows increasing the thermal-aerodynamic efficiency of fins due to the withdrawal of its sites which are in an aerodynamic shade. At the same time the cheap and high-efficiency technology of contact welding of fines can be applied, providing almost ideal thermal contacts to tube surfaces. Moreover, other advantages deal with high parameters of fin factors and the value of specific surface H_1, which are close to the characteristics of best surfaces with completely fining tubes (ψ = 22, H_1 = 1.8 m^2/m), and with the low fining tube aerodynamic resistance.

* Corresponding author: Prof. G. Polupan
Phone: + (52)-55-57296000 Ext. 54754, Fax: + (52)-55-57296000 Ext. 54783
E-mail address: gpolupan@ipn.mx

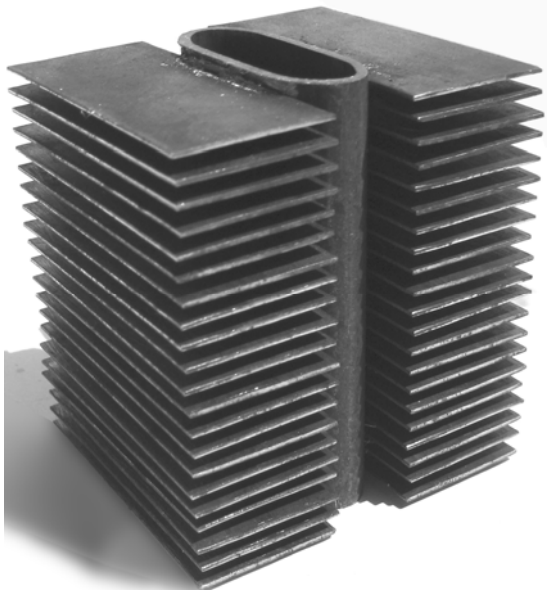

Fig.1. Flat-oval tube with plate rectangular fins.

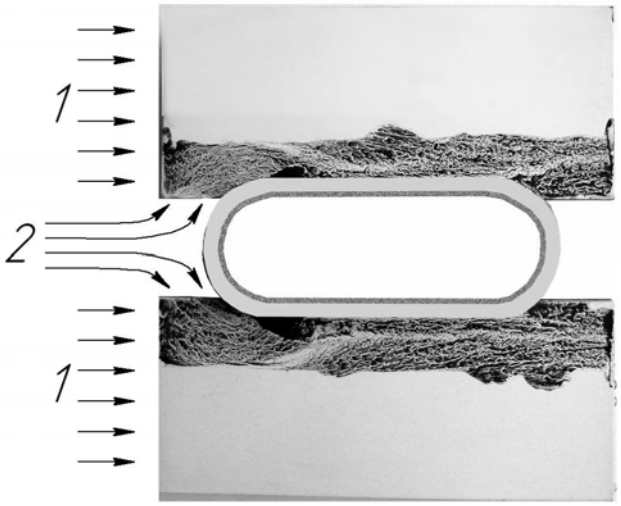

Fig.2. Flow visualization on a surface of fins of a flat-oval tube with plate rectangular fins: 1- a frontal part of stream: 2 - a part of stream getting in inter-fin cavities from the space not occupied by fins at a front part of flat-oval tube.

It is important to notice that due to the design features of flat-oval tubes with plate rectangular fins the turbulisation of stream of external fluid takes place owing to interaction of its components getting in inter costal space from a first line of an fin (Figure 2, a position 1) and from the space not occupied by fins at a front part of a tube (Figure 2, a position 2). Some increase of intensity has been reached in such configuration due to the heat exchange, comparable to effect related to the action of a whirlwind in a front part of completely fining tubes.

The investigation of heat transfer and aerodynamic resistances of tube banks with flat-oval tubes and plate rectangular fins has been carried out with a variation of parameters: i) relative lengths of tube cross-section, $d_2/d_1 = 2.0, \ldots, 2.8$, ii) fin factors, $\psi = 15.2, \ldots, 21.5$ and iii) relations of transversal (S_1) and longitudinal (S_2) steps of tubes in the bank, $S_1/S_2 = 0.99, \ldots, 2.55$ (Figure 3). The comparison of mentioned characteristics for new type of fining tubes has been done with the characteristics of most widespread tube types, such as: steel oval tubes with oval fins coated by zinc, steel round tubes with welding spiral fins and bimetallic tubes (aluminum spiral fins on a steel tube).

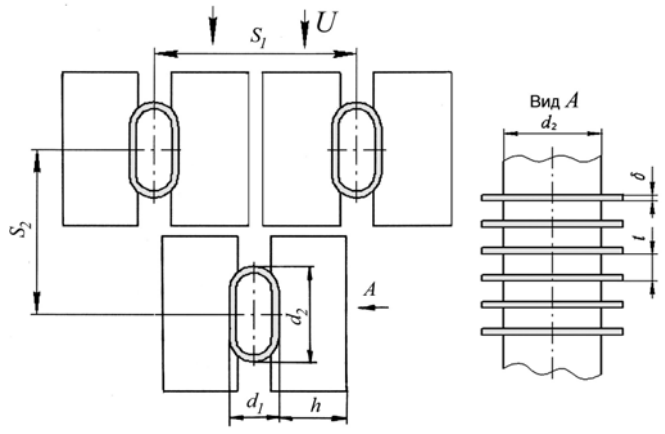

Fig.3. Geometrical characteristics of flat-oval tubes with plate rectangular fins.

The analysis has shown that offered tubes are characterized by the high intensity of convective heat exchange (the same as a round completely fined bimetallic tubes) and by lower aerodynamic resistance than oval tubes with oval fins (Figure 4). These factors allow expecting their high thermo-aerodynamic efficiency, despite the rather low heat conductivity of steel fins in comparison with the aluminum one.

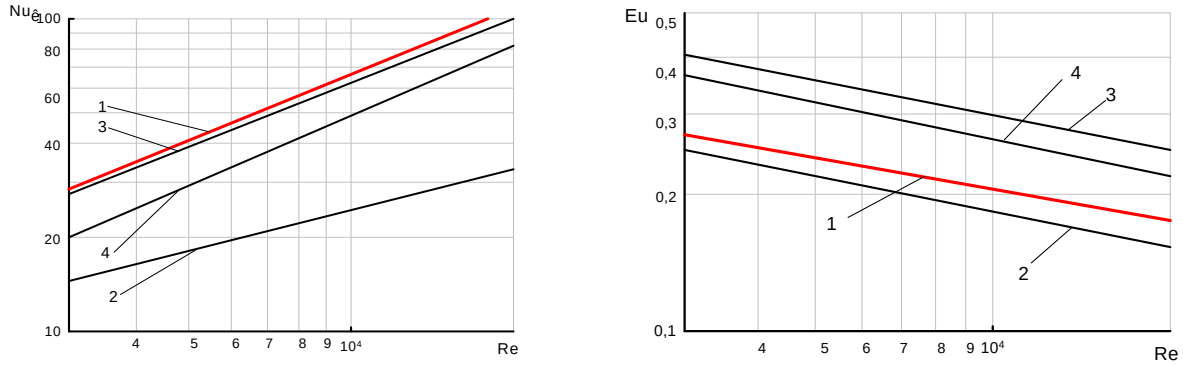

Fig.4. Comparison of the heat transfer intensity (a) and aerodynamic resistance (b) of fining tube banks with flat-oval tubes with plate rectangular fins (1), oval tubes with oval fins coated by zinc (2), round tubes with welding spiral fins (3) and bimetallic tubes with spiral aluminium fins (4).

The comparison of parameters of different air condensers with a capacity of 1280 kW designed on the base of offered tubes and on the tubes specified in Table 1 has been presented as well.

Table1. The comparison of parameters of different air condensers

Variant number		1	2	3	4
Heat surface tube type		Flat-oval tube with plate rectangular fins	Oval tubes with oval fins coated by zinc	Round tubes with welding spiral fins	Bimetallic round tubes with spiral aluminum fins
Transversal tube step, S_1, mm		65	62	65	65
Longitudinal tube step, S_2, mm		60	42	53	60
1	Total length of tubes , L, m	373	865	540	411
2	Thermal capacity removed from 1m of tube, q_1, kW/m	3,43	1,48	2,36	3,11
3	Tube bank aerodynamic resistance, ΔP, Pa	142	138	329	229
4	Compactness factor of heat transfer surface, C, m^2/m^3	393	323	253	421

Results of comparison are presented in Table 1 and in Figure 5. From the analysis follows those former two parameters (L and q_1), almost defining labor input of manufacturing and the cost of heat transfer equipment. Two designs are the best: flat-oval tubes with plate rectangular fins and bimetallic tubes with close to highest possible for pipes of a round profile the degree of surface heat transfer. Taking into account that the high-quality aluminium, (which cost now more than in six-fold exceeds the cost of carbonaceous steel) is necessary for manufacturing of bimetallic tubes, the design from steel flat-oval tubes with plate rectangular fins looks more attractive now concerning the high-efficiency, low-energy-expense and simple technology of their manufacturing. The manufacturing techniques of flat-oval tubes with plate rectangular fins, based on using of simple

contact welding, are integrally connected with an idea of offered design of ridge pipes and completely corresponds to requirements mentioned above.

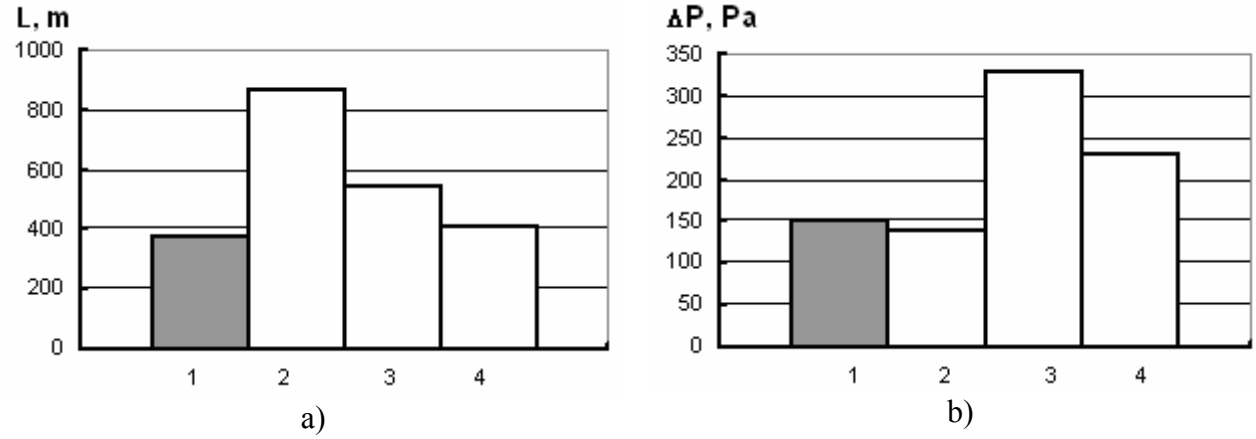

Fig.5. Comparison of total lengths of tubes *L* (a) and aerodynamic resistance *ΔP* (b) for different variants of the air condenser: 1- flat-oval tubes with plate rectangular fins; 2- oval tubes with oval fins; 3 - round steel tubes with welding spiral fins; 4 - bimetallic tubes.

The length of pipes in the cases of # 2 and # 3 in 2.3 and 1.5 times, respectively, exceeds a length of pipes of heat exchanger from flat-oval tubes with plate rectangular fins that considerably reduces competitiveness of corresponding cases of fining tubes in many almost important applications.

The comparison of aerodynamic resistances, actually defining operational expenses, connected with power consumption on a fan drive, and also in the appreciable degree installation expenses caused by necessary capacity of a drive has shown in Figure 5. It is clear that a design of condenser with flat-oval tubes with plate rectangular fins has the same aerodynamic resistance, as a variant of most aerodynamically perfect oval tubes with oval fins. The condensers from bimetallic tubes and from steel pipes with welding spiral fins have in 1.6 and 2.3 times, respectively, higher aerodynamic resistances. It allows to assume that flat-oval tubes with plate rectangular fins will be more preferable: i) in devices for air cooling, and ii) in the design of boiler recuperators of heat of gas turbines, which profitability in a great extent depends on pressure losses in a gas path, and iii) in the design of dry towers with natural draught.

The important characteristic of extended surface (*C*) is its compactness which is estimated as the area of heat transfer surface holding in 1 cubic meter of volume of heat transfer devices. The comparison of these characteristics for different designs has shown that heat transfer surfaces from flat-oval tubes with plate rectangular fins practically do not concede the surfaces from bimetallic pipes, which is characterized by the greatest value of C among developed tubular surfaces. Thus the flat-oval tubes with plate rectangular fins have higher heat power efficiency of surface unit, than in completely fining pipes which surfaces include "badly working" parts located in an aerodynamic shade.

CONCLUSIONS

Thus the offered new type of fining tubes possesses a number of essential advantages in comparison with the pipes used now in the industry. There are:

– an adaptability to manufacture and rather low cost of the manufactures caused by application of technology of contact welding, not demanding the difficult equipment, special materials and the big consumption of energy;

– the higher relative area of heat transfer surfaces, reaching the characteristic for best samples of bimetallic tubes, the use of carbonaceous steels as constructional materials is much cheaper, in comparison with aluminum;

– the high intensity convective heat exchange owing i) to absence of fin parts, working in an aerodynamic shade with low values of local velocities of a stream, and ii) due to turbulization of stream in an inter-fin cavities at the interaction of its components getting there from front and from space not occupied by edges at a front part of the flat-oval tube,

– the ideal thermal contact between fins and flat-oval tubes, caused by the technology of contact welding;

– the low aerodynamic resistance connected with using of flat-oval profile tubes, which provides, in comparison with round tubes of equal cross sections for internal fluids, the considerably smaller area of the block up section;

– the lower thermal resistance in comparison with round tubes at the condensation in tubes of the vapor of technological liquids due to the reduction of condensate film thickness which is localized mainly in the narrow area adjoining to the bottom part of a flat-oval profile.

Presented experimental results have shown the essential advantages of flat-oval tubes with plate rectangular fins. It allows asserting that the heat transfer equipments designed on the base of such tubes will have considerably smaller cost than samples actually used, and will find a wide distribution in various industrial areas.

REFERENCES

1. Pysmennyy, Ye., *Heat exchange and aerodynamic of cross-section-fining tube banks*. Publisher House Altpress, Kyiv, 244 p., 2004.
2. Pysmennyy, Ye., Terekh, O., Rogachov, V., Burley, V., *Heat exchange tube* / Patent for useful model № 25025, Ukraine. 25.07.2007, bul. № 11.

OPPOSING MIXED CONVECTION HEAT TRANSFER IN AN INCLINED FLAT CHANNEL IN A LAMINAR-TURBULENT TRANSITION REGION

R. Poskas*, P. Poskas, G. Drumstas
Lithuanian Energy Institute, Kaunas, Lithuania

ABSTRACT. In this paper we present the results on experimental investigation of the local opposing mixed convection heat transfer in an inclined flat channel (inclination angle $\varphi = 60^o$ from horizontal position) with symmetrical heating in the laminar-turbulent transition region. The experiments were performed in airflow (p = 0.4 MPa) in the range of Re from $1.5 \cdot 10^3$ to $5.3 \cdot 10^4$ and Gr_q up to $1.5 \cdot 10^{10}$ and at the limiting condition $q_{w1} \approx q_{w2} \approx$ const. The experimental data show similar tendencies in the heat transfer as it was revealed in vertical channel, i.e. heat transfer at large x/d_e in vortex flow region ($Re \leq 6 \cdot 10^3$) is more intensive than in case of turbulent flow. But at small x/d_e ($x/d_e \leq 10$) heat transfer variation with Re is different then in case of vertical channel. Analysis revealed also that for the inclination angle $\varphi = 60^o$ there are only minor differences in the local heat transfer for upper (stable density stratification) and bottom (unstable density stratification) walls.

Keywords: *Local heat transfer, opposing mixed convection, inclined flat channel, transition region, experiments*

INTRODUCTION

For modern nuclear and thermal energy technologies, computer, chemistry and other technologies reliability requirements are very important. So, designers of such technologies must have the detailed information about the processes including thermal ones that very often are defining the reliability and operation lifetime of the equipment.

Heat and momentum transfer in single-phase flows in case of complex processes under effect of buoyancy, are still not investigated in details. Due to the importance of the problem for engineering applications a lot of researchers concentrated their attention to the turbulent mixed convection heat transfer investigations in vertical circular tubes. Wide investigations on this problem for turbulent flow in the vertical and horizontal channels were performed at the High Temperature Institute in Moscow [1], at the Manchester University [2, 3] and at the Lithuanian Energy Institute [4 - 6]. At the Lithuanian energy institute also investigations of the turbulent mixed convection in the inclined flat channels with one side heating (under effect of stable and unstable air density stratification) have been performed [7 - 9]. It was revealed that heat transfer is closely related to the channel inclination angle in case of the stable density stratification but heat transfer practically does not depend on the channel inclination angle in case of the unstable air density stratification.

Investigations of heat transfer in the laminar-turbulent transition region under the effect of buoyancy are rather limited. The flow character in pipes in a laminar-turbulent transition region was investigated in [1, 10 - 12]. In paper [13] the results on numerical investigation of the local

* Corresponding author: Dr. R. Poskas
Phone: + (370)-37-401893, Fax: + (370)-37-351271
E-mail address: rposkas@mail.lei.lt

opposing mixed convection heat transfer in a vertical flat channel with symmetrical heating for laminar and vortex airflow (at p = 0.1; 0.2 and 0.4 MPa and Re numbers from 1500 up to 4310, with Gr_q number variation from $1.65 \cdot 10^5$ to $3.1 \cdot 10^9$) were presented. The new correlations were suggested for determination of the non-dimensional distance at which the flow stability is lost in the flat channel with opposing flows. In other paper [14] the detailed results on experimental and numerical investigation of the local opposing mixed convection heat transfer in a vertical flat channel with symmetrical heating ($q_{w1} \approx q_{w2} \approx$ const) in the laminar-turbulent transition region were presented. It was shown that as the influence of the buoyancy becomes stronger the circulating flows appear along the channel. These flows cause asymmetry of velocity profiles and increase in heat transfer up to $Re \approx 8 \cdot 10^3$, when p = 0.4 MPa. The experiments were performed in airflow of different pressures (0.1, 0.2 and 0.4 MPa) in the range of Re from $2 \cdot 10^3$ to $5 \cdot 10^4$ and Gr_q up to $1.5 \cdot 10^{10}$. In the newest paper [15] originated from Lithuanian Energy Institute the results on experimental investigations of the local opposing mixed convection heat transfer in the same vertical flat channel with symmetrical heating in the laminar-turbulent transition region at higher air pressures (0.7, 0.8 and 1.0 MPa) when buoyancy effect is prevailing in the range of Re from $2 \cdot 10^3$ to $4 \cdot 10^4$, and Gr_q up to $1.0 \cdot 10^{11}$ was presented. The experimental data show similar tendencies in the heat transfer at higher air pressures (0.7 – 1.0 MPa) as it was revealed at smaller air pressures (0.2 – 0.4 MPa). But at higher air pressures the transition from the vortical flow regime to the turbulent one does not causes such drastic decrease in heat transfer as it was noticed at smaller air pressures (for p = 0.2 MPa at Re ≈ 4000, for p = 0.4 MPa at Re ≈ 8000). The recent review of the mixed convection in the channels including transition region was presented in [16].

In this paper the results on experimental investigations of the local opposing mixed convection heat transfer in the laminar-turbulent transition region in the same flat channel but with inclination angle $\varphi = 60^o$ from horizontal position is presented. Experiments were performed at air pressure p = 0.4 MPa with symmetrical heating in the range of Re from $1.5 \cdot 10^3$ to $5.3 \cdot 10^4$, and Gr_q up to $1.5 \cdot 10^{10}$.

METHODOLOGY

The same aerodynamic setup was used for the experiments in the transition region in an inclined position as it was used for the experiments in the turbulent region in a vertical or inclined positions [6, 9] and in the transition region in a vertical position [14]. As it was already indicated the experiments are performed at air pressure p = 0.4 MPa. So, the air under a pressure of 0.4 MPa comes from compressors to the group of receivers. Here it loses some moisture. Then it passes one of the three parallel lines with paired flow metering orifices having different flow cross sections and flows into test section. Then the air is released into the atmosphere via bypass valves. The air pressure and flow rates are controlled by bypass valves. A direct electric current generator was used for heating the elements of the experimental section. The current strength was regulated by varying the voltage, applied to an excitation winding of the generator, and determined from the voltage drop on shunts of accuracy class 0.5. The high stability of the generated voltage, which also means the stability of the supplied heating power, was attained by a special electronic control device with feedback of the voltage drop at the test section.

The thermocouples were used for measuring the wall temperature and the voltage drop along the channel. All electric signals from thermocouples and voltage drops along the calorimetric surface and shunt were recorded automatically by a computer-based data acquisition system and processed on line.

A special test section (Fig. 1) for the studies of heat transfer for mixed convection in a flat channel was constructed at the Lithuanian Energy Institute. The flat channel has a height-to-width ratio of about 1 : 10 (40.8 : 400 mm) and it is 6260 mm long. The channel consists of a fluid-dynamic

stabilizer and a calorimeter. The stabilizer is 2370 mm long. Its height and width are the same as that of the calorimeter. The entrance to the channel is fitted with a well-designed smooth intake with an array of laminarizing grids. The calorimeter is 3890 mm ($x/d_e \approx 50$) long. The test section contains two central and two lateral duraluminium plates. The internal side of this duraluminium rig is insulated by 120 mm thick asbestos strips on the central plates and by 60 mm thick asbestos-cement strips on the lateral plates. The calorimetric heated surfaces of the two central plates are made of stainless steel foil 0.38 mm thick and 370 mm wide, fixed at the inlet to the brass contacts.

In order to achieve higher values of Gr_q and higher effects of buoyancy pressurized air up to 1.0 MPa was used. For this purpose the whole test section had to be placed in a pressure vessel of an 870 mm diameter and 7200 mm long. The vessel consists of two halves fixed together by flanges.

The temperature of the calorimeter test-surface (heated foil) was measured by 25 chromel-alumel thermocouples of a 0.3 mm diameter wire, which are fixed to the outer surface of the test foil. Longitudinal voltage drop on this heated foil was measured by the same thermocouples. Thermocouples also measured the temperatures in the insulation layers, which were used to define the losses.

The above construction enables experiments on heat transfer in a flat channel for different pressures of the heat carrier (air). The air was supplied through the top of the channel, so the experiments were accomplished on downward flow with two-side heating of the channel. All experiments were performed at the limiting condition $q_{w1} \approx q_{w2} \approx$ const. The maximum surface temperature was at the rage of 540 K, and the minimum temperature difference between surface temperature and flow bulk temperature was at least 47 K. The air pressure was measured using manometers. Well-type differential manometers filled with distilled water measured the pressure drops across the orifices. Electric signals from thermocouples and pressure probes as well as voltage drops on the calorimetrically measured surface and shunt were all recorded automatically by a computer-based data acquisition system, and processed on line. More detailed description of the test section and methodology of investigations is presented in [7].

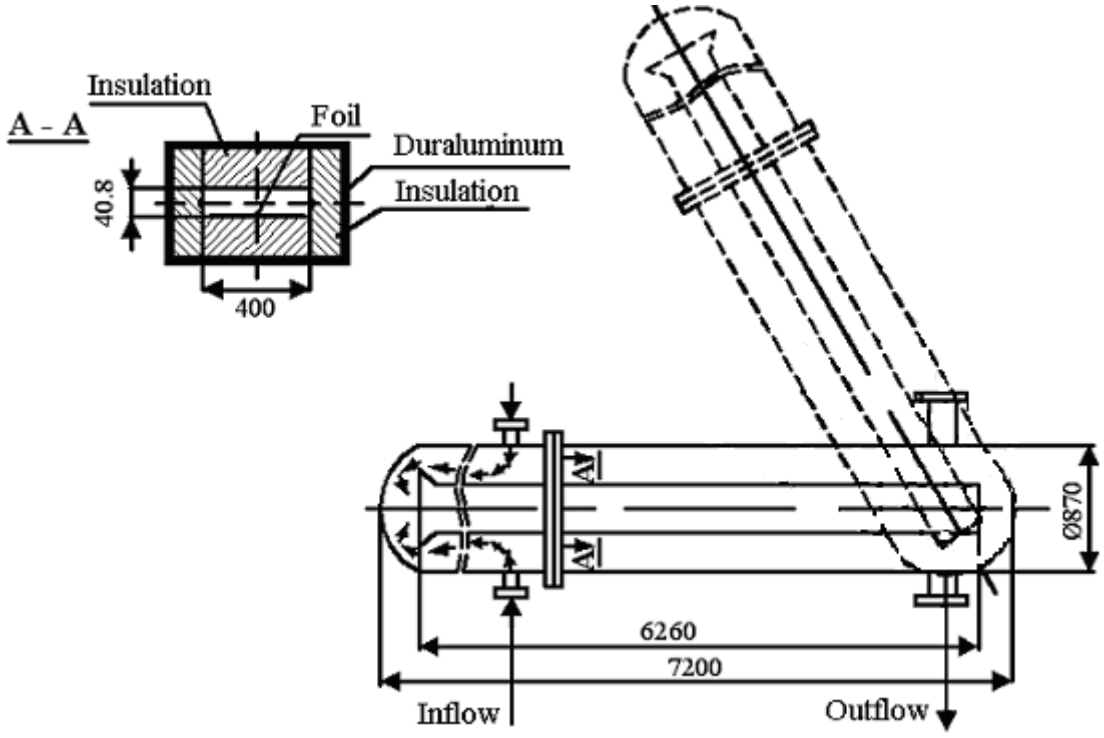

Figure 1. Test section geometry (not to scale)

In the primary interpretation of the data, the values of Nu, Re, Gr_q and Pr were evaluated. Local bulk flow velocity, temperature and equivalent diameter of the channel were used as reference values. Experimental uncertainties were as follows: Re – 3.2-3.4 %, Nu – 3.9-4.1 %, Gr_q – 5.6-5.8 %. The methodology presented in [17] was applied for the evaluation of uncertainties.

RESULTS AND THEIR ANALYSIS

Variation of heat transfer with Re number in stabilized region (x/d_e = 42) of the calorimeter is presented in Fig. 2. From the data obtained for the air pressure p = 0.4 MPa, it is clear that Nu for small Re numbers are higher than the forced turbulent convection heat transfer, but when the Re reaches Re ≈ $6 \cdot 10^3$, a sharp decrease of heat transfer is observed. This phenomenon indicates that in the narrow region of Re = $(6 - 8) \cdot 10^3$, the character of the flow inside the channel changes drastically from the vortex to non-vortex flow. For Re numbers higher then Re = $8 \cdot 10^3$ forced convection heat transfer is prevailing. This is different from the one side heating cases where even for the turbulent region for the same channel geometry (the same channel) and heating loads well expressed mixed convection was identified [7, 8]. It is necessary to notice also that in the region of Re = $8 \cdot 10^3 – 1.5 \cdot 10^4$ heat transfer is les intensive then forced convection one. It is possible that this decrease in heat transfer is caused by the deformation of the velocity profile due to the buoyancy effect, i.e. decrease of the velocity gradient at the wall like in case of the laminar mixed convection with opposing flows.

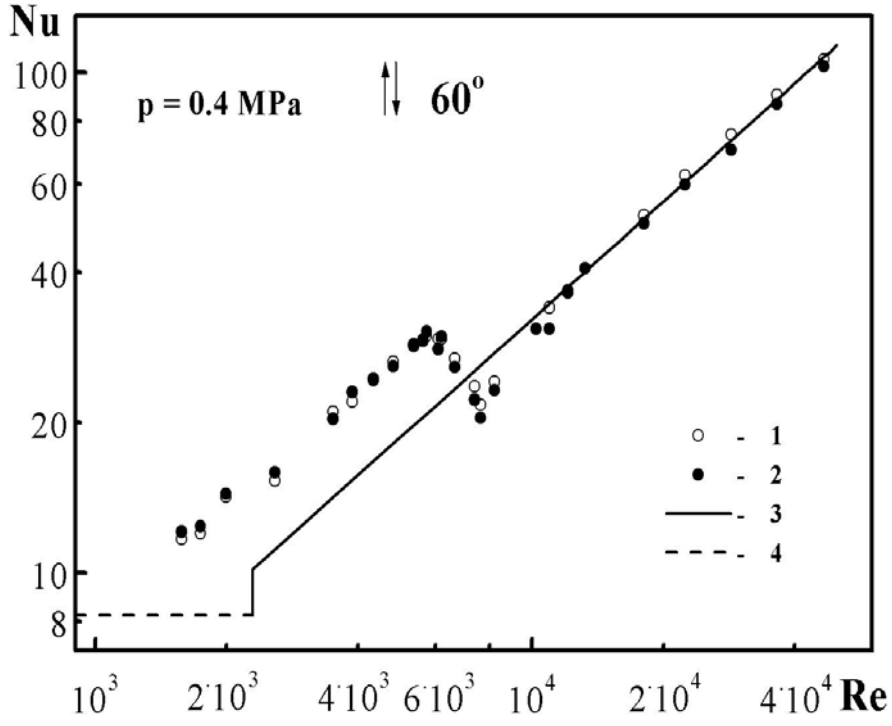

Figure 2. Heat transfer variation with Re (x/d_e = 42). 1 – upper wall, 2 – bottom wall, 3 – turbulent forced convection [1], 4 – laminar forced convection [18]

Heat transfer variation with Re number at p = 0.4 MPa and different x/d_e is presented in Fig. 3. We can notice sharp changes in heat transfer intensity at Re = 5000 – 8000 for larger x/d_e (x/d_e = 22.3 – 42) as we discussed above. It is interesting to notice that in the region close to Re = 4000 heat transfer rate practically does not depend on x/d_e (Fig. 3a). But with small increase in Re, changes in

heat transfer intensity for smaller x/d_e (x/d_e = 3.9 – 10.1) are not in line with the tendency defined for higher x/d_e. There is rather sharp increase in heat transfer at Re ≈ 5000 so different flow structure can be expected at the beginning of the heating section at Re = 5000 – 8000. For the smallest investigated Re numbers it is clear dependence of heat transfer rate on x/d_e. For x/d_e = 42 we have vortex flow regime at Re = 2000 – 6000 and it survives till Re = 6000 – 8000. The length of the vortex region is decreasing with decreasing of x/d_e, and for small x/d_e (x/d_e = 3.9 – 10.1) there is a region where Nu is not dependent on Re (Re = 2000 – 4000). But at Re = 4000 intensity of heat transfer is increasing rather sharply. In the vertical channel in this Re region (Re = 2000 – 4000) heat transfer is dependent on Re for all x/d_e as it is indicated in Fig. 3 by short dashed line.

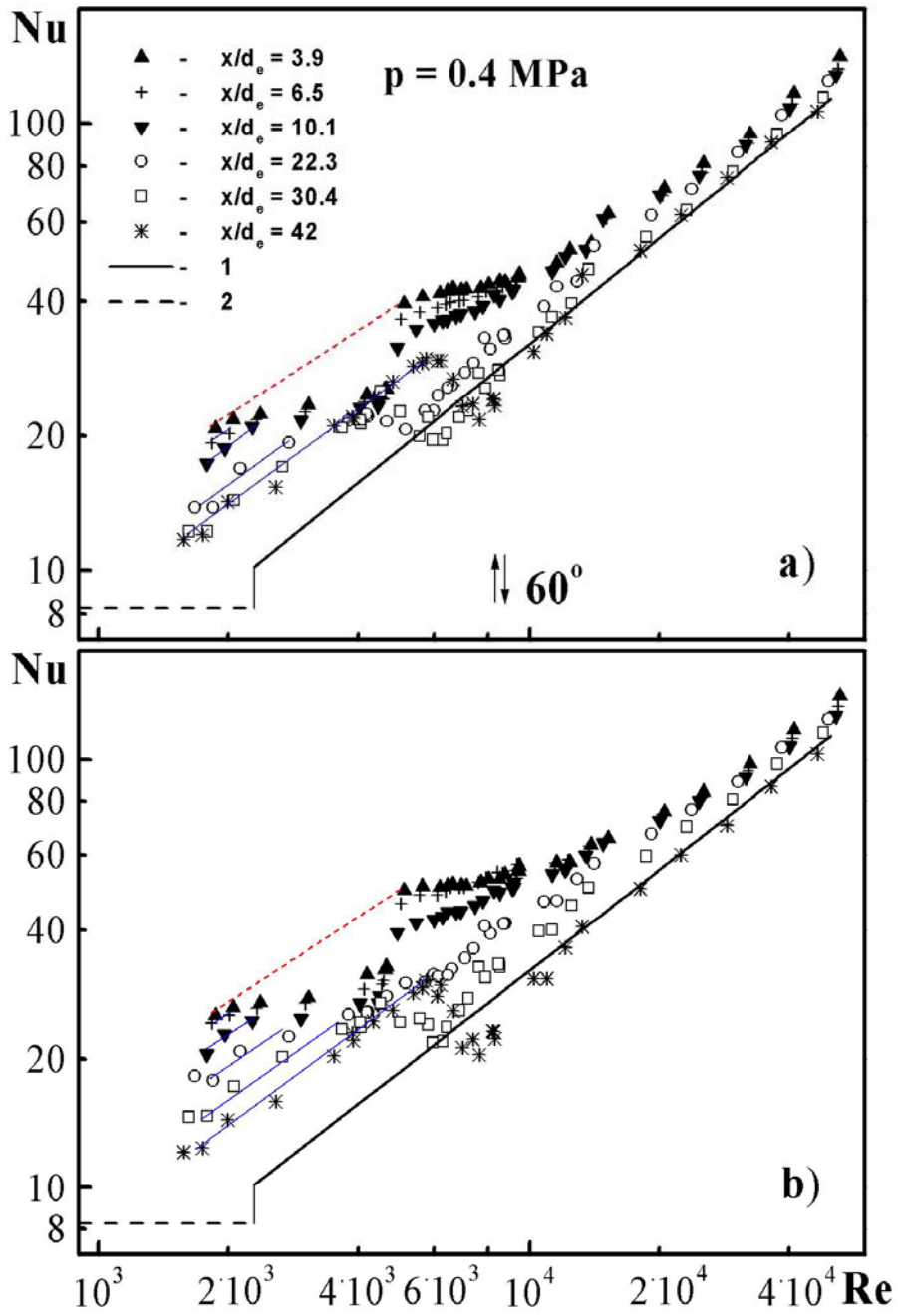

Figure 3. The dependence of the mixed convection heat transfer on Re for different x/d_e. a) – upper wall, b) – bottom wall, 1 – turbulent forced convection [1], 2 – laminar forced convection [18]

Analyzing the heat transfer from the bottom wall (unstable density stratification) (Fig. 3b) we can notice similar tendencies in heat transfer variation but intensity of heat transfer at smaller x/d_e is a little bit higher then for upper wall (stable density stratification). Also, for $x/d_e = 22.3$ at Re = 4000 there is no more heat decrease as it can be noticed for upper wall (Fig. 3a). At small Re (Re = 2000 – 4000) there is also decrease of heat transfer in comparison with vertical channel (short dashed line) as it was indicated for upper wall.

Analysis of the wall temperature variation along the channel for different regimes can provide some additional information to explain heat transfer processes. Fig. 4 presents the results on upper (Fig. 4a) and bottom wall (Fig. 4b) temperature variation along the channel for different regimes at air pressure p = 0.4 MPa. As it is seen from Fig. 4a, for high Re number (Re = 9548–8218) we have forced convection heat transfer and here there is a regime with monotonous variation of the wall temperature along the channel. At smaller Re numbers (Re = 7860–6654 – 5241–4334) we have local temperature maxima at certain x/d_e (for Re = 7860–6654 at $x/d_e \approx 35$, for Re = 6789–5745 at $x/d_e \approx 30$, for Re = 5241–4334 at $x/d_e \approx 25$), and after this maxima there is significant decrease of the wall temperature due to flow separation from the wall and intensification of the heat transfer. But the temperature distributions do not show any drastic temperature changes at the beginning of the channel (at small x/d_e).

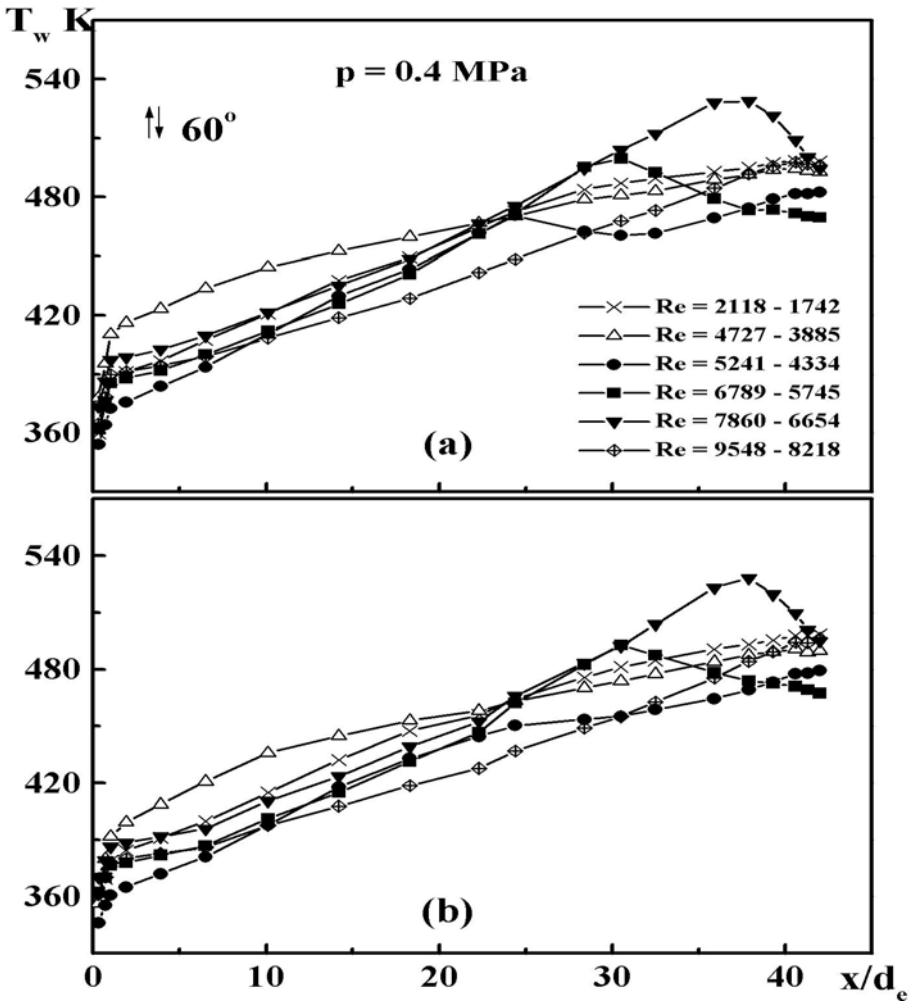

Figure 4. Longitudinal variations of wall temperature for different Re. a) – upper wall, b) – bottom wall. The higher value of Re is at the beginning of the heating and the smaller one is at the end ($x/d_e = 42$) of the channel

There are similar tendencies in temperature variation along the channel for the bottom wall (Fig. 4b). Most significant difference is for the regime with Re = 5241–4334. For the upper wall there is well expressed maximum of the temperature at $x/d_e = 25$, but for the bottom wall a change in temperature variation at $x/d_e = 25$ is observed, but not local temperature maximum.

NOMENCLATURE

d_e	equivalent diameter of the channel (m)	Re	Reynolds number, $Re = ud_e/\nu$
Gr_q	Grashof number defined by the heat flux specified on the surface, $Gr_q = g\cdot\beta\cdot d_e^4\cdot q_w/\nu^2\cdot\lambda$	x	axial coordinate measured from start of heating (m)
		w	at the wall
Nu	Nusselt number ($Nu = \alpha d_e/\lambda$)	in	at the inlet
q	heat flux density (W/m^2)	1,2	first and second wall

CONCLUSIONS

After analysis of the experimental results on local heat transfer for opposing mixed convection flows in an inclined flat channel ($\varphi = 60^o$) with symmetrical heating in the laminar-turbulent transition region the following conclusions can be made:

1. The analysis of the results revealed that depending on the effect of buoyancy different flow modes could be noticed along the channel. For the air pressure of 0.4 MPa at large x/d_e vortex flow regime with intensive heat transfer exists for $Re < 6000$.
2. Heat transfer at small x/d_e practically is not dependent on Re in the region 2000 – 4000 but it is increasing sharply at Re = 4000 – 5000. Such heat transfer variation is characteristic for upper (stable density stratification) and bottom (unstable density stratification) walls, and is different from heat transfer in vertical channels.
3. Analysis revealed that for the inclination angle $\varphi = 60^o$ there are only minor differences in the local heat transfer for upper (stable density stratification) and bottom (unstable density stratification) walls.
4. Further investigations are necessary at smaller inclination angles of the channel to reveal the effect of stable and unstable density stratification on the mixed convection in the transition region.

REFERENCES

1. Petukhov, B. S., Polyakov, A. F. and Strigin, B. K., *Heat Transfer Investigations in Tubes Under Viscous-Gravitational Flow*, Energija, Moscow, Vol. 1, 1968.
2. Jackson, J. D., Cotton, M. A. and Axell, B. P., Studies of Mixed Convection in Vertical Tubes. Review, *Int. J. Heat Fluid Flow*, Vol. 10, No. 1, pp. 2-15, 1988.
3. Jackson, J. D., Influences of Buoyancy on Velocity, Turbulence and Heat Transfer in Ascending and Descending Flows in Vertical Passages, *Proceedings of 4th Baltic Heat Transfer Conference*. *Advances in Heat Transfer Engineering*, Kaunas, Lithuania, August 25-27, 2003, pp. 57-78.
4. Vilemas, J., Poskas, P. and Kaupas, V., Local Heat Transfer in a Vertical Gas-Cooled Tube with Turbulent Mixed Convection and Different Heat Fluxes, *Int. J. Heat Mass Transfer*, Vol. 35, No. 10, pp. 2421-2428, 1992.
5. Vilemas J. and Poskas P., *Effect of body forces on turbulent heat transfer in channels*, LEI-Bigell House, Kaunas-New York, 1999.

6. Poskas, P. and Poskas, R., Turbulent Opposing Mixed Convection Heat Transfer in a Vertical Flat Channel with One Side Heating, *Int. J. Heat Transfer Engineering*, Vol. 25, No. 2, pp. 17-23, 2004.
7. Poskas, P. and Poskas, R., Local Turbulent Opposing Mixed Convection Heat Transfer in Inclined Flat Channel for Stably Stratified Airflow, *Int. J. Heat and Mass Transfer*, Vol. 46, No. 21, pp. 4023-4032, 2003.
8. Poskas, P., Poskas, R. and Sabanskis, D., Local Turbulent Opposing Mixed Convection Heat Transfer in Inclined Flat Channel for Unstably Stratified Airflow, *Int. J. Heat and Mass Transfer*, Vol. 48, No. 5, pp. 956-964, 2005.
9. Poskas, P., Poskas, R. and Sabanskis, D., Comparison of the Turbulent Opposing Mixed Convection Heat Transfer in Inclined Flat Channel for Stably and Unstably Stratified Airflows, *Proceedings of 6th World Conference Experimental Heat Transfer, Fluid Mechanics, and Thermodynamics*, Matsushima, Miyagi, Japan, April 17-21, 2005 (Published on CD-ROM).
10. Scheele, G. F., Rosen, E. M. and Hanratty, T. J., Effects of Natural Convection on Transition to Turbulence in Vertical Pipes, *Can. J. Chem. Eng*, Vol. 38, pp. 67-73, 1960.
11. Scheele, G. F. and Hanratty, T. J., Effects of Natural Convection Instabilities on Rates of Heat Transfer at Low Reynolds Numbers, *AIChE J*., Vol. 9, No. 2, pp. 183-185, 1963.
12. Petukhov, B. S., Polyakov, A. F. and Strigin, B. K., *Heat Transfer Investigations in Tubes Under Viscous-Gravitational Flow*, Energija, Moscow, Vol. 1, 1968.
13. Poskas, P., Poskas, R. and Sirvydas, A., Modelling of the Opposing Mixed Convection Heat Transfer in a Vertical Flat Channel in the Regions of a Laminar and Vortex Flow, *Proceedings of 4th. Int. Heat Transfer Conference, Fluid Mechanics and Thermodynamics*, Cairo, Egypt, September 19-22, 2005 (Published on CD-ROM).
14. Poskas, P., Poskas, R. and Sirvydas, A., Opposing Mixed Convection Heat Transfer in the Vertical Flat Channel in a Laminar-Turbulent Transition Region, *Proceedings of 13th. Int. Heat Transfer Conference*, Sydney, Australia, August 13-18, 2006 (Published on CD-ROM).
15. Poskas, R., Poskas, P. and Sirvydas, A., Opposing Mixed Convection Heat Transfer in the Vertical Flat Channel in a Laminar-Turbulent Transition Region Under Prevailing Effect of Buoyancy, *Proceedings of 5th European Thermal-Sciences Conference*, Eindhoven, the Netherlands, May 18-22, 2008 (Published on CD-ROM).
16. Poskas, P. and Poskas, R., Mixed Convection in the Channel Flows, *Heat Transfer Research*, Vol. 40, No. 1, pp. 31-56, 2009.
17. Schenck, H., *Theories of Engineering Experimentation*, Mir, Moscow, 1972.
18. Petukhov, B. S., *Heat Transfer and Friction in Tubes for Laminar Flow*, Energija, Moscow, 1967.

EXPERIMENTAL INVESTIGATION OF PULSATING HEAT PIPES AND A PROPOSED CORRELATION

Sajad Arabnejad[1], Hamed Jamshidi, M. B. Shafii*, Y. Saboohi
[1]Mechanical Engineering Department, Sharif University of Technology, Tehran, Iran

ABSTRACT. Pulsating heat pipes (PHPs) are complex heat transfer devices, and their optimum thermal performance is largely dependent on different parameters. In this paper, in order to investigate these parameters, first a Closed Loop Pulsating Heat Pipe (CLPHP) was designed and manufactured. The CLPHP was made of copper tubes with internal diameters of 1.8 mm. The length of the evaporator, adiabatic, and condenser sections were 60, 150, and 60 mm, respectively. Afterwards, the effect of various parameters, including the working fluid (water and ethanol), the volumetric filling ratio (30%, 40%, 50%, 70%, 80%), and the input heat power (5 to 70 watts), on the thermal performance of the CLPHP were investigated experimentally. The results showed that the manufactured CLPHP has the best thermal performance for water and ethanol as working fluids when the corresponding filling ratios are 40% and 50%, respectively. Finally, with the available experimental data set of CLPHPs, a power-law correlation based on dimensionless groups was established to predict their input heat flux. Compared with the experimental data, the root-mean-square deviation of the correlation prediction was 19.7% and in addition, 88.6% of the deviations were within ±30%.

Keywords: *Closed Loop Pulsating Heat Pipe, Experimental, Correlation, Modeling*

INTRODUCTION

With the advances in packaging technology, thermal management of electronic components gained new impetus. Novel cooling strategies are required for successful thermal management. Pulsating heat pipes (PHPs) are relatively new innovations in this direction, which have been recently investigated by many engineers and scientists around the world. PHP was introduced by Akachi in the 1990s [1]. Pulsating heat pipes are different from conventional heat pipes in design and working principle. It is made from a long continuous capillary tube bent into many turns, with the evaporator and condenser sections located at these turns. Moreover, an optional adiabatic zone in between may exist (Figure 1). There is no wick structure used in PHPs, so its simple and cheap structure has made PHPs very attractive compared with conventional heat pipes. The diameter of a PHP should be small enough (0.1–5mm) so that vapor plugs can be formed by capillary action. Since the surface tension force is dominant over the gravitation force, the working fluid will be put in slug-plug order in the PHP (Figure 1). These slugs and plugs are randomly distributed in the PHP after it is partially filled with working fluid (Xu et al [2]). The input heat flux, which is the driving force, increases the pressure of vapor plugs in the evaporator, and the heat output decreases the pressure of vapor plugs in the condenser. This pressure difference between the evaporator and condenser results in the oscillation of vapor plugs and liquid slugs in the PHP. Therefore, heat is transported from the evaporator to the condenser region by means of local axial movements of the working fluid (sensible heat) and phase changes (latent heat). Due to the continuous heating of bubbles formed by

* Corresponding author: Prof. M.B. Shafii
Phone: + (98)-21-66165675, Fax: + (98)-21-6000021
E-mail address: Behshad@sharif.edu

nucleate boiling, there will not be steady-state vapor pressure equilibrium for an operating PHP. Therefore, this type of heat pipe is essentially a non-equilibrium heat transfer device.

There are two types of PHPs: (i) open loop PHP (OLPHP), (ii) closed loop PHP (CLPHP). In the CLPHP the two ends of the tube are connected to one another and the working fluid is able to circulate, which enhances the capability of the working fluid in transporting heat from the evaporator region to the condenser region. Unlike the CLPHP, the two ends are sealed in the OLPHP. Compared with the CLPHP, the only advantage of the OLPHP is its cheaper and simpler structure.

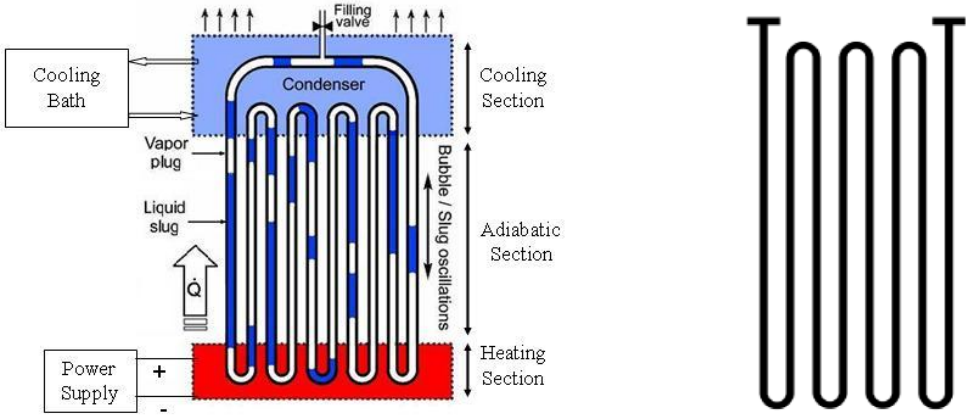

a) CLPHP b) OLPHP

Figure 1. Schematic of Pulsating Heat Pipes.

There are many parameters which affect the PHP operation. These can be summarized as the tube diameter, input heat flux, number of turns, filling ratio (γ), inclination angle, and thermo-physical properties of the working fluid. The filling ratio is defined as the net liquid volume charged into the PHP divided by the total internal volume of the PHP.

Many researchers have investigated these parameters experimentally and analytically [2-11]. Among these researchers, Khandekar et al [3-5,7-8] have done the most comprehensive research on the thermal performance of PHPs. Khandekar et al [3] experimentally investigated the effects of different working fluids (water, ethanol, R-123), input heat flux, and filling ratio (range of 0%-100%) on the thermal performance of a CLPHP. Their experimental set-up was formed from a copper tube (ID 2.0 mm, OD 3.0 mm) with 5 turns in the evaporator section. In their experimental studies, valuable information related to the fundamental characteristics and operational regimes of CLPHPs were obtained. They concluded that for the given input heat flux range, a better performing and self-sustained thermally driven pulsating action of the device is only observed in the filling ratio range of 25–65% depending on the working fluid. Above this range of filling ratio, due to the lack of vapor plugs, the overall degree of freedom and the pumping action of bubbles is insufficient for generating pulsations inside the tubes. Therefore, the thermal performance of CLPHPs would not be suitable. Below a certain range of filling ratio, the probability of partial dry-out of the evaporator and reaching the critical state exists, which causes the evaporator temperature to increase and the thermal performance of CLPHPs to decrease.

Khandekar [4, 5] performed an experimental study on two CLPHPs having 20 turns of copper tubes with inner diameters of 2.0 and 1.0 mm, respectively. The working fluids were water, ethanol, and R-123 with filling ratios of 30%, 50% and 70%. The effect of the inclination angle was also investigated. The results showed that a combination of a large number of turns and a high input heat flux ensures continuous CLPHP operation in any inclination angle. Furthermore, they found that the CLPHPs with 50% filling ratio showed a better thermal performance and a higher performance

limit, while the CLPHPs with 30% and 70% filling ratios experienced a dry-out of the evaporator and reached the critical state at lower thermal performances.

Katpradit et al [6] experimentally studied the heat transfer characteristics of some OLPHPs at the critical state. A set of 27 copper-tube OLPHPs with internal diameters of 2.03, 1.06 and 0.66 mm, consisting of 5, 10 and 15 meandering turns and section lengths of 50, 100 and 150 mm was used in their study. Each OLPHP had a condenser, adiabatic and evaporator section of equal length. The working fluids used were R123, ethanol, and water with a filling ratio of 50% of the total volume of the tube. The results showed that the critical heat flux increases with an increase in the latent heat of vaporization of the working fluid. They also presented two correlations based on dimensionless groups to predict the critical heat flux of the OLPHPs. The correlations were only valid with a filling ratio of 50%. Compared with the experimental data, the standard deviation of the correlation prediction was 29%.

Due to the complicated behavior of PHPs, the published analytical models are very limited in scope and applicability. Therefore, semi-empirical correlations based on dimensionless groups, and an artificial neural network technique could be offered for the modeling of PHPs as a complex system [7, 8]. Therefore, in this study, first a CLPHP was designed and manufactured. Then, the effect of the most important parameters, including the working fluid (water and ethanol), volumetric filling ratio (30%, 40%, 50%, 70%, 80%), and input heat power (5 to 70 watts), on the thermal performance of the CLPHP were investigated experimentally. Finally, with available experimental data sets of the CLPHPs, a correlation based on dimensionless groups was established to predict the input heat flux of CLPHPs.

EXPERIMENTAL SETUP

A schematic diagram of the device used during the experimental tests is shown in Figure 1. A pulsating heat pipe configured as a CLPHP was built using a capillary copper tube with a 3.0 mm OD, 1.8 mm ID, and approximately 4m length to form 10 parallel channels with 9 curves (Figure 2). Therefore, the experimental set-up is a CLPHP with 5 meandering turns. The CLPHP consisted of three regions: a heating section (evaporator), adiabatic section, and cooling section (condenser) with a height of 60 mm, 150 mm, and 60 mm respectively; the whole width of the system was about 250mm. During the tests, the evaporator section was always below the cooling section. The cooling section contains a water-filled tank with an inlet and an outlet for circulating the constant temperature water of cooling bath. The cooling water was always maintained at about 20°C and it flows through the inlet of the water tank, around U-shape bends in the condenser zone. The mass flow rate of the cooling water always ensured that isothermal conditions existed in the condenser.
The evaporator section was in thermal contact with an electrical element, a Ni-Cr heating wire, twisted around U-shape bends on the outer surface and attached to a power supply to deliver a desired heat load (Figure 2). The total electrical resistance of the heater was 45.5Ω at 25°C. The heating power was provided by a precisely designed power supply unit. The input power and consequently the input heat flux were controlled with a rheostat by controlling the heater voltage. Both the evaporator and adiabatic sections were thermally insulated in order to make sure that there is no heat loss in these sections.

Ten Chromel–Alumel (Omaga, K type, accuracy ±0.5^{o}C) thermocouples were applied to measure the system's temperature during the tests. Five thermocouples were placed in each turn of the evaporator section to measure the average evaporator temperature. Three thermocouples were placed at adiabatic zone, and the other two thermocouples measured the inlet and outlet flow temperatures of the cooling section. All these thermocouples were connected to a PC via the data logger, so that the temperatures could be recorded and saved in a spreadsheet on the PC.

Before introducing the CLPHP with any working fluid, the fluid was heated and the CLPHP was placed under vacuum in order to empty the non-condensable gases from the fluid and the CLPHP. The reason for this is that these gases decrease the thermal performance of PHPs [2]. In addition, the minimum purity of all working fluids was about 99.5%.

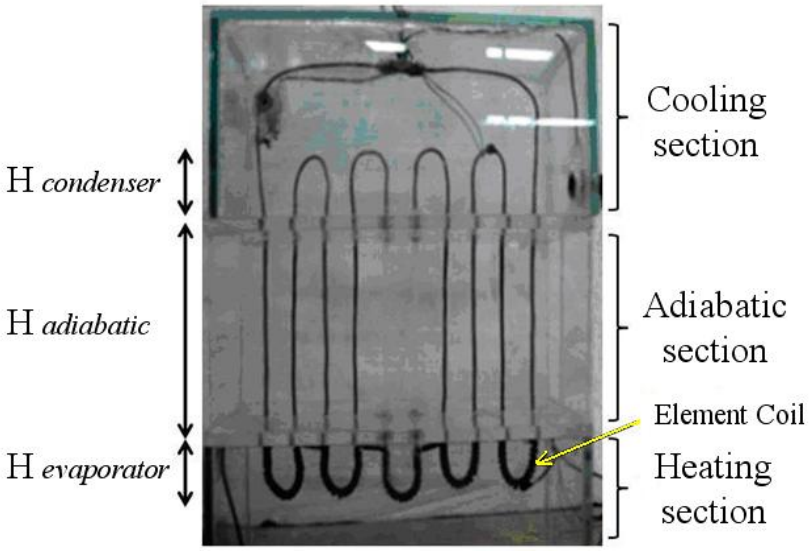

Figure 2. The Manufactured CLPHP

A vacuum and charging system, particularly designed and manufactured in our laboratory, was used to vacuum the CLPHP and to introduce a controlled amount of liquid into the CLPHP tube. This system was also used to empty the undesirable gases from the working fluid.

PROCEDURES AND RESULTS

In the present experiment, two working fluids were employed, which were water and ethanol. Tests were conducted for filling ratios of 30%, 40%, 50%, 70%, 80% for water and 30%, 40%, 50%, 70% for ethanol. The input heat power was in the range of 0 to 70 watts. This input heat power was increased by 5 watts in each step.

In the beginning of the experiment, the CLPHP was partially filled by working fluid. Then, the input heat power was stepwise increased. As a result, the heat flux raises the temperature and pressure in the evaporator region. Therefore, the slugs and plugs moved within the pipe and transferred heat from the evaporator to the condenser. For different input heat fluxes, working fluids, and filling ratios, the average temperature difference between the evaporator and condenser were recorded when the evaporator temperature reached a steady state condition. The experimental results are graphically depicted for ethanol and water in Figures 3 and 4.

It can be seen from Figures 3 and 4 that that the average evaporator temperature increases with increasing input heat flux. Furthermore, it can be concluded from these figures that the CLPHP has different thermal performance at different filling ratios. Figure 3 shows that the manufactured CLPHP has the best thermal performance for water as the working fluid when the filling ratio is 40%. The reason is that in this filling ratio, the CLPHP has the capability to transfer the maximum heat flux with a minimum temperature difference between the evaporator and condenser. When filled with ethanol, the CLPHP has the best thermal performance at a filling ratio of 50% (Figure 4).

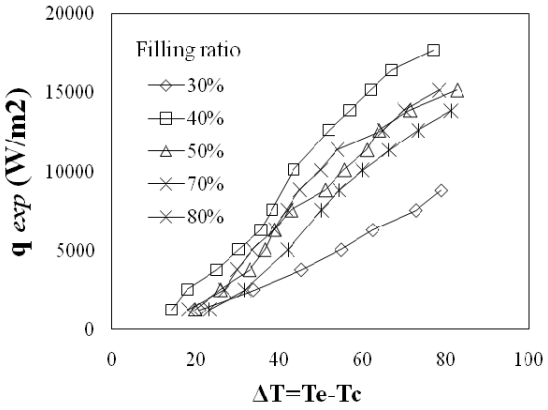

Figure 3: Experimental results for water as the working fluid

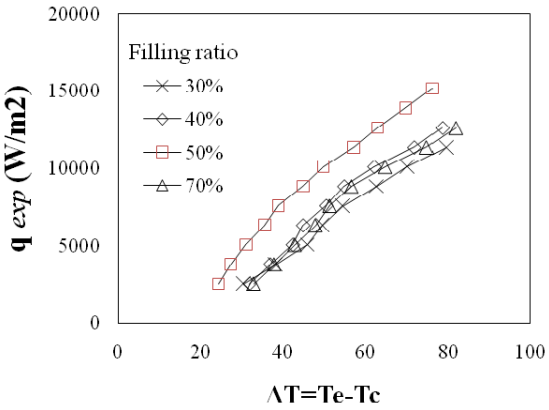

Figure 4: Experimental results for ethanol as the working fluid

Fig. 5 shows the maximum achievable heat flux of the CLPHP when the average evaporator temperature reaches approximately 100°C (for water and ethanol). Figure 5 also shows the comparison between the thermal performance of the CLPHP when it is partially filled with water and ethanol in different filling ratios. It can be concluded from Figure 5 that the CLPHP has better thermal performance when it is partially filled with water because the thermal properties of water, including thermal conductivity, latent heat of vaporization, and constant pressure specific heat, are more suitable than those of ethanol. This result is in complete agreement with previous researches about the effect of working fluid on PHPs performance [3, 6].

It is also expected from Figure 5 that if the filling ratio is below 30% or above 70%, the thermal performance of the CLPHP would decrease. This result is in complete agreement with Khandekar et al's results [3].

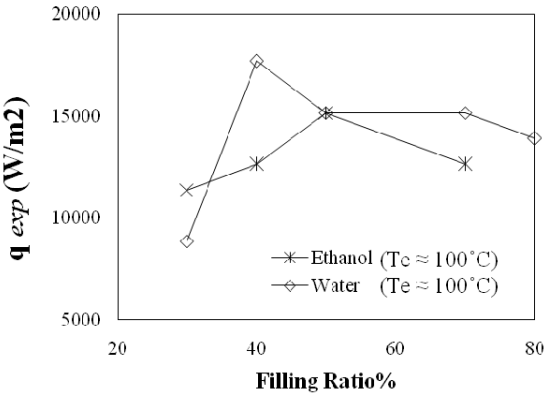

Figure 5. Maximum performance of the CLPHP obtained in different filling ratios.

CORRELATION

In order to find a heat transfer correlation, it is generally convenient to extract effective thermo-physical properties for heat transfer as non-dimensional quantities. In a fixed filling ratio, it was found from the experimental results and physical phenomena analysis of the CLPHPs that the thermo-physical properties of working fluids, the temperature difference between the evaporator and condenser, the internal diameter, and the evaporator section length can affect the thermal performance of the CLPHPs:

$$\dot{q} = \frac{\dot{Q}}{2\pi.D_i.N.L_e} = f\{h_{fg}, K, \mu, Cp, \rho_v, g\Delta\rho, \sigma, \Delta T_{e-c}, D_i, H_{eva}\} \quad (1)$$

By considering M, L, t, T, and J as independent fundamental physical quantities (Incropera and DeWitt [12]), the variables in equation (1) can be grouped into an important set of dimensionless groups including Ku, Ja, Pr, Bo, $\frac{\mu(g\Delta\rho)^{0.25}}{\rho_v^{0.5}\sigma^{0.75}}$ ($Mo^{0.25}$,Morton Number), and aspect ratio ($\frac{D_i}{H_{eva}}$).
These dimensionless groups can be arranged into the following equation:

$$Ku = f\{Ja, \Pr, Bo, Mo, D_i / H_{eva}\} \quad (2)$$

The meaning of each dimensionless parameter in equation (3) can be explained as follows:
Ku is the ratio of the input heat flux of a CLPHP to the critical heat flux in the pool boiling:

$$Ku = \left(\frac{q}{h_{fg}\rho_{vap}^{0.5}[\sigma g(\rho_{liq} - \rho_{vap})]^{0.25}}\right) \quad (3)$$

This dimensionless group represents the pool boiling phenomenon of the working liquid in the evaporator section.
The next numbers of interest are the Jakob number and the liquid Prandtl number, defined respectively as,

$$Ja = \left(\frac{C_{p,liq}.\Delta T_{e-c}}{h_{fg}}\right) \quad (4)$$

$$\Pr_{liq} = \left(\frac{C_{p,liq}.\mu_{liq}}{k_{liq}}\right) \quad (5)$$

The Jakob number indicates the ratio of sensible heat to the latent heat of vaporization in a CLPHP, and the liquid Prandtl number shows the single phase convective effect on heat transfer.
The Bond number is the ratio of the buoyancy force to that of the surface tension of the working fluid and is defined as follows:

$$Bo = D_i\sqrt{g(\rho_{liq} - \rho_{vap})/\sigma} \quad (6)$$

The Morton number shows the interaction between the viscous, buoyancy, inertia, and surface tension forces acting on a bubble formed by nucleate boiling in the evaporator section. In fluid dynamics, the Morton number is used together with the Bond number to characterize the shape of bubbles or drops moving in a surrounding fluid. For more information about the Morton number and its applications, Haberman and Morton [13] or Clift et al. [14] can be investigated.
Using the experimental data of the present and previous research ([3, 4, 5]), it was found that Ku could be described by the following correlation:

$$Ku = a\left(\frac{C_{p,liq}.\Delta T_{e-c}}{h_{fg}}\right)^b\left(\frac{C_{p,liq}.\mu_{liq}}{k_{liq}}\right)^{-0.7}\left(D_i\sqrt{\frac{g(\rho_{liq} - \rho_{vap})}{\sigma}}\right)^{0.85}\left(\frac{\mu(g\Delta\rho)^{0.25}}{\rho_v^{0.5}\sigma^{0.75}}\right)^{0.8}\left(\frac{D_i}{H_{eva}}\right)^{0.7} \quad (7)$$

By considering the effect of the filling ratio on the thermal performance of the CLPHPs, coefficients a and b can be computed from the following equations:

$$a = -2222\gamma^4 + 4704\gamma^3 - 3584\gamma^2 + 1157\gamma - 125.8 \quad (8)$$

$$b = -142.5\gamma^4 + 301.5\gamma^3 - 227.6\gamma^2 + 72.21\gamma - 6.87 \quad (9)$$

For a specific filling ratio, a and b are calculated using equations (8) and (9), and then the input heat flux is obtained by equation (7). In using equation (7), the thermo-physical properties of working fluids are calculated at the evaporator temperature (T_{eva}). Figure 6 shows the comparison between the results obtained from the experiments and those obtained from equation (7).

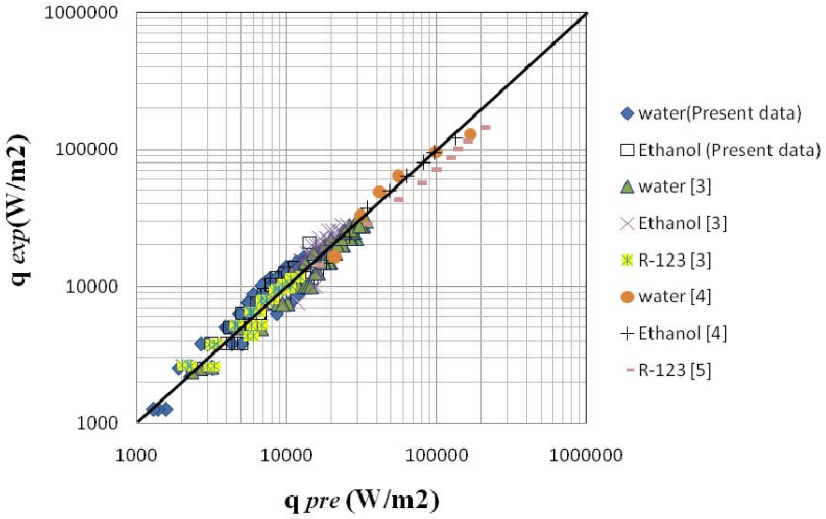

Figure 6: Comparison between the power-law correlation results and those of the experiments

Compared with the experimental data, the root-mean-square deviation of the correlation prediction was 19.7% and approximately 88.6% of the deviations were within ±30%. Therefore, it seems that the correlation can reasonably predict the input heat flux of CLPHPs.

CONCLUSIONS

In this paper, first a CLPHP was designed and manufactured. Then, the effect of various parameters, including working fluid (water and ethanol), volumetric filling ratio (30%, 40%, 50%, 70%, 80%), and input heat power (5 to 70 watts), on the thermal performance of the CLPHP were investigated experimentally. Then, the dimensionless parameters including Ku, Ja, Pr, Bo, Mo, and Di/H_{eva} that affect thermal performance of CLPHPs were obtained. Afterward, a power-law correlation based on dimensionless groups was established to predict the input heat flux of the CLPHPs using available experimental data sets of the CLPHPs. Compared with the experimental data, the root-mean-square deviation of the correlation prediction was 19.7% and approximately 88.6% of the deviations were within ±30%. It seems that the correlation can reasonably predict the input heat flux of CLPHPs.

Acknowledgment
The research is supported by the Iran National Science Foundation under contract no. 85126/68.

List of Symbols

Bo	Bond number	q	Input heat flux W/m^2
C_p	constant pressure specific heat (J/kg.K)	ΔT_{e-c}	temperature difference between evaporator and condenser

D_i	internal diameter (2mm)
g	gravitational acceleration m/s^2
h_{fg}	latent heat of vaporization (J/kg)
Ja	Jakob number
K	Thermal conductivity (W/m.K)
Ku	Kutateladze number
L_e	Evaporator length in each turn
N	Number of turns
Pr	Prandtl number
Q	Input heat power

Greek symbols

γ	Filling ratio
μ	viscosity (Pa .s)
ρ	Density kg/m^3
σ	surface tension (N/m)

Subscripts

liq	liquid
vap	vapor

REFRENCES

1. H. Akachi, US Patent, Patent Number 4921041, 1990.
2. J.L. Xu, Y.X. Li, T.N. Wong High speed flow visualization of a closed loop pulsating heat pipe, Int. J. Heat Mass Transfer, Vol. 48, pp. 3338–3351, 2005.
3. S. Khandekar, N. Dollinger, M. Groll, Understanding operational regimes of closed loop pulsating heat pipes: an experimental study Appl. Therm. Eng., Vol. 23, pp.707–719, 2003.
4. S. Khandekar, Thermo-hydrodynamics of Closed Loop Pulsating Heat Pipes, PhD thesis, Institute of Nuclear Engineering and Energy Systems (IKE), Universitat Stuttgart, Germany, 2004.
5. H. Yang, S. Khandekar, M. Groll, Operational limit of closed loop pulsating heat pipes, Appl. Therm. Eng., Vol. 28, pp. 49–59, 2008.
6. T. Katpradit, T. Wongratanaphisan, P. Terdtoon, P. Kamonpet, A. Polchai, A. Akbarzadeh, Correlation to predict heat transfer characteristics of a closed end oscillating heat pipe at critical state, Appl. Therm. Eng., Vol. 25, pp. 2138–2151, 2005.
7. S. Khandekar, P. Charoensawan, M. Groll, P. Terdtoon, Closed loop pulsating heat pipes Part B: visualization and semi-empirical modeling, Appl. Therm. Eng., Vol. 23, pp. 2021–2033, 2003.
8. S. Khandekar , X, Cui, M. Groll, Thermal Performance Modeling of Pulsating Heat Pipe by Artificial Neural Network, Proceedings of 12th International Heat Pipe Conference, pp. 215-219, Moscow, Russia, 2002.
9. M.B. Shafii, A. Faghri, Y. Zhang, Thermal modeling of unlooped and looped pulsating heat pipes, ASME J. Heat Transfer, Vol. 123, pp. 1159–1172, 2001.
10. T. Wong, B. Tong, S.M. Lim, K.T Ooi, Theoretical Modeling of Pulsating Heat Pipe, Proc.11th Int. Heat Pipe Conf, pp. 159-163, Tokyo, Japan, 1999.
11. S. Arabnejad, H. Jamshidi, M.B. Shafii, Y. Sabohi, Analysis of Liquid-Vapor Pulsating Flow in U-shaped Pulsating Heat Pipe, ISME conference of fluid dynamic Khajeh-Nasir University, Tehran, Iran, 2008.
12. F. P. Incropera, and D. P. DeWitt, Introduction to Heat and Mass Transfer, Wiley, New York, 1996.
13. W.L. Haberman, and R.K. Morton, An experimental investigation of the drag and shape of air bubbles rising in various liquids. David Taylor Model Basin, Washington, Report No. 802, 1953.
14. R. Clift, J. R. Grace, and M. E. Weber, Bubbles Drops and Particles, Academic Press New York, 1979.

HIGH SPEED BOILING VISUALIZATION FOR FINS WITH SUBSURFACE TUNNELS

R. Pastuszko
Kielce University of Technology, Kielce, Poland

ABSTRACT. The paper presents experimental investigations of boiling heat transfer from a system of connected horizontal and vertical subsurface tunnels. The experiments were carried out for water at atmospheric pressure. The tunnel external covers were manufactured out of perforated copper foil of 0.05 mm in thickness (holes diameter 0.5 and 0.3 mm), sintered with the mini-fins, formed on the vertical side of the 10 mm high rectangular fins and horizontal inter-fin surface. Visualization studies were conducted with a real sample and with a transparent structured model of joined tunnels having a cover of perforated foil. The investigations aimed both at identifying differences between pool boiling mechanism for horizontal and vertical tunnels and at determining the diameter and frequency of departing bubbles. The calculated and measured departure bubble frequency for a vertical tunnel showed good agreement at low and medium superheating. The holes in the foil acted as elements feeding the surface tunnel structure. The vapor escaped through the tunnel outlets in vertical tunnels and holes in foil (pores) in horizontal tunnels. Observations of internal and external visualizations confirmed most of the assumptions made for the semi-analytical model for boiling from enhanced structures composed of connected vertical and horizontal tunnels.

Keywords: *pool boiling, visualization, subsurface structure*

INTRODUCTION

Developing an analytical or semi-analytical model for boiling in enhanced subsurface structures requires conducting visualization experiments both for the actual surface and for a selected segment of this structure. The segment, with transparent walls, enables observations of boiling inside the subsurface tunnels. The first method of observation, called external visualization, makes it possible to identify the sites of vapor bubble nucleation and departure, to calculate the diameter and frequency of the departing bubbles and nucleation site density. Internal visualization enables observation of boiling structures, active and inactive pores localization, and the extent to which vertical and horizontal tunnels are filled with vapor.

Nakayama et al. [1] was one of the first to conduct boiling visualization in horizontal structural surfaces (subsurface tunnel covered with foil having triangular holes), using a section of the structure, surrounded by transparent walls. Their visualization study of boiling R-11, water and nitrogen suggested the important role of evaporation inside the tunnel in heat transfer enhancement.
Chien and Webb's [2] visualization experiments conducted for an enhanced tubular surface, having subsurface tunnels and surface pores (micro-fins 0.8 mm in height and pores 0.23 mm in diameter), showed that all the tunnels were vapor filled, except for liquid menisci, just as in the horizontal tube at high heat fluxes. Also Chien and Webb [3] reported bubble dynamics data (diameter, frequency and nucleation site density) for this type of enhanced surface using R-123. In their conclusion they

Corresponding author: Dr. R. Pastuszko
Phone: + (48)-41-3424320,
E-mail address: tmprp@tu.kielce.pl

presented the dependence of nucleation site density on the latent heat generated inside the tunnel, and stated that the latent heat constitutes half of the total heat flux.

Chen et al. [4] also observed the boiling process for structures with subsurface tunnels, on the external surface of tubes, where propane, isobutene and their mixtures were working fluids. The authors focused on the identification of the bubble shapes in different liquids, the generation of small bubbles (of diameters less than 0.5 mm), their arrangement and distribution, and the analysis of their behaviour on different enhanced surfaces. Ramaswamy et al. [5], using a fast camera (1500 frames/sec), determined the data concerning the bubble growth for a silicone structure composed of interconnected mini-channels, and placed in the boiling FC-72. The data included the diameter of departing bubbles (0.61 – 0.66 mm), frequency (150 – 250 Hz), and the density of nucleation sites. It was concluded that the pore diameter had a significant effect on the diameter of the departing bubbles. Visualization for a similar structure, though made from copper and quartz and placed in PF 5060, was also performed by Ghiu and Joshi [6]. They showed different boiling regimes for the investigated materials and confirmed the dynamic nature of the boiling process.

Yu and Lu [7] presented boiling structure visualization results for copper mini-fins (the height: 0.5 – 4.0 mm, the width of the inter-fin space: 0.5 – 2.0 mm), placed in the boiling FC-72 fluid at four different heat fluxes. The departing bubble diameters were estimated to be 0.2 – 0.3 mm. For small and medium heat fluxes (measurements covered the range from 20 to about 1000 kW/m^2) the number of active nucleation sites and frequency of the departing bubbles increased for a small increase in the heat flux. At the highest heat fluxes, emerging „vapor mushrooms" caused the vaporization in the central part of the fin system, which resulted in the sudden superheating.

Pastuszko and Mroczek [8] describe water boiling visualization for subsurface structures in the form of a connected system of horizontal and vertical tunnels. For low values of the heat flux ($q \approx 100$ kW/m^2) the generation of vapor bubbles could be seen in horizontal tunnels and bottom sections of vertical tunnels. The bubbles, which remained separate, were getting out into the inter-fins space via pores of the horizontal tunnel. The increase in the heat flux and superheating ($q \approx 145$ kW/m^2) caused the increase in frequency and diameter of the forming bubbles. At substantial heat flux ($q \approx 185 – 260$ kW/m^2), large vapor structures formed, and through intensive convection, disturbed the steady motion of bubbles visible for low values of q. Pastuszko [9] presented experimental investigations of boiling heat transfer for system of connected narrow tunnels. The experiments were carried out with water at atmospheric pressure. The tunnel external covers were manufactured out of perforated copper foil of 0.05 mm in thickness (hole diameters 0.4 and 0.5 mm), sintered with the mini-fins, formed on the vertical side of the 10 mm high rectangular fins and horizontal inter-fin surface. Visualization studies were conducted with a real sample as well as with a transparent structured model of joined narrow tunnels limited with perforated foil. Diameter and frequency of departing bubbles were determined. The holes in the foil acted as elements feeding the surface tunnel structure and the vapor bubbles generated in menisci in the tunnel corners departed through tunnel outlets in vertical tunnels and holes in foil (pores) in horizontal tunnels.

The objective of the present study is to understand the boiling phenomena for a system of connected horizontal and vertical subsurface tunnels and to verify assumptions for a theoretical model.

EXPERIMENTAL SET-UP AND SAMPLES

External and internal visualization set-up

The diagram of the measurement stand for external visualization is presented in Figure 1. It is modified set-up described in [10]. The main stand module consisted of a cylindrical vessel (7), filled with working fluid, and placed over the investigated sample (9). The sample was soldered to a 170 mm long cylindrical copper bar (10) of 45 mm in diameter.

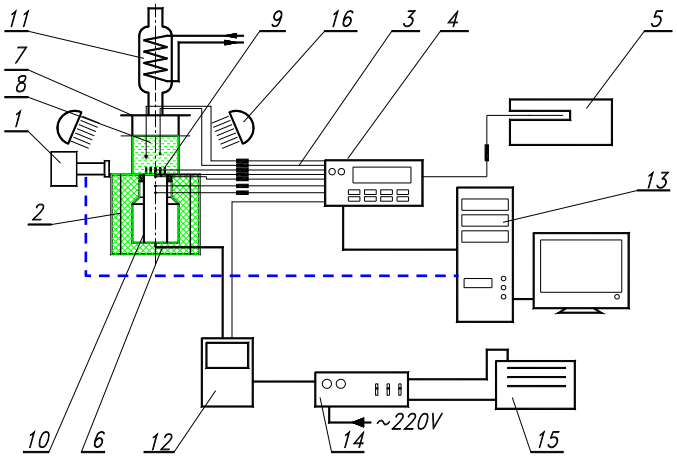

Figure 1. Schematic diagram of the external visualization system: 1 – digital camera; 2 – Teflon casing; 3 – compensating cables; 4 – data logger; 5 – dry-well calibrator; 6 – insulation; 7 – glass vessel; 8 – boiling liquid; 9 – investigated sample; 10 – copper bar with cartridge heater; 11 - condenser; 12 - wattmeter; 13 – PC; 14 – power supply and fuses; 15 – autotransformer; 16 – lights.

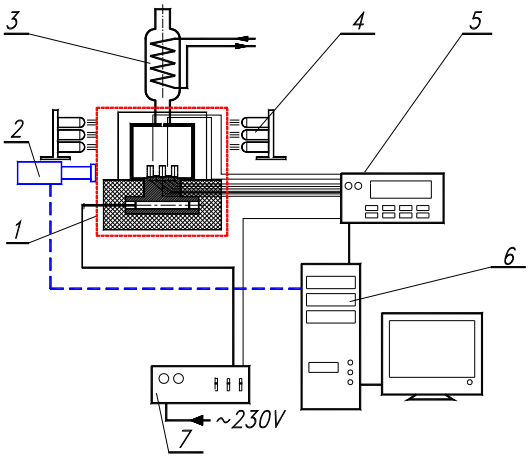

Figure 2. Schematic diagram of the internal visualization system: 1 – main module; 2 – digital camera; 3 – condenser; 4 – lights; 5 – data logger; 6 – PC; 7 – power regulator

The cylinder diameter corresponded to the diagonal of the sample base. A 1000 W electric cartridge heater of 19 mm in diameter and 130 mm in length was installed into the bar.

The estimated uncertainties were as follows:

- low heat flux (20 kW/m^2): heat flux ±15%, wall superheat at the main fin base ±0.2 K, heat transfer coefficient ±18.5%,
- high heat flux (550 kW/m^2): heat flux ±1.2%, wall superheat at the main fin base ±0.42 K, heat transfer coefficient ±2.4%.

The principal part of the internal visualization system is the main module (Figure 2, item 1), which combines a sample segment with a heating system. The visualization images were obtained using a high speed digital monochrome camera PHOT MV-D1024-160-CL (*Photonfocus*) of resolution 1024x1024 pixels as well as high speed camera EX-FH20 (*Casio*) of resolution 480x360 at 210 fps.

Samples

The enhanced structure, which was the focus of the investigations, is shown in Figure 3. A sample with tunnel structure formed a square of 27 mm-long side (w_f). It had three main fins with additional surface modification (mini-fins covered with perforated foil). The visualization studies were conducted with a real sample (external visualization – Figure 3) and with a transparent structured model of joined tunnels limited with perforated foil (internal visualization – Figure 4). Table 1 shows the parameters of the tested samples.

The main stand module for internal visualization (Figure 4) consisted of the base block with the cartridge heater inside, connected with the segment of the sample. Two U-shape copper foils (item 4, Figure 4) having two rows of holes with 0.5 mm in diameter were connected with mini-fins with thermal adhesive. Two transparent plexiglas plates were attached to the edges of the segment and foil by means of epoxy adhesive. The whole module was sealed by high temperature silicone.

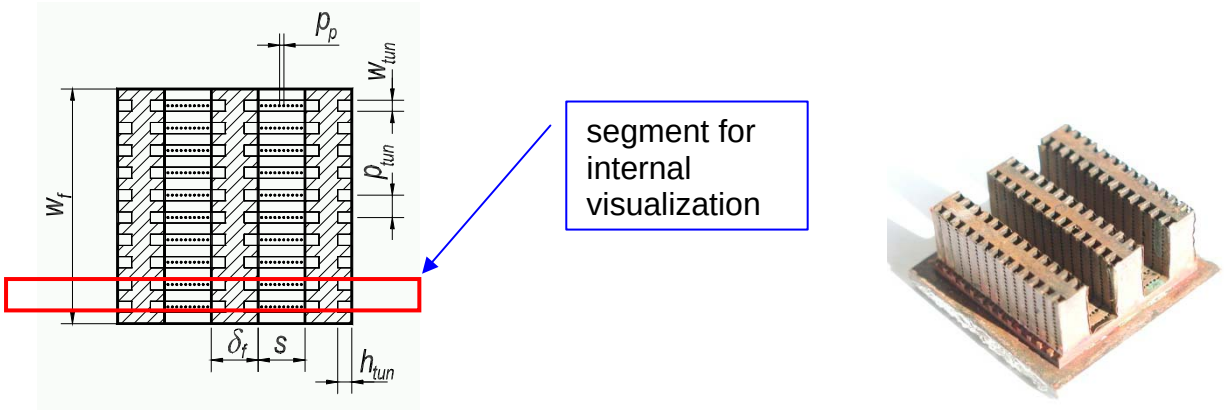

Figure 3. Horizontal section of the tunnel structure and photograph of the sample.

Table 1
Sample code and specifications

sample code	visualization type	pore dia. d_p	pore pitch p_p	tunnel height h_{tun}	tunnel width w_{tun}	tunnel pitch p_{tun}
TS-10-2.50-0.3	external	0.3	0.6	1.6	1.3	2.50
TS-10-2.50-0.5	internal	0.5	1.0	1.6	1.3	2.50

Two plexiglas plates limited the pool space formed also by milled tunnels and perforated foil. The space was filled with boiling liquid. The block was insulated with layers of soft insulation.

RESULTS

External visualization

Figure 5 presents photographs of the phases of bubble growing and departing. The right side presents a magnified cross-section of vertical tunnels. Assumed after [11] direction of the liquid flow (sucking)

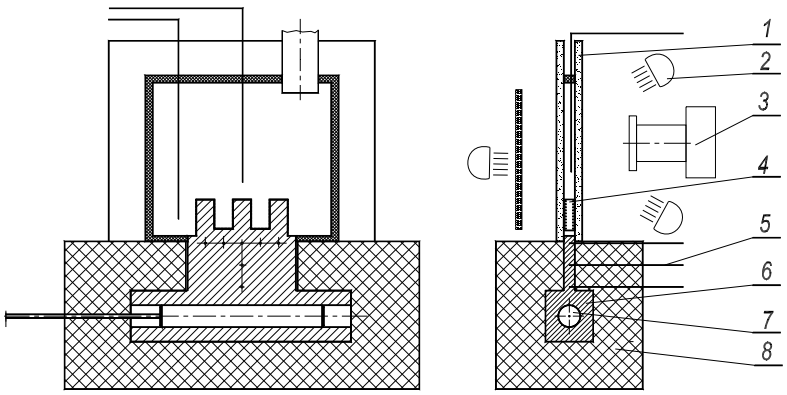

Figure 4. Internal visualization sample and module: 1 – transparent plate; 2 – light; 3 – fast speed camera; 4 – perforated foil; 5 – thermocouples; 6 – copper block with sample segment; 7 – cartridge heater; 8 – insulation.

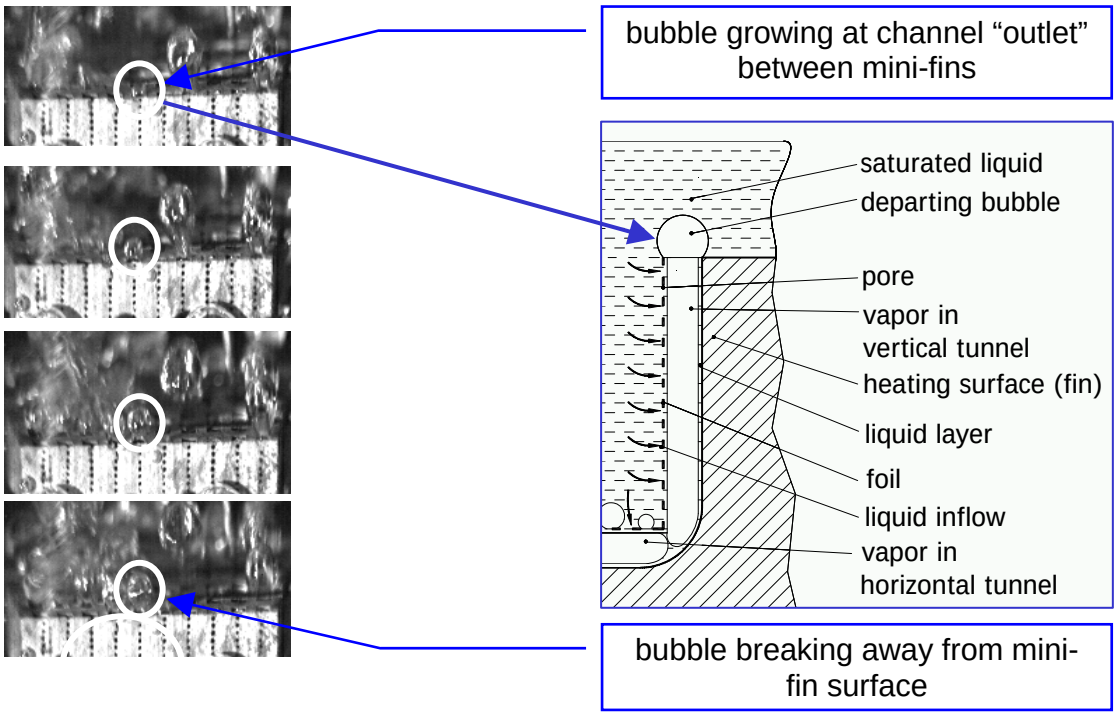

Figure 5. Bubble growing and departing for vertical tunnel outlet, TS-10-2.50-0.3, boiling water $q \approx 40$ kW/m^2, 193 fps.

into pores in the perforated foil, vapor bubble inside tunnels and bubble growth preceding departure are all marked in the figure. Despite small heat flux, one can observe that the majority of vertical tunnels are active.

Bubble departure frequency and diameter

A comparison of the experimentally observed values and the calculated values for bubble departure frequency at boiling water and R-123 in vertical tunnel is shown in Figure 6.

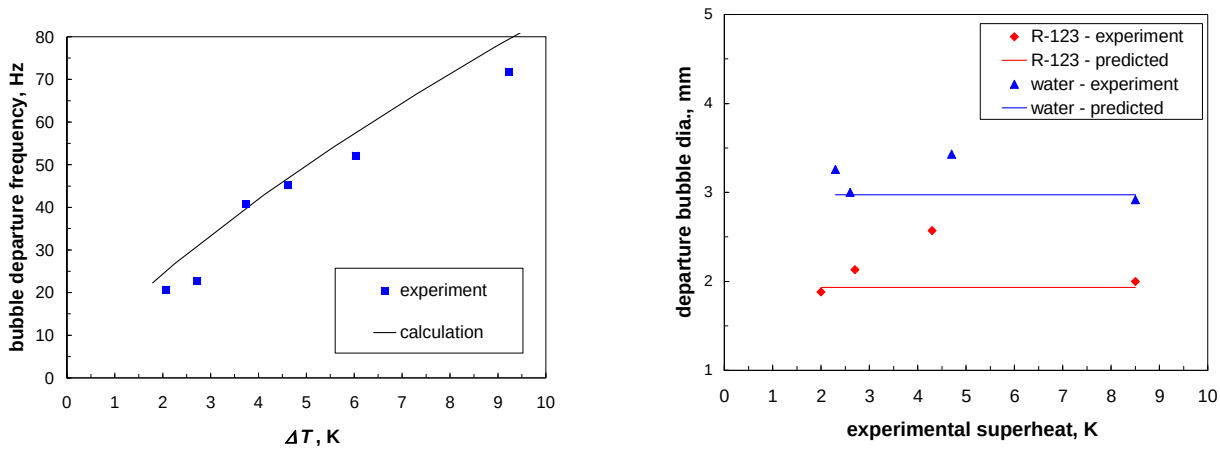

(a) (b)

Figure 6. Comparison of the calculated and measured departure bubble frequency (a) and diameter (b) for the vertical tunnel at the boiling of water and R-123 (data for TS-10-2.50-0.3), according [11].

The experimental data for the vertical tunnel were obtained by means of high-speed photography (193 fps): for each superheat 5 frequency measurements referred to three randomly chosen tunnel outlets were taken and averaged. The measurements show satisfactory agreement with the theoretical calculations.

The maximum error of computed frequencies, compared to the experimental data, do not exceed 30% and occur for small superheats, 2 – 3 K [11]. The discrepancy between the measurement and calculation of bubble diameter reached 15%. The measurements were based on the photographs from a digital camera. The estimated error in defining the diameter was up to 10% (including the error resulting from the non-sphericity of bubbles). The calculations of these parameters were based on semi–analytical approach proposed in [11] for this kind of enhanced structures.

Internal visualization

The internal visualization method allows observation of differences in pool boiling mechanism for the subsurface horizontal and vertical tunnels. At low values of heat flux ($q \approx 130$ kW/m^2) the generation of vapor bubbles can be seen in horizontal tunnels and the bottom regions of vertical tunnels (Fig. 7). In horizontal tunnels, cyclical changes in vapor volume result from cyclical processes of liquid suction by inactive pores, vaporization in menisci and generation of vapor bubbles by active pores [1]. Changes in activity of particular pores take place: an active pore becomes inactive after generating a few bubbles. These findings agree with those of Chien and Webb [2]. In vertical tunnels, all pores in foil remain inactive; vapor escapes through the outlets at the main fin tips. The vapor is generated in the bottom regions of the tunnels, at the contact with vertical tunnels. One may suppose that some of the liquid from horizontal tunnels supplies vertical tunnels. In some vertical tunnels single bubbles can be observed, in other tunnels larger areas are filled with vapor, which results in the increase in the departing bubble diameter.

At medium heat fluxes ($q \approx 180$ kW/m^2) the frequency of bubbles departing through active pores of horizontal tunnels and the number of active pores increase (Figure 8). Increased bubble average diameter is a characteristic feature of bubbles departing from vertical tunnel pores. Most regions of vertical tunnels are filled with vapor, but separate bubbles can also be observed.

At heat flux $q \approx 230$ kW/m^2 (Figure 9) more and more bubbles depart from the horizontal tunnel pores, and the departure frequencies and nucleation site density increase. Bubble coalescence in the space between vertical tunnels intensifies and may affect the whole system of tunnels. The vapor fills nearly the whole space of the horizontal and vertical tunnel, and at the main fin tips the coalescence of bubbles generated by the two analyzed tunnels can be observed.

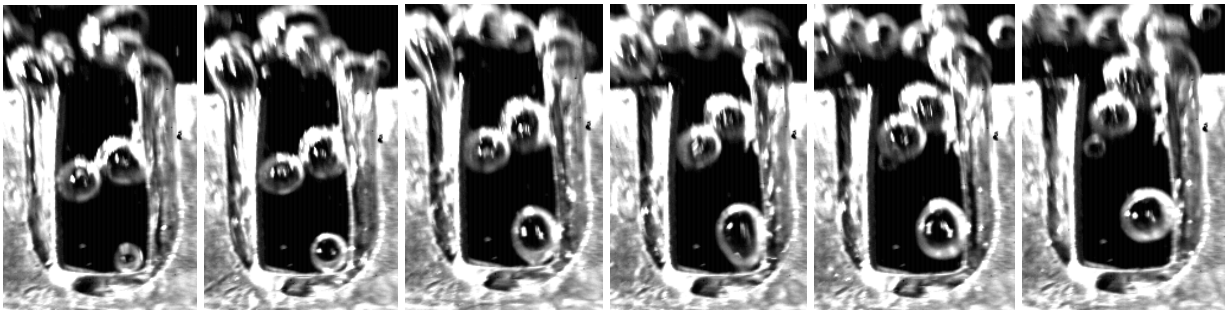

Figure 7. Water boiling internal visualization at small heat flux ($q \approx 130$ kW/m^2), frames every 0.005 s.

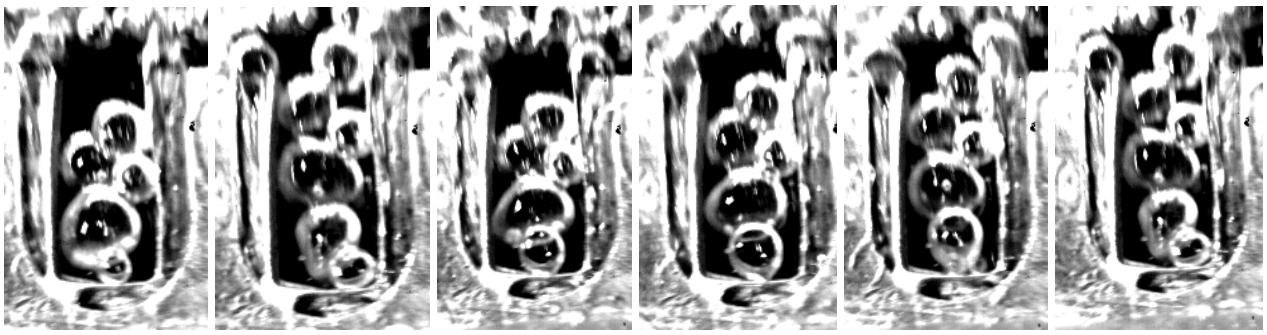

Figure 8. Water boiling internal visualization at medium heat flux ($q \approx 180$ kW/m^2), frames every 0.005 s.

Figure 9. Water boiling internal visualization at high heat flux ($q \approx 230$ kW/m^2), frames every 0.005 s.

CONCLUSIONS

The visualization experiments allow drawing the following conclusions concerning the mechanism of boiling in the system of connected tunnels:

- Passive and active pores were observed for horizontal tunnel. Passive pores make it possible to provide subsurface tunnels with liquid, whereas the active pores act as the vapor outlets.
- Increased heat flux generates a larger number of active pores in the horizontal tunnel, which contributes to higher nucleation site density. Diameters of departing bubbles increase.
- Pores in the perforated foil of vertical tunnel are inactive – their task it to only feed the subsurface space. Liquid layer evaporation takes place inside the tunnel and the vapor bubbles depart through tunnel outlets at the main fin tips.
- Vertical tunnel outlets are active within the whole range of investigated heat fluxes, and the bubbles departing from them have similar diameters at different heat fluxes.
- The tunnels "work" independently, only some fraction of liquid evaporated from the contact area of the horizontal and vertical tunnels.
- The observations based on internal and external visualization confirm most of the assumptions made before developing the semi-analytical model for boiling from enhanced structures composed of connected vertical and horizontal tunnels [11].

REFERENCES

1. Nakayama, W., Daikoku, T., Kuwahara, H., Nakajima, T., Dynamic Model on Enhanced Boiling Heat Transfer on Porous Surfaces. Part I – Experimental Investigation, *ASME Journal of Heat Transfer*, Vol. 102, pp 445-456, 1980.
2. Chien, L.H., Webb, R.L., Visualization of pool boiling on enhanced surfaces, *Experimental Thermal and Fluid Science*, Vol. 16, pp 332-341, 1998.
3. Chien L.H., Webb R.L., Measurement of bubble dynamics on an enhanced boiling surface, *Experimental Thermal and Fluid Science*, Vol. 16, pp 177–186, 1998.
4. Chen, Y., Groll, M., Mertz, R., Kulenowic, R., Visualization and mechanisms of pool boiling of propane, isobutane and their mixtures on enhanced tubes with reentrant channels, *Int. J. Heat Mass Transfer*, Vol.48, pp 2516–2528, 2005.
5. Ramaswamy, C., Joshi, Y., Nakayama, W., Johnson, W. B., High-speed visualization of boiling from an enhanced structure, *Int. J. Heat Mass Transfer*, Vol.45, pp 4761-4771, 2002.
6. Ghiu, C.-D., Joshi, Y.K., Visualisation study of pool boiling from thin confined enhanced dtructures, *Int. J. Heat Mass Transfer*, Vol.48, pp 4287-4299, 2005.
7. Yu, C. K., Lu, D. C., Pool boiling heat transfer on horizontal rectangular fin array in saturated FC-72, *Int. J. Heat Mass Transfer*, Vol. 50, pp 3624–3637, 2007.
8. Pastuszko, R., Mroczek, P.J., Boiling visualization for fins with horizontal and vertical subsurface tunnels, proc. 11th Int. Symp. on Heat Transfer and Renewable Sources of Energy, Miedzyzdroje, 629-636. 2006,
9. Pastuszko, R., Pool boiling visualization for surfaces with narrow tunnels limited by porous structure, *proc. 5th European Thermal-Sciences Conference,* Eindhoven, 18-22 May, 2008, TPF_23.
10. Pastuszko, R., Boiling heat transfer enhancement in subsurface horizontal and vertical tunnels, *Experimental Thermal and Fluid Science*, Vol. 32, pp 1564–1577, 2008.
11. Pastuszko, R., Poniewski, M.E., Semi-analytical approach to boiling heat fluxes calculation in subsurface horizontal and vertical tunnels, *Int. J. Thermal Sciences*, Vol. 47, pp 1169-1183, 2008.

AN INVESTIGATION OF A CONDENSATION PROCESS EFFICIENCY IN AIR-COOLED CONDENSER COILS

T. Bohdal, H. Charun, M. Czapp

Chair of Thermal Engineering and Refrigerating Engineering
Koszalin University of Technology, Koszalin, Poland

ABSTRACT. The authors designed an experimental investigation of the R404A refrigerant condensation process in a long air-cooled coil of length L. The experiments were performed for the following range of the basic parameters: $\dot{m}$ = 100 ÷ 400 kg/(m^2·s), $\dot{q}$ = 4000 ÷ 23000 W/m^2, T_s = 20 ÷ 40°C, L = 10 ÷ 25 m. The experimental setup as well as some of the experimental results are shown in the paper. Heat transfer coefficients on the tube inner surface of the coil within the condensation zone and the influence of the coil length on the efficiency of the condenser are discussed. Based on the experimental results, a correlation describing a R404a condensation process in long coils was worked out. A comparison between results calculated from various formulas and the experimental ones is also given.

Keywords: *heat transfer, condensation, refrigeration, air-cooled condenser, R404A*

INTRODUCTION

Air-cooled condensers have a wide range of applications in refrigerating and air-conditioning units. Heat transfer from the refrigerating medium being condensed by air is a relatively complicated process. It relates to the process of heat transfer from the medium to the tube inner surface as well as the transfer from the outer (finned) surface of a condenser unit to air. Heat transfer occurring during the refrigerating media condensation has been discussed in many papers. Mostly, however, determination of local and average heat transfer coefficients of refrigerating media being condensed in horizontal and straight tubes is discussed. There are not so many research activities concerned with a condensation process inside a cooling coil itself. Such problems as for instance the influence of a cooling coil length on the heat transfer process are considered rather seldom. The designer, however, while working out a air-cooled condenser, should have a lot of that kind of data at his disposal. To analyse the heat transfer process during condensation of a refrigerating media in air-cooled condensers, one has to take into account the specific conditions of their work, i.e. [1, 2, 3]:

1. a small temperature difference between the condensation point and the cooling air temperature (ΔT = 10 ÷ 25 K),
2. small values of the heat flux density ($\dot{q}$ = 500 ÷ 12000 W/m^2),
3. small values of the mass flux density (an order of a few hundred kg/(m^2·s)),
4. condensation of the refrigerating media occurs inside of the coils. Such coils consist of horizontal tube elements joined with elbow connections,
5. condenser coils are supplied with superheated vapour and leave them as supercooled liquid, under real work conditions.

There are three characteristic heat transfer zones:

- superheating zone,
- condensation zone,
- subcooling zone.

Corresponding author: Prof. T. Bohdal
Phone: +(48)-94-3478247, fax: +(48)-94-3425963
E-mail address: tadeusz.bohdal@tu.koszalin.pl

It is relatively simple to calculate heat transfer coefficient h in a single-phase flow (superheating zone or subcooling zone), and this problem is widely discussed in literature. The calculation of the h coefficient in a condensation zone is far more complicated. It is necessary, for instance, to take into consideration the properties of a condensation mechanism itself and a larger amount of data such as properties of vapour and condensate are required. It is not uncommon that differences in the estimation of heat transfer coefficient h for refrigerating media condensation process in straight tubes reach the level of 300 % using formulas from different literature sources. The situation may be even much worse in the case of refrigerating media condensation taking place in tube coils. The further discussion will focus on this problem [5, 6, 7].

EXPERIMENT APPARATUS

The aim of the experimental investigation performed was to determine whether the length of a tube coil influenced the values of heat transfer coefficient α within a condensation zone of an air-cooled condenser. The investigation was performed on a single-coil condenser, finned from the outer (cooling air) surface. It was possible to change the coil length of a condenser in the experiments. The coil was made out of a copper tube (OD = 16 mm) and it consisted of several straight connection tubes (with a unit length equal to 1800 mm), joined together with the elbow type connections. By reducing the number of straight connection tubes, various length coils were obtained: L = 10, 12, 15, 20, 25 m. They had fins of 0.18 mm in thickness, distributed in a pitch of 2.5 mm. The coil under consideration, working as the air-cooled condenser, was put into an isolated cold room. The installation allowed to maintain the assumed inlet air flow as well as refrigerating medium R404A parameters. For different coil lengths, the refrigerant and air parameters were measured. The temperature distribution of R404A lengthwise the coil was measured using thermocouples and a medium flow rate with the use of calibrated tanks. All the measurements were performed as the steady state conditions were achieved. The schematic diagram of the experimental setup is shown in Figure. 1 [8, 9].

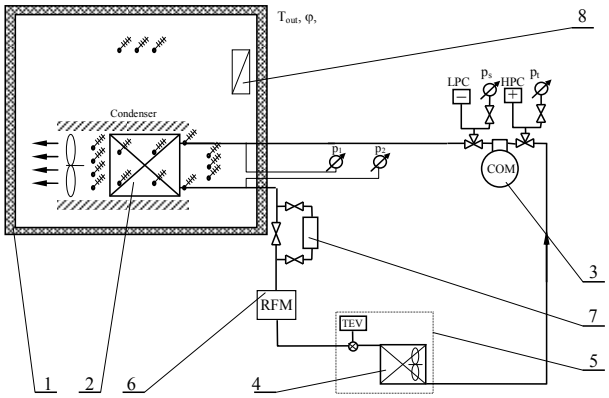

Figure. 1. Schematic diagram of experimetal setup: 1- insulated testing chamber, 2- lamellar condenser subjected to test, 3- compressor unit, 4- fan cooler, 5- cold room, 6- refrigerant flow meter, 7- dewatering filter, 8- stabilising system for air parameters, *T*- temperature measurement, *P*- pressure measurement, *HPC*- high-pressure control valve, *LPC*- low-pressure control valve

RESULTS

The condenser coil was supplied with a superheated vapour of R404A medium and discharged in supbcooled liquid condition. Three zones with an entirely different heat transfer intensity were observed in each condenser, regardless of its coil length. Measuring the medium temperature distribution lengthwise the coil, it was possible to determine the exact position as well as the length of the condensation zone. An example of the temperature distribution is shown in Figure 2 and

Figure 3 and Figure 4 presents an example of the dependence of the pressure drop of the R404A refrigerant in the condenser's coil pipe of length L = 12 m versus the mass flux density $\dot{m}$

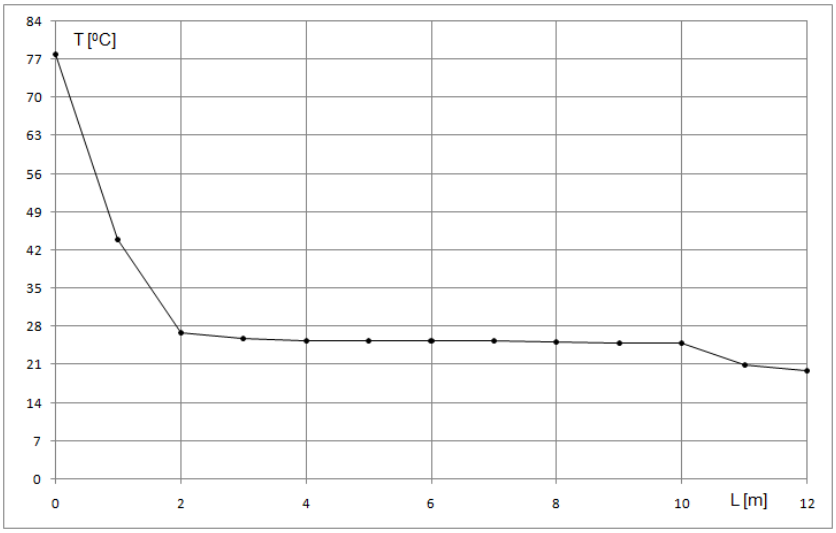

Figure. 2. Distribution of refrigerant temperature while condensing in a coil pipe; $\dot{m}$ = 156 kg/(m^2·s)

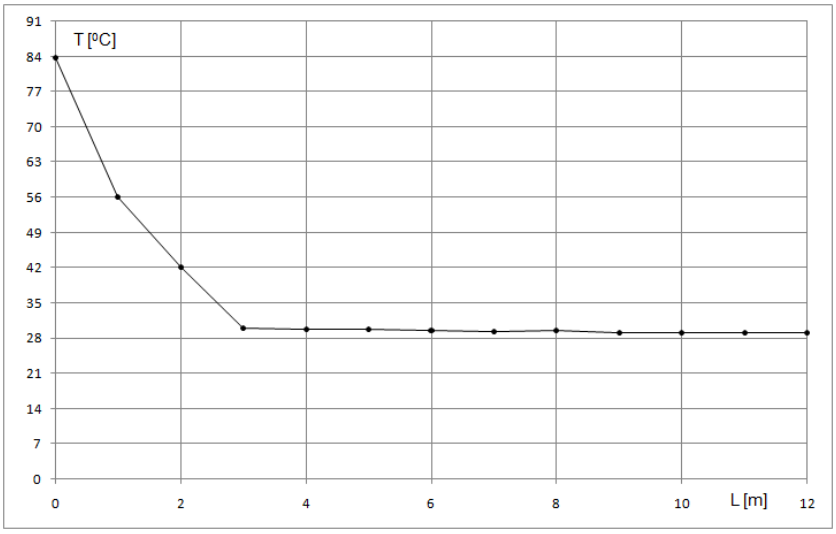

Figure. 3. Distribution of refrigerant temperature while condensing in a coil pipe; $\dot{m}$ = 366 kg/(m^2·s)

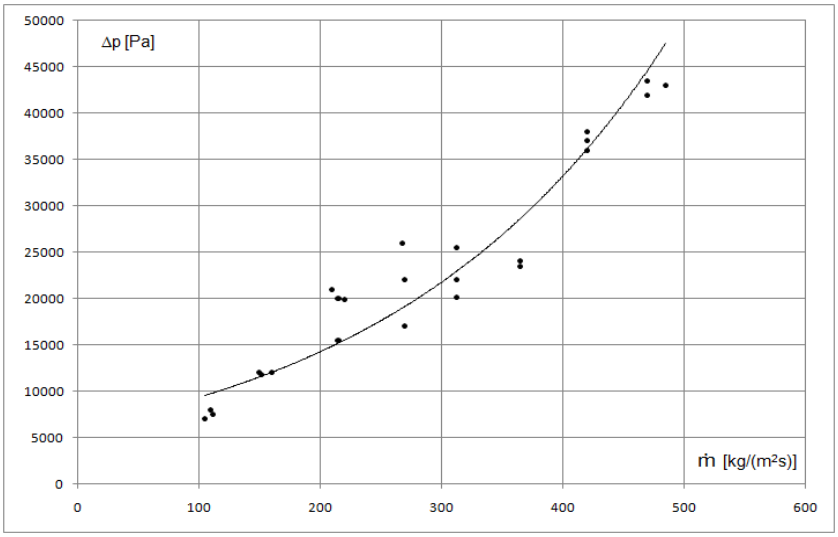

Figure. 4. Results of investigations of flow resistances of R404A refrigerant in condenser's coil pipe depending of mass flux density $\dot{m}$; L = 12 m

Heat transfer coefficients h typical for the condensation zone were determined for the refrigerating media in the experiments. They are shown in Figure 5 and 6 as a function of mass flux density $\dot{m}$, as well as heat transfer flux density $\dot{q}$ for the selected coil investigated. During the experiments, the characteristic parameters were maintained within the scope as given below:

- heat transfer flux density $\dot{q} = 4000 \div 23000$ W/m^2,
- mass flux density $\dot{m} = 100 \div 400$ kg/(m^2·s),
- temperature of condensation $T_s = 20 \div 40$ °C,
- coil length $L = 10 \div 25$ m.

a)

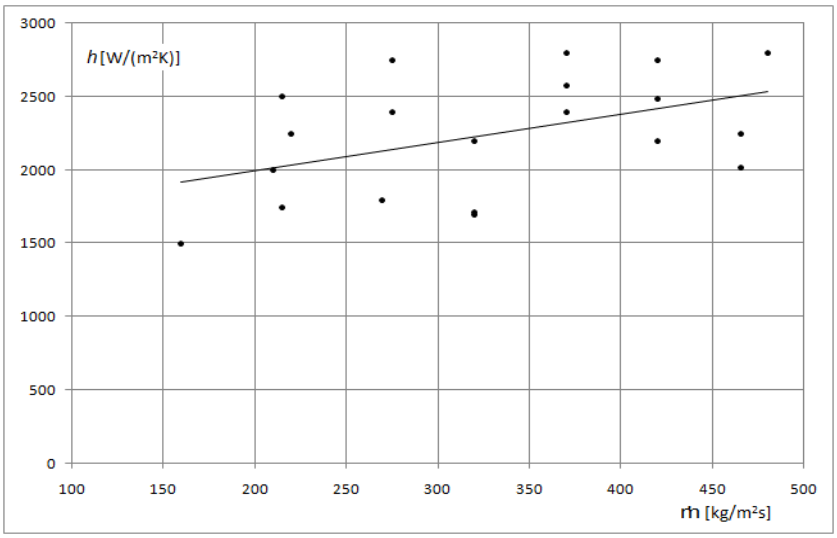

b)

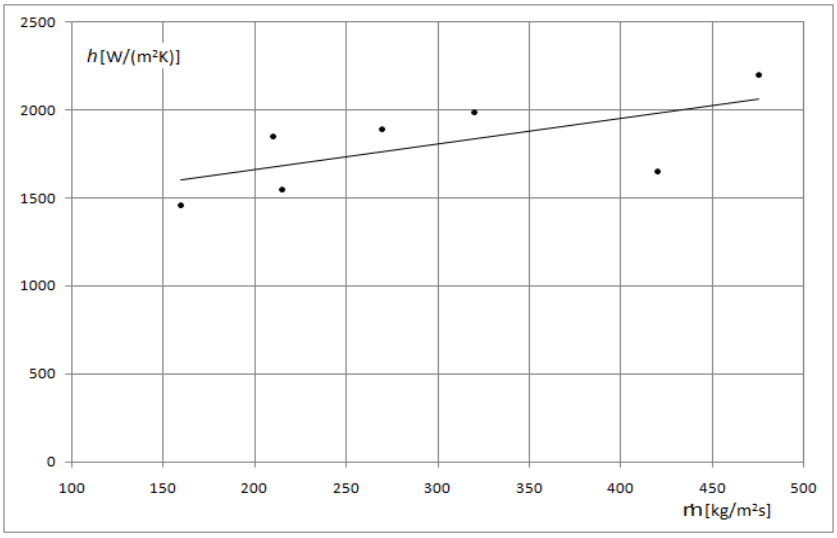

Figure. 5. Experimental mean heat transfer coefficient h versus mass flux density $\dot{m}$: a) $L = 12$ m, b) $L = 20$ m

a)

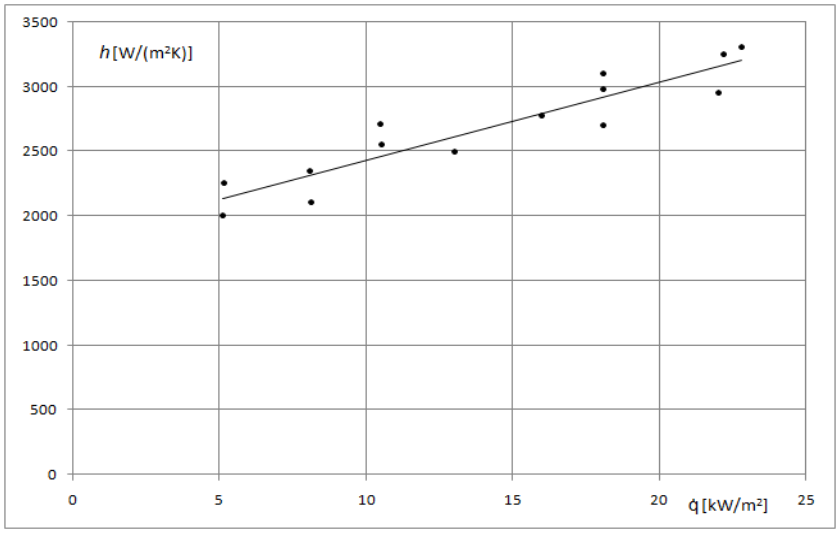

b)

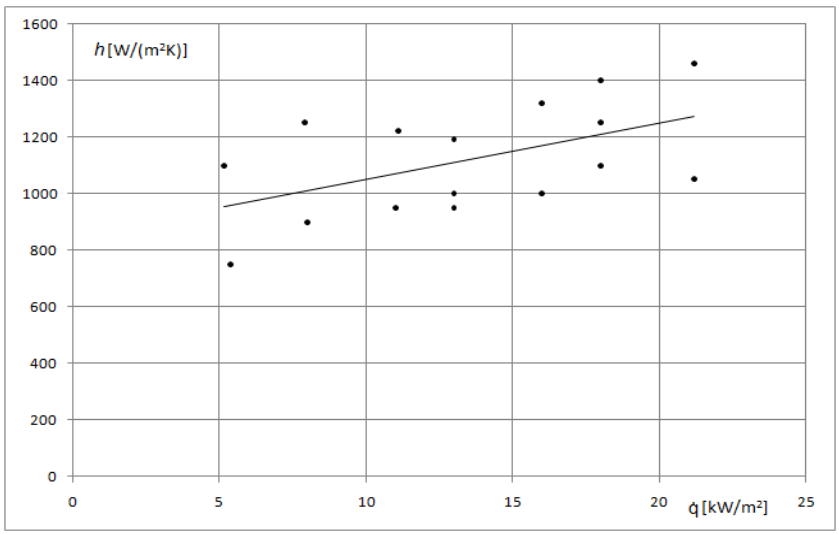

Figure. 6. Experimental mean heat transfer coefficient h versus heat flux density $\dot{q}$: a) L = 10 m, b) L = 25 m

The results presented demonstrate that heat transfer coefficient h increases as the mass flux density $\dot{m}$ and heat transfer flux density $\dot{q}$ rise. Moreover, the h coefficient clearly depends of the coil length. Based on the experimental investigation, the correlation describing a refrigerating media condensation process in long coils is worked out.
The new formula is as below:

$$Nu = 279 \cdot M \cdot \dot{q}_w^{0,21} \cdot L^{-0,61} \cdot D^{0,75} \quad , \tag{1}$$

where:

$$M = \frac{(\rho_l)^{0,1}}{(r \cdot \nu_l)^{0,5} \cdot (\rho_g \cdot \sigma)^{0,3}} \quad , \tag{2}$$

Nu - Nusselt's number,
$\dot{q}_w$ - heat flux density in reference to the internal surface of coil tubes, [W/m^2],
L - length of a coil pipe in a condensation zone, [m],
D - internal diameter of a pipe, [m],
ν_l - coefficient of kinematic viscosity of a saturated liquid , [m^2/s],
ρ_l - saturated fluid density, [kg/m^3],
ρ_g - dry saturated vapour density, [kg/m^3],
r - heat of evaporation, [J/kg],
σ - surface tension, [N/m].

The formula gives the best results in refrigerating media condenser calculations within the scope of parameters investigated by the authors and given previously. A comparison between the calculated results as the formula (1) was applied and the experimental ones, is shown in Figure 7. It can be deduced that 90% of the experimental results are within ±15% scope compared to the values calculated on the basis of correlation (1). The correlation (1) was also verified against the formulas given by the other authors. However, because of the authors' lack of formulas describing the heat transfer coefficient as a function of the coil length, the formulas describing the condensation process in straight tubes were used. The comparison between various formulas is shown in Figures 7 and 8. Within the scope of the $\dot{m}$ and $\dot{q}$ values, being of a real interest in refrigerating engineering, a satisfactory compliance was achieved. The influence of the coil length on the heat transfer coefficient is evident.

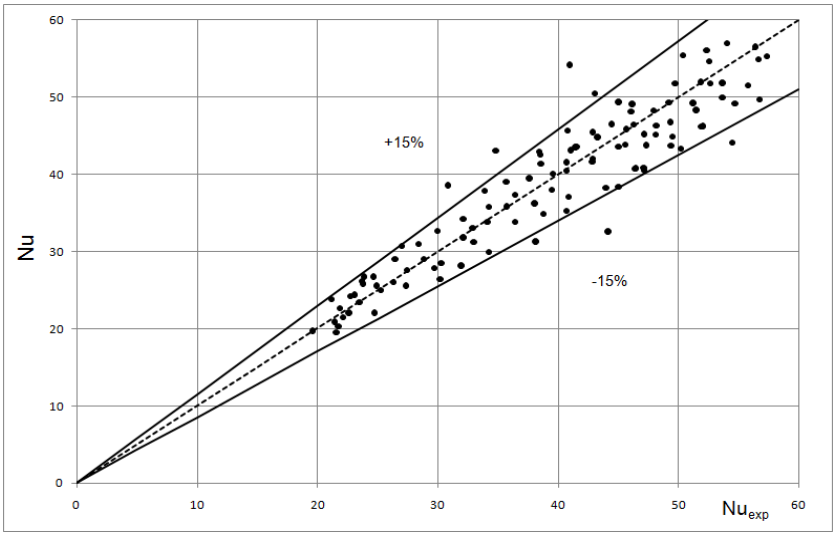

Figure. 7. Comparison of the experimental results Nu_{exp} with the calculations according to correlation Nu_{th}

A comparative listing of the authors' own investigations with the results of the calculations according to the correlations as given by other authors is presented in Figures 8 and 9. Those comparative correlations given by other authors were taken into consideration in which a dependence is noted of the Nusselt's number *Nu* from the coil pipe length. Figure 8 presents a comparison of the dependence of Nusselt's number *Nu* from the density of heat flux $\dot{q}$, while Figure 9 presents a comparison of the authors' own research results and calculations from the correlations given by other authors in the range of characteristics $Nu = f(\dot{m})$, where $(\dot{m})$ is the mass flux density.

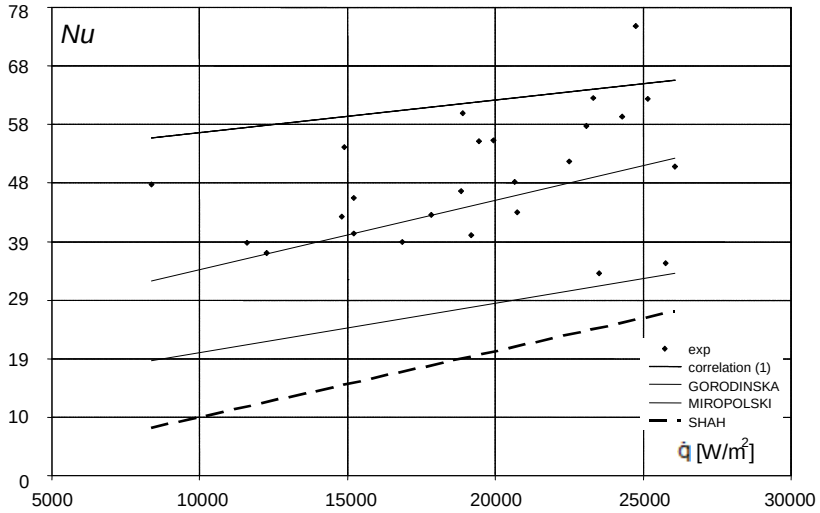

Figure. 8. Comparison of the results of investigations of Nusselt's number $Nu = f(\dot{q})$ with the results of calculations according to correlations provided by other authors [10, 11, 12]

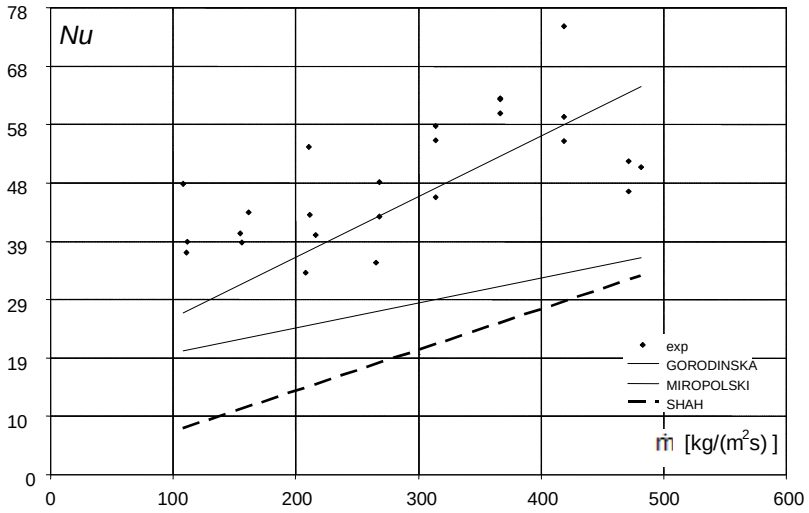

Figure. 9. Comparison of the results of investigations of Nusselt's number $Nu = f(\dot{m})$ with the results of calculations according to correlations provided by other authors [10, 11, 12]

CONCLUSIONS

1. During the condensation of a refrigerant in a flow through a vertical pipe, channel length L has practically no influence on the quantity of heat transfer coefficient h. If this process occurs in a flow through a coil pipe with large length L/D = 1500 (where D – internal diameter), then an influence of the channel length on the value of the coefficient is to be noted. This is so because the mechanism of the refrigerant's condensation changes in a pipe channel of a large length, with a substantial influence of the impeding of the flow through the condensate which leaves subsequent cross-sections of a long channel.
2. The authors conducted their own experimental investigations concerning the condensation of the R404A refrigerant in coil pipes with internal diameter D = 13 mm and length L = 10 ÷ 25 m. For design calculations, formula (1) is recommended, which allows one to calculate the mean h coefficient for coil pipes. The authors had previously checked the usability of formula (1) for engineering calculations with the following refrigerants: R12, R22, R134a and R404A.

REFERENCES

1. Chawla J.M.: Wärmeűbertragung in durchstrőmten Kondensatorrohren. *Kältetechnik-Klimatisierung* 1972, vol 24, s.233 *und Chem. Ing. Tech*. 43 (1971),14, s. 838
2. Cavallini A., Del Col D., Doretti L., Longo G.A. Rosefto L.: Condensation of refrigerants inside plain and enhanced tubes. *3th European Thermal Sciences Conference, Edizioni ETS, Pisa* 2000, pp. 51 – 60
3. Dobson M.K., Chato J.C.: Condensation in smooth horizontal tubes. *Journal Heat Transfer* 1998, vol 120, pp. 774 – 755
4. Rohsenow W.M.: Heat transfer and temperature distribution in laminar film condensation. *Transations of the ASME, Journal of Heat Transfer* 1965, vol. 76, pp. 1645
5. Tandon T.N., Varma H.K., Gupta C.P.: Generalized correlation for condensation of binary mixtures inside a horizontal tube. *An International Journal of Refrigeration* 1986, vol. 9, no 5, pp. 134 – 136
6. Tong L.: Empirical study of new refrigerant flow condensation inside horizontal smooth and micro-fin tubes. *Ph.D. Thesis*, University of Maryland and College Park, 1997, p. 251
7. Tandon T.N., Varma H.K., Gupta C.P.: Generalized correlation for condensation of binary mixtures inside a horizontal tube. *Int. Journal Refrigeration* 1986, vol. 9, No. 5, pp. 134-136

8. Bohdal T., Charun H., Matysko R.: Condensation of refrigerant R-404A in tubular channel. *Archives of Thermodynamics*, Vol. 27(2006) , No 1, pp. 13 - 29
9. Bohdal T., Charun H., Czapp M.: *Refrigeration and compressor steam devices. Theoretical background and calculations.* WNT, Warszawa 2003 (in Polish)
10. Daniłowa G.N., Bogdanov C.N., Iwanov O.P.: Heat exchangers in refrigerating systems, 1986
11. Gorodinskaja S.A.: Problem of generalization of experimental data of heat exchange during vapour condensation inside horizontal pipes, *IZW. Kijewsk,* Politechn. Instituta, t. XVIII, Kijev 1955
12. Shah M. M.: A general correlation for heat transfer during film condensation inside pipes *Journal of Heat Mass Transfer* 1979, Vol. 22 pp.547-555

This study was conducted under Research Project No. NN 512 361834.

EXPERIEMTNAL STUDY ON FLOW BOILING HEAT TRANSFER IN HORIZENTAL METAL-FOAM PARTIALLY FILLED TUBE

Yanping Du [1], Zhiguo Qu [1]*, Huijin Xu [1] , Changying Zhao [1,2] , Wenquan Tao [1] , Tianjian Lu [3]
[1] State Key Laboratory of Multiphase Flow in Power Engineering, Xi'an Jiaotong University, China
[2]University of Warwick, Coventry, England
[3]MOE Key Laboratory for Strength and Vibration, Xi'an Jiaotong University, China

ABSTRACT. In this work, the boiling flow heat transfer in horizontal metal-foam partially filled tubes is experimentally studied using HFC134a with water heating. The interface wall temperature distributions are tested. The effect of mass flow rate, vapour quality, and operation pressure on flow resistance, and two phase heat transfer coefficient are investigated. The two phase flow and heat transfer performance are compared with conventional smooth tube. It is revealed that the boiling heat transfer will be enhanced by increasing vapour quality for high mass flow rates more significantly than in the case of low mass flow rates. The facts are due to different flow patterns occurred inside the metal-foam tubes. The flow pattern can be predicted by monitoring the cross-sectional wall surface temperatures.

Key words: *metal foams, horizontal tube, flow resistance, boiling heat transfer, flow pattern*

INTRODUCTION

High porosity metal foams as a porous media for thermal transport has been a hotspot in the past several decades[1-10]. In order to ignore the effect of thermal radiation ,Calmidi and Mahajan [1] measured the effective thermal conductivity in the condition of low temperatures. As a result, an two-dimensional structure analytical model for predicting the effective thermal conductivity of metal foams was established. Later, a three-dimensional idealized cellular structure model was developped by Boomsma and Poulikakos [2]. The effects of thermal dispersion of metal foams is investigated by Hunt and Tien [3] and Lee et al. [4]. It is noted that high heat fluxes even up to 100 W/cm2 can be dissipated easily by metal foams in the convective condition. Recently, Lu et al. [5] developped an inter-connected cylinders model for analysing the thermal transport characteristics in metal foams, which is approved to be appropriate for most situation. Flow resistance and heat transfer characteristics of metal foams are numerously studyed[6-10]. Calmidi and Mahajan [6] and Kim et al. [7,8] both investigated flow resistance and heat transfer in metal-foam filled pipes through experimental test. It is found that the heat transfer coefficient enhances quickly while the pressure drop increases heavily at the same time. Bastarows et al. [9] found that the heat transfer coefficient in metal foams is as three times as that in conventional microfin. Hwang et al. [10]experimentally investigated the effect of foam porosity on flow resistance and heat transfer coefficient in luminum foams filled pipe.

Forced convection in metal foams without phase change has been studied in recent years[11-16]. Kim etal.[11]carried out experimental studies on single phase convective heat transfer performance in channels. Zhao etal. [12,13] analytically investigated performance of heat transfer and pressure drop and the influencing factors including porosity and pore size of the metal foam and the flow conditions.In contrast, Zhao et al. [14] also conducted experimental test and numerical simulation for

*Corresponding author, Dr. Z.G Qu
Phone:+(086)-29-82668036, Fax:+(86)-29-82668036
E-mail address: zgqu@mail.xjtu.edu.cn

convective flow and thermal transport in foams filled channnels. Mahjoob and Vafai [15] reviewed correlation of flow resistance drop and heat transfer in open cell metal-foam filled channel which will provide help information for heat exchanger design.

Qu and Mudawar[16] investigated the boiling mechanisms in micro channels. It is noted that the nucleation boiling and growth of vapour bubbles are sustained by the difference of temperature of channel wall and fluid by nucleate boiling, while the heat is transferred mainly by single-phase convection through the thin annular liquid film in the convective dominant region. Sondergeld and Turcotte[17] and Zhao et al[18] experimentally investigated boiling heat transfer in closed cavity in porous media. Rahli [19],Topin[20] studyed boiling performance for forced convection in porous media filled channels. The effects of heat flux and mass flux on the distribution of boiling region were discussed. Majumdar[21] and Chung[22] developped a flow model for each phase fluid based on Darcy law. Although research on single phase for metal foams and boiling performance for porous media attract more and more attention, little work was referred to the flow and heat transfer in metal foams with phase change due to complicated boiling mechanism in metal foams.

In this work, the boiling flow heat transfer in horizontal metal-foam partially filled tubes is experimentally studied using HFC134a with water heating. The flow and heat transfer performance are compared with conventional smoothe tube and fully filled foam tube. The effects of mass flow rate and operating pressure on boiling heat transfer and pressure drop are presented in the paper. The flow pattern predicted by monitoring the cross-sectional wall surface temperatures are also referred.

EXPERIMENTAL APPARATUS AND METHOD

Experimental system

Experimental system is comprised of a R134a receiving tank, a R134a pump for refrigerant circulation, a mass flow meter, a pre-heater, a test section, and two chillers. Water-heated method is adopted in the test section, seen in Figure 1(a). Before the refrigerant enters into the mass flow meters, it is firstly sub-cooled in a chiller in case of possible evaporation in pipe. The measurement range of flow meter is between 0.1 and 3 kg/min. A well-insulated pre-heater is used to control the inlet quality of refrigerant to the test section. The enthalpy of the sub-cooled refrigerant before the pre-heater can be determined from its pressure and temperature, thus the refrigerant quality and enthalpy at the inlet of test section can be determined by an energy balance on the pre-heater section. The temperature and pressure of the refrigerant at the inlet and outlet of the test section will be measured. The exit quality is calculated by an energy balance between the imposed heat flux by hot water and enthalpy change of the refrigerant across the test section. The pressure drop in the test section is measured using a differential pressure transducer. A glass tube after the test section will facilitate visualisation of the flow. After the test tube, the refrigerant will enter a separator with the liquid flowing from the bottom of the separator to the refrigerant reservoir and the vapour passing through a condensing heat exchanger where it will condense to liquid before returning to the reservoir.

Test section

The 18mm inner-diameter copper tube is initially used for the tests. The copper foam tube is sintered in the inner pipe with a thickness of 5mm. In addition, 32 T-type thermocouples are attached on 8 outer wall-surface locations along the flow direction. At each location, 4 thermocouples are placed on the circumference of the tube with angles of 0^o , 45^o , 90^o , 180^o, respectively, shown in Figure 1(b). The test tube will be heated by hot water in a double-pipe heat exchanger.

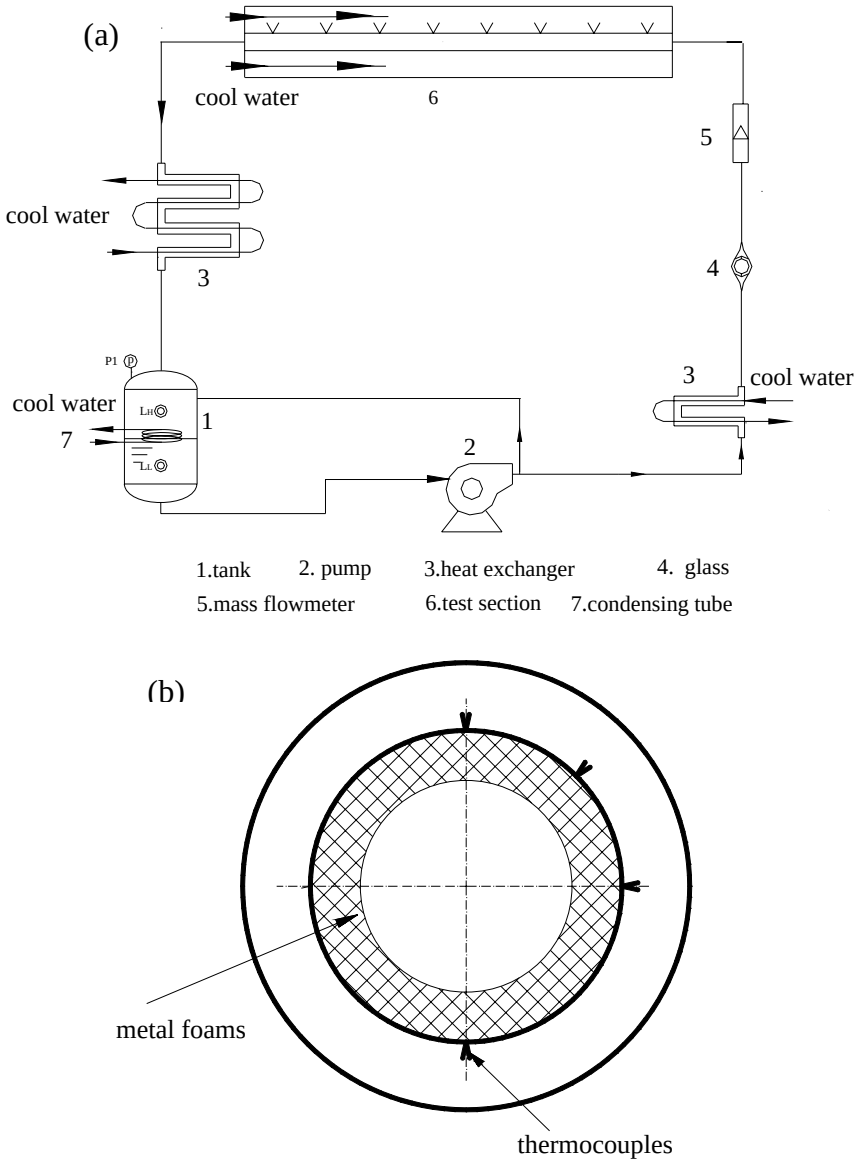

Figure 1. (a) Schematic diagram of test rig. (b) Location of thermocouples at cross section.

RESULT AND DISCUSSION

Experimental results for convective boiling flow resistance

Comparison with smoothe tube. Flow resistance characteristic for convective boiling is compared with that in smoothe tubes, shown in Figure 2(a). As is shown in Figure 2(a), it is noted that flow resistance and friction factor in partially filled tube is one to three magnitudes higher and much more sensitive to the value of vapor quality than that in smoothe tube. It is mostly related to the channel surface drag resistance, which is affected by flow velocity, vapor-liquid composition and the generating and movement of the boiling bubbles.

Effect of mass flux. The effect of mass flux of refrigerant R134a is described in Figure 2(b). Figure 2(b) indicates that pressure drop per unit length is affected obviously by the mass flow rates of R134a

except for vapor quality in the section. The results show that the pressure drop enhances with the increase of mass flux, accorded with Darcy law. Furthermore, it is seen that the difference of pressure drop becomes larger with the increase of vapor quality. It can be attributed to the higher quantity of vapor due to the increase of mass flux. The resistance characteristic is dramatically different from that in smoothe tube.

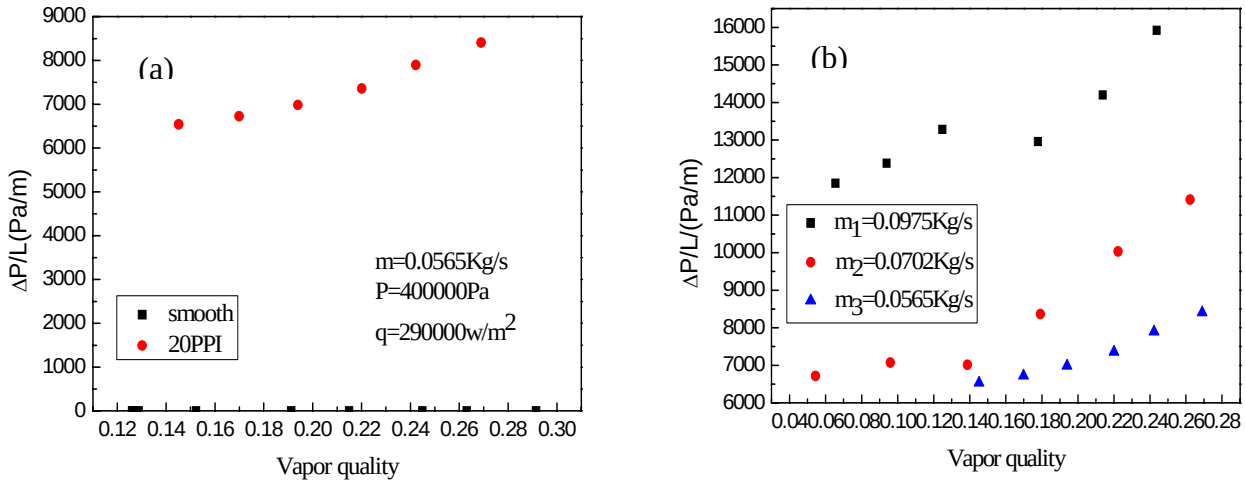

Figure 2. (a) Comparison of pressure drop for convective boiling. (b) Relation of pressure drop and vapor quality.

Effect of operating pressure. Figure 3 is the effect of operating pressure of refrigerant R134a on flow resistance in metal-foam partially filled tube. It indicates that oprerating pressure affects significantly on pressure drop and friction factor due to its influence on vapor density and vapor velocity. With the increase of operating pressure, the pressure drop for convective boiling decreases obviously by reason of the compressed vapor and reduced flow velocity of the vapor-phase, shown in Figure 3(a). It can be concluded that surface drag resistance for vapor- liquid convective boiling is essentially dominated by flow character of vapor-phase in metal foams. However, Figure 3(b) shows that friction factor becomes bigger with the increase of operating pressure, opposite to the pressure character. It can be explained by the definition of friction factor, which indicates that quadric vapor-phase velocity changes much more evidently than the influence of vapor velocity on the pressure drop.

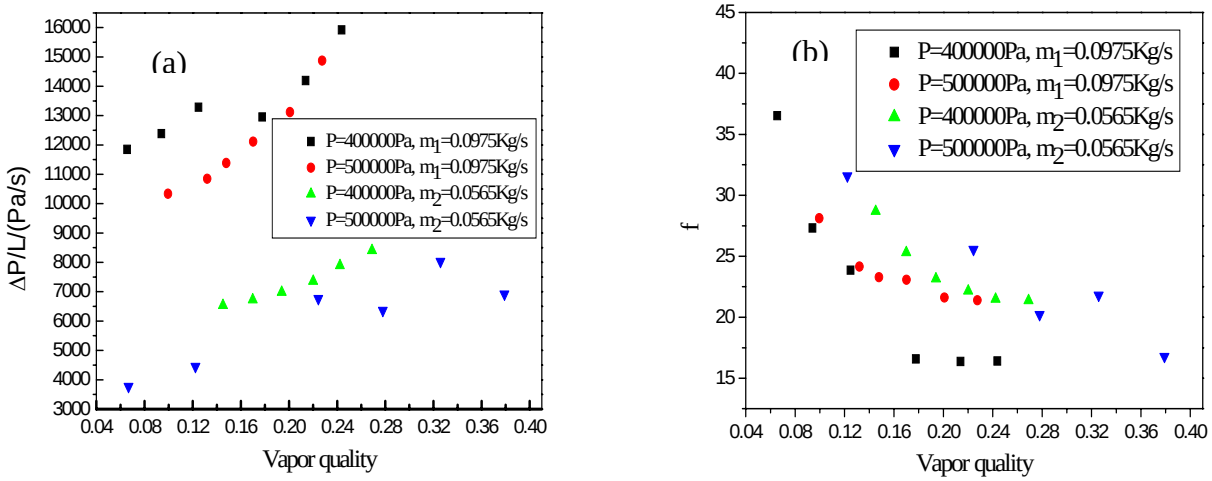

Figure 3. (a)The effect of operating pressure on pressure drop, (b)The effect of operating pressure on friction factor.

Experimental results for boiling heat transfer characteristic

Effect of mass flux of R134a. The boiling heat transfer coefficient is defined in equation (1). Δt represents the difference of refrigerant R134a and the average temperature of inner wall, while q means the uniform heat flux supplied by hot water. Mass flow rate of refrigerant R134a and vapor quality of the test section both influence the performance of boiling thermal transport in metal-foam partially filled tube, as shown in Figure 4. From Figure 4 it is seen that heat transfer coefficient and average Nusselt number along the test section increase with the increase of mass flow rate before the mass flux of 0.0702 *kg/s*, while heat transfer coefficient becomes smaller from mass flow rate 0.0702 *kg/s* to 0.975 *kg/s*. It may be concluded the flow pattern in the metal-foam partially filled tube changed during these two different range of mass flux. It indicates that convective boiling which is affected dramatically by mass flux is mainly processed in metal-foam partially filled tube before mass flux of 0.0702 *kg/s*. For the metal foams filled channel, microstructure of metal foams prevents the growth of bubbles and reduces the diameter of leaving bubbles resulting in uniformity flow and distribution of fluid temperature in metal foams. With the farther increase of mass flux, nucleate boiling whose thermal transport relies on liquid layer nearby the heated wall may become dominant due to the excessive liquid-phase.

$$h = \frac{q}{\Delta t} \tag{1}$$

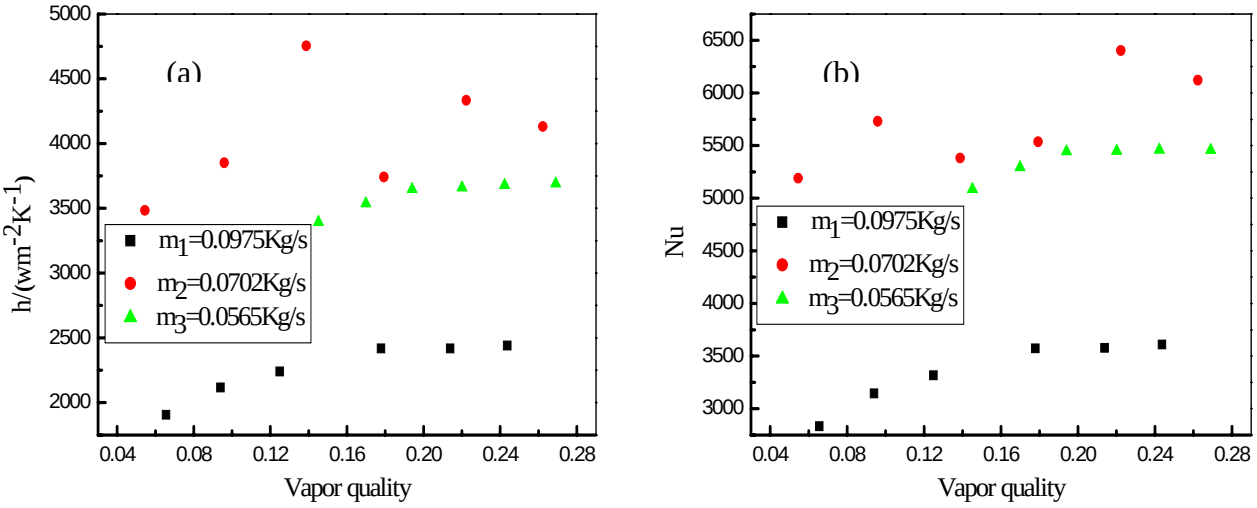

Figure 4. (a) The effect of mass flow rate on heat transfer coefficient, (b) The effect of mass flow rate on nusselt number.

Effect of operating pressure. The effect of operating pressure on convective boiling in metal-foam partially filled tube is shown in Figure 5. It is clear that boiling heat transfer coefficient enhances with the increase of operating pressure of refrigerant R134a. Vapor-phase is compressed and vapor velocity is reduced, attributed to the increase of operating pressure. In the thermal conductivity dominant situation, contact-time of the two phase flow and metal foams extends, resulting in enhanced heat transfer coefficient.

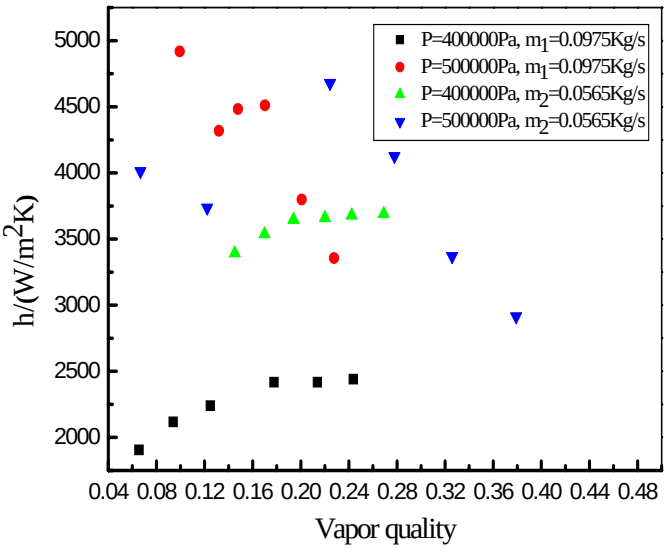

Figure 5. The effect of operating pressure on heat transfer coefficient.

Flow patterns in metal-foam partially filled tube

The flow patterns in metal-foam partially filled tube can not be directly viewed and studied , known from that in smoothe tube. However, it can be partially analysed by the distribution of wall temperature at the cross section. The fluctuations of wall temperature with time for different vapor quality is presented in Figure 6, in which the tempretures of 0 degree , 90 degree and 180 degree are noted down with top, middle and down, respectively.

As well known, refrigerant R134a is accumulated at the bottom of the horizontal tube due to gravity effect. It is proved in Figure 6(a) and Figure 6(b) by the lowest temperature at the bottom. It is also indicated that upper part of the tube is more possibly occupied by vapor-phase while middle part is potentially filled with mixture of vapor-liquid two-phase fluid. The top wall temperature is the highest while the bottom temperature is the lowest due to the component of the vapor-liquid phases, as is shown in Figure 6(a). However, the middle wall temperature is mostly close to the top wall temperature at the vapor quality of *x=0.301*, shown in Figure 6(b), compared to the quality of *x=0.066*, shown in Figure 6(a). It can be noted that proportion of vapor-phase increases heavily at the 90 degree of the cross section. Therefore, stratified flow can be predicted at the vapour quality of *x=0.301*.

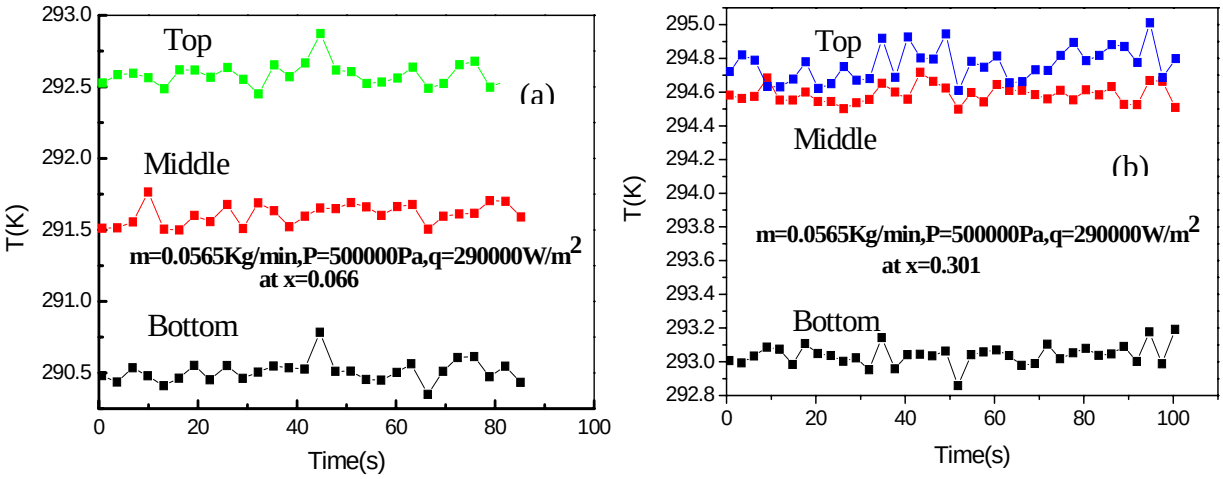

Figure 6. (a)Fluctuations of wall temperature at low vapor quality. (b) Fluctuations of wall temperature at higher vapor quality.

CONCLUSIONS

Flow boiling heat transfer in horizontal metal-foam partially filled tube is experimentally investigated in this paper. It can be concluded as follows:

For convective boiling, flow resistance and friction factor in partially filled tube is one to three magnitudes higher and much more sensitive to the value of vapor quality than that in smoothe tube. However, boiling heat transfer coefficient in metal foams partially filled tube is approximately as three times as that in smoothe tube.

For convective boiling, the pressure drop is increased with the increase of mass flux, or the decrease of operating pressure. However, the characteristic of friction factor for convective boiling is opposite to that of pressure drop.

Boiling heat transfer coefficient is increased with the increase of operating pressure of refrigerant R134a. It is indicated that vaper-phase is compressed and vapor velocity is reduced, attributed to the increase of operating pressure.

The relation of boiling heat transfer coefficient and mass flow rate depends on the flow pattern of the fluid in metal-foam partially filled tube.It can be noted that proportion of vapor-phase enhanced heavily at the 90 degree of the cross section at the vapour quality of $x=0.301$. Therefore, stratified flow can be predicted.

ACKNOWLEDGEMENT

The authors want to give thanks to National Natural Science Foundation of China (No.50806057) and National Basic Research Programme of China (No.2006CB601203) for support.

REFERENCE

1. Calmidi, V. V. and Mahajan, R. L., The effective thermal conductivity of high porosity fibrous metal foams, *ASME J. of Heat Transfer.*, Vol. 121, No. 2, pp 466 – 471, 1999.
2. Boomsma, K. and Poulikakos, D., On the effective thermal conductivity of a three-dimensionally structured fluid-saturated metal foam, Int. J. Heat Mass Transfer., Vol. 44, No. 4 pp 827 – 836, 2001.
3. Hunt, M. L. and Tien, C. L., Effects of thermal dispersion on forced convection in fibrous media, Int. J. Heat Mass Transfer., Vol. 31, No. 2, pp 301-309, 1988.
4. Lee, Y. C., Zhang, W., Xie, H. and Mahajan, R. L., Cooling of a FCHIP package with 100 w, 1 cm2 chip, Proceedings of the 1993 ASME Int. Elec. Packaging Conf., New York, 1993, pp 419-423.
5. Lu, T. J., Stone, H. A. and Ashby, M. F., Heat transfer in open-celled metal foams, Acta Mater ., Vol. 46, No. 10, pp 3619-3635, 1998.
6. Calmidi, V. V. and Mahajan, R. L., Forced convection in high porosity metal foams, J. of Heat Transfer., Vol. 122, No. 3, pp 557 – 565, 2000.
7. Kim, S. Y., Paek, J. W., and Kang, B. H., Flow and heat transfer correlations for porous fin in a plate-fin heat exchanger, J. of Heat Transfer., Vol. 122, No. 3, pp 572 –578, 2000.
8. Kim, S. Y., Kang, B. H., and Kim, J. H., Forced convection from aluminium foam materials in an asymmetrically heated channel, Int. J. Heat Mass Transfer., Vol. 44, pp 1451 – 1454, 2001.
9. Bastarows, A. F., Evans, A.G. and Stone, H. A., Evaluation of Cellular Metal Heat Dissipation Media, Technical Report MECH-325, DEAS, Harvard University, 1998.
10. Hwang, J. J., Hwang, G. J., Yeh, R. H., and Chao, C. H., Measurement of interstitial convective heat transfer and frictional drag for flow across metal foams, J. of Heat Transfer., Vol. 124, No. 1, pp 120 – 129, 2002.

11. Kim, T., Fuller, A.J., Hodson, H.P., Lu, T.J.,An experiment study on thermal transport in lightweight metal foams at high Renolds numbers, Proceedings of the International Symposium of Compact Heat Exchangers,AIAA,Reston,VA,2002, pp 227-232.
12. Lu, W., Zhao, C. Y., Tassou, S. A., Thermal Analysis on Metal-Foam Filled Heat Exchangers, I. Metal-Foam Filled Pipes, Int. J. Heat and Mass Transfer., Vol. 49, No. 15-16, pp 2751-2761, 2006.
13. Zhao, C. Y., Lu, W., Tassou, S. A., Thermal Analysis on Metal-Foam Filled Heat Exchangers, II. Tube Heat Exchangers, Int. J. Heat and Mass Transfer., Vol. 49, No. 15-16, pp 2762-2770, 2006.
14. Zhao, C.Y., Kim, T., Lu, T.J. and Hodson, H.P., Thermal transport in high porosity cellular metal foams, Journal of Thermophysics and Heat Transfer., Vol. 18, No. 3, pp 309-317, 2004.
15. Shadi Mahjoob , Kambiz VafaiA, Synthesis of fluid and thermal transport models for metal foam heat exchangers, International Journal of Heat and Mass Transfer., vol. 51, No.15-16, pp. 3701-3711, 2008.
16. Qu, W. and Mudawar, I., Flow Boiling Heat Transfer in Two-Phase Micro-Channel Heat Sinks — I. Experimental Investigation and Assessment of correlation methods, In. J. Heat and Mass Transfer., Vol. 46, No. 15, pp. 2755-2771, 2003.
17. Sondergeld, C. H., Turcott, D. L., An experimental study of two-phase convection in a porous medium with applications to geological problems, J. Geophys.Res., Vol. 82, pp 2045-2053, 1977.
18. Zhao, T. S., Liao, Q., On capillary-driven flow and phase-change heat transfer in a porous structure heated by a finned surface: measurement and modeling., Int.J.Heat and Mass Transfer., Vol. 43, pp 1141-1155, 2000.
19. Rahli, O., Topin, F., Tadrist, L., et al, Analysis of heat transfer with liquid-vapor phase change in forced flow fluid moving through a porous media, Int. J. Heat and Mass Transfer., Vol. 39, No. 20, pp 3959-3975, 1996.
20. Topin, F., Rahli, O., Tadrist , L., et al, Experimental study of convective boiling in porous medium: Temperature field analysis, J. of Heat Transfer., Vol. 18, pp 230-233, 1996.
21. Majumdar, A., Tien, C. L., Effects of surface tension on film condensation in porous medium, J. Heat Transfer., Vol. 112, No. 3, pp 751-757, 1990.
22. Chung, J. N., Plumb, O. A., Lee, W. C., Condensation in porous region bounded by a cold vertical surface, J. Heat Transfer., Vol. 114, No. 4, pp 1011-1018, 1992.

EXPERIMENTAL ANALYSIS OF THERMOMAGNETIC CONVECTION IN VERTICAL ANNULAR ENCLOSURE

W. Wrobel*, E. Fornalik, J. S. Szmyd
AGH - University of Science and Technology, Krakow, Poland

ABSTRACT. In the present paper an experimental analysis of a thermomagnetic convective flow of paramagnetic fluid in an annular enclosure with a round rod core and a cylindrical outer wall is presented. The convection in the annulus between two vertical coaxial cylinders resulting from gravitational and magnetic environments has been investigated for the first time. In this configuration, natural convection heat transfer is due to the gravity and gravitational buoyancy force. However, it is not always possible to influence this convection at will as physical, technological or economic limitations may arise. A strong magnetic field can be an alternative to heat transfer enhancement. The experimental enclosure was placed in a bore space of a super-conducting magnet of 10 T in three selected positions: 0.09 m above, 0.09 m below and at the centre of solenoid. The axis of bore space was maintained vertically and an aqueous glycerol solution with dissolved gadolinium nitrate hexahydrate (paramagnetic) was employed as the working fluid. The effect of the magnetic field on convection in the annular vessel in selected positions was compared.

Keywords: *thermomagnetic convection, strong magnetic field, paramagnetic fluid, vertical annulus, average heat transfer rate*

INTRODUCTION

The control of fluid convection by a strong magnetic field is an interesting concept that has possible applications for industrial processes. Engineering processes under the influence of magnetic field such as crystal growth using Czochralski method or continuous steel casting are described by Ozoe [1]. The natural convection driving force comes from the density difference between the hot and cold regions of the fluid. If the fluid's magnetic susceptibility varies with temperature, magnetic force can also induce the convective motion.
The magnetic force per unit volume in magnetic field gradient can be defined as [2]:

$$F_{mz} = \mu_0 M \frac{\partial H}{\partial z}, \tag{1}$$

where: M is the magnetization, H is the magnetic field and z is distance.
For paramagnetic fluid, magnetization M is proportional to the applied magnetic field:

$$M = \chi_v H, \tag{2}$$

where χ is the volume magnetic susceptibility which depends on density ρ: $\chi_m = \chi_v / \rho$ and temperature following Curie's law $\chi_m \sim 1/T$. It is important that the magnetic force works only in the non-uniform field. The final expression for the magnetic force, which is based on the mentioned laws, is presented in Table 1. In this expression the most important quantities are the gradient of the square magnetic induction and the magnetization. For the paramagnetics, the gradient of square magnetic induction is equivalent to the gravitational acceleration $\vec{g}$ in the case of natural

* Corresponding author: Witold Wrobel
Phone: + (48)-12-617-26-63, Fax: + (48)-12-617-26-85
E-mail address: witold@agh.edu.pl

convection and the magnetization is equivalent to the thermal expansion coefficient β [2]. A comparison of the natural and thermomagnetic convections is listed in Table 1.

Table 1. Comparison of natural and thermomagnetic convection

Gravitational convection	Thermomagnetic convection
$F_{gz} = -\vec{g}\rho_0\beta(T-T_0)$	$F_{mz} = -\left(1+\frac{1}{\beta T_0}\right)\frac{\rho_0\chi_m\beta}{2\mu_0}(T-T_0)\frac{\partial B^2}{\partial z}$
$\vec{g}$	$\frac{\partial B^2}{\partial z}$
β	$\left(1+\frac{1}{\beta T_0}\right)\frac{\chi_m\beta}{2\mu_0}$

where: μ_0 is the magnetic permeability, B is the magnetic induction, T_0 is the average temperature of fluid, and T is the temperature of fluid.

EXPERIMENTAL SYSTEM

Experimental apparatus

The experimental vessel is presented in Fig. 1.

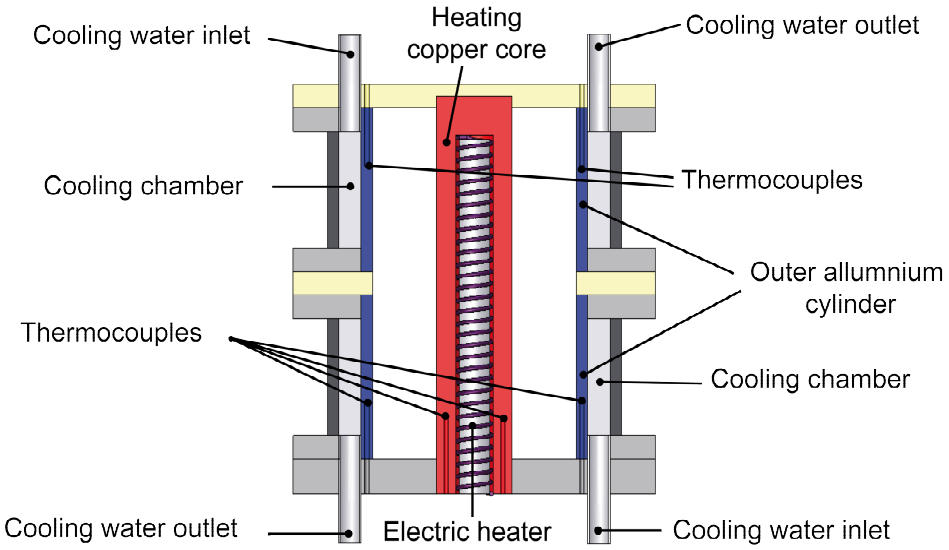

Figure 1. Cross-section of the experimental vessel

The experimental vessel is an annular enclosure with a round rod core and a cylindrical outer wall. The core diameter was 0.02 m and the diameter of the outer cylinder was 0.054 m. The outer cylinder was made of aluminum of 0.003 m thickness, while the core was a copper rod that could be electrically heated. A resistance wire was wound around a ceramic element and placed in a drilled hole inside the copper bar. The electric heater was charged with DC power and the voltage and electrical current were constantly controlled. The outer cylinder was cooled with the water kept at constant temperature inside a thermostating bath. In the middle height a Plexiglas plate of 0.006 m thickness was inserted. The core temperature was measured with two T-type thermocouples and the temperature of the aluminum side wall with three T-type thermocouples. The enclosure was closed by a Plexiglas plate of 0.006 m thickness from one side and an ebonite plate of 0.009 m thickness

from the other. There was a small hole in the closing Plexiglas plate through which the experimental fluid was injected. The total height of the enclosure was 0.092 m. The assembled experimental system is shown in Fig. 2 and the aspect ratio is defined

$$A = \frac{h}{r_o - r_i}, \tag{3}$$

where: h is the height of the enclosure, r_i is the radius of the core, r_o is the radius of the aluminum cylinder. The aspect ratio for the studied geometry was equal to A = 5.41.

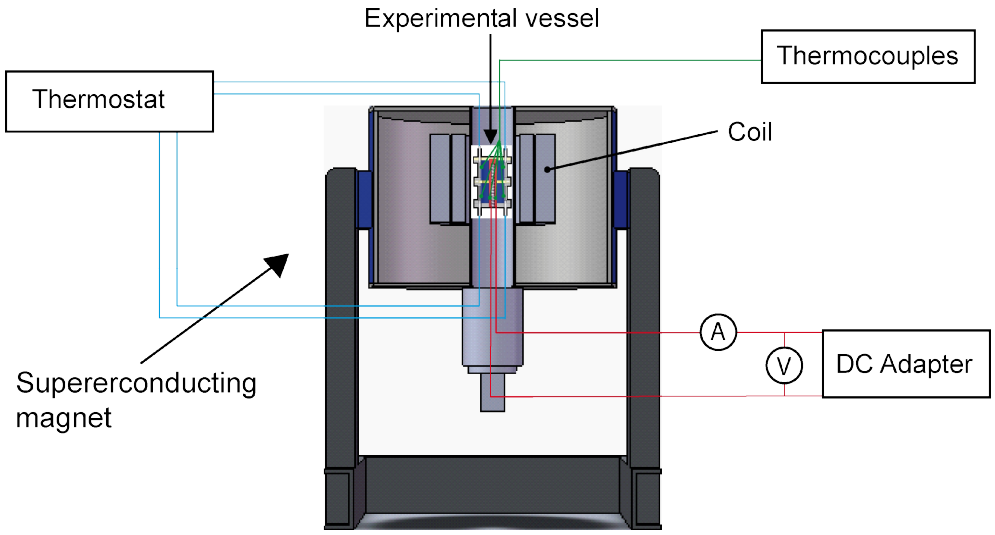

Figure 2. Pictorial drawing of the experimental setup

Fluid

A 50% volume aqueous solution of glycerol with 0.3 mol/(kg of solution) concentration of gadolinium nitrate hexahydradte ($Gd(NO_3)_3 \times 6H_2O$) was used as the working fluid. 150 ml of water and 150 ml of glycerin were mixed to yield 0.320629 kg of solution. To obtain a 0.3 mol/(kg of solution) concentration of gadolinium nitrate hexahydradte of molar mass (0.45136 kg/mol), 0.05030 kg, was added. The thermal expansion coefficient, thermal conductivity, electrical conductivity, density and dynamic viscosity were all found experimentally. The mass magnetic susceptibility of the fluid was measured with the magnetic susceptibility balance. Dynamic viscosity is a function of temperature and the expression describing it was obtained from the experimental data; this equation was subsequently formulated

$$\mu_{(T)} = 0.816 - 5.05 \cdot 10^{-3} T + 7.854 \cdot 10^{-6} T^2 . \tag{4}$$

The properties of 50% volume aqueous solution of glycerol are listed in Table 2.

Table 2. Properties of the fluid at T_0 = 298 K

Properties	Symbol	Value	Unit
Thermal diffusivity	α	$1.14 \cdot 10^{-7}$	m^2/s
Thermal expansion coeff.	β	$3.80 \cdot 10^{-3}$	1/K
Thermal conductivity	λ	0.42	W/m·K
Dynamic viscosity	μ	$1.72 \cdot 10^{-2}$	kg/m·s
Kinematic viscosity	ν	$1.40 \cdot 10^{-5}$	m^2/s
Electrical conductivity	σ	$2.16 \cdot 10^{-6}$	S/m
Density	ρ_0	1230	kg/m^3
V. m. susceptibility	χ_v	$8.3 \cdot 10^{-6}$	[-]

EXPERIMENTAL PROCEDURE

The enclosure was filled with the working fluid with a syringe and needle. The water temperature in the constant temperature bath was set at 18 ^{0}C and the supplied power of electrical heater placed in the core set up at a certain level. The level of supplied power was a variable parameter. Three values of the power were studied in particular detail: 4.45 W, 13.11 W and 27.21 W. The experimental studies were divided into a few steps, the first of which was to examine the natural convection in the presented annular vessel. When the power was set, the apparatus was left to reach steady state. This lasted about 30 to 40 minutes, after which the measured values were recorded and the supplied power set to the next level. The recorded temperature data was averaged and then analysed. The data taken during the last 10 minutes before changing the parameters was included in the average.

When the measurements for various supplied power were done, the next stage was started. The enclosure was placed in a bore of a 10-Tesla superconducting magnet. Three positions were chosen to be studied and are presented in Fig. 3a: (A) the upper maximum value of gradB^2 at the level of 0.101 m from the upper edge of the magnet which corresponds to the 0.090 m above the solenoid centre; (B) the lower maximum value of gradB^2 at the level of 0.281 m from the upper edge of the magnet which corresponds to 0.090 m below the solenoid centre; (C) the centre of the magnetic field – the centre of the enclosure was at the centre of the coils, which means 0.191 m from the upper edge of the magnet, which related to the maximum of magnetic induction.

The distribution of magnetic field inside the bore at 1 T of magnetic induction obtained numerically is shown in Fig. 3b. An example of the gradient square magnetic induction distribution is presented in Fig. 3c. The magnified distributions of the magnetic field induction square gradient inside the experimental vessel for three studied positions A, B and C are presented in Fig. 4. As in Fig. 4a, the vectors in the position above the coil are directed downward, those below the coil (Fig. 4b) are directed upward and in the centre (Fig. 4c) they are directed both upward and downward. The distribution presented in Fig. 4 is important because the magnetic force is proportional to the gradient of square magnetic induction, as listed in Table 1.

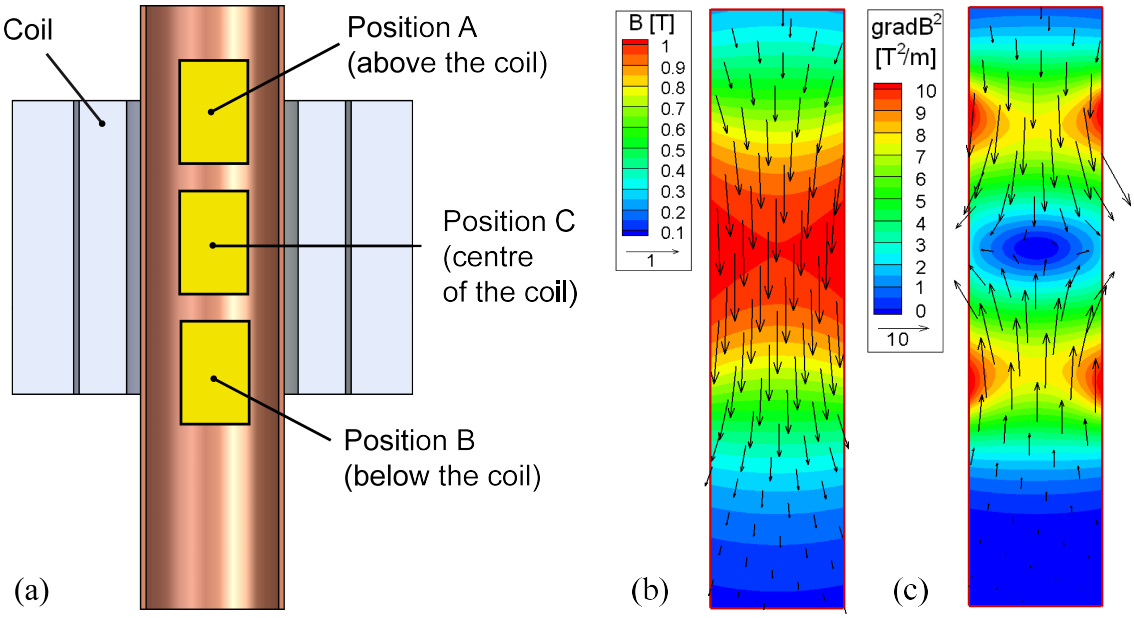

Figure 3. (a) Position of experimental vessel in the bore, (b) distribution of magnetic induction inside the bore from numerical calculation at 1 T of magnetic induction at the centre, (c) distribution of gradient of square of magnetic induction inside the bore at 1 T of magnetic induction

The enclosure was first placed in position A (above the solenoid centre). The temperature of cooling water and certain value of the heater's electric power were set. The system was left to reach a steady state, which took 30-40 minutes. The magnetic field was then applied to the system. At first the magnetic induction of 1 T was set and the apparatus was left to reach the steady state. Then all controlled parameters (temperature, electrical current, voltage) were recorded and the magnetic induction was changed to 2 T. The procedure of setting the controlled parameters, reaching the steady state and recording the data was repeated up to 10 T of magnetic induction. In some cases the magnetic induction was changed from 10 T to 0 T, but the direction change of the magnetic induction (increasing or decreasing) did not have a visible influence on the results. All steps were repeated for three selected power supplies and for the other positions in the magnet bore.
The last stage of the experiment was related to the estimation of heat loss from the enclosure to the environment. The enclosure was emptied and placed inside the magnet bore. It was assumed that the convection and conduction of air was negligible and that the heat loss depended only on the temperature of the heated core. The heat loss measurements were conducted for various powers of the electrical heater.

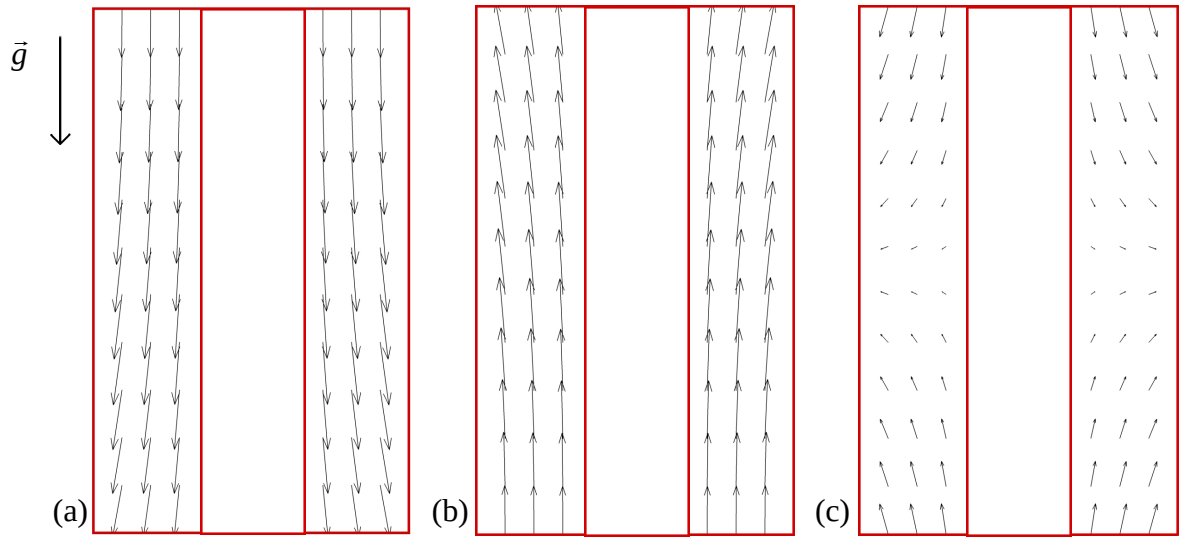

Figure 4. Schematic view of magnetic induction square gradient distribution, (a) above the coil, (b) below the coil, (c) in the centre of the coil

ESTIMATING THE NUSSELT AND RAYLEIGH NUMBERS

To describe the rate of net convection heat transfer, it is easy to use the quantified value known as the Nusselt number. The Nusselt number was calculated as

$$\mathrm{Nu} = \frac{Q_{conv\_net}}{Q_{cond\_theor}}, \tag{5}$$

where Q_{conv_net} indicates the convection heat flux and Q_{cond_theor} is the theoretical heat flux due to the conduction:

$$Q_{conv\_net} = Q_{conv} - Q_{loss}, \tag{6}$$

and:

$$Q_{conv} = U \cdot I, \tag{7}$$

where: U is voltage, and I is electrical current.
The theoretical conduction heat flux Q_{cond_theor} was calculated numerically from the energy equation:

$$\nabla^2 T = 0, \tag{8}$$

and the final form of its definition can be written

$$Q_{cond\_theor} = F_{CFD}\lambda\left(T_h - T_c\right), \tag{9}$$

where F_{CFD} - configurational parameter was calculated for the geometry of the experimental vessel, λ is the thermal conductivity, T_c is the temperature of the cooled wall and T_h is the temperature of the heated wall. The heat loss was calculated from the equation

$$Q_{loss} = 0,082 \cdot (T_h - T)_c, \tag{10}$$

which is a linear approximation of experimental data presented in Fig. 5. It should be emphasized that, due to the configuration of the experimental enclosure, the heat loss was quite small relative to the power supplied.

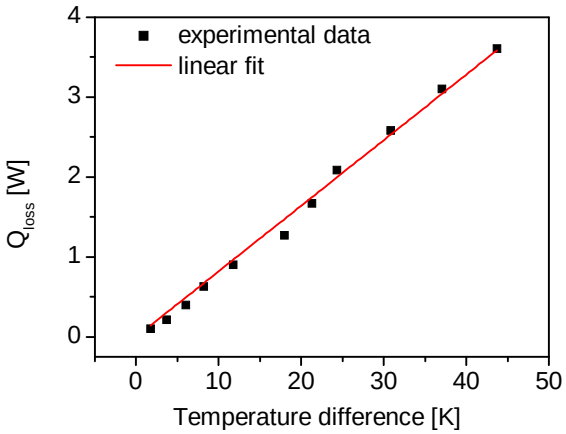

Figure 5. The experimental relation between the heat loss and the temperature difference

The Rayleigh number combines the buoyancy, viscosity, momentum diffusivity and the thermal diffusivity of the fluid in one dimensionless parameter. In the absence of magnetic field, for the annulus in a vertical position [3], the number can be expressed

$$\mathrm{Ra} = \frac{g\beta}{\alpha\nu}(T_h - T_c)(r_o - r_i)^3, \tag{11}$$

where: g is the gravitational acceleration, β the thermal expansion coefficient, α the thermal diffusivity, ν kinematic viscosity, r_i the inner radius of cylinder and r_o the outer radius of the cylinder. For the paramagnetic fluid in the non-uniform magnetic field, following Table 1, the magnetic Rayleigh number can be defined as:

$$\mathrm{Ra_m} = \mathrm{Ra}\left[1 + \frac{\partial B^2}{\partial z}\left(1 + \frac{1}{\beta T_0}\right)\frac{\chi_m}{2\mu_0 g}\right]. \tag{12}$$

RESULTS

Figure 6 presents the Nusselt number values versus the magnetic induction in the centre of solenoid for all studied configurations. In Fig. 6a the data were obtained for the vessel in A configuration (above the solenoid centre). It presents continuous growth from the magnetic induction 1 T. The Nusselt number increased with the magnetic induction. This tendency is observed for the three examined values of power supply. At 10 T of magnetic induction the Nusselt number was two times higher than without the magnetic field. Even the highest studied Rayleigh number did not cause such a high heat transfer rate, which suggests strongly intensified convection. This enhanced heat transfer was obtained due to both forces (gravitational and magnetizing) acting in the same direction. As seen in Fig. 4a, the vectors of gradB^2 are directed downward, similarly to gravity.

In Fig. 6b the Nusselt number values were obtained for the enclosure placed in configuration B (below the coil). At magnetic induction of 0 T to 2 T a decrease in the Nusselt number was observed. A Further increase in magnetic induction up to 10 T caused an increase in the heat transfer rate. The minimum Nusselt number is observed. The same tendency was obtained for three studied power supplies. This data at first suggested the suppression of convection but enhancement of it later.

In configuration C (Fig. 6c), when the magnetic induction was 0 T, 1 T and 2 T, there was no visible influence on the heat transfer rate. At the magnetic induction of 3 T the Nusselt number decreased, which suggests suppression of the natural convection. Increasing the magnetic induction from 4 T to 10 T caused the Nusselt number to increase.

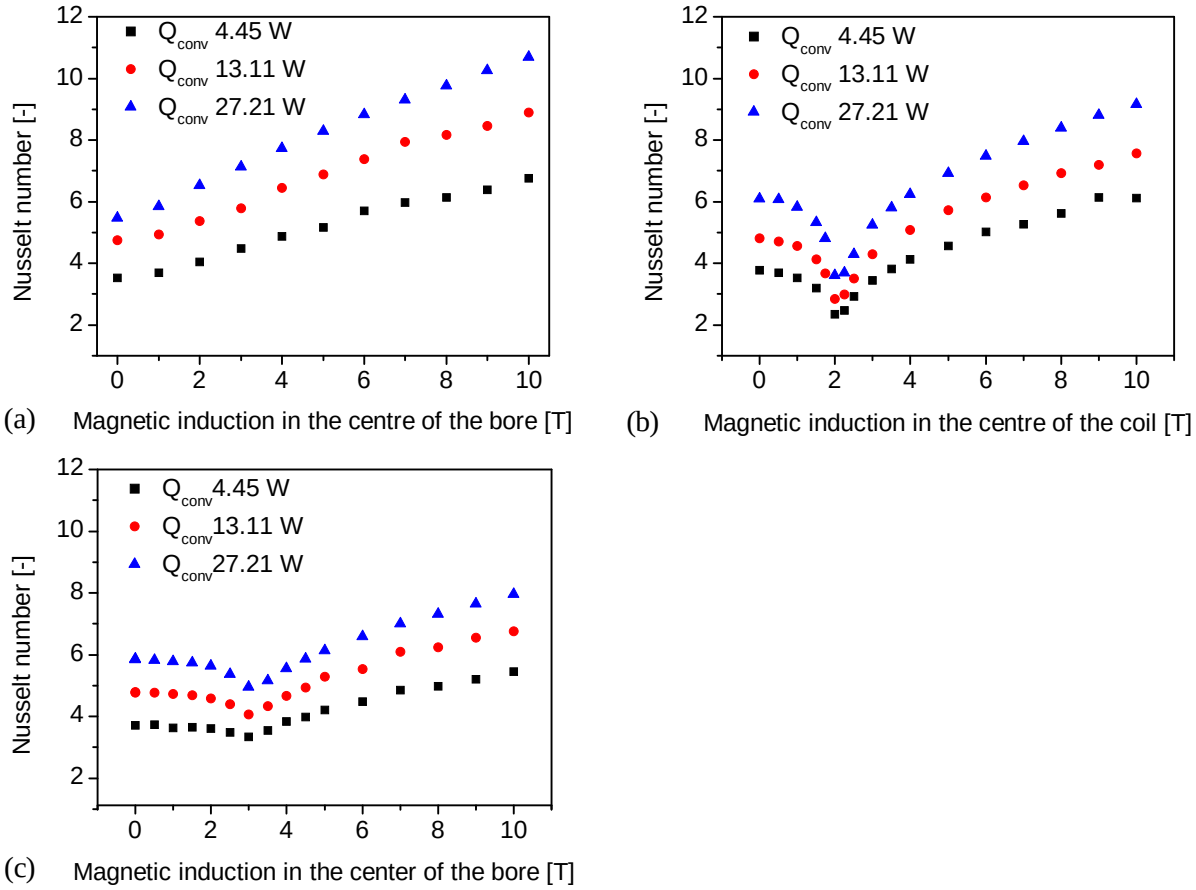

Figure 6. Experimental relationship between the Nusselt number and the magnetic induction: (a) experimental vessel in the configuration above the centre of coil, (b) vessel below the centre of the coil, (c) vessel in the centre of coil

In Fig. 6 the Nusselt number at magnetic induction of 0 T was equal for all studied positions, which indicates the results are repeatable. The results for position B (below the coil centre) and C (at the coil centre) show the minimum. For the position below the coil centre, the Nusselt number was minimal at magnetic induction of 2.0 T while in position at the centre at 2.5 T. A further increase in the magnetic induction in both cases caused the Nusselt number to increase. The highest Nusselt number values were obtained above the coil centre, while the lowest were obtained at position in the coil centre, which was understandable in light of the magnetizing force acting on the fluid in two opposite directions see Fig. 4c.

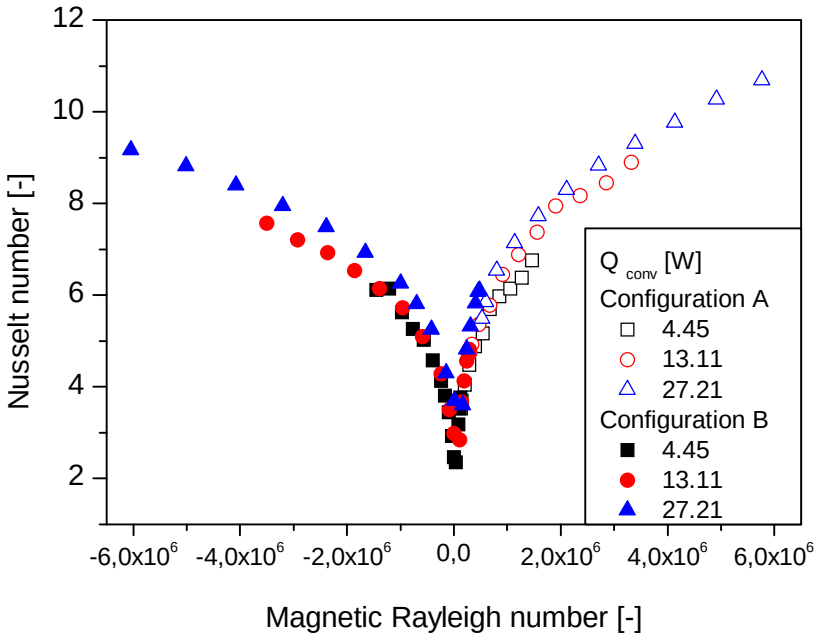

Figure 7. Plot of the Nusselt number versus magnetic Rayleigh number for data obtained in configuration A and B at various values of magnetic induction

Figure 7 presents the Nusselt number versus the magnetic Rayleigh number. The negative values of the Rayleigh number show that the gravitational and the magnetizing forces acted in opposite directions, though the magnetizing force did start to dominate in the system. The magnetic Rayleigh number equal to 0 corresponds to the situation when the gravitational and magnetizing force are equal to each other but moved in opposite directions. The combined data shows that the magnetic Rayleigh number is a parameter which can quantitatively describe the behavior of the fluid in the presence of the magnetic field and temperature gradient.

CONCLUSIONS

The results show that magnetizing force effects the heat transfer rate. A strong magnetic field can control the magnetic convection of paramagnetic fluid. Depending on the direction and the strength of magnetic field, either the enhancement or suppression of convective motion will be observed. The magnetic Rayleigh number is a parameter which can be used to characterize behavior of the fluid in the magnetic field. However, its definition needs to be studied thoroughly, because the behavior of the fluid in the vessel placed in C configuration (in the centre of coil) has not been clearly described.

ACKNOWLEDGEMENTS

This research was supported by grant AGH No. 10.10.210.182

REFERENCES

1. Ozoe H., Magnetic convection, *Imperial College Press*, 2005.
2. Braithwaite D., Beaugnon E., Tournier R. Magnetically controlled convection in a paramagnetic fluid, *Nature*, Vol. 354, pp. 134-136, 1991.
3. Francis N. D., Itamura M. T., Webb S. W., James D. L., CFD Calculation of internal natural convection in the annulus between horizontal concentric cylinders, *Sandia National Laboratories*, 2002.

A RAYLEIGH - BÉNARD CONFIGURATION OF A CUBICAL ENCLOSURE UNDER VARIOUS ORIENTATIONS OF MAGNETIC INDUCTION SQUARE GRADIENT

Ł. Pyrda[1*], E. Fornalik[1], J. S. Szmyd[1]
[1]AGH – University of Science and Technology, Krakow, Poland

ABSTRACT. In the present investigation the influence of a strong magnetic field on paramagnetic fluid is described. The cubical enclosure in the Rayleigh-Bénard configuration was chosen for study. The enclosure was heated from the bottom wall and cooled from the top one. All other walls were adiabatic. The natural convection in this geometry is quite well known. Therefore the influence of magnetic field with various orientations of $\nabla\vec{b}^2$ on the convection phenomena was distinguished easily. The high temperature gradients under a strong magnetic field were also examined.

Keywords: *thermomagnetic convection, strong magnetic field, paramagnetic fluid, cubic enclosure, heat transfer rate*

INTRODUCTION

The influence of temperature gradients on the density of fluid is known, as is that in systems with a temperature gradient, buoyancy forces occur. Such phenomena are commonly called free or natural convection. Control of convection phenomena is important for many heat transfer issues such as mixing devices, air conditioning systems or controlling crystal growth [1]. The buoyancy forces can control the convection but this control is limited. Utilization of magnetic force (Kelvin force) to control convection yields gives more possibilities. Bai et al. [2] formulated their magnetic force equation as follows:

$$F_{mag} = \frac{\chi_v \mu}{2} \nabla \vec{h}^2 \tag{1}$$

where: $\vec{h}$ is the magnetic field [A/m], χ_v is the volume magnetic susceptibility ($\chi_v = \chi_m \cdot \rho$) [-], χ_m is the mass magnetic susceptibility [m^3/kg], ρ *is* density [kg/m^3], and μ is the magnetic permeability [H/m]. This equation is inserted:

$$\mu = \vec{b} / \vec{h} \tag{2}$$

where: $\vec{b}$ is the magnetic induction [T]. According to Curie's law and Bussinesq approximation, the magnetic force equation (1) can be rewritten

$$F_{mag} = -\left(1 + \frac{1}{\beta\theta_0}\right) \frac{\rho_0 \chi_m \beta(\theta - \theta_0)}{2\mu_0} \nabla \vec{b}^2 \tag{3}$$

where β is the thermal expansion coefficient [1/K], θ_0 is the reference temperature [K], θ is the temperature [K], and μ_0 the magnetic permeability of vacuum [H/m].

* Corresponding author: Łukasz Pyrda
Phone: + (48)-12-617-50-54, Fax: + (48)-12-617-26-85
E-mail address: pyrda@agh.edu.pl

The authors studied the influence of strong magnetic field on paramagnetic fluid in an enclosure variously heated. They chose to use a cubical enclosure with a Rayleigh-Bénard configuration in which the bottom wall was heated while the top wall was cooled. They also studied the influence the magnetic field exerted on the heat transfer rate, which is very important from the point of view of engineering. Therefore various relationships between the buoyancy gravitational force and magnetic force were also studied. The reciprocal relationship of these forces was obtained by introducing changes into the enclosure position in the magnet bore. Various phenomena were observed. The high temperature gradients under the influence of the magnetic field from 1 [T] to 10 [T] were also examined. Results are presented and discussed below.

EXPERIMENTAL SYSTEM

Experimental vessel

Figure 1 shows an experimental vessel.

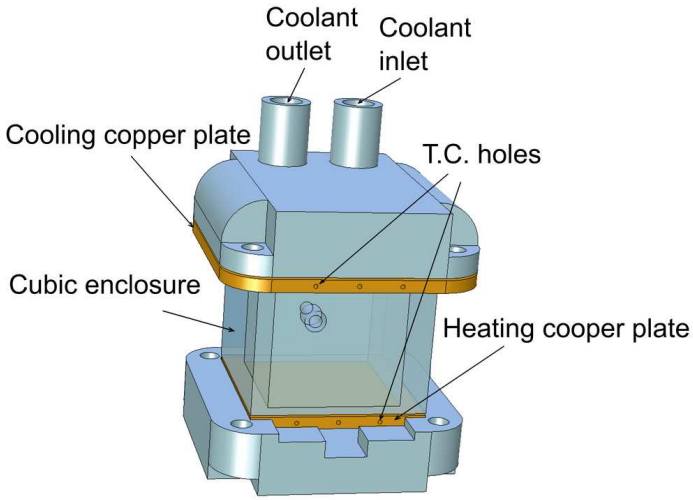

Figure 1. Experimental vessel [3]

The experimental apparatus consists of five elements: two copper plates with three holes in each for T-type thermocouples, cooling and heating chambers and a plexiglass cubical cavity. The cubic cavity had an internal size of 0.032 [m]. The bottom copper plate was heated with a resistance wire placed in the ceramic heating chamber. This wire was connected to a DC power supply which was constantly controlled. The upper copper plate was cooled by water flowing through the cooling chamber from the thermostating water bath. The cubic cavity contained a small hole into which the experimental fluid was injected. The cubical enclosure was placed in the superconducting magnet's bore which generated a strong magnetic field up to 10 [T] of magnetic induction. The assembled experimental setup is shown in Figure 2.

Experimental fluid

An 80% mass glycerol aqueous solution with crystals of gadolinium nitrate hexahydrate ($Gd(NO_3)_3 \times 6H_2O$) was selected as the working fluid. The density and mass magnetic susceptibility were obtained experimentally and the other properties were taken from [3]. Density was measured with a pycnometer. The measurements of mass magnetic susceptibility utilized Magnetic Susceptibility Balance; the magnetic susceptibility measurements were based on Evan's method. The balance measured the force with which the probe was attracted to the pair of permanent magnets and then the magnetic susceptibility was calculated. The properties of the working fluid are listed in Table 1.

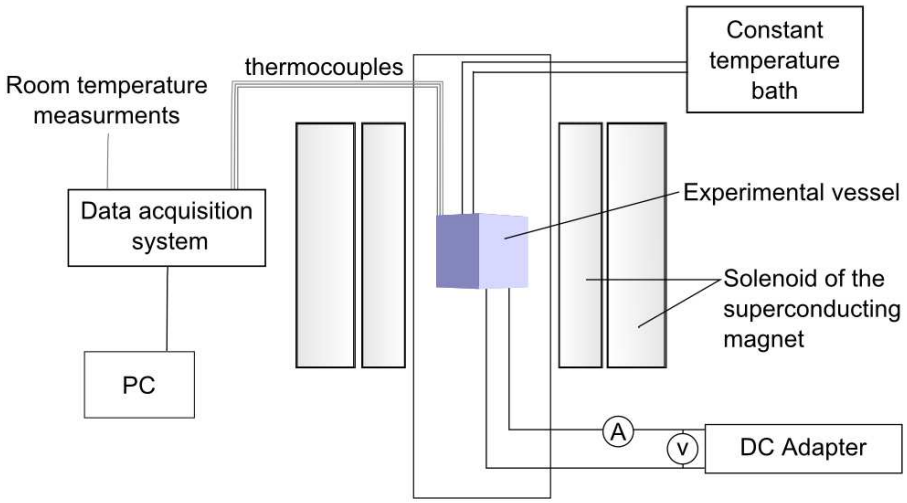

Figure 2. Experimental setup

Table 1. Properties of the fluid

Symbol	Value	Unit
α	1.01×10^{-7}	m^2/s
β	0.52×10^{-3}	1/K
λ	0.3972	W/m·K
μ	86.89×10^{-3}	kg/m·s
ν	5.9×10^{-5}	m^2/s
ρ	1453	kg/m^3
χ	21.776×10^{-8}	[-]

EXPERIMENTAL PROCEDURE

In the first step, a cubical enclosure filled with air was placed in the bore of the turned off magnet in order to measure the amount of heat lost to the environment. Power from the electrical heater attached to the bottom copper plate was set up at chosen levels and a constant temperature of 18 [^{0}C] was set for the cooling bath. After setting one value of power, the whole system was left to reach a steady state, which took roughly 30 minutes, at which point all measured quantities were recorded. Then a new value was set for the power supply, and the system again reached the steady state. This procedure was repeated for various power supply values. The results were used to find the relationship between temperature difference and heat loss. In the second step, convection phenomena under a strong magnetic field were investigated. Figure 3 shows three studied configurations of the system. Position A, placed 0.11 [m] above the centre of the solenoid, corresponded to the maximum of $\nabla \vec{b}^2$ while position B, placed in the centre of the solenoid, corresponded to the maximum value of magnetic induction $\vec{b}$. Position C, placed 0.11 [m] below the centre of the solenoid, corresponded to the second maximum of $\nabla \vec{b}^2$. For this experimental step, the cubic enclosure was filled with working fluid. The temperature of the cooling bath and power supply attached to the heater were then set and the system was left to reach a steady state upon which all measured quantities were recorded. The strength of the magnetic induction was changed stepwise from 1 [T] to 10 [T], with the system each time left to reach a steady state. The entire process lasted approximately half an hour, after which all data were recorded. For each position and each value of the power supply the experimental procedure was the same.

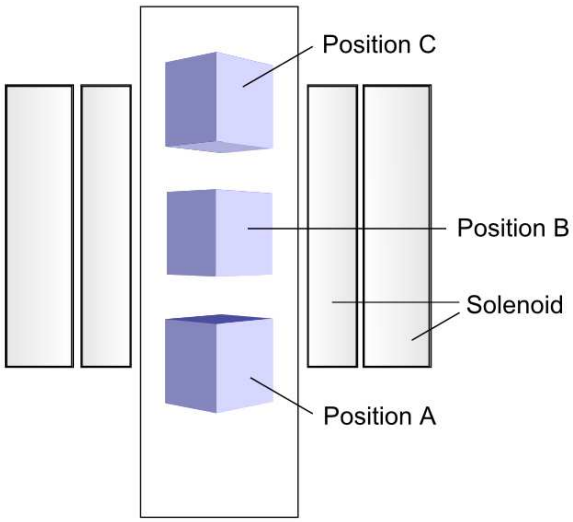

Figure 3. Investigated configurations

Heat transfer rates

To investigate the effect of the magnetic field on the heat transfer rate, thermal measurements were done in all the cases studied. The Nusselt number was calculated from this equation, according to a method invented by Ozoe and Churchill [4]:

$$\mathrm{Nu} = \frac{Q_{net\_convection}}{Q_{theor\_conduction}} \tag{4}$$

where: $Q_{net\_convection}$ is the net convection heat flux, and $Q_{theor\_conduction}$ the theoretical conduction heat flux. The net convection heat flux was obtained as the difference between supplied power ($Q_{convection}$) and the heat loss (Q_{loss}) and

$$Q_{convection} = I \cdot U \tag{5}$$

$$Q_{net\_convection} = Q_{convection} - Q_{loss} \tag{6}$$

The heat loss was estimated from the conduction experiment described in the "Experimental procedure" chapter. It was calculated as the difference between the conduction heat flux and theoretically calculated net heat flux:

$$Q_{loss} = Q_{conduction} - Q_{theor\_conduction} \tag{7}$$

$$Q_{theor\_conduction} = A\lambda(\theta_{hot} - \theta_{cold})/l \tag{8}$$

where A is the conduction area of cross section ($A=l^2$), θ_{hot} is the temperature of the heated wall, θ_{cold} is the temperature of the cooled wall. The definition for the form of the Nusselt number can be rewritten:

$$\mathrm{Nu} = \frac{Q_{convection} - Q_{loss}}{l\lambda(\theta_{hot} - \theta_{cold})} \tag{9}$$

Figure 4 shows the calculated heat losses of the experimental setup for various temperature differences. The data was linearly approximated and the following expression then obtained

$$\Delta\theta = 13.23 Q_{loss} + 0.05 \tag{10}$$

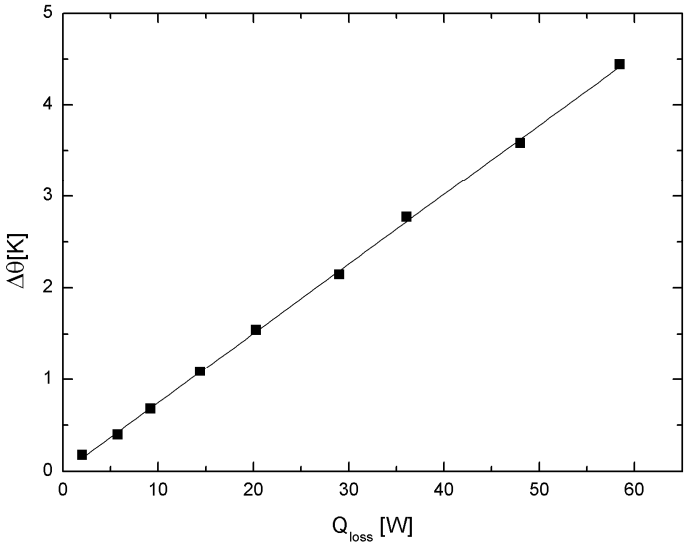

Figure 4. Linear fit of setup heat losses

RESULTS AND ANALYSIS

Figure 5 presents the Nusselt number as a function of magnetic induction in the centre of the bore. Diamonds represents the Nusselt number obtained for the enclosure in Position A (above the solenoid centre) and triangles represents the Nusselt numbers for the enclosure in Position B (in the centre of solenoid), both with about 0.4 W power supply directed to the heating wire.

The Rayleigh number is a very important parameter in the convective heat transfer. It characterise type of flow. It is a product of Prandtl number and Grashof number and near the vertical wall, this number can be defined as:

$$\mathrm{Ra} = \frac{g\beta(\theta_{hot} - \theta_{cold})l^3}{\alpha\nu} \tag{11}$$

where: α is the thermal diffusivity [m^2/s], g the gravitational acceleration, and ν the kinematic viscosity [m^2/s]. The Rayleigh number without magnetic field was equal to Ra = 103025. In Position A, the vectors of ∇b^2 were directed opposite to the gravitational acceleration vector, which produced a convection suppressing effect. From 3 [T] up to 10 [T] of magnetic induction, the Nusselt number was about 1.

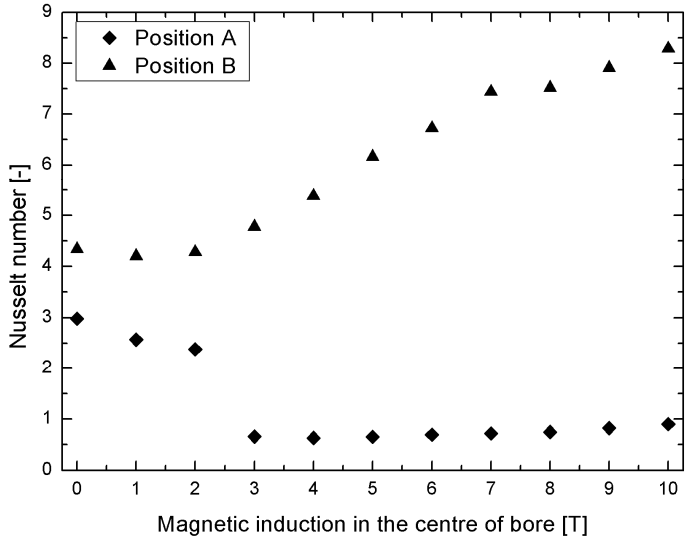

Figure 5. The Nusselt number as a function of magnetic induction in the bore centre for the enclosure placed below (Position A) and in the centre of solenoid (Position B)

In Position B the Nusselt number decreased slightly at 1 [T] of magnetic induction, but for all other values of that number it rise noticeably. It then reached a value two times higher than it was without magnetic field. At 7 [T] of magnetic induction the room temperature dropped and influenced the measurements. Room temperature was roughly 2 [°C] higher than the heated wall, which effected the results. In Figure 6 the Nusselt number values were obtained for the enclosure placed below the solenoid centre in Position C. Here the power supply was ten times higher than it was in other positions. The Nusselt number constantly grew, with increasing magnetic induction reaching a value 2.5 times higher than those without magnetic field. The authors expected the flow type to change from from laminar to transient. However, the data indicated very stable laminar flow even when the Rayleigh was quite high. It would seem that the fluctuations were suppressed and only the mean flow was enhanced.

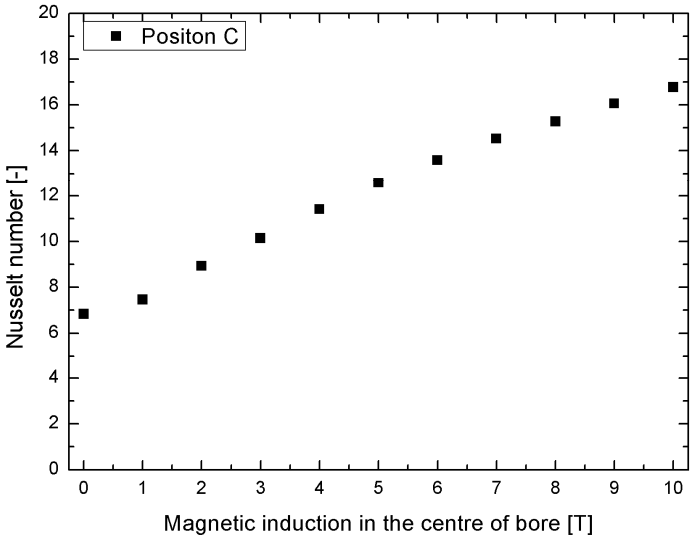

Figure 6. The Nusselt number as a function of magnetic induction in the centre of bore for the enclosure placed below the solenoid (Position C)

CONCLUSIONS

This paper has looked at the influence of a strong magnetic field on the behaviour of paramagnetic fluid in a variously heated cavity. Three different positions of cubical enclosure heated from the bottom and cooled from the top were examined. Enhanced convection was observed in Positions B (the solenoid centre) and C (above the solenoid centre), while the suppression of convection was observed in Position A. The flow was laminar even at a quite high Rayleigh number.

ACKNOWLEDGEMENTS

This research was supported by grant AGH No. 10.10.210.182.

REFERENCES

1. Ozoe H., Magnetic convection, *Imperial College Press*, 2005.
2. Bai B., Yabe A., Qi J., and Wakayama N. I., Quantitative analysis of air convection caused by magnetic-fluid coupling, *American Institute of Aeronautics and Astronautics*, J. 37, 1999, pp. 1538-1543.
3. Bednarz T., Numerical and experimental analyses of convection of paramagnetic fluid in a cubical enclosure, *PhD Thesis*, Kyushu University, Japan, 2004.
4. Ozoe H. and Churchill S., Hydrodynamic stability and natural convection in newtonian and non-newtonian fluids heated form below, *AIChE Symposium Series Heat Transfer 69*, 1973, pp. 126-133.

Large Eddy Simulation in heat transfer and fluid mechanics

DIRECT NUMERICAL SIMULATION OF HEAT-TRANSFER IN ROTATING RAYLEIGH-BENARD CONVECTION

Rudie P.J. Kunnen[a], Bernard J. Geurts[b,c] [1], Herman J.H. Clercx[c,b]

[a]Institute of Aerodynamics, RWTH Aachen University
Wüllnerstrasse 5a, 52062 Aachen, Germany

[b]Department Applied Mathematics, Faculty EEMCS, University of Twente
P.O. Box 217, 7500 AE Enschede, The Netherlands

[c]Fluid Dynamics Laboratory, Faculty Applied Physics, Eindhoven University of Technology
P.O. Box 513, 5600 MB Eindhoven, The Netherlands

ABSTRACT The consequences of rotation on the flow-structuring and the corresponding heat transfer in a cylindrical volume of fluid subjected to a destabilising temperature gradient and rotation about the vertical axis were studied numerically and experimentally. A second order finite volume method was used for direct numerical simulation of the turbulent flow. At small rotation rates the convection is dominated by a large-scale circulation. Conversely, at high rotation rates the flow develops a number of thermal plumes that are strongly localized and roughly aligned along the vertical. The heat transfer is found to be increased by up to about 15% compared to the non-rotating case, which is closely connected to the effect of Ekman pumping in the boundary layers near the upper and lower boundaries. At the highest rotation rates the convective flow is found to be suppressed, as is the heat transfer.

Keywords: *Rayleigh-Bénard, rotation, turbulence, heat-transfer, direct numerical simulation*

INTRODUCTION

More than a century ago, Henri Bénard performed an intriguing experiment in which he heated very thin layers of fluid from below. He observed convective motions that took the shape of a regular pattern of hexagonal cells. The subsequent theoretical analysis of the convective instability of a layer of fluid was due to Lord Rayleigh who pointed out the importance of the temperature gradient, which is nowadays described in dimensionless form by the Rayleigh number. Thus Rayleigh-Bénard convection was coined for the motion of a fluid confined between horizontal plates and heated from below. The addition of rotation in the convective system induces a number of changes. The critical Rayleigh number for the onset of convection is increased with rotation. Furthermore, it is well-known that near solid boundaries in rotating flows active boundary layers are formed that can influence the flow even far away from boundaries, unlike boundary layers in non-rotating flows. An effect that is relevant for strong rotation is described by the Taylor-Proudman theorem: for slow motions in inviscid, strongly rotating flow the vertical gradient of velocity is zero, i.e., a columnar or sheet-like two-dimensional flow is observed. For an overview of literature see [1]. Hence, rotation may induce a macroscopic modulation of turbulence.

[1]Corresponding author: Phone: +31 53 489 4125, Fax: +31 53 489 4833
E-mail address: b.j.geurts@utwente.nl

Fluid flow driven by buoyancy is ubiquitous in nature and technology. In many cases the density differences within the fluid come from differences in temperature, thus the designation thermal convection. Furthermore, some classes of fluid flows are additionally shaped by a rotation. A prime example comes from large-scale motions in the Earth's oceans, which are driven by temperature induced buoyancy, and at the same time have length-scales such that the rotation of the Earth plays a role in the development. An important example is open-ocean deep convection: in winter, in the Arctic and Antarctic seas surface cooling may lead to long-lived vortical downward flow. This deep convection is of paramount importance for the global thermohaline circulation.
A key consequence of the modulation of turbulent flow due to rotation is the change in the capacity of the system to transfer heat. This is the main area of attention in this paper. Ever since the first experiments by Rossby [2], it is known that rotation can have unexpected effects on the heat transfer. Rossby found that, for convection in water, there is a certain range of rotation rates for which the Nusselt number Nu, denoting a dimensionless heat flux, is *increased* relative to its static non-rotating value. The increase was about 10%. Such an increased Nusselt number is counter-intuitive, as it was shown that rotation stabilizes convection (the critical Rayleigh number is increased by rotation). Hence, a reduction of the heat transfer would be expected. At sufficiently high rotation rates, Rossby indeed measured a strongly decreased heat flux. The mechanism behind the increase in Nu in an intermediate range was hinted at by Rossby as being related to so-called Ekman pumping. The boundary layers in rapidly rotating flows have been described by Ekman [3]. These layers can actively influence the surrounding flow: if vorticity is found in the outer fluid the boundary layers will subsequently enact a vertical velocity (Ekman pumping). Since these boundary layers are very thin, the fluid pumped away from the wall will have considerably higher/lower temperature than the surrounding fluid. Thereby the heat-transfer can be enhanced.

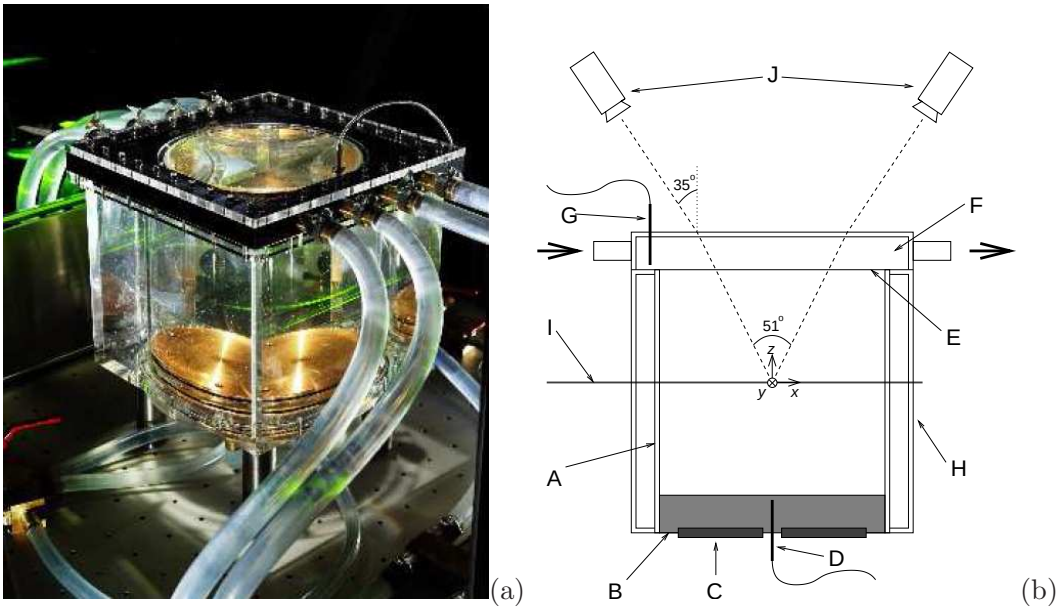

(a) (b)

Figure 1: Impression of the physical experiment (a) and a sketch of the components of the set-up (b) in which two cameras (J) are placed above the vessel that is heated through a copper plate (B) and cooled with a lid (G-F) in between which a laser-sheet is defined (I).

The physics of rotating convection can be investigated in great detail using an experimental set-up as depicted in Fig. 1(a) and sketched in Fig. 1(b) [4]. A cylindrical vessel is heated from below and cooled from above. At different heights through the domain a laser sheet can be generated. The total equipment is placed on a rotating table. Seeding the fluid with tracer particles and adopting two cameras on top of the vessel allows to record all three components of velocity in the illuminated sheet. This stereo PIV (particle image velocimetry) approach allows a precise recording of the instantaneous flow as well as to generate data for a statistical analysis of the flow. Such non-intrusive physical experimentation is complemented with detailed direct numerical simulation.

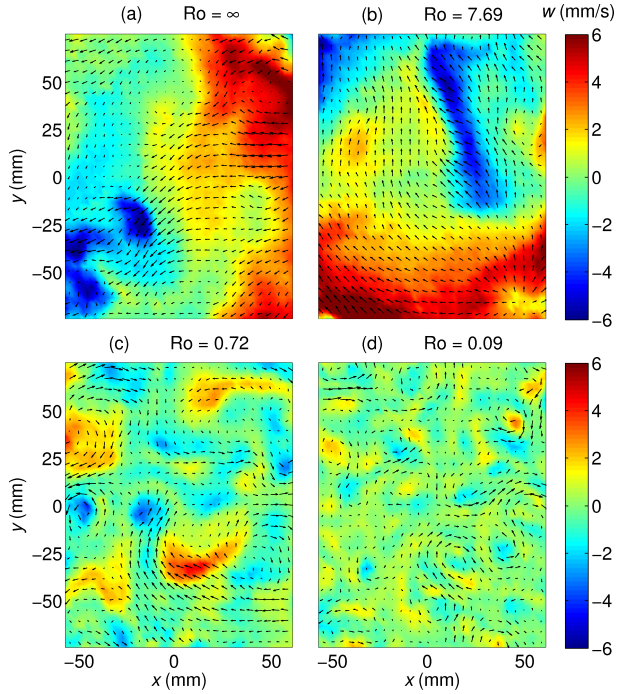

Figure 2: Typical velocity snapshots taken at height $z = 0.8H$, and Rayleigh number $Ra = 1.11 \times 10^9$. Snapshots at four different Rossby numbers Ro are shown. The background coloring depicts the out-of-plane vertical velocity component, while the arrows depict in-plane horizontal motions (only one fourth of the horizontal-velocity arrows is drawn for clarity).

The flow structure that corresponds to the altered heat-transfer display striking features. In fact, flow visualizations in turbulent rotating convection showed that many vertically aligned vortices are formed. An impression of the flow-organization as obtained from the physical experiments is collected in Fig. 2. The colors indicate the level of the vertical velocity w and the arrows correspond to the in-plane velocity components. As the rotation-rate increases (expressed by decreasing Rossby numbers Ro, denoting a dimensionless inverse rotation rate) more localized vortical structures are formed that are pre-dominantly aligned with the axis of rotation. In this paper we will present in some detail the dominant flow structuring, through numerical simulation. We will consider turbulent rotating convection in a cylinder, which can be directly compared to these physical experiments.

The organization of this paper is as follows. In the next Section we present the Boussinesq ap-

proximation to the governing equations and sketch the numerical method used to simulate the flow. Three-dimensional flow in a rotating cylinder that is heated from below and cooled on top is described subsequently. Concluding remarks are contained in a final Section.

MATHEMATICAL MODEL AND NUMERICAL APPROACH

In this section we first describe the mathematical model and then sketch and illustrate the numerical procedures that were adopted.

Mathematical model

The changes in density arising from modest temperature differences are correspondingly small. In this regime the dynamics of fluid flow subject to buoyancy and rotation may be expressed using the Boussinesq approximation. In vector notation the dimensionless set of governing equations can be written as:

$$\begin{aligned} \partial_t \mathbf{u} + (\mathbf{u}\cdot\nabla)\mathbf{u} + \frac{1}{Ro}\mathbf{e}_z \times \mathbf{u} &= -\nabla p + T\mathbf{e}_z + \sqrt{\frac{\sigma}{Ra}}\nabla^2\mathbf{u} \\ \partial_t T + (\mathbf{u}\cdot\nabla)T &= \frac{1}{\sqrt{\sigma Ra}}\nabla^2 T \\ \nabla\cdot\mathbf{u} &= 0 \end{aligned} \tag{1}$$

These equations describe the evolution of velocity $\mathbf{u}$, temperature T and pressure p on the basis of conservation of momentum, energy and mass. Here $\mathbf{e}_z$ denotes the unit vector in the vertical z-direction.

The description of the flow behavior can be done succinctly with dimensionless numbers that give the ratios of different forces in the flow. For horizontally unbounded rotating Rayleigh-Bénard convection, there are six parameters involved, i.e., $\{(g\alpha), \nu, \kappa, \Omega, \Delta T, H\}$ denoting respectively the product of the gravitational acceleration g and thermal expansion α, the kinematic viscosity ν, the thermal diffusivity κ, the rotation rate Ω, the temperature difference between the plates ΔT and the distance between the plates H. These six parameters are formulated in three basic physical dimensions (length, time and temperature) - hence three dimensionless groups arise. A convenient velocity scale is $U = \sqrt{g\alpha\Delta T H}$ in terms of which we have for the Rayleigh Ra and Prandtl number σ:

$$Ra = \frac{g\alpha\Delta T H^3}{\nu\kappa} \quad , \quad \sigma = \frac{\nu}{\kappa} \tag{2}$$

The Rayleigh number is a ratio of buoyancy and dissipation. Diffusive properties of the fluid are described by the Prandtl number. The third basic dimensionless group is the Rossby number defined as

$$Ro = \frac{U}{2\Omega H} \tag{3}$$

which compares inertial and Coriolis forces. For slow rotation ($Ro \gg 1$) buoyancy is dominant, while for strong rotation ($Ro \ll 1$) Coriolis forces are stronger. For convective flow in bounded domains such as a cylinder, it is useful to define an additional parameter, the aspect ratio $\Gamma = D/H$ in which D denotes the diameter of the cylinder.

Numerical approach and validation

For a comparison of numerical simulation results to experiments in a rotating cylinder heated from below it is important to take into account the geometry of the experiment. The choice to perform

simulations in a cylindrical domain is obvious. To match with the experimental conditions the following boundary conditions are applied:

$$\begin{aligned} \text{Bottom plate} \quad (z=0) \quad &: \mathbf{u} = \mathbf{0} \;, \quad T = 1 \\ \text{Top plate} \quad (z=1) \quad &: \mathbf{u} = \mathbf{0} \;, \quad T = 0 \\ \text{Sidewall} \quad (r=1/2) \quad &: \mathbf{u} = \mathbf{0} \;, \quad \partial_r T = 0 \end{aligned} \tag{4}$$

indicating that all walls are no-slip, the bottom and top plates are kept at constant temperatures, and the sidewall is adiabatic.
In cylindrical coordinates the governing equations possess terms that include a factor $1/r$. These need special treatment to be evaluated at the cylinder axis $r = 0$. Verzicco & Orlandi [5] propose to rewrite the equations in terms of $q_r = ru_r$, $q_\phi = u_\phi$ and $q_z = u_z$. This, in combination with the use of a staggered grid, alleviates the discretization problems since $q_r(0, \phi, z) = 0$ and this is the only velocity component that needs to be evaluated at $r = 0$ since the other components are stored all off the axis. The equations are discretized on the staggered grid by central finite-difference formulations of second order accuracy. The solution uses a fractional-step procedure with the elliptic equation inverted using trigonometric expansions in the azimuthal direction and a direct solver for the other two directions. The numerical approach was validated by conducting simulations at a number of gradually finer resolutions. In literature various criteria for 'adequate' resolution were put forward - at a typical resolution of $N_r \times N_\phi \times N_z = 193 \times 385 \times 385$ we verified that these criteria were all satisfied for the simulations conducted. At the range of Rayleigh (10^8-10^{10}), Prandtl (4 and 6.4) and Rossby numbers (0.045 to 11.52) considered, the flow can be well resolved using direct numerical simulation - a systematic parameter-study was compiled.
In the next section we present simulation results of turbulent rotating convection in a cylinder.

ROTATING RAYLEIGH-BENARD CONVECTION IN CYLINDRICAL DOMAIN

We will focus on the numerical prediction of the large-scale flow structuring that occurs in the cylindrical convection cell, its consequences for the various length-scales that are present in the solution, and ultimately in the effect rotation has on the overall heat transfer.
In the physical experiments an organization into coherent structures was observed. Since the numerical simulations provide more detailed velocity and temperature data the development of the vortical plumes and their effect of the flow can be obtained. In order to appreciate the effect of rotation on the flow-structuring we consider the vortex structure in more detail. The vortical plumes that are detected for $Ro < 1$ are the most active components in the flow, as almost all of the vertical transport of fluid and heat is found in the interior of the vortices. Their size and number density are hence important for the total vertical transport through the fluid layer. In order to quantify such vortical structures we adopt the so-called Q-criterion. In [6] a vortex is identified with a spatial region where

$$Q \equiv \frac{1}{2}\Big(\|\mathbf{W}\|^2 - \|\mathbf{S}\|^2 \Big) > 0 \tag{5}$$

where $\mathbf{W}$ and $\mathbf{S}$ denote the symmetric and the antisymmetric parts of the velocity gradient tensor, and $\|\mathbf{A}\| = \sqrt{Tr(\mathbf{A}\mathbf{A}^T)}$ is the Euclidean norm.
A comparison of snapshots of Q at various Ro is presented in Fig. 3. Four Rossby numbers are included: $Ro = 0.09, 0.18, 0.36$ and 0.72. At lower rotation rates (higher Ro) considerably increased vertical variations are found. The columnar flow as expected from the Taylor-Proudman theorem

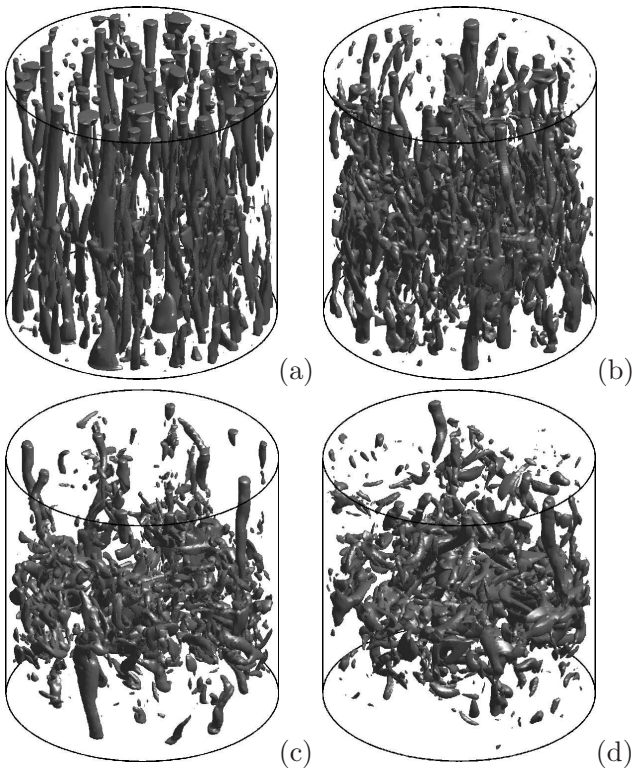

Figure 3: Snapshots of Q isosurfaces at (a) $Ro = 0.09$, (b) $Ro = 0.18$, (c) $Ro = 0.36$, and (d) $Ro = 0.72$.

is only found at the lowest Ro. Especially in the central part of the cylinder an intricate network of entangled tubes is found. Another difference is found in the average thickness of the vortices. It is clear that this is best measured closer to the plates, as there the vortical tubes are still aligned vertically. The average thickness decreases as Ro decreases. The vortex number density shows opposite behavior: more vortices are found at lower Ro.

We have seen that rotation has a profound influence on the phenomenology of turbulent convection. Therefore we also expect considerable changes in the turbulence statistics due to the rotation. The strength of the turbulent fluctuations may be represented by the root-mean-square values of, e.g., velocity, vertical vorticity and temperature. In Fig. 4 we collected the root-mean-square of two velocity components, extracted near the axis. The results correspond at small Ro approximately to a scaling $\sim Ro^{0.2}$ as was also observed in the physical experiments. At very high rotation rates the fluctuations decrease even more rapidly. For the temperature fluctuations the opposite was seen. At high rotation rates the RMS of temperature even increases with $\sim Ro^{-0.32}$. Under rotation the vortical plumes that develop need considerably more thermal contrast to break out from the boundary layer into the bulk fluid, as the critical Ra has increased.

We finally turn to the consequences of rotation for the vertical convective heat transfer as expressed in dimensionless form with the Nusselt number Nu. In Fig. 5 the Nusselt number Nu is presented as function of Ro and scaled with its value at $Ro = \infty$ (no rotation). At very high rotation rates this heat transfer clearly is hindered and Nu decreases. However, next to this asymptotic range, there is a set of rotation rates where Nu is even larger than in the non-rotating situation. The

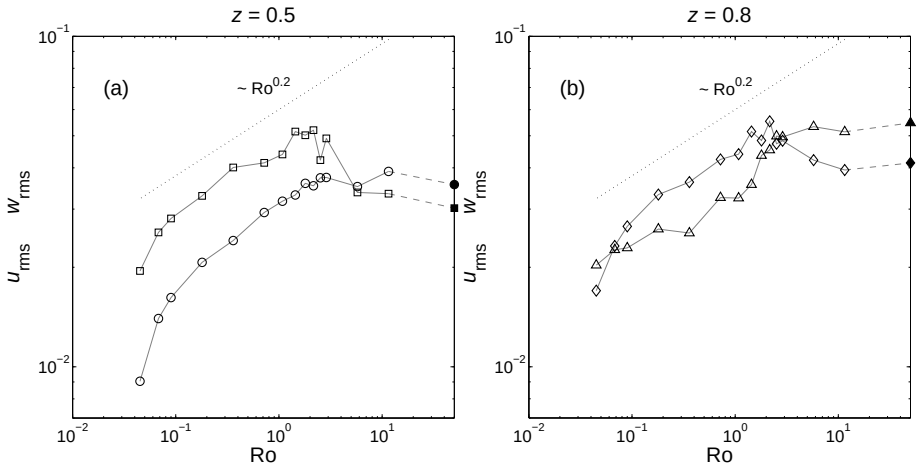

Figure 4: Root-mean-square velocities and their variation with Ro. (a) At $z = 0.5$ the horizontal rms values u_{rms} are indicated with circles and the vertical rms values w_{rms} with squares. (b) At $z = 0.8$ the horizontal components u_{rms} are plotted with triangles, the vertical rms values w_{rms} with diamonds. The filled symbols on the right-hand side of both figures are at $Ro = \infty$. A representative power-law dependence $Ro^{0.2}$ is given by the dotted line.

Ekman pumping taking place inside the vortical plumes is an efficient mechanism for entrainment of boundary-layer fluid (with strong temperature contrast) into the vortical plumes and subsequent transport of this fluid to the vertically opposite side. At higher rotation rates the stabilizing effect of the rotation becomes more and more prevalent and Nu approaches one, for a conductive state with zero flow velocity and a linear temperature gradient over the fluid.

CONCLUDING REMARKS

The problem of rotating Rayleigh-Bénard convection has been investigated through physical experimentation and numerical simulation. Direct numerical simulation has proved to be an excellent tool in the study of turbulent rotating convection in a cylindrical geometry. The agreement of DNS with the physical experiments was very strong. Hence, the phenomenology of rotating turbulent convection could be studied in much more detail, having full access to all flow properties at high spatial and temporal resolution. The effects of rotation on many aspects of the flow could be described and further understood. From the numerical results, a tentative separation into three regimes based on the Rossby number is suggested:

- $Ro \gtrsim 2$ In this range of Rossby numbers the flow behavior is dominated by the presence of the large-scale circulation (LSC). Variation of Ro has only minor effect. The LSC is hardly affected in strength although signs of instability are found near $Ro = 2$.
- $0.1 \lesssim Ro \lesssim 2$ The LSC is replaced by vortical columns as the dominant flow structure. However, in the central region of the cell still a disordered turbulent state is found: the vortices generally do not penetrate far into the fluid bulk. The number of vortices rises when Ro is decreased, and their mean radius decreases. In this range the turbulence intensity drops as rotation is increased. The Nusselt number, is larger than without rotation.
- $Ro \lesssim 0.1$ In the entire fluid volume the vortical plumes are found. Rotation has a more

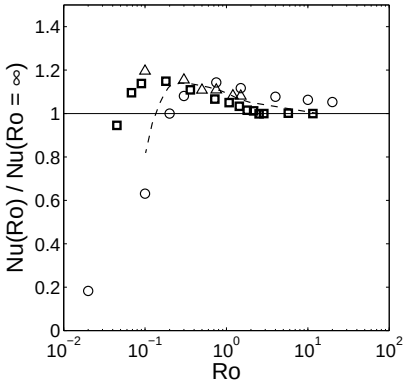

Figure 5: Relative Nusselt number $Nu(Ro)/Nu(Ro = \infty)$ as a function of Ro. The current simulation results are included with squares. The dashed line is taken from [2] at $Ra = 2.5 \times 10^6$, $\sigma = 6.8$, $\Gamma > 6$. Triangles represent results of [7] at $\sigma = 6.3$ and $\Gamma = 0.78$ (cuboid cell), extrapolated to $Ra = 1 \times 10^9$. Circles are taken from [8] at $Ra = 2 \times 10^8$, $\sigma = 0.7$, $\Gamma = 0.5$.

pronounced influence on the turbulence intensities, including vorticity: a considerably steeper dependence on Ro is reported in this range. The heat transfer is also adversely affected by the rotation; for Rossby numbers below 0.1 it is abruptly reduced.

The division into three regimes matches with the classification given in [9]: these authors label the first regime 'thermal turbulence', the second regime 'irregular geostrophic turbulence' and the last regime '(quasi-)regular vortex grid'. Many comparisons between the current numerical results and those from our experiments have been performed. Qualitatively a very good agreement was found. Quantitatively the discrepancies are well-described by stating that turbulent fluctuations in the experiments were generally less intense than in the simulations. The experimental conditions are obviously not as well-defined as in the numerical setting with idealized boundary conditions.

[1] Kunnen, R.P.J. Turbulent rotating convection. *Eindhoven University of Technology* Thesis, (2008).

[2] Rossby, H.T. A study of Bénard convection with and without rotation. *J. Fluid Mech.* **36**, 309-335 (1969).

[3] Ekman, V.W. On the influence of the Earth's rotation on ocean-currents. *Arch. Math. Aston. Phys.* **2**, 1-52 (1905).

[4] Kunnen, R.P.J., Clercx, H.J.H., Geurts, B.J., van Bokhoven, L.J.A., Akkermans, R.A.D. & Verzicco, R. Numerical and experimental investigation of structure function scaling in turbulent Rayleigh-Bénard convection. *Phys. Rev. E* **77**, 016302 (2008).

[5] Verzicco, R. & Orlandi, P. A finite-difference scheme for three-dimensional incompressible flow in cylindrical coordinates. *J. Comput. Phys.* **123**, 402-413 (1996).

[6] Hunt, J.C.R., Wray, A. & Moin, P. Eddies, stream, and convergence zones in turbulent flows. Report CTR-S88, Center for Turbulence Research (1988).

[7] Liu, Y. & Ecke, R.E. Heat transport scaling in turbulent Rayleigh-Bénard convection: effects of rotation and Prandtl number. *Phys. Rev. Lett.* **79**, 2257-2260 (1997).

[8] Oresta, P., Stringano, G., & Verzicco, R. Transitional regimes and rotation effects in Rayleigh-Bénard convection in a slender cylindrical cell. *Eur. J. Mech. B/Fluids* **26**, 1-14 (2007).

[9] Boubnov, B.M. & Golitsyn, G.S. Temperature and velocity field regimes of convective motions in a rotating plane fluid layer. *J. Fluid Mech.* **219**, 215-239 (1990).

NUMERICAL ILLUSTRATIONS OF THE COUPLING BETWEEN LBM AND FINITE-TYPE MACRO-NUMERICAL METHODS

H.B. Luan, H. Xu, L. Chen, Y. L. He, W.Q. Tao*

Xi'an Jiaotong University, Xi'an, China

ABSTRACT Recently, multiscale approaches have had a tremendous impact on the analysis of complex problems in science and engineering. One widely adopted numerical method is "solving in different region individually and coupling the solutions at the interface". The major difficulty for macroscale and micro/mesoscale coupling is how to transform the macroscopic results into the dependent variables adopted in the micro/mesoscale methods. An analytic expression has been proposed by our research group for the exchange from velocity of finite-type method to the single-particle distribution function of lattice Boltzmann method (LBM). In this paper, lid driven cavity flow is selected to implement the coupling between the results of LBM and the finite-volume method (FVM). The final results show that the smoothness and consistency of the streamlines and velocity fields in the coupled region is very good. In addition it is also revealed that for the confirmation of good smoothness and consistence of solutions coupling at the interface vorticity contour distribution is a more appropriate parameter to ensure the quality.

Keywords: *multiscale computation, numerical method, couple method, LBM, FVM*

INTRODUCTION

Challenging multiscale phenomena or processes are widely existed in, e.g., material science, fluid flows, electrical and mechanical engineering [1,2,3]. Examples of multiscale problems include: turbulent fluid flow and heat transfer; transport phenomenon in proton exchange membrane of fuel cell; cooling process in data centre and so on. Multiscale problems can be divided into two categories: multiscale system and multiscale process. By multiscale system we refer to a system that is characterized by large variation in length scales. The processes at different scales are not very closely related and can be studied separately with certain connection. Cooling in data centre is a typical multiscale system problem. The length scale in cooling stream in house is in order of meter, while the cooling process of a chip is in order of millimeter. By multiscale process we mean that the overall behavior is governed by processes occur at different length and/or time scale, and they are inherently connected by process itself. Process in PEMFC, launching a spacerocket from earth surface to outer space and turbulent heat transfer are examples for multiscale process. From simulation point, study of the multiscale processes is more challenging and attractive. The focus of the present paper is in the multiscale process.

It is usually accepted that different scale problem should have different numerical method which is most applicable to that scale. Broadly speaking, there are three levels of simulation methods for fluid flow and heat transfer, the macroscale, mesoscale and microscale. The macro-scale numerical methods include the finite difference, finite volume, finite element and finite analytic methods. The basic feature of the four methods is that the smallest unit for computation is a cell with finite dimension. Thus they can be called finite-type methods. The mesoscale numerical methods include

* Corresponding author: Prof. W.Q.Tao
Phone: + (86)-29-82669106, Fax: + (86)-29-82669106
E-mail address: wqtao@mail.xjtu.edu.cn

the lattice Boltzmann method(LBM), direct simulation of Monte-Carlo method(DSMC). These two methods adopt a concept of computational particles which is much larger than an actual molecular but act as a molecule (simulation molecule). The micro numerical methods include molecular dynamic simulation (MDS) and quantum molecular simulation(QMS). In MDS every molecule is simulated according to the Newton's law of motion. A quantum molecular dynamics simulation solves the coupled time-dependent Schrodinger equations for all particles in the system[4]. This method is largely limited by the present computer source, hence, various approximations have to be used. In this paper QMS will not be concerned.

Recently, Abraham [5] have applied three level schemes FE-MD-QM (finite-element, molecular dynamic, quantum mechanical) to study crack dynamics. Nie et al. [6] adopted MDS and FVM for the lid-driven cavity flow in which the two vertexes are single point in math. Dupuis et al. [7] proposed LB-MD model in simulations of flows of liquid argon past and through a carbon nanotube. Wu et al. [8] proposed a scheme of coupled DSMC-NS using the unstructured mesh. One frequently encountered coupling is the one between some macro numerical method and meso numerical method, such as LBM and/or DSMC. The macro numerical methods usually are the finite-type methods (FDM, FVM, FEM, FAM). In this paper, the adopted method for the multiscale computation is the one in which different regions are solved individually and then the results are coupled at their interfaces.

In the following, we first present a brief overview of the lattice Boltzmann model and the finite volume model in Section 2. Then, we illustrate the basics and implement procedures of the couple strategy in Section 3. After that, we employed this couple strategy to solve the lid driven cavity flow in Section 4. Finally, some conclusions are given in Section 5.

LATTICE BOLTZMANN MODEL AND FINITE VOLUME MODEL

Lattice Boltzmann model

A popular kinetic model adopted in the literature is the single-relaxation-time (SRT) approximation, the so-called Bhatnagar-Gross-Krook(BGK) model [9,10]

$$\frac{\partial f}{\partial t}+\zeta\cdot\nabla f=-\frac{1}{\lambda}\left(f-f^{(eq)}\right) \tag{1}$$

where f is the single particle distribution function, ∇f is the gradient of the function f, ξ is the particle velocity vector, $f^{(eq)}$ is the equilibrium distribution function (the Maxwell-Boltzmann distribution function), and λ is the relaxation time due to collision.

To solve for f numerically, Equation (1) is first discretized in the velocity space using a finite set of velocities $\{\xi_\alpha\}$ without affecting the conservation laws [11, 12],

$$\frac{\partial f_\alpha}{\partial t}+\xi_\alpha\cdot\nabla f_\alpha=-\frac{1}{\lambda}\left(f_\alpha-f_\alpha^{(eq)}\right) \tag{2}$$

In the above equation, $f_\alpha(x,t)\equiv f(x,\zeta_\alpha,t)$ is the distribution function associated with the αth discrete velocity ξ_α and $f_\alpha^{(eq)}$ is the αth equilibrium distribution function. The nine-velocity square lattice model D2Q9 [12] (Figure 1) has been successfully used for simulating 2-D flow. The nine velocities which denoted by $\boldsymbol{e}_\alpha$ are given by:

$$\boldsymbol{e}_0=0, \tag{3a}$$

$$\boldsymbol{e}_\alpha=c\left(\cos\left((\alpha-1)\pi/4\right),\sin\left((\alpha-1)\pi/4\right)\right)\qquad \text{For } \alpha=1,3,5,7 \tag{3b}$$

$$\boldsymbol{e}_\alpha=\sqrt{2}c\left(\cos\left((\alpha-1)\pi/4\right),\sin\left((\alpha-1)\pi/4\right)\right)\qquad \text{FoR } \alpha=2,4,6,8 \tag{3c}$$

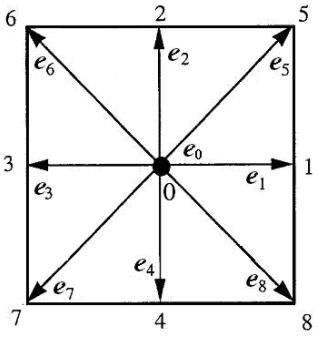

Figure 1. A 2-D, 9-velocity(D2Q9) lattice model

where $c = \delta x / \delta t$, δx is the lattice spacing step size and δt is the time step size. The equilibrium distribution function is given by:

$$f_i^{(eq)} = \omega_\alpha \rho \left[1 + \frac{3}{c^2}(\boldsymbol{e}_\alpha \cdot \boldsymbol{u}) + \frac{9}{2c^4}(\boldsymbol{e}_\alpha \cdot \boldsymbol{u})^2 - \frac{3}{2c^2} u^2 \right] \tag{4}$$

with the weights $\omega_0 = 4/9, \omega_1 = \omega_3 = \omega_5 = \omega_7 = 1/9, \omega_2 = \omega_4 = \omega_6 = \omega_8 = 1/36$ .The macroscopic density ρ and velocity vector $\boldsymbol{u}$ can be evaluated as

$$\rho = \sum_{\alpha=0}^{8} f_\alpha \tag{5a}$$

$$\rho \boldsymbol{u} = \sum_{\alpha=0}^{8} \boldsymbol{e}_\alpha f_\alpha \tag{5b}$$

The pressure of an ideal gas can be calculated from $p = \rho c_s^2$ with the speed of sound being $c_s = c/\sqrt{3}$. In the LBM, Equation (2) is discretized both in time and space, and the completely discretized equation (also the evolution equation) is

$$f_\alpha(\boldsymbol{x}_i + \boldsymbol{e}_\alpha \delta t, t + \delta t) - f_\alpha(\boldsymbol{x}, t) = -\frac{1}{\tau}\left[f_\alpha(\boldsymbol{x}_i, t) - f_\alpha^{(eq)}(\boldsymbol{x}_i, t) \right] \tag{6}$$

with the time step δt , space step $\delta x = \boldsymbol{e}_\alpha \delta t$, $\tau = \lambda / \delta t$ and x_i being a point in the discredited physical space.

Finite volume method

For multiscale simulation a fast converged algorithm of continuum method is highly required. The continuum methods include the finite difference, finite volume, finite element and finite analytic methods. FVM is the most widely adopted one in numerical heat transfer for its conservation properties of discretized equation and clear physical meaning of coefficient. Generally speaking, the macroscale methods (or called continuum methods hereafter) obey the fundamental laws of: mass conservation, momentum conservation and energy conservation.

The corresponding differential equation of the conservation law is:

$$\frac{\partial}{\partial \mathrm{t}}(\rho\phi) + \mathrm{div}(\rho \boldsymbol{U}\phi) = \mathrm{div}(\Gamma_\phi \mathbf{grad}\phi) + S_\phi \tag{7}$$

where ϕ is the dependent variable (such as velocity, temperature), U is the velocity vector, ρ is the fluid density. Γ is the nominal diffusion coefficient and S_ϕ is the source term.

In 1972, Patankar and Spalding proposed a solution procedure called SIMPLE, which is the most widely adopted algorithm for dealing with the coupling between velocity and pressure. There are two major assumptions in the simple algorithm: (1) The initial pressure and initial velocity are independently assumed, leading to some inconsistency between p and u, v ; (2) When the velocity

correction equation is derived, the effects of the neighboring grids velocity corrections are totally neglected.

These two assumptions do not affect the final solution but affect the convergence rate. The first assumption has been overcome by SIMPLER of Patankar(1980) [14]. Researchers have done many efforts to overcome the 2nd assumption, such as SIMPLEC by van Doormaal and Raithby (1984) [15], PISO by Issa (1986) [16], Explicit correction step method by Yen and Liu(1993) [17], MSIMPLER by Yu et al. (2001) [18]. None of the above revised versions could successfully overcome the second assumption. In the recent four years, our group developed CLEAR [19,20], and IDEAL [21,22]. They completely delete the 2nd assumption, making the algorithm fully-implicit. In both the CLEAR and IDEAL algorithms, the improved pressure and velocity are solved directly, rather than by adding a correction term to the intermediate solution. A further improvement of the solution procedure is conducted in the IDEAL algorithm making its convergence rate and robustness better than that of CLEAR.

In this article, the 2-D IDEAL collocated grid algorithm is adopted [23] using the SGSD scheme for the descretization of the convective term [24].

THE PRINCIPLE OF COUPLING LBM AND FINITE TYPE METHOD

First we present a general framework for designing a numerical method that couples marco methods and meso/micro methods. Assuming that a macroscale process is described by a state variable U, and a microscopic process is described by a state variable u. The two processes and state variables are related to each other at the interface of the macro and micro models by compression and reconstruction operation, denoted by Q and R respectively, as follows [1]:

$$U(x,t) = Q\big(u(x,t)\big) \tag{8}$$

$$u(x,t) = R\big(U(x,t)\big) \tag{9}$$

The two operators have the property $QR = I$, where I is the identity operator.

Generally speaking the reconstruction operator does not unique. In fact, the reconstruction procedure leads to a one-to-many mapping, because the microscopic simulator contains more information than that of the macroscopic simulator. In the opposite, the compression operation is usually a local/ensemble average through which a unique parameter can be resulted from lot of micro/meso-scale information. Thus for the coupling between the results from macroscopic and mesoscopic methods the major difficulty is how to transform the macroscopic results, such as velocity, into the dependent variables adopted in the micro/meso-scale methods, for example from velocity of finite-type method to the single-particle distribution function of LBM.

Recently an analytic expression has been derived by our research group which couples the lattice Boltzmann method(LBM) with finite-type macro numerical method as follows [25]

$$f_i = f_i^{(eq)}\{1 - C_s^{-2}\tau\delta t U_{i\beta}(U_{i\alpha}\partial_\alpha u_\beta + \nu\partial_\alpha^2 u_\beta + \nu\frac{1}{\rho}\partial_\alpha \rho S_{\alpha\beta})\} \tag{10}$$

where f_i represent the single-particle distribution function along the direction i, $f_i^{(eq)}$ is the equilibrium distribution function, C_s is the speed of sound of the model, ρ, u denote the density and velocity, respectively, τ is the relaxation time, ν for viscosity, and α, β represent the two coordinate directions.

To illustrate the basic idea, the lid-driven cavity flow is simulated by the coupled LBM-FVM method. The computational domain is decomposed in two regions in which the LBM and FVM methods are used respectively (Figure 2). We can control the coarseness and fineness of grids according to the zone spatial scale in each region. When the grid systems at the interface of the

subregions are not identical, space interpolation at the interface is required when transferring the information at the interface. In this paper, we choose the FVM grid space equals to lattice space for

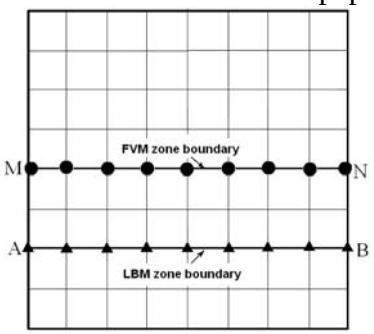

Figure 2. Interface structure between two regions of FVM and LBM

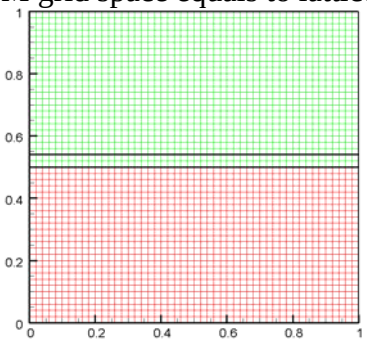

Figure3. Grid layout for a 2-D lid-driven cavity(200×200).

convenience to avoid the spatial interpolation. Line $\overline{MN}$ is the FVM region boundary located in the LBM subregion, while line $\overline{AB}$ is the LBM region boundary located in the FVM subregion. Hence the subdomain between the two lines is the overlapped region (often called hand-shaking region) where both LBM and FVM methods are adopted. This arrangement of the interface is convenient for the information exchange between the two neighboring region.

The coupled computations are conducted as follows. First with some arbitrary assumed velocity at the line $\overline{MN}$, the FVM simulation in the lower region is performed. After a temporary solution is obtained the information at the line $\overline{MN}$ is transformed into the single particle distribution function. The LBM simulation is carried out in the upper region. Then, the temporary solution of LBM at the line is then transported into the macro velocity at the line $\overline{AB}$ and the FVM simulation is repeated. Such computation is repeated until the results at the two lines are remained the same within an allowed tolerance.

RESULT AND DICUSSION

The grid layout is shown in Figure 3. Numerical simulations were carried out for cavity flow using the lattice Boltzmann method for *Re*=100, 400, 1000 on a grid of 200×200. The length of squared cavity is $L=1$. The boundaries of the cavity are still walls, except the upper boundary for which a uniform tangential velocity is prescribed as $u_{Re=100}=3.33\times10^{-3}$, $u_{Re=400}=1.33\times10^{-3}$, $u_{Re=1000}=3.33\times10^{-2}$ for the three Reynolds numbers, respectively.

Figure 4 shows plots of the stream function for the Reynolds number considered. These plots give a clear picture of the overall flow pattern and the effect of Reynolds number on the structure of the recirculating eddies in the cavity. The smoothness of the stream function distribution, especially around the hand-shaking region confirms the correctness of the information transfer at the interface.

To quantify these results, the velocity profiles along the vertical and horizontal centrelines of the cavity are shown in Figure 5 and Figure 6, and the centre locations of the primary vortices, bottom left vortices and bottom right vortices are listed in Table 1. The results are in close agreement with the benchmark solution [26]. As *Re* increases, the primary vortex centre moves towards the right and increasingly becomes circular.

The whole region vector plot is shown in Figure 7. We are interested in the smoothness and consistency of velocity distribution in the "hand-shaking" region. For this purpose, Figure 8 is presented where a local, enlarged view of the vector plot in the rectangle zone of Figure 7 is shown. Clearly, the vectors in the overlap region are quiet consistent between the LBM results and the FVM results, especially the vector arrows at the same location from the two methods in the hand shaking region are almost identical. Figure 9, 10 shows the contours of u_velocity, v_velocity. It is seen that these physical quantities are all smooth across the interface.

Finally the contours of vorticity distribution are presented in Figure 11. It can be observed that at *Re*=100, there is some un-smoothness at the interface in the left half of the cavity. This un-

smoothness may be caused by the un-completeness of iteration for this Reynolds number. This observation gives us a hint: to confirm a good smoothness and consistence when coupling of

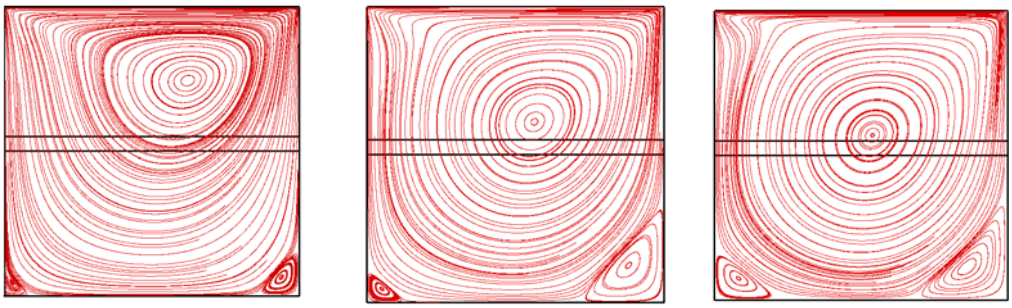

Figure 4. Contour plots of streamline. From left to right, $Re = 100, 400, 1000$, respectively.

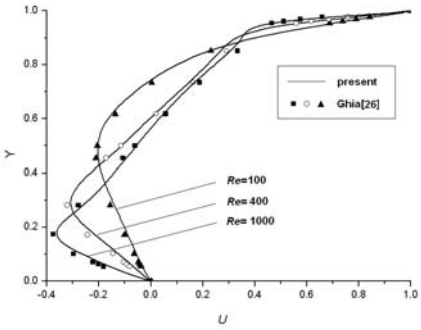

Figure 5. Comparison of U-velocity

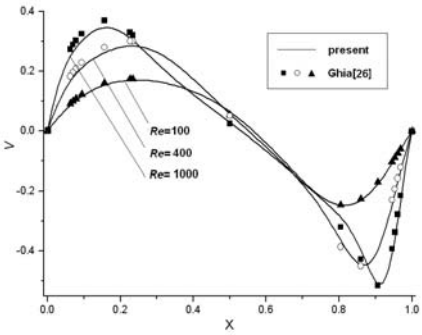

Figure 6. Comparison of V-velocity

Table 1. Comparsion of vortices location between present results and Ref[26]

Re/Vortices		Primary vortices Location (x, y)	Bottom_left vortices Location (x, y)	Bottom_right vortices Location (x, y)
Re=100	Present	(0.615,0.738)	(0.032, 0.039)	(0.936, 0.062)
	Ref.(23)	(0.6172, 0.7344)	(0.0313, 0.0391)	(0.9453, 0.0625)
Re=400	Present	(0.559, 0.608)	(0.051, 0.047)	(0.888, 0.124)
	Ref.(23)	(0.5547, 0.6055)	(0.0508, 0.0469)	(0.8906, 0.1250)
Re=1000	Present	(0.535, 0.568)	(0.083, 0.076)	(0.861, 0.111)
	Ref.(23)	(0.5313, 0.5625)	(0.0859, 0.0781)	(0.8594, 0.1094)

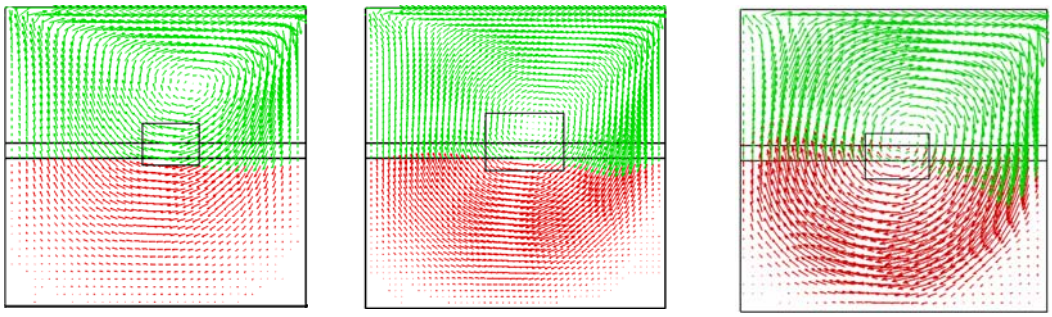

Figure 7. Vector plots of velocity. From left to right, $Re = 100, 400, 1000$, respectively.

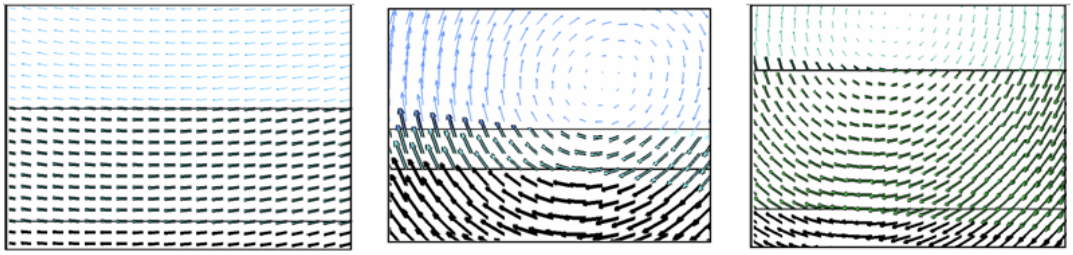

Figure 8. Enlarge Vector plots in rectangle zone of figure (7).

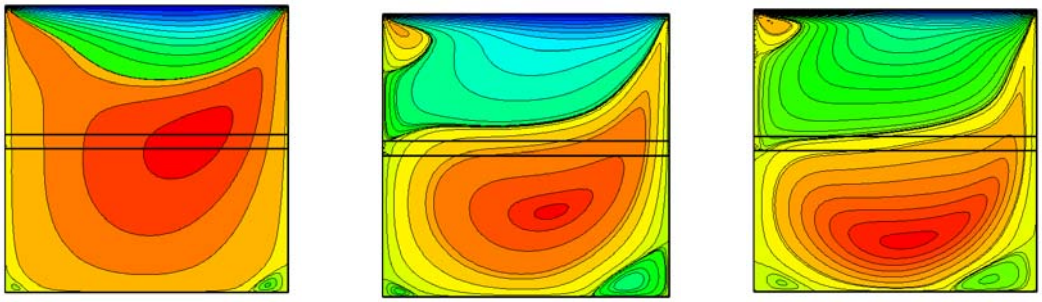

Figure 9. Contour plots of u _velocity. From left to right, $Re = 100, 400, 1000$, respectively.

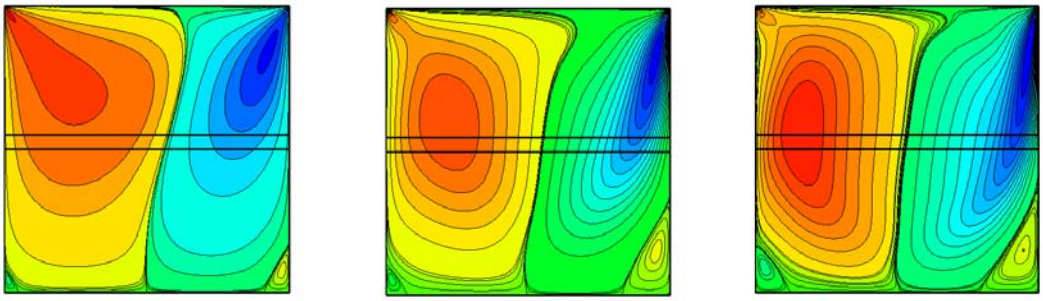

Figure 10. Contour plots of v _velocity. From left to right, $Re = 100, 400, 1000$, respectively.

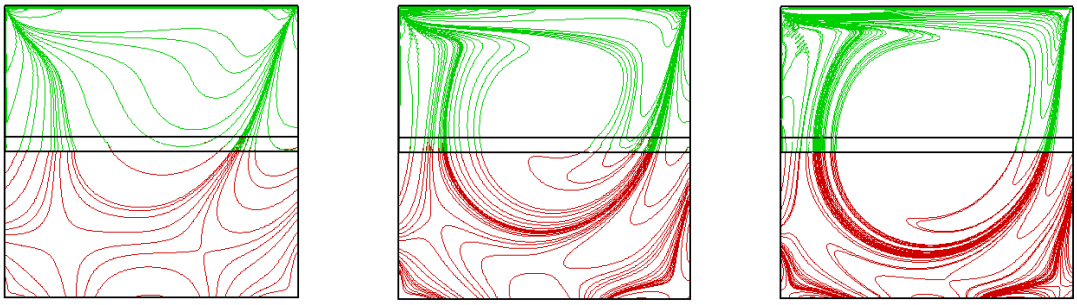

Figure 11. Contour plots of vorticity. From left to right, $Re = 100, 400, 1000$, respectively.

numerical solutions at the interface is investigated, the quality of the vorticity contour plot is more sensible to that of velocity. This is because vorticity is the first derivative of velocity, its smoothness requirement is more strict than that of velocity. The stream function is an integral of the velocity, hence its smoothness is the easiest to be reached.

CONCULUSIONS

In this paper, an coupling approach is used to couple the solutions of LBM and FVM for simulating the fluid flow problems. A reconstruction operator is adopted to lift the macroscopic velocity fields of FVM to mesoscopic distribution functions of LBM. The numerical investigations validate the proposed reconstruction operator and the coupling method.

To confirm a good smoothness and consistence of solutions coupling at the interface the vorticity contours are suggested apart from the velocity distributions. The stream function contours are the most easiest to be smoothed.

ACKNOWLEDGEMENT

This work is supported by the Key Project of National Natural Science Foundation of China. (No. 50636050).

REFERENCES

1. Weinan, E., Engquist, B., Li, X., and Ren, W., and Vanden-Eijnden, E., Heterogeneous multiscale methods: a review, *Commun. Comput. Phys.*, Vol. 2, pp 367-450,2007.
2. Succi, S., Filippova, O., Smith, G., and Kaxiras, The lattice Boltzmann equation to multiscale fluid problems, *Comput. Sci. and Eng.*,Vol 3, pp 26-37, 2001.
3. Zeng, Q. H., Yu, A. B., and Lu, G. Q., Multiscale modeling and simulation of polymer nanocomposites, *Progr. Polymer. Sci.*, Vol 33, pp:191-269, 2008.
4. Chen, G., Nanoscale energy transport and conversion, OXFORD University Press, New York, 2005.
5. Abraham, F. F., Dynamically spanning the length scales from the quantum to the continuum, *Int. J. of Mod. Phys. C*, Vol 11,No 6, pp1135─1148, 2000.
6. Nie, X. B., Chen, S. Y., E. W. N., and Robbins, M. O., A continuum and molecular dynamics hybrid method for micro- and nano-fluid flow, *J. Fluid. Mech.*, Vol 500, pp 55–64, 2004.
7. Dupuis, A., Kotsalis, E. M., and Koumoutsakos, P., Coupling Lattice Boltzmann and Molecular Dynamics models for dense fluids. *Phys. Rev. E.*, Vol 75, No.4, pp 046704, 2007.
8. Wu, J. S., Lian, Y. Y., Cheng, G., Koomullil, P. R.,and Tseng, K. C., Development and verification of a coupled DSMC–NS scheme using unstructured mesh, *J. Comput. Phys.*,Vol 219, pp 579-607, 2006.
9. Bhatnagar, P. L., Gross, E. P., and Krook, M., A model for collision processes in gases, I. small amplitude processes in charged and neutral one-component system. *Phys. Rev.*, Vol 94,pp 511-25, 1954.
10. Yu, D. Z., Mei, R. W., Luo, L. S., and Shyy, W., Viscous flow computations with the method of lattice Boltzmann Equation. *Progr. Aero. Sci.*,Vol 39, pp329-367, 2003.
11. He, X., Luo, L. S., A priori derivation of the lattice Boltzmann equation. *Phys. Rev. E.*, Vol 55, R6333-6, 1997.
12. He, X., and Luo, L. S., Theory of the lattice Boltzmann Equation: from Boltzmann Equation to lattice Boltzmann Equation. *Phys. Rev. E.*, 56:68 11-7, 1997.
13. Qian, Y. H., d'Humiéres, D., and Lallemand, P., Lattice BGK models for Navier Stokes Equation. *Europhys. Lett.*, Vol 15, pp 603-7, 1991.
14. Patankar, S. V., A calculation procedure for two-dimensional elliptic situation. *Numer. Heat. Transfer*, Vol 4, pp 409-425, 1981.
15. van, Doormaal, J. P., and Raithby, G. D., Enhancement of the SIMPLE method for predicting incompressible fluid flow. *Numer. Heat. Transfer*, Vol 7, pp147-163, 1984.
16. Issa, R. I., Solution of the implicit discretized fluid-flow equations by operator splitting. *J. Compt. Phys.*, Vol 62, pp40-65, 1986.
17. Yen, R. H., and Liu, C. H., Enhancement of the SIMPLE algorithm by an additional explicit correction step. *Numer. Heat Transfer, Part B*, Vol24, pp127-141, 1993.
18. Yu, B., Ozoe, H., and Tao, W.Q.. A modified pressure-correction scheme for the SIMPLER method, MSIMPLER. *Numer. Hea. Transfer, Part B*, Vol39, No.5, pp 435-449, 2001.
19. Tao, W. Q., Qu Z. G., and He, Y. L., A novel segregated algorithm for incompressible fluid flow and heat transfer problems-CLEAR (coupled and linked equations algorithm revised) part I: Mathematical formulation and solution procedure, *Numer. Heat. Transfer, Part B*, Vol 45, No 1, pp1-17, 2004.
20. Tao, W. Q., Qu, Z. G., and He, Y. L., A novel segregated algorithm for incompressible fluid flow and heat transfer problems - Clear (coupled and linked equations algorithm revised) part II: Application examples, *Numer. Heat. Transfer, Part B*, Vol 45, No 1, pp19-48, 2004.

21. Sun, D. L., Qu, Z. G., He, Y. L., and Tao, W. Q., An efficient segregated algorithm for incompressible fluid flow and heat transfer problems - IDEAL (Inner Doubly Iterative Efficient Algorithm for Linked Equations) part I--Mathematical formulation and solution procedure. *Numer. Heat Transfer, Part B,* Vol 53, No 1, pp1-17, 2008.
22. Sun, D. L., Qu, Z. G., He, Y. L., and Tao, W. Q., An efficient segregated algorithm for incompressible fluid flow and heat transfer problems - IDEAL (Inner Doubly Iterative Efficient Algorithm for Linked Equations) part II: Application examples. *Numer. Heat Transfer*, Part B, Vol 53, No 1, pp18-38, 2008.
23. Sun, D.L., Qu, Z.G., He Y.L. and Tao W.Q. Implementation of an efficient segregated algorithm－IDEAL on 3D collocated grid system. *Chinese Science Bulletin*, 2009, in press.
24. Li, Z.Y., and Tao, W.Q. A new stability-guaranteed second-order difference scheme. *Numer.* Heat *Transfer, Part B*, Vol 42, pp349-365, 2002.
25. Xu, H., and Tao, W. Q., A reconstruction operator for the interface coupling between LBM and macro-numerical methods of finite-family. *Journal of Xi'an Jiaotong University*, 2009. (accepted)
26. Ghia, U., Ghia, K. N., and Shin, C. T., High-Re Solutions for Incompressible Flow using the Navier-Stokes Equationuations and a Multigrid Method. *J. Compt. Phys.*, Vol 48, pp 387-411, 1982.

HEAT AND FLUID FLOWS IN GAS SPRINGS

U. Lekić*, J.B.W.Kok
University of Twente, Enschede, The Netherlands

ABSTRACT. Thermo-mechanical processes and fluid flow phenomena occurring in an unlubricated piston-cylinder gas spring are investigated. Accurate prediction of the compressed gas thermal behaviour, energy transfer and the fluid flows, together with the heat transport in the surrounding solid structures is of high industrial importance, especially where tight tolerances and the absence of a lubricant are required (e.g. cryo-cooling industry). Existing heat transfer correlations are not applicable for the closed cyclically-compressed volumes. Research on transient fluid and heat flows is done with the use of the ANSYS CFX finite-volume numerical package, modelling the closed fluid domain and the surrounding solid in a valveless piston-cylinder gas spring. Measured pressure and heat-flux data from an unlubricated piston-cylinder experimental setup are compared to the numerically simulated values; very good agreement is observed. Analyses have been made on the forming and propagation of the thermal boundary layer towards the core gas, as a function of the varying operating speed. An analytical expression that determines the boundary layer thickness on the basis of operating conditions is presented.

Keywords: *transient heat transfer, DNS, fluid flow phenomena, boundary layers.*

MOTIVATION

Piston-Cylinder Combinations are in use in a very broad range of industrial applications. Examples are internal combustion engines in the automotive, marine and aerospace applications, compressors in the cooling devices for domestic and commercial applications, for the gas liquefaction, medical purposes and superconductivity technology in electronics. All of them are intrinsically characterized by the reciprocating pistons moving inside cylindrical volumes and compressing the enclosed operating fluid. These parts are conventionally lubricated to reduce the frictional forces and wear and cool the contacts; but unfortunately lubricants also pollute the working medium. In the internal combustion engines this is acceptable in reasonable limits (the lubricant is combusted and removed), but when it comes to the closed cooling-cycle systems, one wants to avoid any presence of impurities in the thermal carrier. Ways to achieve this are thorough filtering of the operating medium and shortening of the maintenance intervals. The other direction, proposed through this project is to omit the lubrication itself and so eliminate the related decrease of performance and increase of the operating costs.

Accurate thermal analysis is crucial in this sort of considerations. Thermal expansion, internal thermal stresses and distortion of the projected geometrical relations can lead to adverse frictional stresses, delamination and destruction of the exposed and interacting parts, wear and fatigue. The oil-free constructions, investigated here, demand extremely narrow tolerances of the functional parts, which again requires much work on understanding and describing the fluid-flow and heat transfer phenomena occurring in the gas and the surrounding solid parts.

* Corresponding author: Ir. U. Lekić
Phone: + (31)-53-4892507, Fax: + (31)-53-4893663
E-mail address: u.lekic@utwente.nl

NUMERICAL HEAT FLUX versus EXPERIMENTS

Conventional Nu-Re correlations, as derived for the steady state developed boundary layer flows, are not applicable for the transient heat transfer from the gas rapidly compressed and expanded, to the surrounding walls. A phase shift can be observed between the peak instantaneous heat flux at the gas spring walls and the peak bulk gas temperature; the peak heat flux precedes the temperature maximum up to as much as 45° (Figure 1), [1, 2, 3]. Attempts have been made and reported in the literature [1, 3, 4] to include this phenomenon in the bulk gas temperature-heat transfer correlation by adding a complex phasing part. This, however, has not lead to a generally applicable correlation. For this reason, in the presented work, numerical heat transfer modelling is performed using computational fluid dynamics, applied on flow and heat transfer in a closed flow domain with transiently changing volume.

The commercially available finite-volume code ANSYS CFX11.0 is used for solving the conservation equations and the numerical modelling of the gas flow field, wall heat flux and heat conduction in the solid wall. A Direct Numerical Simulation (DNS) approach is adopted; no approximating turbulence models are being used. Underlying governing equations are the standard compressible Navier-Stokes conservation equations set up in CFX. In the previous work, [5], k-ω, SAS and LES models were applied, but this was abandoned for the absence of actual developed turbulence in the compressed fluid. Latter will be explained in the following chapter.

Mass and energy conservation in the numerical model are verified with an adiabatic simulation and results are validated with the adiabatic thermodynamic analogy over a period of 10 operating cycles (Figure 2). Discretised models were verified to be sufficiently temporally and spatially refined, to ensure accurate and grid-independent solutions. Subsequently, models are generated also for non-adiabatic cases. These are compared to the available experimental database. Measurements have been performed by A.A.Kornhauser at Massachusetts Institute of Technology-MIT [3], who made the database available to the authors. The experimental setup was a single piston-cylinder crankshaft driven gas spring (no suction/exhaust valves). The geometry of the experimental machine was DxS=50.2x76mm for the compression ratio 2 [3], *S* being the piston stroke. Kornhauser also did experiments with higher compression ratios, but due to the reported uncertainty in the measurement results these will not be discussed here. Two operating-speed test-cases were 2 and 1000 RPM. Measured property was the absolute pressure; the heat flux in [3] and [6] was evaluated as a direct function of pressure, volume and the enclosed mass of the operating fluid, with the use of global thermodynamics (the First Law of Thermodynamics and the Clapeyron equation - ideal gas law). The results of the simulations, as compared to the measurements, are presented in the following pages.

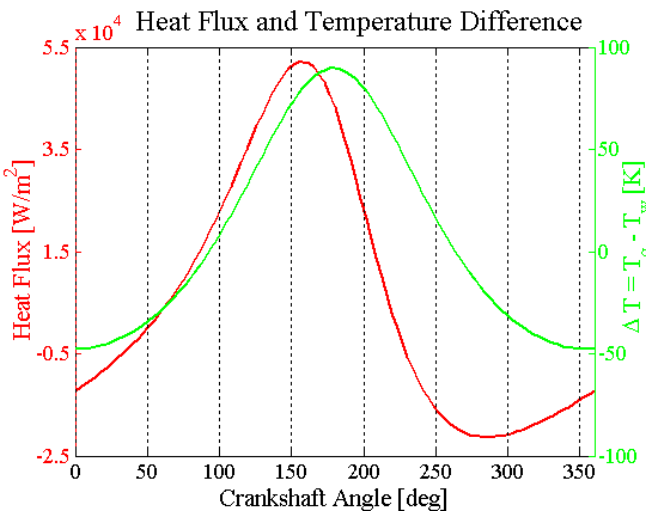

Figure 1. Temperature and heat flux phase shift

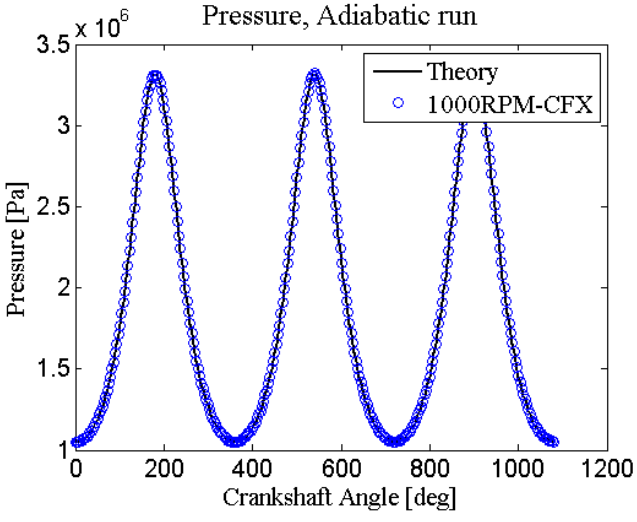

Figure 2. Numerically calculated pressure for an adiabatic run

Results

The CFX-model geometry and mesh are dimensioned according to the MIT experimental setup. For computational time reduction, and assuming the flow to be axi-symmetric, only a 5° cut of the compressed domain is modelled. The moving mesh is uniform, the piston is the only moving boundary (lower boundary) and the mesh elements are allowed to deform and redistribute in axial direction. Every node displacement is specified through an explicit function in order to ensure the uniform cell-distortion and avoid occurrence of negative-volume elements. After consecutive spatial and temporal refinements, the compression-ratio 2 model is optimized to ~28000 nodes (~20000 elements) and 1000 timesteps per cycle. The compressed gas is helium, as in the experiments. In the following discussion 2RPM runs will be regarded to as "*slow*" and 1000RPM as "*fast runs*".

Identical geometry and mesh are used for both slow and fast runs (mesh is optimized on the critical, fast run). All the walls surrounding the gas have a no-slip boundary condition. The piston surface (moving boundary) is set as an adiabatic wall and the cylinder and top (head) walls are defined to have a constant temperature of 295K, equal to the temperature of the coolant on the other side of the gas-spring walls. This assumption was made due to the very small actual oscillations in the wall temperature. This was measured for motored piston engines by several researchers [7, 1], and shown to be lower than ±3K, due to the large thermal time constant of the walls. Validity of this assumption was also examined by [6], and here too it was shown that the wall temperature can be assumed to be constant with a view to the effect on the wall heat flux.

Initial conditions are set to comply with Kornhauser's measured data; the runs are started from the bottom-dead-centre position. Kornhauser's measurements were recorded once the gas spring has reached the cyclic steady state in its operation, i.e. when the mean cycle pressure remained constant (less than 1% deviation). Results of measurements and simulations for the slow runs are presented in Figure 3 and Figure 4, and in Figure 5 and Figure 6 for the fast runs. Please note that *r* in the figure caption denotes the compression ratio and *f* stands for the operating frequency.

Slow runs. As can be seen in Figure 3, the numerically simulated pressure comes very close to the exact measured values. Properties are plotted against the crankshaft angle, 0° being the bottom-dead-centre (BDC) and 180° the top-dead-centre (TDC). The pressure in the steady state is oscillating periodically between approximately 78kPa and 160kPa; the maximum pressure is reached at the TDC. Figure 4 shows the wall heat flux to be well predicted at 0-210° and 300-360° crank angle. It is

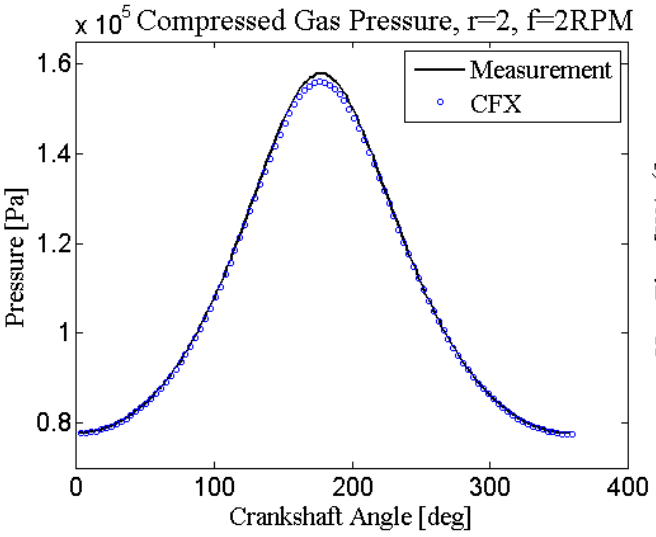

Figure 3. Measured and simulated gas pressure for the slow run, r=2

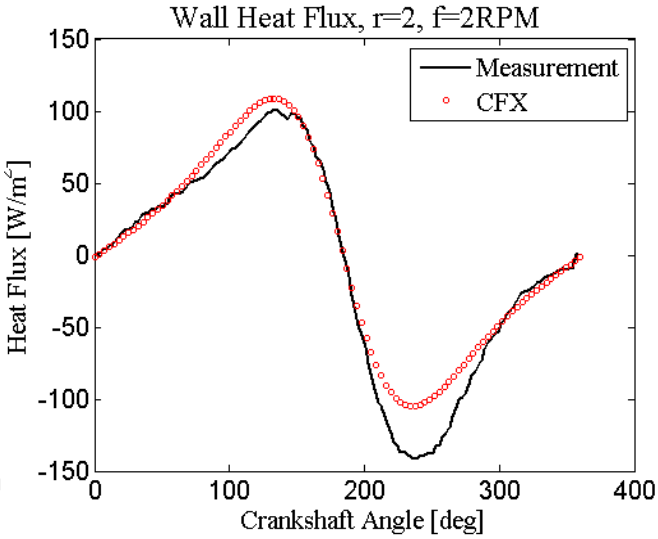

Figure 4. Measured and simulated wall heat flux for the slow run, r=2

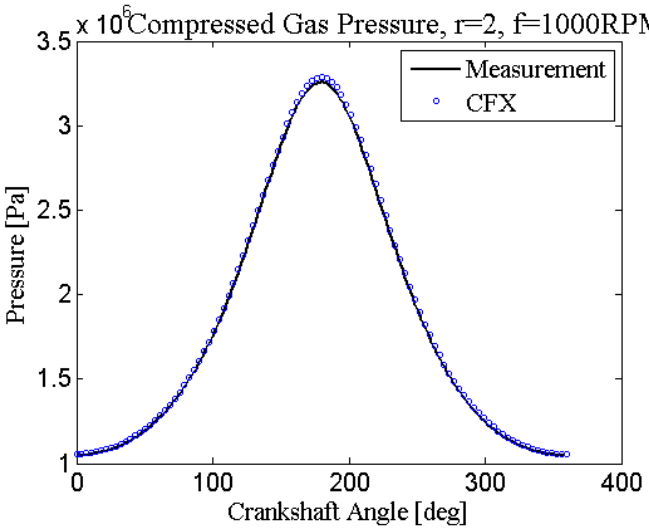

Figure 5. Measured and simulated gas pressure for the fast run, r=2

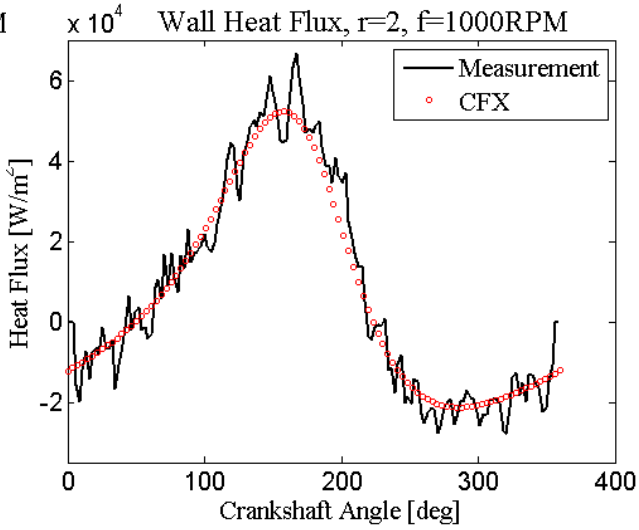

Figure 6. Measured and simulated wall heat flux for the fast run, r=2

positive in the compression phase of the cycle, positive being the heat release from the gas to the cylinder walls. There is no phase shift between the volume and mass averaged temperature and the heat flux for the slow runs (not shown here). Past the top-dead-centre the expansion starts and the heat flux becomes negative, with a negative maximum at approximately 235 degrees crank angle. Here the numerical model under-predicts the reported measured values; the maximum negative heat flux is underestimated by 50%. There is some uncertainty in the measurements at this point, as it appears that more heat is being cyclically accumulated than released. That way the gas spring would actually be producing work while the mean compressed-gas temperature is higher than the environmental (not shown here). Nevertheless, it can be concluded that CFD is very well able to predict the transient pressure and wall heat flux for the slow operating motored gas spring.

Fast runs. Measurements of the fast runs done by Kornhauser are at 1000 RPM and report turbulent flows inside the spring (the latter is discussed in the subsequent chapter). The boundary conditions in this CFD simulation are identical to those in the slow runs. The initial conditions are adapted to the experimental data; starting steady-state pressure is 1.05MPa. The obtained results for pressure and wall heat flux are presented in Figure 5 and Figure 6. The pressure on Figure 5 is observed to vary between 1 and 3.3MPa, with the maximum at the top-dead-centre, 180 degrees crank angle. Wall heat flux is plotted on Figure 6; the amplitude varies from plus 50 kW/m^2 to minus 20 kW/m^2, with the peak heat flux in the compression stroke preceding the temperature by approximately 25° crank angle. With very little error this is reproduced, and in view of the good comparison for the both characteristic test cases, it can be concluded that for the low compression ratio r=2, the CFX numerical model can successfully predict the energy flows and gas properties of the compressed medium in a valveless gas spring.

CYLINDER THERMAL BOUNDARY LAYER THICKNESS CORRELATION

The cylinder's boundary layer characteristics determine the rate of heat transfer and it's phasing with respect to the gas pressure and the bulk-gas temperature. In addition, the boundary layer at the bounding walls carries a significant part of the volume-enclosed gas mass (30-40%, [8]), and its size and shape prediction is a step to the better understanding of the transient instantaneous local heat flux. Here are presented the analysis on the development and propagation of the thermal boundary layer from the convoluting walls towards the centre of the domain. The work is based on the CFX11.0 numerical simulations as elaborated above and the analytical work, for two different piston-cylinder geometries.

Numerical models

The first modelled geometry is the above described Kornhauser's gas spring, while the second is according to the experimental setup built at the University of Twente - UT, Netherlands. Diameter and the piston stroke in the UT setup are 50mm and 52mm, respectively, compression ratio is two. The numerical model is optimized following the same routine as for the first geometry, resulting in ~8500 nodes (~6500 elements) and 1000 timesteps per cycle. The initial pressure in the UT gas spring model was set to 1.5bar and the simulations for every set case were run until the steady state is reached. Investigated operating frequencies for both geometries are 2, 10, 100, 500, 1000 and 1500RPM.

Boundary layers are usually conceptually correlated to the presence of turbulence. Although the swirling motion can be observed in the flow domains for the fast runs discussed above when the piston is at the top and bottom dead centre (Figure 7; left vertical line represents the symmetry axis of the domain 2-D snapshot), no developed turbulence is actually present here for either of the set operating frequencies. This is obvious from the turbulence parameters (eddy-viscosity, Reynolds number), and is in contrast with the reported work of Kornhauser [3]. Computed eddy frequency for the fast runs is in the order 10^3 smaller than the dynamic (molecular); in developed turbulent pipe flows it is three orders higher than the dynamic viscosity [9]. At the same time, Reynolds number is peaked at ~2000. There are no published studies on critical Reynolds numbers in this type of geometries; but it is well known that for pipe flows turbulence is ensured only for $Re>10^4$. Nevertheless, a viscous shear layer with the heat flux affected temperature and a bulk core in inertial motion can be distinguished. During the high speed runs, the shear layer thickness is much smaller than the characteristic length-piston diameter. In the slow runs the shear layer grows to the order of magnitude of the piston diameter.

Typical temperature profiles along the half-diameter, as derived from the computed temperatures for every node, are displayed on Figure 8 and Figure 9. Temperatures are sampled at 3 radius heights (discussed later) between the TDC and the cylinder top, and in the moment of the maximum piston velocities through the cycle (79° and 80° before TDC). Temperatures on these plots are sampled 38.1 and 26mm below the cylinder top (Kornhauser and UT geometry, respectively). As obvious from the figures, the forming and "shrinking" of the boundary layers as the operating frequency of the gas spring rises can be observed. For the fairly slow runs, 2&10RPM, the time scale of the temperature propagation velocity (heat and mass transfer in the gas) is larger than the axial velocity time scale, resulting in the Gaussian-like temperature profile. As the piston speed grows, two regions in the compressed (expanded) volume appear: the distinguished viscous boundary layer and the undisturbed turbulent-like core. Thermal and velocity boundary layers are formed as the consequence of the finite thermal conductivity of the gas and the discrete value of the molecular viscosity, that with the no-slip condition at the wall cause the momentum imposed by the piston displacement to be biased and diffused. Being that there is a time scale related to the propagation of this shear effect, in the fast runs, the turbulent-like core is basically the bulk gas uniformly displaced in the axial direction.

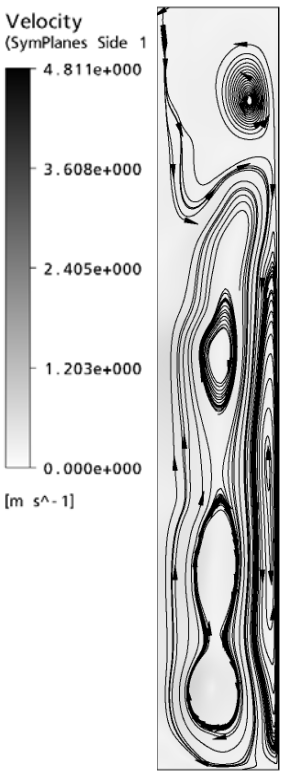

Figure 7. Gas streamlines at the TDC position.

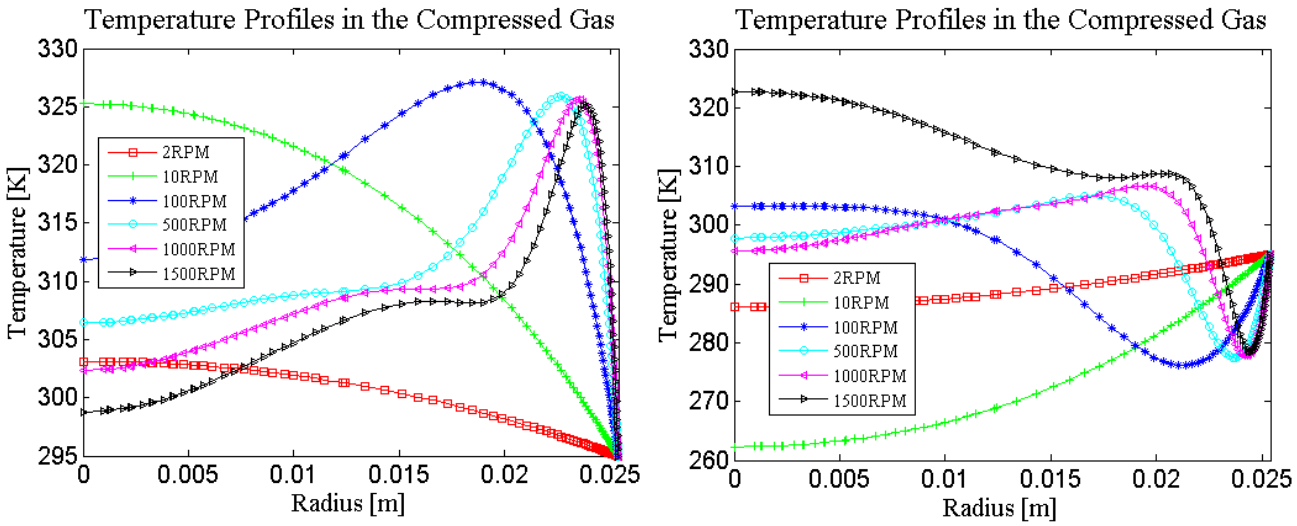

Figure 8. Temperature profiles for in the Kornhauser gas spring, compression (left) and expansion (right) stroke

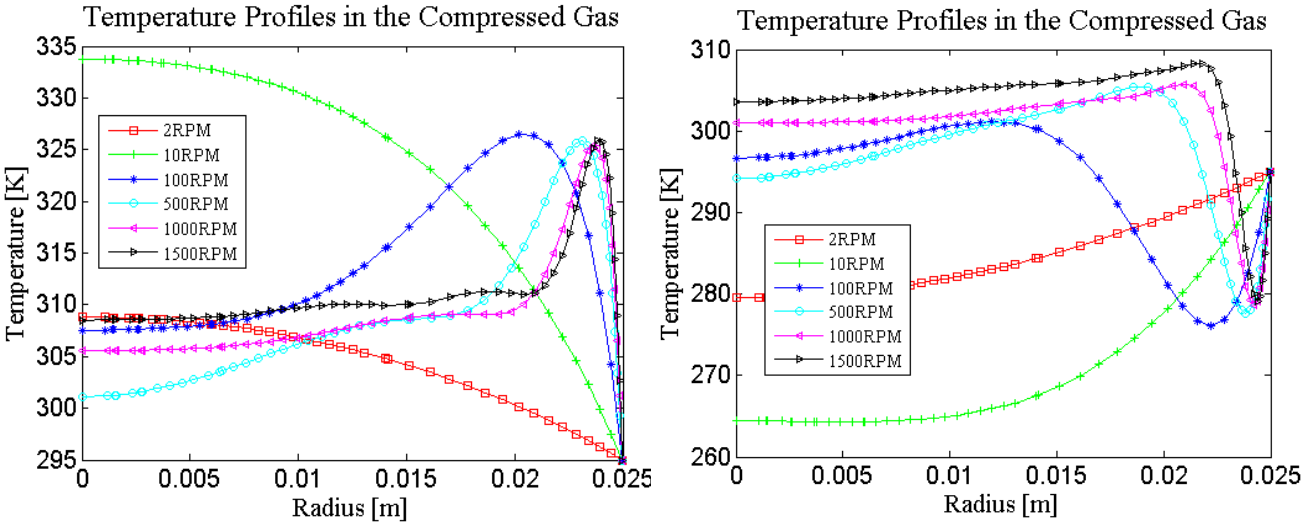

Figure 9. Temperature profiles for in the UT gas spring, compression (left) and expansion (right) stroke

Analytic correlation

Dimensional analysis was used to develop a correlation for the growth of the thermal boundary layer at the cylinder walls. An expression by Lyford-Pike and Heywood [8] for a spark-ignition engine is revised to correlate the thermal boundary layers in the gas springs; the "analytical" boundary layer thickness $\delta_{T,A}$ is fitted to the numerically determined value $\delta_{T,N}$. The question arises what should be defined as the actual boundary layer, i.e. where the transition point should be set. Here, it is proposed to be the point where the temperature gradient dT/dx is changed by 25% when differentiating from the gas core towards the wall (Figure 10). It is very interesting to notice that the shape of the boundary layer through all these runs always follows the rule that this point falls extremely close to three times the distance of the peak-temperature BL thickness (Figure 10). The following quantities were taken as the relevant parameters: gas thermal conductivity k, density ρ, specific heat at constant pressure c_p, viscosity μ, time t, cylinder diameter D and the piston stroke S. All gas properties were evaluated for the mean of the bulk gas and the wall temperature.

The local gas velocity v was evaluated as in [8], varying linearly from the piston velocity v_p to zero at the cylinder head:

$$v = v_p \cdot (x_0/x) \qquad (1)$$

where x_0 is the distance from the sampling point to the cylinder top, and x between the piston crown and the cylinder top. Reynolds number is calculated as $Re = \rho v x_0/\mu$, and the thermal diffusivity $\alpha = k/(\rho c_p)$. Elapsed time for the boundary layer thickness expression begins when the piston passes BDC for the compression, and when it passes TDC for the expansion stroke. The set of sampling locations x_0, as distances from the cylinder top, is quoted in Table 1.

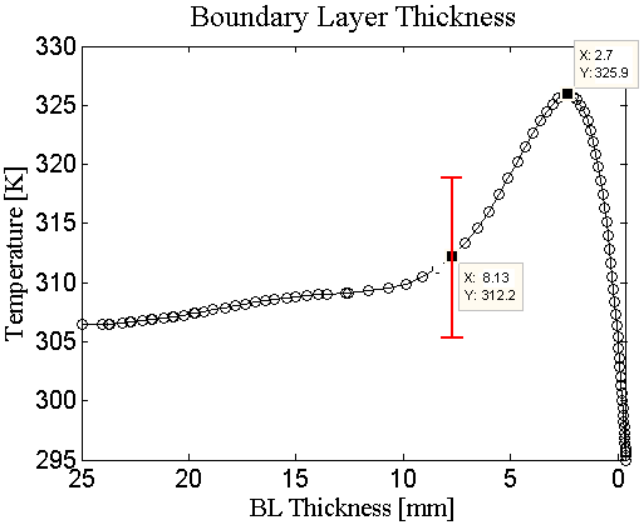

Figure 10. Boundary layer definition

An analytical correlation for the developed boundary layer thickness can be derived and shown to fit the numerically calculated values, during the compression stroke as defined by equation (2):

$$\delta_{T,A,comp} = 4.6\sqrt{\alpha \cdot t} \cdot \frac{1}{\left(Re \cdot \frac{S}{D}\right)^{0.03}}, \qquad (2)$$

and for the expansion stroke by equation (3):

$$\delta_{T,A,exp} = 3\sqrt{\alpha \cdot t} \cdot \frac{1}{\left(Re \cdot \frac{S}{D}\right)^{0.03}} \qquad (3)$$

On Figure 11 are plotted correlations for 3 sampled positions, both geometries and the specified range of operating frequencies. Figures show very satisfactory results for all test cases.

Table 1.
Overview of temperature sampling heights

[mm]	Position 1	Position 2	Position 3
Kornhauser	19.05	38.1	57.15
UT setup	13	26	39

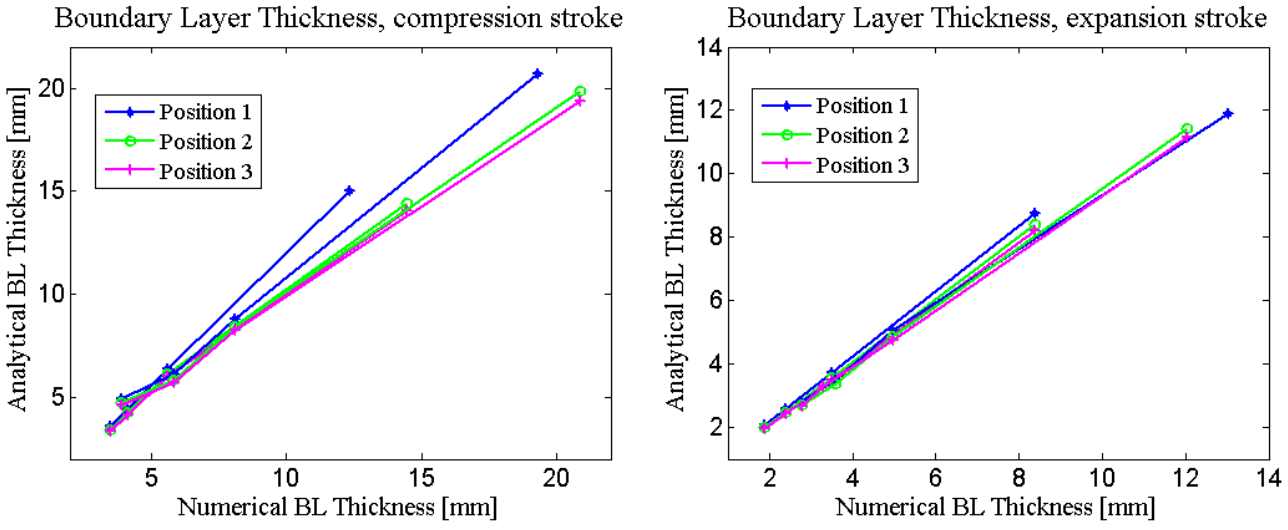

Figure 11. Analytically fitted BL thickness for the compression (left) and the expansion stroke (right)

CONCLUSIONS

Numerical models have been developed with the use of the finite-volume numerical package ANSYS CFX11.0, to simulate the thermodynamic phenomena occurring in a compression ratio 2 helium gas-spring. Characteristic properties such as the mass and energy conservation, pressure of the compressed gas and the heat transfer from the gas to the solid are examined and compared to the experimental database obtained at MIT. For typically slow and fast runs: 2RPM and 1000RPM operating frequency, numerical model very successfully predicts the measured values of pressure and heat-flux, with very little error introduced.

In view of the relevance to the thermodynamic processes and convective heat transfer, the timescale and the depth of the penetration of the thermal boundary layer are analysed in numerical models for two different helium gas-spring geometries and a range of operating frequencies. Derived analytic expressions for determining the thermal boundary layer thickness at the cylinder walls fit the numeric data adequately for various test cases: both compression and expansion stroke, different geometries, charge pressures and operating speeds. It can be concluded that the presented correlation is a good approximation and can be used generally.

Nomenclature:

r – compression ratio, [/], $r=V_{BDC}/V_{TDC}$
f – operating frequency, [RPM]
TDC – Top Dead Centre
BDC – Bottom Dead Centre
$\delta_{T,N}$ – numerically determined boundary layer thickness, [mm]
$\delta_{A,N,\,comp}$ – analytically determined boundary layer thickness during the compression stroke, [mm]
$\delta_{A,N,\,exp}$ – analytically determined boundary layer thickness during the expansion stroke, [mm]
S – piston stroke, [mm]
x_0 – distance from the sampling point to the cylinder top, [mm]
x – distance from the piston crown to the cylinder top, [mm]

Acknowledgments
This project is sponsored by Technologiestichting STW Netherlands. Many thanks also to Prof. Kornhauser presently at Virginia State University for making his measurement data available.

REFERENCES

1. Anand, W.J.D. and Pinfold, D., "Heat Transfer in the Cylinder of a Motored Reciprocating Engine", *SAE Paper 800457, Society of Automotive Engineers*, 1980.
2. Lawton, B., "Effect of compression and expansion on instantaneous heat transfer in reciprocating internal combustion engines", *MIMechE Paper*, Vol 201, No. A3, 1987.
3. Kornhauser, A.A., "Gas-Wall Heat Transfer during Compression and Expansion", PhD Thesis, Massachusetts Institute of Technology, 1989.
4. Lee, K.P., "A Simplistic Model of Cyclic Heat Transfer Phenomena in Closed Spaces", *Proc. 18th IECEC*, 1983, pp. 720-730.
5. Lekić, U. and Kok, J.B.W, "Heat Flows in Piston Compressors", *Proc. 5th EUROTHERM*, FCV_4, 2008.
6. Jak, H.G., "Heat Transfer in a Gas Spring", M.SC.Thesis, University of Twente, 2001.
7. Adair et al., "Instantaneous heat transfer to the cylinder wall in reciprocating compressors", *Proceedings of the 1972 Purdue Compressor Technology Conference*, Purdue University, 1972.
8. Lyford-Pike, E.J. and Heywood, J.B., "Thermal Boundary Layer Thicknesses in the cylinder of a Spark Ignition Engine," M.S. Thesis, Dept. of Mech. Eng., Massachusetts Institute of Technology, 1984.
9. ANSYS CFX, Release 10.0: Installation and Overview Notes", ANSYS Inc, 2005, p.346
10. Pfriem, H., "Periodic Heat Transfer at Small Pressure Fluctuations", *NACA* TM-1048, 1943.

A STUDY OF PARTICLE FEEDBACK IN TURBULENT GAS-PARTICLE FLOWS

T. Strömgren*, G. Brethouwer, G. Amberg and A.V. Johansson
Linné Flow Centre, KTH, Stockholm, Sweden

ABSTRACT. The upward turbulent gas-particle flow in a channel was studied using an Eulerian-Eulerian two-phase model taking into account the feedback from the particles on the gas-phase. The objective is to study the influence of particles with different diameters and volume fractions on the flow and particularly on the accumulation of particles in the near wall region due to the turbophoretic effect. The results were obtained with a two-phase flow model that is presented. The accumulation of particles in the near-wall region was found to be strongest for particles with $\tau_p^+ = 13$. The model also shows that varying the particle diameters leads to different feedback of the particles on the turbulent flow.
Keywords: *Turbulent gas-particle flows, modelling, particle feedback, turbophoresis*

INTRODUCTION

The interaction between turbulent flows and inertial particles is important in both natural and industrial processes. For instance in particulate dispersion in the atmosphere and in processes to remove pollutants generated by power plants fired by fossil fuels. The effect of particles on the turbulence is very complex and it is of importance to increase the understanding of this phenomenon.

Particles tend to accumulate in regions with low turbulence intensity, e.g. in the near wall region of wall-bounded flows, due to the turbophoretic effect [1]. The turbophoretic particle drift caused by gradients in the turbulent kinetic energy is counteracted by turbulent diffusion that transports particles down concentration gradients [2]. These phenomena have been extensively studied by [1, 3, 4, 5, 6].

We have developed a model that takes into account the feedback from the particle-phase on the gas-phase [7]. We use the model to simulate the fully developed turbulent gas-particle flow in a vertical channel. The aim is to study the interaction between the particle-phase and the gas-phase and the accumulation of particles in the near wall region for different particle diameters and mass loadings.

The present paper is organized as follows: first a description of the model and the governing equations are given, then the simulation setup is explained followed by the discussion of the results and the conclusions.

* Corresponding author: «Wiersz pozdrowienia»
Phone: + (46)-8-7907195, Fax: + (46)-8-7989650
E-mail address: tobias@mech.kth.se

MATHEMATICAL FORMULATION

Model equations

An Eulerian-Eulerian model, developed by [7], is used to study turbulent gas-particle flows assuming that the particle-phase can be considered as a continuum. The model is found to be in good agreement with both DNS-data and experiments [7]. The volume fraction weighted averaged continuity equation of the particle-phase can be written as

$$\frac{\partial \Phi_g}{\partial t} + \frac{\partial}{\partial x_i}(U_{gi}\Phi_g) = \frac{\partial}{\partial x_i}(\nu_p \frac{\partial \Phi_g}{\partial x_i}) \tag{1}$$

where Φ_p is the mean particle volume fraction, U_p is the particle velocity and ν_p is the viscosity due to particle-particle collisions. The volume fraction weighted averaged momentum equations for gas- and particle-phase are, respectively

$$\begin{aligned}&\frac{\partial}{\partial t}(\rho_g \Phi_g U_{gi}) + \frac{\partial}{\partial x_j}(\rho_g \Phi_g U_{gi} U_{gj}) = -\Phi_g \frac{\partial P}{\partial x_i} + \\ &\rho_g \frac{\partial}{\partial x_j}((\nu_{tg} + \nu_g)(\Phi_g(\frac{\partial U_{gi}}{\partial x_j} + \frac{\partial U_{gj}}{\partial x_i}))) - \frac{\partial}{\partial x_j}(\frac{2}{3}\rho_g \Phi_g \delta_{ij}(K_g + \nu_{tg}\frac{\partial U_{gl}}{\partial x_l})) \\ &- (1 + 0.15Re_r^{0.687})\frac{\rho_p}{\tau_p}\Phi_p(U_{gi} - U_{pi})\end{aligned} \tag{2}$$

$$\begin{aligned}&\frac{\partial}{\partial t}(\rho_p \Phi_p U_{pi}) + \frac{\partial}{\partial x_j}(\rho_p \Phi_p U_{pi} U_{pj}) = -\Phi_p \frac{\partial P}{\partial x_i} \\ &+ \rho_p \frac{\partial}{\partial x_j}(\Phi_p(\nu_p + \nu_{tp})(\frac{\partial U_{pi}}{\partial x_j} + \frac{\partial U_{pj}}{\partial x_i})) - \frac{\partial}{\partial x_j}(\frac{2}{3}\rho_p \Phi_p \delta_{ij}(K_p + \nu_{tp}\frac{\partial U_{pl}}{\partial x_l})) \\ &+ (1 + 0.15Re_r^{0.687})\frac{\rho_p}{\tau_p}(\Phi_p(U_{gi} - U_{pi})) + \Phi_p(\rho_p - \rho_g)g_i\end{aligned} \tag{3}$$

where U_g, ρ_g, Φ_g, P, K_g, ν_{tg}, and ν_g are the mean velocity, density, mean volume fraction, pressure, mean turbulent kinetic energy, turbulent viscosity and kinematic viscosity of the gas-phase, respectively. ρ_p, K_p and ν_{tp}, are the density, mean turbulent kinetic energy and turbulent viscosity of the particle-phase. The model takes into account the feedback from the particles on the gas-phase through the drag term (last term on the right hand side (R.H.S.) of equation (2)) with a correction term for higher Reynolds numbers according to [8], where $Re_r = D_p|U_p - U_g|/\nu_g$ is the relative Reynolds number, $\tau_p = \rho_p D_p^2/(18\rho_g \nu_g)$ is the particle response time and D_p is the particle diameter.

To model the gas- and particle Reynolds stresses the Boussinesq assumption is used. The turbulent viscosities are modelled according to $\nu_{tg} = K_g/\omega$ [9] and $\nu_{tp} = \nu_{tg}/(1+(\tau_p/T_L)^2)$ [10], where ω is the inverse time scale of the turbulence and T_L is the Lagrangian time scale of the gas-phase. A low Reynolds number K-ω model is used to compute K_g and ω [9]. The equations for K_g and ω are given by

$$\begin{aligned}&\rho_g \frac{\partial K_g}{\partial t} + \rho_g U_{gj}\frac{\partial K_g}{\partial x_j} = 2\rho_g \nu_{tg} S_{ij} S_{ij} - \rho_g C_\mu \omega K_g \\ &+ \frac{\partial}{\partial x_j}[\rho_g(\nu_g + \frac{\nu_{tg}}{\sigma_K})\frac{\partial K_g}{\partial x_j}] - (1 + 0.15Re_r^{0.687})\frac{\rho_p}{\tau_p}\Phi_p(\overline{u'_{gi}u'_{gi}} - \overline{u'_{pi}u'_{gi}})\end{aligned} \tag{4}$$

$$\rho_g \frac{\partial \omega}{\partial t} + \rho_g U_{gj}\frac{\partial \omega}{\partial x_j} = 2\rho_g \alpha S_{ij} S_{ij} - \rho_g \beta \omega^2 + \frac{\partial}{\partial x_j}[\rho_g(\nu_g + \frac{\nu_{tg}}{\sigma_\omega})\frac{\partial \omega}{\partial x_j}] \tag{5}$$

where

$$S_{ij} = \frac{1}{2}(\frac{\partial U_{gi}}{\partial x_j} + \frac{\partial U_{gj}}{\partial x_i}) \tag{6}$$

Equation (4) is derived from the momentum equation of the gas-phase (2). The last term in (4) represents the interaction between the gas-phase and the particle-phase. The model parameters are defined by

$$\alpha = \frac{5}{9}\frac{\alpha_o + Re_T/R_\omega}{1 + Re_T/R_\omega}(\alpha^*)^{-1} \tag{7}$$

$$\alpha^* = \frac{\alpha_o^* + Re_T/R_k}{1 + Re_T/R_k} \tag{8}$$

$$C_\mu = \frac{9}{100}\frac{5/18 + (Re_T/R_\beta)^4}{1 + (Re_T/R_\beta)^4} \tag{9}$$

where $Re_T=K_g/(\omega\nu_g)$. The constants we use are $\beta=3/40$, $\sigma_K=\sigma_\omega=2$, $\alpha_0^*=\beta/3$, $\alpha_0=1/10$, $R_\beta=8$, $R_K=6$ and $R_\omega=27/10$.

ω is decomposed according to

$$\omega = \tilde{\omega} + \omega_w \tag{10}$$

where $\omega_w = 6\nu_g/(\beta y^4)$ and y is the distance to the wall. The rapid variation in the near-wall region is captured by ω_w, whereas the former part is the dominating term far from the boundary [11].

The mean turbulent particle kinetic energy and the fluctuating gas-particle velocity correlation are modelled as

$$\overline{u'_{pi}u'_{pi}} = \overline{u'_{pi}u'_{gi}} = \frac{2K_g}{1 + \frac{\tau_p}{T_L}} \tag{11}$$

where $T_L = (C_\mu\omega)^{-1}$. This closure relation is also used by [12, 13, 14].

In the near wall region, where the particle concentration can be high in dilute gas-particle flows, the viscosity due to particle-particle collisions can be important as shown by [15, 16] through LES and DNS, respectively. To model the particle-particle collisions we adopt the shear induced particle diffusion model by [17]

$$\nu_p = \frac{1}{4}\Phi_p D_p^2 \frac{dU_p}{dy} \tag{12}$$

where dU_p/dy is the shear in the wall normal direction. The model gives a significant contribution only in the near wall region where the velocity gradient dU_p/dy is large and the particle concentration Φ_p can be high.

Simulations

The described Eulerian-Eulerian model is used to simulate the upward turbulent gas-particle flow in a vertical channel. Where channel flow is the flow between two infinite flat plates, so there is only variation in the wall normal direction. The channel half-width δ=0.05 m, ρ_g = 1.3 kg/m^3, ρ_p = 910 kg/m^3 and D_p is varied from 20 to 120 μm. The Reynolds number, $Re=U_{gc}\delta/\nu_g$,= 18500 in all simulations. Here U_{gc} is the centreline velocity of the gas-phase. The velocity components of the gas-phase have a no-slip condition at the wall. The streamwise particle-velocity has a free-slip condition at the wall $dU_p/dx=0$. In the normal direction the particle velocity is zero implying that the net flux of particles at the wall is zero [6]. The pressure and particle volume fraction have Neumann conditions at the wall. We assume that the flow is fully developed in the streamwise direction. Therefore, cyclic boundary conditions are imposed. The model is implemented into a finite element code [18] with grid refinement close to the wall. There are at least 10 grid points in the region below $y^+ = 1$ in order to resolve the steep particle concentration gradients near the wall. Here $y^+=u_\tau y/\nu_g$ where $u_\tau=(\tau_w/\rho_g)^{1/2}$ is the friction velocity and τ_w is the wall shear stress. The simulations are run until a steady state is reached. Simulations are carried out for six particle diameters varying from 20 to 120 μm and four different particle volume fractions.

RESULTS

In figure 1, Φ_p normalised with the initial particle volume fraction, $\Phi_{0,}$ is shown as a function of the wall distance for six different D_p and two different initial particle volume fractions. The particles accumulate in the near-wall region as shown by the large values of Φ_p/Φ_0. This accumulation is due to the turbophoretic effect, which is modelled by the gradient of the mean kinetic energy, i.e. the third term on the R.H.S. in equation (3) [19]. The magnitude of Φ_p/Φ_0 decreases quite substantially with increasing Φ_0, which is explained by an increasing attenuation of K_g for increasing Φ_0, se figure 4.

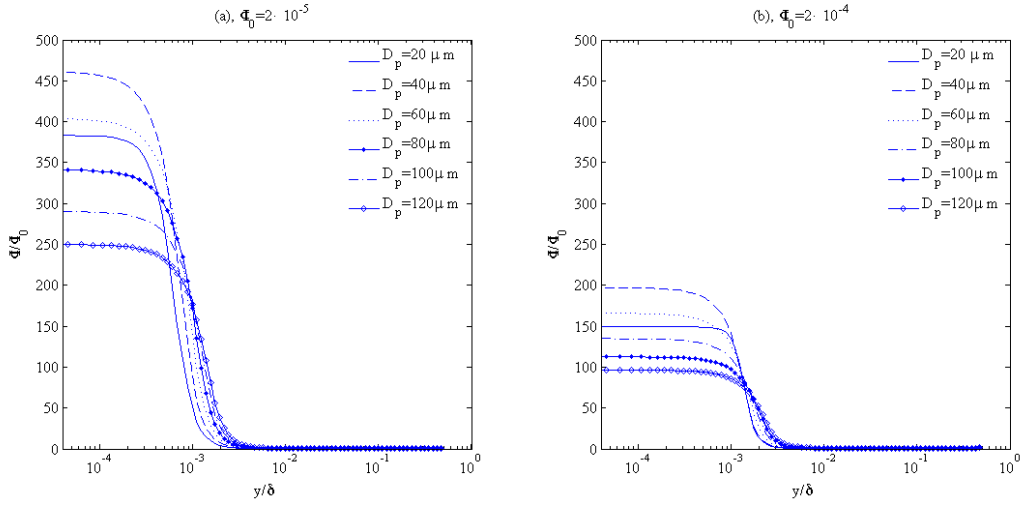

Figure 1. Mean particle volume fraction normalised with the initial particle volume fraction for six different particle diameters and two different particle volume fractions $\Phi_0=2\cdot10^{-5}$ (a) and $\Phi_0=2\cdot10^{-4}$ (b). Note the logarithmic scale in the wall normal direction.

The maximum values of Φ_p/Φ_0 as a function of D_p for four different Φ_0 are shown in figure 2a. The maximum values of Φ_p/Φ_0 occur at the wall due to the turbophoretic effect shown in figure 1. It increases quite substantially for decreasing Φ_0, although K_g changes quite moderately between

$\Phi_0 = 2 \cdot 10^{-5}$ and $1 \cdot 10^{-4}$, see figure 4. The accumulation of particles near the wall due to the turbophoretic effect is strongest for D_p=40 μm, for this particular parameter range, whereafter it decreases. This phenomenon is related to the particle response time. For increasing Reynolds numbers the strongest effect of the turbophoresis will occur for larger D_p.

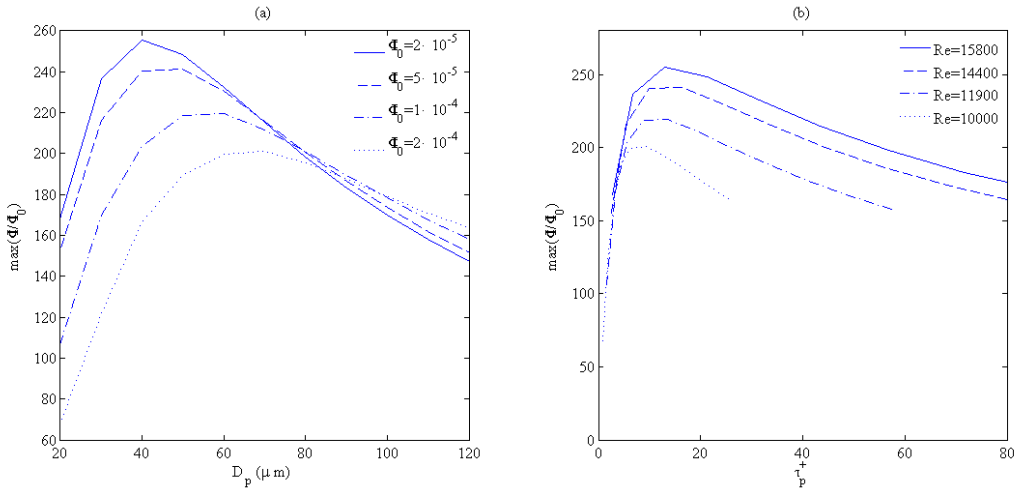

Figure 2. The maximum value of the mean particle volume fraction normalised with initial particle volume fraction as a function of D_p for four different Φ_0 (a) and as a function of τ_p^+ for four different Reynolds numbers with $\Phi_0 = 1 \cdot 10^{-4}$ (b).

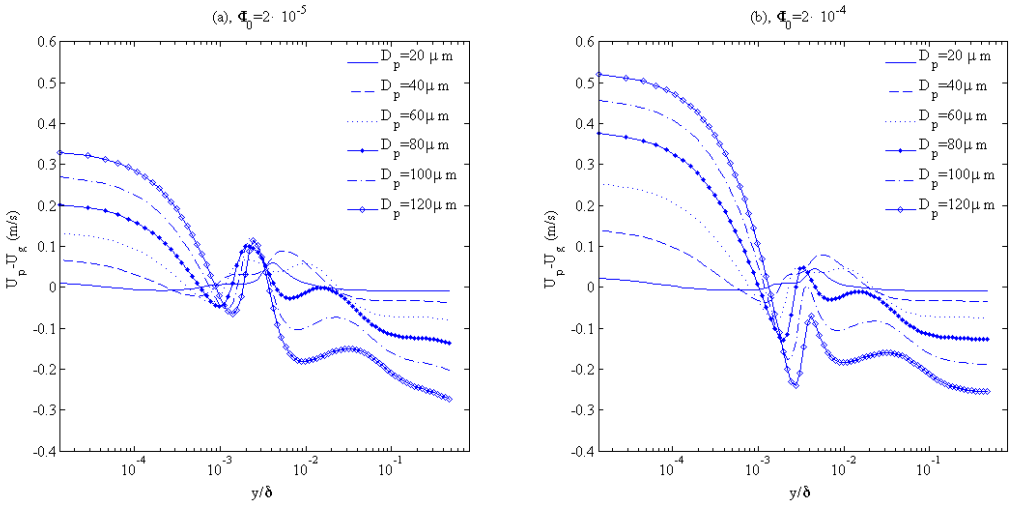

Figure 3. Mean slip velocity between particle- and gas-phase for six different particle diameters and two different particle volume fractions $\Phi_0 = 2 \cdot 10^{-5}$ (a) and $\Phi_0 = 2 \cdot 10^{-4}$ (b). Note the logarithmic scale in wall normal direction.

In figure 2b the maximum value of Φ_p/Φ_0 is shown as a function of τ_p^+ for four different Reynolds numbers, where $\tau_p^+ = \tau_p u_\tau^2/\nu$. Φ_p/Φ_0 reaches a maximum for τ_p^+ around 13 for all Reynolds numbers except for Re=10 000 where the maximum occurs at $\tau_p^+ = 9$. The turbophoretic effect is significant for particles that respond to turbulence but do not perfectly follow the turbulent flow field. This implies

that the turbophoretic effect is weak for particles with large or small τ_p^+, i.e. large or small D_p, because large particles are not affected by the turbulence while very small ones follow the turbulence perfectly.

Figure 3 shows the slip velocity between the particle- and the gas-phase for the same cases as in figure 1. In the core of the channel the particles lag the flow due to gravity. However, in the near-wall region the particles lead the flow due to the inertia the particles gained in the core of the channel [20]. The maximum slip velocity is at the wall since the particles have a free-slip condition at the wall. The slip velocity at the wall increases slightly with increasing particle volume fraction. The magnitude of the slip velocity increases for increasing D_p as shown by figure 3. In figure 4a the mean kinetic energy of the gas phase is shown for D_p=100 μm for four different Φ_0 and for one simulation without particles. Increasing the mass loading leads to a stronger damping of the gas-phase turbulence as shown by the figure. The same behaviour is seen for all D_p between 20 and 120 μm. In figure 4b the mean kinetic energy is shown for $\Phi_0=2\cdot10^{-4}$ for four different D_p. It is seen that K_g decreases with increasing Φ_0. The peak of the turbulence kinetic energy close to the wall is most strongly damped by particles with Dp=20μm. Particles with D_p=120μm have the least effect on K_g. However, at D_p=60μm the maximum value of K_g decreases more than at D_p=40μm. On the other hand, in the centre of the channel particles with D_p=120μm has the largest decrease on K_g and particles with D_p=40μm have the least effect on K_g. The magnitude of the decrease is smaller in figure 4b compared to figure 4a because mass loading is constant in figure 4b. Results with a different diameter have thus a different feedback effect on the gas-phase turbulence even though the mass loading is the same.

Changing the particle diameter D_p gives rise to three different physical mechanisms that counteract each other. A smaller D_p for constant mass loading leads to a larger surface area that increases the friction between the phases. On the other hand, smaller particles have a smaller slip velocity as shown by figure 3, leading to decreased drag. These two effects have opposing effects on the magnitude of the drag term (last term in equation (2)) and the interaction between the gas-phase turbulence and the particle-phase (last term in equation (4)). These terms also depend on Φ_p, which changes with D_p as shown by figure 2a. Therefore the relation between the damping of the gas-phase turbulence and the particle diameter is complex.

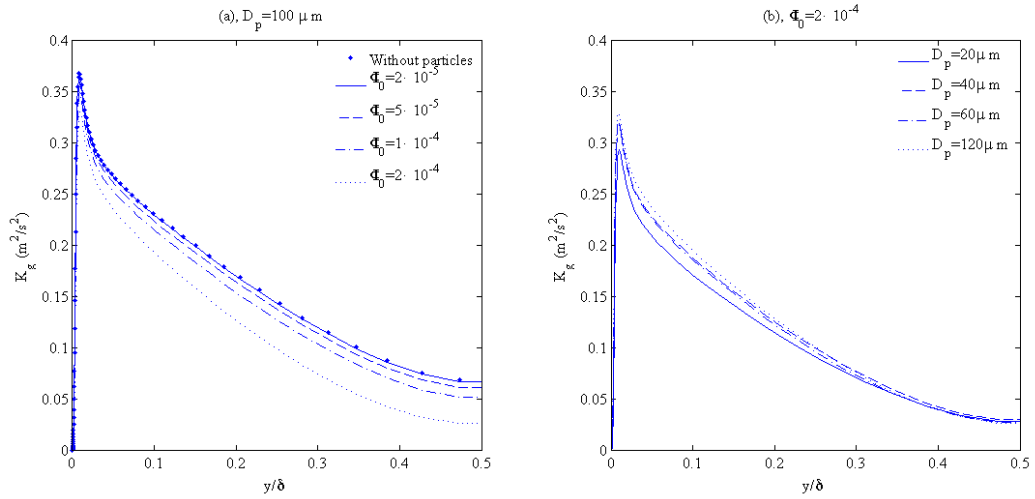

Figure 4. Mean turbulent kinetic energy of the gas-phase. For four different initial particle volume fractions with D_p=100μm (a) and for four different D_p with $\Phi_0=2\cdot10^{-4}$ (b).

The particle velocity in the wall normal direction is shown in figure 5 for the same cases as in figure 4a. We see that the particles move towards the wall in the near wall region whereas in the core of the channel the particles move towards the centreline. The change in sign of the wall normal particle velocity appears where K_g has its peak-value, which clearly shows that the drift of particles in the wall-normal direction is strongly influenced by the gradient in the mean turbulent kinetic energy [19].

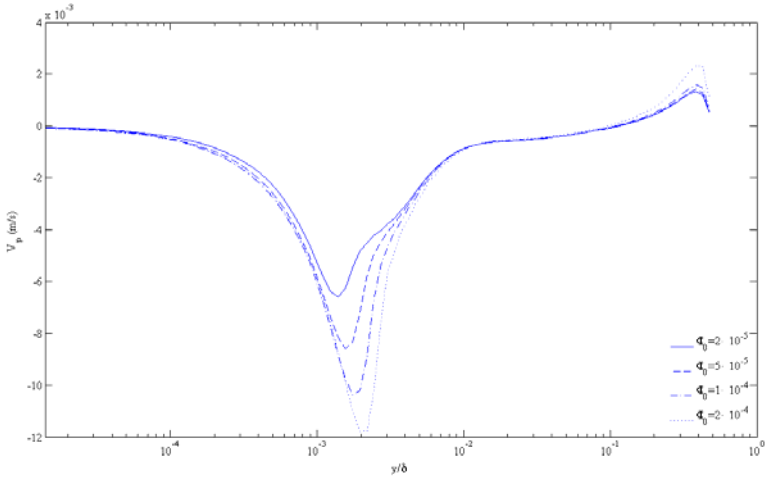

Figure 5. Mean particle velocity in the wall normal direction for four different initial particle volume fractions. Note the logarithmic scale in wall normal direction.

CONCLUSIONS

Upward particle laden turbulent channel flow was studied using an Eulerian-Eulerian two-phase flow model which takes into account the feedback of the particle-phase on the gas-phase. A low Reynolds number K-ω model was used to describe the gas-phase turbulence. Simulations for different particle diameters and particle volume fractions were carried out at constant Reynolds number.

The turbophoresis effect was found to decrease for increasing particle volume fraction. It has a maximum effect for particles with τ_p^+=13. Increasing the particle diameter was found to increase the slip velocity, which increases the drag between the phases. However, increasing the particle diameter decreases the friction between the phases, which decreases the drag. Therefore, the relation between particle diameter and the drag between the phases and the gas-phase turbulence intensity is quite complex.

In this study the centreline velocity of the gas-phase is kept constant between the different cases by changing the pressure gradient. However, when the pressure gradient is kept constant the mean flow will be strongly affected and decreases for decreasing D_p, see [7].

REFERENCES

1. Marchioli, C. and Soldati, A., Mechanisms for particle transfer and segregation in a turbulent boundary layer, *J. Fluid Mech.*, Vol. 468, pp. 283-315, 2002.
2. Haarlem, B., Boersma, B. and Nieuwstadt, F., Direct numerical simulation of particle deposition onto a free-slip and no-slip surface, *Phys. Fluids*, Vol. 17, pp. 2608-2620, 1998.

3. Botto, L., Narayanan, C., Fulgosi, M. and Lakehal, D., Effect of near-wall turbulence enhancement on mechanisms of particle deposition, *Int. J. Multiphase Flow,* Vol. 31, pp. 940-956, 2005.
4. Vreman, A., Turbulence characteristics of particle-laden pipe flow, *J. Fluid Mech.,* Vol. 584, pp. 235-279, 2007.
5. Kulick, J., Fessler, J. and Eaton, J. Particle response and turbulence modification in fully developed channel flow, *J. Fluid Mech.,* Vol. 277, pp. 109-143, 1994.
6. Cerbelli, S., Giusti, A. and Soldati, A., ADE approach to predicting dispersion of heavy particles in wallbounded turbulence, *Int. J. Multiphase Flow,* Vol. 27, pp. 1861-1879, 2001.
7. Strömgren, T., Brethouwer, G., Amberg, G. and Johansson, A.V., Modelling of turbulent gas-paticle flows with focus on two-way coupling effects on turbophoresis, *Submitted to AIChE Journal.*
8. Schiller, L. and Naumann, A., Über die grundlegenden Berechnungen bei der Schwerkraftaufbereitung, *Ver. Deut. Ing.,* Vol. 77, pp 318-320, 1933.
9. Wilcox, D.C., *Turbulence Modeling for CFD,* DCW Ind., Inc. La Cañada, California.
10. Choi Y.D. and Chung, M.K., Analysis of turbulent gas-solid suspension flow in a pipe, *J. Fluids Eng., ASME,* Vol. 105, pp 329-334, 1983.
11. Gullman-Strand, J., Amberg, G. and Johansson, A.V., Turbulence and scalar flux modelling applied to separate flows. *Tech. report,* Dep. Mechanics, KTH, Stockholm, 2004.
12. Young, J. and Leeming, A., A theory of particle deposition in turbulent pipe flow, *J. Fluid Mech.,*Vol. 340 pp. 129-159, 1997.
13. Guha, A., A unified Eulerian theory of turbulent deposition to smooth and rough surfaces, *J. Aerosol Sci.,* Vol. 28, pp. 1517-1537, 1997.
14. Tu, J. and Fletcher, C., An improved model for particulate turbulence modulation in confined two-phase flows, *Int. Comm. Heat and Mass Transfer,* Vol. 21, pp. 775-783, 1994.
15. Vance, M., Squires, K. and Simonin, O., Properties of the particles velocity field in gas-solid turbulent channel flow, *Phys. Fluids,* Vol. 18, pp. 063302, 2006.
16. Li, Y., McLaughlin, J., Kontomaris, K. and Portela, L., Numerical simulation of particle-laden turbulent channel flow, *Phys. Fluids,* Vol. 13, pp. 2957-2967, 2001.
17. Drazer, G., Koplik, J., Khusid, B. and Acrivos, A., Deterministic and stochastic behaviour of non-Browninan spheres in shear suspensions, *J. Fluid Mech.,* Vol. 460, pp. 307-355, 2002.
18. Amberg, G., Törnhardt, R. and Winkler, C., Finite element simulations using symbolic computing, *Mathematics and Computers in Simulation,* Vol. 17, pp. 228-237, 1999.
19. Reeks, M., The transport of discrete particles in inhomogeneous turbulence, *J. Aerosol Sci.,* Vol. 14, pp. 529-546, 1983.
20. Johansen, S., The deposition of particles on vertical walls, *Int. J. Multiphase Flow,* Vol. 17, pp. 355-376, 1991.

NUMERICAL SIMULATION OF TURBULENT FLOW WITHIN A PRECESSING JET NOZZLE

J. W. Zhou*, L. P. Geng, R. Tao
Dept. of Thermal Engineering, China Jiliang University, Hangzhou 310018, China

ABSTRACT. Numerical simulation of unsteady turbulent flow within a precessing jet nozzle is carried out in this paper. The nozzle model comprises of an axisymmetric inlet tube and a large cylindrical chamber. The flow features of a self-excited precessing jet are numerically studied using the large eddy simulation (LES) approach. The simulations show that the precession in axisymmetric sudden expansions develops naturally when the nozzle configuration is within suitable geometric ratios. The bulk axial velocity of the precessing jet is decreased significantly because of the entrainment of ambient air. The swirling flow, the wall attachment effect and the reverse flow region within the nozzle are also found in the numerical flow field and these results accord well with the previous analysis. The simulated oscillating frequency spectrum is also in general agreement with the experimental data.

Keywords: *precessing jet, flow field, large eddy simulation, power spectral analysis*

INTRODUCTION

The precessing jet has found lots of applications in many engineering aspects, such as burners and spray dryers. The precession phenomenon was initially observed in swirling flows. However, the imparted swirl has proved not to be a prerequisite for the generation of a precessing flow instability. Nathan et al. [1] discovered the self-excited precession of an initially axisymmetric jet generated by a fluidic precessing jet nozzle, which has proved beneficial in combustion applications [2]. The precessing jet nozzle in its simplest form is a sudden expansion cylindrical chamber from a small axisymmetric inlet [3, 4]. After entering the chamber via the inlet, the jet expands through entrainment of chamber fluid and reattaches asymmetrically to the chamber wall (see Figure 1). That is the so-called wall attachment effect of fluid (also called Coanda effect). The asymmetric entrainment also feeds back to reinforce an azimuthal pressure difference which causes the reattachment point of the primary jet to move azimuthally around the inner surface of the chamber. This rotating pressure field within the chamber causes the reattaching flow to precess around the inside wall of the chamber and this also produces a precessing exit flow. Simultaneously, external fluid is drawn into the chamber to replenish what is entrained by the primary jet. Thus, the flow emerging from the exit plane is highly three-dimensional and unsteady, with both the exit angle and precession frequency exhibiting considerable cycle-to-cycle fluctuations.

It is important to note that to produce the jet precession the nozzle configuration must be conditioned with the inlet expansion ratio, chamber length-to-diameter ratio and some other parameters [1, 3, 4]. Nathan et al. [1] discovered that, two flow modes, i.e., an instantaneously

* Corresponding author: Prof. J.W. Zhou
Phone: + (86)-571-86875670, Fax: + (86)-571-86914542
E-mail address: jw.zhou@cjlu.edu.cn

highly asymmetric "precessing jet" (PJ) and a quasi-symmetric "axial jet" (AJ), existed simultaneously within the nozzle chamber. The temporal probability (proportion of time) of the PJ mode depends on the nozzle geometry and Reynolds number.

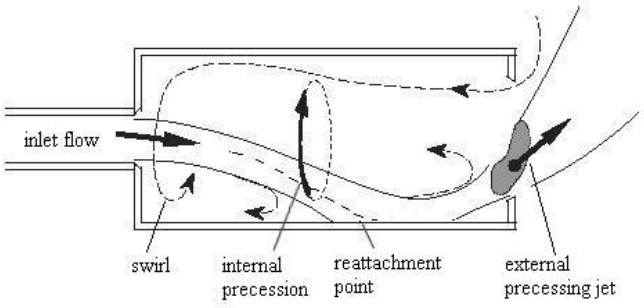

Figure 1. A simplified representation of the flow in a precessing jet nozzle [3, 4]

The configuration of the nozzle usually should be within specific geometric ratios, usually D/d=3.5~6 and L/D=2~3.5 to enable the jet precession although expansion ratio as small as 1.94 or as large as 10 has also been reported [5, 6]. The precessing flow within the nozzle chamber is complex and very sensitive to the geometry. Any alteration to the chamber configuration is expected to cause a significant change to the flow behaviour such as the precession frequency.

Much research has been invested to study the precession behaviour of this naturally oscillating jet flow so far [3, 4]. The particle image velocimetry (PIV) and laser-Doppler anemometry (LDA) techniques are also used to experimentally measure the velocity in the near external field of the precessing jet nozzle [7]. Due to the complexity of the phenomenon, the precessing instability is very difficult to study and the fundamental understanding has thus far remained rather incomplete. There have been relatively few simulation studies of this type of instability [8, 9]. Computational fluid Dynamics (CFD) can be used to provide a better understanding of the complex fluid physics and to provide predictive models for engineering analysis. On the other hand, it is also not easy to get the global information of flow field inside the precessing jet nozzle with experimental approach. Thus, this paper is concerned with the numerical simulation of unsteady turbulent flows behind sudden expansions without inlet swirl. A commercial CFD package, Fluent, is used to simulate the three dimensional, time-dependent flow within precessing jet nozzle in order to explore the phenomena better.

NUMERICAL APPROACH

Mathematical equations

Turbulent flows are extremely complex and time-dependent. Most fluid flows can be described by the full Navier-Stokes equations, which comprise equations for conservation of mass and momentum and, in a non-isothermal flow, energy. Many numerical methods have been developed to simulate the turbulent flow. Among the various methods, the Direct Numerical Simulation (DNS) is only used for low Reynolds numbers in simple geometries and a Reynolds averaging (time-averaging) method (RANS) is usually used to solve for the mean quantities rather than for all details of the turbulence[10,11]. However, swirling or precessing flows are difficult to model with Reynolds-averaged methods due to the effects of mean flow streamline curvature [12]. The Large Eddy Simulation (LES) approach, in which only the small-scale turbulent fluctuations are modelled

and the larger-scale fluctuations are computed directly, is a promising approach for simulation of complex, high Reynolds number turbulent flows. It is especially suitable to the analysis of the precessing flow in abruptly changed geometry channel. Thus LES is used to solve the problems in our study.

There are two key characteristics, i.e., the filter function and the subgrid scale stress (SGS) model, in LES approach. In Fluent, some common filters such as the Fourier cut-off filter, the box filter and the Gaussian filter, are provided and a finite volume method is applied to solve the differential equations. Applying the filtering operation, the governing equations (i.e., the equation of mass conservation and equation of the momentum conservation) are obtained

$$\frac{\partial \rho}{\partial t} + \frac{\partial}{\partial x_i}(\rho \bar{u}_i) = 0 \tag{1}$$

$$\frac{\partial}{\partial t}(\rho \bar{u}_i) + \frac{\partial}{\partial x_j}(\rho \bar{u}_i \bar{u}_j) = \frac{\partial}{\partial x_j}(\mu \frac{\partial \bar{u}_i}{\partial x_j}) - \frac{\partial \bar{p}}{\partial x_i} - \frac{\partial \tau_{ij}}{\partial x_j} \tag{2}$$

where an overline - denotes filtering variables at a computational cell; i (= 1, 2, 3) indicates the spatial dimension; p is pressure; ρ and μ are the fluid density and viscosity, respectively; u is the resolved velocity field; τ_{ij} is the subgrid scale stress defined by

$$\tau_{ij} = \rho \overline{u_i u_j} - \rho \bar{u}_i \bar{u}_j \tag{3}$$

The subgrid scale stresses resulting from the filtering operation are unknown and require modeling. The majority of the SGS models in use today are eddy viscosity models. The most basic of SGS models is proposed by Smagorinsky and further developed by Smagorinsky and Lilly. Most of the other SGS models are the Smagorinsky type variations. In our study the standard Smagorinsky–Lilly SGS model is applied to simulate the complex fluid flows.

Physical model

The geometry in simulation is shown in Figure 2. The ratio of the larger diameter D to the inlet tube diameter d is defined as the expansion ratio E. The inlet tube diameter d is chosen as 3.5mm. The simulation region has been taken as $l=5d$ and the length of the large chamber $L=2\sim4D$. The x-axis of the Cartesian coordinates is on the axis of the pipes and the origin point is defined as the orifice entrance. U_i and U_0 denote the axial bulk velocities for the inlet and outlet.

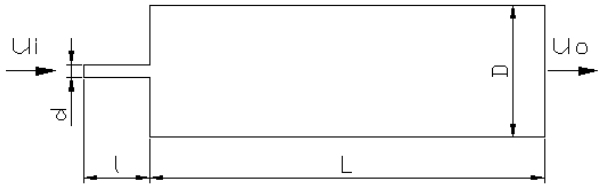

Figure 2. A schematic diagram of the physical model

Drawing and gridding the physical model is the first basic step in a CFD simulation. Fluent offers another software package, GAMBIT, to accomplish the model drawing and meshing. A fully three-dimensional non-structured grid has been used in simulation. The total number of element nodes is approximately between 144000 and 487000 depending on the geometric parameters in the physical model.

Boundary conditions and numerical considerations

Another basic step involved in a CFD simulation is to apply boundary conditions and to solve the problem. For the inlet flow, the velocity is assumed to be parallel to the inlet tube axis without any cross-stream components, with the volumetric flow rate being specified, i.e.,

$$U_{in} = \frac{4Q_{in}}{\pi d^2},\ V_{in} = 0,\ W_{in} = 0 \qquad (4)$$

U, V and *W* denote the averaged velocity components. Q_{in} is the volumetric flow rate and *d* is the inlet diameter.

Neumann boundary conditions are imposed for the outlet, which mean that the velocity components and turbulence quantities are assumed to be fully developed and have a zero normal gradient for the outflow. The relative pressure is set to zero at the outlet. No-slip boundary conditions are applied at the solid walls. A universal log-law wall function is applied for all walls.

A finite volume formulation is used to discretize the Navier-Stokes equations. The PISO algorithm is used for pressure correction. In this algorithm, a second pressure correction equation is solved in order to improve the solution of momentum equations while maintaining continuity and thus reducing the number of global iterations for convergence. Air, assumed to be incompressible and Newtonian gas, is chosen as the working fluid. The physical properties of air are assumed to be constant. The grid and time step independence tests are performed on the above 3-D physical model before the numerical experiments.

RESULTS AND DISCUSSIONS

Although the instantaneous flow field changes with time, the fundamental features remain the same. Many numerical experiments are carried out for various expansion ratios *E*, chamber length *L* and *Re* number in this study. Figure 3 presents the instantaneous axial velocity contour in a plane across the centreline of precessing jet nozzle for the case of *E=5*, *L=4D* at $Re=1\times10^4$ and $Re=2\times10^4$, respectively. From the simulation results, the naturally oscillating phenomena of this turbulent flow are easy to be identified. Because of the instabilities of the flow, the fluid emanating from the inlet tube separates at the expansion, departs from the central axis and moves toward the wall of large cylindrical chamber. It reattaches asymmetrically to the wall and then bends inward toward the other side of the wall. A reverse flow region exits in the flow field and a rapid decay of the bulk axial velocity, due to the strong mixing with ambient air, is found from the simulated results.

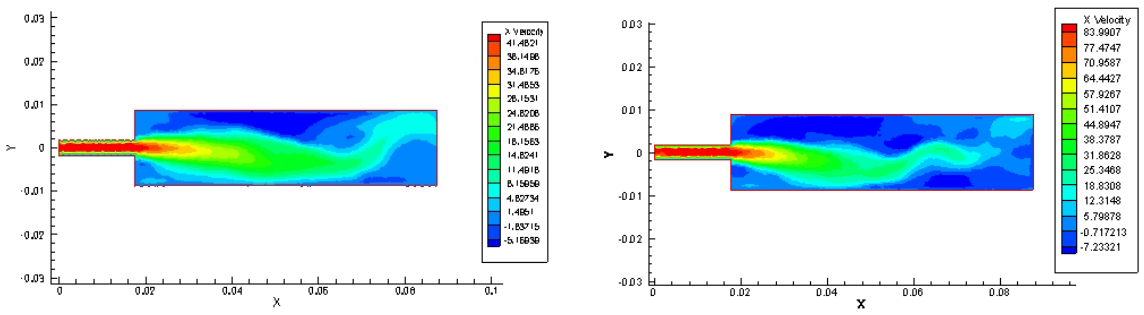

(a) $Re=1\times10^4$ (b) $Re=2\times10^4$

Figure 3. Instantaneous velocity contour maps in PJN (*E=5*, *L=4D*)

Figure 4 shows the instantaneous velocity vectors in a cross-sectional plane just behind the expansion surface (0.2D downstream from the sudden expansion). A non-uniform tangential flow in the circumferential direction is formed although the magnitude of tangential velocity is much smaller than the axial velocity. A significant mixing between the upstream and downstream flows, as well as tangential mixing, is expected inside the precessing jet nozzle.

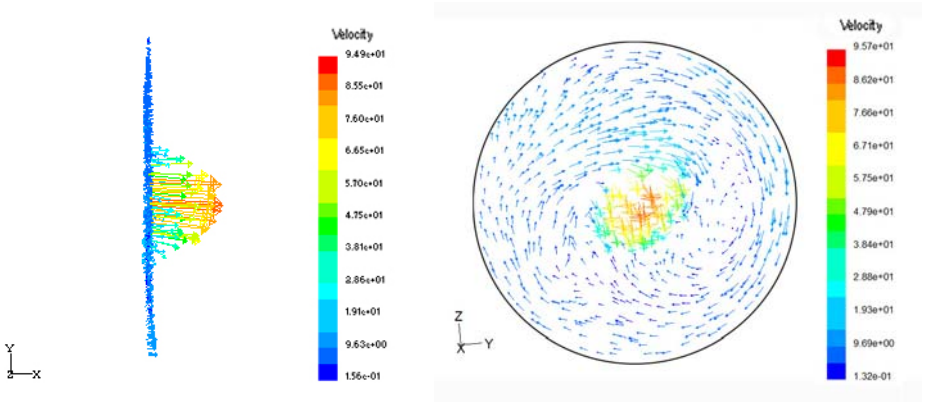

(a) X-Y plane (b) Y-Z plane

Figure 4. Instantaneous velocity vectors in a plane 0.2D downstream from the expansion ($E=5$, $L=4D$, $Re=2\times10^4$)

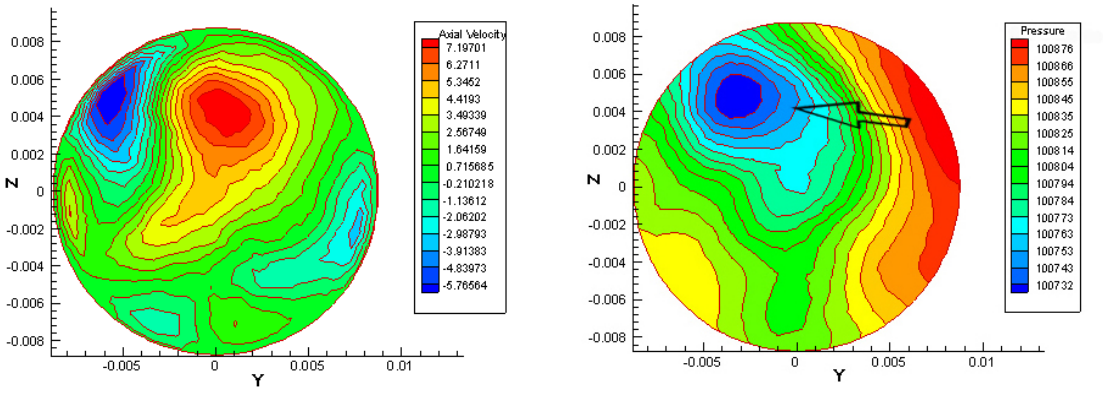

(a) axial velocity (b) pressure

Figure 5. Contour maps in a plane 3.4D downstream from the expansion ($E=5$, $L=4D$, $Re=2\times10^4$)

Figure 5 shows the instantaneous velocity and pressure contour maps in a cross-sectional plane 3.4D downstream from the expansion (i.e., close to the exit of the nozzle). At this moment, the position of the jet and the reverse flow are quite clear in axial velocity contour map (Figure 5(a)). It can be seen, from the corresponding pressure contour map (Figure 5(b)), that the higher pressure occurs on the wall near the jet reattaches and the low-pressure zone locates between the jet and the reverse flow core. A pressure gradient is created across the primary jet (as the arrow shown in Figure 5(b)) and this gradient may drive the jet to move towards the other side of the wall at an oblique angle.

Figure 6 shows two examples of the instantaneous velocity contour maps for different nozzle geometric parameters at $Re=2\times10^4$. Although the flowfield looks not so perfect, the inherent instability or the wall attachment effect of the fluid can be easily found. It demonstrates that the jet

precession within a nozzle depends mainly on the geometric configuration (i.e., ratio of *D/d* and *L/D*) as well as the Reynolds number.

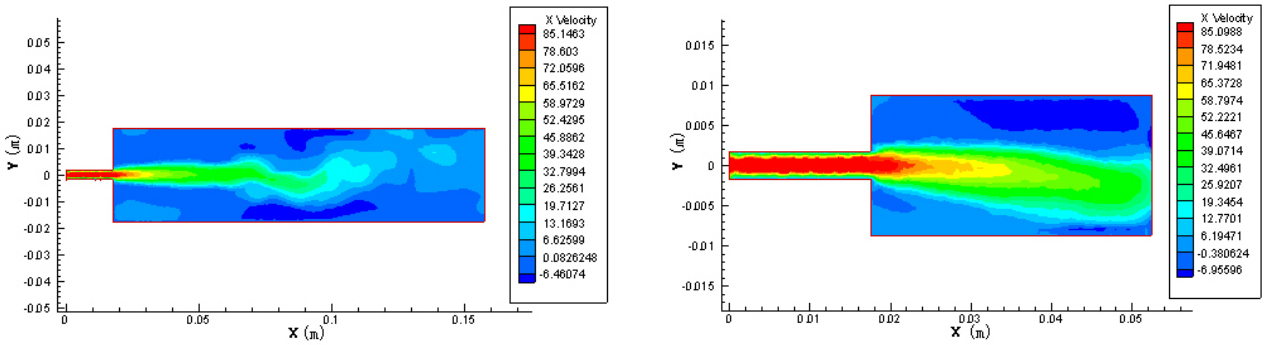

(a) E=10, L=4D (b) E=5, L=2D

Figure 6. Velocity contour maps for different nozzles (Re=2×10^4).

The self-oscillating features of a flow can be characterized by the precession frequency. Some variables, e.g., the velocity and pressure, at a specific location can be monitored during the process of the transient calculation and the resulting time series can be used to the analysis of power spectral density (PSD). The PSD curve obtained from the simulated velocity is compared with the actual experimental PSD result obtained from the same spot hot-wire measurement data. The experimental data was previously obtained from a precessing nozzle with similar geometry and configuration parameters [6]. The results are typically shown in Figure 7(a) and 7(b), respectively. Results show in general agreement between the simulations and the experiments in the sense of the quasi-periodically oscillating features.

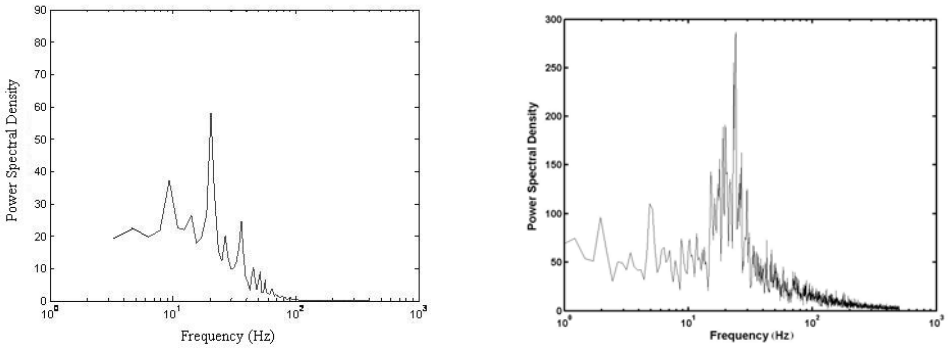

(a) simulated result (b) experimental result

Figure 7. Power spectral density comparison between simulated and experimental data
（E=10, L=2D, Re=2×10^4）

CONCLUSIONS

In this study, the LES turbulence model is used to simulate the complicated turbulent flows within a precessing jet nozzle. The simulations demonstrate that the asymmetry and subsequent oscillations are inherent phenomena within an expansion flow. Strong self-sustained precession can be induced and a reverse flow region can be generated within a precessing jet nozzle. A pressure gradient across the jet in both radial and tangential directions may be the driving force for the precessing motions. The precession phenomena significantly depend on the configuration

parameters of the nozzle and the Reynolds number. The simulated features of self-excited precessing jets are generally consistent with the previous investigations and analysis.

ACKNOWLEDGEMENTS

This work is supported by Natural Science Foundation of China (No. 50676088) and the Qianjiang Program of Zhejiang Province, China (No.2007R10030).

REFERENCES

1. Nathan, G. J., Hill, S. J. and Luxton, R. E., An Axisymmetric 'Fluidic' Nozzle to Generate Jet Precession, *J. Fluid Mechanics*, Vol. 370, pp 347-380, 1998.
2. Nathan, G. J., Turns, S.R. and Bandaru, R.V., The Influence of Jet Precession on NOx Emissions and Radiation from Turbulent Flames, *Combustion Science and Technology*, Vol. 112, pp 211-230, 1996.
3. Mi, J. and Nathan, G. J., Self-excited Jet-Precession Strouhal Number and its Influence on Downstream Mixing Field, *Journal of Fluids and Structures*, Vol. 19, pp 851-862, 2004.
4. Wong, C. Y., Nathan, G. J. and O'Doherty T., The Effect of Initial Conditions on the Exit Flow from a Fluidic Precessing Jet Nozzle, *Experiments in Fluids*, Vol. 36, pp 70–81, 2004.
5. Dellenback, P. S., Metzger, D. E., and Neitzel, G. P., Measurement in Turbulent Swirling Flow Through an Abrupt Axisymmetric Expansion, *AIAA J.*, Vol. 26, No. 6, pp 669–681, 1988.
6. Zhou, J.W. and Herwig, H., Heat Transfer Characteristics of Precessing Jets Impinging on a Flat Plate: Further Investigations, *Int. J. Heat and Mass Transfer*, Vol.50, pp 4488–4492, 2007.
7. Wong, C. Y., Nathan, G. J. and Kelso, R.M., Velocity Measurements in the Near-field of a Fluidic Precessing Jet Flow Using PIV and LDA, *Proc. of 3rd Australian Conference on Laser Diagnostics in Fluid Mechanics and Combustion*, Brisbane, Australia, December2-3, 2002.
8. Guo, B., Langrish, T. A. G. and Fletcher, D.F., Numerical Simulation of Unsteady Turbulent Flow in Axisymmetric Sudden Expansions, *Trans. ASME, J. Fluid Engineering*, Vol.123, pp 574-588, 2001
9. Guo, B., Langrish, T. A. G. and Fletcher, D. F., Simulation of Turbulent Swirl Flow in an Axisymmetric Sudden Expansion, *AIAA J.*, Vol. 39, No. 1, pp 96–102, 2001.
10. Spalart, P. R., Strategies for Turbulence Modelling and Simulations, *Int. J. of Heat and Fluid Flow*, Vol. 21, No. 3, pp 252–263, 2000.
11. Speziale, C. G., Turbulence Modeling for Time-Dependent RANS and VLES: a Review, *AIAA J.*, Vol. 36, No. 2, pp 173–184, 1998.
12. Jakirlic, S., Hanjalic, K. and Tropea, C., Modeling Rotating and Swirling Turbulent Flows: a Perpetual Challenge. *AIAA J.*, Vol. 40, No.10, pp 1984–1996, 2002.

INTERFERENCE METHOD OF CONTROL OF HYPERSONIC SHOCK LAYER DISTURBANCES

T. Poplavskaya[1,2], S. Mironov[1,2] *
[1]Khristianovich Institute of Theoretical and Applied Mechanics SB RAS, Novosibirsk, Russia
[2]Novosibirsk State University, Novosibirsk, Russia

ABSTRACT. The present paper describes comprehensive experimental and numerical investigations of evolution of disturbances generated in the hypersonic viscous shock layer on a flat plate by external acoustic waves and by perturbations introduced into the shock layer from the surface of model. All experiments are performed in the hypersonic nitrogen wind tunnel T-327A based at the Khristianovich Institute of Theoretical and Applied Mechanics with a free-stream Mach number $M_\infty = 21$ and Reynolds number $Re_L = 1.44 \times 10^5$. Direct numerical simulations of propagation of disturbances are performed by solving Navier-Stokes equations with the use of high-order shock-capturing schemes. The results obtained show that periodic blowing and suction of the gas near the leading edge can be used for active control of the transition to turbulence in a hypersonic shock layer through suppressing, by means of destructive interference, the development of instability arising under the action of acoustic perturbations of the free stream. Based on this scheme, wind tunnel experiments on controlling the intensity of density fluctuations in a hypersonic shock layer on a flat plate at a zero angle of attack are performed.

Keywords: *viscous shock layer, receptivity, electron-beam fluorescence method, DNS*

INTRODUCTION

When a flying vehicle moves with a high velocity in the upper atmospheric layers, the regime of a viscous shock layer persists even at a large distance from the leading edges. The viscous shock layer consists of a thick boundary layer and a thin zone of inviscid flow behind the bow shock wave. Disturbances formed in the shock layer are entrained in the downstream direction and affect the evolution of fluctuations and the laminar-turbulent transition in the hypersonic boundary layer on a flying vehicle as a whole.

Understanding the mechanisms of receptivity and instability of the viscous shock layer is a necessary condition for the development of effective methods for controlling the laminar-turbulent transition on flying vehicles in a hypersonic flow.

This problem has not been adequately addressed yet. The previous results of experimental [1-3] and theoretical [4-5] research and control methods developed refer to the boundary-layer flow and cannot be directly transposed to a hypersonic shock layer. The flow in a hypersonic shock layer has some specific features: the influence of a closely located shock wave on the evolution of disturbances, significant nonparallelism of the flow, and a high degree of rarefaction.

The present paper describes the results of a comprehensive numerical and experimental study of a hypersonic viscous shock layer on a flat plate at a zero angle of attack. Based on the data obtained, numerical and experimental modeling of controlling the intensity of fluctuations in the shock layer on a plate model was performed.

* Corresponding author: Dr. T . Poplavskaya
Phone: +7 (383)-330-85-28, Fax: + 7(383)-330-72-68
E-mail address: popla@itam.nsc.ru

EXPERIMENTAL EQUIPMENT AND DIAGNOSTIC METHODS

The experiments were performed in the hypersonic nitrogen wind tunnel T-327A based at the Khristianovich Institute of Theoretical and Applied Mechanics (Siberian Branch, Russian Academy of Sciences). A flat plate model 240 mm long with a sharp leading edge 100 mm wide was inserted into a hypersonic flow with a Mach number $M_\infty = 21$, unit Reynolds number $Re_{1\infty} = 6\cdot10^5$ m^{-1}, and stagnation temperature $T_0 = 1200$ K; the temperature factor of the surface was $T_w/T_0 = 0.26$. The distributions of mean density and the characteristics of density fluctuations were measured by the method of electron-beam fluorescence of nitrogen [6].

The external acoustic disturbances excited in the experiments were slow acoustic waves generated by the turbulent boundary layer formed on the nozzle walls [7]. Internal perturbations localized near the leading edge were generated by an obliquely cut cylindrical aerodynamic whistle located under the plate [8].

NUMERICAL STATEMENT OF THE PROBLEM

With allowance for the moderate magnitude of local Reynolds numbers typical of the viscous shock layer, the most adequate approach to the problem of numerical simulation seems to be the direct numerical simulation (DNS) of disturbances on the basis of solving the full unsteady Navier-Stokes equations. Two-dimensional Navier-Stokes equations were written in the form of conservation laws:

$$\frac{\partial Q}{\partial t}+\frac{\partial F}{\partial x}+\frac{\partial G}{\partial y}=\frac{M_\infty}{\mathrm{Re}_L}\left(\frac{\partial F^v}{\partial x}+\frac{\partial G^v}{\partial y}\right) \tag{1}$$

Here t is the time, x and y are the coordinates along and across the plate, Q is the vector of conservative variables, F, G are the vectors of inviscid fluxes, and F^v, G^v are the vectors of viscous fluxes:

$$Q=\begin{pmatrix}\rho\\ \rho u\\ \rho v\\ e\end{pmatrix},\qquad F=\begin{pmatrix}\rho u\\ \rho u^2+p\\ \rho uv\\ (e+p)u\end{pmatrix},\qquad G=\begin{pmatrix}\rho v\\ \rho uv\\ \rho v^2+p\\ (e+p)v\end{pmatrix},$$

$$F^v=\begin{pmatrix}0\\ \tau_{xx}\\ \tau_{xy}\\ u\tau_{xx}+v\tau_{xy}+\kappa\dfrac{\partial T}{\partial x}\end{pmatrix},\qquad G^v=\begin{pmatrix}0\\ \tau_{xy}\\ \tau_{yy}\\ u\tau_{xy}+v\tau_{yy}+\kappa\dfrac{\partial T}{\partial y}\end{pmatrix}, \tag{2}$$

$$\tau_{xx}=\mu\left(\frac{4}{3}\frac{\partial u}{\partial x}-\frac{2}{3}\frac{\partial v}{\partial y}\right),\quad \tau_{xy}=\mu\left(\frac{\partial u}{\partial y}+\frac{\partial v}{\partial x}\right),\quad \tau_{yy}=\mu\left(\frac{4}{3}\frac{\partial v}{\partial y}-\frac{2}{3}\frac{\partial u}{\partial x}\right).$$

The system is closed by the equation of state of a perfect gas

$$p=\rho T/\gamma\,. \tag{3}$$

In Eqs. (1)-(3), u, v are the x and y components of the velocity vector, p is the pressure, ρ is the density, T is the temperature, $e=p/(\gamma-1)+\rho(u^2+v^2)/2$ is the total energy per unit volume, γ is the ratio of specific heats, μ is the dynamic coefficient of viscosity, and $\kappa=\dfrac{\mu}{(\gamma-1)\mathrm{Pr}}$ is the coefficient of thermal conductivity. The viscosity was calculated with the Sutherland formula $\mu=T^{1.5}\dfrac{1+T_S/T_\infty^*}{T+T_S/T_\infty^*}$, where T_∞^* is the free-stream temperature and T_S is the Sutherland constant

equal to 106.67 K for nitrogen. The Reynolds number Re_L was based on the free-stream parameters and the plate length L^*, and the Prandtl number was Pr= 0.72. Hereinafter, the asterisk indicates dimensional quantities. In writing Eqs. (2), (3) in dimensionless form, the density, temperature, and viscosity were normalized to their free-stream values; the other scaling quantities were the velocity of sound c_∞ for velocity, $\rho_\infty c_\infty^2$ for pressure, and the plate length L for geometric sizes.

Two-dimensional Navier-Stokes equations are solved by high-order shock-capturing schemes. Details of the numerical method can be found in [7,9].

The computational domain was a rectangle with some part of the lower side coinciding with the plate surface. The left (inflow) boundary was located at a distance of a few computational cells upstream from the leading edge of the plate. The height of the computational domain was chosen under the condition that the bow shock wave emanating from the leading edge did not interact with the upper boundary. The right (outflow) boundary was separated from the trailing edge of the plate by some distance so that the flow in the exit section was completely supersonic.

The steady basic flow was first calculated with a uniform hypersonic flow being imposed on the left and upper boundaries. The solution on the right boundary was extrapolated from inside the computational domain. The boundary conditions on the plate took into account the velocity slip and the temperature jump. The results of modeling a steady flow demonstrated good agreement with the values of the Mach number and mean density measured in the shock layer [7].

Then the problem of interaction of a viscous shock layer with external acoustic disturbances propagating in the streamwise direction was solved. The variables on the left boundary were set as a superposition of the steady main flow and a planar monochromatic acoustic wave:

$$\begin{pmatrix} u' \\ v' \\ p' \\ \rho' \end{pmatrix} = A \begin{pmatrix} \pm\cos\theta \\ \mp\sin\theta \\ 1 \\ 1 \end{pmatrix} \exp\left[i\left(k_x x + k_y y - \omega t\right)\right].$$

Here u', v', p', ρ' are the fluctuations of the longitudinal and transverse velocity, pressure, and density, respectively, θ is the angle of propagation of the external acoustic wave, A is the disturbance amplitude, t is the time, $k_x = k\cos\theta, \quad k_y = -k\sin\theta$ are the components of the wave vector related to the frequency $\omega = 2\pi f L / c_\infty$ by the dispersion expression $k = \dfrac{\omega}{\left(M_\infty \cos\theta \pm 1\right)}$. In the above-given relations, the upper (lower) index corresponds to the fast (slow) acoustic wave. In dimensionless relations, the density and temperature disturbances are normalized to their free-stream values, the velocity perturbations are normalized to the velocity of sound in the free stream c_∞, and the pressure disturbances are normalized to $\rho_\infty c_\infty^2$.

In the experiment, artificial disturbances in the form of periodic injection and suction were locally introduced from the leading edge of the plate. In the numerical solution of the problem, they were modeled by imposing the following boundary condition for the transverse flow rate at a certain part of the surface near the leading edge of the plate:

$$\rho v'\big|_{y=0} / \rho_\infty c_\infty = A \sin\left(\pi \frac{x - x_1}{x_2 - x_1}\right) \sin \pi f t$$

Here v' are the velocity fluctuations in the direction normal to the plate surface, ρ is the local density, A is the amplitude, and x_1 and x_2 are the boundaries of the region where the controlled disturbances were introduced.

After introduction of disturbances, the Navier-Stokes equations were integrated until the unsteady solution reached a steady periodic regime. The uniform grid used contained $N_x = 1050$ cells in the streamwise direction and $N_y = 240$ cells in the transverse direction. Up to 20 processors of the Siberian Supercomputer Center were used in the computations.

The simulations of density fluctuations turned out to be in good agreement with the measurements of characteristics of density fluctuations in the shock layer [7,9] and with the computations by the locally parallel linear stability theory with allowance for the influence of the shock wave [10] for the wall temperature of the model T_w = 300 K.

RESULTS

In a hypersonic shock layer under the action of external acoustic waves of slow and fast modes, the main wave processes occur on the shock wave and on the upper boundary of the hypersonic

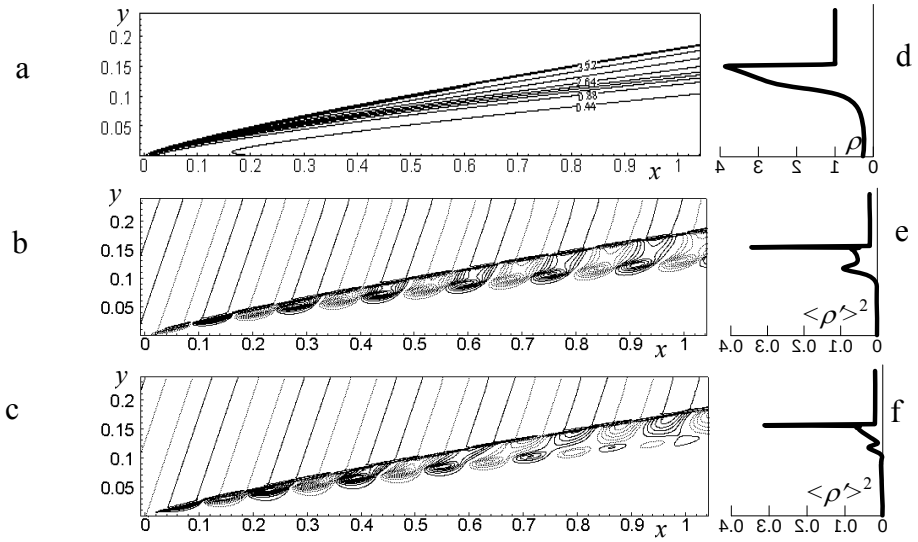

Figure 1. Field of mean density contours (a) M_∞ = 21, $Re_L = 1.44 \cdot 10^5$, field of instantaneous density fluctuations (b,c), and distributions of the root-mean-square fluctuations in the cross section x=0.8 (d,e,f): b,e – disturbances induced by a slow acoustic wave with θ = 20°, A = 0.028, and f=38.4 kHz; c,f – disturbances induced by a fast acoustic wave with θ = 20°, A = 0.028, and f=38.4 kHz.

boundary layer (BL) with vortex disturbances dominating [6,7,]. The fluctuating characteristics of the flow in the hypersonic shock layer have a typical form with two maximums; the greater maximum is located on the SW, and the location of the second maximum coincides with the BL edge (Fig. 1). This is clearly seen both in the field of instantaneous contours of density fluctuations (Fig. 1b,c) and in the distributions of the mean-square fluctuations (Fig.1e,f). For angles of propagation of external acoustic waves θ close to zero, vortex disturbances dominate in the spectrum of disturbance modes in the shock layer [7,9], which agrees with the linear theory of interaction of disturbances with the SW [11]. It should be noted that the prevalence of the entropy-vortex mode is not typical of the boundary layer at moderate hypersonic Mach numbers, where the acoustic instability mode is mainly developed [4,12].

The computations showed that the fields of the mean density and density fluctuations generated by a source of the blowing-suction type are similar to the fields of fluctuations under the action of external acoustic disturbances on the shock layer. Figure 2 shows the instantaneous density fluctuations in the shock layer on a flat plate (a), generated by a blowing-suction source at a frequency f = 20 kHz, which were obtained in direct numerical simulations (a) and in experiments (b). It is seen that the field of intense fluctuations occupies the region between the SW and the BL edge, which corresponds to the maximum gradient of the mean density, as in the case of external acoustic perturbations.

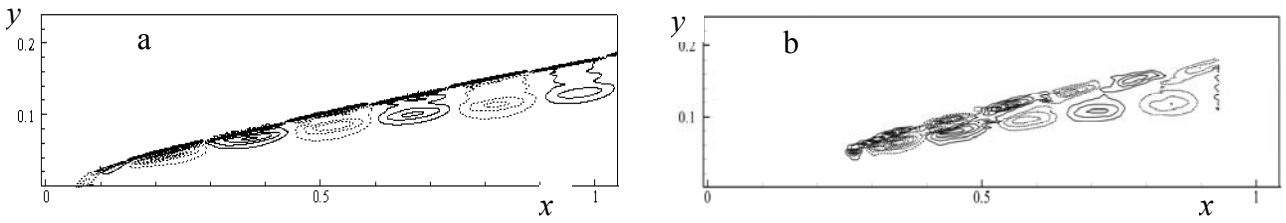

Figure 2. Instantaneous density fluctuations induced by periodic blowing-suction perturbations at a frequency f = 20.5 kHz: a – DNS, A=0.028, b – experiment.

The measurements and the computations of the fields of density fluctuations for disturbances, which are generated by acoustic waves in the external flow, confirmed the similarity of the spatial structure of density fluctuations generated in the shock layer by means of blowing-suction. In particular, there are two maximums of the intensity of density fluctuations; one of the maximums (the greater one) is located on the SW, and the second maximum (the smaller one) is located on the BL edge, and the phases of density fluctuations on the SW and on the BL edge are shifted by 180°. The magnitude of density fluctuations in the shock layer as a function of the amplitude A of the introduced disturbances is considered in the present paper. Such information is important for controlling the intensity of fluctuations in the shock layer by means of injection and suction.

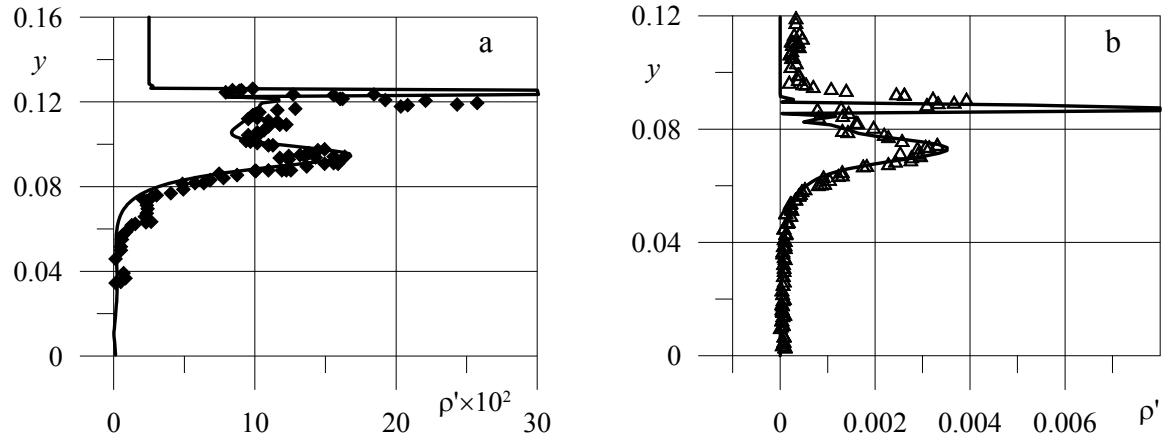

Figure 3. Profiles of density fluctuations across the shock layer for M_∞ = 21 and $Re_L = 1.44 \times 10^5$, which are generated by slow acoustic waves in the external flow ($\theta = 0°$, A = 0.028 and f=38.4 kHz) in the cross section x=0.63 (a) and by a blowing-suction source (f = 20 kHz and A=0.0286) in the cross section x=0.42: the symbols – experimental data; solid curves – computed results.

The computed distributions of density fluctuations across the shock layer are in good agreement with the measured results (Fig.3). A comparison of the data in figure 3b with the distribution of density fluctuations in the shock layer, which are generated by acoustic waves in the external flow (Fig.3a), shows that these profiles also coincide. The position of the maximums of fluctuations correspond to the maximums of the transverse gradient of the mean density, and their intensity corresponds to the magnitude of the local gradient. Thus, the field of density fluctuations is formed by normal-to-the-plate-surface fluctuations of the mean density field in the shock layer, caused by vortices arising behind the SW under the action of external flow perturbations and blowing-suction source.

Thus, the main features of the mechanism of formation of the field of density fluctuations due to shock-layer interaction both with external acoustic perturbations and with blowing-suction perturbations on the plate surface is the emergence and domination of entropy-vortex disturbances inside the shock layer. The spatial structures of disturbances under the action from outside and inside the shock layer are fairly similar. Under these conditions, it is possible to use active methods of disturbance control, which work well in subsonic boundary layers. Oscillations generated by

external perturbations can be suppressed by artificial perturbations introduced, if an appropriate phase and amplitude are chosen for blowing and suction [13].

In the present activities, the possibility of such control was demonstrated numerically and experimentally. Figure 4a shows the calculated field of instantaneous density fluctuations in the shock layer on a flat plate under the action of slow-mode acoustic waves propagating at a zero angle to the external flow centerline. Hereinafter, for the sake of illustration, the field of isolines is supplemented by the root-mean-square (averaged over the period) dependence of density fluctuations on the transverse coordinate y in the cross section x=0.8 (Fig.4e,f,g,h). Figure 4b shows the field of instantaneous density fluctuations in the shock layer on a flat plate, which were generated by blowing-suction of the gas. Qualitative similarity of the fields of fluctuations and quantitative coincidence of the amplitude of density fluctuations on the BL edge are observed. Fig. 4c shows the field of instantaneous density fluctuations in the shock layer on a flat plate under a joint action of external and internal sources of perturbations, when these sources operate exactly in the opposite phases. It is well seen that the density fluctuations on the BL edge decrease substantially, though the oscillations of the shock wave proper remain almost unchanged. For the sake of illustration, Fig.4d shows the field of instantaneous density fluctuations in the case of in-phase operation of the sources of perturbations. As it was expected, the amplitude of fluctuations on the BL edge is doubled.

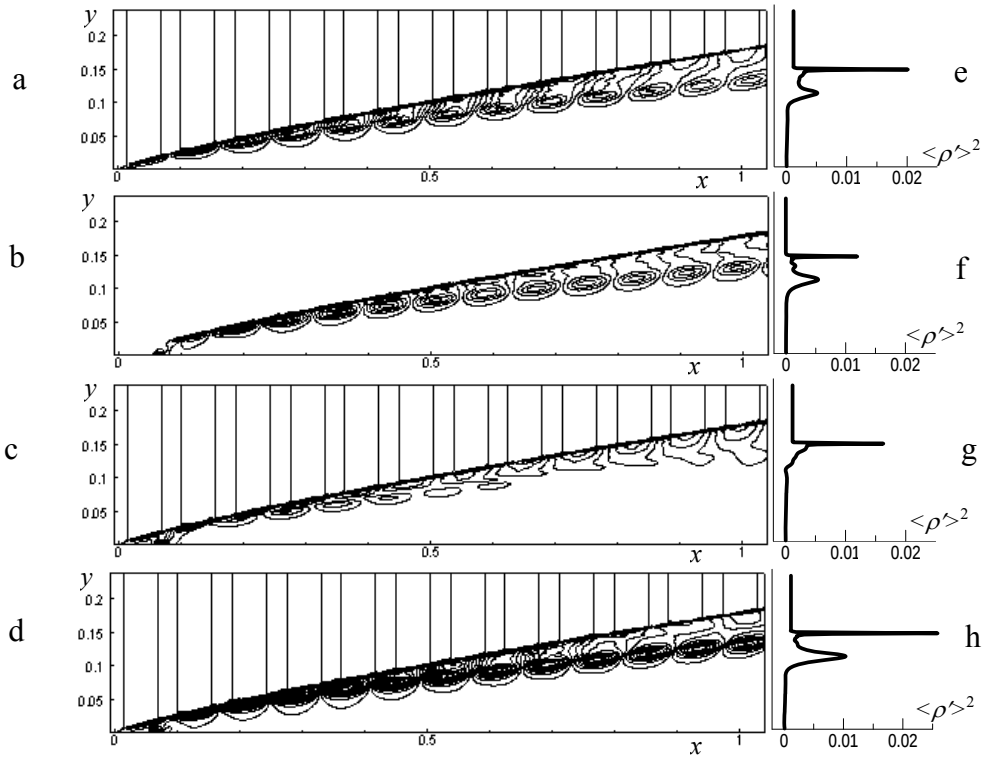

Figure 4. Instantaneous density fluctuations in the shock layer (a,b,c,d) and root-mean-square density fluctuations in the cross section x=0.8 (e,f,g,h) for M_∞ = 21, $Re_L = 1.44 \times 10^5$, $\theta = 0°$, and f=38.4 kHz: a,e) fast acoustic wave A = 0.0017; b,f) blowing-suction of the gas from the plate surface A = 0.0694; c,g) anti-phase action; d,h) in-phase action.

The possibility of controlling the intensity of fluctuations in a hypersonic shock layer on a flat plate was also demonstrated in experiments for fast external acoustic waves. The idea of this experiment is illustrated in Fig.5. Periodic acoustic waves are generated in a hypersonic flow, which interact with the shock layer on the plate and generate fluctuations in the shock layer. The oblique gas-dynamic whistle located under the plate near its tip also excites periodic pressure perturbations in the shock layer. If the frequencies of external flow disturbances and of perturbations excited by the whistle are identical, a certain relation between the phases of these disturbances may lead to

interference suppression (amplification) of fluctuations in the boundary layer on a flat plate. As an illustration, Fig. 5 shows suppression of density fluctuations in the shock layer at the time when the perturbations excited by the whistle have covered half of the plate length

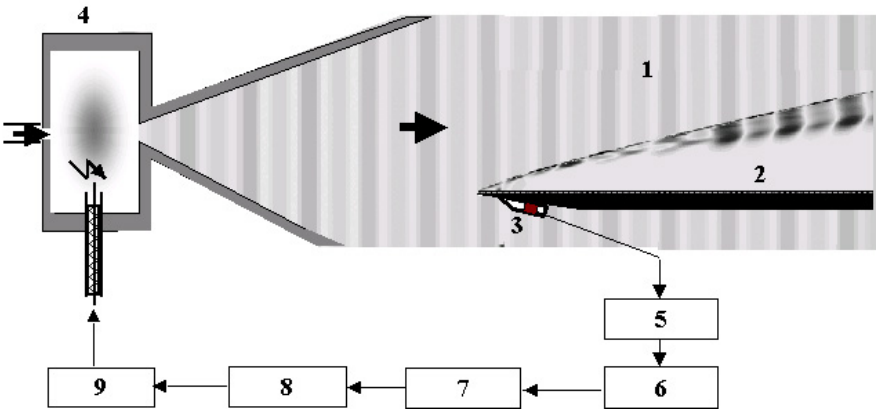

Figure 5. Arrangement of the experiment. 1 – acoustic waves in the external flow; 2 – flat plate; 3 – oblique whistle; 4 – settling chamber; 5 – amplifier; 6 – narrow-band filter; 7 – frequency divider; 8 – generator of pulses for electric discharge initiation; 9 – power unit for the discharge.

For a frequency f = 37.5 kHz, Fig. 6 shows the experimental curves for the amplitude of density fluctuations on the edge of the boundary layer on the plate ρ''/ρ'_{max} in the cross section x/L = 0.63 versus the time shift $\Delta\tau$ between external flow disturbances and perturbations generated by the whistle. Here ρ'_{max} is the level of density fluctuations on the boundary-layer edge in the case of an in-phase action of the external acoustic wave and periodic blowing/suction. The relation between the amplitudes of external and internal disturbances allows almost complete suppression of perturbations in the shock layer. The solid curve in Fig. 6 approximates the experimental values in accordance with the law of interference of two sinusoidal waves of identical frequency and amplitude.

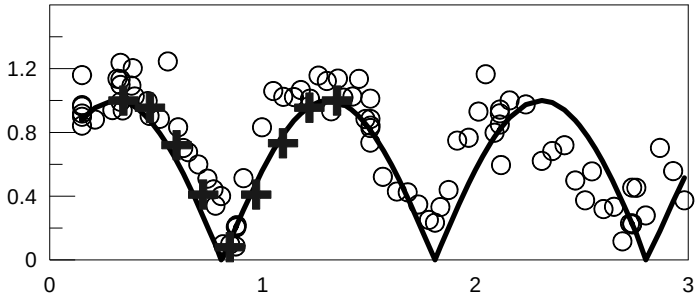

Figure 6. Amplitude of density fluctuations on the boundary-layer edge versus the delay of the initial disturbances.

CONCLUSIONS

The present paper describes comprehensive numerical and experimental studies of receptivity and of disturbance evolution in a hypersonic viscous shock layer on a flat plate at a very high Mach numbers and moderate Reynolds numbers.

It is shown that the main specific feature of the mechanism of formation of the field of fluctuations in the case of shock-layer interaction with external acoustic disturbances and with perturbations of the blowing-suction type is generation and propagation of entropy-vortex perturbations inside the shock layer.

The field of fluctuations induced in the shock layer by external flow perturbations was shown to be similar to the field of fluctuations generated by blowing-suction perturbations; the streamwise phase velocities of fluctuations generated by these sources in the shock layer also coincide. Owing to these features, it became possible to implement interference-based controlling of the intensity of fluctuations in the shock layer by affecting them with the help of controlled perturbations with certain amplitudes and phases.

The interference-based flow-control method was realized both numerically and experimentally. Periodic acoustic waves were introduced into the external flow and generated entropy-vortex disturbances in the shock layer. The latter were suppressed or amplified by periodic perturbations with the opposite phases, which were generated by a blowing-suction source (in numerical simulations) or by an oblique whistle located near the plate tip (in the experiments). Fluctuations on the boundary-layer edge were almost completely suppressed, and fluctuations in the shock layer as a whole were substantially attenuated.

This work was supported by the Russian Foundation for Basic Research (grant 09-08-00557) and by ADTP RNP 2.1.1/3963. The computer time for computations was allocated by the Siberian Supercomputer Center.

REFERENCES

1. Fisher, M.C., Maddalon, D.V., Weinstein, L.M., Wagner, R.D. Jr., Boundary – layer pitot and hot-wire surveys at $M_\infty \cong 20$, *AIAA J*., Vol. 9, No 5, pp. 826-834, 1971.
2. Kemp, J.H., Owen, F.K., Nozzle wall boundary layer at Mach numbers 20 to 47, *AIAA J*., Vol.10, No 7, pp. 872-879, 1972.
3. Smith, J.A., Driscoll, J.F., The electron-beam fluorescence technique for measurements in hypersonic turbulent flows, *J. Fluid Mech*., Vol. 72, No 4, pp. 695-719, 1975.
4. Egorov, I.V., Sudakov, V.G., Fedorov, A.V., Numerical simulation of receptivity of a supersonic boundary layer to acoustic disturbances, *Fluid Dynamics,* Vol. 41, No1, pp. 42-53, 2006.
5. Ma, Y., Zhong, X., Receptivity of a supersonic boundary layers over a flat plate. Part 2. Receptivity to free-stream sound, *J. Fluid.Mech*., Vol. 488, pp. 79-121, 2003.
6. Mironov, S. G., Maslov, A. A., An experimental study of density waves in hypersonic shock layer on a flat plate, *Phys. Fluids A.* , Vol.12, No 6, pp. 1544-1553, 2000.
7. Kudryavtsev, A.N., Mironov, S.G., Poplavskaya, T.V., Tsyryulnikov, I.S., Experimental study and direct numerical simulation of the evolution of disturbances in a viscous shock layer on a flat plate, *J. Appl. Mech. Tech. Phys.*, Vol. 47, No 5, pp. 617-627, 2006.
8. Maslov, A. A., Mironov, S. G., Experimental investigation of the hypersonic low-density flow past a half-closed cylindrical cavity, *Fluid Dynamics* Vol. 31, pp.928-932, 1996.
9. Kudryavtsev, A.N., Maslov, A.A., Mironov, S.G., Poplavskaya, T.V., Tsyryulnikov, I.S., Direct numerical simulation of receptivity of a hypersonic boundary layer to natural and artificial disturbances, *Vych. Tekhnol.* (in Russia), Vol. 11, Pt. 1, pp. 108-115, 2006.
10. Maslov, A.A., Poplavskaya, T.V., Smorodsky, B.V., Stability of a hypersonic shock layer on a flat plate, *Comptes Rendus, Mech*., Vol. 332, No 11, pp. 875-880, 2004.
11. McKenzie, J. F., Westphal, K. O., Interaction of linear waves with oblique shock waves, *Phys. Fluids*, Vol. 11, pp. 2350-2362, 1968.
12. Mack, L. M., Boundary Layer Stability Theory, *JPL, Report* 900-277, 1969.
13. Fomin, V.M., Kudryavtsev, A.N., Maslov, A.A., Mironov, S.G., Poplavskaya, T.V., Tsyryulnikov, I.S., Active control of disturbances in a hypersonic shock layer, *Doklady Physics,* Vol. 52, No 5, pp. 274-276, 2007.

A NEW HYBRYD EULERIAN MONTE CARLO-RANS METHOD FOR SOLVING JOINT SCALAR PDF TRANSPORT EQUATION IN TURBULENT COMBUSTION

M Ourliac[1], V. Sabel'nikov[2*] and O. Soulard[3]

[1] ONERA - Palaiseau, France

[2] ONERA - Châtillon, France

[3] CEA/DAM/DIF, Bruyères-le-Châtel - 91297 Arpajon Cedex, France

ABSTRACT. The joint composition probability density function (PDF) transport equation is widely used for turbulent combustion simulation. Due to the high number of dimensions, traditional finite methods are not suitable for solving this joint PDF transport equation (their computational time increases exponentially with the dimensionality). Monte Carlo methods, on the other hand, yield a linearly growing effort with dimensionality. Eulerian Monte Carlo (EMC) methods are based on stochastic fields that evolve through stochastic partial differential equations (SPDEs) statistically equivalent to the the joint PDF transport equation. EMC methods may be formulated either in non conservative or in conservative forms of SPDEs.
In this paper we devise a new hybrid finite volume/EMC method based on the conservative form of EMC methods, for both stationary and non-stationary turbulent reactive flows. The mean velocity and turbulence fields are solved in the frame of a RANS solver while the species concentrations and enthalpy are treated using SPDEs. The coupling is performed through an additional equation for the mean pressure, in which the source term is calculated using the scalar fields taken from SPDE solver. We validate our algorithm by computing a premixed flame stabilized behind a backward facing step and by comparing with some experimental data obtained in ONERA subsonic combustion rig.

Keywords: *turbulent combustion, probability density function, Eulerian Monte Carlo method, stochastic fields, premixed flame*

INTRODUCTION

In turbulent flames, phenomena of interest, such as pollutant production, soot formation or extinctions/ignitions, mainly arise from a conjunction of rare physical events (peak temperature, weak mixing conditions, ...) and finite rate chemistry effects. Predicting these phenomena thus requires a precise knowledge of the one-point statistics of the species concentrations and temperature, as well as an accurate description of chemical reactions. Regarding both aspects, the one-point joint composition probability function (PDF) appears as a relevant tool: it transports the detailed one-point statistical information of the turbulent scalars and allows chemical source terms to be treated exactly [1].

* Corresponding author: V. Sabel'nikov
Phone: +(33)-1-69936066, Fax: +(33)-1-699936162
E-mail address: vladimir.sabelnikov@onera.fr

These advantages are nonetheless counterbalanced by a severe numerical constraint: the composition PDF possesses a potentially high number of dimensions, which induces heavy computational costs. In particular, the finite methods traditionally employed in computational fluid dynamics (CFD) cannot be used, as their cost increases exponentially with dimensionality. Monte Carlo methods, on the other hand, yield a linearly growing effort and are more adapted to solve PDF equations.

So far, in the field of turbulent combustion, Monte Carlo methods have mostly been considered under their Lagrangian form, following the impulsion given by the seminal work of Pope [1]. Numerous publications document the convergence and accuracy of Lagrangian Monte Carlo (LMC) methods. They have been used in many complex calculations (including LES), and for several years now, they have been implemented in commercial CFD codes. However, the development and evaluation of an alternative Eulerian (Field) Monte Carlo (EMC) method is also useful and stimulating, since the competition between LMC and EMC methods could push both approaches forward.

EMC methods are based on stochastic Eulerian fields, which evolve from stochastic partial differential equations (SPDE) stochastically equivalent to the PDF equation. These SPDEs are the Eulerian counter-part of the stochastic ordinary differential equations (SODEs) used in LMC methods. Their application to simulate the composition PDF in turbulent reactive flows only seems to be dating back from Valiño's work [2], in which the method is named Field Monte Carlo formulation. Sabel'nikov and Soulard [3] proposed a new path to derive SPDEs for solving composition PDF equations. They also presented the details of the theoretical and numerical issues concerning EMC methods. The SPDEs proposed in [3] are written in a non-conservative form. A conservative formulation was later proposed in [4].

In this paper a novel hybrid composition EMC-FV (Finite Volume) algorithm is developed based on the conservative formulation of SPDEs [4]. Correction techniques, time averaging procedure and coupling strategy efficiency are evaluated. This algorithm was implemented into the industrial CFD code ONERA CEDRE. Then, EMC-RANS algorithm was applied to simulate a turbulent premixed methane-air flame stabilized by backward facing step. Computations results were compared with experimental data [5]. The results were found to compare favourably with experimental data.

HYBRID EMC-RANS ALGORITHM

For variable density flows, working with density-weighted (Favre) statistics is a widespread technique. We denote the one-point Favre composition PDF as $\widetilde{f}(\boldsymbol{\Psi}; x, t)$, where $\boldsymbol{\Psi}$ is the vector in the "phase space" for the scalar variables $\boldsymbol{Y}$, where Y_k, $1 \leq k \leq N_s$ are species mass fractions and $Y_{N+1} = h_t$ is the total enthalpy. The exact transport equation for is derived from the species and energy conservations equations, using standard techniques [1]. Mean advection and chemical source terms in this equation are treated exactly, whereas the effects of molecular diffusion and turbulent advection require modelling. Turbulent advection is modelled with an isotropic gradient diffusion assumption. Molecular diffusion effects (micromixing term) are usually described by the simplest model - the interaction by exchange with mean (IEM) [1]. As a result, the following modelled transport equation is obtained for $\widetilde{f}(\boldsymbol{\Psi}; x, t)$:

$$\frac{\partial}{\partial t}\left(\langle\rho\rangle\,\widetilde{f}\right) + \frac{\partial}{\partial x_j}\left(\langle\rho\rangle\,\widetilde{U}_j\,\widetilde{f}\right) = \frac{\partial}{\partial x_j}\left(\langle\rho\rangle\,\Gamma_T\,\frac{\partial \widetilde{f}}{\partial x_j}\right) + \frac{\partial}{\partial \Psi_k}\left(\langle\rho\rangle\,\langle\omega_c\rangle\left(\Psi_k - \widetilde{\Psi}_k\right)\widetilde{f}\right) - \frac{\partial}{\partial \Psi_k}\left(\langle\rho\rangle\,S_k\,\widetilde{f}\right) \tag{1}$$

In this equation, Γ_T is the turbulent diffusivity , $\langle\omega_c\rangle$ is the mean mixing frequency , and $\widetilde{\boldsymbol{U}}$ is the Favre averaged velocity. These quantities are computed from a RANS solver [6].

The Favre averaged continuity and momentum equations are solved and a standard $k-\epsilon$ model is used to compute the turbulent stresses, with k the turbulent kinetic energy and ϵ the turbulent dissipation.

$$\begin{array}{lcl} \textit{Continuity} & : & \frac{\partial \langle\rho\rangle}{\partial t} + \frac{\partial}{\partial x_j}\left(\langle\rho\rangle \tilde{U}_j\right) = 0 \\ \textit{Momentum} & : & \langle\rho\rangle \frac{D\tilde{U}_i}{Dt} = -\frac{\partial \langle P\rangle}{\partial x_j} + \frac{\partial \sigma_{ij}}{\partial x_j} \\ \textit{Turb. kin. energy} & : & \langle\rho\rangle \frac{Dk}{Dt} = \frac{\partial}{\partial x_j}\left(\langle\rho\rangle \frac{\nu_t}{Pr_k}\frac{\partial k}{\partial x_j}\right) + P_k - d_k \\ \textit{Turb. dissipation} & : & \langle\rho\rangle \frac{D\epsilon}{Dt} = \frac{\partial}{\partial x_j}\left(\langle\rho\rangle \frac{\nu_t}{Pr_\epsilon}\frac{\partial \epsilon}{\partial x_j}\right) + P_\epsilon - d_\epsilon \end{array} \tag{2}$$

$\frac{D}{Dt}$ is the substantial derivative. It stands for $\frac{\partial}{\partial t} + \tilde{U}_j \frac{\partial}{\partial x_j}$. σ_{ij} models the turbulent stresses with an eddy viscosity hypothesis:

$$\sigma_{ij} = -\frac{2}{3}\langle\rho\rangle k\delta_{ij} + \langle\rho\rangle \nu_t \left(\frac{\partial \tilde{U}_i}{\partial x_j} + \frac{\partial \tilde{U}_j}{\partial x_i} - \frac{2}{3}\frac{\partial \tilde{U}_k}{\partial x_k}\delta_{ij}\right) \tag{3}$$

P_k and d_k (respectively P_ϵ and d_ϵ) are the production and dissipation terms of the turbulent kinetic energy (resp. dissipation). Standard expressions are used for these terms, as found for instance in [6]. The eddy viscosity is given by $\nu_t = C_\mu \frac{k^2}{\epsilon}$. Standard values are chosen for the $k-\epsilon$ model constants, as given in [6].

The statistics of species mass fractions Y_k and total enthalpy h_t are computed with an EMC solver using SPDEs derived in non-conservative form [3] :

$$\begin{array}{lcl} \textit{Mass fraction} & : & \frac{\partial Y_k}{\partial t}dt + \left(\tilde{U}_j - \frac{1}{2}\frac{\partial \Gamma_T}{\partial x_j} - \frac{1}{\langle\rho\rangle}\frac{\partial\langle\rho\rangle}{\partial x_j}\Gamma_T\right)\frac{\partial Y_k}{\partial x_j}dt \\ & & + \sqrt{2\Gamma_T}\frac{\partial Y_k}{\partial x_j} \circ dW_j(t) = -\langle\omega_c\rangle (Y_k - \tilde{Y}_k)dt + S(Y, h_t)dt \\ \textit{Total enthalpy} & : & \frac{\partial h_t}{\partial t}dt + \left(\tilde{U}_j - \frac{1}{2}\frac{\partial \Gamma_T}{\partial x_j} - \frac{1}{\langle\rho\rangle}\frac{\partial\langle\rho\rangle}{\partial x_j}\Gamma_T\right)\frac{\partial h_t}{\partial x_j}dt \\ & & + \sqrt{2\Gamma_T}\frac{\partial h_t}{\partial x_j} \circ dW_j(t) = -\langle\omega_c\rangle (h_t - \tilde{h}_t)dt + \frac{1}{\langle\rho\rangle}\frac{dP_0}{dt} \end{array} \tag{4}$$

or in conservative form [4] :

$$\frac{\partial}{\partial t}\mathtt{r}\, Y_k + \frac{\partial}{\partial x_j}\left(\mathtt{r}\, Y_k \circ (\widetilde{U}_j + \mathcal{U}^*_j)\right) = -\mathtt{r}\, \langle\omega_c\rangle (Y_k - \widetilde{Y}_k) + \mathtt{r}\, S_k(Y, T) \tag{5}$$

$$\frac{\partial \mathtt{r}\, h_t}{\partial t} + \frac{\partial}{\partial x_j}\left(\mathtt{r}\, h_t \circ (\widetilde{U}_j + \mathcal{U}^*_j)\right) = -\mathtt{r}\, \langle\omega_c\rangle (h_t - \widetilde{h}_t) + \frac{dP_0}{dt} \tag{6}$$

$$\mathcal{U}^*_j = \Gamma_t \frac{1}{\langle\rho\rangle}\frac{\partial\langle\rho\rangle}{\partial x_j} + \frac{1}{2}\frac{\partial \Gamma_t}{\partial x_j} + \sqrt{2\Gamma_t}\dot{W}_j \tag{7}$$

where P_0 is a reference pressure.

In the enthalpy equation, a unity Lewis number assumption has been made and acoustic interactions, viscous dissipation, and body forces were neglected under a low Mach number assumption. In these equations, the turbulent diffusivity is defined by $\Gamma_T = \nu_t / Sc_t$, where Sc_t is a turbulent Schmidt number supposed here to be unity. The mixing frequency is defined by $\langle\omega_c\rangle = C_\phi \frac{\epsilon}{k}$ where C_ϕ is a constant supposed to be equal to 0.7.

For the non-conservative formulation (4), the Favre averaged values of the species mass fraction and total enthalpy are computed by: $\tilde{Y}_k = \frac{1}{N}\sum_{real.} Y_k$ and $\tilde{h}_t = \frac{1}{N}\sum_{real.} h_t$, where the sums are taken over N realisations of the stochastic fields.

For the conservative formulation (5)-(7), the Favre averaged values of the species mass fraction and total enthalpy are computed by: $\widetilde{Y}_k = \sum_{real.} rY_k / \sum_{real.} r$ and $\widetilde{h}_t = \sum_{real.} rh_t / \sum_{real.} r$ where the sums are taken over the N realisations.

Information is transmitted from the RANS solver to the EMC solver via $\langle\rho\rangle$, $\tilde{U}_j$, ν_t and $\langle\omega\rangle$. The influence of the EMC solver on the RANS solver is achieved in the mean momentum equation, through the gradient of the mean pressure, which is computed from the equation of state :

$$\langle P\rangle = \langle\rho\rangle R_0 \sum_k \frac{\widetilde{Y_k T}}{M_k} \tag{8}$$

In this formula, R_0 is the gas constant and M_k is the molecular weight of the species k.
This way of coupling the EMC and RANS solver worked directly for the non-conservative formulation. However, for the conservative formulation, this coupling does not allow to get satisfactory convergence rates. The statistical fluctuations from $\langle \mathtt{r}\rangle_s = \frac{1}{N}\sum_{real.} \mathtt{r}$ and $\widetilde{Y_k T}$ in (8) are large and prevent the convergence. To overcome this difficulty, an equation is considered for the following quantity:

$$\Phi_\gamma = \frac{\langle P\rangle}{\langle\rho\rangle} + \frac{\langle\gamma\rangle - 1}{2}\widetilde{U}_i\widetilde{U}_i \tag{9}$$

where γ is the ratio of specific heats. With some approximation, the following equation is used for Φ_γ:

$$\frac{\partial \langle\rho\rangle \Phi_\gamma}{\partial t} + \frac{\partial}{\partial x_j}\left(\langle\rho\rangle \Phi_\gamma \widetilde{u}_j\right) = \frac{\partial}{\partial x_j}\left(\langle\rho\rangle \Gamma_T \frac{\partial \Phi_\gamma}{\partial x_j}\right) - \sum_k \langle(\gamma - 1)h_k S_k\rangle \tag{10}$$

where h_k is the specific enthalpy of species k and γ is its specific heat ratio. The source term in equation (10) are obtained from the EMC solver. This way of coupling allows to improve the stability and the statistical convergence.

NUMERICAL ASPECTS

Numerical scheme

To be consistent with the Stratonovitch interpretation used in equations (4)-(6), one must respect a "mid-point" rule in temporal integration [7]. For instance, fully explicit schemes are not consistent when used to discretize equations (4)-(6). Another important point is that precision must be evaluated in a weak sense: we are concerned with the error done in solving the PDF equation, not the SPDE.
Thus, we must adapt existing numerical schemes. First, we address the issue of temporal integration. We recast equations (4)-(6) in an SODE form; this allows the use of traditional SODE techniques [7]. An explicit first order scheme is chosen, with a predictor-corrector procedure generalizing the Heun scheme [7].
As for spatial discretization, scalar fluxes are interpolated with a second order Essentially Non-Oscillatory (ENO) scheme and a decentered procedure is used for the advection term. Decentering derivatives yields a correlation between the white noise and the discretization error. As a result, despite being second order accurate for the individual stochastic fields, the numerical scheme only discretizes the PDF equation with a first order spatial accuracy. Higher order numerical schemes can also be constructed.
The timestep is set according to a CFL criterion, built on the stochastic velocity. This guarantees the linear stability of the overall scheme. Because, the advection velocity is stochastic, the CFL criterion that we obtain is different from the usual one, and resembles an advection/diffusion stability criterion.

Boundary conditions

The issue of boundary conditions is also a crucial one. It should be noted that a diffusion equation like the one for the PDF requires boundary conditions to be specified on all the domain frontiers, whereas an hyperbolic equation only requires boundary conditions to be specified on certain parts of

the frontier. Furthermore, the stochastic advection term of SPDEs (4)-(6) can change the specification of boundary conditions in time. The boundaries alternatively become inflow boundaries, with a specified value of the stochastic field or outflow boundaries, with a value of the stochastic field computed from the interior of the domain. A more general discussion on boundary conditions is given in [3].

Correction algorithms

The hybrid algorithm is consistent at the level of the governing equations (i.e. $\langle \mathtt{r} \rangle_s = \langle \rho \rangle$). However due to the limited number of stochastic fields and the accumulation of numerical errors, the condition $\langle \mathtt{r} \rangle_s = \langle \rho \rangle$ may not always be respected during the calculation. In order to limit the statistical error, a correction diffusion term is added to SPDEs (5):

$$\frac{\partial}{\partial t}\mathtt{r}Y_k + \frac{\partial}{\partial x_j}\left(\mathtt{r}Y_k \circ (\widetilde{U}_j + \mathcal{U}_j^*)\right) = -\,\mathtt{r}\,\langle \omega_c \rangle\,(Y_k - \widetilde{Y}_k) + \mathtt{r}S_k(Y,T) + \frac{\partial}{\partial x_j}\left(\langle \rho \rangle\,\Gamma_T \frac{\partial}{\partial x_j}\left(\left|\frac{\langle \mathtt{r} \rangle_s - \langle \rho \rangle}{\langle \rho \rangle}\right| Y_k\right)\right) \tag{11}$$

The correction diffusion term is equal to zero once $\langle \mathtt{r} \rangle_s = \langle \rho \rangle$. The second correction concerns the velocity $\mathcal{U}_j^*$. In theory, the Favre average of this velocity is equal to zero:

$$\left\langle \mathcal{U}_j^* \right\rangle_{\mathtt{r}} = \frac{\left\langle \mathtt{r}\mathcal{U}_j^* \right\rangle_s}{\langle \mathtt{r} \rangle_s} = 0 \tag{12}$$

In the calculations, due to stochastic and numerical errors, condition (12) is not satisfied. To respect condition (12), we correct $\mathcal{U}_j^*$ by substracting its Favre average, as done for LMC methods in [8]. The new stochastic velocity is:

$$\mathcal{U}_j = \mathcal{U}_j^* - \sum_{real.} \mathtt{r}\mathcal{U}_j^* / \sum_{real.} \mathtt{r} \tag{13}$$

To reduce statistical noise, we also applied a time averaging technique similar to the one described in [8].

SIMULATION OF A BACKWARD FACING STEP WITH A HYBRID EMC-RANS ALGORITHM

The EMC-RANS solver described above was validated against experimental data [5] on a configuration consisting in the turbulent combustion of a pre-mixed stoichiometric methane-air mixture. The flame was stabilized by a recirculation zone in a plane channel with a sudden expansion (backward facing step).

Configuration

The physical domain is $L = 1m$ horizontally and $H = 0.1m$ vertically. The height of the step, placed at the lower wall, is $h = 0.035m$, and its extremity is located at $0.2m$ inside the computational domain. Positions will hereafter be given using the step extremity as the origin.

At inlet, a methane/air mixture is injected at $U_0 = 58m/s$ and $T_0 = 525K$, with a stoichiometric equivalence ratio $\phi = 1$. The inlet values of the turbulent quantities are $k_0 = 60m^2/s^2$ and $\epsilon_0 = 800m^2/s^3$. At outlet, the pressure is fixed: $P_s = 1bar$. The geometry and inlet conditions correspond to the experimental ones [5].

At the upper and lower wall, wall functions are applied for k and ϵ, while the enthalpy and mass fractions are set by assuming that the walls are adiabatic. However, the measurements of the temperature in [5] were done in a water-cooled combustion facility. Thus, in the experiment, there were wall heat

fluxes and the redistribution of the heat through metal walls by means of thermal conductivity. As a consequence, the approximation of adiabatic walls overestimates temperature at the lower wall, and underestimates the temperature at the upper wall. This remark has to be taken into account when comparing computed and experimental data.
Methane combustion in air was modeled by a global single-step chemical reaction, which describes complete combustion of methane, the resultant products being CO_2 and H_2O [9]. Though the single-step reaction offers only an approximate description of methane oidation and, in particular, over-predicts the temperature T, it was used for preliminary testing of the hybrid EMC-RANS algorithm developed here.

Results and discussion
The EMC method in non-conservative form (4) was applied to the calculation of the methane-air flame described above in [10]. Comparison against experimental data yielded a qualitatively good agreement between mean temperatures and temperature variances. Statistical and spatial errors were thoroughly analyzed in [10]. It was shown that a grid resolution of $\Delta x = 10^{-2}m$ and $\Delta y = 2.4 \cdot 10^{-3}m$ is sufficient to capture the flame structure.
In this section, we present some results obtained with the EMC method in conservative form (5)-(6). SPDEs (5)-(6) in conservative form yield almost the same restults as those published in [10] with the non-conservative formulation. This is not surprising because the conservative and non-conservative formulations are statistically equivalent to the same PDF equation (1).
Table recapitulates the resolution of the four grids we used. The grid refinement was performed in the near step nose region.

Table 1
Grid Resolution. x: horizontal direction; y: vertical direction

	$\Delta x_{min}(m)$	$\Delta y_{min}(m)$	$N_x \cdot N_y$
Mesh 1	$1.5 \cdot 10^{-2}$	$5 \cdot 10^{-3}$	900
Mesh 2	$6 \cdot 10^{-3}$	$5 \cdot 10^{-3}$	1600
Mesh 3	$4 \cdot 10^{-3}$	$3 \cdot 10^{-3}$	4000
Mesh 4	$1.5 \cdot 10^{-3}$	10^{-3}	8000

We first analyze stochastic convergence. We perform five calculations on *Mesh 3* with $N = 5$, $N = 10$, $N = 25$, $N = 50$, and $N = 100$ stochastic fields. We compare the results once a statistical convergence is attained. This is the case for times on the order of $10L/U_0 = 0.15s$. To better characterize the statistical convergence, we introduce two integrals: $E_1 = \frac{\int |\widetilde{T} - \widetilde{T}_{ref}| dxdy}{\int \widetilde{T}_{ref} dxdy}$ and $E_2 = \frac{\int |\sqrt{\widetilde{T'^2}} - \sqrt{\widetilde{T'^2_{ref}}}| dxdy}{\int \sqrt{\widetilde{T'^2_{ref}}} dxdy}$ where $\widetilde{T}_{ref}$ and $\widetilde{T'^2_{ref}}$ are computed from a high resolution solution with $N = 100$ stochastic fields. Figure (a) shows the evolution of E_1 and E_2 against the number of stochastic fields. A convergence is indeed observed : E_1 decays as $N^{-0.8}$ and E_2 decays as $N^{-0.7}$. These decay rates are slightly higher than the theoretical $N^{-0.5}$ rate that we could expect.
We now analyze spatial convergence. Calculations are done with $N = 50$ stochastic fields, and the number of computational cells is varied from *Mesh 1* to *Mesh 4*. The computation done with *Mesh 4* is considered as a reference solution against which other calculations are compared. The integrals E_1 and E_2, with $\widetilde{T}_{ref}$ and $\sqrt{\widetilde{T'^2_{ref}}}$ computed from *Mesh 4*, are used for this comparison. Figure (b) shows the evolution of E_1 and E_2 against the number of computational cells. Comparison of figures (a) and (b) shows that for $N_c = 4000$ cells the spatial error is on the order of the stochastic error obtained with $N = 50$ fields. Thus, by choosing the most refined mesh $N_c = 8000$ cells for our calculations, we

(a) (b)

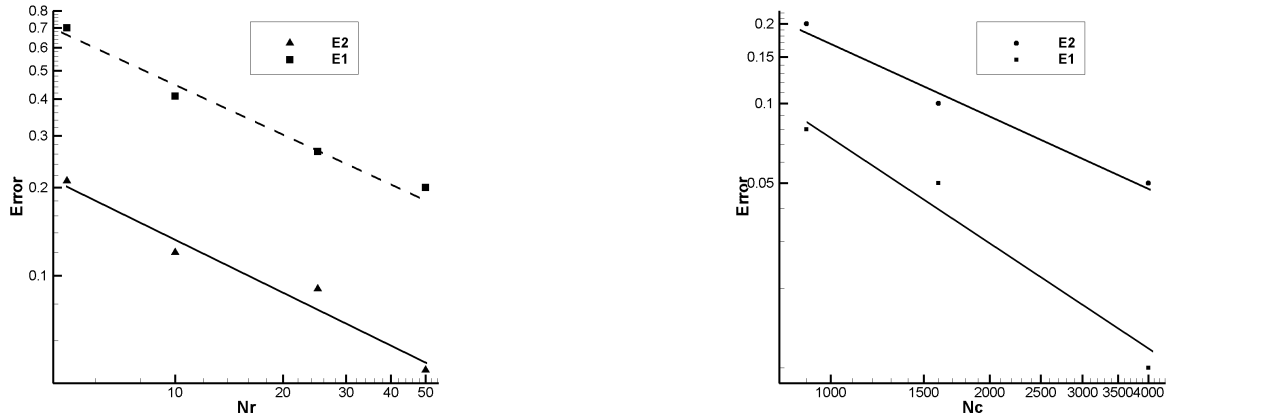

Figure 1: Errors E_1 and E_2 against (a) : the number of stochastic fields N; (b): the number of cells

expect the spatial discretization error to be much smaller than the stochastic error. It then becomes useless to refine further the grid without adding more stochastic fields.
Thus, in the remaining calculations, we will choose *Mesh 3* and $N = 50$ fields as a compromise between precision and calculation cost. Mean and RMS temperature vertical profiles at a given location are shown on figure 2. They are compared against the experimental results obtained by [5]. The main point of this comparison is the satisfactory agreement found between the calculation and the experiment. In particular, the peak location of the calculated RMS temperature is close to the experimental one. The temperature PDFs were also computed and found to compare favorably with experimental data [5]. This comparison is not presented here, but can be found in [10].

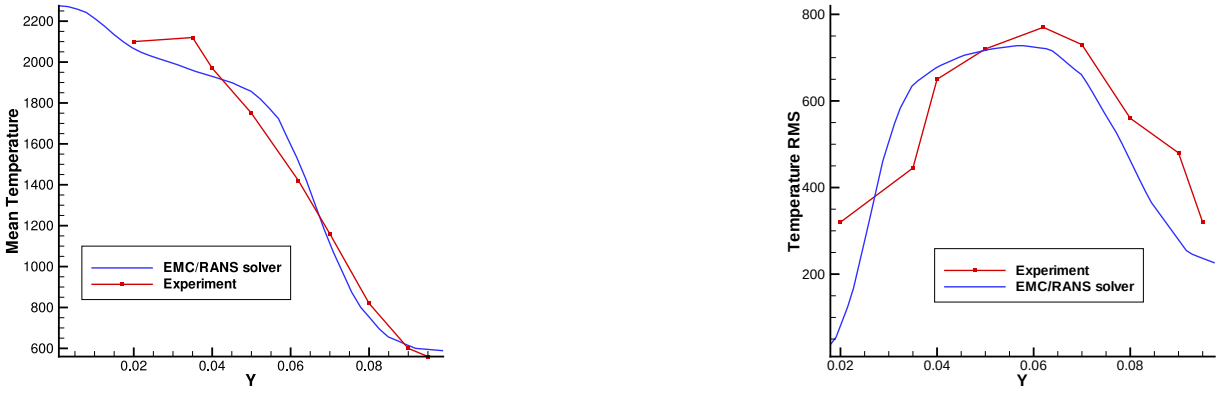

Figure 2: Vertical profiles of $\widetilde{T}$ and T_{RMS} at $x = 250mm$

CONCLUSIONS

Eulerian (Field) Monte Carlo (EMC) methods are employed to construct hybrid algorithms to resolve the composition PDF equations. The composition PDFs in EMC methods are represented by stochastic Eulerian species fields. Stochastic partial differential equations (SPDEs) are statistically equivalent

to the PDF equations. Numerical issues emerging in the solution of the SPDEs are discussed and numerical schemes are adapted. A hierarchy of numerical validation tests is performed. A novel hybrid composition EMC-FV (Finite Volume) algorithm is developed based on the conservative formulation of SPDEs. Correction techniques, time averaging procedure and coupling strategy efficiency are evaluated. This algorithm was implemented into the industrial CFD code ONERA CEDRE. Then, EMC-RANS algorithm was applied to simulate a turbulent premixed methane-air flame stabilized by backward facing step. Computations results were compared with experimental data. The results were found to compare favourably with experimental data.

REFERENCES

1. Pope, S. B., Pdf methods for turbulent reactive flows. *Progress in Energy and Combustion Science*, Vol. 27, pp 119–192, 1985.

2. Valiño, L., A field Monte Carlo formulation for calculating the probability density function of a single scalar in a turbulent flow. *Flow, turbulence and combustion*, Vol. 60, pp 157–172, 1998.

3. Sabel'nikov, V. A. and Soulard, O., Rapidly decorrelating velocity field model as a tool for solving Fokker-Planck PDF equations of turbulent reactive scalars. *Phys. Rev. E*, Vol. 72, pp 016301, 2005.

4. Soulard, O. and Sabel'nikov, V. A., Eulerian Monte Carlo method for the joint velocity and mass-fraction probability density function in turbulent reactive gas flow combustion. *Explosion and Shock Waves*, Vol. 42, No 6, pp 753–762, 2006.

5. Magre, P. , Moreau, P. , Collin, G. , Borghi, R. , and Pealat, M., Further studies by CARS of premixed turbulent combustion in a high velocity flow. *Combustion and Flame*, Vol. 71, No 2, pp 147–168, 1988.

6. Pope, S. B., *Turbulent flows*. Cambridge Univ. Press, 2000.

7. Gardiner, C.W., *Handbook of Stochastic Methods*. Springer, second edition, 1985.

8. Jenny, P. , Pope, S. B. , Muradoglu, M. , and Caughey, D. A., A hybrid algorithm for the joint pdf equation of turbulent reactive flows. *J. Comp. Phys.*, Vol. 166, pp 218–252, 2001.

9. Westbrook, C. K. and Dryer, F. L., Chemical kinetic modeling of hydrocarbon combustion. *Prog. Energy Comb. Sci.*, Vol. 10, pp 1–57, 1984.

10. Sabel'nikov, V. A. and Soulard, O., White in time scalar advection model as a tool for solving joint composition pdf equations: derivation and application. *J. of Flow, Turbulence and Combustion*, Vol. 77, pp 333–357, 2006.

LARGE EDDY SIMULATIONS OF PARTICLE-LADEN TURBULENT CHANNEL FLOWS

M. Jaszczur
AGH University of Science and Technology, Kraków, Poland

ABSTRACT The particle-turbulence interaction is one of the key phenomena important to have a very accurate prediction and a good understanding of the physical process. Due to the interactions with turbulence, the distribution of the particles and their properties can be highly influenced. That behaviour can have serious consequences on the efficiency and direction of many chemical and industrial processes. In presented paper Large Eddy Simulations for the case of flows laden with a large number of small particles were performed. Eulerian-Lagrangian point-particle approach was used to study of the particle-turbulence dynamics. The objective of this work was the analysis of influence of the Smagorinsky constant and wall function on the particle statistics. The influence of the constant models was tested in a comparison between the results obtained with Direct Numerical Simulations and Large Eddy Simulations using a standard Smagorinsky model or combined with Van Driest wall-damping model. Due to the complexity of the particles behaviour, only some computed average profiles of the dispersed phase from the LES simulations show good agreement with the DNS data. Phenomena like clustering and concentration was very difficult to reproduce properly with LES and additional sub grid scale model for dispersed phase seems to be required.
In particular, even though the models reproduces more accurately results for the continuous phase in comparison to results obtained by DNS the properties of the dispersed phase computed using LES do not match the DNS results. The particles tends to be highly concentrated in the region close to the wall but concentration is always lower than for DNS. Moreover, the properties of the particles in terms of concentrations and velocity fluctuation profiles do not show large improvement with the use of different models for LES. This mean that additional model concerning proper preproduction of the dispersed phase needs to be implemented.

Keywords: *LES particle laden flow, multiphase flow, turbulent channel flow*

INTRODUCTION

The multiphase flow laden with a large number of particles has recently received considerable attention due to its relevance to large number of chemical and engineering applications. It is well know that depending on the particle Stokes number and density of the particles the turbulent flow structure can be low or highly influence by the presence of the particles. Numerical computations can play an important role in understanding fundamental interaction between particles and turbulence but is often limited to low Reynolds number cases (Direct Numerical Simulations). To overcome this limitation Large Eddy Simulations has been more often used but in that case suitable subgrid scale model needs to be introduced. In the present work particle transport in fully developed turbulent wall-bounded flow has been investigated with the fluid-particle one way interaction

* Corresponding author: Dr M. Jaszczur
Phone: + (48)-12-6172657, Fax: + (48)-12-6172685
E-mail address: jaszczur@agh.edu.pl

approach and Large Eddy Simulations approach. LES of the incompressible flow, combined with Lagrangian particle tracking technique has been performed to study problem.

Numerical computations using DNS as well as experimental measurements shows that shear flow, mean gradient in the fluid and velocity of the particles have complex effect on the particle fluctuations. In wall-bounded shear flow Rouson and Eaton[1], Pedinotti[2] have shown that particle are preferentially concentrated in the low speed streaks and near-wall region. McLaughlin[3] has shown that particles accumulate in the near wall region.

In order to design industrial devices involving particle-turbulence interaction it is important to have a very accurate prediction of particles behavior in selected processes. Small heavy particles immersed in a turbulent flow tend to accumulate, creating non-homogeneities in concentration [1] in contrast to more welcome for many chemical processes uniformity. This can have important consequences on the direction and efficiency of many chemical and industrial processes. Number of research has been done to study the influence of particle inertia on the dispersion phenomena [2-4]. Most of simulations do not promise to have high reliability and applicability and fail to provide more accurately analysis of the flow.

Several important aspects of particle-turbulence interactions have been analyzed by Maxey and Riley [5], Kulick [6], Fessler and Eaton [7], Chung [8], and Portela [9] among others.

In the most study Direct Numerical Simulations has been used to overcome problem of additional numerical modeling but Large Eddy Simulation method has been also used for particle-laden flows and several work have been published over the last years [9-11]. But the issue is still perceived as open and further work is needed to understand the effect of sub grid-scale fluid flow on particle motion and vice versa. In particular, seems to be very important to model properly the carrier flow. One of the several available models in LES is the Smagorinsky model, which has been widely applied to many different situations. However, one of the main problems of this model is the dependence on a model coefficient, which has to be determined a priori.

In presented paper Large Eddy Simulations for the case of flows laden with a large number of small particles were performed and the objective of this work was the analysis of influence of the Smagorinsky constant and wall function on the particle statistics (dispersed phase). The influence of the constant models was tested by the comparison of the results obtained with Direct Numerical Simulations (performed also here and in reference paper Jaszczur et. al. [12]) and Large Eddy Simulations using a standard Smagorinsky model or combined with Van Driest wall-damping model.

The problem analyzed the transport of small heavy particles in a closed-channel flow coupled with Lagrangian Particle Tracking. The last is done using the point-particle technique, and considering only a one-way coupling situation, i.e., the influence of the particles on the turbulence and particle collisions were not taken into account. Due to the complexity of the particles behavior, only some computed average profiles of the dispersed phase from the LES simulations show good agreement with the DNS data. Phenomena like clustering and concentration was very difficult to reproduce properly with LES and additional sub grid scale modeling for continuous or dispersed phase seems to be required.

MATHEMATICAL MODEL

Equations of motion

In turbulent channel flow laden with particle two different phases can be recognized in the domain: a continuous phase (gas phase) and a dispersed phase (particle phase). Assuming the flow is isothermal, Newtonian and incompressible, for the case of Large Eddy Simulations, the continuous phase can be represented by the filtered Navier-Stokes equations for continuity and momentum presented below:

$$\nabla \cdot \mathbf{u} = \mathbf{0} \tag{1}$$

$$\frac{D\mathbf{u}}{Dt} = -\frac{\nabla P}{\rho_f} + \upsilon \nabla^2 \mathbf{u} + \nabla \cdot \boldsymbol{T} \tag{2}$$

where **u** and P are the fluid velocity and pressure, ρ_f , ν respectively the fluid density, and kinematic viscosity. The stress-tensor, $\boldsymbol{T}$ represented the influence of the sub grid scales on the resolved fluid-velocity. One of the most popular sub grid scale (SGS) stress model is the Smagorinsky model [13]. Even though this relatively easy model has been successfully applied to many different turbulent flows. But there are two limitations on the application of the Smagorinsky model. First of limitation to industrial application is essentially dissipative character of the model, and second more importantly, the value of the Smagorinsky constant C_s has to be defined a priori.
In the standard Smagorinsky model, the residual stress tensor is denoted by $\boldsymbol{\tau}$, and is defined as follows:

$$\tau_{ij} = \overline{u_i u_j} - \bar{u}_i \bar{u}_j \tag{3}$$

This tensor **τ** is parameterized by an eddy viscosity model, as follows:

$$\tau_{ij} - \frac{\delta_{ij}}{3}\tau_{kk} = -2\nu_r \overline{S_{ij}} \tag{4}$$

This is incorporated in the pressure term and the coefficient of proportionally to ν_r and it is modelled by analogy to the mixing length hypothesis as:

$$\nu_r = C\Delta^2 \left|\overline{S}\right| \tag{5}$$

where C is the Smagorinsky constant, $\overline{\Delta}$ is the filter width, and $\left|\overline{S}\right|$ is the magnitude of the large scale strain rate tensor $\overline{S}_{ij}$. Last tensor can be defined as bellow:

$$\overline{S}_{ij} = \frac{1}{2}\left(\frac{\partial u_i}{\partial x_j} + \frac{\partial u_j}{\partial x_i}\right) \tag{6}$$

where the magnitude of the strain-rate tensor can be defined as:

$$|\bar{S}| = \left(2\bar{S}_{ij}\bar{S}_{ij}\right)^{1/2} \tag{7}$$

For the numerical simulations recommended value of the Smagorinsky constant was C=0.01 sometimes defined as C_s=0.1 or in more advanced models this coefficient can be not fixed but determine dynamically (Germano [14]). Also in the case of the standard Smagorinsky model, wall functions has to be implemented to ensure proper values of viscosity at the wall. Influence of the wall function model was tested in the present computation and several simulations was performed with the standard Van Driest wall-damping model, with parameter A=25 and without wall model .

In general the forces acting on the particle immersed in a flow are described properly by Maxey and Riley equations[5]. But in the case of the small heavy particles considered here, the dominant forces acting on the particles are the drag force and gravity force (in order to study fluid particle interactions gravity force will be neglected). With the above assumption the equation of motion for a particle can be written as:

$$\frac{dv}{dt} = C_d \frac{Re_p}{24}\frac{1}{\tau_v}(\boldsymbol{u} - \boldsymbol{v}) \tag{8}$$

where **v**, **u** are the particle velocity and the velocity of the fluid (interpolated at the geometrical center of the particle). The particle Reynolds number Re_p, and the particle relaxation time τ_v, are defined as follow:

$$Re_p = \frac{|(\boldsymbol{u}-\boldsymbol{v})|\, D_p}{\upsilon}, \quad \tau_\upsilon = \frac{\rho_p}{\rho}\frac{D_p^2}{18\upsilon}, \quad C_d = \frac{24}{Re_p} \tag{9}$$

where ρ_p, ρ_f are the density of the dispersed phase (particle) and the continuous phase (fluid), D_p is the diameter of the particles and C_d is the drag coefficient for Stokes flow (valid for small Re_p).

Numerical methods

Figure 1 shows the geometry of the computational domain used in Large Eddy Simulation of a particle-laden channel flow. Mean flow is driven by a streamwise pressure gradient.

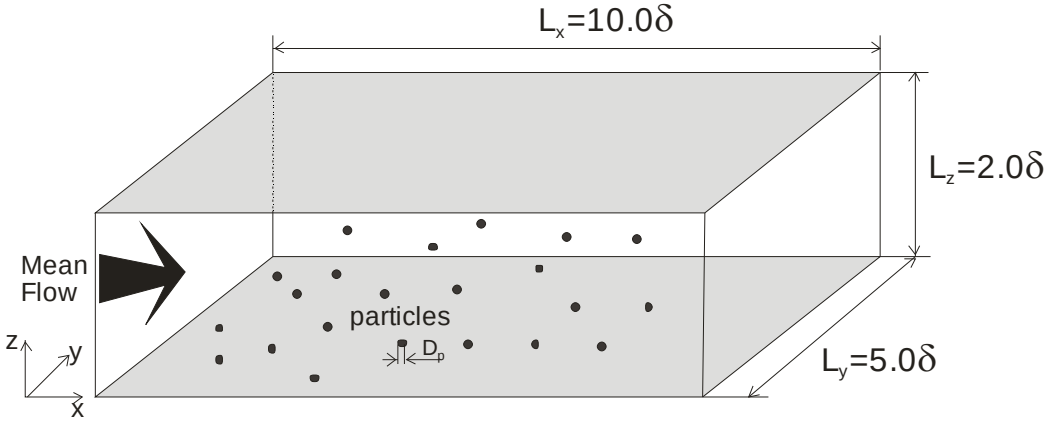

Figure 1. Sketch of computational domain.

The size of the domain, flow and particle quantities are normalized by the channel half-width, δ, and the friction velocity u_τ.

The numerical algorithm was a standard finite-volume method on a staggered grid where the continuous phase was solved using a predictor-corrector solver, with a second-order Adams-Bashforth scheme. The time step was obtained using the Courant stability criterion. In the streamwise and spanwise directions periodic boundary conditions were used.

For the discrete phase, particle equation of motion was integrated using an explicit second-order Runge-Kutta scheme. Tri-linear interpolation has been used to calculate the fluid velocity at the particle position. The time step size for the particles was always equal to or smaller than the fluid time step (a particle can't travel more than ½ of grid cell per iteration). All the conditions for the dispersed phase were the same as in the DNS from Jaszczur et.al. [12]. This means, no model was used to mimic the unresolved flow scales. More details of the code can be found in Portela and Oliemans [9].

RESULTS

Large Eddy Simulations where performed for Re_τ = 150, with the Reynolds number based on the shear velocity and half-channel height. The size of computational domain was 10x4x2δ base on half-channel height and the grid resolution was 64x64x48, with uniform grid spacing in the stream and span-wise directions, and a hyperbolic-tangent stretching in the normal-wise direction, with a high number of grid points in the near-wall region. The simulations started from fully developed DNS (grid size 128x128x64, and domain size 6.4x3.2x2.0) velocity field and particles randomly distributed in computation domain.

When a statistically steady state flow field was obtained, small and heavy particles (density ρ_p=800[kg/m^3]) with particle Stokes number St=1 were introduced in the domain. In order to obtain good statistics for particle the simulations presented here was performed with 1.5x10^5 particles. Their initial velocity assumed to be the same as the fluid in the center of particles location. The particles need to adapt to the new velocity which usually takes few particle response times. But in order to get statistically-steady state for particles conditions much longer time (longer than for flow field) is required. The particles where tracked for t* = 800, and both fluid and particles properties where averaged from t* = 300 till t* = 800. The particle properties were obtained by averaging over a rectangular slices using simple linear model.

Figure 2 presents the mean streamwise velocity profiles for fluid and various constants of LES and compare to DNS as well as no model simulations (C_s=0). On the left hand side are the profiles for model using wall function (Van Driest), while on the right hand side without wall function. Very good agreement between the DNS and LES profiles for mean streamwise velocity was obtain with the use of the wall function model and C_s=0.1. Relatively poor results was obtain without any model C_s=0 or without wall function.

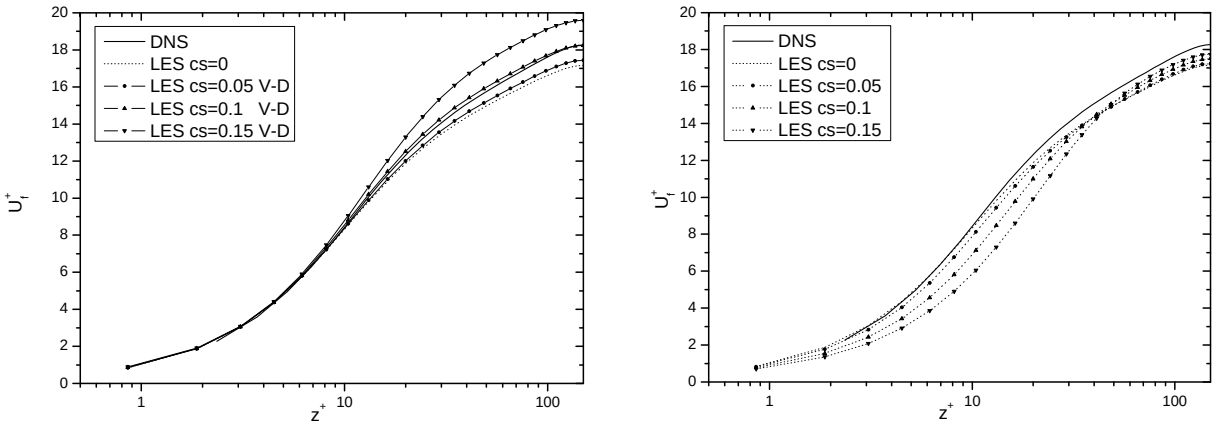

Figure 2: Mean streamwise fluid velocity profiles for LES and DNS and for Re_τ = 150, V-D denotes Van Driest wall function model with A=25.

Figure 3 presents the mean streamwise particle velocity profiles for various constants of LES and DNS. On the left hand side are the profiles for model using wall function while on the right hand side without wall function. Similar to figure 2 very good agreement compare to DNS was obtain with the use of the wall function model and C_s=0.1.

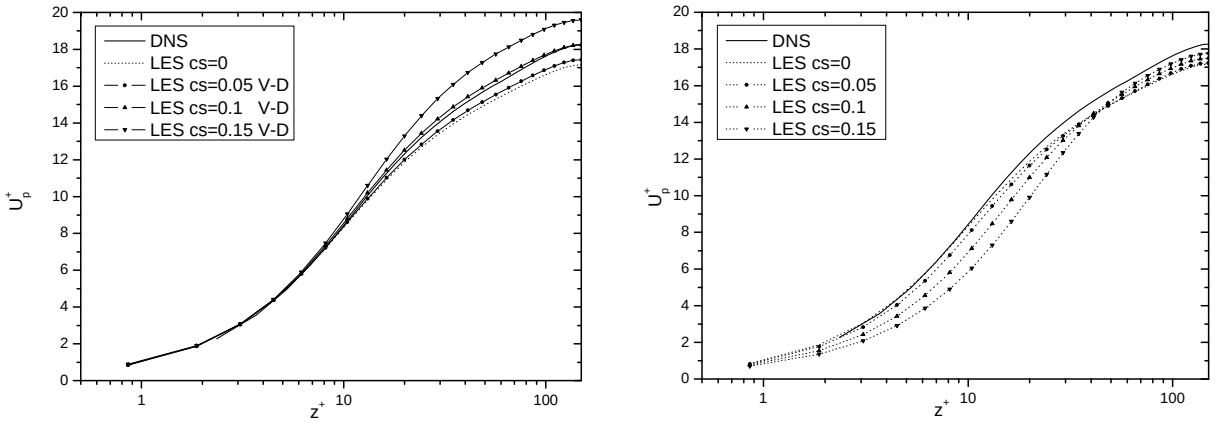

Figure 3. Mean streamwise particle velocity profiles for LES and DNS and for Re_τ = 150, St=1, V-D denotes Van Driest wall function model with A=25.

In contrast to the mean velocity field (where the mean velocity for continuous and for dispersed part computed with DNS and LES shows good agreement for optimal model constant) the stresses differs quite a lot. On figure 4 we can see that value obtained by LES for optimal constant (C_s=0.1) are higher for fluid and lower for particle compare to DNS for correlation <uu>. For the <vv> correlation for continuous phase best result give model with C_s=0.05. This value without wall function model gives better results than for C_s=0.1. Independent of model and constants in all cases prediction of $<w_p w_p>$ and $<u_p w_p>$ is much lower compare to DNS results. Level of fluctuations play key role in particle distributions and, as can be seen from figure 6, large eddy simulation results gives in all cases much lower concentration of the particles close to the wall. This can be in relation to lower fluctuation of the particle in that region. But it need to be emphases that fluid fluctuations depending on model can be relatively well reproduces there. Also, as can be seen on figure 5, the predicted slip velocity with LES is much higher than for DNS. This can be also cause by much smaller particle fluctuation.

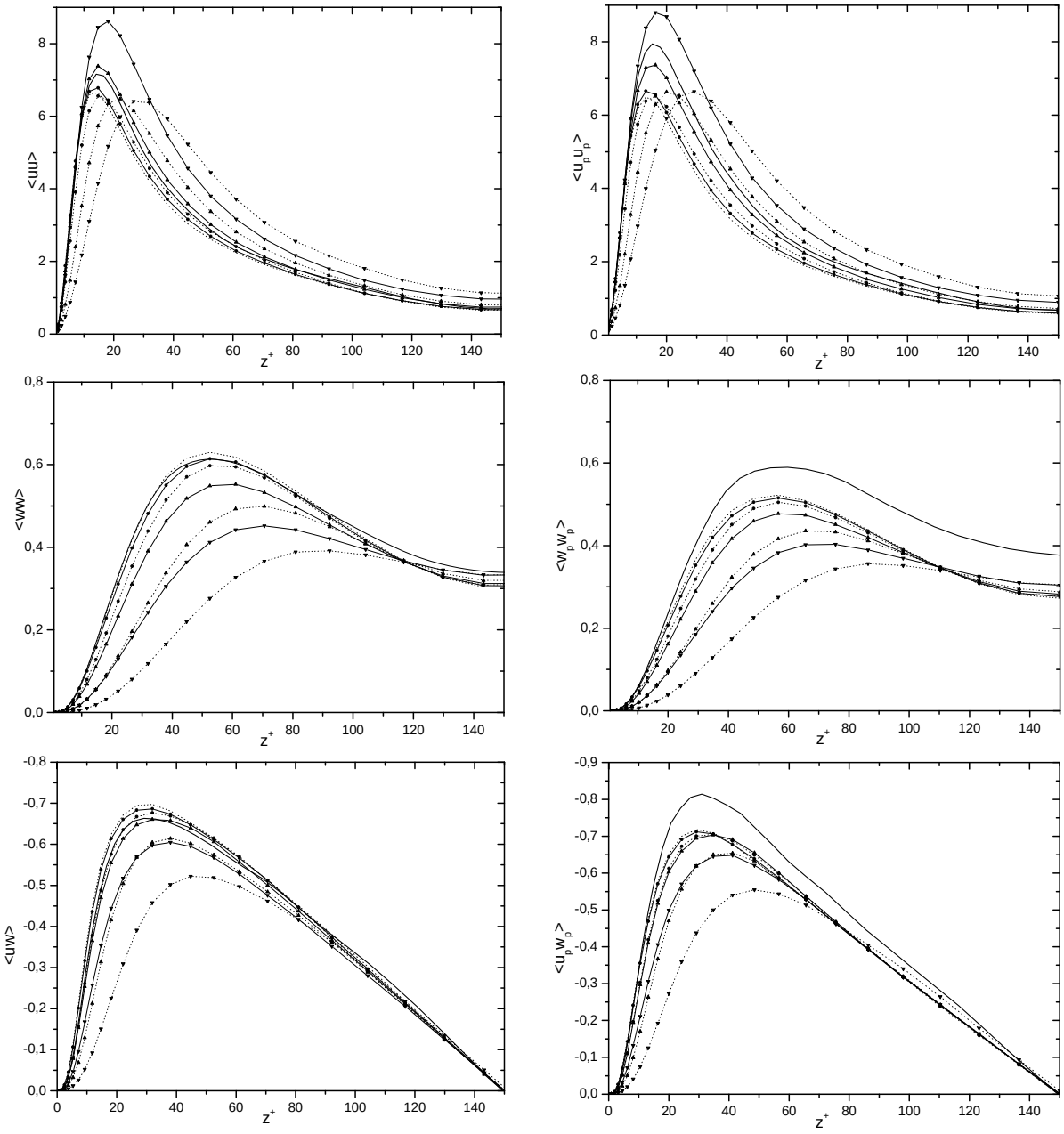

Figure 4: Fluid and particles velocity fluctuation profiles for DNS and large eddy simulations for Re_τ = 150 and St=1(for details see legend on figure 3).

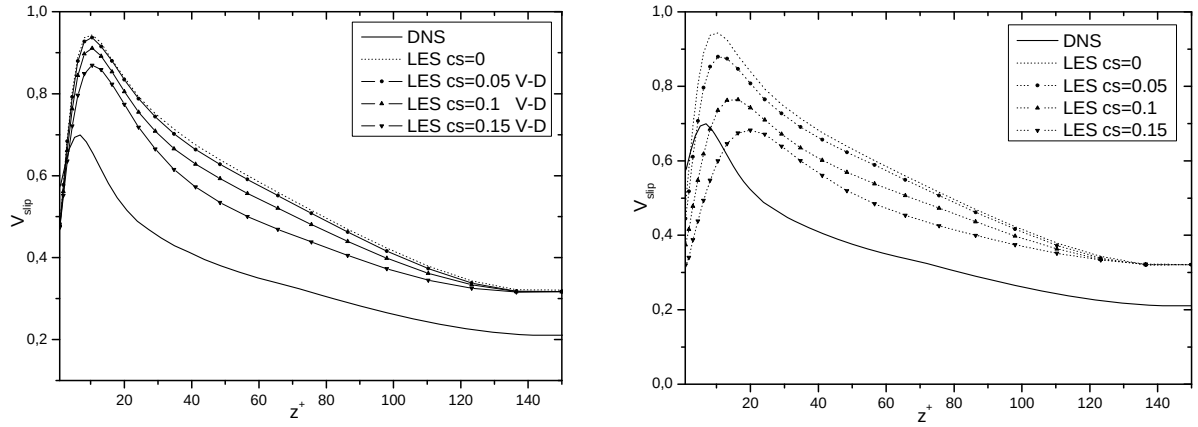

Figure 5: Slip velocity profiles for DNS and large eddy simulations for Re_τ = 150 and St=1, left – with wall model, right – without wall model.

In reference to the fluid and particles fluctuations concentrations for particles in the near wall region is predicted best without any subgrid scale model and with models with Smagorinsky constant C_s=0.05. This tendency is true also for cases without wall-function where predicted concentrations are shifted for all the cases of about 0.25 lower for the first presented point.

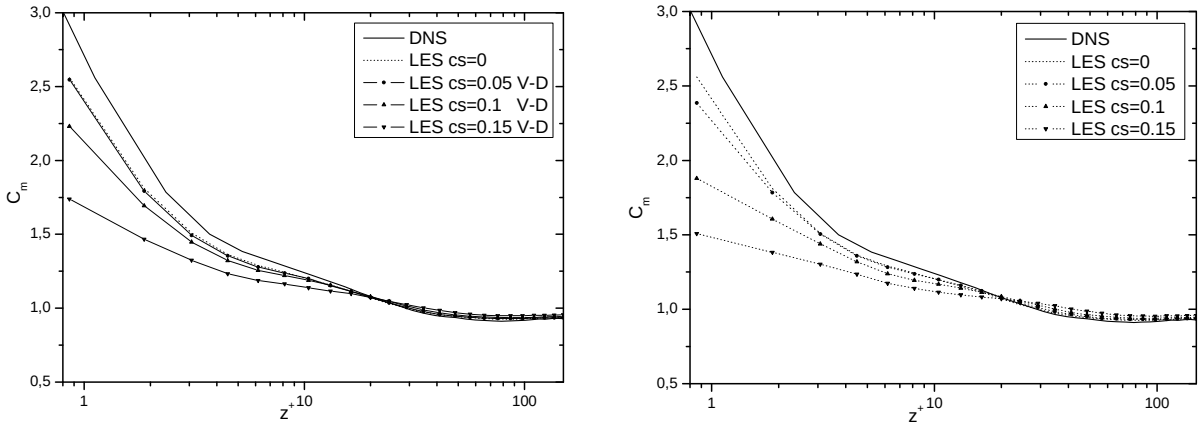

Figure 6: Concentration profiles for DNS and large eddy simulations for Re_τ = 150 and particle Stokes number St=1.

To avoid difference between LES and DNS results due to numerical model, the same procedure was used for particle computation and post-processing (particle statistics). Different numerical model can cause large difference in particle concentration at the wall. This was obtain in benchmark solution [15] where particle concentration at the wall for St=1 and z^+=0.2 was between 3.5 and 7.3 depending on numerical procedure. To avoid influence of averaged time several analysis was done but the difference between results (if statistically steady state was obtain) were very small.

CONCLUSIONS

This paper has shown an analysis of the particle transport in a particle-laden channel flow using Large Eddy Simulations and a point-particle Lagrangian particle tracking. Several statistical quantities for particle velocity and concentrations for both the continuous and the dispersed phase were obtained from the calculations. The results for the fluid phase (mean fluid velocity and correlations) show a good agreement with results obtained by other researchers using DNS for proper model constant. However, the properties of the particles computed from LES do not match DNS results for most properties at all. It was observed that for results obtained using Direct Numerical Simulations particles tend to be highly concentrated in the region close to the wall. This was as a results of particle fluctuation, higher for DNS than with any LES model. Even though the qualitatively behavior of the particles are the same in LES and DNS, this study showed quantitatively differences in the velocity fluctuation and concentration profiles. Moreover, the

properties of the particles in terms of concentrations and velocity fluctuation profiles are not so sensitive to the use of different models for LES, like the standard and can also appears for dynamical models.

Calculations with LES for particle laden flow are still perceived as an open problem, and further work is warranted on the effect of sub grid-scale fluid flow on particle motion. Particle motion similar to continuous phase for proper evaluation of key properties e.g. kinetic energy, preferential concentration, collision statistics, deposition velocity etc, required additional models which will take into account not only local but also global structure of particles. Regarding the treatment of the dispersed phase the way how the fluid velocity is interpolated to the center of the particle can be very important and probably higher order or different method should be introduced. Particles with higher Stokes number can filter itselves velocity field due to high relaxation time and requirement for the sub-grid scale modeling can be less important than in this work.

ACKNOWLEDGMENTS

This research was supported by project COST P20 258/2006

REFERENCES

1. Rouson, D. and Eaton, J., Direct numerical simulation of particles interaction with a turbulent channel flow. *Proc. of 7th Workshop on Two-Phase flow Predictions,* ed. Sommerfeld, Erlangen,1994.
2. Pedinotti, S., Mariotti, G. and Banerjee, S., Direct numerical simulation of particle behavior in the near wall region of turbulent flows in horizontal channels, *Int. J. Multiphase Flow,* Vol. 18, No. 6, pp 927-941, 1992.
3. McLaughlin, J., Aerosol particle deposition in numerically simulated channel flow, *Phys Fluid A*, Vol. 1, No. 7, pp 1211-1224,1998.
4. Wang, L. and Maxey, M., Settling velocity and concentration distribution of heavy particles in homogeneous isotropic turbulence, *J. Fluid Mech.,* Vol. 256, pp 27-68,1993.
5. Maxey, M.R. and Riley, J.K., Equation of motion for a small rigid sphere in a nonuniform flow, *Phys Fluids A*, Vol. 26, pp 883–889, 1983.
6. Kulick, J.D., Feesler, J.R., Eaton, J.K., Particle response and turbulence modification in a fully developed channel flow, *J Fluid Mech*, Vol. 277, pp 109–134, 1994.
7. Fessler, J. and Eaton, J.K., Preferential concentration of particles by turbulence, *Int J Multiphase Flows*, Vol. 20, pp 169–209, 1994.
8. Chung, J., Koch, D.L., Rani, S.L., Clustering of aerosol particles in isotropic turbulence *J Fluid Mech*, Vol. 536, pp 219–251, 2005.
9. Portela, L. M. and Oliemans, R.V.A., Eulerian-Lagrangian DNS/LES of particle turbulence interactions in wall-bounded flows, *Int. J. Numer. Fluids*, Vol. 43, No. 9, pp 1045-1065, 2003.
10. Wang, Q. and Squires, K.D., Large eddy simulation of particle-laden turbulent channel flow, *Phys Fluids*, Vol. 8, pp 1207–1223, 1996.
11. Armenio, V., Piomelli, U. and Fiorotto, V., Effect of the subgrid scales on particle motion, *Phys Fluids*, Vol. 11, pp 3030–3042, 1999.
12. Jaszczur, M., Portela, L.M. and Cargnelutti, M.F., Direct Numerical Simulation of Particle-Laden Turbulent Channel Flow with Heat Transfer, *5th International Symposium on Turbulence, Heat and Mass Transfer*, Dubrovnik, Croatia, September 25-29, 2006.
13. Smagorinsky, J., *Monthly Weather Rev.*, *91*: 99. (1963)
14. Germano, M., Piomelli, U., Moin, P. and Cabot, W.H., A Dynamic Subgrid-scale Eddy Viscosity Mode , *Phys Fluids A* , Vol. 3, pp1760-1765, 1991.
15. Marchioli, C., Soldati, A., Kuerten, J.G.M., Arcen, B., Tanière, A., Goldensoph, G., Squires, K., Cargnelutti, M.F., Portela, L.M., Statistics of particle dispersion in Direct Numerical Simulations of wall-bounded turbulence: results of an international collaborative benchmark test, *Int. J. Multiph Flow*, Vol. 1, pp 879-893, 2008.

Miscellaneous Applications

HIDRODYNAMICS OF JETS FROM GUILLOTINE STEAM GENERATOR TUBE RUPTURE

J.L.Muñoz-Cobo[1,*], L.E.Herranz[2], A.Escrivá[1], A.Geraldo[1]
[1]Universidad Politécnica, Valencia, Spain
[2]CIEMAT, Centro de Investigaciones Energéticas, Madrid, Spain

ABSTRACT. In this work we study the hydrodynamics of characteristic gas jets resulting from guillotine breaks of steam generator tube rupture sequences (SGTR), in pressurized nuclear power reactors. As an initial step towards describing an "in-bundle" gas jet, a hydrodynamic model of free gas jets emerging from a guillotine breach under prototypical SGTR conditions have been developed. The model estimates variables such as trajectories, centreline velocities, and velocity distributions. We have performed model comparisons with experimental data for different experimental conditions with different mass flow rates, and we have found good agreement of the model with the experimental results. Additionally, an "ad-hoc" expression has been derived for the centreline jet velocity ($u_c(s) = C_c / s^{0.92}$), which has been experimentally confirmed. Consistently with data, the model predicts no outflow near the jet centre.

Keywords: *guillotine tube rupture jets, jets in enclosures, hydrodynamics of jets, SGTR*

INTRODUCTION

Steam generators (SG) of nuclear power plants consists of around 4000 U inverted tubes, inside these tubes water flows at high pressure (140 bar) and temperature. These tubes under normal operating conditions are submerged in water at lower pressure (70 bar) and temperature than inside the tubes, the compartment where the tubes are submerged is known as the secondary side of the SG. The heat is transferred by convection and conduction from the primary side of these tubes to the secondary of the SG as result the subcooled water that enters the SG becomes heated and at a given height from the bottom reach saturation conditions, so the heat transferred from the tubes beyond this height is invested only in steam production. Under normal operating conditions the SG secondary is flooded with a biphasic water/steam mixture, so a breach or tube rupture (TR) in one of the tubes produces a discharge of steam into the biphasic mixture and most of the steam condenses and radioactive impurities carried by the steam get absorbed into the secondary side pool. However under accident conditions (SGTR meltdown sequences) the secondary side water level can be located under the tube breach. In this last case a gaseous jet at high velocity and temperature is discharged into the secondary side of the SG. This jet carries radioactive aerosols particles from the primary to the secondary. So the understanding of the hydrodynamics of the jets produced in the tube breach is essential to asses the safety consequences of the tube rupture inside the SG especially when the rupture takes place over the secondary water level. Several experiments in conjunction with computational and analytical studies have been performed in CIEMAT and UPV on this subject as part of the ARTIST international project [1]. This paper shows the accomplishments in modelling the jets produced in SGTR scenarios and the comparison with experimental data.

* Corresponding author: Prof. J.L.Muñoz-Cobo
Phone: + (34)-96-3877631, Fax: + (34)-96-3877639
E-mail address: jlcobos@iqn.upv.es

HIDRODYNAMICS OF JETS FROM GUILLOTINE TUBE RUPTURE

In a first step we analyse the hydrodynamics of free jets from guillotine tube rupture, in a second step we will assume that the jet is produced inside an enclosure of the dimensions of an SG and open in the upper part.

Hydrodynamics of a free jet from a tube with radial symmetry

First we start with the most simple case i.e. a jet from a tube with radial symmetry and free, we will assume that there are not forces that can bend the jet and the initial velocity of the jet has only radial component, the geometry of this jet is displayed in figure 1-a

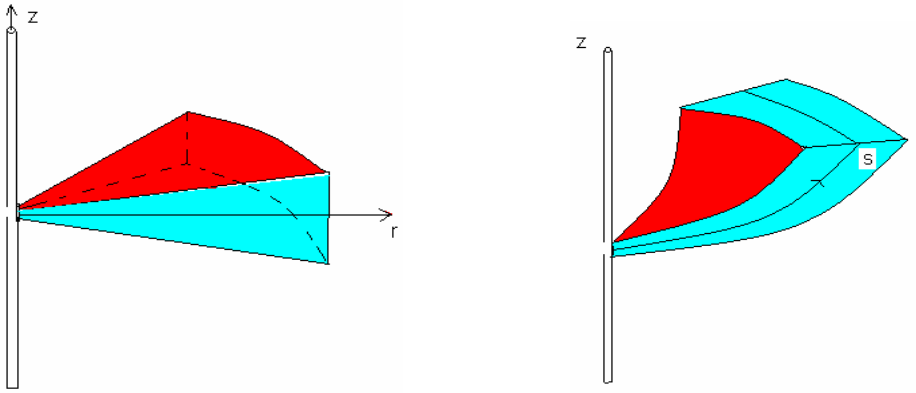

(a) (b)

Figure1 Geometry of a jet from a steam generator tube rupture (SGTR), figure (a) is for an ideal free jet produced in a guillotine tube rupture with only velocity radial component, figure (b) is for a jet with initial velocity components in the radial and axial direction and forces that bend the jet.

If $u_r(r,z)$ denotes the radial velocity component then assuming that the total momentum M_j of the jet in the radial direction is conserved we can write:

$$M_j = 2\pi r_0 \rho u_j^2 D_r = \rho \int_{-\infty}^{+\infty} u_r^2(r,z) 2\pi r \, dz \qquad (1)$$

where u_j is the initial velocity of the jet, and r_0 is the tube radius, and D_r the height of the breach. If we assume that the radial component of the velocity follows a Gaussian distribution [2]:

$$u_r(r,z) = u_c(r) exp\left(-\frac{z^2}{(\delta(r))^2}\right) \qquad (2)$$

where $u_c(r)$ is the centre jet velocity at a distance r from the rupture and $\delta(r)$ is the jet width. From equations (1) and (2) it is deduced:

$$M_j = \rho u_c^2(r)\delta(r)\sqrt{2}\,\pi^{3/2} r \qquad (3)$$

Assuming that the jet width increases linearly with the distance r, i.e. $\delta(r) = c_1 r$, it is obtained from equation (3) that the velocity at the jet centre is given by:

$$u_c(r) = \sqrt{\frac{M_j}{\sqrt{2}\pi^{3/2}\rho}} \frac{1}{\sqrt{c_1 r}} = \frac{C_c}{r} \qquad (4)$$

The continuity equation on account of the symmetry of the problem can be written as follows:

$$\frac{1}{r}\frac{\partial}{\partial r}(r\,u_r(r,z)) + \frac{\partial}{\partial z}(u_z(r,z)) = 0 \qquad (5)$$

And the momentum equation in the radial direction is:

$$\frac{1}{r}\frac{\partial}{\partial r}\left(r\,u_r^2(r,z)\right) + \frac{\partial}{\partial z}\left(u_z(r,z)u_r(r,z)\right) + \frac{\partial}{\partial z}\left(\overline{u_z'(r,z)u_r'(r,z)}\right) = -\frac{1}{\rho}\frac{\partial p}{\partial r} \qquad (6)$$

Where the Reynolds stress is given by $\tau_{Rey} = -\overline{\rho u_z'(r,z) u_r'(r,z)}$. The next step is to integrate the continuity equation between 0 and z, assuming that the axial velocity component is zero at the jet centre, this operation yields the following result for the axial velocity component $u_z(r,z)$:

$$u_z(r,z) = -\int_0^z \frac{1}{r}\frac{\partial}{\partial r}(r\,u_r(r,z))dz = u_c(r)c_1\left(\xi\, exp\left(-\xi^2\right) - \frac{\sqrt{\pi}}{2} erf(\xi)\right) \qquad (7)$$

Where $erf(\xi)$ is the error function and $\xi = z/\delta(r)$. If we plot the ratio $u_z(r,z)/u_c(r)$, of the axial velocity component and the velocity and the jet centre, versus ξ, we obtain the upper curve of figure 2, displayed with (o) circles. We observe that the axial velocity component only shows incoming flow or "inflow" toward the jet from the surrounding, also we observe that the incoming flow velocities from the upper and lower parts of the jet have the same absolute value and opposite directions. The prediction of this model is that it do not occurs outflow in the jet centre. We remind that in the study performed by Agrawad and Prassad [2] with a jet with planar symmetry, they found the existence of "outflow" from the jet centre up to a relative distance of $\xi = 1$. Then the results of the tube rupture with radial symmetry are at this point different from the case of a jet discharge with planar symmetry.

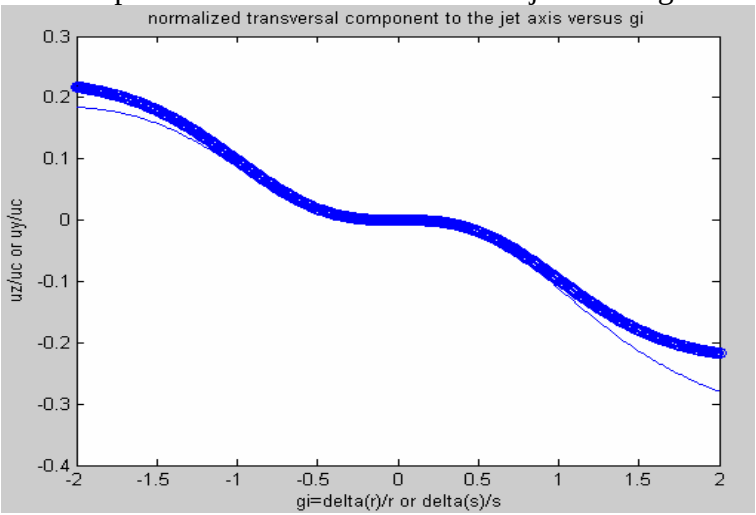

Figure 2 Normalized transversal velocity component to the jet axis versus ξ .The upper curve displays $u_z(r,z)/u_c(r)$, versus $\xi = \delta(r)/r$ for the free radial jet from a SGTR with only radial component at the rupture. The lower curve (thinner line) displays the normalized velocity component $u_y(s,y)/u_c(s)$ versus $\xi = \delta(s)/s$, for a curved jet with radial symmetry.

The next step is to compute the Reynolds stress by integrating equation (5) from jet centre up to the distance z, and assuming that at the jet centre the Reynolds stress vanished by symmetry . This calculation yields:

$$\overline{u_z'u_r'}(r,z) = -\frac{1}{r}\int_0^z \frac{\partial}{\partial r}\left(u_r^2\, r\right) dz - u_z(s,r)u_r(s,r) = c_1 u_c^2(r)\frac{\sqrt{\pi}}{2} exp\left(-\xi^2\right) erf(\xi) \qquad (8)$$

The profile of the normalized shear stress i.e $\overline{u_z'u_r'}/u_c^2$ is the same one that for the planar jet.

Hydrodynamics of a curve jet from a tube with radial symmetry

This case of the jet bending up is displayed in figure 1-b. This is the situation observed experimentally by Velasco, Del Prá, and Herranz [3]. The causative mechanism of the jet bending is that the jet initial velocity has two components one radial and other axial in the positive direction of the z axis, and when it penetrates in the surrounding gas loss radial momentum by friction and because the enclosure is open in the upper part there is an up-flow that produces a drag effect on the jet provoking a progressive jet bending with a pseudo-parabolic trajectory.

To solve the problem we adopt the curvilinear coordinates (natural) displayed in figure (3), i.e. the distance s along the jet centreline, the distance y along the orthogonal to the jet centreline, and the polar angle ϕ. Assuming that this problem has polar symmetry the conservation equations are:

Continuity equation

$$\frac{1}{r}\frac{\partial\left(r\,u_s(s,y)\right)}{\partial s}+\frac{1}{r}\frac{\partial\left(r\,u_r(s,y)\right)}{\partial y}=0 \tag{9}$$

Momentum conservation equation in the jet (stream) direction:

$$\frac{1}{r}\frac{\partial\left(r\,u_s^2\right)}{\partial s}+\frac{1}{r}\frac{\partial\left(r\,u_s\,u_y\right)}{\partial y}=-\frac{1}{r}\frac{\partial}{\partial y}\left[r\left(\overline{u_s'\,u_r'}\right)\right]-\frac{1}{\rho}\frac{\partial p}{\partial s} \tag{10}$$

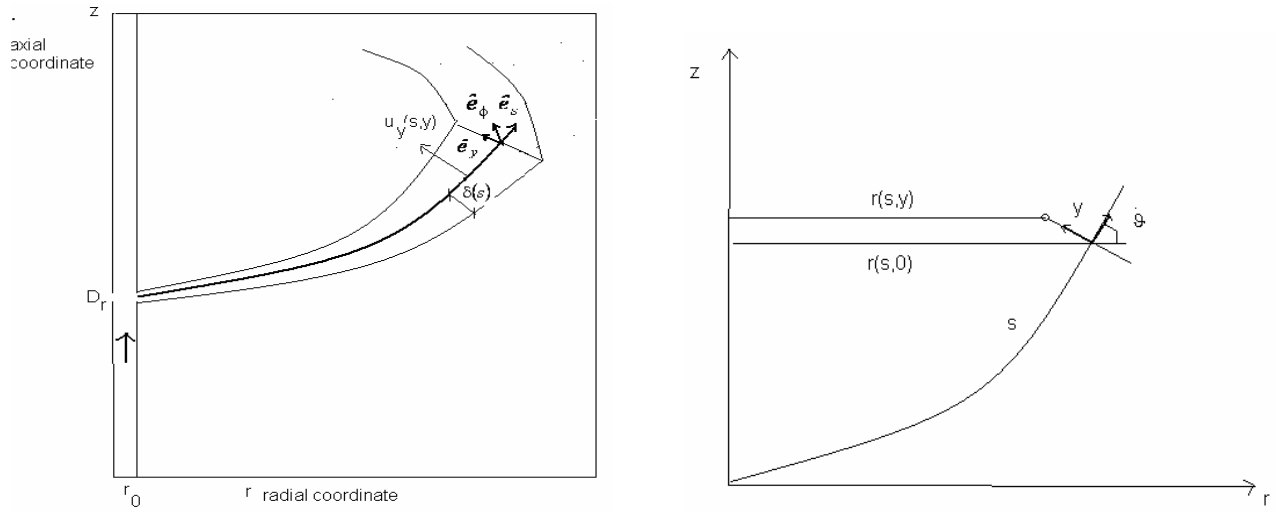

Figure 3 Natural curvilinear coordinates for a jet produced in a guillotine SGTR.

The experiments performed by Velasco et al [3] confirm that 60 mm away from the discharge point, the velocity profile in the direction of the stream is practically Gaussian and symmetric with respect to the jet centreline. We have assumed that the jet width $\delta(s)$ increases linearly with s, this approximation is a standard one for turbulent jets [4]. To have an approximate analytical solution we assume that the velocity component in the stream direction i.e $u_s(s,y)$, can be approximated by a Gaussian distribution, also we assume that the jet momentum is conserved in the s direction. Therefore we write:

$$u_s(s,y)=u_c(s)\,exp\left(-y^2\Big/(\delta(s))^2\right) \tag{11}$$

And the conservation of the jet momentum in the s direction gives:

$$M_j=\rho\int_{-\infty}^{+\infty}u_s^2\,2\pi r(s)dy=\rho\,u_c^2(s)\int_{-\infty}^{+\infty}\left(exp\left(-\frac{y^2}{\delta(s)}\right)\right)^2 dy=\sqrt{2}\;\pi^{3/2}\rho\,(u_c(s))^2\,r(s)\delta(s) \tag{12}$$

The assumption of linear variation of the jet width $\delta(s)$ with the distance s leads to the following expression for the jet centreline velocity:

$$u_c(s)=\sqrt{\frac{M_j}{\sqrt{2}\,\pi^{3/2}\rho}}\;\frac{1}{\sqrt{c_1}\,\sqrt{r(s)}\,s^{0.5}} \tag{13}$$

Next we need to compute the expression that gives the radial distance in terms of s, distance to the jet exit along the jet trajectory. Performing a dimensional analysis similar to the one performed by Ramaprian and Haniu [5], it is found that the jet trajectory obeys the following equation:

$$\frac{z-z_0}{l_m}=C\left(\frac{r}{l_m}\right)^{\alpha} \tag{14}$$

Where z is the axial coordinate assuming the origin in the break point, r is the radial coordinate, and l_m is the momentum length scale, defined for this particular case as the momentum per unit of circumferential length divided by the square of the reference velocity:

$$l_m = \frac{\left(M_j / 2\pi r_0\right)}{v_{j,0}^2} = \left[1 + \left(\frac{u_{j,0}}{v_{j,0}}\right)^2\right] D_r \tag{15}$$

$u_{j,0}$, and $v_{j,0}$ are the radial and axial components of the jet velocity at the tube rupture.

Equation (14) can be used to compute the arc length along the jet trajectory that yields:

$$s(r) = \int_{r_0}^{r} \sqrt{1 + \left[z'(r_1)\right]^2}\, dr_1 = \frac{2}{3b}\left[(1 + br)^{3/2} - (1 + br_0)^{3/2}\right] \tag{16}$$

Where, b is given by the expression:

$$b = \frac{C\,\alpha^2}{(l_m)^{2(\alpha-1)}}, and\ br_0 << 1 \tag{17}$$

From equation (16) it is obtained that de dependence of $r(s)$ with the arc length s is given by:

$$r(s) = \frac{1}{b}\left[\left(1 + \frac{3}{2} b\, s\right)^{2/3} - 1\right] \tag{18}$$

The value of b is approximately equal to 6.7 10^{-3} mm when s is expressed in mm. therefore for small values of s expanding $(1 + 1.5\, b\, s)^{2/3}$ in Taylor series it is obtained that varies linearly with s, however from equation (18) it is deduced that for large values of s, r(s)~$s^{2/3}$. Therefore the velocity at the jet centre diminishes with the law $s^{-\beta}$, where $\beta \in [0.83, 1]$. We have chosen for the decaying parameter β the middle value of the interval i.e. $\beta = 0.92$. As a consequence we have assumed that the velocity at the jet centre follows the law:

$$u_c(s) = C_c\, s^{-\beta},\ with\ \beta = 0.92 \tag{19}$$

The next step is to integrate the continuity equation (9), to do this we need to obtain r(s,y), that according to figure (3-b) is given by:

$$r(s,y) = r(s,0) - y\, sen\vartheta = r(s) - y\frac{\left(\frac{\partial z}{\partial r}\right)}{\sqrt{1 + \left(\frac{\partial z}{\partial r}\right)^2}} = r(s) - c_y\, y \tag{20}$$

To obtain the velocity component $u_y(s,y)$ orthogonal to the jet trajectory , we integrate the continuity equation between the coordinate y=0 at the jet centre and y, and we take on account the fact that at the jet centre the velocity component in the $\vec{e}_y$ direction is zero, so we write:

$$u_y(s,y) = -\frac{1}{r(s,y)}\int_0^y \frac{\partial}{\partial s}\left(u_s(s,y')\, r(s,y')\right) dy' = -\frac{1}{r(s,y)}\int_0^y dy'\left(r(s,y')\frac{\partial u_s}{\partial s} + u_s\frac{\partial r(s,y')}{\partial y'}\right) \tag{21}$$

Performing the calculations that appear in equation (21) with the help of equations (11), (19), and (20) it is obtained after some calculus the following result:

$$u_y(s,y) = \frac{u_c(s) c_1}{4}\frac{r(s)}{r(s,y)}\left\{4\,\xi\, exp\left(-\xi^2\right) - 2\left[(1-\beta) + \frac{\left(\partial r(s)/\partial s\right)}{\left(r(s)/s\right)}\right]\right\}\sqrt{\pi}\, erf(\xi) +$$

$$+ \frac{u_c(s) c_1\, \delta(s)}{r(s,y)} c_y(s)\left\{\left(1 - \frac{\beta}{2}\right) - \left[\left(1 - \frac{\beta}{2}\right) + \xi^2\right] exp\left(-\xi^2\right)\right\} + \frac{u_c(s)\delta^2}{r(s,y)}\frac{\partial c_y(s)}{\partial s}\left\{1 - exp\left(-\xi^2\right)\right\} \tag{22}$$

Equation (22) gives the transversal velocity $u_y(s,y)$ of the curved radial jet, this equation reduces to equation (7) for the free radial jet from a guillotine SGTR if we assume no curvature $c_y(s)=0$, s=r and $\beta=1$.

If we plot $u_y(s,\xi)/u_c(s)$ versus ξ, in the interval [-2, 2], it is obtained the lower curve of figure 2 (thinner line). We observe that in this case we have only incoming flow toward the jet centre, as in the free radial jet from a guillotine SGTR. Also this case differs from the planar jet studied by Agrawal and Prasad that showed outflow near the jet centre. The main differences between the results of the radial free jet from a guillotine SGTR, with only radial velocity component at $r=r_0$ and the case of the curved jet is the loss of symmetry for the inflow velocity from the upper and lower parts of the jets at displayed in figure 2. The inflow transversal velocities are higher at the upper part of the jet or concave side (positive values of ξ), than in the lower part of the jet or convex (negative values of ξ) as displayed in figure 2. This fact has been confirmed experimentally by Velasco et al. [3] that found that the resulting pseudo-parabolic jet gives rise to a non-symmetric gas entrainment around it where suction is more intense at the concave side.

MODEL COMPARISON WITH EXPERIMENTAL DATA AND DISCUSSION

In this section we obtain the model parameters from the experimental data of Velasco et al. [3]. Velasco at al carried out a set of experiments on jets produced in guillotine tube rupture with and without other tubes. The first set of experiments were performed with an isolated tube with a guillotine rupture of height D_r=0.24 D, and a tube diameter D=19.05 mm. Because the upper part of the tube is closed, the flow leaves the tube through the rupture expanding in the enclosure containing the tube. Five runs were performed (see table 1) denoted by its volumetric air flows Q_{air}. As seed material Velasco used TiO_2, injected as aerosol particles. The aerosol generator is based on the fluidized bed technology and allows the injection of 9.75 kg/hr of N_2 doped with aerosol particles of micrometer size. Table 1 displays the experimental conditions.

We performed a fit of the experimental jet trajectories to the curve of equation (14). The value of l_m was obtained from equation (15) and was set equal to 38.86 mm for all the runs. The parameter values C, α and z_0 obtained for the different runs are displayed at table 2, the last column of this table gives the relative error of the fit.

Table 1

Table 1 Experimental conditions for the free jet inside a enclosure [3]

Run Number	Q_{air} Nm^3/hr	p_{in} bar	p_{pri} abs bar	p_{sec} abs bar	T_{pri} ºC	ρ Kg/Nm^3	$\dot{W}_{air}$ Kg/h	$\dot{W}_{air}+\dot{W}_{N_2}$ Kg/h
1	150	3	2	1.3	17.5	1.29	193.88	203.63
2	75	1.9	1.2	1.1	15	1.29	96.94	106.69
3	100	1.3	1.4	1.1	16	1.29	129.25	139.00
4	180	3.2	2.1	1.4	16	1.29	232.20	232.20
5	189	3.2	2.5	1.4	15	1.29	244.28	254.03

Table 2

Parameter values for the trajectories of the jets

Run	C	α	z_0 mm	Relative error %
75	0.456	1.227	6.0	3.24
100	0.345	1.508	8.0	6.24
150	0.283	1.531	9.0	7.90
180	0.285	1.552	9.1	10.55
189	0.295	1.561	10.0	12.03

Figure 4a displays the experimental data for the jet trajectory for run 3 with $Q_{air} = 100\, Kg/hr$, the bubbles are the experimental data, while the continuous line is the result of the fit to equation (14). Due to the inertia of the TiO_2 particles and because they change of direction at the tube rupture, they move near the tube exit at lower velocity than the carrier gas, and the measurements performed with the PIV in the first 30mm from the breach are not reliable. For this reason we use to compute the centreline velocity $u_c(s)$ only the jet velocity data that are 30 mm away from the breach. The expression used to fit the data is $u_c(s) = C_c / s^{0.92}$. The value of C_c for the case of 100 Nm^3/hr was 1006.62. Also we have compared this result with the one obtained using the planar model velocity that for the planar case (x,z) gives $u_c(s) = 176 / \sqrt{s}$ as displayed in the blue line of figure 4-b We can see that the radial model for the curved jet of this paper fits much better the experimental data except at short distances from the break where the TiO_2 particles have not attained the carrier gas velocity.

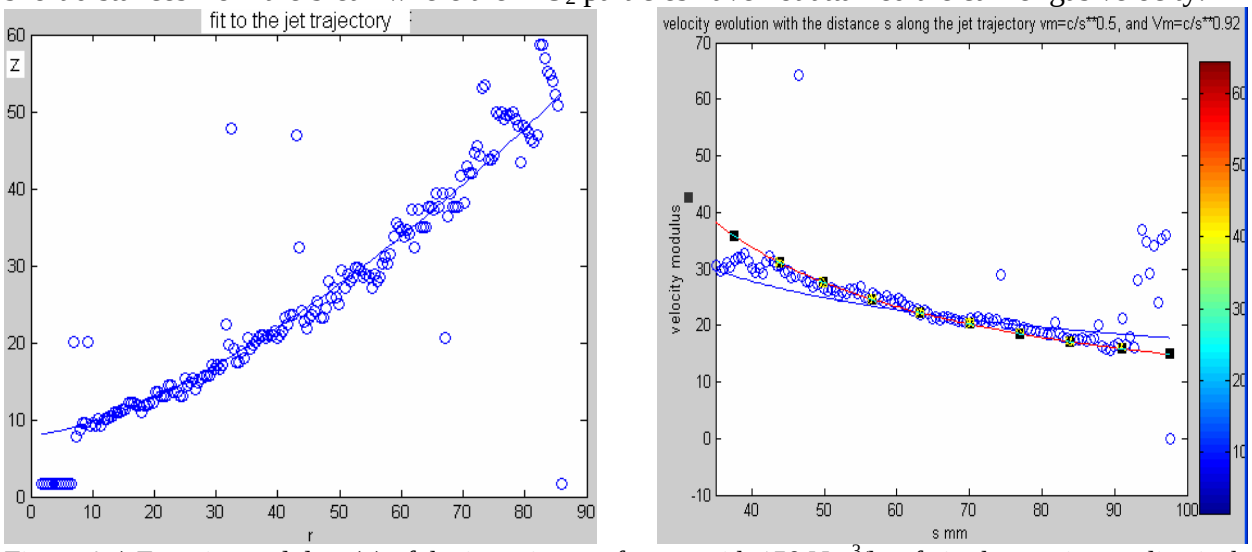

Figure 4 a) Experimental data (o) of the jet trajectory for run with 150 Nm^3/hr of air, the continuous line is the fit with the model of this paper, b) Centre jet velocity for the radial model of this paper (red line), the planar model (blue line) and the experimental data for the run of 100 kg/hr of air flow

.

For the case with an air flow of 75 Nm^3/hr it is clearly seen at figure (5-a) that the radial geometry model of this paper (red line) fit much better the experimental data for the jet centre velocity than the planar jet model. The expression obtained for the radial model was $u_c(s)=769.34/s^{0.92}$, and for the planar model (blue line) $u_c(s)=138/s^{0.5}$.

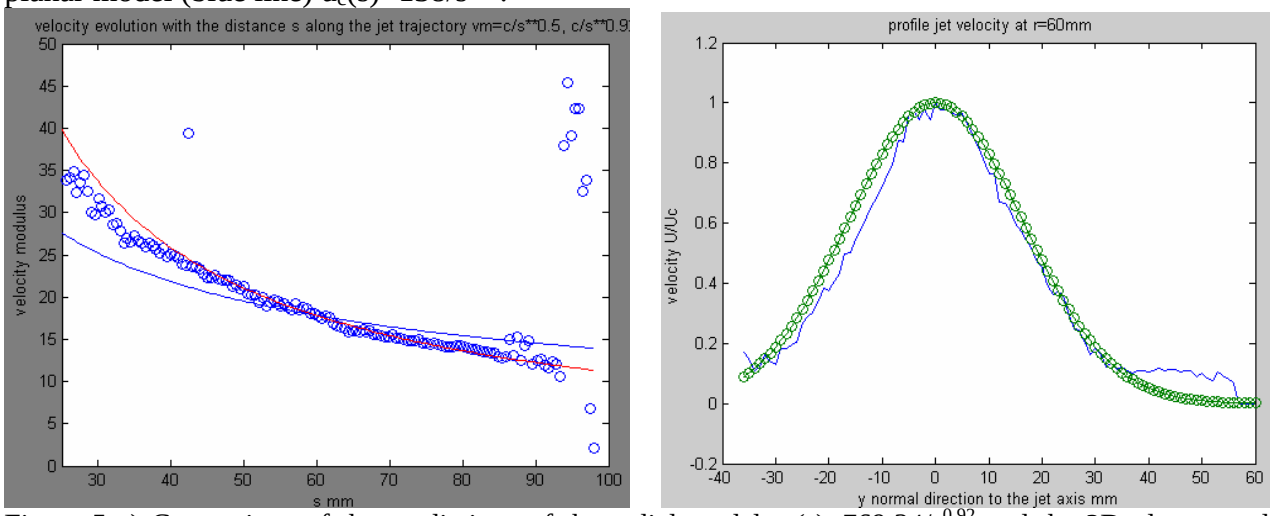

Figure 5 a) Comparison of the predictions of the radial model $u_c(s)=769.34/s^{0.92}$ and the 2D planar model $u_c(s)=138/s^{0.5}$ (blue line) with the experimental data (o). b) Normalized velocity distribution in the jet direction at 70 mm from the rupture for run 75. The experimental data are displayed in blue.

The last issue to be studied is the velocity distribution in the jet direction i.e $u_s(s,y)$. We have seen that at distances equal or bigger than 60 mm from the rupture the shape of the distribution is nearly Gaussian. The value of $\delta(s)$ was obtained by interpolation from the experimental data at 70 mm from the rupture using the spline method and looking for the point where the velocity it is reduced by a factor 1/e. Because we have assumed that $\delta(s) = c_1 s$, we obtain immediately the value of c_1 for this run. Figure (5-b) displays the velocity distribution in the jet direction at 70 mm from the tube rupture for run 75, we see that the distribution is practically Gaussian except at the end of the right hand side.

CONCLUSIONS

The understanding of the hydro-dynamics of jets coming from tube rupture is important to assess the consequences of SGTR accident scenarios of nuclear power plants. Also is important to have analytical expressions for the jet trajectories and velocities in order to have simple models to implement in the reactor safety codes under guillotine tube rupture scenarios. During the SGTR a high velocity steam jet is produced, this jet expands with the distance bending upward due to the initial velocity component in the axial direction, and to the fluid drag produced by the fluid leaving the SG at the dome upper part. We have found that the centre jet velocity diminishes with distance for all the cases with the law $u_c(s) = C_c / s^{0.92}$**,** this law has been compared with experimental data with good results. When we are far away 60mm from the rupture the velocity profile is practically Gaussian, however such symmetry breaks down near the rupture point.

It has been experimentally observed that the gas streamlines over and below the jet are attracted toward the jet producing an incoming transversal velocity toward the jet or inflow that fosters the development of the jet and diminishes the jet velocity at the centreline [3]; the model presented above is capable of capturing with reasonable accuracy gas ingestion and its effects. We have verified also this conclusion by CFD calculations performed with the ANSYS-CFX code. Therefore the tube guillotine SGTR jets display only inflow in the transversal direction to the jet. This behaviour is different in the planar jets that display an outflow region near the jet centre and then beyond $\xi = 1$display inflow.

Acknowelegdments
The authors of this paper are indebted to the National Plant of I+D by the support of the project EXPERTISER ENE2007-68085-C02-01/CON

REFERENCES

1. Güntay, S., Suckow, D., Dehbi, A., Kapulla, R., ARTIST: Introduction and First Results, *Nuclear Engineering and Design* , Vol 231, No 1, pp 109-120, 2004.
2. Agrawal A., Prasad A.K., Integral Solution For The Mean Flow Profiles of Turbulent Jets, Plumes, and Wakes. *ASME Journal of Fluid Engineering*, Vol 125, September 2003.
3. Velasco, F.J.S., López del Prá, C., Herranz, L.E., Expansion of a Radial Jet from a Guillotine Tube Breach in a Shell and Tube Heat Exchanger. *Experimental Thermal and Fluid Science* Vol 32, pp 947-961, 2008.
4. Bejan, A., Convection Heat Transfer, Edited by John Wiley and Sons, Thid Edition 2004.
5. Haniu H., Ramaprian B.R., Studies of Two-dimensional curved Non Buoyant Jets in Cross Flow. *Transactions of the ASME Journal of Fluid Engineering*, Vol 111, pp 78-86, 1989.

MODELLING FLUID FLOW AND HEAT TRANSFER IN CHEMICAL REACTOR WITH USING LASER ENERGY FOR HEATING THE REACTANTS

I. Chernykh[1], T. Mischenko, V. Snytnikov, Vl. Snytnikov[2] *

[1]Institute of Computational Mathematics and Mathematical Geophysics SB RAS, Lavrentjeva ave. 6, Novosibirsk, 630090, Russia
[2]Boreskov Institute of Catalysis SB RAS, Lavrentjeva ave. 5, Novosibirsk, 630090, Russia,

ABSTRACT. There are different organic chemical reactions placed in processes of hydrocarbons refining such as a pyrolysis, oxidation, dehydratation, polymerization, nitration and others. Modelling and improvement of these processes is actual task for chemical industry and science. The efficient use of delivered energy, optimization of gas flows and heat transfer are still remains topical problems.

A flow reactor with the reactants heated by continuous CO_2 laser radiation is proposed for studying the gas phase homogeneous reactions. Ethane pyrolysis yielding ethylene is considered as an example of such chemical process. For this process, a mode of 'energetic catalysis' is feasible, where increasing energy absorption in the volume is related with the increased content of target product. The mode of 'energetic catalysis' was implemented at transformation of laser energy into thermal power using the sensitization properties of ethylene. In the pyrolysis reaction zone, temperature measurements were made for a gas mixture in the laser radiation field with a power density up to 10^2 W/cm^2. The walls and windows were isolated from the high-temperature zone by argon feeding and configuration of the reactor. Three-dimensional calculation of the gas-dynamics reactant flows and their mixing made with the FLUENT software package showed the presence of the modes where reaction zone with a high content of C_2 hydrocarbons is localized in the centre of reactor, which was confirmed by experiments. High values of ethane conversion up to 80 vol. % were obtained at nearby 53% selectivity for ethylene.

Keywords: *ethane pyrolysis, fluent, fluid flow*

INTRODUCTION

Endothermic chemical processes are carried out in the reactors with energy input to the reaction zone. Such reactors are distinguished by the energy source, which can be represented by electric arc, heat from combustion of a part of feedstock with oxygen in reactor, cyclic heating of catalyst, inert gas at a high temperature, or reactor tubes. A wide variety of the heating methods and endothermic chemical processes implies special-purpose designs of chemical reactors: turbulent flow reactors, reactors with shock waves in a tube, and plasma reactors.

The above-listed reactors are used to run the endothermic chemical processes like cracking and pyrolysis of hydrocarbons. However, the efficient use of delivered energy still remains a topical problem. For instance, when acetylene is obtained from methane by electric arc heating, only 30%

* Corresponding author: Dr. I . Chernykh
Phone: + (7)-383-3309665, Fax: + (7)-383-3308783
E-mail address: chernykh@ssd.sscc.ru

of supplied energy can be put into the energy of bond cleavage and formation of new chemicals bond. In this process, high rates of energy input provide fast heating of the reactants, which leads to a temperature gradient in the reaction zone up to 100 - 200 K/mm. However, in this case, spatial heterogeneity of the medium is observed, which decreases the selectivity for target products due to a pronounced temperature dependence of chemical reaction constants.

Another problem is related with optimization of reactants' residence time in the reaction zone to prevent the involvement of target products in secondary reactions. Thus, thermal dehydrogenation of C_2 - C_4 hydrocarbons yielding ethylene and propylene is characterized by high reactivity of these products at the temperatures of pyrolysis. This imposes specific constraints on the reactor design.

The use of laser radiation for heating the reaction medium makes possible the direct input of energy to the gas with the power density of $10^2 W/cm^2$, which exceeds by one and a half - two orders of magnitude the values attained in reactors with metal walls. This circumstance allows decreasing the time of reactants' pyrolysis to milliseconds. Possibility of using laser energy as a powerful energy source for the chemical reactors gives impact to the scientists for studying endothermal chemical processing. There are many different trends initiated in gas-core reactions studying, catalyst preparation, polymer films synthesis, heat-and-mass transfer, interaction between laser energy and gas environment, impact of laser energy on chemical reactions during 70-80 years of twenties century. At the power density below $10^5 \div 10^6 W/cm^2$, energy absorption and reaction occurrence at atmospheric and higher pressures follow the thermal mechanism. A necessary condition for application of laser radiation is that the reaction medium comprises a component which absorption spectrum contains the bands coinciding with the region of laser generation. In this case, the absorbed energy of laser radiation is transmitted at collisional relaxation to the reaction medium, thus heating it. When studying the process kinetics, it is important to provide the gas-phase occurrence of the reactions. A necessary thermal insulation of the reaction zone can be provided by buffer gas supercharging at the sites of laser radiation input and by a relatively cold mixture of reactants in the rest near-wall region of convectively cooled reactor. For cylindrical geometry, such mode can be implemented via a smaller section of laser beam as compared to reactor section.

This work presents results of the study of a flow reactor with laser input of energy for endothermic reactions exemplified by ethane pyrolysis. The reactions were conducted under homogeneous conditions at atmospheric pressure in the reactor with the reaction mixture components heated by the laser energy flux delivered directly into the gas. Ethylene, being among the main reaction products, served as the laser energy absorber. This created the mode of 'energetic catalysis'. Here, increasing energy absorption in the volume is related with the increased content of the reaction product.

The FLUENT software program tested with the experimental data of laboratory setup will allow using numerical methods to search for the reactor design, which will be further implemented in a pilot prototype.

REACTOR DESIGN

A schematic diagram of reactor indicating the temperature gauges layout is displayed in Figure 1. Reactor is made of a quartz tube with the inner diameter 20 mm and length 70 mm. Four inlets (8-1, 4, 5, 9) were used for Ar feeding into reactor to protect optical parts and decrease the effective length of the reaction zone. For the same purpose, stainless steel diaphragms (16) with straight-through diameter 12.5 mm were mounted in the chamber. The ethane-ethylene mixture was fed into reactor via inlet (8-7) in the central section.

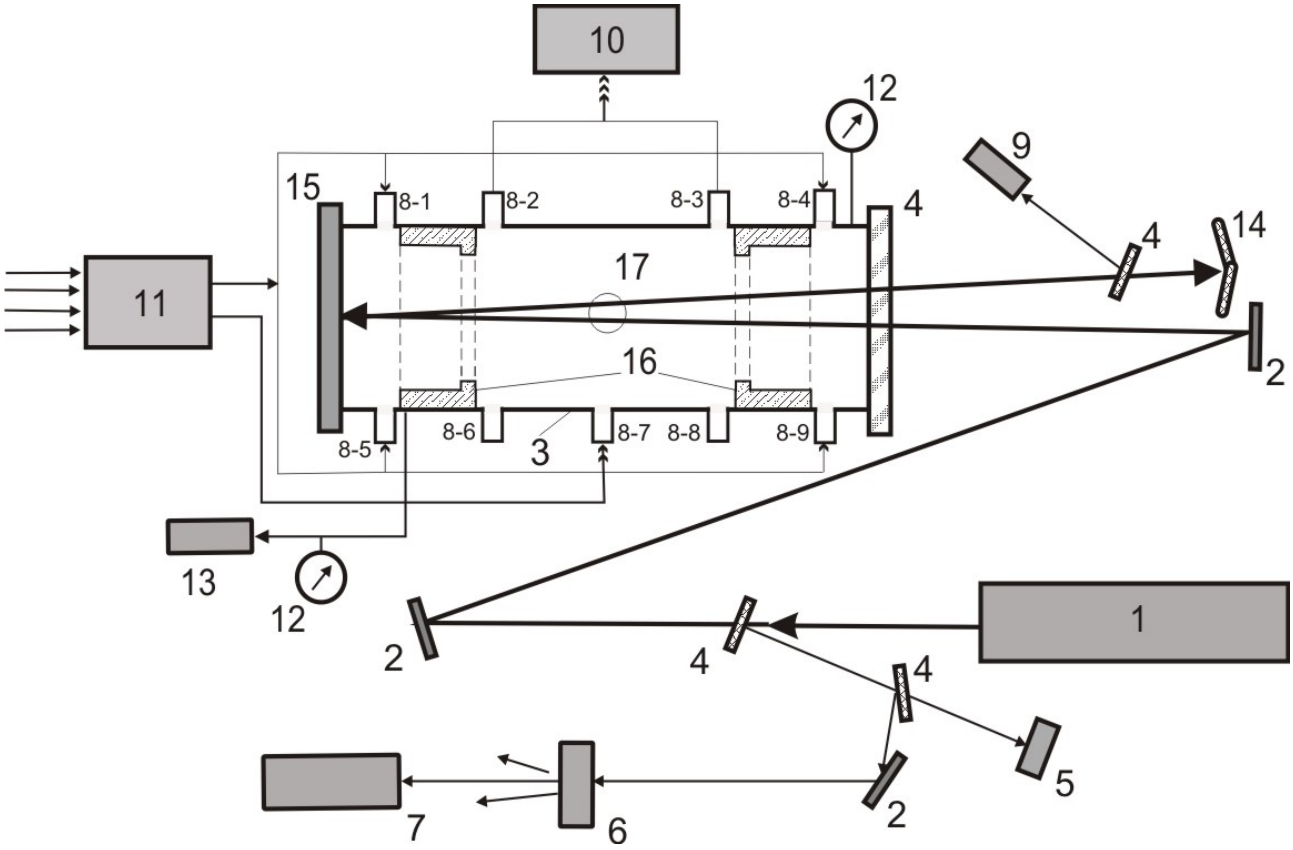

Figure 1. Schematic diagram of the wall-less reactor for ethane pyrolysis.1. CO_2 laser unit. 2. Mirrors of the optical route. 3. Reactor 4. Optical windows (ZnSe). 5. Radiation power meter LM-2 unit. 6. Diffusing window (NaCl). 7. InfraLUM FT-801 Fourier transform spectrometer unit. 8-1,4,5,9 - Ar inputs. 8-2,3 - Gas mixture output. 8-7 - Ethane-ethylene mixture input. 8-6,8 - Closed plugs. 9. Radiation power meter TI-3 unit. 10. Chromatographs Crystal 2000M and LHM-80MD units. 11. UFGP-4 gas flow former. 12. Vacuum manometers. 13. Forevacuum pump unit. 14. CO_2 laser energy absorber. 15. Al mirror of the reactor. 16. Diaphragms.

Four inlets (8-2, 3, 6, 8) symmetric about the central axis were used to remove a mixture of reaction products with argon. In the same section, with a 90° shift, temperature gauges (17) were placed: a heat-insulated Mo plate 50 mkm in thickness and 2.5 mm in diameter - for pyrometric measurements, or a spiral thermistor made of copper wire 70 mkm thick, with coil diameter 3 mm and 0.4 Ω impedance. The axis of six-turn copper spiral and the plane of molybdenum gauge are oriented along the laser beam axis. In the same section with the gauges, a thermocouple is mounted in the chamber to measure the gas temperature at a distance of 0.5÷1 mm from the lateral wall of reactor.

To measure the brightness temperature and calculate the absolute temperature, we used an EOP-66 optical pyrometer with effective wavelength 0.655 mkm. The operating temperature range of pyrometer was 800-10000°C. The total rated measurement error for the luminance temperature in sub-range 800-1400°C did not exceed ±8°C. A correction for determination of the absolute (true) temperature related with the value of spectral radiative ability of Mo in the temperature range 800÷1000°C, $\varepsilon \approx 0.4$, was equal to +(45-60)°C. Irradiation of the pyrometric gauge was recorded through the quartz wall of reactor using a rotary mirror at a distance of nearby 2 m.

There are several reasons for choosing the copper thermistor for temperature measurements. First, the temperatures under consideration range from 300 to 1000°C. Second, thermistor should not affect the

processes in reactor. Third, the thermistor material should be resistant to CO_2 laser radiation with power density up to 200 W/cm^2 and have a low level of radiation absorption. It is necessary also to provide time resolution of ca. 1 s and the possibility of operation with standard measuring equipment.

MODELLING RESULTS

The mixing of gas flows in the 3D reactor geometry was calculated with the FLUENT software package. For all flows, FLUENT solves conservation equations for mass and momentum. Full description of mathematical model that used in FLUENT described in [1]. That was many tests on numerical model with different parameters of reactant and buffer gas flows, radiation model.

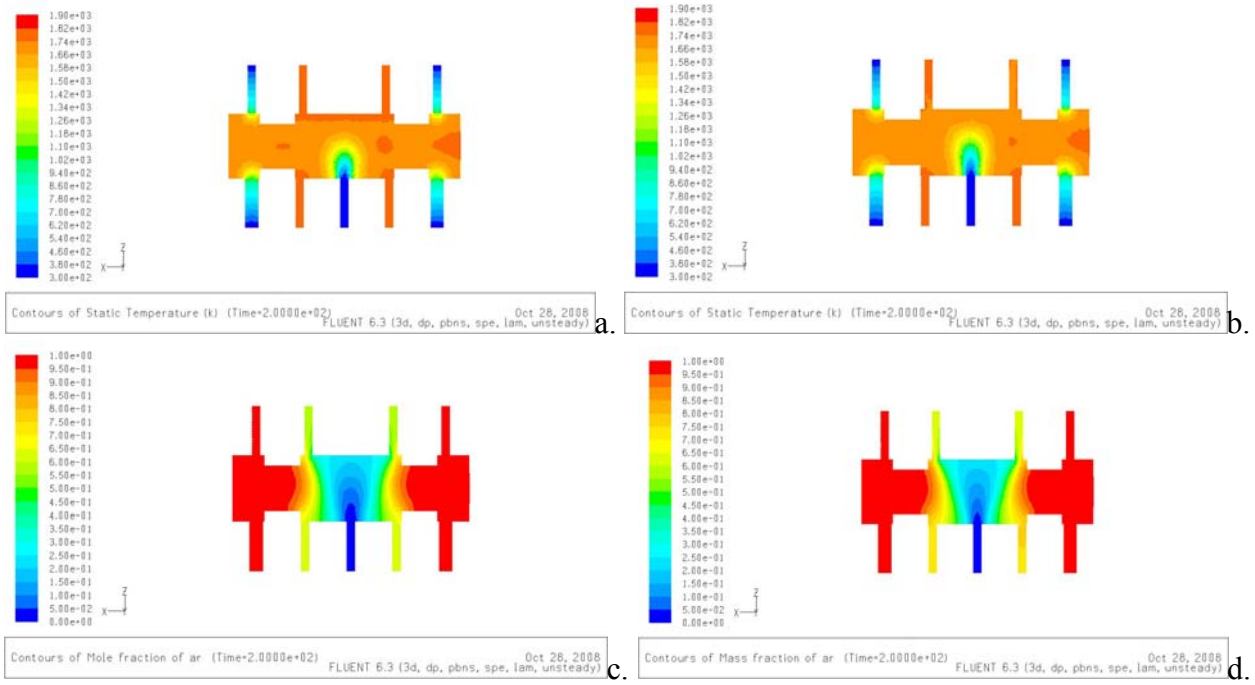

Figure 2. Contours of temperature (a,b) and Ar mass fraction (c,d) for C_2H_6-C_2H_4 mass flow rates 1.1 L/h (a,c), 2.1 L/h (b,d) and Ar mass flow rates 2.5L/h (a,c), 3.45L/h (b,d) at time 200s.

Results of mathematical modelling on the Figure 2 received with using of constant absorption coefficient (absorption of laser energy by reactants gases). This model does not equal to experiment because absorption coefficient depends on C_2H_4 concentration. But we can get the results of modelling gas flows very quickly (2-3 hours of FLUENT work on standard double cores processor) with a 20-30% error to experiment. We can see that Argon block reactant gases from windows 4, 15 on the Figure 1. It means that reaction products did not fall out on the windows and windows will be clear during chemical process.

Results on Figure 3 received with variable absorption coefficient that depends on C_2H_4 concentration. The user defined function for variable absorption coefficient was developed for FLUENT. This scheme is closer to the experiment. But the time of calculation is two times bigger than constant coefficient. The temperature in reaction zone is 1100-1200K that enough for starting of chemical reactions. Concentration of reactants and temperature at windows are very small for starting of chemical reactions.

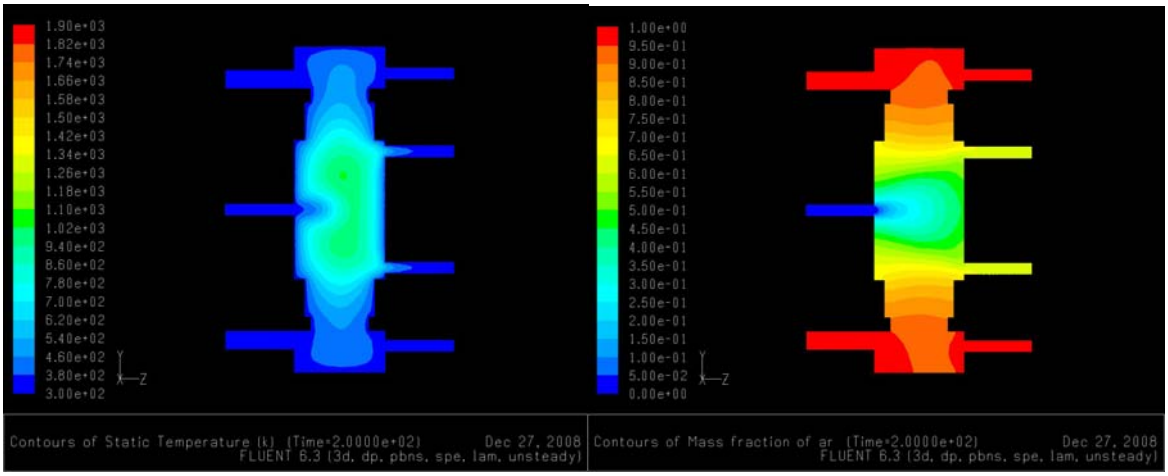

Figure 3. Contours of temperature and Ar mass fraction for C_2H_6-C_2H_4 mass flow rate 1.1 L/h and Ar mass flow rate 2.5L/h at time 200s.

EXPERIMENTAL RESULTS

In the experiments, total flow rate of argon was set at 3 L/h, and that of the ethane-ethylene mixture - at 1.7 L/h, with the 30% content of ethylene. Mixing of the gas flows was studied at 20°C and atmospheric pressure. For the reactor with diaphragms, the fraction of hydrocarbons near the reactor faces was found to be 17%. The axial distribution of hydrocarbons in reactor in the Ar-C_2H_6-C_2H_4 mixture is shown in Figure 4. Dark points correspond to experimental measurements. One may see that in the central part of reactor the fraction of hydrocarbons makes up 60% and far exceeds their amount near the face walls. More widely experiment was described in [2].

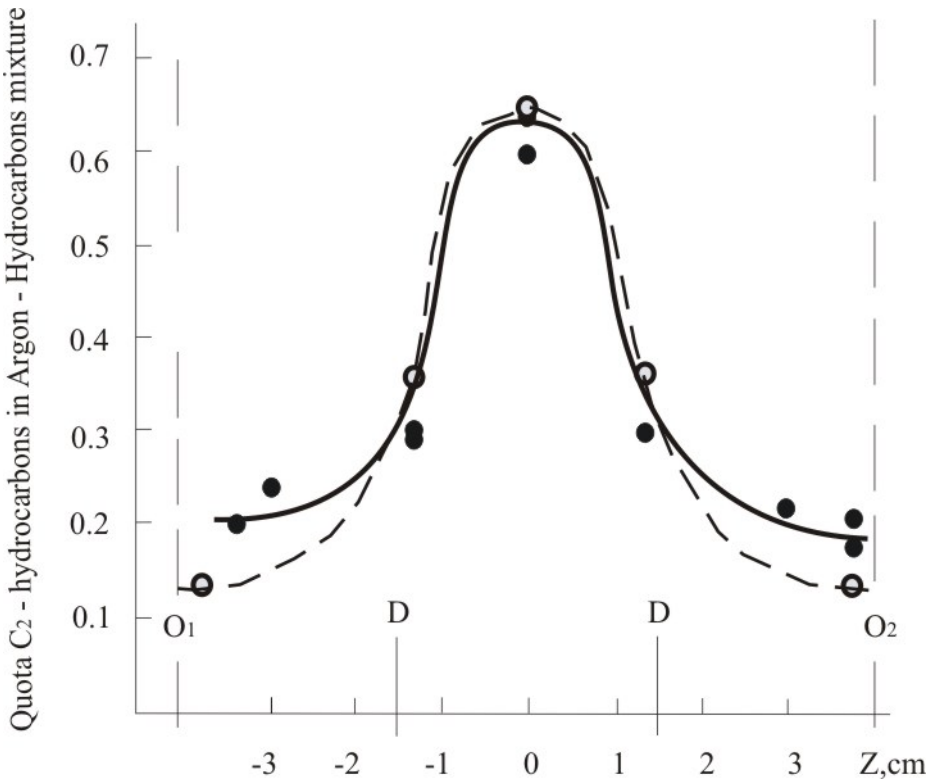

Figure 4. Distribution of hydrocarbons over the length of reactor in the experiments. O1 and O2 - reactor faces, D - diaphragm boundaries in the reaction zone. Dark points - experimental data. Hollow points - calculated data obtained with the FLUENT software.

CONCLUSION

A flow reactor with laser input of energy providing the homogeneous conditions for chemical process occurrence has been devised for the study of gas-phase reactions. Three-dimensional modelling of the gas flow mixing and heat transfer was made using the FLUENT program package for the reactor with geometrical dimensions corresponding to the pilot sample. A qualitative agreement between the calculated and experimental data was obtained. This confirmed applicability of FLUENT for designing of these type reactors. Formation of the reaction zone in the centre of reactor insulated from the chamber face walls with the buffer gas was demonstrated experimentally and supported by numerical modelling. A decreased temperature of the near-wall gas mixture indicates that the reaction zone is insulated also from other reactor walls. Ethylene was shown to be an efficient converter of laser energy to heat power at ethane pyrolysis.

Thus, ethane pyrolysis was performed in the mode of 'energetic catalysis', where energy absorption for endothermic reaction increased with increasing content of the reaction products. In the process, ethane conversion attained 80% at ethylene yield of 43%. As ethane conversion decreased to 70%, ethylene yield increased to 56%. Effective laser energy absorption in reaction zone was from 30% to 70% of total laser energy.

ACKNOWLEDGEMENTS

This work was supported by the Russian Foundation for Basic Research (grant No. 08-01-00615, 08-01-00622 ,09-07-00023); SB RAS integration programs No. 103,113; the RAS program No. 15.

REFERENCES

1. FLUENT. http://www.fluent.com
2. Chernykh I.G., Mischenko T.I., Snytnikov V.N., Snytnikov Vl. N. A reactor for the study of homogeneous processes using laser radiation energy, Chem Eng J., 2009 (in print)

THERMODYNAMIC MODELING OF PETROLEUM FLUIDS CONTAINING ASPHALTENE AGGREGATES: A COMPARATIVE STUDY OF THERMODYNAMIC MICELLIZATION MODEL AND SOLID MODEL

M. Tavakkoli[1, 2, *], R. Kharrat[2], M. Masihi[1], M.H. Ghazanfari[1, 2]

[1] Chemical and Petroleum Engineering Department, Sharif University of Technology, Tehran, Iran

[2] Petroleum Research Center, Petroleum University of Technology, Tehran, Iran

ABSTRACT. There are different thermodynamic models that have been applied for modeling of asphaltene precipitation in various crude oils. However, there is no reported experience in the literature that has compared the predictions of thermodynamic micellization model and solid model under pressure depletion and composition alteration conditions. Moreover, the impacts of different characterization methods on the accuracy of model predictions along with the effects of model parameters are not well understood. In this work, two computer codes which are based on two different asphaltene precipitation thermodynamic models, 1-Thermodynamic Micellization Model and 2- Solid Model, have been developed, and, used for predicting of asphaltene precipitation data reported in the literature under gas/solvent injection condition. The model parameters obtained from sensitivity analysis as well as various characterization methods, were applied in the thermodynamic models. The developed computer code of solid model is able to predict the asphaltene precipitation data under gas/solvent injection condition with a close agreement. Especially, for the maximum value of asphaltene precipitation and for the trend of the curve after the peak point, good agreements were observed which could rarely be found in the available literature. It has been observed that the thermodynamic micellization model, which is more complex than solid model, is able to predict the trend of the asphaltene precipitation curve for gas titration condition reasonably well. Also, its predictions matched well with more experimental data points in comparison to the solid model predictions.

Keywords: *Asphaltene Precipitation, Thermodynamic Modeling, Thermodynamic Micellization Model, Solid Model.*

INTRODUCTION

Asphaltenes are a solubility class of crude oils and are defined as the fraction that precipitates upon the addition of an n-alkane (usually n-pentane or n-heptane), but dissolves in aromatic solvents such as toluene. Asphaltenes can precipitate upon a change in pressure, temperature, and/or composition. For example, when pressure is drawn down around and within a wellbore, asphaltenes can precipitate and significantly reduce production.

For efficient process design, it is important to know *when* and *how much* asphaltene precipitation may affect the production of petroleum in all facets of field development. To predict precipitation, it is useful to develop thermodynamic models for describing the precipitation properties of dead and live oil fluids. Various thermodynamic models such as solubility model, solid model and thermodynamic micellization model have been reported in literature [1, 2, 3]. However quantitative representation is still far from satisfactory.

* Corresponding author: M. Tavakkoli
Phone: + (98)-21-66005819, Fax: + (98)-21-66022853
E-mail address: tavakkoli@che.sharif.edu

The simplest model for precipitated asphaltene is the single-component solid model that was tried by Gupta [4] and Thomas et al. [5]. Nghiem et al. [2] used solid model along with a robust flash calculation procedure for vapor/liquid/asphalt systems to predict asphaltene precipitation data from the literature and the industry under pressure depletion, gas or solvent injection conditions. They observed that their proposed model could not exhibit the correct behavior with increasing solvent concentration under gas/solvent injection condition.
Victorov and Firoozabadi [6] proposed a thermodynamic model that considers that asphaltene precipitation from petroleum fluid is a micellization process. This model has shown promising results in explaining most of the experimentally observed results. However, their proposed approach could not predict asphaltene precipitation data under gas titration condition with a close agreement.
In this work, various characterization methods, including different techniques for estimation of critical properties and acentricities of SCN's and pseudo components, were applied in both thermodynamic micellization model and solid model. The obtained values for matching parameters from sensibility analysis along with the chosen techniques for estimation of critical properties and acentricities of SCN's and pseudo components have been used and the ability of both models to reproduce correct behavior of asphaltene precipitation under gas titration condition has been improved. Finally, the improved ability of the thermodynamic micellization model for predicting asphaltene precipitation data under gas/solvent injection condition has been compared with the enhanced solid model ability.

THERMODYNAMIC MODELING

Solid model

Solid representation of precipitated asphaltene. The precipitate asphaltene is represented as a pure solid. For a given temperature T and pressure P assuming that the solid is incompressible, the fugacity of the solid phase is:

$$\ln f_s = \ln f_s^* + \frac{v_s\left(P - P^*\right)}{RT} \tag{1}$$

where $f_s, f_s^*, P, P^*, R, v_s, T$ are solid fugacity [kPa], reference solid fugacity [kPa], pressure [kPa], reference pressure [kPa], gas constant [$8.314\ kPa\, m^3/kmol\ ^oK$], solid molar volume [$m^3/kmol$], and temperature[$^oK$], respectively.

Oil and gas phases. The oil and gas phases are modeled with a cubic EOS with volume shift parameters. The PR-EOS is used for all calculations in this work. The fugacity of component i in phase j ($j = o, g$) is:

$$\ln f_{ij} = \ln f_{ij}^0 + \frac{s_i b_i P}{RT}; i = 1,...,n_c \quad j = o, g \tag{2}$$

where f_{ij}, f_{ij}^0, s_i are fugacity of component i in phase j with volume shift [kPa], fugacity of component i in phase j without volume shift [kPa], and dimensionless volume shift, respectively and b_i is the EOS "b" parameter for component i, i.e.

$$b_i = \frac{\Omega_b RT_{ci}}{P_{ci}} \tag{3}$$

where P_{ci}, T_{ci}, Ω_b are critical pressure of component i [kPa], critical temperature of component i [^oK], and dimensionless EOS parameter, respectively. The molar volume of phase j with volume shift is:

$$v_j = v_j^0 + \sum_{i=1}^{n_c} y_{ij} s_i b_i ;\ j = o, g \tag{4}$$

where v_j^0 is the EOS molar volume without volume shift.

Representation of asphaltene component. In a mixture of n_c components, let the asphaltene component be the $n_c - th$ component. When a gas phase, an oil phase and a solid phase coexist, the following thermodynamic equilibrium equations are satisfied:

$$\ln f_{ig} = \ln f_{io};\ i = 1,..., n_c \tag{5a}$$

$$\ln f_{n_c o} = \ln f_s \tag{5b}$$

The crucial step in the modeling of asphaltene is the split of the heaviest component in the oil (e.g, C_{31+}) into a non-precipitating component (C_{31A+}) and a precipitating component (C_{31B+}). These two components have identical critical properties and acentric factors, but different interaction coefficients with the light components. The precipitating component has larger interaction coefficients with the light components. Interaction coefficients between components are important parameters for phase behavior predictions. In this work, the interaction coefficients between hydrocarbons are calculated from:

$$d_{ik} = 1 - \left(\frac{2 \cdot v_{ci}^{1/6} \cdot v_{ck}^{1/6}}{v_{ci}^{1/3} + v_{ck}^{1/3}} \right)^e \tag{6}$$

where $d_{ik}, e, v_{ci}, v_{ck}$ are interaction coefficients between component i and k [*dimensionless*], adjustable parameter [*dimensionless*], critical volume of component i [$m^3/kmol$], and critical volume of component k [$m^3/kmol$], respectively. The interaction coefficients between the precipitating component (e.g. C_{31B+}) and the light components (e.g, C_1 to C_5) are set to a constant value, i.e.:

$$d_{ik} = \delta \tag{7}$$

while the interaction coefficients with the remaining heavier components are set equal to zero.

Flash calculations with a solid phase. Given a pressure *P*, a temperature *T*, and a mixture with global composition $z_i (i = 1,..., n_c)$, flash calculations determine the phase molar fraction and composition by solving equation (1). The complexity of multi phase flash calculations is due to the fact that the number of phases in equilibrium is not known a priori. More details can be found in previous works [2, 7].

Thermodynamic micellization model

Victorov and Firoozabadi [6] assumed in their model that an asphaltene-resin micelle is composed by n_1 aggregated asphaltene molecules forming a micellar core, and n_2 bipolar resin molecules which are adhered to the surface of the core. The material balance equations for the case of monodispersed micelles are given by:

$$N_a = N_{a1} + n_1 N_m(n_1, n_2) \tag{8}$$

$$N_r = N_{r1} + n_2 N_m(n_1, n_2) \tag{9}$$

With the precipitation of the asphaltene phase, the material balance equations should include the amount of precipitate. If the precipitated phase (phase γ) contains only pure asphaltene, equation (8) turns out to be:

$$N_a = N_a^{\gamma} + N_{a1} + n_1 N_m(n_1, n_2) \tag{10}$$

In the above equations, N_a and N_r are the number of asphaltene and resin molecules in the crude. N_{a1} and N_{r1} are the number of asphaltene and resin monomeric species, and N_m (n_1, n_2) is the number of micelles containing n_1 asphaltene molecules and n_2 resin molecules.
The micellar-monomer equilibrium equations that govern the aggregation process are:
Micelle chemical potential:

$$\mu_m = n_1 \mu_{a1} + n_2 \mu_{r1} \tag{11}$$

Monomeric resin and monomeric asphaltene chemical potentials:

$$\mu_{a1} = \mu_{a1}^* + kT \ln X_{a1} \tag{12}$$

$$\mu_{r1} = \mu_{r1}^* + kT \ln X_{r1} \tag{13}$$

and

$$\mu_m = G_M^{00} + kT \ln X_m \tag{14}$$

for the micelles.
In above equations, X_i is the mole fraction of species i, μ_{a1}^*, μ_{r1}^* and G_M^{00} are the standard chemical potentials. Equations (12), (13) and (14) lead to:

$$X_m = X_{a1}^{n1} X_{r1}^{n2} \exp(\Delta G_M^{00} / kT) \tag{15}$$

in which

$$\Delta G_M^{00} = n_1 \mu_{a1}^* + n_2 \mu_{r1}^* - G_M^{00} \tag{16}$$

is the standard Gibbs free energy of micellization. It represents the standard free energy difference between all asphaltene and resin molecules present in a micelle.
The standard Gibbs free energy of micellization, ΔG_M^{00}, represents various specific features of the micelle-formation process. These features have been represented in previous works [6, 8]. As the final result, ΔG_M^{00} can be calculated from:

$$\frac{\Delta G_M^{00}}{RT} = n_2 f(\theta) - n_1 \ln X_{a1}^{ons} \tag{17}$$

$$f(\theta) = \ln(1-\theta) + \frac{\Delta U_r}{RT} - \frac{\sigma_0 a(1-\theta)}{RT\theta} \tag{18}$$

θ, the fraction of micellar core covered by resins, can be calculated from:

$$\ln\left(\frac{X_{a1}}{X_{r1} X_{a1}^{ons}}\right) - \frac{\Delta U_r}{RT} - \frac{\sigma_0 a}{RT}(1+b) = \ln(1-\theta) - \frac{\theta}{1-\theta}(1+\theta b) \tag{19}$$

where $b = \frac{v_a}{a}\left(\frac{8\pi}{an_2^s}\right)^{1/2}$.

In above equations, ΔU_r is the energy of desorption per resin molecule, σ_0 is the interfacial tension between a micelle and the petroleum fluid at zero adsorption of resins onto a micelle, a is the surface area of the resin molecule polar head, v_a is the asphaltene molecular volume, n_2^s is the maximum number of the resin molecules which can be accommodated on the flat surfaces of a micellar core and X_{a1}^{ons} is the concentration of asphaltene monomers in the crude in equilibrium with the pure solid asphaltene phase. This last parameter is a characteristic of a given crude and is adjusted from experimental data on asphaltene precipitation for each individual crude mixture.

Having X_{a10}^{ons} at a reference condition, X_{a1}^{ons} can be calculated for other conditions, by using an EOS (In this work, the PR-EOS is used), from equations (20) and (21):

$$X_{a1}^{ons}(T,P,ratio) = X_{a10}^{ons}(T,P,ratio=0)\frac{\varphi_{a10}^{\beta}(T,P,ratio=0)}{\varphi_{a1}^{\beta}(T,P,ratio)} \tag{20}$$

where φ_{a1}^{β} is the fugacity coefficient of monomeric asphaltene species in the petroleum fluid medium β and *ratio* is the dilution ratio.

$$X_{a1}^{ons}(P') = X_{a10}^{ons}(P)\frac{\varphi_{a10}^{\beta}(T,P,x)P}{\varphi_{a1}^{\beta}(T,P',x')P'}\exp\left(\frac{v_a(P'-P)}{RT}\right) \tag{21}$$

where x is the composition at P.

APPLICATION OF THERMODYNAMIC MODEL

In this work, the experimental data of Burke et al. [9] is used to illustrate the modeling of the phase behavior of asphaltene precipitation during gas/solvent injection condition. The behaviors of both models with respect to different techniques for estimation of critical properties and acentricities of SCN's and pseudo components as well as changes in different model parameters are investigated.

Table 1 reports the composition of the oil and the solvent from Burke et al. [9]. The oil was mixed with various amounts of the solvent.

Oil component characterization

Solid model. The plus fraction of the oil was first split into single carbon number components and all the components are then lumped into pseudo-components using the method of Li et al. [10].

Table 1
Burke et al. (1990) Oil and Solvent

Components	Oil Mole%	Solvent Mole%
N_2	0.51	3.17
CO_2	1.42	17.76
C_1	6.04	30.33
C_2	7.00	26.92
C_3	6.86	13.09
i-C_4	0.83	1.26
n-C_4	3.35	4.66
i-C_5	0.70	0.77
n-C_5	3.46	1.26
C_6	3.16	0.78
C_{7+}	66.68	

The heaviest fraction C_{31+} was split into two components: a non-precipitating component, C_{31+A}, and a precipitating component, C_{31+B}. The mole fraction of C_{31+B} is calculated from the average weight percent of total precipitate [2, 7]. Then, the mole fraction of C_{31+A} is calculated from the difference between the mole fractions of C_{31+} and C_{31+B}. The interaction coefficients between all hydrocarbon components up to and including C_{31+A} were calculated from equation (6). The interaction coefficients between C_{31+B} and the light hydrocarbon components up to C_5 are assumed to have the same value δ in equation (7). For gas titration condition, δ affected both the saturation pressures and the amount of precipitates, and had to be adjusted simultaneously.

Thermodynamic micellization model. For modeling the behavior of a crude, it is absolutely necessary to know its composition including the total fractions of asphaltenes and resins. Unfortunately, these data are often missing in the literature. For the considered crude, the total asphaltene weight percent was taken from experimental data. Then, the method of Li et al. [10] for oil component characterization, which is commonly used in the thermodynamic solid model, was used. In this method, the heaviest fraction, C_{31+} is divided into two parts: C_{31+A} and C_{31+B}. C_{31+A} is the non-precipitating and C_{31+B} is the precipitating component. Since in this work we assume no resin precipitation, the amount of C_{31+A} can be set as the resin content of the crude [2]. The interaction coefficients between C_{31B+} and the light hydrocarbon components up to C_5 are assumed to have the same value δ. δ is obtained from sensitivity analysis. We set the interaction coefficients between C_{31A+} and the other hydrocarbon components equal to zero.

RESULTS AND DISCUSSION

Model sensitivity analysis

*Solid model***.** Matching saturation pressure and precipitation data simultaneously, yields e = 1.75 and δ = 0.24. Figure 1 compares calculated and experimental saturation pressures and figure 2 shows the comparison between calculated and experimental precipitates for Burke et al. oil. For solvent concentration above 78 mole percent, the measurements indicated a substantial drop in the precipitate. Burke et al. [9] and Chabak [11] attributed the decrease in the precipitate at high solvent concentration to the switching of the mixture from a bubble-point fluid to a dew-point fluid.

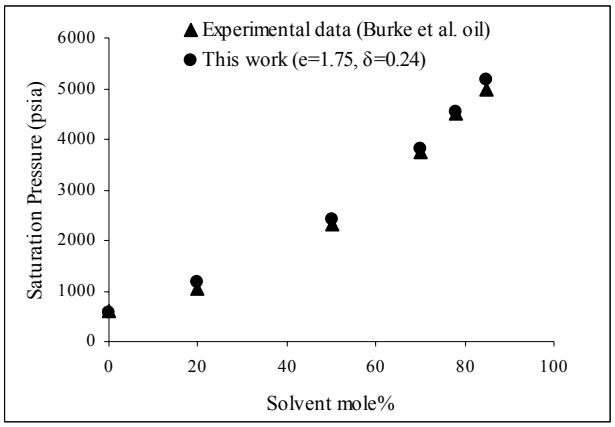

Figure 1. Saturation pressure of Burke et al. oil

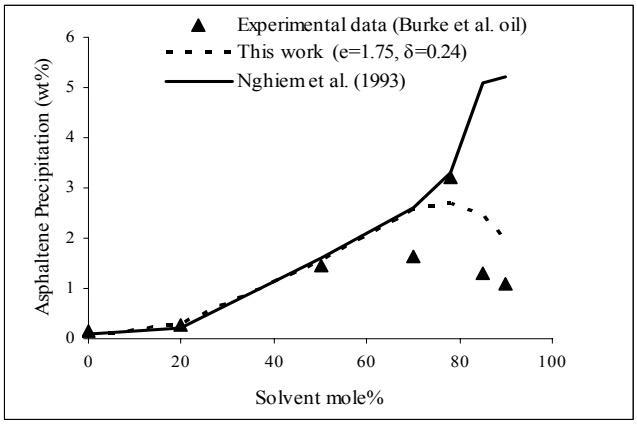

Figure 2. Model predictions for Burke et al. oil

The literature results [2] do not show a decrease in precipitation at high solvent concentration, but do exhibit a change in the precipitation behavior. Here, a significant improvement in model predictions can be observed. This work shows the decrease in amount of precipitation at high solvent concentrations. It can also predict the maximum of precipitation reasonably well. This improvement in the results is due to chosen characterization method including techniques used for estimation of critical properties and acentricities of SCN's and pseudo components, as well as the obtained values for matching parameters e and δ from sensitivity analysis. Various characterization

methods cause different values for fugacities of components and can make changes in final results. Since, at high solvent concentration, the mixture switches from a bubble-point fluid to a dew-point fluid [9], saturation pressure matching is a crucial step which can highly affect the accuracy of the model. Also, the matching is a difficult procedure due to this alteration. Figure 3 shows the effect of δ on model predictions. Larger value for δ, interaction coefficient parameter between C_{31B+} and light components, will cause larger amount of precipitation. Table 2 shows different runs with various characterization methods [12]. It can be found, from figures 4, 5 and 6, that the model is also sensitive to the chosen characterization methods, including techniques for estimation of critical properties and acentricities of SCN's and pseudo components.

Table 2
Characterization Methods for Runs 1 through 6

Run Number	Estimation of Critical Properties of SCN's	Estimation of Critical Properties of Pseudo-Components
(1)	Twu-Correlations	Lee-Kesler Averaging Method
(2)	Twu-Correlations	Molar Averaging Method
(3)	Lee-Kesler Correlations	Lee-Kesler Averaging Method
(4)	Lee-Kesler Correlations	Molar Averaging Method
(5)	Cavett-Correlations	Lee-Kesler Averaging Method
(6)	Cavett-Correlations	Molar Averaging Method

Table 3
Micellization Model Parameters

Model Parameters	Value
a (A^2)	50
X_{a10}^{ons} (fraction)	0.015
$n = n_1 + n_2$	450
v_a (m^3/kmol)	0.5
σ_0 (N/m)	0.060
ΔU_r (J/mol.m^2)	0.070
n^s_2	200
Temperature (^{0}F)	218
δ	0.24

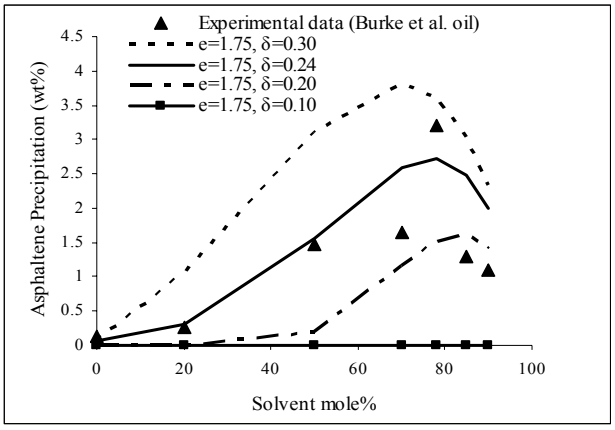

Figure 3. Effect of δ on model predictions

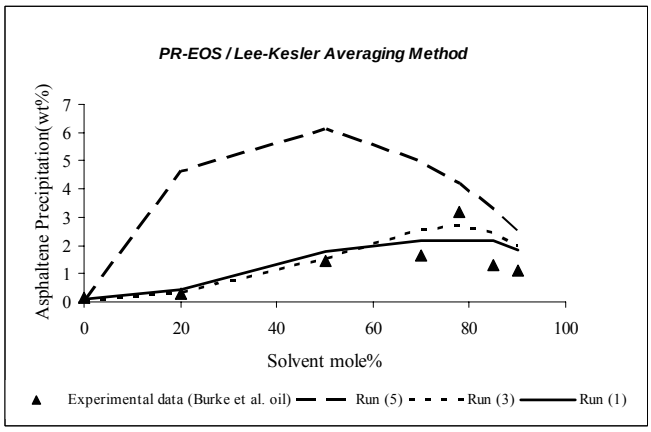

Figure 4. Effect of characterization methods

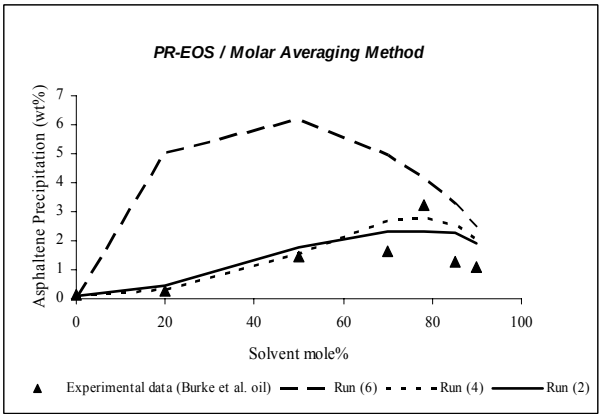

Figure 5. Effect of characterization methods

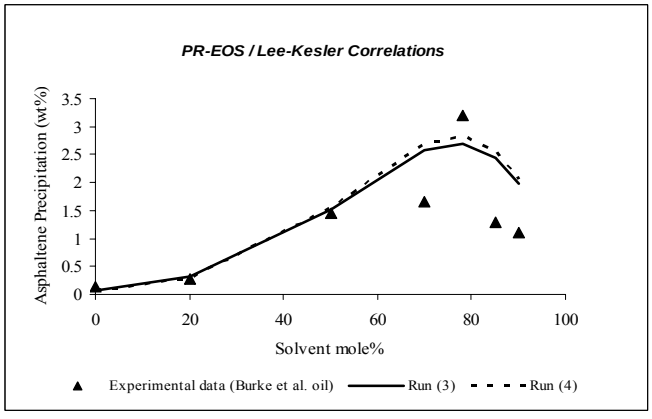

Figure 6. Effect of characterization methods

Thermodynamic micellization model. Figure 7 shows the model predictions using the micellization model parameters given in Table 3. The calculation procedure has been given previously [6]. By

sensitivity analysis, it can be found that the parameters ΔU_r and σ_0 play an important role in the micellization process. Lowering σ_0 will increase the stability of the aggregates. Hence, there is no precipitation for σ_0 = 0.045 N/m, and the model shows much more asphaltene precipitation at low mole percents of solvent with σ_0 = 0.080 N/m. The increase of the ΔU_r shifts the onset of asphaltene precipitation to the higher mole percents of solvent. At the value of 0.075 J/(mol.m^2) no precipitation can be observed. With ΔU_r = 0.065 J/(mol.m^2), the asphaltene precipitation at low mole percents of solvent would increase too much.

Figures 8 and 9 show the effect of chosen values for X_{a10}^{ons} and δ on model predictions. Figures 10 and 11 show the effect of temperature and resin content of the crude. Table 2 shows different runs with various characterization methods [12]. It can be found, from figures 12, 13 and 14, that the model is also sensitive to the chosen characterization methods, including techniques for estimation of critical properties and acentricities of SCN's and pseudo components.

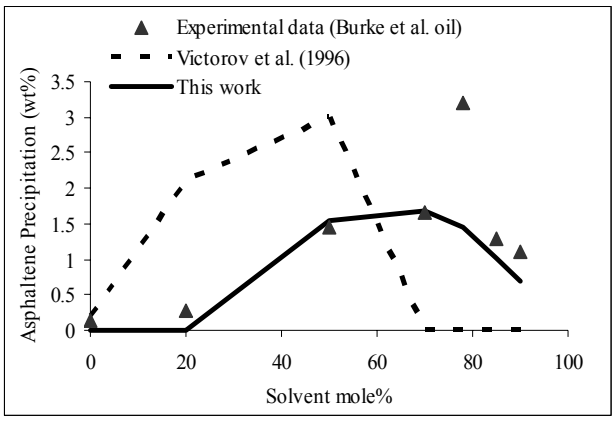

Figure 7. Asphaltene precipitation prediction

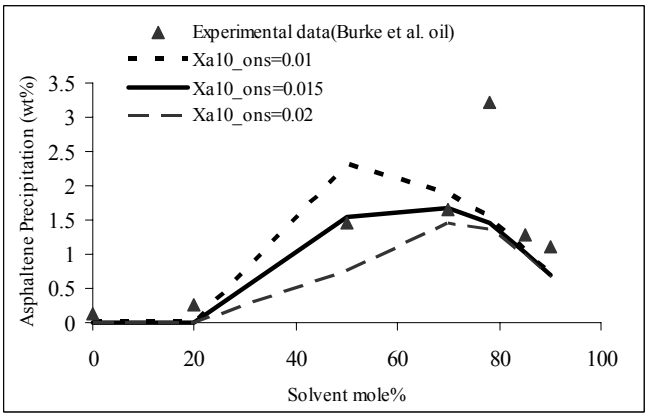

Figure 8. Effect of X_{a10}^{ons} on model predictions

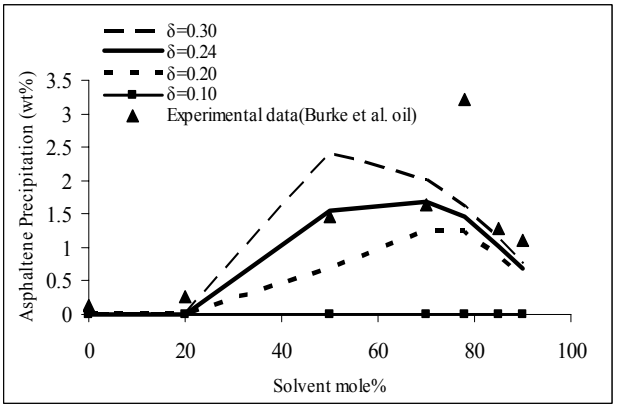

Figure 9. Effect of δ on model predictions

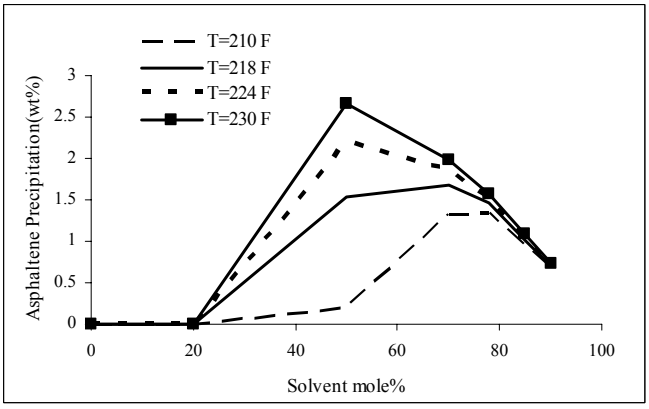

Figure 10. Effect of temperature on model predictions

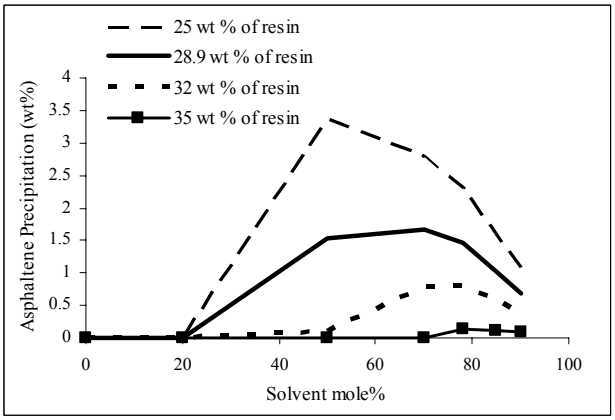

Figure 11. Effect of resin content on predictions

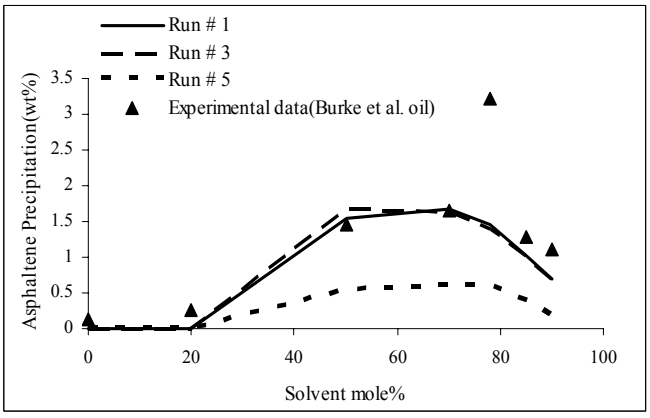

Figure 12. Effect of characterization methods

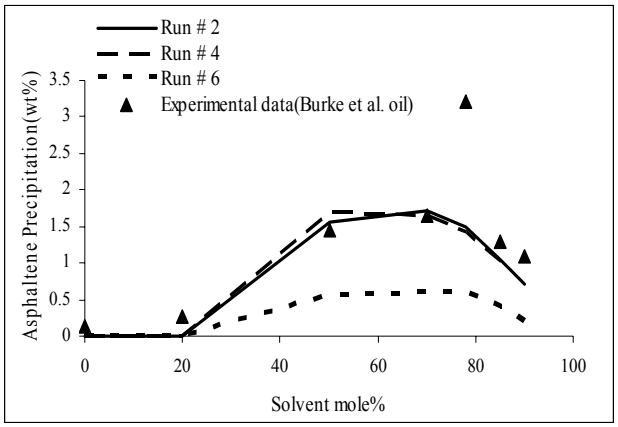

Figure 13. Effect of characterization methods

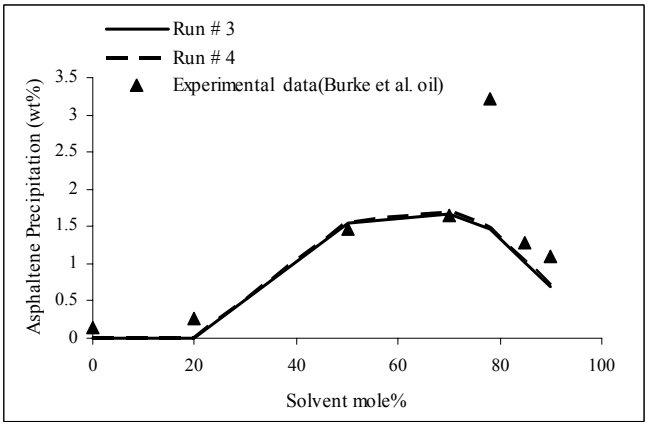

Figure 14. Effect of characterization methods

Comparison of the thermodynamic micellization model and solid model

Figure 15 compares the asphaltene precipitation predictions of the thermodynamic micellization model and solid model under gas titration condition. It can be observed that both models are able to predict the experimental data reasonably well. The predictions of solid model, which is a simple model, show good agreements for the maximum value of asphaltene precipitation and for the trend of the curve after the peak point. In comparison to the solid model, the thermodynamic micellization model is a more complex model and its computational effort is more demanding than for the solid model. The thermodynamic micellization model is able to predict the trend of the asphaltene precipitation envelope reasonably well. It cannot predict the maximum of precipitation as well as the predictions of solid model but, its predictions matched well with more experimental data points in comparison to the solid model.

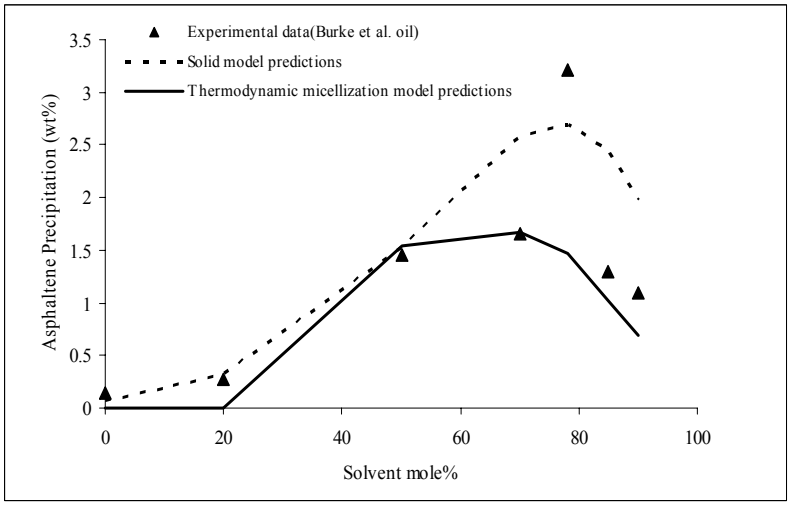

Figure 15. Comparison of the thermodynamic micellization model and solid model predictions

CONCLUSIONS

In this work, two computer codes which are based on two different asphaltene precipitation thermodynamic models, 1-Thermodynamic Micellization Model and 2- Solid Model, have been developed, and, used for predicting of asphaltene precipitation data reported in the literature under gas/solvent injection condition. The obtained values for matching parameters from sensibility analysis along with the chosen techniques for estimation of critical properties and acentricities of SCN's and pseudo components have been used and the ability of both models to reproduce correct behavior of asphaltene precipitation under gas titration condition has been improved. In the case of solid model, two adjustable parameters, e and δ, were required to match the experimental data.

Larger value for δ, interaction coefficient parameter between C_{31B+} and light components, will cause larger amount of precipitation. For thermodynamic micellization model, a characterization method which is commonly used in the thermodynamic solid model, has been applied for oil component characterization. This new approach showed a significant improvement in the thermodynamic micellization model predictions of asphaltene precipitation data under gas injection conditions. The sensitivity analysis on model parameters has shown that the model is highly sensitive to the resin content of the crude, ΔU_r, σ_0, X_{a10}^{ons} and δ. The last two parameters are our main adjustable parameters. The model sensitivity to the parameter δ is due to the new characterization method chosen for the thermodynamic micellization model. Also, it can be found from the sensibility analysis that both models predictions are highly sensitive to the chosen techniques for estimation of critical properties and acentricities of SCN's and pseudo components. Comparison of the thermodynamic micellization model and solid model showed that both models are able to predict the trend of asphaltene precipitation curve reasonably well. The thermodynamic micellization model cannot predict the maximum of precipitation as well as the predictions of solid model but, its predictions matched well with more experimental data points in comparison to the solid model. Also, it can be found that the thermodynamic micellization model is a more complex model and its computational effort is more demanding than for solid model.

REFERENCES

1. Hirschberg, A., and Hermans, L., Characterization of Heavy Oils and Petroleum Residues, *Editions Tech-nip*, p. 492, 1984.
2. Nghiem, L.X., Hassam, M.S., Nutakki, R., and George, A.D.E., Efficient Modelling of Asphaltene Precipitation, SPE 26642 presented at 1993 *SPE Annual Technical Conference and Exhibition*, Houston, 3–6 October, 1993.
3. Pan, H., and Firoozabadi, A., A Thermodynamic Micellization Model for Asphaltene Aggregation and Precipitation in Petroleum Fluids, *SPE Production & Facilities*, Vol. 13, 118-127, 1998.
4. Gupta, A.K., A Model for Asphaltene Flocculation Using an Equation of State, *M.Sc. Thesis*, Department of Chemical and Petroleum Engineering, The University of Calgary. 1986.
5. Thomas, F.B., Bennion, D.B., Bennion, D.W., and Hunter, B.E., Experimental and Theoretical Studies of Solids Precipitation from Reservoir Fluid, *J. Can. Petrol. Technol*., Vol. 31, 22-31, 1992.
6. Victorov, A.I., and Firoozabadi, A., Thermodynamics of Asphaltene Precipitation in Petroleum Fluids by a Micellization Model, *AIChE J*., Vol. 42, 1753-1764, 1996.
7. Nghiem, L.X., and Coombe, D.A., Modeling Asphaltene Precipitation during Primary Depletion, *SPE Journal*, Vol. 2, 170-176, 1997.
8. Victorov A.I. and Smirnova N. A., Description of Asphaltene Polydispersity and Precipitation by means of Thermodynamic Model of Self-assembly, *Fluid Phase Equilibria*., 158-160, 471-480, 1999.
9. Burke, N.E., Hobbs, R.E., and Kashou, S.F., Measurement and Modeling of Asphaltene Precipitation, *JPT 1440; Trans., AIME*, 289, 1990.
10. Li, Y.K., Nghiem, L.X., and Siu, A., Phase Behaviour Computations for Reservoir Fluids: Effect of Pseudo Components on Phase Diagrams and Simulation Results, *J. Can. Petrol. Technol*., Vol. 24, 29-36, 1985.
11. Chaback, J.J., Discussion of Measurement and Modeling of Asphaltene Precipitation, *J. Petrol. Technol*., Vol. 43, 1519-1520, 1991.
12. Danesh A., *PVT and Phase Behavior of Petroleum Reservoir Fluids*, First ed.; Elsevier, 1998.

EFFECT OF NOZZLE GEOMETRY ON HEAT TRANSFER COEFFICIENTS

O. F. P. Lyons[1,*], T. Persoons[1], G. Byrne[1], D.B. Murray[1]
[1]Trinity College, University of Dublin, Dublin, Ireland

ABSTRACT. Much is already known about the heat transfer characteristics of impinging air jets, and they are widely used in many engineering applications. There currently exist many correlations describing such characteristics. However, the complex internal structure of many nozzles can lead these to produce results which deviate from those predicted by correlations. One such nozzle is currently used in this research group to produce a water mist flow. This atomisation nozzle tends to produce a lower stagnation Nusselt number, but higher heat transfer for radial locations beyond two diameters from impingement.

Keywords: *Heat Transfer, Air Jet Cooling, Nozzle Geometry, Mist Jet Cooling*

INTRODUCTION

Length of paper
Impinging air jet nozzles have long been known to achieve superior heat transfer coefficients. The variation in their local heat transfer coefficients also lends itself to application in areas of large temperature gradients. Their ability to achieve effective cooling rates has led to their implementation in many situations including the replacement of lubricants in some machining operations. Previous work in the research group investigated their effect on grinding temperatures [1].

It is believed that the implementation of a fine water mist into the air stream has the potential to further increase the heat transfer rates. Indeed, Lee et al. [2] state that at droplet diameters of 30-80µm, a “superbly effective cooling scheme” is present. Convective heat transfer coefficients can increase by up to 10 times, through evaporation of an “ultra-thin” liquid film (50-100µm). The dispersal of water droplets into an air flow can be characterised as either spray cooling or mist jet cooling. A spray is obtained by pressurising the water in the nozzle in order to atomize it. Mist jets use the air pressure to atomize the water. Mist jets thus allow smaller droplet size [3]. The liquid flow can be controlled with less atomization constraints.

This paper seeks to compare time averaged heat transfer coefficients from two different nozzles. One nozzle is a simple round air jet nozzle, of diameter 4.5mm, made of copper piping. The other nozzle is an atomizing nozzle, Spraying Systems Co., involving a complex nozzle body, with air exiting through an annular hole, nominal diameter 3.5mm, figure 1. This nozzle will ultimately be used to investigate an air flow with entrained mist particles.

* Corresponding author: Prof. X . Yxy
Phone: + (11)-12-345678, Fax: + (11)-12-3456789
E-mail address: my-email@address.edu.pl

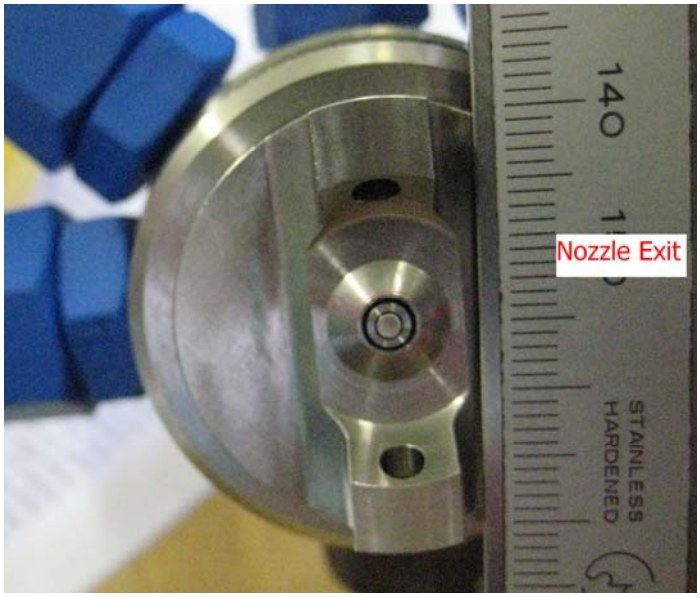

Figure 1. Nozzle profile

Nozzle geometry affects both the flow exit profile and the turbulence characteristics of the resulting flow. The flow structure will influence the local heat transfer distribution, through increased mixing of the thermal boundary layer. The effect of the nozzle exit shape on the velocity profile will also impact on heat transfer distributions [4]. Increased free stream turbulence has been noted by [5] due to the complex internal structure of the nozzle used in this investigation. Thus, the air jet itself is expected to give higher heat transfer coefficients than correlations predict [6, 7].

Chatterjee and Deviprasath [4] showed that the surface heat transfer coefficient can be influenced by the nozzle velocity distribution. The velocity distribution will be controlled by the nozzle exit conditions. Thus, nozzles of different geometries can have different heat transfer profiles. This effect becomes diminished at large H/D values. Kito et al [8] also showed the effect the contraction area ratio can have on surface heat transfer measurements.

The effect of angle of impingement is to relocate the maximum heat transfer coefficient. This occurs because the stagnation point is displaced in the direction of the angle, Goldsteain and Franchett (9)

Heat transfer coefficients tend to increase with increasing Reynolds numbers, in a similar manner to many correlations, e.g. the Lui and Sullivan [10]

$$Nu_0 = 0.585\,\mathrm{Pr}^{0.4}\,\mathrm{Re}^{0.5}$$
$$H/D < 2 \qquad (1)$$

It is expected that the complex nozzle will achieve similar dependencies.

EXPERIMENTAL SET-UP

A rig was built to investigate the effects of nozzle geometry on the heat transfer to an impinging jet. The test surface is an instrumented isothermally heated copper plate. In order to measure the local heat flux transferred from the surface to the jet flow, a hot film sensor and thermopile heat flux sensor are mounted flush with the copper plate. The thermopile sensor is used for obtaining time averaged data whereas the hot film sensor will be used at a later stage of the research to obtain fluctuating heat transfer measurements. Ambient, test surface, and nozzle fluid temperatures are

recorded by several thermocouples. A stepper motor is used to move the test surface with respect to the fixed nozzle, so as to achieve full field measurements.

Data acquisition is via a National Instruments chassis containing analogue and digital input and output modules and a thermocouple module. The microfoil sensors used are RdF 27036 sensors. The signal is amplified before being fed to the data acquisition system. Labview controls all the data handling. Figure 2 shows the schematic of the test apparatus, with H, the nozzle exit to plate distance.

The heat transfer measurement approach has been validated for an impinging air jet against known correlations described in the literature [10, 11, 12] and other experimental rigs. Extensive calibration was performed on the thermocouples with a factory calibrated RTD probe connected to an Omega thermometer. The microfoil sensor was calibrated using an air jet with circular nozzle of diameter 9.5mm. The nozzle was positioned at a jet-to-surface distance H/D of 1. The calibration was performed using the Liu and Sullivan correlation, relating the stagnation Nusselt number to the Reynolds number [10]. The Reynolds number was varied from 10,000 – 20,000.

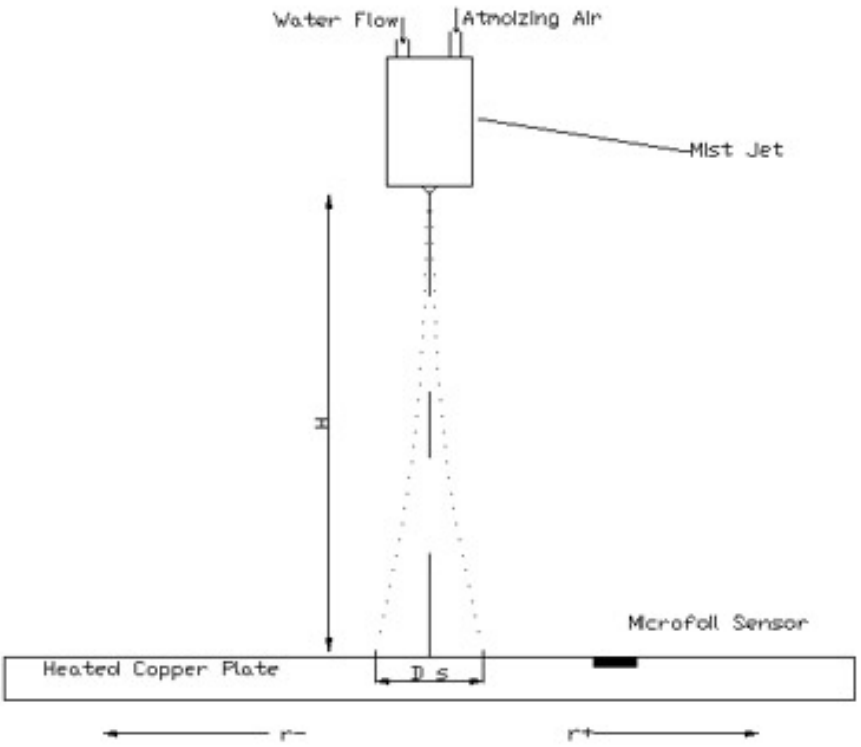

Figure 2. Schematic of the test apparatus

The hydraulic diameter, used for the atomizing nozzle has been defined as four times the cross sectional area (A) divided by the wetted perimeter (U) [13].

$$D = \frac{4A}{U} \tag{2}$$

This value is then used as the characteristic length (D) in all Reynolds number, H/D and r/D spacing. The nozzle exit profile can be seen in figure 1 and is of an annular profile. The nominal or hydraulic diameter has been calculated as 3.5mm. The pipe nozzle was chosen to be close in size to

it; it has a diameter of 4.5mm. As can be seen from figure 2, the nozzle can be varied relative to the test rig, so as to achieve full field measurements.

$$h = \frac{\ddot{q}_{conv}}{T_s - T_{jet}} \tag{3}$$

Heat transfer coefficients associated with the jets are based on the jet temperature of the air flow, eqn 3. This is measured by the air mass flow meter immediately upstream of the nozzle, and is typically 20°C.

The full extent of the rig consists of a water gear pump, pressure and flow meters. This enables water to be pumped to the atomising nozzle at high pressure. Water droplets are thus dispersed into an airstream, creating a mist flow.

RESULTS AND DISCUSSION

Analysis of both atomizing nozzle and pipe nozzle are presented for a range of Reynolds numbers and angles. Comparisons are provided to illustrate the difference in heat transfer obtainable through the complex atomizing nozzle.

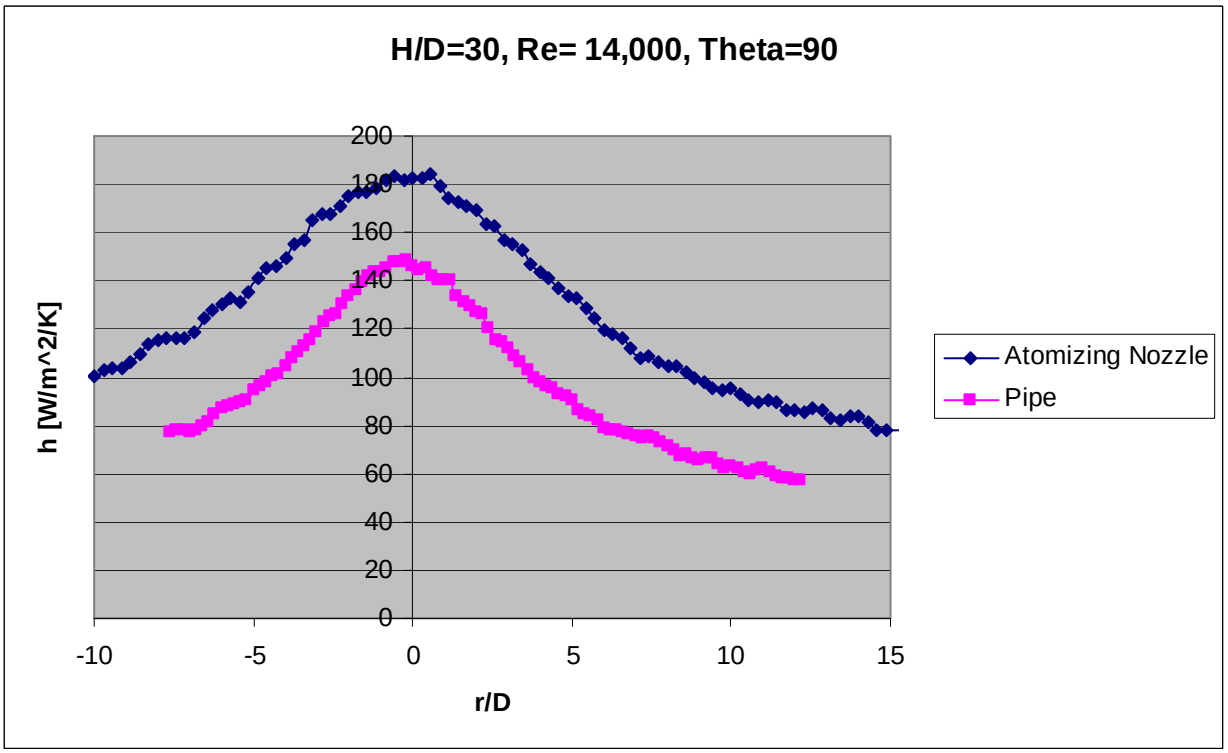

Figure 3. Atomizing vs Pipe Nozzle

Figure 3 shows the heat transfer profiles at a Reynolds number of 14,000, H/D of around 30 and an impingement angle of 90°. The atomizing nozzle shows higher convective coefficients across the r/D profile. It is interesting to note that since the data is for identical Reynolds numbers, yet different nozzle widths, the pipe jet actually has a 40% higher mass flow rate of air, yet achieves lower heat transfer coefficients. Although, corresponding stagnation Nusselt numbers (figure 4) are 10% higher in the pipe jet, and maintain an increase until an r/D of about 2. At such large H/D (>10), the annular exit

profile should not be impacting greatly on the stagnation region. (insert reference). Any potential core effects should have dissipated within 6 diameters, Hrycak et al [14]. Overall Nusselt numbers appear quite similar at large H/Ds similar to that noted by Chatterjee and Deviprasath [4].

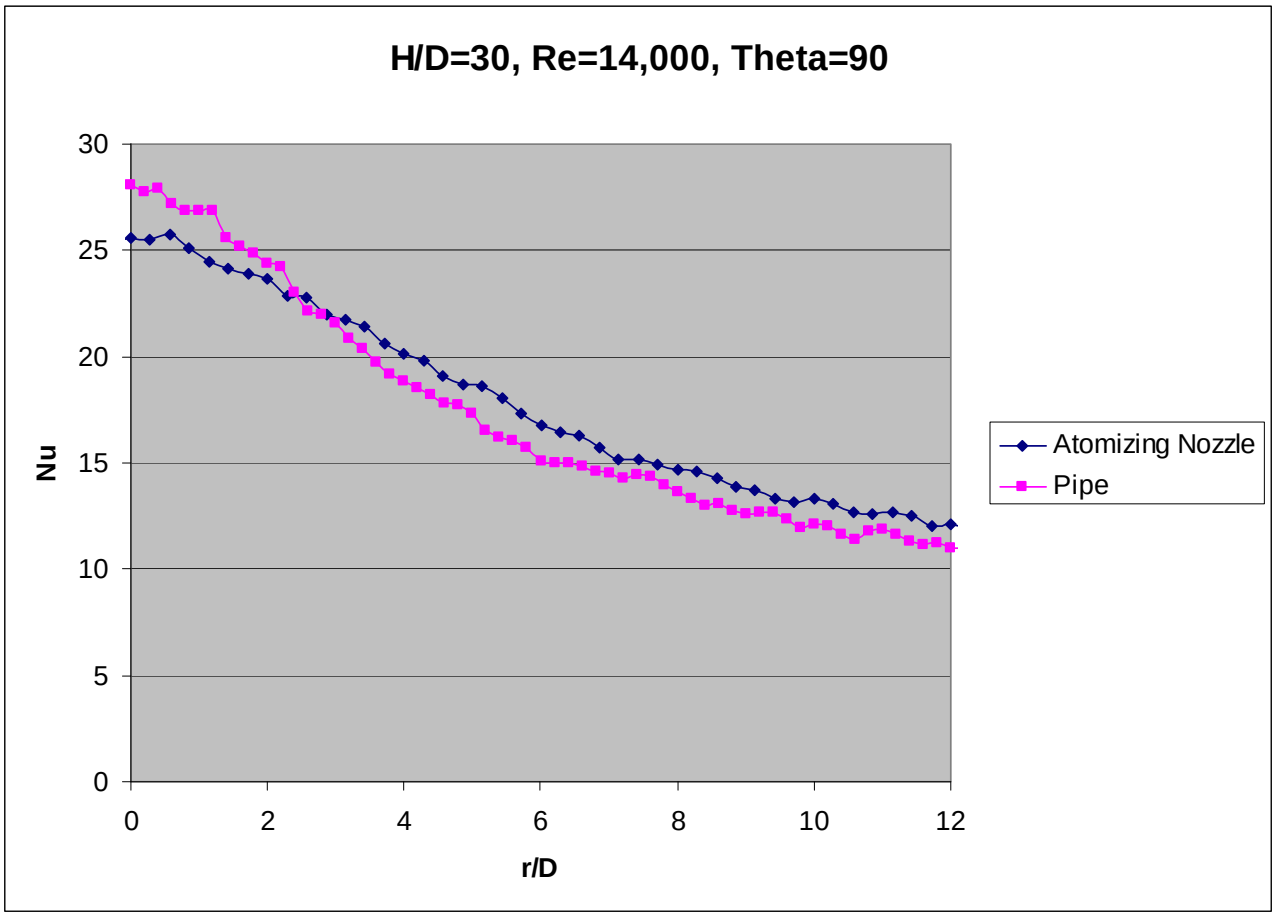

Figure 4. Nusselt number H/D =30

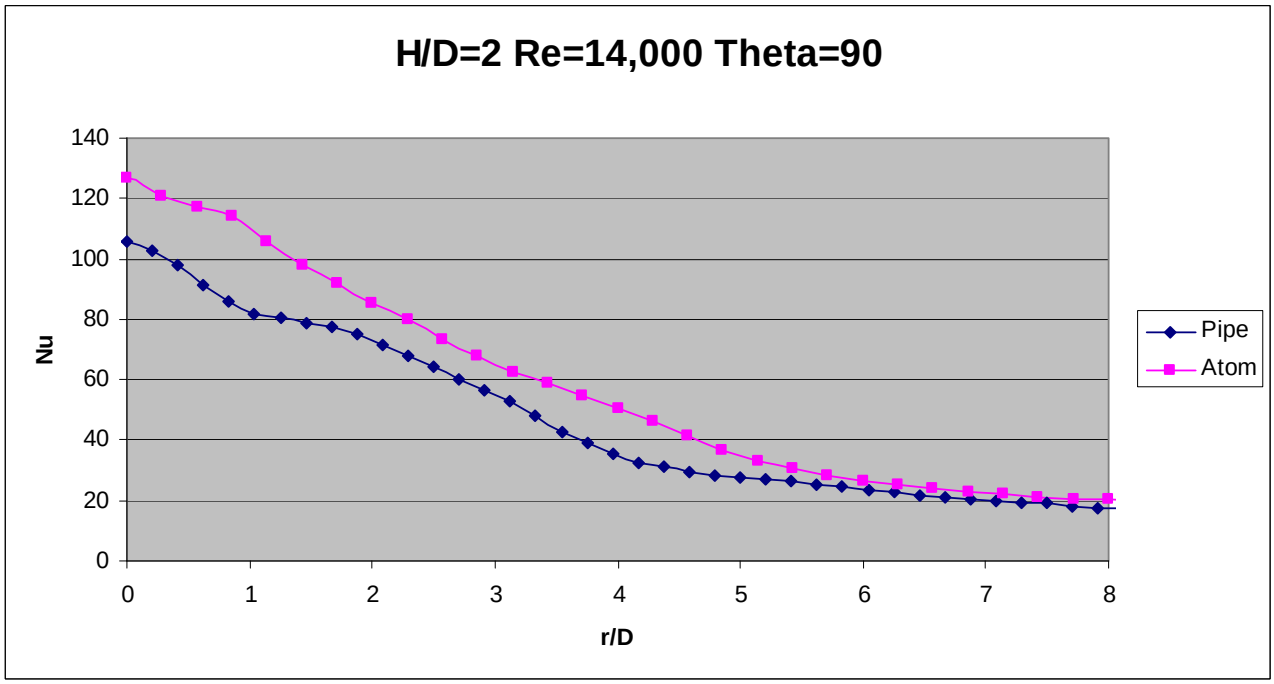

Figure 4b. Nusselt number H/D = 2

Figure 4b shows a comparison of Nusselt numbers for the pipe and atomizing nozzle at an H/D=2. The development of local secondary peaks at approximately one to two diameters can be seen. It is worth noting that the secondary peaks in the pipe nozzle are much more defined than that of the atomizing nozzle. In this case the atomizing nozzle outperforms the pipe nozzle across the radial distribution. The atomizing nozzle exists as an annular profile but shows none of their characteristics; offset maximum heat transfer and reverse stagnation point occurrence in the flow field noted by Chattopadhyay [15] although the Reynolds numbers used in this study are much higher.

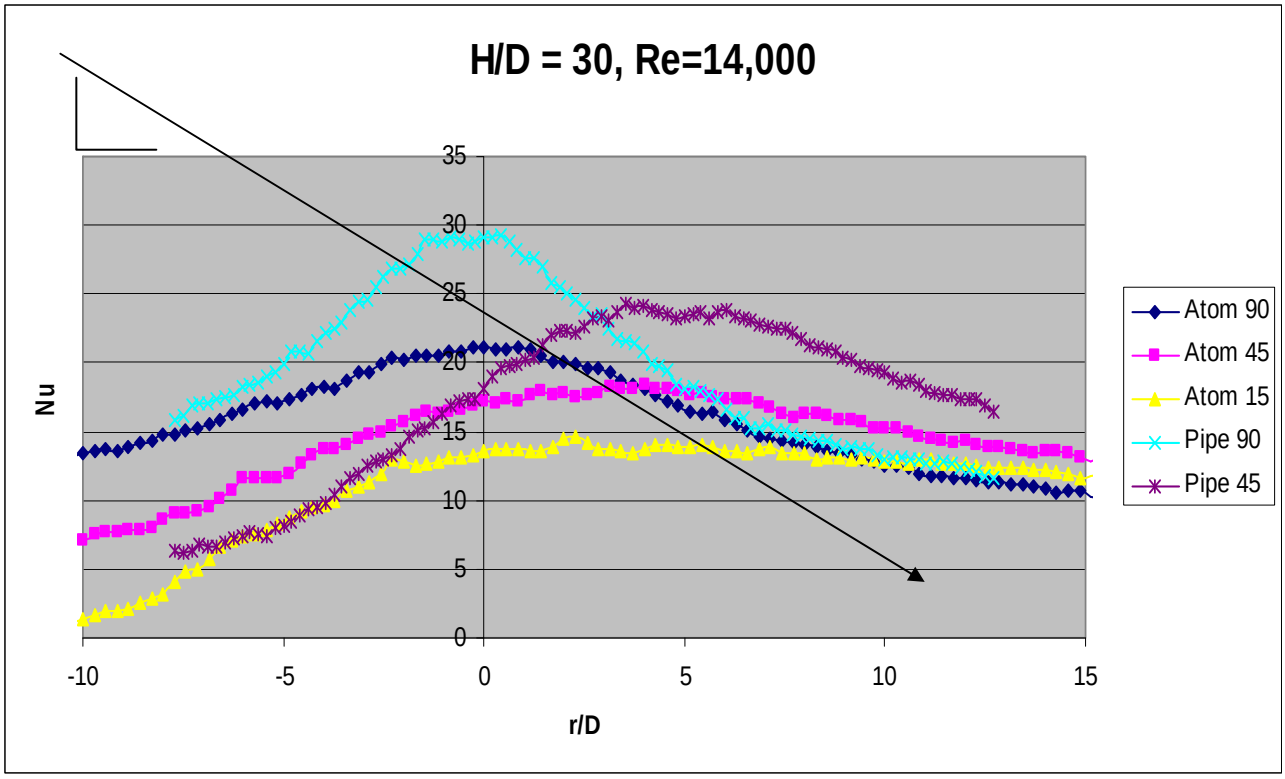

Figure 5. angle of impingement (add in pipe nozzles as well)

Figure 5 shows the variation in heat transfer coefficient against r/D for various angles of impingement. The direction of the angle is represented by the arrow. Again for all flow rates, the atomizing nozzle shows the bell shaped distribution. Upstream, the atomizing nozzle shows a decreasing cooling with increase in angle away from 90. A direct impingement angle has also shown the best degree of cooling in the stagnation region. This is due to a lower mass flux in both stagnation and upstream wall jet regions for angled nozzles. Conversely there is a higher mass flux downstream, and outside of a few diameters the 45 degree data shows an increase in heat transfer. The same is true for the 15 degree data outside approximately seven diameters. Again in these graphs, the stagnation Nusselt number is lower than that of the pipe nozzle.

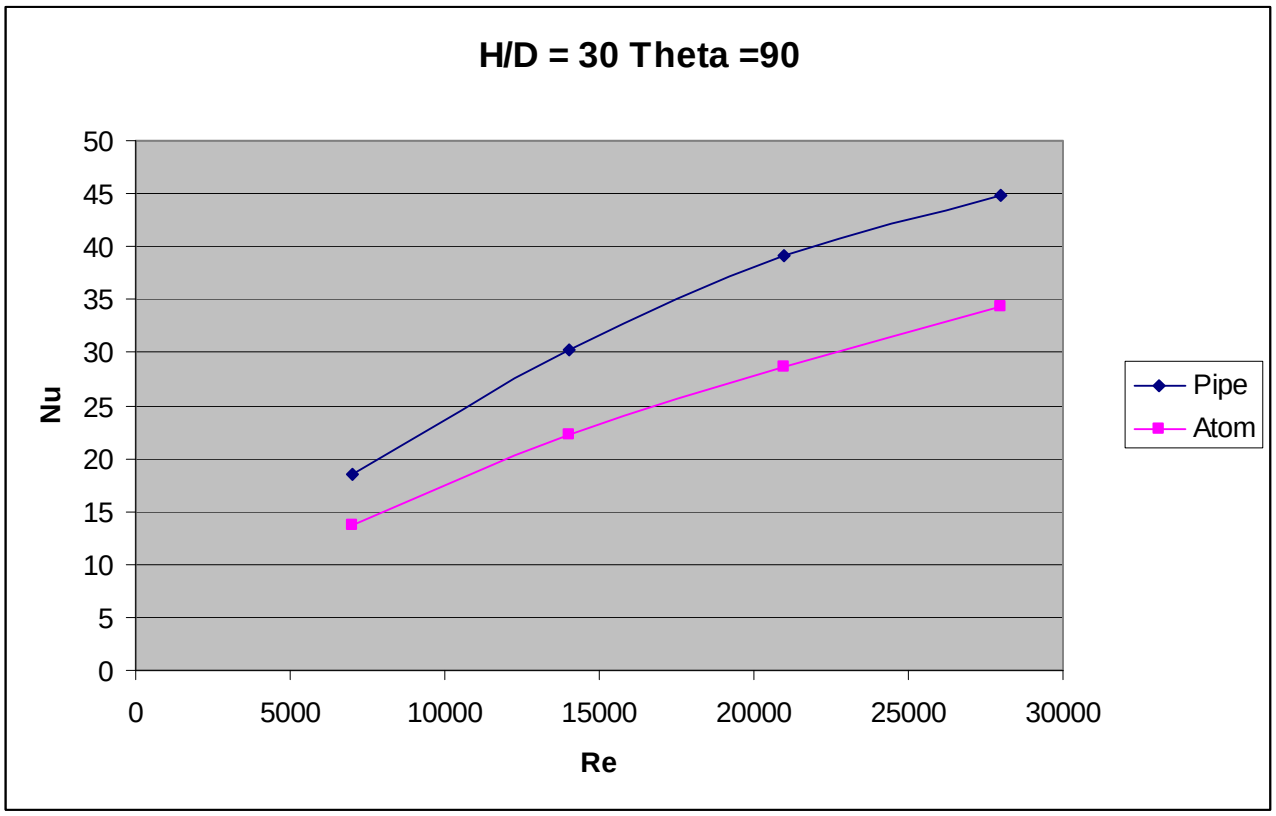

Figure 6. Reynolds number

The stagnation Nusselt numbers are consistently lower for the atomizing nozzle at various Reynolds numbers. It can be seen from figure 6 that the atomizing nozzle has a similar dependence on Reynolds number to that of the pipe nozzle and previous correlations [10].

The atomizing nozzle does appear to be following the typical bell-shaped distribution. Additionally, the effect of Reynolds number and angle of impingement show similar effects to both the pipe nozzle and previous literature (10, 11, 12). Overall Nusselt numbers appear similar, with around 10% higher for the pipe nozzle in the stagnation region at large H/D's. Thereafter the atomizing nozzle achieves higher levels of heat transfer. This effect is not noted at lower H/D's, where the pipe nozzle consistently underperforms.

The data recorded in this experiment has been used to compare a standard pipe nozzle to a more complex nozzle. The aim of these has been to characterise this complex nozzle, which will ultimately be used to generate a mist flow. This analysis has been used so as to determine how much of the increase in heat transfer is due to the mist and how much to that of the complex internal structure of the nozzle.

CONCLUSIONS

A study has been carried out to investigate the effects of nozzle geometry on local heat transfer from an impinging jet to a copper plate.

The atomizing nozzle has been shown to provide superior convective cooling at r/D's greater than two.

The atomizing nozzle has a lower stagnation Nusselt number and tends to be lower in the immediate stagnation region.

The effect of Reynolds number and H/D spacing has been shown to be consistent with that of a straight pipe nozzle.

Further analysis of the flow field, both at nozzle exit and at impingement, is important.

Furthermore, the measurement of fluctuating heat transfer parameters is expected to provide further information on the characteristics of the atomizing nozzle.

REFERENCES

1 O Donovan, T. S., Murray, D. B., Torrance, A.A., Jet Heat Transfer in the Vicinity of a Rotating Grinding Wheel, *Proc. I.Mech. E. Part C-J. Mech.Eng.Sci*, Vol. 220, pp 837-845, 2006.

2 Lee, S.L., Yang, Z.H., Hsyua, Y., Cooling of a Heated Surface by Mist Flow, *Journal of Heat Transfer*, Vol. 116, No. 1, pp. 167-172, 1994.

3 Lee, S., Park, J., Lee, P., Kim, M., Heat Transfer Characteristics During Mist Cooling on a Heated Cylinder, *Heat Transfer Engineering*, Vol. 26, No. 8, pp. 24-31, 2005.

4 Chatterjee, A., Deviprasath, L.J., Heat Transfer in Confined Laminar Axisymmetric Jets at Small Nozzle-plate Distances: the Role of Upstream Vorticity Diffusion, *Numerical Heat Transfer, Part A*, Vol. 39, pp. 777–800, 2001.

5 Viskanta, R. Heat Transfer to an Impinging Isothermal Gas and Flame Jets, *Exp. Therm. Fluid Sci.*, Vol. 6, No. 2, pp. 111-134, 1993.

6 Mehendale, A.B., Han, J.C., Ou, S., Influence of High Mainstream Turbulence on Leading Edge Heat Transfer, *Journal of Heat Transfer*, Vol. 113, No. 4, pp. 843-850, 1991.

7 Choi, J., Teng, S., Han, J., Ladeinde, F., Effect of Free-stream Turbulence on Turbine Blade Heat Transfer and Pressure Coefficients in Low Reynolds Number Flows, *International Journal of Heat and Mass Transfer*, Vol. 47, No. 14-16, pp. 3441-3452, 2004.

8 Kito, M., Shakouchi, T. Sakamoto, T., Tsujimoto, K., Ando, T., Heat Transfer Enhancement of Round Impinging Jet by Orifice Nozzle (Effects of Contraction Area Ratio), *Heat Transfer - Asian Research*, Vol. 37, No. 8, pp 445-459, 2008.

9 Goldstein , R. J and Franchett , M. E., Heat Transfer From a Flat Surface to an Obliquely Impinging Jet, *ASME Journal of Heat Transfer*, Vol. 110, pp. 84-90, 1988.

10 Liu, T.S., Sullivan, J.P., Heat Transfer and Flow Structures in an Excited Circular Impinging Jet, *Int. J. Heat Mass Transfer*, Vol. 39, No. 17, pp. 3695-3706, 1996.

11 Sozbir, N., Chang, Y.W., Yao, S.C., Heat Transfer of Impacting Water Mist on High Temperature Metal Surfaces, *Transactions of the ASME*, Vol. 125, pp. 70-74, 2003.

12 Shadlesky, P.S., Stagnation Point Heat Transfer for Jet Impingement to a Plane Surface, *AIAA Journal*, Vol. 21, pp. 1214-1215, 1983.

13 Rasipuram, S.C., Nasr, K.J., A Numerically-Based Parametric Study of Heat Transfer off an Inclined Surface Subject to Impinging Airflow, *International Journal of Heat and Mass Transfer*, Vol. 47, No 23, 4967-4977, 2004.

14 Hrycak, P., Lee, D.T., Gauntner, J.W., Livengood, J.N.B., Experimental Characteristics of a Single Turbulent Jet Impinging on a Flat Plate, *National Aeronautics and Space Administration*, Nasa TN D-5690, 1970.

15 Chattopadhyay, H., Numerical investigations of heat transfer from impinging annular jet, *International Journal of Heat and Mass Transfer*, Vol. 47, No. 14-16, pp. 3197-3201, 2004.

HEAT TRANSFER CHARACTERISTICS OF LAMINAR FLOW THROUGH A SQUARE RIBBED DUCT WITH WIRE COIL INSERTS

S. K. Saha[1], G. L. Dayanidhi[2]

[1] Professor
[2] Graduate Student
Mechanical Engineering Department,
Bengal Engineering and Science University Shibpur,
Howrah 711 103, INDIA

ABSTRACT. Thermal characteristics of laminar flow through square duct with periodic transverse ribs and through wire coil inserts have been studied experimentally. The duct is under uniform wall heat flux boundary condition. The effect of rib height, rib pitch, coil helix angle and coil wire diameter on axially averaged Nusselt number have been studied. It has been observed that the heat transfer increases with the increase of rib height and decrease of rib pitch, decrease of coil wire diameter and increase of coil helix angle.

Keywords: *Laminar Flow, Forced Convection, Ribbed Duct, Wire Coil Inserts, Enhanced Heat Transfer*

INTRODUCTION

Heat exchangers often operate at low flow velocity for many reasons, e.g. the heat transfer area is usually designed conservatively to be larger than actually needed so that the designed flow velocity is low; or the flow rate of heat exchanging fluid might not be enough; or the load is not full during production; etc. In these circumstances laminar flow occurs for which the heat transfer coefficient is very low. In these cases, different types of heat transfer enhancement techniques are used to increase the heat transfer rate, Webb and Kim [1]. In the present paper, results of experimental work on laminar flow heat transfer characteristics in a square duct with transverse periodic ribs of various height and pitch and through wire coil inserts with various coil helix angle and coil wire diameter have been presented.

EXPERIMENTAL SET UP, OPERATING PROCEDURE AND DATA REDUCTION

The schematic diagram of the experimental setup is shown in Figure 1 below.

1. The Storage Tank— It is a 900 mm×500 mm × 395 mm rectangular box made of PVC. The working fluid is the servotherm medium oil.

*Corresponding author: Prof. S. K. Saha
Phone: 919830493430, Fax: 913326682916
E-mail address: sujoy_k_saha@hotmail.com

2. The Working Fluid Circulating Loop – The working fluid passes through one of the three rotameters, calming section, the test section, mixing chamber, heat exchanger and back to the storage tank. The vane pump pumps the working fluid.

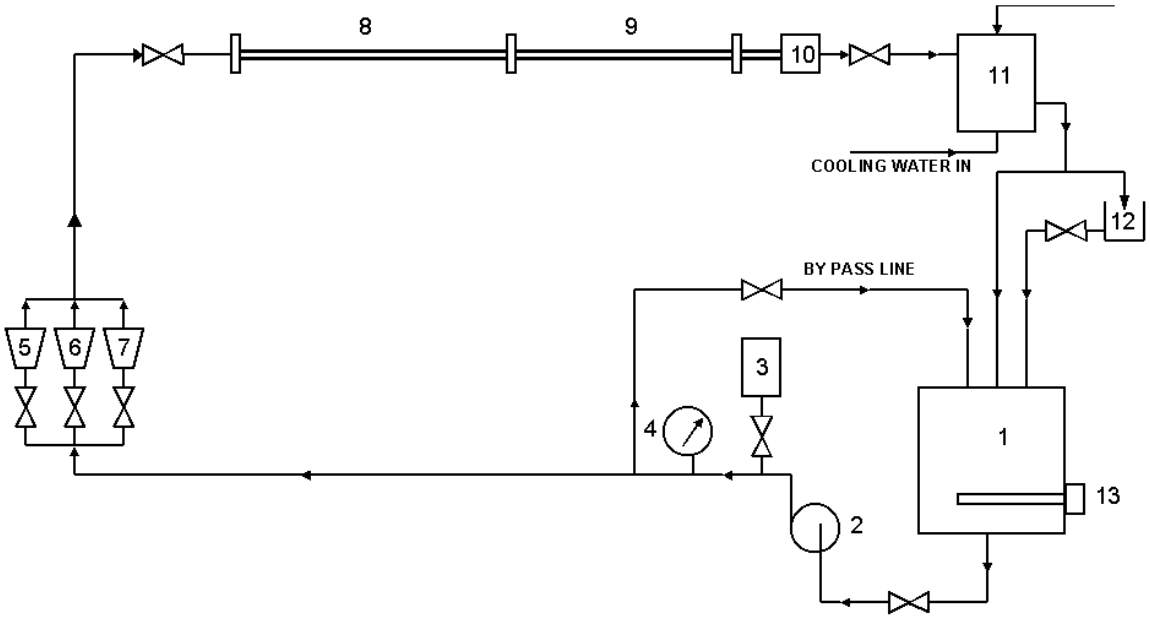

Figure 1.

1.	RESERVOIR	5, 6, 7.	ROTA METERS	11.	HEAT EXCHANGER
2.	PUMP	8.	CALMING SECTION	12.	WEIGHING PLATFORM
3.	ACCUMULATOR	9.	TEST SECTION	13.	HEATER
4.	PRESSURE GAUGE	10.	MIXING CHAMBER		

3. Test Section --- 13 mm × 13 mm square and [13 mm × 26 mm and 13 mm × 39 mm] rectangular SS heat transfer test section, all test sections 2 m long. Heat transfer test sections are wrapped with nichrome (20 gauge, 1.6 Ω /m) heater wire. Heat is supplied to the heat transfer test section by autotransformers. The power input is measured by digital voltmeter and ammeter. Ribs in the test section have heights (e) and pitch (P) such that e/D_h and P/e have pre-determined values, where D_h is the hydraulic diameter of the plain duct.
4. Calming Section – It is 25 mm OD and 1.2 m long GI pipe.
5. Mixing Chamber— It is 50 mm × 50 mm cross section 150 mm long GI piece with 12.5 mm × 12.5 mm helical plate at the centre having φ 6 mm holes in the plate.
6. Heat Exchanger --- Coil-in-shell type. The working fluid passes through the 10 mm ID and 12 mm OD and 15m long copper coil made into two coaxial coils having 150 mm and 120 mm PCD. The shell is a 190 mm OD 260 mm height MS drum with openings at top and bottom for the flow of the coolant.
7. Accumulator--- It is a 150 mm OD 115 mm height vertical MS drum to reduce pressure fluctuations.
8. Thermocouples --- 34 gauge Copper-Constantan, 28 in number; at seven locations (50mm, 500mm, 1000mm, 1250mm, 1500mm, 1750mm and 1950mm from the beginning of the heating); one each in the middle of each of the four edges.
9. Rotameters—3 in number—0.07 –0.7 kg/s; 0.0115—0.115 kg/s, 0.00175—0.0175 kg/s
10. Thermocouples are connected to the digital multimeter via 36-points selector switch box.
11. A centrifugal pump supplies the coolant raised from a reservoir to the overhead tank and then to the heat exchanger.

12. Heat transfer test section is electrically heated by nichrome heater wire giving uniform wall heat flux boundary condition. Nichrome heater wire is having porcelain bead insulation on it. There is no direct contact of the Nichrome heater wire with the duct wall. First, there is fibre glass tape insulation (electrical but not thermal) on the duct wall. Then the porcelain-bead covered Nichrome heater wire is wrapped on the duct wall. Two consecutive turns of the heater wire is seated side by side touching each other in each duct. The thermal conductivity of the duct wall material is high enough and the duct wall thickness is sufficient to ensure uniform wall heat flux. Asbestos rope and glass wool insulates the heat transfer test section after the heater wire. Finally the test section is covered with gunny bag.
13. Oil bulk-mean temperatures at inlet and outlet of the test section are also measured by copper-constantan thermocouples. The oil temperature at outlet is measured after the mixing chamber and this is uniform. The mixing chamber is a cylindrical box of rectangular cross-section. The mixing chamber has rectangular plates arranged inside in such a fashion that the working fluid moves in a serpentine path. This gives a uniform temperature of the working fluid at its exit plane. At other locations, the fluid bulk-mean temperatures are interpolated since the fluid bulk-mean temperature increases linearly for the uniform wall heat flux boundary condition. The duct wall temperature also rises linearly in the downstream fully developed region. Heat input to the test section is evaluated by measuring resistance of and voltage across the heater wires and the enthalpy rise of oil in its passage through the test duct. The electrical energy input and the enthalpy rise of the oil match within 3%. The enthalpy rise of the oil is taken as the thermal energy input to the heat transfer test section. Experimental uncertainty was determined by the method of Kline and McClintock [2]. The uncertainty in Reynolds number, Prandtl number and Nusselt number were $\pm$ 3%, $\pm$5% and ± 8%, respectively. The fluid temperature rise along the heated duct is not very high and fluid thermal properties being well documented, therefore, the uncertainties in fluid properties variation have been neglected without much loss in accuracy,
14. The axial local Nusselt number is determined from the peripherally averaged measured wall temperature and then the axially local Nusselt numbers at seven axial stations are axially averaged by trapezoidal rule.

RESULTS AND DISCUSSION

Figures 2-5 show the experimental heat transfer data. In Figure 2, it is seen that heat transfer is more for a square ribbed duct with wire coil inserts than that for a circular ribbed duct just as it happens for a plain duct. Also, for a larger rib height, the heat transfer is more than that in case of a smaller rib height. This observation is, however, more true for circular duct than that in case of square duct. The observed results can be explained by the fact that more recirculation, mixing with boundary layer separation and reattachment causes flatter temperature profile with increased Nusselt number and heat transfer. Figures 3-5 show the effects of rib pitch, coil wire diameter and coil helix angle, respectively on heat transfer. The larger the rib pitch, the less is the heat transfer as shown in Figure 3. This is true for both circular duct and square duct. The results are explained by the fact that, the number of occasions of boundary layer separation and reattachment is less with larger pitch and hence is the lower heater transfer. Figure 4 shows that the heat transfer is largely unaffected by the coil wire diameter. Figure 5 shows that heat transfer increases with the increase of coil helix angle. In Figures 2-5, X and Y are the multiplying factors.

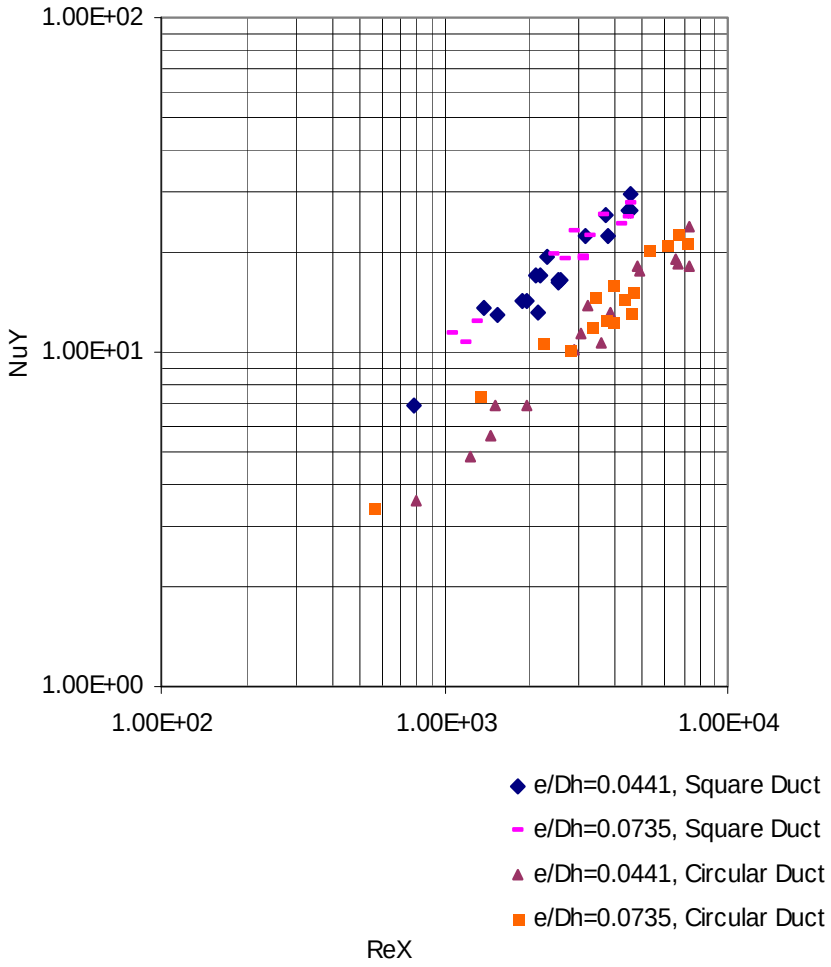

Figure 2. Effect of Rib Height on Nusselt Number---P/e=20, d/D_h=0.07692, Coil Helix Angle= 60^o

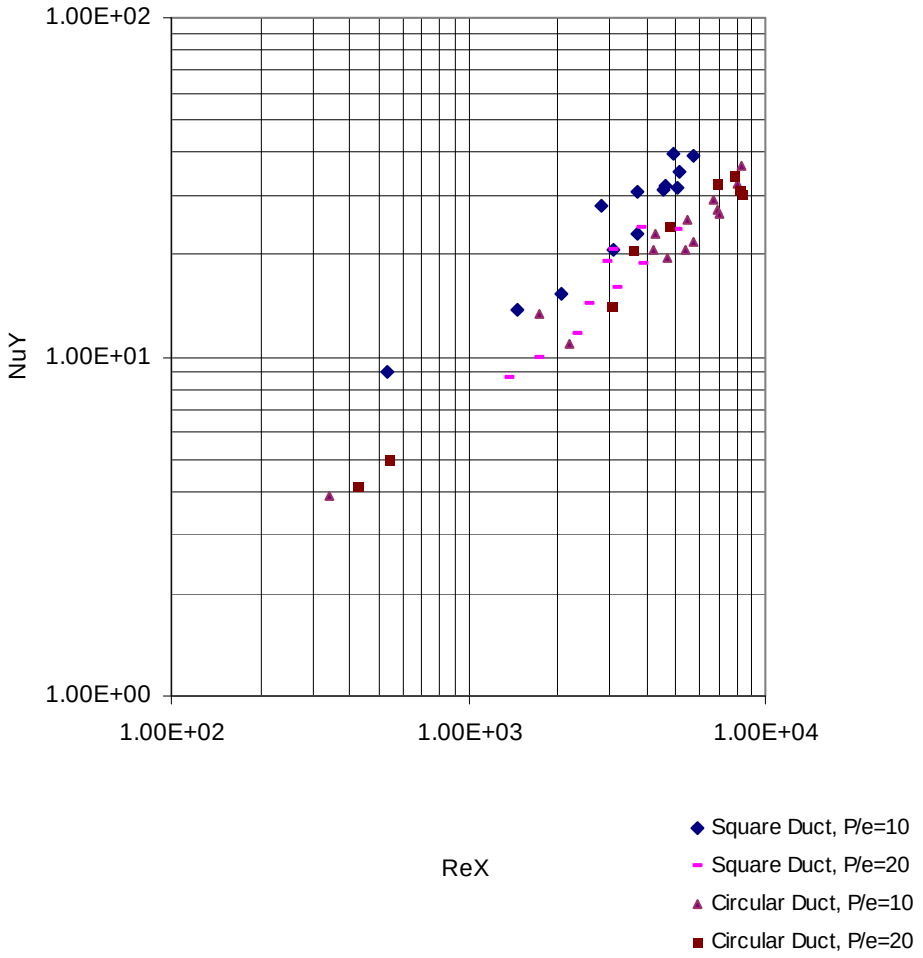

Figure 3. Effect of Rib Pitch on Nusselt Number--e/D_h=0.0735, d/D_h=0.07692, Coil Helix Angle=60^o

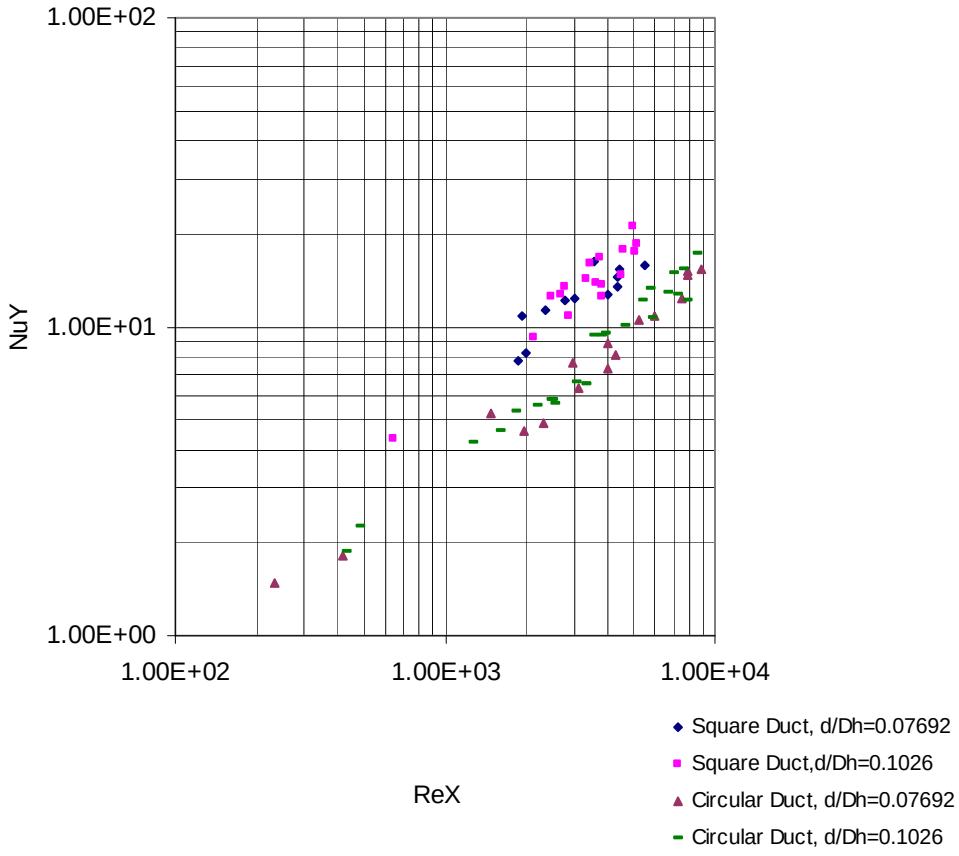

Figure 4. Effect of Coil Wire Diameter on Nusselt Number--e/D_h=0.0441, P/e=20, Coil Helix Angle=30^o

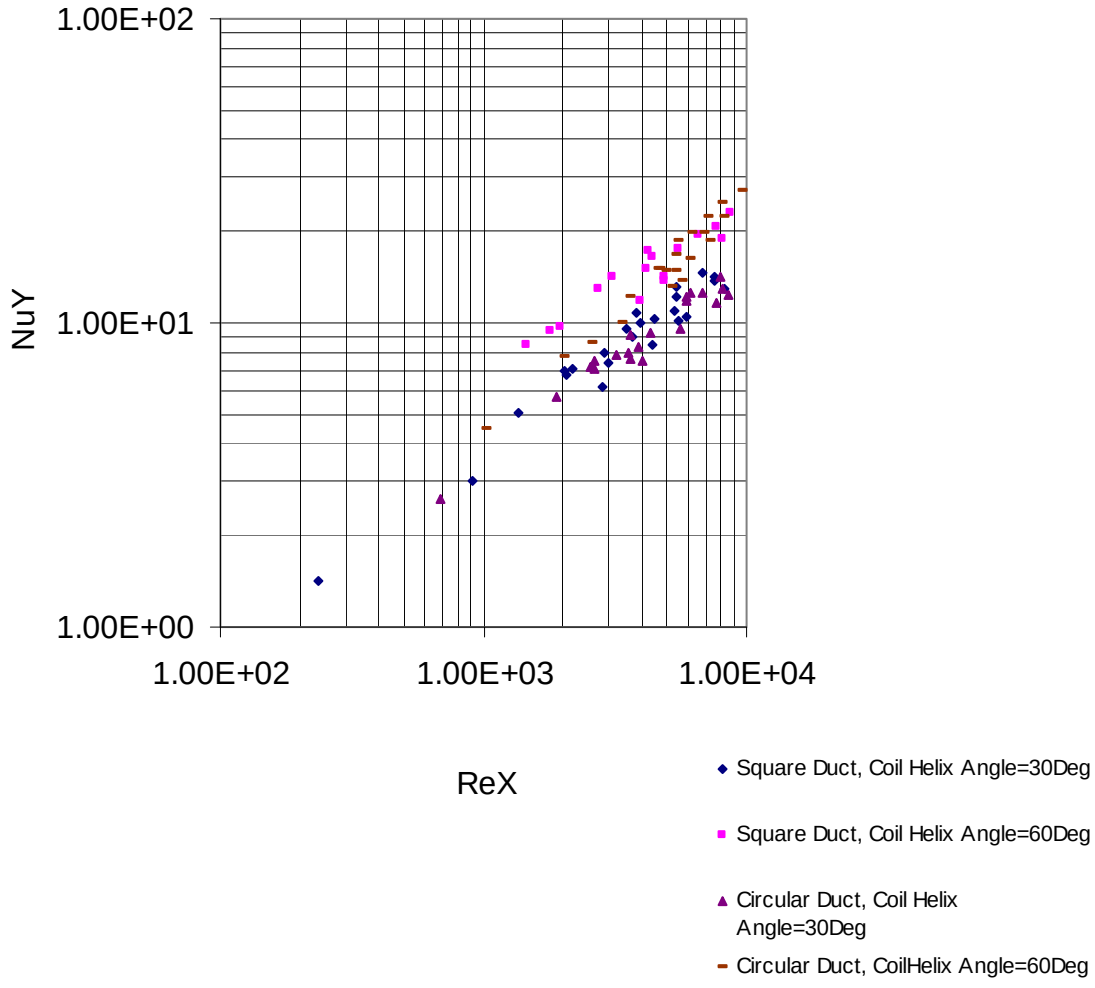

Figure 5. Effect of Coil Helix Angle on Nusselt Number--e/D_h=0.0441, P/e=20, d/D_h=0.07692

CONCLUSION

Thermal characteristics of laminar flow through square duct with periodic transverse ribs and through wire coil inserts have been studied experimentally. The duct is under uniform wall heat flux boundary condition. It has been observed that the heat transfer increases with the increase of rib height and decrease of rib pitch, decrease of coil wire diameter and increase of coil helix angle.

ACKNOWLEDGEMENTS

The authors gratefully acknowledge the financial support received for the research from the AICTE, DST and CSIR, Government of India.

REFERENCES

1. Webb, R. L. and Kim, N-H, 2005, Principles of Enhanced Heat Transfer, Taylor and Francis.
2. Kline, S. J. and McClintock, F. A. , (1953), Describing Uncertainties in Single Sample Experiments, Mechanical Engineering, 75 (1), pp 3-8.

INSTABILITY OF MECHANICAL EQUILIBRIUM AND DIFFUSION IN ISOTERMAL MULTI-COMPONENT GAS MIXTURES

G. Akylbekova,[1], **V.N. Kosov**[1], **S.T. Kuznetsov**[2], **Y.I. Zhavrin**[2]

[1]Kazakh National University named after Abay, 13, Dostyk av., 050100, Almaty, Kazakhstan .
[2]Institute of Experimental and theoretical physics 96a, Tole bi str.,050020, Almaty, Kazakhstan

ABSTRACT. In this particular work is given experimental and numerical study results of temperature gradient influence on concentrating convection, evolving from diffusion in isothermal gas mixtures.

Experiment method is as follows: Binary mixture of helium and argon was blended with nitrogen on the arrangement, realized double-envelope method. The density of helium and argon mixture in the upper envelope at any temperature is less than thickness of nitrogen in the lower part of arrangement. The temperature of the upper envelope was changed in the range of 278-473 K. The temperature of the lower envelope was constant and equal to 298 K. The pressure was 2.5MPa. After every experiment endings the gas mixture structure from both envelopes was analyzed.

As from this experiment, in this system existing unsteadiness mixture mechanical balance. Argon and nitrogen function is considerably more than helium. While growing of temperature convection current intention is decreasing. Convection is discontinued under the temperature definite critical meaning and molecular function became dominant.

Numerical analysis on stability of triple gas mixture mechanical balance shows existence possibility of diffusion and convection. In Relley's terms determined "non-isothermal diffusion - concentrating convection" conversion limit. Results of calculation by non-isothermal diffusion and concentrating convection determination in triple gas mixture depending on channel's temperature, length and radius satisfactory conform to experimental facts.

Keywords: *convection, diffusion, mixtures, instability*

INTRODUCTION

In isothermal binary gas mixture instability of mechanical equilibrium may occur only in case heavier in density gas appears above. Due to Archimedes buoyant force the convection appears in the mixture: heavier gas descends and the lighter one ascends. Convection continues until the lighter gas appears above. Addition of the third component to the mixture may under certain conditions result in disruption of mechanical equilibrium stability and convection shall appear even in case of stable density stratification. This effect can be explained by the fact that in isothermal three-component system convectional currents are induced by two concentration gradients instead of the figure of one. The report will focus on experimental and numerical results related to the investigation of "diffusion – concentration gravitation convection" regimes change in isothermal binary gas mixtures.

*Corresponding author: Prof.Vladimir Kossov,
phone: +7(727) 291 83 82, fax: +7(727) 291 83 82
E-mail: kosov_vlad_nik@list.ru,

EXPERIMENTAL DATA

Experiments on instability study were made on the basis of two-bulb method device (figure 1). Two bulbs of the same size were connected by a vertical canal. Pressure in the bulbs kept equal. The testing method corresponded to the classic scheme. Capillary to connect the bulbs opened and after certain time it was blocked. Mixture composition was being registered in both bulbs. The concentrations that appeared during testing were leveled to diffusions calculated in supposition.

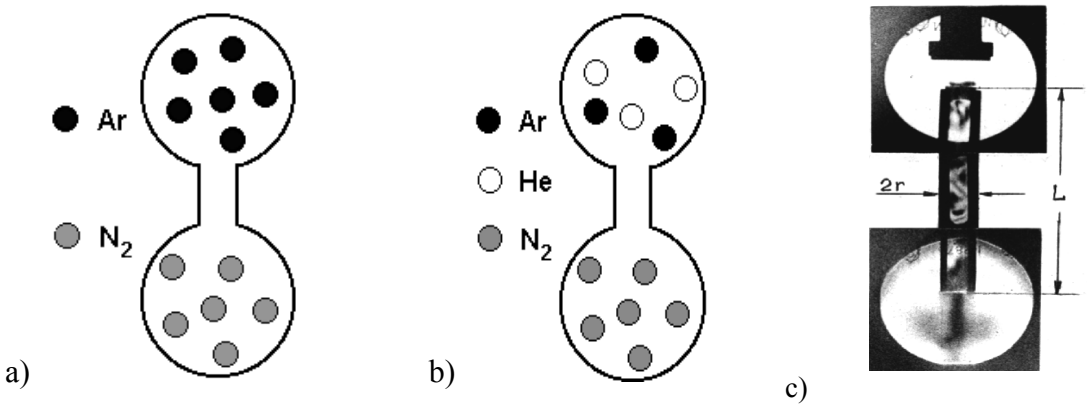

Figure 1. Scheme of diffusion cell.

Binary mixtures

The upper bulb contains gas (or gas mixture) which excels in density the component included into the lower bulb (figure 1a). Instability was studied when occurred as follows:

1) Variation of conditions was made by pressure change, all other thermodynamic parameters and geometrical characteristics of the instrument remained invariable;
2) All parameters were fixed, the system temperature varied;
3) Diffusion canal slope angle was changed relative to the vertical line under the same conditions.

Figure 2(a) shows typical dependence of the parameter thus achieved $\alpha = c_{\text{exp}} / c_{\text{theory}}$ on the pressure for the N_2 – He system. In case of $p < p_*$ pressures usual molecular diffusion occurs. In this case experimental values for concentrations are equal to the diffusion calculated in supposition. Dimensionless parameter α may be approximately equal to the figure of one. Upon pressure p_* =0,58 MPa α parameter exceeds figure of one. Mechanical equilibrium becomes unstable. Convection occurs.

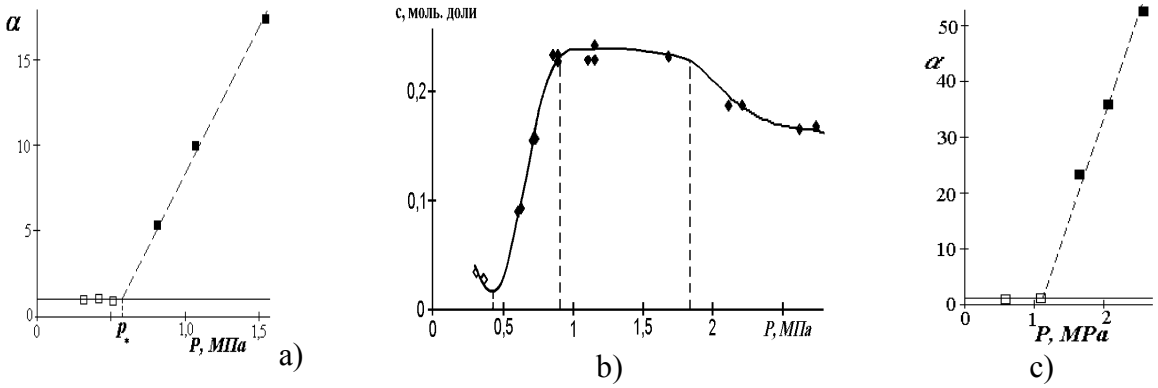

Figure 2. (a) Binary mixture N_2 – He, (gas – helium), T=298 K. □ – diffusion, ■ - convection. (b) System Ar – N_2, T=298 K., points ◇, ◆ – are experimental data for nitrogen. Firm line is the calculation using polynomial dependence. (c) Parameter α_{Ar} at various pressures in the mixture 0,4521 He + 0,5479 Ar – N_2, $T = 298{,}0$ K

Further α starts increasing by linear dependence at the initial stage. Thereby, in binary systems upon certain pressure p_* "diffusion – concentration gravitation convection" change occurs. Further pressure increase results in break of linear dependence. Figure 2(b) shows dependence of gas transferred during experiment on the pressure for system Ar – N_2. After convection appears mass transfer intensity in the system increases drastically to p_{**} pressure. After reaching p_{**} intensity of convection transfer remains relatively constant despite pressure increase. Further, after reaching p_{***} pressure, convection decreases. The dependence of mass transfer intensity on the pressure may be explained by change of current structure in the canal after pressure reaches p_{**} and p_{***}.

Dependence of α parameter on temperature and slope angle are equivalent (figure 2a). The experiments have revealed that pressure increase suppresses convection instability in binary mixtures. Study of the boundary of "diffusion – concentration gravitation convection" change upon changing a canal slope angle in relation to the vertical line showed that canal slope angle increase results in decreasing of instable process intensity. Upon certain angle the system changes its unstable position to the stable one, i.e. diffusion.

Three-component mixtures

Experiments to study "diffusion – concentration gravitation convection" regime change were made by the method used for binary mixtures. The upper bulb included binary mixture of the lighter and heavier components. Medium in density gas was included into the lower bulb. In all cases concentrations of the lighter and heavier components were selected so that mixture in the upper bulb was of a lower density. Thus achieved concentrations were leveled to diffusions in supposition calculated under Stephen-Maxwell equations. Figure 2(c) shows dependence of thus achieved parameter $\alpha_i = c_{i\,\mathrm{exp}} / c_{i\,\mathrm{theor}}$ on the pressure for He + Ar – N_2 system. As it is seen in the figure, α_i parameter under certain critical pressure exceeds figure of one, i.e. mechanical equilibrium of the mixture becomes unstable. Anomalous concentration gravitational convection occurs.

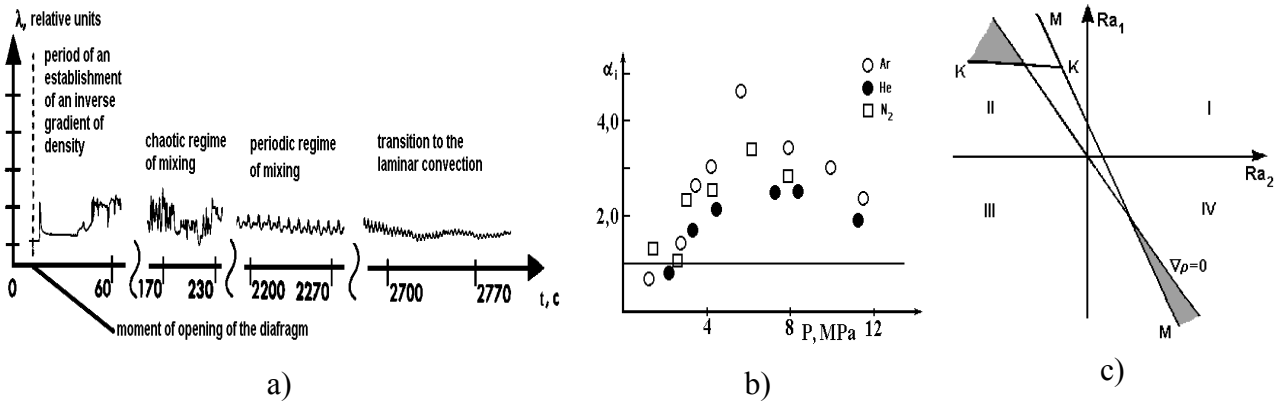

a) b) c)

Figure 3. (a) Change of heat conductivity of a mixture in time, illustrating a change of regimes of convection, (b) Values α_i of rate of flux for various components of a mixture 0,47 *He* + 0,53 *Ar* – N_2, normalized on the settlement charge in conditions of a mechanical equilibrium at change of pressure. $T = 293{,}0$ K. (c) The diagram of stability of three-component system on a plane of partial Rayleigh numbers. Above the line MM the convectional stream in system is stationary, above the semi-infinite line KK the regime of convection is periodic. The straight line passing through the origin of coordinates, divides a plane into areas with negative (below a straight line) and positive gradient of concentration. The shaded areas correspond to conditions of abnormal convection

Studies made in [2-6] have revealed that shift from diffusion to convection mixture is determined by the following critical parameters: pressure, temperature, mixture viscosity, its original composition, difference in diffusion components ratio, geometrical canal characteristics and its orientation in relation to the vertical line. For the purpose of visual registration of shift boundary we used Tepler's shadow method which is based on that rays of light in turbulent layers are deflected in different ways. Canal with transparent walls and right-angled in section was lit by a beam of light. The screen behind the canal was registering heterogeneous light intensity which varied in time. Device construction allowed monitoring convection currents in the device bulbs (figure 1c). Convection regime change may also be registered by quick-response sensors which define gas local heat conductivity. Gas mixture's heat conductivity depends on the component concentration which enables to determine typical periods of regimes being studied (figure 3 a).

Figure 3(b) shows dependence of gas transferred during the test on pressure for system 0,47 He + 0,53 Ar – N_2. There is a certain range of pressures in which anomalous division of mixture components can be seen. Further pressure increase results in stabilization of convective regime.

Theoretical analysis for convective stability of the gas mixture

Boundary of "diffusion – concentration gravitation convection" regime change may be obtained from hydrodynamics equation joint solution. For isothermal three-component gas mixture they are presented as follows:

$$\rho\left[\frac{\partial\vec{u}}{\partial t}+(\vec{u}\nabla)\vec{u}\right]=-\nabla p+\eta\nabla^2\vec{u}+\left(\frac{\eta}{3}+\xi\right)\nabla div\vec{u}+\rho\vec{g},$$
$$\frac{\partial\rho}{\partial t}+div(\rho\vec{u})=0,\ \rho\left(\frac{\partial c_i}{\partial t}+\vec{u}\nabla c_i\right)=-div\vec{j}_i, \qquad (1)$$
$$\vec{j}_1=-\rho\left(D_{11}^*\nabla c_1+D_{12}^*\nabla c_2\right),\ \vec{j}_2=-\rho\left(D_{21}^*\nabla c_1+D_{22}^*\nabla c_2\right),$$
$$\sum_{i=1}^{3}\vec{j}_i=0,\ \sum_{i=1}^{3}c_i=1.$$

Where ρ – density, u – velocity, t – time, p – pressure, η and ξ – ratios of shear and volume viscosity, g- gravity acceleration, c_i –i component concentration, D_{ij}* – multi-component diffusion matrix ratio. Ratios D_{ij}*, η, ξ are not subject to the mixture composition. Equations (1) are added by equalization of conditions $\rho=\rho(c_1,c_2,p),\ T=const.$ After applying traditional procedures to the tasks related to stability studies, which are as follows:

- Use of Boussinesq approximation;
- Neglecting minor squared agitations;
- Minor differences between average mass and number average velocities agitations;
- Neglecting pressure differential as an agitated value;
- Linear distribution of concentration in the vertical canal;
- Selection of typical large measurement units;
- Shift to dimensionless values

The equation system (1) is leveled to agitation equations made as dimensionless ones:

$$\mathrm{Pr}_{22}\frac{\partial c_1}{\partial t}-u=\tau_{11}\frac{\partial^2 c_1}{\partial x^2}+\frac{A_2}{A_1}\tau_{12}\frac{\partial^2 c_2}{\partial x^2},$$
$$\mathrm{Pr}_{22}\frac{\partial c_2}{\partial t}-u=\frac{A_1}{A_2}\tau_{21}\frac{\partial^2 c_1}{\partial x^2}+\frac{\partial^2 c_2}{\partial x^2}, \qquad (2)$$
$$\frac{\partial u}{\partial t}=\frac{\partial^2 u}{\partial x^2}+Ra_1\tau_{11}c_1+Ra_2c_2.$$

$Pr_{ii}=\nu/$ D_{ij}*– Prandtl number; $\nu=$ η/ρ; $Ra_i=g\beta_i A_i d^4/\nu$ D_{ij}*- Rayleigh number; $\tau\beta_i = -\frac{1}{\rho_0}\left(\frac{\partial\rho}{\partial c_i}\right)_{p,T,c_j\neq c_i}$, $_{ij}= D_{ij}$*/ D_{22}*; $A_i\gamma = -\nabla c_{i0}$, γ - unit vector.

Solution (2) results in definition of boundary lines of monotonous (MM) and oscillatory (КК) instabilities showed in figure 3c. Below of both lines the mechanical equilibrium is stable and above – unstable. Density is related to concentrations c_i of the components of

$\tau_{11}Ra_1 = - Ra_2$

In (Ra_1,Ra_2) this condition determines straight line going through origin of coordinates (figure 3б). Below the line $\nabla\rho<0$. Analysis (figure 3б) enables to reveal areas with negative density gradient but located above instability lines MM or КК. In figure 3c these areas are hatched. In the event of special selection of experiment conditions so that the system could appear in the given areas, anomalous convection shall occur. Comparison of experimental data with estimated ones under (1), (2) demonstrates well coordination.

CONCLUSIONS

Linear theory of stability, which takes into account an inversion of a gradient of density, adequately explains experimentally observed phenomenon. However, description of effects observed in the field of parameters considerably exceeding critical, lays out of its limits. To understand, how growing perturbations move over to convective structure it is necessary to refuse assumptions:

- small size of perturbations;
- Linear distribution of concentration on length of the channel.

ACKNOWLEDGMENTS

Authors thank professor Seleznev V.D. for useful discussion of the questions considered in the given work.

This work is supported by Fund of Science of the Ministry of the Science of Republic of Kazakhstan (projects: № 0100 RK 00514, 0103 RK 00617).

REFERENCES

1. V. N. Kosov, Yu. I. Zhavrin, N.B. Ankusheva Convective regimes of mixing in binary systems with the mechanical equilibrium instability of a gas mixture // *J. of Engineering Physics and Thermophysics*.. Vol. 81, No 3, pp. 525 – 532, 2008.
2. Zhavrin Yu.I., Kosov V.N., Seleznev V.D, "Anomalous gravitational instability of mechanical equilibrium during diffusion mixing in isothermal three-component gas mixtures," *Fluid Dynamics*, Vol. 35, No. 3, pp. 464-470, 2000.
3. Zhavrin Yu.I., Kosov V.N., Kulzhanov D.U., Karataeva K.K., "Effect of the pressure on the type of mixing in a three-componeny gas mixture containing a component possessing the properties of a real gas," *Technical Physics Letters*, Vol.26, No. 12, pp. 1108-1109, 2000.
4. Zhavrin Yu.I., Kosov V.N., Kulzhanov D.U., Poyarkov I.V., Ankusheva N.B., "Effect of cell rotation speed upon mutual diffusion in a three-component gas mixture," *Technical Physics Letters*, Vol. 29, No. 2, pp. 108-110, 2003.
5. Kosov V.N., Seleznev V.D., Zhavrin Yu.I., "Separation of components during isothermal mixing of ternary gas systems under free-convection conditions," Zh.T.F., Vol.42, No. 10, pp. 1236-1237, 1997.

6. Yu. I. Zhavrin, M. Mukamedenkyzy, I.V. Poyarkov Diffusive and convective mixing of a propane-carbon dioxide binary mixture with pure nitrogen protoxide // Technical Physics. Vol. 52, No 7, pp. 947-949, 2007.
7. Joseph D.D., Stability of Fluid Motions, Springer, Berlin, 1976.
8. Gershuni G.Z. and Zhukhovitskii E.M., Convective Stability of an Incompressible Fluid, Nauka, Moscow, 1972.

Micro - Electro - Mechanical Systems

MICROCHANNEL HEAT TRANSFER AND PRESSURE DROP PERFORMANCE: SINGLE-PHASE, BOILING AND CONDENSATION

R.K. Shah[1], G.P. Celata[2]
[1]Indian Institute of Technology Bombay, Powai, Mumbai 400 076, India
[2]ENEA, Energy Department, Via Anguillarese 301, 00123 SM Galeria, Rome, Italy

ABSTRACT. Microchannels (smaller than 0.5 mm dia) are emerging geometries for heat and mass transfer applications. The major benefit is to obtain ultra high heat transfer coefficients with equal or somewhat higher pressure drop compared to mini channels and compact heat exchangers depending on the applications. Extensive research efforts are going on world wide to understand the phenomena and develop design data base. As of today, no commercial products are available that use microchannels. In this state-of-the art review, an attempt has been made to summarize heat transfer information for small diameter tubes since this is an area of newer applications to be emerged. The focus will be to summarize the phenomena and design information for single-phase flow, boiling and condensation. Also summarized will be the current challenges and opportunities.

KEYWORDS: *Microchannel Heat Exchanger, Single-phase Convection, Boiling, Condensation*

INTRODUCTION

Microchannels (circular and noncircular) and micropipes are emerging geometries for heat and mass transfer, controlled fluid transport and thermal control in about 0.5 mm and smaller size passages. Since many authors have defined microchannels different way, the definition by Thome (2004) appears to be more technical. He defines microchannels with upper and lower bound for geometrical dimensions as follows: The upper limit (the largest diameter) corresponds to confined bubble flow and the lower limit corresponds to the complete suppression of nucleation and hence threshold to nanochannels for two-phase flows.

Applications include many heat transfer simple and complex devices including microchannel heat sinks, microchannel heat exchangers, micropumps, microelectromechanical systems (MEMS) and biomedical and genetic engineering simulating biological and life science phenomena in the advancing technologies. Microprocessors generate increasingly larger amounts of heat with improved processing speeds from MHz to GHz. This heat must be removed so that the chip does not overheat and deteriorate in performance. In the review here, we will focus primarily on heat transfer and pressure drop aspects and design information in microchannels associated with single-phase and phase-change (two-phase, boiling and condensation) fluids, and will neglect the effects of electrokinetics and electroosmotic forces.

Why do we need microchannel flow passages? There are several reasons depending on the applications: (1) High and ultra high heat transfer rates per unit volume of the heat exchanger. This translates into low physical volume for the heat transfer device generally with lower total cost as the technology advances, and the same pressure drop as the macro heat exchanger if the design is done

* Corresponding author: Dr G.P. Celata
Phone: +39 6 3048 3905, Fax: +39 6 3048 3026
E-mail address: celata@enea.it

properly, i.e., the number of microchannel passages is increased to maintain the same flow area and/or reduces flow length. (2) In microelectronic (PCs, servers, laser diodes, RF devices, etc.) and micromedical devices, higher heat dissipation than was possible in 1993 (~ 200 W/m^2), and this limit is pushed to about 1000 W/m^2 with the temperature differences for heat transfer becoming smaller to a few °C and microchannel size to few microns (Kandlikar and Garimella, 2006). (3) With emerging technology in many fields that use micro devices, they will require cooling where micro heat exchangers will become essential.

The materials used for mini/microchannels are polymers, metal, glass, and ceramics. The choice of material depends on the following factors: temperature resistance, corrosion resistance and thermal properties. Since this is evolving technology, small physical sizes involved and there are not enough applications, there are no codes and standards imposed on micro heat exchangers. The manufacturing technologies used are silicon technologies (dry and wet etching), wet chemical etching, mechanical micro machining, and laser machining. Microstructures like minichannels have many potential applications such as heat transfer, evaporation, mixing, generation of emulsions, and running chemical reactions in the lab-scale range (Brandner et al., 2007).

There are many techniques to realize miniaturized channels but four process technologies are imposing for system miniaturization:

- Micromechanical machining (such as diamond machining, laser processes, focused ion beam, microdrilling);
- X-ray micromachining (such as LIGA LItographie-Galvanoformung-Abformung);
- Photolithographic-based processes (such as Si chemical etching);
- Surface and surface-proximity-micromachining (epimicromachining) processing techniques.

Our focus in this paper will be to provide a state-of-the art review starting with some basic information followed by the recent developments in single-phase, two-phase (with no heat transfer), boiling and condensation heat transfer phenomena in circular and noncircular channels as well as some information on the actual heat exchangers being evaluated.

CLASSIFICATION OF MICROCHANNELS

Most classification methods are rules-of thumb classifications. Based on industrial application viewpoint, Shah (1981, 1998) defined a heat exchanger as compact, meso (laminar flow) or micro heat exchanger based on the surface area density β of the heat transfer surface on one fluid side of the exchanger as follows:

Compact heat exchanger: $\beta > 700$ m^2/m^3 or $D_h \le 6$ mm for gas flows
$\beta > 400$ m^2/m^3 for liquid flows

Laminar flow (or meso) heat exchanger: $\beta > 3000$ m^2/m^3 or $100\ \mu m \le D_h \le 1$ mm for gas flows

Micro heat exchanger: $\beta > 10000$ m^2/m^3 or $1\ \mu m \le D_h \le 100\ \mu m$

Mehendale et al. (2000) proposed the definitions of channels as follows:

Microchannels: $1\ \mu m < D_h \le 100\ \mu m$
Mesochannels: $100\ \mu m < D_h \le 1$ mm
Compact passages: 1 mm $< D_h \le 6$ mm
Conventional passages: $D_h > 6$ mm

Kandlikar and Grande (2002) defined various channel sizes as follows:

Conventional channels: $D_h > 3$ mm
Minichannels: 200 μm < $D_h \leq 3$ mm
Microchannels: 10 μm < $D_h \leq 200$ μm
Transitional Microchannels: 1 μm < $D_h \leq 10$ μm
Transitional Nanochannels: 0.1 μm < $D_h \leq 1$ μm
Molecular Nanochannels: $D_h \leq 0.1$ μm

Cheng and Wu (2006) provided the classification of the small channels based on the relative importance of the buoyancy force to surface tension force (going away from the rules-of-thumb classification), and showed that that this ratio can be translated to a ratio of the hydraulic diameter to the capillary length. This ratio is defined as Bond number as follows.

$$Bo_d = \left(\frac{D_h}{\ell_c}\right)^2 = \frac{g(\rho_\ell - \rho_v)D_h^2}{\sigma} \tag{1}$$

where $\ell_c = [\sigma/\{g(\rho_\ell - \rho_v)\}]^{1/2}$ is the capillary length; D_h is the hydraulic diameter of the channel; g is the gravitational acceleration; σ is the surface tension; and ρ_ℓ and ρ_v are the densities of the liquid and vapor, respectively. Cheng and Wu (2006) then proposed the definitions as

- Microchannel: $Bo_d \leq 0.05$ where the gravity effect can be neglected.
- Minichannel: $0.05 < Bo_d < 3.0$ where the surface tension effect becomes dominant and the gravity effect is small.
- Macrochannel: $Bo_d > 3.0$ where surface tension is small in comparison with gravitational force.

It is relevant to point out that the Bond number, defined by Eq. (1), has taken into consideration the effects of temperature, pressure, and physical properties of the fluid. According to the above classification, the minichannels have the hydraulic diameter 0.5–30 mm at 450 K and microchannels have the hydraulic diameter less than 0.5 mm (at 450 K) for phase change heat transfer if water is used as the working fluid.
It should be emphasized that most of the results presented in the literature do not conform to any of the above definitions, and simply consider any tubes having 2 mm or less hydraulic diameter as the microtube or microchannel!

HEAT TRANSFER AND PRESSURE DROP PHENOMENA AND CORRELATIONS

Single-Phase Flows

Flow and heat transfer phenomena in microchannels and minichannels are the same as those in macrochannels. Shah and Sekulić (2003) have presented extensive data on friction factors, Nusselt numbers, entrance lengths, additional pressure drops due to entrance length, etc. for a large number of flow passages for developed and developing laminar and turbulent flows in channels. Some basic information is provided in Tables 1-2.
Han and Kedzierski (2007) measured pressure drop in microtubes of diameters 97-260 μm and Reynolds number range of 30-3000. Tubes were made of three different materials: fused silica, polyetheretherketone and stainless steel. Three different fluids, distilled water, tap water and deionized water were used to investigate the effect of ionic composition of the fluids on the pressure drop. Other parameters investigated were: influence of surface polarity and the effect of micro-particles. With

systematic variations of tube length, material and diameter, as well as fluid type and filtering, they found that the measurements agreed with the classical theory of flow in a pipe, including no earlier transition from laminar to turbulent flow. They showed that the pressure drop dependence on Reynolds number is the same as that for macrotubes and the classical theory including no significant effect of viscous dissipation, microparticles or small surface roughness of the tubes.

Table 1. Fully developed laminar flow design data for ducts of various geometries. Transition and turbulent flow correlations for ducts of various geometries. (Shah and Sekulić, 2003)

Geometry ($L/D_h > 100$)	Aspect Ratio	Nu_{H1}	Nu_{H2}	Nu_T	$f \cdot Re$	$\frac{j_{H1}}{f}^a$	$K(\infty)^b$	$L_{hy}^{+}{}^c$
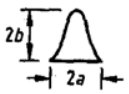	$\frac{2b}{2a}=\frac{\sqrt{3}}{2}$	3.014	1.474	2.39	12.630	0.269	1.739	0.040
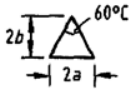	$\frac{2b}{2a}=\frac{\sqrt{3}}{2}$	3.111	1.892	2.47	13.333	0.263	1.818	0.040
	$\frac{2b}{2a}=1$	3.608	3.091	2.976	14.227	0.286	1.433	0.090
		4.002	3.862	3.34	15.054	0.299	1.335	0.086
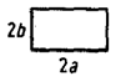	$\frac{2b}{2a}=\frac{1}{2}$	4.123	3.017	3.391	15.548	0.299	1.281	0.085
		4.364	4.364	3.657	16.000	0.307	1.250	0.056
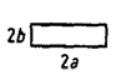	$\frac{2b}{2a}=\frac{1}{4}$	5.331	2.94	4.439	18.233	0.329	1.001	0.078
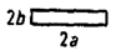	$\frac{2b}{2a}=\frac{1}{6}$	6.049	2.93	5.137	19.702	0.346	0.885	0.070
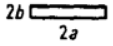	$\frac{2b}{2a}=\frac{1}{8}$	6.490	2.94	5.597	20.585	0.355	0.825	0.063
	$\frac{2b}{2a}=0$	8.235	8.235	7.541	24.000	0.386	0.674	0.011

Additional Effects on Single-Phase Performance due to Microscale of the Geometry

Two most important parameters come into picture for mini and micro channels are: surface roughness and channel straightness along the flow length of the flow passages. Generally, the effect of relatively non-straight flow length on heat transfer is small and is ignored since the tubes are generally not long. Otherwise, the results inferred from curved ducts may be considered. Also, the microchannels are usually short and the entrance length effect may not be negligible and may need to be taken into account.

Table 2. Transition and turbulent flow friction factor and Nusselt number correlations in circular and noncircular channels (Shah and Sekulić, 2003)

Type of Flow and Geometry	Correlations	Eq. No.	Remarks	Reference
Transition and turbulent flow, circular or non-circular duct	$f = A + B \cdot \mathrm{Re}^{-1/m}$ 1. $A = 0.0054$; $B = 2.3 \times 10^{-8}$; $m = -2/3$ 2. $A = 0.00128$; $B = 0.1143$; $m = 3.2154$	(7.70)	Bhatti–Shah correlation 1. $2100 \le \mathrm{Re} \le 4000$ 2. $4000 < \mathrm{Re} \le 10^7$ Accuracy ±2%	Bhatti and Shah (1987)
Turbulent flow in a smooth duct	Blasius: $f = 0.0791\mathrm{Re}^{-0.25}$ McAdams: $f = 0.046\mathrm{Re}^{-0.2}$ Bhatti and Shah: $f = 0.00128 + 0.1143\mathrm{Re}^{-0.311}$	(7.71) (7.72) (7.73)	$4000 < \mathrm{Re} < 10^5$ $30{,}000 < \mathrm{Re} < 10^6$ $4000 < \mathrm{Re} < 10^7$ Accuracy ±2%	Bhatti and Shah (1987)
Turbulent flow in a smooth duct	$\mathrm{Nu} = \dfrac{(f/2)\mathrm{Re} \cdot \mathrm{Pr}}{C + 12.7(f/2)^{1/2}(\mathrm{Pr}^{2/3} - 1)}$ $C = 1.07 + \dfrac{900}{\mathrm{Re}} - \dfrac{0.63}{1 + 10\mathrm{Pr}}$	(7.74) (7.75)	Petukhov–Popov correlation Accuracy ±5% $4000 \le \mathrm{Re} \le 5 \times 10^6$ $0.5 \le \mathrm{Pr} \le 10^6$ Obtain f from Eq. (7.70) or (7.73)	Petukhov and Popov (1963)
Transition and turbulent flow, circular or non-circular duct	$\mathrm{Nu} = \dfrac{(f/2)(\mathrm{Re} - 1000)\mathrm{Pr}}{1 + 12.7(f/2)^{1/2}(\mathrm{Pr}^{2/3} - 1)}$	(7.76)	Gnielinski correlation Accuracy ±10% $2300 \le \mathrm{Re} \le 5 \times 10^6$, $0.5 \le \mathrm{Pr} \le 2{,}000$ Not a good correlation in the transition regime Obtain f from Eq. (7.70) or (7.73)	Gnielinski (1976)
Transition and turbulent flow, circular or non-circular duct	$\mathrm{Nu} = \phi\mathrm{Nu}_{\mathrm{lam}} + (1 - \phi)\mathrm{Nu}_{\mathrm{turb}}$ $\phi = 1.33 - (\mathrm{Re}/6000)$	(7.77) (7.78)	Use $\mathrm{Nu}_{\mathrm{turb}}$ from Eq. (7.74) or (7.76) and $\mathrm{Nu}_{\mathrm{lam}}$ from Table 7.3 Applicable for $2000 < \mathrm{Re} < 8000$	Taborek (1990)
Turbulent flow in a smooth duct	$\mathrm{Nu} = 0.023\mathrm{Re}^{0.8} \cdot \mathrm{Pr}^{0.4}$	(7.79)	So-called Dittus–Boelter correlation Used for approximate calculations	Winterton (1998)

What is considered a smooth tube ($\varepsilon/D_h = 0.0001$ at $\mathrm{Re} = 10^5$) for large diameter tubes (about 3 mm and larger) becomes increasing rough surface (for the same surface roughness height) as the diameter continues to go down in microns. This surface roughness essentially reduces the flow area and/or changes the effective flow cross section shape which in turn affects the fully developed friction factor and Nusselt numbers. Thus the effect of surface roughness should also be taken into account in laminar flow for microchannels by considering an effective diameter what Kandlikar names it as constricted diameter.

As in non-microchannels, the thermal boundary condition for heat transfer through microchannels is also ambiguous and falls in between constant wall temperature and constant heat flux boundary conditions. Not enough data are available to provide a correlation for this effect (Kandlikar and Garimella, 2006), as shown in table 3. Now we provide correlations for laminar and turbulent flow heat transfer and flow friction in microchannel passages.

Single-Phase Flow Friction in Laminar/Turbulent Flow

Kandlikar (2005) suggested to use the constricted diameter $D_{cf} = D - 2\varepsilon$ for the Reynolds number calculation and then use the Moody diagram for the determination of turbulent flow friction factors for microchannels. Here ε is the equivalent roughness and is the same as that used by Nikuradse. The transition Reynolds number reduces from about 2300 for a smooth tube to about 500 for a rough microtube having $\varepsilon/D_{h,cf} = 0.14$. Kandlikar then presented the following laminar-to-turbulent transition Reynolds number criteria as:

$$\mathrm{Re}_{t,cf} = 2300 - 18750\,(\varepsilon/D_{h,cf}) \qquad \text{for } 0 < (\varepsilon/D_{h,cf}) \le 0.08 \tag{2}$$

$$Re_{t,cf} = 800 - 3270\ (\varepsilon/D_{h,cf} - 0.08) \qquad \text{for } 0.08 < (\varepsilon/D_{h,cf}) \le 0.15 \tag{3}$$

Table 3. Fully developed laminar flow Nusselt numbers (Kandlikar and Garimella, 2007)

$\alpha_c = a/b$	$Nu_{fd,3}$	$Nu_{fd,4}$
0	8.235	8.235
0.10	6.939	6.700
0.20	6.072	5.704
0.30	5.393	4.969
0.40	4.885	4.457
0.50	4.505	4.111
0.70	3.991	3.740
1.00	3.556	3.599
1.43	3.195	3.740
2.00	3.146	4.111
2.50	3.169	4.457
3.33	3.306	4.969
5.00	3.636	5.704
10.00	4.252	6.700
>10.00	5.385	8.235

a – unheated side in three-side heated case.

Friction factors in the transition region for rough microtubes ($\varepsilon/D_{h,cf} \le 0.05$) at a given Reynolds number can be obtained by a linear interpolation of (i) the laminar friction factor $f_{cf} = 16/Re_{cf}$ and fully developed turbulent friction factor obtained from the following equations depending on the value of $(\varepsilon/D_{h,cf})$.

$$f_{cf} = \begin{cases} \dfrac{0.25\left[\log_{10}\left(\dfrac{\varepsilon/D_{h,cf}}{3.7} + \dfrac{5.74}{Re_{cf}^{0.9}}\right)\right]^{-2}}{4} & for\ 0 \le \varepsilon/D_{h,cf} \le 0.03 \\ 0.0105 & for\ 0.03 \le \varepsilon/D_{h,cf} \le 0.05 \end{cases} \tag{4}$$

Single-Phase Nusselt Numbers for Laminar/Turbulent Flow

For heat transfer, determine analytical Nusselt numbers for laminar flow through smooth rectangular passages with aspect ratio α_c (1 for square passages to 0 for parallel plates) from the correlations of Shah and Sekulić (2003) as follows for Ⓣ, Ⓗ1, and Ⓗ2 thermal boundary conditions.

$$Nu_T = 7.541(1 - 2.610\alpha_c + 4.790\,\alpha_c^2 - 5.119\,\alpha_c^3 + 2.702\,\alpha_c^4 - 0.548\,\alpha_c^5) \tag{5}$$

$$Nu_{H1} = 8.235(1 - 2.041\alpha_c + 3.0853\,\alpha_c^2 - 2.4765\,\alpha_c^3 + 1.0578\,\alpha_c^4 - 0.1861\,\alpha_c^5) \tag{6}$$

$$Nu_{H2} = 8.235(1 - 10.6044\alpha_c + 61.1755\,\alpha_c^2 - 155.1803\,\alpha_c^3 + 176.9203\,\alpha_c^4 - 72.9236\,\alpha_c^5) \tag{7}$$

It should be mentioned that the reduction in effective hydraulic diameter of a microchannel due to surface roughness would theoretically increase the heat transfer coefficient (for a constant Nusselt number). However, for conservative analysis and not knowing the effect of other factors on Nu, we generally ignore this effect and determine Nu based on the specified full diameter of the microchannels.

Since the rectangular cross section has four sides, the more common boundary condition for microchannel applications is the cross section heated on four sides; however, in experimental studies, heat transfer takes place from three sides and the fourth side has the cover of glass or some material bonded on the top side to form the microchannel. Hence, the fully developed laminar flow Nusselt numbers are presented in Table 3 for three and four side heated rectangular channels (Shah and London, 1978, Kandlikar and Garimella, 2006).
Longitudinal heat conduction in tube walls may not be important for microtubes because of thin walls and having short flow length. However, if the computer programs are used for the design/analysis purpose for a microchannel heat exchanger, this effect is generally taken care in most commercial software.
Kandlikar et al. (Kandlikar and Garimella, 2006) also present some information on enhanced (Offset strip fin geometry) microchannels, as shown in Fig. 1.

Two-Phase Flow in Microchannels: Transition from Macro to Microchannel Phenomena
There are several analytical approaches presented in the literature for quantitative evaluation of the transition regime based on the pertinent dimensionless groups. In the microscale, the surface tension is more important and the influence of gravity diminishes as the tube diameter reduces and hence no stratified flow exists.
Kew and Cornwell (1997) empirically proposed the transition from macro-to-microscale diameter d_{th} to occur at the Bond number Bd = 4. Here,

$$d_{th} = 2\left(\frac{\sigma}{g(\rho_L - \rho_G)}\right)^{1/2} \qquad Bd = \frac{g(\rho_L - \rho_G)d_i^2}{\sigma} \tag{8}$$

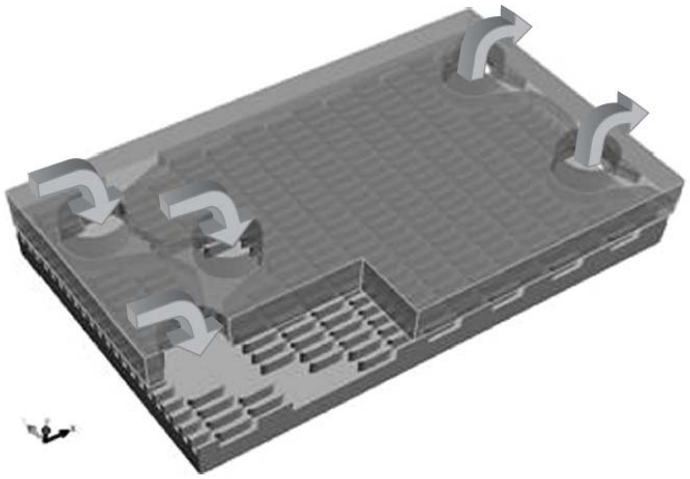

Figure. 1 - Three-dimensional rendition of the IBM enhanced silicon chip with short multiple fluid streams

The $d_{th} < 4$ represents the threshold to confined bubble flow (microscale flow). Some researchers use the confinement number Co instead of the Bond number. Note that Co = Bd/4 by definition.
Kawaji and Chung (2003) refined Kew and Cornwell criterion to include other dimensionless groups to take into account the comprehensive effect of all other acting forces as follows:

Bond number Bd <<4

Weber number $\quad We_{SL} = \frac{\rho_L U_L^2 d_i}{\sigma} << 1 \qquad We_{SG} = \frac{\rho_G U_G^2 d_i}{\sigma} << 1$

Reynolds number $\quad Re_{SL} = \frac{\rho_L U_L d_i}{\mu_L} < 2000 \qquad Re_{SG} = \frac{\rho_G U_G d_i}{\mu_G} < 2000$

Capillary number $\quad Ca_L = \frac{\mu_L U_L}{\sigma} << 1$

Superficial velocity: Gas $U_G = \frac{\dot{Q}_G}{A}$ $\qquad$ Liquid $U_G = \frac{\dot{Q}_G}{A}$

Ullman and Brauner (2007) suggested the transition from macro-to-microchannel threshold to occur at Bd ≈ 0.8, somewhat lower diameter than that of Kew and Cornwell (1997).

Two-Phase Flow Phenomena and Flow Regimes

As mentioned earlier, in the single-phase flow, there are no new fluid flow and heat transfer phenomena in two-phase flow (isothermal, i.e., without heat transfer) and boiling. The results for smooth macrochannels are also applicable to microchannels, except that one has to take into account the wall surface roughness introduced due to microchannel size. In the case of two-phase flow, boiling and condensation in microchannels, this is not the case since the flow regimes are somewhat different in microchannels, and the results for macrochannels may not be applicable to microchannels (D_h < 0.5 mm) due to underlying changes in the physics considerably. For example, surface tension effect (important primarily for condensation) becomes more important as the channel size reduces and the gravitational force becomes weaker. We will summarize these differences now.

Let us start first with the transition from macro-to-micro channel boiling phenomenon followed by the flow regimes. From the phenomena viewpoint, some flow regimes may be suppressed or become of secondary importance while some others may become important as the channel size reduces. These changes are usually gradual as the channel size reduces. Based on published flow visualization results, Thome (2008) concluded that the transition regime for stratified-wavy and fully stratified flow regimes in microchannels occurs in the range 0.5 – 2 mm tube diameter and below 0.5 mm tube diameter it becomes either annular flow or elongated bubble flow. Cheng et al. (2006) conducted an extensive study on flow regimes in vertical tubes (1.01–4.25 mm diameters) with R134a having the pressure range 6–14 bar. They found that none of the macroscale flow regime maps were able to predict their observations. They concluded 2 mm tube size as the boundary between large and small tube behavior with confined flow in the smaller tubes.

Chen et al. (2007) reported that isolated bubble (bubbly flow), confined bubble (plug/slug flow), annular flow and mist flow may exist during flow boiling in microchannels. In the stable flow boiling mode, vapor bubbles grow on the heated wall and carried away by the liquid. In unstable flow boiling mode with long-period oscillations, cyclic variations in pressure and temperature have been observed along with back and forth changing of bubbly flow and annular/mist flow with short-period oscillations.

Two-Phase Pressure Drop

Two-phase pressure drop data are not affected by going from macro-to-microscale in slug and annular flow, and the homogeneous flow model works very well (Thome, 2008).

The pressure drop during flow boiling in multi-microchannels was investigated for R236fa and R245fa, showing that R245fa yields higher pressure drops for chip cooling applications, due to its low vapour density. The total pressure drop was shown to increase almost linearly with vapour quality and as the square of the mass velocity, and to decrease with increasing saturation temperature. The homogeneous model correctly predicted these pressure drop trends and is recommended to be used together with the

inlet and outlet singular pressure drops to predict the total pressure drop in the present multi-microchannel configuration. Furthermore, an analysis showed that for the channel geometry and at the mass velocity and vapour quality required for a chip cooling application, the pressure drop is mainly controlled by the two-phase flow in the microchannels and not the headers with their orifices. However, the outlet pressure drop is not negligible and can represent up to 30% of the total pressure drop.

Flow Boiling

For flow boiling heat transfer in small channels, several studies indicated that as the diameter is reduced, the flow boiling heat transfer coefficient increases, again approximately the 2 mm diameter tube is the boundary between micro-to-macroscale transition, for low vapor quality about 0.25 or so.

Boiling in Microchannels

Thome (2006) provided a review of boiling and two-phase flow in microchannels. His conclusions were: more data are needed to understand and predict the flow boiling phenomena in microchannels: boundary between microchannels and macrochannels, critical heat flux data for circular and noncircular channels, fluid properties, inlet header geometry, two-phase flow transitions, flow instability and flow-induced fluctuations, etc.

Cheng et al. (2007) summarized Yen et al. (2003) work with the following three boiling modes in microchannels (based on the data for a microchannel of 0.186 mm diameter at an inlet subcooling of 35°C):

- Stable flow boiling with no periodic oscillation ($q/G < 0.96$ kJ/kg); isolated bubbles are generated.
- Unstable flow boiling with long-period oscillation (0.96 kJ/kg $< q/G <$ 2.14 kJ/kg); elongated bubbles expand upstream to near the inlet of the microchannel and makes the flow as annular/mist flow.
- Unstable flow boiling with short-period oscillations ($q/G >$ 2.14 kJ/kg) with annular and mist flow appearing alternately with time. Periodic dryout and rewetting has been observed.

Agostini et al. (2008a, 2008b, 2008c) conducted an experimental study in high heat flux flow boiling in silicon multi-microchannels using refrigerants R236fa and R245fa. Their findings were:

- At low heat flux, the heat transfer coefficient increases with vapour quality and is independent of heat flux and mass velocity.
- At medium heat flux, the heat transfer coefficient increases with heat flux as q0.67, is independent of vapour quality, increases slightly with mass velocity for R245fa or is independent of mass velocity for R236fa.
- At high heat flux, the heat transfer coefficient decreases with increasing heat flux and vapour quality and increases with mass velocity. The heat transfer coefficient is found to increase with saturation pressure, particularly for R236fa and the level of subcooling was found to have no influence for saturated boiling, while subcooled boiling data were below those for saturated boiling, similar to other previous studies.

Bertsch et al. (2008) compared 10 data sets on saturated flow boiling in channels of diameters range 0.16-2.01 mm. It included a total of 1847 points and eight fluids. These measured heat transfer coefficients were compared with the predicted values from 25 published correlations for flow boiling. They found a wide variation on the prediction of these experimental data. The best predictions had a

mean absolute error ±40%, less than half of the data were predicted within ±30%, and predictions from 12 out of the 25 correlations exceeded errors of 100%.

Critical Heat Flux

For saturated critical heat flux, the micro-to-macroscale transition occurs approximately in the same tube diameter range.

For the same test conditions, when the tube diameter is reduced from 0.530 to 0.050 and 0.251 to 0.050 mm (two studies), the void fraction deviated from the homogeneous void fraction law (higher void fraction) perhaps suggesting a new smaller scale transition.

Agostini et al. (2008a, 2008b, 2008c) detected CHF when the difference between the wall and the saturation temperatures was greater than 70 K. With increasing mass velocity, the wall critical heat flux also increased. The inlet saturation temperatures ($20.31°C < T_{sat,in} < 34.27$ °C) and the inlet subcoolings ($0.4 < \Delta T_{sub} < 15.3$ K) were found to have a negligible influence on the wall CHF. The best methods were Wojtan et al. (2006) correlation and Revellin and Thome (2008) model. They both predicted 100% of the experimental CHF results to within ±20% with the heated equivalent diameter taken as the characteristic diameter.

Calculating the critical vapor quality from the CHF, an annular-to-dryout transition is also obtained as a design limit in a diabatic microscale flow pattern map. Beyond this transition, damage from overheating would occur for the device being cooled by the microchannels.

Condensation

Condensation in minichannels and microchannels is substantially enhanced because surface tension plays a very important role by pulling the condensate film to the corners of the non-circular passages, more common in automotive air-conditioning condenser passages and some industrial applications. Thus the liquid film away from the corners is thinned out resulting in enhanced heat transfer coefficient in the regions away from the corners. Note that surface tension does not play an important role in boiling as it does in condensation. Some of the geometries investigated or used for condensation in automotive/industrial applications are shown in Fig. 2 (Webb and Ermis, 2001). Other applications of microchannel heat exchangers envisioned as good design data and information on fouling become available. In addition to reduced air-side pressure drop and improved heat transfer, the required refrigerant charge also reduces with minichannels in automotive condensers and some electronic components.

It should be emphasized that surface tension becomes important minichannels and the flow regimes that are dominated by surface tension are: slug, plug and bubble. In contrast, in larger tubes, shear stress dominates and associated flow regimes are mist, annular, wavy and stratified flow. We consider surface tension dominated flows when surface tension force is larger than the sum of shear force plus buoyancy force. As we will describe, in minichannels, the most important flows are intermittent (slug/plug) and annular.

Condensation is extensively studied experimentally in minichannels ($D_h \geq 0.44$ mm) while none in microchannels because of experimentation difficulty. Condensation heat transfer is significantly enhanced as the channel size (hydraulic diameter) becomes smaller and smaller, going from minichannels towards microchannels. We will briefly describe flow regimes in minichannels with circular, rectangular and square cross-sections.

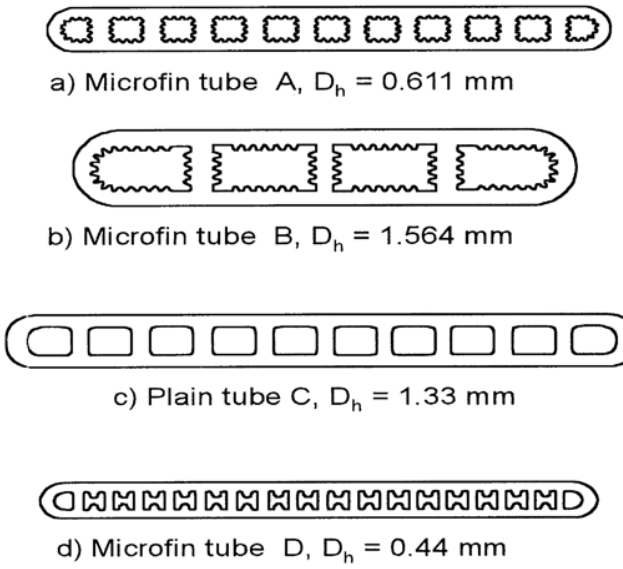

Figure. 2 - Microfin tubes: (a) A: 1.7-18-11M, D_h = 0.611 mm, (b) B: 3-16-4M, D_h = 1.564 mm, (c) C: 2-20 10P, D_h = 1.33 mm; (d) D: 1.4-18-18M, D_h = 0.44 mm (Webb and Ermis, 2001)

Condensation Flow Regimes

Garimella, et al. (2000, 2002, 2005) observed flow regimes during air-water adiabatic flow, and with R134a condensing at 51.7 °C in horizontal tubes and square minichannels with hydraulic diameters ranging from 4.91 to 0.5 mm. The following are their major findings:

- Hydraulic diameter has a substantial effect on flow pattern and transition, while tube shape is less significant.
- For G > 150 kg/m^{2}s, four regimes are identified: annular, wavy (influenced by gravity and with a wavy structure of the liquid film), intermittent (slug, plug), dispersed (bubble).
- As D_h decreases (D_h < 3 mm), overall range of annular flow increases, wavy regime decreases disappearing at D_h = 1 mm, while the intermittent regime increases. The model of intermittent flow is shown in Fig. 3.

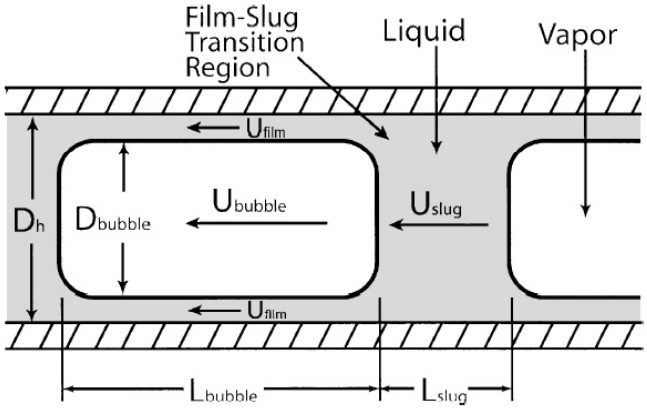

Figure. 3 - Schematic of intermittent flow, Garimella et al. (2005)

Coleman and Garimella (2000) and Garimella et al. (2002) proposed a map for the transition from intermittent to non-intermittent flow (wavy, annular mist, disperse flow) as shown in Fig. 4. This transition occurs at vapor quality x given by

$$x \leq \frac{a}{G + b} \tag{9}$$

where $a = 69.57 + 22.60 \exp(0.259\ D_h)$ and $b = -59.99 + 176.8 \exp(0.383 D_h)$. Here the hydraulic diameter D_h is in mm and G is the total mass flux in kg/m^{2}s.

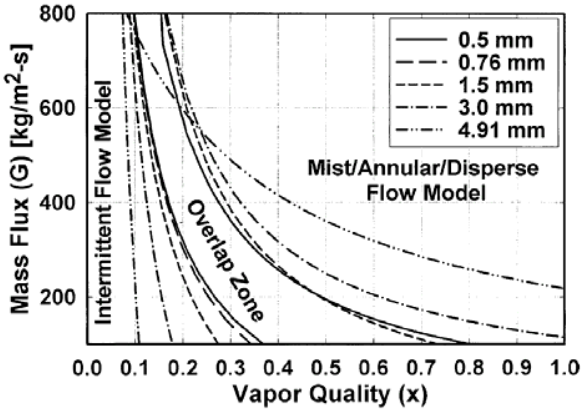

Figure. 4 – Flow regimes in minichannels (Garimella et al. 2002)

Cheng et al. (2007) identified four flow patterns in flow condensation: mist flow, annular flow, slug/plug flow (confined bubble) and bubbly (isolated bubble) flow.

Condensation Pressure Drop

Garimella et al. (2005) studied pressure drop during condensation of refrigerant R134a in horizontal circular channels of diameters range 0.5-4.91 mm. The pressure drops were measured for qualities 0-100% and the mass fluxes 150-750 kg/m^{2}s. Out of a total of 603 experimental data points, 77 data points were in the intermittent regime, 448 data points in disperse/annular/mist flow regime, and the remaining 78 data points in overlap region between the above two flow regimes (see Fig. 4 for flow regimes).

For the intermittent regime modeling, they considered the total pressure drop consisting of three components – the liquid slug ΔP_{slug}, the vapor bubble ΔP_{vb}, and the flow of liquid between the film and slug $\Delta P_{film\text{-}slug}$ as follows. Here it was idealized that the flow was reasonably uniform with large slugs of vapor bubble as shown in Fig. 4.

$$\Delta P_{total} = \Delta P_{slug} + \Delta P_{vb} + \Delta P_{film\text{-}slug} \tag{10}$$

$$\frac{\Delta P}{L} = \left(\frac{dP}{dx}\right)_{film\,bubble}\left(\frac{L_{bubble}}{L_{unit\ cell}}\right) + \left(\frac{dP}{dx}\right)_{slug}\left(\frac{L_{slug}}{L_{unit\ cell}}\right) + \Delta P_{one\,transition}\left(\frac{N_{unit\ cells}}{L}\right) \tag{11}$$

The term in the parenthesis of the last term on the right-hand side of the above equation is the same as $1/L_{unit\ cell}$ and can be determined from the slug frequency measurements or from the following correlation:

$$\frac{D_h}{L_{unit\ cell}} = 1.573\left(Re_{slug}\right)^{-0.507} \tag{12}$$

This model predicted 65% of the intermittent and discrete wave flow data within ±20%. If only intermittent flow regime points were considered, the model would predict 75% of the data within ±20%. In the disperse/annular/mist flow regime, the pressure gradient is given by

$$\frac{\Delta P}{L} = \frac{1}{2} f_i \frac{G^2 x^2}{\rho_V \alpha^{2.5}} \frac{1}{D} \tag{13}$$

where f_i is given by

$$\frac{f_i}{f_l} = A X^a Re_l^b \Psi^c \tag{14}$$

where the constants are given by

$A = 1.308 \times 10^{-3}$; $a = 0.427$, $b = 0.930$ and $c = -0.121$ for laminar region ($Re_l < 2100$)

$A = 25.64$; $a = 0.532$, $b = -0.327$ and $c = 0.021$ for turbulent region ($Re_l > 3400$)

For the transition region, the pressure drop is first independently calculated using the laminar and turbulent constants at the low and high values of the mass flux and quality representing the boundaries of the laminar and turbulent regions. Linear interpolation between these bounding values is then conducted separately based on the quality and mass flux in consideration. The average of these two pressure drops resulting from the interpolation based on G and x represents the two-phase pressure drop for the transition region data point. The above model predicts 87% of the data within ±20%, as shown in Fig. 5.

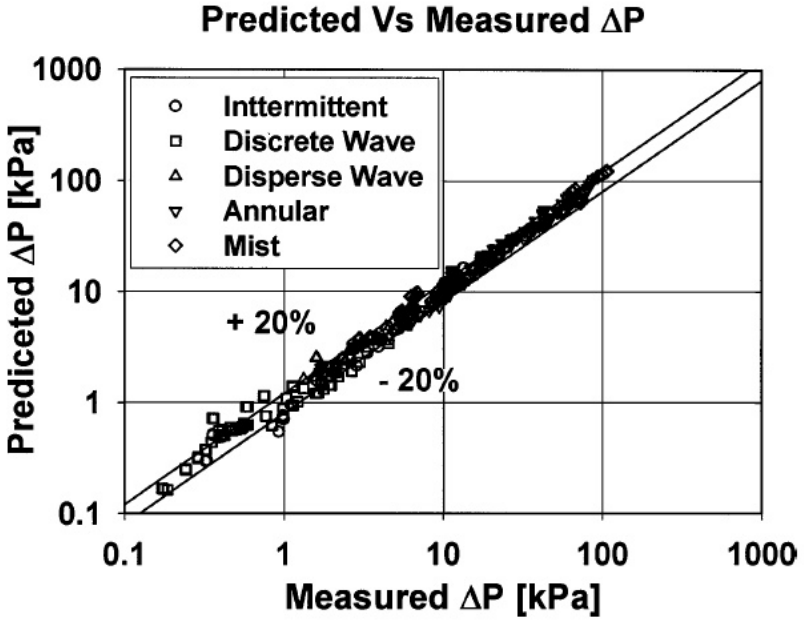

Figure. 5 - Comprehensive pressure drop model predictions (Garimella, et al. 2005)

Condensation Heat Transfer

Due to small channel size, surface tension and viscous dissipation effects become important which may not be that important for large channels.

Several condensation heat transfer studies have been reported in the literature. Cavallini et al. (2005a) reported condensation in a multiport tube (1.4 mm hydraulic diameter) as used in a modern condenser having flat multiport tube and corrugated multilouver air fins. They used R134a and R410a refrigerants and mass velocity range of 200-1000 kg/m^{2}s (for R134a) and 200-1400 kg/m^{2}s (for R410a) with the vapor quality varied as 0.75, 0.50 and 0.25. The measured data were compared with several correlations. There was good agreement of the frictional pressure drop with several published correlations, but the measured heat transfer coefficients were underpredicted by all models. The reason may be different flow regimes for the test results compared to the correlations for annular flow regime.

Cavallini et al. (2005b) extended their work (Cavallini et al. (2005a)) by condensing R134a, R410A and R236ea in 1.4 mm hydraulic diameter multiport tube. They then proposed the following correlation which agreed most of the experimental data within ± 20% in the shear dominated regime, as shown in Fig. 6.

$$Nu_{annular} = Nu_{LO}\,[1 + 1.128\,x^{0.817}(\rho_L/\rho_G)^{0.3685}(\mu_L/\mu_G)^{0.2363}(1-\mu_G/\mu_L)^{2.144}Pr_L^{-0.1}]/(1-E)^{0.08}$$

where

$$E = 0.015 + 0.44\,\log[(\rho_{gc}/\rho_L)(\,\mu_L j_G/\sigma)^2 10^4] \quad \text{and} \quad \rho_{gc} = \rho_G\,(1 + (1-x)\,E/x)$$

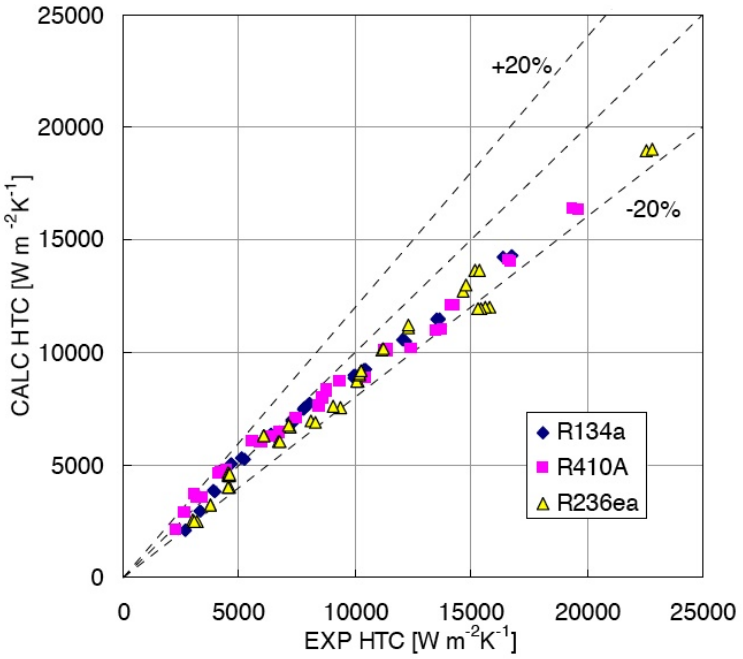

Figure. 6 – Prediction of experimental data for R134a, R410A and R236ea inside l.4 mm inner diameter minichannel, Cavallini et al. (2005a)

Chowdhury et al. (2006) experimentally evaluated pressure drop and heat transfer during condensation of R134a in 7:1 aspect ratio rectangular duct of 0.7 mm hydraulic diameter. They used a unique fabrication technique milling and electroplating to make this channel. They covered the following range of parameters: inlet vapor quality 20-80% and mass flux 130-200 kg/m^{2}s. Outlet conditions were

maintained close to thermodynamic saturated liquid state through a careful experimental technique. The trends of results are similar to those found in recent literature in such microchannels.
Cheng et al. (2007) summarized their findings as follows for condensation in microchannels: At low mass fluxes ($G < 200$ kg/m^{2}s), measured Nusselt numbers are higher than those from macrochannel correlations. At high mass fluxes ($G > 200$ kg/m^{2}s), measured Nusselt numbers can be predicted well with the macrochannel correlations.
Wang and Rose (2006) studied film condensation analytically to determine the effect of tube inclination from +90° (upflow) to -90° (downflow) in square channels with the side 0.5, 1.0 and 3.0 mm. As expected, they found that the effect of inclination was negligible due to surface dominated region and corroborated with the findings of Coleman and Garimella (2003).

Concluding Remarks

Heat transfer information for small diameter tubes are summarized with reference to phenomena and design information for single-phase flow, boiling and condensation.
Micropipes and microchannels as emerging geometries for heat and mass transfer, controlled fluid transport and thermal control are analyzed with reference to manufacturing technologies and possible classification criteria. In this frame the most widely used is the one based on the confinement of bubbles as the tube diameter reduces.
Single-phase fluid flow is examined comparing macro and microscale evidencing the general similarity of behavior provided scaling effects are properly accounted for (entrance length, viscous dissipation). Similarly, single-phase heat transfer does not show any significant change when passing from macro- to microscale, always provided scaling effects are taken into account (thermal entrance length, viscous dissipation, conjugate heat transfer). In single-phase flow there is a common agreement to identify the threshold between micro and macroscale on the basis of scaling effects occurring (depending on fluid properties, velocity and geometry).
Heat transfer with phase change, i.e., boiling and condensation, exhibits large differences between macro- and microscale, the main reason being due to the bubble confinement, which is also the most widely used criterion to identify the transition between micro and macroscale. Although many researches are now available in boiling and condensation, still much has to be studied to accomplish a significant understanding of the microscale heat transfer with phase change.

NOMENCLATURE

D_h	hydraulic diameter, m
G	mass flux, kg/m^{2}s
g	gravitational acceleration, m/s^2
j	superficial velocity, m/s
Nu	Nusselt number, hD_h/k, dimensionless
Pr	Fluid Prandtl number, dimensionless
q	heat flux, kW/m^2
x	vapor mass quality, dimensionless
μ	dynamic viscosity, Ns/m^2
σ	surface tension, N/m
ρ	density, kg/m^3

Subscripts

annulararannular flow regime
G gas
L liquid with its actual mass flow rate
LO liquid with total mass flow rate

REFERENCES

1. B. Agostini, M. Fabbri, J.E. Park, L. Wojtan, J.R. Thome and B. Michel, State of the Art of High Heat Flux Cooling Technologies, *Heat Transfer Engineering*, Vol. 28, No. 4, pp. 258–281 (2007).
2. B. Agostini, J.R. Thome, M. Fabbri, B. Michel, D. Calmi, U. Kloter, High heat flux flow boiling in silicon multi-microchannels – Part I: Heat transfer characteristics of refrigerant R236fa, *Int. J. of Heat and Mass Transfer*, Vol. 51, pp. 5400–5414 (2008a).
3. B. Agostini, J.R. Thome, M. Fabbri, B. Michel, D. Calmi, U. Kloter, High heat flux flow boiling in silicon multi-microchannels – Part II: Heat transfer characteristics of refrigerant R245fa, *Int. J. of Heat and Mass Transfer*, Vol. 51, pp 5415–5425 (2008b).
4. B. Agostini, R. Revellin, J.R. Thome, M. Fabbri, B. Michel, D. Calmi, U. Kloter, High heat flux flow boiling in silicon multi-microchannels – Part III: Saturated critical heat flux of R236fa and two-phase pressure drops, *Int. J. of Heat and Mass Transfer*, Vol. 51, pp. 5426–5442 (2008c).
5. J.J. Brandner, L. Bohn, T. Henning, U. Schygulla and K. Schubert, Microstructure Heat Exchanger Applications in Laboratory and Industry, *Heat Transfer Engineering*, Vol. 28, No. 8-9, pp. 761-771 (2007).
6. A. Cavallini, M. Matkovic, D. Del Col and L. Rossetto, Pressure drop during two-phase flow of R134a and R32 in a single minichannel, HT-08-1175 (2008).
7. A. Cavallini, D. Del Col, L. Doretti, M. Matkovic, L. Rossetto, and C. Zilio, A. Condensation heat transfer and pressure gradient inside multiport minichannels, *Heat Transfer Engineering*, Vol. 26, No. 3, pp. 45-55 (2005a).
8. A. Cavallini, L. Doretti, L. Rossetto, D. Del Col, M. Matkovic, and C. Zilio, A model for condensation inside microchannels, ASME Paper no. HT2005-72528 (2005b).
9. G.P. Celata and G. Zummo, Heat Transfer and Fluid Flow in Microchannels, Chapter 2.13, Heat Exchanger Design Handbook, Begell House, Inc., New York (2002).
10. P. Cheng and H.Y. Wu, Mesoscale and microscale phase-change heat transfer, *Adv. Heat Transfer*, Vol. 39. pp. 461-563 (2006).
11. P. Cheng, H-Y. Wu and F-J Hong, Phase-change heat transfer in microsystems, *ASME J. Heat Transfer, Vol. 129, pp. 101-107 (2007).*, Vol. 39.
12. J.W. Coleman and S. Garimella, Two-phase flow regime transitions in microchannel tubes: The effect of hydraulic diameter, ASME Heat Transfer Division – 2000, Vol. HTD 366-4, pp. 71-83, 2000.
13. J.W. Coleman and S. Garimella, Two-phase flow regimes in round, square and rectangular tubes during condensation of Refrigerant R134a, *Int. J. Refrigeration*, Vol. 26, No. 1, pp. 117-128 (2003).
14. E.G. Colgan, B. Furman, M. Gaynes, W. Graham, N. LaBianca, J.H. Magerlein, R.J. Polastre, M.B. Rothwell, R.J. Bezama, R. Choudhary, K. Martson, H. Toy, J. Wakil, J. Zitz and R. Schmidt, A practical implementation of silicon microchannel coolers for high power chips, *Invited Paper presented at IEEE-Semi-Therm 21*, San Jose, March 15–17 (2005)

15. S. Garimella, J.D. Killion and Coleman, J.W., An experimentally validated model for two-phase pressure drop in the intermittent flow regime for circular microchannels, *J. Fluids Engineering*, Vol. 124, pp. 205-214 (2002).
16. S. Garimella, A. Agarwal and J.D. Killion, Condensation pressure drop in circular microchannels, *Heat Transfer Engineering*, Vol. 26, No. 3, pp. 28-35 (2005).
17. D.H. Han and M.A. Kedzierski, Micro effects for single phase pressure drop in microchannels, *I.J. Trans. Phenomena*, Vol. 10, pp. 103-112 (2008).
18. E.W. Jassim and T.A. Newell, Prediction of two-phase pressure drop and void fraction in microchannels using probabilistic flow regime mapping, *Int. J. Heat Mass Transfer*, Vol. 49, pp. 2446-2457 (2006).
19. S.G. Kandlikar and W.J. Grande, Evolution of microchannel flow passages – thermohydraulic performance and fabrication technology, IMECE2002-32043 (2002).
20. S.G. Kandlikar and S. Garimella, Single-Phase Liquid Flow in Minichannels and Microchannels, *Heat Transfer and Fluid Flow in Minichannels and Microchannels*, Ch. 3, pp. 87-136 (2006).
21. S.G. Kandlikar, High Heat Flux Removal with Microchannels – A Roadmap of Challenges and Opportunities, *Heat Transfer Engineering*, Vol. 26, No. 8, pp. 5-14 (2005).
22. P.A. Kew and K. Cornwell, Correlations for the prediction of boiling heat transfer in small-diameter channels, *Applied Thermal Engineering*, Vol. 17, pp. 705-715 (1997).
23. A.M. Jacobi and R.K. Shah, "Air-side Flow and Heat Transfer in Compact Heat Exchangers: A Discussion of Physics," *Heat Transfer Engineering*, Vol. 19, No. 4, pp. 29-41 (1998).
24. A.M. Jacobi and R.K. Shah, "Heat Transfer Surface Enhancement through the Use of Longitudinal Vortices: A Review of Recent Progress," *Experimental Thermal and Fluid Science*, Vol. 11, pp. 295-309 (1995).
25. M. Matkovic, A. Cavallini, D. Del Col, and L. Rossetto, Experimental study on condensation heat transfer inside a single circular minichannel, *Int. J. Heat Mass Transfer*, Vol. (need to get the details from Prof. Cavallini).
26. S. S. Mehendale, A.M. Jacobi and R.K. Shah, "Fluid Flow and Heat Transfer at Micro- and Meso-Scales with Applications to Heat Exchanger Design," *Appl. Mech. Review*, Vol. 53, No. 7, pp. 175-193 (2000).
27. R. Revellin and J.R. Thome, A theoretical model for the prediction of the critical heat fluxin heated microchannels, *Int. J. Heat Mass Transfer*, Vol. 51, pp. 1216-1225 (2008).
28. R.K. Shah, "Classification of Heat Exchangers," in Heat Exchangers: Thermal-Hydraulic Fundamentals and Design, Eds. S. Kakaç, A.E. Bergles and F. Mayinger, pp. 9-46, Hemisphere Publishing Corp., Washington, DC (1981).
29. R.K. Shah and D.P. Sekulić, "Heat Exchangers," in Handbook of Heat Transfer, Third Edition, Eds. W.M. Rohsenow, J.P. Hartnett and Y.I. Cho, Chapter 17, 169 pages, McGraw-Hill, New York (1998).
30. R.K. Shah and D.P. Sekulić, *Fundamentals of Heat Exchanger Design*, John Wiley, New York (2003).
31. J.R. Thome, Two-phase flow and flow boiling in microchannels, Chapter 20, Engineering Data Book III, Wolverine Tube, Inc. Town, State (2008).
32. J.R. Thome, State-of-the-art overview of boiling and two-phase flows on microchannels, *Heat Transfer Engineering*, Vol. 27, No. 9, pp. 4-19 (2006).
33. A. Ullmann and N. Brauner, The Prediction of Flow Pattern Maps in Minichannels, *Multiphase Science and Technology*, Vol. 19, pp. 49-73 (2007)
34. H.S. Wang and J.W. Rose, A theory of film condensation in horizontal noncircular section microchannels, *ASME J. Heat Transfer*, Vol. 127, pp. 1096-1105 (2005).
35. H.S. Wang and J.W. Rose, Film condensation in microchannels: Effect of tube inclination, Paper No. ICNMM2006-96049, ASME, NY (2006).

36. L. Wojtan, R. Revellin and J.R. Thome, Investigation of critical heat flux in single, uniformly heated microchannels, *Exp. Thermal Fluid Sci.*, Vol. 30, pp. 765-774 (2006).
37. T.H. Yen, N. Kasagi and Y. Suzuki, Forced convective boiling heat transfer in microtubes at low mass and heat fluxes, *Int. J. Multiphase Flow*, Vol. 29, pp. 1771-1792 (2003).

DEVELOPMENT OF MICRO PLASMA ACTUATOR FOR ACTIVE FLOW CONTROL

S. Okochi*, N. Kasagi, Y. Suzuki, S. Ito
Department of Mechanical Engineering, The University of Tokyo, Tokyo 113-8656, Japan

ABSTRACT. We establish the design and fabrication of mm-size plasma actuators through MEMS process. The flow induced by three differently sized actuators fabricated is measured by laser Doppler velocimetry (LDV) in order to clarify these actuators' characteristics. The present experiment first confirms the same dependency of the induced velocity on the imposed voltage as reported in previous work. Then, it is clarified that there exists the optimal frequency to drive a flow unlike previous studies. In the measurement of the flow field, strong suction as well as blowing near the actuator is found in accordance with conventional large plasma actuators. Moreover, distinct suction and blowing in the lateral direction is also identified when reducing the length of actuator. The efficiency of plasma actuator is not changed significantly through miniaturization. These results show that the micro plasma actuator is applicable to various flow controls, particularly, to turbulent flows where small scale structures should be directly manipulated.

Keywords: plasma actuator, miniaturization, MEMS, flow control, turbulence control

INTRODUCTION

Active and flexible flow control has recently attracted much attention due to economical and ecological interests in various industrial applications. For example, efficient flow control systems could modify the laminar-turbulent flow transition in a boundary layer, prevent or induce separation, reduce drag, stabilize or mix air flow in order to avoid undesirable vibration, noise and energy losses [1]. To achieve such flow controls, many actuators have been developed, e.g., mechanical flaps and wall synthetic jets [2, 3]. These actuators have been successfully applied to mixing control in jet, separation control, and so forth. However, they have some drawbacks; generally, they have complicated structures and generate noise, vibration and secondary flow.

In the middle of the 1990s, Roth *et al.* [4] developed a plasma actuator using atmospheric pressure dielectric barrier discharge. Figure 1 shows the configuration of a typical plasma actuator. A plasma actuator (PA, hereafter) consists of two metallic electrodes asymmetrically mounted on both sides of a dielectric plate and lower electrode is covered with dielectric. They demonstrated that a PA drives gas in the area within a few millimeters away from the actuator surface. So far, PAs have been successfully applied to flow separation control or noise reduction. For example, Roth *et al.* [4] have shown the ability of this actuator to modify the properties of a boundary layer over a flat plate, and Göeksel *et al.* [5] have shown lift improvement in stall configuration.

Considering possible advantages such as no moving parts, simple structure and high frequency response, PA is considered promising also for turbulence drag or mixing control. Suppose we consider friction drag reduction in wall turbulence, the momentum transfer is governed by

* Corresponding author: S.Okochi
Phone:+81-3-5841-6419, Fax: +81-3-5800-6999
E-mail address: okouti@thtlab.t.u-tokyo.ac.jp

microscopic coherent structures, whose length and time scales are 10 μm ~ 1 mm and 0.01 ~ 10 ms in practical applications. Therefore, to achieve active and flexible control in such flows, a small PA (1 mm or less) is strongly needed. The most of the PAs reported so far are one with a width of 20 mm and a length of 300 mm. Since the typical length scale of plasma is about a few millimeters, further miniaturization of a PA bellow this length should affect the dynamics of plasma and the resultant performance. We refer to a PA whose electrode width is less than plasma volume (4 mm) as micro PA. Moreover, for the miniaturization of the plasma actuator, to fabricate micro PAs tolerant to high voltage and plasma is a major issue. Therefore, the aim of this paper is: (1) to establish the fabrication process of micro plasma actuator; (2) to clarify the size characteristics of micro and macroscopic plasma actuators; (3) to explore the induced flow velocity and efficiency of micro plasma actuator.

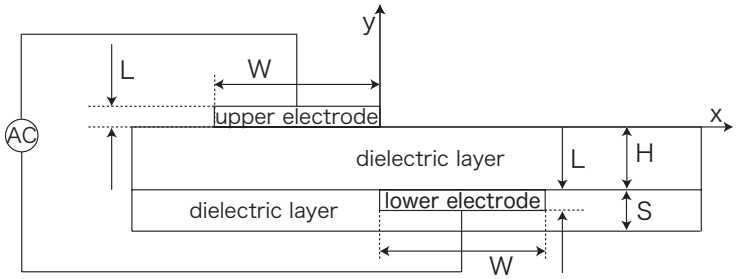

Figure 1. Structure and geometrical parameters of DBD plasma actuator

FABRICATION OF PLASMA ACTUATOR AND EXPERIMENTAL SETUP

Design and fabrication of micro plasma actuator by MEMS

The electrical and mechanical characteristics of a PA depend on various parameters such as electrode width, electrode thickness and dielectric layer thickness. According to Roth *et al.* [4], Forte *et al.* [6] and Hoskinson *et al*. [7], the induced flow is enhanced with decreasing the thicknesses of electrodes and dielectric layer. Based on the knowledge, we designed test actuators are as follows. The electrode width *W* is changed as 1, 4 and 10 mm to investigate the effects of the actuator size on the plasma volume and the induced flow. The electrode thickness *L* is 300 nm, which is the minimum durable thickness through the microelectromechanical system (MEMS) fabrication process we employ. The thickness of a dielectric layer *H* is chosen as 0.525mm, whish is the minimum thickness to avoid dielectric breakdown. The insulate layer thickness *S* is 30 μm to avoid discharge by the lower electrode.

The MEMS fabrication process of micro PA is shown in Fig. 2. The process starts with a 525 μm-thick Pyrex glass wafer. Upper and lower Cr/Au/Cr electrodes are vapour-deposited with a standard lithography process. Then, the lower electrode is covered with Parylene C. Micro PA fabricated by this MEMS process is shown in Fig. 3.

Electric power supply

Figure 4 shows a power supply system used in this experiment. In order to achieve dielectric discharge, the upper electrode is connected to a high voltage amplifier (HEOPT-5B20-L1, ± 5kV) driven by a function generator delivering a sinusoidal waveform. The lower electrode is grounded. A sinusoidal wave voltage with the maximum amplitude up to 5 kV is applied between the electrodes at different frequencies of 0-20 kHz. The voltage and current are monitored by a fast digitizer. The voltage is measured with an internal probe of amplifier, while the current is measured with a Rogowski coil (1kHz-1GHz, 0.1mA-10A).

Velocity measurement

The micro PA is placed flush on the bottom wall surface of the two-dimensional channel, which is about 5 m long and has a test section of 10 × 50 cm^2. A smoke injector is placed at the intake of the channel in order to supply the flow with small oil particles of 1 μm in diameter. The experiment is carried out at low air velocities (Reynolds number based on the channel height and the centerline velocity ~ 1000) in order to easily discriminate the base flow and the flow induced by the micro PA. Although this wind tunnel is designed long enough to reproduce a fully developed turbulence channel flow at the point of measurement, the root-mean-square streamwise velocity fluctuation remains at about 10% of the local mean velocity near the wall region under such a low velocity condition. However, this magnitude of velocity fluctuation is much smaller than the velocity induced by the actuator.

Figure 5 shows the measurement arrangement with a Laser Doppler Velocimeter (LDV) and the coordinate system with its origin being located on the surface just downstream of the center of the upper electrode. The *x*-, *y*- and *z*-axes are defined in the streamwise, wall-normal and spanwise directions, respectively.

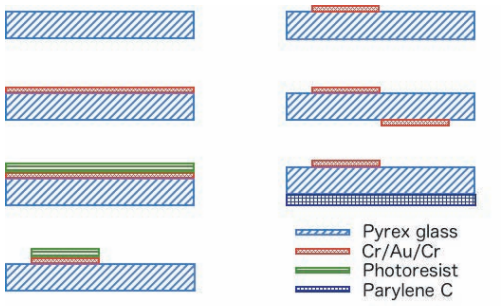

Figure 2. Fabrication process of plasma actuator through MEMS process

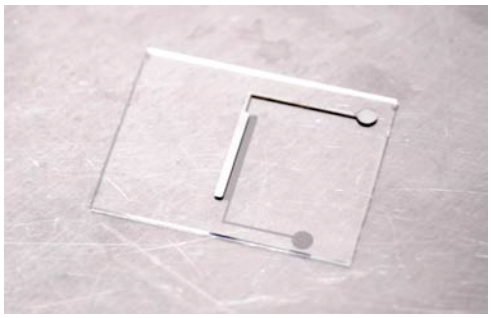

Figure 3. Micro plasma actuator fabricated by MEMS technique (W = 1 mm)

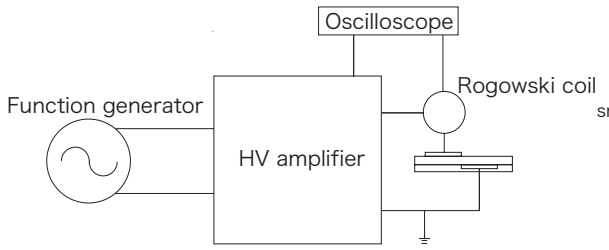

Figure 4. Schematic configuration of the power supply for DBD plasma

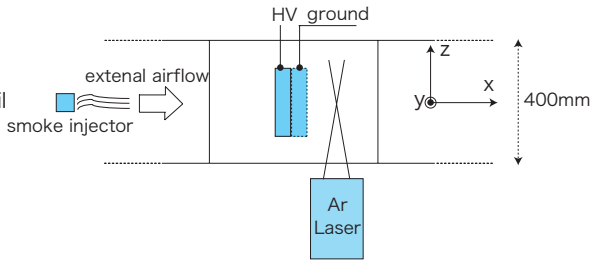

Figure 5. Top view of the LDV system

EXPERIMENTAL RESULTS

Electric discharge and induction of fluid flow

The driving principle of PA is based on the Townsend mechanism, or electron avalanche, which corresponds to the multiplication of some primary electrons in cascade ionization. When a high voltage is applied between two planes, electrons are accelerated towards the anode by the electric field and they ionize the gas by collisions. An avalanche develops because the multiplication of electrons proceeds along their drift from the cathode to the anode. A discharge current is then created.

Figure 6 shows a typical example of the measured voltage and current (W = 1 mm, V_a = 5 kV and F = 10 kHz). It can be seen that the current has two components. One is a sinusoidal wave in

quadrature phase with the voltage. The other is the impulse current due to the dielectric barrier discharge during the positive and negative half-cycles of the voltage waveform. Note that the discharge is asymmetric during the positive and negative cycle. This demonstrated that the discharge is different during the positive and negative cycles as shown in Fig. 6.

Figure 7 presents the instantaneous velocity induced at x = 5 mm, y = 0.5 mm and z = 0 mm by a plasma actuator (V_a = 5 kV, F = 10 kHz, W = 1 mm). The induced flow is fluctuating because the discharge does not behave similarly during the positive and negative cycles. As the barrier discharge is periodic, it seems to generate a pulsating flow. In fact, Forte *et al*. [6] demonstrated that the induced velocity follows the high voltage waveform frequency.

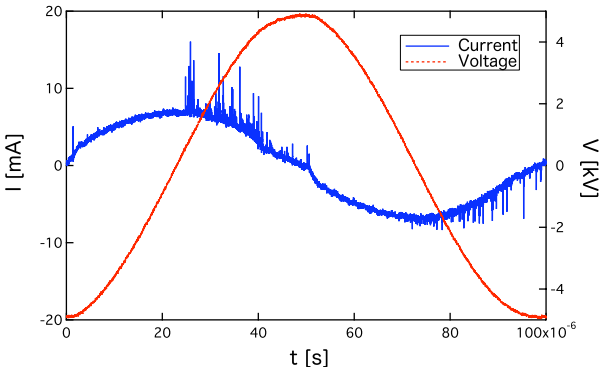

Figure 6. Typical discharge current and voltage waveform

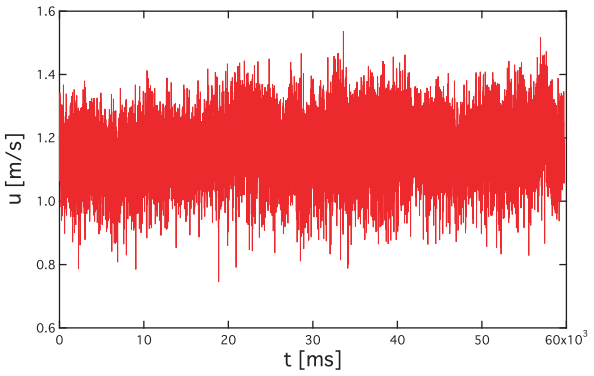

Figure 7. Instantaneous velocity versus time at x = 5 mm and y = 0.5 mm

Time-averaged flow distribution

The velocity field induced by the actuator is measured in the x-y plane with the applied voltage of V_a = 5 kV at the frequency of F = 10 kHz. The time-averaged velocity distributions are shown in Fig. 8. Strong suction is observed between the upper and lower electrodes, and a wall-tangential jet is induced in the vicinity of the wall regardless of the size of plasma actuators. These velocity profiles clearly show the momentum transferred from the plasma to the surrounding air. Specifically, the maximum velocity decreases and the controlled area becomes thicker with increasing streamwise distance x. The maximum induced velocity is enhanced with increasing the actuator size. The peak position of induced velocity in the present study is different from that in the previous research. Forte *et al.* [6] demonstrated that the maximum induced velocity was reached at the end of the plasma, and the induced velocity decreased further downstream. In the present work, in the case of electrode width of 4 and 10 mm, the maximum velocity occurs at the end of the plasma and the height is y = 0.5 mm from the wall. In contrast, in the case of actuator of 1mm width, the maximum velocity is measured at x = 3 mm, not at the end of plasma. This fact is in contrast to the previous results.

Figure 9 shows the flow distribution of the actuator of 1mm in width at different z locations. It is clear that the peak location of induced velocity shifts downstream (x = 3 mm at z = 0 mm, x = 10 mm at z = 3 mm and x = 15 mm at z = 6 mm). Associated with shortening the spanwise length of electrode, it is expected that in the x-z plane where $x < 0$, the induced flow is sucked to the actuator, whereas induced away from it where $x > 0$.

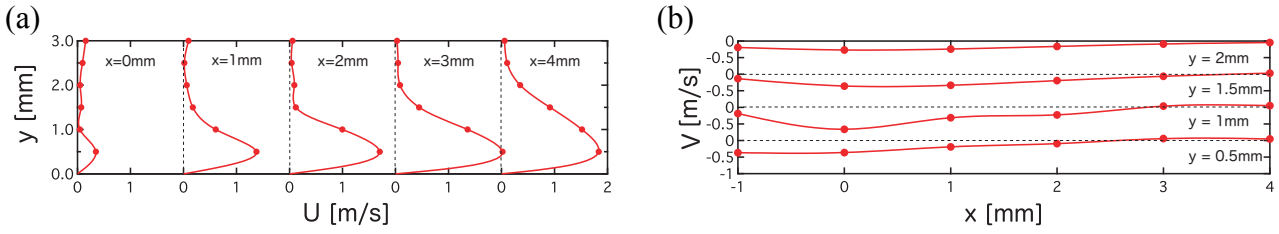

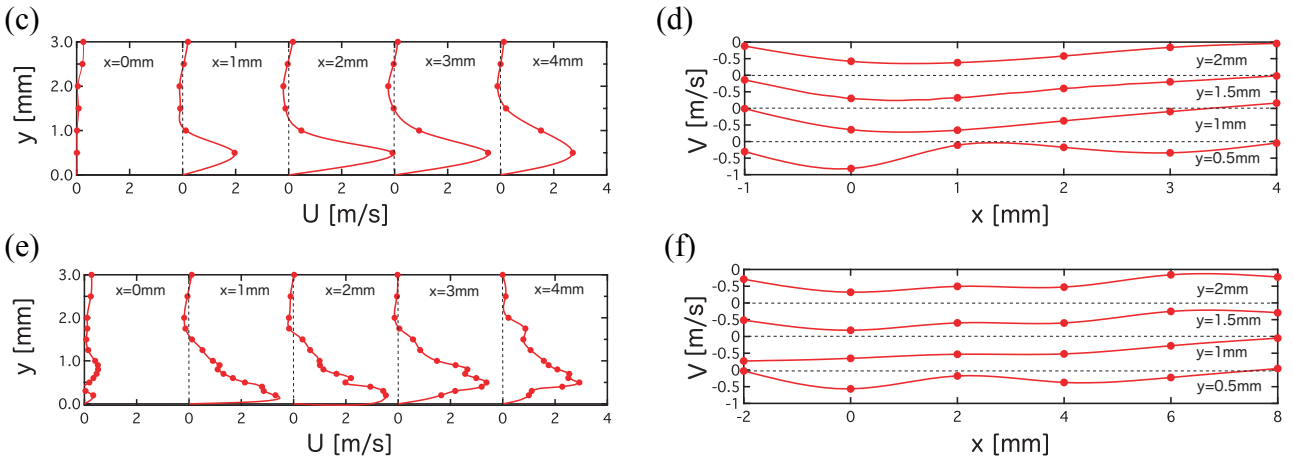

Figure 8. Mean streamwise and wall-normal velocities around the plasma actuator: (a) U with W = 1 mm, (b) V with W = 1mm, (c) U with W = 4 mm, (d) V with W = 4 mm, (e) U with W = 10 mm, (f) V with W = 10 mm

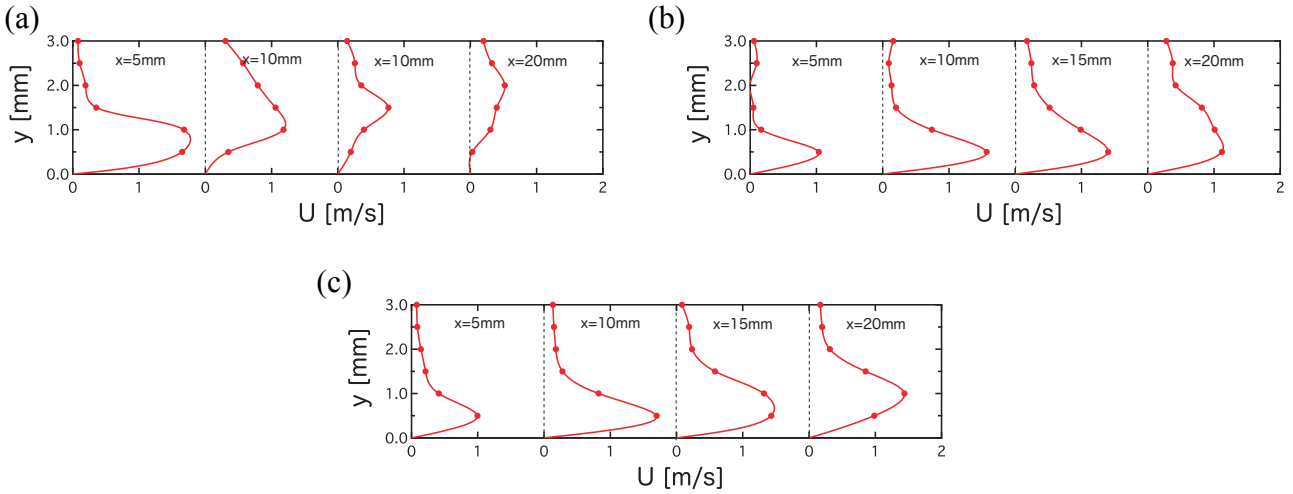

Figure 9. Mean streamwise velocity distributions at different z-planes around the plasma actuator of W = 1 mm: (a) z = 0 mm, (b) z = 3 mm, (c) z = 6 mm

Dependency of induced flow velocity on applied voltage

Figures 10 and 11 respectively show the maximum induced velocity $U_{\max}$, which is measured at the height of y = 0.5 mm, and the electrical power dissipation per unit length P_{elec} at different V_a with F = 5 kHz. The velocity increases monotonously as the applied voltage is increased, because a higher voltage enhances discharge and makes ions undergo stronger Colombian forces. Moreau *et al.* [8] obtained the following empirical equation: $U_{\max} = 0.000166 \times V_a^{3.5}$. In the present work, the relationship between $U_{\max}$ and V_a is approximated as: $U_{max} \propto V_a^{1.8}$, $U_{max} \propto V_a^{1.94}$, and $U_{max} \propto V_a^{2.3}$ for W = 10, 4 and 1 mm, respectively. This difference is due to different discharge modes. It is noted that there is a threshold voltage, at which the discharge mode is changed from glow discharge to filamentary discharge. It is known [6] that the latter filamentary mode of plasma is much less efficient in transferring momentum to neutral gas molecules. However, this threshold voltage is different according to the geometry of PA. Similarly, the electrical power dissipation increases with the applied voltage. The relationship between them is expressed as $P_{elec} \propto V_a^{2.7}$. This result agrees with previous work. For example, Pons [9] and Roth *et al.* [4] demonstrated that $P_{elec} \propto V^n$ with $2 < n < 3$. However, these empirical equations are not based on plasma physics, so that a theoretical approach is needed to establish firm fundamental knowledge.

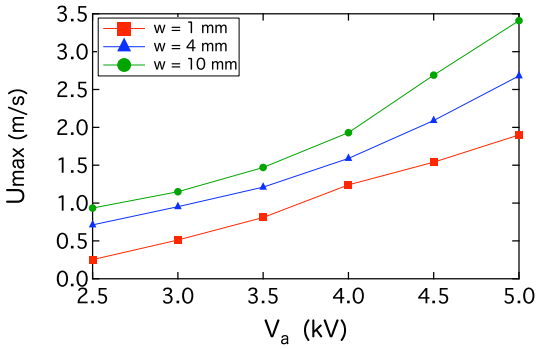

Figure 10. Maximum induced flow velocity versus applied voltage

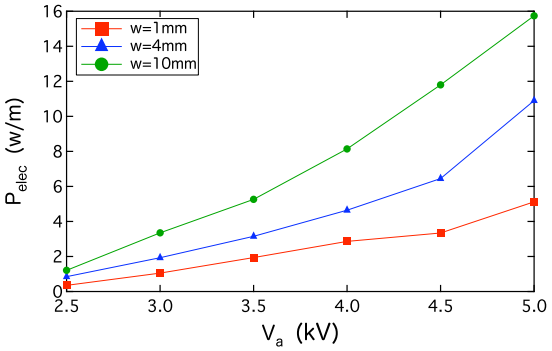

Figure 11. Electrical power dissipation per unit length versus applied voltage

Dependency of induced flow velocity on applied frequency

The maximum induced velocity and the electrical power dissipation per unit length at different frequencies with V_a = 5 kV are shown in Figs. 12 and 13, respectively. It is evident that the optimal frequency to achieve the highest maximum velocity exists and it increases with decreasing the size of the actuator. For example, the optimal frequency is 16 kHz when W = 1 mm, while 12 and 10 kHz for W = 4 and 10 mm, respectively. This fact is in contrast to the previous results, where the induced velocity was monotonically increased with the frequency [6]. The possible reason for this is that, as the frequency is increased, the mean transferred charge increases inducing more collisions between ions and gas and enhancing the induced velocity. However, when the discharge frequency exceeds the ion trapping frequency, the electron avalanche does not grow enough.

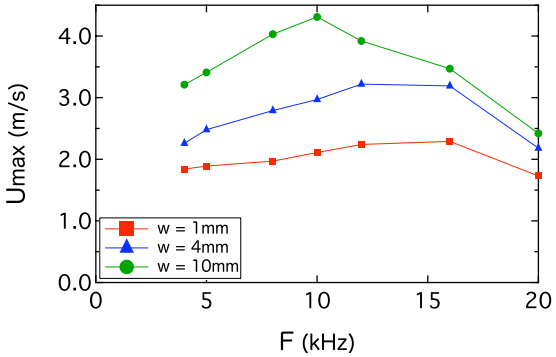

Figure 12. Maximum induced flow velocity versus frequency

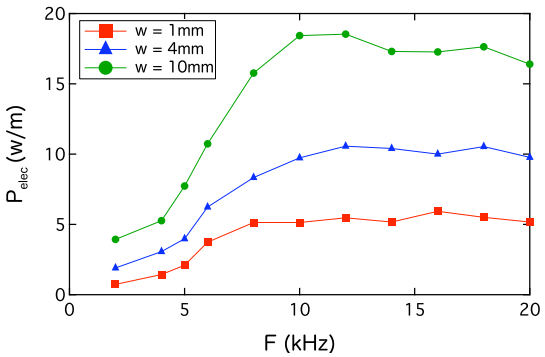

Figure 13. Electrical power dissipation per unit length versus frequency

Efficiency of micro plasma actuator

For a given two-dimensional parallel velocity profile, the corresponding mechanical power delivered to the air can be estimated from the following equation (Moreau [8]):

$$P_{mech} = \int_0^\infty \frac{1}{2}\rho v(y)^3 l dy \ , \tag{1}$$

where ρ is the air density and l is the electrode length. The electrical power dissipation is expressed by the following equation:

$$P_{elec} = \frac{1}{T}\int_0^T V \times I \ dt \tag{2}$$

Then, the mechanical efficiency of a PA is given as:

$$\eta = P_{mech} / P_{elec} \tag{3}$$

The efficiency of micro PA is shown in Fig. 15. It shows that, as the imposed voltage is increased, the electro–mechanical efficiency of a smaller PA reaches its seemingly saturated value faster. Moreover, the efficiency obtained in the present work is much higher than that reported in the previous work. For example, Forte *et al.* [6] demonstrated that the efficiency of PA remains at about 0.03 % as seen in Fig. 15. Figure 16 shows the comparison of maximum induced velocity between conventional and micro PAs. It is clear that the inception voltage of the present micro PA is 2.5 kV and much lower than that reported in previous work. For example, in Forte *et al.* [6], the inception voltage was 8 kV. This is because the employment of a thinner dielectric layer enhances the electric field. Therefore, the efficiency of PA can be even more improved by optimizing design parameters.

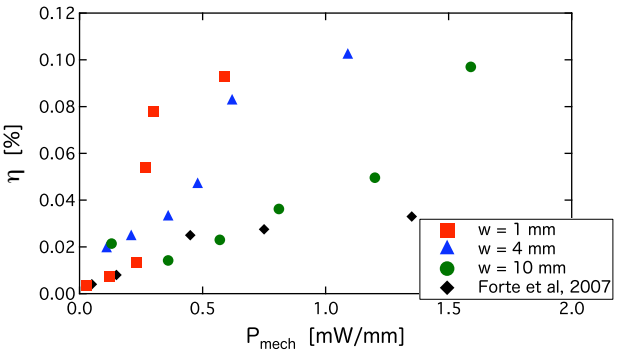

Figure 15. Comparison of the efficiency between conventional and micro plasma actuators

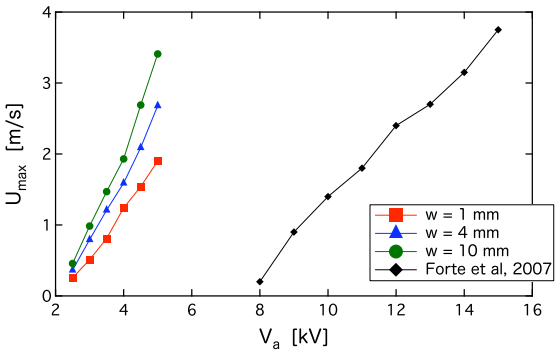

Figure 16. Comparison of the maximum induced velocity between conventional and micro plasma actuators actuator

CONCLUSIONS

In the present work, we proposed and established the MEMS fabrication of micro plasma actuators, of which electrode width is less than the plasma volume size. Then, we experimentally clarified the induced flow characteristics and also the efficiency of the micro plasma actuator. The major findings are summarized as follows:

(1) From the LDV measurement of the flow field, it is confirmed that strong suction and blowing are induced around the plasma actuator regardless of the actuator size tested, i.e., W = 1, 4, and 10 mm. In addition, the induced flow field is essentially three-dimensional because the appreciable spanwise velocity component is also induced, particularly around a smaller plasma actuator.
(2) It is found that the design parameters of plasma actuator affect the discharge and thus the induced velocity considerably. The maximum induced velocity increases with increasing the grounded electrode width and applied voltage, while the optimal driving frequency exists depending upon the size of actuator.
(3) The maximum electro-mechanical efficiency of plasma actuator has weak dependency on the size of the plasma actuator. However, thinning the dielectric layer leads to a higher efficiency.

ACKNOWLEDGEMENTS

We thank Dr. Y. Hasegawa, Messrs. Y. Hamana and D. Ko in the Department of Mechanical Engineering, the University of Tokyo for their discussions and technical supports. The present work was supported through Grant-in-Aid for Scientific Research (A) (No. 20246036) by MEXT, Japan.

REFERENCE

1. Gad-El-Hak M 2000 *Flow Control* (Cambridge: Cambridge university Press)
2. David A and Michael A., Active control of a free jet using a synthetic jet, *International Journal of Heat and Fluid Flow* 29 (2008) 967-984
3. Angele K, Kurimoto N, Suzuki Y and Kasagi N., Evolution of the streamwise vortices in a coaxial jet controlled with micro flap actuators, *Journal of Turbulence*, Volume 7, No. 73, 2006
4. Roth J R and Dai X., Optimization of the Aerodynamic Plasma Actuator as an Electrohydrodynamic (EHD) Electrical Device, *44th AIAA Aerospace Sciences Meeting and Exhibit*, 9 – 12 January 2006
5. B. Göksel, I. Rechenberg, S. Grundmann, C. Tropea, Plasma Actuators for Active Flow Control. DGLR-2005-210, Deutscher Luft- und Raumfahrtkongress, Friedrichshafen, Germany.
6. Forte M *et al.*, Optimization of a dielectric barrier discharge actuator by stationary and non-stationary measurements of the induced flow velocity: application to air flow control, *Experimental Fluids* 43: 917-928, 2007
7. Hoskinson A R, Hershkowitz N and Ashpis D E, Force measurements of single and double barrier DBD plasma actuators in quiescent air, *Journal of Physics D: Applied Physics*. 41 (2008)
8. Moreau E., Airflow control by non-thermal plasma actuators, *Journal of Physics D: Applied Physics*. 40 (2007) 605-636
9. Pons J, Moreau E and Touchard G., Asymmetric surface dielectric barier discharge in air at atmospheric pressure: electrical properties and induced airflow characteristics, *Journal of Physics D: Applied Physics*. 38 (2005) 3635-3642

THE INFLUENCE OF SURFACE EFFECTS ON THE THRUST OF MICRONOZZLES STUDIED BY DSMC AND CONTINUUM METHODS

F. La Torre[1], S. Kenjeres[1], C.R. Kleijn[1], J.L.P.A. Moerel[2]
[1]Department of Multi Scale Physics, Faculty of Applied Sciences, Delft University of Technology, Prins Bernhardlaan 6, 2628 BW Delft, The Netherlands
[2]Department of System Performance and Survivability, TNO Defence, Security and Safety, P.O.Box 45, 2280 AA Rijswijk, The Netherlands

ABSTRACT. Recent trends in small-scale (~1 dm^3) satellites motivate the further development of micro-scale propulsion subsystems with thrusts in the μN - mN range. In the present paper, we focus on the importance of wall effects in such small systems, due to the decrease in the characteristic length and the consequent rapid increase of the surface-to-volume ratio. First, a brief overview is presented of the rarefaction effects that can be expected on the basis of the small characteristic dimensions of the system, and that have been studied through Navier-Stokes based continuum simulations and Direct Simulation Monte Carlo (DSMC). Second, the influence of the gas-surface interaction is studied considering different boundary conditions for the flow in both Navier-Stokes and DSMC, with a special attention for the molecular energy exchange at the gas-solid interface. The precise nature of the boundary conditions is found to have a strong influence on the flow in the region of interest, and consequently on the nozzle performance.

Keywords: *Micro-Thruster, Rarefied Gas Flow, Gas-Surface Interaction, Direct Simulation Monte Carlo, Slip Flow*

INTRODUCTION

Recent trends in small-scale (~1 dm^3) satellites motivate the further development of small-scale, low-mass, low-thrust (μN – mN), microchannel based propulsion systems that allow precise control and manoeuvring of these small spacecrafts. Micro-electromechanical systems (MEMS) technology allows for the fabrication of micronozzles with thrusts suitable for this scale of satellite. In The Netherlands, a large multidisciplinary research program on the development of such propulsion systems is being carried out. An overview of this program is presented in [1], [2].
Micro-propulsion systems differ from large scale propulsion systems: the significant decrease in the characteristic length of such small systems, and the consequent increase of the surface-to-volume ratio, make surface effects strongly influence the flow inside the micro-nozzle. It has been pointed out [3] that while the surface-to-volume ratio is ~1 m^{-1} for a machine with a characteristic length of 1 m, the same ratio for a MEMS device having a size of 1 μm is ~10^6 m^{-1}. As a result, the transport of mass, momentum and energy may be strongly affected by the surface. Some areas of concern, like the inefficiency associated with viscous losses due to the developing boundary layer, and the effect of surface roughness and the way the gas interacts with the solid walls, cannot to be ignored.
Moreover, due to the small characteristic dimensions, comparable to the molecular mean free path, of thrusters in the μN - mN range, rarefaction effects need also to be considered: at these length scales the gas cannot be treated as a continuum, and molecular effects must be taken into account

* Corresponding author: F. La Torre, M.Sc.
Phone: + 31 (0)15-2782839, Fax: + 31 (0)15-2782838
E-mail address: f.latorre@tudelft.nl

[4] [5] [6]. The Knudsen number, defined as the ratio between the mean free path of the gas molecules λ and a characteristic length L of the flow:

$$\mathrm{Kn} = \frac{\lambda}{\mathrm{L}} \tag{1}$$

is an important parameter used to predict flow regions where a continuum method cannot accurately solve the flow. Various flow regimes can be distinguished based on the value of Kn [7]. Here we only want to underline that in micro nozzles the criterion for the validity of the Navier-Stokes solution (Kn<0.01) is not met throughout the entire geometry [8].
Micronozzle hydrodynamics have been studied through numerical CFD simulations in e.g. [9], [10]. Rarefaction effects, that start to play a role for very small scale nozzles, have been accounted for through the use of CFD with wall slip conditions [5], [11], [12] and through the use of Direct Simulation Monte Carlo techniques [4], [6], [11], [13]. Some geometrical aspects, such as the dimension of the throat [6], the shape of the divergent [14], and the 3-dimensional shape of the nozzle [13], [15], have been investigated, also observing the influence of viscous effects in relation to the inlet conditions [15]. The gas-wall interactions have been studied for a nozzle configuration with characteristic length of 1 mm and a very low pressure (~130 Pa) in [9]. Comparisons between numerical data and measurements have been provided in [16].
In the present paper we want to focus on the rarefied effects and the gas-surface interactions in 5–25 μN thrusters for a given geometric configuration (see Figure 1). After a brief introduction of the problem and a discussion of the used numerical techniques used (in the next two sections), we will study rarefaction effects and finally investigate at a molecular level how the way gas particles exchange energy at the gas-solid interface can influence the performance of a μN thruster.

STUDIED MICRONOZZLE CONFIGURATION

The studied nozzle is shown in Figure 1. Two different regions can be distinguished: a convergent part, where the flow is accelerated from the initial subsonic velocity to the sonic condition (which is reached at the throat), and a divergent part, where the flow supersonically expands to the outlet. The throat radius is 3.56 μm, while a sharp angle is considered to connect the convergent and the divergent. Both the convergent angle θ_1 and the divergent angle θ_2 are 20°. The inlet area A_i and the outflow area A_e equal 7.27 and 23.23 times the throat area A_t, respectively. In the inlet, nitrogen gas is introduced at a pressure ranging from P_0=0.5 bar to P_0=3.5 bar and temperature of T_0=300 K. A vacuum condition is assumed outside. The walls are modelled as isothermal at T_0=300 K. Under these conditions, the ideal thrust T_{ideal} computed from the 1D isentropic flow theory [17], is approximately 25 μN for P_0=3.5 bar, and approximately 4 μN for P_0=0.5 bar.

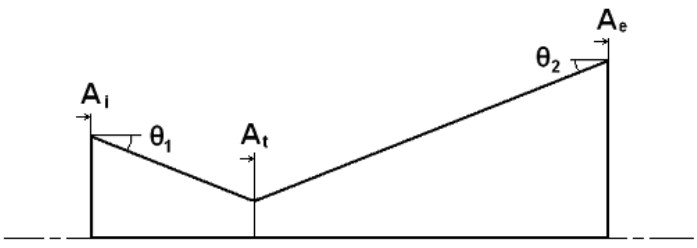

Figure 1. The nozzle geometry configuration considered in the present study, with the geometric parameters of interest.

In order to compare the results obtained through the different numerical models introduced below and to evaluate the performance of different nozzle configurations, two performance parameters will be computed. The first is the efficiency of the nozzle:

$$\eta = \frac{F_{real}}{F_{ideal}} \tag{2}$$

defined as the ratio of the ideal thrust F_{ideal} obtained from 1D isentropic flow theory, and the real thrust F_{real}, computed from

$$F_{real} = \int_{\text{outlet area}} \left[mV_e + (p_e - p_a) \right] dA \tag{3}$$

Where the subscripts e and a refer, respectively, to the conditions at the exit of the nozzle and to the ambient conditions outside the nozzle. The second parameter, the specific impulse, describes the change in momentum of the satellite per unit of propellant weight (on earth)

$$I_{sp} = \frac{F}{mg} \tag{4}$$

NUMERICAL SIMULATION TECHNIQUES

Navier Stokes solver

The Navier Stokes based continuum simulations presented in this paper have been obtained with the general purpose CFD solver Fluent version 6.3 [18]. The studied nozzle has a conical shape and therefore a 2D-axisymmetric flow is considered. The solved equations include the steady state continuity, Navier Stokes and thermal energy equations in compressible form, discretized in space using a second order upwind scheme, and solved using an implicitly coupled pressure based solver. At the nozzle walls, slip flow and temperature jump boundary conditions are imposed according to the formulas derived by Maxwell for the velocity and by Smoluchowski for the temperature [3]:
:

$$V_{gas} - V_{wall} = \frac{2-\sigma_v}{\sigma_v} Kn \left(\frac{\partial V}{\partial n} \right)_{wall} + \frac{3}{4} \frac{\mu}{\rho T} \left(\frac{\partial T}{\partial s} \right)_{wall} \tag{5}$$

$$T_{gas} - T_{wall} = \frac{2-\sigma_T}{\sigma_T} \left[\frac{2\gamma}{\gamma+1} \right] \frac{Kn}{Pr} \left(\frac{\partial T}{\partial n} \right)_{wall} \tag{6}$$

where n and s are the directions normal and the tangential to the wall, respectively, Pr is the Prandtl number and γ is the specific heat ratio. The tangential momentum accommodation coefficient σ_V and the thermal accommodation coefficient σ_T, are defined, respectively, as:

$$\sigma_v = \frac{V_i - V_r}{V_i - V_w} \qquad \sigma_T = \frac{T_i - T_r}{T_i - T_w} \tag{7}$$

where the subscripts i, r and w stand for incident, reflected and solid wall conditions. These parameters are further discussed in the last section. Equations (5) and (6) show that significant slip occurs only if the mean velocity of the molecules varies appreciably over a distance of the mean free path. The slip boundary conditions are approximated by the solver as explained in [18].

DSMC solver

Our 3-dimensional general purpose DSMC code X-Stream [19] has been validated earlier for a wide range of problems [20]. In all simulations presented in this paper, a Variable Soft Sphere (VSS) model has been used, with the corresponding parameter set from the literature [21]. Because of the axi-symmetry, a radial weighting factor [7] has been used such that a computational particle located far from the axis represents more real molecules than one near the axis.
In DSMC, rather than using separate accommodation coefficients for momentum and energy, a single thermal accommodation coefficient α is generally used [7] to account for the fact that incident and the reflected particles have different energies. Several theoretical approaches are available for estimating α [21, 22]. For nitrogen gas and silicon walls, these theories predict $\alpha \approx 0.5\text{-}0.8$. We refer to Section 5 to illustrate how this coefficient is modelled in X-Stream.
Even if DSMC is in principle valid for all Kn numbers, its computational requirements (with respect to the number of particles and time steps) severely increase for decreasing Kn [7]. In order to overcome this problem and to obtain a solution which is accurate both in the low Kn convergent region and in the high Kn divergent region, a hybrid Navier-Stokes/DSMC model has been used, which applies a continuum based CFD approach to model the flow in the low Kn regions where rarefaction effect are unimportant, and the DSMC approach in high Kn regions where rarefaction is important. This approach and a discussion of its results have been discussed in detail in [8]. In particular, it was pointed out how the location of the division between the CFD and DSMC regions may influence the final solution. A vertical division plane located at the throat was used in all the hybrid simulations shown in the present paper.

RAREFACTION EFFECTS

First, a comparison between the solutions obtained from a full CFD simulation (using either no-slip boundary conditions, or slip boundary conditions with $\sigma_V=\sigma_T=0.5$), and the solutions from full DSMC (with $\alpha=0.5$) has been performed for a nozzle with a nominal thrust of ~25 μN.
The DSMC simulation showed the presence of rarefied flow in a large part of the nozzle divergent, leading to a lower pressure and a higher value of the velocity in the exit region, compared to the no-slip CFD solution. In particular, significant differences were observed in the region near the wall, where the presence of a slip velocity strongly influences the thickness of the boundary layer and the mass flow predicted by the model, and, finally, the expansion of the wall. This can be observed from the exit profiles for velocity and pressure, as shown in Figure 2. The CFD simulation with partial slip ($\sigma_V=\sigma_T=0.5$) leads to an outflow velocity profile similar to DSMC, but still leads to a different pressure field. An investigation of the nozzle performance both in terms of thrust and specific impulse (Table 1) showed that the presence of slip velocity allows the flow to reach higher velocities at the outflow with a consequent higher nozzle performance. On the other hand, a full CFD simulation with no-slip wall boundary condition gives an under-prediction of the nozzle thrust compared to full DSMC. It must be stressed however, that the full DSMC solution suffers from the

Table 1
Nozzle Performance evaluated by different Numerical Approaches

Configuration	T, μN	η	I_{sp}, s
full CFD, no-slip wall	19.6	84.52	68.44
full CFD, partial slip wall	20.6	88.78	68.98
Full DSMC	20.0	86.26	66.71
Hybrid CFD slip / DSMC	19.9	86.04	66.85

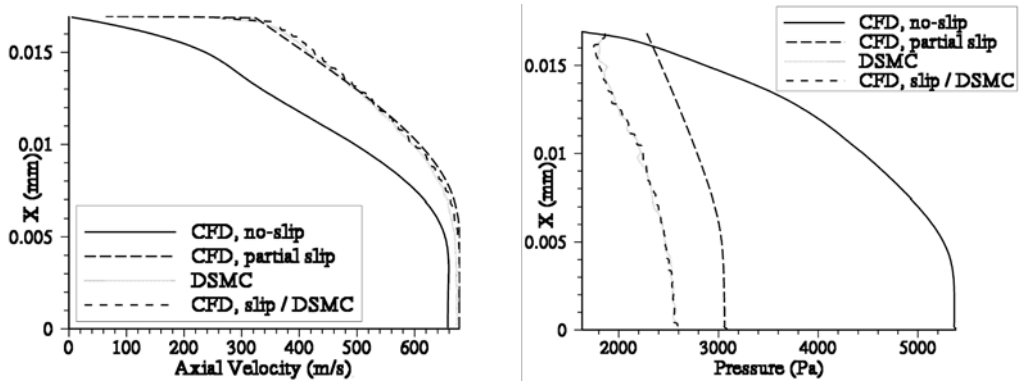

Figure 2. Profiles of exit velocity and pressure obtained by CFD, DSMC and coupled CFD/DSMC

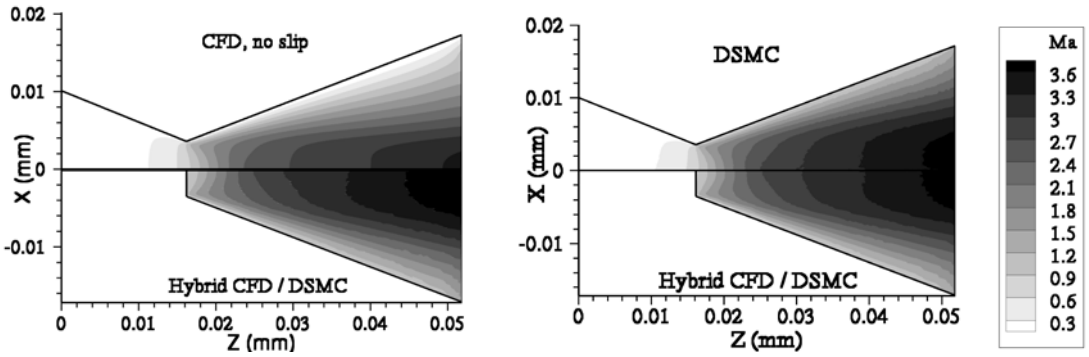

Figure 3. Comparison of Mach number contours from the solution obtained by (1) full CFD with no slip wall velocity, (2) full DSMC with accommodation coefficient α=0.5, and (3) DSMC in the divergent only with inlet boundary conditions in the throat plane obtained from CFD.

fact that the DSMC accuracy requirements cannot be met in the low Kn convergent region. More accurate results can be expected from the hybrid CFD/DSMC solution. A comparison between this approach and full DSMC and full CFD solutions with partial slip are shown in Figure 3.

GAS-SURFACE INTERACTION EFFECTS

It has already been pointed out that the large surface-to-volume ratio makes surface effects become prominent in micro-thrusters. One effect is that common micro system manufacturing techniques lead to surface roughness with length scales that are significant compared to both the characteristic dimensions of micro thrusters and the molecular free path. In [2] we performed an extensive study on the influence of such roughness on the performance of a mN thruster.

In the present paper we study gas-surface interactions in μN nozzles at a molecular level. The result of a collision between a gas molecule and the wall depends on the properties of the molecules hitting the surface and of the surface itself. A perfectly smooth wall would be fully specular, such that hitting particles conserve their tangential momentum and exert no shear on the wall. This would result in perfect slip at the wall. An extremely rough wall reflects the impinging particles at random angles, uncorrelated with their entry angle, leading to an averaged zero tangential momentum to be balanced by a finite slip velocity in order to account for the shear stress transmitted to the wall [3]. In the present DSMC simulations, the accommodation coefficient α is set to be the fraction of particles that reflect diffusely, while (1- α) is the fraction that reflects specularly. So, α=1 and α=0 correspond to purely diffuse and purely reflective surfaces, respectively.

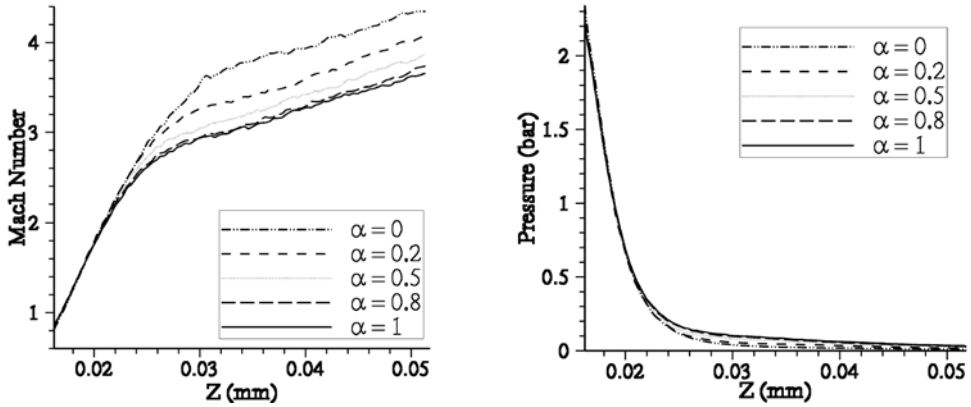

Figure 4. Mach number (left) and Pressure (right) along the nozzle divergent axis, for P_0=3.5 bar

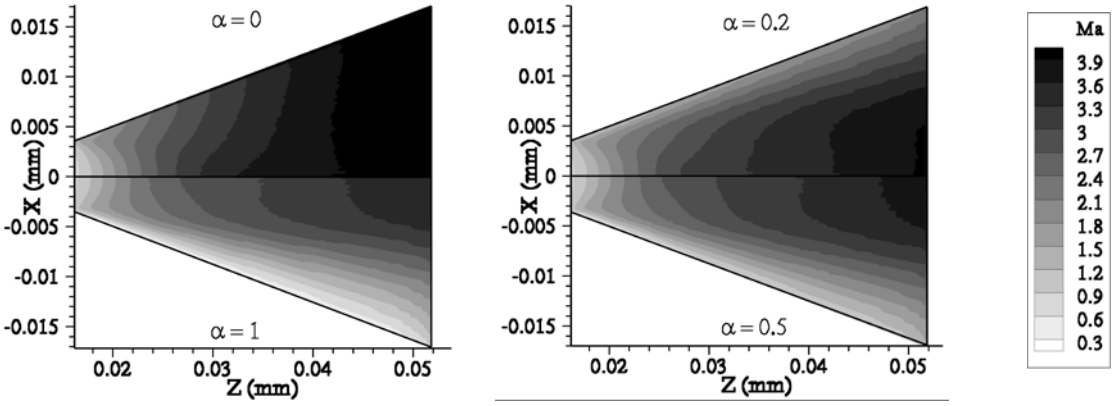

Figure 5. Mach number contours in the nozzle divergent for different values of α, for P_0=3.5 bar

Predictive formulas for thermal accommodation coefficients have been formulated in e.g. [21], [22], but proved to be valid only for a certain range of gas-surface configurations. Experimental data, are provided in [23], [24], [25]. Values between α=0.5 and 0.8 are generally reported for nitrogen molecules interacting with silicon walls. We study the influence of α on the nozzle performance, keeping in mind also that the choice of different gas-surface combinations and the improvement of fabrication techniques may lead to a wide choice in possible values of α.

Figure 4 shows the Mach number and the pressure along the axis of the divergent part of the nozzle, obtained from hybrid CFD/DSMC simulations for P_0=3.5 bar and different values of α. Figure 5 shows Mach number contours, again for P_0=3.5 bar and different values of α. For small values of α, the momentum boundary layers at the walls are thinner and higher velocities and lower pressures are reached at the outflow. This is reflected in the nozzle performance, as reported in Table 2. Thrust, mass flow and specific impulse are significantly higher for low values of α.

Table 2
Nozzle Performance evaluated by the Solutions for Different Values of α, for P_0=3.5 bar

α	T, μN	η	m, g/s	I_{sp}, s
0.0	22.1	95.17	3.19×10^{-5}	70.44
0.2	20.9	90.15	3.10×10^{-5}	68.74
0.5	19.9	86.04	3.04×10^{-5}	66.85
0.8	19.8	85.34	3.02×10^{-5}	66.82
1.0	19.5	84.20	2.98×10^{-5}	66.71

The influence of α was also studied for P_0=0.5 bar. In this case, DSMC was used in the entire nozzle. A fully viscous flow is observed inside the divergent part of the nozzle (Figure 6, left), especially for higher values of α. The flow does not fully expand in the divergent, and the Mach number is not as large as expected. This leads to high losses in terms of thrust and specific impulse, especially for values of α larger than 0.5, as shown in Table 3.

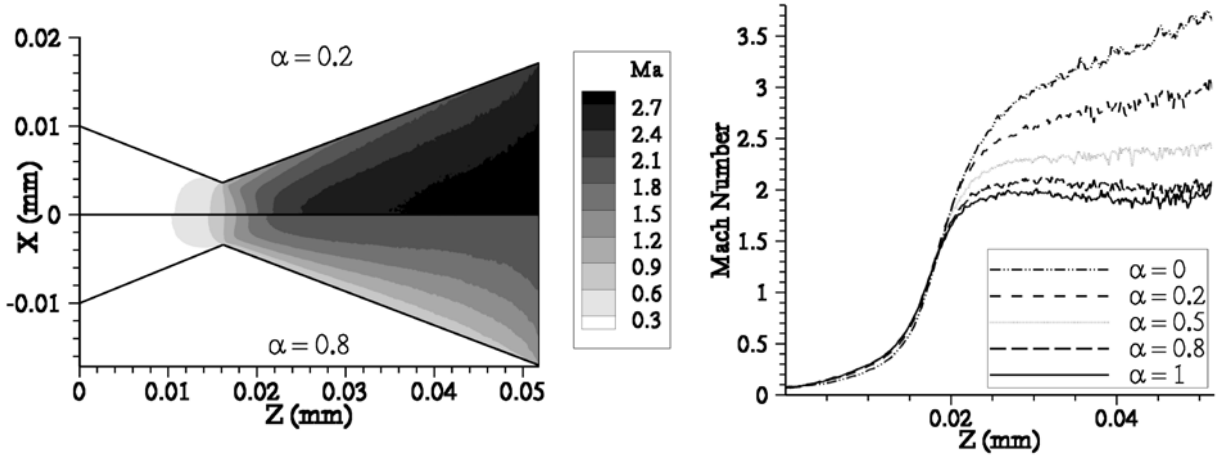

Figure 6. Mach number contours (left) and Mach number profiles along the axis for different values of α, for P_0=0.5 bar

Table 3
Nozzle Performance evaluated by the Solutions for Different Values of α, for P_0=0.5 bar

Configuration	T, μN	η	m, g/s	I_{sp}, s
DSMC – α=0.0	3.16	93.60	4.78×10^{-6}	67.38
DSMC – α=0.2	2.77	82.03	4.43×10^{-6}	63.69
DSMC – α=0.5	2.43	72.08	4.14×10^{-6}	59.87
DSMC – α=0.8	2.26	67.00	3.95×10^{-6}	58.31
DSMC – α=1.0	2.18	64.74	3.84×10^{-6}	57.96

CONCLUSION

CFD with partial slip wall, full DSMC and hybrid CFD/DSMC simulations have been used to study gas flows in ~5-25 μN microthrusters. Due to the small dimensions, the flow was shown to experience strong rarefaction effects in a large part of the divergent. Rarefaction effects lead to increased velocities and decreased pressures in the outflow. This was not correctly predicted by CFD simulations, even when slip flow boundary conditions are used. The thermal accommodation coefficient for gas-surface collisions was found to have a strong influence on the overall nozzle performance, especially for very low thrust nozzles. This suggests that the use of specific coatings or the choice of different gases and wall materials can improve the performance of such devices.

ACKNOWLEDGEMENTS

This project is founded by MicroNed, one of the Dutch BSIK research programs.

REFERENCES

1. Moerel, J.L.P.A., Sanders, H.M., Louwerse, M.C., Jansen, H.V., Boscher, J., Zandbergen, B.T.C., La Torre, F., Kenjeres, S., Kleijn, C.R., Development of Micro Propulsion System Technologies for Minisatellites in The Netherlands, *Proc. 5th Int. Spacecraft Propulsion Conference*, 2008
2. La Torre, F., Kenjeres, S., Kleijn, C.R., Moerel, J.L.P.A., Zandbergen, B.T.C, Influence of Boundary Layer Formation and Surface Roughness on the Thrust of Micro-Nozzle, *Proc.5th Int. Spacecraft Propulsion Conference*, 2008.
3. Gad-el-Hak, M., The Fluid Mechanics of Microdevices – The Freeman Scholar Lecture, *J. Fluids Engineering*, Vol.121 / 5, pp 5-33, 1999.
4. Xie, C., Characteristics of Micronozzle Gas Flows, *J. Physics of Fluids*, Vol.19 (3), 2007.
5. Markelov, G.N., Ivanov, M.S., Ketsdever, A.D., Wadsworth, D.C., Numerical Study of Cold Gas Micronozzle Flows, *Proc. of the 33th Aerospace Science Meeting and Exhibit*, 1999.
6. Mo, H., Lin, C., Gokaltun, S., Skudarnov, P.V., Numerical Study of Axisymmetric Gas Flow in Conical Micronozzle by DSMC and Continuum Methods, *Proc. of the 44th AIAA Aerospace Sciences Meeting and Exhibit*, 2006, AIAA 2006-991.
7. Bird, G.A., *Molecular Gas Dynamics and the Direct Simulation of Gas Flows*, Oxford Science Publications, Oxford, 1994.
8. La Torre, F., Kenjeres, S., Kleijn, C.R., Moerel, J.L.P.A., Evaluation of Micronozzle Performance through DSMC, Navier-Stokes and Coupled DSMC/Navier-Stokes Approaches, *Proc. of Int. Conference of Computational Science 2009*.
9. Buoni, M., Kietz, D., Aslam, K., Subramaniam V.V., Simulation of a Compressible Gas Flow in a Micronozzle, *Proc. of the 35th AIAA Thermophysics Conference*, 2001, AIAA 2001-3073.
10. Thornber, B., Chesta, E., Gloth, O., Brandt, R., Schwane, R., Perigo, D., Smith, P., Numerical Simulation of Micronozzles with Comparison to Experimental Results, *Proc. of the 4th Int. Spacecraft Propulsion Conference*, 2004.
11. Liu, M., Zhang, X., Zhang, G., Chen, Y., Study on Micronozzle Flow and Propulsion Performance using DSMC and Continuum Methods, *Acta Mechanica Sinica*, Vol.22, 2006.
12. Raju, R., Pandey, B.P., Roy, S., Finite Element Model of Fluid Flow inside a Micro-Thruster, *Proc. of the NanoTech 2002 Conference*, 2002, AIAA 2002-5733.
13. Alexenko, A.A., Levin, D.A., Gimelschin, S.F., Collins, R.J., Numerical Modeling of Axisymmetric and Three-Dimensional Flows in MEMS Nozzle, *AIAA J.*, Vol.40 (5), 2002.
14. Engblom, W.A., O'Gara, M., Richards, A., Sypeck, D.J., Investigation of Microthruster Nozzle Performance for Nanosatellite Applications, *Proc. of the 37th AIAA Fluid Dynamic Conference and Exhibit, 2007*, AIAA 2007-3985.
15. Wang, M.R., Li, Z.X, Numerical Simulations on Performance of MEMS-based Nozzle at Moderate Temperatures, *J. Microfluidics and Nanofluidics*, Vol.1, 2004, pagg.67-70.
16. Hao, P., Ding, Y., Yao, Z., He, F., Zhu, K., Size Effect on Gas Flow in Micro Nozzles, *J. of Micromechanical and Microengineering*, Vol.15, 2069-2073, 2005.
17. Sutton, G.P., Biblarz, O., *Rocket Propulsion Elements*, John Wiley&Sons, 2001.
18. *Fluent 6 Tutorial Guide*, Fluent Incorporate, 2005.
19. *CVD-X User Manual*, TNO, 2007.
20. Dorsman, R., Numerical Simulations of Rarefied Gas Flows in Thin Film Processes, *PhD Thesis*, TU Delft Applied Physics Dept., Delft, 2007.
21. Goodman, F.O., Wachman, H.Y., Formula for Thermal Accommodation Coefficients, *J. Chemical Physics*, Vol.46 (6), 1967, pagg.2376-2386.
22. Touloukian, Y.S., Ho, C.Y., Saxena, S.C., Joshi, R. K., *Thermal accommodation and Adsorpion Coefficient of Gases*, McGraw-Hill, New York, 1979.
23. Arkilic, E.B., Breuer, K.S., Schmidt, M.A., Mass Flow and Tangential Momentum Accommodation in Silicon Micromachined Channels, *J. Fluid Mechanics*, Vol.437, 2001.
24. Beskok A., Karniadakis G.E., Trimmer W., Rarefaction and Compressibility Effects in Gas Microflows, *J. Fluid Engineering*, Vol.118, pp. 448-456, 1996.
25. Piekos, E.S., Breuer, K.S., Numerical Modeling of Micromechanical Devices using the Direct Simulation Monte Carlo Method, *J. Fluid Engineering*, Vol.118, pp. 464-469, 1996.

ExHFT-7
28 June – 03 July 2009, Krakow, Poland

MICROFABRICATED SINGLE-JET AND MULTI-JET DEVICE FOR ELECTRONICS COOLING

Y.Won[1], S.Kim[1], E.N.Wang[2], K.E.Goodson[1], T.W.Kenny[1,*]

[1]Stanford University, Stanford, CA, USA
[2]Massachusetts Institute of Technology (MIT)

ABSTRACT. We present an experimental study on microjet cooling performance. While microjets are promising for cooling integrated circuits, there have been few detailed studies on understanding both single and two-phase performance. In this work, we fabricated single-jets and multi-jet arrays with diameters ranging from 50 μm to 100 μm and used infrared thermometry to obtain surface temperature distributions and heat transfer coefficients. We found that heat transfer performance with designed devices. This work offers an improved understanding on single-microjet, and multi microjet.

Keywords: *impingement, microjet, multi-jet, electronic cooling, heat transfer*

INTRODUCTION

As electronic devices continue to scale down to smaller sizes, the increasing power densities in microprocessors motivate new cooling techniques. Jet impingement cooling has been traditionally used in industrial applications such as metal manufacturing and high power lasers in macroscale.[1-2] Similarly, there have been studies about electronic device cooling using microchannels and microscale jets. [3-4] Microscale jet impingement offers a potential solution for cooling high power density microscale electronic devices [5-6]. In addition, an increased temperature uniformity can be achieved with multi-jet arrays. In addition to the high heat capacity, two-phase cooling offers improved performance by utilizing the latent heat of vaporization. [7-8] In this work, we performed detailed heat transfer studies using arrays of jets, and obtained heat transfer coefficient for single phase. We designed, fabricated, and tested new microjet structures for these studies to determine optimized designs for future microjet-based cooling systems.

* Corresponding author: Y.Won, Stanford Univ., Mechanical Eng., Stanford, CA, 94305
Phone: + (1)-650-714-1525, Fax: + (1)-650-723-7657
E-mail address: yoonjin@stanford.edu

EXPERIMENTAL SET UP

Devices

Fabrication. We fabricated silicon microjets using deep reactive ion etching (DRIE). The inlet, top water reservoir, outlet were DRIE etched from both sides with first substrate. With second substrate, jets and a bottom water reservoir were etched from both sides using DRIE. In order to gain optical access to see the jet impingement process, the bottom water reservoir was covered with a glass substrate after the first and second substrates were fusion bonded together. The final step included dicing the wafer into pieces. On one wafer, we were able to obtain several different designs with various numbers of jets, different diameter jets, and jets at various locations. The fabricated jets were connected to inlet and outlet ports from Upchurch Scientific™. The experimental test rigs that contained the jet devices are shown in Figure 1.

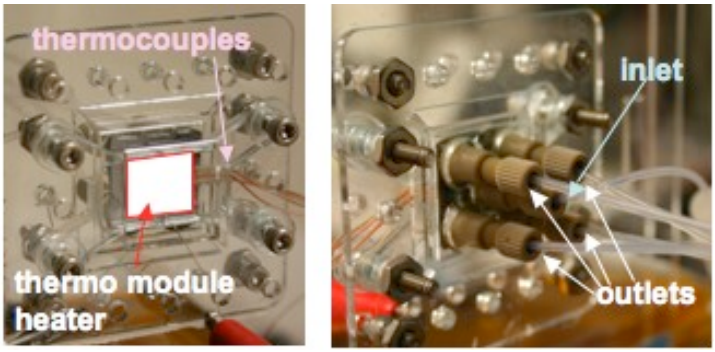

Figure 1. Image of microjet structure in test figure. (a) Front side and (b) back side of microjet device with test fixture.

Design. Figure 2 shows simplified schematics of two different microjet devices used in these studies. The single jet has a 100 µm diameter located at the center, and the 121-jet array has 50 µm diameter jets separated by 150 µm each. There are more design variations, which have 9-jet, 16-jet, 25-jet, 49-jet, we choose two designs to describe jet system in this paper.

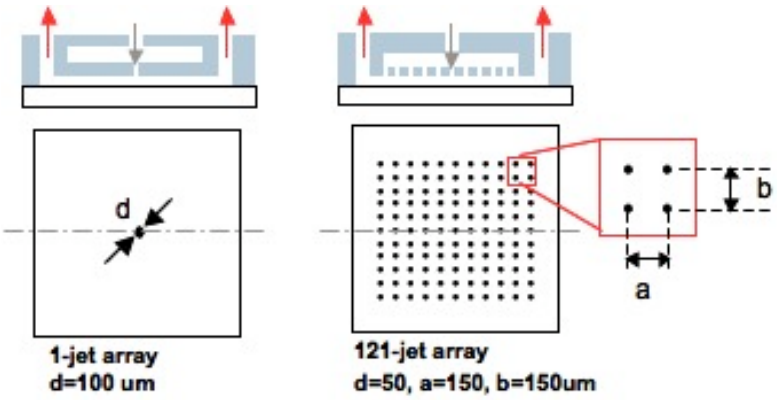

Figure 2. Schematics of example test devices including (a) a single-jet device and (b) 121-jet device.

Experimental work

The jet chip was connected to a syringe pump, which is controlled by the program, to provide fluid with a constant volume rate. De-ionized (DI) water was used as the working fluid. The pressure transducer was also connected to the inlet of the jet chip to see pressure difference between inlet and outlets. Infrared thermometry was used to obtain the surface temperature of the chip. Ti-20 from fluke gives 0.1°C resolution. The images form thermal imager can be used for reading temperatures with different flow rates and power to the heater, and heat transfer coefficients can be calculated. The temperature from thermal imager was calibrated using attached thermocouples and it was compared with the table of emissivities. The emissivity for the chip surface was found to be 0.95.

RESULT AND DISCUSSION

Temperature distribution

We used the data from the thermal imager to extract temperature data with three-dimensional (3-D) surfaces as shown in Figure 3. Figure 3 (a) shows an thermal image with a single-jet device with a flow rate of 0.5ml/min, and 2V bias voltage, which gives 2.4W. The lower temperature region around jet impingement is illustrated in yellow, while the others are red. The 121-jet array with (b) shows almost uniform temperature along the plane, which has mean, minimum, and maximum temperature as 43.2, 42.2, and 45.5 °C, respectively. Each images has x,y axis temperature plots along diagonal lines. These temperature plots explain 1-jet array has a steep region at impingement zone; while 121-jet array has almost const temperature again.

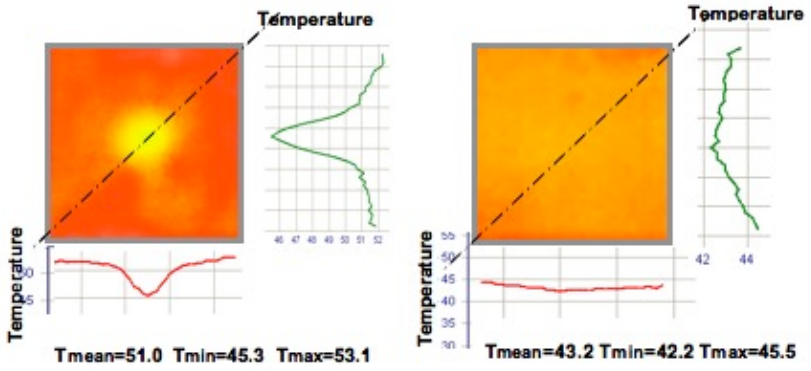

Figure 3. (a) Thermal image with 1-jet array (b) 121-jet array: Thermal image of microjet cooling device with 0.5ml/min, 2V with bias voltage

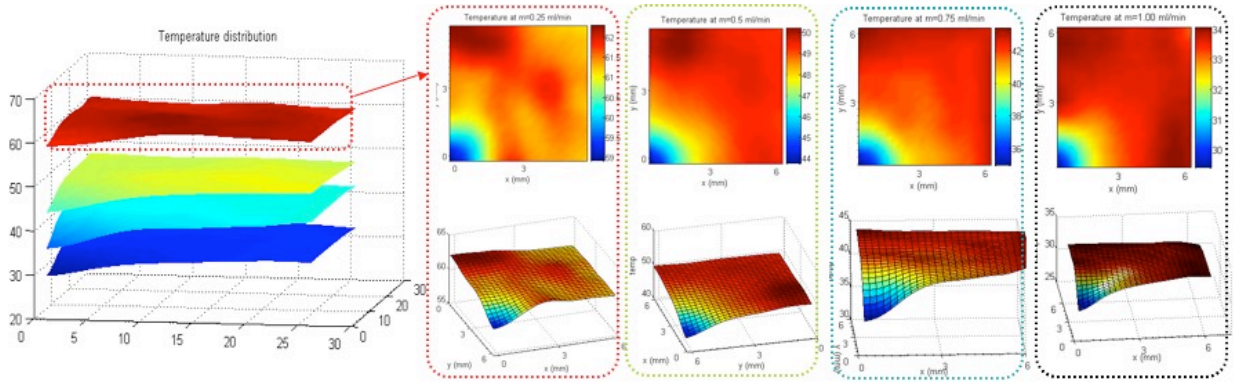

Figure 4. 3-D temperature surface with 1-jet array at m=0.25, 0.5, 0.75, 1 ml/min with voltage 1.8 V.

In figure 4, temperature surface plot has "steep" region at impingement. We can consider steep region as effective region in terms of heat transfer. From the images, there are four plots with different flow rates. At impingement region, which is indicated as origin in figures, each temperature surface plot has minimum temperature, known as the most effective cooling region. Because multi-jet system demonstrates practically uniform temperature, error bars compare the intervals of data for each bias voltage as shown in figure 5. For comparison with different flow rates with different heating power, mean, minimum, maximum temperatures are indicated with bars in figure 5. To make a non-dimensionalized work, real temperatures are divided by the initial temperatures. As shown in graph, higher mass flow rate dissipate with higher removal rates, while plots with lower mass flow rates obtain more effects from higher heating power. The black line is used as a comparison without any liquid cooling impingement. The top black line achieves non-dimensionalized temperature from 1 to 3 with highest heating rates; low mass flow rate experience numbers ranging between 1 to 2.5; while, the highest mass flow rate rises from 1 to 1.2. Therefore more flow flux can lead to more uniformity in terms of large range of heating power. We make comparison work in order to see differences of temperatures with single, multi-jet devices in figure 6. The multi-jet system exhibits much more uniform and lower temperature results.

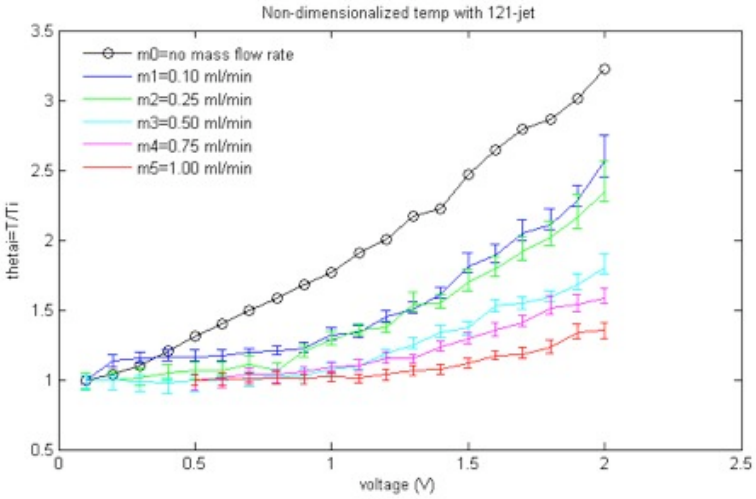

Figure 5. Non-dimensionalized temperature with increasing bias voltage in multi-jet device.

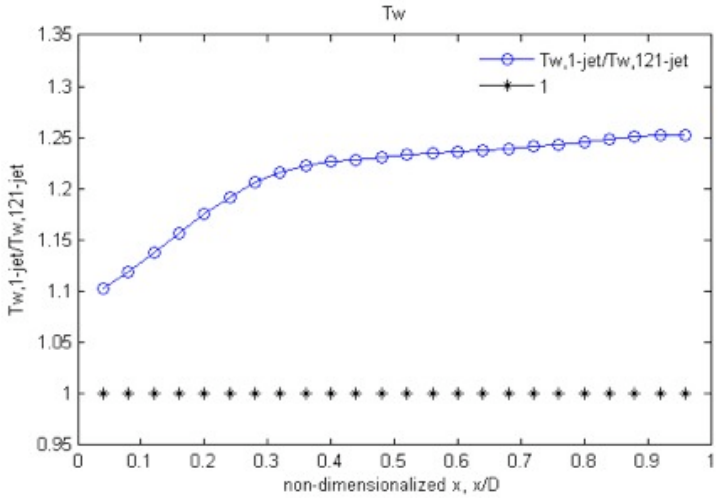

Figure 6. Temperature plots for 1-jet and 121-jet.

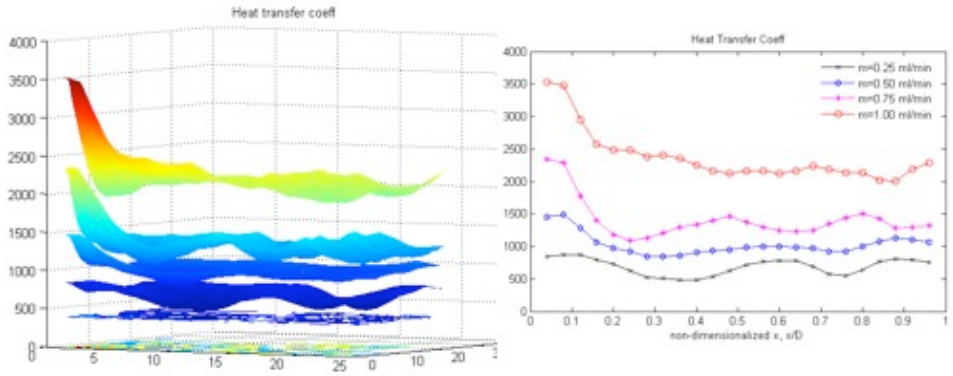

Figure 6. (a) 3-D heat transfer coefficients for m = 0.25, 0.5, 0.75, 1 ml/min with bias voltage 1.8 V. (b) 2-D heat transfer coefficients.

Heat transfer coefficient

From the taken images, we will extract three different temperature sets, which are T_w, taken by imager, T_g as a top glass substrate temperature, T_l as a liquid mean temperature. This simplified jet model shows that convective resistance and conductive resistance exist between different temperautre nods between T_l and T_w as indicated in equation (1). In order to consider additional conductive resistance along x,y axises in 3-D resistances model, we need to consider heat flux from all surrounding points. From equation (2), q (heat flux to the liquid from target point) can be estimated with sum of flux to this point. With known values such as q_{in}, k, material conductivity and geometry numbers (A, cross sectional area, l, length), we can derive a heat flux to the liquid at each point.

$$\frac{T_l - T_w}{q} = R_{conv,z} + R_{cond,z} = \frac{1}{hA} + \frac{l}{kA} \tag{1}$$

$$q = q_{in} + q_{x,i-1} + q_{x,i+1} + q_{y,i-1} + q_{y,i+1} \tag{2}$$

This steep region makes highest heat transfer rate at the origin as shown in figure 6 (a). We achieve higher heat transfer rate with closer to the origin or higher mass flow rates.

Pressure drop

There are two performance goals of microjet design. First, we obtain an enhanced heat transfer coefficient for maximum heat removal from the hot chip surface. Second, we will achieve a small pressure drop to be compatible with micro-pumping technologies. Pressure drop is another important issue in heat sink problems, because engineers have to consider pressure difference to decide a pump capacity.

The total pressure drop is given by [9[

$$\Delta p = n \cdot f\rho \frac{l}{d} v_{jet}^{\ 2} + \rho \frac{v_{out}^{\ 2}}{2} \tag{3}$$

f is the friction factor given by the Blasius correlation for turbulent flow, ρ is the density, d is the diameter of the jet, l is the length of the nozzle, v_{out} is the exit velocity and v_{jet} is the nozzle exit

velocity. The first term on the right hand side of equation (3) gives the losses in the nozzle due to friction, while the second term gives the dynamic pressure loss. While single jet has fewer losses due to friction, compensation with larger dynamic pressure makes comparable value of total pressure drop as shown in figure 8.

CONCLUSION

As a study of micromachined liquid impingement jets, several jet systems with diameters 50 μm-100 μm have been fabricated with silicon substrate. The test structures on single, multi-jet system are used to collect temperature data, extract heat transfer coefficients to make comparison, and analyze optimization of spacing between jet orifices. Images are taken by thermal camera to get plane temperature information. From these images, heat transfer coefficient was calculated. The "effective" region with single jet system only extends to about five times the jet diameter in the 3-D model, while multi-jet array achieves a uniform temperature with plane. The integration of our design will enable high power processors to be run at higher clock frequencies to obtain increased performance, while still ensuring stability and reliability due to sufficient thermal cooling. In addition, liquid impingement cooling has other advantages over traditional air-cooling, such as quieter operation and stable temperature of the processor's operating environment. Future work will aim for an analysis between heat transfer rates and fluid mechanism especially at the impingement region. Optimization of these design parameters will enable an improved design capability for the next generation of jet impingement coolers for electronic circuits.

ACKNOWLEDGMENT

This work is supported by MARCO IFC Program. Work was performed in part at the Stanford Nanofabrication Facility (a member of the National Nanotechnology Infrastructure Network) which is supported by the National Science Foundation under Grant ECS-9731293, its lab members, and the industrial members of the Stanford Center for Integrated Systems.

REFERENCE

[1] Tuckerman, et al., "High-Performance Heat Sinking for VLSI", IEEE Electron Device Letters, Vol. EDL 2, No. 5, May 1981, pp126-129.
[2] Matteo Fabbri, 'A Comparative Study of Cooling of High Power Density Electronics Using Sprays and Microjets', Journal of Heat Transfer, JANUARY 2005, Vol. 127
[3]. L. Jiang, et al., "Two-phase microchannel heat sinks for an VLSI cooling system," Seventeenth Annual IEEE Semiconductor
Thermal Measurement and Management Symposium, San Jose, CA USA, March 20-22, 2001, pp.153-157.
[4] Wang, E.N., et al., "Micromachined Jets for Liquid Impingement of VLSI Chips" J. Microelectromech. Syst., 2004. 13(5): p. 833-842.
[5] Q. Lin, et al., "MEMS Impinging-Jet Cooling," Proceedings of 2000 ASME International Mechanical Engineering Congress and Exposition, Orlando, FL, USA, Nov. 2000, pp.137
[6] Zhang, L., et al., "Microscale Liquid Impingement Cooling", Proceedings of 2001 ASME International Mechanical Engineering Congress and Exposition, New York, NY, USA, CD Vol.2, paper No. 23820, November 11-16, 2001.

[7] L. Zhang, et al, "Enhanced Nucleate Boiling in Microchannels," Fifteenth IEEE International Conference on Micro Electro Mechanical Systems, Las Vegas, Nevada, U.S.A, January 20-24, 2002, pp.89-92
[8] S.V.J. Narumanchil, et al., "Modeling Single-Phase and Boiling Liquid Jet Impingement Cooling in Power Electronics." Technical report, 2005
[9] R.W. Fox and A.T. McDonald, Introduction to Fluid Mechanics, John Wiley & Sons, 1999.

CONVECTIVE HEAT TRANSFER AND FLUID FLOW CHARACTERISTICS OF GRAPHITE FOAM HEAT SINKS WITH COMPLEX STRUCTURES

K.C. Leong[1*], H.Y. Li[1], L.W. Jin[1], J.C. Chai[2]
[1]School of Mechanical and Aerospace Engineering
Nanyang Technological University
50 Nanyang Avenue, Singapore 639798
Republic of Singapore
[2]Amoeba Technologies Inc.
Austin, TX 78733, USA

Abstract. This paper presents a study of forced convection of air flow through porous graphite foams. Three structures, namely stagger, baffle and zigzag were designed to reduce pressure drop while utilizing the thermal properties of Poco graphite foams to enhance the heat transfer. All the structures contain a certain number of thin foam walls perpendicular to the flow direction with empty slots connected throughout the structures. An experimental facility was developed to compare the heat transfer performance of the designed heat sinks with an original block foam under adiabatic condition. The local substrate temperatures, pressure drops and inlet flow velocities were measured. The length-averaged Nusselt numbers of air flow through the samples were calculated. In addition, a numerical simulation was also carried out to explore more details of the fluid flow through the complex structures. It is found that the pressure drops in the designed structures are much lower than that in the block foam. Hence, these heat sinks can remove heat efficiently with relatively low pumping power.

Keywords: *forced convection, porous graphite foam, Nusselt number, pressure drop, pumping power*

INTRODUCTION

The design of electronic packages for modern high-speed computers has led to increased demands for effective cooling methods. The primary concerns in thermal management applications are high thermal conductivity, large specific surface area and low weight. An effective thermal management strategy is to utilize a porous medium to enhance heat transfer by increasing the fluid-solid contact surface area and promoting fluid mixing. As compared to a channel packed with metallic particles or spheres, microcellular materials such as metal and graphite foams are novel porous media with open cell structures. Fluid flow and heat transfer in metal foam have been extensively investigated [1-5]. Recently, the novel porous graphite foam developed at Oak Ridge National Laboratory (ORNL) in USA is a promising heat transfer material because of its high thermal conductivity and low weight-to-volume ratio. The thermal conductivity of the bulk apparent thermal conductivity can be higher than 150 W/m·K, which is almost equivalent to dense aluminum alloys [6].

Motivated by the superior thermophysical properties of graphite compared to its metallic counterpart, several researchers have studied graphite foams for thermal management applications.

* Corresponding author: Prof. Kai Choong Leong
Phone: + (65)-6790-5596, Fax: + (65)-6792-4062
E-mail address: mkcleong@ntu.edu.sg

Porous carbon foam fins were studied as a replacement for aluminum fins in finned tube radiators by Ott *et al*. [7]. Their interest was driven by the unique properties of the foam which reduce the thermal resistance of a heat exchanger without significantly higher pressure drop. Druma *et al*. [8] performed a finite element analysis to determine the thermal conductivity of graphite foams for the complete range of porosity and presented analytical and semi-empirical solutions. Alam and Maruyama [9] conducted an experimental study to determine the thermal conductivity of various graphite foams. Alam *et al*. [10] numerically studied the thermal conductivity of carbon foams with a finite element model. They concluded that the conductivity of carbon foam is influenced mainly by the ratio of the node and ligament thermal conductivities. Williams and Roux [11] evaluated the cooling effects of graphite foam and microfibrous material in an electronics cooling system and concluded that graphite foams showed a good performance.

It is noted that graphite foams possess low permeability. Figure 1 shows the typical internal structure of graphite foams manufactured by Poco Graphite, Inc. observed under a Scanning Electron Microscope. The complex internal structure of the foam results in high flow resistance although most pores are open and interconnected. In this paper, three foam structures were designed (namely stagger, baffle and zigzag) to reduce pressure drop while utilizing the thermal properties of graphite foam to enhance the heat transfer. An experimental facility was developed to perform heat transfer experiments under adiabatic condition. The local substrate temperature, pressure drop and length-averaged Nusselt numbers of air flow through the samples were measured and calculated to compare their performance. In addition, a numerical simulation was also carried out to study the velocity distribution in the complex structures which would be difficult to obtain experimentally.

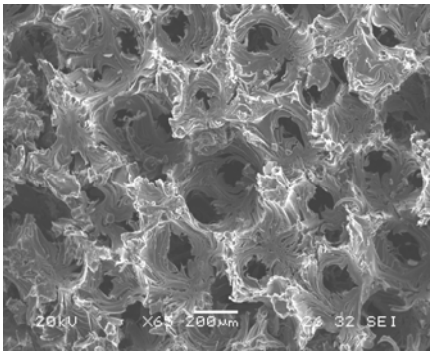

Figure 1 Internal structure of "Poco" graphite foam of 75% porosity

EXPERIMENTAL STUDY

Experimental Setup

Graphite foam configurations. The material used in this study is "Poco" graphite foam of 75% porosity which is licensed by ORNL. It is noted from the literature that the pressure drop for air flow through this graphite foam is rather large. Therefore, the designed structures should be able to reduce the pressure drop significantly while maintaining relatively good heat transfer performance. Three configurations were fabricated into different combinations of thin foam walls and empty slot in a solid block foam (BLK). They are named as baffle (BAF), stagger (STG) and zigzag (ZZG) structures based on their geometric shapes, which are shown in Figure 2.

In these structures, the thickness of the thin foam walls is between 2 to 3 mm and these walls are aligned normally to the flow inlet direction. This arrangement makes the foam dimension comparable to the pore size and therefore part of the inlet fluid can be driven easily through the foam body. Empty slots are connected throughout the structure, which allow the remaining portion of the inlet air to flow through the foam. The wall thickness, length and slot gap are selected based

on the fact that the designed structures should possess approximately the same total wall surface area. Thus, the effect of different surface areas on heat transfer is minimised. Important parameters of the designed configurations are shown in Table 1.

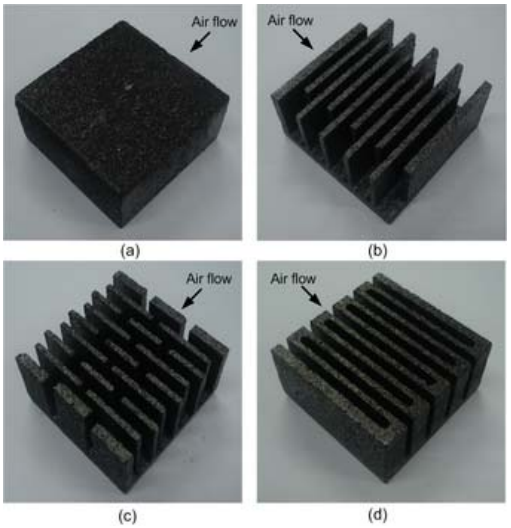

Figure 2 Test structures of (a) block, (b) stagger, (c) baffle and (d) zigzag configurations

Table 1 Parameters of designed structures

Parameters	Baffle	Stagger	Zigzag
External dimension, W×L×H (mm)	50 × 50 × 25		
Foam wall thickness (mm)	2~3	2~3	2~3
Foam wall number	23	10	19
Foam wall length (mm)	14/22	41.5	46
Slot gap width (mm)	3.625	3	3
Base height (mm)	4	4	4
Total surface area (mm^2)	17976	17913	17955

Test facility. The schematic diagram of the experimental facility is shown in Figure 3(a). The graphite foam is placed in a duct made of Teflon for insulation purpose. Two taps for pressure sensors (VALIDYNE DP15) are placed at the two ends of test section to measure the total pressure drop across the sample. Air flow is provided by an auto-balance compressor (SSR EP15SE) and a hotwire (DANTEC 55P11) sensor is placed in the middle of the inlet section to measure the flow velocity. A three-dimensional close-up view of the test section is shown in Figure 3(b). A film heater is installed at the bottom of channel and a 1-mm thick copper plate with ten uniform narrow slots perpendicular to the flow direction is attached on the surface of film heater. Ten K-type thermocouples are placed in the slots at locations of 0.25, 0.75, 1.25, 1.75, 2.25, 2.75, 3.25, 3.75, 4.25, 4.75 cm from the inlet boundary of the test foam. Highly conductive thermal grease (k = 8.5 W/m·K) is applied as filling material to reduce the contact resistances across the interfaces of the film heater, copper plate and test sample. By clamping the channel tightly, the temperatures of the graphite foam surface and copper plate at the bottom of the channel are assumed to be same in the measurements. During the experiments, the temperatures are monitored for a period of three minutes to ensure that steady state has been reached. After that, the inlet flow velocity is increased to obtain results for different Reynolds numbers.

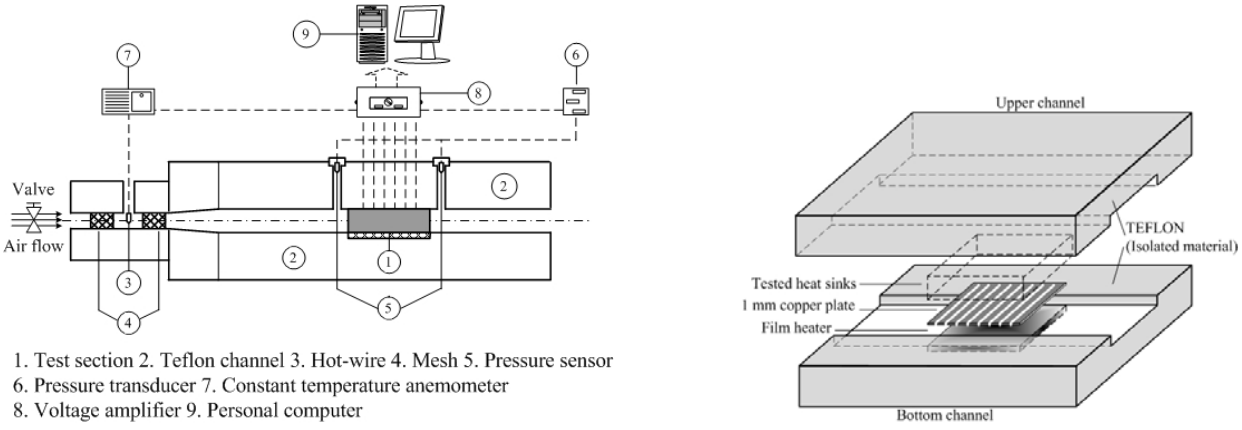

(a) (b)

Figure 3 (a) Schematic diagram of test facility; (b) three-dimensional view of test section

Uncertainty analysis

The data measured by thermocouples, pressure transducer and hot-wire sensors are monitored and acquired by a data acquisition system. The data acquisition system consists of a signal board (NI CB-68LP), I/O boards (NI PCI-6224) and an operating software (NI DAQmx 4.0) within a workstation. The temperatures, pressures and velocities measured by the sensors were fed into the data acquisition board through the differential connections. Experimental errors were estimated based on the accuracies of individual equipment or sensors. The heat loss in the experiment was estimated to be within 6% based on the calculated air enthalpy rise along the test section. The accuracy of the thermocouples used is within ±0.5 °C according to the calibration and the resolution of the data acquisition system. The corresponding value for the pressure transducer is ± 0.25% of full-scale. The accuracy of the hot-wire anemometer is ±0.01 m/s. Using a time-averaging method, the uncertainties of temperature, velocity and pressure are estimated to be 3.0 percent, 2.0 percent and 2.0 percent, respectively. For the calculated parameters, the uncertainties are determined by the method introduced by Taylor [12]. If α, … β, … γ are measured quantities with uncertainties $\delta\alpha$, … $\delta\beta$, … $\delta\gamma$, and the measured values are used to compute the function $q(\alpha,\ldots, \beta,\ldots, \gamma)$, then the uncertainty in q is

$$\delta q = \sqrt{\left(\frac{\partial q}{\partial \alpha}\delta\alpha\right)^2 + \cdots + \left(\frac{\partial q}{\partial \beta}\delta\beta\right)^2 + \cdots + \left(\frac{\partial q}{\partial \gamma}\delta\gamma\right)^2} \tag{1}$$

In the present experiments, the uncertainties of the measured data were assumed to be independent and random with normal distribution. Using Equation (1), the uncertainties of Reynolds number and Nusselt number were calculated to be 3.9 and 5.7 percent, respectively.

NUMERICAL SIMULATION

Formulation

To achieve better understanding of the transport phenomenon in graphite foams, a FORTRAN-based user program was developed to obtain fluid flow and heat transfer characteristics in the designed structures. The local volume-averaging method is used to derive the governing equations. With the assumptions of laminar flow and constant properties, the mass, momentum and energy equations are

$$\frac{\partial \langle u_i \rangle}{\partial x_i} = 0 \tag{2}$$

$$\frac{\rho_f}{\varepsilon}\left(\frac{\partial \langle u_i \rangle \langle u_j \rangle}{\partial x_j}\right) = -\varepsilon \frac{\partial \langle p \rangle}{\partial x_i} + \mu_f \frac{\partial}{\partial x_j}\left(\frac{\partial \langle u_i \rangle}{\partial x_j}\right) - \frac{\varepsilon \mu_f}{K}\langle u_i \rangle - \frac{\varepsilon \rho_f C_E}{\sqrt{K}}\left|\vec{V}\right|\langle u_i \rangle + \varepsilon \rho_f f_i \tag{3}$$

$$\frac{\partial}{\partial x_j}\left(k_{se}\frac{\partial T_s}{\partial x_j}\right) - h_{sf}\alpha_{sf}\left(T_s - T_f\right) = 0 \tag{4}$$

$$\left(\rho C_p\right)_f u_i \frac{\partial T_f}{\partial x_i} = \frac{\partial}{\partial x_i}\left(k_{fe}\frac{\partial T_f}{\partial x_i}\right) + h_{sf}\alpha_{sf}\left(T_s - T_f\right) \tag{5}$$

where ε, C_E and K are the porosity, inertial coefficient and permeability of the porous material, respectively. f is the body force per unit mass and i, j represent the directional components. In energy equations, k_{se} and k_{fe} are the effective thermal conductivities of the solid and fluid, respectively. h_{sf} is the heat transfer coefficient and α_{sf} is the specific interfacial surface area in the porous medium.

The permeability K and inertial coefficient C_E for graphite foam were obtained by experiments using the Darcy-Forchheimer law for porous media given by

$$-\frac{\Delta p}{\Delta L}\frac{1}{\mu u} = \frac{1}{K} + \rho_f \frac{C_E}{\sqrt{K}}\frac{u}{\mu} \tag{6}$$

where Δp is the pressure drop across the graphite foam and ΔL is the length of the test specimen. By plotting $(-\Delta p/\Delta L)(1/\mu u)$ against $\rho_f u/\mu$ for a range of flow rates, the permeability K was obtained as the intercept and the inertial coefficient C_E determined from the slope. The effective thermal conductivities and interior surface area to volume ratio were calculated by the model given by Tee *et al*. [13]. The interfacial heat transfer coefficient h_{sf} was determined by an empirical equation proposed by Klett *et al*. [14]. The main properties of materials used in the numerical code are given in Table 2.

Table 2 Properties of graphite foam

Parameters	Graphite foam, ε = 0.75
Permeability (10^{-10} m^2)	7.74
Inertial coefficient	0.063
Pore diameter (mm)	0.31
Effective thermal conductivity (W/m·K)	16.2
specific surface area (m^2/m^3)	8216

Numerical scheme

The governing equations (2) to (5) were solved using a finite volume method introduced by Patankar [15]. A staggered grid with scalar and vectorial variables defined respectively at the node and surface of the control volumes was employed. The power law is used to treat the combined convection-diffusion effect. The velocity-pressure coupling is handled within the framework of the SIMPLER algorithm. As the energy equations (for the solid and fluid) are decoupled from the continuity and momentum equations, it can only be solved after the converged velocity field is obtained. Both the solid and fluid energy equations are coupled via the convective terms. Different grids were studied to obtain grid independency results. These equations were solved iteratively until both temperature fields converge.

RESULTS AND DISCUSSION

Temperature and Nusselt Number

Figure 4 presents the temperature distribution of air flow through all the tested foams at heating power of 20 W. It can be seen that the temperature variations on the substrate for all samples are similar. The local temperature T_x increases gradually along the dimensionless location X/D_h and decreases with increasing pore diameter based Reynolds number (ud_p/ν_f). Compared to the designed structures, the temperature in the original block is lower at approximately the same Reynolds number. However, it is noted that the pressure drop in original block foam is very high due to its low permeability as mentioned previously. Figure 5 shows the pressure drop versus inlet flow velocity for all the samples. Comparing the pressure drop in designed structures to that in block foam, the results show clearly that the pressure drop is reduced significantly in all the designed structures. This implies that the designed slots and thin foam walls allow air to be driven through the samples easily.

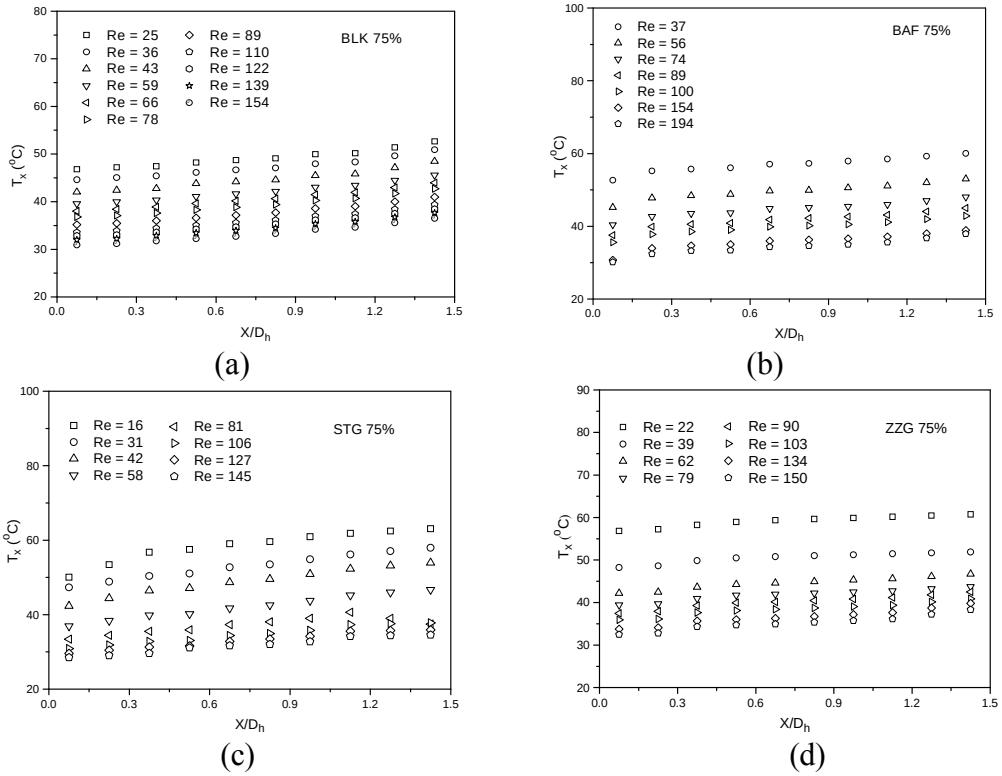

Figure 4 Local substrate temperature variations in (a) block, (b) baffle, (c) stagger and (d) zigzag foams

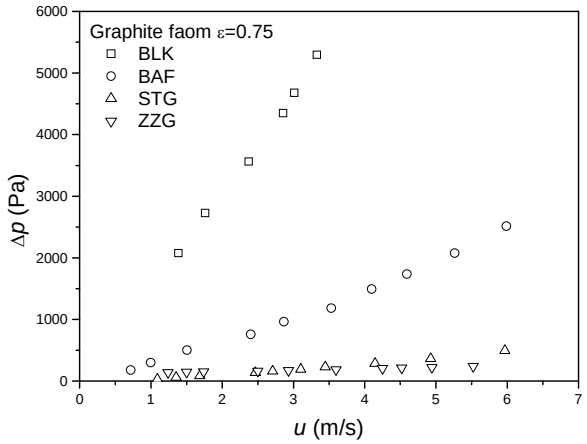

Figure 5 Pressure drop in all the tested samples

To characterize the thermal performance of the samples, we use the length-averaged Nusselt number which is the average of the local Nusselt numbers [Nu=$q''d_p/(T_x-T_{amb})k_f$, where q'' and T_{amb} are the heat flux and ambient temperature respectively] along on the substrate. The experimental and numerical length-averaged Nusselt numbers at various Reynolds numbers are plotted in Figure 6. The simulation results show good agreement with experimental data for all the structures. It can be seen that the block foam has better heat transfer at a given Reynolds number. For Reynolds number from between 10 to 60, the length-averaged Nusselt number in the block foam varies from 4 to 12, while those in the designed structures are between 2 to 7.5. However, the pressure drop is also very high for the block foam for the same Reynolds number.

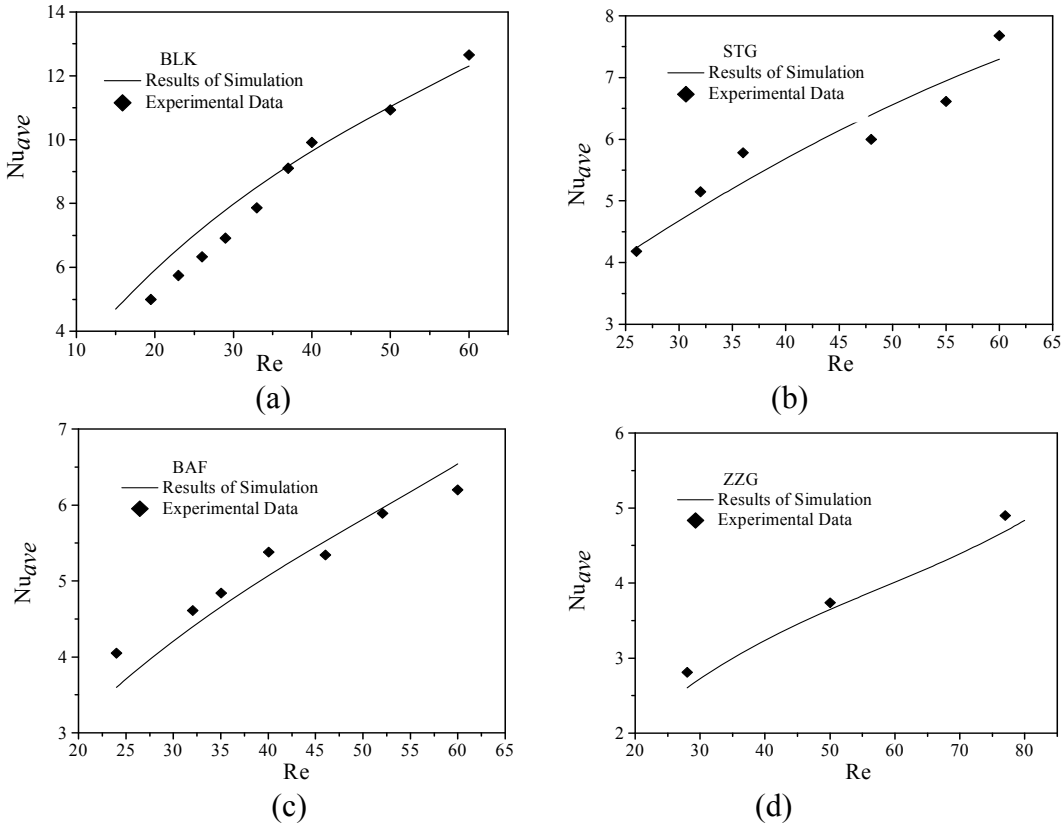

Figure 6 Length-averaged Nusselt number of air flow through (a) block, (b) stagger, (c) baffle and (d) zigzag foams

As analyzed above, the block foam exhibits better enhancement at approximately the same Reynolds number with much higher pressure drop. In practical heat sink design, the driving force for air flow through the structure is a major concern. To quantify the heat transfer of tested samples with consideration of the system driving force, the length-averaged Nusselt numbers are weighted by the pumping power $W_p = \Delta p \dot{V}$ ($\dot{V}$ is the average volumetric flow rate) as plotted in Figure 7. It can be seen that for the same length-averaged Nusselt number, the pumping power for driving air through the block graphite foam is much higher than through the three designed structures for the same heat transfer rate. For instance, to achieve a length-averaged Nusselt number of 10, the pumping powesr for the designed structures are only about 5 to14 W while it is about 70 W for the block foam. This indicates that better heat transfer performance can be obtained from the designed structures as compared to that of block foam at the same pumping power.

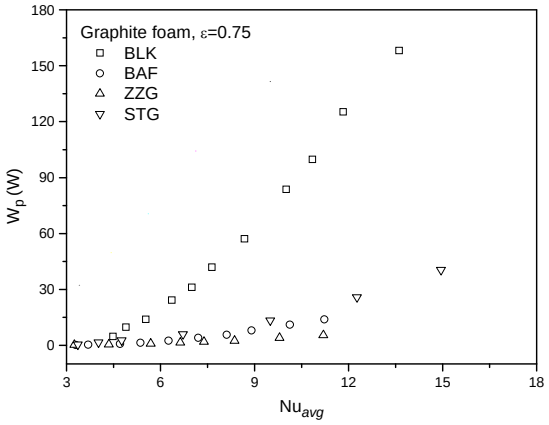

Figure 7 Length-averaged Nusselt number versus pumping power

Velocity Distribution

Figure 8(a) shows the velocity distribution of air flow through block graphite foam. From the simulations, it is observed that the flow characteristics in graphite foams depend mainly on the structure. It is clear that the air flow penetrates the block foam. The velocity profile is uniform throughout the simulated domain. This is expected because the properties of the foam are assumed to be anisotropic in the simulation. Figures 8(b)~8(d) show the velocity distributions in three designed structures. Since the stagger structure is not symmetric, the full size of sample was simulated. It can be seen from these figures that flow in the designed structures is distinctly different from that in the original block graphite foam. Overall, the inlet flow is divided into two streams at the entrance of porous domain. One part of flow penetrates through the foam wall while the rest goes through the foam via the structured empty slots. It is also observed from Figure 8(c) that most of air flows across the zigzag foam through the empty slots and only a small fraction of the air goes through the foam body. This is because the carved slots are parallel to the flow inlet direction and the foam wall area facing the flow is relatively small compared to other structures. Hence, for a given inlet flow velocity, the lowest pressure drop is obtained in the zigzag structure as shown in Figure 5. It can also be observed from the three structures that the magnitude of the velocity vector in the slot area is larger than that in the foam wall due to the low permeability.

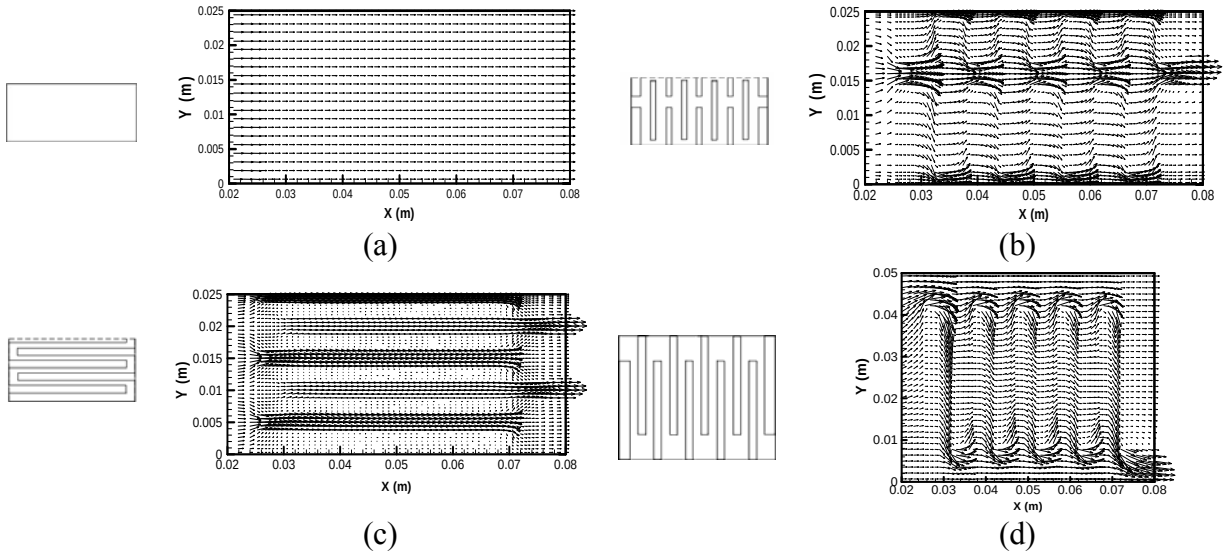

Figure 8 Velocity distributions in (a) block, (b) baffle, (c) zigzag and (d) stagger foams

CONCLUSIONS

In this paper, three configurations of stagger, baffle and zigzag graphite foams were investigated with the aim of reducing pressure drop while utilizing the thermal properties of graphite foam to enhance heat transfer. The experimental results showed that the temperature variations in all the tested samples are similar. It is found that the pressure drops in the designed structures are much lower than that in block foam and that the designed foam heat sinks can achieve relatively good heat removal with lower pumping power. The original block graphite foam requires much more driving force to achieve the same heat transfer rate as compared to the designed structures. The velocity distribution obtained by simulation shows that in the designed structures, one portion of air flow directly penetrates the thin foam wall while the rest goes through the foam via the structured empty slots. This study suggests that high thermal conductivity graphite foams can be appropriately configured for electronics cooling applications with moderate pressure drop.

REFERENCES

1. Bhattacharya, A. and Mahajan, R.L., Finned metal foam heat sinks for electronics cooling in forced convection, *ASME Journal of Electronic Packaging*, Vol. 124, pp. 155-163, 2002.
2. Boomsma, K., Poulikakos, D. and Zwick, F., Metal foams as compact high performance heat exchangers, *Mechanics of Materials*, Vol. 35, pp. 1161-1176, 2003.
3. Leong, K.C., and Jin, L.W., An experimental study of heat transfer in oscillating flow through a channel filled with an aluminum foam, *International Journal of Heat and Mass Transfer*, Vol. 48, pp. 243-253, 2005.
4. Dukhan, N., Picon-Feliciano, R. and Alvarez-Hernandez, A.R., Heat transfer analysis in metal foams with low-conductivity fluids, *ASME Journal of Heat Transfer*, Vol. 128, pp. 784-792, 2006.
5. Leong, K.C. and Jin, L.W., Effect of oscillatory frequency on heat transfer in metal foam heat sinks of various pore densities, *International Journal of Heat and Mass Transfer*, Vol. 49, pp. 671-681, 2006.
6. Klett, J.W., Hardy, R. and Romine, E., High thermal conductivity, mesophase-pitch-derived carbon foam: effect of precursor on structure and properties, *Carbon*, Vol. 38, pp. 953-973, 2000.
7. Ott, R.D., Zaltash, A. and Klett, J.W., Utilization of a graphite foam radiator on a natural gas engine-driven heat pump, *Proceedings of IMECE 2002 ASME International Mechanical Engineering Conference and Exposition*, 2002, Louisiana, USA.
8. Druma, A.M., Alam, M.K. and Druma, C., Analysis of thermal conduction in carbon foams, *International Journal of Thermal Sciences*, Vol. 43, pp. 689-695, 2004.
9. Alam, M.K. and Maruyama, B, Thermal conductivity of graphitic carbon foams, *Experimental Heat Transfer*, Vol.17, pp. 227-241, 2004.
10. Alam, M.K, Druma, A.M. and Druma, C., Thermal transport in graphitic carbon foams, *Journal of Composite Materials*, Vol. 38, pp. 1993-2006, 2005.
11. Williams, Z.A. and Roux, J.A., Graphite foam thermal management of a high packing density array of power amplifiers, *ASME Journal of Electronic Packaging*, Vol. 128, pp. 456-465, 2006.
12. Taylor J.R., *An Introduction to Error Analysis – Study of Uncertainty in Physical Measurements*, Oxford University Press, 1995.
13. Tee, C.C., Klett, J.W., Stinton, D.P. and Yu, N., Thermal conductivity of porous carbon foam. *Proceedings of the 24th Biennial Conference on Carbon*, July 11-16, 1999, Charleston, USA.
14. Klett, J.W., McMillan, A.D. and Stinton, D., Modeling geometric effects on heat transfer with graphite foam, *The 26th Annual Conference on Ceramic, Metal, and Carbon Composites, Materials, and Structures*, 2002, Cocoa Beach, USA.
15. Patankar, S.V., *Numerical Heat Transfer and Fluid Flow*, Hemisphere Publishing Corporation, 1980.

PHENOMENOLOGICAL MODEL OF TWO-PHASE FLOW INCORPORATING FLOW PATTERN PHENOMENA

Jerry K. Keska
Department of Mechanical Engineering, University of Louisiana
Lafayette, LA 70504, USA

ABSTRACT. This paper presents the developed mathematical model of two-phase flow in a minichannel incorporating flow pattern phenomena. Based on the results of the experimental research conducted on air-water mixture flows in the full range of concentration and flow patterns in a horizontal square minichannel, a mathematical model based on in-situ parameters is developed and presented. The model describes pressure losses in two-phase flow incorporating flow pattern phenomena. The presented model significantly reduces the difference between the experimental and simulated values.

Keywords: *Two-phase flow, flow patterns, mathematical model, flow pattern coefficient.*

INTRODUCTION

Many of today's high-tech electrochemical and electromechanical devices that are employed in aeronautical/aerospace and terrestrial applications implement two-phase flow of heterogeneous mixtures. This also includes micro-electronic packages, compact fission and fusion reactor systems, space power and propulsion systems that are exposed to extremely high temperatures, space suits for extravehicular activity (EVA), backpack fuel cells, and thermoelectric power sources. All of these devices require sophisticated and intense thermal control systems in order to perform properly. Other applications of two-phase flow of heterogeneous mixtures include thermal control systems ranging from those used for cryogenic reactant storage devices to primary structures as well as integrated electronic circuits used for communication, guidance and control, and other functions. Whether these systems are very large (active thermal control systems for the Space Shuttle and the International Space Station, bio- and chemical reactors, oil and gas exploration systems) or very small (micro heat exchangers used for the cooling process in CPUs and ICs), all of these systems have one characteristic in common: their proper functioning is heavily dependent on two-phase flow phenomena.

In two-phase flow attempting to incorporate flow patterns into a mathematical model is a critical and challenging process. The determination of flow pattern phenomena is extremely subjective and ambiguous. It relies primarily on the researcher's visual observation skills and judgment, and it cannot cover the entire range of velocities and concentrations. Before 1990, most of the research focusing on two-phase flow used superficial parameters. Most likely, this was due to difficulties in measuring mixture concentration. More recently, however, more and more research in the field uses in-situ parameters such as in-situ velocity and concentration. These new studies also include models for the pressure gradient and other dynamic phenomena in two-phase flow of a heterogeneous mixture. This reduces the differences partially. Flow patterns, however, which are the most dynamic and subjective phenomena in two-phase flow, have not yet to be satisfactorily incorporated into mathematical models.

Corresponding author: Prof. J.K. Keska
E-mail address: jerrykeska@yahoo.com

One possible solution to this problem involves the incorporation of flow patterns by using the flow pattern coefficient.

The paper presents the results of experimental research on the incorporation of flow pattern phenomena into a mathematical model of pressure losses in the two-phase flow of a heterogeneous mixture of air and water in a horizontal square channel (6.35 mm in size). The generated results allowed the flow pattern coefficient to be obtained, which, when incorporated into the pressure loss model, significantly reduced the differences between experimental and predicted values. Based on the results of the experimental research conducted on air-water mixture flows within the full range of concentration and flow patterns in a horizontal square minichannel, a mathematical model based on in-situ parameters has been developed and presented. The model describes pressure losses in two-phase flow incorporating flow pattern phenomena and significantly reduces the difference between the experimental and simulated values. This model incorporating flow pattern phenomena can be used for applications in two-phase flow of air and water mixtures in minichannels. The model, however, also incorporated parameters such as mixture viscosity and the channel's diameters, which allows it to be potentially useful in other two-phase mixtures and channel sizes.

This work is a continuation of research presented in [2, 6, 7]. Due to space constraints, however, many sections of this paper that would normally be presented have either been omitted or abridged. These sections, including the literature analysis, experimental system, and experimental data, can be found in the above mentioned publications [1, 3, 4, 5, 8].

TWO-PHASE FLOW MODEL WITH FLOW PATTERNS

In order to develop and design a compact heat exchanger with phase transition, it is necessary to develop mathematical models for the two-phase flow and heat transfer processes. Starting from assuming one-dimensional flow and a constant pressure gradient, the pressure drop in a channel/conduit can be expressed by the equation [2, 6, 7]:

$$\Delta P = \frac{dP}{dL}\Delta L. \qquad (1)$$

The total pressure gradient can be formulated as a superposition of three components accounting for mixture acceleration, skin friction and gravity or buoyant forces. This is expressed by the following equation:

$$\frac{dP}{dL} = \left.\frac{dP}{dL}\right|_a + \left.\frac{dP}{dL}\right|_f + \left.\frac{dP}{dL}\right|_g. \qquad (2)$$

For steady-state conditions and for small and moderate pressure differences for a horizontal or short vertical channel/conduit, the total pressure gradient is caused solely by the frictional pressure gradient and is written as:

$$\frac{dP}{dL} = \left.\frac{dP}{dL}\right|_f. \qquad (3)$$

The frictional pressure gradient of a two-phase mixture can be viewed as a superposition of two separate frictional pressure gradients due to the gas component and liquid component as follows:

$$\left.\frac{dP}{dL}\right|_m = \left.\frac{dP}{dL}\right|_l + \left.\frac{dP}{dL}\right|_g, \qquad (4)$$

where for steady-state flow conditions and homogenous spatial and temporal distribution of phases in the mixture with the in situ overall spatial concentration (c_v), the theoretical frictional pressure loss of the mixture is [6, 7]:

$$\Delta P_{theoretical} = \frac{dP}{dL}\Delta L = \frac{\Delta L}{2D}\left[f_g v_g^{\,2} \rho_g \left(1 - c_v\right) + f_l v_l^{\,2} \rho_l c_v \right]. \qquad (5)$$

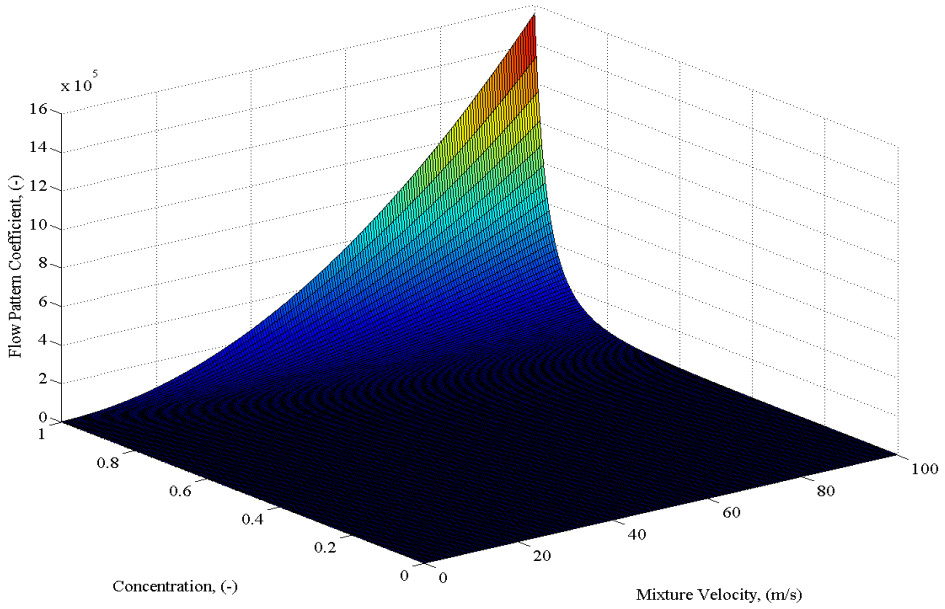

Figure 1. Flow pattern coefficient vs. mixture velocity and in-situ spatial concentration

This represents a surface for an ideal distribution of mixture concentration as a function of mixture velocity and concentration. The friction factors can be determined for the liquid and gas, respectively, in the laminar flow regime by the equation f = 64/Re, and for turbulent flow using either the Colebrook equation or direct numerical values from the Moody diagram for a given Reynolds number and roughness coefficient (ε/D):

$$\frac{1}{f^{1/2}} = -2.0\,\mathrm{Log}_{10}\left(\frac{2.51}{f^{1/2}\mathrm{Re}} + \frac{\varepsilon / D}{3.7} \right) \qquad (6)$$

where Re is the Reynolds number of the mixture, calculated separately for in situ conditions:

$$\mathrm{Re}_m = \frac{v_m D \rho_m}{\mu_m} \qquad (7)$$

Comparing the experimental results for pressure gradient to the theoretical pressure gradients (calculated by Eq. 5), with the flow conditions for given in-situ concentrations and velocities for the various flow patterns, it is not surprising to observe significant differences between the theoretical and experimental pressure gradients caused by the complexity of the flow patterns. These differences are significant, and they are indicative of the need for a significant revision of the model, specifically, through the incorporation of another flow-related independent parameter. A very significant

phenomenon, and one that is not included in Eq. 5, is the flow pattern phenomenon, which includes both the spatial and temporal heterogeneity of the mixture. By the incorporation of the flow pattern phenomenon in the form of a flow pattern coefficient, where the axial pressure gradient becomes a function of in-situ component velocities, friction coefficients, in-situ concentration, and the flow pattern coefficient (Fp), the difference between the theoretical and experimental values should be significantly reduced. This modified correlation can be expressed as:

$$\left(\frac{\Delta \mathrm{P}}{\Delta \mathrm{L}}\right)_{tested} = \frac{1}{2D}\left[f_g v_g{}^2 \rho_g \left(1-\mathrm{c_v}\right) + f_l v_l{}^2 \rho_l \mathrm{c_v} \right] Fp. \quad (8)$$

The application of dimensional and similitude analysis based on Equations 5, 7 and 8 for a steady-state heterogeneous mixture flow of gas and liquid in the horizontal channel results in the following equation for the flow pattern coefficient (Fp):

$$Fp = \frac{1}{E}\left(\frac{\nu_m}{\nu_m}\right)^2 (c_v)^F D^2 \quad (9)$$

where E and F are constants, which could be found experimentally.

The flow pattern coefficient model developed here (Eq. 9) is expressed by the use of in-situ and measurable parameters such as the in-situ mixture concentration and velocity, mixture kinematic viscosity, and channel diameter. In this case, the value of the flow pattern coefficient is independent of the flow pattern visual observations since the flow pattern coefficient is a function of the in-situ measurable parameters. The incorporation of flow patterns occurred through the incorporation of the flow pattern coefficient, which is proportional to the square of in-situ mixture velocity, in-situ concentration to the power of F, the square of channel diameter and reverse proportional to the square of the mixture kinematic viscosity and the constant E (as shown in Eq. 9). The conducted experiments were focused on the collection of data, which allowed for the discovery of the correlation between simulated and measured values of flow pattern coefficients for a two-phase air-water mixture flow in a horizontal minichannel. From Eq. 9, it can be inferred that Fp is a dimensionless number, which varies along with the temporal and spatial distribution of in-situ concentration and the mixture velocity. A graphical image of this is presented in Fig. 1. Thus, two-phase flow of heterogeneous mixtures is extremely dynamic. It is a continuously changing process and any observation of flow patterns is highly observer-dependent. Therefore, in order to obtain accurate experimental results, it is

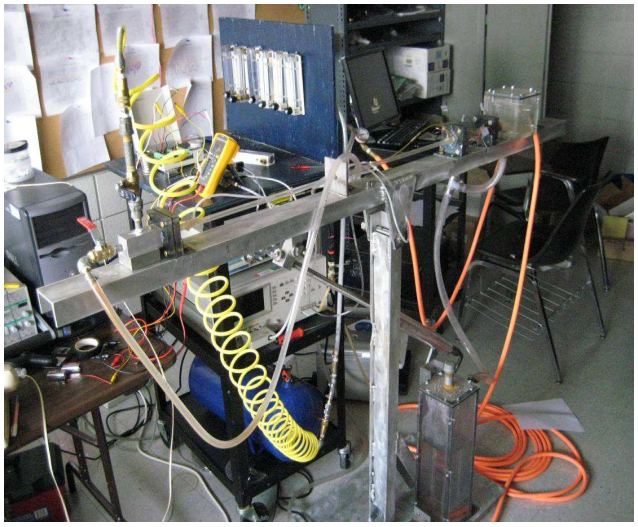

Figure 2. View of the CADAS for two-phase mixture flow in horizontal square channel

critical to use objective, accurate measurement tools for the measurement of the in-situ parameters and for data validation, as well as for the elimination of system-dependent or unique parameters such as flow patterns, superficial parameters, or the quality of the mixture.

EXPERIMENTAL SYSTEM, EXPERIMENTAL DATA AND RESULTS

An experimental system for investigating two-phase flow in minichannels was developed (see Fig. 2), which consisted of a flow set-up with unique measurement systems for concentration using both capacitive and conductive sensors, an optical system, and pressure measurement devices. All of these were interfaced into a computer-aided data acquisition system (CADAS) based on LabVIEW and MatLab software. The experimental apparatus consisted of a horizontal transparent minichannel (cross-section 6.35 mm x 6.35 mm), which was supplied by controlled air and water flow from a mixing chamber. The mixing chamber allows the air and water flows to become fully mixed before entering the test section. The input and output flow rates of air and water are controlled and measured by various instruments, such as cylinders, rotameters, scale, and time and length meters. The system is operated in an closed-loop mode. The controlled, steady-state experiment runs were conducted for all flow pattern types over the full range of concentration (0 – 1.0) and mixture velocity (0 - 20 m/s). These runs were conducted using all five measurement systems (optical, two pressures, conductive, and capacitive) simultaneously in the same space and time for the air-water mixture flow. From this experimental data, the friction factor vs. mixture Reynolds number was calculated using mixture density, velocity and viscosity. Reynolds numbers indicate that the experiments were conducted in laminar and turbulent flow regimes and fit into the classic Moody diagram (Fig. 3). The experimental flow pattern coefficient values change in the range from 0 to 1.7 in function of the Reynolds number values. The Fp values starting from zero for Re = 0, increase to maximum value for Re = 1900 and decrease as the mixture Re continues to increase. It reaches its lowest values at the highest Re, which is 9000.

The conducted experiments were focused on the collection of data, which allowed for the discovery of the correlation between simulated and measured values of flow pattern coefficients for a two-phase air-water mixture flow in a minichannel. Thus, two-phase flow of heterogeneous mixtures is extremely dynamic. It is a continuously changing process and any observation of flow patterns is highly observer-dependent. Therefore, in order to obtain accurate experimental results, it is critical to use objective, accurate measurement tools for the measurement of the in-situ parameters and for data validation, as well as for the elimination of system-dependent or unique parameters such as flow patterns, superficial parameters, or the quality of the mixture. The flow pattern coefficient *Fp* from Equation 9 is defined for the experimental conditions. From obtained experimental data (shown if Fig.4) we could get the values of the constants (E and F) by the application of best fit approach for a steady-state heterogeneous mixture flow of gas and liquid in a horizontal channel, results:

$$Fp = \frac{1}{110000}\left(\frac{\nu_m}{\nu_m}\right)^2 (c_v)^{3.5} D^2 \qquad (10)$$

The presented surface is a graphical representation of the flow pattern coefficient as simulated by Eq. 10 and the points represent experimental values of Fp (Fig.4). The visually observed good fit of experimental points into the calculated surface indicates a high potential for the significant reduction of discrepancies between measured and calculated values of pressure losses. Indeed, the application of the flow pattern coefficient Fp into Eq. 10 reduces the error in the calculated results by very significant values. Using the sum of squares of error values as the measure of error, the value of the error is reduced up to 94% after applying and incorporating the flow pattern coefficient (Fp). The reduction of the error can be visualized by plotting the length pressure gradient, obtained from the theoretical

formula along with the experimental results, with and without considering the Fp, against the in-situ concentration and mixture velocity. This is shown in Fig. 5.

As shown in Fig. 5, the separation of points without the application of Fp from theoretical surface is significantly larger as compared to points with the application of Fp. This indicates that the incorporation of Fp significantly closes the deviation gap between measured and calculated values of the length pressure gradients.

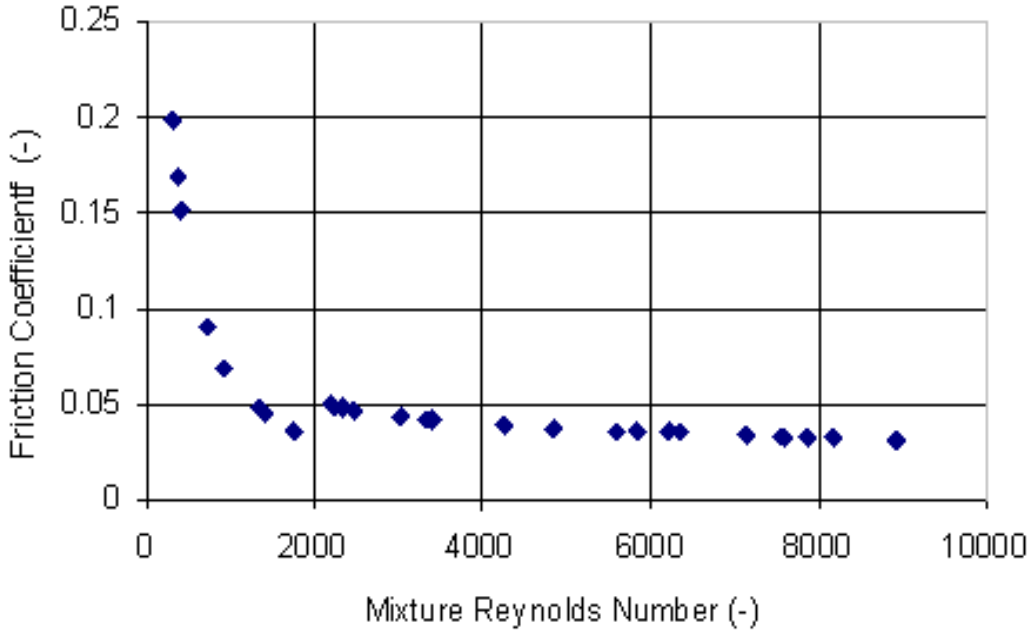

Figure 3. Experimental friction factor vs. Reynolds number for air-water mixture flow.

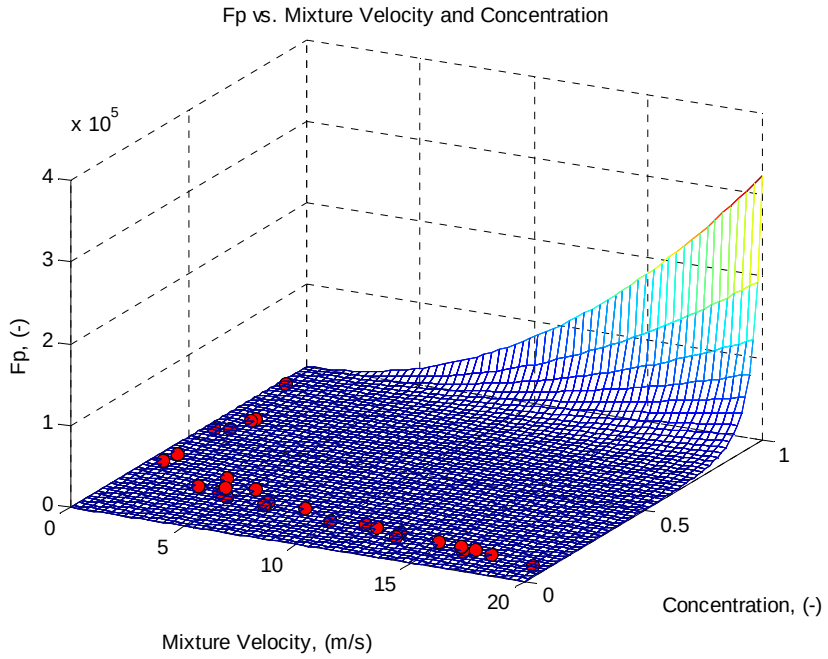

Figure 4. Flow pattern coefficient (surface from simulation and points are experimental values) vs. mixture velocity and in-situ spatial concentration

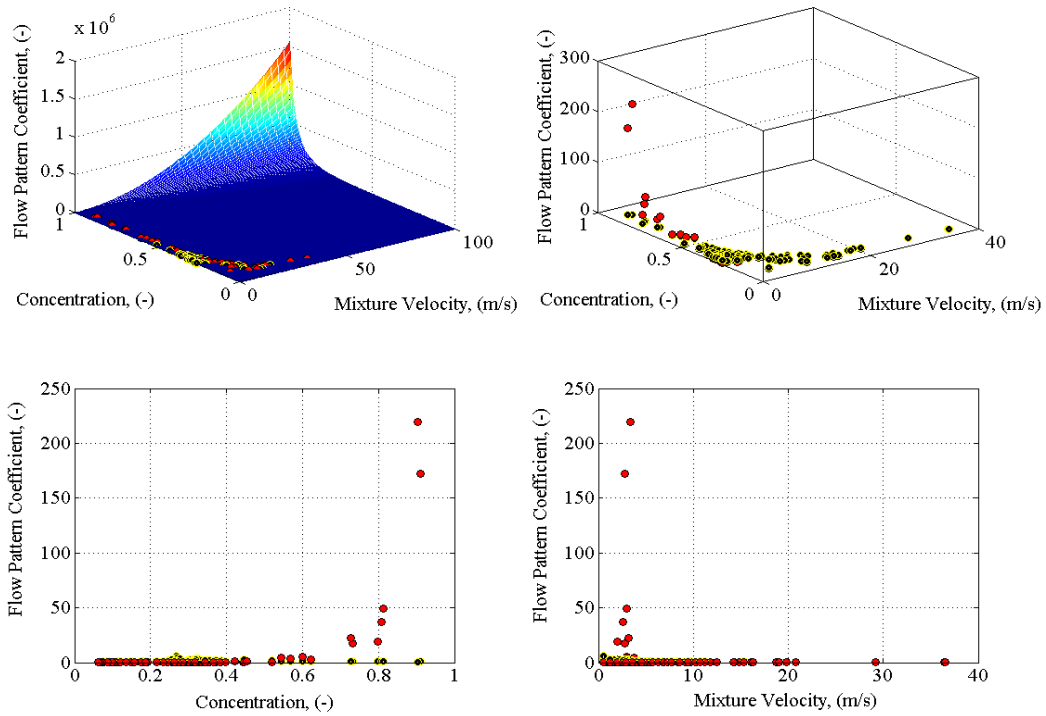

Figure 5. Simulated and experimental values of length pressure gradient losses vs. mixture concentration and velocity.

Figure 5 represents experimental points of the length pressure gradient vs. pair of values of in-situ spatial concentration and mixture velocity, which generated a 3D graph. In analyzing these figures, however, one always needs to keep in mind that those two graphs are reduced from 3D and always have a third parameter, which is depth. From Fig. 5, it is difficult to observe a clear trend for error analysis of the length pressure gradient vs. pair of values of in-situ spatial concentration and mixture velocity for the both cases. The data, however, clearly indicates the importance of considering flow pattern phenomena by using the flow pattern coefficient as defined by Eq. 10.

CONCLUSIONS

This experimental study was performed in an adiabatic minichannel system constructed to generate an air-water steady-state mixture flow over the full range of concentration from 0 (all gas) to 1.0 (all liquid) and with mixture velocities up to 20 m/s. This covered the full range of possible flow patterns and involved the simultaneous measurement of in situ parameters. From this research, the following conclusions can be drawn:

(1) An objective procedure for flow pattern determination and data validation were developed and incorporated into a mathematical model based on in-situ parameters (Eqs. 9 and 10).

(2) The developed mathematical model for the pressure gradient incorporates flow pattern phenomena by integrating a flow pattern coefficient. In this model, the axial pressure gradient is expressed as a function of in-situ mixture concentration and velocity, and the flow pattern coefficient. Although the experiments were limited to mini and microchannels and to water and air mixtures, the proposed model could be expanded for other channel sizes and for other mixtures with different components and mixture properties.

(3) The flow pattern phenomenon significantly affects the process of two-phase flow. This phenomenon is represented by the flow pattern coefficient (Fp) which, when it is incorporated into a mathematical model, reduces significantly the cumulative errors.

NOMENCLATURE

c_v = spatial concentration (V_w/V_m)
Fp = flow pattern coefficient (-)
$\Delta P/\Delta L$ = length pressure gradient (Pa/m)
S = slip ratio (v_g/v_l)
V = volume (m^3)
$\dot{V}$ = volume flow rate (m^3/s)
v = velocity (m/s)
x = quality of mixture (-)

Subscripts

a = air
g = gas
l = liquid
m = mixture
v = vapor
w = water

REFERENCES

1. Lockhart, R. W., and Martinelli, R. C., "Proposed Correlation of Data for Isothermal Two-Phase Two-Component Flow in Pipes," *Chemical Engineering Progress*, **45**, pp. 39-48, 1949.
2. Keska, Jerry K. and William E. Simon, "In Search of Physical Parameters Influenced by Flow Patterns in a Heterogeneous Two-Phase Mixture in Microchannels Using Concomitant Measurements", *International Journal of Multiphase Flow*, p.483 - 498, Vol. 32, 2006..
3. Barnea, D., Luninski Y. and Taitel Y., "Flow Patterns in Horizontal and Vertical Two-Phase Flow in Small Diameter Pipes", *Canadian Journal of Chemical Engineering*, **61**, pp. 617-620, 1983.
4. Coleman, J. W. and Garimella, S., "Characterization of Two-Phase Flow Patterns in Small Diameter Round and Rectangular Tubes," *Int. J. Heat and Mass Transfer*, **42,** 2869-2881 (1999).
5. Triplett, K. A., Ghiaasiaan, S. M., Abdel-Khalik, S. I., and McCord, B. N., 1999, "Gas-Liquid Two-Phase Flow in Microchannels Part II: Void Fraction and Pressure Drop," *International Journal of Multiphase Flow*, **25**, pp. 337-410.
6. Keska, J. K., and Wang, G., "Pressure Gradient Calculation for Air-Water Heterogeneous Mixture Flow in A Small Square Horizontal Channel Based on the In-Situ Parameters And Flow Pattern Coefficient," *Experimental Thermal and Fluid Science*, **30**, pp. 403-413, 2006.
7. Keska, J. K. and Miller, A. C., "Micromechanical Devices: An Enhanced Micro-Heat Exchanger for Applications in High Integrated Microprocessors and Laser Diode Arrays," p. 1-6, 98-WA/EEP-19, 1998. Proceedings of the 1999 International Mechanical Engineering Congress and Exposition, November 1998, Anaheim, CA
8. Vance, M.A. and Lahey, R.T., "On the Development of an Objective Flow Regime Indicator," *International Journal of Multiphase Flow*, **8**, 93-124 (1982).

INFLUENCE OF THE FLASHING PHENOMENA ON THE BOILING CURVE OF REFRIGERANT R134A IN MINICHANNELS

T. Bohdal, H. Charun, K. Dutkowski *, W. Kuczyński
Koszalin University of Technology, Koszalin, Poland

ABSTRACT. The results of experimental investigations of the heat transfer during the flow of R134a in a minichannel are presented here. The experimental investigations were conducted using a minichannel of a 500 mm total length, and 1.68 mm of the internal diameter. The heated length of the minichannel was 200 mm, the total mass flow rate of the refrigerant (uρ) = 200 ÷ 450 kg/m^{2}s, the inlet subcooling ΔT_s = 5 ÷ 15 K, while the heat flux density q'' = 1.7 ÷ 60.3 kW/m^2. The results of experimental investigations as a curve boiling are presented. The phenomena of the zero boiling crisis, and the influence of the flashing phenomena on the boiling curve show the importance of these elements on a single-phase and a two-phase heat transfer.

Keywords: *experimental investigations, minichannels, boiling curve, zero boiling crisis, flashing*

INTRODUCTION

There are numerous papers dedicated to the general aspects of the heat exchange and flow resistance, especially of two-phase flow in minichannels. However, it is necessary to focus on details, such as the start of the boiling process, the critical heat flux, the flashing, the boiling curve, the phenomena of the zero boiling crisis (boiling hysteresis).
The boiling curve is a curve which represents the influence of the heat flux (q") on the difference of temperatures ($\Delta T = T_w - T_f$), where T_w - the temperature of the heated wall and T_f – the temperature of the fluid. The temperature of the fluid is equal to the temperature of saturation T_s when the process of boiling lasts. Figure 1 presents a fragment of a classical boiling curve. When q" = 0, the temperature of the wall is equal to the temperature of the fluid (ΔT = 0). The increase of heat flux results in an increase of the temperature difference. This means that the temperature of the wall is greater than the temperature of the liquid. The process clearly runs as a straight line and is presented in Figure 1 as section 0-B. In the point B, the temperature of the wall is much higher than the temperature of the liquid, and also the temperature of the wall is higher than the saturation temperature. This is a metastable condition. At a certain moment, the boiling process will occur. Vapour bubbles constitute heat sinks, which results in a reduction of the temperature of the wall. Therefore, with a constant value of q", a sudden drop of ΔT is observed – the line from the point B to the point C. This phenomena is known as a zero boiling crisis. A further increase of heat flux results in an increase of the number of bubble sites. The difference of temperature is slowly increasing. This is so until the Critical Heat

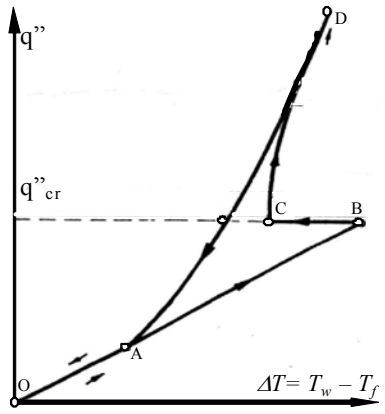

Figure 1. Classical boiling curve

* Corresponding author: Dr. Eng. K. Dutkowski
Phone: + (48)-94-34 78 378
E-mail address: krzysztof.dutkowski@tu.koszalin.pl

Flux (CHF), at which a born-out can occur. During the reduction of the heat flux, the process does not run in the same manner. The ΔT values during the reduction of the heat flux are different from those when the heat flux was being increased. The boiling process lasts until the point A. The abovementioned processes presented in Figure 1 are known as the boiling hysteresis.
The flashing phenomena in minichannels occurs when the pressure at some cross-section of the minichannel drops below the vapor pressure of the fluid being passed, and the whole bulk of the liquid becomes superheated: metastable. The unique characteristic of the flashing processes is a withdrawal of the latent heat of evaporation from the internal energy of the superheated liquid (Hahne E. and Barthau G. [1]). In that cross-section, vapor is suddenly generated in an explosive manner (Elias E. and Chambre P.L. [2]). When flashing occurs, bubbles are formed in the flow stream. These bubbles carry large amounts of energy.
The present paper is focused on the experimental investigation of the influence of the flashing phenomena on the boiling curve. The R134a refrigerant was used as the working fluid considering its widespread application in refrigerating and air conditioning systems. The refrigerant flowed through a stainless steel pipe with the internal diameter of 1.68 mm and 500 mm of the total length. Ten thermocouple sensors were set on a 200 mm electrically heated section in even intervals (18.2 mm). For each location, individual characteristics were prepared. This allowed the determination of the place where flashing started and its influence on the boiling curve. Another issue is to show that the area before the incipience of boiling, considered in all the papers as a single-phase flow area, can be a two-phase flow area (the presence of flashing). Therefore, a proposal is made to introduce the following nomenclature as more correct: first zone - *before incipience of boiling* and the second zone *with boiling*, because as it was further shown in the paper, the flow before the incipience of the boiling process can be both single or two-phase.

LITERATURE REVIEW

Lists of results in the form of boiling curves in minichannels occur more and more frequently in publications. This is so owing to a larger number of experimental data, which as a result of the use of precise measuring equipment and measuring methods have become comparable regardless of the research centre.
Numerous papers include information about the possibility of the occurrence of the flashing phenomena (Schneider et al. [3], Bergles and Kandlikar [4], Revellin et al. [5], Lee and Mudawar [6]). However, there are no publications which would discuss this issue more extensively. One of the few papers is the paper by Warrier et al. [7]. The authors assume that: a two-phase flow starts when a rapid increase of the heat transfer coefficient occurs, and the local vapor quality should also take the flashing phenomena into account.
During the experimental investigations of the liquid nitrogen boiling process conducted by Qi et al. [8] in minipipes with internal diameters of 0.531, 0.834, 1.042 and 1.931 mm the existence of the zero boiling crisis phenomena was noted. The investigations were carried out in the range of mass flow rate ($u\rho$) = 440 – 3000 kg/m^{2}s and heat flux q" = 5.09 – 21.39 W/cm^2. It was noted that a drop of the temperature of the wall at ONB moment reached 5.0 K. Only these authors analyzed the influence of the flashing phenomena on the local vapor quality. An increase of the vapor quality was 18% when flashing phenomena was taken into account.
It is characteristic than in each of the papers above mentioned, the authors speak about the zone of a single and two-phase flow. There are two cases:

- absence of the zero boiling crisis phenomena, then the single-phase flow zone finishes when the trend of the boiling curve changes;
- the zero boiling crisis phenomena occurs - the single-phase flow occurs until the moment of a rapid temperature drop. This moment is considered to be the start of the boiling process and incipience of a two-phase structure. This is also written in those papers where the flashing phenomena is observed.

EXPERIMENTAL APPARATUS AND PROCEDURE

The test loop

A schema of the test loop is presented in Figure 2. The liquid of the R134a refrigerant pumped from tank 12 by pump 2 flowed through filter 3 and precooler 4. Next the Coriolis mass-flowmeter 5 was installed (mass flow rate: 0 - 20 kg/h, accuracy 0.075% of measured value). A liquid with the known flow rate was fed to the set of heat exchangers 6, 7 and 8. There was a possibility to use these exchangers alternatively, which allowed one to obtain the proper conditions of the refrigerant on the test section inlet 1. The parameters of the refrigerant (pressure and temperature) were measured on the inlet (p_1, T_1) and outlet (p_2, T_2) of heat exchangers. The designed set of heat exchangers enabled experimental tests of the heat transfer and pressure drop during a single-phase flow of the refrigerant, subcooled and saturated boiling.

The refrigerant was directed to the test section. The following parameters were measured here: the pressure in the initial cross section of the tested part of minichannel p_{in}, the pressure drop Δp on the tested part of the minichannel, the wall temperature T_1-T_{10} of minichannel, temperature on the inlet T_{in} and outlet T_{out} of the tested part, as well as supplied electric power q_{el}. All the voltage signals of the measured values were connected with data acquisition system 18 which cooperates with computer 17.

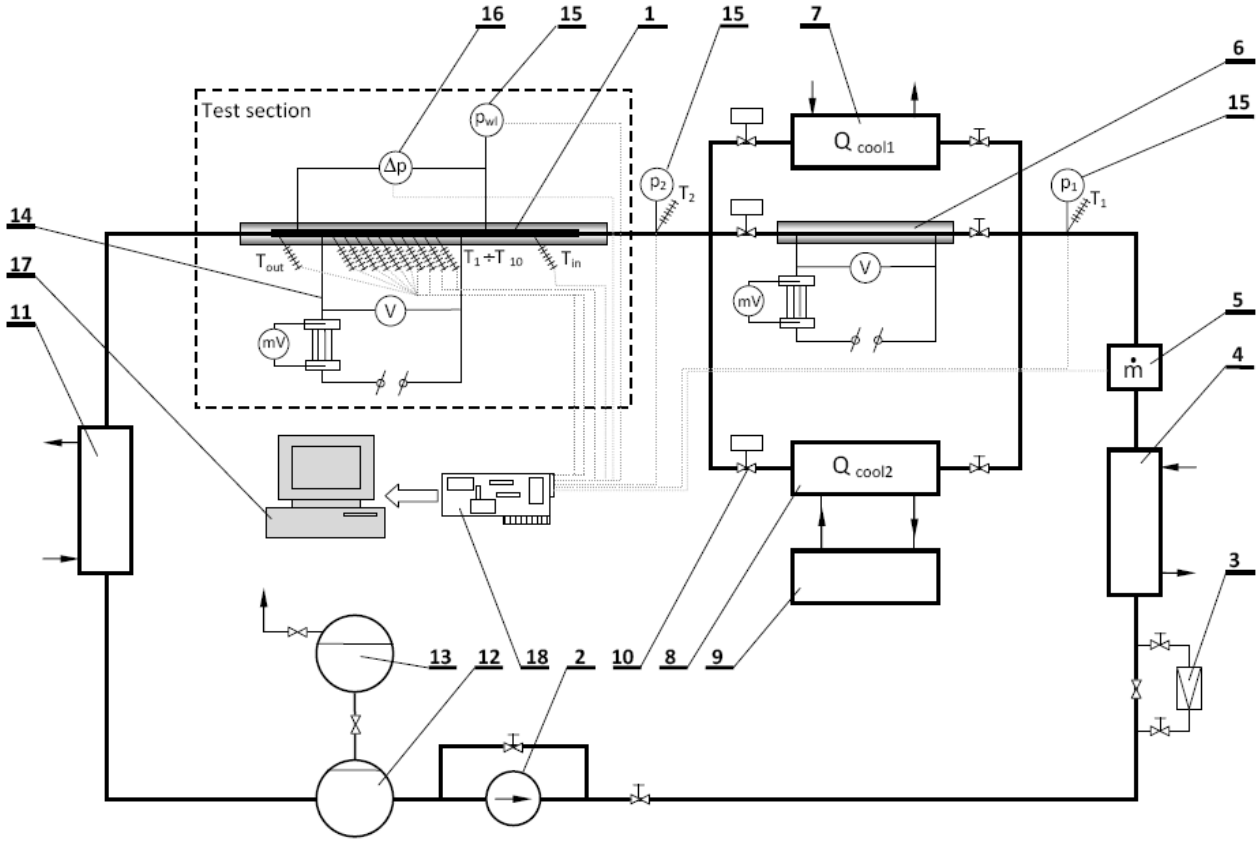

Figure 2. Experimental set-up: 1 – minichannel, 2 – pump (with instrumentation), 3 – filter, 4 – precooler, 5 – flowmeter, 6 – preheater, 7 – cooler no. 1 (cooling with water), 8 – cooler no. 2 (cooling with refrigerant), 9 – additional cooling system, 10 – valves, 11 – condenser (cooled with water), 12 – tank of refrigerant, 13 – spare tank of refrigerant, 14 – system of electric heating of measuring section, 15 – pressure sensors, 16 – differential pressure sensor, 17 – computer, 18 – data acquisition system

The test section

The test section was made from stainless steel pipe 1 with a total length of 500mm and an internal diameter of 1.68mm. The pipe was divided into several sections. The first one, 150 mm long, constituted a hydraulic stabilization area, the further one (300 mm) was the proper test part of minichannel and the third one, 50 mm long, was the outlet section.

The proper test section was electrically heated on the length of 200. Using a high voltage adjustable transformer, a high voltage shunt 150A/60 mV and voltmeters, it was possible to change the heat flux and to measure the parameters required for its determination.

On the measuring section, 10 thermocouples K type and diameter of wire ϕ = 0.2 mm were installed. Using these sensors, the temperature of the external surface of the minichannel wall was measured. Just right before the heated area and after it, the same two thermocouples were additionally fixed to the pipe surface in order to measure the refrigerant's temperature on the inlet and the outlet of the test section. Before the sensors were installed, their individual experimental thermo-electric characteristics were prepared in relation to the precise thermometer with accuracy of 0.1^{o}C.

In the pipe, 50 mm before the heated section and 50 mm after it, holes were made. They made it possible to measure the working fluid pressure and pressure drop on the minichannel's tested part. For the measurement of the pressure, manufactured by Endress+Hauser, a piezoresistant sensor with a transducer was used (Deltabar S PMD75). Measuring range of this device was 0 ÷ 4 MPa and an accuracy of 0.075. The measurement of the pressure drop was conducted with use a differential pressure transducer (Deltabar S PMD75) with a basic measuring range of 0 ÷ 1.6 MPa and an accuracy of 0.075. The uncertainty of the pressure and the pressure drop was ± 3 kPa and ± 1.2 kPa respectively.

The whole test section was insulated in order to have conditions closer to adiabatic ones. The total heat losses to the environment were assessed to be smaller than 5% of the supplied electric power.

The test procedure

All the data was collected once steady state conditions were achieved. The required mass flow rate was set as first. The refrigerant with a required flow rate was directed to one of 3 heat exchangers in the preparation section. The selection of the exchanger depended of the expected value of the refrigerant's temperature on the minichannel inlet. The value of the refrigerant's saturation temperature depended on the working pressure of the refrigerant in the minichannel. This value could be changed with a valve installed behind the test section. When the mass flow rate, pressure, pressure drop and the refrigerant's temperature were constant, data registration began. The averaged values from several measurements were the basis for further calculations. It should be mentioned that in some cases, oscillations of the abovementioned parameters were registered, and then the registration was conducted in a quasi steady state conditions.

The experiments were conducted using R134a refrigerant in the following range of parameters: D = 1.68 mm, $(u\rho)$ = 260 - 2144 kg/m^{2}s, q" = 1.7–60.3 kW/m^2, T_{in} = 13.1 – 23.5 ^{0}C.

Data reduction

The heat transfer rate to the refrigerant in the minichannel is obtained on the basis of the net power input q and the total internal surface area of the minichannel A. The total power input is calculated by subtracting heat loss from electrical power

$$q'' = q/A = (q_{el} - q_{loss})/A. \quad (1)$$

It is accepted that the temperature of the wall on the internal surface of the minichannel is equal to the temperature of the external surface of minichannel. It is assumed that the liquid temperature changes linearly on the length of the channel, and in the single-phase flow it is calculated from the heat balance, while in the two-phase flow region it corresponds to the saturation temperature being the result of the local pressure inside the minichannel:

$$T_f(i) = \begin{cases} T_{in} + q'' \cdot \dfrac{\pi d\ L(i)}{\dot{M} \cdot c_p} - \text{single-phase region} \\ T_s(i) = f(p_s) \quad - \text{two-phase region} \end{cases} . \tag{2}$$

The following was assumed in formula (2): T_{in} – temperature of the liquid measured on the inlet to the heated minichannel section, L(i) - distance measured from the beginning of the heated section, m – refrigerant's flow rate, c_p – specific heat of the liquid, $T_s(i)$ – saturation temperature in cross-section (i) dependent on local saturation pressure - p_s.

RESULTS AND DISCUSSION

Boiling curves without flashing phenomena

Figure 3 presents boiling characteristics of refrigerant R134a determined for the mass flow rate (uρ) = 450 kg/(m^2·s), with the liquid subcooling ΔT_n = 10 K. By the liquid subcooling ΔT_n should understand the difference of saturation temperature T_s and temperature of inflowing liquid T_f. Figure 3a shows the dependence of temperature difference ΔT ($\Delta T = T_w - T_f$) on heat flux density q". T_w denotes the temperature of the wall. Considering the fact that on heated part of minichannel ten thermocouples were placed, it was possible to determine the difference of temperature ΔT= f(L) in ten cross-sections.

In the first phase of heating the difference of temperature in each measuring cross-section on length L had the same value. An increase of the heat flux density resulted in the growth of value ΔT. This corresponds to the conditions of the heating of a liquid during forced convection, which characterizes section O – B in Figure 1. For the parameters of the experiment given in Figure 3, it is observed that a single-phase liquid flow in a minichannel occurs to the value of heat flux q" = 22.4 kW/m^2 (each thermocouple confirms the trend of the process in compliance with section O – B). A further growth of the heat flux caused an increased difference of temperature ΔT, while this process is in a meta stable condition of the system. Any disturbances of the meta-stable equilibrium lead to the initiation of the zero boiling crisis, which was accompanied by an rapid drop of the minichannel wall temperature. For example presented here, this took place when the heat flux was q" = 27 kW/m^2.

The measurement of temperature showed the boiling process occurred initially only on a part of the minichannel length, and covered those cross-sections which were located above 91 mm from the inlet cross-section of the minichannel. It was observed that in this part of the measuring section where five first temperature sensors were installed (18,2 ÷ 91 mm), there was no zero boiling crisis effect (i.e., the states of the refrigerant remained on the part of section O – B of the characteristics from Figure 1). This means that a single-phase liquid flow continued there. An increase of the heat flux to q" = 36.6 kW/m^2 caused the zero boiling crisis to cover also this part of the minichannel, and it was accompanied by a drop of the wall temperature. Only then almost the whole volume of the pipe minichannel was covered by boiling. It should be noted that the temperature recorded by the first sensor, installed in the distance of 18.2 mm from the inlet cross-section to the section heated confirmed a single-phase flow of the R134a liquid in this part of the length of the minichannel. During the zero crisis, the boiling front moved in the direction contrary to the liquid flow in the pipe minichannel. This manner of the movement of the boiling front also occurs in conventional channels [1]. Twice the zero boiling crisis was recorded, and the front of nucleation occurred in range L = 91 ÷ 109.2 mm from the inlet cross-section of the minichannel for q" = 27.0 kW/m^2, and then in range L = 18.2 ÷ 36.4 mm for q" = 36.6 kW/m^2. For the given experiment conditions, this was the maximum value of the heat flux. Then, the heat flux was decreased. With a decreasing heat flux the characteristic points of the boiling curve moved and connected one by one to the straight line of the single-phase liquid flow.

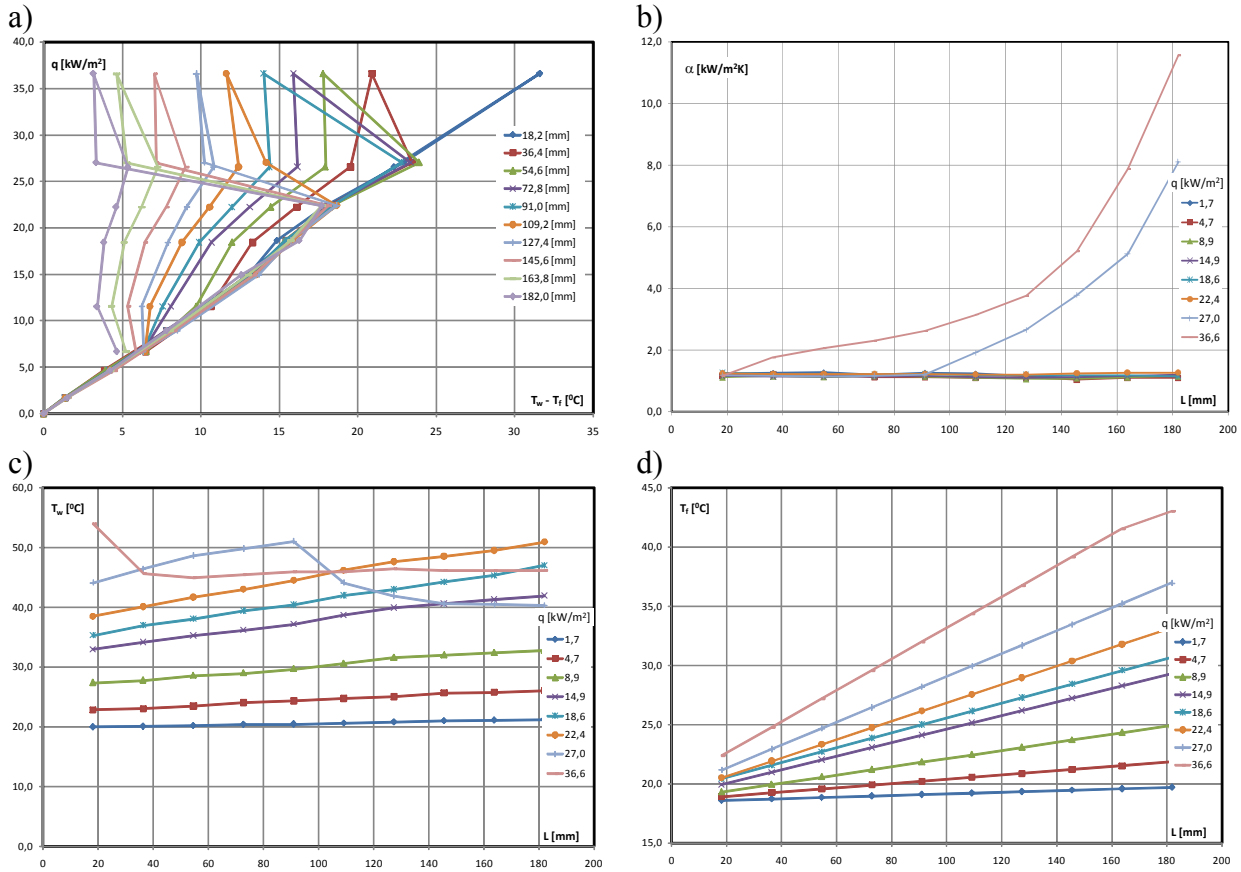

Figure 3. Results of experimental investigation: R134a, D = 1.68 mm, (uρ) = 450 kg/(m^2·s), $\Delta T_n = T_s - T_f = 10$ K; q" = 1.7 - 36.6 kW/m^2
a) heat flux q" versus temperature difference $\Delta T = T_w - T_f$
b) local heat transfer coefficient on the length of the test section
c) temperature of the wall T_w on length of the test section
d) temperature of the refrigerant T_f on length of the test section

The distribution of the local heat transfer coefficient (for selected values q" = const) during a single-phase liquid flow and during boiling is presented in Figure 3b. A clear and significant increase of heat transfer coefficient is observed in the boiling region. The changes of the channel wall temperature during a single-phase liquid flow and after the incipience of boiling (for q" = 27 kW/m^2 and q" = 36.6 kW/m^2) are presented in Figure 3c. Figure 3d presents the distribution of the refrigerant temperature along the minichannel. A linear growth of the refrigerant temperature occurs in the region where it doesn't exceed the level of the saturation temperature.

Boiling curves with flashing phenomena

Figure 4 refer heating of R134a refrigerant in a minichannel with the same internal diameter, but in the conditions of the occurrence of flashing. The results demonstrated that this phenomena has an influence not only on the heat transfer during a single-phase liquid flow but also during flow boiling. Figure 4 presents the results of experimental investigations with following conditions: (uρ) = 280 kg/(m^2·s), $\Delta T_n = 4$ K. During increase of the heat flux, the refrigerant's states should occur in the same manner as for the previously discussed case (in the graphical interpretation along straight line O – B in Figure 1). It appeared that the points which represent the location of these states on the diagram depart clearly from straight line O – B. First of all, this concerned those positions which were placed at the end of the minichannel. For the higher values of the heat flux, the deviation concerned the cross-section situated more and more closely to the inlet cross-section. This can be explained by a drop of the refrigerant temperature on the minichannel length, which causes a

growth of temperature difference $\Delta T = T_w - T_f$. This is clearly visible in Figure 4d, which presents the distribution of the refrigerant temperature on the minichannel length for various values of the heat flux. This undoubtedly is the result of the occurrence of the flashing phenomena, which initially ($q'' = 15.7$ kW/m^2) covered only two last cross-sections of the minichannel located nearest of the outlet cross-section, and moved in the direction opposite to the refrigerant flow. For conventional channels, it is considered that along straight line O - B (Figure 1), heat transfer is realized during a single-phase forced convection. In the case when the flashing phenomena occurs there is in fact a two-phase structure of refrigerant (however, this is not classical flow boiling). In these experimental conditions the value of heat flux $q'' = 54.4$ kW/m^2 can be treated as a maximum one, at which boiling has not yet occurred. Its increase up to 55.1 kW/m^2 resulted in a meta-stable condition. Sufficient overheating of the wall occurred and a boiling process with its zero crisis was initiated. New temperatures of the wall were established as in Figure 4c. As a result a drop of temperature difference ΔT occurred. Also, a rapid growth of the heat transfer (Figure 4b) serves to confirm the fact of flow boiling. It is characterized by a growth of the local heat transfer coefficient. The value of this coefficient significantly exceeds those values which are obtained in forced convection conditions during a single-phase flow and a flow with flashing. The technical potential of the experimental set-up did not allow for tests at the growth of the heat flux above $q'' = 55.1$ kW/m^2.

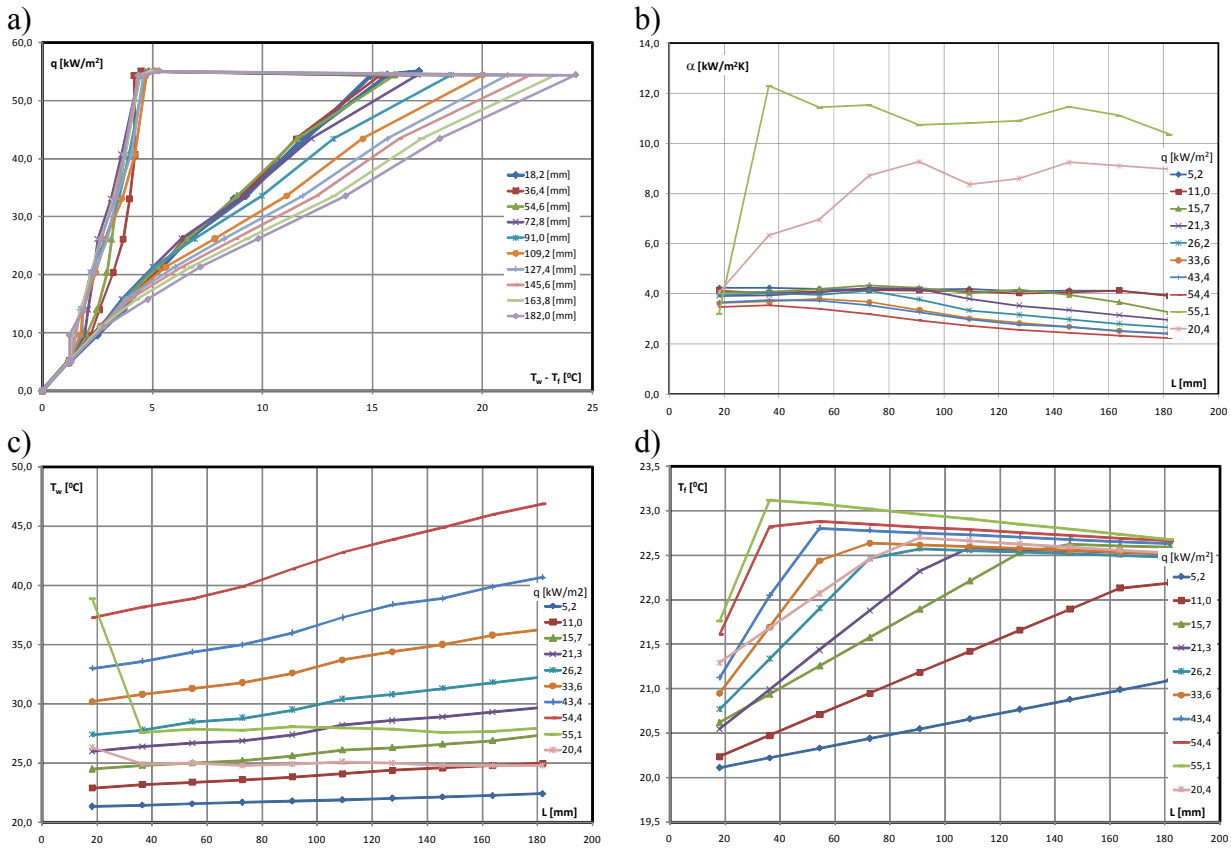

Figure 4. Results of experimental investigations: R134a, D = 1.68 mm, (uρ) = 280 kg/(m^2·s), $\Delta T_n = T_s - T_f = 4$K; $q'' = 5.2 – 55.1$ kW/m^2, flashing
a) heat flux q'' versus temperature difference $\Delta T = T_w - T_f$
b) local heat transfer coefficient on the length of the test section
c) temperature of the wall T_w on length of the test section
d) temperature of the refrigerant T_f on length of the test section

Also, tests were conducted where the heat flux was decreased. A characteristic feature of the boiling process in the flow with the flashing phenomena is overlapping states of the refrigerant in each

cross-section of the minichannel. In practice, this meant that for each value of heat flux density q" which occurred in the conditions of boiling with the flashing phenomena temperature difference $\Delta T = T_w - T_f$ had the same value in all the cross-sections on the whole length of the minichannel. This can be explained by a significant growth of vapour bubbles, which make flow more homogeneous by making it turbulent.

CONCLUSIONS

1. The experimental investigations conducted with the R134a refrigerant during a flow in a heated minichannel with an internal diameter of 1.68 mm, enabled the presentation of boiling curves. A description of boiling curves, known for conventional channels, proved to be insufficient for a minichannel. Instable phenomena have a special significance during heat transfer in minichannels. These are especially the zero boiling crisis and the flashing phenomena.
2. The mechanism of the boiling process in the flow in minichannels is substantially different from the one which has already been well recognized as regards conventional channels. The surface tension and a large drop of the pressure in the flow have a special impact on this mechanism. On the basis of the results of their research, the authors confirmed that boiling in conventional channels and in minichannels cannot be compared directly.
3. The so-called flashing phenomena, which is usually leaved out in an analysis of boiling in conventional channels, which consists in the occurrence of a two-phase structure as a result of the pressure lowering (below the saturation pressure) as a result of large flow resistances in the minichannel, plays a significant role and has an impact on boiling curves.
4. The impact of flashing on the boiling curves in a pipe minichannel constitutes a new look at the description of the boiling mechanism in channels.

REFERENCES

1. Hahne, E., Barthau G.: Evaporation waves in flashing processes, *Int. Journal of Multiphase Flow*, vol. 26, pp. 531-547, 2000.
2. Eliasa, E., Chambre, P.L.: Bubble transport in flashing flow, *Int. Journal of Multiphase Flow*, vol. 26, pp. 191-206, 2000.
3. Schneider, B., Kosa, A., Peles, Y.: Hydrodynamic cavitation and boiling in refrigerant (R-123) flow inside microchannels, *Int. Journal of Heat and Mass Transfer*, vol. 50, pp. 2838–2854, 2007.
4. Bergles, A. E., Kandlikar, S. G.: Critical heat flux in microchannels: experimental issues and guidelines for measurement, *First International Conference on Microchannels and Minichannels*, New York, 2003.
5. Revellin, R., Thome, J. R.: Adiabatic two-phase frictional pressure drops in microchannels, *Experimental Thermal and Fluid Science*, vol. 31, pp. 673-685, 2007.
6. Lee, J., Mudawar, I.: Two-phase flow in high-heat-flux micro-channel heat sink for refrigeration cooling applications: Part I—pressure drop characteristics, *Int. Journal of Heat and Mass Transfer*, vol. 48, pp. 928-940, 2005.
7. Warrier, G.R., Dhir, V.K., Momoda, L.A.: Heat transfer and pressure drop in narrow rectangular channels, *Experimental Thermal and Fluid Science*, vol. 26, pp. 53-64, 2002.
8. Qi, S.L., Zhang, P., Wang, R.Z., Xu, L.X.: Flow boiling of liquid nitrogen in micro-tubes: Part I – The onset of nucleate boiling, two-phase flow instability and two-phase flow pressure drop *Int. Journal of Heat and Mass Transfer*, vol. 50, pp. 4999 - 5016, 2007.
9. Bohdal, T., Chatun, H., Czapp, M., Dutkowski, K.: Wrzenie perspektywicznych czynników w parownikach chłodniczych, *Wyd. Politechniki Koszalińskiej*, Koszalin, 1999.

This paper was realized under Research Project No. N513 012 31/2188.

EXPERIMANTAL STUDY OF SINGLE-PHASE FLOW HEAT TRANSFER IN A MINICHANNEL

T. Bohdal, H. Charun, K. Dutkowski *, W. Kuczyński
Koszalin University of Technology, Koszalin, Poland

ABSTRACT. In this article the results of experimental investigations are presented. The experiment was conducted with the liquid R134a in a minichannel with an internal diameter of 1.68 mm. The results of the experiment were compared with the calculations of the correlations provided by other authors. Correlations for the calculation of Nusselt number during the heat transfer in a flow known in conventional channels as well as new correlations proposed for the use in minichannels were applied. The usefulness of some correlations used so far in the conventional channels was demonstrated.

Keywords: *experimental investigations, minichannels, single-phase flow, heat transfer*

INTRODUCTION

Widely conducted experiments of two-phase flow in minichannels has demonstrated that both flow resistances and heat transfer coefficients differ significantly from the values obtained from calculations with the dependences used for conventional channels [1, 2, 3]. In order to propose dependences which could be useful for the purpose of a flow in minichannels with a heat transfer analysis, a lot of experimental investigations were conducted. In this research, very accurate measuring devices are used, whose aim is to exclude the influence of the measuring error on the discrepancies occurring. One of the ways to check the correctness of the applied methodology is testing of the set-up during single-phase flow heat transfer [4, 5, 6, 7, 8, 9]. Obtained results of experimental investigations during single-phase flow heat transfer which are compliant with general trends constitutes a guarantee of the correctness of an experiment conducted with boiling. The analysis covered by this paper concerns a comparison of various correlations which describe the heat transfer in a single-phase flow of refrigerants in a minichannel. Those dependences which are recommended for conventional channels and new dependences which are proposed for minichannels were used.

EXPERIMENTAL SET-UP AND DATA REDUCTION

Experimental set-up

The liquid of the R134a refrigerant pumped from tank by pump flowed through filter and precooler. Next, the Coriolis mass flowmeter was installed. A liquid with a known flow rate was fed to heat exchangers. It was able to use these exchangers alternatively, which allowed one to achieve the proper refrigerant conditions on the test section inlet. The refrigerant (with suitable outflow parameters) was directed to the test section. The following parameters were measured: the pressure in the initial cross section of the tested part of the minichannel, the pressure drop on the tested part of the minichannel, the profile of the minichannel wall temperature, temperature on the inlet and outlet of the tested part, and the supplied electric power. All of the voltage signals of the measured values

* Corresponding author: Dr. Eng. K. Dutkowski
Phone: + (48)-94-34 78 378
E-mail address: krzysztof.dutkowski@tu.koszalin.pl

were connected with data acquisition system which cooperates with computer. A detailed description of experimental set-up is presented in paper [10].

Data reduction

The heat flux supplied to the refrigerant on length L(i) of the minichannel (measured from the location of the inlet cross-section) can be described with the following formula:

$$\dot{Q}(i) = \dot{M} \cdot c_p \cdot \left[T_f(i) - T_{in}\right], \tag{1}$$

where $T_f(i)$ is the temperature of the single-phase refrigerant in a cross-section L(i), while c_p is the mean specific heat of the refrigerant determined at the refrigerant's mean temperature on length L(i). From equation (1), the refrigerant's temperature is determined in i^{th} cross-section of the minichannel, from the following equation:

$$T_f(i) = T_{f,in} + \frac{\dot{Q}(i)}{\dot{M} \cdot c_p}, \tag{2}$$

which after a rearrangement takes on the following form:

$$T_f(i) = T_{f,in} + q'' \cdot \frac{\pi \cdot D \cdot L(i)}{\dot{M} \cdot c_p}. \tag{3}$$

Local convective heat transfer coefficient - h(i) was calculated from the below dependence:

$$h(i) = \frac{q''}{\left[T_w(i) - T_f(i)\right]}. \tag{4}$$

Experimental local Nusselt number was determined as:

$$Nu(i) = \frac{h(i) \cdot D}{k_f(i)} \tag{5}$$

where: $k_f(i)$ is the heat conductivity of liquid (calculated for the mean in the cross-section liquid temperature).

METHODOLOGY OF THE CORRELATION SELECTION

It was found on the basis of an analysis of the papers by many authors that two problems need to be addressed in the description of the heat transfer process during a forced convection in a single-phase flow. The first one is the proper determination of the thermal entrance length - L_T, while the other one is the selection of the equation for the calculation of Nusselt number depending of the nature of the refrigerant's flow.

Selection of the thermal entrance length correlation

Selection of thermal entrance length L_T plays a significant role in the calculations of minichannels because in practice (e.g. in compact evaporators) minichannels with small and very small lengths are usually used. Therefore, it is very difficult to guarantee the proper thermal entrance length for all cases. Therefore, it is necessary to consider in which area the measurement is made. This should be taken into account while choosing the suitable correlation.

In the further discussion, the thermal entrance length was according to the formula presented e.g. in articles by Yang and Lin [11] or by Fernando et al. [12, 13]:

$$L_T/D = 0{,}05 \cdot Re \cdot Pr \tag{6}.$$

Selection of the Nusselt number correlation

While selecting comparative correlations for the Nusselt number calculation, the nature of the flow (laminar/turbulent) and zone (thermal entrance length/thermally developed flow) should be taken into account.

Review of the conventional channel Nusselt number dependences

Laminar flow (thermal entrance length)

- For the calculation of local Nusselt number, the authors of paper [11] propose Shah and Bhatti formula:

$$Nu = 1302 \cdot Gz^{1/3}, \text{ for } 1/\text{Gz} \le 0.00005, \tag{7}$$

$$Nu = 1.302 \cdot Gz^{1/3} - 0.5, \quad \text{for} \quad 0.00005 \le 1/\text{Gz} \le 0.0015, \tag{8}$$

$$Nu = 4.364 + 8.68 \cdot 10^{-3} (Gz)^{0,506}, \text{ for } 1/\text{Gz} \ge 0.0015, \tag{9}$$

where: Gz – local Graetz number expressed with the following equation:

$$Gz = \text{Re} \cdot \text{Pr} \cdot D / L(i), \tag{10}$$

while L(i) is the distance between the analyzed cross-section and the inlet cross-section of the heated region.

- Sieder and Tate (1936) provided a dependence which describes the mean Nusselt number in the thermal entrance length for a hydraulically developed flow, with the influence of the fluid properties. The „w" index concerns the liquid properties in the wall temperature, while „f"– in the temperature of the flow core. The formula is recommended for the following range: 0.48 < Pr < 1670 and 0.004 < (μ_f/μ_w) < 9.75 [12, 14, 15]

$$Nu = 1.86 \left(\text{Re} \cdot \text{Pr} \frac{D}{L} \right)^{1/3} \left(\frac{\mu_f}{\mu_w} \right)^{0,14}. \tag{11}$$

- The formula of Shah and London (1978) calculation of the local Nusselt number has the following form [12, 14,16]:

$$Nu = \begin{cases} 1.953 \left(\text{Re} \cdot \text{Pr} \cdot \dfrac{D}{L} \right)^{1/3} \\ 4.364 + 0.0722 \left(\text{Re} \cdot \text{Pr} \cdot \dfrac{D}{L} \right)^{1/3} \end{cases} \quad \text{for} \quad \begin{cases} \text{Re} \cdot \text{Pr} \cdot \dfrac{D}{L} \ge 33.3 \\ \text{Re} \cdot \text{Pr} \cdot \dfrac{D}{L} < 33.3 \end{cases}. \tag{12}$$

- According to Hausen (1943) and Kays (1955) [12], the mean Nusselt number can be calculated from the following formula:

$$Nu = 3.66 + \frac{0.0668 \left(\text{Re} \cdot \text{Pr} \cdot \dfrac{D}{L} \right)}{1 + 0.04 \left(\text{Re} \cdot \text{Pr} \cdot \dfrac{D}{L} \right)^{1/3}}. \tag{13}$$

Turbulent flow

- According to Dittus – Boelter (1930) for Re ≥ 10 000, 0.7 < Pr < 16 700, $L_H/D > 10$ (smooth channels), for the calculation of the mean Nusselt number, the following formula is proposed [12, 15, 16, 17, 18, 19, 20]:

$$Nu = 0.023 \cdot \text{Re}^{0.8} \, \text{Pr}^{0.4}, \tag{14}$$

- Gnielinski (1976) for 3000 < Re < $5 \cdot 10^6$, 0,7 < Pr < 160 (rough channels), recommends the following dependence [12, 15, 18, 20]:

$$Nu = \frac{(f/8)(\text{Re} - 1000)\text{Pr}}{1 + 12.7 (f/8)^{1/2} \left(\text{Pr}^{2/3} - 1 \right)}, \tag{15}$$

where friction factor f is calculated from the following formula:

$$f = \left[1.82 \cdot \log(\text{Re}) - 1.64 \right]^{-2} \tag{16}$$

or the following dependence which gives very similar results:

$$f = \left[0.79 \cdot \ln(\text{Re}) - 1.64 \right]^{-2}. \tag{17}$$

- According to the proposal put forward by Kakac (1987), for the range of 2 300 < Re < 10 000 [12], the formula has the following form:

$$Nu = 0.116 \cdot \left(\mathrm{Re}^{2/3} - 125\right) \cdot \mathrm{Pr}^{1/3} \left[1 + \left(\frac{D}{L}\right)^{2/3}\right] \left(\frac{\mu_f}{\mu_w}\right)^{0,14} . \tag{18}$$

- Petukhov's correlation [15] for $1000 < \mathrm{Re} < 5 \cdot 10^6$ (rough channels) has the following form:

$$Nu = \frac{(f/8)\mathrm{Re} \cdot \mathrm{Pr}}{K + 12.7(f/8)^{1/2}\left(\mathrm{Pr}^{2/3} - 1\right)}, \tag{19}$$

where K coefficient:

$$K = 1.07 + \frac{900}{\mathrm{Re}} - \frac{0.63}{1 + 10\,\mathrm{Pr}} , \tag{20}$$

while friction factor f is calculated according to the formulae (14 or 15).

- According to Petukhov-Popov, for Re ≥ 10 000 (rough channels) [21], the following correlation is applicable:

$$Nu = \frac{(f/8)\mathrm{Re} \cdot \mathrm{Pr}}{1 + 3.4 \cdot f + \left(11.7 + \frac{1.8}{\mathrm{Pr}^{1/3}}\right)(f/8)^{1/2}\left(\mathrm{Pr}^{2/3} - 1\right)} \tag{21}$$

where f is the friction factor.

Review of the minichannel Nusselt number dependences

Laminar flow (thermally developed flow)

- According to Choi et al. (1991), for Re < 2000 [14] the correlation has the following form:

$$Nu = 0.000972 \cdot \mathrm{Re}^{1.17}\,\mathrm{Pr}^{1/3} . \tag{22}$$

Turbulent flow (thermally developed flow)

- Wu and Little (1983) proposed for 3000 < Re < 20 000 [12, 15, 20] the following dependence:

$$Nu = 0.002222 \cdot \mathrm{Re}^{1.09}\,\mathrm{Pr}^{0.4} . \tag{23}$$

- According to Choi et al. (1991), for 2 500 < Re < 20 000 [12, 15]:

$$Nu = 3.82 \cdot 10^{-6} \cdot \mathrm{Re}^{1.96}\,\mathrm{Pr}^{1/3} . \tag{24}$$

- Yu et al. (1995) proposed for 6 000 < Re < 20 000 correlation [15]:

$$Nu = 0.0007 \cdot \mathrm{Re}^{1.2}\,\mathrm{Pr}^{0.2} . \tag{25}$$

- Adams (1988) modified Gnielinski correlation for 2 300 < Re < 23 000 [15, 20] to the following form:

$$Nu_{Adams} = Nu_{Gnielinski}(1 + F), \tag{26}$$

where:

$$F = 7.6 \cdot 10^{-5}\,\mathrm{Re}\left[1 - \left(\frac{D}{D_o}\right)\right], \tag{27}$$

while D_o=1.164 mm

RESULTS OF EXPERIMENTAL INVESTIGATION

Figure 1 shows a comparison of the experimental local Nusselt number. The mass flow rate was changed in the range (uρ) = 245 ÷ 2150 kg/(m^2·s). The comparison was prepared depending of the Reynolds number. The experiments were conducted during a flow of R134a through a minichannel with an internal diameter of 1.68 mm until boiling occurred. It is noted that with the increase of Reynolds number, Nusselt number increase, as well. In the zone of larger values of Reynolds number, a greater scattering of the measuring results is observed. This is so because of the occurrence of the flashing phenomenon, which decrease the local Nusselt number. The flashing phenomenon consists in the generation of vapor bubbles, which is the result of the decreasing of the saturation temperature of the refrigerant caused by a significant pressure drop on the minichannel length. Then, a two-phase structure is created, however it is not the result of the classical boiling phenomenon.

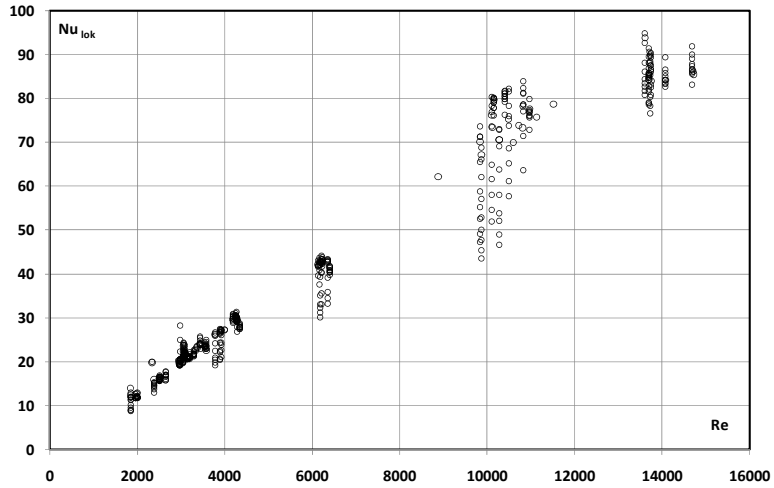

Figure 1. Experimental local Nusselt number versus Reynolds number

COMPARISON OF THE THEORETICAL AND EXPERIMENTAL RESULTS

Results of own experimental investigations as the experimental mean Nusselt number are compared to the theoretical Nusselt numbers obtained from above mentioned correlations.

Laminar thermally developing flow - conventional channel correlations

Figure 2 presents a comparison of the mean Nusselt number obtained from the experiment with the results of calculations made on the basis of dependences applied for conventional channels, as proposed by Sieder and Tate - formula (11), Shah and London – formula (12) and Hausen and Kays - formula (13). It is evident from the comparative analysis placed in Figure 2 that these correlations are useless for calculations for minichannels.

Turbulent thermally developed flow - conventional channel correlations

Figure 3 presents a comparison of the mean Nusselt number obtained from the experiment and from calculations applied for conventional channels, and proposed by Dittus & Boelter – formula (14), Gnielinski – formula (15), Kakac – formula (18), Petukhov – formula (19) and Petukhov & Popov – formula (21).

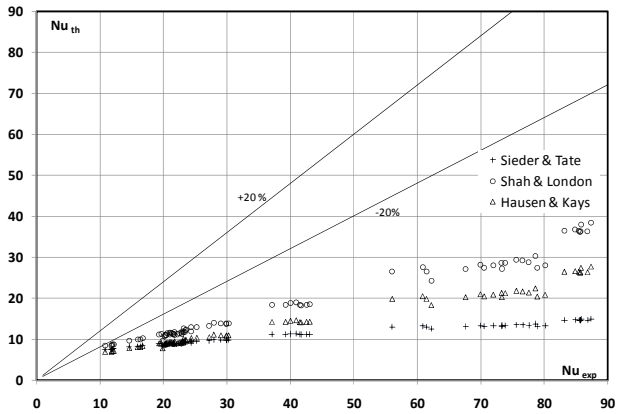

Figure 2. Experimental Nusselt number versus theoretical Nusselt number (Sieder & Tate, Shah & London, Hausen & Kays)

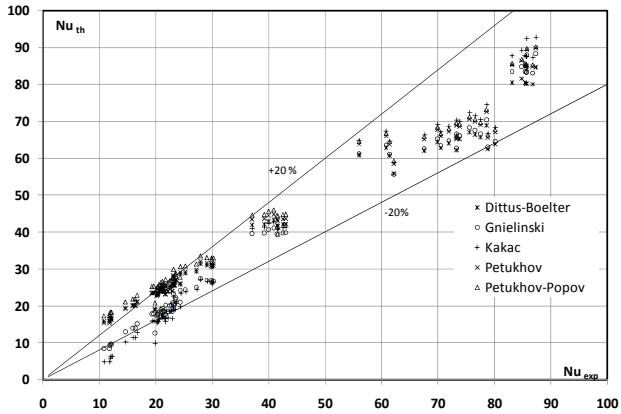

Figure 3. Experimental Nusselt number versus theoretical Nusselt number (Dittus & Boelter, Gnieliński, Kakac, Petukhov, Petukhov & Popov)

The results of calculations made on the basis of the correlations mentioned above, are in the range of ±20% as compared with the experiment. Only in those cases when Nusselt number is smaller than 20, which corresponds to number Re < 3000 (laminar and intermediate flow), the deviations

are larger. This confirms the possibility to use those formulae which have so far been used for conventional channels now in relation to minichannels.

Laminar thermally developed flow – new minichannel correlations

Figure 4 presents a comparison of the mean Nusselt number values obtained from the experiments with the results of the calculations on the basis of the dependences proposed for minichannels by Choi et al. – formula (22). It is interesting to note that the formula recommended by these authors for a thermally developed flow in the area of laminar flow is good for a turbulent flow in the experiment (Re = 1 840 ÷ 14 000). It was found that correlation (22) proposed by Choi is useful for the calculation of the mean Nusselt number also in the thermal entrance length of turbulent flow R134a in minichannels.

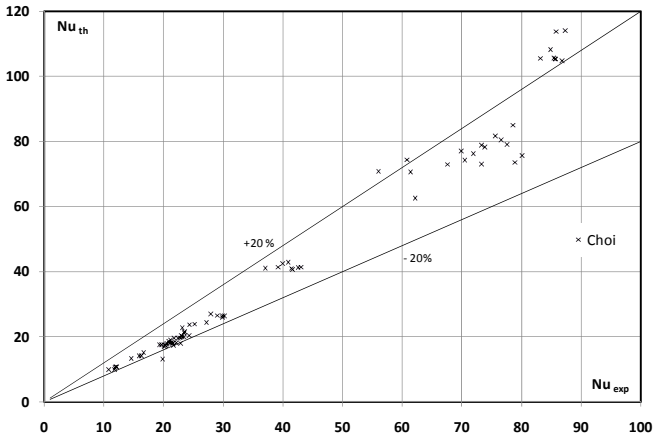

Figure 4. Experimental Nusselt number versus theoretical Nusselt number (Choi et al. – formula 22)

Turbulent thermally developed flow - new minichannel correlations

Figure 5 presents a comparison of the mean Nusselt number obtained from the experiments and from the calculations on the basis of the dependences for minichannels proposed by Wu & Little – formula (23), Choi et al. – formula (24), Yu et al. – formula (25) and Adams – formula (26). The results of the mean Nusselt number obtained from the formulae proposed by Choi et al. – formula (24) and Adams – formula (26), significantly depart from the experimental values. The correlation proposed by Yu et al. (25) gives satisfactory results in the range of ±20%. For Nusselt numbers $Nu_{exp} < 30$, which corresponds to the value of Reynolds number Re < 5 000, the error exceeds 20% (Figure 6). The correlation proposed by Wu & Little overpredicts results of experiment and could be proposed for use after an introduction of a correction factor.

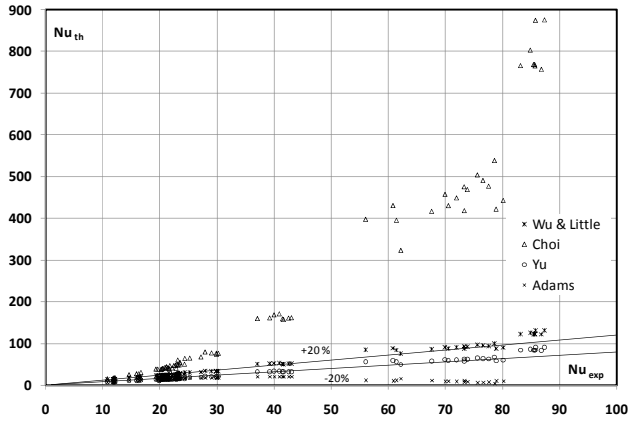

Figure 5. Experimental Nusselt number versus theoretical Nusselt number (Wu & Little, Choi, Yu, Adams)

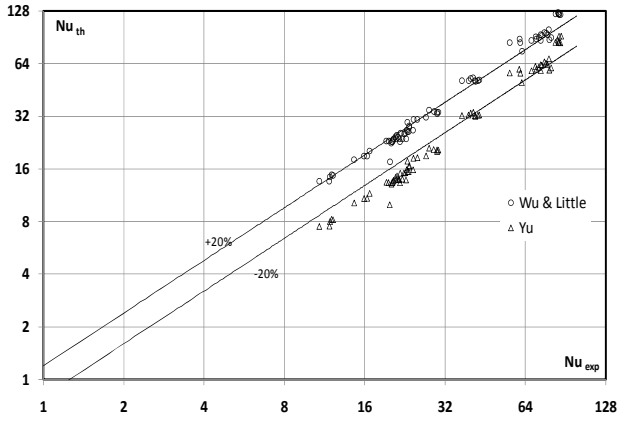

Figure 6. Experimental Nusselt number versus theoretical Nusselt number (Wu & Little, Yu)

For each correlation the value of the mean absolute error (MAE) was calculated. The MAE is described with the following dependence:

$$MAE\ [\%] = \frac{1}{n} \cdot (\sum \frac{\left| Nu_{th} - Nu_{\exp} \right|}{Nu_{\exp}}) \cdot 100\%, \tag{28}$$

where n is the number of measurements. Table 1 includes a list of the results of the calculations of the Nusselt number mean absolute error for each analyzed correlation.

Table 1
List of the Nusselt number mean absolute error (MAE)
R134a liquid flow in a minichannel with internal diameter d=1.68 mm

	Conventional channels								Minichannels				
	Laminar flow			Turbulent flow					Lam. flow	Turbulent flow			
	Sieder & Tate	Shah & London	Hausen & Kays	Dittus-Boelter	Gnielinski	Kakao	Petukhov	Petukhov-Popov	Choi	Wu & Little	Choi	Yu	Adams
MAE [%]	66,4	50,6	61,3	**12,8**	**9,78**	15,3	12,2	17,2	**12,13**	**22,25**	290	**24,3**	56,5

CONCLUSIONS

The following from the investigations of a heat transfer during a single-phase flow of the R134a is evident:

- the value of the mean Nusselt number in a single-phase turbulent flow of the liquid R134a refrigerant in a minichannel can be calculated from the formulae used for conventional channels, especially the Gnielinski or Dittus-Boelter correlations;
- the dependence recommended by Choi et al. (20), which describes Nusselt number during a flow in a minichannel in a laminar flow area, can also be applied in a turbulent flow area;
- from many proposals of the correlations for the calculation Nusselt number during a turbulent flow of refrigerant in a pipe minichannel, satisfactory results are obtained by Yu et al. correlation (applicability as specified by the authors must be preserved).

REFERNCES

1. Agostini, B., Bontemps, A.: Vertical flow boiling of refrigerant R134a in small channels, *Int. Journal of Heat and Fluid Flow*, vol. 26, pp. 296-306, 2005.
2. Cortina Diaz, M., Schmidt, J.: Experimental investigation of transient boiling heat transfer in microchannels, *Int. Journal of Heat and Fluid Flow*, 28, pp. 95-102, 2007.
3. Tran, T.N., Chyu, M.-C., Wambsganss, M.W., France D.M.: Two-phase pressure drop of refrigerants during flow boiling in small channels: an experimental investigation and correlation development, *Int. Journal of Multiphase Flow*, vol. 26, pp. 1739-1754, 2000.
4. Dutkowski, K.: Single-phase pressure drop of laminar and turbulent water flow in minichannels, *Proceedings of the 5th International Conference on Transport Phenomena in Multiphase Systems, HEAT 2008*, Białystok, pp. 283 - 288, 2008.
5. Grohmann, S.: Measurement and modeling of single-phase and flow-boiling heat transfer in microtubes, *Int. Journal of Heat and Mass Transfer,* vol. 48, pp. 4073-4089, 2005.

6. Hetsroni, G.: Flow and heat transfer in micro-channels, 4th International Conference on Heat Transfer, *Fluid Mechanics and Thermodynamics HEFAT 2005*, paper number: K3,Cairo, Egypt, 2005.
7. Kandlikar, S. G.: Microchannels and minichannels – history, terminology, classification and current research needs, *First International Conference on Microchannels and Minichannels*, New York, 2003.
8. Lelea, D., Nishio, S., Takano, K.: The experimental research on microtube heat transfer and fluid flow of distilled water, *Int. Journal of Heat and Mass Transfer*, vol. 47, pp. 2817-2830, 2004.
9. Li, Z., He, Y.-L., Tang, G.-H., Tao, W.-Q.: Experimental and numerical studies of liquid flow and heat transfer in microtubes, *Int. Journal of Heat and Mass Transfer*, vol. 50, pp. 3447-3460, 2007.
10. Bohdal, T, Charun, H., Dutkowski, K., Kuczyński, W., Influence of the flashing phenomena on the boiling curve of refrigerant R134a in minichannels, *7th World Conference on Experimental Heat Transfer, Fluid Mechanics and Thermodynamic*s, Krakow, Poland, 2009 (in progress).
11. Yang, C.-Y., Lin, T. - Y.: Heat transfer characteristics of water flow in microtubes, *Experimental Thermal and Fluid Science*, vol. 32, pp. 432 – 439, 2007.
12. Fernando, P., Palm, B., Ameel, T., Lundqvist, P., Granryd, E.: A minichannel aluminium tube heat exchanger – Part I: Evaluation of single-phase heat transfer coefficients by the Wilson plot method, *Int. Journal of Refrigeration*, vol. 31, pp. 669 – 680, 2008.
13. Owhaib, W., Martín-Callizo, C., Palm B.: Flow boiling visualization and heat transfer in a single vertical microchannel, *6th World Conference on Experimental Heat Transfer, Fluid Mechanics, and Thermodynamics,* Matsushima, Miyagi, Japan, 2005.
14. Li, Z., Huai, X., Tao, Y., Chen, H.: Effects of thermal property variations on the liquid flow and heat transfer in microchannel heat sinks, *Applied Thermal Engineering*, vol. 27, pp. 2803 – 2814, 2007.
15. Owhaib, W., Palm, B.: Experimental investigation of single-phase convective heat transfer in circular microchannels, *Experimental Thermal and Fluid Science*, vol. 28, pp. 105-110, 2004.
16. Shuai, J., Kulenovic, R., Sobierska, E., Hertz, R., Troll, M.: Flow boiling heat transfer in a vertical narrow chanel, *3rd International Symposium on Two-Phase Flow Modelling and Experimentation*, Pisa, 2004.
17. Agostini, B., Watel, B., Bontemps, A., Thonon, B.: Friction factor and heat transfer coefficient of R134a liquid flow in mini-channels, *Applied Thermal Engineering*, vol. 22, pp. 1821-1834, 2002.
18. Agostini, B., Watel, B., Bontemps, A., Thonon, B.: Liquid flow friction factor and heat transfer coefficient in small channels: an experimental investigation, *Experimental Thermal and Fluid Science*, vol. 28, pp. 97-103, 2004.
19. Lie, Y.M., Su, F.Q., Lai, R.L., Lin, T.F.: Experimental study of evaporation heat transfer characteristics of refrigerants R-134a and R-407C in horizontal small tubes, *Int. Journal of Heat and Mass Transfer,* vol. 49, pp. 207-218, 2006.
20. Qi, S.L., Zhang, P., Wang, R.Z., Xu, L.X.: Single-phase pressure drop and heat transfer characteristics of turbulent liquid nitrogen flow in micro-tubes, *Int. Journal of Heat and Mass Transfer*, vol. 50, pp. 1993-2001, 2007.
21. Yu, W., France, D.M., Wambsganss, M.W., Hull, J.R.: Two-phase pressure drop, boiling heat transfer, and critical heat flux to water in a small-diameter horizontal tube, *Int. Journal of Multiphase Flow,* vol. 28, pp. 927-941, 2002.

This paper was realized under Research Project No. N513 012 31/2188.

EXPERIMENTAL INVESTIGATIONS OF THE CONDENSATION PROCESS OF REFRIGERANT R134a IN PIPE MINI-CHANNELS

T. Bohdal, H. Charun, K. Dutkowski, W. Kuczyński

Chair of Thermal Engineering and Refrigerating Engineering
Koszalin University of Technology, Koszalin, Poland

ABSTRACT. In the era of the miniaturization of power equipment, the application of compact systems is a very advantageous solution. Compact heat exchangers which are used in refrigerating systems do not only transfer a large density of the heat flux but also perform environment-friendly functions; a refrigerant occupies a small volume, and when there is no leak tightness, there is little threat to the natural environment. The basic part of the paper is constituted by the presentation of the author's own experimental research into heat exchange in the condensation process of R134a refrigerant in pipe mini-channels with an internal diameter of 0.98 ÷ 3.3 mm. On the basis of a comparative analysis, the usefulness of *Akers* and *Shah's* correlations was stated for the determination of the heat transfer coefficient in this process

Keywords: *heat transfer, condensation, mini-channels, refrigeration, R134a*

INTRODUCTION

In the recent years, a global trend has been observed in the construction of refrigeration heat exchangers, which consists in the miniaturization of their structures. The requirements must be met of transferring a large heat flux density, with thermal-economic criteria being preserved in the scope of the reduction of power and material consumption of heat exchangers. One of the ways of a heat intensification understood in this way in relation to the abovementioned criteria, is the use of the phase changes of a refrigerant, especially of boiling and condensation in the flow in mini- and macro-channels of the exchangers. In this manner, the concept was created of the so-called *compact heat exchangers* (evaporators and condensers), which are included in the refrigerating system [10]. In relation to the small internal volume of mini-channels, additionally the ecological criterion is fulfilled, as in the unfavourable case of unsealing of such a system, the quantity of the refrigerant carried off to the environment will be scanty.

The designers of compact heat exchangers are facing today the same problem concerning the suitable selection of computational procedures as they faced some time ago in relation to conventional exchangers. It needs to be stated, however, that their problems are much more difficult, as the procedures proposed for conventional exchangers have already been tested on numerous occasions, while this is not true of compact exchangers as yet. Two basic problems remain to be solved: the calculation of the required heat exchange surface, and calculations of the resistance of the refrigerant's flow through the exchanger. The first problem consists chiefly in the selections of a dependence for the calculation of the heat transfer coefficient in a two-phase flow with a heat exchange in a mini-channel [11].

It needs to be emphasized that the number of the papers published which present a description of the heat exchange and flow resistances during boiling in mini- and micro-channels is significantly larger that the number of those which deal with condensation in these channels. The state of

Corresponding author: Prof. T. Bohdal
Phone: +(48)-94-3478247, fax +(48)-94-3425963
E-mail address: tadeusz.bohdal@tu.koszalin.pl

knowledge to date covering conventional channels proves that the processes of boiling and condensation in a flow cannot be treated as "symmetric" phenomena in the computational sense. In the boiling process of a refrigerant with heat supplied to the channel, the flow is accelerated, while during condensation with heat being carried off, there is a delay in the direction of the flow, connected with an increase of the condensate created [1]. Apart from that, there are no well-motivated premises so far so that this description of phase changes phenomena could be transferred to mini-channels, as well. However, it was noted that in the scope of the application of computational procedures of flow resistances during boiling and condensation in mini-channels, there exist possibilities to use some of the joint dependences for two-phase mixtures in conventional channels and in mini-channels, while there are relatively large discrepancies in the area of the heat exchange.

The present study covers selected results of an analysis of literature data and the results of the authors' own experimental investigations concerning calculations of heat transfer coefficients and flow resistances during the condensation of the R34a refrigerant in the pipe mini-channels of compact condensers. The analysis was narrowed down to the case of condensation in a single mini-channel. This allows one to indicate those correlations for calculations which have been suitably tested at the present state of knowledge.

RESEARCH ISSUES

The authors reviewed those correlations published in the literature which allow one to calculate heat transfer coefficient α and flow resistances of refrigerants in pipe mini-channels [4, 6, 7]. However, the results of the analysis did not give an explicit answer as regards the selection of the best correlation. It was found for the R134a refrigerant which condensates in pipe mini-channels that the discrepancies of the calculation results of heat transfer coefficient h are at times very large, which is illustrated in Fig. 1. For example, condensation of the R134a refrigerant was taken into account in a pipe mini-channel with an external diameter of 2.75mm in the saturation temperature of +35°C, for heat flux density $\dot{m}$ = 400 kg/(m^2·s). The values of heat transfer coefficient α, depending of dryness level x were calculated with the use of the correlations proposed by the following authors: *Shah* [12], *Cavalli* et al. [5], *Dobson* and *Chato* [8], as well as *Bandhauer* [2]. Relatively large discrepancies were found of the results of calculations, especially in the range of dryness level x = 0.8 ÷ 1.

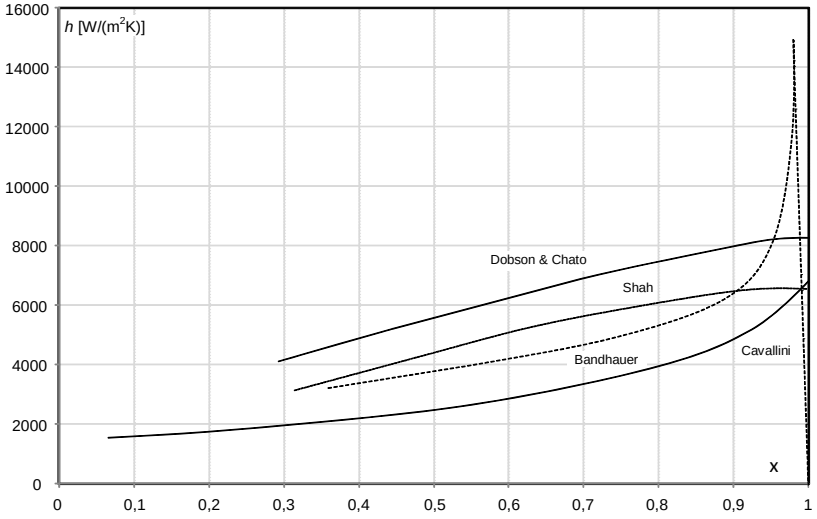

Figure. 1. Dependence of heat transfer coefficient α from dryness level x during condensation of R134a refrigerant in pipe mini-channel with diameter D = 2.75 mm, with heat flux density $\dot{m}$ = 400 kg/(m^2·s) and saturation temperature +35°C according to calculations from correlations of *Shah*, *Cavallini et al*, *Dobson* and *Chato* as well as *Bandhauer*

The results of the calculations of heat transfer coefficient *h* according to the correlations proposed by *Dobson* and *Chato* and the correlations proposed by *Akers* [1] allowed a characteristic to be built which described the dependence of the *h* coefficient from internal diameter *D* of the pipe mini-channel. Figure 2 presents a diagram of dependence *h* = f(*D*) for the R134a refrigerant. A reduction of the internal diameter of a pipe mini-channel leads to an increase of the values of the heat transfer coefficient, while large discrepancies are observed of the results of calculations according to the two correlations given above. These discrepancies increase together with the drop of the measurement of the channel's diameter *D*.

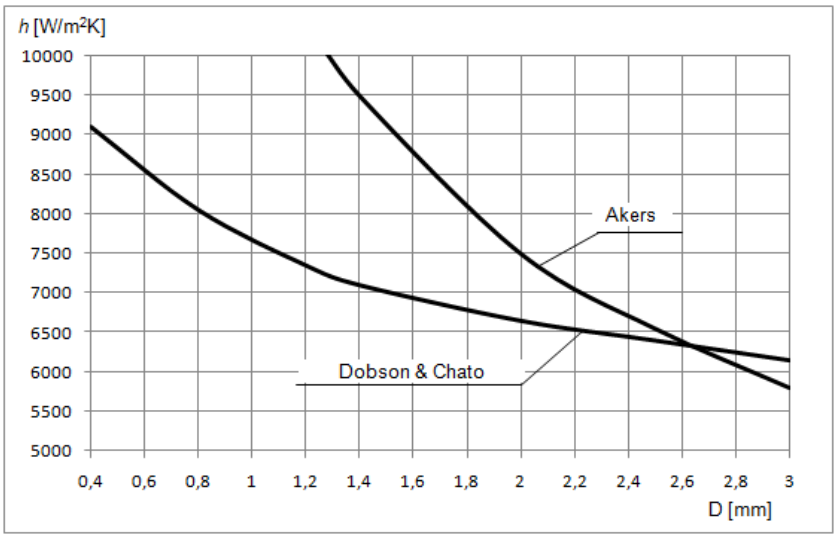

Figure. 2. Influence of diameter *D* of pipe mini-channel on the quantity of heat transfer coefficient *h* during condensation of R134a refrigerant on the basis of calculations according to correlations given by *Akers* and *Dobson* and *Chato*; $\dot{m}$ = 400 kg/(m^2·s), *x* = 0.6

Also, as an example, comparative calculations were conducted with the application of various correlations to calculate the frictional pressure drop for a pipe mini-channel with a diameter of 1.4 mm, in which the R134a refrigerant condenses (Figure 3).

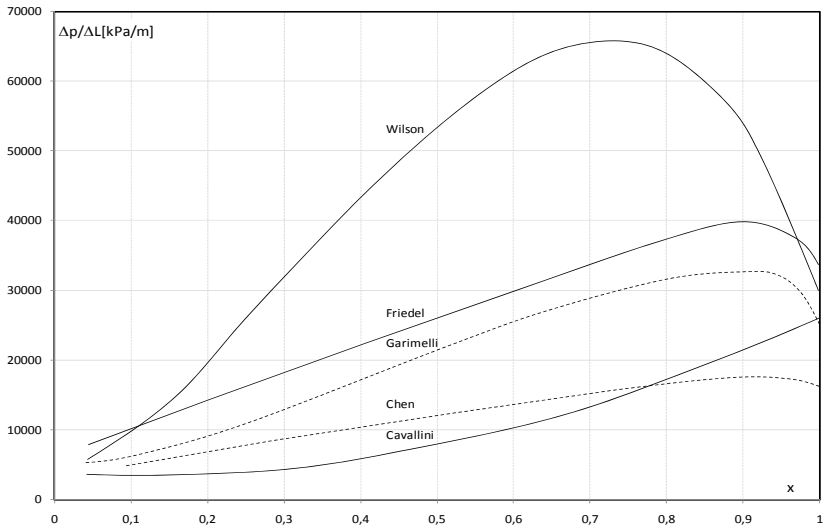

Figure. 3. Comparative listing of the dependence of frictional flow resistance ($\Delta p/\Delta L$) from dryness level *x* during condensation of R134a refrigerant in pipe mini-channel with internal diameter *D* = 1.4 mm, $\dot{m}$ = 400 kg/(m^2·s), T_s = +40^{0}C; for calculations, correlations proposed by *Friedel*, *Chen*, *Wilson, Cavallini* and *Garimell* were used.

Taking into consideration the computational characteristics which describe the heat transfer coefficient during the condensation of the R134a refrigerant and the discrepancies of the calculation

results, the authors decided to conduct their own comparative experimental investigations with this refrigerant in the application for condensation in pipe mini-channels with internal diameter $D = 0.98 \div 3.3$ mm and made of stainless steel [3].

STAND FOR EXPERIMENTAL RESEARCH

An original research stand was designed and built in the Laboratory of the Chair of Thermal Engineering and Refrigerating Engineering, the Koszalin University of Technology. Figure 4 presents the schematic diagram of the stand. On the diagram of the test stand, two refrigeration systems need to be distinguished with the R134a refrigerant, which cooperate in parallel, i.e. a single-stage refrigeration system fed by a compressor and condenser unit, and a refrigeration system which feeds the measuring section of the pipe mini-channel.

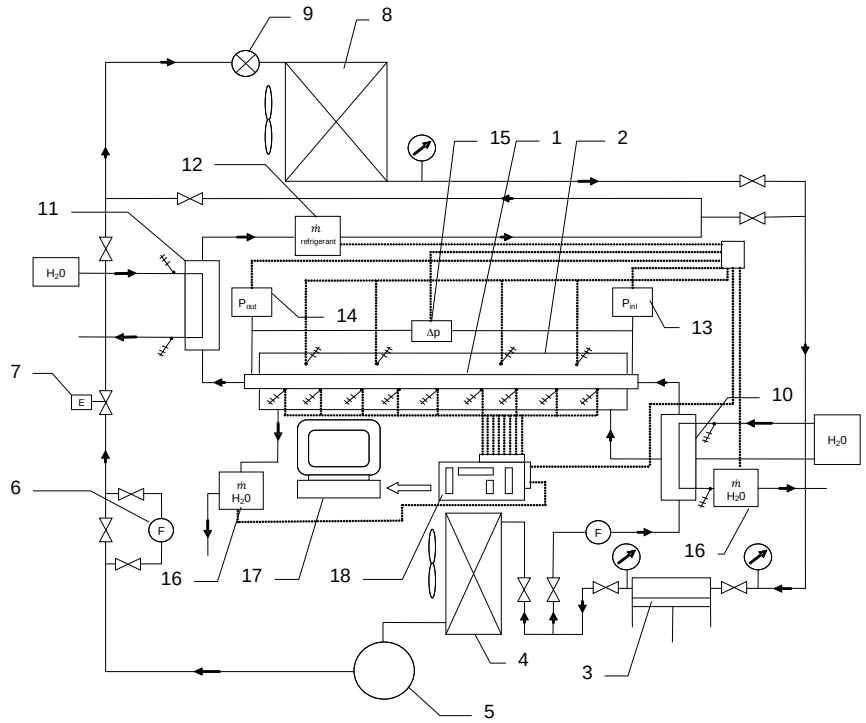

Figure. 4. Schematic diagram of research stand: 1 – measuring section of pipe mini-channel with length $L = 1000$ [mm], 2 – water channel, 3 – refrigeration compressor installation, 4 – condenser cooled with air, 5 – refrigerant liquid tank, 6 – filter and dryer of refrigerant, 7 – electromagnetic valve, 8 – lamelled air cooler, 9 – expansion valve which feeds the cooler, 10 - heat exchanger to collect refrigerant's superheat, 11 – subcooler of refrigerant's liquid, 12 – electronic flowmeter of refrigerant, 13 – sensor of refrigerant's pressure on the inlet to measuring section, 14 - sensor of refrigerant's pressure on the outlet from measuring section, 15 – differential pressure sensor, 16 – electronic water flowmeter, 17 – computer, 18 – data canvassing system

RESULTS OF EXPERIMENTAL RESEARCH

Figures 5 present examples of the experimental investigations of the condensation of the R134a refrigerant in a flow through pipe mini-channels with an internal diameter of 2.3 and 3.3 mm. The diagrams were presented of thermal characteristics in the form of dependence $h = f(x)$, that is the local heat transfer coefficient from dryness level x. A significant influence is to be noted of the heat flux density $\dot{m}$ on the course of the characteristics.

a) b)

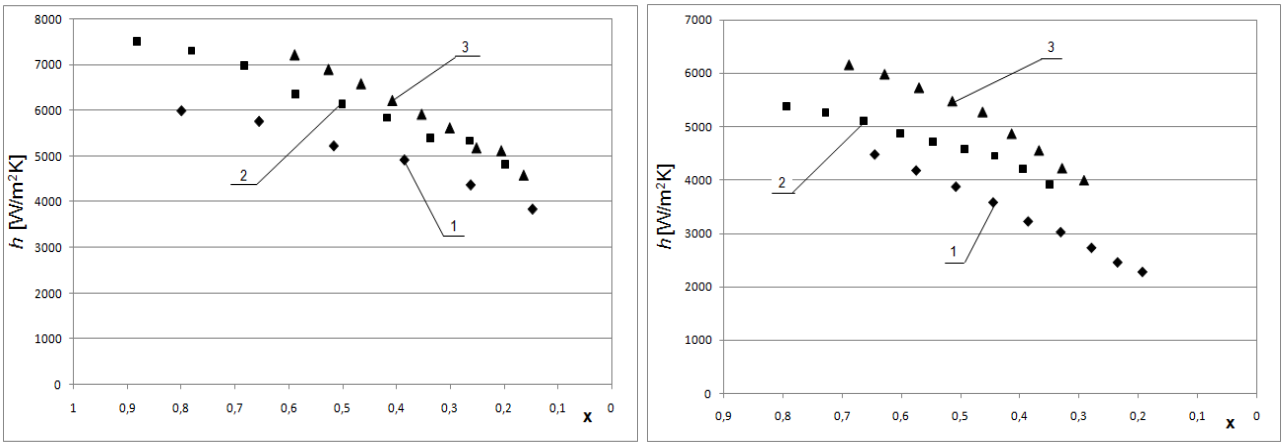

Figure. 5. Results of experimental investigations of characteristics $h = f(x)$ during condensation of R134a refrigerant in pipe mini-channel with internal diameter; a) $D = 2.3$ mm, $\dot{q} \cong 30$ KW/m^2; *1* - $\dot{m} = 337$ kg/(m$^2\cdot$ s), *2* - $\dot{m} = 497$ kg/(m$^2\cdot$ s), *3* - $\dot{m} = 709$ kg/(m$^2\cdot$ s), b) $D = 3.3$ mm, $\dot{q} \cong 30$ KW/m^2; *1* - $\dot{m} = 300$ kg/(m$^2\cdot$ s), *2* - $\dot{m} = 404$ kg/(m$^2\cdot$ s), *3* - $\dot{m} = 543$ kg/(m$^2\cdot$ s)

Also, thermal characteristics were performed of type $h = f(x)$ for other diameters of pipe mini-channels. The results obtained were compared with the results of calculations according to the correlations given by other authors, including *Dobson* and *Chato*, *Cavallini* and *Zecchin*, *Akers*, *Shah* and *Tang* [13]. Figure 6 presents comparative listings of the research results. Their analysis demonstrated that the results of the calculations of the heat transfer coefficients from the correlations proposed by *Akers* and *Shah* correspond best with the results of the experimental investigations (Figure 7). Figure 8 presents examples of the results of investigations of the pressure drop during a complete condensation of the R134a refrigerant (in range $x = 1 \div 0$) in a pipe mini-channel in the form of characteristics $\Delta p = f(\dot{m})$, while Figure 9 presents a comparison of the results of the author's own investigations of flow resistances with the research results of other authors.

a) b)

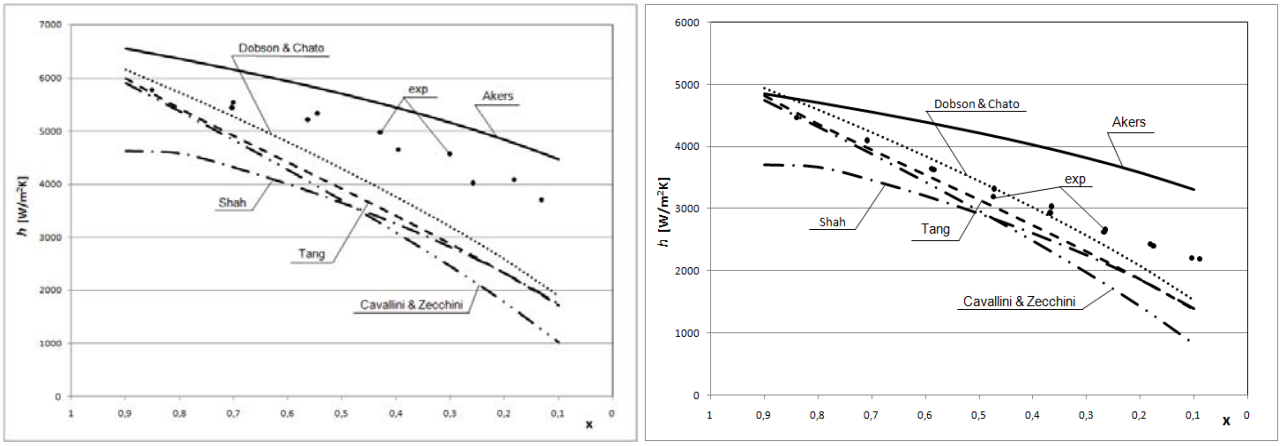

Figure. 6. Comparison of thermal characteristics $h = f(x)$: experimental and computational characteristics for the condensation of R134 a refrigerant in pipe mini-channels; a) $D = 2.3$ mm, $\dot{m} = 300$ kg/(m$^2\cdot$ s), $T_s = 40^oC$; b) $D = 3.3$ mm, $\dot{m} = 200$ kg/(m$^2\cdot$ s), $T_s = 40^oC$

a) b)

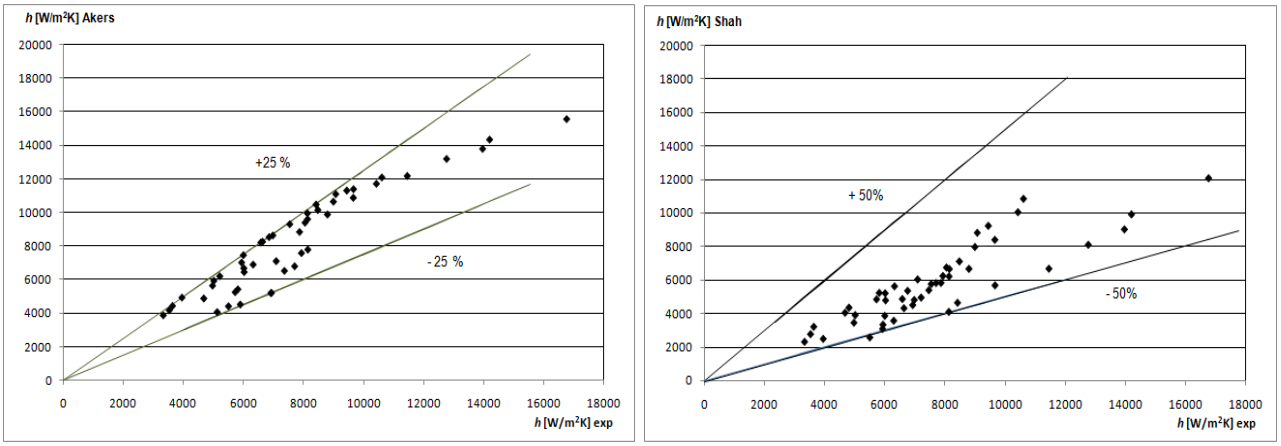

Figure.7. Comparison of the results of experimental tests of heat transfer coefficient during condensation of refrigerant with the results of calculations according to *Akers'* and *Shah's* correlations; a) comparison with calculation results according to Akers' correlation, b) comparison with calculation results according to *Shah's* correlation

a) b)

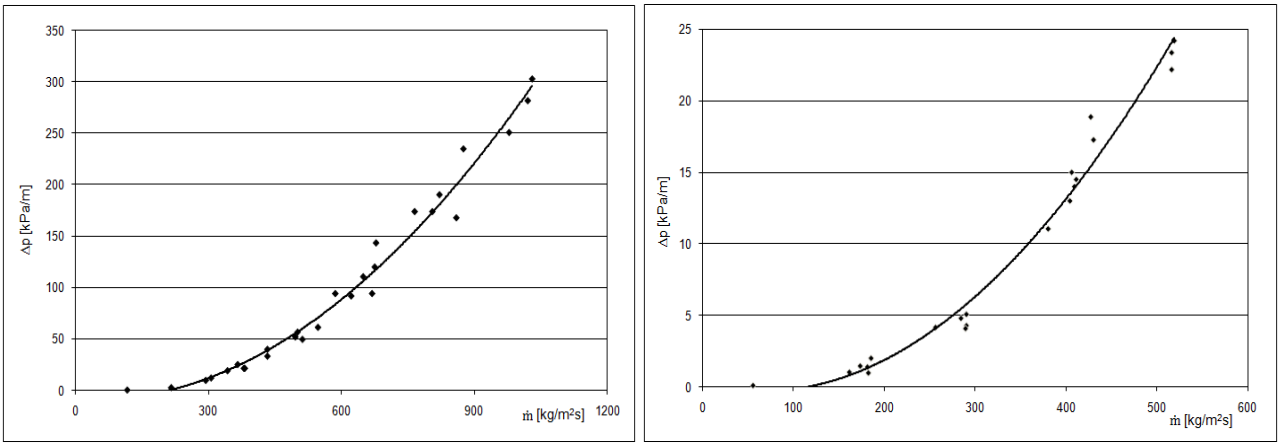

Figure. 8. Results of experimental investigations of pressure drop during condensation of R134a refrigerant in pipe mini-channel with mass flux density $\Delta p = f(\dot{m})$, in range $x = 1 \div 0$; a) $D = 1.4$ mm, b) $D = 3.3$ mm

a) b)

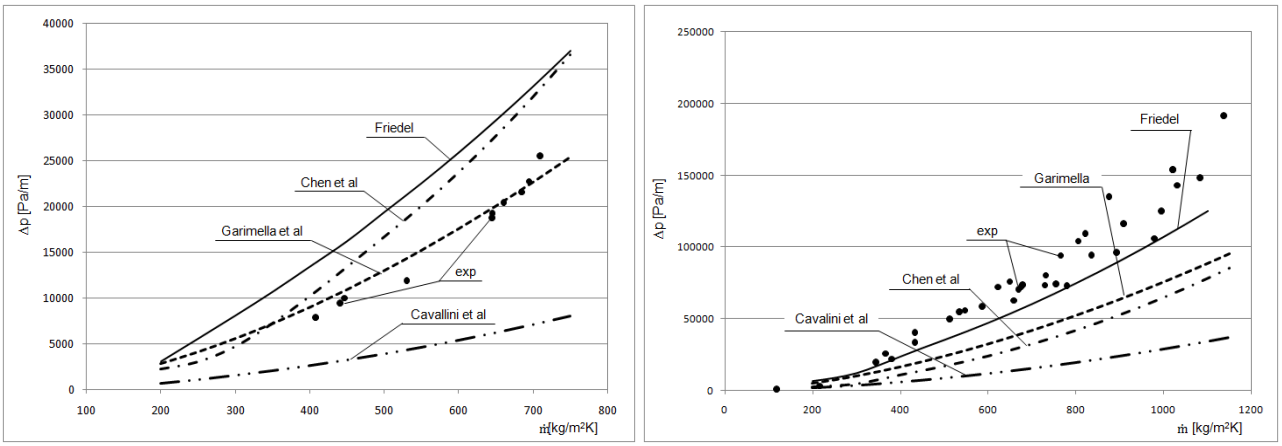

Figure. 9. Comparison of authors' own investigations of flow resistances during condensation in mini-channels with results of investigations conducted by other authors; a) $D = 1.94$ mm, $x_{śr} = 0.35$; b) $D = 1.40$ mm, $x_{śr} = 0.45$

CONCLUSIONS

The authors conducted thermal comparative investigations of the condensation of the environment-friendly R134a refrigerant in pipe mini-channels with internal diameters $D = 0.98 \div 3.3$ mm, which confirmed the usefulness of the application of the correlations proposed by *Akers* and *Shah* for the calculations of the heat transfer coefficient (used for the calculations for conventional channels). The discrepancies of the experimental results and the calculations according to the correlation of *Akers* were in the range of ±25%, and for this reason this correlation can be recommended to designers. The experimental tests were conducted in the following range of parameters: saturation temperature $T_s = 35 \div 40^{o}$C, mass flux density $\dot{m} = 200 \div 600$ kg/(m^2·s), and heat flux density $\dot{q} = 5 \div 50$ kW/m^2.

REFERENCES

1. Akers W., Deans O.K., Crosser O.K.: Condensation heat transfer within horizontal tubes. *Chemical Engineering Progress Symp*. 1959, vol. 55, pp. 171-176.
2. Bandhauer T.M., Agarwal A., Garimella S.: Measurement and modeling of condensation heat transfer coefficients in circular microchannels. *Journal of Heat Transfer Transactions of ASME* 2006, vol. 128, pp. 1050-1059.
3. Bohdal T., Charun H., Piątkowski P., Więckiewicz D.: Skraplanie czynników chłodniczych w minikanałach rurowych. *Międzynarodowa Konferencja Chłodnicza,* Poznań 2008, XL Dni chłodnictwa, pp. 59 – 75.
4. Bohdal T., Charun H.: Przegląd procedur obliczeniowych skraplania czynnika chłodniczego R134a w minikanałach. *Chłodnictwo* 2008, nr 8, pp. 2-5 – Part 1 and no. 9, pp. 2-7 - Part 2.
5. Cavallini A., Censi G., Del Col D., Doretti L., Longo G.A., Rosetto L.: Condensation of halogenated refrigerants inside smooth tubes. *HVAC &R Research* 2002, vol. 8, no 4, pp. 429-451.
6. Del Col D.: Condensation in minichannels and microchannels. *Proc. VII Scuola estiva UIT, Tecniche Sperimentali in Termofluidodinamica,* Portignano 2007, pp. 1-34.
7. Dhanani H., Schmidt S., Metzger C.: Condensation in mini- and microchannels. *Heat and Mass Transfer Laboratory*, 2007.
8. Dobson M.K., Chato J.C.: Condensation in smooth horizontal tubes. *I. Heat Transfer*, ASME 1998, vol. 120, pp. 193-213.
9. Garimella S.A., Agarwal A., Killion J.D.: Condensation pressure drop in circular microchannels. *Heat Transfer Engineering* 2005, vol. 26, no 3, pp. 1-8.
10. Gnutek Z., Nemś A.: Tendencje rozwoju maszyn i urządzeń energetycznych w erze miniaturyzacji. *Materiały XXX Zjazdu Termodynamików,* Wrocław 2008, vol. I , pp. 318-324.
11. Kandlikar S.G.: Microchannels and minichannels- history, terminology, classification and current research needs. *First International Conference on Microchannels and Minichannels*, New York, 2003.
12. Shah M.M.: A general correlation for heat transfer during film condensation inside pipes. *Int. J. of Heat and Mass Transfer* 1979, vol. 22, pp. 547-556.
13. Tang L.: Empirical study of new refrigerant flow condensation inside horizontal smooth and micro-fin tubes. *University of Maryland at College Park, Ph.D. Thesis*, 1997, p. 251.

This study was conducted under Research Project No. NN 512 2315 33

VARIOUS APPROACHES TO THE CALCULATION OF MINICHANNEL FLOW BOILING HEAT TRANSFER

S. Hozejowska[1,*], M.E. Poniewski [2]
[1] Kielce University of Technology, Kielce, Poland
[2] Warsaw University of Technology, Plock Campus, Poland

ABSTRACT. The paper deals with a numerical determination of heat flux and the heat transfer coefficient between boiling liquid flowing through a vertical, rectangular and asymmetrically heated minichannel, and a heating foil. The one-dimensional approach includes the foil temperature change only along the flow direction, whereas the two-dimensional one also in the direction perpendicular to the flow. The two-dimensional approach uses heat polynomials – functions satisfying Laplace's differential equation. The results of exterior foil surface temperature measurements based on the thermosensitive liquid crystal technique are applied. Due to that the only possible method to identify sought local values on the foil interior surface in the two-dimensional approach is to solve the inverse heat conduction problem. Known temperature measurement errors allow employing equalizing calculus and help refine the numerical method in the two-dimensional approach. The equalizing calculus-based criterion for the correctness of numerical method selection is presented.

Keywords: *minichannel, flow boiling, inverse problem, heat polynomials, equalizing calculus*

STATING THE PROBLEM AND OBJECTIVES

The investigated system consists of the flowing boiling liquid (R123) and two walls, a quasi-adiabatic wall on one side and the heating foil with a covering glass on the other, see Figure 1[1,2]. The liquid, whose temperature is lower than its boiling point, flows into a minichannel. Thermo-sensitive liquid crystal technique and design of the experimental stand see Figure 1, only allow measurements of the heating foil temperature on its surface from the side of the glass. We are seeking to identify the local values of temperature, the heat flux and the heat transfer coefficient on the foil interior surface, contacting the boiling liquid. That is an inverse problem in which, on the basis of temperature measurement at the system interior points and the measurement of the electric power supplied to the foil, it is possible to determine the unknown boundary conditions [2,3,4]. We assume a steady state of the entire system but omit the crystal layer thickness and changes in glass, foil and liquid temperature along the minichannel width.

The objectives of the investigations discussed in this paper are as follows: a) to develop one- and two-dimensional approaches for determining local temperature of foil, the heat flux and the heat transfer coefficient at the foil-liquid contact; b) to refine calculation procedures through the use of the known foil exterior surface temperature measurement errors; c) to propose a criterion for verifying the quality of temperature measurement fitting by means of a suitable polynomial.

* Corresponding author: Sylwia Hozejowska
Phone: + (48)-41-3424394, Fax: + (48)-41-3424306 ,
E-mail address: ztpsf@tu.kielce.pl

ONE-DIMENSIONAL APPROACH

The investigations took into account the dimension along the flow direction (x), but the dimension perpendicular to it (y) was related only to the foil or glass thickness, see Figure 1. The glass pane, owing to its very low conductivity ($\lambda_G = 0.71$ Wm^{-1}K^{-1}), quite large thickness ($\delta_G = 5$mm) and a low heat transfer coefficient on its exterior surface, may be treated as a perfect insulator. Consequently, it may be assumed that the entire volumetric heat flux generated inside the foil, is transferred by heat conduction across the foil thickness to the flowing liquid, and the heat flux on the surface contacting the liquid is given by the equations:

$$-\lambda_F \frac{\partial T_F(x,\delta_G+\delta_F)}{\partial y} = q_V\,\delta_F = q_w \quad \text{(a)} \qquad \text{where} \qquad q_V = (U\,I)(\delta_F\,W_F\,L_F)^{-1} \quad \text{(b)} \tag{1}$$

At the boundary surface $y = \delta_F + \delta_G$ heat is dissipated by convection, therefore

$$-\lambda_F \frac{\partial T_F(x,\delta_G+\delta_F)}{\partial y} = \alpha(x)\big(T_F(x,\delta_G+\delta_F) - T_l(x)\big) \tag{2}$$

where $T_l(x)$ changes, for simplicity, linearly from $T_{l,inlet}$ to $T_{l,outlet}$. Since δ_F is very small, it is possible to replace the partial derivative in equation (1a) with a finite difference, and after taking condition (2) into account we get a simple formula for the heat transfer coefficient:

$$\alpha_{1D}(x) = (q_V\lambda_F\delta_F)\,(\lambda_F(T_F(x,\delta_G) - T_l(x)) - q_V\cdot\delta_F^2)^{-1} \tag{3}$$

In equation (3), $T_F(x,\delta_G)$ is obtained from approximation of the liquid crystal measurement results T_k by an n – degree polynomial.

TWO-DIMENSIONAL AAPROACH

The stationary heat transfer process in a two-layer partition is expressed with the equations:

$$\text{• in glass: } \nabla^2 T_G = 0\,\text{(a)} \qquad \text{and} \qquad \text{• in foil: } \nabla^2 T_F = -\frac{q_V}{\lambda_F}\ \text{(b)} \tag{4}$$

At the glass – foil contact the equality of both temperatures and their gradients is found:

$$T_F(x_k,\delta_G) = T_G(x_k,\delta_G) = T_k\ ,\ k = 1,2,...,K \quad \text{(a)} \qquad -\lambda_F\frac{\partial T_F}{\partial y} = -\lambda_G\frac{\partial T_G}{\partial y}\ ,\ \text{y} = \delta_G,\ 0 \le x \le \text{L} \quad \text{(b)} \tag{5}$$

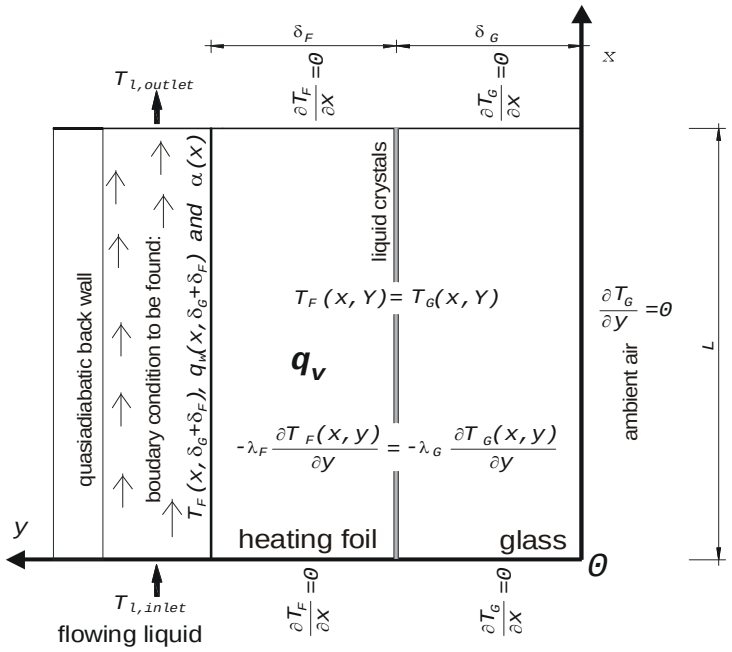

Figure 1. Diagram of flow boiling process in the investigated minichannel and boundary conditions.

It is assumed that the remaining boundaries are isolated, see Figure 1. The unknown $T_G(x,y)$ is approximated with a linear combination of the heat polynomials $u_n(x,y)$, which satisfy equation (4a), whereas the foil temperature $T_F(x,y)$ is given as the sum of the function being a specific solution $\tilde{u}(x,y)$ to equation (4b) and the linear combination of polynomials $u_n(x,y)$ [2,5]:

$$T_G(x,y) \approx \sum_{i=0}^{N} a_i u_i(x,y) \quad \text{(a)} \qquad T_F(x,y) \approx \tilde{u}(x,y) + \sum_{j=0}^{M} b_j u_j(x,y) \quad \text{(b)} \tag{6}$$

Unknown coefficients a_i and b_j are calculated by the least squares method which leads to the minimization of error functionals. Those functionals describe the mean squared errors between approximates and prescribed boundary conditions in Figure 1. This is the heat polynomials method [2,5]. $T_G(x,y)$, which is computed first, and $T_F(x,y)$, determined in this way, satisfy accurately equations (4), and approximately boundary conditions (5). If we know the function $T_F(x,y)$ on the boundary $y = \delta_G+\delta_F$, we can compute the heat flux and the heat transfer coefficient from the condition (3).
The function $T_G(x,y)$ satisfies equation (4a) and the assumed boundary conditions. Thus, in order to determine coefficients a_i, equation (6a), we rely on the error functional J_G defined as follows [2,4]:

$$J_G = \int_0^L \left(\frac{\partial T_G(x,0)}{\partial y} \right)^2 dx + \int_0^\delta \left[\left(\frac{\partial T_G(0,y)}{\partial x} \right)^2 + \left(\frac{\partial T_G(L,y)}{\partial x} \right)^2 \right] dy + \sum_{k=1}^{K} \left(T_G(x_k,\delta_G) - T_k \right)^2 \tag{7}$$

When in (7) $T_G(x,y)$ is substituted with dependence (6a), the minimum of functional J_G is determined from the solution for the system of equations:

$$\frac{\partial J_G}{\partial a_i} = 0, \quad i = 0, 1, ..., \mathrm{N} \tag{8}$$

Coefficients b_j are determined in the same manner as in equation (8). For function $T_F(x,y)$, the minimized functional J_F has a similar form to the functional (7).

TECHNIQUES TO IMPROVE THE ACCURACY OF NUMERICAL CALCULATIONS

Equalizing calculus

In the heat polynomials method measurements T_k can be expressed as a sum of unknown accurate measurements $\tilde{T}_k$ and temperature measurements corrections ε_k, that is,

$$\tilde{T}_k = T_k + \varepsilon_k \tag{9}$$

Corrections ε_k are assumed to have a normal distribution with a mean of zero and finite variance σ_k^2 [6,7], where σ_k are local temperature measurement errors discussed in [1,2,3,4]. They are the errors in estimating values of the foil temperature, based on the hue indicated by liquid crystals.
The normal distribution density function for corrections ε_k is expressed by:

$$\varphi_k = (\sigma_k \sqrt{2\pi})^{-1} \exp(-1/2(\varepsilon_k \sigma_k^{-1})^2) \tag{10}$$

For K independent measurements T_k the density of occurrence probability of given measurement results and corrections ε_k is defined by the product $\Phi = \varphi_1 \varphi_2 ... \varphi_K$ of the density functions φ_k, which is called a reliability function.

The identification of corrected measurements $\tilde{T}_k$ given by equation (9), leads to the determination of the maximum of the reliability function Φ. Corrected measurements $\tilde{T}_k$ are congruent and asymptotically effectual, that is, with the growing number of measurements K the estimation result approaches the real value; the variance of estimator $\tilde{T}_k$ will then be the lowest [6]. The reliability function Φ reaches its maximum when the quadratic form below fulfills the following condition:

$$W = \varepsilon^T V \varepsilon \rightarrow \min \tag{11}$$

where $V = \left[\sigma_k^{-2}\right]$ is the weights matrix [1,3,6,7].

Let T denotes a respective vector hereafter and T_k - the elements of this vector. Additionally, we assume that condition (5a) is fulfilled for corrected measurements $\tilde{T}$

$$\tilde{T}_F - \tilde{T} = 0 \tag{12}$$

where $\tilde{T}_F$ is the corrected temperature of the foil, computed from equation (6b). By solving problem (11) with condition (12), we can find the minimum of the Lagrange function

$$\Omega = \varepsilon^T V \varepsilon + 2\omega^T (\tilde{T}_F - \tilde{T}) \rightarrow \min \tag{13}$$

where: ω is K dimensional vector of Lagrange multipliers [1,6,8]. For the smoothed results - $\tilde{T}$, obtained from conditions (12) and (13), their measurement errors - $\tilde{\sigma}$ - are calculated following the procedure described in [3,8]. As expected, equalizing calculus smoothes the measurement data of temperature, $T \rightarrow \tilde{T}$, and reduces the errors, $\sigma \rightarrow \tilde{\sigma}$. Similar results are obtained when in condition (12) we assume that $\tilde{T}_G - \tilde{T} = 0$, where $\tilde{T}_G$ is corrected glass temperature. If we know the $\tilde{T}$ values, it is possible to calculate new approximations of glass and foil temperatures, and consequently the new heat fluxes and heat transfer coefficients.

Equalizing calculus was used in the same way for the one - dimensional approach [8].

Experimental errors implementation

Originally, when forming error functionals J_G and J_F, equation (7), it was assumed that liquid crystals temperature measurements were error-free [2,3]. The modification is based on the assumption that $T_F(x_k, \delta_G) - T_k$ and $T_G(x_k, \delta_G) - T_k$ have a normal distribution with a zero mean value and variance σ_k^2. In functionals J_G and J_F, the last terms $\sum_{k=1}^{K}\left(T_G(x_k, \delta_G) - T_k\right)^2$, $\sum_{k=1}^{K}\left(T_F(x_k, \delta_G) - T_k\right)^2$ describe how accurately the computed approximations of glass and foil temperatures satisfy the conditions (5). In the modified heat polynomials method, taking into consideration temperature measurement errors σ_k in functionals J_G and J_F will result in reducing the difference between the calculated approximations and measured temperature values [2,3,4]. Modified are only the last components in functionals J_G and J_F, which have the following new forms:

$$\text{a) for glass:} \quad \sum_{k=1}^{K}((T_G(x_k, \delta_G) - T_k)\sigma_k^{-1})^2 \quad \text{b) for foil:} \quad \sum_{k=1}^{K}((T_F(x_k, \delta_G) - T_k)\sigma_k^{-1})^2 \tag{14}$$

In formulas (14), errors σ_k are weights for individual temperature measurements.

The higher the accuracy of the measurement the smaller the error and the greater the weight. The described modification improves conditioning of systems of equations (8) [2,3,4].

For the modified heat polynomials method equalizing calculus was also used [1,3,8].

EVALUATION OF IMPROVEMENTS IN ACCURACY OF HEAT TRANSFER CALCULATIONS

The numerical calculation results presented below are for the experimental data, showed in Figure 2 as hue distributions on the foil external surface obtained through liquid crystal thermography. In the one-dimensional approach the measurements of temperature T_k were approximated using a 5-degree polynomial, i.e. n=5. In the two-dimensional approach it was assumed that $\tilde{u}(x, y) = -0.5 q_v \lambda_F^{-1} y^2$

and $N = M = 5$, which means that six heat polynomials were used to determine glass and foil approximates expressed by equation (6).

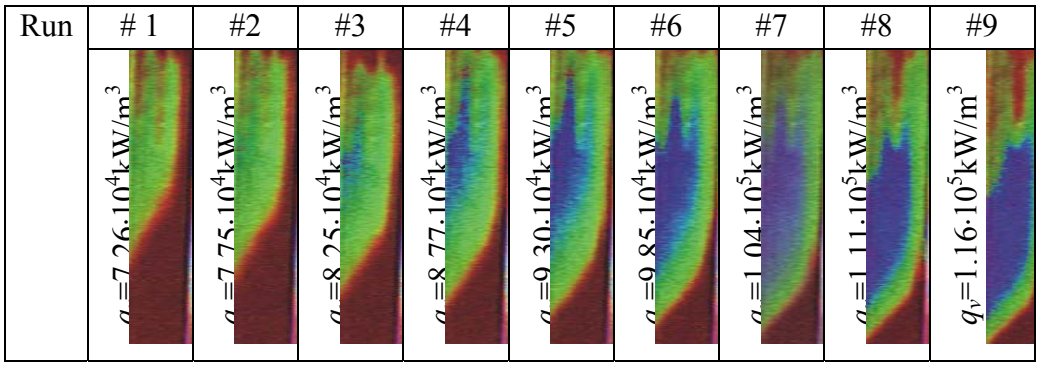

Figure 2. Images of hue distribution on the minichannel external surface while increasing the heat flux supplied to the heating foil; parameters of the runs: mass flow rate = 120 kg m^{-2}s^{-1}; Reynolds number = 543; inlet pressure = 197 kPa; inlet liquid subcooling = 9.6 K.

Further, diagrams for computed heat transfer coefficients α_{1D}, shown in Figure 3(a), and α_{2D}, shown in Figure 3(b), are presented for particular runs. Both coefficients have similar values. The character of coefficient α_{1D}, computed for run #7, is different from diagrams in the remaining runs and different from the character of the diagram for α_{2D}, compare Figure (3a) and Figure 3(b). The differences result from the temperature measurement approximation by a 5-degree polynomial, which causes over fitting. To avoid this effect, in calculations we should either use measurement data instead of approximates, or apply the equalizing calculus in the one-dimensional approach [8].

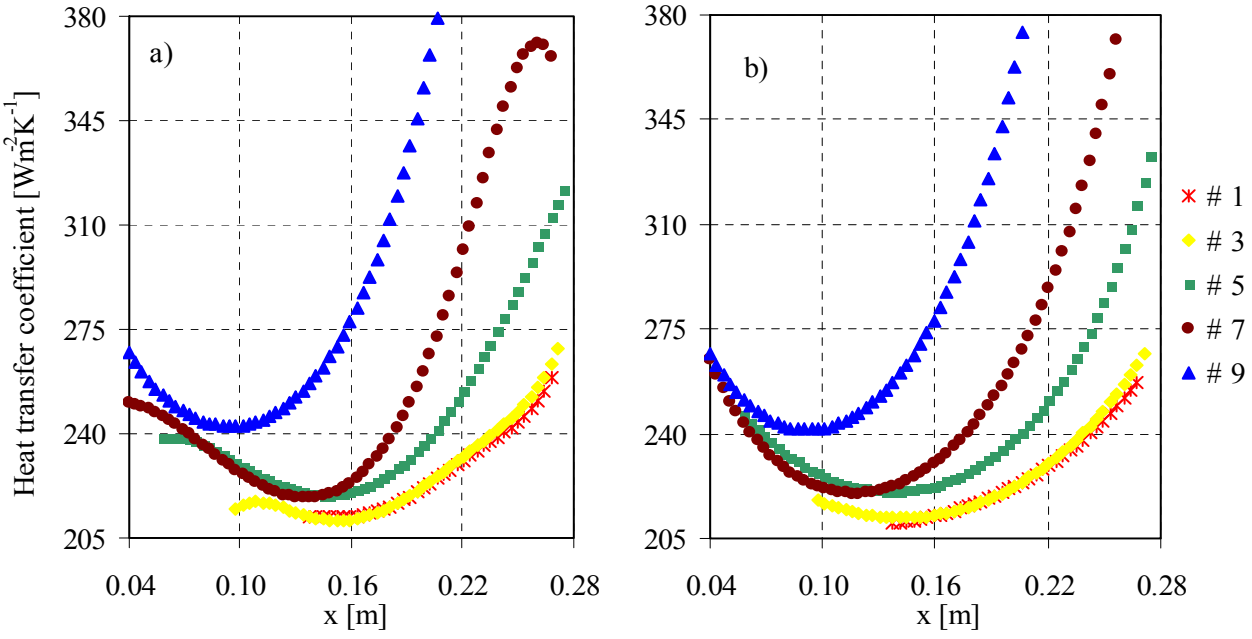

Figure 3. Heat transfer coefficient dependence on the distance along the channel length: (a) α_{1D}, (b) α_{2D}; experimental data as in Figure 2.

The use of the equalizing calculus in the one-dimensional approach and in the heat polynomials method resulted in a smaller standard deviation of the smoothed measurements $\tilde{T}$, when compared with temperature measurements T, see Figure 4b. This means that the equalizing calculus reduces the errors of the smoothed temperature measurements. For instance, for run #5, measurement errors

σ_k change from 0.5K (x=0.06) to 1.63K (x=0.18.), whereas the smoothed measurement errors have values from 0.11K to 0.25K (for one-dimensional approach) and from 0.11K to 0.19K (for heat polynomials method).

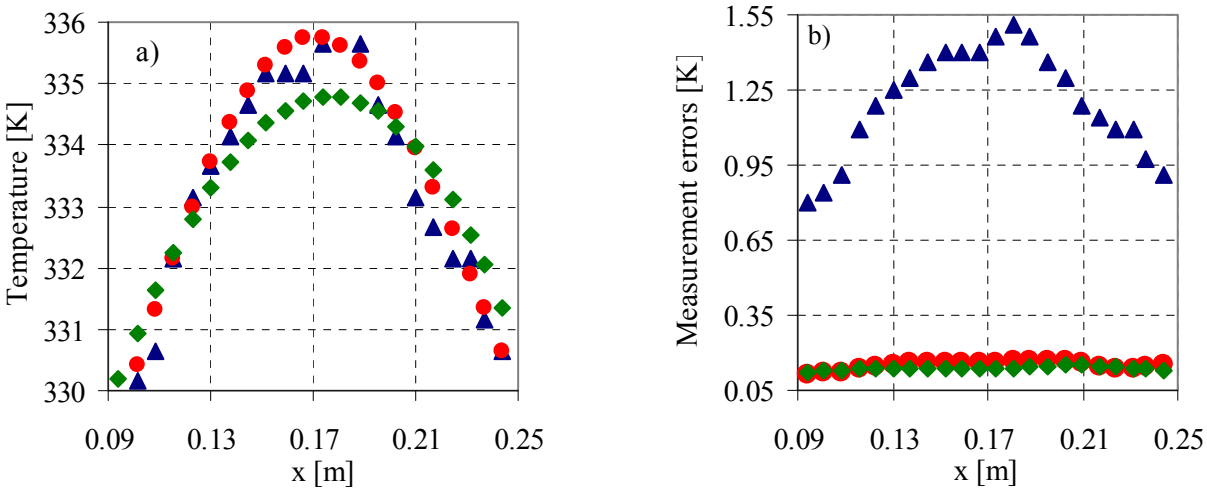

Figure 4. Temperature distribution and measurement errors for run#5:
a) temperature: ▲ – measurements, ● – smoothed measurements (one-dimensional approach), ♦ – smoothed measurements (heat polynomials method); b) ▲ – measurement errors (σ_k), ● – measurement errors for smoothed measurements (one-dimensional approach), ♦ – measurement errors for smoothed measurements (heat polynomials method) .

The corrections ε_k given by equation (17), to temperature measurements T_k are assumed to have the normal distribution with a mean of zero and finite variance σ_k^2, and they should fulfill condition [7]:

$$|\varepsilon_k| < 3\sigma_k \tag{15}$$

For one-dimensional model, 98.4% of corrections meet condition (15); run #7 is an exception. For the heat polynomials method (modified and classical) condition (15) is always fulfilled.

With the assumed corrections ε_k, function W given by equation (11), has a distribution χ^2 with *K-n-1* number of the degrees of freedom in the one-dimensional approach, and *K-N-1* in the heat polynomials method [6]. The calculations confirm that the value of function W in each run is lower than the number of freedom degrees. This makes the calculations reliable (except for run #7, see Table 1). Function W helps test the fitting of measurement data by means of an *n*-degree polynomial (one-dimensional approach) or a combination *N+1* of heat polynomials (for the heat polynomials method). With the use of χ^2 we can verify the correct fitting hypothesis for measurement data T_k using a 5-degree polynomial (one-dimensional approach) or a combination of six heat polynomials (for the heat polynomials method) [6]. The assumed hypothesis is rejected when at the significance level β:

- in the one-dimensional approach: $W > \chi^2_{1-\beta}(K-n-1)$ (a)
- for the least squares method: $W > \chi^2_{1-\beta}(K-N-1)$ (b) (16)

Table 1 presents the values of the functions given by equations (11) determined for one-dimensional approach (W_1), the heat polynomials method (W_2), the modified heat polynomials method (W_3) and the values $\chi^2_{0.99}$ at the significance level of 1% and the suitable number of degrees of freedom. Conditions (16) are fulfilled only in the case of run #7. Thus, there are no grounds for adopting the assumed hypothesis of a correct fitting of measurement data using a 5-degree polynomial (one-dimensional approach) or a linear combination of six heat polynomials (heat polynomials method).

Table 1
Values W_1, W_2, W_3 and $\chi^2_{0.99}$, at the significance level of 1%, and a suitable number of degrees of freedom (*K-n-1* or *K-N-1*, depending on the applied model).

Run	W_1	$\chi^2_{0.99}$	W_2	$\chi^2_{0.99}$	W_3	$\chi^2_{0.99}$
1	38.82	< 182.98	41.59	< 184.12	24.63	< 184.12
3	30.32	< 234.91	44.99	< 236.03	33.69	< 236.03
5	74.69	< 286.14	76.95	< 287.45	84.21	< 287.45
7	**352.89**	**> 304.94**	**414.11**	**> 306.04**	**500.36**	**> 306.04**
9	26.85	< 239.39	25.88	< 240.51	28.56	< 240.51

The application of the equalizing calculus to the heat polynomials method improved the percentage of calculated approximations $T_G(x,y)$ and $T_F(x,y)$ which fulfill conditions (2) and (3). Also, the conditioning of system of equations (8) improved. In order to verify the changes introduced by the equalizing calculus, the mean squared error between randomly chosen functions of two variables *f* and *g* was defined with the formula

$$d(f,g) = (K^{-1}\sum_{k=1}^{K}\left(f\left(x_k,\delta_G\right)-g\left(x_k,\delta_G\right)\right)^2)^{1/2} \tag{17}$$

T_F and T_G denote respectively foil and glass temperature approximates obtained from the classical method; $T_{F,1}$ and $T_{G,1}$ - foil and glass temperature approximates obtained from the classical method after introducing the equalizing calculus; $T_{F,2}$ and $T_{G,2}$ - foil and glass temperature approximates obtained from the modified method; $T_{F,3}$ and $T_{G,3}$ - foil and glass temperature approximates obtained from the modified method after the equalizing calculus application. Table 2 lists mean squared errors calculated from formula (17), between a suitable foil and glass temperature approximate and measurements: T - for the classical method; $\tilde{T}$ - for the classical method after the equalizing calculus application; $\approx{T}$ - for the modified method after the equalizing calculus application. Moreover, for all the runs from #1 to #9 computed foil and glass temperature approximates (T_F and T_G; $T_{F,1}$ and $T_{G,1}$; $T_{F,2}$ and $T_{G,2}$; $T_{F,3}$ and $T_{G,3}$) fulfill condition (5b) with the mean squared error not exceeding 0.012 Wm^{-2}; most often the error is 0.002 Wm^{-2}. The analysis of data presented in Table 2 shows that equalizing calculus reduces mean squared errors in both classical and modified methods. This means that equalizing calculus improves the accuracy with which the calculated approximates fulfill conditions (5). The smallest mean squared errors occur for approximates $T_{F,3}$ and $T_{G,3}$, that is, for functions obtained from the modified heat polynomials method combined with the equalizing calculus. Approximate $T_{F,3}$ is the most accurate when approximating unknown temperature distribution in the foil, thus the heat transfer coefficient based on this approximate corresponds to the actual heat transfer coefficient.

Table 2
Mean squared errors expressed by formula (17) for run #5.

	The method	Mean squared errors $d(f,g)$ [K]		
1	Classical heat polynomials	$d\left(T_G,T_F\right)=0.72$	$d\left(T,T_G\right)=0.97$	$d\left(T,T_F\right)=0.63$
2	Classical combined with equalizing calculus	$d\left(T_{G,1},T_{F,1}\right)=0.67$	$d(\tilde{T},T_{G,1})=0.70$	$d(\tilde{T},T_{F,1})=0.03$
3	Modified heat polynomials	$d\left(T_{G,2},T_{F,2}\right)=0.67$	$d\left(T,T_{G,2}\right)=1.09$	$d\left(T,T_{F,2}\right)=0.67$
4	Modified combined with equalizing calculus	$d\left(T_{G,3},T_{F,3}\right)=0.02$	$d(\approx{T},T_{G,3})=0.02$	$d(\approx{T},T_{F,3})=0$

The smallest mean squared errors occur for approximates $T_{F,3}$ and $T_{G,3}$, that is, for functions obtained from the modified heat polynomials method combined with the equalizing calculus.

Approximate $T_{F,3}$ is the most accurate when approximating unknown temperature distribution in the foil, thus the heat transfer coefficient based on this approximate corresponds to the actual heat transfer coefficient.

CONCLUSIONS

• The calculated heat transfer coefficients α, based on all the presented approaches, have similar values, see Figure 3.The results verify one another, which confirms the correctness of the assumed approaches and the used numerical procedures.
• The application of equalizing calculus in the one-dimensional approach and the heat polynomials method „smoothed" temperature measurements and reduced standard deviations of the „smoothed" measurements considerably, see Figure 4.
• Test χ^2 verifies the hypothesis of measurement data fitting using an *n*-degree heat polynomial (for the one-dimensional approach) or a linear combination *N*+1 of heat polynomials. Measurement data fitting is fulfilled for nearly all the runs, Table 1.
• The modification of the heat polynomials method helped obtain foil and glass temperature approximates which fulfil boundary conditions (5) with a mean squared error smaller than in the classical method. The smallest mean squared error was obtained for the modified method combined with the equalizing calculus, Table 2.

REFERENCES

1. Hozejowska S., Piasecka M. and Poniewski M. E., Boiling heat transfer in vertical minichannels. Liquid crystal experiments and numerical investigations, *Int.J. of Thermal Sciences*, accepted for publication - http://dx.doi.org/10.1016/j.ijthermalsci.2008.11.013, 2008.
2. Piasecka M., Hozejowska S. and Poniewski M.E., Experimental evaluation of flow boiling incipience of subcooled fluid in a narrow channel, *Int. J. Heat & Fluid Flow*, Vol. 25, pp.159-172, 2004.
3. Hozejowska S., Piasecka M. and Poniewski M.E., Equalizing calculus in minichannel flow boiling heat transfer calculation, *Proc. ECI Int. Conf. on Heat Transfer and Fluid Flow in Microscale*, Castelvecchio Pascoli, 2005, paper #25, p.8.
4. Piasecka M., Hozejowska S. and Poniewski M.E., Experimental error analysis and heat polynomial method improvement for boiling heat transfer numerical calculations in minichannels, *Proc. 3rd Int. Conf. on Microchannels and Minichannels*, Toronto , 2005, paper # ICMM2005-75142.
5. Cialkowski M. and Frackowiak A., Heat functions and their application to solving heat conduction and mechanical problems, Poznan Univ. of Technology, Poznan, 2000, in Polish.
6. Brandt S., Data analysis, statistical and computational methods for scientists and engineers, Springer Verlag, New York, 1999.
7. Szargut J.,Equalizing calculus in heat engineering, Ossolineum,Katowice, 1984, in Polish.
8. Piasecka M., Poniewski M.E., Hozejowska S. and Hozejowski L., Various models and numerical procedures of boiling heat transfer calculations in minichannels, *Proc. Euromech Colloquium #472 on Microfluidics and Transfer*, Grenoble, 2005, p.4.

Material Processing

DEVELOPMENT OF A VACUUM INSULATION PANEL WITH A STAGGERED BEAM STRUCTURE

C.H. Jang[1], H. Jung[1], J. S. Kwon[1], T. H. Song[1,*]
[1]School of Mechanical, Aerospace and System Engineering
Korea Advanced Institute of Science and Technology, Daejeon, KOREA

ABSTRACT. Recently, thermal insulation technique having higher thermal resistance is highly required to save energy and space. A superior thermal insulation can be achieved by VIPs (vacuum insulation panels) having designed inner structures. For this purpose, staggered beam structure is designed and tested. Its effective thermal conductivity is investigated theoretically and experimentally. Heat transfer in VIP occurs via solid conduction, gaseous conduction and radiation. Radiation can be reduced to a negligible order when radiation shields are installed. To minimize gaseous conduction, the core structure is evacuated to below 1.33×10^{-1} Pa and sealed in aluminium laminated film envelope after a baking process. The material is selected as polycarbonate thanks to its relatively low thermal conductivity and high strength. The calculated result is compared with experimental one. It shows the effective thermal conductivity as low as 0.89×10^{-3} W/m·K, which means about 30 times higher thermal resistance than the conventional insulators such as polystyrene or polyurethane foams. This proves the practical applicability of the proposed VIP structure and further, there is a room for further improvements.

Keywords: *Vacuum insulation panel*, *Thermal conductivity*, *Staggered beam structure*

INTRODUCTION

About half of the energy in the world is consumed for HVAC (heating, ventilating and air conditioning) of buildings [1]. Thermal insulation of buildings is thus becoming the key element to improve energy utilization efficiency. Although most insulation materials are developed in the early 20th century, their insulation performances are stagnant at the level of 0.03 W/m·K of thermal conductivity for a century. If we can develop an excellent insulator, this is the most promising solution for the energy crisis. The VIPs being developed lately are the very candidates. Thermal resistance of VIPs is by a factor of ten to hundred times greater than the conventional insulation materials such as polystyrene and polyurethane foams at the same thickness. This means that much thinner insulation layer will save the energy and the building space.

VIPs usually have filling materials to withstand the external atmospheric pressure. Filling materials must have maximum thermal path to enhance the insulation performance. Many studies of the VIPs are performed during the last two decades. Early studies include PU (polyurethane) foam and fumed silica [2, 3]. These bulk-type materials have random structure. Most of the core materials are not loaded up to the ultimate compression strength, which means they do not have the maximum possible thermal resistance. Hence, these are not optimized. Accordingly, an optimized design is highly required. The purpose of this study is to develop a super insulator having outstanding insulation performance. As one of such insulators, staggered beam structure is investigated in this

* Corresponding author: Prof. T. H. Song
Phone: + (82)-42-350-3032, Fax: + (82)-42-350-3032
E-mail address: taehosong@kaist.ac.kr

study. It is designed considering strength and deflection. Effective thermal conductivity is obtained by theoretical and experimental methods. The calculated result is compared with experimental one.

DESIGN OF THE STAGGERED BEAM STRUCTURE

To the authors' knowledge, the first practically realized VIP with designed inner structure which is the vacuum glazing of Collins et al. [4]. They install support pillars between two layers of glass. Though simple in its shape, the overall heat transfer coefficient is lowered to about 1/5 of that of a single glass plate [5]. This demonstrates the potential possibility of designed inner structure of VIPs. In this study, a staggered beam structure is proposed to enable multi-layered structure (see Figures 1 and 2). As can be seen from the figures, a layer of beam is placed at a right angle on another layer. A third layer, then is placed half pitch staggered from the first layer. Heat conduction thus occurs along the beam in a spiral manner.This design is similar to that of G. Kawaguchi and K. Nagai [6].

Consider a staggered beam under compression load. The beam cross-section should be minimal to decrease the thermal conduction. Two design conditions are thus derived considering the maximum stress constraint [7]. First, bending strength constraint is expressed as

$$\frac{3}{4}\frac{P_{atm}}{\sigma_t} \le \frac{bh^2}{w^3} \tag{1}$$

where P_{atm} is the atmospheric pressure, σ_t is the tensile strength of core material, w is span between beams, b is width and h is height of the beam. Second, the deflection of staggered beam should not be greater than $h/2$ to avoid beam-to-beam contact (for example, beams of layers 1 and 4 may contact each other). Therefore, stiffness constraint by deflection of beam is expressed as

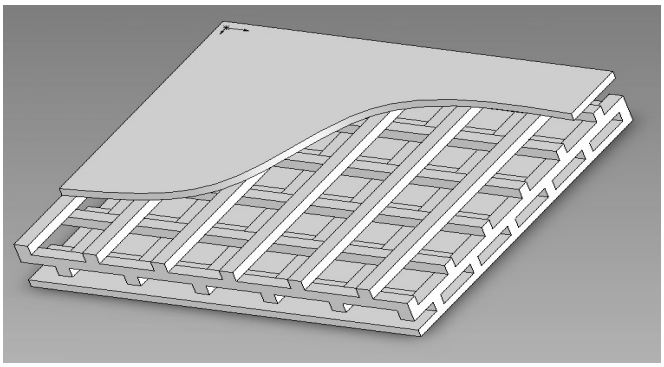

Figure 1. Super insulator with staggered beam structure

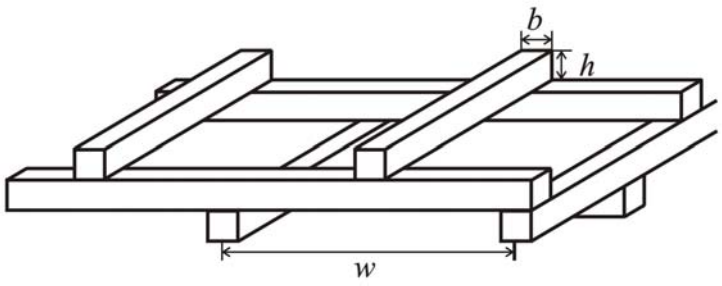

Figure 2. Schematic diagram of the super insulator with staggered beam structure

Table 1
Mechanical and Thermal Properties of Polycarbonate

Thermal conductivity	Tensile Strength	Compressive strength	Young's modulus
0.192 W/m·K	65.5 MPa	74.5 MPa	2,380.0 MPa

$$\frac{\delta}{w} \le \frac{P_{atm} w^4}{16 E b h^3} \tag{2}$$

where δ is the maximum deflection and E is Young's modulus. Staggered beam structure having a pair of layers is fabricated based on these design conditions by injection molding. The pairs can be stacked in series in a staggering manner to any total height. Its parameters are determined as b = 1mm, h = 1mm and w = 7.6mm. The material of staggered beam is selected as PC (polycarbonate) for its relatively high tensile strength and low thermal conductivity. Its mechanical and thermal properties are shown in Table 1 [8].

ANALYSIS OF THE THERMAL TRANSPORT MECHANISM OF THE VIP

Thermal transport in VIPs occurs via solid conduction, gaseous conduction and radiation. The solid conduction depends on the structure and material properties of the core. The gaseous conduction depends on the gas pressure which increases with time by permeation of atmospheric gases and outgassing of the inner material. Thermal radiation depends on the structure and optical properties of the core. The total effective conductivity k_{eff} of VIPs can be determined by summation of the solid conductivity k_s, the gaseous conductivity k_g and the radiative conductivity k_r as

$$k_{eff} = k_s + k_g + k_r \tag{3}$$

Separate study of each contribution is required to improve the thermal insulation performance of the VIP. In the meanwhile, experimental separate measurement of these contributions is not easy because any of them cannot be fully eliminated.

Solid conductivity

Consider staggered beam structure having $N \times N$ beams and M layers. The total resistance is given as

$$R_{total} = k_{eff}^{-1} \frac{hM}{w^2 N^2} \tag{4}$$

There exists contact resistance because contact region is not perfectly flat. Total resistance is determined by summation of total beam and contact resistances. So, the effective solid conductivity k_s neglecting beam deflection is given as

$$k_s = \frac{k_{s0}}{\frac{w^2}{8 r_c h} + \frac{w^3}{4 b h^2}} \tag{5}$$

where k_{s0} is thermal conductivity of core material and r_c is contact radius. In a denominator of this equation, first term is related to contact resistance and second one is related to beam resistance. It is

assumed that plastic deformation occurs in the contact region, which has the minimum contact area and thus maximum contact resistance. The contact radius is given as

$$r_c = \frac{w}{\sqrt{\pi}}\left(\frac{P_{atm}}{\sigma_c}\right)^{\frac{1}{2}} \tag{6}$$

where σ_c is the compressive strength of the core material. If equation (1) determines w for given b and h with a safety factor S, equation (1) is rewritten as

$$\frac{w^3}{4bh^2} = \frac{1}{3S}\left(\frac{\sigma_t}{P_{atm}}\right) \tag{7}$$

This equation determines the ratio w/h as

$$\frac{w}{h} = \left(\frac{b}{h}\frac{4\sigma_t}{3SP_{atm}}\right)^{\frac{1}{3}} \tag{8}$$

The contact radius and this equation are substituted in equation (5). Then, the solid conductivity can be expressed as

$$k_s = \frac{k_{s0}}{\frac{\sqrt{\pi}}{8}\left(\frac{b}{h}\frac{4\sigma_t}{3SP_{atm}}\right)^{\frac{1}{3}}\left(\frac{\sigma_c}{P_{atm}}\right)^{\frac{1}{2}} + \frac{1}{3S}\frac{\sigma_t}{P_{atm}}} \tag{9}$$

The parameters and properties of fabricated VIP are substituted in equitation (9). In the denominator, the value of first term becomes 45.4 and second one becomes 107.8. Thus, it is found that the effect of beam resistance is more dominant than the contact resistance for this case. It is also found that the contact resistance can be increased by increasing b/h. Also, it is important to choose core material having great FOM (figure of merit), which is given as

$$FOM = \frac{\sigma_t}{k} \tag{10}$$

Gaseous conductivity

Thermal conductivity of gas is independent of pressure as far as the gaseous conduction may be treated as continuum because the pressure is inversely proportional to the mean free path [9]. However, it is considerably reduced when the mean free path is almost same as or longer than the gap or pore size. The mean free path λ (m) for air in room temperature is given as [9]

$$\lambda = \frac{6.65\times10^{-3}}{P} \tag{11}$$

where P is the pressure in Pa (N/m^2). If the pore size of the VIP's core material is known, the pressure level which gaseous conduction is significantly lowered is determined by this equation. The fabricated VIP must be evacuated to below 3Pa by this equation because the pore size of staggered beam structure is 2mm. However, it is evacuated to below 1.33×10^{-1} Pa in this experiment to have a long durability.

Next, the gaseous conduction is expressed. A theory of gaseous conduction in rarefied gas is developed by Smoluchowski [10]. It is based on the concept of temperature jump and discontinuity. For two surfaces separated by distance d, the heat flux q is given as

$$\dot{q} = \frac{k_{g0}}{d + 2\beta}(T_1 - T_2) \tag{12}$$

where k_{g0} is the thermal conductivity of free gas. Here, β is given as [11]

$$\beta = \left(\frac{9\gamma - 5}{2\gamma + 1}\right)\left(\frac{2 - \alpha}{\alpha}\right)\lambda \tag{13}$$

where γ is specific heat ratio of gas and α is the accommodation coefficient. Common gases have α between 0.7 and 1.0 at room temperature [12]. Equation (11) and γ=1.4, α=0.8 for air in room temperature are substituted in equation (13). Equation (13) is then rewritten as β=0.016/P. Thus, the gaseous thermal conductivity is derived by Fourier's heat conduction equation and equation (12) as

$$k_g = \frac{k_{g0}}{1 + \dfrac{0.032}{Pd}} \tag{14}$$

Radiative conductivity

Generally, radiative heat transfer is important when the system is at an elevated temperature. However, it can not be ignored even in VIPs because its effective thermal conductivity has very small order of magnitude. If reflective surfaces are installed in the gap of VIPs, radiative heat transfer is considerably lowered, for they function as radiation shields. An advantage of staggered beam structure is that many radiation shields can be installed between the beam layers. There may exist evanescent wave in the gap if the gaps are as small as micro-meter. It, then, is very complicated to analyze the heat transfer rate. Yoon and Song [13], after performing the analysis, conclude that radiative transfer can be treated using simple ray theory if the gap size between the shields is more than 5 μm at room temperature. Here, it is assumed that radiation by staggered beam itself is ignored. Then, the radiative thermal conductivity having N gaps is given as

$$k_r = \frac{t_{core}\sigma T_m^3}{N\left(\dfrac{2}{\varepsilon} - 1\right)} \tag{15}$$

where t_{core} is the thickness of the VIP, T_m is the average temperature in the VIP, σ is Stefan-Boltzmann coefficient and ε is emissivity of the radiation shield surface. This is as small as 6.25×10^{-5} W/m·K for the real system to be explained later in detail.

Table 2
The Patameters of Fabricated Staggered Beam

w	h	b
7.6mm	1mm	1mm

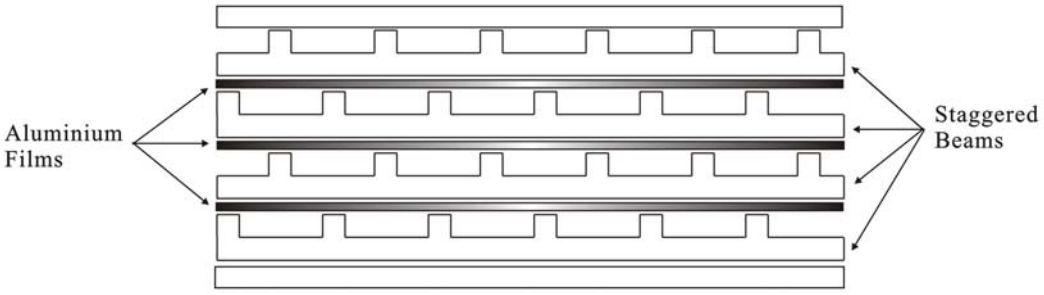

Figure 3. Fabricated staggered beams with aluminium films.

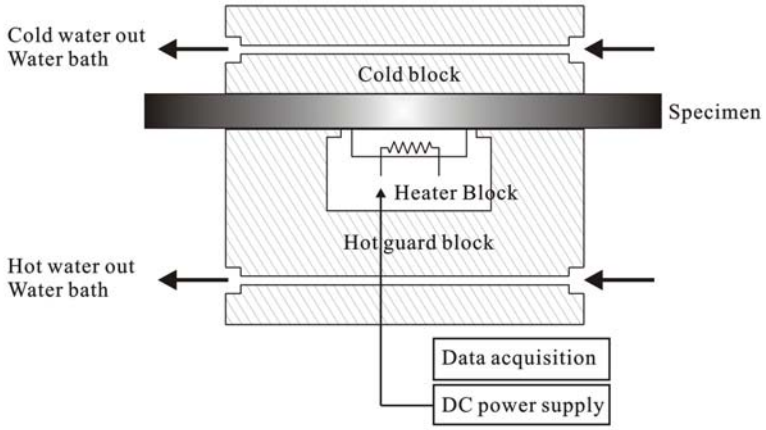

Figure 4. Guarded hot-plate apparatus

EXPERIMENT

The fore mentioned staggered beam structure is fabricated. Strength constraint is determined by equation (7) with negligible deflection given by equation (2). Staggered beam pair having 2 layers is made by injection molding. VIP having 8 layers is made for the experiments (see Figure 3). As mentioned above, the material of staggered beam is selected as PC (polycarbonate) for its large FOM (= 340 $\frac{MPa}{W/m\cdot K}$). See Table 2 for the detailed dimensions, *w*, *h*, and *b*. Aluminium films of 7 μm thickness are installed between the beam pairs to reduce the radiative heat transfer. A getter, product from SAES Getters®, is inserted in the VIP for maintenance of the vacuum level. Laminated core structure is evacuated to below 1.33×10^{-1} Pa. Also, it is baked at 80℃ for 24 hours to avoid the outgassing from PC itself. Envelope material to minimize permeation and leak from the atmosphere is a laminated film consisting of PET (polyethylene terephthalate), LDPE (low density polyethylene), aluminium and L-LDPE (linear low density polyethylene).

The total effective thermal conductivity k_{eff} is measured using a guarded hot-plate apparatus [14]. The principle of this apparatus is shown in Figure 4. Two copper blocks are in good contacts with the VIP surfaces. One block is located in the guard side which is maintained as high temperature T_h, while the other is at low temperature T_c. High temperature T_h and low temperature T_c are maintained using constant temperature water bath. Heater block temperature T_m is precisely controlled to be equal to T_h. Then heat transfer does not occur between the heater block and the hot guard. All electrical energy supplied to heater block flows as heat to the cold guard in a one-

dimensional manner. Using the electric power Q, overall heat transfer coefficient U of VIP can be calculated as

$$U = \frac{Q}{A_c(T_h - T_c)} \tag{16}$$

where A_c is the effective area of heater block. The thermal conductivity of a reference insulation material (SRM 1450C) is measured to check the accuracy of this apparatus [15]. The relative errors between the standard conductivity (0.0333 W/m·K) and measured one (0.0350 W/m·K) are found to be 5.1%, which proves the reliability of the proposed apparatus. Thermal conductivity of fabricated VIP is measured by this apparatus. Note, however, that the apparatus basically measures the overall heat transfer, rather than the thermal conductivity itself. The error 5.1% is that of the overall heat transfer coefficient when it is about 1 W/m^2·K. For super insulators of about 1cm thickness, the overall heat transfer coefficient is as low as 0.1 W/m^2·K. If the absolute error of the overall heat transfer coefficient remains the same, it may result in a significant relative error for the super insulators. More investigations are necessary in this problem.

RESULTS AND DISCUSSIONS

Before presenting the experimental results, the theoretical thermal conductivity of VIP is calculated as based on the fabricated one. The parameters, properties and safety factor S = 2 (see Tables 1 and 2) are substituted in equation (9). Then, the solid conductivity k_s is determined as 1.25×10^{-3} W/m·K. The fabricated VIP is evacuated to below 1.33×10^{-1} Pa. Its gap size is 2mm with the installed radiation shields. The gaseous conductivity k_g is calculated by equation (14) as 2.14×10^{-4} W/m·K. The fabricated VIP has 4 gaps over its total thickness of 8mm. The average temperature T_m is taken as 300K. The emissivity of the aluminium radiation shield is 0.04. Then, the radiative conductivity k_r becomes 6.25×10^{-5} W/m·K from equation (15). It is found that the solid conduction mostly contributes to the overall heat transfer of VIP.

The thermal conductivity of fabricated VIP is measured by guarded hot-plate apparatus. It is 0.89×10^{-3} W/m·K as contrasted to the calculated one in Table 3. The analytical results are slightly overpredicting k_{eff}. The discrepancy is considered to be primarily due to the measurement error of the guarded hot-plate as mentioned before. Secondly, the predictions may be containing some errors, especially the error in k_s, with additional uncertainty in k_g. It is impressive that k_{eff} is as small as 1/30 of those of conventional insulation materials. This strongly proves the usefulness of the current super insulator. Remember, also, that there is a significant room to improve the insulation performance by adjusting the safety factor and/or allowing beam deflection.

Table 3
Theoritical and Experimental Thermal Conductivity of VIP

Thermal conductivity	Analytical result (W/m·K)	Experimental result (W/m·K)
k_s (solid conductivity)	1.25×10^{-3}	-
k_g (gaseous conductivity)	2.14×10^{-4} @ 1.33×10^{-1} Pa	-
k_r (radiative conductivity)	6.25×10^{-5}	-
k_{eff} (total conductivity)	1.53×10^{-3} @ 1.33×10^{-1} Pa	0.89×10^{-3} @ 1.33×10^{-1} Pa

CONCLUSIONS

A staggered beam VIP (vacuum insulation panel) is proposed and fabricated using PC (polycarbonate) by injection molding. Its effective thermal conductivity is experimentally and theoretically investigated. Thermal conductivity of VIP via solid conduction, gaseous conduction and radiation is theoretically calculated. The effective thermal conductivity is measured by guarded hot-plate apparatus. The performance of the fabricated VIP in this study is proved through experimental and theoretical investigations. It has about 30 times higher thermal resistance than the conventional insulators such as polystyrene or polyurethane foams. Also, further improvements are possible through parameter adjustments. The proposed experimental and theoretical methods are useful for further VIP developments.

RERERENCES

1. Department of Trade and Industry, Energy Trends, London, 2003.
2. J. Fricke, U. Heinemann, H. P. Ebert, Vacuum insulation panels – From research to market, Vacuum, Vol. 82, Issue 7, pp. 680-690, 2008.
3. J. W. Wu, W. F. Sung, H. S. Chu, Thermal conductivity of polyurethane foams, International Journal of Heat and Mass Transfer, Vol. 42, Issue 12, pp. 2211-2217, 1999.
4. R. E. Collins, G. M. Turner, A. C. Fischer-Cripps, J. Z. Tang, T. M. Simko, C. J. Dey, D. A. Clugston, Q. C. Zhang, J. D. Garrison, Vacuum glazing-a new component for insulating windows, Building and Environment, Vol. 30, Issue 4, pp. 459-492, 1995.
5. B. H. Lee, I. S. Yoon, T. H. Song and H. S. Kwak, Experimental Study on Manufacturing of Insulation Vacuum Glazing and Measurement of the Thermal Conductance, Journal of the Korean Society of Mechanical Engineers B in Korean,Vol. 30, No. 8, pp. 772-779, 2006.
6. G. Kawaguchi, K. Nagai, Vacuum insulation spacer, US Patent 4409770, 1983.
7. F.P. Beer, E.R. Johnston, Jr. and J.T. DeWolf, Mechanics of Materials, 2nd ed., McGraw-Hill, London, pp. 183-217, pp. 478-529, 1991.
8. J. E. Mark, Polymer Data Handbook, Oxford University Press, New York, pp. 363-367, 1999.
9. A. Roth, Vacuum Technology, 3rd ed., Elsevier, Amsterdam, pp. 37-56, 1990.
10. J. M. Lafferty, Foundations of Vacuum Science and Technology, John Wiley & Sons, New York, pp. 50-51, 1998.
11. E, H, Kennard, Kinetic theory of gases with an Introduction to Statistical Mechanics, McGraw-Hill, New York, pp. 311-318, 1938.
12. T. M. Thomas, Cryogenic Engineering, 2nd ed., Marcel Dekker, New York, pp. 459-460, 2005.
13. I. S. Yoon, T. H. Song, Thermal conductance of multiple vacuum/plate layer, Thermal Science and Engineering, Vol. 13, No. 2, pp. 29-32, 2005.
14. R. E. Collins, C. A. Davis, C. J. Dey, S. J. Robinson, J. Z. Tang, G. M. Turner, Measurement of local heat flow in flat evacuated glazing, International Journal of Heat and Mass Transfer, Vol. 36, Issue 10, pp. 2553-2563, 1993.
15. R. R. Zarr, Standard Reference Materials: Glass Fiberboard, SRM 1450c, for Thermal Resistance From 280 K to 340 K, National Institute of Standards and Technology Special Publication, pp. 130-260, Gaithersburg, MD, 1997.

OSCILLATORY THRERMOCAPILLARY FLOW IN ANNULAR POOL OF SILICON MELT

WY Shi[1], M. K. Ermakov [2], YR. Li[1], L. Peng[1], N. Imaishi*[3]
[1] College of Power Engineering, Chongqing University, Chongqing, China
[2] Institute for Problems in Mechanics of the R.A.S., Moscow, Russia
[3] Institute for Materials Chemistry and Engineering, Kyushu University, Japan

ABSTRACT . The influence of buoyancy force on the thermocapillary convection instability in the annular pools (R_i = 20 mm, R_o = 40 mm, and depth d ranging from 1 mm to 10 mm) of silicon melt (Pr = 0.011), differentially heated at the outer wall and cooled at the inner wall, is investigated numerically. The critical Marangoni numbers (Ma_c) for the incipience of oscillatory flow are determined by linear stability analysis (LSA) under both microgravity and normal gravity conditions. The results indicate that the buoyancy force destabilizes the thermocapillary convection under different liquid layer depths from 3mm to 10mm. With increasing the layer depth, the critical Ma number, critical azimuthal wave number and critical phase velocity decrease. Some of 3-D simulation results are compared with those of LSA. 3-D results are found consistent with the LSA results.

Keyword: Thermocapillary flow, Buoyancy, Hydrothermal wave, Silicon melt, Annular pool

INTRODUCTION

It is well known that the thermocapillary force may cause unstable fluid flow in single-crystal growth processes such as the Czochralski (Cz) methods [1-3]. Spatiotemporal changes of flow and temperature distributions in the melt may cause inhomogeneous distributions of impurities and point defects in the grown crystals. Related to the flow instability in the melt pool of Cz crystal growth furnaces, many research works have been reported for thermocapillary flow and the hydrothermal wave [4] (HTW) type instability in annular pools. So far, many reports are available on HTW in annular pools of silicone oils [5-16]. Schwabe et al. [5-7] revealed, through their on-ground and microgravity experiments, that buoyancy force tends to suppress the incipience of HTW in annular pool of silicone oil (0.65 cSt). Schwabe [7] experimentally determined the critical temperature difference for the incipience of oscillatory flow for different liquid depths. Wakitani [8] observed surface temperature patterns on annular pools of silicone oil (Pr=18). 3-D numerical simulations have been also applied for the thermocapillary flow instabitlities in annular pool of silicone oils [9-12]. Recently, Shi and Imaishi [11] performed a series of numerical simulations of HTW in an annular pool of silicone oil (Pr = 6.7) with the same Ri and Ro as those of Ref. 7 but the depth 1 mm. They compared their results for microgravity (0G) and normal gravity (1G) conditions and concluded that gravity tends to stabilize the basic steady thermo-capillary flow. Linear stability analysis (LSA) is also a powerful tool for determining the critical conditions for the incipience of flow instabilities. Hoyas et al. [13-15] performed linear stability analysis and obtained a stability diagram for the incipience of stationary or oscillatory secondary flow in annular pools of

* Corresponding author: Prof. N. Imaishi
Phone: + (81)-92-583-7615, Fax: + (81)-92-583-7615
E-mail address: imaishi@cm.kyushu-u.ac.jp

silicone oil heated at the inner wall. In our previous work [16], both LSA and 3-D numerical simulations were applied to determine the critical conditions for the incipience of HTW in annular pool of silicone oil (Pr=6.7) with a depth d=1mm under 0G.

On the other hand, little is known for thermocapillary flow instabilities in annular pool of low Pr fluids. Azami et al. [17] speculated that hydrothermal wave (HTW) type instability may play an important role in the formation of such unstable melt flow in Cz crucible, based on their experiment of silicon melt flow in shallow annular pool (R_i = 15 mm, R_o = 63.5 mm). So far, numerical analysis related to their experiments in annular pool of silicon melt is quite sparse [18, 19]. In this study, a series of LSA is conducted to determine the critical conditions for the incipience of oscillatory flow of silicon melt (Pr=0.011) in differentially heated annular pools with the same geometry with those used for silicone oil problems [5-7, 9,12,16] and with various liquid depths (from 1mm to 10mm) under both 0G and 1G conditions so as to evaluate the effect of the buoyancy on the stability of steady axisymmetric basic flow and the results are qualitatively compared with the critical conditions determined by 3-D numerical simulations [18].

MODELS AND METHODS

Physical and mathematical models

Figure 1 shows the model system of an annular pool, with an open top free surface, a solid bottom, an inner solid wall (radius R_i = 20 mm), an outer solid wall (radius R_o = 40 mm), and depth d varied from 1 to 10 mm. This geometry is the same as that of Ref. 7 and Ref. 11. The fluid is silicon melt, and its physical properties are listed in Table 1.

The outer wall is maintained at a constant temperature T_h while the inner wall at a lower temperature T_c ($T_h > T_c$ and $\Delta T = T_h - T_c$). The top and bottom surfaces are assumed to be adiabatic. The silicon melt is considered to be an incompressible Newtonian fluid with constant properties except for the temperature dependence of surface tension. Thermocapillary force acts on the free surface. The flow is considered to be laminar and the liquid top surface is assumed to be flat and non-deformable.

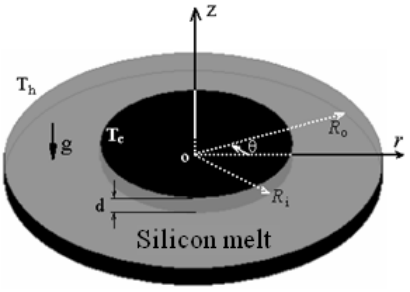

Figure 1 Configuration of the model system.

Table 1
Physical properties of silicon melt

Prandtl number:	$Pr = 0.011$
Density:	$\rho = 2530$ kg/m^3
Thermal diffusivity:	$\alpha = 2.53 \times 10^{-5}$ m^2/s
Dynamic viscosity:	$\mu = 7.0 \times 10^{-4}$ m^2/s

Under the above assumptions, the mathematical model is expressed by the following non-dimensional equations. In the cases of axisymmetric steady simulations, we assume that all gradients in the azimuthal direction are zero.

$$\nabla \cdot \boldsymbol{V} = 0 \tag{1}$$

$$\frac{\partial \boldsymbol{V}}{\partial \tau} + \boldsymbol{V} \cdot \nabla \boldsymbol{V} = -\nabla \boldsymbol{P} + \nabla^2 \boldsymbol{V} + Gr\Theta \boldsymbol{e}_z \tag{2}$$

$$\frac{\partial \Theta}{\partial \tau} + \boldsymbol{V} \cdot \nabla \Theta = \frac{1}{Pr} \nabla^2 \Theta \tag{3}$$

Here, $\boldsymbol{e}_z$ is the axial unit vector. The boundary conditions are obtained as follows:
at the top surface ($z = D$, $r_i < r < r_o$, $0 \le \theta \le 2\pi$, $\tau > 0$):

$$\frac{\partial u}{\partial z} = -\frac{Ma}{Pr}\frac{\partial \Theta}{\partial r}, \quad \frac{\partial v}{\partial z} = -\frac{Ma}{Pr}\frac{\partial \Theta}{r\partial \theta}, \; w=0, \; \frac{\partial \Theta}{\partial z} = 0 \tag{4a, b, c, d}$$

at the bottom ($z = 0$, $r_i < r < r_o$, $0 \le \theta < 2\pi$, $\tau > 0$): $u = v = w = 0$, $\dfrac{\partial \Theta}{\partial z} = 0$ (5a, b, c, d)

at the inner wall ($r = r_i$, $0 \le z \le D$, $0 \le \theta < 2\pi$, $\tau > 0$): $u = v = w = 0$, $\Theta = 0$ (6a, b, c, d)

at the outer wall ($r = r_o$, $0 \le z \le D$, $0 \le \theta < 2\pi$, $\tau > 0$): $u = v = w = 0$, $\Theta = 1$. (7a, b, c, d)

where u, v and w are non-dimensional velocities in the r, θ, and z directions, respectively. The length, time τ, pressure P and velocity are scaled by $(R_o–R_i)$, $(R_o–R_i)^2/\nu$, $\nu\mu/(R_o–R_i)^2$ and $\nu/(R_o–R_i)$, respectively. The non-dimensional temperature is defined as $\Theta = (T - T_c)/\Delta T$, where, $\Delta T = T_h - T_c$. The Marangoni number, Prandtl number and Grashof number are defined as $Ma = \gamma_T(R_o–R_i)\Delta T/\mu\alpha$, $Pr = \nu/\alpha$, $Gr = g\rho_T\Delta T(R_o–R_i)^3/\nu^2$, respectively. Here, μ is the viscosity; γ_T, the temperature coefficient of surface tension ($\gamma_T = -\partial\gamma/\partial T$, where γ is the surface tension); ν, the kinematic viscosity; and α, the thermal diffusivity of silicon melt. g is the gravitational acceleration; the case with g =0 (microgravity case) is indicated by 0G, while g =9.8m/s^2 (normal gravity case) by 1G in the following. The non-dimensional stream function ψ is defined as follows:

$$u = -\frac{1}{r}\frac{\partial \psi}{\partial z} \text{ and } w = \frac{1}{r}\frac{\partial \psi}{\partial r} \tag{8}$$

The numerical method for 3-D simulations based on this mathematical model is described in [18].

Linear stability analysis

2-D axisymmetric steady flow and temperature fields, a basic flow, are obtained by solving Eqs. 1-7 numerically [11]. Stability of the basic flow against small 3-D perturbations is investigated by means of LSA.

The fully unsteady 3-D equations, equations(1)-(7), are linearized for perturbations $(u',v',w',p',\phi)^T$ in the vicinity of the basic solution $(u_0,v_0,w_0,p_0,\Theta_0)^T$ and the perturbations are approximated by the superposition of integer-valued azimuthal normal modes.

$$\begin{pmatrix} u \\ v \\ w \\ p \\ \Theta \end{pmatrix}(r,\theta,z,\tau) = \begin{pmatrix} u_0 \\ v_0 \\ w_0 \\ p_0 \\ \Theta_0 \end{pmatrix}(r,z) + \begin{pmatrix} u' \\ v' \\ w' \\ p' \\ \phi \end{pmatrix}(r,z)e^{\lambda\tau + im\theta} \tag{9}$$

The resulting non-dimensional linearized equations and boundary conditions will be found in our previous paper [16]. These are discretized at the same staggered grid as that used for the basic flow calculation. Therefore, the problem is reduces to a generalized eigenvalue problem

$$\boldsymbol{A}\boldsymbol{x} = \lambda \boldsymbol{B}\boldsymbol{x}, \qquad \boldsymbol{x} \in \mathbf{C}^n \tag{10}$$

where $\boldsymbol{A}$ and $\boldsymbol{B}$ are sparse square matrices with 5n×5n elements; n is the total grid number in the r-z plane. The vector $\boldsymbol{x}$ indicates the unknown perturbation variables $(u',v',w',p',\phi)^T$ in the discretized equations. **C** represents a complex matrix set. Further, $\boldsymbol{A}$ is the coefficient complex matrix of all

terms except those involving λ, while $\boldsymbol{B}$ is the coefficient matrix of terms involving λ, which is a diagonal singular sparse matrix. The singularity arises due to the continuity equation and the boundary conditions included in the problem formulation. In contrast to reference [20], the azimuthal velocity is not excluded from the formulation due to the continuity equation; moreover, this equation is not transformed into the equation for pressure. Based on reference [20], the inverse iteration [21] is applied to the solution of the generalized eigenvalue problem. Since the linear stability of the system is defined by the eigenvalue of the maximum real part, the minimum value of *Ma* at which the system attains the eigenvalue with a nonnegative real part is the critical Marangoni number (Ma_c) and the corresponding *m* value is the critical azimuthal wave number (m_c). The grid-independence has been carefully checked [16].

RESULTS AND DISCUSSIONS

Basic flow

It is well known that thermocapillary flow in shallow pools is not so much influenced by the buoyancy force. This is also true for the present annular pool of silicon melt for D<0.15. However, the buoyancy force tends to enhance the thermocapillary flow in deep pools. Figure 2 compares the basic flow fields for D=0.5 (d=10mm) at Ma=79.05 (ΔT=1K) under 0G and 1G conditions. Figures 2(a) and 2(b) indicate that the temperature and radial velocity on the surface under 1G are larger than those under 0G condition. These are caused by the change of induced vortexes near the hot wall. Under 0G, a large positive valued vortex appears near the hot wall as well as the small corner vortex near the cold wall, both are driven by the main vortex driven by the Marangoni effect. There is another very weak negative valued corner vortex near the hot wall but is too weak to be plotted in the figure The buoyancy force acting near the hot wall takes significant role to suppress the positive vortex near the hot wall. Thus the main vortex becomes stronger.

Critical conditions for the incipience of oscillatory flow

Linear stability analysis provides us with the critical condition for the onset of flow instability in annular pool of silicon melt with different depth as summarised in Table 2. The critical Marangoni number Ma_c, the critical azimuthal wave number m_c and the critical phase velocity ω_c decrease steeply with increase in the pool depth, D in a range from 0.05 to 0.1 and their changes become less significant at $D \geq 0.1$. Comparison of those critical conditions indicates that the buoyancy force gives small effects on the critical conditions for shallow pools ($D \leq 0.1$). However, for deeper pools (D>0.1), the buoyancy force slightly destabilizes the basic 2-D steady flow fields and decreases m_c and ω_c.

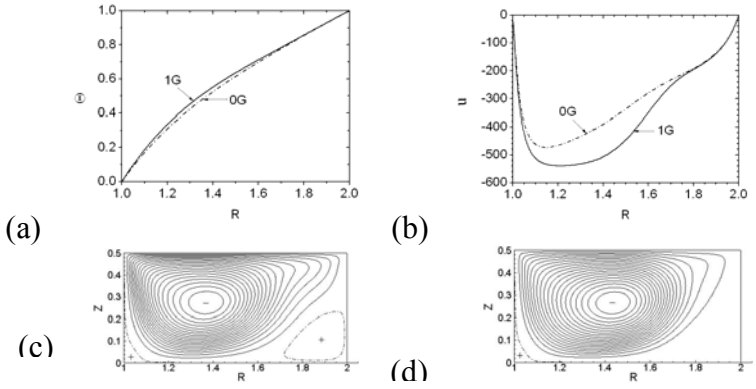

Figure 2 Basic fields for Ma=79.05 (ΔT=1K) and D=0.5 under 0G and 1G.
(a) Radial distribution of surface temperature. (b) Radial distribution of surface velocity u.
(c) Stream function on a R-Z plane under 0G,(ψ_{min}= −42.3, ψ_{max} =0.37).
(d) Stream function on a R-Z plane under 1G, (ψ_{min}= −78.7, ψ_{max} =0.078).

Table 2
Critical conditions for the incipience of flow instability in annular pool of silicon melt.

D	0G			1G		
	Ma_c	m_c	ω_c	Ma_c	m_c	ω_c
0.05	3927.7	39	44.95	3912.7	39	44.41
0.1	1033.9	20	22.15	994.31	20	21.52
0.15	531.22	15	17.10	474.62	15	15.58
0.25	289.18	12	13.85	200.00	11	11.22
0.5	151.79	13	7.369	83.18	12	8.71

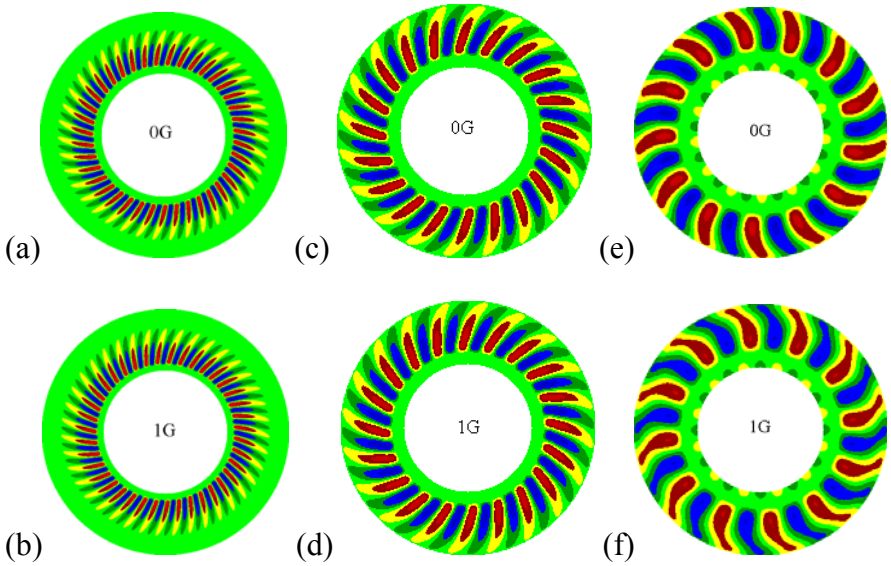

Figure 3 Distribution of temperature eigenfunction on the surface at the critical conditions.
(a) D=0.05, 0G, m_c=39. (b) D=0.05, 1G, m_c=39.
(c) D=0.10, 0G, m_c=20. (d) D=0.10, 1G, m_c=20.
(e) D=0.50, 0G, m_c=13. (f) D=0.50, 1G, m_c=12.

However, ω_c shows an increase at D=0.5. Figure 3 compares the temperature eigenfunctions on the surface for D=0.05, 0.10 and 0.5 under both 0G and 1G at each critical state. For the cases of D=0.05 and 0.10, patterns of the temperature eigenfunction under both gravity levels are quite similar, while they are slightly different for D=0.5.
It should be noted here that the influence of the buoyancy force on the critical Marangoni number Ma_c for the silicon melt is quite different from that for silicone oil (Pr=6.7) via experiments [7] and non-linear numerical simulations [11] (i.e. the buoyancy force stabilizes the basic steady 2-D flow field in annular pools of silicone oil). The difference in the effect of the buoyancy force on the critical Marangoni number for low and high Pr fluids is related to the difference in the physical mechanism of HTW, i.e., waves derive their energy from the imposed horizontal temperature gradient through horizontal convection when the Prandtl number is small and from the vertical temperature gradient through vertical convection when it is large [4,23].

HTW by 3-D numerical simulation

Several 3-D numerical simulations are conducted under slightly super critical condition. Some of the surface temperature distributions obtained by the numerical simulation are shown in Figure 4 in which the $\delta\Theta$ (temperature deviation from the average temperature (averaged in the azimuthal direction) is adopted, i.e.,

$$\delta\Theta(r,\theta,z,\tau) = \Theta(r,\theta,z,\tau) - \frac{1}{2\pi}\int_0^{2\pi}\Theta(r,\theta,z,\tau)\,\mathrm{d}\theta \tag{11}$$

Figure 4(a) is a result for D=0.1 (d=2mm) at Ma= 1.19×10^3 (ΔT=15K and ε=(Ma–Ma_c)/Ma_c=0.15) under 0G, and Figure 4(b) is a spatiotemporal diagram (STD) (a plot of $\delta\Theta$ at r=1.25 during 10 seconds). (For this simulation, a grid (n_r, n_θ, n_z=202, 303, 41) was used.) These figures indicate that the basic flow in the melt pool is unstable and an oscillatory flow with a wave number m=20 is induced at this condition. The STD indicates the oscillation of surface temperature is a pulsating type with ω=26.7, although the LSA predicts a HTW with a temperature distribution shown in Figure 3(a) traveling in the azimuthal direction (m_c=20 and ω_c=22.15) at ε=0. Movie of surface temperature pattern shows that the black and white fringes shown in figure 4(a) move outward and then the phase is changed. This time history of the pattern is explained as an interference of two HTWs of m=20 (similar to that shown in figure 3(c)) propagating in the opposite azimuthal directions to each other.

Figure 4(c) is a snapshot of surface temperature deviation at Ma=118.6 (ΔT=1.5K, ε=0.43) in a deep melt pool (D=0.50) under 1G. The STD (Figure 4(d)) shows 8 bend spokes which propagate in the azimuthal direction with ω= −7.07 (f=0.039Hz). The shape of the spoke is similar to that of the temperature eigenfunction shown in Figure 3(f) but number of spokes and the oscillation frequency are different from the critical values (m_c=12, ω_c=8.71). These differences can be attributed to the large super criticality for this simulation. It should be noted here that a 3-D simulation run at Ma=118.6 under 0G end up with a steady 2-D flow. This is quite reasonable because the Marangoni number is smaller than Ma_c (=151.79) for 0G condition. These confirm the result of present LSA for deep pools, i.e., the buoyancy force destabilizes the basic thermocapillary flow in deep annular pool of silicon melt. (For this simulation, a grid (n_r, n_θ, n_z= 82, 123, 51) was used.)

YR. Li *et al*. [18] determined critical conditions for the incipience of oscillatory flow in annular pool of silicon melt with adiabatic free surface under 0G by means of 3-D numerical simulations.

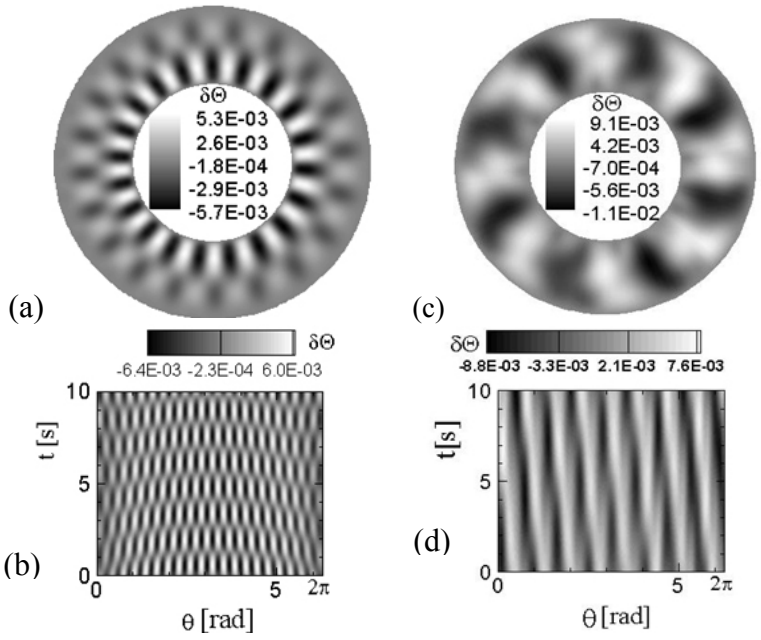

Figure 4 Snapshots and STD of surface temperature deviation, obtained by 3-D numerical simulations.

(a) Snapshot at Ma=1190, D=0.10, 0G. (b) STD on a circle at radius r=1.25: m=20, ω=26.7.

(c) Snapshot at Ma=118.6, D=0.50, 1G. (d) STD on a circle at radius r=1.25: m=8, ω=–7.07.

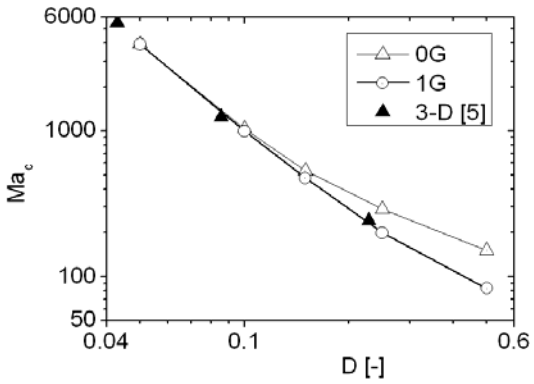

Figure 5 Comparison of the Ma_c determined by 3-D simulations [18] with the present LSA results (Table 2) for annular pools of silicon melt.

Although the radiuses of their pool are slightly different from those of the present ones, i.e., R_i=15mm and R_o=50 mm, it is worth to compare their results with the present LSA results. They obtained critical Marangoni numbers for the incipience of oscillatory flow in three different pool depths, Ma_c =5504 for D=0.0429 (d=1.5mm), Ma_c=1244 for D=0.0857 (d=3.0mm) and Ma_c=242 for D=0.229 (d=8mm). They used relatively coarser grids in Ref. 5, i.e., (n_r, n_θ, n_z= 80, 120, 20), (n_r, n_θ, n_z= 80, 92, 20) and (n_r, n_θ, n_z= 80, 60, 30), for layers of d=1.5 mm, 3 mm and 8 mm, respectively. Figure 5 indicates that their critical conditions are also closely correlated together with those of LSA if these critical conditions are plotted as a function of the non-dimensional depth D ($=d/(R_o-R_i)$: i.e., reciprocal of the aspect ratio of the pool). However, for the case of d=8mm, their Ma_c value falls much lower than the present LSA's prediction for 0G and closer to that for 1G. It should also be noted that they reported a different type of pulsating oscillatory flow for a pool of d=8mm. These may be partly attributed to the coarser grid they used for d=8mm.

CONCLUSIONS

The critical Marangoni numbers for the incipience of oscillatory flow in small annular pools of silicon melt are determined by means of LSA under both microgravity and normal gravity conditions. The results indicate that the buoyancy force destabilizes the thermocapillary convection in the annular pools with depth ranging from 3mm to 10mm. With an increase in layer depth, the critical Ma number, critical azimuthal wave number and critical phase velocity decrease. Most of the 3-D numerical simulations are found consistent with those obtained by LSA.

ACKNOWLEDGEMENTS

This work was supported by Natural Science Foundation Project of CQ CSTC (2008BB4301), China Postdoctoral Science Foundation funded project and Innovation Ability Training Foundation of Chongqing University.

REFERENCES

1. D. C. Miller and T. L. Pernell, Fluid flow patterns in a simulated garnet melt, *J. Crystal Growth*, **58**, pp.253-260, 1982.
2. K. -W. Yi, K. Kakimoto, M. Eguchi, M. Watanabe, T. Shyo and T. Hibiya, Spoke patterns on molten silicon in Czochralski system, *J. Crystal Growth*, **144**, pp. 20-28, 1994.
3. K. Kakimoto, H. Ozoe, Heat and mass transfer during crystal growth, *Computational Materials Science*, **10**, pp.127-133, 1998.

4. M. K. Smith, S. H. Davis, Instabilities of dynamic thermocapillary liquid layers, Part 1. Convective instabilities, *J. Fluid Mech.*, **132**, pp. 119-144, 1983.
5. D. Schwabe, S. Benz, Thermocapillary flow instabilities in an annulus under microgravity-results of the experiment MAGIA, *Adv. Space Res*. **29**, pp. 629-638, 2002.
6. D. Schwabe, Buoyant-thermocapillary and pure thermocapillary convective instabilities in Czochralski systems, *J. Crystal Growth*, **237-239**, pp.1849-1853, 2002.
7. D. Schwabe, A. Zebib, B-C. Sim, Oscillatory thermocapillary convection in open cylindrical annuli. Part 1. Experiments under microgravity, *J. Fluid Mech.*, **491**, pp. 239-258, 2003.
8. S. Wakitani, Experiments on instabilities of thermocapillary convection in shallow annular liquid layers, J. Physics: Conference Ser., **64**, 012006, 2007 (2nd Int. Symp. Instability and Bifurcation in Fluid Dynamics)
9. B.C. Sim, A. Zebib, D. Schwabe, Oscillatory thermocapillary convection in open cylindrical annuli, Part 2 Simulations, *J. Fluid Mechanics*, **491**, pp. 259-274, 2003.
10. B-C. Sim, A. Zebib, Thermocapillary convection in cylindrical liquid bridges and annuli, *Comptes Rendus Mecanique*, **332**, pp. 473-486, 2004.
11. W. Y. Shi, N. Imaishi, Hydrothermal waves in differentially heated shallow annular pools of silicone oil, *J. Crystal Growth*, **290**, pp.280-291, 2006.
12. Peng, Y-R. Li, W. Y. Shi, N. Imaishi, Three-dimensional thermocapillary-buoyancy flow of silicone oil in a differentially heated annular pool, *Int. J. Heat Mass Transfer*, **50**, 872-880, 2007.
13. S. Hoyas, H. Herrero, A. M. Mancho, Bifurcation diversity of dynamic thermocapillary liquid layers, *Phys. Rev. E*, **66**, pp.057301-1-4, 2002.
14. S. Hoyas, H. Herrero, A. M. Mancho, Thermal convection in a cylindrical annulus heated laterally, *J. Phys. A: Math. Gen.*, **35**, pp.4067-4083, 2002.
15. S. Hoyas, A. M. Mancho, H. Herrero, N. Garnier, A. Chiffaudel, Bénard–Marangoni convection in a differentially heated cylindrical cavity, *Phys. Fluids*, **17**, pp. 054104-1-12, 2005.
16. W. Y. Shi, M. K. Ermakov, N. Imaishi, Effect of pool rotation on thermocapillary convection in shallow annular pool of silicone oil, *J. Crystal Growth*, **294**, pp.474-485, 2006.
17. T. Azami, S. Nakamura, M. Eguchi, T. Hibiya, The role of surface-tension-driven flow in the formation of a surface pattern on a Czochralski silicon melt, *J. Crystal Growth*, **233**, pp. 99-107, 2001.
18. Y-R. Li, N. Imaishi, T. Azami, T. Hibiya, Three-dimensional oscillatory flow in a thin annular pool of silicon melt, *J. Crystal Growth*, **260**, pp.28-42, 2004.
19. L. Peng, Y.R. Li, Y.J. Liu, N Imaishi, T.C. Jen, Q.H. Chen, Bifurcation and hysteresis of flow pattern transition in a shallow molten silicon pool with Cz configuration, Numerical Heat Transfer, Part A, Applications, **51**, 211-223 (2007)
20. M. Wanschura, V. M. Shevtsova, H.C. Kuhlmann, H.J. Rath, Convective instability mechanisms in thermocapillary liquid bridges, *Phys. Fluids*, **7**, pp.912-925, 1995.
21. Y. Saad. Iterative methods for sparse linear systems, 2nd ed., SIAM, 2003.
22. M. K. Ermakov, M. S. Ermakova, Linear-stability analysis of thermocapillary convection in liquid bridges with highly deformed free surface, *J. Crystal Growth*, **266**, pp.160-166, 2004.
23. M. K. Smith, Instability mechanisms in dynamic thermocapillary liquid layers, *Phys. Fluid*, 29, pp.3182-3186, 1986.

STUDY OF DRYING BEHAVIOR REMAINING LIQUID FILM / DROPLET ON MARANGONI DRYING

Y. Miyamoto*, J. Kamoshida and J. Yamada
Shibaura Institute of Technology, Tokyo, Japan

ABSTRACT. To clarify the drying mechanisms of droplets remaining on a silicon wafer in the Marangoni drying process, the dry-up time of droplets during organic gas dissolution has been investigated using a CCD camera. The concentration of the organic component in the droplets has also been measured using a micro-optical concentration sensor. In addition, numerical calculations of dry-up time and the organic component concentration based on phase equilibrium methods were performed. The numerical results were found to be in good qualitative agreement with the experimental data. Finally, optimal concentrations of the organic component and water vapor were determined to reduce the formation of watermarks on the silicon wafer.

Keywords: *Marangoni drying, Watermark, Mass transfer*

INTRODUCTION

In semiconductor manufacturing, cleansing and drying technologies are of paramount importance for achieving ultra-clean surfaces and improving production efficiency. Marangoni drying is a process that has become widely used for silicon wafers due to its superior drying effects [1-2]. However, even with this method, residual water traces (watermarks) and particles are sometimes present after drying, leading to a decrease in the yield ratio. Normally, such residues have been prevented by optimizing various operating conditions used during the cleansing/drying process [3]. However, in recent years, as wafer sizes become larger, the occurrence of residues has become an increasing problem, and improvements are needed in the drying method itself. To achieve this, it is necessary to understand the mechanism for remnant formation in order to develop preventive measures.

In the Marangoni drying process, following cleaning, a silicon wafer is drawn from the rinse bath in an atmosphere containing an organic gas, typically isopropyl alcohol (IPA). As shown in figure 1, this gives rise to a higher concentration of the organic component in the thin top part of the meniscus than in the thicker bottom root. Since the organic component causes a reduction in the surface tension of the liquid, a surface tension gradient is formed in the meniscus, which increases from the top to the bottom. As a result, the Marangoni force is produced, which causes the meniscus to be pulled back to its root, enhancing the drainage.

Previously, the mechanisms of Marangoni drying were clarified by measuring the IPA concentrations in the meniscus and the liquid surface far from the meniscus and visualizing with ammonia gas [4].

* Corresponding author: Y. Miyamoto
Phone: + (81)-3-5859-8066, Fax: + (81)-3-5859-8001
Email address: m605108@shibaura-it.ac.jp

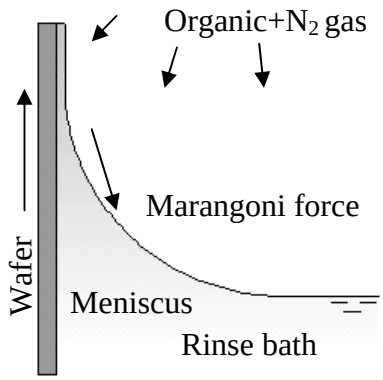

Figure 1. A tentative mechanism of Marangoni drying.

In addition, in the same study, the formation mechanism for residual liquid films or droplets that are thought to be the origin of residual particles and watermarks was examined. The results revealed that the leftover films/droplets are produced when a wave occurs on the liquid surface in the rinse bath.

Residue particles in the cleaning liquid are difficult to avoid if the drainage failed and liquid films/droplets remain on the wafer and dry up. To prevent this, it is necessary that the drainage is performed with no remaining liquid present, or that higher purity cleaning liquid is used. Watanabe et al. studied the mechanism of watermark formation and concluded that it was caused by the elution of Si from the silicon wafer into the rinse liquid and subsequent oxidation due to the presence of dissolved oxygen [5]. If this mechanism is correct, then the formation of watermarks may be suppressed if residual liquid films/droplets can be made to evaporate faster, since the time available for Si elution would be reduced. Furthermore, Koo et al. showed that if the concentration of the organic component is high, watermark formation can be suppressed even for longer dry-up times [6]. It is believed that the amount of Si elution is reduced when the wafer is in contact with an organic solution instead of pure water.

These results imply that control of the IPA concentration in the droplets and the dry-up time are effective methods for suppressing the formation of watermarks. However, Marangoni drying is a complicated process in which the remaining liquid films/droplets are drying concurrently with IPA gas dissolution. Therefore, it is difficult to predict which parameters would have a dominant effect on IPA concentration and dry-up time.

It is likely that even if the influence of temperature is ignored, since the drying process is generally performed at room temperature, the concentrations of IPA and water vapor (relative humidity) in the atmosphere will affect both the dry-up time and the IPA concentration in the liquid. In this study, the effects of the organic component and water vapor concentration in the drying atmosphere on the dry-up time of the droplets have been investigated using a CCD camera, and the concentration of organic gas in the droplets has been measured using an unique optical fiber probe concentration sensor. In addition, numerical methods based on phase equilibria have been used to evaluate the dry-up time and organic component concentration for the liquid, and to determine the optimum concentrations of water vapor and organic gas for suppressing the formation of watermarks.

EXPERIMENTAL EXAMINATION

Experimental equipment and method

Figure 2 shows a schematic diagram of the experimental apparatus. In this set-up, a single liquid droplet is placed on a horizontal silicon wafer. The test cell is almost airtight and has a volume of 1×10^{-3} m^3. Water is stored in a container at the cell bottom to obtain water vapor. To produce IPA

gas, N_2 gas is flowed through a container of liquid IPA at a rate of 4×10^{-3} m^3/min. The concentration probe sensor used to measure the IPA concentration of the droplet consists of an optical fiber that can measure the refractive index of the droplet. Details of the design of the sensor are given in [7]. The probe is set at a position 0.15 mm distant from the wafer surface in the vertical direction, and a LED is used as a light source. The test sample was a specular silicon wafer (width: 25 mm, height: 40 mm, thickness: 0.72 mm), with a hydrophilic surface. The method used to obtain a hydrophilic surface is described in [8]. The contact angle between the droplet and the wafer surface was 10 deg as a result of the sessile droplet method. Droplets with volumes of 0.5 and 2×10^{-9} m^3 were used in this study. It is difficult to perform this type of experiment on droplets produced during practical wafer cleaning because of the very small sizes involved. Therefore, extrapolations were performed from the droplet volumes used in this work to predict the tendencies as the volume is reduced. The initial IPA concentration (x_{IPA}) of the droplets was 0.016 mole fraction as a result of IPA gas dissolution while the droplet was on the silicon wafer. The atmospheric IPA concentration (Rh_{IPA}) was varied from 40% to 90%, and the relative humidity (Rh_{water}) was varied from 0% to 50%. The humidity values are based on an assumed temperature of 25 ^{o}C. Rh_{IPA} is controlled by changing the IPA liquid surface height and Rh_{water} by changing the surface area of the water in the container.

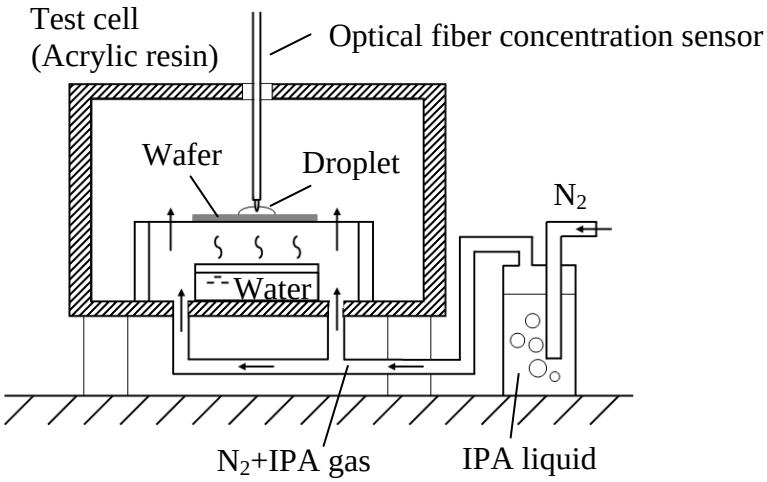

Figure 2. Schematic diagram of experimental apparatus

Dry-up time measurements

Figure 3 shows the dry-up time of the droplets on the silicon wafer during the IPA gas dissolution. In this experiment, the concentration probe was not used. Solid lines in the figures are the results of

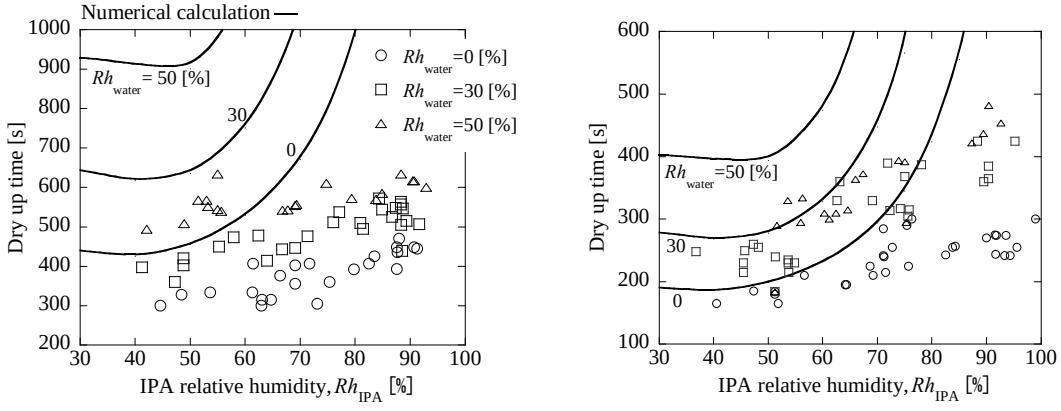

(a) 2×10^{-9} m^3 (b) 0.5×10^{-9} m^3

Figure 3. Influences of water and IPA relative humidities on the liquid droplet dry-up time.

a numerical calculation that will be described later. Figure 3 (a) is for a droplet volume of 2×10^{-9} m^3. As seen in this figure, the dry-up time increases as Rh_{IPA} and Rh_{water} increase. A similar tendency is found for the droplet with a volume of 0.5×10^{-9} m^3 (figure 3 (b)). Practical drying processes usually take between about 180 and 300 seconds, and thus figure 3 (b) is close to the practical situation. Therefore, it is considered that a similar tendency would be found for very small droplets.

IPA concentration measurements

Figure 4 (a), (b) shows the time variation of x_{IPA} in the droplet during the IPA gas dissolution, whereas figure 4 (c), (d) shows the results of a numerical calculation that will be described later. The final values of x_{IPA} could not be measured since the droplet height decreased to less than 0.15 mm due to evaporation, which is the distance of the probe from the wafer surface. Therefore the dry-up times are also shown as tables in these figures. x_{IPA} was measured only for the droplet with a volume of 2×10^{-9} m^3. As seen in figure 4 (a), x_{IPA} is found to increase with Rh_{IPA}, since the IPA gas readily dissolves in the droplet. Furthermore, it appears that the droplet changes completely to liquid IPA for very high values of Rh_{IPA}. The reason for the very long dry-up times (as shown in the table in figure 4 (a)) when Rh_{IPA} is very high is due to the fact that these IPA droplets cannot evaporate into the IPA-saturated atmosphere. A similar tendency is found for the case where Rh_{water} is high (50%), although the increase in x_{IPA} is much slower. Again, this is due to the fact that evaporation of the water component of the droplet is inhibited by the large amount of water vapor in

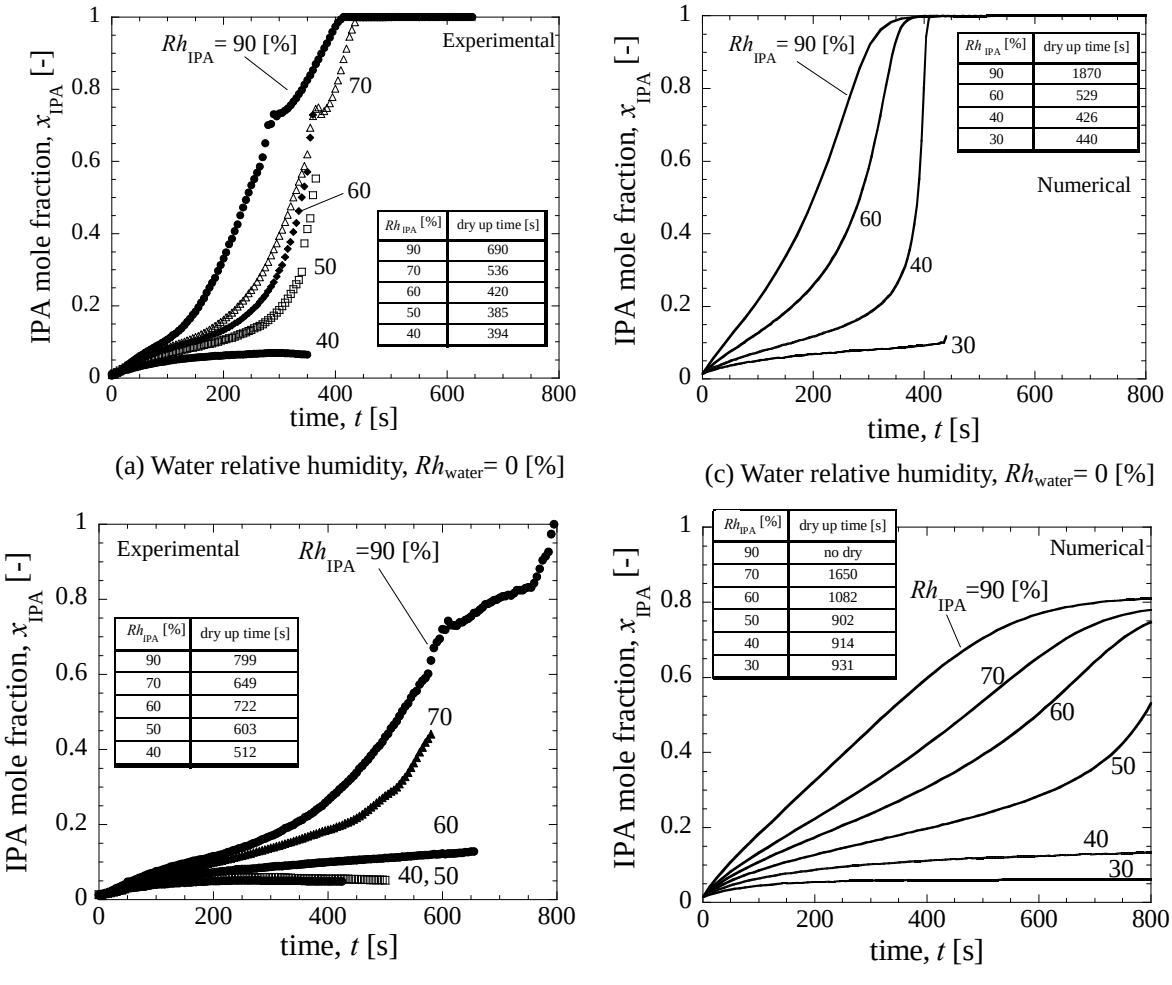

(a) Water relative humidity, Rh_{water}= 0 [%]

(c) Water relative humidity, Rh_{water}= 0 [%]

(b) Water relative humidity, Rh_{water}= 50 [%]

(d) Water relative humidity, Rh_{water}= 50 [%]

Figure 4. Time variation of IPA concentration in a liquid droplet during IPA gas dissolution.

the atmosphere. The discontinuities in the plots for x_{IPA} = 0.7-0.75 are due to a limitation of the concentration sensor, in that a reversal occurs in the relationship between the concentration and the refractive index of IPA-water. Next, numerical analysis based on phase equilibrium diagrams was carried out to investigate the drying process in more detail.

NUMERICAL CALCULATION

Calculation model

Figure 5 shows the phase equilibrium diagram for the IPA-water system [9]. The horizontal axis is the liquid or gas phase concentration and the vertical axis is vapor pressure. This figure represents the equilibrium diagram, but the system in this study is in a non-equilibrium condition. The evaporation of the droplet is investigated by first assuming that the droplet comes close to an equilibrium point, which is the atmosphere gas situation. The outline of the calculation is then as follows. If x_{IPA} of the droplet is given by the dotted line in the diagram, the vapor pressure at the surface will be described by the symbol □. This vapor pressure is the sum of the IPA and water vapor pressure, as indicated by the symbols ▲ and ■. If the IPA and water vapor pressure of the atmosphere are given at △ and □, the amount of evaporation or dissolution per unit time will be determined by the difference between each vapor pressure, which represents the driving force. For the example shown in figure 5, the IPA gas dissolves and the water vapor evaporates. If these vapour pressure differences are decided, to calculate the droplet volumes and x_{IPA} momentarily are easy. The details of the calculation model to determine the amount of evaporation and dissolution per unit time will now be presented.

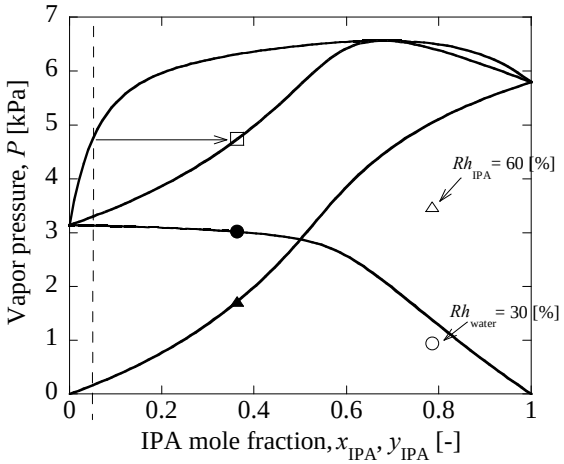

Figure 5. Phase equilibrium diagram for the system IPA-water

This calculation assumes that droplet evaporation is enhanced by the airflow that carries the IPA gas. In addition, the following assumptions are made:

[1] The droplet on the silicon wafer is a hemisphere and the system is isothermal.

[2] The droplet volume is very small, and there is enough IPA gas in the atmosphere to dissolve uniformly in the droplet. Therefore, the concentration distribution of each phase is uniform without the need to consider the diffusion resistance of each phase.

The amount of evaporation or dissolution per unit time is determined by the following equation:

$$\sum_{i=1}^{2} W_i = \frac{1}{2}\pi d^2 h_i(\rho_{is} - \rho_{i\infty}) \tag{1}$$

W_i is the amount of evaporation or dissolution for component i, d is the droplet diameter, h_i is the mass transfer coefficient for component i, and ρ_i is the vapor density for component i. Since there is no mass transfer coefficient suitable for the experimental system, a formula related to droplet evaporation proposed by Ranz-Marshall, shown in equation 2, is used instead [10].

$$\frac{h_i d}{D_i} = 2 + 0.60\,\mathrm{Re}_i^{1/2}\, Sc_i^{1/3} \tag{2}$$

The value of ρ_{is} is given by the following equation of state for an ideal gas.

$$\rho_{is} = \frac{P_{is} M_i}{RT} \tag{3}$$

P_{is} is the surface vapor pressure, and M_i the molecular weight of component i. R is the gas constant and T is the temperature. P_{is} can be written as

$$P_{is} = y_{is} \sum_{i=1}^{2} \gamma_i P_{i,sat} x_i \;,\; y_{is} = \frac{\gamma_i P_{i,sat} x_i}{\sum_{i=1}^{2} \gamma_i P_{i,sat} x_i} \tag{4}$$

Moreover, $\rho_{i\infty}$ is given by the equation.

$$\rho_{i\infty} = \frac{Rh_i P_{i,sat} M_i}{100RT} \tag{5}$$

For each component i, γ_i is the activity coefficient, x_i is the mole fraction of the liquid phase, y_{is} is the mole fraction of the gas phase, and Rh_i is the relative humidity. Each diffusion coefficient D_i is obtained from the data of Thurener et al. [11]. The kinematic viscosity of air is also taken into account in these calculations. The value of $P_{i,sat}$, which is the saturated vapor pressure of component i, is estimated from the Antoine equation for water and the Wagner equation for IPA. The activity coefficient γ_i is obtained from the Wilson equation based on the phase equilibrium data of Sazonov [9]. A gas velocity of 0.1 m/s in the test cell is used in these calculations. This value is close to that measured by an anemometer, although the accuracy of the measurement is not very high. Since equation 2 does not perfectly describe the current system, the mass transfer coefficients obtained in this study are approximate values.

Dry-up time

The numerical results together with the experimental data are shown in figure 3 (a), (b). The solid lines in these figures are the numerical results. In each figure, both the numerical and experimental results show a similar behavior in that the dry-up time increases with increasing Rh_{i}. However, the magnitude of the effect is different. In particular, the dry-up time in the numerical data increases much faster than that for the experimental data. This is probably due to the fact that the actual Rh_{IPA} value in the test cell is less than the theoretical value, since some of the IPA gas is swept away by the N_2 gas before it has a chance to fully diffuse. The differences in the dry-up times between the numerical and experimental data as the value of Rh_{water} is increased are likely due to a similar effect.

Time variation of IPA concentration

The numerical results for IPA concentration are shown in figure 4 (c),(d). Figure 4 (c) shows the case for low Rh_{water} (0%). The curves are qualitatively in good agreement with the experimental data. Specifically, the tendency of x_{IPA} to increase rapidly at certain times, and the influence of Rh_{IPA} on this rapid increase, are reflected in both the experimental and numerical data. Similar agreement is found for the high Rh_{water} (50%) case (figure 4 (d)). However, the calculated x_{IPA} curves never reach a value of 1.0, whereas this does occur in the experimental data. This is again most likely due to the fact that Rh_{water} does not reach its theoretical value due to being removed by the gas flow. Slight differences between the numerical and experimental results are expected since the proposed model is not a rigorous representation of the experimental system and certain parameters (surrounding environment, gas velocity etc.) related to the mass transfer coefficient are based on assumptions and predictions. However, the level of agreement that is observed indicates that this model has potential for predicting the dynamics of the drying process.

GUIDELINES FOR SUPPRESSING WATERMARK FORMATION

As mentioned previously, to decrease watermarking, dry-up times should be as short as possible, or the x_{IPA} value in the droplet should be increased as rapidly as possible. In this section, the optimum values of Rh_{IPA} and Rh_{water} are discussed. A droplet volume of 0.5×10^{-9} m^3 is used, since this is thought to be more representative of practical drying processes. Figure 6 shows a contour map of dry-up time, where the horizontal axis is Rh_{IPA}, the vertical axis is Rh_{water}, and the dry-up time is indicated by shade and numerical values. The scale is logarithmic and darker regions represent longer dry-up times. When Rh_{IPA} is comparatively low (0-50%), the dry-up times are dependent on Rh_{water} and independent of Rh_{IPA}. On the other hand, when Rh_{IPA} is high, the contour map takes on a longitudinal striped appearance. In this case, the dry-up times are dependent on Rh_{IPA} and independent of Rh_{water}. Therefore, to achieve short dry-up times, the value of Rh_{water} should be low, and Rh_{IPA} should be maintained at moderate levels. As mentioned previously, a rapid increase in x_{IPA} is also effective in reducing watermarking. According to Koo at al., Si elution ceases at a x_{IPA} value of 0.26 (corresponding to a volume fraction of 0.6) [6]. Figure 7 shows the time required to increase the mole fraction of IPA to 0.26 for different values of Rh_{IPA} and Rh_{water} referred to as the

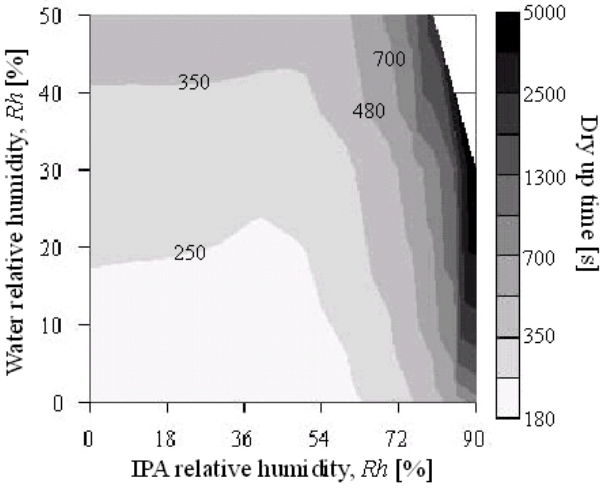

Figure 6. Contour map for dry-up time.

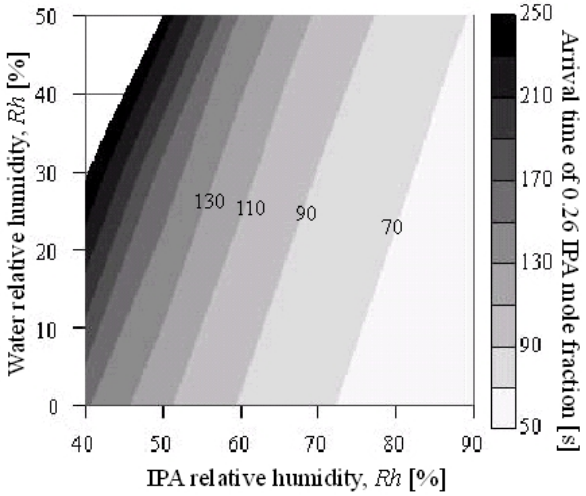

Figure 7. Contour map for IPA exchange.

"arrival time". The horizontal axis is Rh_{IPA}, and the vertical axis is Rh_{water}, similar to figure 6. However, the scale of the arrival time is linear in this case. As seen in this figure, the contour map has a longitudinal striped appearance, which indicates that the arrival time is strongly dependent on Rh_{IPA}. It is seen that high values of Rh_{IPA} lead to short arrival times. In addition, it is also confirmed that the similar tendencies were found for very small droplets, e.g. 0.3×10^{-9} m^3.

CONCLUSIONS

To clarify the drying mechanisms of droplets remaining on a silicon wafer in the Marangoni drying process, the dry-up time of droplets during organic gas dissolution has been investigated using a CCD camera. The concentration of the organic component in the droplets has also been measured using a micro-optical concentration sensor. In addition, numerical calculations of dry-up time and the organic component concentration based on phase equilibrium methods were performed. The numerical results were found to be in good qualitative agreement with the experimental data. Finally, optimal concentrations of the organic component and water vapor were determined to reduce the formation of watermarks on the silicon wafer.

REFERENCES

1. A. F. M., Leenaars, J. A. M. Huethorst and J. J. Van Oekel, Marangoni drying: a new extremely clean drying process, *Langmuir* Vol. 6**,** pp 1701-1703, 1990
2. J. Marra and J. A. M., Huethorst, Physical Principle of Marangoni drying, *Langmuir* Vol. 7, 2748-2755, 1991.
3 J. Tang, W. Lu, B. Xie and E. Martinez, Marangoni dryer integrated high performance cleaner for cu/low k post strip for 45 nm technology node and beyond, *Solid State Phenomena* Vol. 134, pp 337-340, 2008.
4. Y. Miyamoto, J. Kamoshida and J. Yamada, Three phase contact line behaviour and remaining liquid film/droplet formation in Marangoni drying, *Thermal Science Engineering* Vol. 47**,** No. 16, pp 113-120, 2008.
5. M. Watanabe, M. Hamano and M. Harazono, The role of atmospheric oxygen and water in the generation of watermarks on the silicon surface in cleaning processes, *Materials Science and Engineering: B* vol. 4, pp 401-405, 1989.
6. J. Koo, T. Kim, C. Jung, J. Lee and T. Kim, Effect of water and iso-propyl alcohol relative humidities on single wafer cleaning system performance, *International Journal of Heat and Mass Transfer* Vol. 50**,** pp 4275-4285, 2007.
7. J. Kamoshida, Y. Suzuki, T. Oouchi and N. Isshiki, Development of fiber-optic refractometer for measuring local concentration of aqueous libr solution, *Proc. Absorption Heat pump Conf.* vol. 2, pp 547-554, 1996.
8. W. Kern, The Evolution of Silicon Wafer Cleaning Technology, *Journal of the Electrochemical Society*, Vol.137, No.6, pp 1887-1892, 1990.
9. V. P. Sazonov, Isothermal equilibrium of liquid-liquid-vapor in the system nitromethane-isopropylalcohol-water, *Zhurnal Prikladnoi Khimiji,* Vol. 59, No.7, pp 1451-1456, 1986.
10. W. E. Ranz. and W. R. Marshall, Evaporation from drops part II, *Chemical Engineering Progress,* Vol. 48, No.4, pp 173-180, 1952.
11. F. Thurener and E. U. Schlünder, Progress towards Understanding the Drying of Porous Materials Wetted with Binary Mixtures, *Chemical Engineering Process*, Vol. 20, pp 9-25, 1986.

A STUDY OF LASER ENGINEERED NET SHAPING PROTOTYPING TECHNOLOGY

R.S. Amano[1*], Z.Xu[1], P.K. Rohatgi[1]
[1]University of Wisconsin, Milwaukee, USA

ABSTRACT. The objectives of this work are to study Laser Engineered Net Shaping (LENS^{TM}) produced materials and identify the microstructures. Numerical method was used to examine the influence of materials' type and LENS^{TM} process parameters on the forming of the specific microstructures from thermodynamics and fluid dynamics point of view. Samples of 316L stainless steel were examined, microstructures of samples were used to estimate the corresponding cooling rate, and the cooling rate was compared with the results of three different level of simplified models..

Keywords: *Laser assisted manufacturing, LENS, Rapid Prototyping*

NOMENCLATURE

E	=	Energy (Jm^3/kg)
H	=	Enthalpy (Jm^2/kg/s)
p	=	Pressure (kgm^{-1}s^{-2})
Q_j	=	Heat Transfer (J)
t	=	time (s)
V_i	=	x_i component of velocity (m/s)
V_j	=	x_j component of velocity (m/s)
x_j	=	Cartesian coordinate (m)

Greek Symbols

ρ	=	Density (kg/m^3)
$\tau_{ij}^{(l)}$	=	Laminar Shear Stress Tensor (N/m^2)
$\tau_{ij}^{(T)}$	=	Turbulent Shear Stress Tensor (N/m^2)
λ_1	=	Dentritic Arm Spacing (DAS) (m)
ε	=	Cooling Rate (K/s)

INTRODUCTION

LENS^{TM} is a type of Rapid Prototyping (RP) technology, which is unique in fabricating fully dense metal parts directly from Computer Aided Design (CAD) solid models by layer additive methods[1-9]. The LENS^{TM} process can be thermodynamically described as the following four steps:

* Corresponding author: Prof. R.S. Amano
Phone: + (1)-414-229-2345, Fax: + (1)-414-229-6958
E-mail address: amano@uwm.edu

1. The Laser hits on the substrate and creates a melting pool with a size of 1-2 mm[1].
2. The micro or nano powders of desired material are injected into the melting pool; the powders are melted and deposited.
3. As the substrate traverses forward, the laser heat moves away relatively, the temperature of the melting pool begin to fall, And at the same time, the melting pool with deposited powders experience a solidification process.
4. The substrate keeps traverse back and forth, and the powders are added on layer by layer.

The thermo history plays an important role in this process, particularly; the heating and cooling history are the critical factors to determine the microstructure of the produced part.

In this paper, the microstructures of LENS^{TM} produced 316L stainless steel were examined and corresponding cooling rates were calculated using the experimental relations [2]. At the same time, numerical method was enrolled and the results were compared with experiment data.

.

NUMERICAL METHOD

When the substrate traverses under the laser, metals are melted for the closing up of laser spot and solidified for the parting away of laser spot. Simultaneously, powders are injected into the melting pool, there are following several phenomena involved: convection, conduction and radiation heat transfer; metal's melting and solidification, heat and mass exchange between discreet particle powders and continuum melting pool.

Navier-Stokes (N-S) equations are the governing equation for simulating the flow field and thermal field in and around the melting pool. In addition, Lagrange-Eulerian method is used to track the motion of powders and heat transfer between powders and melting pool. The Volume of Fluid (VOF) method was used to track the interface between liquid metal and environment gas, Argon. Mushy zone melting / solidification model is used to mark the interface of liquid metal and solidified metal.

RESULTS

This paper simplifies the real LENS system as shown in Figure. 1. The upper stationary part represents the laser & powder nozzles assemble and the surrounding environmental gas, while the under moving part represents the moving metal substrate. The dimension of upper part is $0.18m \times 0.06m \times 0.03m$ and the dimension of under part is $0.10m \times 0.06m \times 0.03m$.

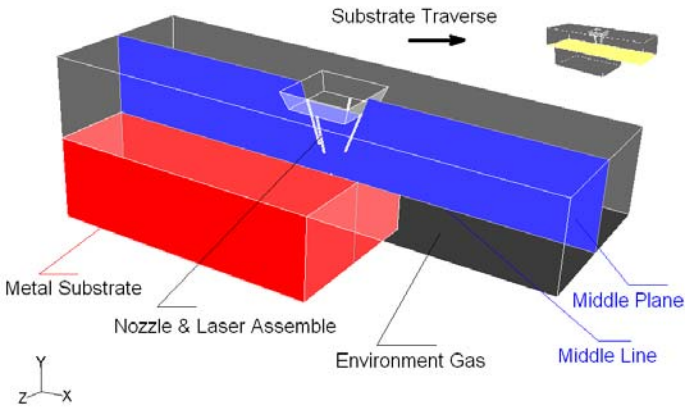

Figure 1. Real and Simplified LENS^{TM} System

As shown in Fig. 2, the mesh size of the whole model is 480,000. There are heat flux boundary condition exerted on position of laser spot and the value is coming from the calculation of laser

power used and laser spot diameter; Powder injections are set on each nozzle and the powder size, flow rate and injection speed is directly from the sample making parameters. The surrounding boundary is to be constant temperature wall, this is reasonable with high precision, because the heat infected zone is small, around 5-10mm [3], this will be verified when the temperature distribution is calculated out.

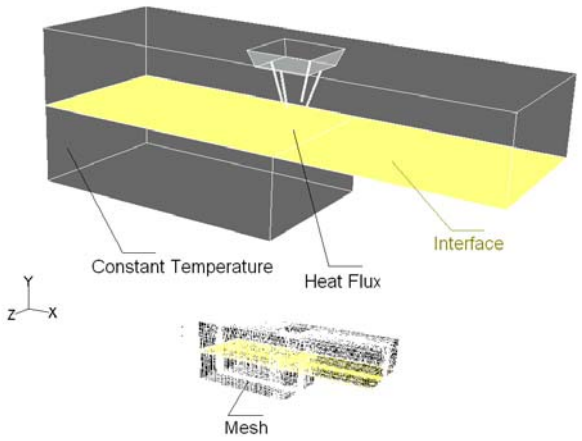

Figure 2. Boundary Conditions & Mesh

In this paper, three real samples are studied; correspondingly, three simulations were carried out. The parameters are collected in Table 1.

Table 1

Simulation Parameters

Density (kg/m^3)	7730
Specific Heat Cp (J/kg/K)	450
Thermal Conductivity (W/m/K)	21.5
Viscosity (kg/m/s)	0.0055
Solidus Temperature (K)	1390
Liquidus Temperature (K)	1440
Laser Power (W)	220
Beam Diameter (m)	0.0005
Traverse Velocity (m/s)	0.0148
Powder Feeding Rate (kg/s)	3.34E-5*4
Powder Injection Velocity (m/s)	6.37
Powder Diameter (m)	1.00E-07
Heat Flux (W/m^2)	1.12E+09
Environment Temperature (K)	320
Environment Pressure (Pa)	101325

In case 1, the powder injection model, VOF model, and Melting/Solidification model were used. In case 2, the powder injection model was taken off form case1, so case 2 didn’t take the effect of

powder's absorption of energy in to count. While in the metal was only treated as a solid, so the whole effect of melting pool was get rid of. The cases descriptions are as table 2 shown.

Table 2
Cases Description

	Case 1	Case 2	Case 3
VOF Model	√		
Melting/Solidiffication Model	√	√	
Powder Injection Model	√		

Figure 3 shows the temperature distribution of three cases along the middle line at time t=1s separately. the temperature remains unchanged as the environment temperature; only in the small area around laser spot (x=0m) the temperature shoots up suddenly.

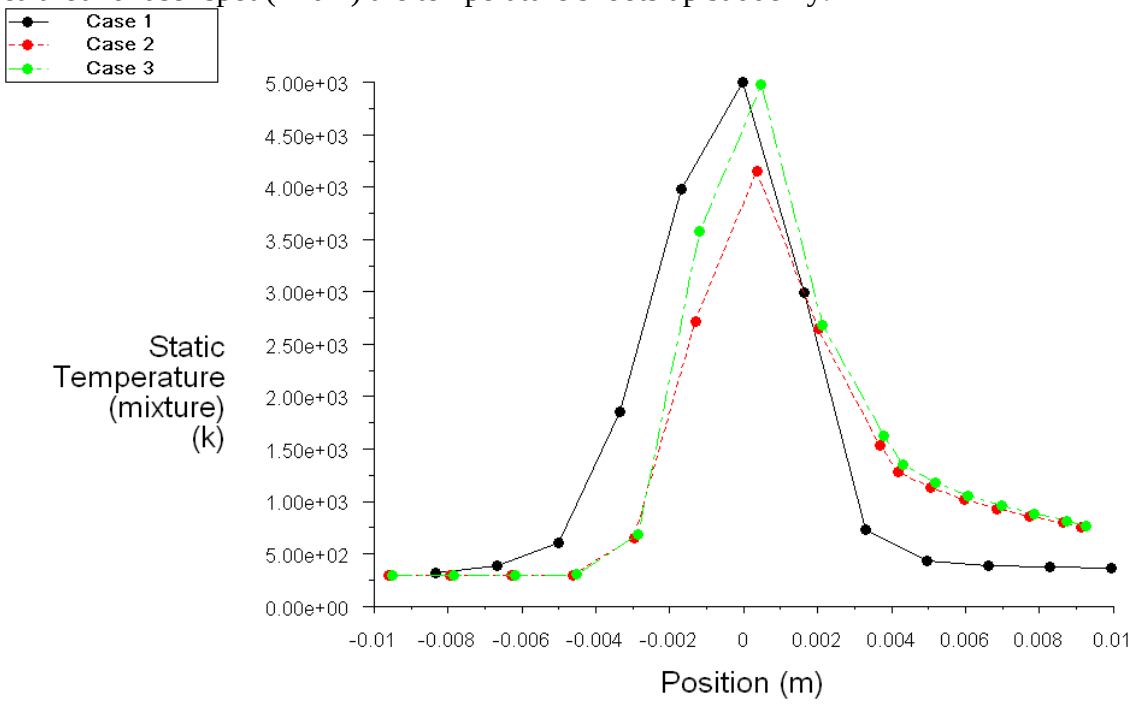

Figure 3. Temperature Distribution along the middle line at different time: t=1s

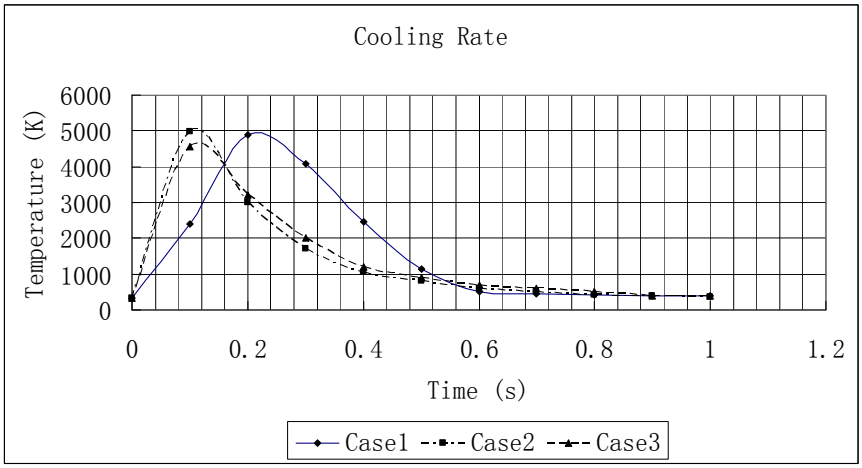

Figure 4 Temperature Changing with time

Figure 4 shows the temperature changing with time of three cases; from this figure, the heating rate and cooling rate is easy to find. The numerical results and experimental sample results on cooling rate is listed in Table 3.

Table 3
Cooling Rate (K/s)

	Experimental Data	Numerical Data
Case 1	11000	9163
Case 2	11000	7954
Case 3	11000	6163

Further work can be done to refine to dig out more precise mass transfer between powder and melting pool, so that more precise cooling rate can be measured.

CONCLUSION

Compared with previous work [4], the case 2 yield more accurate results by compared with experimental data for the refined mesh. While in case 2, because the powder injection model was ignored, so as the energy transfer between the powder and continuum metal was ignored, so the final average cooling rate is smaller than the experimental data. In case 3, the melting pool effects was also get rid of, so the results between case 2 and case 3 differ from each other. From the comparison of three cases, the cooling rate largely depends on the metal's solid metal' material properties, at the same time, the powder's injection also contribute much to the final cooling rate.

ACKNOWLEDGMENTS

The authors are thankful for US Army's support on this project under contract #W56HZV-04-C-0784.

REFERENCES

1. Su, W.N., Erasenthirian, P., & Dickens, P.M, Investigation of fully Dense Laser Sintering of Tool Steel Powder using Nd:YAG (neodymium-doped yttrium aluminum garnet) Laser. *Mechanical Engineering Science Journal*, Vol. 217 PartC02202. UK, 2003.
2. Watkins, K.G., Achieving the Potential of Direct Fabrication with Lasers. *3rd International Conference on Laser Assisted Net Shaping (LANE 2001)*, Erlagen. PP. 25-38, 2001.

3. Boddu, M.R., Musti, A., Landers, R.G., Agarwal, S., & Liou, F.W., Empirical Modeling and Vision Based Control for Laser Aided Metal Deposition Process. *Solid Freeform Fabrication Symposium Proceedings*. PP. 452-459, 2001.
4. Susan, D.F., Puskar, J.D., Brooks, J.A., & Robino, C.V., Porosity in Stainless Steel LENS Powders and Deposits. PP. 50-57, 2000.

VALIDATION AND VERIFICATION PROCEDURE OF THE FREE SURFACE MAPPING IN AN ELECTRICAL TRANSFORMERS MOULDING PROCESSES

Z. P. Buliński*, A. J. Nowak
Institute of Thermal Technology, Silesian University of Technology, Gliwice, Poland

ABSTRACT. Paper presents a numerical simulation, verification and experimental validation of an electrical transformer moulding process. For this purpose an experimental stand, which would allow us to carry out and monitor such a process, was designed and built. Two types of experiments were preformed. First was an isothermal experiment in ambient conditions, in which an analog liquid was used. As an analog liquid substance with highly non-Newtonian properties was used. The second experiment was done in non-isothermal conditions with an epoxy resin as a working fluid. In this experiment epoxy resin was used and the internal transformer parts were heated up to the process temperature before filling the mould with epoxy resin. The course of transformer casting process highly depends on the rheological and surface properties of the epoxy resin and their dependency on temperature and degree of polymerisation. This properties were carefully measured. In case of non-isothermal simultaneously to moulding process, polymerization reaction of the epoxy resin take place. This effect was also considered in the mathematical model of the process, for this purpose DSC measurements of the epoxy resin was carried out to estimate curing kinetics. Geometrical and numerical models of both experiments were created with the use of the commercial Computational Fluid Dynamics code *Fluent*. Mathematical model of the moulding process considered free surface flow with Volume Of Fluid method, in this model also surface tension and wall adhesion were include with Continuum Surface Model. In the non-isothermal case transport properties of epoxy resin were assumed to be a function of temperature and curing degree. Calculations were preformed on several numerical grids with different mesh densities based on which the spatial discretisation error was estimated using Richardson extrapolation rule. Finally obtained results for both cases were compared with experimental measurements showing satisfactory agreement.

Keywords: *Moulding Process, Multiphase Modelling, Free Surface Flow, Computational Fluids Dynamics, Validation*

INTRODUCTION

During the last thirty years or so, an incredible development and a dramatic cost decrease in computers has caused them to become one of the most important tools in the work of a modern engineer in the field of modelling fluid and heat flows. Computational Fluid Dynamic (CFD) techniques are efficiently used in conceptual studies of new designs, detailed product development, troubleshooting or redesign, optimisation and control of many industrial processes, etc. Broad use of CFD in industrial applications has resulted in more complicated problems being solved. However, each CFD code and simulation needs to be inspected if the obtained results are reliable. This objective is accomplished by means of a credibility analysis (or Validation & Verification - V&V analysis) of the numerical model [1].

* Corresponding author: Z. P. Bulinski
Phone: + (48)-32-2372974, Fax: + (48)-32-2372872
E-mail address: zbigniew.bulinski@polsl.pl
www: http://www.itc.polsl.pl/bulinski

Dry-type resin-impregnated electrical transformers are very important parts of many industrial power supply systems. In those devices all electrical circuits are enclosed in tight casings made of epoxy resin, whose main function is the electrical insulation of the device. It must ensure that it carries away heat produced inside the transformer. To assure the proper fulfilment of these tasks, the transformer epoxy casing must be free of any internal failures, such as air voids or material discontinuities. This type of electrical transformers are produced in so called Vacuum Casting Technology. In this technology the internal elements of the transformer are placed in a mould which is then filled with an epoxy resin composition. After the introductory curing in the mould, the casting is further cured outside the mould by heating it in a tunnel furnace. One of the types of transformers produced in this technology are instrument electrical transformers, which are commonly used in measuring and controlling systems of power plants. They separate measuring instruments from primary circuits, and prevent any damage due to short-circuit currents. They can also extend the measuring range of standard devices.

EXPERIMENTAL RIG

Based on the dimensions of the common voltage transformer UMZ-24 produced in ABB's plant in Poland, the experimental stand for the casting of such a transformer is designed and built. On this experimental stand two experiments were carried out, the first isothermal one with analog liquid and the second non-isothermal one with epoxy resin [2]. The experimental stand was the same in both experiments (see Figure 1) and consists of: glass tank (casting mould), inner transformer elements and resin feeding system. The mould in the experiment has been made of glass to allow us the tracing and filming the position and shape of the liquid free surface. The main internal parts of the voltage transformer are: core made of steel sheets, primary and secondary coils wounded concentrically around one arm of the core, connectors which establishes connections between windings and phase terminals (Figure 2).

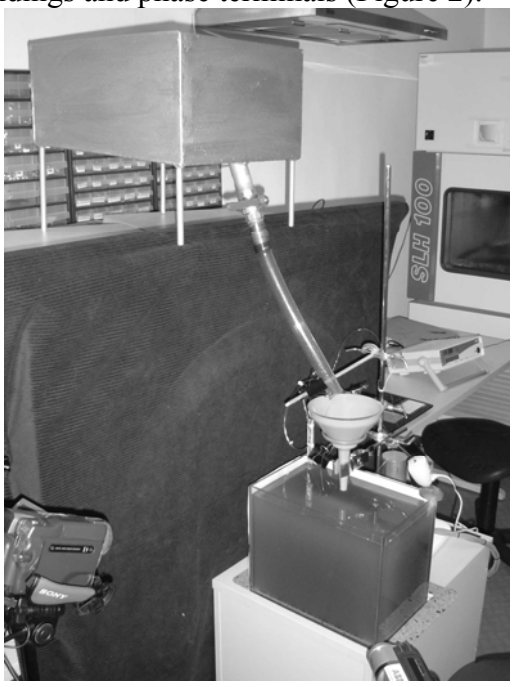

Figure 1. Casting experimental rig.

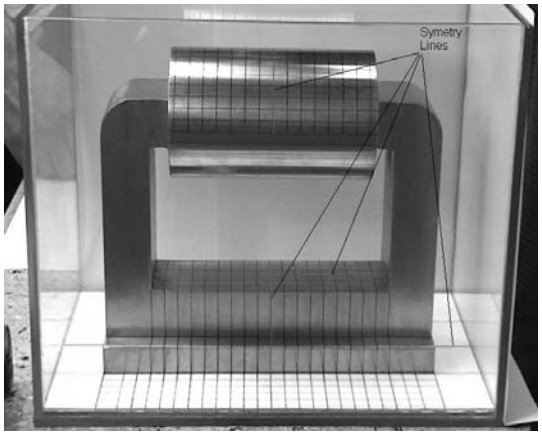

Figure 2. Mould made of glass and Internal parts of the transformer.

Original geometry of internal transformer parts has been simplified. Moreover the core and the coil have been made of one solid piece of steel whose properties are well defined. The feeding system was designed as a gravitational one (Figure 1) where the driving force is the difference between the free surface of the liquid in the main tank and the level of the inlet to the mould. On the surfaces of

the selected internal elements, grids have been plotted which would allow us to validate the free surface mapping. Three digital cameras were used to film both experiments. Their location assured the best capture of the shape of the flowing free surface. Two experiments were carried out on the experimental stand [3]. The first one was isothermal experiment with analog liquid with highly nonlinear viscosity. In the second one, performed in non-isothermal conditions, epoxy resin was used. In the non-isothermal experiment temperature of the epoxy composition during the experiment was measured with a coat thermocouples placed in the funnel and inside the mould.

MATHEMATICAL MODEL OF THE CASTING PROCESS

Numerical model in case of isothermal experiment encompassed mould inner and a part of the feeding pipe. In case of the non-isothermal experiment, computational domain was extended to include also mould walls. Geometrical model and numerical grid was created with use of commercial code *Gambit*. Since two symmetry planes can be spotted in the mould, numerical models were restricted to its quarter. Calculations for isothermal experiment were preformed on three different grids with 145753, 255278 and 509420 hexahedral cells. Therefore the numerical model consists of the mould interior, internal transformer elements and the walls of the mould. For these calculations only one grid is used with 314374 hexahedral cells [3]. Mathematical model and CFD calculations were carried out with commercial code *Fluent*.

Governing equations

The Volume of Fluid (VOF) formulation was chosen to describe multiphase flow [5] in casting process. In this approach, for each phase the volume fraction α_i of that specific phase in a computational cell of the domain is defined. In analysed problem two phases were considered: liquid phase *l* and gas phase *g*. Liquid phase volume fraction α_l is governed by the following transport equation:

$$\frac{\partial \alpha_l}{\partial \tau} + \nabla \cdot (\alpha_l \mathbf{w}) = 0 \tag{1}$$

where **w** is the fluid velocity vector. The volume fraction of the gas phase is calculated using following formula:

$$\alpha_g = 1 - \alpha_l \tag{2}$$

Transport equation for polymerization reaction progress β (degree of cure):

$$\frac{\partial \beta}{\partial \tau} + \nabla \cdot (\beta \mathbf{w}) = R_\beta \tag{3}$$

where R_β is the reaction rate.
A single momentum equation is solved throughout whole domain:

$$\frac{\partial \rho \mathbf{w}}{\partial t} + \nabla \cdot (\rho \mathbf{w}\mathbf{w}) = \rho \mathbf{g} - \nabla p + \nabla \cdot \left(\mu \left(\nabla \mathbf{w} + \nabla \mathbf{w}^T\right)\right) + \mathbf{F}_\sigma \tag{4}$$

where ρ is the density, p pressure, μ dynamic coefficient of viscosity and $\mathbf{F}_\sigma$ is the body force due to surface tension:

$$\mathbf{F}_\sigma = 2\sigma \frac{\rho \kappa_l \nabla \alpha_l}{\rho_g + \rho_l} \tag{5}$$

where σ is the surface tension between liquid and gas phase and κ_l is curvatures of phases interface. The energy equation is shared by both phases:

$$\frac{\partial \rho h}{\partial t} + \nabla \cdot \left[\mathbf{w}(\rho h + p) \right] = \nabla(\lambda \nabla T) + R_\beta \Delta H \tag{6}$$

last term on the right hand of equation is a heat source due to polymerization reaction, h is enthalpy of the two-phase mixture and ΔH is the heat of reaction. The properties which appear in the governing equations are calculated as a volume-weighted average.

Physical properties

Most important properties which influence a real-life process and numerical computation as well are viscosity, surface tension and in case of epoxy resin polymerization reaction kinetics. Since both fluids used in experiments were not described in available literature, their properties were measured. Surface tension was determined with du Nouy ring tensiometer Krüss K-800. Rheological properties were measured with AR2000ex rheometer from TA Instruments. Epoxy resin reaction kinetics were established with use of Netzsch STA409 differential scanning calorimeter. Obtained rheological and kinetics models where implemented in mathematical model through user defined functions capability.

Analog liquid rheological model. Analog liquid used in isothermal experiment revealed highly non-Newtonian rheological properties, which successfully can be described by Cross model:

$$\frac{\mu - \mu_\infty}{\mu_0 - \mu_\infty} = \frac{1}{1 + (k\dot{\gamma})^n} \tag{7}$$

where μ_0, μ_∞, k, n are the model parameters and $\dot{\gamma}$ is shear rate. Figure 3 presents measured flow curve fitted with Cross model.

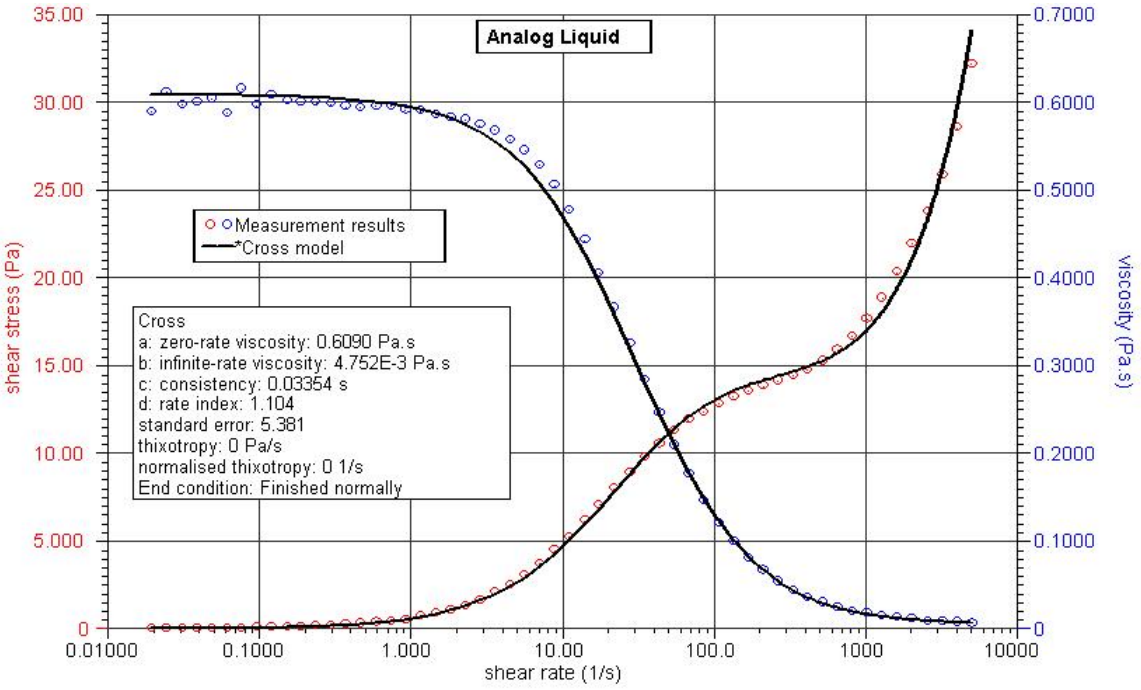

Figure 3. Flow curve of analog liquid.

Epoxy resin rheo-kinetic model. In non-isothermal experiment commercial epoxy composition EPR04820+EPH860 from Bakelite AG was used. To resolve coupling between rheological properties, temperature and reaction progress, simultaneous rheological and calorimetric measurements were done. First calorimetric data were elaborated and reaction kinetics model determined [6]:

$$R_\beta = \frac{\partial \beta}{\partial \tau} = \exp\left(-\frac{E_\beta}{RT} \right) \left[k_1 \beta^{m_1} (1-\beta)^{n_1} + \left(k_2 + k_3 \beta^{m_2} \right) (1-\beta)^{n_2} \right] \tag{8}$$

where E_β, k_1, k_2, k_3, m_1, m_2, n_1, n_2 are model parameters, R is the universal gas constant and T is temperature. Obtained reaction rate model as a function of reaction progress (degree of cure β) for a few different temperatures is presented in figure 4. Having reaction rate kinetics, parameters of Macosko-Cross rheological model were calculated [4]:

$$\mu = \mu_0 \exp\left(\frac{E}{RT}\right)\left(\frac{\beta_g}{\beta_g - \beta}\right)^{c_1 + c_2\beta} \tag{8}$$

where μ_0, E, c_1, c_2 are the model parameters, β_g is resin gelation point. Figures shows resin viscosity measurement results compared with Macosko-Cross model.

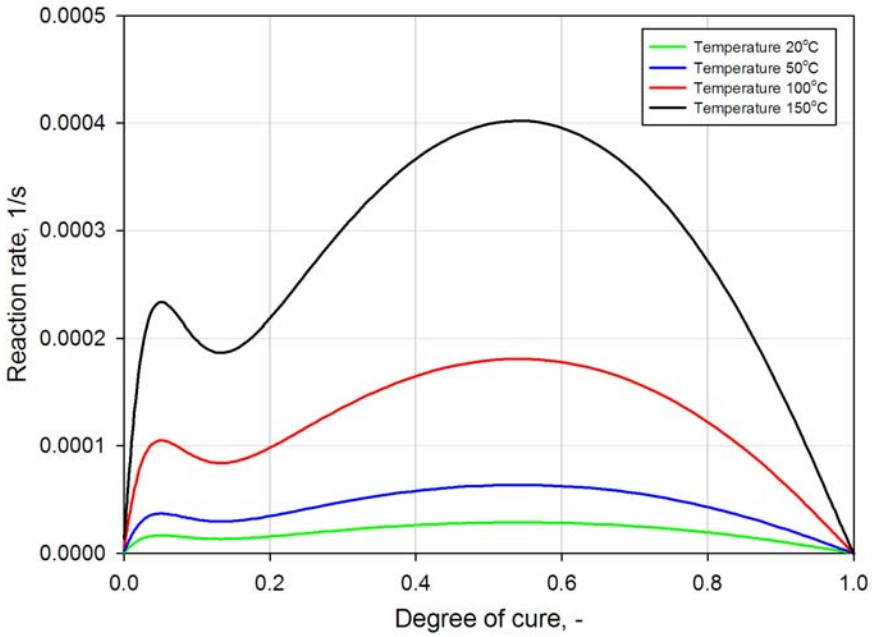

Figure 4. Plot of reaction rate kinetics model against degree of cure for a few different temperatures.

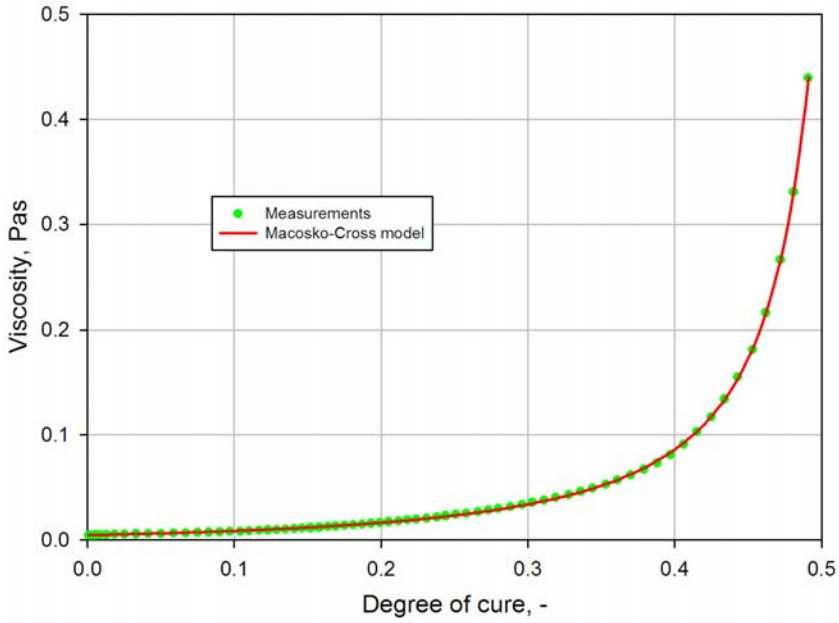

Figure 5. Comparison of measured resin viscosity fitted with Macosko-Cross model at temperature 150°C and shear rate 143 1/s.

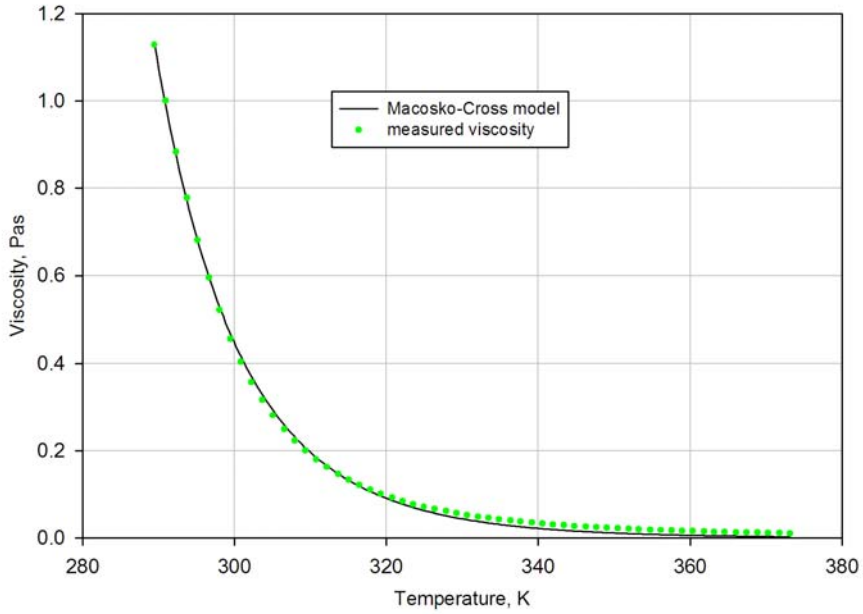

Figure 6. Comparison of measured resin viscosity fitted with Macosko-Cross model in temperature range from 15 ^{o}C to 100^{o}C at shear rate 143 1/s.

RESULTS AND CONCLUSIONS

Main objective of this work was to developed validation procedure for casting process. To be able to quantitatively compare experimental results with simulations on some of surfaces inside the mould measuring grid was plotted. This allowed us to measure some of the two phase flows features, giving the means for simulation validation. One of measured quantity was the liquid film width formed at the transformer coil. In tables 1 and 2 results for isothermal and non-isothermal experiments are compared with computations results. Since for isothermal experiment calculations were done on a few numerical grids it allowed us to calculate extrapolated solution with Richardson extrapolation rule (see Table 1).

Table 1.
Comparison between experimental and simulation results for isothermal experiment.

Time, s	First grid, 145753 cells			Second grid, 255278 cells			Third grid, 509420 cells			Experiment		
	liquid stream width, cm	extrapolated solution, cm	relative discretisation error	liquid stream width, cm	extrapolated solution, cm	relative discretisation error	liquid stream width, cm	extrapolated solution, cm	relative discretisation error	liquid stream width, cm	absolute error, cm	relative error
0.2	4.40	—	—	4.50	4.99	0.10	4.50	4.50	0.00	4.1	0.3	0.08
1.0	8.18	—	—	8.16	8.06	0.01	8.18	8.26	0.01	7.2	0.2	0.02
2.0	9.43	—	—	9.53	10.02	0.05	9.36	8.70	0.08	7.9	0.2	0.02
5.0	10.42	—	—	10.40	10.30	0.01	10.35	10.16	0.02	8.7	0.2	0.02
10.0	10.60	—	—	10.70	11.19	0.04	10.63	10.36	0.03	9.3	0.2	0.02
30.0	10.78	—	—	10.75	10.60	0.01	10.63	10.17	0.05	10.2	0.2	0.02
50.0	10.78	—	—	10.75	10.60	0.01	10.63	10.17	0.05	10.2	0.2	0.02
70.0	10.78	—	—	10.75	10.60	0.01	10.63	10.17	0.05	10.3	0.2	0.02
90.0	10.78	—	—	10.75	10.60	0.01	10.63	10.17	0.05	10.4	0.2	0.02
100.0	10.84	—	—	10.78	10.49	0.03	10.69	10.34	0.03	10.6	0.2	0.02

Table 2.
Comparison between experimental and simulation results for isothermal experiment.

time, seconds	measurements			calculations
	liquid stream width, cm	absolute error, cm	relative error	liquid stream width, cm
2.0	6.6	0.2	0.03	5.2
10.0	6.9	0.2	0.03	5.7
50.0	7.0	0.2	0.03	6.2
100.0	7.3	0.2	0.03	6.5
200.0	7.5	0.2	0.03	6.7
250.0	7.5	0.2	0.02	6.7
270.0	7.5	0.2	0.02	6.7

In case of non-isothermal experiment thermocouple were placed inside the mould to compare with simulation results. In figure 7 exemplary temperature reading from one of thermocouples is compared with simulation result.

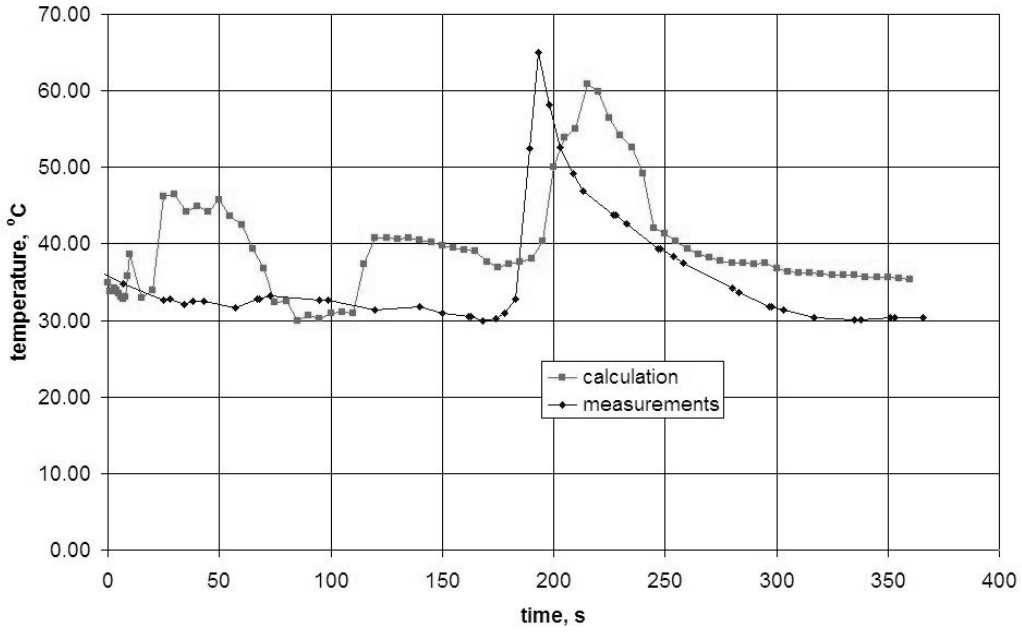

Figure 7. Comparison of temperature reading from thermocouple placed inside the mould with calculation results.

Summarizing, simulation results show good agreement with the experimental data. Solutions found with the use of the Richardson extrapolation method corresponded very well with the measured value of width of liquid stream at the transformer's top. Although the Richardson extrapolation procedure is restricted to smooth solution which is in asymptotic grid convergence region and to grids with uniform spacing, it was successfully applied in this complex case with a nonuniform grid present and solution discontinuities.
The results obtained for the second case are not as good and discrepancy between the calculated and measured results were significant. However, still some of the effects observed during the experiment were successfully captured by the numerical simulations e.g. the liquid stratification.

ACKNOWLEDGEMENTS

Research has been financed by the Polish Ministry of Science and Higher Education within the grant N512 022 31/2577 and by the BK funds. This help is gratefully acknowledged herewith.

REFERENCES

1. Babuska, I., Oden, L.T., Verification and validation in computational engineering and science: basic concepts, *Computer Methods in Applied Mechanics and Engineering*, Vol. 193, No 36-38, pp 4057–4066, 2004.
2. Brackbill, J.U., Kothe, D.B., Zemach, C., A Continuum Method for Modelling Surface Tension, *Journal of Computational Physics*, Vol. 100, pp 335-354, 1992.
3. Buliński, Z. P., Nowak, A.J., Numerical analysis and experimental validation of the free surface flow and heat transfer in electrical transformers moulding processes, *International Journal for Numerical Methods in HEAT and Fluid Flow*, Special Issue, Vol. 18, No 3/4, pp 356–377, 2008.
4. Castro, J.M., Macosko, C.W., Kinetics and rheology of typical polyurethane reaction injection molding system, *Society of Plastics Engineering Annual Technical Conference*, Vol. 26, pp 434-438.
5. Hirt, C.W., Nichols, B.D., Volume of fluid (VOF) method for dynamics of free boundaries, *Journal of Computational Physics*, Vol. 39, No 1, pp 201-225, 1981.
6. Kamal, M.R., Sourour, S., Kinetics and Thermal Characterization of Thermoset Cure, *Polymer Engineering and Science*, Vol.13, No. 1, pp 59-64, 1973.

EXPERIMENTAL INVESTIGATION OF THE SWIRL OF THE LIQUID METAL FLOW PRODUCED BY THE NON-UNIFORM ELECTRIC CURRENT

V. Zhilin, Yu. Ivochkin, A. Oksman, I.Teplyakov*
Joint Institute for High Temperatures RAS, Moscow, Russia

ABSTRACT. The results of the experimental and numerical investigation of the electrovortex flow formed at non-uniform electric current passing through the liquid metal volume are presented. The experiments were carried out on the working section which was the copper hollow hemispherical container filled with eutectic alloy In–Ga–Sn. The electric current value was up to 400 A. Experimental data on the velocity fields are presented. Measurements of different velocity components were carried out by the unique fiber-optical transducers. A swirl of the flow in azimutal plane was revealed and it was shown that the cause of this swirl is the external magnetic field. A numerical calculation of the electrovortex flow subject to the external magnetic field was carried out and satisfactory correspondence between calculation results and experimental data was received.

Keywords: *liquid metal, electric current, magnetic field, velocity, swirl*

INTRODUCTION

Among the different types of magnethydrodynamic flows with liquid-metal heat-transfer medium, the so-called electrovortex flows (EVF) formed as a result of the interaction between of the electric current passing through the electroconductive liquid and the electric current's own magnetic field are of special interest for investigators [1]. Investigation of the electrovortex flows has not only fundamental orientation but also is of great importance for different branches of machine-building, energetics and metallurgy. For example, EVF affects the quality of the weld at submerged arc welding and the presence of EVF changes the evolution dynamics of electroslag remelting.

Usually electroslag technological processes of welding and remelting are investigated by physical modeling method by the apparatus where electric current spreads into the volume of electroconductive liquid from the point source (electrode) located on the surface of the liquid metal [2]. It is assumed that under this condition EVF formed as the result of the electric force action $\mathbf{F_{el}}=\mathbf{j}\times\mathbf{B}$ is the toroidal curl with a jet directed down under the electrode. Such 2D axisymmetric approximation is convenient for the numerical and theoretical investigation of EVF and demonstrates value in practice of application of the velocity stream structure reconstruction method in the volume of liquid metal by the shape of surface flows. However, observation results both in model experiments and in industrial apparatus are evidence of conditions under which the azimutal swirl appears and the stream becomes 3D. Evidently, the effect of swirl can raise due to the increase of instability in convergence flow or can be connected with the influence of magnetic field of the

* Corresponding author: Mr. I . Teplyakov
Phone: + 7(495)-361-1673
E-mail address: vortex@iht.mpei.ac.ru

Earth and power wires, and Coriolis effect. In our opinion the second factor out of the listed above is the most important one. The aim of the presented investigation was to verify this suggestion.

EXPERIMENTAL APPARATUS AND MEASUREMENT METHOD

The experiments were carried out on the apparatus the scheme of which is shown on fig.1. An eutectic alloy In-Ga-Sn with content by weight Ga – 67%, In – 20.55, Sn – 12.5% (melting temperature +10.5 ^{0}C) was used as a working liquid. The hollow copper hemispherical container with 188 mm diameter serving as a big electrode was filled with the alloy. The small electrode was made of copper, too, in the form of a convex hemisphere and its diameter could be varied from 3 up to 6 mm. The source developed on the basis of three-phase rectifier of alternating current was used for power supply of experimental installation. The electric current value was varied in the range 50 – 400 A. The power wire containing both vertical and horizontal sections was located in 0.15 – 1 m from the apparatus axis. To measure velocity in the volume of current-carrying liquid the fiber-optical transducer (fig.2) was used. Its construction and working principle are described in [3].

The probe of the fiber-optical transducer (as well as the temperature sensor) was L-shaped and attached to the traverse gear which allowed moving the probe in three perpendicular directions. The output signal form measuring sensors (of temperature and velocity) was amplified and filtered by the signal forming units and then applied to analog-to-digital converter and then was processed on the computer.

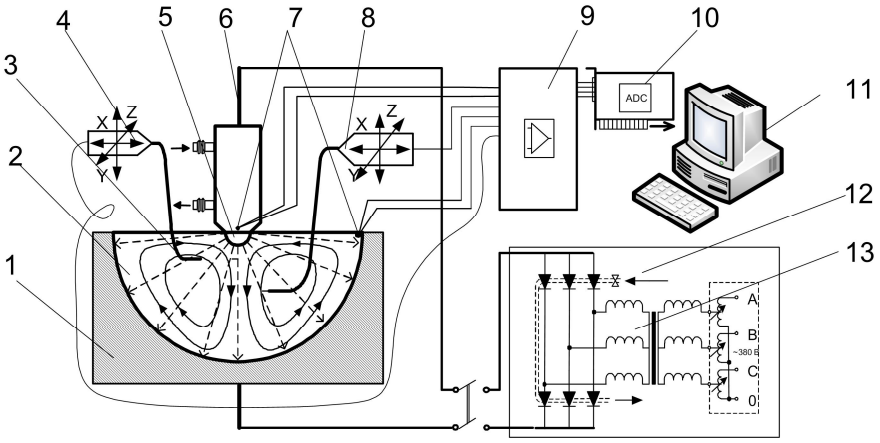

Figure 1. Experimental apparatus. 1 – copper container; 2 – eutectic alloy; 3- sensor of fiber-optical transducer; 4 – probe; 5 – small electrode; 6 – power wire; 7 – thermocouples; 8 – thermocouple probe; 9 – amplifier; 10 – analog-to-digit converter; 11 – computer; 12 – water-cooling system; 13 - power source.

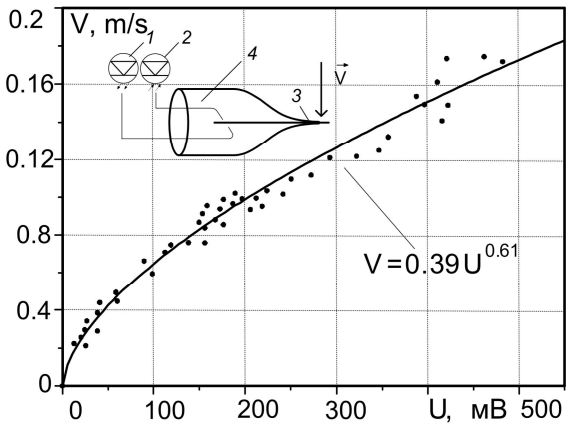

Figire 2. Scheme of fiber-optical transducer and calibration curve. 1 – photodiode; 2 – light-diode; 3 – sensor;4 – fibre.

The calibration of the fiber-optical transducer was carried out in the air jet and then was calculated for eutectic alloy stream. The form of the gauge dependence typical for fiber-optical probes (for range of velocity 0 – 0.2 m/s) is shown on fig. 2. The thermocouple probe made of two copper and constantan wires with 0.075 mm diameter was used to measure temperature.

The analog-to-digital converter La2M3 by *Rudnev-Shilyaev* with 16 channels and 12 digits allowing to make a numbering with a maximum frequency of 500 kHz was used as secondary equipment as well as the set of measuring devices by *National Instruments.* An original precision amplifier with 8 channels of our own production was used to coordinate the electric signal level of the fiber-optical transducer and thermocouple with this ADC. The visualization of the surface flow with the help well observed hydrogen bubbles produced at the contact of 3% HCl and the liquid metal surface was carried out.

MATHEMATICAL DESCRIPTION OF PROCESSES AND CALCULATION METHOD

As mentioned above EVF is formed as the result of the interaction of the non-uniform electric current with density **j** with its own magnetic field **B** (fig.4). Navier-Stokes's equation describing hydrodynamics of the electrovortex flows looks like:

$$\rho\left(\frac{\partial V}{\partial t}+(V\nabla)V\right)=-\nabla p+\rho\nu\nabla^2 V+\rho g+F_{el} \qquad (1)$$

Where $\mathbf{F}_{el}=\mathbf{j}\times\mathbf{B}$ – electromagnetic force producing the movement of electroconductive liquid.

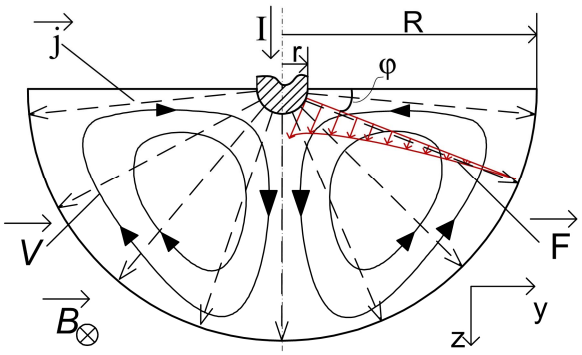

Figure 3. Scheme of EVF forming

For hemispherical geometry where current density depends on radius R as $j=\frac{I}{2\pi R^2}$, the expressions for magnetic field and electromagnetic force in liquid metal have the following form:

$$B_{evf}=\frac{\mu_0 I(1-\cos\varphi)}{2\pi R\sin\varphi} \text{ and } F=\frac{1}{4}\frac{\mu_0 I^2(\cos\varphi-1)}{\pi^2 R^3\sin\varphi}$$

Taking into account the external magnetic field produced by power wire the summary magnetic field in container has the form:

$\mathbf{B}_\Sigma=\mathbf{B}_{evf}+\mathbf{B}_\parallel$ for vertical power wire and $\mathbf{B}_\Sigma=\mathbf{B}_{evf}+\mathbf{B}_\perp$ for horizontal power wire.

The configuration of the magnetic fields produced by EVF proper and two current wires variously arranged in relation to the experimental installation axis is shown on fig.4.

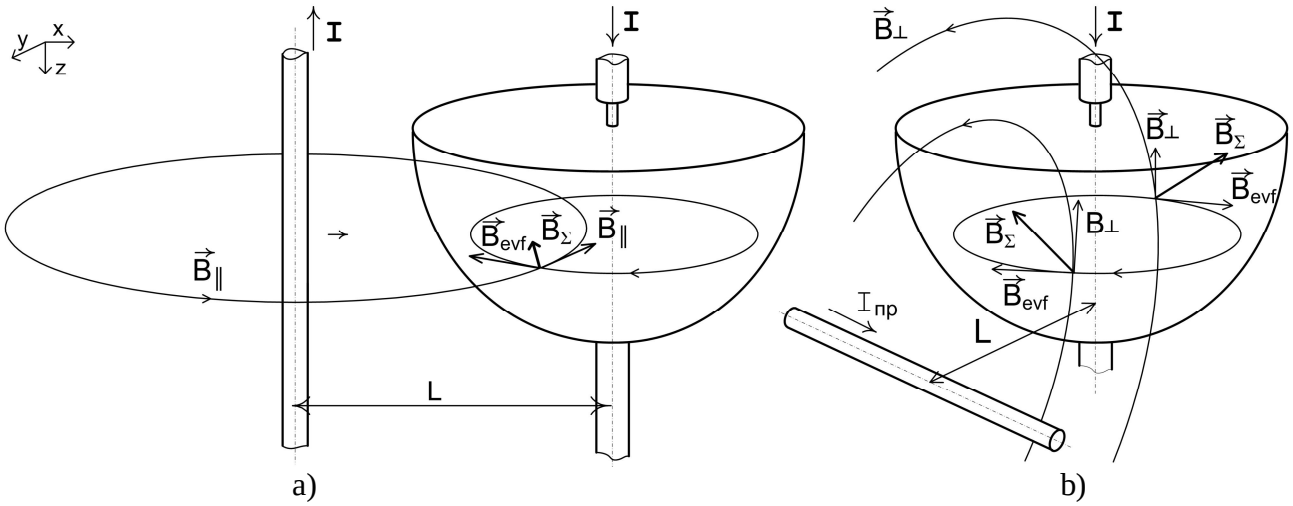

Figure 4. Configuration of the magnetics fields (a) verical wire, (b) horizontal wire.

The calculation area was the concentric hemisphere with radiuses corresponding to the small and big electrodes. Computation mesh consisted of the ~80000 tetrahedral elements. 3D steady and unsteady Navier-Stokes's equation with specified electric force was solved with the control volume method in Cartesian coordinate. K–ε turbulent model with standard parameter was used. As the motionless oxide film is formed on the free surface of liquid metal, the condition of the solid stationary wall was specified on the surface. The cases of absence of the external magnetic field and the presence of the field of vertical and horizontal power wire were considered.

RESULTS OF THE INVESTIGATION

At the same time the result of visual observation showed that there is flow swirl in horizontal plane (photo on fig. 6) accompanied by the formation of the funnel near the small electrode at the current over 400A. This funnel deepens as the electric current increases up to the electric arc forming and break of a circuit.

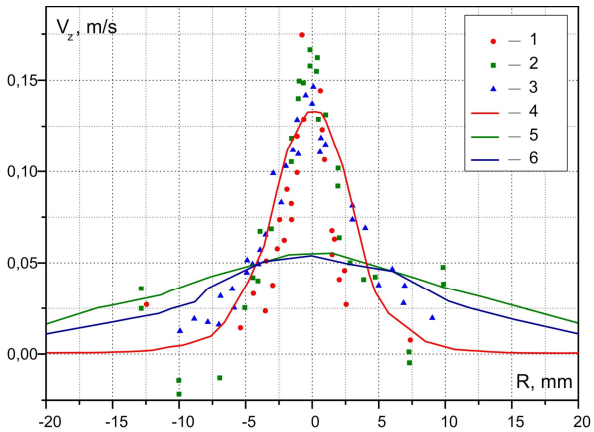

Figure 5. Velocity profile at different depth. Experiment: 1 – 2.5 mm; 2 – 20 mm; 3 – 30 mm; calculation 4 – 2.5 mm; 5 – 20 mm; 6 – 30 mm; I=250A.

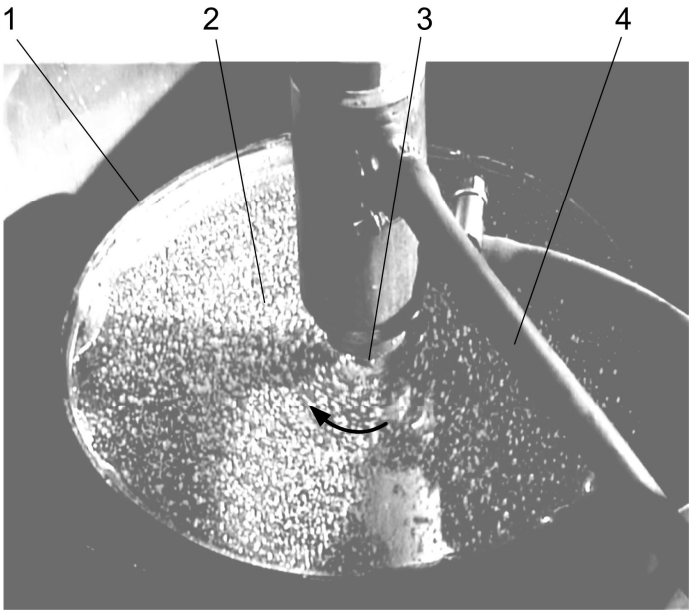

Figure 6. Visualizaton of rotation. 1 – Big electrode; 2 – surface of liquid metal with bubbles of hydrogen; 3 – small electrode; 4 –water-cooling system.

Theoretical estimates confirmed by calculation results show that the magnetic field of the vertical power wire (parallel to experimental installation axis) does not lead to the swirl of the stream and do not distort flow on the whole. On the contrary force interaction of the magnetic field of the horizontal power wire and electrovortex flows leads to the swirl of the liquid metal in the horizontal plane. This process is accompanied by the formation of the axis upward flow suppressing EVF
The latter effect is registered by fiber-optical transducer of velocity. (Fig. 7).

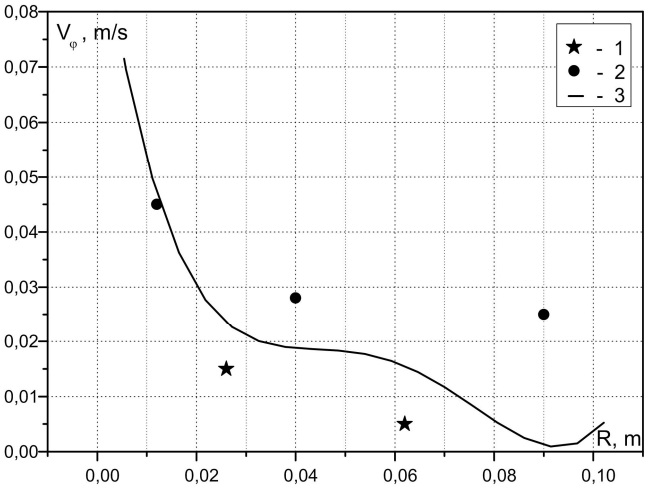

Figure 7. Dependence of azimutal velocity on radius. 1 – Experiment with fiber-optical transducer (z=5 mm); 2 – visualization; 2 – calculation (z=5 mm). I=400A.

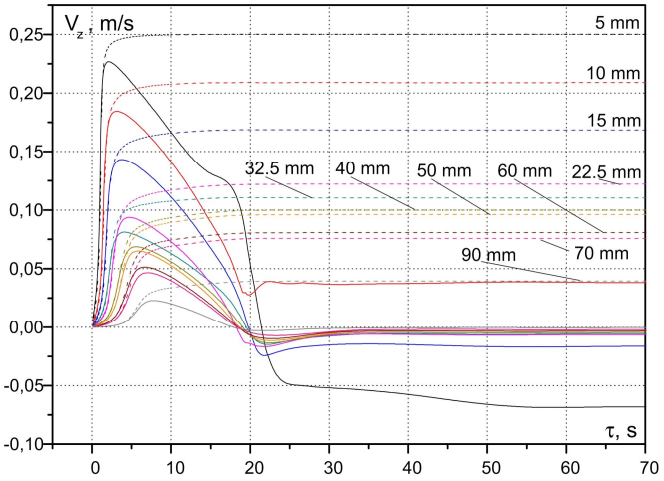

Figure 8. Dependence of vertical velocity on time with external magnetic field (—) and without (---) at different depth. I=400A.

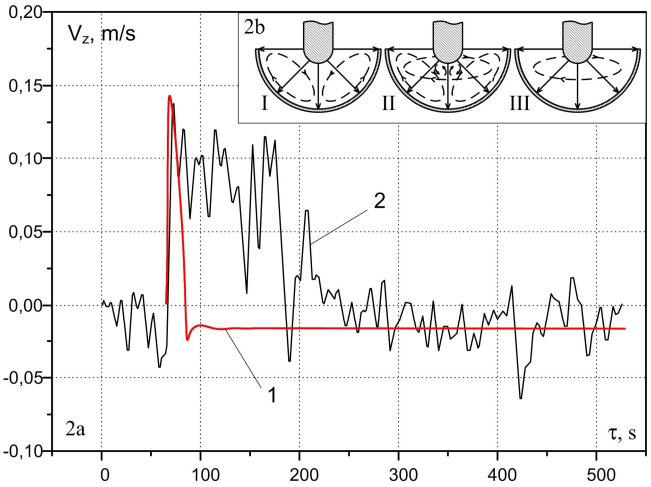

Figure 9. Comparison of the results of the unsteady calculation of the axis velocity under electrode and measurement results. 1 – calculation; 2 – experiments. I=400A, z=11.5 mm.

On the ground of the received data we can suggest the following scheme of the evolution of the electrovortex flow with presence of the external magnetic filed of the horizontal power wire. At first the toroidal curl with the central part in the shape of the jet directed to the bottom of the container is formed. (Fig. 9-I). Then the azimutal rotation appears and the upward flow is developed. (Fig. 9-II). And at last the upward flow is superimposed on EVF and suppresses it forming the stagnant zone. (Fig. 9-III).

CONCLUSIONS

The received experimental data supported the results of the calculations demonstrates the complicated 3D structure of electrovortex flow. The received experimental data supported the results of the calculations demonstrates the complicated 3D structure of electrovortex flow. This structure substantially differs from simplified two-curl flow model on the free surface of current-carrying liquid which is usually used as EVF [1].

Three-dimensionality of the flows in question is produced by azimutal swirl of stream stipulated by the strong dependence of EVF stability from external magnetic field which always present in model and industrial experiments.

The authors express gratitude to Belov K.I and Lozina E.Y. for the help in carrying out the experiments and the calculations.

This work was carried out with support of Russian Foundation for Basic Research.
Project № 07-08-00464-a.

REFERENCES

1. Bojarevish V., Freibergs Ya., Shilova E.I., Shcherbinin E.V, Electrically Induced Vortical Flows (Mechanics of Fluids and Transport Processes),Springer, 1988.
2. Zhilin V., Ivochkin Yu., Igumnov V., Oksman A, Experimental study of the electrovortex flow in the hemispherical volume. *High temperature,* Vol. 33, № 1, pp 3 – 6, 1995.
3. Zhilin V.G., *Optical–fiber velocity and pressure transducers*, Hemisphere publishing corporation, New York, 1990.

EFFECT OF HELIUM ON HEAT TRANSFERS IN ALUMINIUM CASTING

S. Rouquette[1*], J-C. Gebelin[2], A. Caden[2], N. Prabhu[3], W. Griffiths[2]
[1] Laboratory of Mechanics and Civil Engineering (UMR 5508 CNRS), Montpellier, France
[2] University of Birmingham, Birmingham, United Kingdom
[3] National Institute of Technology Karnataka, Karnataka, India

ABSTRACT. The solidification and cooling of Al alloys elaborated under helium have been thoroughly investigated. Al alloys cast under helium in steel mould have solidified and cooled faster than the ones made under air. The solidification time has been reduced by up to 25% and the overall cooling time has been decreased by up to 45% in steel mould. A second set of experiments were carried out in order to estimate the improvement of the heat transfer coefficient under Helium. Thermal inverse analysis was employed in order to estimate the heat flux at the interface chill/aluminium. Then heat transfer coefficient was deduced from the estimated heat flux and calculated temperatures on both sides of the interface chill/aluminium. Heat transfer coefficient values of 3300 $W.m^{-2}.K$ have been calculated under helium against 1800 $W.m^{-2}.K$ under air.

Keywords: *Aluminium alloys, casting under Helium, inverse heat flux problem.*

INTRODUCTION

Aluminium (Al) alloys are attractive due to its high mechanical properties to weight ratio. The use of Al alloys in the transport industry allows reducing the weight of the vehicles and, consequently, leads to low petrol consumption. Mechanical properties of Al alloys rely heavily on the cooling rate during casting. Greater is the cooling rate, smaller will be the grain size and the secondary dendrite arm spacing what leads to better tensile strength and ductility [1].

In casting process, the heat is transferred from the core (casting) to the mould (sand, steel, copper…) and, finally dissipated by either radiation, convection or a cooling system. In die casting, the interface mould/casting represents a barrier to heat transfer because of the air gap. Furthermore, during the solidification the casting shrinks what leads to larger air gap and low heat transfer at the interface. In the aim to improve the heat transfer at the interface mould/casting, air was replaced with helium. Helium thermal conductivity (0.275 $W.m^{-1}.K$) is 4 times greater than Air (0.058 $W.m^{-1}.K$) at same temperature. Argyropoulos et al. investigated the addition of Helium at the interface mould/casting [2]. They showed an increase of 30% of the heat transfer coefficient. The Helium was mainly applied to one surface of the casting. In this work, the mould and the casting are totally surrounded with Helium what allows a thorough investigation of the Helium effect from a thermal, metallurgical and mechanical points of view. The thermal point of view is proposed in this communication. A first experiment has been carried out to evaluate the helium effect on the solidification and the overall cooling of the casting.

The knowledge of the heat transfer coefficient at the mould/casting interface is necessary in order to perform accurate modelling of Al casting solidification. Better understanding of casting processes is made by simulation tools. The process is optimised by avoiding solidification defects such as shrinkage or better design of the feeding system, etc. A good solidification model requires

* Corresponding author: Dr Sébastien Rouquette
Phone: +33 (0)4-66-62-85-83, Fax: +33 (0)4-66-62-85-31
E-mail address: sebastien.rouquette@iut-nimes.fr

an accurate thermal modelling, good thermophysical properties of the material studied, a good knowledge of initial temperatures and thermal boundary conditions (namely heat transfer coefficient). A second experiment has been dedicated to the estimation of the heat transfer coefficient under helium. Temperature measurements in a steel chill and in Al casting have been done. Thermal inverse analysis was used in the aim to estimate the heat flux at the interface chill/casting. Then heat transfer coefficient (HTC) has been deduced from the estimated heat flux. HTC could have been evaluate by taking into account all the thermal resistance at the mould/casting interface (gaseous gap size, areas of contact, coating thickness, etc.) as did Hallam et al. [3]. HTC has been calculated for both cases: helium and air. Inverse thermal analysis allowed knowing the HTC at each time of the experiment.

In this communication, the first section deals with the effect of helium versus air on the cooling of the Al casting. Secondly, the experiment dedicated to the estimation of the HTC is described as well as its thermal modelling and its inverse thermal problem. Then the inverse analysis results are presented and discussed.

HELIUM EFFECT

Helium effect on the improvement of the heat transfer has been investigated in Argyropoulos et al[1]. Unfortunately their experiment could not show the overall effect of the helium on casting microstructure and mechanical properties. The developed experimental procedure answers to these points: the casting procedure is carried out entirely under helium. Thus, the effect of helium on the microstructure and the mechanical properties of the Al casting can be analysed in addition of the measured temperatures in the casting. In this communication, only the helium effect on the heat transfers is discussed.

In order to evaluate correctly the effect of the helium, an airtight chamber has been built connected to a vacuum pump and helium gas cylinder. Inside the chamber, a 12 kg furnace is used to melt the aluminium bars. Then the molten aluminium is poured in the cast iron mould. The cast iron mould has been used to make aluminium plates of several thicknesses (5 mm, 15 mm and 25 mm). Cooling curves for the 15 mm thickness aluminium plates are presented in figure 1. 15 mm thickness plates have been cast in air and in helium.

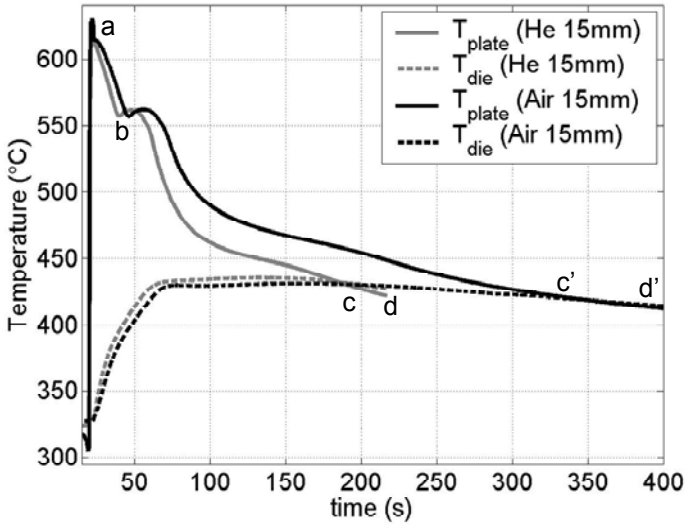

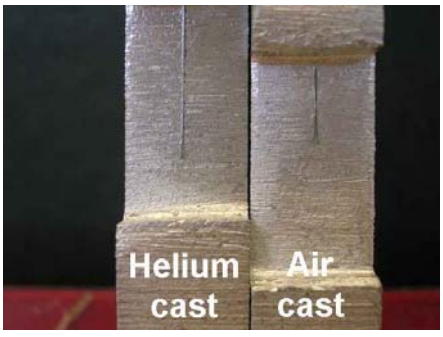

Figure 1. Cooling curves in the cast iron mould (dashed lines) and in the aluminium plate (full lines). Two cases are exhibited: one aluminium plate has been cast in air (black curves) and the second one in helium (grey curves). Picture on the left: position of the thermocouple head in the aluminium plates.

The operating conditions were:

- Melt the aluminium and keep the temperature of the molten aluminium around 770-780ºC (the chamber is set under partial vacuum to avoid any hydrogen absorption by the molten aluminium);
- Warm the cast iron mould to 360-370ºC;
- Fill the chamber with helium until its concentration is equal or upper to 95%.

The temperatures of the molten aluminium and the cast iron mould were almost the same for each experiment undertaken under air and under helium (within ±5ºC).

The cooling temperatures for each Al castings are presented in figure 1. The black curves denote the experiment carried out under air while the grey ones symbolise helium experiment. Similar thermal behaviours have been observed with plates of 5 mm and 25 mm thickness plates. The start of the solidification process is noticed with the first dentritic formation (point a, figure 1) around 615ºC followed with the eutectic plateau (point b, figure 1) around 555ºC. The solidification of the aluminium under helium started earlier than under air.

The reduction of the solidification time was about 25% under helium. Moreover the temperature of the aluminium under helium has reached the mould temperature in less than 3 min (c) while it was about 5 min and a half under air (c'). That means a decrease of 43%-45% of the cooling time of the plate. Then the cooling curve of the casting-mould set beyond point (d) under helium seems to decrease faster than the one at point (d'). Helium affects both the solidification and the global cooling of the casting. Its effect is not linear with the time: firstly the solidification time has decreased about 25%, secondly the global cooling of the casting is superior to 40%.

The position of the type K thermocouples located into the Al castings have been checked, figure 1 left. The thermocouples were both well positioned in the middle of the plates.

The modelling of the casting process is an approach to better understand the different casting mechanisms. One of the most important parameters is heat transfer coefficient at the metal-mould interface. The effect of helium atmosphere on the casting process is significant but the heat transfer coefficient at interface is not known so far. An experiment has been designed in order to evaluate it.

ESTIMATION OF THE HEAT TRANSFER COEFFICIENT

Experimental setup

The experiment consists in casting an aluminium bar in a refractory tube inserted on a H13 steel chill as depicted in figure 2. The steel chill is water cooled as it is commonly done industrially.

The operating conditions were the following:

- Firstly, the still chill is heated until the temperature of the steel at the interface steel / aluminium is about 250ºC.
- Then, the molten aluminium (A356), average temperature of 820ºC, is poured in the refractory tube.
- The water cooling system is switched on.

Three 0.5 mm diameter mineral-insulated type-K thermocouples were inserted into the chill, at distances of 5, 37.5, and 75 mm from the top of the chill. Other 0.2 mm homemade type K thermocouples were inserted in the casting and in the refractory tube. The thermocouple outputs were connected to a data-logger itself connected to a laptop, which recorded the thermal histories at these points in the chill, in the casting and in the refractory tube every 0.025 seconds, for approximately 10-15 minutes.

Measured temperatures inside H13 steel chill were used to estimate the heat flux at the interface steel / aluminium. An inverse heat flux problem has been developed for. Heat transfer coefficient

was deduced from this heat flux and the measured temperatures in the aluminium and in the steel chill. First of all, an accurate thermal modelling of the steel chill is required.

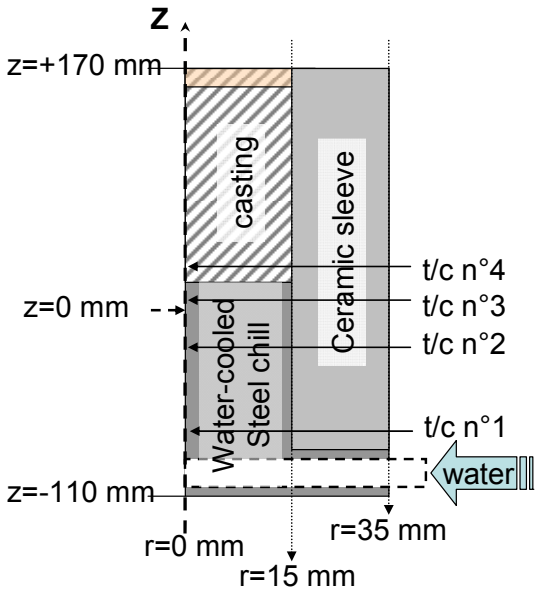

Figure 2. Experimental H13 steel chill used for the estimation of the heat transfer coefficient at the interface steel / aluminium. The steel chill is water cooled at the bottom and the molten aluminium is poured in a refractory tube (thermal insulator) put on the steel chill.

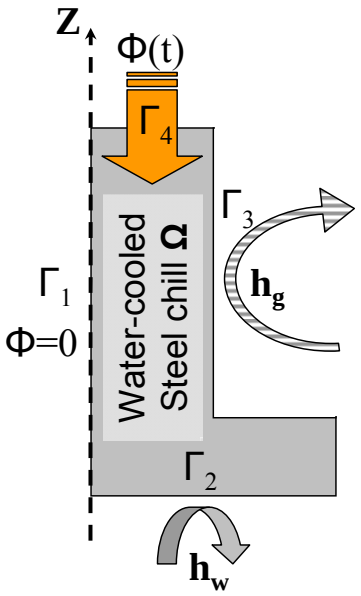

Figure 3. thermal modelling of the H13 steel chill. A global convective coefficient (h_g) is considered on the lateral frontier of the steel chill to take into account the refractory tube. The interface steel/aluminium is subjected to a heat flux. The water cooling is modelled as a convective exchange.

Thermal modelling

A sketch of the thermal modelling of the steel chill is presented in figure 3. Problem geometry is two dimensional axi-symmetric. Lower part of the steel chill is cooled with water, figure 3. Heat loss on the lateral frontier of the steel chill is modelled with convective exchange (the inverse of the refractory thermal resistance: R_g with $h_g = 1/R_g$). The heat transfer at the steel/aluminium interface is modelled with a time dependent heat flux $\phi(t)$.

The stated thermal modelling is described with the following equations:

- the heat conduction equation in the H13 steel chill (domain Ω) during the studied time interval I :

$$\rho(T)C_p(T)\frac{\partial T}{\partial t} - \nabla(\lambda(T)\nabla T) = 0 \quad in\ \Omega \times I \tag{1}$$

- the boundary conditions:

$$-\lambda(T)\frac{\partial T}{\partial n_1} = 0 \quad on\ \Gamma_1 \times I \tag{2}$$

$$-\lambda(T)\frac{\partial T}{\partial n_2} = h_W(T - T_W) \quad on\ \Gamma_2 \times I \tag{3}$$

$$-\lambda(T)\frac{\partial T}{\partial n_3} = h_g(T - T_{room}) \quad on\ \Gamma_3 \times I \tag{4}$$

$$-\lambda(T)\frac{\partial T}{\partial n_4} = \varphi(t) \quad on\ \Gamma_4 \times I \tag{5}$$

- the initial condition:

$$T(r,z;t=0) = T_{room} \quad in\ \Omega \tag{6}$$

where $\rho(T)$, $C_p(T)$ and $\lambda(T)$ are respectively the density, the specific heat and the thermal conductivity of the H13 steel. h_W, T_W, h_g and T_{room} are respectively the water convective exchange coefficient, the water temperature, the inverse of the refractory tube thermal resistance and the ambient temperature. $\phi(t)$ is the heat flux exchanged between the steel chill and the aluminium.

The heat transfer coefficient HTC can be defined as follows:

$$\phi(t) = HTC.(T_{chill} - T_{casting}) \quad \text{on } \Gamma_4 \times I \tag{7}$$

Therefore HTC can be deduced from the heat flux when steel and aluminium temperatures are known at the interface. The statement of the inverse heat flux problem is briefly described in the next section.

Inverse Heat Flux Problem

The inverse heat flux problem can be stated as follows:

Let's find $\phi(t)$, the unknown heat flux, such as $T(r,z,t;\phi) = \hat{T}_m(t;\phi)$ where $T(r,z,t;\phi)$ are the calculated temperatures from the thermal modelling, $\hat{T}_m(t;\phi)$ are the measured temperatures at the thermocouples and $m = 1, n_{th}$ is the number of thermocouples.

This expression can be formulated to least square sense, so the problem consists in minimizing the following cost function $J(T,\varphi)$:

$$J(T,\varphi) = \int_{t_0}^{t_f}\int_{\Omega}\sum_{m=1}^{n_{th}}\left(T(r,z,t;\varphi) - \hat{T}_m(t)\right)^2 \delta(\vec{x} - \vec{x}_m)dtd\Omega \tag{8}$$

Due to the high non-linearity of the thermal problem (temperature dependent parameters, high temperature variations) and the high number of heat flux parameter to estimate (one for each time step of the simulation), a regularization technique is necessary in order to solve and stabilize the formulated inverse problem. The conjugate gradient method developed by O.M. Alifanov [4] has been employed to solve this inverse heat flux problem.

The overall principle of the inverse heat flux problem regularized with the conjugate gradient method is the following (details of the method are given in Alifanov [4]):

Load experimental data

[1] Inverse heat flux loop starts:

Solve **Direct problem** (thermal problem),

Export calculated temperatures $T(x,t)$ at each sensor positions,

Compute cost function $J^n = \sum\left(\theta(x_i,t) - \hat{\theta}_{meas}(t)\right)$, test if $J^n < J_{stop}$ else go to [2],

Solve **Adjoin problem** (derivated from the thermal problem in the order to compute the cost function gradient $J'(T,\phi)$),

Compute the descent direction $d^n = J'(T,\phi) + \beta_n d^{n-1}$,

Solve **Variational problem** (in order to compute the descent depth γ_n),

Compute the descent depth γ_n,

Compute the new estimated heat flux $\bar{\phi}^{n+1} = \bar{\phi}^n + \gamma_n \bar{d}^n$ go back to [1]

End loop

[2] Display estimation results.

EXPERIMENTAL RESULTS

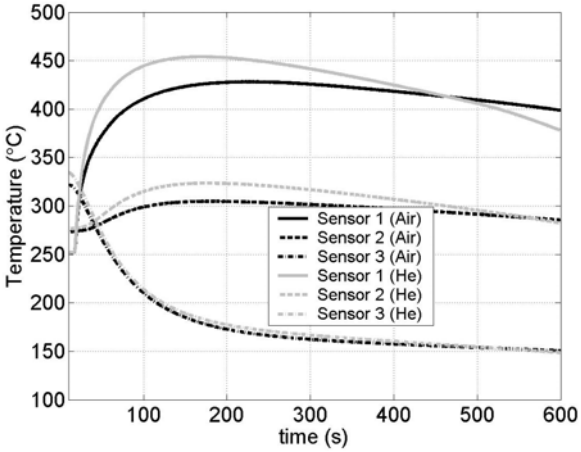

Figure 4. measured temperatures through the depth of the steel chill under air (black curves) and under helium (grey curves).

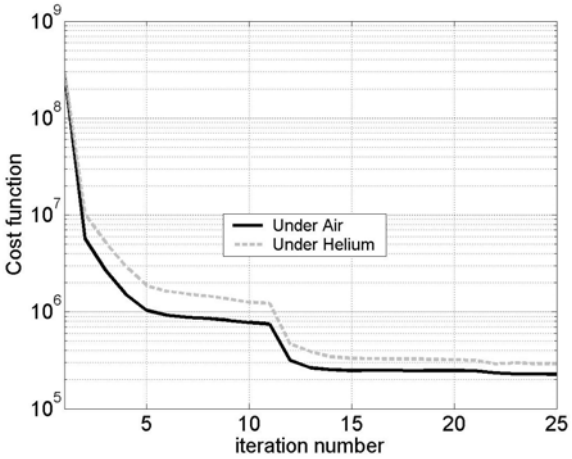

Figure 5. Cost function evolutions for each investigated inverse heat flux problems.

Let's compare the measured temperatures in the steel chill for both conditions: under air and under helium. These experimental data are plotted in figure 4: black curves denote air experiment while the grey curves are for helium. The steel chill heated higher and faster under helium than under air. The thermocouple located to the closest to the interface has risen slightly over 450ºC while it was only 425ºC under air. Steel chill started cooling faster under helium than in air after it has reached his maximum temperature.

These experimental data were used in the inverse heat flux problem in order to estimate the heat flux at the interface mould/casting under helium and under air. Evolutions of the two cost functions are presented in figure 5. The two cost functions have the similar trend. An important decrease is observed in the first 5 iterations as the inverse heat flux problem converges towards the solution. The two cost functions stabilized around a value of 2.10^5 what corresponded to an average standard deviation about $\pm 8°C$ between measured and calculated temperatures as it can be seen in figure 6.

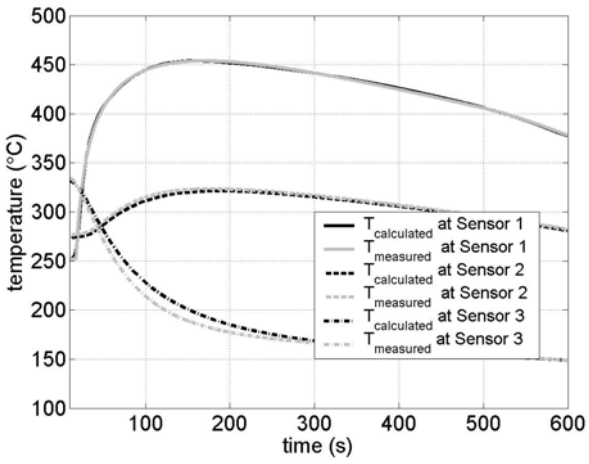

Figure 6. Comparison between measured and calculated temperatures once the inverse heat flux problem was solved (helium experiment).

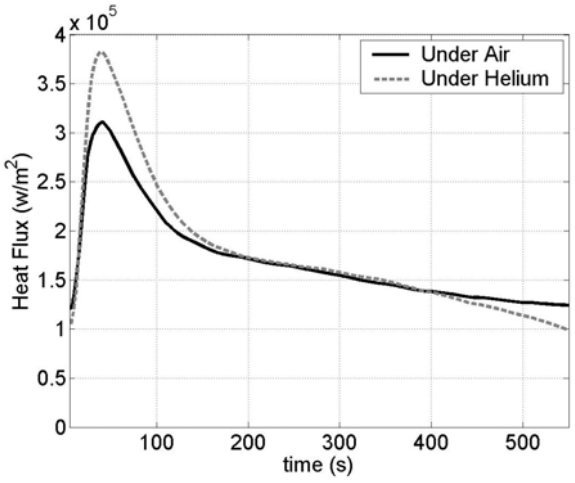

Figure 7. Estimated heat fluxes at the interface mould / casting. Air experiment: black curves; Helium experiment: grey curves.

Calculated and measured temperatures fit quite well except for the thermal sensor which is the closest to the water cooling boundary. The convective exchange coefficient was underestimated on this boundary.

The two heat flux solutions of their respective inverse problem are reported in figure 7. Maximum heat flux values can be of few $kW.m^{-2}$ with sand moulds to few $MW.m^{-2}$ with copper moulds [5]. Maximum heat flux values under helium are about 23% higher than the one under air. The heat flux values under helium are greater than the one under air in the first 180 seconds of the experiments. Then these values remains quite similar between $180\ s$ and $400\ s$. Heat flux values under helium dropped beyond $t \geq 400\ s$. The decrease of both estimated heat fluxes can be decomposed in two parts: the first one starts from the maximum reached value to time $t \sim 110\ s$ and the second one beyond $t \geq 110\ s$. This special time corresponds to a temperature about $555°C$ in the aluminium at the interface mould/casting, figure 9 (temperature of the eutectic plateau). Heat flux rate slowed as the aluminium is solid at the interface mould/aluminium and shrinks, generating a gaseous gap at the interface mould/aluminium what slows the heat transferred through the interface.

Estimated heat fluxes have been used in a second thermal simulation (including the refractory tube and the solidifying aluminium). This thermal simulation allowed calculating the temperature of the aluminium at the interface chill/casting. Then heat transfer coefficients (HTCs) were deduced from previous heat fluxes according to the formula (7). HTCs are presented in figure 8. The HTC calculated under air reached a maximum value of $1700\ W.m^{-2}.K^{-1}$, in the first $50\ s$. Then this value stabilized around $1600\ W.m^{-2}.K^{-1}$ over the remaining time. These HTC values are typical as regards to the literature [1,2].

HTC estimated under helium reached maximum values of $3200\ W.m^{-2}.K^{-1}$ in the first $50\ s$. HTC values stabilized around $2500\ W.m^{-2}.K^{-1}$ until $t \leq 400\ s$ and started decreasing beyond this point to reach $1800\ W.m^{-2}.K^{-1}$ at the end of the time interval. HTC values stabilized over the eutectic transformation and dropped once the casting was totally solidified, see figure 9, probably due to the end of heat release by latent heat of solidification.

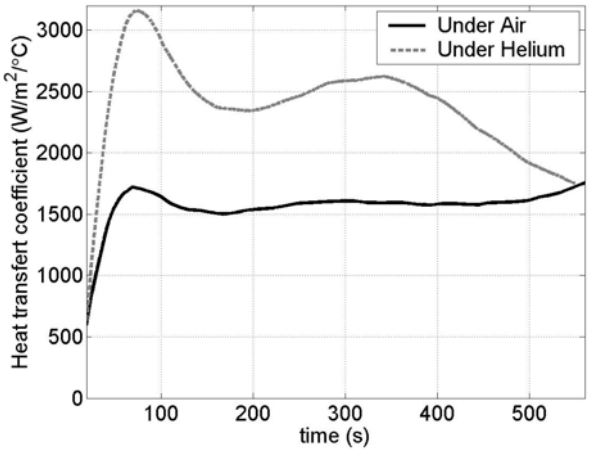

Figure 8. Deduced heat transfer coefficients at the interface mould / casting (Air: black curves and helium: grey curves).

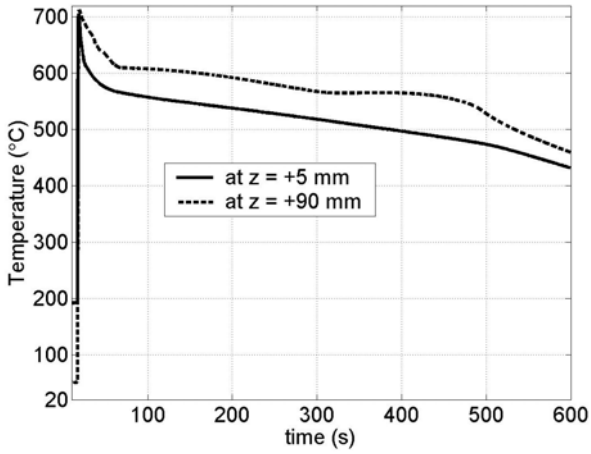

Figure 9. Measured temperatures in the Al casting at different distance from the interface, see figure 3. Helium experiment.

Several phases have been distinguished:

- During the solidification, the HTC values under helium are twice larger than the one under air.
- During the eutectic transformation, the HTC values under helium keep a stabilized value. This one is 1.5 times greater than under air.
- HTC values dropped off once the aluminium is totally solidified. This behaviour has not been observed under air as the temperature measurements were stopped after 10 minutes.

CONCLUSIONS

1. The influence of the helium on the aluminium solidification duration is important. This duration has been shortened by up to 25% in comparison with Al casting under air. Improvement of the heat transfer at the interface mould/casting is due to helium's high thermal conductivity. This reduction of the solidification times should lead to a refinement of grain size [1] and hopefully to an improvement of aluminium mechanical properties.
2. The influence of the helium on the overall cooling of the aluminium casting and steel mould is also significant: the aluminium casting reaches the steel mould temperature 45% faster in comparison with air experiment. Heat losses at exterior mould surfaces are enhanced due to the helium atmosphere as well as the heat transfer at the casting/mould interface. Productivity is almost divided by two according to our results.
3. Heat transfer coefficient values under helium atmosphere are 2 times greater than under air during the solidification of the aluminium. The ratio drops to 1.5 times during the eutectic transformation.

The use of helium in casting industry sounds promising. At least, it should improve the productivity. At this productivity time, the time used to evacuate the air out of the chamber and the time used to refill in the chamber with helium have to be added. In order to decrease the preparation time (air vacuum and helium refilling), it should be interesting to investigate the percentage of helium required to get a good preparation/casting productivity time. The presented experiments have been made with at least 95% of helium. What would have happened with 50% of helium in the chamber?

The effect of the helium on the micrography and mechanical is not known yet but it is currently investigated on the aluminium alloys cast in this work. A last remark: it should be interesting to add some special elements such as sodium, at low concentration, which has the property to help refining the grain size. A study made by Kumar et al [5] showed a grain size refinement and an improvement of the heat flux at the interface. How fast would be the cooling?

REFERENCES

1. E. W. Miguelucci, the aluminium association cast alloy test program: interim report, *AFS Trans.*, vol. 93, 1985, pp 913-916.
2. S. A. Argyropoulos and H. Carletti, Comparisons of the effects of air and helium on heat transfer at the metal-mold interface, *Metallurgical and Materials Transactions B,* Vol. 39, issue 3, 2008, pp 457-468.
3. C.P. Hallam and W.D. Griffiths, A model of interfacial heat transfer coefficient for the aluminium gravity die-casting process, *Metallurgical and Materials Transactions B,* Vol. 35B, 2004, pp 721-733.
4. O.M.Alifanov**,** E.A.Artyukhin et S.V. Rumyantsev, Extreme Methods for Solving Ill-Posed Problems with Applications to Inverse Heat Transfer Problems**,** *Begell house Inc.*, pp 306, 1995.
5. G. Kumar, S. Hedge, K.N. Prabhu, Heat transfer and solidification behaviour of modified A357 alloy. Journal of Materials Processing Technology. 182, 2007, pp 152-156.

A THERMAL MODEL OF FRICTION STIR WELDING APPLIED TO SC-MODIFIED AL-ZN-MG-CU ALLOY EXTRUSIONS

C. Hamilton[1,*], A. Sommers[1], S. Dymek[2]
[1]Miami University, Department of Mechanical and Manufacturing Engineering, Oxford, OH USA
[2]AGH University of Science and Technology, Faculty of Metals Engineering and Industrial Computer Science, Kraków, Poland

ABSTRACT. A thermal model of friction stir welding is presented that proposes an energy-based formulation of the Johnson-Cook plasticity model in order to account for heat generation due to plastic deformation. The proposed formulation is derived from an empirical relationship between the ratio of the maximum welding temperature to the solidus temperature of the alloy and the welding energy. The thermal model is applied to Sc-modified Al-Zn-Mg-Cu alloy extrusions joined by friction stir welding at 225, 250, 300 and 400 RPM (all other weld parameters held constant). With the incorporation of heat generation due to plastic deformation, the thermal model accurately predicts the maximum weld temperatures and temperature profiles at the higher energy weld conditions. At the lower energy welds where plastic deformation contributes a larger portion to the total heat generation, the model under predicts the maximum weld temperatures under the tool shoulder but shows good agreement with the remaining experimental temperature data.

Keywords: *friction stir welding, thermal model, slip factor, heat flux, aluminum alloys*

INTRODUCTION

Friction stir welding (FSW) is a novel solid-state joining process that is gaining popularity in the manufacturing sector and, in particular, the aerospace industry [1, 2]. The plastic deformation and temperature profile during FSW produce a microstructure characterized by a central weld nugget surrounded by a thermo-mechanically affected zone (TMAZ) and heat-affected zone (HAZ). The welded joint is fundamentally defect-free and displays excellent mechanical properties when compared to conventional fusion welds [3]. Since its introduction, numerous researchers have sought to characterize the principles of FSW and to model the microstructural evolution and temperature behavior. The current status of FSW research has been well summarized by Mishra and Mahoney [4].

Researchers have found success in modeling the heat transfer characteristics of FSW. Frigaard et al. [5] developed a finite difference thermal model for a moving heat source and correlated the predicted temperature profile with the measured temperature profile for friction stir welded AA6082-T6 and AA7108-T79 extrusions. Khandkar et al. [6] introduced a model of heat input based on tool torque and successfully modeled the temperature history of friction stir welded AA6061-T651 plate. Early thermal models, such as those of Colegrove and Shercliff [7], however, did not account for the slip that occurs when the tool/workpiece interface softens as the welding temperature approaches the solidus temperature of the alloy. As a result, these models significantly over predicted the maximum temperature for “hot” welding conditions.

* Corresponding author: Dr. Carter Hamilton
Phone: + (1) 513-529-0722, Fax: + (1) 513-529-0717
E-mail address: hamiltbc@muohio.edu

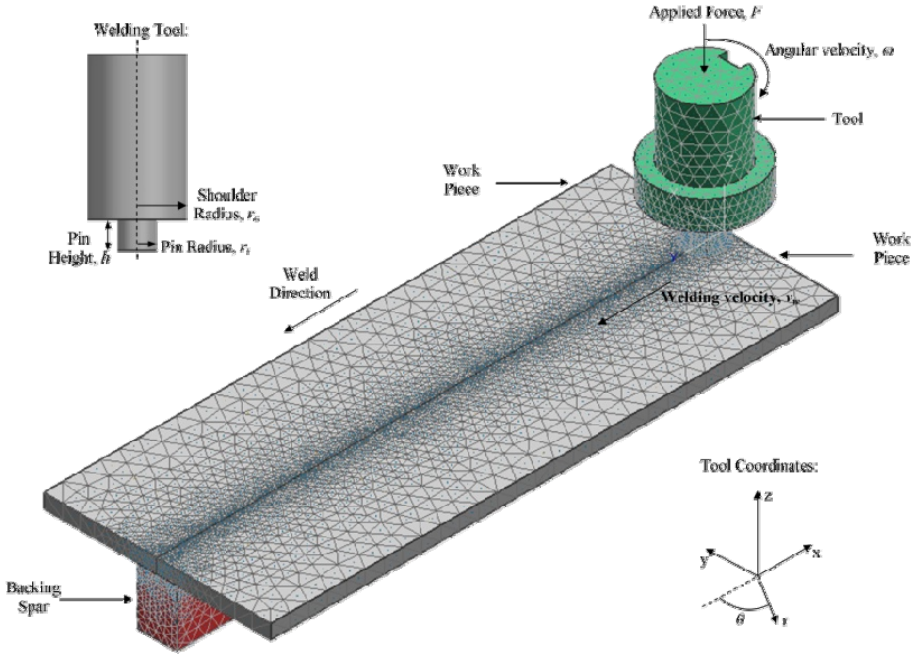

Figure 1. Finite element model of FSW, tool coordinate system and tool geometry

Utilizing Khandkar's torque model, Hamilton et al. [8] proposed an energy-dependent expression for the slip factor for aluminum alloys based on a relationship between the ratio of the maximum weld temperature to the solidus temperature of the alloy and the energy per unit length of weld. The model, however, did not take into account heat generation due to plastic deformation. As a result, the predicted maximum temperatures for low energy welds deviated from experimental data. The current investigation incorporates heat generation due to plastic deformation into this thermal model and demonstrates better agreement between the predicted temperature distributions and the experimental data. A new formulation of the Johnson-Cook plasticity model is also proposed that, like the slip factor, is based upon the weld energy.

EXPERIMENTAL PROCEDURE

Sc-modified Al-Zn-Mg-Cu billets (SSA038 [9]) were extruded as 50.4 mm x 6.35 mm bars and heat treated to a –T6 temper. The extrusions were then sectioned into eight 305 mm sections and sent to the Edison Welding Institute (Columbus, OH) to produce four friction stir welded samples with the configuration shown in Figure 1.The diameter of the FSW tool shoulder was 17.8 mm, the pin diameter tapered linearly from 10.3 mm at the tool shoulder to 7.7 mm at the tip, and the pin depth was 6.1 mm. More specific details of the tool design are proprietary to EWI, but Mishra and Mahoney [4] have reviewed many FSW tool designs that are similar to those utilized in this investigation. With a weld velocity of 2.1 mm/s and an applied force of 22 kN, welds were produced at the following tool rotational speeds: 225, 250, 300 and 400 RPM. Since the force oscillated during welding, the average load values were determined to be 21.4, 20.1, 22.8 and 20.1 kN for 225, 250, 300 and 400 RPM, respectively. The recorded data verified that the weld velocity remained constant at 2.1 mm/s for all welding trials. The temperature profile across the weld was experimentally recorded using a Mikron M7815 Infrared Thermal Imaging Camera. These data were used to verify the efficacy of the numerical model developed during this investigation. The uncertainty in these measurements was ± 2% (or approximately ± 9°C). The thermal emissivity for the infrared data was calibrated by imaging an extrusion length heated to 460°C and adjusting the emissivity value until the recorded temperature of the camera matched the reference temperature. The appropriate thermal emissivity value was determined to be 0.285 which is typical of a lightly oxidized surface.

RESULTS AND DISCUSSION

Energy Contribution due to Plastic Deformation

During friction stir welding, the total energy imparted by the tool to the workpieces, E_{total}, is partitioned between the energy required for plastic deformation and material flow, $E_{plastic}$, and the energy due to friction between the tool and workpieces, $E_{friction}$. The total energy per unit length of weld may be derived from Khandkar's [6] torque-based model for which the total torque, T_{total}, is expressed as the sum of torque contributions from the tool shoulder against the workpiece, the bottom of the tool pin against thickness material and the pin surface against thickness material. If the taper of the welding pin is ignored for simplification, then for the FSW representation in Figure 1, the total torque then becomes:

$$T_{total} = 2\mu F\left(\frac{r_o}{3} + \frac{r_i^3}{r_o^2}h\right) \tag{1}$$

where r_o is the radius of the tool shoulder, r_i is the radius of the pin, h is the pin height, τ is the shear stress during welding, F is the applied force and μ is the coefficient of friction between the tool and the workpieces. The coefficient of sliding friction between aluminum and steel depends on the temperatures produced by the welding conditions. Frigaard et al. [5] reasoned that the coefficient of friction between aluminum and mild steel should be set as the average value between 0.5 for sticky friction and 0.25 for dry sliding. For this investigation, a coefficient of friction 0.5 was used in all calculations. The total energy per unit length of weld, E_{total}, is found by dividing the average power, P_{avg}, by the weld velocity to yield the expression in equation (2):

$$E_{total} = \frac{P_{avg}}{v_w} = T_{total}\frac{\omega}{v_w} \tag{2}$$

where v_w is the welding velocity and ω is the tool angular velocity.

The energy leading to plastic deformation, $E_{plastic}$, may be estimated by considering the stress-strain behavior of metallic materials. The energy required to deform a volume of material to a desired strain is given by the area under the stress-strain curve, and for the idealized case of an elastic, perfectly plastic material:

$$E_{plastic} = V\left(\frac{1}{2}\sigma_y\varepsilon_y + \sigma_y(\varepsilon_f - \varepsilon_y)\right) \tag{3}$$

where V is the volume of material deformed, σ_y is the yield strength of the material, ε_y is the strain value at yield and ε_f is the final strain level of deformation. Hamilton et al. [10] hypothesized that the tool shoulder extrudes a volume of material from an interaction layer into the workpieces to form the weld. The volume of material is contained within a ring centered on the tool at the extrusion distance, r_e (the calculation of which is found in [10]). Thus, the volume of material extruded into the weld center per unit length, V_l, is given by the following expression:

$$V_l = 2\pi r_e w t\frac{\omega}{v_w} \tag{4}$$

where t is the thickness of the interaction layer, w is the width of the extruded column and all other terms have their previous meaning. Based on experimental observations in [10], w was estimated as the tool advance per revolution, $2\pi v_w/\omega$, and t was found to be 0.1 mm. Substituting V_l from equation (4) into equation (3) for V and evaluating at the onset of plastic deformation to simplify the analysis (i.e. $\varepsilon_f = \varepsilon_y$), the energy due to plastic deformation during FSW becomes:

$$E_{plastic} = 2\pi^2 r_e t\sigma_y\varepsilon_y = 2\pi^2 r_e t\frac{\sigma_y^3}{E} \tag{5}$$

where E is the modulus of elasticity.

The yield strength, σ_y, which is dependent on the temperature and the strain rate, is typically modeled using the Johnson-Cook material law that is of the form [11]:

$$\sigma_y = (A + B[\bar{\varepsilon}^{pl}]^n)\left(1 + C\ln\frac{\dot{\bar{\varepsilon}}^{pl}}{\dot{\varepsilon}_0}\right)\left(1 - \left(\frac{T - T_{ref}}{T_{melt} - T_{ref}}\right)^m\right) \quad (6)$$

where $\bar{\varepsilon}^{pl}$ is the effective plastic strain, $\dot{\bar{\varepsilon}}^{pl}$ is the effective plastic strain rate, $\dot{\varepsilon}_0$ is the normalizing strain rate and *A, B, C, n, T_{melt}, T_{ref}* and *m* are material/test constants for a particular alloy. As the welding energy of FSW increases, the welding temperature also increases, thereby decreasing the yield strength of the material. Hamilton et al. [8] proposed that during FSW a characteristic relationship exists for aluminum alloys between the ratio of the maximum weld temperature to the solidus temperature of the alloy, T_{max}/T_s, and the total energy per unit length of weld, E_{total}. From that relationship, the following energy-dependent expression for the slip factor was offered:

$$\delta_E = \exp\left(-\frac{E_{total}}{(E_{total})_{max}}\right) \quad (7)$$

where $(E_{total})_{max}$, the maximum effective total energy, is defined as the energy level for which the maximum welding temperature is equal to the solidus temperature of the alloy (i.e. $T_{max}/T_s = 1$). Thus, one possible energy based expression for the temperature dependence of the yield strength during FSW is then:

$$(\sigma_y)_T = (\sigma_y)_o \exp\left(-\alpha\frac{E_{total}}{(E_{total})_{max}}\right) \quad (8)$$

where $(\sigma_y)_T$ is the yield strength at the welding temperature corresponding to an energy level of E_{total}, $(\sigma_y)_o$ is the room temperature yield strength, α is a scaling factor and all other terms have their previous meaning.

Figure 2 plots the Johnson-Cook model for the temperature-dependent yield strength of AA6061-T6 and the energy-dependent relationship given by equation (8) applied to the AA6061-T6 FSW-data taken from [6] and [8]. The $\bar{\varepsilon}^{pl}$ and $\dot{\bar{\varepsilon}}^{pl}$ inputs for the Johnson-Cook model were selected such that the predicted yield strength at room temperature equaled the value of the *A* coefficient. These inputs and coefficients are summarized in Table 1 [11]. Figure 2 demonstrates that with the scaling factor, α, in equation (8) set to 1.4, the two models show excellent agreement with one another over a temperature range from 100°C to 500°C, typical FSW temperatures. The perturbation in the energy-dependent model beyond 400°C results from a change in the coefficient of friction value for higher weld energies, as discussed in [8]. Therefore, by substituting equation (8) into equation (5), the plastic energy per unit length of weld during friction stir welding becomes:

$$E_{plastic} = \frac{2\pi^2 r_p^2}{E}(\sigma_y)_o^2 \exp\left(-2\alpha\frac{(E_{total})_{eff}}{(E_{total})_{max}}\right) \quad (9)$$

Table 1
Johnson-Cook plasticity model coefficients and input parameters

Coefficients		Input Parameters	
A	324 MPa	$\bar{\varepsilon}^{pl}$	0.0001
B	114 MPa	$\dot{\bar{\varepsilon}}^{pl}$	0.001 s^{-1}
C	0.002		
n	0.42		
m	1.34		
$\dot{\varepsilon}_o$	1.0 s^{-1}		
T_{melt}	925 K		
T_{ref}	294 K		

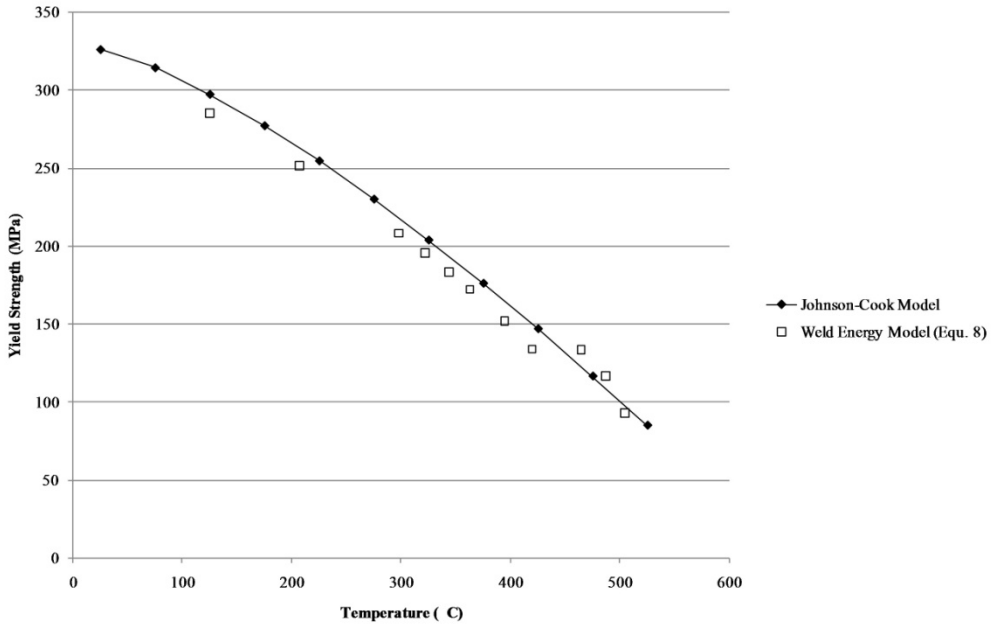

Figure 2. Comparison of the Johnson-Cook material model for AA6061-T6 with the proposed welding energy model presented in equation (9)

The energy expression in equation (9) approximates the plastic energy during FSW, but underestimates the actual plastic energy due to three assumptions that were employed in its derivation. First, although the yield strength and tensile strength for certain alloys can be similar in magnitude (for example, the tensile strength of SSA038-T6 is 663 MPa, and the yield strength is 605 MPa), some strain-hardening is expected to occur and increase the amount of plastic energy over the elastic, perfectly plastic condition assumed in this analysis. Second, during FSW, the strain level will exceed the strain at yield resulting in higher plastic energies than predicted by this model. Finally, the volume of material calculated using equation (4) is conservative and represents only a portion of the total volume that is actually plasticized during FSW. Despite these assumptions, this method of accounting for the heat generation due to plastic deformation improves the correlation between the experimental temperature data and the temperature distributions predicted by the thermal model.

Heat Equation and Heat Flux

For the FSW representation and tool coordinate system shown in Figure 1, the heat flux, q, is typically presented in the following form [12]:

$$q = \left[(1-\delta)\eta\tau_y + \delta\mu P_N\right](\omega r - v_x sin\theta) \tag{10}$$

where v_x is the welding velocity in the x-direction, δ is Nandan's slip factor from [12], η is the mechanical efficiency (the amount of mechanical energy converted to heat energy), τ_y is the maximum shear stress at yielding, P_N is the normal pressure relative to a tool face and θ is the radial angle measured about the tool axis. For typical welding velocities, the $v_x sin\theta$ term in equation (10) is small relative to the ωr term; therefore, the ($\omega r - v_x sin\theta$) expression can effectively be replaced by ωr.

The first term in equation (10) represents heat generation due to plastic deformation, and the second term represents heat generation due to friction between the tool and workpiece. Thus, as presented in the equation, δ represents the partition of heat generated from plastic deformation to heat generated from friction. The slip factor proposed by Hamilton et al. [8], δ_E, however represents the efficiency of frictional heat transfer rather than the partition of heat between plastic deformation and friction. Therefore, if one defines the energy partitioning factor, γ, as the ratio of the plastic

energy to the total energy (i.e. $\gamma = E_{plastic}/E_{total}$) and introduces δ_E as the slip factor, an alternate representation for equation (10) becomes:

$$q = \gamma\eta\tau_y\omega r + (1-\gamma)\delta_E\mu P_N\omega r \tag{11}$$

The value of γ decreases with increasing welding energy, reflecting the decreasing contribution of plastic deformation to heat generation and the increasing contribution of friction. The maximum shear stress in the first term of equation (11) can be estimated from the von Mises yield criterion, such that $\tau_y = (\sigma_y)_T/\sqrt{3}$, where $(\sigma_y)_T$ is the welding temperature dependent yield strength defined in equation (8).

For the tool shoulder and pin bottom, the normal pressure, P_N, is the applied pressure on the workpiece during welding. For the interface between the side of the pin and the workpiece, however, the heat flux is assumed to be zero since the normal pressure here is significantly less than the applied pressure on the workpiece under typical welding conditions. Therefore, the thermal model developed in the following sections utilizes the average heat flux on the pin bottom, $q_{pinbottom}$, and tool shoulder, $q_{shoulder}$, to calculate the welding temperatures. Assuming axisymmetric heat generation, these heat flux equations given in equations (12) and (13) are:

$$q_{pinbottom} = \frac{\int_0^{r_i}\gamma\eta\tau\omega r+(1-\gamma)\delta_E\mu P_N\omega r dr}{r_i} = \frac{\gamma\eta\tau\omega r_i+(1-\gamma)\delta_E\mu P_N\omega r_i}{2} \tag{12}$$

and

$$q_{shoulder} = \frac{\int_{r_i}^{r_o}\gamma\eta\tau\omega r+(1-\gamma)\delta_E\mu P_N\omega r dr}{r_o-r_i} = \frac{\gamma\eta\tau\omega(r_o^2-r_i^2)+(1-\gamma)\delta_E\mu P_N\omega(r_o^2-r_i^2)}{2(r_o-r_i)} \tag{13}$$

where all terms have their previous meaning. Based on other FSW research, the value of the mechanical efficiency factor, η, is taken as 0.5 [12].

Thermal Model: Material Properties and Boundary Conditions

Using NX 5.0, a thermal model of friction stir welding was developed that included tool articulation. Figure 1 shows the finite element model of the FSW process that utilizes a backing spar. Due to the applied pressure during FSW, most heat flows from the workpiece to the backing plate at the interface under the tool resulting in high localized heat transfer in this region. Some thermal models introduce a variable gap conductance to simulate the workpiece/backing plate interface, but in this treatment, the thermal model uses a spar, reducing the number of equations to be solved while still capturing the flow of heat between the workpiece and backing plate. The width of the backing spar is equal to the tool diameter with a height of 25.4 mm, consistent with the spar dimensions used by other researchers [6, 7].

Since the chemistry of SSA038 is similar to that of AA7050, the thermal model utilizes the thermal conductivity and specific heat capacity for AA7050 [9]. For the tool material, the thermal model uses 410 stainless steel. The model assumes perfect contact between the workpieces along the weld line and assumes perfect contact between the tool shoulder and the workpieces. A gap thermal conductivity of 157 W/m·K, the average thermal conductivity of AA7050 between 300 K and 700 K, was applied between the pin bottom and the bottom of the workpieces. For the boundaries exposed to ambient conditions, the convective heat transfer coefficient was set to 15 W/m^2·K to approximate free convection on these surfaces. For the tool top and spar bottom, a convection coefficient of 200 W/m^2·K was applied, and for the area outside of but adjacent to the backing spar (and therefore removed from tool articulation), a convective coefficient of 100 W/m^2·K was used. Heat dissipation due to radiation was ignored.

Table 2
Total energies and maximum weld temperatures for each weld condition

RPM	E_{total} (J/mm)	Maximum Welding Temperature (°C)		
		Experimental	Plastic Def.	No Plastic Def.
225	938	346	313	294
250	977	350	320	301
300	1331	372	365	356
400	1567	390	391	385

Thermal Model: Execution and Results

The thermal model was then used to determine the maximum welding temperatures and temperature profiles of SSA038-T6 for the four, unique total energy levels (see Table 2), and these predicted results were then compared with the experimental temperature data. The model was executed for each weld condition with heat fluxes calculated from equations (12) and (13) to include the effect of heat generation due to plastic deformation. For comparison, the model was also run without heat generation due to plastic deformation (i.e. the partitioning factor, γ, was set equal to zero). The maximum welding temperature stabilized after approximately 26 simulated seconds of friction stir welding. (Note: The model did not utilize a dwell time prior to tool advance.) Table 2 summarizes the predicted maximum welding temperatures and the experimental temperatures for each weld trial.

As seen in the table, inclusion of plastic deformation brings the predicted temperatures of the thermal model into better agreement with the actual welding temperatures. At 225 RPM, without plastic deformation, the thermal model predicts a maximum temperature of 294°C, a 15% error with respect to the experimental value. Introducing plastic deformation into the model raises the predicted temperature to 313°C and reduces the error to 9.5%. At 400 RPM, without plastic deformation, the predicted welding temperature is 385°C, a 1.3% error. But with plastic deformation taken into account, the predicted temperature rises to 391°C and shows good agreement with the experimental value (< 1.0% error). The efficacy of the model with plastic deformation, however, is primarily observed in the lower energy welds. Since the flow stress is greater at the lower weld energies, the contribution to heat generation from plastic deformation represents a greater portion of the total heat generation at lower weld energies (225 and 250 RPM), than at higher weld energies (300 and 400 RPM). This behavior is captured in the partitioning factor, γ, introduced in equation (11).

Figure 3 plots the experimental temperature data for each weld trial with the profiles predicted by the thermal model for the same location. The profiles extend from the weld centerline into the workpiece along the top surface of the FSW configuration. As seen in each figure, inclusion of plastic deformation shifts the predicted temperature profiles toward the experimental profiles. For the lower weld energies, the thermal model under predicts the maximum weld temperature but shows relatively good agreement with respect to the magnitude and shape of the experimental temperature profile beyond 9 mm, the approximate radius of the tool shoulder. The conservative approach utilized to calculate the plastic energy may explain the observed discrepancy between the maximum weld temperatures that were experimentally observed and numerically predicted. For the higher weld energies, the predicted maximum weld temperatures show good agreement with the experimental values, but the temperature profiles beyond 9 mm generally under predict the temperature as compared to the experimental data.

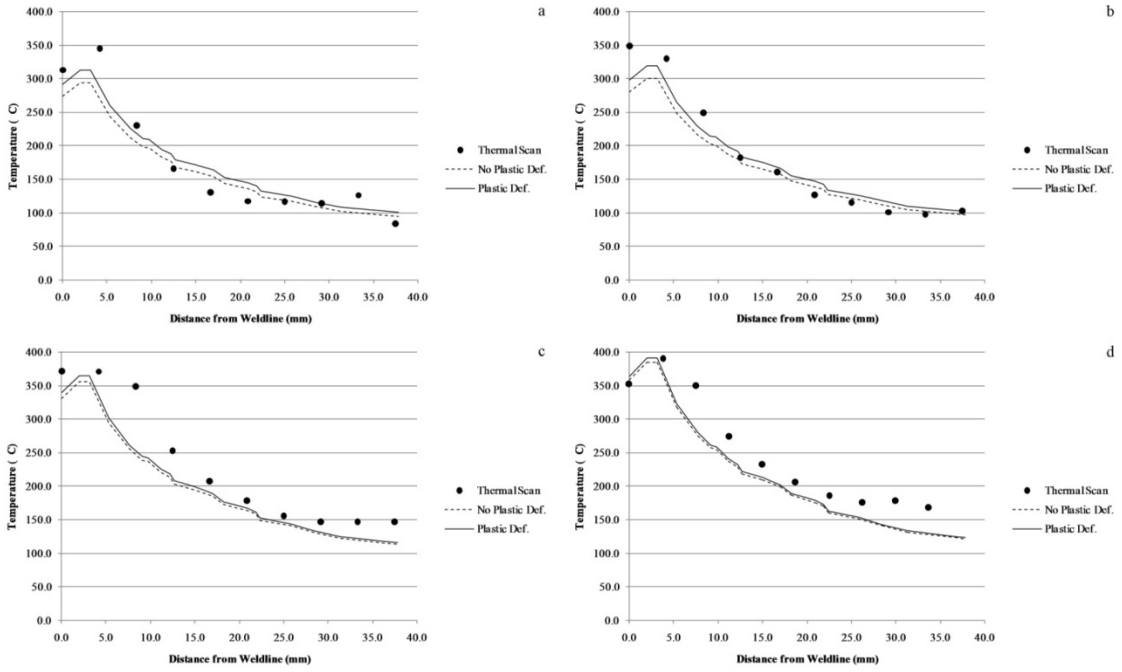

Figure 3. Experimental temperature and predicted temperature profiles: a) 225 RPM, b) 250 RPM, c) 300 RPM and d) 400 RPM

CONCLUSIONS

A thermal model of the friction stir welding of aluminum alloys is presented that incorporates heat generation due to plastic deformation and partitions the heat generation between friction and plastic deformation based on the ratio of the plastic energy to the total effective energy. To calculate the plastic energy and to account for the change in the yield strength with welding temperature, a formulation of the Johnson-Cook material model based on welding energy is utilized. This energy-based formulation shows good agreement with experimental yield strength/temperature data found in the literature for AA6061-T6; however, its application to other aluminum alloys has not yet been verified due to a paucity of published experimental data.

For the Sc-modified Al-Zn-Mg-Cu alloy examined in this work, the thermal model successfully predicts the maximum welding temperatures and temperature distributions over the energy range investigated. The model, however, shows its greatest potential at higher energy welds (i.e E_{total} > 1000 J/mm) where heat generation due to friction dominates. At lower energy levels (i.e. E_{total} < 1000 J/mm), the predicted temperature profile shows good agreement with experimental temperature data in terms of magnitude and shape away from the tool shoulder, but the model under predicts the maximum welding temperatures due to the assumptions/simplifications that were used in the calculation of the plastic energy.

ACKNOWLEDGEMENTS

The authors acknowledge the Polish Ministry of Science and Higher Education (Grant No. N 507 094 32/2648), for their support of this research.

REFERENCES

1. W. M. Thomas et al., Great Britain Patent Application No. 9125978.8, December 1991.
2. C. Dawes, W. Thomas, TWI Bulletin 6, November/December (1995) 124.

3. C. Hamilton, S. Dymek, M. Blicharski, Comparision of mechanical properties for 6101-T6 extrusions welded by friction stir welding and metal inert gas welding, Archives of Metallurgy and Materials 52 (2007) 67 – 72.
4. R. S. Mishra and M. W. Mahoney, Friction stir welding and processing, Metals Park, OH, ASM International, 2007.
5. O. Frigaard, O. Grong and O. T. Midling, A process model for friction stir welding of age hardening aluminum alloys, Metallurgical and Materials Transactions A 32 (5) (2001) 1189 – 1200.
6. M. Z. H. Khandkar, J. A. Khan and A. P. Reynolds, Predictions of temperature distribution and thermal history during friction stir welding: input torque based model, Science and Technology of Welding and Joining 8 (3) (2003) 165 – 174.
7. P. A. Colgrove and H. R. Shercliff, Experimental and numerical analysis of aluminium alloy 7075-T7351 friction stir welds, Science and Technology of Welding and Joining 8 (5) (2003) 360 – 368.
8. C. Hamilton, S. Dymek and A. Sommers, A thermal model of friction stir welding in aluminum alloys, International Journal of Machine Tools and Manufacture 48 (2008) 1120 – 1130.
9. S. V. Senkova, O. N. Senkov, D. B. Miracle, Cryogenic and elevated temperature strengths of an Al-Zn-Mg-Cu alloy modified with Sc and Zr, Metallurgical and Materials Transactions A, 57 (12) (2006) 3569 – 3575.
10. C. Hamilton, S. Dymek, M. Blicharski, A model of material flow during friction stir welding, Material Characterization 59 (2008) 1206 – 1214.
11. G. R. Johnson and W. H. Cook, A constitutive model and data for metals subjected to large strains, high strain rates and high temperatures, Proceedings of the 7th International Symposium on Ballistics, The Hague, The Netherlands, 1983.
12. R. Nandan, G. G. Roy, T. J. Lienert and T. Debroy, Three-dimensional heat and material flow during friction stir welding of mild steel, Acta Materialia 55 (2007) 883 – 895.

EXPERIMENTAL ESTIMATION OF HEAT TRANSFER COEFFICIENT IN HOT STAMPING PROCESS: OMEGA CONFIGURATION

B.Abdulhay[1,2,*], B.Bourouga[1], C.Dessain[2], G.Brun[2] and J.Wilsius[2]
[1]LTN, UMR CNRS 6607, BP 50609, La Chantrerie, 44306 Nantes Cedex 3, France
[2]ArcelorMittal R&D Automotive Applications, BP 30109, 60761 Montataire Cedex, France

ABSTRACT. Hot stamping is a novel process that comes out as a combination of hot forming and simultaneous quenching of the blank. In this paper, an original experimental procedure developed to estimate the thermal conductance at the Part-Tools interfaces during a hot stamping process, is presented. The tools set (punch and die) has been designed to form samples with an omega shape. Reproducibility tests carried out under a pressure contact of 10MPa demonstrated the good reliability of the device. In order to describe correctly the thermal boundary conditions at Part-Tools interfaces, the adopted procedure consists in estimating accurately the thermal contact resistance *TCR* at different contact points. We noticed a good repeatability of thermal conductance time evolution and particularly, of the final reached value $R_c = 2.88*10^{-4}\ m^2.K/W$. The analysis of experimental results showed that the heat transfer intensity is maximum at the bottom of the die.

Keywords : *Thermal Contact Resistance TCR, Pressure, Phase change, static contact.*

NOMENCLATURE

a	Thermal diffusivity (m²/S)
C_P	Specific heat (KJ/Kg.K)
e_O	Position of 2nd thermocouple in the tool (m)
e_P	Position of the thermocouple in the sample (m)
E	The young's modulus (P)
g	The gravity acceleration (m/S²)
M_S	Martensitic transformation temperature
P	Pressure (P)
t	Time (S)
T_O	Tool temperature (K)
TCR	Thermal contact resistance (m².K/W)
$\overline{R_C}$	Mean average of thermal resistance (m².K/W)
Y_O	Temperature (K)
α	Thermal expansion
ε	Nominal strain
λ_O	Thermal conductivity of the tool (W/m.°C)
ρ	Density (Kg/m^3)
σ	Nominal stress (P)
φ	Flux density (W/m²)

INTRODUCTION

Safety improvement and weight reduction has become the major objectives of automotive manufacturers in the design of new BIW components. Therefore, it is essential to realize parts presenting not only a high mechanical properties but also significant thinner sheet thickness [1]. Hot stamping of a quenchable steel comes out as a quite novel process which allow reaching strength levels which are far above those of best-in-class cold stamping steels. Moreover, the traditional balance between high strength and low formability is overcome by hot stamping: as the forming is done at high temperature, the austenitic material exhibits a very good ductility and complex shapes can be realized in a single step [2].

* PHD student :Bakri ABDULHAY
Phone :+(33)02 40683143
E-mail address: bakri.abdulhay@univ-nantes.fr

A specific steel grade, called Usibor 1500P, dedicated to the hot stamping process has been developed by ArcelorMittal [3]. Usibor1500P is a coated Aluminium-Silicon boron steel designed to reach an ultimate tensile strength above 1500MPa after hot stamping. This forming technique consists, first, in heating blanks until complete austenitization (900°C to 950°C) during 4 to 10 minutes. Afterwards the hot sheet is transferred, as fast as possible, to the press and immediately stamped in order to take advantage of the excellent formability at high temperature (600°C to 800°C). The tool is held closed for 20 seconds for quenching the sheet below the martensite finish temperature M_f (figure 1).

To determine the feasibility of Usibor1500P components and help the hot stampers in the fast evolution of this innovative technology, the numerical simulation of this thermo-mechanical process is paramount. It requires a good knowledge of thermal and mechanical material characteristics that are needed as input data in any finite element code.

In this objective, thermal study is of a fundamental importance for the hot stamping process modelling. It requires a proper control of the temperatures and thus, the heat transfer coefficient at the part-tools interfaces during the different process steps, from the blank positioning in the die until the blank quenching in the closed tools.

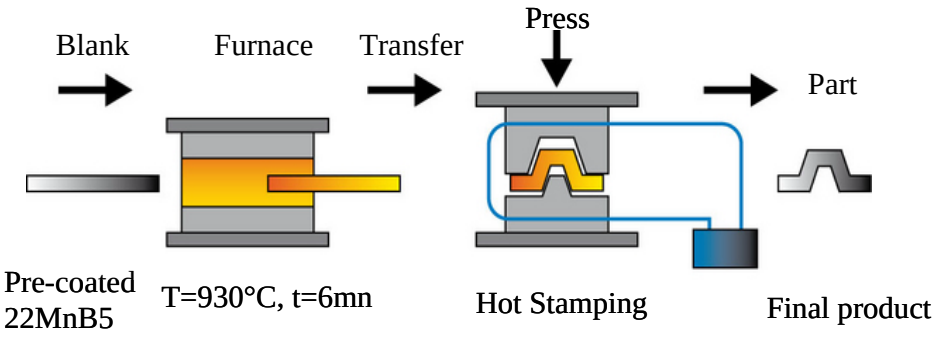

Figure 1. Schematic sketch of the hot stamping process of Usibor1500P.

In this paper, we present a brief description of the experimental procedure developed in order to determine the thermal contact resistance *TCR* at the part-tool contact interface. In the second section of this work, the experimental results of tests carried out at a contact pressure of 10 MPa are described. The last section details the analysis of the experimental results at different contact pressures.

THE EXPERIMENTAL PROCEDURE

After blanking, the first step of the hot stamping process is austenization. The blank is heated in a continuous furnace above material's specific AC_3-temperature for a defined duration in order to guarantee a homogeneous micro-structural phase transformation from ferrite-pearlite to austenitic. The aluminium-silicon coating is transformed to Al-Si-Fe alloyed layer which avoids corrosion and decarburization of the base material. Then, the blank is transferred very quickly to the press where it stays a short time on the die during punch approach (Approach step ~2sec). Afterwards, the hot blank is stamped between the moving punch and the static die to get a final Omega shape when the tool is completely closed (Forming step ~2sec). Finally, the formed part is quenched between the die and the punch (Quenching step ~20sec). Figure 2 summarizes the different steps of hot stamping procedure.

As the objective of this study is the heat transfer estimation at the part-tools contact, one or more flux sensors made of at least two thermocouples are placed in the close vicinity of the tools surface. Four thermocouples are also inserted in the half thickness of the blank sample at various positions judiciously chosen.

The measurement principle and the experimental device, particularly the thermal instrumentation, are fully described in [4]. So, a brief description is presented in this paper.

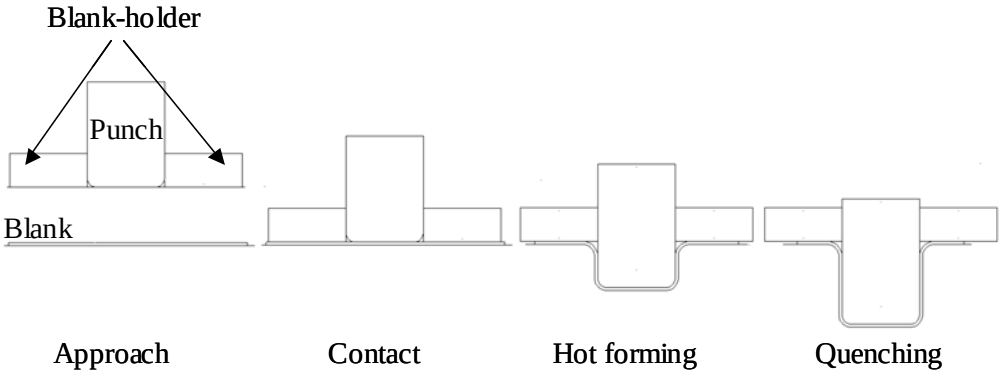

Figure 2. Sketch of different phases in hot stamping process (the die is not shown).

The measurement principle

The principle of the method is based on the transitory analysis of the temperature fields recorded on both sides of the interface. An example of the *TCR* estimation at a specific position is presented in figure 3:

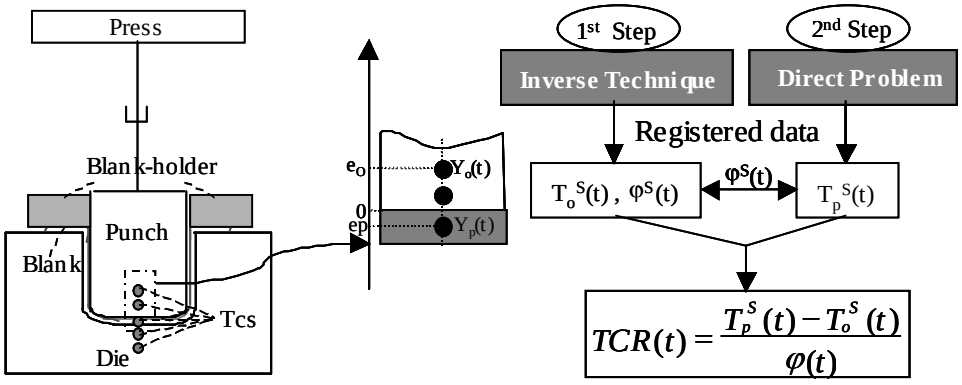

Figure 3. The measurement principle.

The formulation of the direct problem in the part is as follows:

$$(\rho.C_p)_p \frac{\partial T_p(x,t)}{\partial t} + P_p(T) = \frac{\partial}{\partial x}[\lambda_p . \frac{\partial T_p(x,t)}{\partial x}] \qquad 0 \le x \le e_p \ , \qquad t > 0 \tag{1.1}$$

$$-\lambda_p \left.\frac{\partial T_p}{\partial x}\right|_{x=0} = \varphi(t) \qquad t > 0 \tag{1.2}$$

$$T_p(e_p,t) = Y_p(t) \qquad t > 0 \tag{1.3}$$

$$T_p(x,0) = Y_p(0) \qquad 0 \le x \le e_p \ , \qquad t > 0 \tag{1.4}$$

P_p is the internal source due to the metallurgical transformation from austenite to martensite. It is obtained from the literature. The formulation of the direct problem in the tools is similar by replacing the index p (work-piece) by O (tool). The heat conduction equation in this case becomes homogeneous ($P_O = 0$). To summarize, the estimation procedure is as follows:

a- Considering the data recorded by the two thermocouples and the direct problem in the tool, we estimate the flux density $\varphi(t)$ and the temperature at the surface on the tool side $T_O(0,t)$ by the inverse technique based on the sequential method of Beck.

b- Then, knowing the heat flux density at the contact interface and the temperature measured by the thermocouple placed on the blank, we can calculate the surface temperature on the blank $T_p(0,t)$ by resolution of the heat conduction problem.

c- Finally, knowing the two surface temperatures on the blank and the tool sides as well as the flux density at the contact interface, we estimate *TCR(t)*:

$$TCR(t) = \frac{T_P(0,t) - T_O(0,t)}{\varphi(t)} \tag{2}$$

The experimental device

The *TCR* measurement at the Blank-Tool interface suggests us to develop an experimental device made up of five elements as represented in Figure 4: the forming press, the furnace, instrumented blanks and tools and the acquisition system.

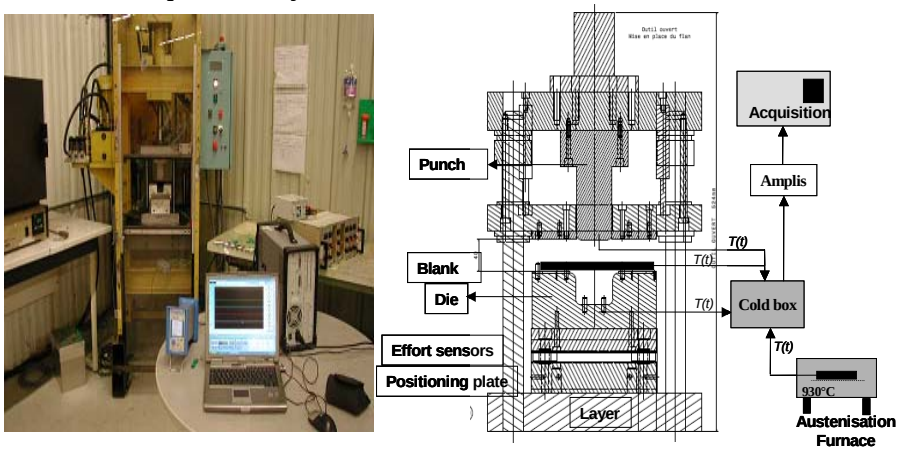

Figure 4. The experimental device.

The sample is designed as a 165x50x1.5 mm^3 plane blank and made in Usibor 1500P. The hot stamping tool designed for the study is made up of a die and a punch made in Z160CDV12 steel material. One or more flux sensors made of at least two thermocouples are placed in the immediate vicinity of the tool surface. The positions of the measurement points are selected based on the sensibility and the precision of the *TCR* estimation. Thus, certain rules that govern parietal instrumentation by thermocouple have to be considered [5].

The tool dimensions (die and punch) and the technological choices for the implementation of the measurement system described above, were specified in a way to respect the ability and the capacity of the press (speed, maximal stamping force,…). Therefore, we choose the thermocouple type K ($d = 100\,\mu m$) sheathed with silky glass in order to avoid the saturation phenomenon of thermocouples at high temperature. The blank and the tools dimensions and the positions of different flux meters are presented on figure 5:

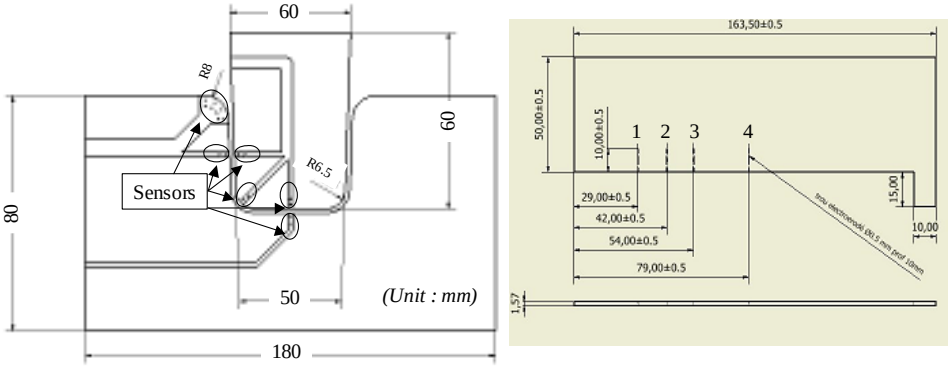

Figure 5. Part and tools dimensions and thermocouples positions.

EXPERIMENTAL RESULTS

In order to ensure the repeatability of the results, six instrumented samples made in Usibor 1500P are successively hot stamped. Each sample is first homogenously heated in a furnace up to 930°C until its complete austenization. It is, then, transferred from furnace to press and put on the die. The hot sample is rapidly formed and finally quenched by direct contact with the tools.
The post processing of recorded data is conducted according to the measurement principle. In this section, we will focus on the *TCR* estimation during the quenching phase where the part-tools contact is static. A typical temperature variation registered by the thermocouples inserted in the blank and in front of the bottom of the die at the end of forming is presented in figure 6:

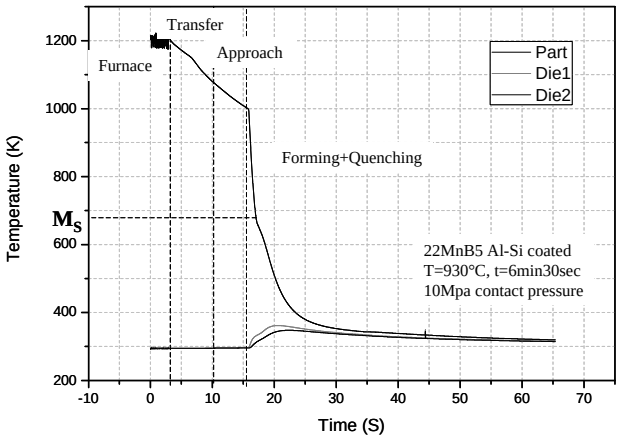

Figure 6. Typical cooling rate under a contact pressure of 10MPa.

This figure shows the temperature variation given by the thermocouples implanted in the sample and the die (the thermocouples are aligned on the symmetric vertical plane of the tool). We notice that the cooling rate during the transfer phase is roughly identical to the approach phase (~15 K/S). The blank temperature decreases from 930°C to 730°C which is considered as acceptable as the blank keeps its high formability at this temperature. Thus, the forming phase begins still at the austenitic phase ($T > M_S$).

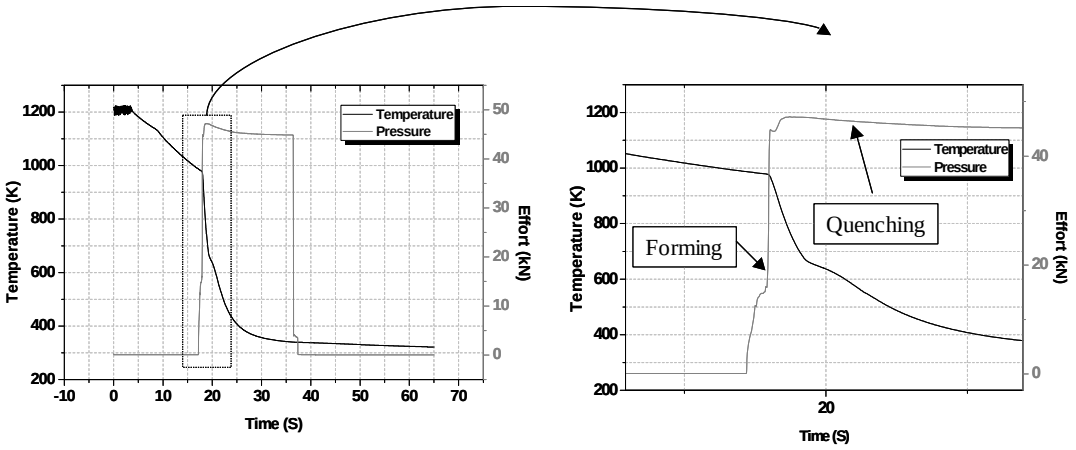

Figure 7. The part temperature and the pressure evolution.

Figure 7 shows the blank temperature given by the thermocouple #4 and the stamping force evolution. We observe that the blank temperature at this very point is not influenced by the forming. In fact, in this zone, the punch is not in contact with the blank during the forming phase, as illustrated on Figure 8.

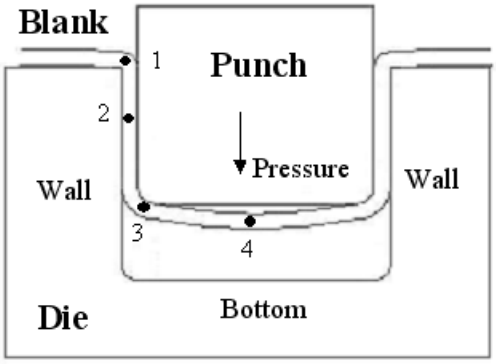

Figure 8. Position of the thermocouples in the blank during the forming phase.

First, reproducibility tests were carried out at a contact pressure of 10MPa. We estimate the *TCR* evolution as function of time at different contact positions during the quenching phase. Figure 9 illustrates the good repeatability of the *TCR* results. In this figure, a singularity is also observed on the *TCR* curves that appears systematically at the thermal level corresponding to the metallurgical transformation from austenite to martensite.

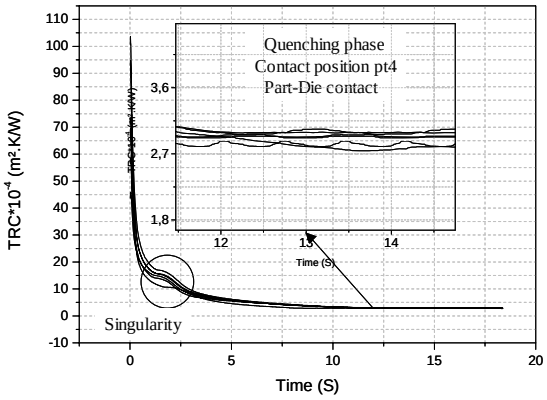

Figure 9. The *TCR* evolution as function of time under a contact pressure of 10MPa.

The *TCR* decreases to reach a constant value around $\mathrm{TCR} = 3.0\mathrm{x}10^{-4}\ \mathrm{m^2.K/W}$. A mean value of $\overline{\mathrm{R_C}} = 2.88\mathrm{x}10^{-4}\ \mathrm{m^2.K/W}$ is obtained with a dispersion that doesn't exceed $1.9\mathrm{x}10^{-5}$. All results have a dispersion of about 5 % which is considered as acceptable, considering the high influence of surface parameters of each samples and the difficulty of the temperature measurement. The singularity observed on the *TCR* curves is due to microstructure transformation in the sample. Indeed, the rapid cooling by tool quenching induces a transformation of the austenite into martensite. The martensitic transformation takes place through a process of nucleation and growth. Literature shows that this microstructure transformation causes the release of an elastic energy (volume change due to the difference in structure of austenite and martensite) and dissipative energy (latent heat release). The volume change of the sample caused by the martensitic transformation leads to a normal stress that tends to antagonize the punch force:

$$\sigma_{A-M} = \varepsilon * E = \alpha * \Delta T * E \tag{3}$$

In a second step, we compared the heat transfer at the blank-tool interface at two different contact positions during the quenching phase (with a contact pressure of 10MPa). The sample-bottom of the die (position #4) and the sample-vertical wall of the die (position #2) contact areas were analyzed (Figure 8).

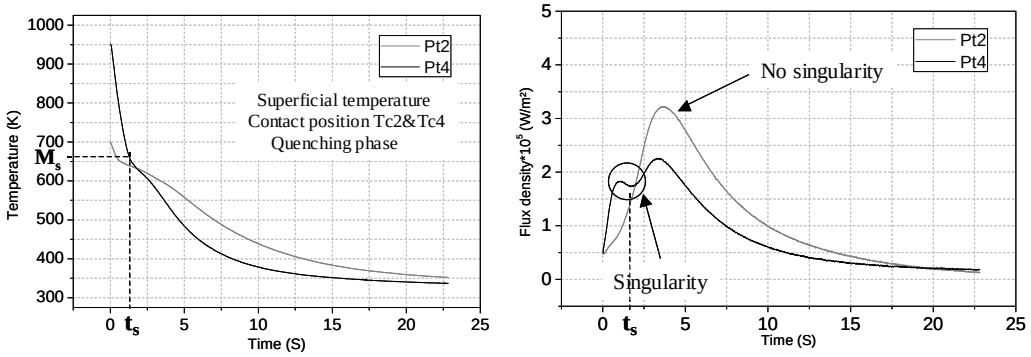

Figure 10. Superficial temperature and flux density evolutions at position #2 & #4.

The surface temperature of the blank and the flux density absorbed by the die at position #2 & #4 are presented in figure 10. It can be noticed that the cooling velocity at position #4 is significantly higher than in position #2. This is due to the reduction of heat transfer between the blank and the die wall. In fact, during the forming step, the blank slides along the die wall leading to an increase of the die surface temperature. Thus, the temperature difference between the blank and the die at this contact point becomes lower than the one observed at point #4, where the die has not been in contact with the hot blank. On the flux density curves shown in Figure 10, we notice also the presence of the singularity at contact position #4 while the superficial heat flux density at position #2 remains unchanged. It is due to the influence of the normal stress induced by the martensitic transformation on the punch force. This normal stress at position #2 is not captured by the force sensors placed under the die.

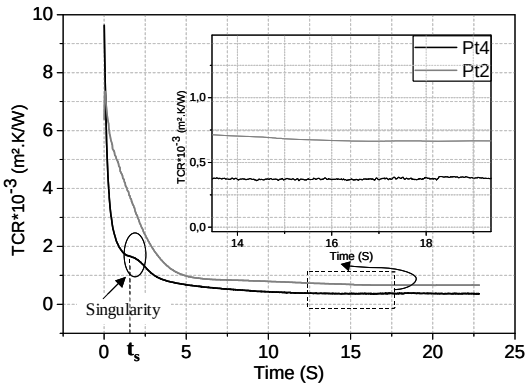

Figure 11. The *TCR* curves as function of time at position #2 & #4 during the quenching.

Figure 11 gives the *TCR* evolution as function of time at position#2 and #4 during quenching. Here also it is noticed that the singularity linked to the phase transformation is only observed at position #4.

Finally, tests under different contact pressure values were carried out in order to determine the law governing heat transfer between the blank and the die during the quenching phase. Figure 12 shows the comparison of the *TCR* curve as function of the contact pressure at both contact positions (#2 & #4) during the quenching phase. TCR values are lower at position #4 than at position #2. As mentioned earlier, it is due to the sliding of the hot blank against the die wall during the forming phase which warms up the die surface.

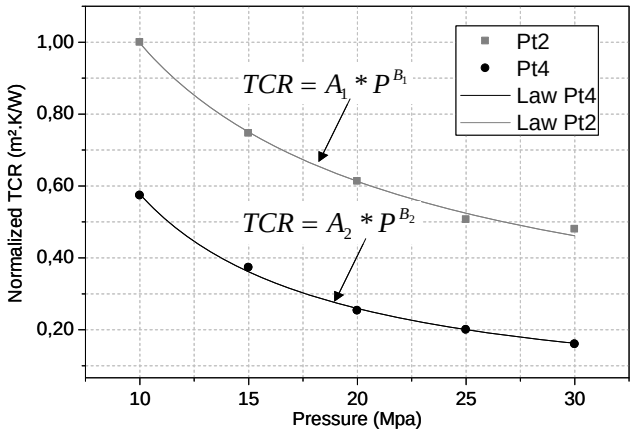

Figure 12. The *TCR* curve as function of contact pressure at position#2 & #4 during quenching.

CONCLUSION

In this paper, an experimental device which has been designed and developed to measure the Thermal Contact Resistance under hot stamping conditions was presented. Reproducibility tests were carried out and showed repeatable and accurate values of TCR at blank-tool interface. Hot stamping trials were conducted with various contact pressures to determine the TCR law as function of pressure. A comparison of thermal conductance values measured in two different contact areas (respectively sample-bottom of the die and sample-die wall) during the quenching phase, was presented. It appears that the heat transfer of the sample with the bottom of the die is higher than with the die walls due to different contact conditions.

REFERENCES

1. Moersdorf, W.: Moderne Werkstoffe und ihre Anwendungen in der Karosserieentwicklung. Proc. Of Neuere Entwicklungen in der Blechumformung, Stuttgart, Germany, 2006, p. 1/11.
2. Geiger, M.; Merklein, M.; Hoff, C.: Basic investigation on the Hot Stamping Steel 22MnB5. Advanced Materials Research. Vols 6-8. May 2005. pp. 795-802.
3. Wilsius, P. ; Hein, P. ; Kefferstein, R.: Status and Future Trends of Hot Stamping of Usibor 1500P. Erlangen Workshop Warmblechumformung, Erlangen (Germany), 2006.
4. Abdulhay, B.; Bourouga, B.; Dessain, C.; Brun, G.; Wilsius, J.: Experimental Study of Heat Transfer In Hot Stamping Process. International conference on advances in mechanical engineering and mechanics. (Sousse, 16-18 December 2008).
5. Bourouga, B. ; Goizet, V.; Bardon, J.P. : Les aspects théoriques régissant l'instrumentation d'un capteur thermique pariétal à faible inertie, *Int. J. Therm. Sci*., vol. 39, pp 96-109, 2000.

THE EXPERIMENTAL TEMPERATURE PROFILES IN THE CZOCHRALSKI MELT UNDER THE STATIC AND ROTATIONAL MAGNETIC FIELD

M. Iwamoto[1*], J. Matsuhisa[1], M.Akamatsu[2] and H.Ozoe[3]

[1]Oita University, Oita, Japan
[2]Yamagata University, Yonezawa, Japan
[3]Professor Emeritus, Kyushu University, Kasuga, Japan

ABSTRACT. A model experiment is carried out for the Czochralski crystal growth configuration under the horizontal rotational magnetic field. The transient temperatures at various locations in the melt are measured by thermo-couples. A pair of permanent magnets is placed at the outside of crucible sidewalls and the magnet is rotated by a motor. Asymmetric temperature distributions occur in the melt and rotate in the crystal rotating direction without or in a static magnetic field. Under the rotational magnetic field, the temperature distributions rotate in a rotating direction of the magnetic field under the strong and/or the large rotating rates of magnetic field even against to the rotating direction of the crystal rod. The periodic temperature oscillation is caused due to the rotation of the asymmetric temperature distribution in the melt. The oscillation period strongly depends on the rotational magnetic field.

Keywords: *Liquid Metal, Czochralski Method, Static and Rotational Magnetic Fields, Temperature Distribution*

INTRODUCTION

The silicon single crystal for the semiconductor has been mainly manufactured by the Czochralski (Cz) method and the fluid flow of melt affects the quality of grown crystal [1]. Therefore, the fluid flow in the crucible has been controlled by the crystal and the crucible rotation under the traditional system. However, recently horizontal or vertical static magnetic field has been applied to the Cz melt to control the melt convection [2, 3]. Lorentz force works for electrically conductive fluid under the magnetic field and the fluid flow can be suppressed in a static magnetic field. However, the non-homogenous oxygen concentration and the other various positive and/or negative characteristics occur in the melt under the static magnetic field [4]. Previously, we reported [5] the oxygen concentration in the melt under the horizontal and the rotational magnetic field numerically. The oxygen concentration at the crystal-melt interface was decreased under the rotational magnetic field compared to the horizontal static magnetic field for the same magnetic induction. The 3-dimensional numerical computation of Cz melt convection was also reported [6] under the rotational magnetic field, and the temperature distribution and the concentration of oxygen transfer changed from the spoke to the 2-folded one with increasing the magnetic flux density and the rotational rates of magnetic field.
In this study, the temperature distribution in the Cz melt is measured under the horizontal and the rotational magnetic field. A pair of permanent magnets is used to generate the magnetic field and

* Corresponding author: Prof. Mitsuo Iwamoto
Phone: + (81)-97-554-7806, Fax: + (81)-97-554-7790
E-mail address: iwa@cc.oita-u.ac.jp

the magnets are rotated with the motor. This system is simple and the low frequency (0.05 - 1.5 Hz) rotational magnetic field can be applied to the melt. The magnetic flux density and the rotational rates of magnetic field are changed and the temperature oscillation period and the temperature distribution in the melt are measured.

EXPERIMENTAL CONDITIONS

Experimental apparatus is described in detail in the accompanying paper in this meeting and is not repeated herein. Experimental conditions are summarized in Table 1. Four different strengths of magnetic field are employed. They are case A at 0 mT, case B at 1.8 mT, case C at 2.7 mT and case D at 4.5 mT. The rotating rates of magnetic field are changed for each case from +10 rpm to -30 rpm.

The gallium melt is selected as the experimental fluid. The physical properties of gallium melt [7, 8] are shown in Table 2 at the average temperature ($T_{ave.}$= 319.69 K) of this experiment. The melting point of gallium is 302.93 K and the electrical conductivity is high.

Table 1
Experimental conditions

N_{rod}= 35 rpm, N_{cru}= 0 rpm, D_{rod}= 23.0 mm, D_{cru}= 46.0 mm, H_{melt}= 47.1 mm,
Th_{water}= 322.15 K (60.0 degree Celsius), Tc_{water}= 273.15 K (0.0 degree Celsius),
Th_{wall} = 318.87 ~ 320.05 K, Tc_{wall} = 307.79 ~ 314.40 K

Case	Average magnetic flux Density **B** (mT)	Rotating rates of magnetic field $\mathbf{N_B}$ (rpm)
A	0	0
B	1.8	+10, + 5, 0, - 5, - 7, - 10, - 13, - 15, - 20, - 25, - 30
C	2.7	+10, + 5, 0, - 3, - 5, - 7, - 10, - 15, - 20, - 25, - 30
D	4.5	+10, + 5, 0, - 3, - 5, -7, - 10, - 15, - 20, - 25, - 30

Table 2
Physical properties of Gallium melt (at $T_{ave.}$=319.69K) [7, 8].

Item	**Physical property**
Density	6.083×10^{3} kg/m^3
Viscosity	1.832×10^{-3} kg/(m·s)
Kinematic viscosity	3.011×10^{-7} m^2/s
Coefficient of thermal expansion	1.269×10^{-4} 1/K
Thermal conductivity	32.71 W/(m·K)
Electric conductivity (at 313.15K)	3.850×10^{6} 1/(Ω·m)
Specific heat	3.976×10^{2} J/kg·K
Thermal diffusivity	1.352×10^{-5} m^2/s
Magnetic permeability	$4\pi \times 10^{-7}$ H/m
Melting point	302.93 K

EXPERIMENTAL RESULTS

No magnetic field.

At first, temperature measurement is carried out without a magnetic field for Case A. Figure 1 shows the measured temperatures at four locations in a circumferential direction. Figure 1 (c) shows these locations in the melt. They are located at $\pi/4$ shifted in a horizontal plane and are named as TC2, TC3, TC4 and TC6. As shown in Figure 1(a), the temperature in the melt is periodically oscillating at all measuring positions in this experimental condition. The temperature oscillation period is found to be τ = 391s. Temperatures at four locations are shifted due to the shifted locations in the circumferential direction.

Figure 1(b) shows the instantaneous temperature distribution is defined as the temperature difference from the average of oscillating temperature to the measuring temperature at each angular location. Radial locations are indicator of temperature difference from its average temperature. At the center it corresponds to - 1 [K] and at the outer most locations it corresponds to + 1 [K]. This is possible since the temperature oscillation amplitude is less than 1 [K] as seen in Figure 1(a). Four different timings in one oscillating period τ are shown in a sine function as shown schematically in the top right of Figure 1(b). The top views of these temperature distributions show different peak values depending on the timings in one cyclic oscillation period. The peak locations rotate in the same circumferential direction as the crystal rod rotation which is indicated with a bold arrow in the left lower side of this picture.

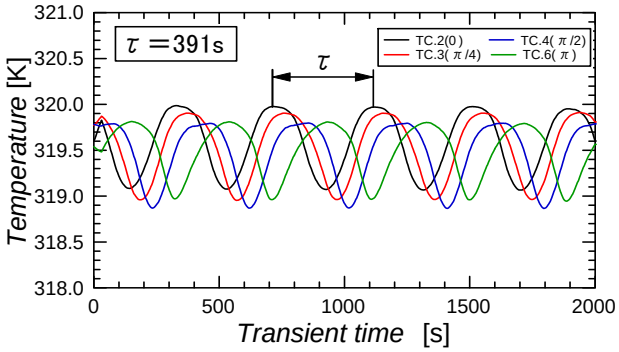

(a) Transient temperature

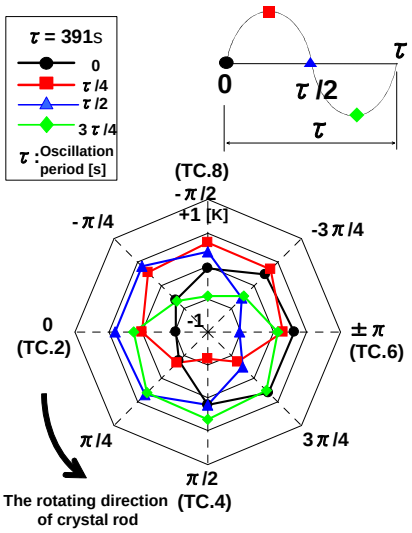

(b) The top view of temperature distribution

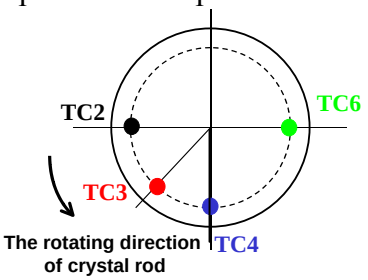

(c) Measuring position

Figure 1. Transient temperature and the top view of temperature distribution in the melt for B = 0 mT (Case A).

Horizontal rotational magnetic field

The horizontal rotational magnetic field is applied to the melt. The magnetic flux density and the rotational rates of magnetic field are varied. Figure 2 shows the transient temperature at B = 1.8 mT (Case B) and the rotating rates of magnetic field are from N_B = + 10 to - 25rpm. The positive symbol of rotating rates of magnetic field N_B shows the same rotating direction as that of crystal rod and the negative symbol shows the opposite direction. The oscillation period for each case are varied with the rotating rates of magnetic field and the rotating direction. Under the positive rotating direction, the oscillation period is shorter than that of the negative rotating direction and the oscillation period at N_B = + 10 rpm is shorter than that at N_B = + 5 rpm. For the cases of negative rotating direction of Figures 2(d)-(f), the oscillation period at N_B = - 5 rpm is longer than that of the static horizontal magnetic field (N_B = 0 rpm) in Figure 2(c). The transient temperatures at N_B = - 15 rpm are almost constant and the

temperature oscillations occur at N_B = - 25 rpm again. However, the temperature oscillation turns from black to green, blue and red at N_B = - 25rpm. This transition is reverse to those at $N_B \geq -5rpm$.

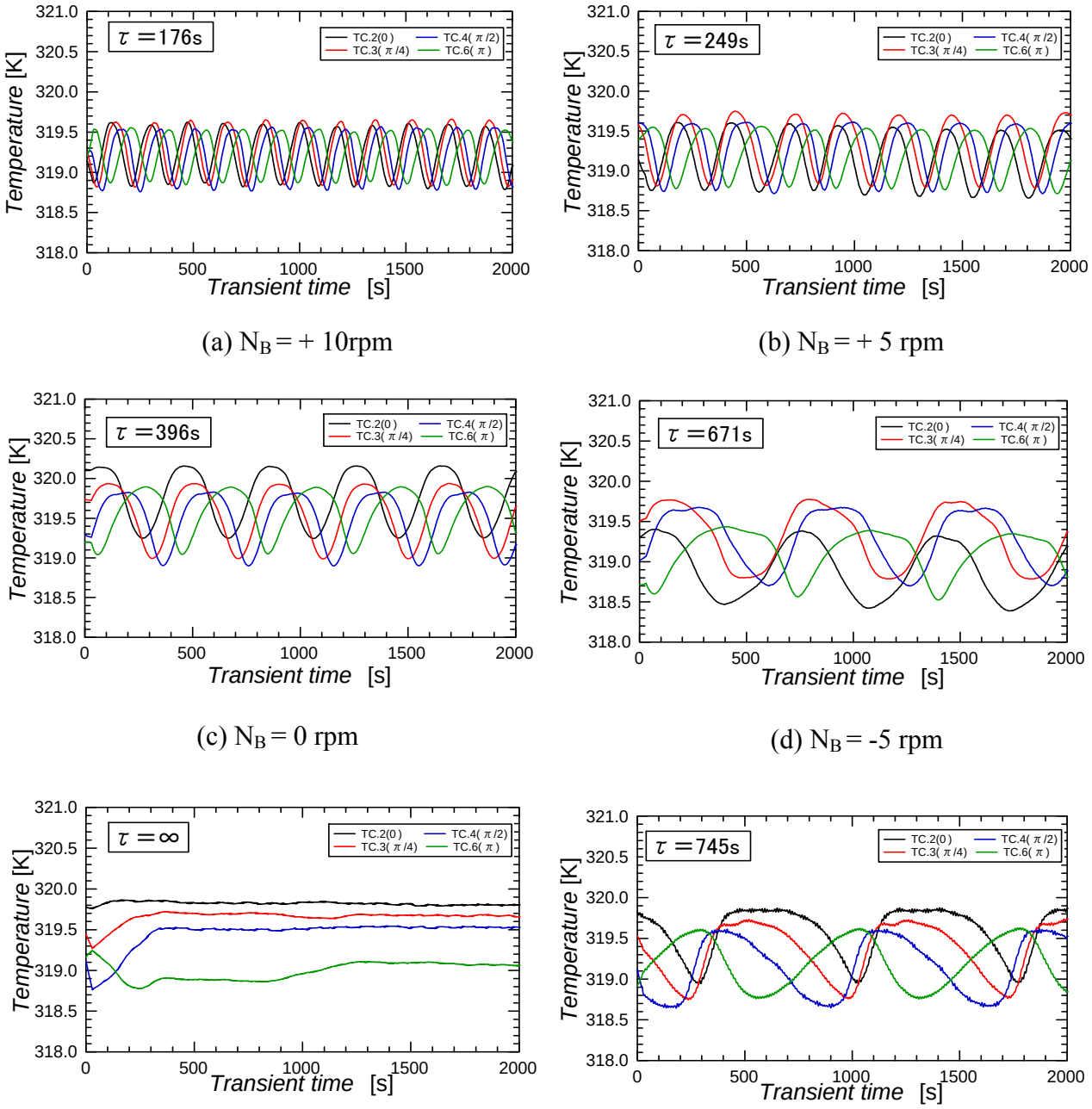

(a) N_B = + 10rpm

(b) N_B = + 5 rpm

(c) N_B = 0 rpm

(d) N_B = -5 rpm

(e) N_B = - 15 rpm

(f) N_B = - 25 rpm

Figure 2. Transient temperature in the melt for B = 1.8 mT (Case B).

Figure 3 shows the top view of temperature distribution in the melt at B = 1.8 mT (Case B). The red arrow with symbol B indicates the rotating direction of magnetic field. The temperature distributions are asymmetry and rotate in the crystal rotating direction (counter clockwise) at N_B = + 5, 0 and - 5 rpm. However, the temperature distribution at N_B = - 25 rpm rotate clockwise in the same rotating direction as that of a magnetic field. The rotating direction is switched under the large rotating rates of magnetic field. At N_B = - 25 rpm, the Lorentz force appears to overcome the strength of the crystal rod rotation.

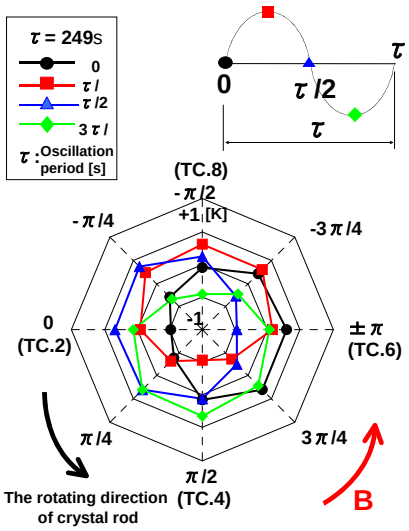

(a) N_B = + 5 rpm

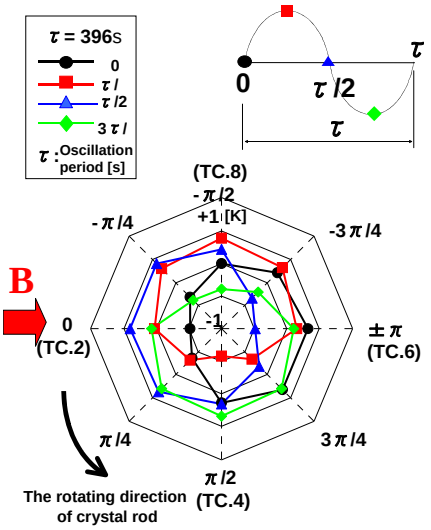

(b) N_B = 0 rpm

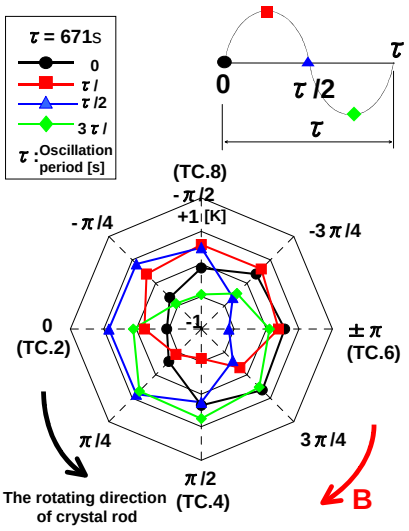

(c) N_B = - 5 rpm

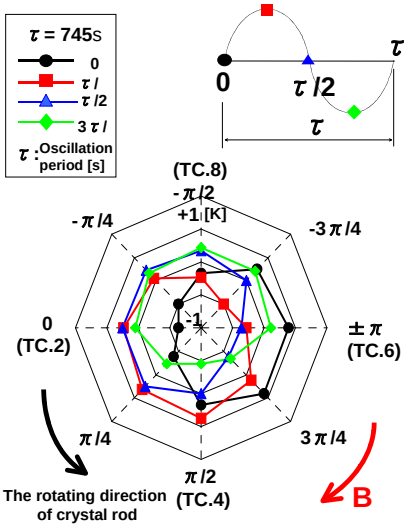

(d) N_B = - 25 rpm

Figure 3. The top view of temperature distribution in the melt for B= 1.8 mT (Case B).

Figures 4 and 5 show the transient temperature at B = 2.7 mT (Case C) and B = 4.5 mT (Case D). For the positive rotating direction of N_B = + 5rpm in Figures 4 (a) and 5(a), the oscillation period of temperature is shorter than that of the static horizontal magnetic field at N_B = 0 rpm for each case. The oscillation period at B=4.5mT is shorter than that at B = 2.7 mT at N_B = + 5 rpm. For the static horizontal magnetic field at N_B = 0 rpm, the oscillation period slightly increases with the increase in the magnetic flux density. At N_B= - 5 rpm and B = 2.7 mT in Figure 4(c), the temperature is almost constant which appears to be similar to Figure 2(e) (B = 1.8 mT, N_B = - 15 rpm). At N_B = - 5 rpm and B = 4.5 mT in Figure 5(c), the temperature distribution turns from black to green, blue and red. This transition is reverse to those at N_B = + 5 and 0 rpm.

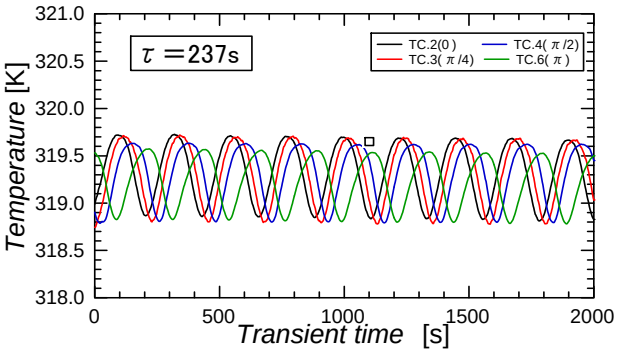

(a) N_B = + 5 rpm

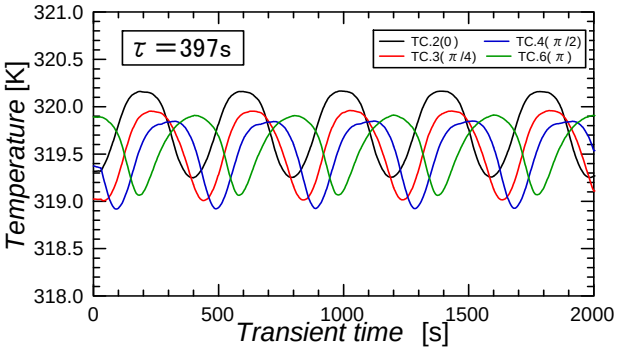

(b) N_B = 0 rpm

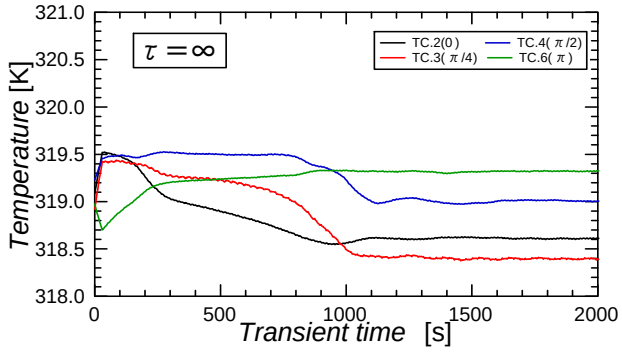

(c) N_B = - 5 rpm

Figure 4. Transient temperature in the melt for B = 2.7 mT (Case C).

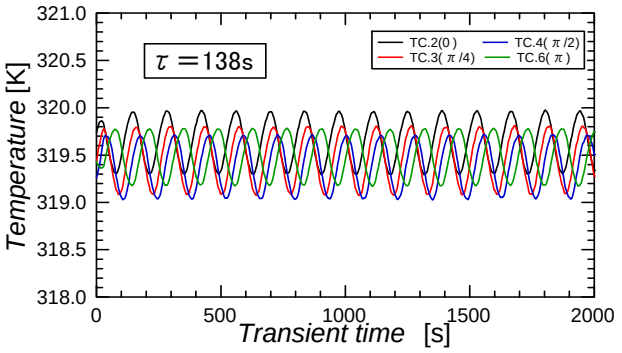

(a) N_B = + 5 rpm

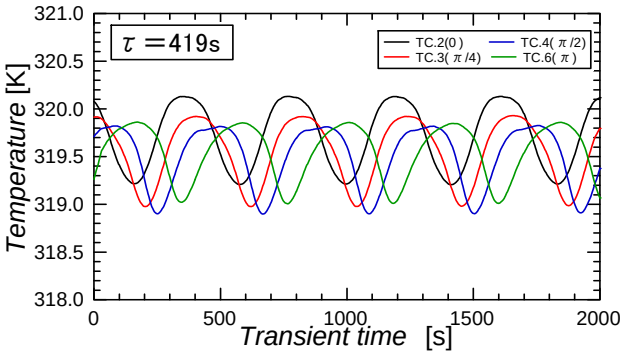

(b) N_B = 0 rpm

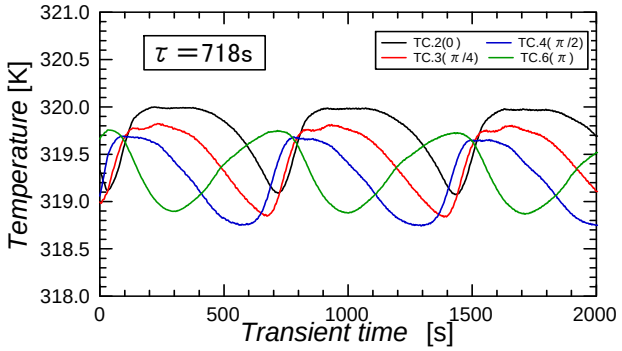

(c) N_B = - 5 rpm

Figure 5. Transient temperature in the melt for B = 4.5 mT (Case D).

Figure 6 shows the top view of temperature distribution in the melt at B = 4.5 mT (Case D). The temperature distribution at N_B = + 5 and 0 rpm rotates in the crystal rotating direction. At N_B = - 5 rpm, the temperature distribution rotates in the opposite rotating direction of crystal rod. The rotating direction of temperature distribution is switched with the increase of magnetic flux density at the same rotating rates of magnetic field in comparison to that at B = 1.8mT in Figure 3(c).
Figure 7 shows the inverse of oscillation period of temperature $1/\tau$ versus the rotating rates of magnetic field N_B. N_B = 0 rpm corresponds to the static horizontal magnetic field. Each symbol corresponds to the strength of the magnetic flux density B. All data show the similar characteristic that $1/\tau$ takes the minimum value of zero ($\tau \to \infty$) somewhere between 0 and - 20 rpm depending on the strengths of the magnetic field. As shown above in detail, disappearance of temperature oscillation is due to the reverse rotation of the horizontal magnetic field against to that of a crystal rod at N_{rod} = 35 rpm in this experiment. Therefore, this characteristics should depend on the magnitude of the rotating rate of the crystal rod N_{rod} as well as the rotating rate of crucible, though N_{cru}=0 in this study.

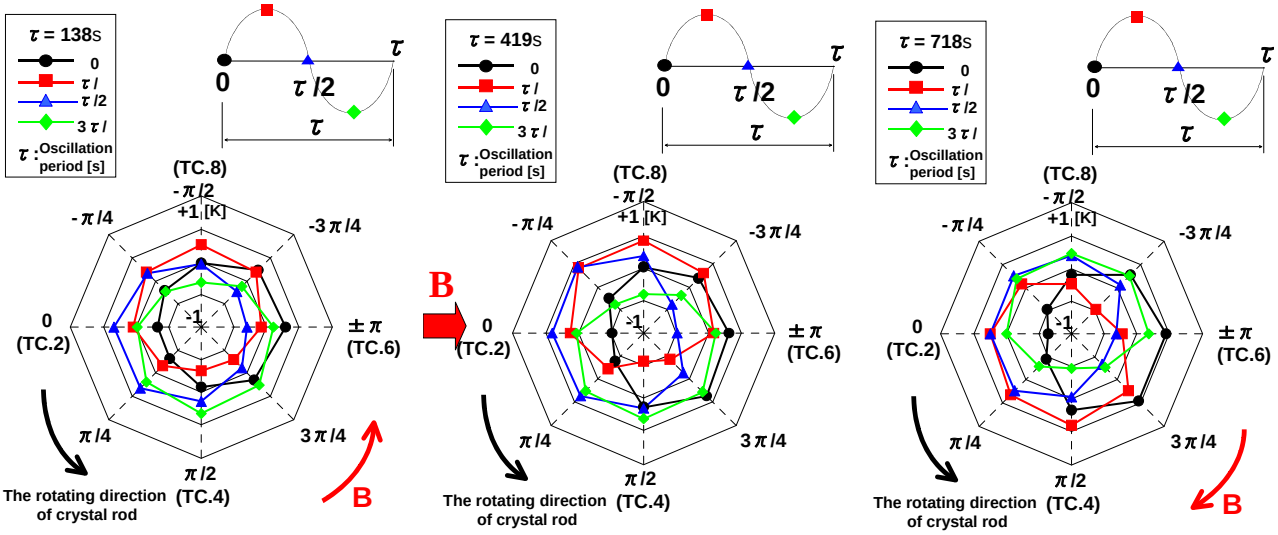

(a) N_B = + 5 rpm (b) N_B = 0 rpm (c) N_B = - 5 rpm

Figure 6 The top view of temperature distribution in the melt at B = 4.5 mT (Case D).

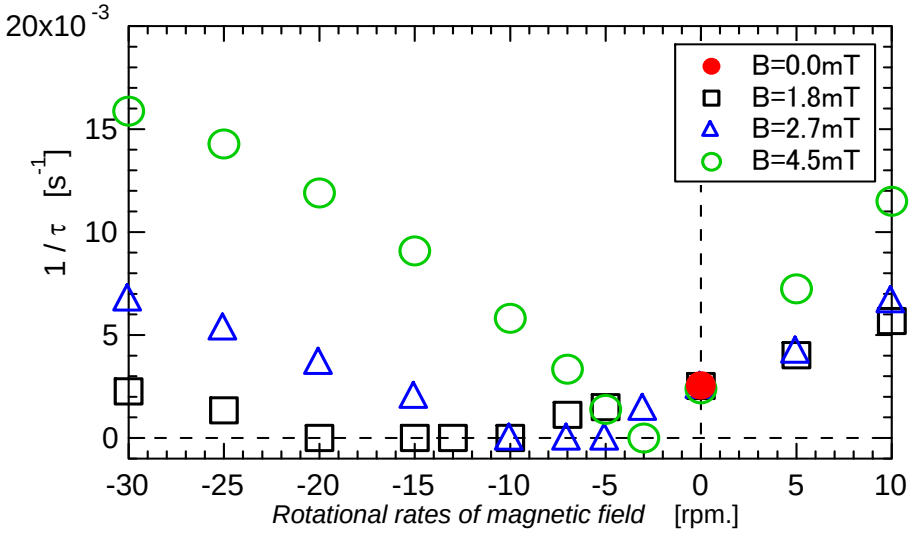

Figure 7. The inverse of the oscillation period of temperature in the melt versus the rotating rates of magnetic field at N_{rod} = 35 rpm and N_{cru} = 0 rpm.

CONCLUSION

The temperature distribution and the transient temperature in the Czochralski melt are measured under the rotational magnetic field. The periodic temperature oscillation is observed in this experimental condition and the temperature distribution rotates in a crystal rotating direction under the non-magnetic field. The oscillation period slightly increases with the increase in the magnetic flux density in a static horizontal magnetic field, though the rotating direction of temperature distribution is the same as that of the crystal rotating direction. Under the rotational magnetic field, the oscillation period decreases with the increase in the rotating rates of magnetic field in the same rotation direction as that of a crystal rod. For the counter rotation of the magnetic field against to that of the crystal rod, the oscillation period becomes longer for faster rotation rates of a magnetic field. Finally, the melt becomes almost stagnant and starts to be rotated in the same direction as that of a magnetic field at larger strength or at faster rotation rates of a magnetic field.

NOMENCLATURE

B	= Magnetic flux density	[mT]
D	= Diameter of crucible or crystal rod	[mm]
H_{melt}	= Height of melt	[mm]
N	= Rotating rates	[rpm]
Tc	= Cooling temperature	[K]
Th	= Heating temperature	[K]
τ	= Temperature oscillation period	[s]

Subscript

ave = Average value
B = Magnetic field
cru = Crucible
rod = Crystal rod
water = Heating or cooling water
wall = Crucible or crystal surface

REFERENCES

1. Pimputkar, S., M., Ostrach, S., Convection effects in crystals grown from melt, *Journal of Crystal Growth*, **55**, pp.614-646, 1981
2. Witt,A.F., Herman,C.J. and Gatos,H.C., Czochralski-type Crystal Growth in Transverse Magnetic Field, *Journal of Material Science*, **5**, 822-824, 1970
3. Hoshi,K., Suzuki,T., Okubo,Y. and Isawa,N., Cz Silicon Crystal Growth in Transverse Magnetic Field, *The Electrochemical Society Extended Abstracts*, 811-813, 1980
4. Ozoe, H., Magnetic Convection, Imperial College Press, London, 2005.
5. Iwamoto, M., Akamatsu,M., Tagawa,T., Ozoe, H., The Concentration Profile in the Czochralski Oscillating Bulk Flow under the Rotational and Horizontal Magnetic Field, *10th The Asian Pacific Confederation of Chemical Engineering Congress*,3P-13-013, (2004),Japan, (CD-ROM,10pages)
6. Kakimoto, K., Effects of Rotating Magnetic Fields on Temperature and Oxygen Distributions in Silicon Melt, *Journal of Crystal Growth*, **237-239**, pp.1785-1790, 2002.
7. Spells, K.E., The Determination of the Viscosity of Liquid Gallium over an Extended Range of Temperature, *Proc. Phys. Soc*., **48**, pp.299-311, 1936.
8. Cubbery, W.H., Metals Handbook II, 9th Ed., ASM, pp.735-737.

EXPERIMENTAL PREPARATION OF THE ROTATIONAL MAGNETIC FIELD FOR THE CZOCHRALSKI CONFIGURATION SYSTEM

M. Iwamoto[1*], J.Matsuhisa[1], M.Akamatsu[2] and H.Ozoe[3]

[1]Oita University, Oita, Japan
[2]Yamagata University, Yonezawa, Japan
[3]Professor Emeritus, Kyushu University, Kasuga, Japan

ABSTRACT**.** The experimental preparation of the rotational magnetic field is studied for the configuration of Czochralski crystal growing system. A pair of permanent magnet is used for generating the magnetic field and the magnet is rotated by the motor. This system enables to vary low rotational frequency (0.05 Hz -1.5 Hz) of magnetic field in contrast to the previous one with using 3-phase electromagnet and inverter power supply. The test experiments for confirming this system are carried out and the temperature distribution and the transient temperature in the melt are measured under the variation of the magnetic flux density and the rotational rates of magnetic field. The horizontal rotational magnetic field is found to affect the melt convection more than the static horizontal magnetic field with relatively weak magnetic strength.

Keywords: *Liquid Metal, Czochralski Method, Rotational Magnetic Field, Permanent Magnets*

INTRODUCTION

The Czochrakski crystal growing method was invented by a Polish chemist, Czochralski [1] and has been widely employed to manufacture the single crystal rods of silicon to be used for semi-conductor integrated circuits. Recent development and economic requirement force to enlarge the crystal rod diameter from current 300 mm to a larger size. This inevitably requires the larger depth and diameter for a crucible for silicon melt and makes the melt convection faster and more chaotic. It is important to calm the convection of melt for the successful seeding and/or stable growing with a constant diameter single crystal rod, etc. To calm the melt convection, various magnetic fields have been proposed and employed such as vertical, horizontal or cusp-shaped field (Figure 1(a)-(c)). However, these have various positive and/or negative characteristics [2-4]. On the other hand, a rotational magnetic field could rotate the melt with relatively weak magnetic strength, although there are many unknown characteristics..
The Czochralski crystal growing apparatus includes various complicated scheme such as rotation of a crystal rod, rotation of a crucible, heating system for a crucible, cooling system for growing a

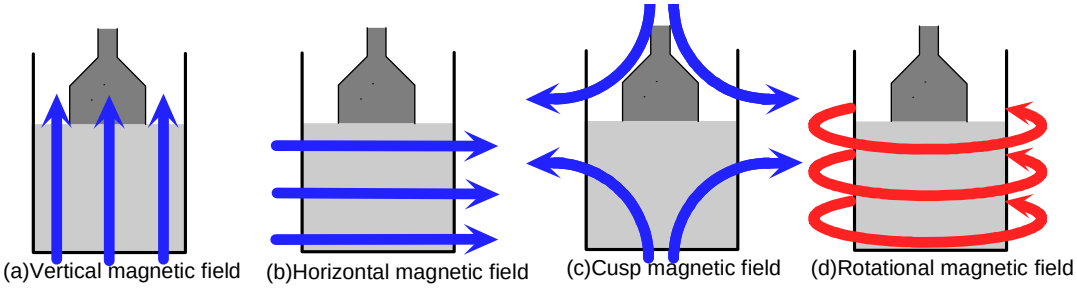

Figure 1. Magnetic control systems for the Czochralski method.

* Corresponding author: Prof. Mitsuo Iwamoto
Phone: + (81)-97-554-7806, Fax: + (81)-97-554-7790
E-mail address: iwa@cc.oita-u.ac.jp

crystal rod as well as a lifting system of a grown crystal rod. The application of additional rotational magnetic field makes the system more complicated even for the simple laboratory experimental system like the present study. The detailed description of this complicated experimental system is the motivation of the present report. Figure 1(d) shows the scheme of the rotational magnetic field. A transverse magnetic field passes through the melt and rotates with time. Some experimental studies were carried out for the rotational magnetic field under the Czochralski system [5,6]. The 3-phase electromagnet and inverter power supply were used to generate the rotational magnetic field. In their system, they had a difficulty to apply the low rotating frequencies of magnetic field at less than 20 Hz due to the limitation in the inverter power supply. Previously, we [7] carried out the model experiment of Czochralski system under the rotational magnetic field for which magnetic field was applied with using 3-phase and 2-pole electromagnet with the inverter power supply. In that system, the inverter power supply was limited up to 10Hz and the output voltage varied with the frequency of output power. It was difficult to fix the magnetic flux density for the general inverter power supply, for which the magnetic flux density of electromagnet was controlled by three phase transformer and the gauss meter. On the other hand, our present experimental apparatus can supply the low frequency transverse rotating magnetic fields with a simple magnetic system for the Czochralski configuration. The experimental results will be reported in an accompanied paper in this same meeting.

EXPERIMENTAL APPARATUS

Figure 2 shows total scheme of the experimental system in which each apparatus is numbered and named. Followings are the system configuration.

Scheme of the system

The apparatus in Figure 2 is a model for a Czochralski crystal growing system. No.1 is a model for a crucible which is made of a Plexiglas cylindrical enclosure. Its inner diameter is 46 mm, height 90 mm and the bottom wall 3 mm thick. Outside of this cylinder is a water jacket (No.3) through which hot water is circulated from a constant temperature bath (No.5) kept at 60 degree Celsius. The model for a crystal rod (No.2) is a cylindrical copper plate whose bottom surface is in contact with a melt surface. This copper plate is connected to a bottom of a cooling water jacket (No.4) in which water is filled and this water is cooled at a lower temperature with an annular cylindrical jacket. In this jacket, cooling water is run from another constant temperature bath (No.5) kept at 0 degree Celsius. This cylindrical model for a crystal rod is rotated by a motor (No.7) which is controlled on its rotational rate by a motor control unit (No.8). The experimental fluid is molten gallium which is filled in a model of a crucible. The free surface of gallium is easily oxidized and solidified in air. Furthermore, low temperature at 0 degree Celsius produces the water droplets over

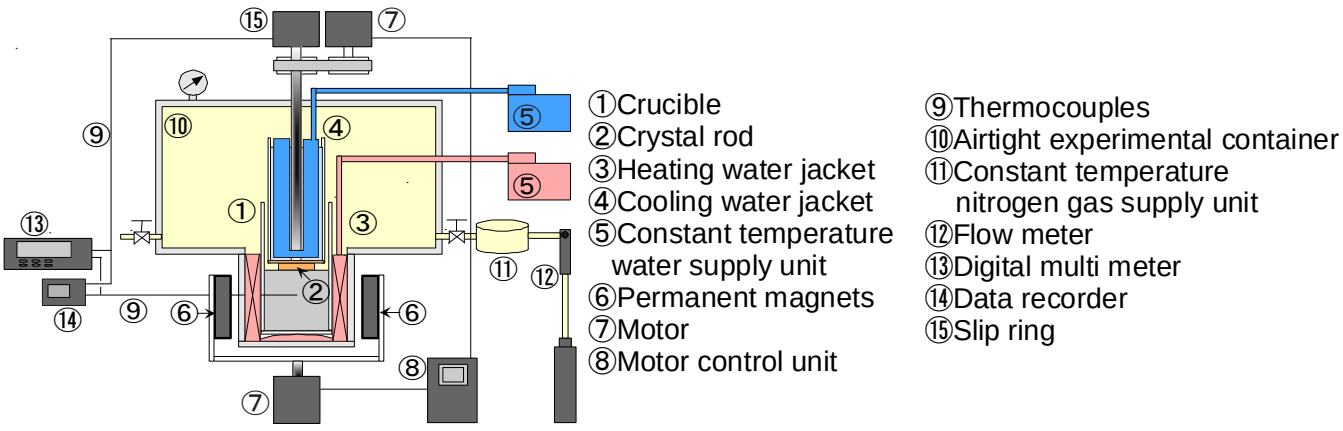

Figure 2. Schematic drawing of an experimental apparatus.

the surface of the model of a crystal rod. To avoid these anomalies, the whole experimental system is kept in an air-tight nitrogen gas chamber (No.10). Nitrogen gas is circulated in this chamber. The nitrogen gas is supplied through a constant temperature supply unit (No.11) and through a constant flow rate controller (No.12). Horizontal magnetic field is applied with a pair of permanent magnet (No.6). This pair of magnet is rectangular shaped and connected to a U-shaped steel plate which is rotated by another motor (No.7). This motor is controlled by a unit (No.8). This magnet provides an almost horizontal magnetic field through a crucible cylinder and is rotated to provide a rotational magnetic field. Rotational direction of this motor is taken as positive for an anti-clockwise one seen from top. This rotational direction is the same as that of a crystal rod. The clockwise rotation is taken as negative.

K-type (Alumeru-Chromeru) thermo-couples (No.9) of 0.1 mm diameter are placed at various locations in a melt, inside and outside of a crucible, crystal rod surface and inside an air-tight nitrogen gas room. These outputs are processed in a digital multi-meter (No.13) and a data logger (No.14).

The gallium melt is selected as the experimental fluid. The physical properties of gallium melt are reported in an accompanied paper in this same meeting.

Magnetic system

Figure 3 shows the sets up of magnets. Two permanent magnet plates of neodymium are fixed on the U-shape steel plate which is 19 mm wide and the distance of magnets (Symbol L) can be varied. The magnets are set at the outside of crucible and the magnetic field passes through the melt in a horizontal direction. The size and the distance of magnets are changed for varying the magnetic intensity. Four kinds of magnets are used for this experiment. The size of magnets and the magnetic flux density on the surface of magnets are listed in Table 1. Various magnetic intensities are tested in this operation. These magnets are rotated by the speed controlled motor with the reduction gear (ratio 1:18) and their rotating rates are controlled from 3 rpm to 90 rpm. The rotating direction of motor can be changed. Rotating rates of magnetic field are from 0.05Hz to 1.5Hz. The other rotating rates of magnetic field can be applied by the exchange of reduction gear unit.

The distribution of magnetic flux density in the x-, y- and z-directions is measured with a gauss meter as shown in Figure 4. The x-direction is normal to the magnet plates and the y-direction is parallel to the magnet plates in the horizontal plane. The z-direction is vertical. The origin of the horizontal axis is the center of melt height and diameter. The distribution of magnetic flux density

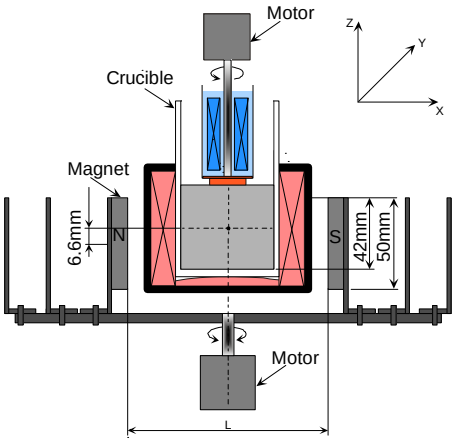

Figure 3. A set up of

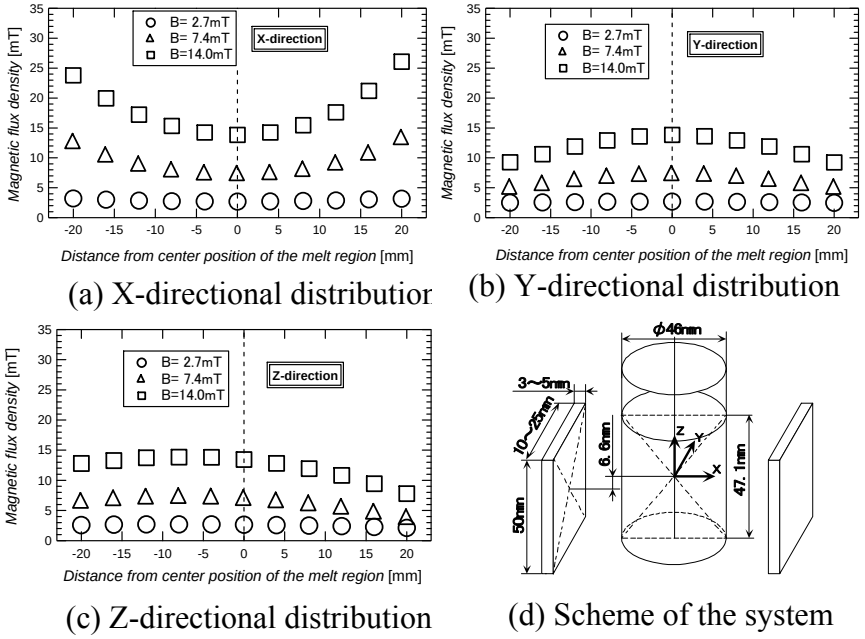

Figure 4. The magnetic flux distribution in the melt.

Table 1
Example of the magnetic set up.

Average magnetic flux density **B**	Magnet size (thickness, wide, height) (The magnetic flux density on the magnet surface)	The distance of magnets **L**
1.0 mT	3x10x50 mm (3300 Gauss)	194 mm
2.7 mT	5x25x50 mm (3400 Gauss)	190 mm
4.5 mT	4x20x50 mm (2800 Gauss)	146 mm
7.4 mT	3x10x50 mm (3300 Gauss)	94 mm
14.0 mT	5x15x50 mm (3200 Gauss)	90 mm

in the x-direction in Figure 4(a) is symmetric and the intensity of magnetic flux density is smallest at the centre. The components of magnetic flux density in the y- and z-directions are largest at the centre. The distribution of magnetic field in the z-direction is asymmetry since the centre of magnet is 6.6 mm lower than the centre of melt in the z-direction. The magnetic flux density varies with the position, so that the average magnetic flux density in the x-, y- and z-directions in the melt region is used for the definition of magnetic flux density B. The relation of the average magnetic flux density B, the size of magnet and the distance of magnets L are shown in Table 1.

Temperature measurement

The temperature distribution in the melt is measured with the K-type (Alumeru-Chromeru) thermo-couples and the locations of thermo-couples are shown in Figure 5. The eight thermo-couples are set in the melt 5.1 mm below the crystal rod. These thermo-couples are located with 45-degree ($\pi/4$ *rad*.) angular interval in the horizontal plane and the distance from the centre is 18 mm. The temperature of crystal rod surface is measured by the K-type thermo-couples whose output is connected to the slip-ring and recorded by the data logger. The temperature of melt, crucible side and bottom walls, ambient gas and crystal rod surface are measured and total measuring points are 20.

In this experiment the temperature is oscillatory and the amplitude of temperature oscillation is less than 1 K. Therefore, the high resolution recorder is necessary for the accurate measurement of transient temperature. The output voltage of thermo-couples in the melt is recorded by the digital multi-meter (KEITHLEY MODEL2000) with multi-scanner card. The resolution of voltage is 0.1 μV (for voltage range of 100 mV) which corresponds to 0.0025 K for the K-type thermo-couples. The cold junction of thermo-couples is kept in the 0 degree Celsius of the distilled water and ice mixture.

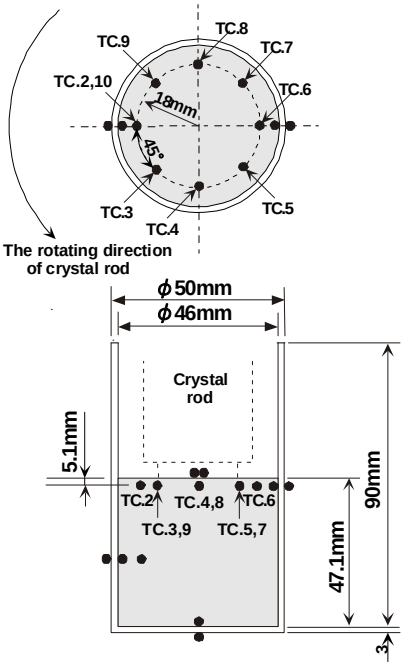

Figure 5. A set up of thermo-couples.

Heating and cooling system

The dummy crystal rod is used in this experimental apparatus. The circular copper plate is set at the bottom of rod which is 23 mm in diameter and 5mm thick. Its surface is covered with the Teflon coating to protect the dissolution of copper surface due to gallium melt. The upper side of this plate is attached to a glass cylinder whose inside is filled with water. The cooling pipe made of aluminium is dipped in the water and the cooling water is circulated through the cooling pipe and the temperature of cooling water is set at 0.0 degree Celsius. The cooling pipe is connected with constant temperature water supply unit (LAUDA RM6S) whose control accuracy is 0.01 degree Celsius. The dummy crystal rod is rotated with the speed controlled motor from 3 to 90 rpm. The outside of crucible side and bottom walls are heated by the hot water. The temperature of water is kept at

60.0 degree Celsius. The hot water is supplied from another constant temperature water supply unit. The nitrogen gas is circulated in the experimental chamber to protect the gallium melt from oxidization. The nitrogen gas temperature and the flow rates affect the heat loss from the gas-melt interface on the gallium melt, and the temperature and the flow rates of nitrogen gas are fixed at 30 degree Celsius and 20 liter per minute.

TEST MEASUREMENTS

The temperature of the melt is measured in the melt. The experimental conditions are shown in Table 2. The crystal rod is rotated and the crucible is fixed. The temperature of crucible inner side wall, inner bottom wall and the crystal rod surface slightly change with varying the magnetic flux density and the rotating rates of magnetic field. The rotational rates of crystal rod, the magnetic flux density and the rotational rates of magnetic field are varied in this experiment.

Non magnetic field

Figure 6 shows the transient temperature in the melt for the crystal rotating rates N_{rod} = 30 and 35 rpm with the static crucible and the non-magnetic field (B = 0 mT). Each line corresponds to the measuring position of temperature in Figure 6(c). The temperature in the melt is periodically oscillating for all measuring points. Kakimoto et al. [8] reported the Czochralski melt convection of silicon by using the double X-ray radiography with the tracer. The particle path of tracer was asymmetry and the velocity components in the x-, y- and z-direction were periodically fluctuating. The experimental conditions of this paper are selected to have the oscillatory flow condition to measure the effect of rotational magnetic field. The oscillation period decreases with the increase in the rotating rates of crystal rod. The oscillation periods of temperature at each measuring position are almost the same but the peak timing of each oscillation shifts each other due to the shifted positions in the circumferential positions.

Figure 7 shows the top view of temperature distribution in the melt for the crystal rotating rates N_{rod} =35 rpm under the non magnetic field. This temperature distribution is defined as the temperature difference from the average of oscillating temperature to the measuring temperature at each angular point. Each colour line in the figure corresponds to the time transition of temperature with the interval of τ /4. The temperature distributions turn from black to red, blue and green with time. The temperature distribution is asymmetry and rotates with time. The rotating direction of temperature distribution is counter clockwise whose rotating direction is the same as the crystal rotation for all rotating rates of

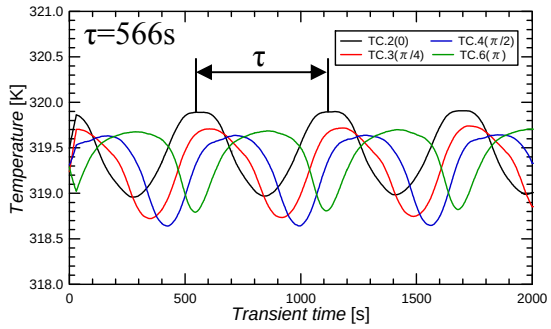

(a) N_{rod} = 30 rpm

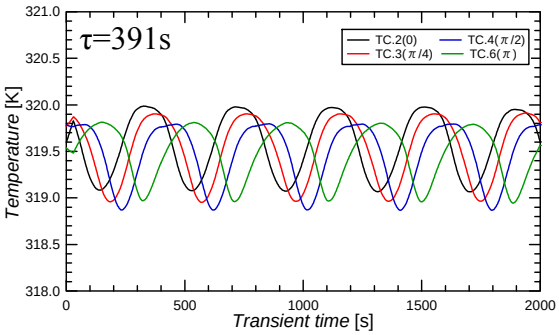

(b) N_{rod} = 35rpm

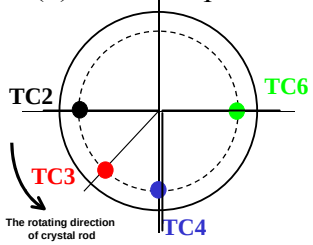

(c)Measuring position

Figure 6. Transient temperature in the melt under the non-magnetic field.

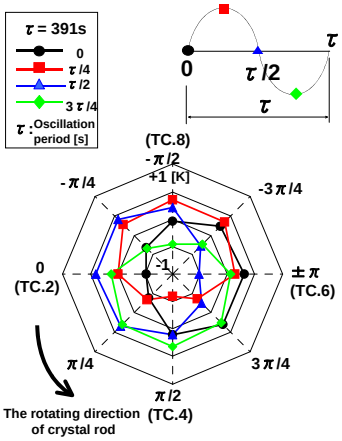

Figure 7. The top view of temperature distribution in the melt under the non-magnetic field at N_{rod} = 35 rpm.

crystal rod. The periodical temperature oscillation at each measuring point in Figure 6 is caused by the rotation of asymmetric temperature distribution.

Static horizontal magnetic field

The static horizontal magnetic field is applied to the melt from B = 1.0 to 19.5 mT and the crystal rotating rate 35 rpm. The other conditions are shown in Table 2.

Figure 8 shows the transient temperature in the melt at B = 2.7 and 14.0 mT. The measuring positions of temperature are the same as those in Figure 6. The observed oscillation period is 397 s at B = 2.7 mT. The oscillation period under the non-magnetic field (B = 0 mT) is 391 s in Figure 6(b), therefore the oscillation period of the horizontal magnetic field is slightly larger than that at non-magnetic field. Temperatures at all four locations are almost constant at B = 14.0 mT to mean infinite long periods.

Figure 9 shows the top view of temperature distribution in the melt at B = 2.7 mT. The bold arrow on the left hand side of picture shows the direction of magnetic field B. The temperature distributions are asymmetric and rotate in the crystal rotating direction. The rotational rate of asymmetric temperature distribution decreases with the strength of the horizontal magnetic field, although the other data are not shown.

Figure 10 shows the inverse of the oscillation period of temperature in the melt versus the magnetic flux density. Lorentz force works for electrically conductive fluid and the oscillation period becomes longer with the strength of magnetic field. Finally, the rotation of fluid flow becomes almost stagnant condition under the strong magnetic field.

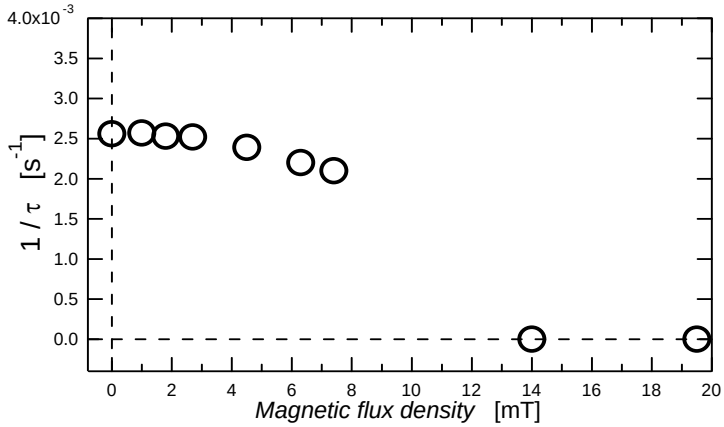

Figure 10. The inverse of oscillation period versus the magnetic flux density under the static horizontal magnetic field at N_{rod} = 35 rpm.

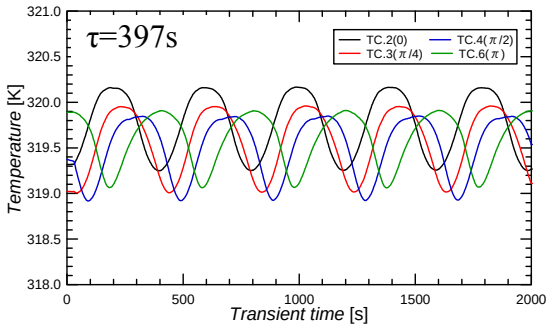

(a) B = 2.7 mT

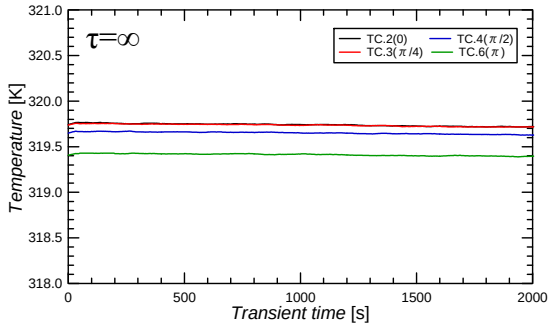

(b) B = 14.0 mT

Figure 8. Transient temperature in the melt under the static horizontal magnetic field at N_{rod}=35rpm.

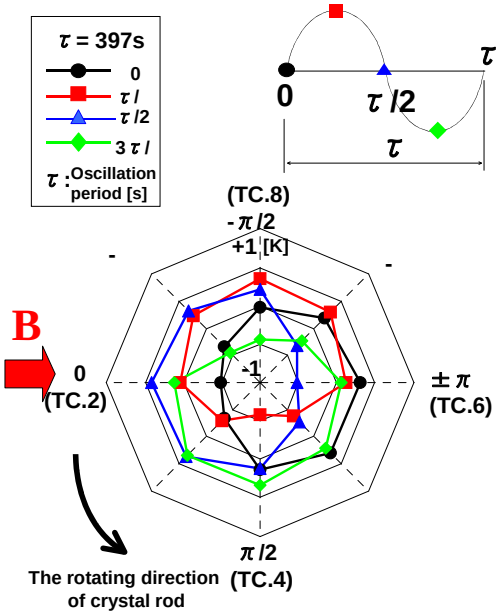

Figure 9. The top view of temperature distribution in the melt under the static horizontal magnetic field at B = 2.7 mT and N_{rod} = 35 rpm.

Table 2
Experimental conditions

Item	System parameter
Rotational rate of crystal rod (N_{rod})	30, 35, 40 rpm.
Magnetic flux density (B)	1.0 ~ 19.5 mT
Rotational rate of magnetic field (N_B)	+ 30 ~ − 50 rpm.
Diameter of crystal rod	23.0 mm
Diameter of crucible	46.0 mm
Height of melt	47.1 mm
Temperature of heating water (Th_w)	333.15 K (60.0 degree Celsius)
Temperature of cooling water (Tc_w)	273.15 K (0.0 degree Celsius)
Temperature of heating surface (Th)	318.87~320.05 K
Temperature of cooling surface (Tc)	307.79~314.40 K

Horizontal rotational magnetic field

Figure 11 shows the transient temperature at four points and the top view of temperature distribution under the rotational magnetic field. The rotating rate of crystal rod is N_{rod} = 35 rpm, the magnetic flux density B = 2.7 mT and the rotating rate of magnetic field N_B = - 15 rpm. The negative symbol of N_B means the opposite rotating direction against to the crystal rotation. Under the rotational magnetic field, an induction current may be caused in the thermo-couples due to the variation of magnetic flux density. Therefore, the high frequency noise from the output of thermo-couples is removed by the moving average processing. The oscillation period in Figure 11(a) is 493s and the phase transits from black to green, blue and red. The rotational direction of temperature distribution in Figure 11(b) is the same direction as that of the magnetic field. The rotating direction is opposite in comparison to that for the static horizontal magnetic field in Figures 7 and 9. The rotating direction is switched under the large rotating rates of magnetic field. The detail of experimental result under the rotational magnetic field will be reported in the accompanying paper in this same meeting.

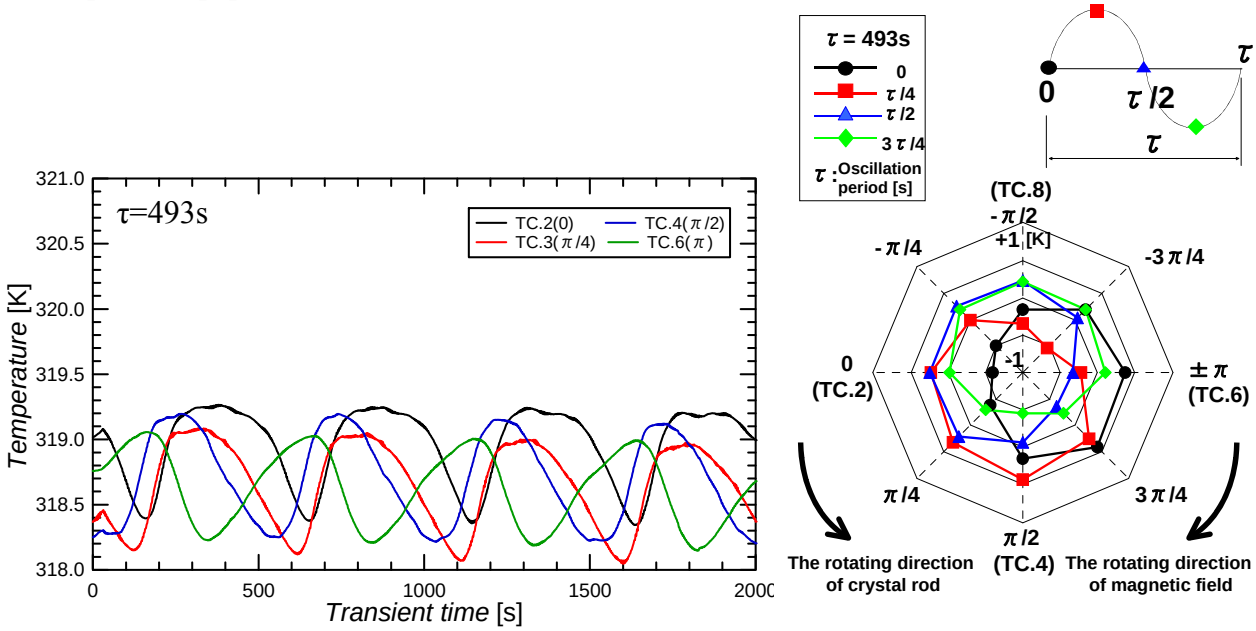

(a) Transient temperature

(b) Top view of temperature

Figure 11. Transient temperature and the top view of temperature distribution in the melt under the rotational magnetic field (N_{rod}= 35 rpm, B = 2.7 mT, N_B = - 15 rpm)

CONCLUSION

The experimental preparation of the rotational magnetic field is described for the Czochralski configuration system. The static horizontal magnetic field and the horizontal rotational magnetic field are applied to the melt and the temperature distribution is measured. The oscillation period of temperature in the melt becomes longer with the increase in the magnetic flux density under the static horizontal magnetic field. The top view of the temperature distribution in the melt is asymmetric and rotates in the crystal rotating direction under the static magnetic field. On the contrary, the temperature distribution rotates in the opposite direction against to the crystal rotation under the reverse directional rotation of magnet field.

NOMENCLATURE

B	= Magnetic flux density	[mT]
L	= Distance of magnets	[mm]
N_B	= Rotational rates of magnetic field	[rpm]
N_{rod}	= Rotational rates of crystal rod	[rpm]
τ	= Oscillation period of temperature	[s]

REFERENCES

1. Czochralski,J.,Ein neues verfahren zur messung der kristallisationsageschwindigkeit der metalle, *Z.Phys. Chemie.* **92**, pp.219-221, 1918.
2. Toh,K., Ozoe,H., Dopant Concentration Profile in a Czochralski Flow of Liquid Metal in a Vertical or Horizontal Magnetic Field, *Journal of Crystal Growth* **130**, pp.645-656, 1993.
3. Kakimoto,K., Ozoe,H., Oxygen Distribution at a Solid-Liquid Interface of Silicon under Transverse Magnetic Fields, *Journal of Crystal Growt* , **212**,pp.429-437, 2000.
4. Ozoe, H., Magnetic Convection, Imperial College Press, London, 2005.
5. Spitzer,K.H., Application of Rotating Magnetic Fields in Czochralski Crystal Growth, *Progress in Crystal Growth and Characterization of Materials,* pp.39-58, 1999.
6. Dold,P., Benz,K.W."Rotating, Magnetic Field:Fluid Flow and Crystal Growth Applications, *Progress in Crystal Growth and Characterization of Materials*, pp.7-38, 1999.
7. Iwamoto,M., Akamatsu,M., Hirata,T., Yamaguchi,K., Ozoe,H., Experimental Study of Natural and Forced Convection of Liquid Metal under a Rotational Magnetic Field, *Proceedings of the 4th JSME-KSME Thermal Engineering Conference,* **3**, pp.225-228, 2000.
8. Kakimoto,K., Watanabe,M., Eguchi,M., Hibiya,T., Ordered structure in non-axisymmetric flow of silicon melt convection, *Journal of Crystal Growth*, **126**, pp.435-440, 1993.

EFFECT OF HYDROGEN ON MARTENSITIC TRANSFORMATION OF TiNi SHAPE MEMORY ALLOY PRODUCED BY MECHANICAL ALLOYING

T. Saito*, A. Takasaki
Shibaura Institute of Technology, Tokyo, Japan

ABSTRACT. Ti and Ni elemental powders with composition of $Ti_{50}Ni_{50}$ were mechanically alloyed for 30 h, compacted, sintered at 973 K, and annealed at 773 K. Both cathodic and gaseous hydrogen charging were conducted for the bulk samples. The martensitic transformation behavior for the bulk samples after hydrogenation was investigated. The elemental powders turned into amorphous state after mechanical alloying (MA). After compacting, sintering and annealing, however, a B2-TiNi phase with a small amount of Ti_2Ni phase formed in the sample. Martensitic and reverse transformation behaviors were observed in the bulk sample after annealing. The martensitic and reverse transformation enthalpies were reduced by approximately 40% after cathodic hydrogen charging for 24 h in martensitic transformation, while 58% in reverse transformation, although the transformation temperature was not affected by the charging. No martensitic transformation behavior was observed after gaseous hydrogen charging for 120 h, but it was observed again after dehydrogenation.

Keywords: *hydrogen, martensitic transformation, mechanical alloying, current sintering, TiNi shape memory alloy*

INTRODUCTION

TiNi shape memory alloy has been widely used for various industrial fields because of their good mechanical properties, corrosion resistance and fascinating behaviors due to shape memory effect. Especially the application to biomaterials has been increased recently. In terms of the biological application of TiNi shape memory alloy, there are several problems that have to be investigated for the view point of biocompatibility. The influence of hydrogen on TiNi shape memory alloy is one of the issues. It was reported that hydrogen charging in TiNi shape memory alloy resulted in shape recovery phenomenon in martensitic phase, which showed that shape recovery took place during hydrogen charging even below transformation temperature (A_s) [1], martensitic transformation temperature was lowered by cathodic hydrogen charging [2] and hydrogen embrittlement of work-hardened Ni-Ti alloy occurred in acid fluoride solutions [3]. Powder metallurgy has attracted much attention because of the simplicity, cheapness and superior technique to make a complex shape and high quality product as a near-net-shape. Mechanical alloying (MA) process has some advantages to produce intermetallic compounds. It helps to change the local microstructure in the alloys [4], which has possibilities to produce new compositions to improve material properties. In this study, the influence of hydrogen on martensitic transformation behavior of TiNi shape memory alloy produced by a combination of MA and current sintering was investigated.

* Corresponding author: T. Saito
Phone: + (81)-3-5859-8072, Fax: + (81)-3-5859-8001
E-mail address: m408030@shibaura-it.ac.jp

EXPERIMENTAL PROCEDURE

Commercially pure Ti (99.9%) and Ni (99.9%) powders with composition of $Ti_{50}Ni_{50}$ were mechanically alloyed in stainless steel vials (45 ml) with stainless steel balls whose atmosphere was argon. The MA was performed by a planetary ball mill. The powder after MA was compacted, and sintered at a temperature of 973 K and a pressure of 20 MPa for 10 min under a vacuum condition (2 Pa) by using a current sintering equipment. The bulk samples after sintering were then annealed at 773 K for 1 h under a high vacuum condition (10^{-3} Pa) in a furnace.

Hydrogen charging was conducted by cathodic electrolysis using a 0.9% NaCl aqueous solution at a current density of 50 A/m^2 for several charging times at room temperature. Gaseous hydrogen charging was also conducted at a hydrogen pressure of 4 MPa and a temperature of 473 K for 120 h. The phases of the sample were determined by X-ray diffraction (XRD) measurement using Cu-Kα radiation at 20 kV and 30 mA. The martensitic transformation behavior was investigated by differential scanning calorimetry (DSC). The hydrogen desorption property was measured by thermal desorption spectroscopy (TDS).

RESULTS AND DISCUSSION

Figure 1 shows XRD patterns for the elemental powders after several alloying times. The elemental powders, Ti and Ni, remain at an early stage of MA (10 h). However, a new broad diffraction peak at about $2\theta = 42^\circ$ is observed after MA for 20 h, showing that the elemental powders turned into amorphous state. Compacting, sintering and annealing were conducted for the powders after MA for 30 h.

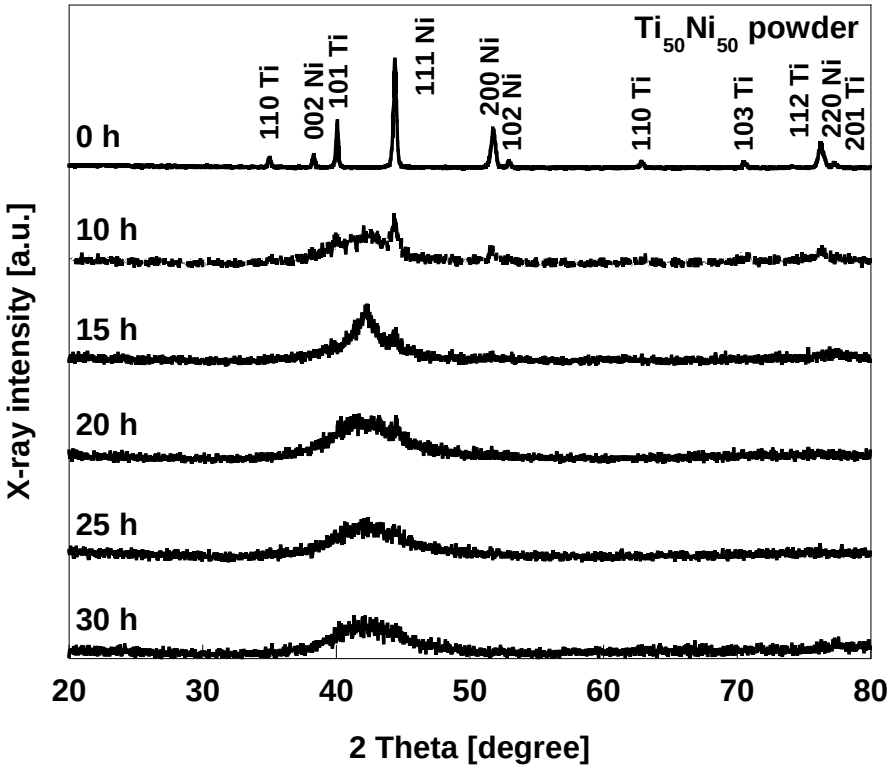

Figure 1. XRD patterns for the powder samples after MA for several alloying times

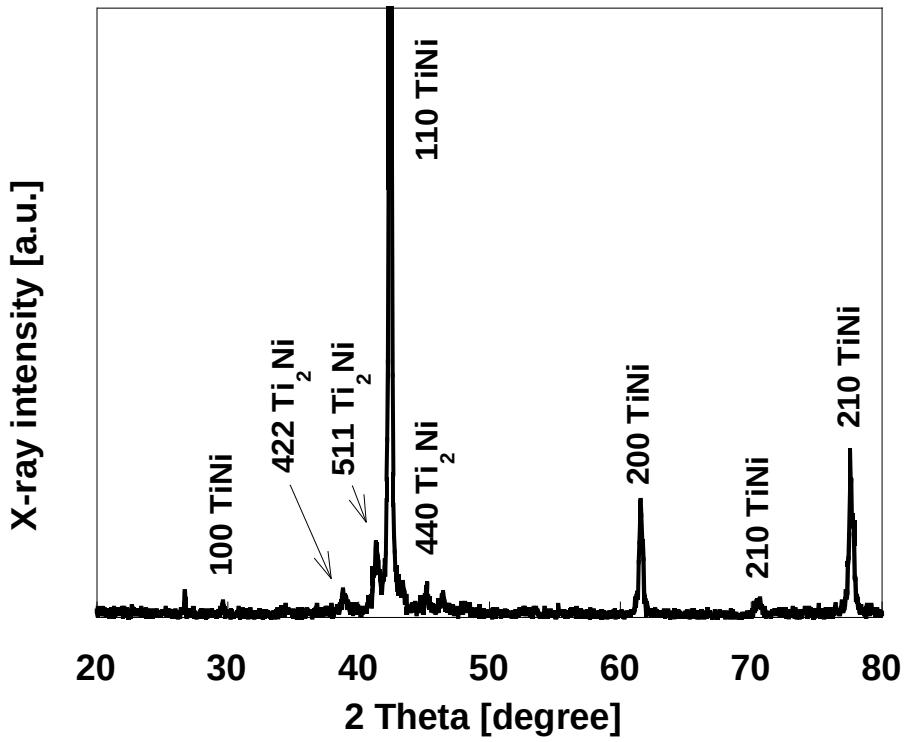

Figure 2. XRD pattern for the compacted sample after sintering at 973 K and annealing at 773 K

Figure 2 shows XRD pattern for the compacted sample after sintering at 973 K and annealing at 773 K. After sintering and annealing, a B2-TiNi phase with a small amount of Ti_2Ni phase formed. Because the B2-TiNi is an intermetallic phase, it shows fundamental and superlattice diffractions in XRD pattern [4]. Both fundamental diffraction at 2θ = 42, 61 and 78˚ and superlattice one at 2θ = 29 and 70˚ are observed. The B2-TiNi is well known as the phase showing shape memory effect (SME) due to thermoelastic martensitic transformation. Bulk density of the compacted sample after sintering at 973 K was 4.8 g/cm^3, which is smaller than that of theoretical calculation, around 6.45 g/cm^3. Therefore it indicates that the sample was porous material.

Figure 3 shows DSC curves for the compacted sample after sintering and annealing. Clear peaks for martensitic transformation (exothermic) and reverse transformation (endothermic) are observed. A transformation temperature width between M_s and M_f (or A_s and A_f) is approximately 20 K. No martensitic transformation behavior was observed for the compacted sample (after sintering) before annealing even if B2-TiNi phase existed in the sample, suggesting that the sample compacted before annealing was not homogenized (martensitic transformation depends deeply on homogenization of the sample). The annealing process homogenized and changed the local microstructure of the sample. In terms of the martensitic and reverse transformation enthalpies, the enthalpies were calculated as 1.65 J/g in the martensitic transformation, while 1.91 J/g in the reverse transformation. However it was reported that a heat of martensitic transformation was 310 cal/mol [5], which is 24.34 J/g. The value is larger than the enthalpies of the sample.

Figure 4 shows XRD patterns for the compacted sample after cathodic hydrogen charging for several times. The XRD intensities of B2-TiNi phase were decreased with increasing charging times and disappeared after charging for 24 h. A TiNi hydride phase, which is thought to form on the sample surface, is observed after charging for 4 h. In case of gaseous hydrogen charging, the TiNi hydride phase is observed after charging for 120 h, as shown in Figure 5. However, the B2-TiNi phase was not detected.

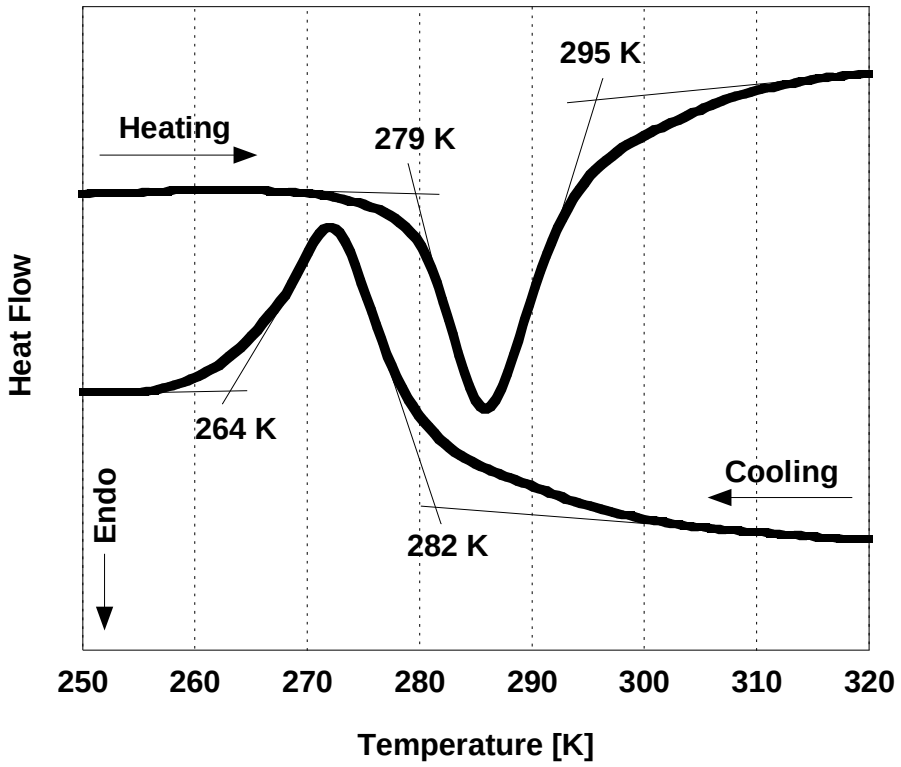

Figure 3. DSC curves for the compacted sample after sintering at 973 K and annealing at 773 K

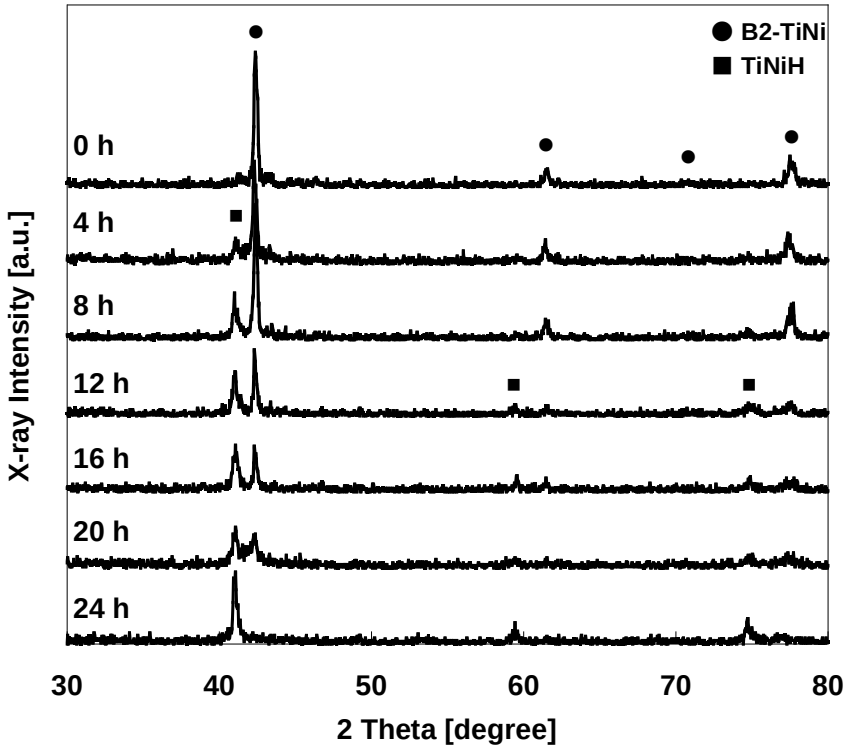

Figure 4. XRD patterns for the compacted sample after cathodic hydrogen charging for several times

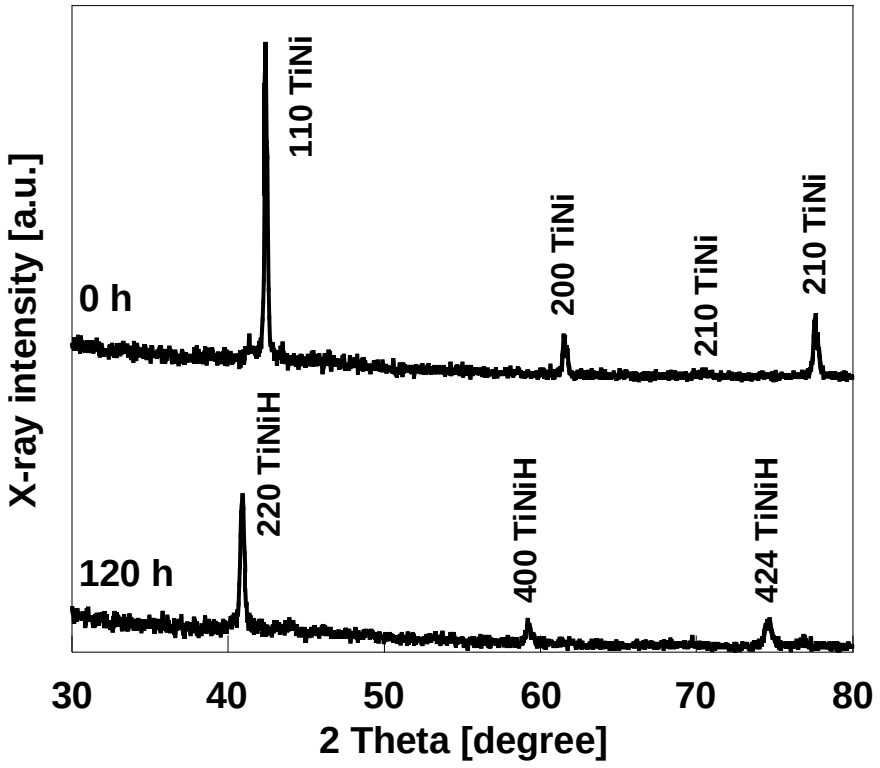

Figure 5. XRD patterns for the sample before and after gaseous hydrogen charging for 120 h

Figure 6 shows DSC curves for the compacted sample after cathodic hydrogen charging for several charging times. Martensitic and reverse transformation behaviors are observed even if the TiNi hydride phase forms after hydrogen charging. Martensitic and reverse transformation enthalpies were reduced with increasing charging times. However, martensitic and reverse transformation temperatures are not affected even after cathodic hydrogen charging. Table.1 summarizes martensitic and reverse transformation enthalpies after several charging times. It shows that martensitic and reverse transformation enthalpies were reduced with increasing charging times, which was reduced by 41% after charging times of 24 h in martensitic transformation, while 58% in reverse transformation.

Figure 7 shows hydrogen desorption curve, measured by TDS, for the compacted sample after gaseous hydrogen charging. Two TDS peaks are observed at 566 and 633 K, showing two different energy levels for the hydride in the sample. Besides, the first peak at 566 K is sharper and more intensive than the second one at 633 K, suggesting that hydrogen bonding of the first peak at 566 K was weaker than the second one at 633 K and the energy level of second peak is stable compared to that of first peak.

Figure 8 shows DSC curves for the hydrogenated sample, by gaseous hydrogen charging, after hydrogen desorption by TDS. Martensitic and reverse transformation behaviors are observed after hydrogen desorption. Therefore, the TiNi phase was recovered after heating the sample because of the hydrogen release. However, the peaks are not clear and the transformation widths between M_s and M_f (or A_s and A_f) is approximately 50 K, which is broader than that before gaseous hydrogen charging. The martensitic and reverse transformation temperatures and enthalpies are lower than those before gaseous hydrogen charging.

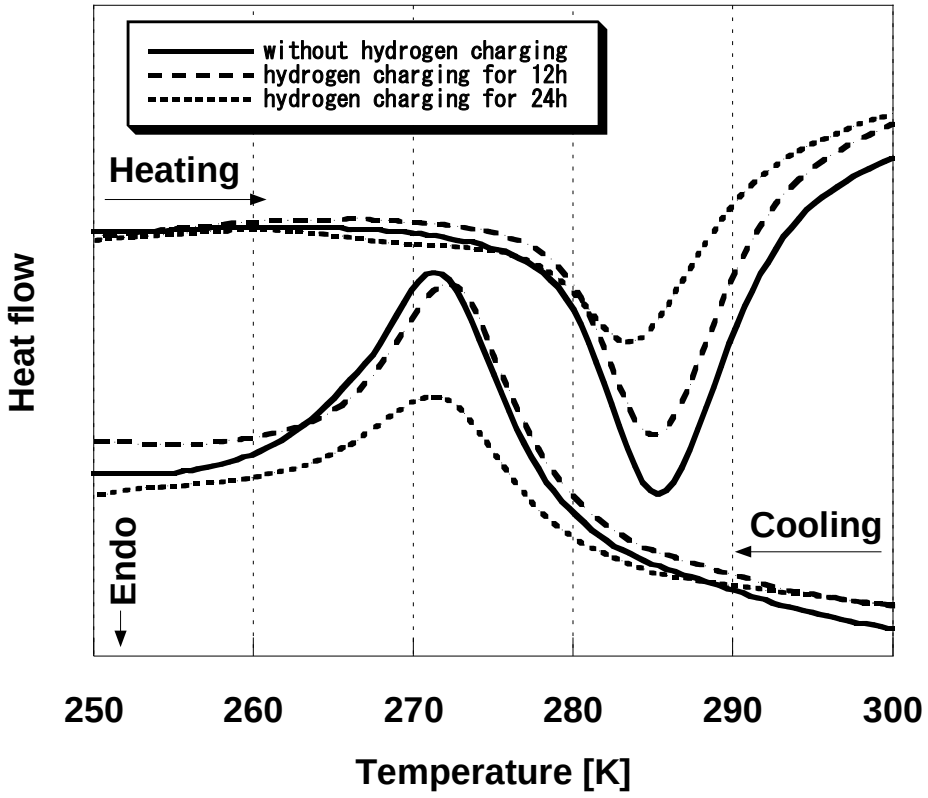

Figure 6. DSC curves for the compacted sample after cathodic hydrogen charging.

Table.1
Martensitic and Reverse Transformation Enthalpies at Several Charging Times

Hydrogen charging time [hour(s)]	Martensitic transformation enthalpy [J/g]	Reverse transformation enthalpy [J/g]
0	1.65	1.91
4	1.49	1.51
8	1.44	1.30
12	1.38	1.42
16	1.32	1.28
20	0.99	1.04
24	0.98	0.80

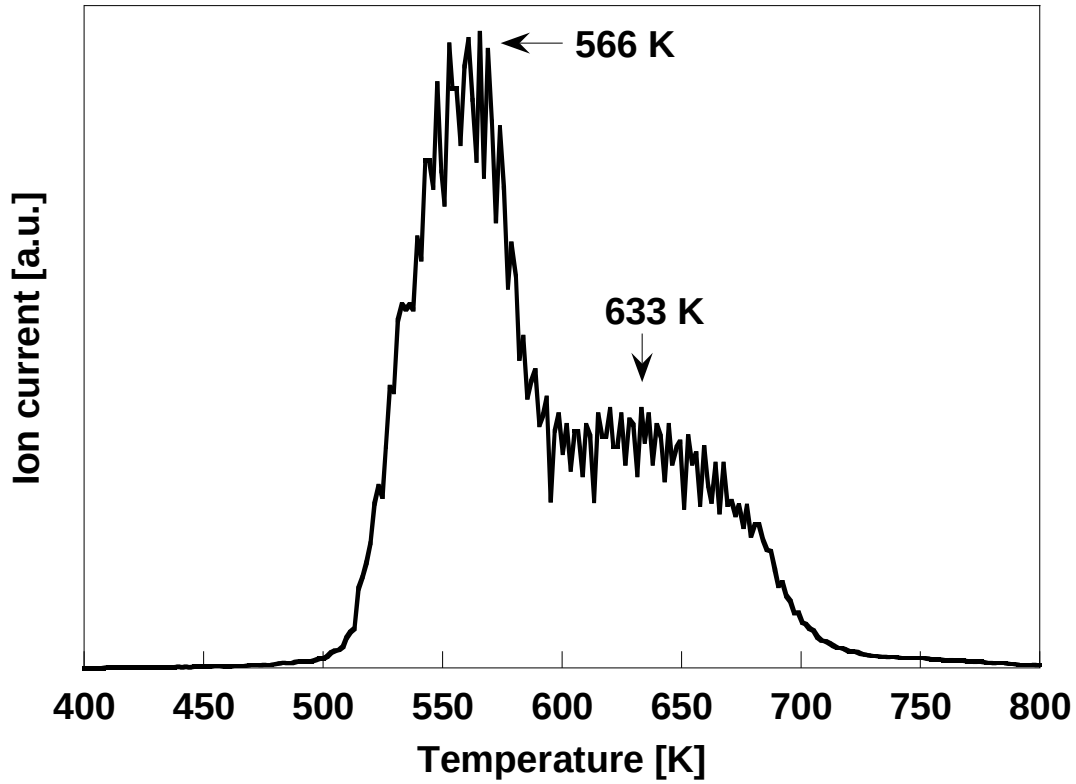

Figure 7. Hydrogen desoprption curve for the compacted sample after gaseous hydrogen charging

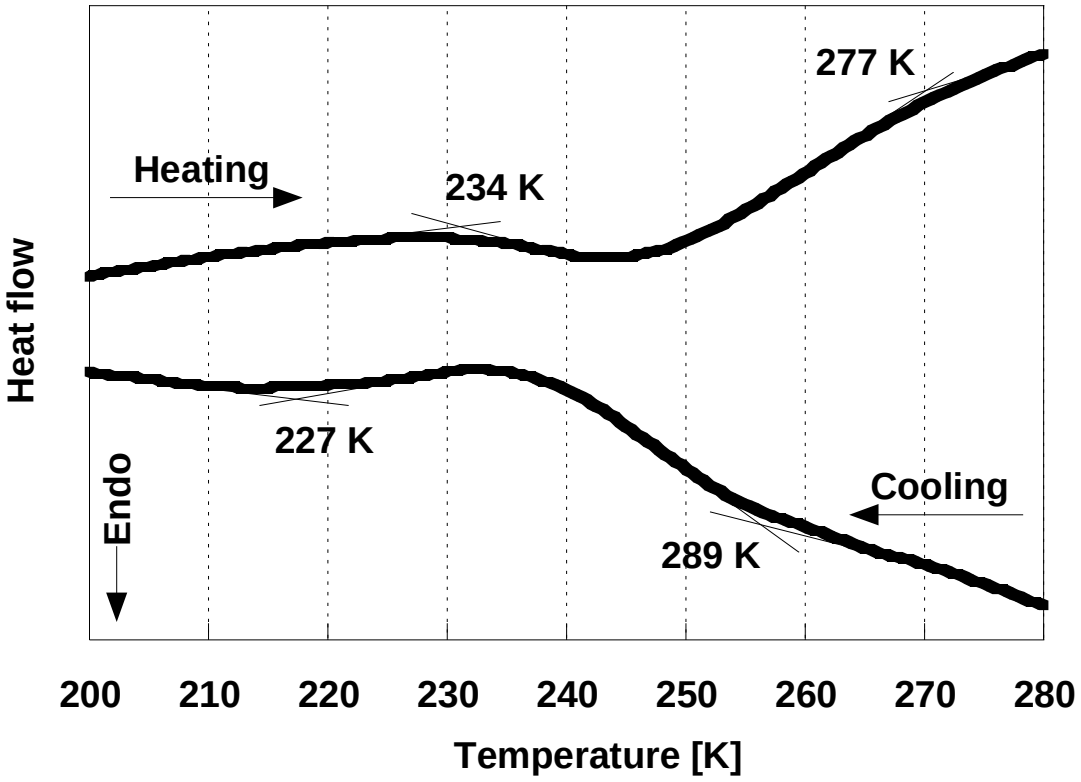

Figure 8. DSC curves for the hydrogenated sample after hydrogen desorption.

CONCLUSIONS

Ti and Ni elemental powders with composition of $Ti_{50}Ni_{50}$ were mechanically alloyed, compacted, sintered, and annealed. The obtained bulk samples were then hydrogenated by both cathodic and gaseous charging, and the martensitic transformation behaviors were investigated. The results obtained are summarized as follows,

1. The martensitic transformation behavior was not observed for the bulk samples after sintering. The annealing treatment after sintering the bulk sample was required for a recovery of the martensitic transformation behavior.
2. TiNi hydride phase was observed after both cathodic and gaseous hydrogen charging. In case of the cathodic hydrogen charging, XRD intensities of B2-TiNi phase were decreased with increasing hydrogen charging times and disappeared after charging for 24 h. On the other hands, TiNi hydride phase was observed after gaseous hydrogen charging for 120 h. However, the B2-TiNi phase was not detected.
3. The martensitic and reverse transformation enthalpies were reduced with increasing hydrogen charging times, which was reduced by approximately 40% after charging for 24 h in martensitic transformation, while 58% in reverse transformation, however the martensitic and reverse transformation temperatures were not affected by cathodic hydrogen charging.
4. Two different energy levels of hydrogen in the TiNi hydride were identified. The matensitic transformation behavior was observed after hydrogen desorption. However, the martensitic transformation temperature and enthalpy were lowered.

REFERENCES

1. N. Wade, Y. Adachi, Y. Hosoi, Scripta Metall. Mater. 24 (1990) 1051.
2. W. Jihong, Z. Xiaotao, W. Zhiguo, L. Yanzhang, Rare metals, 24 2 (2005) 190
3. K. Yokoyama, K. Kaneko, T. Ogawa, K. Moriyama, K. Asaoka, J. Sakai, Biomaterials, 26 1 (2005) 101-108
4. A. Takasaki, Phys. Stat. Sol. (a), 169 (1998) 183-191.
5. Dautovich, D. P., Melkvi, Z., Purdy, G. R., Stager, G. V., J. Appl. Phys., 37 (1966) 2513

LANGER & MULLER-KRUMBHAAR CRITERION IN THE DESCRIPTION OF THE LIQUID CONCENTRATION AT A GROWING DENDRITE TIP

W. Wołczyński[1,*], R. Martynowski[2], J. Kowalski[2], W. Wajda[1]
Institute of Metallurgy and Materials Science, Polish Academy of Sciences, Kraków, Poland
CELSA "Steelworks Ostrowiec", Ostrowiec Świętokrzyski, Poland

ABSTRACT. Columnar dendrites growth is observed during solidification of some massive ingots of steel or cast iron. The columnar dendrites zone is of special interest in the case of a cast iron rolls solidification. It is postulated that dendrite tip growth follows the criterion of marginal stability formulated by Langer and Muller-Krumbhaar (LMK) as a result of some numerical simulations. An application of the criterion as well as some measurements of *Peclet Number* for a given condition of steel solidification allowed to formulate not only the growth law for a columnar dendrite but the equation for solute concentration ahead of a dendrite tip as well. The differential equation for the solute redistribution after back-diffusion inside the columnar dendrite is also suggested. The solute concentration at the dendrite tip is treated as a boundary condition in solution of above equation for some parts of dendrite appearing sequentially at different growth rates. Each part of dendrite is treated separately in the current analysis. The current model improves the precision of calculation of solute redistribution within a growing dendrite by introducing a new boundary condition changeable with the dendrite growth rate. Additionally a simplified temperature filed for a solidifying ingot or roll is delivered. The simulation of temperature field allows to show the period of time for the columnar dendrite into equiaxed dendrite transition. It is postulated that the period of transition time could be simulated more precisely when the changing solute concentration at the dendrite tip will be taken into account in the simulation of temperature field.

Keywords: *marginal stability, solute redistribution, columnar ➔ equiaxed transition,*

INTRODUCTION

Columnar dendrites or columnar cells zone extends over a large area, especially in some massive ingots of steel or cast iron, Fig.1. The existence of columnar dendrites/cells promote some fissures along the grooves created between dendrites or cells. The fissures propagation could be observed during plastic deformation of some steel ingots (example: forging ingots produced in CELSA "Huta Ostrowiec", Company Limited, Ostrowiec Świętokrzyski) or even during the work of rolls made of steel or cast iron (example: rolls produced in Huta Buczek, Company Limited, Sosnowiec).
The columnar dendrite/cell tip plays essential role in the growth in such kind of morphology. It can be proved that the tip undercooling, ΔT, supersaturation, Ω, and solute concentration of the liquid adjacent to the tip, C_L^*, depend on the radius of curvature of the tip of the dendrite, R.
Additionally, the growth law for columnar dendrite/cell morphology can be developed mathematically to show correlation between three control technological parameters like: tip radius, R, dendrite/cell growth rate, v, nominal solute concentration, C_0, and some material parameters of steel or cast iron.
Finally, the influence of tip radius on solute redistribution and temperature field will be considered.

* Corresponding author: Prof. W . Wołczyński
Phone: + (48)-12-295 2887, Fax: + (48)-12-295 2804
E-mail address: nmwolczy@imim-pan.krakow.pl

Fig. 1 presents the massive ingot (as produced in CELSA) with columnar dendrites/cells zone.

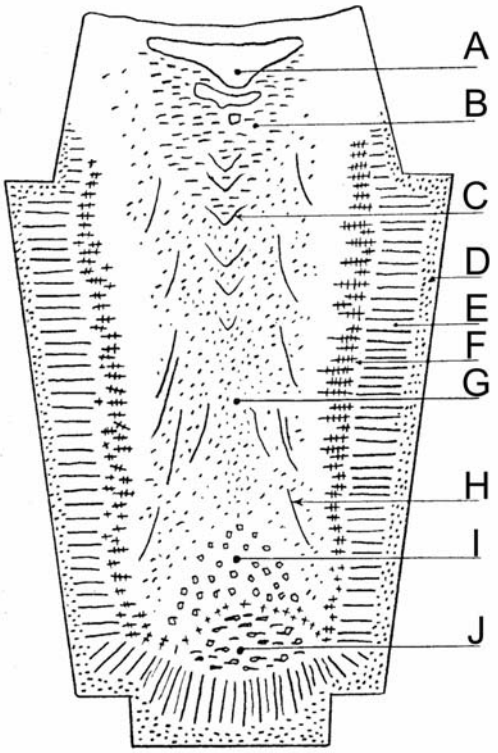

Figure 1. Phenomenological model of the ingot showing some morphological zones:
A – shrinkage cavity,
B – maximum positive segregation area,
C – "V" – type segregation areas,
D – chilled crystals, (equiaxed grains),
E – columnar dendrite/cells,
F – oriented dendrites,
G – high segregation and central porosity,
H – inverted "V" – type segregation areas,
I – negative segregation, (equiaxed dendrites)
J – sedimentary area: oxides and inclusions,
The E and F zones formation is the subject of current model considerations.
The so-called marginal stability criterion shown by Langer and Muller-Krumbhaar, [1] will be applied to a description of the two above zones formation. The LMK criterion is as follows:

$$R_S = \lambda_S \tag{1}$$

MODEL FOR SOLUTE CONCENTRATION AT THE TIP OF GROWING DENDRITE

The LMK marginal stability criterion (equation (1)) which refers to the Glicksman *et al.* [2] measurement and some numerical simulations replaced the conventional maximum velocity condition describing dendritic growth.
The LMK criterion corresponds to the Mullins and Sekerka [3] theory (MS theory) for the solid / liquid (s/l) interface instability.
The minimum wavelength λ_S for planar instabilities results from the MS theory, Fig. 2, and is defined as follows:

$$\lambda_S = 2\pi\sqrt{l\,d_0} \tag{2}$$

The tip radius, R, measurement, Fig. 2, was performed for the set of directional solidification experiments made for steel by the closed *Bridgman* system, [4], to estimate the *Peclet* Number defined:

$$P = 0.5\,v\,R\,D^{-1} \tag{3}$$

The measured *Peclet* Number for carbon steel fulfils the inequality $0.5 < P < 1$ with D - diffusion coefficient. Some observations of dendritic growth proved that the dendrite tip is a paraboloid of revolution, [2]. Therefore, its curvature is equal to $\widehat{K} = 2/R$.
An appearance of the primary branches takes place at a distance which is a number of times greater than the tip radius, R. This behaviour of dendrite / cell is typical and is in good agreement with the LMK analysis of the s/l interface perturbation. It is evident that tip radius plays an essential role in the description of the s/l interface instability (perturbation analysis) and the LMK theory seems to deliver the best criterion to study columnar dendrite growth (is more applicable than conditions of: maximum velocity, or minimum undercooling, or minimum entropy production).

Mode of the dendrite / cell tip radius measurement is shown in details in Fig. 2.

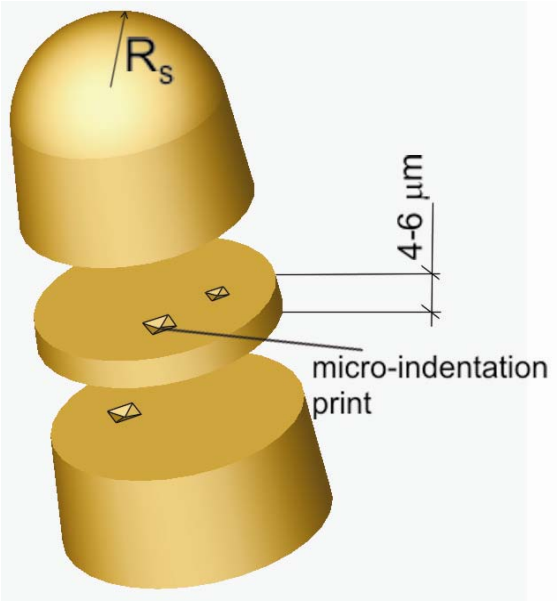

Figure 2. Principle of the dendrite / cell tip radius measurement by the gradual polishing of the smooth part of a dendrite (until first side instability). The polishing allows to measure and reproduce some perimeters of removed slights of 4-6 μm of the thickness. The set of studied perimeters gives possibility of the computer 3D reproduction of the paraboloid of revolution approximately similar to the dendrite tip. The method verifies a hypothesis given by equation (1). $R_{exp.} \approx 22 \pm 4$ μm for the steel containing 0.32 wt % of carbon and solidifying with 1.67 10^{-3} cm/s by the *Bridgman* system. The dendrite is treated as a single crystal so that the 1D mode of solidification is expected for each columnar dendrite / cell, [4].

Transport equations for the columnar structure growth

Mass transport around the dendrite tip growing under steady-state can be successfully described by the *Ivantsov* function, $I(P)$. When the values of *Peclet* Number fulfill inequality $0 \le P \le 1$ the second *Ivantsov* function, $I_2(P)$, is sufficient to be equalized to the supersaturation, Ω,

$$\Omega = I_2(P) = P\exp(P)E_1(P) \approx 2P/(2P+1) \tag{4}$$

The supersaturation is defined as a parameter describing a deviation of the system from an equilibrium:

$$\Omega = \left(C_L^* - C_0\right)/\left[(1-k)C_L^*\right], \qquad 0 \le \Omega \le 1, \tag{5}$$

Both capillarity limit and diffusion limit decide on the value of two control parameters: R and v. An experiment indicates that the tip radius, R, chosen by the solid / liquid system is approximately equal to the lowest wavelength of perturbation of the tip, which is close to the λ_S, Fig. 3. This is referred to growth at the limit of marginal stability for which $R \Rightarrow R_S$, (equation 1).

Perturbation analysis for the dendrite tip

The analysis of perturbation resulting from the MS theory, [3] is shown schematically in Fig. 3.
The rate of a development of perturbation formulated by the MS theory, [3], is given as follows:

$$\frac{\dot{\varepsilon}}{\varepsilon} = \left(\frac{v}{mG_C}\right)\left[-\omega^2\Gamma\left(\omega^* - (1-k)\frac{v}{D}\right) - G\left(\omega^* - (1-k)\frac{v}{D}\right) + mG_C\left(\omega^* - \frac{v}{D}\right)\right] \tag{6}$$

$$\omega = 2\pi/\lambda \tag{7a}$$

$$\omega^* = \frac{v}{2D} + \left[\frac{v^2}{4D^2} + \omega^2\right]^{0.5} \tag{7b}$$

Equation (6) can be useful in characterization of the analysed materials that is steel.

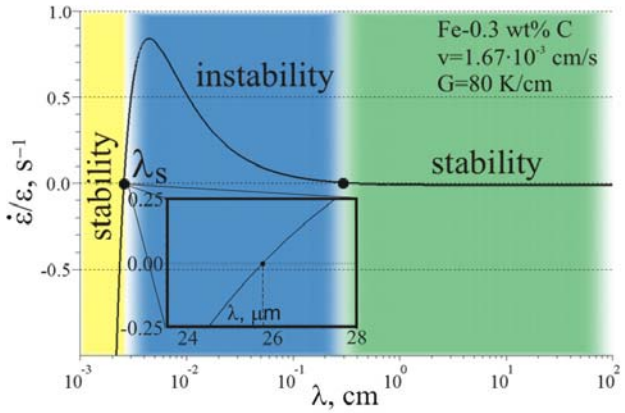

Figure 3. Rate of a perturbation development at the constitutionally undercooled s/l interface. At a very short wavelengths, the value of the $\dot{\varepsilon}/\varepsilon$ parameter (equation (6)) is negative due to curvature damping and the perturbation vanishes. At wavelengths greater than λ_S the instability of solid / liquid interface is observed. The second stability (r.h.s. part of the curve) results from a difficulty of mass transfer over large distances. $\lambda_S \approx 26$ μm according to the calculation.

When $\lambda = \lambda_S$, then the term contained in the square brackets in equation (6) is equal to zero. This occurs when $\dot{\varepsilon} = 0$. As a result the following formula can be obtained:

$$\omega^2 \Gamma = m G_C \xi_C - G, \qquad \xi_C = 1 - 2k / \left\{ \left[1 + (2\pi / P)^2 \right]^{0.5} - 1 + 2k \right\} \tag{8}$$

For $\lambda \le \lambda_S$ the curve is below $\dot{\varepsilon}/\varepsilon = 0$ since the solid /liquid interface curvature damps any perturbation, Fig. 3. At wavelengths greater than λ_S the perturbed interface becomes stable and for high values of the λ again stable plane interface is observed because of the difficulty of mass transfer over large distances.
When the interface is completely stable, the curve will remain below the $\dot{\varepsilon}/\varepsilon = 0$, again.
When the *Peclet* Number is sufficiently small, $0 \le P \le 1$, then $\xi_C \to 1$.
Additionally, a combination of equation (7) and equation (8) with the application of the LMK criterion, equation (1) yields:

$$\lambda_S = 2\pi \left(\Gamma / \left(m G_C \xi_C - G \right) \right)^{0.5}, \qquad \Gamma = \sigma / \Delta S \tag{9}$$

Some rearrangements of equation (4) and equation (5) allows to define one of the important parameters associated with the dendrite tip that is the solute concentration in the adjacent liquid:

$$C_L^*(R,v) = C_0 / \left[1 - (1-k) I_2(P) \right] \tag{10}$$

Simultaneously, the total undercooling of the dendrite tip can be given:

$$\Delta T = \Delta T_C(R,v) + \Delta T_{\bar{K}}(R) = m\left(C_0 - C_L^*(R,v) \right) + 2\Gamma / R = m C_0 \left[1 - 1/\left(1 - (1-k) I_2(P) \right) \right] + 2\Gamma / R \tag{11}$$

Additionally, the solute concentration gradient at the dendrite tip is:

$$G_C(R,v) = dC/dz = -(v/D)(1-k) C_L^*(R,v) = -(v/D)(1-k) C_0 / \left[1 - (1-k) I_2(P) \right] \tag{12}$$

The equation (9) can be simplified when $\xi_C \to 1$ which is justified for the steel/cast iron solidification:
Combination of equations (12) and (9) gives:

$$\lambda_S = 2\pi \left\{ \sigma / \left[\Delta S \left(m (v/D)(k-1) C_0 / \left(1 - (1-k) I_2(P) \right) - G \right) \right] \right\}^{0.5} \tag{13}$$

Growth law for the columnar dendrites /cells array formation

Introducing criterion (1) the following rearrangement of equation (13) can be given:

$$R_S^{\,2}\left(m G_C - G\right) = 4\pi^2 \sigma / \Delta S \tag{14}$$

and after application of equation (12) equation (15) becomes:

$$R_S^{\,2}\left\{m(v/D)(k-1)C_0 / \left[1-(1-k)I_2(P)\right] - G\right\} = 4\pi^2 \sigma / \Delta S \tag{15}$$

According to measurement shown in Fig. 2 the experimental radius of dendrite tip $R_{\text{exp.}} \cong R_S$. Thus,

$$I_2(P) = 2P/(2P+1) = R_{\text{exp.}}\, v/\left(R_{\text{exp.}}\, v + D\right) \tag{16}$$

Taking into account criterion (1) verified experimentally, Fig. 2, and equation (16) it can be given that:

$$m v (k-1) C_0 \left(R_S\, v + D\right)/\left[D\left(D + k\, R_S\, v\right)\right] - G = 4\pi^2 \sigma / \Delta S / R_S^{\,2} \tag{17}$$

Finally, after some rearrangements the so-called growth law for columnar dendrites / cells array formation is obtained:

$$R_S^{\,3}\left[\Delta S\, v\left(m(k-1)C_0\, v - G\, D\, k\right)\right] + R_S^{\,2}\left[\Delta S\, D\left(m v (k-1) C_0 - G\, D\right)\right] - R_S\left[4\pi^2 \sigma\, D\, k\, v\right] - 4\pi^2 \sigma D^2 = 0$$

Equation (18) is a mathematical relationship in which control parameters: R_S, v, C_0, G and materials parameters: $\Delta S, m, k, D, \sigma$ are contained. This formula makes possible to predict R_S - tip radius. However, values of temperature gradient are necessary to be applied in calculation. The temperature gradient can be obtained from a simulation of the temperature field in the solidifying ingot or roll.

MODEL OF TEMPERATURE FIELD IN SOLIDIFYING INGOT / ROLL

In order to predict a period of time during which columnar dendrites transform into equiaxed dendrites a temperature field in solidifying ingot / roll was simulated with the use of the *Fourier* equation, Fig. 4.

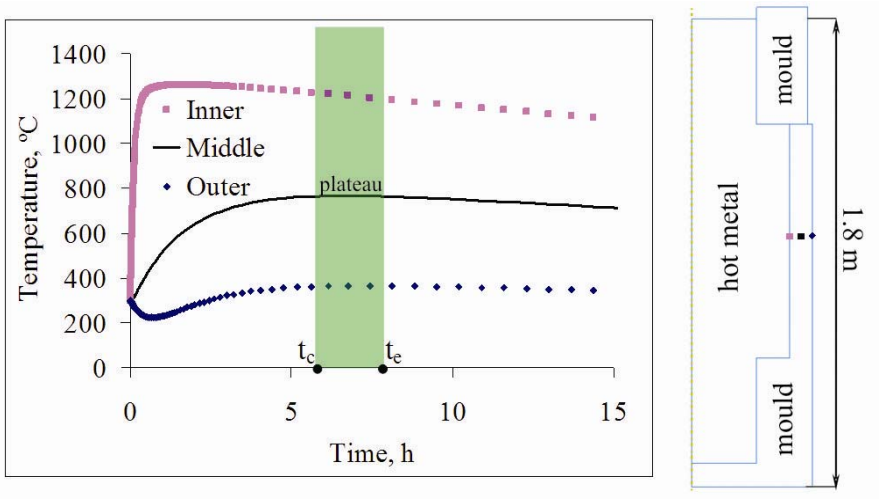

Figure 4. Predicted temperature change in the middle of mould (additionally in inner and outer side) The transition period of time from columnar into equiaxed dendrites is marked as $t_c \leftrightarrow t_e$.

The calculation was performed in the Academic Computer Centre CYFRONET AGH (computer named '*baribal*' was financed from the project MNiSW/SGI3700/PAN/021/2009.
The commercial Finite Element software ABAQUS was used to calculate temperature change in ingot and mould.
The simulation of temperature field includes latent heat, however the convection was neglected. The temperature change in the middle of the mould was associated with period of time necessary for dendrites transition.
It is concluded that the transition occurs when the heat flow through the mould is stable which is visible in Fig. 4 as a plateau, at the middle of the mould curve plotted versus time.

MODEL OF SOLUTE REDISTRIBUTION IN THE GROWING DENDRITE / CELL

Physical bases for present model have already been formulated, [5], in order to improve differential equation, shown by Brody and Flemings, [6]. There are:

- complete mixing in the liquid within the volume element, assumed in Fig. 5,
- increase of solute concentration in advance of the tips of growing dendrites or cells is negligible,
- equilibrium crystal growth and non-equilibrium freezing are integral parts of the current model,
- no assumption is made associated with the movement of the solid/liquid interface,
- a formula for $d\left(x\overline{C}_S\left(x;\alpha\right)\right)$- increment of average solute concentration inside a crystal contains all the factors, which decide on back-diffusion; there are: coefficient of the diffusion in the solid, D_S, amount of growing crystal, x, size of half cell / dendrite, λ^F, rate of dendrite / cell thickening, v_p, and gradient of the solute concentration, $dC_S^*\left(x;\alpha\right)/dx$ in a given layer, dx.

The above assumptions allow to formulate a new differential equation for solute microsegregation, $C_S^*\left(x;\alpha\right)$, as observed at the moving solid / liquid interface:

$$d\left(x\,\overline{C}_S\left(x;\alpha\right)\right)=C_S^*\left(x;\alpha\right)dx+D_S\,/\left(L\,v_p\right)x\left(dC_S^*\left(x;\alpha\right)/dx\right)dx \tag{19}$$

The l.h.s. of equation (19) presents the amount of solute, which entered inside the crystal due to back-diffusion, when the newly growing dx- layer appeared; the first term of r.h.s. of equation (19) presents the amount of solute, which is actually within this layer, (at a solid / liquid interface); the second term of r.h.s. of equation (19) presents the amount of solute which passed across the solid / liquid interface and entered inside the crystal. Equation (19) causes mass balance in the solid-liquid system to not yet be satisfied. Equation (19) determines increase of solute, which is passing from the liquid to the solid across the solid / liquid interface, only, while considering the increment, dx. Taking into account the average thickening rate, v_p, perpendicular to the direction of crystal growth, Fig. 5, the definition of the α - back-diffusion parameter, [6],

$$\alpha=D_S\,t^F\,(\lambda^F)^{-2}=D_S\,/\left(\lambda^F\,v_p\right) \tag{20}$$

can be separated from equation (19). Combining equation (19), equation (20), mass balance consideration for the solid – liquid system, Fig. 5, and assuming that back-diffusion parameter is constant for a given dendrite / cell growth at $v=const.$ the final differential equation is:

$$dC_L^*\left(x;\alpha\right)/dx=\left(1-k\right)C_L^*\left(x;\alpha\right)/\left(1+\alpha\,k\,x-x\right),\qquad k=C_S^*\left(x;\alpha\right)/C_L^*\left(x;\alpha\right) \tag{21}$$

The following initial condition $C_L^*(0,\alpha)=C_0$ allows to solve equation (21):

$$C_S^*(x;\alpha)=k\,C_0\left(1+\alpha\,k\,x-x\right)^{\frac{k-1}{1-\alpha\,k}} \qquad x\in[0,x_K], \quad x_K\in[0,1] \tag{22}$$

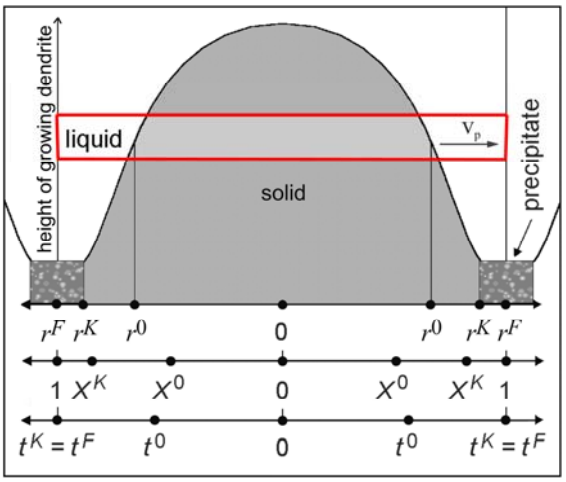

Figure 5. Scheme of the dendrite / cell tip: distance (growing crystal size) ➔ r - axis; crystal amount, dimensionless, ➔ x - axis; local solidification time ➔ t - axis. v_p is the rate of the movement for a generating line of the paraboloid of revolution (rate of the solid / liquid interface motion). r^0, X^0, t^0 define a position on a stopped solid / liquid interface at an intersection with an observation window (solid – liquid volume). r^K, x^K, t^K is a boundary between a crystal and precipitate, at the end of a crystal thickening ($t^K = t^F$).

Finally, the solute redistribution after the back-diffusion inside a dendrite / cell is given as follows:

$$C_B\left(x;X^0,\alpha\right)=C_S^*(x;\alpha)[1+\beta^{ex}\left(x;X^0\right)\beta^{in}\left(X^0,\alpha\right)/k] \tag{23}$$

where $x=X^0$ is a parameter responsible for arrested solid / liquid interface.

CONCLUDING REMARKS

The equation (10) describing the solute concentration at the growing columnar dendrite can be applied to the solution of equation (19) as an initial condition for each section of dendrite. This is explained in Fig. 6 where $C_B(x;1,\alpha)$ means the solute redistribution inside the growing columnar dendrite / cell.

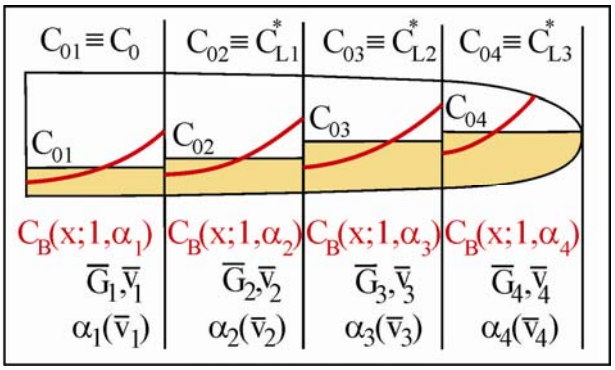

Figure 6. A dendrite / cell divided into four sections. A steady-state growth is attributed to each section. Therefore, average growth rate is $\overline{v}_i = const.$ and average temperature gradient $\overline{G}_i = \partial T/\partial x = const$ in each section. $C^*_{L(i-1)}$ solute concentration at the tip becomes the initial condition for differential equation (19) which should be solved for each section. Thus $C^*_{l(i-1)} \to C_{0i}$ where i is the section number.

The equation (23) describing the solute redistribution after back-diffusion into the growing dendrite / cell can be perfectly mathematically reduced to the description of the equilibrium solidification while applying $\alpha = 1$ and to the description of the non-equilibrium solidification while applying $\alpha = 0$.
The use of $C_L^*(R,v)$ solute concentration (equation (10)) can modify temperature field and localization of the $t_c \leftrightarrow t_e$ zone in Fig. 4. Geometry of mould has also an influence on this localization.

NOMENCLATURE

d_0 thermal capillary length,
D coefficient of diffusion in the liquid,
G temperature gradient in the liquid just at the solid / liquid interface,
G_C solute concentration gradient in the liquid just at the solid / liquid interface,
k equilibrium partition ratio of the solute between the solid and the liquid,
l thermal diffusion length,
m slope of the liquidus line,
β^{ex} coefficient of the extent of solute redistribution inside a growing dendrite / cell, [4],
β^{in} coefficient of the intensity of solute redistribution inside a growing dendrite / cell, [4],
ΔS entropy of melting,
ΔT solid liquid interface undercooling,
ε amplitude of the planar instabilities (perturbation),
Γ capillarity parameter (*Gibbs-Thomson* relationship),
λ wavelength for planar instabilities,
λ_S minimum wavelength for planar instabilities,
σ interfacial energy in the *Gibbs-Thomson* relationship.

ACKNOWLEDGEMENTS

The financial support from the Polish Ministry of Science and Higher Education (MNiSW) under contract N R15 006004 is gratefully acknowledged.

REFERENCES

1. Langer, J. S., and Muller-Krumbhaar, H., Stability Effects in Dendrirtic Growth, *Journal of Crystal Growth,* Vol. 42, pp 11-14, 1977.
2. Glicksman, M. E. Schaefer, R. J. and Ayers, J. D., Dendritic growth – A Test of Theory, *Metallurgical Transactions A,* Vol. 7A, pp 1747-1759, 1976.
3. Mullins, W. W. and Sekerka, R. F., Stability of a Planar Interface during Solidification of a Dilute Binary Alloy, *Journal of Applied Physics*, Vol. 35, pp 444-451, 1964.
4. Wołczyński, W., *Phenomenes de Segregation aux Pointes des Dendrites Colonnaires dans les Aciers au Carbone*, Rapport Confidentiele, RP.246, IRSID – Maizieres-les-Metz, 1988.
5. Wołczyński, W., *Back-diffusion Phenomenon During the Crystal Growth by the Bridgman Method*, chapter 2. in the book: Modelling of Transport Phenomena in Crystal Growth, eds. J.S. Szmyd and K. Suzuki, ed. WIT Press, Southampton – Boston, 2000, pp 19-59.
6. Brody, H. D., and Flemings, M. C., Solute Redistribution in Dendritic Solidification, *Transactions of The Metallurgical Society of AIME*, Vol. 236, pp 615-623, 1966.
7. Hunt, J. D., Steady State Columnar and Equiaxed Growth of Dendrites and Eutectics, *Materials Science and Engineering,* Vol. 65, pp 75-83, 1984.

MAGNETIC FIELD CONTROL OF CONVECTION IN AN INCLINED FERROCOLLOID LAYER

A. Bozhko[1,*], G. Putin[1], T. Tynjälä[2]
[1]Perm State University, Perm, Russia
[2]Lappeenranta University of Technology, Lappeenranta, Finland

ABSTRACT. Thermomagnetic convection is a feasible method to augment or suppress free convection in non-conducting magneto-polarizable natural media and artificial magnetic nanoparticle fluids (ferrocolloids) especially for small length scale applications or in microgravity. As a rule, nonuniform magnetic fields with gradient directed along or against the acceleration of gravity are used for these manipulations. Present work shows that in the case of an inclined ferrocolloid layer heated from below the similar promotional or overwhelming magnetic field action may be realized by means of external uniform magnetic fields. The understanding of the relation between an applied magnetic field and the resulting heat transfer is necessary for the proper design and control of thermomagnetic devices.

Keywords: *convection, inclined layer, magnetic field, ferrocolloid*

INTRODUCTION

Rayleigh-Bérnard convection in a horizontal cavity heated from below is traditional case to study the formation of convection patterns [1]. Symmetry of the Rayleigh-Bernard convection of horizontal cavity may be destroyed by tilting the layer. As known, thermally driven shear flow in an inclined layer draws up convection rolls in the direction of inclination. In addition, for ferrocolloid with nonuniform magnetic permeability, an external uniform transverse field may cause onset of magnetoconvective motion similar to buoyancy driven natural convection whereas longitudinal magnetic field has orienting effect on convection rolls as in the case of shear flow [2]. For moderate inclination angles a wide variety of different patterns such as longitudinal rolls, tick-like patterns or travelling undulating rolls. Similar observations have been recently made in the absence of magnetic field in [3] and for magnetic liquids with a free surface in [4]. Besides one should note that in the case of ferrocolloids the gradients of magnetic permeability may arise due to both temperature and particle concentration gradients. When ferrocolloid is exposed to the temperature or magnetic field gradient, density gradients within the fluid will be developed due to thermal expansion of the carrier fluid as well as ordinary, thermal and magnetic diffusion mechanisms. In contrast to a horizontal layer in an inclined layer the direction of buoyancy or gravity sedimentation is not parallel with other effects as shown in Figure 1.

One should note that there are two main reasons the generation of concentration inhomogeneities induced by gravity. The former, an effective height of inclined layer increases with the inclination rise and the density drops of barometric origin begin to play a larger role. The latter, the rising–sinking shear flow appearing due to the inclination of a layer, also amplifies the colloidal particles inhomogeneities that is similar to the separation effect in the thermodiffusion column.

* Corresponding author: Dr. A. Bozhko
Phone: + (7)-342-396836, Fax: + (7)-342-2371611
E-mail address: bozhko@psu.ru

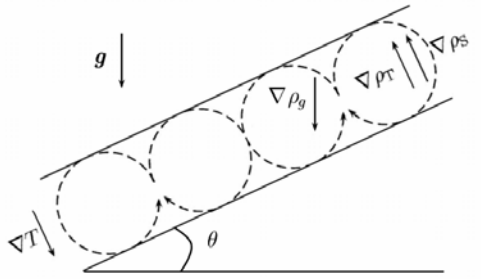

Figure 1. Inclined layer convection - in an inclined layer the direction of temperature gradient is not parallel with gravity acceleration vector. In the absence of magnetic field density gradients inside the layer will be developed due to thermal expansion, gravity sedimentation $\nabla\rho_g$, ordinary $\nabla\rho_T$ and thermal diffusions $\nabla\rho_S$.

RESEARCH METHODS

The stability of buoyancy-driven shear flow and heat transfer in an inclined layer of a ferrocolloid is investigated by experiments and numerical simulations. The stability of mechanical equilibrium as well as intensity of convective motion of non-isothermal ferrocolloid subjected to gravity and magnetic fields are determined by gravitational and magnetic Rayleigh numbers, Ra and Ra_{m}, defined as,

$$Ra = \frac{g\beta\Delta T h^3}{\nu\kappa} \tag{1}$$

$$Ra_{\mathrm{m}} = \frac{\mu_0(\beta_{\mathrm{m}} M\Delta T h)^2}{\rho\nu\kappa(1+\chi)}, \tag{2}$$

where ΔT is the temperature difference across the fluid layer, h is the layer thickness and g is the acceleration due to the gravity. β and β_{m} are thermal expansion and relative pyromagnetic coefficient, M, χ, ρ are the magnetization, susceptibility and density of the ferrocolloid and μ_0 is the vacuum permeability. Whereas gravitational Rayleigh number describes the ratio of buoyant and viscous forces, the magnetic Rayleigh number is ratio of magenetic and viscous forces. Critical Rayleigh number for the onset of convection in horizontal layer is $\mathrm{Ra_{cr}} = 1708$ [1], and for inclined layer longitudinal rolls are predicted to occur at $\mathrm{Ra_{cr}}(\theta) = 1708/\cos\theta$ [3]. The sidewalls influence the formation of the convection patterns significantly when the aspect ratio $A = D/h$ is order of 30 or less [5]. In our case the aspect ratio was varied between 20 and 37.5. Studied ferrocolloid consists of magnetite particles suspended in kerosene carried fluid. The average magnetite particle size was equal to 10 nm, particle volume fraction was 10 % and saturation magnetization $M_{\mathrm{s}} = 48$ kA/m.

Experimental methods

Cross-sectional view one of the test enclosures is presented in Figure 2 [6]. Test enclosures were placed inside of a Helmholtz coil to create uniform external magnetic field parallel to the plane of the layer and while system was tilted in order to study different inclination angles. The cavities with different aspect ratios were used. For the visualization upper copper heat exchanger was replaced with a plexiglass heat exchanger and a temperature sensitive liquid crystal film was attached to the test enclosure. The liquid crystal sheet undergoes its entire color change from brown to blue at temperature interval 24–27^{0}C.

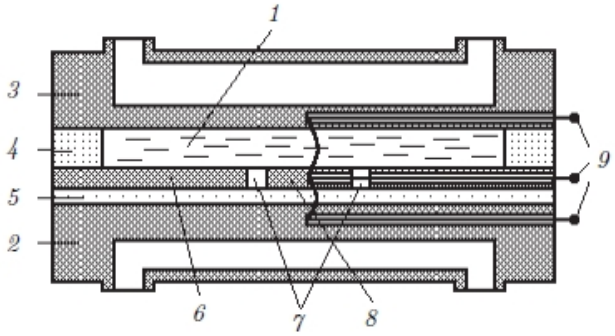

Figure 2. Cross-sectional view of the test enclosure. 1 – ferrocolloid layer; 2, 3 – copper heat-exchangers; 4 – circular plexiglass frame; 5 – fluoroplastic layer; 6 – copper plate; 7 – circular heat-insulating groove; 8 – integral heat flux sensor; 9 –thermocouples. [6]

The onset of convection is determined with the help of thermocouples by well-known method of Schmidt and Milverton [7], where the temperature difference over a fluoroplastic layer was compared with the temperature difference over the cavity filled with the ferrocolloid. As long as the heat across the fluid layer is transported by conduction, the heat flux will increase linearly with temperature difference. This linear relation breaks down at the onset of thermal instability because other modes of heat transport become operative. Average Nusselt number was determined with the help of integral sensor 17 mm in diameter situated in the middle of the cavity [6].

Numerical simulations

Numerical calculations were conducted using a commercial software Fluent. Solver uses finite volume method (FVM) to solve discretized conservation equations. Conservation equations for mass (3), energy (4) and momentum (5) as well as flux function for magnetic scalar potential (6) were solved. In the simulations all fluid properties were defined in mean temperature and held constant, expect for the density and fluid magnetization, for which a Boussinesq type approximation was used. In the method, coefficient of thermal expansion and pyromagnetic coefficient take into account for the temperature dependence of density and magnetization [8]. Fluid properties used in the simulations are shown in Table 1.

$$\nabla \cdot \mathbf{u} = 0 \tag{3}$$

$$\rho_0 \left(\frac{\partial u}{\partial t} + \mathbf{u} \cdot \nabla \mathbf{u} \right) = -\nabla p + \rho_0 \beta (T - T_0)\mathbf{g} + \eta \nabla^2 \mathbf{u} + \mu_0 \beta_{\mathrm{m}} M_0 (T - T_0) \nabla H \tag{4}$$

$$\left(\frac{\partial T}{\partial t} + \mathbf{u} \cdot \nabla T \right) = \frac{k}{\rho c_{v,H}} \nabla^2 T \tag{5}$$

$$\nabla \cdot (\mu \nabla \phi_m) = -\beta_m M_0 \nabla T \tag{6}$$

Subscript 0 in above equations refers to the base state at applied external magnetic field H_0 and average temperature between top and bottom walls T_0. Boundary conditions were no slip at the walls, constant temperatures for bottom and top walls, and sidewalls were assumed insulated.

Magnetic scalar potential ϕ_m is use to describe magnetic field inside the simulation domain. Magnetic scalar potential is defined as

$$\mathbf{H} = -\nabla \phi_m \tag{7}$$

According to the Maxwell equations for non-conducting media, following statements for the magnetic induction field B and magnetic field H can be written

$$\nabla \cdot \mathbf{B} = 0 \quad \text{and} \quad \nabla \times \mathbf{H} = 0\,. \tag{8}$$

Magnetic induction field is defined as

$$\mathbf{B} = \mu_0(\mathbf{H} + \mathbf{M}) = \mu_0(\mathbf{H} + \chi\mathbf{H}). \tag{9}$$

In equation (9) χ stands for susceptibility defined as the ratio of magnetic field H and magnetization M. From equations (8) and (9) it can be shown that normal component of the magnetic induction field and tangential component of the magnetic field are continuous across the border between materials with different magnetic permeability. In terms of magnetic scalar potential this means that Laplacian of the magnetic scalar potential is constant at the sidewalls and gradient of the magnetic scalar potential is constant at bottom and top walls. Diameter of the studied cell was 75 mm, height was 3.5 mm were taken as in experiment [6]. The simulation mesh was composed of more than 400 000 tetrahedral cells.

Table 1
Properties of the studied ferrocolloid.

Density	ρ	1250 kg/m^3
Specific heat capacity	c_p	2100 J/kg/K
Dynamic viscosity	η	0.01 kg/ms
Thermal conductivity	k	0.15 W/mK
Coefficient of volume expansion	β	0.001 1/K
Pyromagnetic coefficient	β_m	0.001 1/K

RESULTS AND DISCUSSION

Magnetic field was applied horizontally parallel to the plane of cavity as shown in Figure 3 (a). Due to boundary effects, large magnetic field gradients exist next to the boundaries. Especially for large magnetic field magnitude, boundary effects will create torus like disturbances, as shown in Figure 3 (b). Despite the fact that heat flux was measured only from the center part of the cavity, boundary disturbances are causing some peculiarities to the heat flux calculations at large magnetic field. For moderate aspect ratios, the same effect will limit the simulations to small and medium magnetic field strengths. In the absence of magnetic field, the effect of boundary disturbances will decrease. Liquid crystal visualization of the shear flow in the absence of magnetic is represented in Figure 3 (c). Here white and black regions correspond to hot and cold fluids.

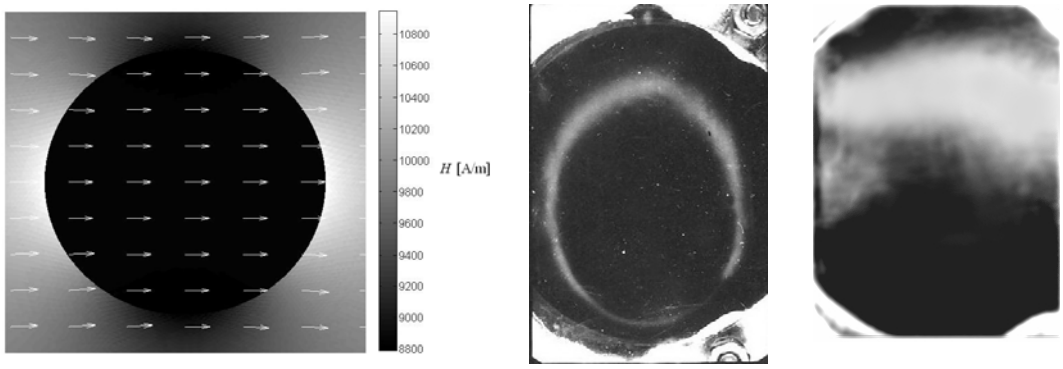

Figure 3. (a) Magnetic field within the horizontal cylinder in the absence of temperature gradient. Arrows show the direction of magnetic field lines. (b) Liquid crystal visualization of torus flow due to boundary disturbances for case $H = 27$ kA/m, $\Delta T/\Delta T_{cr} = 4$, $\theta = 20°$. Magnetic field is parallel with the plane of photo. (c) Temperature stratification in the case of base shear flow for $H = 0$, $\theta = 90°$. The temperature variation from cool (black) to warm (white) liquid is approximately 3 K.

In Figure 4 the Nusselt numbers have been presented for inclination angles 15° and 30°, in the absence of magnetic field. In the absence of magnetic field the increase in convection is more abrupt for smaller inclination angles that for larger ones. Critical temperature difference used in the figures is calculated from horizontal case and for inclined cases at $\Delta T/\Delta T_{cr} = 1$. The spread in experimental values of Nusselt numbers is connected with temperature oscillations which observed in wave convective regimes in inclined ferrofluid layer [6].

In the case of uniform magnetic field, the comparable contribution of mutually perpendicular orientation mechanisms - shear flow and magnetic field - leads to the formation of different types of wave structures in the form of oblique rolls and their superposition. At modest inclination angles it is possible to decrease or increase the heat flux intensity with the help of modulation of the magnetic field value. The decreasing of heat transfer is connected with suppression of gravitational convection rolls whereas the increasing is due to the development of convection rolls oriented along the magnetic field direction.

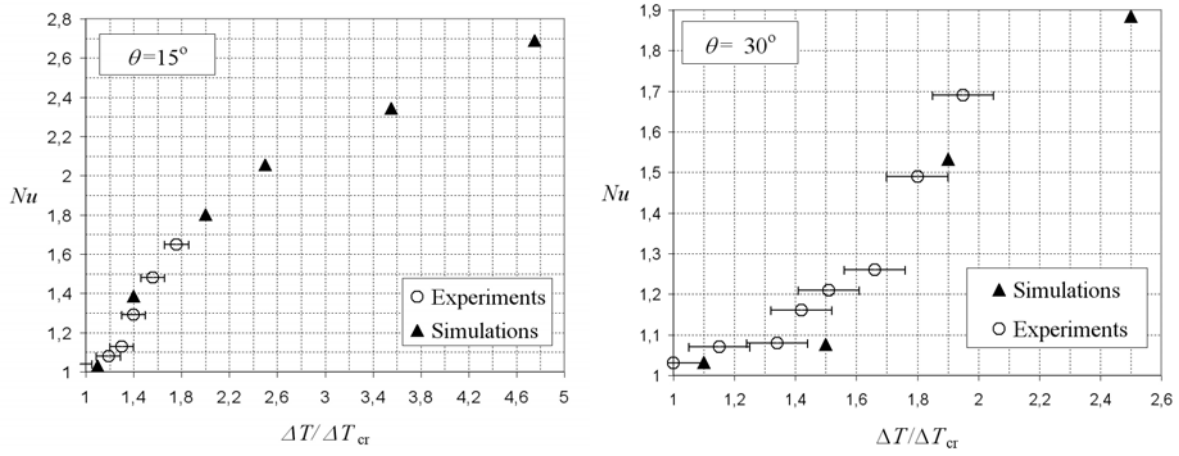

Figure 4. Nusselt number as the function of critical temperature difference for the onset of convection in horizontal layer in the absence of magnetic field for inclination angles 15º (left) and 30º (right).

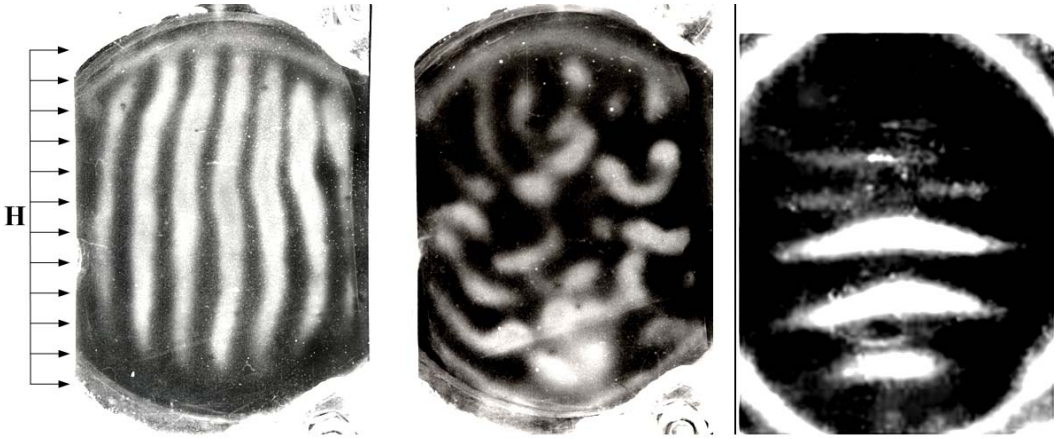

Figure 5. Development of convection rolls in an inclined layer at θ= 15º. Magnetic field is increasing from left to right H = 0, 2 and 10 kA/m. In the figure the upper part of the cavity is elevated

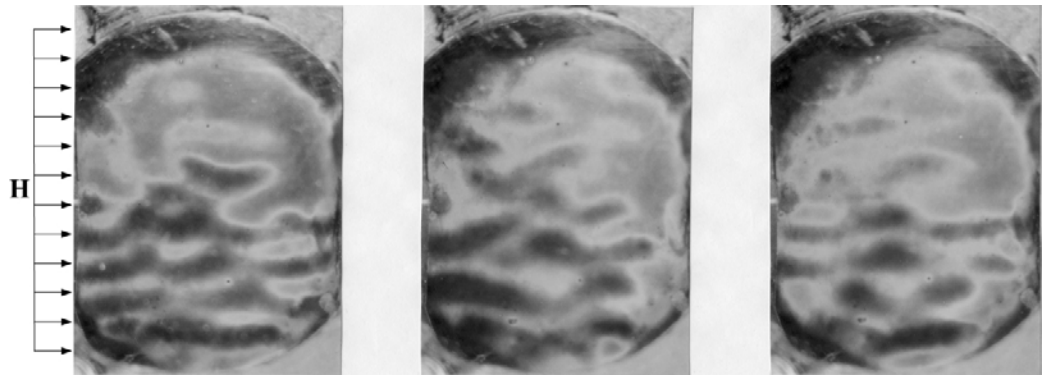

Figure 6. Development of convective rolls for H = 2.5 kA/m and θ= 15°. The time intervals between snapshots are 1 min. In the figure the upper part of the cavity is elevated

Figure 5 shows orientation effect of convection rolls as the magnetic field magnitude increases. If the magnetic field strength and inclination angle are large enough the complete stabilization of Rayleigh convection occurs. The drastic change of heat flux is observed in regimes of travelling rolls and solitary vortices which arise near the boundary of the intersection of gravity and magnetic orientation mechanisms. For small angles and moderate fields, there exist large oscillations in the recorded heat flux. The large oscillations at small magnetic fields correspond to tick-like patterns in Figure 5 for H = 2 kA/m or traveling undulating rolls as shown in Figure 6 for H = 2.5 kA/m.

When the magnetic field is applied the convection rolls orientated in the direction of shear flow are replaced by cells beginning from the lower part of the cavity. In Figure 7 simulation results are shown for the inclination angle 15° after the magnetic field of H = 10 kA/m is turned on. In the upper part of the cavity convective rolls still exist. Increase of inclination angle has an opposite effect on formation of convection. As inclination angle is increased the shear flow takes more place as shown in Figure 8, where simulated convection patterns have been plotted for inclination angles 0°, 15° and 30°, in the presence of magnetic field H = 10 kA/m.

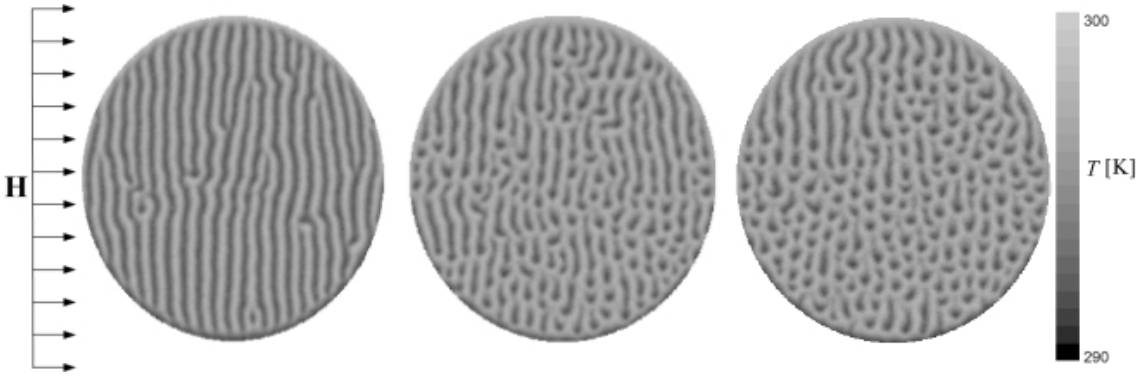

Figure 7. Simulated temperature contours in an inclined layer $\theta = 15°$. When the magnetic field is applied the convection rolls orientated in the direction of shear flow are replaced by cells. In the elevated upper part of the cavity convective rolls still exist.

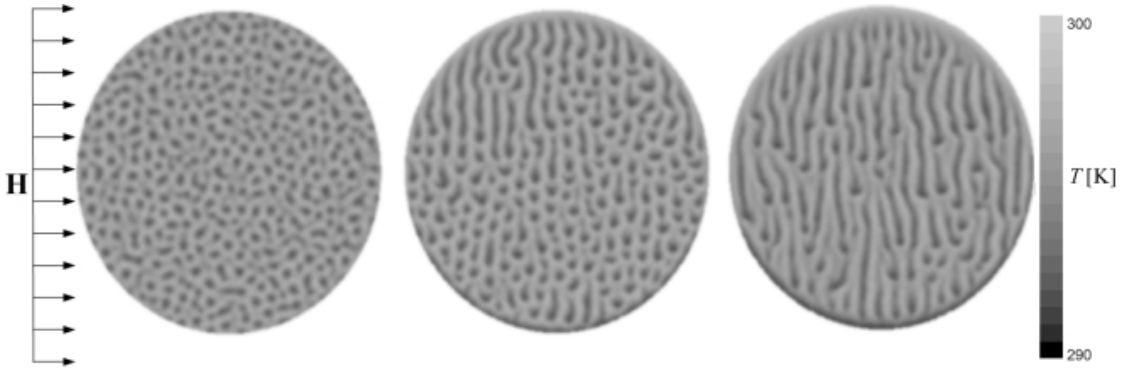

Figure 8. Simulated temperature contours at increasing inclination angles 0°, 15° and 30° from left to right. Here $\Delta T/\Delta T_{cr} = 2$ and $H = 10$ kA/m. In the figure the upper part of the cavity is elevated.

CONCLUSION

Magnetic field control of heat transfer when applied field is applied from the side, parallel with the fluid layer and perpendicular to the inclination angle, may be fulfilled by two main ways. The former is the extinguishing of the convection perturbations along the magnetic field direction at enough large inclination angles. The latter is the alternation of the weakening and strengthening of heat transfer with magnetic field growth when inclination angles are smaller than $\theta = 20°$ and various realignments of convection patterns occur.

NOMENCLATURE

Symbol	Quantity	Unit
B	Magnetic induction	T
H	Magnetic field magnitude	A/m
M	Magnetization	A/m
$\chi = 1 + \mu$	Susceptibility	-
ϕ_m	Magnetic scalar potential	A/m^2
μ	Relative permeability	-
μ_0	Vacuum permeability	$4\pi \times 10^{-7}$ H/m

ACKNOWLEDGEMENTS

The work was supported by the Russian Foundation for Basic Research and Government of Perm Region, Russia, under grant No 07-08-96039, and Finnish Academy grant No 110852.

REFERENCES

1. Chandrasekhar, S., *Hydrodynamic and Hydromagnetic Stability*, Dover Publ. Co., USA, 1961.
2. Bozhko, A. A., Putin, G. F. and Tynjälä, T., Magneto-hydrodynamic interaction in an inclined layer of ferrocolloid heated from below, *Solid State Phenomena*, Vol. 152-153, pp 159-162, 2009.
3. Daniels, K. E., Plapp, B. B. and Bodenschatz, E., Pattern formation in Inclined Layer Convection, *Phys. Rev. Lett.*, Vol. 84, pp 5320-5323, 2000.
4. Groh, C., Richter, R., Rehhberg, I. and Busse, F. H., Reorientation of a hexagonal pattern under broken symmetry: The hexagon flip, *Phys. Rev. E*, Vol. 76, pp 055301-1-4, 2007.
5. Busse, F. H., Non-linear properties of thermal convection, *Rep. Prog. Phys.*, Vol. 41, pp 1929-1967, 1978.
6. Bozhko, A. A. and Putin, G. F., *Heat transfer and flow patterns in ferrofluid convection*, *Magnetohydrodynamics*, Vol. 39, pp 147–169, 2003.
7. Schmidt, R.J. and Milverton, S.W., On the instability of a fluid when heated from below, *Proc. Roy. Soc. London. Ser. A.,* Vol. 152, pp 586-594, 1935.
8. Tynjälä, T. Theoretical and numerical study of thermomagnetic convection in magnetic fluids, *PhD Thesis*, LUT Energy, Lappeenranta, Finland, 2005.

COALESCENCE PHENOMENA OF LIQUID DROPLETS IN A TUBE

M. Muraoka[1*], N. Ogawa[2], R. Fujita[3], I. Ueno[1], and H. Mizoguchi[1],
[1]Tokyo University of Science, Noda, Chiba, Japan
[2]Undergraduate, Tokyo University of Science (present: Graduate School at Tokyo Univ. Science)
[3]Undergraduate, Tokyo University of Science (present: Hitachi Cable, Ltd.)

ABSTRACT. We focus on coalescence phenomena of liquid droplets with/without suspended particles in confined geometry; in a horizontal creeping tube flow and in a vertical tube in a quiescent fluid. Correlation between the droplets' size and the coalescence time (i.e., period between instances when the relative velocity of two droplets becomes zero after their contact and when the coalescence takes place) are examined. Effects of suspended particles in the droplets on their coalescence are discussed.

Keywords: *Coalescence, Droplet, Creeping motion, Tube, Flow visualization*

INTRODUCTION

Creeping motion of liquid droplets through a capillary tube is generally employed as a fundamental problem for analyzing the flow of multiphase fluids through porous media [1]. Such a phenomenon can be seen, for instance, in enhanced oil recovery, breaking of emulsions in porous coalescers, fluid handling technique, controlling chemical reaction and so on. Preceding works have indicated coalescence time in this system. There exists little information, however, on effects of suspended particles in the droplets concerned on their coalescence. We have paid our attention to coalescence phenomena in the creeping motion of liquid droplets through a capillary tube. In the present study, we focus on this simple, but complex phenomenon in the system that droplets are confined in a narrow tube. We examine two cases; coalescence in a horizontal tube with a forced flow, and that in a vertical tube with a quiescent fluid. We especially focus on effects of particles suspended in the coalescing droplets on coalescence time and induced behavior of the particles as well as the liquid in the droplets.

EXPERIMENT

Figure 1 is a schematic of the experimental apparatus in the case of a horizontal tube creeping flow. Glass tube of 2 or 5 mm in inner diameter, D, and of 1500 mm in length is used as test tube. Silicones oil of 5, 10, 50, 100, 300, 1000 and 10000cSt are employed as the test fluid for the droplet. Glycerol or a mixture fluid of glycerol and pure water is used for a surrounding fluid in the tube. The density of the droplets is matched to that of the surrounding fluid by adding carbon tetrachloride. Ratio of the viscosity between the droplet and the surrounding fluid is defined as $\alpha = \mu_d/\mu_s$, in which the subscript d and s indicate droplet and surrounding fluid, respectively. An over flow tank is used to keep the flow in the tube steady at a designated averaged velocity, V. The test tube is surrounded by a tank filled with a temperature-controlled water to keep the temperature of

* Corresponding author: Assistant Prof. M. Muraoka
Phone: + (81)-4-7124-1501 Ext.3908 , Fax: + (81)-4-7123-9814
E-mail address: masal@rs.noda.tus.ac.jp

the system constant. Droplets are successively injected into the test tube using two pairs of micro-syringes fixed to the tube. Diameters of the leading and following droplets, d_1 and d_2, respectively, are separately controlled. Thus we can control the initial interval between the droplets and their diameters independently. Behaviors of droplets and suspended particles are monitored by a digital video camera placed on a sliding stage. The motion of the stage is electrically controlled to follow the travelling droplets in the tube.

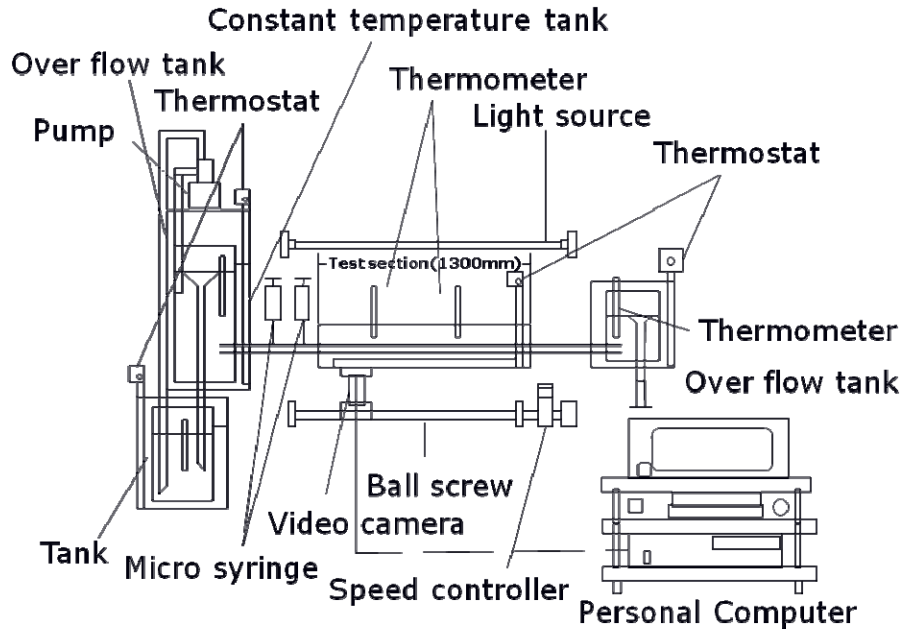

Figure 1. Experimental apparatus for the case of horizontal tube.

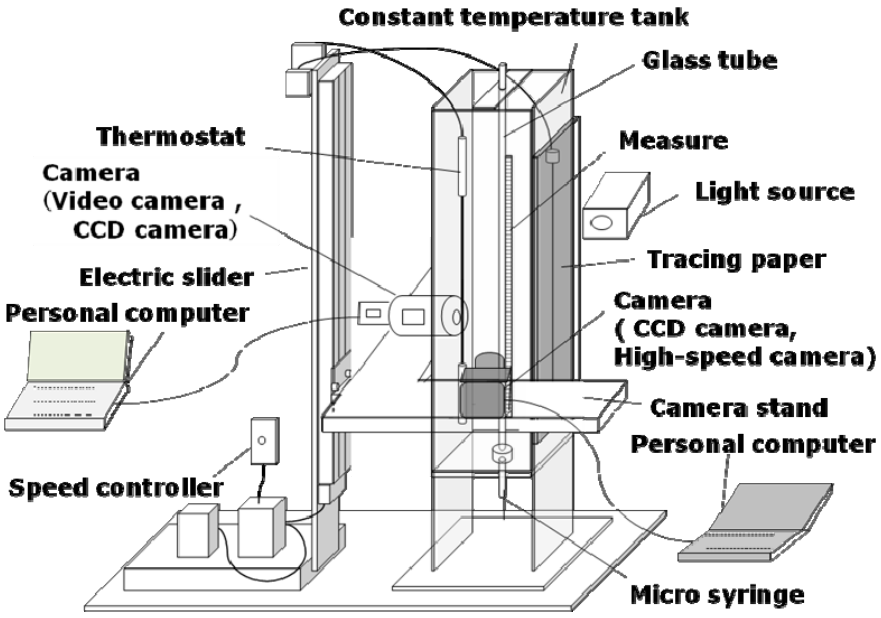

Figure 2. Experimental apparatus for the case of a vertical tube with a quiescent fluid.

Figure 2 is a schematic of the experimental apparatus for the case of a vertical tube with a quiescent fluid. A glass tube of 3.5 mm in inner diameter, 8 mm in outer diameter, and 1500 mm in

length is used as a test tube. Silicone oil droplets are successively injected into the test tube using a single micro-syringe. In this series of experiment, effect of particles suspended in the droplet(s) is examined; gold-coated acrylic particles of 30 μm in diameter and 1490 kg/m^3 in density are employed. Volume concentration of the particles is fixed at 0.13 % in the present study. In the observation system a high speed camera is also employed as well as the digital video camera. The stage for the camera, the test fluid for the surrounding fluid filled with the tube, and the thermal control system for the test section are the same as employed for the experiments with the horizontal tube.

RESULTS & DISCUSSION

Figure 3 shows a typical example of successive images of coalescing droplets without any particles in the tube of D = 5 mm. Experimental condition of this example is $d_1/D = 0.91$, $d_2/D = 0.81$, V = 7.9 mm/s and $\alpha = 0.09$. The kinematic viscosity of droplets is of 564 cSt. Temporal interval between each frame is of 0.5 s. The droplets are colored by adding oil orange for the leading droplet and oil blue for the following. One can clearly see an axisymmetric dynamical motion of following droplet blowing off into the leading one.

Figure 4 indicates coalescence time for different α in the case of D = 2 mm, V = 2.6 mm/s and $d_1/D = 0.984$ against the diameter of the following droplet. Results in the cases of ν_d = 15 cSt ($\alpha = 0.058$), 102 cSt ($\alpha = 0.405$) and 990 cSt ($\alpha = 3.94$) are presented (A surrounding fluid is a mixture fluid of glycerol and pure water). The coalescence time indicates a period between instances when the relative velocity of two droplets becomes zero after their contact and when the coalescence takes place. The coalescence time is non-dimensionalized with D/V followed by a preceding work [2]. In the range of $d_2/D < 0.8$, which corresponds to the experimental range by Ref. [2], the coalescence time decreases as d_2/D increases. This trend corresponds to the one indicated in Ref. [2] In the range of $d_2/D > 0.8$, on the other hand, the coalescence time increases as d_2/D. In order to explain this tendency, one must consider a thin liquid film of R in radius formed between two droplets before the coalescence. Figure 5 represents a diameter of the contact area between the droplets, that is, a diameter of the confined film, against d_2/D. The film diameter takes a maximum value at $d_2/D \sim 0.85$. This value corresponds well with the condition of the minimum coalescence time. This result indicates that the larger the contact area between the droplets, the easier the coalescence takes place.

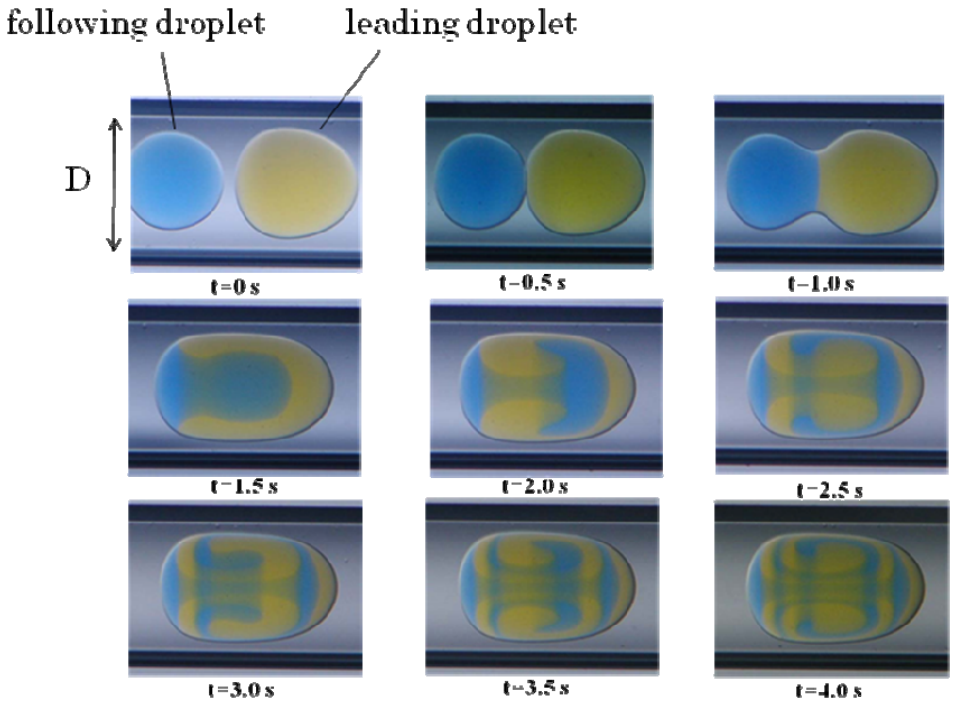

Figure 3. Typical example of coalescence of two droplets flowing in horizontal tube; $d_1/D = 0.91$, $d_2/D = 0.81$, D = 5 mm, V = 7.9 mm/s, $\nu_d = 564$ cSt and $\alpha = 0.09$. Direction of the flow in the tube is left to right.

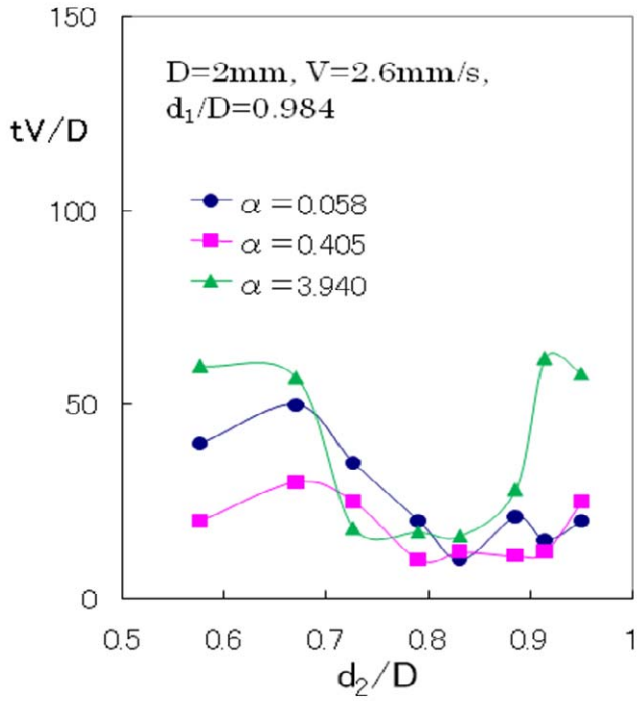

Figure 4. Coalescence time against following droplet diameter for various α in the case of horizontal tube; D = 2 mm, V = 2.6 mm/s and $d_1/D = 0.984$.

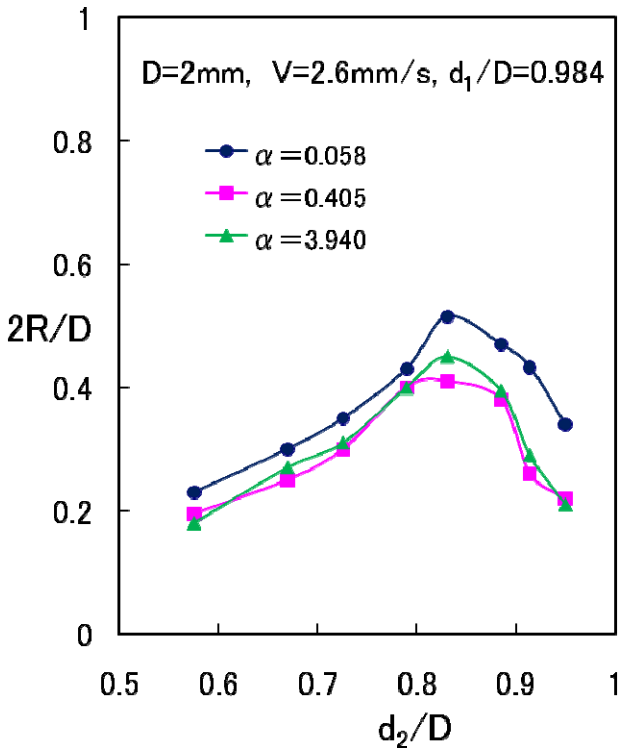

Figure 5. Diameter of contact area between the droplet against following droplet diameter for various α in the case of horizontal tube; conditions are the same as indicated in Fig. 4.

Figure 6 shows an example of temporal variation of droplets' velocities before/after the coalescence in the vertical tube case; U_1 and U_2 indicate the velocities of the leading and following droplets, respectively, and U_3 a velocity of the coalesced droplet. The experimental conditions are $d_1/D = 0.8$, $d_2/D = 0.46$, and the coalesced droplet diameter $d_3/D = 0.87$, and $\alpha = 8.87$. At an early stage of the droplets' travel in the tube, the following droplet pursuits the leading droplet at almost constant velocities. At an instance, interaction between the droplets emerges, and results in making the leading droplet decelerate and the following one accelerating. The relative velocity gradually becomes zero, and they make a contact and flow at a constant velocity for a while. Then the contacted droplets finally coalesce to form a larger droplet, and the coalesced droplet flows at a constant velocity slower than that of the contacted droplet before coalescence. In this case the coalescence time is 21.2 s.

Figure 7 indicates the coalescence time against the diameter of the following droplet under a fixed diameter of the leading droplet and a fixed viscosity ratio. In this figure the coalescence time of the droplets with and without the suspended particles are plotted. The coalescence time takes a minimum value at around $d_2/D = 0.52$ for both cases. Significant effect of the suspended particles is not seen on the coalescent time under this condition.

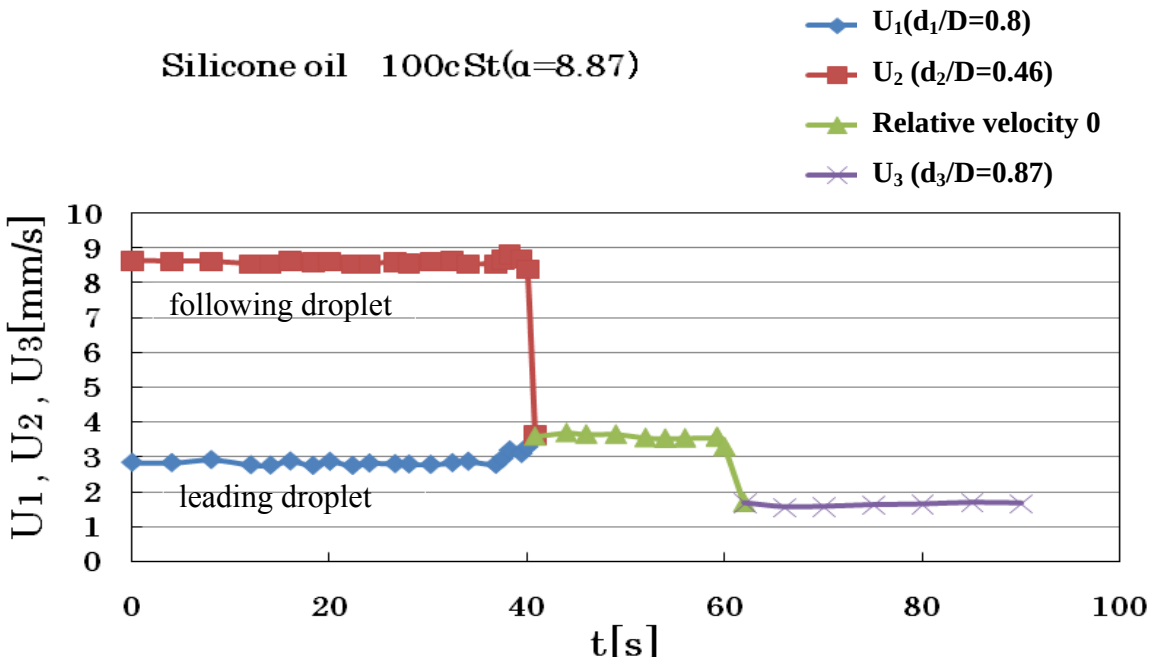

Figure 6. Temporal variations of velocities of leading and following droplets before/after the contact and coalescence.

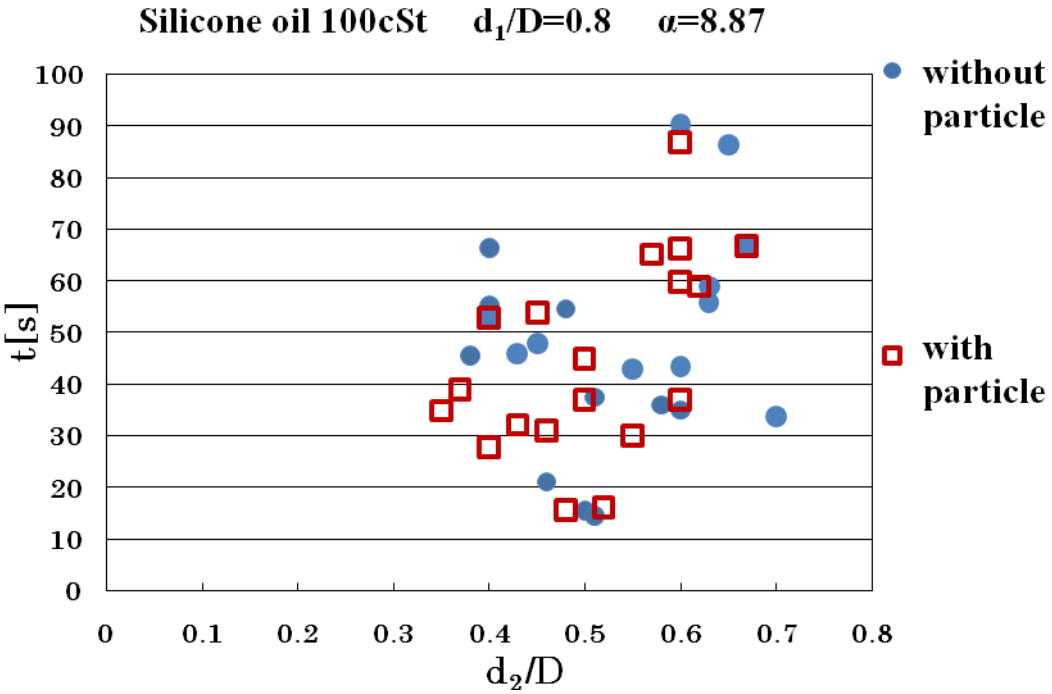

Figure 7. Coalescence time against following droplet diameter; results of droplets with and without suspended particles are plotted.

CONCLUSIONS

Contact and coalescence of droplets in a confined geometry is investigated experimentally. In the case of the horizontal tube creeping flow, induced flow by coalescence of the leading and the following droplets is successfully visualized, and a correlation between the coalescence time (period between the

instances when the droplets make a contact and when they start coalescing) and the contact area between the droplets is illustrated as a function of the following bubble diameter for a various viscosity ratio between the fluids of the droplets and the surrounding fluid in the test tube. In the case of the vertical tube filled with a quiescent fluid, the coalescence time is described as a function of the following droplet diameter for various viscosity ratios. Effect of particles suspended in the droplets on their coalescence of two droplets is examined to find out rather small under this experimental condition.

NOMENCLATURES

d : equivalent diameter of droplet
D : inner diameter of tube
R : radius of contact area between the droplets
U : droplet velocity
V : average velocity of the two-phase flow
α : viscosity ratio ($=\mu_d/\mu_s$)
μ : viscosity
ν : kinematic viscosity

Subscripts
1 : leading droplet
2 : following droplet
3 : coalesced droplet
d : droplet
s : surrounding fluid

ACKNOWLEDGMENTS

We express our thanks to Mr. H. Kambara, Mr. T. Shizuka & Mr. K. Hayashi, ex-students of Tokyo University of Science who carried out a part of the present experiments.

REFERENCES

1. Olbricht, W. L., Pore-scale prototypes of multiphase flow in porous media, *Ann. Rev. Fluid Mech.* 28, pp.187-213,1996.
2. Olbricht, W. L. & Kung, D. M., The Interaction and coalescence of liquid droplets in flow through a capillary tube, *J. Colloid Interface Sci.* 120, pp.229-244, 1987.

THE MODEL OF GRAIN LAYER-TO-LAYER DRYING IN HETEROGENEOUS ENVIRONMENT

S. Arhipovs*
Latvian University of agriculture, Jelgava, Latvia

ABSTRACT. Currently, grain drying theory mainly concerns the phenomena of heat and humidity transfer within a grain and the phenomena of heat and mass exchange between grain through space. The nature of drying process is best described by drying curves (humidity - time), drying speed curves (drying speed- humidity) and temperature curves (temperature - humidity). Experimental data is used to construct the curves. However, there system interpretation is difficult because of the separation of the analyses of the diffusion process in the grain and its surrounding environment. The common solution of grain drying problem should consist of full system integration diffusion equations both in the internal environment of a grain layer and in an external environment of a diffusing drying agent.

Keywords: *grain, drying, thermo and moisture diffusion*

INTRODUCTION

The great amount of grain drying experiments prove linear model of this process

$$\frac{dM(t)}{dt} = K(M_e - M) \tag{1}$$

where M - is material moisture, M_e - is material equilibrium moisture, K - is drying coefficient. However, the given model has limits: temperature and speed of drying agent have to be constant, the grain layer, which is exposed to drying, has to be quite thin, but the humidity and the temperature of grain – equally divided through the whole layer when the drying process has an adjusted character.

The differential equation

$$\frac{\partial M(x,t)}{\partial t} = \mu \frac{\partial^2 M(x,t)}{\partial x^2} \tag{2}$$

of moisture transfer is the simplified mass M model diffusion in the homogeneous and passive environment of coordinates x and time t. However in reality natural process of moisture diffusion is often deformed by additional heating of the thermal agent and its compulsory convection. During the drying process the coefficients of moisture and heat transfer usually are not constants. Real diffusion systems are heterogeneous, and there is always an interaction between diffusion mass and environment which changes the conditions of diffusion process passing. Homogeneity and passivity of environment is determined by a diffusion coefficient which is equal to $\mu=\Delta h^2/2\Delta t$ where Δh is a range of diffusion particle in any point of environment for an infinitesimal interval Δt at any moment of system existence. The linear equation of diffusion with constant coefficient is a limit of time and model distance of the elementary scheme particles migration (Figure 1.). Generalization of the elementary discrete scheme

* Corresponding author: assist. prof. S.Arhipovs
Phone: + (371)-29506423
E-mail address: sergejs.arhipovs@llu.lv

of particles migration leads to continuous integral-differential model of diffusion. Thus the dividing condition has to be formulated as a condition of fields overlapping of corresponding heat and humidity potentials of drying agent and grain. The system complexity increases with the variation of environment potentials with time and with integrated heat and mass streams dependencies.

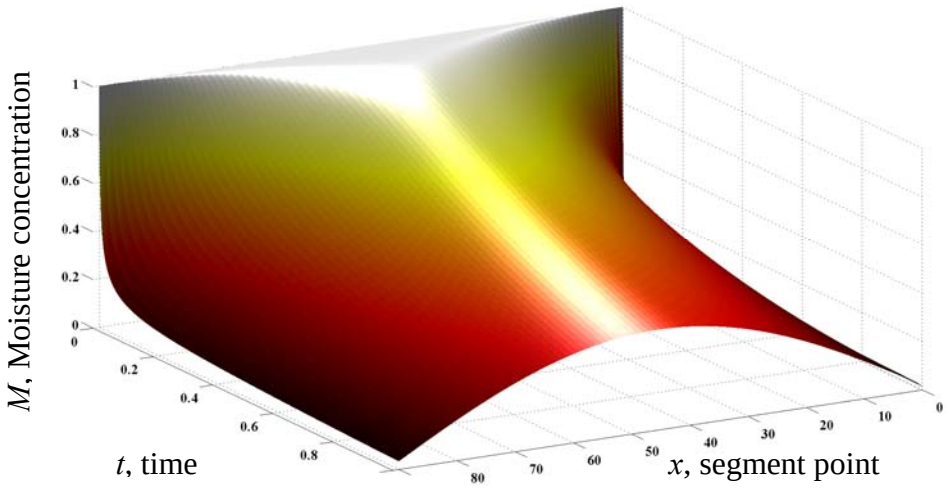

Figure 1. Moisture distribution in segment, during diffusion process with zero moisture concentration on segment boundaries.

For example, the equations describing the process of the drying of a grain layer, where the humidity and the thermal diffusivity are changed with time are so complex that are not always able to be solved analytically. Therefore, in the grain-air system it is necessary to simulate the dynamics of temperature and moisture of the drying agent while it is going through the grain mass, layer-by-layer warming up of grain mass, and also dynamics of coefficients, such as thermal and humidity diffusivity of grain and drying agent.

The solution of such system gives the precise definition of the nature of the drying process under conditions of continuous contact with air. Semantic interpretation of the solution shows not only such concepts as front of drying and its speed, but also allows the analysis of the real mechanism of moisture and heat transfer in grain and the estimation of the influence of various factors on drying process [3]. This also helps to identify the dominant factors of the process and provide an analytical approach to improvements in the process.. This paper describes the construction of the system models for the layer-by-layer drying process of static grain mass with two interactive dynamic potentials of temperature and a moisture. The realization of the given model is related to the integro- differential diffusion equations system solution, which are used in order to model the dynamics of transfer coefficients.

LINEAR MODEL OF GRAIN DRYING

The common solve of a drying problem consists of system integration of the transfer equations in two components - in the material and environment, which surrounds a material [4]. Thus parameters of components depend on each other and dynamically change in time and space. The difficulty of the solving of such systems in engineering calculations leads to used model simplification of drying and very often to its linearization. The use of experimental data linear approximation leads to linear model of drying process (1). The experimental-statistical approach to drying process modeling assumes linear dependence of speed material drying on its humidity and does not explain the nature of process and, moreover, introduces a system error at the initial stage of material warming up , even if to assume that environments is uniform and isotropic.

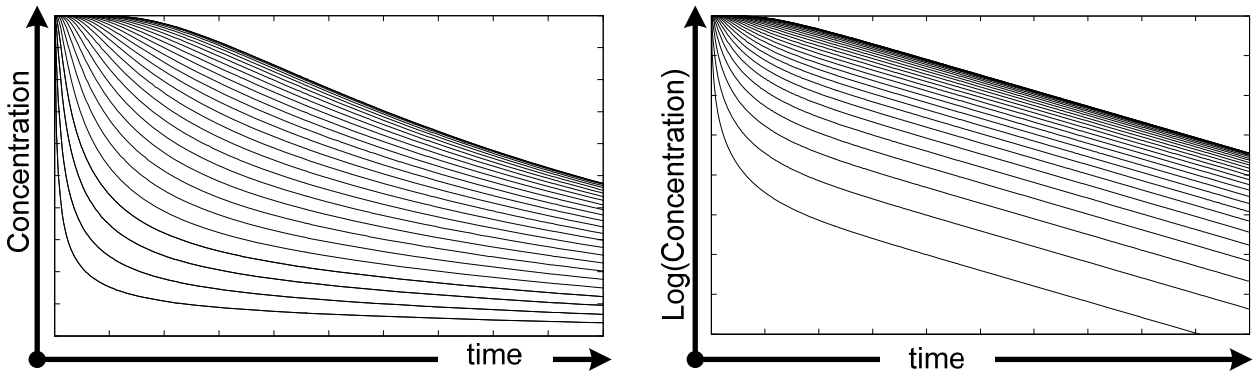

Figure 2. Sub segments humidity concentration curves in dependence on time (left graph) and logarithm of concentration in dependence on time (right graph)

The solution of the linear differential equation well approximates not only experimental data, but also gives good approximation for solutions of the diffusion classical equation (figure 1). In figure 1 distribution of moisture in a one-dimensional core is represented at natural diffusion of moisture through its boundary points. In figure 2 (left graph) drying curves of modelling separate segments core are represented. The bottom curve describes process of core boundary segment drying. An average segment drying of a core is shown by the top curve. The result of drying curves logtransformation is shown in figure 2 right graph. Tails of these data correspond for 100 % to the linear regression model. Thus, the linear model (1) of drying process in some cases adequately describes not only real experiments but also can replace under certain conditions the model of classical diffusion. The purpose of this work is to establish dynamics of moisture and heat moving in one-dimensional thick layer of grain through compulsory aeration from below upwards by the drying agent with the set temperature. The grain bulk is considered in a projection as one-dimensional core of the given length with heat isolated lateral surface. There is a diffusion of a moisture and heat in a core. On the right end of a core there is a constant heat source, the temperature of the core's left end is maintained at temperature equal to zero. Heat moves inside the core with primary and constant drift from the right to the left, that models compulsory aeration or moving of drying agent inside the grain layer aside its surfaces. The moisture moves inside the core with variable diffusion coefficient in each point of a core and which is proportional to the temperature of the core in the given point. At the beginning temperature of a core is equal to zero, the moisture is uniformly distributed on all length of a core and the system "moisture - heat" is in an equilibrium condition [1].

While heating the right end of a core dynamic balance is broken, there is a warming up and, as a result of diffusion increase of moisture coefficient, there is a carrying out of heat and moisture through the right end of a core. It is necessary to construct fields of temperature and moisture distribution on all length of a core in each moment of time.

DIFFUSION OF TWO COMPONET IN GRAIN BULK DRYING

Uniformity and passivity of environment is defined by a constancy of diffusion coefficient. The equation of diffusion (2) with constant diffusion coefficient is a limit on time and model distance of the elementary scheme of particles wandering. The given diffusion model assume that in one-dimensional space the infinitesimal particle in infinitesimal time interval moves from the current position into one of two infinitely neighbour positions. Quantity of particles N in the given point x at any moment $t+1$ is proportional to quantity of the particles which have come from two adjacent points at last time moment and is equal to:

$$N_{x,t+1} = \tfrac{1}{2}\left(N_{x-1,t} + N_{x+1,t}\right) \qquad (3)$$

However, in a reality natural process of moisture diffusion is often deformed by additional heating of the thermal agent and its compulsory convection. At aeration and drying the grain bulk and intergrain air space becomes non-uniform and not isotropic.

Integro- differential equation of diffusion

While drying process coefficient of moisture and heat transfer usually are not constants in time and space. Real diffusion systems are heterogeneous, and between mass and environment there always is an interaction which changes conditions of diffusion process. Therefore generally the particle can change the position for any another and not necessarily adjacent, as in the elementary case. The balance of particles in this case is calculated from recurrent expression

$$N_{x,t+1} = N_{x,t} + \sum_{s \neq x} P(s,x,t) \cdot N_{s,t} - \left[\sum_{s \neq x} P(x,s,t) \right] \cdot N_{x,t} \qquad \sum_{x} P(s,x,t) = 1 \qquad \forall s,t \tag{4}$$

Where *P(s,x,t)* is probability of one particle transition from position *s* into position *x* by the moment of time *t* with restriction on the sum of probabilities. The sums in a limit become integrals and continuous analogue of this relation is the equation [5]:

$$\frac{\partial N}{\partial t} = \int K(s,x,t) N(s,t) ds - \left[\int K(x,s,t) ds \right] \cdot N(x,t) \tag{5}$$

For any particle there can be any preferences in a choice of the new position and, on the contrary, unattractive points for visiting. Such approach leads to necessity of consideration not only classical model of diffusion, but also the generalized diffusion equations, start with the kinetic equation of statistical physics [2].

Heterogenic environment characteristics

The phenomena of heat and moisture transfer inside of grain thick layer during drying are interconnected and mutually caused. Connection among these phenomena is expressed in the form of dependence between temperature and a moisture or an expense of heat for heating of a material and evaporation of a moisture from it during drying. At storage, drying and aeration of real grain bulks in them non-uniform fields of temperature and moisture are created. Thus parameters of heat and moisture transfer also can be dependent on each other. The system "air-grain" is in dynamic balance when absorption or feedback of moisture from air stops.

Dynamic balance is broken as a result of moisture moving in grain bulk among separate grains, and as a result of a temperature difference in various parts of grain bulk. Change of temperature in any site of grain layer is accompanied by moisture moving in a direction of heat stream from places more heated to less heated. Physical assumptions of considered system are expressed in the form of requirements to a kernel $P(s,x,t)$ in the equation (4). If diffusion environment is homogeneous, i.e. the conditions of diffusion are identical in all points, then the kernel $P(s,x,t)$ depends only on distance between points and $P = P(x-s)$. If diffusion environment is homogeneous and isotropic, then $P(x-s) \equiv P(s-x) \equiv P(|x-s|)$. Thus, the relation (3) is a special case of the generalized approach (4), when

$$\forall t \quad P(s,x,t) = \begin{cases} \frac{1}{2} & when \quad |s-x| = 1 \\ 0 & when \quad |s-x| \neq 1 \end{cases} \tag{6}$$

Distribution of probabilities (4) defines equiprobable transition of a particle in one of the adjacent positions for one moment of time. For two moments of time the particle does two equiprobable

jumps and distribution of probabilities corresponds to decomposition members of a degree $\left(\frac{1}{2}+\frac{1}{2}\right)^2=\frac{1}{4}+\frac{1}{2}+\frac{1}{4}$ under the formula of Newton. For three moments of time the particle does three equiprobable jumps and decomposition $\left(\frac{1}{2}+\frac{1}{2}\right)^3=\frac{1}{8}+\frac{3}{8}+\frac{3}{8}+\frac{1}{8}$ answers probabilities of various transitions.

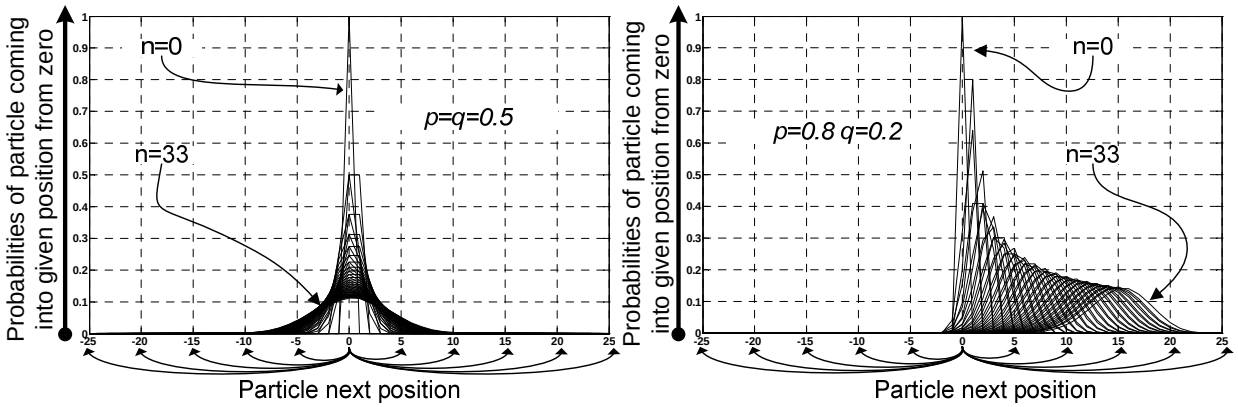

Figure 3. The increase of parameter n in binomial distribution leads to increase in speed of particles transfer in diffusion environment

Thus, if environment is homogeneous and isotropic, then eventually the diffusion process can be slowed down or accelerated, using values of binomial distribution $\frac{n!}{n!\cdot(n-k)!}\cdot\left(\frac{1}{2}\right)^n$ at various values n.

At increase in value n for one discrete moment of time environment is changed also as for n moments of time, only at distribution of probabilities (4).

Uniformity and isotropic of environment is kept if the kernel $P(s,x,t)$ satisfies the binomial distribution $C_n^k p^k q^{n-k}$ at $p=q=0.5$. In this case the discrete relation (4) in a limit aspires to the classical equation of diffusion. At infringement of this relation at diffusion particles there is a drift in the certain side because values of binomial distribution become not symmetric. In figure 3 values of binomial distribution for various probabilities of particle transition which is in a point with zero coordinate are represented. In charts on a horizontal axis there are noted possible positions in which the particle can jump to the present moment from the zero position.

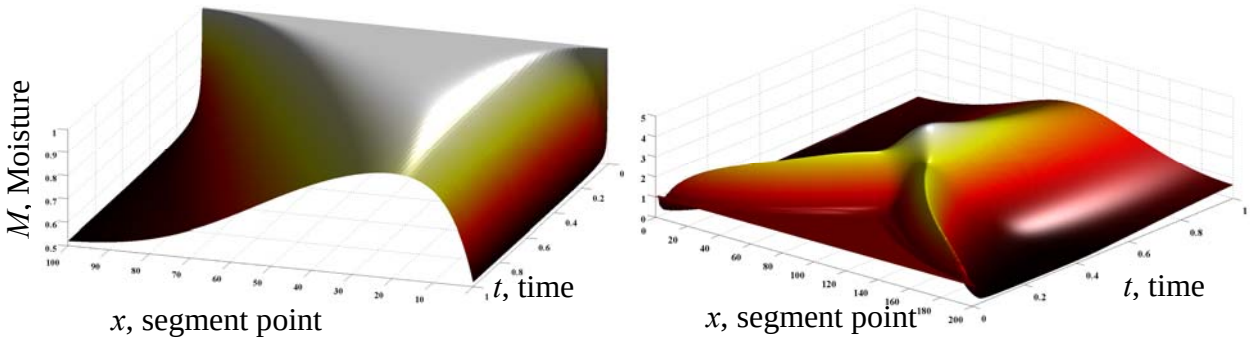

Figure 4. Heating (left graph) and drying (right graph) of one grain layer

On the left chart diffusion environment is characterized by uniformity and isotropy because the identical probabilities the particle can jump as on the left and on the right. When $n=0$ the particle remains on a place. It is the highest peak on the left chart in figure 3. When $n=1$ with probability ½ the particle moves to one position to the left or to the right. With increasing n the cloud of transitions symmetrically creeps away and it increases the speed of particles diffusion. On the right chart coefficients of binomial distributions are represented at $p=0.8$ *and* $q=0.2$, that defines greater

preference to moving to the right and smaller preference to moving on the left. When *n* is high - it is the lowest and most right bell on the right chart, the particle from zero position with the greatest probability will get in position with coordinate *15*, with smaller probability will get in a vicinity of coordinate *15*.

Change of parameter *p* concerning value *0.5* leads to change of environment uniformity. In figure 4 distribution of a mass concentrations field in time are shown. In the beginning the mass has been uniformly concentrated in a all segment, then during time the mass was redistributed as a result of diffusion process (4) with binomial kernel *P (s, x, t)* within parameters *n=33* and *p=0.49*. Discrete process of diffusion was modeled on a segment [0; 100], during an absolute time interval [0;1]. On the ends of a segment the mass value was supported on zero.

Integro- differential model of drying

The task of finding humidity and temperatures fields is related to the solution of integro- differential equations system which is possible to write down as

$$\begin{cases} \dfrac{\partial M}{\partial t} = \int K_M(s,x,t)\cdot M(s,t)ds - \left[\int K_M(x,s,t)ds\right]\cdot M(x,t) \\ \dfrac{\partial Q}{\partial t} = \int K_Q(s,x,t)\cdot Q(s,t)ds - \left[\int K_Q(x,s,t)ds\right]\cdot Q(x,t) \end{cases} \tag{7}$$

$$K_M = K_M(s,x,t,Q),\ K_Q = K_Q(s,x,t,M). \qquad \int K_i(s,x,t)\cdot dx = 1, \quad i=\{Q,M\} \tag{8}$$

Sense of kernels K_M and K_Q consists not only in relative speed of transfer (density of probability of transfer, attributed to time unit) of humidity *M* and temperature *Q* in the moment *t* from position *x* in position *s*. Movement of moisture in grain mass can take place by virtue of temperature difference in the different points of grain mass, therefore a kernel K_M which describes redistribution character of moisture can depend on the environment temperature . A kernel K_Q describes a character of temperature conduction which can depend on humidity consistence in environment. In the case of new particles generation absence on kernels K_M and K_Q limitation of mass saving is laid on because all particles which are in position s in the next moment of time necessarily must appear somewhere. At some additional limits on kernels K_M and K_Q integro- differential equations can be taken to differential equations with particular derivations. The process of drying is modeled by the discrete analogues of integro- differential equations

$$\begin{cases} M_{x,t+1} = M_{x,t} + \sum\limits_{s\neq x} P_M(s,x,t)\cdot M_{s,t} - \left[\sum\limits_{s\neq x} P_M(x,s,t)\right]\cdot M_{x,t} \qquad \sum\limits_x P_M(s,x,t) = 1 \quad \forall s,t \\ Q_{x,t+1} = Q_{x,t} + \sum\limits_{s\neq x} P_Q(s,x,t)\cdot Q_{s,t} - \left[\sum\limits_{s\neq x} P_Q(x,s,t)\right]\cdot Q_{x,t} \qquad \sum\limits_x P_Q(s,x,t) = 1 \quad \forall s,t \end{cases} \tag{9}$$

Distributions of probabilities coincide with the coefficients of the binomial distributing $P_Q = \left\{ \ ...C_{n_Q}^k p_Q{}^k (1-p_Q)^{n_Q-k}... \ \right\}$ and $P_M = \left\{ \ ...C_{n_M}^k p_M{}^k (1-p_M)^{n_M-k}... \ \right\}$, the parameters of which functionally depend on descriptions of environment thermodynamicses characteristics.

Speed n_Q and direction p_M heat propagation can be constants or depend on moisture countenance in the system $n_Q=n_Q(M)$ and $p_Q=p_Q(M)$. Accordingly, speed n_M and direction p_M moving of moisture can be constants or depend on the temperature of the system $n_M=n_M(Q)$ and $p_M=p_M(Q)$ in current time.

SISTEM OF INTEGRO- DIFFERENTIAL EQUATIONS AND HETEROGENIC ENVIRONMENT CHARACTERISTICS

The purpose of conducted numerical experiments is a construction of moisture and temperature fields by the solution of the recurrent expressions system (7) for an analysis and comparison of the summarized results with the classic diffusion equation solutions. A behaviour of the two component system "grain - air" is modelled by a one dimensional segment. In the initial moment of time a temperature equals to zero in all points, and humidity in every point equals the conditional unit. During all time the right border of segment is heated and system temperature component propagate with constant speed which sets to be $n_Q = 22$ in the binomial distribution $P_Q = \left\{ \quad ...C_{n_Q}^k p_Q{}^k \left(1 - p_Q\right)^{n_Q - k} ... \quad \right\}$. The forced aeration of grain mass is imitated by the temperature parameter $p_T = 0.45$ and by temperature values reflection into a segment in relation to his right border. On the left graph of figure 5 the layer segment temperatures dynamics is represented at the constant heating of it border in a point.

Character of moisture distribution is imitated with the use of probabilities distribution $P_M = \left\{ \quad ...C_{n_M}^k p_M{}^k \left(1 - p_M\right)^{n_M - k} ... \quad \right\}$ with the parameter of diffusion speed $n_M = Q_{x,t}$, which is equal to an absolute value the temperature of environment in this point in current time. Like a temperature, the values of layer moisture are reflected into a segment. Analysing dynamics of moisture, on the right graph the characteristic peak of moisture concentration is seen in every layer.

Comparing two graphs it is seen that motion of moisture peak coincides with the layer segment warming up period on all its length. The practical supervisions of grain drying process confirms the brief increase of humidity of corn intermediate layers on the initial drying stages.

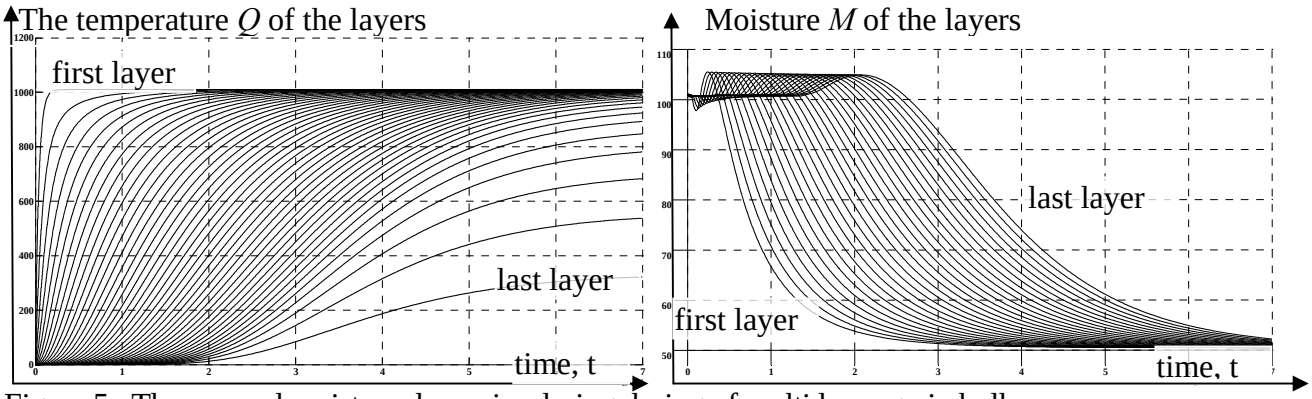

Figure 5. Thermo and moisture dynamics during drying of multi layer grain bulk

EXPERIMENTAL DATA OF GRAIN LAYER-TO-LAYER DRYING

In order to check adequacy of numerical experiment of real processes, a laboratory stand has been planned (figure 6) which is intended for the receipt of information about the amount of moisture in the separate layers of grain mass during all time of the experimental drying, is planned.

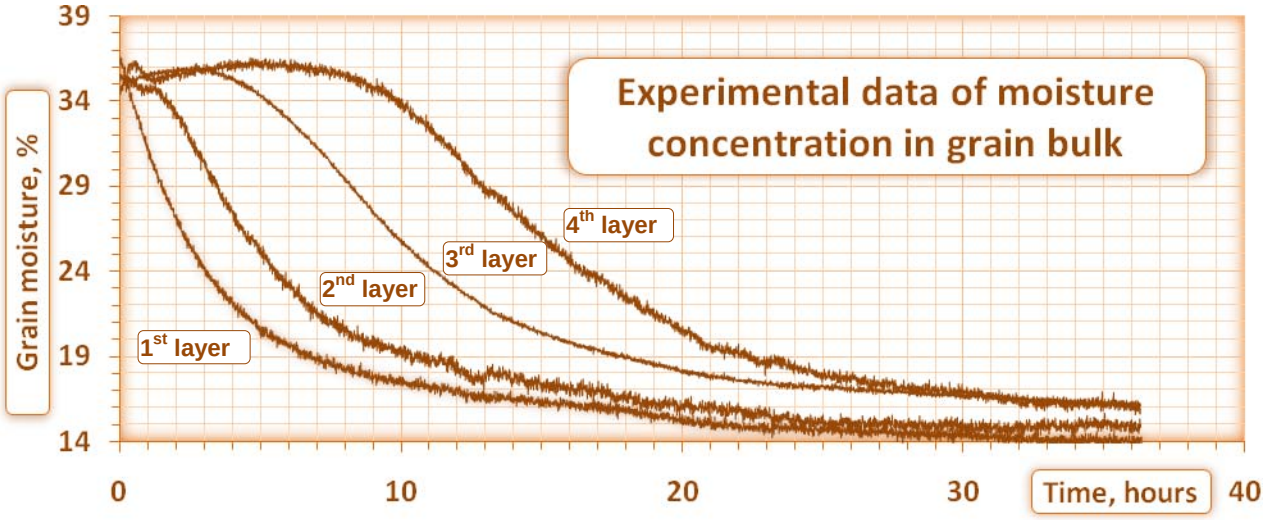

Figure 6. Moisture concentration in four sequences layers of grain bulk during 36 hours of it aeration.

CONCLUSIONS

Generalization of the elementary discrete scheme of particles migration leads to continuous integral-differential model of diffusion. Generally the particle can change the position for another and not necessarily for the next one, as in the elementary case. Movement of a particle can be linear diffusion superposition and convection component. Using the coefficients of the binomial distributing, in integro-differential diffusion model, it is possible to regulate speed of moisture and direction transfer of its motion in time depending on descriptions of thermodynamics environments, which, in same line, can depend on humidity of environment or on other indicators, – for example, pressures. Similarly as classic diffusion, a decision integro-differential diffusion model possesses smoothing property. When numerically solving the system of recurrent correlations – the analogues of integro-differential model, it is possible to build the fields of two or more interactive diffusion component of the system.

REFERENCES

1. Eckert E.R.G., Robert M. Jr. Drake, Analysis of Heat and Mass Transfer, Springer, 1997.
2. Kampen N.G., 1981, Stochastic processes in physics and chemistry, North Holland.
3. Mills A.F., 1999, Basic Heat and Mass Transfer, Prentice Hall.
4. J.Crank, The mathematics of diffusion, Clarendon Press Oxford, 1975
5. Zeldovich J.B, Mishkis A.D, 1973, Elements of mathematical physics, Nauka. (In Russian)

INVESTIGATION OF THE HEAT TRANSFER COEFFICIENT DURING QUENCHING IN VARIOUS COOLING AGENTS

A. Buczek, T. Telejko*
AGH University of Science and Technology, Kraków, Poland

ABSTRACT. The paper presents a method of identifying the local heat transfer coefficient (LHTC) at the surface of cooled metal sample during quenching. The quenching speed strongly impacts the product quality and depends mainly upon the type of cooling agent. The choice of the cooler is therefore essential for the elaboration of proper quenching technology. This can be supported by the numerical simulations involving calculations of temperature profiles in the steel product, which enables to trace the rate of cooling and arising thermal stresses. The determination of the temperature field in the cooled body requires unity conditions of the heat conduction equation to be estimated including heat transfer at the surface usually described by the heat transfer coefficient at the cooled item surface. For the extremely intensive and dynamic process it is impossible to measure it directly, so some indirect methods are frequently applied. The boundary heat transfer inverse problem has been solved by the authors to measure LHTC. The basis of the theory and numerical procedures as well as estimation results are also shown for the selected quenchants.

Keywords: *heat transfer, boundary conditions, inverse solution, quenching*

INTRODUCTION

Quenching is the thermal process used to ensure the required mechanical properties of the steel product. The steel item is heated up to the temperature above austenitization and subsequently cooled down at a sufficiently fast rate of cooling. The desired quenching speed is achieved by providing the properly chosen coolants, like water, water polymer solutions, oils, etc. Frequently a choice of the agent is made upon the base of cooling rate curves elaborated in the experimental procedure according to the ISO 9950 [5]. The cylindrical sample 12.5 mm in diameter and 60mm in length manufactured from the Ni-Cr-Fe alloy (INCONEL 600) is cooled down from the temperature equal to approximately 850^{o}C. The temperature measurements made by a sensor placed at the geometrical centre of the sample are recorded. The maximum cooling rate, the respect temperature and the cooling rate at 300^{o}C are the characteristic parameters of the quenchant. The more effective technique is the application of numerical simulation of heat transfer during quenching, when the temperature profiles at selected points of the body can be observed. It also allows to determine the thermal stresses arising from temperature gradients. However solution of heat transfer requires boundary conditions to be known, which can be described by the temperature of coolants and the heat transfer coefficient at the surface. Quenching is the type of heat treatment for which the heat transfer varies with the phase of cooling and heat process is therefore highly nonlinear. The effective procedure applied in such cases is the solution of the boundary inverse problem [2, 4, 6]. The method consists in numerical selection of boundary heat transfer conditions providing a temperature distribution in the body not differing, within the necessary accuracy limits, from the assumed one. The temperature profile is measured by the sensors placed at the selected internal

* Corresponding author: Prof. T. Telejko
Phone: + (48)-12-6172612, Fax: + (48)-12-6172612
E-mail address: telejko@metal.agh.edu.pl

points of the sample during cooling in the different agents and compared with computation results. Therefore the numerical simulation of the quenching process coupled with the experiment enables identification of heat transfer coefficient at the sample surface.

PROBLEM FORMULATION

In the boundary inverse problem we look for the boundary conditions of heat transfer. The effects of the cooling process are expressed by the temperature variation at the selected points of the test sample. In the calculus procedure the general form of the function approximating the heat transfer coefficient or the heat flux density is assumed. The problem is solved when the particular form of that function is determined under assumed quality criterion. That criterion consists in the minimum error norm value expressed by equation (1)

$$\Phi = \sum_{i=1}^{n} \sum_{j=1}^{m} \left[t_{i,j}^{num}(\tau) - t_{i,j}^{ex}(\tau) \right]^2 \tag{1}$$

Computed temperature values $t_{i,j}^{num}(\tau)$ were obtained from the solution of heat conduction equation given below

$$\rho c \frac{\partial t}{\partial \tau} = \frac{1}{r} \frac{\partial}{\partial r} \left(r k_r \frac{\partial t}{\partial r} \right) + \frac{\partial}{\partial z} \left(k_z \frac{\partial t}{\partial z} \right) + \dot{q}_v \tag{2}$$

The boundary conditions are formulated in the following form

$$-k_r \frac{\partial t(r = R,\, z,\, \tau)}{\partial r} = \alpha_R(\tau) \left[t_w - t(R, z, \tau) \right] \tag{3}$$

$$-k_z \frac{\partial t(r,\, z = 0,\, \tau)}{\partial r} = \alpha_{z=0}(\tau) \left[t_w - t(r, z = 0, \tau) \right] \tag{4}$$

$$-k_z \frac{\partial t(r,\, z = l,\, \tau)}{\partial r} = \alpha_{z=l}(\tau) \left[t_w - t(R,\, l, \tau) \right] \tag{5}$$

while the initial condition is as follows

$$t(r,\, z,\, \tau = 0) \tag{6}$$

The computation was performed using finite element model and self–developed computer program. The inverse problem was solved by conjugate gradients and Choleski methods. The approximation function was formulated by spline function of the Hermite polynomials over the total time of computation $\langle 0, \tau_{end} \rangle$. For each elementary time interval $\langle \tau_a, \tau_b \rangle$ the polynomial describing the heat transfer coefficient *versus* time relation has the form

$$\alpha(\tau) = a_1 H_1^0(\xi) + a_2 H_1^1(\xi) + a_3 H_2^0(\xi) + a_4 H_2^1(\xi) \tag{7}$$

$H_1^0(\xi) = 1 - 3\xi^2 + 2\xi^3$

$H_2^0(\xi) = 3\xi^2 - 2\xi^3$

$H_1^1(\xi) = \left(\xi - 2\xi^2 + \xi^3 \right) \Delta\tau$

$H_2^1(\xi) = \left(\xi^3 - \xi^2 \right) \Delta\tau$

$\xi = \dfrac{\tau_i - \tau_a}{\Delta\tau} \qquad \tau_a \le \tau_i \le \tau_b, \qquad \Delta\tau = \tau_b - \tau_a$

The coefficients a_1, a_2, a_3, a_4 were yielded from the solution of inverse problem for every time interval and for the total time range $\langle 0, \tau_{end} \rangle$. The number and the position of spline nodes were adjusted regarding to the minimal value of the mean temperature error given by equation (8)

$$\Delta t = \frac{1}{m\,n} \sum_{i=1}^{n} \sum_{j=1}^{m} \left| t_{i,j}^{num}(\tau) - t_{i,j}^{ex}(\tau) \right|. \tag{8}$$

The temperature data $t_{i,j}^{ex}, t_{i,j}^{num}$ were obtained from the measurements at some points inside the test sample and numerical simulation of the quenching process respectively. As a result the LHTC *versus* time relation has been found in the form of a spline function of polynomials given by equation (7). For the practical use in numerical applications the heat transfer coefficient was expressed as a function of a surface temperature. That temperature was yielded from the direct solution of the heat conduction equation carried out at every time step.
The validation of mathematical and numerical models have been performed replacing the measurement data with the values obtained from a solution of a direct problem. For the simple boundary condition the numerical model gives the temperature profiles calculated from the inverse procedure were almost identical to the input temperature data [2]. The error of the LHTC approximation did not exceeded 0.5%.

EXPERIMENTAL PROCEDURE

The method of investigations is based upon temperature measurements made at selected locations of the previously warmed-up sample after immersing it in an investigated quenchant.
Thus, the response of the sample temperature profile to an unknown (sought) boundary input was determined in the test. The sample was designed in such a way to achieve nearly unidirectional heat transfer along the sample axis. The schematic sketch is shown in Figure 1.
The main part of the sample is the metal cylinder 20mm in length and diameter placed in a cylindrical casing. The thickness of the casing was equal to 0.5mm. Both cylinder and casing were made of INCONEL 600. Four temperature sensors were located in the holes drilled to the sample axis at the distance 2, 4, 6 and 19 mm from active surface. Temperature was measured using ***K*** type thermocouples with 80 μm diameter wires protected by a 500 μm diameter sheath. The output signal was measured and recorded by high accuracy AC/DC data acquisition system allowing data registration at extremely high frequencies. The sample was heated up to temperature about 850^{o}C in the resistance furnace. After equalizing the temperature profile inside the sample it was immersed in the coolant having various, but steady in time, temperature. The experimental stand allowed to investigate heat transfer in stationary and moveable liquid (Figure 2). In the first case the sample was placed in a agent tank **1**, in the second one – in the column **6** after setting the desired value of liquid flow velocity performed by circulating pump **5** and inverter **12**.

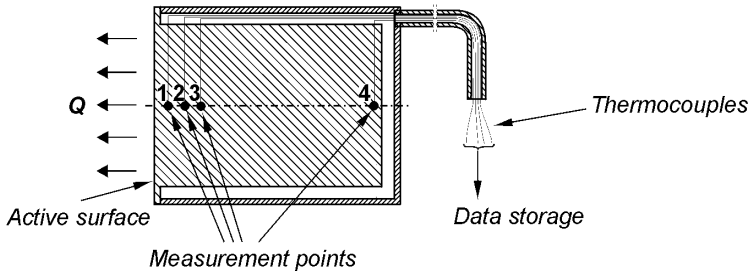

Fig. 1. Test sample equipped with temperature sensors

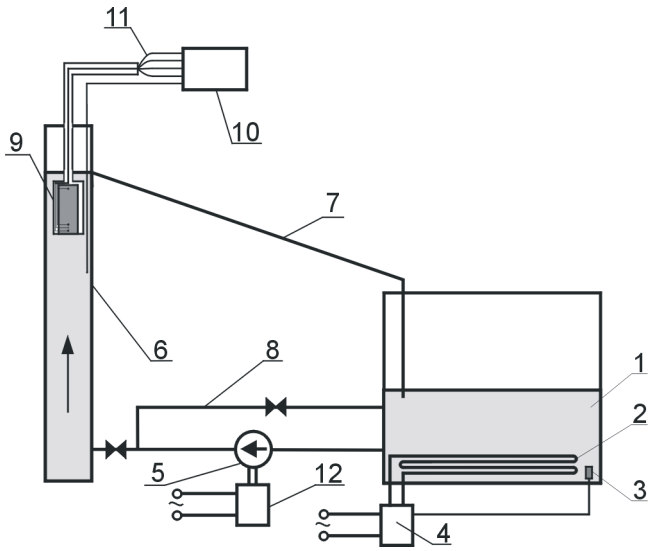

Fig. 2. Experimental stand

1–tank of coolant; 2–resistance heater, 3–resistance temperature sensor, 4–temperature controller, 5–circulating pump, 6–vertical column, 7–coolant overflow, 8–bypass, 9–test sample, 10–data acquisition system, 11–thermocouples, 12–inverter.

RESULTS OF EXPERIMENTS AND NUMERICAL SIMULATION

The numerous experiments and simulations have been performed for various quenchants. The example of the experimental temperature change recorded by the sensors at different locations is shown in Figure 3. The experiment was carried out during quenching in oil **A** having temperature equal to 40^{o}C. The recorded temperature in points 1, 2 and 3 were supplied to the inverse procedure. The LHTC versus time function was approximated by a spline function consisted of fifteen Hermite polynomials. The nodes of the spline was established at the time equal to 0;1;2;3;4;5;6;7;8;10;15;25;50;100;200s. The mean temperature error given by equation (8) has been checked to establish the number and position of spline nodes. The higher concentration of the nodes at the beginning of the quenching process allowed to provide better accuracy of the simulation results. In this case the calculated mean temperature error using equation (8) was equal to 1.53K. The dependence of the LHTC from time is presented in Figure 4. Surface temperature computed from the direct problem enable to get more practical LHTC *versus* temperature relation (Figure 5). This form can be easily applied in heat transfer calculations of the cooling in liquids. Qualitative estimation of the relation shown in Figure 5 suggests that cooling process proceeds in the way characteristic for local boiling in liquids whereas the quantitative differences occur for various quenchants. The relatively low temperature of the sensor at the start of cooling results in nucleate boiling phase with remarkable first boiling crisis. Figure 6 presents the selected drawings of the LHTC versus surface temperature relations for two different oil quenchants.

In the industrial quenching process the coolant temperature increases with time in spite of applying cooling systems. The temperature growth can achieve even 20K. It is therefore important to know, how the temperature of cooling medium impacts the heat transfer process. The selected results of investigations are plotted in Figure 7. It can be clearly seen that the small coolant temperature change significantly affects the value of LHTC, particularly at the neighborhood of the first boiling crisis. The effect of total working life of coolant on cooling ability can be also interesting for the user regarding its high price and considerable quantities applied under industrial circumstances. It is obvious, that this factor should influence the cooling properties of the medium.

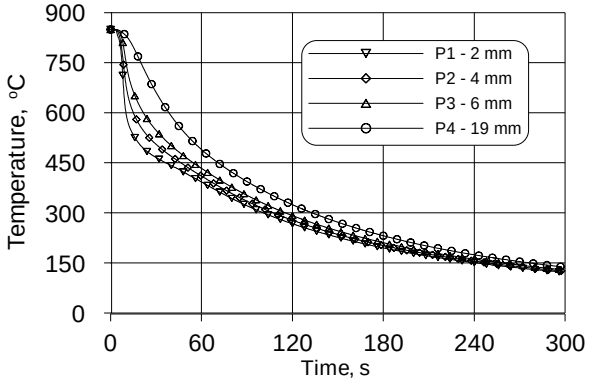

Fig. 3. Temperature at internal points of the sample. Oil **A** maintained at 40°C

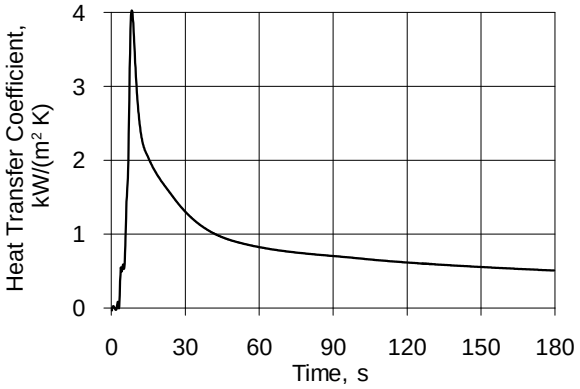

Fig. 4. Dependence of LHTC from time. Oil **A**, maintained at 40°C

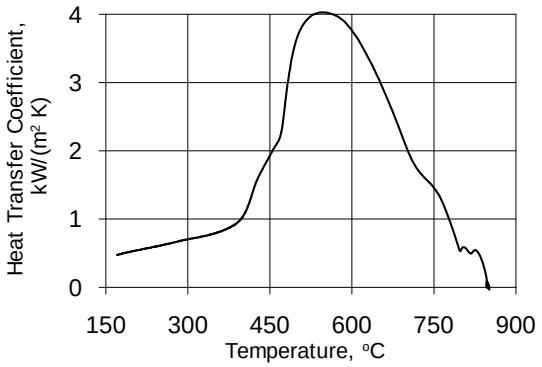

Fig. 5. LHTC–surface temperature curve for oil **A** maintained at 40°C

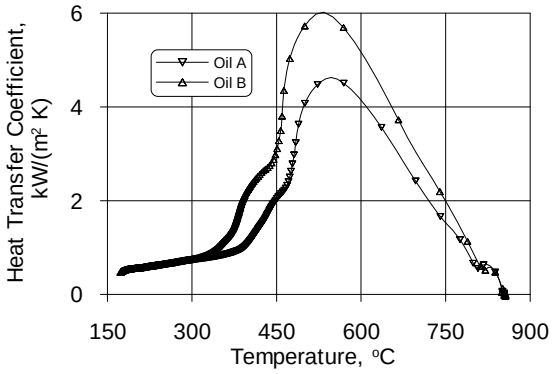

Fig. 6. LHTC for two different oil coolants

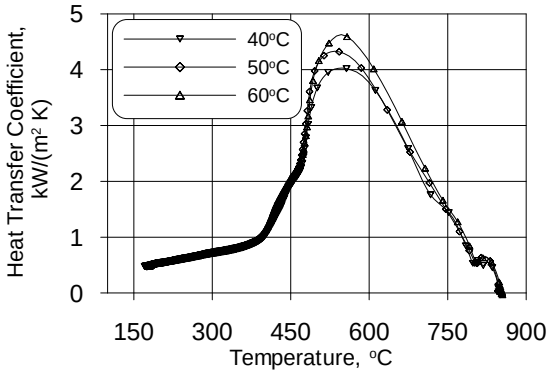

Fig. 7. The effect of quenchant temperature on LHTC for oil **A**

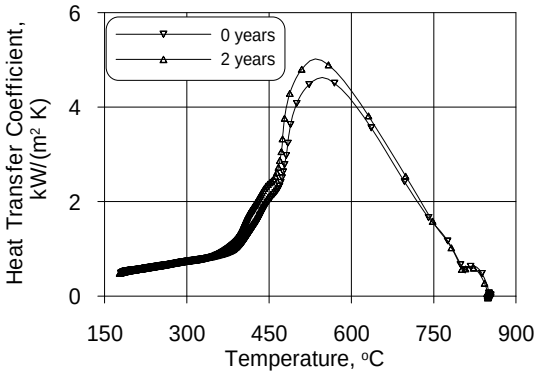

Fig. 8. The effect of quenchant working life on LHTC for oil **A**

Figures 8 and 9 show the results illustrating the two examples of LHTC curves for the same quenchant differing in working life. There is no an unequivocal direction of the change of coolant properties. In the case of oil **A** the longer exploitation time results in increasing heat transfer coefficient, whereas LHTC significantly decreases for the oil **C**.

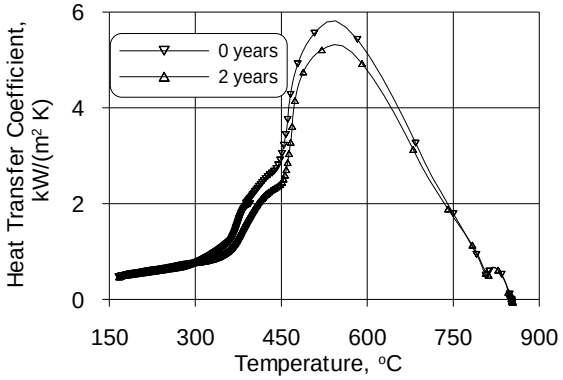

Fig. 9. The effect of coolant working life on LHTC for oil **C**

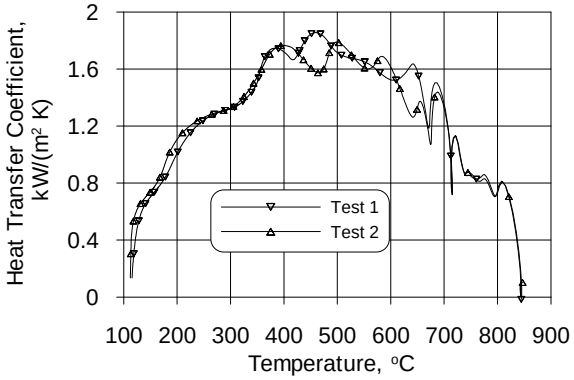

Fig. 10. LHTC for polymer solution in water maintained at temperature 40°C. Agent flow rate equal to 0.2 m/s

The synthetic cooling oils are frequently substituted with solutions of organic polymers in water. They have many advantages comparing to other quenchants: they are nonflammable, do not produce smoke or fumes under operation, provide the wide flexibility of quenching speed. On the other hand they are corrosive to tanks and products despite of additions of corrosion inhibitors, so the application are limited only to selected quenching technologies.

The quenching characteristics can be modified by the agent temperature and/or polymer concentration. The performed laboratory tests has proved, that the proposed method can be easily adopted for investigations of heat transfer during quenching in polymer water solutions. The heat transfer characteristic for quenching in water solution at 20% polymer concentration is presented in Figure 10. The polymer has oil-like heat transfer coefficient characteristic, but at some stages the local disturbances are observed, particularly in the range of surface temperature 400–800°C. In this case the sample was immersed in the flowing agent at a rate of 0.2m/s. It should ensure uniform temperature of the quenchant, but agitation resulted in LHTC instabilities. This phenomena can be explained by the inverse polymer solubility in water resulting in reversible creating and disappearing of a polymer film at a cooled surface.

The effect of the investigated factors on temperature profiles in the quenched item can be determined from the numerical simulations using the experimentally estimated boundary conditions defined by heat transfer coefficient. This allows to follow the structure and mechanical properties of the metal and select the proper quenchants and quenching technology to satisfy the quality demands of a final product.

SUMMARY

The presented investigations indicated the succesfull application of the proposed technique for determination of LHTC in quenching process. The tests have been carried out using the different quenchants including cool oils and polymer solutions of water. The heat transfer in these coolants is relatively less intensive comparing to water, so quenching process is easier to controll. The high sensivity of the method enables to examine the effect of various quenching parametrs on the heat transfer. The impact of coolant temperature on LHTC can be pointed out as an example. The variations in LHTC occuring in a limited range of surface temperature can be observed when coolant temperature changes in a narrow interval equal 10K (Fig. 7). The method belongs to dynamic ones, so its accuracy strongly depends on the relatively high temperture differences in the sample affected by cooling process. Therefore it is very important to provide the proper design of the test sample and the precise system of temperature measurement. The boundary inverse problem is ill-posed, so the measurement errors must be limited as much as possible. This remark reffers

both to the quality of the data acquisition system and to exact determination of temperatue sensors location.

It is also worth to underline, that under local boiling circumstances heat transfer at the cooled surface of the sample is limited by the heat conduction in the sample. The transport of heat from the center part of the body to the surface region is limited by thermal parameters of the cooled item, like thermal conductivity, heat capacity and density. In case of numerous materials this factor can not be ommited in investigations of coolant characteristics. The discussion of this problem for metals is presented in literature [3]. The use of the same quenching curves for different materials to be quenched can lead to significant quality loses in final product. This factor is not included in standard quenching characteristics advised by International Standard Organization (ISO 9950).

The presented method was applied to the investigations of cooling process using a sample manufactured of INCONEL 600. Thermal properties of that alloy do not differ much from the most of thermally treated steels. The main advantage of tests using INCONEL is the lack of phase transition in a wide temperature interval (from ambient temperature up to 1000^{o}C). The precise LHTC determination for steel requires modelling heat effect of phase transition, which faces remarkable difficulties. However the ommitting that heat source results in significant errors of LHTC estimation results.

NOMENCLATURE

a_1, a_2, a_3, a_4	–	coefficients of Hermite polynomial
c	–	specific heat
H	–	Hermite polynomial shape function
k	–	thermal conductivity
l	–	length of cylindrical sample
m	–	number of time steps
n	–	number of temperature measurement points
$\dot{q}$	–	heat flux density
r, z	–	cylindrical coordinates
R	–	radius of cylindrical sample
t	–	temperature

Greek symbols

α	–	heat transfer coefficient
Δt	–	mean temperature terror
Φ	–	error norm
ξ	–	supportive variable
τ	–	time

Subscripts

a,	–	the beginning and the end of time interval respectively
end	–	the end of computation time
i, j	–	index
m	–	number of time steps in numerical calculus
n	–	number of temperature measuring points (sensors)
w	–	quenchant
v	–	internal heat sources

Superscripts

num	–	numerical simulations
ex	–	experimental measurements

ACKNOWLEDGEMENT

Financial assistance of the Faculty of Metals Engineering and Industrial Computer Science, Department of Heat Engineering and Environment Protection, is greatly acknowledged.

REFERENCES

1. Beck J.V., Blackwell B., Clair Jr. Ch. R. St., Inverse Heat Conduction, A Wiley-Interscience Publ., New York, 1985.
2. Buczek A., Zastosowanie brzegowego zagadnienia odwrotnego do identyfikacji współczynnika przejmowania ciepła podczas chłodzenia, Rozprawy Monografie, nr 140, Uczelniane Wydawnictwa Naukowo-Dydaktyczne, Kraków, 2004, (in Polish).
3. Buczek A., Telejko T., Inverse determination of boundary conditions during boiling water heat transfer in quenching operation, J. Mater. Process. Technol. vol. 155–156, 2004, pp 1324–1329.
4. Hammad J., Mitsutake Y., Monde M., Movement of maximum heat flux and wetting front during quenching of hot cylindrical block, Int. J. Therm. Sci. 43, 2004, pp 743–752.
5. International Standard ISO 9950. Industrial quenching oils. Determination of cooling characteristics. Nickel-alloy probe test method. First edition, 1995.
6. Raynaud M., Beck J.V., Methodology for comparison of inverse heat conduction methods, Trans. ASME 110, 1998, pp 30–37.

HYDRODYNAMICS OF A CYCLONE WITH WASH WATER INJECTION

J. Dueck[1], A. Krokhina[2], L.L. Minkov[3], T. Neesse[1]*
[1] Friedrich-Alexander-University, Erlangen-Nuremberg, Germany
[2] Bauman Technical University, Moskow, Russia
[3] Tomsk State University, Russia

ABSTRACT. Hydrodynamics of the hydrocyclone using an additional water injection is presented. The tangential water injection influence on the main hydrodynamic characteristics is investigated for different feed pressure drop and varied injection water flow rate.
The water injection markedly changes the hydrodynamic field in the hydrocyclone. The effect of non monotonic dependence of the injected water allocated through the underflow aperture has been found.
Based on the experimental results and supported by calculations, the mechanism of injection can be explained. The mechanism is based on the modification of the axial streams which determine the transport of the fines solid material.

Keywords: *hydrocyclone, hydrodynamics, water injection, flow distribution water*

INTRODUCTION

The hydrocyclone is widely used in different fields of process engineering for particle classification, solid-liquid separation or sludge thickening. One of the methods to improve the hydrocyclone characteristics is the injection of water in the conical part [1-6]. In the present work the influence of water injection on the hydrodynamics inside the hydrocyclone is investigated.
The schema of the water injection through the wall at the lower part of the hydrocyclone cone is shown in Fig.1.
Preliminary experiments have shown that the water injection is most effective if installed near the underflow discharge. Water injection is expected to remove fine particles from the wall boundary layer to the axis where these particles are picked up by the upward flow and then discharged through the overflow. Thus, fine particles will not missreported through the underflow discharge. Obviously, the characteristics of the injection (amount of injected water, jet power, zone of injection) have to be optimised.

Experimental test rig and procedures

The water injection cyclone which was used in this work is a conventional hydrocyclone with a modified conical part to have a water injection facility.
The test rig (Fig. 1) consists of a 50 mm hydrocyclone (1) with injector (2), placed above the tank filled with water (3). The water is fed into the hydrocyclone by the pump. The bypass with hydraulic valve (4) regulates the required pressure in the hydrocyclone, which was measured using a pressure gauge (5), located at the entrance of the hydrocyclone. The water injection rate was measured by a digital flow meter (6).

* Corresponding author: Dr. J. Dueck
Phone: + (49)-9131-8523189, Fax: + (49)-9131-8523002
E-mail address: johann.dueck@uvt.uni-erlangen.de

The water injection assembly (2) consists of 2 inlet openings at equal distances. This assembly is connected with a control valve through which the water can be injected through these openings. A digital manometer was fixed near the water injection to indicate the water injection rate.

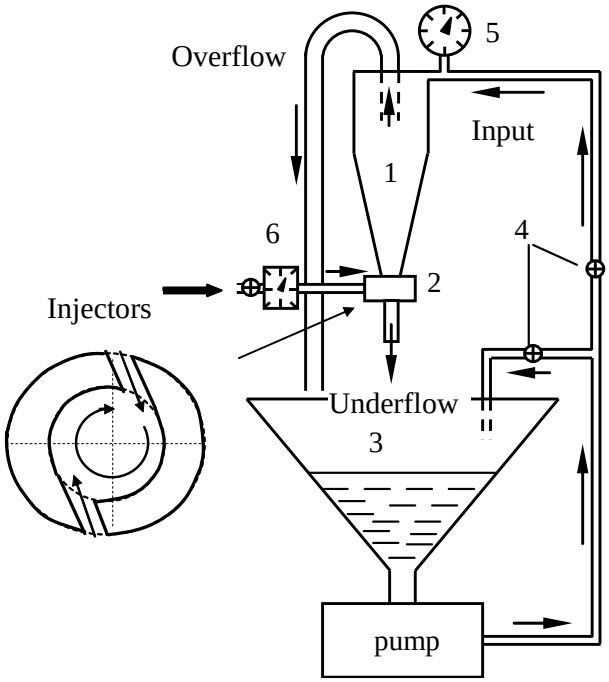

Figure 1. The experimental test rig and the schema of water injection into the hydrocyclone along the tangential velocity of the main flow.

The water was injected in tangential direction with the same swirling direction as the main flow inside the hydrocyclone.
The water injection part was added near the apex of the cyclone without causing any extension of the total cyclone length.
To investigate the effect of water injection rate on the hydrodynamics, samples of the overflow and the underflow were taken at different injection flow rates. From these samples, the feed flow rate, overflow flow rate, and underflow rate can be calculated for every test from which the split - parameter can be estimated.

RESULTS AND DISCUSSIONS

To study the impact of the injection on the hydrodynamics in the apparatus the water flow rates through the underflow and the overflow openings were measured for different injection flow rates and the inlet pressures.

The hydrocyclone without water injection

The measured characteristics of investigated hydrocyclone without injection are: water flow through the feed inlet, which shows the feed water flow rate Q_F^0, flow through underflow opening Q_{UF}^0 and flow through overflow opening Q_{OF}^0.
All measurements are performed for the different values of inlet pressure.

The Fig.2 shows an increasing of feed flow rate approximately proportional to the square root of pressure. This finding agrees with the reviewed empirical equations given by many authors collected in [7]. For example:

$$Q_F^0 = 27.7\, d_{in}\, d_0\, \sqrt{p} \qquad (1)$$

Higher feed pressure results in an increase of both outlet flows in different proportions as shown in Fig. 2.

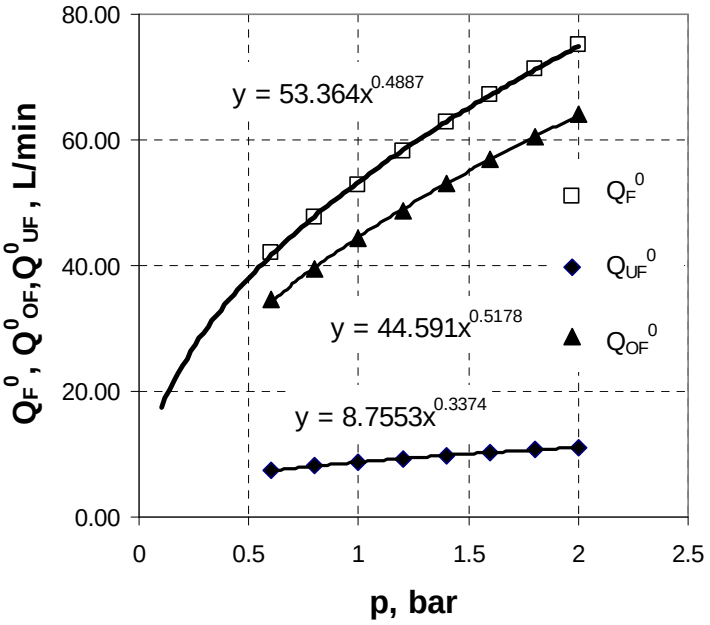

Figure. 2. Dependences of the feed flow rate, underflow rate and overflow rate versus feed pressure.

Empirical relations [8-10], given for the split-parameter $S^0 = \frac{Q_{OF}^0}{Q_{UF}^0}$ assume simplifying only a dependence of S^0 on the diameters of the outlet openings.
The experiments show a moderate dependence of split-parameter on the inlet pressure drop:

$$S^0 = 5p^{0.18} \qquad (2)$$

Other measurements of split-parameter depending on pressure can be found in [11] with much stronger power. Probably the power of dependence S^0 on p is not the universal value and has to be measured for every individual hydrocyclone.

The hydrocyclone with water injection
The hydraulic characteristics of hydrocyclone with water injection depend on the construction of injector.
The experimental results using two tangential openings with the same swirling direction as the main flow inside the hydrocyclone (construction – Fig.1) are presented below in Fig. 3 and Fig. 4.

The flow rate $\Delta Q_{OF} = Q_{OF}^{inj} - Q_{OF}^{0}$ through the overflow due to additional water injection increases monotonically with the growth of flow rate Q_{inj} of injected water.

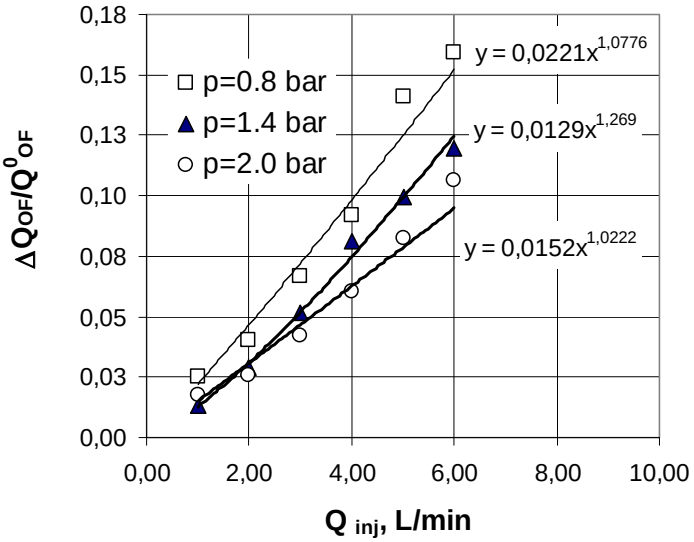

Figure 3. Influence of water injection rate on the overflow of the hydrocyclone.

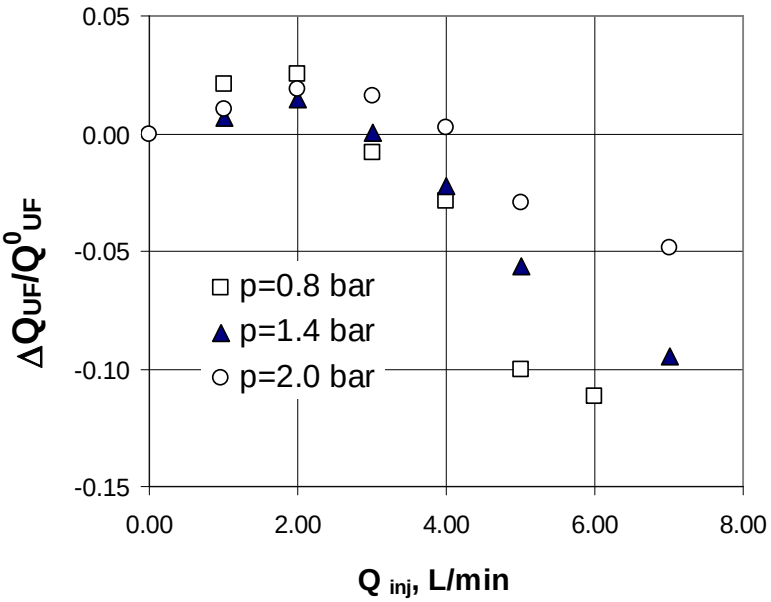

Figure 4. Influence of water injection rate on the underflow of the hydrocyclone.

The dependence of flow rate through the underflow ($\Delta Q_{UF} = Q_{UF}^{inj} - Q_{UF}^{0}$) is more complicated: experiments show that the increase of injection rate Q_{inj} at low values (up to 2-3 litres per minute in dependence of inlet pressure) leads to an increase in the underflow throughput Q_{UF}^{inj}, while at higher Q_{inj} underflow throughput decreases if injection rate increases.

At low injection rates the power of injection flow is relatively weak and is not high enough to overcome the strong swirling motion of the hydrocyclone mean flow. Therefore, it becomes not able to penetrate through the main flow to reach the hydrocyclone axis. Accordingly, it will discharge through the underflow apex which is located near the injection.
The decrease of Q_{UF}^{inj} at higher Q_{inj} can be explained by high hydraulic resistance of the underflow opening which diameter is rather smaller as the overflow opening.
The curves in Fig.3 and Fig.4 demonstrate relatively high influence of the feed pressure.
Based on dimensionless analysis all the measurements can be united to one curve by using the variable Q_{inj}/Q_F^{inj}, where Q_F^{inj} is the feed water flow rate which is influenced by the flow rate of injected water.

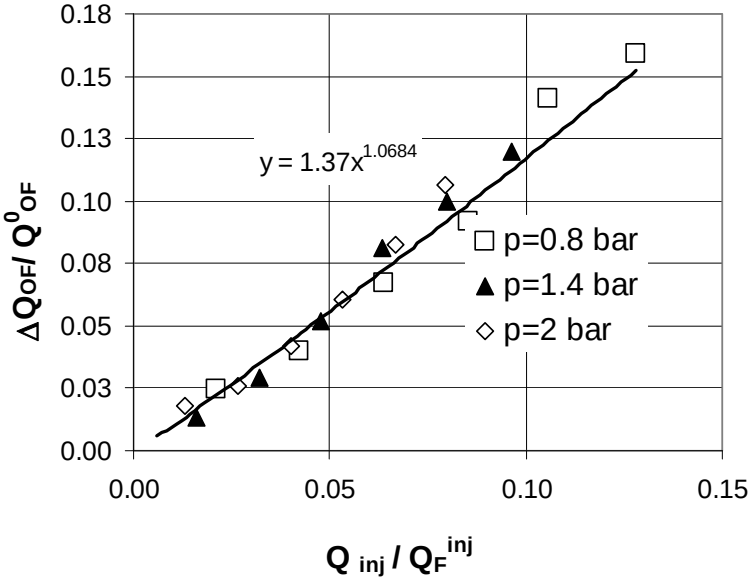

Figure 5. The relative water flow rate through overflow versus the relative injection rate

On the base of graph presented in Fig.5 the equation for the overflow is given in the form:

$$Q_{OF} = Q_{OF}^{0}\left[1+1.37\left(\frac{Q_{inj}}{Q_F^{inj}}\right)^{1.07}\right]. \tag{3}$$

For the underflow (Fig.6) the equation has a more complicated form:

$$Q_{UF} = Q_{UF}^{0} + Q_f\left[0.89\left(\frac{Q_{inj}}{Q_F^{inj}}\right) - 14.85\left(\frac{Q_{inj}}{Q_F^{inj}}\right)^{2}\right]. \tag{4}$$

Q_F^{inj} can be calculated on the base of experimental measurements as follows:

$$\frac{Q_F^{inj}}{Q_F^{0}} = 1 - 0.12\,\frac{Q_{ing}}{Q_F^{0}} \tag{5}$$

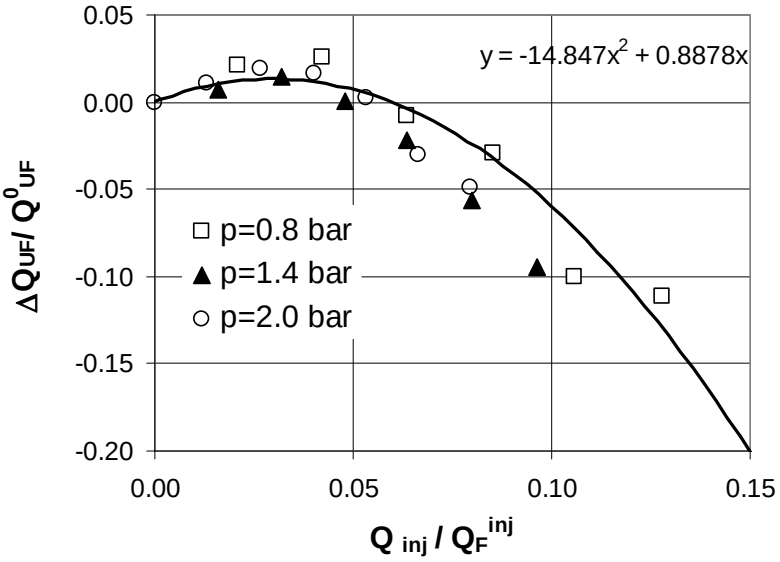

Figure 6. Water flow rate through underflow as a dependence on universal variable

Ratio of flow rates at outlets.

The split-parameter is of great importance to the separation process. Small particles are divided proportional to the ratio of the water flows through these outlets. Fig. 7 shows the change of the split parameter dependent on the throughput of the injected water Q_{inj} at different feed pressures.

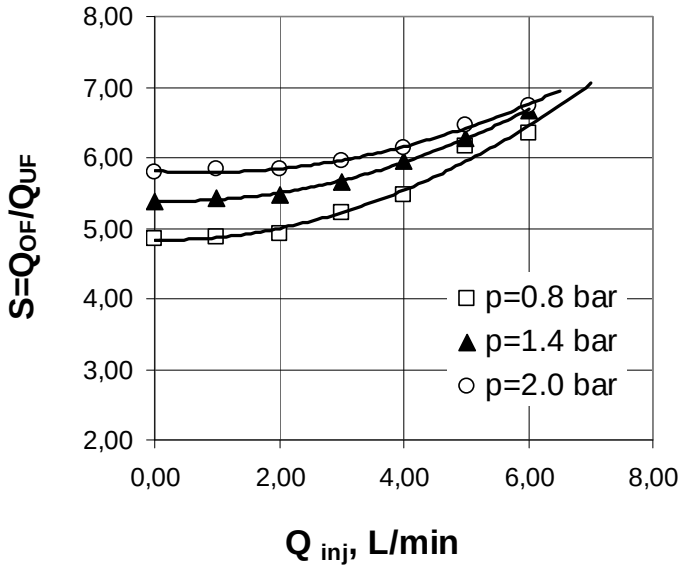

Figure 7. Split-parameter dependent on injected water flow rate

The increase of split-parameter with the increase of injected water flow rate is explained by strong increase of spigot hydraulic resistance compared to the vortex finder hydraulic resistance. Even

here, the dependence of the split-parameter can be presented in dependence on the related injection rate:

$$\frac{S - S^0}{S^0} = 22.1\left(\frac{Q_{inj}}{Q_F^{inj}}\right)^2, \qquad (6)$$

where the equation for S^0 is given by Equation (2).

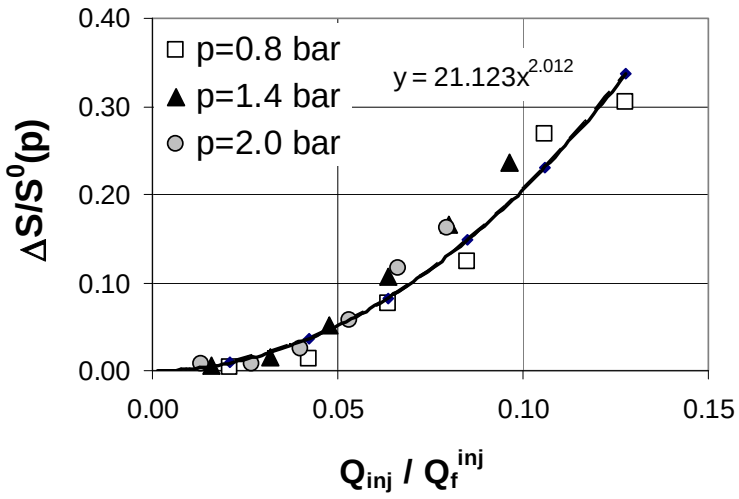

Figure 8. Split-parameter versus related injection rate

The experiments are supported by computer simulations using Fluent 6.3.23.

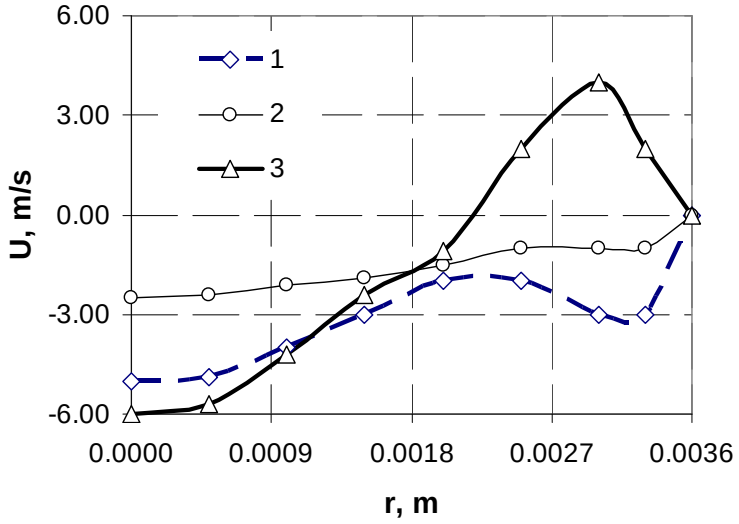

Figure 9. Dependence of the axial velocity distributions above the injector position on radial coordinate r for various water injection rates Q_{inj}. 1 - Q_{inj} = 0 m/s, 2 - Q_{inj} = 4 m/s, 3 - Q_{inj} = 9 m/s.

In Fig. 9 are shown the computed radial profiles of the axial velocity U in the apparatus directly above the injector.
Positive values indicate the flow directed to the overflow.
The injection changes the profiles of water velocity. For high Q_{inj} the rebuilding of the stream as an arousing of strong bottom-up flow can be observed.
In the absence of injection at the observed point no up-stream flow exists and all water is directed downwards to the underflow aperture. In the case of intensive injection because the hydraulic resistance at the underflow is higher than at the overflow, the injected water causes an intensive upstream at the wall.
This suggests a mechanism for the effects of tangential injection: fine particles are attracted by water in the direction to overflow where they are carried by main flow and leave the apparatus through the upper discharge.

REFERENCES

1. Heiskanen, K., *Particle Classification*, Chapman and Hall, London–Glasgow–New York–Tokyo–Melbourne–Madras, 1993, 321 pp.
2. Patil D.D., Rao T.C., Technical Note. Classification evaluation of water injected hydrocyclone, *Mineral Engineeering*, Vol. 12, No.12, pp 1527- 1532, 1999.
3. Kelsall D.F., Holmes J.A., Improvement in classification efficiency in hydraulic cyclones by water injection In: *Proc. 5th Mineral processing Congress, Paper 9*, Inst. Of Mining and Metallurgy, 1990, pp 159-170.
4. Honaker R.Q., Ozsever A.V., Singh N., Parekh, B. K., Apex water Injection for improved hydrocyclone classification efficiency, *Mineral Engineeering*, Vol. 14, No.11, pp 1445- 1457, 2001.
5. Bhaskar K. Udaya, Govindarajan B., Barnawal J.P., Rao K.K., Rao T.C., Modelling studies on a 100 mm water-injection cyclone, *Physical Separation in Science and Engineering*, Vol. 13, No. 3-4, pp 89 – 99, September-December 2004.
6. Bhaskar K. Udaya, Govindarajan B., Barnawal J.P., Rao K.K., Gupta B.K., Rao T.C., Classification studies of lead-zinc ore fines using water-injection cyclone, *Intern. Journ. Mineral Processing*, No. 77, pp 80-94, 2005.
7. Ternovsky I.G., Kutepov A.M., *Hydrocycloning*, Nauka, Moscow, 1994, 350 pp.
8. Tarjan, G., Some theoretical questions on classifying and separating hydrocyclones, *Acta tech. Acad. Sci*., No. 32, pp 357 – 388, 1961.
9. Plitt, L. R., A Mathematical Model of the the Hydrocyclone Classifier, *CIM Bulletin*, No. 69, pp 114 – 123, 1976.
10. Schubert, H., *Mechanische Verfahrenstechnik*, Deutscher Verlag für Grundstoffindustrie, Leipzig, 1990.
11. Mittal Manju, Adaptation of Hydrocyclone to Varying Solid Load by Air Injection, *Chem. Eng. Technol*., Vol.19, pp 510-513, 1996.

NUMERICAL AND EXPERIMENTAL INVESTIGATIONS OF MARANGONI DRIVEN FLOW REVERSALS IN LIQUID STEEL WELDING POOLS

Z.S. Saldi[1, 2, *], C. Zhao[1, 3], S. Kenjeres[2, 4], I.M. Richardson[3], C.R. Kleijn[2, 4]
[1]Materials Innovation Institute, Delft, The Netherlands
[2]Department of Multi-Scale Physics, Delft University of Technology, The Netherlands
[3]Department of Materials Science & Engineering, Delft University of Technology, The Netherlands
[4]J.M. Burgers Centre for Fluid Mechanics, The Netherlands

ABSTRACT. Combined numerical and experimental studies have been performed in order to provide insights into the dynamics of the surface flow of welding pools. The primary focus of the study is on the influence of the oxygen concentration on the Marangoni convection in the liquid metal pool during laser spot welding of 304 stainless steel. Since during the experiment no shielding gas was employed, the material was exposed to open air, causing an accumulation of oxygen in the weld pool and at its surface. Consequently, the surface tension and its temperature coefficient ($d\sigma/dT$) are altered, affecting the direction of Marangoni stress that can cause the reversal of the weld pool flow.

Keywords: *laser welding, weld pool hydrodynamics, Marangoni convection*

INTRODUCTION

A laser welding process is a typical example where complex interactions between multi-physics phenomena take place. These include intensive heat transfer from a laser beam to an initially solid metal, melting of the metal, combined natural and Marangoni (surface tension) driven convection in the liquid metal pool, and dynamical behavior of the free-surface. In a laser welding process, the character of the fluid flow inside of the liquid metal weld pool is primarily determined by surface tension gradients at the free-surface. This flow plays an important role in the energy transfer from the weld pool to the surrounding heat-affected zone. Additionally, the shape of the weld pool also highly depends on the magnitude and the direction of the liquid velocities in the weld pool. Altering the temperature coefficient of surface tension due to the – intentional or unintentional – addition of surface active elements is known to affect the direction of the Marangoni shear stress at the pool surface [1, 2, 3]. Pure metals usually feature negative values of temperature coefficient of surface tension, causing the weld pool flow to be in the radially outward direction. The presence of surface active elements at a sufficiently high concentration can change temperature coefficient of surface tension to a positive value, resulting in radially inward flow. The temperature coefficient of surface tension as function of temperature and composition of surface active element was formulated in [4], and has been used in many weld pool models. This variable plays important role in the mechanism of flow reversal in the weld pool. The understanding of the flow reversal phenomena is important for a better control of weld pool shapes and weld quality.

* Corresponding author: Z.S. Saldi
Phone: + (31)-15-2787084, Fax: + (31)-15-2782838
E-mail address: z.s.saldi@tudelft.nl

MATHEMATICAL FORMULATION

In this work we study the influence of surface active elements on the weld pool flow in a laser welding process. The physical domain of interest is a rectangular stainless steel plate of SS304 type subjected to a laser beam on its top surface, as shown in Figure 1. The present study considers the laser spot welding, i.e. the position of the laser beam is fixed during the process. Additionally, it is assumed that the surface of the weld pool during melting is flat.

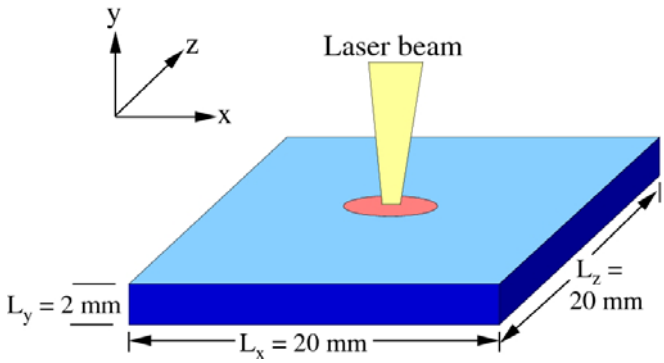

Figure 1. Laser spot welding of SS304

Conservation equations

The mathematical formulation for the above problem is based on a set of conservation equations, namely conservation of mass, momentum, and energy, described as follows.

$$\frac{\partial \rho}{\partial t} + \nabla \cdot (\rho \mathbf{U}) = 0 \tag{1}$$

$$\frac{\partial (\rho \mathbf{U})}{\partial t} + \nabla \cdot (\rho \mathbf{U}\mathbf{U}) = -\nabla p + \nabla \cdot (\mu \nabla \mathbf{U}) + \rho \mathbf{g} \beta (T - T_{ref}) - \mathbf{S}_{\mathbf{U}} \; ; \qquad \mathbf{S}_{\mathbf{U}} = \frac{C(1 - f_l^{\,2})}{f_l^{\,3} + b} \mathbf{U} \tag{2}$$

Here, ρ is the liquid steel density, $\mathbf{U}$ velocity, μ dynamic viscosity, β coefficient of thermal expansion, and p the pressure. $\mathbf{S}_{\mathbf{U}}$ is a momentum sink that accounts for deceleration of the flow due to solidification [5]. It decreases with increasing liquid fraction f_l. C is a large constant, typically 10^6 kg/(m^{3}s), and b is a small number, chosen as 10^{-12}, to avoid division by zero. This formulation leads to zero velocities in the solid region ($f_l = 0$) and a smooth transition of velocities from solid to liquid region ($f_l = 1$).

$$\frac{\partial (\rho C_p T)}{\partial t} + \nabla \cdot (\rho C_p \mathbf{U} T) = \nabla (k \nabla T) + S_T \qquad ; \qquad S_T = -\frac{\partial (\rho \Delta H)}{\partial t} - \nabla (\rho \mathbf{U} \Delta H) \tag{3}$$

In equation (3), C_p is the specific heat and k the thermal conductivity. S_T is the source term contributed by the latent heat ΔH. The latent heat and the liquid fraction are calculated as follows

$$\Delta H = \begin{cases} L & : \quad T > T_L \\ L(T - T_S)/(T_L - T_S) & : \quad T_S \le T \le T_L \\ 0 & : \quad T < T_S \end{cases} \; ; \qquad f_l = \frac{\Delta H}{L} \tag{4}$$

where L is the latent heat of melting.

Boundary and initial conditions

At the top surface, a laser beam of power Q and radius r_q is directed perpendicularly to the center of the domain. The absorbed heat flux from the laser is described by a Gaussian distribution

$$q''(r) = \eta \frac{k_q Q}{\pi r_q^2} \exp\left(- k_q \frac{r^2}{r_q^2} \right) \tag{5}$$

where η is the laser absorption coefficient and k_q is a constant associated with the shape of the Gaussian function. The thermal boundary condition for the top surface is given by the contribution from the absorbed laser heat flux and convective and radiative heat losses.

$$-k \frac{\partial T}{\partial y} = -q''(r) + h\left(T_{top} - T_\infty\right) + \varepsilon\sigma\left(T_{top}^4 - T_\infty^4\right) \tag{6}$$

Here, h is the coefficient of convective heat transfer between the plate and air, T_{top} the top surface temperature, T_∞ the ambient temperature, ε the surface emissivity, and σ the Stefan-Boltzmann constant. At the top surface, the viscous force is balanced by the force due to surface tension. Assuming flat weld pool surface, the vertical velocity is zero.

$$\mu \frac{\partial u_x}{\partial y} = \frac{\partial \sigma}{\partial T} \frac{\partial T}{\partial x} \quad ; \quad u_y = 0 \quad ; \quad \mu \frac{\partial u_z}{\partial y} = \frac{\partial \sigma}{\partial T} \frac{\partial T}{\partial z} \tag{7}$$

At the four side boundaries and the bottom boundary, the thermal boundary condition is given by

$$-k \frac{\partial T}{\partial n} = h\left(T - T_\infty\right) \tag{8}$$

where n is the normal direction pointing outward from the surface. At these boundaries, a no-slip condition for velocities is imposed.

Initial conditions for temperature and velocities are $T = T_\infty = 298$ K and $u_x = u_y = u_z = 0$ m/s, respectively.

Temperature coefficient of surface tension

On the top surface of the weld pool, the dependence of the temperature coefficient of surface tension on the temperature is taken into account according to the following formulation [4]

$$\frac{d\sigma}{dT} = -A - R\Gamma_s \ln\left(1 + Ka_i\right) - \frac{Ka_i}{\left(1 + Ka_i\right)} \frac{\Gamma_s \left(\Delta H^o - \Delta \overline{H}_i^M\right)}{T} \quad ; \quad K = k_1 \exp\left(\frac{-\Delta H^0}{RT} \right) \tag{9}$$

Here, A is the value of surface tension coefficient for pure metal, Γ_s the surface excess at saturation, K the equilibrium constant for segregation, ΔH^0 the standard heat of adsorption, $\Delta \overline{H}_i^M$ the partial molar enthalpy of species mixing in the solution, and a_i the activity of the surface active element (in % weight). In this study, the surface active element of interest is oxygen and the

corresponding constants in equation (9) for the steel-oxygen system [4] are given in table 1, leading to the curves in Figure 2.

Table 1
Constants for formulation of temperature coefficient of surface tension

Constants	Units	Value
A	N/(m K)	4.3 x 10^{-4}
R	J/(kg mole K)	8314.3
Γ_s	kg mole/m^2	2.03 x 10^{-8}
k_1	-	1.38 x 10^{-2}
ΔH^0	J mole/kg	-1.46 x 10^8
$\Delta \overline{H}_i^M$	J mole/kg	0

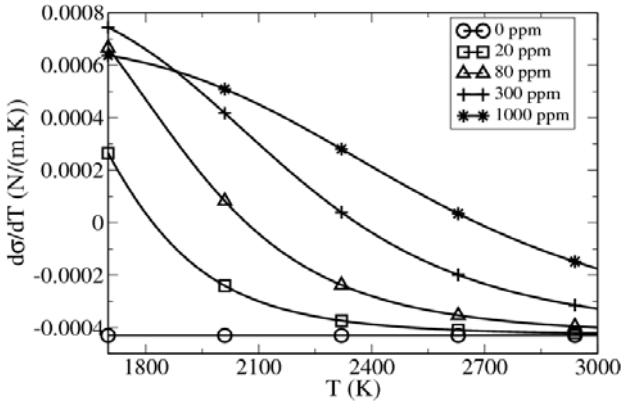

Figure 2. Temperature coefficient of surface tension for different oxygen concentration

The above mathematical model equations have been implemented into the open-source CFD toolbox OpenFOAM [6], which is based on the finite volume method to solve systems of partial differential equations.

SIMULATION SETTINGS

The physical domain in Figure 1 is decomposed into a $N_X \times N_Y \times N_Z = 70 \times 50 \times 70$ grid system, with fine grid spacings in the center and top parts of the domain. The typical cell size near the center of top surface is $\Delta x \times \Delta y \times \Delta z = 50 \times 10 \times 50$ μm. The simulation time step is chosen to be 0.0002 s. The physical properties of the material and process parameters are listed in Table 2. The differential equations are spatially discretized using a second-order central difference scheme. The unsteady terms are treated using a first-order fully implicit time integration scheme.

In the simulation, we try to mimic qualitatively our experimental observation in the weld pool in which we found a flow reversal as time progressed. Since in the experiment the weld pool is exposed to open air, the surface oxygen concentration increases in time. At present, we are assuming that the surface oxygen concentration increases linearly with time, based on the following expression

$$a_O(t) = a_{O,0} + Mt \tag{10}$$

where a_O is oxygen activity, t is time, $a_{O,0}$ is the initial oxygen activity and set as zero, and M is the rate of oxygen increase. The above expression is evaluated every time step and combined with the surface temperature field solution for the calculation of the temperature coefficient of surface tension according to equation (9). Simulations have been carried out for M = 5, 10, 20, and 40 part per million per second.

Table 2
List of physical properties and process parameters

Property/parameter	Units	Value
Solid and liquid density, ρ	kg/m^3	7200
Liquid viscosity, μ	kg/(m.s)	0.1
Solidus temperature, T_S	K	1697
Liquidus temperature, T_L	K	1727
Specific heat of solid, $C_{p,S}$	J/(kg.K)	711.76
Specific heat of liquid, $C_{p,L}$	J/(kg.K)	837.36
Thermal conductivity of solid, k_S	W/(m.K)	19.25
Thermal conductivity of liquid, k_L	W/(m.K)	209.2
Latent heat of melting, L	J/kg	1.23×10^6
Coefficient of thermal expansion, β	1/K	1.96×10^{-5}
Top surface emissivity, ε	-	0.3
Stefan-Boltzmann constant, σ	W/(m^{2}K^4)	5.67×10^{-8}
Convective heat transfer coefficient, h	W/(m^{2}K)	10
Laser power, Q	kW	3
Laser absorption coefficient, η	-	0.27
Laser Gaussian distribution constant, k_q	-	3
Laser beam radius, r_q	mm	3.75

EXPERIMENTAL SETUP

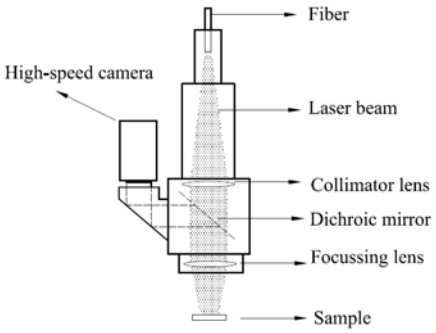

Figure 3. Experimental setup

The experimental welding setup is shown in Figure 3, which includes a high speed camera directed towards the top side of the weld pool. The light reflected from the weld pool surface passes the laser lens and reaches the high speed camera. The high speed camera worked at 3000 frames per second to capture the weld pool surface flow motions and surface particle flow. Chromium oxide (Cr_2O_3) particles formed in the weld pool are used to trace the surface velocities using a Particle Image Velocimetry (PIV) method. The images were post-processed using commercial software (Davis 6.2, LaVision). A more detailed description can be found in [7, 8].

RESULTS AND DISCUSSION

Top views and cross-sectional views of the weld pool at t = 0.65 s for different oxygen increase rates *M* are shown in Figure 4 and 5, respectively. At this time instant, an outward flow is observed for *M* = 5, 10, and 20 ppm/s. For these cases, at 0.65 s the surface oxygen concentrations are 3.25, 6.5 ppm, and 13 ppm, respectively. According to Figure 2, at those concentration levels the temperature coefficient of surface tension is negative over the temperature range in the weld pool. Combined with a negative value of *dT/dr*, this causes the flow to be directed outward. Interestingly, for *M* = 40 ppm/s, two counter-rotating flows are observed because two regions exist with different sign of the temperature coefficient of surface tension. At 0.65 s, the corresponding oxygen concentration is 26 ppm, and the temperature coefficient of surface tension is positive below approximately 1820 K, which is the temperature at approximately halfway from the pool center to the melting front. This causes outward flow in the center part of the pool and inward flow in the outer part of the pool.

Figure 6 shows the radial velocity at the surface as a function of time, for various values of *M*. Except for *M* = 40 ppm/s, the flow is always in the outward direction (positive value of radial velocity) because up to 0.65 s the surface oxygen concentrations still do not reach the level that causes change of sign of $d\sigma/dT$. On the other hand, inward flow (negative value of radial velocity) is observed for *M* = 40 ppm/s in the outer region of the weld pool for t = 0.4 and particularly 0.65 s.

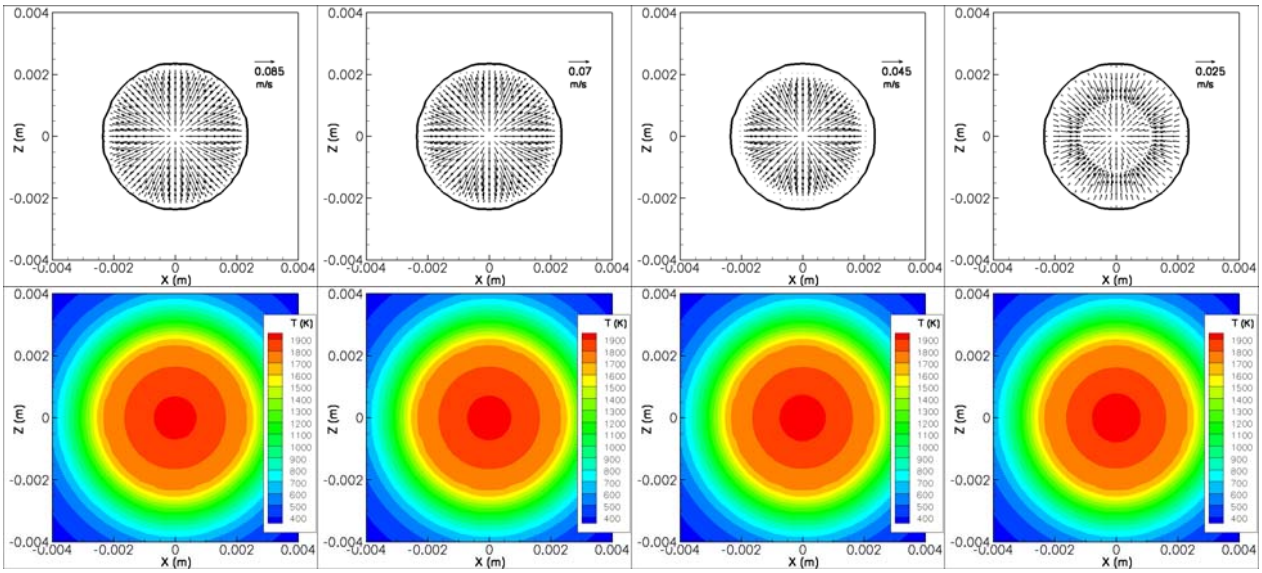

Figure 4. Weld pool velocity vectors (top) and temperature contours (bottom) at t = 0.65 s. From left to right: M = 5, 10, 20, and 40 ppm/s.

Experimental snapshots of the weld pool surface obtained using the high-speed camera are shown in Figure 7 for t = 0.244, 0.403, and 0.813 s. In the first snapshot, the flow is outward, while in the other two the flow is inward. The flow reversal is more quantitatively shown by the experimental velocity vectors obtained by PIV in Figure 8, in which a fully outward flow is initially observed (t = 0.27 s), followed by a combined outward and inward flow (t = 0.413 s), and a fully inward flow (t = 0.954 s). Comparison between simulation and experimental results shows that the predicted weld pool surface velocity behaves more orderly than that in the experiment. This difference is mainly caused by the assumption of linear increase of surface oxygen concentration used in the simulation. In the experiment, where the weld pool is exposed to the open air, the oxygen increase is most likely to be non-linear and not perfectly controlled as in the simulation. Moreover, in the simulation the spatial variation of surface oxygen concentration is not taken into account, whereas in reality a

much more complex mechanism involving adsorption kinetics and convection of surface active elements is present. Accordingly, the spatial variation of surface tension becomes much more complicated and so does the surface flow pattern.

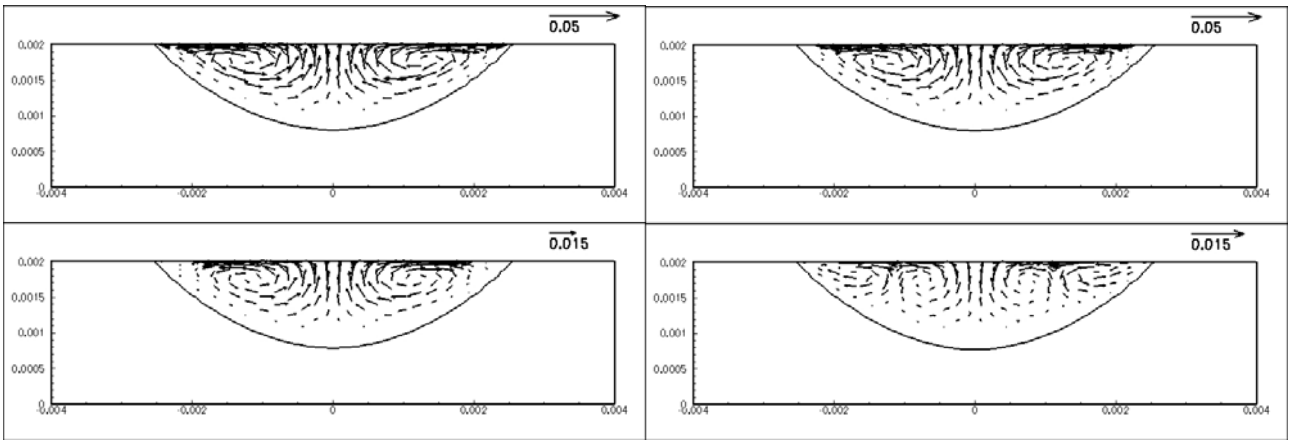

Figure 5. Cross section view of velocity vectors in weld pool, at t = 0.65 s, for M = 5, 10, 20, and 40 ppm/s (top left to bottom right)

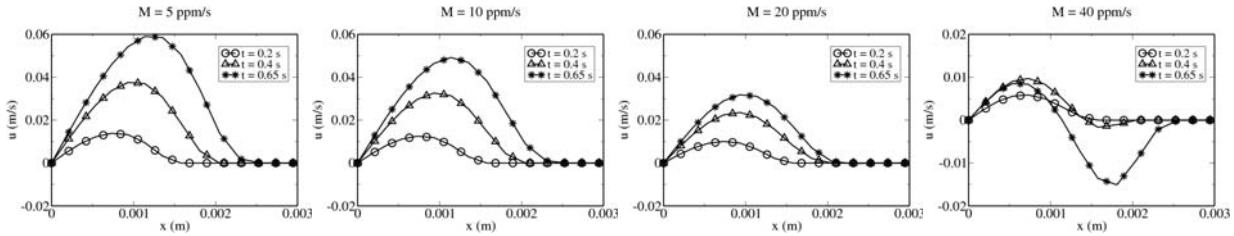

Figure 6. Radial velocity along the center line of weld pool surface

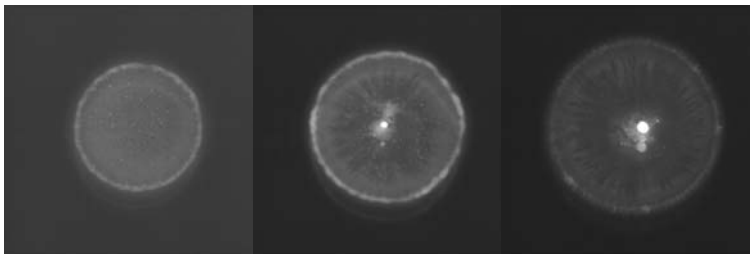

Figure 7. Snapshots of weld pool obtained using high-speed camera.
Left: t = 0.244 s; *Center:* t = 0.403 s; *Right:* t = 0.813 s.

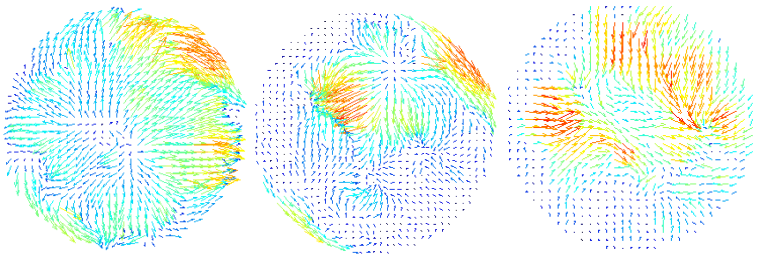

Figure 8. Surface velocity vectors obtained from experiment.
Left: t = 0.27 s, U_{max} = 0.043 m/s; *Center:* t = 0.413 s, U_{max} = 0.292 m/s;
Right: t = 0.954 s, U_{max} = 0.304 m/s.

CONCLUSION

A mathematical model describing the three-dimensional fluid flow and heat transport in a weld pool for laser spot welding process is presented. The model includes surface tension driven (Marangoni) stress at the weld pool surface due to surface temperature gradients. The temperature coefficient of surface tension is calculated as a function of surface temperature and concentration of oxygen as surface active element. The assumption of linear increase of surface oxygen concentration over time is employed and leads to the prediction of a flow reversal in the weld pool as time progresses. The flow reversal occurs if at any given time the surface oxygen reaches a level at which in the weld pool two regions with different signs of temperature gradient of surface tension exist. Comparison with experiment shows that the current model can only qualitatively predict the flow reversal. The current model can not yet reproduce the dynamics of the surface velocity observed in the experiment, since transport of oxygen at the weld pool surface that involves adsorption kinetics and convection mechanism is not taken into account. This suggests that there is a need for implementation of transport of surface oxygen into the current model.

ACKNOWLEDGEMENT

The work reported in this paper is carried out under the project number MC8.05240 in the framework of the research program of Materials Innovation Institute (www.m2i.nl), formerly Netherlands Institute for Metals Research (NIMR).

REFERENCES

1. Pitscheneder, W., DebRoy, T., Mundra, K., Ebner, R., Role of Sulfur and Processing Variables on the Temporal Evolution of Weld Pool Geometry during Multikilowatt Laser Beam Welding of Steels, *Supplement to the Welding Journal*, pp 71-s, 1996.
2. Ehlen, G., Ludwig, A., Sahm, P., Simulation of Time-Dependent Pool Shape during Laser Spot Welding: Transient Effects, *Metallurgical and Materials Transactions A*, Vol. 34A, pp 2947 – 2961, 2002.
3. Xu, Y.L., Dong, Z.B., Wei, Y.H., Yang, C.L., Marangoni Convection and Weld Shape Variation in A-TIG Welding Process, *Theoretical and Applied Fracture Mechanics*, Vol. 48, pp 178 – 186, 2007.
4. Sahoo, P., DebRoy, T., McNallan, M., Surface Tension of Binary Metal – Surface Active Solute Systems under Conditions Relevant to Welding Metallurgy, *Metallurgical Transactions B*, Vol. 19, pp 483 – 491, 1988.
5. Brent, A., Voller, V., Reid, K., Enthalpy-Porosity Technique for Modeling Convection-Diffusion Phase Change: Application to the Melting of Pure Metal, *Numerical Heat Transfer B*, Vol. 13, pp 297 – 318, 1988.
6. www.opencfd.co.uk
7. Zhao, C.X., van Steijn, V., Richardson, I.M., Saldi, Z.S., Kleijn, C.R., Experimental Observation for Weld Pool Surface Velocity Field of GTAW, *8th Trends in Welding Research Conference*, June 1 - 6 Pine Mountain, Georgia, USA, 2008.
8. Zhao, C.X., van Steijn, V., Richardson, I.M., Kleijn, C.R., Kenjeres, S., Saldi, Z.S., Unsteady Interfacial Phenomena for Weld Pool Inward Flow with an Active Surface Oxide, *Sci. Technol. Weld. Joi*., Vol. 14(2), pp 132 – 140, 2009.

Measurement Techniques

1969

A NOVEL SOUND RESONANCE METHOD FOR MEASUREMENT OF EVAPORATION COEFFICIENT

S. Nakamura[1], T. Yano[2], M. Watanabe[1] and S. Fujikawa[1*]
[1]Division of Mechanical and Space Engineering, Hokkaido University, Sapporo, Japan
[2]Department of Mechanical Engineering, Osaka University, Suita, Japan

ABSTRACT. A new method for measurement of the evaporation coefficient using sound resonance experiment is developed. To demonstrate the applicability of this method, we measure the amplitude of standing sound wave generated in a closed space filled with air at a resonance frequency. The experiments are conducted in two types of resonators, one is closed by a solid wall and the other by a liquid water layer, under the atmospheric condition and a reduced-pressure condition at 0.5 atm. We find that the first few harmonic components are produced by the nonlinearity of sound. The amplitude of the second harmonics appreciably decreases when the liquid water layer is formed on the closed end and this enables us to evaluate the evaporation coefficient with the help of the theory of molecular gas dynamics.

Keywords: *evaporation coefficient, sound wave, wave absorption, resonance, second harmonics*

INTRODUCTION

Evaporation and condensation are physical phenomena having attracted attention of engineers and scientists, because these are concerned with not only a fundamental aspect on their molecular mechanism but also a wide range of practical applications. One of unresolved problems in the fundamental aspect is the kinetic boundary condition at a vapor-liquid interface [1]. It is used as the boundary condition for the Boltzmann equation, i.e. the governing equation for statistical behavior of gas molecules in non-equilibrium states. The kinetic boundary condition contains two unknown parameters called the evaporation coefficient and condensation coefficient. There has been a history over these coefficients for more than one century, and it is still open.

The kinetic boundary condition is given by

$$f^{out} = \left[\alpha_e + (1-\alpha_c)\frac{\sigma}{\rho^*}\right] f^* \quad (\xi_1 - v_l) > 0 \tag{1}$$

where f^* is the distribution function at equilibrium state, ξ_1 is the velocity of molecules normal to the interface between a vapor and its liquid phase, ρ^* is the saturated vapor density, v_l is the velocity of the interface, σ is defined by the incident mass flux, α_e is the evaporation coefficient and α_c is the condensation coefficient. These coefficients are defined by molecular mass fluxes at the interface as follows:

$$\alpha_e = \frac{J_{evap}}{J^*_{out}} \quad \alpha_c = \frac{J_{cnds}}{J_{coll}} \tag{2}$$

where J_{evap} is the evaporation mass flux, J^*_{out} is the outgoing mass flux at equilibrium state, J_{cnds} is the condensed mass flux and J_{coll} is the incident mass flux. From the definitions of the evaporation and condensation coefficients, they are equal in an equilibrium state.

* Corresponding author: Prof. S. Fujikawa
Phone: + (81)-11-7066429, Fax: + (81)-11-7066429
E-mail address: fujikawa@eng.hokudai.ac.jp.

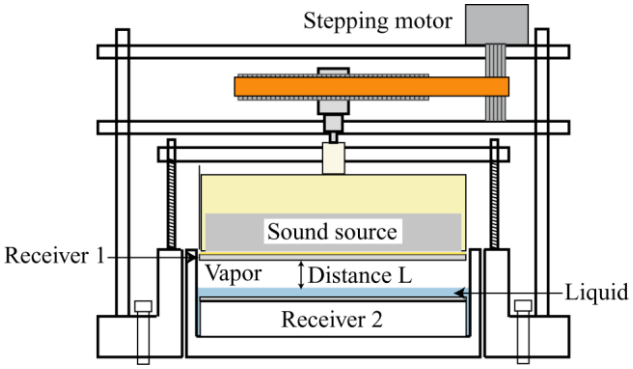

Figure 1. Schematic diagram of experimental setup

The aim of this study is to measure the evaporation coefficient by using sound wave near a very weak non-equilibrium state. In such a state, we can regard these two coefficients as an almost identical one, i.e. evaporation coefficient. In this paper, we describe a new method of evaporation coefficient measurement by sound wave.

MEASUREMENT METHOD

The method by using sound wave was originally proposed by Kogan and Nosik in 1988 [2]. It was theoretically predicted that the evaporation coefficient can be measured using sound absorption by the boundary layer formed on the interface when evaporation or condensation occurs at the interface. Based on this paper, we develop a new method for measurement of the evaporation coefficient, which is based on combination of both sound resonance experiment in a closed vessel with a planar sound source and a liquid layer opposing against the generator and molecular gas dynamics analysis as the counterpart of experiment. Since the variations of pressure, velocity and temperature induced by the sound wave are usually sufficiently small compared with those in a reference state, we conduct the measurement in a weak non-equilibrium state.

Figure 1 shows the schematic diagram of experimental setup. The apparatus consists of the sound source (PZT, diameter: 50 mm, thickness: 10 mm, resonance frequency: 201 kHz), the receiver 1 (PVDF, diameter: 54 mm, thickness: 0.2 mm), the receiver 2 (PVDF, diameter: 54 mm, thickness: 0.2 mm) and the liquid holder. The receiver 1 is attached to the surface of sound source and the receiver 2 is attached to the acrylic plate. The sound source is supported by six columns with springs and its position is controlled by a micrometer which is connected to a stepping motor at the center of top surface. This enables us to change the distance between the sound source and liquid surface L accurately by rotation of the stepping motor. In the measurement, we put the apparatus into the vacuum vessel and adjust the tilt of sound source to make the surface of sound source parallel to the acrylic plate on which the receiver 2 is mounted. Then we infuse the sample liquid into the liquid holder to form a uniform layer (depth: about 2 mm) on the surface of the receiver 2. After that, we close a lid of vacuum vessel and evacuate the contained gas by a rotary pump until the pressure inside the vessel reaches below the saturated vapor pressure. After a while, a condition that the vessel is filled only with the vapor of sample liquid is attained.

The sound source, parallel to the liquid surface, is driven continuously. After a few seconds, the standing wave is formed in the closed space between the sound source and the liquid surface. Also on the surface, evaporation and condensation take place cyclically by the pressure variation induced by the sound wave and part of sound wave is transmitted into the liquid. This affects the amplitude of standing wave. We utilize the sound resonance in the vapor space to increase the amplitude of standing wave and obtain the effect of evaporation and condensation more clearly. At resonance

points, harmonic components are excited. To eliminate the continuous noises generated from the sound source in the received signals, we also use the second harmonics. In this method, we measure the variation of the amplitude of second harmonics by the receiver 1. By comparison with the theoretical analysis using molecular gas dynamics, we can evaluate the value of the evaporation coefficient.

EXPERIMENTAL RESULTS

To demonstrate the applicability of our new method, we conduct preliminary measurements as mentioned below. In this section, we show experimental conditions and results.

The actual measurements are to be conducted under the saturated vapor pressure of sample liquid. In the case of methanol, the saturated vapor pressure at 323 K is about 0.5 atm (55.7 kPa). Under the reduced pressure, owing to the decrease of efficiency of sound emission from PZT and the increase of attenuation rate of sound wave in comparison with the case of atmospheric condition, it is expected that output amplitude obtained from the receiver 1 is decreased. We therefore examine the output of receiver 1 at the following four conditions: (i) solid wall and atmospheric pressure, (ii) solid wall and 0.5 atm, (iii) liquid water and atmospheric pressure, (iv) liquid water and 0.5 atm. In particular, we focus on the amplitude of second harmonics at the resonance point. Note that the saturated vapor pressure of water is 3.2 kPa at the room temperature.

It was extremely difficult tasks to set the distance between the sound source and the liquid (or solid), L, as the predetermined value accurately, and to measure the absolute distance after the experimental device was organized; hence we discuss the relative distance L_1. First the distance between the sound source and the liquid (or solid) was approximately set as one wavelength. We refer to this distance as L_0 hereafter. This distance L_0 was defined as the reference distance, and then L_1 was defined as the relative distance to the reference L_0. The output amplitudes, by changing L_1 from zero to the half of the wavelength with the increment of 0.01 mm, obtained from the receiver 1 are shown in Figures 2 and 3. These amplitudes are mainly composed of three components, i.e., the driving frequency f (f=201 kHz), the second harmonics 2f and the third harmonics 3f. The ambient temperature of the apparatus, T, is shown in the figures. The horizontal axes in Figures 2 and 3 are the relative distance L_1. The left side of vertical axes corresponds to the amplitude of component of driving frequency f and the right side of vertical axes corresponds to 2f and 3f.

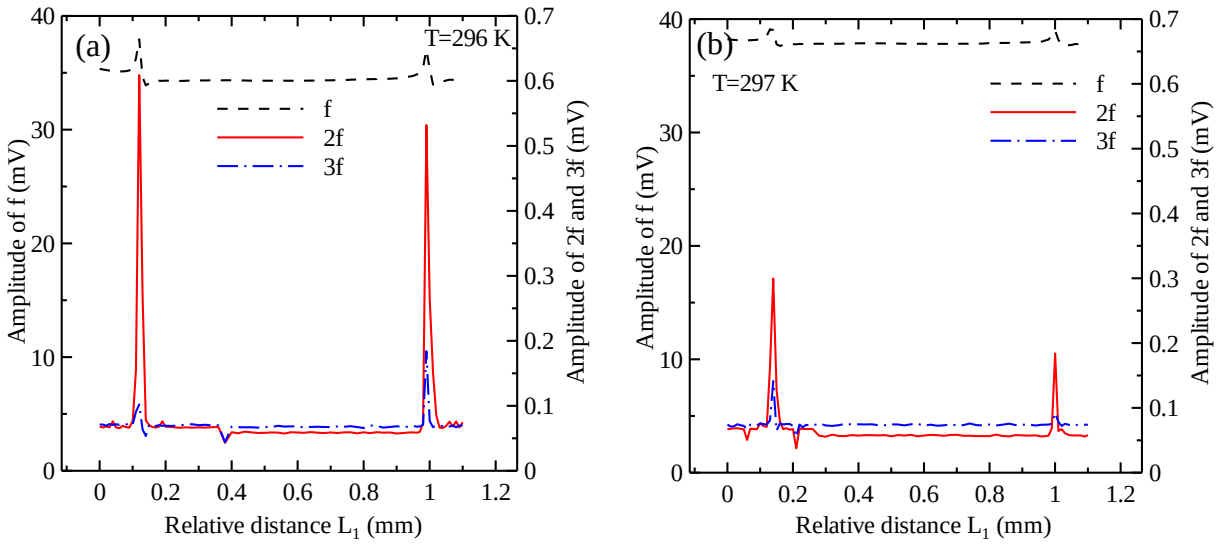

Figure 2. Output amplitude for solid wall: (a) atmospheric pressure, (b) 0.5 atm

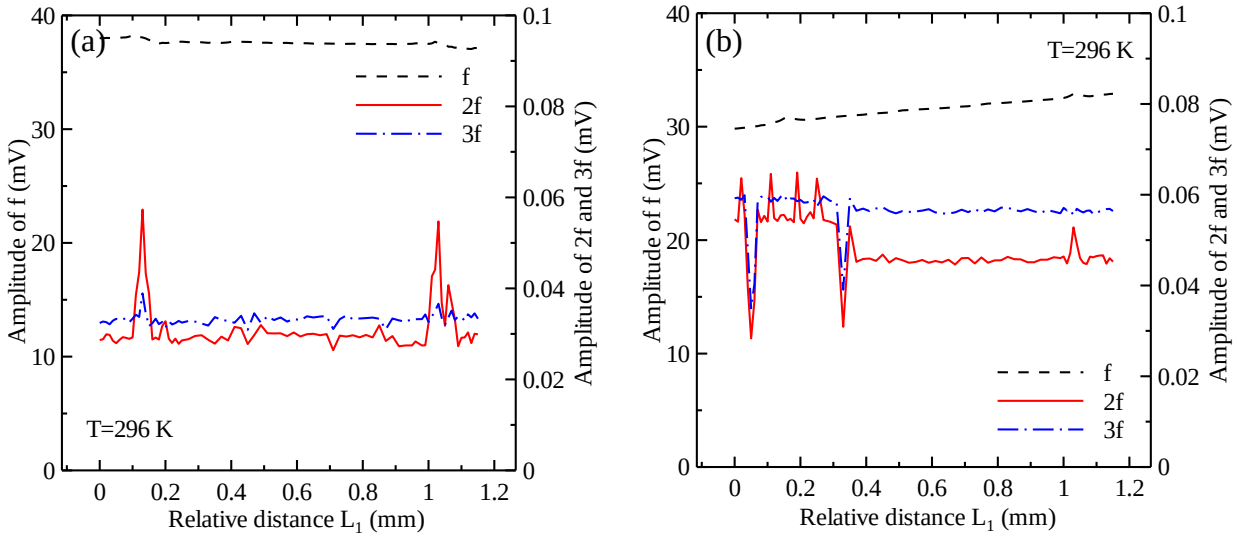

Figure 3. Output amplitude for water: (a) atmospheric pressure, (b) 0.5 atm

Two peaks in Figures 2(a) and 2(b), the results for a solid wall case, show the sound resonance excited in the vapor space, because these differences between two peaks (Figures 2(a) 0.87 mm and 2(b) 0.86 mm) are approximately equal to half wavelength obtained from the sound speed in the air. By comparing Figures 2(a) and 2(b), the maximum amplitude of the second harmonics in the case of Figure 2(b) 0.5 atm is decreased by 50 % as against the case of Figure 2(a) atmospheric pressure.

In Figures 3, the results for the case of liquid water layer, we find two peaks caused by the sound resonance for Figure 3(a). Meanwhile, for Figure 3(b), we can identify only one peak near L_1=1.03 mm as the resonance point because of the noise around L_1=0.17 mm. The maximum amplitudes of second harmonics for Figures 3(a) and 3(b) are comparable. In the measurement for atmospheric pressure, we can find the oscillation of water surface at the resonance point and it weakens with decreasing pressure. Therefore, we suppose the oscillation of water surface affects the output amplitude.

CONCLUSION

For the determination of the evaporation coefficient of methanol in an equilibrium state, we have proposed the evaporation coefficient measurement method using sound wave near the equilibrium state. From the results measured in the atmospheric pressure and 0.5 atm, when the distance L is equal to the integral multiple of half wavelength, the sound resonance occurs in the vapor space and the harmonic components are excited. Even for the case of liquid water layer, the effect of sound resonance, i.e. increase in amplitude of the second harmonics, is actually measurable, although it significantly decreases compared with the case for the solid wall. Therefore, we conclude that our method using sound resonance and second harmonics is effective for the measurement of evaporation coefficient.

REFERENCES

1. Ishiyama, T., Yano, T. and Fujikawa, S., Molecular dynamics study of kinetic boundary condition at an interface between a polyatomic vapor and its condensed phase, *Phys. Fluids*, Vol. 16, pp 4713-4726, 2004.
2. Kogan, M. N. and Nosik, V. I., Reflection of a sound wave by an evaporating surface, *Fluid Dynamics*, Vol. 23, pp 608-613, 1988.

EXPERIMENTAL MEASUREMENT OF THE INCIDENCE ANGLE DURING GAS BUBBLE GROWTH AND DETACHMENT

P. Di Marco

Department of Energetics "L.Poggi", University of Pisa, Pisa, Italy

ABSTRACT. A simple experimental apparatus was built to generate nitrogen bubbles in different fluids; high speed images of bubbles were processed via a dedicated software to obtain the main geometrical parameters, i.e. bubble volume, curvature radius at top and incidence angle. From these parameters, it was possible to evaluate the forces acting on the bubbles during quasi-static growth and detachment and compare them with theoretical predictions, to check the overall momentum balance. The agreement with theory was fairly good, although improvement in measurement of incidence angle should be sought.
Keywords: *gas bubble, bubble growth, bubble detachment, incidence angle, bubble momentum balance*

FOREWORD

The study of bubble detachment has interest not only *per se*, but it is mainly intended to open the way to the comprehension of more complex boiling phenomena, in which mass transfer and bubble dynamics play a determinant role. Experimental and theoretical works on this topic are also useful for the optimization of a wide class of industrial processes which involve mass and thermal exchange in bubbly flows. Although the problem of growth and detachment of a bubble in a still liquid can be stated exactly in terms of governing conservation equations, its complete solution is currently beyond our capabilities, even with numerical techniques, due to the variety and complexity of the involved momentum, heat and mass transfer phenomena. The first step is therefore limiting the attention to a simpler system, constituted by a single gas bubble detaching from a circular orifice in a still liquid, which can give useful information for the growth and detachment process. In this way, mass transfer phenomena are suppressed, and for a wide spectrum of conditions the bubble base is bounded to the orifice rim [1], [2], [3], giving a clear boundary condition for comparison with theory. The aim of the present paper is to compare the theoretical prediction of the forces acting on a detaching gas bubble, during its quasi-static growth and detachment, with their experimental evaluation. The conditions under which the detachment can be considered quasi static are discussed in the following section.

MOMENTUM BALANCE ON A GROWING AND DETACHING BUBBLE

Consider a growing gas bubble stemming from an orifice A_o, delimited by a contact line *CL*, with no mass transfer at the surface, but through the inlet orifice (Fig.1). The overall momentum balance on a control volume surrounding the bubble, bounded by the liquid side of the vapor-liquid interface, *S*, and by the gas side of the orifice A_o, can be written in a very general way as

$$\frac{\mathrm{d}}{\mathrm{d}\,t}\int_V \rho_g\,\mathbf{v}_g\,\mathrm{d}V = \int_{CL}\sigma_{fg}\mathbf{t}_{fg}\,\mathrm{d}L + \int_V \rho_g\,\mathbf{g}\,\mathrm{d}V + \\ + \int_S\left[\underline{\underline{\mathbf{T}}}_{v,f} - p_f\,\underline{\underline{\mathbf{I}}}\right]\cdot\mathbf{n}\;\mathrm{d}S + \int_{A_o}\left[\underline{\underline{\mathbf{T}}}_{v,g} - p_g\,\underline{\underline{\mathbf{I}}} + \rho\mathbf{v}_g\,\mathbf{v}_g\right]\cdot\mathbf{n}\;\mathrm{d}A \tag{1}$$

* Corresponding author: Paolo Di Marco
Phone: + (39)-050-2217107, Fax: + (39)-050-2217150
E-mail address: p.dimarco@ing.unipi.it

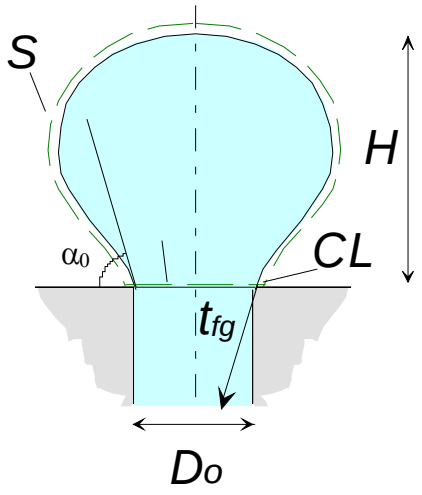

Figure 1. Application of momentum balance on a growing bubble.

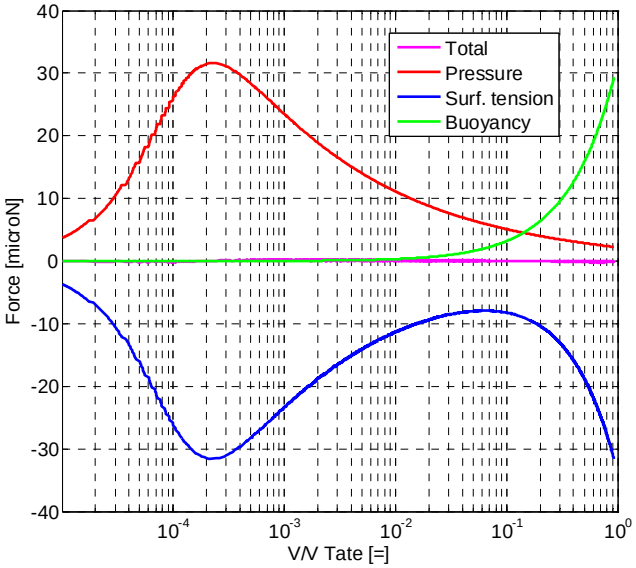

Figure 2. Theoretical force balance for a growing bubble (water properties).

Where, **n** and **t** are the normal outward and tangent (in the meridian plane) unit vectors, respectively, p is the pressure, **v** is the velocity, **g** is the gravity acceleration, $\underline{\underline{\mathbf{T}}}_v$ is the viscous stress tensor, σ is the surface tension. The suffixes g, f are referred to gas, and liquid, respectively. The inertial term in LHS is generally negligible, as only the inertia of the gas has to be taken into account here. Dynamical effects (including the surrounding liquid inertia) are accounted for in the normal and tangential stress distribution around the bubble, which must be evaluated taking into consideration the surrounding fluid motion. Additional surface forces, like the electrical one, may be added to the RHS via an appropriate stress tensor [1].

Influence of dynamical effects on bubble growth

The momentum influx through the orifice gives a lifting force of the form

$$F_u = \int_{A_o} \rho_g \, \mathbf{v}_g (\mathbf{v}_g \cdot \mathbf{n}) \, dA = \beta \rho_g \frac{\pi D_o^2}{4} u_o^2 \tag{2}$$

where D_o the orifice diameter, u_0 the mean flow rate velocity and the parameter β depends upon the velocity profile in the inlet orifice. In particular, for a flat profile, β = 1 while for a parabolic one β = 4/3.

The Rayleigh-Plesset equation describes the pressure p_b inside a spherical bubble growing in a still liquid as

$$\frac{p_b - p_\infty}{\rho_f} = \frac{2\sigma}{\rho_f R_b} + \left[R_b \frac{d^2 R_b}{dt^2} + \frac{3}{2}\left(\frac{dR_b}{dt} \right)^2 \right] + \frac{4\mu_f}{\rho_f R_b} \frac{dR_b}{dt} \tag{3}$$

Although this is not exactly the case of a bubble growing at the wall, an order-of-magnitude estimate of the viscous and inertial contributions to bubble growth may be obtained as the second and third tem in the RHS. In case of constant volumic growth rate, that is

$$Q = \pi D_b^2 \frac{dR_b}{dt} = \text{const} \tag{4}$$

the three dynamic contributions in equations (2) and (3), can be easily evaluated and scaled to the surface tension force, $\pi \sigma D_o$. After some manipulation [1], according to this approach, inlet momentum, inertia and viscous effects are expected to become important when, respectively

$$Eo\,Fr\,\frac{\rho_g}{\rho_f-\rho_g}\gg 1 \quad , \quad Eo^2\,Fr\left(\frac{R_o}{R_b}\right)^3\gg 1 \quad , \quad Ca\left(\frac{R_o}{R_b}\right)^2\gg 1 \tag{5}$$

Where Eötvos, Froude and capillary numbers are defined in the Nomenclature. It is worth noting that both inertial and viscous effects result more significant when the bubble radius is of the same order of magnitude as the orifice radius, i.e. in the early stage of bubble growth. In particular, the second of equations (5) justifies the use of the parameter $Fr^{0.5}\,Eo$, introduced by Tsuge [4] to distinguish static and dynamic regimes of detachment.

Quasi-static bubble detachment

Neglecting momentum, viscous and inertial terms, the integration of the *z*-component (**j** unit vector) of equation (1) can be put as a balance of buoyancy, internal overpressure, and surface tension forces, respectively

$$V(\rho_f-\rho_g)g+\frac{\pi D_o^2}{4}\left(\frac{2\sigma}{R_0}-\rho_f g H\right) = \pi D_o \sigma \sin\alpha_0 \tag{6}$$

where V is the bubble volume, R_0 the radius of curvature at bubble apex, and H the bubble apex height over the orifice. This balance must hold at any stage of bubble growth, by means of an adjustment of the incidence angle α_0 at the orifice rim. Bubble detachment occurs when, further to a volume increase, it is no longer possible to fulfill it. The equation above shows the importance of the incidence angle α_0 in the phenomenon, which determines the amount of the force keeping the bubble attached to the orifice. The term "incidence angle" is intentionally used here in place of "contact angle" to stress the fact that, for a bubble growing on a sharp orifice rim, it may assume a range of values and it is not determined uniquely by a surface tension balance, as in the Young equation. It is clear that the surface tension force has a maximum when the incidence angle is 90°.

It is well known that the shape of a static liquid-gas interface is ruled by the capillary equation [1]:

$$\sigma\left(\frac{1}{R_1}+\frac{1}{R_2}\right)=\frac{2\sigma}{R_0}-(\rho_f-\rho_g)\,g\,y \tag{7}$$

From equation (7) it cam be seen that in the absence of other stresses, the gravitational head is responsible of deviation of the bubble from spherical shape. Starting from Bashfort and Adams in 1892 [5], equation (7) has been integrated numerically with a variety of methods: among the others, in [2], [6], [7], [8], [9], [10], [11], [12]. Detachment of the bubble occurs for the maximum volume compliant with the boundary condition at the orifice [11].

One may wonder about the coherence between the force and capillary approaches. In fact, when capillary equation is solved and the related forces, as in equation (6), are derived from the profile shape, it can be checked that the force equilibrium holds at any stage of the bubble growth, as shown in Figure 2 [1]. Furthermore, it can be noted that initially, for small bubble volume the growth is essentially ruled by a balance of surface tension and overpressure; later on, as the volume increases, the balance is mainly between surface tension and buoyancy, with overpressure playing a reduced but still significant role.

Traditionally, the occurrence of bubble detachment has been considered a tradeoff between buoyancy and surface tension forces. This approach has been extensively credited either to Fritz [7] or Tate [14] although, actually, the related derivation does not appear in their papers. By balancing the two forces, the so-called Tate's detachment volume is obtained:

$$V_T = \frac{\pi D_o \sigma}{(\rho_f-\rho_g)g} \tag{8}$$

In the following paragraph it will be shown that Tate's volume is rather a close approximation of real detachment volume.

Departure volume and detachment volume

According to the preceding analysis, bubble detachment volume may differ from Tate's one, equation (8), for the following two reasons.

- The internal overpressure force gives an additional contribution: this is demonstrated by an elaboration like Figure 2, where it can be noted that all the lines end for a value of $V/V_T = 0.928$. For all the cases considered here, the overpressure force has a lifting role and the departure volume of the bubble is always lower than Tate's one. The discrepancy is larger when the overpressure force is significant, that is for smaller bubbles. From equation (6), by putting $\alpha_0 = 90°$, the departure volume can be derived and scaled to Tate's one as

$$\frac{V_d}{V_T} = 1 - \frac{D_o}{2R_0} + Eo\frac{H}{4D_o} \tag{9}$$

- Once the bubble has departed from equilibrium, the pinch-off of its neck does not occur instantaneously. During the breakup phase, gas is still injected in the bubble, and hence a detached volume greater than the static prediction (but not necessarily greater than the Tate's one) results.

Further to these considerations, it seems appropriate to distinguish a "departure volume" from a "detaching volume", the second being larger than the former one. Wong et al. [10] pointed out that the neck contraction is very rapid and hence the viscous force comes into play, and estimated the pinch-off time of the bubble as

$$t_{p.o.} = 3.8\,\frac{\mu_f\, D_o}{\sigma} \tag{10}$$

which makes it particularly significant in viscous liquids. According to equation (10), the volume increment between departure and detachment, $\Delta V_{p.o.}$, can be scaled to the Tate's volume as

$$\frac{\Delta V_{p.o.}}{V_T} \cong Eo\ \ Ca \tag{11}$$

This is in agreement with Table 1 of [10], where this difference is deemed negligible for low values of *Eo* and *Ca*.

EXPERIMENTAL APPARATUS AND MEASUREMENTS

The experimental cell (Figure 2) consisted of a polycarbonate box of about 2.5 dm^3 volume, open to the atmosphere and monitored by a temperature sensor [11], [13]. A circular orifice (0.14±0.05 mm diameter) was drilled in a polished, flat brass plate 30x30 mm^2, laid horizontally inside it, and gas (nitrogen) was injected through it into the fluid. In order to check the influence of physical properties, four different working fluids were adopted, as detailed in Table 1. The level of the liquid above the plate was varied from a fluid to another in order to keep the hydraulic head constant and equal to 980 Pa (100 mm H_20). To control nitrogen mass flow, a digital mass flow controller (model El-Flow by Bronkhorst) was used: this device guaranteed a stable inlet mass flow (proportional to an input voltage) in the chamber below the orifice. The outlet flow rate from the orifice stabilized at the same value within some seconds. The apparatus was intended to work in a "constant flow" condition, which was achieved mainly by reducing the volume of the gas chamber under the orifice: in fact, the Hughes' parameter, has been calculated as $N_c \approx 10^{-4}$, and "constant flow" conditions are expected to hold until $N_c<1$ [15], [11]. Several consecutive tests were carried out by varying the gas flow rate and hence the bubble frequency and detachment volume.

Measurements and related uncertainties

During the experiments reported herein, measurements of bubble volume V_B was obtained by digital processing of video images taken with a high speed camera (Phantom V4.0 by Vision Research) at a frame rate up to 1500 fps and with a resolution of about 130 pixel/mm. After some attempts, back

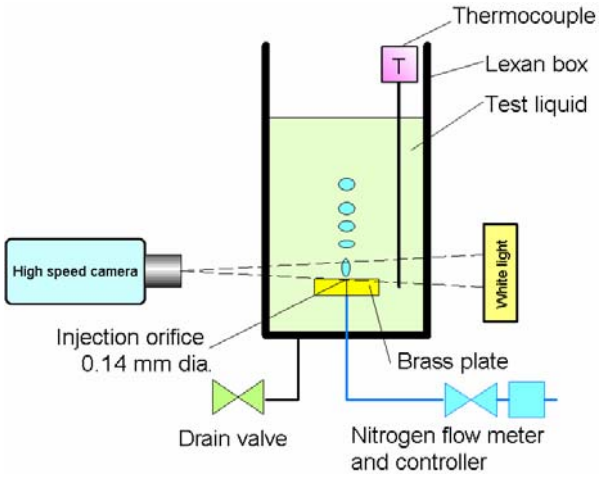

Figure 3. Experimental apparatus.

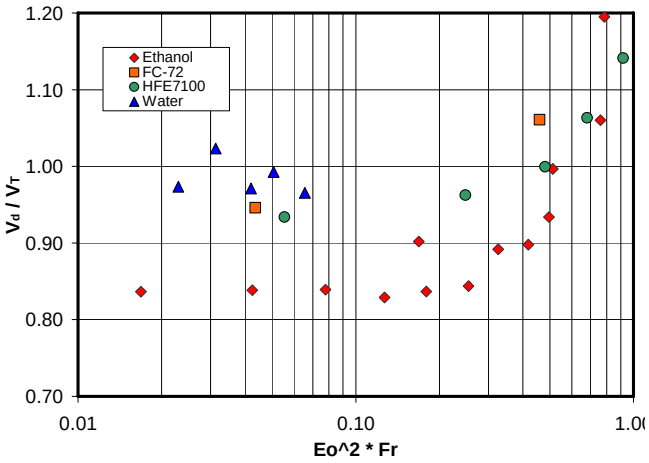

Figure 4. Bubble detachment volumes (scaled on Tate's value vs. $Eo^2\,Fr$.

Table1
Properties of the adopted fluids.

Fluid	Chemical formula	σ @ 20°C (N/m)	μ @ 20°C (mPas)	ρ_f @ 20°C (kg/m^3)	l_L (mm)	$\log_{10} Mo$
FC72	C_6F_{14}	0.012	0.68	1670	0.9	-9.1
Distilled water	H_2O	0.073	1	998	2.7	-10.6
Ethanol	C_2H_5OH	0.022	1.2	790	1.7	-8.6
HFE7100	$C_4F_9OCH_3$	0.014	0.57	1492	1.0	-9.6

illumination with a dc halogen lamp was selected. The digital processing software is based on Matlab "Image Acquisition" toolbox. At first, the region occupied by the bubble is identified by an edge detection routine. Then relevant properties of this region (number and coordinates of pixels, area center of gravity, principal axes of inertia and so on) are evaluated by Matlab's **`regionprops`** utility. It is assumed that the bubble is an axisymmetric body, with its axis inclined of an angle φ with respect to the vertical (φ is determined by image processing and is very close to 0° in any instance). The volume of each bubble is evaluated as

$$V_B = L_s^3 \sum_{j=1}^{N_H} 2\pi r_{p,j} \tag{12}$$

where $r_{p,j}$ is the distance (in pixels) of the pixel j of the bubble region from the symmetry axis, and L_s is the length scale, determined before each test by taking an image of a rod with marks at known distances. In this way, remarkably, no other assumption on bubble shape but axial symmetry is made. To check this assumption, the volume evaluation is performed separately on the N_H pixels on left and right side of the symmetry axis, the two values are compared and an error message is issued if the difference is greater than 1%. The resulting bubble volume is the average of the measured volumes over all the images of the bubbles taken after its detachment (typically 3 to 5 different bubbles, with 15-40 images for each of them). Notwithstanding in some cases the bubble exhibits relevant shape oscillations, in most of cases the sample standard deviation of the volume is less than 1%, and this is another proof of the adequacy of the method.

The volumic flow rate was also evaluated by digital processing of images, by measuring the volume of bubbles crossing a fixed line in the image over a certain time. This method provided more reliable and consistent values with respect to the output of the flow controller, although the agreement was generally good. The detachment period could be determined by counting the frames

intercurring between the passage of two consecutive bubbles across the same line. The period was averaged among 4 to 6 consecutive passages.
The coordinates of the bubble profile were also extracted and stored. From these, it was possible to determine the bubble curvature at its top, R_0, by fitting a quadratic interpolation in the band of the upper five pixels of the bubble. The incidence angle at orifice rim, α_0, was also evaluated by interpolating the bubble profile in the form.

$$r = \sum_{i=1}^{N} A_i \, y^i \tag{13}$$

where r is the bubble radius (from the symmetry axis) and y the height over the orifice, and taking the derivative for $y = 0$. After several attempts, a quadratic interpolation (N=2) over the lower 10 or 15 pixels of the bubble profile was selected as the better compromise between noise reduction and accuracy.

RESULTS AND DISCUSSION

Detachment volume

Bubble detachment volumes, scaled to Tate's one, are reported versus $Fr\ Eo^2$, in Figure 4. The bubble volume is nearly constant for $Fr\ Eo^2 < 0.2$, thus demonstrating that the dynamical effects are negligible in the range considered, according to the criterion in equation (5). It can be noted that , in quasi-static regime, detachment volumes are lower than the Tate's one.
The velocity of the center of gravity of the bubble is reported for some cases in Figure 5 versus the volume $V' = V/V_d$ (i.e., scaled on the departure volume predicted by equation (9)). it can be seen that the velocity increases for $V' > 1$: this seems to indicate that the bubble has started its detachment, departing from equilibrium.

Contact angle and curvature at bubble top

The measured values of the radius of curvature at bubble top, R_0, scaled on the Laplace length, $a = \{\sigma / [(\rho_f - \rho_g)\ g]\}^{0.5}$, are plotted versus dimensionless bubble volume in Figure 6, and compared with the theoretical prediction based on integration of the capillary equation: the agreement is quite good, and proves the validity of the adopted measurement technique.
In a similar way, the measured values of incidence angle are plotted versus dimensionless bubble volume in Figure 7, and compared with the theoretical prediction. The agreement, although qualitatively good, is less accurate in this case. It can be seen that generally the incidence angle is overestimated at small values of the bubble volume and underestimated for large bubble volume. This tendency is the same regardless of the degree of the interpolating polynomial and the chosen interpolation range over the bubble base. The reason for that is very probably the insufficient resolution of the region of the interface close to the orifice, where the incidence angle undergoes large variations.

Overall balance of forces

The overall force balance on the growing bubble, evaluated on the basis of experimental parameters, is reported for different fluids in Figures 8, 9 and 10. The results are qualitatively good, but are clearly affected by the inaccuracy in the measurement of the incidence angle. It is thus evident that a further improvement in the measurement techniques of the incidence angle, both in terms of optical resolution of the images and mathematical methods in digital processing, is necessary to accomplish a more accurate evaluation of the forces acting on a growing bubble in quasi-static regime.

CONCLUSIONS

The aim of the present paper is to compare theoretical consideration on quasi-static bubble growth with experimental measurements. Conditions in which the detachment can be considered quasi static are discussed in the paper, and a link was established between momentum balance and

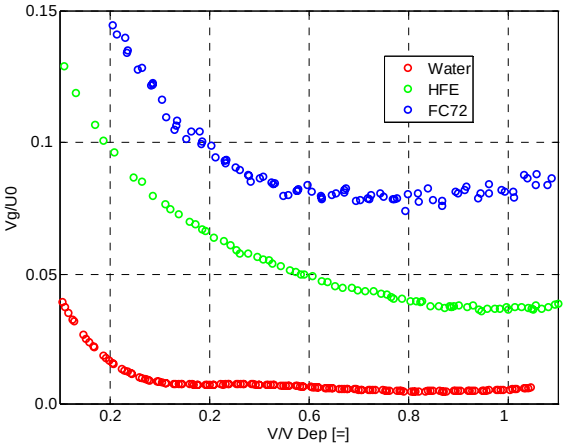

Figure 5. Velocity of center of gravity of the bubble (scaled on u_0) versus bubble volume, scaled on departure value, equation(9).

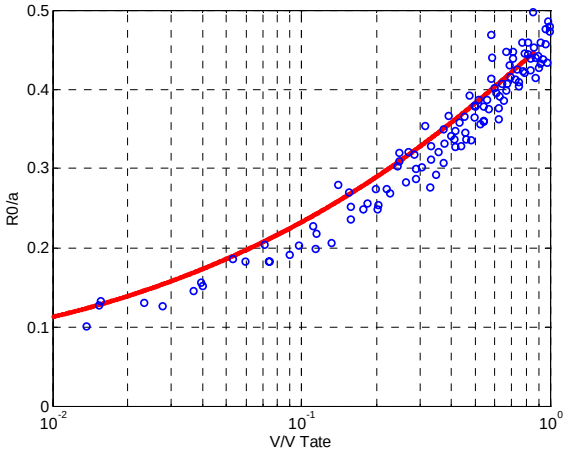

Figure 6. Measured dimensionless curvature radius versus dimensionless volume and comparison with theory (FC-72).

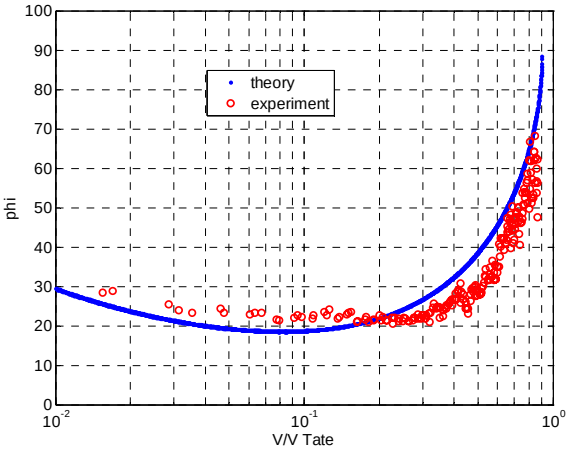

Figure 7. Measured incidence angle versus dimensionless volume and comparison with theory (Ethanol).

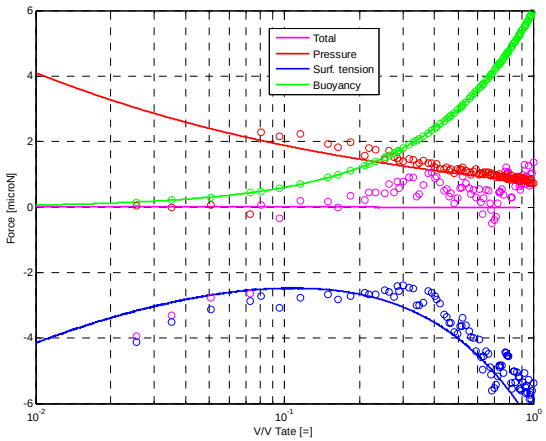

Figure 8. Experimental force balance for a growing bubble (symbols) and comparison with theory (lines) (HFE-7100).

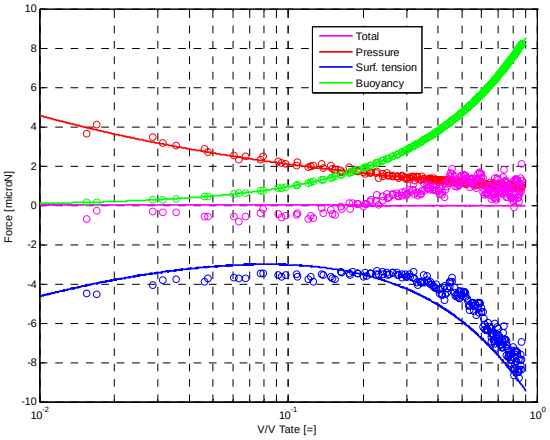

Figure 9. Experimental force balance for a growing bubble (symbols) and comparison with theory (lines) (Ethanol)

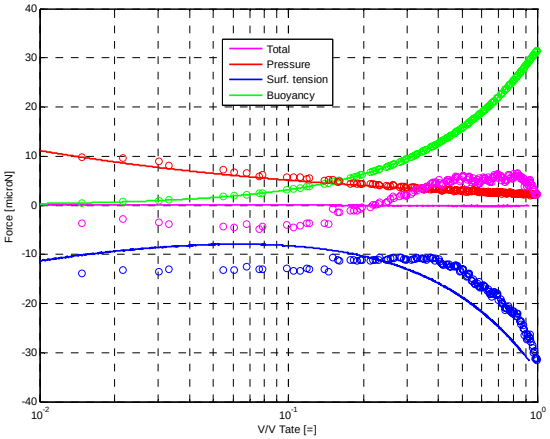

Figure 10. Experimental force balance for a growing bubble (symbols) and comparison with theory (lines) (Water)

capillary equation. A simple experimental apparatus was built to generate nitrogen bubbles in different fluids. Bubble images were taken with a high speed camera and processed via a dedicated software to obtain the main geometrical parameters, i.e. bubble volume, curvature radius at top and incidence angle. From these parameters, it was possible to evaluate the forces acting on the bubble to check the overall momentum balance during bubble growth. The experimental results show a generally good agreement with theory: the main source of discrepancy is the measurement of contact angle, whose measurement technique should be further improved

NOMENCLATURE

$Eo = \frac{\left(\rho_f - \rho_g\right) g\, D_o^2}{\sigma}$, Eötvos number $\qquad Fr = \frac{u_0^2}{g\, D_o}$, Froude number $\qquad Ca = \frac{\mu_f\, u_0^2}{\sigma}$, capillary number

ACKNOWLEDGEMENTS

Thanks are due to Roberto Manetti for the design and the assembling of the electronics of the test apparatus. Gianluca Memoli gave a fundamental contribution to the development of the image processing software; Andrea Cosentino and Antonello Cattide, collected and processed part of the experimental data.
This work has been partly funded by the European Space Agency (ESA, MAP AO99-45) and by the Italian Ministry of Research and Education (MIUR) under the grant PRIN 2002.

REFERENCES

[1] Di Marco P., Bubble growth and detachment: current status and future prospects, *HEAT 2008, Fifth International Conference on Transport Phenomena In Multiphase Systems*, June 30 - July 3, 2008, Bialystok, Poland, Invited Paper.

[2] Gerlach D., Bishwas G., Durst F., Kolobaric V., Quasi-static bubble formation on submerged orifices, *Int. J. Heat Mass Transfer*, 48, 2005, pp. 425-438.

[3] Dyson, D.C.., Contact line stability at edges: comments on Gibbs' inequalities, *Phys Fluids*, 31, 1988, pp. 229-232.

[4] Tsuge H., Hydrodynamics of Bubble Formation from Submerged Orifices, from *Encyclopedia of Fluid Mechanics*, Chap. 9, 1986, pp. 191-232.

[5] Bashforth F., Adams J.C., *An attempt to test the theory of capillary action*, Cambridge Un. Press, 1892.

[6] Longuet-Higgins M., Kerman B.R., Lunde K., The release of air bubbles from an underwater nozzle, *J. of Fluid Mech.*, 230, 1991, pp. 365-390.

[7] Fritz, W., Berechnung des maximalvolumes von dampfblasen, *Phys Z.* 36, 1935, pp.379-384.

[8] Pitts, E., The stability of pendent liquid drops. Part2. Axial symmetry, *J. of Fluid Mech.*, 63, 1974, pp. 487-508.

[9] Chesters A.K., An analytical solution for the profile and volume of a small drop or bubble symmetrical about a vertical axis, *J. of Fluid Mech.*, 81, 1977, pp. 609-624.

[10] Wong H, Rumschitzki D., Maldarelli C., Theory and experiment on the low-Reynolds-number expansion and contraction of a bubble pinned at a submerged tube tip, *J. Fluid Mech.*, 356, 1998, pp.93-124.

[11] Di Marco P., Forgione N., Grassi W., Quasi-static formation and detachment of gas bubbles at a submerged orifice: experiments, theoretical prediction and numerical calculations, *XXIII UIT National Heat Transfer Conference*, Parma, 20-22 Giugno 2005, pp.237-243.

[12] Oguz H.N., Prosperetti A., Dynamics of bubble growth and detachment from a needle, *J. Fluid Mech.*, 257, 1993, pp.111-145.

[13] Cosentino A., Di Marco P., Grassi W., Memoli G., Detachment of Nitrogen Bubbles in Various Fluids: Effects of Electric Field, *6th World Conference on Experimental Heat Transfer, Fluid Mechanics, and Thermodynamics*, Matsushima, Japan, April 17-21, 2005, (CD-ROM), paper 6-a-2, pp.1-7.

[14] Tate T., On the magnitude of a drop of liquid formed under different circumstances, *Phil. Mag. S.*, 27, 181, 1864, pp. 176-180.

[15] Hughes R.R, Handlos A.E, Evans H.D and Maycock R.L, Formation of bubbles at simple orifices, *Chem. Eng. Prog.*, 51, 1955, pp. 557-563.

CONJUGATE GRADIENT METHOD APPLIED TO INFRARED THERMOGRAPHIC DATA FOR THE INVERSE ESTIMATION OF THE CONVECTIVE HEAT TRANSFER COEFFICIENT

F. Bozzoli*, S. Rainieri and G. Pagliarini
Department of Industrial Engineering, University of Parma, Italy

ABSTRACT. The conjugate gradient method formulated with the adjoint problem is here employed to solve the 2-D Steady State linear Inverse Heat Conduction Problem with the aim of estimating the local convective heat transfer coefficient on a given surface by using the temperature distribution, acquired by an infrared acquisition system, as input data. This solution technique, already successfully adopted in literature for the Unsteady formulation of the Inverse Heat Conduction Problem, is here newly applied to state state tempertaure maps in order to restore the local heat transfer performance of a surface in a turbulent channel air flow by reconstructing the local energy balance in the wall.

Keywords: *Parameter Estimation, Inverse Problem, Infrared Thermography*

INTRODUCTION

In the estimation of the local convective heat transfer coefficient at the interface between a fluid and a given surface, it is mandatory to solve the Inverse Heat Conduction Problem (IHCP) in the solid domain. The well known difficulties involved in IHCPs stem primarily from the fact that they are often ill-posed and, consequently, very sensitive to small perturbations in the input data. A simple application of this approach consists in adopting the steady state temperature surface distribution as input data of the so called Steady State Inverse Heat Conduction Problem in which the unknown quantity is represented by the local heat transfer coefficient. A suitable experimental technique for this application is based on infrared thermography, which enables to acquire high spatially resolved temperature maps without disturbing the fluid layer adjacent to the wall.

A growing number of papers published in the open scientific literature report solution techniques of the Unsteady Inverse Heat Conduction Problem (UIHCP) while the Steady Inverse Heat Conduction Problem (SIHCP) has been less extensively investigated. Although it can be regarded as a special case of the UIHCP, some care is needed in the application of standard inverse solution strategies. In fact the elliptic nature of the partial difference equation, expressing the steady state local energy balance, makes the estimation procedure based on the solution of the SIHCP more complex, being the destructive effect of noise amplified by the necessity of estimating the wanted information from the signal Laplacian and not from the signal first temporal derivative, as it often happens in the classical formulation of the IHCP. The peculiar difficulties of the SIHCP in which the unknown is the spatial distribution of the heat transfer coefficient are mainly related to the high number of degrees of freedom of the problem, and therefore to the computational cost of the solution algorithm. This peculiarity makes most of the available solution strategies unfeasible.

A general approach, capable of recovering the local surface heat transfer coefficient in 2-D domains, is the one formulated by Rainieri and Pagliarini [1,2]. It is based on an iterative procedure aimed to the forced matching between experimental data and calculated data, derived by the solution of the corresponding direct problem. A more sophisticated methodology, based on the consecutive

* Corresponding author: F. Bozzoli
Phone: + (39)-0521-905859, Fax: + (39)-0521-905705
E-mail address: fabio.bozzoli@unipr.it

application of the Wiener filter on the raw infrared thermograhyic data has been successfully applied to the same problem [3]. The same steady state energy balance equation is instead solved directly by Ay et al. [4] by processing temperature distributions, acquired by infrared thermography, in order to recover both local and average heat transfer coefficient in a tube-and-fin assembly both in in-line and staggered arrangements. The authors perform a direct calculation of the discrete Laplacian of the temperature distribution without specifying the approach followed to handle the well-known ill-posed nature of the problem with regards to the estimation of the signal's second derivative.
To the Authors' knowledge no other inverse solution techniques have been applied to this problem, which can be regarded as a fundamental problem in the design of heat exchanger. In fact the heat transfer coefficient is the fundamental parameter which is likely unknown not only on some portions of the domain's boundary, as it is often assumed, but on the whole heat transfer surface.
The present investigation is intended to extend the study of this inverse problem by adopting the conjugate gradient method with adjoint problem formulation as solution method. This well known method [5] has been here newly applied to the two-dimensional SIHCP in which the unknown quantity is represented by the local distribution of the surface heat flux and then by the local convective coefficient, which is recovered by estimating the Laplacian of the experimental temperature maps acquired by means of an infrared thermographic system.

THE ESTIMATION PROCEDURE

Under the assumption of constant thermal properties, thin fin approximation and steady state condition, the local energy balance is expressed in Cartesian coordinates x,y by the following elliptic partial differential equation:

$$\frac{\partial^2 T(x,y)}{\partial x^2} + \frac{\partial^2 T(x,y)}{\partial y^2} = \frac{g(x,y)}{s \cdot \lambda} \quad , \qquad (x,y) \in D \tag{1}$$

where $g(x,y)$ is the arbitrarily distributed heat flux density over the domain D, s and λ the wall respectively thickness and thermal conductivity. By assuming a Dirichlet's condition on the domain's boundary, the partial differential equation is completed as follows:

$$T(x,y) = T_b(x,y) \quad , \quad (x,y) \in \partial D \tag{2}$$

In the inverse formulation here considered the heath flux distribution $g(x,y)$ is regarded as being unknown, while surface temperature is assumed to be known from experimental data. This condition is then expressed by the following constraint:

$$T(x,y) = \Theta(x,y) \quad , \qquad (x,y) \in \partial D \tag{3}$$

where $\Theta(x,y)$ is the measured temperature map. The extreme sensitivity of the governing equation to even small errors or noise in the input experimental data, makes the problem ill-conditioned and then ill-posed. The strategy here adopted to inversely estimate the unknown heat flux distribution $g(x,y)$ is the Conjugate Gradient Method (CGM) with the adjoint equation approach which represents a suitable solution strategy in problems involving many design variables and a limited number of cost function [6]. It is a gradient-based optimization procedure which, by using the steepest descent method firstly evaluates the search direction, the gradient of the objective function with respect to the design variables and, secondly, it searches iteratively in this direction the minimum of the performance function.
Under the adjoint equation approach, such minimization procedure requires the solution of auxiliary problems, known as the sensitivity and the adjoint problem. These equations are then solved

iteratively in order to minimize the objective function, represented by the error between the estimated and measured temperature distributions [5].The functional to be minimized in the problem under investigation is then:

$$J[g(x,y)] = \sum_{i=1}^{M} [T(X_i, Y_i) - \Theta(X_i, Y_i)]^2 \tag{4}$$

where matrix $T(X_i,Y_i)$ and $\Theta(X_i,Y_i)$ express respectively the estimated and measured temperature discrete map, having a total number of elements equals to M. The above equation can be suitably rewritten on the whole domain D as follows:

$$J[g(x,y)] = \iint_{(x,y)\in D} [T(x,y) - \Theta(x,y)]^2 \cdot \delta(x - X_i) \cdot \delta(y - Y_i) \cdot dxdy \tag{5}$$

where δ is the Dirac delta function. With the aim of estimating $g(x,y)$, the iterative procedure of the CGM is written as follows

$$g^{K+1}(x,y) = g^K - \beta^K q^K(x,y) \ , \quad K=0,1,2,\ldots \tag{6}$$

where β^k is the search step size at iteration K, and q^K is the direction of descent, obtained as a linear combination of the gradient direction with descent direction of the previous iterations. The step size β^k is determined minimizing the functional $J[g(x,y)]$ given by Eq. (5) with respect to β: after rearrangement, the following expression can be obtained for the search step size β^k

$$\beta^K = \frac{\int_{(x,y)\in D} \Delta T[q^K(x,y)] \cdot [T[g^K(x,y)] - \Theta(x,y)] \cdot \delta(x - X_i) \cdot \delta(y - Y_i) \cdot dxdy}{\int_{(x,y)\in D} [\Delta T[q^K(x,y)]]^2 \cdot \delta(x - X_i) \cdot \delta(y - Y_i) \cdot dxdy} \tag{7}$$

The calculation of $\Delta T[q^K(x,y)]$, representing the change in $T(x,y)$ with respect to a change in the heath flux distribution $g(x,y)=q^K(x,y)$, can be performed either by direct calculation of incremental ratios for each term, unfeasible in the present problem because of the high computational cost consequent to the high number of variables, or by solving the sensitivity problem:

$$\frac{\partial^2 \Delta T(x,y)}{\partial x^2} + \frac{\partial^2 \Delta T(x,y)}{\partial y^2} = \frac{\Delta g(x,y)}{s \cdot \lambda} \ , \quad (x,y) \in D \tag{8}$$

$$\Delta T(x,y) = 0 \ , \quad (x,y) \in \partial D \tag{9}$$

In which $\Delta g(x,y)$ is set equal to $q^K(x,y)$ [4]. Considering equation (6), the direction of descent for the CGM can be written as:

$$q^o(x,y) = J'^o(x,y), \quad q^K(x,y) = J'^K(x,y) + \gamma^K q^{K-1}(x,y) \tag{10}$$

where $J'^K(x,y)$ is the gradient of the functional $J(g(x,y))$ and γ is the conjugation coefficient obtained as follows:

$$\gamma^0 = 0 \ , \ \gamma^K = \frac{\int_{(x,y)\in D} \left[J'^K(x,y)\right]^2 dxdy}{\int_{(x,y)\in D} \left[J'^{K-1}(x,y)\right]^2 dxdy} \qquad K=1,2,... \tag{11}$$

The convergence of above the above iterative procedure in minimizing the functional J is proved by Alifanov [5].
The calculation of the gradient $J'^K(x,y)$ of the functional $J[g(x,y)]$ to be minimized, under the adjoint equation approach, ends in the solution of a single direct problem.

$$2\cdot\left[\Theta(x,y)-T(x,y)\right] = \frac{\partial^2 J'(x,y)}{\partial x^2} + \frac{\partial^2 J'(x,y)}{\partial y^2} \quad , \quad (x,y)\in D \tag{12}$$

$$J'(x,y) = 0 \ , \quad (x,y)\in \partial D \tag{13}$$

After developing the expressions for the search step size β^k and for the gradient direction, the iterative algorithm of the CGM can be implemented until a given stopping criterion is satisfied, as discussed in the following.
Since the experimental temperature data are inevitably affected by uncertainties the stopping criterion can be defined by adopting the approach formulated by Alifanov [5], named *discrepancy principle*. According to this principle, the inverse problem solution is regarded to be sufficiently accurate when the difference between estimated and measured temperatures is close to the standard deviation σ of the measurements. Thus the stopping criterion is as follows:

$$J\left[g^K(x,y)\right] = \sum_{i=1}^{M}\left[T(X_i,Y_i)-\Theta(X_i,Y_i)\right]^2 \cong M\cdot\sigma^2 \tag{14}$$

where M is the total numbers of experimental data. The direct, sensitivity and adjoint problems are here solved by adopting the finite-difference method implemented in Matlab® environment.
Once the heat flux density has been restored, the convective heat transfer coefficient distribution can be estimated by knowing the wall to fluid temperature difference, as follows:

$$h(x,y) = \frac{g(x,y)}{T(x,y)-T_f} \tag{15}$$

EXPERIMENTAL VALIDATION

The above described estimation technique has been applied to experimental data regarding a typical condition to be found in plate and fins heat exchangers, that is to the surface temperature distribution occurring on the wall of a plane channel which delimits a turbulent air flow. The experimental apparatus adopted consists of a closed-loop wind tunnel schematically shown in figure 1. In order to regulate the air temperature, the stream is forced, by a fan with adjustable output power, through a finned tube heat exchanger connected to a heat bath. It enters then into a settling chamber and then into a methyl methacrylate (Perspex®) channel, 2 m long and having a rectangular section with a width to height ratio of 10, where the test section is arranged. On one vertical wall of the Perspex channel, a window with a section of 300 mm×180 mm and fitted with a 3 mm thick aluminium plate, is placed.

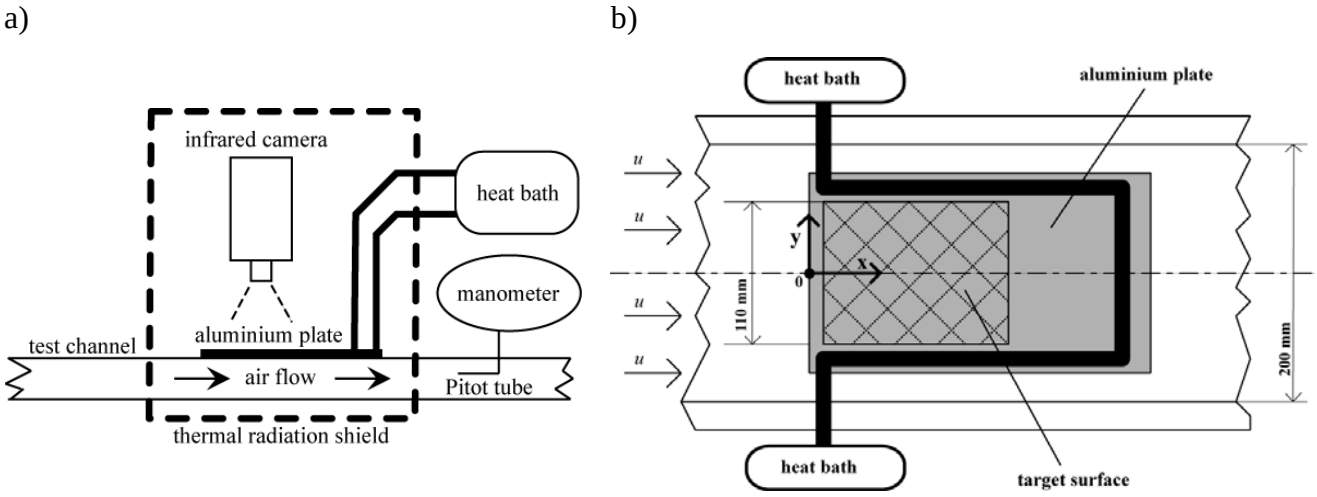

Figure 1. Scheme of the experimental apparatus

A particular attention has been paid to not creating surface geometrical discontinuities on the channel's wall on which the aluminium plate is fitted. The test section is located 1.20 m downstream the channel inlet section, in order to assure that a fully developed boundary layer is achieved for the whole Reynolds number range under investigation.
The temperature along three sides of the metallic fin is controlled by means of direct contact with a copper tube where a fluid coming from a circulator bath flows, as shown in figure 2.
The external surface of the metallic plate has been coated by a thin film of opaque paint with uniform and known emissivity. The surface temperature distribution has been acquired by means of an infrared thermographic system, namely the ThermoVision A20-M by Flir Systems.
By adopting Focal Plane Array Technology, it measures the energy emitted by the object surface by means of 180x120 microbolometer sensors matrix, active in the wavelength range 7.5-13 μm. The sensitivity reported by the instrument manufacturer is 0.12 K at 303 K, while the stated accuracy is ± 2 K. The instrument performance, declared by the manufacturer, can be significantly enhanced, in relation to the aim of restoring the Laplacian of the surface temperature distribution, by adopting the optimal data acquisition and data processing methodology addressed in [7].
The mean inlet and outlet air temperature is measured with a precision of 0.1 K by means of type-K thermocouples connected to a precision HP multimeter, model 3458A.
A Pitot tube, fitted in the downstream end of the test section and connected to a micro-manometer Kimo, model MP120, having a 3mm external diameter, has been used to measure the fully developed air flow velocity profile in the test channel.
The whole experimental equipment has been shielded by using black curtains in order to limit the effects of uncontrollable radiation coming from the surroundings.

RESULTS AND CONCLUSIONS

The investigation has been performed by heating the aluminium plate on the frame and considering two different stream air velocity values. The corresponding Reynolds number values, together with the corresponding stream and average surface temperature values are reported in Table 1.
Figure 2 reports the experimental temperature map obtained for the representative case corresponding to the highest velocity value. The inevitable presence of noise makes the direct calculation of its Laplacian unfeasible, by making necessary the inverse solution approach.

Table 1
Test conditions

Test	u (m/s)	Re	T_f (K)	$\overline{T(K)}$
1	10.7	$24 \cdot 10^3$	295.4	318.1
2	17.6	$40 \cdot 10^3$	295.4	316.0

In the present investigation the local heat flux density, and then the heat transfer coefficient distribution on the surface have been restored by adopting the conjugate gradient method with the adjoint problem formulation previously described. In particular, the convective heat transfer coefficient has been estimated by subtracting from the total heat flux density the heat exchanged by radiation and by natural convection evaluated under the assumption of grey surface behaviour for both the internal and external surfaces and of free convection laminar boundary layer for the external side.

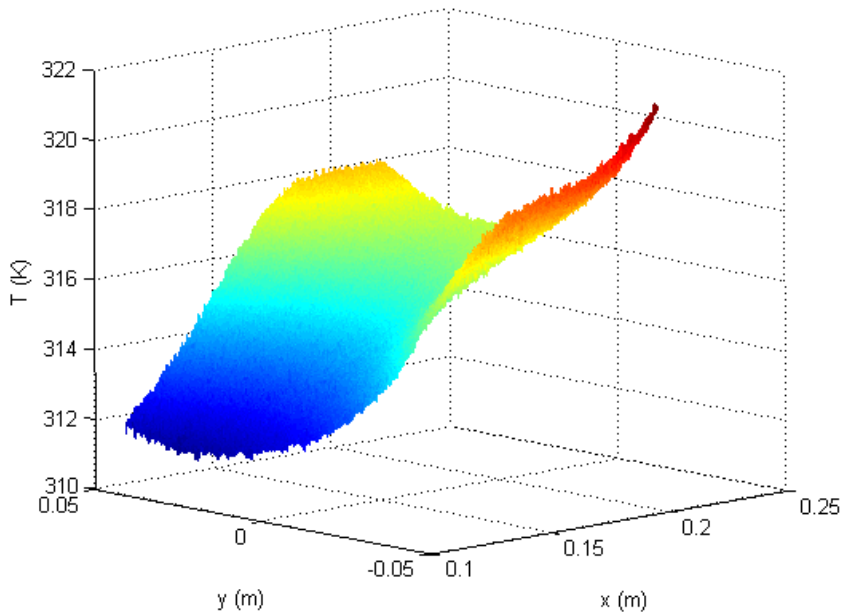

Figure 2. Experimental temperature map for u=10.7 m/s

In the formulation of the stopping criterion based on the discrepancy principle, a data standard deviation of 0.1 K has been assumed. Figure 3 compares the raw temperature map and the restored function on the domain centreline which, as expected, results to be a smooth function, doubly differentiable, in which the experimental noise has been filtered out. Figure 4 shows the estimated convective heat transfer coefficient on the centreline of the aluminium plate versus the longitudinal coordinate for the two different air flow velocity values considered in the present investigation.
The classical method of Kline and McClintock [8] has been applied in order to estimate the uncertainty to be associated to the heat transfer coefficient values: the maximum value for the uncertainty on the local heat transfer coefficient results of ± 10%. Further considerations on the uncertainty of the above experimental apparatus and data processing technique are reported in [2].

The results are also compared to the values predicted by the Dittus-Böelter correlation, holding for the fully developed turbulent internal flow in which all the fluid properties have been evaluated at the inlet mean air temperature and in which the channel hydraulic diameter has been adopted as the characteristic length.

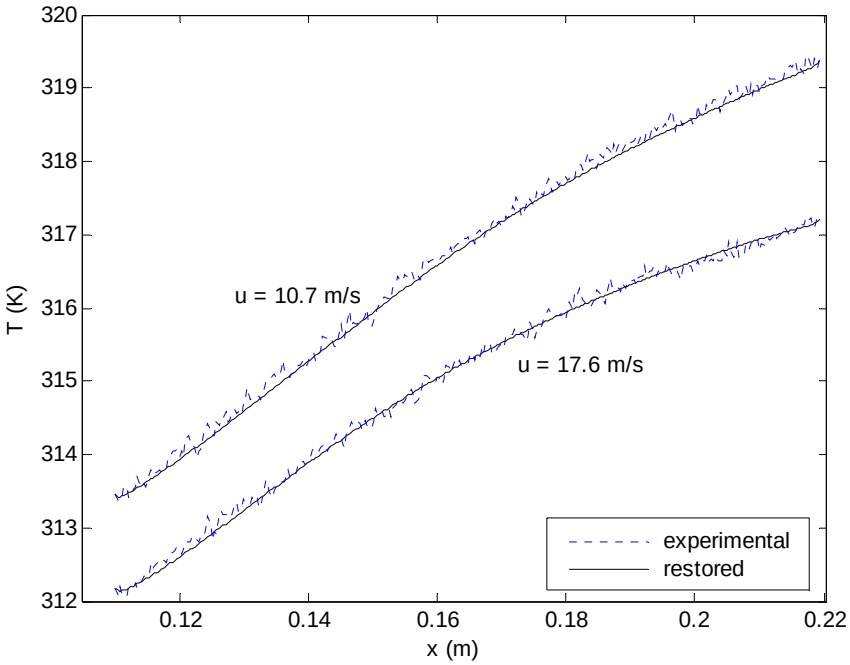

Figure 3. Experimental and restore temperature distributions on the centreline of the plate

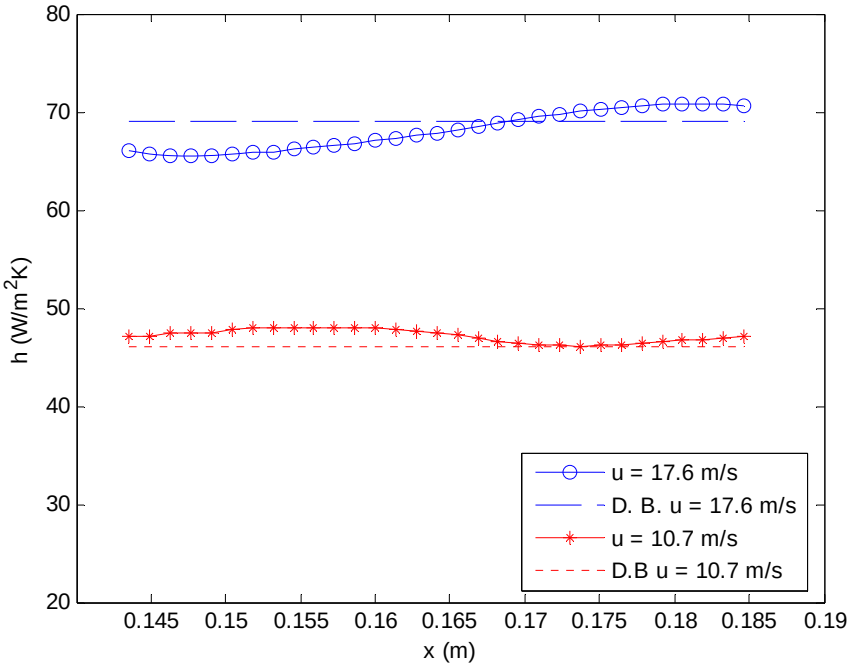

Figure 4. Experimental heat transfer coefficient on the centreline of the plate and comparison with the Dittus-Böelter correlation.

The good agreement between the reconstructed distribution of te convective heat transfer coefficient and the asymptotic fully developed values predicted by the Dittus-Böelter correlation confirms the

robustness of the Conjugate Gradient Method in the solution of the 2-D SIHCP characterized by a high number of degrees of freedom, that is in the inverse heat transfer problem aimed to the restoration of the convective heat transfer coefficient distribution. This approach provides then an effective strategy in the estimation of the heat transfer performance of a given surface by offering a useful tool in heat exchanger design.

NOMENCLATURE

D	Spatial domain	
g	Heat flux density	W/m^2
J	Performance function	K^2
M	Total number of sensors	
q	Direction of the descent	W/m^2
s	Thickness	m
T	Temperature	K
x,y,X,Y	Spatial coordinates	m
β	Search step size	
γ	Conjugate coefficient	
η	Lagrange multiplier	$m^2 \cdot K$
Θ	Measured temperature	K
λ	Thermal conductivity	$W/m \cdot K$
σ	Standard deviation	K

REFERENCES

1. Rainieri, S., Pagliarini, G., Estimation of Local Heat Transfer Coefficient in Corrugated Plates Intended for Fin and Tube Heat Exchanger, *Proc. 3rd European Thermal Sciences Conference*, vol. II, pp. 1095-1100, Heidelberg, 2000.
2. Rainieri, S., Bozzoli, F., Pagliarini, G., Effect of a Hydrophobic Coating on the Local Heat Transfer Coefficient in Forced Convection under Wet Conditions, *Exp. Heat Transfer*, in press.
3. Rainieri, S., Bozzoli, F., Pagliarini, G., Wiener Filtering Technique Applied to Thermographic Data Reduction Intended for the Estimation of Plate Fins Performance, *Exp. Therm. Fluid Sci.*, 28 Issue 2-3, pp. 179-183, 2004.
4. Ay, H., Jang, J., Yeh, J., Local heat transfer measurements of plate finned-tube heat exchangers by infrared thermography, *Int. J. Heat Mass Transf.,* 45, 4069-4078, 2002.
5. Alifanov, O.M., *Inverse heat Transfer Problems*, Springer-Verlag, New York, 1994.
6. Rainieri, S., Bozzoli, F., Pagliarini, G., Characterization of an Uncooled Infrared Thermographic System Suitable for the Solution of the 2-D Inverse Heat Conduction Problem, *Exp. Therm. Fluid Sci.*, vol. 32 Issue 8, pp. 1492-1498, 2008.
7. Park, H.M., Chung, O.Y., Comparison of various conjugate gradient methods for inverse heat transfer problems, *Chem. Eng. Comm.*, 176, 210-228, 1999.
8. Kline, S.J., McClintock, F.A., Describing uncertainties in single-sample experiments, *Mech. Eng.*, vol. 75, pp. 3–8, 1953.

HEAT TRANSFER AND FLOW CHARACTERISTICS AROUND FINNED TUBE BANK HEAT EXCHANGERS

H. Umekawa[1*], R. Honda, G. Kommoda and M.Ozawa[1*]
[1]Kansai University, Osaka, Japan

ABSTRACT. Fluidized-bed has high heat transfer performance which mainly caused by the particle convection. This particle convection is generated by the void movement, thus the visualization of the fluidized-bed is very useful mean to understand the heat transfer characteristics. In this investigation, simulated fluidized-bed heat exchanger with annulus fin was visualized by using the neutron radiography, and local and overall heat transfer characteristics were measured. This annuls fin also worked as the annulus obstacles of the particle movement, and it made clear the difference of the influence of the tube arrangement. As the result the staggered-arrangement took higher heat transfer performance than the in-line arrangement under low fluidized velocity, and the opposite tendency was observed under higher fluidized velocity. These tendencies could be explained by the bed-material movement well.

Keywords: *Fluidized-bed, Heat exchanger, Finned-tube banks, Heat transfer, Void fraction, Neutron radiography*

INTRODUCTION

Heat transfer characteristics of fluidized-bed heat-exchanger have been widely investigated so far[1-10], and the dominant heat transfer mechanism could be classified into three categories, i.e. solid convection, gas convection and radiation. Characteristics of these principal components depend on the particle size, and the solid convection is dominant in the particle size of the fluidized-bed heat exchanger.

The high heat transfer characteristics of solid convection is caused by the large specific surface of the particle, the large heat capacity of the particle, and the high mixing rate of particles. Thus to keep the high heat transfer ability as heat exchanger, continuous high exchange rate of the solid particle will be required. This characteristic, of course, is strongly influenced by the particle diameter, tube diameter, tube arrangement and fluidized velocity, etc.

Consequently, understanding of the solid movement around the heat exchanger is important to understand the fluidized bed heat exchanger. For this purpose, the movement of the individual solid has also been investigated so far [3,6,7]. As alternative approach, Author evaluated the void fraction characteristics around the fluidized-bed heat exchanger, and this manner based on the concept the solid movement is caused by the void fraction movement [8-10]. In this investigation, similar estimation has been done against the fluidized-bed heat exchanger with annulus fin.

EXPERIMENT

Experimental setup

* Corresponding author: Prof. H . Umekawa
Phone: + (81)-6-6368-0804, Fax: + (81)-6-6368-0804
E-mail address: umekawa@kansai-u.ac.jp

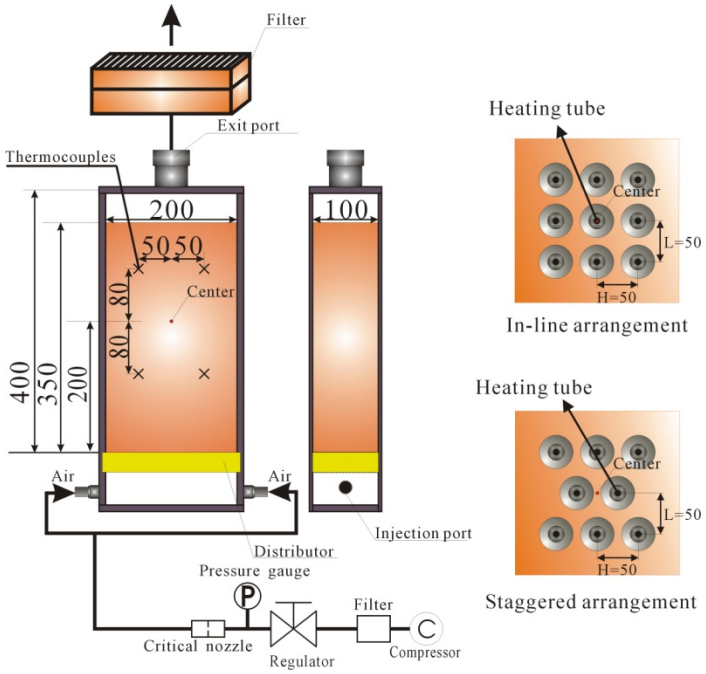

Figure 1 Experimental apparauts

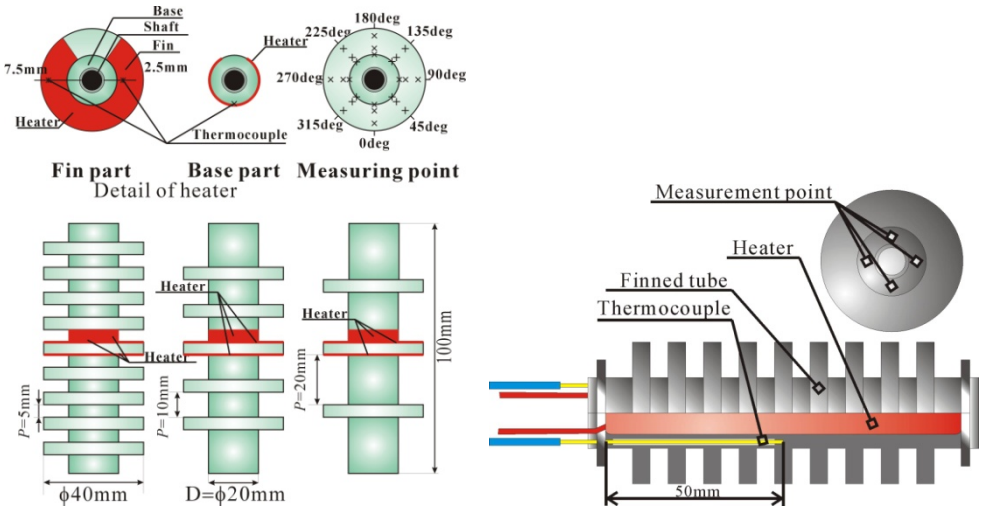

Figure 2 Detail of the fin-tube

The experimental setup, shown in Figure 1, is a slender rectangular fluidized-bed with inside dimensions of 200mm width, 400mm height and 100mm depth. The wall material of the test-section was aluminium which is transparent against the thermal neutron, and the bed material was silica sand (mean diameter 0.17mm, density 2555kg/m^3). The stagnant bed height is 350mm, and the minimum fluidization velocity J_{Gmf}=0.045m/s. The detail of the tube is shown in Figure 2, and the core tube diameter D=20mm. The thickness of the fin is 5mm and outer diameter of fin is 40mm, and fin pitches are 5mm, 10mm and 20mm, respectively. In the experiments, these tubes are arranged in staggered or in-line arrangements as shown in Figure 1, and the centre of these arrangements locate at 200mm height from the distributor plate. The horizontal pitch H/D=2.5, the lateral pitch L/D=2.5. Bulk temperatures of the fluidized-bed were measured at four points as shown in Figure 1 by using the Φ=1mm sheathed thermocouples (Type-K).

In this investigation, three kinds of the experiments, i.e. the visualization by neutron radiography, the measurements of the local heat transfer characteristics and the measurements of the overall heat transfer characteristics, were conducted. In the experiment of the neutron radiography and the

experiment of the overall heat transfer characteristics, fin-tubes were made of aluminium. In the case of the overall heat transfer characteristics, cartridge heater (Φ=20mm × 100mm) and four Type-K sheathed thermocouples(Φ=1mm) are inserted. For the experiment of the local heat transfer characteristics, fin-tube was made of acrylic resin, and the 3 μ m nichrome foil heater is pasted upon the surface. Nichrome foil was heated by Joule heating of A.C. power. Under the nichrome heater, three Type-K bare thermocouples (Φ=0.2mm, surface of core-tube, surface of fin (Δr=2.5, 7.5mm)) are equipped, and the heating tube was rotated every 45deg. Consequently, the number of measuring points around the heating surface becomes twenty-four locations as shown in Figure 2.
The fluidized gas was air supplied from the compressor through the oil filter and mist separator, was regulated by means of a critical flow nozzle. The volumetric gas flux J_G was set in the range of 0.04-0.18m/s (J_G/J_{Gmf}=1.0-4.0), and injected into the fluidized-bed through the distributor. After the test section, air ejected to the ambient through the HEPA filter.
The thermal neutron radiography system of JRR-3 in Japan Atomic Energy Agency (JAEA) was used for the visualization, and the image processing will be briefly described in the next section.

Image processing

Thermal neutron radiography is one of non-destructive inspection methods, and is quite similar to X-ray radiography. Owing to the difference of the attenuation characteristics, the neutron radiography is suitable for the visualization of fluidized-bed. In the case of this investigation, aluminium of test-section and silica sand are both transparent against the neutron radiography. Moreover the attenuation of the silica-sand is easily controlled by using the aqueous solution of gadolinium sulfate.
The visualization area of thermal neutron radiography system of JRR-3 is 220mmwidth and 250mm height, and the visualization image was recorded by using SIT-tube camera in video rate.
The visualization image can be expressed as next equation,

$$S_{(x,y,t)} = G_{(x,y)} \exp\left\{\rho_W \mu_W \delta_{W(x,y)} - \left[1-\varepsilon_{(x,y,t)}\right]\rho_S \mu_S \delta_S\right\} + O_{(x,y)} \tag{1}$$

and by using the image of the test section without fluidized bed material $S_{W(x,y)}$, fluidized-bed under static condition $S_{0(x,y)}$ and dark current image $O_{(x,y)}$, the void fraction can be estimated by using next equation.

$$1-\varepsilon_{(x,y,t)} = \frac{\log(S_{W(x,y)} - O_{(x,y)}) - \log(S_{(x,y,t)} - O_{(x,y)})}{\left[\log(S_{W(x,y)} - O_{(x,y)}) - \log(S_{0(x,y)} - O_{(x,y)})\right]\left(1-\varepsilon_{0(x,y)}\right)} \tag{2}$$

The error of the measurement accuracy of the void fraction is less than 10%, and more detail information of the visualization of the neutron radiography can be found elsewhere[8,9].

Flow pattern and void fraction distribution

The examples of the visualization results of void fraction are shown in Figure 3 as successive image. As shown in this figure, the void fraction movement is clearly obtained as the projection image. In the case of the staggered arrangement, the direction of the void movement is strongly controlled by the tube which located at the upstream position, and the void directly hits to the bottom of the tube which located at the downstream position. These movements of void in staggered arrangement can be observed under all gas volumetric flux conditions.
On the contrary, the movement of the void fraction in-line arrangements depends on the gas volumetric flux value. In the case of the low gas volumetric flux condition, the void simply rises up through the path between tubes. But, under high gas volumetric flux condition, inrush of void to the bottom of the tubes can be observed.

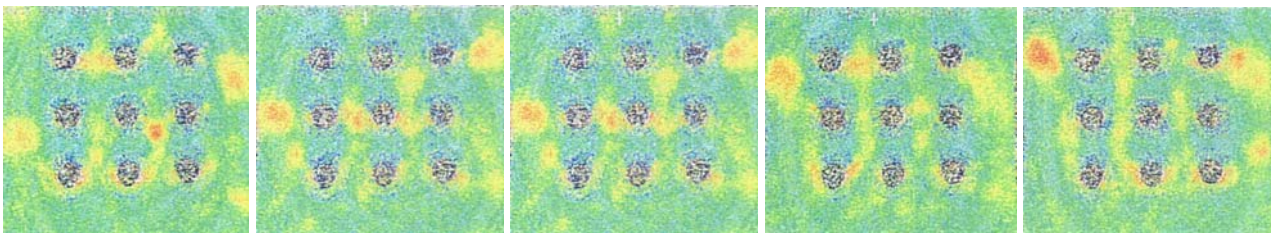

0/30s 2/30s 4/30s 6/30s 8/30s

(a) In-line arrangement J_G/J_{Gmf}=2

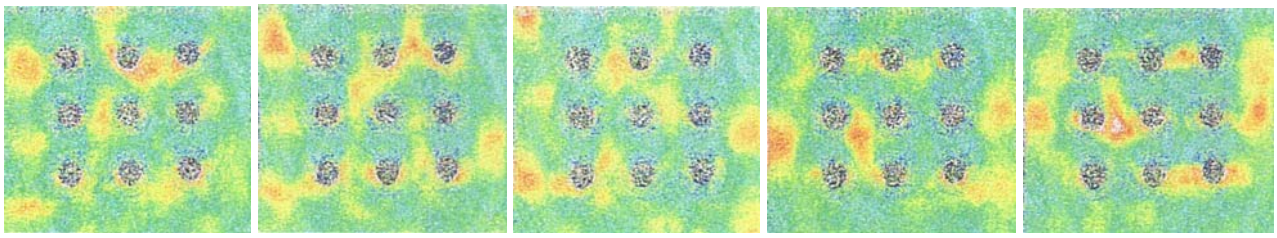

0/30s 2/30s 4/30s 6/30s 8/30s

(b) In-line arrangement J_G/J_{Gmf}=4

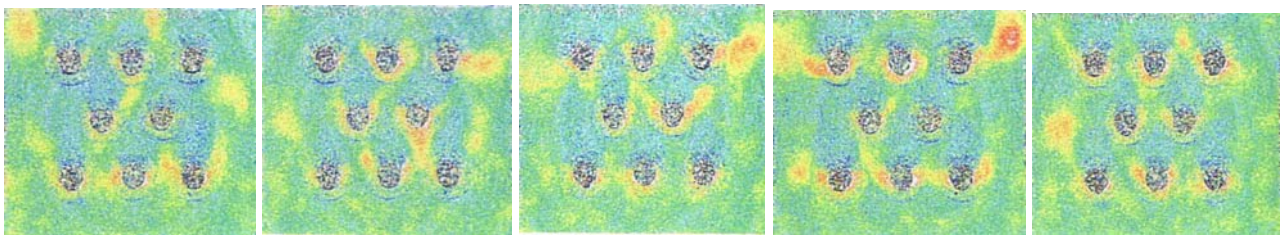

0/30s 2/30s 4/30s 6/30s 8/30s

(c) Staggered arrangement J_G/J_{Gmf}=2

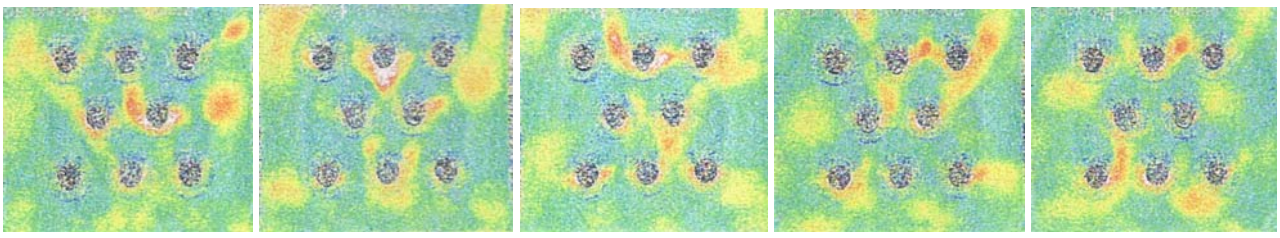

0/30s 2/30s 4/30s 6/30s 8/30s

(d) Staggered arrangement J_G/J_{Gmf}=4

Figure 3 Successive image of the void fraction movement (P=5mm)

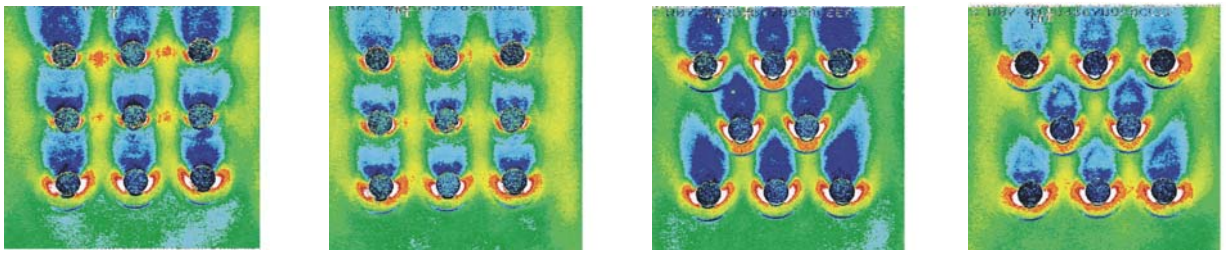

(a) J_G/J_{Gmf}=2 (b) J_G/J_{Gmf}=4 (c) J_G/J_{Gmf}=2 (d)J_G/J_{Gmf}=4

Staggered arrangement In-line arrangement

Figure 4 Time averaged void fraction image

These successive image, or video image, is useful to understand the movement of the void fraction, but

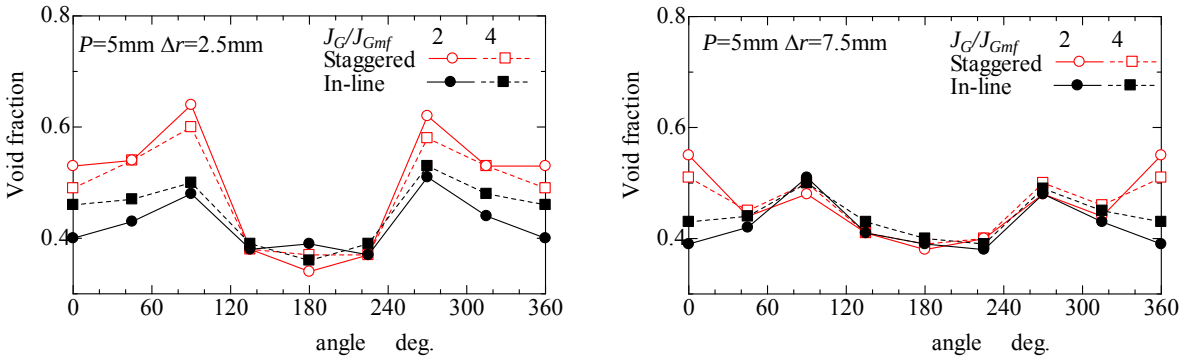

Figure 5 Void fraction along the circumferential direction

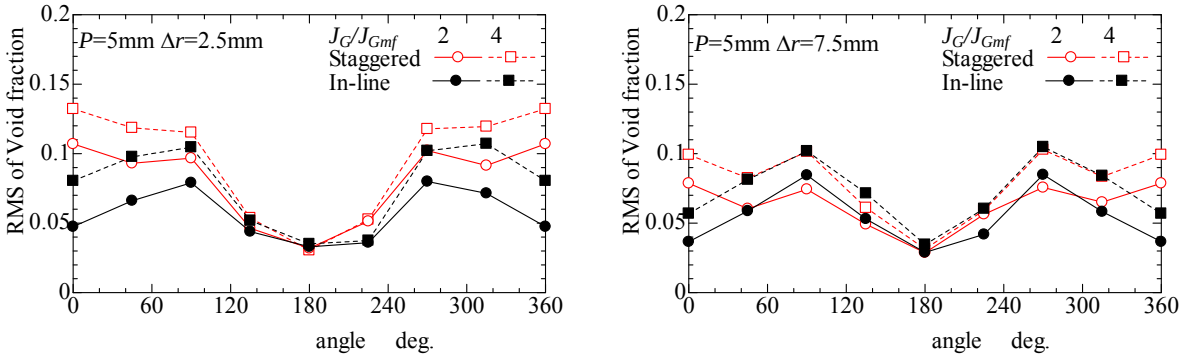

Figure 6 RMS of void fraction along the circumferential direction

it is difficult to use as the information of the heat exchanger design. To understand the flow characteristics of fluidized-bed heat exchanger in macroscopic view point, the time averaged images, "flow pattern", are calculated as Figure 4. These figures are the time averaged value among 20 seconds, and the flow characteristics which mentioned above can be perceived.

On the basis on these data, the void fraction profile along the circumferential direction and RMS of void fraction are plotted in Figure 5 and 6, respectively. An each estimated region of the data in Figures 5 and 6 was the area with dimensions of a.2mm×a.3mm at the temperature measuring point in Figure 2.

Firstly general tendency of void fraction and RMS will be explained.

At the top of the tube (180deg) the stagnant cap is constructed, and the void fraction takes the quite low value under all conditions. On the other side, the bottom of the tubes (0, 360 deg.) take the slightly high value which corresponds to the gas-packet. But, the peaks of the void fraction locate at the side (90, 270deg). It is because the void which hit the tubes is ejected to the side as clearly observed in Figure 4.

Similar profiles are also observed in RMS, and high RMS value means the frequently contact of void, and it may correspond to the intense movement of the bed material. These tendencies are common characteristics of this experiment, and next the detailed characteristics will be explained.

At the middle of the fin (Δr=7.5mm), influences of the tube arrangements and J_G/J_{Gmf} on void fraction can be observed at only the bottom part, but the influences of J_G/J_{Gmf} on RMS value are clearly observed. This means that the bubble frequency increases with the increase in J_G/J_{Gmf}, but the bubble passes through these locations. Thus the influence on the void fraction did not clearly appear, except the extremely high frequency part at the bottom.

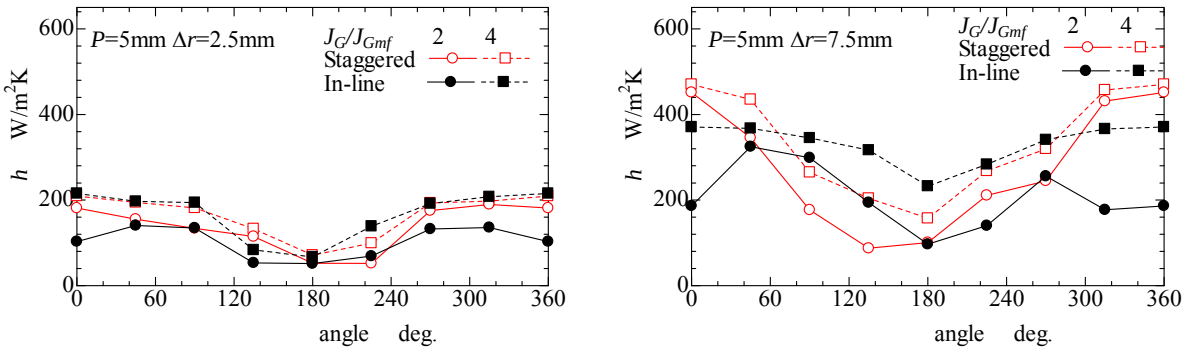

Figure 7 Local heat transfer coefficient

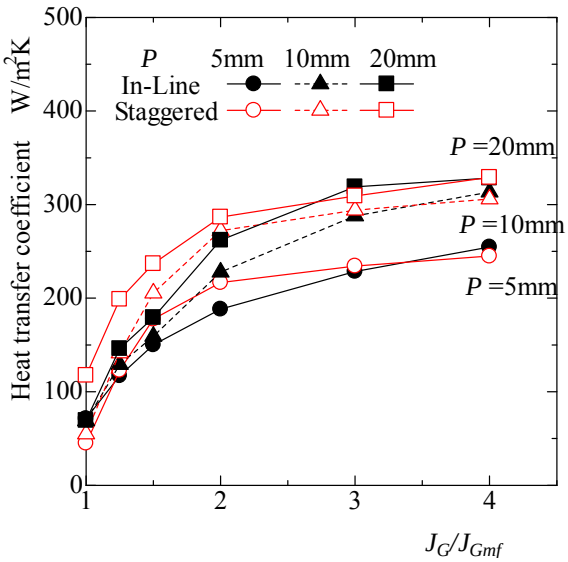

Figure 8 averaged heat transfer coefficient

At the adjacent region of the core tube (Δr=2.5mm), void fraction and RMS take the quite different tendency with the results of Δr=7.5mm. In this region, high void fraction is observed at the wide region of bottom part. Although the influence of the tube arrangement can be observed clearly in both figures of void fraction and RMS, the influence of the J_G/J_{Gmf} is not clear in the case of the void fraction of the staggered arrangement. The increasing of the void and RMS at the bottom of the tube is caused by the sliding of bubble along the core tube, and the weak influence of void fraction may mean the saturation of the void.

Heat transfer characteristics

Figure 7 is the local heat transfer coefficient at Δr=2.5mm and 7.5mm. These heat transfer coefficient characteristics can be roughly correlated with the void fraction and RMS except the data at J_G/J_{Gmf}=4 of in-line arrangement. Generally, high void fraction and high RMS value means the intense of the solid movement, thus the heat transfer coefficient at those locations become the high value.

The reason of that the heat transfer of Δr=2.5mm is roughly half of that of Δr=7.5mm can be considered as the results of the dilution of solid. On the contrary, the high heat transfer coefficient at Δr=7.5mm may be partially induced by drag of the wake by the void movement at Δr=2.5mm.

The heat transfer mechanism of the top of the tube at J_G/J_{Gmf}=4 of in-line arrangement may be caused by the different movement. On the basis on the visualization results, the stagnant cap causes the oscillatory movement with constant void fraction, and strong oscillation was especially observed in the case of the in-line arrangement. This oscillatory movement cause the mixing of the solid particle, thus the high heat transfer coefficient, but it cannot be detected by the void fraction or RMS.

Figure 8 is the overall heat transfer plotted against the J_G/J_{Gmf}. In this experimental range, heat transfer coefficient increases with the increase in J_G/J_{Gmf}, and decreasing tendency is not observed.
As shown in this figure, overall heat transfer coefficient of the staggered arrangement takes the higher value than that of the in-line arrangement. As the explanation of the local heat transfer coefficient, this difference is caused by the void movement induced by the influence of the upstream tubes. Under high J_G/J_{Gmf} condition, heat transfer coefficient of inline arrangement becomes slightly higher than that of the staggered arrangement owing to the difference of the particle movement at top of the tubes.
In this paper, the influence of the tube arrangement has been mainly explained. As final part of this paper, the influence of the fin pitch will be explained briefly. As shown in Figure 8, the strong deterioration of heat transfer coefficient can be observed in P=5mm compared with another fin pitches. Of cause this deterioration can be considered as the results of the restriction of the bed material caused by the annulus fin. But in the view point the heat transfer performance, P=5mm takes the highest value owing to the large heat transfer area.

CONCLUSION

In this paper, heat transfer characteristics and void fraction characteristics of fluidized-bed heat exchanger with annulus fin were experimental explained. In this investigation, simulated fluidized-bed heat exchanger with annulus fin was visualized by using the neutron radiography, and local and overall heat transfer characteristics were measured. This annuls fin also works as the annulus obstacles of the particle movement, and it makes clear the difference of influence of the tube arrangement. As the result the staggered-arrangement took higher heat transfer performance than in-line-arrangement under low fluidized velocity, and the opposite tendency was observed under higher fluidized velocity. These characteristics can be explained by the void movement characteristics well.

REFERENCES

1. Saxena, S.C., Grewal, N.S., Gabor, J.D., Zabrodsky, S.S. and Galsershtein, D.M., Heat Transfer between a Gas Fluidized Bed and Immersed Tubes, Advances in Heat Transfer, Vol.14, p.149-247, Academic Press, N.Y., 1978.
2. Saxena, S.C., Heat Transfer between Immersed Surface and Gas-Fluidized Beds, Advances in Heat Transfer, Vol.19, pp.97-190, Academic Press, N.Y., 1989.
3. Kim, S.W., Ahn, H.Y, Kim, S.D and Lee, D.H., Heat Transfer and Bubble Characteristics in a Fluidized Bed with Immersed Horizontal Tube Bundle, Int. J. Heat Mass Transf., Vol.46, pp.399-409, 2003.
4. Rasouli, S., Golriz, M.R. and Hamidi, A.A., Effect of Annular Fins on Heat Transfer of a Horizontal Immersed tube in Bubbling Fluidized Beds, Powder Tech., Vol. 154, pp.9-13, 2005.
5. Masoumaifard, N., Mostoufi, N., Hamidi, A. and Sothudeh-Gharebagh, R. Investigation of Heat Transfer Between a Horizontal Tube and Gas-solid Fluidized Bed, Int. J. Heat Fluid Flow, Vol. 29, pp.1504-1511, 2008.
6. Kurosaki, Y., Satoh, I. and Ishize, T., Mechanism of Heat Transfer Enhancement of Gas-Solid Fluidized Bed: Estimation of Direct Contact Heat Exchange from Heat Transfer Surface to Fluidized Particles using an Optical Visualization Technique, Trans. ASME, J. Heat Transfer, Vol.117 No.1, pp.104-112, 1995.
7. Miyamoto, M., Takahashi, K., Jin, R.J., Katoh, Y. and Kurima, J., Unsteady Heat Transfer and Particle Behaviour around a Horizontal Tube Bundle near an Expanded Bed Surface of a Gas Fluidized Bed: Conditional Sampling Statistical Analysis, Int. J. Heat Trasf., Vol.38, No.17, pp.3263-3273, 1995.
8. Ozawa, M., Umekawa, H., Matsuda, T., Takenaka, N. and Matsubayashi M., Flow Pattern and Heat Transfer in Tube Banks of a Simulated Fluidized-bed Heat Exchanger, JSME Int. J., Ser.B, Vol.41, No.3, pp.720-726, 1998.

9. Ozawa, M., Umekawa, H., Takenaka, N. and Matsubayashi, M., Quantitative Flow Visualization of Fluidized-bed under Normal- and Down-flow-mode Operations by Neutron Radiography, Experiments in Fluids, Vol.28. pp.413-424, 2000.
10. Hondam R, Umekawa, H. and Ozawa, M, Heat Transfer and Flow Characteristics around a Finned-tube Bank Heat Exchanger in Fluidized Bed, Nuclear Instruments and Methods in Physics Research A, doi:19.1016/j.mima.2009.01.151(2009)

MEASUREMENT OF THERMAL CONDUCTIVITY AND THERMAL DIFFUSIVITY OF A FINE WIRE USING A T TYPE PROBE

J.L. Wang[1], M. Gu[1], G. P. Wu[2], X. Zhang[1, *]

[1] Key Laboratory for Thermal Science and Power Engineering of Ministry of Education, Department of Engineering Mechanics, Tsinghua University, Beijing 100084, China

[2] Institute of Coal Chemistry, Chinese Academy of Sciences, Taiyuan 030001, China

ABSTRACT. We describe a method and an experimental system to measure the thermal conductivity and the thermal diffusivity of a fine wire simultaneously by a T type probe. In T type probe, a short hot wire is subjected to both an alternating and a direct current, and a thermally infinite long test wire is attached to the midpoint of the hot wire with an interstitial material. Theoretical analysis shows that, the thermal effusivity of the test wire can be obtained when the hot wire is heated by an alternating current, and the thermal conductivity is determined by the conventional steady state method. The present method is tested by measuring a platinum wire at room temperature, our results agree well with the literature reported values.

Keywords: *T type probe, thermal conductivity, thermal diffusivity, thermal effusivity*

INTRODUCTIONS

Investigations of measurement techniques for thermophsical properties, including the thermal conductivity and thermal diffusivity, of solid materials are of great importance in relation to new material research, space technology and applications of solar energy. For wire specimen, a number of measurement techniques have been developed, including Ångström method [1], transient heating method [2], constant-rate heating method [3], self-heating 3ω method [4] and others [5, 6]. The first periodic temperature method to gain widespread acceptance was Ångström method to accurately determine the thermal diffusivity, where one end of the long rod was subjected to a periodic temperature as the boundary condition [1]. The self-heating 3ω method [4] was well developed to measure both thermal conductivity and thermal diffusivity of a metallic wire in low and high frequency range, respectively. However, it can not be applied to the nonmetallic wire, and the fit results have the frequency dependence [4].

The present authors developed a technique for the measurement of the thermal conductivity and thermal diffusivity of a fine wire, using a T type probe. The conventional steady state T type probe was introduced by Zhang *et al.* [7], to measure the thermal conductivity of fine wires. In the steady state T type probe, a short hot wire is subjected to a direct current, and the test wire, nonmetallic or metallic wire, is attached to the midpoint of the hot wire at one end using an interstitial material, with the other end connected to a heat sink to maintain a constant temperature. Then, the thermal conductivity of the test wire, λ_s, can be obtained by comparing the average temperature rise of the hot wire with and without the test wire.

* Corresponding author: Prof. X. Zhang
Phone: 0086-10-62772668, Fax: 0086-10-62781610
E-mail address: x-zhang@tsinghua.edu.cn

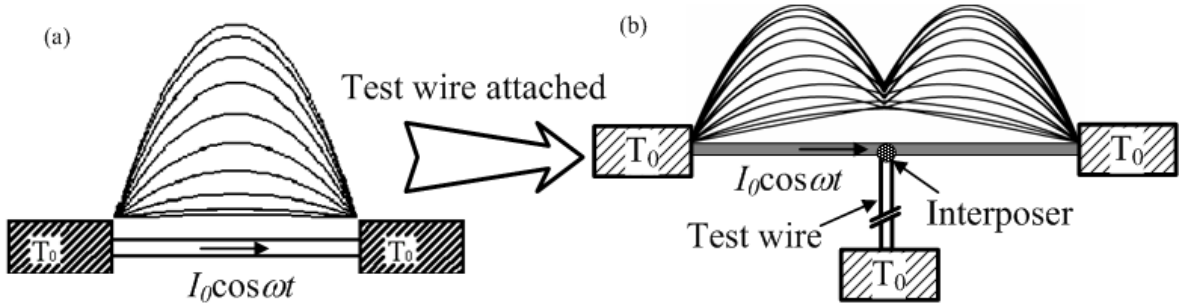

Figure 1. Principle for the present method to determine the thermal effusivity of a fine wire, (a) temperature distribution of the hot wire without test wire attached; and (b) that with the test wire.

To measure the thermal diffusivity, we apply an alternation current (ac) to the hot wire in the T type probe. If the thermal penetration depth [8], given by $4(\alpha_s/2\omega)^{1/2}$ (α_s is the thermal diffusivity of the test wire, ω the current angular frequency), in the test wire is much smaller than its length, the thermal effusivity, b_s, defined by $b_s=(\lambda\rho C_p)_s^{1/2}$ with the thermal conductivity λ, density ρ, and specific heat C_p, of the test wire can be obtained. Thus, the thermal diffusivity, α_s, is calculated by $\alpha_s=(\lambda/b)_s^2$.

MEASUREMENT PRINCIPLE

Figure 1(a) shows the temperature distribution of the hot metallic wire in the self-heating 3ω method, where an ac current, $I_0\cos(\omega t)$, was applied to the hot wire, which serves both as a thermometer and the heater. Neglecting the radial heat loss from convection or radiation, the heat conduction equation for the hot wire can be written as

$$\frac{1}{\alpha}\frac{\partial \Delta T}{\partial t}-\frac{\partial^2 \Delta T}{\partial x^2}+\frac{I_0^{\,2}R'}{\lambda l S}\cos^2(\omega t)\Delta T=\frac{I_0^{\,2}R}{\lambda l S}\cos^2(\omega t) \tag{1}$$

where ΔT is the temperature variation from the initial temperature, $\Delta T=T-T_0$, R' is the temperature coefficient of electrical resistance, R is the initial electrical resistance, λ is the TC of the hot wire with length l and cross section area S. If the heating power inhomogeneity caused by the resistance fluctuation is neglected, Lu *et al*. [4] gives exact solution using the impulse theorem. For this classical 3ω heating problem, only the steady transient temperature component needs to be concerned. The solution of equation (1) is in the form of $\Delta T(x)=\mathrm{Re}\{u(x)e^{i2\omega t}\}$, where Re denotes the "real part of ", i is the imaginary unit, and the complex temperature oscillation, $u(x)$, containing both the amplitude of the temperature oscillation and phase relative to the driving current, is expressed as

$$u(x)=\frac{I^2R}{lS\lambda\beta}\left[1-\frac{\cosh(\sqrt{\beta}x)}{\cosh(\sqrt{\beta}l/2)}\right] \tag{2}$$

Here, β is defined by $i2\omega/\alpha$, I is the root mean square (rms) value of I_0. As a sequence, the average temperature oscillation of the hot wire is

$$\bar{u}=\frac{I^2R}{lS\lambda\beta}\left[1-\frac{2}{\sqrt{\beta}l}\tanh(\sqrt{\beta}l/2)\right] \tag{3}$$

As shown in Figure 1(b), one end of the test wire is contacted to the midpoint of the hot wire using an interstitial material (interposer), with the other end connecting to the heat sink. If an ac

current with relative higher frequency to keep the thermal penetration depth shorter than the test wire, the temperature distribution along the test wire can be written as

$$\frac{1}{\alpha_s}\frac{\partial \Delta T_s}{\partial t} - \frac{\partial^2 \Delta T_s}{\partial x^2} = 0 \tag{4}$$

In this quasi steady state experiment, the thermal impedance of the interposer at the junction is assumed to be equivalent to the thermal contact resistance multiplying a ratio function, f. Taken into the account of the thermal impedance at the junction between the hot wire and the test sample, the boundary condition at the junction is

$$\frac{\Delta T\left(x = l/2\right) - \Delta T_s(x_s = 0)}{fR_r} = -\left(\lambda S\right)_s \left.\frac{\partial\left(\Delta T_s\right)}{\partial x_s}\right|_{x_s=0}$$

$$2\lambda S \left.\frac{\partial\left(\Delta T\right)}{\partial x}\right|_{x=\frac{l}{2}} = \left(\lambda S\right)_s \left.\frac{\partial\left(\Delta T_s\right)}{\partial x_s}\right|_{x_s=0}$$

As a consequence, the average temperature oscillation of the hot wire with the test wire attached is obtained as

$$\bar{u} = \frac{I^2 R}{\lambda S \beta l} + \frac{2I^2 R}{\lambda S \beta^{3/2} l^2}\left\{e^{-\sqrt{\beta} l/2} - 1 - \left[\cosh(\sqrt{\beta} l/2) - 1\right] \times \frac{b_s S_s\left(1 - e^{-\sqrt{\beta} l/2}\right) + 2bSe^{-\sqrt{\beta} l/2}\left(1 + \sqrt{i2\omega} b_s S_s f R_r\right)}{b_s S_s \sinh(\sqrt{\beta} l/2) + 2bS\cosh(\sqrt{\beta} l/2)\left(1 + \sqrt{i2\omega} b_s S_s f R_r\right)}\right]\right\} \tag{5}$$

where b is the thermal effusivity of the hot wire, R_r is the thermal contact resistance at the junction, b_s is the thermal effusivity of the test wire with cross section S_s. Compared with the average temperature oscillation of the bare hot wire using equation (3), equation (5) introduces two unknown parameters: thermal impedance, fR_r, indicating the influence of the interposer; and the thermal effusivity multiplying across area of the test wire, $(bS)_s$.

As long as the average temperature oscillation is obtained, the third harmonic voltage (rms value) across the hot wire with and without the test wire can both be calculated by

$$V_3 = \frac{1}{2} I R' A B S\{\bar{u}\} \tag{6}$$

by substituting equation (3) and equation (5) into equation (6), respectively. For bare hot wire, the result from equation (3) is consistent with that of Lu *et al*. [4], but in another expression.

As in the steady state T type probe, the thermal effusivity measurement also proceeds in two steps: The thermal properties of the hot wire is calibrated using the self-heating 3ω method, by fitting the experimental data using equations (3) and (6), the thermal conductivity and thermal diffusivity are simultaneously obtained. Thus, the thermal effusivity of the hot wire is derived from:

$$b = \frac{\lambda}{\sqrt{\alpha}} \tag{7}$$

In the next step, the test wire is attached to the midpoint of the hot wire [as shown in Figure 1(b)], and the third harmonic voltages across the hot wire are measured again. By fitting the data to equations (5) and (6), the thermal effusivity of the test wire can be obtained.

THERMAL IMPEDANCE OF THE INTERPOSER

As in the previous discussion, the thermal impedance of the interposer at the junction in 3ω measurement is different from the steady state thermal contact resistance, which is taken to be the steady state thermal resistance multiplying a complex ratio function, f. The ratio function, which is

a function of the frequency, is introduced to take account for the effect of the geometrical and thermal properties of the interposer.

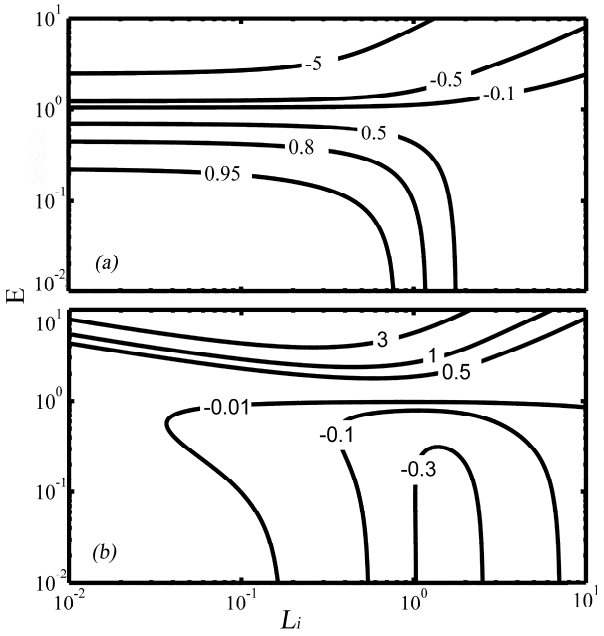

Figure 2. Ratio function, *f*, varies with dimensionless thickness L_i and dimensionless thermal effusivity multiplying cross area *E*, the values illustrated in plotted lines denote (a) the real part and (b) the imaginary part of the ratio function.

Theoretical analysis [9] shows that, *f* depends on two dimensionless ratios, including dimensionless thickness, L_i, i.e., the ratio of the idealized thickness of the interposer to its thermal penetration depth, and dimensionless thermal effusivity multiplying cross area, *E*, i.e., the ratio of the thermal effusivity multiplying cross area of the interposer to that of the test wire. Figure 2 shows the real part [Figure 2(a)] and imaginary part [Figure 2(b)] of the ratio function at various L_i and *E*. It is found that, when these two dimensionless ratios are much smaller than 1, the real part of *f* approaches to the limit of 1, and the corresponding imaginary part can be neglected, i.e., the thermal impedance of the interposer is equivalent to its thermal contact resistance. In the case of E>>1, *f* is a complex value, and the thermal characterization of the interposer is a function of frequency. In the case of E~1, the thermal impedance of the interposer can be ignored.

For the preliminary experiment in this study, platinum wire with diameter of about 100μm is used as the test wire. As a result, a small amount platinum black is used as the interposer. The platinum black, with purity over 99.9%, was manufactured by Ishifuku Metal Industry Corporation in Japan, the average grain diameter was about 0.5μm. A stable junction is formed when the platinum black is solidified, which can be easily washed off by ethanol. If the idealized interposer thickness is assumed to be 1 μm and has the thermal properties of platinum, the thermal penetration depth is calculated to be 5.6 to 17.8 mm with the corresponding heating frequency 1 to 0.1Hz. In such case, as shown in Figure 2, the ratio function, *f*, is taken to be a real number, and the thermal impedance of the interposer is so small that can be neglected.

EXPERIMENTAL TESTS

Replacing the commercial lock-in amplifier, a Labivew-based virtual lock-in is developed to measure the third harmonic voltages. The schematic of the experimental apparatus and the electrical

circuit is as shown in Figure 3. The experiment system consists of a function generator (Agilent 33220A), a series resistor (ZX74B), A/D board (PXI 5922), industrial computer (PXI 8106) and a homemade pre-amplifier. PXI 5922 can trade sampling rate for resolution to sample from 24 bits at rates of 500 kS/s to 16 bits at 15MS/s. Other than the third harmonic voltages of the hot wire, the virtual lock-in can simultaneously measure the first harmonic voltage across the series resistor to get the supplied current. Using the commercial lock-in amplifier, e.g., to measure 0.1Hz signal, the corresponding time-constant of 100s is needed, thus, it is tedious to get a single data out. Comparatively, the virtual lock-in simplifies the measurement to get rid of the time constant setting, and takes few minutes to get the stable voltage, even when current frequency is 0.1Hz.

In the measurements, platinum wire (purity over 99.98%) is used as the hot wire with about 30 μm in diameter and 8mm in length. With a precision resistance spot welder, both ends of the hot wire were welded to 1mm diameter copper leads, which are mounted on a homemade copper substrate. In order to insulate the copper leads and the substrate, each lead was first inserted into a ceramic tube, and the ceramic adhesive was used among the ceramic tubes, copper leads and the substrate. The substrate was then loaded into a vacuum chamber (Oxford Instrument, Optistat DN-V), which was continuously evacuated by a vacuum pump (R5614Y-Z, 1400 rpm) and a molecular pump (Leybold TW70H, 72000 rpm). All the measurements are carried out at a vacuum level of below 1×10^{-3}Pa, and the convection heat transfer could be neglected.

When the chamber temperature is stable (TC601, 0.1K), a very small direct current, such as 0.1mA, is supplied to the hot wire to get the initial electrical resistance, R, in equation (2). The steady state measurement system is detailed in [10]. Then, the third harmonic voltages of the hot wire are measured in the frequency range of 0.1 to 6Hz. The fitting procedure is performed using the least square method based on the relative error for the frequency dependent third harmonic voltages. By fitting the experimental data using equation (6) [substituting equation (3) into equation (6)], the thermophysical properties, including the thermal conductivity and thermal diffusivity, of the hot wire are obtained. Finally, the thermal effusivity is calculated using equation (7). After calibrating the metallic sensor, the test wire is attached to the midpoint of the hot wire with fine powder platinum black, and the third harmonic voltages of the hot wire are measured again. As for the bare hot wire, the fit results vary with the applied frequency range, therefore, the same frequency range is applied in the measurement when the test wire is attached.

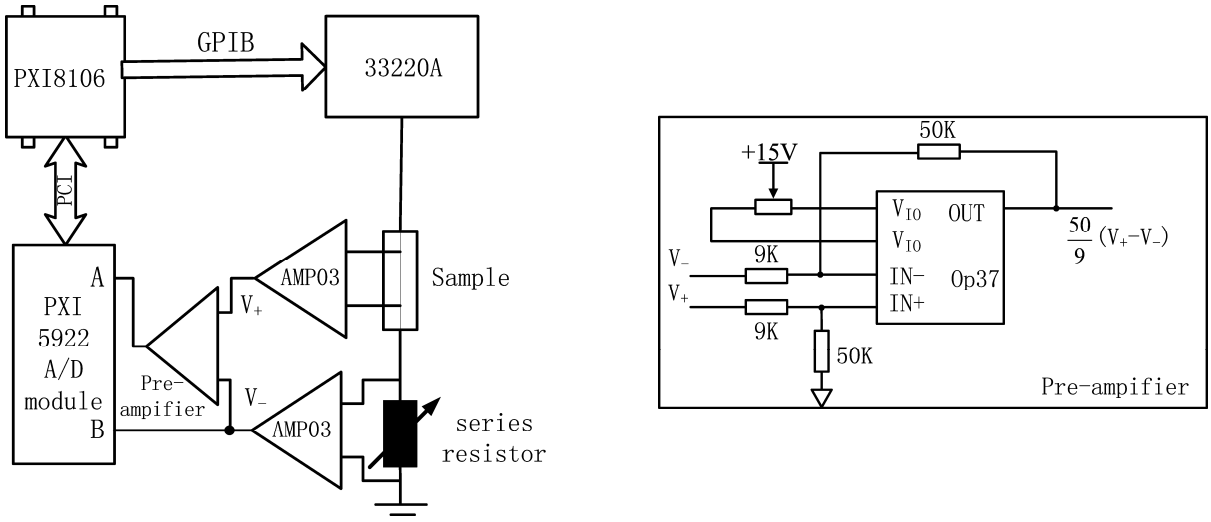

Figure 3. Schematic of the experimental apparatus and the electrical circuit, right block is a schematic diagram of the homemade pre-amplifier circuit.

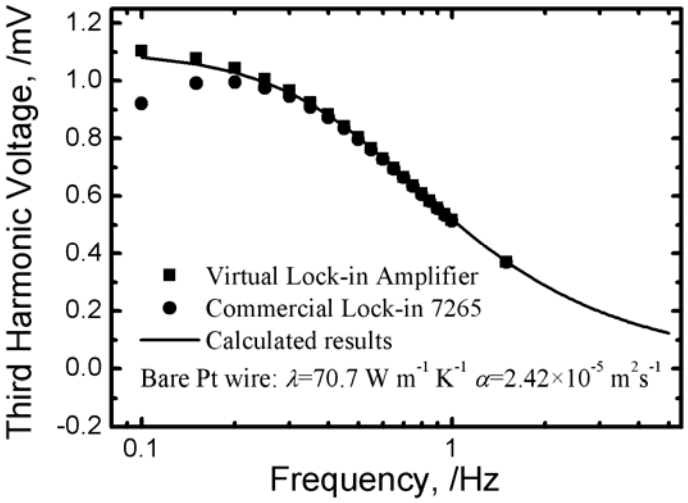

Figure 4. Comparison of the third harmonic voltages measured by virtual lock-in with that by commercial lock-in amplifier 7265, the solid line is the fit using equations (3) and (6), giving the thermal conductivity of a platinum wire 70.7 Wm^{-1} K^{-1}, and thermal diffusivity 2.42×10^{-5} m^2 s^{-1}.

RESULTS AND DISCUSSIONS

Before the thermal effusivity measurement, the accuracy of the virtual lock-in is first verified by measuring a bare platinum hot wire. The measured third harmonic voltages are compared with that by commercial lock-in amplifier 7265, as shown in Figure 4. Using the commercial lock-in amplifier, the external reference mode is selected with TTL reference signal. It is found that, in low frequency range, the third harmonic voltages measured by virtual lock-in are in good agreement with the theoretical predictions using equations (3) and (6), but always larger than that measured by the commercial lock-in amplifier. The possible explanation for the poor performance of the commercial lock-in amplifier in low frequency range is the frequency tracking, e.g., 0.099Hz is detected while the exact current frequency is 0.1Hz, leading to a smaller voltage value. The relative difference in frequency tracking decreases with the increasing frequency, as shown in Figure 4, causing the voltages measured by commercial lock-in amplifier first increase and then decrease with the frequency. In high frequency, the same third harmonic signal is obtained for both virtual and commercial lock-in.

The present method is then verified by measuring a high purity platinum wire (99.98%, diameter ~100μm), which is purchased from Ishifuku Metal Industry Corporation in Japan. Figure 5 shows the measured third harmonic voltage with respect to the current frequency. In high frequency, the third harmonic voltages of the hot wire with and without the test wire are close to each other, since the influence range of the temperature oscillation along the test wire decreased with the increasing frequency. In the frequency range of 0.1 to 1Hz, obvious difference is achieved between these two voltages, indicating the thermal properties of the test wire have a non-negligible effect on the hot wire temperature distribution. Thus, the thermal effusivity of the test wire is fitted to be 1.41×10^4 J m^{-2} K^{-1} $s^{-0.5}$, using equation (6) [substituting equation (5) into equation (6)], with the thermal properties of the hot wire which are obtained from the bare hot wire measurement. From equation (5), the across area of the test wire has a significant effect on the thermal effusivity measurement, as a result, the diameter is accurately measured to be 95.40μm with a Scanning Electron Microscopy.

The previous quasi steady state measurement can be easily transfer to measure the thermal conductivity of the test wire using the conventional steady state method, without changing the test T type probe. The schematic of experimental apparatus for the steady state T type probe is presented in [9]. Figure 6 shows the average temperature rise of the hot wire with respect to the heating rate. Neglecting the radial heat loss from convection or radiation, the thermal conductivity of the test platinum wire is found to be 69.8 W m^{-1} K^{-1}. Finally, the thermal diffusivity of the test wire is calculated to be 2.45×10^{-5} m^2 s^{-1} using $\alpha_s=(\lambda/b)_s^2$. Both the thermal conductivity and thermal diffusivity agree well with the literature reported value [11].

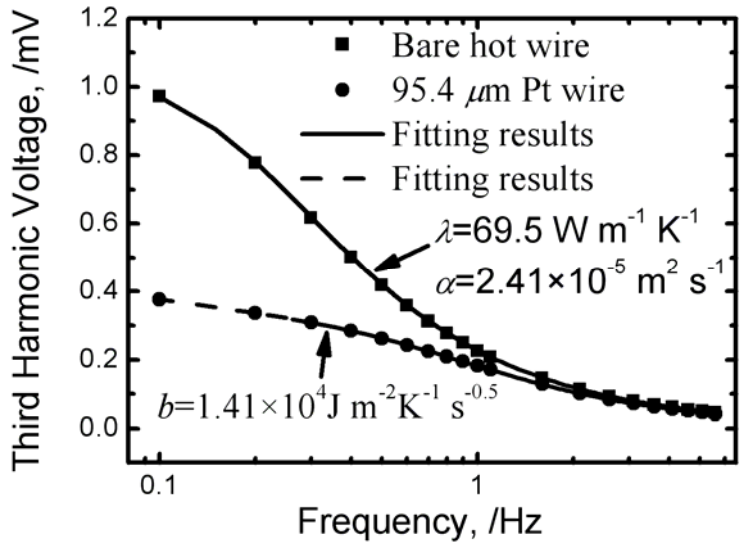

Figure 5. Third harmonic voltage *vs.* frequency, the obtained thermal effusivity of the platinum wire is 1.41×10^4 J m^{-2} K^{-1} $s^{-0.5}$, the solid line is the fit using equations (3) and (6), and the dashed line is the fit using equations (5) and (6).

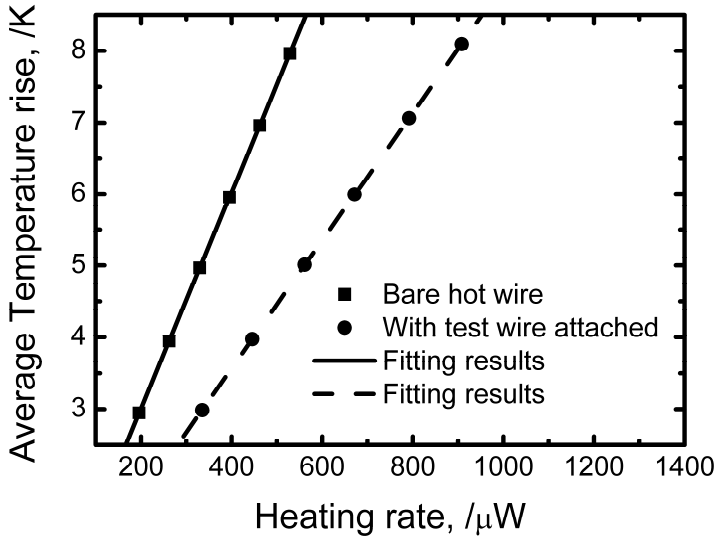

Figure 6. Average temperature rise vs. heating rate, the obtained thermal conductivity of the platinum wire is 69.8 W m^{-1} K^{-1}. (■) denotes the hot wire without the test wire attached, and (●) denotes that with the test wire.

CONCLUSIONS

We have developed a quasi steady state T type probe to measure the thermal effusivity of a fine wire, when the hot wire is supplied by an ac current. A Labview-based virtual lock-in has been designed to obtain the third harmonic voltage across the hot wire. Compared with the commercial lock-in amplifier, the virtual lock-in has the advantage in low frequency detection. To eliminate the influence of the thermal impedance of the interstitial material, a fine powder platinum black with high purity is selected to contact one end of the test platinum wire to the midpoint of the hot wire. The thermal effusivity is fitted from the third harmonic voltage with respect to the current frequency. If a direct current is applied to the hot wire, the same T type probe can be transfer to measure the thermal conductivity of the test wire. Thus, both thermal conductivity and thermal diffusivity of the test wire can be obtained. To verify the present method, a fine platinum wire is measured, the thermal conductivity and thermal diffusivity of is found to be 69.5 W m^{-1} K^{-1} and 2.41 m^2 s^{-1}, both agree well with the literature reported value.

ACKNOWLEDGMENTS

This work was supported by the National Natural Science Foundation of China (Grant Nos. 50676046 and 50730006).

REFERENCES

1. Danielson, G. C. and Sidles, P. H., Thermal diffusivity and other non-steady-state methods, in: R.P. Tye (Eds.), *Thermal conductivity*, Vol. 2, Academic, London, UK, 1969.
2. Sasaki, S., Masuda, H., Kou, H. and Takahashi, H., A transient heating technique for measuring the thermal diffusivity of metals, *Int. J. Thermophys.* Vol. 19, No. 1, pp 259-279,1998.
3. Flynn, D. R., Measurement of thermal conductivity by steady-state methods in which the sample is heated directly by passage of an electric current, in: R.P. Tye (Eds.), *Thermal conductivity*, Vol. 1, Academic, London, UK, 1969
4. Lu, L., Yi, W. and Zhang, D. L., 3 omega method for specific heat and thermal conductivity measurements, *Rev. Sci. Instrum.*, Vol. 72, pp 2996-3003, 2001.
5. Yamane, T., Katayama, S.-i. and Todoki, M., Thermal diffusivity measurement of single fibers by an ac calorimetric method, *J. Appl. Phys.*, Vol. 80, No. 8, pp 4358-4365, 1996.
6. Hou, J. B., Wang, X. W. and Guo, J. Q., Thermal characterization of micro/nanoscale conductive and non-conductive wires based on optical heating and electrical thermal sensing, *J. Phys. D: Appl. Phys.*, Vol. 39, pp 3362-3370, 2006.
7. Zhang, X., Fujiwara, S. and Fujii, M., Measurements of thermal conductivity and electrical conductivity of a single carbon fibre, *Int. J. Thermophys.*, Vol. 21, No. 4, pp 965-980, 2000.
8. Incropera, F. P., Dewitt, D. P., Bergman, T. L. and Lavine, A. S., *Fundamentals of heat and mass transfer*, 6th ed., J. Wiley, New York, 2007.
9. Wang, J. L., Gu, M., Zhang, X. and Wu, G. P., Dynamic characteristic of thermal impedance of the interstitial material at a junction, unpublished.
10. Wang, J. L., Gu, M., Ma, W. G., Zhang, X. and Song, Y., Temperature dependence of the thermal conductivity of individual pitch-derived carbon fibers, *New Carbon Mater.*, Vol. 23, No. 3, pp 259-263, 2008.
11. David, R. L., *CRC Handbook of Chemistry and Physic*, 85th ed., CRC Press, Boca Raton, 2004.

EVAPORATION IN SQUARE CAPILLARY TUBES: OPTICAL MEASUREMENT OF THE CORNER FILMS THICKNESS

F. Chauvet[1, 2, *], P. Duru[1, 2], M. Prat[1, 2]
[1]Université de Toulouse ; INPT, UPS ; IMFT (Institut de Mécanique des Fluides de Toulouse) Allée Camille Soula - F 31400 Toulouse, France
[2]CNRS ; IMFT - F 31400 Toulouse, France

ABSTRACT. Evaporation of volatile liquids in capillary tubes of square internal cross section is studied experimentally. The distinguishing feature of evaporation in a square tube is the presence of liquid films which are trapped by capillarity along the tube internal corners and which control the evaporation kinetics. Gathering experimental data on these liquid films is therefore crucial to better understand and model the evaporation process. An experimental technique allowing measurement of the liquid films thickness during evaporation is presented. Together with measurements of the evaporation rate and of the liquid films length, the film thickness data are used to analyse the result of a typical evaporation experiment and to shade light on the physical mechanisms at play.

Keywords: *Evaporation, capillary tubes, corner flow, meniscus, geometrical optics.*

INTRODUCTION

Evaporation from a meniscus plays an important role in many applications such as capillary pumped loops, heat pipes, fuel cells and drying of porous media. In this context, the study of evaporation of a liquid confined in a capillary tube can be regarded as a first step before more complex situations such as, for example, networks of interconnected capillaries [1]. Here, we study evaporation from a single capillary tube of square internal cross section when evaporation is driven by the vapour diffusion mass transfer between the air-liquid interface and the surrounding air. This corresponds to the classical situation of slow evaporation of a volatile liquid in stagnant air at room temperature. As sketched in Figure 1a, the distinguishing feature of evaporation in a square tube when the volatile liquid is sufficiently wetting is the presence of liquid films trapped by capillarity along the internal corners of the tube as the bulk meniscus recedes into the tube. These corner films provide a pathway for the capillary-driven transport of the liquid from the receding bulk meniscus up to the film tips. This explains why evaporation is generally much faster in a square tube compared to a classical circular tube where the only mechanism to transport the volatile species up to the tube entrance is the poorly efficient vapour diffusion transport. As discussed in previous modelling works, [2, 3], the evaporation kinetics depends on the dynamic of the corner films, which depends in turn on the competition between the capillary, viscous and gravitational forces acting in the system. This leads to delineate different regimes depending on the relative influence of these forces. However, there is a lack of experimental data and therefore of quantitative comparisons between the available models and the experimental data. The general objective of the present work is to contribute to fill this gap by combining careful experimental studies with a proper modelling.

Experimentally, a major difficulty is to obtain quantitative measurements of the corner films characteristics (length and thickness), both due to the capillary tube small size (inferior to 1 mm)

[*]Corresponding author: F. Chauvet
Phone: (+33) 05 61 28 58 75, Fax: (+33) 05 61 28 58 99
E-mail adress: chauvet@imft.fr

and the tricky geometry of the system. In [4], we described how an infrared thermography technique could be used to measure the evolution of the film length during evaporation. Notably, it was shown that there is a maximal film extension, beyond which the films tip ceases to be pinned at the tube entrance and begins to recede into the tube. This maximal film extension is caused by the limiting effects of gravity and viscous forces that oppose to the capillary pumping of the evaporating fluid within the films from the bulk meniscus up to the tube entrance. In the present work, we present an optical technique allowing the study of the evolution of the film thickness during the evaporation experiment. Together with the infrared thermography technique, this opens up the way to a complete characterization of the liquid films. In the following, the experimental set-up is presented first. Then, details on the experimental techniques are presented and, finally, some typical results are discussed.

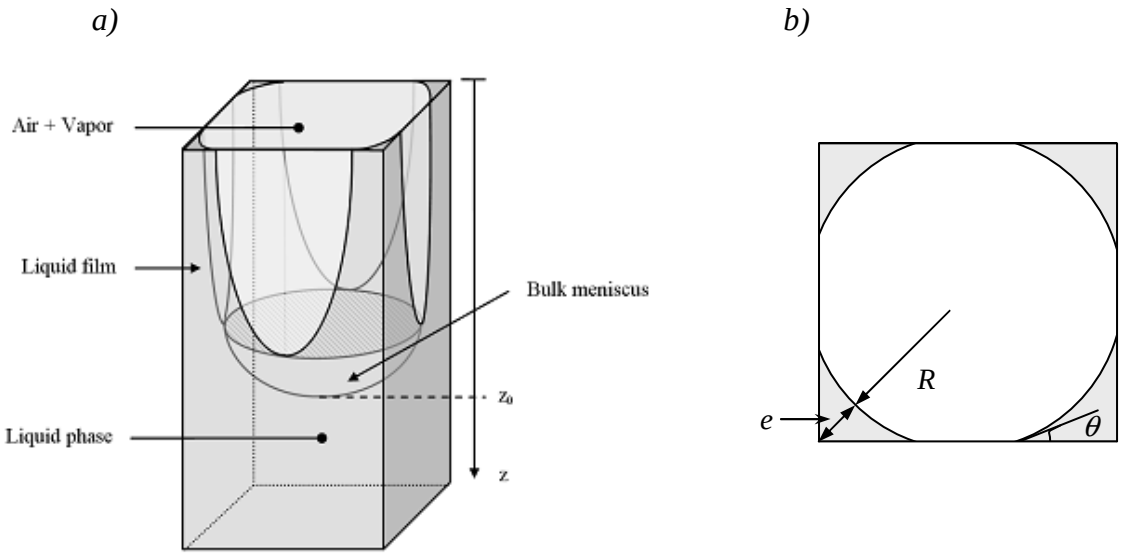

Figure 1. *a)* Sketch of liquid films in a square capillary tube. *b)* Radius of curvature R and film thickness e, in the tube cross section plane; $e = (\sqrt{2}\cos\theta - 1)R$, where θ is the fluid contact angle.

EXPERIMENTAL SET-UP

The 10 cm long square (Vitrocom) capillary tubes used in the present study are made of borosilicate glass: the internal side length d of the tubes is either 1 mm or 0.4 mm, the wall thickness is 0.2 mm. The capillary tube is glued by an epoxy resin silicone adhesive directly to a syringe tip. The syringe is placed on a precision syringe pump (PHD 2000, Harvard apparatus) allowing accurate filling of the tube by the volatile liquid (n-hexane). The room temperature is controlled by an air-conditioning system. The experimental set-up is placed inside a Plexiglas enclosure, see Figure 2, which helps further stabilize the temperature in the environment of the tube. The air temperature inside the enclosure is monitored by thermocouples and remains constant for the entire duration of the experiment, which can last several hours. This temperature control is crucial to avoid the possible effect of dilatation/contraction of the liquid with variations of the ambient temperature, which can distort the evaporation rate measurement.

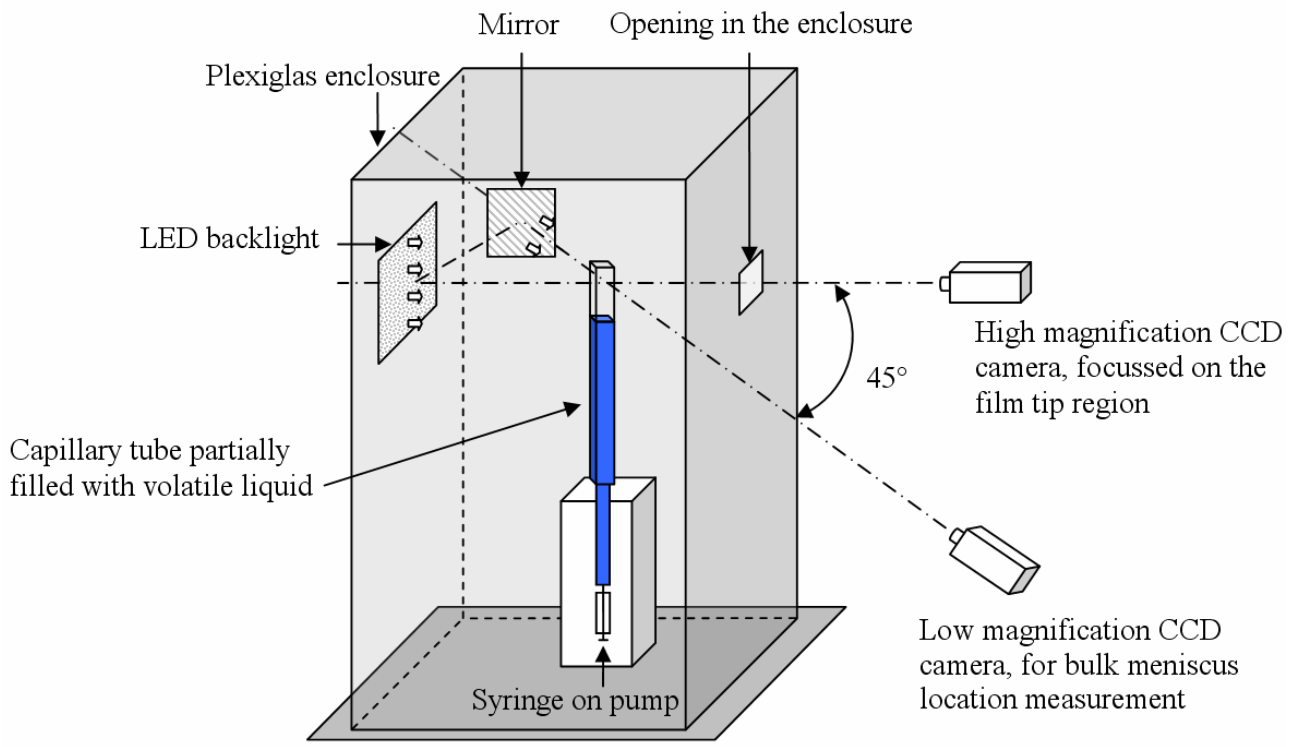

Figure 2. Sketch of the experimental set-up.

The tube is visualized with two CCD cameras (Sensicam, PCO). The first one, equipped with a regular 60 mm objective, images the whole tube and is used to determine the evolution of the bulk meniscus position along the tube (spatial resolution: 13 pixels/mm). The second one is equipped with a 200 mm Medical Nikon objective and images the tube top at high magnification (spatial resolution: 654 pixels/mm). The corresponding visualizations, see Figure 3 for a typical image, are used to measure the corner films thickness (see next section). As shown in Figure 2, the two optical axes make an angle of 45°. The first camera is facing one of the tube sides, and the second one is then focused on one of the corner of the square capillary. This latter relative positioning of the camera and the tube was chosen to limit parallax effects. A Phlox white LED backlight is used as a light source. It provides a constant and uniform light intensity and does not release heat in the strobe mode used in the present experiments. The backlight is facing the CCD camera equipped with the high magnification objective. An opening in the Plexiglas enclosure permits to avoid any distortion of the light rays, while a mirror is used to reflect some of the light towards the other camera. As the tube is placed between the light source and the cameras, an ombroscopy configuration, often used to detect gas-liquid interface, is obtained. As far as the camera imaging the whole tube is concerned, the liquid and gas phases regions appear as bright on the images whereas the bulk meniscus appears as dark because light rays are deviated by the curved interface. Therefore, after binarization of the images, the bulk meniscus position, defined as the most advanced point of the gas phase into the tube (see Figure 1a), can easily be detected. The way to obtain the liquid film thickness from the high magnification visualizations is detailed in the next section.

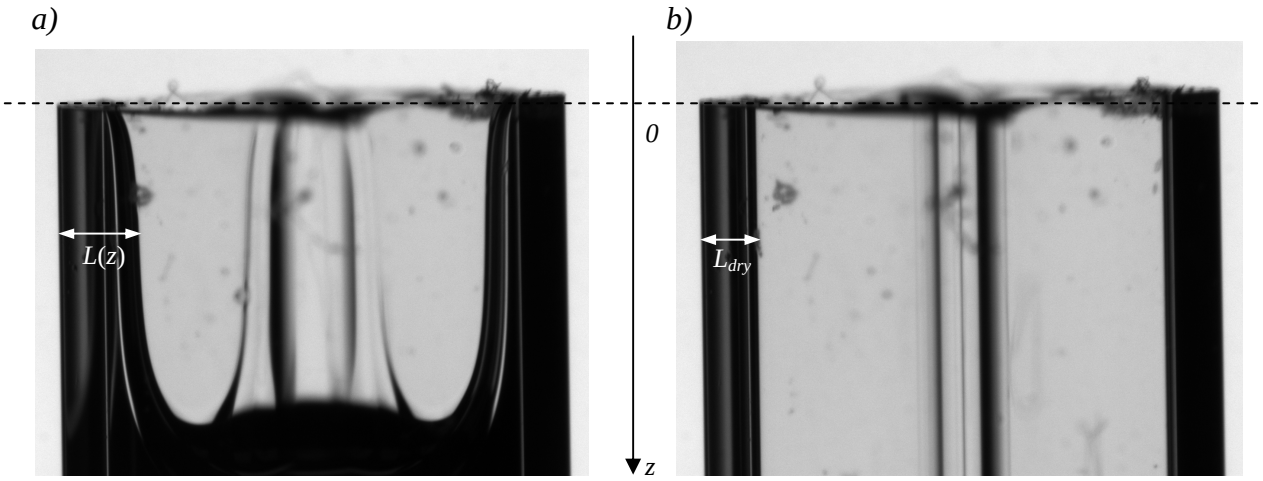

Figure 3. Typical images of the capillary tube top, at high magnification. *a)* This image was taken at the beginning of an evaporation experiment. The bulk meniscus is still in the field of view. The width of the dark region L can be measured at any z position. *b)* Image obtained at the end of the experiment when the tube is dry. The width of the dark region L_{dry} can then be measured.

CORNER FILM THICKNESS MEASUREMENT

Using the ombroscopy configuration presented above, the curvature radius R of the corner film meniscus in the tube cross-section plane can be obtained from the images obtained with a high magnification. Note that the curvature radius R and the film thickness e are directly related, see caption of Figure 1b. This measurement is performed at least one tube diameter below the tube entrance, so that the axial curvature (i.e. along the z direction) of the corner meniscus can be neglected. Note this is an usual assumption in the analysis of corner flows, which is correct in the developed film region but is in error at the film tip, as can be appreciated in Figure 3a. As far as the measurement of R is concerned, the argument is based on the tracing of the light rays paths through the imaged capillary tube corner, using the Snell-Descartes' law (with the respective indices of refraction of air, liquid and glass being such that $n_{air} < n_{liq} < n_{glass}$), and the assumption that the LED backlight is a parallel light source. As sketched in Figure 4, a distinction can be made between light rays that remain parallel to the optical axis after they have travelled through the many interfaces present in the system and those that are deviated, for instance by the curved liquid-gas interface. The latter are not collected by the receiving optics as the camera is positioned far enough from the tube.

Consequently, a dark region of width L is expected on the images and is indeed observed as can be seen from Figure 3a. The width L (in pixels) is a function of the corner film curvature radius R and can be measured after image binarization for any given distance z from the tube entrance. As can be seen from Figure 3b, such a dark region, of width L_{dry}, also exists when the tube is empty because of the roundedness of the tube internal and external corners. When the fluid contact angle is 0, the value of the corner film curvature radius, R, is given by:

$$R - r_0 = \frac{L - L_{dry}}{S \sin \phi}, \tag{1}$$

where S is the spatial resolution, in pixels/mm, ϕ is the angle between the optical axis and the normal to the tube face located between the camera and the observed corner (see Figure 4) and r_0 is the curvature radius of the tube internal corner. By imaging a cross section of each capillary tube used in the present study, it was found that the corners internal shape could be well fitted by a

quarter-circular arc. The corresponding values for the curvature r_0 were found to be r_0 = 0.100 mm for d = 1 mm, r_0 = 0.032 mm for d = 0.4 mm (these values are an average over the four corners, the standard deviation being lower than 10 %).

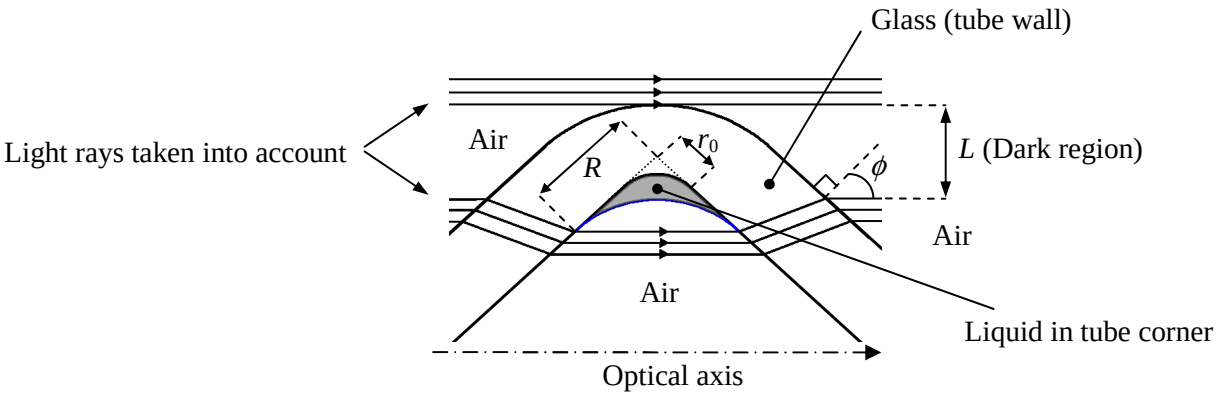

Figure 4. Light rays trajectories used for film curvature radius measurement.

The validity of this measurement technique, which only involves simple geometric optics, is first tested within the framework of a simple experiment of hydrostatic equilibrium. To this end, a capillary tube held vertically is partially filled with a silicone oil. The oil is non volatile and perfectly wetting on borosilicate glass so that corner films develop and reach a hydrostatic equilibrium state. Several corner film lengths are obtained, by tuning the capillary tube filling. Visualizations are performed taking care to avoid any liquid films dynamic state by waiting until the liquid films return to a hydrostatic equilibrium state after each bulk meniscus displacement imposed by the syringe pump. The meniscus curvature radius is determined using the measurements of L and L_{dry} as explained above and compared to the expected value that can be predicted from a simple hydrostatic analysis, [4]:

$$Bo(z_0^* - z^*) = \frac{1}{R_h^*(z^*)} - \frac{1}{R_h^*(z_0^*)} \qquad 0 \le z^* \le z_0^* \tag{2}$$

where $Bo = (\rho_l g d^2)/\gamma$ is the Bond number, ρ_l is the liquid density, g is the gravitational acceleration and γ is the surface tension. In equation (2), R_h is the curvature radius provided by the hydrostatic analysis, z_0 is the bulk meniscus position and the superscript * denotes that the variables are made dimensionless by d. As shown in [5], $R_h^*(z_0^*) = 1/3.77$ for a perfectly wetting liquid in a square tube geometry.

Figure 5 shows the hydrostatic curvature radius R_h predicted by equation (2) as a function of the measured curvature radii difference R-r_0 obtained from experimental measurements of L and L_{dry} and the use of equation (1), for the two tube internal sizes, d = 1 mm and d = 0.4 mm. In both cases, the measured curvature radii difference R-r_0 is proportional to R_h. As can be seen, the data are well fitted by linear functions (shown as solid lines in Figure 5a and 5b). However, the proportionality coefficient is not equal to 1 and is different for the two tube sizes. This could come from the oversimplified vision of the optical problem presented above. Also, it must be noted that it is tricky to perfectly set the angle ϕ at the required value of 45 ° because of the small tube size compared to the size of the others elements in the set-up, which may induce another uncertainty in the use of equation 1. Nevertheless, the linearity between the measured and the predicted values allows for measurement of the films curvature radius value evolution, relative to its initial value or to the curvature radius at the bulk meniscus, which is sufficient to get valuable pieces of information in the present case.

As can be seen from Figure 5, the value of the constant of the linear regression is very close to the value of the tube internal corner curvature radius r_0. This is fully consistent with the hydrostatic analysis since R_h cannot become lower than r_0 in a square tube with rounded internal corners. In other words, equation (2) can be used to predict the maximum film length of a non volatile liquid in a square capillary tube with a non zero internal corner curvature radius.

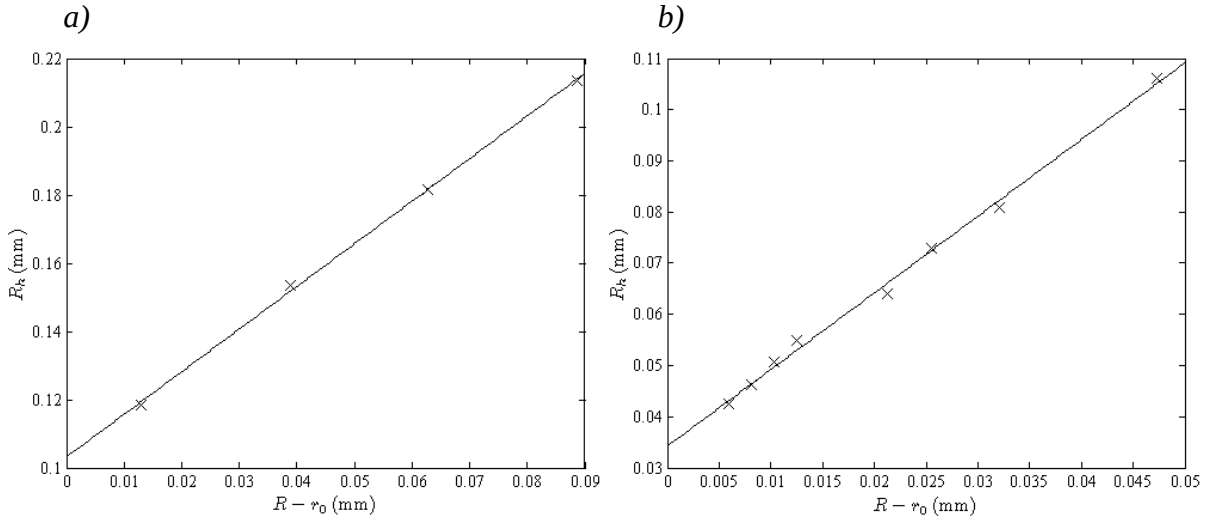

Figure 5. Curvature radius R_h, obtained from the hydrostatic analysis, equation (2) as a function of the optically measured curvature radii difference R-r_0, for several static liquid films lengths. *a)* d = 1 mm, measurement and prediction are made at $z^* = 1$. *b)* d = 0.4 mm, measurement and prediction are made at $z^* = 1.7$. For both cases, the best fitting linear function is shown as a solid line. The linear regression gives $y = 1.25x+0.103$ and $y = 1.50x+0.034$ for the 1 mm and 0.4 mm tubes, respectively.

EXPERIMENTS WITH A VOLATILE LIQUID

In this section, we present some typical experimental results on evaporation of a volatile liquid in a capillary tube of square cross section. The insights on the evaporation process brought by the measurement of the corner films thickness, together with the evaporation rate measurement, will be emphasized.

A tube of internal side length d = 0.4 mm is held vertically and filled with n-hexane (a volatile and perfectly wetting fluid on borosilicate glass). The tube opened top is placed in a stagnant air environment under ambient temperature and atmospheric pressure. The evaporation rate E is obtained straightforwardly from the measurement of the evolution of the bulk meniscus location as a function of time, $z_0(t)$, $E=\rho_l(d^2-\lambda R_h(z_0)^2)(dz_0/dt)$, where λ is a geometrical coefficient, [6]. In Figure 6a, E is plotted as a function of the bulk meniscus position z_0. In Figure 6b, the film thickness, made dimensionless by its value e_0 at the bulk meniscus, is plotted as a function of z_0 (note that because of the tube internal corner roundness, the film thickness is given by $e = (\sqrt{2}-1)(R-r_0)$).

As already discussed in [4], two main evaporation periods can be distinguished. In the first one, the corner films tip stays located at the tube entrance. The second period starts when the films tip ceases to be pinned at the tube entrance and start to recede inside the tube. Measurements of the critical film length z_{0c} when the depinning occurs was obtained in [4] by infrared thermography and it was found to be $z_{0c} \approx 11$ mm. Interestingly, as be seen from Figure 6a, the evaporation rate remains essentially constant during a significant part of the first period, i.e. up to $z_0 \approx 9$ mm. This can be explained by the diffusional screening effect in the tube exit region. As illustrated in previous

numerical simulations of the vapour diffusion transport in the gas phase, [2, 7], the diffusional screening effect refers to the fact that the hexane vapour partial pressure field in the $z = 0$ tube cross section plane is uniform and very close to the hexane saturation vapour pressure (the air is saturated in hexane vapour) when the films are sufficiently thick in the tube entrance region.

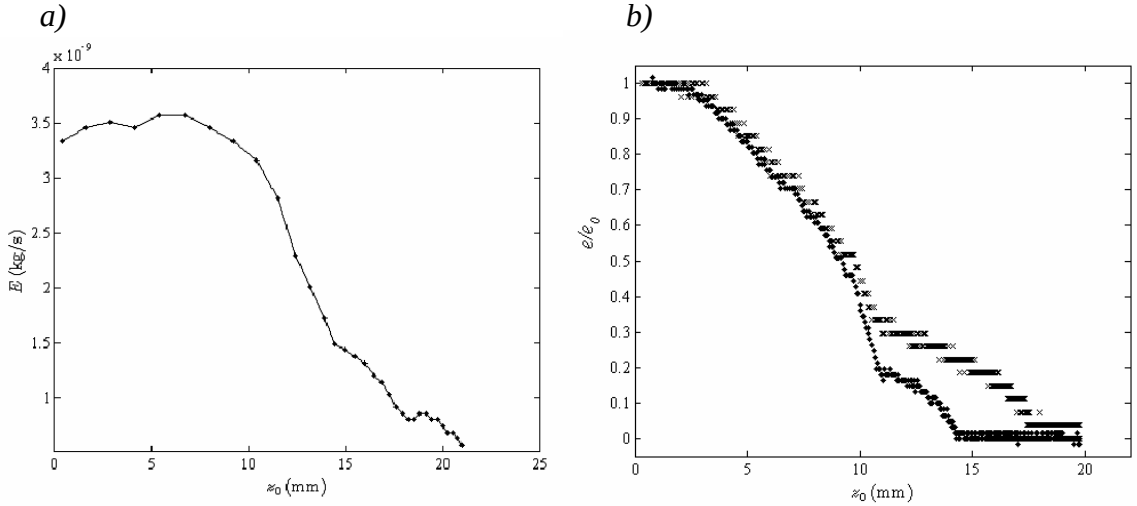

Figure 6. *a)* Evaporation rate E as a function of the bulk meniscus position z_0. *b)* Film thickness e, made dimensionless by its value at the bulk meniscus $e_{0,}$ as a function of z_0, for two different distances from the tube exit, $z = 0.45$ mm (dots) and $z = 1.15$ mm (crosses).

Hence, in the presence of a sufficiently effective diffusional screening effect, the evaporation rate does not depend on the respective distribution of the liquid and gas phases in the tube entrance region and therefore must be constant, which is confirmed by the present experimental results. Note this remains true for $0 < z_0 < 9$ mm, even though the film thickness decreases in the meantime under the conjugated action of gravity and viscous effects. However, just before the films depinning, the evaporation rate begins to decrease slightly as soon as $z_0 > 9$ mm, even if the film tips are still "attached" at the top of the tube, see Figures 6a and 6b. This would simply indicate that the diffusional screening effect becomes less effective when the films become sufficiently thin in the tube entrance region. Hence, the hexane vapour partial pressure field would no longer be uniform at $z = 0$ and would begin to become lower than the hexane saturation vapour pressure on average.

As can be seen from Figure 6, the transition towards the second period takes place at the critical film length $z_{0c} = 11$ mm, which is in good agreement with the infrared thermography result. As already mentioned, the curvature radius of the film was not measured at the very top of the film, where the effect of the axial curvature cannot be neglected. As can be seen from figure 6b, the film thickness is not yet 0 at the two locations where the film thickness is measured, $z = 0.45$ mm and $z = 1.15$ mm when the films depinning occurs at the tube top. The curves in Figure 6b, for $z_0 \geq 11$ mm, display in fact the film tip shape when it passes in front of these two measurement locations. Note that the depinning of the four corner films does not occur simultaneously (the observed differences in term of films length are always lower than one tube size d), which may explain, together with the end of the period of very effective diffusional screening effect, why the evaporation rate decreases before the films depinning. Elucidating the relative importance of these two mechanisms is crucial for a good understanding of evaporation in a square capillary tube and is the subject of ongoing works.

CONCLUSION

In this work an experimental method to measure the corner film curvature radius of a liquid film in a square glass capillary was presented. It is based on simple geometrical optics considerations and on the use of a high magnification ombroscopy visualization technique. Despite the fact that this method does not lead to an absolute measurement of the film thickness, it was shown that it permits to access to the evolution of the film thickness. This technique was used to measure the evolution of the film thickness during the evaporation of a volatile liquid in a square capillary tube. Insights on the evaporation process were obtained by combining this measurement with the determination of the evaporation rate, which was deduced from the evolution of the bulk meniscus position using also a visualization technique. In particular, these measurements reveal that the evaporation rate remains constant during a first period despite the decrease in the film thickness within the tube entrance region. As confirmed by an independent measurement based on an infrared thermography technique, the presented experimental visualization technique also permits to determine the films tip depinning, i.e. the exact moment when the films tip begins to recede into the tube as well as the shape of the film tip as it recedes inside the tube. The experimental data presented here will be exploited in a future work to assess the validity of theoretical models of evaporation in square tubes.

ACKNOWLEDGMENTS

Financial support from GIP ANR “Intensifilm” (Project ANR-06-BLAN-0119-01) is gratefully acknowledged.

REFERENCES

1. Prat, M., Recent advances in pore-scale models for drying of porous media, *Chemical Engineering Journal*, 86 (1-2) 153-164, 2002.
2. Camassel, B., Contribution à l'étude du changement de phase liquide vapeur en milieu poreux, *Ph.D. Thesis*, Institut National Polytechnique de Toulouse, 2003.
3. Coquard, T., Camassel, B. and Prat, M., Evaporation in capillary tubes of square cross section, *Proceedings of ASME Heat Transfer Conference (HT2005)*, San Fancisco, CA, USA, 2005.
4. Chauvet, F., Duru, P. and Prat, M., Study of evaporation in capillary tubes by infrared thermography and ombroscopy technique, *Proceedings of ASME International Conference on Nanochannels, Microchannels and Minichannels (ICNMM08)*, Darmstadt, Germany, 2008.
5. Mason, G. and Morrow, N., Meniscus curvatures in capillaries of uniform cross-section, *Journal of the Chemical Society Faraday Trans*. 1 80 (9) 2375–2393, 1984.
6. Prat, M., On the influence of pore shape, contact angle and film flows on drying of capillary porous media, *International Journal of Heat and Mass Transfer*, 50 1455-1468, 2007.
7. Yiotis, A.G., Boudouvis, A.G., Stubos, A.K., Tsimpanogiannis, I.N. and Yortsos, Y.C., The effect of liquid films on the drying of porous media, *AIChE Journal*, 50 (11) 2721-2737.

DIODE LASER ABSORPTION SENSOR WITH 2F DETECTION FOR COMBUSTION CONTROL BY SECONDARY FUEL INJECTION

M. Shimura[1,*], T. Seo[1], G.-M. Choi[2], M. Tanahashi[1], T. Miyauchi[1]
[1]Tokyo Institute of Technology, Tokyo, Japan
[2]Pusan National University, Busan, Korea

ABSTRACT. Diode laser absorption sensor with 2f detection of wavelength modulation spectroscopy is developed and applied to the swirl-stabilized combustor controlled by secondary fuel injection. The sensor provides temperature of H_2O molecule in the path of laser beams at 1 kHz. The combustor is operated without secondary fuel injection and with continuous or intermittent injections. Mean and rms values of temperature measured at several positions of the combustor show that the sensor provides important information related to the pressure fluctuation in combustor and combustion noise even for measurement in the recirculation zone near the exit of swirl nozzle. In addition, characteristics of temperature oscillations which are related to the interaction between premixed flame and secondary fuel can be detected by applying the sensor to middle of recirculation zone. These results prove that the diode laser absorption sensor with 2f detection is effective for detection of the combustion condition controlled by secondary fuel injection.

Keywords: *diode laser absorption sensor, wavelength modulation spectroscopy, 2f detection, swirl-stabilized combustor, secondary fuel injection*

INTRODUCTION

In active controls of combustion, sensors with high temporal resolution and high accuracy have been required to monitor combustion condition and to give appropriate control signals for controllers. Pressure transducers used in many researches on active combustion control only provide global information on combustion condition, which may limit control algorithm, since combustion is one of the complicated three-dimensional phenomena. Diode laser absorption techniques have been developed for monitoring of combustion fields. In the previous studies, diode laser absorption techniques for H_2O [1], CO and CO_2 [2], CO and H_2O [3] and NO_2 [4] have been developed. Wavelength modulation spectroscopy, such as 2f detection, is used to improve signal-to-noise-ratio (SNR) of the sensor. Theory of wavelength modulation spectroscopy was experimentally verified by Reid and Labrie [5]. Since these techniques can provide characteristics of selected molecule along the line of sight, the diode laser absorption sensor is a candidate for space-resolved sensors monitoring combustion state in many engineering applications. For combustion controls, the diode laser absorption sensors have been utilized for monitoring combustion state of Hencken burner [6], 5 kW dump combustor [7], a pulse detonation engine [8]. Li et al. [9] applied the sensor to a swirl-stabilized combustor controlled by a loudspeaker. Effectiveness of the sensor, however, should be confirmed with a greater variety of control actuators or algorithms.

In this study, diode laser absorption sensor with 2f detection has been developed and applied to measurements of temperature of H_2O molecule in the recirculation zone which is generated in a swirl-

* Corresponding author: Mr. M. Shimura
Phone: + (81)-3-57342505, Fax: + (81)-3-57342505
E-mail address: mshimura@navier.mes.titech.ac.jp

stabilized combustor without and with passive controls by secondary fuel injection. Availability of the diode laser absorption sensor for active combustion control using secondary fuel injection is investigated.

EXPERIMENTAL METHOD

Second-harmonic detection of wavelength modulation spectroscopy

The theory of wavelength modulation spectroscopy was extended to account for effects of intensity modulation of laser on 2f signal by Philippe and Hanson [10]. Wavelength and intensity of laser modulated by a cosine wave of angular frequency ω and amplitudes, a and i_0, can be represented by

$$\nu(t) = \bar{\nu} + a\cos\omega t \tag{1}$$

$$I_0(t) = \bar{I}_0 + i_0\cos(\omega t + \phi) \tag{2}$$

where $\nu(t)$ is the instantaneous optical frequency and $I_0(t)$ is the incident intensity of laser and ϕ is the difference of phase between modulations of optical frequency and laser intensity. Averages of the frequency $\bar{\nu}$ and the intensity $\bar{I}_0$ are scanned slowly relative to ω across the range of absorption feature (scanned-wavelength method). Transmission coefficient $\tau(\nu(t))$ is an even function of time and can be expanded in Fourier cosine series.

$$\tau(\nu(t)) = \sum_{n=0}^{\infty} H_n(\bar{\nu}, a)\cos n\omega t \tag{3}$$

$$H_0(\bar{\nu}, a) = \frac{1}{2\pi}\int_{-\pi/\omega}^{\pi/\omega} \tau(\bar{\nu} + a\cos\omega t)dt \tag{4}$$

$$H_n(\bar{\nu}, a) = \frac{1}{\pi}\int_{-\pi/\omega}^{\pi/\omega} \tau(\bar{\nu} + a\cos\omega t)\cos n\omega t dt \tag{5}$$

where $H_n(\bar{\nu}, a)$ is the n-th Fourier component. Transmitted intensity can be represented by

$$\begin{aligned} I(t) &= I_0(t)\tau(t) \\ &= \{\bar{I}_0 + i_0\cos(\omega t + \phi)\}\left(\sum_{n=0}^{\infty} H_n(\bar{\nu}, a)\cos n\omega t\right) \end{aligned} \tag{6}$$

2f signal $S_2(\bar{\nu}, a)$ can be obtained by multiplying equation (6) by cosine wave of frequency 2ω and arbitrary phase ψ, and by extracting direct component.

$$S_2(\bar{\nu}, a) = \frac{i_0}{4}H_3(\bar{\nu}, a)\cos(2\psi + \phi) - \frac{\bar{I}_0}{2}H_2(\bar{\nu}, a)\cos(\psi + \phi) + \frac{i_0}{4}H_1(\bar{\nu}, a)\cos\phi \tag{7}$$

The arbitrary phase ψ should be set to $-\phi$ to increase signal-to-noise-ratio. 2f signal is mainly dominated by the second harmonic component $H_2(\bar{\nu}, a)$ due to small intensity modulation. At the line center of absorption, 2f signal is not affected by $H_1(\bar{\nu}, a)$ and $H_3(\bar{\nu}, a)$ components, since the components are odd functions of $\bar{\nu}$.

Temperature measurement

2f signal can provide original absorption feature theoretically. However, loss of incident intensity due to particles or dirty optical access may disturb the conversion. Effect of loss can be removed by calculating peak ratio of 2f signals as follows;

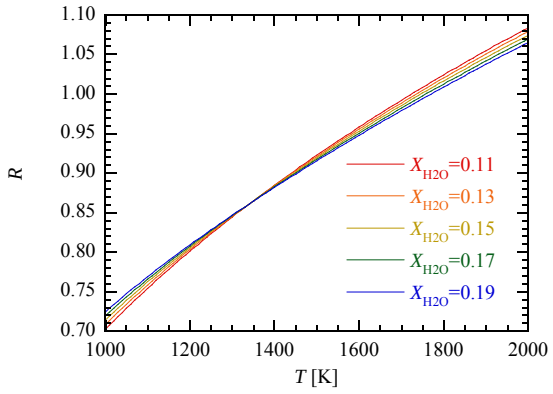

Figure 1. Ratio of simulated 2f signals around 7185 cm^{-1} and 7444 cm^{-1} as a function of temperature for several cases of H_2O mole fraction in burnt gases.

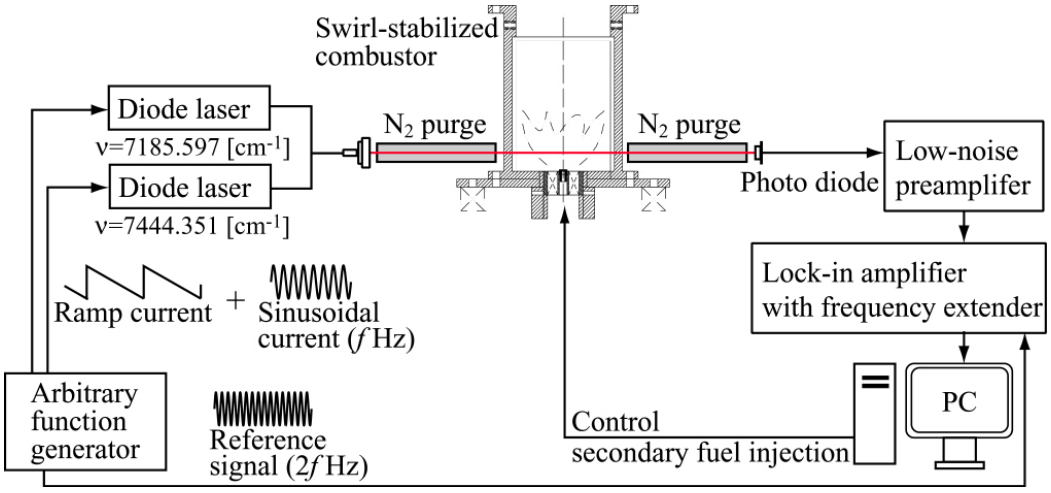

Figure 2. Schematic diagram of diode laser absorption sensor with 2f detection of wavelength modulation spectroscopy

$$R_{2\,fpeak} = \frac{\bar{I}_{0,1}\int_{-\pi/\omega_1}^{\pi/\omega_1} \tau(\nu_1(t))\cos 2\omega_1 t dt}{\bar{I}_{0,2}\int_{-\pi/\omega_2}^{\pi/\omega_2} \tau(\nu_2(t))\cos 2\omega_2 t dt} \tag{9}$$

The ratio depends not only on temperature, but also composition of absorption medium. Figure 1 shows ratio of simulated 2f signals around 7185 cm^{-1} and 7444 cm^{-1} as a function of temperature for several cases of H_2O mole fraction in simulated burnt gas. This set of wavelength was used by Baer et al. [1]. Although relation between the ratio and temperature varies in accordance with the composition of the burnt gas, effect of variation of H_2O mole fraction on temperature measurement is small. For instance, 0.04 variation of H_2O mole fraction correspond to difference of 30 K in the case of $R = 1.0$. In addition, fluctuations of peak heights cause some errors. In the measurement in constant temperature and humidity cell, rms of fluctuation of peak height ratio was about 1.2 %. This fluctuation corresponds to difference of about 30 K.

Experimental setup

Scanned-wavelength method with 2f detection of wavelength modulation spectroscopy is adopted to monitor temperature fluctuations of burnt gas in inner and outer recirculation zones of the swirl-stabilized combustor. Figure 2 shows schematic diagram of experimental set-up. Lasers near 7185 cm^{-1} (1392 nm, $2\nu_1$ and $\nu_1 + \nu_3$ bands transitions) and 7444 cm^{-1} (1343 nm, $\nu_1 + \nu_3$ band transition) are

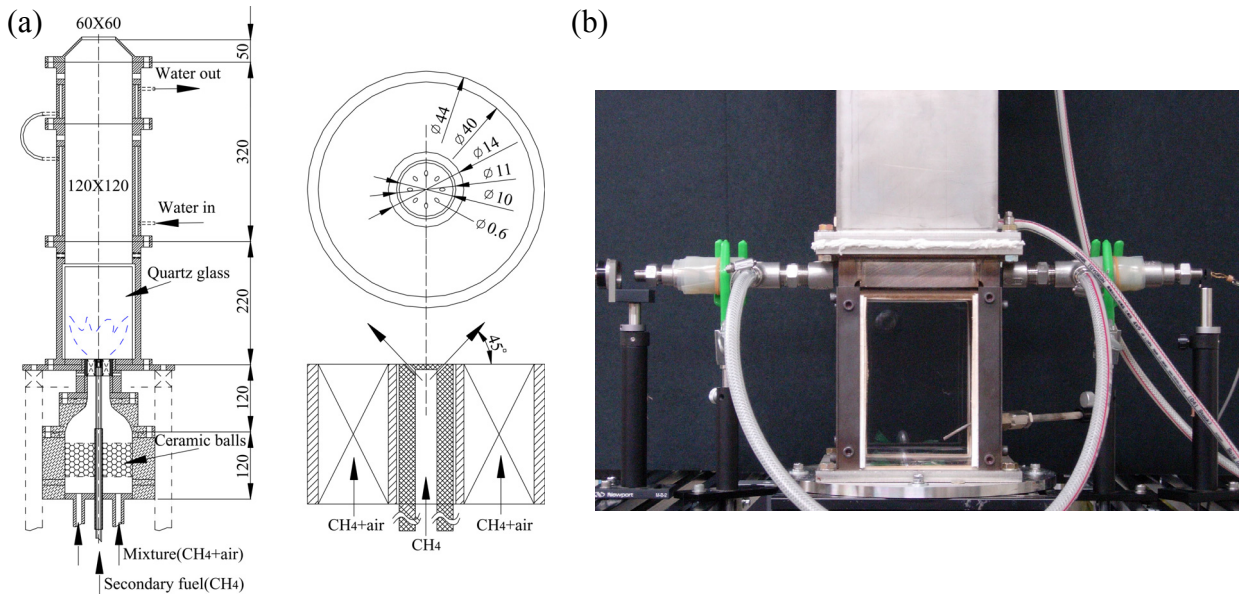

Figure 3. Apparatus of swirl-stabilized combustor and swirl nozzle with hub of secondary fuel injection holes (a) and photo of diode laser absorption sensor installed to the combustion chamber (b)

driven by 1 kHz ramp current summed with 250 kHz and 410 kHz sinusoidal current, respectively. Therefore fluctuations of temperature up to 500 Hz can be detected. Absorption by H_2O in ambient air is eliminated by N_2 purged pipes. In one side of the pipe near photodiode, focusing lens is installed to suppress beam steering. Transmitted signal is amplified and led to lock-in-amplifiers with frequency extenders. Pressure transducer is attached to the combustion chamber about 500 mm downstream from the exit of swirl nozzle.

Figure 3 (a) shows apparatus of swirl-stabilized combustor. The combustor is comprised of a contraction section, the swirl nozzle and the combustion chamber. The swirl nozzle of 14 mm inner diameter and 40 mm outer diameter is mounted on the contraction section and has 8 swirl vanes inclined at 45° from central axis of the combustor. A hub of secondary injection hole is attached at the center of the swirl nozzle and has 8 injection holes inclined at 45° from main stream direction. Secondary fuel injection can be modulated by solenoid valve installed at the position of 750 mm upstream from exit of injection holes. On each side of the combustion chamber, silica glass plate is installed to allow optical access. Figure 3 (b) shows a photo of installation of diode laser absorption sensor to the combustion chamber. Relative position of the sensor to the chamber can be changed in the region of the silica glass. In the previous study [11], characteristics of the swirl-stabilized combustor have been investigated in detail. For the case of ϕ=0.790 and 300 L/min, the sound level is about 110 dB. If the secondary fuel is injected continuously, peak frequency of the pressure fluctuation changes and noise level reduces to about 100 dB. If the secondary fuel is injected intermittently with appropriate frequency of 40 Hz, the pressure fluctuation becomes the minimum and the combustion noise is further reduced by about 5 dB [12]. Note that pressure fluctuation and noise level increases again if frequency of the secondary fuel injection exceeds 40 Hz. Noise levels are 98 dB for 10 Hz, 95 dB for 40 Hz and 104 dB for 70 Hz, respectively [12].

Experimental conditions

Experiments were conducted for the cases of no secondary fuel injection, continuous injection and intermittent injections at 10 Hz, 40 Hz and 70 Hz. Flow rate of main methane-air premixed gas was set in 300 L/min and equivalence ratios of the premixed gas were 0.790 for no control case and 0.717 for the cases of continuous and intermittent injections. Total equivalence ratio for injection cases was 0.819 including 3 L/min of secondary pure methane fuel. Note that air used in premixed gas is once

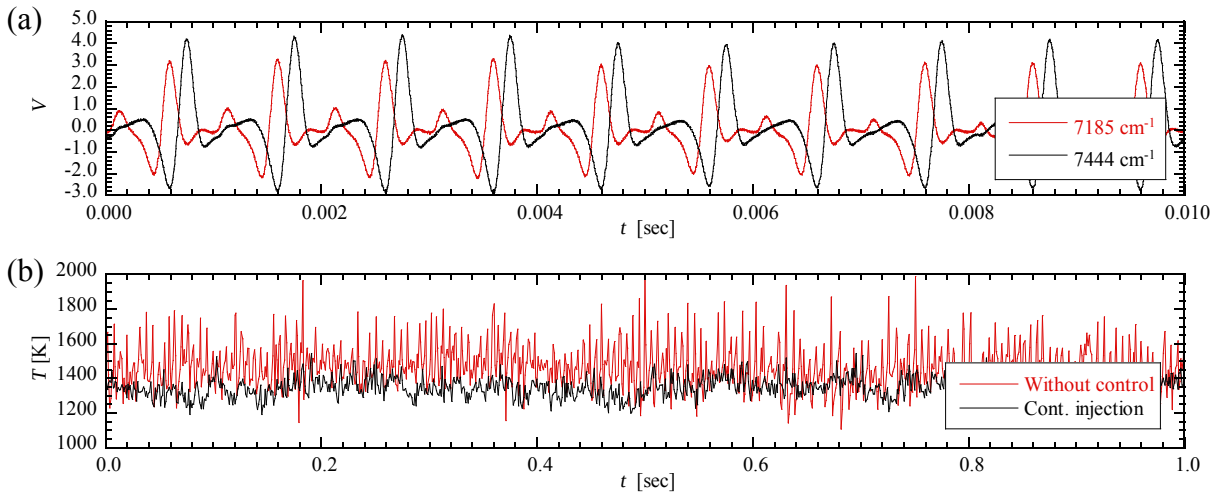

Figure 4. Examples of time series data of 2f signals of 7185 cm^{-1} and 7444 cm^{-1} without control (a) and temperature without control and with continuous secondary fuel injection (b)

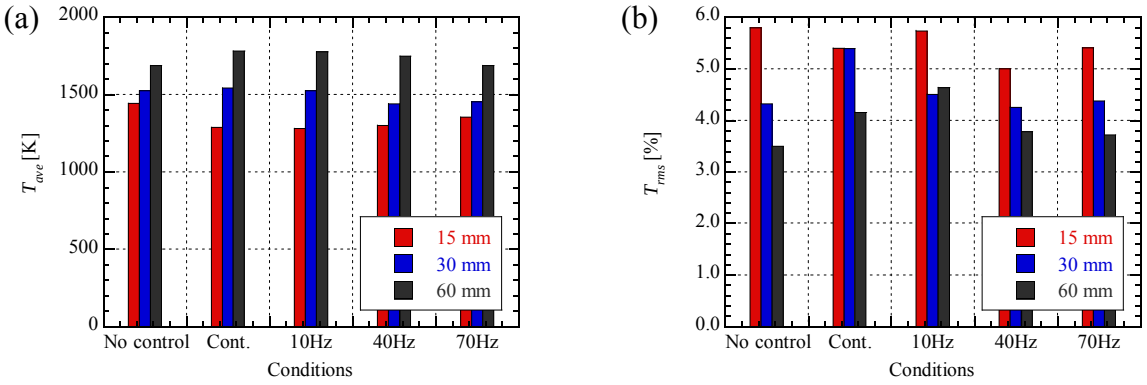

Figure 5. Mean (a) and rms (b) values of measured temperature for each injection case at three measurement heights

compressed to about 8 atm and dried, and therefore most of H_2O in the air is removed. As for the position of path of laser beams, lines passing the center axis of the combustor at 15, 30 and 60 mm downstream from exit of swirl nozzle are selected.

RESULTS AND DISCUSSIONS

The sensor for active control of combustors should detect the characteristics of the combustion state. Figure 4 (a) shows examples of time series data of 2f signals of 7185 cm^{-1} and 7444 cm^{-1} without control. The ratio of peak heights of 2f signals provides temperature in the path of laser beams at 1 kHz. Figure 4 (b) shows examples of time series data of obtained temperature without control and with continuous injection. In the case without control, the diode laser sensor detects large fluctuations of temperature. For the case of continuous injection, the diode laser absorption sensor reveals that fluctuations of temperature are suppressed. On the other hand, temperature becomes low, which might be caused by spread of flame due to secondary fuel jet as shown in the previous study [13]. Figure 5 (a) and (b) show mean and rms values of measured temperature at three measurement height. As for the case without injection, mean temperature at 15 mm is higher than that for the other cases and that at 60 mm is lower. Therefore, spatial variance of mean temperature is relatively small in the range of measurements. However, rms of temperature at 15 mm is larger than the other cases. This result corresponds to the large fluctuation of pressure and noise. In contrast, rms values are relatively small in

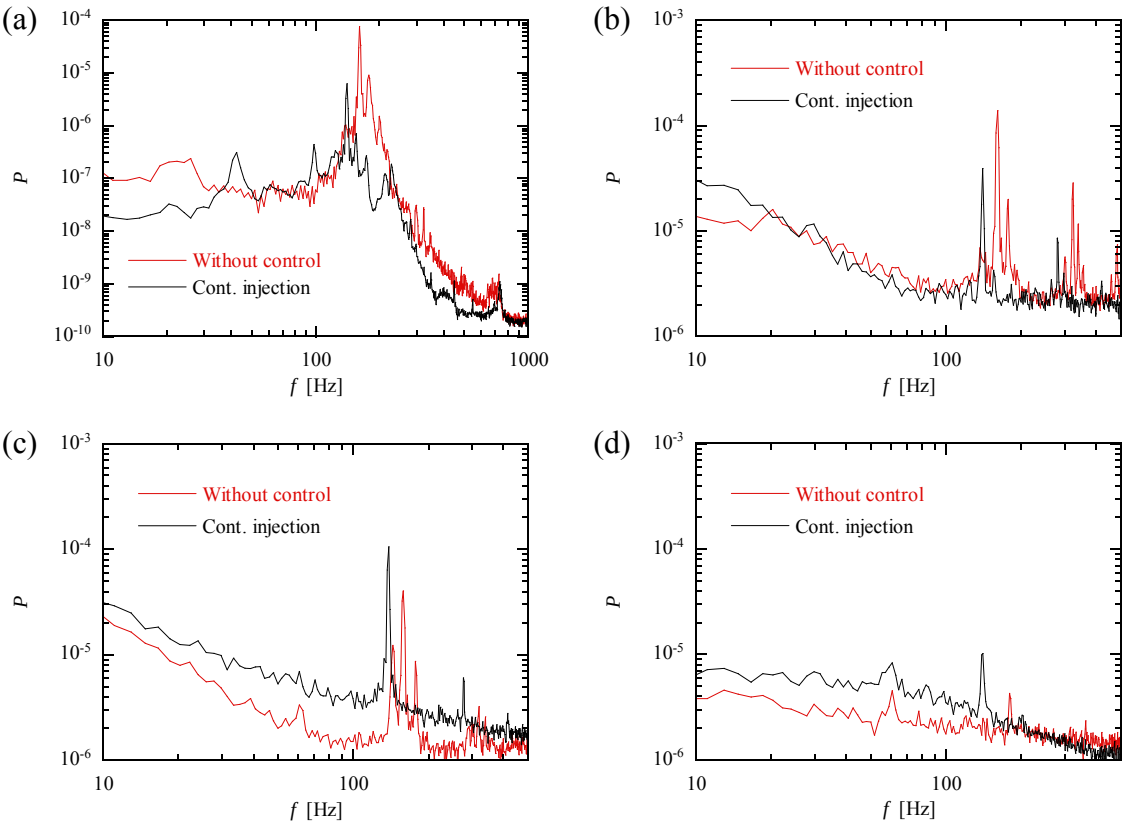

Figure 6. Power spectra of pressure fluctuation (a) and temperature at 15 mm (b), 30 mm (c) and 60 mm (d) without control and with continuous injection

the downstream regions, such as 30 mm and 60 mm. For continuous secondary fuel injection case, spatial variance of mean temperature is larger than the other injection cases. Rms values at 15 mm are reduced compared with no secondary fuel injection case. However, those at 30 mm and 60 mm show high value. In the cases of intermittent secondary fuel injections, mean temperature at 15mm increases and that at 60 mm decreases with increase of injection frequency. Compared with continuous injection case, rms values at 15 mm for 10 Hz and 70 Hz are larger and, on the other hand, rms value at 30 mm for intermittent injection cases is lower, which means that intermittent injection suppresses fluctuations of flame front and resultant burnt gas near flame region. In addition, 40 Hz injection case shows lower value than the other cases at 15 mm and 30 mm, which correspond to the results that noise is reduced by 40 Hz secondary fuel injection [12]. Note that diode laser absorption sensor which is assuming homogeneous absorption medium cannot provide distributions of precise temperature in combustion fields. However, these results suggest that diode laser absorption sensor with 2f detection can indicate characteristics of pressure fluctuation and noise by measuring temperature of H_2O in recirculation zone near the exit of swirl nozzle.

Figure 6 represents power spectra of pressure and temperature fluctuations without control and with continuous injection for 3 height cases. The peak frequencies of pressure fluctuation are found in about 160 Hz and 180 Hz without control in Figure 6 (a). The energy at the peak frequency is decreased by the secondary fuel injection in accordance with the decrease of the combustion noise measured in the previous study [11], and peak frequency is shifted from about 160 Hz to 140 Hz. Peak frequencies of power spectra of temperature at 15 mm (shown in Figure 6 (b)) coincide with those of pressure fluctuation. At 30 mm (Figure 6 (c)), energy at peak frequency for continuous injection case is larger than that for no injection case. At 60 mm (Figure 6 (d)), energies at peak frequencies for no injection case and even for continuous injection case are much lower. Since apparent peaks are observed in power spectra of pressure fluctuation, it seems that temperature fluctuation of burnt gas is not small as

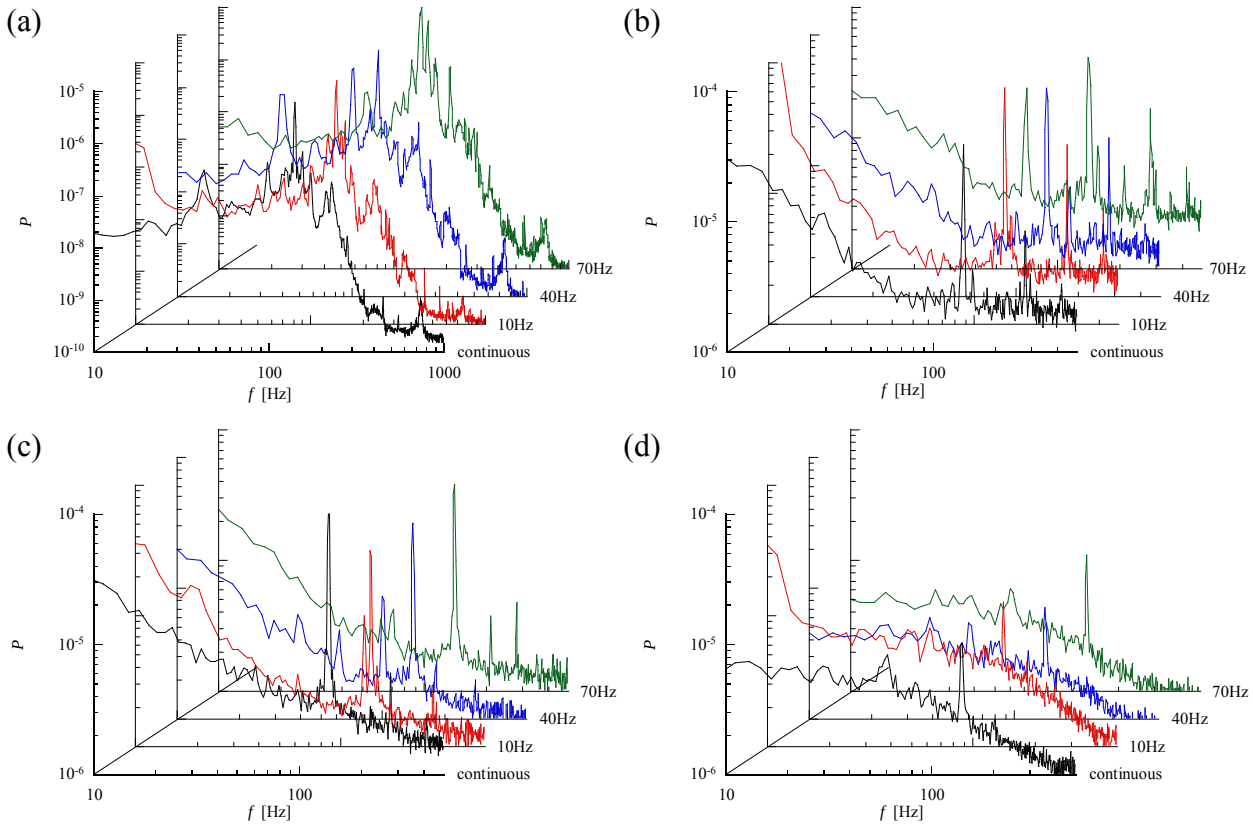

Figure 7. Power spectra of pressure fluctuation (a) and temperature at 15 mm (b), 30 mm (c) and 60 mm (d) for continuous and intermittent secondary fuel injection cases

a whole. Therefore, measurement at 60 mm is not suitable for detection of combustion oscillation.

Figure 7 shows power spectra of fluctuations of pressure and temperature at 15 mm, 30 mm and 60 mm for continuous and intermittent secondary fuel injection cases. In addition to the dominant frequency of about 140 Hz, pressure oscillation occurs at the same frequency with injection and beat between the dominant and injection frequencies. In the case of 10 and 70Hz, temperature measured at 15mm oscillates largely at injection frequencies, whereas 40 Hz injection does not induce large temperature fluctuation. As for 30 mm shown in Figure 7 (c), continuous injection case which has large value of rms shows large energy at the dominant frequency. In the cases of intermittent injections, peaks both at the injection and beat frequencies appear even for 40 Hz injection. The beat caused by the interaction between premixed flame and secondary fuel can be detected at the height. As for the case of 60 mm shown in Figure 7 (d), energy at the dominant frequency is most reduced for 40 Hz injection. For the cases of continuous and intermittent secondary fuel injections, oscillation at the dominant frequency can be observed even in relatively downstream region. However, the energy shows lower value than that in upstream region. Therefore, SNR of the sensor for detection of combustion oscillation can be set higher by applying it to lower positions in the recirculation zone. The diode laser absorption sensor provides characteristics of temperature fluctuations depending on the measurement path. Therefore, installation to the proper positions makes the sensor effective for the active combustion control by secondary fuel injection.

CONCLUSIONS

Diode laser absorption sensor with 2f detection of wavelength modulation spectroscopy was developed and applied to the swirl-stabilized combustor. The combustor was operated without

secondary fuel injection and with continuous and intermittent secondary fuel injections. The sensor can indicate characteristics of pressure fluctuation and noise by measuring temperature of H_2O molecule in recirculation zone near the exit of swirl nozzle. In addition, oscillation characteristics can be detected by applying the sensor to lower positions. The sensor provides information depending on the position of laser path. The characteristics of interaction of premixed flame and secondary fuel can be apparently measured only in the middle of measurement position. Therefore, space-resolved sensor has potential to innovate control algorithms different from those for the traditional active combustion control which defines pressure fluctuation as a control object. These results prove that the diode laser absorption sensor with 2f detection is a great candidate for active combustion control by secondary fuel injection.

ACKNOWLEDGEMENTS

This work is partially supported by Grant-in-Aid for Young Scientists (S) (No. 20676004) of Japan Society for the Promotion of Science and by Grant-in-Aid for JSPS Fellows (No. 19-10540) of Japan Society for the Promotion of Science.

REFERENCES

1. Baer, D. S., Nagali, V., Furlong, E. R., Hanson, R. K. and Newfield, M. E., Scanned- and Fixed-Wavelength Absorption Diagnostics for Combustion Measurements Using a Multiplexed Diode-laser Sensor System, *AIAA Paper-95-0426*, 1995.
2. Sonnenfroh, D. M. and Allen, M. G., Observation of CO and CO_2 Absorption near 1.57μm with an External-cavity Diode Laser, *Appl. Opt.*, Vol. 36, No. 15, pp 3298-3300, 1997.
3. Teichert, H., Fernholz, T. and Ebert, V., Simulataneous in situ measurement of CO, H_2O, and gas temperature in a full-sized coal-fired power plant by near-infrared diode lasers, *Appl. Opt.*, Vol. 42, No. 12, pp 2043-2051, 2003.
4. Mihalcea, R. M., Baer, D. S. and Hanson, R. K., Tunable Diode Laser Absorption Measurements of NO_2 near 670 nm and 395 nm, AIAA Paper-96-0173, 1996.
5. Reid, J. and Labrie, D., Second-Harmonic Detection with Tunable Diode Lasers – Comparison of Experiment and Theory, *Appl. Phys. B,* Vol. 26, pp 203-210, 1981.
6. Furlong, E. R., Baer, D. S. and Hanson, R. K., Combustion Control Using a Multiplexed Diode-laser Sensor System, *Proc. Combust. Inst.*, Vol. 26, pp 2851-2858, 1996.
7. Furlong, E. R., Baer, D. S. and Hanson, R. K., Real-Time Adaptive Combustion Control Using Diode-Laser Absorption Sensors, *Proc. Combust. Inst.*, Vol. 27, pp 103-111, 1998.
8. Mattison, D. W., Brophy, C. M., Sanders, S. T., Ma, L., Hinckley, K. M., Jeffries, J. B. and Hanson, R. K., Pulse Detonation Engine Characterization and Control Using Tunable Diode-Laser Sensors, *J. Propul. Power*, Vol. 19, No. 4, pp 568-572, 2003.
9. Li, H., Zhou, X., Jeffries, J. B. and Hanson, R. K., Sensing and Control of Combustion Instabilities in Swirl-Stabilized Combustors Using Diode-Laser Absorption, *AIAA Journal*, Vol. 45, No. 2, pp 390-398, 2007.
10. Philippe, L. C. and Hanson, R. K., Laser Diode Wavelength-Modulation Spectroscopy for Simultaneous Measurement of Temperature , Pressure, and Velocity in Shock-Heated Oxygen Flows, *Appl. Opt.*, Vol. 32, No. 30, pp 6090-6103, 1993.
11. Choi, G.-M., Tanahashi, M. and Miyauchi, T., Control of Oscillating Combustion and Nose Based on Local Flame Structure, *Proc. Combust. Inst.*, Vol. 30, No. 2, pp 1807-1814, 2005.
12. Tanahashi, M., Murakami, S., Miyauchi, T. and Choi, G.-M., Control of oscillating combustion and measurements of turbulent flames, *Proc. 5th Symp. Smart Control of Turbulence*, pp 75-84, 2004.
13. Tanahashi, M., Inoue, S., Shimura, M., Taka, S., Choi, G.-M. and Miyauchi, T., Reconstructed 3D Flame Structures in Noise-Controlled Swirl-Stabilized Combustor, *Exp. Fluids.*, Vol. 45, No. 3, pp 447-460, 2008.

ENHANCEMENT BEHAVIOR OF COMBUSTION AND HEAT TRANSFRER IN FOUR TYPES OF CONSTANT-VOLUME COMBUSTORS

Norio Ohiwa[1,*], Yojiro Ishino[1], Jiro Oda[2], Ken-ichi Miyata[2], Yo-ichiro Koike[2]
[1] Graduate School of Engineering, Nagoya Institute of Technology, Nagoya, Japan
[2] Technical Research Development, Makita Corporation, Anjo, Japan

ABSTRACT. Based on the qualitative considerations that the flow durability in the combustor plays an important role not only in combustion enhancement but also in heat transfer enhancement, the main attention is paid on the flow durability in the cooling period after the pressure attains maximum. Four types of constant-volume combustors are used; a cylindrical combustor with a hemi-sphere-shaped divided chamber, one with a pan-cake-shaped divided chamber, a fan-stirred combustor and a simple cylindrical combustor. The latter is used for getting standard combustion properties. Enhancement behavior of combustion and heat transfer is examined by analysing pressure histories after the spark ignition. Flow visualization in the fan-stirred combustor is made using a cold water flow. It is found that the fan-stirred combustor can realize and maintain a complex flow pattern in the cooling period and realize simultaneously strong heat transfer enhancement and moderate combustion enhancement.

Keywords: *Premixed combustion, Combustion enhancement, Heat Transfer augmentation, Constant volume combustion, Flow visualization*

INTRODUCTION

To develop a combustion-driven, portable, reciprocal and self-sustainable impact machine, which utilizes the steep pressure increase due to combustion as driving force; basic properties of combustion and heat transfer enhancement have already been studied using a quasi-constant volume and divided chamber combustor [1, 2]. In these papers the physical and chemical properties of multiple flame jets and their influences on the combustion augmentation mechanism have been qualitatively elucidated by making basic reference to the accumulated information concerning the divided chamber combustors [3 ~ 9]. Detailed considerations on the results can clarify that the laminar flame propagation in the sub-chamber produces multiple radial flame jets issuing into the main chamber and the multiple radial flame jets realize effective combustion enhancement for its small sub-chamber volume, through homogeneous and thorough mixing all over the main chamber. Even in this case, however, cooling of combustion gas by heat transfer to the walls after the pressure reaches to its maximum becomes insufficient and results in slow and incomplete returning of the piston to its original position.

The main attention in this investigation is focused on the qualitative considerations that the long flow durability in the main chamber may effectively promote not only the burning process in the main chamber just after the ignition in the main chamber, but also the cooling process after the combustion terminates. To clarify the difference in the enhancement processes in combustion and heat transfer, four types of constant-volume combustors using DME-air mixture are prepared; two types of divided chamber combustors of hemi-sphere type and pan-cake type, a fan-stirred constant volume combustor and a normal cylindrical constant volume combustor. In this paper the burning and cooling processes are examined for four types of constant-volume combustors by analysing the pressure histories in the

* Corresponding author: Prof. N. Ohiwa
Phone: + (81)-52-735-5327, Fax: + (81)-52-735-5327
E-mail address: oiwa.norio@nitech.ac.jp

main chamber. Their fundamental properties; such as the maximum pressure, the maximum pressure increasing rate, the total burning time, the net burning time and the total cooling time are then compared with those of the normal cylindrical combustor for examining qualitatively the interrelation between the enhancement effects for burning and cooling. Finally a cold flow pattern in the fan-stirred combustor without combustion is visualized by replacing it with a cold water flow field under the standard pressure and temperature conditions.

EXPERIMENTAL APPARATUS AND METHODS

The schematic diagram of the experimental system is shown in Fig. 1. The system is composed of a constant volume combustor, a mixture supply line, a measuring circuit for main chamber pressure, an ignition circuit and a control PC-circuit. The construction of four types of constant volume combustors is given in the inset to Fig. 1, as indicated by each abbreviated character; FD: fan-stirred, NC: normal cylindrical, HS: hemi-spherical type divided chamber and PC: pan-cake type divided chamber. All combustors have a cylindrical shape of 84.5 mm diameter and 46.5 mm height and a total volume of $V_m = 260$ cm^3, except for the fan-stirred combustor of $V_m = 266$ cm^3.

The hemi-sphere is made of iron of 2 mm thickness and has a volume of $V_s = 62.4$ cm^3. The ratio of the sub-chamber volume to the main chamber volume, $a = V_s/V_m = 24$ %. Forty small nozzles having a diameter of $d = 1.6$ mm are regularly arranged over the hemi-sphere surface and has a total sectional area of 80.4 mm^2. The pan-cake type divided chamber combustor is constructed by dividing the main chamber into two parts using a flat plate. The sub-chamber volume is $V_s = 106$ cm^3 and has a volume ratio of $a = 40$ %. The flat plate has a thickness of 3.2 mm and a diameter of 84.5 mm, and six nozzles with a diameter of 2.1 mm and six nozzles having a diameter of 3.2 mm are coaxially and alternately arranged on the plate. The total sectional area of 12 nozzles is 69.0 mm^2. A fan consisting of four blades of a twisted angle of 30° and having a diameter of 60 mm is driven by a DC-motor in the range of n = 6,000 ~ 12,000 rpm. The configuration and dimensions of four kinds of combustors are summarized in Table 1. By the way, the specifications of two divided chamber combustors are so determined based on the preceding studies [1, 2] that they indicate the highest enhancement effect in the main chamber combustion.

The fuel used is dimethyl ether, abbreviated to DME in the following, whereas air is supplied by a compressor. DME and desiccated air are filled into a mixing chamber at an absolute pressure of 0.13 MPa to form mixture having an assigned equivalence ratio. The mixing chamber is equipped with a fan, which is driven indirectly by magnetic force of a rotating magnet. The equivalence ratio is varied in the range of $\phi = 0.8 \sim 1.4$ at 0.2 intervals. The mixture with an assigned equivalence ratio is charged into the combustor, which is discharged to a vacuum in advance. After balancing the combustion chamber pressure against the atmospheric one using a control valve, an electric plug is discharged at

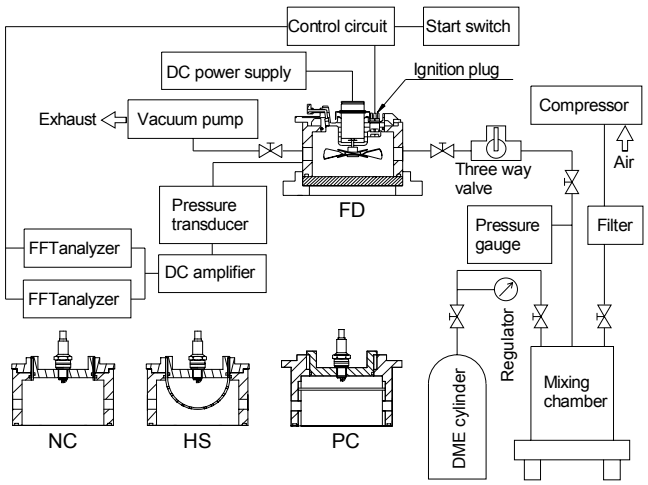

Figure 1. Schematic of the experimental apparatus and four kinds of constant-volume combustors

Table 1
Configurations and dimensions of four kinds of constant-volume combustors

	Hemi-sphere (HS)	Pan-cake (PC)	Fan-stirred (FD)	Cylindrical (NC)
Main chamber volume, V_m (cm^3)	260		266	260
Sub-chamber volume, V_s (cm^3)	62.4	106	–	–
Volume ratio, a ($=V_s/V_m$) (%)	24	40	–	–
Nozzle diameter, number and their total area, d (mm) and A (mm^2)	$\phi 1.6 \times 40$ 80.4	$\phi 2.1 \times 6 + \phi 3.2 \times 6$ 69.0	–	–
Fan revolution, n ($\times 10^3$ rpm)	–	–	6~10	–
Fuel and equivalence ratio, ϕ	DME, 0.8 ~ 1.4			

ignition energy of 24.5 mJ. Synchronizing with the spark discharge, the main chamber pressure is measured using a water-cooled semi-conductor type pressure transducer having a maximum response frequency of 10 kHz (Toyota Koki Co. Ltd., PMS-5M-20H).

In this paper flow visualization is also made by replacing the mixture flow in the fan-stirred combustor before ignition with a fan-stirred water flow in the model combustor, while Reynolds number is kept constant. The model combustor with the same dimensions as those of the FD-combustor is made of transparent plastics. Reynolds number is defined using the fan diameter and the tangential velocity at the fan diameter as the characteristic length and velocity. In this case the kinematic viscosity of air at room temperature of 300 K is greater than that of water by about 16 times. This enables visualization of the water flow under extremely low fan revolution ranging 320 ~ 640 rpm. Fine polyethylene terephthalate resin powder, abbreviated to PET-powder in the following, having a density of $\rho = 1.38 \times 10^3$ kg/m^3 and diameters ranging in $d = 100 \sim 125$ μm is used as tracer particles. One gram of PET-powder is added to the deaerated water and incandescent light is applied in the side direction. Reflected light from PET-particles is photographed using a high-speed CCD video camera (Photron; FASTCAM-PCI) at a framing speed of 500 fps.

EXPERIMENTAL RESULTS AND DISCUSSION

Combustion behavior in four types of constant-volume combustors

Comparison of pressure characteristics. Temporal variations of the pressure and its increasing rate are presented in Fig. 2 for four types of combustors; the HS-, PC-, FD- and NC-combustor, where the equivalence ratio is assigned to $\phi = 1.0$. The upper figure gives the pressure history and the lower the pressure increasing rate, where the abscissa shows the time after the spark ignition in the sub-chamber. The upper figure of Fig. 2 shows that a moderate pressure increase and a relatively low maximum pressure are obtained in the NC-combustor due to the slow and smooth laminar combustion. In cases of the divided chamber combustors the same moderate pressure increase as that in the NC-combustor is observed in the initial stage of combustion. This is because the initial stages in both the HS- and PC-combustors do not substantially differ from that in the NC-combustor, but is dominated by the same slow laminar flame propagation. The pressure histories in the HS- and PC-combustors, therefore, overlap with each other in the first stage. During the initial stage, however, multiple jets are driven by the laminar flame propagation through the nozzles and thoroughly disturb the mixture in the main chamber. Due to the thorough mixing by the multiple jets, rapid turbulent flame propagation follows multi-point ignitions by flame kernels and/or flamelets in the main chamber and realizes steep pressure increase and high maximum pressure. It is confirmed that the multiple jets exert extreme effects on combustion enhancement in the constant volume combustors. Also found is that, although the volume ratio of the HS-combustor of 24 % is smaller than that of the PC-combustor of 40 %, being only 0.6 times, the effects of combustion enhancement in the former due to a series of radial and multiple flame jets can compare with those of the latter caused by a coaxial set of flame jets.

The combustion behavior in the FD-combustor can be clearly distinguished from those in the other

two types of constant volume combustors. In the divided chamber combustor, the multiple flame jets are suffered from intense cooling both by the nozzle walls in their passages through them and the cold mixture entrained by the high-speed flame jets just after the nozzle exits, resulting in an extreme long ignition delay time. In the ND-combustor, no disturbance extends to all over the combustion chamber at the beginning of spark ignition, resulting in the slow and moderate laminar flame propagation. These differences in the burning conditions realize not only early ignition due to laminar flame propagation from the flame kernel around the spark discharge, but also quick transition from laminar to turbulent flame propagation. As a result, the early pressure rise and steep pressure increase appear.

The lower figure of Fig. 2 presents clearly the differences in the pressure properties caused by the ignition patterns and the methods of combustion enhancement. The maximum pressure increasing rates in the four combustors indicate the following numerical values; $(dp/dt)_{max}$ = 1.02 MPa/ms in the HS-type, 0.87 MPa/ms in the PC-type, 0.38 MPa/ms in the FD-type and 0.06 MPa/ms in the NC-type. These numerical values clarify the extreme effects of multiple flame jets on the process of combustion enhancement in the constant volume combustors [6 ~ 9].

Variations of the maximum pressure and maximum pressure increasing rate with the equivalence ratio.
Variations of the maximum pressure, p_{max} and maximum pressure increasing rate, $(dp/dt)_{max}$ with the equivalence ratio of DME-air mixture are given in Fig. 3(a) and (b) respectively by simply averaging over eight data, where the equivalence ratio is varied in the range of ϕ = 0.8 ~ 1.4 at 0.2 intervals. Figure 3 shows that both the maximum pressure and the maximum pressure increasing rate become larger as the types of combustors change in turn of NC, FD, PC and HS. However, a small difference in the maximum pressure up to about 10 ~ 12 % appears among the four types of combustors, whereas a great difference can be found in the maximum pressure increasing rate. In cases of ϕ = 1.0 and 1.2 the maximum pressure increasing rate in the divided chamber combustors of HS and PC takes a value much greater than that in the NC-combustor by about 12 times and greater than that of the FD-combustor by about 2.4 times. This fact shows again the remarkable influence of the multiple jets on combustion augmentation in the constant-volume combustors. It is found that the HS-type divided

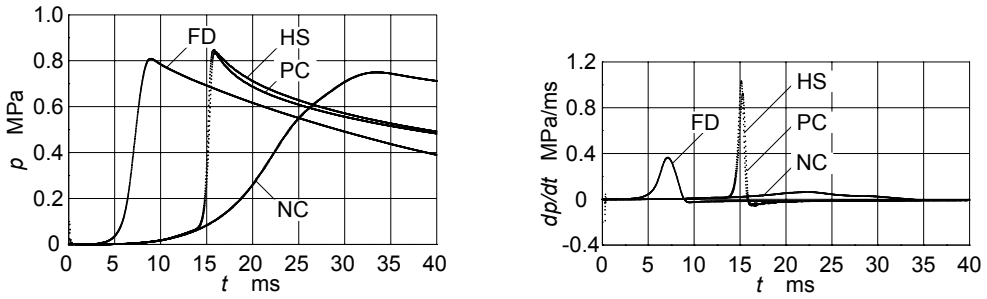

(a) Pressure histories (b) Pressure increasing rates

Figure 2. Temporal pressure profiles and their increasing rate in four types of constant volume combustors, where ϕ = 1.0

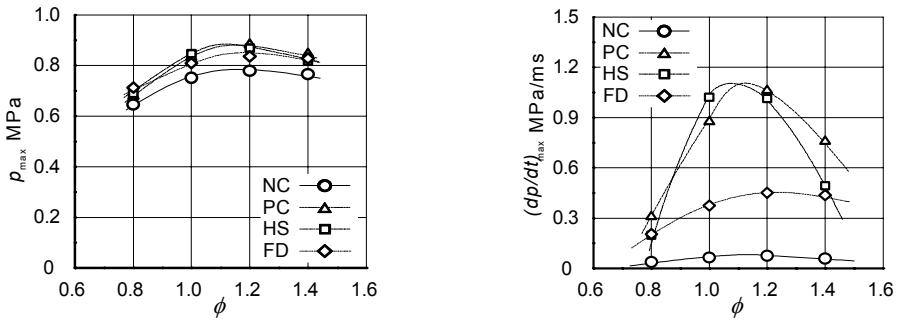

(a) Pressure profiles (b) Pressure increasing rates

Figure 3. Variations of the pressure increasing rate (upper) and maximum pressure (lower) with the equivalence ratio in four types of constant volume combustors

chamber combustor is most useful and effective, when the instantaneous and intense pressure increase in the combustor is focused in the portable, reciprocal and self-sustainable impact machine.

In the divided chamber combustors of HS- and PC-types, the maximum pressure increasing rate exhibits rather strong dependency on the equivalence ratio by comparing with other two types of FD- and NC-combustors. This is because that the thorough mixing and intense turbulence due to high-speed continuous and multiple jets exert more prominent cooling effects on the flame propagation processes of weak mixture of $\phi = 0.8$ and 1.4 than those of strong mixture of $\phi = 1.0 \sim 1.2$.

Variations of three characteristic times with the equivalence ratio. Variations of three kinds of characteristic times with the equivalence ratio; the total burning time τ_t, the net burning time τ_n and the total cooling time τ_c are given in Fig. 4(a), (b) and (c) respectively by simply averaging over eight data. The first is defined as the time when the pressure attains its maximum after the spark ignition, whereas the second is defined as the time duration between the time of initiation of pressure rise and the time of maximum pressure. The third is estimated, on the other hand, using the pressure history by evaluating the time duration between the time of maximum pressure and the time when the pressure decreases to 10 % of its maximum. Figure 4 indicates entirely that three characteristic times exhibit the concave dependency to the equivalence ratio, showing minimum at $\phi \approx 1.2$. The total and net burning times in the NC-combustor take values in the ranges of $\tau_t = 29 \sim 56$ ms and $\tau_n = 15 \sim 28$ ms, respectively, indicating that the slow and moderate laminar flame propagation dominates the entire combustion process in the constant volume combustor.

The dependency of total burning time τ_t on the types of combustors is then considered. The HS- and PC-combustors have longer total burning times than the FD-combustor by 1.7 ~ 2.1 times due to the slow and moderate laminar flame propagation in the sub-chamber. Augmented by the thorough mixing by the multiple jets, however, they complete overall combustion in the main chamber in shorter time periods than the NC-combustor by about 0.5 times. When the behavior of net burning time is focused in Fig. 4(b), it is found that the divided chamber combustors can accomplish such short net burning times ranging in $\tau_n = 1.1 \sim 2.4$ ms that they become about a half of that of the FD-combustor in the range of $\tau_n = 2.2 \sim 4.9$ ms. This experimental fact indicates the effects of combustion enhancement due to the multiple flame jets in the divided chamber combustor are superior to those by the stirring fan in the FD-combustor.

In the reciprocal and self-sustainable impact machine under consideration, the returning time of the piston to its original position after the spark ignition constitutes another key factor. The interrelation between the cooling effects and the methods of combustion enhancement is examined, based on the dependency of τ_c on the types of combustors. Figure 4 (c) indicates that the total cooling time becomes longer as the types of combustors change in turn of FD, HS, PC and NC, and that in the FD-combustor τ_c takes a very short time in the range of $\tau_c = 0.11 \sim 0.13$ s and is almost kept constant. Also found is that τ_c in the NC-combustor becomes longer than the other three combustors by about 2

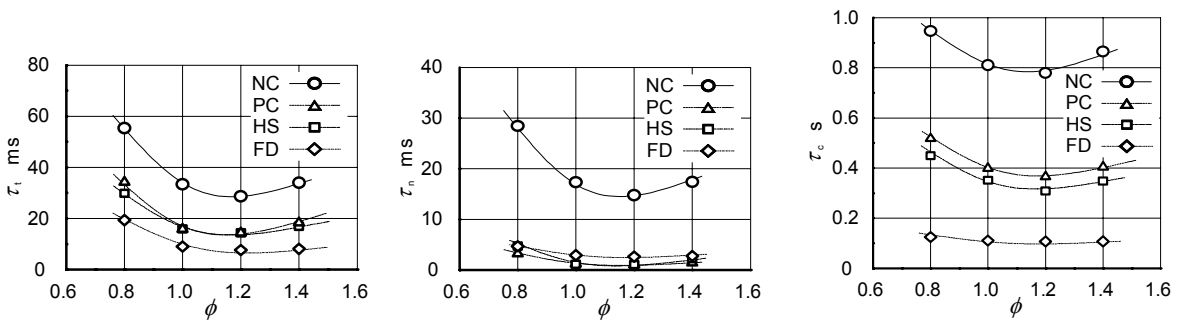

(a) Total burning time (b) Net burning time (c) Total cooling time

Figure 4. Variations of the total and net burning times and the total cooling time with the equivalence ratio in four types of constant volume combustors

~ 9 times and has a value in the range of $\tau_c = 0.79 \sim 0.96$ s.

The total cooling time in the divided chamber combustors of HS- and PC-types is then considered. As discussed earlier in this paper, the multiple flame jets issue into the main chamber, stir the entire main chamber and promotes effectively combustion after ignition in the main chamber. In spite of these positive influences of the multiple jets particular to the divided chamber combustor, the cooling time short enough to realize reciprocal and self-sustainable combustion can not be attained. The following two reasons are considered. First, the stirring effect of multiple jets in the divided chamber combustor is effective only in the combustion period in the main chamber and does not continue to the cooling stage after the combustion terminates. Second, the highly viscous character of high temperature combustion gas may attenuate flow and turbulence and result in quick disappearance of stirring motion in the main chamber. The combined effects of these two negative factors are the key reason for producing longer cooling times than the FD-combustor. In the FD-combustor the stirring motion is forcedly sustained in the entire combustion and cooling periods and promotes heat transfer to the entire walls of combustor and piston. It is concluded that the FD-type constant volume combustor which combines both remarkable enhancement effects of combustion and heat transfer is most suitable for applying it to the potable, reciprocal and self-sustainable impact machine.

High-speed photographing of combustion process and cold flow visualization in the fan-stirred combustor

Combustion process in the fan-stirred combustor. Eight images extracted from a series of high-speed movie of the combustion process in the FD-combustor are presented in Fig. 5 on the pressure history, where the number of fan revolution is set at $n = 8000$ rpm, the mixture equivalence ratio is set to $\phi =$ 1.0, and the framing speed is 1000 fps. The timings of eight images correspond to the typical stages shown on the pressure profile. In the images the direction of fan revolution is anti-clockwise, as indicated by a white arrow circle. Although ambiguity in the images is indispensable in photographing high-speed phenomena such as combustion in the constant volume combustor, the following characteristic behavior can be observed in Fig. 5. The pressure begins to increase at $t = 3 \sim 4$ ms after the spark ignition, whereas weak but uniform flame emission is apparent in the entire combustion chamber at $t = 6$ ms almost in accordance with the appreciate pressure rise. Once combustion due to turbulent flame propagation occurs, the steep pressure increase proceeds almost synchronized with quick spreading of flame emission in the short time duration of about 4 ms. Following its maximum at $t \approx 10$ ms, the pressure decreases gradually with the uniform and gradual reduction of flame emission. Temporary variation of flame emission from its appearance to disappearance takes place almost uniformly in the entire volume of combustor, being one of the typical behaviors in the FD-combustor.

Flow visualization in the fan-stirred cold water model flow. Nine reflection images extracted from a

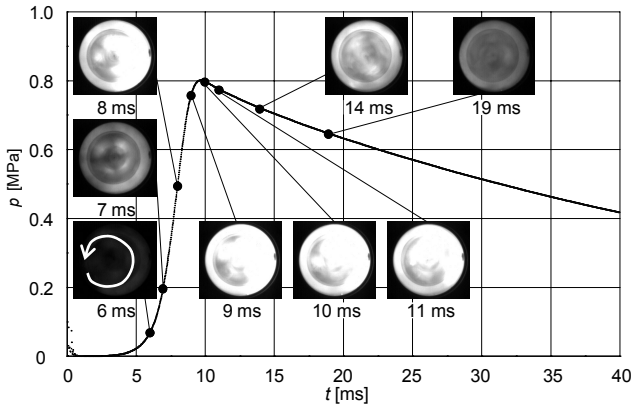

Figure 5. Typical eight images of combustion process on a typical pressure profile in the FD-combustor, where the fan is rotated at $n = 8000$ and $\phi = 1.0$

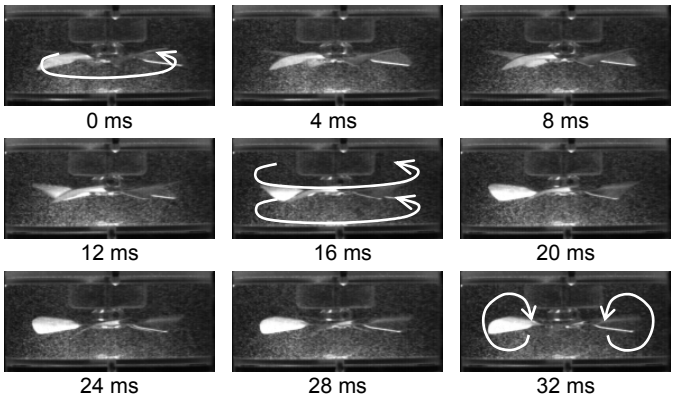

Figure 6. A series of high-speed reflection images from PET particles in the fan stirred model water flow, where the fan is driven at n = 340 rpm

movie of cold water flow in the model FD-combustor are presented in Fig. 6, where the fan rotates at n = 340 rpm and the framing speed of the movie is 500 fps. The water flow simulates the cold gas flow generated in the FD-combustor at the fan revolution of n = 6,500 rpm. As indicated by a white arrow circle in the first image of Fig. 6, the fan rotates in the clock-wise direction. Although it is difficult to understand and construct the flow patterns in the combustor based on still images such as given in Fig. 6, detailed and careful observation of the high-speed movie makes clear the following two basic flow patterns particular to the fan-stirred constant volume combustor.

As indicated by two sets of white arrow circles in the image at t = 16 ms, at first, the fan induces a strong swirling flow in the cylindrical combustion chamber due to the centrifugal force. The swirling flow may play an important role in heat transfer enhancement to the cylindrical wall. The fan produces another flow, secondly, as illustrated by two white rings in the image at t = 32 ms. The axial flow driven by the fan flows downward across the fan, diverges radially and uniformly outward at the bottom, ascends up along the cylindrical wall and join the original downward flow to constitute a doughnut-like ring flow. The ring flow may also play an important role in thorough mixing in the combustor. Based on detailed observation of the high-speed movie, it can be considered that the flow field in the FD-combustor consists of the two typical flows; one is the strong fan-induced swirling flow and the other is the doughnut-like ring flow, and constitutes a complex composite flow.

Flow measurements using a hot-wire anemometer show that, by the way, the time-averaged maximum velocities of the swirling and ascending flows take values of about 10 m/s and 5 m/s, respectively, and the turbulence intensity takes high values in the range of 0.5 ~ 2.0 m/s. Although quantitative discussion on the flow properties is difficult because of the peculiarity of flow measurements using the hot-wire anemometer, the fan-driven composite flow with intense turbulence is found to plays effective roles in combustion enhancement. However the convergent and divergent flows along the upper and bottom end walls and the composite ascending flow along the cylindrical wall may exert negative effects, suppressing turbulent flame propagation near the combustor wall through enhanced heat transfer from hot combustion gas to the wall. Based on the considerations on the pressure characteristics, these flow properties particular to the FD-combustor reduce both the maximum pressure and maximum pressure increasing rate on one hand, and enable to shorten the returning time of the piston to its original position due to augmented heat transfer after the pressure attains to its maximum, on the other.

Detailed considerations concerning the pressure histories and high-speed movies suggest that the FD-combustor combining simultaneous enhancement of combustion and heat transfer is suitable for the portable, reciprocal and self-sustaining impact machine. However, since the HS-type divided chamber combustor exhibits conspicuous enhancement for combustion, it is still extremely useful for the same application. To obtain the best configuration of the HS-combustor which realizes simultaneously enhancement of combustion and heat transfer, the overall influences of the volume ratio and the number, arrangement and diameter of nozzle on the enhancement mechanisms of both combustion

and heat transfer should be precisely examined, being the future experimental problems.

CONCLUDING REMARKS

The results obtained in this paper are summarized as follows.

(1) When the dependency of the pressure on the equivalence ratio is examined from the viewpoint of combustion enhancement, the mixture of $\phi \approx 1.2$ indicates the highest pressure, the steepest pressure increasing rate and the shortest net burning time. Concerning the dependency of the maximum pressure increasing rate on the methods of combustion enhancement, the HS-combustor realizes the most pronounced effects and the shortest net burning time.

(2) Concerning the dependency of the total cooling time on the equivalence ratio, it varies moderately in the concave manner and takes the minimum at $\phi \approx 1.2$, independent of the types of combustors. The dependency of the total cooling time on the types of combustors, however, becomes remarkable and the cooling time becomes longer as the types of combustors change in turn of FD, HS, PC and NC. The total cooling time in the FD-combustor takes the shortest value of $\tau_c \approx 0.10$ s.

(3) The intense and continuous turbulent flow in the FD-combustor realizes simultaneously moderate combustion enhancement and continuous heat transfer augmentation. As a result, the combustion process consists of the initiation of weak but uniform flame emission, the steep but uniform growth of flame emission and the gradual but uniform attenuation of flame emission. It is found that the FD-combustor combines suitable combustion enhancement and intense heat transfer promotion.

(4) The fan-induced flow pattern in the FD-combustor consists of two basic flows; one is the strong swirling flow and the other is the doughnut-like ring flow, both being driven by the fan. This complex composite flow makes possible simultaneous enhancement of combustion and cooling in the constant volume combustor and constitutes one of the most suitable combustion patterns for realizing the combustion-driven, portable, reciprocal and self-sustainable impact machines.

ACKNOWLEDGMENT

The authors acknowledge Mr. H. SUGIURA, Mr. K. MORITA, Mr. J. MATSUMOTO and Mr. Y. SUGINO for their valuable and faithful contributions during this research and development.

REFERENCES

1. N. Ichikawa, et al., *Proc. 42nd Chugoku-Shikoku Branch Regular Meeting of the JSME* (in Japanese), No. 045-1, pp. 277-278, 2004.
2. N. Naito, et al., *Proc. 43rd Chugoku-Shikoku Branch Regular Meeting of the JSME* (in Japanese), No. 055-1, pp. 217-218, 2005.
3. S. Kumagai and I. Kimura, *Proc. the Combustion Institute*, Vol. 4, pp. 667-669, 1953.
4. K. Iinuma, *Proc. 14th National Symposium on Combustion* (in Japanese), pp. 142-144, 1981.
5. K. Wakai, et al., *Trans. JSME* (in Japanese), Vol. 47, No. 417, Ser. B, pp. 872-879, 1981.
6. N. Ohiwa and S. Yamaguchi, *Trans. JSME* (in Japanese), Vol. 49, No. 444B, pp. 1799-1809, 1983.
7. S. Yamaguchi, N. Ohiwa and T. Hasegawa, *Combust. Flame*, Vol. 59, No. 2, pp. 177-187, 1985.
8. N. Ohiwa, S. Yamaguchi, T. Hasegawa and M. Ogiso, *Trans. JSME* (in Japanese), Vol. 52, No. 482B, pp. 3609-3615, 1986.
9. Y. Ishino, H. Seo, S. Yamaguchi and N. Ohiwa, *Trans. JSME* (in Japanese), Vol. 66, No. 642, pp. 571-578, 2000.
10. *Open Patent Official Reports of Japan* (in Japanese), P2001-162561A, pp. 1-11, 2001.
11. *Patent Application Official Notices of Japan* (in Japanese), 1989-34753, pp. 1-17, 1989.
12. H. Sugiura, J. Matsumoto, Y. Ishino and N. Ohiwa, *Proc. 42nd Tohoku Branch Regular Meeting of the JSME* (in Japanese), No. 2007-1, pp. 123-124, 2007.
13. K. Morita, Y. Sugino, Y. Ishino and N. Ohiwa, *Proceedings of the Okinawa Joint Meeting of Kyusyu and Chugoku-Shikoku Branches of the JSME* (in Japanese), No. 078-2, pp. 245-246, 2007.

MEASURING OF THERMAL CONDUCTIVITY OF LIQUIDS USING PHOTOTHERMAL RADIOMETRY

A. Kusiak [*], C. Pradère, J.-L. Battaglia
Laboratoire TREFLE "Transfert, Ecoulement, Fluide, Energétique", UMR CNRS 8508, Esplanade des Arts et Métiers, 33405 Talence Cedex, FRANCE

ABSTRACT. A method for the estimation of thermal conductivity of liquids is proposed. The measurement is based on the front face modulated photo thermal radiometry usually used for studies of solid deposit (thin film) on substrate systems. The system considered here, is in the three-layers form, the intermediate layer being the investigated liquid. An experimental setup has been developed in order to avoid the drawbacks of the classical methods like flash or hot wire measurement. The measurement is carried out with low temperature oscillations and the studied liquid is confined in specific (low thickness) container. This configuration leads to very low Rayleigh number and permits to eliminate the convection phenomena during the experiment and to characterize very small (~1 µl) volume of liquid. This is an important feature for metrology of expensive or hazardous samples.
According to the knowledge of the thermo physical properties of the two external to liquid solid layers, the phase lag between the thermal perturbation and the response of the sample is used as the experimental data. The measurement was validated using two well known liquids: water and sunflower oil.

Keywords: *photo thermal radiometry, thermal conductivity, liquid*

INTRODUCTION

The knowledge of thermal conductivity of liquids is very important in many industrial sectors. The estimation of this thermal parameter is well treated in the literature. The principle of the methods used for this purpose is similar as for the solids. The studied medium is submitted to a calibrated thermal solicitation and then the temperature response is recorded. The fitting of a theoretical model of heat transfer in the used experimental configuration to the carried out measurement leads to the required thermal parameter.
The principal classification of the existent methods is based on the temporal evolution of thermal solicitation. In this way, it can be found some techniques based on steady state heat transfer [1]. The technique seems to ensure good results but requires relatively complex and expensive equipments. Moreover, the minimal volume of liquid that can be characterized is generally large what is the major inconvenient in the case of expensive fluids. Another family of methods is based on the response of the studied sample to a transient excitation. The hot wire, the flash or the thermal oscillation are the common techniques. The hot wire measurement is performed using electrically heated metallic wire immersed in the liquid [2, 3, 4, 5, 6]. The change of the electrical resistivity with temperature leads to the simultaneous measurement of temperature and imposed heat flux. The measurement is easier to carry out but the question of the large volume of liquid is still present. On the other hand, the measurement must be carry out with precautions in order to avoid the convection phenomena. The flash method has been initially developed for measurement of the thermal diffusivity of solids [7]. In

* Corresponding author: Dr. A. Kusiak
Phone: + (33)-556845426, Fax: + (33)-556845436
E-mail address: andrzej.kusiak@u-bordeaux1.fr

this method the studied sample is heated by a short and high heat flux pulse and the temperature at the rear face is measured. Temporal evolution of this temperature permits to determine the diffusivity of the sample. Such an application for liquids can be found for example in [8, 9, 10]. The major drawback of this technique is that the convection phenomena may occur due to high temperature elevation at the short times. To avoid such phenomenon, the temperature oscillation measurement seems to be the best compromise. The temperature variation during the measurement may rest small and an appropriate design for the sample container permits to study a small volume of liquid. This an important advantage face to the convection phenomena and the price of the sample [11, 12]. New approaches based on photo thermal radiometry or pump-probe technique appeared recently [13, 14].
In this work we present a method for the determination of the thermal conductivity of liquids. The measurement is an extension of the periodic front face photo thermal radiometry developed for studies of thin film on substrate systems [15, 16]. The system considered here is in the three-layer form, the intermediate layer being the investigated liquid considered here as opaque for thermal (infrared) radiation. The thickness of the liquid layer is very small (500 µm). This value with low temperature oscillation (2 K) ensures that no natural convection occurs in the liquid layer. Therefore only the heat diffusion is considered for the modelling of heat transfer in the sample. In section EXPERIMENTAL SETUP, the experimental heating-measuring system and the sample are presented. Section HEAT TRANSFER MODEL describes the governing equations used for the heat transfer description in the studied system. The behaviour of this model according to its different parameters is presented in section SENSITIVITY OF THE MODEL. Finally, the results of validation and the measurement using water and sunflower oil are presented in section RESULTS OF VALIDATION.

EXPERIMENTAL SETUP

The schematic view of the experimental setup is presented in Figure 1 a).

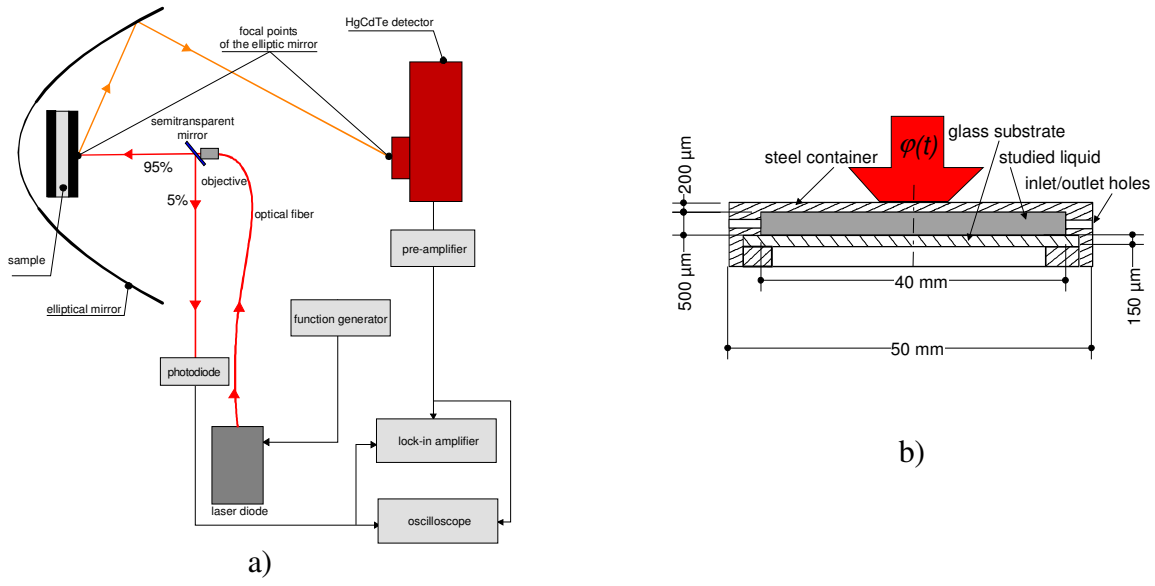

Figure 1. Schema of: the experimental setup a), the sample b)

The thermal excitation is generated on the sample front face by a laser diode of 920 nm wavelength and 2.5 W maximal power. The laser diode is directly modulated by its driver using the sinusoidal signal issued from a function generator. The allowed modulation frequency range is up to 20 kHz. The laser beam is brought to the sample by an optical fiber equipped with a microscope objective allowing to focus the laser beam at desired diameter on the sample surface. The laser beam has a Gaussian profile of power repartition on the spot of 5 mm in diameter at $1/e^2$. A very fast photodiode (Thorlabs DET10A/M) is used to measure the reference signal in order to avoid the phase lag due to the laser

diode driver. The thermal response is measured by an infrared detector based on HgCdTe (Infrared Associates 2C-13-1.0). The measurement wavelength range is comprised between 5 and 13 µm. The elliptical mirror coated with high reflective rhodium (reflectivity of 98% in the infrared detector wavelength band) is used to collect the emitted infrared radiation and to focus it on the infrared detector. In fact, the heated surface of the sample is located at the interior focal point of the mirror and the sensitive element of the detector at the exterior one, what results in a conjugate focuses system. The incident laser beam is centred and aligned on the focal axis of the mirror. The detector wavelength band is largely greater than that of the laser, what gives the advantage that the measurement is not disturbed by the excitation source. The zone viewed from the detector is the image of the infrared sensitive element on the sample; it corresponds to a circle of 1 mm in diameter.

The signal from the detector is amplified with an adapted preamplifier (Infrared Systems MCT-1000), and then is visualized on a digital oscilloscope with the photodiode signal. A lock-in amplifier is used to measure the amplitude and the phase lag between the reference source and the detector signals versus the frequency.

For the sample, the system considered here is in three layers form. The first layer is constituted of steel. This metallic layer submitted to the laser beam leads to surfacic absorption of the heat flux. The second layer is the studied liquid (opaque for thermal radiation), and finally the last one made of glass, is transparent in the visible band and opaque in the infrared. This glass layer permits to verify that the sample is well filled with liquid.

For the sample size, a large ratio between the diameter and the thickness was chosen in order to neglect the heat transfer at the periphery and to emphasize the heat diffusion in the transverse direction of the sample. In fact, considering the thermal diffusivity of the first steel layer (that is the highest in this system) the radius of the sample (20 mm) was chosen to ensure the heat diffusion time from the centre to the periphery be largely greater than that corresponding to the frequency explored during the measurement. The geometrical characteristics of the sample are represented in Figure 1 b).

HEAT TRANSFER IN THE SAMPLE

During the experiment the cylindrical sample is submitted to a heat flux from a laser on its metallic layer ($z = 0$) (see Figure 2). r_0 and r_m correspond to the heating and the measurement radius respectively, e_i describes the thickness of each layer.

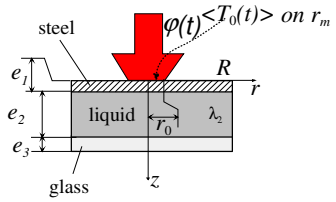

Figure 2. Schema of the geometrical configuration of the sample considered for the model

Such a heat flux is applied at the centre of the sample in order to ensure the axis-symmetry condition. The external surfaces of the steel and the glass layer are submitted to natural convection described by the coefficient h. The convective exchange at the periphery is neglected because of the small surface and the heat diffusion time largely exceeding the heat flux modulation period. The temperature in the system is described by the set of equations in the cylindrical coordinates with r, z space, and t time variables:

$$\frac{1}{r}\frac{\partial}{\partial r}\left(r\frac{\partial T(r,z,t)}{\partial r}\right)+\frac{\partial^2 T(r,z,t)}{\partial z^2}-\frac{1}{\alpha_i}\frac{\partial T(r,z,t)}{\partial t}=0$$
$$i=1,\ 2,\ 3 \tag{1}$$
$$0<r<R,\ 0\le z\le e_1,\ e_1\le z\le e_2,\ \ e_2\le z\le e_3,\ \text{t>0}$$

The index i corresponds to the layer 1: steel, 2: liquid and 3: glass and α_i and λ_i are the thermal diffusivity and the thermal conductivity of the layer i. The used initial and boundary conditions are:

$$\frac{\partial T(r,z,t)}{\partial r}=0,\ r=0,\ r=R,\ 0<z\le e_1+e_2+e_3,\ t>0 \tag{2}$$
$$-\lambda_1\frac{\partial T(r,\ z,\ t)}{\partial z}=\begin{cases}\varphi_0(r,\ t)+hT(r,\ z,\ t)\ \ 0\le r\le r_0\\ hT(r,\ z,\ t)\ \ r_0\le r\le R\end{cases} \tag{3}$$
$$z=0,\ t>0$$
$$-\lambda_3\frac{\partial T(r,\ z,\ t)}{\partial z}=hT(r,\ z,\ t) \tag{4}$$
$$0\le r\le R,\ z=e_1+e_2+e_3,\ t>0$$
$$T(r,\ z,\ t)=0$$
$$0\le r\le R,\ 0\le z\le e_1+e_2+e_3,\ t=0 \tag{5}$$
$$\lambda_1\frac{\partial T(r,\ z,\ t)}{\partial z}=\lambda_2\frac{\partial T(r,\ z,\ t)}{\partial z} \tag{6}$$
$$0\le r\le R,\ z=e_1,\ t>0$$
$$\lambda_1\frac{\partial T(r,\ z,\ t)}{\partial z}=\lambda_2\frac{\partial T(r,\ z,\ t)}{\partial z} \tag{7}$$
$$0\le r\le R,\ z=e_1+\mathrm{e}_2,\ t>0$$

The application of Laplace and Hankel integral transforms on the time t and radius r variables [16] in this set of equations leads to the expression of the average temperature investigated on the metallic surface as a function of the applied heat flux in the Laplace domain:

$$\left\langle\theta(z=0,\ p)\right\rangle=Z(p)F(p) \tag{8}$$

$Z(p)$ being the transfer function:

$$Z(p)=\frac{r_0^2}{R^2}\frac{\beta_z}{1-h\beta_z}+\sum_{k=0}^{\infty}\frac{4r_0^2J_1(\alpha_k r_m)}{\alpha_k r_m R^2 J_0(\alpha_k R)^2}\frac{\beta_z}{1-h\beta_z}\exp\left(-\frac{\alpha_k^2 r_0^2}{4}\right) \tag{9}$$

where:

$$\beta_z=\frac{M^*_{1,1}+hM^*_{1,2}}{M^*_{2,1}+hM^*_{2,2}},\ M^*=\prod_{i=1}^{3}M_i,\ M_i=\begin{pmatrix}A_i & B_i\\ C_i & D_i\end{pmatrix} \tag{10}$$

and:

$$A_i = \cosh\left(\sqrt{\frac{p}{\alpha_i} + {\alpha_k}^2 e_i}\right),\ B_i = \frac{1}{\lambda_i\sqrt{\frac{p}{\alpha_i} + {\alpha_k}^2}} \sinh\left(\sqrt{\frac{p}{\alpha_i} + {\alpha_k}^2 e_i}\right), \tag{11}$$

$$C_i = \lambda_i\sqrt{\frac{p}{\alpha_i} + {\alpha_k}^2}\ \sinh\left(\sqrt{\frac{p}{\alpha_i} + {\alpha_k}^2 e_i}\right),\ D_i = \cosh\left(\sqrt{\frac{p}{\alpha_i} + {\alpha_k}^2 e_i}\right)$$

$$\alpha_k = \pi\left(k + \frac{1}{4}\right) - \frac{3}{8\pi\left(k + \frac{1}{4}\right)},\ \alpha_0 = 0,\ k = 1...\infty \tag{12}$$

The equivalence of $p = j\omega$ permits to compute the phase of the transfer function as:

$$\phi(j\omega) = \arctan\left(\frac{\mathrm{Im}\left(Z(j\omega)\right)}{\mathrm{Re}\left(Z(j\omega)\right)}\right) \tag{13}$$

with j imaginary unit and $\omega = 2\pi f$ the heat flux (laser) pulsation.
The heat transfer model in the sample only takes into account the heat diffusion in the three layers. To ensure the best reliability of the estimation of the thermal conductivity it is important to avoid the natural convection phenomena while heating during the measurement. This phenomenon, characterized by Rayleigh number, depends on the type of fluid, the dimensions of the container and the temperature oscillations. Several transition regions those occur in a horizontal layer of fluid for a given Rayleigh number in the function of Prandtl number are given in the literature [17]. These numbers are defined as:

$$\mathrm{Ra} = \frac{g\beta\Delta T {e_2}^3}{\upsilon\alpha_2} \text{ and } \mathrm{Pr} = \frac{\upsilon}{\alpha_2} \tag{14}$$

where g is the gravity acceleration; β is the thermal expansion coefficient; ΔT, υ, α_2, e_2 are the temperature variation, the kinematic viscosity, the thermal diffusivity and the thickness of the studied liquid. For a wide range of Prandtl number (10^{-2} to 10^4, that cover the majority of liquids) and the Rayleigh inferior to 2.10^3 the region where no motion occurs exists. The sample of studied liquid must be designed to fulfil the Ra limit. For this purpose, the two parameters ΔT and e_2 may be adjusted. The simulation using precedently described model with absorption of 50% (largely exceeding the experimental configuration) of the maximal laser power leads to the temperature oscillation around 2 K, therefore the thickness e_2 was fixed equal 500 µm in order to cover a wide spectrum of liquids, keeping Ra inferior to the mentioned limit 2.10^3.

SENSITIVITY OF THE MODEL

The described previously thermal model (equation 1) depends on different geometrical (the heating and the measurement radius r_0 and r_m and the thickness e_i of each layer) and thermo physical parameters (the thermal diffusivity α_i, the thermal conductivity λ_i, and the convective heat transfer coefficient h on the front and back face of the sample).
The geometrical parameters may be measured directly and are considered here as perfectly known. The properties of the steel and the glass layer were obtained by using the Hot Disk technique for the thermal conductivity and the Differential Scanning Calorimetric technique for the specific heat.

The specific heat and the density of the studied liquid are considered also as known. In the application, the literature values are used for water ($C_2 = 4180$ J.kg^{1}.K^{-1} and $\rho_2 = 1000$ kg.m^{-3}) and sunflower oil ($C_2 = 2741$ J.kg^{1}.K^{-1} and $\rho_2 = 918$ kg.m^{-3}) [18, 19]. For an unknown liquid, these parameters may be obtained by DSC experiment and volumetric measurement. The coefficient h was taken equal to 5 W.m^{-2}.K^{-1}. The simulations have shown that the model is not sensitive to this convective parameter on frequency range exploited in the application. In this way, it leads that the thermal conductivity of the liquid layer is the unique parameter to estimate.

Table 1
Known parameters used in the measurement and the analysis of model

i	1	2	3
λ_i [W.m^{-1}.K^{-1}]	24,8	-	1,1
ρ_i [kg.m^{-3}]	7784	-	2600
C_i [J.kg^{-1}.K^{-1}]	438	-	384
e_i [µm]	200	500	150
r_0 [mm]	r_m [mm]		R [mm]
5	0,5		20

In order to determine the frequency range where the measurement of phase varies with the thermal conductivity of liquid, a simulation using the parameters reported in Table 1 for solid layers and those for water as liquid (second layer) was performed. Figure 4 a) shows that the phase varies strongly in the frequency range from 10^{-2} to 10^{2} Hz. To make the experiment as rapid as possible and to fulfil the experimental conditions (frequency response band of the infrared detector) the frequency range between 1 and 50 Hz seems interesting for the measurement. The variations of the phase in this frequency range are sufficient to estimate the thermal conductivity of the liquid. Figure 4 b) represents the variation of the phase with the thickness of liquid layer. It clearly shows that over the chosen frequency range the measurement is not affected by small variations/errors of the second layer thickness. This ensures also that the third layer (glass) does not influence the measurement. Meanwhile, the thermal properties of the first (steel) layer must be perfectly known to make a reliable identification of the thermal conductivity of the second layer.

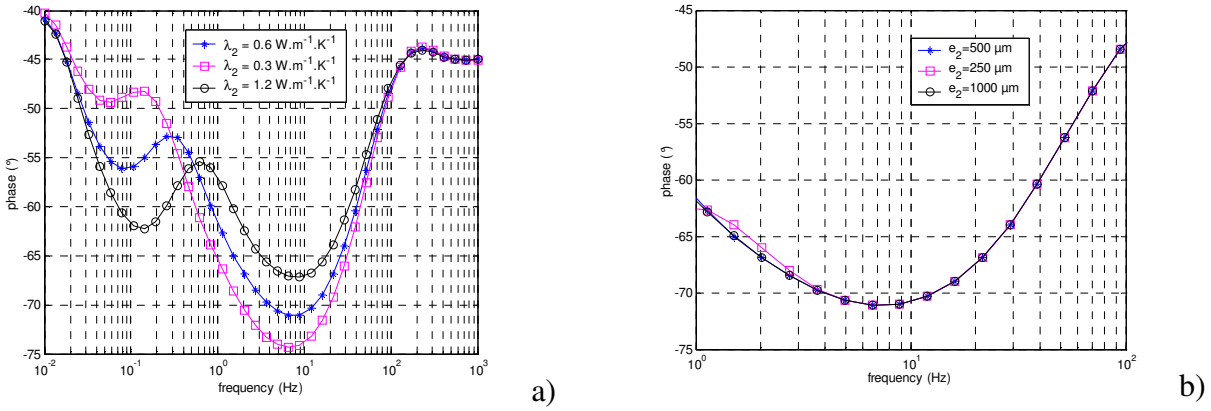

a) b)

Figure 4. Sensitivity to: the thermal conductivity of liquid a), the thickness of the liquid layer b)

RESULTS OF VALIDATION

Two series of measurements were performed: one on water filled sample and the second with sunflower oil. The Rayleigh numbers are equal to 6,56 and 0,55 and the Prandtl numbers are 5,42 and 410 for water and for oil respectively. These values were obtained using the literature data [18, 19, 20, 21, 22].
The values of Ra numbers are very small in comparison with the limit given by [17]. This allows assuming that no convective motion occurred during the experimentation. The used frequency range resulting from the sensitivity analysis is comprised between 5 and 50 *Hz* . The thermal conductivity of liquid is estimated by minimizing the quadratic gap between the theoretical and the experimental values of the phase [23]. The fits of the experimental points of phase lag measurement are presented in Figure 5.

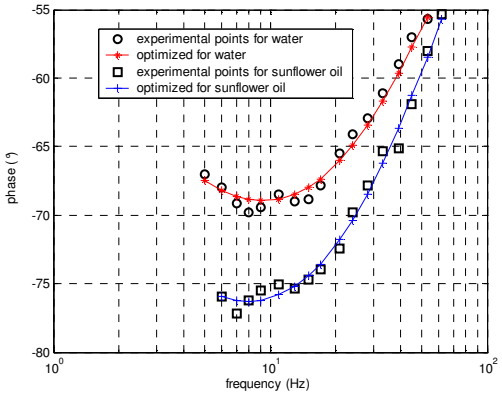

Figure 5. Optimization of the experimental points of phase lag in water and sunflower oil measurement

These fits lead to the following values of thermal conductivity: $0,61 \pm 0,02$ W.m^{-1}.K^{-1} for water and $0,22 \pm 0,02$ W.m^{-1}.K^{-1} for sunflower oil. These values are in agreement with the literature and the tests performed using the hot wire measurement. The uncertainty is lower than 5%. The obtained results prove the reliability of the used method.

CONCLUSION

An application of photo thermal radiometry to the measurement of thermal conductivity of liquids at ambient temperature was presented. The developed small sample dimensions and the low temperature oscillation ensure that the convection does not occur during the measurements and only heat conduction model for describing the experiment may be used. The measurement requires only a small quantity of liquid (~1 µl) what gives an important advantage for studies of expensive or hazardous samples.
The proposed system of measurement may be easily extended for studies at different temperatures by controlling of the temperature of the sample cell. For the liquids transparent or partially transparent in IR band the modelling of heat transfer must be completed by the radiative part.

REFERENCES

1. Celik D. and Van Sciver S.W., Thermal conductivity of subcooled liquid oxygen. Cryogenics, 45:620-625, 2005.
2. De Groot J. J., Kestin J., and Sookiazian H., Instrument to measure the thermal conductivity of gases. Physica, 75:454-482, 1974.

3. Hwang Y.J., Ahn Y.C., Shin H.S., Lee C.G., Kim G.T., Park H.S., and Lee J.K., Investigation on characteristics of thermal conductivity enhancement of nanofluids. Current Applied Physics, 6:1068-1071, 2006.
4. Lee S., Choi U.-S., Li S., and Eastman J. A., Measuring thermal conductivity of fluids containing oxide nanoparticles. Journal of Heat Transfer, 121:280-288, 1999.
5. Parsons J. R. Jr and Mulligan J. C., Measurement of the properties of liquids and gases using a transient hot-wire technique. Review of Scientific Instruments, 49:1460-1463, 1978.
6. Zhang X., Gu H., and Fujii M., Effective thermal conductivity and thermal diffusivity of naonfluids containing spherical and cylindrical nanoparticles. Experimental Thermal and Fluid Science, 31:593-599, 2007.
7. Parker W. J., Jenkins W., Butler C. P., and Abbot G. L., Flash method determining thermal diffusivity, Heat capacity and thermal conductivity. Journal of Applied Physics, 39:1679-1684, 1961.
8. Tada Y., Harada M., Tanigaki M., and Eguchi W., Laser flash method for measuring thermal conductivity of liquids - application to low thermal conductivity liquids. Review of Scientific Instruments, 49:1305-1314, 1978.
9. Remy B. and Degiovanni A., Parameters estimation and measurement of thermophysical properties of liquids. International Journal of Heat and Mass Transfer, 48:4103-4120, 2005.
10. Blumm J., Lindemann A., and Min S., Thermal characterization of liquids and pastes using the flash technique. Thermochimica Acta, 455:26-29, 2007.
11. Kuntner J., Kohlb F., and Jakoby B., Simultaneous thermal conductivity and diffusivity sensing in liquids using a micromachined device. Sensors and Actuators A, 130-131:62-67, 2006.
12. Bhattacharya P., Nara S., Vijayan P., Tang T., Lai W., Phelan P.E., Prasher R.S., Song D.W., and Wang J., Characterization of the temperature oscillation technique to measure the thermal conductivity of fluids. International Journal of Heat and Mass Transfer, 49:2950-2956, 2006.
13. Sreekumar K. and Vaidyan V. K., Measurement of thermal effusivity of liquids using a photothermal imager. Measurement Science and Technology, 17:666-669, 2006.
14. Schmidt A., Chiesa M., Chen X., and Chen G., An optical pump-probe technique for measuring the thermal conductivity of liquids. Review of Scientific Instruments, 79:064902-064902-5, 2008.
15. Kusiak A., Battaglia J. L., Gomez S., Manaud J. P., and LePetitcorps Y., Cuo thin films thermal conductivity and interfacial thermal resistance estimation. European Physical Journal Applied Physics, 35:17-27, 2006.
16. Battaglia J. L., Kusiak A., Bamford M., and Batsale J. C., Photothermal radiometric characterization of a thin deposit using a linear swept-frequency heat flux waveform. International Journal of Thermal Sciences, 45:1035-1044, 2006.
17. Krishnamurti R., Some further studies on the transition to turbulent convection. Journal of Fluids Mechanics, 60:285-303, 1973.
18. Weast R. C. et al., CRC Handbook of Chemistry and Physics. CRC Press, 1988.
19. Santos J. C. O., Santos M. G. O., Dantas J. P., Concei Marta M., Athaide-Filho P. F., and Souza A. G., Comparative study of specific heat capacities of some vegetable oils obtained by DSC and microwave oven. Journal of Thermal Analysis and Calorimetry, 79:283-287, 2005.
20. Balderas-Lopez J. A. and Mandelis A., Self-consistent photothermal techniques: Application for measuring thermal diffusivity in vegetable oils. Review of Scientific Instruments, 74:700-702, 2003.
21. Knothe G. et al., The biodiesel handbook. Urbana, AOCS Press, 2005.
22. Quinchia L. A., Delagado M. A., Valencia C., Franco J. M., and Gallegos C., Viscosity modification of high-oleic sunflower oil with polymeric additives for the design of new biolubricant formulations. Environmental Science and Technology, XX:XXX-XXX, 2009.
23. More J. J., The Levenberg-Marquardt algorithm: Implementation and theory. Numerical Analysis, ed. G. A. Watson, Lecture Notes in Mathematics, 630:105-116, 1977.

EXPERIMENTAL INVESTIGATION OF TEMPERATURE DISTRIBUTIONS IN BULK MATERIALS

F. Weigler*, T. Hoffmann, M. Naumann, M. Peglow, E. Tsotsas
Thermal Process Engineering, Otto-von-Guericke-University Magdeburg, Universitaetsplatz 2, 39106 Magdeburg, Germany

ABSTRACT. In view of a better description of the heating behavior of bulk systems, a new experimental method which permits the measurement of temperature distributions of single particles in beds of spheres was developed. The experimental investigations are carried out with particles which are coated with thermo-chromic pigments. By change of particle temperature the pigment color changes as a result of structural phase transition. With the help of a suitable calibration the change of pigment color, which corresponds to the change of particle temperature, is correlated in a way that allows the temperature distribution in the bed to be measured by photo-optical analysis. The measuring technique enables the experimental description of temperature distributions in the disperse phase, so that the heat transfer process can be described at the single-particle level. In the present work first measurements carried out in stagnant particle systems are presented and compared with DEM (discrete element method) simulations. The DEM provides the possibility to treat the problems of mechanical movement and heat transfer between particles simultaneously, so that it is easily extendable to agitated beds.

Keywords: *heat penetration, thermal DEM, thermo-chromic pigments, particle systems*

INTRODUCTION

The thermal treatment of powdery or granular products in tray, drum or paddle equipment by contact with the hot wall, shaft or inserts of the apparatus belongs to the most common processes in chemical engineering. Mixing in rotating drums is often coupled with heating from the wall of the drum, and has often a large influence on the rate of heat transfer to the particles. To control the drying process in contact dryers one needs to determine the heating behavior of the material in the dryer. In order to evaporate the moisture, heat must be transferred from a heating surface to the static or mechanically bed of particles. The heat transfer takes place by first overcoming a thermal conduction resistance between heating surface and the bed (first particle layer) and then by overcoming a penetration resistance inside the bed. The two heat transfer resistances are connected in series.
Continuum models are traditionally used for the description of the process [1]. An example is the penetration model (PM), which approximates the heating process of the particles by means of a sequence of penetration periods and subsequent mixing periods. This means that the bed is assumed to lie motionless for a certain time, followed by a perfect mixing of the particles, which is assumed to take place instantaneously. This cycle is then repeated, starting with a further static period.

The most important limitations of the penetration model are that the link to the mechanics of motion of the granular material is missing and that quasi-homogeneous behavior is assumed. Therefore, the use of the thermal version of the Discrete Element Method (thermal

*Corresponding author: Dipl.-Ing. Fabian Weigler
Phone: +(49)-391-67-11059, Fax: +(49)-391-67-11160,
E-mail address: Fabian.Weigler@st.ovgu.de

DEM) is a new and promising approach [2, 3]. By the thermal DEM the mechanical behavior (including deterministic patterns of particle motion) is directly coupled to the heat transfer and vice versa. This would be a change of paradigm for the considered class of problems, opening (due to easier scale-up and real access to the density functions of distributed particle properties) completely new opportunities for process and product engineering. In fact, mechanical DEM has attained maturity in the last decade and demonstrated many successes in the solution of problems, including mixing of granules by mechanical agitation. However, several issues concerning thermal DEM are still open, with experimental validation probably being the most important [2, 3].
Therefore, the goal of the present work is to develop an experimental setup to validate the numerical simulations of inter-particle heat transfer in stagnant and agitated beds.
To this purpose, the presumably simplest possible problem of thermal equilibration between two groups of spherical particles in a two-dimensional drum without inserts will be considered. The two particle groups are initially stratified in the drum and have different temperatures (cold and hot particles).
The experimental setup and the functional principle of thermo-chromic pigments are first described in this paper. Then, the experimental procedure and modeling by thermal DEM are discussed. Subsequently, selected experimental results (measured distributions of particle temperature) are presented and compared with the results of thermal DEM. The paper ends with a brief summary and outlook.

EXPERIMENTAL SETUP

To validate the thermal DEM simulation a novel experimental system has been developed. With this system the temperature distributions emerging in beds of particles during heat transfer processes can be measured. In the present investigation the particles were alumina spheres coated with thermo-chromic pigments. Thermo-chromic pigments are pigments that change from colored to colorless by increasing the temperature. This color change is reversible. It is the result of a structural phase transition of the pigment with temperature (see figure 1). The structural phase transition is accompanied by a change of the absorption spectrum of light. Optical thermometers are a typical, every-day application of thermo-chromic pigments.

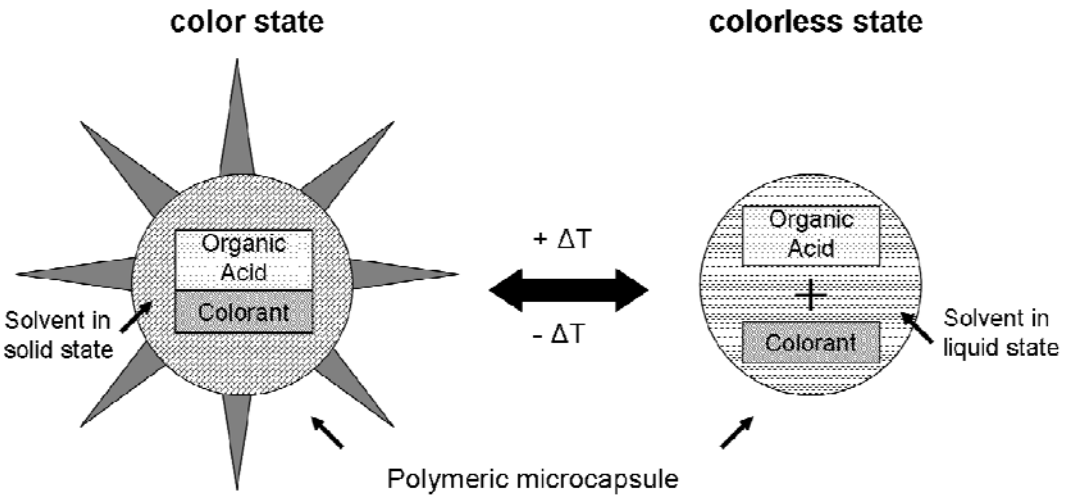

Figure 1. Functional principle of thermo-chromic pigments

The interrelation between the hue of the pigments (that means the color within the range of visible light wavelengths) and the temperature is non-linear and depends on several parameters, for example on the viewing angle and the source of light. To eliminate external influences on the intensity of the hue and to guarantee steady lighting conditions, the whole experimental setup, which consists of an acrylic glass box, is mounted on a lighting rack. Each source of light of the lighting rack consists of two fluorescent lamps. Since our goal is to investigate the heat transfer between particles, heat transfer from the particles to their surroundings should be controlled and minimized. To this purpose, the entire box is tempered to a constant temperature by means of air heated by a heating element and circulated by a radial fan with a permanent and constant flow rate. Two thermocouples and one mercury thermometer measure and control the gas temperature in the box. In the front side of the acrylic glass box an optical window is inserted, which allows to film into the box without disturbing the process. The video system that is used to record the color change of the spheres stands in front of the box. To minimize the reflection of light on the windowpane, the video system is aimed vertically at the window and at the drum, where the thermal equilibration process between the particles takes place (see figure 2).
To be consistent during the entire experimental investigation, the parameters of the used high-resolution video camera such as screen (iris), signal strengthening (gain), focus, zoom, white comparison and the distance to the drum are kept constant. In order to recognize unwanted changes in the experimental set-up, a test stripe with three basic colors (red, green and blue) is placed beside the test drum. The hue values of the test stripe must be the same in every experiment in order to ascertain the precise reproduction of the hue values of the particles. The recorded images of the color change of the particles are evaluated photo-optically by an image analysis program from Olympus called AnalySIS pro**.**
AnalySIS pro determines the hue of every single pixel from the image. The hue represents the dominant wavelength, which depends on temperature. With the help of a suitable calibration the hue can be correlated with the temperature of the particle. The calibration is the main focus for the analysis of the thermal experiments. The calibration curve provides an explicit correlation between the temperature and the hue. Though the temperature measurement is based on the RGB model (Red-Green-Blue), RGB information alone is not sufficient for an explicit correlation of hue and temperature. The latter is therefore achieved by the HSI model (Hue-Saturation-Intensity). The HIS model is based on the physiological perception of colors by the human eye. Because of the separation of intensity and color, the HSI model is often used in image processing.

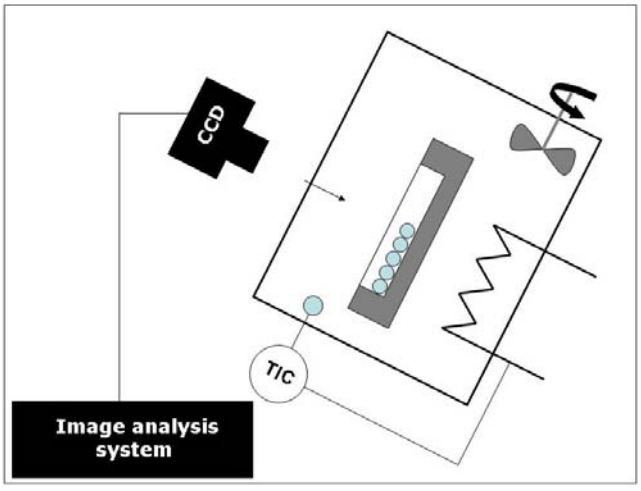

Figure 2. Scheme of the experimental setup

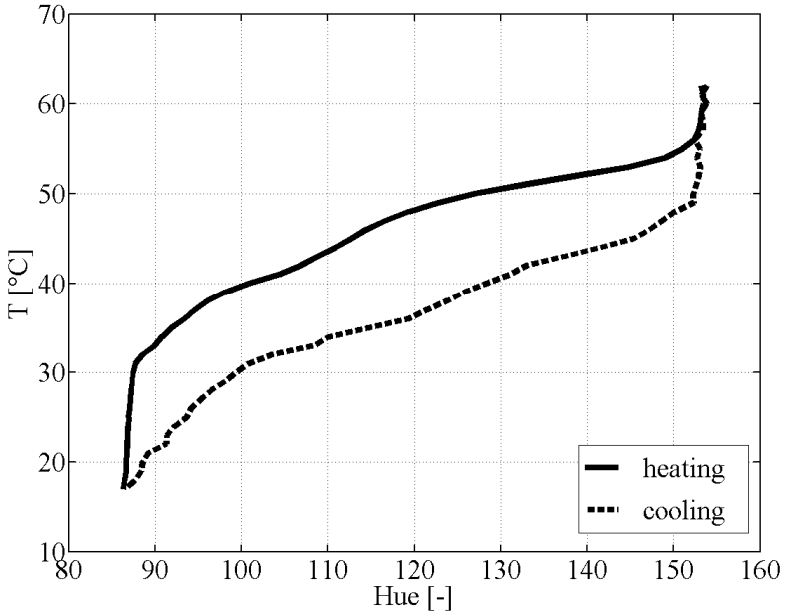

Figure 3. Calibration – correlation of the hue with the temperature of the pigment mixture (red RT38 / green GT43 / blue BT50 / orange OT55)

Calibration was conducted in-situ, by imposing selected temperatures on the acrylic glass box, the drum and the particles and measuring the respective values of the hue. The already mentioned tempering facilities were used to this purpose. This was done twice, once with incrementally increasing and a second time with incrementally decreasing temperature, in order to account for the hysteresis behavior between heating and cooling of the pigments (see figure 3). Such behavior is well known and characteristic for thermo-chromic pigments. The examined temperature measuring range goes from 18°C to 62°C.

THERMAL EXPERIMENTS

For the thermal experiments, alumina spheres with a diameter of 4 mm were coated in a fluidized bed process with a mixture of pigments (red RT38 / green GT43 / blue BT50 / orange OT55). This was done to increase the working range for the experiments, because every pigment has a different color change temperature. All experiments were carried out in a flat drum with an internal diameter of D = 0.05 m with the mentioned spherical particles (d = 4 mm). The particle density for alumina is $\rho = 2700$ kg/m^3 and the specific heat capacity is c_p = 900 J/kg K. All experiments were conducted with 70 coated alumina spheres divided in two equal fractions (35 particles each). One fraction was tempered with the help of a thermostat to 50°C and the other fraction to 25°C. Then, the two fractions were piled up successively in the insulated flat drum, resulting in a stratified arrangement with one fraction at initially 25°C and the other at initially 50°C (see figure 4). The arrangement is two-dimensional (it has a thickness of just one particle diameter in the direction parallel to the axis of the drum). Then the drum with the spheres was put in the preheated isothermal acrylic glass box and was exposed to the camera. The recording with the high-resolution camera started while putting the drum in the box. To quantify the influence of heat exchange between the particles and their surroundings (which is undesired but unavoidable) the temperature of the chamber and the material of the drum (polyurethane, polystyrene) were varied.

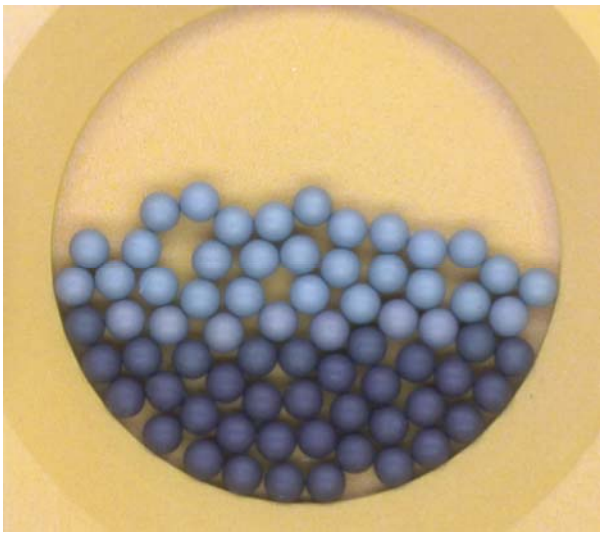

Figure 4. Coated alumina spheres of different temperature piled up in an insulated drum in a two-dimensional way

The experiment runs until equilibration of the temperature inside the bed (until all particles have reached the same, then constant temperature). The temperature of every individual particle during this thermal relaxation process can be evaluated with the help of the image analysis program. To this purpose, the temporal change of the hue was analyzed out of the recorded images. The received information about the hue of every single sphere is correlated with the temperature using the calibration curve. Because of the hysteresis behavior of the calibration curve, it is necessary to carefully distinguish between hot spheres and cold spheres. Therefore, the average bulk temperature must be determined. Spheres with a temperature higher than the average bulk temperature are assumed to cool down and spheres with a temperature lower than the average bulk temperature are assumed to heat up. With this method, the two groups of hot and cold spheres corresponding to the two branches of the calibration curve can be separated from each other. The individual temperatures obtained for each of the 70 spheres at a certain point of time define the distribution of temperature in the bed at that time.
The first thermal experiments were carried out with stagnant beds. Then, experiments with a rotating drum were also realized. The rotational speed of the drum was 12 rpm – with otherwise the same conditions as in the stagnant drum experiments. Due to the inclination of the flat drum (see figure 2), the 70 spheres stay in two-dimensional arrangement throughout the run. The analysis of the resulting images was more complicated and more time-consuming than for stagnant beds, because of the motion of spheres of different temperature. However, it is possible to derive the temperature distribution of the bed with the previously mentioned method even in the case of rotating drum.

MODELING

The penetration model traditionally used for the heating of agitated beds in contact with a hot wall [1] is not applicable to the present problem of temperature equilibration. Therefore, simulations in this work are realized with discrete methods. Specifically, the discrete element method (DEM) is employed to simulate both the thermal and the mechanical behavior of the particle system in 2D. The DEM treats the particles individually, instead of considering the bed as a continuum.
All simulations are carried out for a drum with an internal diameter of D = 0.05 m and spherical particles with d = 4 mm. The particle density and specific heat capacity of the alumina particles

are set to ρ = 2700 kg/m^3 and c_p = 900 J/kg K, respectively. Since the heat transfer between the spheres is expected to be the dominant heat transfer mechanism, the particle-to-particle heat transfer coefficient α_{pp} is the key model parameter. In the present work, α_{pp} was calculated from heat conduction in the gas gap between two spheres according to an equation developed by Schlünder [4]:

$$\alpha_{pp} = \frac{2 \cdot k_g}{d}\left[\left(1+\frac{2 \cdot l}{d}\right)\cdot \ln\left(1+\frac{d}{2 \cdot l}\right)-1\right] \qquad (1)$$

For the present materials and experimental conditions a value of $\alpha_{pp} = 93\ [W \cdot m^{-2} \cdot K^{-1}]$ is obtained from equation (1).

The equalization of temperature inside a stagnant bed was simulated in two different ways.

The first way establishes a network of heat reservoirs representing the single particles, incorporating the heat transfer mechanisms between particles, wall and gas. The alignment of the spheres (particle coordinates) is obtained directly from the experimental images and used as a contact network in a Matlab program (see figure 5) to simulate the structure of the bed and the contacts of each particle. The heat transfer in the bed is calculated by means of an enthalpy balance for each particle. Heat transfer between the spheres is assumed to be the main heat transfer mechanism, expressed by the coefficient α_{pp}. Heat transfer from the spheres to the gas by convection, as well as heat transfer from the spheres to the drum wall by radiation and conduction are combined in one further heat transfer coefficient denoted by α_{CRW}.

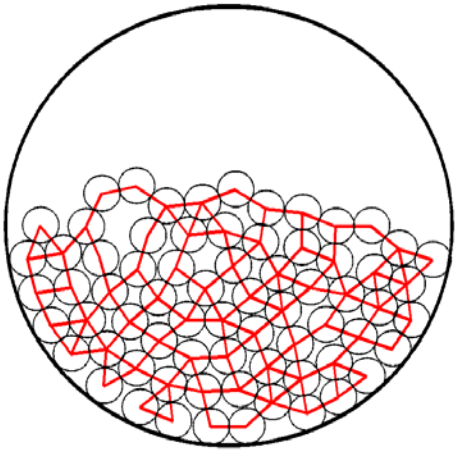

Figure 5. Network of thermal contacts / Simulation with Matlab

This coefficient must be established empirically, because it is hardly possibly to exactly compute separate heat transfer coefficients for convection between the spheres and the gas, for conduction between the spheres and the wall, and for radiation between the spheres and their entire external surroundings. Additionally, the surfaces available for each of these heat loss mechanisms can also not be defined exactly, because the spheres are exposed to the gas at their one side and simultaneously contact the rear wall of the drum, which is made of insulating material, at their other side. Therefore, the product $\alpha_{CRW} \cdot A$ is determined experimentally and incorporated in the heat balance

$$\frac{d\vartheta}{dt} = \frac{\alpha_{PP} \cdot A_{PP}}{m_P \cdot c_P} \cdot \overline{CM} \cdot \overline{\vartheta} + \frac{\alpha_{CRW} \cdot A}{m_P \cdot c_P} \cdot \left(\vartheta_g - \overline{\vartheta} \right) \tag{2}$$

Here, $\overline{CM}$ is a structural parameter called the contact matrix. In this matrix, the contact information between all spheres in the bed is saved. $\overline{\vartheta}$ is the sphere temperature vector.

Another way to compute particle temperatures is simulation with commercial DEM software. In the present work the DEM software from Itasca called PFC, which is an upgrade of the discrete element method introduced by Cundall and Strack [5], was used. In this software, the interaction of the particles is treated as a dynamic process with states of equilibrium developing whenever the internal forces are balanced. The contact forces and displacements of an assembly of particles are found by tracing the movement of individual particles. The program associates to each particle a heat reservoir and a thermal pipe to each contact. Starting with an initial temperature field, the temperature of each particle is updated. The simultaneous solution of the mechanical and the thermal problem in PFC increases the computational time by a factor of 10 in comparison to the Matlab simulation. Therefore, the Matlab simulation is used for comparison between experimental and simulation results for stagnant beds in the present work.

RESULTS

Only results with a stagnant bed will be presented here. Experimental results of this kind are plotted in figure 6 in form of cumulative temperature distributions. The two plots correspond to gas temperatures closely below and closely above the average caloric temperature of the particle system (here: 37.5°C). The average caloric temperature of the particles would be the equilibrium temperature if heat losses were not present. In presence of heat losses, the final temperature is equal to the gas temperature. It is approached from above or from below, depending on whether the average caloric temperature of the particles is larger or smaller than the gas temperature.

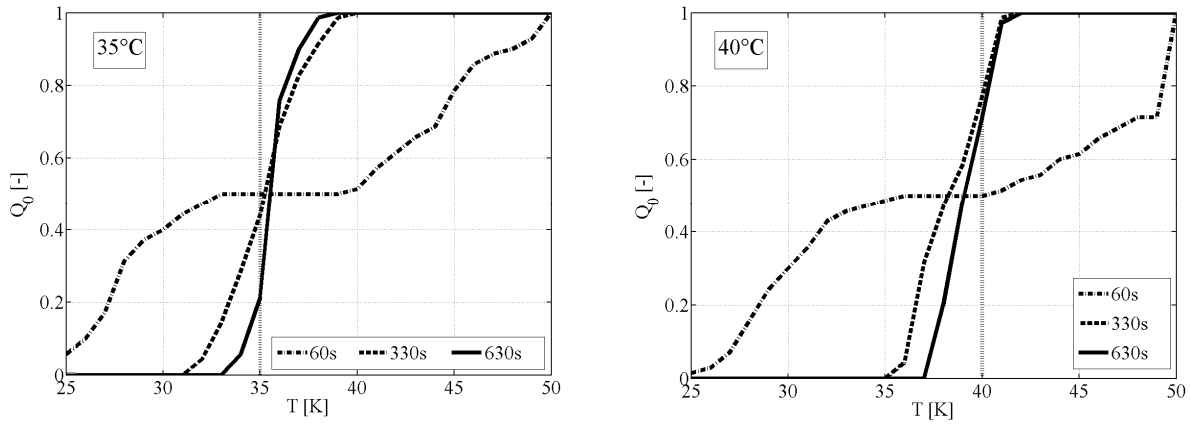

Figure 6. Measured temperature distributions in a stagnant bed, initial temperatures of spheres 25°C and 50°C, α_{PP} = 93 W·m^{-2}·K^{-1}, ϑ_g = 35°C, ϑ_g = 40°C

Because of the discrete recording of sphere temperatures, temperature distributions such as those depicted in figure 6 are available and can be compared with the results of discrete thermal simulations. Simulation results were obtained with the parameter $\alpha_{CRW} \cdot A$ fitted to a

value of $\alpha_{CRW} \cdot A = 4,0 \cdot 10^{-4} [W \cdot K^{-1}]$. Related to the surface of one sphere, this corresponds to a value of $\alpha_{CRW} = 8\ [W \cdot m^{-2} \cdot K^{-1}]$. In comparison to the heat transfer coefficient between the spheres $\alpha_{PP} = 93\ [W \cdot m^{-2} \cdot K^{-1}]$, the loss heat transfer coefficient α_{CRW} is much smaller. This confirms the assumption that – despite unavoidable heat losses – the heat transfer between the spheres is the dominant factor in the conducted experiments. Simulated temperature distributions are compared with measured temperature distributions in figure 7. This figure is typical for the good agreement that could be reached between experiment and simulation (both discrete).

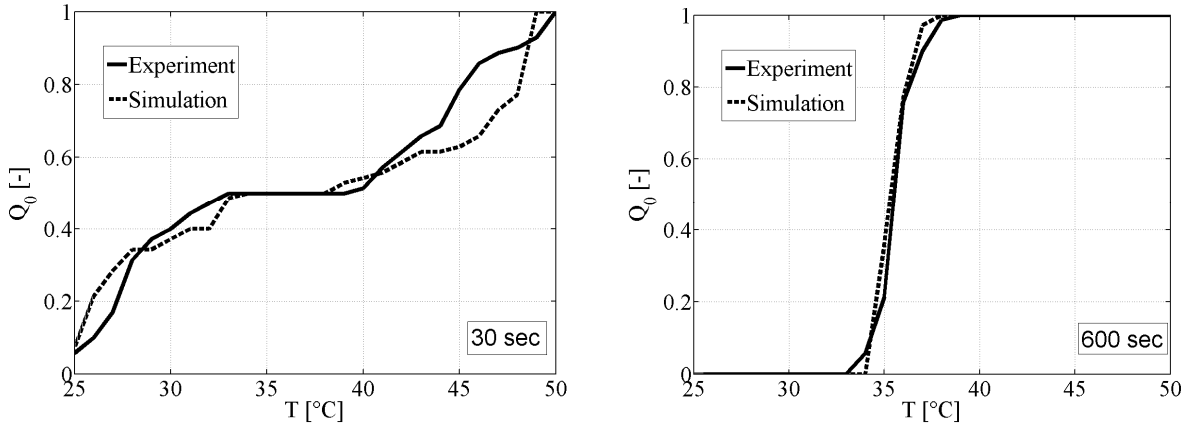

Figure 7. Measured and calculated temperature distributions in a stagnant bed, initial temperatures of beads 25°C and 50°C, α_{PP} = 93 W·m^{-2}·K^{-1}, ϑ_g = 35°C

SUMMARY

Heat transfer between the particles in flat drum has been determined for stagnant and agitated beds with a novel experimental setup by means of thermo-chromic coated alumina spheres. The experimental technique allows the determination of temperature distributions in the disperse phase, so that data for quantitative comparison with the results of discrete simulations are provided. Such comparison has been conducted with the thermal version of the Discrete Element Method (DEM). A combined heat transfer coefficient accounting for heat losses by radiation and convection had to be fitted to the experimental results, but simulations were otherwise predictive. The comparison between the simulated and measured distributions of particle temperature shows for stagnant beds a good agreement. In future the experimental investigation should be expanded to agitated beds and systems of higher particle number. The first experimental results and the results of the discrete thermal simulation indicate that we are at the beginning of the development of a powerful new tool to interpret thermal processes in contact apparatuses.

REFERENCES

[1] Schlünder, E.-U., Tsotsas, E., Georg Thieme Verlag Stuttgart, 1988, 166 - 189
[2] Kwapinska, M., Saage, G., Tsotsas, E., Powder Technol., 161 (2006), 69-78
[3] Tsotsas, E., Kwapinska, M., Saage, G., Drying Technology, 25 (2007), 1377-1391
[4] Schlünder, E.-U., Chem-Ing.-Tech., 43 (1971), 651-654
[5] Cundall, P.A., Strack, O.D.L., Geotechnique 29 (1979), 47-65

COMPARISON BETWEEN TIME AVERAGED AND INSTANTANEOUS PIV AND HOTWIRE MEASUREMENTS DOWNSTREAM OF A DELTA WINGLET PAIR

D. Hernon[1]*, M. G. Hyde[2], N. Patten[1, 3]
[1]Bell Labs, Alcatel-Lucent, Dublin, Ireland
[2]TSI Instruments Ltd, High Wycombe, England
[3]Dept. of Mechanical and Aeronautical Engineering, University of Limerick, Ireland

ABSTRACT. Vortex generators (VGs) have been studied extensively in the literature owing to their ability to enhance heat transfer at modest pressure drop penalties. VGs are incorporated in heat exchanger design and are more fundamentally studied on heated flat surfaces or in channel flow. The techniques used to investigate the flow phenomena associated with VGs are classically IR imaging, particle image velocimetry (PIV), five hole pressure probes and the naphthalene sublimation technique which relates mass transfer to heat transfer by evoking the heat and mass transfer analogy. Typically, the results presented using these techniques are in time-averaged form and this implies that the majority of information that relates to enhanced heat transfer, i.e. unsteady flow phenomena, is lost.

Hotwire and PIV images were obtained downstream of a delta winglet pair placed on an unheated flat surface and comparisons are made between instantaneous and time-averaged flow features using both techniques. Reasonable comparisons were obtained between the time-averaged PIV and hotwire measurements demonstrating that useful information can be gained with the use of a 1D hotwire measurement in a complex 3D flow.

Examining the instantaneous flow features reveals the true nature of the unsteadiness and also elucidates some of the more complex flow phenomena. Some of the key observations from the instantaneous PIV are that at any given time the vortices shed from each delta winglet can vary in size, strength, and location from wall. These variations cause the two counter rotating vortices to sweep across the lower wall while at the same time they move towards and away from the wall causing compression and extension of the underlying boundary layer. All of these complex unsteady flow phenomena may result in enhanced heat transfer.

Keywords: Vortex generator, Boundary layer, Delta winglet, PIV, Hotwire

INTRODUCTION

Vortex generators increase heat transfer by a number of mechanisms; (a) they enhance mixing due to the swirling motion of the vortices; (b) secondary flows are set up normal to the main streamwise flow which cause local thinning of the boundary layer, i.e. when the secondary flow is directed towards the surface and (c) the unsteady separation of the flow from the VG causes unsteady flow downstream of the VG. VGs are examined extensively in heat exchanger design due to their use in varied applications such as automotive, air conditioning, process plant and geothermal [1]. Extensive reviews of the literature are available from a number of sources [2, 3]. A brief review of some of the more important results relating to the present investigation are given here.

* Corresponding author: Domhnaill Hernon
Phone: + (353)-1-692148, Fax: + (353)-1-8864782
E-mail address: hernon@Alcatel-Lucent.com

Gentry and Jacobi [4] examined the effects of introducing delta wing VGs into flat plate and channel flow. They used flow visualization, vortex strength measurements and naphthalene sublimation techniques to characterize the vortices. They found local heat transfer enhancements of up to 300% compared to the baseline measurements. They found that the vortex strength increased with Re, Aspect ratio and Angle of Attack (AoA) and that the vortex strength decayed downstream of the VG. Similar results have been shown by a number of investigators into enhanced heat transfer using VGs [5-8].

It has been shown that longitudinal vortices maintain their coherence over long streamwise distances and for this reason they exhibit better heat transfer characteristics over transverse vortices [4, 9]. Counter rotating vortex pairs have been shown to create the greatest heat transfer enhancement [10, 11]). These studies illustrate the benefits of using vortex generators for enhanced heat transfer applications. It is for the above reasons that in the current investigation a delta winglet pair is studied in the common-flow-down condition with an angle of attack resulting in a longitudinal vortex.

It is noted that for the most part only time-averaged results are presented in the majority of investigations available in the literature, as described above. There are few investigations that examine the instantaneous flow structures and heat transfer characteristics downstream of delta winglets. One investigation performed numerical simulations of the unsteady flow downstream of bars and baffles that acted as vortex generators [12]. In [12] they presented instantaneous isotherms, instantaneous Nusslet number and friction factors illustrating the influence of the VGs.

This investigation examines the flow downstream of a delta winglet pair using PIV and hotwire anemometry. The two main goals of the current study are: (1) gain greater insight into the underlying flow mechanisms that lead to enhanced heat transfer by examining the instantaneous PIV and hotwire results and (2) compare the time-average hotwire results to those gained using the PIV thereby allowing an estimation of the accuracy of measuring an inherently 3D flow with a 1D hotwire measurement.

EXPERIMENTAL FACILITY AND MEASUREMENT TECHNIQUES

Experimental facility

The PIV and hotwire measurements were performed in a small size wind tunnel. The wind tunnel consists of honeycomb, contraction and screen sections upstream of the test section inlet to reduce the background turbulence intensity of the flow. The test section is made from Plexiglas of internal dimension 610x406x77mm and is powered by two 12W axial fans that are placed downstream of the diffuser section. The inlet turbulence intensity of the wind tunnel at the test section entrance was measured at 0.4% using the hotwire system detailed below.

One delta winglet pair was tested in this investigation with a height of 15mm and chord length of 30mm (Figure 1a). The VG had a wall thickness of 1mm and was made from plastic. The delta winglet pair was placed on one surface of the test section wall using double sided tape and one AoA was examined in the current investigation (Figure 1) with the leading edge transverse separation between each winglet maintained at 4mm and the trailing edge separation of 30mm resulting in an AoA of 26°.

A boundary layer traverse was obtained with a single-normal hotwire probe without a VG in place and this served as a baseline measurement for boundary layer profile shape, boundary layer thickness and RMS measurements. Each boundary layer traverse consisted of 60 measurement locations away from the wall with the measurement resolution increasing closer to the wall. A number of boundary layer traverses were obtained downstream of the VG as illustrated in Figure 1b. Four spanwise locations were investigated at three different streamwise distances at the given AoA. In the results sections, the measurement location is described by the streamwise (X) and the spanwise (Z) location, e.g., the measurement in the centreline of the VG (Z0) and at the first streamwise position downstream of the VG (X30) is described as X30Z0.

The cross plane PIV measurements were obtained at the same streamwise distances downstream of the VG at 30, 70 and 110mm. In the cross plane measurements, the laser is directed in the z-plane and the camera is directed in the x-plane. The cross plane measurements are used to demonstrate the decay in vorticity downstream of the VG and also the instantaneous vortical flow patterns. PIV data were also obtained in the streamwise plane where the laser was directed in the x-plane and the camera was directed in the z-plane. These measurements are used to obtain the mean streamwise velocities.

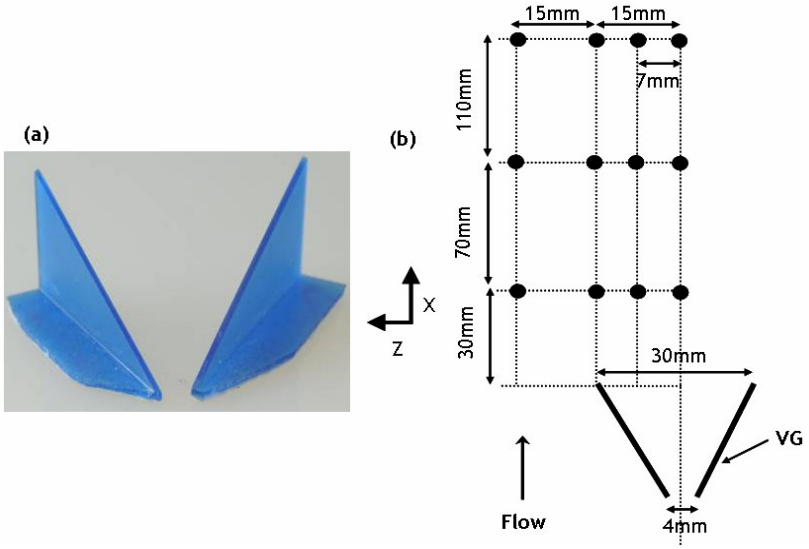

Figure 1. (a) Picture of the delta winglet pair. (b) Schematic of the VG placement and downstream measurement locations indicated by the filled circles. Measurement locations shown are for 26° AoA.

Measurement techniques

Mean and fluctuation velocities were measured using a TSI IFA300 constant temperature anemometer system. The hotwire was operated at an overheat temperature of 250°C and measurements were recorded over 13 seconds at a sampling rate of 20 KHz and were then low-pass filtered at 10KHz to remove any noise at higher frequencies. During any boundary layer traverse the temperature in the test section was maintained to within ±0.1%. The hotwire calibration was achieved by measuring the velocities in the wind tunnel with a Pitot-static probe and relating these velocities to the bridge output voltage from the IFA300 via a 5^{th} order polynomial fit. The hotwire is mounted to a Velmex slide and stepper motor which are powered by Parker ViX drives and a parker power supply. In the current investigation the smallest incremental movement was 10µm in the near-wall region.

PIV measurements were obtained using a TSI PowerView digital particle image velocimetry (DPIV) system [13]. The PIV system consisted of a 200mJ double-pulsed New Wave Nd-YAG laser with a cylindrical lens and spherical lens combination which was used to generate the laser sheet of thickness less than 1mm at the measurement plane. The camera used was TSI PowerView 4MP CCD camera having a resolution of 2048 X 2048 pixels and 12 bit greyscale. Data was obtained at a frame rate of 7Hz and a total of 40 image-pairs were captured per acquisition set. Data was acquired and processed using TSI Insight 3G software. The PIV algorithm used to process the particle images was a 2D fast Fourier transformation algorithm with 50% overlap on the interrogation spots. Spot sizes of 64 by 64 pixels initially set, going down to 32 by 32 using a recursive processing scheme [14]. Erroneous vectors were removed using a global velocity magnitude and local median filtering mechanism. Data was interpolated using a local mean interpolation scheme [15]. Seeding in the wind tunnel was implemented using a TSI six-jet atomizer generating oil particles of 1µm diameter.

RESULTS

Comparison between time-averaged PIV and hotwire measurements

Figure 2 illustrates the comparison between time-averaged velocity profiles obtained via hotwire and PIV measurements. Two profiles are shown in Figure 2, one at X30Z15 and one at X70Z15. This location (Z15) was chosen as the worst case scenario for comparing the hotwire and PIV measurements as it represented the flow downstream of the VG tip and hence should contain highly 3d flow. It can be seen from Figure 2 that the PIV and hotwire measurements are qualitatively similar and both measurements compare reasonably well.

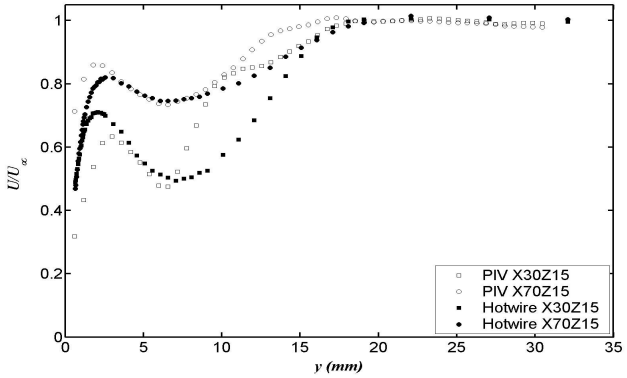

Figure 2. Comparison between time-averaged hotwire and PIV measurements of the mean velocity downstream of a delta winglet pair at 26° AoA.

It must be noted that after the PIV measurements were obtained it was discovered (while obtaining a detailed hotwire traverse across the depth of the test section) that there was a problem with the flow conditioning within the wind tunnel test section entrance. It was found that the rubber seal between the contraction and test sections was protruding slightly into the flow causing unsteadiness and disruption to the mean velocity in the centre line of the test section. This protrusion was removed for the hotwire measurements presented in this paper but the PIV measurements remain affected beyond the 35mm position shown in Figure 2. It is not believed that the flow field modified by the VG is significantly affected by the disruption to the centreline flow. Further PIV measurements will have to be performed to fully understand the effect of the protrusion on the flow field.

Hotwire measurements

It was shown in the last section that good comparison between the PIV and hotwire measurements from a single-normal hotwire probe was possible. This section will present detailed hotwire measurements downstream of the VGs. One of the main advantages of hotwire measurements over PIV measurements is the greater temporal and spatial resolution which can further elucidate some critical flow features that may lead to enhanced heat transfer.

All of the mean velocity profiles obtained with the hotwire downstream of the VG are shown in Figure 3 and the effect of placing a VG in the flow is seen immediately. In Figure 3a it is observed that in the centreline between the two delta winglets (Z0), the near-wall velocity has increased substantially (approximately doubled) over that without the VG in place. Another interesting point to observe from Figure 3a is that the boundary thickness in the VG centreline is less than that without the VG in place. This corresponds to previous studies which have demonstrated the effect of the counter rotating vortex pair on thinning the boundary layer in the centreline thereby resulting in enhanced heat transfer. Figures 3b and 3c illustrate the mean velocity profiles at Z7 and Z15, respectively. The effect of the downward flow directed towards the lower wall and the effect of the vortex core are observed in these figures. Near the wall there is an increase in the mean streamwise velocity due to the compression of

the flow owing to the downward motion of the counter rotating vortex pair. As the hotwire traverses towards the vortex core, there is a decrease in velocity. Similar phenomena are also seen in the PIV images discussed in the next section. Different trends are observed when examining Figure 3d. The near-wall velocity does not increase substantially above the no VG case and the trends also show a widening of the vortex in the spanwise direction at X=110mm. This widening effect is evident due to the fact that in the near-wall region the velocity has increased above the no VG case and as the hotwire traverses farther away from the wall a constant velocity region in encountered which is indicative of the vortex core.

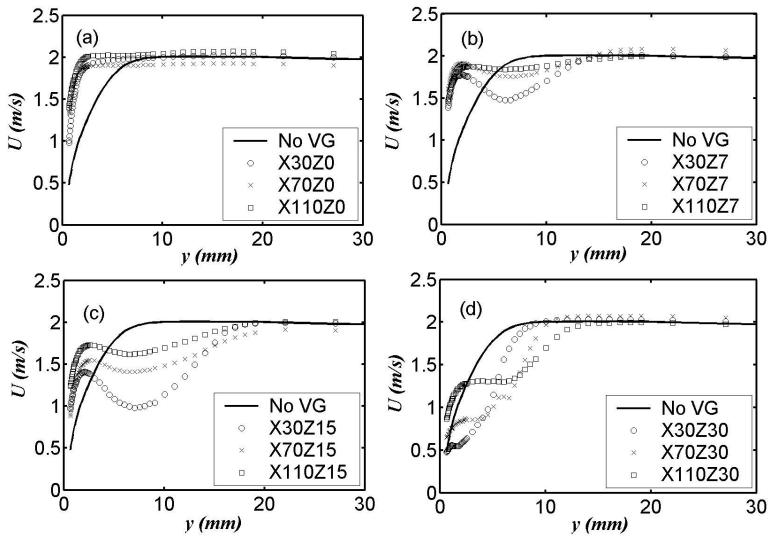

Figure 3. Time-averaged hotwire measurements of the mean velocity downstream of a delta winglet pair at 26° AoA.

Figure 4 illustrates the RMS profiles for the same conditions shown in Figure 3. In Figure 4a it can be seen that when the VG is placed in the flow there is an immediate enhancement in the unsteady flow phenomena due to the increase in peak RMS over the no VG case. Figure 4a also illustrates that a peak develops in the RMS close to the wall farther downstream. This peak RMS value and its proximity to the wall (Figure 4a) along with the increase in near-wall velocity (Figure 3a) aids in explaining the enhanced heat transfer measured in this region by other investigators. In Figure 4a the peak RMS increased with downstream distance from the VG. In Figures 4b and 4c, as the hotwire moves well into the vortex enhanced flow, it can be seen that the peak RMS increases significantly over the no VG and Z0 cases. The peak RMS values have now moved farther away from the wall and occupy a much broader region of the flow. It is noted that near the wall in Figure 4b and 4c the RMS values are reasonably low but higher than the peak values shown in Figure 4a. In Figures 4b and 4c the trend of increasing RMS values downstream of the VG (as shown in Figure 4a) has reversed where the streamwise location nearest to the VG now has the highest peak RMS value. A change in the flow structure is observed as the hotwire moves to the Z30 location (Figure 4d). In Figure 4d it can be seen that at X30Z0 the vortex has not spread to the Z30 location and only causes a slight change to the flow at y~6mm where a small peak is observed.

Figure 5 illustrates the development of the boundary layer thickness downstream of the VG at each transverse location estimated from the hotwire profiles. These measurements again corroborate other studies that demonstrated in the centreline of the VG (Z0) there is a thinning of the boundary layer while in the vortex enhanced flow there is a thickening of the boundary layer at Z7 and Z15.

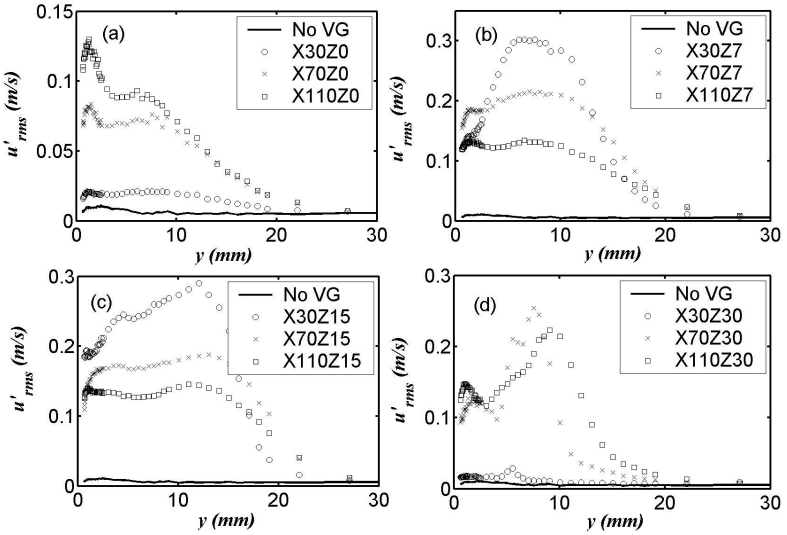

Figure 4. Time-averaged hotwire measurements of the RMS velocity downstream of a delta winglet pair at 26° AoA.

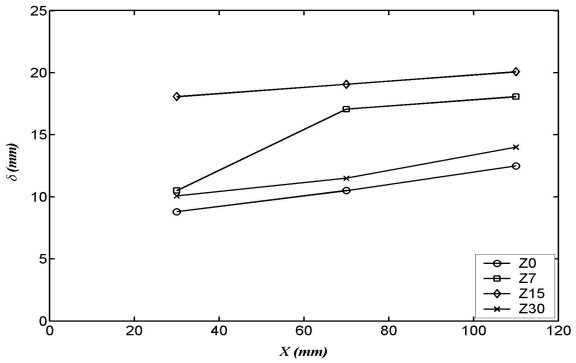

Figure 5. Boundary layer thickness (δ) development downstream of the VG.

Instantaneous PIV and hotwire measurements

Figures 6a and 6b are instantaneous cross plane PIV images of the flow 30mm downstream of the VG. The colour bar represents the vorticity and the vectors show the direction of the flow. Figure 6c is the time-averaged image of the vortex pair. There is a marked difference between the instantaneous images of the flow which seem almost chaotic compared to the time-averaged view showing a nicely formed counter rotating vortex pair. In Figure 6c it can be seen that the VGs significantly disrupt the flow and increase the boundary layer thickness from 8mm (no VG case) to 20mm in Figure 6c. To the right hand side of Figure 6c are two fluctuating velocity traces from the hotwire. In the near-wall region the fluctuation levels are significant over both the positive and negative range. As the edge of the boundary layer is reached it can be seen that the mean fluctuating velocities are reduced considerably; however, large negative spikes in the fluctuating velocity are observed (at t~0.4s).

Figures 7a and 7b are instantaneous PIV images of the flow 70mm downstream of the VG. Figure 7c is the time-averaged PIV image. Comparing Figure 6c and 7c it is clear that the peak vorticity levels are reduced with downstream distance and also the size of the vortices has increased and they have spread farther apart. This effect was also observed in the hotwire measurements (Figures 3b and 3c) where the velocity profiles flattened with downstream distance.

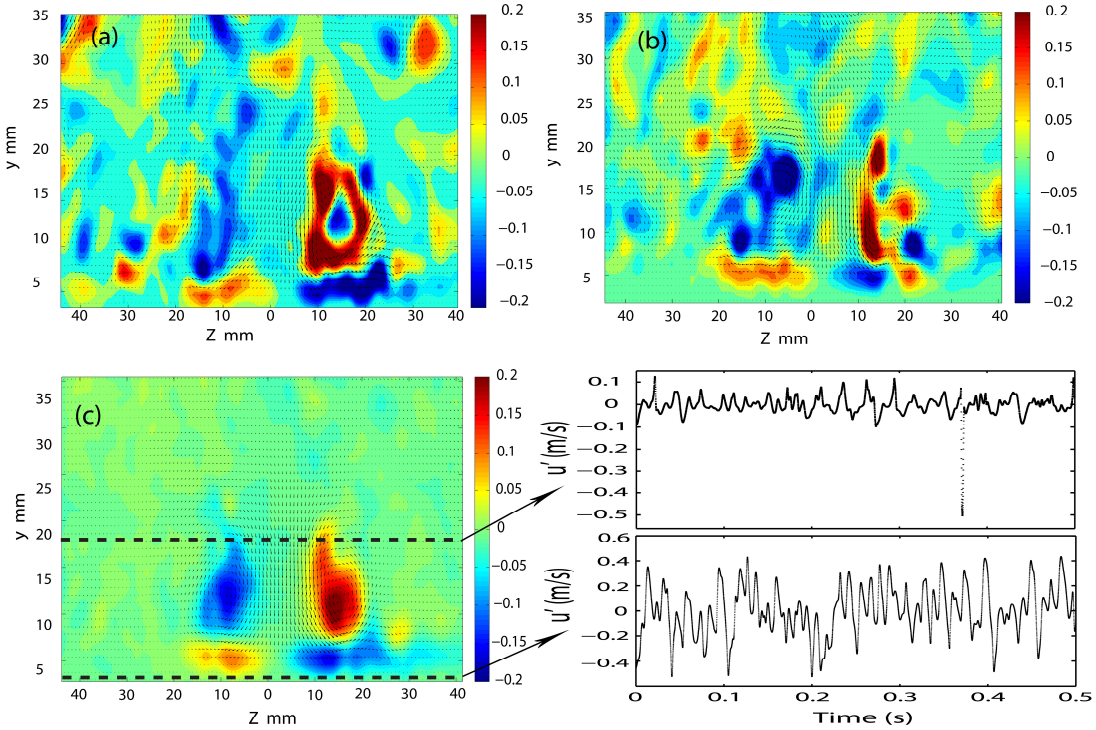

Figure 6. (a) and (b) are instantaneous PIV images of the vorticity generated 30mm downstream of the delta winglet pair at 26° AoA and (c) is the time-averaged image of the flow and on the right hand side of (c) are instantaneous hotwire traces of the flow at y ~ 0.6mm and 19mm.

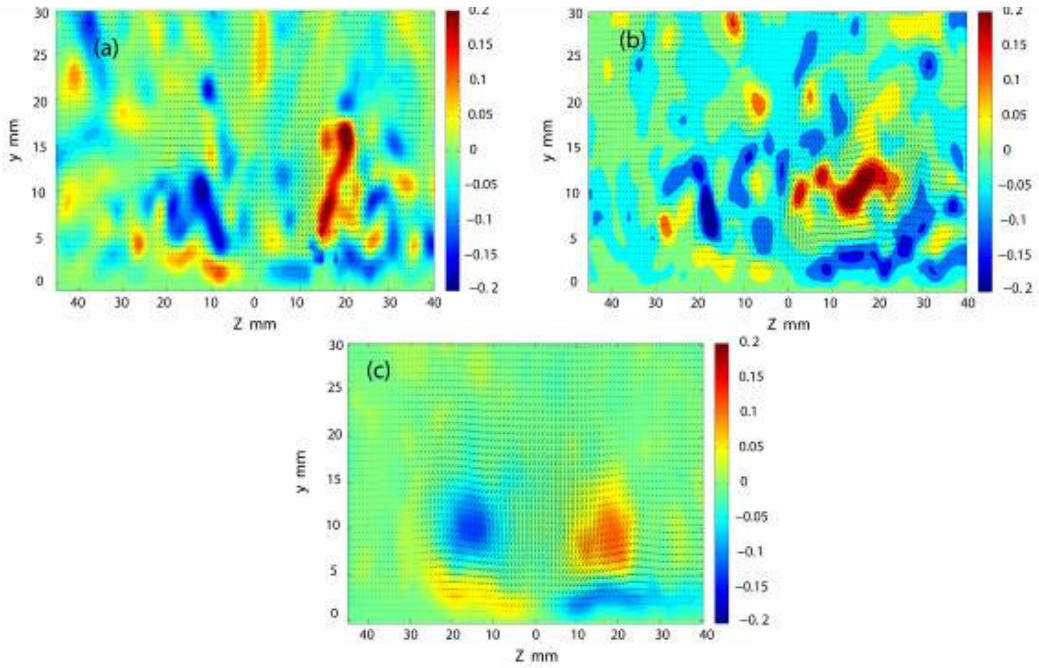

Figure 7. (a) and (b) are instantaneous PIV images of the vorticity generated 70mm downstream of the delta winglet pair at 26° AoA and (c) is the time-averaged image of the flow.

Figures 8a and 8b are the instantaneous PIV images of the flow 110mm downstream of the VG. Figure 8c is the time-averaged PIV image. It is again clear that farther downstream of the VG the peak vorticity decreases and the size of each vortex increases and spreads away from the centreline.

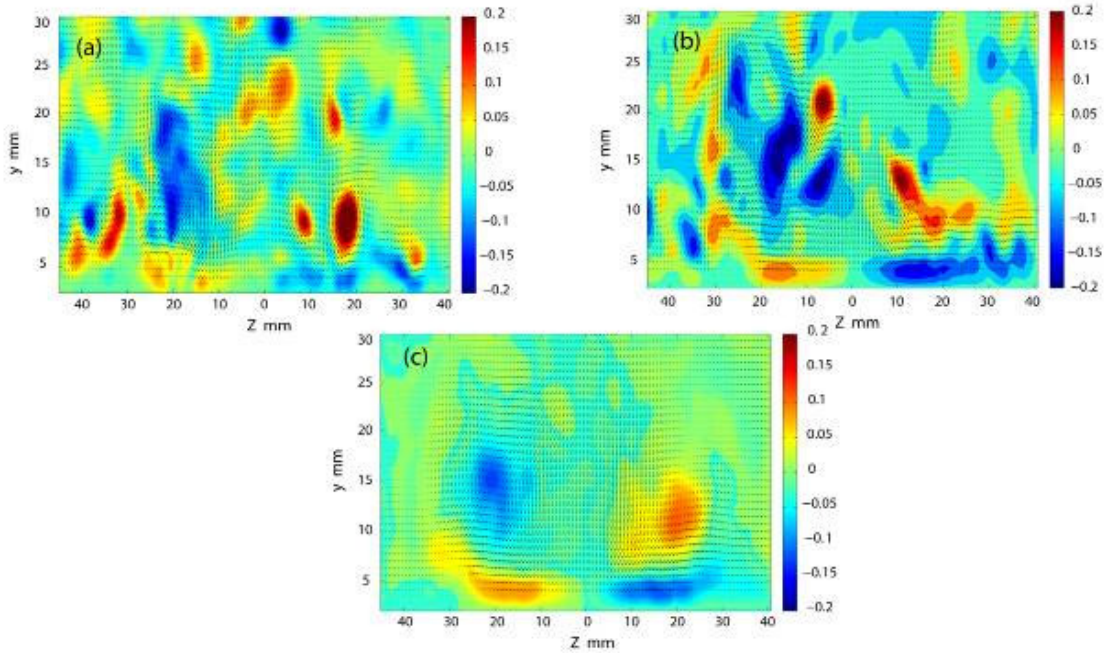

Figure 8 (a) and (b) are instantaneous PIV images of the vorticity generated 110mm downstream of the delta winglet pair at 26° AoA and (c) is the time-averaged image of the flow.

CONCLUSIONS

Hotwire and PIV measurements were taken downstream of a delta winglet pair at 26° angle of attack on an unheated flat surface within a wind tunnel test section. Time-averaged PIV and hotwire measurements were compared in 3D flow to determine the applicability of using a single normal (1D) hotwire probe to obtain data in a 3D flow field. Comparison between mean velocity profiles using both of these techniques was promising allowing interesting conclusions to be drawn from the hotwire measurements downstream of the VGs. The hotwire measurements demonstrated the extent to which the introduction of a VG disrupts an otherwise laminar flow field. The hotwire measurements demonstrated the regions of the flow most affected by the VG and allowed for detailed insight into the change in flow structure via RMS profiles and instantaneous fluctuating velocity traces.

Instantaneous PIV images of the flow were examined and compared to the time-averaged image of a nicely formed counter rotating vortex pair. It was shown that the instantaneous flow structures are complex and highly random. This instantaneous view of the flow field helps to further elucidate the complex flow features that lead to enhanced heat transfer with the inclusion of VGs in an otherwise uninterrupted laminar flow. The time-averaged PIV data also demonstrated the decrease in vortex strength (decrease in vorticity) and the enlarging vortex flow downstream of the delta winglet. These results also compared well with the time-averaged hotwire measurements which show qualitatively similar flow features.

ACKNOWLEDGEMENTS

Bell Labs Ireland would like to thank the Irish Development Agency (IDA) for their continued financial support. The authors would like to thank Liam McGarry and John Mullins for their technical assistance during the measurement phase and TSI Incorporated for supplying the PIV equipment.

REFERENCES

1. Torii, K., Kwak, K.M. and Nishino, K., Heat Transfer Enhancement Accompanying Pressure-loss Reduction with Winglet-type Vortex Generators for Fin-tube Heat Exchangers, Int. J. Heat and Mass Transfer, vol. 45, pp. 3795-3801, 2002.
2. Jacobi, A.M. Shah, R.K., Heat Transfer Surface Enhancement Through the use of Longitudinal Vortices: A Review of Recent Progress, Exp. Thermal and Fluid Science, vol. 11, pp. 295-309, 1995.
3. Joardar, A. and Jacobi, a.m., Impact of Leading Edge Delta-wing Vortex Generators on the Thermal Performance of a Flat Tube, louvered-fin Compact Heat Exchanger, Int. J. Heat and Mass Transfer, vol. 48, pp. 1480-1493, 2005.
4. Gentry, M.C. and Jacobi, A.M., Heat Transfer Enhancement by Delta-wing –Generated Tip Vortices in Flat Plate and Channel Flows, J. Heat Transfer, vol. 124, pp. 1158-1168, 2002.
5. Deb, P., Biswas, G. and Mitra, N.K., Heat Transfer and Flow Structure in Laminar and Turbulent Flows in a Rectangular Channel with Longitudinal Vortices, Int. J. of Heat and Mass Transfer, 38, pp. 2427-2444, 1995
6. Edwards, F.J. and Alker, C.J.R., The Improvement of Forced Convection Surface Heat Transfer using Surface Protrusions in the form of (A) Cubes and (B) Vortex Generators, Proc. 5th Int. Heat Transfer Conf., pp. 244-248, 1974.
7. Torii, K., Yanagihara, J.I. and Y. Nagai, Heat Transfer Enhancement by Vortex Generators, Proc. ASME/JSME Thermal Eng. Joint Conf., pp. 77-83, 1991.
8. Joardar, A. and Jacobi, A.M., Heat Transfer Enhancement by Winglet-type Vortex Generator Arrays in Compact Plain-Fin-and-Tube Heat Exchangers, Int. J. Refrigeration, doi:10.106/j.ijrefrig.2007.04.011, 2007.
9. Hiravennavar, S.R., Tulapurkara, E.G. and Biswas, G., A Note on the Flow and Heat Transfer Enhancement in a Channel with Built –in Winglet Pair, Int. J. Heat and Fluid Flow, vol. 28, pp. 299-305, 2007.
10. Yanagihara, J.I. and Torii, K., Heat Transfer Augmentation by Vortices Rows, Proc. 3rd World Conf. on Experiment Heat Transfer, Fluid Mechanics, and Thermodynamics, pp. 560-567, 1991.
11. Kim, E., and Yang, J.S., An Experimental Study of Heat Transfer Characteristics of a Pair of Longitudinal Vortices using Color Capturing Technique, Int. J. Heat and Mass Transfer, vol. 45, pp. 3349-3356, 2002.
12. Valencia, A. and Sen, M., Unsteady Flow and Heat Transfer in Plane Channels with Spatially Periodic Vortex Generators, Int. J. Heat and Mass Transfer, vol. 46, pp. 3189-3199, 2003.
13. Adrian, R.J., Particle-Imaging Techniques for Experimental Fluid Mechanics, Ann. Rev. Fluid Mech., 23, pp. 261–304, 1991.
14. McKenna, S.P. and McGillis, W.R., Performance of Digital Image Processing Techniques, Experiments in Fluids, 32, pp. 106-115, 2002.
15. Westerweel, J. and Scarano, F., Universal Outlier Detection for PIV Data, Experiments in Fluids, 39, Pp. 1096–1100, 2005.

HEAT FLUX EFFECTS ON FALLING FILM EVAPORATION INSIDE A VERTICAL TUBE

Th. Storch, Ch. Philipp, A. Doeg, U. Gross*
Institute of Thermal Engineering, Technische Universität Bergakademie Freiberg
D-09596 Freiberg, Germany

ABSTRACT. Falling film evaporation has widely been investigated in the past. This has been done for pure liquids and mixtures covering wide ranges of liquid Re and Pr numbers, various geometries, cocurrent and countercurrent vapor flow and stagnant, and finally at heating conditions yielding nucleate boiling or not. Nevertheless, for Re < 100 and conditions without bubble formation in the superheated liquid film, only a few references are published. Therefore the heat-flux effect has been investigated while measuring the evaporation heat transfer coefficient inside a vertical tube at zero shear stress. Results for isopropanol are presented in the article where influences of Re, Pr and Ka numbers on heat transfer are discussed, correlated and compared with the literature.

Keywords: *Falling film evaporation, Heat flux, Heat transfer, Vertical tube, Wave factor*

INTRODUCTION

Falling film evaporation and condensation inside vertical tubes is found in industrial applications like heat exchangers and chemical process columns where heat transfer is always affected by the vapor-side shear stress. This acts cocurrent or countercurrent to the liquid film depending on the vapor flow direction. The open literature provides lots of publications about heat transfer measurements, both for evaporation and condensation, and also studies of the hydrodynamics of falling liquid films. For this see, e.g., [1] regarding falling film evaporation, [2] for condensation, and [3] for the hydrodynamics.

Film structure and heat transfer results are found to depend on the wall-surface geometry which may be concave (with the film flow at the inner surface of a tube), flat or convex (film flow at the outside surface, which possibly may be part of an annular flow passage).

The present authors performed extended reflux-condensation heat transfer measurements inside a vertical tube with water, ethanol, and isopropanol in the countercurrent flow situation with the focus directed to shear stress effects on heat transfer, see [4], [5] and [2]. The excellent reproducibility (± 1 % for water, ± 0.5 % for isopropanol) allows extrapolation of the measured data to zero shear stress. The resulting Nusselt number, see Fig. 1, has been referred to Nusselt's solution [6] and F_{wave} has been obtained as the enhancement factor, see Fig. 2. The condensation heat transfer data have been correlated in the range of laminar-wavy film flow, see [7] and [8], evaluated from experiments with water, ethanol and isopropanol. This was done for three sub-ranges corresponding to wave characteristics as obtained from visual observations (for definitions, see equations (4) - (10) below):

* Corresponding author: Prof. U. Gross
Phone: + 49 (0) 3731-392684, Fax: + 49 (0) 3731-393963
E-mail address: gross@iwtt.tu-freiberg.de

$$F_{wave} = 1.028 \qquad (Re\,Ka^{0.09} < 0.8) \qquad (1)$$

$$F_{wave} = 1.096\ Re^{0.141}\ Ka^{0.0126} \qquad (0.8 \le Re\,Ka^{0.09} < 4.2) \qquad (2)$$

$$F_{wave} = 1.270\ Re^{0.040}\ Ka^{0.0036} \qquad (4.2 \le Re\,Ka^{0.09} < 7.3) \qquad (3)$$

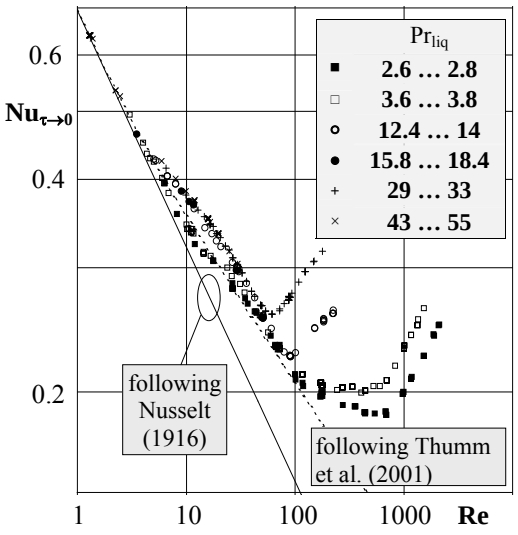

Figure 1. Condensation heat transfer for the limiting case of zero shear stress

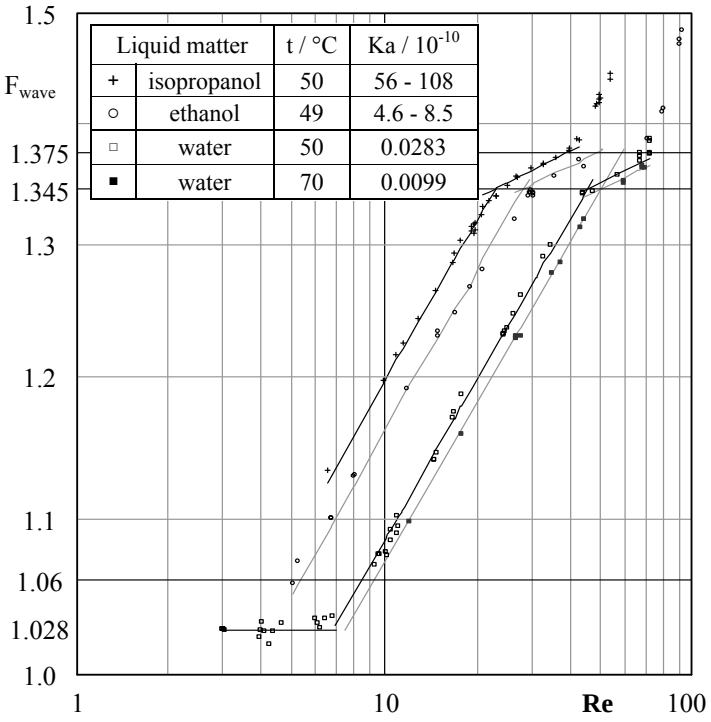

Figure 2. Wave factor vs. Re number (condensation heat transfer data)

Based on additional visual observations of surface waves, the effective wave frequency as the leading effect on heat transfer enhancement has been evaluated from slow motion videos, see [9]. Various characteristic ranges have been obtained from both studies with clear criteria for the transition from the range of occasional small waves with a limited heat transfer enhancement of about 2.8 %, equation (1), to two-dimensional waves with low effective wave frequency, equation (2), and finally three-dimensional waves with increased effective wave frequency, equation (3), bringing enhancement factors up to 34.5 % and 37.5 %, respectively.

EXPERIMENTS

Test plant

The falling-film evaporation experiments have been carried out after some modifications of the test facility. These enable both cocurrent and countercurrent vapor flow, and the limiting case of zero shear stress can now be established by means of a special control system.

The experimental plant (Fig. 3) consists of a vertical brass tube with a total length and inner diameter of 4.2 m and 28 mm, respectively. Three cycles are established, one for the liquid and two for vapor, which can be operated independent from each other. Liquid isopropanol is pumped at a constant temperature to the top of the tube where it penetrates a porous sintered steel section. A uniform liquid film is created which flows downward at the inner wall surface with a total hydrodynamic entrance length of about 1580 mm. The uppermost part of the tube is surrounded by

a water jacket for heating where the liquid film is partially vaporized. The heating water can be fed into three different inlets of the evaporation section, permitting three different lengths of the heating zone (378, 828, 1628 mm). The measuring level of local heat transfer coefficients is located in the middle of the third heated section. The present experiments have been done with the thermal entrance length of 740 mm (mainly) and 1540 mm. Vapor is created in the evaporation section and it can be forced to flow upwards, i.e. countercurrent to the liquid film (vapor cycle I), and / or downwards, cocurrent to the liquid film (vapor cycle II). This is managed by the respective operation of two condensers. The condensate is finally brought together with the excess liquid coming from the separation device at the bottom of the tube.

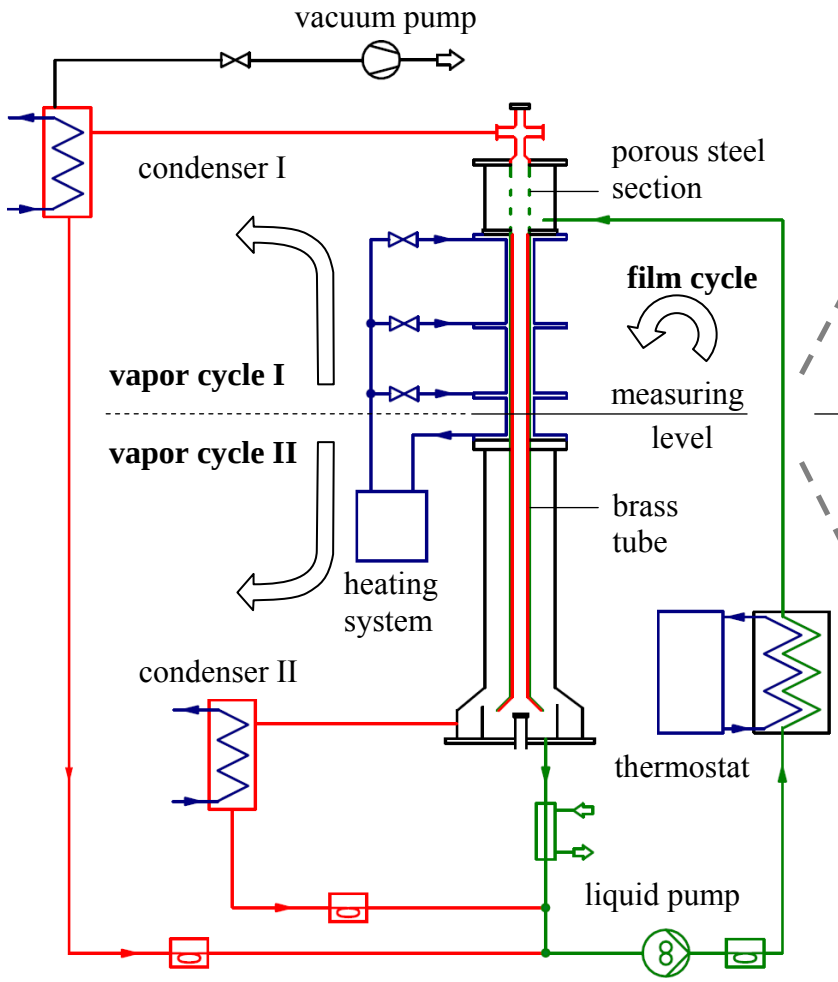

Figure 3. Schematic drawing of the test plant

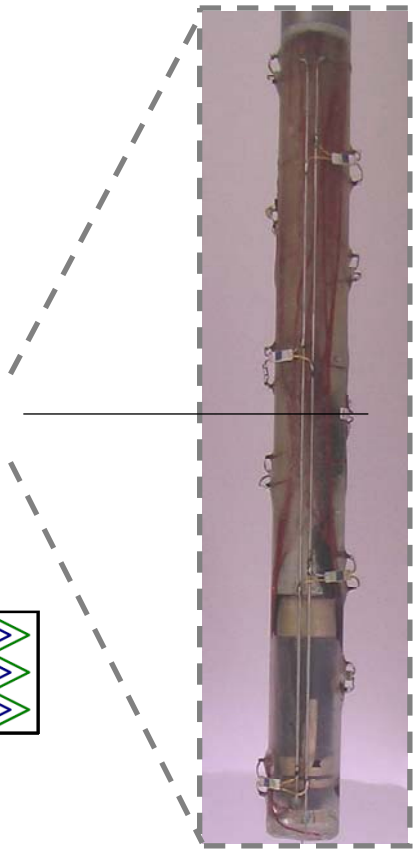

Figure 4. Measuring probe

Using a very fine condenser setting the ratio between the two vapor flow rates (upward and downward) can be controlled in a specific way for shifting the level of zero velocity (vapor) exactly to the heat transfer measuring level. This vapor flow condition is comparable to experiments outside a tube where the vapor volume is big enough to be considered at rest.

For identification of the zero-velocity point a special measuring probe has been designed, installed and tested inside the tube, see Fig. 4. It consists of 8 micro resistance thermometers (PT 1000) mounted at equal distances of 20 mm and situated along the tube axis being centered in the measuring level. These resistance thermometers are self heated, and they are cooled by the vapor flow, see [8]. The resulting temperature distribution along the tube axis directly corresponds to the vapor velocity and the location of maximum temperature is obtained at the zero-velocity level. By measuring this temperature distribution the condenser settings were aligned until the vapor stagnation zone is situated in the measuring level.

The particular mass flow rates were measured after liquification by means of Coriolis flow meters with an accuracy of about ± 0.15% on the measured value. Before entering the porous steel section the liquid temperature is controlled by a thermostat.

RESULTS AND DISCUSSION

Evaluation of data

The film Re number in the measuring level has been evaluated from the liquid mass flow rate corrected for the liquid evaporated above the measuring level.

$$\mathrm{Re}_{\mathrm{film}} = \dot{m}_{\mathrm{liq}} / (\pi\, d_{\mathrm{inside}}\, \mu_{\mathrm{liq}}) \qquad (4)$$

Measured heat transfer coefficients are expressed as the Nu number (accuracy ± 5.04%)

$$\mathrm{Nu} = \frac{h\,(\nu_{\mathrm{liq}}^2 / g)^{1/3}}{\lambda_{\mathrm{liq}}} \quad \text{with} \quad h = \dot{q}_{\mathrm{wall,inside}} / \Delta T_{\mathrm{film}} \qquad (5), (6)$$

The heat transfer coefficients (condensation and evaporation) typically exceed those predicted by Nusselt's theory by a certain amount due to wave formation and turbulence. The improvement in the range of laminar-wavy film flow is usually expressed by the wave factor F_{wave} relating the measured heat transfer coefficients to those predicted by Nusselts's theory [6]:

$$F_{\mathrm{wave}} = \frac{\mathrm{Nu}_{\mathrm{exp.}}}{\mathrm{Nu}_{\mathrm{laminar,Nusselt\,[6]}}} \qquad (7)$$

Further the Pr and Ka numbers are evaluated with the temperature-sensitive liquid properties due to

$$\mathrm{Pr}_{\mathrm{liq}} = \frac{c_{\mathrm{p,liq}}\, \mu_{\mathrm{liq}}}{\lambda_{\mathrm{liq}}} \text{ and } \mathrm{Ka} = \frac{\mu_{\mathrm{liq}}^4\, \rho_{\mathrm{liq}}}{\sigma_{\mathrm{liq}}^3\, g} \qquad (8), (9)$$

The liquid properties are taken at a reference temperature

$$T_{\mathrm{ref}} = T_{\mathrm{wall,inside}} - f_{\mathrm{ref}}\,(T_{\mathrm{wall,inside}} - T_{\mathrm{vap}}) \qquad (10)$$

with f_{ref} = 0.25 for the viscosities and f_{ref} = 0.5 for all other. As exception for $\mathrm{Pr}_{\mathrm{liq,\ freesurface}}$ the properties are taken at vapor temperature with f_{ref} = 1. Extended experiments have been carried out at zero-velocity conditions. Local heat transfer coefficients have been measured for falling film evaporation of isopropanol covering film Reynolds numbers up to 100, inner wall heat flux up to 12,500 Wm^{-2}, and vapor temperatures ranging from 8.5 °C to 36 °C.

Reynolds number effects

The results are plotted in Fig. 5 in terms of F_{wave} versus Re number. Various heat-flux classes ranging from 2,000 ± 500 Wm^{-2} to 12,500 ± 500 Wm^{-2} are represented by a variety of symbols (there is one exception for 6,550 Wm^{-2} with only ± 150 Wm^{-2} as the interval). In general, the wave factor F_{wave} is found to increase along with the Re number. This is sketched in Fig. 5 by the yellow trend line interconnecting data points at 6,550 Wm^{-2} and t_{vap} = 36 °C.
Five characteristic Re number ranges are found with limits as indicated in Fig. 5 by vertical yellow lines:

(a) Re < 2.5: F_{wave} is nearly constant (obtained for heat fluxes 7.500 - 9.500 Wm^{-2});

(b) 2.5 < Re < 4: The wave factor starts to rise moderately;

(c) 4 < Re < 25: The increase becomes stronger …

(d) 25 < Re < 70: … and weaker again …

(e) Re > 70: … and finally a re-intensification is obtained with a significantly stronger slope of the yellow curve.

The various Re number ranges correspond to respective ranges for the wavy-film flow characteristics: Only occasional, so-called "very small" and first small waves (both two-dimensional circled) are found in (a) as reported in Gross et al. [7]. Range (b) represents transition to two-dimensional waves with rising mightiness, (c), characterized by increasing wave frequency and heat transfer enhancement, whereby a fluid transition from two to two-dimensional-inclined and further on to three dimensional wave shape is found. Range (d) with fully three-dimensional waves brings first indications for the transition to local turbulence with further increased frequency showing, however, only moderate additional enhancement of heat transfer which finally is further increased at about Re > 40 with the transition to developed turbulence in range (e).

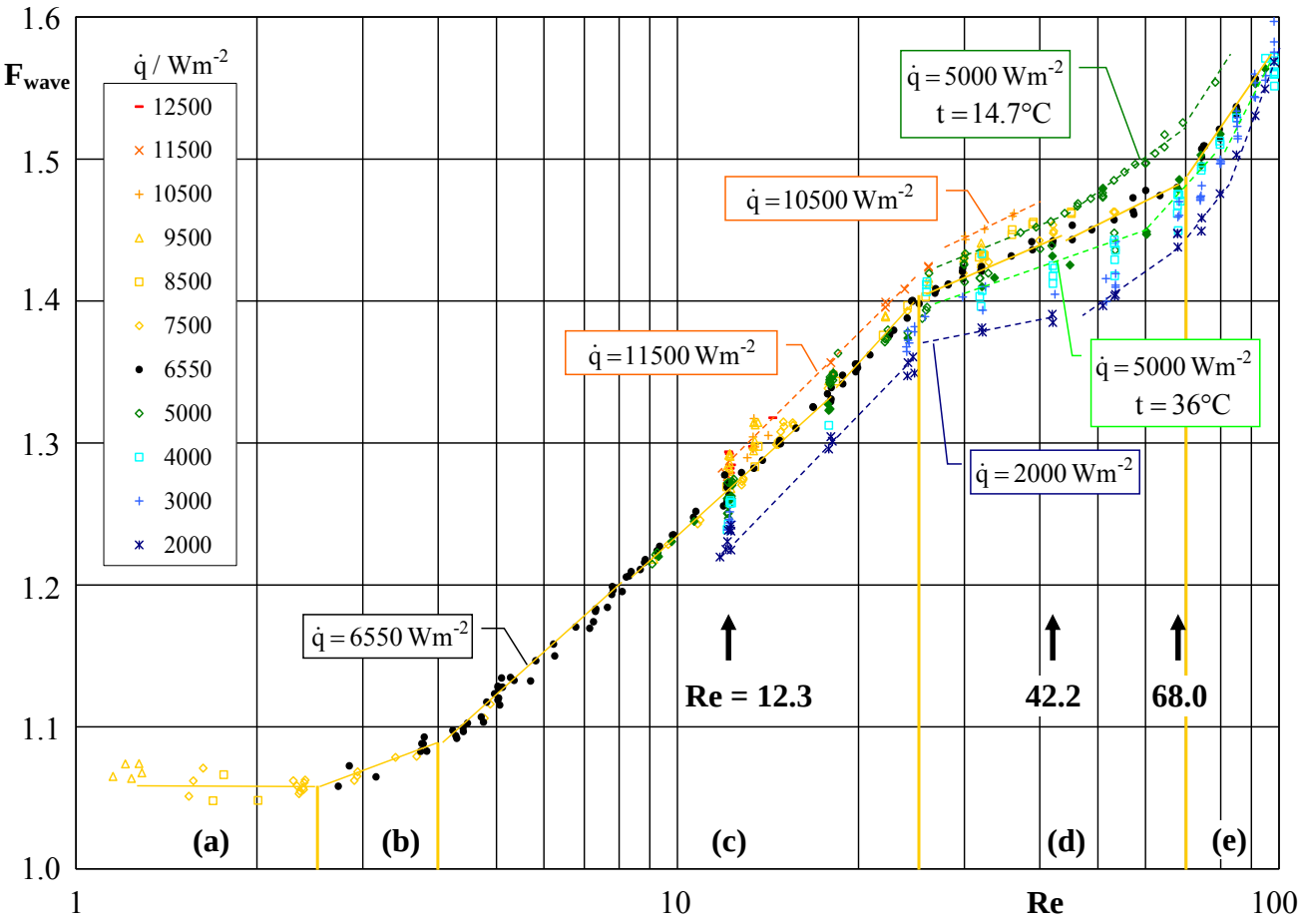

Figure 5. Wave factor vs. Re number (evaporation heat transfer data)

This general Re number effect on F_{wave} is found to be superposed by a certain influence of the wall heat flux. This is clearly seen in Fig. 5 for range (c) showing some increase of F_{wave} when the heat flux is raised from 2,000 Wm^{-2} to 11,500 Wm^{-2}. This influence seems to by even stronger in range (d), i.e. in presence of developing turbulence. Here an additional temperature effect becomes visible showing a decrease of F_{wave} when the temperature is raised from 14.7 °C to 36 °C (as measured for 5,000 Wm^{-2}). This strange behavior asks for analysis and clarification.

Heat flux and temperature effects

Three different Re numbers have been selected. They represent the ranges of two-dimensional waves (Re = 12.3), the begin of transition from three-dimensional waves to local turbulence (Re = 42.2), and finally transition to developed turbulence (Re = 68.0).

The Nu number versus heat flux plot, Fig. 6, shows characteristic rising curves for each of the selected Re numbers with a weak superposed vapor-temperature effect as already seen in Fig. 5. Both the temperature effect and the heat flux effect (i.e. temperature-difference effect) are caused by respective thermophysical property variations in the evaporating liquid film.

A vapor temperature decrease results in an increase of the Kapitza number caused by the combined effects of surface tension, liquid density and viscosity variations. An intensification of the wave activity is observed, see Gross et al. [7], and subsequently the Nusselt number is forced to rise.

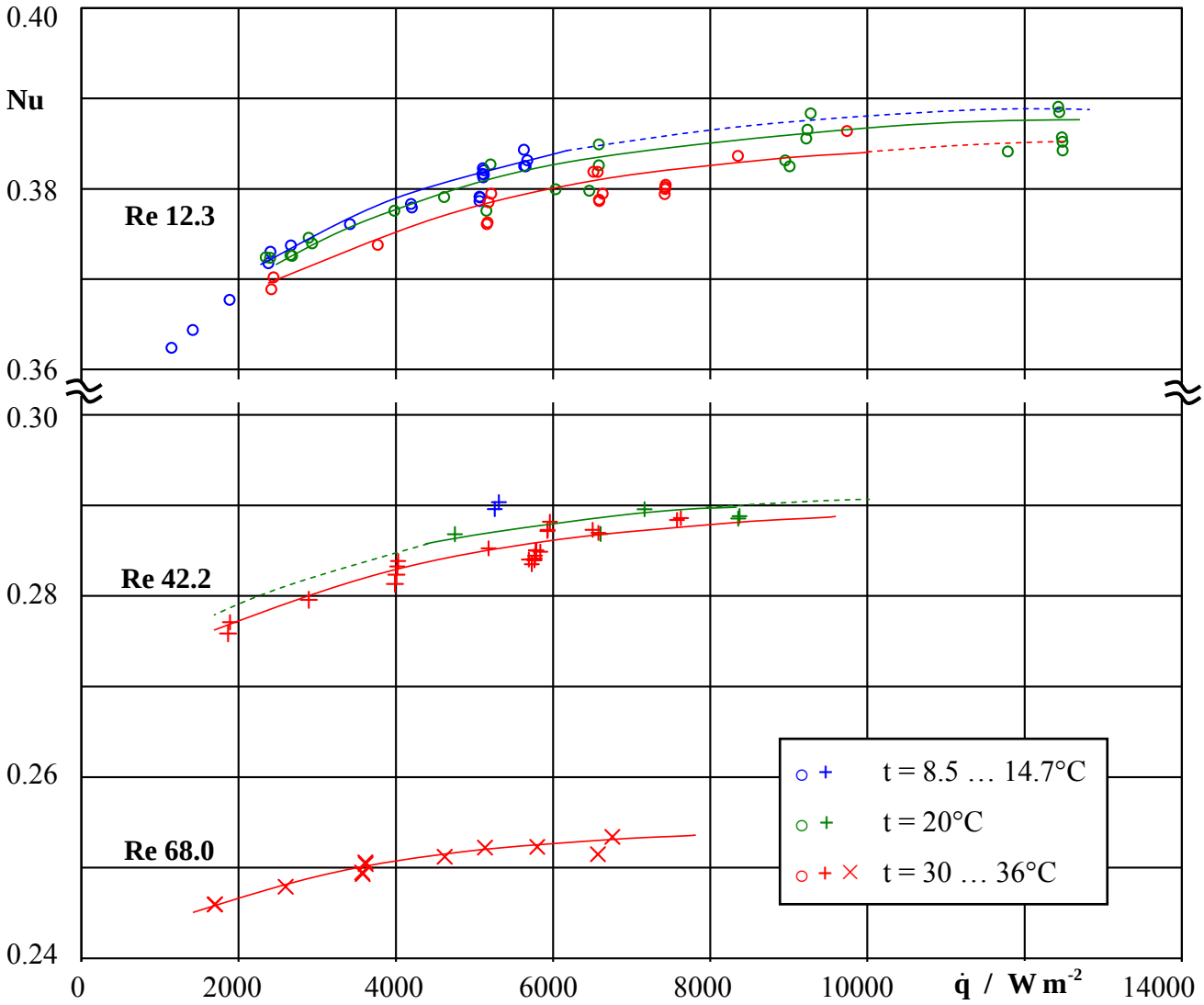

Figure 6. Nu number vs. heat flux

Increasing heat flux at a constant vapor temperature brings proportionally increasing temperature differences across the evaporating liquid film. The latter one becomes increasingly superheated next to the wall surface. The following effects have to been taken into account:

- Superheated liquid is in a metastable thermodynamic state with the latent chance for the formation of vapor bubbles. If the excess temperature is large enough, transition to nucleate boiling is obtained with strongly increased heat transfer coefficients on one side and an increasing danger of dry-patch formation on the other. These phenomena are outside the scope of the present investigation which is pure related to evaporation from the falling film surface.

- Evaporating films show characteristic temperature profiles with the gradient orthogonal to the wall surface and respective variations of the temperature-dependent thermophysical properties. The heat transfer experiments have been evaluated by taking mean values of the properties, equation (10), ignoring their variations across the liquid film. The liquid viscosity as the most sensitive property exhibits increasingly big differences between the wall surface (where it is low) and the vapor-side surface (where it is large) when the heat flux is being raised.

This phenomenon is not generally new. Heat flux effects on single-phase convection heat transfer in tubes has already been studied by Sieder and Tate [10] who introduced $(\mu_{liq} / \mu_{liq,\ wall})^{0.14}$. This concept has been modified by M.A. Mikheev and by V.V. Yakovlev in the 1950's for turbulent flow situations, and based on their suggestion Hufschmidt et al. [11] found $(Pr_{liq} / Pr_{liq\ ,wall})^{0.11}$ as an optimized correction term which finally is suggested in the VDI Wärmeatlas [12] for both laminar and turbulent internal convection. This concept will now be applied to consideration of heat flux effects on falling film evaporation heat transfer.

Correlation

All experimental heat transfer data, in terms of F_{wave} , have been correlated with Re and Ka numbers using the following power law equation:

$$F_{wave} = C\ Re^{a}\ Ka^{b} \left(\frac{Pr_{liq,\ freesurface}}{Pr_{liq,wall}} \right)^{0.11} \qquad (11)$$

This has been done separately for the ranges (b) to (d), see table 1. In (a) the wave factor has been obtained to be constant at about $F_{wave} = 1.06$. For the fully turbulent liquid film in range (e), the enhancement factor concept based on Nusselt's solution looses its sense.

Table 1
Results of data correlation following equation (11)

Range	Re number range	Constant	Re number exponent a	Ka number exponent b
(b)	2.5 < Re < 4	1.040	0.0467	0.0021
(c)	4 < Re < 25	1.096	0.1450	0.0126
(d)	25 < Re < 70	1.217	0.0593	0.0036

The strongest Re and Ka number effects are clearly found in range (c), i.e. for the developed two-dimensional wavy film flow situation with continuous transition to two-dimensional-inclined and further to three dimensional wave shape.

The remaining deviations between correlated and experimental data are plotted in Figs. 7 and 8 versus Re and Ka number respectively. The correlation proves to be extremely good with deviations typically within ± 3%. This is, of course, due to the limited width of the data set regarding Re number and also Ka number ranges. It is not the intension of this article to provide correlations for design engineers. This will be done in future after completing the data base by measurements with further liquids like ethanol, water and others. The basic intension of this presentation is a

comparison of the characteristics in the various Re number ranges, and also a comparison with the earlier condensation results as reported in equations (1) to (3).

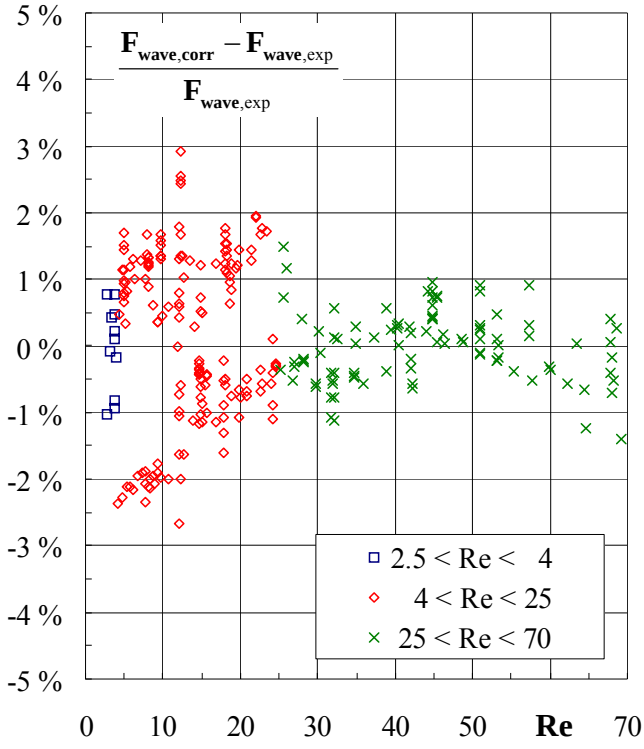

Figure 7. Deviation of correlation vs. Re

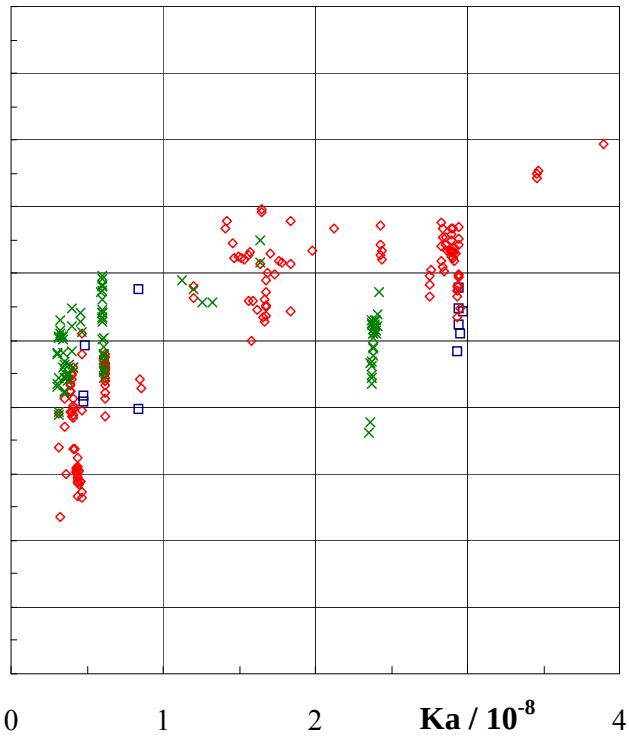

Figure 8. Deviation of correlation vs. Ka

Comparison with the literature

The open literature contains only a few references regarding the heat flux effect. For conditions without bubble formation in the superheated liquid film, only a fistful of earlier studies is found.

Struve [13] and Elle [14] investigated falling film evaporation heat transfer of refrigerant R11 outside a vertical tube. No heat flux effect has been found by them below the limit of first bubble formation.

Shah and Darby [15] studied surfactant effects on evaporation heat transfer in a liquid film flowing downward a vertical flat plate. Among many other findings they obtained results for the limiting case of pure water at Re numbers in the range of developing turbulence. There are clear signs of heat transfer promotion for increasing heat flux which is found to be moderate in case of surface evaporation. Beyond the onset of bubble nucleation, at about $\Delta t = 5$ K, the heat flux effect becomes much stronger.

Alhusseini et al. [16] measured mean heat transfer coefficients for evaporation of water and propylene glycol outside a vertical tube and they provided the following correlation valid for the laminar-wavy region:

$$Nu = 2.65\,Re^{0,175}\;Ka^{0.0563} \tag{12}$$

which may be rewritten for the wave factor as

$$F_{wave,Alhusseini\,et\,al[16]} \propto Re^{0,175}\;Ka^{0.0563} \tag{13}$$

Both the Re and Ka number effects are obviously much stronger than in the present investigations.

Weise and Scholl [17] present falling film evaporation results for liquids in the high Prandtl number range with Pr_{liq} = 40 to 130. Overall heat transfer measurements have been carried out with the heat flux, i.e. the driving overall temperature difference, as one of the parameters. Only a few of the results are found for the laminar range with no significant heat flux effects. In the turbulent range, however, there is a heat transfer enhancement in the order of 20 % when the driving temperature difference is increased from Δt = 10 K to 20 K. This effect has been found for Pr = 40 and 58 and it seems to vanish for larger Prandtl numbers, i.e. $Pr \geq 78$.

CONCLUSION

For isopropanol, the authors' local heat transfer measurements of falling film evaporation have been evaluated at zero shear stress inside a vertical tube with systematic variations of Re number, heat flux and vapor temperature. Basically the new results verify the earlier condensation heat transfer results. Nevertheless, a deviation in the range of transition from three-dimensional wave shape to turbulence (Re = 25 to 70) was found. Heat flux effects have been detected and correlated. Thereby the ratio of Pr numbers at vapor temperature and wall temperature, as known from pipe flow correlations, have been used. Prospective investigation with other fluids will follow to verify the presented effects.

ACKNOWLEDGMENT

The authors like to thank Alexander Köhler, Tobias Nell, Nick Trümmel and Volkmar Wörner for their contributions. The support by the Deutsche Forschungsgemeinschaft (DFG) is greatly appreciated.

REFERENCES

1. Weise F., Experimentelle Untersuchungen zur Strömung und Wärmeübertragung von Reinstoff-Fallfilmen mit hohen Prandtl-Zahlen, *PhD thesis*, TU Braunschweig, Cuvillier Verlag, Göttingen, 2007.
2. Gross, U., Philipp, Ch., Conjugated shear stress and Prandtl number effects on reflux condensation heat transfer inside a vertical tube, *Int. J. Heat Mass Transfer,* Vol.49, pp.144-153, 2006.
3. Adomeit P., Experimentelle Untersuchung der Strömung laminar-welliger Rieselfilme, *PhD thesis*, RWTH Aachen, 1996.
4. Thumm S., Philipp Ch., Gross U., Film condensation of water in a vertical tube with countercurrent vapour flow, *Int. J. of Heat Mass Transfer*, Vol. 44, pp. 4245-4256, 2001.
5. Gross U., Philipp Ch., Thumm S., Effect of countercurrent vapour flow on film condensation heat transfer inside a vertical tube, Heat Transfer 2002, in: *Proc. 12th Int. Heat Transfer Conf.*, Grenoble, pp. 923–928.
6. Nusselt W., Surface condensation of steam (in german: Die Oberflächenkondensation des Wasserdampfs), *Z. Ver. Dt. Ing.* 60 (1916) 541 – 546, 569 – 575.
7. Gross U., Storch Th., Philipp Ch., Doeg A., Wave frequency of falling liquid films and its effect on reflux condensation in vertical tubes, *Int. J. Multiphase Flow*, Vol. 35, No. 4, pp. 398 – 409, 2009.
8. Storch, Th., Philipp, Ch., Gross, U., Zero shear-stress experiments of falling film evaporation inside a vertical tube, *Eurotherm 2008 - 5th European Thermal-Sciences Conf.*, Eindhoven, 2008, CD-Rom, ISBN 978-90-386-1274-4.

9. Philipp, Ch., Doeg, A., Tellefsen, Kufaas S., Groß, U., Wave characteristics of liquid films – correlation of heat transfer data with visual observations. *Proc. of 13th International Heat Transfer Conference*, Sydney, 2006, CD-ROM, ISBN 1-56700-226-9.

10. Sieder E.N., Tate G.E., Heat Transfer and Pressure Drop of Liquids in Tubes, *Ind. Eng. Chem.*, Vol. 28 (1936) 12, 1429-1435.

11. Hufschmidt W., Burck E., Riebold W., Determination of local and averaged heat transfer coefficients inside tubes at high heat flux (in german, Die Bestimmung örtlicher und mittlerer Wärmeübergangskoeffizienten in Rohren bei hohen Wärmestromdichten), *Int. J. Heat Mass Transfer*, Vol. 9 (1966) 539-565.

12. VDI Wärmeatlas, Section Ga, Forced convection heat transfer in tubes (in german, Wärmeübertragung bei der Strömung durch Rohre), Springer Verlag Berlin Heidelberg, 2006, ISBN-10 3-540-25504-4.

13. Struve H., Heat Transfer to an Evaporating Falling Refrigerant Film, *Proc. 12th Congress Int. Inst. Refrigeration*, Madrid, 1967, 635-640.

14. Elle C., Falling film evaporation of refrigerant R11 and refrigerant-oil-mixture R11 – 51KM33 (in german, Der Wärmeübergang bei der Rieselfilmverdampfung des Kältemittels R11 und des Kältemittel-Öl-Gemisches R11 – 51KM33), *PhD thesis*, Dresden University, Germany, 1970.

15. Shah B.H., Darby R., The effect of surfactant in evaporative heat transfer in vertical film flow, *Int. J. Heat Mass Transfer*, Vol.16 (1973) 1889-1903.

16. Alhusseini A.A., Tuzla K., Chen J.C., Falling film evaporation of single component liquids, *Int. J. Heat Mass Transfer*, Vol. 41 (1998) 1623-1632.

17. Weise F., Scholl S., Fluid Dynamics and Heat Transfer in Falling Film Evaporation of Pure High-Prandtl-number Liquids (in german: Fluiddynamik und Wärmeübergang bei der Fallfilmverdampfung von Reinstoffen mit hohen Prandtl-Zahlen), *Chemie Ing. Technik* ,Vol. 79 (2007) 8, 1145-1153.

AXIAL DEVELOPMENT OF TWO-PHASE FLOW STRUCTURE IN A VERTICAL PIPE : EXPERIMENTAL DATA USING CONDUCTIVITY PROBES AND LASER DOPPLER ANEMOMETRY

S. Chiva[1,*] , S. Mendez[2] , J.L. Muñoz-Cobo[2], E. Julia[1], L. Hernandez[1]
[1]Department of Mechanical Engineering and Construction , Universitat Jaume I, Spain,
[2]Department of Chemistry and Nuclear Engineering, Polytechnic University of Valencia, Spain

ABSTRACT. An upward isothermal co-current air-water flow in a vertical pipe (52 mm inner diameter) has been experimental investigated. Local measurements of void fraction, interfacial area concentration (IAC), interfacial velocity and Sauter mean diameter were measured using a four sensor conductivity probe. Liquid velocity and turbulence intensity were measured using Laser Doppler Anemometry (LDA). Different air-water flow configurations was investigated for a liquid flow rate ranged from 0.491 m/s to 3 m/s and a void fraction up to 25 % .For each two-phase flow configuration twenty five radial position and three axial locations were measured by the conductivity probe methodology, and several radial profiles was measured with LDA at different axial positions..

Keywords: *double sensor conductivity probe, LDA, Interfacial Area Concentration, two-phase flow structure*

INTRODUCTION

One of the most important key in the two-phase flow is the existence of multidimensional interfaces between both phases. The correct behaviour prediction of this interfaces, and its quantification is one of the frontiers in the theoretical and experimental studies of this kind of flow, and up to now, there is not an effective technique and methodology for the multidimensional interface characterization in two-phase flow measurement [1] . Then, experimental works play a very important role in the development of new theoretical models and it is essential for design, analysis and behaviour analysis of existing and futures scenarios. In this work a detailed experiments are performed in order to have a good data base about the main parameters in two-phase flow characterization in upward co-flow in vertical pipes.

The basic structure of a two-phase flow can be characterized by three fundamental parameters. These are the void fraction, Sauter mean diameter (for bubbly flow mainly) and interfacial area concentration (IAC) [2]. The void fraction expresses the phase distribution and it is a required parameter for hydrodynamic and thermal design in various industrial processes. On the other hand, the interfacial area describes available area for the interfacial transfer of mass, momentum and energy, and it is a required parameter for a two-fluid model formulation. Various transfer mechanisms between phases depend on the two-phase interfacial structures. Therefore, an accurate knowledge of these parameters is necessary for any two-phase flow analyses.

The void fraction measurement is not so complicated using intrusive methods like conductivity probes with only two sensors. But IAC, defined by the quantity of interface between both phases, measured in area units per each unit of mixture volume, is quite complex itself, and with a large difficulties to be

* Corresponding author: Prof. S. Chiva
Phone: + (34)-964-728141, Fax: + (34)-964-728106
E-mail address: schiva@emc.uji.es

measured. [3] defined the local time-averaged IAC at a fixed position in space derived on the basis of velocities measurements according to the expression:

$$\bar{a}^t = \frac{1}{\Omega}\sum_l \frac{1}{|\vec{V}_{il}\cdot\hat{n}_{il}|} \qquad (1)$$

That definition opens the door to measure the interfacial area using the velocity of the interphase , if it is measured with enough detail together its vector components. The theoretical fundaments for this technique was originally proposed by Kataoka [4], and during the last fifteen years numerous researcher have used and improved that technique using intrusive probes of two, four and five sensors. In this work we have used four-sensor probes in order to characterize the two-phase flow parameters. The double–sensor sensor conductivity probe technique is useful for 1D flow when spherical bubble can be assumed, which could be easily supposed in flows trough vertical pipes with relative small diameter and with gas moderated flow. The IAC and interface velocity can be calculated using the distance between the probe tips, but a calibration factor, based in a Mote-Carlo methodology, is proposed to relate the real magnitude to that measured from the experimental signal. It is necessary to introduce a calibration factor, based on statistical methods, to be able to take on account the possible deviation from the vertical direction and the presence of missing bubbles, bubbles that produces bad signals or bubble that only produce a signal in only one of the tips. Interfacial velocity, void fraction, Sauter mean diameter and IAC were measured using double-sensor probe. Also in this work, we include a detailed liquid velocity and turbulence intensity measurements using LDA which it is not usual in other research works where it is measured using hot-wire anemometer (HWA) . LDA is a not intrusive method and it give a more precise results and easier to interpret than HWA when bubbles are present in a liquid flow. Accurate magnitude information about liquid is basic for a good results interpretation.When spherical bubbles can not be assumed, it is necessary to introduce a four-sensor conductivity probe to perform the measurements, since no hypotesis for the bubble shape is necessary in the mathematical formulation to calculate the local interfacial area concentration.

EXPERIMENTAL FACILITY AND INSTRUMENTATION

The experimental work was performed using a thermo-hydraulic loop placed at the Energy Engineering Institute in Polytechnic University of Valencia (Spain). The loop is schematically illustrated in Figure 1. It consists of a test section, a round transparent tube made by Plexiglas with constant section, an upper plenum and a lower plenum where air and water are mixed. The test section has a 52 mm inner diameter and a length of 3340 mm. The water was circulated by two centrifugal pumps controlled by a frequency controller.

The air was supply by a compressor, and it was introduced to the test section through a porous sinter element with a average pore size of 10 mm installed below the mix chamber. The air and water temperature was kept constant during the test assay. The air mass flow rate was measured with a thermal mass flow meter and controller (Bronkhorst ® , EL-FLOW model), liquid flow rate with a Electromagnetic flow meter (Badger Meter ®), and the pressure with a precision pressure transmitter, DRUCK ® PTX 600 series.(INF position: range [0..1] bar, MED, SUP position range [0..250] mbar (Prec. 0.5% F.S.)

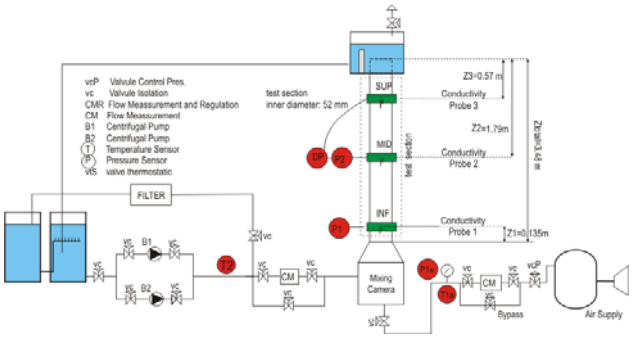

Figure 1. PUMA Facility scheme

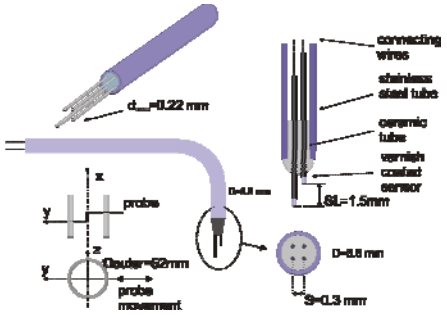

Figure 2. Schematic diagram of four sensor conductivity probe

The LDA equipment consists of a 0.5W Ar+ Ominichrome laser, Dantec Fiberflow beam separator, Dantec FVA 58N40 processor and a PC using the software Floware for data acquisition. A lens of 0.125 m focal length was used and the system was operated in backscattering mode. The vertical component was determined with green (λ=514.5 nm) beams and the horizontal component with blue (λ=488 nm) beams. A preshift frequency of 500 kHz was used. The flow was seeded with hollow particles which were neutrally buoyant with a 10 □m mean size (Dantec HGS-10); therefore, only the liquid velocity was measured [7]. The time series obtained were 60 seconds long. The LDA system provides the liquid phase velocity moments. However, a number of data-processing steps are required before calculating the velocity moments. Firstly, the multiple validation, i.e. the multiple detection of the burst caused by a single particle, was handled by first rejecting velocity realizations with $V_i - \overline{V_i} > 4\sigma$ (σ is the standard deviation of the signal, $\overline{V_i}$ a single velocity realization and the averaged velocity over the measurement time). Then, the bursts which follow other bursts within a 1 ms interval were removed. Finally, the velocity bias, i.e. higher velocities over-representation, was corrected using the so-called 2D+ weighting: inversely weighting the data with the velocity [8]. Since only two components are known, the magnitude of the third component is estimated from the variance of the second component: the weighting factor w is,

$$w = 1/\sqrt{V_x^2 + V_z^2 + (d_m / l_m)^2 \overline{V_z'^2}} \qquad (2)$$

with dm/lm as the diameter-to-length ratio of the ellipsoidal measurement volume. The use of only two components is justified since the magnitude of the vertical and lateral fluctuations will be close, and the influence of the third component is slight since d_m/l_m is also small. In this way, pairs of vertical and lateral velocity realizations, which have arrival times inside coincidence windows with a length of 200 μs, are searched. More technical details about the data processing can be found elsewhere [9],[10].

Sensor conductivity probe methodology

The four- sensor probe is basically a phase identifier. It consists of two sensors made of stainless steel, coated with gold, with a diameter of 0.22 mm. The vertical distance between both tips was about 1.5 mm . Each sensor is insulated using a insulating varnish except its tips. If the probe is connected to a power supply with a fixed voltage, due to the large difference in conductivity between the liquid phase and the gas phase, the impedance signal acquired rises sharply when a bubble passes through one of the sensor tips, obtaining a more or less square signal. With a suitable signal processing methodology is possible extract precise information from that raw signal.

From the time lag, between the impedance signals of the front and back tips, we can know the time that needs the front of the bubble to travel from one tip to the other that is far away a distance, S. Then a measurable value of the bubble velocity, Vm, can be easily obtained. If the bubble moves with its velocity vector parallel to the conductivity probe orientation then the measurable value Vm of the velocity match the true value of the bubble speed. However, as the bubble velocity fluctuates in response to the turbulence of the liquid phase then the bubble's lateral motion along with the finite value of the distance between both tips of the probe, and the bubble curvature can cause problems in the measurement of the true value of the bubble velocity. To quantify this difference it is possible to define a calibration factor as the ratio between the mean value and the measured value of the bubble including the missing bubbles. The most common model used are: Kataoka statistical model, Wu statistical model or Hibiki statistical model.

In this work we have chosen the methodology carried out by Muñoz-Cobo et al. [5] to determine the calibration factor. In his study the effects of bubble motions, and probe spacing have been included. The value measured is related to the local bubble interface velocity in the surface normal direction. The probability density function of each variable is identified with the suitable coordinate transformation. Two theoretical calibration factors are defined to relate the mean measurable parameter to the interfacial area concentrations obtained and the measured bubbles, including the missed bubbles. These calibration factors have been obtained through analytical and numerical method, using a Monte Carlo approach. The results of these calculations show that the total interfacial area correction factor is very close to 2, and depends very weakly on the velocity fluctuation, and the relative distance between tips. For the velocity calibration factor, the Monte-Carlo results show that for moderate values of the relative bubble velocity fluctuation and values of the relative distance between tips not too small, the correction velocity factor for the bubble sensor conductivity probe is close to unity.

EXPERIMENT RESULTS AND CONCLUSIONS

The flow conditions have been chosen measuring the superficial liquid and air velocity and the average void fraction on z/D=56 in each condition. All the conditions (Table 1) are in the bubbly flow regime, and only in the highest void fractions appears some large cups, near the transition . For each liquid velocity conditions we have at least five gas conditions from 5 % to up 25% . That void fraction was measured by a pressure sensors at z/D=56. For the probe sensors, two different configurations were used, as it can see in Figure 5 and 6, in order to study the best configuration, mainly near the wall. Details about the experiments and the facility can be found in [11]

Table 1
Experimental Flow Condition

j_f = 0.5 m/s			j_f [m/s] = 1.0 m/s			j_f = 2.0 m/s			j_f = 3.0 m/s		
	j_g [m/s]	<α>		j_g [m/s]	<α>		j_g [m/s]	<α>		j_g [m/s]	<α>
F01G00	0	0	F02G00	0	0	F03G00	0	0	F04G00	0	0
F01G01	0.035	5.14	F02G01	0.058	4.99	F03G01	0.097	4.5	F04G01	0.166	3.12
F01G02	0.077	10.03	F02G02	0.142	10.3	F03G02	0.233	9.73	F04G02	0.389	4.72
F01G03	0.125	15.11	F02G03	0.235	14.32	F03G03	0.47	12.39	F04G03	0.662	7.56
F01G04	0.176	19.95	F02G04	0.396	18.57	F03G04	0.72	19.66	F04G04	1.023	9.03
F01G05	0.257	21.7	F02G05	0.67	23.96	F03G05	1.181	21.8	F04G05	1.695	9.51
F01G06	0.338	24.38									

The bubble diameter at the inlet depends on the gas flow and liquid flow, for a pressure and a bubble generator system given. The initial diameter was not controlled in this experiment, we only measure it. With liquid velocities at the inlet below 2 m/s the turbulence does not produce bubble

disintegration, then the initial bubble determinates the developing profile. The bubble diameter at the inlet was in the range [2–4] mm, Figure 4, file 1, and by pressure reduction along the flow direction, the bubble diameter change increasing its diameter, Figure 4, file 2. For jf = 0.5 , G05 (20%) and G06 (25 %) conditions large cup bubble were detected.

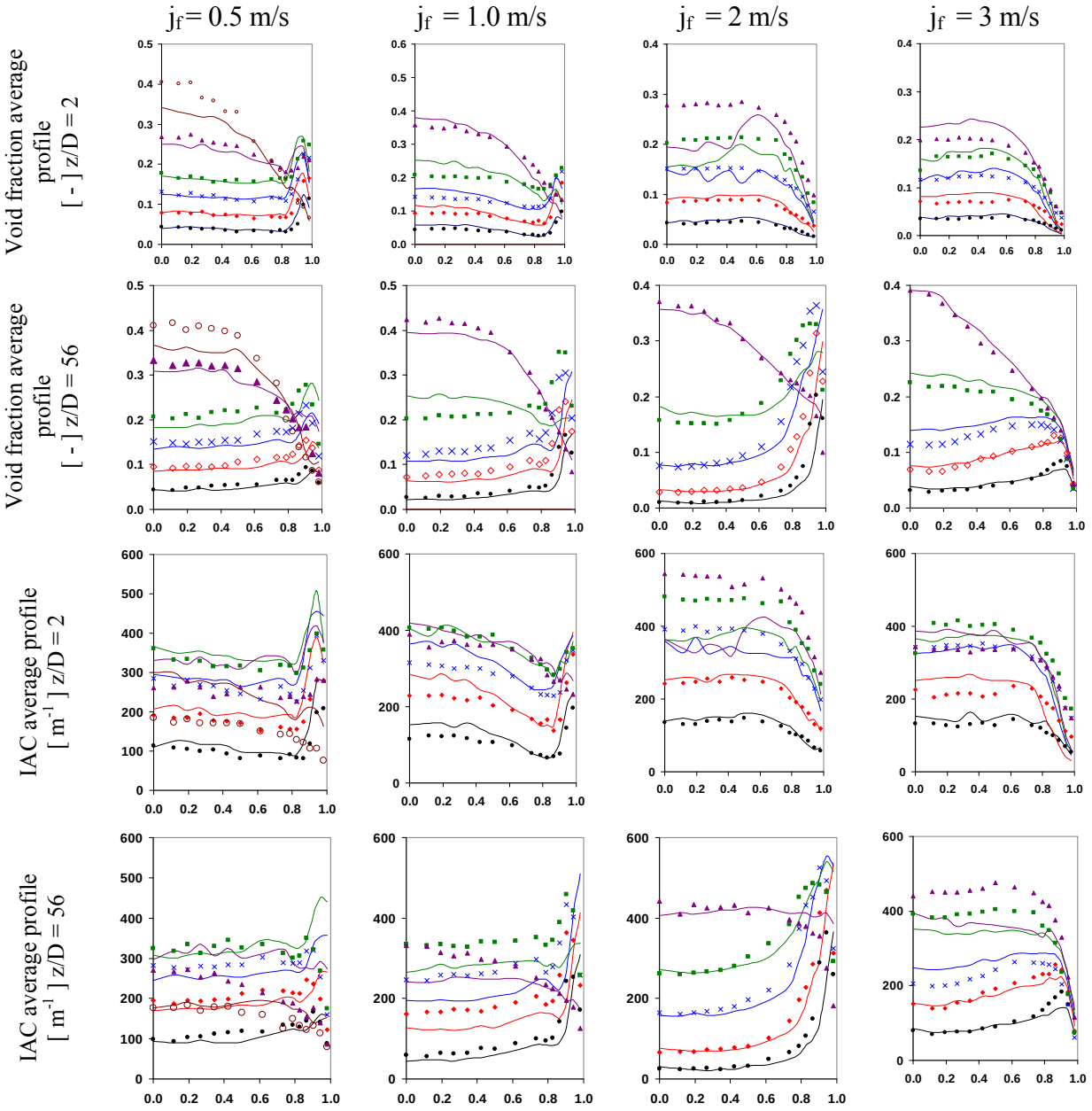

Figure 3. Results: Average profile (r/R) for IAC and void fraction for two axial position. Solid symbol correspond to F0A probe configuration, and without symbol for F0.. The legend for the graphs are as follow: Black (●) G01, Red (◊) G02, Blue (X) G03, Green (■) G04, Violet (▲) G05, light Violet (○) G06

The radial distribution of the bubble, gas phase, depends on the diameter, and the liquid velocity gradient. Small bubbles tend to move toward the wall , while large bubble migrate preferable to the center. This lateral movement is determinate by the lift force, and its sign change as function of the bubble diameter. We must consider other later force, the wall lubrication force, which acts to drive the bubble away from the wall, but its effect decreases very fast. The balance, from those two forces, produces the peak near the wall. Figure 3, file 1 and 2, shows the void fraction behaviour. We can observe the three typical profiles, wall-peak, transitional and core-peak. For, F01, F02 and

F03, j_f = [0.5 – 2] m/s the void fraction show a wall-peak profile for G01,G02 and G03, typically [0-15%]. The local void fraction profile have a typical evolution of the pressure reduction, it match with lack of bubble break-up o coalescence due to the reduced liquid velocity and the moderated void fraction. The peaks in the void fraction profile match quite good with the peaks position described in the literature, the peaks were located more or less at one bubble diameter from the wall. For jf = 2 m/s and 3 m/s at lower position no wall-peak profile was observed for void fraction , perhaps, the development zone at the entrance produces bubble migration toward the center, since the bubble diameter is small. For G04 (20%), the profile has an evolution to transitional shape, due, mainly, to the tendency to migrate toward the channel center by the large bubble, and only shows wall-peak for jf=0.5 and 1 m/s at z/D=2. For jf=2 m/s and 3 m/s at z/D=2 the void fraction has a transitional profile for all the void fraction concentration. The core-peak profile appears when large quantity of gas is injected to the system and large bubbles appears (Figure 4, file 1 and 2) , migrating toward the center of the tube. For void fraction average largest than 20% a core-peak profile appears, mainly in the upper part of the section.

Since, in the cases without cups, the Sauter diameters are quite uniform, Figure 4, file 1 and 2, in all the profile, the IAC profile (Figure 3, file 3 and 4) shows a similar behaviour of its respective void fraction profile. Special attention needs the F01 case, jf=0.5 m/s , when large cups appears in G05 and G06 cases, since although a core-peak is showed in its void fraction profile, the IAC have a flat profile. It could be explained by the minor IAC were cup are presents.

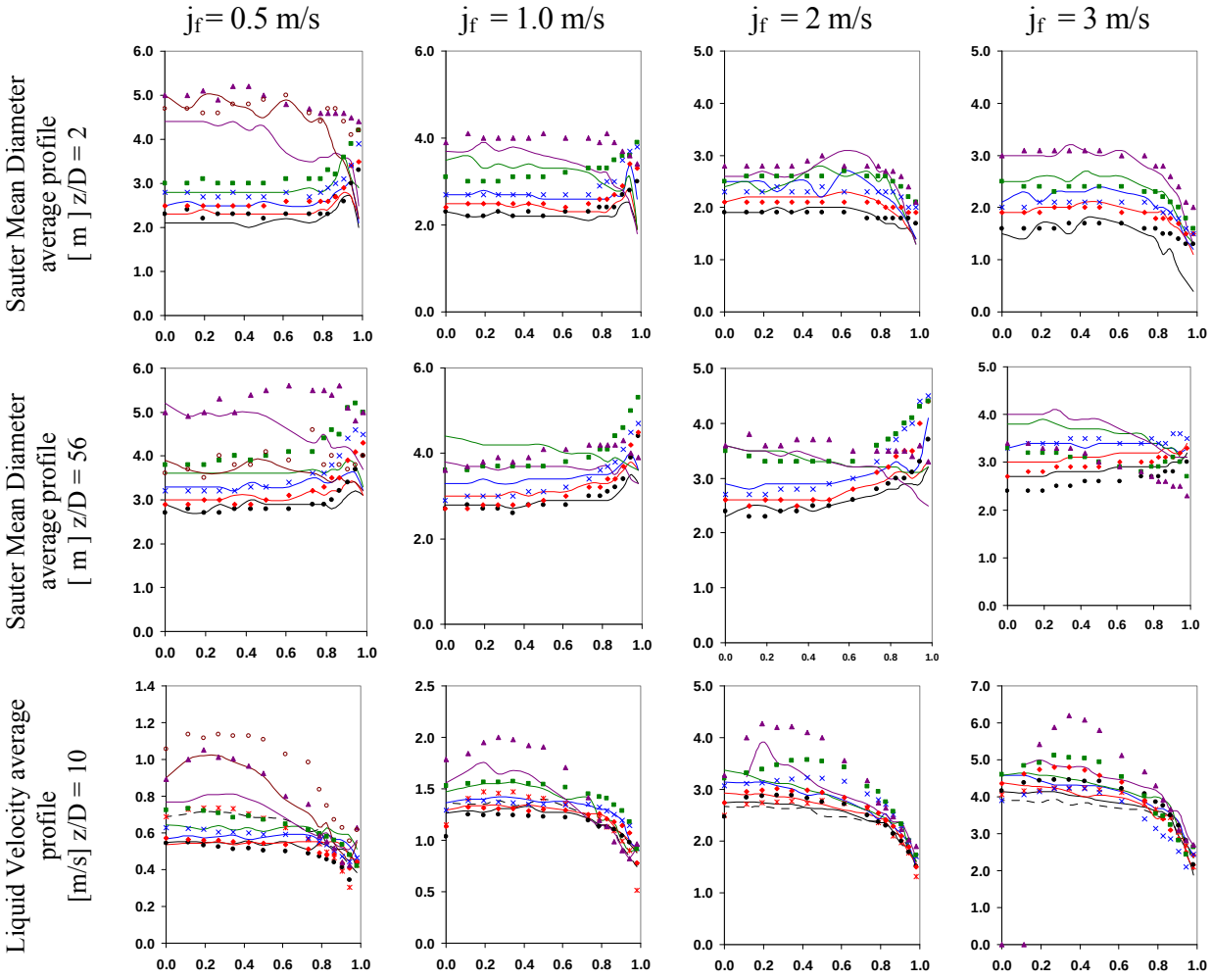

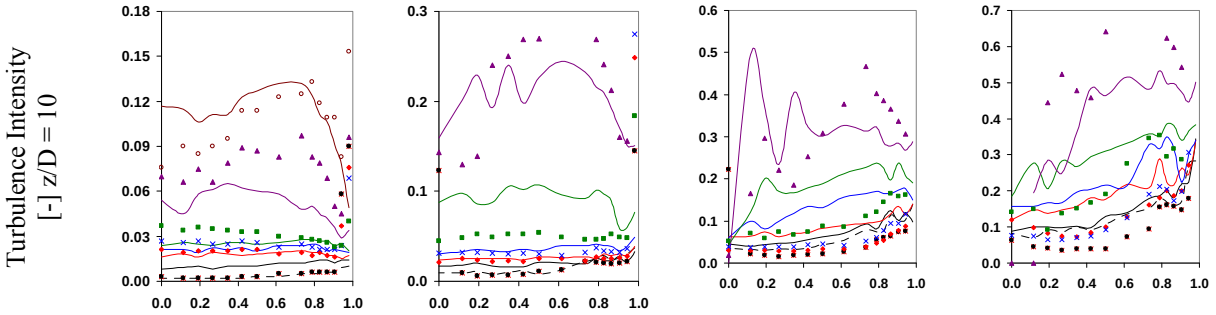

Figure 4. Results: Average profile (r/R) for Sauter Mean Diameter for two axial position, Velocity and Turbulence intensity for liquid phase at z/D = 10. Solid symbol correspond to F0A probe configuration, and without symbol for F0.. The legend for the graphs are as follow: Red (X) G00, Black (●) G01, Red (◊) G02, Blue (X) G03, Green (■) G04, Violet (▲) G05, light Violet (○) G06

The liquid velocity (Figure 4, file 3) and its turbulence intensity (Figure 4, file 4) were measured using LDA. In each figure, a red line is included, that line shows the single phase behaviour. For each liquid velocity a velocity profile was measured for single phase condition, where only liquid flows through the test section. The liquid flow rate calculated from the velocity profile was compared to the liquid flow rate measured with the flowmeter with very good results. The liquid velocity profile , in general, is more flatted when bubbles appear, but this effect is quickly saturated when the quantity of bubble increase, but when the liquid velocity increases, $\geq$ 1 m/s, the liquid profile is not largely affected by the bubbles, and the shape of the profile in single phase is maintained. The cups produce an increase in the liquid velocity, with a more pronounced core peak profile, , i.e. Figure 7, file 3, for void fraction largest than 20%

In general, the wall-peak profile in the turbulence intensity can be explained by the large gradient of the velocity and shear stress distribution near the wall, mainly in the lower part of the test section, where the flow is developing. In the center part of the pipe the turbulence is quite constant and lower than near the wall. It could explain why the bubbles are not disintegrated in the center of the pipe. When caps appear, the turbulences is enhanced (void fraction > 20%). It is interesting to comment that in certain flow conditions, as it was pointed out by Serizawa and Kataoka [11], locally, bubbles can reduce the turbulence intensity, when the liquid velocity is equal or bigger than 1 m/s. That could explain the turbulence intensity behaviour of G01, as you can see at Figure 4, file 4, for jf > 1 m/s.

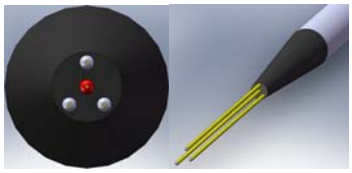

Figure 5.- Probe Configuration F0X

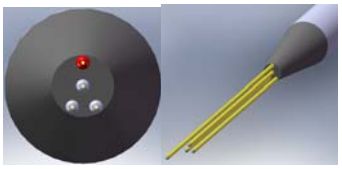

Figure 6.- Probe Configuration F0A

Both geometrical configurations give good and very similar results. The F0X configuration gives better results in position very close to the wall, with more robust physical sense. The second configuration, F0A, gives the best results when we need detect large bubbles or the velocity of the liquid is high. More experimental work and a detailed redesign are been done in order to give more answers about the election of the suitable design.

CONCLUSIONS

As it is showed in the paper, the results maintain a good agreement with those published by authors like Hibiki [6] and co-workers, with a very good prediction of the peaks in the profiles and its tendencies. The liquid velocity and its turbulence intensity were measured using LDA, with more accurate results. Then, the experimental methodology developed to build the four-sensor conductivity probe and to process the data set obtained, give good and repeatable results about the two-phase flow parameters. This methodology could be considered a suitable tool to study two-phase flow sceneries together the use of LDA to measure the liquid magnitudes.

ACKNOWLEDGMENTS

This research was supported by the Plan Nacional de I + D + I. Project EXPERTISER ENE2007-68085-C02-02

REFERENCES

1. Shen X, Y. Saito, K. Mishima, H. Nakamura, 2005, *Methodological improvement of an intrusive four-sensor probe for the multi-dimensional two-phase flow measurement*, International Journal of Multiphase Flow, Vol. 31, pp. 593-617
2. Delhaye J.P., P. Bricard, 1994, *Interfacial area in bubbly flow: experimental data and correlations*, Journal of Nuclear Engineering Design, Vol. 151, pp. 65-77
3. Ishii M. , 1975, *Thermo-fluid Dynamic Theory of Two-phase flow* , Eyrolles Paris
4. Kataoka I., M. Ishii, A. Serizawa, 1986, *Local formulation and measurement of interfacial area concentration in two-phase flow*, International Journal of Multiphase Flow, Vol. 12, pp. 505-529.
5. Muñoz-Cobo J.L., J. Peña, S. Chiva, S. Mendez, , 2006 *Monte-Carlo calculation of the calibration factors for the interfacial area concentration and the velocity of the bubbles for double sensor conductivity probe,* Nuclear Engineering and Design, Volume 237, Issue 5, March 2007, Pages 484-496
6. Hibiki T.,M. Ishii, Z. Xiao, 2001, *Axial interfacial area transport of vertical bubbly flow*, International Journal of Heat and Mass Transfer, Vol. 44, pp. 1869-1888
7. Groen, J. S., Mudde R. F. and Van den Akker H. E. A. 1999. *On the application of LDA to bubbly flow in the wobbling regime*. Exp. in Fluids 27, 435 - 449.
8. Tummers, M. J. 1999. *Investigation of a turbulent wake in an adverse pressure gradient using Laser Doppler Anemometry*. PhD thesis, Delft University of Technology, The Netherlands.
9. Harteveld, W. K., Mudde, R. F. and Van den Akker, H. 2003. *Dynamics of a bubble column: influence of gas distributions on coherent structures*. Can. J. Chem. Eng. 81, 389-394.
10. Harteveld, W. K., Juliá, J. E., Mudde, R. F. and Van den Akker, H. 2004. *Large scale vertical structures in bubble columns for gas fractions in the range of 5%-25%*. CHISA conference.
11. Mendez Diaz, Santos, *Medida Experimental De La Concentración De Area Interfacial* , PhD Thesis, Politechnic University of Valencia, Spain, 2008

EFFECT OF SURFACTANTS ON BOILING PHENOMENA

A.T.Pise*[1], A.R. Acharya[1] and I. I. Momin[1]
[1] Department of Mechanical Engg. Govt. College of Engineering. Karad M.S. 415124, India

ABSTRACT. The heat transfer in boiling can be enhanced by adding small amount of additive in fluid. Presence of small amount of additive in the fluid changes the physical behavior of the boiling phenomenon. These surfactants change thermo-physical properties of the fluid. Experiments on pool boiling were carried in presence of the surfactant in pure water. Ammonium Chloride NH_4Cl, Sodium Lauryl Sulphate SLS, Hydroxyethyl Cellulose HEC-H and Betel Nut served as test surfactants and added separately in water with varying concentration. The results of surfactants namely SLS, HEC-H and betal nut in pure water showed the heat transfer enhancement up to 500ppm and NH_4Cl up to 2800ppm concentration, above this range no enhancement was observed. Enhancement was more for SLS as compared to other surfactants. Also the trend of boiling curves in presence of these surfactants in the water, shifted towards the lower temperature difference side. Presence of Betel nut (Areca Catechu) in water showed the value of critical heat flux low as compared to other surfactants. Also the kinetics of vapor bubble in pool boiling phenomena for pure water with and without surfactants were observed in terms of bubble nucleation, growth and their departure.

Keywords: *Surfactant, Boiling, additive, Surface Tension, Bubble behavior Flow Visualization.*

INTRODUCTION

There is a general need to increase the heat transfer rate in pool boiling applications for saving the energy required to phase change. Now lots of efforts are taking place to save the energy from different applications due to energy crisis and global warming. Hence the main motive is to reduce the energy i.e. increase the heat transfer in pool boiling. Researchers found enhancement techniques in heat transfer for the boiling. The addition of surfactant as additive in the solution is the cost effective technique and simple to handle. Some of the researchers had conducted the experiments on pool boiling enhancement-using additives.

Hetstroni and his group [1,2] in their study of pool boiling on horizontal stainless steel tube inside a transparent glass vessel observed the bubble behaviors. They observed that boiling in surfactant solution when compared with that in pure water was more vigorous and more activation of nucleation sites in clustered mode. For the boiling curve, wall temperature of the heated tube decreased with an increase in the concentration of the alkyl polyglucosides. Bubble form in Habon-G solution was very much smaller than those in water and surface becomes covered with them faster. Kotchaphakdee et al., [3] studied the effects of Polyacrylamide, PA and Hydroxyethyl Cellulose, (HEC) solute concentrations ranged from 62 to 500 ppm liquids in water boiled at atmospheric pressure on a

* Corresponding author: Prof. Dr. A.T. Pise
Phone: +(91)-2164-271711/271712, Fax: +(91)-2164-271713
E-mail address: ashokpise@yahoo.com

horizontal steam heated chrome-plated surface. They observed that amount of polymers in water increases nucleate boiling heat flux. PA leads to significantly improved heat transfer coefficient over the entire range of excess temperature. The peak heat flux is considerably higher than for water. Klein et al., [4] investigated the effects of APG surfactant solution flows through a micro-channel heat sink in which heat generated due to electronic components were removed. Surfactants mixed solution-boiling phenomena were also found to stabilize the maximum and average surface temperatures for a wide range of applied heat fluxes. Further effort invested on revealing proper surfactant additives and performing experiments of surfactant solutions flowing through a various micro-channel heat-sink configurations. Urquiola, et al., [5] did the boiling experiments with pure water and surfactant solutions of SDS on horizontal heating surface. Surfactant behavior was studied in terms of static contact angle directly related with the surface conditions, rather than the surface tension value. Higher contact angle leads the boiling curve of a specific liquid or solution to show better heat transfer characteristics. Wen and Wang [6] observed the effects of surface wettability on nucleate pool boiling heat transfer for Sodium Dodecyl Sulphate (SDS) and Triton (X-100) surfactant in water. They found that both SDS and Triton X-100 could increase boiling heat transfer coefficient. Also the boiling phenomena is mainly depends on thermo physical properties of fluid that are density, surface tension and kinematic viscosity. The addition of small amount of surfactant does not affect the density of solution but it slightly increases the viscosity and measure reduction in surface tension if surfactant is polymeric. Number of researchers measured the surface tension data with and without surfactants in water, [2,8] which shows with increase in surfactant concentration surface tension decreases.

After the extensive literature reviewed some of the conclusions are contradictory. Selection of the additive and its optimum quantity. Whether it mix or not? The mechanism of enhancement is not yet properly understood, but a reduction in surface tension changes the boiling behavior. Better understanding of this process is needed. So in this work, the effect of surfactants in pool boiling for enhancement of heat transfer is experimentally investigated. Ammonium Chloride NH_4Cl, Sodium Lauryl Sulphate SLS, Hydroxyethyl Cellulose HEC-H and Betel Nut served as test surfactants and added in water with varying concentration in search of to find optimum quantity. The overall aim of this work is to understand the phenomenon of nucleate pool boiling of water with and without surfactants, as it is very complex in nature.

EXPERIMENTAL METHOD

Experimental setup

The apparatus as for experimental studies on pool boiling is shown in Figure1. It consists of cylindrical glass container housing, the test heater and the heating coil for the initial heating of the water. The heater coil is directly connected to the mains (Heater R1) and the test heater (Nichrome wire) is connected also to mains via a dimmerstat. An ammeter (range 0-10A) is connected in series while the voltmeter across it to read the current and voltage. Voltage selector switch is used to select the voltage range 50/100V. These controls are placed inside the control panel.

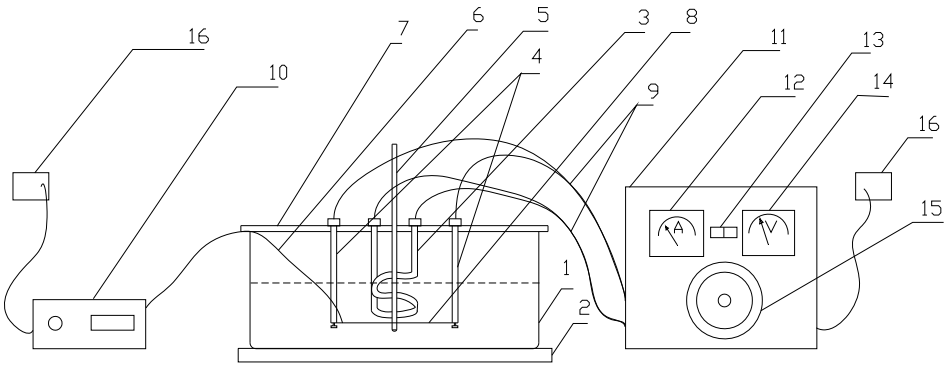

Figure 1. Schematic Figure of Experimental Setup

1.Glass Container **2**.Wooden Platform **3**.Auxilary Heater (R1) **4**.Test Heater (R2) **5**.Thermometer **6**.Thermocouple **7**.Clay Lid **8**.Nichrome Wire **9.**Heater Connecting Cable **10**.Digital Temperature Indicator **11**.Control Panel **12**.Ammeter **13**.Voltage Range Selector Switch **14**.Voltmeter **15**.Dimmerstat **16**.Electric Power Switch

Test Procedure

The glass container was filled with 2.5 liters of water and it kept on a stand, which is fixed on a wooden platform. The temperature of bulk water i.e. saturation temperature of water was measured using mercury thermometer with least count of 0.5^{o}C Cr-Al k-type thermocouple. It is connected to nichrome heater wire to measure the temperature of wire using digital temperature scanner having least count 0.1^{0}C. The kinetics of boiling (bubble nucleation, growth and departure) i.e. bubble behavior with and without surfactants in water was recorded by Handy camera (800X) video recording. Each experiment was repeated three times to maintain the repeatability.

RESULTS & DISCUSSION

The extensive experimentation of pool boiling was carried for pure water with and without surfactants of varying concentrations namely SLS, HEC-H, NH_4Cl and Betel nut. From the obtained experimental data results are plotted in terms of boiling curve as a heat flux vs. heater excess temperature. Also the some images of kinetics of boiling (bubble nucleation, growth and departure) i.e. bubble behavior for water and water with surfactants were recorded by Sony Handy camera (800X). Comparative studies of results of surfactant were broadly discussed into two categorize as boiling behavior and boiling curves.

Boiling Behavior

The kinetics of vapor bubble in pool boiling phenomena for pure water with and without surfactants was observed in terms of bubble nucleation, growth and departure the evolution of vapor bubble. The growth of bubble is one of the parameters determining the intensity of the heat transfer from a heated surface. All the pool boiling experiments were carried out under atmospheric pressure. The phenomenon of foaming, often observed during boiling in the presence of surfactant in water. The foam formed on the surface of the solution and its height increased with the heat flux. The bubble behavior was recorded at 24 frames per second by the video camera and recording was done for varying the concentration of the surfactants and heat flux. The typical stages of bubble growth analyzed for this study are shown in Figs. 2–4.

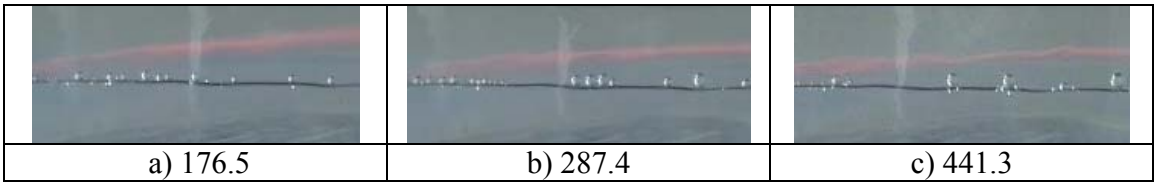

a) 176.5	b) 287.4	c) 441.3

Figure 2. Images of boiling of pure water for heat fluxes (kW/m^2): a) 176.5 b) 287.4 c) 441.3

Figure 2 (a-c) show typical images of deionized water boiling on the nichrome wire at heat fluxes 176.5, 287.4 and 441.3 kW/m^2 respectively. Population of bubbles was observed in the vicinity of the heated wire. The bubble dynamics for water were seen to depend on heat flux, similar to well-known boiling visualization data. After the onset of nucleate boiling, the regime of single bubbles occurred close to the heated wall (Figure 2a). As the heat flux increased, bubble coalescence takes place (Figure 2b). This phenomenon was more pronounced at heat flux 441.3 kW/m^2 (Figure 2c). For pure water, the average bubble size was observed to slightly increase with increasing heat flux. The bubbles have an irregular shape at all values of heat flux. Same heat fluxes with SLS, HECH-H of 400 ppm and NH_4Cl of 1200 ppm in pure water was observed and the images of 400ppm with SLS are shown in Fig. 3(a-c).

a) 176.5;	b) 287.4;	c) 441.3

Figure 3. Images boiling of 400 ppm SLS in water for heat fluxes (kW/m^2): a) 176.5; b) 287.4; c) 441.3

The SLS additive reduces significantly the tendency of coalescence between vapor bubbles. Here too, there is a weak tendency toward increasing the average diameter as heat flux increased. In this case, the shape of bubbles is closer to spherical than for pure water. It presents cluster of small bubbles, which rise from the cavity. The bubbles are adjacent to each other and the cluster neck is not observed. Effect of the surfactant concentration on the boiling phenomena was also recorded at the 300 kW/m^2. Surfactant concentrations were varied from 100 to 600 ppm for the SLS, HEC-H and betal nut and 200 to 2800 ppm NH_4Cl in water.

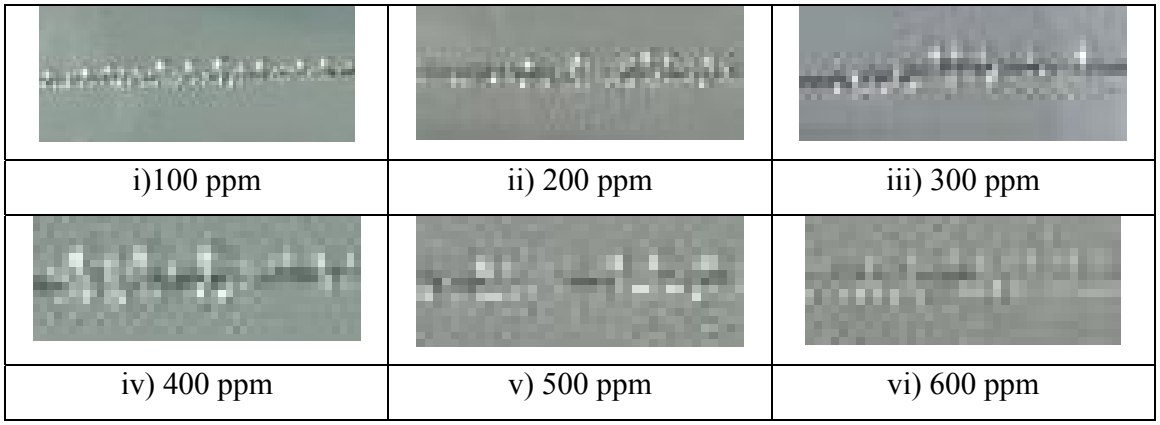

i)100 ppm	ii) 200 ppm	iii) 300 ppm
iv) 400 ppm	v) 500 ppm	vi) 600 ppm

Figure 4. Photographs of 100-600 ppm SLS in water for heat flux 300 kW/m^2

Figure 4 show the boiling images of SLS water having concentrations 100–600 ppm at heat flux 300 kW/m^2. It was observed that with increased in heat flux i.e. temperature, bubble size also increased and detaching time of the bubble was less as compared to pure water. Diameter of bubble in surfactant solution is smaller as compared to water. Bubbles form a blanket over the wire, which could not observed in pure water. This might be due to addition of SLS in water, decreases the surface tension of solution and hence the forces acting on bubbles are smaller and detach rapidly from the surface. Also surfactant activates the number of nucleation sites on the same wire. The time between detaching bubbles from wire and reaching the bubble up to free surface is measured in Windows Movie Maker and the distance between wire and free surface was measured using Adobe Photoshop 7.0 software. The same procedure was repeated in three times for each concentration and average velocity was calculated. The results show that the velocity of bubble slightly increased with varying concentrations from 100 to 600 ppm. This might be due to addition of surfactant, surface tension force decreases and hence resistance to bubble motion is also decreases [2,8]. Similar boiling phenomena were observed HEC-H, NH_4Cl and betel nut used as surfactant. The phenomenon of foaming was observed after 1200-ppm concentration for NH_4Cl and velocity of bubbles are slightly increased with varying concentrations from 200 to 3000 ppm. Up to 800ppm NH_4Cl in the water the boiling behavior quite similar to that of water.

Boiling Curves

The saturated pool boiling curves are plotted with varying concentrations of surfactant in pure water as a function of the heat flux q (kW/m^2) vs. the heater excess temperature (T_w-T_{sat}) ^{0}C (Figs.5-6). Figure (a) show the surface temperature of the heated nichrome wire decreased monotonically with an increase in the concentration of the SLS solution up to 500 ppm, also noted that the effect of surfactant additives on nucleate boiling heat transfer slightly decreases or almost constant, when the concentration of SLS in water solution was higher than 500 ppm. The analogues data on the decrease in the heat transfer for 1060 ppm Habon-G solution also reported by Hetsroni et al [2].

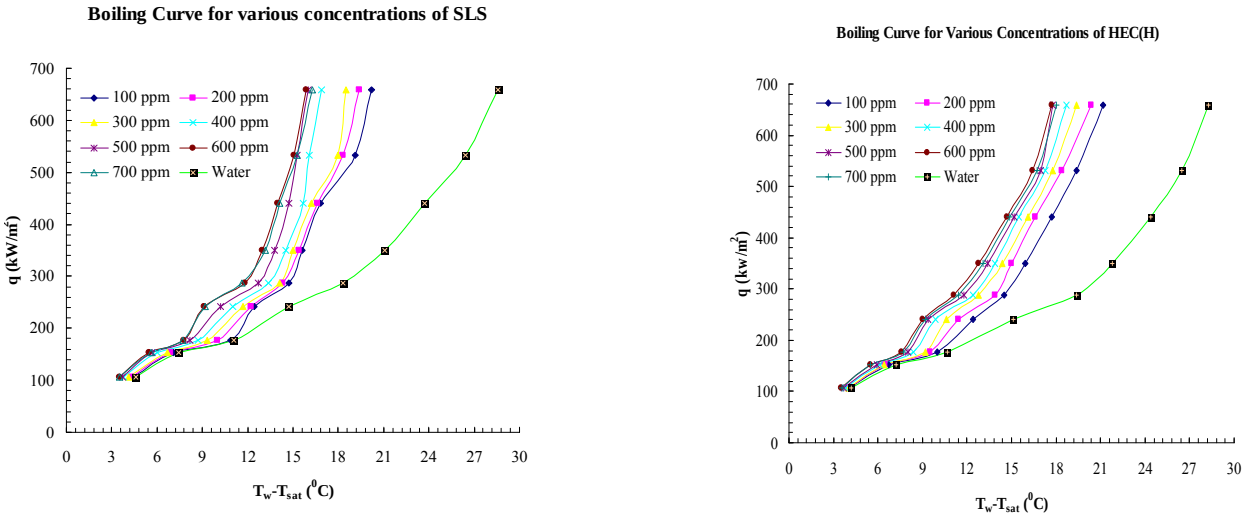

a) SLS **b) HEC-H**

Figure 5. Pool boiling curves of pure water with SLS & HEC-H

The effect of SLS additives on nucleate boiling heat transfer slightly decreases, when the concentration of SLS solution is higher than 500 ppm. Figure 6(b) the saturated pool boiling curves of water with varying concentrations of HEC-H. HEC-H is the polymeric surfactant with viscous in nature. An increase in concentration of HEC-H in pure water increases the viscosity with significantly decreases the surface tension [8]. The general effect of increasing concentration of HEC-H additive in pure water is to increase the heat transfer. The similar effect of concentrations was observed as that of

the SLS. Upto 500-ppm heat transfer increased above that there is slightly decreased in heat transfer and cross over of the curve towards right for 600 ppm at heat flux 152 kW/m^2. Similarly check the effects of NH_4Cl as a surfactant in pure water are also checked. The surface temperature of the heated nichrome wire decreased monotonically with an increased in the concentration of the NH_4Cl solution up to 2800 ppm, also noted that the effect of surfactant additives on nucleate boiling heat transfer slightly decreased, when the concentration of NH_4Cl solution is higher than 2800 ppm. Figure 6(a) shows the boiling curve for various concentrations of NH_4Cl in water.

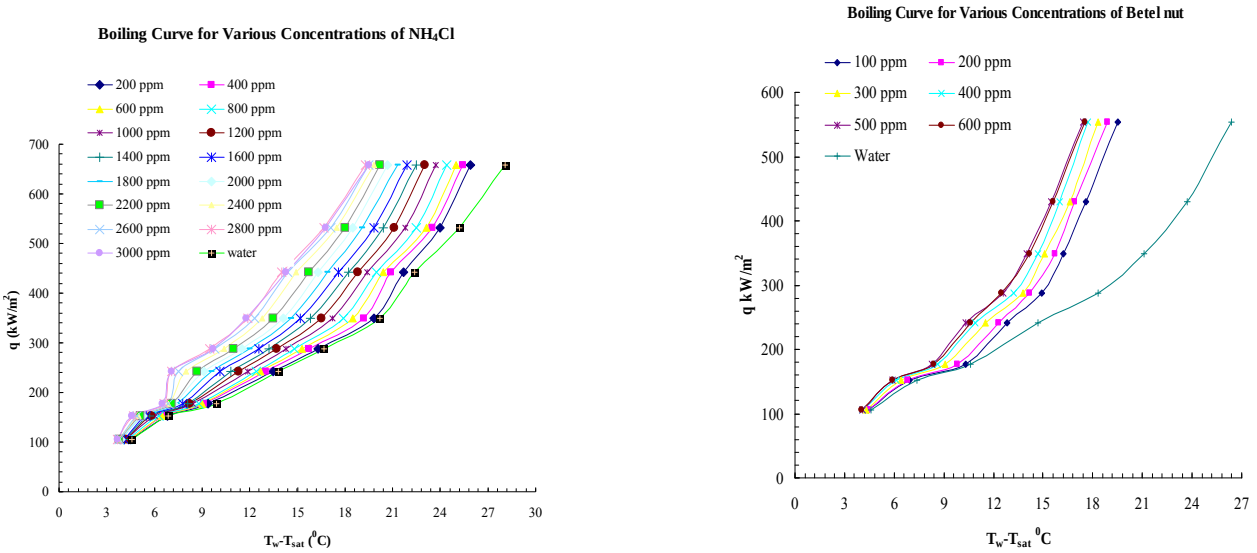

(a) NH_4Cl **(b) Betel Nut**

Figure 6. Pool boiling curves of pure water with NH_4Cl & Betel Nut

The effects of varying concentrations of Betel nut in the water were studied. It was observed that increase in concentrations up to 500 ppm the heat transfer rate increased. The power required to reach the critical heat flux is low as compared to other surfactant solutions means heat required to reach the maximum heat flux is low but use of betel nut has some limitations that, it adversely affects the solution properties and its less solubility in water. The excess betel nut was floating. Also changes the solution color with remains red marks left on the glass surface. Figure 6(b) shows boiling curve for varying concentrations of Betel nut in water. The general effect of increasing concentration of Betel nut additive is to increase the heat transfer up to 500 ppm, above that heat transfer is constant. Similarly the heat transfer coefficient increased as the heat flux and concentration are increased, except when the concentration is higher than 500 ppm.

CONCLUSION

From the experimental results of this study the following major conclusions are drawn. The bubbles formed in water with surfactant solutions are much smaller than pure water and they covered the surface of wire faster. Presences of the surfactant reduce the boiling excess temperature ΔExcess it results the boiling curves shifted to the left side and promotes activation of nucleation sites in a clustered mode. For pure water average bubble size was observed to slightly increase with increasing heat flux. Up to 800-ppm ammonium chloride NH_4Cl in the water the boiling behavior quite similar to that of water. This might be the slight reduction in surface tension up to 800 ppm and due to its higher solubility limit in the water. The addition of small amount of anionic surfactant Sodium Lauryl Sulphate SLS and polymeric surfactant Hydroxyethyl Cellulose HEC-H in water makes the boiling behavior quite different from that of pure water. It might be that reduction in surface tension results in

a decrease of energy required creating a bubble. All the surfactant showed the heat transfer coefficient was increased up to solubility limit of the surfactant in water. The addition of the surfactant beyond the solubility limit was almost constant or slightly decreases the heat transfer coefficient. Presence of surfactant in water increases average bubble velocity.

REFERENCES

1. Hetsroni G., Gurevich M., Mosyak A., Rozenblit R. and Segal Z, "Boiling Enhancement with Environmentally Acceptable Surfactants", Int. Jou.of Heat and Fluid Flow 25, 2004, pp. 841-848
2. Hetsroni G., J.L. Zakin, Z. Lin, A. Mosyak, E.A. Pancallo and R. Rozenblit, "The effect of surfactants on bubble growth, wall thermal patterns and heat transfer in pool boiling", International Journal of Heat and Mass Transfer 44, pp. 485-497, 2001.
3. Kotchaphakdee P., and. Williams M. C., "Enhancement of Nucleate Pool Boiling with Polymeric Additives", International Journal of Heat and Mass Transfer 13, pp. 835-848,1970.
4. Klein D., Hetsroni G., & Mosyak G., "Heat Transfer Characteristics of Water and APG Surfactant Solution in a Micro-Channel Heat Sink", International Journal of Multiphase Flow 31, pp. 393-415, 2005.
5. Urquiola Erwin & Fujita Yasunobu, "Contact Angle Effects in Boiling Heat Transfer" Memoirs of the Faculty of Engineering, Kyushu University, Japan 62(1), pp. 55-65,2003.
6. Wen D.S., & Wang. B.X., "Effects of Surface Wettability on Nucleate Pool Boiling Heat Transfer for Surfactant Solutions", International Journal of Heat and Mass Transfer 45, pp.1739-1747,2002.
7. Inoue, T., Teruya T. & Monde. M., "Enhancement of Pool Boiling Heat Transfer in Water and Ethanol/Water Mixtures with Surface Active Agent", International Journal of Heat and Mass Transfer 4, pp. 5555-5563, 2004.
8. "Handbook of Pharmaceutical Excipients", A joint publication of the American Pharmaceutical Association and The Pharmaceutical Society of Great Britain, 1989.
9. Momin I.I. "Effects of Surfactants on Boiling Phenomena" Thesis, M.E. Department of Mechanical Engineering, Government College of Engineering, Karad, India, 2007.

AN EXPERIMENTAL AND NUMERICAL INVESTIGATION OF A COMBUSTOR OPERATING IN THE FLAMELESS OXIDATION REGIME

A. Rebola, M. Costa* and P. J. Coelho
Mechanical Engineering Department, Instituto Superior Técnico, Technical University of Lisbon, Avenida Rovisco Pais, 1049-001 Lisboa, Portugal

ABSTRACT. Flameless oxidation is a combustion regime that may allow a significant reduction of the NO_x emissions without compromising the combustion efficiency. The present study investigates this combustion regime both experimentally and computationally. The experiments have been performed in a small-scale combustor, fired with methane, and include flue-gas measurements for various combustor operating conditions that allowed for the quantification of the dependence of the NO_x emissions and combustion efficiency on the stoichiometry, thermal input and inlet temperature of the combustion air. Subsequently, detailed measurements of local mean gas species concentrations and local mean gas temperatures for one representative combustor operating condition have also been performed. In the parallel modeling work, a computer code was employed to predict the temperature and species concentration fields. The experimental data revealed that NO_x emissions are always low regardless of the combustor operating conditions. The prediction of the temperature and major species concentration is in satisfactory agreement with the measurements, except in the near burner region, where the predicted temperature rise is too steep in comparison with the experimental data.

Keywords: *flameless oxidation, pollutant emissions, combustion efficiency*

INTRODUCTION

Flameless oxidation is a combustion regime where the reactants are highly diluted with hot combustion products causing the reaction to occur in a distributed reaction zone with a reduced temperature maximum and low O_2 partial pressure. In this regime, distinct flame fronts, as they occur in typical lean premixed or diffusion flames, are replaced by a volume type flame mode. As a consequence, the temperature distribution is nearly uniform and the NO_x emissions are very low. The reduction of the aero-acoustic fluctuations and the extended stability limits are additional benefits of this combustion regime. This technology has received various names, namely flameless oxidation (FLOX) [1], moderate and intense low oxygen dilution (MILD) combustion [2] and colorless distributed combustion (CDC) [3], with a number studies revealing the success of this technology as a NO_x control technique.

Related experimental studies include those of references [1-9], among others. Wünning and Wünning [1] and Plessing et al. [5] presented data from recuperative furnaces operating under flameless oxidation conditions and showed that the temperature increase in the near burner region was rather smooth and that the thermal NO formation was largely suppressed owing to the nonexistence of temperature maxima. Plessing et al. [5] concluded that under flameless oxidation conditions combustion takes place in a regime similar to that of a well-stirred reactor, where no

* Corresponding author: M. Costa
Phone: + 351218417186, Fax: + 351218475545
E-mail address: mcosta@ist.utl.pt

ignition and quenching events occur, which explains the low level of the combustion noise associated with this combustion regime. Dally et al. [6] studied the effects of the fuel dilution on the flameless oxidation structure in a recuperative furnace, for a variety of fuel mixtures. The results showed that the fuel stream dilution with inert gases helps to establish flameless oxidation conditions and to reduce NO_x emissions. Weber et al. [4] and Flamme [7] reported data from semi-industrial furnaces operating under flameless oxidation conditions. Weber et al. [4] observed that the furnace operated under conditions resembling a well-stirred reactor, and almost all furnace volume was filled with combustion products containing 2-3% of O_2, with high and uniform radiative heat fluxes, while Flamme [7] showed the capacity of achieving low NO_x emissions using this technology even with high preheated air levels. Recently, Weber et al. [2] demonstrated the potential of the technology for the combustion of liquid and solid fuels, and Flamme [8] and Schieper et al. [9], among others, evaluated its potential in gas turbine combustion chambers.

Related numerical studies include those of references [10-16], among others. Coelho and Peters [10] carried out numerical simulations of a flameless oxidation burner from a recuperative furnace. The numerical simulation was based on the Reynolds averaged Navier-Stokes (RANS) equations and the turbulence-chemistry interaction was accounted for by means of the non-premixed flamelet–PDF approach. The NO_x emission was calculated by the Eulerian Particle Flamelet Model (EPFM) in a post-processing step. They argued that the steady flamelet library was unable to correctly describe the formation of NO_x, since this is a chemically slow process, which is sensitive to transient effects, while the unsteady flamelet model was able to predict the correct order of magnitude of the NO_x emissions. Mancini et al. [11, 12] presented numerical simulations of a laboratory burner. The standard k-ε turbulence model was used together with three combustion sub-models: the eddy-breakup model (EBU) with a two-step reaction scheme, the eddy-dissipation concept model (EDC) with chemical equilibrium and the mixture fraction/PDF model with equilibrium tables. The uniformity of the temperature and O_2 fields was reproduced correctly, but the combustion models, which provided similar predictions, could not describe the chemistry and the temperature field in the fuel jet region.

Christo and Dally [13] performed simulations of high temperature and highly diluted turbulent reacting jets using three variants of the k-ε model (standard, renormalization group and realizable). The combustion/turbulence interaction was simulated using the conserved scalar approach along with an assumed PDF and equilibrium tables, the non premixed flamelet model, the eddy dissipation (EDM) and the EDC with skeletal and detailed chemical kinetics. They concluded that the standard k-ε turbulent model with a modified dissipation equation constant ($C_{\varepsilon 1}$) provides the best agreement with the experimental data, and the EDC model with skeletal and detailed chemistry performs better when compared to the conserved scalar models like PDF and flamelet models. Paul and Mukunda [14] presented numerical simulations of a flameless combustion test facility using the EDC model, a skeletal chemical reaction mechanism and including an extinction model based on the Da number. The predictions of this model compared well with the experimental results. Very recently, Duwig et al. [15] presented numerical simulations of a flameless oxidation combustor using the LES (Large Eddy Simulation) technique and a combustion model based on a tabulation technique proposed by Duwig and Fuchs [16] that includes detailed chemical kinetics based on the stirred reactor approach.

In spite of the studies above, the present knowledge on the theoretical foundations of flameless oxidation phenomena is still limited. In particular, there is a lack of detailed experimental data available to provide increased insight into the underlying physics, and there is no consensus about which combustion models are able to simulate accurately this combustion mode. The present article is aimed at contributing to overcome these shortcomings, by providing new experimental data and employing two different partially premixed combustion models. Both models combine a steady laminar flamelet approach for diffusion flames with another approach for premixed flames.

EXPERIMENTAL

Figure 1 shows schematically the combustor used in this study. The combustion chamber is a cylinder with a diameter of 150 mm and a length of 300 mm. The burner is placed at the top end of the combustion chamber and the exhaust of the burned gases is made by the bottom end through a convergent nozzle with a length of 50 mm and an angle of 35º. Along the length of the combustion chamber there are 5 ports, each with a diameter of 20 mm, which allow for the introduction of probes inside the combustion chamber. The chamber is equipped with electrical elements that allow preheating the combustor walls up to ≈ 900 ºC. Two thermocouples installed in the combustion chamber (Fig. 1) are used to monitor the wall temperatures and to evaluate the temperature gradients along the combustor. The burner consists of a central gas gun and a combustion air supply in a conventional double concentric configuration. The combustion air is preheated by an electrical system that allows inlet temperatures up to 750 ºC. The sampling of gases for the measurement of local mean O_2, CO, CO_2, unburned hydrocarbons (HC) and NO_x concentrations was achieved using a stainless steel water-cooled probe. The analytical instrumentation included a magnetic pressure analyzer for O_2 measurements, non dispersive infrared gas analyzer for CO_2 and CO measurements, a flame ionization detector for HC measurements and a chemiluminescent analyzer for NO_x measurements. Local mean temperature measurements were obtained using uncoated 76 μm diameter fine wire platinum/platinum: 13% rhodium thermocouples. The analog outputs of the analyzers and of the thermocouple were transmitted via A/D boards to a computer where the signals were processed and the mean values computed. Flue-gas data were obtained using the same procedures.

MATHEMATICAL MODEL

The mathematical model is based on the numerical solution of the Favre-averaged governing equations for mass, momentum and energy and on transport equations related to the turbulence and combustion models. The standard k-ε model was used to model the turbulence, the thermal radiation was taken into account using the discrete ordinates method and the radiative properties of the participating medium are modelled by the weighted-sum-of-grey gases model. Combustion models for diffusion flames employed in the past have revealed difficulties in modeling flameless oxidation phenomena, since the fuel mixes and reacts with a mixture of air and recirculated combustion products, rather than with pure air, as in conventional diffusion flames. In an attempt to describe this process, two different combustion models, hereafter referred to as models A and B, were employed. Both of them assume that the reactants are partially premixed and combine the steady laminar flamelet model for diffusion flames with a model for premixed flames. In the steady laminar flamelet model, the balance equations for the species mass fractions and temperature in the mixture fraction space were solved assuming unity Lewis number for all species. The turbulent effects were accounted for by integrating the laminar values over the mixture fraction space using an assumed beta PDF. The mean mass fractions of the species are stored in a library as a function of the mean mixture fraction, its variance and the scalar dissipation rate. Model A is a partial premixed turbulent combustion model based on the solution of a transport equation for a non-reacting scalar variable G, which represents the normal distance to the flame front. This G-equation may be derived from the local kinematics relation between the propagation velocity of a flame front in the unburnt mixture and the local flow velocity [17]. The model B is based on the premixed model presented in [18] and involves the solution of a transport equation for the reaction progress variable.

RESULTS AND DISCUSSION

The experiments performed in the small-scale combustor (Fig. 1), fired with methane, included initially flue-gas measurements for various combustor operating conditions as summarized in Table 1. They encompass various experimental flames which quantify the effects of the excess air

coefficient (tests 1 to 9), thermal input (tests 10 to 14) and combustion air inlet temperature (tests 15 to 18) on NO_x emissions and combustion efficiency from the present combustor. Subsequently, detailed measurements of local mean gas species concentrations of O_2, CO_2, CO, HC and NO_x and local mean gas temperatures for one representative combustor operating condition (test 10 in Table 1) have also been performed.

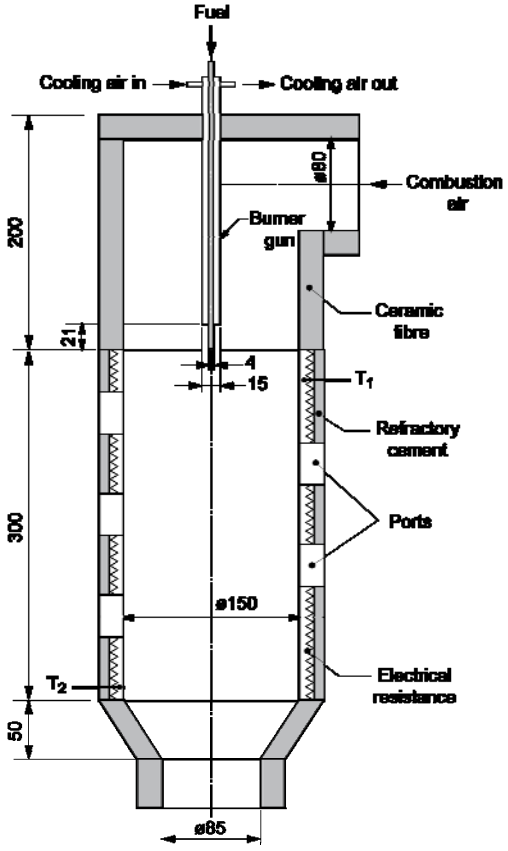

Figure 1. Small-scale combustor.

Table 1
Test conditions

Test	Thermal input (kW)	λ	T_{in} (ºC)	T_{gases} (ºC)
1	13.0	1.2	590	-
2	13.0	1.3	551	-
3	13.0	1.4	540	-
4	13.0	1.5	570	-
5	13.0	1.6	543	-
6	13.0	2.0	538	-
7	10.0	1.1	700	1396
8	10.0	1.6	700	1271
9	10.0	2.5	700	1146
10	15.6	1.6	700	1355
11	12.0	1.6	700	1338
12	10.0	1.6	700	1278
13	8.0	1.6	700	1271
14	6.0	1.6	700	1211
15	10.0	1.6	700	1271
16	10.0	1.6	600	1265
17	10.0	1.6	500	1256
18	10.0	1.6	400	1220

Flue gas measurements

Figure 2 shows the effect of the excess air coefficient (λ) on CO and NO_x emissions. It is seen that NO_x emissions are extremely low, as expected for flameless oxidation conditions, even near stoichiometry with a relatively high level of air preheating. The CO emissions are also extremely low, in particular for small values of λ. For values of $\lambda > 2$, however, the CO emissions become important. This is because an increase in λ causes a reduction in the temperature inside the combustor, as typified by the temperature of the exhaust gases displayed in Table 1, which slows down the reaction rate and hence increases the level of CO emissions.

Figure 3 shows the effect of thermal input and air inlet temperature on NO_x and CO emissions. Both NO_x and CO emissions are extremely low regardless of the thermal input. This suggests that the thermal density in the combustor does not affect the combustion performance provided the combustor wall temperature is kept constant. Fig. 3 also reveals that above 500 ºC the inlet air temperature has no significant effect on NO_x emissions. The reduction of the air inlet temperature reduces the temperatures inside the combustion chamber. This slows down the reaction rate which causes CO emissions to increase. Moreover, the reduction of the air inlet temperature causes a decrease in the air injection velocities which may affect the mixing process and thus CO emissions.

Figure 4 shows the effect of λ and $T_{in}/T_{wall} \times R_m$ on NO_x emissions and combustion efficiency, R_m

being the ratio of the inlet fuel to inlet air momentum fluxes. It should be noted that the data presented in both graphs of Fig. 5 include all the experimental conditions shown in Table 1. Combustion efficiency is here defined as $\varepsilon = 100\times\left[1-10109\times(EI_{CO}/\Delta h_c)-EI_{HC}/1000\right]$, where the emissions are expressed as emissions index (EI) and Δh_c is the lower heating value expressed in J/kg. The results show that increasing λ beyond ≈ 1.6 causes a reduction in ε. Large values of λ reduce the temperature inside the combustor, which in turn decreases the reaction rate, increases the CO emissions and penalizes the combustion efficiency. In addition, the parameter $T_{in}/T_{wall} \times R_m$ appears to correlate well with ε. This suggests that R_m affects the mixing process in the combustor and thereby the combustion efficiency.

In-flame data: measurements and modeling

The present calculations were carried out using a collocated, two-dimensional axisymmetric, non-uniform grid. The grid has a higher density in the region near the burner exit and in the vicinity of the centreline. In the inlet boundaries the radial velocity component at the burner exit was taken as zero, and the axial velocity was calculated from the fuel and air mass flow rates, respectively. The inlet turbulent kinetic energy, $\tilde{k}_{in}$, was estimated by assuming that the turbulence intensity is 10%.

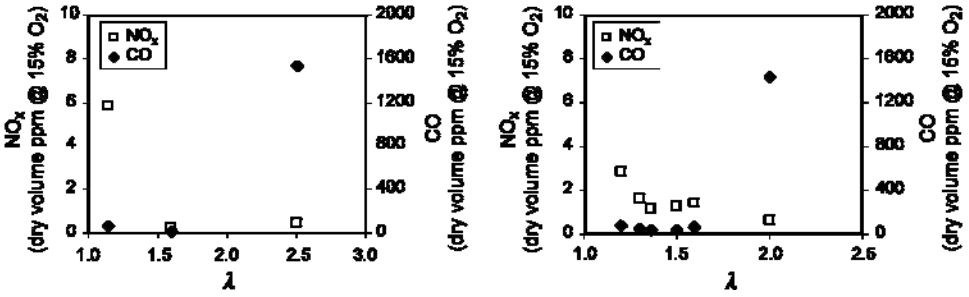

Figure 2. Effect of λ on CO and NO_x emissions. Left: tests 7 to 9; right: tests 1 to 6.

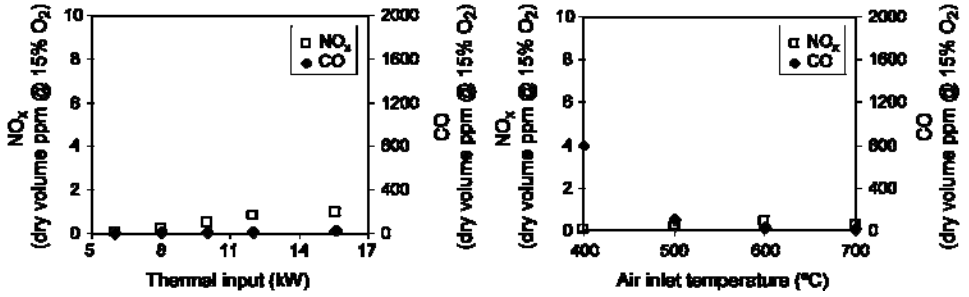

Figure 3. Effect of thermal input (left) and air inlet temperature (right) on NO_x and CO emissions.

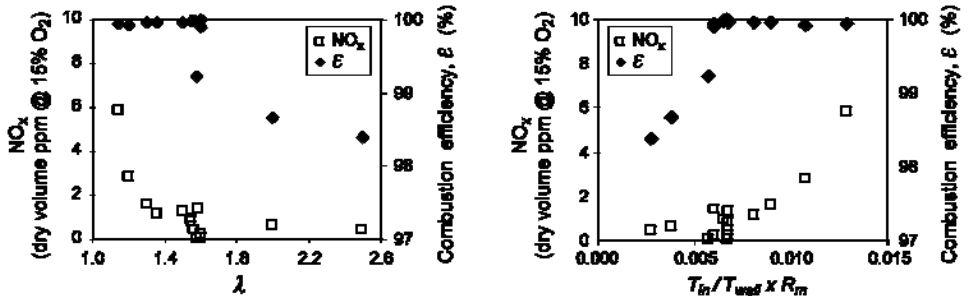

Figure 4. Effect of λ (left) and $T_{in}/T_{wall} \times R_m$ (right) on NO_x emissions and combustion efficiency.

The inlet values of the dissipation rate of the turbulent kinetic energy were determined from $\tilde{\varepsilon}_{in} = 0.169\,\tilde{k}_{in}^{1.5}/l$. The mixing length, l, was taken as the hydraulic radius of the fuel and air injector. The wall temperature was predefined and considered equal to the measured value and the wall emissivity was taken as 0.7. The commercial software COSILAB was used to compute the laminar flame velocity for different degrees of premixing and temperatures of the unburnt mixture. The laminar flame velocity computed is stored in a library as a function of the mean mixture fraction and the unburnt temperature. The values of temperature and mixture fraction upstream of the flame front were used to interpolate the laminar flame velocity and calculate the turbulent flame velocity.

Figure 5 shows the axial profiles of predicted temperature and O_2 and CO_2 mole fractions together with the measurements for test 10, while Figs. 6 and 7 show the radial profiles of temperature and O_2 also for test 10. The experimental data reveal that the temperature field inside the combustor is relatively uniform. The axial temperature profile is smooth and the radial profiles do not present the pronounced gradients typical of those encountered in conventional flames. The maximum measured temperature exceeds a little 1400 ºC in a small region of the combustor which explains the low NO_x emissions measured in the flue gases. As expected, the CO_2 molar fraction profiles present qualitatively the same trends as those of the temperature, being the O_2 molar fraction profiles complementary of those of the CO_2 and relatively uniform, except in the region where mixing is intense.

The predictions of both models are similar and, in general are in fair agreement with the experimental data, except in the near burner region where important differences between the computational results and the experimental data occur. Both models predict a moderate evolution of the temperature downstream of the burner. However, after this initial zone the models predict a strong gradient of the temperature and species concentrations, which is not supported by the experiments. In the computational domain, where the variable G is lower than zero, the molar fraction of the species and the temperature change only due to the mixing process between the combustion air, the recirculated products and the fuel. After this initial region, the variable G becomes greater than zero, and outside the thin layer that represents the turbulent flame thickness, the model becomes identical to the flamelet model for diffusion flames. This explains the predicted strong rise of the temperature and of the molar fraction of CO_2 and the reduction of the O_2 concentration. This is also valid for model B, *i.e.*, after the initial region of the combustor, where the variable c has values between zero and one, the model is identical to the flamelet model for diffusion flames. A possible source of inaccuracy common to both models may be the calculation of the laminar flame velocity, which does not account for the presence of the recirculation combustion products in the flame front. So, the laminar flame velocity computed by COSILAB and used in both models is likely to over predict the real value of the flame velocity in the conditions of the flameless oxidation regime. The same limitation affects the laminar flamelet data used to build the library of the chemicals species.

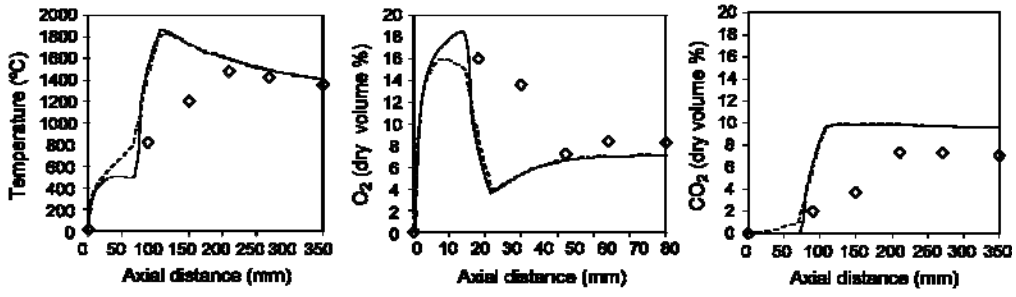

Figure 5. Measured and predicted axial temperature and mole fraction profiles for test 10. Symbols, measurements; —, model A; -----, model B.

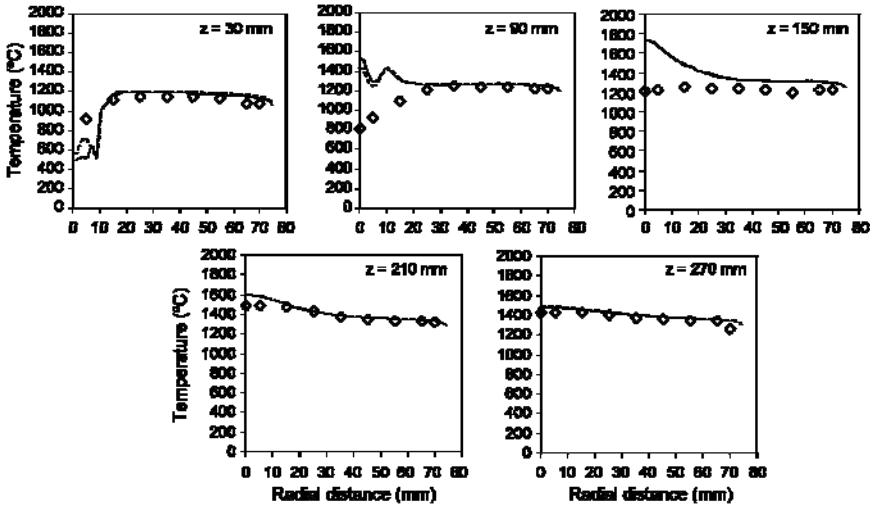

Figure 6. Measured and predicted radial temperature profiles for test 10. Symbols, measurements; —, model A; -----, model B.

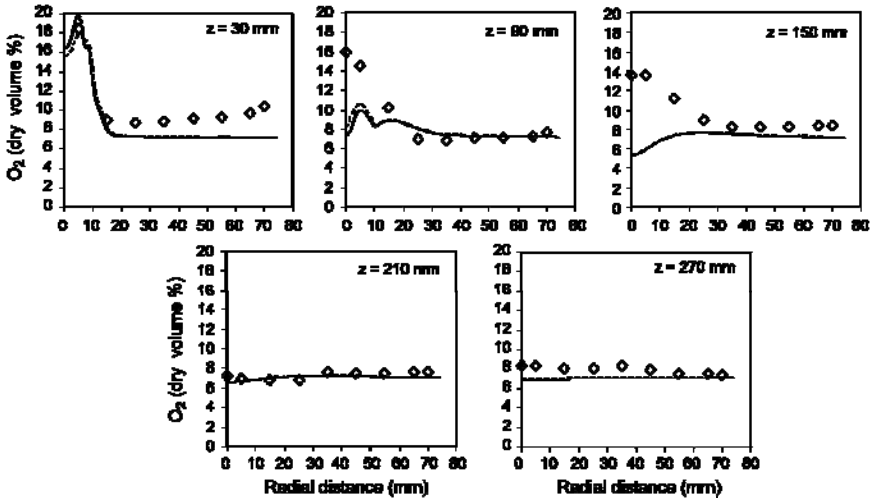

Figure 7. Measured and predicted radial O_2 mole fraction profiles for test 10. Symbols, measurements; —, model A; -----, model B.

CONCLUSIONS

The main conclusions of this study are as follows:

- The flue gas data reveal that NO_x emissions are always low regardless of the combustor operating conditions. The CO emissions, and thus the combustion efficiency, are however strongly affected by the excess air level.
- The in-flame data disclose that the temperature field inside the combustor is relatively uniform, without the pronounced gradients typical of those encountered in conventional flames. The major species mole fraction profiles present, however, a less pronounced uniformity.
- The prediction of the temperature and major species mole fractions are in satisfactory agreement with the measurements, except in the near burner region, where the predicted rise in temperature and CO_2 mole fraction are too steep in comparison with the experimental data. The reduction of the O_2 concentration downstream of the fuel ignition is also over predicted.

ACKNOWLEDGEMENTS

This work was developed within the framework of project PPCDT/EME/57480/2004, which is financially supported by Fundação para a Ciência e a Tecnologia, project nº 3599. A. Rebola is pleased to acknowledge the FCT for the provision of a scholarship (SFRH/BD/23619/2005).

REFERENCES

1. Wünning, J. A. and Wünning, J. G., Flameless Oxidation to Reduce Thermal NO-Formation, Progress Energy Combustion Science, Vol. 23, pp 81-94, 1997.
2. Weber, R., Smart J. P. and Kamp W., On the (MILD) Combustion of Gaseous, Liquid, and Solid fuels in High Temperature Preheated Air, Proceedings of the Combustion Institute, Vol. 20, pp 2623-2629, 2005.
3. Arghode, V. H., Gupta, A. K. and Yu, K. H., Colorless Distributed Combustion (CDC): Effect of Flowfield Configuration, 47th AIAA Aerospace Sciences Meeting Including the New Horizons Forum and Aerospace Exposition, Orlando, Florida, 5-8 January 2009.
4. Weber, R., Orsino, S., Lallemant, N. and Verlaan, A., Combustion of Natural Gas with High-Temperature Air and Large Quantities of Flue Gas, Proceedings of the Combustion Institute, Vol. 28, pp 1315-1321, 2000.
5. Plessing, T., Peters, N. and Wünning, J. G., Laseroptical Investigation of Highly Preheated Combustion with Strong Exhaust Gas Recirculation, Proceedings of the Combustion Institute, Vol. 27, pp 3197-3204, 1998.
6. Dally, B. B., Riesmeier, E. and Peters, N., Effect of Fuel Mixture on Moderate and Intense Low Oxygen Dilution Combustion, Combustion and Flame, Vol. 137, pp 418-431, 2004.
7. Flamme, M., Low NO_x Combustion Technologies for High Temperature Application, Energy Conversion and Management, Vol. 42, pp 1919-1935, 2001.
8. Flamme, M., New Combustion systems for Gas Turbines (NGT), Applied Thermal Engineering, Vol. 24, pp 1551-1559, 2004.
9. Schlieper, M., Scherer, V. and Wirtz, S., Low-NO_x Combustion of Liquid Fuels in Gas Turbines Using Flameless Oxidation, *Proceedings of the 9th International Conference on Energy for a Clean Environment*, Póvoa de Varzim, Portugal, 2-4 July 2007.
10. Coelho P. J. and Peters N., Numerical Simulation of a Mild Combustion Burner, Combustion and Flame, Vol. 124, pp 503-518, 2001.
11. Mancini, M., Roman, W. and Bollettini, U., Predicting NO_x Emissions of a Burner Operated in Flameless Oxidation Mode, Proceeding of the Combustion Institute, Vol. 29, pp 1155-1163, 2002.
12. Mancini, M., Schwoppe, P., Weber, R. and Stefano, O., On Mathematical Modelling of Flameless Combustion, Combustion and Flame, Vol. 150, pp 54-59, 2007.
13. Christo, F. and Dally, B., Modeling Turbulent Reacting Lets Issuing Into a Hot and Diluted Coflow, Combustion and Flame, Vol. 142, pp 117-129, 2005.
14. Kumar, S., Paul, P. J. and Mukunda, H. S., Prediction of Flame Liftoff Height of Diffusion/Partially Premixed Jet Flames and Modeling of Mild Combustion Burners, Combustion Science and Technology, Vol. 179, pp 2219-2253, 2007.
15. Duwig, C., Stankovic D., Fuchs, L., Li, G. and Gutmark, E., Experimental and Numerical Study of Flameless Combustion in a Model Gas Turbine Combustor, Combustion Science and Technology, Vol. 180, pp 279-295, 2008.
16. Duwig, C. and Fuchs, L., Modeling of Flameless Combustion using Large Eddy Simulation. *Proceedings of the ASME Turbo Expo*, ASME Paper GT-2006-90063, 2006.
17. Peters, N., Turbulent Combustion, Cambridge University Press, 2000.
18. Zimot, V., Polike, W., Bettelini, M. and Weisenstein, W., An Efficient Computational Model for Premixed Turbulent Combustion at High Reynolds Numbers Based on a Turbulent Flame Speed Closure, Journal of Engineering for Gas Turbines and Power, Vol. 120, pp 526-532, 1998.

EXPERIMENTAL POOL BOILING INVESTIGATIONS OF VERTICAL COALESCENCE FOR FC-72 ON SILICON FROM AN ISOLATED ARTIFICIAL CAVITY

C. Hutter[1], A. Sanna[2], K. Sefiane[1,*], D.B.R. Kenning[2], T.G. Karayiannis[2], R.A. Nelson[3], H. Lin[1], G. Cummins[1], A.J. Walton[1]
[1]University of Edinburgh, Edinburgh, United Kingdom
[2]Brunel University, London, United Kingdom
[3]Los Alamos National Laboratory, Los Alamos, USA

ABSTRACT. In this study bubble growth from an isolated artificial cavity micro-fabricated on a horizontal 380 µm thick silicon wafer was investigated. The horizontally oriented boiling surface was heated by a thin resistance heater integrated on the rear of the silicon test section. The temperature was measured using an integrated micro-sensor situated on the boiling surface with the artificial cavity located in its geometrical centre. A resistive track was used as the sensor, which when calibrated, exhibited a near-linear behaviour with increasing temperature. To conduct pool boiling experiments the test section was immersed in degassed fluorinert FC-72. Bubble nucleation, growth and detachment at different pressures were observed using high-speed imaging. Coalescence was observed at the boundary between the isolated bubble and interference regimes. The occurrence of vertical coalescence was found to be more frequent, with increasing wall superheat and decreasing pressure.
The equivalent sphere volumes of two bubbles before and after coalescence were evaluated from area measurements. It was observed that the second nucleated bubble is always smaller than its predecessor. The vapour generation appears not to stop during coalescence as the volume of the merged bubble was typically 5-18% larger than the sum of the bubble volumes just before coalescence.

Keywords: *Nucleate Pool Boiling, Vertical Coalescence, Artificial Cavity*

INTRODUCTION

Nucleate boiling heat transfer remains as a potential cooling solution for high-performance micro-processors. Despite the intensive research over the last decades, a comprehensive understanding of many aspects and mechanisms is still not available. One of these aspects is vertical coalescence. In general, coalescence is a hydrodynamic direct interaction between bubbles, as they collide and hence merge into one larger bubble.
Zuber [1] separated nucleate boiling into two regions, the regime of isolated bubbles and the region of interference. The isolated bubble regime in nucleate pool boiling has been discussed in many publications [2]. In this regime, bubbles are produced intermittently and do not interfere with each other. When the wall superheat increases, the waiting time between the nucleation of a new bubble and the departure of the previous bubble, grown from the same site, becomes shorter. If a certain critical temperature is reached, succeeding bubbles merge to form a mushroom-like bubble. This merger can also involve pairs consisting of a large bubble followed by a small one departing from

* Corresponding author: C. Hutter
Phone: + (44)-0131-6505685, Fax: + (44)-0131-6506551
E-mail address: C.Hutter@ed.ac.uk

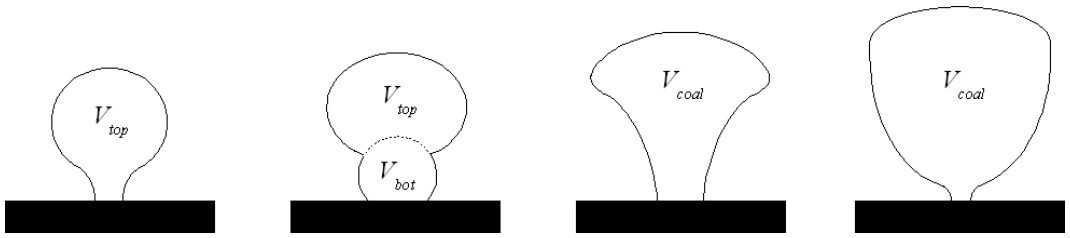

Figure 1. Vertical coalescence of two succeeding bubbles from an artificial nucleation site. The bubble with the volume V_{top} merges with the bubble with the volume V_{bot} to form a bubble of the volume V_{coal}.

the same nucleation site. This is known as the region of interference; bubbles interfere with each other and form continuous vapour columns and patches.

Buyevich and Webbon [3] investigated the limit of the isolated bubble regime. They identified four contributing mechanisms that lead to this limit, a) the upward flow of the rising bubble which obstructs the downward flow of liquid required to compensate for the vapour removal from the wall, b) lateral coalescence of bubbles from several nucleation sites to form large bubbles and extended vapour patches on the surface, c) longitudinal coalescence close to the wall, which results in the departure of dissimilar sized bubble pairs as mentioned before, d) longitudinal coalescence in the bulk, which leads to the formation of vapour columns. Buyevich and Webbon identified the last case as the most important effect for the termination of the isolated bubble region, as it can lead to the boiling crisis and trigger the critical heat flux.

Zhang and Shoji [4] classified 3 types of coalescence, i.e. vertical, horizontal and declining coalescence. Vertical coalescence occurs when during its growth phase a bubble touches the previously departed bubble, which is then drawn into and pulled away from the hot surface as illustrated in Figure 1.

Horizontal coalescence happens between two or more adjacent growing bubbles, which merge to form one large bubble. The merger of a growing bubble with an already departed bubble from an adjacent nucleation site is called declining coalescence. Zhang and Shoji concluded that bubble coalescence near the heated wall promotes growing bubbles to depart from the nucleation site. However, because vertical coalescence can occur for single and adjacent multiple nucleation sites, only horizontal and declining coalescence were thoroughly analysed. Although vertical coalescence is mentioned in several publications, this type of bubble interaction is usually not given much attention in the boiling heat transfer literature.

The bubbles in this study are growing from one isolated artificial cavity acting as nucleation site, allowing control of the location of the active site. Artificial cavities are widely used in boiling heat transfer research and mainly manufactured using microfabrication. Vapour or gas trapped in a cavity acts as a nucleus for the growth of a bubble. Bankoff [5] formulated the first criterion for pre-existing nuclei. This paper focuses on vertical coalescence occurring during nucleate pool boiling in the region of interference from an isolated artificial cavity. Coalescence is a hydrodynamic direct interaction between bubbles, as they collide and hence merge into one larger bubble. This is only of interest when occurring close to the heated surface, because away from the surface the impact on the boiling heat transfer is small [6].

EXPERIMENTAL SETUP

The working fluid was fluorinert FC-72, which is widely used for boiling experiments due to its non-toxicity, non-flammability and its low boiling temperature (T_{sat} = 57.15 °C at p = 1 bar). Its good dielectric properties make it possible to immerse the bare electrical connections to the 380 µm thick

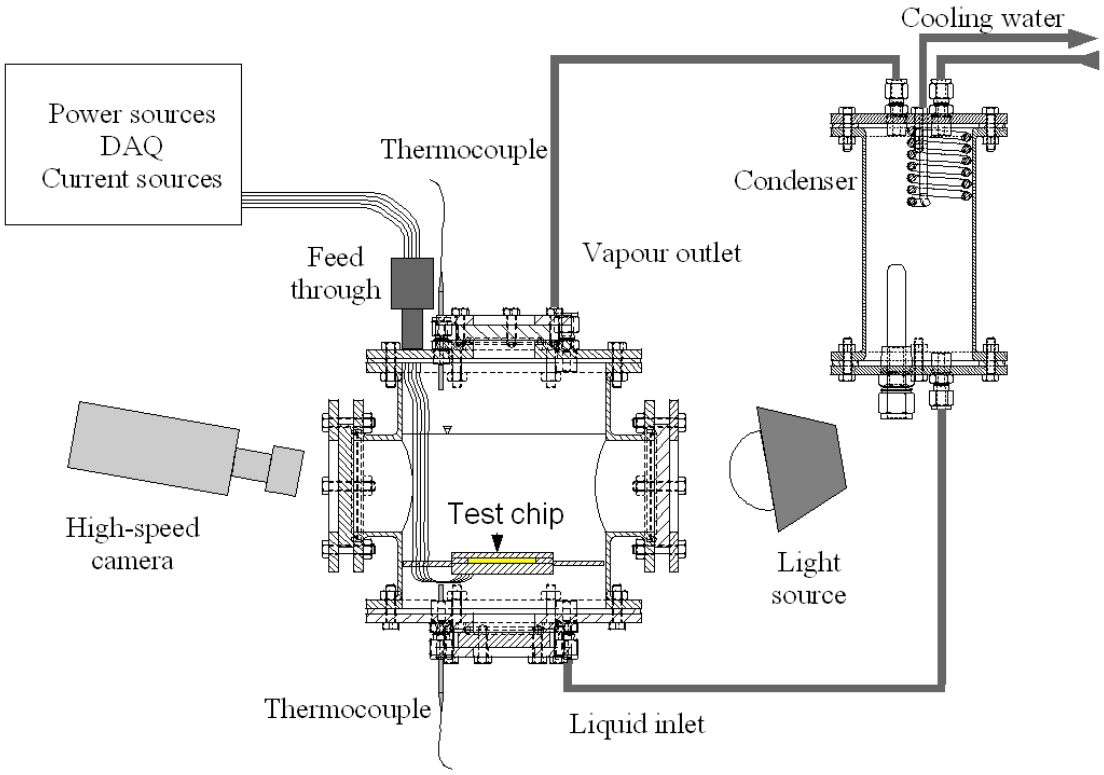

Figure 2. Experimental setup including the main parts boiling chamber with test section, condenser, high-speed camera and backlight source.

silicon test section into the liquid. Electrical connections from the silicon chip are made through an air-tight feed-through in the wall of the stainless steel boiling chamber to provide the interconnect to the DAQ, the power supply for the integrated resistance heater and the constant current sources for the integrated micro-sensors. The chamber has four windows for optical access to the test section as shown in Figure 2. The wall temperature of the chamber is controlled by two silicone heater pads wrapped around the chamber. Four heater elements at the bottom of the chamber are used for degassing and bringing the liquid to the set temperature. Two thermocouples inside the chamber measure the temperature of the liquid and the vapour. If they indicate the same temperature, the saturation pressure has been reached and saturated boiling is taking place. The pressure in the chamber is measured by a calibrated pressure transducer with measurement error smaller than 0.2%. Boiling can be maintained at any pressure between 0.5 and 3 bar by adjusting the condenser cooling water flow with a valve and the temperature with a heating bath.

An isolated cylindrical artificial cavity with a mouth diameter of 10±0.5 µm and a depth of 80±5 µm was micro-fabricated on the top surface of the silicon test section. A Ti/Ni micro-sensor with a square shape covering an area of 0.84 mm x 0.84 mm was deposited around the artificial cavity. The silicon chip was held in place and, except for the actual boiling surface, insulated with a frame made of PEEK, which has similar thermal properties to PTFE. Spring probes were used, in order to ensure a good electrical contact between the integrated heater and sensor on the chip and the wires. The resistance of the sensor was calibrated using a standard thermometer and exhibits a near linear behaviour with temperature.

After the boiling liquid is thoroughly degassed and the set pressure reached, boiling from the artificial cavity is initiated with the resistance heater integrated on the rear of the silicon wafer. Bubble growth is observed with a high-speed camera and a backlight source positioned on the opposite side. The temperature readings from the micro-sensor are simultaneously acquired through a trigger. Synchronisation is necessary to correlate measurements to video recordings and will be

essential to link small changes in local wall temperatures to the bubble dynamics in future studies. In this paper the sensors are used to measure the time averaged wall surface temperature in the immediate vicinity of the nucleation site for the duration of recording. The limit of error is 0.5 K for all wall superheat measurements and the standard deviation is within the error. However, no error bars are indicated in the plots in order to improve legibility. The heat flux was measured with a voltage and current meter and has an error of ±1%.

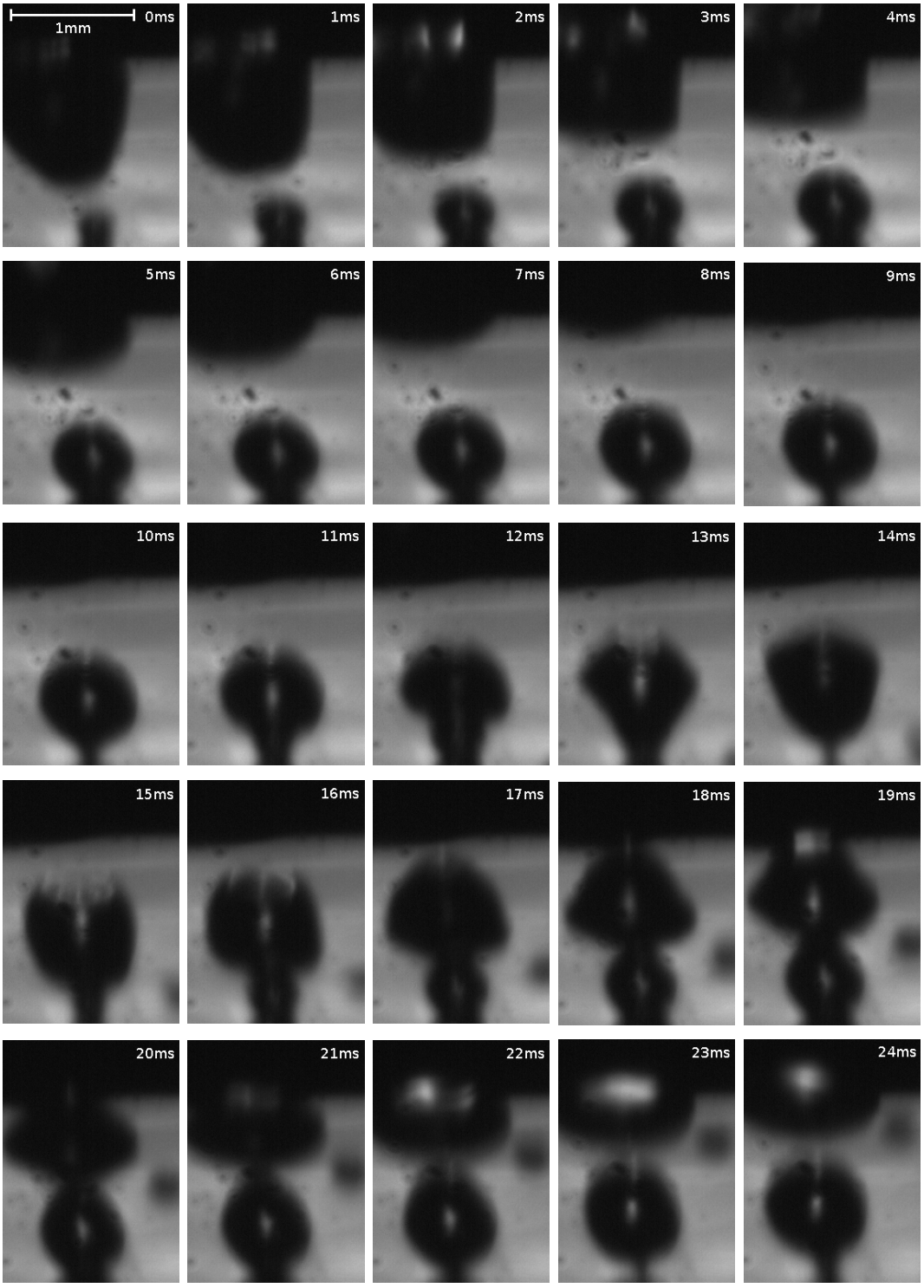

Figure. 3: Bubble growth sequence including vertical coalescence for a wall superheat of 7.9 K (applied heat flux 4.8 kW/m^2) at an absolute pressure of 0.5 bar. The first frame includes a scale.

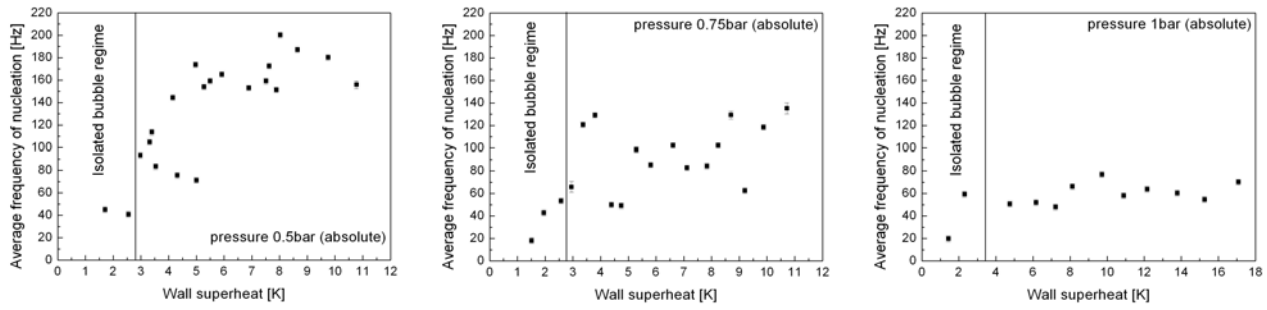

a) b) c)

Figure 4. Average frequency of nucleation with increasing wall superheat for a) 0.5 bar, b) 0.75 bar and c) 1 bar.

EXPERIMENTAL RESULTS AND DISCUSSION

The lowest possible wall superheat is limited by the internal temperature of the nucleus, which must equal the saturation temperature for the pressure of the vapour phase in order for the nucleus not to shrink. It is calculated from the Laplace equation:

$$p_g - p_l = \frac{2\sigma}{r_b} \tag{1}$$

where p_g is the vapour pressure, p_l the pressure of the liquid, σ the surface tension and r_b the nucleus curvature radius which equals the cavity mouth diameter r_c. For 0.5 bar, 0.75 bar and 1 bar the minimum temperature differences are 1.98 K, 1.29 K and 0.94 K.

The average frequency of nucleated bubbles and vertical coalescence from an isolated single cavity were measured using high-speed images for absolute pressures of 0.5 bar, 0.75 bar and 1 bar with increasing wall temperature superheat. Figure 3 presents a sequence of bubble growth at 0.5 bar absolute pressure and a wall superheat of 7.9 K (applied heat flux 4.8 kW/m^2) with camera set to 1000 fps. Bubble nucleation occurs at 0 ms and for the first 11 ms the bubble growth follows the common behaviour of a single bubble. At 11 ms a second bubble nucleates from the same artificial cavity and within 3 ms completely merges with the previously departed upper bubble. At 15 ms a third bubble nucleates, but does not coalesce with its predecessor during growth. The occasionally visible widening of the bubble base is due to reflection of the bubble on the silicon surface.

Figure 4 shows the average nucleation frequency with increasing wall superheat for the above three pressures. With increasing pressure the number of nucleations per second decreases. With increasing wall superheat this number of nucleations initially increases sharply and seems to level off, with this behaviour being more pronounced for the 0.5 bar pressure case. The results for 0.75 bar are rather scattered and for 1 bar the initial increase is less noticeable.

Figure 5 presents the average frequency of vertical coalescence for the same three pressures with increasing wall superheat. Lowering the pressure or increasing the wall superheat increases the occurrence of coalescence. The average frequency of bubble nucleation corresponds to an increase in the average frequency of vertical coalescence, as coalescence tends to reduce the bubble growth time. Bubbles are pulled away from the surface at much smaller size and this increases the number of nucleations for the same time period but increases the total growth time of the two bubbles only by a few milliseconds.

Figure 6 compares the average frequency of vertical coalescence with the number of nucleations (*VC*/*Nu*). At 0.5 bar approximately 50% of the bubbles coalesce for higher wall superheats. The

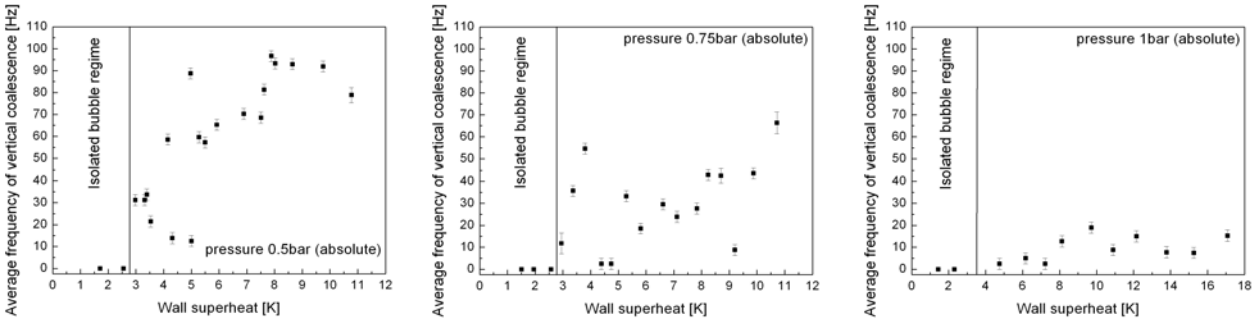

a) b) c)

Figure 5. Average frequency of vertical coalescence with increasing wall superheat for a) 0.5 bar, b) 0.75 bar and c) 1 bar.

ratio remains at this level even with increasing wall superheats. A possible explanation for this behaviour might be the fact that vertical coalescence most commonly appears only in pairs, i.e. only very rarely does a third bubble coalesce with already vertically coalesced bubbles. As the pressure increases, the ratio between vertical coalescence and nucleations decreases. For 1bar the maximum ratio is around 0.2 for high wall superheats. This means that around three bubbles depart as single bubbles before vertical coalescence occurs between the two that follow. Measurements for 0.75 bar tend to lie in between the results for the lower and higher pressure.

Following the above observations the volumes of ten bubble pairs immediately before and after coalescence are presented. The pressure was 0.5 bar with a wall superheat of 7.9 K (applied heat flux 4.8 kW/m^2). Bubble vapour volumes were estimated from high speed image sequences and Figure 7 presents an example sequence. The original images were processed with the software PCO Picture Viewer and a suitable threshold helped to identify the bubble area. The program then solved the equation:

$$V = \pi \int_0^y r_b(y)^2 dy \tag{2}$$

where $r_b(y)$ is the bubble radius depending on the vertical position. The volume was scaled with a reference image loaded into the software. The measurement error was estimated to be ±0.005mm for the bubble radius. Due to the invisibility of the intersection between the top and bottom bubble the shape of the bottom bubble was assumed to be spherical. Since small single bubbles have a small Eötvös or Bond number, gravitational effects are negligible and the shape is near spherical.

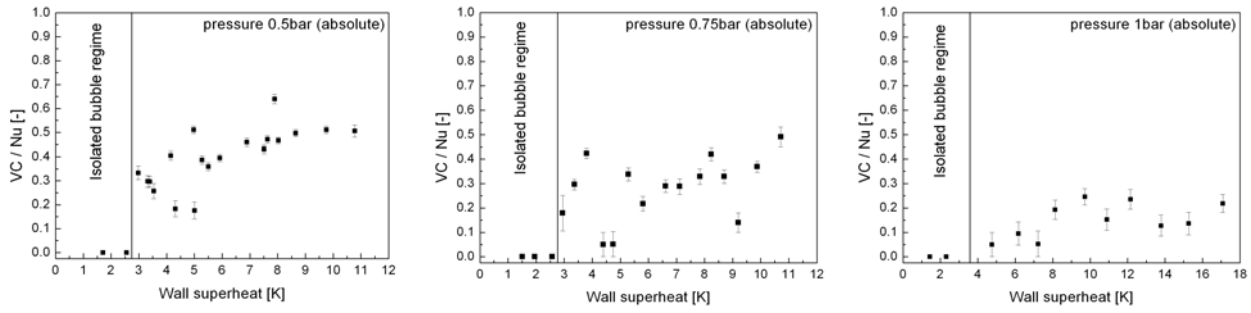

a) b) c)

Figure 6. Ratio of the average frequency of vertical coalescence and bubble nucleation with increasing wall superheat for a) 0.5bar, b) 0.75bar and c) 1bar.

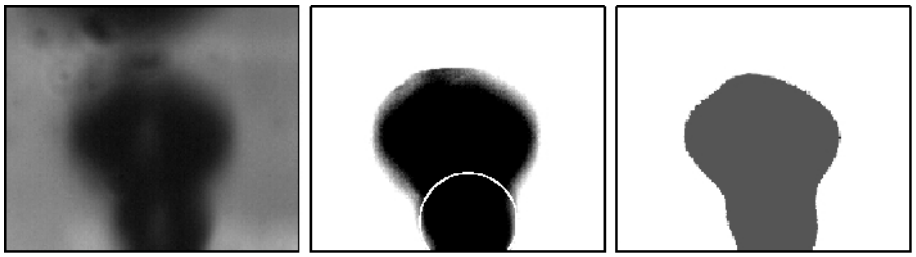

a) b) c)

Figure 7. a) Original image during bubble growth with vertical coalescence. b) Processed picture with the assumed shape of the bottom bubble indicated. c) Area measured with PCO Picture Viewer software. From this area the volume of revolution is calculated.

Figure 8 a) shows the results with the systematic measurement error indicated. The newly nucleated bubble (bottom bubble) is always smaller than the previously departed one (top bubble) and the total volume immediately after coalescence is larger than the sum of volumes before the coalescence. Figure 8 b) shows the ratio between the volume of the bottom bubble V_{bot} and the top bubble V_{top} with error bars indicating the propagated systematic measurement error. The volume of bottom bubble never exceeds one third of the volume of the top one. The smallest bottom bubble compared to its top one is 10 times smaller than its predecessor. Figure 8 c) illustrates the ratio between the sum of the volumes of the two bubbles $V_{bot}+V_{top}$ immediately before coalescence and the total volume V_{coal} just after (1ms). After coalescence the total volume is 5-18% larger than before. This suggests that the process of coalescence causes a brief increase in heat transfer to the liquid-vapour interface. This might occur at the base of the second bubble, or by heat transfer from a thin superheated liquid layer trapped between the bubbles, or by rapid motion close to the line of coalescence.

CONCLUSIONS

Bubble growth from an isolated artificial cavity at the end of the isolated bubble regime and the beginning of the regime of interference, where vertical coalescence appears, has been experimentally investigated. The phenomenon of vertical coalescence was visualised and quantified using high-speed imaging. Further studies of longer sequences at different wall superheats and pressures of 0.5 bar, 0.75 bar and 1 bar revealed the dependence of vertical coalescence on these properties.

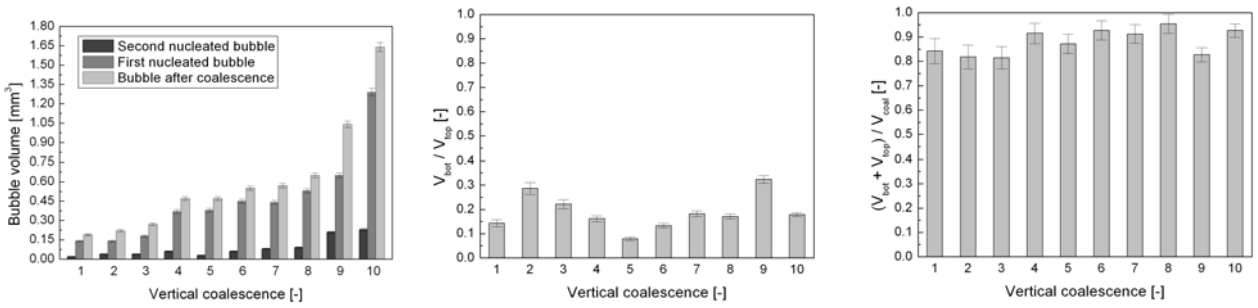

a) b) c)

Figure 8. a) Bubble volume immediately before coalescence and the total volume after for 10 pairs of bubbles. b) Ratio between the volume of the newly nucleated bubble (bottom bubble) and the previously departed bubble (top bubble) for the same 10 bubble pairs. c) Ratio of the total volume of the top and bottom immediately before coalescence and the volume of the coalesced bubble.

With increasing wall superheat bubble growth changes from the isolated bubble regime into the regime of interference. The average frequency of bubble nucleation and vertical coalescence increased with the wall superheat. Decreasing the pressure, increases the average frequency of vertical coalescence and therefore subsequently the average frequency of nucleated bubbles from the artificial cavity. At 0.5 bar every two nucleated bubble pairs merge into one for high wall superheats. At 1 bar up to three single bubbles depart from the artificial cavity, before two coalesce.
The equivalent volume of a sphere was calculated for ten pairs of bubbles immediately before and after they coalesced. The second nucleating bubble is always smaller than its departed predecessor. During coalescence the vapour volume still increases, as the merged bubble is between 5 and 18% larger than the summarised volumes of the two bubbles before coalescence.

NOMENCLATURE

Nu	number of bubble nucleations	[-]
p	pressure	[Pa]
p_g	vapour pressure	[Pa]
p_l	liquid pressure	[Pa]
r_b	bubble radius	[m]
r_c	cavity mouth radius	[m]
T_{sat}	saturation temperature	[°C]
V	volume	[m^3]
V_{bot}	bottom bubble vapour volume	[m^3]
V_{coal}	upper bubble vapour volume	[m^3]
V_{top}	coalesced bubble vapour volume	[m^3]
VC	number of vertical coalescence	[-]
y	variable in vertical direction	[m]
σ	surface tension	[N/m]

ACKNOWLEDGEMENTS

This work was funded by the UK Engineering and Physical Sciences Research Council (EPSRC) by grant EP/C532813/1.

REFERENCES

1. Zuber, N., Nucleate Boiling. The Region of Isolated Bubbles and the Similarity with Natural Convection, *Int. J. Heat Mass Transfer*, vol. 6, pp. 53-78, 1963.
2. Dhir, V.K., Boiling Heat Tranfer, *Annu. Rev. Fluid. Mech.*, 30, pp. 365-401, 1998.
3. Buyevich, Y.A. and Webbon, B.W., The Isolated Bubble Regime in Nucleate Boiling, *Int. J. Heat Mass Transfer*, vol.2, no.2, pp. 365-377, 1997.
4. Zhang, L. and Shoji, M., Nucleation Site Interaction in Pool Boiling on the Artificial Surface, *Int. J. Heat Mass Transfer*, 46, pp. 513-522, 2003.
5. Bankoff, S.G., Entrapment of Gas in the Spreading of a Liquid over a Rough Surface, *AIChE Journal*, vol. 4, no. 1, pp. 24-26, 1958.
6. Bonjour, J., Clausse, M. and Lallemand, M., Experimental Study of the Coalescence Phenomenon During Nucleate Pool Boiling, *Exp. Therm. Fluid Science*, 20, pp. 180-187, 2000.

EXPERIMENTAL STUDY OF HEAT TRANSFER INSIDE A HYDROGEN COMBUSTION ENGINE: MEASUREMENTS UNDER MOTORED CONDITIONS

J. Demuynck*, M. De Paepe, H. Huisseune, C. T'Joen, S. Verhelst
Ghent University, Gent, Belgium

ABSTRACT. This paper presents the first stages of an experimental study of heat transfer inside a hydrogen combustion engine. A heat transfer model for hydrogen engines is under development and measurements are carried out for validation. The current paper describes heat transfer measurements in the cylinder under motored conditions. Transient heat flux is evaluated at the cylinder head and liner with a commercially available sensor. The influence of the compression ratio and measuring position is investigated. Results show that the peak of the heat flux trace rises with increasing compression ratio. The position of the peak remains the same for all the compression ratios. The heat flux is negative during the intake and differs from position to position because of differences in the local air flow field. The flux varies less in the compression and expansion stroke but a large cyclic variation is present in that part of the cycle.

Keywords: *hydrogen, engine, model, heat transfer, experimental*

INTRODUCTION

Hydrogen-fuelled internal combustion engines are attractive as they offer the potential of near-zero noxious emissions, high efficiency and zero greenhouse gas emissions. Computer simulation of the performance enables a cheap and fast optimization of engine settings for operation on hydrogen. A quasi-dimensional simulation model, the GUEST-code (Ghent University Engine Simulation Tool), has been developed by Verhelst and Sierens [1]. Up until now the GUEST-code has simulated power output and efficiency of hydrogen engines with good accuracy. The simulation tool has been validated for varying mixture richness, ignition timing and compression ratio.

In a next step emission calculations will be added to the GUEST-code. In hydrogen engines NO_x emissions occur at high loads. It is important to describe the heat transfer from the burning gases to the cylinder walls in a sub-model in order to calculate the maximum gas temperature which influences the NO_x emissions. Several models exist but they have been developed for fossil fuels and are cited to be inaccurate for hydrogen engines [2, 3]. The maximum possible heat transfer in an engine operating on hydrogen is expected to be higher than in a hydrocarbon-fuelled one. The shorter quenching distance of hydrogen leads to a thinner thermal boundary layer, the higher flame speed causes an intensified convection and hydrogen has a higher thermal conductivity. A new model for the heat transfer in hydrogen engines is under development and measurements inside an engine are carried out for validation.

A stepwise investigation of the heat transfer inside a cylinder is performed in order to fully understand the process and all the effects which take part in it. First of all measurements under motored operation are investigated to decouple the flow and turbulence from combustion. The

* Corresponding author: ir. J. Demuynck
Phone: + 32-(0)9-2643302, Fax: + 32-(0)9-2643590
E-mail address: Joachim.Demuynck@UGent.be

Reynolds and Nusselt number should be the same under motored and fired operation according to Nijeweme [4], so it is interesting to look at the heat transfer without having combustion. The stepwise investigation also allows an exploration of the possibilities of the heat flux sensor. In this paper a sensor is mounted in a CFR-engine (CFR: Cooperative Fuel Research) and measurement results under motored conditions are discussed. The flow field inside this type of engine (modified for optical access) has been investigated by Namazian [5] with Schlieren visualisation techniques. The flow field inside the CFR engine can be summarized as follows. It takes a while after IVO for the gases to enter during the intake stroke. A shrouded intake valve induces a counter clockwise swirl and a vortex flow is created in the top left and right hand corners of the cylinder (see Figure 1). This vortex is present through the intake process, persist during compression and still influences the flow field during expansion. Again it takes a while after valve opening before the gases start to move during the exhaust stroke.

EXPERIMENTAL EQUIPMENT

Test engine. Heat transfer is measured in the cylinder of a CFR-engine. This single cylinder engine has a variable compression ratio (ε) and a constant rotation speed of 600 rpm. The cylinder liner and head are one piece so it is difficult to install sensors. However, four holes with an M18 thread are available in the cylinder head for sensor mounting (see Figure 1). One hole is lost in case of fired operation because of the spark plug. The geometrical properties and valve timing of the engine are summarised in Table 1. The intake valve is shrouded and induces a swirl as mentioned above.

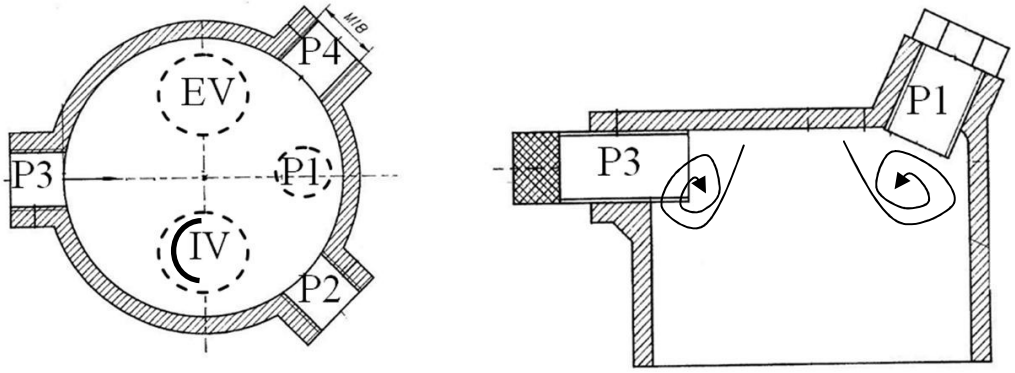

Figure 1. Top and side view of the CFR-engine, P1-P4: sensor positions, IV: shrouded intake valve, EV: exhaust valve

Table 1
Geometrical Properties and Valve Timing of the CFR-engine

Bore	82.55 mm
Stroke	114.2 mm
Connecting rod length	254 mm
Stroke volume	611.7 cm³
Intake valve opening (IVO)	17 °ca ATDC (After Top Dead Centre)
Intake valve closing (IVC)	26 °ca ABDC (After Bottom Dead Centre)
Exhaust valve opening (EVO)	32 °ca BBDC (Before Bottom Dead Centre)
Exhaust valve closing (EVC)	6 °ca ATDC

Heat transfer sensor. The sensor used for heat transfer measurements in the engine is a custom-made HFM-7 E/L (Heat Flux Microsensor) from Vatell Corporation [6]. The sensor has two signal outputs. Firstly an HFS-channel (Heat Flux Sensor) which is the voltage of a thermopile proportional to the heat flux, secondly an RTS-signal (Resistance Temperature Sensing) which is the resistance of a platinum RTD (Resistance Temperature Detector) proportional to the temperature of the substrate of the thermopile. Figure 2 shows the head of the sensor with the thermopile in the centre (diamond shape) and the RTD in a loop around it.

The basic principle of a heat flux sensor is to measure the temperature gradient over a layer with known thermal properties. The thermopile however measures the heat flux over a thin layer (in the order of 1 µm) so the temperature gradient is very small and one thermocouple pair would result in an immeasurable signal. That is why several thermocouple pairs are connected in series to give a measurable signal output which is in the order of 150 µV for 1 W/cm² in the case of the HFM (see Figure 3, TL&TH: temperatures at each side of the layer, A&B: the two different metals of the thermocouples). The temperature measured with the RTD is used to correct the HFS signal because the thermal properties of the sensor substrate are temperature dependent.

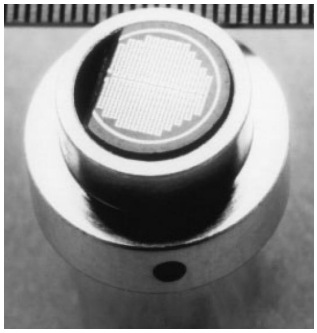

Figure 2. HFM-7 E/L sensor

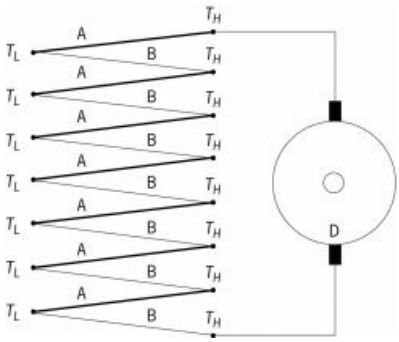

Figure 3. Construction of a thermopile

The HFS and RTS signal are sent to an AMP-6 amplifier from Vatell Corp. It sends a current of 100 µA through the RTD and measures the corresponding voltage drop. The two signals are amplified with a selectable gain. The sensor is calibrated by Vatell Corp. and the calibration coefficients make it possible to calculate the heat flux and sensor temperature out of the two measured voltage signals. At the beginning of each measurement the HFS and RTS signal have to be zeroed at zero heat flux and a known temperature.

Other sensors and data acquisition. Two pressure transducers are mounted, one in the intake manifold and one in the cylinder. The transducer in the intake manifold is of the piezoresistive type and the one in the cylinder of the piezoelectric type. An encoder is mounted on the crankshaft in order to sample the measured signals at certain degrees crank angle (°ca). A 12-bit Keithley data acquisition card collects the data of the four channels every 0.1 °ca.

MEASUREMENTS

Test conditions. The commercially available film type heat flux sensor is mounted in the CFR-engine in four different positions (P1-P4) as shown in Figure 1. The pressure transducer is mounted in P2 or P4. Measurements under motored conditions at 600 rpm are executed, investigating the influence of the compression ratio and the measuring position on the heat flux. The compression ratio is varied from 6 to 15 during measurements in P1 and heat flux is measured in the four positions for ε equal to 10. Only air is sucked into the engine. The heat flux and pressure traces are averaged over 20 cycles (unless it is mentioned otherwise).

Results and discussion. Heat flux is positive when heat is transferred from the walls to the gases and negative when the gases cool the wall. If the heat transfer is negative and the flux trace decreases, an enhancement in heat transfer occurs. So an observed decreasing in the heat flux trace will be described as an improved heat transfer. Heat flux is plotted on the left vertical axis and pressure on the right one if they are given in one figure.

The heat flux traces at P1 for varying compression ratio are shown from Figure 4 to Figure 6. In Figure 4 it can be seen that during intake the heat flux is negative so heat is flowing from the wall to the air which is colder. The heat transfer increases for increasing ε because the wall temperature rises and there is a bigger temperature difference between the air and the wall. The heat flux starts to decrease at an earlier degree crank angle for increasing ε because there is a larger difference between the inlet and cylinder pressure so air enters the cylinder more rapidly.

The peak of the heat flux trace during compression increases with increasing ε (see Figure 5) because of rising gas temperature, the average heat flux trace peaks a little bit before TDC for every ε. The flux decreases more for higher ε at the end of the expansion stroke, except for ε=12. It will be investigated with more measurements around this compression ratio whether this is a measuring error or an anomaly. The trend for lower and higher compression ratios may differ from those around ε=12 because of contradictory effects.

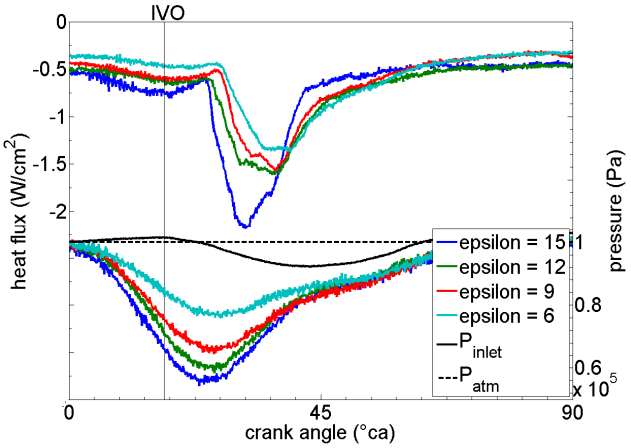

Figure 4. Heat flux and pressure (cylinder and inlet) for varying compression ratio at P1 during intake stroke

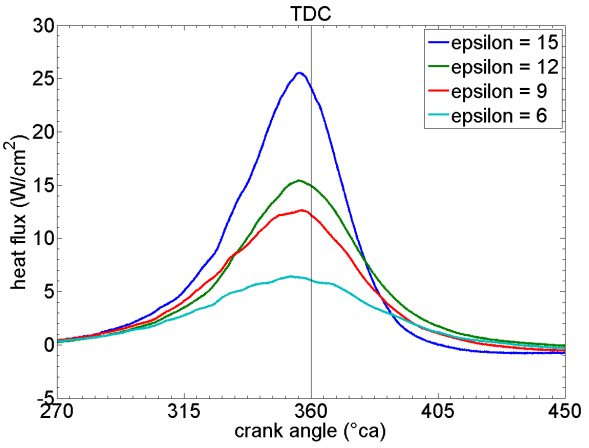

Figure 5. Heat flux for varying compression ratio at P1 during the compression and expansion stroke

Figure 6 shows the heat flux and cylinder pressure during the exhaust process. It appears that the cylinder pressure is lower than atmospheric pressure at EVO so air from the exhaust manifold flows into the cylinder. The pressure rises because of the inflowing air and the actual exhaust process starts a while after BDC which causes the heat flux to level off. The heat transfer (negative again) increases before BDC with increasing compression ratio, but again ε=12 is an exception.

No consistent difference can be found between the four measuring positions during the compression and expansion stroke. Certain measurements show equal heat fluxes for varying measuring positions (see Figure 7). Others show differences, but these are never consistent. The reason is shown in Figure 8. The cyclic variation of the heat flux during the compression and expansion stroke is higher as one might expect under motored conditions. The difference between the peak of the mean and the maximum flux trace is around 10 W/cm², which is 67% of the mean peak value. This cyclic variation is not present during the intake and the exhaust stroke.

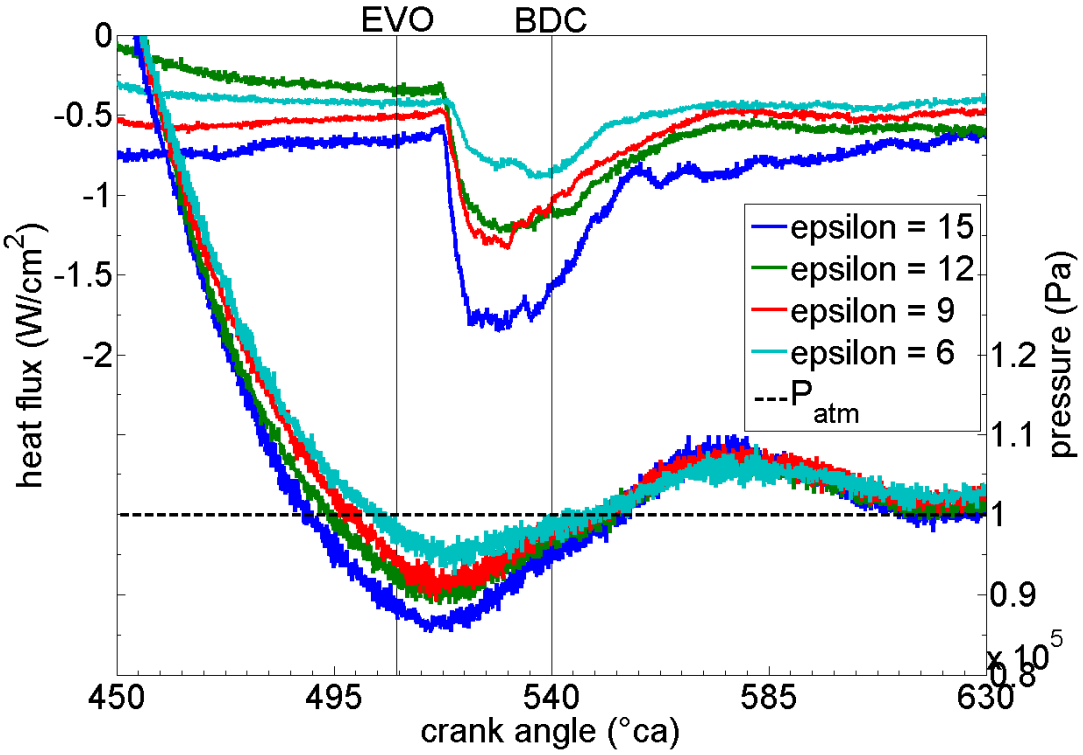

Figure 6. Heat flux and cylinder pressure for varying compression ratio at P1 during the exhaust process

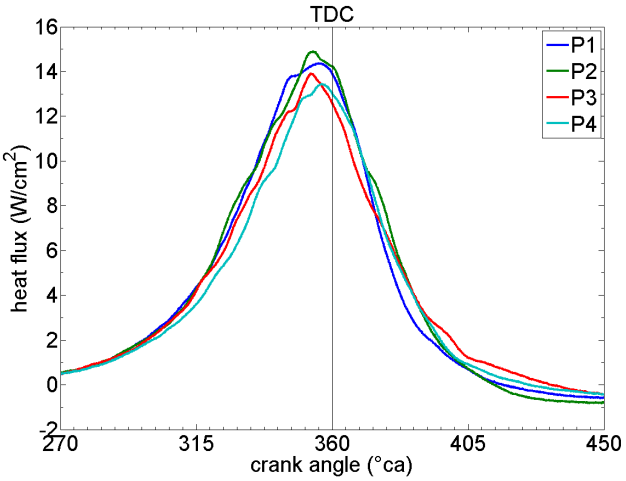

Figure 7. Heat flux for varying measuring position during the compression and expansion stroke (ε=10)

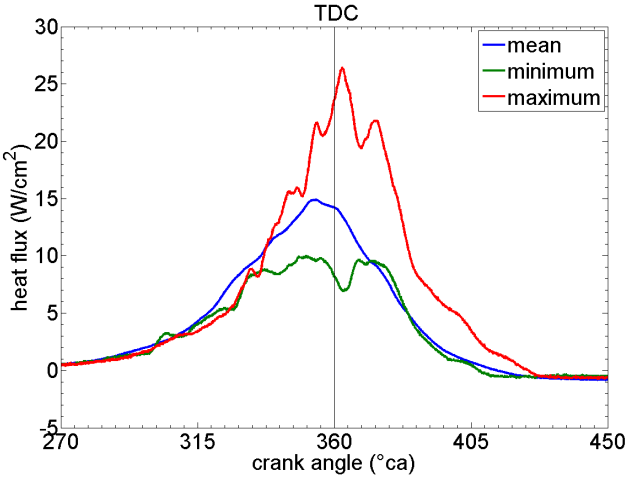

Figure 8. Cyclic variation of heat flux at P2 (ε=10)

This indicates that turbulence and gas motion (with a large cyclic variation) influence the heat flux trace during compression. The temperature and the amount of mass of air entering or exiting the engine do not fluctuate much over cycles and have to be the driving forces of the heat transfer in the intake and exhaust process. The heat flux traces in Figure 9 support this idea. A throttle in the intake manifold is stepwise closed to create extra turbulence. At first the heat flux rises during compression. When the gas temperature decreases too much because of lower cylinder pressure (throttle is almost closed and causes a strong expansion of the inflowing air so cylinder pressure at IVC is beneath atmospheric pressure), the heat flux starts to decrease again.

Two important differences can be seen in the heat flux traces (negative again) during the exhaust stroke (Figure 10). It takes a while for the incoming exhaust air to reach P2 which lies furthermost away from the exhaust valve, so the heat transfer augments at a later degree crank angle than at the other positions. Less air reaches P3 so the minimum in the heat flux trace is less deep. The heat flux remains constant a little bit after BDC when the actual exhaust process occurs.

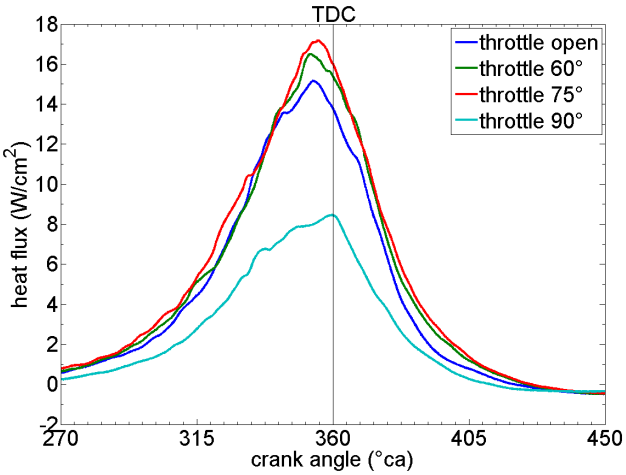

Figure 9. Heat flux for varying throttle opening during the compression and expansion stroke at P1 (ε=10)

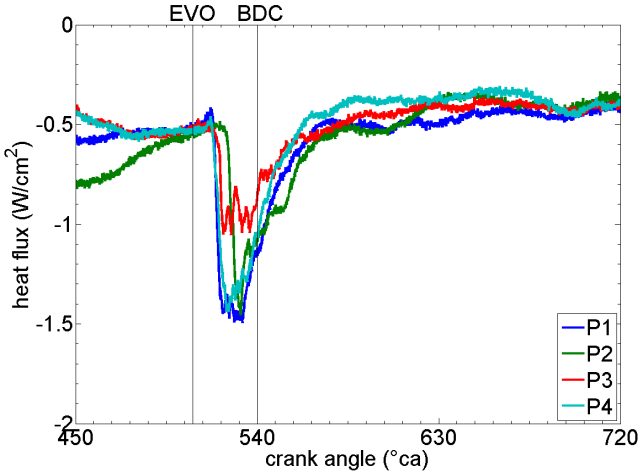

Figure 10. Heat flux for varying position at P1 during the exhaust stroke (ε=10)

There is more variation in heat transfer from position to position during the intake process. A bigger temperature difference between wall and gas, more inflowing air and a shrouded intake valve are the causes for this pronounced variation. The shroud opens in the direction of P1 as drawn in Figure 1 so a counter clockwise swirl is induced. First the existence of the swirl will be demonstrated. Then a general description of the heat flux traces in the four positions will be given starting at IVO going to IVC. The heat flux traces are negative again, so a decrease actually means an increase in heat transfer.

The existence of this swirl can be seen in Figure 11 if one only focuses on the heat flux traces at P2 and P4. The heat transfer at P4 starts to increase at a later degree crank angle than at P2 because it takes a while for the swirl to reach P2. The minimum in the flux trace at P4 is less deep because the incoming air warms up in its way towards P4. The second drop in the heat flux trace at P2 (starting around 48 °ca) can also be found with a delay at P4 (starting around 80 °ca). The drop at P4 is less profound again. The heat transfer at P3 and P1 starts to increase simultaneously with the one at P2. The minimum at P1 is less deep than at P2 so more fresh air reaches P2. Strangely the heat transfer at P3 increases at the same time as at P2 (but less profound) because one should expect no air reaching P3 because of the shrouded intake valve. Two reasons could explain this phenomenon. Firstly a little bit of air could flow at the left side of the shroud in the direction of P3. Secondly a general change in gas speed following the start of the intake process could cause an enhancement in heat transfer without fresh air reaching P3.

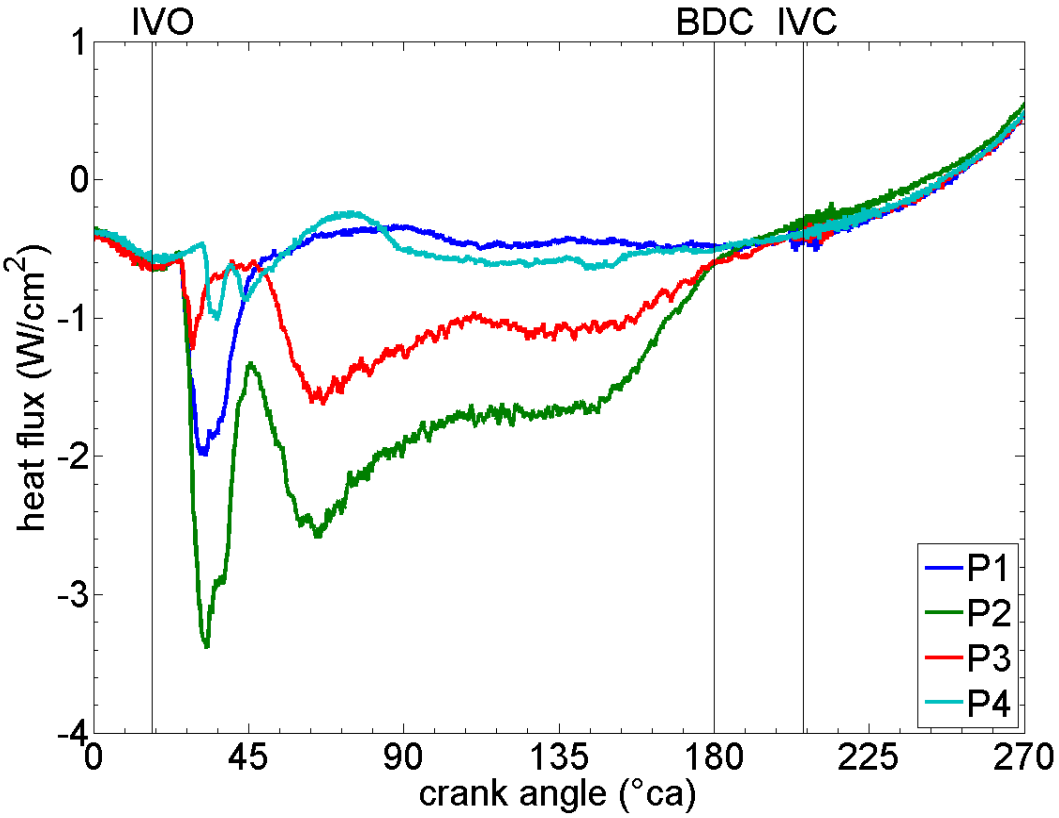

Figure 11. Heat flux for varying measuring position during the intake stroke (ε=10)

Now a general overview of the heat flux traces in Figure 11 will be given starting around IVO. Before the heat transfer at P1, P2 and P3 increases around 8 °ca after IVO, they decrease a little bit because gas speed is dropping after EVC. This counters the effect of dropping cylinder pressure and gas temperature which create a bigger temperature difference between the gas and the wall, hence an increase in heat transfer. After 10 °ca the heat transfer at P1 and P2 drops again because the rising cylinder pressure starts to increase the gas temperature in the cylinder (see the pressure traces in Figure 4). The heat transfer at P3 drops earlier. Only the heat transfer at P4 then increases again around 40 °ca. Perhaps the swirl coming from P2 has just reached P4 causing this augmentation which could mean the first increase at 33 °ca is caused by the possible general change in gas speed (mentioned above) reaching P4.

The transfer at P2 and P3 increases again around 48 °ca. This could be caused by the pressure wave in the intake manifold which increases the mass flow rate at that moment. This increase occurs simultaneously again at P2 and P3 (less profound). One could imagine the swirl travelling around the entire cylinder causing the increase in the heat transfer at P2, but this should then be visible earlier at P3. The heat flux at P1 remains constant after 48 °ca because of the vortex in the top right hand corner of the combustion chamber as mentioned above. The heat transfer reduces again because of lowering gas speed and rising cylinder pressure and temperature. The levelling off at P2 and P3 from 110 °ca until 150 °ca can be explained by the pressure wave in the intake manifold which causes a second increase in the mass flow rate of the incoming air.

CONCLUSIONS

Heat transfer measurements have been carried out in an engine under motored operation as a first part of the stepwise research on heat transfer in a hydrogen engine. The influence of the compression ratio and measuring position is investigated with following conclusions:

- The heat transfer augments with increasing compression ratio. A bigger temperature difference between wall and gas is the cause of this enhancement during the intake and exhaust stroke. The heat transfer starts to increase earlier with increasing compression ratio because of a bigger pressure difference between intake or exhaust manifold and cylinder. The increasing gas temperature is the cause of the increasing heat transfer during the compression and expansion stroke.
- The trend around ε=12 could be different and this will be investigated with extra measurements.
- The heat transfer varies along the cylinder wall surface during the intake and the exhaust stroke. The delay between the heat flux trace at P2 and P4 shows the effect of the shrouded intake valve. No significant difference in heat transfer for varying measuring position can be seen during the compression and expansion stroke.
- Cyclic variation in turbulence causes a large cyclic variation in the heat flux around TDC during the compression and expansion stroke.

NOMENCLATURE

ε	Compression Ratio	A	After
IV	Intake Valve	B	Before
EV	Exhaust Valve	HFM	Heat Flux Microsensor
O	Opening	HFS	Heat Flux sensor
C	Closing	RTS	Resistance Temperature Sensing
TDC	Top Dead Centre	RTD	Resistance Temperature Detector
BDC	Bottom Dead Centre	AMP	Amplifier

ACKNOWLEDGEMENTS

Research funded by a Ph.D. grant (SB-81139) of the Institute for the Promotion of Innovation through Science and Technology in Flanders (IWT-Vlaanderen).

REFERENCES

1. Verhelst, S. and R. Sierens, *A quasi-dimensional model for the power cycle of a hydrogen-fuelled ICE.* International Journal of Hydrogen Energy, 2007. **32**(15): p. 3545-3554.
2. Shudo, T. and H. Suzuki, *Applicability of heat transfer equations to hydrogen combustion.* Jsae Review, 2002. **23**(3): p. 303-308.
3. Wei, S., *A Study on Transient Heat Transfer Coefficient of In-cylinder Gas in the Hydrogen Fueled Engine*, in *KHES and HESS, the 6th Korea-Japan Joint Symposium on Hydrogen Energy*. 2001.
4. Nijeweme, D.J.O., et al., *Unsteady in-cylinder heat transfer in a spark ignition engine: experiments and modelling.* Proceedings of the Institution of Mechanical Engineers Part D-Journal of Automobile Engineering, 2001. **215**(D6): p. 747-760.
5. Namazian, M., et al., *Schlieren Visualization of the Flow and Density Fields in the Cylinder of a Spark-Ignition Engine.* SAE paper 800044, 1980.
6. Vatell. *Heat Flux Microsensor*. 2007. http://www.vatell.com/hfm.htm.

HOW TO ESTIMATE THE HEAT TRANSFER DUE TO DROPLETS IMPINGING ONTO A HOT SLAB?

F. Lelong[1,2], M. Gradeck[1,*], A. Ouattara[1], D. Maillet[1], N. Seiler[2]
[1]LEMTA Nancy University/CNRS, Vandoeuvre lès Nancy, France
[2]IRSN/DPAM/SEMCA/LEMAR, Cadarache, France

Abstract: The present work achieved in collaboration between LEMTA (Laboratoire d'Energétique et de Mécanique Théorique et Appliquée) and IRSN (Institut de Radioprotection et de Sûreté Nucléaire) aims at accurately characterizing the heat flux removed by single droplet (50-300µm diameter) impinging onto a hot surface. As the interaction between the droplet and the wall is very fast (a few of ms), the experimental set-up to measure the heat flux during the resident time of the droplet at the wall has been carefully designed. The heat flux due to the droplet impingement is estimated using a semi-analytical inverse heat conduction model. The resolution of the inverse heat conduction problem (IHCP) is based on an analytical solution of the direct problem. The unsteady heat equation is double transformed in the Laplace-Hankel space. As the transform temperature can be expressed as a linear function of the transform heat flux, a least square method can be used to estimate the heat flux. The goal of this paper is to described the experimental method for measuring this cooling flux.

Keywords: *Droplet, Leidenfrost, Bouncing regime, Integral transform, LOCA, IHCP*

INTRODUCTION

Liquid cooling is unavoidable in applications where the required power dissipation must be very important. Possible liquid cooling technologies include single-phase boiling, immersion flow boiling, jet impingement cooling, spray cooling. This study is concerned with the safety of nuclear pressurized water reactor (PWR). During a LOCA (Loss of Coolant Accident, basic designed accident for PWR), a pipe rupture in the primary circuit could lead to an important rise of the fuel rod temperature because of the water vaporization in the nuclear core reactor. This is followed by the thermal mechanical swelling of the clad and consequently by the rupture of the fuel clad, Fig.1. The reflooding phase is initiated by water injection after the activation of security system. During this phase, liquid water is injected into the reactor core in order to cool down the fuel rod heated by the nuclear residual power. This water, rising along the rods, is instantaneously vaporized because of the very high wall temperature. The important amount of vaporized water leads to create a high vapor flow, which pulls up and drags some water droplets above the quenching front. As one of the safety issues is the coolability of the fuel assemblies in the blockage regions, the capacity of the generated mist flow to cool down the fuel blockage region must be accurately evaluated. Thus, it is necessary to characterize the mist flow in these zones and its effect on the heat transfers to be able to predict the transient of the nuclear core during a LOCA. Up to now, no measurement of heat transfer for single droplet impinging a hot wall has been experienced. These experiments are now performed at LEMTA located in Nancy (France). An experimental program, with droplet and wall

* Corresponding author: Dr. M . Gradeck
Phone: + (33)-383-555-559, Fax: + (33)-383-595-514
E-mail address: michel.gradeck@ensem.inpl-nancy.fr

characteristics (velocity, diameter and temperature) in agreement the LOCA conditions, is performed.

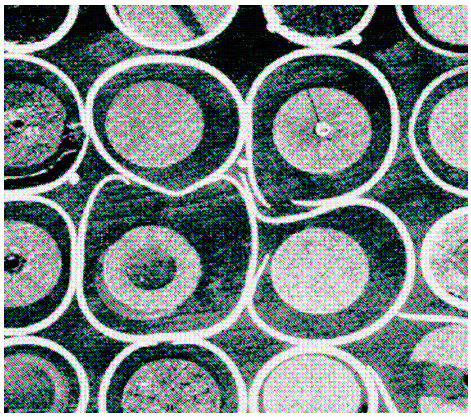

Figure 1 : view of a real ballooned zone from the experiment PHEBUS LOCA

LITTERATURE SURVEY

The estimation of the heat transfer removed from the wall by the impinging droplets is thus one part of the work devoted to LOCA safety studies. A lot of experimental studies of droplets impacting onto a heated surface are extensively reported in the literature. When a droplet interacts with a hot wall, the impact regime is determined by two important dimensionless parameters : the Weber number $We = \frac{\rho_L D_d u^2}{\sigma}$ which is the ratio of the impact inertial force to the surface tension force and the dimensionless temperature $T^* = \frac{T_w - T_{sat}}{T_{Leid} - T_{sat}}$. So, depending on these two parameters, the droplet would either rebound without disintegration (perfect bouncing regime), partially rebound (bouncing regime with secondary atomization), or splash on the wall after the impact (splashing regime). As the temperature of the fuel rod is much higher than the Leidenfrost temperature, the expected impact regime will be the bouncing one. Some models of heat transfer are reported in the literature. Andreani et al. [1] proposed a correlation for the estimation of the heat flux, q_{DC}, between a single droplet that impinges a hot wall in the case of the Leidenfrost regime. They assumed that only a few part of the droplet evaporates, thus the heat flux removed at the wall by the direct contact of the droplet is known if the effectiveness ε of the heat exchange can be estimated. The effectiveness ε is the ratio between the energy E_{DC} exchanged during direct contact of the droplet and the hot wall and the energy necessary to completely evaporates this droplet :

$$\varepsilon = \frac{E_{DC}}{\rho_L h_{LV} V_d} \text{ and } Q_{DC} = \frac{\varepsilon}{\Delta t_C} \rho_L h_{LV} V_d \quad (1)$$

Guo et al. [2] estimated the heat transfer due to the contact of droplets bouncing on the wall using the following equation. This one has been established by solving mass, momentum and energy equations in the vapour cushion beneath the flatten droplets above the hot wall in the Leidenfrost regime :

$$Q_{DC} = \dot{m}_d (T_w - T_{sat}) \left[\frac{18 \lambda_V{}^3 \Delta t_C{}^3 \rho_V \Delta h_V u_d}{D_d{}^5 \rho_L{}^3 \mu_v (T_w - T_{sat})} \right]^{0.25} \quad (2)$$

Correlations of post-dry out heat transfer have been compared with experimental data of Evans [3] and Gotulla [4]. The agreement seemed to be good. In a recent review, Mishima [5] concluded that : "*However, direct droplet-wall contact and vapor-wall radiation have significant contributions to*

the wall superheat and to the vapor superheat. Ignoring any of these two heat transfer processes will result in unacceptable errors".

A simple calculation using (1) or (2) shows that, considering only one droplet impinging on a hot wall, the value of Q_{DC} is very small (about one hundred mW) and thus is difficult to measure. In what follows, we describe the experimental method, which has been developed to measure such low cooling fluxes.

EXPERIMENTAL SET-UP

The experimental set-up has been designed in order to be able to make a full energy balance of the droplet-wall interaction, Figure 2. A thin nickel Slab (1) is heated thanks to an electromagnetic device (not represented here). When the temperature of the wall has reached a value much over the Leidenfrost temperature, the heating is stopped and the slab is cooled down by a controlled monodisperse droplet stream. At the same time, the temperature field on the rear face of the nickel disk is measured using an infrared camera (2). The monodisperse droplet stream is generated with a home-made device (3) ; the available droplets have a diameter ranging between 80 and 200μm and their velocities are close to 2-5 m.s^{-1}. Velocities, temperatures and diameters will be measured thanks to the lacer-induced fluorescence technique [6] and interferometry set-up. Since the interaction between the droplet and the wall is very short (a few of ms [7]), the estimation of the resident time of the droplet at the wall can be accurately measured from picture recorded thanks to a high speed camera (4). An example of droplet stream impinging onto the hot slab is given in Fig. 3.

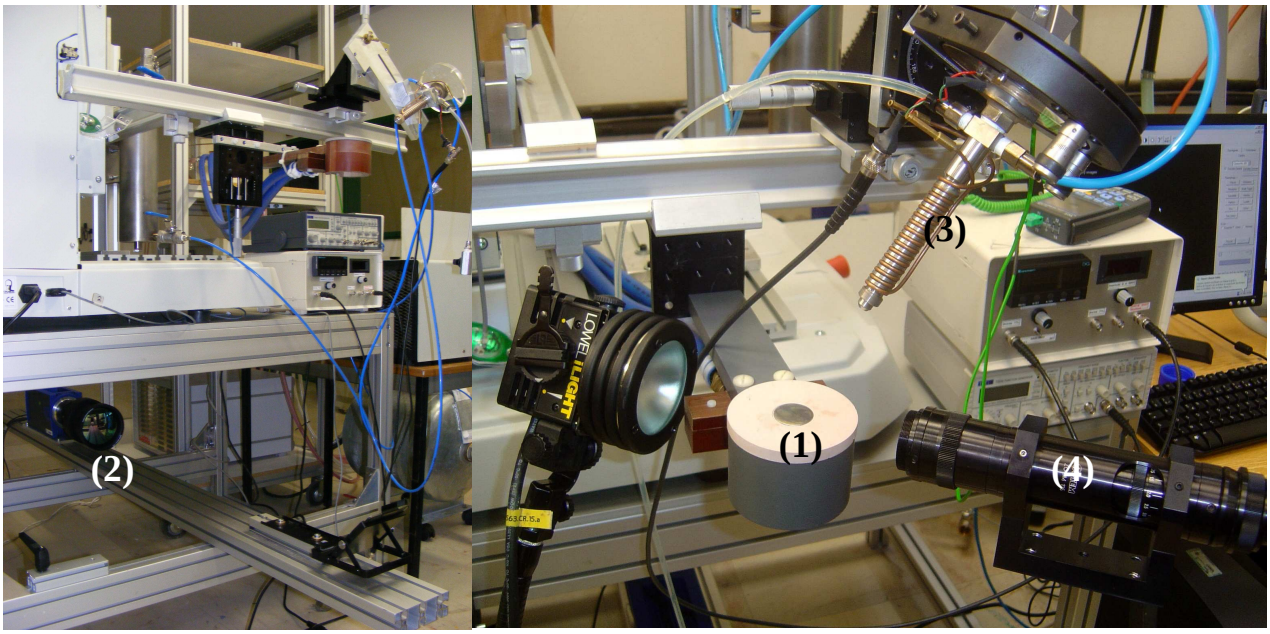

Figure 2 : experimental device

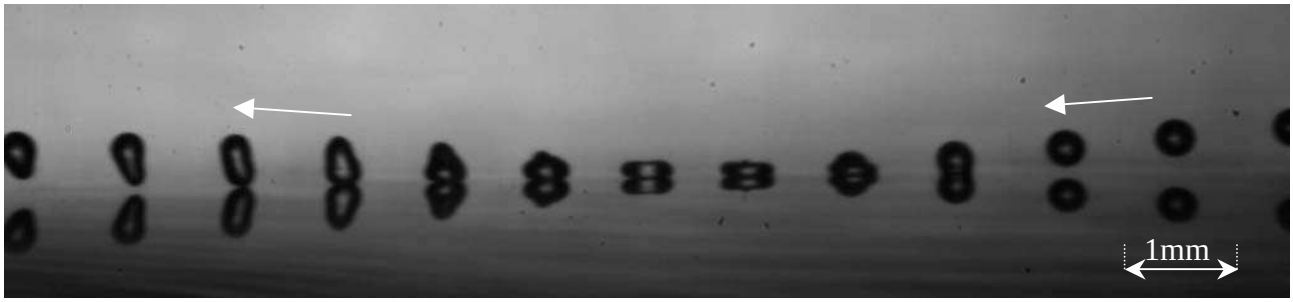

Figure 3 : example of 300 µm droplet stream impinging onto the slab (T_w > 300°C)

As mentioned before, the heat flux is estimated using an inverse heat conduction problem through the rear face temperature profile, measured thanks to the infrared camera. In the following parts, this estimation and this inverse model will be exposed.

HEAT FLUX ESTIMATION – INVERSE MODEL

Solution of the direct heat transfer problem

One consider the internal transient conduction within a finite circular disk whose radius is *R*=25mm and thickness *e*=500µm. Assuming constant thermophysical properties, the basic set of equations are thus the followings, assuming constant thermophysical properties :

$$\frac{\partial^2 T}{\partial r^2}+\frac{1}{r}\frac{\partial T}{\partial r}+\frac{\partial^2 T}{\partial z^2}=\frac{1}{a}\frac{\partial T}{\partial t} \tag{3}$$

$$T=T_\infty \text{ at } t=0\ ;\ \lambda_{NI}\left.\frac{\partial T}{\partial z}\right|_{z=0}=h_{SUP}^{EQ}(T-T_\infty)+q_{DC}(r,t) \tag{3a}$$

$$-\lambda_{NI}\left.\frac{\partial T}{\partial z}\right|_{z=e}=h_{INF}^{EQ}(T-T_\infty)\ ;\ -\lambda_{NI}\left.\frac{\partial T}{\partial r}\right|_{r=R}=0 \tag{3b}$$

Laplace (⁻) and Hankel (~) transforms are performed so that equation (1a) can be solved :

$$\frac{\partial \tilde{\bar{\theta}}_n^2}{\partial z}-(\alpha_n^2+\frac{p}{a})\,\tilde{\bar{\theta}}_n=0 \quad \text{with } \theta=T-T_\infty \tag{4}$$

with *p*, the Laplace parameter, $\alpha_n=\frac{u_n}{R}$ and u_n solutions of $J_1(u_n)=0$

Finally, the quadrupole method [8] yields a linear relationship between the rear face temperature (*z* = *e*) and the cooling heat flux (z = 0) :

$$\tilde{\bar{\theta}}_n=\tilde{Z}_n(p+a\alpha_n^2)\,\tilde{\bar{q}}_n \tag{5}$$

where: $\bar{Z}(p)=\dfrac{1}{((h_{SUP}^{EQ}+h_{INF}^{EQ})\cosh(e\sqrt{p/a})+\dfrac{h_{SUP}^{EQ}h_{INF}^{EQ}}{\lambda_{NI}\sqrt{p/a}}\sinh(e\sqrt{p/a})+\lambda_{NI}(\sqrt{p/a})\sinh(e\sqrt{p/a}))}$

Laplace inversion of equation (2) makes a convolution product appears:

$$\tilde{\theta}_n(t)=\int_0^t e^{-a\alpha_n^2(t-t')}\tilde{Z}_n(t-t')\,\tilde{q}_n(t')\,dt' \tag{6}$$

Finally, the real temperature in time-space domain is obtained through the following relation :

$$\theta(r,e,t)=\frac{2}{R^2}\sum_{n=0}^{\infty}\tilde{\theta}_n(e,t)\frac{J_0(\alpha_n r)}{J_0^2(\alpha_n R)} \tag{7}$$

Inverse heat transfer problem

Inverse Heat conduction Problem (IHCP) is a specific estimation technique that consists in using discrete temperature measurements inside a solid or at one of its external wall in order to recover a time and/or space boundary condition (in our case the distribution of cooling flux at the droplet impact). This estimation problem is not well-posed, which means that low magnitude perturbation in the temperature measurement (noisy temperature) can generate large deviations on the estimated wall heat flux. This is due to the discrete features of measurements while the information that is looked for is a continuous function of time and/or space. Different regularization techniques such as the least square method (used in this paper) have been designed to overcome this effect and to efficiently stabilize the inversion algorithm. In our case, it can be easily solved because the solution of the direct heat transfer problem is known (see equations 5 and 6).

Equation (6) which is expressed in Hankel domain (~) is the starting point of the inverse heat conduction problem ; the integral form in that equation (6) can be expressed using a truncature :

$$\tilde{\theta}_n(t_k) = \sum_{j=1}^{k} e^{-a\alpha_n^2 (k-j)\Delta t}\ \tilde{Z}_n((k-j)\Delta t)\,\tilde{q}_n(t_j)\,\Delta t = \sum_{l=1}^{k} S_{kj}\ \tilde{q}_n(t_j) \tag{8}$$

where Δt is the time step of the infrared camera or a multiple and $t_k = k\,\Delta t$, $t_l = l\,\Delta t$.

The harmonics of heat flux (noted '^') can be thus estimated using a least square method. In our case, a Gauss-Markov estimator was used to estimate the temperature in the hankel domain to take into account a non uniform noise variance (ie the input temperature field is obtained from a conversion and averaging of the initial field from Cartesian to cylindrical frame) :

$$\tilde{\theta}_n = (X_n^t\,\Omega X_n)^{-1}\,\Omega X_n^t\,\theta \ \text{ with } \ \Omega = \begin{bmatrix} \sigma_1^2 & 0 & 0 & 0 \\ 0 & . & 0 & 0 \\ 0 & 0 & . & 0 \\ 0 & 0 & 0 & \sigma_{k\max}^2 \end{bmatrix} \tag{9}$$

$$\text{with } \ X_{ln} = \frac{2}{R^2}\frac{J_0(\alpha_n\, r_l)}{J_0^2(\alpha_n R)}$$

$$\tilde{\theta}_n = \begin{bmatrix} \tilde{\theta}_n(t_1) \\ . \\ . \\ \tilde{\theta}_n(t_{k_{\max}}) \end{bmatrix} = \mathrm{S}_k^n\,\tilde{\mathrm{q}}_n = \begin{bmatrix} S_{11}^n & 0 & 0 & 0 \\ . & . & 0 & 0 \\ . & . & . & 0 \\ S_{k_{\max}1}^n & . & . & S_{k_{\max}\,k_{\max}}^n \end{bmatrix} \begin{bmatrix} \tilde{q}_n(t_1) \\ . \\ . \\ \tilde{q}_n(t_{k\max}) \end{bmatrix} \tag{10}$$

$$\hat{\tilde{q}}_n = (S_n^t\,S_n)^{-1}\,S_n^t\,\hat{\tilde{\theta}}_n \tag{11}$$

The return to time-space domain yields:

$$q_{DC}(r,t_k) = \frac{2}{R^2}\sum_{n=0}^{n_{\max}} \frac{J_0(\alpha_n\, r)}{J_0^2(\alpha_n\, R)}\,\hat{\tilde{q}}_n(t_k) \tag{12}$$

Heat flux estimation from real temperature data

The temperature *T(x,y,t)* obtained from the infrared camera is available in a Cartesian reference frame while the input data *T(r,t)* of the model must be known in a cylindrical reference frame. Thus, it requires the conversion and the averaging of the initial Cartesian temperature field in order to obtain the input data. As a consequence, we can not access to the real heat flux $q_{DC}(x,y,t)$ but only to an averaged heat flux $q_{DC}(r,t)$. So, *the first step* of the inversion procedure is to obtain the input temperature by averaging the initial field. In *a second step*, the Hankel transform (~) of the temperature $\tilde{\theta}_n$ will be estimated using a Gauss-Markov estimator (equation 9) because the temperature distribution *T(r,t)* shall be subject to a non uniform noise variance. Then, the harmonics of heat flux (in the Hankel domain) can be estimated using the equation (12). As the cooling flux is very weak, we must consider all the heat loss by conduction, convection and radiation.

PRELIMINARY RESULTS

The previous inverse model has been tested with some data obtained from simulations of the direct problem. Indeed, these tests are necessary to calibrate the robustness of our model. Dewitte [9] gave a relation which help us to estimate the efficiency of the droplet evaporation (about 2.5% for a 100 µm droplet diameter of water impinging a hot slab with u=2m/s, T_d=20°C and We=7). This low value is due to the fact that the interaction time Δt_C is very short, typically about 1ms for a 100µm droplet diameter and that the incoming droplet evolves in an environment being saturated in vapour by the preceding droplets. All the input data are given in the table 1. Q_{DC} is estimated using (1) and we assumed that the droplet does not slip on the surface and impinges at $r = 0$ so that the heat flux $q_{DC}(r,t)$ of each incoming droplet is expressed as :

$$q_{DC}(r,t) = \frac{Q_{DC}}{S\Delta t_C}\left[H(r) - H(r - \frac{D_d}{2})\right]\left[H(t) - H(t - \Delta t_C)\right] \tag{13}$$

where H is the Heaviside function.

Table 1
Input data for the direct simulations

Q_{DC} (mJ)	$S.10^8$ (m²)	Δt_C (ms)	h_{LV} (kJ/kg)	ε
0.0295	7.85	0.198	2258	0.025

T_d (°C)	h_{SUP}^{EQ} (W/m².K)	h_{INF}^{EQ} (W/m².K)	λ (W/m.K)	a (m²/s)
20	68	55	90.9	$2.3\ 10^{-5}$

A white noise (variance about 0.8°C) is added to the calculated temperature field in order to test a near experimental condition. Indeed, as we used an infrared camera, the signal on each sensor pixel will be noised. The inversion has been made with a number of harmonic n_{max}=20 and is compared to the input heat flux on the figure 4. This shows that the inversion is still possible even if the measured temperature field is noised. All the losses are estimated from the temperature field which relaxes naturally. In figure 5, we show the initial temperature field in the Cartesian frame and compare the average temperature distribution *T(r,t)* with the reconstructed field using n_{max} Hankel harmonics. In this example, we considered n_{max}=60.

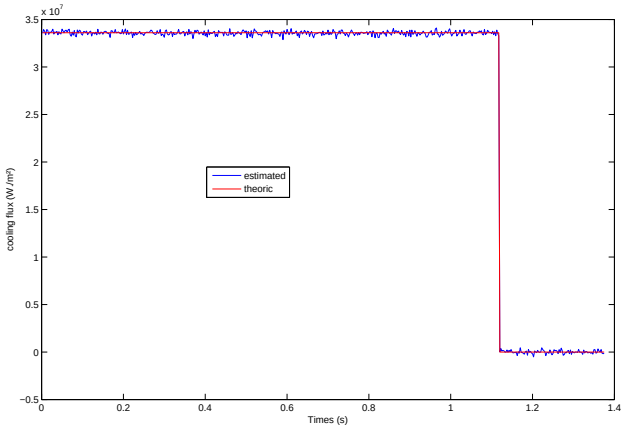

Figure 4: comparison between theory and estimation

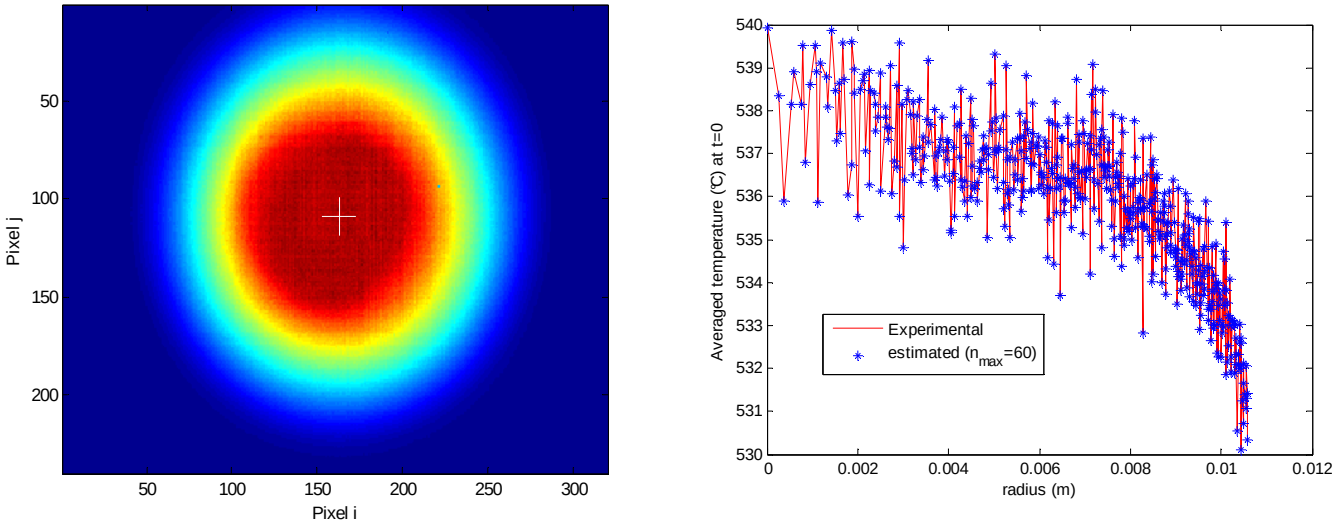

(a) (b)

Figure 5: initial temperature field measured by infrared camera (a) and average temperature distribution (b)

CONCLUSIONS

In this preliminary work, we described the experimental method to measure cooling flux due to single droplet impacting onto a hot slab. As these fluxes are very low, the model must take into account all the unavoidable losses when we experienced droplet impacts. For the moment, it is not possible to obtain a better estimation than the average cooling flux removed by the impact of drops. For better resolution, a new inverse model could be developed in the initial Cartesian frame but the experimental data of the average of this flux is sufficient to check and/or derive correlations used in simulations of LOCA transients.

NOMENCLATURE

a	=	thermal diffusivity, $m^2.s^{-1}$
D_d	=	droplet diameter, m
h_{LV}	=	enthalpy of phase change, J/kg
h_{SUP}^{EQ} , h_{INF}^{EQ}	=	equivalent heat exchange coefficient, $W.m^{-2}.K^{-1}$
J_0	=	Bessel function

q_{DC}	=	heat flux density, $W.m^{-2}$
Q_{DC}	=	heat flux, W
R	=	radius, m
T_w, T_{sat}, $T_{lei.}$, T_d	=	wall, saturation, Leidenfrost and droplet temperatures, $°C$
u	=	velocity, $m.s^{-1}$
V_d	=	droplet volume, m^3
We	=	Weber number, dimensionless

Greek symbols :

θ	=	shift temperature, °C
σ_i	=	variance of the measured temperature, °C
α_n	=	Eigenvalue
Δt_c	=	Resident time, s
Δh_{LV}	=	modified latent heat of evaporation, $(h_{LV} + C_p(T_v\text{-}T_{SAT}))$, $J.kg^{-1}$
ρ	=	density, $kg.m^{-3}$
μ	=	dynamic viscosity, $Kg.m^{-1}.s^{-1}$
λ	=	thermal conductivity, $W.m^{-1}.K^{-1}$
σ	=	surface tension, $N.m^{-1}$

subscripts

L	=	Liquid
n	=	harmonic number
V	=	vapour

REFERENCES

1. M. Andreani, G. Yadigaroglu, 1997, A 3-D Eulerian-Lagrangian model of dispersed flow film boiling including a mechanistic description of the droplet spectrum evolution—I. The thermal-hydraulic model, *International Journal of Heat and Mass Transfer*, Volume 40, Issue 8, pp. 1753-1772
2. Guo Y., Mishima K., "A non equilibrium mechanistic heat transfer model for post dryout dispersed flow regime", Experimental Thermal and Fluid science, Vol 26, pp 861-869, 2002.
3. D. G. Evans, S. W. Webb, et al, June 1983, Measurements of Axially Varying Non-Equilibrium in Post-Critical-Heat-Flux Boiling in a Vertical Tube, *NUREG/CR-3363*, Vols. 1 and 2.
4. R. C. Gottula, R. A. Nelson, et al, 1983, Forced Convective Non-Equilibrium Post-CHF Heat Transfer Experiments in a Vertical Tube, *ASME-JSME Thermal Engineering Conference*, Honolulu.
5. Kaichiro Mishima, Review on Post-CHF Heat Transfer and Rewetting Phenomena, *5th International Conference on Multiphase Flow, ICMF'04*, Yokohama, Japan, May 30–June 4, 2004Paper No. K14- 1
6. G. Castanet, T. Liénart, F. Lemoine, 2009, Dynamics and temperature of droplets impacting onto a heated wall, *International Journal of Heat and Mass Transfer*, Volume 52, Issues 3-4, Pages 670-679
7. Chen R.H., Chiu S.L. & Lin T.H., 2007, Resident time of a compound drop impinging on a hot surface, *Applied Thermal Engineering*, 27, 2079-2085
8. D. Maillet,S.André, J.Barsale, A. Degiovanni, C. Moyne, 2000, Thermal Quadrupoles – Solving the heat equation through integral transforms, *Wiley, Chichester, UK.*
9. Dewitte J., 2006, Modélisation de l'impact d'un brouillard de gouttes en évaporation et sous pression sur une paroi chauffée, *Thèse de Doctorat ENSAE Toulouse.*

EXPERIMENTAL STUDIES ON THERMAL CONDUCTIVITY OF POLYMER SOLUTIONS AS A FUNCTION ON SHEARING RATE AND THEIR RHEOLOGICAL PROPERTIES

L. Broniarz-Press*, K. Pralat[2]

[1]Poznan University of Technology, Department of Chemical Engineering and Equipment, Poznan, Poland
[2]Higher Vocational State School of President Stanislaw Wojciechowski, Polytechnic Institute, Kalisz, Poland

ABSTRACT. In the present paper the results of the experimental studies directed to the correlation between the non-Newtonian fluids rheological behaviour and thermal conductivity taking into account shear rate effect, have been presented. In the experimental tests 3 Newtonian liquids (water, drive oil, aqueous solution of glycerol) as well as 18 aqueous solutions of polymers (non-elastic shear thinning fluids), have been used. It was confirmed that the thermal conductivity k of Newtonian liquids at $T = \text{const}$ is independent of shear rate. For the non-Newtonian aqueous solutions studied the effect of shear rate is evident and should be taken into account in all design practices. The thermal conductivity increases linearly with shear rate increase.

Keywords: *thermal conductivity, power-law fluids, shear effect, temperature effect*

INTRODUCTION

Many important industrial fluids, which are non-Newtonian or rheologically complex in their flow characteristics are often used in the chemical processes and food industries, as well as in many other practical applications. For the unavailability of another literature data in previous works on non-Newtonian fluid heat transfer the thermal conductivity was accepted to be identical with that one in the clear solvent. It was essentially a rough approximation that existed long. Additionally, it must be emphasized that until now the kinetic-molecular theory for liquids does not exist, and the relationships proposed for thermal conductivity in Newtonian liquids are empirical and very different in their form.

Of the significance is the fact that in non-Newtonian fluids the most experimental studies on thermal conductivities were performed under static conditions [1, 2]. Bellet, Sengelin and Thirriot [1] have determined the volume specific heat at constant pressure and thermal conductivity using an analytical identification method (Figure 1). Authors showed that the volume specific heat is independent of shear rate. In both, carboxymethylcellulose sodium salt solution (Na-CMC RC 197) and Carbopol 960 aqueous solutions in the range of temperature $293 \le T \le 333$ K thermal conductivity increased with increasing of temperature and decreased with an increase of polymer concentration in a solution. Lee, Cho and Hartnett [2] have tested the aqueous solutions of polyethylene oxide, polyacrylamide, carboxymethylcellulose sodium salt, Carbopol 960 and Attagel 40 (specialty attapulgite product, fine-milled grade, thickener of waterborne systems) in the range

*Corresponding author: Prof. Lubomira Broniarz-Press:
Phone: +48 61 6652789; mobile: + 48 604 918734, Fax : + 48 61 8103003
E-mail adresses : mirka@box43.pl, Lubomira.Broniarz-Press@put.poznan.pl

of concentrations changed from 100 to 10,000 w.ppm under static conditions. As a result they stated an increase of thermal conductivity when the concentration of the polymer in a solution increased, thus indicating the contrary effect in reference to the study presented above [1].

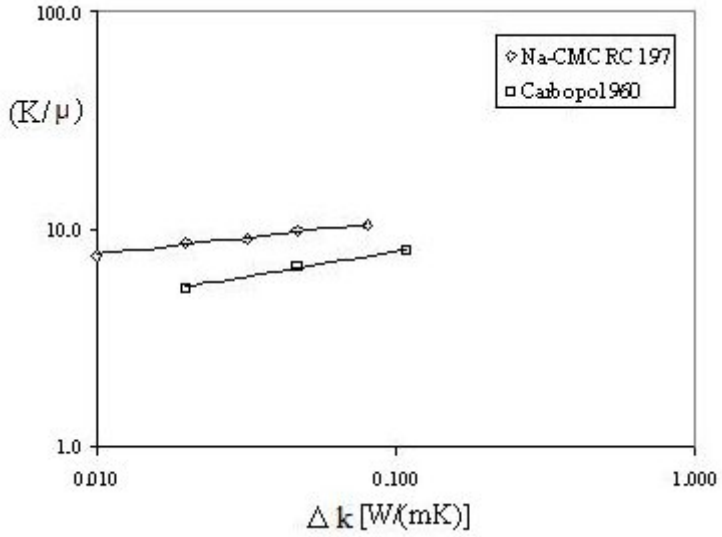

Figure 1. Change of thermal conductivity in non-Newtonian polymer aqueous solutions [1]

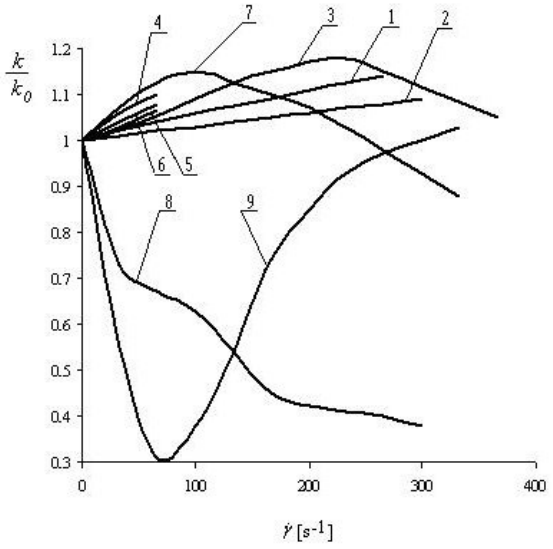

Figure 2. Comparison of the shear rate dependent thermal conductivity of non-Newtonian fluids resulted from literature [10]:
1 – Cocci and Picot [3], Dow 200, T = 288,7K; 2 – Cocci and Picot [3], Dow 200, T = 327K; 3 – Chitrangad and Picot [4], Dow 200, T = 298K; 4 – Chaliche *et al*. [8], Na-CMC, 8%, T = 298K; 5 – Loulou *et al*. [7], Carbopol, 0.1%, T = 298K; 6 – Loulou *et al*. [7], Carbopol, 0.2%, T = 298K; 7 – Picot *et al*. [5], polyethylene melt, T = 423K; 8 – Wallace *et al*. [6], low molecular weight polyethylene melt, T = 433K; 9 – Wallace *et al*. [6], high molecular weight polyethylene melt, T = 433K

The measurements of non-Newtonian fluid thermal conductivity should be made when the fluid is in a motion. Only few previous works studying the effect of shear rate on thermal conductivity in non-Newtonian polymer solutions have been found, whereas their results are contradictory [3-13] The exemplary graphs of the shear rate dependent thermal conductivity of non-Newtonian fluids resulted from these studies are presented in Figure 2.

Shin [14] has presented theoretical study where the empirical linear model for shear rate dependent thermal conductivity was adopted (Figure 3). The model can be formulated as follows:

$$k = k_0 + \left(\dot{\gamma} - \dot{\gamma}_0 \right) tg\alpha \tag{1}$$

where k_0 represents the stationary thermal conductivity of fluid, and $\dot{\gamma}_0$ indicates the bound of the linear region below of which the thermal conductivity seems to be invariable and independent of shear rate.

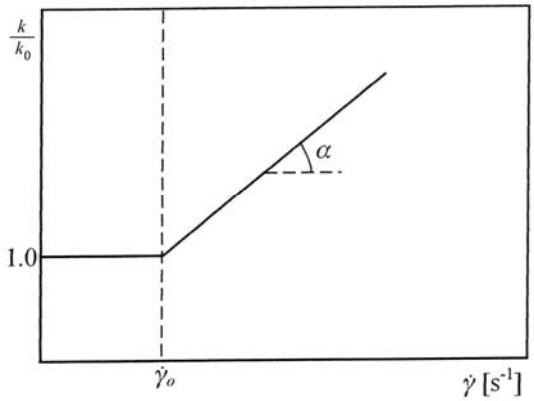

Figure 3. Theoretical model of thermal conductivity for non-Newtonian fluids [9]

The present study is concerned with determination of viscous properties of chosen non-Newtonian liquids with a view to correlate the viscous and thermal properties of these fluids. In the fluids studied the thermal conductivity was measured both, in static and dynamic conditions, over a shear rate range where the viscous properties significantly vary with shear rate.

EXPERIMENTAL SET-UP

To measure the heat conductivity the new experimental installation was designed (Figure 4) which permitted to determine thermal conductivity for power-law fluids basing on the rheometric technique and very accurate temperature measurement on outer cylinder. The main parts of the system were two coaxial cylinders while the inner cylinder is mounted as stationary and the outer cylinder is rotating. Cylinders made of steel chosen as the one permitted to use in food technology are of the following dimensions: outer cylinder with inner diameter 72 mm and inner cylinder with outer diameter 69 mm. The test fluid was located in the annular gap of 1.5 mm between two cylinders. The inner cylinder included the resistance sensors and the heater, which was designed and realized especially for experiment. The heater consisted of three sections: main and two guards (Figure 5). Three calibrated sensors were used to measure the surface temperature of the inner cylinder. The resistance sensors were positioned in the middle of the test section, and uniformly distributed at 120° interval. Analogically, three sensors were mounted in the surface of the outer cylinder. The novel element of experimental setup to measure the temperature of the outer cylinder consists of two parts as integrated circuits: transmitter and receiver. Transmitter was mounted on the outer cylinder. Receiver was connected with measurer which indicated temperature on the rotating cylinder. This innovatory element of temperature measurement of the outer cylinder based on wireless communication. Transmitter, changed sensors resistance signal into light signal, which was transmitted from diode. The receive diode, changed light signal into voltage signal, which was registered on measurer.

a) b)

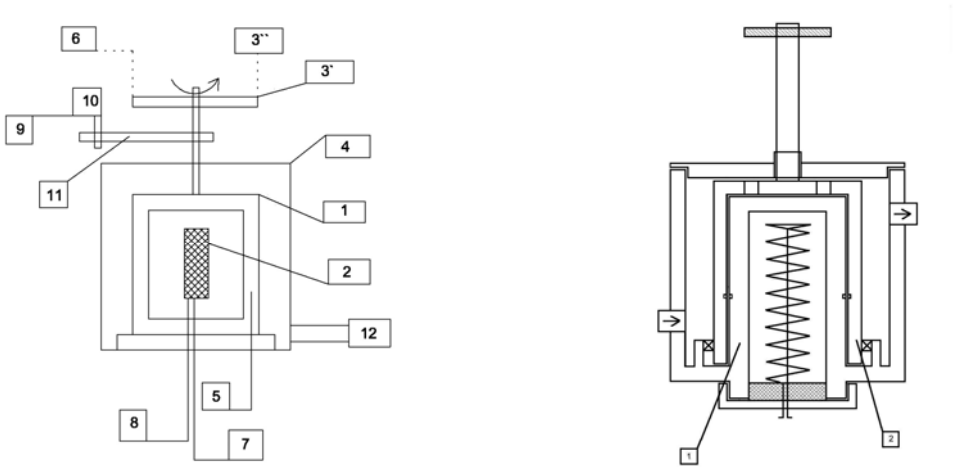

Figure 4. Scheme of the experimental set-up (a) and coaxial cylinders used (b):
1 – coaxial cylinders, 2 – heater, 3 – integrated circuit to measure temperature of outer cylinder, 4 – water jacket, 5 – meter to measure temperature of inner cylinder , 6 – tachometer, 7 – power supply, 8 – ammeter/voltmeter, 9 – motor speed controller, 10 – motor, 11 – rotating mechanism, 12 – water bath

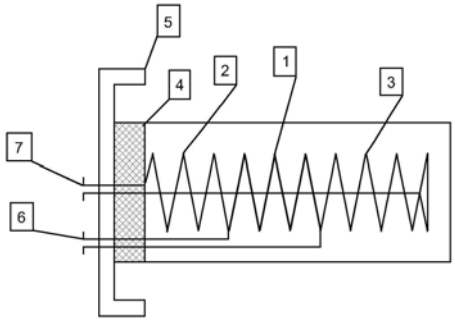

Figure 5. The novel heater mounted in the inner cylinder:
1 – main heater, 2,3 – two guards heaters, 4 – isolation, 5 – cover, 6,7 – wires

The two guard-heaters are controlled in such a way to maintain uniform axial temperature in the central, main-heater region. The latter heat flux is virtually in the radial direction only. The guard heaters will prevent end effects and heat losses.

Provided that Fourier`s law of conduction is applicable, the apparatus is operated at steady state, the shear rate variation across the gap is negligible, and the thermal conductivity of the liquid in the gap is considered to be independent of temperature, the following equation is used to calculate the thermal conductivity:

$$k = \frac{Q \ \ln\left(\frac{d_o}{d_i}\right)}{2\,\pi\, L\, \Delta T} \tag{2}$$

where Q was calculated from the measurements of current and voltage through the main heater:

$$Q = I \ V \tag{3}$$

EXPERIMENTAL RESULTS

The liquids tested were water, glycerol (50%) and petrol as Newtonian fluids, and aqueous solutions of: carboxymethylcellulose sodium salt (delivered by Aldrich Company, of the molecular masses 250,000 and 700,000 and of the polyelectrolyte concentrations in solutions ranged from 1,000 to 5,000 w.ppm) and high-molecular polyacrylamide $M \approx (2 \div 4) \cdot 10^6$ (kg kmol^{-1}) (Rokrysol WF1, delivered by Rokita S.A.), partially hydrolyzed polyacrylamide $M \approx (2 \div 4) \cdot 10^6$ (kg kmol^{-1}) (Rokrysol WF2, delivered by Rokita S.A.) as well as their mixtures as non-Newtonian fluids. All polymer solutions used were non-elastic power-law fluids:

$$\tau = K \dot{\gamma}^{n} \tag{4}$$

Experiments were performed at temperatures changed in the range from 299 K to 315 K. The shear rate range studied was $0 \le \dot{\gamma} \le 750\,(\mathrm{s}^{-1})$.

It was confirmed that thermal conductivity of Newtonian liquids at constant temperature is independent of shear rate. On the ground of experimental studies the relationships $k = f(T)$ for analyzed model Newtonian fluids were found (Table 1).

Table 1
Newtonian liquids used

Name	ρ (kg m^{-3})	$\mu \times 10^3$ (Pa·s)	Authors' experimental data correlations
diesel oil	844.0 ÷ 849.2	2.76 ÷ 3.53	$k = 33.5 \cdot T^{-0.803}$
water	991.5 ÷ 996.8	0.630 ÷ 0.900	$k = 1.11 \cdot 10^{-5} T^{1.91}$
aqueous solution of glycerol (50 %)	1116 ÷ 1125	2.06 ÷ 5.30	$k = 1.57 \cdot 10^{-7} T^{2.6}$

For all non-Newtonian solutions used thermal conductivity values obtained in static conditions increase with the temperature increase. The maximal values were obtained for aqueous solutions of carboxymethylcellulose sodium salt of the averaged molar mass M = 700,000 (kg kmol^{-1}).

In Figures 6 and 7 the experimental relationships of thermal conductivity vs. shear rate for the inelastic non-Newtonian solutions studied are presented. The evident increase of the thermal conductivity compared to water in all polymer solutions used has been observed. The thermal conductivity at a higher temperature at a certain shear rate is greater than at a lower temperature. The temperature effect is significant, and the increase in thermal conductivity at higher temperatures with respect to shear rate is larger than at lower temperatures. The general trends of the curves are similar in all graphs. The solution of the lowest concentration (1,000 w.ppm) has a greater change in thermal conductivity with shear rate in comparison with the solution of the highest concentration (5,000 w.ppm). The generalized relationship has the form:

$$k = a_o + a_1 \cdot \dot{\gamma} + a_2 \cdot T + a_3 \cdot \dot{\gamma} \cdot T \tag{5}$$

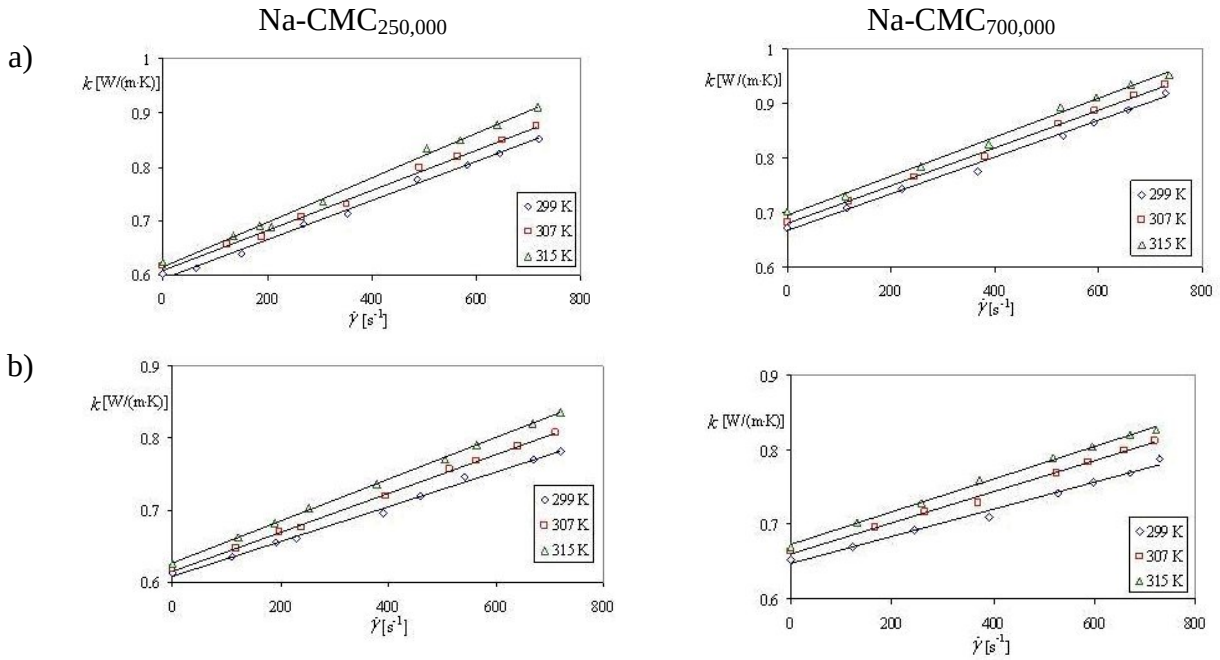

Figure 6. Heat conductivity coefficient k vs. shear rate $\dot{\gamma}$ for polymer Na-CMC solutions of concentrations of:
a) u_p = 0.001 (kg p kg^{-1}), b) u_p = 0.005 (kg p kg^{-1})

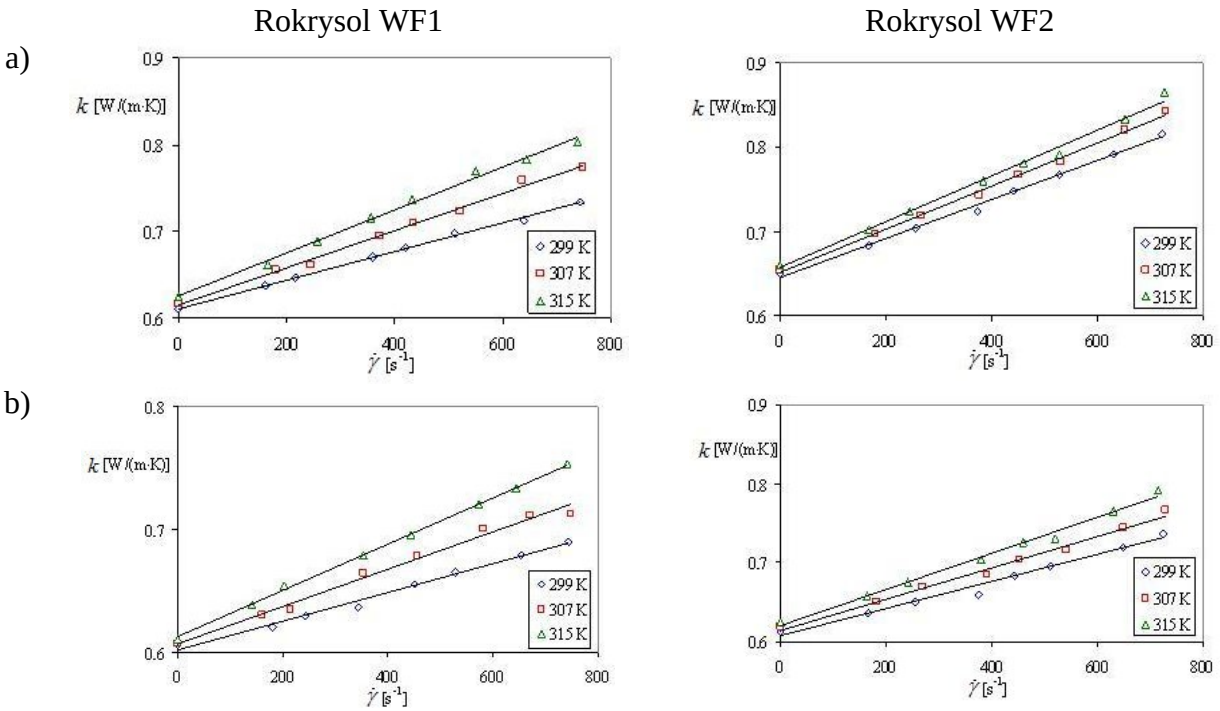

Figure 7. Thermal conductivity coefficient k vs. shear rate $\dot{\gamma}$ for polyacrylamide solutions of concentrations of:
a) u_p = 0.001 (kg p kg^{-1}), b) u_p = 0.005 (kg p kg^{-1})

The increase of the polymer concentration in a solution caused the decrease of the thermal conductivity k. The increase of the molar mass or hydrolyzation degree of a polymer caused the

increase in the values of k. The maximal values of $k = 0.992$ (W m^{-1} K^{-1}) were obtained for the solution of mixture III (Na-CMC$_{700,000}$: $u_p = 0.001$ (kg p kg^{-1}) and Rokrysol WF1: $u_p = 0.005$ (kg p kg^{-1})) at temperature of 315 K and shear rate of $\dot{\gamma} = 750$ (s^{-1}). Additionally the existing of the critical values of shear rate $\dot{\gamma}_o$ below of whose the thermal conductivity for non-Newtonian fluids was independent of shear velocity and equal to the static one, has been observed. The increase of the shear rate at the values greater than $\dot{\gamma}_0$ caused the effect of the shear rate on thermal conductivity, related to the Shin [9] suggestion. The critical values of shear velocity increase with the polymer concentration in a solution.

a)

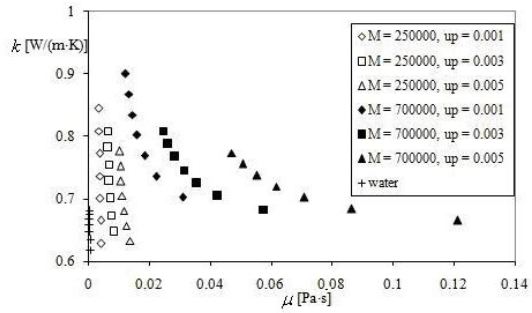

b)

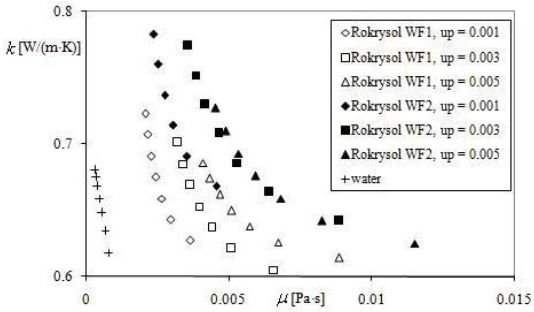

Figure 8. Comparison of the non-Newtonian viscosity effect on heat conductivity coefficient values at temperature 299 K:
a) aqueous solutions of carboxymethylcellulose sodium salt, b) aqueous solutions of high-molecular polyacrylamide

Next, basing on thermal conductivity and rheological measurements the effect of the non-Newtonian viscosity μ on thermal conductivity, has been determined. It has been shown that the relation of k vs. μ depends considerably on molecular mass of the polymer studied and temperature (Figure 8). It seems evident that thermal conductivity decreases when the Newtonian or non-Newtonian viscosity increases. It was affirmed that for all liquids used the relationship of thermal conductivity vs. viscosity can be well approximated by the third degree multinomial function of the form as follows:

$$k = C_0 - C_1 \cdot \mu + C_2 \cdot \mu^2 - C_3 \cdot \mu^3 \tag{6}$$

In the final step of the experimental data elaboration the special attempt was undertaken to express the relationship between the ratio of non-Newtonian viscosity to heat conductivity coefficient and rheological parameters of polymer solutions used. Basing on thermal conductivity vs. shear rate and viscosity vs. shear rate correlations, we proposed new formula for all non-Newtonian fluids:

$$\frac{\mu}{k} = 2.095 \cdot K^{0.95} \cdot \dot{\gamma}^{0.881 \cdot n - 1.021} \tag{7}$$

valid at $n \in (0.51, 0.98)$ and $K \in (0.003, 1.140)$ (Pa·s^n).

CONCLUSIONS

The effect of temperature, shear rate, molecular mass of polymer present in non-Newtonian solution and its concentration on thermal conductivity, has been observed. The increase of the molar mass or

hydrolyzation degree of a polymer caused the increase in the values of *k*. The increase in concentration of polymer in an aqueous solutions caused the decrease in values of thermal conductivity *k*. It has been stated that the values of thermal conductivity for aqueous solutions of polymers as well as their mixtures increase linearly with the increase of both, shear velocity $\dot{\gamma}$ and temperature. Additionally the existing of the critical values of shear velocity $\dot{\gamma}_o$ below of whose the values of thermal conductivity for non-Newtonian fluids were independent of shear velocity and equal to the static ones, has been observed. The increase of the shear velocity at the values greater than $\dot{\gamma}_o$ caused the effect of the shear velocity on thermal conductivity, related to the Shin's suggestion. For all liquid systems tested (Newtonian and non-elastic shear thinning) the decrease of the thermal conductivity with the increase of liquid viscosity was observed. The relationship between the ratio of non-Newtonian viscosity to thermal conductivity and rheological parameters of polymer solutions has been proposed.

REFERENCES

1. Bellet, D., Singelin, M. and Thirriot, C., Détermination des Propriétés Thermophysiques des Liquides non-Newtoniens à l'Aide d'une Cellule à Cylindres Coaxiaux, *Int. J. Heat Mass Transfer*, Vol. 18, pp 1177-1186, 1975.
2. Lee, W. Y., Cho, Y. I. and Hartnett, A., Thermal Conductivity Measurements of non-Newtonian fluids, *Letters Heat Mass Transfer*, Vol. 8, pp 255-259, 1981.
3. Cocci, A. A. and Picot, J. J. C., Rate of Strain Effect on the Thermal Conductivity of a Polymer Liquid, *Polym. Eng. Sci*., Vol. 13, pp 337-341, 1973.
4. Chitranged, B. and Picot, J. J. C., Similarity in Orientation Effects on Thermal Conductivity and Flow Birefringence for Polymers: Polydimethylsilioxane, *Polym. Eng. Sci*., Vol. 21, pp 782-786, 1981.
5. Picot, J. J. C., Goobie G. I. and Mawhinney, G. S., Shear-induced Anisotropy in Thermal Conductivity of a Polyethylene Melt, *Polym. Eng. Sci*., Vol. 22, pp 154-157, 1982.
6. Wallace, D. J., Moreland, C. and Picot, J. J. C., Shear Dependence on Thermal Conductivity in Polyethylene Melts, *Polym. Eng. Sci*., Vol. 25, pp 70-74, 1985.
7. Loulou, T., Peerhossaini, H. and Bardon, J. P., Etudé Experiméntale de la Conductivite Thermique de Fluids non-Newtoniens sous Cisaillement Application aux Solutions de Carbopol 940, *Int. J. Heat Mass Transfer*, Vol. 35, pp 2557-2562, 1992.
8. Chaliche, M., Delaunay, D. and Bardon, J. P., Transfert de Chaleur dans une Configuration Cone-Plateau et Mesure de la Conductivite Thermique en Presence d`une Vitesse de Cisaillement, *Int. J. Heat Mass Transfer*, Vol. 37, pp 2381-2389, 1994.
9. Shin, S., The Effect of the Shear Rate-Dependent Thermal Conductivity of non-Newtonian fluids on the Heat Transfer in a Pipe Flow, *Int. Comm. Heat Mass Transfer*, Vol. 23, pp 665-678, 1996.
10. Lee, D.-L. and Irvine T. F., Shear Rate Dependent Thermal Conductivity Measurements of non-Newtonian fluids, *Exp. Thermal Fluid Sci*., Vol. 15, pp 16-24, 1997.
11. Kostic, M. and Tong, H., Investigation of Thermal Conductivity of a Polymer Solution as Function of Shearing Rate, *HTD*, Vol. 364-4, pp 15-21, ASME, New York, 1999.
12. Shin, S. and Lee, S. H., Thermal Conductivity of Suspension in Shear Flow Fields, *Int. J. Heat Mass Transfer*, Vol. 43, pp 4275-4284, 2000.
13. Lin, S. X. Q., Chen, X. D., Chen, Z. D. and Bandopadhayay, P., Shear Rate Dependent Thermal Conductivity Measurement of Two Fruit Juice Concentrates, *J. Food Eng*., Vol. 57, pp 217-224, 2003.

A NOVEL EXPERIMENTAL SETUP FOR INVESTIGATION OF PERFECT MIXING AND PERFECT DISPLACEMENT SCAVENGING PROCESS IN A CAVITY

Adil Rasheed[1], Kausik Nandi, and A W Date[2,*]
[1]Ecole Polytechnique Federale de Lausanne, Switzerland
[2]Mechanical Engineering Dept., IIT Bombay, Mumbai-400076, India

ABSTRACT. In this paper, design of a novel experimental set-up for study of scavenging process in a rectangular cavity is described. The real scavenging process has two idealized extremes: (1) Scavenging by Perfect Mixing and (2) Scavenging by Perfect Displacement. In Two-Stroke Internal Combustion engines, the scavenging and the scavenged fluids are in gaseous state and, therefore, process visualization is not possible. In the present set-up, the scavenging fluid is water. The scavenged fluid is KMnO4 in the perfect mixing experiment whereas in the perfect displacement experiment, the scavenged fluid is Engine Oil. Transient measurements of scavenging process are made and illustrative results are presented.

Keywords: *Two Stroke IC Engine, Perfect Mixing Model, Perfect Displacement Model*

INTRODUCTION

Background

In Two-Stroke IC engines, the burnt charge in the engine-cylinder is driven out of the cylinder in two stages. At the end of the expansion stroke, as the piston approaches Bottom-Dead-Center (BDC) position, exhaust port opens and the low-density hot burnt gas is driven out by the higher pressure in the cylinder. As the piston moves further towards BDC, however, higher density fresh charge (fuel + air) is introduced through the inlet port while the exhaust port opens further. Ideally, the fresh charge should drive out the burnt charge in the cylinder completely as if the scavenged (burnt gas) and the scavenging (fresh charge) were immiscible. However, since both the fresh charge and the burnt gases are in gaseous state, fluid mixing takes place. As a result, during the scavenging transient, some of the fresh charge exits through the exhaust port as unburnt fuel while at the end of the scavenging process (when both the inlet and exhaust ports are closed due to upward movement of the piston towards Top-Dead-Center TDC) , some burnt gas remains in the engine-cylinder. The loss of fresh fuel through exhaust is associated with scavenging efficiency whereas the failure to remove all the burnt gas is associated with Trapping Efficiency. It is important to note that during the entire scavenging process (from exhaust port opening to closure of both the inlet and exhaust ports), the cylinder volume changes but, only by a very small amount. As such, the scavenging process may be idealized as a Constant-Volume process. The real process is extremely rapid and the cylinder interiors are inaccessible for direct measurements of concentration and temperature distributions. Also, flow visualization is not possible. As such, the scavenging process is idealized by two extremes: Perfect Mixing Model and Perfect Displacement Model [1]; the real process being a weighted combination of the two models. In more recent times, the entire engine-cycle is simulated by CFD [2]. Nonetheless, scavenging and trapping efficiencies can be estimated from exhaust-gas analysis.

Present Contribution

* Corresponding author: Prof. A . W. Date
Phone: + (91)-22-25767517, Fax: + (11)-12-3456789
E-mail address: awdatel@me.iitb.ac.in

In this paper, our aim is to mimic the two extremes of transient scavenging process in a Constant Volume cavity under iso-thermal conditions. Like in the real process, we use water as the scavenging fluid whose density is greater than or equal to the scavenged fluid. We employ KMnO4 (whose density is nearly equal to that of water) to mimic the perfect mixing model, water and KMnO4 being miscible in each other. In order to mimic the perfect displacement model, we employ Engine Oil (whose density is less than that of water). In both experiments, the processes are made visible and therefore filmed using a Handy Cam. Also, the amounts of fluids scavenged are measured as functions of time. Next section describes the experimental set-up and the procedure. The measured results are presented in the subsequent section. Finally, conclusions are reported in the end.

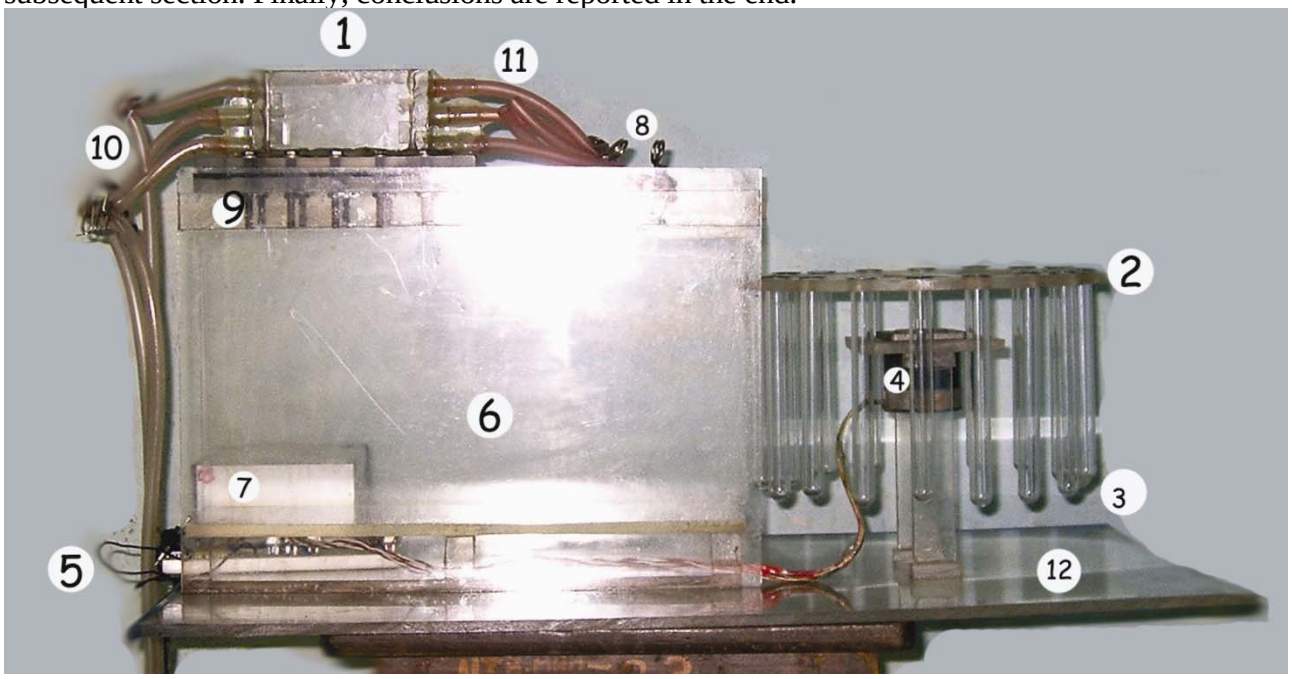

Figure 1: Experimental Setup

EXPERIMENTAL SET-UP AND PROCEDURE

The set-up (see Figure 1) consists of a 80 x 60 x 10 mm cavity (1) made from 8 mm thick Acrylic sheet. The cavity has 3 inlet and 3 outlet ports (10 and 11) of 5 x 10 mm (see Figure 2). The cavity is secured on a perspex mounting (6). Initially, the cavity is filled with a liquid to be scavenged with all ports closed. This liquid is driven out of the cavity by forcing water from a constant-head overhead tank (not shown) with a rubber tube connection to any one pre-selected inlet port. Both the inlet and the pre-selected outlet port are opened at the same instant. The discharge from the outlet port is intermittently collected in calibrated Test-Tubes (3) mounted on a horizontal 28 cm diameter rotating Wheel (2). The wheel is rotated by means of a Stepper Motor (4) at a pre-selected speed. The rotation of the motor (typically, 1.8 degree in one step) is controlled by Control Circuit PCB (5) (see Figure 3).

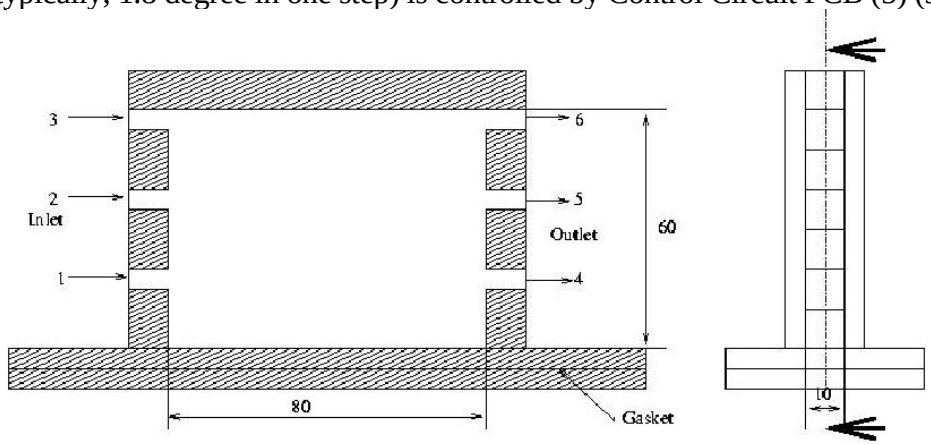

Figure 2: Schematic diagram of the test section

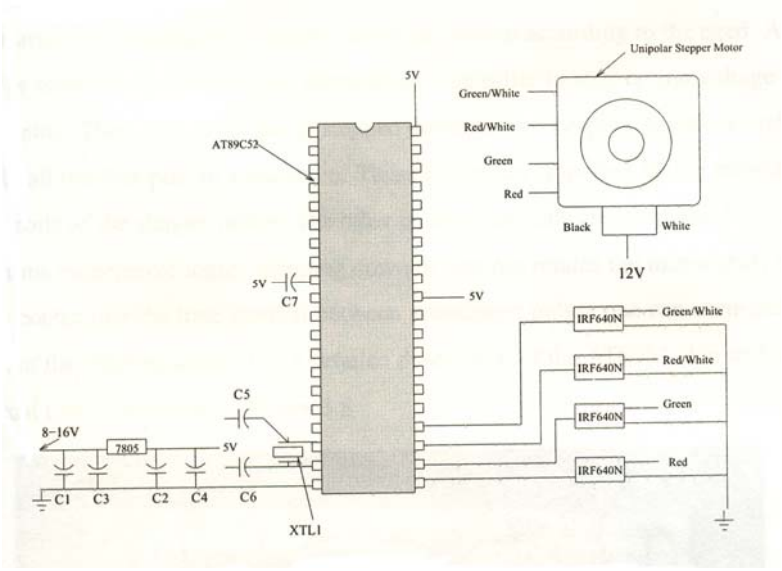

Figure 3: Schematic diagram of the electronic circuit

The supply voltage and current to the motor are regulated by Eliminator and Adaptor (7). In the Perfect Mixing experiment, the cavity is initially filled with 1 Normal KMnO4 solution. The scavenged liquid-mixture is collected in Test-Tubes at pre-set intermittency. The inlet port is kept open till the entire cavity is scavenged and is filled only with water and steady-state is established. In order to measure time-variation of the amount of liquid scavenged, at the end of the experiment, the collected mixture is titrated against Anhydrous Oxalic Acid in the presence of small amounts of Sulphuric Acid which acts as a catalyst. The mixture is also mildly heated before titration to speed-up the chemical reaction. In the Perfect Displacement experiment, the cavity is filled with a liquid (Engine Oil or Castor Oil) immiscible in water. In this experiment, a clear interface between water and the liquid is observed in the cavity. Depending on the water flow rate, the two-fluid cavity flow reaches either completely steady or periodically steady-state with some liquid entrapment in the cavity in both cases. In this case, the amount of scavenging is easily estimated because the two immiscible liquids naturally separate in the Test Tubes. Both experiments are repeated for different combinations of inlet-outlet port openings and different heads of water to change the scavenging water flow rates. The measured concentrations/volume fractions of the collected fluid are recorded as functions of time for a given flow rate of scavenging water. Concentration distributions and Interface evolutions are captured using a Handy Cam. Typical experimental results are presented in the next section.

PRESENTATION OF RESULTS

Perfect Mixing Experiment

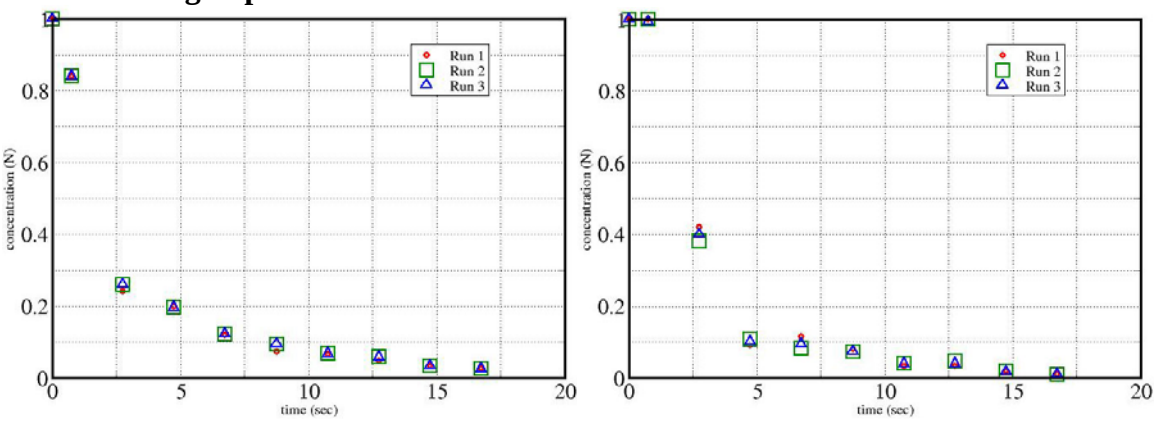

(a) (b)

Figure 4: Variation of $KMnO_4$ concentration with time for a) 1-4 configuration b) 3-4 configuration

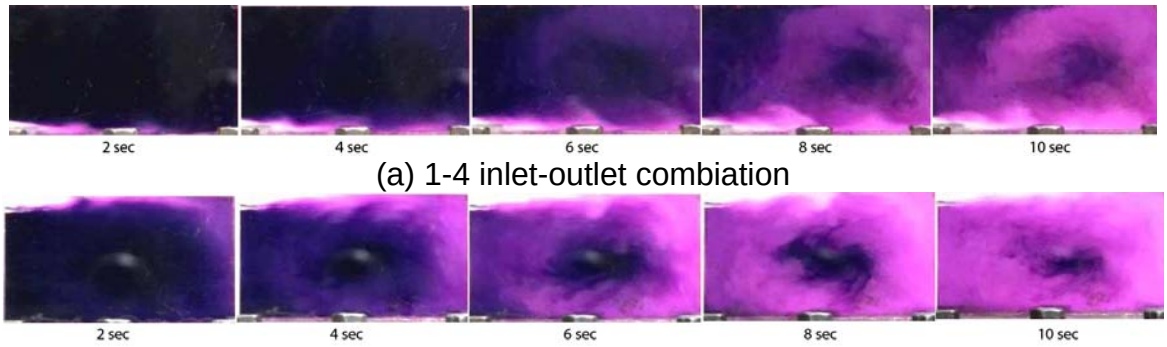

(a) 1-4 inlet-outlet combiation

(b) 3-4 inlet-outlet combination

Figure 5 Snapshots of the test section at 2 sec time interval (Perfect Mixing case)

Initially, the cavity is filled with KMnO4 solution. Three runs Run1, Run2 and Run 3 (to ensure repeatability) are conducted corresponding to a volumetric flow rate of 20.43ml/sec. A given pair of Inlet and Outlet ports is opened simultaneously. The time-variations of the concentrations (of KMnO4) of the collected fluid are plotted for two combinations of inlet-outlet ports viz 1-4 and 3-4 in Figure 4. As is seen, in both cases and for all flow rates of injected water, after initial near-perfect-displacement, the concentrations decline and ultimately are reduced to zero because KMnO4 in the cavity is diffused out completely and only water remains in the cavity. Thus, scavenging is 100 %. Figure 5 gives a snapshot of the test section as a function of time. Figure 6 presents the scavenging time for six different combinations at different flow rates Q1, Q2 and Q3 corresponding to 20.43, 26.3 and 31ml/sec. Quite expectedly the scavenging time decreases with increasing flow rate for any inlet-outlet combination. Also one can see that the inline combination is the best for achieving lowest scavenging time.

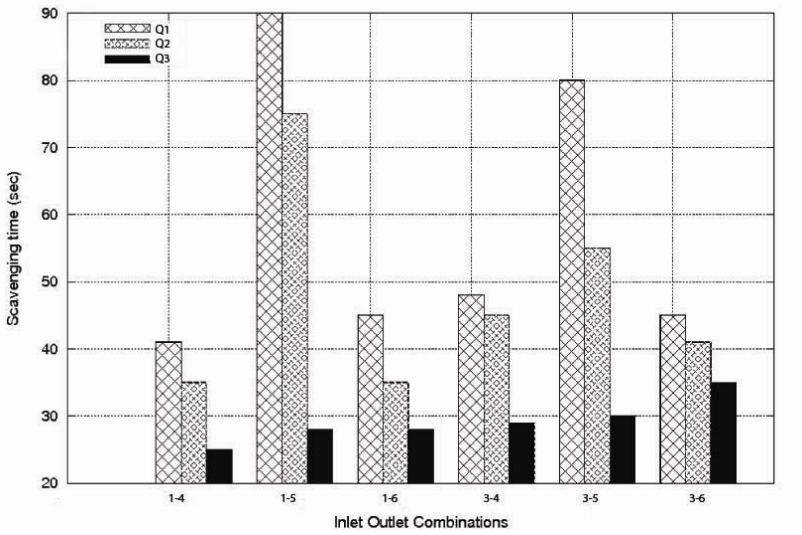

Figure 6: Scavenging time for different inlet-outlet combinations

Perfect Displacement Experiment

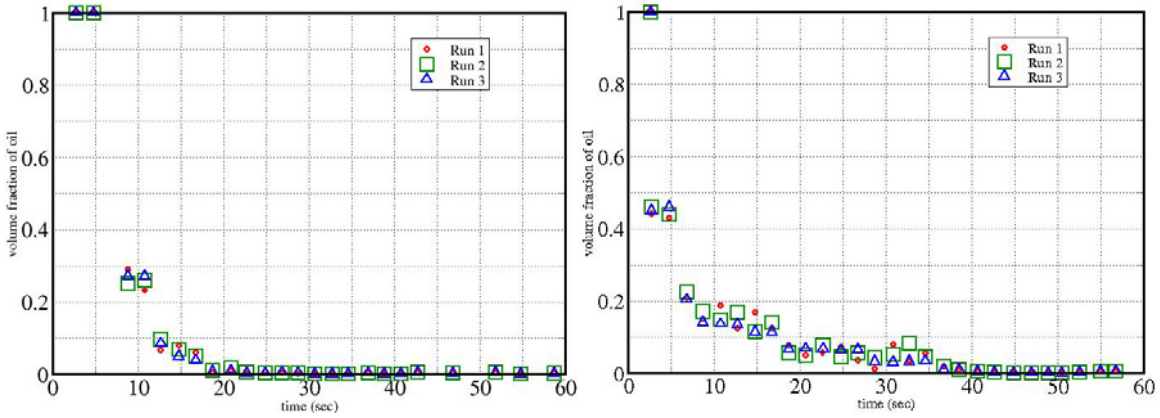

(a) (b)

Figure 7: Variation of engine oil concentration with time for a) 1-4 configuration b) 3-4configuration

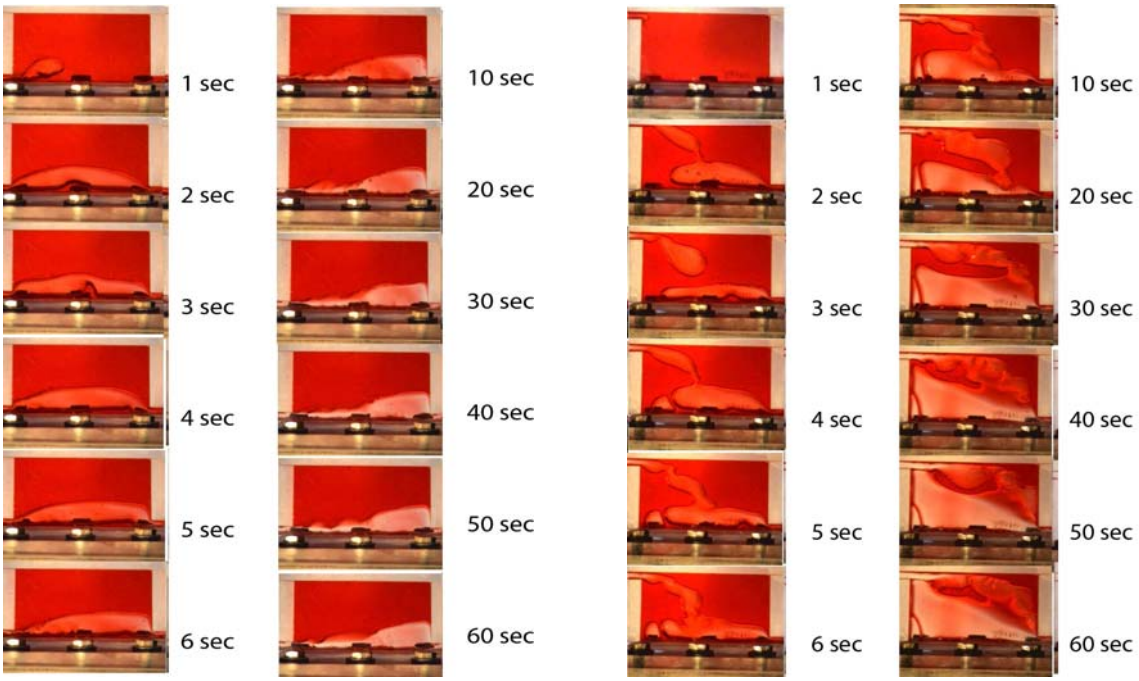

(a)1-4 (b) 3-4

Figure 8: Snapshot of the test section at different time (Perfect Displacement Case)

In this experiment, the cavity is initially filled with Engine oil which is displaced by injected water forming a clear interface. Figure 7 shows the time variations of volume fraction of oil in water collected in the test-tubes for the 1-4 and 3-4 port combinations. Three runs Run 1, Run 2 and Run 3 are conducted to ensure repeatability. The water flow rate is 8.33 ml/s in each of the 3 runs. It is seen that the volume fractions decrease with time but attain a steady finite value at large times. This suggests that scavenging is not complete. Figure 8 shows the snapshots of the test section at different times. It is seen that due to fluid circulations, the interface distorts; ultimately creating dead-zones at large times with trapped oil. For measuring the residual volume of oil two approaches are used. In the first approach the ejected volume in the test tubes are computed. This volume when subtracted from the volume of the test section gives the residual volume. In the second approach the residual volume was directly calculated using an image processing tool called GetData.

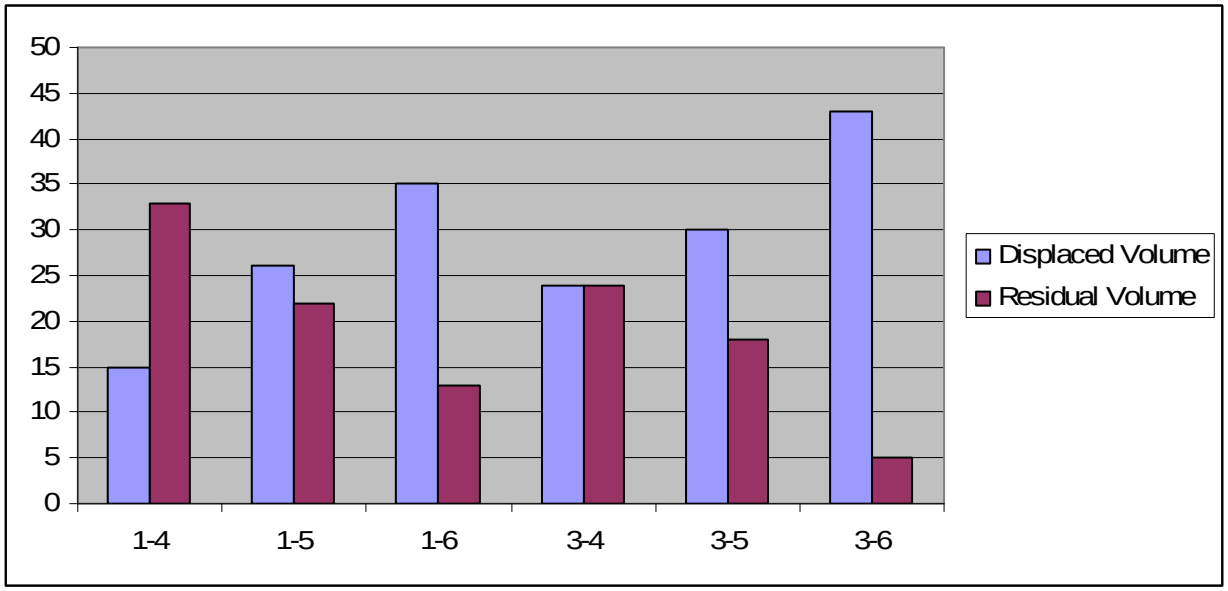

Figure 9: Displaced and Residual volume for a flow rate of 8.33ml/sec

In Figure 9 the displaced and residual volume of oil for different inlet-outlet combination is presented. It is clear from the figure that for any particular outlet increasing the height of inlet results in better scavenging as the displaced volume of oil increases. An interesting fact that comes to surface from the study is that the 1-4 combination which is best in the Perfect Mixing case turns out to be the worst in Perfect Displacement case. The reason for this is short circuit of the fresh charge through the exit port.

CONCLUSIONS

A novel experimental set-up is designed to capture essentials of Perfect Mixing and Perfect Displacement models of scavenging phenomena in two-stroke IC engines. Although, the density and viscosity of ratios of the burned and unburned gas mixture cannot be mimicked exactly, the experiment qualitatively shows features that can be used in design of cylinder interior (shape of cylinder head, for example) and relative locations of inlet and exhaust ports. A refined version of the experimental setup with sophisticated instrumentation can be used to generate high quality data set for validating CFD codes for both diffusion and interface tracking.

REFERENCES

1. Blair GP, *Design and Simulation of Two Stroke Engines*, Warrendale: SAE, 1994.
2. Stiesch G, *Modelling Engine Spray and Combustion Processes*, Springer, 2003.
3. Kenneth J Ayala, The 8051 *Microcontroller: Architecture, Programming and Applications, Penram International Publishing*, Mumbai, 1996.

HEAT TRANSFER DURING HIGH TEMPERATURE OXIDATION OF MOLYBDENUM FILAMENT

S. Orlovskaya, F.Karimova, M. Shkoropado
Odessa Mechnikov's National University, Odessa, Ukraine

ABSTRACT**.** High temperature oxidation of molybdenum filaments was studied experimentally. The detailed investigation of filament heating by dc over the range 0.5A ÷ 7A was fulfilled by means of electrothermography and optical pyrometry. The conditions of stationary and non-stationary oxidation modes realization were established. The filaments temperature histories for a number of dc values were obtained. Heat transfer modelling results are in good agreement with the data obtained.

Keywords: *molybdenum, filament, oxidation, electrothermography, stationary, non-stationary*

INTRODUCTION

Refractory metals – molybdenum and tungsten are typically used in high temperature applications and their oxides have wide prospects in microelectronics, solar and green energy. So peculiarities of these metals high temperature oxidation are of great interest. In the present work we studied experimentally high temperature oxidation and heat transfer of molybdenum filaments heated electrically in air.

So called "hot filament" method now is used to produce diamond films, carbon nanotubes, but it is also promising method to produce high-quality metal-oxide films with a desired chemical composition [1]. We investigated molybdenum filaments heating by dc over the range 0.5A ÷ 7A by means of electrothermography and optical pyrometry. We defined heat transfer time characteristics and the conditions of stationary and non-stationary oxidation modes.

Computer-assisted electrothermography method consisted in programmed electric heating thin metal filament (with diameter in the range 100–300 mcm) and continuous registration its volt-ampere characteristic. Current value of the filament temperature was derived from the change of it's resistivity [2].

ELECTROTHERMOGRAPHY AND OPTICAL PYROMETRY

The experimental set-up included a reaction chamber provided with gas feed and pressure regulating system; electric power supply; ampere and volt meters; analog to digital converter, optical pyrometer, digital camera.

At first we defined experimentally the limits of stationary oxidation mode. We raised the heating current step by step and controlled temperature time behavior for every dc value. If the filament temperature approached some stationary value, i.e. the process became stabilized than we considered this dc value corresponding to some stationary oxidation mode. In so way we defined the upper limit of stationary oxidation mode existence. The minimum current value corresponding to non-stationary mode we named the current critical value I_{cr}.

* Corresponding author: D-r. S . Orlovskaya
Phone: + (38)-048-7236227, + (38)-048-7236227
E-mail address: svetor@rambler.ru

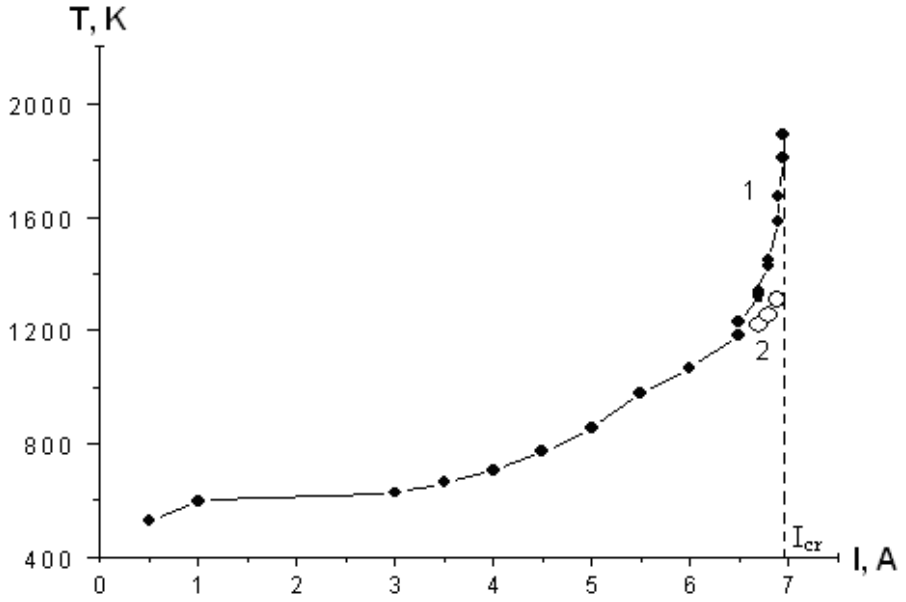

Fig. 1. Stationary filament temperature as function of heating current (d = $3 \cdot 10^{-4}$ m, L = 10^{-1} m): a) ♦–♦ the temperature defined by electrothermography; b) ○–○ the temperature in the central zone measured by optical pyrometer.

It depended on filament diameter, gaseous phase temperature and composition. On Figure 1 the experimental dependence of the filament stationary temperature on heating current is presented.

When heating current exceeded I_{cr} the accelerating oxidation due to oxide evaporation led to quick filament failure. The electrothermography gave us an averaged temperature value whereas during non-stationary oxidation the filament failure took place in the zone of maximum local temperature.

So we measured the temperature in the hottest zone by pyrometer with disappearing filament. In order to correlate the optical pyrometry temperature and the electrothermographical one we defined the temperature profile along the filament by use relative brightness pyrometry.

We took the pictures of hot filament by digital camera Canon 450D through narrow-band filter (λ=$0.77 \cdot 10^{-6}$ m). Than the images were processed using MATLAB 7.0. The temperature distribution was calculated by formula derived from Wien's law:

$$\frac{1}{T(x)} = \frac{1}{T_0} + \frac{\lambda}{C_2} \ln\left(\frac{S_0}{S(x)}\right) \tag{1}$$

here T_0 – the temperature measured by optical pyrometer in the filament centre; S_0 – the camera response in corresponding image pixel; $S(x)$– the response in the point x. We approximated the temperature profile near cold contacts by linear function.

The temperature profile along the filament was computed also numerically. Mathematical model of the heating process was based on solution of stationary heat transfer equation with account of the surface chemical reaction (every term of the equation is heat flux per unit filament length):

$$q_\lambda - q_\alpha - q_\varepsilon + q_{ch} + q_{DJ} = 0 \tag{2}$$

The first term of the equation (2) corresponds to heat flow to the filament ends:

$$q_\lambda = \lambda S \frac{d^2 T}{dx^2}$$

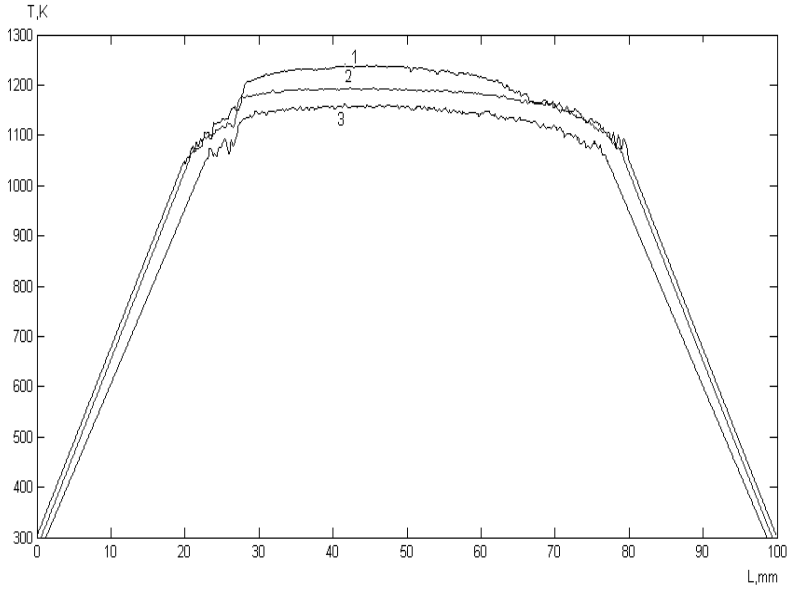

Figure 2. Temperature profile along the filament (d = $3 \cdot 10^{-4}$ m, L = 10^{-1} m):
1– I = 6.9 A, 2 – I = 6.8 A, 3 – I = 6.7 A, T_g = 293 K

The first term of the equation (2) corresponds to heat flow to the filament ends:

$$q_\lambda = \lambda S \frac{d^2 T}{dx^2}$$

The second term corresponds to convection heat loss:

$$q_\alpha = \alpha P\left(T - T_g\right),\ \alpha = \frac{\lambda_g Nu}{d}$$

Radiation heat loss is the next term:

$$q_\varepsilon = \varepsilon\sigma P\left(T^4 - T_g^4\right)$$

Oxidation reaction calorific effect equals

$$q_{ch} = QW_{O_2} P = Q\frac{k}{h} n_{O_2} \rho_g P$$

here

$$k = k_0 \exp\left(-\frac{E}{RT}\right) \quad n_{O_2,S} = n_{O_{2,\infty}}\left(1 + \frac{k}{h\beta}\right)^{-1} \quad \beta = \frac{NuD_{O_2}}{d}$$

where P – filament perimeter, k is oxidation reaction constant; k_0 – coefficient of reagents diffusion through oxide film; E – activation energy; h – oxide film thickness; ρ_g – air density; D_{O2}– oxygen diffusion coefficient; $n_{O_2,S}$ – oxygen relative mass concentration on the surface; $n_{O_{2,\infty}}$ – oxygen relative mass concentration at infinity; Q_a – heat of the reaction, T_g – gas temperature is supposed to be equal to one of the experimental chamber walls; α and β – heat and mass transfer coefficients.

The Joule heat equals:

$$q_{DJ} = \frac{I^2 \rho_0 \left(1 + \gamma\left(T - T_0\right)\right)}{S};$$

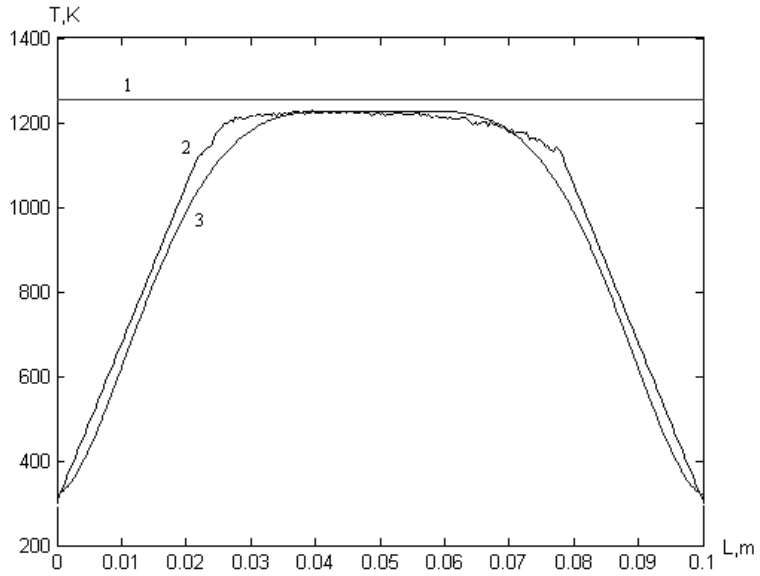

Figure 3. The temperature profiles: 1 – the electrothermography value; 2 – the experimental curve; 3 – the computed profile.

Figure 3 shows that the experimental curve T(x) computed by formula (1) is in a good agreement with the numerical solution of the equation (2), whereas the mean temperature defined by filament resistivity change is significantly higher. It is possible, that filament diameter change owing to metal oxidation resulted in significant error. So it is necessary to take into account the change of the filament conductive core diameter.

Non-stationary oxidation heat transfer was studied by use of electrothermography and optical pyrometry. Experimental thermogram (filament temperature history) is presented on Fig. 4. The thermogram allows identifying three successive stages of heat transfer during molybdenum filament high temperature oxidation.

After switching on the current the filament temperature quickly went up quasi-stationary value. At this stage of fast heating the filament temperature quickly increased due to Joule heat release. It is known that molybdenum is oxidation resistant up to 523 K. Further heating led to quick oxide film formation and growth. Initial oxide film consisted mainly of molybdenum dioxide and was rather dense. Usually the scale includes at least two layers: MoO_2 and MoO_3.

When the filament temperature attained trioxide melting point (point A) oxide scale began to melt. Molybdenum trioxide was highly volatile so oxidation and evaporation processes were parallel at the second stage – so called quasi-stationary oxidation stage, while the temperature increased relatively slowly at this stage.

When the the temperature in the filament centre attained the oxide boiling point (point B) the evaporation from the surface accelerated – at the third stage the scale practically didn't prevent from fast oxidation so the temperature increased sharply and went up to metal melting point (point C), corresponding to the filament failure.

In so way the oxide phase transitions were supposed to affect significantly molybdenum oxidation. Molybdenum oxide melting and boiling points defined the limits of high temperature oxidation succesive stages.

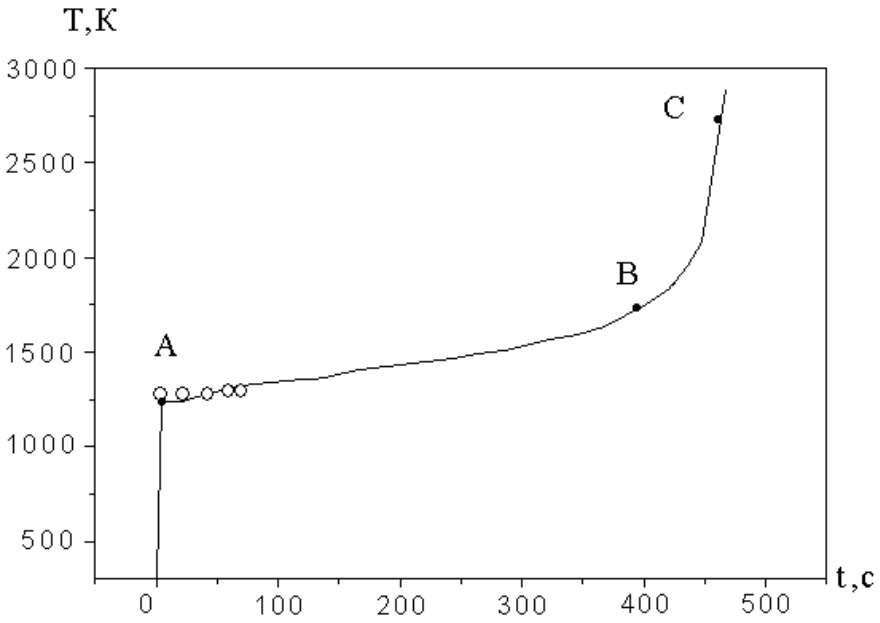

Figure 4. The molybdenum filament temperature history during non-stationary oxidation.

CONCLUSIONS

High temperature oxidation of molybdenum filaments in air was studied experimentally. It was shown that stationary oxidation mode realized when heating current was below some critical value.

The dependence of filament stationary temperature on heating current was found by means of electrothermography.

Temperature profile along the filament was found experimentally and numerically. The computed and experimental curves were in good agreement.

The temperature history was registered during non-stationary oxidation process. Three successive stages of the process were identified. It was shown that oxide melting point and boiling point delimited the succesive stages.

REFERENCES

1. F. Paulo Rouxinol, B. Cláudio Trasferetti, Richard Landers and Mário A. Bica de Morales. Hot-Filament Metal Oxide Deposition (HFMOD): A Novel Method for Depositing Thin Films of Metallic Oxides, J. Braz. Chem. Soc., Vol. 15, No. 2, pp 324-326, 2004.
2. S. Orlovskaya, V. Kalinchak, F. Karimova. High Temperature Heat Transfer and Oxidation Kinetics of Metal Filaments Heated Electrically, Proceedings of VI Minsk International Heat and Mass Transfer Forum - Minsk, May 19-21, 2008, pp 52-53.

RECIRCULATION BEHAVIOR IN SUBSCALE GAS TURBINE COMBUSTOR

H. Moriai[1,2*], P. Wang[3], J. Hayashi[3], N. Nakatsuka[3], F. Akamatsu[3], R. Kurose[2], S. Komori[2]
[1]Mitsubishi Heavy Industries, Ltd., Komaki, Japan
[2]Kyoto University, Kyoto, Japan
[3]Osaka University, Osaka, Japan

ABSTRACT. Understanding internal flow field in combustors is very important to design and improve the low-NOx combustor for aircraft engines. The subscale (1/2) combustor model with swirl nozzle (air-blast nozzle) is newly fabricated, and the visualization and measurement of the internal flow in the combustor using PDA (Phase Doppler Anemometer) technique are conducted. The results show general feature of flow field in the combustor and effect of the air/fuel flow on the axial velocity and size distribution of the spray.

Keywords: *Gas Turbine Combustor, Spray Combustion, Swirl Flow, Recirculation Zone, PDA measurement*

INTRODUCTION

The aircraft gas-turbine combustor has to meet many requirements such as combustion efficiency, NOx/CO/UHC (Unburned Hydrocarbon) emission, combustor exit temperature profile, altitude relight capability, and blowout characteristics. To satisfy the combustion efficiency and emission requirements, air-blast swirl nozzle is commonly used. However, this type of nozzle sometimes causes problems associated with altitude relight capability and blowout performance [1]. Since these characteristics are closely related to the recirculation zones that work as flame holder of the combustor, it is very important to understand the relationship between the recirculation flow behaviour and swirler design in order to optimize the nozzle performance.

Figure 1 shows the general development cycle of the combustors (including the nozzle and the combustion liner). The precise predictions of the combustion behaviour and emission are so difficult that the cycle is generally repeated again and again to reach the spec requirements of the combustor. This means the try-and-error characteristics of the combustor development, in which quite a long time and high cost are needed. To reduce the development time and cost, CFD (Computational Fluid Dynamics) is strongly expected to be useful in the near future [2,3]. However, the reliability of the CFD has not been established yet, since the spray combustion in the aircraft gas-turbine combustors is a complex phenomenon in which swirling and recirculating flow, fuel jet breakup, evaporation, and chemical reactions and so on take place simultaneously and interact each other, and therefore the experimental data for the validation of the CFD are not enough.

The purpose of this study is, therefore, to provide the experimental data of the spray combustion in the aircraft gas-turbine combustors for the understanding of the spray combustion and the CFD validation. In this study, the fuel droplet velocity and size near the burner in the 1/2-scale combustor model are measured using PDA (Phase Doppler Anemometer).

* Corresponding author: H. Moriai
Phone: + (81)-568-794123, Fax: + (81)-568-794348
E-mail address: hideki_moriai@mhi.co.jp

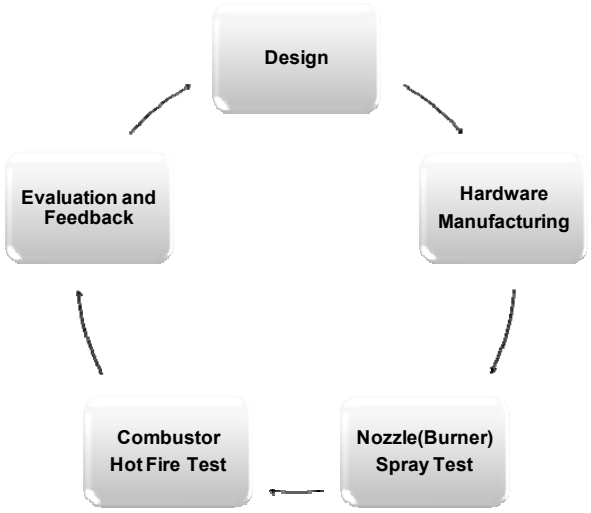

Fig. 1 General development cycle of the combustors for aircraft gas turbine engines

EXPERIMENT

Figure 2 shows the PDA measurement system and the spray combustion combustor used in this study. The spray combustion combustor is a 1/2-scale combustor model with single burner (nozzle) and optical windows, and installed as a subscale combustor in the combustion test facility of Osaka University.

Test conditions are summarized in Table 1. The changed parameters are air flow rate and fuel flow rate. The measurements are conducted under atmospheric pressure condition (the measurements under the high pressure condition will be conducted in the near future). The PDA measurement points are shown in Figure 3. The nozzle has two swirlers (inner swirler and outer swirler) for spray atomization and recirculation zone that works as flame holder. In this figure, ● shows the measurement points at which the enough number of droplets are not detected, and ○ with numbers are the measurement points.

Table 1
Experimental Conditions

CASE NO.	Air Flow (L/min)	Fuel Flow (kg/h)	Equivalence Ratio
CASE 1	200	0.75	0.79
CASE 2	176	0.75	0.90
CASE 3	126	0.75	1.25
CASE 4	126	0.5	0.83
CASE 5	126	1	1.67

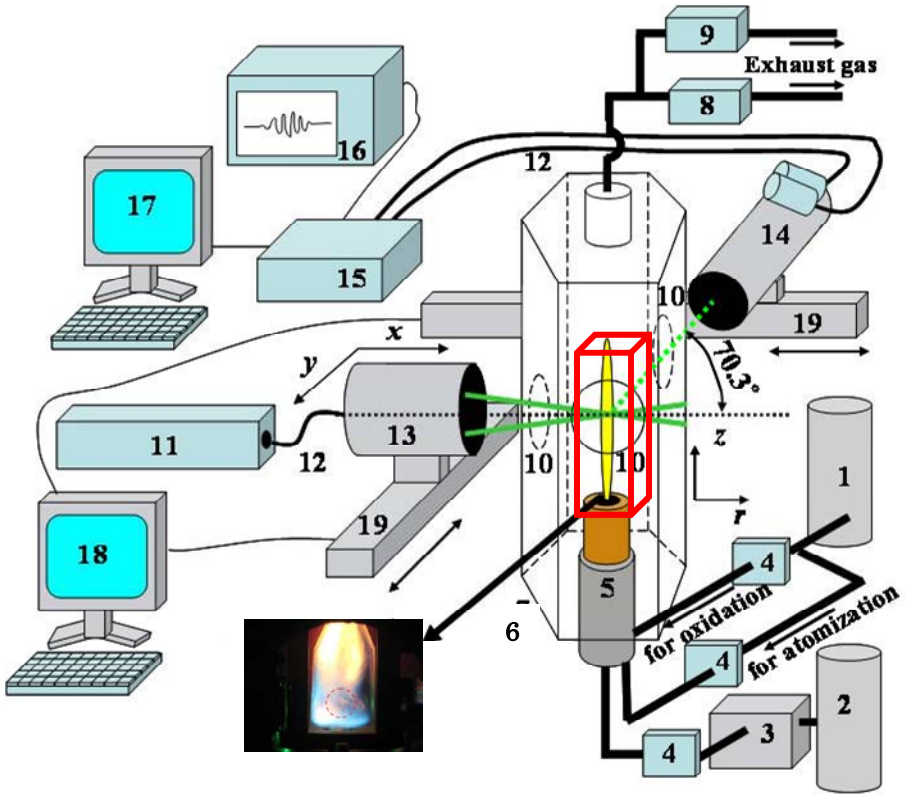

1: Air compressor
2: N2 tank
3: Liquid fuel tank
4: Mass flow controller
5: Burner (air-blast nozzle)
6: Combustor
8: Relief valve
9: Pressure control valve
10: Quartz window
11: Ar^+ laser
12: Optical fiber
13: PDA transmitter
15: Signal processor
16: Oscilloscope
17: PC for PDA
18: PC for traverse
19: Optical rail

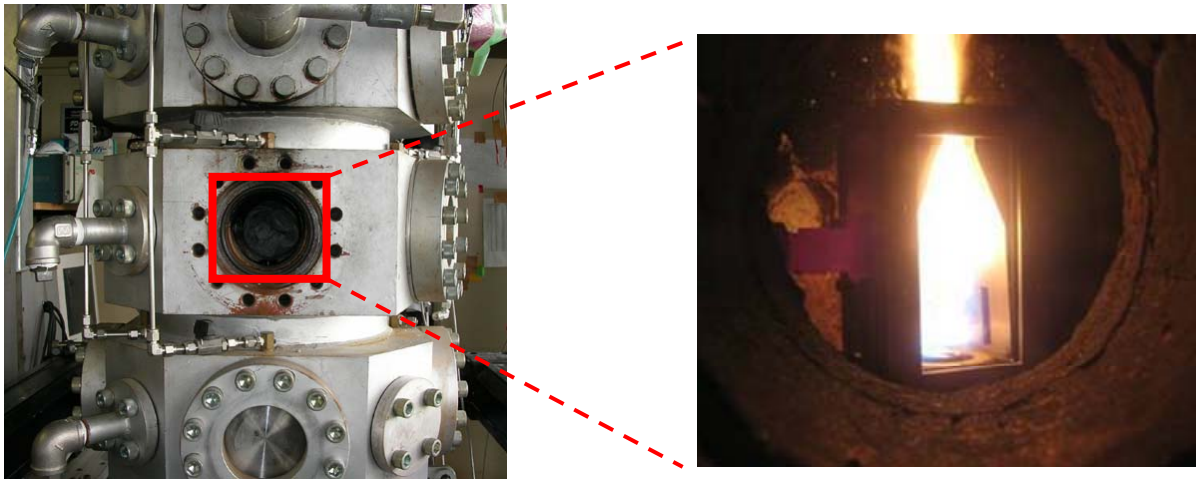

Fig. 2 PDA measurement system and spray combustion combustor

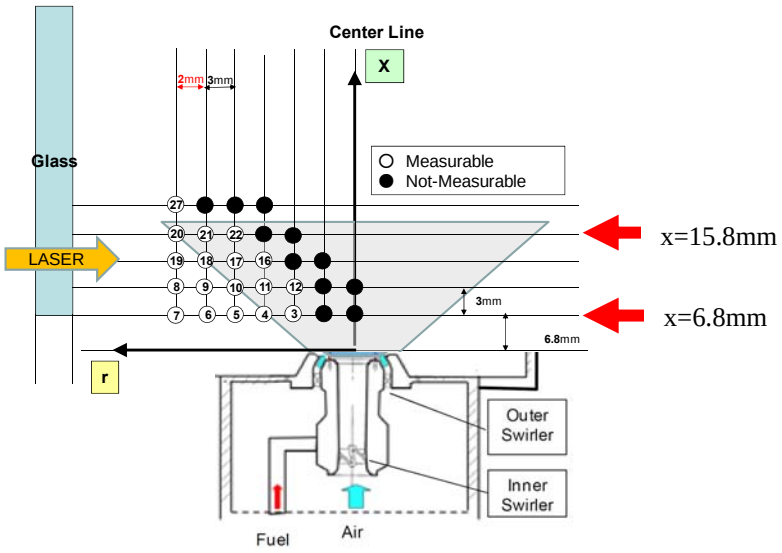

Fig. 3 Measurement points for PDA

RESULTS & DISCUSSION

General Feature of Spray Flame

In Figure 3, it is found that the spray droplets do not exist in the centre of the spray cone. This is because the spray cone angle is very wide (strong swirl flow) and little spray droplets exist in the downstream direction. Another reason is that there exists a recirculation zone around the centre line right downstream of the nozzle but only burned gas (after vaporization, mixing and chemical reaction) in the downstream is recirculating to the upstream central region.

Figure 4 shows the direct photographs of spray flame for fuel-lean (equivalence ratio ϕ <1) and fuel-rich (equivalence ratio ϕ >1) combustion. Blue flame is observed in the fuel-lean condition and visualization and measurement are easier because little amount of soot generates on the quarts window surface. In the fuel-rich condition, on the other hand, luminous flame is observed and soot grows considerably on the window in short time.

Effect of Air Flow Rate

Figures 5 and 6 show the effect of air flow rate on the radial distribution of fuel droplet velocity *U* at two axial points from the nozzle exit of x = 6.8 mm and 15.8 mm. In the region close to the nozzle exit of x = 6.8 mm, very narrow recirculation zone exists and *U* increases with the air flow rate (almost in proportion to the air flow rate). In the downstream region of x = 15.8 mm, on the other hand, the recirculation zone gets wider (with wider cone width) and *U* becomes larger. The increase in *U* is mainly due to the thermal expansion of reacting flow.

Figures 7 and 8 show the effect of air flow rate on the radial distribution of fuel droplet size *D32* at x = 6.8 mm and 15.8 mm. It is found that *D32* decreases with the air flow rate. This is due to the fact that shear force for atomizing the fuel liquid becomes larger as the air flow rate increases.

Effect of Fuel Flow Rate

Figures 9 and 10 show the effects of fuel flow rate on the radial distributions of fuel droplet velocity *U* and size *D32* at x = 6.8 mm. Compared to the effect of the air flow rate, the effects of the fuel flow rate are found to be less on both *U* and *D32* in the measured region.

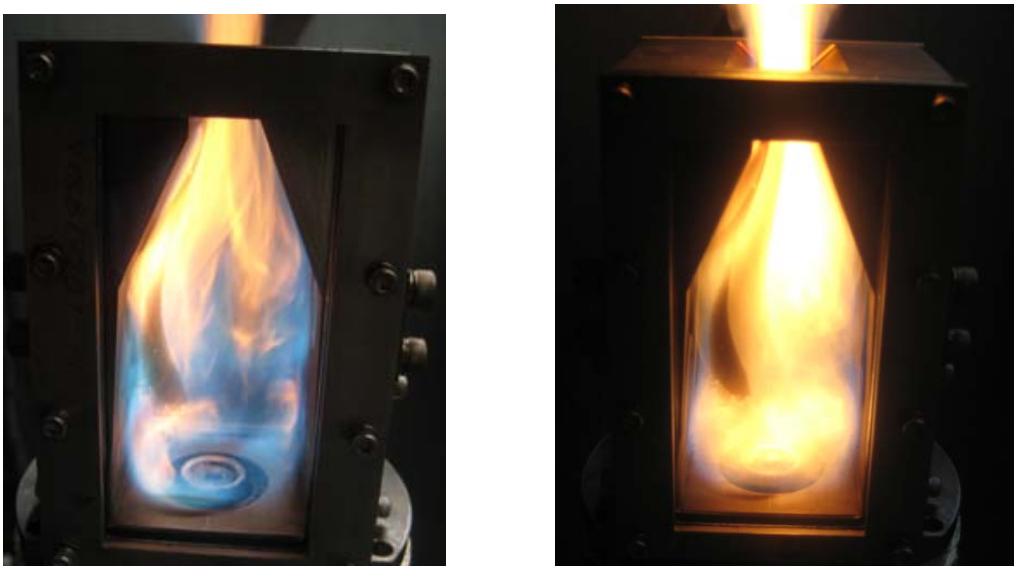

Fig. 4 Direct photographs of spray flame for fuel-lean (left) and -rich (right) combustion

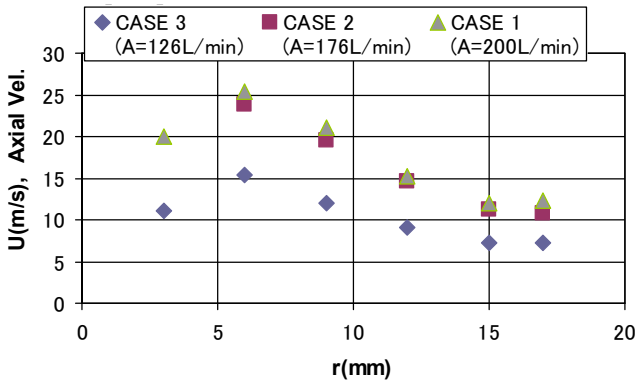

Fig. 5 Effect of air flow rate on radial distribution of axial droplet velocity *U* at x = 6.8 mm

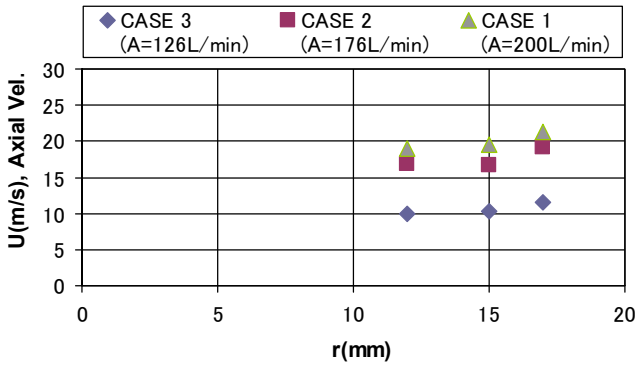

Fig. 6 Effect of air flow rate on radial distribution of axial droplet velocity *U* at x = 15.8 mm

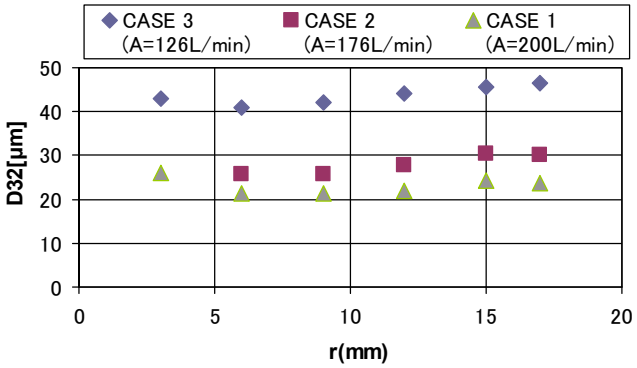

Fig. 7 Effect of air flow rate on radial distribution of droplet size *D32* at x = 6.8 mm

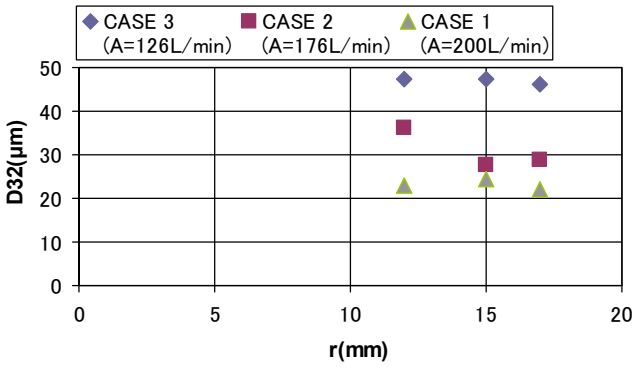

Fig. 8 Effect of air flow rate on radial distribution of droplet size *D32* at x = 15.8 mm

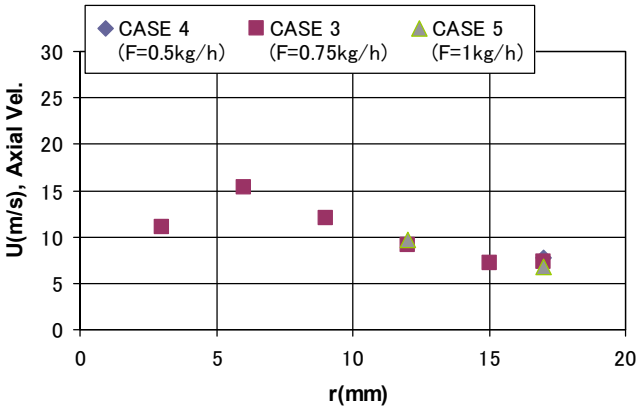

Fig. 9 Effect of fuel flow rate on radial distribution of axial droplet velocity *U* at x = 6.8 mm

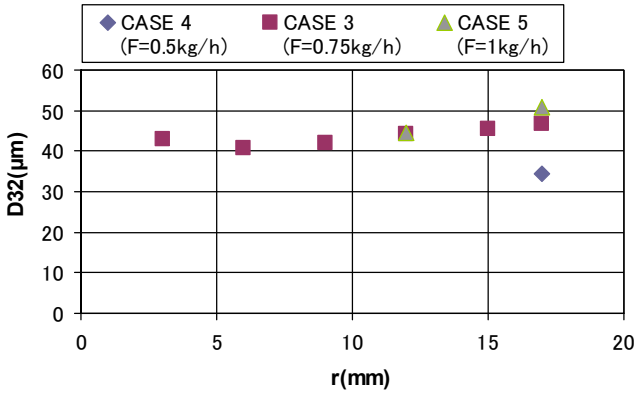

Fig. 10 Effect of fuel flow rate on radial distribution of droplet size *D32* at x = 6.8 mm

CONCLUSIONS

In this study, the subscale (1/2) combustor model of an aircraft gas-turbine combustor was newly fabricated for the laboratory-scale experiments. In addition, general feature of the spray combustion was visualized and the effects of the air and fuel flow rates on the fuel droplet velocity and size were investigated using PDA technique. It was found that the recirculation zone is formed in the central region close to the nozzle, and that the fuel droplet behaviour is strongly affected by the air flow rate but not by the fuel flow rate very much.

ACKNOWLEDGEMENTS

This work is part of "environmentally-compatible small aero engine (eco-engine) research and development" supported by NEDO (New Energy and Industrial Technology Development Organization).

REFERENCES

1. Moriai, H., et.al., Research and Development of a Combustor for an Environmentally Compatible Small Aero Engine, *Technical Review, MHI*, Vol. 45, No. 4, 2008, pp 9-15.
2. Moriai, H., et.al., Flow Dynamics of Gas Turbine Swirl Nozzle, *In Proc. of Asian Joint Conference on Propulsion and Power 2008*, Gyeongju, Korea, 2008, Paper No. A2-6.
3. Kurose, R., Large-eddy Simulation of Turbulent Combustion - Application to Spray Combustion, *Journal of the Gas Turbine Society of Japan*, Vol. 35, No. 4, pp 243-252, 2007.

EXPERIEMNTAL COMPARISON OF CALCUIM SULFATE ($CaSO_4$) SCALE DEPOSTION ON COATED CARBON STEEL AND TITANIUM SURFACES

L. Al-Hadhrami[1*], D. Al-Otaibi[2], A. Quddus[3]

[1,3]Center for Engineering Research, King Fahd Univesity of Petroleum & Minerals, Dhahran 31261, Saudi Arabia
[2]Aramco, Consulting Service Department, Dhahran, Saudi Arabia

ABSTRACT. Calcium Sulfate ($CaSO_4$) deposit reduces heat exchange in heat transfer equipment which adversely affects the equipment performance and plant production. Experimental studies were conducted using Rotating Cylinder Electrode (RCE) equipment to study the effect of Calcium Sulfate ($CaSO_4$) scale deposition on coated carbon steel and titanium surfaces. In this study the rotational speed was varied from 100 to 2000 RPM to study the behavior of Calcium Sulfate ($CaSO_4$) accumulation on both materials. Based on the experimental results, Calcium Sulfate ($CaSO_4$) scale obtained in the present study was almost constant on coated carbon steel. However, it increased as speed increased for deposition observed on titanium material

Keywords: *Scale Deposition, Calcium Sulfate (CaSO4), Coated Carbon Steel, Titanium*

INTRODUCTION

Fouling formation, and under deposit corrosion caused by scale deposits are major concerns for heat transfer equipment such as boilers, process fired heaters and heat exchangers in petroleum refineries, chemical and power plants. To mitigate corrosion and fouling, expensive corrosion-resistant alloys are used as construction materials for shell and tube heat exchangers. The use of titanium tubes in heat exchangers is a common practice now-a-days which has resulted in an exceptional increase of service life in many refinery heat exchangers. The copper based alloys such as Copper-Nickel (Cu-Ni) are the most effectiveness tube material used in desalination plants, however, due to seawater corrosion, the leak developed could cause serious problems. Titanium has been used either as original equipment or for retubing. Capital and maintenance costs of heat exchangers can be reduced considerably if inexpensive carbon steel tubes are coated with a low-cost, thermally conductive coating that provides corrosion resistance as well, equal to that of costly high-grade alloy materials. In aggressive environments, heat exchangers capital and maintenance costs are high due to the use of expensive corrosion resistance materials [1]. Heat exchanger fouling or deposition accumulation in general is a major economic problem accounting to 0.25 % of the total gross domestic product (GDP) in highly industrialized countries [2].

A methodology was developed earlier in laboratory by the use of Rotating Cylinder Electrode (RCE) to study scale build up on different metal surfaces. RCE is used to simulate conventional pipe flow [3]. The technique has some advantages over conventional flow loop test methods due to the ease of creating turbulent flow conditions and the simplicity in handling and operating the whole test

* Corresponding author: Dr. Luai Al-HAdhrami
Phone: + (966)-3-8602888, Fax: + (966)-3-8603996
E-mail address: luaimalh@kfupm.edu.sa

equipment. Although the boundary conditions in conventional flow loop and are different, scientists had successfully modelled the velocity affected corrosion mechanism. This was accomplished by equating the wall shear stresses in RCE to the pipe geometry under similar hydrodynamic conditions, for example turbulence, which resulted in identical mass transfer coefficients of both geometries [3]. In the present work the effect of solution hydrodynamics is studied at different rotational speeds (RPM) to obtain Calcium Sulfate ($CaSO_4$) scale deposition on coated carbon steel and titanium surfaces.

Fouling or deposit accumulation is a severe problem in heat transfer surfaces. Fouling is resulted from the accumulation of suspended particles in liquid or gas streams onto heat transfer surfaces [5]. Particles accumulation due to gravity is referred to as sedimentation. The suspended particles could include ambient pollutants such as sand, iron, and microbial organisms in cooling water.

It occurs when the process conditions lead to supersaturation of the dissolved inorganic salts on the heat transfer surfaces. These process conditions which lead to supersaturation involve evaporation beyond solubility limits, cooling/heating beyond solubility limits or mixing of the process stream. The industrial systems and operations in which the problem of precipitation fouling is significant are: Saline Desalination Plants, Geothermal Brine Systems, Cooling Water Systems, Steam Generation Systems and Potable Water Supply Systems. Some dissolved species show inverse solubility versus temperature behavior. In this case the substance tends to precipitate on a heated rather than a cooling surface as seen in cooling water application. Calcium Sulfate ($CaSO_4$) which is our main focus in this research study is one of the salts that exhibit this behavior. The driving force for crystallization is the chemical potential difference between the substances in the solution and deposit formed on the metal surface [5].

The effect of supersaturation, pH, Reynolds number and concentration of ions in the brine solution on the formation of silica scale in heat-exchanger tubes were discussed and also a silica deposition model was proposed by Neusen et al. [6]. Chemical reaction fouling includes deposits that are formed as a result of chemical reactions within the process fluid. Although heat exchanger surface doesn't act as reactant, it sometime behaves as a catalyst [7]. This type of fouling is commonly occurring in chemical process industries, refineries and dairy process.

Brian et al. [8]; investigated the use of titanium tubes in petroleum refining heat exchangers. The investigation was conducted on forty in-service heat exchangers. The investigation results revealed that the use of titanium tubes for heat exchangers resulted in an exceptional increase of service life in many refinery heat exchangers. The service life of the exchangers and plant production were improved by the use of titanium tubes. Scholl [9]; reported that capital costs of a typical heat exchanger can be reduced to 67% if polymer-coated carbon steel tubes, tube sheets, and headers are used in place of titanium tubes and titanium-clad plates. Scale deposit on coated surfaces is reduced tremendously compared with non-coated parts. Scale mitigation on heat transfer equipment improves equipment performance and reduces plants production losses.

Calcium Sulfate ($CaSO_4$) is considered to be one of the most commonly found scale in Arabian Gulf and Red Sea regions. Scale formation impacts heat transfer mechanism and affects equipment performance. The objective of this experimental work is to study the deposition of Calcium Sulfate ($CaSO_4$) scale on coated carbon steel and titanium surfaces

EXPERIMENTAL SET UP

The rotating cylinder equipment (RCE) used for conducting the experiments is shown in Figure 1 RCE consists of supersaturated solution tank, adjustable speed motor, Teflon-coated shaft, Teflon ring, specimen, Teflon cap, glass cell and hot water circulation bath. Coated carbon steel and titanium samples were fitted on the shaft that was attached to a rotating motor. The shaft holding the sample was completely immersed in double wall glass cell that contained supersaturated solution. The supersaturated, Calcium Sulfate ($CaSO_4$), solution was supplied to the glass cell from the tank. All the experiments were conducted at 60 ºC temperature and atmospheric pressure.

The solution tank which contained Calcium Chloride ($CaCl_2$) and Sodium Sulfate (Na_2SO_4) supersaturated solutions had a volume of four (4) litres. It was connected to the cylindrical double wall glass cell via ¼ inch (6.35 mm) tubing. The glass cell was 13.0 cm long with inner diameter of 3.4 cm. The supersaturated solution flowed to the glass cell at a rate of 1.0 to1.5 liter/hour. Overflow fluid was drained though an outlet ¼ inch (6.35 mm) tubing. Replenishment of the supersaturated solution in the tank was done when necessary by adding equal amount of $CaCl_2$ and Na_2SO_4 solutions. Continuous flow of the fresh solution to glass cell assured that the test specimen was exposed to a solution of constant composition. Motor speed was adjustable which enabled the sample rotation speed to be varied. The rotation speeds used in the experiments were varied from 100 to 2000 Revolution Per Minute (RPM).

At the beginning of each experiment, supersaturated solution was prepared and filled in supersaturated solution tank (1). Solution was allowed to flow to the glass cell (7) and heated to the required set temperature 60 °C, by circulating hot water. Hot water was circulated through the jacket surrounding the cylindrical glass cell. Water in glass cell was circulated by the use of constant temperature water-circulating bath arrangement (8) as shown in Figure 1. Each experiment was conducted at a certain rotational speed and preset solution temperature of 60 °C under atmospheric pressure. The duration selected for each experiment was six (6) hours.

When supersaturated solution reached to a temperature of 60 °C and the motor was set to the required rotational speed, test rig was ready to start. Before starting the experiment, each specimen (see Figure 2 and 3) was thoroughly cleaned with distilled water and acetone, weighed and mounted on the shaft of the rotating equipment. The shaft was immersed in the glass cell and the test started. At the end of each experiment the specimen was rinsed with water and carefully removed from the shaft. It was dried in the oven for two (2) hours. The oven temperature was set at 70 °C. Then, the test sample was re-weighed to determine the mass of scale gained by the specimen.

Before starting the next experiment the glass cell and solution tank were soaked overnight with dilute acid (HCl) then thoroughly cleaned with normal tap water followed by cleaning with distilled water.

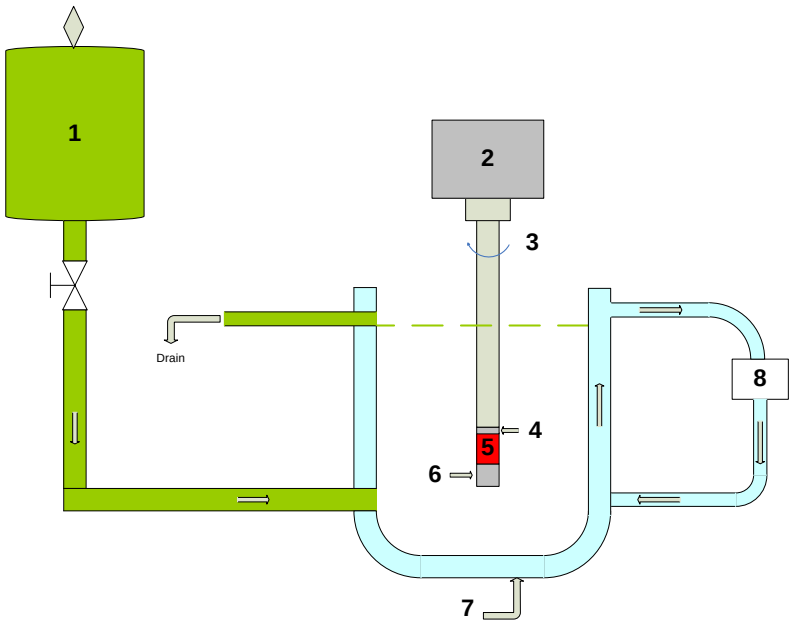

1 Supersaturated solution
2 Adjustable Speed Motor
3 Teflon-coated shaft
4 Teflon ring
5 Specimen
6 Teflon cap
7 Glass cell
8 Hot water circulation bath

Figure 1. Schematic of the Experimental Setup of RCE Apparatus

Figure 2. Photograph of Coated Carbon Steel Samples

Figure 3. Photograph of Titanium Samples

DATA REDUCTION AND UNCERTAINTY ANALYSIS

The weight gained (W_g) by the specimen was resulted from the weight difference of specimen after the test and its initial weight before the test. The deposition rate (D_r) is calculated as the weight gained (W_g) of the scaled specimen in grams (g) divided by the surface area of the specimen in square meter (m^2), and the experiment time in hour (hr). The deposition rate (D_r) therefore has units of g. m^{-2}. hr^{-1}.

Calcium Sulfate ($CaSO_4$) deposition rate on coated carbon steel and titanium samples was calculated by the following reduction equation.

$$D_r = W_g * A_s^{-1} * t^{-1} \qquad (1)$$

Where;

D_r	Deposition rate ($g.m^{-2}.hr^{-1}$)
W_g	Weight gained by the specimen (g)
A_s	Surface area of the specimen [π*D*L] (m^2).

t Duration of the experiment work (hr).

The deposition rate uncertainty for Coated carbon steel was ± 8% and for Titanium was ±12 %

For each rotational speed, equivalent Reynolds numbers (Re) were calculated using the equation proposed by Gabe [3].

$$Re = R_1 \omega [(R_2-R_1)/\nu] \quad (2)$$

Where

Re	equivalent Reynolds number
R_1	radius of the rotating specimen (cm)
R_2	radius of the glass cell (cm)
ω	angular velocity of the rotating specimen (rad/sec)
ν	fluid kinematics viscosity (cm^2/s).

The Reynolds number uncertainty for coated carbon steel and Titanium ±4 %

RESULTS AND DISCUSSION

The following graphs are for titanium samples. Each graph shows three repetitions to compare the deposition accumulation at same Re (or rotational speed -RPM). These three tests are presented by Set 1, Set 2 and Set 3 respectively

Figures 4 and 5 show Calcium Sulfate ($CaSO_4$) deposition rates on the coated carbon steel and Titanium samples. For each rotation number, the experiment was performed three times to determine the deposition rate. In each experiment that was conducted a new sample was installed in the rotating shaft.

Figures 4 shows the behaviour of Calcium Sulfate ($CaSO_4$) deposition rates on the coated carbon steel samples. The deposition rate shows almost asymptotic line. It is an indication that mechanism of deposition and removal existing continuously regardless of the Reynolds number.

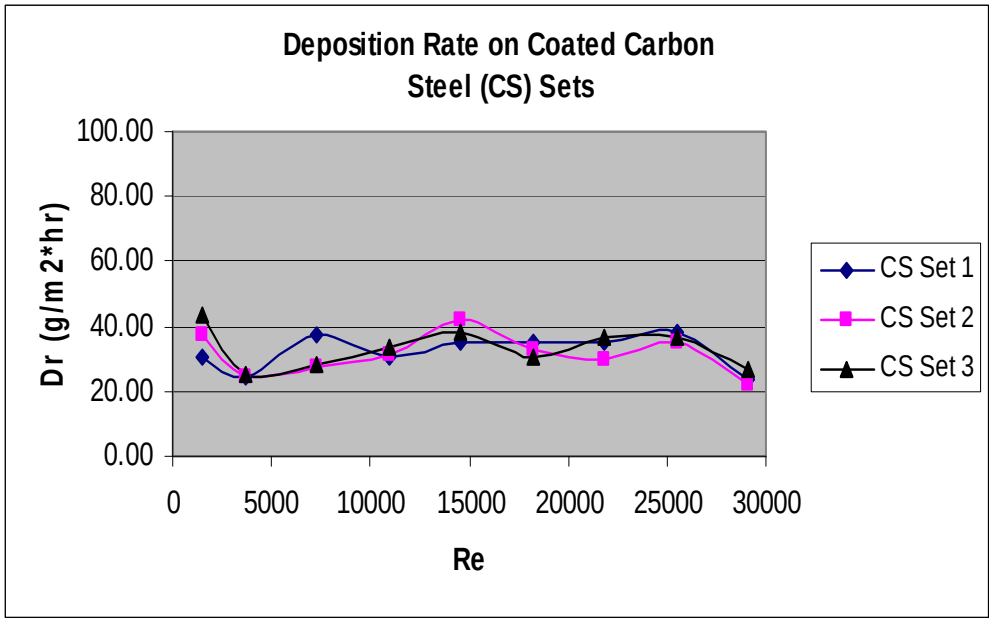

Figure 4. Deposition Rate on Coated Carbon Steel for Three Sets

Figure 5 shows the Calcium Sulfate ($CaSO_4$) deposition rate on Titanium samples. The deposition rate of Calcium Sulfate ($CaSO_4$) increases as the Reynolds number increases on titanium samples.

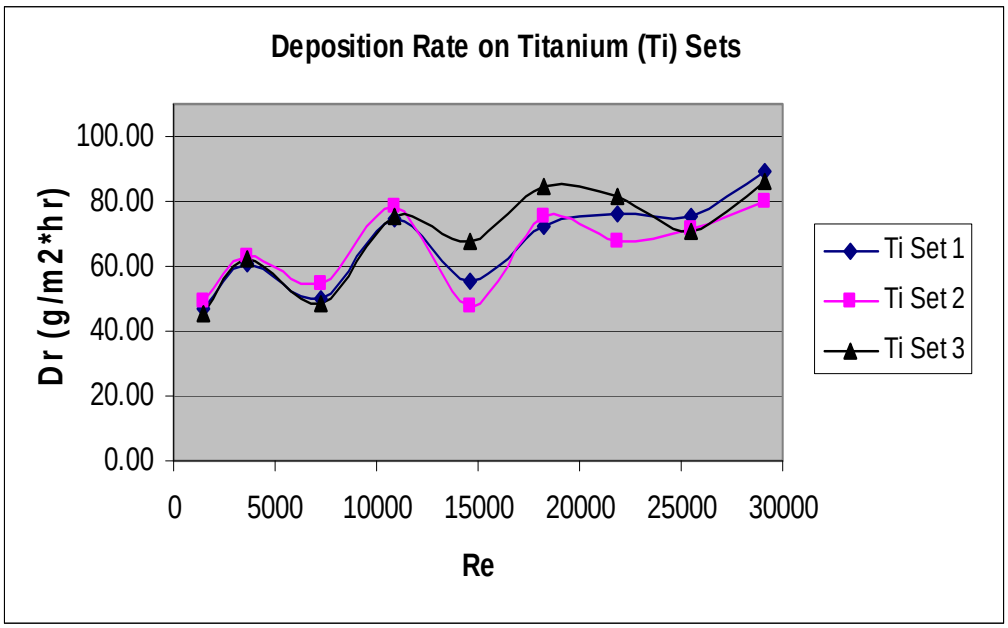

Figure 5. Deposition Rate on Titanium for Three Sets

Figure 6 shows the average deposition rate on Coated Carbon Steel and the Titanium samples. It can be seen that the deposition rate on the titanium samples are increasing proportionally to Reynolds number compared to coated carbon steel samples.

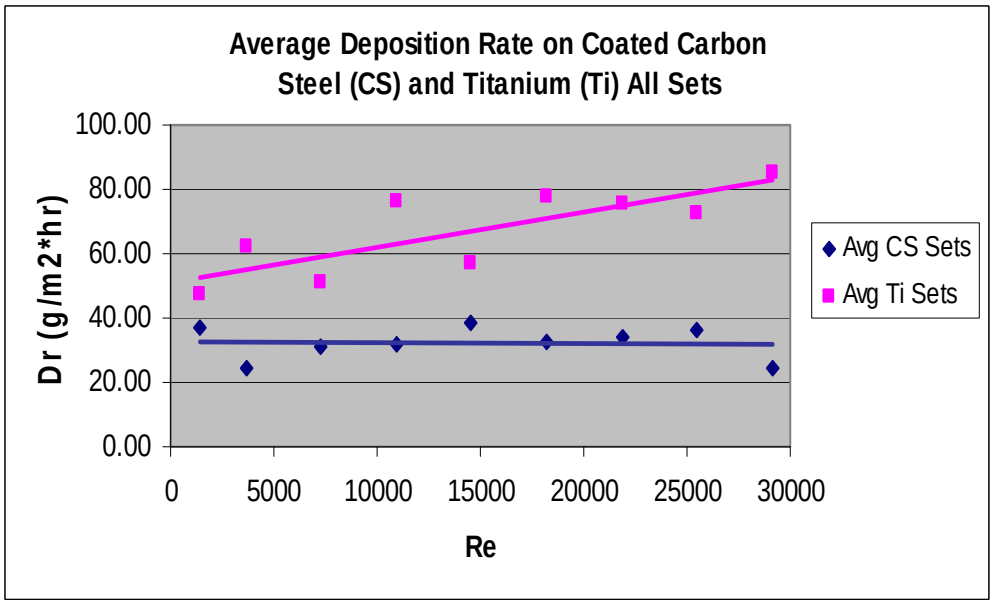

Figure 6. Average Deposition Rate on Coated Carbon Steel and Titanium Samples

According to the analysis done by Levich [11], the mass transfer coefficient should increase with the square root of Reynolds number - $(Re)^{0.5}$. For such case, the Log-Log plot should give a straight line with theoretical slope of 0.5. It is obvious from Figure 7 that the log-log plot of deposition rate

(D_r) versus Reynolds number shows a linear relationship,. a straight line with a slope of 0.45. This result is in close agreement with the theoretically predicted value of 0.5, obtained when the mass transfer coefficient is proportional to the square root of Reynolds. Hence, this shows that the process is diffusion controlled.

Based on the results presented in Figure 7, Coating on carbon steel samples reduced scale buildup and decelerated fouling accumulation on the external surfaces of the samples. However, in the case of titanium samples the scale growth was significantly more as the rotational speed was increased. Therefore, coated carbon steel samples showed better resistance to fouling and deposition compared to titanium samples

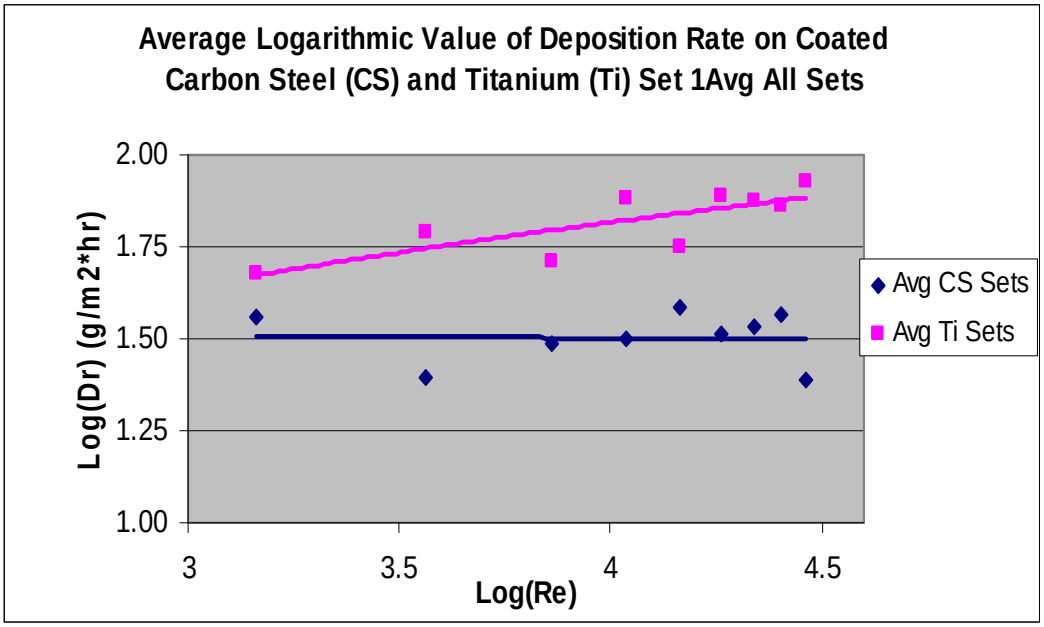

Figure 7. Average Logarithm (Deposition Rate) vs. Logarithm (Reynolds number)

CONCLUSION

Based on the results of the present experimental study, the following conclusions can be made:

- Scale buildup on the metal surfaces is proportional to the rotational speed. This is clear in case of titanium samples. As the rotational speed increased, the deposition rate increased which also was represented by more weight gained on the specimen surface.

- Another interesting point which was seen is the uniform distribution of Calcium Sulfate ($CaSO_4$) crystal on the metal surface. It was clearly seen that once a thin layer of scale is formed, the subsequent scale layer growth on it is much faster because of the readily available abundant nucleation sites as compared to the initially polished surface. Another perception could be that the scaled surface becomes sufficiently rough which promotes deposition process compared to the bare surface.

- The data analysis of Calcium Sulfate ($CaSO_4$) scale deposition rate showed that the rotational speed and the mixing of the solution have a strong influence on the rate of Calcium Sulfate deposition on coated carbon steel and titanium surfaces. The higher the speed of rotation the more scale crystals adhered to the metal surface. Deposition rate increased linearly with the square root of the Reynolds number, which showed that the process is diffusion controlled. It was noticed that, for both coated carbon steel and titanium

that were investigated, the deposition rate had clear linear relationship with the speed of rotation.

ACKNOWLEDGMENT

The authors would like to thank King Fahd University of Petroleum and Minerals for supporting the research work under the project number (SB080012)

REFERENCES

1. Keith Gawlik, Stephen Kelley, Toshifumi Sugama, Ronald Webster and Walter Reams; "Development and Field Testing of Polymer-Based Heat Exchanger Coatings", Proceeding World Geothermal Congress, pp. 3161-3165, 2000.
2. R. Steinhagen, H. Muller-Steinhagen and K. Maani, "Problems and Costs Due to Heat Exchanger Fouling in New Zealand Industries", Heat Transfer Engineering, Vol.14, no.1, pp. 19-30, 1992.
3. Silverman D.C.; "Rotating Cylinder Electrode – Geometry Relationships for Prediction of Velocity – Sensitive Corrosion", Corrosion, Vol. 44, pp.42-48, NACE, 1988.
4. Gabe D. R., "The Rotating Cylinder Electrode", Journal of Applied Electrochemistry, Vol. 4, pp.91-108, 1974.
5. H. M. STEINHAGEN; "Fouling of heat exchanger surfaces", Chemistry & Industry, Vol. 50, pp. 62-76, March 6, 1995.
6. Neusen K. F., Chan S. H. and Zhou D. Z; "Heat transfer in Geophysical and Geothermal System", Vol. 76, pp. 45-50, ASME HTD, New York, 1987.
7. Gudmundson J. S.; "Particulate Fouling", Fouling of Heat Transfer Equipment, Hemisphere Publishing Company, Washington D. C., pp. 357-387, 1981.
8. Brian E. Hopkinson and Fermin S. Hernandez O.; "Use of Titanium in Petroleum Refining", Material Performance, vol. 29, no. 9, pp. 48-52, Sep. 1990.
9. K. Scholl, "Report on Liner Application/Heat Exchanger Construction Techniques", National Renewable Energy Laboratory, NREL Milestone Report 2.2.3, July 1997.
10. Neville A., Hodgkiess T. and Morizot A. P.; "Electrochemical assessment of calcium carbonate deposition using a rotating disc electrode (RDE)", Journal of Applied Electrochemistry, Vol. 29, pp. 455-462, 1999.
11. V. G. Levich, "Physicochemical Hydrodynamics", Prentice-Hall, Englewood Cliffs, NJ, 1962.

INVESTIGATION OF TWO-PHASE REFRIGERANT FLOW IN THE VERTICAL ACCUMULATOR OF A REFRIGERATOR

A. Celik[1,*], O. Unal[2], H. Kerpicci[1], I. Teke[2]
[1]Arcelik A.S., Istanbul, Turkey
[2]Yildiz Technical University, Istanbul, Turkey

ABSTRACT. This paper covers the transient two-phase isobutane (R-600a) refrigerant flow visualization and analyses, which were performed in the accumulator located after the fresh food evaporator of a two-compartment refrigerator. The inlet of the accumulator in such systems has very high refrigerant mass qualities between 0,9-1,0 during the on-cycle of the compressor. Effects of several system parameters have been taken into account during the experimental studies such as refrigerant mass flux and ambient temperature. High-speed camera pictures were taken to measure the liquid refrigerant droplet diameter and velocity for different test conditions. The refrigerant droplet size distribution and liquid refrigerant level increase inside the accumulator have been determined for different system parameters. Separation efficiency has been analysed based on force balance on the liquid droplet. Liquid refrigerant droplets ranging from 180µm-2000µm have been found in the experimental studies. Refrigerant mass flux has a profound effect on the liquid refrigerant diameter. Due to high variation in droplet diameter, calculated Sauter Mean Diameter (SMD) for the liquid droplets are found to be generally 32-50% higher than the calculated mean diameter of the droplets.

Keywords: *accumulator, two-phase flow, flow visualization, droplet distribution, high speed camera*

INTRODUCTION

Two-phase gas-liquid flows very often occur in industrial processes as well as in small capacity refrigeration systems. For instance, in household refrigeration systems, the refrigerant frequently leaves the specific heat exchanger named evaporator as in two-phase condition. There is a specific risk with these systems concerning the compressor. If two-phase flow occurs at the outlet of the evaporator, liquid phase of refrigerant will enter the suction line of the compressor in the refrigeration system without an accumulator. Slugging condition occurs when liquid refrigerant enters the suction line of the compressor. This is quite an important problem since the slugging condition may cause serious mechanical damage to the compressor. In most cases, an accumulator is installed vertically or horizontally between the evaporator and the compressor to prevent the occurrence of slugging condition. The basic function of the commonly used vertical accumulator is collecting the excess liquid phase refrigerant by gravity-driven separation of liquid-vapour mixture. Thus, the compressor is protected from damages caused by liquid refrigerant slugging.

Monnery and Svrcek (2000) established the separation efficiency of flare knock-out drums and determined the expected entrained liquid droplet diameter. Todd B. Jekel et al. (2001) reviewed the literature on the principles governing gravity-driven separation of liquid-vapour mixtures and

* Corresponding author: A. Celik
Phone: + (90)-216-5858440, Fax: + (90)-216-4233045
E-mail address: aydin.celik@arcelik.com

design methods for separators. They developed a model that predicts separator performance given operating requirements such as size or velocity and design droplet size. Sang-Joon Lee et al. (2003) investigated the flow structure inside the accumulator of a rotary compressor experimentally using a hybrid particle tracking velocimetry (PTV) velocity field measurement technique. C.M. Winkler and J. E. Peters (2002) determined the centerline droplet size in the header of a typical evaporator. They used a phase-doppler particle analyser to characterize the spray along the centerline of the header for 1, 2 and 3 g/s total mass flow rate. During the experiments the thermodynamic quality is varied in the header from 0 to 0,15. Cemil Inan et al. (2002) investigated the transient behaviour of a domestic refrigerator by an X-ray system. X-ray images were recorded by focusing to on the dryer, capillary exit, evaporator inlet, and accumulator regions specifically. They visualized the change in liquid level in the accumulator with R-134a refrigerant.

In this study, motion of droplets is visualized by Phantom v5.1 high-speed camera in order to understand dynamic and kinetic behaviour of liquid refrigerant droplets. Accumulator prototype is made of plexiglass for the flow visualization purposes. During the experimental study, ambient temperature is held at 25°C. Real time high-speed video images of the sight accumulator are taken during cyclic periods. The set of experiments are conducted to measure liquid refrigerant droplet diameter and velocity flowing with vapour phase.

THEORY AND MODELING

The droplet of any liquid in a vapour flow is under the influence of gravity, buoyancy and drag forces. The resulting net force on the droplet affects the velocity and separation of the droplet depending on the direction of the net force. The gravity force must be greater than the sum of buoyancy and drag forces in order to separate the droplet from the vapour flow. Figure 1 shows the forces acting on liquid droplet entrained in vapour flow.

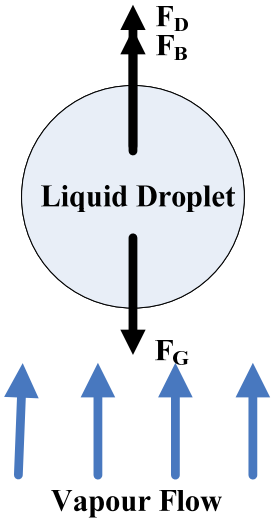

Figure 1. Forces on liquid droplet in vapour flow

According to Todd B. Jekel et al. (2001) [2], the forces acting on the liquid droplet and the force balance can be established by application of Newton's Law:

$$\sum_{i=1}^{n} \vec{F}_i(t) = m_d \vec{a}(t) \tag{1}$$

$$F_G = \rho_L V_d g \tag{2}$$

$$F_B = -\rho_V V_d g \tag{3}$$

$$F_D = -\rho_V U^2 C_D \frac{A_d}{2} \tag{4}$$

The signs in the above equations are given considering that the gravity force is always directed downward, the buoyancy force is opposite the gravity force and the direction of the drag force on the liquid is opposite to the gravity force.

When sizing the accumulator, SMD can be used for the force balance equations. According to ASTM E799-92, Kröger and Alkidas SMD is defined as [8]

$$d_{32} = \frac{\sum n d_d^{\,3}}{\sum n d_d^{\,2}} \tag{5}$$

The accumulator separation efficiency ηs describes the ability of an accumulator in separating the refrigerant phases. [6] Separation efficiency can be estimated as following

$$\eta s = \frac{\sum_{i=1}^{n} \rho_{l,i} d_{s,i}^{\,3}}{\sum_{i=1}^{n} \rho_{l,i} d_{s+e,i}^{\,3}} \tag{6}$$

EXPERIMENTAL SETUP

Tests were conducted with Phantom v5.1 high speed camera at 1000pps. The refrigerant droplet size distribution and liquid refrigerant level increase inside the accumulator have been determined for different system parameters. To capture minimum diameter of a liquid droplet, which is in the order of 50-100 µm, high magnification is required in the experimental setup. To achieve this, macro lens is used and an extension tube is mounted between the camera sensor and the macro lens. A cold light source and a boroscobe system are used for illumination of the test section to measure liquid refrigerant level in the accumulator. Temperature measurements are made with T-type thermocouples attached to different locations on the whole cooling circuit. ImageJ software is used for analyses of the liquid droplets. Minitab software is used for statistical analyses of the liquid droplets. Agilent 34970A acquisition system is used for temperature measurements. Accuracy of temperature measurement is ±0,25°C.

The original metallic accumulator in the refrigeration system of a refrigerator is replaced with a sight accumulator prototype made by plexiglass tubing capable of sustaining 6-10 bar pressure. Inlet and outlet pipes of the accumulator were kept in the system. The tube connections to the sight accumulator have been made by a unique epoxy designed for these type of low temperature, low pressure applications. The sight accumulator is placed vertically at the outlet of the fresh food evaporator, which is mounted in the insulation of the refrigerator through an opening. To determine droplets sizes, a ruler located near the accumulator prototype and glycol is applied to accumulator surface to prevent condensation. The visualisation section has a cover that is made of polyurethane to minimize heat gain when the flow is not being visualized. Figure 2 shows the experimental setup.

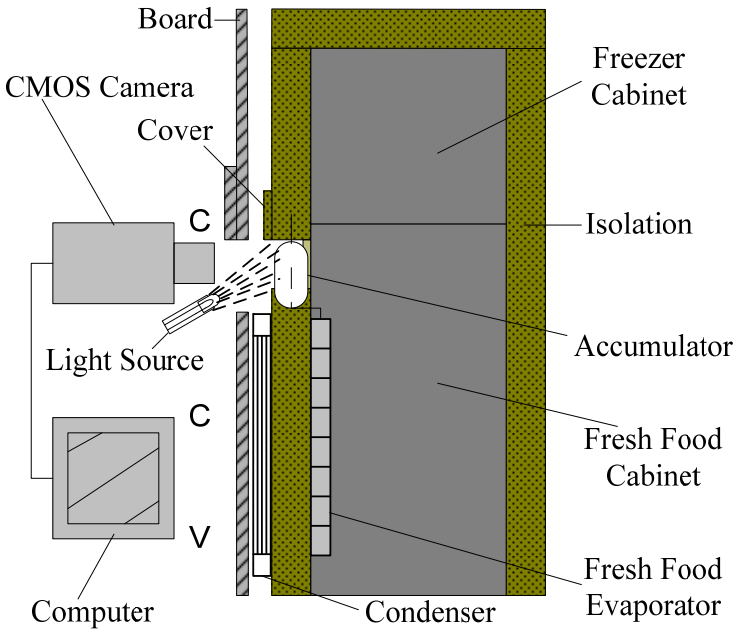

Figure 2. Experimental setup for liquid droplet visualisation

EXPERIMENTS

The refrigerator is placed in the conditioned room where ambient temperature is set to 25 ± 0,2°C. Temperature data collection has been synchronized with video recording by high-speed camera and boroscobe system. The high-speed videos are recorded at different times of on period of the refrigerator at 1000pps. For the real working conditions of the refrigerator, the droplet SMD was measured where the ambient temperature is 25°C by high-speed camera and analyzed with ImageJ. Figure 3 shows the real time captured picture and modified picture for the particle analysis with ImageJ.

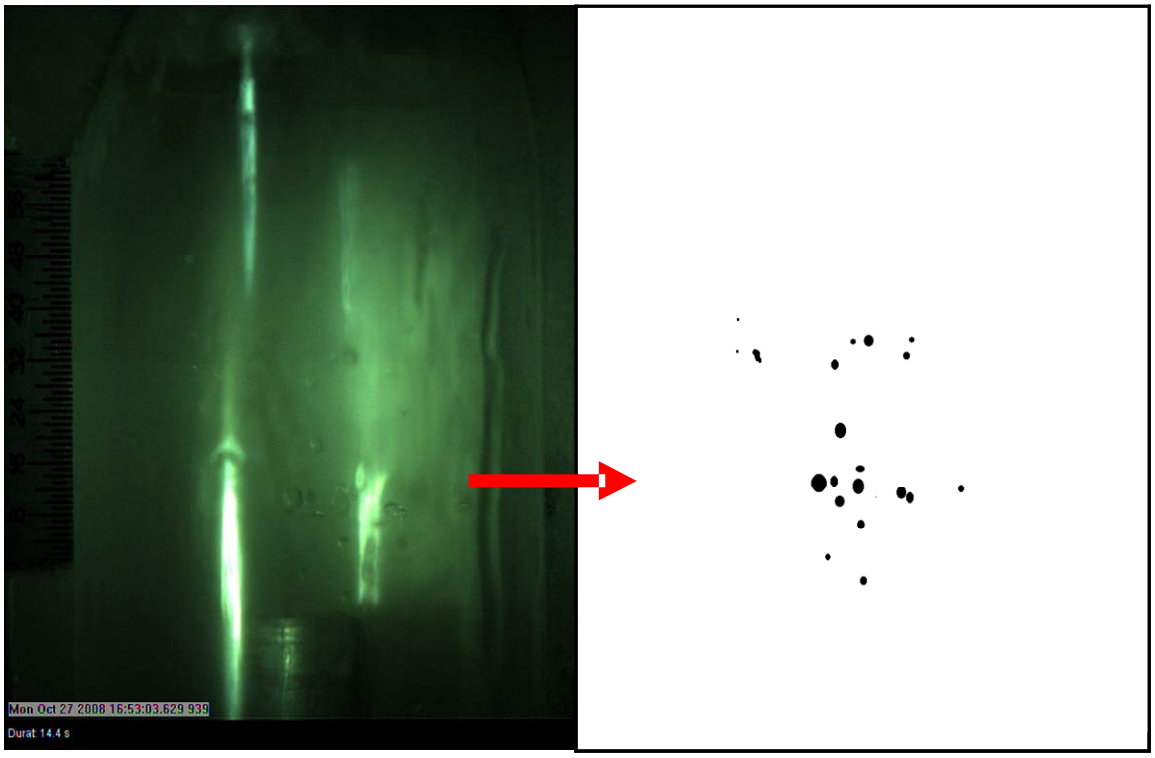

Figure 3. a) Real time captured picture b) Modified picture for particle analysis

Probability distribution and normal distribution of liquid droplet diameters are shown in Figure 4 and Figure 5 respectively. Liquid refrigerant droplets ranging from 180µm-2000µm have been found in the experimental studies. Entrained and separated droplets in vapour flow are visualized to determine the separation efficiency of the accumulator. The calculated separation efficiency (η_s) from Equation (6) for this droplet diameter distribution is 96,7%.

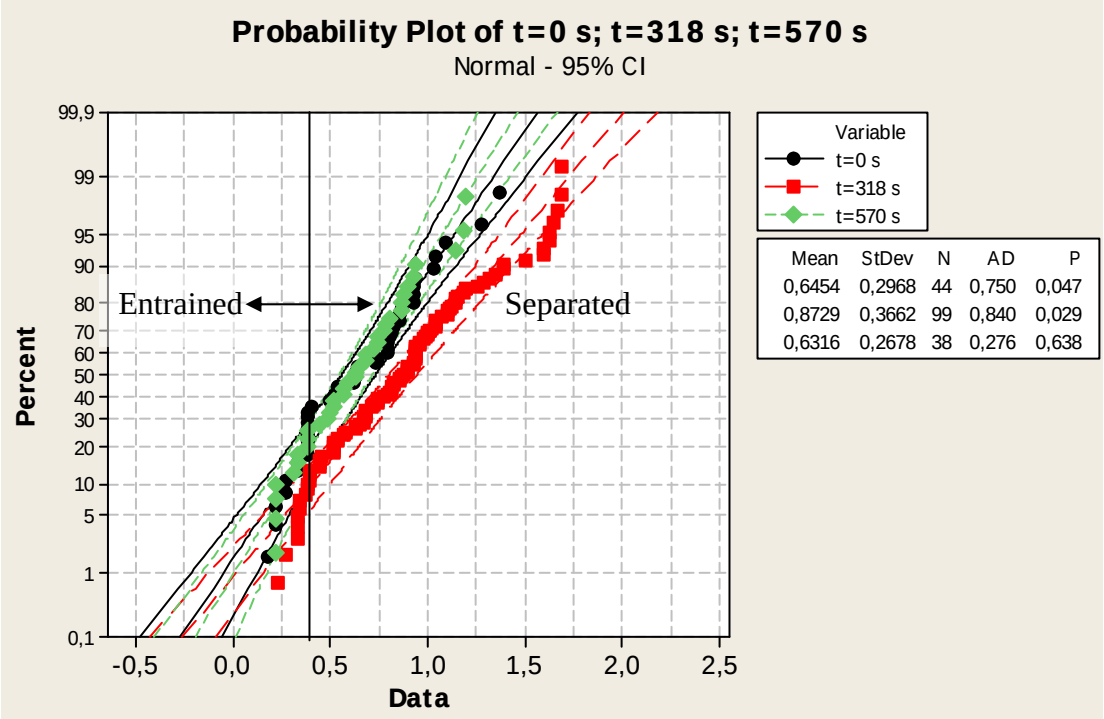

Figure 4. Probability distribution of liquid droplets

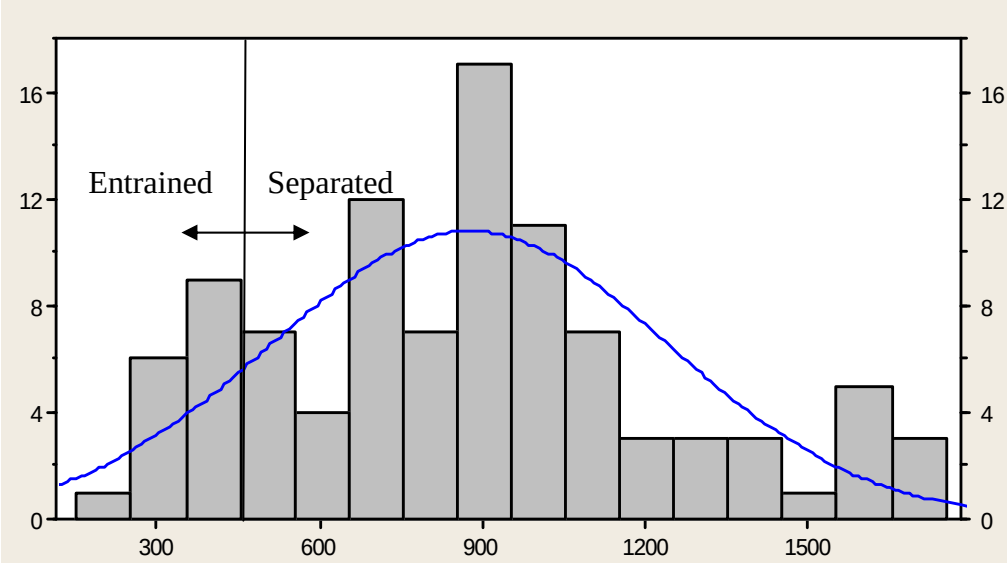

Figure 5. Normal distribution of liquid droplets

During the experiments, droplet size measurements are conducted at different total refrigerant mass fluxes on the time domain. Figure 6 shows the calculated mean diameter and SMD for the liquid droplets at different mass fluxes entering the accumulator. Due to high variation in droplet diameter, calculated SMD for the liquid droplets are found to be generally 32-50% higher than the calculated mean diameter of the droplets.

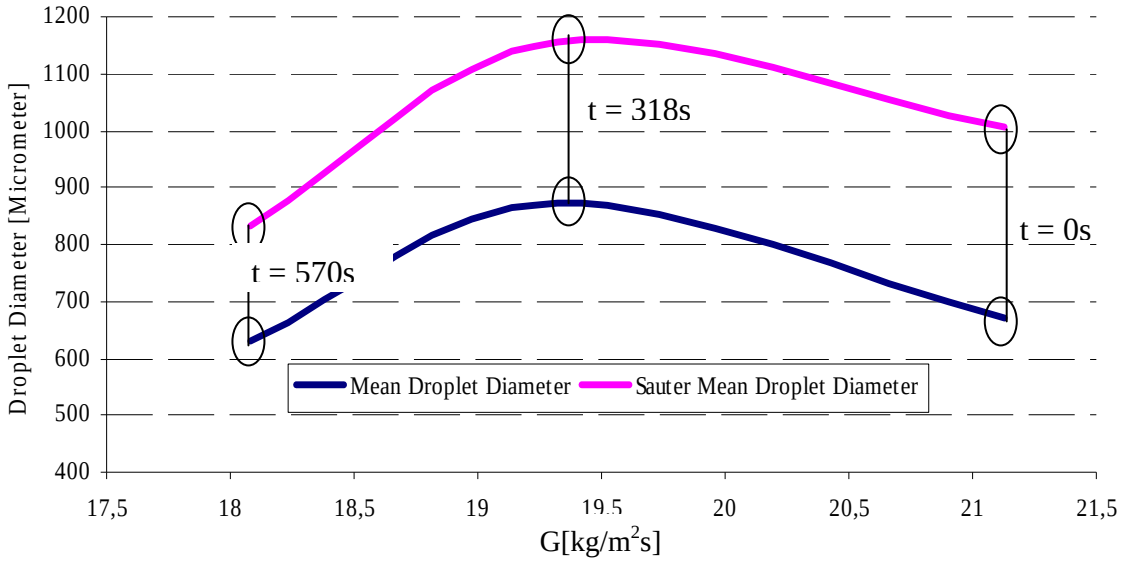

Figure 6. Mass flux versus mean droplet diameter and the SMD

Due to separation of liquid droplets from the vapour phase, continuous increase in the liquid level inside the accumulator has been observed. There are three important phases during on cycle of the refrigerator. First, the accumulator is filled up suddenly. This is due to high mass flux and low thermodynamic quality. Second, we observe a decrease in the liquid level due to partial evaporation of the stored liquid refrigerant. Third, increase in the liquid level with additional storage of liquid refrigerant due to low mass flux, but high thermodynamic quality. Figure 7 shows the change in the liquid level during the on period of the refrigerator.

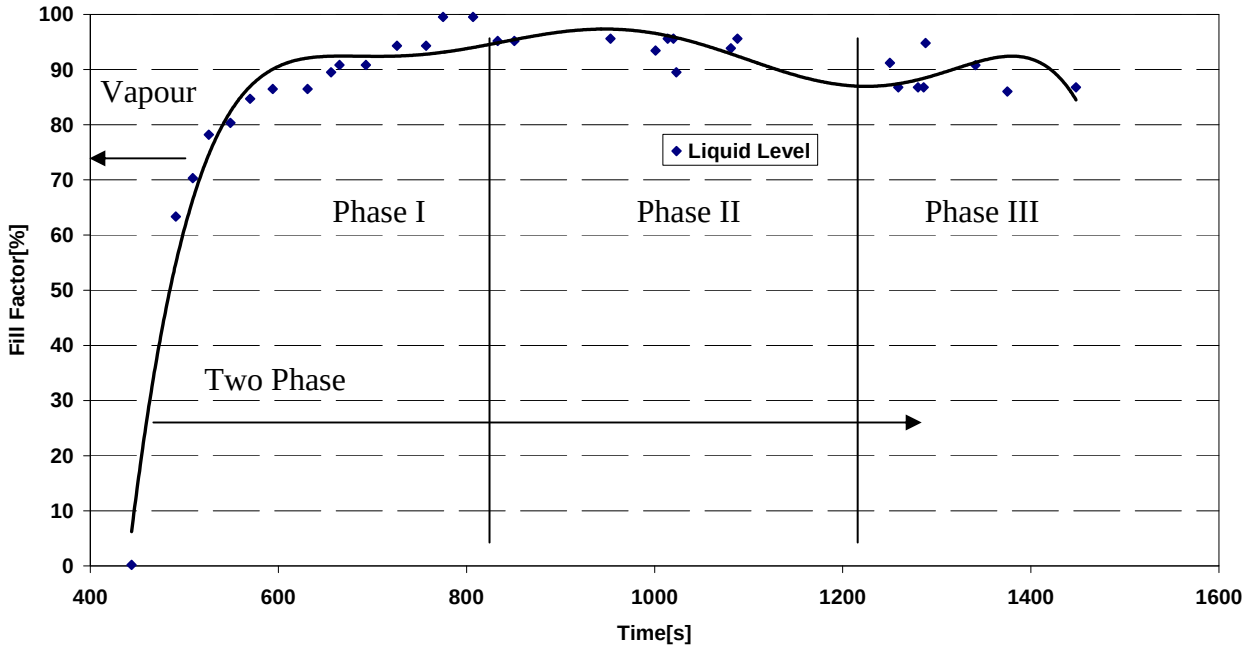

Figure 7. Change in the liquid refrigerant level during the on period of the refrigerator

The velocity, diameter and distance from the center of the accumulator inlet tube are measured instantaneously by the high speed camera. As shown in Figure 8, droplet velocity changes with the droplet diameter and the distance from the center of the accumulator inlet tube. It has been found that the velocity distribution of the liquid droplets also has a normal distribution along the axial direction. The positive and negative velocities indicate the entrained and the separated liquid droplets respectively.

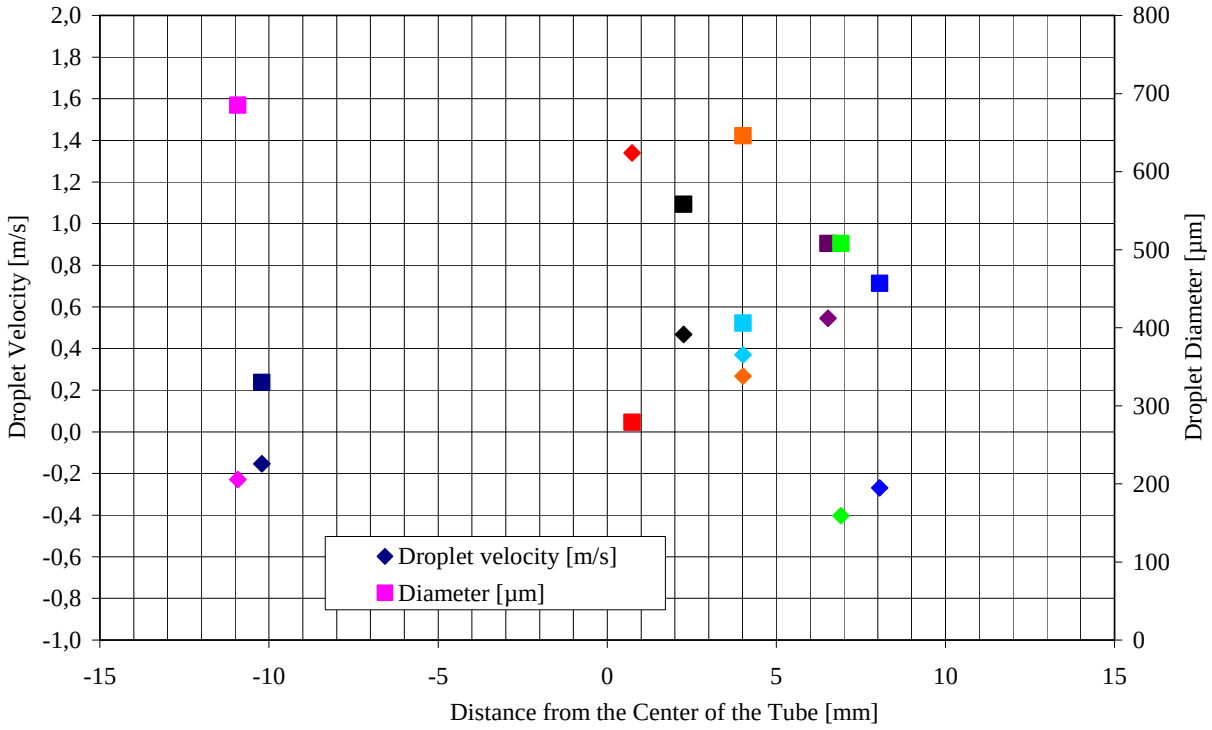

Figure 8. Velocity and diameter of liquid droplets in the accumulator

CONCLUSIONS

The transient two-phase isobutane (R-600a) refrigerant flow visualization and analyses in the accumulator provides important information on the flow characteristics. In this study, the refrigerant droplet size distribution and the increase of liquid refrigerant level inside the accumulator have been determined for different mass fluxes.

1. Liquid refrigerant droplets ranging from 180µm-2000µm have been found in the experimental studies.
2. Due to high variation in droplet diameter, calculated SMD for the liquid droplets are found to be generally 32-50% higher than the calculated mean diameter of the droplets.
3. Refrigerant total mass flux has a profound effect on the liquid droplet diameter.
4. Separation efficiency has been analysed based on force balance on the liquid droplet. The calculated separation efficiency (η_s) from Equation (6) for this droplet diameter distribution is 96,7%.
5. It has been found that droplet velocity changes with respect to the droplet diameter and the distance from the center of the accumulator inlet tube.
6. The velocity distribution of the liquid droplets also has a normal distribution along the axial direction.

NOMENCLATURE

Quantity	**Symbol**	**Coherent SI Unit**
A	Area	m^2
D	Diameter	m
F	Force	$N = kgm/s^2$
ρ	Density	kg/m^3
V	Volume	m^3
G	Mass flux	kg/m^2s

U	Velocity	m/s
a	Acceleration	m/s^2
g	Gravitational acceleration	m/s^2
d	Diameter	m
t	Time	s
pps	Picture per second	s^{-1}
C_D	Coefficient of drag	
η_s	Separation efficiency	

Subscripts

d	Liquid droplet
V	Vapour
L	Liquid
D	Drag
B	Buoyancy
G	Gravitational
s	Separated droplet
e	Entrained droplet

REFERENCES

1. Gas Processors Suppliers Association, *Engineering Data Book*, Volumes 1&2, Section 7, 2004.
2. Todd B. Jekel, Douglas T. Reindi, Micheal Fisher, *Gravity Separator Fundamentals and Design*, IIAR 2001 Ammonia Refrigeration Convention & Exhibition Long Beach, CA, 2001.
3. W.D. Monnery, W.Y. Svrcek, *Analytical Study of Liquid/Vapour Separation Efficiency*, Department of Chemical & Petroleum Engineering University of Calgary, Calgary, AB T2N 1N4, 2000.
4. Cemil Inan, Turgay Gonul, M. Yalcin Tanes, *X-Ray Investigation of a Domestic Refrigerator. Observations at 25°C Ambient Temperature,* ARCELIK A.S., Research and Technology Development Center, 81719 Tuzla-Istanbul, Turkey, 2002
5. 5. C. M. Winkler, J. E. Peters, *Refrigerant Droplet Size Measurements in Conjuction with a Novel Method for Improving Flow Distribution in Evaporators*, Department of Mechanical and Industrial Engineering, University of Illinois at Urbana-Champaign, Urbana, Illinois, 2002
6. Marcos Bockholt, Wilhelm Tegethoff, Nicholas Lemke, Nils-Christian Strupp, Christoph Richter, *Transient Modelling of a Controllable Low Pressure Accumulator in CO_2 Refrigeration Cycles*, Modelica, 2008
7. Dongbei Yue, Yudong Xu, Rasool Bux Mahar, Fuqiang Liu, Yongfeng Nie, *Analytical Solution of Gravity Separation Model (GSM): Separation of Water Droplets from Vapour in Submerged Combustion Evaporator*, Department of Environmental Science and Engineering, Tsinghua University, Beijing 1000084, China, 2006
8. R. Terblache, H.C.R. Heuter, D. G. Kröger, *Drop Size Distribution Below Different Wet Cooling Tower Fills*, Department of Mechanical and Mechatronic Engineering, University of Stellenbosch, Private Bag X1, Matieland, 7602, South Africa, 2008
9. Sang-Joon Lee, Hyoung-Bum Kim, Jeong-Ki Huh, Seung-Joon Lee, Byoung-Ha Ahn, *Quantitative Analysis of Flow inside the Accumulator of a Rotary Compressor*, International Journal of Refrigeration, 2003

ANALYSIS OF BOILING HEAT TRANSFER ON THE NON-ISOTHERMAL SURFACE COVERED WITH SELECTED WIRE MESH STRUCTURES

Ł.J. Orman[1,*], T. Orzechowski[2]
[1,2]Kielce University of Technology, Kielce, Poland

ABSTRACT. The paper presents the experimental results of distilled water and ethyl alcohol boiling heat transfer on the non – isothermal surface of a fin covered with wire mesh structures. The coating consists of 1, 2 and 3 layers of copper mesh whose wire diameter is 0.20 mm and mesh aperture 0.32 mm. The layers have been sintered to each other and to the copper fin in a reduction hydrogen atmosphere. The work covered the investigation into the impact of the number of mesh layers on heat flux, analysis of physical phenomena during the process and comparison of the results with selected heat transfer models. It has been concluded that the application of such porous structures enhances boiling heat transfer - the heat flux for mesh coated surfaces is several times higher comparing to the smooth surface. The thickest 3 – layer coating proves to be most favourable, especially at small superheats. For high superheats the heat flux approaches a certain limiting value, which seems to be caused by a capillary pumping crisis and the fact that a significant amount of vapour remains in the voids of the structure.

Keywords: *boiling, heat transfer enhancement, thermovision*

INTRODUCTION

Boiling heat transfer enables to dissipate significant heat fluxes at relatively small temperature differences. However, in order to further increase dissipated heat fluxes smooth surfaces of heat exchangers can be covered with some additional coatings: capillary porous, wire mesh and others. Such layers enhance boiling heat transfer comparing to smooth surfaces. Nevertheless, up to now it has not been possible to form a general model of heat transfer during boiling on such coatings, because the knowledge of physical fundamentals of the phenomenon is still insufficient.
Smirnov et al. [1] describe the boiling phenomenon in porous structures, which are modelled as arrays of microfins in which heat transfer under nucleate boiling regime occurs. The local heat transfer coefficients are determined considering hydraulic pressure loss of the counter flow of the vapour and liquid phase. A disadvantage of the model is a need to determine a constant that depends on the experiment conditions, sample properties and etc. A dependence of heat flux vs. superheat (defined as a difference between the wall and saturation temperatures) is given in the form of [2]:

$$q \sim \theta^m \tag{1}$$

where the contact m for mesh structures is nearly linear and in the range of $0.8 \div 1.0$.
In a semi – empirical model of Rao et al. [3] it is assumed that the pressure loss in the porous layer can be determined from the Darcy equation. A formula to calculate heat flux as a dependance of superheat, surface microgeometry and liquid physical properties is given. The model was verified

* Corresponding author: Ł. Orman
Phone: + (48)-413424278, Fax: + (48)-413424450
E-mail address: orman@tu.kielce.pl

with experimental data of independent researchers for different flat surfaces and tubes covered with porous layers and good agreement was found.
A very simple and easy to use model to determine the heat flux was proposed by Nishikava et al. [4]. Heat is assumed to be transferred from the heating surface to the liquid by means of a 1-D heat conduction. The application of the model, however, might results in heat flux values well above the experimental data, as verified e.g. by Orzechowski et al. [5].
In order to propose a reliable model of boiling heat transfer it is necessary to properly conclude about the physical phenomena occurring in porous coatings. Brausch et al. [6] investigated water boiling on surfaces with 1, 3 and 5 layers of stainless steel mesh. Four kinds of mesh were used whose wire aperture ranged from 0.087 mm to 0.318 mm. It was observed that one layer of mesh improved heat transfer in comparison to the smooth surface at superheats up to 15 K, while at higher temperature differences the wire mesh made bubble removal from the structure more difficult, which resulted in the formation of a vapour film, which insulated the heating surface from the liquid. Franco et al. [7] made similar observations from the exerimental tests of pool boiling of the dielectric refrigerant R141b. The heating surface was covered with copper, aluminium, brass and stainless steel mesh structures. It was assessed that mesh layers of small aperture enhanced heat transfer comparing to the smooth surface for small heat fluxes. Higher values of heat flux in this case led to limiting heat transfer, which was due to an unfavourable effect of vapour dry out conditions and resulted in lowering the critical heat flux. However, contradictory conclusions can be drawn from the experimental investigations of Rannenberg et al. [8] focused on R11 and R113 boiling on surfaces covered with 2 – 9 layers of mesh, which generally showed no impact of the number of layers on heat transfer.
Boiling heat transfer measurements are widely conducted on experimental stands whose main element is an isothermal heating block. However, real heat exchanging surfaces are usually non-isothermal and in order to properly design heat exchangers there is a need to carry out experiments on real non – isothermal surfaces. Consequently, an experimental stand was constructed that enables to conduct measurements on such surfaces. An important element of the stand is a thermovision camera, which registers a thermal map of an object.
In the paper the mesh coatings were selected as enhancing coverings since they have a regular geometrical structure as opposed to some porous layers. Thus, there is a possibility to conclude about the impact of their geometry on heat flux and, basing on the results, draw conclusions regarding the physical phenomena inside the layers.

EXPERIMENTAL SET – UP

The main element of the experimental stand is a copper fin, which is part of the wall of a vessel (Figure 1). It is in contact with the boiling liquid on one side and with the air on the other. Heat is supplied to the base of the fin with an electric heater. A thermovision camera is used to observe the outer surface of the fin in order to determine temperature along its height. The measured temperature distribution is then used to determine local values of the heat transfer coefficient. An auxiliary heater is installed at the bottom of the vessel to maintain stable pool boiling regime. A detailed description of the apparatus and the research method has been given in [9].

The inner surface of the fin in contact with the boiling liquid was covered with copper wire mesh coatings of mesh aperture 0.32 mm and wire diameter 0.20 mm. Four kinds of surfaces were tested: surfaces with 1, 2 and 3 layers of mesh, while a smooth surface served as a reference surface. The meshes were sintered to each other and to the copper fin in reduction atmosphere of hydrogen. The applied technology ensures strong and large bonds between the elements. In this way a contact resistance is eliminated. The tests were conducted for distilled water and ethyl alcohol as boiling liquids at ambient pressure.

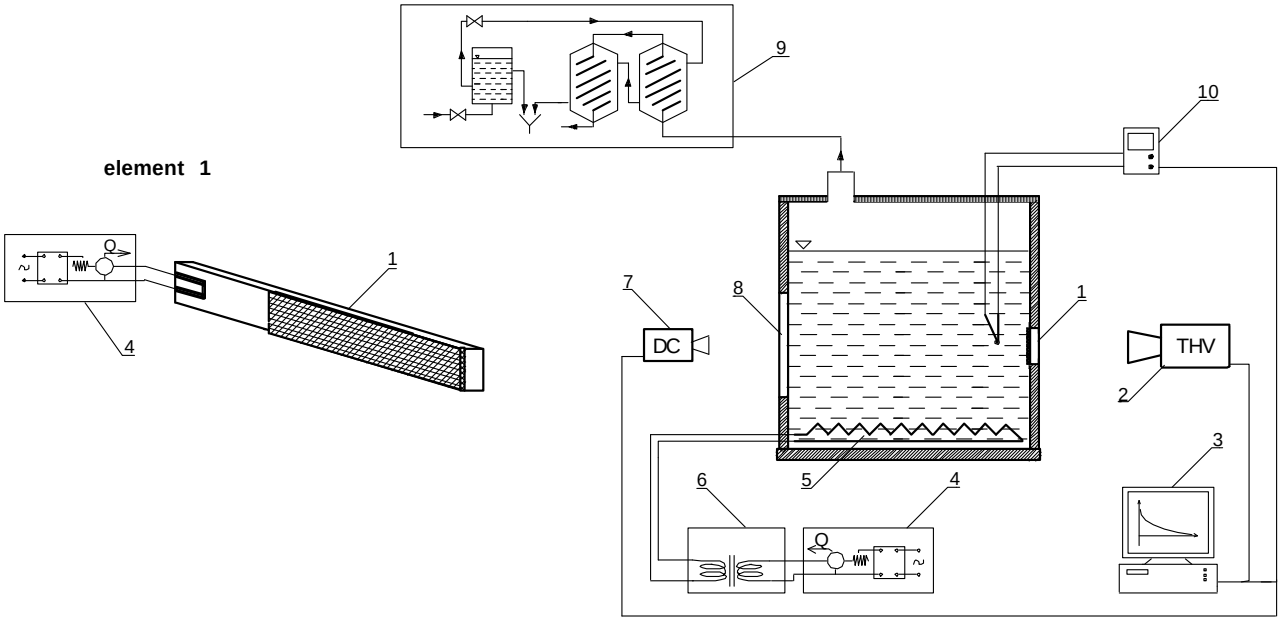

Figure 1. Schematic of the experimental set - up: 1 – copper fin, 2 – thermovision camera, 3 – data acquisition system, 4 – autotransformer, 5 – auxiliary heater, 6 – electrical current separation unit, 7 – digital camera, 8 – observation window, 9 – cooling and condensate retrieval unit, 10 – temperature measurement device [5]

RESULTS

The temperature distribution along the fin and its numerical differentiation enable to determine local values of the heat transfer coefficient according to the method presented in [9]. It has been assumed that the heat transfer coefficient between the fin and the liquid depends exponentially on superheat:

$$\alpha = a\,\theta^{n} \tag{2}$$

where a, n are constants, whose experimental determination leads to a formula for the boiling curve. Having considered (2) and the simplifing assumptions for 1-D heat conduction, a formula for temperature distribution along the fin is produced in the form of:

$$\frac{d^2\theta}{dx^2} = m^2\theta^{n+1} \tag{3}$$

which was analyzed by Ünal in [10].
After differentiation of (3) the superheat gradient in logarithmic coordinates is then calculated as:

$$\ln\left(\frac{d\theta}{dx}\right)^2 = \ln\left(\frac{2m^2}{n+2}\right) + (n+2)\ln\theta \tag{4}$$

where $n \neq 2$, while m^2 is defined as:

$$m^2 = \frac{a\,P}{\lambda F} \tag{5}$$

P and F are the circumference and surface area of the fin, respectively, while λ is the thermal conductivity of the fin's material. For fins of significant length, as in the analyzed case, no heat transfer at the tip can be assumed. In such a case an integration constant C in (4) equals 0.
Basing on the temperature distribution along the fin recorded with the infrared camera and its numerical differentiation the constants: a and n can be determined from (4), which is done applying the linear regression to research data. Consequently, it is possible to draw boiling curves as a function of heat transfer coefficient or heat flux and wall superheat using (2).
In order to more precisely determine the heat flux the results for ethyl alcohol have been analysed with a modified method, assuming the non - linear dependance for heat transfer coefficient [9]:

$$\alpha = a_1 + a_2\theta + a_3\theta^2 + a_4\theta^3 + \ldots \tag{6}$$

The infrared temperature measurements have been conducted with a long-wave (8 – 14 μm) thermovision camera VIGOcam v50 (Vigo System). The device is equipped with 22°x16° lens and a detector of 384x288 pixels whose thermal sensivity is 0.08 K at 30°C.
The measurement results have been presented in Figures 2a and 2b as heat flux vs. wall superheat for surfaces with 1, 2 and 3 layers of wire mesh. The porous layers have mesh aperture of 0.32 mm and wire diameter of 0.20 mm. The coating covers a surface of a copper fin of 4 mm thickness, 12 mm height and 90 mm length. For comparison the smooth surface test results for a bare surface are also given as in [11].

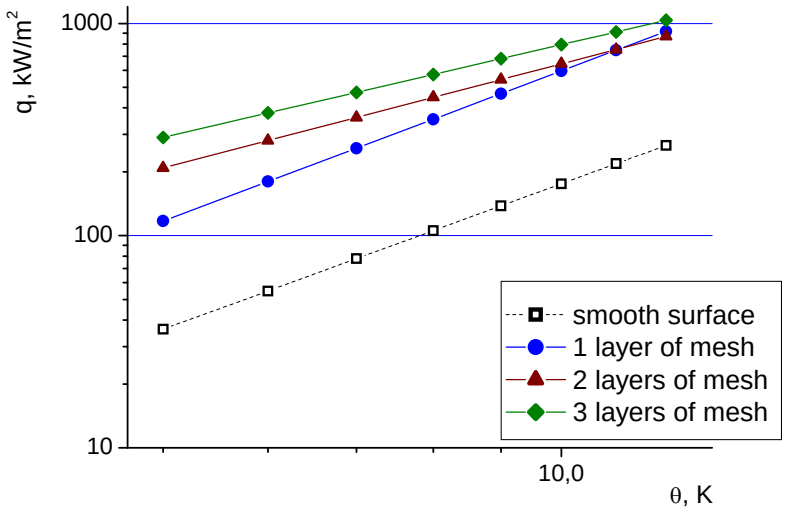

Figure 2a. Boiling curves for distilled water

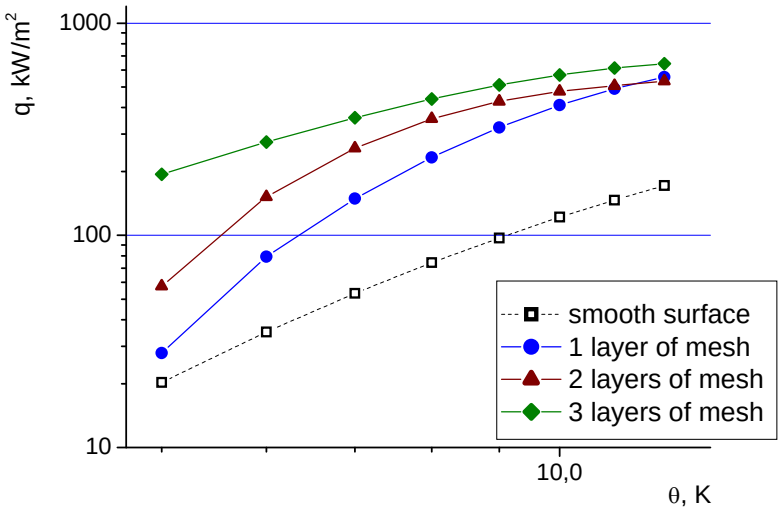

Figure 2b. Boiling curves for ethyl alcohol

As can be seen in the figures the porous coatings enhance boiling heat transfer comparing to the smooth reference surface. As the coating becomes higher (as more layers of mesh are applied – from 1 to 3) heat flux increases, which is most apparent for small superheats for both water and ethanol. For high superheats the heat flux approaches a certain value, which almost does not depend on the number of mesh layers. It seems to be caused by a crisis of capillary pumping and the fact that a significant amount of vapour remains in the interlayer's voids of the structure.
Figures 3a and b present a dependence of the enhancement factor expressed as a ratio of the heat flux for the surface with a microcoating (q_m) and for the smooth reference surface (q_s) as a function of the number of layers.

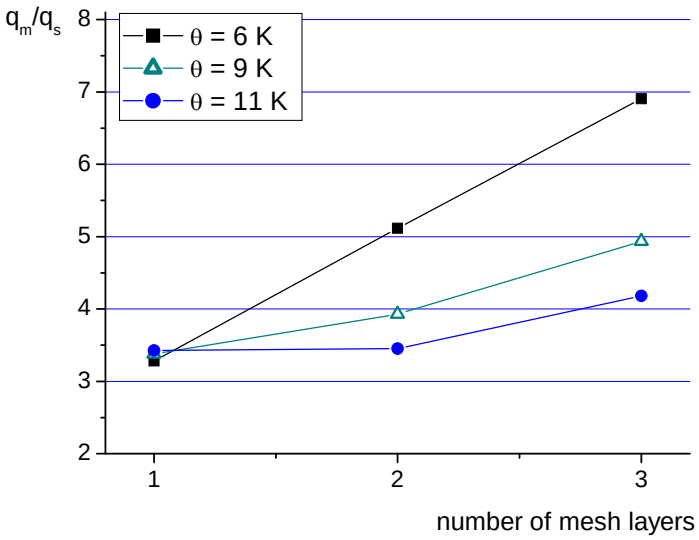

Figure 3a. Enhancement factor for distilled water

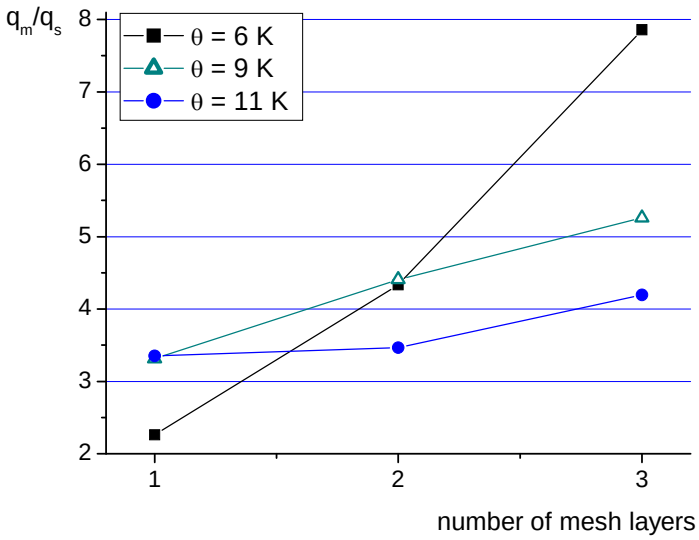

Figure 3b. Enhancement factor for ethyl alcohol

The analysis of Figures 3a and b reveals that the most significant impact of the application of the porous coatings is observed for small superheats. At the superheat of 6 K the heat flux for the surface with the 3 – layer mesh structure is almost 8 times higher for ethanol and 7 times higher for water in comparison to the smooth surface. It might be related to a higher active nucleation sites density. All the curves show a proportional dependence of the enhancement factor on the number of mesh layers, however, at high superheats this dependence is weakest, which might be caused by significant vapour flow resistance in such thick structures. It is worth noting that the results for the superheat of 11 K and the surfaces of 1 and 2 mesh layers are very similar to each other, while the 3 – layer coating performs much better. It might indicate that the transport of liquid into the structure by the side area of the sample is significantly improved for the thickest coating comparing to the other two structures, which might be verified by further visualisation studies.

Strong similarities between distilled water and ethyl alcohol results lead to a conclusion about the same mechanisms of heat transfer for both liquids. The enhancement factors for fully developed nucleate boiling (superheat of 11 K) have almost the same values for water and ethanol and they become more similar as superheat increases. It could indicate that in this regime coating properties have a dominant role.
In order to compare the present results with a model for boiling heat transfer obtained for isothermal surfaces the Smirnov model [1] has been selected. In this model the wire mesh structure is modelled as a system of regular microfins covered with a liquid film. The calculations are carried out according to the general formula:

$$q = C \sqrt[6]{\frac{r \sigma \lambda_l^3}{\nu_l}} (1-\varepsilon)^{\frac{5}{6}} \sqrt[3]{\lambda_{eff}} \left(\frac{\Delta T - \Delta T^*}{L_0} \right)^{\frac{5}{6}} \tag{7}$$

where L_0 is a structure parameter which depends on the mesh aperture and wire diameter, while ΔT - temperature differences.

The test results for a 2 – layer coating are compared with the calculation results in Figure 4. For both water and ethanol the congruity between the theoretical and experimental values is acceptable only for superheat of 5 K. Almost in the whole range of studied superheats the model

underestimates the experimental values, which might prove that it is unsuitable to successfully predict the heat flux for non – isothermal surfaces.

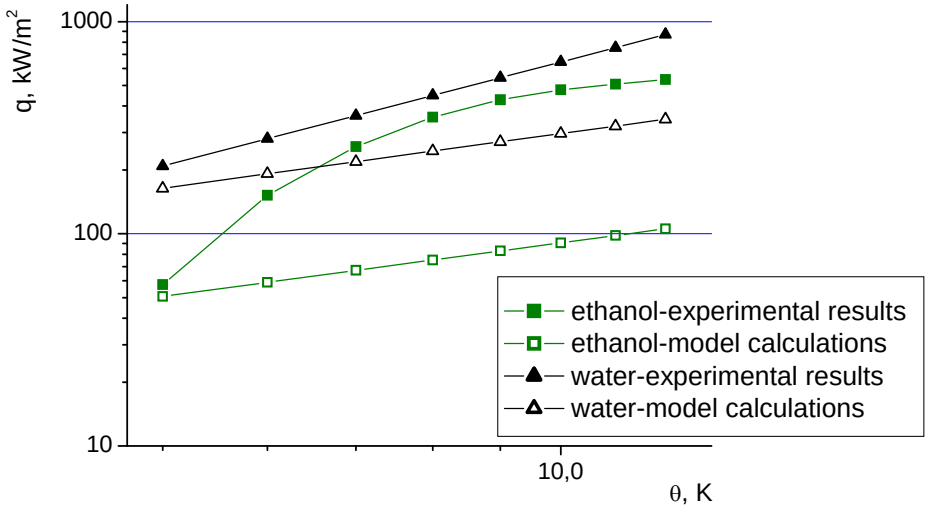

Figure 4. Comparison of the experimental data and calculation results according to the Smirnov model [1] in case of the 2 – layer coating

CONCLUSIONS

The application of porous structures enhances boiling heat transfer. The heat flux for surfaces with the investigated wire mesh structures is several times higher comparing to the smooth surface. The thickest 3 – layer coating proves to be most favourable, especially at small superheats. The present findings are congruous with the work of Kovalev et al. [12]. Moreover, as can be seen in Figure 2b, on the boiling curves for ethyl alcohol a region of significant increase in heat flux (for small superheats) is observed and than the curves become flatter, which is also described in [12] as a characteristic feature. However, the comparison of the results with the Smirnov model shows poor agreement. Consequently, there is a need to develop a correlation for the non – isothermal surfaces basing on the fundamental analysis of the boiling phenomenon in the porous coatings.
It is worth noting that for the tested mesh structures of mesh aperture of 0.32 mm, wire diameter of 0.20 mm and the number of layers from 1 to 3 heat flux increases as the coating becomes higher for supeheats up to 11 K. For high superheats the heat flux approaches a certain value, which seems to be caused by a capillary pumping crisis and the fact that a significant amount of vapour remains in the voids of the structure.

Nomenclature:
ε - porosity
σ - surface tension
C - constant
r - latent heat of vaporisation
eff - subscript of an effective value
l - subscript describing a liquid property

REFERENCES

1. Smirnov G.F., Coba A.L., Afanasiev B.A., The heat transfer by boiling in splits, capilaries, wick structures, *AIAA Paper,* 1978, 78-461.
2. Smirnov G.F., The Generalised Model of Boiling Heat Transfer, *Proceedings of 8th Int. Heat Pipe Conference*, 1992, pp 60-64.
3. Rao M. S., Balakrishnan A.R., Analysis of pool boiling heat transfer over porou surfaces, *Heat and Mass Transfer*, No. 32, pp 463-469, 1997.
4. Nishikava K., Ito T., Tanaka K., Augmented heat transfer by nucleate boiling on a sinterer metal layer, *Heat Transfer – Japanese Reseach*, Vol. 8, pp 65-81, 1979.
5. Orzechowski T., Orman Ł.J., Boiling heat transfer on surfaces covered with copper fibrous microstructures, *Proceedings of XI Int. Symposium „Heat Transfer and Renewable Sources of Energy”*, Szczecin, September 13-16, 2006, pp 613-619.
6. Brausch A., Kew P.A., The effect of surface condition on boiling heat transfer from mesh wicks, *Proceedings of 12th Int. Heat Transfer Conference*, Grenoble, vol. 3, 2002.
7. Franco A., Latrofa E.M., Yagov V.V., Heat transfer enhancement in pool boiling of a refrigerant fluid with wire nets structures, *Experimental Thermal and Fluid Science*, vol. 30, pp 263-275, 2006.
8. Rannenberg M., Beer H., Heat transfer by evaporation in capillary porous wire mesh structures, *Letters in Heat and Mass Transfer*, vol. 7, pp 425-436, 1980.
9. Orzechowski T., Local values of heat transfer coefficient determination on fin's surface. *Experimental Thermal anf Fluid Science*, 31 Issue: 8, pp 947-955, 2007.
10. Ünal H.C., Determination of the temperature distribution in an extended surface with non – uniform heat transfer coefficient, *Int J Heat Mass Transfer*, vol. 28, pp 2279 – 2283, 1985.
11. Orman Ł.J., Nucleate boiling heat transfer on a smooth surface of a fin*, Proceedings of XII Int. Symposium „Heat Transfer and Renewable Sources of Energy”*, Szczecin, September 11-14, 2008, pp 363-369.
12. Kovalev S.A., Solov'ev S.L., Ovodkov O.A., Liquid boiling on porous surfaces, *Heat Transfer-Soviet Research*, vol. 19, pp 109-120, 1987.

AN EXPERIMENTAL STUDY ON PRESSURE DROP OF INLET AND EXIT MANIFOLDS AND PORTS OF PLATE HEAT EXCHANGERS

C.-Y. Yang*, Y.-H. Lin and H.-T. Lo
Department of Mechanical Engineering
National Central University, Chung-Li, Taiwan

ABSTRACT. Precise pressure drop estimation is critical for an optimum plate heat exchanger design. Numerous studies have been conducted on the pressure drop within the plate passages but studies on pressure drop of flow through inlet/outlet ports are very limited. The present study is intending to derive a relation between the ports losses and the ports/core geometries. Four plate heat exchangers with various inlet/outlet port diameters and plate number were tested in the present study. The test results show that the port and manifold pressure drop predicted by Shah and Focke [1] is almost twice of the measure value for large plate number heat exchangers. The core friction coefficients for different pate number heat exchangers were also examined. There is a drastic difference between the heat exchangers with the same plate geometry but different plate number if the Shah and Focke [1] predicted manifold and port losses were used to evaluate core friction coefficients. However, while the measured manifold and port losses were used to evaluate core friction pressure drop and friction coefficients, the friction coefficients for both type heat exchangers agree very well with each other.

Keywords: *Plate Heat Exchanger, Pressure Drop, Manifolds and Ports*

NOMENCLATURE

A_c	total core cross-section area, m^2
A_{c1}	core flow passage cross-section area, m^2
A_p	port cross-section area, $A_p = \pi D_p^{\,2}/4$, m^2
D_h	flow passage hydraulic diameter, m
D_p	port diameter, m
f	plate passage frictional coefficient, dimensionless
G_c	plate passage mass velocity, $G_c = \dot{m}/A_c$, kg/m^2 s
G_p	port mass velocity, $G_p = \dot{m}/A_p$, kg/m^2 s
K_p	inlet and outlet manifolds and ports pressure losses coefficient, dimensionless
$\dot{m}$	mass flow rate, kg/s
Re_{D_h}	core Reynolds number, $Re_{D_h} = G_c D_h/A_c$, dimensionless
Re_{D_p}	port Reynolds number, $Re_{D_p} = G_p D_p/A_p$, dimensionless

Greek symbol

* Corresponding author: Prof. C.-Y. Yang
Phone: + (886)-3-4267347, Fax: + (886)-3-4254501
E-mail address: cyyang@ncu.edu.tw

Δp_{cn} connecting parts pressure drop, Pa
Δp_f core frictional pressure drop, Pa
Δp_p inlet and outlet manifolds and ports pressure drop, Pa
Δp_t total pressure drop, Pa
ρ density, kg/m^3
σ cross-section area ratio, $\sigma = A_p/A_c$, dimensionless

Sbuscripts
i inlet
o outlet

INTRODUCTION

Plate heat exchangers have been popularly used in industrial applications and air-conditioning systems for several decades. Owing to its complicate corrugate flow passages, the pressure drop in a plate heat exchanger is relatively higher than other type of heat exchangers. Precise pressure drop estimation is critical for an optimum plate heat exchanger design. The pressure drop in a plate heat exchanger consists of flow through inlet and exit manifolds and ports, flow through plate passages and the effects of elevation and momentum change. Numerous studies have been conducted on the pressure drop within the plate passages but studies on pressure drop of flow through inlet/outlet ports are very limited. In a well designer heat exchanger, the inlet/outlet ports pressure drop is kept below 10 % of the total pressure drop. Most of the designers applied a simplified correlation proposed by Shah and Focke [1], $\Delta p_p = 1.5\ G_p^2/2\rho$, to evaluate the manifold and ports pressure drop. However, for some high plates number exchangers, the ports pressure drop may exceed 40 % of the total pressure drop. The above Shah and Focke [1] correlation may course significant error on port pressure drop calculation.

The present study measured the pressure drop in inlet and exit ports and manifolds of plate heat exchangers directly by putting pressure probes into the manifolds of the heat exchangers. It is intending to derive the relation between the ports losses and the ports/core geometries.

EXPERIMENTAL SETUP AND DATA REDUCTION

Four plate heat exchangers with various inlet/outlet port diameters (16 and 28 mm) and plate number (10 and 60) were tested in the present study. All heat exchangers have the same flow passage height δ = 2 mm, passage width λ = 7 mm, chevron angle $\beta = 65^o$ and hydraulic diameter D_h = 4 mm. The cross section area for each port $A_p = \pi/4\ D_p^2$, each flow passage $A_{c1} = \delta(W - 4)$, total core $A_c = A_{c1}\ N/2$ and port/core cross section area ratio $\sigma = A_p/A_c$. Details dimensions of the plate heat exchangers tested are listed in Table 1. The relative geometric parameters are shown in Figure 1.

Table 1.
Dimensions of test heat exchangers (mm)

type	port D_p (mm)	Plates number, N	length L (mm)	width W (mm)	cross section area (mm^2)			$\sigma = A_p/A_c$
					port, A_p	passage, A_{c1}	core, A_c	
D28 x 10	28	10	304	124	615.44	240	1200	0.513
D28 x 60	28	60	304	124	615.44	240	7200	0.085
D16 x 10	16	10	194	80	200.96	152	760	0.264
D16 x 60	16	60	194	80	200.96	152	4560	0.044

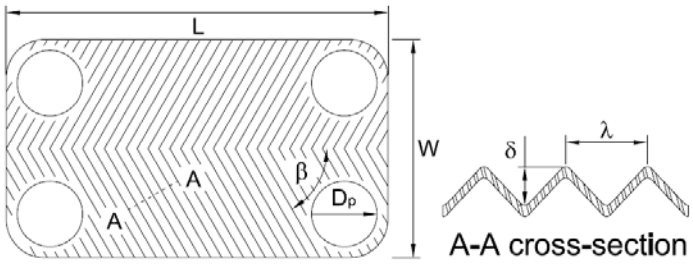

Figure 1. Geometric parameters of the heat exchangers

A schematic diagram of the test facility is shown in Figure 2. Water was pumped from the storage tank to the test section and return to the storage tank to complete a close loop by a variable speed centrifugal pump. A gear type flow meter was placed between the pump and the test section to measure the water flow rate. A RTD was installed near after the flow meter to measure the water temperature which is based for evaluating water properties. Three differential transducers were installed between the external inlet/outlet port, inlet port/upstream of the core inside the plate heat exchanger and outlet port/downstream of the core inside the plate heat exchanger to measure the total (Δp_t), inlet (Δp_i) and outlet (Δp_o) pressure drops respectively.

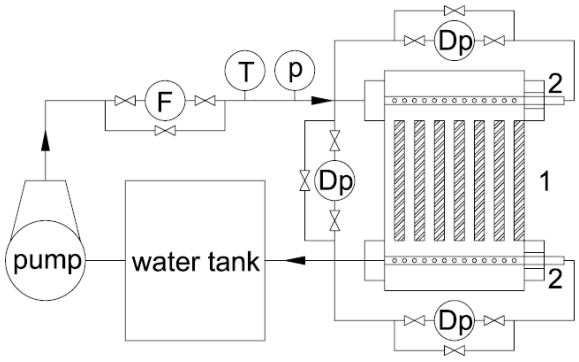

Figure 2. Schematic diagram of the test facility

As shown in Figure 3, the measured total pressure drop, Δp_t, consists of (a) pressure drop associated with the inlet and outlet external connecting parts for installing pressure transducer, Δp_{cni} and Δp_{cno}, (b) pressure drop associated with the inlet and outlet manifolds and ports inside the heat exchanger, Δp_{pi} and Δp_{po}, (c) frictional pressure drop within the core plate passages, Δp_f, and (d) pressure drop due to the elevation change. Since the test heat exchangers were placed horizontally, there is no elevation effect on the pressure drop measurement. The total measured pressure drop can be expressed as:

$$\Delta p_t = \Delta p_{cni} + \Delta p_{cno} + \Delta p_{pi} + \Delta p_{po} + \Delta p_f \quad (1)$$

Since the connecting parts losses, Δp_{cni} and Δp_{cno}, can be evaluated from the conventional correlations [2], the inlet and outlet ports losses, Δp_{pi} and Δp_{po}, can be obtained by direct subtracting the connecting losses from the measured inlet/outlet losses.

$$\Delta p_{pi} = \Delta p_i - \Delta p_{cni} \text{ and } \Delta p_{po} = \Delta p_o - \Delta p_{cno}$$

We may combine the ports and connecting parts losses as:

$$\Delta p_p = \Delta p_{pi} + \Delta p_{po} \text{ and } \Delta p_{cn} = \Delta p_{cni} + \Delta p_{cno}$$

The core friction coefficient, f, can be calculated as:

$$f = \frac{\Delta p_f D_h}{4L} \frac{2\rho}{G_c^{\ 2}} \tag{2}$$

where G_c is the mass velocity through the core area.

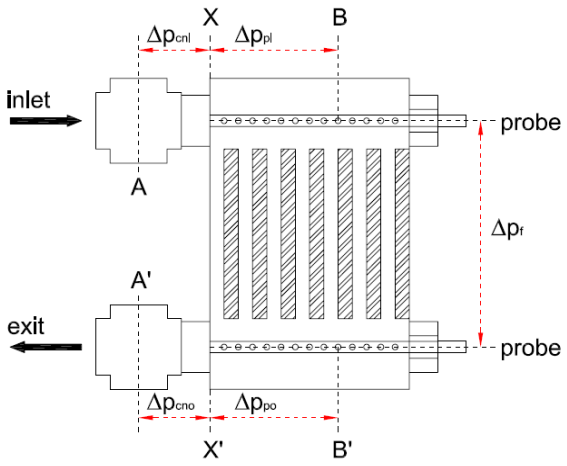

Figure 3. Schematic diagram of each pressure drop component

EXPERIMENTAL RESULTS AND DISCUSSIONS

Figure 4 shows each measured pressure drop components in the heat exchanger D28x10 which has larger port diameter and fewer plates. The manifold and port pressure drop predicted by Shah and Focke [1] is also sketched for comparison. The figure shows that the predicted value is slightly lower than the measured values. However, since the flow rate is low, the ports pressure drop is less than 10 % of the total pressure drop; the prediction discrepancy does not make significant error for core frictional pressure drop evaluation. The same experimental results for the heat exchanger D16x10 is shown in Figure 5. Since the port diameter of D16x10 is smaller than that of D28x10, the manifold and port pressure drop is higher than that of D28x10 and, therefore, the prediction discrepancy by Shah and Focke [1] is larger than D28x10.

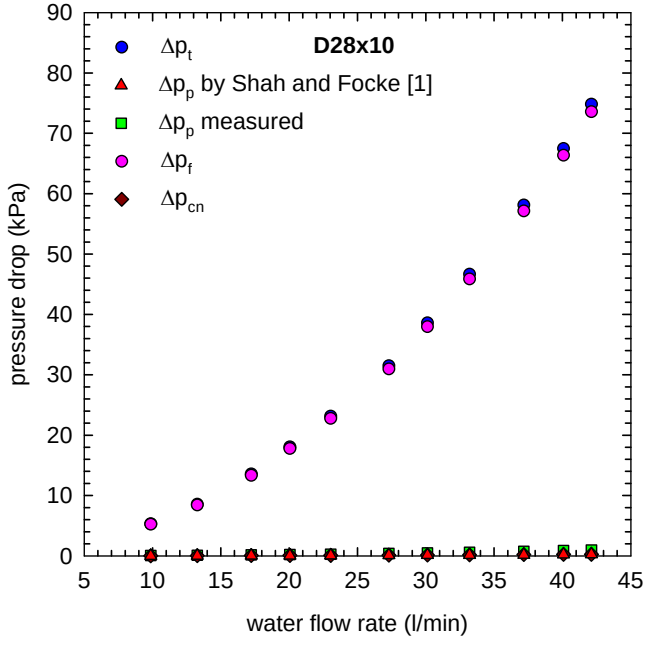

Figure 4. Measured and predicted pressure drops components of D28x10

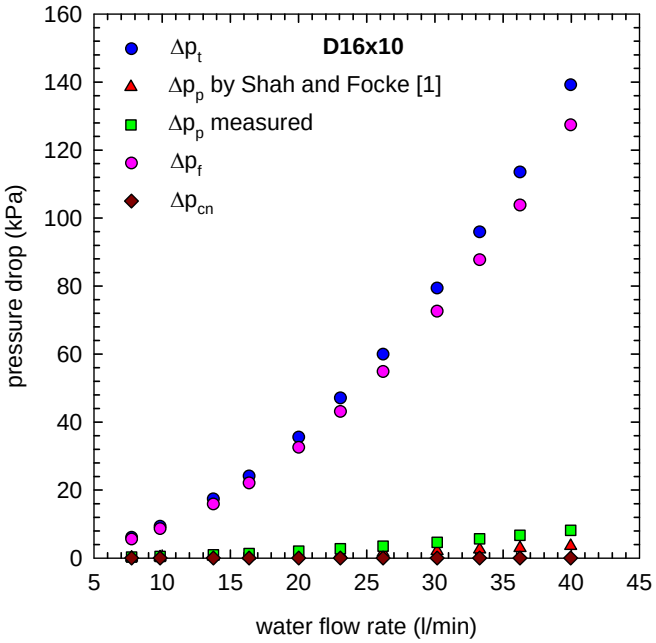

Figure 5. Measured and predicted pressure drops components of D16x10

As shown in Figures 6 and 7, for the larger plate number heat exchangers D28x60 and D16x60, the ratio of port and manifold pressure drop to the total pressure are larger than 10 %. Especially for the smaller port diameter heat exchanger D16x60, the pressure drop ratio is greater than 36 %. The port and manifold pressure drop predicted by Shah and Focke [1] is almost twice of the measure value. This causes a significant error for deriving friction coefficient. The discrepancy caused by the Shah and Focke [1] prediction is no longer negligible.

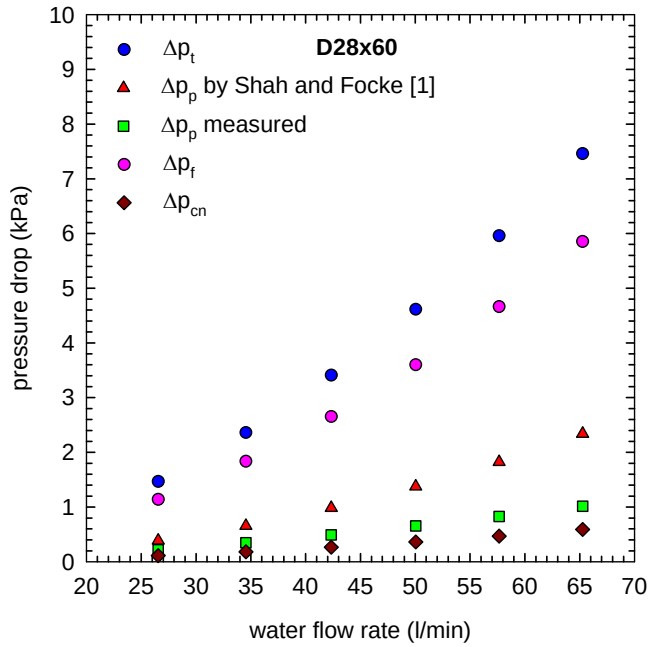

Figure 6. Measured and predicted pressure drops components of D28x60

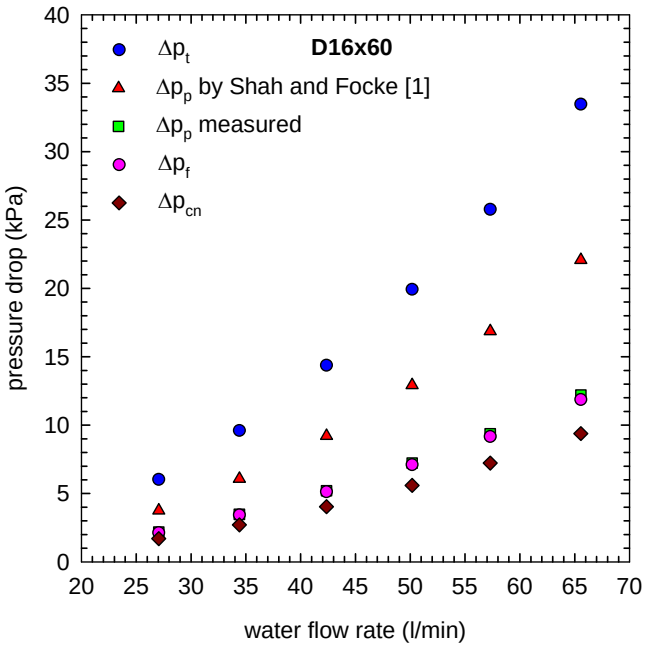

Figure 7. Measured and predicted pressure drops components of D16x60

For examining the correctness of the prediction port losses by Shah and Focke [1], the core friction coefficients based on the predicted and measured manifold and port losses were plotted in Figures 8 and 9. Figure 8 shows that if the Shah and Focke [1] predicted manifold and port losses were used in Equation (1) to evaluate core friction pressure drop and friction coefficients, there is a drastic difference between the heat exchangers with the same plate geometry but different plates number, especially for the smaller port heat exchangers (D16). This is not reasonable because the same plate geometries heat exchangers should have the same core friction coefficients. While the measured manifold and port losses were used in Equation (1) to evaluate core friction pressure drop and friction coefficients, Figure 9 shows that the friction coefficients for both type heat exchangers are agree very well with each other. This results shows that the Shah and Focke [1] correlation over predicted the port and manifold losses for high plate number heat exchangers.

Since the manifold and ports losses occur while the fluid flows through the sudden change of cross section area and direction from the ports to the core passage, they depend on the geometry of the inlet and outlet ports and core. It is expected that the manifold and port losses are in the form of conventional minor losses shown in Equation (3) and the loss coefficient, K_p, is a function of Reynolds number and port/core area ratio, $\sigma = A_p/A_c$.

$$\Delta p_p = \Delta p_{pi} + \Delta p_{po} = K_p \frac{G_p^{\,2}}{2\rho} \tag{3}$$

$$K_p = K_p\left(Re_{Dp}, \sigma\right) = C\sigma^n \, Re_{D_p}^{\,m} \tag{4}$$

Figure 10 shows that the loss coefficient K_p can be well correlated if the exponent of the area ratio, n = 0.5. More study for establishing accurate correlation is necessary for those kinds of plate heat exchangers.

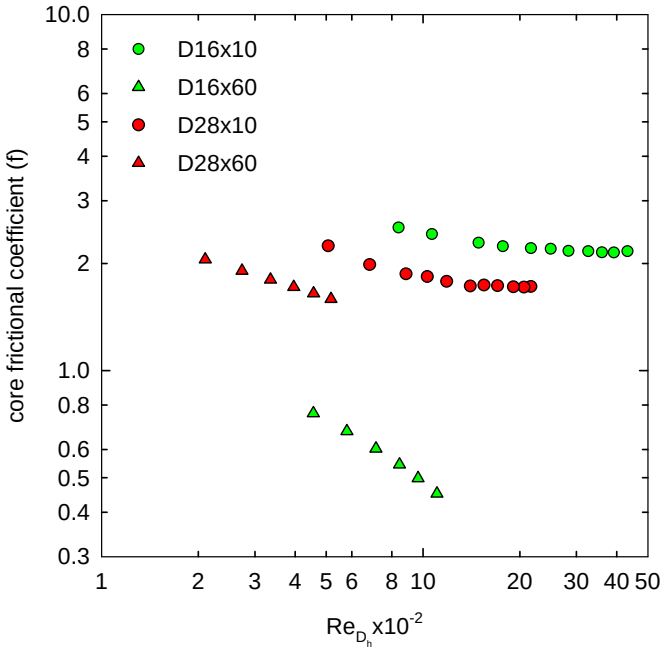

Figure 8. Core frictional coefficients based on the port losses predicted by Shah and Focke [1]

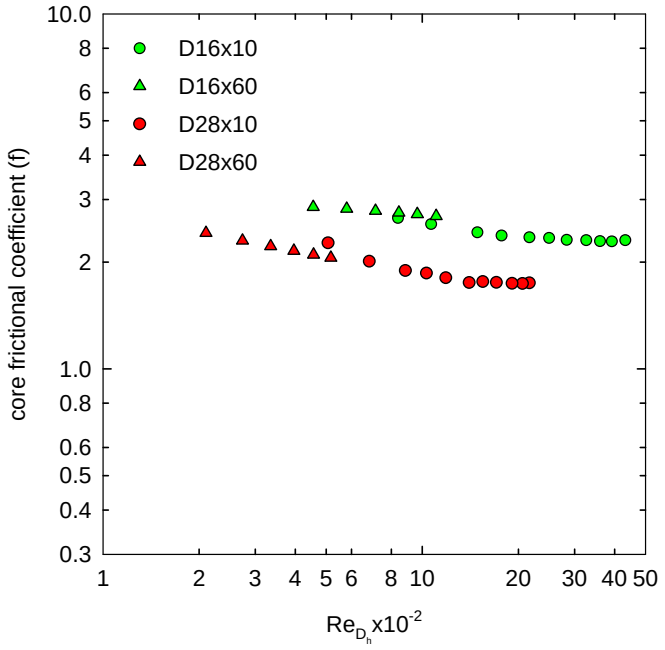

Figure 9. Core frictional coefficients based on the measured port losses

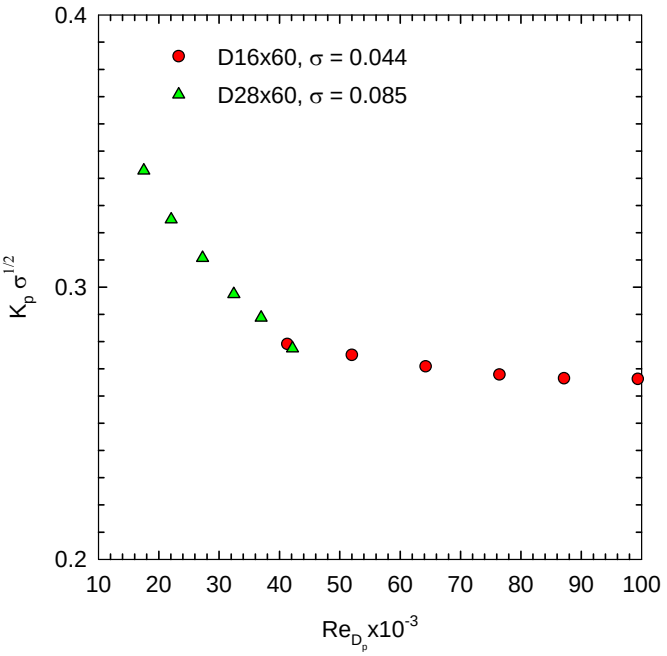

Figure 10. Relation of the loss coefficient K_p to Reynolds number and area ratio

CONCLUSIONS

Four plate heat exchangers with various inlet/outlet port diameters and plate number were tested in the present study. The test results show that the port and manifold pressure drop predicted by Shah and Focke [1] is almost twice of the measure value for large plate number heat exchangers. The discrepancy caused by the Shah and Focke [1] prediction is not negligible.

The previous test results were examined by plotting the core friction coefficients for different pate number heat exchangers. The Results show that if the Shah and Focke [1] predicted manifold and port losses were used to evaluate core friction coefficients, there is a drastic difference between the heat exchangers with the same plate geometry but different plates number, especially for the smaller port heat exchangers. However, while the measured manifold and port losses were used to evaluate core friction pressure drop and friction coefficients, the friction coefficients for both type heat exchangers agree very well with each other.

REFERENCES

[1] Shah, R. K., and Focke, W. W., 1988, “Plate Heat Exchangers and their Design Theory,’’ published in Heat Transfer Equipment Design, edited by Shah R. K., Subbarao, E. C. and Mashelkar, R. A., pp. 227-254, Hemisphere Publishing Corp. Washington, D. C.

[2] Munson, B. R., Young D. F., and Okiishi T. H., 1990, Fundamentals of Fluid Mechanics, 3rd Edition, pp. 496-501, John Wiley & Sons, Inc., Canada.

HEAT TRANSFER ENHANCEMENT FROM A CIRCULAR CYLINDER TO DISTILLED WATER BY ULTRASONIC WAVES: PRELIMINARY REMARKS

F. Baffigi, C. Bartoli *
Energetic Department "L.Poggi", University of Pisa, Via Diotisalvi 2, Italy

ABSTRACT. An experimental investigation was carried out to research the effects of ultrasonic waves on heat transfer, in subcooled boiling conditions, from a stainless steel horizontal cylinder, heated by Joule effect, to distilled water. Actually the acoustical streaming induces turbulence through the cinematic field and so an increase of the heat transfer coefficient. In this preliminary paper, the authors have studied the heat transfer enhancement for two-phase conditions. The dependence on such parameters as ultrasonic wave power, subcooled ΔT and convection heat flux is also examined. The aim of this paper is to find out the parameters that maximise the heat transfer coefficient. After our preliminary tests we had found that the maximum heat transfer coefficient increase occurs at the difference between the water saturation temperature and prefixed water temperature is higher, as also the ultrasonic generator power.

Keywords: *experimental methodologies, heat transfer enhancement, subcooled boiling, ultrasonic waves, cooling systems.*

INTRODUCTION

Since the 1960s the cooling effect induced by ultrasonic waves was investigated. Firstly R.M. Fand, in 1965, [1] reported the heat transfer data obtained in an experimental study to determine the influence of acoustic vibrations on solid-liquid interface process involved in the desalination of water. The heat transfer test section is a cylinder, 0.011 mm. O.D.. The tests were performed at constant bulk water temperature and frequency. The sound pressure level, measured by a calibrate hydrophone, varied from 0 to 10^5 Pa and the acoustic frequency was 6.5 kHz for all tests. The bulk water temperature was 300 K and the difference in temperature between the cylinder and bulk of water varied from 255.4 to 311 K. The maximum increase in the heat transfer coefficient, due to acoustically induced cavitation observed in these experiments, was 33%.
K.-A. Park and A.E. Bergles, in 1988, [3] undertook a study to confirm the effects of ultrasonic cooling of microelectronic components, in saturated boiling conditions, using R-113 as working fluid. They noticed that a degradation of low heat flux boiling occurred when the pool was saturated, but boiling was improved when the pool was subcooled. Burnout heat fluxes for saturated and subcooled conditions were slightly increased by an ultrasonic field.

In 1967, K.W. Li and J.D. Parker [2], had investigated the acoustical effects in free convection heat transfer to water. The heating surface consisted of a platinum wire ($2 \cdot 10^{-4}$ m. in diameter), immersed in water at the temperature of 302.6 K. Experimental results showed that the heat transfer rates were affected by the presence of sound waves in the vicinity of the wire. The sound frequency was set up at 20 kHz. The tests were carried out at a given temperature difference (ΔT = 288.7 and 299.7 K). It might be noticed that the influence of the acoustical field on free convection was greater at lower temperature difference. Moreover the heat transfer coefficient increased until a

* Corresponding author: Prof. C. Bartoli
Phone: + (39)-050-2217113, Fax: + (391)-050-2217150
E-mail address: c.bartoli@ing.unipi.it

certain level of sound, above which the heat transfer coefficient started to decrease. Actually the sound waves propagated through the water, induced a cavitation process in the water. As the sound pressure was greater than 53.4 kPa, this process due to the presence of the sound waves was significant.

In 1992 Y. Iida and K. Tsutsui [4] carried out a series of experiments to make clear systematically the effects of ultrasonic waves, at 28 kHz in frequency and 33.6 W in maximum power, on natural convention, nucleate boiling, and film boiling from a heated 0.2 mm diameter platinum wire to saturated water or ethyl alcohol. A distinctive augmentation effect on heat transfer was observed in both the natural convection and film boiling heat transfer regions. Though no effects were observed in nucleate boiling of water, a small effect was attained in low heat flux nucleate boiling of ethyl alcohol. An increase of about 20% in the maximum heat flux in both liquids was obtained by applying ultrasonic waves. The minimum heat flux point was raised at higher values of both the degree of superheat and the heat flux. Moreover it might be noticed that the heat transfer coefficients attained under ultrasonic waves were depended largely on the distance from the vibrating surface to the test position.

In 1993 S. Nomura and M. Nakagawa [5] explained the mechanism of heat transfer enhancement on a narrow surface by ultrasonic vibration, cavitation intensities and measured the heat transfer coefficients changing the width of the surface from 0.1 to 8 mm. It might be noticed that the heat transfer coefficient on a narrow surface without ultrasonic increased due to the heat conduction with decreasing width. Moreover, the authors found out that the ultrasonic waves induced at the same time cavitation and a perturbation of the dynamic field. They had measured the cavitation intensity, by measuring the erosion loss of the aluminium foil attached to the surface of a heater, and they could evaluated the contribution due to the only ultrasonic vibrations. The large-scale motions induced by acoustic streaming would be effective for cooling large heating surfaces, while the very-small motions induced by cavitation would be more effective for cooling small heating surfaces.

In 1997 S. Bonekamp and K. Bier [6] had been investigated the effect of ultrasound on pool boiling heat transfer to mixtures of the refrigerants R23 and R134a, in a wide range of heat flux and saturation pressure. The main result was that the enhancement of the heat transfer coefficient, which could be achieved by ultrasound, was much more pronounced than for pure substances.

In 1998 H. Yamashiro, H. Takamatsu and H. Honda [7] had studied experimentally the effect of ultrasonic vibration on the heat transfer during the rapid quenching of a thin horizontal wire in subcooled water. They had examined the parametric effects of the sound pressure and the frequency of ultrasonic vibration on the transient boiling curve and the first minimum heat flux point with a higher wall superheat.

H.-Y. Kim, Y.G. Kim and B.-H. Kang, in 2004 [8] reported the relationship between the flow behaviour induced by ultrasonic vibration and the consequent heat transfer enhancement in natural convection and pool boiling regimes. Experimental results showed that the effects of ultrasonic vibration on flow behaviour were vastly different depending on the heat transfer regime and the amount of dissolved gas. In natural convention and subcooled boiling regimes, behaviour of cavitation bubbles strongly affects the heat transfer enhancement. In saturated boiling, no cavitation occurs, thus the reduced bubble size at departure and acoustic streaming are major factors enhancing heat transfer rate. The highest enhancement ratio was obtained in natural convection regime, where the effect of ultrasonic vibration was manifested through violent motion of cavitation bubbles.

In 2004 B.-G. Loh and D.-R. Lee [9] found out that the cooling effect on the heat source had a correlation with the gap between the ultrasonic vibrator and heat source; the cooling effect was maximized when the gap corresponds to the multiple of half-wavelength of the ultrasonic wave and this effect was attributable to the resonance of the sound wave.

This introduction highlights that the scientific works about the cooling effect by ultrasonic waves aren't so clear, so the authors had been begun a systematic series of experimental tests, to try to understand the mechanism. Moreover, the aim of this work will be to find out the parameters that maximize the heat transfer coefficient from a circular cylinder to water. The first results are referred

to subcooled boiling conditions, because the heat transfer coefficient is higher than in single-phase conditions; in fact in saturated boiling [8] the effect of ultrasonic waves is negligible. Later on we could apply this basic research to the cooling of electronic components.

EXPERIMENTAL APPARATUS

The experimental set-up consisted of a rectangular stainless steel ultrasonic tank (300x230x200 mm^3). The ultrasonic waves generator worked at the frequency of 40 kHz (ν), with a combined transducer output from 200 to 400 W. An electrical resistance was put inside the tank, in order to heat the water. Cold water circulating into a copper coil (8-mm. O.D., 6-mm. I.D, length 2000-mm.), connected to an external refrigerator, was used to control the pool temperature. The heating element was a stainless steel horizontal cylinder (3-mm. O.D, 2-mm. I.D., length 192- mm.), immersed in water. The cylinder was heated by a direct current power supply (maximum value of current and voltage respectively 450 A and 20V).The experimental apparatus is shown in Figures 1 and 2. The test length, which was the distance between two voltage sensors, was 70 mm.. This two voltage sensors, made of 0.5-mm. diameter copper wires, were connected to a digital multimeter to measure the voltage drop across the test section. The amperage instead was measured by means of the voltage drop across a calibrated resistance. The cylinder axial temperature was measured by means of one sliding thermocouple. The results reported here refer to a test length, which was the central part of the heater, where the temperature is axially uniform to within ± 0.1 K. The water temperature near the heater, was measured by means of a thermocouple.

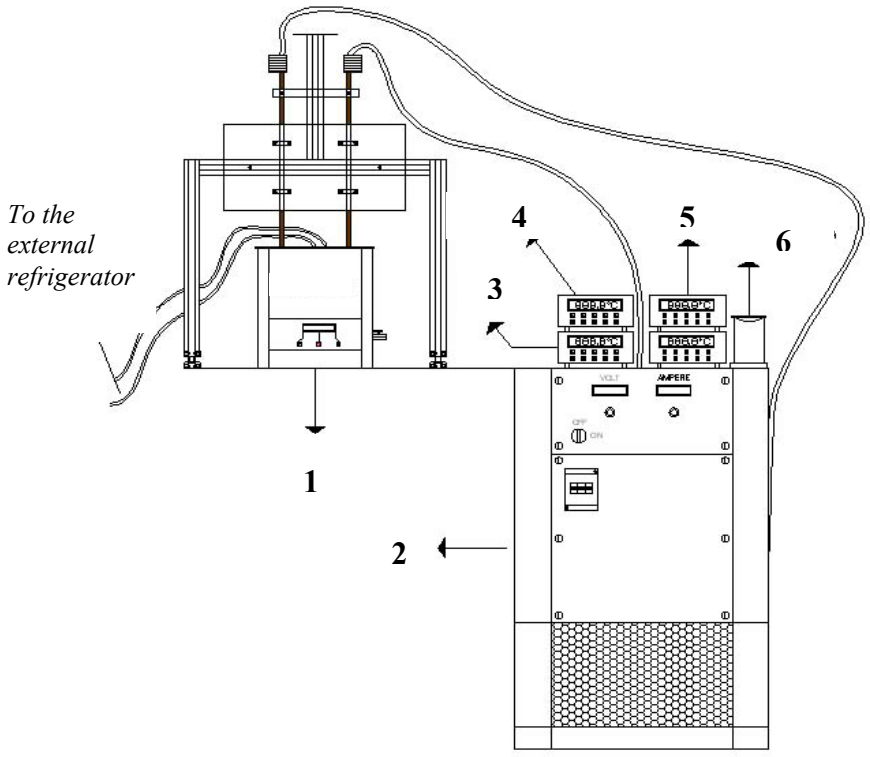

Figure 1. Experimental apparatus
(1. Ultrasonic generator; 2. DC power supply; 3, 4, 5.Digital multimeter; 6. Calibrated resistance)

PROCEDURE AND ANALYSIS OF UNCERTAINTY

The distilled water was set at the temperature of 338.15 K (ΔT_{sub} = 35 K) by the electrical resistance inside the tank. Then we supplied electrical power, $\dot{q}$, by the direct current power supply, varying from $80 \cdot 10^3$ W/m^2 to $160 \cdot 10^3$ W/m^2. The water remained at the same temperature by means

of the external cooling coil. When the steady state conditions had been reached, we activated the ultrasonic generator, and at first we changed the ultrasonic power, P_{gen}, from 200 to 400 W. Each parameters ($\dot{q}$ and P_{gen}) was been varied one by one.

(a) **(b)**

Figure 2. Experimental apparatus ((a) ultrasonic generator, (b) Stainless steel circular cylinder immersed in water inside the tank)

The circumferentially averaged external temperature of the heater was calculated, assuming cylindrical symmetry, after the circumferentially averaged internal temperature, the dissipated power, the thermal conductivity, and the thickness were known. The inner temperature (T_i) of the hollow cylinder is measured by a 0.5 mm in diameter T – type thermocouple. The external temperature (T_{wall}) is calculated through the Fourier equation as a function of the dissipated electric power per unit volume and of the hollow cylinder radii, as shown in equation (1):

$$T_{wall} = T_i + \frac{\dot{q}^*}{4 \cdot k} R_i^2 \cdot \left[1 + 2 \cdot \ln\left(\frac{R_e}{R_i}\right) - \left(\frac{R_e}{R_i}\right)^2 \right] \tag{1}$$

The flux per unit surface was been calculated by the equation (2):

$$\dot{q} = \frac{V \cdot I}{\pi \cdot De \cdot L} \tag{2}$$

Finally, we could calculate the heat transfer coefficient, by the Newton's equation, without and with the ultrasonic waves, as shown in equation (3):

$$\dot{q} = hA(T_{wall} - T_{H_2O}) \tag{3}$$

Radial conduction is assumed as being dominant. Indeed, investigations performed with a sliding thermocouple showed that the temperature variation along the test length of the cylinder didn't exceed the value of measurement uncertainties. Angular dependence, was not considered here, as an average value was sought. A thermocouple at the cylinder measured the water temperature. Uncertainty analysis has been carried out according to [10]. Uncertainty sources are reported in Table 1, while calculated values for q and ΔT are 4.2% and ±0.5 K respectively.

Table 1
Uncertainty Sources

Measured Quantity	Reference Value	Overall Uncertainty
Cylinder temperature	T_{wall}-T_{H2O}=60 K	0.5 K
Water bulk temperature	338.15 K	0.5K
Current	84 A	0.3%
Voltage	1.2 V	0.2%
Cylinder thickness	$0.5 \cdot 10^{-3}$ m	2%
Heater area	$6.6 \cdot 10^{-4}$ m^2	3.7%

DISCUSSION OF EXPERIMENTAL RESULTS

In this preliminary paper we had studied the subcooled boiling regime, because our aim was to find out the optimal conditions to maximize the heat transfer coefficient. Firstly we had tried some tests to investigate the ΔT_{sub} influence on the heat transfer coefficient (Table 2). These data were obtained at $\dot{q}$ =135·10^3 W/m^2, ν = 40 kHz and P_{gen}= 400W. The experimental results had shown that the optimal ΔT_{sub} is 35 K, at which one the h increase amounts to 53%. These data had highlighted that h increases with ΔT_{sub} increasing. For this reason we had chosen this value of subcooling for each next test.

Table 2
Trend of h without and with ultrasound waves versus ΔT_{sub}

ΔT_{sub}[K]	**h (without ultrasonic waves) [W/Km^2]**	**h (with ultrasonic waves) [W/Km^2]**	**Δh [%]**
35 K	2450	3750	53
25 K	2840	3510	24
20 K	3147	3347	6

Then we had investigated the P_{gen} influence on h. As shown in Table 3 we had found a trend monotonically of h versus P_{gen}. For this reason the next tests had been carried out at 400W.

Table 3
Trend of h without and with ultrasound waves versus P_{gen}

P_{gen} [W]	**h (without ultrasonic waves) [W/Km^2]**	**h (with ultrasonic waves) [W/Km^2]**	**Δh [%]**
200W	2091	2690	28.6
300W	2091	2675	28
400W	2091	2838	35

The data in Table 3 were obtained at ΔT_{sub} =35 K, $\dot{q}$ =84·10^3 W/m^2, ν = 40kHz.

In Figure 3 is shown the $\dot{q}$ trend versus the difference T_{wall}-T_{H2O} . The tests were carried out in the previous optimal conditions for ultrasonic generator power (P_{gen} = 400W) and ΔT_{sub}=35 K, with or without ultrasound waves. At the presence of ultrasound waves the trend of the experimental points is significantly horizontally translated: at the same heat flux we had found a decrease of the difference

T_{wall}-T_{H2O} from 25 to 10 K. This result showed that the ultrasound waves could be used to decrease the cylinder temperature and also could be applied for cooling electronics components.

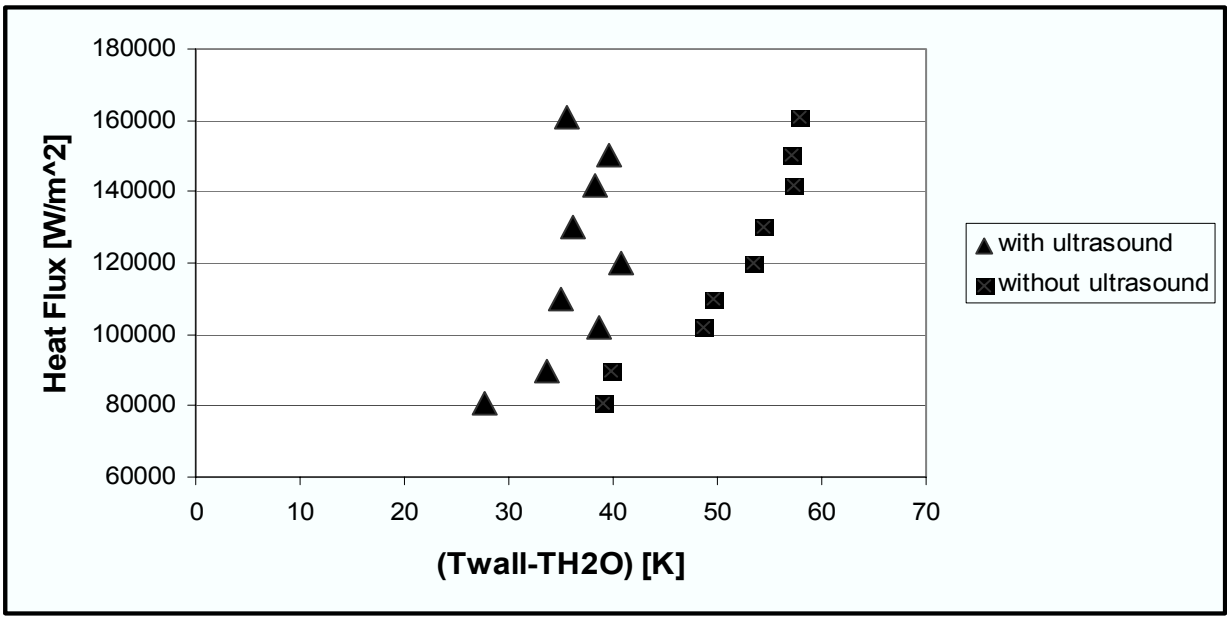

Figure 3. Trend of q versus (T_{wall}-T_{H2O}) at ΔT_{sub} =35 K, ν= 40 kHz and P_{gen} =400W

Figure 4 shows clearly that the presence of the ultrasound increases significantly the heat transfer coefficient, with the following parameters

1) ΔT_{sub} =35 K 2) ν =40kHz 3) P_{gen} = 400W.

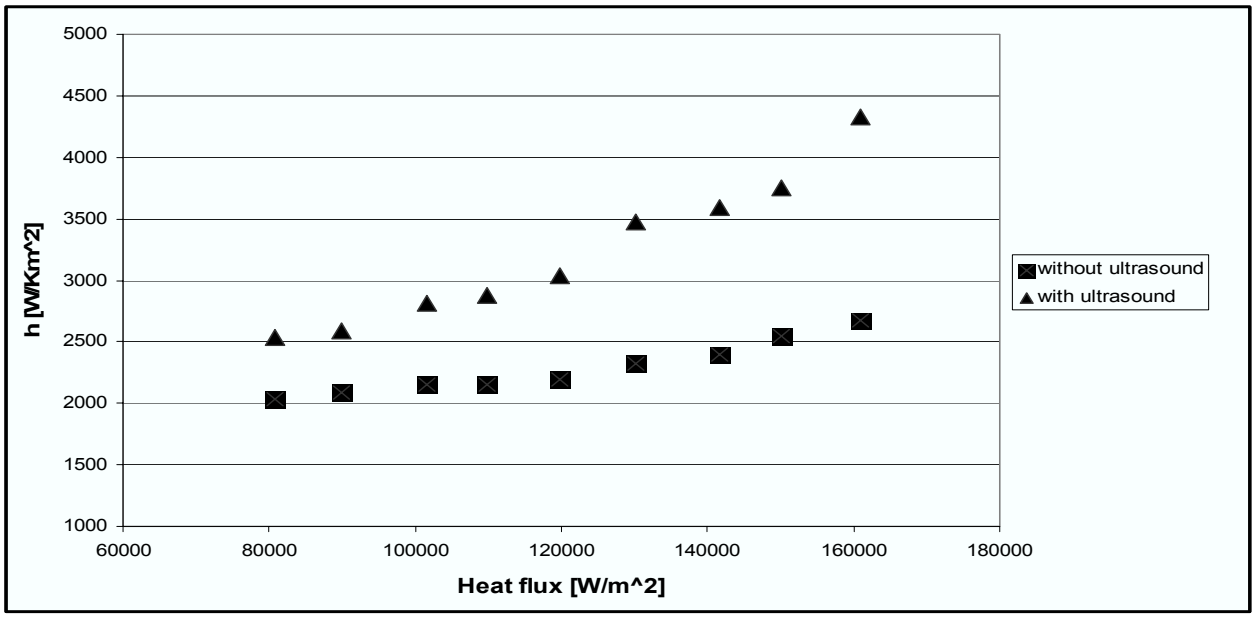

Figure 4. Trend of h versus at q (ΔT_{sub} =35 K, ν 40 kHz and P_{gen} = 400W)

In Table 4 we had summarized the data of figure 4.

Table 4

Trend of h without and with ultrasound waves versus $\dot{q}$

Heat flux [W/Km^2]	h (without ultrasonic waves) [W/Km^2]	h (with ultrasonic waves) [W/Km^2]	Δh [%]
$80 \cdot 10^3$	2032	2533	24
$90 \cdot 10^3$	2090	2585	23,7
$100 \cdot 10^3$	2151	2817	31
$110 \cdot 10^3$	2154	2876	33,5
$120 \cdot 10^3$	2192	3035	38
$130 \cdot 10^3$	2323	3477	50
$140 \cdot 10^3$	2398	3588	49,6
$150 \cdot 10^3$	2542	3757	48
$160 \cdot 10^3$	2678	4330	61,6

.

CONCLUSIONS

Afterwards we had been an exhaustive bibliography review, we had put right a new experimental research about ultrasonic waves. Our aim was to find out the parameters that maximize the heat transfer coefficient, in this case only in subcooled conditions. Each test had been carried out at the prefixed water temperature of 65 K and at the prefixed ultrasonic frequency, 40 kHz. After our preliminary tests we had found that the maximum h increase occurs at the difference between the water saturation temperature and prefixed water temperature is higher, as also the ultrasonic generator power. In this condition the presence of ultrasonic waves involves an h increase of about 53%, with heat flux of $135 \cdot 10^3$ W/m^2. In the future we firstly will complete the experimental study in subcooled regime, varying others different parameters, as the generator frequency and the gap between the cylinder and the bottom of the tank. Finally we will examine a narrow surface.

ACKNOWLEDGEMENTS

This work was supported by the NOVATEC S.r.l and his owner, Mr. Nello Franco, located in San Martino di Lupari (PD), which had donated to us the ultrasonic generator.

NOMENCLATURE

Symbol	Description	Units
T_{wall}	Cylinder outer temperature	[K]
Ti	Cylinder inner temperature	[K]
$\dot{q}^*$	Heat flux per unit volume	[W/m^3]
R_i	Cylinder inner radius	[m]
R_e	Cylinder outer radius	[m]
V	Voltage drop	[V]
I	Amperage	[A]
D_e	Cylinder outer diameter	[m]
L	Distance between the sensing leads	[m]

T_{H2O}	Reference water temperature	[K]
$(\Delta T)_{sub}$	Value of subcooling	[K]
P_{gen}	Ultrasonic power generator	[W]

REFERENCES

1. R.M. Fand, The influence of acoustical vibrations on heat transfer by natural convection from a horizontal cylinder to water*, Journal of heat transfer*, pp 309-310, 1965.
2. K.W Li and J.D. Parker, Acoustical effects on free convective heat transfer from a horizontal wire, *Journal of heat transfer*, pp 277-278, 1967.
3. K.-A. Park and A.E. Bergles, Ultrasonic enhancement of saturated and subcooled pool boiling, *International Journal of Heat and mass Transfer*, Vol.31, No.3, pp 664-667, 1988.
4. Yoshihiro Iida, Kentarou Tsutsui, Effects of ultrasonic waves on natural convection, nucleate boiling and film boiling heat transfer from a wire to a saturated liquid, *Experimental thermal and fluid science*, Vol.5, pp108-115, 1992.
5. S. Nomura and M. Nakagawa, Ultrasonic enhancement of heat transfer on narrow surface, Heat transfer- Japanese RESEARCH, Vol. 22, No 6, pp 546-558, 1993.
6. S. Bonekamp, K. Bier, Influence of ultrasound on pool boiling heat transfer to mixtures of the refrigerants R23 and R134a, *International Journal of Refrigeration,* Vol.20, No.8, pp 606-615, 1997.
7. H.Yamashiro, H.Takamatsu and H.Honda, Effects of ultrasonic vibration on transient boiling heat transfer during rapid quenching of a thin wire in water, *Transactions of the ASME*, Vol.120, pp282-286, 1998.
8. Ho-Young Kim, Yi Gu Kim, Byung Ha Kang, Enhancement of natural convection and pool boiling heat transfer via ultrasonic vibrations, *International Journal of Heat and Mass Transfer,* Vol. 47, pp2831-2840, 2004.
9. B.-G. Loh and D.-R. Lee, Heat transfer characteristics of acoustic streaming by longitudinal ultrasonic vibration, Journal of thermophysics and heat transfer, Vol.18, No 1, pp 94-99, 2004
10. R. J. Moffat, Describing Uncertainties in Experimental Results, *Experimental Thermal and Fluid Science,* Vol. 1, pp 3-17, 1988.

EXPERIMENTAL STUDY ON THE BRDF MEASUREMENT FOR SURFACE OF SOME MATERIALS

M. Xie*, X.C. Wang, H.H. Zhao, H.P. Tan
School of Energy Science and Engineering, Harbin Institute of Technology, 150001, China

ABSTRACT. Bidirectional Reflectance Distribution Function (BRDF) is a physical quantity that describes space reflection and scattering distribution characteristic of material surface. The concept of the BRDF defined by F.E.Nicodemus in 1970, is from the view of ray radiation and gets further development combined with the electromagnetic scattering theory of rough surface. Bidirectional Reflectance Distribution Function can describe the surface reflection and scattering characteristic of solid materials better, so considering the influence of material surface roughness, using lasers with band of 0.6328 μm, 1.34 μm and 3.39 μm, at different incident angles, we measured the BRDF of various materials including granite, aluminum plate, copper plate、aluminum foam, graphite fiber magnesium, carbon fiber (aluminum) through a self-built experiment table, by using the white standard plate made of polytetrafluoroethylene powder(approximate Lambert body) as a single sample for reference, and based on experimental data, we analyzed the reflection and scattering characteristic of the material surface.

Keywords: *BRDF, Reflection, Ray radiation, Characteristic*

INTRODUCTION

Bidirectional Reflectance Distribution Function (BRDF) is a physical quantity that describes space reflectance and scattering distribution characteristic of material surface. The concept of the BRDF defined by Nicodemus in 1970, is from the view of ray radiation [1] and gets further development combined with the electromagnetic scattering theory of rough surface. The BRDF can be used to evaluate reflection、absorption and scattering characteristic of varieties of material surfaces to the visible and infrared lights. So it can be used for telemetry or stealthy technology of the material surface and military target, and also be used for remote sensing measurement of satellites and other planets [2].

Considering that the BRDF influencing factors include material surface roughness, dielectric constant, incident angle and polarization etc, in this paper we used a self-built experiment table, according to a single reference method [3, 4, 5]—namely by using the white standard plate made of polytetrafluoroethylene powder(approximate Lambert body) as a single sample for reference, with band of 0.6328 μm, 1.34 μm and 3.39 μm, at different incident angles, considering the influence of material surface roughness at the same time, we measured the BRDF of various materials including granite, aluminum plate, copper plate, aluminum foam, graphite fiber magnesium, carbon fiber (aluminum), and based on experimental data, we analyzed the reflection and scattering characteristic of the material surface.

ANALYSIS OF INFLUENCE FACTORS

* Corresponding author: Prof. M. Xie
Phone: 0451-86413117
E-mail address: xieming@hope.hit.edu.cn

Surface roughness

With the increase of the measured material surface roughness, electromagnetic wave will change continuously from specular reflection to diffuse reflection, even cause shadowing and masking effect or polarization. So the experimental date of surface roughness is one of the major factors in this study.

Dielectric constant

When the measured material surface consist of different dielectric constant mediums, part of the energy projected to the underlying medium is scattered back again by inhomogeneous medium, the latter goes through the interface back to the upper medium [6]. The experimental samples of granite, aluminum plate, copper plate, aluminum foam, graphite fiber magnesium, carbon fiber (aluminum) selected in this paper all consist of opaque single medium, so dielectric constant is not considered.

Incident angle

Under the same condition of surface roughness, the factors below will change as a result of incident angle change: incident light flux, surface reflectivity and shadowing effect [4, 7]. If the sample used in the experiment is slightly roughness surface, then with incident angle increasing, there will be scattering peak in the corresponding specular reflection direction, the peak goes down with incident angle increasing, this is the result of interaction of three factors related to incident angle. As the surface is a bit gentle, the shadowing effect is not significant, the bidirectional shadowing functions in each incident angle is basically coincident, and there are a few differences only when the incident angle is very large. So incident intensity is decided mainly by the effective incident flux. As incident flux decreases with incident angle increasing, and specular scattering intensity goes lower and lower, so the change trend is contained in general effect under three factors above.

Polarization

The theoretical analysis shows that the surface roughness of the sample has an obvious effect on polarization: the bigger surface roughness, the more obvious polarization effect. Polarization scattering makes theoretical analysis more complex, it normally needs 4 Stokes parameter to describe polarization scattering fully; if the roughness surface described is random surface, then it needs one 4×4 Muller matrix, and all these parameter are functions of scattering field, which makes numerical calculation increase a lot [7]. So we only provided the experimental result of the BRDF in this paper, but did not do theoretical analysis on polarization effect.

EXPERIMENTAL PRINCIPLE

Classification and measurement of surface roughness

Classification of surface roughness. Material surface roughness, to a great extent, affects the reflection and scattering of light projected to the surface. Optics principle holds that surface rough or not is compared with incident wavelength. Here we give surface roughness condition divided by incident light wavelength λ and incident angle θ in optics aspect [8]:

Lubricous surface $$h < \frac{\lambda}{25\cos\theta} \quad (1)$$

Medium rough surface $$\frac{\lambda}{25\cos\theta} < h < \frac{\lambda}{8\cos\theta} \quad (2)$$

Rough surface $$h > \frac{\lambda}{8\cos\theta} \quad (3)$$

Where, h denotes relative height of two observation or measuring points on the surface.

As rough surface structure is random, we use surface height standard deviation σ_h instead of *h*, that is

$$\sigma_h = \sqrt{\frac{\sum_i^n f_i^2 - n(\mu)^2}{n-1}} \tag{4}$$

Where, *n* is measurement time, f_i is surface roughness is the *i*-th time measurement result, μ is the average of *n* times measurement.

The measurement of surface roughness. In this paper we adopt stylus tracing method to measure sample surface roughness, and use multi-parameter surface roughness inspection instrument [9]. The instrument uses a very small and fine diamond stylus (the arc radius of its contact is usually only 0.50mm), to touch the measured surface directly and do transverse move on the surface. When the stylus moves, its needle tip skates slightly over the measured surface(perpendicular to machining trace). As the measured surface is not smooth, the stylus will fluctuate vertically along with surface geometric shape, so we should change the signal of displacement, which gets from the stylus fluctuating vertical along with the measured surface tiny peak-valley, into electrical parameter, and amplify it, then do operation processing [9]. We choose 8 measurement points from every sample above to do measurement, 10 times every point. This paper gives only granite and aluminum foam surface roughness measurement curves (Figure 1 and 2). The measurement result substituted into formula (4), Table 1 shows the height standard deviation value σ_h of each material surface above.

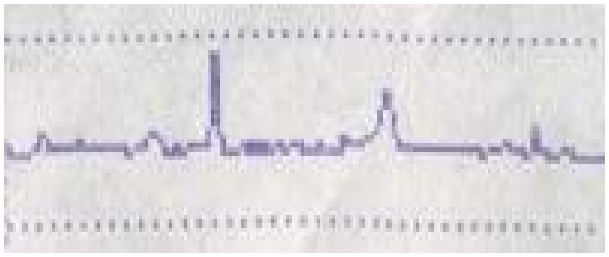

Figure 1. The curve of granite surface roughness (σ_h =0.280)

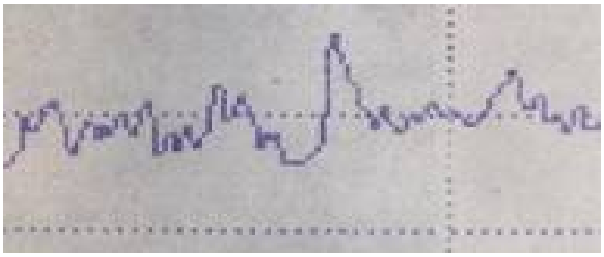

Figure 2. The curve of aluminum foam surface roughness (σ_h =0.374)

Table 1
The Height Standard Deviation Value σ_h of Each Material Surface Measuring Point

Sample	Granite	Aluminum plate	Copper plate	Aluminum foam	Graphite fiber magnesium	Graphite fiber aluminum	Carbon fiber (aluminum)
σ_h	0.280	0.305	0.133	0.374	0.367	0.381	0.352
Roughness	Medium rough surface		Lubricous surface	Rough surface			

The measurement of the BRDF

The principle of measurement. According to the concept of the BRDF and combining with rough surface electromagnetic scattering theory, we usually define the BRDF as [3, 4]:

$$f_r(\theta_i,\varphi_i,\theta_r,\varphi_r) = \frac{L_r(\theta_i,\varphi_i;\theta_r,\varphi_r)}{E_i(\theta_i,\varphi_i)} \tag{5}$$

Where, θ,φ denote the zenith and azimuth angle in spherical coordinates respectively, the subscripts *i, r* denote the incident light and reflection light respectively. $L_r(\theta_i,\varphi_i;\theta_r,\varphi_r)$ is the reflective brightness in the direction of (θ_r,φ_r), $E_i(\theta_i,\varphi_i)$ is the incident illuminance in the direction of (θ_i,φ_i). f_r ranges between $0 \sim \infty$, with dimension sr^{-1}.
Make the incident condition equal to the receiving, the reflective brightness of test sample could be obtained by voltage output of the receiving detector:

$$V_s = \tau_s \Re_s L_s A_s \cos\theta_s A_d \cos\theta_d / d_s^2 \tag{6}$$

Incident illuminance of test sample and standard board are equal to each other, Incident illuminance of standard board could be obtained by voltage output of receiving detector:

$$V_B = \tau_B \Re_B f_B E_B A_B \cos\theta_B A_d \cos\theta_d / d_B{}^2 \tag{7}$$

Where, s、B is the test sample and standard board, τ is the transmissivity of light, $\Re$ is the responsivity of detector, A_s, A_B is the area of test sample and standard board, A_d is the area of detector, θ_s,θ_B is the reflective zenith angle of test sample and standard board, θ_d is the incident zenith angle, d is the distance from detector to test sample, f_B is the BRDF quantity of standard board, so:

$$BRDF(f_s) = f_B \frac{V_s}{V_B} \frac{\tau_B \Re_B E_B A_B \cos\theta_B A_d \cos\theta_d / d_B{}^2}{\tau_s \Re_s E_s A_s \cos\theta_s A_d \cos\theta_d / d_s^2} \tag{8}$$

Where, $f_B = L_B / E_B$, choose parameters in the formula appropriately, $\tau, \Re, A, E, A_d \cos\theta_d / d_r{}^2$ are all constants, so the BRDF of test sample is expressed by the output voltage as:

$$BRDF_r(\theta_i,\varphi_i;\theta_r,\varphi_r) = f_B \frac{V_s}{V_B} \frac{\cos\theta_B}{\cos\theta_s} \tag{9}$$

The measurement system. The BRDF measurement system in this paper consists of optical debugging system、mechanical rotation system、heating system(not used in the experiment of this paper)and circuit receiving system. The lamp-house of testing system includes four wavelength lasers: visible light 0.6328μm, near-infrared 1.34μm, mid-infrared 3.39μm and mid/far-infrared 10.6μm. It completed multi-band measurements very well. Figure 3 shows measuring device system diagram.

The measurement method. The BRDF measurement can be divided into absolute and relative measurements [3]. The absolute measurement is carried out without any reference standard; while relative measurement is carried out by comparing the reference standard (reflectance known) with samples. The relative measurement can be divided into comparing measurement and single reference method. This experiment uses the single reference method, that is to say, firstly measures the voltage value of sample surface, and then measures the voltage value of standard white board surface (approximate Lambert body)(reflectance known) under the same geometric condition, finally obtains the BRDF value of sample by comparing the voltage of sample surface with standard white board.

Error analysis. We calibrate the error of the BRDF experimental table by a measurement method comparing three standard white boards with known reflectance, the measurement error can be controlled within 20% [10].

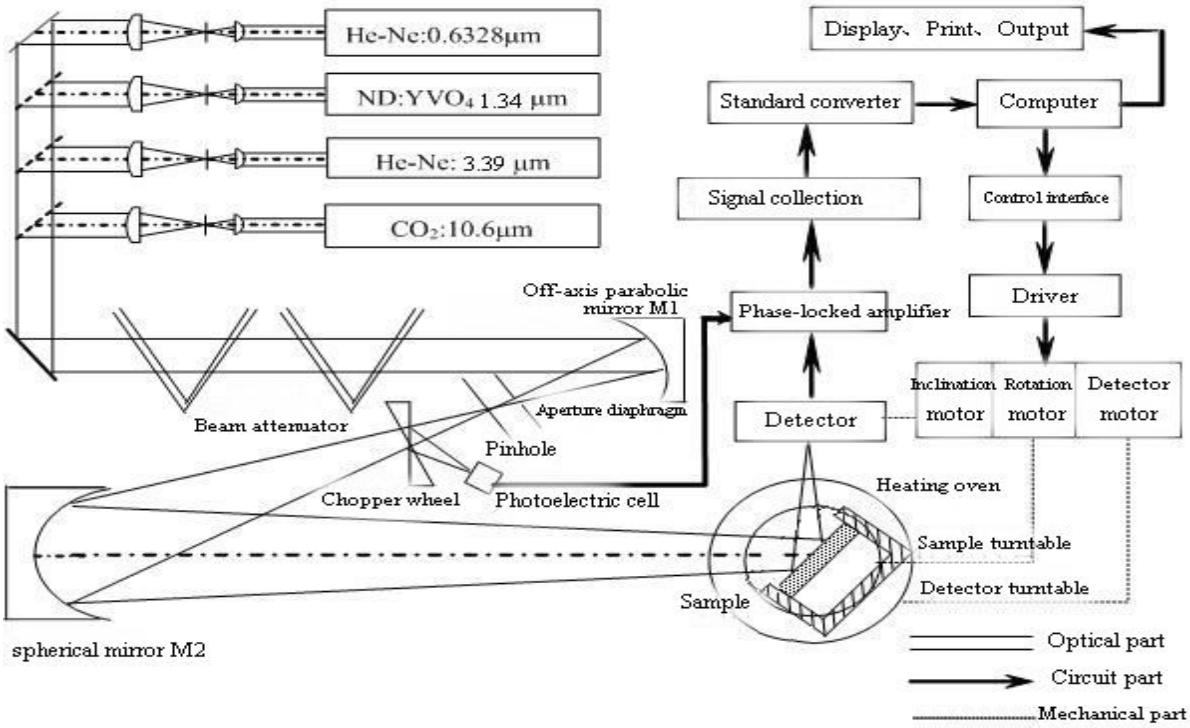

Figure 3. The measurement system diagram of temperature controllable BRDF

EXPERIMENTAL RESULTS AND DISCUSSION

In this paper, we carried out the measurement of the BRDF of the above materials with various bands at room temperature. Because of the limit of the space, we chiefly discussed partial experiment results with bands of 0.6328μm, 1.34μm and 3.39μm.

The measurement results of the BRDF with the band of 0.6328μm

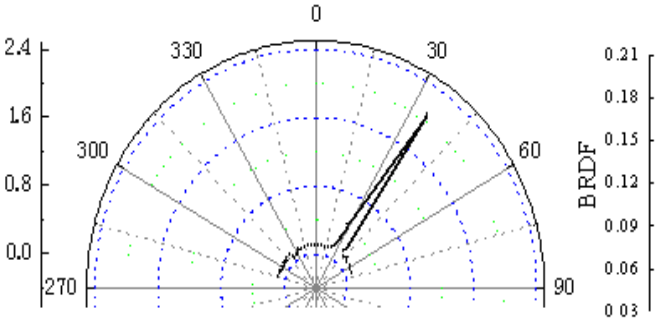

Figure 4. The BRDF distribution of granite surface at the incident angle of 35°

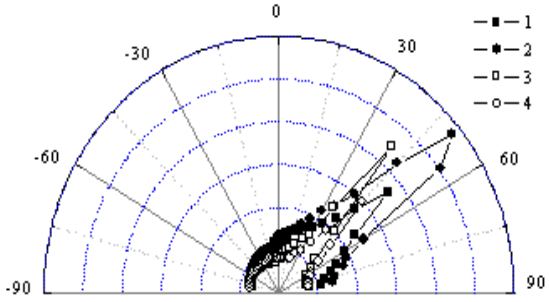

Figure 5. The BRDF distribution of the four composite surface ($\theta = 60^0, \varphi = 30^0$)

In this paper, we carried out the measurement of the BRDF of the above materials with the band of 0.6328μm and at different incident angle. Figure 4 shows the BRDF distribution of granite surface at the incident zenith angle of 35° [4]; Figure 5 shows the BRDF distribution of the four composites surface at incident zenith angle of $\theta = 60^0, \varphi = 30^0$. Case 1 in Figure 5 shows aluminum foam, case 2 shows aluminum-based graphite fiber, and case 3 shows magnesium-based graphite fiber, case 4 shows carbon fiber (aluminum).

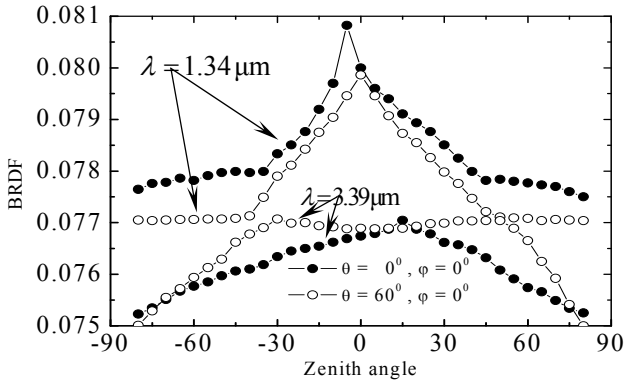

Figure 6. The infrared BRDF distribution of aluminum plate surface

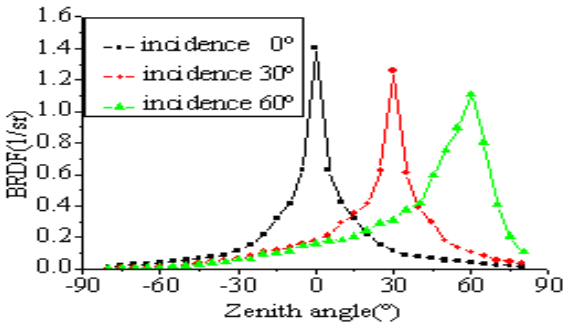

Figure 7. The BRDF distribution of copper plate surface with the band of 1.34μm as the incident angle change

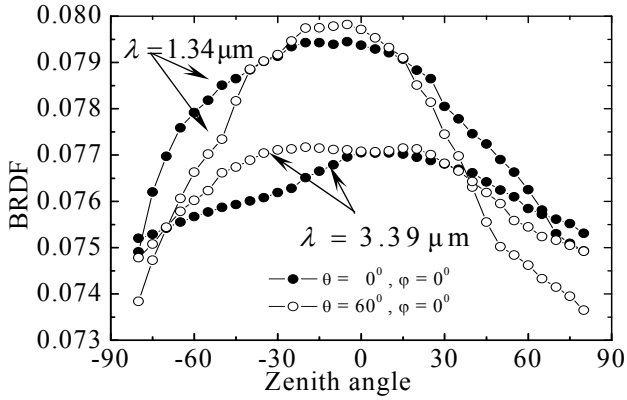

Figure 8. The infrared BRDF distribution of aluminum foam fiber surface

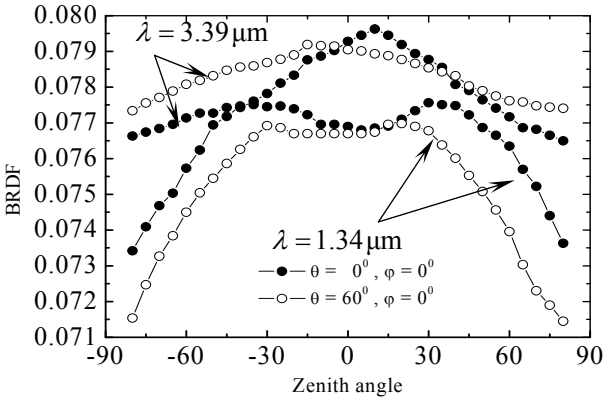

Figure 9. The infrared BRDF distribution of aluminum-based graphite fiber surface

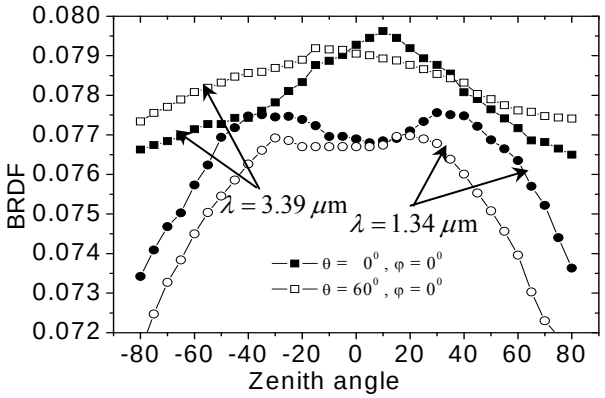

Figure 10. The infrared BRDF distribution of magnesium-based graphite fiber surface

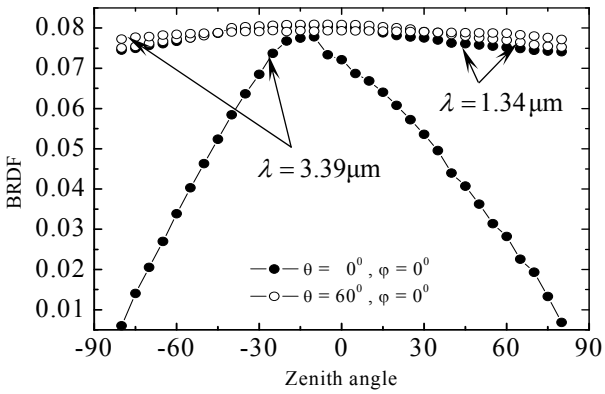

Figure 11. The infrared BRDF distribution of carbon fiber (aluminum) surface

The measurement results of the BRDF with the band of 1.34μm and 3.39μm

Figure 6 shows the BRDF distribution of aluminum plate surface at the typical incident zenith angle; Figure 7 shows the BRDF distribution of copper plate surface with the band of 1.34μm as the incident angle change; Figure 8 shows the BRDF distribution of aluminum foam fiber surface at the typical incident zenith angle; Figure 9 shows the BRDF distribution of aluminum-based graphite fiber surface at the typical incident light zenith angle; Figure 10 shows the BRDF distribution of magnesium-based graphite fiber surface at the typical incident zenith angle; Figure 11 shows the BRDF distribution of carbon fiber (aluminum) surface at the typical incident zenith angle.

EXPERIMENTAL RESULT ANALYSIS

From Figure 4, we know that, with the band of visible light, the BRDF distribution of granite surface presents more concentrative mirror reflection component, though the surface is medium roughness, the granite is treated by water mill and polishing, mirror reflection effect appears at the incident angle of 35° [4]. However, the BRDF distribution of the four composites surface is more divergent at incident angle $\theta = 60^0, \varphi = 30^0$ than granite (as shown in Figure 5), that is because of the shadowing effect of rough surface. Besides, the BRDF value of the four composites surface is lower than granite evidently. After analysis, we consider that, the composite material surface mentioned above has obvious absorbency to the wavelength.

From Figure 6 and Figure 7, we know that, with the infrared band, copper plate surface is smoother than aluminum plate, the BRDF distribution of copper plate presents mirror reflection effect when the incidence angle has changed three times with the band of 1.34μm; while the BRDF distribution of aluminum plate shows scattering as the incidence angle and band change. Besides, the BRDF value of aluminum plate is lower than copper plate evidently, the same reason as granite.

From Figure 8 to Figure 11, we know that, with the infrared band, due to the rough surfaces, the whole presents scattering characteristic. The BRDF values of the four materials changed little as the azimuth angle increases when the incident angle is 0° , the corresponding zenith angle of the peak value is near 0° . The BRDF values of the four materials drive to diffuse reflection characteristic as the azimuth angle increases when the incident angle is 60° , the peak value has deviated from the direction of mirror reflection. At the same time, the whole reflects that, to different infrared bands, the BRDF distributions of aluminum foam fiber and graphite fiber adding metal are different. Besides, they have selectivity to the wavelength and the degree of reflection or scattering is different too.

CONCLUSION

An experimental investigation was conducted of the BRDF distribution of various material surfaces through a self-built experiment table by using single reference method. The results indicate that the influencing factors in BRDF distribution are surface roughness, incident wavelength and incident angle, it reflects the reflection and scattering characteristic of various material surfaces. Besides, other factors can also affect the reflection or scattering characteristic of material surface, including the shadowing and polarization effect、dielectric constant、surface temperature and material color and so on, which remain for further theoretical and experimental study.

REFERENCES

1. F. E. Nicodemus, Reflectance Nomenclature and Directional Reflectance and Emissivity, Applied Optics, Vol. 9, No.6:1474-1475, 1970.6.
2. X.B. Zheng, Review on research and application of light scattering from randomly rough surfaces, Chinese Journal of Quantum Electronics, 1999, 16(2): 97-103.
3. C. Qi, M.H. Yang, J.M. Dai, Technique for BRDF Measurement from Visible to Infrared, Chinese Journal of Lasers, 2003, (30), supplement: 134-136.
4. M. Xie, H. Xu , Y. Zou, L.M. Ruan, H.P. Tan. Experimental methodology of moorstone's surface BRDF. Journal of Engineering Thermaophysics, Vol. 26, No.4:683-685 7.2005.
5. B.S. Zhang, W.Q. Liu, Q.N. Wei, Analysis of scattering characteristic of the sample based on BRDF experiment measurements, Optical Technique, 2006,32(2):180~182.
6. Xiao D.He, Kenneth E.Torrance, Francois X.Sillion, Donald P.Greenberg. A Comprehensive Physical Model for Light Reflection.ACM Computer Graphics, 1991, Vol.25, No.4, 175-186
7. Bourlier C, Berginc G, Saillard J. The oretical Study of the Kirchhoff Integral from Two-dimensional Randomly Rough Surface with Shadowing Effect: Application to the Backscattering Coefficient for a Perfectly-conducting Surface. Waves in Random Media, 2001, 11(1):91-118
8. D.H. Xie, Modeling the Characteristics of Light Scattering from Target and Background on the Earth, Chinese excellent graduate papers, Library of Xidian University, 2002.
9. Q.G. Mao, Evaluation and Measurement of Surface Roughness, China Machine Press, 1991.
10. M. Xie, H. Ren, Y. Zou, Y. Li, H.P. Tan, The check and error analysis of the BRDF experiment bench**,** Journal of Harbin Institute of Technology, Vol. 14, N o. 6:784-787, 2007.12.

Thermodynamics

CO-GENERATION SYSTEMS WITH COMBUSTION ENGINES AND WASTE HEAT USE BY TWO STAGE ORGANIC RANKINE CYCLE

S. Smolen[1 *], J.T. Cieslinski[2]
[1] Hochschule Bremen, "J.R. Mayer Institute for Energy Engineering"
Neustadtswall 30, D 28199 Bremen, Germany
e-mail: Slawomir.Smolen@hs-bremen.de

[2] Gdansk University of Technology
Narutowicza 11/12, 80952 Gdansk, Poland
e-mail: jcieslin@pg.gda.pl

ABSTRACT. The possible optimization of co-generation systems with combustion engines by the means of the ORC-Cycle for power generation from waste heat has been presented. The practical basis for this concept was the operational power and heat performance analysis of co-generation units with diesel engines using gaseous and liquid fuels (especially biogas installations). The key issue of the presented publication is simulation and thermodynamic analysis of the original concept with two-stage ORC process for waste heat utilisation as possible optimization measure. Due to process-related factors, the waste heat use in the exhaust gas heat exchanger and from the engine cooling system is performed at different temperature levels and is realised in the ORC cycle in two stages by the means of a micro-turbine and a screw engine. The special calculation procedure has been elaborated and the representative results are presented.
The next phase of the project will involve a practical analysis of the plant concept, e.g. the options regarding different expansion machines, regulation concepts, real losses, and other aspects.

Keywords: *waste heat use, combustion engines, ORC – two-stage process*

INTRODUCTION

One of the key challenges on the area of energy engineering is the system development for increasing the efficiency of primary energy conversion and use. From this perspective, low-and middle temperature heat as waste heat from various processes is becoming more and more "attractive" as a secondary energy source. The temperatures of the exhaust gas and other industrial processes and power plants are mostly less than 350°C – 400°C. Using conventional methods for waste heat recovery is in most instances technically and economically infeasible.
One of the typical examples is the utilisation of waste heat in the co-generation units with combustion engines, which was in many investigated installations non-optimal. A special case are biogas plants, where the heat use is often limited only to utilisation of thermal energy for the biogas generation process, while the remaining heat is either not used at all, or used only partially. In terms of total energy utilisation ratio, this situation is dissatisfactory and results primarily from the fact that there are no major consumers of thermal energy in the vicinity of biogas plants which would have a suitable and continuous requirement for thermal energy.

* Corresponding author: Prof. Dr.- Ing. Slawomir Smolen
Phone: 0049-(0)421-5905-3579, Fax: 0049-(0)421-5905-3505
E-mail address: smolen@fbm.hs-bremen.de

In these circumstances, optimising the biogas plants by converting the waste heat into electricity in an ORC (Organic Rankine Cycle) process at medium or low temperature is a relatively complicated and cost-intensive solution due to the investment involved, but one that leads directly to higher efficiency and, given the conditions described, is the only conceivable alternative. Since the ORC consumes virtually no additional fuel for the added power, emissions and pollutants would be decreased and according to the local demand, the ORC output heat could be further utilized for example to drive absorption chillers to supply cooling systems [1].

CONCEPT OF THE TWO-STAGE ORC CYCLE FOR HEAT RECOVERY IN CO-GENERATION SYSTEMS WITH COMBUSTION ENGINES

The presented concept evolves from own research activities about optimization measures of waste heat utilisation in biogas plants. Figure 1 shows a typical biogas installation with the two potential waste heat sources at middle and low temperature levels, it means the "exhaust gas heat exchanger" (EGHE) and the engine cooling "system heat exchanger" (SHE). In this example of the circuit diagram the both heat exchangers are in series connection.

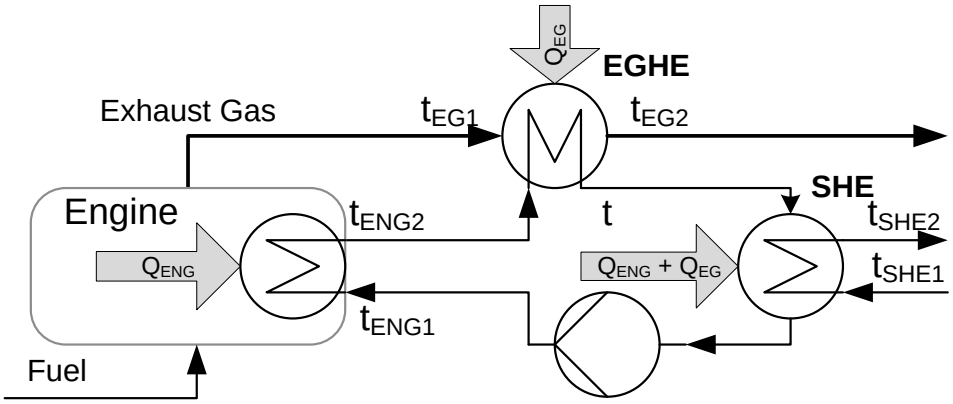

Figure. 1. Circuit diagram of a biogas installation (one of the possible typical variants)

As a result of the practical investigations and requirements a special procedure and program for the thermal operational analysis of the co-generation system with combustion engines were elaborated. Different variants of circuit diagrams, fuels and frame conditions can be taken into consideration by the means of the elaborated procedure. It is also possible to analyse the part load operation on the basis of the quasi-steady method. The possibilities and chosen results from this work were presented in other papers [2, 3] and are not matter here.

One of the analysed measures was the heat recovery by Organic Rankine Cycle. The efficiency of the ORC-Process and the total system depends (among other things) on finding an optimised working fluid [4] for biogas power plants with respect to properties and characteristics and on the working conditions connected to the temperature level of the waste heat. The following two diagrams show the representative results of the theoretical calculations of the investigated object [2, 3]. Figure 2 illustrates influence of the evaporating temperature, and Figure 3 – influence of the temperature difference by the heat recovery (an indicator of the irreversibility) on the efficiency of the ORC-Process. This was shown exemplarily for the chosen (partly environmentally unfriendly) refrigerants R 113, R 123, R 600, R 600a.

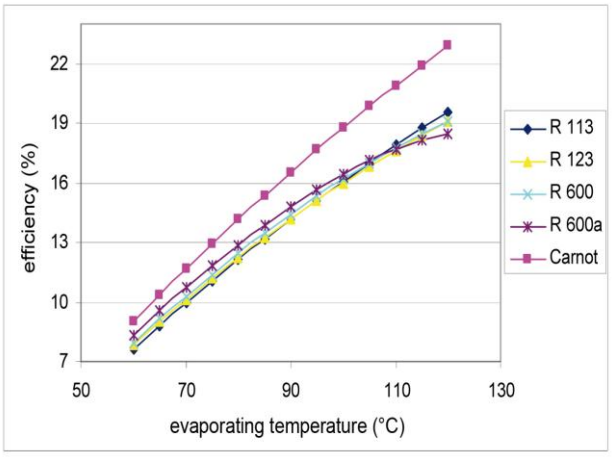

Figure. 2. Influence of the temperature difference by the heat recuperation on the efficiency of the Organic-Rankine-Cycle for different working fluids (theoretical calculation results).

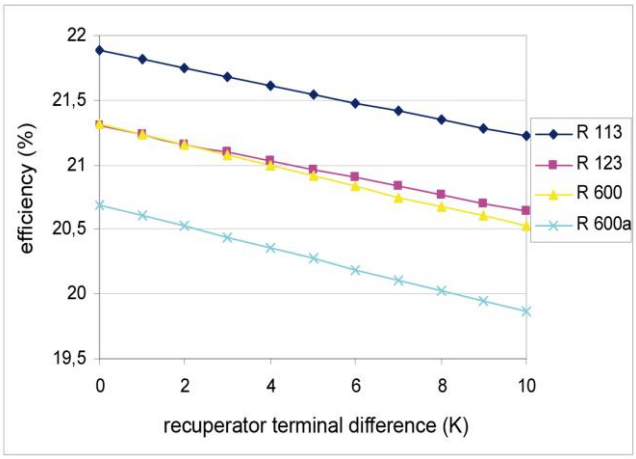

Figure. 3. Influence of the evaporation temperature on the efficiency of the Organic-Rankine-Cycle for different working fluids (theoretical calculation results).

An original concept of two-stage Organic Rankine Cycle [3,5] (shown in Figure 4) was elaborated, which arise from the practical experiences and requirements. The measurement results carried out from the real objects and characteristic of waste heat sources from co-generation systems with combustion engines were the basis for the proposed solution. The two temperature levels of heat input correspond to the heat transfer temperatures and ratios in the exhaust gas heat exchanger of a combustion engine - specifically a gas motor in a biogas plant - and in the cooling system of the engine. High-pressure expansion is carried out in a micro-turbine, and the residual expansion is coupled to expansion of the working fluid from the low-temperature heat input in a screw engine. In Fig. 5 the simplified view of the two-stage ORC process in the form of a T-s diagram is presented.

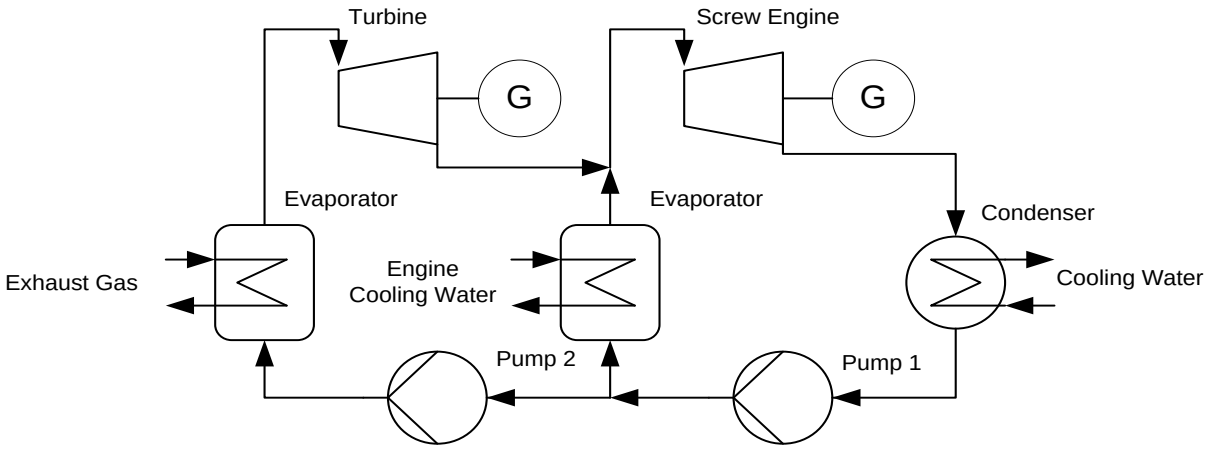

Figure. 4. Overall concept for a two-stage ORC plant

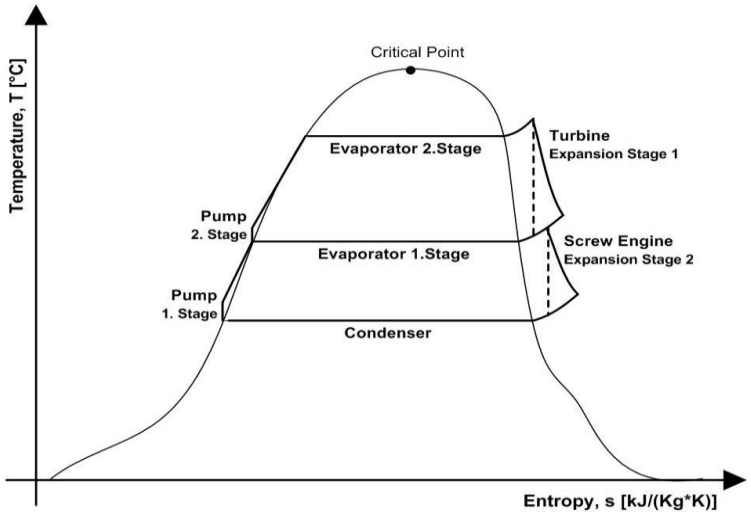

Figure. 5. Simplified view of the two-stage ORC process in the form of a T-s diagram

ANALYSIS OF THE TWO-STAGE ORC CONCEPT AND REPRESENTATIVE RESULTS

The concept was investigated theoretically by the means of the carried out calculations procedure and program and some chosen results of this analysis will be presented in this chapter.
An elaborated calculation procedure and program which is partly based on experience gathered by other researchers, e.g. [1, 6-10], is rather universal and which also matches the special requirements of the proposed plant concept was developed in order to conduct extensive arithmetic simulation, analysis and optimisation of the reference system [11]. The program consists of a database mainly containing the properties of different media, and a calculation and optimisation algorithm providing a range of options and possibilities. The calculation algorithm contains different switch variants (one- and two-stage, with and without regeneration) and permits simulation of the process for broad ranges of thermal parameters of the working fluid, and of the parameters of the available heat sources.
A large database containing the material properties of the working fluids is based on known media whose properties are generally available. In the course of the work carried out, no research on media (either theoretical or practical) was conducted, but the results of research work in this field, e.g. [4, 12] flowed into the optimisation measures being studied, of course.
The calculation method can also be applied in combination with a program for simulating the utilisation of exhaust heat from combustion engines [3]. In this way, it is possible to optimise the adaptation of the ORC process to the available heat source under both steady and quasi-steady operating conditions. In the quasi-steady method, operation of the engine under partial load conditions is simulated arithmetically in such a way that dynamic processes can also be taken into account.

Representative results obtained with the aid of the ORC calculation and simulation program developed are presented in the following, mainly in relation to the plant concept presented in the previous section and for pentafluoropropane R245–fa [13] as the selected working fluid.
In the first step, the influence of the internal efficiency of the two expansion machines on the total efficiency of the plant was examined. (The total efficiency of the plant, as shown in the following, ignores the work performed by the pump or pumps). Figure 6 summarises the representative findings that were obtained.

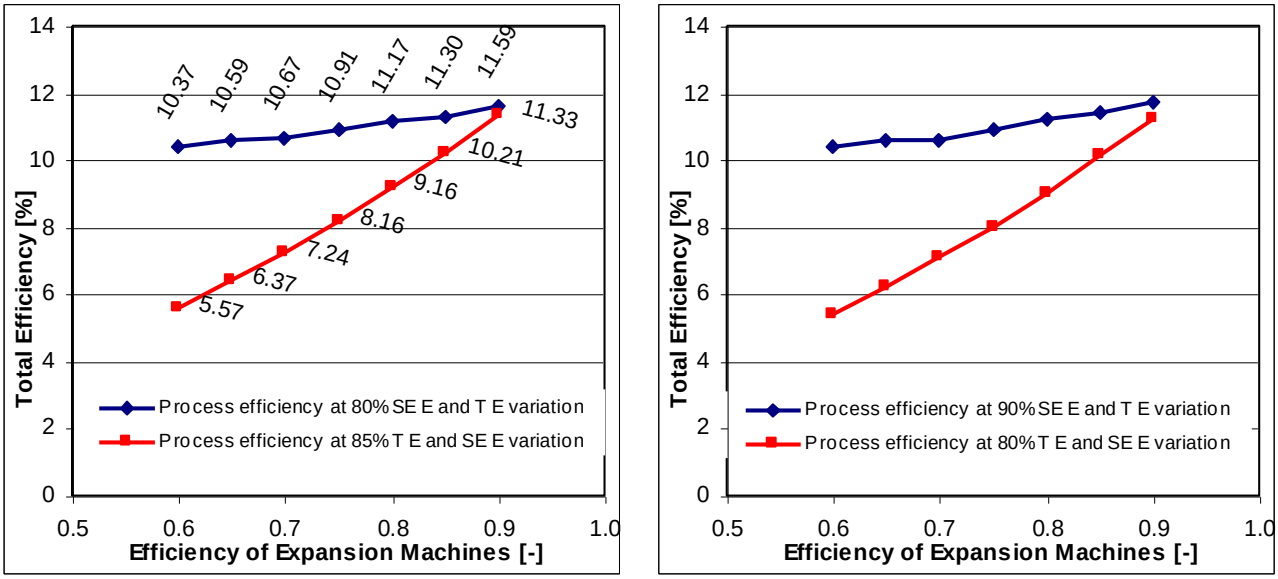

Figure 6. Influence of the internal efficiencies of the two expansion machines on the total efficiency of the ORC plant. (TE: turbine efficiency, SEE: screw engine efficiency)

In Fig. 6 the total efficiency of the ORC plant is shown as a function of the internal efficiency of the respective expansion machine used, with the efficiency of the other expansion machine assumed to be constant. In general terms, one can see from the gradients of the curves that the influence of the low-pressure stage is much greater than that of the high-pressure stage.

The selection of the intermediate pressure is also related to the total efficiency. Figure 7 shows the influence exerted on the total efficiency of the plant by the pressure upstream from the second expansion stage, based on the design parameters of the reference system, with the range of pressure variation corresponding to the options for technical realisation. It can be seen from the curve that the influence observed is relatively small in the parameter range that is technically feasible. Of course, this statement is specific to the plant and is dependent on the design parameters.

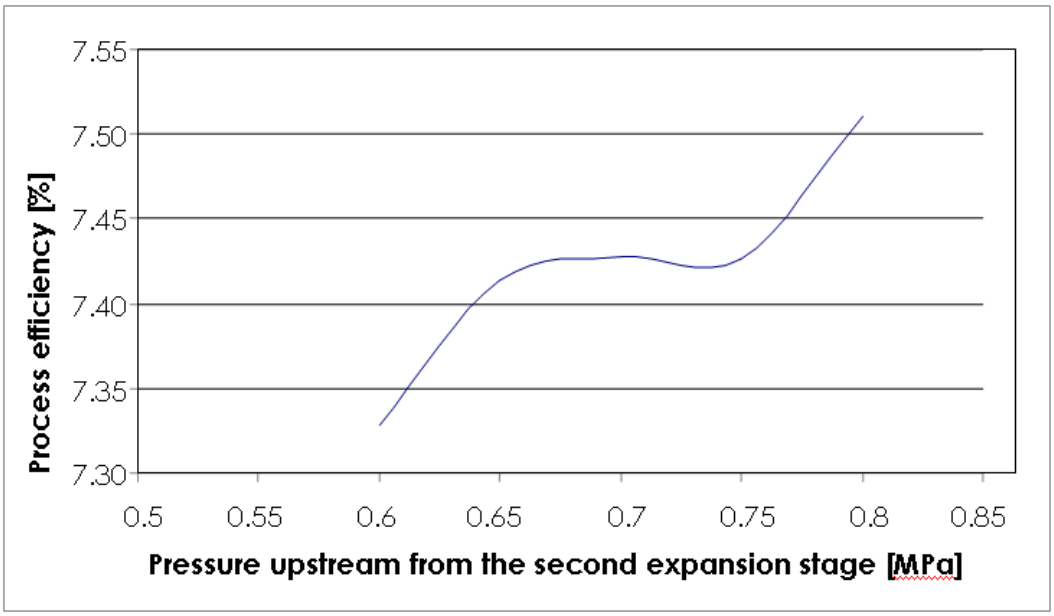

Figure 7. Influence of intermediate pressure on the total efficiency of the ORC plant

A standard question concerns, the influence of the condenser pressure on the efficiency of the plant, as illustrated in Fig. 8 for different initial pressures. As expected, lowering the condensation pressure (mainly achieved by reducing the temperature difference in the condenser) provides substantial optimisation potential. The irregularities found in the individual graphs result primarily from inaccuracies in determining the material properties, and from other sources of inaccuracy in the calculation method.

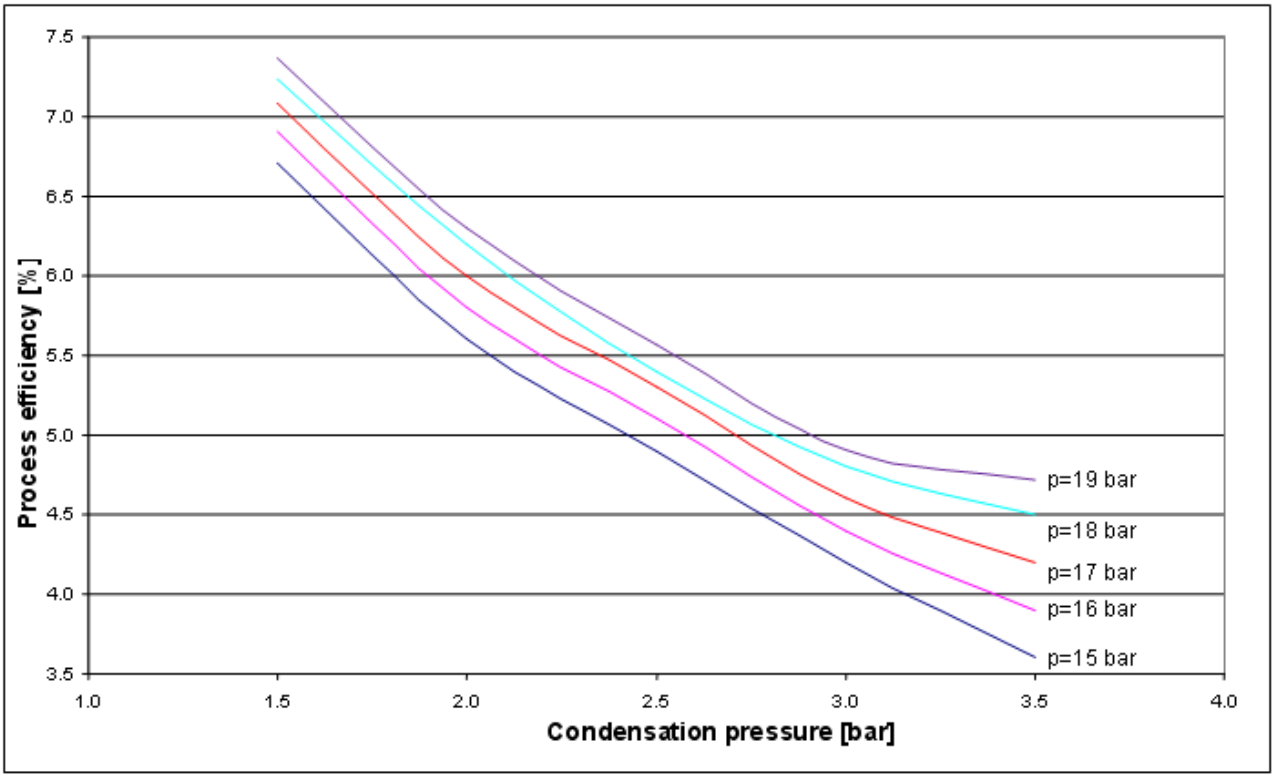

Figure 8. Change in total efficiency in relation to the pressure in the condenser

The influence of the initial pressure and of the level of superheating is relatively small, as can be seen in Fig. 9. Here, too, the irregularities in the curves are the result of inaccuracies in programming the characteristic values for the working fluids being used. This problem has a general impact on the accuracy of calculations. Depending on source, the material properties can be entered with a certain degree of precision, and the effects are particularly apparent in the range where two parameters (pressure and temperature) can vary, i.e. in the region of the superheated steam. However, with a more exact error propagation analysis it is possible to prove that the resultant errors are within a range that is acceptable for the technical calculations (less than one percent). Increasing the level of accuracy would require data sources that provide more precise details of the material properties.

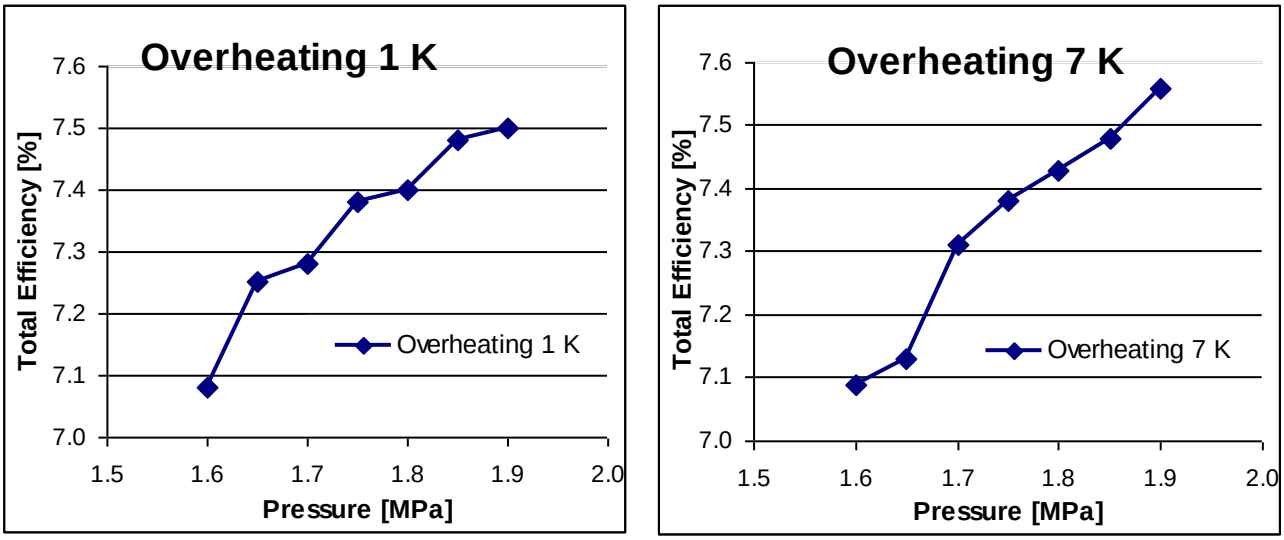

Figure 9. Total efficiency of the ORC plant as a function of initial pressure, for two different levels of steam superheating (1 K and 7 K)

The results presented in this section are intended to show, by way of example, the possibilities of the software developed, specifically in relation to the planned demonstration plant and the chosen working fluid. One important optimisation measure that has not been discussed here involves adapting the parameters of the ORC plant to the characteristics and temperature level of the available heat source.

CONCLUSIONS AND OUTLOOK

An original concept with a two stage ORC Cycle for waste heat utilisation from co-generation systems with combustion engines has been presented and analysed. The proposed solution results from the practical research work at the real objects, especially biogas installation with diesel engines. The special, innovative feature of the concept consists in adaptation of the two expansion stages to the characteristics of most biogas plants (two-stage heat input at different temperature levels). The expansion machines (small turbine and screw engine) should also be used in the realistic and optimal area of expansion ratios.

In the course of the work carried out, a calculation method and software were developed with which it was possible to analyse and optimise the two-stage plant system. The program and its procedures (including the database) are not limited solely to the plant in question, but are suitable in general for theoretical analysis of ORC processes. On the basis of the design parameters for the envisaged prototype plant, numerous simulations were carried out to investigate the complex interrelationships and influences at work. The influences of the thermal parameters in the key elements of the process and of the characteristics of the two expansion stages on die efficiency of the plant were analysed.

Simulation of the interaction between the two systems (the biogas plant and the ORC process) was also a part of the calculation procedure. With the present database of material properties, it is also possible to analyse the system efficiency with different working fluids for the specific applications in question. In the future the possible application of multicomponent working fluids [14] will be taken into consideration too.

The next step of the project will involve a practical part; it means the installation of the demonstration and test bench. First of all the application of the screw engine should be investigated practically. After that the total plant concept, regulation concepts, real losses, and other aspects will be researched and analysed.

REFERENCES

[1] Donhong Wei, Xuasheng Lu, Zhen Lu, Jianming Gu: Performance Analysis and Optimization of Organic Rankine Cycle (ORC) for Waste Heat Recovery, Energy Conversion and Management 2006

[2] Smolen S. Part Load Operation and Heat Recovery Optimization in Cogeneration Units with Diesel Engines, International Conference on Automation, Quality and Testing, Robotics AQTR, IEEE Computer Society – Test Technology Technical Council; Technical University of Cluj-Napoca, May 2008

[3] Smolen S. Part Load Operation and Heat Recovery Optimization in Cogeneration Units with Diesel Engines, 18. International Symposium "Research – Education – Technology", ISBN 978-83-88579-12-7, Gdansk University of Technology, Faculty of Mechanical Engineering, June 2008

[4] Bo-Tau Liu, Kuo-Hsiang Chien, Chi Chuan-Wang: Effect of Working Fluids on Organic Rankine Cycle for Waste Heat Recovery, Energy 2004, 29: 1207-1217

[5] Holze C., Meier M.: Development of a compact ORC- unit for power generation from waste heat of biogas plants (Entwicklung eines kompakten ORC-Moduls zur Stromerzeugung aus Restwärme von Biogasanlagen), 1. International Conference: "Low- Temperature and Waste Heat Use in Communal and Industrial Energy Supply Systems, Theory and Practice", Conference Proceedings, JRMayer Institut für Energietechnik, Hochschule Bremen, Germany, November 2007

[6] Drescher U., Brüggemann D.: Fluid Selection for the Organic Rankine Cycle (ORC) in Biomass Power and Heat Plants, Applied Thermal Engineering 2007, 27: 223-228

[7] Gnutek Z., Baryszewska-Mazurek A. The Thermodynamic Analysis of Multicycle ORC Engine, Energy 2001, 26: 1075-1082

[8] Invernizzi C., Iora P., Silva P. Bottoming Micro-Rankine Cycles for Micro Gas Turbines, Applied Thermal Engineering 2007; 27: 100-110

[9] Tzu-Chen Hung, Waste Heat Recovery of Organic Rankine Cycle Using Dry Fluids, Energy Conversion and Management 2001, 42, 539-553

[10] Takahisa Yamamoto, Tomohiko Furuhata, Norio Arai, Koichi Mori; Design and Testing of the Organic Rankine Cycle, Energy 2001, 239-251

[11] Smolen S., Köhler M., Redich E. Algorithm and calculations procedure for optimization of ORC-Processes in part load operation (Berechnungsalgorithmus und -programm zur Optimierung von ORC-Prozessen im Teillastbereich), 1. International Conference: "Low-Temperature and Waste Heat Use in Communal and Industrial Energy Supply Systems, Theory and Practice", Conference Proceedings, JRMayer Institut für Energietechnik, Hochschule Bremen, Germany, November 2007

[12] Saleh B., Koglbauer G., Wendland M., Fischer J. Working Fluids for Low Temperature Organic Rankine Cycles, Energy 2005

MEASUREMENT OF TEMPERATURE TRANSIENTS IN THE SUCTION SYSTEM OF A RECIPROCATING COMPRESSOR

A. Morriesen, C. J. Deschamps*
Federal University of Santa Catarina, Florianopolis, Brazil

ABSTRACT. The present paper reports an experimental investigation of thermal transients in the suction chamber of a small reciprocating compressor, operating at 3600 rpm. Due to the small time scales associated with the phenomenon, a hot-wire system was employed to measure temperature and velocity transients. Results for valve displacement and pressure in the suction chamber were also obtained to complement the analysis. It has been observed a considerable increase in the gas temperature during the period in which the suction valve is closed. On the other hand, the results allowed identifying temperature transients correlated with pressure pulsation in the suction chamber.

Keywords: *thermal transients, anemometry, thermodynamics.*

INTRODUCTION

Figure 1 presents a schematic view of a reciprocating compressor and its indicator diagram for a typical cycle. When the piston moves downwards, it reaches a position where low pressure vapor is drawn in through the suction valve, which is opened automatically by the pressure difference between the cylinder and the suction chamber. The vapor keeps flowing in during the suction stroke as the piston moves towards the bottom dead center (BDC), filling the cylinder volume with vapor at suction pressure, p_s. The suction process is represented by curve A-C in the indicator diagram of Fig. 1b. After reaching the BDC, the piston starts to move in the opposite direction, the suction valve is closed, the vapor is trapped, and its pressure rises as the cylinder volume decreases. Eventually, the pressure reaches the pressure in the discharge chamber, p_d, and the discharge valve is forced to open. After the opening of the discharge valve, the piston keeps moving towards the top dead center (TDC), represented by point A. It should be noted that suction and discharge processes do not take place at constant pressure. This phenomenon is associated with the dynamics of the valves and the restriction imposed by the valve passage areas. This appears on the indicator diagram, with compression continuing after pressure p_d is reached and the same happening for the expansion stroke after pressure p_s.

In household refrigeration compressors, a significant portion of the energy losses is associated with refrigerant superheating along the suction path. This useless superheating provokes a reduction in volumetric efficiency and an increase in compression work per unit mass. A detailed thermal analysis of the suction system can lead to a considerable improvement in its performance, mainly through the reduction of gas superheating. However, a complete analysis of the involved phenomena requires also data for gas temperature transients. This is a very difficult task because the time scale of such variations is similar to that of compressor valves. Thermocouples are the most commonly used sensors in compressors but, nevertheless, their slow response time make them

* Corresponding author: Prof. C. J. Deschamps
Phone: + (55)-48-32345166, Fax: + (55)-48-32345691
E-mail address: deschamps@polo.ufsc.br

inappropriate for measurements of steep transients of gas temperature that occur in the suction system. This is a consequence of their thermal inertia, which can be substantially decreased with the adoption of micro-thermocouples.

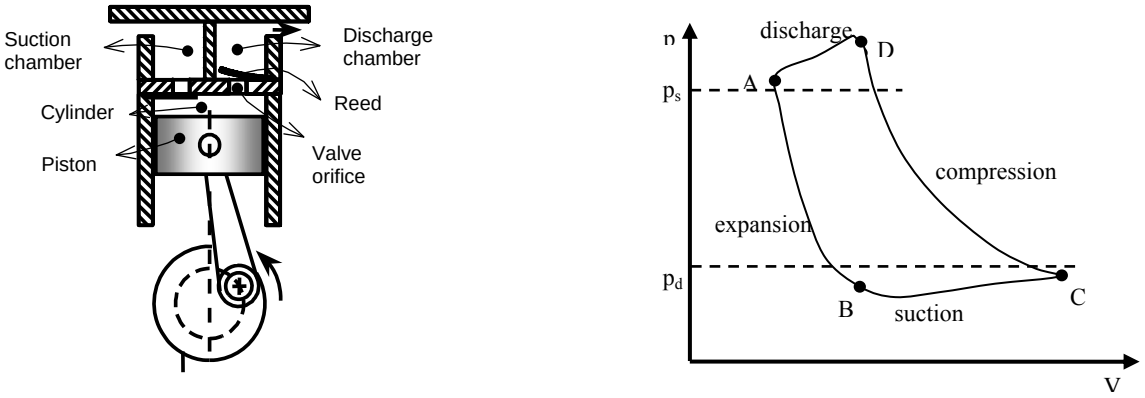

Figure 1. Dimensionless calibration curve and experimental obtained with argon.

Shiva Prasad [1] built a 12.7μm diameter chromel-constantan wire thermocouple especially designed for temperature measurements in a two stage, double acting, compressor running at approximately 900 rpm. He successfully measured the instantaneous temperature inside the cylinder, which suggested a large gas suction heating.

Experiments of flow in inlet manifolds of IC engine were conducted by Bauer *et al.* [2] with the purpose of analyzing heat exchange for different flow parameters. The instrumentation of the manifold was made with thermocouples, distributed in 5 positions along the manifold, and four heat flux sensors in each section. Next to the exit, the port was arranged to fit, alternatively, a hot-wire, a cold-wire and a heat flux sensor. The cold-wire probe calibration was made to allow temperature measurements up to 100°C, with a correction for thermal inertia using a fixed time constant of 2 ms, derived from energy balance and heat transfer correlations for the wire sensor. The authors concluded that the period in which the flow is stagnated contributes strongly to the total heat transfer to the fluid in the inlet manifold.

Zend and Assanis [3] analyzed heat transfer in inlet manifolds of IC engines, pointing out that during the operation cycle, the air flow inside the manifold is composed of two phases, associated with periods in which the admission valve is either open or closed. The authors developed a new correlation to characterize the transient nature of the flow.

In an experimental investigation of flow through inlet and discharge manifolds of diesel engines, Olczyk [4] identified that the main difficulties in measurements of temperature transient are related to the sensor time response and the signal interpretation. The experiments adopted thermocouples, hot-wires and cold-wires in an apparatus capable of generating pulsating flows with frequencies up to 180 Hz. A methodology was proposed to take into account thermal inertia in the measurements carried out with the cold-wire sensor, which does not require any information about its constructive parameters.

From the review given, it is clear that single point measurement techniques such as cold-wires and micro-thermocouples have been used to measure temperature transients in suction systems of IC engines, including the analysis of effects associated with thermal inertia. Yet, there is only one study dedicated to reciprocating compressors, considering a 900 rpm operation speed. In this paper, an experimental investigation of thermal transients is carried out in the suction chamber of a small

high speed reciprocating compressor, operating at 3600 rpm. Results for temperature, velocity, pressure in the suction chamber are used to analyse gas superhating.

EXPERIMENTAL SETUP AND PROCEDURE

A reciprocating compressor operating with R134a was selected for the analysis, being submitted to two operating conditions, represented by two pairs of evaporation and condensation temperatures: (-23.3ºC/54.4ºC) and (-35.0ºC/54.4ºC). The first condition defines the pressure in the suction and discharge lines as 1.149 bar and 14.71 bar, respectively. When the evaporation temperature is lowered to -35.0ºC, the suction pressure becomes equal to 0.6617 bar.

Measurements of pressure, valve displacement and crankshaft position

Piezoelectric pressure transducers were selected for the measurements in the suction chamber, due to their high response frequency, small size and reliability regarding the hostile conditions inside the compressor. To correlate the pressure measurement with the crank angle, a sensing winding was assembled to the crankcase to collect the signal emitted by a magnet fixed to the crankshaft. The instantaneous crankshaft position is calculated taking into account the compressor mechanism characteristics. Small sensing windings were also assembled into the valve plate seat to give the valve lift according to the crankshaft position.

Measurements of temperature and velocity

Measurements of temperature were conducted with a DANTEC anemometer system composed by a constant current module (90C20). Yet, for velocity measurements, a DANTEC mini-CTA system (54T30) was adopted. A single 5 μm diameter tungsten wire sensor (55P11) was employed for both velocity and temperature measurements. The sensor was calibrated for velocity measurements by using a DANTEC calibration unit (90H10), with a temperature sensor (55A76) being employed to register any significant variation during the process.

It should be mentioned that a number of aspects may affect measurements of velocity and temperature with anemometry sensors. For instance, Weiss *et al.* [5] has shown that the presence of oil droplets in the flow can increase the sensor diameter with running time, leading to a reduction of its frequency response. Such a contamination process requires testing and cleaning the wire steadily in order to keep a significant frequency response. This is particularly relevant in compressors because oil is always present in the suction system.

Calibration procedure

The calibration of a cold-wire sensor aims to establish a relationship between the temperature of the environment in which the sensor is inserted and the resulting tension read by the system; i.e. a relation between the temperature and the electric resistance of the sensor wire. In the present work, the calibration procedure for temperature consisted in placing the cold-wire sensor inside a cavity next to a thermistor. Then, by adjusting the power of a heater inside the cavity to different levels, the signal of both the sensor and the thermistor were registered, allowing a calibration curve to be obtained for the cold-wire sensor.

As far as the hot-wire sensor is concerned, the calibration was carried with a DANTEC calibration unit (90H10), in which the sensor is exposed to a range of flow velocities typically found in the suction chamber. A number of 20 different velocity levels was employed to adjust a calibration curve to express the velocity, U, as a function of the voltage indicated in the anemometry system, E. During the calibration procedure, pressure and temperature prevailing in the flow were also registered so as specify the fluid properties at each velocity level.

Tetrafluoroethane (R134a) is the working fluid of the compressor selected for the present study, which is a common choice for household refrigeration systems. Therefore, after the hot-wire sensor was calibrated in air, the resulting calibration curves were made dimensionless, by characterizing the fluid flow conditions through Reynolds and Prandtl numbers. There are a number of proposals for such dimensionless relationship in the literature [6]. Here, the relation proposed by Kramers [7],

$$Nu = A\,Pr^{a} + B\,Pr^{b}\,Re^{c}\,, \tag{1}$$

was chosen to express the dimensionless calibration curve. This correlation takes into account variations in fluid properties with temperature, which are evaluated at the film temperature rather than at the fluid temperature. Equation (1) is strictly valid only for hot-wire sensors with very high L/d ratios, where L and d are the length and diameter of the wire, respectively.

The coefficients and exponents A, B, a, b and c in equation (1) are adjusted for an adequate fit in relation to the experimental data. The adoption of this calibration curve requires that fluid properties (density, thermal conductivity, specific heat and viscosity) must be known for each measurement in the suction chamber. It was assumed that fluid properties could be evaluated from data of pressure and temperature acquired in the flow during the compressor operation.

Before proceeding to measurements in the compressor, the calibration curve obtained with air was validated through measurements of velocity in argon flow. To this extent the calibration unit was again used to specify different levels of velocity, following the aforementioned procedure. Figure 2 shows a comparison between the dimensionless calibration curve previously obtained for air and the new data acquired for argon. As can be seen, there is a good agreement between both results, with a maximum deviation of 2.2%. Therefore, the dimensionless curve was found to be also accurate for measurements in R134a.

Experimental procedure

A calorimeter facility was employed to investigate the compressor under the specified operating conditions. The uncertainties associated with measurements taken with the calorimeter are $\pm$ 3% for mass flow rate and power consumption. Further details of the experimental facility can be found in [8]. The compressor was tested three times for each operating condition.

The acquisition system is composed of a computer, a National Instruments converter analogue/digital (A/D), model 6071E, and a program for data acquisition and reduction, developed using LabView 6i [9].

As illustrated in Figure 3, the anemometry sensor was assembled at the entrance of the suction chamber, allowing measurements of velocity and temperature. A small tap hole (1 mm diameter) was used to connect the suction chamber to a larger orifice (7 mm diameter), in which the piezoelectric pressure transducer is mounted.

The first step in the experimental procedure is to submit the compressor to an adequate vacuum condition, in order to remove air, humidity and any other contaminant inside the system. Then, the system receives a charge of refrigerant and the flowmeter reading is set to zero. After the compressor is switched on, a period of approximately 6 hours is needed to establish a fully periodic operating condition because of compressor thermal inertia. When this condition is satisfied, data for energy consumption and mass flow rate are acquired during a period of 10 minutes. Finally, data for temperature, velocity and pressure in the suction chamber and displacement of suction valve are collected for 240 operation cycles of the compressor, allowing the evaluation of an average value for each quantity.

A total of 1000 measurements were acquired to properly characterize the compressor operation cycle. Since the compressor operates at a velocity of 3600 rpm, an acquisition rate of 60 kHz was needed. The 240,000 experimental data collected along 240 cycles were submitted to a statistical analysis, with ensemble average results being expressed as function of the crankshaft angle.

Measurements of velocity at the entrance of the suction chamber were used to allow a correction in the experimental data for temperature, associated with the sensor thermal inertia. The corresponding temperature and pressure in the suction chamber were also measured to specify physical properties. Then, based on the Nusselt number, *Nu*, for each crankshaft position an estimate for the time constant τ related to the sensor was obtained.

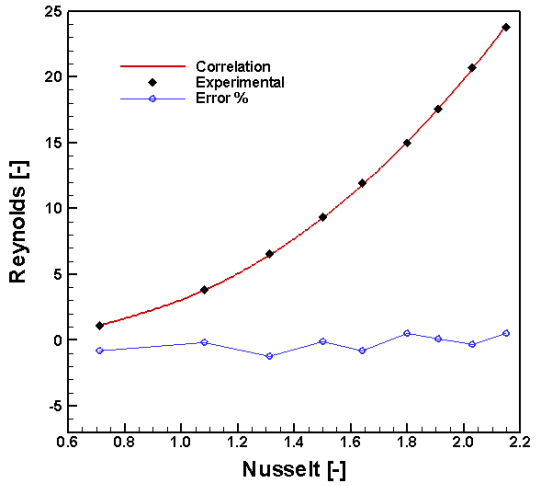

Figure 2. Dimensionless calibration curve and experimental obtained with argon.

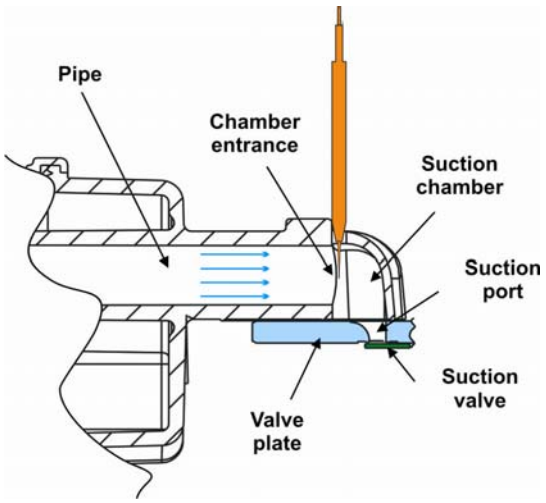

Figure 3. Detail of anemometry sensor assembly.

RESULTS AND DISCUSSIONS

Figure 4 shows results for temperature variation along the compressor cycle for the operating condition of -23.3°C/54.4°C, with and without correction for thermal inertia of the cold-wire sensor. It can be noticed some noise in the temperature data when the correction is applied to the sensor measurement. In this study, a smoothing process was adopted to remove such a noise, in which a discrete Fourier transform is initially applied to the temperature data. With the signal in the frequency domain, high frequencies are removed and then, via an inverse transform, the smoothed signal is finally corrected for thermal inertia.

As can be seen, the correction adopted for thermal inertia allows one to recover part of the temperature transient information lost in the measurement. For instance, the sensor was originally able to follow the temperature variation of 4.2°C/ms occurring in the cycle between 240° and 263°. Considering thermal inertia, a response of 4.9°C/ms is seen for the corrected data between 230° and 251°. Furthermore, the maximum value for temperature in the cycle is increased from 54.2°C to 54.9°C, with a shift of 12° in the crankshaft position.

In Figure 5, results for pressure, velocity and valve displacement are shown along the compressor cycle. It can be observed that the valve opening occurs at the angle of 230°, followed by a pressure drop and an increase in velocity, which reaches a maximum value of 32.2 m/s at the crankshaft angle of 264°. It is interesting to note that the points of maxima for velocity and valve displacement are not in

the same crankshaft position. Since the hot-wire sensor was installed at the entrance of the suction chamber, the distance the fluid has to flow before reaching the suction port contributes for a delay between the data for velocity and valve displacement. The other aspect taking part in this situation is valve dynamics, since inertia does not allow the valve to instantaneously respond to steep variations of velocity and pressure.

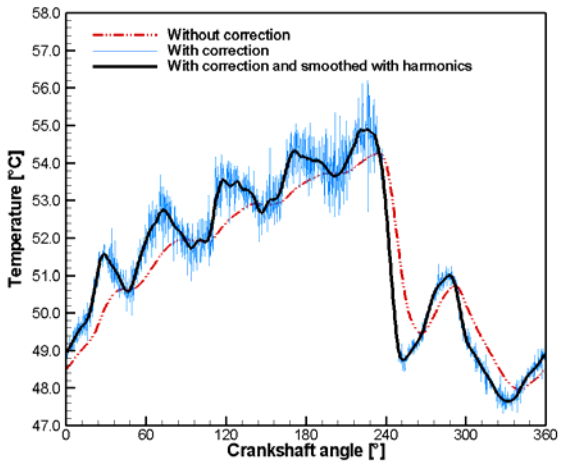

Figure 4. Correction in the temperature due to the sensor thermal inertia.

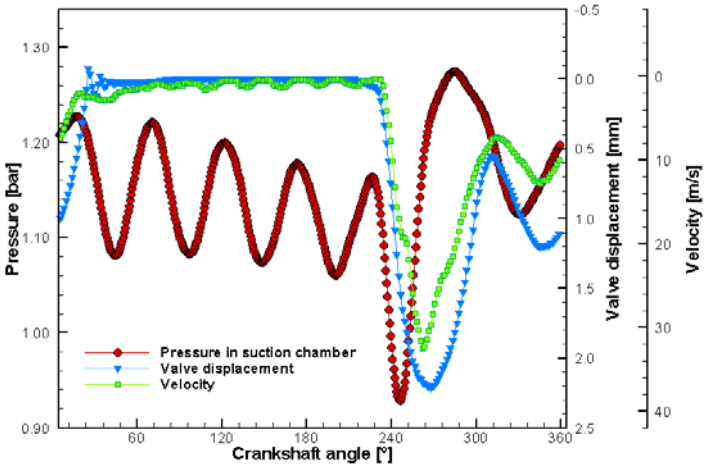

Figure 5. Measurements for temperature, pressure and velocity in the suction chamber.

Despite the difficulty originated by the two aforementioned aspects, it is clear that the velocity reaches its maximum value when the valve is fully open. It is also worthwhile noticing subtle variations in the velocity gradient around crankshaft positions 250° and 270°, probably due to perturbations in the flow. When the valve is closed, the sensor indicates the presence of velocity oscillations with amplitude of approximately 3 m/s. This phenomenon is associated with expansion and compression pressure waves traveling forward and backward in the duct that feeds the suction chamber. Naturally, the hot-wire sensor is insensitive to the velocity direction and, therefore, cannot detect an outflow condition in the suction chamber. Therefore, velocity magnitudes are always shown as positive.

Temperature variation in the suction chamber is due to heat transfer between the gas and the chamber walls, as well as pressure pulsation and interaction with the flow in the suction system. As can be seen in Figure 6 for the condition -23.3°C/54.4°C, pressure waves present during the suction process induce temperature oscillations. However, at the cycle positions 16, 28, 246 and 255°, within the period in which the valve is open, such variations are not perfectly in phase. The maximum and minimum temperature values in the suction chamber are equal to 54.8°C and 47.5 °C at the angles 227° and 331°, respectively. The temperature decrease observed when the valve opens can be attributed to the pressure drop to which the fluid in the suction chamber is submitted.

For the period in which the valve is closed, between 26° and 230°, there is an increase of approximately 3.5°C in the suction chamber temperature. Considering that such a time period corresponds to 9.4 ms, this temperature increase indicates a high intensity heat transfer between the gas and the chamber walls.

Figure 7 shows a comparison between results for temperature in the suction chamber obtained at two operation conditions: -23.3°C/54.4°C and -35°C/54.4°C. As can be noticed, the average cycle temperature is increased from 51.4°C to 57.3°C when the condition is changed to -35°C/54.4°C. Moreover, the temperature reduction observed when the valve opens is almost 1°C greater for this

condition. The other aspects already analyzed for the condition -23.3°C/54.4°C remains very similar in this new situation but, nevertheless, with a phase shift of 15° in the temperature and pressure oscillations.

It is interesting to observe the presence of two temperature oscillations during the period in which the valve is open for the condition -35°C/54.4°C. The first one occurs between the crankshaft positions of 280 and 330° and is linked to an increase of pressure in the suction chamber. On the other hand, the second oscillation can be attributed to heat transfer, since after the angle 330° the valve is almost closed and the fluid inside the chamber is virtually stagnated.

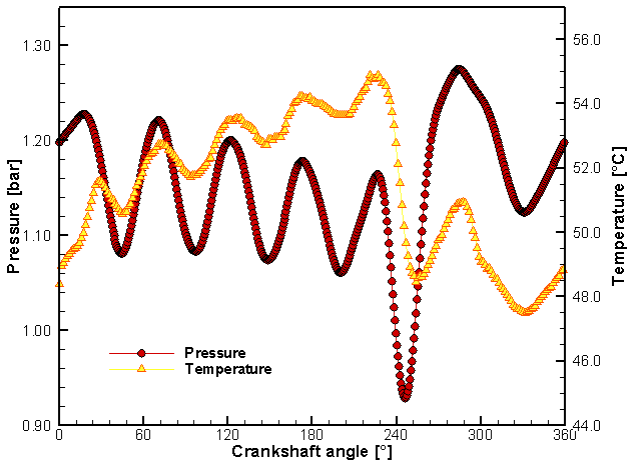

Figure 6. Pressure and temperature during the compressor operation cycle.

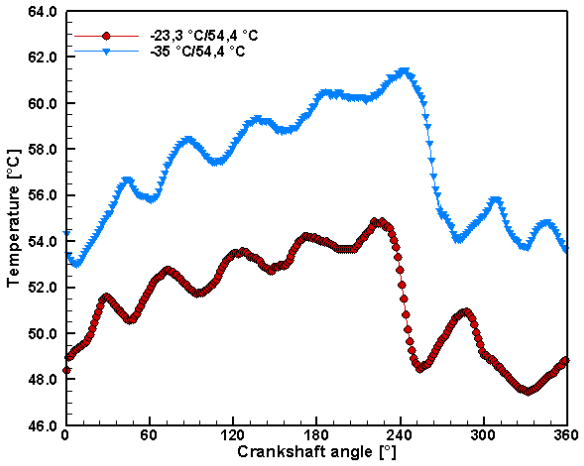

Figure 7. Temperature variation along the compressor cycle for two operating conditions.

CONCLUSIONS

An experimental setup was developed to investigate thermal transients in the suction chamber of high speed refrigeration compressors. To this extent, a hot-wire system with a 5μm diameter wire probe was adopted for temperature and velocity measurements. A calibration procedure was specially elaborated due to the impossibility of using the refrigerant as the working fluid. Additionally, corrections were made available to temperature measurements at each position of the compressor operation cycle, by estimating the sensor thermal inertia. Results for valve displacement and pressure pulsation in the suction chamber were also obtained to complement the analysis. Measurements indicated abrupt variations in all flow properties, strongly linked to the valve motion. When the valve is open, velocity reach levels of approximately 32 m/s, in comparison with 3 m/s when it is closed. It has been observed a considerable increase in the gas temperature during the period the suction valve is closed associated with heat transfer between the gas and the suction chamber walls.

ACKNOWLEDGEMENTS

This study forms part of a joint technical-scientific program of the Federal University of Santa Catarina and EMBRACO. Support from FINEP (Federal Agency of Research and Projects Financing) and CAPES (Coordination for the Improvement of High Level Personnel) is also acknowledged.

REFERENCES

1. Shiva Prasad, B. G., Fast Response Temperature Measurements in a Reciprocating Compressor. *Proc. of the 1992 Purdue Compressor Tech. Conf. Purdue*. pp. 1385-1395. 1992.
2. Bauer, W. D.; Wenisch, J.; Heywood, J. B. Averaged and Time-Resolved Heat Transfer of Steady and Pulsating Entry Flow in Intake Manifold of a Spark-Ignition Engine. *Int. J. of Heat and Fluid Flow*. v. 19. pp. 1-9. 1998.
3. Zend, P.; Assanis, D. Time-Resolved Heat Transfer in Engine Intake Manifold. *Int. Symposiun on Transient Convective Heat and Mass Transfer in Single and Two-Phase Flows*. 2003.
4. Olczyk, A. Problems of Unsteady Temperature Measurements in a Pulsating Flow Gas. *Meas. Sci. and Technol***.** v. 19. pp. 1-11. 2008.
5. Weiss, F., Paranthöen, P., Lecordier, J.C. Frequency Response of a Cold-Wire in a Flow Seeded with Oil Particles. *Experiments in Fluids*. v. 39. pp. 935-940, 2005.
6. Bruun. H. H., *Hot-Wire Anemometry: Principles and Signal Analysis*. 1995.
7. Kramers. H. Heat Transfer from Spheres to Flowing Media. *Physica*, v. 12*,* pp. 61-80, 1946.
8. Pereira, E.L.L., Deschamps, C.J., Ribas Jr, F.A. Performance Analysis of Reciprocating Compressors through Computational Fluid Dynamics. *Proc. IMechE, Part E: J. Process Mechanical Engineering*, v. 222, pp. 183-192, 2008.
9. National Instruments Inc. *LabView – User manual. Part Number 320999C-01*, 2000.

PERFORMANCE, EMESSIONS, AND COMBUSTION DEPOSIT CHARACTERISTICS OF A DIECT INJECTION DIESEL ENGINE FUELED WITH WASTE SUNFLOWER OIL METHYL ESTER

Chris Steyn, Makame Mbarawa *
Department of Mechanical Engineering,
Tshwane University of Technology, Private Bag X680, Pretoria 0001, South Africa

ABSTRACT. In this study, performance, emission and combustion deposit (CD) characteristics of a direct injection (DI) diesel engine fuelled with the pure waste sunflower oil methyl ester (WSOME) and its blends at proportions of 30 %, and 70% (v/v) were investigated. The results showed the WSOME/blends presented better brake thermal efficiency than diesel fuel. This is due to the higher density and lower heating value of the WSOME than that of diesel fuel. Engine tests showed that the performance parameters of the WSOME/blends fuels did not differ greatly from those of diesel fuel. Slight power losses were experienced with the WSOME/blends fuels. This may be due to the lower heating value of the blends fuels. The engine operated on the WSOME100 and their blends resulted in higher NOx, HC, CO and lower exhaust smoke concentrations than the diesel fuel case. Further, it was found that the WSOME100 produced lowest fraction of carbon deposits as compared to diesel fuel and other WSOME blend fuels.

Keywords*: performance,; emission, combustion deposits, methyl ester, diesel engine*

INTRODUCTION

The rapid depleting of fossil fuels deposits, increasing global concern due to air pollution caused by internal combustion engines as well as escalating oil prices have catalysed efforts to look for alternative energy sources that are both renewable and environmentally friendly. In this respect, various investigations in many countries have been carried out to see the possibility of replacement of diesel fuel with oxygenated fuels such as biodiesel, ethanol etc. One of the oxygenated fuels that shows a great potential is biodiesel (BD). BD, an alternative fuel obtained from vegetable oils or animal fats, has a number of technical advantages over diesel fuel which include reduction of most exhaust emissions, improved lubricity and biodegradability, higher flash point, reduced toxicity, and renewable. In the case of viscosity, calorific value and cetane number, BD and diesel fuel show similar behaviour.

The raw material costs and limited availability of vegetable oil feedstocks are always critical issues for the BD production and are the major obstacles to its commercialization. The high costs of vegetable oils, which could be up to 75% of the total manufacturing costs, have led to the production costs of BD becoming approximately 1.5 times higher than diesel. The price of waste cooking oils (WCO) is still remains 2-3 times cheaper than the net vegetable oils, depending on the base stock, geographic area, variability in crop production from season to season, the price of the crude petroleum and other factors. Exploring ways to reduce the high cost of BD is of much interest in recent BD research, especially for those methods concentrating on minimizing the raw material

* Corresponding author: Prof. M. Mbarawa
Phone: + (27)-12-382 5171, Fax: + (11)-12-382 5022
E-mail address: mbarawamm@tut.ac.za

costs. One way to reduce the cost of BD is to use less expensive feedstock such as WCO from restaurants. WCO is a promising alternative to vegetable oil due to its reduced cost.

Although, there have been numerous studies on the performance and emission of the WCO based BD, there are limited studies in the literature concerning the comprehensive evaluation of BD from WCO as an alternative fuel for diesel engine. Hence, more detailed research is need. With this background, the present study is aimed in investigation the engine performance, emission and combustion deposit (CD) rate formation of a direct injection (DI) diesel engine fuelled with waste sunflower oil methyl ester (WSOME) and its blends.

EXPERIMENTAL SET-UP AND PROCEDURES

Experimental Equipment and performance and emission test procedures

Experiments were conducted on a four cylinders, four stroke, naturally aspirated, water cooled, direct injection Isuzu diesel engine with a bore of 93 mm, stroke of 92 mm and compression ratio of 18.4:1. The engine was directly coupled to an eddy current dynamometer using a flexible coupling and a stub shaft assembly. The maximum torque of the engine was 162 Nm at 2000 rpm and the rated power was 43 kW at 2800 rpm. No adjustment was made at the fuel injection timing, i.e**.** at 20^{o} before top dead centre (BTDC).

Testing was performed at maximum fuelling at different engine speeds to produce a power curve. This mode was performed at increasing speed starting at 1000 rpm, and incrementing in step of 200 rpm to 2800 rpm. The experimental procedures started with a preliminary investigation of the engine running on the pure diesel fuel in order to determine the engine's operating characteristics and exhaust emission levels, constituting the 'baseline' that is compared with the corresponding cases when the blended fuels were used. Before the significance of the performance and exhaust emissions results can be considered, it is important to establish if the engine operating conditions were reproduced consistently, as any deviation in operating conditions can have an overriding influence on performance and emissions. The reproducibility of the dynamometer speed control set points was generally within ± 5 rpm of the desired engine speed, while torque settings were generally achieved to within 1.5 %. All of the torque and power results were corrected using SABS 013-correction factor [1] to adjust for atmospheric variation. Exhaust gases: (CO (%), NO_X (ppm), HC (ppm) and CO_2 (%)) were measured on line by an Ultra-Tune gas analyser. The relative standard deviation of NOx, CO, HC and carbon dioxide (CO_2) concentrations was 1%, 3%, 3% and 0.3% respectively.

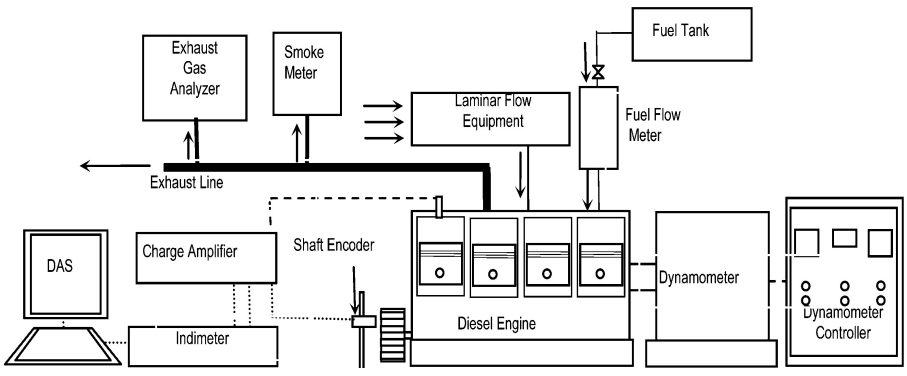

Figure 1. Schematic diagram of the experimental set-up

Combustion chamber deposits generation and analysis procedures

The same engine used in performance and emission testing was operated for 40 h under cycled conditions that approximated city-suburban driving conditions to generate CD from the test fuels.

The CD test cycle is shown in Table 2. At the end of each cycle, the engine was dismantled, visually inspected and rated according to the Coordinating Research Conical (CRC) test procedures [2].

After rating process, the deposit from each of the four combustion chamber region, cylinder head region and piston top region was scraped using gasket scraper and fine wire brush. The sample material from respective region of the four cylinders was then mixed together to form on large average sample for the respective region. After scraping, the cylinder head was washed using an organic solvent (acetone) assisted with sand paper and a wire brush for removing the remaining deposits. Then, compressed air was used to remove the loose carbon from cleaning areas. After that, cylinder head was assembled to the engine and used lubrication oil was discharged and refilled with new one before performing a new test.

Quantitative analysis of combustion deposit formation was carried out by weighting the scraped deposit samples from the test fuels. Then, the analytical analysis was characterised by using a scanning electronic microscopy (SEM) for morphology, X-Ray diffraction (XRD) for elemental composition and the nitrogen adsorption for surface area and pore size distribution. In addition, thermo-gravimetric analysis was carried out so that weight changes of combustion deposit could be measured qualitatively while being heated.

Biodiesel Preparation

In the present investigation, WSOME used was produced from sunflower WCO collected from different local restaurants. WSOME was prepared using alkali catalyzed method. Methanol (1:3 molar WCO: alcohol) was mixed with NaOH (1 wt. % of oil) added to the reactor containing oil. The reaction mixture was refluxed for 2-4 hrs. After completion of the reaction the material was transferred to separating funnel for separation and washing process. Although several blends with a wide composition spectrum were prepared by splash blending, the tests were carried out with WSOME30 (30% WSOME-70% diesel by volume), WSOME70 (70% WSOME-30% diesel by volume), WSOME100 (net WSOME). These blend ratios were chosen to see whether clear difference could be detected in their performance ability, emission and CD formation.

Table 2. Sample Test cycle for combustion chamber deposit

Hours	Engine speed(rpm)	Engine Load (Nm)
2	2800	100
2	2600	100
4	2500	110
Engine off for 8hrs		
6	2500	110
2	2400	110
Engine off for 16hrs		
8	2400	110
Engine off for 16hrs		
8	2200	90
Engine off for 16hrs		
2	2200	90
6	2200	90
Overall cycle duration: 40hrs		

REUSLTS AND DISCUSION

Performance Parameters

The effect of the WSOME addition to the blends on the engine torque output for various speeds is shown in Figure 2a. The engine torque output of all test fuels increases as engine speed increases, reaches a maximum and then, as engine speed increases further, torque decreases. The torque decreases because the engine is unable to ingest a full charge of air at the higher speeds. This is due to the fact that as engine speed increases, there is less time for the engine cylinders to be filled with fresh air and expel exhaust gases. Comparison of engine torque between WSOME100, WSOME70, WSOME30 and diesel fuel generally shows reduction in torque that are approximately the same as the reduction in energy content of the blend relative to diesel fuel. It is shown that the maximum torque of 158 Nm was developed by the engine on the diesel fuel. The corresponding engine speed was 2400 rpm. The engine developed maximum torque of 156.1, 154.9 and 153.5 Nm at 2200 rpm when the engine was operated on WSOME30, WSOME70 and WSOME100 respectively. The lower specific heating value of WSOME is the reason for the reduction in torque.

Figure 2b shows the brake power output versus engine speeds for WSOME100, WSOME70, WSOME30 and diesel fuel. There is slightly difference between the brake power values developed by the test fuels. The increase in the amount of the WSOME in the blend fuels consistently shows a decreasing trend of the brake power output. This trend can be explained by the lower heating value of the WSOME-diesel blended fuels with increasing biodiesel concentration in the blends.

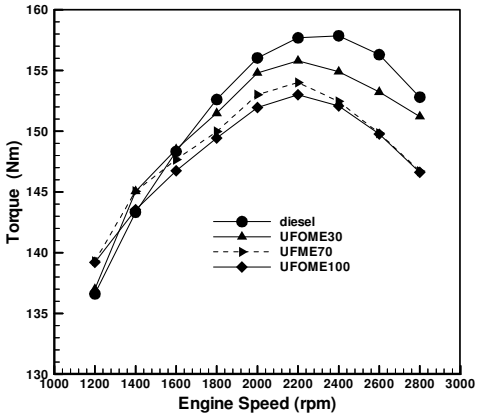

Figure 2a. Effects WSOME on engine toque

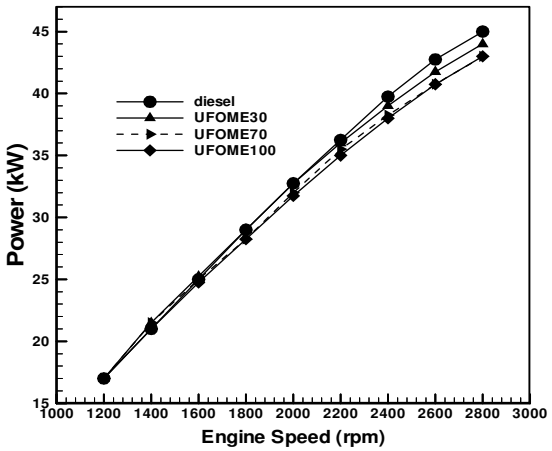

Figure 2b. Effects of the WSOME on engine power output

If different biodiesel fuel blends with different heating values are compared, their heating values decrease with the increase of biodiesel in the blend and for this reason; brake thermal efficiency is shown in Figure 3a instead of brake specific fuel consumption (BSFC). As shown in the figure, WSOME-diesel blends present better brake thermal efficiency than diesel fuel. These results concur with those obtained by Ramadhas et al. [3] who compared the performance of a diesel engine

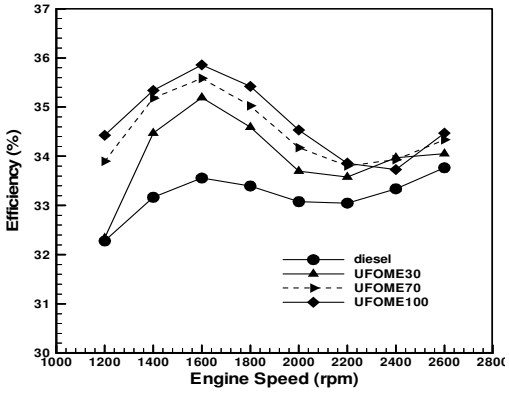

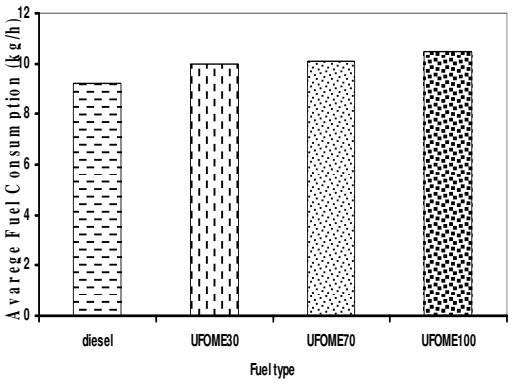

Figure 3a Effects of the WSOME on engine thermal efficiency

Figure 3b Effects of the WSOME on average fuel consumption

running on blends of diesel fuel and biodiesel derived from rubber seed oil. Elsewhere, Raheman and Phadatare [4] recorded a slightly different behaviour. The better engine performance with WSOME is probably due the oxygenated nature of WSOME, and also due to its higher viscosity and lower calorific value, which have a major bearing on spray formation and initial combustion. Figure 3b compares the average fuel consumption rates of the test fuels that were observed over the range of tested engine speeds. The diesel fuel had a slightly lower fuel consumption rate primarily because it had the largest heating value among the test fuels. In contrast, the WSOME100, which had the lowest heating value, had a slightly higher fuel-feeding rate to attain the maximum engine load required.

Regulated Gas Emissions

NOx as function of engine speed and percentage of WSOME is shown in Figure 4a. The results show that NOx increase gradually with the load and their values depend largely on the engine speed and the percentage of WSOME in the blend. The use of the WSOME100 and their blends resulted in quite considerably increased NOx emissions. This is due to the presence of fuel oxygen within the blend fuels. This observations are in line with many other biodiesel fuel emission studies (e.g. [5- 7]). Among the test fuels, WSOME70 produced the highest NOx for engine speed between 1400 and 2600 rpm while WSOME100 gave the highest NOx emissions at the engine speeds of 2800 rpm. As shown in Figure 4b, the engine running on WSOME and its blends showed higher HC concentration than those of diesel fuel. Among these fuels, WSOME70 produced the highest HC emissions while diesel fuel gave lowest HC emission for all engine speeds. Humke and Barsic [8] reported that the physical properties of fuel such as density and viscosity can have a greater influence on hydrocarbon emissions than its chemical properties. The viscosity of WSOME and its blends are higher than that of diesel fuel. High viscosity causes poor fuel atomization during the spray and may lead to higher fuel spray droplet sizes. As a result, the fuel spray for WSOME and its blends may not propagate deeper into the combustion chamber and gaseous hydrocarbons remain along the cylinder wall, the crevice volume and left unburned fuel [9].

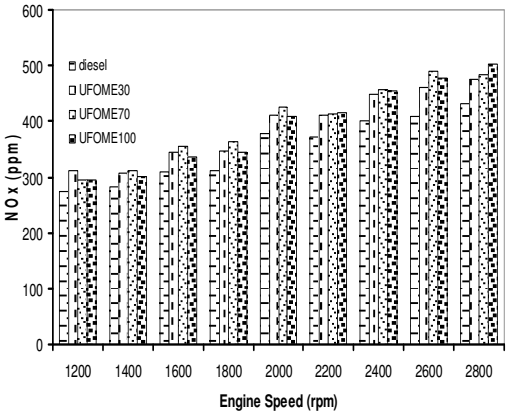

Fig 4a Effects of the WSOME on NO_X emissions

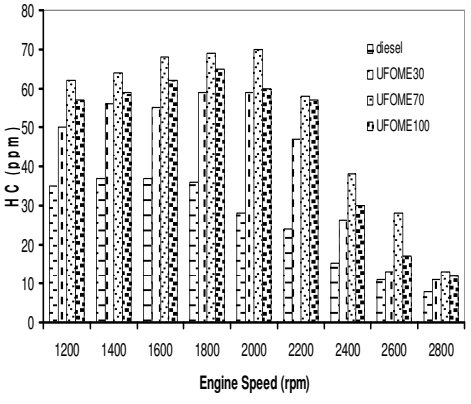

Fig 4b Effects of the WSOME on HC emissions

The CO emission in the exhaust gas indicates the lost chemical energy that is not fully utilized in the engine. Generally, CO emission depends on equivalence ratio, fuel type, atomization ratio, injection timing, engine load and speed. Figure 5a shows the changes in the CO emissions for different test fuels at different engine speeds. WSOME30 produced the highest CO emissions, while diesel fuel produced lowest CO emissions for all engine speeds. The CO emissions are found to be increasing with increase in engine speed to the maximum values at 2600 rpm and then decreases as the engine speed increases. Generally, the CO emission emitted by the blend fuels is higher than

that by the corresponding diesel fuel case. Relatively poor atomization and lower volatility of biodiesel compared to diesel oil is responsible for this trend.
Figure 5b shows that the CO_2 concentration increased with increasing engine speeds for all test fuels. WSOME30 produced the highest amount of CO_2 than other fuels for all engine speeds. The CO_2 emission from biofuel engines can be absorbed by plants for photosynthesis purposes, so that the CO_2 level in the atmosphere is kept in balance.

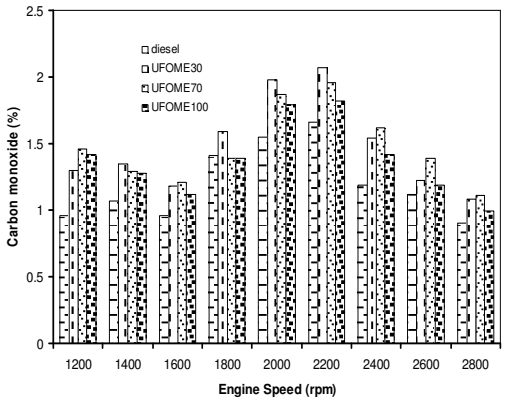

Fig 5a Effects of the WSOME on CO emissions

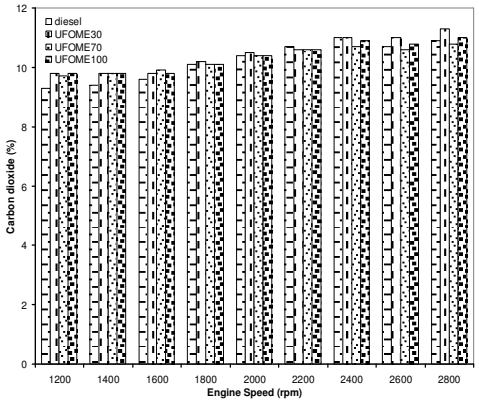

Fig 5b Effects of the WSOME on CO_2 emissions

Smoke opacity is a direct measure of smoke and soot. The exhaust smoke generated by different fuels depends on the engine load, engine speed, air turbulence velocity inside engine cylinder and the amount of oxygen content in the blend. As it is obvious from the Figure 8a, the exhaust smoke concentrations from the engine using WSOME100 were lower than the other test fuels for all engine speeds and WSOME blend fuels produced lower concentration than diesel fuel. The significant reduction in smoke emission for WSOME fuelled engine operation mode may be due to the oxygenated blends. Smoke is mainly produced in the diffusive combustion phase; the oxygenated fuel blends lead to an improvement in diffusive combustion for the biodiesel operation. These results are similar with the results obtained in previous studies [10, 11, 12, 13].

Combustion deposits formation

Figure 6 shows the CD build up in the cylinder head from the test fuels. It can be clearly seen that the CD for WSOME70 and WSOME100 operated engines are substantially lower than diesel-fuelled operated engine. The dark flat deposit is seen around the periphery of the cylinder head (Figure 5a). This area is where average temperatures are lower, promoting accelerated CD formation. WSOME blends produced less amount of CD compared with diesel fuel. Figure 7 also shows CD on piston top of the tested fuels. It can be clearly noticed that the CD formation for the WSOME- fuelled engines are substantially lower than diesel-fuelled engine.

Shown in Figure 8b are the CD weights on the cylinder head and piston tops of the test fuels. The differences in CD weights were found to be very small between diesel fuel and WSOME30. A reduction in CCD is observed with an increase in percentage of WSOME in the blend. WSOME70 and WSOME100 samples produced smaller amounts of CCD as compared to diesel fuel and WSOME30 samples. Lowest amount of deposits was recorded on WSOME100 fuelled engine. This may be due to more complete combustion resulted from the higher amount of oxygen in the WSOME. These results agree with those obtained by Agrawal et al. [14] who compared CD on cylinder head of biodiesel-fuelled engine after 512 h of engine operation.

Figure 9 presents scanning electron micrographs of diesel, WSOME30, WSOME70 and WSOME100 sample deposits. The diesel sample deposit is characterized by a relatively homogeneous appearance with plenty of tiny back particle materials (Figure 9a). These materials

become larger at the outer layer of combustion chamber suggesting agglomeration of small particle materials such as KCl which condensed on the surface of particles of more rich in silicates. WSOME-diesel blend

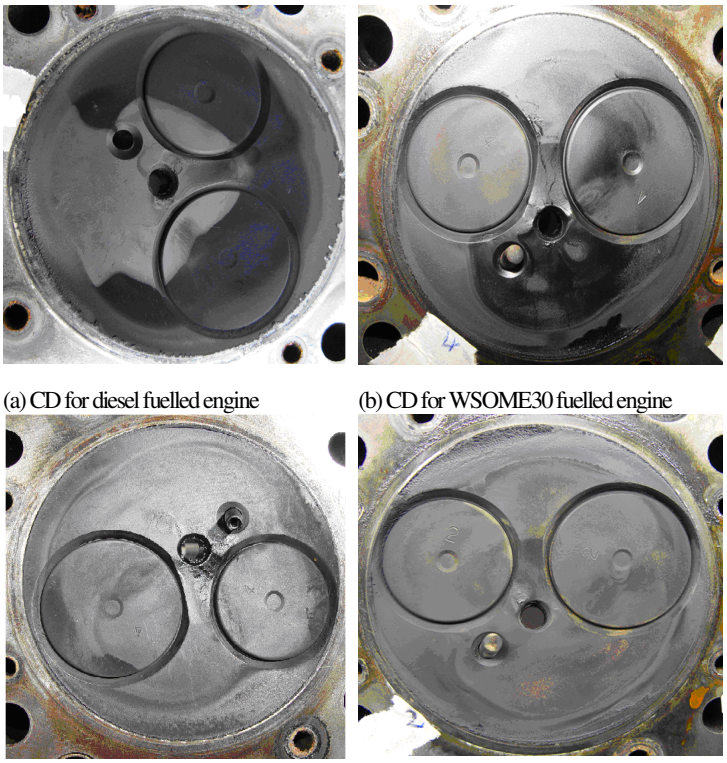

(a) CD for diesel fuelled engine (b) CD for WSOME30 fuelled engine

(c) CD for WSOME70 fuelled engine (d) CD for WSOME100 fuelled engine

Figure 6 Carbon deposits on cylinder head after 40 h of engine operations

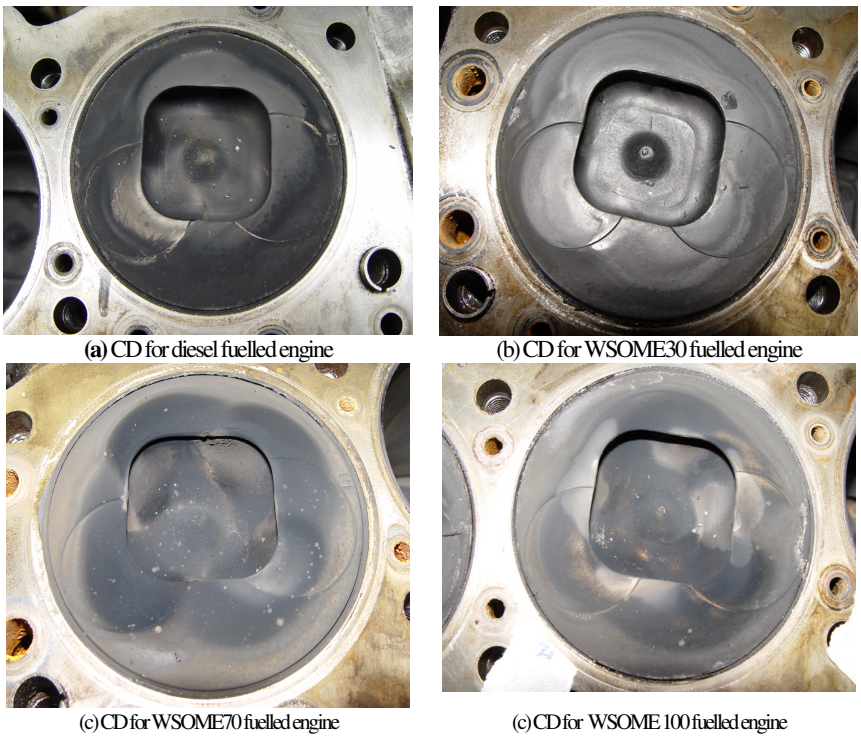

(a) CD for diesel fuelled engine (b) CD for WSOME30 fuelled engine

(c) CD for WSOME70 fuelled engine (c) CD for WSOME 100 fuelled engine

Figure 7 Carbon deposits on piston top after 40 h of engine operations

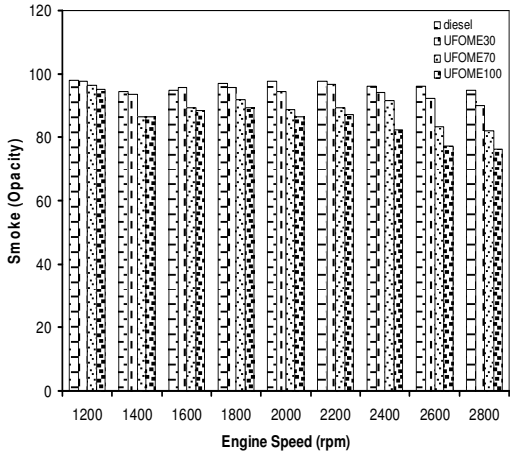

Figure 8a Effects of the WSOME on smoke

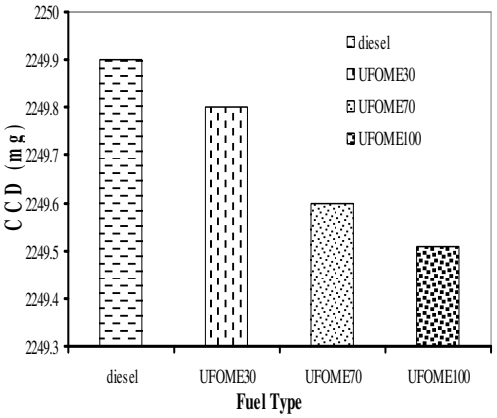

Figure 8b. Effects of fuel type on CD formation

WSOME resulted in more varied particle morphology (Figure 6c and 6d) with smaller particles, microspheres or agglomerates. WSOME and diesel have different portion of volatile and non-volatile matters. The non-volatile matter (carbon residue) in diesel is about 0.2% by mass, while in WSOME is approximately 0.36%. The larger amount of non-volatile matter in WSOME may cause the development of larger particles in WSOME30. On the other hand, the presence of oxygen in WSOME enables the reduction of soot particles in fuel rich regions. It was also observed that the deposits from diesel appear darker compared with WSOME-diesel blend deposits.

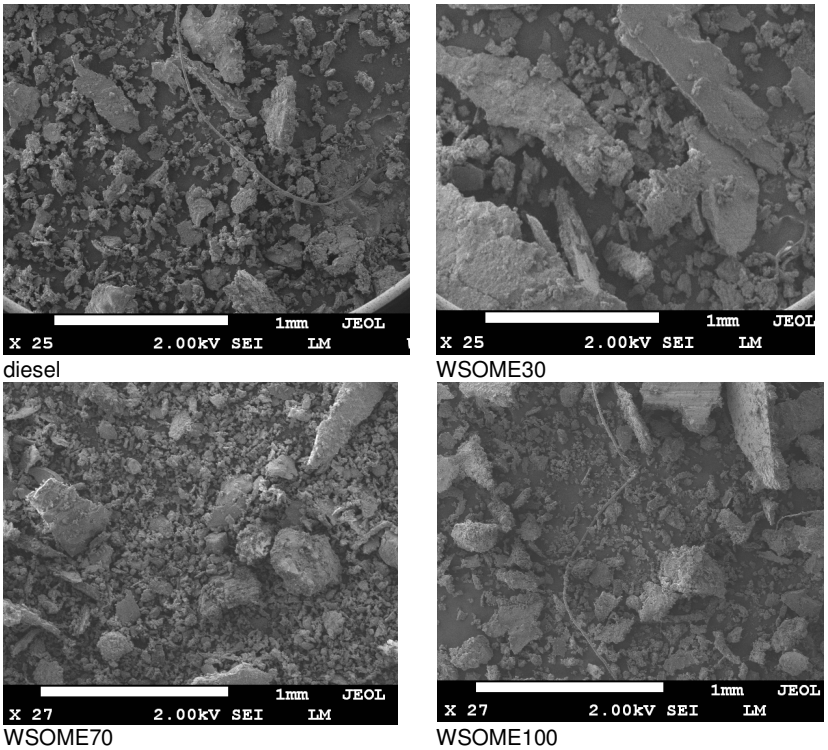

Figure 9. SEM micrograph of combustion chamber deposits for test fuels

CONCLUSIONS

The performance, emission and deposit characteristics of the diesel engine fuelled with the WSOME and its blends were investigated and the following conclusions can be drawn:

- WSOME/blends presented better brake thermal efficiency than diesel fuel. This is due to the higher density and lower heating value of the WSOME than that of diesel fuel. Increasing fuel density increases the energy content of the fuel brought into the engine at a given injector setting.
- Engine tests showed that the performance parameters of the WSOME/blends fuels did not differ greatly from those of diesel fuel. Slight power losses were experienced with the WSOME/blends fuels. This may be due to the lower heating value of the blends fuels.
- The engine operated on the WSOME100 and their blends resulted in higher NOx, HC, CO and lower exhaust smoke concentrations than the diesel fuel case.
- From the deposit characteristic results, it was found that the WSOME100 produced lowest fraction of carbon deposits as compared to diesel fuel and other WSOME blends fuels.

Acknowledgments
The authors sincerely thank the Natural Research Foundation-South Africa for financial grant (Grant Number 65429 and 65297) to carryout this research work. The authors also thank Tshwane University of Technology for financial support.

REFERENCES

1. South African Bureau of Standards: SABS, 342, Pretoria, South African, 2003.
2. Proceedings of the CRC workshop on combustion chamber deposits, 1993, Orlando, Florida, USA.
3. Ramadhas AS, Jayaraj S, Muraleedharan C, Characterization and effect of using rubber seed oil as fuel in the compression ignition engines, Renew Energy 2005; 30:795–803.
4. Raheman H, Phadatare AG, Diesel engine emissions and performance from blends of karanja methyl ester and diesel, Biomass Bioenergy 2004; 27:393–397.
5. Dorado MP, Ballesteros E, Arnal JM, Gomez J, Lopez FJ. Exhaust emissions from a diesel engine fuelled with transesterified waste olive oil. Fuel 2003; 82:1311–5.
6. Yage Di, Cheung C.S., Huang Z, Experimental investigation on regulated and unregulated emissions of a diesel engine fuelled with ultra-low sulphur diesel fuel blended with biodiesel from waste cooking oil, Science of the Total Environment, 407, 2009; 835-846.
7. Tsolakis A. et al. Engine performance and emissions of a diesel engine operating on diesel-RME (rapeseed methyl ester) blends with EGR (exhaust gas recirculation). Energy 2007; 32:2072–80.
8. Humke AL, Barsic NJ. Performance and emissions characteristics of a naturally aspirated diesel engine with vegetable oil fuels. SAE paper No. 810955.
9. Nagarajan G, Renganarayanan S, Rao AN. Emission and performance characteristics of neat ethanol fuelled DI diesel engine. Int. J. Ambient Energy 2002; 23(3):149–58.
10. Agarwal AK. Vegetable oil versus diesel fuel: development and use of biodiesel in a compression ignition engine. TERI Inform. Dig. Energy 1998;8(3):191–204.
11. Scholl KW, Sorenson SC. Combustion of soybean oil methyl ester in a direct injection diesel engine. SAE paper No. 930934, 1983.
12. Kalligeros S, Zannikos F, Stournas S, Lois E, Anastopoulos G, Teas Ch, et al. An investigation of using biodiesel/marine diesel blends on the performance of a stationary diesel engine. Biomass Bioenergy 2003; 24:141–9.
13. Agarwal AK, Das LM. Biodiesel development and characterization for use as a fuel in compression ignition engine. J. Eng Gas Turbines Power 2001; 123:440–7.
14. Agarwal AK, Bijwe J, Das LM. Wear assessment in biodiesel fuelled compression ignition engine. J. Eng Gas Turbine Power (ASME J) 2003; 125(3):820–6.

INTERFACIAL ENERGY AND ENERGY BALANCE IN WATER-IN-HEAVY-OIL EMULSIONS

V. Karcher, A. Bannwart*
State University of Campinas, Campinas-SP, Brazil

ABSTRACT. The aim of this study is to investigate the interfacial properties of water-in-oil (w/o) emulsions composed by water and a Brazilian heavy crude oil. For such purpose an experimental set-up was built in order to measure the different energy terms involved in the emulsification, including the interfacial energy of the emulsion being generated. Different w/o emulsions were prepared in a batch calorimeter by using a high-shear rotating homogenizer. Two experimental techniques were used, namely, the calorimetric method based on the energy balance for the emulsification and the standard method based on the measurement of the droplet size and distribution by means of a digital microscope. The uncertainties in the interfacial energy provided by both techniques were determined, in order to compare their feasibility. The main result is that the interfacial energy may be accurately determined from the drop size distribution and interfacial tension. The relative magnitudes of the different terms in the energy balance are established for the selected process.

Keywords: *emulsion, oil-water, interface energy, energy balance droplet size*

INTRODUCTION

In the production operations for heavy crudes, water is commonly present within the oil phase as a finely dispersed phase. This situation may originate from the oil recovery method (e.g. water injection in the reservoir), presence of connate water inside the own reservoir [1, 2] and/or water injection in the production pipeline for friction reduction purposes. The turbulent shear associated with fluid flow within a pump, gas lift system and pipeline flow may cause the formation of water-in-oil emulsions (w/o). These remain stable for a long time, due the presence of naturally emulsifying agents in the crude oil phase, high oil viscosity and small droplet size. Thus, emulsion separation at surface facilities requires specific equipment which contribute to increase the production costs [2]. Besides, the viscosity of w/o emulsions is still higher than the viscosity of the heavy oil alone, with a typically non-Newtonian behavior [3, 4].

Oil-water emulsions can be encountered at many locations such as hydrocarbon reservoirs, well bores, pumps, production pipelines, surface facilities, refineries and at many stages during drilling, producing, transporting and processing of crude oils [2]. In oilfield, w/o emulsions are called 'regular', with drop sizes usually in the micron range. Oil-in-water emulsions (o/w) are termed 'inverse' or 'reverse'. In both cases their structure is complex and may include water-in-oil-in-water (w/o/w) or oil-in-water-in-oil (o/w/o) sub-systems [5].

It is well-known the influence of surfactant compounds naturally present in the crude oil itself on the stability of w/o emulsions. Crude oils, especially heavy oils, contain significant amounts of asphaltenes (high molecular weight polar components) and resins, both acting as natural emulsifiers

* Corresponding author: Prof. A.C. Bannwart
Phone: + (55)-19-35213202, Fax: + (55)-19-32894999
E-mail address: bannwart@dep.fem.unicamp.br

because of their active surface and structure-forming properties, which tend to accumulate at the interface and hence have pronounced effects on emulsion stabilization [5-7].
Interfacial properties of oil-water emulsions are strongly important to determine the mechanisms involved in their stability [6]. The process of emulsion generation, due to external forces such as shear, causes an increase in the total surface energy. However, there is a natural tendency for the coalescence of droplets to take place, which tends to reduce the total interfacial area and consequently the total surface energy [6, 7].
The dispersion of two immiscible fluids can be obtained by mechanical agitation. First, the interface is deformed and breaks up into many droplets under the action of shear or inertial forces in either laminar or turbulent flow. The droplet deformation is achieved if energy input creates a pressure differential of the same magnitude of Laplace pressure $2\sigma/R$ (where σ is the interface tension and R the radius of the droplet). This condition can be produced by intense agitation which requires a significant amount of energy [8]. However, it has been reported that only a small fraction of the energy input is spent in the increase of free energy of the interface [9, 10].
The intensity of agitation can be represented by the energy input per unit volume of mixture. For an emulsion prepared in an agitated vessel, not only the physical properties of the phases, but also the operational parameters affect the energy input. Earlier studies have investigated the behavior of the emulsion prepared mechanically in stirred vessels. Several correlations were proposed to determine the mean droplet size as a function of power input and operational parameters [10-13].
The objective of this study is to investigate the interfacial energy and the energy balance for w/o emulsions composed by distilled water and a heavy crude oil. Determination of the interfacial energy was based on the droplet size and distribution obtained by means of a digital microscope. An experimental set-up was built in order to measure the terms of the energy balance during the emulsion generation. The w/o emulsions were prepared in a calorimeter vessel in which a high-speed rotating impeller was inserted. The main result of this research is the determination of the relative magnitudes of the different terms in the energy balance during emulsification. The interfacial energy was compared with the energy provided by the impeller and the other terms of the energy balance.

EXPERIMENTAL SETUP AND PROCEDURE

The emulsions, composed by heavy crude oil (17 ºAPI) and distilled water, were prepared in water volume fractions of 0.1, 0.25 and 0.4 and stirrer speeds of 14000 and 22000 rpm. The total volume of the mixture (water and crude oil) was 90 cm³. Even for the water fraction of 0.4, coalescence was not observed in experiments.
Measured physicochemical properties of the crude oil are presented in Table 1. Measurements of surface/interfacial tension were carried out using an automatic tensiometer KSV Instruments, model Sigma 701. Oil-water interfacial tension was measured by the ring method and is provided in Table 2 at several controlled temperatures.
A specially designed calorimeter to determine the relative terms of the energy balance for the emulsification is shown in Figure 1. It consisted of a hermetically closed aluminum vessel of 100 cm³ capacity. The impeller of a homogenizer (IKA Ultra Turrax T18 Basic) was inserted into the vessel to disperse the fluids. A system of helicoidal fins of 1 mm in thickness with 5 mm pitch was machined externally to allow cooling of the stirred vessel by a water jacket. The ensemble was placed into a cylindrical 2 cm thick Teflon box to get good isolation.
The electric power input to the homogenizer was measured by means a wattmeter. The cooling water was supplied by a centrifugal pump, from a temperature controlled bath toward the calorimeter and returned to the same bath. Inlet (T_{inlet}) and outlet (T_{outlet}) temperatures of the coling jacket were recorded by using two platinum resistance temperature detectors (± 0.05 ºC). The internal temperature of the vessel ($T_{emulsion}$) was also recorded by a resistance temperature detector (± 2 ºC). The flow rate was controlled by valves and measured with a Coriolis mass flowmeter. All

the temperatures and water flow rate were collected and recorded by means of a LabView Signal Express data acquisition system (National Instruments). Thus the instantaneous heat transfer from the stirred vessel could be determined.

Table 1
Properties of Crude Oil

Property	Value	Measurement method
Viscosity (25 ºC)	2000 mPa.s	Haake RheoStress reometer
Specific gravity (25 ºC)	0.96	Densimeter
Superficial Tension (25 ºC)	33×10^{-3} N.m^{-1}	KSV tensiometer by Wilhelmy plate method
Water Content (25 ºC)	0.24 %	Karl Fisher method
Specific Heat (20-100 ºC)	1.65 J.g^{-1}.K^{-1}	DSC

Table 2
Oil-Water Interfacial Tension $\sigma_{w\text{-}o}$ at several Temperatures.

Temperature (ºC)	$\sigma_{w\text{-}o}$ (N.m^{-1})
15	0.02823
25	0.02760
35	0.02632
45	0.02508

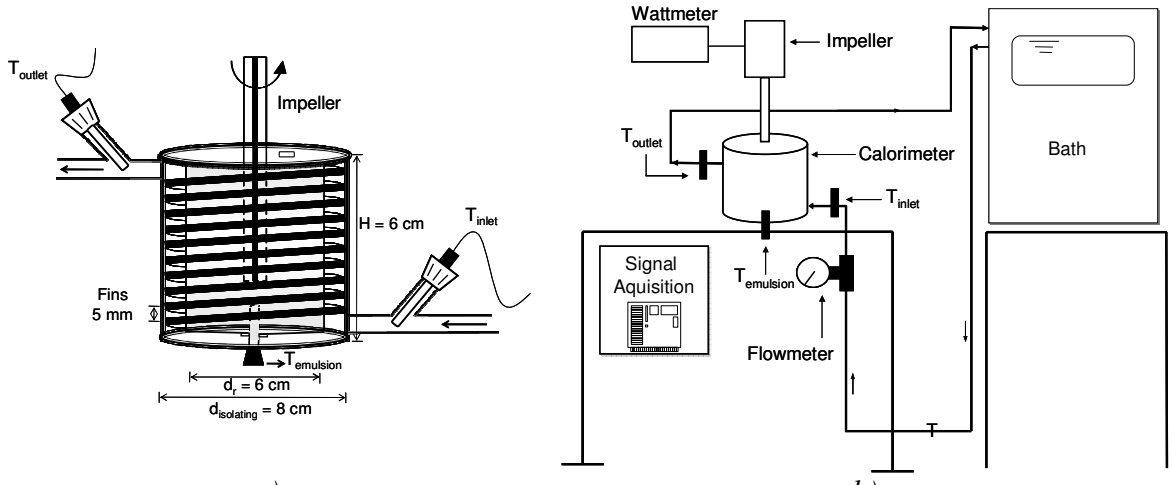

a) *b)*

Figure 1. *a)* Calorimeter and *b)* Experimental setup.

The experiments were performed at 25ºC in the beginning of the runs. Each run lasted approximately 12 minutes, which was far enough to homogenize the emulsion and attain a steady state operating condition. The uncertainty of experimental results depended, of course, on the accuracy of each instrument. To reduce the uncertainty in the cooling heat transfer, the water mass flow rate in the jacket was set to 300 g/min for all the experiments. Heat transfer uncertainties in the range of 5-8 % were obtained with this selection. The experiments were carried out in duplicates to ensure its repeatability.

Immediately after each emulsion generation experiment, six samples of the emulsion were withdrawn, placed between two slides and observed at the microscope (Coleman model NT 200 connected to a Sony 6.0 digital camera). A photograph was taken and analyzed in a laptop with specific image processing software (Image Tool) in order to measure the drop sizes.

INSTANTANEOUS ENERGY BALANCE

Considering the scheme of Figure2 the following energy balance can be formulated [14]:

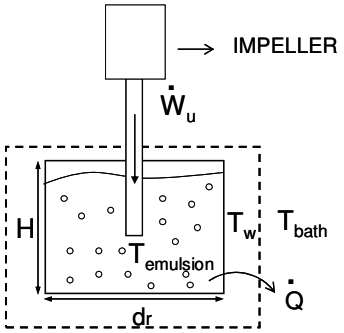

Figure 2. Schematic view of the emulsion generation experiment

$$\dot{W}_u = \dot{Q} + \left(\rho_1 \mathcal{V}_1 c_1 + \rho_2 \mathcal{V}_2 c_2 + m_{vessel} c_{vessel}\right) \frac{d\,T_{emulsion}}{d\,t} + \frac{d\left(u_i A_i\right)}{d\,t} + \frac{dE_k}{d\,t} \tag{1}$$

where $\dot{W}_u$ is the power transferred to the emulsion by the impeller; $\dot{Q}$ is the rate of heat transfer from the vessel, E_k the average kinetic energy of the emulsion (caused by the impeller), ρ_j is the density of phase (j = 1, 2 for oil and water respectively), $\mathcal{V}_j$ is the phase volume, c_j is the specific heat, m is the mass; $T_{emulsion}$ is the emulsion temperature, u_i the specific energy per unit of interface area and A_i the total interface area of the emulsion. Thermal resistance inside the vessel was neglected due to the strong internal convection caused by the impeller and, since aluminum is a very effective heat conductor, its temperature can be considered to be same as the emulsion. In steady equation (1) becomes:

$$\dot{W}_u = \dot{Q} \tag{2}$$

Thus, if the electric power input, $\dot{W}_{input}$, is known then the internal losses of the homogenizer are $\dot{W}_{input} - \dot{Q}$ and its efficiency η becomes :

$$\eta = \dot{W}_u / \dot{W}_{input} = \left[\dot{Q} / \dot{W}_{input}\right]_{steady\ state} \tag{3}$$

This efficiency can be assumed to depend on the rotation speed and fluid being stirred.
The specific interfacial energy of the emulsion is ruled by the interfacial tension [7]:

$$u_i = \sigma - T_i \frac{d\sigma}{dT_i} \tag{4}$$

where σ is the interfacial tension and T_i the interface temperature.
The interfacial area A_i can be related to the Sauter mean drop diameter, d_{32}, defined by:

$$d_{3,2} = \sum_{k=1}^{n} d_k^3 \Big/ \sum_{k=1}^{n} d_k^2 \tag{5}$$

through the relation:

$$\frac{A_i}{\mathcal{V}} = \frac{6\alpha}{d_{3,2}} \tag{6}$$

where α is the water volume fraction in the emulsion. From equations (4) and (6) the interfacial energy per unit emulsion volume is:

$$\left(\frac{u_i A_i}{\mathcal{V}}\right)_{emulsion} = \frac{6\alpha}{d_{3,2}}\left(\sigma - T_i \frac{d\sigma}{dT_i}\right) \tag{7}$$

RESULTS AND DISCUSSION

Typical time evolutions of temperature, power input and cooling heat transfer are shown in Figure 3 for a water fraction of 0.1, 14000 rpm stirrer speed and a constant temperature 25 ºC in the water bath. Those results indicate that 12 minutes was enough to achieve steady state and are in agreement with the behavior of single phase tests, previously run in order to validate the system.

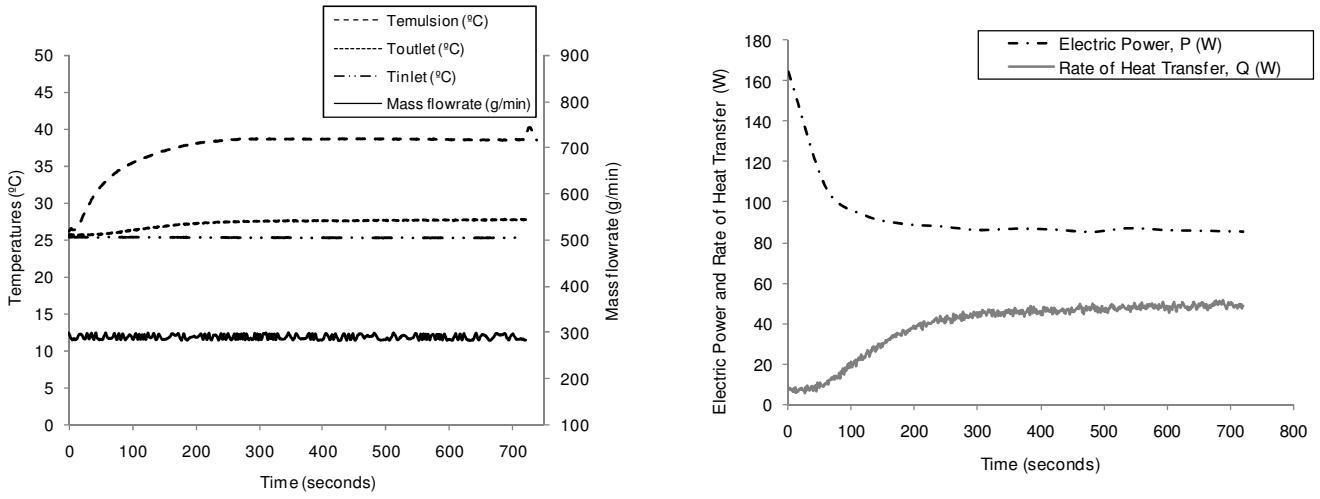

a) *b)*

Figure 3. Typical time evolutions of temperatures, power input and heat transfer.

In Fig 3a, at t = 0 sec, all the temperatures were 25 ºC, i.e. the same temperature of the water bath. Then the emulsion temperature grows continuously due to the shear produced by the impeller. This fact resulted in an increase of the outlet temperature of the water jacket. At the same time, the increase of emulsion temperature caused a decrease in its viscosity, thus the power input decreases. At t = 720 s the impeller was turned off, but a peak in emulsion temperature was noticed (Figure 3a). It can be attributed to the dissipation of kinetic energy of the emulsion due to the high speed induced by the stirrer; the kinetic energy was dissipated into heat causing an extra raise of approximately 3ºC in emulsion temperature.

It is clear in Figure 3 that the steady state was achieved at approximately t = 300 sec. In this run the final values of $\dot{W}_{input} \cong 86\,\mathrm{W}$ and $\dot{W}_u = \dot{Q} \cong 50\,\mathrm{W}$ are found. Table 3 summarizes the final values These results are in agreement with those obtained by other researchers e.g. [10].

The uncertainties in heat transfer were around 3 % and electric power input is 5 %. The average efficiency was 50 % for any experimental condition. Tests carried out with single-phase fluids (water, glycerin and crude oil), also provided the same average efficiency. It can be also noted in

Table 3 that the power input and heat transfer both increase as the rotation speed increases, for a given water fraction, as expected.

Table 3
Steady State Energy Balance Terms for the Emulsion Generation Experiments

Agitation speed (rpm)	Water volume fraction (%)	$\dot{W}_{input}$ (W)	$\dot{Q}$ (W)	$\dot{W}_{losses}$ (W)	η (%)
14000	0.1	86	48.3	37.7	56
	0.25	97.3	51	46.4	52
	0.4	95.5	51.8	43.7	54
22000	0.1	196	93	103	47
	0.25	203	102.7	100	51
	0.4	196.7	97.6	99	50

Integrating the above instantaneously measured energies between t = 0 and t = 720 s, gives the results shown in Table 4. Considering that the kinetic energy (E_k) was dissipated as heat, this term was calculated as an extra increase in internal energy (U) at the end of the run as explained above.

Table 4
Overall Energy Terms between t = 0 and t = 720 s

Agitation speed (rpm)	Water volume fraction, α	$W_u/\mathcal{V}\Big\|_0^{12}$ (J/cm³)	$Q/\mathcal{V}\Big\|_0^{12}$ (J/cm³)	$U/\mathcal{V}\Big\|_0^{12}$ (J/cm³)	$E_k/\mathcal{V}\Big\|_0^{12}$ (J/cm³)
14000	0.1	443.1	349.7	80.2	13.2
	0.25	442.7	321.1	103.2	18.3
	0.4	438.7	305.6	111.1	22.0
22000	0.1	813.2	702.7	96.6	14.0
	0.25	796.8	659.4	121.2	16.2
	0.4	828.6	658.3	147.6	22.6

It can be observed the energy cost to disperse two immiscible fluids is high, however about 80 % of such energy is dissipated into heat and only 20 % is expended to increase the total energy of the emulsion (internal energy, kinetic energy). The energy input increases with a increasing speed rotation. The increase in water content causes an increase in internal and kinetic energy and a decrease in heat transfer. The energy stored at the interface has a much lower magnitude and can not be accurately determined from integration of equation (1). Thus, this term was evaluated with the help of equation (7).

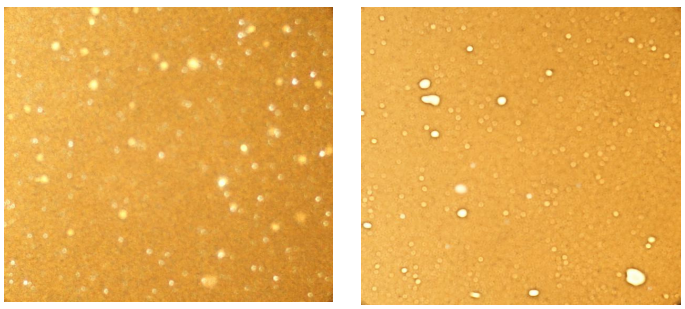

Figure 4. Micrographs of water-in-oil emulsions.

Figure 4 illustrates photographs of sampled w/o emulsions. Droplet size evaluation was accomplished from the micrographs obtained at the microscope. Through the images it could be concluded that the droplet sphericity could be considered as 1. The sizes of 500 – 900 droplets were measured and were distributed in 10 μm ranges. The histograms of Figure 5 show a log-normal distribution for all experiments. The polidispersity observed, mainly at 14000 rpm, may be related to high viscosity of continuous phase and non-uniformity in shear distribution within the emulsion which tends to cause a larger distribution of droplet sizes.

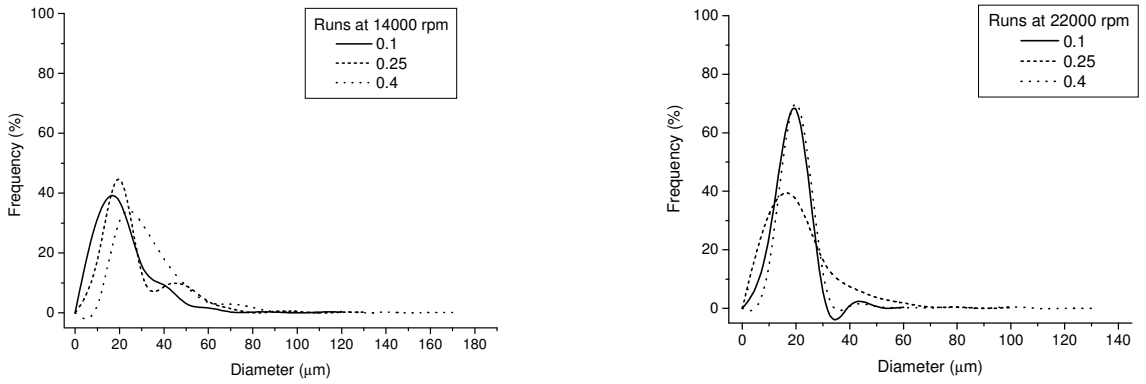

Figure 5. Histograms obtained from experimental runs.

Table 5 summarizes the values of the Sauter, mean, maximum and minimum drop diameters. Through this table the differences between the techniques become clear. The Sauter mean diameter, used in studies related to interface phenomena is significantly higher than the mean diameter. The standard deviations of different runs were around to 30 %, and can be attributed to poli-dispersed distribution of droplet sizes.
It can be observed that d_{32} decreases with increasing rotation speed at a given water fraction, as expected, and increase with increasing water fraction at a given rotation speed. The same trends are reported by other authors [12].

Table 5
Comparison between Different Definitions of Average Drop Size

Speed Agitation	Water Volume Fraction	d_{32} (μm)	Mean diameter (μm)	Mininum diamter (μm)	Maximun diameter (μm)
	0.1	45	18	3	113
14000 rpm	0.25	50	23	4	121
	0.4	60	30	8	163
	0.1	21	14	3	57
22000 rpm	0.25	37	18	3.5	92
	0.4	42	16	2	132

Figure 6 shows that interfacial tension (σ) decreases with increasing temperature, reproducing the commonly accepted result. The specific interfacial energy, u_i, was obtained from equation (4) and is also shown in Figure 6. The term $d\sigma/dT$ was determined by curve fitting of the data in Table 2 using a third degree polynomial. It is interesting to note that the specific interfacial energy is significantly higher than the interfacial tension and increases with increasing temperature. This is due to the second term of the r.h.s. of equation (4), which represents the thermal contribution to u_i .

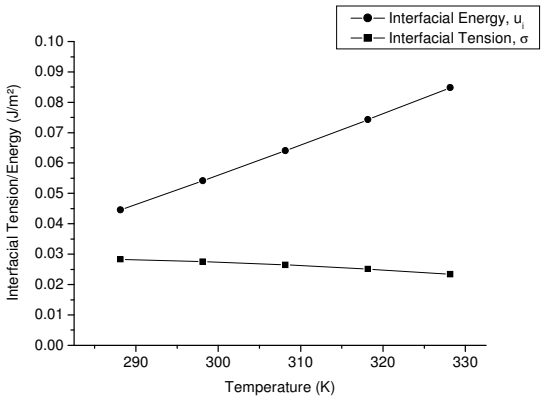

Figure 6. Interfacial tension and specific interfacial energy versus temperature.

The interfacial area per unit volume as calculated from equation (6) is shown in Table 6. This quantity clearly increases with increasing agitation speed and water volume fraction, as expected. The obtained values are much higher than reported in other studies; the difference may be attributed to the higher speed of the impeller used in the present study.

The interfacial energy per unit volume, $u_i A_i/\mathcal{V}$, is also shown in Table 6. This energy also depends on the specific interfacial energy which is related to the final temperature of each experiment. Their values range from 0.09 to 0.26 J/cm³, which represent a very small fraction of the total energy per unit of volume provided to the emulsion (Table 4.

Table 6
Total Interfacial Area and Interfacial Energy per Unit Volume of Emulsion, $u_i A_i/\mathcal{V}$

Speed Agitation	Water Content	$A_i/\mathcal{V}$ (m^{-1})	$u_i A_i/\mathcal{V}$ (J/cm³)
	0.1	13 000	0.09 ± 0.03
14000 rpm	0.25	31 000	0.22 ± 0.05
	0.4	42 000	0.26 ± 0.05
	0.1	30 000	0.22 ± 0.09
22000 rpm	0.25	42 000	0.20 ± 0.05
	0.4	58 000	0.10 ± 0.03

CONCLUSION

In this study the different terms of the energy balance during the generation of a water-in-oil emulsion in laboratory were measured. The method used for emulsion generation was that of shearing the emulsion with a high speed impeller in a hermetically closed vessel. The measured terms include: impeller work, heat transfer, internal energy, kinetic energy and interfacial energy. The later term was very small and could only be determined from drop size information (Sauter diameter) and interfacial energy data. Uncertainties in all energy terms except interfacial energy where within 8 %, whereas for interfacial energy it reached 30 %. The stirring method provided high kinetic energy dissipation in the vessel. From the energy provided to the emulsion about 80 % was converted into heat, and just 20 % caused a change in internal and kinetic energies (this transformed into internal energy by dissipation after the impeller was turned off). This energy partition is due to the highly dissipative nature of the method used for emulsion generation.

It was observed that the Sauter mean diameter decreases with increasing agitation speed and increases with increasing water fraction. A high average interfacial area (~ 30000 m^{-1}) was found due to the high speed of the impeller in comparison with conventional devices.

Despite the relatively high interfacial area per unit volume, the interfacial energy per unit of volume obtained was roughly 0.20 J/cm³ for both rotation speeds, which represents a vanishing fraction of the energy provided to the emulsion (440 J/cm³ at 14000 rpm and 800 J/cm³ at 22000 rpm). This means that the energy required to disperse two immiscible fluids is very high, but just a very small portion of it will be expended to creation of further interfacial area,

REFERENCES

1. Kokal, S., Crude Oil Emulsions: A State-of-the-Art Review, paper SPE 77947, *SPE Annual Technical Conference and Exhibition*, San Antonio - Texas, USA, 2002.
2. Langevin, D., Langevin, D., Pateau, S., Héanult, I., Argilier., J.F., Crude Oil Emulsion Properties and Their Application to Heavy Oil Transportation, *Oil & Gas Science and Technology*, Vol.59, No. 3, pp.511-521, 2004.
3. Pal, RA., Novel Method to Correlate Emulsion Viscosity Data, *Colloids and Surfaces A*, Vol.137, pp.275-286, 1998.
4. Dan, D. & Jing, G. Apparent Viscosity Prediction of non-Newtonian Water-in-Crude Oil Emulsions, *Journal of Petroleum Science & Engineering*, Vol.53, pp.113-122, 2006.
5. Manning, F. S., Thompson, R. E. *Oilfield Processing – II: Crude Oil*, Penn Well Publishing Company, University of Tulsa, Tulsa, Oklahoma, 1995.
6. Djuve, J., Yang, X. & Fjellanger, L. J. Chemical Destabilization of Crude Oil Based Emulsions and Asphaltene Stabilized Emulsions, *Colloid and Polymer Science*, Vol. 279, pp.232-239, 2001.
7. Adamson A.W., *Physical Chemistry of Surfaces*, 4th ed., John Willey and Sons, 1982.
8. Becher, P., *Encyclopedia of Emulsion Technology*, Vol. 1, New York, Marcel Dekker Inc., 1985.
9. Mc Lean, J. and Kilpatrick, K.K., Effects of Asphaltenes Solvency on Stability of Water-in-Crude-Oil Emulsions, *Journal of Colloid and Interface Science*, Vol. 189, pp.242-253, 1997.
10. Lemenand, T., Della Valle, D., Zellouf, Y., Peerhossaini, H., Droplets Formation in Turbulent Mixing of Two Immiscible Fluids in a New Type of Static Mixer, *International Journal of Multiphase Flow*, Vol. 29, pp.813-840, 2003.
11. Zhou, G., Kresta, S.M., Correlation of Mean Drop Size and Minimum Drop Size with the Turbulence Energy Dissipation and the Flow in an Agitated Tank, *Chemical Engineering Science*, Vol.53, pp.2063-2079, 1998.
12. Sulaimann, A., Ramachandran, K. B., Hansan, M., Investigation of Specific Interfacial Area of a Palma Oil-Water System, *J. Chem. Technol. Biotechnol*., Vol.79, pp.706-710, 2004.
13. Calderbank, P.H., Physical Rate Processes in Industrial Fermentation - Part I: The Interfacial Area in Gas-Liquid Contacting with Mechanical Agitation, *Trans I. Chem. Eng.*, Vol. 36, pp. 443-463, 1958.
14. Delhaye, J.M., Jump Conditions and Entropy Sources in Two-Phase Systems - Local Instant Formulation, *International Journal of Multiphase Flow*, Vol.1, pp.395-409, 1974.
15. Behrend, O.K. and Schubert, H., Influence of Continuous Phase Viscosity on Emulsification by Ultrasound, *Ultrasonics Sonochemistry*, Vol.7, pp.77-85, 2000.

INTERACTION BETWEEN TWO NEIGHBOURING GAS BUBBLE COLUMNS - MODELLING AND EXPERIMENTAL INVESTIGATION

R. Mosdorf*, K. Jagielski
Białystok Technical University,
15-351 Bialystok, ul. Wiejska, Poland,

ABSTRACT. In the paper the results of simple experiment of investigation of interaction between two neighboring bubble columns have been presented. The video recorded by high speed camera has been used to determine the bubbles departure frequency and theirs paths and velocities. The process of mixing neighboring bubble columns has been observed. To explain this phenomenon the simulation of gas bubble movement in the liquid has been made with using the stabilized finite element method (FEM) and level set method. The interaction between two columns with different spacing between columns and different location of bubbles has been discussed. It has been shown that when vertical locations of bubbles in neighboring columns are different and the distance between columns is small then bubbles located higher attract bubbles from the neighboring column. Finally two columns attract each other and form the single bubble column.

Keywords: Bubbles, bubble columns interaction, FEM, level set.

INTRODUCTION

The knowledge of bubble and bubble columns dynamics is of key importance in industrial applications such as aeration, fermentation, saturation, homogenisation, degassing, fluidization, smelting, froth flotation, boiling, etc. Despite of numerous experimental and theoretical investigations a reliable model even for the simplest case of single bubble formation still remains a formidable task. The investigations of the hydrodynamic behavior of bubble columns involve both the large-scale phenomena and the local phenomena. The local phenomena refer to the dynamic of single bubble, the large-scale phenomena are connected with the flow regime around the bubble column.

Numerous modelling studies have been conducted on the bubble formation from a single orifice or nozzle submerged in liquids [1, 2-5], among others. The basis of many theoretical models is in the assumption that the bubble is spherical and by application of a force balance acting on the bubble due to the main effects of buoyancy, surface tension, gas momentum effects and liquid inertia effects the motion of the bubble can be predicted. Lately, in [6] a comprehensive model has been presented that takes into account instantaneous interactions between successive bubbles as well as incorporates the wake effect of the previous bubble. Furthermore, it is known that the volume of the gas chamber connected to the orifice (nozzle) is an important factor in determining the initial bubble size and frequency of bubble emission. Two limiting modes of bubble formation are distinguished: constant flow rate regime (CFRR) and constant pressure regime (CPR). The CFRR can be obtained by imposing a strong restriction between the settling chamber and the injection point, in such a way that the incoming flow of the bubbles will be controlled and therefore be constant [7, 8, 9]. The CPR occurs whenever the chamber volume is sufficiently large and the pressure in the gas chamber is maintained constant. With progression of time and the extent of bubble formation, the pressure drop across the

* Corresponding author: dr hab. inż. R. Mosdorf
Phone: + (48)- 85-746-90-50, Fax: + (48)- 85-746-90-57
E-mail address: mosdorf@ii.pb.bialystok.pl

orifice (nozzle) varies and thereby results in a non-constant flow rate. In [10] has been suggested that the bubbles are formed under CFRR provided that the orifice Reynolds number is larger than 1000, and CPR prevails for orifice Reynolds number smaller than 1000. Lately, it has been stated [9], that it is impossible to obtain a CFRR, even using a sonic hole.

According to [11] bubble motion and bubble shape are controlled by deterministic forces, such as body force and drag force caused by the convective motion, and the complex and non-linear input of the liquid motion including wake and turbulent motion surrounding the bubbles. Therefore new approaches based on fractal and deterministic chaos analyses have been applied to investigate the complex phenomena of multi-phase systems [12-14]. The concept of non-linear dynamics systems has also been applied to study chaotic features of gas bubbling from a single nozzle (orifice) [11, 15- 19].
When the distance between nozzles is relatively large then bubble motion in each column is independent of the processes occurring in the neighbour column. The bubble flow in column depends only on the hydrodynamic forces occurring inside the column. Therefore the single bubble column can be treated as the dynamical system with complex properties. Behaviours of this system can be periodic or chaotic as it has been shown in papers [6,17-19]. When the distance between nozzles become smaller then the bubble motion in each column depends on processes occurring in neighbour column. The paths of the bubbles from neighbouring columns cross each other and finally create the common bubble column. For investigation of the dynamic of bubble columns it is necessary to track paths of bubbles emitted from all nozzles.

The main aim of the paper is to test the method of estimation of bubble velocities and bubbles departure frequency basing on the high speed video with using the cheep camera Casio EX FX1. The investigation presented in the paper has a preliminary character. The investigation is the first phase of preparing the special software for automatic investigation of dynamic of bubbles in interacting columns. In the paper the preliminary results of experimental investigation of bubble velocities in the interacting bubble columns have been presented. The simple model based on the stabilized finite element method and level set method has been used to investigate the liquid velocity structure in interacting bubble columns.

PRELIMINARY EXPERIMENTAL INVESTIGATION

The main aim of experimental investigation is to test the method of estimation of bubble velocities and bubbles departure frequency basing on the high speed video. It has been tested usability of the cheep camera Casio EX FX1(1200 fps) for identification of bubble departure frequency and movement.

In the experiment the air bubbles motion in the tank (40cmx50cmx5cm) filled with distillated water has been investigated. The bubbles were generated from 5 mm diameter plastic nozzles. The behavior of bubbles in case of spacing between nozzles in the range of 6-30 mm has been investigated. Each nozzle had its own simple air supply system. In the air supply system the aquarium air pumps has been used. The observation of the single bubble trajectory has been used to estimate bubble velocity.

The typical behavior of interacting bubble columns has been presented in Figure 1. Bubbles departing from neighboring nozzles attract each other and finally form a common bubble column located between twin nozzles. The bubble motion in this column is characterized by the large oscillation of bubbles horizontal location.

In Figure 1d the reconstruction of bubble path in case of two columns interaction has been shown. This is reconstruction of the path of bubble departing from the left nozzle. This path may be divided into three parts are schematically shown in Figure 1d. In the area ‘1’ the bubble is moving into direction of neighbour column. In the area ‘2’ bubbles from two nozzles move straight up forming the common bubble column. In the area ‘3’ bubbles in single column become separate because of horizontal movement of the bubbles.

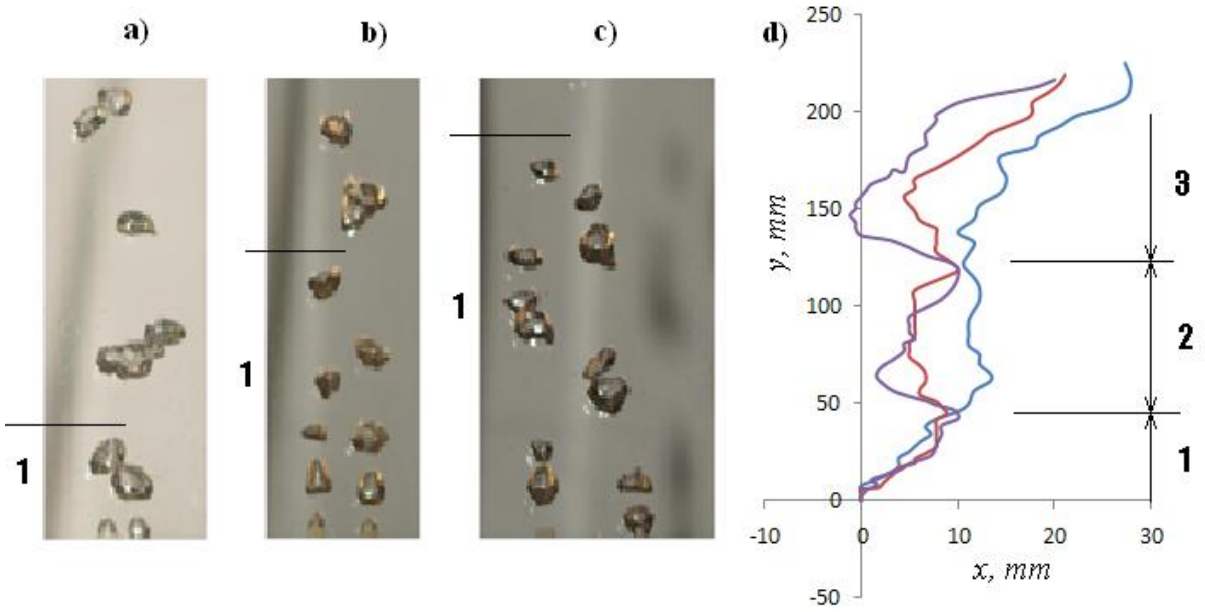

Figure.1. Interacting bubble columns for different spacing between nozzles. a) 6 mm. b) 12 mm. a) 26 mm. d) Paths of single bubbles.

For a single isolated spherical bubble, the terminal velocity can be estimated using formula [23]:

$$u_\infty = 0.707\sqrt{g d_e} \tag{1}$$

where g is the gravity acceleration, d_e is an equivalent bubble diameter (diameter of a sphere with the same volume as the bubble) can be predicted by the following equation [24]:

$$d_e = 2\left[\frac{\sigma R_o}{g(\rho_l - \rho_g)}\right]^{1/3}, \tag{2}$$

σ is the surface tension of water, R_o is the radius of the gas nozzle, ρ_l is the density of liquid and ρ_g is the density of gas.

For water and air bubble the terminal velocity calculated with using equation (1) is equal to 198 mm/s.

The bubbles vertical velocity has been calculated with using the recorded video. The example of results has been shown in Figure 2. The bubble departure frequency in case of single nozzle was about 11 bubbles/s and in case of twin nozzles - 30 bubbles/s for each nozzle. In Figure 2a it has been shown the vertical velocity of single bubble in single bubble column presented in Figure 2c, where the tracking bubble was marked with a red circle on the beginning and the end of the recorded path. In Figure 2b it has been shown the vertical velocity of separated single bubble mowing up when two bubble columns interact. The tracked bubble has been shown in Figure 2d.
In both mentioned cases vertical velocities of bubbles are greater than terminal velocity calculated using equation (1). It happens because the equation (1) calculates the velocity in stagnate liquid but the bubbles which are moving in the column create the liquid circulation around the column, finally they flow in moving liquid. The measured velocity is a sum of liquid velocity and bubble velocity in liquid.

In the common bubble column created by bubbles departing from two nozzles the standard deviation of horizontal velocity of bubbles is greater than in case when bubbles depart from the single nozzle. The mean standard deviation of vertical bubble velocity in the column from single

nozzle (Figure 2c) is equal to 70 mm/s, while in case of common bubble column (Figure 2d) it is equal to 120 mm/s.

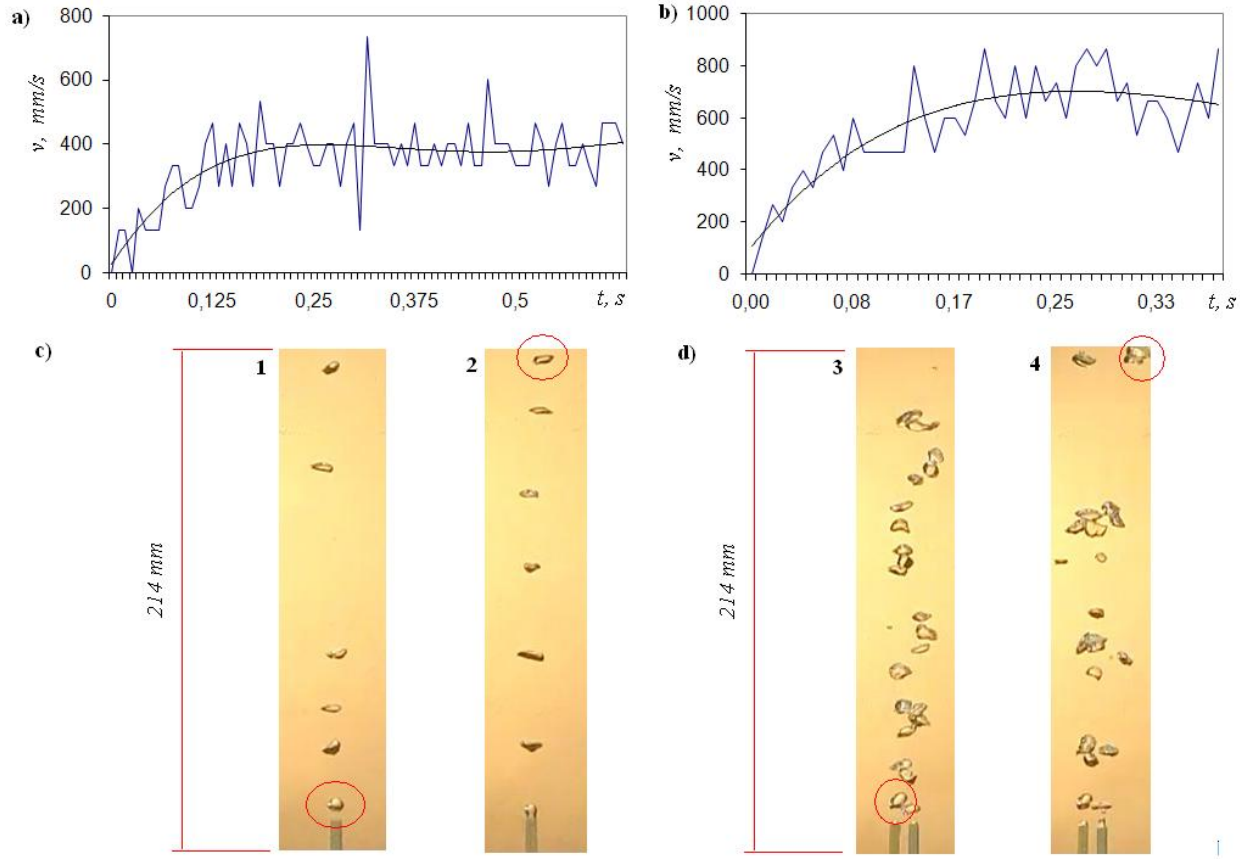

Figure.2. The vertical velocity of air bubbles. a) The vertical bubble velocity changes in time in case of single nozzle. b) The vertical bubble velocity changes in time in case of twin nozzles. c) bubble location at the beginning and the end of the bubble motion in case of single nozzle. d) bubble location at the beginning and the end of the bubble motion in case of two nozzles. Bubble departure frequency in case of single nozzle is 11 bubbles/s and in case of twin nozzles - 30 bubbles/s for each nozzle. The nozzles diameter is equal to 5 mm, the equivalent bubble diameter is equal to 6.7 mm, distance between two nozzles is equal to 14 mm.

MODELLING OF GAS BUBBLES INTERACTION

The simulation of gas bubble movement in liquid has been made with using the stabilized finite element method and level set method. The time-dependent COMSOL Multiphysics solver [20] with streamline diffusion (Petrov-Galerkin/Compensated, tuning parameter equal to 0.25) has been used for solving 2D Navier-Stokes equations [20]:

$$\rho\left(\frac{\partial \vec{u}}{\partial t}+\vec{u}\cdot\nabla\vec{u}\right)-\nabla\cdot\left[\mu\left(\nabla\vec{u}+\nabla\vec{u}^{T}\right)\right]+\nabla p=\sigma\kappa\vec{n}\delta+\rho\vec{g}$$
$$\nabla\cdot\vec{u}=0 \qquad (3)$$

In the level set method the zero level set at $\varphi = 0$ determines the position of the interface. The changes in time of level set function φ have been described by the following equation [21]:

$$\frac{\partial \varphi}{\partial t} + \vec{u} \cdot \nabla \varphi = 0 \tag{4}$$

In the simulation the fluid density has been described by the following equation [21]:

$$\rho = \rho_g + H(\varphi) \cdot (\rho_l - \rho_g) \tag{5}$$

where $H(\varphi) = \begin{cases} 0 & if \quad \varphi < 0 \\ 1 & if \quad \varphi > 0 \end{cases}$

Under the evolution of equation (4), the values of the level set function that are close to zero may move with velocities different than those of the zero values of level set function. Therefore, the φ distance field gets distorted ($|\nabla \varphi|$ becomes different than 1). In this case the gas volume changes during the simulation. The re-initialization of the level set function in regular intervals in order to rebuild the signed distance function is necessary. The direct application of re-initialization procedure in the Comsol solver is difficult because of their small ability to modification of solving procedure. Therefore the Comsol proposes a slight modification of equation (6) by adding the diffusion at the interface to maintain the bubble volume during the simulation. Finally, the following equation:

$$\frac{\partial \varphi}{\partial t} + \vec{u} \cdot \nabla \varphi = \delta(\varphi) \cdot \nabla \cdot (D \nabla \varphi) \tag{6}$$

has been solved instead of equation (6) [20].

The simulation has been made for air and water: ρ_l = 1000 kg/m^3, ρ_g = 1 kg/m^3, σ = 0.07 N/m, g = 10 m/s^2, μ = 0.075 Pa·s. The two dimensional air bubbles flow in tank (60 mm*60 mm) filled with water has been considered. The area of container has been divided into square elements (80*80). The velocity and pressure has been set to zero at t = 0. Boundary settings: no-slip conditions, u = 0, have been used on boundary of liquid container.

In Figure 3 it has been shown the results of simulation of bubble flow in two neighboring bubble columns, each one containing two bubbles. It has been considered two initial spacing between columns. The grey area indicates where the vertical velocity of liquid is greater than zero. When the spacing between columns is enough large (Figure 3a) then the liquid between columns flows down. In case of small spacing between columns (Figure 3b) the structure of liquid flow between bubbles becomes complex and liquid between columns flows up.

In Figure 4 it has been shown the time evolution of two initial location of bubbles in neighboring columns. In Figure 4a and b the initial horizontal locations of bubbles in columns are different. Finally, after the time 0.1 s two bubbles in the right column join and all bubbles start to form common bubble column. This process has been observed in the experiment. In Figure 4c and d the initial locations of bubbles in columns are the same. Finally, after 0.1 s bubbles in both columns join and new bubbles start to repeal. The area of liquid between bubbles where liquid flows down (Figure 4d) is responsible for bubbles repealing. This area disappears when initial locations of bubbles are different in both columns (Figure 4b).

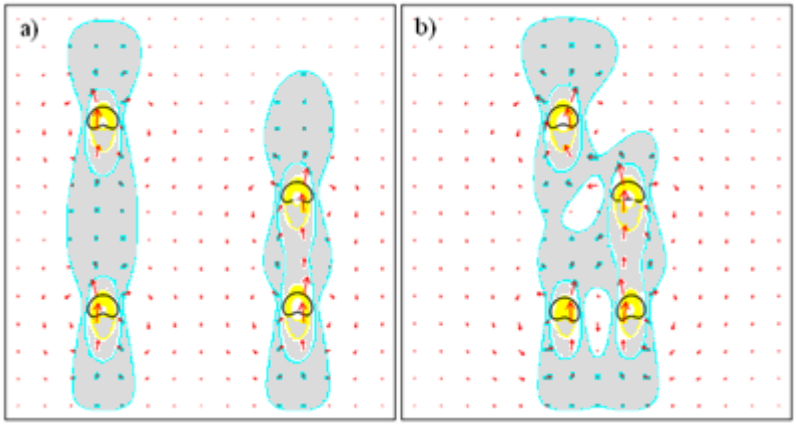

Figure.3. Liquid velocities in two interacting bubble columns. a) Distance between columns is equal to 25 mm. b) Distance between columns is equal to 15 mm.

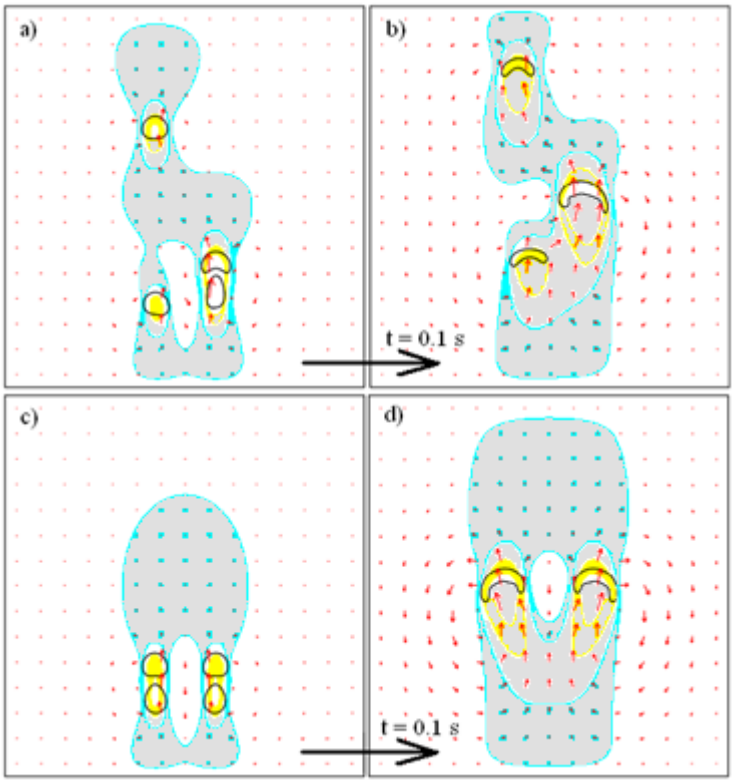

Figure.4. Bubbles displacement in 0.1 s. a), b) Creation of single bubble columns. c), d) Increasing distance between bubbles.

CONCLUSIONS

In the paper the results of simple experiment of interaction between two neighboring bubble columns has been presented. The video recorded by high speed camera has been used to determine the bubbles departure frequency and bubble paths and velocities. It has been found that bubble paths may be divided into three parts. In the first part the bubbles are moving into direction of neighbour column, in the second one the bubbles are forming the common bubble column. In the third one the bubbles movement in common column becomes instable. It has been found that the vertical velocity of bubbles was greater than terminal velocity of bubble in the stagnate liquid.

For explanation of the mechanism of mixing the neighboring bubble columns the simulation of gas bubble movement in the liquid has been made with using the stabilized finite element method (FEM) and level set method. It has been shown that when vertical locations of bubbles in neighboring columns are different then higher located bubbles attract bubbles from neighboring column. Finally, the columns attract each other and form the common bubble column.

The investigation presented in the paper have a preliminary character.

ACKNOWLEGMENT

The authors are grateful for the financial support of Białystok Technical University (grant: W/WI/6/2007)

REFERENCES

1. Davidson J.F., Schüler B.O.G., Bubble formation at an orifice in an inviscid liquid, *Trans. Instn. Chem. Engrs*, 38, pp 335-345, 1960
2. Ramakrishnan S., Kumar R., Kuloor N.R., Studies in bubble formation-I: Bubble formation under constant flow conditions. *Chemical Engng Sc.*, 24, pp 731-747, 1969.
3. Clift R., Grace J.R., Weber M.E., *Bubbles, Drops and Particles*, Academic Press, New York, 1978.
4. Pinczewski W.V., The formation and growth of bubbles at submerged orifice. *Chemical Engng Sc.*, 36, pp 405-411, 1981.
5. Raymond F., Rosant J. M., A numerical and experimental study of the terminal velocity and shape bubbles in viscous liquids. *Chemical Engng Sc.*, 55, pp 943-955, 2000.
6. Zhang L., Shoji M., Aperiodic bubble formation from submerged orifice. *Chemical Engng Sc.*, 56, pp 5371-5381, 2001.
7. Manasseh R., Acoustic sizing of bubbles at moderate to high bubbling rates. *Proceedings of Exp. Heat Transfer, Fluid Mech. and Thermodynamics*, Brussel, pp 943-947, 1997.
8. Kumada T., Sakashita H., Yamagishi H., Pool boiling heat transfer-I. Measurements and semi-empirical relations of detachment frequencies of coalesced bubbles, *Int. J. Heat Mass Transfer*, 38, pp 969-977, 1995.
9. Dias M.I., Breit R., Riethmuller M.L., Non-intrusive measurement technique to analyze bubble formation. *Proc. Experimental Heat Transfer, Fluid Mechanics and Thermodynamics*, Brussel, pp 949-956, 1997.
10. Costes J., Alran C., Models for the formation of gas bubbles at a single submerged orifice in non-Newtonian fluid, *Int. J. Multiphase Flow*, 4, pp 535-551, 1978.
11. Luewisutthichat W., Tsutsumi A., Yoshida K., Chaotic hydrodynamics of continuous single-bubble flow system. *Chemical Engng Sc.*, 52, pp 3685-3691, 1997.
12. Li H.Z., et al., Chaotic bubble coalescence in non-Newtonian fluids. *Int. J. Multiphase Flow*, 23, pp 713-723, 1997.
13. Femat R., Ramirez J.A., Soria A., Chaotic flow structure in a vertical bubble column. *Physics Letters A*, 248, pp 67-79, 1998.
14. Kikuchi R., et al. Diagnosis of chaotic dynamics of bubble motion in a bubble column. *Chemical Engng Sc.*, 52, pp 3741-3745, 1997.
15. Tritton D.J., Egdell C., Chaotic bubbling, *Phys. Fluids A*, 5, pp 503-505, 1993.
16. Tufaile A., Sartorelli J.C., Chaotic behaviour in bubble formation dynamics. *Physica A*, 275, pp 336-346, 2000
17. Mosdorf R., Cieśliński J.T., Fractal analysis of pressure changes during gas bubble emission. *Int. Symp. on "Multiphase Flow and Transport Phenomena*", Antalya, Turkey. (D.M. Maron, Ed.). New York, Wallingford, Begell House, pp 70-77, 2001
18. Cieśliński J.T., Mosdorf R., Identification of chaotic attractors in gas bubbling. *Proc. of the 5th World Conf. on Experimental Heat Transfer, Fluid Mechanics and Thermodynamics* 2001. Thessaloniki, (G.P. Celata, P. Di Marco, A. Goulas, A. Mariani, Eds). Pisa: Edizioni ETS, vol. 2, pp 1233-1236, 2001.
19. Mosdorf R., Shoji M., Chaos in bubbling – nonlinear analysis and modelling. *Chemical Engng Sc.*, 58, pp 3837-3846, 2003.

20. Comsol Multiphysics. Rising Bubble Modeled with the Level Set Method solved with Comsol Multiphysics 3.2. <http://www.comsol.com/showroom/gallery/177.php?highlight=bubble>.
21. Nagrath S., Jansen K. E., Lahey R.,T., Three dimensional simulation of incompressible two-phase flows using a stabilized finite element method and a level set approach. (Preprint).
22. R. Mosdorf, M. Shoji. Hydrodynamic aspects of interaction between nucleation sites. *Int. J. Heat Mass Transfer.* Vol.51, nr 13/15, pp 3378-3386, 2008.
23. Davies R. M., Taylor G. I., "The mechanics of large bubbles rising through liquids in tubes", Proc. of Roy. Soc., London, 200, Ser. A, pp 375-390, 1950.
24. Wallis G.B., One Dimensional Two-phase Flow. McGraw-Hill, New York, 1969.

APPLICATION OF TWO-PHASE EJECTOR AS SECOND STAGE COMPRESSOR IN REFRIGERATION CYCLES

M. Bergander[1,3]*, D. Butrymowicz[2], J. Karwacki[2], J. Wojciechowski[3]
[1]University of Hartford, 200 Bloomfield Avenue, West Hartford, CT 06117, USA
[2]Institute of Fluid-Flow Machinery, Polish Academy of Sciences, Gdansk, Poland
[3]AGH University of Science & Technology, Cracow, Poland

ABSTRACT. Paper deals with analysis of application of two-phase ejector as a second stage compressor in refrigeration compression systems. The thermodynamic reason for the efficiency improvement due to application of the ejector is effect of difference in compression work for liquid and vapour phases. The own approach of the calculation of the compression-ejector refrigeration cycle has been proposed in the paper. This approach is based on the set of two performance characteristics: one for the ejector and the second one for the rest of the refrigeration installation. On the basis of the above approach the limiting conditions of operation of the systems have been established for selected refrigerants. It has been showed that possible increase of coefficient of performance of the system strongly depends on the entrainment ratio of the two-phase ejector.

Keywords: *refrigeration cycle, ejector, two- phase flow, compression*

COMPRESSION – EJECTION REFRIGERATION SYSTEM

The paper deals with aspects of application of two-phase ejector as a second stage compressor in refrigeration compression systems. The schematic of the investigated system is presented in Figure. 1. Vapour compressed in the mechanical compressor is sucked by the ejector. The motive fluid in the ejector is liquid delivered by a mechanical pump. The presented configuration is totally novel approach for improving of the efficiency of the refrigeration systems by means of two-phase liquid-vapour ejector. This configuration was proposed and patented by Bergander [1,6].

The thermodynamic reason for the efficiency improvement is effect of difference in compression work for liquid and vapour phases. Therefore increasing the efficiency of the standard single-stage vapour compression cycle is caused through a reduction of mechanical compression at the expense of harnessing kinetic energy of vapour in the ejector device.

The compression-ejection cycles in *p-h* and *T-s* diagrams are presented in Figure. 2. The suction point 1 is located at the saturation line. However, there is no obstacles to take into consideration also superheating of the sucked vapour in the analysis. The isentropic compression process in the mechanical compressor was assumed in these charts. However, the internal efficiency of the mechanical compressor has been included in the analysis presented in this paper. The only reason the isentropic process was chosen is the problem with the appropriate representation of the discharge parameters from real mechanical compressors in refrigeration systems. Moreover assumption of the isentropic compression process in the mechanical compressor is the common approach made in the calculations of the compression refrigeration systems.

* Corresponding author: Dr. Mark Bergander
Phone: 203-421-3562
E-mail address: mark@mdienergy.com

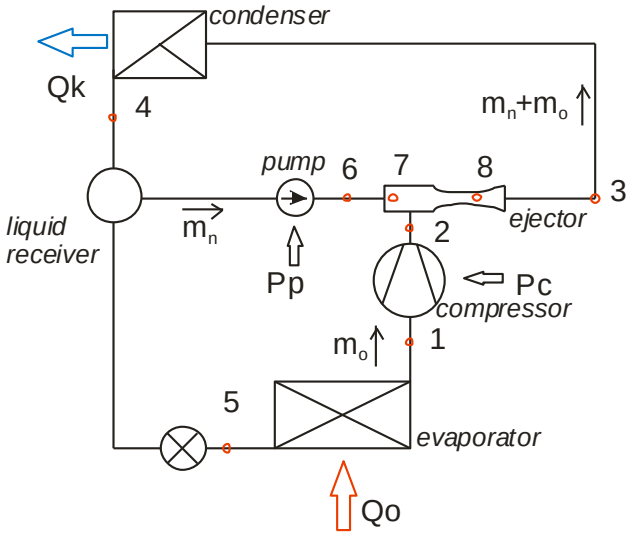

Figure. 1. Schematic of refrigeration compression system with two-phase ejector as a second stage compressor.

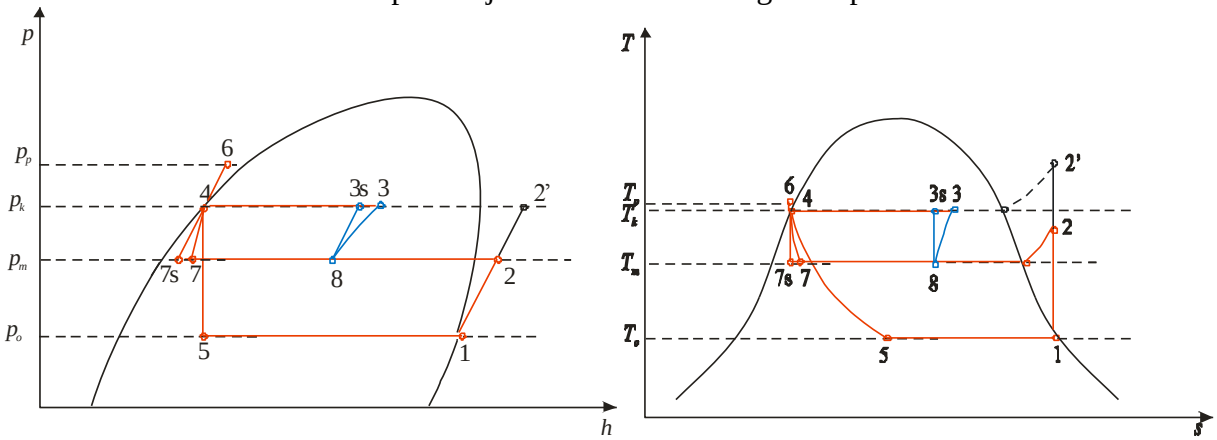

Figure. 2. Compression-ejection cycle of the system presented in Figure. 1.

Important feature of the system is two additional pressures, i.e. inter-stage pressure p_m and corresponding inter-stage saturation temperature T_m, as well as pump motive pressure p_p and liquid phase temperature T_p. Therefore the discharge of the mechanical compressor in the discussed system is represented by point 2 while in classic one-stage system the discharge will be located at the point 2'.

The next assumption made in Figure. 2 deals with liquid parameters at the outlet of the condenser. No subcooling was taken into account in these charts. Therefore liquid state is represented by point 4 located at the liquid saturation line. Isentropic process of liquid compression was assumed in Figure. 2. If the expansion process of the liquid phase occurs isentropically then the outlet of the ejector motive nozzle is represented by the point 7s. Taken into account efficiency of the motive nozzle – real outlet is located at the point 7. In most practical cases wet vapour may be expected at the outlet of the motive nozzle as the flashing process will occur. The quality of the vapour emanating from the motive nozzle depends on the nozzle efficiency as well as possible liquid subcooling for the given operation pressures in the system.

A good representation of the operation of the ejector at the thermodynamic charts is by no means a simple task as a combination of compression and mixing processes occur at the mixing chamber simultaneously. Therefore processes occurring inside the mixing chamber of the ejector may be presented by assumed representation process lines. In Figure. 2 common approach was applied: the mixing process and compression process due to momentum exchange were separated. Moreover,

the mixing process is assumed as the isobaric process of the discharged vapour from mechanical compressor 2 and fluid expanded in the motive nozzle 7. Therefore the mixing process 7-8-2 was assumed in Figure. 2. Compression process due to momentum and energy transfer between motive fluid and secondary fluid (vapour discharged form mechanical compressor) is represented by compression line 8-3s for the ideal case of isentropic compression and 8-3 for real compression in the mixing chamber and the diffuser. At this stage of research the possible discussion on share of the compression process between mixing chamber (due to momentum and energy transfer between motive and secondary streams) and the diffuser (due to increasing of cross-section area) is not possible, and moreover there is no clear need for it. Location of point 8 as well as point 3 depends on the entrainment ratio of the ejector which is not visible in the thermodynamic charts.

Condensation process is represented by line 3-4. It means that wet vapour enters the condenser. Liquid phase flows to the receiver and then is delivered to pump to motive the ejector and main part of the liquid is delivered to the expansion valve feeding the evaporator. The operation of the evaporator (process line 5-1) should not be affected by reorganisation of the system due to two-phase ejector. The saturated vapour at the evaporator outlet was assumed. However, in the case of feeding of the evaporator by means of the thermostatic expansion valve superheated vapour enters the mechanical compressor. This may be included in the analysis without any obstacles.

COMPRESSION-EJECTION CYCLE ANALYSIS

The general purpose of this paper is to provide with rational methodology based on which it is possible to assess possible improvement of the *COP* due to application of the second stage compression in two-phase ejector in compression refrigeration system. Moreover, there is a clear need to apply such methodology in order to establish the range of the operation parameters of the refrigeration system in order to establish a preliminary geometry of the two-phase ejector and the pump performance.

The proposed approach is based on the set of two performance characteristics: one for the ejector and the second one for the rest of the refrigeration system, as it was depicted in Figure. 3. The operating parameters of the whole system can be determined then by the intersection of these two characteristic lines. This is the very similar method as in the case of the well known calculation procedure of the pressure rise and liquid flow rate of the pump system. The similar approach has been applied by the authors for the case of two-phase ejector as a booster compressor in refrigeration systems [2,3]. However, in the case of the discussed system the configuration is completely different and this methodology has to be applied taken into consideration the specific system features.

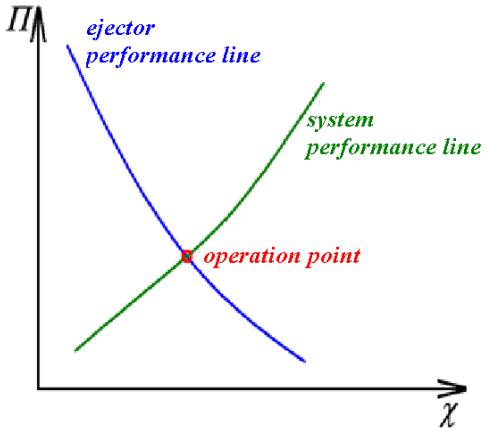

Figure. 3. Idea of the performance line approach: Π is the dimensionless compression ratio, see eq. (21); χ is the volumetric entrainment ratio.

It necessary to define the main operation parameters and classify them as fixed for the discussed application and parameters dependent on the ejector operation. The following quantities are assumed as fixed for given application of the refrigeration system:

- evaporation temperature t_o and corresponding evaporation pressure p_o (because of saturated state in the evaporator);
- condensation temperature t_k and corresponding condensation pressure p_k (because of saturated state in the condenser);
- refrigeration capacity $\dot{Q}_o$;
- vapour superheating at the outlet of the evaporator ΔT_o and condensate subcooling at the outlet of the condenser ΔT_k.

The internal efficiency of the compressor η_{ci}; mechanical efficiency of the compressor η_{cm}; and liquid mechanical pump efficiency η_p have to be also treated as known quantities. There are assumed as constant in this paper. The following cycle points can be established unambiguously on the basis of the above parameters (see Figure. 2): 1, 4, 5, and 2'. If so, then the mass flow rate through the evaporator is also known as (see Figure. 1):

$$\dot{m}_o = \frac{\dot{Q}_o}{h_1 - h_5}. \tag{1}$$

The following quantities depend on the operation of the ejector and pump, i.e. depend on the performance which is not known:

- inter-stage pressure p_m and corresponding inter-stage temperature t_m (because of saturated state in the mixing chamber and the diffuser of the ejector at the thermodynamic equilibrium conditions);
- pump discharge pressure p_p (discharge temperature t_p of liquid depend on the efficiency of the pump and may be calculated on the basis of the discharge pressure);
- motive liquid mass flow rate $\dot{m}_n$ flowing through the pump.

The rest of the characteristic cycle points may be predicted on the basis of the above parameters: 2, 6, 7s, 7, 8, 3s and 3. Therefore:

$$h_2 = h_2(p_m);\ h_6 = h_6(p_p);\ h_{7s} = h_2(p_m, p_p);\ h_7 = h_2(p_m, p_p); h_8 = h_8(p_m, p_p, \dot{m}_n);\ h_3 = h_3(p_m, p_p, \dot{m}_n).$$

These points may be calculated only the performance of the ejector is known. The specific theoretical power consumption by the mechanical compressor:

$$P_{tc} = \dot{m}_o(h_2 - h_1), \tag{2}$$

as well as theoretical power consumption by the mechanical pump:

$$P_{tp} = \frac{\dot{m}_n}{\rho_4}(p_p - p_k). \tag{3}$$

The actual power consumptions may be calculated as follows:

$$P_c = \frac{1}{\eta_{ci}\eta_{cm}} P_{tc}, \tag{4}$$

and

$$P_p = \frac{P_{tp}}{\eta_p} = \frac{1}{\eta_p}\frac{\dot{m}_n}{\rho_4}(p_p - p_k). \tag{5}$$

The coefficient of performance of the whole system is defined as follows:

$$COP = \frac{\dot{Q}_o}{P_p + P_c}. \tag{6}$$

Note that all above quantities cannot be calculated without specific knowledge about the operation of the ejector.

ANALYSIS OF EFFICIENCY INCREASE DUE TO EJECTOR APPLICATION

The general reason for application of the ejector in compression system in the discussed configuration (see Figure. 1) is possible increase of the *COP* defined by eq. (6). It may be assumed that in the case of classic compression system the following system efficiency can be defined:

$$COP_c = \frac{\dot{Q}_o}{P_{cc}}, \tag{7}$$

where the power consumption by the compressor in classic compression system is equal to:

$$P_{cc} = \frac{1}{\eta_{ci}\eta_{cm}} \dot{m}_o \left(h_{2'} - h_1\right), \tag{8}$$

The following condition for increase of the system efficiency can be established:

$$P_{cc} - P_c > P_p, \tag{9}$$

so the following relationship can be found:

$$\frac{1}{\eta_{ci}\eta_{cm}} \dot{m}_o \left(h_{2'} - h_2\right) > \frac{1}{\eta_p} \frac{\dot{m}_n}{\rho_4} \left(p_p - p_k\right). \tag{10}$$

Now it is possible to introduce the entrainment ratio:

$$U = \frac{\dot{m}_o}{\dot{m}_n}, \tag{11}$$

the efficiency modulus:

$$E = \frac{\eta_{ci}\eta_{cm}}{\eta_p}, \tag{12}$$

as well as thermodynamic dimensionless work potential:

$$W = \frac{p_p - p_k}{\rho_4 \left(h_{2'} - h_2\right)} = W\left(U, p_m, p_p\right). \tag{13}$$

Therefore the condition for the system efficiency increase is as follows:

$$\frac{1}{E} \frac{U}{W\left(U, p_m, p_p\right)} > 1. \tag{14}$$

Note that from direct relationship describing specific enthalpies *W* does not depend directly on *U*. However, because compression produced by the ejector depends on *U*, therefore the dimensionless work potential has to depend on *U*. If the theoretical case is considered for isentropic processes, then $E = 1$, and the following condition has to be fulfilled in order to increase the efficiency of the cycle:

$$U_s > W\left(U_s, p_m, p_p\right), \tag{15}$$

where U_s is the mass entrainment ratio for isentropic ejector and compressor, and ideal pump.
Note that the following compression may be defined:

$$\pi_p = \frac{p_p}{p_m} \quad ; \quad \pi_k = \frac{p_k}{p_m} \quad ; \quad \Pi = \frac{p_k - p_m}{p_p - p_m} = \frac{\pi_k - 1}{\pi_p - 1} < 1, \tag{16}$$

Therefore:

$$W = \frac{p_p - p_k}{\rho_4 \left(h_{2'} - h_2\right)} = \frac{p_k}{\rho_4} \left(\pi_p - 1\right) \frac{1}{h_{2'} \left(1 - \frac{h_2}{h_{2'}}\right)} = W\left(U, \pi_p, \pi_k\right). \tag{17}$$

It is clear now that *W* may be interpreted as the ratio of the specific work of isochoric liquid compression between pressures p_p and p_k to the specific work of isentropic vapour compression between points 2 and 2'. It is not possible to draw any conclusion from eq. (17) without any specific information on the ejector performance or the system performance.

REFRIGERATION SYSTEM AND EJECTOR PERFORMANCE

Graphical representation of this approach is presented in Figure. 3. The performance line of the system may be written as the following relation:

$$U = f_s(\Pi). \tag{18}$$

Physically equation (18) describes system demands for the ejector performance based on energy balance for the ejector:

$$\dot{m}_n h_6 + \dot{m}_o h_2 = (\dot{m}_n + \dot{m}_o) h_3, \tag{19}$$

Therefore from eq. (19) mass entrainment may be calculated:

$$U = \frac{h_3(U) - h_6(p_p)}{h_2(p_m) - h_3(U)} = f_s(\Pi, U). \tag{20}$$

Assuming initially the entrainment ratio U, then enthalpy at outlet from ejector can be found from eq. (20). Energy balance equation between inlet and outlet of the motive nozzle can be written as:

$$h_6 = h_7 + \frac{1}{2} w_7^2. \tag{21}$$

Energy equation for mixing chamber may be written as follows:

$$h_7 + \frac{1}{2} w_7^2 + U h_2 = (1+U)\left(h_8 + \frac{1}{2} w_8^2 \right) = h_6 + U h_2. \tag{21}$$

The mixture velocity in the mixing chamber before compression is calculated on the basis of the momentum equation as well as assumption of the isobaric mixing:

$$w_8 = \frac{w_7}{1+U}. \tag{22}$$

Combining eqs. (21) and (22):

$$h_6 + U h_2 = (1+U)\left[h_8 + \frac{1}{2} \frac{w_7^2}{(1+U)^2} \right]. \tag{23}$$

From eq. (23) it is possible to calculate the specific enthalpy at the point 8, so:

$$h_8 = \frac{h_6 + U h_2}{1+U} - \frac{1}{2} \frac{w_7^2}{(1+U)^2}. \tag{24}$$

If the compression process will be isentropic, then the specific enthalpy at the point 3 is equal to:

$$x_8 = \frac{h_8 - h'_m}{h''_m - h'_m}, \tag{25}$$

where h'_m and h''_m are the specific enthalpies of saturated liquid and saturated vapour, respectively, at the inter-stage pressure p_m. Then:

$$x_3 = \frac{s'_m + x_8 (s''_m - s'_m) - s'_k}{s''_k - s'_k}, \tag{26}$$

where s'_m and s''_m are the specific entropies of saturated liquid and saturated vapour, respectively, at the inter-stage pressure p_m, s'_k and s''_k are the specific entropies of saturated liquid and saturated vapour, respectively, at the condensation pressure p_k. Then:

$$h_3 = h'_k + x_3 (h''_k - h'_k), \tag{27}$$

where h'_k and h''_k are the specific enthalpies of saturated liquid and saturated vapour, respectively, at the condensation pressure p_k. Combining eq. (20) and (27) make possible finding relation defined by eq. (18). Note that this is indirect relationship and therefore numerical calculations are necessary to find relation between compression ratio and entrainment ratio demanded by the system.

The performance line of the ejector may be written as the following relation:

$$U = f_e(\Pi). \tag{28}$$

Physically equation (28) describes ejector possibilities based on given ejector geometry and operation parameters. Butrymowicz [2,3,4] developed the theoretical model of the two-phase ejector. However, this model cannot be directly applied to the discussed case because it is dedicated for the isothermal compression case. It should be noted that there are some simple equations describing roughly two-phase ejectors performance, e.g. Sokolov and Zinger [5] proposed the following equation:

$$\frac{1}{\Pi} = 2\frac{\varphi_n}{\varphi_s} b\left[\varphi_n\varphi_m\varphi_s - \left(1 - \frac{\varphi_m}{2\varphi_n}\right) b(1+\chi)^2\right]. \tag{29}$$

Here: φ_s - velocity coefficient for the suction nozzle; φ_m - velocity coefficient for the mixing chamber. Basing on eq. (29) it is also possible to find out relationship (28). However, it should be noticed that eq. (29) may be treated as a very rough estimation of the water-air ejector.

CALCULATION RESULTS FOR ISENTROPIC CYCLE

The most important results are given by eq. (20) for the case of isentropic processes. The relationship between dimensionless work W and pumping compression ratio are given in Figure. 4 and Figure. 5 for the two cases of refrigerants: R-507 (and R-404A), and R-22, respectively.

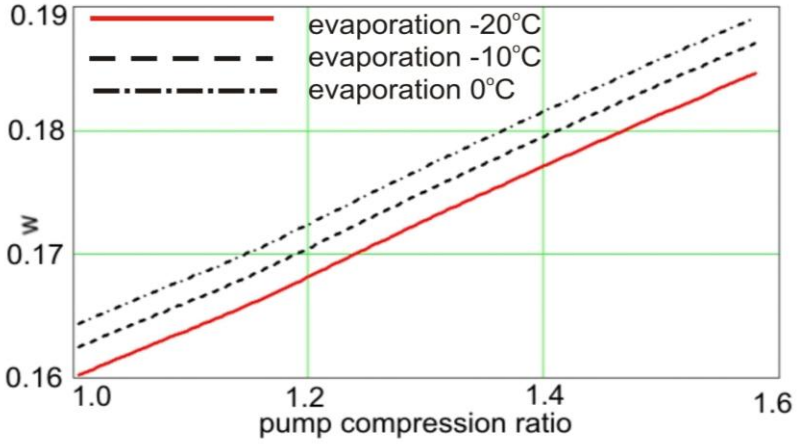

Figure. 4. Calculation results of the dimensionless work potential W versus pump compression ratio π_p for refrigerant R-507 (and R-404A); condensation temperature t_k = +40 °C; E = 1.

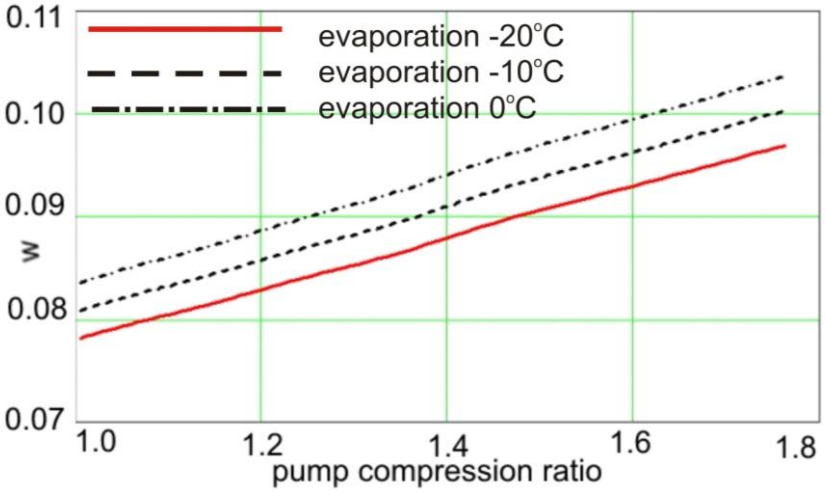

Figure. 5. Calculation results of the dimensionless work potential W versus pump compression ratio π_p for refrigerant R-22; condensation temperature t_k = +40 °C; E = 1.

It is evident from these results that the condition given by eq. (20) should be always fulfilled for both refrigerants only if the mass entrainment ratio will be higher than numerical values of W given in these figures. For refrigerant R-22 this condition should be fulfilled more easier than for refrigerant R-507 (and R-404A as well). The volumetric entrainment ratio required by eq. (15) are $\chi < 5$ in most cases. That means it should be possible to prepare the appropriate geometry of the ejector to ensure the required range of the entrainment ratio.

CONCLUSIONS

The own approach of the analysis of the operation of the ejection-compression system has been proposed in this paper. Based on this analysis the limiting entrainment ration of the two-phase ejector has been predicted for given operation conditions. However, the experimental research of the operation of high-pressure two-phase ejector is required in order to operate with reliable ejector performance in the analysis.

ACKNOWLEDGEMENT

This material is based upon work supported by the US Department of Energy, under Award Number DE-FG36-06GO16049 and by the National Science Foundation, STTR Phase II Project No. 0822525.

REFERENCES

1. Bergander M., Schmidt D.P., Herbert D.A., Wojciechowski J., Szklarz M.: Condensing ejector for second step compression in refrigeration cycles, *International Refrigeration and Air Conditioning Conference*, Purdue, USA, Paper No. 2174, 2008.
2. Butrymowicz D.: Improvement of compression refrigeration cycle by means of two-phase ejector, *21st International Congress of Refrigeration*, Washington D.C., USA, Paper No. ICR0310, 2003.
3. Butrymowicz D., Karwacki J., Miąskowska D., Trela M.: Performance of two-phase ejector of various geometries, *22nd International Congress of Refrigeration*, Beijing China, 2007, Paper No ICR07-B1-1269.
4. Butrymowicz D.: Problems of improving of effectiveness of refrigeration cycles (in Polish), *Scientific Notes of the Institute of Fluid-Flow Machinery of PASc*, No. 538/1497/2005, Gdańsk, 2005.
5. Sokolov E.I., Zinger N.M.: Jet apparatuses (in Russian), Moscow, 1989.
6. Bergander M.: Refrigeration cycle with two-phase condensing ejector, International Refrigeration and Air Conditioning Conference, Purdue, USA, Paper No. R008, 2006.

DISCLAIMER

IMPROVING PERFORMANCE OF SPLIT-AIR-CONDITIONER WITH AN EVAPORATIVELY COOLED CONDENSER UNDER VARIOUS AMBIENT TEMPERATURE

E. Hajidavalloo*, H. Eghtedari
Mechanical Engineering Department, Shahid Chamran University, Ahvaz, Iran

ABSTRACT. Increasing coefficient of performance of split type home-air-conditioners is a challenging problem especially in hot weather conditions. Application of evaporatively cooled air condenser instead of commonly used air condenser is a solution to this challenge. In this paper an evaporative cooler was designed and coupled to the existing air condenser of a split air conditioner to evaluate its effect on the cycle performance under various ambient air temperatures up to 49°C. Experimental results show that application of evaporatively cooled air condenser has significant effect on performance improvement of the cycle and improvement increases as ambient air temperature increases. It is found that by using evaporatively cooled air condenser in hot weather conditions, power consumption can be reduced up to 21% and performance of the cycle can be improved up to 52%.

Keyword: *evaporative cooler, split air conditioner, energy saving, condenser*

INTRODUCTION

Power consumption is a major concern in vapor compression cycle especially in the home air conditioners with air cooled condensers working in hot weather conditions. Temperature of air cooled condenser is directly depended on the ambient air temperature, therefore, in the area with very hot weather in summer, the condenser temperature and pressure increase considerably which consequently increases the power consumption of the air conditioner due to increase in pressure ratio. Increasing condenser temperature also decreases cooling capacity of the cycle due to reduction of liquid content in the evaporator. These two effects decrease performance of air conditioner considerably [1]. In order to increase the performance of air conditioner it is required to decrease the condensing temperature. To reach this goal, one of the easiest ways is the application of direct evaporative cooler in front of the condenser to cool down air temperature before passing over the condenser. Using evaporative cooler in front of the air condenser can be considered as energy efficient, environmentally friendly and cost-effective method to enhance the performance of air conditioners. Since huge numbers of air conditioners are used in the residential sector, therefore, any small improvement in the performance of the cycle will have huge effect on the power consumption of the whole network.
Water consumption in this system is very small and there is not any risk of scale or rust on the condenser tubes because there is not any direct contact between water and tubes.
There is little work to address the different aspects of using direct evaporative cooler in front of the air condenser. Goswani et al. [2] employed an evaporative cooler on the existing 2.5 ton air conditioning system by using media pad and reported 20% power saving for the retrofitted system

* Corresponding author: E. Hajidavalloo
Phone: + (98)-611-3738532, Fax: + (98)-611-3336642
E-mail address: hajidae_1999@yahoo.com

when ambient air temperature was 34°C. Zhang et al. [3] investigated on the evaporative cooler filled with corrugated holed aluminum foil and presented correlations to predict the performance, pressure drop and temperature outlet of the cooler. They used correlations to predict the improvement of an air-cooled chiller by comparing the exit temperature of evaporative cooler with performance curve of the chiller and reported that COP of the chiller could be improved bout 39%. Yu and Chan [4] simulated an air–cooled chiller equipped with a direct evaporative cooler and showed up to 14.4% reduction in power consumption and up to 4.6% increase in the refrigeration effect. Hajidavalloo [5] investigated the effect of using evaporative cooler in the window air conditioner by injecting water on the media pad installed in front of the condenser entrance and reported 16% reduction in power consumption and 55% improvement in total performance.
Despite large potential of evaporative cooling system to reduce power consumption of split air-conditioners, there is few investigation in this area and it seems much work are required to address different aspect of this system. In this work experimental investigation was used to evaluate the effect of using an evaporative condenser on the behavior of a split air conditioner under variable ambient air conditions.

SYSTEM DESIGN AND EXPERIMENTAL SET-UP

An existing split air-conditioner (1.5 ton) made by Mitsubishi Electric was used in the experiments. Consistent with the shape of condenser, a frame was built and filled by cellulous media pad (packing) with 5 cm thickness and installed in front of the air condenser as shown in Figure 1. A water circulation system was built to inject water on the top of the media pad by using a pump. Hot ambient air passed over the evaporative media pad and get cooled and then passed over the condenser and finally exits from back side of the condenser. Digital AC clamp power meter [Kyoritsu 2017, with 1.5% accuracy] was used to measure the electrical current of the compressor. The pressure in inlets of condenser and evaporator were measured by special type Bourdon gauges suitable for refrigeration system with accuracy of ±0.05 bar. Based on the experimental evidence, pressure drop in condenser and evaporator was considered 7% and 5% respectively. Calculations show that the pressure drop has no significant effect on the results.

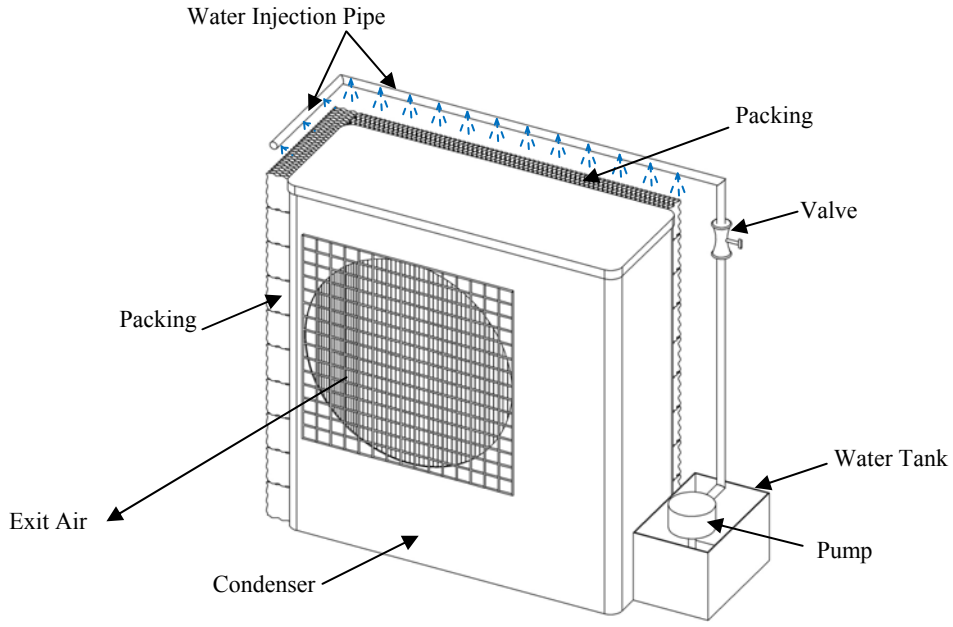

Figure 1. Schematic view of the retrofitted condenser

Temperatures of refrigerant and circulation air at different points were recorded with K-Type thermocouples and the signals were connected to the computer by using data acquisition system type MIO-64E-3 and analyzed by LabView program from National Instrument. Before temperature measurement, the surface of tube was polished for removing any dust or rust and then the thermocouple probe was laid down on the surface. In order to reduce the thermal contact resistance between thermocouple probe and tube surface, thermal grease was used in the point of contact. Insulating tape was wrapped around the tube to push the probe against the tube surface and also prevent any convection effect of ambient air on the temperature readings. The water consumption rate due to evaporation effect was measured by using water level change in the tank during the test period.

Table 1
Experimental Results of two Condensers at Three different Air Temperatures

Parameter	Unit	AC	EC	AC	EC	AC	EC
Ambient dry bulb temperature	°C	35.0		44.0		49.0	
Ambient wet bulb temperature	°C	24.0		25.0		24.0	
Inside dry bulb temperature	°C	24.0		24.0		24.0	
Inside wet bulb temperature	°C	20.0		20.0		20.0	
Compressor exit temperature	°C	89.5	75.2	100.5	83.6	102.5	87.2
Condensing temperature	°C	45.5	38.5	51.9	44.2	54.9	45.0
Condenser exit temperature	°C	37.9	29.1	47.0	29.1	50.2	37.0
Evaporating temperature	°C	8.5	7.5	11.4	10.9	11.4	9.9
Compressor inlet temperature	°C	23.2	21.4	23.4	25.9	20.0	21.0
Condenser pressure	bar	17.5	14.8	20.3	17.0	21.7	17.3
Evaporator pressure	bar	6.5	6.3	7.1	7.0	7.1	6.8
Air temperature after pad	°C	-	26.0	-	29.0	-	32.0
Air temperature at condenser exit	°C	47.5	40.1	57.0	42.4	61.9	45.8
Outlet air from evaporator	°C	6.5	5.8	7.5	5.0	9.0	6.5
Electric current	A	7.1	6.2	8.2	6.7	8.5	6.7
Water evaporation rate	cm^3/min	-	201	-	222	-	231

AC: Air Condenser, EC: Evaporative Condenser

EXPERIMENTAL RESULTS

In order to estimate the effect of evaporative cooling on the system and compare the results of two different types of air conditioners, experimental tests were performed in two consequent stages. In the first stage, air cooled condenser was used and in the second stage evaporative cooled condenser was used. Data were recorded after steady state condition was established and the properties of refrigerant and air remained constant (after 20 min.). Many experimental tests were performed at different ambient temperature. The results of tests at three different temperatures (35, 44, 49°C) are shown in Table 1. As shown in this table electric current, condenser pressure, compressor exit temperature increase considerably as ambient temperature increases.

Figure 2 shows the experimental results on the P-h diagram when ambient temperature was 35.0°C. The results show condenser and evaporator pressure of the retrofitted system reduced about 15% and 3% respectively and the pressure ratio reduces about 13%. Also in the retrofitted system the temperature of the condenser dropped down about 7°C while the evaporator temperature reduced about 1°C. Electric current consumption of system reduces about 12%.

Figure 3 shows the experimental results on the P-h diagram when ambient temperature was 49.0°C. As shown, condenser pressure reduced from 21.7 to 17.3 bar which shows 20% reduction and evaporator pressure reduced from 7.1 to 6.8 bar which shows only 4% reduction. The pressure ratio across the cycle reduces from 3.05 to 2.54 which shows 17% reduction. Also in the retrofitted

system the temperature of the condenser dropped down about 10°C while the evaporator temperature reduced about 1.5°C. Electric current consumption of system reduces about 21%.

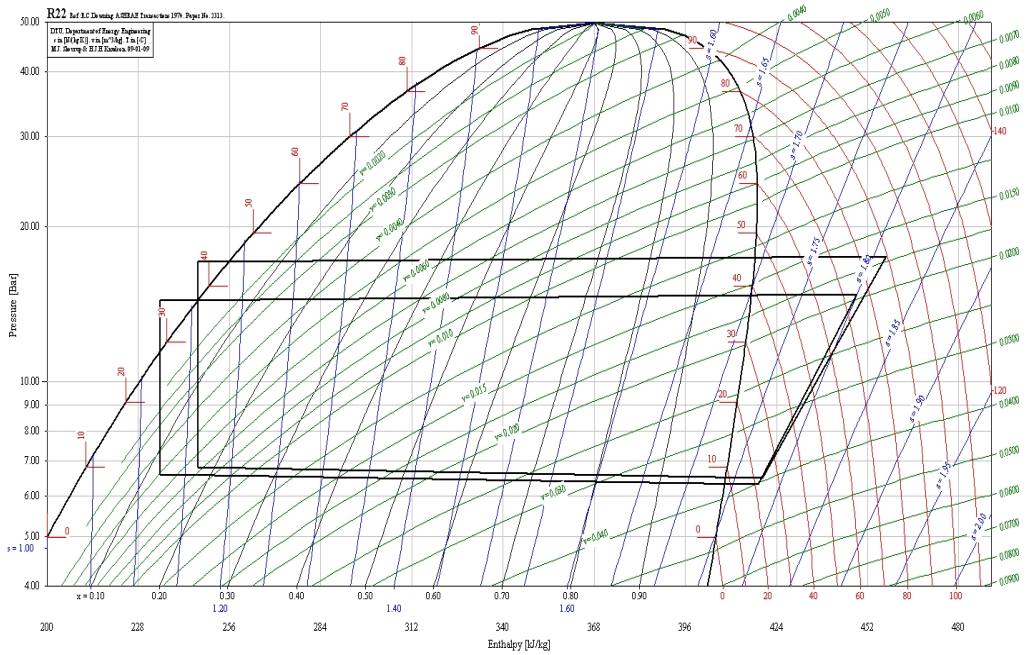

Figure 2. The P-h diagram of conventional and evaporative cooling cycle at T_{amb}=35.0°C

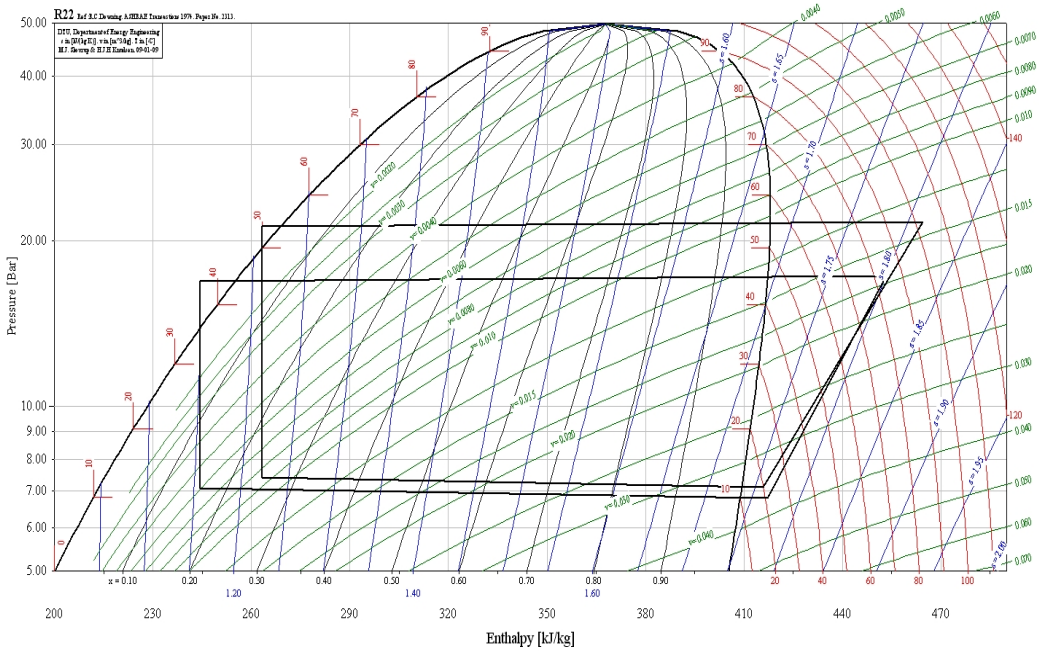

Figure 3. The P-h diagram of conventional and evaporative cooling cycle at T_{amb}=49.0°C

PERFORMANCE RESULTS AND DISCUSSION

Based on the experimental results, thermodynamic properties of refrigerant at different points of the cycle were obtained (Figure 2 and 3) in order to calculate mass flow rate, cooling capacity and COP. Equations (1-4) are used to calculate the desired parameter. Actual power consumption can be obtained by using Eq. (1) since the voltage, current and cosφ are known. Mass flow rate can be obtained by Eq. (2). Cooling capacity and COP can be obtained by using equation. (3) and equation.

(4) respectively. In all equations, subscripts (1), (2), (3) and (4) stand for exit conditions from compressor, condenser, capillary tube and evaporator respectively.

$$Wc = VI\cos\phi \tag{1}$$

$$m = \frac{W_c}{h_2 - h_1} \tag{2}$$

$$Q_c = \dot{m}(h_1 - h_3) \tag{3}$$

$$COP = \frac{h_1 - h_3}{h_2 - h_1} \tag{4}$$

Table 2 and 3 shows the results of calculation for tests at ambient temperatures at 35.0 and 49.0°C respectively. Comparing the results of two tables shows that as ambient temperature increases effect of using evaporative air cooling increases. Power reduction improvement increase from 12% to 21%, refrigeration effect improvement increase from 6.1% to 13.3% and COP improvement increases from 33.0% to 52.2%. The results are in consistent with findings of other researches [3-5].

Table 2
Performance results of air conditioner after retrofitting (T_{amb}=35.0°C)

Parameter	Unit	Conventional	Evaporative	Variation
W_c	kW	1.484	1.295	-12.6%
m	gr/sec	0.03905	0.04286	9.7%
q_c	kJ/kg	173.2	183.8	6.1%
Q_c	kW	6.763	7.877	16.4%
β	-	4.56	6.08	33.0%

Table 3
Performance results of air conditioner after retrofitting (T_{amb}=49.0°C)

Parameter	Unit	Conventional	Evaporative	Variation
W_c	kW	1.776	1.400	-21.1%
m	gr/sec	0.03661	0.03876	6.0%
q_c	kJ/kg	152.4	172.7	13.3%
Q_c	kW	5.579	6.693	20.1%
β	-	3.14	4.78	52.2%

Effect of ambient temperature on the cycle performance

Many tests at different ambient conditions ranging between 35.0 to 49.0°C were performed in order to have better understanding of the cycle behavior. Figure 4 compares the variation of refrigeration effect for two condensers in terms of ambient air temperature. It can be seen that the performance of the evaporative cooled condenser is much better than the air cooled condenser and the improvement increases as ambient temperature increases. Figure 5 compares the variation of compressor work for two condensers in terms of ambient air temperature. As seen, with increasing air temperature compressor work is increased and there is considerable difference between two condensers performance. Figure 6 shows variation of COP versus ambient air temperature for two type condensers. As the experimental results show the difference between two curves is very large and it increases as ambient air temperature increases.

Decreasing the COP of evaporative cooled air condenser with ambient air temperature is the result of increasing the air temperature after the pad. Figure 7 shows the temperature of air after the pad in

terms of ambient air temperature. The air temperature after the pad depends on many parameters like ambient wet bulb temperature, rate of water injection, air velocity and thickness and shape of the pad [3]. It is possible to decrease air temperature after the pad to approach ambient wet bulb temperature in order to get the best performance. This needs many other tests and changes in the experimental set up like increasing the pad thickness and water injection rate which was not in the scope of this paper.

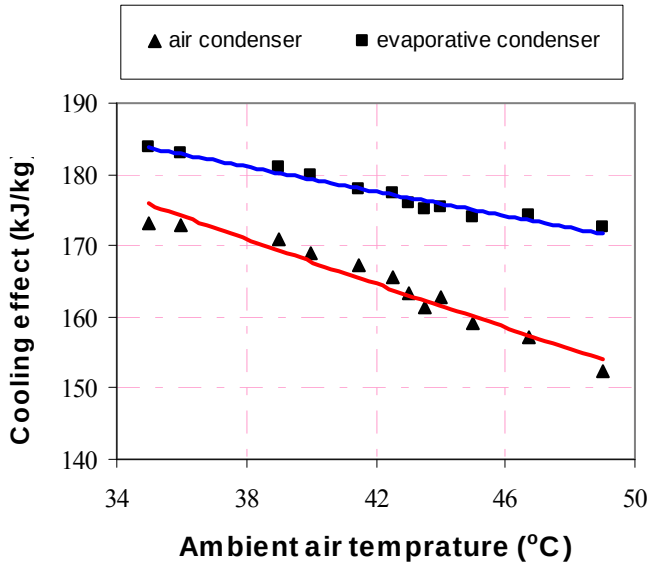

Figure 4. Cooling effect variation at different ambient air temperature

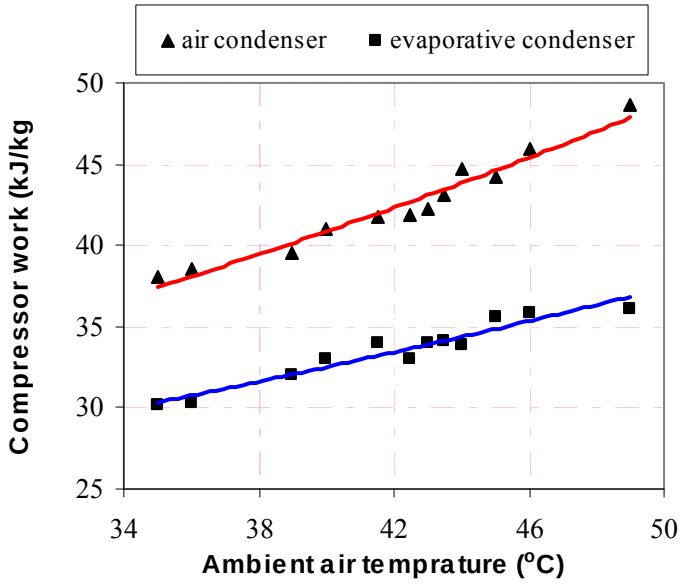

Figure 5. Compressor work variation at different ambient air temperature

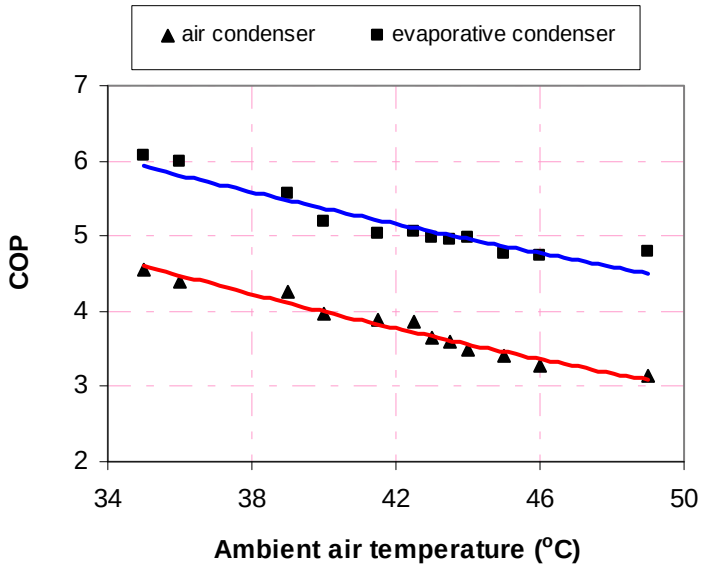

Figure 6. COP variation at different ambient air temperature

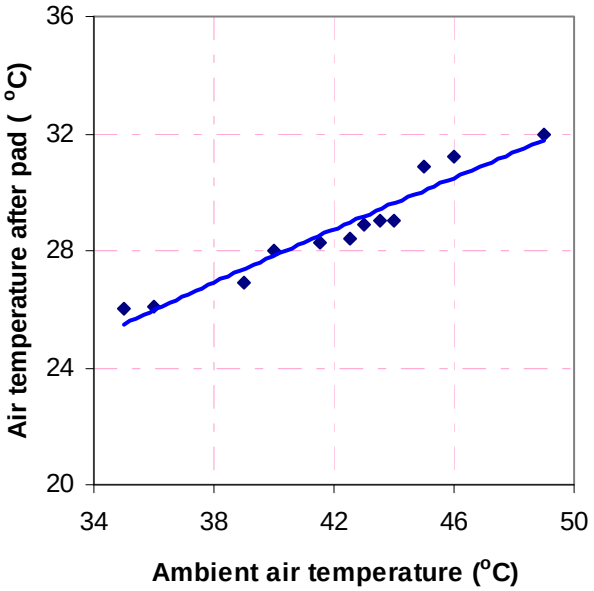

Figure 7. Air temperature after pad

Error analysis

Error analysis for estimating the maximum uncertainty in experimental results was done [6]. It was found the maximum uncertainty in the results is belonging to COP by 3.4%.

CONCLUSIONS

Effective use of energy sources needs more efficient use of air conditioners. Evaporative cooler coupled to the air condenser is an efficient, reliable and cost-effective method to increase the performance of split type air conditioner. Experimental results show that increasing ambient air temperature decreases the coefficient of performance of air cooled condenser considerably but it has less effect on the performance of evaporatively cooled condenser. Power consumption can be decreased up to 21% and performance can be improved up to 52% by application of evaporative condenser. It is found that evaporatively cooled air conditioner works more efficiently as air

temperature increases, therefore, its application in very hot weather condition is highly recommended.

NOMENCLATURE

COP	coefficient of performance (-)
h	enthalpy (kJ/kg)
I	electric current (A)
m	mass flowrate (kg/sec)
q_c	refrigeration effect (kJ/kg)
Q_c	cooling capacity (kW)
V	electric voltage (V)
W_c	compressor power (kW)

REFERENCES

[1] Dossat, R. J., *Principal of Refrigeration*, Prentice Hall, New Jersey, 1991.
[2] Goswami, D. Y., Mathur, G. D., and Kulkarni, S. M., Experimental Investigation of Performance of a Residential Air Conditioning System with an Evaporatively Cooled Condenser, *J. Sol. Energy Eng.*, Vol. 115, pp 206-211, 1993.
[3] Zhang, H., You, S. J., Yang, H. X., and Niu, J. L., Enhanced Performance of Air-Cooled Chillers Using Evaporative Cooling, *Build. Services Eng. Res. Technol.*, Vol. 21 No. 4, pp 213-217, 2000.
[4] Yu, F. W. and Chan, K. T., Application of Direct Evaporative Coolers for Improving the Energy Efficiency of Air-Cooled Chillers, *J. Sol. Energy Eng.*, Vol. 127, pp. 430-433, 2005.
[5] Hajidavalloo, E., Application of Evaporative Cooling on the condenser of Window Air-Conditioner, *Applied Thermal Engineering*, Vol. 27 pp. 1937-1943, 2007.
[6] Holman, J. P., *Experimental Method for Engineers*," 4th Ed. McGraw-Hill, 1984.

FLOW STABILITY IN TUBE – THERMODYNAMIC ANALYSIS

P. Novotný[1, 2, *], F. Maršík[2]
[1]Faculty of Mechanical Engineering CTU in Prague, Prague, Czech Republic
[2]Institute of Thermomechanics AS CR, v.v.i., Prague, Czech Republic

ABSTRACT. Flow stability in tube is analysed by using the new thermodynamic condition of stability. This condition is derived from the thermodynamics, especially from the extremal condition for the total energy. In this paper is indicated the theoretical solution of the flow between two rotating cylinders. The Poiseuille and the Couette flow into the annulus are taken as the examples. This analysis supports the experimental findings, i.e., the strong influence of vortex core rotation on the enhancement of flow stability.

Keywords: *vortex, flow stability, hydrodynamics stability, balance of entropy*

INTRODUCTION

Flow field instabilities play important part for the distribution of the substances and are important in flows in the atmosphere, in the ocean, in blood vessels, around streamlined bodies, in jets, mixing layers; in fact, in almost any flows. The flow stability can be defined based on the kinetic energy of disturbances or based on critical Reynolds number, see [4]. Inviscid stability theorems like Rayleigh's inflexion point theorem, Fjörtoft's theorem are used at present, see [4, 3]. On the other hand the flow stability problem can be solved based on the new thermodynamic stability conditions, which is now under development at the Institute of Thermomechanics AS CR. This thermodynamics stability condition is derived from the new formulation of thermodynamics and represents the measure of the attenuation of the fluctuations of the total energy. This theoretical research is accompanied by the experimental research, which will be published later.

CONDITION OF STABILITY

General form for the balance of entropy is, see [2]

$$\frac{DS}{Dt} - J(S) = P(S) \geq 0 \tag{1}$$

Where S is the entropy, $J(S)$ denotes the total flux of the entropy through the system and $P(S)$ denotes the production of the entropy of the system. The entropy production $P(S)$ gives the important information about the fluid flow stability of thermoviscose fluid. To obtain the convenient form of needed stability condition we have to use for analysing of the fundamental thermodynamic inequality the total enthalpy

* Corresponding author: Pavel Novotný
Phone: + (420)-224-352690, Fax: + (420)-233-322482
E-mail address: Pavel.Novotny@fs.cvut.cz

$$h_c(s,p) = \frac{|v^2|}{2} + u + \frac{p}{\rho} + \phi \tag{2}$$

The final form of the thermodynamic condition of stability for the thermoviscose fluid has following form

$$\pi = -\frac{q^j}{T} \cdot \frac{\partial T}{\partial x^j} + v_i \cdot \frac{\partial t_{dis}^{ij}}{\partial x^j} + t_{dis}^{ij} \cdot \frac{\partial v_i}{\partial x^j} \geq 0 \tag{3}$$

Inequality (3) is so called the modified fundamental thermodynamic inequality and for our purposes is taken as ***the thermodynamic criterion of stability of thermoviscose flow***.

The cylindrical coordinates are convenient for the tube flow ($x^1=r$, $x^2=\varphi$, $x^3=z$). Relation between the Cartesian coordinates ($x^1=x$, $x^2=y$, $x^3=z$) and the cylindrical coordinates ($\xi^1=r$, $\xi^2=\varphi$, $\xi^3=z$) are given as follows $x = r\cdot\cos\varphi$, $y = r\cdot\sin\varphi$, $z = z$. For the isentropic flow with constant density ρ, viscosity μ , constant temperature T a rotational flow in the axial direction i. e. $\vec{v} = (v^r, v^\varphi, v^z) = (0, v^\varphi(r), v^z(r))$ is supposed. The general thermodynamic condition of stability (3) for the isothermal fluid has after transformation the following form

$$\pi = \mu \cdot v^\varphi \cdot \frac{\partial^2 v^\varphi}{\partial r^2} + \mu \cdot \left(\frac{\partial v^\varphi}{\partial r} - \frac{v^\varphi}{r}\right) \cdot \left(-\frac{v^\varphi}{r}\right) + \mu \cdot \left(\frac{\partial v^\varphi}{\partial r} - \frac{v^\varphi}{r}\right) \cdot \left(\frac{\partial v^\varphi}{\partial r}\right) +$$
$$+ \mu \cdot \left(\frac{\partial v^z}{\partial r}\right)^2 + \mu \cdot v^z \cdot \left(\frac{\partial^2 v^z}{\partial r^2} + \frac{1}{r} \cdot \frac{\partial v^z}{\partial r}\right) \geq 0 \tag{4}$$

APPLICATION TO THE COUETTE – POISEUILLE FLOW

The total flow is assumed as superposition of the two flows – Poiseuille flow in the axial direction and Couette flow in the tangential direction, Figure 1.

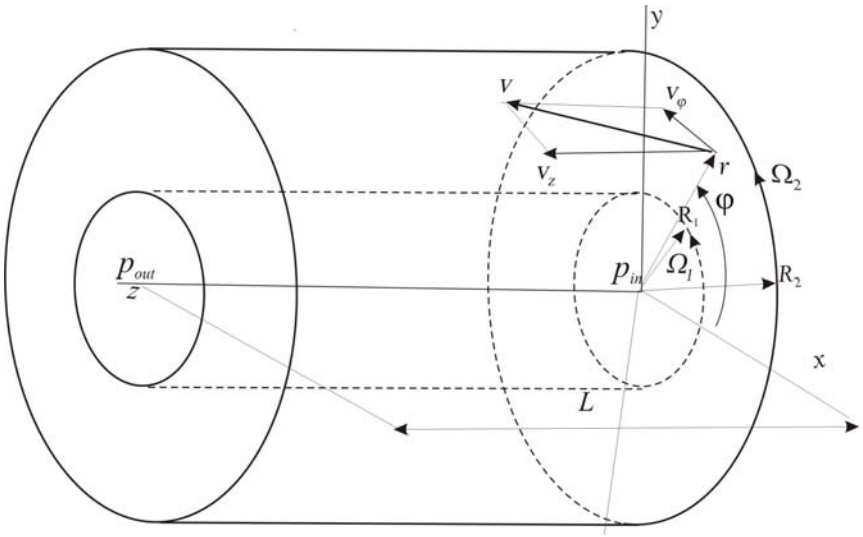

Figure 1. Scheme of the vortex tube.

The velocity profile in the annulus for the Poiseuille flow is given as the analytical solution of the Navier-Stokes equations in the form

$$v^z(r) = A_p \cdot R_2^2 \cdot \left\{ 1 - \left(\frac{r}{R_2}\right)^2 + \left[1 - \left(\frac{R_1}{R_2}\right)^2 \right] \cdot \frac{\ln\left(\frac{r}{R_2}\right)}{\ln\left(\frac{R_2}{R_1}\right)} \right\} \tag{5}$$

Where the flow parameter $A_p = \frac{p_{in} - p_{out}}{4 \cdot \mu \cdot L} = const.$ represents the driving pressure gradient. Analogously to tube flow, the exact solution of the Navier-Stokes equations between two rotating cylinders (so called the Couette flow) is given as, [1]

$$v^{\varphi}(r) = r \cdot \omega(r) \tag{6}$$

Where

$$\omega(r) = A + \frac{B}{r^2} \tag{7}$$

The parameters A and B have the form

$$A = -\Omega_1 \cdot \eta^2 \cdot \frac{1 - \frac{\overline{\mu}}{\eta^2}}{1 - \eta^2}, B = \Omega_1 \cdot \frac{R_1^2 \cdot (1 - \overline{\mu})}{1 - \eta^2}, \overline{\mu} = \frac{\Omega_2}{\Omega_1}, \eta = \frac{R_1}{R_2} \tag{8}$$

To obtain the non-dimensional form of the thermodynamic condition of stability (4) in the radial coordinate $\tilde{r} = r/R_2$, we put in the formulas (5), (6), (7) and (8) into inequality (4). After some algebra the thermodynamic stability condition has the final form, where are the contributions both of the Poiseuille flow and Couette flow to the global stability, separated

$$\frac{\pi}{\Omega_1^2 \cdot \mu} = \frac{2 \cdot \eta^2 \cdot (1 - \overline{\mu})}{\tilde{r}^2 \cdot (1 - \eta^2)} \cdot \left[\frac{3 \cdot \eta^2 \cdot (1 - \overline{\mu})}{\tilde{r}^2 \cdot (1 - \eta^2)} - \eta^2 \cdot \frac{1 - \frac{\overline{\mu}}{\eta^2}}{1 - \eta^2} \right] +$$

$$+ CP \cdot \left[8 \cdot \tilde{r}^2 - 4 - 4 \cdot \frac{1 - \eta^2}{\ln\left(\frac{1}{\eta}\right)} \cdot \ln(\tilde{r}) - \frac{4 \cdot (1 - \eta^2)}{\ln\left(\frac{1}{\eta}\right)} + \frac{(1 - \eta^2)^2}{\tilde{r}^2 \cdot \ln\left(\frac{1}{\eta}\right)^2} \right] \geq 0 \tag{9}$$

The parameter CP (the coupling number) indicates an interaction of both velocities fields from point of view their stability and is defined as follows

$$CP = \frac{A_p^2 \cdot R_2^2}{\Omega_1^2} \sim \frac{v_{z\max}^2}{(R_2 \cdot \Omega_1)^2} \tag{10}$$

where $v_{z\max}^2$ is maximal axial velocity. For the low value of *CP* the influence of the disturbances of the Poiseuille flow on the total flow is insufficient.

APPLICATION TO THE VORTEX TUBE

We consider the vortex tube, see Figure 1, where is R_1 = 4.4 mm, R_2 = 8.8 mm, Ω_1 = 30 rad/s, A_p = 4500 Pa/Pa·s·m. We apply the new thermodynamic stability condition (9) to the three following flow regimes; for $\overline{\mu} = 1$, $\overline{\mu} = 0.5$ and $\overline{\mu} = 0$. The viscosity is taken as the constant ($\mu = 1 \cdot 10^{-3}$ Pa·s).

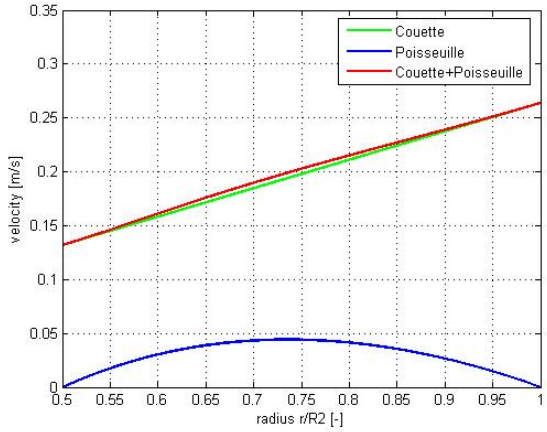

Figure 2. Velocity field of the Couette (green line), of the Poiseulle (blue line) and the total flow (red line) for $\overline{\mu} = 1$.

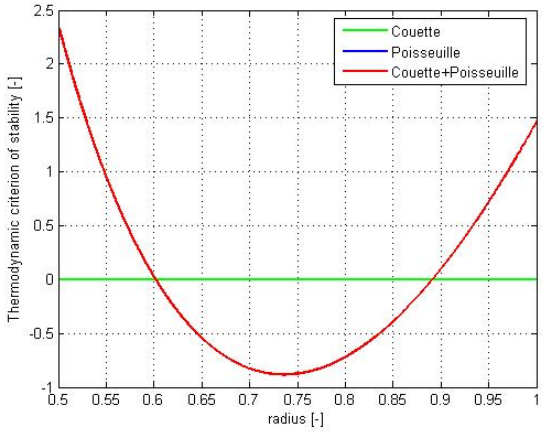

Figure 3. The stability condition for the Couette (green line), of the Poiseulle (blue line, it coincides for this case with red line) and the total flow (red line) for $\overline{\mu} = 1$.

Angular velocities of the inner cylinder and the outer cylinder are for $\overline{\mu} = 1$ equal, i.e. $\Omega_1 = \Omega_2$ and $v_{\varphi\max} = R_2 \cdot \Omega_2$. The Couette flow has the linear character; the Poiseuille flow has the parabolic character in this case. The total flow, which is composed from the Couette and the Poiseuille flow, is plotted in the Figure 2 (red line). The Couette flow is for this case at the margin of the stability, see Figure 3. So that the Couette flow has not the influence on the stability of the total flow. It is the reason why is the total flow core unstable alike the Poiseuille flow core, the stability curves of both flows coincide.

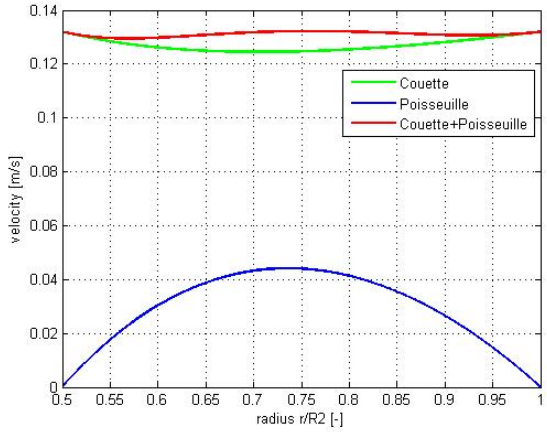

Figure 4. Velocity field of the Couette (green line), of the Poiseulle (blue line) and the total flow (red line) for $\overline{\mu} = 0.5$.

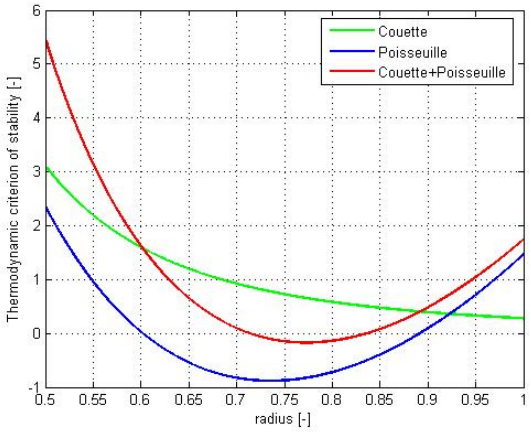

Figure 5. The stability condition for the Couette (green line), of the Poiseulle (blue line) and the total flow (red line) for $\overline{\mu} = 0.5$.

The similar case ($\overline{\mu} = 0.5$) is shown in the Figure 4. The value of the stability criterion (9) is for the Couette flow positive, see Figure 5; so that the Couette flow has the stabilizing influence on the stability of the total flow, nevertheless the total flow core is still unstable, see Figure 5.

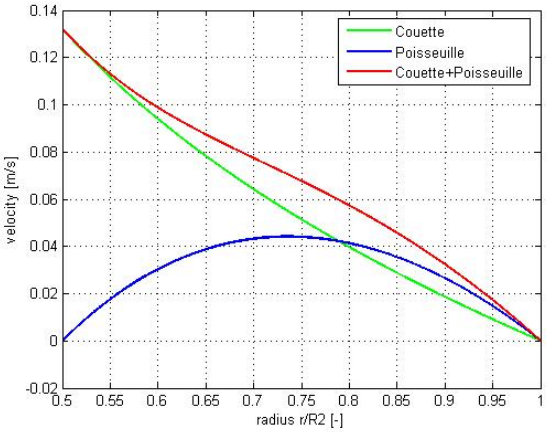

Figure 6. Velocity field of the Couette (green line), of the Poiseulle (blue line) and the total flow (red line) for $\overline{\mu} = 0$.

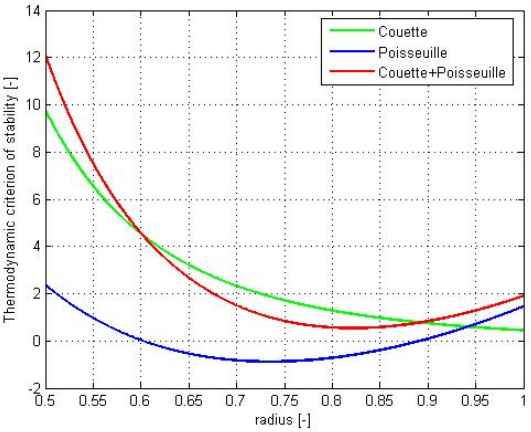

Figure 7. The stability condition for the Couette (green line), of the Poiseulle (blue line) and the total flow (red line) for $\overline{\mu} = 0$.

The strong stabilizing influence of the Couette flow on the Poiseuille flow and consequently on the total flow, is reached for $\overline{\mu} = 0$, see Figure 6. The stability criterion of the Couette flow in this case prevailing, see Figure 7. The total flow is for $\overline{\mu} = 0$ completely stable. This case is physically very close to the potential vortex flow.

CONCLUSION

The Couette flow for $\overline{\mu} = 1$ (solid body rotation) is at the margin of the stability and the Poiseuille flow core is unstable, see Figure 1 and Figure 2. The unstable core of the Poisseuille flow

predominates over the Couette flow so that the core of the total flow, which is composed from the Couette and the Poiseuille flow, is unstable too. However, for $\overline{\mu} = 0.5$, the Couette flow is stable and the core of the Poiseuille flow is unstable, see Figure 3 and Figure 4. The total flow core is more stable then the Poseuille flow core itself, nevertheless the total flow core is still unstable. For $\overline{\mu} = 0$ the stabilizing effect of the Couette flow is strong enough, Figure 6 and Figure 7, so the total flow, which is composed from the Couette and the Poiseuille flow, is completely stable. The possibility to stabilize Poisseuille flow by the given Couette flow follows directly from the thermodynamic stability condition (9) only. Such condition cannot be obtained from the Rayleigh's criterion itself.

We can conclude, that the stable annular flow can be reached in such vortex tube configuration, where the Couette flow is dominant.

Thermodynamic criterion of stability is in comparison with the Rayleigh theory more general and includes as well the influence of the viscosity. This theory is in general applicable not only for steady flows, but even for unsteady flows.

ACKNOWLEDGEMENT

This work was supported by MSM 6840770012 'Transdisciplinary Research in the Field of Biomedical Engineering II' and project No. 1M06031 of the Ministry of Education, Youth and Sports of the Czech Republic

REFERENCES

1. Chandrasekhar, S., *Hydrodynamic and Hydromagnetic Stability*, International Series of Monographs on Physics, Oxford: Clarendon, 1961.
2. Marsik, F., *Continuum thermodynamics*, Prague, Academia, 1999, (in Czech).
3. Novotny, P., Marsik, F., Chlup, H., Stability of Velocity Fields, *9th Workshop of Applied Mechanics*, ISBN 978-80-01-04161-1, pp 52-54, 2008.
4. Schmid, P.J., Henningson, D.S., *Stability and Transition in Shear Flows*, New York, Springer – Verlag 2001.

EFFICIENCY DEPENDENCE ON FUEL IN THE BRAYTON CYCLE

I. López*, R. Nieto, C. González, A. Jiménez
ETSI Industriales
Universidad Politécnica de Madrid, Madrid, Spain

ABSTRACT. This study belongs to a broader line of research on exergy analysis of industrial systems. The paper presents a comparison between the efficiencies of a standard Brayton cycle when run on different fuels. The fuels are the first compounds of the alkane series. The main goal of this study is to characterize the exergetic performance of the series in order to identify a trend, so as to understand the influence of C2+ components in alternative fuels to methane: syngas and unprocessed natural gas. The study has centred on cycle thermodynamics, leaving aside turbine design issues and other concerns of new fuels. Simulations have been carried out with the proprietary software PATITUG. Gases have been modelled as Lewis-Randall mixtures with truncated virial equations. Methane proves to be the most exergetic-efficient. A decreasing trend in efficiency has been observed as the series progresses, justified by a linear rise in the specific power at the turbine against an exponential growth of the chemical exergy.

Keywords: *Gas turbine fuels, Exergy analysis, Combined cycle, Power Generation.*

INTRODUCTION

The current complex economic, strategic and energetic scenarios lead to a strong drive for alternative fuels or fuel interchangeability in many sectors, and especially in the power generation sector [1, 2]. Unprocessed methane has been traditionally the preferred fuel. However, it is not always available at new plant sites and its prices are rising [3]. Besides, other fuels and technologies such as coal or biomass in integrated gasification combined cycle, IGCC, present a significant environmental potential when combined with carbon dioxide capture facilities [4, 5, 6].

This situation results in two main alternative fuels to processed methane for power generation: unprocessed natural gas and syngas [7], obtained from coal or biomass [8]. However, the properties of these fuels may differ significantly from processed methane in many aspects, from reachable flame temperatures to maintainability issues.

Although there exist a number of application studies related to alternative fuels and their associated processes, there exists a need for systematic studies of their thermodynamic implications [11, 12, 13, 14]. In this line, this paper attempts to portrait the different performance trends of the first elements of the alkane series as fuels for power generation. Alkanes are relevant to the current alternative fuels. Unprocessed natural gas may contain up to 20% of non-methane compounds, of which the most part are alkanes, usually up to pentane and exceptionally heavier. Similarly occurs with syngas [14, 15].

* Corresponding author: Prof. I. López
Phone: + (34)-913363150, Fax: + (34)-913364262
E-mail address: ilopez@etsii.upm.es

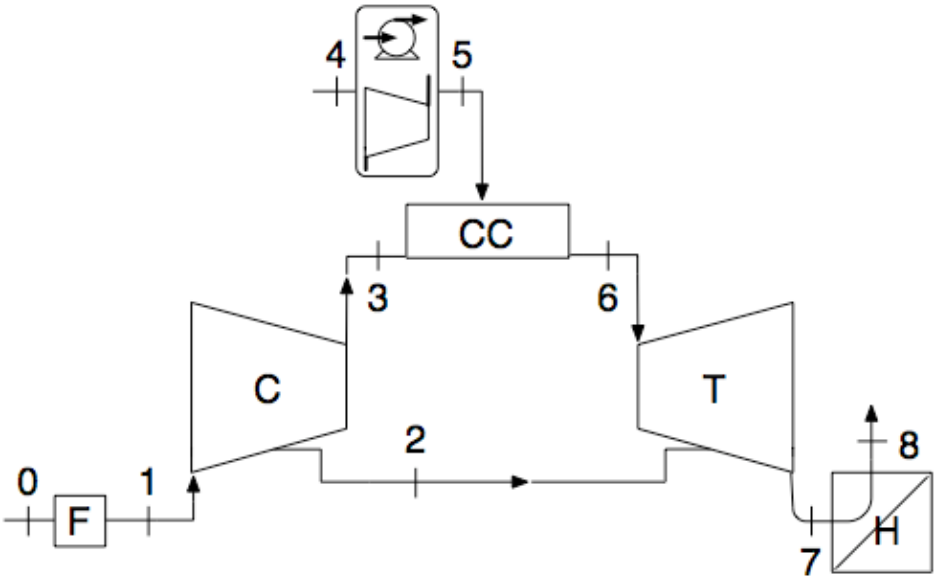

Figure 1. Diagram of the standard Brayton cycle considered

The study presented here consists in a series of simulations of a standard Brayton cycle for power generation, in which the different pure alkanes are considered as fuels. Different turbine inlet temperatures and compression ratios are considered for each. Practical considerations such as corrosion or turbine maintenance are not treated. A series of curves is obtained showing the trend of exergetic efficiency with the number of carbons of the compound.

Simulations have been carried out with the PATITUG software developed at ETSII. It is oriented to themodynamic design and analysis of elements and cycles. It allows configuring the different thermodynamic parameters of all elements in the considered plant, not being restricted to commercial devices. It also provides accurate thermodynamic treatment of pure substances, mixtures and chemical reactions through different models that can be selected. Although PATITUG is normally used for academic purposes, other studies related with this paper have been carried out in the past [16].

DESCRIPTION OF THE STUDY

The considered Brayton cycle is represented in figure 1. Air enters the cycle at point 0, and is filtered before entering the compressor at 1. A partial extraction for turbine refrigeration is made at 2. The output of the compressor enters the combustion chamber at 3, where it reacts with the fuel being compressed or pumped from 4 and entering the chamber at 5. After a complete combustion, the gases enter the turbine at 6, and are expanded. The gases leave the turbine at 7, entering a heat exchanger, where exergy is assumed to be transferred to a steam cycle. Finally, the gases leave the plant at 8.

This setting has been adjusted to standard values in order to make it representative of a general configuration. For each fuel, an exergy analysis is performed for a range of working temperatures and pressures.

Exergetic Efficiency

The exergetic efficiency of the cycle is calculated as the ratio between the net exergy obtained and the chemical exergy of the fuel, e_4, as indicated in equation (1).

Thus, the net exergy obtained is the power balance of the cycle, allowing a factor η for mechanical losses in turbine, compressor and fuel injection, plus the exergy obtained at the heat exchanger, assumed 0.7 of the total:

$$\xi = \frac{\eta(\dot{W}_T + \dot{W}_C + \dot{W}_{4-5}) + 0.7(\dot{E}_7 - \dot{E}_8)}{\dot{m}_4 e_4} \quad (1)$$

In order to isolate the effect of the fuel and to ensure comparability of results, the turbine has been assumed to be designed specifically for the particular fuel of the studied case. In this way, the possible influence on efficiency of running a turbine on a different fuel to that it was designed for is eliminated.

Operating Conditions

For the sake of simplicity and representativeness of the study, only turbine inlet temperature, T6, and compressor ratio, P3/P1, are varied. T6 is studied in the range 1000-1450 ºC, and P3/P1 in 10-40.

However, the operating conditions of the cycle are determined by a large series of factors which shall be assumed in standard values, as will be described following.

Pressure losses at the inlet filter, F, are taken 196.3 Pa. Isentropic efficiencies of compressor, C, and turbine, T, 0.845. Fuel compressor or pump (in the case of liquid fuels) have isentropic efficiencies of 0.84. Pressure losses at the combustion chamber, CC, are modelled as P6=0.9601P3. Heat losses in CC are taken 0.34% of m_4e_4. The mass flow at 2 has been assumed 6.2% of intake flow. Pressure at 7 has been assumed 2499 Pa over ambient pressure, P0. Temperature at 8, 120 ºC. Finally, air is assumed to enter at ISO conditions, 15 ºC, 1.01325 bar and 60% RH, and fuel is assumed to enter at 4 at 15 ºC and 10.34 bar.

Considered Fuels

Considered fuels: methane, ethane, propane, n-butane, isobutane, n-pentane, hexane and heptane.

Chemical Reaction

The combustion reaction considered is a simplification of the real case. Dry air has been modelled as a mixture of O2, N2, Ar and CO2. Minor components of air such as metals has been neglected [5]. The quantity of water in air has been adjusted to the considered RH. No formation of NOx has been considered. Finally, combustion has been assumed to take place in excess of air with respect to the stoichiometric ratio, in the proportion necessary to obtain the considered turbine inlet temperatures (calculated by PATITUG for each case). Thus, the basic reaction is:

$$C_kH_{2k+2} + \frac{3k+1}{2}O_2 \longrightarrow kCO_2 + (k+1)H_2O$$

Thermodynamic Properties of Substances

As it has been mentioned by some authors [11], thermodynamic properties of combustion gases may vary significantly from the perfect gas. Thus, an adequate thermodynamic model may be critical for obtaining meaningful results.

In this study, air flow and combustion gases have been treated as a Lewis-Randall ideal mixture. Pure components have been modelled with virial equations of state truncated after the second term.

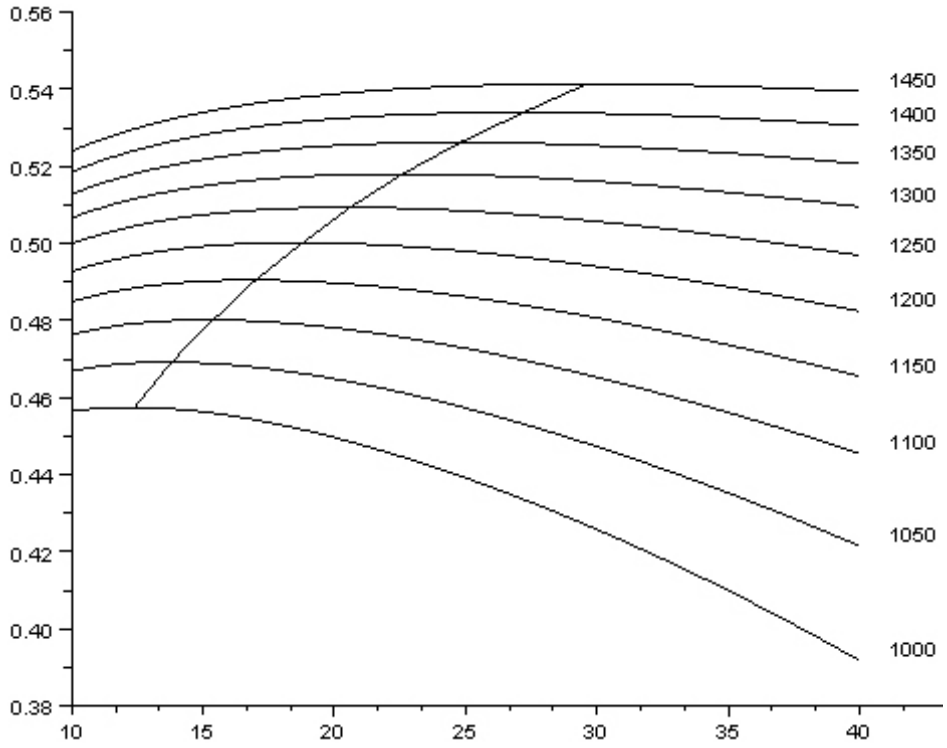

Figure 2. Exergetic efficiency curves for methane

Fuel, in the 4-5 process, is modelled by the Lee-Kesler equation of state. This is necessary to treat adequately the liquid state in which most alkanes enter at point 4.

In both liquids and gases, specific heat has been modelled as a function of temperature. Properties have been obtained from [17]. The chemical exergies of alkanes have been obtained from [18] and adapted to the conditions of the cycle.

RESULTS

Reference Case

Combustion of methane has been taken as the reference case. The excess of air over stoichiometric ratio has been adjusted for the different values of turbine intake temperatures, T6.

Results are shown in figure 2. Exergetic efficiency of the combined cycle is represented against the ratio P3/P1. Each line corresponds to the indicated temperature (in ºC).

Alkanes up to pentane are the most common C2+ components in unprocessed natural gas. The following figures represent the difference between the exergetic efficiencies of ethane and heptane with methane. Intermediate compounds are not shown but follow the trend.

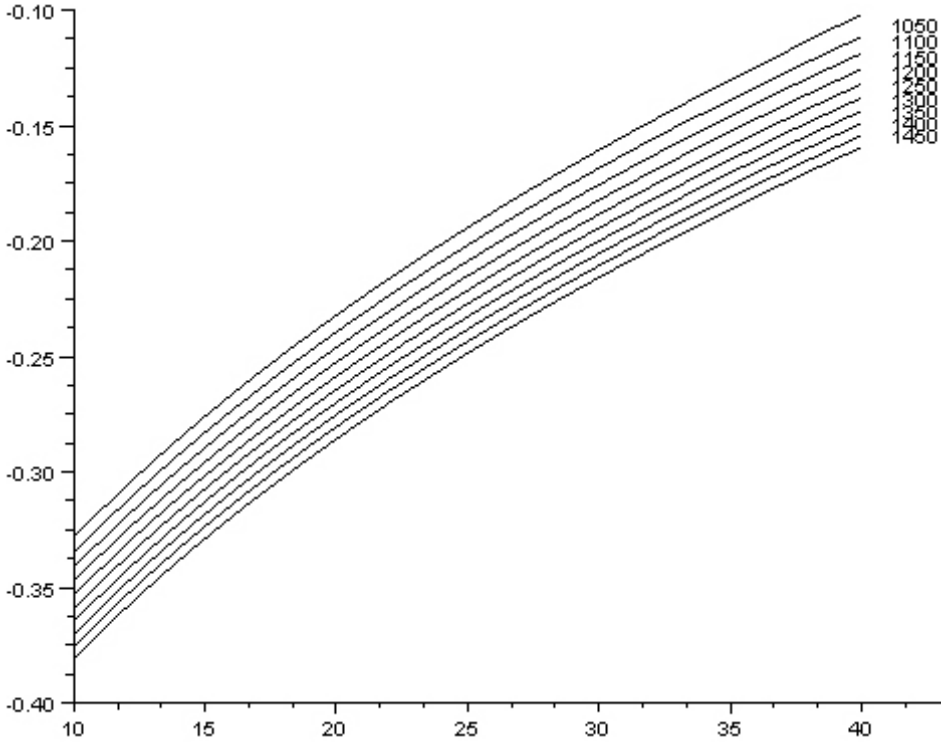

Figure 3. Difference of exergetic efficiencies between ethane and methane

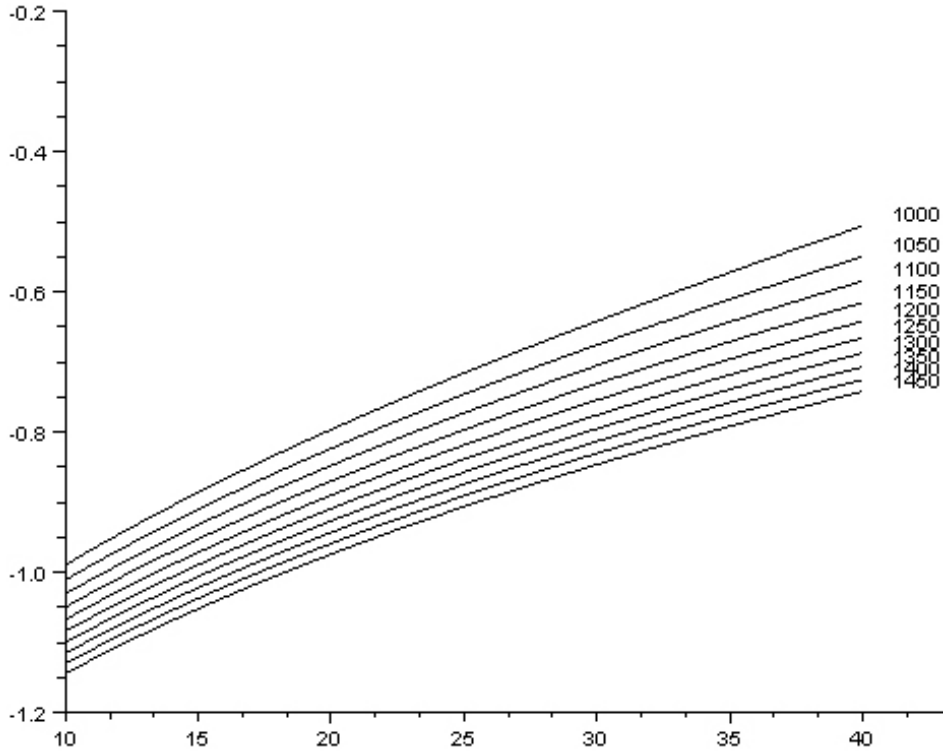

Figure 4. Differences of exergetic efficiencies between heptane and methane

DISCUSSION AND CONCLUSIONS

At a given turbine inlet temperature, a clear decreasing trend in the exergetic efficiency of the combined cycle can be observed along the considered series of alkanes, shown in figures 3 and 4. It can also be observed, although the curves for intermediate compounds have not been shown, that the difference of exergy efficiencies is narrower between consecutive compounds of higher order than between the first of the series. This effect seems correlated with the decrease of the molar fraction of water in combustion gases, which decreases significantly between the first elements of the series but tends asymptotically to 0.5.

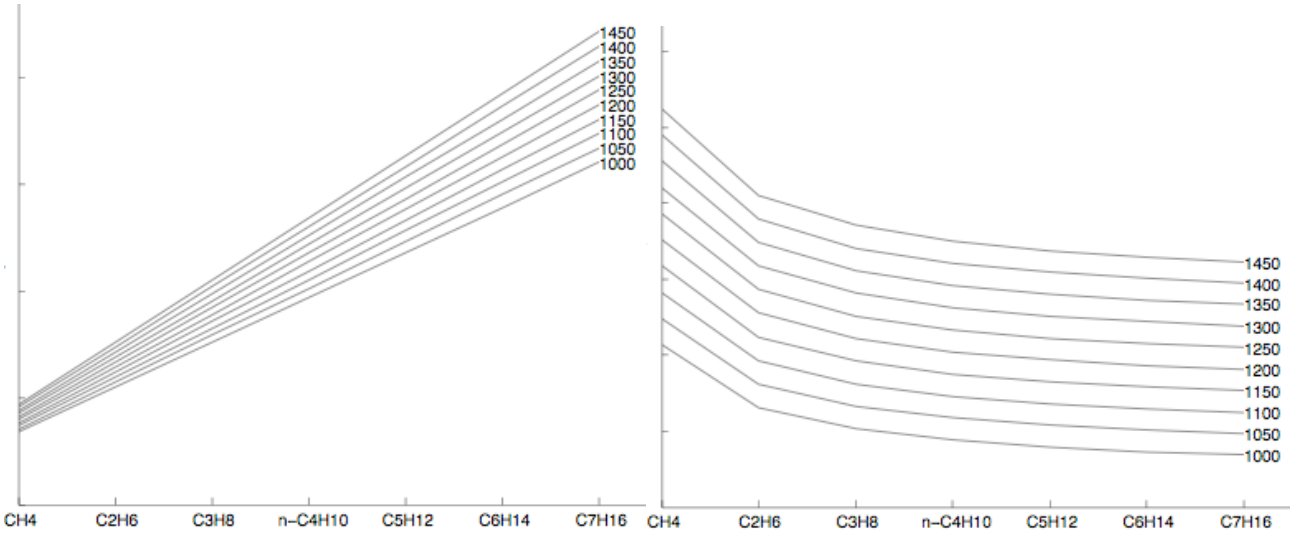

Figure 5. Left: Evolution of the specific power at the turbine for a given P_7/P_6 ratio
Right: Evolution of the turbine power contribution to exergetic efficiency

We may realize that, with respect to the turbine, the only difference between cases is the composition of the gases, and therefore their specific heat. A clear, rising trend with the number of carbons of the compound can be observed in the specific power produced at the turbine, as shown in figure 5 (left).

Given that heavier compounds exist as liquid at the input conditions considered in this study, meaning less compression power needed between 4 and 5, this could lead to expecting higher exergetic efficiencies for these substances. However, it can be seen in the previous section that the real trend is the opposite.

This can be explained by analyzing the evolution of the main contribution to exergetic efficiency, the turbine power term in equation (1). While the rising trend of specific power is clearly linear, in figure 5 (right) it can be seen that for a given turbine outlet/inlet pressure ratio, the decrease of the turbine term is exponential.

In summary, we may conclude that although there exists a decreasing trend with the number of hydorcarbons in exergetic efficiency, the differences are relatively small. Given that the content of C2+ compounds in turbine fuels will in general not exceed 20%, it is expectable that the effect in the overall efficiency will be negligible. However, this study has assumed several simplifications such as no

formation of NOx and total combustion, and bypassed turbine design questions. The influence in exergy of some of these aspects will be assessed in future stages.

REFERENCES

1. Gökalp, I. and Lebas, E., Alternative fuels for industrial gas turbines (aftur) alternative fuels for industrial gas turbines (aftur), *Applied Thermal Engineering*, 24:1655–1663, January 2004.
2. Nag, P., LaGrow, M., Wu, J., Abou-Jaoude, K. and Engel, J., LNG Fuel Flexibility in Siemens' Land-Based Gas Turbine Operations, *Electric Power Conference*, Chicago, May 1-3, 2007.
3. McMillan, R., Martin, P., Noden, R. and Welch, M.. Gas fuel flexibility in a dry low emissions combustion system. *Technical report*, Siemens. Demag Delaval Industrial Turbomachinery Ltd., UK, October 2006.
4. C. A. R. Board. Summary of the joint workshop on natural gas quality standards. *Technical Report* CEC-600-2005-012, CEC 04-IEP-01, CPUC R.04-01-025, California Department of Conservation. Division of Oil, Gas and Geothermal Resources, April 2005.
5. Rising, B. Wu, J. and Sorurbakhsh, P., Survey of ultra-trace metals in gas turbine fuels. In *Proceedings of the 11th Annual International Petroleum Environmental Conference*, October 12-15, 2004, 2004.
6. Anheden, M., Analysis of Gas Turbine Systems for Sustainable Energy Conversion. *PhD thesis*, Department of Chemical Engineering and Technology. Royal Institute of Technology KTH. Sweden., Stockholm, Sweden, 2000.
7. Elmegaard, B., Henriksen, U. and Qvale, B., Thermodynamic analysis of supplementary-fired gas turbine cycles. *International Journal of Applied Thermodynamics*, 6:2, 2003.
8. Gadde, S., Wu, J., Gulati, A., McQuiggan, G., Koestlin, B. and Prade. B., Syngas capable combustion systems development for advanced gas turbines. In ASME, editor, *Proceedings of the ASME Turbo Expo 2006, Power for Land, Sea and Air*. Barcelona, May 8-11, 2006. ASME, May 2006.
9. Shortt, A. A., The use of di-methyl ether as alternative fuel in gas turbines for power generation. *Technical report*, Bateman Power and Energy, 2005.
10. Basu, A., Gradassi, M., Sills, R., Fleisch, T. and Puri, R., Use of dme as a gas turbine fuel. In ASME, editor*, Proc ASME Turbo EXPO GT2001*, June 2001.
11. Kurzke. J., Achieving maximum thermal efficiency with the simple gas turbine cycle. In *9th CEAS European Propulsion Forum*: "Virtual Engine - A Challenge for Integrated Computer Model ling". 15- 17 October 2003, Roma, Italy. CEAS, October 2003.
12. Lee, M. C., Seo, S. B., Chung, J. H. , Joo Y. J., and Ahn, D. H., Industrial gas turbine combustion performance test of dme to use as an alternative fuel for power generation. *Fuel*, In Press, Corrected Proof:–, 2008.
13. Sudiro, M., Bertucco, A., Ruggeri, F. and Fontana, M., Improving process performances in coal gasification for pwer and synfuel production*. Energy Fuels*, 22(6):3894–3901, September 2008.
14. N. E. T. Laboratory. LNG interchangeability/gas quality: Results of the national energy technology laboratory's research for the ferc on natural gas quality and interchangeability. *Technical Report* DOE/NETL-2007/1290, US Department of Energy, June 2007.
15. Erstevag, I. S., Kvamsdal, H. M. and Bolland. O., Exergy analysis of a gas-turbine combined-cycle power plant with precombustion co2 capture. *Energy*, (1):5–39, January 2005.
16. Lacalle, J. M., Nieto, R. and González, C., The impact of new trends in gas turbine design: A thermodynamic analysis. In ASME, editor, 1995 *ASME Cogen-Turbo Power Conference*, number 95-CTP-23. American Society of Mechanical Engineers, 1995.
17. Daubert, T. E. and Danner, R. P., Physical and Thermodynamic Properties of Pure Chemicals: Data Compilation. Hemisphere Publishing Corporation, 1989.
18. Kotas, T. J. The Exergy Method of Thermal Plant Analysis, Butterworths, 1985.

Turbulence

TURBULENT FLOW IN A RIBBED CHANNEL ANALYSED BY THE PROPER ORTHOGONAL DECOMPOSITION

L. Wang[1*], M. Salewski[2], B. Sundén[1]
[1] Lund University, Lund, Sweden
[2]Risø National Laboratory for Sustainable Energy, Technical University of Denmark, Roskilde, Denmark

ABSTRACT. Particle image velocimetry (PIV) measurements and proper orthogonal decomposition (POD) are used to explore the turbulent structures in a ribbed channel. In this study, only one channel wall is equipped with square ribs which are oriented transversely to the main stream direction. The ribs obstruct the channel by 20% of its height and are arranged 10 rib heights apart. The results include mean streamlines, Reynolds shear stresses, two-point correlation coefficients, POD eigenvalues and eigenfunctions. By means of the POD analysis, the underlying flow features are identified, which are the strong upward ejections from the leading edge of the rib. Essentially, these motions give rise to the sharp peaks in the fluctuating turbulent kinetic energy and make great contributions to the Reynolds shear stress.

Keywords: *Particle image velocimetry, proper orthogonal decomposition,*

INTRODUCTION

The proper orthogonal decomposition (POD), which is based on the Karhunen-Loéve (K-L) expansion [1], was proposed by Lumley [2] as an unbiased technique for studying the coherent structures in turbulent flows. Unlike many other techniques, for instance conditional sampling, POD does not need any assumptions about the flow. The method decomposes the fluctuating velocity field into a sum of mutually orthonormal eigenfunctions weighted by random coefficients. The best correlated structures, in an average sense, of the turbulent velocity field are extracted [3]. An important feature of this decomposition is that the contribution of the extracted structures to second-order turbulence statistics can be determined [4].

Turbulent flows in a channel roughened with periodic transverse ribs are frequently encountered in various engineering applications, for example gas turbine cooling. Numerous experimental studies have been carried out to investigate the heat transfer characteristics in a ribbed channel. In the present study, the proper orthogonal decomposition technique is employed to study the flow structures in a ribbed channel. Two-dimensional particle image velocimetry is used to generate the instantaneous velocity data in a streamwise vertical plane. In this study, only one channel wall is fitted with periodic transverse square ribs. The ribs obstruct the channel by 20% of its height and are arranged 10 rib heights apart. The organization of this paper is as follows. Section 2 describes the experimental setup and measurement technique. Section 3 briefly formulates the theory of POD. The results and discussions are presented in section 4. The conclusion is given in section 5.

* Corresponding author: Dr. L. Wang
Phone: + (46)-46-222 9439, Fax: + (46)-46-222 4717
E-mail address: lei.wang@energy.lth.se

EXPERIMENTAL PROCEDURE

The experimental setup consists of a 750 mm long smooth channel followed by a rib-roughened section of equal length. The cross section of the channel is 50 mm × 50 mm. In the ribbed section, only one wall is quipped with periodic transverse ribs. The ribs obstruct the channel by 20% of its height and are arranged 10 rib heights apart. Two-dimensional velocity measurements are made in the vertical symmetry plane, as shown in Figure 1. The Reynolds number, based on the bulk-mean velocity U_0 and the height of the channel, is fixed at 22,000 throughout this paper.

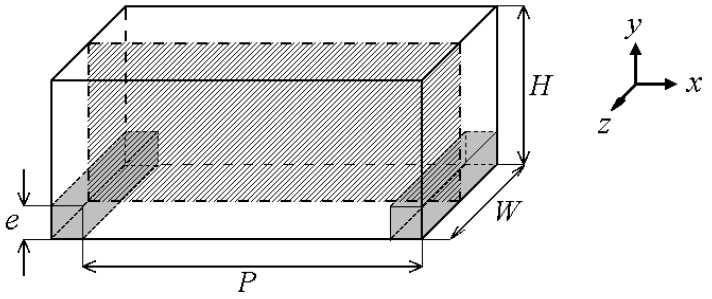

Figure 1. Rib configuration and measurement plane

A commercially available PIV system developed by Dantec Dynamics is used in the present investigation. A Quantel Q-switched Nd:YAG laser provides the pulsed illumination with a wavelength of 532 nm. The duration of each pulse is 10 ns and the maximum output energy is 120 mJ. The size of interrogation window is 32 × 32 pixels with 50% overlapping. The spatial domain contains 79 × 34 vectors, and the spacing between vectors is 0.67 mm. An ensemble of 1000 instantaneous velocity samples is generated with acquisition rate 4 Hz. Throughout this paper, reference quantities for length and velocity are rib height e and U_0, respectively. For the sake of convenience, all the times are normalized by 0.25s, which is the reciprocal of the acquisition rate in PIV.

OVERVIEW OF POD

The POD is a non-prejudiced technique for studying the structures in turbulent flows. The resulting structures are optimal in the sense that they represent the most common events occurring in the fluctuating fields. Consider, for example, an ensemble of fluctuating velocity fields $u'_i(x_j,t)$ which is time-dependent, non-homogeneous, and square-integrable (with finite kinetic energy) on a finite domain Ω (i, j = 1, 2, 3). We seek functions such that the mean-square energy projection onto them is maximized. By applying the calculus of variations, this leads to the following integral eigenfunction problem:

$$\int_{\Omega} R_{ij}(x_l,x'_k)\phi_j(x'_k)dx'_k = \lambda\phi_i(x_l) \tag{1}$$

where the kernel $R_{ij} = < u'_i(x_l,t)u'_j(x'_k,t) >$ is the two-point velocity correlation tensor. Each eigenfunction $\phi_i^{(n)}(x_l)$ is associated with a real positive eigenvalue $\lambda^{(n)}$, and the eigenfunctions form a complete set. That is, the random velocity field $u'_i(x_j,t)$ can be expressed as the linear superposition of the eigenfunctions

$$u'_i(x_j,t) = \sum_{n=1}^{M} a_n(t)\phi_i^{(n)}(x_j) \tag{2}$$

in which $a_n(t)$ are time-dependent coefficients. By projecting the $u'_i(x_j,t)$ on each of the eigenfunctions, we have

$$a_n(t) = \int_\Omega u'_i(x_j,t)\phi_i^{(n)}(x_j)dx_j \tag{3}$$

In addition, it is shown that temporal coefficients are uncorrelated and that the eigenfunctions are mutually orthonormal to each other. That is,

$$< a_n(t)a_m(t) >= \lambda^{(n)}\delta_{mn} \tag{4}$$

$$\int_\Omega \phi_i^{(n)}(x_j)\phi_i^{(m)}(x_j)dx_j = \delta_{nm} \tag{5}$$

It is useful to define the fluctuating kinetic energy E(t)

$$E(t) = \int_\Omega u'_i(x_j,t)\cdot u'_i(x_j,t)dx_j = \sum_{n=1}^{M} a_n(t)\cdot a_n(t) \tag{6}$$

To compute the eigenfunctions effectively, the snapshots technique is employed which was introduced by Sirovich [5] . The eigenvalues are arranged in descending order with $\lambda^{(1)}$ as the largest eigenvalue. As a result, $\phi^{(1)}(x,y)$ represents the 'dominant' turbulent structure.

RESULTS

Prior to presenting the various turbulence statistics and POD results, it is helpful to display some global flow features. Figure 2 shows the mean streamlines around the rib. The most striking feature is the formation of a large recirculation bubble downstream of the rib which is bounded between the free separated shear layer and the wall. A secondary vortex is also perceived in the leeward corner as the backward flow approaches the vertical surface. In addition, another vortex is observed in the windward corner in which the flow is subjected to a strong adverse pressure gradient.

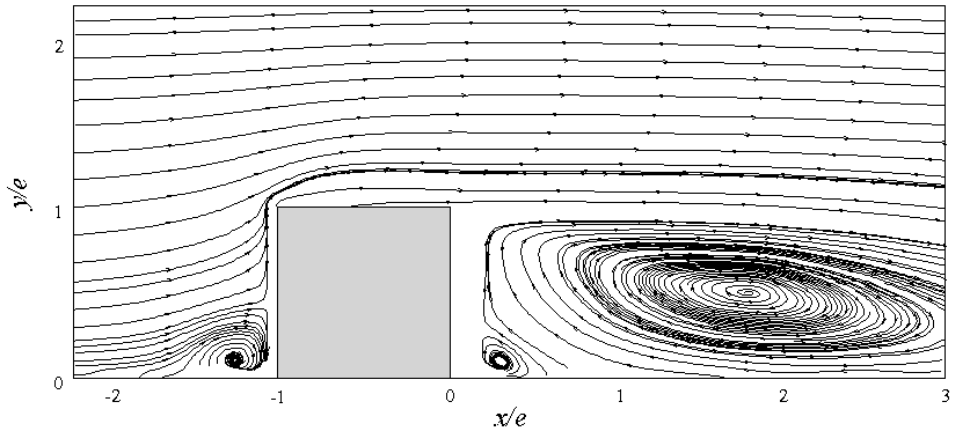

Figure 2. Mean streamlines around the sixth rib

The contours of Reynolds shear stresses are given in Figure 3. In this figure, only the quantities greater than $0.5<-u'v'>_{max}$ are demonstrated in order to highlight the region with large Reynolds shear stresses. It is clear that the maximum Reynolds shear stresses reside in the region upstream of the leading edge of the rib. In the separated shear layer, the general trend is that the Reynolds shear stresses rise up gradually with increasing distance from the rib.

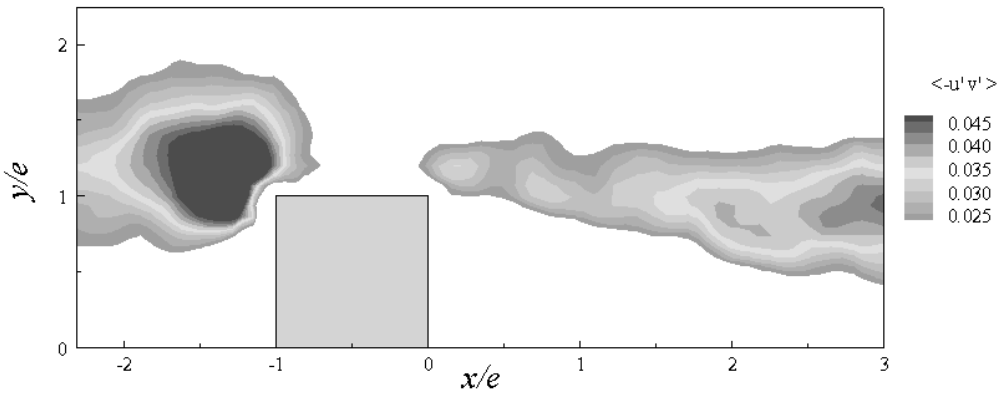

Figure 3. Contour of Reynolds shear stress, the quantities are normalized by U_0^2

Since the extraction of POD modes is based on the autocorrelation tensor R_{ij}, it is of interest to examine the two-point correlation coefficients of original data to give an indication of the spatial structure of the flow. The correlation coefficient is defined as

$$R_{u_i u_j} = \frac{< u'_i(x_l) u'_j(x_k) >}{\sqrt{< u'^2_i(x_l) >< u'^2_j(x_k) >}} \tag{7}$$

where $u'_i(x_l)$ and $u'_j(x_k)$ are two instantaneous velocity fluctuations. In this paper, we only consider the correlation coefficient of the u' and v', denoted R_{uu} and R_{vv}, respectively. Figures 4a and 4b show the contours of R_{uu} and R_{vv} in the x-y plane, respectively. The reference location is point A (x/e = 1.1, y/e =1.1) which resides in the separated shear layer. In order to highlight the strongly-correlated events, the quantities below the value 0.3 are discarded. In Figure 4a, the elongated contours of R_{uu} are nearly aligned in the x-direction. For highly correlated regions (R_{uu} > 0.6), the contours are almost symmetrical. Further away from the reference point, the contours are obviously asymmetrical. The downstream extent of R_{uu} is much larger than the upstream extent which is shortened by the presence of rib. In Figure 4b, the contours of R_{vv} are approximately aligned in the y-direction. For the contour R_{vv} = 0.3, the normal extent of correlation is about twice as large as the streamwise extent. Comparing Figure 4a to Figure 4b, it is found that the spatial extent of R_{uu} is considerably greater than that of R_{vv}. This may be attributed to the generation of roller vortices (a series of vortices) in the separated shear layer which gives rise to a fairly long length scale for R_{uu}.

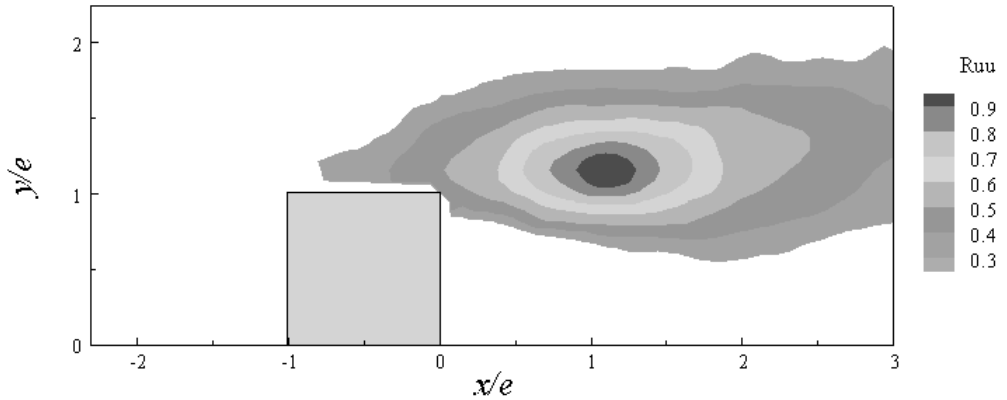

(a)

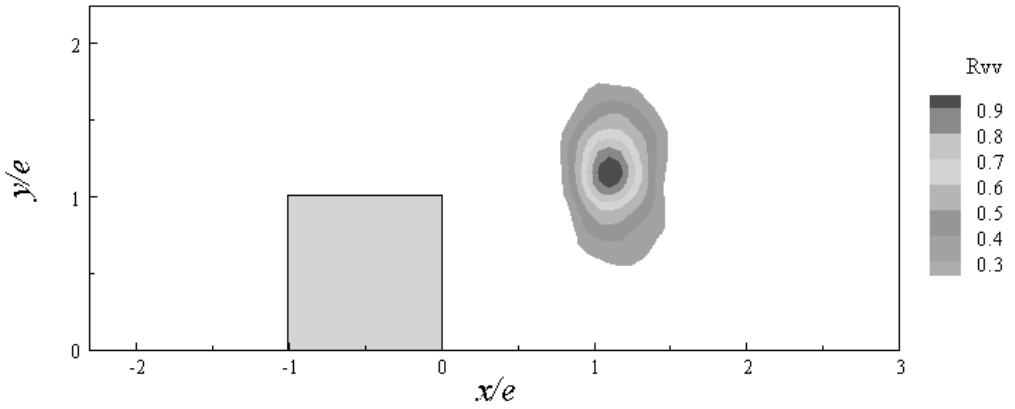

(b)

Figure 4. Contours of two-point correlation coefficients. (a) R_{uu} , (b) R_{vv}

POD decomposes the flow field into modes having various scales, and it allows us to evaluate the distribution of energy as a function of scale. Figure 5 shows the energy content, i.e. the summation of eigenvalues, versus the number of POD modes. It is shown that the first 100 modes contain 90% of the turbulent kinetic energy (TKE) in the flow domain. This cannot be considered as an effective convergence when comparing to decomposition of other flows. The slower convergence, generally speaking, is attributed to a large variety of scales present throughout the flow. As energy cascades across a fairly large range of scales, a wide range of energy distribution over POD modes is expected. Specifically, two causes lead to the increase in the range of scales. One is the additional length scales imposed onto the turbulence owing to the presence of rib, for example the rib height or the reattachment length; the other is the relatively high Reynolds number used in the present study. In turbulent flows, the higher Reynolds number always characterizes the broader range of scales.

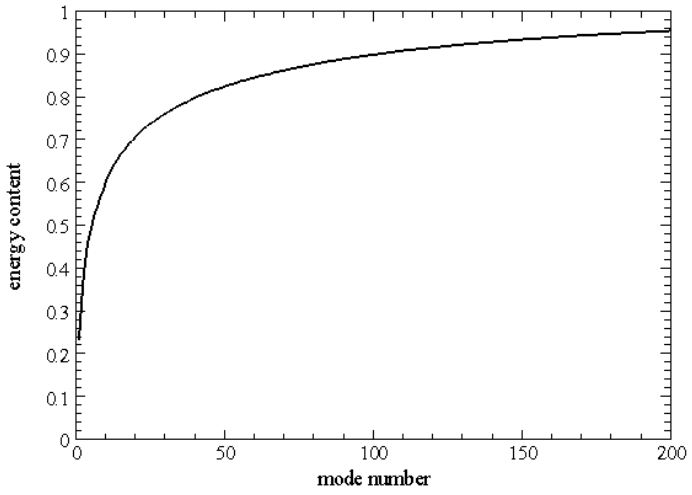

Figure 5 Energy content, sum of the eigenvalues versus the number of modes

In what follows, attention is paid to the fluctuating kinetic energy of the flow E(t), which can be calculated directly from the time-dependent coefficients a_n(t) in Eq. (6). Figure 6 plots the temporal evolution of E(t) based on 100 modes. Most noticeable are two sharp peaks at $t^+ = 33$ and $t^+ = 195$, in addition to a number of smaller peaks. The sharp rise of turbulent kinetic energy, essentially, is

attributed to the characteristic events occurring in flow fields. To gain further insights into the turbulent structures, a reconstructed instantaneous velocity field corresponding to the sharp peak is examined. Figures 7a and 7b demonstrate the reconstructed instantaneous velocity fields at $t^+ = 33$ and $t^+ = 195$, respectively. It should be noted that the velocities are obtained by adding the mean flow field $< U(x,y) >$ to the reconstructed fluctuating velocity field, i.e. $u(x,y,t) = < U(x,y) > + \sum_{n=1}^{100} a_n(t)\phi^{(n)}(x,y)$. In Figures 7a and 7b, the pronounced flow feature is the strong upward ejection from the leading edge of the rib. The magnitude of normal velocity is so large that it is comparable to the mean streamwise velocity <*U*> in the centre of the channel. When the rapid upward motion encounters the incident main stream, a sharp inclined shear layer is observed. The fluids, once ejected from the leading edge, move towards the central region along a curved path. In addition to $t^+ = 33$ and 195, we also analyze the instantaneous flow fields at $t^+ = 19$, 177, 599, 674, 698, 771, 836, and 964, which correspond to the smaller peaks in *E*(t) (where *E*(t) > 3). Except for the instant $t^+ = 599$, the upward ejection from the leading edge of the rib is a common flow feature.

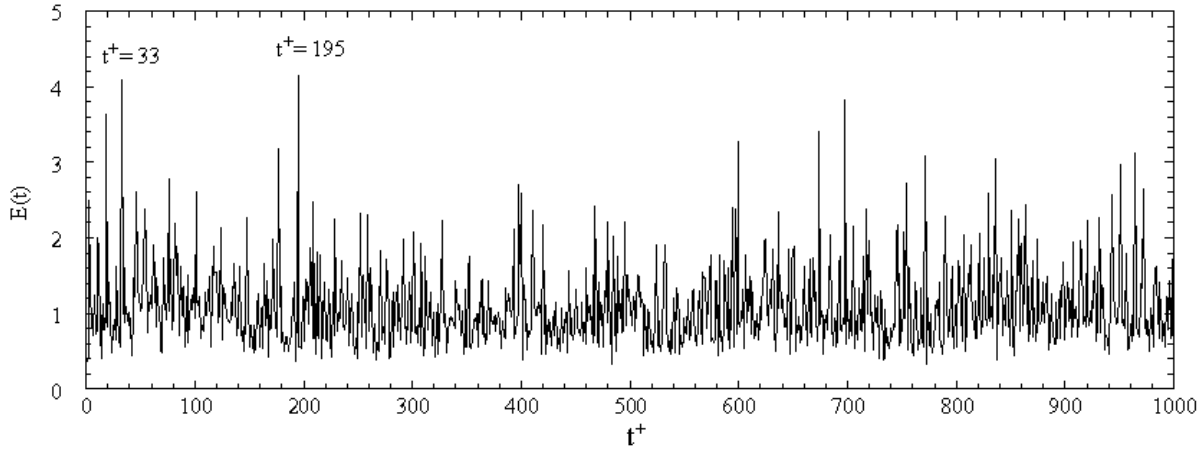

Figure 6. Temporal evolution of the fluctuating turbulent kinetic energy *E*(t)

Apart from the strong upward ejections, Figures 7a and 7b illustrate the vortical structures as well. In Figure 7a, a big recirculation bubble is visible downstream of the rib; in Figure 7b, three vortices are recognized in the separated shear layer. In order to view the vortical structures in great detail, Figure 8 presents the scaled-up velocity field corresponding to Figure 7b. In this figure, three distinct vortices are observed at *x/e* = 0.6, 1.6, and 2.6, respectively. These provide strong evidence that the roller vortices are generated by the Kelvin-Helmholtz instability. The vortex at *x/e* = 0.6, to the first order, is circular. However, the obvious asymmetry around its core suggests that its principal axis is inclined to the *x*-*y* plane. The vortex at *x/e* = 1.6 shows an apparent spiral pattern. The vortex at *x/e* = 2.6 begins to lose its coherence which may be attributed to the secondary instabilities applied on the primary Kelvin-Helmholtz rollers. In contrast to the roller vortices in the separated shear layer, the vortex in the wall region (*x/e* = 2.2, *y/e* = 0.2) seems to characterize the boundary layer development as the backward flow approaches the upstream rib.

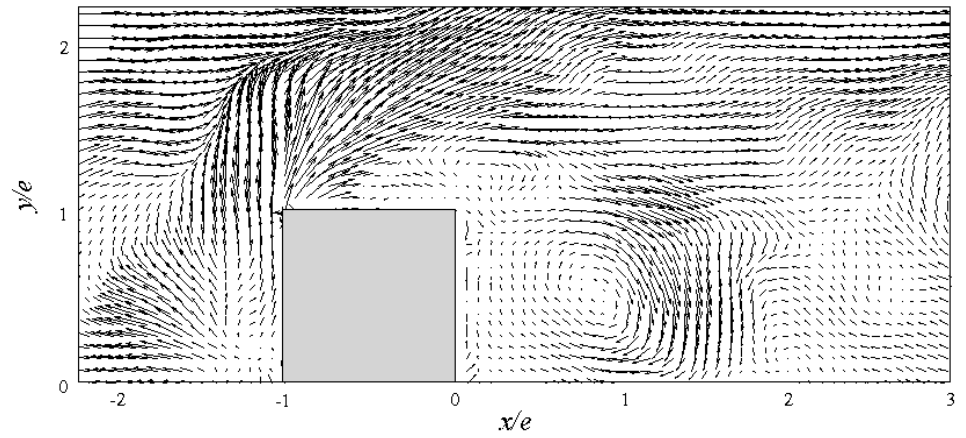

(a)

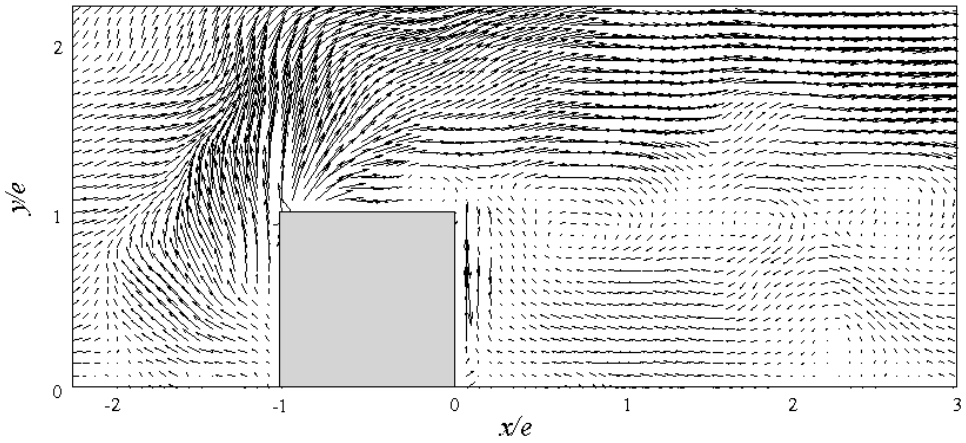

(b)

Figure 7. Reconstructed instantaneous velocity fields. (a) $t^+ = 33$; (b) $t^+ = 195$

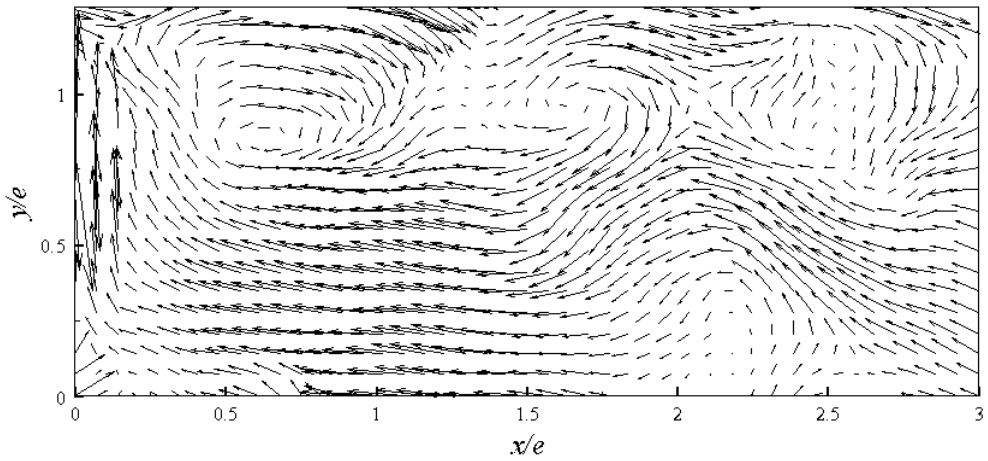

Figure 8. Scaled-up velocity field corresponding to Figure 7b

CONCLUSIONS

By applying POD, the underlying flow features are extracted, and the second-order turbulence statistics are reconstructed. In this study, the most noticeable flow features are the strong, highly-intermittent upward ejections from the leading edge of the rib. Essentially, these underlying motions result in the sharp peaks in the fluctuating turbulent kinetic energy and make great contributions to the Reynolds shear stress. It is supposed that the upward ejections are triggered by the large-scale motions which are swept downward from the outer region as the separated shear layer curves and reattaches on the wall.

REFERENCES

1. Loéve, M., 1955. *Probability theory*. Van Nostrand.
2. Lumley, J. L., 1967. The structure of inhomogeneous turbulent flow. In atmospheric turbulence and radio wave propagation (ed. A. M. Yaglom and V. I. Tatarski), Nauka, Moscow, 166-178.
3. Juttijudata, V., Lumley, J. L., and Rempfer, D., 2005. Proper orthogonal decomposition in Squire's coordinate system for dynamical models of channel turbulence. J. Fluid Mech. 534, 195-225.
4. Moin. P., and Moser, R. D., 1989. Characteristic-eddy decomposition of turbulence in a channel. J. Fluid Mech. 200, 471-509.
5. Sirovich, L., 1987. Turbulence and dynamics of coherent structures. Quart. Appl. Math. 5, 561-590.

EFFECTS OF WALL PERMEABILITY ON TURBULENCE

K. Suga*, Y. Matsumura, Y. Ashitaka, S. Tominaga, M. Kaneda
Osaka Prefecture University, Sakai, Japan

ABSTRACT. PIV measurements are carried out for turbulent flows in a channel with a porous bottom wall. It is found that the laminar to turbulent transition occurs even at the bulk Reynolds number of Re_b=1300 and the flows become more turbulent in the case of high permeability. To confirm the effects of the wall roughness and the wall permeability, detailed discussions are made assuming the effective wall roughness for the porous media. The results clearly indicate that the turbulence is induced by not only the wall roughness but the wall permeability. The measurements have also revealed that as Re_b and /or the wall permeability increase, the wall normal fluctuating velocity is amplified drastically near the porous wall due to the effects of the wall permeability. This leads to the increase of the turbulent shear stress resulting in the higher friction factor of turbulent porous boundary layer flows.

Keywords: *PIV measurement, porous wall, permeability, turbulent channel*

INTRODUCTION

Highly permeable materials are used in various engineering devices such as catalytic converters, fuel cells, etc. due to the advantages of heat and mass transfer and chemical reaction by their large contact area. It is readily understandable that to provide the gas/fuel inside the porous media for chemical reaction, mass transfer enhancement over the porous wall is crucially important. Flows and mass transfer around porous media are thus of interest in industrial designing processes. However, not so much knowledge is available about the flow physics near highly permeable walls particularly in turbulent flow regimes though many research studies were historically performed.

Beavers and Joseph [1] firstly reported that the friction over porous walls of laminar flow regimes reduced due to the porosity. However, in turbulent flow regimes, the friction factors over porous walls were found to be higher than those over impermeable rough walls (e.g. Zagni and Smith [2], Zippe and Graf [3]). Kong and Schetz [4] assumed that the increase of the skin friction was due to the combined effects of roughness and porosity. Recently, the numerical study by Breugem et al. [5] revealed the turbulence structure over permeable walls and that the turbulent transfer was weakly blocked at the porous wall leading to weak streaky structures. In their simulation, they applied a volume averaging for the porous layer with the assumption that the permeability was a function of the porosity and hence it was unclear whether such phenomena were due to the porosity or due to the permeability of the wall.

Therefore, those studies in the literature did not try to discuss separately on the effects of the wall permeability from those of the porosity. Although the modern experimental techniques are far advanced, studies on highly permeable turbulent boundary layer have not been done yet and the detailed flow physics to explain such specific phenomena is still undeveloped. Therefore, in the

* Corresponding author: Prof. K. Suga
Phone: + (81)-72-254-9224, Fax: + (81)-72-254-9904
E-mail address: suga@me.osakafu-u.ac.jp

present study, to discuss and understand the turbulence mechanism over porous permeable materials, two velocity components of the turbulent fields over porous walls are measured by the modern PIV.

EXPERIMENTAL METHODS AND PROCEDURES

Figure 1(a) illustrates the present experimental setup. Tap water is pumped up from the tank, and the water flow is rectified by the honeycomb-bundled nozzle. Then the flow is introduced into the channel whose length is 3.0 m to achieve the full flow development. The channel consists of a solid smooth acrylic top wall while the bottom wall is made of a porous medium (foamed ceramics whose photo is included in the figure). The thickness of the porous wall is 0.03 m which is the same as the channel height H for the clear fluid region whose width is 0.3 m. Thus the aspect ratio of the cross section is 10. The channel continues to the 1m-length test section where the flow fields are measured by PIV (Dantec, Nd:YAG laser system). This device consists of a double-pulse Nd-YAG laser with the frequency of 532nm, a CCD camera of 30 fps, a camera lens and a computer for the data acquisition. The laser light is expanded to a sheet light with approximately 1mm-thickness and irradiates the symmetry plane of the channel where the instantaneous images are recorded by the CCD camera. The recorded area is $30\times30\text{mm}^2$ with 2048×2048 pixels.

For the PIV measurement, acrylic colloid particles, whose diameters and specific gravity are respectively 0.1-1 μm and 1.19, are used as the tracer particles. The number of the particle is adjusted over 5 in one control volume whose size is set to 64×16 pixels. The lens magnification is adjusted so that one particle is captured by 3.1 pixels and more. The image sampling rate is varied depending on the maximum particle moving distance in Δt. In the present experiments, the maximum moving distance is limited to 25 % length of the control volume.

After the recordings, recorded data are calculated by fast Fourier transform [6] with 50 % overlapping for the data precision in the normal velocity component. Therefore, the number of the control volume in the recorded area is 63×255. The velocity vectors are calculated from non-overlapped sequential 159 image pairs due to the limitation of the device specifications. For the sufficient precision, this procedure is repeated at least 20 times and integrated (3180 image pairs in total), and then the final vector data are obtained by averaging in the streamwise direction. Thus, totally 200340 velocity signals are used for the statistics at the single point in the wall normal direction.

The experimental parameters are the type of the porous media and the bulk Reynolds number Re_b. The representative characteristics of porous media are the porosity φ, the permeability K and the mean pore diameter D_p. The porosity is the ratio of the void volume to the total volume. The void volume is obtained by measuring the residual volume soaked into water. The permeability is obtained from the Darcy-Forchheimer equation [7] with the measured pressure difference, the Darcy velocity and fluid viscosity using the rig shown in Figure 1(b). The mean pore diameter D_p is measured from photographic images. The resultant three characteristics of the presently used porous media are listed in Table 1. In this study, three types of the foamed ceramics are employed as the bottom wall. Those media have quite same porosity, however, the permeability varies. Indeed, as in Table 1, the permeability of case #06 is 4.5 times as large as that of case #20.

Another experimental parameter Re_b is defined as $\text{Re}_b = U_b H/\nu$ where U_b is the bulk mean velocity and ν is the kinematic viscosity of the fluid. By averaging the integrated velocity profile across the channel, U_b is calculated. (Even if the flow rates inside the porous walls are included to calculate U_b , only a few percent increase of U_b can be estimated. In fact, the flow rate inside the porous wall estimated by using the Brinkman equation is 2% of the clear channel region's at Re_b=1300 of the highest permeability case #06.) In the present experiments, Re_b is set approximately between 1000 and 10000 covering both the laminar and turbulent flow regimes.

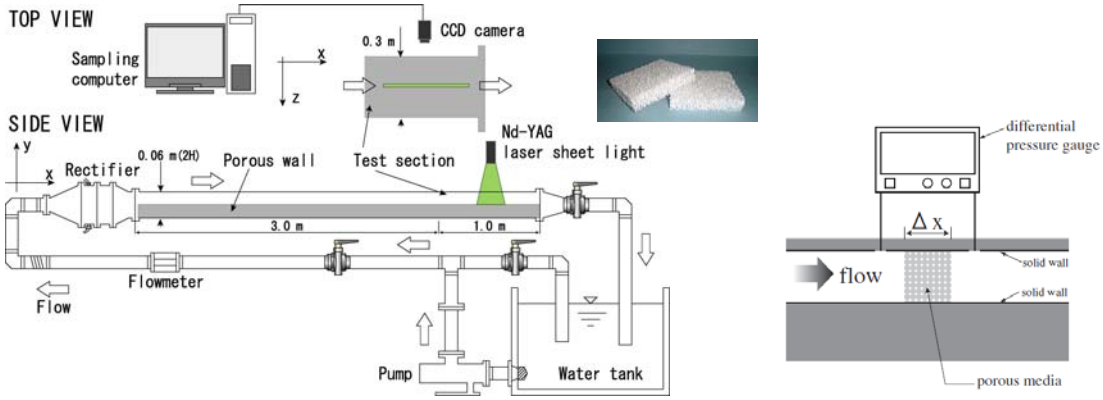

(a) Experimental setup (b) Permeability measurements

Figure 1. Experimental apparatus

Table 1 Characteristics of the porous media

porous media	φ	K [$\times 10^{-7}$ m^2]	D_p [mm]
case #06	0.80	0.9	3.8
case #13	0.81	0.3	2.8
case #20	0.82	0.2	1.7

RESULTS AND DISCUSSIONS

Mean velocity profiles

Figure 2 shows the mean velocity distribution presently measured. Velocity distribution across the channel is normalized by the bulk velocity U_b. The surface of the foamed porous ceramics (y/H = 0) is determined as the outermost perimeter. The other side (y/H = 1.0) represents the solid acrylic wall. Near the top wall (y/H ~ 1.0), the velocity converges to 0 due to the non-slip boundary. On the contrary, the velocity near the porous wall (y/H ~ 0.0) increases as $\mathrm{Re_b}$ increases. This indicates the flow has an effective "slip velocity" at the surface of porous media due to the streamwise space averaging. (This slip velocity is further discussed later.) As the velocity slip becomes remarkable, the velocity profile changes into that of turbulent flow. The onset of the turbulence is shifted to the smaller $\mathrm{Re_b}$ than the ordinary critical Reynolds number. This effect is more apparent for case #06 than in case #20. Indeed, it is clearly indicated in Figure 2 that in case #06 the flow is turbulent from $\mathrm{Re_b}$ = 1300 while in case #20 the flow is still laminar even at $\mathrm{Re_b}$ = 2100. This can then confirm that porous media enhance the onset of the turbulence. It can be guessed that this enhancement is due to the wall permeability since all the tested porous media have nearly the same porosity.

To characterize the turbulent flow induced by the porous media, log velocity profiles are obtained for the mean velocity near the porous wall, which is shown in Figure 3. (Due to the page limit, the profiles of case #13 are omitted hereafter.) Superscripts p represents 'porous' and the U^{p+} and y^{p+} are normalized using the friction velocity u_τ^{p} obtained by extrapolating the measured Reynolds shear stress distribution (shown later). As $\mathrm{Re_b}$ increases, U^{p+} decreases and the turbulent regime sifts away from the wall, which is remarkable for the high permeable wall (case #06). This means the increase in the friction velocity. The turbulent region can be fitted by the least-square law to the equation:

$$U^{p+} = \frac{1}{\kappa}\ln y^{p+} + B \tag{1}$$

The corresponding fitted line is added in the figures and coefficients κ and B are listed in Table 2. Obviously, the Kármán constant κ varies ($0.3 < \kappa \leq 0.4$) according to $\mathrm{Re_b}$ and the porous media. This

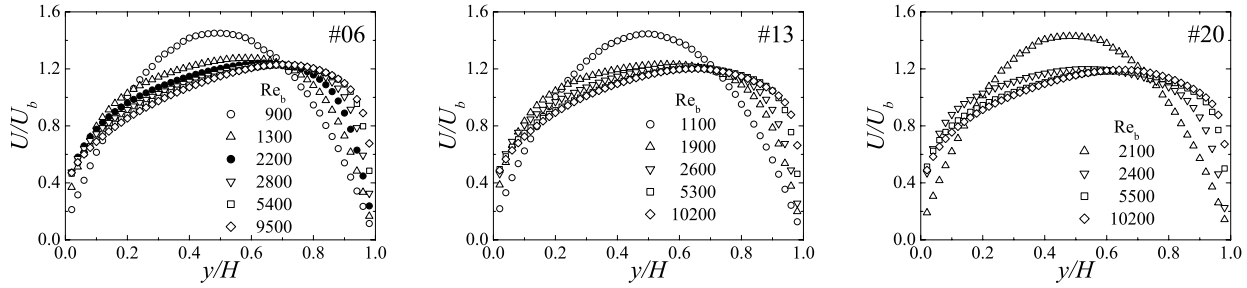

(a) case #06 (b) case #13 (c) case#20

Figure 2. Mean velocity profiles

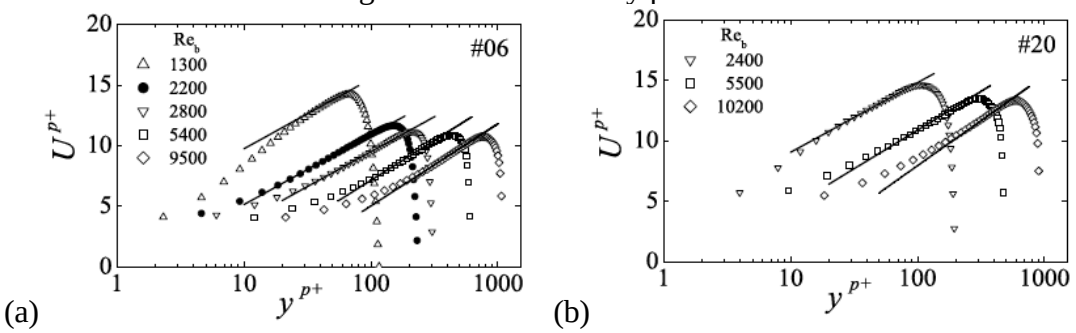

(a) (b)

Figure 3. Mean velocity in semi-log scale

Table 2 Coefficients for the fitted line in Figure 4 by equation (1)

porous media	Re_b	κ	B
case #06	1300	0.40	4.0
	2200	0.40	-0.6
	2800	0.40	-2.0
	5400	0.35	-6.0
	9500	0.34	-8.5
case #20	2400	0.40	3.3
	5500	0.36	-1.9
	10200	0.31	-6.9

suggests that as Re_b increases the turbulence structure near a porous wall differs from those along rough walls since the Kármán constant does not change so much in rough wall turbulence [8].

Transition in the slip velocity

In Figure 2, the velocity near the porous wall has a jump depending on Re_b. The dependence of the slip velocity U_w on the Re_b is further discussed. Figure 4(a) shows the transitional behaviour of the slip velocity estimated by the extrapolation of the velocity distribution to the wall surface. In all the cases, there can be found narrow transitional regions where U_w/U_b increases steeply. In fact, in case #20, the transition begins at $Re_b > 2000$, while it does at $Re_b > 1000$ in case #06. In case #13 the tendency shown is in between those of cases #06 and #20. Consequently, apparent effects of the porous characteristics can be found on the turbulence transition. After the transition to the turbulence, the slip velocity becomes almost constant and the value of U_w/U_b tends to be larger in higher permeability cases. These characteristic profiles of the slip velocities have a quite unified profile against the permeability Reynolds number Re_K ($=u_\tau^p K^{1/2}/\nu$) as shown in Figure 4(b). This means Re_K can be a good measure for permeable turbulent boundary layers.

Roughness effects

Through the above discussions, it is confirmed that turbulence is induced by the porous surface. However, it is still unclear that the role of the wall permeability for the turbulence enhancement since wall roughness also induces turbulence. To clarify the factor to induce the turbulence by the wall permeability, the effects of surface roughness are discussed.

Although the turbulence is induced by both the wall roughness and permeability, the discussions here assume that all the turbulence effects come from the wall roughness only. The velocity profiles in Figure 3 are re-plotted in Figure 5 with the consideration of the effective roughness height Δy. Since the porous wall does not have a definite bottom, the present study estimates Δy by applying the extended Brinkman equation [5] to the flow profile inside the porous media as schematically shown in Figure 5. Then the velocity profile can be fitted by using Cebeci-Bradshaw's correlation [9]. This correlation is based on the assumption that all the turbulent enhancements come from the wall roughness and its profile is as follows;

$$U^{p+} = \frac{1}{\kappa}\ln\left(y+\Delta y\right)^{p+} + 5.2 - \left(5.2 - 8.5 + \frac{1}{\kappa}\ln h^{p+}\right)\sin\left(0.4258[\ln h^{p+} - 0.811]\right), \quad \text{if} \quad 2.25 < h^{p+} < 90$$

$$U^{p+} = \frac{1}{\kappa}\ln\frac{\left(y+\Delta y\right)^{p+}}{h^{p+}} + 8.5, \quad \text{if} \quad h^{p+} \geq 90 \qquad (2)$$

where h^{p+} is the dimensionless equivalent sand grain roughness height. The fitted line is added in Figure 5 and the obtained κ, h^{p+} and corresponding dimensional equivalent sand grain roughness height h are summarized in Table 3. The gradient of the slopes is not constant in $\mathrm{Re_b}$ and thus the corresponding κ varies. The height h increases as $\mathrm{Re_b}$ and the value of h in case #06 is larger than that in case #20. This corresponds to that the roughness effects are remarkable in case #06 and depend on $\mathrm{Re_b}$.

However, this fact does not agree with the original concept of the correlation since the dimensional equivalent sand grain roughness height does not normally change by $\mathrm{Re_b}$ in the rough wall turbulence. Therefore, the tendency in the present experimental data implies that the other effects also contribute to the turbulence. The permeability is thus the factor to be considered and its contribution to the turbulence is discussed in the next section in terms of the turbulent intensities.

Figure 6 shows the profiles of κ, h^{p+} and Δy^{p+} listed in Table 3 against the permeability Reynolds number Re_K. It clearly shows that those profiles can be unified with single correlation lines:

$$\kappa = 0.23\,\mathrm{Re}_K^{-0.23}, \quad h^{p+} = 25.6\,\mathrm{Re}_K^{1.6}, \quad \Delta y^{p+} = 36.8\,\mathrm{Re}_K^{1.2} \qquad (3)$$

With those correlations, the experimental correlation of the mean velocity over permeable walls can be derived.

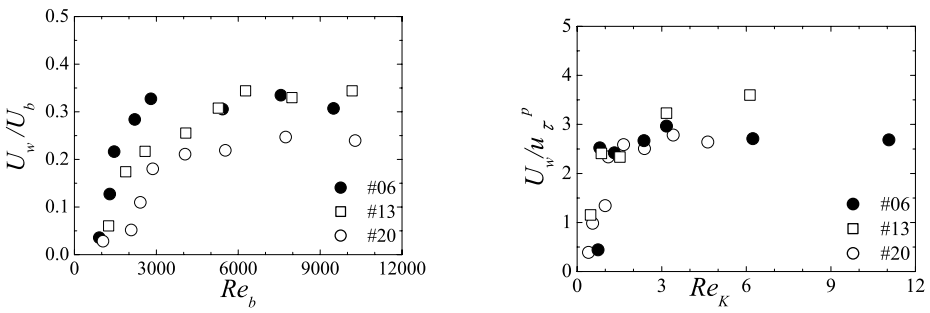

(a) (b)

Figure 4. Slip velocity at the porous wall - fluid interface

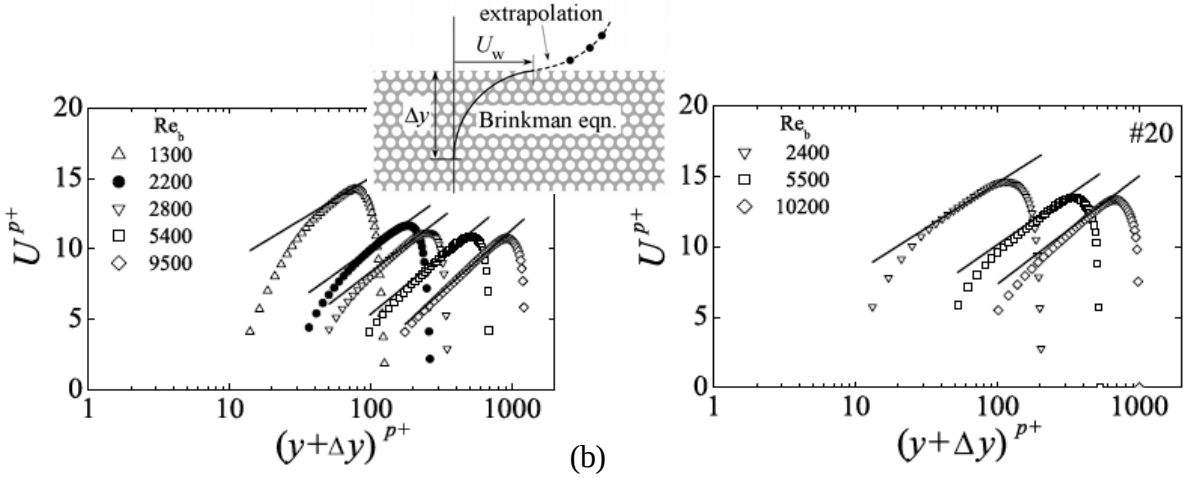

(a) (b)

Figure 5. Correlation with Cebeci-Bradshaw's profiles; (a) case #06, (b) case #20

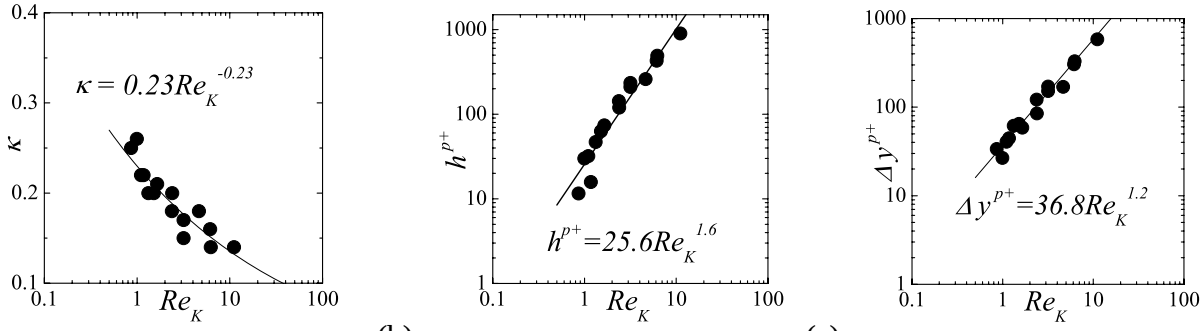

(a) (b) (c)

Figure 6. Distribution profiles of parameters in equation (2)

Table 3
Effective roughness height and equivalent sand grain roughness height for the equation (2)

porous media	Re_b	Δy [mm]	κ	h^{p+}	h [mm]
case #06	1300	11	0.22	15.8	4.0
	2200	15	0.18	143	18
	2800	16	0.15	235	22
	5400	16	0.14	490	23
	9500	16	0.14	900	24
case #20	2400	3.8	0.26	30	4.2
	5500	5.0	0.20	120	6.9
	10200	5.1	0.18	260	7.9

Turbulent intensities and Reynolds stress

The turbulent intensities are calculated to clarify the effect of the wall permeability. The distribution profiles of the turbulent root mean square velocity components u'^{t+}, v'^{t+} are plotted in Figure 7. (The values with the superscripts "$t+$" mean the normalized value using the top wall friction velocity u_τ^t obtained by extrapolating the measured Reynolds shear stress.) In case #06, u'^{t+} near the porous wall ($y/H \sim 0$) is not affected by Re_b, except $1300 < Re_b < 2200$ where transition to turbulence occurs. On the contrary, v'^{t+} keeps increasing as the increase of Re_b even after the transition to turbulence. This apparently represents that the normal velocity fluctuation is enhanced by Re_b, which suggests the promotion of the penetrating flow into the porous media at high Re_b. In case #20 the flows have the same tendency. Therefore, the mechanism of the turbulent enhancement by the

porous media can be explained by the increase in the wall normal velocity fluctuation related to the bulk flow velocity.

Comparing at almost the same Re_b, the value of v'^{+} in case #06 is larger than that in case #20. As shown in Table 1, case #06 has larger permeability than in case #20 despite the same porosity. These facts imply that the penetration flow is affected by the permeability in addition to Re_b. In other words, the blocking effects by the porous wall are reduced by the wall permeability, which become remarkable at higher Re_b.

The Reynolds shear stress $-\overline{u'v'}$ is plotted in Figure 8. Due to the large contribution of v'^{+} shown in Figure 7, $-\overline{u'v'}$ near the porous wall monotonically increases as the permeability and Re_b. In addition, the value of $-\overline{u'v'}$ in case #06 is larger than that in case #20 compared at the corresponding Re_b. This represents that the turbulent shear stress depends on the permeability and Re_b. That is, the higher wall permeability can obtain higher turbulence effects at lower Re_b.

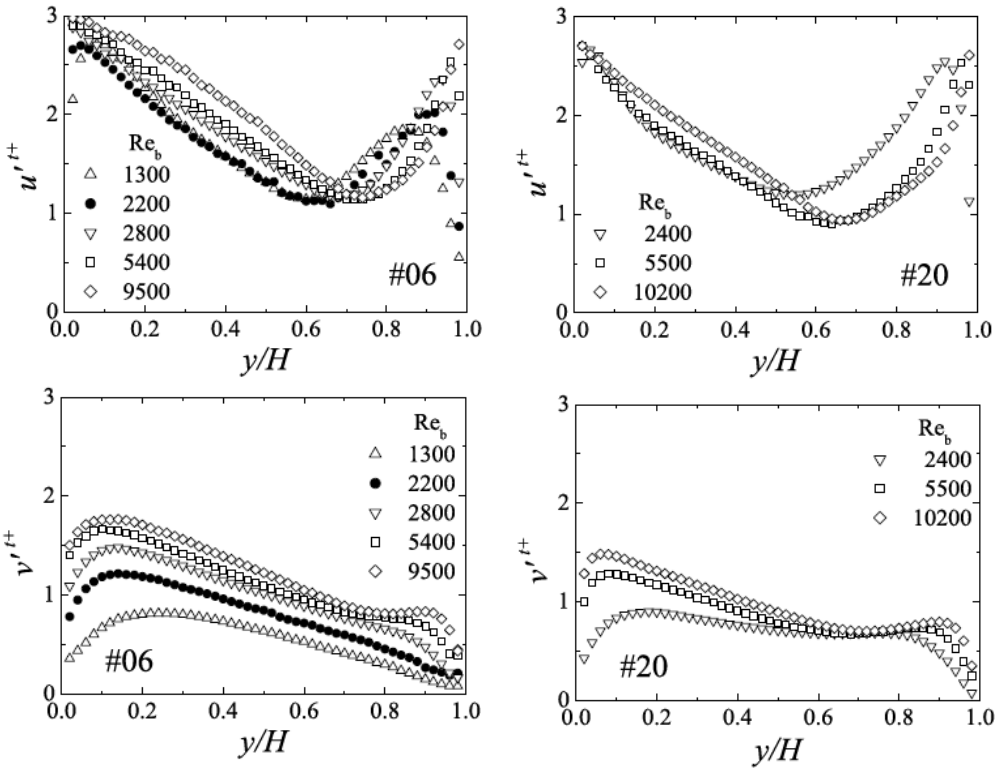

(a) case #06 (b) case #20

Figure 7. Turbulent root mean square velocity

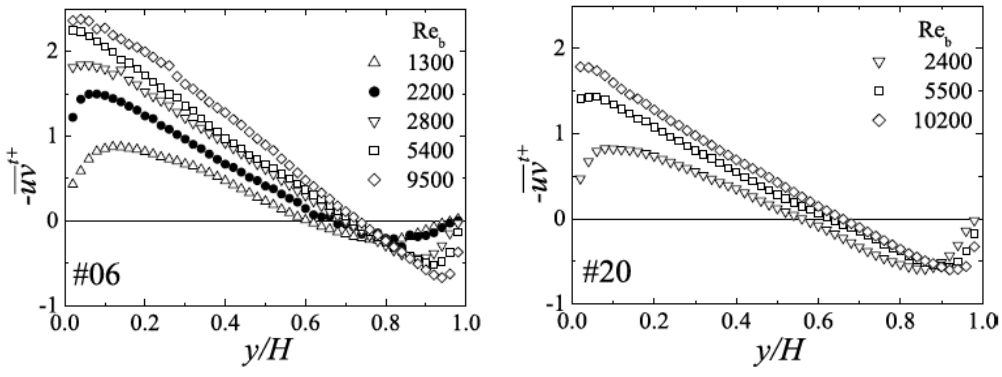

(a) case #06 (b) case #20

Figure 8. Reynolds shear stress

CONCLUSIONS

The turbulent flows over permeable walls are studied by using PIV measurements at different wall permeability and Reynolds numbers. The velocity slip occurred on the porous wall and simultaneously the turbulence is induced at the low Reynolds number. The velocity slip transits in a narrow range of the bulk Reynolds number. The velocity distribution near the porous wall becomes different to that for a solid wall. The estimated effective sand grain roughness height is found to be affected by the Reynolds number, which suggests that the turbulent flow is induced not only by the porous roughness but by the wall permeability. From those data, an experimental correlation of the logarithmic layer of the mean velocity is deduced. The wall normal velocity fluctuation component reveals that the flow penetration into the wall is a key factor to induce the turbulence on the permeable wall and its contribution is affected by the permeability. The increase in the wall normal velocity fluctuation also enhances the turbulent shear stress. Consequently, on the permeable walls, both the wall roughness and the wall permeability are important to induce turbulence. The higher permeable wall flow at lower Reynolds numbers can posses the same turbulence effects as those in the lower permeable wall flow at higher velocity, which can be applied to the engineering devices.

ACKNOWLEDGEMENTS

This study was financially supported initially by the Iwatani Naoji Foundation's Research Grant and then by the Strategic Development of PEFC Technologies for Practical Application: Development of Technology for Next-generation Fuel Cells of New Energy and Industrial Technology Development Organization (NEDO) Japan.

REFERENCES

1. Beavers, G.S., Joseph, D.D., Boundary conditions at a naturally permeable wall, *J. Fluid Mech.*, Vol. 30, pp. 197-207, 1967.
2. Zagni, A.F.E., Smith, K.V.H., Channel flow over permeable beds of graded spheres, *J. Hydraul. Div.*, Vol.102, pp.207-222, 1976.
3. Zippe H. J. and Graf, W. H., Turbulent Boundary-layer Flow over Permeable and Non-permeable rough surfaces, *J. Hydraul. Res.*, Vol. 21, pp. 51-65, 1983.
4. Kong, F.Y., Schetz, J.A., Turbulent boundary layer over porous surfaces with different surface geometries, AIAA Paper 82-0030, 1982.
5. Breugem, W. P., Boersma, B. J., Uittenbogaard, R. E., The Influence of Wall Permeability on Turbulent Channel Flow, *J. Fluid Mech.*, Vol. 562, pp 35-72, 2006.
6. Willert, C. E. , Gharib, M., Digital Particle Image Velocimetry, *Experiments in Fluids*, Vol. 10, pp. 181-193, 1991.
7. Straatman, A. G., Callego, N. C., Yu, Q., Tompson, B. E., Characterization of Porous Carbon Form as a Material for Compact Recuperators, *Trans. ASME J. Eng. Gas Turbines & Power*, Vol.129, pp.326-330, 2007.
8. Nikuradse, J., Strömungsgesetze in Rauhen Rohren, VDI-Forschungsheft, 361, 1933.
9. Cebeci, T., Bradshaw P., Momentum Transfer in Boundary Layers, Hemisphere Publishing Corporation, New York, 1977.

ASSESSMENT OF ANISOTROPY IN THE NEAR FIELD OF A RECTANGULAR TURBULENT JET

A. Cavo[1], G. Lemonis[2], T. Panidis[1, *]
[1] Laboratory of Applied Thermodynamics, University of Patras, Patras, Greece
[2] Hellenic Aerospace Industry S.A., Schimatari, Greece

ABSTRACT. The anisotropy in the near field of a rectangular turbulent jet with aspect ratio 6 is experimentally assessed. The presented data were obtained using an in-house constructed 12-sensor hot wire probe consisting of three closely separated orthogonal 4-hot wire velocity arrays. Measurements have been conducted in a jet with Reynolds number Re_D = 21000 at distances from the nozzle exit, x/D =1, 3, 6 and 11, where D is the width of the nozzle. The results of the present study indicate that the direct production of turbulent energy by the mean shear leads to a strong anisotropy in the fluctuating fields for $0<x/D<11$. Moreover, it is clear that the large scales have not relaxed to isotropy in spite of the absence of the mean shear at the centreline of the jet.

Keywords: *Rectangular jet, turbulent jet, mixing layers, plane jet, free jet*

INTRODUCTION

A rectangular turbulent jet has many practical applications in aerospace, in mechanical and chemical engineering. There were many experimental investigations in jets issuing from rectangular nozzles which have enhanced our understanding of the underlying physics of these flows mainly from information on the velocity field (Krothapalli et al. 1981, Sfeir 1979, Sforza & Stasi 1979, Grinstein 2001, etc). It has been well documented from many researchers that aspect ratio of the nozzle and initial conditions at the jet exit play an essential role in the distribution of the rectangular jets' properties, especially in the near field (Quinn 1992, Lazanova & Stankov 1998, Deo et al. 2007, etc). The intention of this work is to assess the anisotropy in the near field of a rectangular turbulent jet an issue not extensively covered in current literature, due to inherent difficulties in measuring the relevant characteristic properties. A unique attribute of the present study is that the spatial derivatives in all three directions of the three components of the fluctuating velocity field have been directly measured using a 12-sensor hot wire anemometry probe. The performance of the 12-sensor probe in the near field of a rectangular turbulent jet has been assessed by Cavo et al. (2007) in comparison with corresponding measurements with an X-wire probe and other experimental and numerical studies.

EXPERIMENTAL ARRANGEMENT

The jet exits from a rectangular nozzle with length L=300 mm and width D=50 mm (Figure 1). The aspect ratio is AR=L/D=6. The experiment was conducted at a Reynolds number $Re = U_0 D/\nu = 21000$, where U_0 is the exit velocity from the nozzle and ν is the air's kinematic viscosity at environmental temperature (23°C). The streamwise turbulence intensity distribution at

* Corresponding author: Prof. T. Panidis
Phone: + 30 2610-997242, Fax: + 30 2610-997271
E-mail address: panidis@mech.upatras.gr

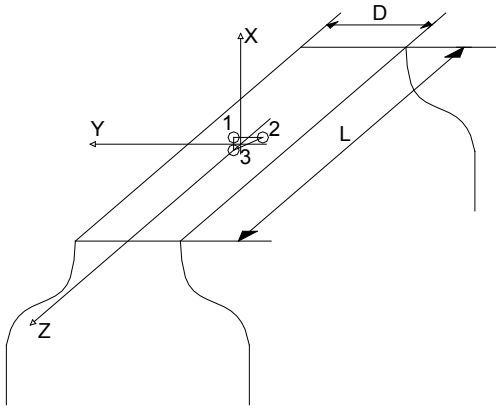

Figure 1 Jet nozzle and coordinate system

the nozzle exit was uniform and had a constant value of about 1%, except in the boundary layers adjacent to the nozzle lips, where the maximum value was about 2%. The initial boundary layers developed on the nozzle lips are characterised as laminar (Cavo et al. 2007).

The 12-sensor probe manufacturing, probe calibration and data reduction techniques rely upon previous work of Lemonis (1995), and have been further improved and refined at the Laboratory of Applied Thermodynamics of the University of Patras. The probe composing of three 4-wire arrays (Figure 2) measures simultaneously the three-dimensional velocity vector components at the centroids of the three arrays on a cross plane of the flow field. Spatial velocity derivatives are estimated using a forward difference scheme of first order accuracy. Streamwise velocity derivatives are estimated using Taylor's frozen turbulence hypothesis. Details regarding the design and operation of the 12-sensor probe as well as the experimental facility, used in the present experiment can be found in Cavo et al. (2007).

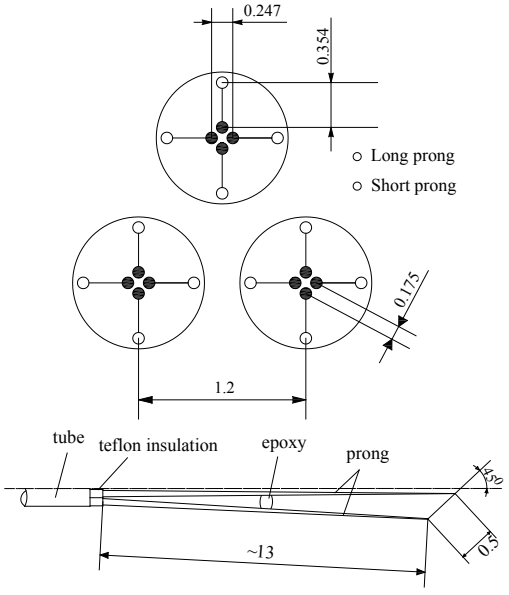

Figure 2. Schematic diagram showing the 12-sensor probe front view and a 45° inclined hot-wire with supporting prongs

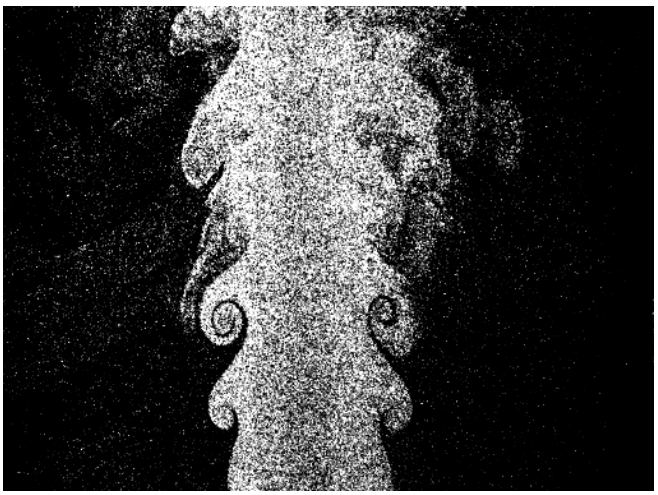

Figure 3. Flow visualization of a rectangular jet in the near field region

EXPERIMENTAL RESULTS

The behaviour of the planar jet due to the merging of the mixing layers is consistent with the eventual breakdown of the structures generated from the rollup and pairing of spanwise vortices ($0 \le x/D \le 4 \div 5$) to strongly three-dimensional turbulence. Figure 3 shows a characteristic flow visualization image of the rectangular jet in the near field region. Rockwell & Niccolls (1972) results, as well as the present visualization, indicate that near the nozzle exit the large-scale structures in the flow field are predominately symmetric for flat exit profiles. When the shear layers interact downstream, these structures reorganize into an asymmetric configuration in the fully developed region of the jet.

Measurements of the present study have been conducted in the jet at distances from the nozzle exit, x/D =1, 3, 6 and 11. Experimental results based on measurements with the 12 wire and the X wire probe are compared with several experimental and computational (DNS) data of other investigations on plane jets (Browne et al. 1983, 1984, Everitt and Robins 1978, Gutmark and Wygnanski 1976, Ramaprian and Chandrasekhara 1985, Stanley et al. 2002), rectangular jet (Quinn 1992) and two stream mixing layer (Bell and Mehta 1990, Spencer and Jones 1971, Wygnanski and Fiedler 1970) of various Reynolds numbers.

Mean velocity-vorticity field

The mean streamwise velocity, U, profiles normalized by the centreline velocity, U_c, at different stations are shown in Figure 4, in comparison with corresponding measurements of the X-wire probe (Cavo et al. 2007) and experimental results of other investigators. The velocity at the exit plane of the nozzle presented an almost top hat profile as evidenced by x/D=1 measurements. Further downstream the profiles assume a bell shaped distribution and are in agreement with corresponding profiles of Quinn (1992) and Browne et al. (1984). The presented results at x/D=6 and 11 indicate that planar jet similarity as far as the mean velocity distributions are concerned may be claimed at least for a limited range, within the two dimensional region of rectangular jets.

In rectangular jets downstream derivatives of mean velocity components are expected to be small compared to cross-stream derivatives, $\partial/\partial x << \partial/\partial y$. Under these conditions, the dominant mean vorticity component $\Omega_z = \partial V/\partial x - \partial U/\partial y$ can be estimated approximately as $-\partial U/\partial y$ and a reasonable estimate of Ω_z may be obtained by differentiating the distribution U(y).

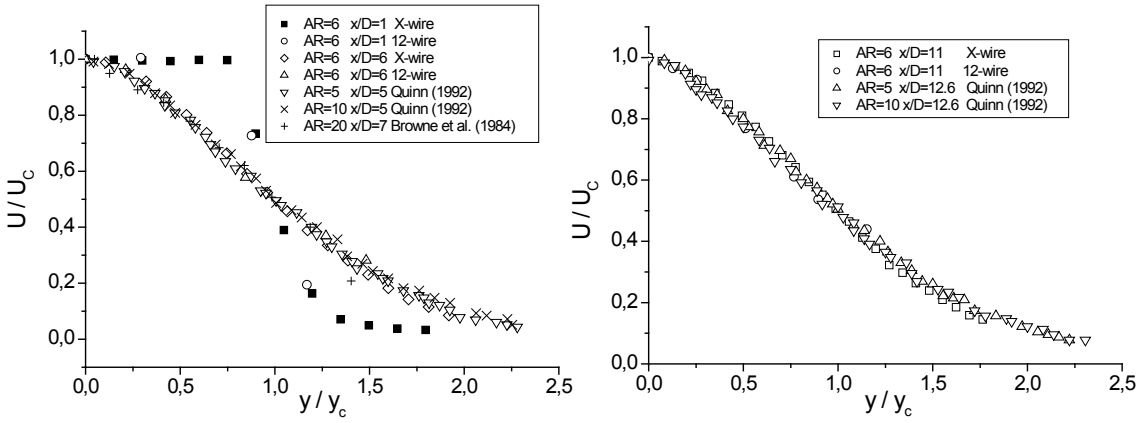

Figure 4. Mean streamwise velocity profiles (x/D=1, 3, 6, 11)

Figure 5 depicts lateral profiles of mean spanwise vorticity, Ω_z, at different locations downstream (Cavo et al. 2007). Two kinds of estimates are presented. Based on the above analysis Ω_z is first estimated calculating the $\partial U/\partial y$ derivative, differentiating U(y) curve measured with the X wire. The second Ω_z estimate is obtained by averaging the time series of local instantaneous spanwise vorticity results of the 12-wire probe. Close to the nozzle exit high values of vorticity are observed in the shear layers developing between the jet and the ambient fluid, whereas doesnsteam measurements indicate the diffusion of vorticity from the shear layers towards the centre and the edges of the jet.

Turbulent velocity-vorticity field

Figure 6 shows measurements of the root mean square (rms) values of the three fluctuating velocity and vorticity components at x/D=1, 3, 6, 11. The profiles have been normalized with U_0 and U_0/D respectively. These results demonstrate the growth of velocity-vorticity fluctuations in the potential core region (x/D=1, 3) within the shear layer due to rollup and pairing of spanwise vortices. The lateral distributions of the velocity-vorticity components are significantly changed downstream by the interaction of the shear layers. This change is associated with the growth of fluctuations around

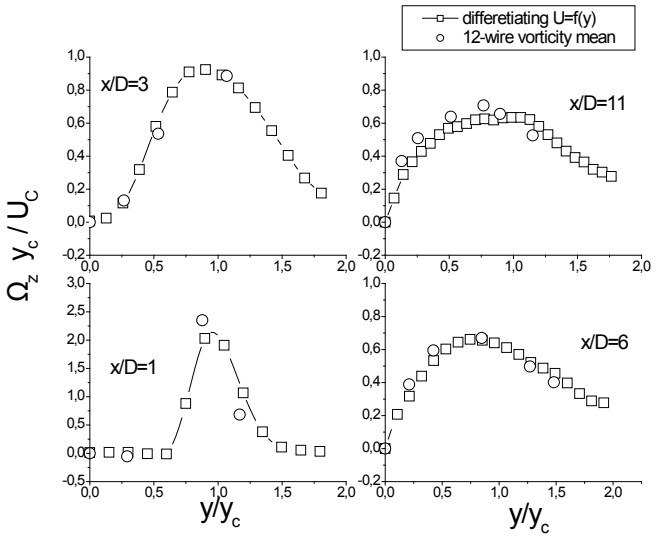

Figure 5. Mean spanwise vorticity distributions (x/D=1, 3, 6, 11)

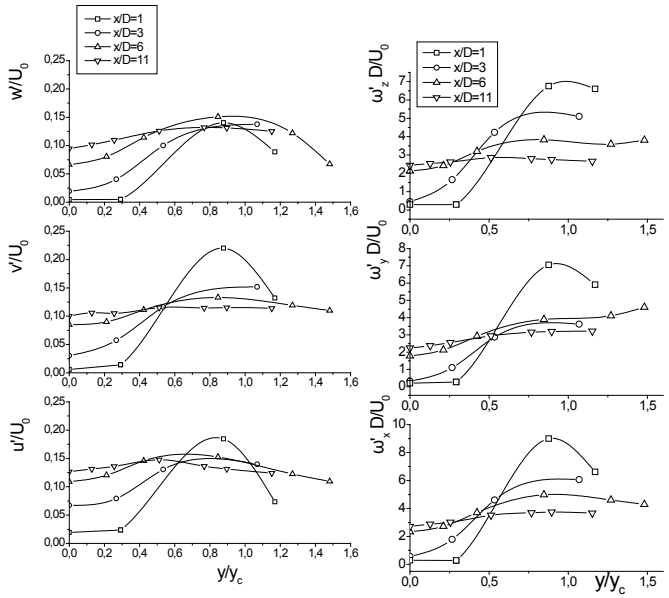

Figure 6. Measured rms value of the three fluctuating velocity-vorticity components

the axis area and with decrease of rms values within the shear layers (x/D=6, 11). This behaviour is characterized by the turbulence diffusion from shear layers towards the centre and edges of the jet. It seems that areas with low or high levels of velocity turbulence are associated with corresponding levels of vorticity turbulence respectively.

Assessment of anisotropy

The normal Reynolds stresses anisotropy levels at $y/y_c \approx 1$ in the near field region of the rectangular jet are shown in Table 1 compared to available experimental and numerical (DNS) data. The direct production of energy by the mean shear at x/D=1 seems to lead to a strong anisotropy in the fluctuating field in this region of the jet, amplifying the $\overline{vv}/q^2$ component. As expected this anisotropy is reduced downstream and jet development seems to be characterized by a redistribution of energy between the three directions probably due to pairing, which is the main mechanism of the evolution of the shear layer (Grinstein 2001). This process results in the augmentation of the other two normal stresses at the expense of the $\overline{vv}$ component, which eventually becomes less than the isotropic value. Differences with Stanley et al. (2002) results should probably be attributed to the different initial and boundary conditions whereas all other results on plane jets depicted in table 1 have been obtained in the full development region.

On the jet centreline at x/D=11 (Table 2) the streamwise component is higher than the isotropic level while the lateral and spanwise components are below this level. It is clear that the large scales have not relaxed to isotropy in spite of the absence of mean shear at the centreline. As shown in Table 2, the present results are in a good agreement with the experimental results of Gutmark & Wygnanski (1976) and Browne et al. (1983) for fully developed jets.

Table 3 lists the normal velocity derivative variances on the centreline as well as in the high-shear regions. While DNS results are very close to the isotropic value, the deviations of the present results from it are significant. The different values between the two cases should be attributed to the different stage of the flow development, since the results of Stanley et al. (2002) indicate that at x/D=11 the jet has reached full development. As stated in their work the large scales of the flow relax slowly to isotropy in the absence of mean shear at the centreline whereas the small scales

Table 1
Comparison of the jet turbulence intensities for $y/y_c \approx 1$ in the near filed region at x/D=1, 3, 6 and 11 with several experimental and computational (DNS) data of other researchers (x/D>30 characterises the full development region)

Source	Position	$\overline{uu}/\overline{q^2}$	$\overline{vv}/\overline{q^2}$	$\overline{ww}/\overline{q^2}$	$\overline{\lvert uv \rvert}/\overline{q^2}$
Present study	x/D=1	0.33	0.47	0.19	0.09
	x/D=3	0.32	0.37	0.31	0.12
	x/D=6	0.37	0.28	0.36	0.14
	x/D=11	0.36	0.28	0.36	0.15
Stanley et al (2002) (DNS)	x/D=4	0.42	0.27	0.31	0.20
	x/D=11	0.37	0.35	0.28	0.13
Wygnanski & Fiedler (1970)	x/D>30	0.43	0.26	0.31	0.13
Spencer & Jones (1971)	x/D>30	0.53	0.23	0.23	0.20
Bell & Mehta (1990)	x/D>30	0.44	0.27	0.29	0.14
Gutmark & Wygnanski (1976)	x/D>30	0.59	0.19	0.22	0.14
Ramaprian & Chandrasekhara (1985)	x/D>30				
	$y/y_c \approx 1$	0.40^+	0.27^+	-	0.15^+
	$y/y_c \approx -1$	0.42^+	0.24^+	-	0.14^+

$^+$ assumes $\overline{q^2} = (3/2)(\overline{u^2} + \overline{v^2})$

Table 2
Comparison of the jet turbulence intensities for $y/y_c=0$ in the near filed region at x/D=11 with several experimental and computational (DNS) data of other researchers (x/D>30 characterises the full development region)

Source	Position	$\overline{uu}/\overline{q^2}$	$\overline{vv}/\overline{q^2}$	$\overline{ww}/\overline{q^2}$
12-wire	x/D=11	0.46	0.29	0.26
DNS Stanley (2002)	x/D=11	0.37	0.39	0.23
Gutmark & Wygnanski (1976)	x/D>30	0.48	0.27	0.24
Ramaprian & Chandr. (1985)	x/D>30	0.37+	0.29+	-
Everit & Robins (1978)	x/D>30	0.38	0.34	0.28
Browne et al. (1983)	x/D>30	0.47	0.24	0.29

$^+$ assumes $\overline{q^2} = (3/2)(\overline{u^2} + \overline{v^2})$

Table 3
Normal-derivative variances in the near filed region at x/D=11

	$\frac{\overline{(\partial u/\partial x)^2}}{(\varepsilon/15\nu)}$	$\frac{\overline{(\partial v/\partial y)^2}}{(\varepsilon/15\nu)}$	$\frac{\overline{(\partial w/\partial z)^2}}{(\varepsilon/15\nu)}$
Isotropic Value	1.0	1.0	1.0
Present work			
$y/y_c \approx 1$	0.26	2.41	1.34
$y/y_c = 0$	0.12	1.95	1.76
Stanley et al. (2002)			
$y/y_c \approx 1$	0.883	1.034	1.095
$y/y_c = 0$	1.014	0.975	1.019

adjust quite rapidly. The results of the present work indicate that the jet has not reached the full development region in accordance with experimental results of previous studies indicating that full development of planar jets is attained at distances x/D>30-40.

The development of rectangular jet in the near field after the interaction of the shear layers which occurs beyond the tip of the jet potential core, similar to that of a plane jet, is controlled by large-scale coherent vortical structures which are characterized by their persistence. On the other hand, vortices in the full development region have lost most of their energy. Consequently it is expected that the near field region will be characterized by anisotropy whereas the flow may relax towards isotropic attributes in the fully developed region. Table 4 shows the variance of the cross-derivative terms at x/D=11, where the same differences between the two investigations are observed. This behaviour is attributed also to the different initial and boundary conditions of the two studies. As is well known jet development in the near field is expected to be influenced mainly by aspect ratio and factors such as jet exit formation, Reynolds number and room turbulence (Cavo et al. 2007).

Table 4
Cross-derivative variances in the near filed region at x/D=11

	$\frac{\overline{(\partial u/\partial y)^2}}{\overline{(\partial u/\partial x)^2}}$	$\frac{\overline{(\partial u/\partial z)^2}}{\overline{(\partial u/\partial x)^2}}$	$\frac{\overline{(\partial v/\partial x)^2}}{\overline{(\partial v/\partial y)^2}}$	$\frac{\overline{(\partial v/\partial z)^2}}{\overline{(\partial v/\partial y)^2}}$	$\frac{\overline{(\partial w/\partial x)^2}}{\overline{(\partial w/\partial z)^2}}$	$\frac{\overline{(\partial w/\partial y)^2}}{\overline{(\partial w/\partial z)^2}}$
Isotropic Value	2.0	2.0	2.0	2.0	2.0	2.0
Present work						
$y/y_c \approx 1$	5.63	5.90	0.34	0.73	0.29	1.13
$y/y_c = 0$	16.94	21.35	0.12	0.83	0.10	0.70
Stanley et al. (2002)						
$y/y_c \approx 1$	2.36	2.30	1.58	2.07	1.61	2.20
$y/y_c = 0$	2.06	2.13	1.95	1.96	1.95	1.91

CONCLUSIONS

The anisotropy in the near field of the turbulent rectangular jet of aspect ratio 6, at Re=21000 has been illustrated and discussed in detail. The results obtained with a 12 sensor hot wire probe indicate that the formation and development of large-scale vortices in the shear layers of the rectangular jet lead to the anisotropy of the flow. A strong advantage of the current results in comparison with other studies is that the spatial derivatives of the three components of the fluctuating velocity field in all three directions have been directly measured.

REFERENCES

1. Bell, J. H. and Mehta, R. D., Development of a two-stream mixing layer from tripped and untripped boundary layers, *AIAA J.*, Vol. 28, pp 2034-2042, 1990.
2. Browne L. W. B., Antonia R. A, Rayagopalan S., Chambers, A. J., Interaction region of a two – dimensional turbulent plane jet in still air, *In structure of complex turbulent shear flow (ed. R. Dumas & L. Fulachier)*, Springer, pp 411-419, 1983.
3. Browne, L. W. B., Antonia, R. A., Chambers, A. J., The interaction region of turbulent plane jet, *J Fluid Mech.*, Vol. 149, pp 355-373, 1984.
4. Cavo, A., Lemonis, G., Panidis, Th., Performance of a 12-sensor vorticity probe in the near field of a rectangular turbulent jet, *Exp. in Fluids*, Vol 43, pp 17-30, 2007.
5. Deo, R. C., Mi, J., Nathan, G. J., The influence of the nozzle aspect ratio on the plane jets, *Exp. Therm. and Fluid Sci.*, Vol. 31, pp 825-838, 2007.
6. Everitt, K. W. and Robins, A. G., The development and structure of turbulent plane jets, *J. Fluid Mech.*, Vol. 88, pp 91-122, 1978.
7. Gutmark, E. and Wygnaski, I., The planar turbulent jet, *J. Fluid Mech.*, Vol. 73, pp 465-495, 1976.
8. Grinstein, F., Vortex dynamics and entrainment in rectangular free jets, *J. Fluid Mech.*, Vol. 437, pp 69-101, 2001.
9. Krothapalli, A., Baganoff, D., Karamacheti, K., On the mixing of a rectangular jet, *J. Fluid Mech.,* Vol. 107, pp 201-220, 1981.
10. Lozanova, M. and Stankov, P., Experimental investigation on the similarity of a 3D rectangular turbulent jet, *Exp. in Fluids*, Vol. 24, pp 470-478, 1998.
11. Lemonis G. C., An experimental study of the vector fields of velocity and vorticity in turbulent flows, *PhD Thesis, Swiss Federal Institute of Technology,* Zurich, 1995.
12. Quinn, W. R., Turbulent free jet flows issuing from sharp-edged rectangular slots, The influence of slot aspect ratio, *Exp. Thermal Fluid Sci.*, Vol. 5, pp 203-215, 1992.
13. Ramaprian, B. R. and Chandrasekhara, M. S., LDA measurements in plane turbulent jets, Trans. ASME: *J. Fluids. Engng*., Vol. 107, pp 264-271, 1985.
14. Rockwell, D. O. and Niccols, W. O., Natural breakdown of planar jets, *Trans. ASM, J. Basic Engng.*, Vol. 94, pp 720-730, 1972.
15. Sfeir, A. A., Investigation of three-dimensional turbulent rectangular jets, *AIAA J.*, Vol. 17(10), pp 1055-1060, 1979.
16. Sforza, P. M and Stasi, W., Heated three-dimensional turbulent jets, ASME, *J. Heat Mass Transfer*, Vol. 101, pp 353-358, 1979.
17. Spencer, B. W. and Jones, B. G., Statistical investigation of presure and velocity fields in the turbulent two mixing layer, *AIAA Paper*, pp 71-613, 1971.
18. Stanley, S. A., Sarkar, S., Mellado, J. P., A study of the flow-field evolution and mixing in a planar turbulent jet using direct numerical simulation, *J Fluid Mech.,* Vol. 450, pp 377-407, 2002.
19. Wygnanski, I. and Fiedler, H. E., The two-dimensional mixing region, *J. Fluid Mech*., Vol. 41, pp 327-361, 1970.

PRESSURE FLUCTUATIONS PRODUCED BY A JET IMPINGING ON A WALL AT NORMAL AND OBLIQUE INCIDENCE

M. El-Anwar [1], K. Zhang[2], A. Naguib[2, *], A.M. Abouel-Fotouh[1]
[1] National Research Centre, Giza, Egypt
[2] Michigan State University, East Lansing, MI-44824, USA

ABSTRACT. The spatio-temporal characteristics of the wall pressure produced by an axisymmetric jet impinging on a round plate are examined. The particular emphasis of this examination is to study the influence of the jet impingement angle on the unsteady wall-pressure field. This is accomplished by measuring the surface-pressure fluctuations using an array of 30 microphones that are arranged in radial as well as azimuthal configurations. Data are reported for a jet Reynolds number of 16500, a plate-to-jet-exit separation distance of 4 and normal as well as oblique impingement angles. The results show that oblique impingement leads to substantial asymmetry in the wall-pressure field involving both magnification as well as attenuation of the pressure fluctuations. The former is found in the half plane where the jet experiences more obtuse turning relative to normal impingement and the latter in the half plane where the jet makes a sharper turn.

Keywords: *jets, free-shear flows, turbulence, pressure fluctuations*

INTRODUCTION

Impinging jets are significant to many practical engineering applications, including heating, cooling and drying. Many studies of impinging jets have focused on the examination of the heat transfer from the impingement plate (e.g. Yan *et al.* [1], Viskanta [2], Lytle and Webb [3] and Webb and Ma [4]) and the flow field (Didden and Ho [5], Popiel and Trass [6] and Landreth and Adrian [7]). In contrast, there is little information regarding the space-time characteristics of the pressure fluctuations (p') acting on the impingement plate. The exceptions are two recent studies by Hall and Ewing: one [8] where two-point wall-pressure measurements are employed and the other [9] based on the use of extensive wall-pressure-sensor-array measurements. Such information has direct relevance to unsteady loading on the impingement plate as well as flow-induced noise and vibration. Moreover, the intensity of p' is indicative of the strength of the associated turbulent flow structures, which are responsible for significant enhancement in heat transfer in impinging jets.

In the vicinity of the impingement plate, the flow field of a round impinging jet may be divided into two regions: a stagnation region ($r/D < 1$; r is the radial coordinate measured from the centre of the jet and D is the jet diameter), where the turning of the jet to become parallel to the plate takes place, and a wall-jet region ($r/D > 1$). Using data from azimuthal wall-pressure arrays, Hall and Ewing [9] found the dominant p' modes to be helical in the stagnation region. The strength of these modes, which the authors linked to the flow structures existing in the jet prior to its impingement on the plate, increased with increasing distance between the jet exit and impingement plate. In the wall-jet region, Hall and Ewing [9] found axisymmetric and helical structures to be significant. Both modes had the same frequency, which was different from the much lower frequency of the helical modes found in the

* Corresponding author: Prof. A.M. Naguib
Phone: + (1)-517-4321616, Fax: + (1)-517-3537179
E-mail address: naguib@egr.msu.edu

stagnation zone, and they decayed in strength with increasing separation between the jet exit and the plate. This led the authors to conclude that the helical modes identified for $r/D > 1$ were not the same as those originating in the jet and found in the stagnation zone. Instead, Hall and Ewing [9] hypothesized that an asymmetric interaction of the jet's flow structure with the impingement plate caused the formation of the helical modes observed in the wall jet.

Although the investigations of Hall and Ewing [8] and [9] provide considerable insight into the spatio-temporal characteristics of the wall pressure, similar information is lacking for oblique jet impingement. The present study employs an approach similar to that of Hall and Ewing to fill this gap for a round jet impinging on a circular disc.

EXPEIMENTAL SETUP

The experimental setup is illustrated in Figure 1: an axisymmetric air jet with a top-hat exit velocity profile and a diameter D = 25.4 mm impinges on a flat, circular disc. The diameter of the disc is 12D, which is more than an order of magnitude larger than the jet diameter in order to minimize disc-edge effects on the measurements. The impingement disc is located at a distance H away from the jet exit and could be inclined to cause deviation from normal impingement by an angle γ (see Figure 1).

Unsteady-surface-pressure (p') data are acquired using 30 microphones embedded in the impingement plate. Each microphone is a Panasonic WM-61A electret microphone with a package diameter of 6 mm and a sensing-hole diameter of 2 mm (approximately 0.08D). The frequency response of all microphones is obtained from calibration against a Brüel and Kjær ¼" microphone (model 4938-A-011) in a plane wave tube. The calibration procedure is similar to that employed by Daoud and Naguib [10]. The sensors are configured into one radial array at an azimuthal angle θ = 90°, and two azimuthal arrays at r/D = 1 and 2.33, as depicted in Figure 2 (also note the coordinate-system's definition in the figure). The radial array contains eight microphones that are spaced 0.33D apart starting from r/D = 0. On the other hand, the azimuthal array at r/D = 1 contains eight uniformly distributed microphones, while the one at r/D = 2.33 has sixteen microphones with an angular spacing of 22.5°. Microphone signals are sampled simultaneously at the rate of 5000 samples/s for a jet exit velocity U_j = 10 m/s, H/D = 4, and γ = 0 and 30°. The corresponding jet Reynolds number based on diameter is $Re_D \approx 16500$.

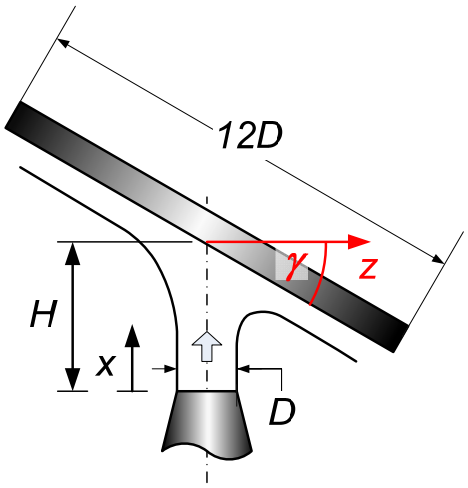

Figure 1. A schematic drawing of the experimental setup

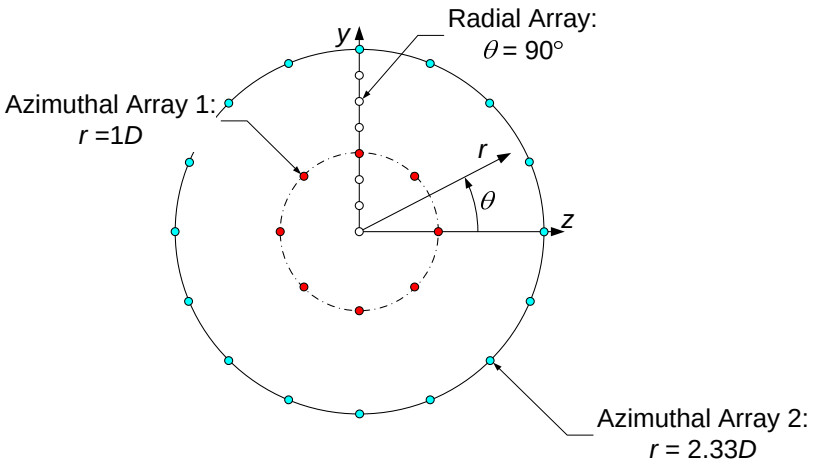

Figure 2. Microphone-array configuration

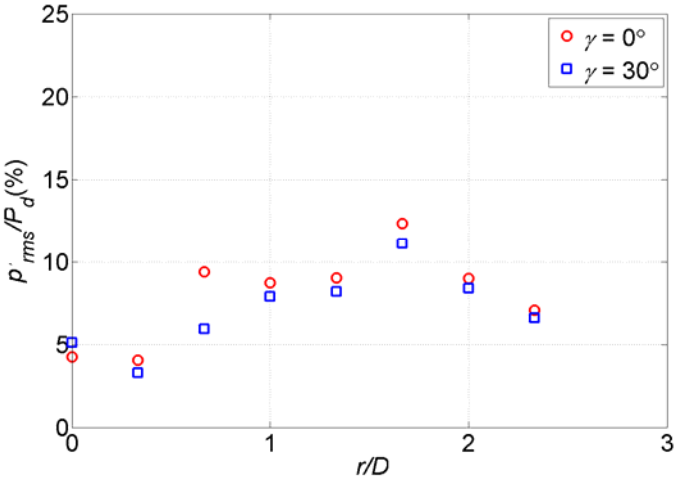

Figure 3. Radial distribution of the *rms* pressure fluctuations along the ray $\theta = 90^o$ for normal ($\gamma = 0^o$) and oblique ($\gamma = 30^o$) impingement. P_d is the dynamic head based on jet velocity: $P_d = \frac{1}{2}\rho U_j^2$

RESULTS AND DISCUSSION

Figure 3 depicts the radial distribution of the root-mean-square (*rms*) pressure fluctuation normalized by the dynamic head ($P_d = \frac{1}{2}\rho U_j^2$) for normal (red circles) and oblique (blue squares) impingement. The distribution is obtained along the line corresponding to $\theta = 90^o$, which coincides with the axis around which the impingement plate is rotated. Overall, no significant differences are seen in the pressure fluctuation distribution between the two cases. One exception is at $r/D = 0.67$, where p'_{rms} is larger for normal impingement. This location is inside the stagnation zone ($r/D < 1$) in the vicinity where the shear layer interacts with the plate. The deviation is possibly indicative of a stronger interaction of the shear layer with the plate at normal incidence.

The normal-impingement p'_{rms} results are consistent with those obtained recently by Hall and Ewing [9]. In particular, the latter authors find two peaks in the *rms* distribution: one in the stagnation zone, where the shear-layer interacts with the plate, and the other in the wall-jet region at $r/D = 1.5$. Hall and Ewing associated the latter peak with the formation of secondary vortices caused by the interaction of the convecting vortex structures, which originate in the jet shear layer, with the impingement plate. The present results show a subtle peak at $r/D = 0.67$ in the stagnation zone, and a prominent one at $r/D = 1.67$ beneath the wall jet. The stagnation-zone peak is substantially less observable than that identified by Hall and Ewing. The more energetic peak in the latter study is believed to result from the turbulent character of the jet flow, which forms at the exit of a fully-

developed turbulent pipe flow. In contrast, in the present study, the jet discharges from a plenum at the exit of a contoured nozzle.

The power spectral density ($\phi_{p'p'}$) plots corresponding to the *rms* data of Figure 3 are displayed in Figures 4 and 5 for normal and oblique impingement respectively. With the exception of the spectrum at r/D = 0.67, which contains more fluctuation energy in the former case, no major deviation in the behaviour of the spectra is seen between the two cases. Focusing on Figure 4, a local spectrum peak is found at a normalized frequency $fD/U_j \approx 0.4$ near the stagnation point (r/D = 0 and 0.33). At larger r/D values, but still within the stagnation zone, the spectrum becomes broader, the fluctuation energy increases (as seen from the rise in the spectrum) and the spectral peak shifts to $fD/U_j \approx 0.3$ at $r/D = 0.67$. The increased broadness of the spectrum presumably results from broadband turbulence in the shear layer influencing the pressure fluctuation at locations where the shear layer interacts with the wall. As will be seen from the analysis of the cross spectra, the superposition of these broadband fluctuations onto those produced by the coherent motion causes the shift in the spectrum-peak frequency found at r/D = 0.67. In other words, the change in spectrum-peak frequency is not a manifestation of the change in the frequency of the pressure-signature of the convecting coherent structures in the flow.

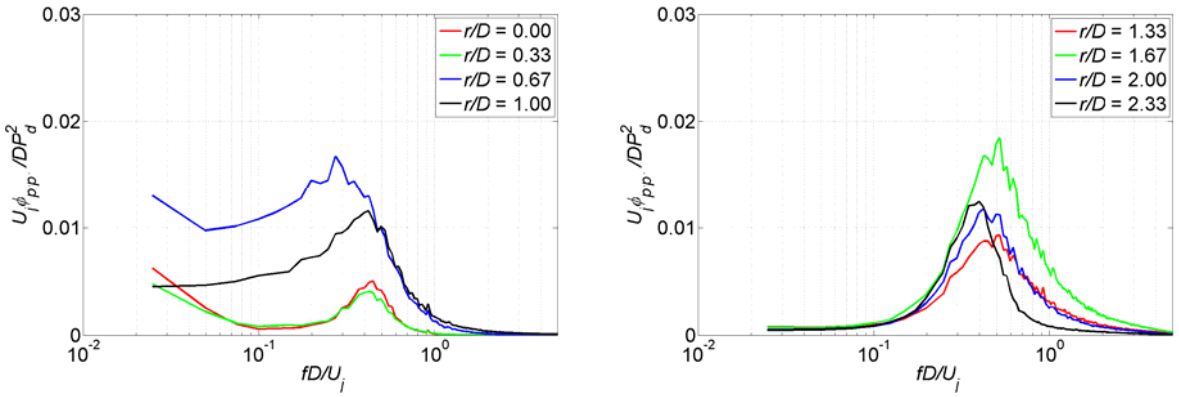

Figure 4. Power spectral density at different radial locations along the ray $\theta = 90^o$ for normal impingement: stagnation zone (left); wall-jet zone (right)

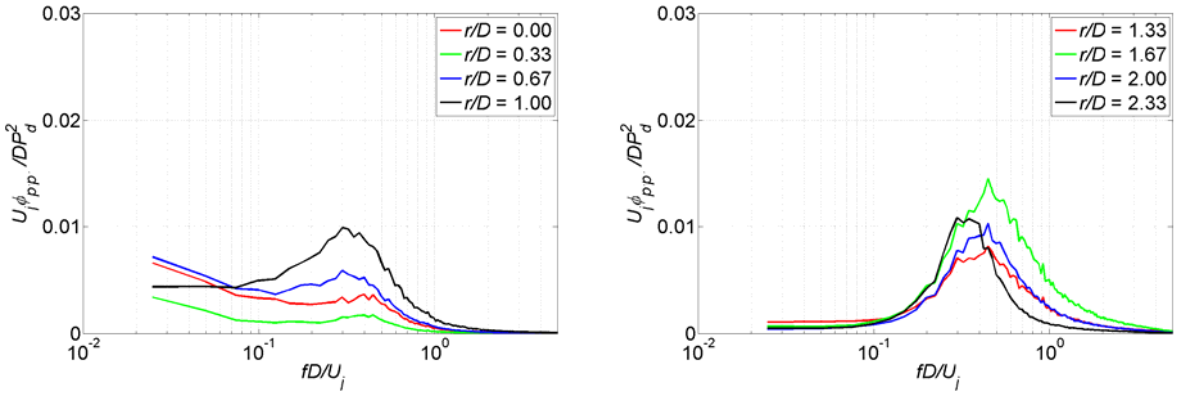

Figure 5. Power spectral density at different radial locations along the ray $\theta = 90^o$ for oblique impingement: stagnation zone (left); wall-jet zone (right)

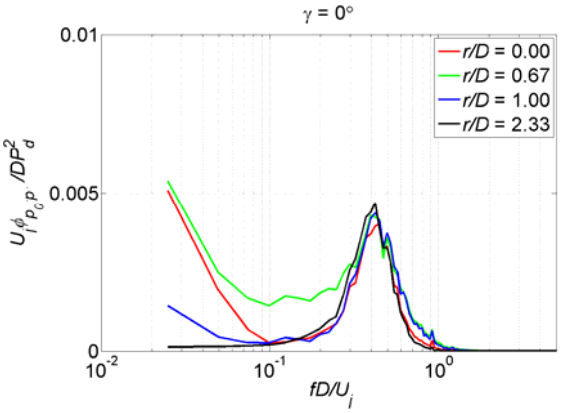

Figure 6. Radial distribution of the cross spectral density of the wall pressure for normal impingement. Lines with different colours indicate different radial locations

In the wall-jet region ($r/D \geq 1.33$: right plot in Figure 4), the spectrum peak shifts to $fD/U_j \approx 0.5$ and is unaffected by the increase in r/D up to a value of 2.0. Farther downstream at $r/D = 2.33$, the peak shifts back to the value found near $r/D = 0$; i.e. $fD/U_j \approx 0.4$.

The back/forth shift of the dominant spectrum peak with increasing r/D leads to ambiguity in identifying the frequency of the convective coherent flow structures. These structures are presumably vortices that originate in the jet shear layer, impinge on the wall and spread outwards along the radial direction. To clarify this issue, the cross spectral density between the pressure signal measured at $r/D = 0$ (p'_0) and that measured at different radial locations along $\theta = 90^o$ ray is computed and displayed in Figure 6. Unlike the power spectral density, which depicts fluctuations produced by all flow structures, peaks in the cross spectral density correspond to frequencies at which the pressure fluctuations at $r/D = 0$ are highly correlated with those found at other radial locations. Figure 6 shows that in fact the cross-spectrum peak remains at $fD/U_j \approx 0.4$ over the *entire* radial range of observation. As discussed earlier, the shift in the spectrum peak in Figure 4 (left) to $fD/U_j \approx 0.3$ at $r/D = 0.67$ is likely an artefact of the pressure signature of broadband turbulence from the shear layer. On the other hand, the shift to higher frequency of $fD/U_j \approx 0.5$ in the range $1.33 \leq r/D \leq 2.00$ (Figure 4; right) is in the zone where researchers have found secondary vortices to form through interaction of the convecting primary vortices with the wall. The cross-spectrum analysis provides unambiguous evidence that the pressure signature of the convective coherent flow structures (i.e. those producing a coherent pressure signature at all microphones in the radial array) occurs at $fD/U_j \approx 0.4$. Although Figure 6 only provides information on the coherence of these structures, independent evidence of their convective nature is found later when considering the cross-correlation results.

It is somewhat surprising that the above results don't show striking difference in the level and frequency content of the wall-pressure fluctuation between the normal and oblique impingement. However, so far the discussion has focused on the pressure fluctuations along the axis around which the impingement plate is rotated, which in fact remains in the same spatial location relative to the jet in both cases. Thus, to better understand the effect of the jet's impingement angle, attention is redirected to the azimuthal structure of the wall-pressure field. Figure 7 displays polar contour plots of the power spectra at different azimuthal angles for $r/D = 2.33$ and $\gamma = 0$ & 30°. The colour bar shown on the right side of the figure gives the spectrum magnitude normalized by the largest peak, and fD/U_j values are given by the radial coordinate (shown in red). Note that for $\gamma = 30°$, the jet turning angle becomes more acute relative to $\gamma = 0°$ for $270^o < \theta < 90^o$ and more obtuse for $90^o < \theta < 270^o$. The results in Figure 7 show that the oblique impingement causes the pressure fluctuations to become asymmetric and more dominant on the side where the jet turning angle is more obtuse (i.e. $90^o < \theta < 270^o$). This asymmetry is associated with substantial decrease in p' level relative to

normal impingement in the range $270^o < \theta < 90^o$. To see this, the power spectral density of the pressure fluctuations at $\theta = 0^o$ and $r/D = 2.33$ is displayed for the normal and oblique impingement cases in the left plot in Figure 8. The figure clearly demonstrates the substantial reduction in the level of pressure fluctuations for the case of more acute turning of the jet. On the side where the jet experiences more obtuse turning, the opposite scenario takes place and the pressure fluctuations are much higher than in the case of normal impingement, as seen from the comparison of the spectra in the right plot in Figure 8.

Another significant effect of oblique impingement is found when examining the azimuthal distribution of the convection velocity (u_c). Here, u_c along a given θ direction is computed from the cross-correlation between the pressure signal measured by one microphone in the smaller aziumthal array ($r/D = 1$) and its counter part at the same azimuthal angle in the bigger azimuthal array ($r/D = 2.33$). An example of the correlation results for $\theta = 180^o$ is depicted in Figure 9 in which the correlation coefficient ($R_{p'p'}$); i.e. the correlation magnitude normalized by the product of p'_{rms} at $r/D = 1$ and 2.33, is plotted versus the time delay between the signals measured at the two different locations. As seen in the figure, the largest correlation is found at a time delay of $\tau_p U_j/D \approx 2$. That such a time delay is required between the observance of a pressure signature at $r/D = 1$ and the occurrence of a similar signature at $r/D = 2.33$ is reflective of the existence of convective pressure-producing flow structures. The radial convection velocity can be computed by dividing the radial offset between these two locations by the time delay of the correlation peak, or: $u_c/U_j = 1.33/2 \approx 0.67$ at $\theta = 180^o$.

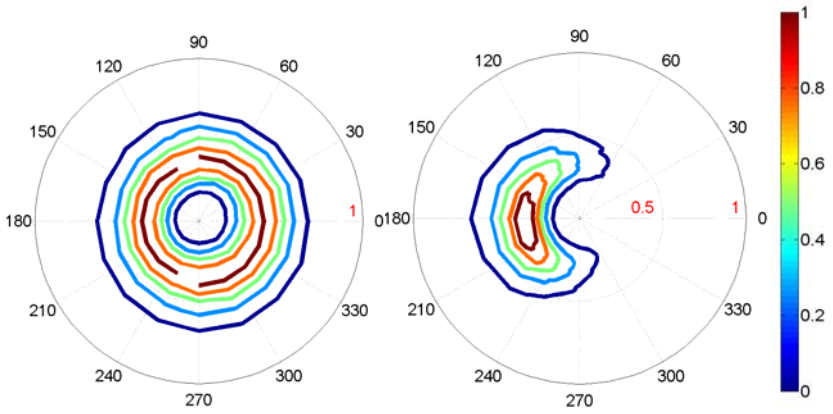

Figure 7. Contour plot of the azimuthal distribution of p' spectra at $r/D = 2.33$: $\gamma = 0$ (left) and 30° (right). The colour bar gives the spectrum magnitude normalized by the largest peak, and the normalized frequency fD/U_j values are given by the radial coordinate (shown in red)

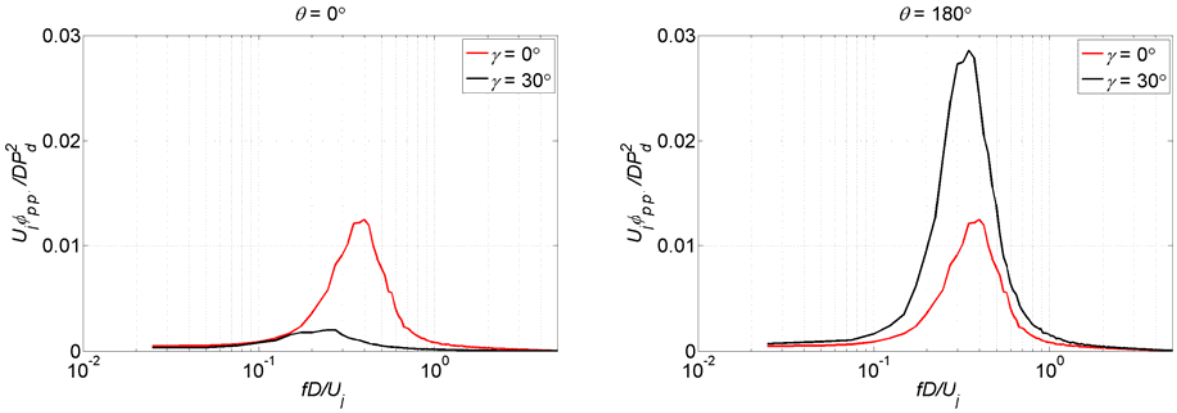

Figure 8. Comparison between the wall-pressure power spectral density for normal and oblique impingement at $r/D = 2.33$: $\theta = 0^o$ (left) and $\theta = 180^o$ (right)

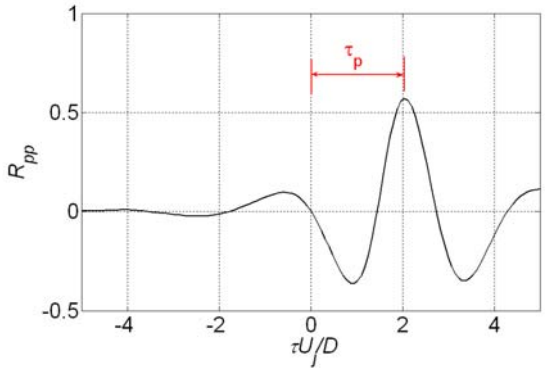

Figure 9. Cross-correlation between p' at $r/D = 1$ and p' at $r/D = 2.33$ along the azimuthal ray $\theta = 180°$ for $\gamma = 30°$

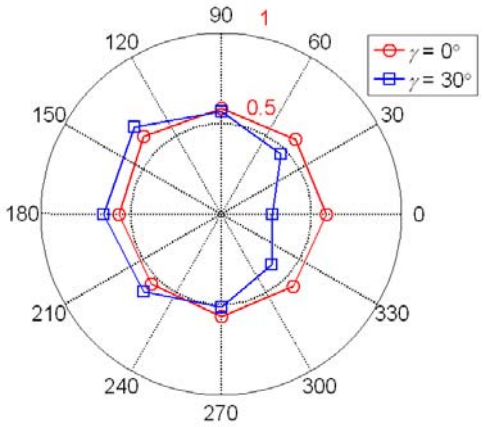

Figure 10. Azimuthal distribution of u_c/U_j for normal ($\gamma = 0^o$) and oblique ($\gamma = 30^o$) impingement (values given by red text)

The full azimuthal distribution of u_c may be seen in Figure 10. The figure contains a polar plot, the radial coordinate of which gives the value of u_c/U_j at different azimuthal angles for normal (red circles) and oblique (blue squares) impingement. Examination of the results clearly demonstrates that whereas the convection velocity is axisymmetric for normal impingement, the inclination of the jet by 30^o relative to the impingement plate causes the establishment of asymmetry in the azimuthal distribution of u_c/U_j. The asymmetry is such that the convection velocity is larger than in the case of normal impingement on the side where the jet experiences more obtuse (i.e. more gradual) turning ($90^o < \theta < 270^o$), and vice versa.

CONCLUSIONS

It is found here that oblique impingement of an axisymmetric jet on a flat wall causes an asymmetry in the wall-pressure distribution relative to a jet at normal incidence. The asymmetry is such that the wall-pressure fluctuations increase in the half plane where the jet experiences more obtuse turning relative to normal incidence, and vice versa. These larger pressure fluctuations, which are reflective of the enhancement in the strength of the flow structures, are associated with a larger convection velocity than in the normal jet. An interesting implication of the present results is the possibility of the existence of an optimum obtuse turning angle where the enhancement in the strength of the flow structures is maximized.

ACKNOWLEDGEMENT

This work is funded by US-Egypt Joint Board on Scientific and Technological Cooperation through contract no. OTH10-028-002 and NSF grant number OISE-0611984.

REFERENCES

1. Yan, X., Baughn, J.W. and Mesbah, M., The Effect of Reynolds Number on the Heat Transfer Distribution from a Flat Plate to an Impinging Jet. *Fundamental and applied heat transfer research for gas turbine engines. ASME Heat Transf. Div.* Vol. 226, pp 1-7, 1992.
2. Viskanta, R., Heat Transfer to Impinging Isothermal Gas and Flame Jets. *Exp. Therm. Fluid Sci.* Vol. 6, pp 111-134, 1997.
3. Lytle, D. and Webb, B.W., Air Jet Impingement Heat Transfer at Low Nozzle-Plate Spacings. *Int. J. Heat Mass Transf.* Vol. 37, pp. 1687-1697, 1994.
4. Webb, B.W. and Ma, C.F., Single-phase Liquid Jet Impingement Heat Transfer. *Adv. Heat Transf.* Vol. 26, pp. 105-217, 1995.
5. Didden, N. and Ho, C., Unsteady Separation in a Boundary Layer Produced by an Impinging Jet. *J. Fluid Mech.* Vol. 160, pp 235-256, 1985.
6. Popiel, C.O., Trass, O., Visualization of a Free and Impinging Round Jet. *Exp. Therm. Fluid Sci.* Vol. 4, pp 253-264, 1991.
7. Landreth, C.C. and Adrian, R.J., Impingement of a Low-Reynolds Number Turbulence Circular Jet onto a Flat Plate at Normal Incidence. *Exp. Fluids* Vol. 9, pp 74-84, 1991.
8. Hall, J.W. and Ewing, D., The Development of the Large-scale Structures in Round Impinging Jets Exiting Long Pipes at Two Reynolds Numbers. *Exp. Fluids* Vol. 38, pp 50-58, 2005.
9. Hall, J.W. and Ewing, D., On the Dynamics of the Large-Scale Structures in Round Impinging Jets. *J. Fluid Mech.* Vol. 555, pp 439-458, 2006.
10. Daoud, M. and Naguib, A.M., A Doppler Sensor for High Spatial Resolution Measurements of Unsteady Surface Pressure. *Meas. Sci. Technol.* Vol. 14, pp 13-23, 2003.

DYNAMIC LOCAL QUENCHING PHENOMENA OF LEAN PREMIXED AND DIFFUSION IMPINGING FLOW

I. Makino[1], R. Kaminishi, Y. Yahagi [2*]
6-611 Aramaki-Aoba, Aoba-ku Sendai 980-8579 Japan, Tohoku University
3-7-5, Toyosu, Koto-ku, Tokyo 135-8548 Japan, Shibaura Institute of Technology

ABSTRACT. The dynamic local quenching and recovery phenomena of impinging lean premixed CH_4 air flame (LPF) and lean CH_4 diluted or N_2 diffusion flame (LDF) have been investigated experimentally for fundamental studies of the heterogeneous lean combustion. The reacting flows are visualized by a high speed time series of particle image velocimetry (PIV).

The local quenching phenomena can be observed frequently when approaching the extinction limit. The large scale local quenching may trigger to develop the global extinction. However, in many cases, the flame can recover from the local quenching phenomena.

Two distinct local quenching recovery mechanisms exist. One is a passive local quenching recovery mode and other is an active local quenching recovery mode. In the passive local quenching recovery mode, the local quenching occurs slightly outside of the stagnating point. The local quenching area drifts outward from the stagnating point. Finally, the flames can be automatically recovered from the local quenching phenomena in accordance with the opposite flow properties. In the active local quenching recovery mode, local quenching occurs including the stagnating point. In this case, the flame recovers by the self-propagating wrinkled flamelet. From these results, an active local quenching recovery mechanism is useful to extend the extinction limits. The mechanism works well in the turbulence added in the premixed gas and also the mixture has to be in the self-propagating condition. In addition, the local quenching area might recover by the reacting flow transported by the eddy.

Keywords: *lean combustion, premixed flame, diffusion flame, turbulent flow, quenching*

INTRODUCTION

Extinction is one of the important subjects in combustion studies. In order to understand extinction phenomena, we need to know extinction is induced by many factors. Heat loss and flame stretch are two major factors. Lewis number effects are also important as an additional factor to discuss a stretched laminar flame which is under controlled by molecular level heat and mass diffusion. Up to now, many studies were carried out and the extinction mechanism and phenomena are summarized in combustion textbooks [1]. The extinction mechanism can be clearly understood in the laminar flame. When we measured extinction limits of turbulent flames, extinction limits do not fall on the same line as with laminar flames. The extinction limits of turbulent flames are plotted on the belt [2].

In the region of wrinkled laminar flamelets, stretched laminar flame concepts can be applied in the local flame structure. It is worthwhile to forces that the extinction in turbulent flame induced by compound factors such as the heat loss, the stretch, the Lewis number and so on. The extinction occurs suddenly while one of the stronger factors may become the trigger. The powers of each

*Corresponding author: Prof. Y. Yahagi
Phone: +(81)-3- 5859 - 8022, Fax: +(81)-3-5859-8001
E-mail address: yahagi@sic.shibaura-it.ac.jp

extinction induced factors are fluctuating due to turbulence energy. The extinction limits of the turbulent flame, therefore, may not show the line. It has been made clear by a high speed move that instantaneously the flamelet of turbulent flame is locally quenched and the local quenching becomes trigger to develop whole flame extinction. However, the flame may sometimes recover from the local quenching [3, 4]. We would like to recommend distinguishing the technical terms, "extinction" and "quenching". The "extinction" here refers to whole flame is extinguished such as there is no flame in the burner. The "quenching" here refers to partially flame front is extinguished such as one or more part of the flame front disappear but the flame is still reacting in the burner.

Our questions to start this study are: how to induce the whole extinction by the local quenching, how to recover the flame from the local quenching and also to define the extinction limits in a turbulent flame that exist within the wrinkled laminar flamelet regime. Our selected flow filed is an opposite flow that impinges with lean premixed flame and lean non-premixed or diffusion flame. The one of the great success to reduce the fuel consumption rate is a heterogenous combustion in internal combustion engines [5, 6]. In fact, commercially, the modern Diesel engines and gasoline direct injection engines are operated within the stratified combustion regime. This is not only the trend in the internal combustion engines but also the practical combustors in premixed combustions are shifting from homogeneous combustion to heterogeneous combustion. Recently, some studies have been made numerically in the turbulent premixed flames within the heterogeneous mixture condition [6, 7]. However, up to now, the combined combustion phenomena, such as the lean premixed flame and lean diffusion flame have not been performed in experimentally. Therefore, we are focusing the premixed and diffusion combined lean combustion in turbulent flow namely a combined lean turbulent combustion.

Our proposed flow filed turbulent premixed and diffusion combined flames are one of the suitable geometry for the fundamental modeling of the heterogeneous combustion on the turbulent flow such as the stratified charged internal combustion engines since the reactants compositions and turbulence conditions of each burner can be controlling individually [8]. In the present study, we discussed the global extinction induced local quenching and recovery phenomena in an opposite turbulent flow burner by using the time series particle image velocimetry (PIV).

Nomenclature

U	mean velocity, m/s
d	diameter of burner nozzles, mm
L	distance between two nozzle exit, mm
r	radial coordinate, mm
y	axial coordinate, mm
Re_0	Reynolds number
υ_0	viscosity of air room temperature, m^2/s
l_0	integral length scale, m/s
u_0'	turbulent intensity, m/s
φ	equivalence ratio
χ	mole fraction of fuel
F_{st}	stoichiometric mixture fraction
W	mean molecular weight
υ	stoichiometric coefficient
y_f	flame location, mm
y_s	stagnation plane location, mm
T_o	temperature, K

Subscripts

U	upper stream
L	lower stream
st	stoichiometric

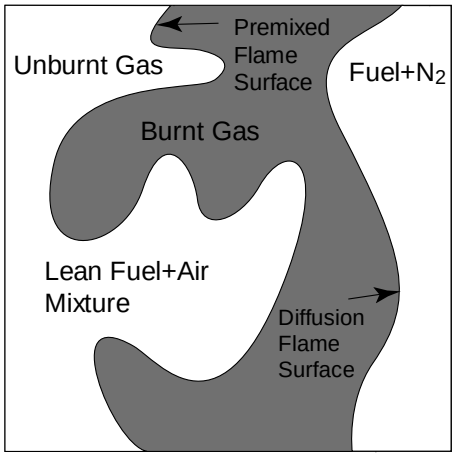

Figure 1. A schematic model of combined structure lean turbulent combustion in the heterogeneous reactants.

co co-flow

EXPERIMENTAL SETUP

Figure 1 shows the schematic model of combined lean turbulent combustion. In the case of combined turbulent lean combustion, a lean premixed flame is impinged with a diluted fuel then two flames are formed in the stagnating regions. The lean fuel diluted with inert gas will be reacting with the high temperature and low oxygen concentration oxidizer from the lean or ultra lean premixed flame. In the burnt gas of the lean premixed flame, the oxidizer has the potential to re-react with the diluted fuel even though the concentration is much less than an ordinary diffusion flame. Especially, the condition of the stoichometric mixture fraction (F_{st}) defined as equation 1 is a very important index to characterize the diffusion flame structures formed in the opposite flow where χ is the mole fraction of reaction gas in a reactant flow, W is a mean molecular weight, υ is a stoichiometric coefficient, and subscripts O and F refer to the oxidizer and the fuel, respectively.

$$\mathrm{F_{st}} = (1 + \chi_F \cdot \mathrm{W}_O \cdot \upsilon_O / \chi_O \cdot \mathrm{W}_F \cdot \upsilon_F)^{-1} \quad (1)$$

In the diffusion flame formed in an opposite flow, the flame location can be divided by 3 modes depending on the F_{st} [9, 10]. In the case of F_{st}<0.5, the flame is formed in the oxidizer flow side. For the F_{st}=0.5, the flame is formed on the impinging surface. For the F_{st}>0.5, the flame is formed in the fuel flow side. If the combined flames are formed under the condition of F_{st}<0.5, it is expected that the mole fraction of the oxygen can be reduced just like in oxidizer preheating combustion [9].

Figure 2 shows the opposite burner system. The burner system consist two symmetrical nozzle type burners placed in line vertically. The exit diameters of both nozzles (d) are 40mm and the distance (L) between the two nozzle exits is set to 80mm. The mean velocity of each nozzle is set at up to 2.0m/s. The turbulence generator, namely P_4, is used as turbulence generators and it can be installed between the converging nozzle and the straight tube. Then the generated turbulent intensity is 0.37m/s and the turbulence Reynolds number ($Re_0=u'_0 l_0/\upsilon_0$) is 52, where l_0 is the integral length scale, and υ_0 is the kinematic viscosity of air at room temperature. The flow condition in the present

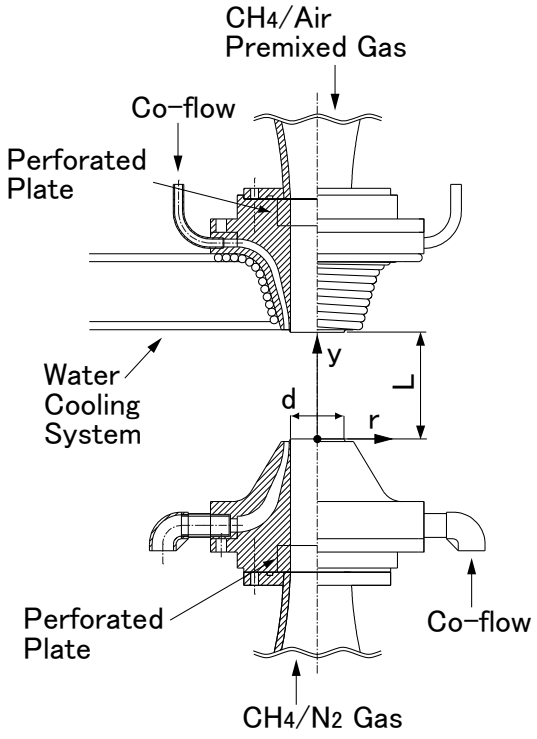

Figure 2. Opposite turbulent flow burner system, d=40mm L=2d.

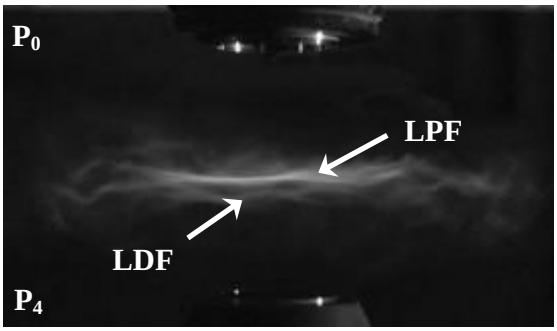

(a) Upper burner lean laminar premixed flame φ_U=0.85, Lower burner turbulent N_2 diluted CH_4 χ_L=10.0%, F_{st}=0.12.

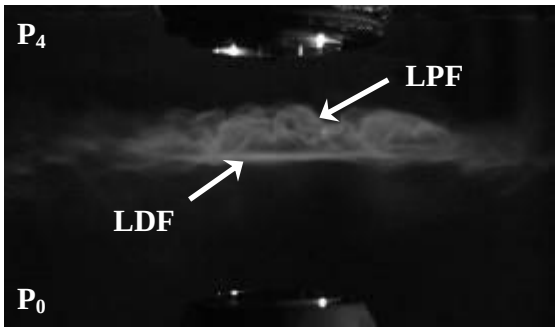

(b) Upper burner lean turbulent premixed flame φ_U=0.8, Lower burner laminar N_2 diluted CH_4 χ_L=10.0%, F_{st}=0.16.

Figures 3. Direct photographs of combined lean premixed flame and diffusion flame formed in the opposite flow. The photos took by Nikon D2x having a 12.4M pixel

study is in the wrinkled laminar flame regime. P_0 means that no perforated plate is used and laminar stagnating flow is formed. The experiments are conducted for 2 flow combinations; one side is a laminar flow while the other side is a turbulent flow (P_0/P_4 or P_4/P_0). The CH_4 and air premixed gas flow is supplied from the upper side burner and the CH_4 diluted with N_2 non-premixed gas flow is issued from the lower side burner. Ring shape co-flows are supplied from both burners to reduce the shear turbulence generated and to extinguish secondary combustion of the unburned fuel. The co-flow velocities (U_{co}) are set equal to the main flow velocity. The coordinate y is defined as the upstream direction from the lower nozzle exit.

Figure 3(a) and (b) show the typical flame image for the turbulent premixed and diffusion combined flames formed in the opposite flow.

FLAMELET STRUCTURE OF PREMIXED AND DIFFUSION COMBINED FLAMES

Figure 4 shows the flamelet structure for premixed and diffusion combined flames in the opposite flow for three different flow conditions. Fine alumina particles about 1μm in diameter were added in the premixed gas side while silicone oil droplets were added in the fuel + N_2 side. When both flows are laminar (Fig. 4 (a)), the lean premixed flame (LPF), lean diffusion flame (LDF) and the impinging surface (IS) are formed in parallel. In this case, F_{st}=0.36, that is F_{st}<0.5, and the LDF is formed in the burnt gas side which is a high temperature and low oxygen concentration oxidizer

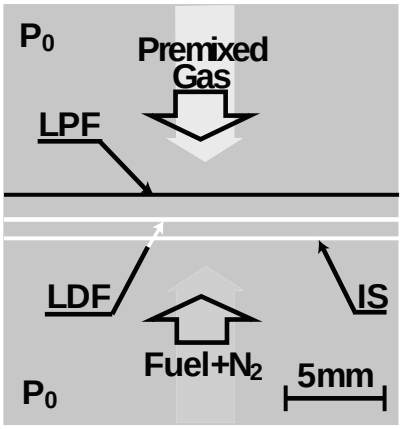

(a) P_0/P_0: laminar to laminar

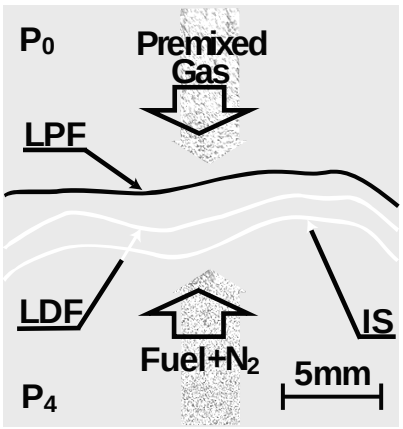

(b) P_0/P_4: laminar to turbulent

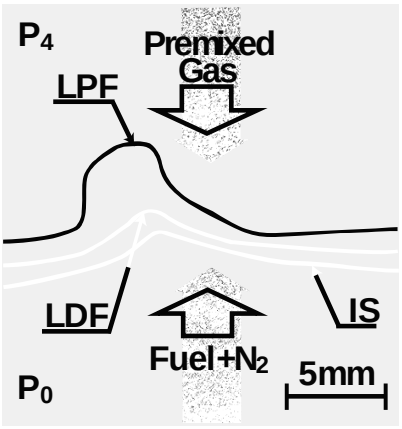

(c) P_4/P_0: turbulent to laminar

Figures 4. Flamelet structure of premixed and diffusion combined flames in for three different flow conditions visualized by a laser tomography. LPF, LDF and IS corresponds lean premixed flame, lean diffusion flame and impinging surface.

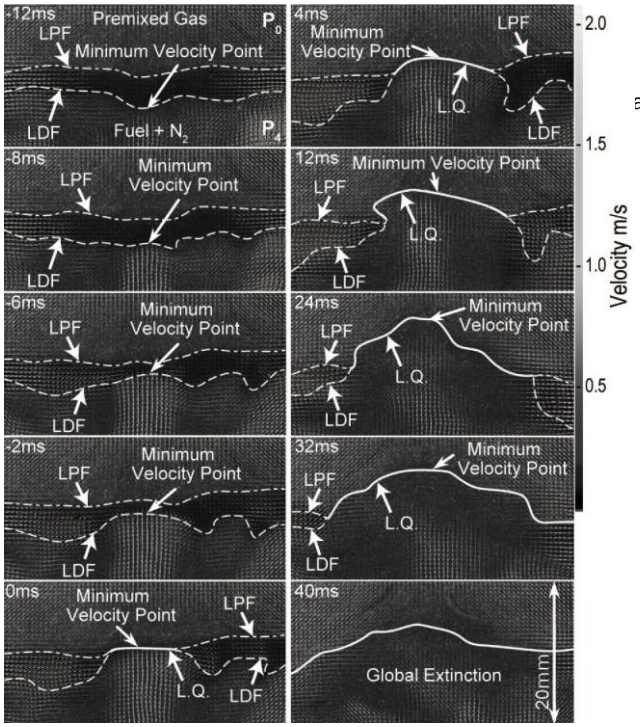

Figure 5. Local Quenching develops to Global Extinction phenomena. P_0/P_4, φ_U=0.6, χ_L=10.0%, F_{st}=0.27, L.Q.: Local Quenching.

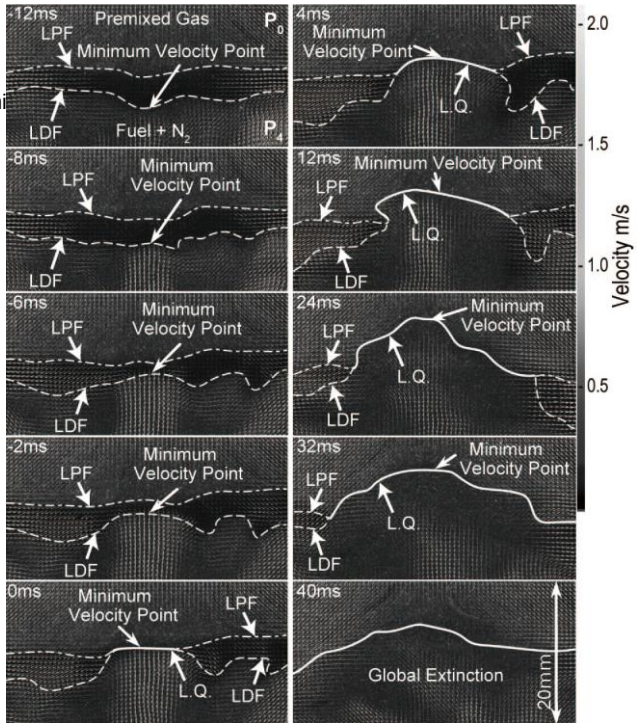

Figure 6. Local Quenching recovery phenomena. P_0/P_4, φ_U=0.6, χ_L=10.0%, F_{st}=0.27, L.Q.: Local Quenching.

region. When the turbulence added only on the premixed gas side as shown in Fig. 4 (b) the flame front of the LPF side has a more complex structure than that of the LDF. And a LDF is also formed in the burnt gas side because of the F_{st}<0.5. The wrinkled flame front of the LDF becomes more complicated than a LPF when the turbulence is added to the diffusion flame. In this case, a LDF is also formed in the burnt gas. In the present study, the fuel of CH_4 diluted with nitrogen may react with the oxygen in the burnt gas of the lean premixed flame.

GLOBAL EXTINCTION PHENOMENA

Figure 5 shows a high speed time series of capture PIV images taken by a high speed camera Photoron Fastcam-1024PCI 100K having 1024×1024 resolution at 1000 frame/sec. The measurement field is 40mm×40mm. Fine alumina particles about 1μm are used as scattering particles added via both nozzles. A Q-Switched YAG laser having a 200mW output power and 3 kHz pulse (Photonics Industries DC 10-527) is used as a light source. The flow condition of the upper burner is laminar premixed gas flow, while that of lower burner is turbulent CH_4+N_2 flow. These frames indicate the minimum velocity point, which is identified by PIV data seems to be stagnating points. (As mentioned by Kostiuk et al [11,12], in the turbulent opposite flow the stagnating stream line moves three dimensionally near the center axis of the flow. Therefore, it is difficult to correctly identify the stagnating point from the 2D flow data so we use the minimum velocity point; the stagnating point will probably be located near there.) The first frame (see -12ms), lean premixed flame (LPF) and the lean diffusion flame (see LDF) surfaces are formed individually. In the second frame (see -8ms), the convex part of the LDF surface moves to upward. The local velocity of that region exceeds 1.5m/s and finally the LDF surface attaches to the LPF surface (see 0ms). In this part, both flames are locally quenched. The local quenching area (L.Q.) is developing to outer direction as shown in frames 0ms to 32ms. Finally (see 40ms), the local quenching area developed to the global extinction (G.E.). The local quenching developed to the global extinction phenomena at about 30~40ms. It is worthwhile to note that the minimum velocity point does not move.

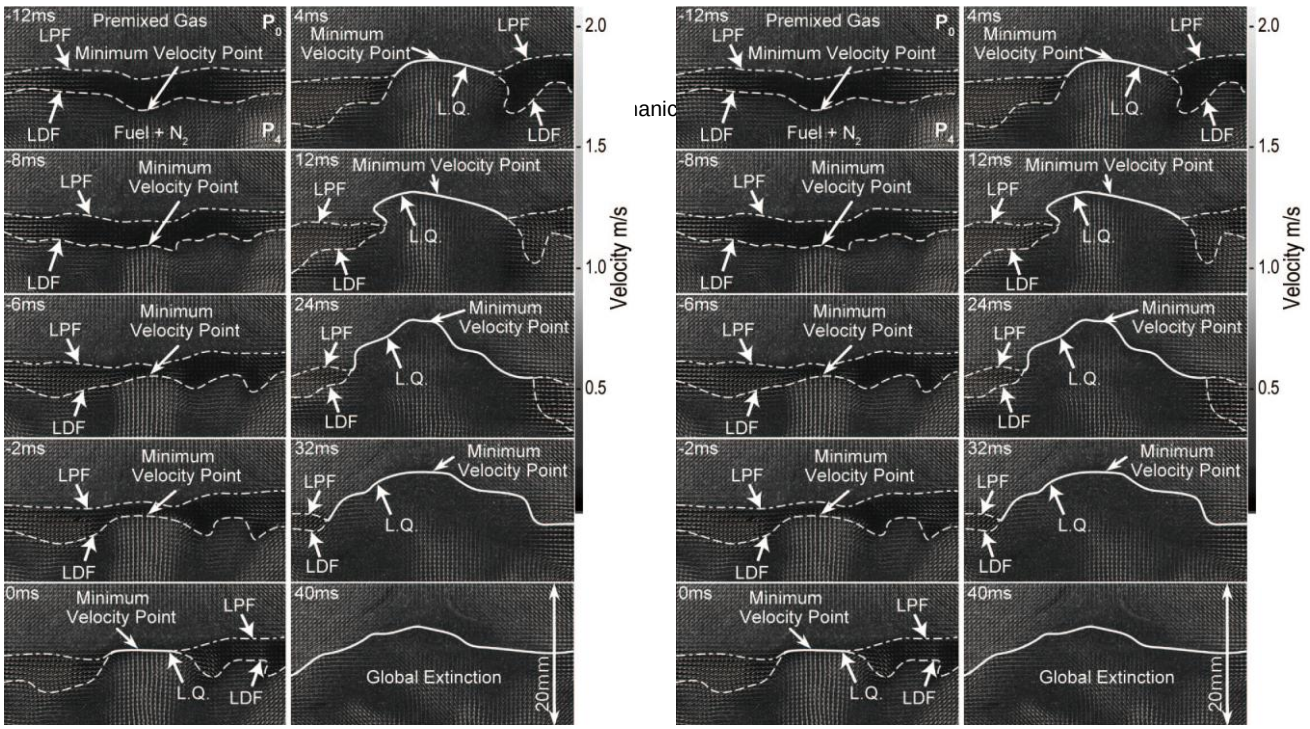

(a) Passive Local Quenching recovery (b) Active Local Quenching recovery

Figures 7. Local quenching recovery mechanism for turbulence added lean premixed gas side. (P_4, P_0, ϕ_0=0.6, χ_L=7.8%, T_{st}=0.33, shutter speed: 1/100 seconds)

Figures 8. Local Quenching possibility. The regions (A), (E), and (F) are corresponding as an active, an eddy and a passive local quenching recovery modes, respectively. Definition of the extinction limit is that the flames are formed 2 seconds is the opposite flow without a pilot flame burner which is used as an igniter.

LOCAL QUENCHING RECOVERY MECHANISM

Near the extinction limit, the local quenching phenomena can be observed frequently. As shown in Fig.5, if the large area of the local quenching occurs at the stagnating point, the local quenching area develops to the global extinction. However, the local quenching does not always lead to global extinction. In many cases, the flame can recover from the local quenching phenomena. Figure 6 shows the local quenching recovery mechanism in the same flow conditions as Fig. 5. The difference between this case and Fig. 5 is that the local quenching occurs slightly outside of the minimum velocity point (see frame 0ms). In frames 4ms to 12ms, the local quenching area develops slightly. However, the local quenching area leaves the minimum velocity point (see frames 16ms to 26ms). In this case, the local quenching area cannot be spread to the whole region. The local quenching flows to outside, then the flame can automatically recover from the local quenching (see frame 30ms).

TWO DIFFERENT LOCAL QUENCHING RECOVERY MECHANISMS

Figure 7 (a) and (b) show two distinct local quenching recovery mechanisms. In these cases, the turbulence generator is set on the upper burner, while the lower approaching flow is laminar. That is, the lean premixed flames are turbulent and the lower flow diffusion flame surface will be wrinkling to receive the turbulence energy from turbulent premixed flames.

There are two distinct local quenching recovery mechanisms. In the case of passive local quenching mode shown in Fig. 7 (a), the local quenching occurs slightly outside of the minimum velocity point (see frame 0ms). The local quenching area is drifting outward from the minimum velocity point as well as Fig. 6 and then it is displaced by the stable flames. Finally, the flames can be automatically recovered from the local quenching phenomena in accordance with the opposite flow properties. We called this mechanism a passive local quenching recovery mode.

As the other local quenching recovery mechanism, Fig. 7 (b) shows an active local quenching recovery mode. In this case, the local quenching occurs at the center including the minimum velocity point (see frames 0ms~4ms). The local quenching area can spread to the whole region. The flames are active in 3-dimensional space though the flames seem globally extinguished in 2-dimensions. In fact,

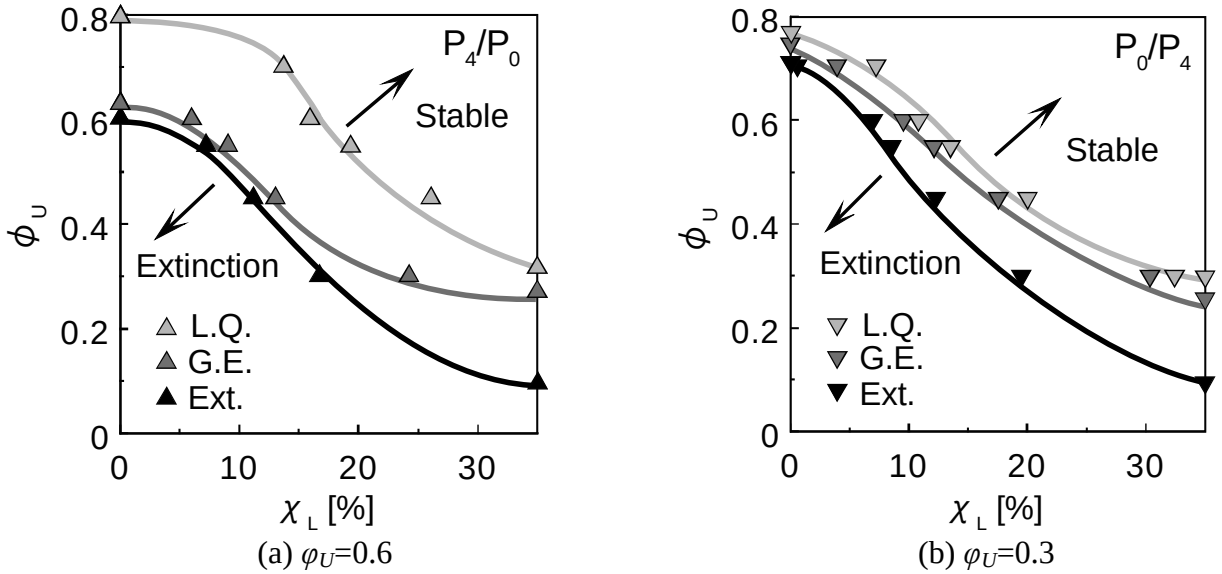

Figures 9. Extinction and Quenching boundary. L. Q., G. E. and Ext. are corresponding with the local quenching start line, the global extinction start line and the extinction limits, respectively.

the LPF propagates from the right side (see 20ms). In the 24ms frame, a LPF island also appears. These flame fronts are spreading until reaching the quenching surface. In the 28ms frame, the recovered LPF surface appears and spreads to the whole area. Finally, the flames can be recovered from the local quenching phenomena. We called this recovery mechanism induced by the flame propagation an active local quenching recovery mode.

As the common feature of local quenching phenomena of Fig. 5 and Fig. 7 (b), it is worthwhile to pay attention that the local quenching occurs in the regions of the minimum velocity point. Without the self-propagation, the flame may not recover from large scale local quenching if the quenching occurs within the minimum velocity point. Therefore, with the turbulence added in the premixed flame side shown in Fig. 7 (b), the wrinkled flamelet propagation plays a very important role for the recovery mechanism.

POSSIBILITY OF LOCAL QUENCHING TO GLOBAL EXTINCTION

As discussed previously, the local quenching is a trigger to induce global extinction. Tthe possibility of local quenching to global extinction mechanisms is affected by two factors. One is that the premixed flame side can propagate self-sustainably or not. Another factor is including the turbulence in the premixed flame side or in the diffusion flame side. Figure 8 (a) and (b) show the local quenching possibility of P_0/P_4 and P_4/P_0 for φ_U=0.6 and φ_U=0.3, respectively, where the number of local quenching or global extinction is normalized by the total image number of tomographic data (N/N_0) and shown on the ordinate, while the lower burner CH_4 mole fraction (χ_L) is shown on the abscissa. The three regions, (A), (E), and (P), in these figures correspond with the quenching mode difference. In the region (A), only an active local quenching recovery mode is observed. In the region (P), a passive local quenching recovery mode is mainly observed. In the region (E), an eddy transport local quenching recovery mode is additionally observed with a passive local quenching recovery mode.

In the case of the premixed flame side having self-propagation as shown in Fig. 8 (a), the region (A) is wider than region (P). In addition, for P_0/P_4 which has turbulence only in the fuel flow side, the extinction limit corresponds to the border of the regions (A) and (P). On the other hand, for P_4/P_0, the flame can be formed even passing the extinction limit of P_0/P_4 flame and the extinction limit may extend to the end of region (A). The difference of the extinction limits between P_0/P_4 and P_4/P_0 are 7.6% based on the χ_L. That is, the extinction limit of the P_4/P_0 can be extended 7.6% by an active local quenching recovery mechanism in this experimental condition.

In the case of the premixed flame not self-propagating as shown in Fig. 8 (b), we have two regions (E) and (P), where region (E) is narrower than region (P). To work the active local quenching recovery mode in the premixed flame not having self-propagation, the flame should be supporting from diffusion flame side. However, in this condition the premixed flame side is φ_U=0.3. So it is difficult to conclude that the quenched flame can recover by the active local quenching recovery mechanism. In fact, we have observed a similar recovery mechanism to an active local quenching recovery mode. It seems the local quenching area might recover by the reacting flow which is transported by the eddy. Therefore, in this stage we would call this recovery phenomenon an eddy transport local quenching recovery mode. The extinction limit of P_0/P_4 in Fig. 8 (b) also corresponds the boundary of (E) and (P).

EXTINCTION AND QUENCHING BOUNDARY

Figure 9 (a) and (b) show the extinction and quenching limits for P_4/P_0 and P_0/P_4, respectively, where the upper burner equivalence ratio (φ_U) on the ordinate and the lower burner CH_4 mole fraction diluted with N_2 (χ_L) on the abscissa. The extinction condition at χ_L=0 means lean premixed gas impinging on 100% N_2 gas flow and corresponds to a single premixed flame extinction limit. Here, we have three boundaries which are the local quenching start line (L. Q.), the global extinction start line (G. E.) and the extinction limits (Ext.). As mentioned previously, when the fuel concentration is decreasing, the flame front is locally quenched. However, the flame front easily can recover in the first stage. In the second stage the flame may suddenly extinguish, however, if we try to reignite the flame may reform. At the extinction limits, the flame very easily extinguishes and the flame cannot be sustained for 2 seconds even if we try to reignite.

In the case of P_4/P_0 shown in Fig. 9 (a), the boundary between the G. E. and L. Q. is wider than that of P_0/P_4 shown in Fig. 9 (b). The clearance of the G. E. and Ext. in the P_4/P_0 are getting wider and increases with χ_L. On the other hand, in the case of the P_0/P_4 the clearance of the G. E. and L. Q. is nearly constant regardless of χ_L. From these results, an active local quenching recovery mechanism is useful to extend the extinction limits. The mechanism works well with turbulence added to the premixed gas and when the mixture has the self-propagating condition.

CONCLUSIONS

The local quenching and recovery phenomena of impinging lean premixed CH_4 air flame (LPF) and lean CH_4 diluted with N_2 diffusion flame (LDF) with different turbulence conditions have been investigated experimentally for fundamental understanding of heterogeneous lean combustion. The reacting flows are visualized by a high speed time series of particle image velocimetry (PIV).

The local quenching phenomena can be observed frequently when approaching the extinction limit. If the large area of the local quenching occurs in the minimum velocity point, which corresponds to the stagnating point, the local quenching area leads to global extinction. However, local quenching does not always trigger global extinction. In many cases, the flame can recover from the local quenching phenomena.

Two distinct local quenching recovery mechanisms exist. One is a passive local quenching recovery mode and the other is an active local quenching recovery mode. In the passive local quenching recovery mode, the local quenching occurs slightly outside of the minimum velocity point. The local quenching area drifts outward from the minimum velocity point. Finally, the flames can be automatically recovered from the local quenching phenomena in accordance with the opposite flow properties. In the active local quenching recovery mode, local quenching occurs including the minimum velocity point. In this case, the flame recovers by the self-propagating wrinkled flamelet. Only when the turbulence is added to the premixed flame side, an active local quenching recovery mode is observed. From these results, an active local quenching recovery mechanism is useful to extend the extinction limits. The mechanism work well if the turbulence is added to the premixed

gas and the mixture has the self-propagating condition. In addition, the local quenching area might recover by the reacting flow transported by the eddy.

REFERENCES

1. Law, C. K., Combustion Physics, Cambridge University Press, 2006.
2. Yahagi, Y., Ueda, T., and Mizomoto, M., *Proc. Comb. Inst.*, 24, pp.537-542, 1992.
3. Yahagi, Y., Ueda, T., and Mizomoto, M., Proceedings of 15th International Colloquium on the Dynamics of Explosions and Reactive System, pp.114-117, 1995.
4. Yahagi, Y., and Katahara, K., The proceedings of the 6th Pacific Symposium on Flow Visualization and Image Processing, pp1-6, 2007.
5. Takagi, Y., *Proc. Comb.Inst.*, 27, pp.2055-2068, 1998.
6. Haworth, D. C., Blint, R. J., Cuenot, B., and Poinsot, T. J., *Combust. Flame,* Vol.121, pp395-417, 2000.
7. Jimenez, C., Cuenot, B., and Poinsot, T., and Haworth, D., *Combust. Flame,* Vol.128, pp1-21, 2002.
8. Yahagi, Y., and Nihei, H., *Proceedings of the Second Joint Meeting of the U.S. Sections of the Combustion Institute,* pp.1-7, (CD-R), 2001.
9. Yahagi, Y., Nakahara, S., Hamatsu, K., and Takeuchi, M., *Proceedings of The Second Joint Meeting of the U.S. Sections of the Combustion Institute*, pp.1-7, (CD-R), 2003.
10. Du, J. and Axelbaum, R. L., *Proc. Comb.Inst.*, 26, pp.1137-1142, 1996.
11. Kostiuk, L. W., Bray, K. N. C., and Cheng, R. K., Combust. Flame, Vol.92, pp.396-409, 1993.
12. Kostiuk, L. W., Shepherd, I. G., and Bray, K. N. C., Combust. Flame, Vol.118, pp.129-139, 1999.

LIQUID MIXING IN A BUBBLE COLUMN

N. Shimada[1,*], R. Saiki[1] and A. Tomiyama[2]
[1]Sumitomo Chemical Co. Ltd., Sobiraki-cho 5-1, Niihama, Ehime, Japan
[2]Garduate School of Engineering, Kobe University, Rokkodai 1-1, Nada, Kobe, Japan

ABSTRACT. The performance of a bubble column strongly depends on the liquid mixing induced by bubbles in the column. It is, therefore, important to evaluate the degree of liquid mixing for column design. However, few quantitative investigations have been carried out on two-phase turbulence and liquid mixing. In this study, a one-dimensional liquid mixing coefficient has been measured using a tracer detection method and compared with numerical simulations using a multi-fluid model. A parameter ϕ, which determines the contribution of shear-induced turbulence, was adopted in a two-phase turbulence model based on a linear superposition of bubble-induced turbulence and shear-induced turbulence. Good predictions were obtained for a wide range of gas superficial velocity and liquid superficial velocity by adding 10% contribution of shear-induced turbulence to bubble-induced turbulence, i.e. by setting $\phi = 0.1$.

Keywords: *bubble column, liquid mixing, conductance method, turbulence flow, simulation*

INTRODUCTION

The performance of a bubble column strongly depends on the liquid mixing induced by bubbles. For example, if intermediate products in successive reactions are desired, the column performance may be deteriorated by strong mixing [1]. Figure 1 shows a comparison of yields in successive reaction (A→R→S) between perfectly mixed flow and piston flow (i.e, flow without back mixing). The selectivity of R in the piston flow is larger than that in the perfectly mixed flow at any conversion of A. It is, therefore, important to evaluate the degree of liquid mixing when designing bubble columns. Though several efforts [2, 3] have been made to quantitatively measure liquid mixing in a bubble column, it is very difficult to deduce a liquid mixing model applicable to various bubble columns only from limited experimental data.

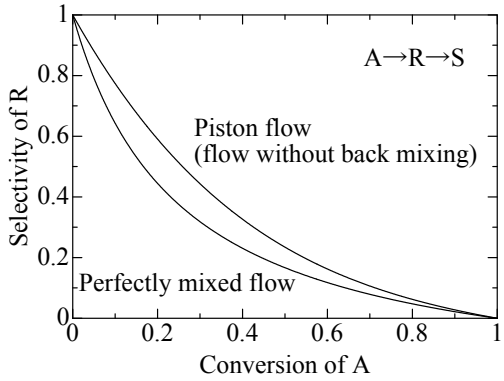

Fig. 1 Effect of mixing for yield in successive reactions [1]

* Corresponding author: Dr. N. Shimada
Phone: + (81)-897-37-4138, Fax: + (81)-897-37-4181
E-mail address: shimadan@sc.sumitomo-chem.co.jp

If we can develop a reliable numerical method for predicting turbulent bubbly flow in a bubble column, we will be able to overcome this situation and use the method as a tool for designing bubble columns. Hence the authors [4-8] have been developing a three-dimensional CMFD (Computational Multi-Fluid Dynamics) method based on a hybrid combination of an interface tracking method and a multi-fluid model, which we refer to as NP2-3D because it can deal with N bubble groups Plus 2 continuous phases simultaneously.

In this study, a one-dimensional liquid mixing coefficient in a bubble column has been measured using a tracer detection method and compared with NP2 predictions. Since bubbly flow in bubble columns is turbulent and liquid mixing is strongly affected by the flow, we have focused our attention on two-phase turbulence models implemented in NP2-3D.

EXPERIMENTAL SETUP

Figure 2 shows a schematic of the experimental apparatus. The column diameter is 0.3 m, and the height is 1 m. The column wall is made of transparent polyvinyl chloride. Tap water was fed from the bottom of the column, and air was sparged from the two ring-type spargers installed in the column. The spargers are 0.25 m in diameter, and have equally spaced eight holes. They are aligned at heights of 0.25 m and 0.75 m from the bottom of the column. There is one outlet at the top of the column. Table 1 shows the experimental conditions. Experiments were carried out under eight sets of conditions. All conditions were within the homogeneous flow regime as shown in Fig. 3. The system temperature and pressure were about 20.8 deg C and 0.1 MPa, respectively.

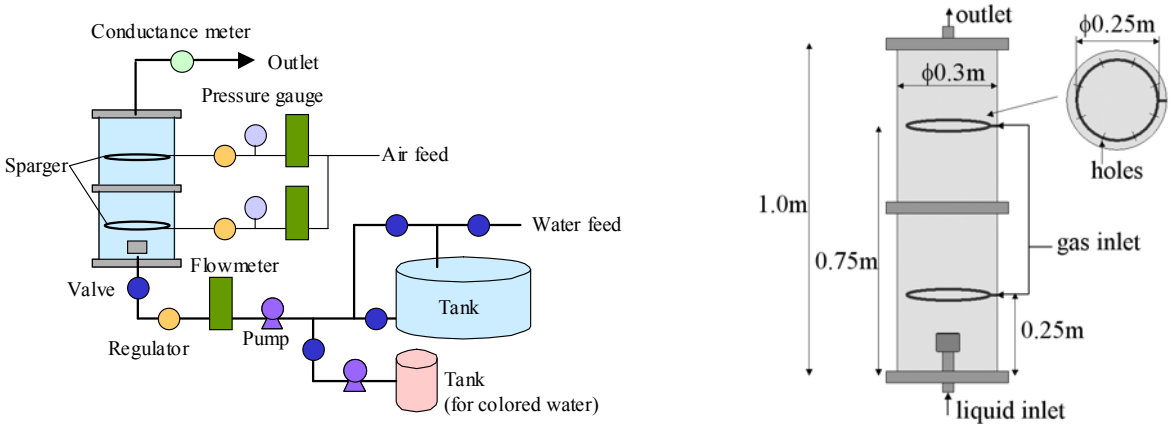

(a) Schematic of system (b) Detail of the column

Fig. 2 Schematic of experimental apparatus

Table 1 Experimental Condition

Run No.	Superficial velocity of liquid [cm/s]	Gas flow rate	
		Upper/Total ratio [%]	Total superficial velocity [cm/s]
1	1.0	50	1.50
2	0.5	50	0.75
3	1.0	50	3.00
4	1.0	50	2.25
5	1.0	50	0.75
6	1.0	50	0.38
7	1.0	25	1.50
8	1.0	75	1.50

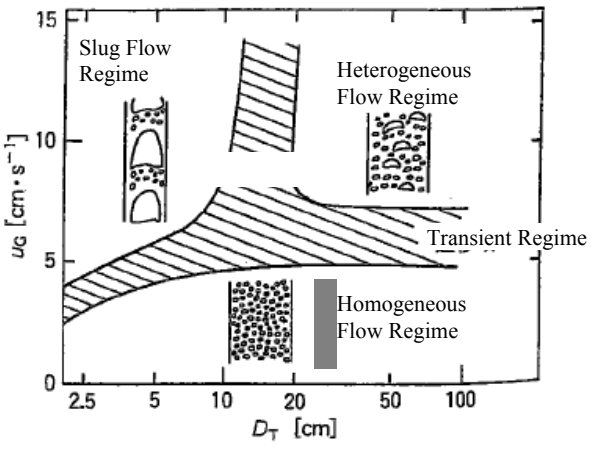

Fig. 3 Flow regime in a bubble column [9]

After a steady state was established, salt and coloring agent were stepwisely injected into the feed water. The salt concentration was 0.07 wt%. Figure 4(a) shows an example of observed tracer motion in Run 1. A conductance meter measured the concentration of salt solution at the outlet (Fig. 4(b)), from which the one-dimensional liquid mixing coefficient D was evaluated using the following equation:

$$\frac{\partial C}{\partial t} + U_{\mathrm{L}} \frac{\partial C}{\partial z} = D \frac{\partial^2 C}{\partial z^2} \tag{1}$$

where t is the time, C the salt concentration, U_{L} the liquid superficial velocity and z the axial coordinate. Measured values of C were substituted into Eq. (1), and Eq. (1) was solved for D [10]. The Euler explicit method was used for the time difference, and QUICK[11] and the central difference schemes were used for convection and diffusion terms, respectively.

Bubble size distributions in the column were also measured. A high speed video camera (Photoron, FASTCAM-512PCI) was used to obtain close-up images of bubbles. Figure 5(a) shows the effect of the superficial gas velocity U_{G} on bubbles. The peripheral length and area of each bubble were measured, from which the Sauter mean diameter was obtained by assuming spheroidal bubble shapes. Figure 5(b) and Table 2 show the measured size distributions. These data were used in the simulations described below.

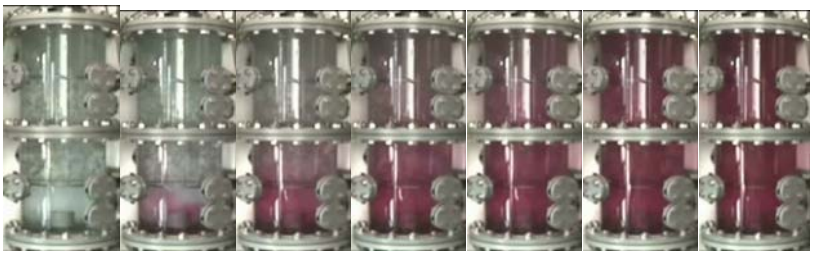

(a) Mixing process of tracers (red-colored)

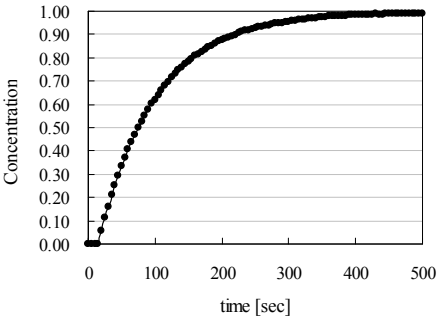

(b) Transient pattern of salinity at the outlet of the column

Fig. 4 Example of tracer measurements (Run 1)

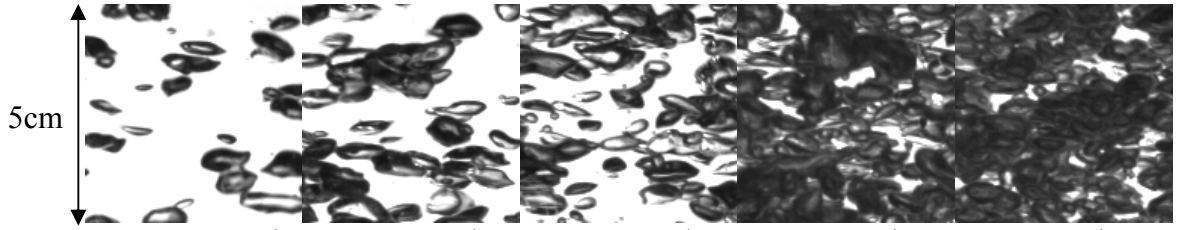

U_{G}=0.0019m/s 0.0037m/s 0.0075m/s 0.0112m/s 0.0150m/s

(a) Snapshots in the column (U_{G}: Superficial Gas Velocity)

OUTLINE OF NP2-3D

The hybrid method, NP2-3D, which is based on the combination of multi-fluid and interface tracking methods [7], was used to simulate the flow. This model classifies the phases in a flow into N+2 groups: one continuous gas phase (G), one continuous liquid phase (L) and N dispersed bubble groups (B_m, m = 0, 1, ..., N). When the length scale of a gas-liquid interface is much larger than the cell size Δx, the two phases separated by the interface are regarded as continuous gas and liquid fields. Bubbles smaller than or comparable to Δx are classified into N groups in terms of their sizes. The volume fraction α of each phase field satisfies

$$\alpha_{\mathrm{G}} + \alpha_{\mathrm{L}} + \sum_{m=1}^{N} \alpha_{\mathrm{B}m} = 1 \tag{2}$$

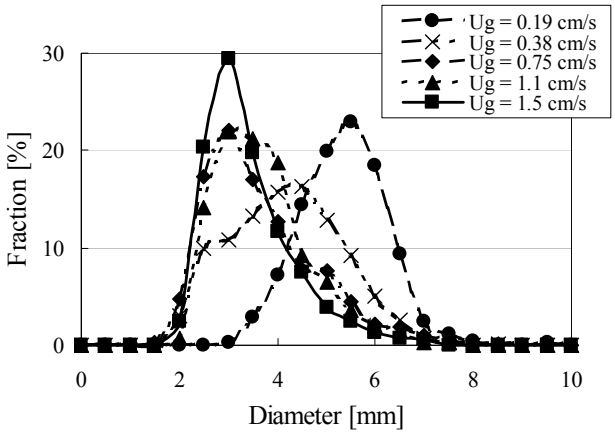

(b) Bubble diameter distribution

Fig. 5 Bubble behavior in a column

Table 2 Bubble group in each case

Run	Superficial velocity of liquid [cm/s]	Gas flow rate		Bubble diameter[mm]/fraction[%]		
		Upper/Total ratio [%]	Total superficial velocity [cm/s]	1	2	3
1	1.0	50	1.50	3.2/33.8	4.7/37.4	6.4/28.8
2	0.5	50	0.75	3.7/39.0	5.0/37.2	6.1/23.8
3	1.0	50	3.00	3.1/48.5	4.6/35.1	6.2/16.4
4	1.0	50	2.25	3.3/39.0	4.6/40.7	6.2/20.3
5	1.0	50	0.75	3.7/39.0	5.0/37.2	6.1/23.8
6	1.0	50	0.38	4.5/27.5	5.5/46.6	6.6/25.9
7	1.0	25	1.50	3.4/20.5(upper) /45.3(lower)	4.7/55.7(upper) /31.8(lower)	4.7/23.8(upper) /22.9(lower)
8	1.0	75	1.50	3.4/45.3(upper) /20.5(lower)	4.7/31.8(upper) /55.7(lower)	4.7/22.9(upper) /23.8(lower)

For simplicity, the gas and liquid phases are assumed to be incompressible Newtonian fluids without phase change, and viscous and turbulent diffusion in the dispersed phases is postulated to be negligible. The cell-volume averaged mass and momentum equations are then given by

$$\frac{\partial \alpha_{\mathrm{B}m}}{\partial t}+\nabla\cdot\left(\alpha_{\mathrm{B}m}\boldsymbol{V}_{\mathrm{B}m}\right)=\frac{1}{\rho_{\mathrm{B}m}}\left(\sum_{m'=1}^{N}\Gamma^{\mathrm{CB}}_{\mathrm{B}m\mathrm{B}m'}-\Gamma^{\mathrm{CB}}_{\mathrm{GB}m}\right) \tag{3}$$

$$\frac{\partial \alpha_{\mathrm{G}}}{\partial t}+\nabla\cdot\left(\alpha_{\mathrm{G}}\boldsymbol{V}_{\mathrm{C}}\right)=\frac{1}{\rho_{\mathrm{G}}}\sum_{m=1}^{N}\Gamma^{\mathrm{CB}}_{\mathrm{GB}m} \tag{4}$$

$$\frac{\partial \alpha_{\mathrm{L}}}{\partial t}+\nabla\cdot\left(\alpha_{\mathrm{L}}\boldsymbol{V}_{\mathrm{C}}\right)=0 \tag{5}$$

$$\frac{\partial \boldsymbol{V}_{\mathrm{B}m}}{\partial t}+\boldsymbol{V}_{\mathrm{B}m}\cdot\nabla\boldsymbol{V}_{\mathrm{B}m}=-\frac{1}{\rho_{\mathrm{B}m}}\nabla P+\boldsymbol{g}-\frac{1}{\rho_{\mathrm{B}m}\alpha_{\mathrm{B}m}}\left(\boldsymbol{M}^{\mathrm{F}}_{\mathrm{LB}m}+\boldsymbol{M}^{\Gamma}_{\mathrm{LB}m}\right) \tag{6}$$

$$\frac{\partial \boldsymbol{V}_{\mathrm{C}}}{\partial t}+\boldsymbol{V}_{\mathrm{C}}\cdot\nabla\boldsymbol{V}_{\mathrm{C}}=-\frac{1}{\rho_{\mathrm{C}}}\nabla P+\boldsymbol{F}^{\mu}+\boldsymbol{F}^{\mathrm{S}}+\boldsymbol{g}+\frac{1}{\rho_{\mathrm{C}}\alpha_{\mathrm{C}}}\sum_{m=1}^{N}\left(\boldsymbol{M}^{\mathrm{F}}_{\mathrm{LB}m}+\boldsymbol{M}^{\Gamma}_{\mathrm{LB}m}\right) \tag{7}$$

where $\boldsymbol{V}$ is the velocity, ρ the density, $\Gamma^{\mathrm{CB}}_{\mathrm{GB}m}$ the gas volume transfer from the bubble group m to the continuous gas phase, $\Gamma^{\mathrm{CB}}_{\mathrm{B}m\mathrm{B}m'}$ the gas volume transfer to the group m due to bubble coalescence and breakup, P the pressure, $\boldsymbol{g}$ the gravity, $\boldsymbol{M}^{\mathrm{F}}_{\mathrm{LB}m}$ the interfacial momentum transfer between the bubble group m and the liquid phase, $\boldsymbol{M}^{\Gamma}_{\mathrm{LB}m}$ the momentum transfer associated with the mass transfer $\Gamma_{\mathrm{GB}m}$,

$\boldsymbol{F}^{\mu}$ the viscous diffusion, and $\boldsymbol{F}^{S}$ the surface tension force. Note that we do not need two momentum equations for the two continuous phases because NP2-3D is based on the one-field approximation for the two continuous phases. Hence the volume fraction α_{C} in equation (7) is defined by $\alpha_{\mathrm{C}} = \alpha_{\mathrm{G}} + \alpha_{\mathrm{L}}$, and ρ_{C} is defined by

$$\rho_{\mathrm{C}} = \frac{\rho_{\mathrm{L}}\alpha_{\mathrm{L}} + \rho_{\mathrm{G}}\alpha_{\mathrm{G}}}{\alpha_{\mathrm{L}} + \alpha_{\mathrm{G}}} \tag{8}$$

When no dispersed phases are present, i.e. when $N = 0$, Eqs. (2)-(8) reduce to the field equations for interface tracking methods (ITM). On the other hand, they reduce to the (N+1)-fluid model (MFM; [8]) when $\alpha_{\mathrm{G}} = 0$. Thus NP2-3D includes ITM and MFM as subsets.

The interfacial momentum transfer term $\boldsymbol{M}^{\mathrm{F}}_{\mathrm{LB}m}$ is given by:

$$\begin{aligned}\boldsymbol{M}^{\mathrm{F}}_{\mathrm{LB}m} &= \boldsymbol{M}_{\mathrm{D}m} + \boldsymbol{M}_{\mathrm{VM}m} + \boldsymbol{M}_{\mathrm{LF}m} + \boldsymbol{M}_{\mathrm{TD}m} \\ &= \frac{1}{8} a_{\mathrm{int}\,m} C_{\mathrm{D}m} \rho_{\mathrm{L}} \left|\boldsymbol{V}_{\mathrm{B}m} - \boldsymbol{V}_{\mathrm{C}}\right| \left(\boldsymbol{V}_{\mathrm{B}m} - \boldsymbol{V}_{\mathrm{C}}\right) + \alpha_{\mathrm{B}m} C_{\mathrm{VM}m} \rho_{\mathrm{L}} \left[\frac{D_{\mathrm{B}m}\boldsymbol{V}_{\mathrm{B}m}}{Dt} - \frac{D_{\mathrm{C}}\boldsymbol{V}_{\mathrm{C}}}{Dt}\right] \\ &\quad + \alpha_{\mathrm{B}m} C_{\mathrm{LF}m} \rho_{\mathrm{L}} \left(\boldsymbol{V}_{\mathrm{B}m} - \boldsymbol{V}_{\mathrm{C}}\right) \times \nabla \times \boldsymbol{V}_{\mathrm{C}} + C_{\mathrm{TD}m} \rho_{\mathrm{L}} k_{\mathrm{L}m} \nabla \alpha_{\mathrm{B}m}\end{aligned} \tag{9}$$

where a_{int} is the interfacial area concentration, $\boldsymbol{M}_{\mathrm{D}}$ the drag force, $\boldsymbol{M}_{\mathrm{VM}}$ the virtual mass force, $\boldsymbol{M}_{\mathrm{LF}}$ the lift force, $\boldsymbol{M}_{\mathrm{TD}}$ the turbulent dispersion force, C_{D} the drag coefficient, C_{VM} the virtual mass coefficient, D/Dt the substantial derivative, C_{L} the lift coefficient, C_{TD} the turbulent dispersion coefficient, and k_L the turbulence kinetic energy. The viscous diffusion is given by

$$\begin{aligned}\boldsymbol{F}^{\mu} &= \nabla \cdot \left[\alpha_{\mathrm{C}} \mu_{\mathrm{C}} \left\{\nabla \boldsymbol{V}_{\mathrm{C}} + \left(\nabla \boldsymbol{V}_{\mathrm{C}}\right)^{\mathrm{T}}\right\}\right] \\ \mu_{\mathrm{C}} &= \frac{\mu_{\mathrm{L}}\alpha_{\mathrm{L}} + \mu_{\mathrm{G}}\alpha_{\mathrm{G}}}{\alpha_{\mathrm{L}} + \alpha_{\mathrm{G}}}\end{aligned} \tag{11}$$

where μ_{L} and μ_{G} are the viscosities of the continuous liquid and gas phases, respectively. Details on closure relations and solution procedure can be found in [4,7].

The viscosity μ_{C} of the continuous liquid must be accurately modeled for good predictions of the liquid mixing in the column. The liquid viscosity μ_{L} can be estimated by

$$\mu_{\mathrm{L}} = \mu^{\mathrm{Re}} + \mu^{\mathrm{M}}$$

where μ^{M} and μ^{Re} are the molecular and turbulent eddy viscosities, respectively.

Lopez de Bertodano *et al*. [12] proposed a two-phase turbulence model based on a linear superposition of bubble-induced turbulence (BI) and shear-induced turbulence (SI). In this model, μ^{Re} is given by

$$\mu^{\mathrm{Re}} = \mu^{\mathrm{BI}} + \mu^{\mathrm{SI}}$$

Hereafter, this model is referred to as “Model A”. Then, a model which accounts for only shear-induced turbulence is called “Model B”:

$$\mu^{\mathrm{Re}} = \mu^{\mathrm{BI}}$$

Equation (14) is based on the intuition that the effects of walls in a bubble column are much smaller than those in pipe flows.

The bubble-induced and shear-induced turbulences were calculated using Sato's model [13] and the k-ε model [14], respectively:

$$\mu_{\mathrm{BI}} = C_{\mu\mathrm{B}} \sum_{m=1}^{N} \alpha_{\mathrm{B}m} d_{Bm} \rho_{\mathrm{L}} \left(\boldsymbol{V}_{\mathrm{B}m} - \boldsymbol{V}_{\mathrm{C}} \right) \tag{15}$$

$$\mu_{\mathrm{SI}} = \rho_{\mathrm{C}} C_{\mu} \frac{k_{\mathrm{SI}}^2}{\varepsilon} \tag{16}$$

$$\alpha_{\mathrm{c}} \frac{D}{Dt} k_{\mathrm{SI}} = \nabla \cdot \alpha_{\mathrm{c}} \left(\frac{\nu_{\mathrm{cL}}}{\sigma_{\mathrm{k}}} \nabla k_{\mathrm{SI}} \right) + \alpha_{\mathrm{c}} \left(p_{\mathrm{k}} - \varepsilon \right) \tag{17}$$

$$\alpha_{\mathrm{c}} \frac{D}{Dt} \varepsilon = \nabla \cdot \alpha_{\mathrm{c}} \left(\frac{\nu_{\mathrm{cL}}}{\sigma_{\varepsilon}} \nabla \varepsilon \right) + \alpha_{\mathrm{c}} \left(C_{\varepsilon 1} \frac{\varepsilon p_{\mathrm{k}}}{k_{\mathrm{SI}}} - C_{\varepsilon 2} \frac{\varepsilon^2}{k_{\mathrm{SI}}} \right) \tag{18}$$

$$p_{\mathrm{k}} = \nu_{\mathrm{cL}} \left(\nabla \boldsymbol{V}_{\mathrm{C}} + \nabla \boldsymbol{V}_{\mathrm{C}}^{\mathrm{T}} \right) : \nabla \boldsymbol{V}_{\mathrm{C}} \tag{19}$$

where k_{SI} is the turbulence energy, p_{k} the production term, and ε the turbulent dissipation rate. The recommended parameters are used in Eqs. (15)-(19): $C_{\mu} = 0.09$, $C_{\mu\mathrm{B}} = 0.6$, $\sigma_{\mathrm{k}} = 1.0$, $\sigma_{\varepsilon} = 1.3$, $C_{\varepsilon 1} = 1.44$, $C_{\varepsilon 2} = 1.92$. The tracer concentration is computed using the following transport equation:

$$\frac{\partial C}{\partial t} + \nabla \cdot \left(C \boldsymbol{V}_{C} \right) = 0 \tag{20}$$

COMPARISON AND DISCUSSION OF TURBULENCE MODEL

Simulations were compared with the experiments to verify the models. The grid size was $\Delta x = \Delta y = \Delta z = 0.02$ m. The total number of cells was 19×19×55=19855. Our previous studies confirmed that good predictions of void fraction distributions can be obtained using a grid size less than 0.1 m (eg. [4]). After 150 sec from the start of gas and liquid injection, the steady state was established. Then tracers (C = 1) were introduced from the liquid inlet. Calculation for t = 650 sec required about 11 hours using a personal computer (CPU: Xeon 3.0 GHz, Memory: 2GB).

Figure 6 shows comparisons between measured and predicted D. The effects of U_{L} and U_{G} on D were investigated. In addition, the effect of the ratio γ of the gas flow rate from the upper sparger to that from the lower one,

$$\gamma = \frac{Q_{\mathrm{G\,upper}}}{Q_{\mathrm{Gtotal}}} = \frac{Q_{\mathrm{G\,upper}}}{Q_{\mathrm{Gupper}} + Q_{\mathrm{Glower}}} \tag{21}$$

was also examined. Here Q_{Gupper} is the gas flow rate from the upper sparger, Q_{Gtotal} the total gas flow rate, and Q_{Glower} the gas flow rate from the lower sparger.

The experimental data show that (1) the effect of U on D is small, (2) D increases with U_{G}, (3) D depends on γ at constant Q_{Gtotal}. The Model A prediction was 30-50% lower than the measured D. This means Model A overestimates μ^{Re}, which has been also pointed out by Sokolichin and Eigenberger [15]. On the other hand, Model B underestimates μ^{Re}. Menzel [16] has pointed out that there are convex distributions of liquid velocity in the cross section even at U_{L}=0 cm/s. This indicates that shear-induced turbulence is not negligible even at low U_{L}.

To examine the contribution of shear-induced turbulence, we tested the turbulence eddy viscosity μ^{Re} given by

$$\mu^{\mathrm{Re}} = \mu^{\mathrm{BI}} + \phi\mu^{\mathrm{SI}} \tag{22}$$

where ϕ ($0 \le \phi \le 1$)is a parameter representing the contribution of SI.

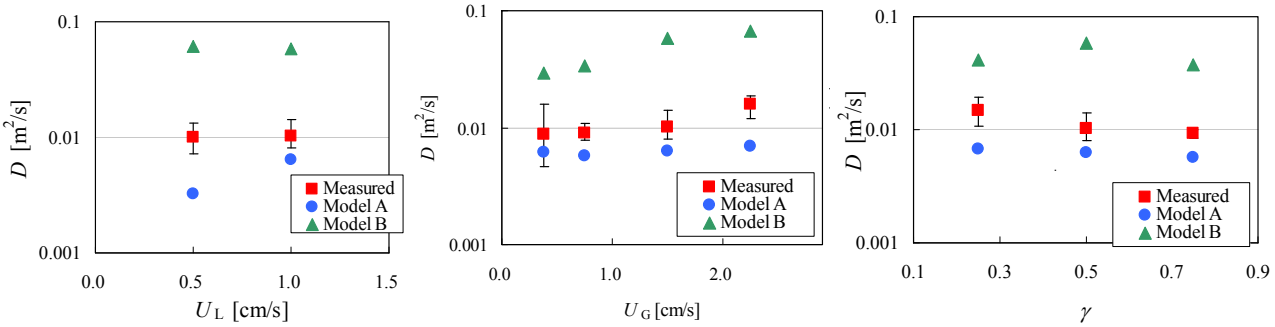

(a) Effect of U_{L} (b) Effect of U_{G} (c) Effect of γ

Fig. 6 Comparison with available models

Figure 7(a) shows the tracer motion predicted by using $\phi = 0.1$, which is close to Fig. 4(a). Figure 7(b) shows a comparison of the tracer concentration at the outlet. Figure 8 shows comparisons of D by taking U_{L}, U_{G} and γ as parameters. These comparisons clearly show that $\phi = 0.1$ gives good predictions.

As a result, we could confirm that the liquid mixing in a given bubble column can be well predicted, provided that we can find an appropriate value of ϕ in Eq. (22) for the given column.

This kind of information is of great use in the column design. In addition to the liquid mixing, the gas hold up, gas absorption rate, temperature and so on are also obtained in the simulation. Further studies should be, however, indispensable to make the method as a reliable engineering tool, especially on sparger design, column diameter, internal structure, and so on.

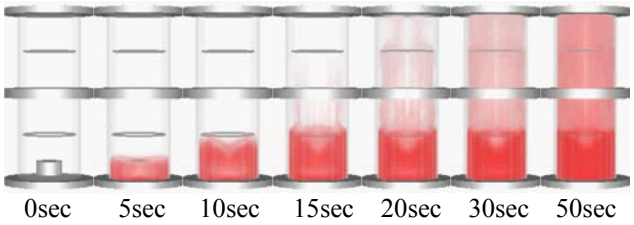

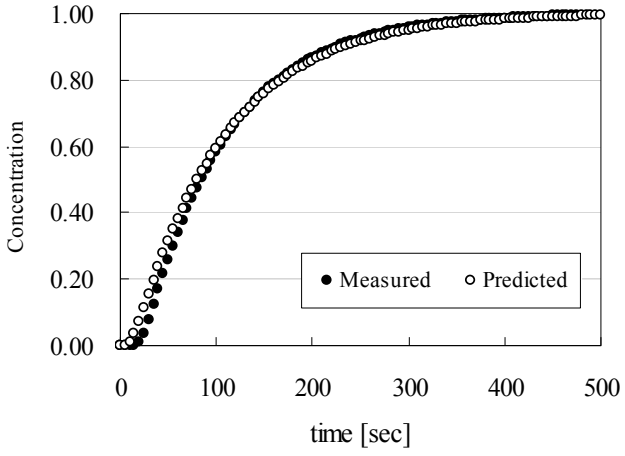

(a)Predicted tracer motion(U_g=1.5cm/s, ϕ=0.1) (b)Tracer concentration at the outlet

Fig. 7 Example of tracer motion (Run 1)

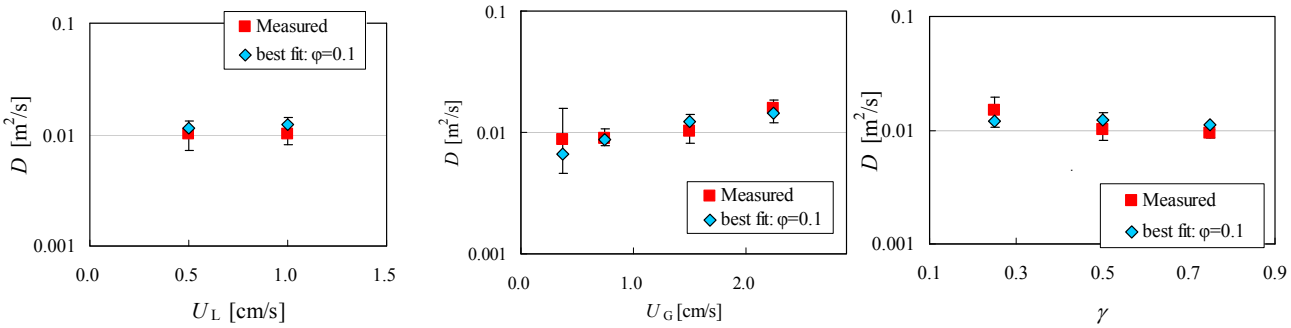

(a) Effect of U_L (b) Effect of U_G (c) Effect of γ

Fig. 8 Comparison with best fit ϕ=0.1

CONCLUSION

A one-dimensional liquid mixing coefficient has been measured using a tracer detection method and compared with numerical simulations using a multi-fluid model. A parameter ϕ, which determines the contribution of shear-induced turbulence, was adopted in a two-phase turbulence model based on a linear superposition of bubble-induced turbulence and shear-induced turbulence. Good predictions were obtained for a wide range of gas superficial velocity and liquid superficial velocity by adding 10% contribution of shear-induced turbulence to bubble-induced turbulence, i.e. by setting ϕ = 0.1. This means that the degree of liquid mixing in a given bubble column can be well predicted by taking into account an appropriate amount of contribution of shear-induced turbulence.

REFERENCES

1. Hashimoto, K., Chemical reaction engineering, Revised Edition (Kaiteiban Hanno Kogaku), Baifukan, Tokyo, Japan (1993)
2. Aoyama, Y., *et al.*, *J. chem. Eng. Jpn.*, 1, 158 (1968)
3. Towell and Ackerman, *Proc. Fifth European 2nd Int. Symp. Chem. React. Eng.*, B3-1. (1972)
4. Shimada N., *et al*, *Kagakukougaku Ronbunshu*, 29 (6), 778-786 (2003)
5. Shimada N., *et al*, *Kagakukougaku Ronbunshu*, 31 (6), 377-387 (2005)
6. Shimada N. *et al.*, *Proc. Int. Conf. Multiphase Flow, CD-ROM* (2007)
7. Tomiyama A. and Shimada N., *CFD Journal*, 9 , 418-426 (2001)
8. Tomiyama A. and Shimada N., *Trans. ASME, J. Pressure Vessel Technology*, 123, 510-516 (2001)
9. Decker, D. *et al*., *Ind. Eng. Chem., Process Des. Dev.*, 19, 699 (1980)
10. Kuroda, H., Computational Programing using Visual Basic (Visual Basic niyoru Suuchikaiseki Program), CQ shuppan, Tokyo, Japan (2002)
11. Leonard B. P., *Comput. Meths. Appl. Mech. Eng.*, 19, 59-98 (1979)
12. Lopez de Bertodano *et al*., *Int. J. of Multiphase Flow*, 20(5), 805-818 (1994)
13. Sato *et al.*, *Int. J. of Multiphase Flow*, 7, 179-190 (1981)
14. Launder B. E. and Spalding D. B., *Computer Methods in Applied Mechanics and Engineering*, 3, 269-289,(1974).
15. Sokolichin and Eigenberger, *Chem. Eng. Sci.*, 49(24B), 5735-5746 (1994)
16. Menzel, T. *et al*., *Ind. Eng. Chem. Res.*, 29, 988–994. (1990)

THE STRUCTURE OF VELOCITY AND VORTICITY FLOW FIELDS IN THE NEAR WAKE REGION OF A COROTATING VORTEX PAIR

A. Romeos, D. Triantafyllidou, T. Panidis*
Laboratory of Applied Thermodynamics, University of Patras, Patras, Greece

ABSTRACT. The formation-interaction field of a pair of corotating vortices, generated by a split wing configuration, with equal and opposite angles of attack has been studied experimentally, using an in-house designed and constructed 12-sensor hotwire vorticity probe. Simultaneous measurements of all three components of the velocity and vorticity vectors were conducted for Re_c = 133,000, on a cross plane grid, at a distance of 0.3 wing cord lengths, *c,* behind the trailing edge. Due to the proximity of the wings the two streams, which fold around the tips to generate the vortices, collide creating on the cross plane flow a stagnation point and an "impermeable" line joining the two vortex centres. Along this line fluid is directed towards the two vortices, expanding their cores and increasing their separation distance. Vortices' cores are characterised by the presence of a dipole of opposite sign streamwise mean vorticity and a significant streamwise velocity deficit. The turbulent flow field is the result of fluctuations of the intensity of formation and wandering effects.

Keywords: *vortex pair, co-rotating vortices, multisensor hot wire anemometry,*

INTRODUCTION

Vortices generated at the wing tips of an aircraft, constitute a probable hazard affecting the capacity, the safety and the environmental impact of the air transport system. They also represent an intriguing challenge for modern fluid dynamics since they represent distinctive unit coherent structures. The importance of tip vortices has motivated many research efforts during the last decades. Understanding the interaction and merging process of counter and co-rotating vortices is an important element in the study of the vortex system of an aircraft. The interaction of co–rotating vortices generated by aircraft wings is characterized by turbulence that influences the lifetime of the wake. The vortex pairing process, in most of the cases, leads to the formation of a single, stable and significantly larger vortex.

Regarding the interaction and merging process for a pair of corotating vortices, Cerretelli & Williamson [1] suggested a mechanism incorporating four phases, namely: i) an initial stage of diffusive growth, ii) a convective merging phase, iii) a second diffusive stage in which vorticity is reorganized and iv) a final stage where the merged vortex diffuses. Initially, the two cores move away from each other until a critical growth of their radius. The rotational velocity field around each core induces a rotational velocity to the other core and thus the two cores are converging, developing a braid of spiralling vortices, which finally merges to a new stable linear vortex (Devenport et al. [2], Chen et al. [3]).

* Corresponding author: Prof. T. Panidis
Phone: + 30 2610-997242, Fax: + 30 2610-997271
E-mail address: panidis@mech.upatras.gr

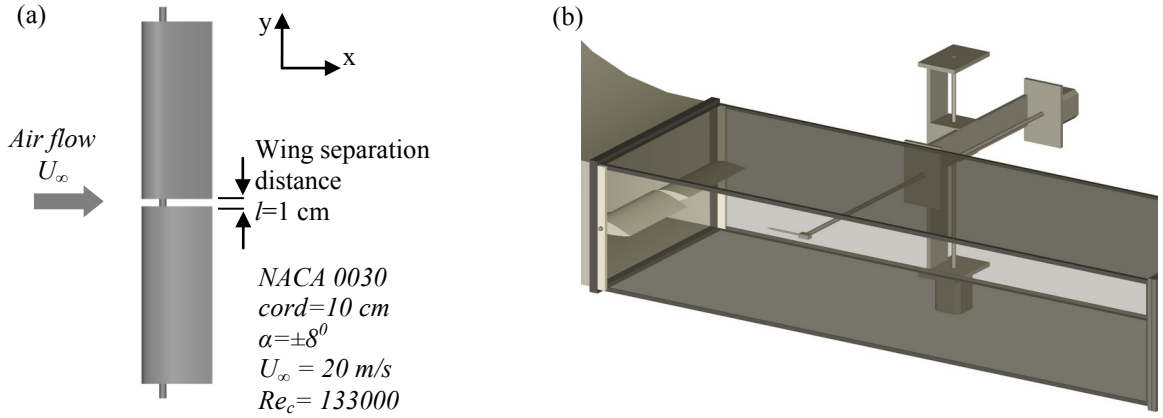

Figure 1. (a) Split-wing arrangement, (b) Wings and hotwire probe placed at the test section

As vortices start to interact, the two cores lose their symmetry and obtain an elliptical formation. Previous studies on two-dimensional vortex interaction attributed the distortion of the vortex cores into an ellipse to the existence of strain rate field of one vortex action upon the other (Moore & Saffman [4], Melander et al. [5, 6]).

In case of three – dimensional vortex interaction, the viscous phase before merging lasts long enough and a three – dimensional short – wavelength elliptic instability is developed (Meunier & Leweke [7], Dizes & Verga [8], Jacquin et al. [9]). This significant feature of corotating vortex interaction plays dominant role in the total flow evolution. This instability is different compared with Crow's [10] long-wavelength elliptic instability, which develops in counter rotating vortices and controls the vortex cores deformation. Furthermore, as proved by Jimenez [11], Crow's instability is not active in corotating vortex systems. Important aspects, as well as open issues, on the physics of trailing vortices have been presented and discussed in several review papers (Rossow [12], Spalart [13]).

The present work is part of ongoing research on corotating vortex interaction (Romeos et al. [14]) and provides experimental information on particular aspects associated with the formation and initial interaction of a pair of corotating vortices produced by a split wing configuration. These phenomena are encountered between vortices generated at wing tips and flaps or fuselage and also on many wake vortex alleviation devices. The flow field is characterized by a number of significant mechanisms that appear to determine the formation of the vortex pair flow field as well as the life expectancy of the vortical scheme. Most of the previous research has been focused on the interaction of vortices produced and formed almost independently with a considerable distance between the wing tips, whereas in the present study a small clearance between the differential wings was used. Detailed 3-D velocity and vorticity experimental measurements providing the mean and statistical characteristics of the interacting vortex–pair flow field were conducted by using an in-house developed and constructed 12-sensor hotwire probe.

EXPERIMENTAL APPARATUS

An open-circuit, subsonic, wind tunnel, with a test section of dimensions 30cm x 50cm x 300 cm, a maximum velocity of 20 m/s and turbulence level <0.2% was used as the experimental test bed. Vortices were generated, using two half-wings placed at the entrance of the test section (Figure 1). Both wings had a rectangular planform with NACA 0030 profile. The length of the cord was c=0.1 m with an effective half span of b=24.5 cm. The half–wings were placed at angles of attack α=±8

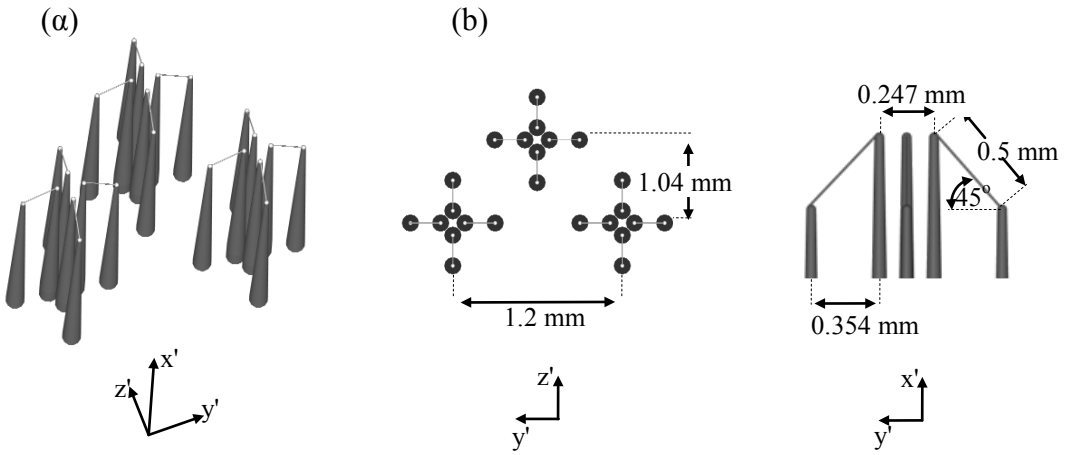

Figure 2. In-house manufactured, 12-hotwire vorticity probe, (a) 3-D view, (b) Probe dimensions

degrees, connected with a circular cylinder of diameter d=1cm at a wing separation distance l=0.1c (1cm). All measurements were made at a cord based Reynolds number, Re_c=133000 corresponding to a free – stream velocity, U_∞, of 20 m/s. Based on initial circulation, Γ_o, the Reynolds number was estimated as, $Re_{\Gamma o}$=58400.

An in–house manufactured, 12–hotwire vorticity probe, consisting of three closely separated orthogonal 4–hotwire velocity arrays (Figure 2), measures simultaneously the three dimensional velocity vector at three locations on a cross plane of the flow field. The design of the probe as well as the data reduction techniques rely upon the work of Lemonis [15], Lemonis & Dracos [16] and have been further improved and refined at the University of Patras. Probe's wires are made of Pt-Rh 10% alloy and are oriented at 45 degrees to the downstream direction. Their length is l_w =0.5 mm with a diameter, d_w =2.5 μm, giving a length/diameter ratio of about 200. Each sensing wire is welded on two separate prongs, uniformly tapered to ~20 μm at the tip, to overcome cross talking and thermal interference effects of previous common prong constructions (Kastrinakis et al. [17]).

Spatial resolution criteria indicate that the sensor length has to be in the range of 2-4 Kolmogorov length scales, η, in order to be able to ideally resolve the flow scales, whereas a similar criterion with the same range is suggested for the separation of sensor arrays in relation to velocity gradients estimation (Vukoslavčević et al. [18], Klewicki & Falco [19], Antonia et al. [20]). The minimum Kolmogorov scale of the present flow was estimated to be η=0.09 mm, in the core region where the dissipation rate attains maximum values. Thus the sensor length to the Kolmogorov length scale ratio deviates marginally from the suggested range only in a small area in the vortex cores where it attains a maximum value of 5.5. The spacing between sensor array centres, over which the velocity gradients are estimated, is 1.04 and 1.2 mm or in relation to the smallest Kolmogorov length scale 11.5η and 13.2η. Thus the probe is expected to almost fully resolve the velocity fluctuations field, whereas spatial filtering of the smallest flow scales in the velocity derivatives estimation within the vortex cores is expected to result in the attenuation of vorticity rms by 15% in the average (Honkan & Andreopoulos [21]).

Probe calibration is performed in-situ in the core of a round jet. The jet is rotatable about the pitch and yaw directions with an accuracy of better than 0.01 deg. Analysis of measurement data is based on the approximation of the calibration response of the wires by three dimensional B-splines and the solution of non-linear, three equations system to determine the components of the velocity vectors at the location of each 4-hot-wire array. Cross plane spatial velocity derivatives are

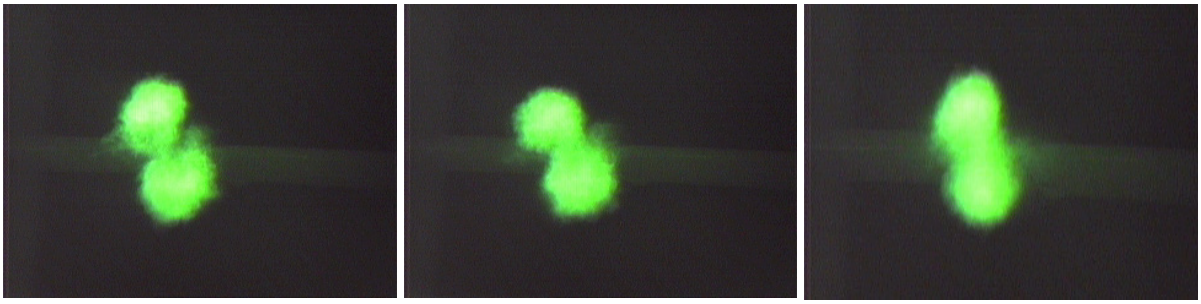

Figure 3. Characteristics visualization pictures of corotating vortex interaction at a cross plane

estimated using a forward scheme of first order accuracy. The streamwise velocity derivatives are obtained making use of Taylor's hypothesis of frozen turbulence using the local average velocity as the convection velocity. The uniqueness domain of a similar probe in combination with the present data reduction method has been assessed by Lemonis & Dracos [16]. Using reverse computations of calibration data they were able to recover correctly all data within a cone of pitch and yaw angles in the range $\pm 40^{o}$. In the present study the corresponding vectors never exceeded 30 degrees.

Flow visualization experiments (Figure 3) were used prior to the measurements to qualitatively characterise the formation and the interaction processes between the co-rotating vortices towards merging and select suitable configurations and measurements' locations. Measurements were obtained at several points, forming a closely spaced grid covering the area occupied by the vortices on a cross plane. At every point 80000 samples of each wire signal were recorded at a rate of 10 kHz, over a total sampling time of about 8 sec. Present results were obtained on a cross plane 3 cm (x/c=0.3) from the trailing edge. All data presented in this work, refer to a right hand Cartesian coordinate system (x, y, z) with corresponding velocities U, V and W (Figure 1).

MEAN FLOW FIELD

The mean velocity flow field, as measured by the 12-wire vorticity probe is presented in Figure 4. The streamwise velocity component, U, clearly depicts the form of two vortices with a characteristic velocity deficit reaching 50% of U_{∞} at the core centres (defined as the rotational centres of the flow field, see Figure 5). Contour lines of elliptical shape surround the vortex centres, illustrating the distortion of the vortex cores which can be attributed to the strain rate field of one vortex action upon the other (Melander et al. [5, 6]). The two transverse mean velocity components,

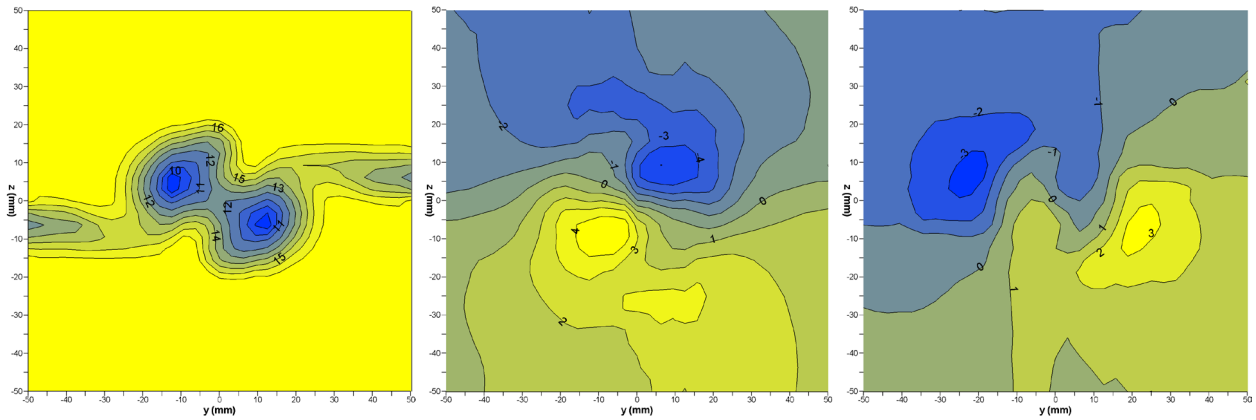

Figure 4. Mean velocity components, U(m/s), V(m/s), W(m/s), measured by 12-wire sensor

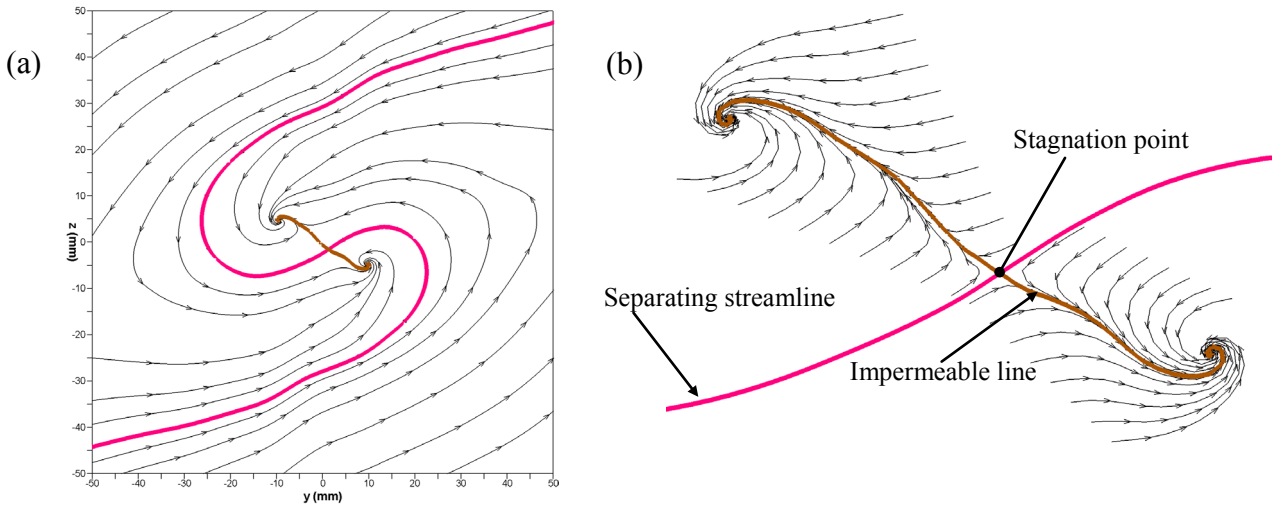

Figure 5. Streamlines and flow topology, (a) cross plane field, (b) enlargement vortex centers area

V, *W*, indicate the rotational character of the cross plane flow field, clearly demonstrated in the "streamline" plot based on the cross plane velocity components (Figure 5). The thick (red) "*S*" curve dividing the flow field in two similar antisymmetric parts represents segments of four limiting streamlines. Fluid travelling on the two sides of these curves will eventually reach a stagnation point at the middle of the "*S*" curve and diverge towards different vortex centres. Therefore, the "*S*" curve is dividing the flow field in two areas, each one comprising fluid which is directed to a different vortex centre. The limiting streamlines reaching the stagnation point continue towards the centres of the two vortices along an "impermeable" line formed between the centres (thick line, brown).

The mean vorticity flow field measured by the 12-wire sensor is presented by contour plots in Figure 6. The distribution of the streamwise mean vorticity component, Ω_x, is characterized by a dipole of positive and negative vorticity in the region of each vortex. The cores' centres are located in an area between the two maxima. Since the measurement technique assumes zero mean velocity gradients in the streamwise direction, both lateral components of mean vorticity are solely determined by the streamwise velocity gradients in the corresponding lateral directions.

The mean flow field indicates the presence of two flow streams, rolling up due to the pressure

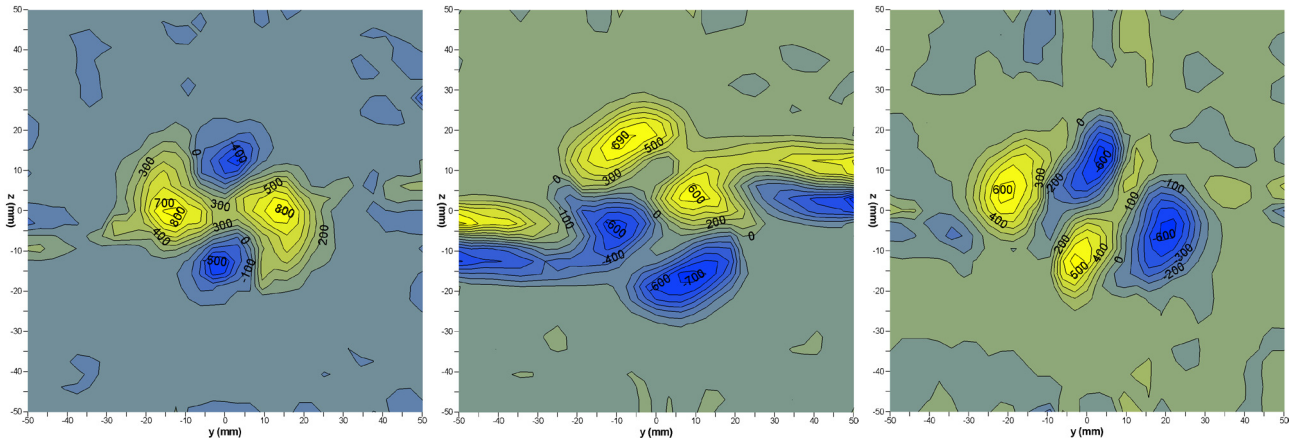

Figure 6. Mean vorticity components, Ω_x(1/s), Ω_y(1/s), Ω_z(1/s), measured by 12-wire sensor

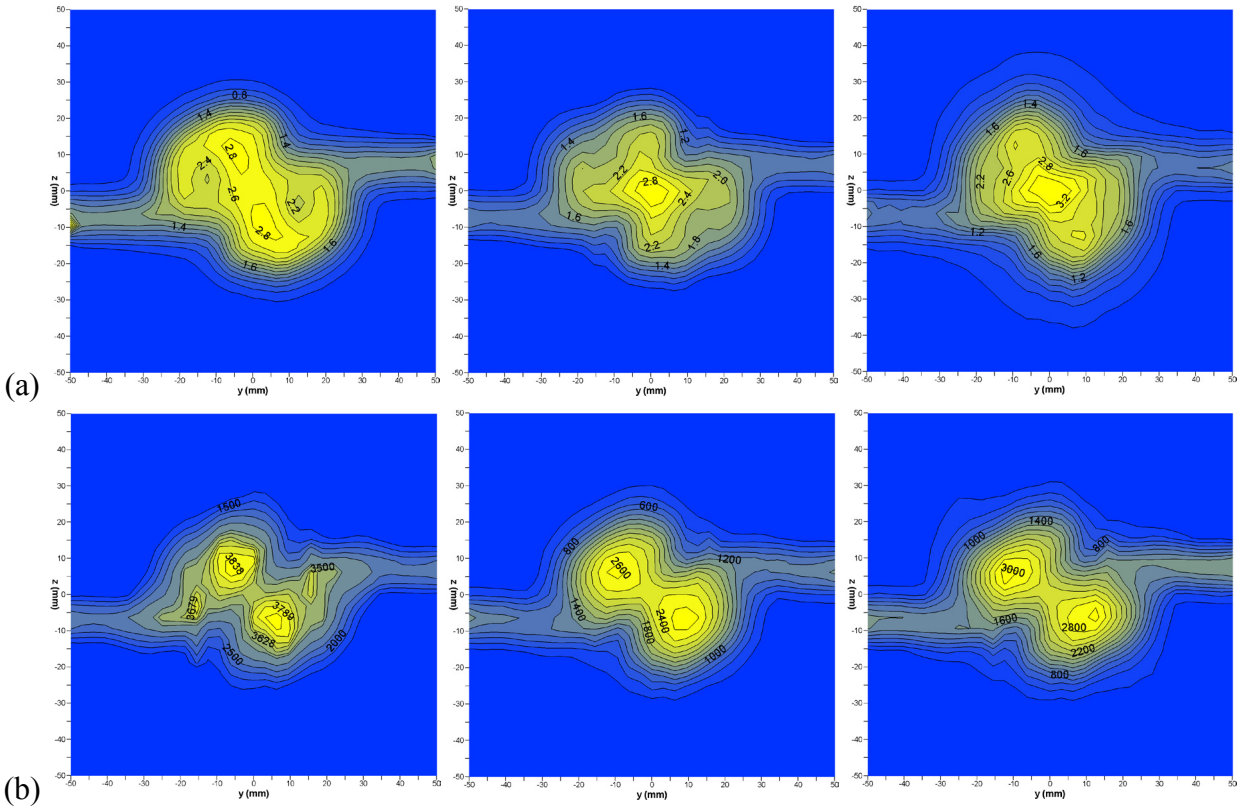

Figure 7. Rms values of (a) velocity fluctuations, $\sqrt{u^2}\ (m/s)$, $\sqrt{v^2}\ (m/s)$, $\sqrt{w^2}\ (m/s)$, (b) vorticity fluctuations, $\sqrt{\omega_x{}^2}\ (1/s)$, $\sqrt{\omega_y{}^2}\ (1/s)$, $\sqrt{\omega_z{}^2}\ (1/s)$

difference at the wing tips. These streams are led to a head on collision at the "impermeable" line. Along this line fluid is travelling towards the vortex centres leading to the expansion of the vortex centres and the increase of their separation. This motion in the absence of an external flow would have generated a counter rotating mushroom type vortex pair. The shear of the external rotational flow enhances the corotating vortex of the pair but eliminates the counter rotating one. Remnants of the counter rotating vortex are the existence of corresponding negative vorticity. This counter rotating vorticity can be also associated with the evolution of a secondary vortex during the formation of a single tip vortex on the wing observed by several investigators (Ghias et al. [22]) and considered as important for the development of the vortex.

TURBULENT FLOW FIELD

Contour plots of the Root Mean Square (RMS) of velocity and vorticity fluctuations are shown in Figure 7. Each vortex is characterized by a significant peak in streamwise velocity rms, $\sqrt{u^2}$, reaching 15% of the mean undisturbed velocity, U_∞. Vortex centres are surrounded by a band of high rms contour lines while a local minimum is observed within them. Cross stream rms velocity components, $\sqrt{v^2}$, $\sqrt{w^2}$, attain highest values, of the same order as the streamwise component, at the centre of the flow field, at the location of the stagnation point. The large values of all normal stresses inside the core region do not necessarily indicate intense turbulent mixing, but may result from inactive motions as it is buffeted by surrounding turbulence (Devenport et al. [2]). All the distributions are affected by the elliptic shape of the vortices and seemingly by specific characteristics of the mean field as for example the location of the mean streamwise vorticity peaks.

Vorticity fluctuations attain very high values, reaching more than 300% of the corresponding mean values. The streamwise component, $\sqrt{\overline{\omega_x^2}}$, also presents two peaks in each vortex, having the vortex centre in between them. The peaks on the clockwise side of vortex centres corresponding to the negative mean vorticity area are broader and higher, whereas those on the counter – clockwise side corresponding to the positive mean vorticity peaks are lower and more concentrated. Cross stream vorticity components' fluctuations rms, $\sqrt{\overline{\omega_y^2}}$, $\sqrt{\overline{\omega_z^2}}$, present one peak in each vortex, on or very close to the vortices' centres. The shape of the vortices and the wing wakes' regions can also be inferred from all vorticity fluctuations plots.

CONCLUSIONS

Simultaneous measurements of the mean and turbulent characteristics of the three-dimensional velocity and vorticity fields of a mutually interacting turbulent corotating vortex-pair have been conducted, using an in-house manufactured 12-hotwire probe. The flow field is characterized by a substantial streamwise velocity deficit at the vortex cores. The formation of the vortices seems to be dominated by the head on collision of the two rolling up flow streams generated due to the pressure difference at the wings' tips. This process results in the development of a dipole of counter-rotating vorticity at each vortex core. Visualization experiments show that the instantaneous flow field of the vortices preserves at all times the structural characteristics of the mean flow field. The vortices are continuously formed close to the wing tips and the fluctuating flow field depicted in the measurements is the result of changes in the intensity of the formation or changes in the position of the cores.

ACKNOWLEDGMENTS

The authors would like to acknowledge the financial support of the European Commission through GROWTH contract G4RD-CT-1999-00141 (C-Wake). Part of the multi-sensor hotwire anemometry development has been accomplished thanks to the support of GSRT (PENED 2001).

REFERENCES

1. Cerretelli, C. and Williamson, C. H. K., The physical mechanism for vortex merging, *J. Fluid Mech.*, 475 pp. 41-77, 2003
2. Devenport, W. J., Vogel, C. M., Zsoldos, J. S., Flow structure produced by the interaction and merger of a pair of co-rotating wing-tip vortices, *J. Fluid Mech.,* 394, 357-377, 1999
3. Chen, A. L., Jacob, J. D., Savas, O., Dynamics of co-rotating vortex pairs in the wakes of flapped airfoils, *J. Fluid Mech.*, 382, 155-193, 1999
4. Moore, D. W. and Saffman, P. G., Structure of a line vortex in an imposed strain, *In Aircraft Wake Turbulence and its Detection* (ed. J. H. Olsen, A. Goldburg & M. Rogers), pp. 339-354 Plenum, 1971
5. Melander, M. V., McWilliams, J. C., Zabusky, N. J., Axisymmetrization and vorticity gradient intensification of an isolated vortex through filamentation, *J. Fluid Mech.*, 178, 137-159, 1987
6. Melander, M. V., Zabusky, N. J., McWilliams, J. C., Symmetric vortex merger in two dimensions: causes and conditions, *J. Fluid Mech.*, 195, 303-340, 1988
7. Meunier, P. and Leweke, T., Elliptic instability of a co-rotating vortex pair, *J. Fluid Mech.*, 533 125-159, 2005
8. Dizes S. and Verga, A., Viscous interactions of two co-rotating vortices before merging, *J. Fluid Mech.*, 467, 389-410, 2002

9. Jacquin, L., Fabre, D., Sipp, D., Coustols, E., Unsteadiness, instability and turbulence in trailing vortices, *C.R. Physique*, 6, 399-414, 2005
10. Crow, S. C., Stability theory for a pair of trailing vortices, *AIAA J.*, 8 (12) 2172–2179, 1970
11. Jimenez, J., Stability of a pair of co-rotating vortices, *Phys. Fluids*, 18 (11) 1580-1581, 1975
12. Rossow, V. J., Lift-generated vortex wake of subsonic transport aircraft, *Progress in Aerospace Sciences*, 35, 507-660, 1999
13. Spalart, P. R., Airplane trailing vortices, *Annu. Rev. Fluid Mech.*, 30:107-108, 1998
14. Romeos, A., Lemonis, G., Panidis, T. and Papailiou, D. D., Multisensor Hot Wire Vorticity Probe Measurements of the Formation Field of Two Corotating Vortices, *Flow Turbulence and Combustion*, DOI: 10.1007/s10494-008-9193-8, 2009
15. Lemonis, G., Three-dimesional measurements of velocity, velocity gradients and related properties in turbulent flows, *Aerospace Sci. Tech.*, 7:453-461, 1997
16. Lemonis, G. and Dracos, T., A new calibration and data reduction method for turbulence measurement by multi-hot wire probes, *Exp. in Fluids*, 18, 319-328, 1995
17. Kastrinakis, E. G., Eckelmann, H., Willmarth, W. W., Inf1uence of the flow velocity on Kovasznay type vorticity probe, *Rev. Sci. Instrum.*, 50, 759-767, 1979
18. Vukoslavčević, P., Wallace, J. M., Balint, J. L., The velocity and vorticity vector fields of a turbulent boundary layer. Part 1. Simultaneous measurement by hot-wire anemometry, *J. Fluid Mech.*, 228, 25 – 51, 1991
19. Klewicki, J. C. and Falco, R. E., On accurately measuring statistics associated with small scale structure in turbulent boundary layers hot-wires probes, *J. Fluid Mech.*, 219, 119 – 42, 1990
20. Antonia, R. A., Zhu, Y., Kim, J., On the measurement of lateral velocity derivatives in turbulent flows, *Exp. Fluids*, 15, 65 – 69, 1993
21. Honkan, A. and Andreopoulos, Y., Vorticity, strain-rate and dissipation characteristics in the near-wall region of turbulent boundary layers, *J. Fluid Mech.*, vol. 350, pp. 29-96, 1997
22. Ghias, R., Mittal, R., Dong, H., Study of tip-vortex formation using large-eddy simulation, *AIAA 43rd Aerospace Science Meeting and Exhibit*, pp. 10853-10865, 2005

EXPERMENTAL INVESTIGATION ON TURBULENT DRAG REDUCTION WITH BLOWING POLYMER SOLUTION FROM THE WALL

M. Motozawa[1]*, Y. Onose[1], S. Sugita[1], K. Iwamoto[2], H. Ando[3], T. Senda[3], Y. Kawaguchi[1]
[1]Tokyo University of Science. Chiba, Japan
[2]Tokyo University of Agriculture and Technology, Tokyo, Japan
[3]National Maritime Research Institute, Tokyo, Japan

ABSTRACT. Experimental investigation on the turbulent drag reduction with blowing polymer solution from the channel wall was performed. Measurement of the drag reduction has been carried out with changing condition of blowing polymer solution (e.g. blowing rate and concentration) and Reynolds number based on the channel height and bulk mean velocity ranging from 20000 to 50000. The obvious drag reduction was obtained with blowing polymer solution and the maximum drag reduction rate achieved about 20 %. In addition, it seems that there is close relationship between the drag reduction rate and the mass flux of polymer. The drag reduction rate as the function of the mass flux has asymptotic curve limiting the maximum drag reduction. Because it is the merit of wall blowing that polymer can exist in the whole near-wall region, we discussed the difference between our results (wall blowing) and the effect of slot injection. Based on these results, the effect of wall blowing polymer solution on the heterogeneous drag reduction was discussed.

Keywords: *Drag Reduction, Polymer Solution, Wall Blowing*

INTRODUCTION

Adding dilute polymer solution or surfactant to turbulent wall-bounded flow can show obvious reduction in the skin frictional drag compared with the turbulent water at the same Reynolds number. This phenomenon is well known as Toms effect[1]. The drag reduction by additives can be classified into homogeneous drag reduction and heterogeneous drag reduction.

In the homogeneous drag reduction, Virk[2] reviewed the drag reduction by dilute polymer solutions in turbulent pipe flow and obtained 75 % drag reduction comparing with the solvent. Although several studies by polymer solution[3] and surfactant additives[4] have been performed for more than 50 years, the interaction of polymer solution with the near-wall turbulence and coherent structure in turbulent wall-bounded flow are still unclear.

On the other hand, as the heterogeneous drag reduction is the most efficient for applications to the external flow, it becomes remarkable theme in the recent. This heterogeneous drag reduction with injecting polymer solution into the boundary layer can be classified into the drag reduction in the pipe or in the channel. In case of injection into pipe flow, the most successful application of heterogeneous drag reduction by polymer solution is used in the Trans-Alaska-Pipeline. Adding the polymer solution to the crude oil in this pipeline, the desired discharge of 2 million barrels per day could be achieved.

In this study, we focused on the heterogeneous drag reduction with injecting polymer solution into the boundary layer of the channel flow. There are also many studies about heterogeneous drag reduction with injecting polymer solution into the boundary layer from the slot on the channel wall.

* Corresponding author: Dr. M. Motozawa
Phone: + (81)-4-7124-1501 (Ext.3963), Fax: + (81)-4-7123-9814
E-mail address: motozawa@rs.noda.tus.ac.jp

(a) Slot injection (b) Wall blowing

Figure 1. Schematic image for the distribution of near-wall polymer concentration: (a) slot injection and (b) wall blowing.

Walker and Tiederman[5] measured the profiles of the instantaneous polymer concentration in turbulent water channel flow with injecting polymer solution from the slot. They examined the action of polymer solution in the turbulent flow, but there were no discussions the relation between the polymer concentration and drag reduction. Winkel et al.[6] measured the drag reduction and near-wall polymer concentration with injecting polymer solution from the slot. They investigated the relation between the local drag reduction and the polymer concentration. Hou et al.[7] employed the PIV measurement to study the relation between the drag reduction and the near-wall polymer concentration.

It is revealed that the polymer in near-wall region is effective to reduce the skin frictional drag. However, the injected polymer from the slot is diffused into the boundary layer and drag reduction does not sustain for long region in the downstream of the slot as shown in Figure 1(a). More effective injection method is dissolving or blowing the polymer solution from the wall because the polymer will remain near the wall before it is diffused into the bulk flow and the polymer additive is expected to interact with the coherent structure near the wall as shown in Figure 1(b). If we can apply this effect to industrial applications such as ship bottom paint, it has great benefit of savings of fuel, cost of marine transportation and travel time. Actually, we are developing a new concept ship bottom paint applying this effect.

In this paper, as the first step of the development of ship bottom paint with polymer diffusion, we evaluated the drag reduction in the skin friction with blowing polymer solution from the permeable blower wall attached on the channel wall. Based on these results, the relation between the blowing mass flux of polymer and the drag reduction was discussed.

EXPERIMENT

Experimental Facility

Figure 2 shows experimental facilities including (a)flow system and (b)cross section of the channel with blower wall. Flow system consists of a closed-circuit water loop with two-dimensional channel test section. This test section is made of transparent acrylic resin, having 6.0 m in length, 0.04 m in inner height (H) and 0.5 m in spanwise width. There is a honeycomb rectifier with 0.15 m length at the channel entrance for removing large eddies. An electromagnetic flow meter with uncertainty of ±0.01 m^3/min is installed upstream of the channel. Storage tank of the flow loop contained a heater and an agitator to adjust a temperature of flowing fluid. The temperature of fluid is stabled at 25 °C.

The wall for blowing polymer solution is made of sintered metal, having 0.45m × 0.45m in size. Three blower walls are attached to one side of the channel. Polymer solution is oozing from whole surfaces of these walls. The blowing rate of polymer can be adjusted by the pump and the flow meter for polymer solution as shown in Figure 1(b). The blowing velocity normal to the wall is less than 0.09 mm/s.

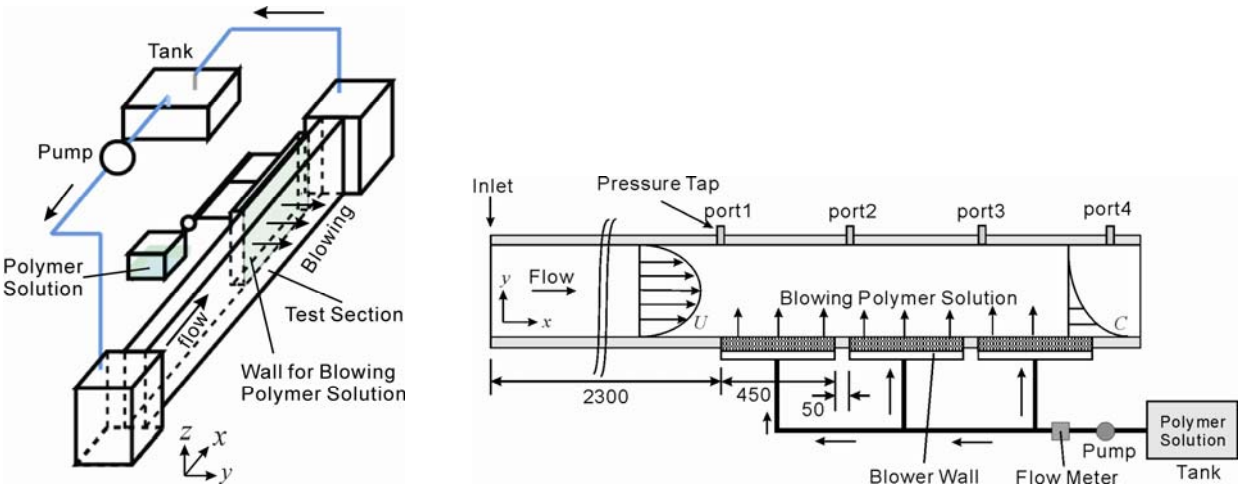

(a) Flow system (b) Cross section of the test section

Figure 2. Experimental facility: (a) Flow system and (b) Cross section of the test section.

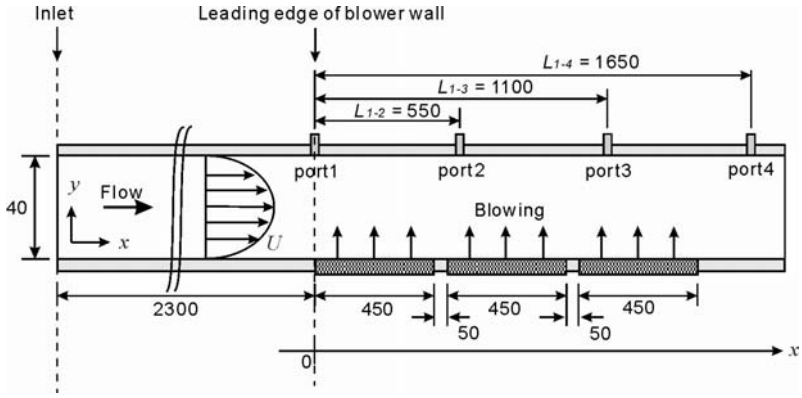

Figure 3. Detailed structure of the test section.

Reynolds number based on the kinematic viscosity of the solvent (ν), the channel height (H) and bulk mean velocity (U_b) is defined as $\mathrm{Re}=U_bH/\nu$. Re can be varied ranging from 20000 to 50000.

Detailed structure of the test section. Figure 3 shows the detailed structure of the test section. We defined the position of the leading edge of the blower wall as x=0. There are four pressure taps at the wall opposite side of the blower wall. These taps located x=0 (pressure port1), x=550 mm (port2), x=1100 mm (port3) and x=1650 mm (port4) at the downstream from the edge. The wall shear stress of between the ports1-2 ($\tau_{1\text{-}2}$), ports1-3 ($\tau_{1\text{-}3}$) and ports1-4 ($\tau_{1\text{-}4}$) can be calculated from static pressure gradient based on port1. Drag reduction rate (DR%) is defined by $(\tau_{water}-\tau_{blowing})/\tau_{water}\times 100$, where $\tau_{blowing}$ and τ_{water} are the wall shear stress of the water flow with and without blowing polymer solution, respectively. We can estimate the drag reduction rate at port 2, port 3 and port 4 based on port 1.

Polymer Solution

The polymer solution used in this experiment is Polyox WSR-205, produced by the Dow Chemical Company, dissolving in pure water. Major component of WSR-205 is 0.6 million in molecular weight water-soluble polyethylene oxide (PEO). This polymer is known to have large drag reduction ability in aqueous solution by other experiment. We prepared following weight concentration of polymer solution: 5, 10, 25, 50 and 100 ppm.

Table 1
Blowing Mass Flux $\dot{m}$ each Blowing Rate and Polymer Concentration.

	C ppm				
	5	10	25	50	100
Q L/min	$\dot{m}$ mg/(min ·m^2)				
0.5	4.1	8.2	20.5	41.0	82.0
1.0	8.2	16.4	41.0	82.0	164.0
1.5	12.3	24.6	61.5	123.0	246.0
2.0	16.1	32.8	82.0	164.0	328.0
2.5	20.5	41.0	102.5	205.0	410.0

Blowing Rate of Polymer Solution

As mentioned above, the polymer solution is blowing from the blower wall in this experiment. The blowing rate Q can be adjusted 0.5 L/min to 2.5 L/min. The blowing mass flux of polymer $\dot{m}$ can be calculated as follows:

$$\dot{m} = \frac{CQ}{S} \tag{1}$$

where, S is the total area of the blower wall (0.45m×0.45m×3) and C is weight concentration of polymer solution for blowing. The blowing mass flux of polymer $\dot{m}$ each Q and C is shown in Table1.

RESULTS AND DISCUSSION

Blowing Condition Dependence on the Drag Reduction

Figure 4 shows the polymer concentration dependence on the drag reduction evaluated between the ports 1 and 4 for Re=(a)20000, (b)40000 and (c)50000. These figures indicate that the obvious drag reduction is obtained with blowing polymer solution from the wall. The drag reduction for Re= 40000 is larger than that for Re=20000. However, comparing Re=40000 with 50000, the drag reduction rate is almost same and the profiles are similar. Moreover, the drag reduction becomes large in blowing condensed polymer for Re=20000, but it seems that there is saturation of the drag reduction in 50ppm for Re=40000 and 50000. About 20% of maximum drag reduction was obtained.

The blowing rate dependence on the drag reduction rate evaluated between ports 1 and 4 for Re=(a)20000, (b)40000 and (c)50000 are shown in Figure 5. As the blowing rate of polymer solution increases, the drag reduction rate becomes large and also saturates at 2.0 L/min of blowing rate for Re=40000 and 50000. Thus, the drag reduction rate saturates with the polymer concentration and the blowing rate as shown in Figure 4(c) and 5(c). These saturation behaviours were also observed in the slot injection study. It is believed that the drag reduction rate is determined by the local polymer concentration at the buffer layer. Therefore, though the blowing condition is different between Re=40000 and 50000, almost same amount of polymer seems to be existence at the buffer layer. Then once the polymer suppresses the turbulence, the surplus of polymer cannot work any more and the polymer diffuses to the logarithmic layer. As a result of this polymer behaviour, almost same drag reduction rate was obtained.

Streamwise Development of Drag Reduction

Figure 6 shows the drag reduction rate evaluated between ports1-2 (550 mm), ports1-3 (1100 mm) and ports1-4 (1650 mm) for Re=(a)40000 and (b)50000. The blowing rate is 0.5 L/min. This figure indicates that the drag reduction rate develops at the downstream from the leading edge of the blower wall. Though the drag reduction becomes large in blowing condensed polymer, this rate saturates in 50 ppm similar to Figure 4(b) and (c). The track of the change of drag reduction is similar between

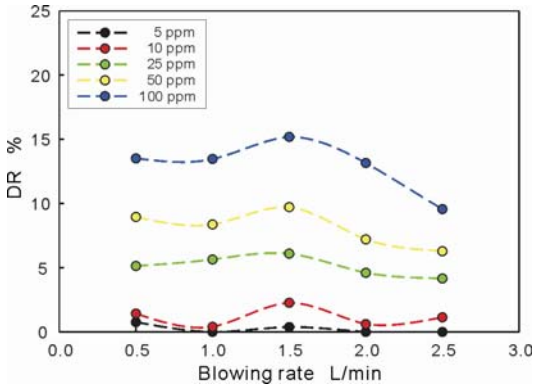

(a) Re=20000

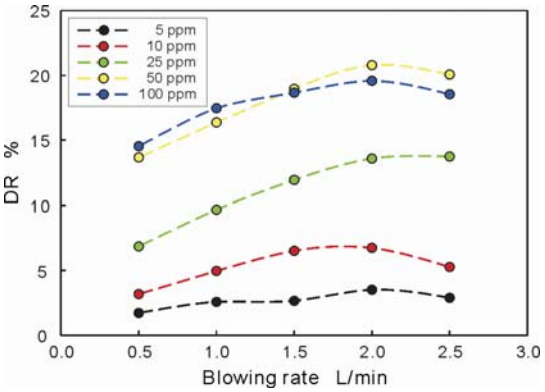

(b) Re=40000

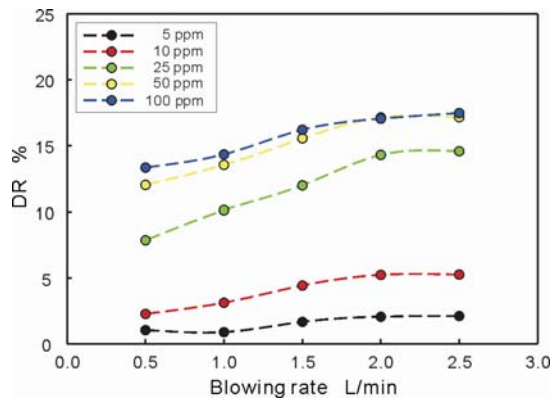

(c) Re=50000

Figure 4. Polymer concentration dependence on the drag reduction rate: Re=(a)20000, (b) 40000 and (c)50000.

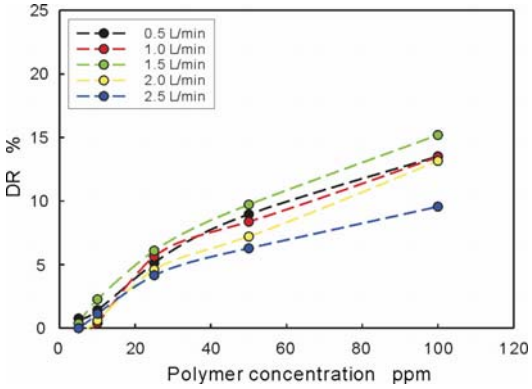

(a) Re=20000

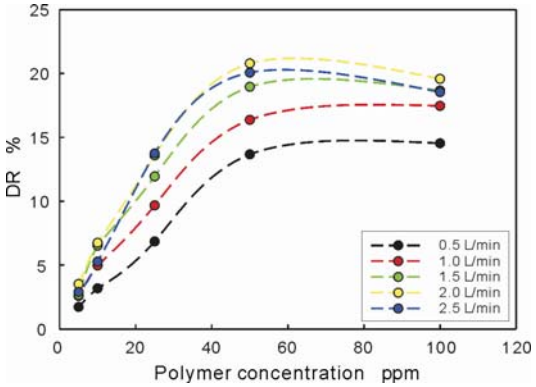

(b) Re=40000

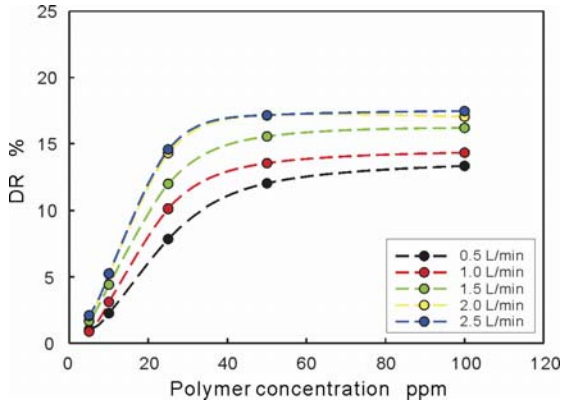

(c) Re=50000

Figure 5. Blowing rate dependence on the drag reduction rate: Re=(a)20000, (b)40000 and (c)50000.

Re=40000 and 50000, and about 15 % of maximum drag reduction was obtained in this blowing condition. If we experiment with large blowing rate or large polymer concentration, about 20 % of maximum drag reduction can be expected.

There appeared the region where the drag reduction rate is kept at a constant level toward downstream. We call this region as “Steady region” in this study. This steady region is obtained remarkably for 5, 10 and 25 ppm at Re=50000. If the blower wall is longer, the steady region can be observed for 50 and 100 ppm. In this region, the polymer seems to be provided continuously at the buffer layer. As a result, the same drag reduction can be kept to the downstream.

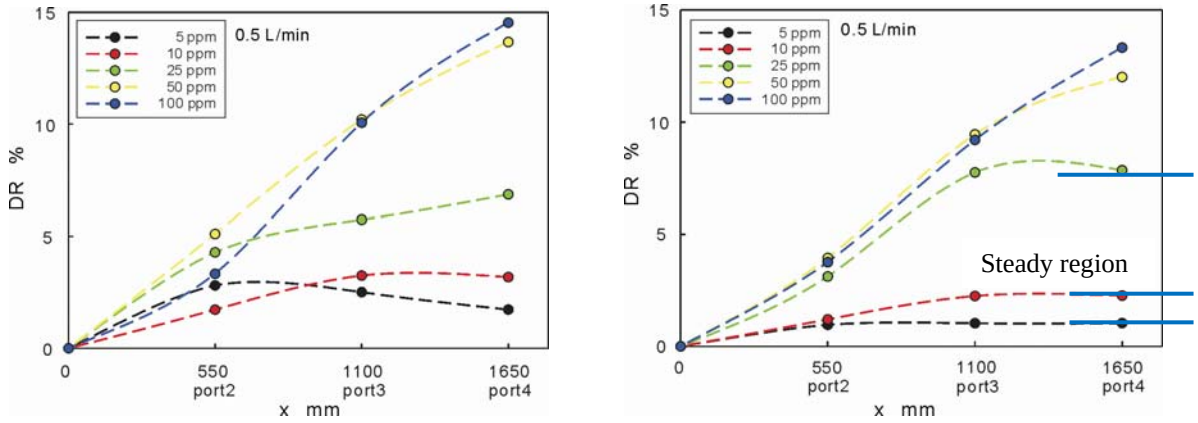

(a) Re=40000 (b)Re=50000

Figure 6. Streamwise development of the drag reduction: Re=(a)40000 and (b)50000.

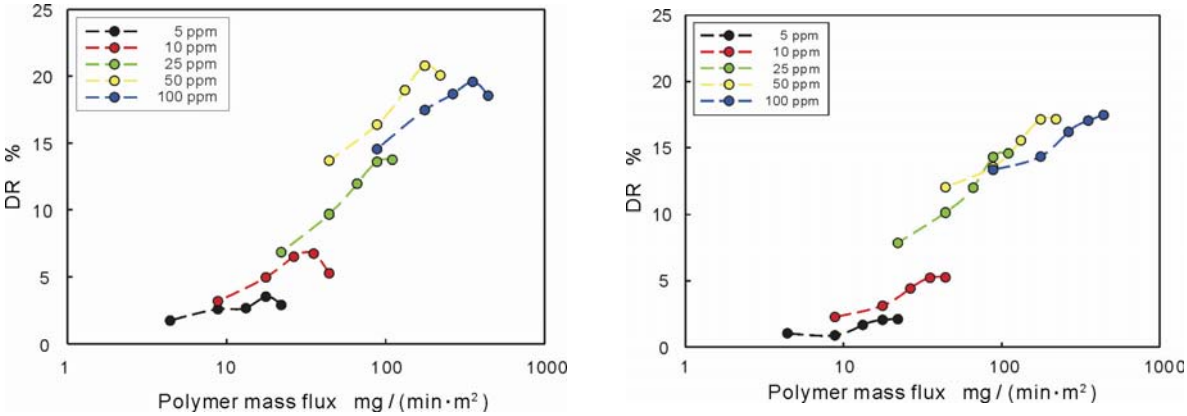

(a)Re=40000 (b)Re=50000

Figure 7. Relation between the blowing mass flux of polymer and the drag reduction: Re=(a)40000 and (b)50000.

In comparing with the slot injection[6,7], the steady region is also obtained, but it is necessary to inject very high concentration of polymer solution (e.g. 1000 ppm or 500 ppm). Moreover, the steady region cannot be kept to the downstream, the drag reduction decreases immediately at the downstream of the slot. As mentioned above, in the wall blowing, the steady region can be obtained with blowing low concentration of polymer solution and kept to the downstream. This ability to keep the drag reduction is one of the merits of wall blowing.

Relation between Mass Flux and Drag Reduction

Figure 7 shows the relation between the blowing mass flux of polymer and the drag reduction rate for Re=(a)40000 and (b)50000. This figure indicates that the amount of blown polymer has close relationship with the drag reduction. The tendency of results is similar between Re=40000 and 50000. It seems that the drag reduction rate as the function of the mass flux has asymptotic curve with limiting the maximum drag reduction 20%.

The profiles of the relation between the mass flux and drag reduction rate for each Re are shown in Figure 8. Though the profiles of Re=40000 and 50000 is observed in similar tendency, the profiles of Re=20000 shift to the right region. Because the wall shear stress for Re=20000 is smaller than that for Re=40000, the effect of polymer is lower relatively at Re=20000 and the profiles are observed at the right region. However, there is limitation in the effect of polymer and the tendency of result becomes similar for Re=40000 and 50000.

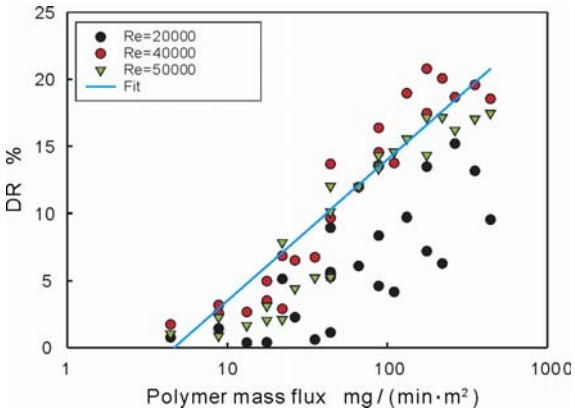

Figure 8. Relation between the blowing mass flux of polymer and the drag reduction.

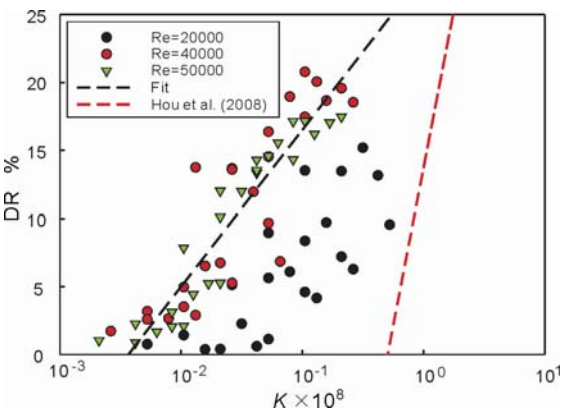

Figure 9. Relation between the *K* plot and drag reduction.

The solid line in Figure 8 is a fit to left side of these profiles. This line seems to represent the effective amount of blown polymer for getting the target drag reduction. However, the drag reduction rate has a limitation of 20 %. Eventually, the drag reduction is depend on the blowing mass flux of polymer $\dot{m}$ as a function of polymer concentration C and blowing rate Q represented by Equation (1) having limitation.

Comparison with Slot Injection

About K parameter. The drag reduction rate with slot injection can be plotted as a function of the *K* parameter developed by Vdovin and Smol'yakov[8]. It is useful to relate the amount of injected polymer from the slot and the drag reduction rate. This *K* parameter is defined as

$$K = \frac{Q_i C}{\rho X_i U_b} \tag{2}$$

where, Q_i is volumetric injection rate per unit span, C is the weight concentration of polymer solution, ρ is the density of the solvent (water), X_i is the downstream distance and U_b is the bulk mean velocity. The drag reduction rate is observed to be linearly proportional to $\log_{10}(K)$ and reaches maximum drag reduction.

Comparison with slot injection by K parameter. Figure 8 shows the profiles of the relation between $K\times10^8$ and the drag reduction rate. The black broken line is a linear fit to the experimental data with following equation:

$$\mathrm{DR} = 11.5\times\log_{10}(K\times10^8) + 28 \tag{3}$$

On the other hand, the red broken line is obtained by Hou et al.[7] This line is represented as:

$$\mathrm{DR} = 46.3\times\log_{10}(K\times10^8) + 13.7 \tag{4}$$

As mentioned above, there are two methods of diffusing polymer, wall blowing (our experiment) and slot injection (Hou et al.[7]). Equations (3) and (4) refer to the effective condition of blowing polymer from the wall and injecting polymer from the slot, respectively. The profiles of *K* for the wall blowing exist in the region where the value of *K* is smaller than that for the slot injection representing in Equation (4). This result indicates that the method of wall blowing can obtain the large drag reduction with blowing small amount of polymer in comparison with the slot injection. This ability is the excellent merit of wall blowing. However, the maximum drag reduction for wall blowing is smaller than that for slot injection.

CONCLUSIONS

We carried out precise measurement of a drag reduction rate with blowing polymer solution from the permeable blower wall attached on the channel wall. Measurements have been conducted with changing condition of blowing polymer and Reynolds number based on the channel height and bulk mean velocity ranging from 20000 to 50000. The main conclusions were drawn as follows:

1. Obvious drag reduction was obtained with blowing polymer solution from whole surface of the wall. The drag reduction becomes large in blowing condensed polymer. However, it seems that there is saturation of drag reduction in 50 ppm of polymer weight concentration and 2.0 L/min of the blowing rate. Maximum drag reduction is 20 % in this experiment.
2. The drag reduction rate develops at the downstream from the leading edge of the blower wall. The "Steady region" where the drag reduction can be kept at a constant level was observed. This steady region was obtained remarkably for 5, 10 and 25 ppm at Re=50000. In the slot injection, this steady region cannot be obtained with injecting low concentration polymer and the drag reduction rate decreases to the downstream. It is one of the merits of wall blowing that the drag reduction rate can be kept at the same level toward the downstream.
3. The drag reduction rate is dependent of the blowing mass flux of polymer. The drag reduction rate as the function of the mass flux has asymptotic curve with limiting the maximum drag reduction 20%.
4. In comparison wall blowing (our experiment) with slot injection, though the maximum drag reduction with wall blowing is smaller than that with slot injection, wall blowing can obtain the large drag reduction with blowing small amount of polymer comparing with the slot injection.

ACKNOWLEDGMENT

This study was carried out under the support of research project of the New Energy and Industrial Technology Development Organization (NEDO). We would like to thank Dr. L.Q. Kang, Mr. T. Ikegami and Mr. T. Satou of the Tokyo University of Science and Mr. E. Yoshikawa of the Chugoku Marine Paints, Ltd. for the supporting in this study.

REFERENCES

1. Toms, B. A., Some Observations on the Flow of Linear Polymer Solutions through Straight Tubes at Large Reynolds Numbers, *Proc. 1st Int. Cong. Rheology*, Amsterdam, 1948, pp. 135-141.
2. Virk, P. S., Drag Reduction Fundamentals, *AIChE J.*, Vol. 21, pp. 625-656, 1975.
3. White, C. M. and Mungal, M. G., *Annu. Rev. Fluid Mech.*, Vol. 40, pp. 235-256, 2008.
4. Li, F.Ch., Kawaguchi, Y., Hishida, K. and Oshima, M., Investigation of Turbulence Structures in a Drag-reduced Turbulent Channel Flow with Surfactant Additive by Stereoscopic Particle Image Velocimetry, *Exp.Fluids*, Vol. 40, pp. 218-230, 2006.
5. Walker, D. T. and Tiederman, W. G., The Concentration Field in a Turbulent Channel Flow with Polymer Injection at the Wall, *Exp. Fluid*, Vol. 8, pp. 86-94, 1989.
6. Winkel, D. R. *et al.*, Friction Drag Reduction at High Reynolds Numbers with Wall Injected Polymer Solutions, *Proc. 26th Sym. Naval Hydrodynamics*, Rome, Sept. 2006, pp.17-22.
7. Hou, Y. X., Somandepalli, V. S. R. and Mungal, M. G., *J. Fluid Mech.*, Vol. 597, pp. 31-66, 2008.
8. Vdovin, A. V. And Smol'yakov, A. V., Turbulent Diffusion of Polymers in a Boundary Layer, J. Appl. Mech., Vol. 22, pp. 526-531, 1981.

ANALYSIS OF MOMENTUM AND HEAT TRANSFER IN COUNTER – CURRENT JETS

B. Wojciechowska[1,*], P. Domagała[1], S. Drobniak[1]
[1]Częstochowa University of Technology, Częstochowa, Poland

ABSTRACT. The paper presents the results of experimental analysis of the flowfield in isothermal and non-isothermal countercurrent round jets. The velocity measurements were carried out by means of a hot-wire anemometry and Laser Doppler Anemometry. The instantaneous signals collected during the experiment were digitally processed and used to determine the statistics and spectra of velocity fields and the distributions of turbulence scales. The results revealed, that both the fluid aspiration at the jet periphery and the density ratio between the inner and outer jet significantly influence mixing and entrainment in the flow considered.

Keywords: *countercurrent jets, turbulence intensity, turbulence scales, coherent structures*

INTRODUCTION

The countercurrent jet is the subject of a number of publications which appeared mostly during the recent decade. The reason for this interest is twofold, i.e. the applicability of this type of flow in many practical technologies and the appearance of interesting flow phenomena like absolute instability. The motivation for research in counter-current jets was initiated by the experiment of Strykowski and Niccum [1], which revealed the great potential of that way of flow stimulation in terms of an intensification of transport processes. The phenomenon had local character, i.e. intensive mixing took place in limited space of the flow only, and was accompanied by flow "laminarisation" (i.e. damping of turbulent fluctuations) in the remaining jet regions. Another motivation for investigations of counter-current jets is the appearance of absolute instability, found experimentally in heated jets by Monkewitz et al [2] and in helium jets by Kyle and Sreenivasan [3]. The theoretical justification for absolute instability triggered by external counter flowing jet was shown theoretically by Jendoubi and Strykowski [9], but so far no convincing experimental evidence was found for the existence of this phenomenon in countercurrent jets. Presented study resulted from the research performed at ITM CzUT within the framework of TIMECOP A.E. project, devoted to modelling of liquid fuel atomization and combustion in jet engines. The counter-current jet was selected as the test flow for investigations of fuel droplets evaporation [4] due to possibility of changing the structure of turbulence at the given point by changing the velocity ratio between the inner and outer jets. The results concerning the influence at suction velocity in outer jet upon the flow characteristic in isothermal jet was presented recently in [5, 8] but the problem of mixing enhancement in non – isothermal jets still needs clarification which was the main motivation for the present study.

EXPERIMENTAL FACILITY AND CONDITIONS

In Figure 1 the sketch off nozzles is given together with most important dimensions given in Table 1. In the experiment with countercurrent jets two regions of special interest were selected,

* Corresponding author: MSc Barbara Wojciechowska
Phone: + (48)-34-3250502, Fax: + (48)-34-3250555
E-mail address: bwoj@imc.pcz.czest.pl

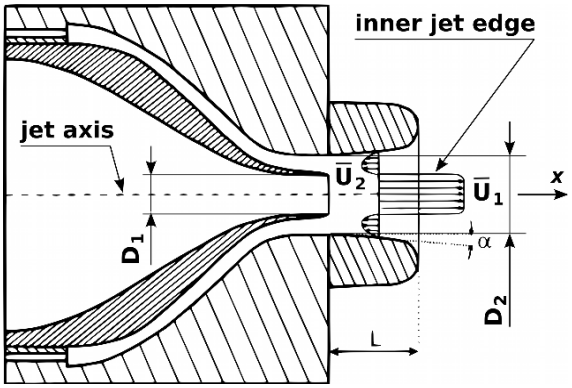

Figure 1. The test rig main components

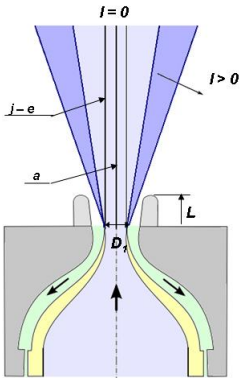

Figure 2. The sketch of the characteristic lines in countercurrent jets.

Table 1
Basic dimensions of the nozzles.

	Dimensions
D_1	15 mm
D_2	30 mm
L	D_1, $7D_1$
α	7°

the first one along the symmetry axis of the jet (denoted "a") and the second located along the edge of the inner jet (denoted "j – e"), as can be seen in Figure 2. From this sketch one may observe that the spreading rate of main stream may be changed by the aspiration parameter I, which is defined as the ratio of the inner to outer velocity. When aspiration is applied, the spreading rate of the inner jet increases and in all points of the flow the mean and fluctuating parameters are changed.

One of main components of the test rig is an inner nozzle which is made of brass. This nozzle generates air stream with low turbulence level and "flat" profile of mean velocity at the exit. The key parameter for this type of outflow is the roughness of inner surface of the nozzle. For this reason the inner surface has been done as turn surface. Additionally to reduce influence of backflow on the velocity field in the channel between inner and outer nozzle a profiled collar has been mounted at the inner nozzle.

The extension collars with different lengths L have been used to change the exit boundary layer thickness δ, because there is experimental evidence [7] that the ratio δ / D_1 may appear important in further investigations. The key parameter for the outer nozzle is also the inner surface, because its shape determines the shape of the reversed flow channel. Additionally, the design of the outer nozzle allows for change of orifices which determine the inlet width of the suction channel. The outer nozzle and orifices are made of aluminium.

Instrumentation of Test Rig and Measured Quantities

The flow rate of the inner jet was controlled by measurement of static pressure at the nozzle. Since the inner jet was heated the static pressure readings were corrected for air temperature measured with thermocouples. The flow rate of the outer jet was measured with a set of rotameters, which could be connected in parallel in order to cover the entire range of flow rates.

The temperature of the fluid flow was measured with type K thermocouple with uncovered joint. This thermocouple was introduced to the main flow only for controlling the airflow temperature. During measurements of the velocity profile at the nozzle exit this thermocouple was removed to avoid

flow disturbances. Detailed information about design of test rig and previous test conditions can be found in [7, 8].

The isothermal jet measurements were carried out with the use of DANTEC single channel hot-wire anemometer, the details of the setup are shown schematically in Figure 4. Constant temperature anemometer was used to recover the instantaneous velocity of flow. Velocity measurements were performed with DANTEC gold-plated wire probe 55P05. Instantaneous voltage signals of CTA were sent to the signal conditioners and data analysis system. In order to enable the continuous monitoring of the experiment, all signals were visualized by oscilloscopes and their average values were controlled by mean voltage meters. Signal processing, i.e. recovering the instantaneous velocity value U as well as the evaluation of the statistical moments and spectral density functions, was performed digitally by HP signal analyzer.

The measurements of velocity field for the cold jet were performed along the jet radius in several control planes covering the area $x/D_1 = 0 \div 11D_1$ as well as along the inner jet axis (line "a") and along the line being the extension of the edge of the inner nozzle (line "j-e"). The spreading rate of main stream could be changed by the parameter I, which was defined as the ratio of the inner to outer velocity. The main flow parameters of the reported experiment Reynolds number $Re = U_1D_1/\nu$ was 10000 and 20000, aspiration intensity expressed as the ratio of the mean velocities of the reverse flow and main stream was varied in the range $I = U_2/U_1 = 0 \div 0.4$.

The hot jet measurements were carried out with the use of DANTEC 2D Laser Doppler Anemometry in backscatter mode, equipped with Ar–Ion laser which generated two beams i.e. green (515nm) and blue (488nm) with total power 300mW, the details of the set up are shown schematically in Figure 5. Velocity measurements were performed with 2D DANTEC LDA probe with focal length 310mm. Instantaneous LDA signals were sent to FVA/BSA processor and then they were recorded on PC. For the case with overheat of the inner jet the experiment was performed for Re = 10000, the test conditions were controlled by aspiration ratio, and the overheat of the inner jet described by the density ratio "s" between the inner jet and the ambient fluid. The mean velocity, its gradient and turbulence intensity, as well as mean and temperature fluctuations were measured, furthermore the scales of turbulence and spectra of velocity and temperature were investigated for the following test conditions:

- Reynolds number Re = 10000, 20000
- Aspiration ratio $I = U_2/U_1 = 0 \div 0.4$
- Dimension ratio $L / D_1 = 7$
- Density ratio s = 1.0, 0.7, 0.5

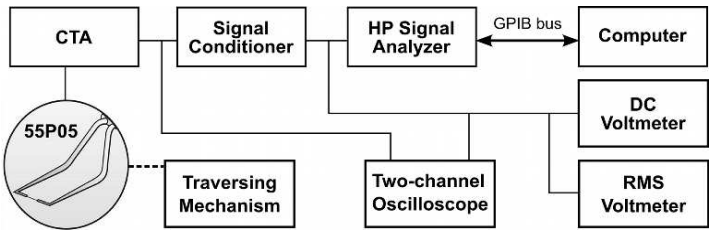

Figure 4. Scheme of CTA measuring equipment used in cold jet experiment

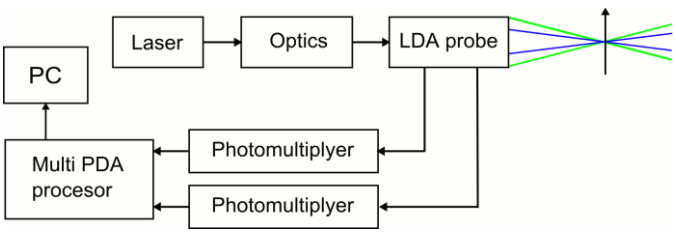

Figure 5. Scheme of LDA measuring equipment used in hot jet and in flame experiment

RESULTS

The first stage of the experiment was the comparison of present experimental data for mean velocity and turbulence intensity with literature data [6] for Reynolds number Re = 20000 along the symmetry axis for the isothermal (s = 1.0) jet with no suction (I = 0). The investigations were intended as the verification of the test-rig conditions [6]. Results for mean velocity (Figure 6) are in very good agreement with literature data. Also the data for turbulence intensity (Figure 7) are very similar except for the first region where some differences can be noticed. These differences are most probably due to much lower turbulence intensity at the jet exit obtained during the present experiment, which may be attributed to corrected shape of the nozzle and better selection of gauzes in the plenum chamber. One may conclude therefore, that the inner jet characteristics are in agreement with previous investigations.

The next part of investigation was devoted to the analysis of mixing enhancement due to countercurrent external flow and the overheat of the inner jet. Both countercurrent flow and overheat should create the conditions for the appearance of the absolute instability phenomenon, as it was reported in [2, 3]. These investigations were performed for two values of Reynolds number i.e. Re = 10000 and Re = 20000, the sample results shown in Figures 8 and 9 for Re = 10000 case reveal, that both the decay of the potential core (Figure 8) and the increase of turbulence intensity along the jet symmetry line (Figure 9) caused by suction are visible, these pictures present the measurements obtained in consecutive cross-sections from the jet exit up to normalized distance x/D1 = 11D_1. Both the mean velocity and RMS of velocity fluctuations have been normalized with inner jet velocity $\bar{U}_0$ at the exit. The influence of suction is not monotonous, the smallest value of suction parameter I = 0.1 causes faster decay of potential core and bigger increase of turbulence intensity than for I = 0.2, for larger values of I the faster decay of mean velocity and increase of Tu is restored, for all values of I the maximum of Tu moves upstream. One may see that due to change of variable I flow parameters change considerably at every point located at the jet axis. One may conclude therefore, that the results presented here is in full agreement with previous investigations [5] and confirms that external counter flow is effective way of mixing enhancement.

Consecutive Figures 10 and 11 present the comparison of the isothermal (s = 1.0) and non-isothermal (s = 0.5 and 0.7) jet when the counter flow was absent i.e. for the ratio I = 0. The distance x and velocity U are again normalized by jet diameter D_1 and inner jet velocity at the exit $\bar{U}_0$.

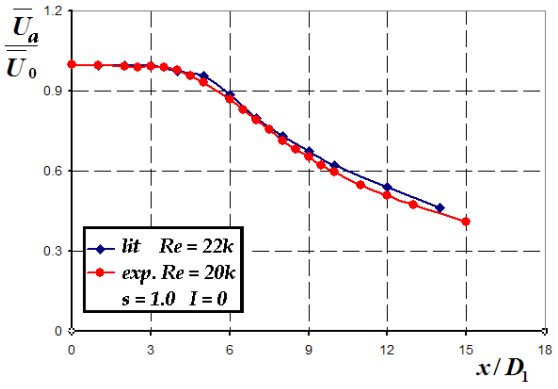

Figure 6. The comparison of present experimental data for turbulence intensity with literature [6] (measurements along the jet axis)

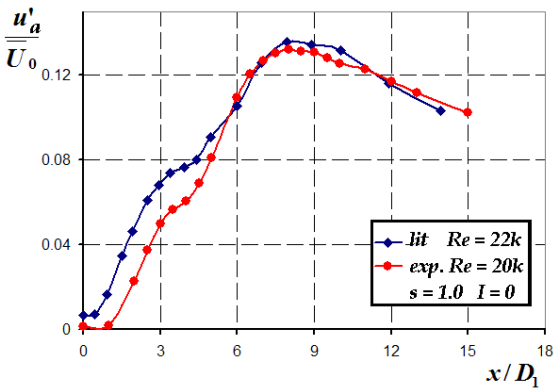

Figure 7. The comparison of present experimental data for mean velocity with literature [6] (measurements along the jet axis)

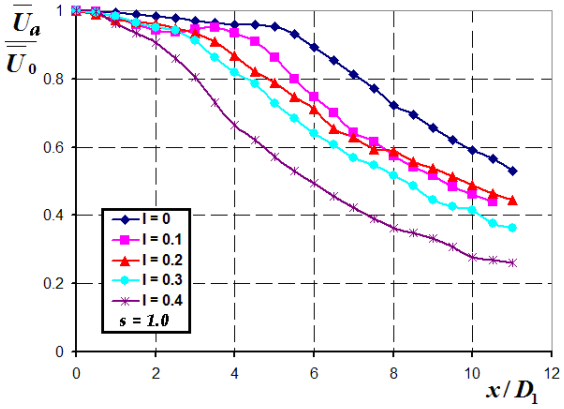

Figure 8. The decay of the potential core for Re = 10000 for various ratios of suction intensity I

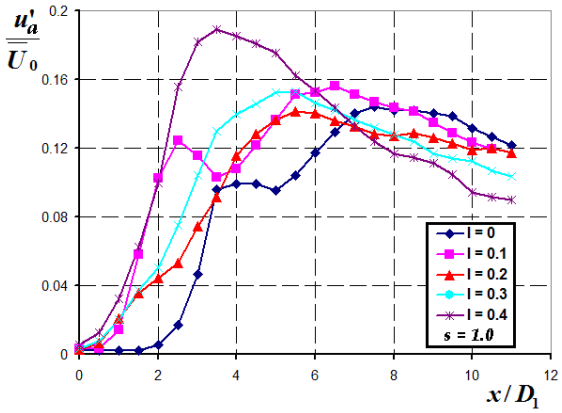

Figure 9. Turbulence intensity evolution for Re = 10000 for various ratios of suction intensity I

The decay of potential core (Figure 10) and the increase of turbulence intensity (Figure 11) behave differently, then before i.e. for smaller overheat s = 0.7 the decay of mean velocity is slower, while for s = 0.5 the decay of mean velocity along the jet axis is faster than isothermal flow. This behaviour is consistent with the data for turbulence intensity (Figure 11), which reveals slower increase rate for s = 0.7 and faster increase for s = 0.5. It may be observed, that contrary to counter flow the jet overheat influences the flow behaviour in complex and first of all not monotonous way. The measurements in non – isothermal flow required the application of LDA, and to the optical probe limitations the measurements could not be performed at the outlet plane (see Figures 10 and 11). The final stage at the investigations was the joint application of both counter flow and overheat.

This series of measurements was performed for Re = 10000 and for two values of overheat ratio i.e. s = 0.7 and s = 0.5,the suction ratio was varied in the range I = 0 ÷ 0.4. Sample results for s = 0.5 and s = 0.7 given in Figures 12 and 13 reveal, that the both mean and fluctuating velocity fields react to countercurrent flow but this reaction is the less effective the higher is the inner jet overheat. It may suggest that new phenomenon appears in this type of flow, that requires more elaborate investigations.

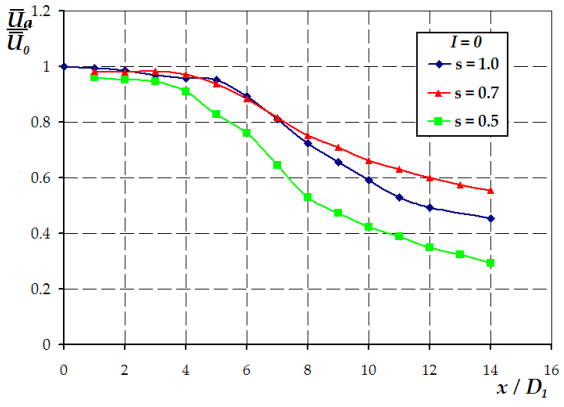

Figure 10. The decay of potential core for I = 0 for various ratios of density s.

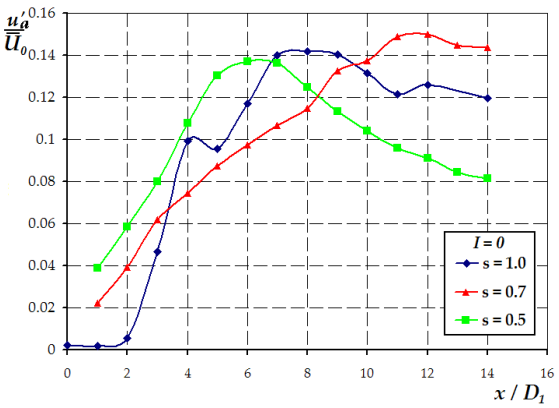

Figure 11. Turbulence intensity evolution for I = 0 for various ratios of density s.

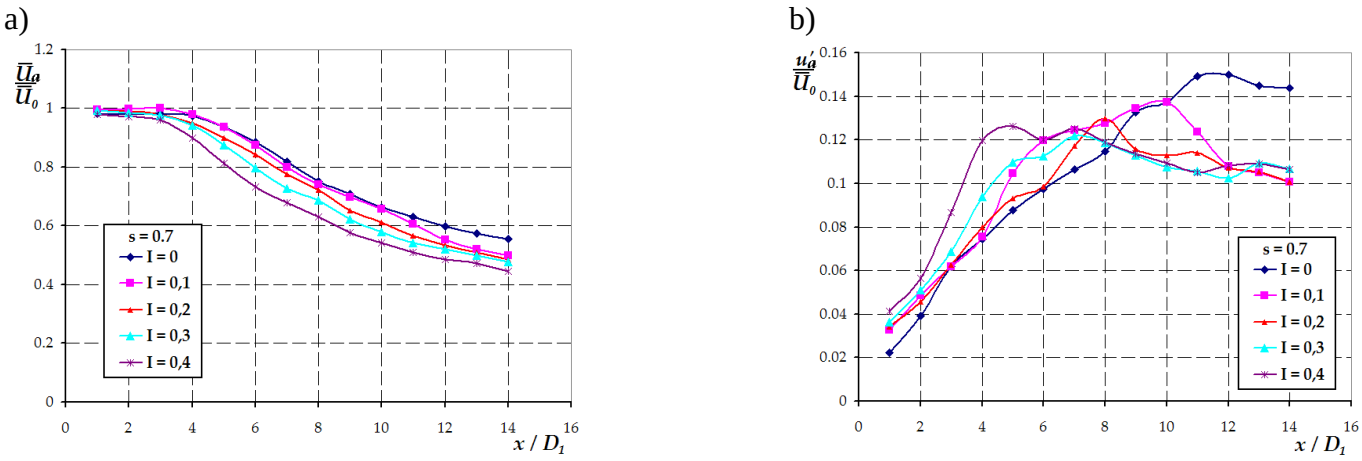

Figure 12. The influence of suction intensity upon the mean a) and fluctuating b) velocity along the jet axis for countercurrent jet with density ratio s = 0.7

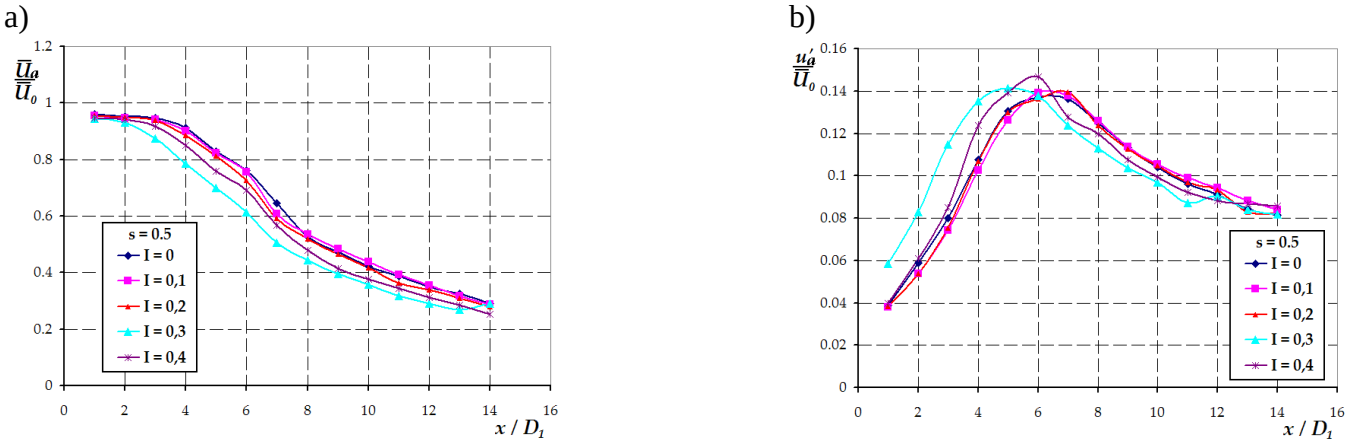

Figure 13. The influence of suction intensity upon the mean a) and fluctuating b) velocity along the jet axis for countercurrent jet with density ratio s = 0.5

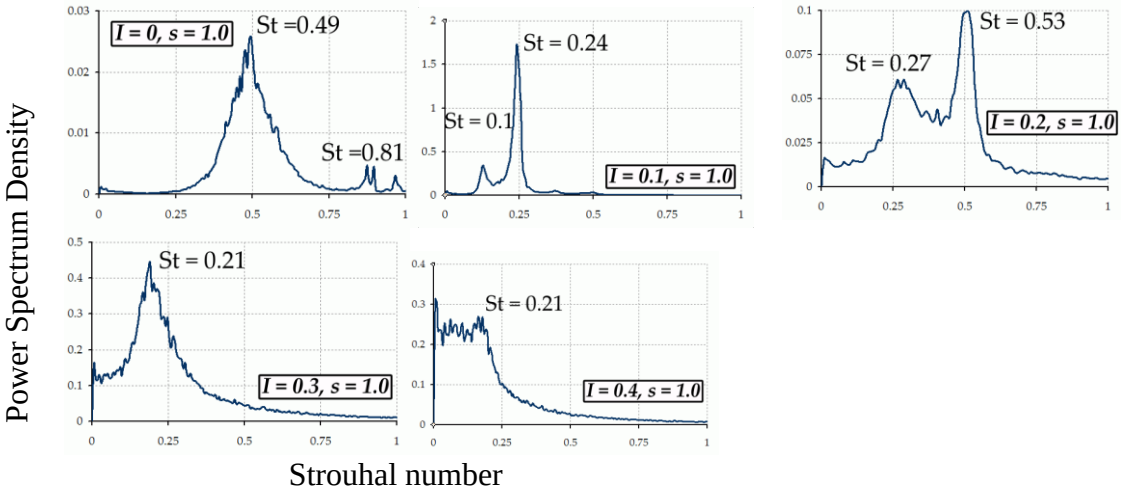

Figure 14. The evolution of the power spectrum density function of velocity fluctuation at the axial location $x/D_1 = 3$ for various ratios of suction intensity I

Since the pioneering paper of Crow & Champagne [10] it is a well established fact that the dynamics of a free jet is mainly governed by the large – scale vortices, which first are characterized by

the dominant frequency and then are transformed during pairing phenomenon when they travel downstream. Consecutive stages of pairing create more coherent structures which in turn contribute to larger amplitudes of periodic velocity oscillations. Vortex phenomena may be most precisely investigated by spectral analysis and that is why these measurements have been performed in the present research. The sample results in Figure 14 present power density spectra (*psd*) of velocity fluctuations recorded at the isothermal jet (s = 1.0) centreline at the distance $x / D_1 = 3$ from the nozzle exit, that for isothermal jet corresponds to the end of potential core. Figure 14 presents the centreline spectra measured at $x / D_1 = 3$ for all the values of aspiration ratio "I". These plots were expressed in terms of Strouhal number.

One may notice that for undisturbed jet (I = 0) the *psd* plot obtained at the end of potential core reveals the presence of peak for $St \approx 0.8$, that corresponds to the first stage of formation of column mode vortex rings. The lowest level of aspiration ratio (I =0.1) leads to the appearance of well established column vortex rings with the typical frequency $St \approx 0.24$, one may also notice the presence of pairing phenomenon, that leads to the formation of peak at half the dominant frequency ($St \approx 0.2$). Application of higher aspiration ratio (I=0.2) intensifies the vortex pairing phenomenon as it is indicated by the growing amplitude of the peak corresponding to half the dominant frequency. One should notice however, that for I= 0.2 aspiration ratio the dominant frequency was slightly shifted towards higher frequencies, as it is indicated by the $St \approx 0.5$ value of the dominant peak for I=0.2 (instead of $St \approx 0.24$ observed for I=0.1). This phenomenon may result from the change of exit boundary layer thickness, but the more convincing explanation requires more elaborate studies. The increase of aspiration ratio to I=0.2 leads to the formation of peak at half the column mode dominant frequency ($St \approx 0.2$), while further increase of aspiration (I=0.4) leads to the *psd* shape, which is characteristic for fully developed turbulence (see that only slight trace of $St \approx 0.2$ peak is visible at Fig. 14 for I=0.4). One may conclude therefore, that aspiration ratio I acts as an effective means of vortex dynamics control in a free jet, and the changes in spectra of velocity fluctuations due to the increase of I are identical as the psd transformation observed in undisturbed jet when the measuring point is moved downstream along the jet axis. A similar analysis was performed for the non – isothermal counter – current jet but this discussion is beyond the scope of the paper.

SUMMARY

The paper presents the experimental study describing of flow field characteristics in isothermal countercurrent round jets. The experiment confirmed that both the reverse outer flow and the overheat of the inner jet may substantially change the flow pattern of inner jet, proving that it can be utilised for the active flow control. In particular, the results obtained prove that these parameters affect the process of coherent vortex rings formation that in turn intensifies the momentum and heat transport in the flow considered.

NOMENCLATURE

δ – the thickness of boundary layer

v – kinematic viscosity coefficient

CTA – Constant Temperature Anemometer

D_1 – diameter of inner jet

D_2 – diameter of outer jet

I – the ratio of the outer to inner velocity [$I = \overline{U}_2 / \overline{U}_1$]

L – extension collar length

LDA – Laser Doppler Anemometer

Re – Reynolds number based on D_1

s – the density ratio between the jet and the ambient fluid

St – Strouhal number [$St = fD_1 / \overline{U}_1$]

$u'/\overline{U}$ – turbulence intensity

$\overline{U}_1$ – mean velocity of main (inner) jet

$\overline{U}_2$ – aspirated reverse (outer) mean velocity

$\overline{U}_0$ – mean reference velocity at the exit of the inner nozzle

$\overline{U}$ – local mean velocity

u' – turbulence component of $\overline{U}_1$ (RMS)

Acknowledgements

The research was performed under the TIMECOP EU project (contract No STREP 030828) and SPB TIMECOP funded by MNiSzW.

This work received funding from the European Community through the project TIMECOP-AE (Project #AST5-CT-2006-030828). It reflects only the author's views and the Community is not liable for any use that may be made of the information contained therein.

REFERENCES

1. Strykowski P.J., Niccum D.L. 1991, The Stability of Countercurrent Mixing Layers in Circular Jets, *J. Fluid Mech.*, vol. 227, 309-343, 1991.
2. Monkewitz P.A., Bechert D.W., Barsikow B., Lehman B., Self-excited oscillations and mixing in a heated round jet, *J. Fluid Mech.,* vol. 213, 611-639, 1990.
3. Kyle D.M., Sreenivasan K.R., The instability and breakdown of round variable density jet, *J. Fluid , Mech.,* vol.249, 1993
4. http://timecop-ae.com/
5. Wojciechowska B., Drobniak S., Domagała P., Experimental Analysis of Velocity Field Structure In Isothermal Countercurrent Jets, *J. of Theor. and Applied Mech.,* vol.47, No. 1, s. 3-17, 2009,.
6. Asendrych D., Drobniak S. Experimental Analysis of the Flow field in Nonisothermal Countercurrent Jets, *Advances in Turbulence*, IX, 839, 2002.
7. Asendrych D. Intensification of Transport Processes in Free Round Countercurrent Flows, Cieplne Maszyny Przepływowe, *"Turbomachinery"*, 117, II, 27-32, 2000.
8. Asendrych D. Active Flow Control by Countercurrent Jets, *J. of Theor. and Applied Mech.*, vol. 45, No. 3, s. 463-478, 2007.
9. Jendoubi S., Strykowski P. J.: Absolute and Convective Instability of Axisymmetric Jets with External Flow, *Phys. Fluids* 6 (9), 1994.
10. Crow S. C., Champagne R. S.: Orderly structure in jet turbulence, *J. Fluid Mech.*, vol, 48, 567, 1971.

EDDY GENERATION AND HEAT-TRANSFER CONTROL IN RIBBED SYSTEMS COMPOSED OF SEVERAL STREAMLINED RIBS

Ya.I. Smulsky, V.I. Terekhov*, N.I. Yarygina
Kutateladze Institute of Thermophysics SB RAS,
Novosibirsk, Russia

ABSTRACT. In the present work, experimental data are reported concerning the development of turbulent separated flow and heat transfer in systems of several transverse or inclined ribs at different levels of free-stream turbulence. Visualization data and data on pressure and heat-transfer coefficients are presented. It is shown that there is the extremely unstable vortex formation in the second inter-rib cell under condition of natural turbulence of main stream, but high external turbulence stabilizes flow. The approximately identical promoting action of high turbulence on pressure coefficients and heat transfer coefficients is demonstrated. It was obtained that the secondary flows caused by the inclined ribs create a significant spanwise variation of heat transfer coefficients with appreciable increase of heat transfer on the part of a sharp angle at the ward side. Average on heated surface heat transfer coefficients slightly depend on ribs orientation. The maximal values of heat transfer intensity take place at an inclination angle of 60 degrees.

Keywords: *experiment, flow, separated flow, turbulence, heat transfer*

INTRODUCTION

In the present work, experimental data are reported concerning the development of turbulent flow and heat transfer in systems of several ribs at different levels of free-stream turbulence. On the one hand, this problem is related with the necessity of developing advanced heat transfer intensification methods providing simultaneously for an acceptable level of hydraulic losses in heat-and-power plant applications. On the other hand, this study is aimed at the development of physical foundations for heat and mass-transfer processes in high-turbulent flows with separation.

Rib turbulators are frequently in the form of rectangular cross-sectional bars mounted along the surface, which are often angled with respect to the bulk flow direction. Because they protrude into the flow, they act to trip the flow, mix the flow, and also generate vortices and three-dimensional velocity gradients. Today, many reported studies are available in which the flow structure and heat transfer in ribbed channels were examined [1-9]. Nonetheless, the multiparameter nature of the problem and the action of such factors as initial conditions, high flow turbulence, mutual influence of flows separated from obstacles, etc., did not allow a reliable calculation procedure to be developed for predicting heat transfer intensification in ribbed channels.

In our previous studies [10-13], the vortex-formation pattern and heat transfer behind a transverse rib streamlined by turbulent flow were thoroughly examined. The rib height and the free-stream turbulence were found to be parameters permitting an efficient control of the separated flow and heat transfer intensification. The separated flows behind steps [10] and flows in transverse cavities [14] are flows even more sensitive to external conditions, including the free-stream

* Corresponding author: Prof. V.I. Terekhov
Phone: + (7)-383-3306736, Fax: + (7)-383-3308480
E-mail address: terekhov@itp.nsc.ru

turbulence. According to [15], the flow pattern in an inter-rib cell differs substantially from the flow pattern in a similarly sized rectangular cavity. Unfortunately, reported studies of the flow structure and heat transfer over the initial length of flow in system of cross-flow ribs are few in number. Over this length, a most pronounced influence of external conditions on the separated flow is exerted, defining the formation of downstream flow features throughout the surface. Considering the evolution of the flow, establishing the conditions that make the flow over the ribbed surface self-similar also seems to be an important matter.

In the present work, we experimentally examined the dynamic and thermal characteristics of the separated flow in systems of two to five flat flow-normal ribs and oblique to flow direction ribs. The vortex formation patterns, and the fields of temperature, pressure and heat transfer coefficients, were investigated. Visualization data, and also data on pressure and heat transfer coefficients, are reported. The effect due to free-stream turbulence is analyzed.

EXPERIMENTAL SETUP

The tests were carried out in the subsonic flow of the wind tunnel of the Institute of Thermophysics SB RAS with rectangular working channel 1000 mm long, 200 mm wide and 200 mm high. A 600-mm long model was installed at a height of 600 mm over the lower wall. The step nose of the model, of length 100 mm, was used to produce on the surface a 1/7-power-law turbulent boundary layer about 10 mm thick [10].

In measuring the dynamic and thermal characteristics, identically sized models were used. Both models were made of 20-mm thick textolite. The dynamic model was provided with pressure taps located in five longitudinal cross-sections across the channel, spaced 5 mm apart over the initial length of 300 mm and 10 mm apart on the remaining part of the plate. The 500-mm thermal model was heated ohmically in the regime q_w = const with the help of a ribbon heater made of 20-μm thick aluminum foil which covered the entire surface of the model. In the central longitudinal cross-section, twenty thermocouples were provided, mounted flush with the surface. The heat leaks by thermal conduction were determined from the temperature drop across the model. The distribution of temperature over the entire heat-exchanging surface was examined thermographically, with the help of a THERMO TRACER TH7102 IR imager (Japan). The gained temperature fields were digitized using reference thermocouples and special software.

To visualize the surface flow pattern in the ribbed system by the soot-oil film method, we used another similar-sized model coated with 3-mm thick Plexiglas. The visualizing mixture was a mixture of offset black and lamp oil.

A system of two to five ribs, sufficiently wide to completely span the channel, was mounted on the model surface; the first rib was installed 50 mm from the leading edge of the model. The ribs were made of Plexiglas, the rib height being H = 60 мм, and were 4 mm thick. Like the rib height, the spacing between the ribs was 60 mm; the used cells were therefore square. In the systems of oblique ribs, the rib height was 3, 6 and 10 mm. In the majority of experiments, the free-stream velocity U_0 = 20 m/s. The Reynolds number for this velocity calculated from the rib height was $1.2 \cdot 10^5$.

The experiments were carried out at two, a low and a high, free-stream turbulence levels $Tu_0 = \sqrt{\overline{u'^2}}/U_0$ = 1.5 and 15 %. The high turbulence level was achieved by tripping the flow with a flag turbulence generator installed 330 mm upstream of the first rib. The polyethylene flags were fastened to a perforated grid with 20-mm diameter holes. This grid completely spanned the channel.

EXPERIMENTAL DATA

Flow visualization. The visualized patterns of the flow at the bottom of inter-rib cells were obtained for all ribbed systems comprising one to five ribs. A typical picture for the systems of four and five ribs at the low and high level of free-stream turbulence is shown in Fig. 1. In the figure, the

flow is directed from the left to the right. The vortex-formation pattern observed in the first cell at Tu_0 = 1.5 % closely resembles the pattern observed in a rectangular cavity [14].

Near the trailing wall of the cell a most intense eddy forms, with a secondary eddy registered near the leading wall. Similar patterns were also registered in the third and fourth cells, the flow in these cells being more stable. The flow in the second cell was very unstable because of the development of a reverse flow directed against the mainstream flow and moving out of the third cell into the second cell. This effect was reported previously in our early studies (see [15]). Flow instability in the second cell was also observed in the systems of three and four ribs. In these systems, the flow behind the last rib always resembled the flow behind a single rib. Under the action of the external turbulence, the flow in the second cell gets stabilized to become a flow most stable among all cells. Flow instability was also registered in the first cell; accordingly, a reverse flow, yet less intense compared to the low-turbulence case, was observed in the region over the second rib. An appreciable reconstruction of the vortex structure was exhibited by the secondary flow in the third and fourth cells.

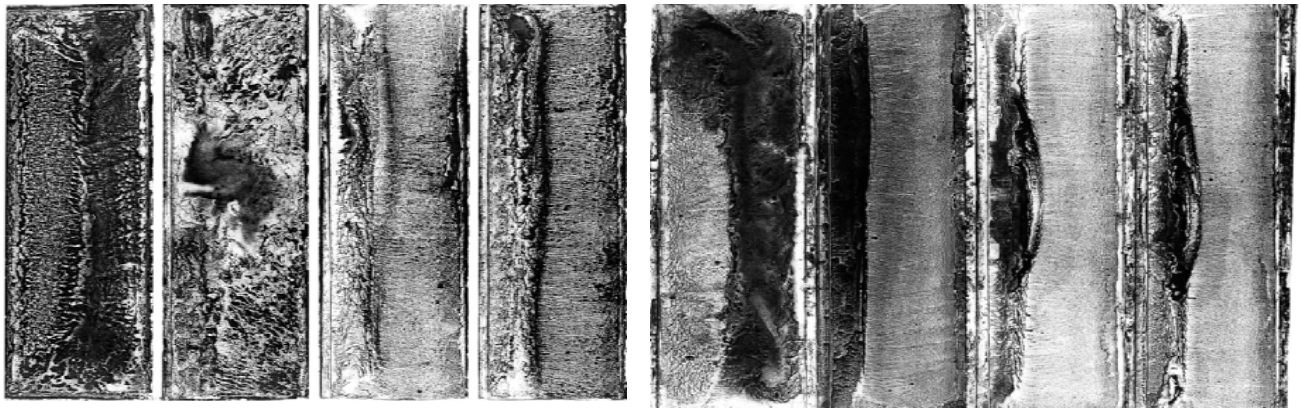

a) b)

Figure 1. Vortex-formation pattern at the bottom surface in the system of five ribs
a) Tu_0 = 1.5 %; b) Tu_0 = 15

Distribution of pressure coefficients. Our experiments showed that the distributions of pressure measured inside inter-rib cells in different cross-sections of the channel were almost identical.

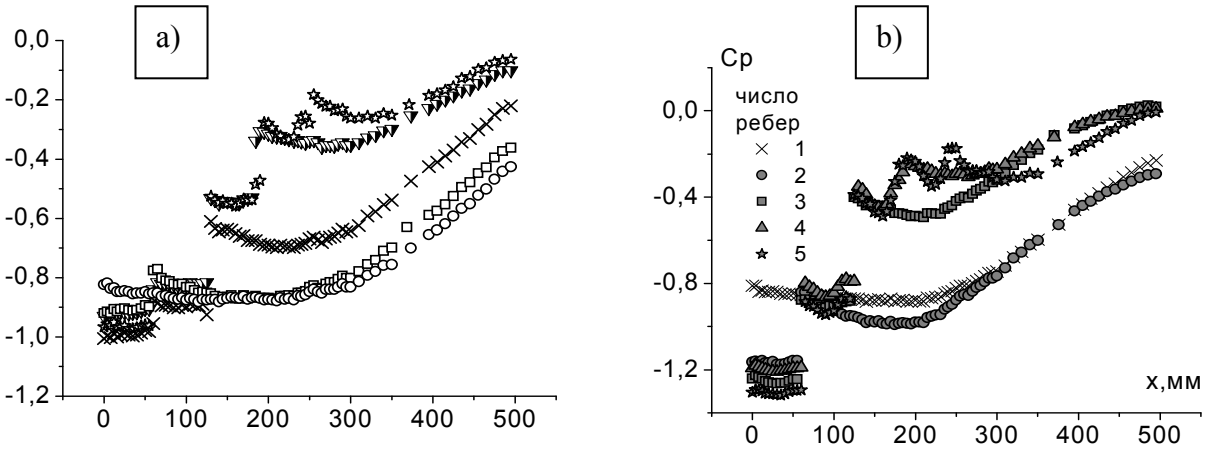

Figure 2. Distribution of pressure coefficient in inter-rib cells in systems with different number of ribs a) - Tu_0 = 1.5 %; b) - Tu_0 = 15 %

The distributions of the pressure coefficients $C_p=2(p_i - p_0)/\rho U_0^{\,2}$ at the bottom of inter-rib cells are shown in Fig. 2. Here, p_i is the wall pressure, and p_0 and U_0 are the reference pressure and the flow-core velocity un the region over a rib. In the downstream region of the last rib, a characteristic distribution of pressure is observed that closely resembles the similar distribution behind a single rib. Behind the last rib, the pressure recovers over a length of 14 calibers [5]. As it follows from Fig. 2, with each additional rib installed in the system the pressure recovers more and more rapidly. In the system of four or five ribs the pressure recovery lengths are identical, extending to a distance of nine calibers from the leading wall of the first rib. In the tripped flow, a decrease in the absolute value of C_p in the downstream region of the last rib is observed, especially in systems made up by small number of ribs, and also in the second cell of the system comprising three ribs, this finding being indicative of some reconstruction of the flow.

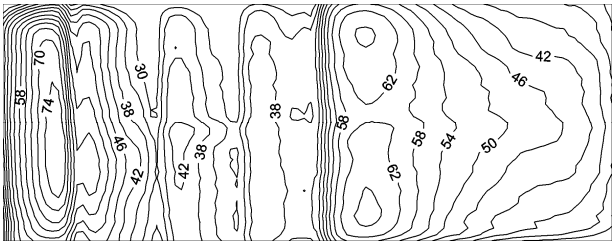

Figure 3. Isotherms of the bottom surface under heating the bottom in the system of five ribs

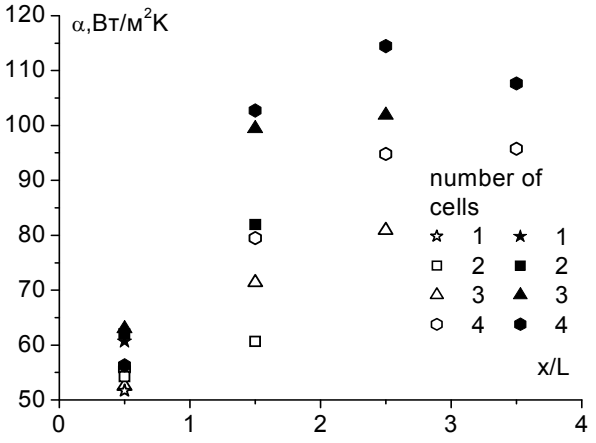

Figure 4. Distribution of cell surface-average heat transfer coefficient α in the systems of two to five ribs (open symbols - Tu_0 = 1.5%, full symbols - Tu_0 = 15 %)

Heat transfer. The temperature field revealed thermographically at the natural turbulence level in the system of five ribs and in the downstream region of the last rib is shown in Fig. 3. The flow instability in the second inter-rib cell is seen to have a most pronounced influence on the distribution of temperature in this cell. The temperature field in the second cell is symmetric with respect to the temperature field in the first cell. A weak reconstruction of temperature distributions is also observed in the third and fourth cells, the isotherm distribution behind the last rib being the same as behind a single rib.

The gained temperature fields were used to calculate the local heat transfer coefficients α. The longitudinal distributions of the lengthwise-local values of α obtained in systems with different numbers of ribs showed that, for both turbulence levels, a considerable growth of heat transfer in the second cell is observed, most pronounced in the system of five ribs. In subsequent cells, the growth of heat transfer coefficients somewhat weakens. In the low-turbulence flow over the system of five ribs the rate of heat transfer attains its highest in the two last cells. This observation is also confirmed by Fig. 4, which shows the surface-average heat transfer coefficients for each cell. In compliance with the vortex-formation pattern, the most pronounced heat transfer intensification due to the external turbulence (up to 30 %) is observed in the second cell.

The visualization tests performed with systems of low-height (6 mm) oblique ribs inclined at angles of 45, 60, and 75° to the flow proved the temperature and thermal fields to differ from the fields observed in systems of flow-normal ribs. Figure 5 shows visualization data for 60° angled ribs represented in the form of distributions of local heat transfer coefficients.

It is seen from Fig. 5 that, compared to systems of flow-normal ribs, the heat transfer coefficient in systems of oblique ribs are substantially redistributed in the spanwise direction with markedly enhanced heat transfer behind ribs on the acute-angle side.

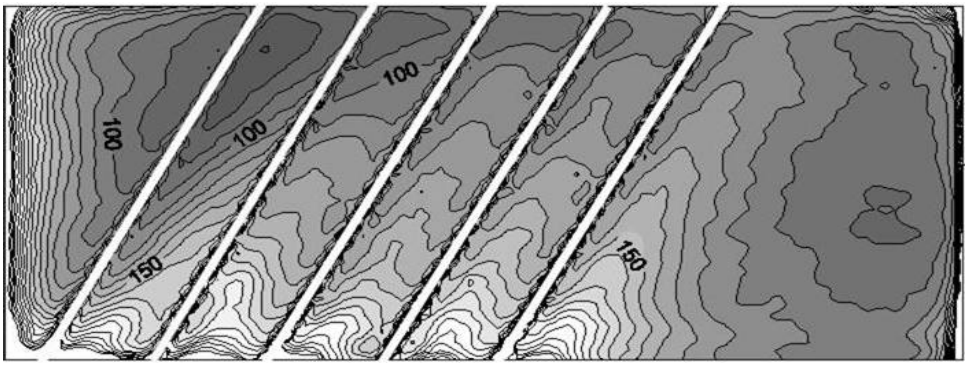

Figure 5. Distribution of local heat transfer coefficients in the system of 60° angled ribs

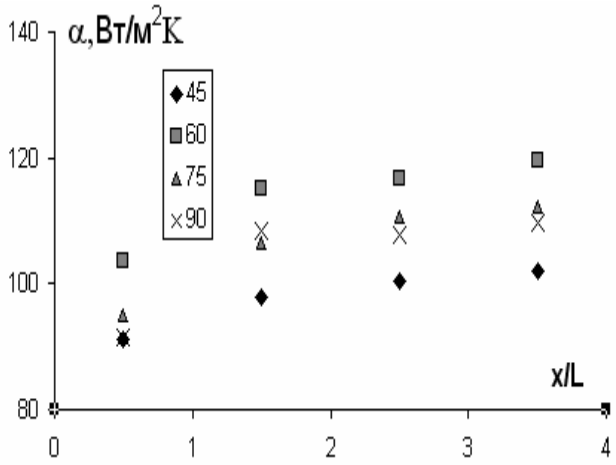

Figure 6. Distribution of cell surface-average heat transfer coefficient in the system of ribs with different inclination angles

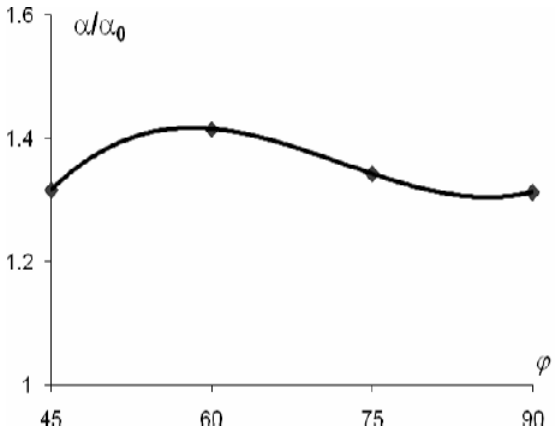

Figure 7. All heated surface-average heat transfer coefficient normalized to the same coefficient on a flat plate for four angular configurations of the system of five ribs

Overall picture of heat transfer distribution in each cell is similar. For all angular configurations the first cell has the least heat transfer augmentation in comparison with the subsequent cells that Fig. 6 proves to be true. However the level of heat transfer for various angles of a ribs orientation is slightly differs. According to Fig. 7, the surface-average heat transfer coefficients in the system of five ribs also depend, although insignificantly, on the rib angle φ. All data, including those for flow-normal ribs, were obtained for 6-mm high obstacles. A maximum values of α_{mean} was observed at φ=60°.

Figure 8 shows the surface-average heat transfer coefficients in the low-turbulent flow normalized to the flat-plate heat transfer coefficients versus the total number of installed ribs. High flow-normal ribs are seen to be good heat transfer intensifiers only in the high-turbulent flow due to the high level of free-stream turbulence. In the case of low-height ribs installed obliquely to the flow (Fig.8 b), the rate of heat transfer increases with increasing number of such ribs.

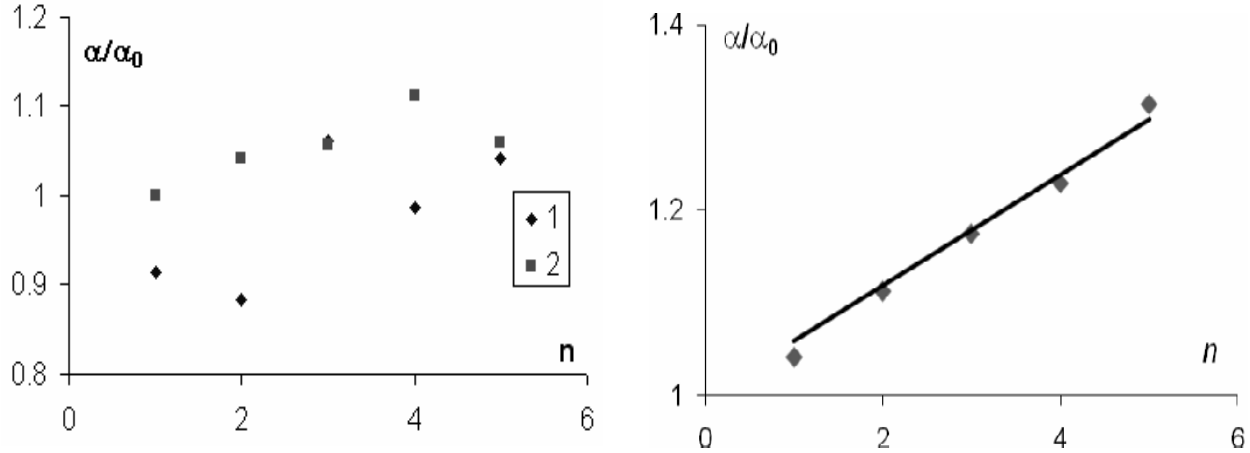

a) b)

Figure 8. Cell surface-average heat transfer coefficient versus the total number of installed ribs
a) H = 60 mm, 1 - φ = 90°, Tu_0 = 1.5%; 2 - φ = 90°, Tu_0 = 15%;
b) H = 6 mm, φ = 45°, Tu_0 = 1.5%.

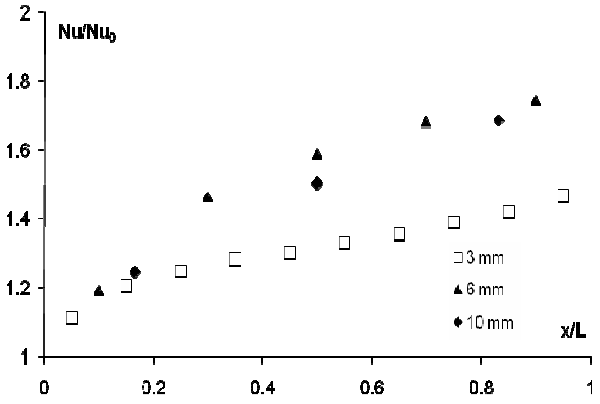

Figure 9. Cell surface-average Nusselt number normalized to the same coefficient on a flat plate for φ = 60°

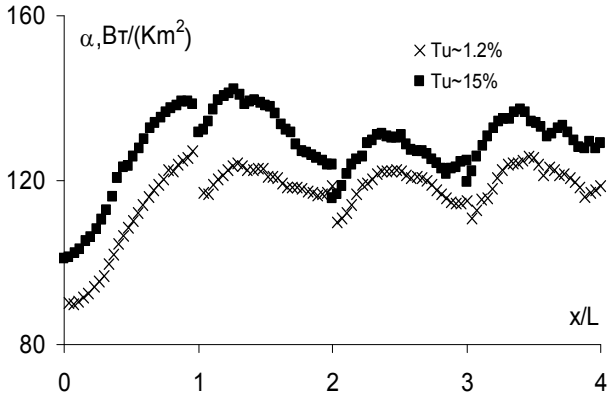

Figure 10. Distribution of local heat transfer coefficient in the system of 45° angled ribs at two turbulence levels

Distribution of average heat transfer coefficient calculated on the area of a cell of for system of ribs with an attack angle of 60° is submitted at three values of height of a rib in Fig. 9. The system has consisted of 4 ribs with step of 100 mm at height of rib H=10 mm on heat-release surfaces, from 6 ribs with step of 60 mm at height H=6 mm and from 11 ribs with step of 30 mm at H=3 mm. In Fig. 9, Nusselt number grows with increase in height for ribs of small height.

Distribution of local coefficient α along an axis of symmetry of model (at φ =45° and H=6 mm, Fig. 10) differs from distribution local heat transfer in system of direct ribs (Fig. 4) a little. There is influence of external turbulence upon α up to 30 % in the system of 45° angled ribs the same as in system of direct ribs. As a whole it is shown, that the augmentation of heat transfer in separated

flows behind obstacle such as ribs can be effectively control both change of orientation of a main stream and a level of turbulence in the external flow.

CONCLUSIONS

An experimental study was performed to examine the formation of the vortex structure, and also the pressure and temperature fields, in inter-rib cells of ribbed systems at two turbulence numbers, 1.5 % and 15 %.

The visualization tests showed that in the low-turbulent flow over a system of three or more ribs a very unstable flow forms in the second cell, related with the rarefaction induced mass suction behind the second rib and with the development of a reverse flow in the region over the third rib. Under conditions of high free-stream turbulence, this instability was found to be displaced into the first cell.

With each additional rib installed in the system, the flow separation region behind the last rib and the pressure recovery region become less extended in the downstream direction, and the coordinate at which the pressure attains its maximum, decreases.

A sharp increase in the rate of heat transfer in the second inter-rib cell was identified. The rate of heat transfer in the flow over a system of five ribs under the low-turbulence conditions attains its highest in the third cell, at a distance of three calibers over the rib height, whereas in the flow over a single rib this distance amounts to 15 calibers. High free-stream turbulence intensifies heat transfer. In the second cell, the heat transfer intensification amounts to 30 %.

In the systems of oblique ribs, some redistribution of temperature profiles is observed, most pronounced for obliquely ribbed systems with $\varphi = 60°$. Unlike systems with high ribs, under natural-turbulence conditions low-height ribbed systems ($H \leq 10$ mm) serve good heat transfer intensifiers.

This work was partly supported by the Russian Foundation for Basic Research (Grant No. 09-08-00076).

NOMENCLATURE

C_p – pressure coefficient, $C_p=2(p_i-p_0)/\rho U^2$;
H – rib height, mm;
L – расстояние между ребрами,mm;
q – heat flux, W/m^2;
Re – Reynolds number, $\mathrm{Re}_H = U \cdot H/\nu$;
U – free-stream velocity, m/s;
u' - longitudinal velocity fluctuation, m/s;
Tu_0 – free-stream turbulence number, $\sqrt{\overline{u'^2}}\ /U$;
x – streamwise coordinate, m, mm;
α – heat-transfer coefficient, W/m^{2}K;
φ – angle of rib inclination to the free-stream direction, deg.

SUBSCRIPTS

mean – average values;
0 – conditions in the free stream;
i – local values;
w – values at the wall.

REFERENCES

1. Han, J.C., Park, J.S., Developing heat transfer in rectangular channels with rib turbulators, *Intern. J. Heat Mass Transfer,* Vol. 31, No. 1, pp 183–195, 1988.

2. Chyu, M.K., Wu, L.X., Combined effects of rib angle-of-attack and pitch-to-height ratio on mass transfer from a surface with transverse ribs, J. Experimental Heat Transfer, Vol. 2, pp 291–308, 1989.
3. Olsson, C.-O., Sunden, B., Experimental study of flow and heat transfer in rib-roughened rectangular channels, *J. Exp. Thermal Fluid Sci.,* Vol. 16, No. 4, pp 349–365, 1998.
4. Kiml, R., Mochizuki, S., Murata, A., Effects of rib arrangements on heat transfer and flow behavior in a rectangular rib-roughened passage: Application to cooling of gas turbine blade trailing edge, *J. Heat Transfer*, Vol. 123, No. 4, pp 675-682, 2001.
5. Gao, X., Sunden, B., Heat transfer and pressure drop measurements in rib-roughened rectangular channels, *J. Experimental Thermal and Fluid Science*, Vol. 24, pp 25–34, 2001.
6. Mahmood, G., Ligrani, P.M., Chen, K., Variable property and temperature ratio effects on Nusselt number in a rectangular channel with 45 deg angled rib turbulators, *J. Heat Transfer*, Vol. 125, No. 5, pp 769–778, 2003.
7. Mahmood, G., Ligrani, P.M., Won, S.Y., Spatially-resolved heat transfer and flow structure in a rectangular channel with 45° angled rib turbulators, *Proceedings of ASME TUPBO EXPO 2002*, Amsterdam, The Netherlands, June 3-6 , 2002, Gt-2002-30215, pp 1-12.
8. Ligrani, P.M., Oliveira, M.M., Comparison of heat transfer augmentation techniques, *AIAA Journal*, Vol. 41, No 3, pp 337-361, 2003.
9. Oyakawa, K., Fukami, S., Islam, M., Miyafuji, Y., Heat transfer enhancement of votex generation fin, *Proceedings of Int. Conf. on Jets, Wakes and Separated Flows, ICJWSF-2008*, Berlin, Germany, September 16-19, 2008, pp 1-8.
10. Terekhov, V.I., Yarygina, N.I., Zhdanov, R.F., Heat transfer in turbulent separated flows in the presence of high free-stream turbulence, *Int. J. Heat Mass Transfer*. Vol. 46, pp 4535-4551, 2003.
11. Terekhov, V.I., Yarygina, N.I., Smulsky, Ya.I., Three-dimensional turbulent separated flow behind a flat obstacle with different orientations relative to the flow, *Proceedings of the Sixth World Conference on Experimental Heat Transfer, Fluid Mechanics and Thermodynamics (ExHFT-6)*, Matsushima, Japan, April 17-21, 2005, Paper No 3-a-5, pp 1–5.
12. Terekhov, V.I., Yarygina, N.I., Smulsky, Ya.I., Thermal and dynamic characteristics of the separated flow behind a flat rib with different angles of alignment toward the flow, *J Appl.Mechan. and Techn. Physics,* Vol. 48, No 1, pp 85-90, 2007.
13. Terekhov, V.I., Yarygina, N.I., Smulsky, Ya.I., Heat transfer peculiarities in separated flow past an oblique rib under different external turbulence, *J. Thermophysics and Aeromechanics,* Vol. 15, No 2, pp 205-213, 2008.
14. D'yachenko, A.Yu., Terekhov, V.I., Yarygina, N.I. Vortex formation and heat transfer in turbulent flow past a transverse cavity with inclined frontal and rear walls, *Int. J. Heat Mass Transfer*, Vol. 51, No 13-14, pp 3275-3286, 2008.
15. Terekhov, V.I., Tretyakov, S.P., Yarygina, N.I. Heat transfer in turbulent separated flows behind large obstacles on the plate, *Heat Transfer Research*, Vol. 25, No. 5, pp. 615-619, 1993.

NUMERICAL AND EXPERIMENTAL EVALUATION OF THE VELOCITY PROFILES IN TEST SECTION OF AN OPEN LOW SPEED WIND TUNNEL

C.Soares[1], C.Maia[2,], L. Cabezas-Gómez[3], S. Hanriot[4*]

[1]Federal Center of Technological Education of Minas Gerais-CEFET-MG, Belo Horizonte, Brazil
[2,3,4]Pontifical Catholic University of Minas Gerais-PUC-MG, Belo Horizonte, Brazil

Abstract. Aerodynamic forces are function of the relative velocity between the air and the body model. In a wind tunnel, this relative velocity is achieved moving the air over a stationary model. In the past years, several wind tunnels are being designed and built to measure aerodynamic forces and moments. It is observed that, even with the recent computational advances, wind tunnels are still an essential tool to the study of the aerodynamics. This paper presents a comparison between numerical and experimental data in the test section of a low speed wind tunnel. Numerical results were obtained for three turbulence models, namely the k-ε, *RNG k-ε and* shear stress transport *SST* models. The simulation results were compared with the mean time experimental velocity profiles as a function of several values of inlet mass flow rate, as well as with the experimental turbulent kinetic energy.

Keywords: *wind tunnel, hot wire anemometry, CFD*

INTRODUCTION

A wind tunnel is a research tool used to help the study of the effects of air moving over or around a body. Geometrical shapes or models (such as cars or plane wings) are mounted inside a duct and air is blown or sucked through this duct, creating a relative movement between the air and the object. Although the first wind tunnels predated the advent of aeroplanes, with Wenham in 1871, the wind tunnel was developed along with the aeronautical industry, between 1900 and 1960. In this period, the wind tunnel was seen as an essentially research tool. Between 1960 and 1980, it became a reliable and robust tool for commercial design purposes. From 1980, there have been significant advances in wind tunnel testing techniques, particularly in terms of instrumentation [1]. Even with the computational advances, wind tunnels still represent an essential tool to aerodynamic studies. Wind tunnel measurements are being used to validate Computational Fluid Dynamics (CFD) calculations, and CFD can be used as a tool to support wind tunnel design, wind tunnel testing and the interpretation of the test results [2].

Several reports of experiments performed in wind tunnels are available in literature. Wind tunnels are used to evaluate the drag and lift forces in objects [3, 4, 5], to investigate mean and fluctuating wind loads on buildings and atmospheric boundary layers [6, 7, 8] and to investigate turbulent boundary layers [9], among other studies.

* Corresponding author: Prof. S. Hanriot
Phone: + (55)-31-33194323, Fax: + (55)-31-33194910
E-mail address: hanriot@pucminas.br

With the improvement of computational capabilities, CFD techniques have been used to predict the behaviour of the airflow over and around solid bodies and to predict the acting forces and moments over them. Experiments in wind tunnels are performed to validate the numerical models [10, 11].

This paper presents numerical and experimental investigations of the airflow inside an open wind tunnel. The wind tunnel tests were carried out in the test section of a low-speed wind tunnel. Velocity and pressure were measured in an array of points in the test section. The instantaneous velocity and turbulent intensity were measured in the central point of the exit region of test section. The numerical predictions were performed using three turbulence models: the standard k-ε, the *RNG* k-ε and the *SST* model (see next section).

2.1 Numerical Methodology

A Computational Fluid Dynamics (CFD) technique comprehends the numerical solution of the governing flow equations. In the analysis, the solution domain is divided into a large number of infinitesimal control volumes and the governing equations are solved for each of them. The main governing equations of fluid flow are mass conservation, momentum conservation and energy conservation.

For turbulent flows, it is necessary to take into account the effects of turbulence. In this paper it is done through application of turbulence models. Three turbulence models were evaluated: k-ε model [12], the *RNG* k-ε model [13] and the *SST* model. The *SST* model was proposed by [14] from the k-ω turbulence model, initially formulated by [15]. The models are presented in the above-mentioned order, considering only the main equations used in the numerical simulations. Models constants are also introduced. It is important to note that are presented the model definitions and formulation used in [16], since the numerical simulations were performed with this commercial code. The main interest is to study how different models can lead to different computational results only considering the defaults definition of each model, including the default boundary conditions.

The mass conservation and momentum conservation equations are used in the same form for all the models evaluated.
Mass conservation:

$$\frac{\partial \rho}{\partial t} + \vec{\nabla} \cdot (\rho \boldsymbol{U}) = 0 \tag{1}$$

Momentum conservation:

$$\frac{\partial (\rho U)}{\partial t} + \vec{\nabla} \cdot (\rho U \otimes U) = -\vec{\nabla} p + \vec{\nabla}\left(\mu (\vec{\nabla} U)\right) + B \tag{2}$$

where B is the sum of body forces, μ_{eff} is the effective viscosity accounting for turbulence, and p' is the modified pressure. μ_{eff} and p' are given respectively by:

$$\mu_{eff} = \mu + \mu_t \tag{3}$$

$$p' = p + \frac{2}{3}\rho k \tag{4}$$

2.2 Standard k-ε model

The k-ε model uses the eddy viscosity concept, assuming that the turbulence viscosity μ_t is computed by:

$$\mu_t = C_\mu \rho \frac{k^2}{\varepsilon} \tag{5}$$

where C_μ is a model constant.

The standard k-ε model [17] introduces two new variables into the equation system: the turbulent kinetic energy, k, m^2/s^2; and the turbulence eddy dissipation,ε, m^2/s^3. The new variables are obtained through the solution of transport equations, given by:

$$\frac{\partial(\rho \boldsymbol{k})}{\partial t} + \vec{\nabla} \cdot (\rho \boldsymbol{U} k) = \vec{\nabla} \cdot \left[\left(\mu + \frac{\mu_t}{\sigma_{\boldsymbol{k}}} \right) \vec{\nabla} k \right] + \boldsymbol{P_k} - \rho\varepsilon \tag{6}$$

$$\frac{\partial(\rho\varepsilon)}{\partial t} + \vec{\nabla} \cdot (\rho \boldsymbol{U} \varepsilon) = \vec{\nabla} \cdot \left[\left(\mu + \frac{\mu_t}{\sigma_\varepsilon} \right) \vec{\nabla} \varepsilon \right] + \frac{\varepsilon}{k} \left(C_{\varepsilon 1} \boldsymbol{P_k} - C_{\varepsilon 2} \rho\varepsilon \right) \tag{7}$$

In the equations, $C_{\varepsilon 1}$, $C_{\varepsilon 2}$, σ_k and σ_e are the model constants and P_k is the turbulence production tensor due to viscous forces. The buoyancy forces are not considered in the present work.

The *RNG* k-ε model is based on renormalization group analysis of the Navier-Stokes equations. The transport equations for turbulence generation and dissipation are the same as those for the standard k-ε model, but the model constants differ. The equations for the momentum and continuity are also the same.

The other two-equation turbulence model refers to the Shear Stress Transport model taken from [12]. This model was proposed by [14], and grew from the denominated baseline k-ω model in [12]. The baseline k-ω model makes use of the k-ε model in regions far away from the walls and the k-ω Wilcox model (cf. [15]) near the surface. The *SST* model is an improvement of the baseline k-ω model, taking into account the transport of the turbulent shear stress by a limitation of the eddy viscosity ν_t by the following equation:

$$\nu_t = \frac{a_1 k}{\max(a_1 w, SF_2)} \tag{8}$$

where: $\nu_t = \mu_t / \rho$ and S represents an invariant measure of the strain rate. F_2 is a blending function, which restricts the limiter to the wall layer computed by:

$$F_2 = \tanh(\arg_2^2) \tag{9}$$

with:

$$\arg_2 = \max\left(\frac{2\sqrt{k}}{\beta' \omega y'} \frac{500\nu}{y^2 \omega} \right) \tag{10}$$

3. Experimental setup

The experiments were conducted in an open wind tunnel type shown in Figure 1. This setup has a square cross-sectional test section of 200 mm wide and 790 mm of extension. Before the test

section removable grids can be installed to homogenize the flow turbulence. The rotation speed of the fan is controlled to modify the mass airflow inside the wind tunnel. The tests were carried out for several values of rotation speeds, ranging from 1800 rpm up to 3200 rpm.

In order to measure the mean time axial velocity a Pitot-static probe was used in several points of the exit test section region. Considering that [18] establishes a minimum of 25 measurement points, 36 measurement points were used to characterize the velocity profile in the exit of the test section. These points are shown in Figure 2, where (0,0) corresponds to the centre of the section and the values are in mm.

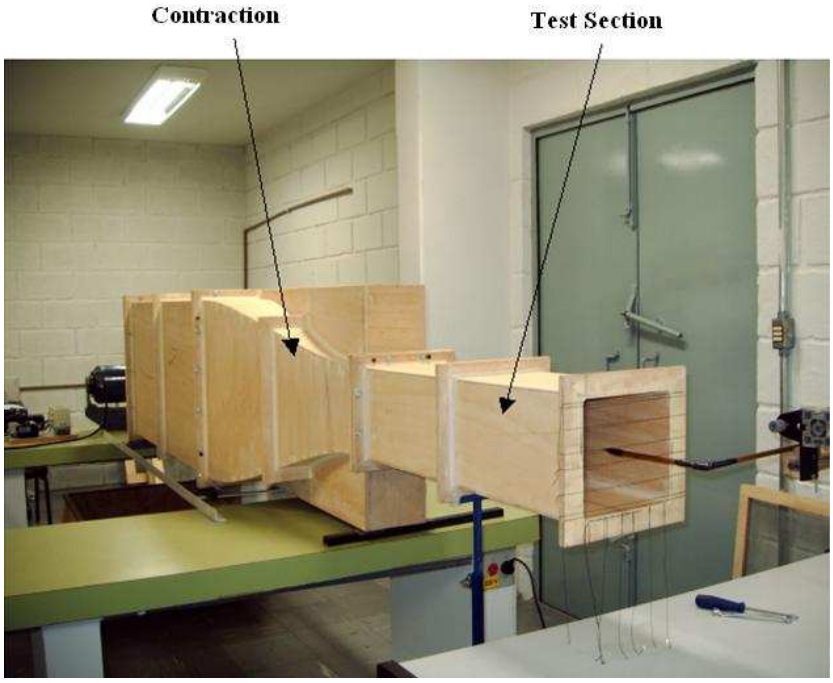

Figure 1. Wind tunnel[19]

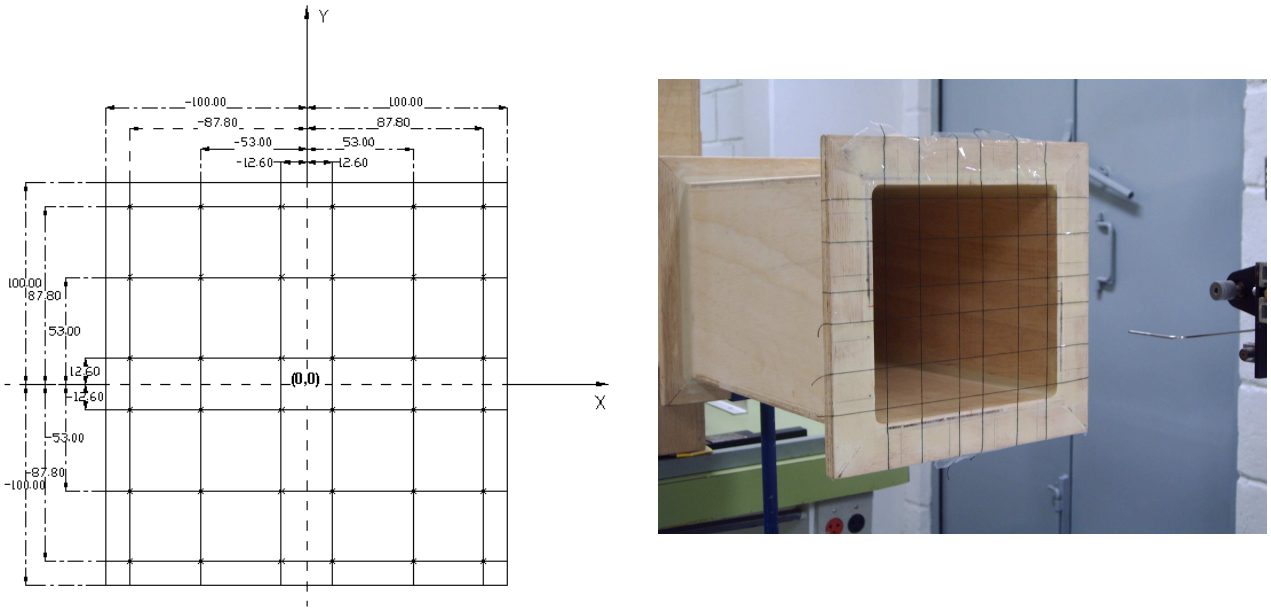

Figure 2. Velocity measurement points at the exit of the test section [19].

A hot wire anemometer was placed in the centre of the test section (0,0 coordinates) to evaluate the instantaneous velocity and the intensity of turbulence of the airflow at this point. In the experiments, the room temperature was 294 K and the atmospheric pressure was 0,906 bar.

RESULTS AND DISCUSSIONS

The employed computational domain (see Figures 5 and 6) includes the wind tunnel test section and additional region, after the wind tunnel exit, which was used in order to guarantee a zero value of the relative pressure. In all the simulations was employed a computational mesh with a total number of elements and nodes equals to 1386313 and 339286, respectively. A mass flow rate, obtained from experimental results, was used as inlet boundary condition. The outlet region (additional region in Figures 5 and 6) considered a zero value of the relative pressure in all outlet surfaces and was set out as an opening condition in the CFX code. This condition allows a mass flow across the outlet surfaces. A no slip condition was considered for the wind tunnel test section walls. The flow was considered as isothermal with a temperature value of 293 K. For the necessary turbulent quantities at boundaries were employed the CFX default boundary conditions assumed for each turbulence model. The models constants also were assumed as the default values considered in the CFX code.

Figure 3 shows the numerical results and experimental data of the cross-sectional mean time axial velocity profiles at position ($x = 0.1126$ m, $0 \leq y \leq 0.2$ m) in the exit plane of the wind-tunnel test section. In terms of the mean time axial velocity, it is not observed significant differences in the numerical results obtained for each turbulence model and each fan rotational speed. In the present case this behaviour is expected because the flow does not present a strong adverse pressure gradient at the exit region, which commonly lead to unsatisfactory results when the k-ε and *RNG* k-ε models are used (see [14] for more details).

Comparing with the experimental data, the major differences are observed in the regions near the tunnel walls, especially in the left side. This behaviour can be explained to small distortions of the wood wind tunnel walls; which produce an asymmetry of the experimental velocity profiles.

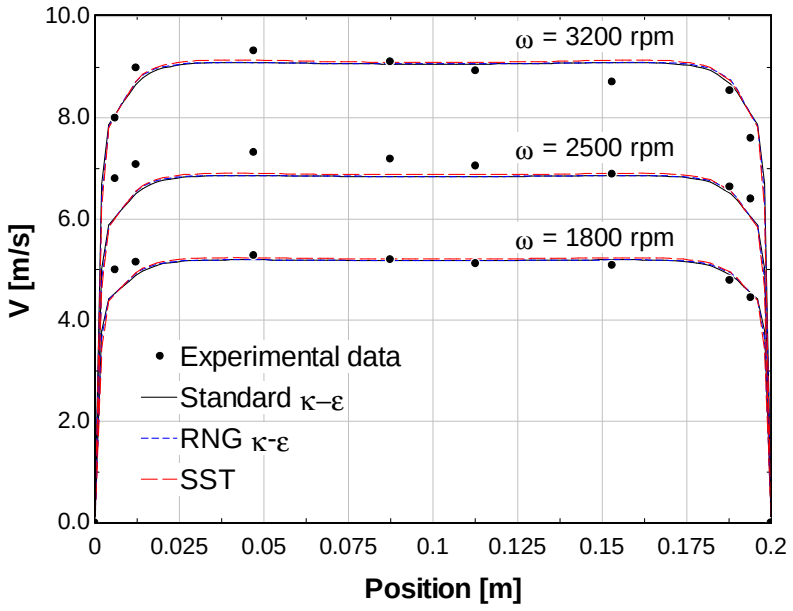

Figure 3. Velocity profile versus position at exit wind tunnel section.

The turbulent kinetic energy profiles for the three turbulence models are shown in Figure 4. The experimental data was obtained in the centre of the tunnel using the hot wire anemometer sensor. The turbulent kinetic energy is associated with the rms velocity fluctuations. Laufer [20] using a hot wire anemoter showed that the rms fluctuations in a turbulent developed pipe flow are small in the

regions near walls and have a sharp maximums near the edges of the laminar sublayers, existing a strong movement of kinetic energy away from this point (laminar sublayer). This behavior was obtained only with the *SST* turbulence model, as shown in Figure 4. The *k-ε* and *RNG k-ε* models were not able to predict this feature. Considering the experimental value of the turbulent kinetic energy in the tunnel centre it is also noted that the best prediction was obtained with the *SST* model.

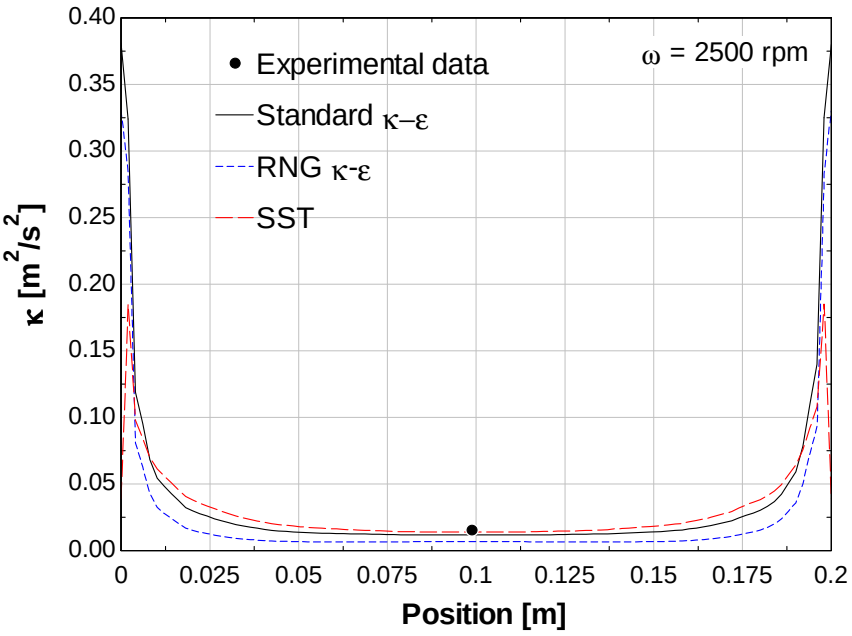

Figure 4. Turbulent kinetic energy versus position at exit section.

Figure 5 shows the numerical velocity field in the test section of a wind tunnel. It can be seen a free jet and a recirculation region in the outlet section after the test section, properly of this type of flow. The maximum velocity equals to 9.18 m/s, in accordance with experimental data.

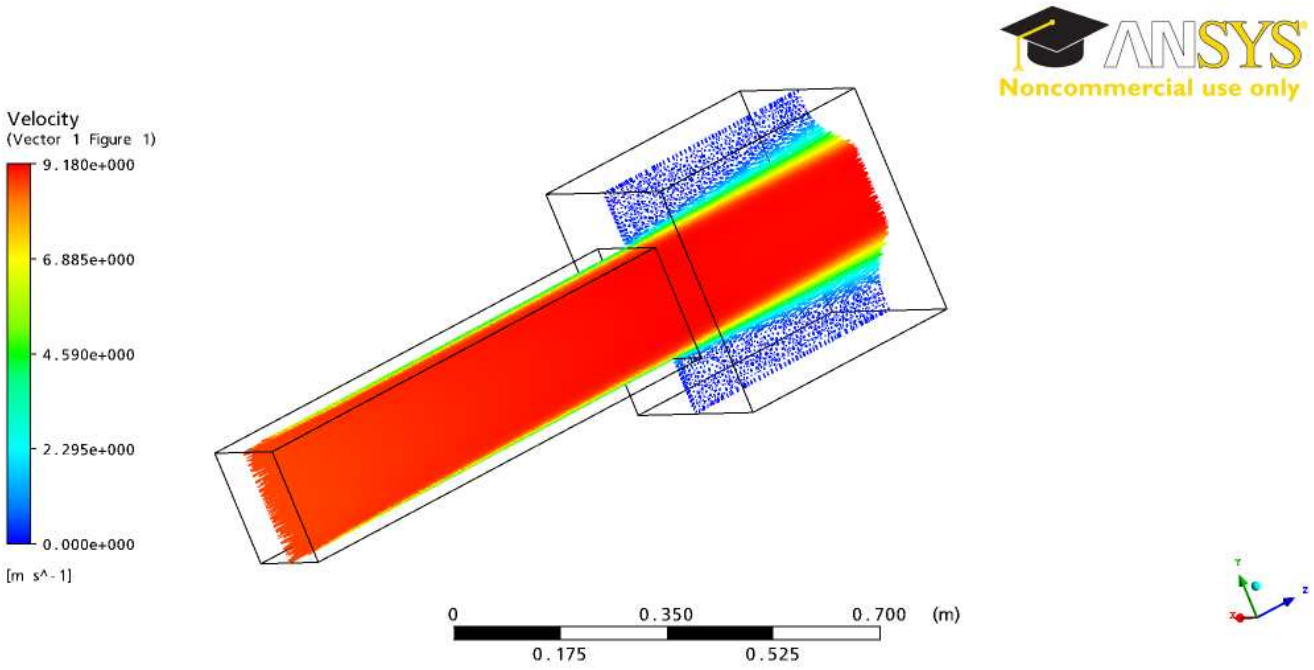

Figure 5. Numerical results of velocity field section (w= 3200 rpm)

Figure 6 shows the numerical pressure field in the test section of wind tunnel. It can be seen that the highest relative pressure is at the inlet of the test section, decreasing towards the exit region, as expected. It should be observed that the present turbulent flow is characterized by very small pressure gradient and pressure values, which was not possible to measure experimentally with the available measurement devices. However, the displayed pressure gradient seems to be physically correct, and will be validated in future works.

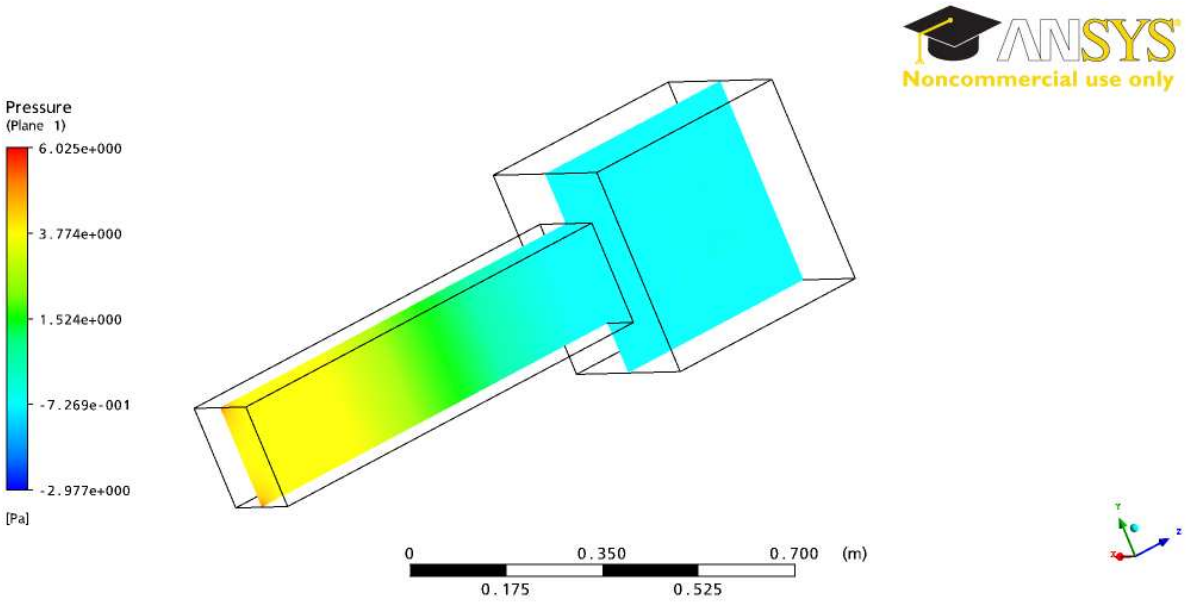

Figure 6. Numerical results of pressure field section (w= 3200 rpm)

CONCLUSIONS

This paper presents a comparison between numerical and experimental data in the test section of a low speed wind tunnel. Detailed Pitot tube and hot wire anemometry measurements were made to examine the flow behavior in the exit region of a wind tunnel build from wood. Numerical results were obtained for three turbulence models, namely the *k-ε, RNG k-ε and* shear stress transport *SST* models. The simulation results were compared with the mean time experimental velocity profiles as a function of three values of inlet mass flow rate, as well as with the experimental turbulent kinetic energy in the centre of the exit region of wind tunnel. The comparison of the numerical and experimental data showed that the *SST* model appears to be the one that produces the best results. More advances studies must be carried on to confirm the present observations.

ACKNOWLEDGMENTS

Authors are grateful to Foundation for the Support of Research of the State of Minas Gerais-Brazil (FAPEMIG) who supports this work.

REFERENCES

1. C.J. Baker. Wind engineering—Past, present and future. *Journal of Wind Engineering and Industrial Aerodynamics* 95 (2007) 843–870

2. Peter Moonen, Bert Blocken, Staf Roels, Jan Carmeliet. Numerical modeling of the flow conditions in a closed-circuit low-speed wind tunnel. *Journal of Wind Engineering and Industrial Aerodynamics* 94 (2006) 699–723
3. M. Kämpchen, A. Dafnis, H.-G. Reimerdes, G. Britten, J. Ballmann. Dynamic aero-structural response of an elastic wing model. *Journal of Fluids and Structures* 18 (2003) 63–77
4. G.L. Larose, A. D'Auteuil. Experiments on 2D rectangular prisms at high Reynolds numbers in a pressurised wind tunnel. *Journal of Wind Engineering and Industrial Aerodynamics* 96 (2008) 923–933
5. Xianzhi Liu, Marc Levitan, Dimitris Nikitopoulos. Wind tunnel tests for mean drag and lift coefficients on multiple circular cylinders arranged in-line. *Journal of Wind Engineering*
6. Arun K.S. Iyengar, Cesar Farell. Experimental issues in atmospheric boundary layer simulations: roughness length and integral length scale determination. *Journal of Wind Engineering and Industrial Aerodynamics* 89 (2001) 1059–1080
7. Cesar Farell, Arun K.S. Iyengar. Experiments on the wind tunnel simulation of atmospheric boundary layers. *Journal of Wind Engineering and Industrial Aerodynamics* 79 (1999) 11-35.
8. Aishe Zhang, Ming Gu. Wind tunnel tests and numerical simulations of wind pressures on buildings in staggered arrangement. *Journal of Wind Engineering and Industrial Aerodynamics* 96 (2008) 2067–2079.
9. S. Finnveden, F. Birgersson1, U. Ross, T. Kremer. A model of wall pressure correlation for prediction of turbulence-induced vibration. *Journal of Fluids and Structures*, 20 (2005) 1127–1143
10. F. Cluni,V. Gusella, G. Bartoli. Wind tunnel scale model testing of suspended cables and numerical comparison. *Journal of Wind Engineering and Industrial Aerodynamics* 96 (2008) 1134–1140
11. Christof Gromke, Riccardo Buccolieri, Silvana Di Sabatino and Bodo Ruck. Dispersion study in a street canyon with tree planting by means of wind tunnel and numerical investigations – Evaluation of CFD data with experimental data. Atmospheric Environment Volume 42, Issue 37, December 2008, Pages 8640-8650.
12. Launder, B. E. and Spalding, D. B., *The Numerical Computation of Turbulent Flows*. *Comput. Methods Appl. Mech. Eng*., 3:269-289 (1974).
13. Yakhot, V., Orszag, S. A., Thangam, S., Gatski, T. B. and Speziale, C. G., Development of Turbulence Models for Shear Flows by a Double Expansion Technique. *Physics of Fluids A*. 4(7):1510-1520 (1992).
14. Menter, R. F., Two-equation Eddy-viscosity Turbulence Models for Engineering Applications. *AIAA Journal*. 32(8):269-289 (1994).
15. Wilcox, D. C., *Turbulence Modeling for CFD*. DCW Industries, La Cañada, CA, 1993. ANSYS-CFX® Solver Theory manual, Release 10.0, 1996.
16. ANSYS-CFX® Solver Theory manual, Release 10.0, 1996.
18. *INTERNATIONAL ORGANIZATION for STANDARDIZATION. ISO 3966:1977* – Measurements of fluid flow in closed conduits velocity area method using Pitot static tubes-First Edition – 1977.
19. SOARES, Cleide Barbosa; Experimental Study of the Velocity Profiles in Test Section of an Open Low Speed Wind Tunnel 2008. 138f. Master degree dissertation, Pontifical Catholic University of Minas Gerais, Belo Horizonte, Brazil.
20. Laufer, J., The structure of turbulence in fully developed pipe flow, NACA report 1174, 1954.

NUMERICAL SIMULATION OF COMBUSTION INSTABILITIES FROM THE METASTABLE STATE TO THE LIMIT CYCLE

H. J. Kim, H. D. Shin*
Korea Advanced Institute of Science and Technology, Daejon, Korea

ABSTRACT. This paper describes the dynamic behaviours of the limit cycle for combustion instability. The time evolution of pressure oscillations usually demonstrates growth and saturation behaviours when combustion instability occurs. This saturation behaviour is known as limit cycle behaviour and it occurs due to nonlinear oscillations. Until now, the limit cycle behaviour was usually determined by the time evolution of pressure oscillation. However, the total disturbance equation was derived from the linearization of governing equations in 1965 instead of the acoustic energy equation which was derived under isentropic assumption. The total disturbance equation includes three main variables: pressure, velocity and entropy. In this study, numerical simulation was performed for combustion instabilities from the metastable state to the limit cycle. The limit cycle region was redefined as a fixed trajectory of pressure, velocity and entropy in three-dimensional phase space. In conclusion, considering entropy oscillation, in addition to pressure and velocity oscillations, may be important when determining the time step in which the limit cycle starts.

Keywords: *Combustion Instability, Meta Stable State, Limit Cycle*

INTRODUCTION

Combustion instabilities have caused serious problems in industrial applications such as the use of gas turbines for electricity and in high performance propulsion systems including liquid rocket and scramjet. The most serious problems resulted from large pressure oscillations and damage to the combustor by detonation. Researchers have tried to reduce combustion instabilities for a long time, because many industrial applications and propulsion systems can not endure large pressure oscillations. The instability mechanisms in combustion are categorized into acoustic, shock and fluid dynamics [1, 2]. Many studies have been conducted to experimentally or theoretically determine the relationship between acoustics and heat releases [3-9].

Numerical simulation is based on the pioneering works of Benelli (1990) [10], who first simulated unsteady combustion using FLUENT v2.97 software and Vax 8530 hardware. The main objective of his experiment was to observe the time evolution of turbulence, mixing rates and reaction rates under acoustic perturbation. Benelli et al. (1993)[11] observed combustion instability under the oscillations of a turbulent reaction rate. It was initially believed that the turbulent reaction rate determined the combustion rate. However, the experiment revealed that the velocity oscillation caused by acoustic waves led to fluctuation in the turbulence. The reaction rate oscillation occurred as a result of the oscillations of the turbulent variables. Hantschk and Vortmeyer (1999)[12] studied thermoacoustic instability in a Rijke tube using the FLUENT commercial code. They simulated combustion instability in a combustor and studied the time evolution of pressure oscillation, time-lag variables and the pressure oscillation frequencies in 2002 [8]. In 2000, Steele et al. performed

* Corresponding author: Prof. H. D. Shin
Phone: + (82)-42-3503057, Fax: + (82)-42-3503095
E-mail address: hdshin@kaist.ac.kr

numerical simulation for two-dimensional geometry using CFD-ACE+ software. The axial distance from the fuel injection was an important factor in creating unstable combustion. The predicted frequency value was similar to the measured value and the predicted stable operating conditions were in agreement with the experimental range for stable combustion. The three-dimensional Large Eddy Simulation (LES), three-dimensional Unsteady Reynolds-Averaged Navier-Stokes (URANS) and two-dimensional URANS were simulated and compared by Cannon et al. Their predicted results of the frequency and pressure histories for the three cases were nearly identical to the measured values despite the different frequencies. These studies indicated that the time evolution of pressure reached the limit cycle, the oscillations of variables were delayed on the time axis and the resonant frequencies were predicted by unsteady calculation.

The time evolution of pressure oscillation normally shows growth and saturation behaviour when combustion instability occurs. This saturation dynamic occurs due to nonlinear oscillation and is called limit cycle behaviour. Previously, limit cycle behaviour was characterized by the time evolution of pressure oscillation [8, 13]. However, the total disturbance energy equation was derived by Chu [14] and rederived by Nicoud and Poinsot (2005)[15] based on Chu's results from the linearization of governing equations instead of the acoustic density equation that is typically derived under the isentropic assumption. The total disturbance energy equation is composed of three main variables: pressure, velocity and entropy. The left-hand side of the resulting equation ($e_{tot}= \rho_0 \mathbf{u}_1^2/2+p_1^2/2\rho_0 c_{sound,0}^2+p_0 s_1^2/2Rc_p$) indicates that pressure, velocity and entropy are very important in the non-isentropic method. Although the total disturbance energy equation was derived from linear analysis, the time evolutions of the three variables need to be examined further. In addition, the entropy oscillation portion of the equation was numerically investigated because it was difficult to measure directly.

In this study, the dynamic behaviours of combustion instabilities were analysed using numerical simulation from the metastable state to the limit cycle. The limit cycle region was also redefined as a periodic trajectory of pressure, velocity and entropy oscillations in the three-dimensional phase space. The time evolutions of the three variables were observed and their trajectories were investigated in phase space. In conclusion, the time step in which the limit cycle began was redefined through the investigation of the trajectories in three-dimensional phase space.

EXPERIMENTAL AND NUMERICAL METHODS

Numerical Models

The Favre-averaged conservation equations for mass, momentum and energy can be readily found in the literature [16, 17]. It is important to simulate the interaction between the turbulence and chemical reactions. The Direct Numerical Simulation (DNS), LES and RANS are all models for turbulence treatment. The RANS method generally costs less than the other methods. Furthermore, the 2-dimensional URANS and the 3-Dimensional LES and URANS were simulated and compared by Cannon et al.[18] Their results showed that the three cases followed the same pressure histories. Therefore, the standard k-ε turbulent model was used in this study because the URANS provided similar results to the other models despite its low cost.

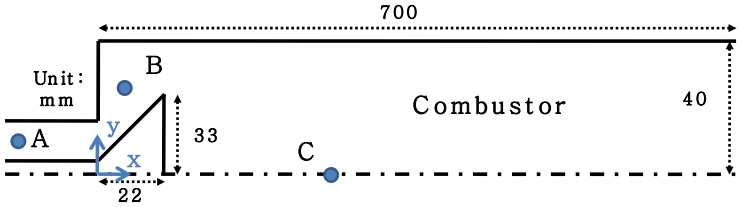

Figure 1. The position for data acquisition; (A) position A, (B) position B and (C) position C

Combustion models are based on statistical methods and turbulent mixing. The statistical method refers to the technique using probability density function (PDF) and the turbulent mixing model indicates combustion that is dominated by the turbulent time scale. Therefore, the latter model has stronger physical meaning. Particularly in the case of the latter, the eddy dissipation model (EDM) is the simplest model to simulate turbulent flames. This model was developed by Magnussen and Hjertager [19] and assumes that combustion occurs immediately when fuel and oxidizer meet. The chemical reaction for turbulent reacting flow does not occur that quickly. For example, the turbulence effect on combustion is not dominant enough that the turbulent mixing and kinetically controlled reaction effects should simultaneously be considered. For numerical simulation, the kinetically controlled reaction rate is a function of the Arrhenius rate coefficient and mass fraction, and the turbulence controlled reaction rate is a function of the turbulent time scale and mass fraction. Furthermore, the minimum values of the reaction rate representing the above two effects should be applied to the computational domain. This method is usually referred to as the hybrid model (eddy dissipation model and kinetically controlled model) [16]. Hantschk and Vortmeyer [8] investigated combustion instabilities using this model and found that the predicted frequency was in agreement with the measured value.

Experimental and Numerical Method

In this study, axisymmetric geometry was applied to the combustor, which was the same type of combustor as that used by Hong [20]. This geometry prevented the flame from lifting off and reduced the calculation cost, because the geometry could be treated as a two-dimensional model for numerical simulation using a bluff-body burner instead of a swirl burner. Liquefied petroleum gas (LPG; approximately 98% C_3H_8) was used for fuel and was injected from a 0.3 mm diameter hole pierced at an interval of 90° and x=-0.285 m based on the distance from the dump plane to the mixing pipe for air flow. The bluff-body burner was lozenge shaped and had a diameter of 66 mm at the y-axis and 22 mm at the x-axis. Therefore, the flame could exist in the vicinity of the burner without swirl flow, because the flame had such a radial flow structure that the resident time was extended at the upstream field of the flame. The height of the combustion chamber was fixed at 700 mm, which was designed for the dominant longitudinal mode. The pressure was measured with a piezoelectric pressure sensor (PCB Model 106B) installed under the dump plane and surrounded with a water jacket to protect it from the high temperature.

Numerical simulation was performed by FLUENT. The combustion chamber was made of quartz and had a diameter of 80 mm. The exit pressure of the combustion chamber was set to the pressure boundary condition. The overall grid was a non-uniform, hexagonal grid of 145012, which was refined in the vicinity of the injection hole. In order to investigate the grid dependency of the solution, the number of grids was increased twice and an error of less than 1% was computed from steady calculations. Therefore, the grid dependency was negligible. After obtaining the steady solutions, unsteady simulation was completed on them with a small pressure perturbation and the sinusoidal function was used in the simulation for 2 ms. Then self-excited pressure oscillations evolved from the metastable state to the limit cycle.

Figure 1 shows the positions for data acquisition. The position A is at x=-40 and y= 12 mm, position B is at x=10 and y=30 mm and position C is at x=300 and y=0 mm in the dump plane.

VALIDATION AND TRAJECTORY ANALYSIS

Frequency Spectra Result

Figure 2 shows the frequency spectra of the calculated pressure plotted from 0.2 sec to 0.3 sec. The values obtained by the pressure sensor for the pressure amplitude (peak-to-peak $\Delta p \approx 10$kPa) and frequency (~256Hz) were nearly identical to the first harmonic value (~244Hz) predicted by

numerical simulation. The reaction zone was positioned near the downward plane of the bluff body and the upward plane of position B where the chemical reaction was dominant, however it did not exist in positions A and C.

The Trajectories Near The Meta Stable State

Figure 3 shows the trajectories near the metastable state at each position. The pressure oscillation in the time domain appeared with different growth constants (*k)* for each position. The value of *k* (exponential function e^{kt}) was approximately 173.3 for position A, 187.6 for position B and 184.2 for position C. The pressure oscillation was higher at position A and therefore it started at approximately 900 Pa in Fig. 3 (A-1), while it started at approximately 0 Pa in Fig. 3 (B-1) and Fig. 3 (C-1). The history of pressure oscillation in Fig. 3 (A-1), (B-1) and (C-1) exhibited identical behaviour in respect to the linear growth rate.

Figure 3 (A-2), (B-2) and (C-2) showed the trajectories near the metastable state in two-dimensional phase space (pressure and axial velocity). The linear behaviour was observed for 2 ms due to the forced sinusoidal pressure oscillation and the trajectories gradually shifted far away from the metastable state because of self-excited dynamic behaviour. All of the trajectories appeared to have a spiral structure in each position. Their behaviours were identical, including their movement counter-clockwise in two-dimensional phase space.

The trajectories are shown in Figure 3 (A-3), (B-3) and (C-3) in two-dimensional phase space (pressure and entropy) near the metastable state. These trajectories had spiral structures and were not near the metastable state. They moved clockwise in Fig. 3 (A-3) and (B-3), while they moved counter-clockwise in Fig. 3 (C-3).

The trajectories between axial velocity and entropy are shown in Figure 3 (A-4), (B-4) and (C-4) near the metastable state. Dynamic behaviours in Fig. 3 (A-4) and (C-4) moved counter-clockwise, while the one in Fig. 3 (B-4) moved in the reverse direction. Noisy trajectories in Fig. 3 (A-3) and (A-4) seemed to be caused by the smallest entropy oscillation.

The trajectories of three variables (pressure, axial velocity and entropy) appeared to have a spiral pattern in three dimensional phase space in Fig. 3 (A-5), (B-5) and (C-5). It was difficult to characterize the pattern of the trajectory found in Fig. 3 (A-5), because the entropy changed with little fluctuation. The other trajectories in Fig. 3 (B-5) and (C-5) clearly exhibited their identical patterns (spiral structure).

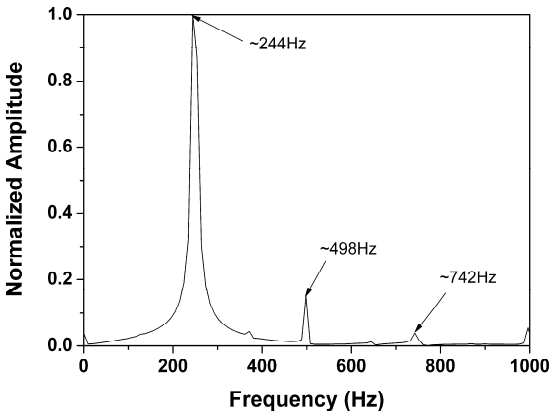

Figure 2. Frequency spectra of the calculated pressure from 0.2 sec to 0.3 sec (at the limit cycle region)

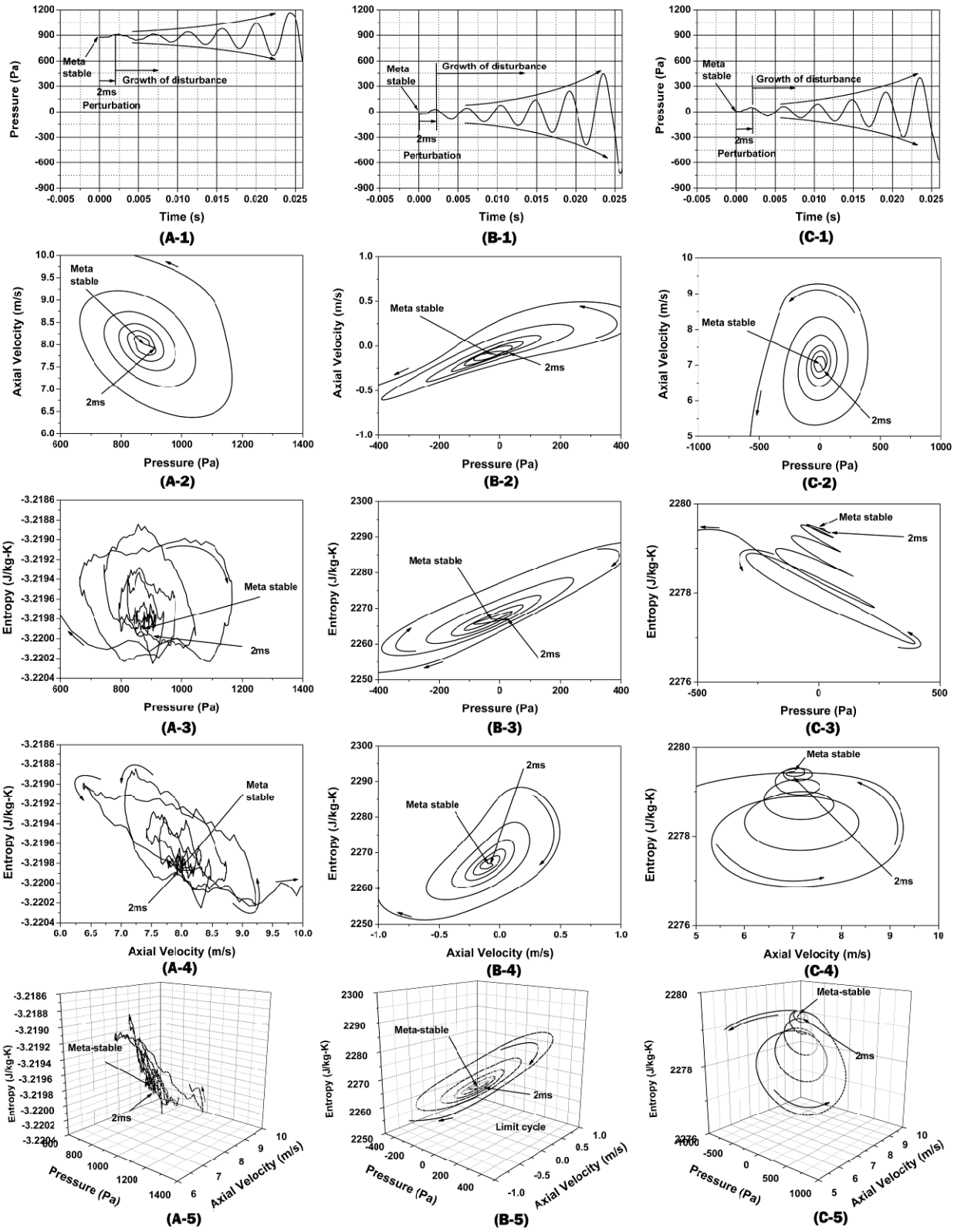

Figure 3. The time evolution of the pressure oscillations (A-1), (B-1) and (C-1); the trajectories in two–dimensional phase space, which consisted of pressure-axial velocity: (A-2), (B-2) and (C-2), pressure-entropy: (A-3), (B-3) and (C-3) and axial velocity-entropy: (A-4), (B-4) and (C-4); and the trajectories in three–dimensional phase space (A-5), (B-5) and (C-5). All graphs were plotted near metastable states for 0.025 seconds.

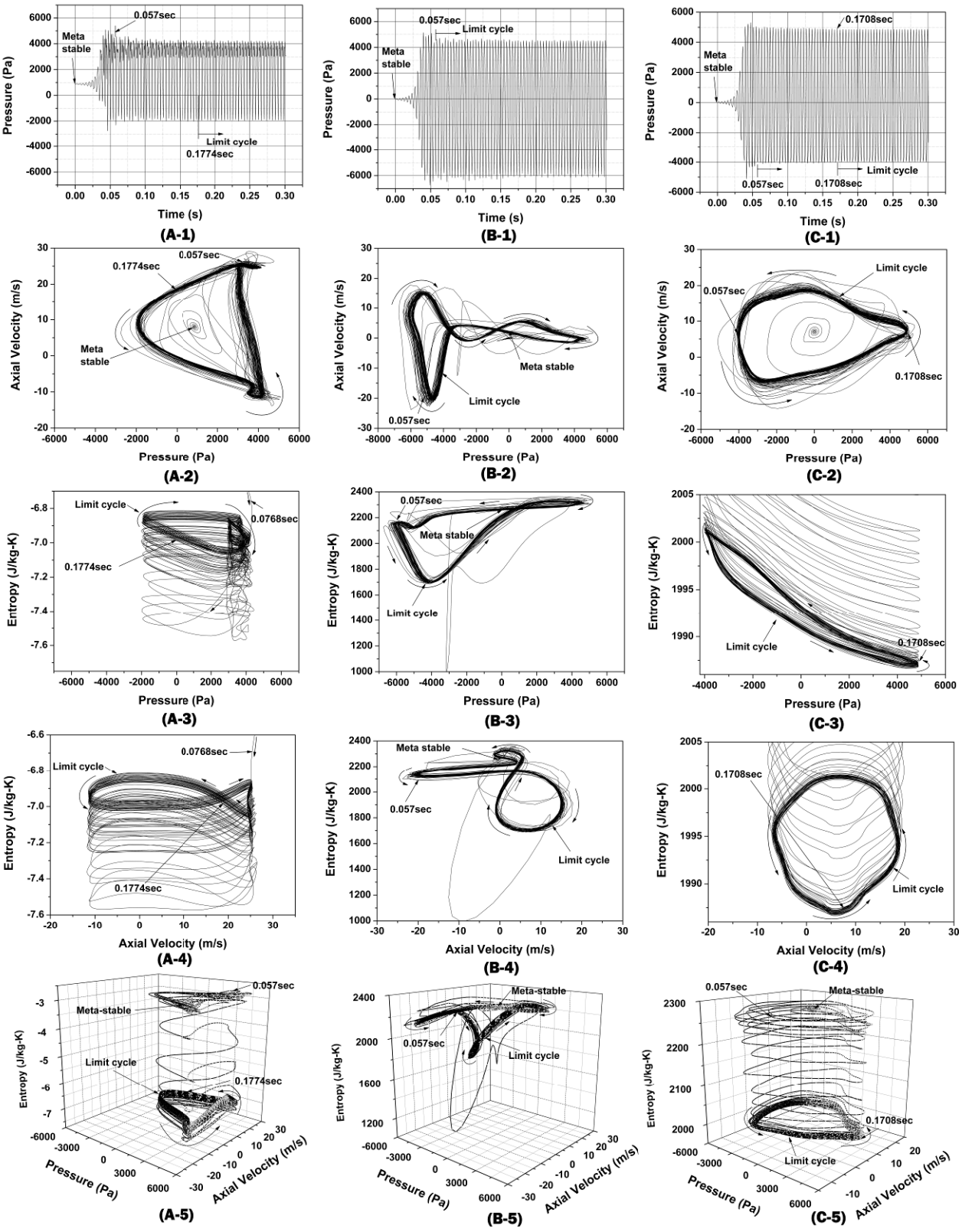

Figure 4. The time evolution of the pressure oscillations (A-1), (B-1) and (C-1); the trajectories in two–dimensional phase space which consisted of pressure-axial velocity (A-2), (B-2) and (C-2), pressure-entropy (A-3), (B-3) and (C-3) and axial velocity-entropy (A-4), (B-4) and (C-4); the trajectories in three–dimensional phase space (A-5), (B-5) and (C-5). All graphs were plotted on limit cycle regions for 0.3 seconds.

The Trajectories Near The Limit Cycle Region

Figure 4 shows the full trajectories to the limit cycle state at each position. The time evolution of the pressure oscillation, which changed from the metastable state to the limit cycle, was identical for all positions. It appeared that the pressure oscillation at all positions reached the limit cycle region after nearly 0.057 seconds. Until now, the limit cycle had been defined as the saturation behaviour of the pressure oscillation's time evolution in Fig. 4 (A-1), (B-1) and (C-1). However, the starting point of the limit cycle needed to be changed through investigation of the dynamic movement, including entropy fluctuation, in the phase space as shown in Fig. 4 (A through C, 3 through 5).

To investigate the starting point of the limit cycle in detail, the trajectories were observed in two dimensional and three dimensional phase space in Fig. 4 (A through C, 2 through 5). The trajectories evolved to the limit cycle in three and two-dimensional phase space, and they moved around a fixed trajectory after reaching the limit cycle region. The trajectories at the limit cycle region appeared as bold curves which were amassed as a periodic trajectory in phase space. Therefore, the limit cycle could have been defined as the point when the time evolution of the three variables reached periodic trajectory in the phase space.

The starting point of the limit cycle in Fig. 4 (A-2), (B-2) and (C-2) was nearly the same as that after 0.057 seconds in Fig. 4 (A-1), (B-1) and (C-1). The overall trajectories near the limit cycle region moved counter-clockwise in Fig. 4 (A-2) and (C-2) and clockwise in Fig. 4 (B-2), although their intersection occurred in the border of the limit cycle. However, the trajectories in the phase space which included the entropy variable had a different starting point of the limit cycle as shown in Fig. 4 (A and B, 3 through 5). The trajectories of the variables in the phase space reached the limit cycle in approximately 0.1774 and 0.1708 seconds in Fig. 4 (A-3 through 5) and (C-3 through 5), respectively, and the trajectories reached the limit cycle in approximately 0.057 seconds in Fig. 4 (B-3 through 5) similar to the timing in Fig. 4 (A-, B- and C-, 1 and 2). Consequently, the trajectories in the phase space not including entropy reached the limit cycle earlier than those that included entropy in the position where the flame didn't exist. Those trajectories that did not include entropy appeared to have the same starting point for the limit cycle as those including entropy in the flame position, because the flame produced the entropy and only existed at position B.

CONCLUSIONS

The frequency value that was obtained by the pressure sensor was compared to that calculated by numerical simulation, and the values were in good agreement. The time step in which the limit cycle starts in the time evolution of the pressure oscillation was the same as that in two-dimensional phase space (pressure-axial velocity). The starting point of the limit cycle in the time evolution of the pressure oscillation was the same as that in the phase space in the flame position where the entropy was produced. The starting point of the limit cycle in the phase space including entropy differed from that in the time evolution of the pressure oscillation and in two-dimensional phase space (pressure-axial velocity) in the positions where the flame didn't exist. The method that was used to determine the limit cycle region from the time evolution of pressure oscillation and the trajectories in the phase space which consisted of pressure and velocity could not produce accurate results for determining the starting point of the limit cycle. Therefore, it is necessary that the starting point of the limit cycle is determined in the phase space including entropy.

ACKNOWLEDGMENTS

This research was supported by the Combustion Engineering Research Center (CERC) through KOSEF. This work was also supported by the Brain Korea 21 (BK21) program, Ministry of Education, Science, and Technology.

REFERENCES

1. McManus, K.R., Poinsot, T. and Candel, S.M., A Review of Active Control of Combustion Instabilities, *Prog. Energy Combust. Sci.*, Vol. 19, pp. 1-29, 1993.
2. Seo, S.H., Parametric Study of Lean Premixed Combustion Instability in a Pressurized Model Gas Turbine Combustor, Ph.D. Thesis, Pennsylvania State Univ., 1999.
3. Putnam, A.A. and Dennis, W.R., A Study of Burner Oscillations of the Organ Type, *Trans. ASME*, Vol. 75, pp. 15-28, 1953.
4. Kim, H.J., Hong, J.G., Kim, D.H. and Shin, H.D., Numerical Simulation of Self-Excited Combustion Oscillation in a Dump Combustor with Bluff-Body, *Transaction of the KSME (B)*, Vol. 32, No. 9, pp. 659-668, 2008.
5. Kim, H.J., Numerical Simulation on Thermoacoustic Instability in the Dump Combustor, M.S. Thesis, KAIST, 2005.
6. Keller, J.J., Thermoacoustic Oscillations in Combustion Chamber of Gas Turbines, *AIAA Journal*, Vol. 33, No. 12, pp. 2280-2287, 1995.
7. Hatout, J.P., Thermoacoustic Instability, in *Reacting Gas Dynamics Computational Lab*. 1999, MIT report.
8. Hantschk, C.C. and Vortmeyer, D., Numerical Simulation of Self-Excited Combustion Oscillations in a Non-Premixed Burner, *Combust. Sci. and Tech.*, Vol. 174, pp. 189-204, 2002.
9. Crocco, L. and Cheng, S.I., Theory of Combustion Driven Instabilities in Liquid Rocket Motors. 1956, London, United Kingdom: Butterworths Scientific Publications.
10. Benelli, G., Cossalter, V. and Da, L.M. Numerical Simulation of the Cross-Coupling between Acoustic Waves and Heat Release (Turbulence-Controlled Reaction Rate) in a Tube-Like Combustor. *Joint Meeting of the Soviet and Italian Sections of the Combustion Institute*. 5-9 Nov. 1990. Pisa(Italy).
11. Benelli, G., Cossalter, V. and Lio, M.D., Advances in Numerical Simulation of Pulsating Combustion at Enel, *Combust. Sci. and Tech.*, Vol. 94, pp. 317-335, 1993.
12. Hantschk, C.C. and Vortmeyer, D., Numerical Simulation of Self-Excited Thermoacoustic Instabilities in a Rijke Tube, *Journal of sound and vibration*, Vol. 277, No. 3, pp. 511-522, 1999.
13. Poinsot, T. and Veynante, D., Theoretical and Numerical Combustion. 2001.
14. Chu, B.T., On the Energy Transfer to Small Disturbances in Fluid Flow (Part I), *Acta Mech.*, pp. 215-234, 1965.
15. Nicoud, F. and Poinsot, T., Thermoacoustic Instabilities: Should the Rayleigh Criterion Be Extended to Include Entropy Changes?, *Combustion and Flame*, Vol. 142, pp. 153-159, 2005.
16. Fluent User's Guide, pp., Dec. 2001.
17. Peters, N., Turbulent Combustion. 2000: *Cambridge University Press*.
18. Cannon, S.M., Adumitroaie, V. and Smith, C.E. 3d Les Modeling of Combustion Dynamics in Lean Premixed Combustors. 2001: ASME.
19. Magnussen, B.F. and Hjertager, B.H. On Mathematical Modeling of Turbulent Combustion with Special Emphasis on Soot Formation and Combustion. *16th symposium(International) on Combustion*. 1977: The Combustion Institute.

20. Hong, J.G., Lee, M.C., Lee, U.D., Oh, K.C. and Shin, H.D., An Experimental Study on the Instability of Combustion in a Dump Combustor with Respect to Fuel and Air Mixing and Flow Conditions, *Transaction of the KSME(B)*, Vol. 29, No. 8, pp. 963-970, 2005.

DATA ASSESSMENT ON TWO ERCOFTAC TRANSITION MODELLING TEST CASES FOR CFD VALIDATION

D. Di Pasquale[*1], A. Rona[1]

[1] Department of Engineering, University of Leicester, Leicester, UK

ABSTRACT. This paper aims to demonstrate the use of the Ercoftac database to validate a 2D CFD code, giving more details of the approach adopted, and how to use the Ercoftac experimental data to generate the inflow condition, and in doing so to inform the community on the consistency of the information in this dataset by testing it for the known trend in the mean velocity components and their statistical fluctuations. The objectives are to expose some limitations of the dataset and to evaluate the performance of the RANS transition model implemented in the in-house code Cosmic. Velocity measurements from two boundary layer test cases under zero pressure gradient are considered.

Keywords: *Ercoftac, transition, intermittency, boundary layer, CFD*

INTODUCTION

Transition is a complex phenomenon, defined as the whole process of change from laminar to turbulent flow. The origin of turbulence and the accompanying transition from laminar to turbulent regime, as often happens, for example, on aircraft wings or past turbine blades, is of fundamental importance for the whole science of fluid mechanics. The European Research Community on Flow, Turbulence and Combustion (ERCOFTAC) is a scientific association of research, education and industry groups in the technology of flow, turbulence and combustion. The Special Interest group of Ercoftac (SIG10) on Transition Modelling is organized into five sub-groups focussing on different aspects of transition modelling. In particular the Sub-group 5 focusing on experimental Real-Flow data in order to provide a sufficiently experimental databases to validate predictive capabilities of transition codes, on the identification of directions for future model developments and applications, and to focus model refinement on the key elements which influence accuracy of predictions under real operating conditions; in addition to establish a fundamental experimental analysis of the flow physics of bypass transition with the aim to build up basic understanding of the phenomenon.

DESCRIPTION OF THE TEST CASES

The Ercoftac test cases T3A- and T3A [1] include both laminar and transitional boundary layers over a 1.7m long flat plate which is 20mm thick and 710mm wide, with the test surface extremely flat that employs a small leading edge radius of 0.75mm. These cases have zero pressure gradient and a nominal air temperature maintained at 20°C±0.1°C The T3A- case has a freestream velocity U_∞=19.8 m/s and a FST level of 0.9%. The second test case, T3A, has U_∞=5.2 m/s and a higher FST level of 3.3%. The wind tunnel used in these experiments is of the closed circuit type. Its major elements include a centrifugal fan blowing through a large plenum fitted with turbulence reducing honeycomb gauzes, a small 2-D contraction, leading to a highly versatile working section, and a

* Corresponding author: Mr. D. Di Pasquale
Phone: + (44)-11-62231334, Fax: + (44)-11-62522525
E-mail address: ddp2@le.ac.uk

wide-angle diffuser. The working section is of 2m length, 0.71m width and 0.26m height with full-length perspex sidewalls for good optical access as it is shown in Figure 1.

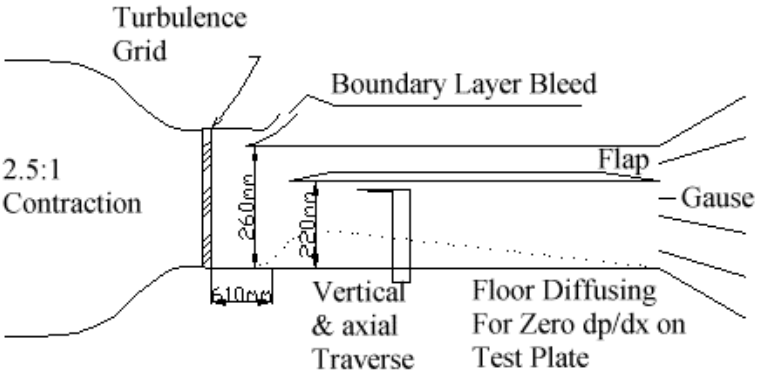

Figure1. Detail of the wind tunnel and test plate

DATABASE INTEGRITY

The database is a valuable tool for the transitional flow community. Still, in both datasets, some discrepancies were found from what is stated in the description of the experiment and in the database information, specifically with respect to the normal velocity component, the turbulence isotropy, and the pressure gradient.

In the Ercoftac database, case T3A, as well as in the case T3A-, the sign of the cross-stream velocity V is negative, as shown in Figure 2(a) and 3(a) respectively. However, V should be positive definite, as the displacement thickness grows monotonically along the flat plate, giving a negative $\partial U/\partial x$ and a positive $\partial V/\partial y$ so that the incompressible continuity equation (1)

$$\frac{\partial U}{\partial x}+\frac{\partial V}{\partial y}=0 \tag{1}$$

is satisfied.

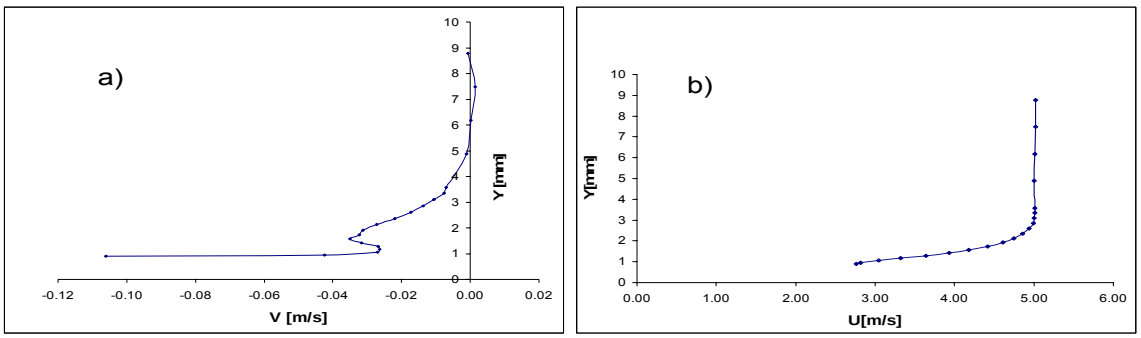

Figure 2. (a) cross-stream and (b) stream-wise velocity measurements. Case T3A.

Moreover, the first data points closest to the wall in Figure 2(a) and 3(a) are suspect; the velocity magnitude above this points decrease monotonically, whereas at these points the trend reverse; it is only possible to assume that the odd behaviour of V near the wall is associated with measurements problems with the hot-wire when this was very close to the flat plate surface. Therefore, they should not be inserted in the dataset.

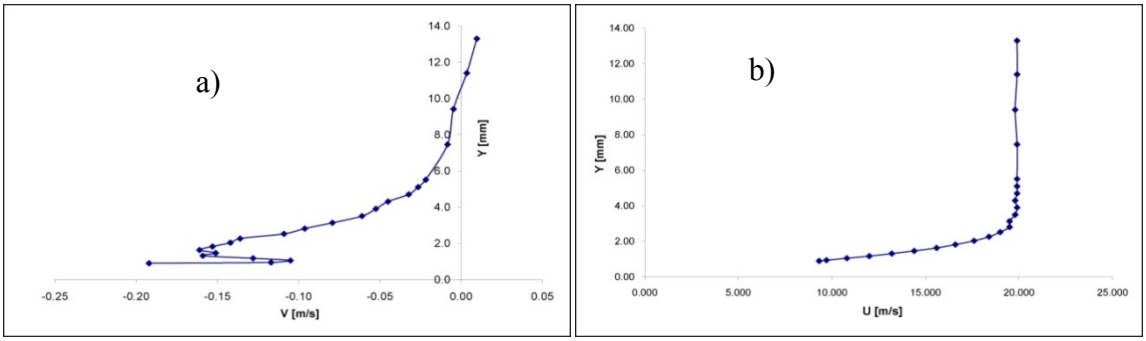

Figure 3. (a) cross-stream and (b) stream-wise velocity measurements. Case T3A-.

As far the free-stream turbulence is concerned, it is found to be not isotropic, contrary what is stated in the Ercoftac explanatory note for this database, which report that the generated turbulence is extremely homogeneous and isotropic with a streamwise-to-normal fluctuating velocity ratio of about 1.005, obtained with a turbulence generating grid located at the entrance plane of the working section, at the downstream end of the 2-D contraction, made of square or round bars and woven wire mesh, and it is positioned 610mm upstream of the test plate leading edge. Table 1 reports the data taken from the database at approximately four δ above the wall. The ratio of the streamwise-to-normal velocity fluctuations, u'/v' and u'/w', are quite far from 1.005.

Table1
Fluctuations of Velocity Components

Test case	x-coord. [mm]	δ (99%) [mm]	y-coord. [mm]	u' [m/s]	v' [m/s]	w' [m/s]	u'/v'	u'/w'
T3A	495	3.33	13	0.130	0.100	0.117	1.300	1.111
T3A-	95	2.71	8.78	0.124	0.101	0.118	1.227	1.051

The next aspect over our attention is focussed on the pressure gradient. In the Ercoftac documentation it is declared possible in the wind tunnel in use inclining both the test plate and the opposite tunnel wall in such a way as to ensure zero pressure gradient over the bulk of the test plate length. But using the database for ρ and T values and making use of the equation of state for ideal gas $P = \rho RT$ it is possible determine a non-constant value of pressure along the flat plate. In fact, the experimental data does not show a constant value of the free-stream velocity along the flat plate, as shown in Figure 4.

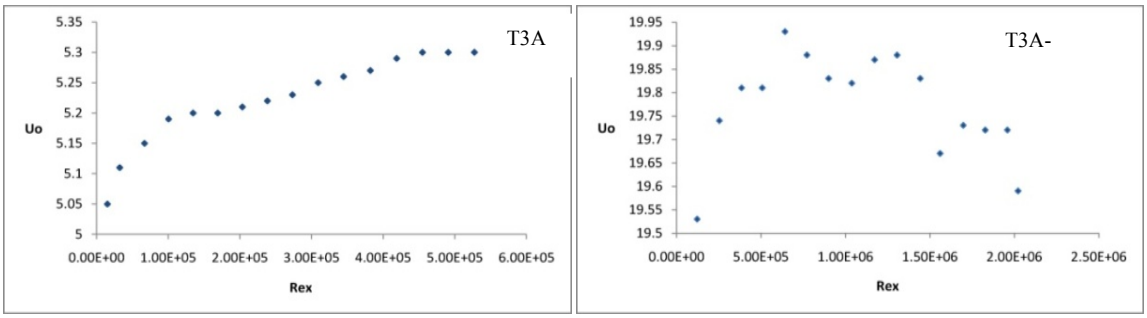

Figure 4. Free-stream velocity along the flat plate for both test cases.

This is also confirmed by applying the Thwaites method as it is shown in Figure 5, an empirical relationship, based on the observation that laminar boundary layer obey the following relationship:

$$\frac{u_e}{\upsilon}\frac{\partial\theta^2}{\partial x} = 0.45 - 6\frac{\theta^2}{\upsilon}\frac{\partial u_e}{\partial x} \tag{2}$$

The above equation (2) may be analytically integrated to find the momentum thickness θ. After θ is found, the following relations (3) and (4) are used to compute the shape factor $H = \delta^*/\theta$

$$H = 2.61 - 3.75\lambda + 5.24\lambda^2 \quad for\ 0 \le \lambda \le 0.1 \tag{3}$$

$$H = 2.472 + \frac{0.0147}{0.107 + \lambda} \qquad for -0.1 \le \lambda \le 0 \tag{4}$$

where, $\lambda = (\theta^2/\upsilon)(\partial U/\partial x)$ is the dimensionless pressure gradient.

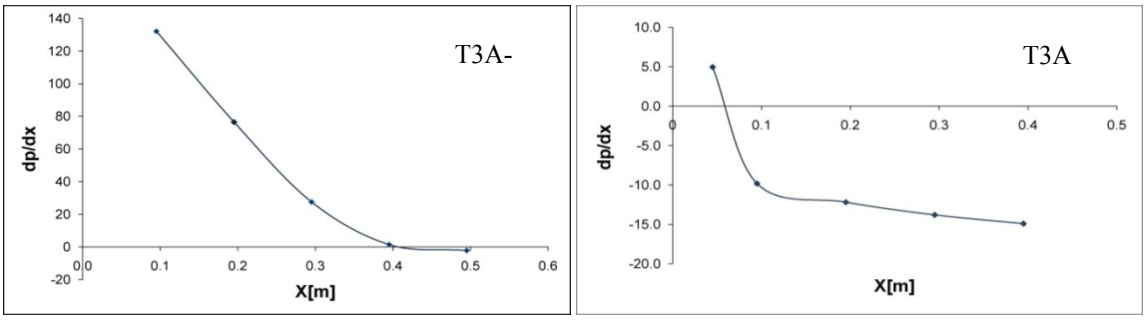

Figure 5. Pressure gradient evaluated with the Thwaites method for both test cases in the laminar part of the boundary layer

The start of transition is taken as the location where the skin friction coefficient starts to deviate from its analytical laminar value.
This is shown to be at $Re_x \approx 1.3*10^5$ in Figure 6(b). In a flow with zero pressure gradient, the shape factor before transition should be constant and equal to 2.61. As it can be seen from Figure 6(a), the shape factor H reduces below the laminar value of 2.61 in the region before the transition starts. This can be explained by a non-zero streamwise pressure gradient in the flow field.

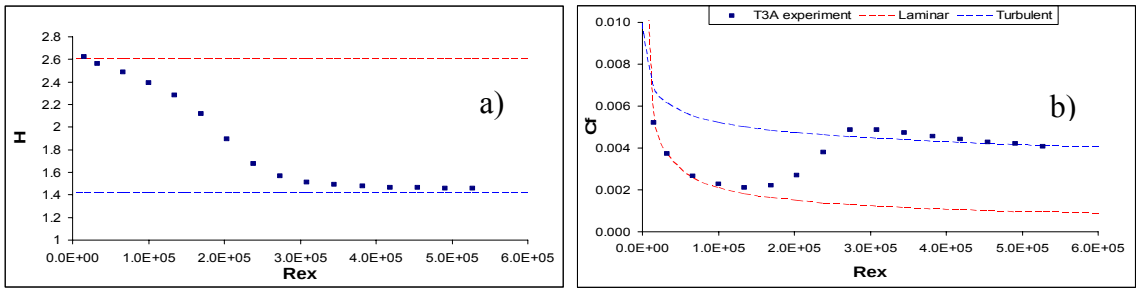

Figure 6. (a) Shape factor and (b) Skin friction coefficient distribution along the flat plate for the T3A test case.

VALIDATION OF RANS 2D TRANSITION CFD MODEL

This project aims to evaluate the performance of the transition RANS transition model implemented

in the in-house code Cosmic. The in-house multi-block finite volume time-resolved RANS scheme is used to compute the seven conservative variables (density, specific momentum, specific stagnation energy, specific turbulent kinetic energy, specific turbulent dissipation rate and intermittency) that define the flow state in the discretized Navier-Stokes equations. The code uses a 2D finite-volume four-point stencil approximate Riemann solver with a Monotone Upstream-centred Scheme for Conservation Laws (MUSCL) interpolation by Van Leer et al. [2] to compute the convective fluxes. This gives up to a third order accurate reconstruction of the spatial gradients in regions of smooth flow. To prevent numerical oscillations in region of rapidly changing flow, the spatial gradients are limited by the introduction of a Total Variation Diminishing Scheme (TVD) by Sweby [3]. The scheme is explicit and a standard multi-stage second-order Runge-Kutta (RK) integration is used to time-march the flow. The turbulent flux vector is estimated using a second order accurate gradient reconstruction method, based on the Gauss divergence theorem.

The creation of a transitional flow solver combining an in-house laminar flow solver and a RANS k-ω solver through incorporating an intermittency transport model into the computation. The intermittency transport model uses empirical correlations that have shown some success in predicting transitional flows past conventional geometries. A two-equation turbulence model was modified to incorporate the varying turbulence intermittency of transitional flow. Further to the flow solver already in place a γ transport equation, balancing its production, destruction, convection and diffusion, was implemented. The flow is governed by the compressible Navier- Stokes equations. These are suitably averaged into time-dependent discrete Navier-Stokes equations, so that in 2D the flow state is described by 7 conservative variables. Seven conservative laws plus algebraic auxiliary equations are solved by the numerical scheme. The implementation of the transition model of Suzen & Huang [4] it is presented. Suzen & Huang developed an intermittency transport model which can produce both the experimentally observed streamwise variation of intermittency and a realistic profile in the cross-stream direction. The model combines the transport equation models of Steelant & Dick [5] and Cho & Chung [6]. Specifically, the transport of intermittency, γ, is given by the following equation (5):

$$\frac{\partial \rho\gamma}{\partial t}+\frac{\partial u_j\gamma}{\partial x_j}=(1-\gamma)\left[(1-F)C_0\rho\sqrt{u_k u_k}\beta(s)+F\left(\frac{C_1\gamma}{k}\tau_{ij}\frac{\partial u_i}{\partial x_j}-C_2\gamma\rho\frac{k^{\frac{3}{2}}}{\varepsilon}\frac{u_j}{(u_k u_k)^{\frac{1}{2}}}\frac{\partial u_i}{\partial x_j}\frac{\partial \gamma}{\partial x_j}\right)\right]+C_3\frac{k^2}{\varepsilon}\frac{\partial \gamma}{\partial x_j}\frac{\partial \gamma}{\partial x_j}+\frac{\partial}{\partial x_j}\left(\left((1-\gamma)\gamma\sigma_{\gamma t}\mu+(1-\gamma)\gamma\sigma_{\gamma t}\mu_t\right)\frac{\partial \gamma}{\partial x_j}\right) \tag{5}$$

Where the modelling constant are: $\sigma_{\gamma t}=1.0$, $C_0=1.0$, $C_1=1.6$, $C_2=0.16$, $C_3=0.15$

Further details of the transport model algorithm are given in Suzen & Huang. Equation has been implemented explicitly in the scheme. The convective and diffusive terms are treated separately. Specifically, the upwind Riemann solver of Roe convects γ around the flow field. The γ-diffusion term has been implemented using the Gauss divergence theorem around cell interfaces. All derivatives in the source terms are discretized by central differencing. The intermittent behaviour of transitional flows is modelled by modifying the eddy viscosity μ_t by the intermittency factor γ. Turbulent quantities are predicted by using the Wilcox [7] two-equation k-ω turbulence model. While the intermittency transport equation defines the intermittency distribution for transitional flows in the simulation, the onset of transition is defined by correlations. The onset of attached flow transition is determined as a function of the turbulence intensity, Tu, for zero pressure gradient. Specifically, for by-pass transition, the Abu-Ghannam & Shaw [8] correlation (6) is used.

$$Re_{\theta t} = 163 + exp(6.91 - Tu) \tag{6}$$

The length of transition region is obtained from the Suzen correlation (7).

$$\hat{n}\sigma = \left(\frac{n\upsilon^2}{U^3}\right)\sigma = 1.8 \cdot 10^{-11} Tu^{\frac{7}{4}} \tag{7}$$

The predicting capabilities of this model have been validated against the ERCOFTAC T3A- and T3A experiments of Roach & Brierley. The computational domain is made up of 260352 rectangular computational cells, with 1357 nodes points in the x-direction and 193 nodes in the y-direction. For accuracy grid points are clustered in regions of large gradients, but spread out elsewhere for economy. The stretching factor has been chosen in order to have a value of $y+ < 0.2$ for the first point away from the wall, and such that the viscous region of the BL ($y+ < 30$) contains more than 40 cells (see Figure 7).

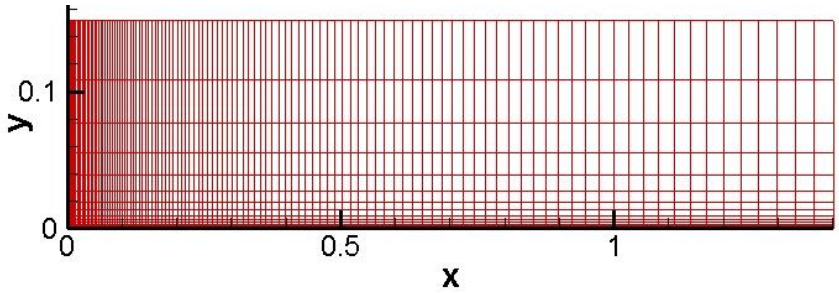

Figure 7. Computational mesh: the total length of the test section is 1.4m. For clarity, one point every 12 in both x and y direction is shown, and the x-axis to y-axis ratio is 0.4

At the streamwise distance of x=495mm and x=95mm, respectively, from the leading edge, a laminar profile (γ=0) is imposed as the inflow of the computational domain. As far as the inflow boundaries in the computation, these are derived from a numerical solution of the Blasius equation that is re-scaled to match the experimental laminar boundary layer parameters, see Table 2, in order to have a turbulent kinetic energy and its specific dissipation rate profiles.

Table2
Boundary layer parameters at inflow (95mm) for T3A case

T3A	C_f	δ^* [mm]	θ [mm]	Re_θ	H
Experimental	0.003723	0.882	0.344	117.4	2.562
Numerical	0.003731	0.918	0.354	118.1	2.593

This has been done, because transition is strongly affected by the decay of turbulence in the free-stream; therefore, it is very important for a correct analysis of the results to assign the appropriate inlet boundary condition. It is not possible starting from experimental initial condition supplied to computors in the form of tabulated hot-wire probe traverse results both for the uncertainty of the experimental data and because it is not easy to estimate the dissipation profile starting from velocity data. The inlet turbulent kinetic energy is fixed according to the freestream turbulence level. Initially gamma is set to zero throughout the flow field. On solid wall boundaries and at the freestream, a zero gradient of gamma is assumed. On outflow boundaries gamma is extrapolated from inside the domain to the outer boundaries. The temperature distribution across the boundary

layer was determined using Crocco's law. Adiabatic wall temperature due to frictional heating was given by the equation (8):

$$T_w = T_\infty \left[1 + \sqrt{P} \frac{\gamma - 1}{2} \left(\frac{\bar{U}}{\sqrt{\gamma R T}} \right)^2 \right] \tag{8}$$

and the wall's one modelled as adiabatic by the use of the temperature recovers factor the square root of Prandlt number. The static pressure was imposed as constant across the boundary layer.
Finally, the computational result for the T3A case is shown in Figure 7. The predicted skin friction coefficients and shape factor variation have been compared with the experimental data. The plot (a) shows the shape factor which indicates the region where the boundary layer tends to be turbulent. A decrease in H implies the transition is about to occurs. As before mentioned the experimental data showed a premature decline of H from the laminar value, on the other hand, the computation showed a pure laminar flow before the transition onset. Also for the skin friction as well as the streamwise velocity profile (see Figure 8), the computational results are in good agreement with the experimental ones.

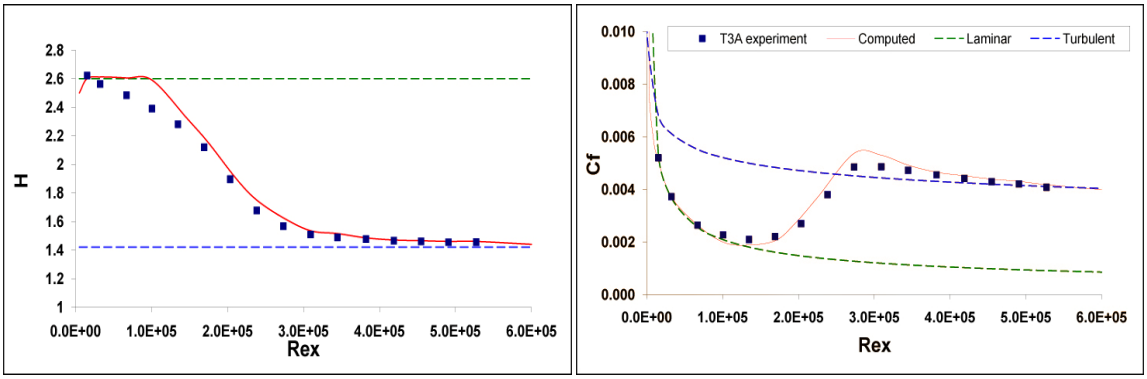

Figure 7. Comparison of the experimental shape factor and skin friction coefficient against computational results for the T3A test case

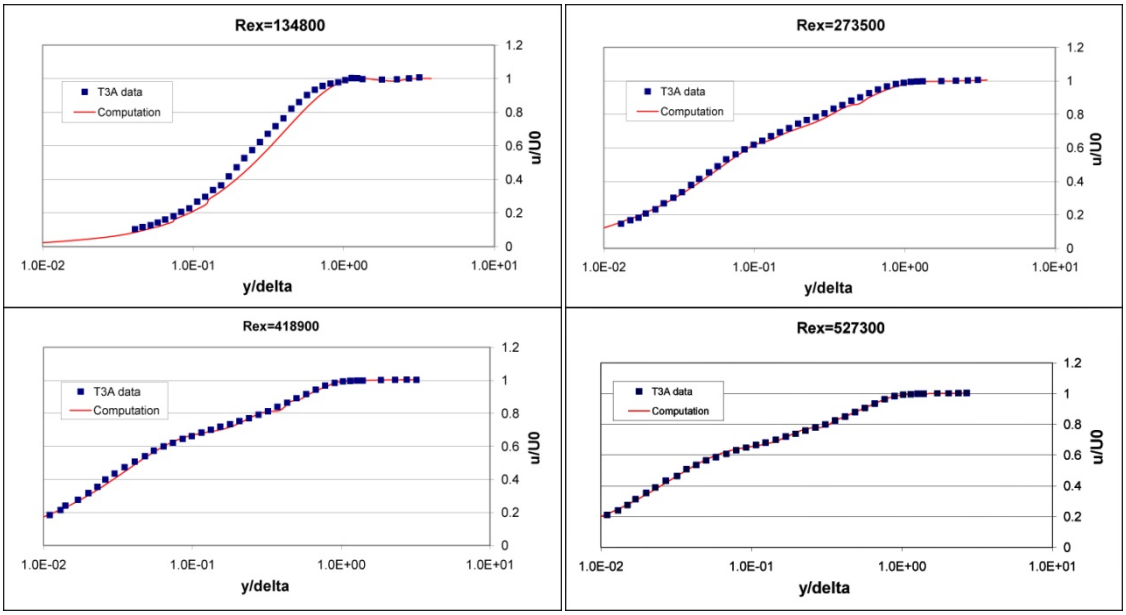

Figure 8. Numerical against experimental stream-wise velocity profile at different location along the flat plate

CONCLUSIONS

The dataset for the two Ercoftac test cases analysed has to be used with care, so the practitioners should be aware of the issue encountered. Perhaps an extension of the explanatory notes accompanying the database should be done. The transition model works well at a moderate FST level and less well at lover FST intensity. This different behaviour is probably due to the different physics of the two transition mechanisms in the two test cases. Possibly in the T3A- test case with a FST level of 0.9% the influence of Tollmien-Schliting waves might be not entirely negligible.

ACKNOLEDGEMNTES

This research project has been supported by a Marie Curie Early Stage Research Training Fellowship of the European Community's Sixth Framework Programme under contract number MEST CT 2005 020301.
This work was performed using the University of Leicester Mathematical Modelling Centre's supercomputer which was purchased through the HEFCE Science Research Investment Fund.

REFERENCES

1. Roach, P. E. and Brierley, D. H., "The influence of a turbulent free stream on zero pressure gradient transitional boundary layer development. Part 1: testcases T3A and T3B," *Cambrige University .press*, 1990.
2. Van Leer B., Thomas J., Roe P. and Newsome R., "A Comparison of numerical flux formulas for Euler and Navier-Stoke equation" , *AIAA 8th Computational Fluid Dynamics Conference*, Ed., No. 87-1104, pp. 36–41, 1987.
3. Sweby P., "High resolution schemes using flux limiters for hyperbolic conservative laws", *Journal of Numerical Analysis*, Vol. 21, No.5, pp. 995–1011, 1984.
4. Suzen, Y. B. and Huang, P. G., "Model of Flow Transition Using an Intermittency Transport Equation," *Journal of Fluid Engineering*, Vol. 122, pp. 273–284, 2000.
5. Steelant, J. and Dick, E., "Modeling of Bypass Transition with Conditioned Navier-Stokes Equations Coupled to an Intermittency Transport Equation," *International Journal for Numerical Methods in Fluids*, Vol. 23, pp. 193–220, 1996.
6. Cho, J. R. and Chung, M. K., "A k-ε-γ equation turbulence model," *Journal of Fluid Mechanics*, Vol. 237, pp. 301–322, 1992.
7. Wilcox, D. C., *Turbulence Modeling for CFD*, 1993.
8. Abu-Ghannam, B. J. and Shaw, R., "Natural Transition of Boundary Layers -The Effects of Turbulence, Pressure Gradient, and Flow History," *Journal of Mechanical Engineering Science*, Vol. 22, No. 5, pp. 213–228, 1980.

STUDY OF VORTICAL STRUCTURES IN IMPINGING JETS - NEW METHODS AND APPROACHES

V. Tesař [*], **V. Němička**
Institute of Thermomechanics AS CR v.v.i., Praha, Czech Republic

ABSTRACT. Heat transfer characteristics of impinging jets are strongly affected by complex, not yet fully understood vortical structures that develop due to hydrodynamic instability in the outer mixing layer**.** The paper describes the new techniques used in experiments with impinging jets: periodically triggered vortex formation, visualisation by laser light scattered from water mist particles added to the jet, and using advanced processing of image sequences. Particularly interesting is "frozen motion" evaluations of the correlations between frames of a sequence, revealing the investigated structures by using their higher coherence in contrast to the uncorrelated surrounding turbulence.

Keywords: *impinging jets, flow visualisation, image processing, vortical structures, turbulence*

INTRODUCTION

Impinging jets, Figure 1, are an especially important case of fluid flows used in heat transfer applications, because they make possible achieving the highest thermal power transfer rates between a fluid and a solid surface – higher than any other known convective transport method [5].

It has been for a long time recognised that impinging jet flowfields, and their resultant heat transfer properties, are strongly influenced by the vortices - as well as by more complex vortical structures that gradually evolve from the initially regular vortex motions – that arise and evolve due to hydrodynamic instability in the mixing layer surrounding the jet core. They are apparent features in the example in Figure 2. All aspects of this influence have not yet been fully elucidated [1]. For example, experimental results obtained with the nozzles positioned at a small relative distance h/d,

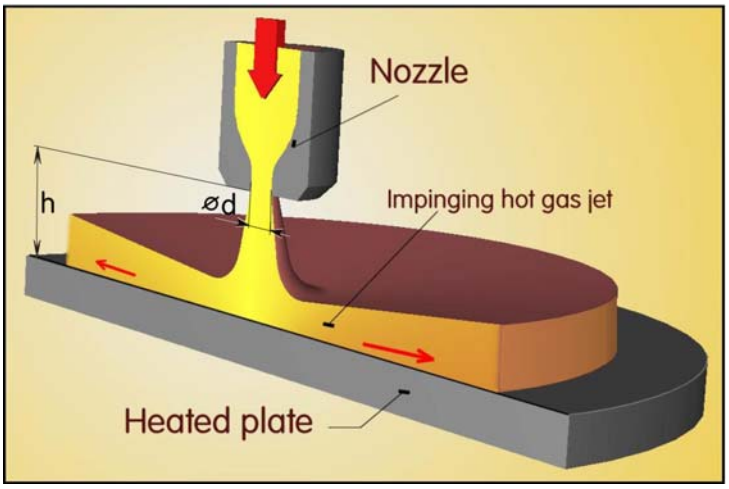

Figure 1. Schematic representation of heating by a hot gas in the impinging jet configuration. The jet issues from a nozzle usually oriented in perpendicular direction towards the heated surface. Reynolds number of the jet is usually high enough for vortical motions, associated with hydrodynamic instability of the flow, developing in the mixing layer on the outer edge of the jet.

* Corresponding author: Prof. Ing. Václav Tesař, CSc.
Phone: 420 2 6605 2270
E-mail address: tesar@it.cas.cz

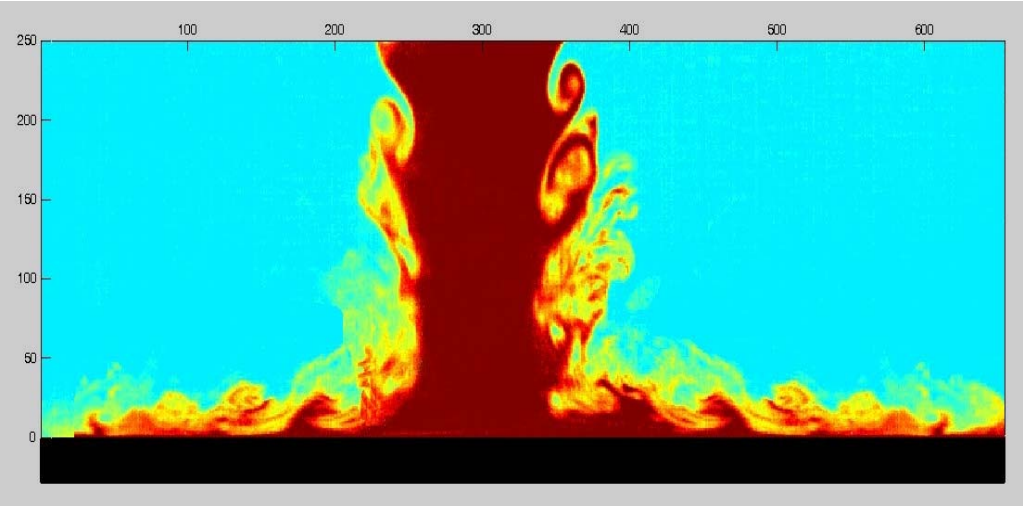

Figure 2. A typical example of a visualised impinging jet at a Reynolds number value typical for heat transfer applications, with prominent vortices initially developing in the mixing layer on the outer edge of the jet, gradually losing the coherence and finally evolving into chaotic turbulence.

(Figure 1) above the impingement wall exhibit strange off-axis transfer rate maxima [2], which are now accepted to be caused by the vortical motions [3, 11, 14], but the details of generating the maxima are not fully understood, especially since the vortices apparently decompose before reaching wall proximity.

The main difficulty encountered in investigations of these vortical objects is their variation in time. They appear with certain periodicity, but with chaotic phase jitter, and are not easy to follow as they are carried with the jet flow. Particularly troublesome problem is the influence of chaotic turbulence by which the structures are surrounded and within which they finally disappear.

The authors made three important steps in eliminating these problems in experimental investigations. First, they applied a periodic triggering action so that the vortices are formed in precisely reproducible periodicity. Second, the triggering of vortex formation was synchronised, at an adjustable phase angle, with the instants at which the camera recorded the frames showing the visualised jet. Finally, the image frames are processed in a novel way making apparent the investigated structures by using their higher coherence property in contrast to the uncorrelated surrounding turbulence.

This paper describes the basic features of these newly developed techniques.

EXPERIMENTS

General features

The investigated flow was a jet of air issuing from a $d = 40$ mm i.d. nozzle. The nozzle properties were studied as described in [6]. It was located in the centre of a large horizontal surface perpendicular to the jet axis. The jet impinged upon a parallel impingement surface positioned at a distance $h = 100$ mm, i.e. at $h/d = 2.5$. The air was supplied by an adjustable-speed blower [7] through a settling chamber provided with sieves. The flow rate was varied so that Reynolds numbers of the jet were of the order $1 .10^3 – 10 .10^3$. The jet was visualised by addition of water mist particles. These scattered the light of an illuminating "laser knife". The images of the scattered light were captured by a digital camera oriented perpendicularly to the light sheet. Essentially, they pro-

* Corresponding author: Prof. Ing. Václav Tesař, CSc.
Phone: 420 2 6605 2270
E-mail address: tesar@it.cas.cz

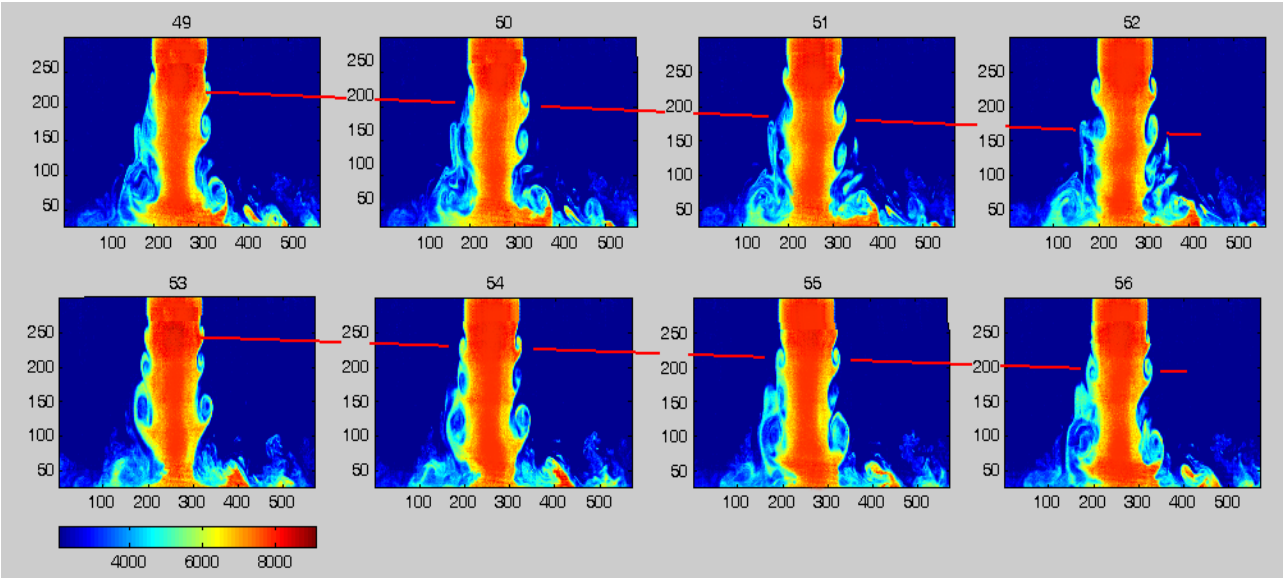

Figure 2. A typical sequence of video frames of an impinging jet visualised by addition of water mist particles and presented using the false-colour mapping that replaced the actually photographed various levels of grey by an arbitrarily assigned colour according to the scale at bottom left. These frames show the vortices as they form in unexcited impinging jet. The red line connects the positions of a particular vortex as it progresses towards the wall.

vided an information on local intensities of the scattered light. The scattering particles were made by evaporating water and passing it through a bed of crushed ice, so that the vapour condensed before it was introduced into the air flow in the entrance into the blower. This placement of the injection ensured homogeneous mixing by the blower blades before the mist containing air entered the nozzle.

The laser used for generating the "*laser light knife*" was a diode-pumped solid state green light (wavelength 532 nm) Nd:YAG laser DPGL-2200L-45 supplied by Shanghai Uniwave Tech-nology Ltd. Its maximum output power is 200 mW; but the power was adjustable and during the experiment the values were usually lower than this maximum. The laser is provided with a cylindrical optics generating the light sheet of fan angle 45^{o} and guaranteed width < 5 mm at 5 m distance. The distance actually used, 700 mm, was shorter so that the sheet thickness was ~0.7 mm.

The camera used was Vision Research Phantom v7.3 with continuously recording 14-bit monochrome SR-CMOS sensors giving 800 x 600 pixels resolution and top speed of 6 688 frames per second – which was not used in the present case. In the unexcited jet pictures in Fig. 2 the data acquisition speed was 100 frames per second while with the excitation the picture taking was synchronised to the excitation frequency. From the images, sequences of 8 frames were chosen and processed. The original pictures presented various levels of grey. The entrained outer air containing no water droplets appeared black and the numerical value stored for the corresponding pixel of the image should be theoretically 0. There is always some inevitable light dispersion inside the test space and also the absorbance of the background (which was black textile) is not perfect, so that the minimum values are higher. On the other hand, no pictures contained the full 14 bit white extreme. Also the camera sensitivity is practically never set so as to utilise the 14 bit resolution. Instead of the theoretical range 0 to 16 384, in practical situations the values were in a more narrow range, which was shifted down to make the lowest value zero. Typically, after the shift, the highest value were typically near to 9 000. This is seen in the colour coding bar in the lower left corner of Figure 2. To facilitate visual inspection of the images, the levels of grey were replaced by a false colour using an assignment function which could be completely arbitrary and has to be presented in the form of the colourbar accompanying the images.

Phase synchronisation

Among the complicating factors that make a closer study of the vortical structures not easy, is their motion from the nozzle towards the impingement wall, as it is clearly seen from the slope of the red connecting line in Figure 2. In our experiment, we managed to virtually "stop" this motion when taking flow visualisation pictures by utilising the stroboscopic effect [8]: the pictures are taken at the same phase of a periodic process. With natural generation of vortices only very roughly periodic, the periodicity was to be secured by triggering the vortex formation. An essential part of the experimental rig used by the authors is an actuator for periodic excitation of the jet flow. It should be stressed that this is no generation of the vortices - the excitation is very weak. Due to the hydrodynamic instability the vortices are ready to appear even if there were no excitation at all so that even the very weak triggering disturbance suffices to start the vortex formation. Because of maintaining a precise excitation frequency, the stroboscopic effect makes the pictures of subsequently appearing vortices to look like if there were permanently only a single, stationary vortex – as is, e.g., the vortex A in Figure 3.

The ultimate target of the planned investigations (not discussed in the present paper) are the rather strange properties of helical instability structures [10]. This is why the chosen excitation mode in the experiments is azimuthal, acting on the jet in the plane of the nozzle exit. It has the form of two waves running, one after another, along the exit circumference. The actuator producing it consists of 8 electro/acoustical transducers - standard commercially available low-frequency woofer loudspeakers ARN-165-01/4. Four neighbouring transducers supplied by harmonic electric current with phase shifting by one quarter of the period generate the first acoustic perturbance. The azimuthal wave coupled with the axial translation of the jet produces a helical object upon leaving the outer part of the nozzle. Similarly, the remaining quartet of the loudspeakers produces another wave, phase shifted by 180 deg. The two waves follow one another and this generates two interleaved helical structure objects in the mixing layer of the jet. It should be noted that because of this arrangement, the Strouhal number values Sh are twice as high than if they were simply computed from the given frequency f.

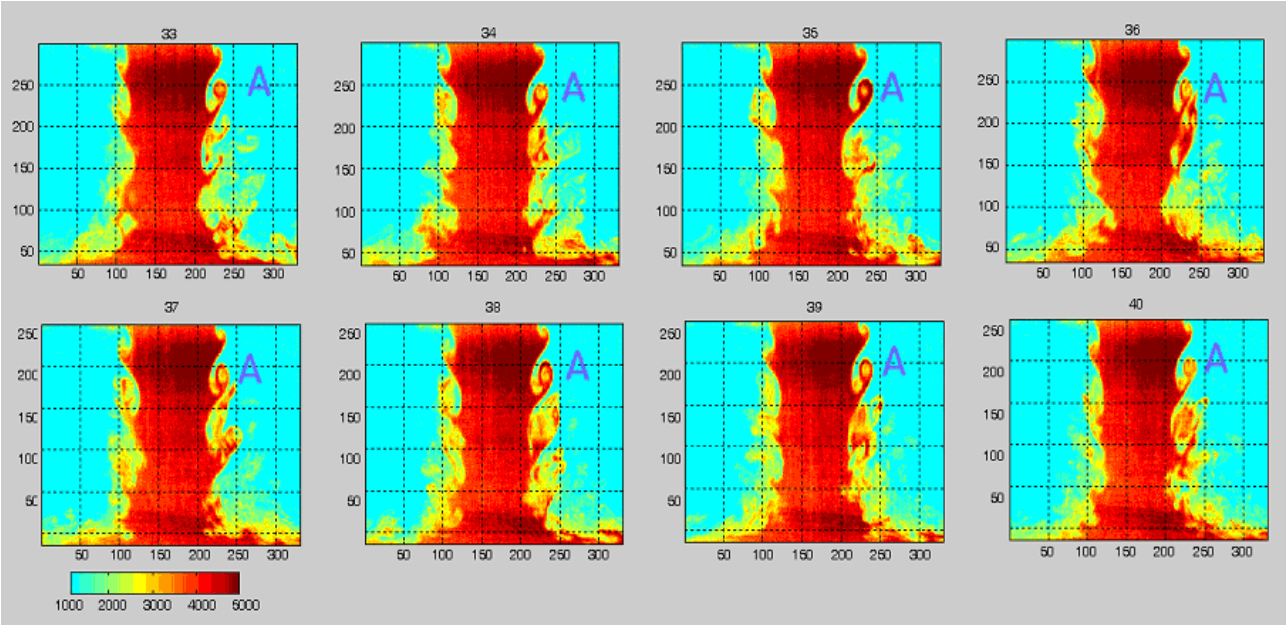

Figure 3. An example of video frames sequence demonstrating the success of the phase synchronisation. The impinging jet, same as in Figure 2, was excited by azimuthal acoustic waves in the nozzle exit plane. Taking of the pictures at a particular phase of the excitation resulted in seeing in each frame the excited jet in the same phase of the excitation. In this case, different subsequently generated vortices A are captured in the same phase of their development so that they seem to be the same stationary object.

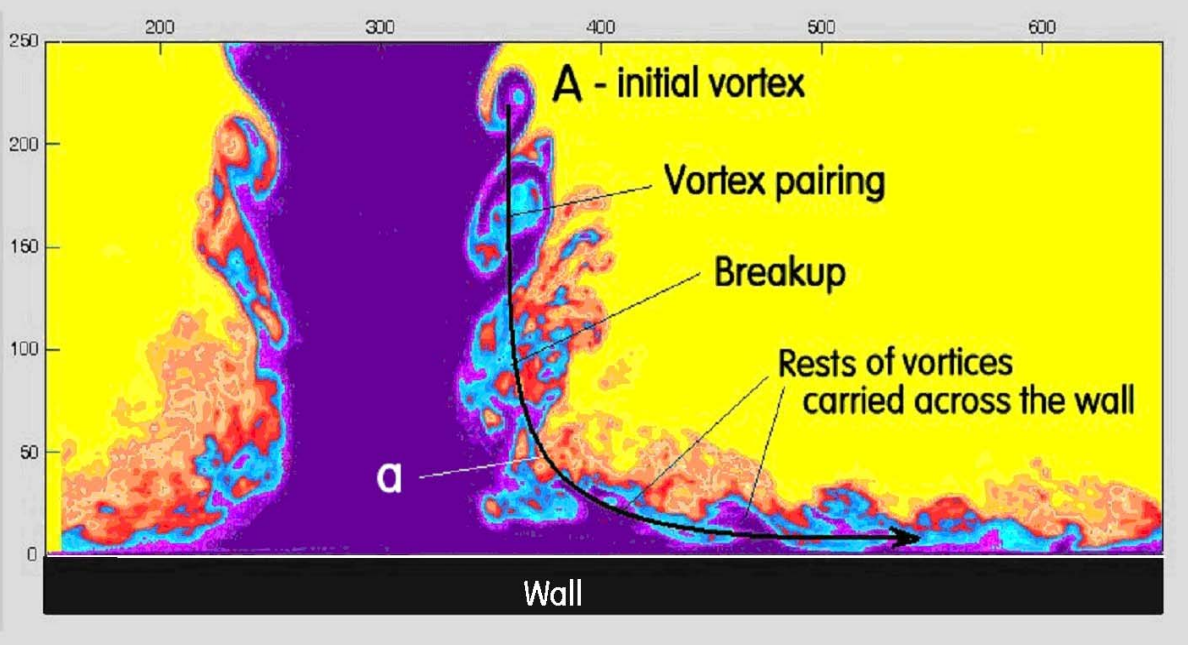

Figure 4. The constant phase processing of video frames – here enhanced by posterisation (reduction of colour palette) makes possible a close study of the development of progressing vortices and their rests remaining in the flowfield after the vortex breakup.

The signal for camera release was derived, by a phase-shifting circuit, from the generator of the excitation signal. This way, taking each picture in the sequence was synchronised with acoustic triggering of vortex generation. As a result, the coherent components of the structures (best seen in the initial stages when the vortices are still coherent — such as is the case of the topmost vortices A in the accompanying Figure 3) became virtually "frozen", non-movable. Further downstream, the vortical structure breaks down and loses its coherence. Because the main periodic component of the motion of the structures keeps them at a particular, virtually steady location in the frame, the pictures make possible evaluating the uncorrelated components of their behaviour – e.g. by statistical processing of the time-mean and fluctuating components of the structures. A single-picture example that demonstrates the possibilities offered for the study of the breaking-up of the vortices by this synchronisation is presented in Figure 4. Of course, these processes are incoherent and the results are therefore different in each frame – as is seen in following further downstream the decomposing vortices in the frames of Figure 3.

Figure 4 also demonstrates one of the simple but useful methods of the image processing – the ***posterisation*** approach used to make better apparent the basic features, as introduced by Tesař and Barker in [11]. The colour palette of the picture is drastically reduced to only a few colours. Also the contours between the different hue areas were traced to make better recognisable the demarcation lines between the coloured areas. The posterisation procedure is somewhat of a psychological paradox. It, in fact, decreases the information contents of the processed image rather than increasing it, yet can make some essential features better recognisable visually. Its certain disadvantage is the considerable degree of subjective aspects in the procedure – the demarcation lines between the coloured areas may be chosen differently by different investigators. Usually, posterisation is not a structure-revealing procedure itself, but may be usefully applied to images processed by some more advanced procedure.

Correlation

More sophisticated and for the visual identification more convincing detection criterion used to identify the instability structures is the use of correlation techniques [4]. This is based on the fact

that the information about the local intensity of the scattered light in a flow visualisation frame is stored in the form of a matrix, e.g. a matrix $\underline{A}$ in one frame and matrix $\underline{B}$ in the following one, the numerical values at a particular element of a matrix being the stored numerical value at the corresponding pixel. There are standard library procedures for computing correlations of two matrices. The procedure admits a considerable degree of freedom in choosing the pixels entering the evaluation. In the accompanying example in Figure 5, for each interrogated pixel the evaluation procedure took the surrounding 5 x 5 pixels in the RoI (Region of Interest). This selection leads to formation of the submatrix

$$\text{sub}\,\underline{A} = \begin{bmatrix} A_{k-2,l-2} & A_{k-2,l-1} & A_{k-2,l} & A_{k-2,l+1} & A_{k-2,l+2} \\ A_{k-1,l-2} & A_{k-1,l-1} & A_{k-1,l} & A_{k-1,l+1} & A_{k-1,l+2} \\ A_{k,l-2} & A_{k,l-1} & A_{k,l} & A_{k,l+1} & A_{k,l+2} \\ A_{k+1,l-2} & A_{k+1,l-1} & A_{k+1,,} & A_{k+1,l+1} & A_{k+1,l+2} \\ A_{k+2,l-2} & A_{k+2,l-1} & A_{k-2,l} & A_{k+2,l+1} & A_{k+2,l+2} \end{bmatrix} \quad \ldots (1)$$

The comparison vector may be then formed from the elements of this submatrix as follows:

$$\mathbf{A} = [\, A_{k-2,l-2},\ A_{k-2,l-1},\ A_{k-2,l},\ A_{k-2,l+1},\ A_{k-2,l+2},\ A_{k-1,l-2},\ A_{k-1,l-1},\ A_{k-1,l},\ A_{k-1,l+1},\ A_{k-1,l+2},\ A_{k,l-2},\ A_{k,l-1},\ A_{k,l},\ A_{k,l+1},$$
$$A_{k,l+2},\ A_{k+1,l-2},\ A_{k+1,l-1},\ A_{k+1,l},\ A_{k+1,l+1},\ A_{k+1,l+2},\ A_{k+2,l-2},\ A_{k+2,l-1},\ A_{k-2,l},\ A_{k+2,l+1},\ A_{k+2,l+2}\,]$$

and analogously in the comparison vector of the second frame there are

$$\mathbf{B} = [\, B_{k-2,l-2},\ B_{k-2,l-1},\ B_{k-2,l},\ B_{k-2,l+1},\ B_{k-2,l+2},\ B_{k-1,l-2},\ B_{k-1,l-1},\ B_{k-1,l},\ B_{k-1,l+1},\ B_{k-1,l+2},\ B_{k,l-2},\ B_{k,l-1},\ B_{k,l},\ B_{k,l+1},$$
$$B_{k,l+2},\ B_{k+1,l-2},\ B_{k+1,l-1},\ B_{k+1,l},\ B_{k+1,l+1},\ B_{k+1,l+2},\ B_{k+2,l-2},\ B_{k+2,l-1},\ B_{k-2,l},\ B_{k+2,l+1},\ B_{k+2,l+2}\,]$$

The correlation coefficient R is then computed as

$$R = \frac{\mathbf{A}\,\mathbf{B}}{|\mathbf{A}||\mathbf{B}|} \quad \ldots (2)$$

The order of the components in the vectors may be selected differently [9] so as to identify the direction of the studied motion changes of the compared vortical structures during their. In principle,

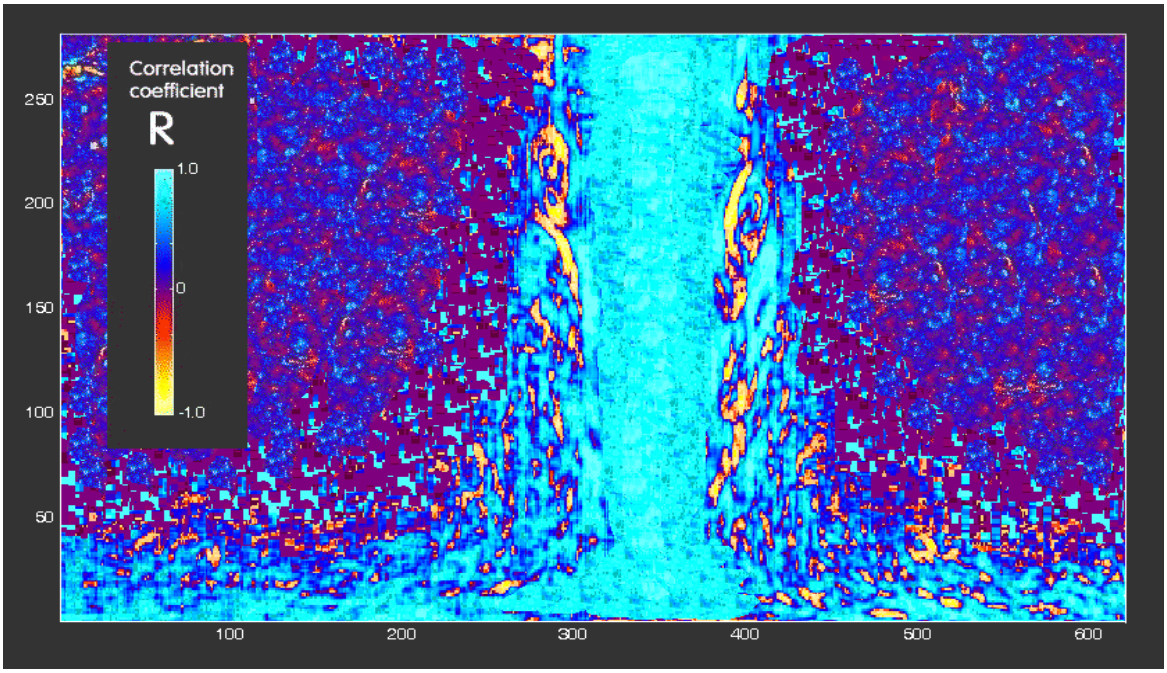

Figure 5. An example of image processed by computing correlations between two frames in a sequence, using the absolute values of the optical intensity data. In the locations coloured light blue the flow features do not change between the instants at which the pictures were taken. Of interest are the yellow coloured areas of large negative correlation coefficient. They are indicative the motions of coherent structures and are mainly found on the structure edges.

the correlation is computed as the normalised scalar product of the vectors [9]. Because of the normalisation, the resultant correlation coefficient may be interpreted geometrically as the cosine of the (multi-dimensional) "angle" between the two vectors. If the two vectors are identical or parallel, their correlation coefficient is $R = 1$. The corresponding area is coloured light blue in Figure 5. If the two vectors have nothing in common at all, or are mutually "perpendicular", the correlation coefficient is zero $R = 0$. The corresponding area should appear black in Figure 5, but the ideal value is rarely attained and the areas are coloured dark blue or dark red. This is the region of uncorrelated turbulence. Most interesting in the present context are the locations in which the comparison vectors from the two frames in the interrogation point are anti-parallel $R = -1$. The corresponding areas should be marked light yellow in the picture. This is usually indicative of movement of instability structures that move coherently. In particular, such a change is mainly found on the structure edges.

By choice of the pixels in the RoI that are used to set up the components of the comparison vectors it is possible to detect the ***direction*** of structure motion between two correlated image frames.

The correlations may be also computed using comparison vectors from the differences with subtracted mean value of a sequence. We store the scattered light intensity data in six matrices A, B, C, D, E, F, each containing an information acquired at a different instant of time. The mean value $M_{k,l}$ at each k and l location is simply evaluated as

$$M_{k,l} = (A_{k,l} + B_{k,l} + C_{k,l} + D_{k,l} + E_{k,l} + F_{k,l}) / 6 \quad \ldots (3)$$

The differences, such as e.g. $A_{k,l} - M_{k,l}$, are particularly sensitive to even small changes taking place during the time interval between which the frames were captured. Evaluating the correlations from these relative values makes in the results particularly apparent the structure evolutions in time and their motion in space.

CONCLUSIONS

The subject of this paper are new techniques introduced by the present authors for detecting instability structures in impinging jet flows and for evaluation of the dynamics of their development. The basic problem is how to extract information about three-dimensional objects – in particular vortical structures – from two-dimensional flow visualisation images. The problem is made more difficult by the objects of interest appearing quasi-periodically (i.e. with large variations in the phase), moving as they are carried away with the flow, and submerged in stochastic turbulence that complicates even their mere identification. Because of the unsteady character of the detected objects, the turbulence cannot be simply filtered out by statistical averaging.

The discussed approach to solving these problems operates with triggering the vortex formation by a periodic signal from which is derived the camera releasing signal. This way one obtains a sequence consisting of a relatively small number of monochrome pictures taken at periodic time intervals, each of them capturing only a section through the object (which makes them insufficient for a tomographic reconstruction). The images are then analysed using as the basic idea the difference in the rates of change of the identified object and of the surrounding chaos. Using subtraction of local mean values and evaluation of correlation coefficients, supplemented by false colour coding and posterisation, can reveal interesting and significant information.

ACKNOWLEDGEMENTS

The authors acknowledge gratefully the support by the grant IAA200760705 from the Grant Agency of the Academy of Sciences of the Czech Republic, and by the grant 101/07/1499 from the Grant Agency of the Czech Republic.

REFERENCES

1. Chung Y.M., Luo K. H., Unsteady Heat Transfer Analysis of an Impinging Jet, *Trans. ASME, Journal of Heat Transfer*, Vol. 124, p. 1039, December 2002
2. Tesař V., The Problem of Off-Axis Transfer-Effect Extremes in Impinging Jets, *Proc. of XVIIth Internat. Scientific Conference of Depts. of Fluid Mechanics and Thermomechanics*, p. 187, ISBN 80-88896-19-3, Herlany, Slovakia, June 1998
3. Meola C., de Luca L., Carlomagno G. M., Influence of Shear Layer Dynamics on Impingement Heat Transfer, *Experimental Thermal and Fluid Science*, Vol.13, p. 29, July 1996
4. Tesař V., Němička V., Extracting Information about 3D Structures from 2D Flowfield Images, in Press, *Journal of Visualization*, Japan, 2009
5. Tesař V., Trávníček Z., Increasing Heat and/or Mass Transfer Rates in Impinging Jets, *Journal of Visualization*, Vol. 8, No. 2, pp. 91-98, ISSN 1343-8875, Japan, 2005
6. Tesař V., Characterisation of Subsonic Axisymmetric Nozzles, Chemical Engineering Research and Design, p. 1253, Volume 86, Issue 11, 2008
7. Tesař V., Kukačka L., Kellnerová R., Investigation of Characteristics of a Blower used as an Air Source in an Experimental Rig for Studies of Helical Instabilities in Flowing Fluids, *Proc. of Colloquium ' Fluid Dynamics 07'*, Inst. of Thermomechanics Acad. of Sciences of the Czech Republic, v. v. i., , ISBN 978-80-87012-07-09, Prague, 2007
8. Tesař V., Němička V., Šonský J., Kukačka L., Pavelka M., Effect of Azimuthal Excitation in the Nozzle Exit on Structures Formed in Submerged Jets, Proc. of Colloq. "Fluid Dynamics 2008", Inst. of Thermomechanics AS CR, v.v.i., Prague, Czech Republic, 2008
9. Němička V., Hlína J., Šonský J., Krejčí L., Application of the Correlation Analysis to Identification of Coherent Structures in Free Plasma Flow, *Acta Technica CSAV*, ISSN 0001-7043, Vol.. 48, Nr. 2 , p. 175, 2003
10. Tesař V, Zimmerman W.B.J., Regunath G., Helical Instability Structures in Swirling Jets, *Proc of the 8th International Symposium on Fluid Control, Measurements, and Visualization FLUCOME 2005*, Chengdu, China, 2005
11. Tesař V., Barker J., Dominant Vortices in Impinging Jet Flows, *Journal of Visualisation*, Japan, ISSN 1343-8875, Vol.5, No.2, p. 121, 2002
12. Regunath G.S., Zimmerman W. B., Tesař V., Hewakandamby B. N.: "Experimental investigation of helicity in turbulent swirling jet using dual-plane dye laser PIV technique", *Experiments in Fluids*, ISSN 0723-4864, Springer Berlin/Heidelberg, Vol. 45, pp. 973-985, December 2008
13. Hewakandamby B. N., A numerical study of heat transfer performance of oscillatory impinging jets, *International Journal of Heat and Mass Transfer* Vol. 52, pp. 396–406, 2009
14. Vejrazka J., Tihon J., Effect of an external excitation on the flow structure in a circular impinging jet, *Physics of Fluids,* Vol. 17, 105102, 2005
15. Tesař V., Randa Z., Impinging Jet Heat Transfer Experiments – Quantitative Evaluation Using Thermochromic Liquid Crystals, *Proc. of Conference 'Topical Problems of Fluid Mechanics 2008*', p. 117, Institute of Thermomechanics AS CR, Prague, February 20 – 22, 2008
16. Trávníček Z., Kopecký V., Maršík F., Tesař V**.,** Bifurcated and Helical Impinging Jet Controlled by Azimuthally Arranged Synthetic Jets, *Proc. of HEFAT2007, 5th International Conference on Heat Transfer, Fluid Mechanics and Thermodynamics*, Paper TZ1; p.35 in Book of Abstracts; full text on the CD Proceedings ISBN:978-1-86854-6435, Sun City, South Africa, July 2007
17. Regunath G., Tesar V**.,** Zimmerman W.B.J., Hewakandamby B.N., Russell N.V., Experimental Investigation and Visualization of Helical Structures in a Novel Swirling Jet, *Proc. of FEDSM06, ASME Joint U.S. – European Fluids Engineering Summer Meeting*, Technical 32-5 Optical Methods 2, Miami, FL, July 2006

Author index

Author index

Keywords index

Keywords index

Sponsors

Conference Sponsors:

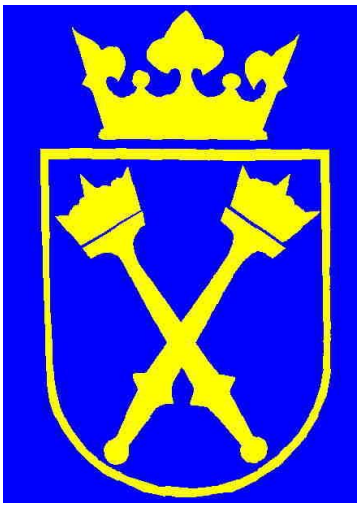

COST action P20: LES-AID

Conference Co-sponsor:

ISBN 978-837464-235-4

ExHFT-7

www.exhft-7.agh.edu.pl

AGH

2415